European Community on Computational Methods in Applied Sciences

ECCOMAS Thematic Conference

COMPDYN 2019

7th International Conference on Computational Methods in Structural Dynamics and Earthquake Engineering

PROCEEDINGS

Volume III

M. Papadrakakis, M. Fragiadakis (Eds)

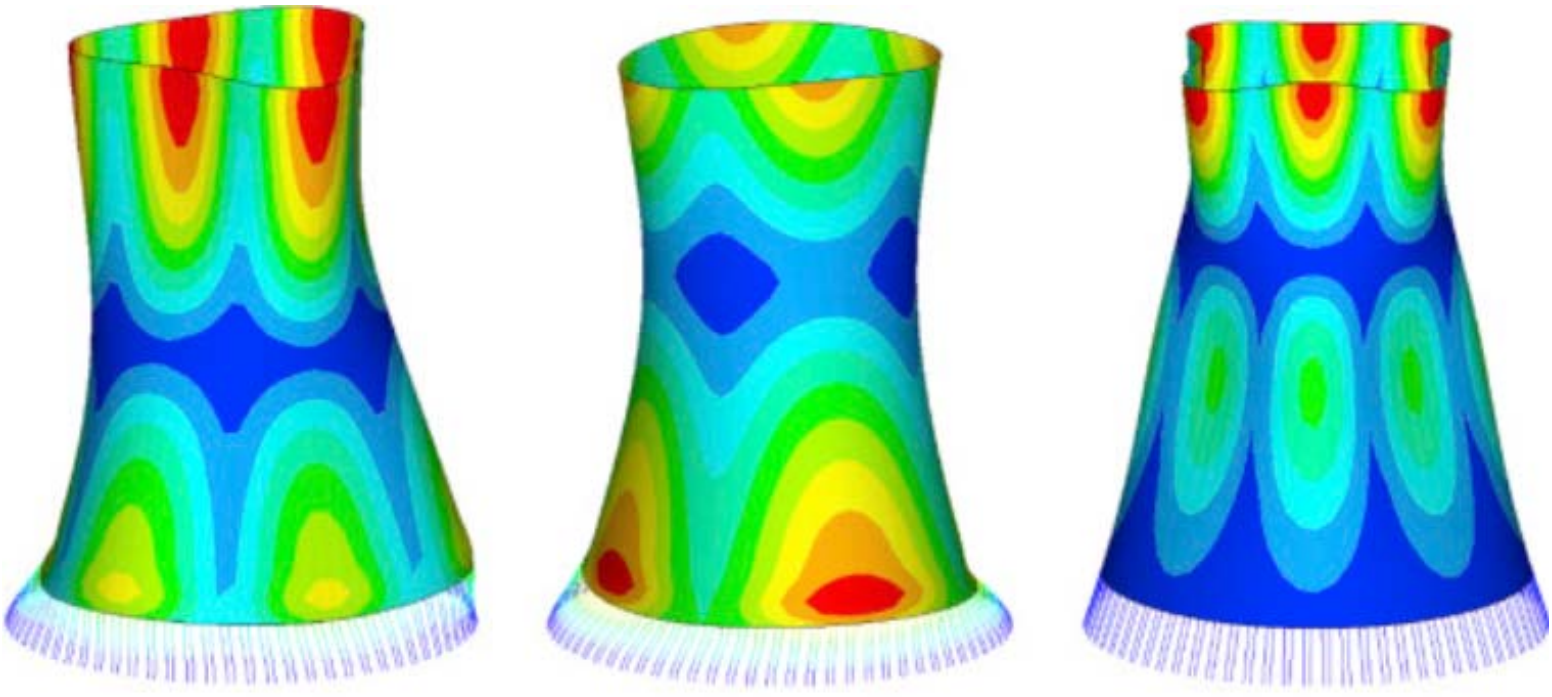

An IACM Special Interest Conference

COMPDYN 2019

Computational Methods in Structural Dynamics and Earthquake Engineering

Proceedings of the 7th International Conference on Computational
Methods in Structural Dynamics and Earthquake Engineering
Held in Crete, Greece
24-26 June 2019

Edited by:

M. Papadrakakis
National Technical University of Athens, Greece

M. Fragiadakis
National Technical University of Athens, Greece

A publication of:

Institute of Structural Analysis and Antiseismic Research
School of Civil Engineering
National Technical University of Athens (NTUA)
Greece

COMPDYN 2019
Computational Methods in Structural Dynamics and Earthquake Engineering
M. Papadrakakis, M. Fragiadakis (Eds)

First Edition, October 2019

ISBN (set): **978-618-82844-5-6**
ISBN (vol III): **978-618-82844-8-7**

PREFACE

This volume contains the full-length papers presented in the 7th International Conference on Computational Methods in Structural Dynamics and Earthquake Engineering (COMPDYN 2019) that was held on June 24-26, 2019 in Crete, Greece.

COMPDYN 2019 is one of the 32 Thematic Conferences of the European Community on Computational Methods in Applied Sciences (ECCOMAS) to be held in 2019 and is also a Special Interest Conference of the International Association for Computational Mechanics (IACM). The purpose of this Conference series is to bring together the scientific communities of Computational Mechanics, Structural Dynamics and Earthquake Engineering, to act as the forum for exchanging ideas in topics of mutual interests and to enhance the links between research groups with complementary activities. We believe that the communities of Structural Dynamics and Earthquake Engineering will benefit from their exposure to advanced computational methods and software tools which can highly assist in tackling complex problems in dynamic and seismic analysis and design, while also giving the opportunity to the Computational Mechanics community to be exposed to very important engineering problems of great social interest. The COMPDYN 2019 Conference is supported by the National Technical University of Athens (NTUA), the European Association for Structural Dynamics (EASD), the European Association for Earthquake Engineering (EAEE), the Greek Association for Computational Mechanics (GRACM).

The editors of this volume would like to thank all authors for their contributions. Special thanks go to the colleagues who contributed to the organization of the Minisymposia and to the reviewers who, with their work, contributed to the scientific quality of this e-book.

M. Papadrakakis
National Technical University of Athens, Greece

M. Fragiadakis
National Technical University of Athens, Greece

ACKNOWLEDGEMENTS

The conference organizers acknowledge the support towards the organization of the "7th International Conference on Computational Methods in Structural Dynamics and Earthquake Engineering", to the following organizations:

- European Community on Computational Methods in Applied Sciences (ECCOMAS)
- European Association for Structural Dynamics (EASD)
- European Association for Earthquake Engineering (EAEE)
- Greek Association for Computational Mechanics (GRACM)
- Hellenic Society for Earthquake Engineering (HSEE)
- School of Civil Engineering, National University of Athens (NTUA)
- Hellenic Republic-Region of Crete
- Municipality of Heraklion

Plenary Speakers and Invited Session Organizers

We would also like to thank the Plenary and Semi-Plenary Speakers and the Minisymposia Organizers for their help in the setting up of a high standard Scientific Programme.

Plenary Speakers: Michel Bruneau, Álvaro Cunha, Michael Fardis, Charbel Farhat, Christian Soize, Alexander Vakakis

Semi-Plenary Speakers: Christoph Adam, Gian Paolo Cimellaro, Eleni Chatzi, Geert Degrande, Boris Jeremic, Shinobu Yoshimura

MS Organizers: Günther Achs, Christoph Adam, Hamid Ahmadi, António Arêde, Rui Carneiro Barros, Michael Beer, Amadeo Benavent-Climent, Manuel Braz-Cesar, Alessandro Cabboi, Silvia Caprili, Claudia Casapulla, Serena Cattari, Nicola Cavalagli, Liborio Cavaleri, Jianbin Chen, Dimitris Chronopoulos, Alice Cicirello, Gian Paolo Cimellaro, Francesco Clementi, Marco Corradi, Flavia De Luca, Carlo Del Gaudio, Ciro Del Vecchio, Pedro Delgado, Raimundo Delgado, Raffaele Di Laora, Marco Di Ludovico, Luigi Di Sarno, Fabio Di Trapani, Francisco Alejandro Diaz de la O, Marco Domaneschi, Stefanos Dritsos, Hossein Ebrahimian, Antonio Formisano, Michalis Fragiadakis, Linda Giresini, Jose Gonzalez, Alexander Idesman, Alper Ilki, Maria Iovino, Fatemeh Jalayer, Hector Jensen, Andreas Kappos, Jin-Gyun Kim, Radek Kolman, Davide Lavorato, Guido Magenes, Charilaos Maniatakis, George Manos, Gabriele Milani, Stergios Mitoulis, Naoto Mitsume, Fabrizio Mollaioli, Paolo Morandi, Lukas Moschen, George Mylonakis, Jiri Naprstek, Ehsan Noroozinejad, Camillo Nuti, Roger Ohayon, Georgios S. Papavasileiou, K.C. Park, Vagelis Plevris, Nikos G. Pnevmatikos, Maria Polese, Laura Ragni, Andrei M. Reinhorn, Paolo Ricci, Hugo Rodrigues, Emmanouil Rovithis, Juan Chiachío Ruano, Manuel Chiachío Ruano, Walter Salvatore, Fabrizio Scozzese, Anastasios Sextos, Castorina Silva Vieira, Andrei L. Smirnov, Sergey Sorokin, Enrico Spacone, Daniele Spina, Constantine Spyrakos, Francesca Taddei, Anton Tkachuk, Petr Evgen'evich Tovstik, Savvas Triantafyllou, Yiannis Tsompanakis, Enrico Tubaldi, Marcos Valdebenito, Humberto Varum, Ioannis Vayas, Gerardo Mario Verderame, Stefania Viti, Shinobu Yoshimura

SUMMARY

VOLUME II

Minisymposia

VOLUME III

Regular Sessions

CONTENTS

VOLUME I

MS 3: EXPERIMENTAL MEASUREMENTS AND NUMERICAL SIMULATION ON PROBLEMS IN THE FIELD OF EARTHQUAKE ENGINEERING AND STRUCTURAL DYNAMICS

MS 6: SEISMIC SAFETY ASSESSMENT OF STRUCTURES

MS 7: RECENT ADVANCES IN THE DEVELOPMENT OF APPROXIMATE MATHEMATICAL TECHNIQUES FOR SOLVING COMPLEX SIMULATION-BASED PROBLEMS INVOLVING UNCERTAINTY

MS 8: RIGID BLOCK MODELING APPROACHES FOR STATIC AND DYNAMIC ANALYSIS OF MASONRY STRUCTURES IN SEISMIC AREAS

MS 9: NON-LINEAR DYNAMICS, WAVE PROPAGATION AND CONTACT-IMPACT PROBLEMS

MS 10: PROGRESS AND CHALLENGES IN RAIL TRACK DYNAMICS

MS 11: POST-EARTHQUAKE ASSESSMENT FOR BUILDINGS AND INFRASTRUCTURES AND REPARABILITY DECISIONS

MS 12: REPAIR AND RETROFIT OF STRUCTURES

MS 13: RECENT NUMERICAL MODELLING TRENDS FOR THE PRESERVATION OF HISTORICAL MASONRIES IN SEISMIC AREAS

MS 15: ADVANCES IN NUMERICAL METHODS FOR LINEAR AND NON-LINEAR DYNAMICS AND WAVE PROPAGATION

MS 17: SEISMIC RISK ASSESSMENT OF BUILDING PORTFOLIOS

MS 18: POTENTIAL OF VIBRATIONS MONITORING FOR IMPROVING THE RELIABILITY OF BUILDINGS SEISMIC ASSESSMENT

VOLUME II

MS 24: INFLUENCE OF INFILL MASONRY WALLS IN THE RESPONSE AND SAFETY OF BUILDINGS

MS 25: SPECIAL DESIGN AND ANALYSIS OF STRUCTURES

MS 26: RECENT ADVANCES ON ENERGY-BASED SEISMIC DESIGN

MS 27: ADVANCES IN MODEL REDUCTION TECHNIQUES IN COMPUTATIONAL STRUCTURAL DYNAMICS

MS 28: NEW ADVANCES IN COMPUTATIONAL MODELLING AND EXPERIMENTAL TESTING OF INFILLED FRAMES

MS 29: AFTERSHOCK RISK ASSESSMENT: STATE OF THE ART AND FUTURE CHALLENGES

MS 30: STRUCTURAL PERFORMANCE OF NEW AND EXISTING REINFORCED CONCRETE BUILDINGS IN SEISMIC AREAS: NUMERICAL AND EXPERIMENTAL APPROACHES FOR MODELLING

MS 31: MUSEUMS' COLLECTIONS AND SEISMIC PREVENTION: RESEARCH DEVELOPMENTS AND CASE-STUDIES

MS 36: SEISMIC ASSESSMENT OF EXISTING STRUCTURES BEFORE AND AFTER STRENGTHENING

MS 38: RELIABILITY ASSESSMENT AND DESIGN OF STRUCTURES EQUIPPED WITH ISOLATION AND DISSIPATION DEVICES

MS 39: PERIODICITY EFFECTS IN VIBRO-ACOUSTICS

MS 40: DYNAMICS OF BUILDINGS AND BRIDGES AND CONTROL STRATEGIES WITHIN STRUCTURAL ENGINEERING

MS 41: THIN-WALLED STRUCTURES, STRENGTH, VIBRATION AND STABILITY

MS 42: NOVEL METHODS FOR SEISMIC DESIGN AND INTERVENTION OF CONVENTIONAL AND INTEGRAL BRIDGES

MS 44: DYNAMIC BEHAVIOUR OF JOINTS AND JOINTED STRUCTURES: MODELLING AND EXPERIMENTS

MS 45: ADVANCES ON EXPERIMENTAL AND COMPUTATIONAL SEISMIC ASSESSMENT AND RETROFIT OF MASONRY STRUCTURES

VOLUME III

Regular Sessions

RS 2: ALGORITHMS FOR STRUCTURAL HEALTH MONITORING

RS 3: CONSTITUTIVE MODELLING UNDER EARTHQUAKE LOADING

RS 4: DYNAMICS OF CONCRETE STRUCTURES

RS 5: DYNAMICS OF COUPLED PROBLEMS

RS 7: DYNAMICS OF STEEL STRUCTURES

RS 8: GEOTECHNICAL EARTHQUAKE ENGINEERING

RS 9: IMPACT DYNAMICS

RS 10: INVERSE PROBLEMS IN STRUCTURAL DYNAMICS

RS 12: NONLINEAR DYNAMICS

RS 13: NUMERICAL SIMULATION METHODS FOR DYNAMIC PROBLEMS

RS 14: OPTIMUM DESIGN AND CONTROL IN STRUCTURAL DYNAMICS AND EARTHQUAKE ENGINEERING

RS 16: PERFORMANCE-BASED EARTHQUAKE ENGINEERING

RS 20: SEISMIC RISK AND RELIABILITY ANALYSIS

RS 26: STEEL STRUCTURES

RS 27: STOCHASTIC DYNAMICS

RS 29: WAVE PROPAGATION

COMPDYN 2019
7th ECCOMAS Thematic Conference on
Computational Methods in Structural Dynamics and Earthquake Engineering
M. Papadrakakis, M. Fragiadakis (eds.)
Crete, Greece, 24–26 June 2019

DEVELOPMENT AND VERIFICATION OF REAL-TIME DAMAGE ASSESSMENT BASED ON STATISTICAL PATTERN RECOGNITION TECHNOLOGY FOR STRUCTURE MAINTENANCE

GwangHee Heo[1], ChungGil Kim[1], ChinOk Lee[2], ByeongChan Ko[3], ChaeRin Park[3]

[1] Civil Engineering Dept. Professor, Konyang University
e-mail: {heo, cg-kim}@kyu.ac.kr

[2] Civil Engineering Dept. Professor, Chungnam University
e-mail: colee@cnu.ac.kr

[3] Department of Disaster Safety Engineering Dept. Master's Candidate, Konyang University
e-mail: {yunil-0, cherish_7169}@naver.com

Abstract

This study focuses on the development of a real-time damage detection technology based on statistical pattern recognition methods to detect damages in a complex structure, such as a cable-stayed bridge. Further, the performance of the proposed method is evaluated experimentally. The real-time damage detection method is devised on a statistical pattern recognition technology from a damage data assessment section and a simulation based on a non-damage data generation section. The damage data assessment section applies the improved Mahalanobis distance theory from among the available statistical pattern recognition technologies. Further, the non-damage data generation section comprises logic based on the state-space equation. To verify the performance of the technology developed, a damage detection test was conducted on the model structure of the cable-stayed bridge. The experiment confirms that the real-time damage detection technology determines the location of damages in the cable-stayed bridge in real time.

Keywords: Statistical pattern recognition, Real-time damage assessment, Mahalanobis distance, State-space equation, Maintenance, Cable-stayed bridge

1 INTRODUCTION

Owing to the development of modern society, human beings now live in more densely populated spaces. Structures that are built recently consider service loads, but old structures are always exposed to loads that exceed the serviceability limit of the structure itself. In addition, the safety of structures is always threatened by typhoons and earthquakes whose intensity increases with global climate changes.

Researchers have perceived such threats to the safety of structures and studied diverse technologies for the inspection and assessment of structure safety. Such an assessment technology is called structural health monitoring (SHM). SHM is a technology that can determine damages or unsafe elements in structures by conducting a statistical analysis of the data measured from the structures and clarifies the current conditions of the structures [1,2]. The method of statistical analysis on the current conditions of the structures is divided primarily into supervised learning and unsupervised learning. Supervised learning is a high-level damage detection method that can assess the current conditions of the structures using both non-damage data and damage data. For such a damage assessment, it is essential to secure non-damage data and a large volume of data learning is required. Unsupervised learning that has improved the problems of supervised learning is a convenient method of assessing the current conditions of structures without learning a damaged structure; however, the level and degree of damage assessment [2] are limited. Recently, such a limit of unsupervised learning is overcome by applying the data mining technology that extracts new information hidden in data by analyzing the correlation between data [3,4]. The Mahalanobis distance (MD) theory is a diverse data mining technology that has been studied by many researchers; it uses a simple method of perceiving the data pattern and can analyze a large data volume [5,6]. However, the Mahalanobis distance theory presents drawbacks even though it is an unsupervised learning, as it requires non-damage data for setting a threshold and is a post-treatment method that analyzes data only after the occurrence of a damage.

The objective of this study is to overcome the limit of the statistical analysis method used for the existing SHM method and to develop a technology that enables a real-time damage assessment. A real-time damage assessment technology was developed by offering non-damage data required for supervised learning as a simulation based on the information of a structure and by using a complex learning method that adopted the Mahalanobis distance for unsupervised learning. To verify the developed real-time damage assessment method, damage detection tests were performed on a cable-stayed bridge. The result proved that the real-time assessment method developed for this study can approximately yield the location of damages in a cable-stayed bridge.

2 REAL-TIME DAMAGE ASSESSMENT TECHNOLOGY

2.1 Statistical Pattern Recognition Technology

The assessment of damages in structures using the Mahalanobis distance theory was proposed in 2007 by Nair and Kiremidijian, who applied a specific vector obtained using the Gaussian mixture model (GMM) to calculate the Mahalanobis distance; this assessment method was verified using the ACSE benchmark structure's interpreted data [5]. Heo et al. proposed an improved Mahalanobis distance theory to resolve issues with the existing theory and verified it by conducting damage detection tests on a cable-stayed bridge [7].

This study used the improved Mahalanobis distance theory for real-time damage assessment. Equation (1) represents the improved Mahalanobis distance (IMD) that offsets the de-

crease following a substantial variability between data; this was a shortcoming of the existing MD. that the improved method can reduce large variability in data by utilizing the differences in the data before and after damage occurrence.

$$IMD = \sqrt{(\Delta x - m)^T R^{-1} (\Delta x - m)} \tag{1}$$

In the equation, x is the measurement value obtained from a structure; m is the average value of x; R is the covariance matrix of the measured x value. Δx is the difference between x before damage and x' after damage.

2.2 Simulation to Obtain Non-Damage Data

The most general technique of assessing damage in a structure is to compare the responses between the damaged and undamaged structures. However, the majority of structures built before the development of a monitoring system do not contain information about their initial condition. In this study, a simulation logic was created based on the basic information of a structure to obtain non-detection data for real-time damage assessment and was included in the real-time damage detection system. The simulation logic for obtaining the non-damage data was established based on the motion equation. Information on the mass, hardness, and damping obtained from a detailed finite element (FE) modeling and interpretation of the target bridge that used NX Nastran were used as the basic information of the structure. To ensure reliability of the obtained information, the modal assurance criteria (MAC) was used to compare the response data obtained from a model test with the target bridge, and the data was interpreted through FE analysis.

$$MAC(A, X) = \frac{\left| \sum_{j=1}^{n} (\Phi_X)_j (\Phi_A)_j^* \right|^2}{\left(\sum_{j=1}^{n} (\Phi_X)_j (\Phi_X)_j^* \right) \left(\sum_{j=1}^{n} (\Phi_A)_j (\Phi_A)_j^* \right)} \tag{2}$$

Here, Φ_X and Φ_A are the mode shapes calculated and obtained from interpretation and experiment, respectively, and the MAC value approaches 1 as the two compared modes correspond more with each other. The result of the FE interpretation of the target bridge indicated an approximately 4% of maximum error when compared to the result of the model test. To resolve such a problem, model updating was performed. Table 1 and Fig. 1 below indicate the MAC results for which model updating was performed.

		FE Analysis Modes (Updating)		
		1st	2nd	3rd
Exp. Modes	1st	1	0.016348	0.010044
	2nd	0.016091	1	0.003991
	3rd	0.010122	0.003648	1

Table 1: FE Interpretation and MAC Value from Modal Test

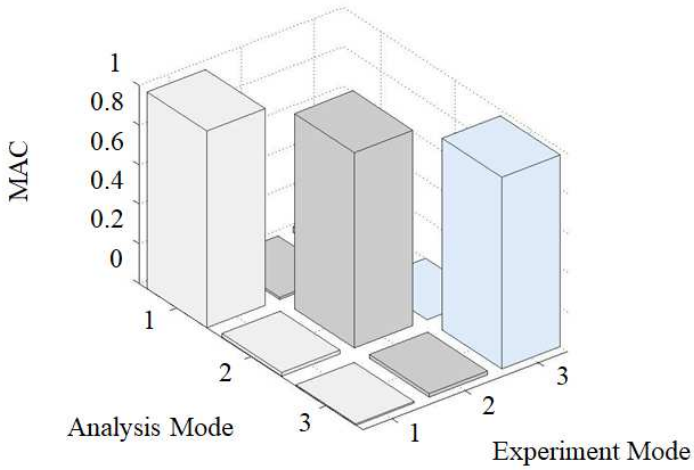

Figure 1: MAC Plot

2.3 Real-Time Damage Assessment Program

For the experimental verification of the developed real-time damage assessment technology, programming was performed using Matlab & Simulink, as shown in Fig. 2 below.

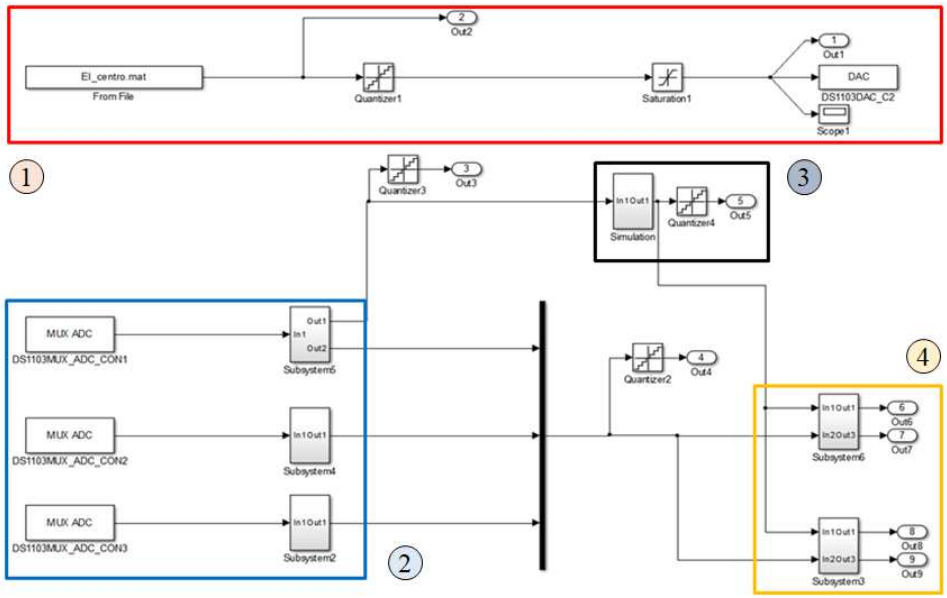

Figure 2: Real-Time Damage Assessment Program

For the real-time damage assessment program shown in Fig. 2, programming was performed separately for a seismic excitation signal output section for the vibration experiment, a measurement section that measures the response from the structure, and a damage detection section that is used to assess damages. Here, the damage assessment section is divided into a simulation section that provides the non-damage data of the structure based on measured seismic excitation signals and a statistical analysis section that compares the measured response from the structure and non-damage data by applying the IMD theory.

3 REAL-TIME DAMAGE ASSESSMENT TEST

3.1 Model Cable-Stayed Bridge for Damage Assessment Test

A model cable-stayed bridge that is a 1/200 replica of the Seohaedaegyo Bridge in Korea was used as the target for the verification of the developed real-time damage assessment method. The model bridge had 4,200 mm length, 170 mm width, and 1,000 mm pylon height, as displayed in Fig. 3. The seats at both ends of the bridge were of the roller type and the seat of the pylon was of the roller and hinge type.

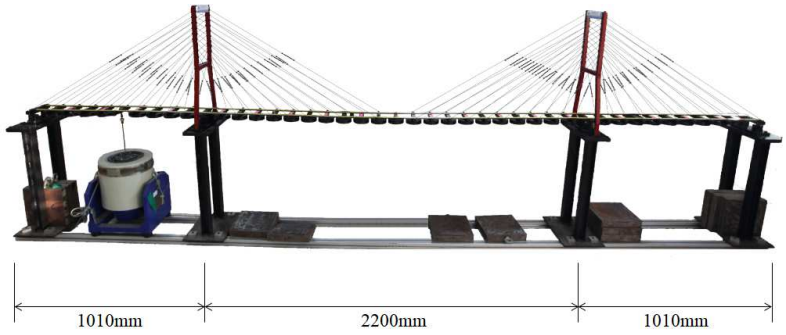

Figure 3: Model Cable-Stayed Bridge

As shown in Fig. 3, a shaker was located at the bottom of the left-side span to generate vibrations by imposing an external force to the cable-stayed bridge.

3.2 Damage Detection Test

Damage assessment tests were performed to assess the performance of the developed real-time damage assessment technology experimentally. For the output of the structure's seismic excitation signal and the measurement of its response, dSPACE 1103 was used. Control Desk based on Matlab & Simulink that is an operation-dedicated program was used for the operation of dSPACE 1103. Dytran's 3055B3 acceleration sensor was used for the measurement of the structure's response. Eight sensors were selected using kinetic energy optimization techniques, and one sensor on each of the left-side and right-side spans were positioned as illustrated in Fig. 4.

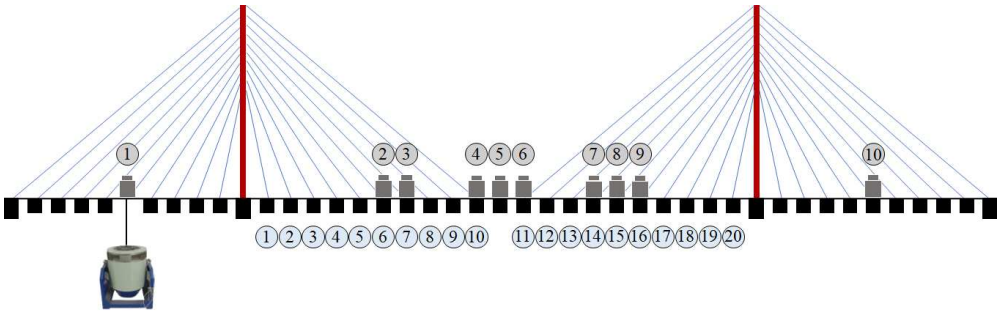

Figure 4: Measuring Instrument Locations and Cable Numbers

As shown in Fig. 4, the damage assessment test was implemented by removing the cables that support the span between two pylons in consecutive order. A set of cables in the front and back in the same section was removed together.

4 DAMAGE DETECTION PERFORMANCE OF DEVELOPED REAL-TIME DAMAGE ASSESSMENT TECHNOLOGY

Three damage tests were conducted for each case for the assessment of the damage detection performance of the newly developed real-time damage assessment technology to ensure the reliability of the test result. Fig. 5 below expresses the result of the response from the No.6 sensor out of the data obtained from the damage test in a graph.

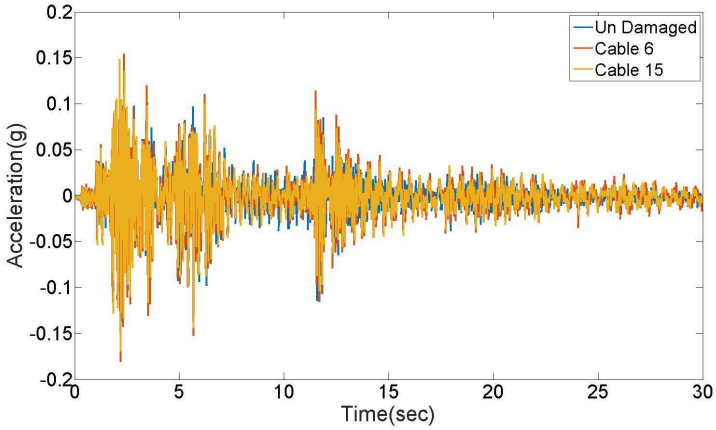

Figure 5: Acceleration Response Following Cable Damage

Fig. 5 compares the non-damage response and the acceleration response by damages in the No. 6 and No. 15 cables. As illustrated in the graph, the response following cable damage was similar to a non-damage response to the extent that the difference between the two could not be detected. Such results were observed in the other damage cases and sensors as well.

Subsequently, the result of damage detection that utilized the improved statistical pattern recognition technology was compared. IMD was calculated using data measured from ten sensors. Further, the root mean squared (RMS) value of each IMD was compared to detect the damage in 20 test cases. Fig. 6 below shows the result of damage detection using the improved statistical pattern recognition technology.

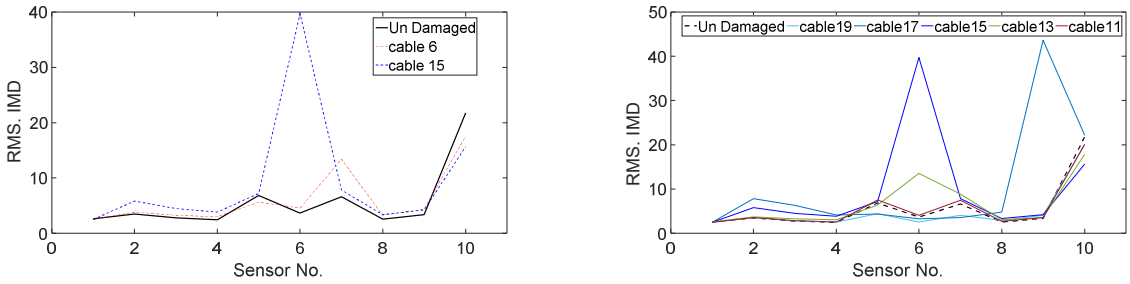

(a) A difference result (b) Indeterminate result

Figure 6: Result of Damage Detection that Utilizes Statistical Pattern Recognition Technology

As shown in Fig. 6(a), the IMD by cable damage was significantly different from non-detection IMD. However, a pattern that enables the damage location to be detected by simply comparing the IMD is not shown, as illustrated in Fig. 6(b).

Heo et al. compared the data obtained from one sensor to detect the degree of cable damage by utilizing the improved statistical pattern recognition technology [7] Such a data analysis method may be appropriate for assessing the degree of damage; however, it is not sufficient to detect the damage location in a bridge out of various responses from the bridge. In addition, as indicated by Fig. 6(b), the IMD calculated from each sensor did not offer a pattern for accurate damage detection.

Hence, the variability of the IMD and the RMS values of each test case are analyzed in this study to detect the damaged location from the IMD and RMS results from each sensor. As demonstrated in Fig. 6(b), the IMD and RMS values of each sensor did not indicate a significant variability for sensors No. 1 to 5; however, the variability between sensors was shown in sensors No. 6 to 10. Accordingly, the variability of the IMD and RMS values of sensors No. 6 to 10 were analyzed for each test case. Fig. 7 shows the variability of the IMD and RMS values in a graph.

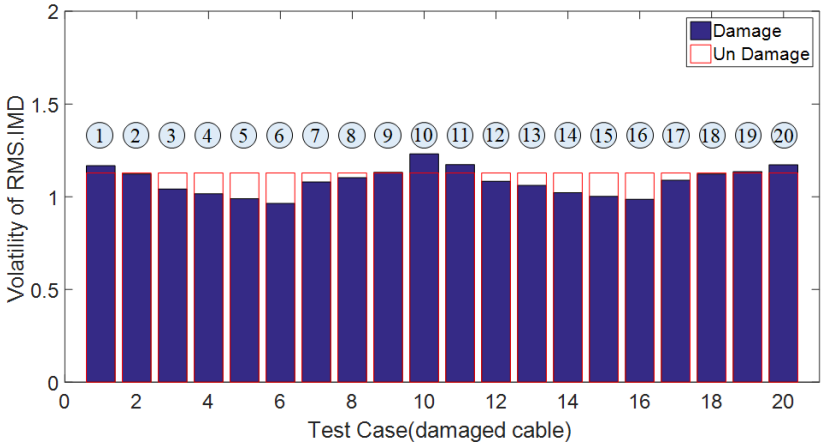

Figure 7: Detection of Damage in a Structure Using IMD Variability

Fig. 7 shows the RMS results from the IMD based on the data obtained from sensors No. 6 to 10 in 20 test conditions (cable damage) and the variability of each case. In Fig. 7, the red bars represent the result from a non-damage condition and the blues bars represent the result from damaged conditions. As the graph indicates, the variability of the damage is greater for the positions nearer to the pylon or the middle of the spans than the variability of the non-damaged conditions, while the variability was reduced at the 1/4 and 3/4 positions of the span.

5 CONCLUSIONS

Bridges are exposed to the threat of external loads frequently, even though they are critical in the transportation network. This study aimed at developing a technology that can perform a real-time damage assessment for bridges using a statistical pattern recognition technology. The real-time assessment technology was developed by applying a complex learning method that combined a simulation section offering non-detection data required for supervised learn-

ing and the Mahalanobis distance theory, which is the most well-known method of unsupervised learning. Notably, to overcome the limits of the newly improved Mahalanobis distance theory that resolved the shortcomings of the original version, a new method of analysis that considered the variability between the responses of a structure was proposed. Damage assessment tests were performed on a model cable-stayed bridge to verify the result of the study experimentally. The test result proved that the real-time damage assessment technology newly developed in this study could approximately detect the location of cable damage. The conclusion of this experimental study is as follows:

1) For the damage detection technology newly developed in this study, non-damage data were offered through simulations and the improved Mahalanobis distance theory utilizing such data was confirmed to demonstrate a difference by damage. However, the technology presented a drawback in that it did not exhibit a pattern that could detect the damage location;
2) This study proposed an analysis method that considered the variability between data for overcoming the limit in detecting the damage locations. The result of real-time damage assessment utilizing the proposed method proved its ability to approximately detect the location of cable damage.

Finally, it was confirmed that the real-time damage assessment technology and data analysis method developed in this study could perform the detection of damage location in a structure while non-damage data have not been obtained. However, the performance should be further verified on cases of damages in mass and in diverse structure types, as it was verified only on the cable of a cable-stayed bridge in this study.

ACKNOWLEDGMENTS

Research Foundation of Korea (NRF) grant funded by the Korea government (MIST) (No: 2016R1A2A1A05005499, 2016R1A6A3A11931945, and 2018R1A6A1A03025542). Many appreciation and acknowledgements go to the National Research Foundation who made this research possible.

REFERENCES

[1] Wang Z, Ong KCG, *Structural damage detection using autoregressive-model-incorporating multivariate exponentially weighted moving average control chart*, Eng Struct, *Vol 31(5)*, pp. 1265–1275. 2009.

[2] Charles, R, F, Hoon, S, *Pattern recognition for structural health monitoring*, Workshop on Mitigation of Earthquake Disaster by Advanced Technologies, Las Vegas, NV, USA, LA-UR- 00-5565, 2000.

[3] Ruotolo, R, and Surace, C, *Damage detection using singular value decomposition," Structural Damage Assessment Using Advanced Signal Processing Procedures*, Proceedings of DAMAS '97, University of Sheffield, UK, pp. 87-96, 1997.

[4] Worden. K, Manson. G, and Fieller, N. R. J, *Damage detection using outlier analysis, Journal of Sound and Vibration, Vol. 229,* No. 3, pp. 647-667, DOI: 10.1006/jsvi.1999.2514, 2000.

[5] Nair. K. K, Kiremidjian. A, S, *Time series-based structural damage detection algorithm using Gaussian mixtures modelling*, Journal of Dynamic Systems, Measurement, and Control, *Vol. 129*, pp.129-293, DOI: 10.1115/1.2718241, 2007.

[6] Kiremidjian. A. S, Kiremidjian. G, Sarabandic. P, *A wireless structural monitoring system with embedded damage algorithms and decision support system*, Structure and Infrastructure Engineering, *Vol. 7*, No. 12, pp. 881-894, DOI: 10.1080/15732470903208773. 2011

[7] Gwanghee. H, Chunggil. K, Chinok. L, Jieun. Hur, Sanggu, S, *A Damage Assessment Technique based on a Revised Statistical Pattern-Recognition Technique (SPRT)*, KSCE Journal of Civil Engineering, 21(3), 882-888, 2017

COMPDYN 2019
7th ECCOMAS Thematic Conference on
Computational Methods in Structural Dynamics and Earthquake Engineering
M. Papadrakakis, M. Fragiadakis (eds.)
Crete, Greece, 24–26 June 2019

MODAL IDENTIFICATION FROM MOTION MAGNIFICATION OF ANCIENT MONUMENTS SUPPORTED BY BLIND SOURCE SEPARATION ALGORITHMS

Vincenzo Antonio Fioriti[1], **Ivan Roselli**[1], **and Gerardo De Canio**[1]

[1]ENEA Casaccia R. C.
Via Anguillarese 301, 00123- Rome
{vincenzo.fioriti, ivan.roselli, gerardo.decanio}@enea.it

Abstract

Motion Magnification (MM) is an emerging video processing methodology that acts like a microscope for motion in digital videos. Hardly visible motions are magnified leaving unchanged the general topology of the image. Therefore, the micro-displacements produced by vibrations can be amplified greatly and made available to the standard frequency domain analysis. The MM was recently successfully explored as a viable method to perform modal identification, at least in laboratory. In outdoor environment ambient vibration acquisitions are unavoidably affected by significant noise disturbing the modes identification. However, the first three or four modes, which are usually the most relevant to the dynamic behaviour of most structures, can be identified with little supervision, possibly reducing the calculation requirements as much as possible. All these tasks may be accomplished using MM together with the Blind Source Separation (BSS) algorithm. BSS allows the separation of mixed signals without previously known information about the mixture. MM provides the data while the BSS improves the identification of the modes by separating their contribution within the mixed noisy signals. A case-study is proposed to explore the application of the methodology to large ancient masonry structures, which represent very challenging objects for their structural complexities and heterogeneities. In particular, the studied structure was represented by an ancient bridge, the Ponte delle Torri, Spoleto. Due to the outdoor environmental difficulties, to the state of damage of the bridge and to the high level of noise in the video footages, this case-study has to be considered a very demanding one, nevertheless the modes were identified with good approximation in comparison to the results by Operational Modal Analysis (OMA) techniques, applied to ambient vibration data from seismographs equipped with accurate triaxial velocimeters.

Keywords: Motion Magnification, Blind Source Separation, Modal Identification.

1 INTRODUCTION

Monuments in the urban environment are affected by strong vibrations caused by anthropic activities, besides the natural events, therefore the health monitoring of these ancient constructions is required periodically. The standard procedure for the monitoring is the frequency domain analysis since a significant variation of the frequency response suggests that a damage has occurred, but expensive equipment, time-consuming elaborations and, last but not least, trained personnel are needed. Moreover, if the monument to be analysed is a large building, sensors have to be positioned to cover critical areas, but often is not possible to reach these points easily and sometimes it is impossible at all [1]. Even more important, since to perform reliable elaborations high density data should be collected, that is, the number of devices to be deployed to provide the full coverage of the building should be huge or alternatively, many measurement repetitions should be done. As a matter of fact, usually one chooses carefully some points, hoping that they will suffice to the analysis purpose. Once data have been collected, their processing and analysis may result in a long, hard and complex task.

To face these difficulties in the field of the mode identification, we propose the recently developed motion magnification (MM) digital video methodology [2] together with the Blind Source Separation (BSS) [3] algorithm. Motion magnification acts like a microscope for micro-motions in video sequences, saving the topology of the images but unveiling tiny visual patterns hardly visible with the naked eye. The magnification enables the spatial resolution of the videocamera to extract physical properties from images, to make inferences about the dynamical behaviour of the object no matter its dimensions, since any point on its surface can be considered a “virtual sensor”.

Recently, a number of laboratory experiments have ascertained the reliability of the MM methodology compared to standard techniques of modal identification, but regrettably, an extensive on-the-field experimentation for real buildings is still lacking.

On the other hand, the BSS original algorithm [3] allows the separation of randomly mixed signals, without previously known information about the mixture. Therefore, the MM provides the data, while the BSS (in the second-order statistical BSS formulated by McNeill’s [4]) improves the identification of the modes, separating their contributions within the mixed signals semi-automatically.

In the present paper, a case-study is proposed about the analysis of the *Ponte delle Torri*, a mediaeval bridge located in Spoleto, Italy. The McNeill approach properly adapted to the modal identification [4-6] was applied to video footages of the bridge processed through phase based MM. The analysis was limited to the first four modal frequencies and a comparison with the results obtained by Operational Modal Analysis (OMA) of velocimeters data is discussed.

Figure 1. The Ponte delle Torri of Spoleto.

2 THE PONTE DELLE TORRI OF SPOLETO

Our case study is the so-called *Ponte delle Torri* of Spoleto (Figure 1). It is a large historical construction that connects Colle Sant'Elia with Mount Monteluco in Spoleto, which used to be an important city in central Italy during the middle-ages.

The bridge superstructure is made up of a pedestrian deck, provided with a water canal on one side, supported by lancet arcades and stone piers known as "towers".

The bridge has a stone structure with shoulders and piers made up of rubble walls in a square matrix assembled by mortar and lime. The structure is only apparently regular. In fact, piers and arches have all different shapes and sizes, as well as the walls towards Colle Sant'Elia and Monteluco are also diverse in the masonry texture, due to their different construction timing and subsequent rebuilding interventions. The bridge has an overall length of about 230 m, while the highest tower is over 70 m. The bridge has a state of damage typical of historic masonry bridges. At the top of the arches, especially those on the slope of Monteluco, there are heavy water infiltrations resulting in losses of mortar binder and wall apparatus skiving. Moreover, a widespread damaged layer, especially in the lower part of the piers, was detected. This has caused the expulsion of some cornerstones of the piers, the disarticulation of the masonry texture and the collapse of portions of the outer layers. The bridge showed a widespread and extended state of damage already prior to the Central Italy sequence. The cracks present in the bridge seem mostly to be related to the heterogeneity of the construction materials, as usually befalls to ancient structures that are subjected to a series of structural interventions, architectural modifications and functional changes during their long history. The upper part of the piers is generally made up of better quality masonry with mortar of good consistency. In the lower piers, widespread damages caused the expulsion of some cornerstones, local dislocations of the masonry and some partial detachments of the outer layers. The fourth pier from West displayed two very large cracks that are clearly visible [1, 4].

3 THE MM AND BSS ALGORITHMS

Now we present briefly the two main algorithms used to perform the blind modal output-only identification, just the necessary to the comprehension of the proposed methodology, since the complete mathematical formalization is rather cumbersome.

3.1 The Magnified Motion algorithm

In the present work we have used the phase based version of the MM algorithm [7] to process the digital videos. It is important to observe that within the MM processing a band-pass derivation step is included, so that to magnify the motion displacements, either the initial Taylor's expansion or the amplification factor α do not have to be too large. In practice, slowly changing scenes and small amplifications permit to remain into the linearity bound needed.

Moreover, the algorithm implies a certain noise amplification too [8]. Physical sources of noise are lighting conditions, presence of shadows, camera unwanted vibrations, poor pixel resolution, presence of unexpectedly large motions, excessive camera-object distance. In particular, the scene lighting conditions should remain constant, as changing the background light could produce apparent motions. In general, the video duration heavily affects the computation time of the whole processing and may be a major problem. Obviously, according to the Shannon-Nyquist Theorem the frame rate should be appropriate as it represents the sampling frequency f_{fps} of the data. The general condition to be respected is given by:

$$f_{\text{fps}} \geq 2f_{\text{max}} \tag{1}$$

where f_{max} is the maximum frequency of interest.

3.2 The Blind Source Separation algorithm

The Blind Source Separation is an Independent Component Analysis (ICA) signal processing technique, that extracts n original signals $\boldsymbol{s}$ from their random mixtures $\boldsymbol{x}$, observed by a certain number m of sensors and possibly polluted by noise. Thus the *blind* source separation consists in identifying the mixing matrix $\mathbf{A}$ and retrieving the source signals $\boldsymbol{s}$ without resorting to any *a priori* information about $\boldsymbol{s}$, the mixing process, or the signals propagation medium. The only hypothesis is that the source signals are mutually statistically independent [4]. ICA algorithms are based on an objective function to be optimized according to a measure of independence of the source in the direction of the increasing independence. The physical phenomenon is represented by:

$$\boldsymbol{x}(t) = \mathbf{A}*\boldsymbol{s}(t) + \boldsymbol{\eta}(t) \tag{2}$$

where, given m sensors and n sources of signal, $\boldsymbol{x}$ is the observed signals vector that originate from the mixture, and vector $\boldsymbol{\eta}$ is the noise of unspecified distribution, $\mathbf{A}$ is the random "mixing matrix". The number of sensor m must be at least equal to the number of sources n, otherwise the reconstruction will be affected by very large errors. There are two important types of mixing models: instantaneous mixtures and convolutive mixtures. The first one is a mixing model which does not take into account any delays whereas the convolutive mixture involves some delays in the mixing process. In our case we admit no delays.

Originally, the BSS was developed to solve the "cocktail party" problem, whose simplest formulation is this: two people are speaking during a party, while two distant microphones record the overlapping voices amid noise. We want to separate voices $\boldsymbol{s}$ using only their registrations $\boldsymbol{x}$ from at least two microphones.

Thus, $m = n = 2$ and the mixing system is:

$$x_1(t) = a_{11}s_1(t) + a_{12}s_2(t) + \eta(t) \tag{3}$$
$$x_2(t) = a_{21}s_1(t) + a_{22}s_2(t) + \eta(t) \tag{4}$$

If the sources are statistically independent, the problem is solvable estimating the matrix $\mathbf{W} = \mathbf{A}^{-1}$, called the de-mixing matrix (up to some constants scaling factors):

$$\boldsymbol{s}(t) = \mathbf{W}* \boldsymbol{x}(t) \tag{5}$$

Today many ways to calculate $\mathbf{W}$ are known. Usually a cost function is chosen according to geometric information or theoretical considerations and minimized by the gradient descent, the simulated annealing or a genetic algorithm, resulting in an estimation of $\mathbf{W}$ [3].

Here we use the McNeill BSS version [4], to obtain the separation of signals from noise and, at the same time, the output-only calculation of vibration modes. The underlying idea is quite simple: the physical responses $\boldsymbol{x}$ of the dynamic system are constructed from the modal response $\boldsymbol{q}$, through the modal matrix $\boldsymbol{\Phi}$:

$$\boldsymbol{x}(t) = \boldsymbol{\Phi} * \boldsymbol{q}(t) \tag{6}$$

hence using the BSS framework to calculate $\mathbf{W} = \boldsymbol{\Phi}^{-1}$:

$$\boldsymbol{q}(t) = \mathbf{W} * \boldsymbol{x}(t) \tag{7}$$

the modes $\boldsymbol{q}$ are obtained.

This decomposition allows for the estimation of the natural frequencies and damping ratios too. The modal matrix and modal responses are formed by real values if the topology of the damping matrix results in a proportional damping, otherwise are formed by complex values (for details see [4-6]).

4 APPLICATION TO THE PONTE DELLE TORRI

We validated the methodology on the case-study of the *Ponte delle Torri*, using the modal frequencies by OMA as a reference ground-truth. Besides the magnified motion that provides a very large number of "virtual sensors", the major advantages coming from the McNeill-BSS algorithm are the semi-automation of the mode calculations and the separation of the signals from most of disturbances. Two sets of time-series are used as inputs to the BSS: those from the MM and those from a velocimeter.

4.1 Modal identification by OMA of velocimeters data

Ambient vibration was measured by SL06 recorders (SARA Instruments) equipped with triaxial electrodynamic velocimeters, set to 200 Hz sampling frequency [8]. The instruments were positioned along the bridge deck, on top of each pier and in the middle between piers. Also the basis of the central pier and both abutments were recorded. All configurations were acquired for at least 20 minutes.

The OMA techniques implemented in the ARTeMIS Modal Pro software were used to elaborate the experimental data of the velocimeters. Among the several OMA techniques available, the Frequency Domain Decomposition (FDD), the Enhanced Frequency Domain Decomposition (EFDD) and the Stochastic Subspace Identification (SSI) were utilized. EFDD provides also an estimation of modal damping, SSI is a more sophisticated and automatic procedure based on time-domain approach. The results of the identification of the modal frequencies averaged over the OMA techniques are resumed in Table 1. Also a finite element analysis (FEM) has been carried out along with the experimental campaign, further confirming results of Table 1 [1, 4].

4.2 BSS with velocimeters data

We firstly applied the BSS to SARA velocimeters data in order to validate the algorithm efficiency by comparison with the OMA results of the same dataset. A velocimeter channel $y(t)$ was considered for the following processing steps. The segmentation can be expressed as follows:

$$\begin{aligned} y_1 &= y(t_i : t_{f1}); \\ y_2 &= y(t_{f1} : t_{f2}); \\ y_3 &= y(t_{f2} : t_{f3}); \\ y_4 &= y(t_{f3} : t_f); \end{aligned} \tag{8}$$

The above segmentation is correct only if the ergodic hypothesis holds, otherwise the BSS error could be quite large. It is not easy to demonstrate the ergodicity of the system under consideration, however, as a matter of fact, the errors with respect to OMA modes are small

(Figure 2, Table 1). This reduced error could be quite predictable by means of specific tests and will be the object of future investigations.

In the Fast Fourier Transform (FFT) of the velocimeter signal, the peaks are well defined and separated, allowing a clear identification of modes (Figure 3). This is clearly due to the good quality of the high-performance velocimeters mounted on the SARA recorder. Therefore, BSS proved to be an effective tool for frequencies identification with good-quality vibration data.

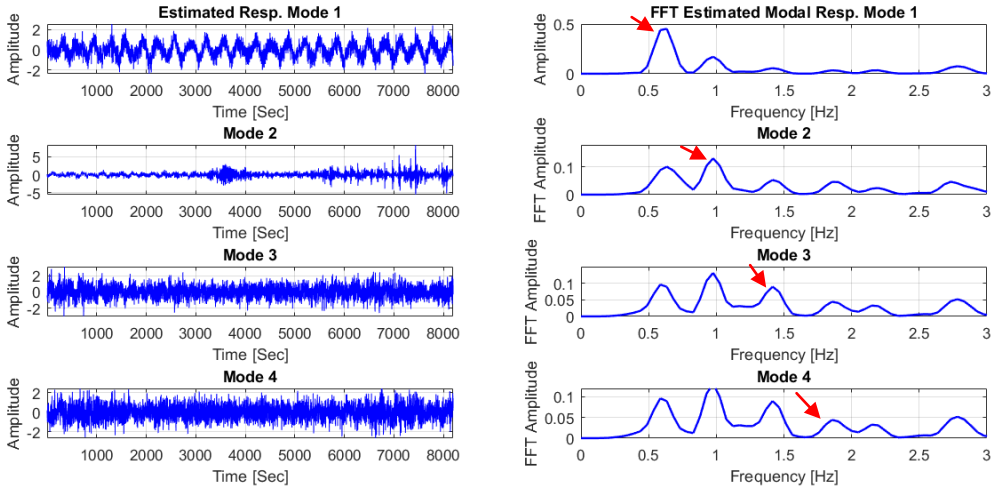

Figure 2. The first four vibration modes indicated by the red arrows (right column) and on the left their amplitude time-series. Each subgraph shows the related peak, according to the mode order. Here the signal is from a velocimeter, direction y.

Mode	BSS-vel (Hz)	OMA (Hz)	% error
1	0.635	0.632	-0.44
2	0.977	1.011	-3.40
3	1.416	1.496	5.34
4	1.855	1.975	-6.08

Table 1. Modal frequencies calculated by BSS of velocimeter data (BSS-vel), the reference values of OMA, and the percentage errors with respect to the OMA values.

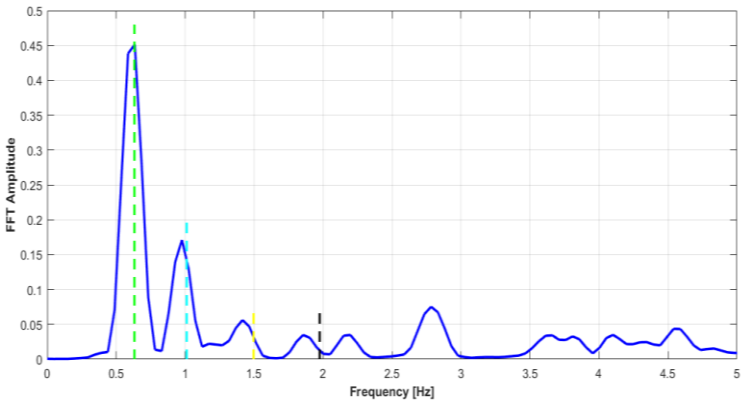

Figure 3. FFT amplitude of the velocimeter signal processed by BSS. Dotted coloured vertical lines represent the modes identified by OMA. The peaks are well defined and separated, allowing a clear identification of modes.

4.3 The Magnified Motion data

A video footage of the bridge was recorded contemporarily to the ambient acquisition of velocimeters data during the campaign of 29th May 2017. Large motions, such as people passing by in front of the camera and swinging objects, were avoided [10]. The presence of large motions is one of the most important sources of noise for the MM, requiring the experimenter to isolate part of the image, although usually this is not a feasible option. Video footage was recorded by means of a commercial low-cost camera (pixel resolution 360 x 445, frame rate of 50 fps). The basic methodology is to take advantage of the large number of pixels contained in the camera view. Theoretically, we could have 160,200 "virtual sensors", meaning that each pixel provides a time history of intensity variation (colour or grey scale), from the first frame to the last one. These time series contain the information about the displacements of the physical points related to the pixels (although they are not real displacements). Of course, not all the surface of the structure generates useful information, therefore we identify a small area with high signal-to-noise ratio (SNR). The identification of the region of interest (ROI) is a crucial point of the procedure.

In Figure 4 the first frame of the MM video, note also the field of view. The red box enlarged on the right is the selected region of interest used to extract the MM intensity time-series and finally the average over all the pixel time series (bottom).

It is not mandatory to perform the PSD on this averaged signal, but it is useful to exploit the low-passing action of the mean to reduce noise disturbances. The main source of vibrations is the wind, although a road flanks the monument on the right side. In any case, man-made vibrations may be considered of low intensity. The camera is positioned on the road near the monument hence wind and traffic affect its stability too [11].

To run the MM algorithm [3] we need to set some parameters. In particular, the magnification band and the amplification factor are the most important. We chose a band of 0.5-2.5 Hz and an amplification factor of 140. Similar values would be also acceptable, nevertheless, since the MM acts as a pass-band filter, choosing a band close to the actual modes gives better results. In our case we have been supported by the previous analysis [1], but generally one must rely on experience to decide a suitable band. After the MM phase based magnification step [3], we have to select the region of interest of the virtual sensors, meaning to pick some pixels whose time history of colour variation will be translated into the frequency domain. We choose the area as in the red box of Figure 5, because it is morphologically different from the wall and provides some edges to the algorithm.

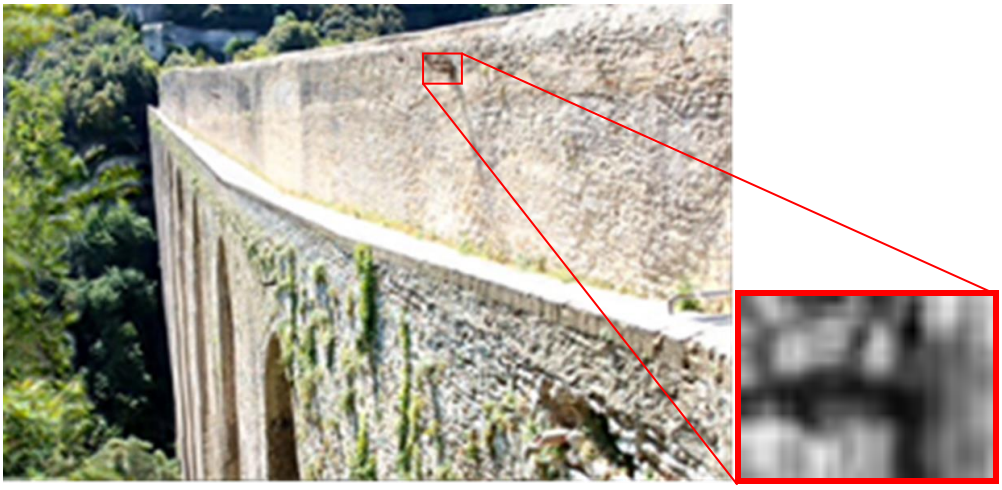

Figure 4. The camera view of the bridge. The red box enlarges the lamppost selected for analysis.

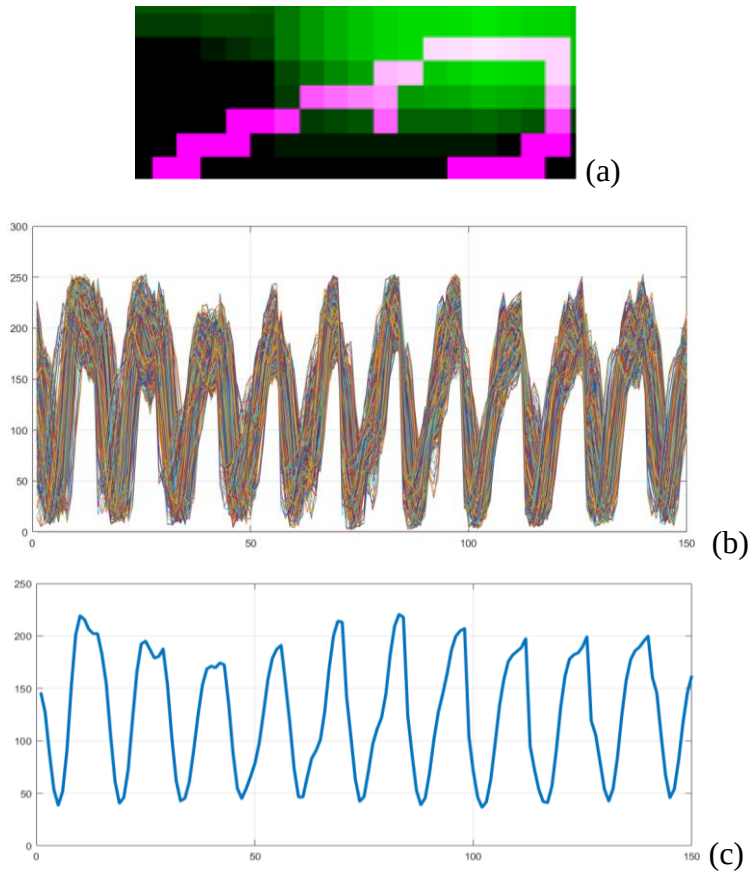

Figure 5. Signals time histories (b) from the selected pixels (a) and the related average signal (c).

The presence of marked edges or texture would be very helpful for the MM, but unfortunately the surface of the monument is rather homogeneous. These circumstances produce a large amount of noise, to be added to other disturbances. Also the angle of the camera is much less than 90° (Figure 4), therefore the magnification will be affected by a distortion. Also the air refraction and the wind provide a substantial source of noise, affecting the algorithm. No attempt to compensate for these distortions has been made.

The ROI is part of a lamppost, in-built to the wall about 40 m from the camera; however only the red box pixels are able to supply low-noise information, because are close to the structure. In fact, the upper part of the lamppost spreads spurious frequencies, due to its own resonances. Other choices of the ROI have not improved the measurements.

Signals provided by MM do contain displacement information, but they cannot be used immediately as real displacements. Anyway, acceleration may be calculated just like it can be done with the velocimeter displacement measurements, and the PSD obtained as well.

The ROI area of Figure 4 may be identified qualitatively by trial and error considering the number of peaks in the PSD and their inter-distance; a dense presence of peaks suggests a high level of noise and of course is misleading, therefore only PSD spectra with identifiable frequencies are acceptable. In practice, to avoid a biased choice, one may select manually the area several times, repeat the calculation and average the results. In our case, we find that ten iterations of the MM-PSD procedure is a good trade-off between speed and precision (intended as closeness to the mean value). The smooth appearance of the MM-PSD depends on the short time span of the video that decreases the PSD frequency resolution. Another selection criterion of the ROI could be based on the entropy calculation for the single pixel time-series, choosing the high information content suggested by the entropy.

4.4 BSS with Magnified Motion data

Having extracted the time-series from the digital video as described above, we take the temporal average on four sets of selected pixels to simulate the signal obtained from four sensors, in order to match the basic BSS requirement, then we apply the McNeill calculation to unveil the modes [5-6]. Focusing on the first four modes, we must consider at least 4 signals, thus $m = 4$.

$$m = n = 4 \tag{9}$$

where eq. 9 is the BSS requirement condition. To such purpose we took four segments of the original averaged MM signal s (Figure 3, bottom) as follows:

$$\begin{aligned} s_1 &= s(t_i \ : t_{f1}); \\ s_2 &= s(t_{f1} : t_{f2}); \\ s_3 &= s(t_{f2} : t_{f3}); \\ s_4 &= s(t_{f3} : t_f); \end{aligned} \tag{10}$$

The eq. 10 is the formalization of the signal segmentation of s, in analogy to eq. 8. Each of the above four signals can be considered as the measurement time-series received from some "virtual sensors" (i.e. a group of pixels, see Figure 3), acting as input to the second order-BSS algorithm [9]. The first four modes obtained are shown in Figure 6. Each subgraph shows the related peak, according to the mode order. The smoothness of the peak depends on the particular choice of the algorithm parameters, which introduce a certain amount of unwanted arbitrariness. From the FFT amplitude of signal s (Figure 7), it can be noted that the peaks are ,ore noisy and not as well-separated as in the case of velocimeters data. Here the noise is introduced mostly by the MM mechanism, but usually noise sources may be related also to a variety of factors, and anyway they are hardly avoidable. In such cases, the McNeill's algorithm contributes to resolve the hardly distinguishable frequency peaks. In fact, the first four modes could be identified with interesting accuracy with respect to the modes identified by OMA (Table 2). Therefore, integrating the MM with the BSS proved interesting potential as a vibration measurement technique for fundamental frequency identification. It must be remarked that this achievement was due to the proper choice of the pixels to process by MM.

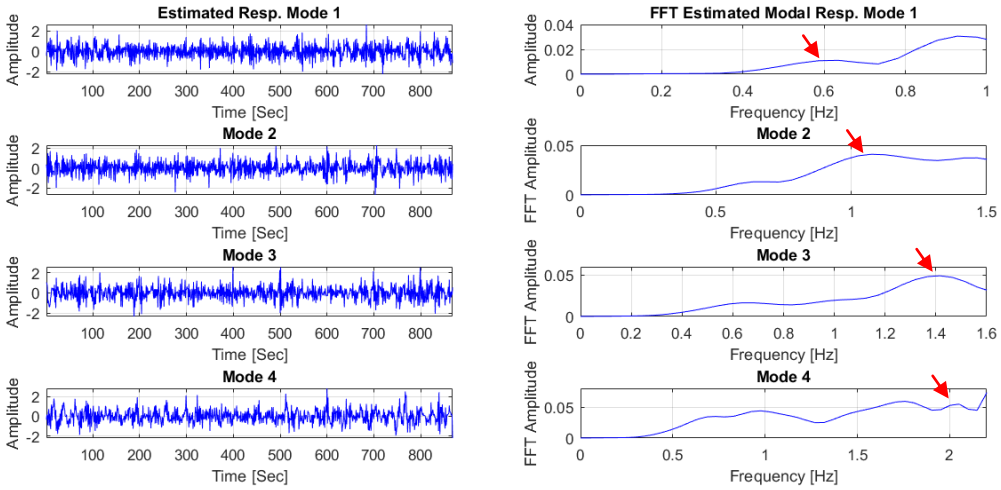

Figure 6. The first four vibration modes indicated by the red arrows (right column) and on the left their amplitude time-series. Each subgraph shows the related peak, according to the mode order.

Mode	MM (Hz)	OMA (Hz)	% error
1	0.635	0.632	-0.44
2	1.074	1.011	-6.23
3	1.416	1.496	5.34
4	2.051	1.975	-3.85

Table 2. Modes calculated from MM data, the reference values of OMA, and the MM errors.

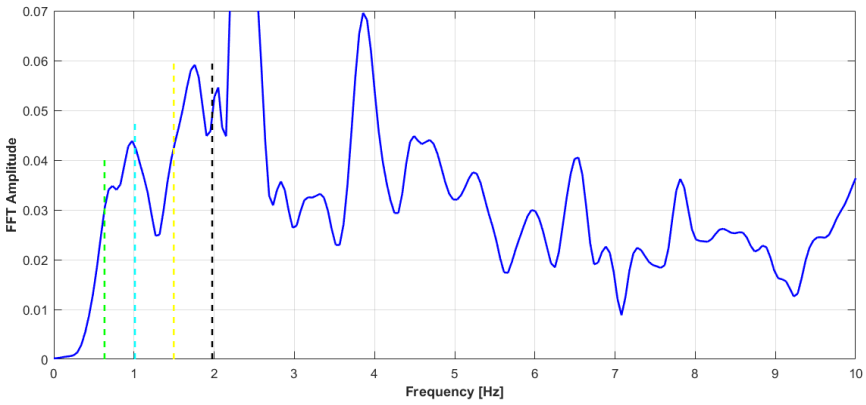

Figure 7. FFT amplitude of the MM signal processed by BSS. Dotted coloured vertical lines represent the modes identified by OMA.

5 CONCLUSIONS

Ambient vibration monitoring of large buildings is a difficult task both in terms of data collection and elaboration. Several sensors must be deployed on the structure, which is quite expensive and often demand specialized operators. After on-the-field collection, vibration data must be pre-processed, elaborated and finally analysed. In the presented case-study, about the *Ponte delle Torri*, the data were collected also as video footages for the application of MM technique. The large number of virtual sensors extracted from the acquired scene were processed with a semi-automatic procedure through the second order BSS to identify the modes of the analysed structure. Although the used McNeill algorithm for BSS still needs a complete automatization, the number of parameters to be set is limited, making it already quite easily usable for non-expert operators. On the other hand, it proved to be very stable and well-integrated with the MM. Moreover, it must be stressed that the proposed case-study was particularly tricky with regard to the noise/disturbance issues. Nevertheless, the overall procedure performed well in terms of speed, simplicity and accuracy of modal frequencies identification (6%-error accuracy with respect to the frequencies obtained with velocimeters data processed by OMA techniques). Improvements of both the basic MM and the BSS algorithms are definitely within reach, paving the way to the perspective of very easy, speedy and low-cost data acquisition for modal identification of monitored structures.

REFERENCES

[1] G. De Canio, M. Mongelli, I. Roselli, A. Tatì, D. Addessi, M. Nocera, D. Liberatore, Numerical and Operational modal analyses of the Ponte delle Torri, Spoleto, Italy. *10th International Conference on Structural Analysis of Historical Constructions (SAHC)*, 752-758, Leuven, Belgium, 13-15 September, 2016.

[2] H. Yu-Wu, et al., Eulerian Video Magnification for Revealing Subtle Changes in the World. *ACM Transactions on Graphics (TOG),* **31**(4), 65, 2012.

[3] A. Hyvarinen, J. Karhunen, E. Oja, *Independent Component Analysis*. https://www.cs.helsinki.fi/u/ahyvarin/papers/bookfinal_ICA.

[4] S. McNeill, D. Zimmermann, A framework for blind modal identification. *Mech. Sys. Sig. Proc*., **22**(7), 1526-1548, 2008.

[5] S. McNeill, An analytic formulation for blind modal identification. *Journal of Vibration and Control*. **18**(14), 2111-2121, 2012.

[6] S. McNeill, *Modal identification using blind source separation techniques*. PhD Dissertation, Houston, Department Mechanical Engineering, University of Houston, Texas, 2007.

[7] N. Wadhwa, H. Wu, A. Davis, M. Rubinstein, E. Shih, G. Mysore, J. Chen, O. Buyukozturk, J. V. Guttag, W. T. Freeman, F. Durand, Eulerian Video Magnification and Analysis. *Communications of the ACM*, **60**(1), 87-95, 2017.

[8] V. Fioriti, I. Roselli, A. Tatì, R. Romano, Motion Magnification Analysis for Structural Monitoring of Ancient Constructions. *Measurement* **129**, pp. 375-380, 2018.

[9] I. Roselli, M. Malena, M. Mongelli, N. Cavalagli, M. Gioffrè, G. De Canio, G. de Felice, Structural health monitoring by ambient vibration testing of the 'Ponte delle Torri' of Spoleto during the 2016-2017 Central Italy seismic sequence. *Int. J. Civil Struct. Health Monitor.*, **8**(2), 199-216, 2018.

[10] V. Fioriti, I. Roselli, A. Tatì, G. De Canio, Motion magnification for urban buildings. *12th International Conference on Critical Information Infrastructures Security (LNCS 10707, 253-260)*, Lucca, Italy, October 8-13, 2017.

[11] I. Roselli, A. Tatì, V. Fioriti, I. Bellagamba, M. Mongelli, R. Romano, G. De Canio, M. Barbera, M. Magnani Cianetti, Integrated approach to structural diagnosis by non-destructive techniques: the case of the Temple of Minerva Medica. *ACTA IMEKO*, **7**(3), 13 - 19, 2018.

COMPDYN 2019
Equation7th ECCOMAS Thematic Conference on
Computational Methods in Structural Dynamics and Earthquake Engineering
M. Papadrakakis, M. Fragiadakis (eds.)
Crete, Greece, 24–26 June 2019

IDENTIFICATION THROUGH SEISMOMETRIC MEASUREMENTS OF TRANSIENTS PROPAGATING INSIDE THE ASINELLI AND GARISENDA TOWERS (BOLOGNA, ITALY), IMPLICATION ON STRUCTURAL MODELING AND STATE OF HEALTH MONITORING.

Simonetta Baraccani[1], Riccardo M. Azzara[2] , Giada Gasparini[1], Andrea Morelli[3], Michele Palermo[1]Tomaso Trombetti[1] , Lucia Zaccarelli[3]

[1] University of Bologna
Viale del Risorgimento 2, Bologna, Italy
e-mail: simonetta.baraccani2@unibo.it

giada.gasparini4@unibo.it

michele.palermo7@unibo.it

tomaso.trombetti@unibo.it

[2] Istituto Nazionale di Geofisica e Vulcanologia, Arezzo, Italy
riccardo.azzara@ingv.it

[3] Istituto Nazionale di Geofisica e Vulcanologia, Bologna, Italy
andrea. morelli@ingv.it
lucia.zaccarelli@ingv.it

Abstract

The SHM has a very important role in the diagnostic process of cultural heritage buildings, for which generally, the identification of the structural behaviour is affected by many uncertainties. The use of ambient vibration tests allow to characterize the dynamic behavior of the structures, providing also information to validate numerical modeling. Moreover, continuous monitoring allows to record streams of seismic ambient noise for long time intervals in order to retrieve the temporal evolution of the structural characteristics and to highlight the response of them to seasonal variations of environmental parameters (temperature, humidity) and the stresses due to the human activities or to the rapid (daily or weekly) changes in the ambient conditions (temperature, wind velocity and intensity).
Three seismic monitoring experiments were performed in 2012, 2013 and 2014 at the Asinelli and Garisenda Towers, two masonry leaning tower built in the center of Bologna (Italy). The aim of this work is to present the results of the analysis of the data recorded by seismic monitoring that allowed to clearly identify the normal modes of oscillation of the Two Towers. A particular attention was devoted to the identification of transient that, propagating inside the structures, produce beating effects at the top stations. Implication to the structural modeling and to the State of health monitoring are discussed.

Keywords: Dynamic Structural Health Monitoring, Masonry tower, Ambient vibration

1 INTRODUCTION

The assessment of the structural heath of the historical buildings, through non-destructive techniques, is fundamental in order to preserving their cultural integrity. For this purpose, Structural Health Monitoring (SHM) plays a crucial role in providing information both on the dynamic properties of the structures and the damage caused by earthquakes, impacts or traffic loads. In the last decade, the number of SHM systems designed and implemented on historic structures increased considerably. SHM perfectly meets principles and guidelines of Italian and European seismic codes concerning the historical buildings, which require the preservation of the structural architectural integrity, promoting removable, non-invasive and compatible solutions in the knowledge process, restoration and strengthening [1], [2]. The data obtained from a dynamic monitoring system shall provide information regarding the intrinsic properties of the structure that can be used to develop more accurate models and thus to plan effective strengthening interventions. Vibrations are one of the main factors for fatigue in structures. For this reason, with the increase of heavy traffic in the cities the study of the effects of the road traffic vibrations induced on the historical buildings is becoming another important issue. Continuous monitoring allows to record streams of seismic ambient noise for long time intervals in order to retrieve the temporal evolution of the structural characteristics, the influence on them of the ambient conditions (temperature, wind velocity and intensity) and the stresses due to the human activities (traffic loads). Three seismic monitoring experiments were performed in 2012, 2013 and 2014 at the Asinelli and Garisenda Towers, two masonry leaning tower built in the center of Bologna (Italy). The aim of this work is to present the results of the analysis of the data recorded by seismic monitoring, that allowed to identify the dynamic properties of the Two Towers, and to investigate the effects of the vibrations induced by the traffic loads on the Towers. The information obtained from the monitoring are also used to calibrate FEM models with the purpose of identify models able to better simulate the real behavior of the Towers. Particular attention was paid to the evidence of particular signals propagating inside the Towers that point out clear effects of beatings at the top.

2 GARISENDA AND ASINELLI TOWER

Garisenda and Asinelli Towers, commonly referred to as “The Two Towers”, are the main monument of the city of Bologna, North Italy (Figure 1). The Asinelli Tower is the taller one (97 m) and was built between 1109 -1119. During the Second World War, the Tower was used as a watchtower. It tilts toward South-West of 2.23 m [3]. The external walls were built using solid bricks for the outer skins and rubble masonry fill. The total thickness of the masonry decreases almost linearly from 3.15 m at the base to 0.45 m at the top. Three main discontinuities are present at 11.5 m, 34.0 m and 56.0 m (Figure 1b) [4]. The Garisenda, the older one, can be dated around the last two decades of the eleventh century. During the construction phases, the foundation soil underwent important subsidence phenomena, which caused a visible tilt of the tower [5]. The tower is 48 m high and has a slope of 3.40 m towards South-East. The base of the Garisenda tower presents an external selenitic layer that cover the external wall for the first 3.5 m. The Tower cross section above the selenitic base (built using solid bricks for outer skins and rubble masonry fill) reduces with height as the common construction practice at the time of construction (Figure 1c) [6]. The knowledge of actual state of health the towers is a crucial issue in order to preserve these monuments. For this reason, at the beginning of the 2011 the Municipality decided to installed a static SHM systems in both the Towers [7], [8]. In addition, following the Emilia earthquakes (20th May 2012 and 29th May 2012, respectively 5.8 and 5.6 Mw), seismic monitoring experiments were commissioned to the Istituto Nazionale di Geofisica e Vulcanologia (INGV) in conjunction with the

University of Bologna with the purpose of obtaining information on the dynamic behaviour of the Two Towers.

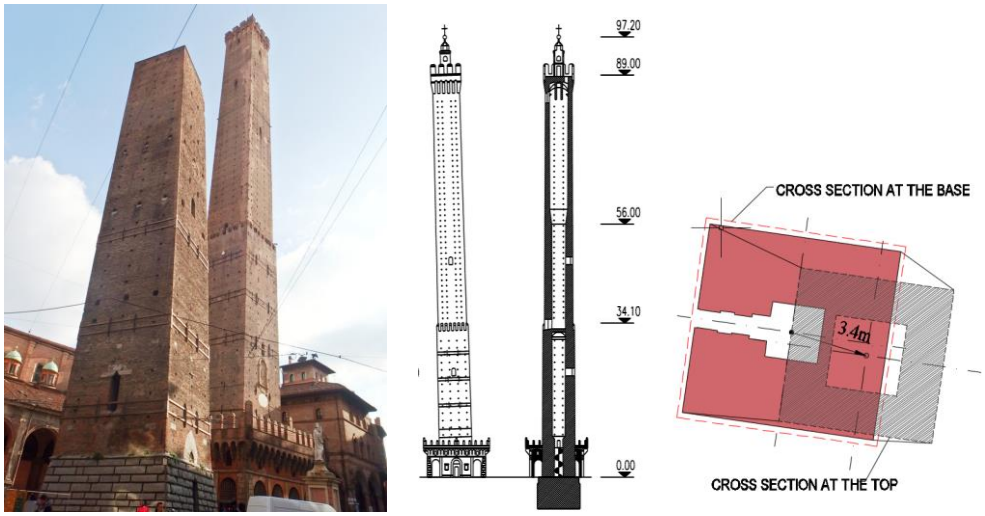

(a) (b) (c)

Figure 1- (a) The Two Towers of Bologna, (b) The Asinelli Tower elevation with the indication of the main discontinuities, (c) Garisenda Tower cross section at two different heights

2.1 The monitoring system and the tests developed

The Towers' vibrations induced by natural or artificial sources (ambient noise) have been recorded in order to evaluate their dynamic properties. The first experiment [9] was performed from June 2012 to September 2012. Six seismic stations, equipped with three-axial seismometers (Lennartz Le3d5s coupled to 24-bit digitizers Reftek 72A-07/08) were installed along the height of each Towers (4 in the Asinelli, 2 in the Garisenda), see Figure 2. A second experiment was repeated the year after, from September 2013 to March 2014 (Lennartz Le3d5s coupled to 24-bit digitizers Reftek 130). A third experiment was performed from August to October 2014 (three seismic stations in the Asinelli, SS20 2Hz seismometer coupled to a SL06 24 bit DAS from Sara Electronics S.r.l.).

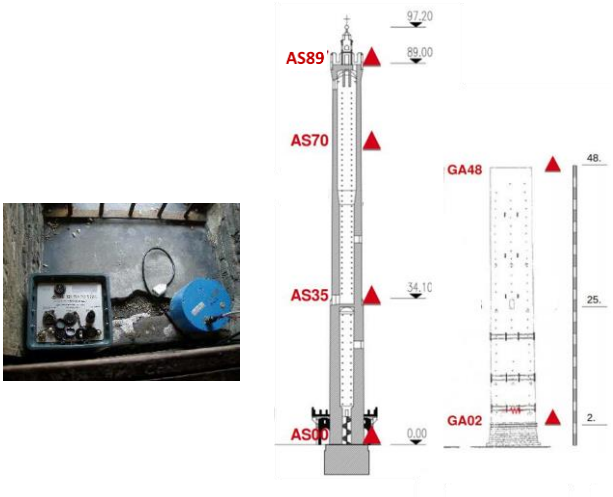

(a) (b)

Figure 2-a) Three-axial seismometers (Lennartz Le3d5s coupled to 24-bit digitizers Reftek 72A-07/08; (b)Position of the seismometers on the Asinelli tower (left) and Garisenda tower (right)

At the end of the third experiment (October 2014) additional experimental measurements have been carried out in order to study the effects of the transit of a heavy vehicle on the Asinelli tower, at the end of the monitoring period. For this aim, the oscillations produced by the transit of an heavy truck at different speed along Strada Maggiore (the road at the base of the Asinelli Tower, Figure 3) were recorded by the three seismometric stations, installed at the base, at 35 m high and at the top of the Asinelli Tower.

Figure 3-a) View of the position of the Two Towers (Google Earth);b)Picture of the transit of a truck along Strada Maggiore during the experimental measurements.

3 AMBIENT MODAL FREQUENCIES IDENTIFICATION AND MODELING

Recording natural vibration on built structures gives a way to identify their fundamental frequencies of vibration. Since the use of these techniques allows to make measurements without any damage to the building and without interfering with its normal use, it appear particularly suitable for the analysis of structures of historical and monumental interest. Also, from the spectral-analysis point of view, taking into account the wide frequency band covered by the natural vibration, it is possible to recognize the principal modal frequencies in a single step.
Figure 4 and 5 show the average spectra computed over the entire monitoring period of 2013 for the three components of the top station for the Asinelli and Garisenda, respectively [7, 8]. The first three fundamental flexural frequencies (indicated as F1, F2, F3 in the spectrum of figure 4a) of the Asinelli Tower fall within the range of 0.32-0.33 Hz, 1.3-1.5 Hz and 3.0-3.3 Hz. The third peak (indicated as R1 in figure 4a) of the spectrum of the horizontal components may be associated with a torsional motion. The first three fundamental frequencies of the Garisenda tower, instead, fall within the range of 0.71- 0.73 Hz, 3.7-4 Hz and 8.8 9.0 Hz respectively (Figure 5). It can be noticed that these peaks are split and characterised by different amplitudes between the two horizontal components (figure 4b and 5b). The frequency splitting, not existing in a symmetrical structure, is probably due to the asymmetry in building characteristics and to the leaning angle of the Towers.
A more detailed observation of the spectral response of the Garisenda Tower (Figure 5a) allows to capture a quite interesting phenomena, that is the presence of two small spectral peaks at frequencies corresponding to the fundamental frequencies of the Asinelli Tower. Such phenomena can be interpreted as a mutual induction effect of oscillation. The same effect, on the other hand, is visible only on the vertical average spectrum of the Asinelli Tower that exhibits in this frequency band the minimum spectral amplitude (Figure 4a).
In the last years, the assessment of the structural health was mostly focused on the Asinelli Tower rather than on the Garisenda Tower, mainly because being the larger height of that would probably make it more vulnerable to the effects of lateral vibrations, such as those in-

duced by earthquakes. In the past, some of the authors have conducted numerical studies based on the use of Finite Element Method (FEM) to asses to seismic response of the Tower. FE models of increasing complexity (mono and bi- dimensional models considering different base conditions) have been developed and the results of modal analysis were compared with the data recorded by the dynamic monitoring. Details are available in [10].

In this work, to investigate the phenomenon of frequency splitting and of beating (that will be presented in the next sections), a further FE model of the Asinelli Tower has been developed. considering isotropic shells elements using the commercial softwareSAP2000. The model reflects faithfully the geometry in the following aspects: inclination, thickness of the walls at the differed sections, windows, holes used to install the scaffolding during the construction phases and steel ties installed during the years to confine the masonry walls. In particular, the openings could influence the structural response of the Tower and could be a possible cause of the frequency splitting detected through the dynamic monitoring. Figure 4c displays the mode shapes obtained by the FE model. It can be noticed that the fundamental periods obtained from the model analysis are in good agreement with those obtained from the measurements. Time history analyses, using the recorded data at the base of the Tower as input, are under development to better investigate the cause of the beating phenomenon observed.

In 2018, a possible material degradation at the base of the Garisenda tower has been revealed pointing out the necessity to assess its current structural health. Several models (bi-dimensional and three-dimensional finite element models) of the Garisenda have been developed. Particular attention has been paid to the modelling of the base of the Tower composed by an external and internal perimeter of selenitic stones (thickness of around 50-60 cm) and an internal filling. The measured frequencies have been used to calibrate these models, which will be used to investigate the consequences of the natural decay of material properties in terms of safety and stability. For sake of brevity, only the mode shapes as obtained by the bi-dimensional model are reported in Figure 4c. The material properties used in the models of both Towers, characterized through in situ tests (both destructive and non-destructive), are summarized in Table 1.

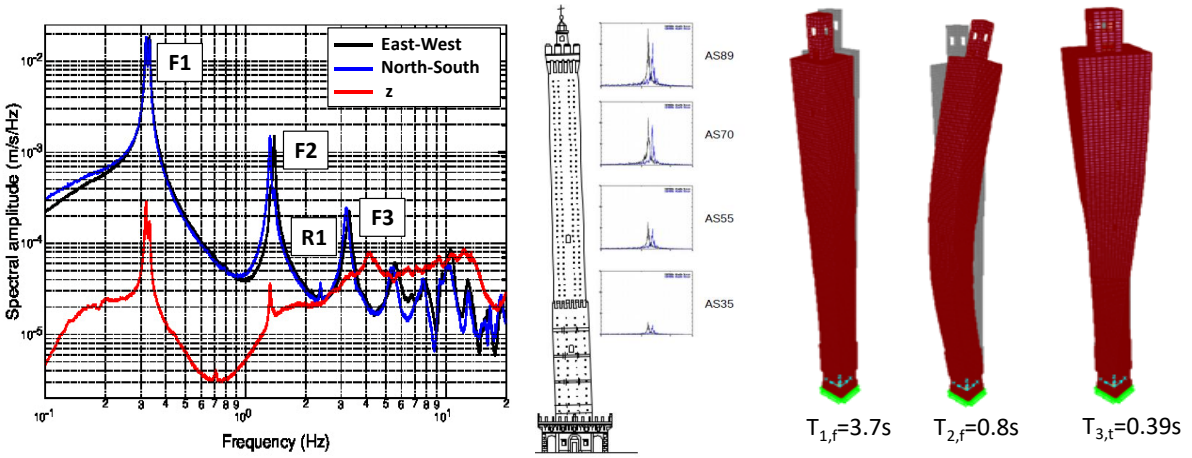

(a) (b) (c)

Figure 4- a) Average spectra computed over the entire monitoring (2013) for the top station. b) Example of the distribution of the FFT spectra along the vertical profile inside the Asinelli Tower. c) Modal shape obtained by a finite element model developed by the authors.

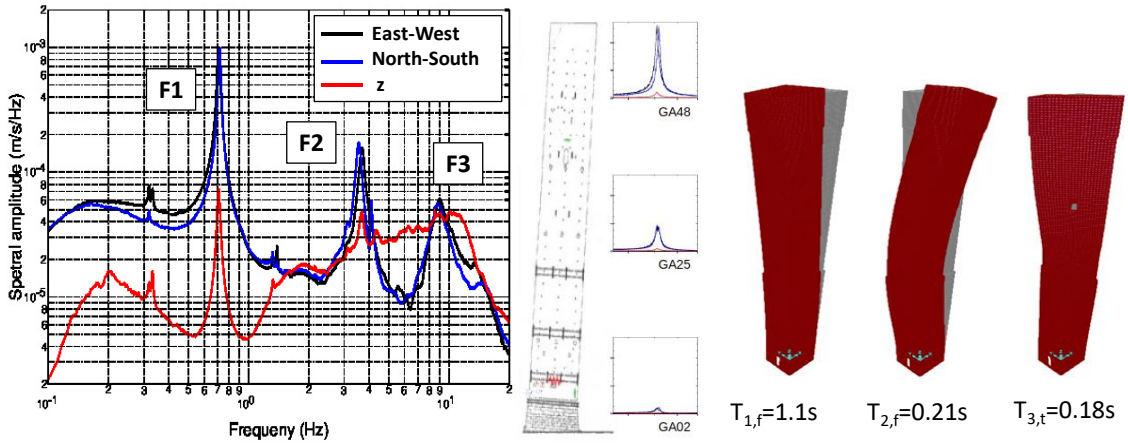

(a) (b) (c)

Figure 5- a) Average spectra computed over the entire monitoring (2013) for the top station. b) Example of the distribution of the FFT spectra along the vertical profile inside the Garisenda Tower.
c) Modal shape obtained by a finite element model developed by the authors.

Material	Specific Weight γ	υ	Elastic Modulus E_m	Compressive strength f_m	Shear strength $f_{v,m}$
	[KN/m^3]		[MPa]	[MPa]	[MPa]
Masonry bricks	18	0.2	3000	4	0.5
Selenitic stone	24	0.2	5000	7	0.7
infill	17	0.2	2500	4	0.5

Table 1: Material properties of the Asinelli and Garisenda towers

4 CHANGES IN THE OSCILLATION DUE TO VARIATION OF AMBIENT CONDITION

Dynamic monitoring, if performed continuously and for a long period, can be an effective tool to describe the health status of a built structure. The recording of long data flows allows to follow the variation of the modal parameters with time and to correlate it to the changes in the environmental conditions, natural or artificial, that can influence the behavior of the structure and can produce fatigue or rapid modification of the mechanical-physical properties. It is the case of the Two Towers, which have been monitored for several months over several years, allowing not only to depict a snapshot of the modal parameters but also to observe how the Towers are solicited by the variation of ambient parameters.

A first aspect taken into account was to measure the variation of the amplitude of oscillation with the variation of anthropic noise due to the daily increment of the vehicular traffic at the base of the Towers. As representative example of an average behaviour for both Asinelli and Garisenda Tower, Fig. 6 shows the daily oscillation recorded at the Asinelli top station during August 2012 between 1–20 Hz, the frequency band where the seismic ambient noise is known to be dominated by “cultural sources”. It is clear the similarity of the trend during the working days, showing a sharp increment in the amplitude of oscillation when the human activity rises (about at 6: am, local time), a reduction during the evening and an almost instant decrease in the night, after the 01 a.m. (local time). On the other hand, also during holidays (15, 17, 18 August 2012) the pattern is similar but the interval when the oscillation amplitude is increasing reduces its duration only in the central part of the day.

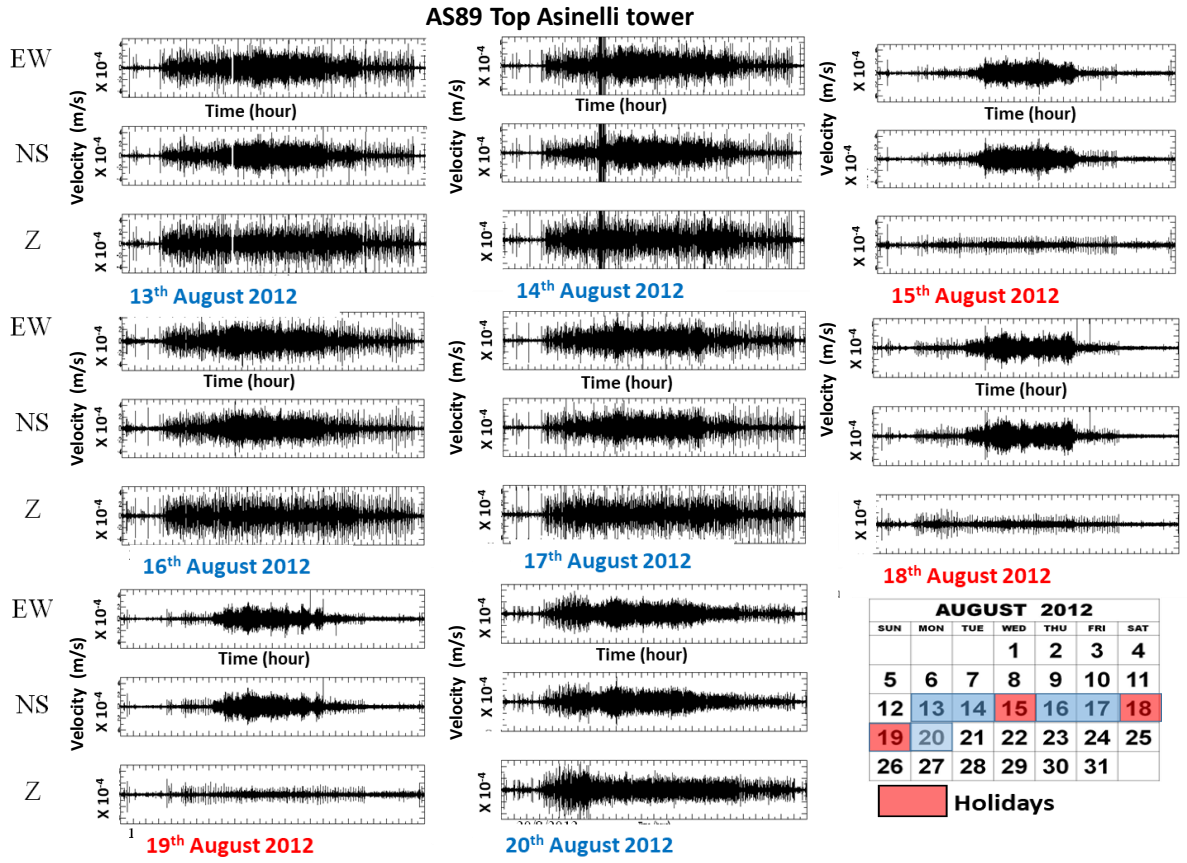

Figure 6- Daily trend of the oscillation recorded by the top station of the Asinelli Tower from 13th to 20th August 2012. The signal has been filtered in the 1-20 Hz frequency band, in order to point out the content associated with the anthropic noise surrounding the Tower.

To evaluate the amplitude ratio of the oscillation between night and day periods and between weekdays and holidays, the trends of the maximum amplitudes of oscillation in the different periods have been calculated, performing the averages of the maximums. It can be noticed that the oscillation between day and night is between 2 and 6 times greater on weekdays and doesn't exhibit evident differences between weekday and holidays.

The continuous monitoring has allowed recognizing the propagation inside the Towers of transients that trigger beatings at the top of the Asinelli Tower. Figure 7 shows the time history of the three components of recorded signals (200 s) recorded by the three stations. The signals recorded by the station at the top clearly show beatings. The phenomenon has been investigated by some of the authors Palermo et al [11] using a simplified eccentric planar model with an equivalent eccentric and torsional stiffness. The results indicated that the equivalent eccentricity could be compatible with some partial wall disconnections due to cracks propagating along the openings.

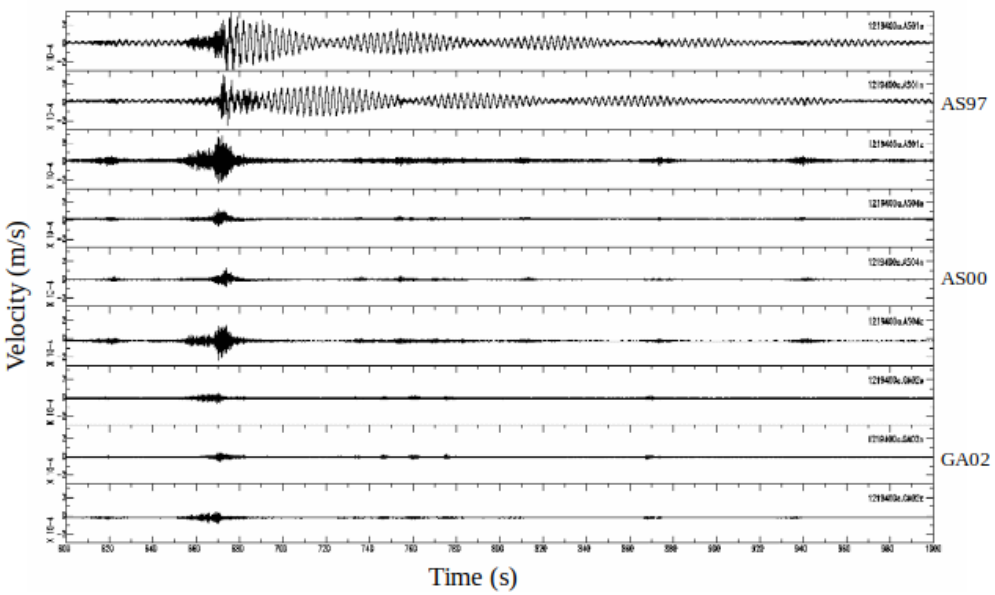

Figure 7. Example of transient propagating inside the Towers and triggering beatings at the Top level of Asinelli Tower. Each set of three signals are the waveforms on the Z, NS, EW directions, from down to top respectively for GA02, AS00 and AS97 measurements point.

In order to individuate the possible source of the impulse at the base, a horizontal particle motion analysis of the signal recorded at the base of the Two Towers has been performed. Figure 8 shows that the cross point of the composition of the horizontal components, taking into account the position of the instrumentation inside the Towers, points toward the intersections of roads “Via Rizzoli” and “Strada Maggiore”, daily traveled by heavy vehicular traffic.

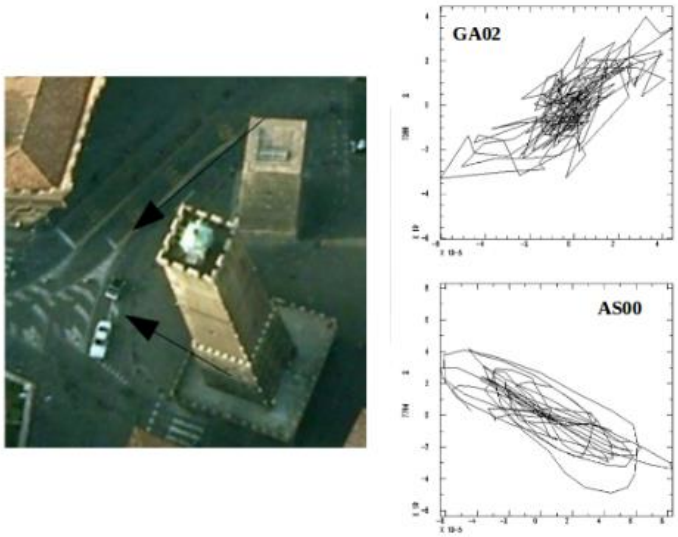

Figure 8. Particle motion analysis along the horizontal directions for the two seismic stations installed at the base of the Two Towers

5 VIBRATION INDUCED BY HEAVY TRAFFIC: EXPERIMENTAL TEST

In October 2014, during the execution of some maintenance works along road "Strada Maggiore" that required the road closure, an experimental test has been performed in order to record the Asinelli Tower vibrations induced by the passage of a heavy truck along the road (Figure 3). Three seismic station equipped with three-axial seismometrs (SARA SS20 and SL06) were installed at the base, at 35 m and at the top level of the Tower. The signal was sampled at 100 sps. The truck made five passages at different speeds (10, 20, 30 km / h). The presence of a sudden discontinuity in the pavement was also accounted for by placing an obstacle in the road, namely a wooden beam in the direction perpendicular to the road. For each measurement, the following tests have been conducted (Figure 9):

A. truck moving at 20km/h with no obstacle
B. truck moving at 30km/h with no obstacle
C. truck moving at 10km/h in correspondence of the storm drain
D. truck moving at 30km/h with obstacle
E. truck moving at 10km/h with obstacle

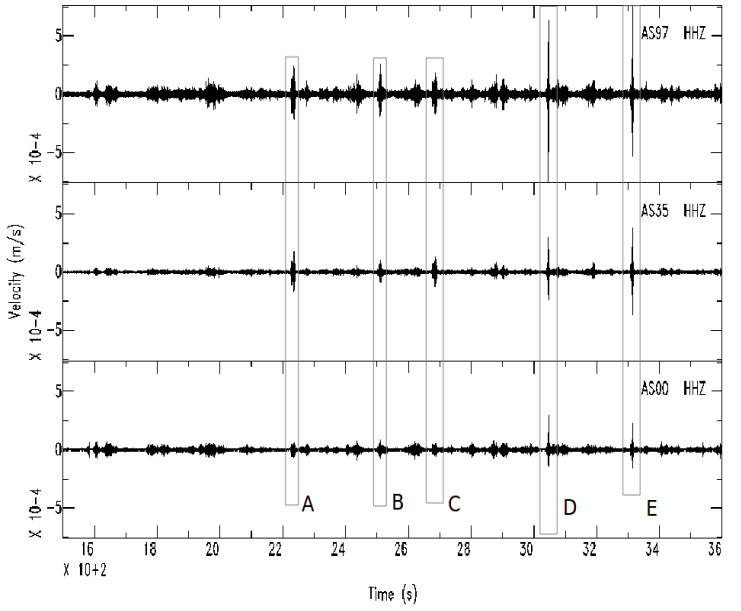

Figure 9. Vertical component waveforms recorded at the three measurement points during the five passages of the truck.

As is evident from Figure 9, during the first three passages (A,B,C) the amplitude of motion along the vertical component of the base didn't exceed the maximum average vibration recorded in absence of input. During the last two tests (D and E), the input at the base was significantly stronger. In these cases at both the stations inside the Tower beatings were recorded, similar to those observed during the continuous monitoring (Figure 10). This seems to confirm that the input at the base produced by heavy traffic along the roads surrounding the Towers is responsible for the observed beatings. The acceleration and displacement peak values (PGA and PGD) recorded during the tests were computed and collected in Table 2. The maximum values of PGA and PGD recorded at the top along the horizontal direction refer, as expected, to the two most energetic tests (D, E). They are equal to 3 mg and 0.4 mm respectively (Table 2).

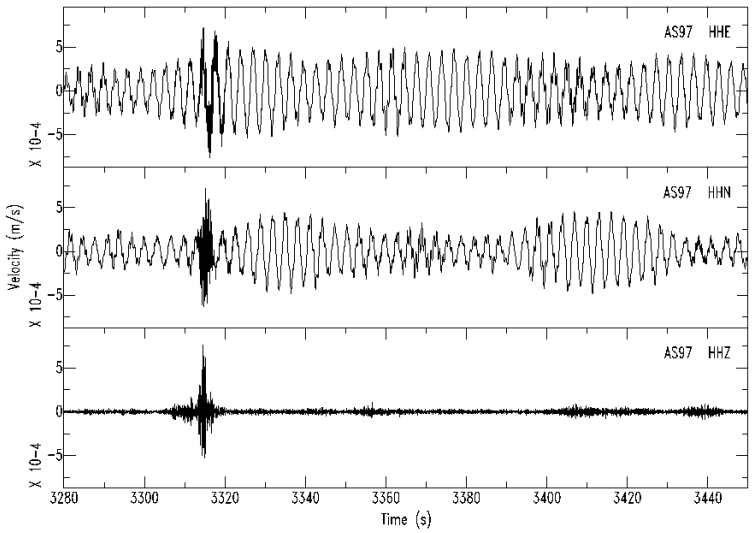

Figure 10. Waveforms recorded during the most energetic test (E) at the top level station, from top to down respectively EW, NS and Z components.

Acceleration		Test A	Test B	Test C	Test D	Test E
		mg	mg	mg	mg	mg
AS00	E	0.08	0.11	0.05	0.28	0.19
	N	0.07	0.10	0.05	0.48	0.33
	Z	0.24	0.45	0.19	1.71	1.08
AS35	E	0.36	0.45	0.21	1.31	0.62
	N	0.34	0.34	0.18	1.41	0.91
	Z	0.38	0.37	0.25	1.13	1.09
AS97	E	0.62	0.84	0.50	1.23	1.24
	N	0.86	0.64	0.49	2.71	1.41
	Z	0.63	1.14	0.53	2.89	1.81
Displacement		Test A	Test B	Test C	Test D	Test E
		μm	μm	μm	μm	μm
AS00	E	1.72	1.93	1.81	1.96	2.12
	N	2.16	1.55	2.02	2.03	1.89
	Z	3.40	2.13	2.81	5.06	4.56
AS35	E	50.7	72.2	66.6	73.7	62.7
	N	32.4	55.0	43.5	95.8	67.0
	Z	10.7	8.63	9.51	12.4	16.4
AS97	E	162.9	193.0	278.8	369.5	261.8
	N	138.9	286.0	260.2	375.0	204.2
	Z	16.1	11.92	11.32	19.3	24.6

Table 2: The acceleration and displacement peak values (PGA and PGD) recorded during the tests.

CONCLUSIONS

The main conclusions of the study can be summarized as follows:

- The experimental modal frequencies determined from the dynamic monitoring performed between 2012 and 2014 result in good agreement with those obtained from modal analysis performed on the FE models.
- The long duration and the repetition over several years of the survey allowed to recognize a typical trend of the vibration of the Towers that at high frequency (1-20 Hz) seems to be strongly correlated to the surrounding anthropic sources. In particular, some specific transients propagating inside the Asinelli Towers triggered beatings that are evident at the top of the Tower.
- The passage of an heavy truck monitored during one specific experiment induced beatings that resulted to be similar to those evidenced during the long term monitoring.
- Further analyses are necessary to better interpret the observed beatings in order to identify possible relations between structural and material irregularities and the peculiar dynamic response.

ACKNOWLEDGEMENT

The authors gratefully acknowledge Dott. Ing. Gilberto Dallavalle who provided valuable information related to geometrical and material properties. The experimental activities have been partially funded by a collaboration contract between Bologna Municipality and INGV.

REFERENCES

[1] ISCARSAH (International Scientific Committee for Analysis and Restoration of Structures of Architectural Heritage), "Recommendations for the analysis, conservation and structural restoration of Architectural Heritage," *Icomos*, no. June, pp. 3–6, 2003.

[2] Guidelines for Evaluation and Mitigation of Seismic Risk to Cultural Heritage, "Guidelines for Evaluation and Mitigation of Seismic Risk to Cultural Heritage," *Gazz. Uff.*, vol. 47, 2011.

[3] F. Cavani, *Sulla pendenza e sulla stabilità della torre degli Asinelli di Bologna.* 1912.

[4] M. Palermo, S. Silvestri, G. Gasparini, S. Baraccani, and T. Trombetti, "An approach for the mechanical characterisation of the Asinelli Tower (Bologna) in presence of insufficient experimental data," *J. Cult. Herit.*, vol. 16, no. 4, pp. 536–543, 2015.

[5] C. Ceccoli, P. Diotallevi, P. Pozzati, L. Sanpaolesi, and G. Dallavalle, "Indagini inerenti le strutture murarie e fondali e consolidamento delle parti in elevazione della Torre Garisenda"." 2001.

[6] G. Francisco, *La Torre Garisenda*. 2000.

[7] S. Baraccani, M. Palermo, R. M. Azzara, G. Gasparini, S. Silvestri, and T. Trombetti, *Structural interpretation of data from static and dynamic structural health monitoring of monumental buildings*, vol. 747 KEM. 2017.

[8] S. Baraccani, G. Gasparini, M. Palermo, S. Silvestri, and T. Trombetti, "A possible

interpretation of data acquired from monitoring systems," *Civil-Comp Proc.*, vol. 106, 2014.

[9] R. M. Azzara, A. Cavaliere, S. Danesi, and A. Morelli, "Il monitoraggio sismico della Torre degli Asinelli e della Garisenda. Risultati preliminari dell'analisi dei dati.," 2014.

[10] M. Palermo, S. Silvestri, G. Gasparini, S. Baraccani, and T. Trombetti, "An approach for the mechanical characterisation of the Asinelli Tower (Bologna) in presence of insufficient experimental data," *J. Cult. Herit.*, vol. 16, no. 4, 2015.

[11] M. Palermo *et al.*, "Measurements of the Free Vibration Response of the Asinelli Tower in Bologna and Its Interpretation," in *Second European Conference on Earthquake Engineering and Seismology*, 2014, pp. 1–12.

COMPDYN 2019
7th ECCOMAS Thematic Conference on
Computational Methods in Structural Dynamics and Earthquake Engineering
M. Papadrakakis, M. Fragiadakis (eds.)
Crete, Greece, 24-26 June 2019

DENOISING CORRUPTED STRUCTURAL VIBRATION RESPONSE: CRITICAL COMPARISON AND ASSESSMENT OF RELATED METHODS

Gabriele RAVIZZA[1], Rosalba FERRARI[1], Egidio RIZZI[1*], Vasilis DERTIMANIS[2] and Eleni N. CHATZI[2]

[1]University of Bergamo, Department of Engineering and Applied Sciences,
viale G. Marconi 5, I-24044 Dalmine (BG), Italy
*Corresponding Author, e-mail: egidio.rizzi@unibg.it

[2] ETH Zürich, Institute of Structural Engineering,
Department of Civil, Environmental and Geomatic Engineering,
Stefano-Franscini-Platz 5, CH-8093 Zürich, Switzerland

Keywords: Noise-corrupted signal; Noise-to-Signal (N/S) ratio; Denoising methods; Discrete Wavelet Transform (DWT); Singular Value Decomposition (SVD); Seismic response; Ambient vibration.

Abstract. *Vibration-based Structural Health Monitoring (SHM) is receiving increasing attention due to the high technological level that the developed methodologies are nowadays reaching, together with the increasing quest for the implementation of effective, but ideally of low-cost, monitoring instrumentation. The latter is relatively easy to deploy and allows for the recording of the structural vibration response at multiple locations, which, for large strategical infrastructures, such as high-rise buildings, bridges, wind farms, etc. may be of critical importance. On the other hand, low-cost instrumentation may typically be accompanied by high Noise-to-Signal (N/S) ratios, contaminating the structural response, increasing the induced uncertainties and rendering the implementation of SHM methods more difficult. This calls for appropriate and effective denoising processes. In tackling such an associated denoising problem, several methods have been proposed and are currently under further development. Among specific variants, the utilization of multi-rate filter banks, especially the one based on Discrete Wavelet Transform (DWT), as well as the application of Singular Value Decomposition (SVD), have revealed to be rather effective. Yet, they have mostly been applied to problems where structural vibration response signals originate from specific behavioral classes, as, e.g., in monitoring applications of rotating machinery. In this study, the aforementioned methods are reconsidered and reimplemented; then, assessed on noise-corrupted vibration response signals related to civil engineering applications. Different Noise-to-Signal (N/S) ratios and excitation types are considered, i.e. earthquake and ambient vibration input. Advantages and limitations of both denoising approaches are presented and discussed, with a critical comparison. The outcomes prove the effectiveness of the considered methods in clarifying earthquake response signals, yet also their difficulty in purifying ambient vibration signals, motivating further specific research on the filtering of this latter common class of structural response.*

1 INTRODUCTION

Due to ever increasing structural requirements and loading condition magnitudes to which civil engineering structures are continuously subjected, an effective and accurate evaluation of the safety of existing structures, as well as an appropriate estimation of their remaining lifetime, become more and more necessary. In particular, in the last few years, the increasing interest in predicting the potential deterioration and collapse of such critical infrastructures by collocating on them various sensors for detecting data related to their dynamic response, has led to the emergence of the field of Structural Health Monitoring (SHM). Many case studies in which the structural vibration response has been employed as a critical and directly measurable quantity for evaluating structural safety, may be found in the literature [1–4]. From all these examples, the availability of reliable data on structural safety, usability and fatigue resistance, represents an essential point for efficient SHM, aiming at preserving structural integrity over time. However, often either no updated information on the structural characteristics is available or it may result incomplete, or even noise affecting the signals may considerably alter the useful information embedded within the response signals themselves. Consequently, in many cases, the application of denoising techniques aiming at enhancing the data quality by removing the noise affecting the signals, might become necessary.

Several denoising approaches for dealing with signals have been developed and reported in the literature [5–7]. In particular, the application of band pass filters, such as high-pass and low-pass filters, may be considered as a most simple and rudimentary denoising method. The Fourier Transform might also be employed for denoising purposes [8]. However, all these mentioned approaches are ineffective when the noise is concentrated in a frequency band similar to that of the useful part of the signal, and this occurs in several real cases. In fact, this would mean removing not only the noise but also a relevant portion of the meaningful signal, which instead should be preserved.

In the last two decades, this has led to search for alternative denoising approaches able to overcome this issue, by removing the contaminated part of the signal without losing the important information contained within it. In particular, two important denoising approaches are identified, as focus herein, i.e., one based on a Discrete Wavelet Transform (DWT) implementation [9] and one based on a Signal Value Decomposition (SVD) algorithm [10]. In addition, a further interesting approach to the problem of signal denoising is the effectuated use of a Kalman Filter (KF), as a powerful tool to enhance noise-corrupted data, as presented in recent publications [11–13]. Specifically, in Ravizza et al. [13], a KF algorithm has been integrated into a Heterogeneous Data Fusion (HDF) scheme, aiming at improving the quality of displacement response signals detected on a numerical dynamic system.

In this paper, DWT- and SVD-based denoising approaches are reconsidered and independently implemented, in order to explore their effectiveness in dealing with signal typologies typical of civil engineering contexts, namely structural vibration response signals. This may open up to new perspectives in the post-processing of such signals; in fact, although these techniques have been already tested, for instance, on gravity and magnetic signals, biological signals such as electrocardiograms (ECG) or electroencephalograms (EEG), or even acoustic signals and pressure signals, their application on structural vibrational signals, typical of the civil engineering field, has not been deeply inspected yet. Furthermore, structural response data are crucial for SHM purposes, as their observation over time, also supported by the wide development of modal identification techniques for the acquisition of the structural modal features [14–16], may reveal variations in the physical properties of the monitored structure. This

might be related to the possible appearance of damage and, consequently, it could lead to a decay of the structural performance characteristics.

In particular, within the present analysis, seismic response and ambient vibration signals, in terms of acceleration, will be considered. This choice is motivated by the fact that, since these signals display a very different nature, i.e., non-stationary (seismic excitation) vs. stationary (ambient vibration), they could bring out different aspects inherent to the process of denoising, depending on the performed approach. A ten-story shear-type building is assumed as a benchmark reference structure, in order to generate simulated response signals, which are then subsequently contaminated with different levels of noise, and further denoised by means of the proposed techniques.

The main goal which this study aims to achieve is twofold:

- to inspect the effectiveness of denoising methods in dealing with response signals which are typical of the civil engineering context, i.e., ambient vibration and seismic acceleration response signals, through the assessment of their performance based on the comparison between the reconstructed denoised signal and the original clean one;
- to shed light on strengths and limitations of DWT- and SVD-based denoising approaches, depending on the amount of noise that affects the data, and as referring to the type of the response signal (ambient vs. seismic).

The paper is organized as follows. In Section 2 a brief description of the analysis procedure is provided, through the presentation of the benchmark dynamical system, the synthetic generation of last-floor's acceleration response signals (considering both seismic excitation and ambient vibration), and the process of their distortion by adding a Gaussian white noise. In Section 3, DWT- and SVD-based denoising approaches are performed on data affected by increasing noise levels, and results are presented and commented on. A critical comparison based on the performance evaluation of the two considered techniques is also presented. Conclusions and global remarks are finally outlined in Section 4, together with some possible future research perspectives.

2 ANALYSIS PROCEDURE

2.1 Problem statement

The traditional formulation of a generic signal denoising problem may be expressed according to the following relation:

$$\mathbf{y} = \mathbf{x} + \mathbf{n} \tag{1}$$

where $\mathbf{y} = (y_1, ..., y_i, ..., y_n)$ is the noise-affected signal which has to be processed, and that may be interpreted as the sum of a clean (noise-free) signal $\mathbf{x} = (x_1, ..., x_i, ..., x_n)$, which embeds the useful information to be preserved, and an additive noise signal $\mathbf{n} = \sigma(n_1, ..., n_i, ..., n_n)$, of intensity given by standard deviation σ, which may be modeled as a stationary independent zero-mean Gaussian term [17, 18], superimposed on the useful signal and altering its content.

The application of each numerical denoising technique aims at achieving a best approximation $\widehat{\mathbf{x}} = (\widehat{x}_1, ..., \widehat{x}_i, ..., \widehat{x}_n)$ of original (noise-free) signal $\mathbf{x}$, starting from noise-affected signal $\mathbf{y}$, removing most of the unwanted noise without losing the useful information. It is

worth mentioning that, at least at this preliminary stage of research, all signals involved within the analyses are constituted by *synthetic signals*, since this assumption allows to more deeply explore all possible strengths and limitations of the two studied denoising methods, rather than and before eventually considering *real signals*.

Several approaches have been presented in the literature in order to assess the effectiveness of denoising techniques [19–21]. Here, since both original (clean) signal $\mathbf{x}$ and denoised signal $\widehat{\mathbf{x}}$ are available, the Percentage Root Mean Square Difference (PrmsD) [22] value can be employed toward such purposes:

$$\text{PrmsD} = 100 \cdot \sqrt{\frac{\sum\limits_{i=0}^{n}(x_i - \widehat{x}_i)^2}{\sum\limits_{i=0}^{n} x_i^2}} \tag{2}$$

Small values of PrmsD are desirable for achieving a reliable approximation of original signal $\mathbf{x}$. In this study, PmrsD is considered as an evaluation term to compare the performances of DWT- and SVD-based denoising approaches in processing both stationary and non-stationary response signals.

2.2 Description of benchmark structure

In order to generate simulated acceleration response signals, a one-bay ten-story shear-type building is taken as a reference structure. For making the analysis as truthful as possible, realistic values of mass, stiffness and damping are assumed. In particular, for the first-floor, values of mass $m_1 = 100$ t and stiffness $k_1 = 4 \cdot 10^6$ kN/m are considered, while the upper floors are characterized by values of mass $m_i = 80$ t and stiffness $k_i = 3 \cdot 10^6$ kN/m, with $i = 2, ..., 10$. Furthermore, a modal damping ratio $\zeta_i = 5\%$, as typical of reinforced concrete structures, is assumed, for all the modes.

During the analysis, two different input typologies are considered acting on the structure, i.e. an earthquake acceleration excitation, acting at the base, and an ambient vibration force distribution, applied along the structure with a linear variation (increasing from bottom to top of the building). In both cases, the last-floor acceleration response signal is solely monitored, as it shall be associated to the most critical response values and, consequently, it may be enough to well characterize the whole structural response of the analyzed building.

2.3 Generation of noise-affected response signals

In this section, the procedure of generation of noise-affected response signals is shown. In particular, a zero-mean Gaussian white noise is added to the original (noise-free) signals, aims at simulating the intrinsic error characterizing the sensor technology, as well as the errors which might occur *"in situ"* at the signal acquisition stage. The fact that the added Gaussian white noise affects each single frequency component indifferently over the whole length of the signal, makes its removal always a challenging task. Here, the Noise-to-Signal (N/S) ratio is used to quantify the amount of noise, in relation to the useful signal. Although in today's sensor technology N/S ratios greater then 20% might be considered as unrealistic, or extremely rare, for a complete understanding of the limitations of the explored denoising techniques, in the present analysis N/S ratios up to 50% are taken into account. Two different types of excitation

are considered as acting on the benchmark structure, i.e., seismic input and ambient vibration input; whereupon, performing a classic direct analysis, the dynamic response of the system is obtained.

The analyzed non-stationary input is the earthquake excitation that struck Kalamata (Greece) in 1986, characterized by a Peak Ground Acceleration (PGA) of 0.24 g, magnitude of $M = 5.9$ and focal depth of 22 km. Such a seismic excitation has been assumed acting at the base of the reference building. The numerically-determined acceleration response signal related to the tenth floor is first obtained and then contaminated by adding a white Gaussian noise level of 25% N/S ratio, as depicted in following Fig. 1.

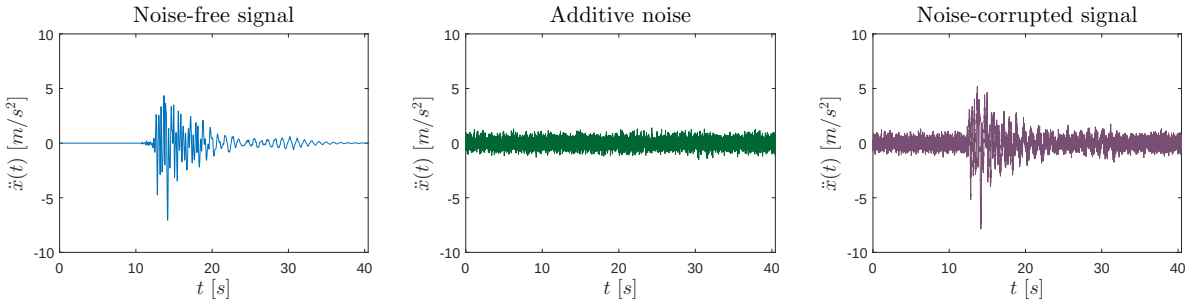

Figure 1: *10th-floor acceleration response signal of the benchmark structure under earthquake excitation input and subsequent noise addition process (25% N/S ratio).*

Ambient vibration, instead, represents the stationary excitation to which the structure is subjected to during its regular operating condition, and is commonly associated to environmental loads like wind, traffic load or wave motion. The last-floor dynamic acceleration response of the benchmark structural system under ambient vibration input is represented in Fig. 2, as well as the process of data corruption through the addition of a Gaussian white noise characterized by a N/S ratio of 25%.

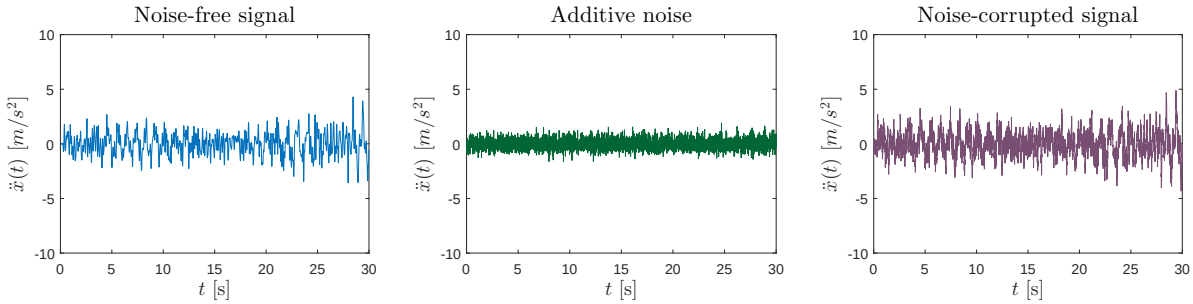

Figure 2: *10th-floor acceleration response signal of the benchmark structure under ambient vibration input and subsequent noise addition process (25% N/S ratio).*

The so generated noise-corrupted signals are now processed within a denoising implementation based on the application of DWT and SVD. The outcomes of the analysis are presented in next Section 3.

3 ANALYSIS RESULTS

3.1 DWT-based denoising application

The optimal calibration of the DWT-based denoising approach for dealing with seismic response signals has been first investigated through a criterion of minimization of the PmrsD index between the original (noise-free) signal and the denoised one. For this purposes, several mother wavelets (i.e. *Symlet, Coifet, Daubechies, Biorthogonal, Reverse Biorthogonal* and *Discrete Meyer*) and thresholding rules (i.e. *Heuristic SURE, Sqtwolog, Minimax* and *Rigorous SURE*) have been explored, with the optimal solution being identified in the adoption of *Smylet* with two oscillations in its mother wavelet combined with *Heursure* hard thresholding, at decomposition level 2. The results of the DWT-based denoising performed on a seismic acceleration response signal corrupted with a 25% N/S ratio are shown in Fig. 3. The small error which may be appreciated between the original signal and the denoised one reveals the effectiveness of the method in the clarification of such a non-stationary signal.

A similar procedure has then been applied for the denoising of an ambient vibration response signal. However, even though the denoising method based on DWT has been suitably recalibrated for dealing with this specific class of signals, in this latter case, the error which occurs between the original signal and the denoised one becomes more visible, as observed in the last graph in Fig. 4. In particular, here, the combination of *Coifet*, featuring two oscillations in its mother wavelet and *Minimax* hard thresholding at decomposition level 3 is adopted. The difficulty in the denoising of stationary signals and, in general, the relevant discrepancy in the obtained results seems to clearly show how the typology of the processed signal strongly affects the performances of the DWT-based denoising technique.

3.2 SVD-based denoising application

The SVD-based implementation exploited in this study for denoising purposes is based on the computing of the singular values associated to so-called Hankel matrix $\mathbf{A}$, which contains the noise-corrupted signal components that ought to be denoised. Since it has been shown that the noise mainly affects the small singular values of the signal, it follows that by removing those lower than a selected threshold, a new matrix $\hat{\mathbf{A}}$ (of a lower rank) containing solely the denoised signal components, may be obtained. Thus, in this process, the critical point is represented by the choice of the threshold value. To this end, here, a criterion based on the minimization of the PrmsD index between the noise-free and denoised signal has been adopted, which has led to the selection of a threshold value of 10.

In Fig. 5, the results of the SVD-based denoising approach performed on the non-stationary seismic response signal are shown. It may be asserted that, through the proposed SVD implementation, and despite the considered significant level of noise (i.e. 25% N/S ratio), the original signal has been almost completely reconstructed, as demonstrated by the very small error that can be appreciated.

A similar analysis has then been performed on the stationary ambient vibration response signal and, contrary to what was seen for the denoising approach based on DWT, in this case, satisfactory outcomes may still be achieved, as represented in Fig. 6. Thus, the SVD-based denoising technique seems to better fit the different nature of the considered input, providing a more stable solution and, thus, leading to a more reliable estimate of the original reference signal.

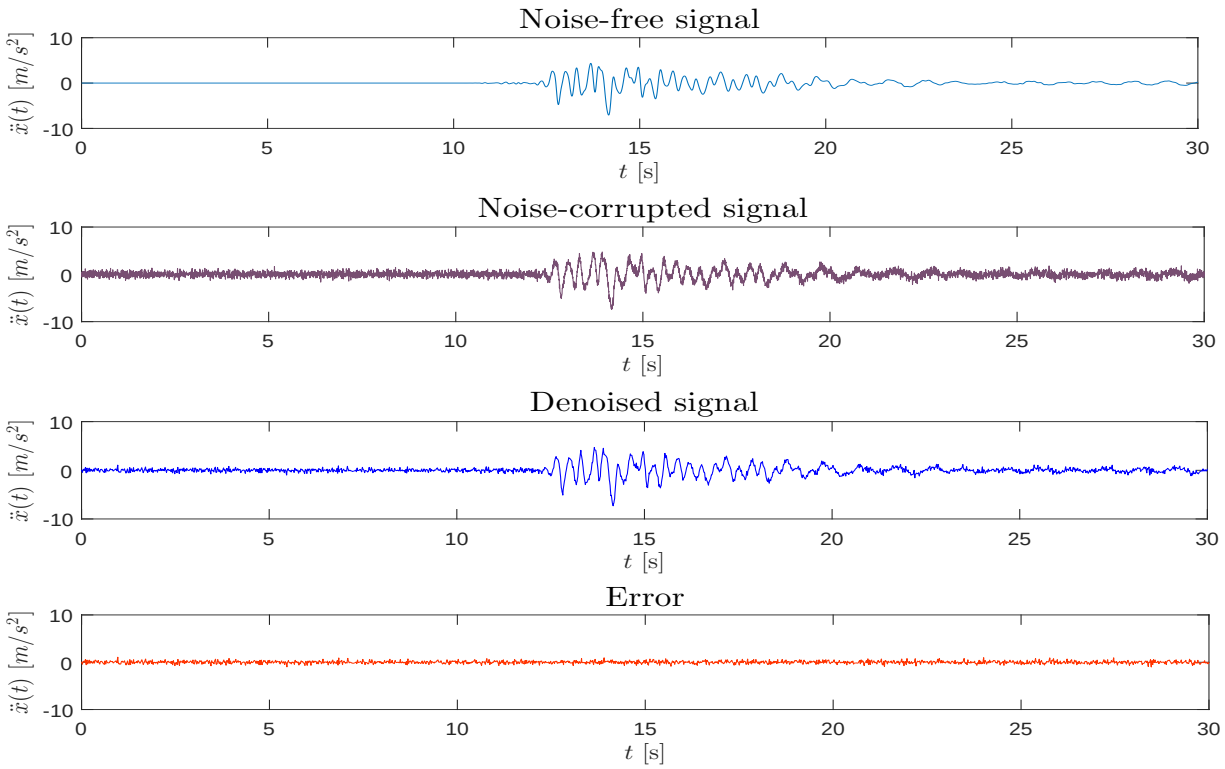

Figure 3: *DWT-based denoising of a noise-corrupted* $\ddot{x}(t)$ *response signal under seismic input (*25% *N/S ratio).*

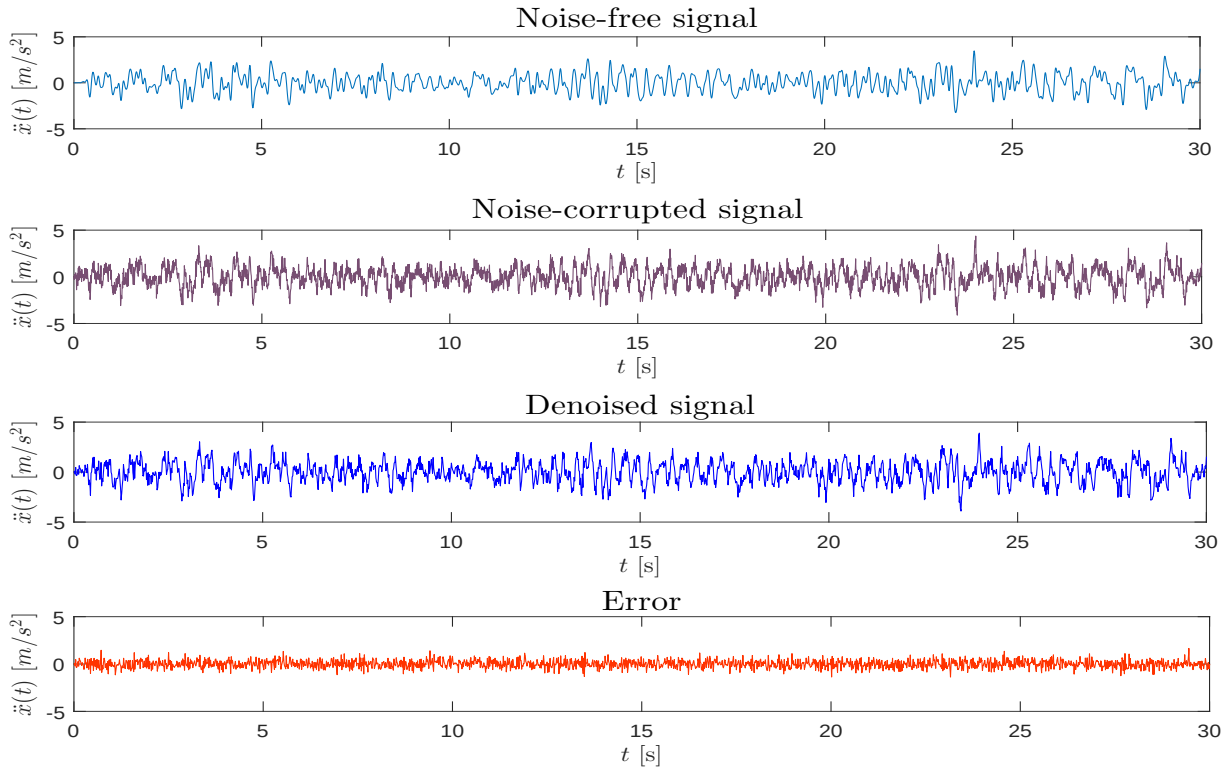

Figure 4: *DWT-based denoising of noise-corrupted* $\ddot{x}(t)$ *response signal under ambient vibration (*25% *N/S ratio).*

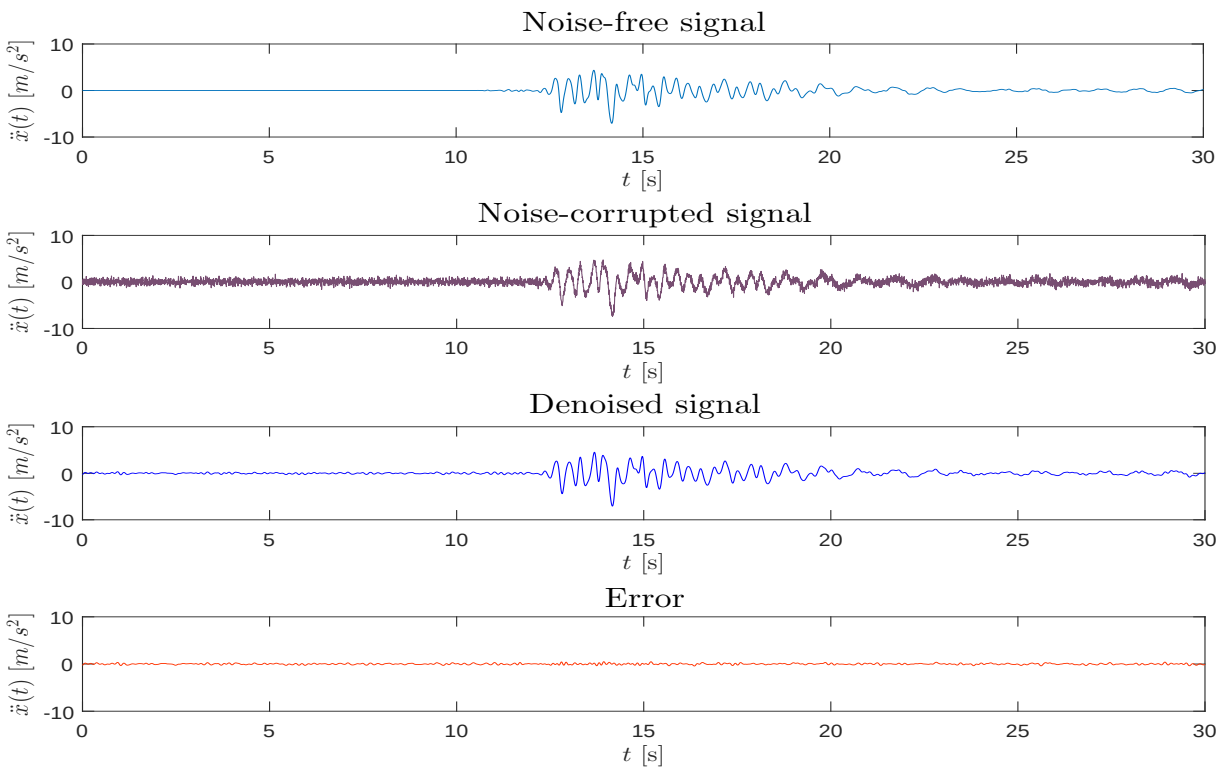

Figure 5: *SVD-based denoising of a noise-corrupted $\ddot{x}(t)$ response signal under seismic input (25% N/S ratio).*

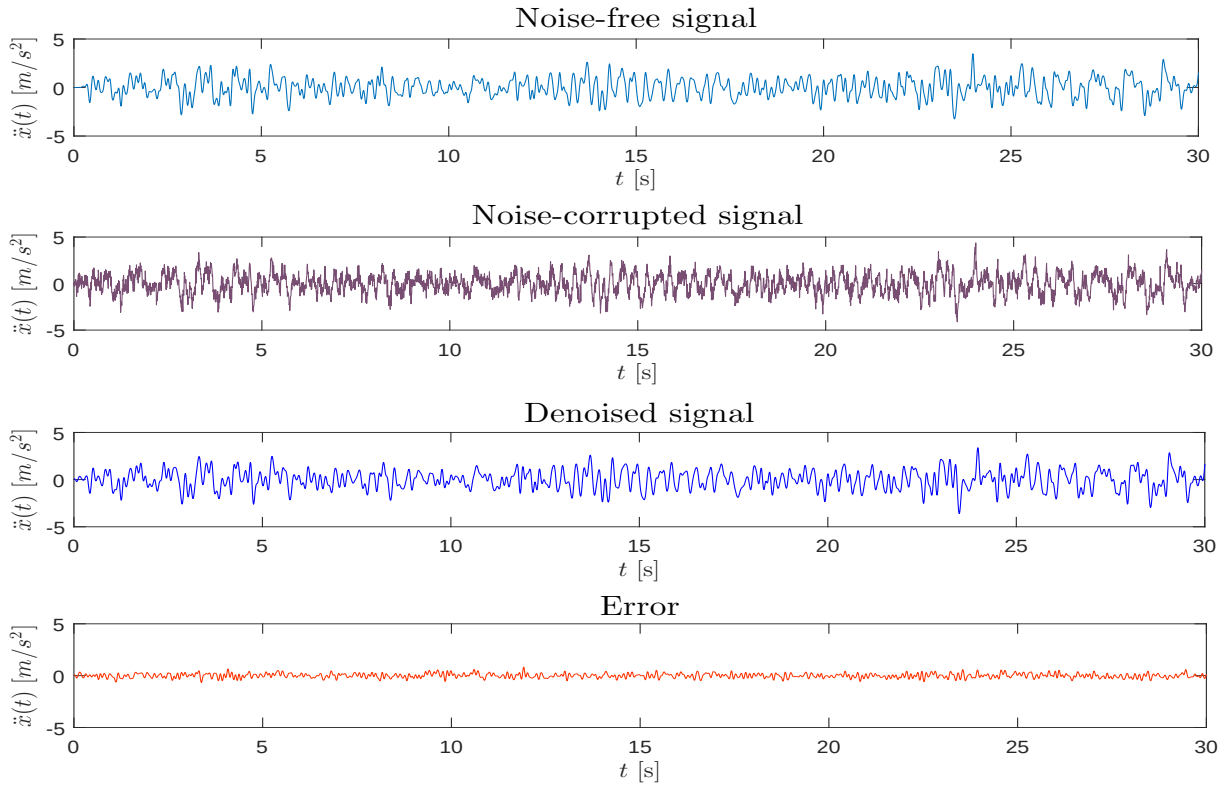

Figure 6: *SVD-based denoising of a noise-corrupted $\ddot{x}(t)$ response signal under ambient vibration (25% N/S ratio).*

3.3 DWT- vs. SVD-based denoising techniques

In this section, a critical comparison based on the performance evaluation of the two analyzed denoising approaches in clarifying noise-affected response signals is presented. The effectiveness of both methods is assessed, depending on the typology of the processed signal (non-stationary vs. stationary) and on the level of Gaussian white noise added to the source data. For academic purposes, N/S ratios up to 50% are considered within the analysis, and a PrmsD value between the reference signal and the denoised one is computed for each noise level. Results are summarized in following Table 1, and depicted in Fig. 7.

N/S ratio [%]			**5**	**10**	**15**	**20**	**25**	**30**	**35**	**40**	**45**	**50**
PrmsD [%]	Seismic excitation	DWT	0.06	0.13	0.18	0.20	0.88	1.18	1.23	1.39	2.11	2.69
		SVD	0.23	0.34	0.46	0.55	0.44	0.69	0.59	0.55	0.60	0.71
	Ambient vibration	DWT	0.59	1.25	2.64	3.80	4.58	4.93	5.23	5.90	6.21	6.82
		SVD	0.15	0.07	0.21	0.39	0.57	0.53	0.66	1.19	2.33	2.88

Table 1: *PrmsD [%] index between original and denoised signal for different signal typologies and N/S ratios: DWT vs. SVD.*

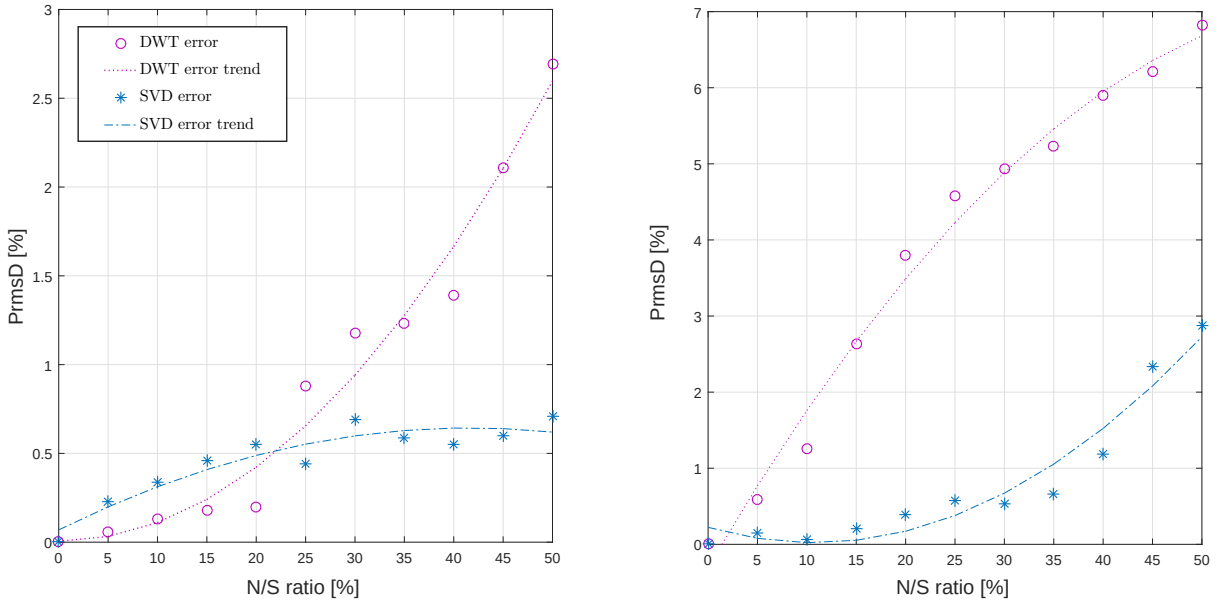

Figure 7: *Effectiveness evaluation of DWT- and SVD-based denoising techniques for increasing N/S ratios and different signal typologies: (a) earthquake excitation; (b) ambient vibration. Notice that scales on the PrmsD axes are different, almost twice for (b). Indicated trends come from a polynomial fit of degree 2.*

From the obtained outcomes it may be deduced that both considered denoising approaches seem to be well suited for dealing with non-stationary signals, and in particular for seismic response. However, the analysis performed on ambient vibration response has shown that, for the denoising of stationary signals, only the SVD-based technique leads to reliable estimates. This technique seems less affected by the level of noise considered in the source signals, in comparison to the DWT-based approach. Its robustness may also be better appreciated by the

graphs in Fig. 7, which plot the data in Table 1, where the error trends (in terms of PrmsD index) of the two denoising approaches are compared, considering the two studied typologies of source response signals.

4 CONCLUSIONS

In this paper, two different approaches for the denoising of (acceleration) structural response signals have been presented, i.e. one based on Discrete Wavelet Transform (DWT) and one based on Singular Value Decomposition (SVD). These two denoising techniques have been implemented with reference to simulated response signals typical of the civil engineering context, such as earthquake excitation and ambient vibration response signals. A ten-story shear-type building has been assumed as a benchmark structure, in order to generate the source noise-affected signals, and the last-floor acceleration response has been monitored.

Salient research contributions which this study is bringing to light may be briefly summarized as follows:

- stationary signals proved more problematic to purify than non-stationary ones, due to their almost constant distribution in time and frequency;
- the effectiveness of the SVD-based denoising method has been fully proven. It can be stated that it constitutes a rather robust technique, which is able to return reliable estimates of the original (noise-free) signal, despite for the significant amount of additive noise assumed on the source data. Moreover, this technique seems to be suitable for both non-stationary and stationary signals;
- The DWT-based approach may be considered as useful for the denoising of non-stationary signals, such as seismic response signals, especially for N/S ratios lower than 20%, where it may provide even better results than those for the SVD-based approach. However, the performed analysis has proven also its limitations in the processing of stationary signals, for which the application of the denoising method based on SVD is instead suggested.

Finally, after this first necessary phase of effectiveness assessment of the two denoising methods, in which only simulated signals have been considered, future developments shall concern the employment and denoising of real response signals (accelerations but also displacements), within the developed denoising procedure.

Acknowledgments
Public research support from *"Fondi di Ricerca d'Ateneo ex 60%"* and a ministerial doctoral grant and funds at the ISA Doctoral School, University of Bergamo, Department of Engineering and Applied Sciences (Dalmine), are gratefully acknowledged.

REFERENCES

[1] Lee, J.J., Fukuda, Y., Shinozuka, M., Cho, S. and Yun, C.B. (2007), Development and application of a vision-based displacement measurement system for structural health monitoring of civil structures. *Smart Structures and Systems*, 3(3): 373–384.

[2] Ferrari, R., Froio, D., Chatzi, E.N., Gentile, C., Pioldi, F. and Rizzi, E. (2015), Experimental and numerical investigation for the structural characterization of a historic RC arch bridge. In: *COMPDYN 2015, 5th ECCOMAS Thematic Conference on Computational Methods in Structural Dynamics and Earthquake Engineering*, Crete Island, Greece, 25-27 May 2015, 1: 2337–2353, available online in Eccomas Proceedia,

www.eccomasproceedia.org/conferences/thematic-conferences/compdyn-2015/3542.

[3] Ferrari, R., Pioldi, F., Rizzi, E., Gentile, C., Chatzi, E.N., Klis, R., Serantoni, E. and Wieser, A. (2015), Heterogeneous sensor fusion for reducing uncertainty in Structural Health Monitoring. In: *UNCECOMP 2015, 1st ECCOMAS Thematic Conference on International Conference on Uncertainty Quantification in Computational Sciences and Engineering*, Crete Island, Greece, 25-27 May 2015, pp. 511–528, available online in Eccomas Proceedia, www.eccomasproceedia.org/conferences/thematic-conferences/uncecomp-2015/4289.

[4] Ferrari, R., Pioldi, F., Rizzi, E., Gentile, C., Chatzi, E.N., Serantoni, E. and Wieser, A. (2016), Fusion of wireless and non-contact technologies for the dynamic testing of a historic RC bridge. *Measurement Science and Technology*, 27(12): 1–19.

[5] Buades, A. and Coll, B. (2006), A review of image denoising algorithms, with a new one. *Multiscale Modelling and Simulations*, 4(2): 490–530.

[6] Chen, G. and Bui, T. (2003), Multiwavelets denoising using neighboring coefficients. *IEEE Signal Processing Letters*, 10(7): 211–214.

[7] Portilla, J. and Strela, V. (2003), Image denoising using scale mixtures of Gaussians in the wavelet domain. *IEEE Transactions on Image Processing*, 12(11): 1338–1351.

[8] Gopinathan S., Kokila R. and Thangavel P. (2015), Wavelet and FFT-based image denoising using non-linear filters. *International Journal of Electrical and Computer Engineering*, 5(5): 1018–1026.

[9] Jiang, X., Mahadevan, S. and Adeli, H. (2007), Bayesian wavelet packet denoising for structural system identification. *Structural Control and Health Monitoring*, 14(2): 333–356.

[10] Zhao, M. and Jia, X. (2017), A novel strategy for signal denoising using reweighted SVD and its applications to weak fault feature enhancement of rotating machinery. *Mechanical Systems and Signal Processing*, 94(September 2017): 129–147.

[11] Chatzi, E.N. and Fuggini, C. (2012), Structural identification of a super-tall tower by GPS and accelerometer data fusion using a multi-rate Kalman filter. In: *Proceedings of the 3rd International Symposium on Life-Cycle Civil Engineering*, Delft, Netherlands, 3-6 October 2012, 10: 144–151.

[12] Chatzi, E.N. and Fuggini, C. (2015), Online correction of drift in Structural Identification using artificial white noise observations and an Unscented Kalman filter. *Smart Structures and Systems*, 16(2): 296–328.

[13] Ravizza G., Ferrari R., Rizzi E. and Chatzi E.N. (2018), Effective heterogeneous data fusion procedure via Kalman filtering. *Smart Structures and Systems*, 22(5): 631–641.

[14] Pioldi, F., Ferrari, R. and Rizzi, E. (2015), *Output-only modal dynamic identification of frames by a refined FDD algorithm at seismic input and high damping*. Mechanical Systems and Signal Processing, 68-69(February 2016):265–291.

[15] Pioldi, F., Ferrari, R. and Rizzi, E. (2015), *Earthquake structural modal estimates of multi-storey frames by a refined FDD algorithm*. Journal of Vibration and Control, 23(13):2037-2063.

[16] Pioldi, F., Ferrari, R. and Rizzi, E. (2017), *Seismic FDD modal identification and monitoring of building properties from real strong-motion structural response signals*. Structural Control and Health Monitoring, 24(11):1-20.

[17] Moulin P. and Liu J. (1999), Analysis of multiresolution image denoising schemes using generalized Gaussian and complexity priors. *IEEE Transactions on Information Theory*, 45(3): 909–919.

[18] Alfaouri M. and Daqrouq K. (2008), ECG signal denoising by wavelet transform thresholding. *American Journal of Applied Sciences*, 5(3): 276–281.

[19] Gradolewski D. and Redlarski G. (2013), The use of wavelet analysis to denoising of electrocardiography signal. In: *XV International PhD Workshop OWD*, 19-22 October 2013, pp. 456–461.

[20] Al-Qazzaz N.K., Ali S., Ahmad S.A., Islam M.S. and Arif M.I. (2015), Selection of mother wavelets thresholding methods in denoising multi-channel EEG signals during working memory task. *Sensors*, 15(11): 15–35.

[21] Sadooghi S.S. and Khadem E.K. (2016), A new performance evaluation scheme for jet engine vibration signal denoising. *Mechanical Systems and Signal Processing*, 76–77(2016): 201–212.

[22] Karthikeyan P., Murugappan M. and Yaacob S. (2012), ECG signal denoising using wavelet thresholding technique in human stress assessment. *International Journal of Electrical Engineering and Information*, 4(2): 306–319.

COMPDYN 2019
7th ECCOMAS Thematic Conference on
Computational Methods in Structural Dynamics and Earthquake Engineering
M. Papadrakakis, M. Fragiadakis (eds.)
Crete, Greece, 24–26 June 2019

DRIVE-BY DAMAGE MONITORING OF TRANSPORT INFRASTRUCTURE USING DIRECT CALCULATION OF THE PROFILE

J. Keenahan[1], E.J. OBrien[2], and Y. Ren[3]

[1] School of Civil Engineering, University College Dublin, Ireland
e-mail: jennifer.keenahan@ucd.ie

[2] School of Civil Engineering, University College Dublin, Ireland
e-mail: eugene.obrien@ucd.ie

[3] School of Civil Engineering, University College Dublin, Ireland
e-mail: ren.yifei@ucdconnect.ie

Abstract

Roads and railway tracks are a major focus of interest in transport infrastructure monitoring. Settlement in a road or railway track profile changes the dynamic excitation applied to passing vehicles. This, in turn, results in a changed dynamic response in the original source of loading, such as a passing vehicle. These changes in dynamic excitation make it possible to detect damage in transport infrastructure from the vehicle response. In this paper, the profile is calculated using accelerations in a passing vehicle and used to monitor transport infrastructure.

Keywords: Direct Integration, Drive-by, Profile, Railway Track, Acceleration, SHM.

1 INTRODUCTION

Roads and railway tracks are critical parts of transport infrastructure. They routinely become damaged with features emerging such as potholes in the roads and 'soft spots' in the railway track. These damages may influence the serviceable and safe operation of the transportation network. Therefore, infrastructure monitoring is an important area of research.

Railway tracks are subject to reductions in stiffness due to deteriorating foundations and to permanent fatigue deformations that result in a change in the track profile. The objective of this research is to identify local reductions of profile or stiffness that can help with the identification of problems related to track settlement, vehicle-ride comfort, track geometry and even ground-borne vibrations [1]. Railway track stiffness can currently be measured using specialised medium-speed vehicles or stationary equipment. A track recording vehicle (TRV) is a traditional method used by railway infrastructure managers to assess the condition of their network. A TRV is a specialised, instrumented train which periodically collects geometric data of the railway track including track gauge, longitudinal profile, alignment, super-elevation irregularity (cross level or cant) and twist. European Standard EN13848 defines the method of measurement of railway track using TRVs in Europe [2]. TRVs are the current preferred method of measurement for these parameters. However, they are expensive to operate and may disrupt regular services during operation. Using in-service vehicles to determine at least some of these parameters represents a possible alternative that can provide much more frequent measurements at much less cost [3].

In this method, sensors mounted on in-service vehicles collect accelerations and possibly other dynamic parameters. Improvements in band-width of wireless communications, reductions in sensor and data acquisition electronics cost have allowed the development of unattended track geometry inspection systems that are compact and robust enough to be mounted on in-service vehicles [4]. This concept of using trains in regular service to measure track stiffness has the potential to provide inexpensive daily 'drive-by' track monitoring to complement data collected by other less frequent (but more accurate) monitoring techniques.

Railway track longitudinal profile is also regard as indicator of serviceability condition. Perfectly level track profiles can minimise dynamic responses of the vehicle, which can increase passenger comfort, reduce power consumption and reduce wear on vehicle components. A reduction in vehicle dynamics also reduces the vehicle load on the track. Therefore, keeping a good vertical longitudinal profile helps maintain overall track condition through a reduction in vehicle dynamic effects [5].

Accelerometer(s) mounted on a vehicle also provide a way to measure road profile which is of low cost. González et al identify the relationship between vehicle accelerations and the power spectral densities of road surfaces using a transfer function [6]. The road condition is accurately classified by Fourier analysis which is used to calculate the power spectral density (PSD) function of the surface. OBrien et al present a drive-by method to monitor transport infrastructure (such as bridges and pavements) by analysing vehicle accelerations [7]. An algorithm is proposed to identify the dynamic vehicle-bridge interaction forces using the vehicle response. It is suggested that this method could be used to identify the global bending stiffness of the bridge and to predict the pavement roughness. This paper will use a new direct integration approach to calculate track and/or road profiles using vehicle accelerations. Points of low stiffness in the track are also determined as it is loaded track profile that is measured which is a combination of permanent deformation/profile and deflection in response to the weight of the train.

2 MODEL DESCRIPTION

2.1 Vehicle Model

The vehicle is represented by a 4 degree-of-freedom half-car model travelling on a beam-on-elastic-foundation track (Figure 1(a)) and rigid road (Figure 1(b)). The four independent degrees of freedom correspond to sprung mass bounce displacement, u_s, sprung mass pitch rotation θ_s and axle hop displacements of the unsprung masses at axles 1 and 2, u_{u1} and u_{u2} respectively. The vehicle body is represented by sprung mass, m_s. The axle components are represented by unsprung masses, m_{u1} and m_{u2}. The sprung mass connects to the axle masses via a combination of springs and dampers. The damping coefficients of viscous dampers are $C_{s,i}$ and stiffnesses of springs are $K_{s,i}$ which represent the suspension components for the front and rear axles ($i = 1,2$). The axle masses connect to the road or railway track surface via springs with linear stiffnesses, $K_{t,i}$ which represent the tyre components for the front and rear axles ($i = 1,2$). Finally, I_s is the sprung mass moment of inertia and the distances of the axles to the centre of gravity are D_1 and D_2. Table 1 gives the property values of the half-car.

Property	*Unit*	*Symbol*	*Half-Car and track model*	*Half-Car and road model*
Body mass	kg	m_s	16 200	16 200
Axle mass	kg	m_{u1}	700	700
		m_{u1}	1100	1100
Suspension stiffness	N/m	$K_{s,1}$	4×10^5	4×10^5
		$K_{s,2}$	1×10^6	1×10^6
Suspension damping	N s/m	$C_{s,1}$	1×10^4	1×10^4
		$C_{s,2}$	2×10^4	2×10^4
Tyre stiffness	N/m	$K_{t,1}$	1.75×10^6	1.75×10^6
		$K_{t,2}$	3.5×10^6	3.5×10^6
Pitch moment of inertia	kg m^2	I_s	111 193	93 457
Distance of axle to centre of gravity	m	D_1	4.13	2.375
		D_2	4.13	2.375

Table 1: Vehicle model properties.

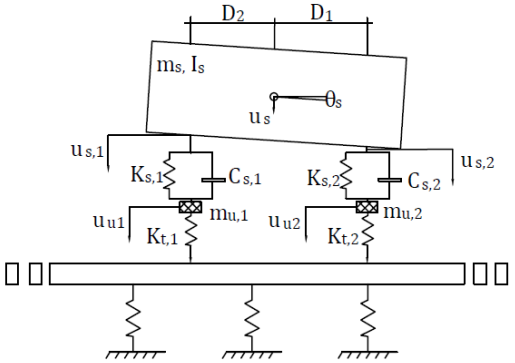

Figure 1(a): Half-Car and track model.

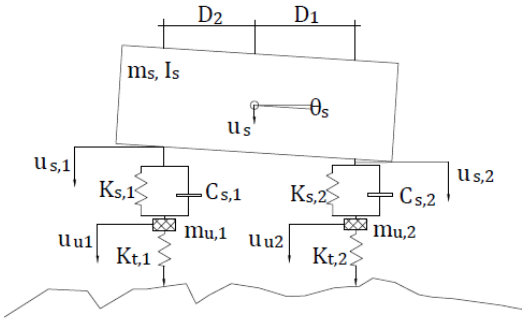

Figure 1(b): Half-Car and road model.

The equations of motion of the vehicle are obtained by imposing equilibrium of all forces and moments acting on the vehicle:

$$\mathrm{M}_v\ddot{u}_v + C_v\dot{u}_v + \mathrm{K}_v u_v = f_v \tag{1}$$

where M_v, C_v, and K_v are the mass, damping and stiffness matrices of the vehicle respectively. The vehicle accelerations, velocities and displacements are represented by vectors, $\ddot{u}_v$, $\dot{u}_v$ and u_v respectively, where the displacement vector of the vehicle is,

$$u_v = \{u_s, \theta_s, u_{u1}, u_{u2}\}^T \tag{2}$$

The time-varying dynamic interaction force vector is,

$$f_v = \{0,0,F_{t1},F_{t2}\}^T \tag{3}$$

The dynamic interaction force at wheel *i* is,

$$F_{ti} = K_{t,i} \times y_i \tag{4}$$

$i = 1,2$, where y_i is the road or track profile. The mass, damping and stiffness matrices are:

$$\mathrm{M_v} = \begin{bmatrix} m_s & 0 & 0 & 0 \\ 0 & I_s & 0 & 0 \\ 0 & 0 & m_{u,1} & 0 \\ 0 & 0 & 0 & m_{u,2} \end{bmatrix} \tag{5}$$

$$\mathrm{C_v} = \begin{bmatrix} C_{s,1}+C_{s,2} & D_1C_{s,1}-D_2C_{s,2} & -C_{s,1} & -C_{s,2} \\ D_1C_{s,1}-D_2C_{s,2} & {D_1}^2C_{s,1}+{D_2}^2C_{s,2} & -D_1C_{s,1} & D_2C_{s,2} \\ -C_{s,1} & -D_1C_{s,1} & C_{s,1} & 0 \\ -C_{s,2} & D_2C_{s,2} & 0 & C_{s,2} \end{bmatrix} \tag{6}$$

$$\mathrm{K_v} = \begin{bmatrix} K_{s,1}+K_{s,2} & D_1K_{s,1}-D_2K_{s,2} & -K_{s,1} & -K_{s,2} \\ D_1K_{s,1}-D_2K_{s,2} & {D_1}^2K_{s,1}+{D_2}^2K_{s,2} & -D_1K_{s,1} & D_2K_{s,2} \\ -K_{s,1} & -D_1K_{s,1} & K_{s,1}+K_{t,1} & 0 \\ -K_{s,2} & D_2K_{s,2} & 0 & K_{s,2}+K_{t,2} \end{bmatrix} \tag{7}$$

2.2 Road model

In this paper, a 100 m road profile is generated by Monte Carlo simulation according to the ISO standard [8]. It simulates a class 'A' road which is a 'very good' profile, typical of a well-maintained highway. The geometric spatial mean is 8×10^{-6} m^3/cycle. A moving average filter

is applied to the generated road profile heights, y_i. It is over a distance of 0.24 m to simulate the attenuation of short wavelength disturbances by the tyre contact patch [7,9].

2.3 Track Model

In past work, the railway track is represented using a beam-on-elastic-foundation model [1]. This model features a single layer of discrete elastic springs. Figure 1(a) shows the beam-on-elastic-foundation track model. It features an elastic beam (the rail) supported on some springs with different stiffness, k. Track supports have regular interval spacing, L_s, representing the spacing between the sleepers. A UIC60 rail is simulated as a finite element Euler-Bernoulli beam with one beam element per sleeper spacing. Each track element has 2 nodes with 2 degrees of freedom (DOF), vertical translation and rotation, at each node. Rail irregularities are not considered in this research which means the track profile is entirely from deflection of the springs under the loaded train.

3 DIRECT SOLUTION OF PROFILE CALCULATION

The forward problem and the inverse problem are features of any profile calculation. The forward problem is to find vehicle accelerations, velocities and displacements for a given profile. The inverse problem, in contrast, uses given $\ddot{u}$ and $\dot{\theta}_s$to find the profile. In previous research, the inverse problem is solved using a complex optimisation procedure [10]. It repeatedly solves the problem for thousands of trial profiles, until a good match is achieved between measured and theoretical accelerations. It also should repeat this for each segment of track/road. In this paper, the direct integration approach is proposed to solve the inverse problem directly to find the profile.

The forward problem is solved first. In the forward problem calculation, a 'true' profile is used to generate the 'measured' sprung mass accelerations and sprung mass pitch rotational velocity. Then, to test the method of solving the inverse problem, the profile y_i is calculated with these 'measured' sprung mass accelerations and sprung mass pitch rotational velocities. All problems are solved here using the Newmark-Beta integration scheme and simulated in MATLAB.

In the Newmark-Beta integration scheme, a value of γ=0.5 is used to ensure unconditional stability of the algorithm. In the Newmark-Beta method, the integration constants are chosen as:

$$\text{Time step } \Delta t,\ \ \gamma = 0.5, \beta = \ 0.25 \times (0.5 + \gamma)^2$$

$$a_0 = \frac{1}{\beta \times \Delta t^2},\ a_1 = \frac{\gamma}{\beta \times \Delta t},\ a_2 = \frac{1}{\beta \times \Delta t}, a_3 = \frac{1}{\beta \times 2} - 1, a_4 = \frac{\gamma}{\beta} - 1, \tag{8}$$

$$a_5 = \frac{\Delta t}{2} \times \left(\frac{\gamma}{\beta} - 2\right), a_6 = (1 - \gamma) \times \Delta t, a_7 = \ \gamma \times \Delta t$$

The profile is calculated step by step in the process as follows: The sprung mass bounce acceleration, $\ddot{u}$ and the sprung mass pitch rotational velocity, $\dot{\theta}_s$ are taken to be known at first. Then the sprung mass bounce displacement, u_s, and velocity, $\dot{u}_s$, sprung mass pitch rotational displacement, θ_s, and accelerations, $\ddot{\theta}_s$, can be calculated using the Newmark-Beta integration scheme:

$$u_{s,t+\Delta t} = (\ddot{u}_{s,t+\Delta t} + a_2 \times \dot{u}_{s,t} + a_3 \times \ddot{u}_{s,t})/a_0 + u_{s,t} \tag{9}$$

$$\dot{u}_{s,t+\Delta t} = \dot{u}_{s,t} + a_6 \times \ddot{u}_{s,t} + a_7 \times \ddot{u}_{s,t+\Delta t} \tag{10}$$

$$\theta_{s,t+\Delta t} = (\dot{\theta}_{s,t+\Delta t} + a_4 \times \dot{\theta}_{s,t} + a_5 \times \ddot{\theta}_{s,t})/a_1 + \theta_{s,t} \quad (11)$$

$$\ddot{\theta}_{s,t+\Delta t} = a_0 \times (\theta_{s,t+\Delta t} - \theta_{s,t}) - a_2 \times \dot{\theta}_{s,t} - a_3 \times \ddot{\theta}_{s,t} \quad (12)$$

According to Equations (1) to (7), the equations of motion of the sprung mass can be found:

$$m_s \times \ddot{u}_{s,t+\Delta t} + (C_{s,1} + C_{s,2}) \times \dot{u}_{s,t+\Delta t} + (D_1 C_{s,1} - D_2 C_{s,2}) \times \dot{\theta}_{s,t+\Delta t} - C_{s,1} \times \dot{u}_{u1,t+\Delta t} - C_{s,2} \times \dot{u}_{u2,t+\Delta t} + (K_{s,1} + K_{s,2}) \times u_{s,t+\Delta t} + (D_1 K_{s,1} - D_2 K_{s,2}) \times \theta_{s,t+\Delta t} - K_{s,1} \times u_{u1,t+\Delta t} - K_{s,2} \times u_{u2,t+\Delta t} = 0 \quad (13)$$

$$I_s \times \ddot{\theta}_{s,t+\Delta t} + (D_1 C_{s,1} - D_2 C_{s,2}) \times \dot{u}_{s,t+\Delta t} + ({D_1}^2 C_{s,1} + {D_2}^2 C_{s,2}) \times \dot{\theta}_{s,t+\Delta t} - D_1 C_{s,1} \times \dot{u}_{u1,t+\Delta t} + D_2 C_{s,2} \times \dot{u}_{u2,t+\Delta t} + (D_1 K_{s,1} - D_2 K_{s,2}) \times u_{s,t+\Delta t} + ({D_1}^2 K_{s,1} + {D_2}^2 K_{s,2}) \times \theta_{s,t+\Delta t} - D_1 K_{s,1} \times u_{u1,t+\Delta t} + D_2 K_{s,2} \times u_{u2,t+\Delta t} = 0 \quad (14)$$

The terms, $\dot{u}_{u2,t+\Delta t}$ and $u_{u2,t+\Delta t}$ can be removed by combining Equations (14) with Equations (13), scaled by D_2:

$$D_2 m_s \times \ddot{u}_{s,t+\Delta t} + D_2(C_{s,1} + C_{s,2}) \times \dot{u}_{s,t+\Delta t} + D_2(D_1 C_{s,1} - D_2 C_{s,2}) \times \dot{\theta}_{s,t+\Delta t} + D_2(K_{s,1} + K_{s,2}) \times u_{s,t+\Delta t} + D_2(D_1 K_{s,1} - D_2 K_{s,2}) \times \theta_{s,t+\Delta t} + I_s \times \ddot{u}_{s,t+\Delta t} + (D_1 C_{s,1} - D_2 C_{s,2}) \times \dot{u}_{s,t+\Delta t} + ({D_1}^2 C_{s,1} + {D_2}^2 C_{s,2}) \times \dot{\theta}_{s,t+\Delta t} + (D_1 K_{s,1} - D_2 K_{s,2}) \times u_{s,t+\Delta t} + ({D_1}^2 K_{s,1} + {D_2}^2 K_{s,2}) \times \theta_{s,t+\Delta t} = (D_2 C_{s,1} + D_1 C_{s,1}) \times \dot{u}_{u1,t+\Delta t} + (D_2 K_{s,1} + D_1 K_{s,1}) \times u_{u1,t+\Delta t} \quad (15)$$

In the Newmark-Beta method,

$$\dot{u}_{u1,t+\Delta t} = a_1 \times (u_{u1,t+\Delta t} - u_{u1,t}) - a_4 \times \dot{u}_{u1,t} - a_5 \times \ddot{u}_{u1,t} \quad (16)$$

Substituting (16) into (15), the unsprung mass displacement can be calculated:

$$u_{u1,t+\Delta t} = (D_2 m_s \times \ddot{u}_{s,t+\Delta t} + I_s \times \ddot{\theta}_{s,t+\Delta t} + (D_2 C_{s,1} + D_1 C_{s,1}) \times \dot{u}_{s,t+\Delta t} + (D_2 D_1 C_{s,1} + {D_1}^2 C_{s,1}) \times \dot{\theta}_{s,t+\Delta t} + (D_2 K_{s,1} + D_1 K_{s,1}) \times u_{s,t+\Delta t} + (D_2 D_1 K_{s,1} + {D_1}^2 K_{s,1}) \times \theta_{s,t+\Delta t} + (D_2 C_{s,1} + D_1 C_{s,1}) \times (a_1 \times u_{u1,t} + a_4 \times \dot{u}_{u1,t} + a_5 \times \ddot{u}_{u1,t}))/(D_2 K_{s,1} + D_1 K_{s,1} + (D_2 C_{s,1} + D_1 C_{s,1}) \times a_1) \quad (17)$$

Unsprung mass acceleration and velocity can be calculated using the Newmark-Beta method:

$$\ddot{u}_{u1,t+\Delta t} = a_0 \times (u_{u1,t+\Delta t} - u_{u1,t}) - a_2 \times \dot{u}_{u1,t} - a_3 \times \ddot{u}_{u1,t} \quad (18)$$

$$\dot{u}_{u1,t+\Delta t} = \dot{u}_{u1,t} + a_6 \times \ddot{u}_{u1,t} + a_7 \times \ddot{u}_{u1,t+\Delta t} \quad (19)$$

This is used to calculate $f_{v,t+\Delta t}$ at time step, $t + \Delta t$,

The effective stiffness matrix is:

$$\bar{K} = K_v + a_0 \times M_v + a_1 \times C_v \quad (20)$$

The effective force is:

$$\bar{f}_{v,t+\Delta t} = \bar{K} \times u_{v,t+\Delta t} \quad (21)$$

and,

$$f_{v,t+\Delta t} = \bar{f}_{v,t+\Delta t} - \mathrm{M}_v \times (a_0 \times u_{v,t} + a_2 \times \dot{u}_{v,t} + a_3 \times \ddot{u}_{v,t}) - C_v \times (a_1 \times u_{v,t} + a_4 \times \dot{u}_{v,t} + a_5 \times \ddot{u}_{v,t}) \quad (22)$$

According to Equation (3), $f_{v,t+\Delta t} = \{0,0,F_{t1,t+\Delta t},F_{t2,t+\Delta t}\}^T$, so $F_{ti,t+\Delta t}$ is known, and the profile can be found according to Equation (4):

$$y_{i,t+\Delta t} = F_{ti,t+\Delta t}/K_{t,i} \tag{23}$$

The calculated road profile and track profile are shown in the Figure 2(a) and Figure 2(b) respectively. The results show that the profiles are found with a great degree of accuracy. This direct integration approach allows the calculation to be completed in a very short time which is massively more efficient than an optimisation approach.

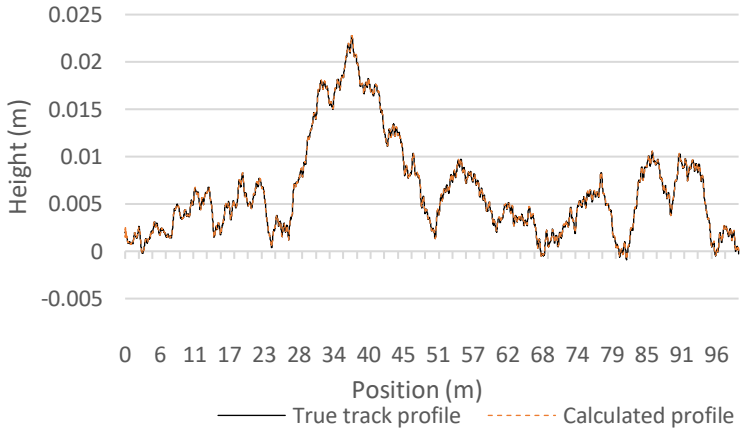

Figure 2(a): Calculated road profile and true profile.

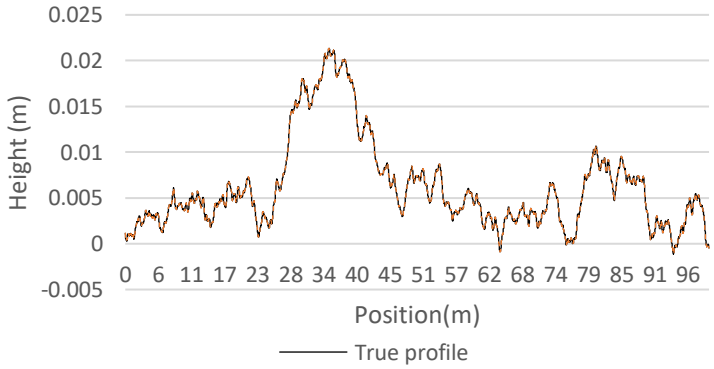

Figure 2(b): Calculated track profile and true profile.

4 DAMAGE IN RAILWAY TRACK

Local variations in the track stiffnesses can be detected from the calculated track profile which is effectively a combination of profile and deformations under load. In this example, there is a 50% loss in the track stiffness from 60 m to 65 m. This changes the 'measured' accelerations and rotational velocities. Using these changed signals, the new deflected profiles are calculated. The calculated track profile with and without a local reduction in railway track stiffness are shown in Figure 3. The results show that calculating track profile is a good means of identifying defects in the track.

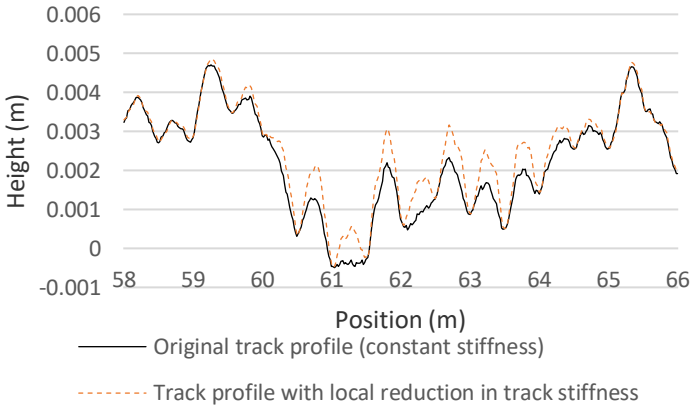

Figure 3: Calculated track profile with variations in railway track stiffness.

5 CONCLUSIONS

This paper introduces a new method of monitoring transport infrastructure. A direct integration approach is proposed to calculate road and railway track profiles using measured accelerations from vehicles. The direct method is used to calculate profiles using these 'measured' accelerations. The results show that the calculated profiles are the same as the 'true' profiles which are from the forward problem (used to generate the accelerations). What is more, direct integration is much more efficient and allows the calculation to be completed much more quickly in comparison to the optimisation procedure used by previous researchers. Also, the calculated track profile can be used to detect local variations in railway track stiffness. It has good potential as a means of detecting areas where railway tracks have suffered a reduction in stiffness.

ACKNOWLEDGMENTS

Mr. Yifei Ren acknowledges the Ph.D. scholarship received jointly from University College Dublin and the China Scholarship Council.

REFERENCES

[1] P. Quirke, D. Cantero, E. J. OBrien, C. Bowe, Drive-by detection of railway track stiffness variation using in-service vehicles. *Proceedings of the Institution of Mechanical Engineers, Part F: Journal of Rail and Rapid Transit*, **231**, 498-514, 2017.

[2] IS EN 13848: Railway Applications - Track - Track Geometry Quality - CEN European. Committee for Standardisation.

[3] E. J. OBrien, C. Bowe, P. Quirke, and D. Cantero, Determination of longitudinal profile of railway track using vehicle-based inertial readings. *Proceedings of the Institution of Mechanical Engineers, Part F: Journal of Rail and Rapid Transit*, **231**, 518-534, 2017.

[4] P. Weston, C. Roberts, G. Yeo, E. Stewart, Perspectives on railway track geometry condition monitoring from in-service railway vehicles. *Vehicle System Dynamics*, **53**, 1063-1091, 2015.

[5] R. D. Frohling, Deterioration of railway track due to dynamic vehicle loading and spatially varying track stiffness. PhD Thesis, University of Pretoria, South Africa, 1997.

[6] A. González, E. J. OBrien, Y. Y. Li, K. Cashell, The use of vehicle acceleration measurements to estimate road roughness. *Vehicle System Dynamics*, **46**(6), 483-499, 2008.

[7] E. J. OBrien, P. J. McGetrick, A. González, A drive-by inspection system via vehicle moving force identification. *Smart Structures and Systems*, **13**(5), 821-848, 2014.

[8] ISO 8608: Mechanical vibration-road surface profiles - reporting of measured data, 1995

[9] N. K. Harris, E. J. OBrien, A. González, Reduction of bridge dynamic amplification through adjustment of vehicle suspension damping. *Journal of Sound and Vibration*, **302**(3), 471-485, 2007.

[10] E. J. OBrien, J. Keenahan, Drive-by damage detection in bridges using the apparent profile'. *Structural Control and Health Monitoring*, **22**(5), 813-825, 2015.

COMPDYN 2019
7th ECCOMAS Thematic Conference on
Computational Methods in Structural Dynamics and Earthquake Engineering
M. Papadrakakis, M. Fragiadakis (eds.)
Crete, Greece, 24–26 June 2019

REAL TIME DAMAGE DETECTION THROUGH SINGLE LOW-COST SMART SENSOR

Said Quqa[1], Luca Landi[1], and Pier Paolo Diotallevi[1]

[1] DICAM, University of Bologna
Viale del Risorgimento 2, 40136, Bologna, Italy
e-mail: {said.quqa2, l.landi, pierpaolo.diotallevi}@unibo.it

Abstract

Continuous vibration-based structural monitoring is increasingly used to assess the state of health of existing structures and infrastructures in environmental conditions through non-invasive methods that allow, in most cases, an early identification of damage. To date, the innovative wireless smart sensor networks are the subject of numerous researches in the field of structural health monitoring, but their use on real structures is still limited, due to problems related to energy consumption and algorithmic optimization. In fact, most of the traditional identification algorithms work in centralized topology and are not suitable for electronic elements with low computational capacity. Nevertheless, the high energy consumption of wireless communication does not allow continuous data transmission for centralized processing in real time. However, the limited costs of new technologies, compared to traditional wired acquisition systems, shifts the interest towards innovative solutions, both from an algorithmic and hardware point of view, in order to provide innovative monitoring systems that can also be used on minor structures, for which traditional systems would be inaccessible. This paper presents a first practical application of a structural identification algorithm specifically designed for low-cost embedded electronic systems on a scaled laboratory model. The proposed solution consists of a single sensing node able to identify natural frequencies in real time, even in conditions of non-stationary excitation and variable structural characteristics. The estimated parameters are periodically uploaded to a cloud platform, where a preliminary real-time damage detection takes place.

Keywords: Structural Health Monitoring, Real Time Modal Identification, Damage Detection, Smart Sensors, Teager Energy Operator, Wavelet Packet Transform.

1 INTRODUCTION

In order to ensure the reliability and efficiency of existing civil structures, they have to be properly maintained. Because of the strict constraints of architectural conservation, the preservation of historical buildings mainly means monitoring [1]. For this reason, in recent decades, infrastructures and buildings of strategic and monumental importance have been equipped with advanced vibration-based structural health monitoring systems that allow to detect any changes in the dynamic characteristics potentially connected with ongoing damage [2-3]. Nevertheless, recent news has highlighted the fact that maintenance, and then monitoring, is of the utmost importance also for minor structures and infrastructures, which could undergo fatigue load cycles or other forms of degradation during their rated life time. However, providing each viaduct or building of traditional monitoring systems would be difficult due to the prohibitive costs of traditional sensors and related equipment.

Nowadays, by using the most recent Micro Electro-Mechanical Systems (MEMS) sensors combined with low-cost microcontrollers and wireless transmission modules, it is possible to design innovative monitoring solutions having less impact from the visual and economic point of view with respect to the traditional configurations based on wired piezoelectric sensors [4-5]. Furthermore, thanks to the computational capacity of the microcontrollers, part of the processing activities can be performed directly on board, making the system particularly suitable for applications in the Internet of Things (IoT) [6-11].

However, these systems have important limitations related with the weak computational abilities of processing units [5]. It is therefore of fundamental importance that the operational algorithms are simple and use few resources, both in terms of memory and energy consumption. For this reason, most of the traditional techniques used for modal identification and damage estimation are not suitable for applications through the innovative low-cost systems.

In this paper, we propose a variant of a structural identification algorithm previously presented for multi-node monitoring networks [12]. This variant is specifically designed for single-node embedded systems and is able to estimate the first natural frequencies of the monitored structure in real time, in order to notice any changes that could be related with damage.

A first application on a scaled laboratory model is also presented. In particular, two acceleration channels collected by a single triaxial sensor are analyzed in order to compute the instantaneous natural frequencies of the first three vibration modes of the structure. The results are automatically uploaded to the cloud through a platform that allows the real-time visualization of data from any device connected to the Internet. Moreover, a simple procedure for measuring frequency variations with respect to the initial condition is implemented within the online platform in order to perform an early damage detection.

2 MONITORING SYSTEM

In this section, a brief description of the hardware and software parts is given. Both these aspects have been designed in order to exploit the computational capabilities of the implemented low-cost electronic devices.

2.1 Hardware configuration

The hardware implemented in this study consists of a sensing node and a gateway (Fig. 1). The node is an embedded system composed of a MEMS triaxial accelerometer connected to a microcontroller on which the preliminary signal processing procedures take place through the proposed identification algorithm. In the presented application, the node communicates via a wired one-to-one connection with the gateway, consisting of a single board computer with a

microprocessor that performs the modal identification. The gateway is wirelessly connected to the Internet in order to upload the identification results to a programmable data-logging application that allows simple post-processing activities, mainly aimed at data representation.

The sensor implemented in the proposed system is the digital low-power and low-noise-density ADXL-355 triaxial MEMS accelerometer by Analog Devices, with incorporated 20-bit analog-to-digital converter. An amplitude limit of ±2g has been selected, corresponding to a sensitivity of 256000 LSB/g and noise density of 20 μg/√Hz for an output data rate of 500 Hz. The accelerometer is connected via the serial peripheral interface (SPI) to an ARM Cortex-M3 microcontroller unit with 64 kB of flash memory and 20 kB of Random Access Memory (RAM). Some additional LEDs are connected to the microcontroller for debugging purposes.

The sensing node is connected via the Universal Asynchronous Receiver-Transmitter (UART) interface to the gateway, consisting of a Raspberry Pi 3 model B.

The overall cost of the hardware used in this study is very low, and much lower than the cost of traditional piezoelectric sensors, which are usually connected to onerous external monitoring stations.

In order to evaluate the quality of the signal collected through the implemented MEMS sensor, two mono-axial piezoelectric accelerometers 333B40 by PCB Piezotronics have been installed, with a sensitivity of 500 mV/g and noise density equal to 0.4 μg/√Hz for an output data rate of 1 kHz.

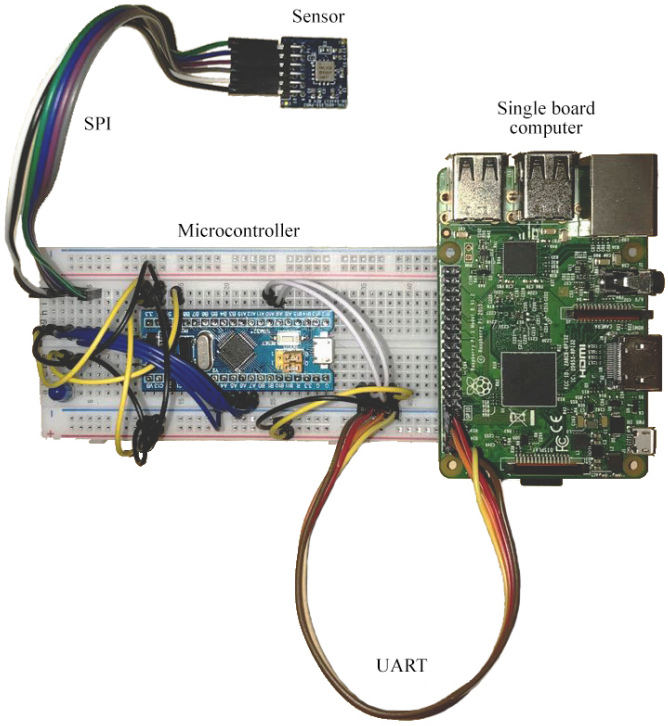

Figure 1: Hardware setup.

2.2 Algorithm description

The identification algorithm consists of two steps that are recursively performed to generate a signal-adaptive procedure. The first step involves the construction of a wavelet filter bank used to decompose the acquired signal in separate modal responses, while the second step lies in the real-time estimation of the instantaneous dynamic parameters (frequencies and amplitudes) for each component.

In particular, the first step involves the preliminary decomposition of the acceleration time histories collected on the structure in different positions and/or directions over a limited time window. The decomposition is performed through a wavelet filter bank, whose properties depend on the parameters selected at the base of the algorithm (i.e., the implemented wavelet function, its order, and the transform level). The signals are therefore decomposed into a series of components, each characterized by a narrow frequency band, which are subsequently grouped into clusters. Then, the signals associated to the same cluster are merged together and only the clusters whose energy (computed as the root mean square of the merged signals) is higher than a user-defined threshold (e.g., the mean value over all the clusters) are selected. Finally, a new filter bank is generated in order to extract by convolution only the selected components. This filter bank is used in the second step of the algorithm, that involves the real-time decomposition of acquired signals and the simultaneous identification of modal parameters.

In the algorithm presented in [12], the clustering procedure is based on the similarity of the operational deflection shapes computed for each component. Since in this application only one sensing node is used, in order to carry out the clustering procedure, the components extracted from two orthogonal channels collected by the same triaxial sensor are analysed, considering a bidirectional element of the operational deflection shape as clustering variable. This method is based on the assumption that the signal window used to build the filter bank is collected under 360° broadband input excitation.

Moreover, in this application, the modal identification is performed by using the Teager Energy Operator (TEO) [13], that allows to compute the instantaneous frequency and amplitude of each component by analysing extremely reduced signal windows. In particular, by implementing the Discrete-Time Energy Separation Algorithm-1 (DESA-1), only five samples per component are required to estimate an instantaneous parameter value, allowing a real-time and relatively simple evaluation of frequencies and amplitudes, easily performed on board low-cost electronic devices.

In this study, the first step is entirely performed on the gateway, while the second step is carried out partly on the node and partly on the gateway, exploiting the computational capacity of both the devices. The algorithm has been converted into a script for the microprocessor and a firmware for the embedded sensing system, the first aimed at the filter bank construction and modal identification, and the latter used to extract the modal components in real time, as illustrated in Fig. 2.

If the filter bank is no longer suitable for decomposing the modal responses due to a variation of modal parameters, it should be updated. For this reason, each identified frequency value is compared to the limits of the bandpass filters. If these limits are exceeded, the first step of the procedure is repeated.

The natural frequencies are temporarily stored on the on-board memory and, after applying a median filter and a downsampling, are logged on an online platform specifically designed for IoT applications. Here, the variation in terms of frequency for each vibration mode is calculated and plotted in real time, in order to allow users to access the identification results from any location at any time.

In addition, a simple script for damage detection has been written within the online platform. In a “training” window of user-defined duration, the median values of all the identified frequencies are determined. Then, the instantaneous variation of frequency for each mode and an average trend over all the identified modes are computed in the same window with respect to the median values. Finally, the maximum term in the averaged variation is multiplied by a user-defined factor and used as a threshold in damage detection (i.e. as the maximum allowed average frequency variation to consider the structure as undamaged).

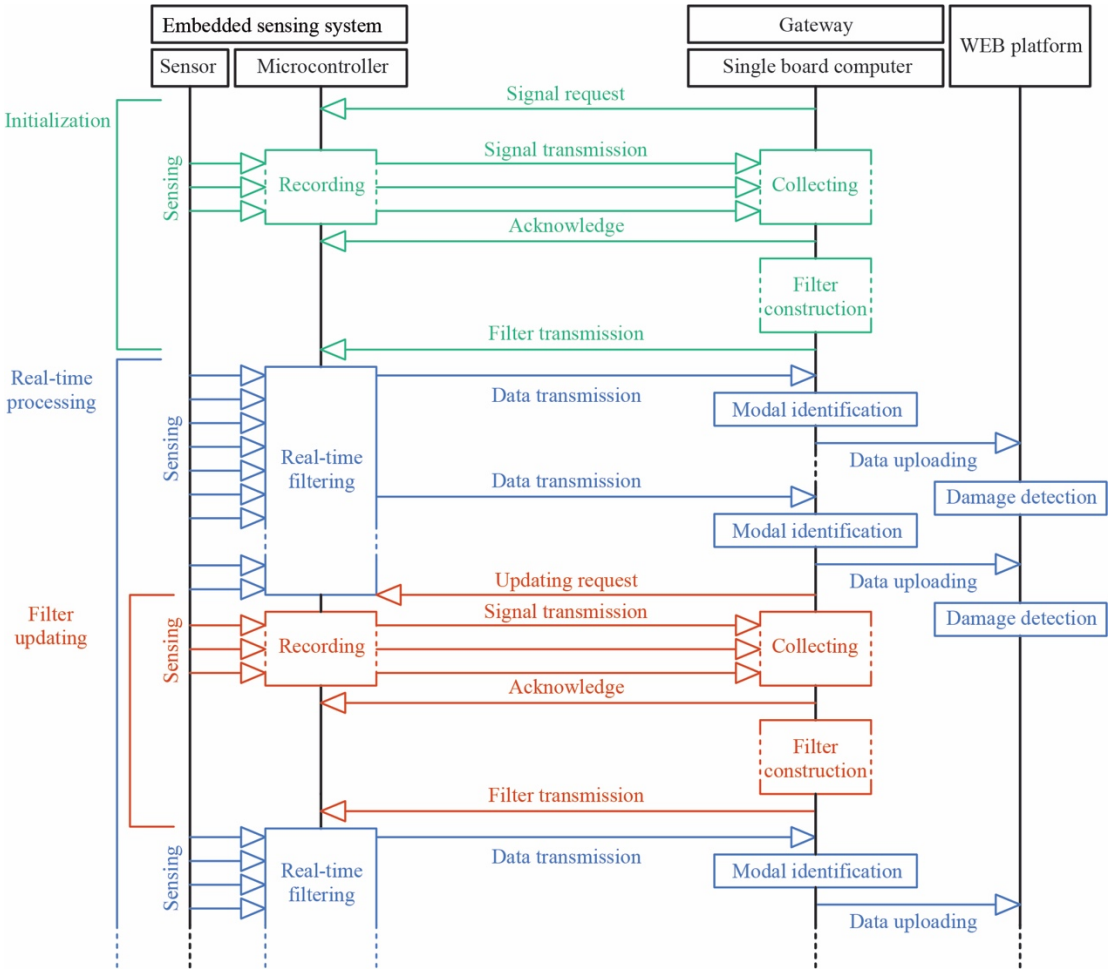

Figure 2: Workflow of the proposed algorithm.

3 APPLICATION

As a first application, the proposed monitoring system has been tested on a scaled steel laboratory model. The experimental tests have been conducted to evaluate the reliability of low-cost electronic devices for structural monitoring purposes and the effectiveness of the algorithm in estimating instantaneous natural frequencies.

This section gives a brief description of the specimen and the discussion of the results obtained during the experimental campaign. First, the accelerations recorded through the MEMS sensor implemented in the embedded system are compared with those obtained through a traditional piezoelectric acquisition system during an impulsive test, in order to evaluate the differences in the recorded signals. Subsequently, the results of real-time identification procedure performed through the proposed monitoring system under ambient vibration are reported.

3.1 Model description and experimental setup

The model is a three-level steel frame structure (Fig. 3) with a total height of 916 mm, whose base is formed by a 16 mm thick rectangular plate with main dimensions of 460x300 mm. Each level consists of a 12 mm thick plate measuring 400x300 mm and is supported by rectangular columns with a section of 40x3 mm. The connections between columns and plates are formed by L30x3 angle profiles and 72x40x3 mm flat plates held together by couples of M4 bolts with washers, as illustrated in Fig. 4. The net distance between each floor plate is 288 mm. The base plate and the top plate are connected to the columns through stud bolts.

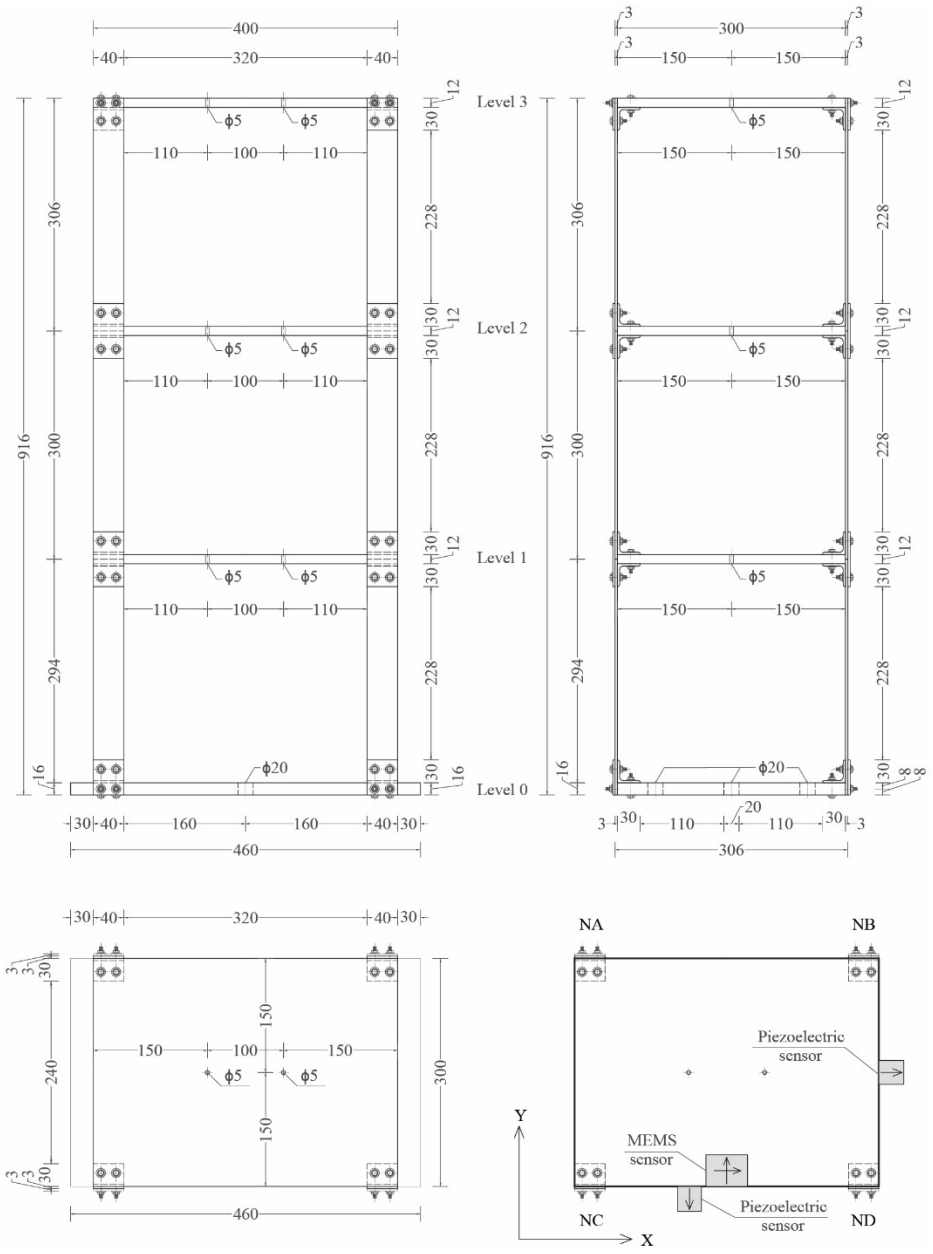

Figure 3: Front, side, and top view of the case study with sensor layout.

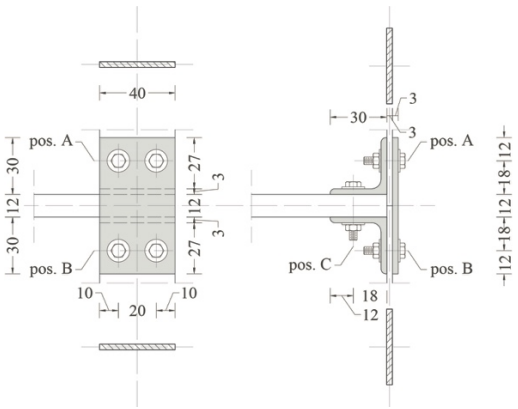

Figure 4: Detail of the connection between columns and plates.

In a preliminary analysis, the proposed monitoring system and two mono-axial piezoelectric sensors have been mounted on the last level of the structure, as shown in Fig. 3 and 5, in order to collect the response of an impulsive excitation along the same two acceleration channels (i.e., X and Y with reference to Fig. 3).

In a second analysis, only the proposed embedded system has been used to monitor the structural conditions under environmental excitation. In this case, several structural configurations (described in Tab. 1) have been reproduced in row, in order to simulate different operative and damaged conditions. After a "training" phase with the reference setup (U, represented in Fig. 3 and 5), four configurations characterized by different mass distributions have been considered. The first three conditions consist of an increase in the floor masses of around 12% (i.e., 1.5 kg steel elements placed on the floor plates), at the first level (MA), at the first and second levels (MB), and at all three levels (MC). Then, in condition MD, an additional mass of 1.5 kg has been introduced at the third level. Subsequently, all the additional masses have been removed in order to bring the structure back to its initial state (R). Then, two damaged configurations have been induced: the first consisted of loosening two bolts in position A for the node NA (with reference to Fig. 3 and 4) at the second level, while in the second configuration two additional bolts in the same position at the first level have been loosened.

Condition	Description	Duration [s]
U	Initial configuration	585
MA	Additional mass of 12% at level 1	605
MB	Additional masses of 12% at levels 1 and 2	610
MC	Additional masses of 12% at levels 1,2 and 3	550
MD	Additional masses of 12% at levels 1 and 2, 24% at level 3	605
R	All additional masses removed	605
DA	Loosened bolts at level 2	590
DB	Loosened bolts at levels 1 and 2	650

Table 1: Summary of the progressively induced structural conditions.

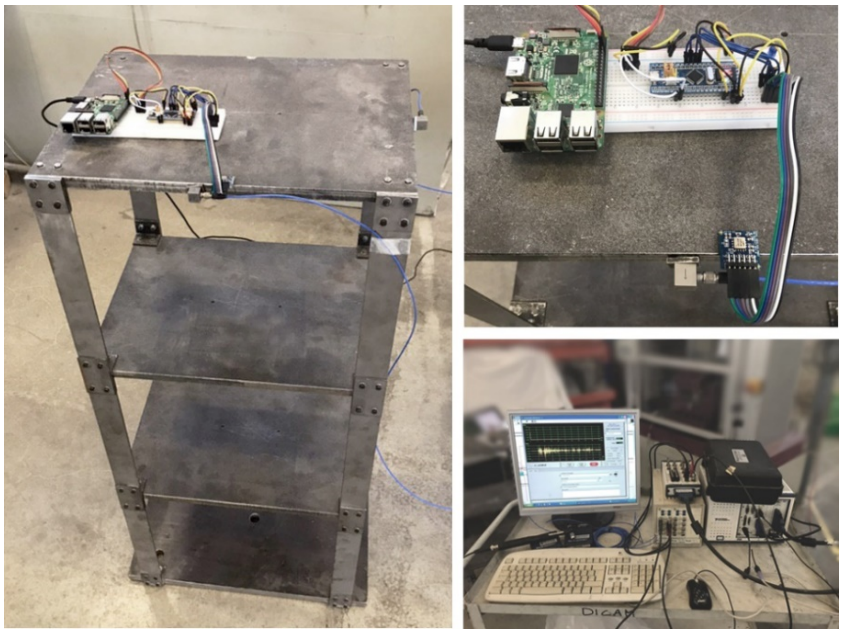

Figure 5: Model equipped with the proposed technology and the traditional sensors (left), detail of the sensor disposition (right-up), and traditional monitoring station used with piezoelectric sensors (right-down).

Acceleration data on all channels have been collected with a sampling rate of 100 Hz through the MEMS sensor and 1000 Hz through the piezoelectric accelerometers. The total duration of the experimental tests of the second analysis is 4800 seconds.

3.2 Considerations on the signal quality

The acceleration data collected by piezoelectric sensors have been first compared to those collected using the MEMS sensor. In Fig. 6, the time histories collected along direction Y (with reference to Fig. 3) after an impulsive excitation in the same direction, over a 30-second time window, are reported. Moreover, in Fig. 7 the intervals 0-50 Hz of the Fourier spectra of these signals are represented.

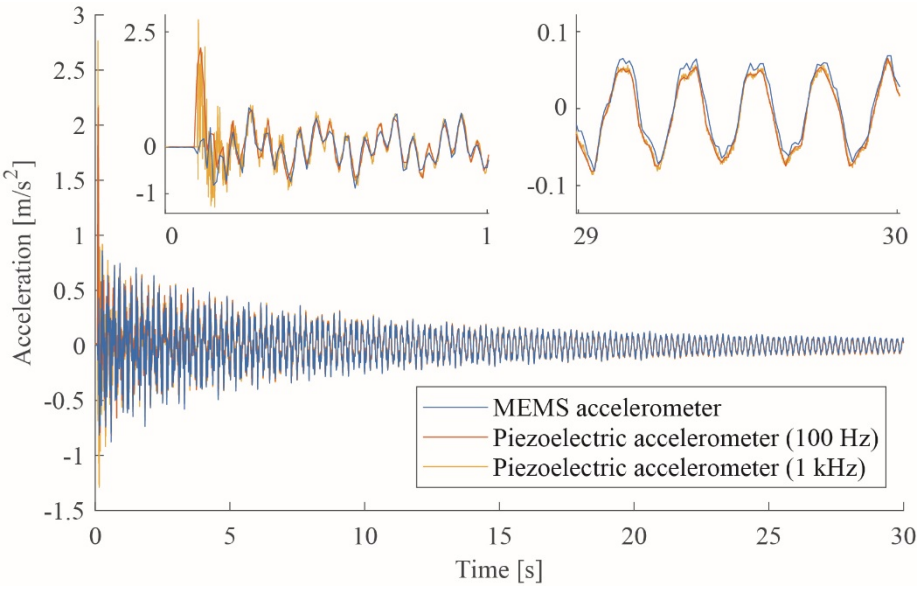

Figure 6: Comparison between the acceleration impulse responses in Y direction collected by the piezoelectric and MEMS accelerometers. In the upper part of the figure, two zoomed windows of 1 second are reported.

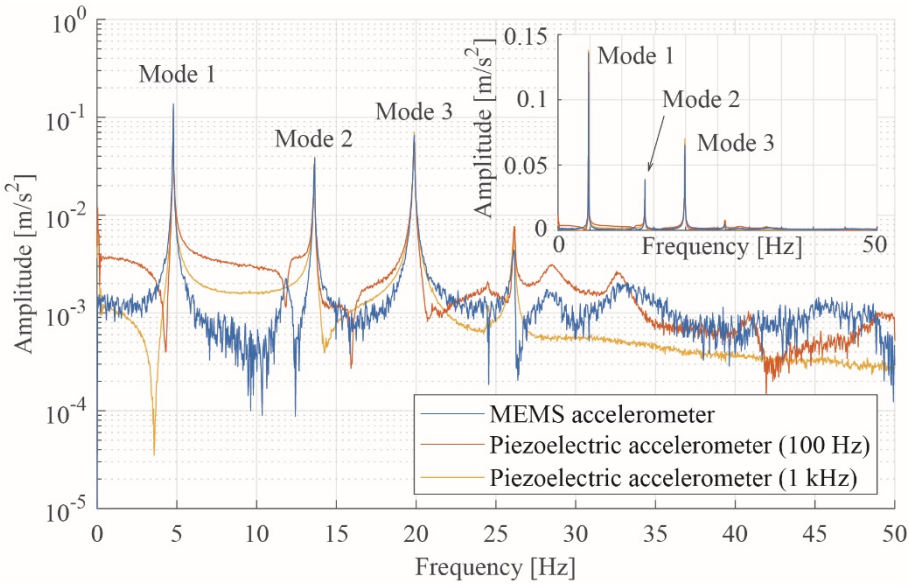

Figure 7: Fourier spectra obtained from the impulse responses. The main figure is represented on logarithmic scale, while the upper graph is on linear scale.

In particular, the first signal is the acceleration collected by the MEMS sensor, which is compared to the second signal obtained through the piezoelectric accelerometer, downsampled by a factor 10 in order to have the same sampling rate as the first. The third signal is the original acceleration recorded by the piezoelectric sensor, reported as a reference.

From Fig. 6 it is possible to observe, especially in the first part of the recording, how the signal obtained by using the piezoelectric sensor is considerably more accurate than the one measured through the MEMS sensor, also for the downsampled version. In fact, the ratio between the root mean square (RMS) of the difference between the two signals (considering the downsampled version for the piezoelectric sensor) and the RMS of the signal obtained through the MEMS sensor is equal to 0.42. However, it is possible to observe how the upper parts of first three peaks in the frequency spectra reported in Fig. 7, are almost coincident. In particular, the main differences are for lower amplitudes, and noticeable only by representing the spectrum on a logarithmic scale. For this reason, even if the MEMS sensor is less accurate, it still allows to correctly identify the first natural frequencies. The three identified peaks also correspond to the natural frequencies associated with the first three translational vibration modes in the Y direction of a finite element model designed to confirm the results obtained from modal analysis.

3.3 Results of the proposed system

Following the analyses performed to evaluate the signal quality, the modal identification algorithm has been applied using only the MEMS sensor under environmental vibration.

The wavelet function Fejér-Korovkin 14 has been chosen to build the filter bank used in the first phase of the identification algorithm. The wavelet transform has been performed up to the fifth order, generating a bank of 32 bandpass filters. Following the clustering procedure, based on the parameters computed over a 10-seconds initialization window, three signal components have been selected, associated with the first three modal responses.

With the application of DESA-1 algorithm, each value of the instantaneous natural frequencies has been computed considering only 5 acceleration samples. In order to lighten the computed parameters, a median value of the frequency has been calculated every 5 seconds. The results obtained for each vibration mode have been then uploaded to the cloud platform. The instantaneous frequency for each identified mode is represented over time in Fig. 8 as a solid line, while the state representing the reference condition, computed as the median value of each natural frequency over a training window of 50 samples obtained during the state U, is reported as dotted line.

During the real-time processing procedure, the estimated frequencies exceeded the limits of bandpass filters in two instants, indicated as vertical violet dashed lines in Fig. 8, where the filter bank has been updated following the scheme of Fig. 2. It can be noted that the proposed algorithm has shown particularly suitable also for detecting sudden changes in modal parameters, since the results reported in Fig. 8 has been calculated continuously, without interrupting the identification procedure during the changes in structural conditions.

Within the cloud platform, a script has been written to evaluate the frequency variation with respect to the baseline, in order to indicate any possible state of damage. The frequency variation has been evaluated with respect to the reference value computed during the training window. The results for the three identified modes and an average trend are reported as functions of time in Fig. 9. In this application, the criterion selected to define a condition as probably damaged consists in evaluating whether the average instantaneous frequency variation exceeds more than twice the maximum average variation value encountered in the training window.

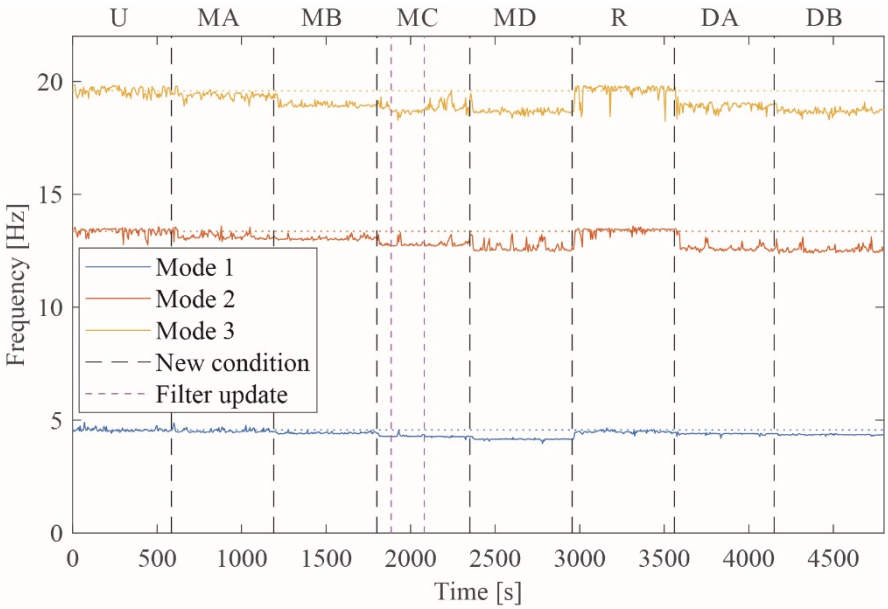

Figure 8: Instantaneous frequencies estimated through the proposed system during the experimental tests.

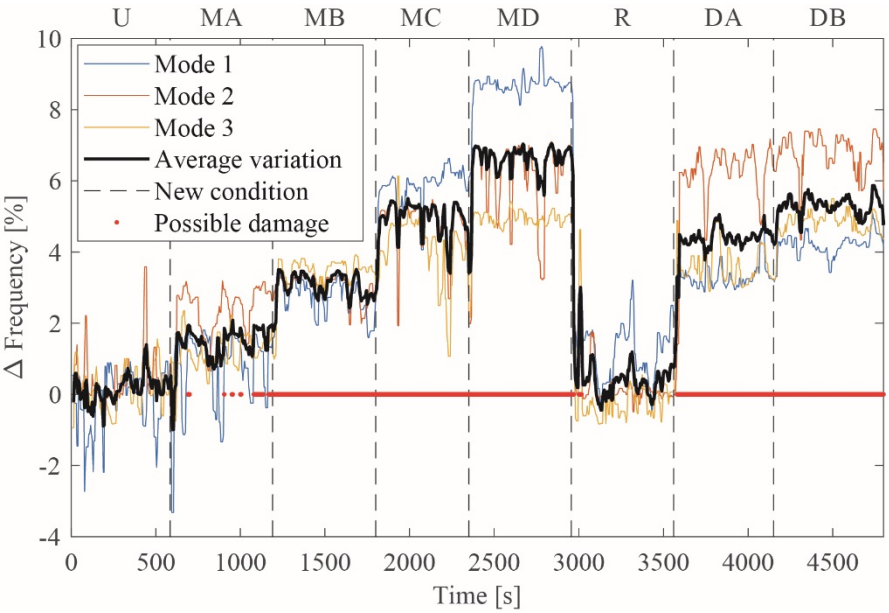

Figure 9: Instantaneous variation of frequency and damage detection performed through the algorithm written within the online platform.

In Fig. 9, the red dots represented on the time axis indicate the instantaneous detection of a "possibly damaged" configuration. Where the red sign appears continuous, a persistent damaged condition is detected, in which the frequency variation does not return within the bounds evaluated during the training interval. It is observable how all the operational and damaged condition have been indicated as "possibly damaged", with some missing alarms for the MA condition, where the frequency variation is in some parts comparable with the values of the training window. However, by applying a median filter with a window of 10 samples to the instantaneous frequency variations, the whole condition MA would be referred to as "possibly damaged" and the detection would become more robust.

4 CONCLUSIONS

In this paper, the implementation of a modal identification and damage detection algorithm on a specifically-designed electronic monitoring system has been presented. The algorithm proved to be particularly effective for the identification of dynamic parameters of a scale laboratory model, even if the quality of the accelerations obtained through the implemented MEMS sensor is lower than the quality of the recordings collected by piezoelectric accelerometers. In fact, also small variations in natural frequencies have been evaluated with sufficient accuracy to allow the distinction between all the considered structural configurations.

On-board processing was made possible by the simplicity and low amount of memory required by the identification algorithm. This allows to apply the proposed method through small, non-invasive and low-cost smart devices.

REFERENCES

[1] ICOMOS charter (2003) Principles for the Analysis, Conservation and Structural Restoration of Architectural Heritage. Ratified by the ICOMOS 14th General Assembly, in Victoria Falls, Zimbabwe, October 2003.

[2] A. Saisi, C. Gentile, A. Ruccolo, Continuous monitoring of a challenging heritage tower in Monza, Italy. *Journal of Civil Structural Health Monitoring*, **8(1)**, 77–90, 2017.

[3] Z. Chen, X. Zhou, X. Wang, L. Dong, Y. Qian, Deployment of a smart structural health monitoring system for long-span arch bridges: a review and a case study. *Sensors*, **17(9)**, 2151, 2017.

[4] A.B. Noel, A. Abdaoui, T. Elfouly, M.H. Ahmen, A. Badawy, M.S. Shehata, Structural health monitoring using wireless sensor networks: a comprehensive survey. *IEEE Communications Surveys & Tutorials*, **19(3)**, 1403–1423, 2017.

[5] J.P. Lynch, K.J. Loh, A summary review of wireless sensors and sensor networks for structural health monitoring. *The Shock and Vibration Digest*, **38(2)**, 91–128, 2006.

[6] H. Jo, S.-H. Sim, T. Nagayama, Development and application of high-sensitivity wireless smart sensors for decentralized stochastic modal identification. *Journal of Engineering Mechanics*, **138(6)**, 683-694, 2012.

[7] Y. Gao, B.F. Spencer Jr, M. Ruiz-Sandoval, Distributed computing strategy for structural health monitoring. *Structural Control and Health Monitoring*, **13**, 488-507, 2006.

[8] A.T. Zimmerman, M. Shiraishi, R.A. Swartz, J.P. Lynch, Automated modal parameter estimation by parallel processing within wireless monitoring systems. *Journal of infrastructure systems*, **14(1)**, 102-113, 2008.

[9] S.-H. Sim, J.F. Carbonell-Márquez, B.F. Spencer Jr, H. Jo, Decentralized random decrement technique for efficient data aggregation and system identification in wireless smart sensor networks. *Probabilistic Engineering Mechanics*, **26**, 81-91, 2011.

[10] A. Sadhu, S. Narasimhan, A decentralized blind source separation algorithm for ambient modal identification in the presence of narrowband disturbances. *Structural Control and Health Monitoring*, **21**, 282-302, 2014.

[11] S. Jeong, Y. Zhang, R. Hou, J.P. Lynch, H. Sohn, K.H. Law, A cloud-based information repository for bridge monitoring applications. J.P. Lynch ed. *Proceedings of the SPIE Smart Structures/NDE Conference*, Baltimore, Maryland, USA, 2016.

[12] S. Quqa, L. Landi, P.P. Diotallevi, Vibration-based structural damage detection using a decentralized network with limited sensors. *16th European Conference on Earthquake Engineering (16ECEE)*, Thessaloniki, Greece, 2018.

[13] P. Maragos, J.F. Kaiser, T.F. Quartieri, Energy separation in signal modulations with application to speech analysis. IEEE Transactions on Signal Processing, **41(10)**, 3024-3051, 1993.

COMPDYN 2019
7th ECCOMAS Thematic Conference on
Computational Methods in Structural Dynamics and Earthquake Engineering
M. Papadrakakis, M. Fragiadakis (eds.)
Crete, Greece, 24–26 June 2019

BRIDGE-PIER SAFETY EVALUATION METHOD USING NONDESTRUCTIVE IMPACT TESTS

Mintaek, Yoo[1], Myungjae, Lee[1], Kihyun, Kim[1], Jungjun, Park[1] and Il-Wha Lee[2]

[1] Railroad Structure Research Team, Korea Railroad Research Institute, 176 Cheoldobangmulgwan-ro, Uiwang-si, Gyeonggi-do, 16105, Republic of Korea.
e-mail: thezes@krri.re.kr, myoungjae@krri.re.kr, kimkh738@krri.re.kr, jjpark@krri.re.kr

[2] Advanced Infrastructure Research Team, Korea Railroad Research Institute, 176 Cheoldobangmulgwan-ro, Uiwang-si, Gyeonggi-do, 16105, Republic of Korea.
e-mail: iwlee@krri.re.kr

Abstract

This study aims to establish an evaluation method for bridge pier safety. To achieve this aim, a full-scale bridge pier was constructed, and a series of nondestructive tests were conducted using impact loads. The overburden loaded in the full-scale bridge pier was increased from 0 tonf up to 25 tonf by increments of 2.5 tonf. Impacts were applied to the upper and lower parts of the bridge pier in longitudinal, transverse, and lateral directions to analyze the behaviors of the bridge pier. Accelerometers were used to measure acceleration responses to impacts. Test results were converted to natural vibration frequencies according to impact direction and overburden using a fast Fourier transform algorithm. In addition, phase differences were utilized to analyze the behaviors of the bridge pier from the 1st to 4th modes. The effect of scouring was numerically analyzed. Ultimately, the safety of the bridge pier could be reasonably evaluated through the 2nd and 3rd modes.

Keywords: Full-Scale Bridge Pier, Nondestructive Test, Overburden, Mode Number.

1 INTRODUCTION

Special structures, such as railway bridges, and their social and economic impact are receiving more attention than ever. When a structure demands careful maintenance, an appropriate maintenance technology is needed to retain a target performance in accordance with the processes of rational inspection, measurement, evaluation, decision-making, maintenance, and reinforcement. In practice, however, most inspection works depend on manpower. Maintenance works also often lack data about past works, major drawings, and construction records, which are necessary for sufficient examination. Railway bridges do not collapse suddenly; they give signs in advance. The conventional practices of occasional manpower-centered inspection or regular inspection using a vehicle at a considerably long interval have limitations in identifying such signs. Many studies have been performed to develop a technology of detecting the collapse of bridge pier in advance, both at home and abroad. In Schoharie creek, New York, USA, in April, 1987, a bridge was washed away because of scour at the bottom of the footing foundation. This accident caused enormous financial damages and many casualties. After the tragic accident, the research fund for only the scour issue received nearly USD11M. Since then, research projects have been supported at the national level under the remit of National Cooperation Highway Research Program (NCHRP). Additionally, based on the outcomes of active research and assessment programs after 1987, the Federal Highway Administration (FHWA) prepared technical manuals (e.g., Hydraulic Engineering Circular (HEC)-18 (2012), HEC-20 (2001), and HEC-23 (1997)) for bridge scour, channel stabilization, and countermeasures and applied them to the analysis and designs of bridge scour.

However, most studies have focused on bridges built on sandy soils. Therefore, they did not consider the scour characteristics of the ground. The formula proposed by HEC-18 is commonly used for scour analysis. Because this formula is based on experimental data about sand, it is not valid or applicable to different soil conditions. Recently, the scour rate over time and time effects are considered for clay soils [1], and a new approach using erosion index is applied to rock sites [2].

In the Netherlands, the national project called “Dutch Delta Works” has been conducted to systematically and comprehensively investigate scour tendencies since 1953. This research project is led by Delft Hydraulics and the Ministry of Transport, Public Works, and Water Management. Delft Hydraulics performs numerous indoor experiments by considering various parameters about hydraulic characteristics and scour materials. A semi-empirical formula comprising functions of time and locations was derived. A comprehensive technical manual about the scour phenomenon was also proposed. This is the Breusers-equilibrium method and leverages the mean velocity of flow at the maximum scour depth, relative turbulent intensity, and dominant time characteristics [3].

In Japan, a method of evaluating the safety of foundations is being developed, utilizing the variation of natural frequency based on the vibration of the bridge pier caused by water-flow force. A soundness diagnostic index is also being prepared [4]. Keita and Michiko [5] proposed a soundness diagnostic index correlated to natural variation frequency by using the results of model experiments and field measurements. Bridge-collapse accidents are most likely to occur because of the scour, settlement, and cracks of bridge piers. The stability of the bridge substructure is closely related to bridge safety. Unfortunately, most safety inspections and tests in South Korea focus on issues about

bridge materials and superstructures. Thus, no quantitative evaluation method for substructure has been established. This study leverages a full-scale bridge pier where nondestructive impact tests were performed to achieve a method of deriving natural frequencies that could be used to assess the safety of bridge piers. Furthermore, a mode number analysis was conducted to ascertain the tendency of bridge behaviors under impact conditions.

2 NATURAL MODE NUMBER ANALYSIS OF BRIDGE PIER

2.1 Dimensions of full-scale bridge pier

We used a direct foundation type bridge pier to evaluate the characteristics of deteriorated foundations. The slab of the bridge foundation was 5.15-m long, 2.42-m wide, and 0.50-m tall. The pier was constructed to have a height of 4.5 m by repeating the process of placing 1.5-m thick concrete sections and curing three times. The length and width of the pier were 4.15 m and 1.42 m, respectively. Fig. 1 shows the dimensions of the full-scale bridge pier.

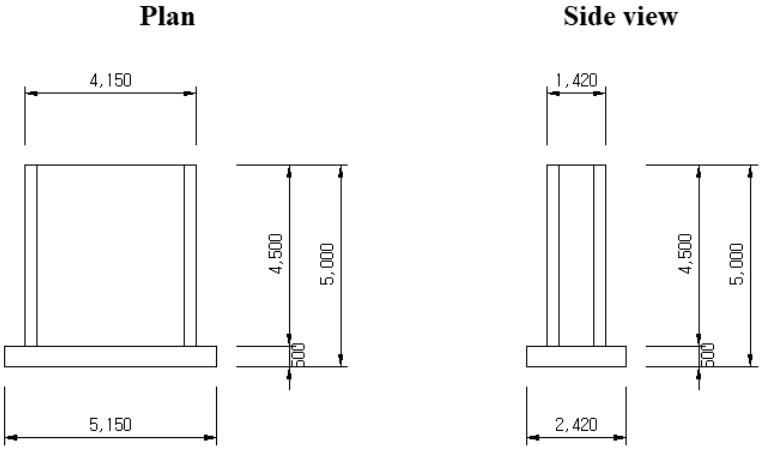

Figure 1: Dimension of full-scale bridge pier.

2.2 Mode number analysis of bridge pier

Before the full-scale bridge-pier test was conducted, the eigenvalues of the bridge pier were derived by using [6], a finite element program, to analyze the behaviors of the pier. The dimensions of the full-scale bridge pier were applied to the analysis. Accordingly, the behaviors of the bridge pier from the 1st to 4th modes could be analyzed according to the eigenvalues. The analysis result is illustrated in Fig. 2. In the 1st mode, the displacement occurred in the longitudinal direction. In the 2nd mode, the displacement occurred in the transverse direction. In the 3rd mode, the bridge pier showed a torsional behavior. In the 4th mode, the middle part of the pier had the largest displacement. The mode number analysis revealed that the transverse impacts caused natural vibration frequencies corresponding to the 2nd mode, whereas the longitudinal impacts generated natural frequencies corresponding to the 1st, 3rd, and 4th modes. Table 1 presents natural frequencies for the 1st, 2nd, 3rd, and 4th modes. Based on the analysis of eigenvalues of the bridge pier, impact directions could be selected to derive the mode numbers of the full-scale bridge pier.

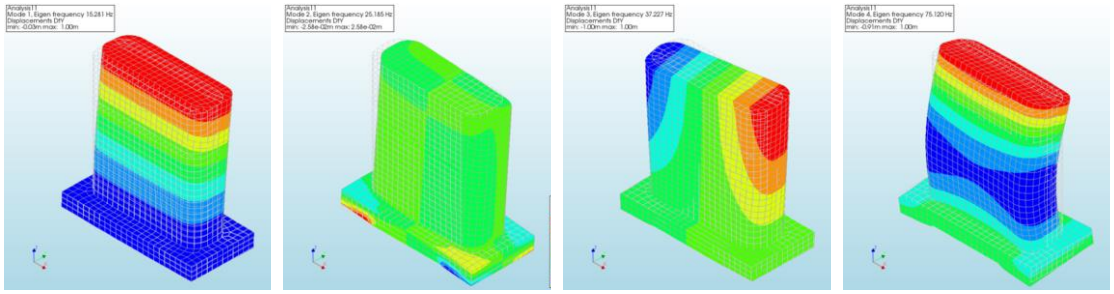

(a) 1st mode (b) 2nd mode (c) 3rd mode (d) 4th mode

Figure 2: Mode numbers of the bridge pier through a numerical analysis.

Mode number	**Natural vibration frequency (Hz)**	**Direction of a test impact where a mode number can be driven**
1	**15.28**	**Longitudinal**
2	**25.19**	**Transverse**
3	**37.23**	**Longitudinal (lateral)**
4	**75.12**	**Longitudinal**

Table 1: Natural frequencies and impact directions for the full-scale bridge-pier test through the analysis of eigenvalues.

3 TEST CONDITIONS AND RESULTS

3.1 Test method

Eight accelerometers and an impact hammer were used to evaluate the safety of the bridge pier in a series of nondestructive tests. Fig. 3 illustrates the test cases according to impact directions. The accelerometers were installed at 3 points: 50 cm from the top; 50 cm from the bottom; and at the middle point of the bridge pier. Two accelerometers were attached to each point to measure accelerations in both longitudinal and transverse directions. Apart from the six accelerometers, another two were attached to the external side of the bridge pier in order to measure accelerations in the transverse direction. Impacts were applied in six directions. Table 2 presents the information of the test cases.

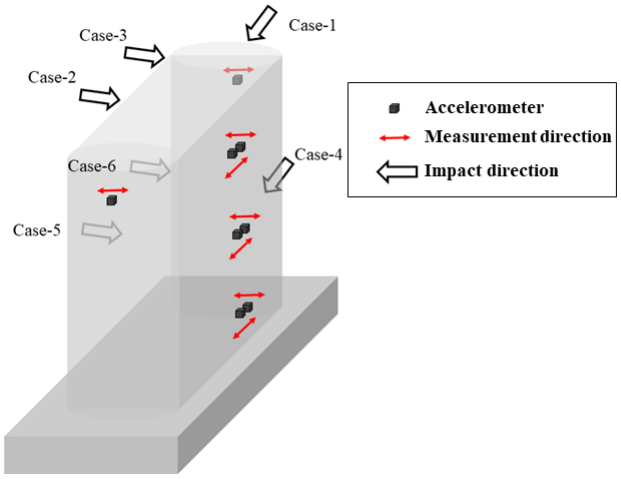

Figure 3: Schematic of accelerometer locations and impact directions.

Test case	**Impact direction**	**Impact location**
Case-1	Transverse	Top
Case-2	Longitudinal	Top
Case-3	Longitudinal (lateral)	Top
Case-4	Transverse	Middle
Case-5	Longitudinal	Middle
Case-6	Longitudinal (lateral)	Middle

Table 2: Natural frequencies through the analysis of eigenvalues and the selection of impact directions for the full-scale bridge-pier test.

3.2 Analysis method of test data

Figure 4(a) shows the accelerations measured in the test. In the case of an impact/vibration test, natural vibration frequencies and modes can be determined by analyzing a spectrum of repeated waveforms obtained from by repeating recorded waveforms multiple times. The fast Fourier transform (FFT) method, which can divide signals at each frequency, is the most appropriate for spectrum analysis. As shown Fig. 4(b), the natural vibration frequencies of the bridge pier in a frequency domain could be derived using FFT. Fig. 4(c) displays the phases of measurement locations. Accordingly, the overall behavior of the bridge pier could be analyzed by obtaining the phase differences among accelerometers.

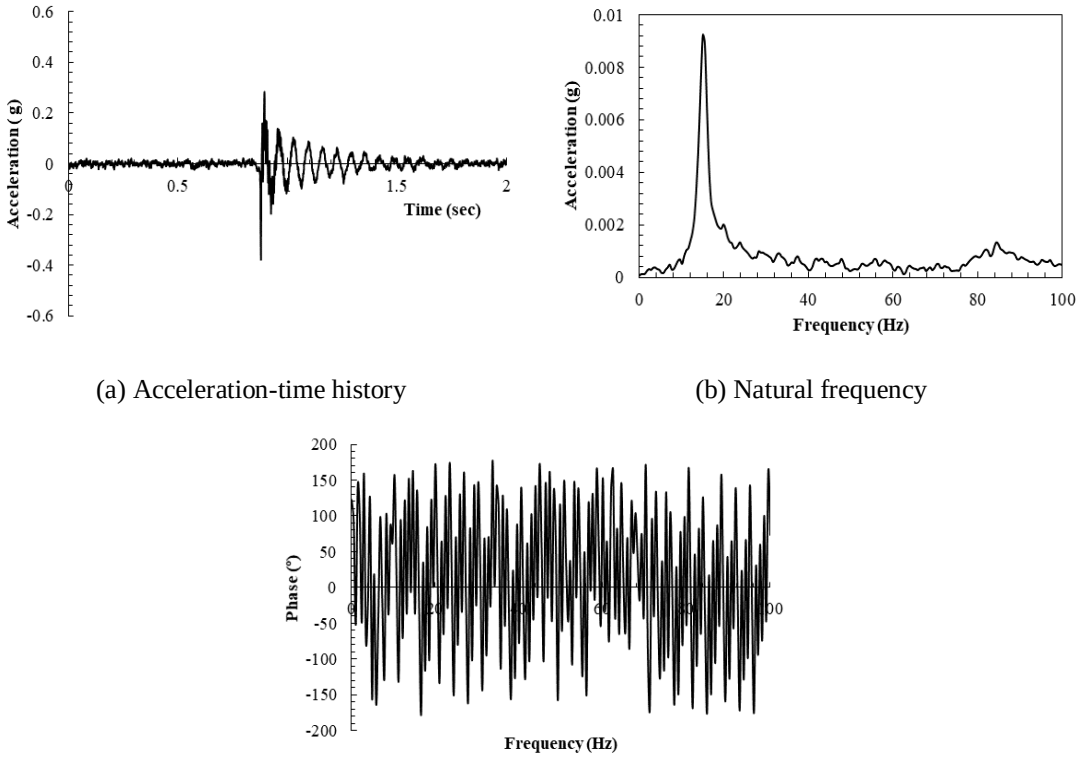

(a) Acceleration-time history

(b) Natural frequency

(c) Phase

Figure 4: Results of the analysis using accelerometers.

3.3 Derivation of mode numbers in the full-scale bridge pier test

Mode numbers of the bridge pier were analyzed, and the natural vibration frequencies for each mode were derived in a series of tests. Fig. 5(a) shows the natural vibration frequencies of Case 2, where the impacts were applied to the top of the bridge pier in the longitudinal direction. The natural vibration frequencies were around 15.24 Hz. Additionally, phases were calculated from measurements of each height to analyze the behavior of the bridge pier. Fig. 5(b) illustrates the phase differences among the different locations. All phase differences, where a natural frequency occurred, tended to converge on 0°. This indicates that all the accelerometers at each height were displaced in the same direction. Thus, the bridge pier moved in the same direction. This was analyzed to show a similar tendency to the 1st mode of the eigenvalue analysis. Fig. 5(c) shows the result of Case 1, where the natural vibration frequencies were derived at each height by applying a transverse impact to the top of the bridge pier. The natural vibration frequencies were about 22.4 Hz, which was higher than those in the longitudinal direction by about 7 Hz. This difference of natural vibration frequency was analyzed to be attributable to the fact that the bridge pier had a large stiffness in the transverse direction than in the longitudinal direction. Thus, the difference of stiffness was influential on natural vibration frequencies. As shown in Fig. 5(d), the phase difference was analyzed to identify the behavior of the bridge pier in the transverse direction. Like the behavior of the 1st mode, the phase difference was analyzed to converge on 0° when a natural vibration frequency occurred. This was similar to the behavior of the 2nd mode, which was identified by the eigenvalue

analysis of the bridge pier. Fig. 5(e) presents the natural vibration frequencies of Case 3, where acceleration was measured by applying an impact to the lateral part of the top of the bridge pier. Clearly distinct natural vibration frequencies occurred at two locations. These natural vibration frequencies were 15.14 Hz and 54.19 Hz. Regarding the phase differences of Fig. 5(f), one phase difference at around 15.14 Hz tended to converge on 0°. Because this natural vibration frequency was similar to the behavior of the 1st mode, it was predicted. However, the phase difference at around 54.19 Hz converged on 180°. This result indicates opposite behaviors in the lateral part of the bridge pier: a torsional behavior. This behavior was similar to that of the 3rd mode. Accordingly, when a longitudinal impact was applied to the lateral part of the bridge pier, the 1st mode occurred followed by the 3rd mode: a torsional behavior. Fig. 5(g) magnified the range of 60~100 Hz in the result of Case 2. Whereas there was no clear natural frequency in the range of 60~100 Hz, unlike the other results, the phase difference between the top and the bottom of the bridge pier converged on 0°. Both the phase difference between the middle and the top of the bridge pier and that between the middle and the bottom were 180°, indicating an opposite behavior. This was similar to the behavior of the 4th mode in the eigenvalue analysis. Thus, the 1st mode occurred first. Then, as the impact vibration decreased, the 4th mode appeared.

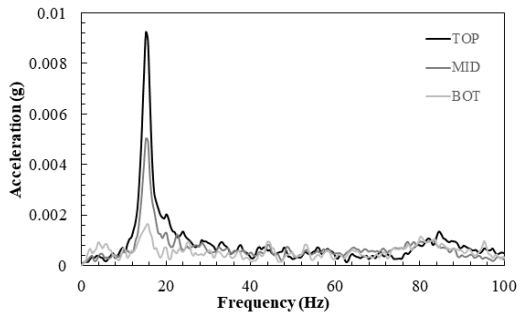

(a) Natural frequency of 1st mode

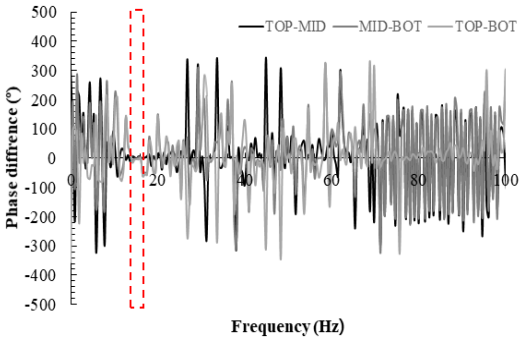

(b) Phase difference of 1st mode

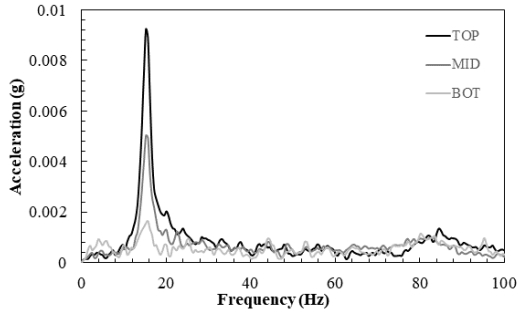

(c) Natural frequency of 2nd mode

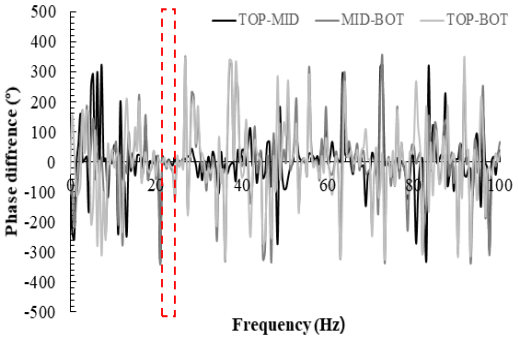

(d) Phase difference of 2nd mode

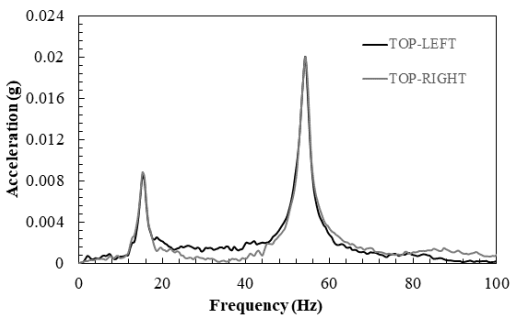

(e) Natural frequency of 3rd mode

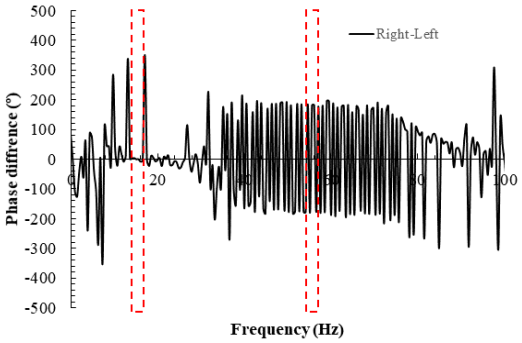

(f) Phase difference of 3rd mode

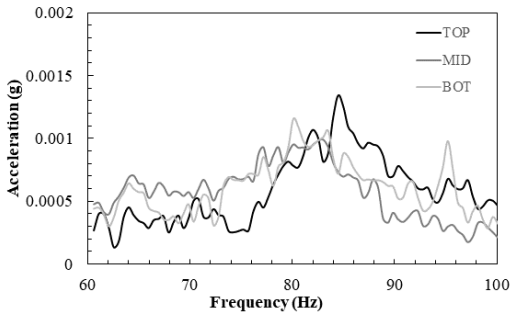

(g) Natural frequency of 4th mode

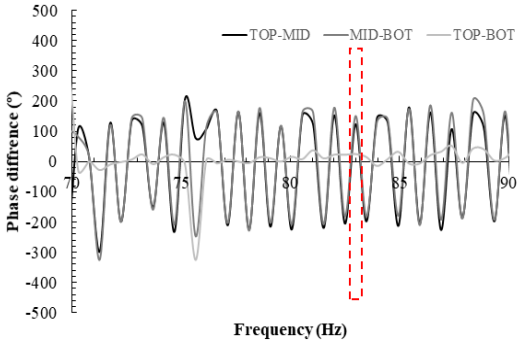

(h) Phase difference of 4th mode

Figure 5: Natural frequency and phase difference of each mode.

In a series of the full-scale bridge-pier tests, the natural vibration frequencies of the bridge pier were derived using accelerations, and the behaviors from the 1st to 4th modes were analyzed based on phase differences. As presented in Table 3, the natural vibration frequencies of the full-scale bridge-pier test were compared with the results of the numerical eigenvalue analysis. The full-scale bridge-pier test and the eigenvalue analysis showed natural vibration frequencies in a similar range at an error rate of less than 5% in all the modes (1st to 4th).

Classification	**1st mode**	**2nd mode**	**3rd mode**	**4th mode**
Natural frequency of the eigenvalue analysis (Hz)	15.39	23.18	52.04	88.30
Natural frequency of the full-scale test (Hz)	15.14	22.4	54.19	83.94
Error rate (%)	1.62	3.37	-4.13	4.94

Table 3: Comparison of natural frequencies in each mode.

4 ANALYSIS OF PARAMETERS

4.1 Numerical analysis of scour effect

Owing to the limitations of the full-scale bridge pier test, the effect of scour on the na tural vibration frequency was examined by a numerical analysis. Regarding the analysis condition, the scour progress was described by removing one side of the soil under the a butment by increments of 10% until 50% remained. Fig. 6 illustrates the analysis conditi on.

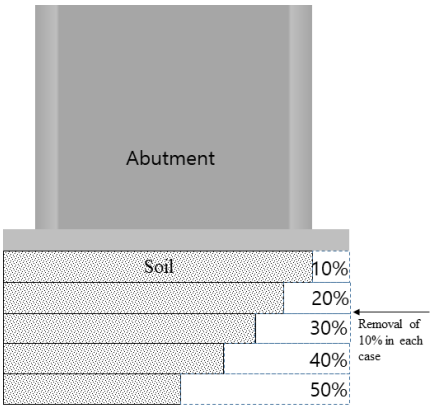

Fig. 6 Numerical analysis condition for the effect of scour progress

The scour effect was analyzed by setting the scour progress to five cases. Figure 7 shows the variation of natural vibration frequencies according to scour progress, which was obtained with the numerical analysis. As the scour proceeded, every natural vibration frequency from the 1st to 4th modes decreased. As presented in Table 4, the natural vibration frequency decreased from 15.39 Hz to 10.24 Hz along with the increase of overburden in the 1st mode. Thus, the maximum decreasing rate of natural vibration frequency was 33% in the 1st mode. The maximum decreasing rates of natural vibration frequency were 57%, 55%, and 23% in the 2nd, 3rd, and 4th modes, respectively. The scour was analyzed to be significantly influential in the 2nd and 3rd modes. Therefore, the test methods of the 2nd and 3rd modes turned out to be reasonable for identifying the effects of soil scour. Moreover, as the 3rd mode indicated a torsional behavior of the bridge pier. It was appropriate to evaluate the scour effect.

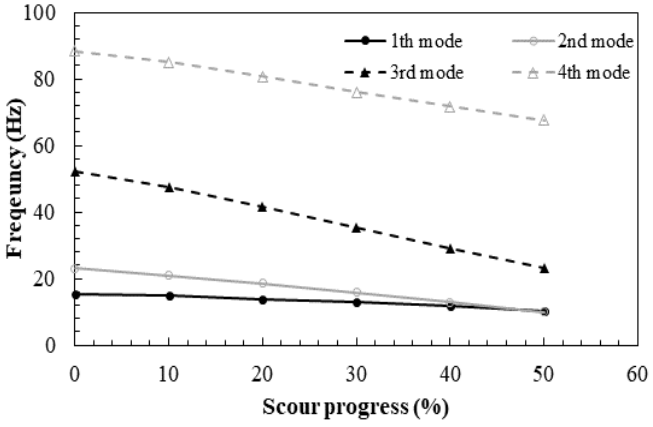

Figure 7: Variation of natural vibration frequency according to scour progress.

Scour progress (%)	1st mode	2nd mode	3rd mode	4th mode
0	15.39 Hz	23.18 Hz	52.04 Hz	88.30 Hz
10	15.14 Hz	22.40 Hz	54.19 Hz	83.94 Hz
20	13.95 Hz	18.53 Hz	41.56 Hz	80.65 Hz
30	12.92 Hz	15.80 Hz	35.23 Hz	76.01 Hz
40	11.69 Hz	12.90 Hz	28.98 Hz	71.65 Hz
50	10.24 Hz	9.95 Hz	23.28 Hz	67.52 Hz

Table 4: Natural vibration frequencies of each mode according to scour progress.

5 CONCLUSIONS

This study leveraged a full-scale bridge pier to conduct an indoor test. The scour effect was also numerically analyzed. Acceleration was measured for the bridge pier under an impact load, and both natural vibration frequencies and phase differences were obtained from the measurements. In this way, a new method of evaluating the safety of bridge piers was established. Moreover, all mode numbers of the bridge pier were analyzed. The results of this study can be summarized as follows.

- (1) Eigenvalues and mode numbers of the bridge pier were derived by conducting a numerical analysis. Thus, based on the full-scale bridge pier test, a method of evaluating the safety of bridge piers was established, which could derive 1^{st}, 2^{nd}, 3^{rd}, and 4^{th} modes.
- (2) The effects of scour on the natural vibration frequency of bridge pier was numerically analyzed. As the scour progress increases, the natural vibration frequency of every mode decreases. The scour effect was largest in the 2^{nd} and 3^{rd} modes. The scour progress at the soil under the bridge-pier foundation can be identified by utilizing the 3^{rd} mode, showing the torsional behavior of the bridge pier.

ACKNOWLEDGMENT

This research was supported by a grant from R&D program of the Korea Railroad Research Institute, Republic of Korea.

REFERENCES

[1] J.L. Briaud, H.C. Chen, K.W. Kwak, S.W. Han, F.C.K. Ting, Multiflood and multilayer method for scour rate prediction at bridge piers. *Journal of Geotechnical and Geoenvironmental Engineering*, **127**(2), 114-125, 2001.

[2] G.W. Annandale, R.J. Wittler, J.F. Ruff, T.M. Lewis, Prototype validation of erodibility index for scour in fractured rock media. *Water Resources Engineering '98*, 1096-1101, ASCE, 1998.

[3] H.N.C. Breusers, *Conformity and time scale in two-dimensional local scour*. 1966

[4] Masahiko S., Satoshi W., Akira F., Tomoyasu S., and Katsuya O. (2010) "Proposal on a method for identifying the natural frequency of a railway piers during river rising." *Proceedings of the Japan Society of Civil Engineers* F, Vol. 66, No 4, pp. 524-535. (*In Japanese*)

[5] K. Abe, M. Endo, State Monitoring Method on the Soundness of River Bridge Pier (Special Issue Disaster Management Technology), *Report of Railway Research Institute–RTRI report: Railway Integrated Technology Journal*, **30**(3), 29–34. 2016. (*In Japanese*)

[6] F. Diana, *Finite element analysis user's manual-release 10.2*. TNO DIANA. 2017.

COMPDYN 2019
7th ECCOMAS Thematic Conference on
Computational Methods in Structural Dynamics and Earthquake Engineering
M. Papadrakakis, M. Fragiadakis (eds.)
Crete, Greece, 24–26 June 2019

SEISMIC ANALYSIS OF AN EMERGENCY HOSPITAL IN SOUTH OF SWITZERLAND INCLUDING SOIL-PILE-STRUCTURE INTERACTION EFFECTS

Niloufar Ghazanfari[1], Mohsen Rostami[1], Setayesh Rotami[1], Rolf Liechti[2], and Sassan Mohasseb[1]

[1] Department of Civil Engineering, Smteam GmbH, Zurich, Switzerland
E-mail: Smteam.gmbh@gmail.com

[2] Technical Manager, Mange and Müller AG Engineers, Bern, Switzerland

Abstract

In this study the effects of (SPSI) forces on the seismic response of a hospital in Brig, Switzerland were investigated. The building is an existing reinforced concrete construction with concrete columns. The primary lateral loads are resisted by a reinforced concrete core and a number of shear walls and massive concrete columns. Due to the importance of the building and its potential danger in failure cases of the loadbearing structure, earthquake analysis was first carried out by using a 3D finite element model for the entire structure and FCONE program for the soil under the structure. FCONE program was developed by Smteam for soil modeling based on CONE Model which was proposed by J.P.Wolf from ETH. This program utilizes the equivalent dynamic modeling concept in the analysis of soil dynamics and pile-foundation interaction. The implementation of simulation was conducted in two different conditions: namely fixed-base behavior and soil-structure interaction are considered. In this case, soil-structure interaction is considered by assigning equivalent springs and dashpots located under foundation and the analyses were carried out directly in the time domain for considering the effects of interaction. It is shown that the effects of soil-structure-interaction are demonstrated as increasing the period of vibrations and the displacements. Based on the results obtained by using CONE method, the period of vibration in the case of concentrated piles with the correction factor for pile-group action, exhibiting the value of (1.2 seconds), which is increased up to 42% compared with the case of fixed-based (0.7 seconds). Besides, a comparison was made between the structural responses of the obtained Cone method and 3D finite element simulation in ABAQUS which indicated that these results were in good agreement with direct results. It was concluded that Cone model as a convenient, fast and rather accurate method can be applied for foundation vibration and dynamic soil-structure-interaction analysis in a practical engineering projects whenever possible.

Keywords: Seismic analysis, Soil-Pile-structure Interaction (SPSI), Pilegroup effect, CONE Model, FEM method

1 INTRODUCTION

The soil-pile-structure interaction (SPSI) plays an important role in assessing the dynamic response to seismic ground motions or vibrations internally generated within the structural system. It is very important to note that the SPSI can alter the superstructure's performance by influencing the dynamic properties of structure. A fundamental understanding of this complex phenomenon is essential for improvements of the structural design and construction practices, and, as a result, for reduction of loss of life and monetary damages caused by earthquakes. Extensive field testing and experimental investigations on different aspects of pile behavior have resulted in a number of empirical and approximate analytical methods for the pile-foundation design [1-6]. In addition, other studies have resulted in more rigorous schemes for pile analysis. The results of research from various studies also back up the point that dynamic impedance of foundation is affected by several geometric and material factors such as foundation shape (i.e., disk, rectangular, strip), type of soil profile (i.e., deep uniform or multi-layer deposit, shallow stratum on rock), foundation embedment (i.e., surface foundation, embedded foundation, pile foundation), shear wave velocity and type of loading (static, dynamic) [7-8]. Generally, three direct numerical approaches have so far been evolved for predicting the dynamic pile behavior. The first approach represents soil as an elastic continuum, the second represents the soil-pile system by a set of discrete masses, springs and dashpots, and the third one uses either boundary element or finite element methods based on the actual soil properties [9, 10]. The continuum model was considered to be a generalized Winkler model. The major contribution regarding this approach was carried out by Novak [11], who introduced an approximate method based on the analytical solution of Baranov [12]. The soil was considered to be made of a set of independent infinitesimally thin horizontal layers in this model. Therefore, it automatically considered wave propagation in the horizontal direction. A set of equations for stiffness and damping ratio based on frequency independent parameters were provided for a single pile under vertical vibration. Thereafter, further progress on this model was made by Novak et al. [13] and Dobry and Gazetas [14]. The reduction in soil stiffness and the increase in damping associated with strong shaking are sometimes modelled crudely in these analyses by making arbitrary reductions in shear moduli and arbitrary increases in viscous damping. Moreover, several researchers developed dynamic nonlinear finite element analysis in the time domain using the full 3-dimentional wave equations to investigate the seismic soil structure interaction [15], but is not feasible for engineering practice at present because of the time needed for the computations. A rigorous finite-element analysis of a pile foundation subjected to lateral loading was done by Kaustell et al. [16]. These numerical methods have an advantage in that they can analyze the soil–pile system as a whole. Therefore, no separate analysis is required to calculate the dynamic interaction factors for pile group analysis [17].

The major drawbacks of analytical and numerical models in prior research studies were overcome with the introduction of Cone model which applies only for shallow foundations. Wolf has rearranged and extended the concept of the cone model to cover a complete range of dynamic excitations and physical situations. This model was based on one dimensional wave propagation in cone segments with reflections and refractions at layer interfaces. Due to the simplification of the physical problem, the mathematics of the cone models can be solved rigorously [18-20].

The present study investigates the effectiveness of applying the CONE model to analysis the dynamic response of pile groups in a critical hospital in south of Switzerland. For this purpose, FCONE program were developed for soil modeling. This program utilizes the equiv-

alent dynamic modeling concept in the analysis of soil dynamics and soil-pile-structure interaction.

2 THE CONCEPT OF CONE MODEL

The dynamic response of pile foundations embedded in a horizontally stratified soil profile is determined using the Cone model (Meek and Wolf 1994). Linear behavior of the site is assumed; hence the soil is assumed to remain linearly elastic with hysteretic material damping during dynamic excitation. Figure 1 shows the loaded disk on the surface of a homogeneous half-space, modelled in the one-dimensional strength-of-materials approach as a truncated semi-infinite bar with a vertical axis [20].

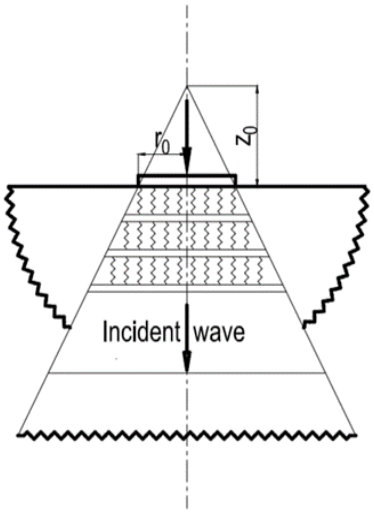

Figure 1: Translational truncated semi-infinite cone model of a loaded disk on a half-space.

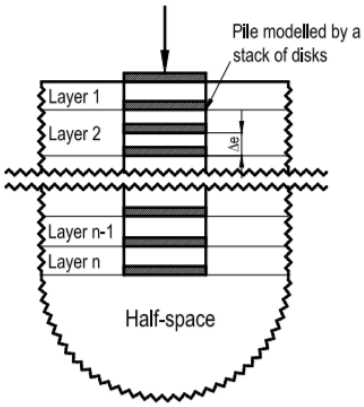

Figure 2: Pile modelled by a stack of disks

The soil region is divided into several segments by massless rigid disks (Figure 2). The disks will coincide with the interfaces of the half-space. In addition, further disks are selected to adequately represent the dynamic behavior. After assemblage, the dynamic stiffness matrices of all the cone frustum segments are then calculated and subsequently assembled together with the underlying half-space to form the dynamic stiffness matrix of the corresponding backbone cone. Applying a unit load at the disk and solving for the displacement amplitudes at all disks leads to a column in the flexibility matrix [$G(w)$] of the free field condition. Thus, the force-displacement relationship is obtained as (Eq.1); where $\{u(w)\}$ is the displacement amplitudes, and $\{P(w)\}$ is the force amplitudes:

$$\{u(w)\} = [G(w)]\{P(w)\} \tag{1}$$

This procedure is repeated for all disks to obtain all columns of the dynamic flexibility matrix [G(w)]. The dynamic stiffness of a single cone $S_1(w)$ modeling an incident wave induced by a disk load of radius r_0 on a half space is given by (Eq.2), where K_s is the static translational stiffness coefficient of the cone modelling the incident wave, c is the relevant wave velocity, w is the load circular frequency and ρ is the soil density. The value of the aspect ratios of a particular cone are shown in (Table 1) for each type of motion.

$$S_1(w) = K_s(1 + i\frac{wz_0}{c}) \qquad K_s = \frac{\rho c^2 \pi r_0^2}{z_0} \tag{2}$$

Table1: Aspect ratios for different types of motion

Motion	Horizontal	Vertical	Rocking	Torsional
Aspect ratio $\frac{z_0}{r_0}$	$\frac{\pi}{8}(2-\upsilon)$	$\frac{\pi}{4}(1-\upsilon)(\frac{c}{c_s})^2$	$\frac{9\pi}{32}(1-\upsilon)(\frac{c}{c_s})^2$	$\frac{9\pi}{32}$
Poisson's ratio υ	all υ	$\upsilon \le \frac{1}{3}$, $\frac{1}{3} < \upsilon \le \frac{1}{2}$	$\upsilon \le \frac{1}{3}$, $\frac{1}{3} < \upsilon \le \frac{1}{2}$	all υ

The dynamic stiffness matrix of the cone frustum segments is obtained by inverting the dynamic flexibility matrix $[S^f(w)]=[G^{-1}(w)]$, and then the forces acting on the top and bottom disks and their corresponding displacements are related as:

$$\{P(w)\}=[S^f(w)]\{u(w)\} \tag{3}$$

It is well known that the behavior of a pile in a compact group is quite different from that of a single pile because of pile-soil-pile interaction. These interaction effects depend mainly on pile spacing. These dynamic interactions incorporated into the analysis by a factor which is defined as the ratio of fractional increase in displacement amplitude at receiver pile to the displacement amplitude at the loaded source pile. The dynamic normal-axial interaction factor $\alpha_\upsilon(w)$ can be obtained from (Eq.4), where C_s = shear-wave velocity; ζ_g = hysteretic damping ratio; w = frequency of excitation; r_0 = radius of the pile; and d = distance between two piles.

$$\alpha_\upsilon(w)=\frac{{u_r}^f(w)}{u_s(w)}=\sqrt{\frac{r_0}{d}}e^{-\zeta_g w\frac{d}{c_s}}e^{-iw\frac{d}{c_s}} \tag{4}$$

$${u_\theta}^f(w)=-Sin\theta.{u_r}^f(90°,w)$$

$${u_{rad}}^f(w)=Cos\theta.{u_r}^f(0°,w)$$

When analyzing soil-structure interaction, two types of damping have to be taken into account, namely the geometric attenuation (radiation attenuation) that results from the distance of the excitation source to the object and the material damping due to the friction between the individual soil particles. The latter can be taken into account by substitution of G and G (1 + 2iζ) and E by E (1 + 2iζ), with ζ as the degree of attenuation of the soil. The material damping is independent of the excitation frequency.

When the distance between the piles is large (greater than about 20 diameters) the piles do not affect each other and the group stiffness and damping are simply the vector sums of the individual pile stiffness and damping. The dynamic stiffness matrix of the pile embedded in the half space can be obtained by replacing the properties of the soil between two consecutive disks with the mechanical properties of the pile section. This can be performed by adding the difference between the dynamic stiffness matrix of the pile and that of the corresponding soil cylinder, $[\Delta S(w)]$ leading to:

$$S(w)=S^f(w)+\Delta S=S^f(w)+[\Delta K]-w^2[\Delta M] \tag{5}$$

$$\{P(w)\}=[S(w)]\{u(w)\} \tag{6}$$

Where *P(w)* is force amplitudes, and ΔK and ΔM is the difference between stiffness matrices and mass matrices of the pile and soil cylinder, respectively. (Eq.6) can be written as

$$\begin{bmatrix} P_z \\ P_x \\ p_y \\ m_z \\ m_x \\ m_y \end{bmatrix} = \begin{bmatrix} K_{vz}(w) & 0 & 0 & 0 & 0 & 0 \\ 0 & K_{hx}(w) & 0 & 0 & 0 & K_{hxry}(w) \\ 0 & 0 & K_{hy}(w) & 0 & K_{hyrx}(w) & 0 \\ 0 & 0 & 0 & K_{tz}(w) & 0 & 0 \\ 0 & 0 & K_{hyrx}(w) & 0 & K_{rx}(w) & 0 \\ 0 & K_{hxry}(w) & 0 & 0 & 0 & K_{ry}(w) \end{bmatrix} \begin{bmatrix} u_z \\ u_x \\ u_y \\ \varphi_z \\ \varphi_x \\ \varphi_y \end{bmatrix} \tag{7}$$

Where *v*, *h*, *r* and *t* denote vertical, horizontal, rocking and torsional motions respectively. It can be noted that coupling occurs between horizontal and rocking motions. Furthermore, the dynamic stiffness coefficient obtained from the analysis is then decomposed into two parts:

$$K_{ij}(w) = K_{st}[k_{ij} + ia_0c_{ij}] \tag{8}$$

In (Eq.7), K_{st} is the static stiffness, i the imaginary unit, k_{ij} and c_{ij}, respectively called stiffness and damping coefficients, are dimensionless coefficients depending on the Poisson's coefficient of the soil and the frequency parameter.

$$a_0 = \frac{w(2r_0)}{C_s} \tag{9}$$

Where $Cs = \sqrt{G/\rho}$ is the shear wave velocity in the soil. Finally, the total displacement of receiver pile(i) due to lateral load of source pile(j) can be written as:

$$u_i(w) = \sum_{j=1}^{i-1} \alpha_v(d_{ij}, w)u_{jj}(w) + u_{ii}(w) + \sum_{j=i+1}^{n} \alpha_v(d_{ij}, w)u_{jj}(w) \qquad ,(i = 1,..,n) \tag{10}$$

or

$$u_i(w) = \frac{1}{S(w)}\left[\sum_{j=1}^{i-1} \alpha_v(d_{ij}, w)P_j(w) + P_i(w) + \sum_{j=i+1}^{n} \alpha_v(d_{ij}, w)P_j(w)\right] \quad , \quad (i = 1,..,n) \tag{11}$$

In order to achieve a sufficient accuracy, the number of disks n has to be selected so that the length L of a pile element does not exceed about one tenth of the shortest wavelength propagating from the pile. Because the shear wave velocity is less than the dilatational wave velocity in the soil, the wavelength of shear waves is lesser than that of longitudinal ones and the number of disks can be chosen as:

$$n \geq 1 + \frac{5}{\pi}\left(\frac{L}{2r_0}\right)a_0 \tag{12}$$

3 CASE STUDY (AN EMERGENCY HOSPITAL IN SOUTH OF SWITZERLAND)

The building is of a general rectangular shape with the overall dimensions of 73 meters in the longitudinal direction, 25 meters in the width direction, and a height of 35.6 meters. The building is a new reinforced concrete construction with concrete columns. The primary lateral load carrying system consists of three reinforced cores and an integrated reinforced concrete exterior frame system. For the earthquake resistance evaluation a special micro zoning map and a response spectrum developed by Resonance Ltd for Brig was used. The building is classified as a category III construction with an importance factor of 1.4. This is the highest class

of building categories in Switzerland. The building was modeled in three dimensions (3D) and calculated for non-ductile behavior according to the SIA Standard 262 (2013 edition). The summary of the building characteristics and modeling assumptions is given below:

3.1 Modeling assumptions:

- Longitudinal direction

The earthquake loads are carried by the three reinforced concrete cores and two shear walls together with the reinforced concrete framework. As the geometry of all floors is similar, continuous transfer of earthquake loads is guaranteed from the roof to the foundation. Additionally, due to the layout and stiffness differences the mass center and the stiffness center of the building do not match resulting in torsional stresses due to lateral earthquake effects.

- Lateral (short) direction

Three reinforced concrete core and two reinforced concrete frames transfer the horizontal equivalent loads corresponding to the earthquake effects from the higher levels through the lobby level to the basements of the building. There is a concern of soft story in the building. As a result, high shear stress concentrations occur in the building due to this irregularity.

3.2 Numerical Investigation:

The earthquake loads are determined according to the Swiss Code SIA 260-262; Merkblatt SIA 2018. The following material characteristics have been used;

Concrete: Ec = 20,000Mpa (Elastic modulus); f ’c= 19.2 Mpa (compressive strength)

For the seismic structural analysis four computer programs were used:

- ETABS which is a well-known structural analysis and design software, CSI, Berkeley, USA

- OpenSees Open System for earthquake engineering Simulation. This is an earthquake simulation software based on the displacement based structural analysis considering material nonlinearities. The program is very suitable for assessing the behavior of buildings in seismic situations. The purpose of modeling with OpenSees is to perform a nonlinear static pushover (NSP) analysis of the reinforced concrete system with concrete cores, shear walls, and the heavy concrete columns. The modeling is based on ASCE 41-13 (2014). Material nonlinearities and hysteretic behavior are considered for the elements under normal forces, bending and shear effects. For the calculations, both force-based and displacement-based methods have been used. For the displacement-based method ASCE 41 procedures have been implemented in the calculation of target displacements.

- FCONE program was developed at Smteam based on the CONE model for soil modeling. This program utilizes the equivalent dynamic modeling concept in the analysis of soil dynamics and pile- foundation interaction [22,23].

-Abaqus/Cae was used to investigate the structure response according to seismic soil-pile-structure interaction effect. The finite element simulation phase of the present study along with a description of boundary conditions, the meshing and analysis techniques and the materials’ constitutive laws is also presented below.

3.2.1 Pile group effect

When piles are used as part of a building foundation system, they are usually configured in groups to support continuous mat foundations or discrete pile caps for individual load-bearing elements. The impedance of a pile group cannot be determined by simple addition of individual pile impedances because grouped piles interact through the soil by "pushing" or "pulling" each other through waves emitted from their periphery. This is called a group effect, and it can significantly affect the impedance of a pile group as well as the distribution of head loads among individual piles in the group. Group effects depend primarily on pile spacing, frequency, and number of piles. They are more pronounced in the elastic range, and dynamic group effects decrease in the presence of material nonlinearity. Numerical analysis methods of soil-pile-structure interaction (SPSI) problems can be classified into two approaches: direct method and substructure method. In the direct method for analysis of SPSI it is necessary to model underlying soil, foundation and structure with best precision and accuracy since they are supposed to be analyzed together. In substructure method, soil-structure system is divided into two parts: first part is structure and the second part is the soil that has common boundary with foundation and each part can be modeled in detail (Wolf 1985) [21]. In order to consider the influence of the piles on the dynamic response of the structure, the substructure method was used in this study. This consists of three consecutive steps:

(1) Calculation of foundation input motion in the absence of superstructure inertia (kinematic interaction) includes translational displacements and rotational components.
(2) Calculation of the dynamic impedances (spring and damping coefficients) for horizontal rotation and the combination of base foundation and pile system.
(3) Calculation of the seismic response of the building supported on the springs and dashpots of step-2 and subjected at its base to the foundation input motion of step-1.

The method of Fan and Gazetas [7], based on the BDWF model (Beam on Dynamic Winkler Foundation) is used to determine the foundation input motion. In this method, the displacement of the pile head (U11) as a function of the free-field motion (Uff) is calculated as follows:

$$U_{11} = \Gamma\, U_{ff} \tag{13}$$

Here Γ is a function of spring and damping constants, frequency, mechanical characteristics of the piles such as Ip, Ap, Mp, Ep.

A detailed study of gazetas shows that the kinematic factor $Iu = U_{11} / U_{ff}$ for small frequencies, like the first frequency of the hospital Brig (0.7 Hz), is equal to 1; This means: no increase in the amplitude of the freefield earthquake motions. Therefore, in the case of the Brig hospital, the kinematic interaction effect was neglected.

The arrangement of pile group in rectangular foundation is shown in Figure 3. In this case, both rigid and flexible foundations are considered. In fixed-base model, the structure is being analyzed without soil and foundation with fixed boundary condition to resist all displacements or rotations at the bottom.

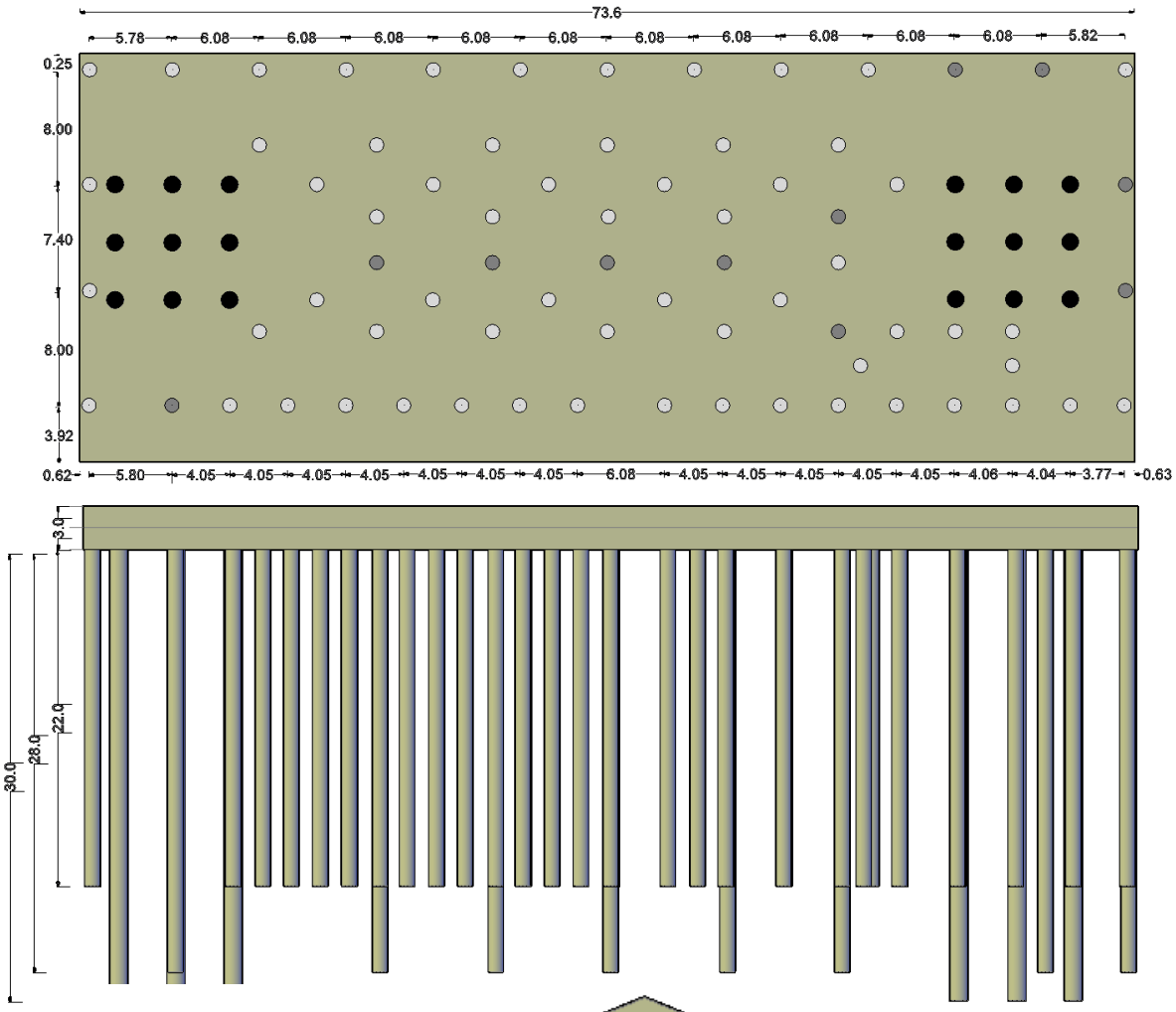

#	Pile Type	Diameter (Cm)	Length (m)
	1	100	22
	2	100	28
	3	120	30

Figure 3: The arrangement of pile group in rectangular foundation

In Cone model the structure is built on a rigid foundation with springs and dashpots in the bottom in place of soil. The response spectrum method was used for determining the displacements and accelerations.

To determine the vertical axial load in the upper part of the piles, a finite element model of the building was created using the ETABS program. In the modeling of the core 3D shell elements were used. The elastic modulus E of concrete has been reduced to 60% of the design value to include the effects of cracking in concrete. The (q) factor (response factor) is set to 2, and the importance factor is assumed 1.4. In 2015, a new earthquake hazard map of Switzerland (Figure 4) was issued with a corresponding design spectrum, which was used for the present study. The modal analysis was performed to determine natural modes of frequencies for the structural model in two different conditions: namely fixed-base behavior and behavior including SPSI (containing embedded piles with pile group effect).

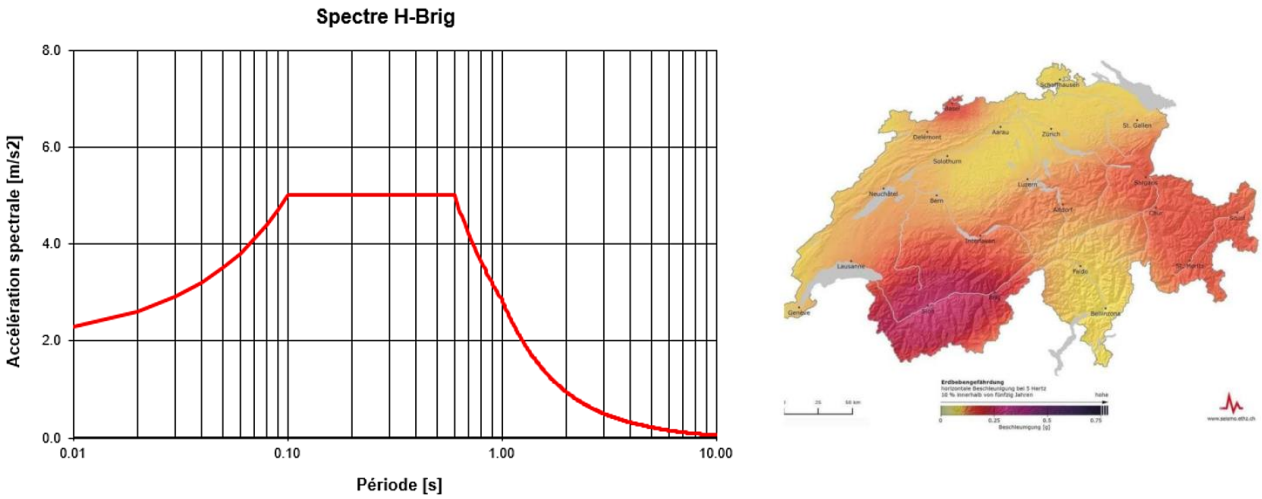

Figure 4: The response spectrum for the Brig ground motion and
The Seismity map of Switzerland

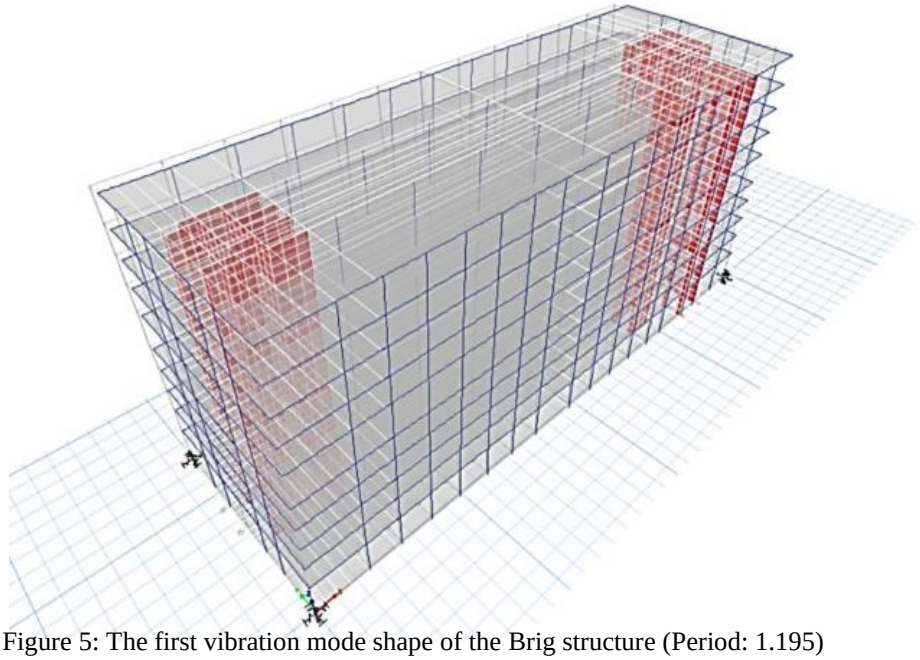

Figure 5: The first vibration mode shape of the Brig structure (Period: 1.195)

The results of ETABS analysis are given in table 2, and the first vibration mode shape of the building with dynamic pile group effect obtained from the ETABS is shown in Figure 5.

Table 2: The results of two analysis obtained from the ETABS model

	Period of vibration (s)	The Roof displacement (cm)
Fixed based foundation (No Piles)	0.7	6.5
Flexible foundation (Including Piles)	1.2	11.5

3.2.2 Target Displacements

The calculated target displacement in long direction and short direction according to the Euronorm 8 and ASCE 41-13, 2014, are found to be 12cm and 15cm, respectively. These values represented the demand on the structure to have a sufficient ductility level under earthquake loads before a collapse of the building can occur.

3.2.3 Nonlinear Pushover Analysis

A pushover analysis involves the application of static lateral loads distributed over the height of the structure, and calculation of the resulting displacements in a model of the SPSI system. A pushover analysis of a structure with a flexible base is schematically illustrated in Figure 6. A non-linear pushover analysis was reported for the reinforced concrete system model of the building with the parameters defined in ASCE 41-13. Behavior of each wall was determined based on the wall thickness, the wall length and the material properties as provided by the ETABS model. At each point on the pushover curve, the deformations of all components in the structural system are related to the reference displacement. The ETABS model has been read into OpenSees for conducting the pushover analysis.

The pushover analysis resulted in displacement capacities of 20 cm in the transverse direction, and 22 cm in the longitudinal direction, as shown in Figure 7. This compared with the target displacements, found from ASCE 41-13, of 12 cm in longitudinal direction and 15 cm in the transverse direction.

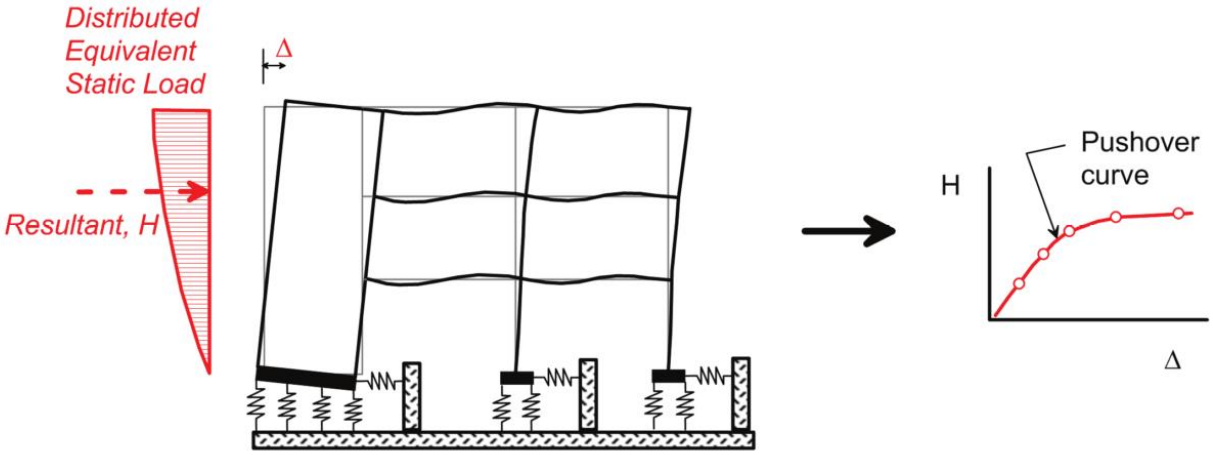

Figure 6: Schematic illustration of a pushover analysis and development of a pushover curve for a structure with a flexible base [24]

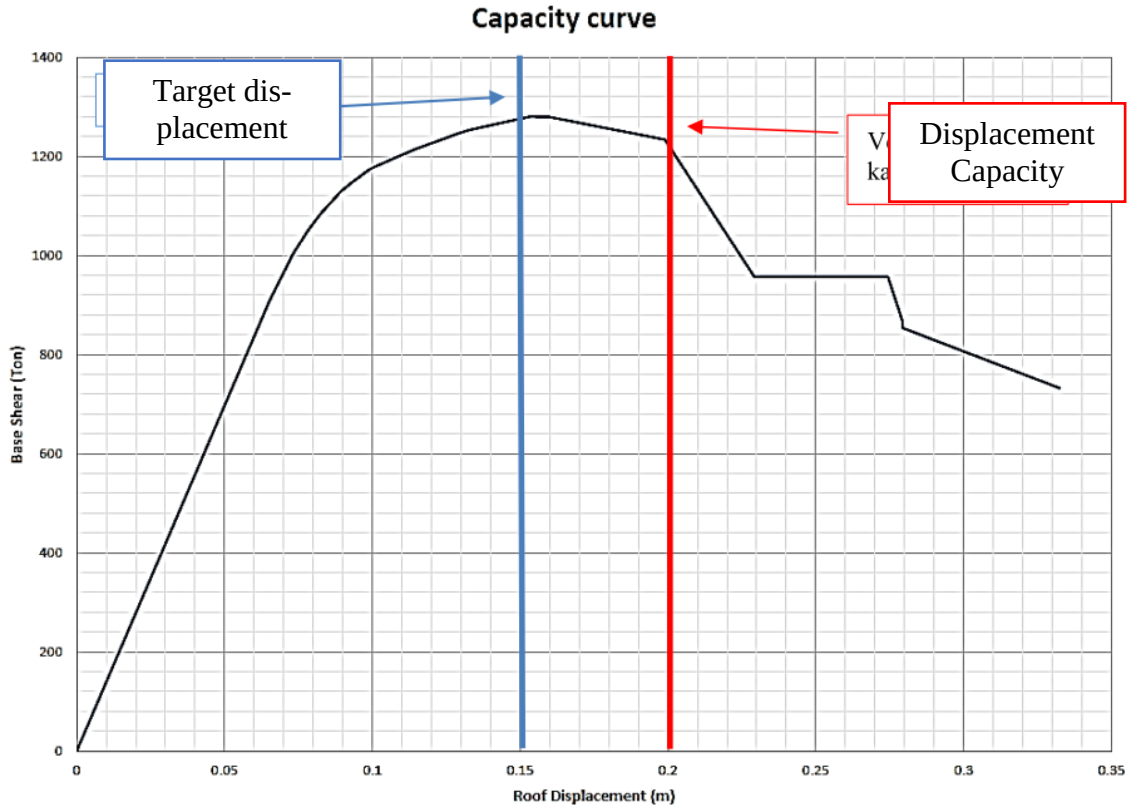

Figure 7: The pushover curve obtained by OpenSees analysis

3.2.4 Dynamic Stiffness of pile groups

Dynamic stiffnesses (spring and damping coefficients) for a pile group are strongly frequency-dependent. Therefore, the dynamic stiffnesses for different blocks (pile groups) as a function of frequency were calculated using the cone method according to John P. Wolf [20]. For the determination of stiffness, a new method of solving dynamic interaction problems was developed at Smteam, which, the seismic behavior of Pile-Soil-Pile structure interaction (SPSI) system is investigated as a whole considering both pile group effect and soil constitutive model according to the CONE theory. Results of the program for one 3×3 block under a core (i.e., spring and damper constants as a function of frequencies) are attached at the end of this report.

The spectral values have been reduced to take account of the radiation and material damping of the soil. It turns out that in the case of the flexible-base structure, in addition to the added rocking component to the horizontal motion of the structure, a part of the structure vibration energy will transmit to the soil layer and can be dissipated. This results in a reduction of the natural frequency in comparison to the fixed-base model and an increase of the damping (mainly due to radiation damping resulting from the wave propagation and hysteresis damping of the soil materials).

Detaied mechnaical characteristics of the soil has been explained in Table 3 where E is Elastic modulus, G_s is shear modolus, ρ is unit weigth, C_s is shear wave velocity, υ is poisson's ratio and ξ is material damping ratio. The soil region was assumed to be homogeneus with uniform shear modulus and density during analysis. The horizontal, vertical, and rotational dynamic

stiffness and damping ratios of a soil layer captured by using FCONE program,which are shown as a function of dimensionless frequency in Figure 8.

Table 3: The mechanical characteristics of the soil

Parameter	E (MPa)	Gs (MPa)	ρ (KN/m3)	Cs (m/s)	υ	ξ (%)
Quantity	350	125	16.45	276.00	0.4	0.05

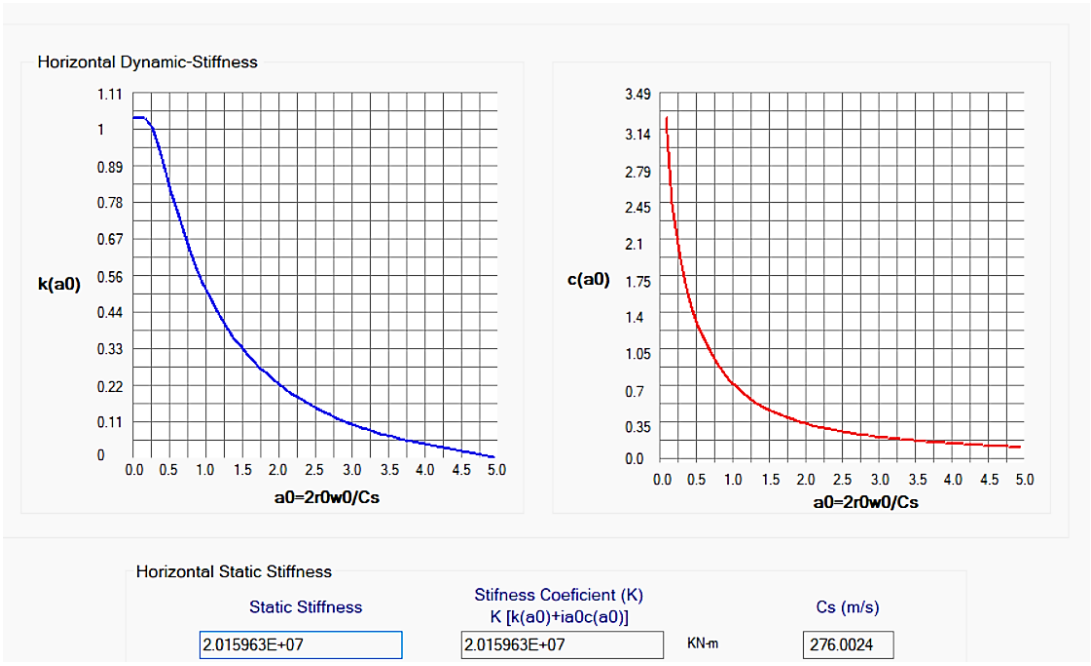

a) Horizontal Stiffness for a 3×3 Pile group

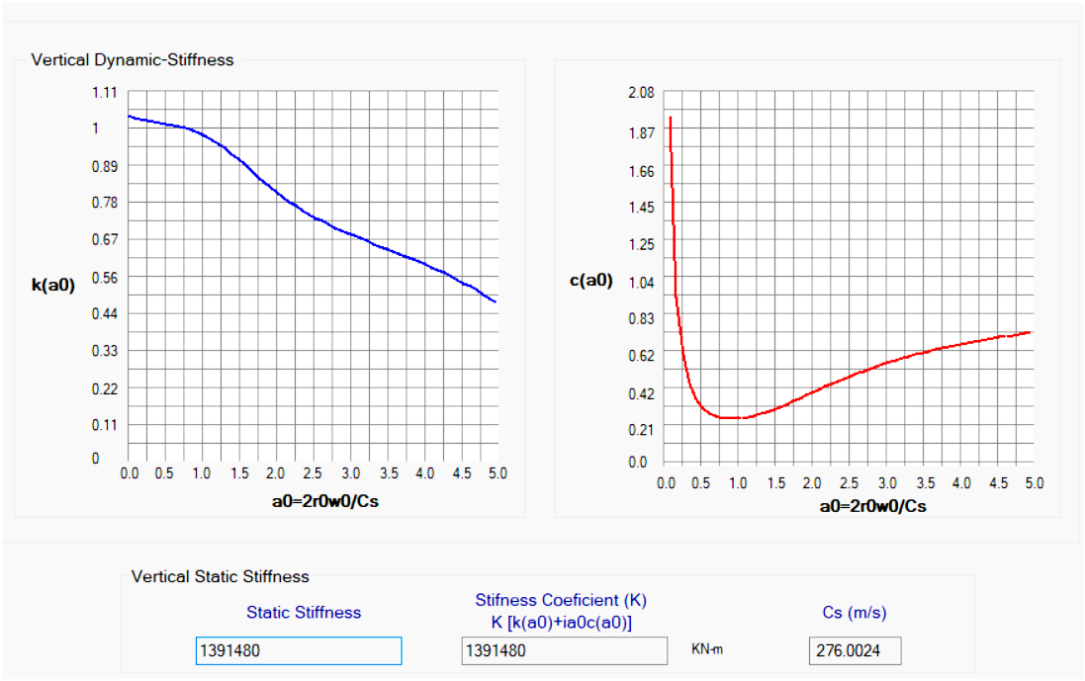

b) Vertical Stiffness for a 3×3 Pile group

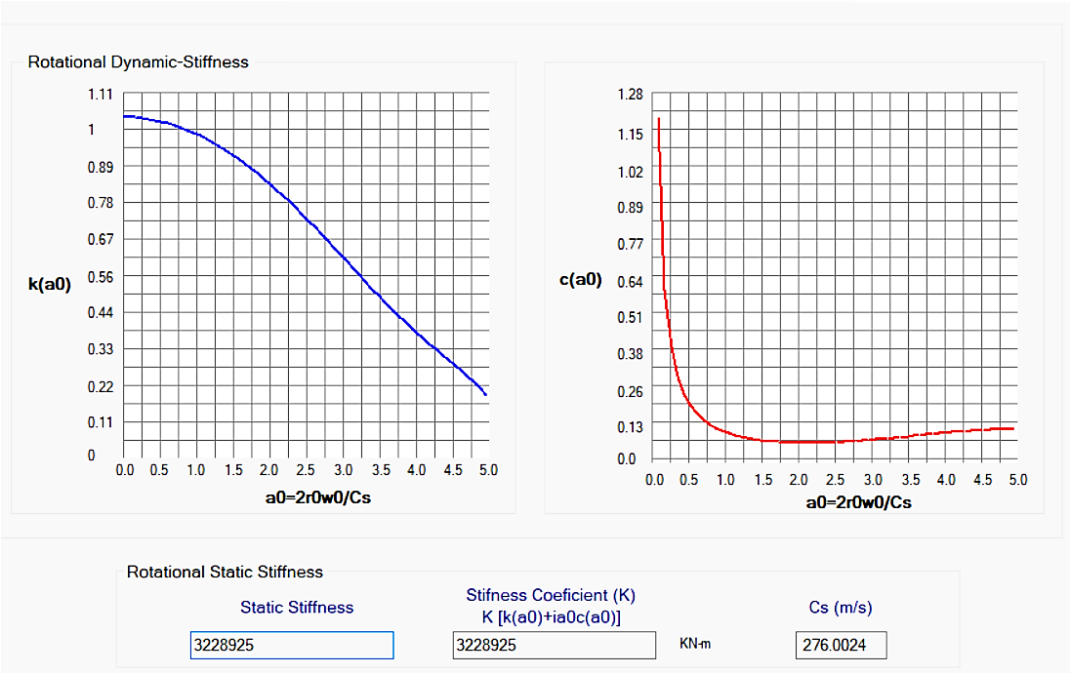

c) Rotational Stiffness for a 3×3 Pile group

Figure 8: The vertical, horizontal, and rotational dynamic stiffness for a 3×3 Pile group

3.3 The Finite-Element Simulation:

The finite element code ABAQUS/Cae model as an accurate direct way was used to investigate the seismic behavior of the structure under SPSI effect. For this purpose, the infinite soil medium is reduced to a finite region using infinite element boundaries. In this case, an elastic perfectly plastic model was adopted for modeling the concrete piles with a modulus of elasticity of 30 MPa (C30). In the 3D finite element model developed using Abaqus/Cae, both the pile and the soil were modeled using eight-nodded solid continuum elements (C3D8R) to account for the continuum nature of the soil. This element has quadratic shape function which is well suited to model the medium with bending dominated deformation. A too coarse mesh may deviate from the expected response, whereas a too fine mesh requires very long computational time. Hence, a relatively fine mesh was adopted for the pile and a coarser mesh was adopted for the soil. Overall 11089 elements for the piles and 10205 elements for 10-story SPSI model was used. Soil was modeled using 98400 elements and the soil-pile interaction was modeled by defining the tangential and normal behavior of the contact surfaces in the FE model.

A strain hardening model using Mohr–Coulomb failure criterion was adopted for the soil which uses the five significant soil parameters, such as shear modulus (G), Poisson's ratio (ν′), shearing resistance angle (φ′), effective cohesion (c′), and angle of dilatancy (ψ) as shown in Table 4. An angle of internal friction of 35° was used in the definition of the Mohr–Coulomb failure criterion. The geometrical details adopted for the SPSI analysis is shown in Figure 11.

Table 4: The soil parameters used in the finite element code ABAQUS/Cae model

Elastic Parameters		Plastic Parameters (Mohr–Coulomb failure criterion)	
Mass density, ρ (KN/m3)	16.45	Shearing resistance angle, φ′	34
Modulus of Elasticity, E (MPa)	350	Angle of dilatancy, ψ	0.1
Poisson's ratio, ν′	0.4	Effective Cohesion, c′ (kPa)	22

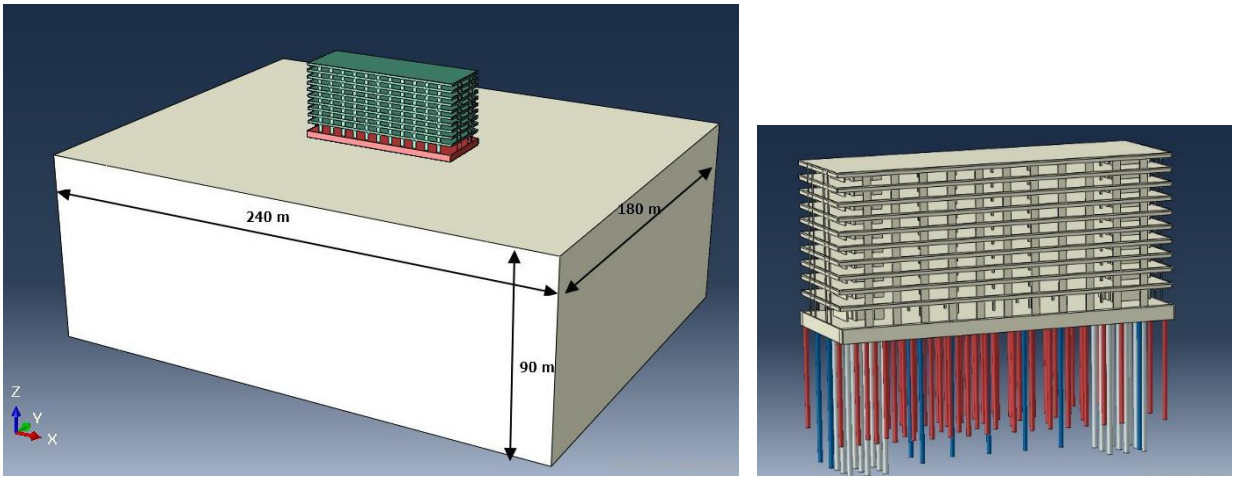

Figure 11: The geometrical details of SPSI model using ABAQUS/Cae

Results of 3D numerical prediction of first mode of vibration in Eigenvalue analysis for both cases (fixed-base and SPSI interaction), and maximum lateral displacements in short direction are shown in Figure 12, 13 respectively.

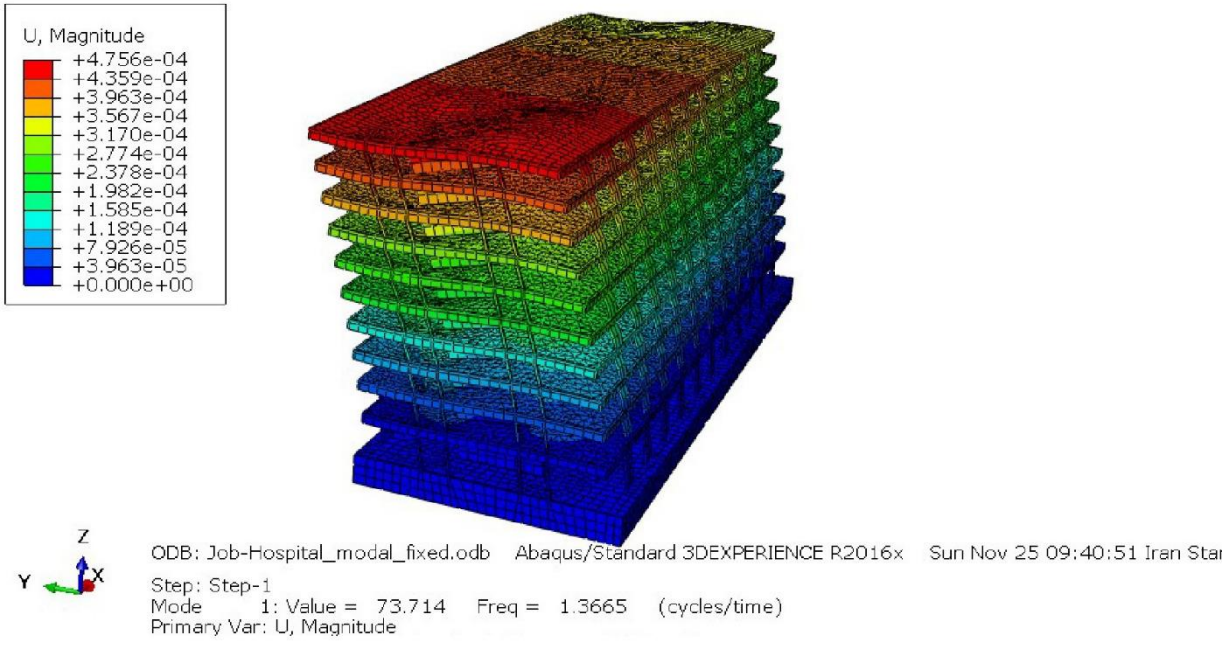

a) Fixed base behavior (period of vibration: 0.73)

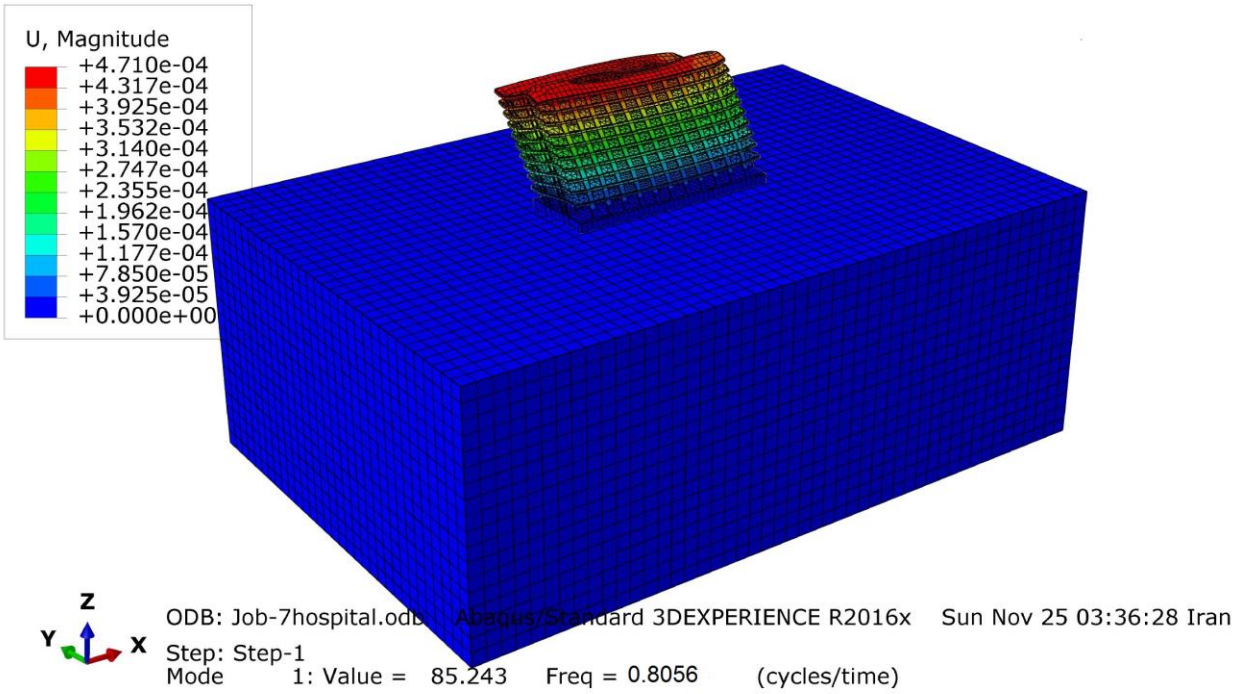

(b) SPSI analysis (period of vibration: 1.24)
Figure 12: The first mode of vibration in Eigenvalue analysis

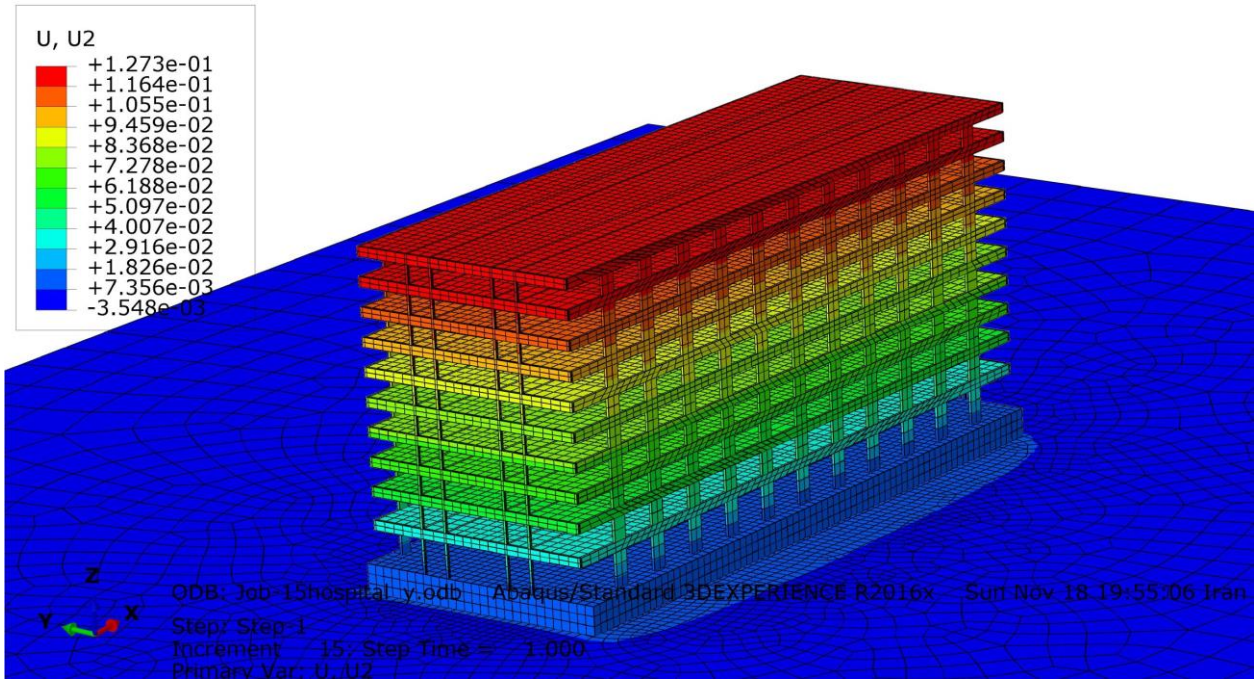

Figure 13: The maximum lateral displacements in short direction

Table 5 provides a good comparison between the results of SPSI analysis obtained by Cone method and FEM solution, which indicate that the results of Cone method are in close agreement with FEM results. As the structural stiffness in comparison with soil or building height increases, the period rate increases as well. For first mode of vibration in modal analysis a

good tendency with negligible difference was observed. Therefore, the Cone model provided reasonable accuracy of modal analysis for the high-rise building responses because the deviation was limited to 3%.

Table 5: Comparison between the results of SPSI analysis obtained by Cone method and FEM solution

	The period of vibration (s) (First-mode)		The lateral displacement in short direction (Cm)	
	Fixed base	SPSI	Foundation	The roof story
CONE Model	0.7	1.20	0.28	11.50
FEM Model	0.73	1.24	0.30	12.73

From the comparison between the maximum lateral displacements, it can be seen that the foundation displacements results obtained from Cone method give good agreement with FEM analysis results with about 6% and the most difference was observed in the roof displacement with around 10%. As expected, nonlinear modeling of soil results in increased lateral displacements of stories. It can be also concluded that the maximum lateral displacement of structures increases with the increasing number of stories, and the upper stories displacements are more affected with SPSI than the lower stories.

4 CUNCLUSION

The FCONE program we designed at Smteam is a new method of solving dynamic interaction problems, in which the seismic behavior of pile-soil-pile structure interaction on a large building is investigated as a whole considering pile group effect and soil constitutive model according to the CONE theory. The capability of the CONE method to predict the dynamic SPSI effects giving it an advantage over other time-consuming rigorous methods. This approach leads to physical insight with conceptual clarity, is simple to use and solve, as the mathematical solution is simplified, and provides sufficient generality (layered site, embedment, all frequencies) and acceptable engineering accuracy. The accuracy of any analysis is limited anyway, because of the many uncertainties, some of which can never be eliminated (for instance the definition of the dynamic loads and the values of the dynamic soil properties in the analysis of a structure). The analysis with cones fits the size and economics of practical engineering projects. Thus, the results presented in this article can contribute to relevant engineers in designing safe and economical structures based on foundation vibration and dynamic SPSI analysis in practical projects whenever possible.

REFERENCES

[1] Craig, R. R. J., and Kurdila, A. J. (2006). Fundamentals of structural dynamics, Wiley, Hoboken, NJ.

[2] Han, Y. (2002). "Seismic response of tall building considering soil-pile-structure interaction." Earthquake Eng. Eng. Vib., 1(1), 57–65.

[3] Guin, J., and Banerjee, P. K. (1998). "Coupled soil-pile-structure interaction analysis under seismic excitation." J. Struct. Eng., 10.1061/(ASCE) 0733-9445(1998)124:4(434), 434–444.

[4] Kaynia, A. M. (1982). Dynamic stiffness and seismic response of pile groups (Doctoral dissertation, Massachusetts Institute of technology).

[5] Dobry, R., & Gazetas, G. (1988). Simple method for dynamic stiffness and damping of floating pile groups. *Geotechnique*, 38(4), 557-574.

[6] Chore, H. S., Ingle, R. K., & Sawant, V. A. (2010). Building frame-pile foundation-soil interaction analysis: a parametric study. Interaction and multiscale mechanics, 3(1), 55-79.

[7] Fan, K., Gazetas, G., Kaynia, A., Kausel, E. & Ahmad, S. Kinematic seismic response of single piles and pile groups. J. *Geotech. Eng., ASCE, 1991*, 117(12), 1860-79.

[8] Pitilakis, D., Dietz, M., Wood, D.M., Clouteau, D. and Modaressi, A. (2008) Numerical simulation of dynamic soil-structure interaction in shaking table testing. *Soil Dynamics and Earthquake Engineering* 28, 453-467.

[9] Kaynia AM, Kausel E. Dynamics of piles and pile groups in layered soil media. *Soil Dynamic Earthquake Engineering 1991*;10(8):386–401.

[10] Massumi A, Tabatabaiefar HR. Effects of soil–structure interaction on seismic behavior of reinforced concrete buildings with moment resisting system (using direct method, Tehran, Iran: *International Institute of Earthquake Engineering and Seismology (IIEES); 2007.*

[11] Novak, M., 1987, "Discussion of dynamic response of arbitrarily shaped foundations: experimental verification," *Journal of Geotechnical Engineering, Vol. 113, No. 11, pp. 1410-1412.*

[12] Baranov, V. A. 1967. On the calculation of excited vibrations of an embedded foundation. Voprosy Dinamiki Prochnocti, 14. Riga, Latvia: Polytechnic Institute Riga.

[13] Novak, M. and Nogami, T. (1977): "Soil-Pile Interaction in Hori- zontal Vibration," *International Journal of Earthquake Engineering and Structural Dynamics,* Vol. 5, pp. 263-281.19.

[14] Dobry, R., and G. Gazetas. 1988. "Simple method for dynamic stiffness and damping of floating pile groups." Geotechnique 38 (4): 557–574

[15] Ismail, S., Kaddah, F., & Raphael, W. (2018, November). Seismic Soil Structure Interaction of a Midrise Frame Structure. In International Congress and Exhibition" *Sustainable Civil Infrastructures: Innovative Infrastructure Geotechnology" (pp. 73-88). Springer, Cham.*

[16] Ülker-Kaustell, M., Karoumi, R., & Pacoste, C. (2010). Simplified analysis of the dynamic soil–structure interaction of a portal frame railway bridge. *Engineering structures*, 32(11), 3692-3698.

[17] Sadeghi Hokmabadi, A., Fatahi, B., Far, H., & Samali, B. (2012). Effects of soil-pile-structure interaction on seismic response of moment resisting buildings on soft soil. *In 3rd International Conference on New Developments in Soil Mechanics and Geotechnical Engineering. Near East University Press, Turkey.*

[18] Pal, A. S., & Baidya, D. K. (2018). Dynamic Analysis of Pile Foundation Embedded in Homogeneous Soil Using Cone Model. *Journal of Geotechnical and GeoEnvironmental Engineering, 144(8), 06018007.*

[19] Jaya, K. P., & Prasad, A. M. (2004). Dynamic behaviour of pile foundations in layered soil medium using cone frustums. Géotechnique, 54(6), 399-414.

[20] Meek, J. W., and J. P. Wolf. 1994. "Cone models for an embedded foundation." J. Geotech. Eng. 120: 60–80.

[21] Wolf, J.P. (1985) Dynamic soil-structure interaction. Prentice-Hall, Englewood Cliffs, New Jersey.

[22] Mohasseb. S., Ghazanfari. N., Davoodi. R., (2018), "Project management in construction projects: Negotiation Engineering", *Mahnevisan publication*

[23] Mohasseb. S., Nayeri. A. (2015), "Theory to practice", *Mahnevisan publication*

[24] Stewart, J., Crouse, C. B., Hutchinson, T. C., Lizundia, B., Naeim, F., & Ostadan, F. (2012). *Soil-structure interaction for building structures (No. Grant/Contract Reports (NISTGCR)-12-917-21).*

COMPDYN 2019
7th ECCOMAS Thematic Conference on
Computational Methods in Structural Dynamics and Earthquake Engineering
M. Papadrakakis, M. Fragiadakis (eds.)
Crete, Greece, 24–26 June 2019

A COMPUTATIONAL METHOD FOR PERFORMING NONLINEAR ADAPTIVE PUSHOVER ANALYSIS OF STRUCTURES THROUGH ABAQUS SIMULATION

Konstantinos A. Skalomenos[1], **George Papazafeiropoulos**[2]

[1]Department of Civil Engineering, University of Birmingham
Birmingham B15 2TT, United Kingdom
e-mail: k.skalomenos@bham.ac.uk

[2]Institute of Structural Analysis and Antiseismic Research, National Technical University of Athens
Zografou Campus, Athens 15780, Greece
e-mail: gpapazafeiropoulos@yahoo.gr

Abstract

A computational method which uses the nonlinear adaptive static (pushover) analysis to evaluate the static force-deformation response of a planar moment resisting frame (MRF) is presented. The MRF considered in this study is a seismic-resisting frame of a prototype five-storey five-bay steel building structure designed based on the Japanese seismic design code.

The frame model is simulated by the finite element software ABAQUS. Failure on members is captured by adopting shell elements for beams and columns combined with a refined meshing. The lateral force distribution is adapted during the pushover analysis according to the first eigenmode of the structure by utilizing a novel inverse optimization algorithm. A new stop analysis criterion is introduced that overcomes the numerical difficulty of the available static-solution algorithms to terminate the analysis in the degrading region of the load-deformation response. The effects of load distribution and first (fundamental) small strain eigenperiod on the force-deformation pushover curve are studied.

The monotonic adaptive pushover procedure is implemented using the programming language MATLAB. The new tool effectively combines the advanced modeling and analysis capabilities of ABAQUS with the programming simplicity of MATLAB, thus leading to a user-friendly environment. The last offers a robust implementation of pushover analysis and superior numerical results can be obtained, especially the descending branch of the pushover curve and collapse mechanism.

Keywords: Pushover, Adaptive, Finite element, Descending branch, Collapse.

1 INTRODUCTION

Static pushover analysis has been widely used in earthquake engineering and design of buildings, such as in the Capacity Spectrum Method (CSM) [1]. In general, pushover analysis is used for seismic evaluation of existing buildings and design verification for new construction in order to identify damage states and their correlation with the amplitude of the seismic ground motion. Among the advantages of the pushover analysis method are that it is simple, fast and provides all the capacity points of a structure until collapse [2,3].

In an attempt to increase the accuracy of the results of the pushover analysis, adaptive force or displacement patterns are considered during the analysis. Adaptivity is realized in a way that ensures that the force or displacement pattern imposed on the building during the pushover analysis is continually updated depending on the instantaneous dynamic characteristics of the structure and/or a site-specific spectrum. Among the first studies that have introduced procedures to utilize fully adaptive patterns for pushover analysis is [4], where the various eigenproperties of the structure and the associated spectral quantities are used primarily to determine the demands to develop a capacity spectrum envelope.

A comprehensive presentation of the importance and various special traits of the pushover curve can be found in [5,6]. It is shown that the slope of the descending branch of any pushover curve depends strongly on the level of modelling sophistication, elastic unloading of the stories not participating in the collapse mechanism, and on the static or dynamic nature of the pushover algorithm. This implies that the reduction of a MDOF system in an equivalent SDOF system or use of simplified plastic hinge formulations may not apply for tracing the descending branch accurately.

An advanced modelling through FEA would be beneficial to accurately capture the descending branch of a pushover curve and finally the collapse mechanism. However, to trace accurately the descending branch in a force-controlled pushover analysis is generally difficult (almost impossible with normal static analysis) since once the maximum capacity is reached the lateral loads cannot increase further. In addition, the use of advanced modelling approaches often generate convergence errors (strain concentration etc.) that terminate the analysis at an early stage. To overcome these problems, FEA softwares have adopted computational techniques, such as the arch-length control static analysis or advanced stabilization algorithms.

In this study, a computational platform that combines ABAQUS [7] and MATLAB [8] is developed and used for the generation of pushover curves of buildings. The key points of this new computational tool are:

a. It uses “active” advanced modelling methods for members and materials instead of “passive” plastic hinge models with fixed material parameters.
b. Failures related to strength and stiffness reduction, such as local buckling, overall buckling etc. are captured accurately through advanced FEA modeling.
c. It utilizes the common static analysis of Abaqus without obscure stabilization algorithms or arc-length methods that may become uncontrollable or give erroneous results under certain circumstances.
d. It is mainly a force-based pushover analysis after the post-peak strength point and captures the collapse mechanism that is not captured in displacement-based pushover analysis.
e. The load distribution is updated based on subsequent modal analysis (adaptive procedure) for accounting the stiffness reduction. The loading pattern is closer to that of a dynamic analysis.

2 NUMERICAL MODELING

2.1 Description of the Analyzed Building

The building under consideration is a five-floor steel structure designed by the Japanese seismic code [9,10] using the A_i force distribution. It has a rectangular floor plan with aspect ratio equal to 1.70. The longitudinal dimension L_X has length 32.0m and five bays, while the transverse dimension L_Y has length 18.6m and three bays. In Fig. 1a, the structural system of a typical floor plan is presented while in Fig. 1b a general view of the building side is shown. The total building's height is 20.50m. The structural system illustrated in Fig. 1a consists of three plane moment resisting frames (MRFs) along the X axis and two MRFs along the Y axis. The building have square tube column sections and H beam sections. The cross-section of the columns and beams are given in Table 1. The seismic design of the building was achieved through a characteristic factor D_s = 0.25 (i.e., behavior factor q = 4.0), while the drift limitation requirement 1 / 200 was satisfied for a base shear coefficient C_0 = 0.20. Table 2 provides the weight of each floor, the Ai load distribution, the strength-based and drift-based seismic forces, the total story strength determined by the cross-sections, and the normalized first mode. The period of the building is 0.94 sec along the X axis and 0.90 sec along the Y axis.

The A_i force distribution is described by the following relation:

$$A_i = 1 + \left(\frac{1}{\sqrt{a_i}} - a_i \right) \frac{2T}{1+3T} \tag{1}$$

where a_i and T is obtained by:

$$a_i = \frac{\sum W_i}{W} \tag{2}$$

and:

$$T = H \cdot (0.02 + 0.01 \cdot \alpha) \tag{3}$$

In the Eq. (2), W is the total weight of structure, ΣW_i is the summation of the weight of all stories above of the story i, H the total building height and α equals 1.0 for steel buildings (along the height). The structural period T was estimated equal to 0.615 sec.

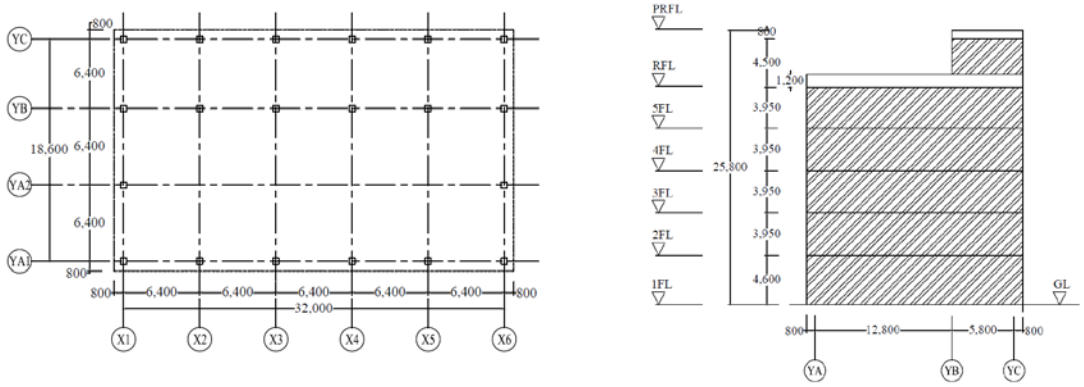

(a) (b)

Figure 1: (a) Plan view of the building; and (b) side view of the building.

Floor	Columns	Beam Ends	Beam Middle	Columns	Beam Ends	Beam Middle
5	500×22	H-600×250×12×19	H-600×250×12×19	BCP325	SN490B	SN490A
4	500×22	H-600×250×12×19	H-600×250×12×19	BCP325	SN490B	SN490A
3	500×22	H-600×250×12×19	H-600×250×12×19	BCP325	SN490B	SN490A
2	500×22	H-600×250×12×22	H-600×250×12×19	BCP325	SN490B	SN490A
1	500×22	H-600×250×12×22	H-600×250×12×19	BCP325	SN490B	SN490A

Table 1: Column and beam cross-sections, and steel materials.

Floor	Floor Weights W_i (kN)	Distribution A_i	Drift-Based Design Q_i (kN)	Strength-Based Design Q_{un} (kN)	Floor strength Q_u (kN)	Over-strength Factor Q_u/Q_{un}	Modal Analysis
5	6600	1.743	2662	3328	6844	2.06	4.70
4	5523	1.459	3841	4801	9874	2.06	4.17
3	5523	1.275	4753	5953	12243	2.06	3.33
2	5538	1.128	5463	6829	14044	2.06	2.22
1	5567	1.000	5974	7446	15313	2.06	1.00

Table 2: Seismic demand and seismic capacity.

2.2 FEA Model of the Building

One plane frame of the three along the X direction shown in Figure 1 was modelled by the finite element analysis software Abaqus [7]. The overall view of the plane frame (YA) is shown in Figure 2a, while modeling details can be seen in Figure 2b. The model developed is a mixed shell/beam element model that combines the powerful nonlinear S4R shell elements with beam-column elements. Shell elements were used in the critical regions of the building, such as beam-column connections and column at the base, where strong geometrical nonlinearities (e.g., local buckling) are expected to take place. Beam-column elements were used for the rest length of beams and columns which tend to remain mainly in the elastic region. The beam-column connection is fully restrained by diaphragm plates located at the bottom and top of the panel-zone height thus simulating a rigid welded connection. The welding access hole was not modelled. Shell elements were used for a length equal to two times the width of column and depth beam, respectively.

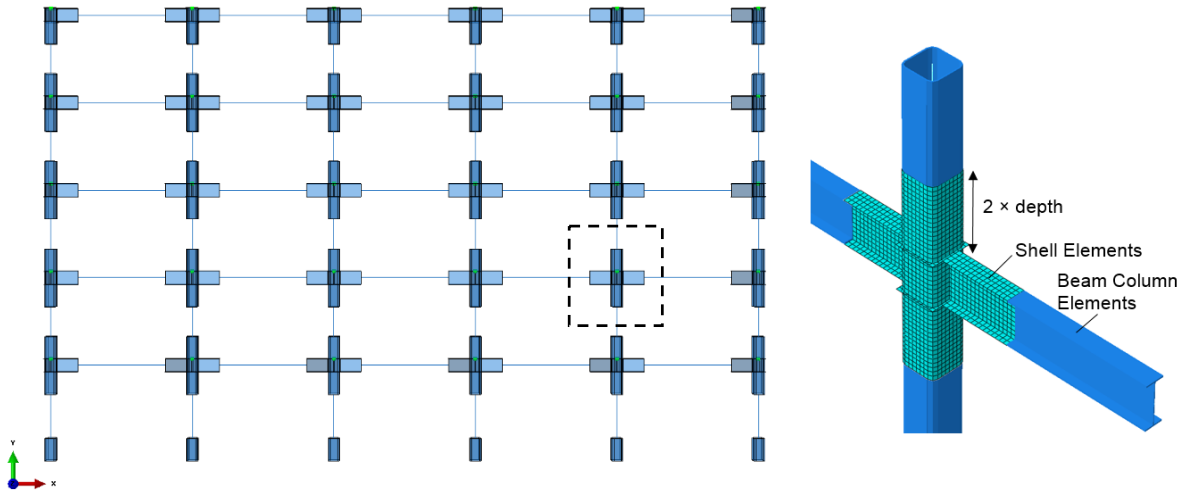

(a) (b)

Figure 2: (a) Overall view of the frame model in Abaqaus; and (b) Modelling details of a beam-column connection.

2.3 Material properties

For sufficiently small straining, steel is modeled as a linear elastic isotropic material with density ρ=7850kg/m^3, modulus of elasticity E=205GPa and Poisson ratio ν=0.3. The constitutive model used for steel includes pressure-independent plasticity with kinematic hardening and is suitable to simulate the inelastic behavior of metals. The evolution of the backstress for the isothermal (temperature independent) material response follows the Ziegler's hardening rule. According to this evolution law, the yield surface is translated in the stress space through the backstress, the rate of which due to plastic straining is in the direction of the current radius vector from the center of the yield surface. The equivalent stress remains constant throughout the analysis, and is equal to its initial value which defines the size of the yield surface at zero plastic strain. The kinematic hardening modulus is linear, and for temperature independent analyses it requires only two stress-strain pairs for its definition: the yield stress at zero plastic strain and a yield stress at a finite plastic strain value. A strain hardening equal to 1.0% of the modulus of elasticity was assigned.

2.4 Analysis

The force distribution that is applied to the structure in each increment of the static adaptive pushover analysis carried out in this study is updated according to the first eigenmode of the structure. This eigenmode is calculated with the use of a shifted block Lanczos algorithm, similar to that developed and described in detail in [11,12]. It is noted that in order to perform an adaptive pushover analysis in Abaqus, none of the analysis types offered by Abaqus can be used since (in the best case) they preserve the load distribution until the analysis is ended. Two types of nonlinear static analysis procedures can be carried out in Abaqus finite element software in order to perform static pushover analysis of any structural model, which are described below, along with their limitations:

- Static analysis with force, displacement and/or force/displacement control. Even in a non-adaptive pushover analysis, it is recognized that this type of Abaqus analysis cannot be used with force-control to trace the descending branch of the material response. Therefore, neither for an adaptive, nor for a non-adaptive constant load pattern pushover analysis can this type of analysis be used.

- Static analysis with arc-length control (Riks). Assuming that the model is loaded with forces of constant pattern, although this analysis can trace the descending branch of the material response, it can trace only a single loading path during the analysis and does not allow the user for control over the force distribution pattern during the pushover analysis. Therefore, for an adaptive load pattern pushover analysis, this type of analysis cannot be used.

Abaqus offers the capability of the restart analysis, which enables the user to stop the analysis at a desired time point and restart at the same or another time point the analysis of an updated version of the model already analyzed. Actually, each increment of the proposed pushover analysis procedure includes a restart analysis, in which the model definitions and all information of the current analysis state is written in a set of restart files. The Abaqus input file is properly updated based on the specified loading definitions in conjunction with the response of the structure calculated so far, and finally the updated input file along with the restart files written at the current increment are read by the restart Abaqus analysis calculating thus the structural response at the next increment.

Since the static Riks analysis with arc-length control cannot distinguish between loading and unloading directions, if the step of the restart analysis is a static Riks step, there is the possibility that the analysis starts from a point different from the last converged equilibrium point, and apply the loading in a direction opposite to the one specified, leading thus the structure to unexpected unloading instead of reloading condition.

For the above reasons, in this study the restart analysis is used only with general static analysis with mixed force and displacement control, as will be shown in a later section. Displacement control is applied by directly specifying the desired displacement at the top of the structure. Force control is applied indirectly through an optimization procedure which ensures that the force pattern is maintained or appropriately updated throughout the pushover analysis. With repeated use of the restart capability, ABAQUS [7] can be consistent with the quasi-static structural loading response.

In each increment of the novel adaptive pushover analysis procedure that is proposed in this study, a static analysis is performed in which both forces and displacements are imposed at the structure. The forces and displacements are imposed in a controlled manner that ensures the linear dependence between the actual force distribution imposed at the structure, $\left\{\tilde{F}_i\right\}$, and the desired force distribution that is based on its fundamental eigenmode, $\left\{\bar{F}_i\right\}$, i.e. that the following relation is satisfied at all storeys of the structure:

$$\tilde{F}_i\left(j\right)=\lambda_i\bar{F}_i\left(j\right),\ j=1,...,5 \tag{4}$$

Since the way of computation of the load proportionality factor λ_i at the i^{th} increment of pushover analysis is not straightforward, it is indirectly calculated through the implementation of an optimization procedure. The optimization problem that is considered at each increment of the

pushover analysis is to find the optimum load proportionality factor λ_i that minimizes the variance of the vector defined by the division of $\{\tilde{F}_i\}$ to $\{\bar{F}_i\}$ in an element-wise manner:

$$R_i(j) = \frac{\tilde{F}_i(j)}{\bar{F}_i(j)},\ j = 1,...,5 \tag{5}$$

If $\mathrm{var}(R_i) = 0$ this means that all the elements of the vector R_i are equal with each other, and equal to λ_i, since it is always $\mathrm{var}(R_i) \geq 0$ by definition. The design variable of the optimization problem is the scalar λ_i and the objective function to be minimized is equal to $F_i^{obj} = \mathrm{var}(R_i)$.

Matlab [8] is employed for carrying out the optimization analysis associated with the mixed force-displacement control static analysis at each increment and operate Abaqus [7] analysis. The optimization algorithm considered in this study for the solution of the optimization problem is the Interior Point Algorithm (IPA). The application Abaqus2Matlab [13] (developed by Papazafeiropoulos et al. [14]) which integrates between Matlab [8] and Abaqus [7] is adopted in this study as a suitable tool for post-processing the analysis results.

3 RESULTS

Figure 3a shows the pushover curves for building model as obtained by utilizing the developed algorithm. The curve is presented in the typical fashion: total lateral force on the building (base shear force) normalized by the total building's weight W on the vertical axis versus roof drift on the horizontal axis. The building is seen to have an over-strength of more than 2 relative to its design base shear of 0.09W. The pushover curve reaches 0.192 W at a roof drift of 0.048 and then descends. The descending branch drops more steeply after reaching a roof drift of 0.10. Gravitational instability is observed at a roof drift of 0.22. Figure 3b shows the normalized by the total weight base shear of each column. External columns reached lower values since they subjected to higher axial loads. The normalized axial loads sustained by each column during the lateral loading are shown in Figure 3c and the bending moment reached is shown in Figure 3d. The building deforms in a collapse mechanism that involves the first two stories. Active plastic hinges are formed in the columns at the building base and just below the second floor level and in the intermediate beams. Figure 4 illustrates the overall view of the collapse mechanism as identified with the proposed method. The failure of local buckling at the columns of second floor level is highlighted.

An additional analysis was also performed utilizing the conventional static algorithm in a single step. Figure 3a compares the conventional pushover curve against the one obtained by utilizing the proposed algorithm scheme. In conventional static pushover analysis, the scaler λ_i is increased over time. However, once the peak of the pushover curve is reached, a converged solution cannot be obtained because the total pushover load being applied is greater than the lateral strength of the structure (assuming there is not a higher peak further out).

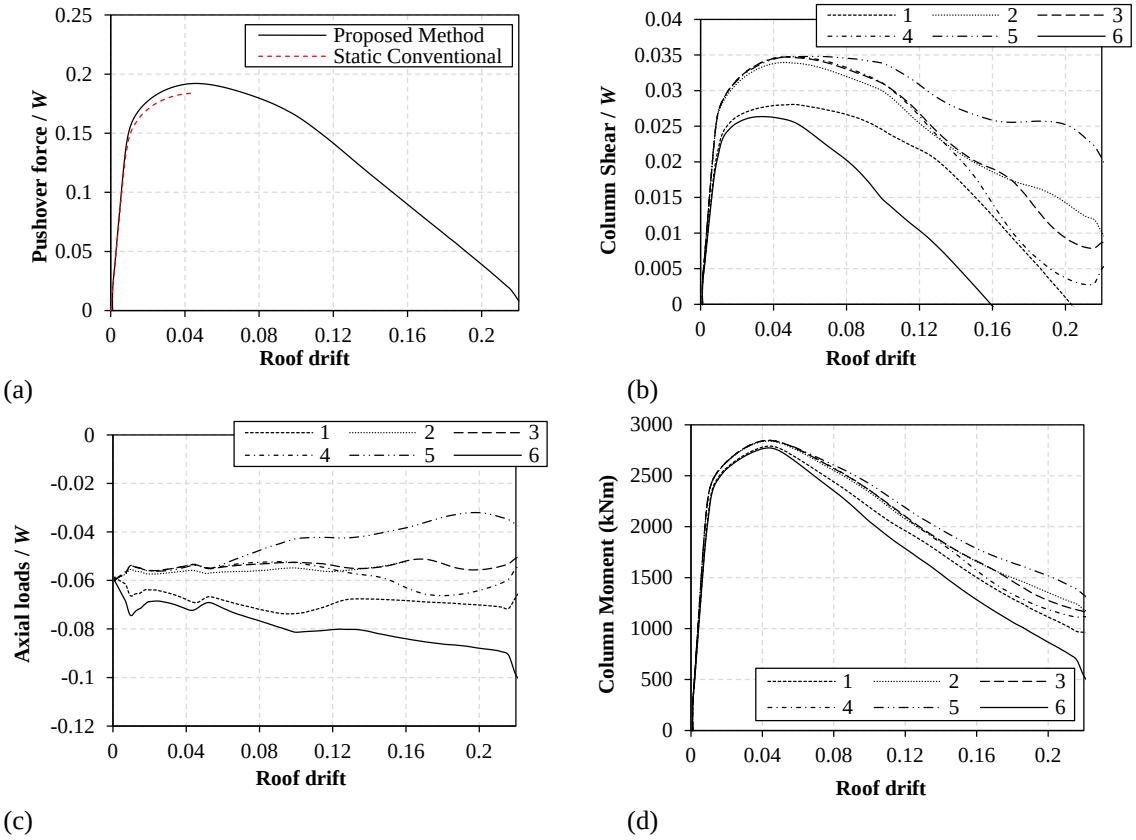

Figure 3: (a) Pushover curve; (b) Base shear at each column; (c) Axial loads; and (d) Bending moment at each column.

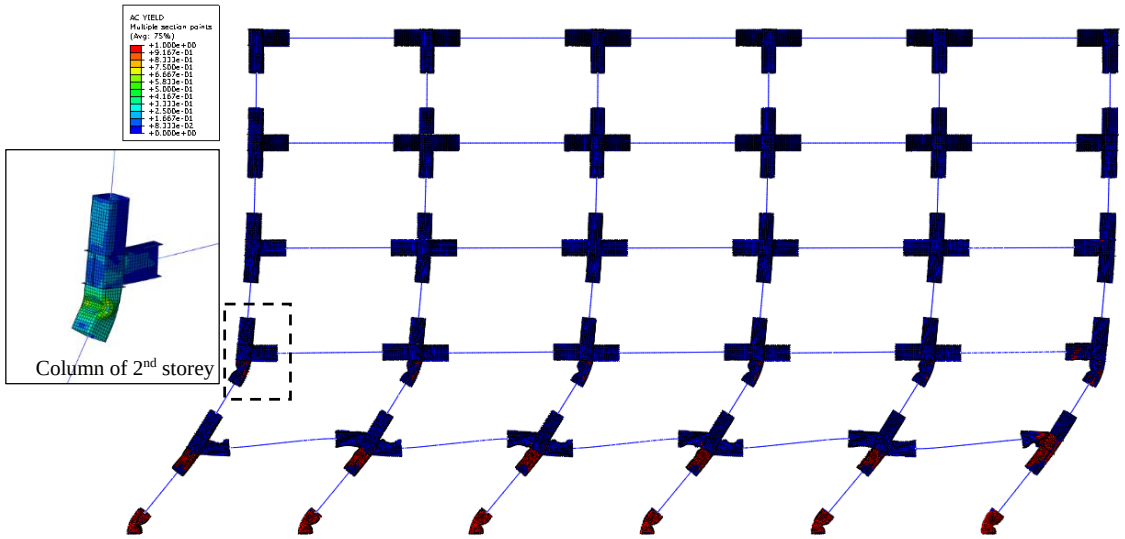

Figure 4: Overall collapse mechanism of the frame model.

Based on the frequency analysis conducted at the first step of the adaptive pushover analysis, the period T of the frame model is equal to 1.02 sec. The mode shape is [1.00; 2.22; 3.33; 4.17; 4.70] while the load proportion factor (LPF) is [1.00; 2.22; 3.28; 4.11; 5.55]. Figure 5a shows the normalized by the building's weight applied loads per floor level and Figure 5b the normalized mode shapes for roof drifts equal to 0.0, 0.072, 0.10, 0.14, 0.202 and 0.22. The modes are

representative ones from those determined during the proposed adaptive pushover analysis. In the following roof drift at which gravitational instability was observed (i.e., 0.22 roof drift), the roof control displacement obtained a negative value for maintaining the force equilibrium of the reduced stiffness forces and applied loads. At this point the analysis was terminated.

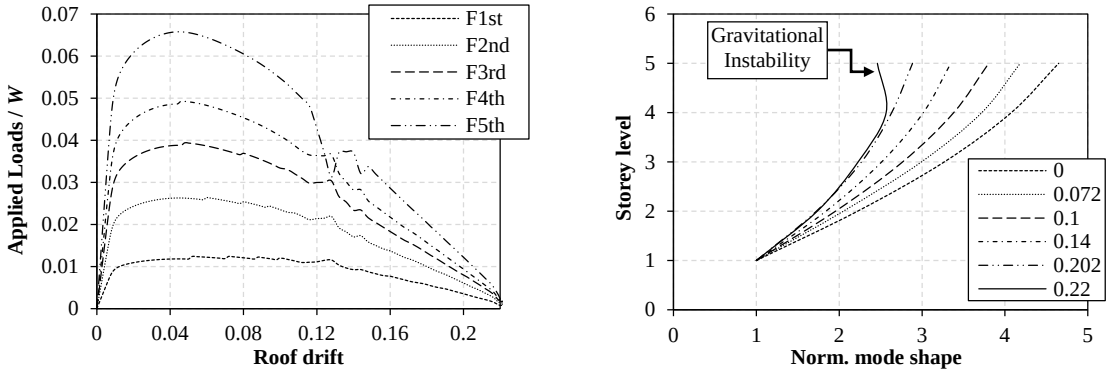

(a) (b)

Figure 5: (a) Applied loads at each storey; and (b) Normalized mode shape for roof drifts 0.0, 0.072, 0.10, 0.14, 0.202 and 0.22.

4 CONCLUSIONS

A computational method which uses the nonlinear adaptive static (pushover) analysis to evaluate the static force-deformation response of structures is presented. The method is validated on a five-storey five-bay steel moment-resisting frame (MRF) designed based on the Japanese seismic design code. Main conclusion of the present study are as follows:

- The computational platform uses finite element modelling methods for members and materials. Failures related to strength and stiffness reduction, such as local buckling, are captured accurately. The load distribution is updated based on subsequent modal analysis (adaptive procedure) accounting for the stiffness reduction.
- The computational platform utilizes the common static analysis of Abaqus without obscure stabilization algorithms or arc-length methods that may become uncontrollable or give erroneous results under certain circumstances. It is mainly a force-based pushover analysis after the post-peak strength point and captures the collapse mechanism.
- The building is seen to have an over-strength of more than 2 relative to its design base shear of 0.09W. The pushover curve reaches 0.192 W at a roof drift of 0.048 and then descends. The descending branch drops more steeply after reaching a roof drift of 0.10. Gravitational instability is observed at a roof drift of 0.22.

REFERENCES

[1] S.A. Freeman, Review of the development of the capacity spectrum method. *ISET Journal of Earthquake Technology*, **41**(1), 1-13, 2004.

[2] A.K. Chopra, R.K. Goel, A modal pushover analysis procedure for estimating seismic demands for buildings. *Earthquake Engineering and Structural Dynamics*, **31**, 561–582, 2002.

[3] P. Panyakapo, Cyclic pushover analysis procedure to estimate seismic demands for buildings. *Engineering Structures*, **66**, 10-23, 2014.

[4] J.M. Bracci, S.K. Kunnath, & A.M. Reinhorn, Seismic performance and retrofit evaluation of reinforced concrete structures. *Journal of Structural Engineering*, **123**(1), 3-10, 1997.

[5] A. S. Elnashai, Advanced inelastic static (pushover) analysis for earthquake applications. *Structural Engineering and Mechanics*, **12**(1), 51-69, 2001.

[6] J.F. Hall, On the descending branch of the pushover curve for multistory buildings. *Earthquake Engineering and Structural Dynamics*, 1–12, 2017.

[7] Dassault Systèmes, Simulia Corp. ABAQUS version 2016 documentation. Providence: Dassault Systèmes, Simulia Corp.; 2016.

[8] MathWorks, Inc. MATLAB R2016a. Natick, MA: MathWorks, Inc., 2016.

[9] BSL, Building standard law, 2000 [in Japanese].

[10] BCJ, Structural provisions for building structures. Tokyo: Building Center of Japan, 1997 [in Japanese].

[11] R. G. Grimes, J. G. Lewis, H. D. Simon, A shifted block Lanczos algorithm for solving sparse symmetric generalized eigenproblems. *SIAM Journal on Matrix Analysis and Applications*, **15**(1), 228-272, 1994.

[12] ABAQUS, Analysis User's Manual version 6.14, Dassault Systems, 2014.

[13] Abaqus2Matlab, 2017, http://www.abaqus2matlab.com.

[14] G. Papazafeiropoulos, M. Muñiz-Calvente, E. Martínez-Pañeda, Abaqus2Matlab: A suitable tool for finite element post-processing. *Advances in Engineering Software*, **105**, 9–16, 2017.

COMPDYN 2019
7th ECCOMAS Thematic Conference on
Computational Methods in Structural Dynamics and Earthquake Engineering
M. Papadrakakis, M. Fragiadakis (eds.)
Crete, Greece, 24-–26 June 2019

IMPACT OF EARLY AGE DAMAGE ON THE SEISMIC RESPONSE OF REINFORCED CONCRETE STRUCTURES

Chaimaa Jaafari[1], Fabien Delhomme[1], David Bertrand[1], Jean-François Georgin[1], Stéphane Grange[1]

[1]Univ. Lyon, INSA-Lyon, GEOMAS, F-69621, Villeurbanne.
20 Avenue Albert Einstein 69100 Villeurbanne.
e-mail: {chaimaa.jaafari, fabien.delhomme, david.bertrand, jean-francois.georgin, stephane.grange}@insa-lyon.fr

Keywords: Early age, pseudo-dynamic, damage, concrete, vulnerabiliy, earthquake.

Abstract. *Reinforced concrete damage over time can cause severe structural problems (e.g. Morandi Bridge in Italy [1]). Many factors contribute to concrete deterioration (Thermal conditions, chemical attacks, shrinkage, creep, carbonatation, corrosion, etc.) [2]. Reinforced concrete deterioration starts at early-age and continues with structure aging. Early-age shrinkage, creep and thermal conditions or initial cracks can have a significant impact on the dynamic behavior of concrete structures. As shown in [3], the natural frequency of a beam subjected to early-age restrained shrinkage is highly affected. In order to quantify the impact of early-age concrete damage on the dynamic behavior of structures, the GEOMAS Lab at INSA Lyon is working on a research project combining both numerical modeling and pseudo-dynamic tests on two groups of reinforced concrete portal frames. The first group is a reference group kept in endogenous conditions during its early age period in a way to limit drying effects leading to cracks while the second group is kept in non-endogenous conditions similar to construction site conditions, which induces damage. The present paper focuses on the enhanced multifiber beam model developed for the portal frames and that allows describing their behavior when subjected to a seismic loading while taking into account their initial damage due to early age effects. Future papers will deal with experimental results obtained using the pseudo-dynamic technique. In the numerical model developed, concrete shrinkage and thermal deformation are calculated independently using a THC 3D model [4] , while creep is described by a series of three Kelving-Voigt models [5] and calculated using strain superposition in series with concrete μ Damage model [3]. Then values are implemented into a multifiber finite element model. Damage evolution of the RC structures over time is followed using the numerical model during 28 days and then their dynamic response when subjected to a seismic event is simulated numerically.*

1 INTRODUCTION

In 2018 the Morandi Bridge collapsed in Italy as well as buildings in France causing many deaths. Such dramatic events remind us that during their aging process reinforced concrete structures get damaged and become more vulnerable. This damage starts at early age and continues during the life time of the structure (Figure 1). It can be caused by creep, shrinkage, corrosion, thermal deformation, carbonatation and so on [2]. As a consequence of this damage, the structure becomes more vulnerable and can collapse either due to its self weight and live loads or due to accidental hazards such as an earthquake or an impact. This paper focuses on the impact of the initial damage that takes place during the early age period (0-28 first days) on the seismic response of reinforced concrete structures. In RC design, early age damage is often neglected and it is roughly assumed that the structure is initially undamaged when put into service. Early age effets on structure dynamic performances need to be quantified.

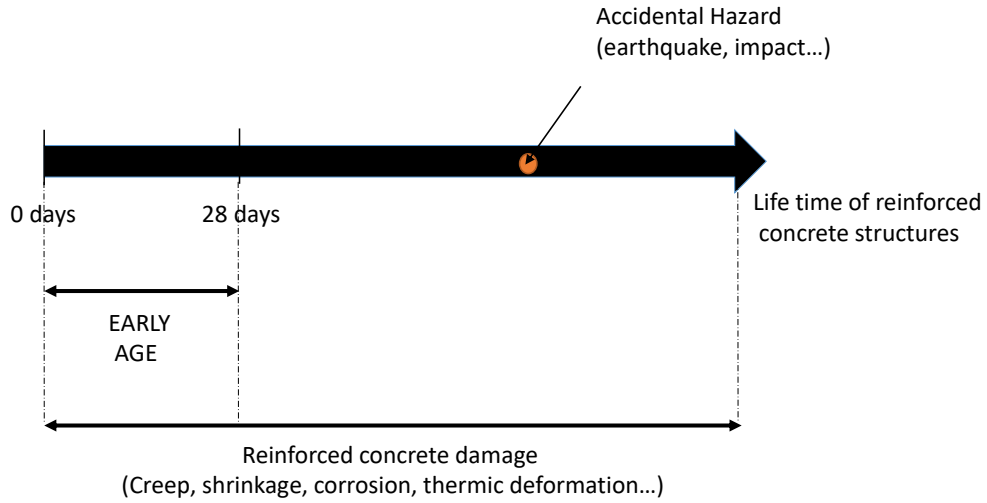

Figure 1: RC deterioration over time

1.1 Methodology

Two types of reinforced concrete portal frames are considered (Figure 2). A first group kept during its early age period in endogenous conditions (by covering it using a plastic sheet) in a way to limit drying effects leading to cracks. It's supposed to be a reference group where almost no damage should happen. The second group will be kept in non-endogenous conditions that are similar to the ones found on construction sites. Consequently, its initial damage will be more important. An enhanced multifiber beam model was developed for each group which allows following their early age damage due to creep, shrinkage, thermal deformation and to evaluate their response under an earthquake. It is based on the THC model of Buffo Lacarrière [4], on the creep model of Briffaut [5] and on the μ damage model [3].The enhanced concrete non-linear constitutive law used will be explained in details. Results obtained with this numerical model will be presented in this paper. In parallel, pseudodynamic tests on the two portal frame groups are still undergoing. Using such technique, which is an interesting alternative to shaking table

tests [6], the same seismic load will be applied on the two types of portal frames after their early age period in order to determine their dynamic response.

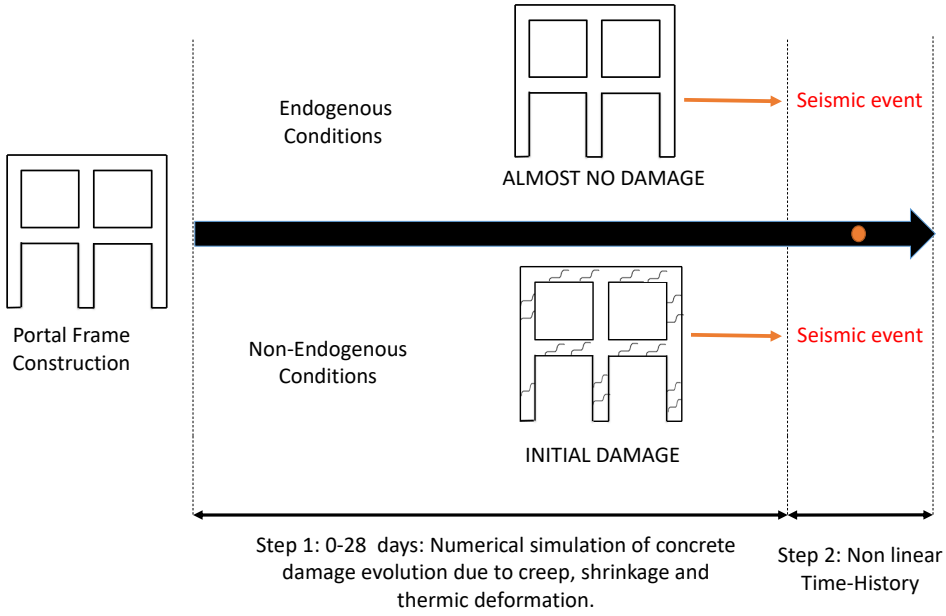

Figure 2: Methodology

Ultimately, the objective of the research project undergoing will be to compare purely numerical results with pseudo-dynamic resuls in order to validate the numerical model and to determine the impact of early age damage on the seismic response of reinforced concrete structures.

2 NUMERICAL MODEL

This section presents in details the numerical model developped for the portal frames.

2.1 Geometry of the structures

Studied portal frames are 1.05 meter by 1.1 meter structures as shown in Figure 3a. Longitudinal and transverse reinforcements were designed in a way to comply with Eurocodes requirements. Chosen longitudinal and transverse reinforcements have a diameter of 6 mm (Figure 3b). Figure 3c presents the experimental set up that will be used in portal frames pseudo-dynamic tests.

2.2 Material properties

Concrete used in the portal frames has a compressive strength of 30 MPa and a tensile strength of 3.7 MPa. Steel reinforcements have a yield stress of 500 MPa.

2.3 Finite Element discretization

Figure 4b gives node numbers that were used in the finite element model that was developed for the portal frames. The structures are subjected to 3 concentrated masses (M_1, M_2 and M_3)

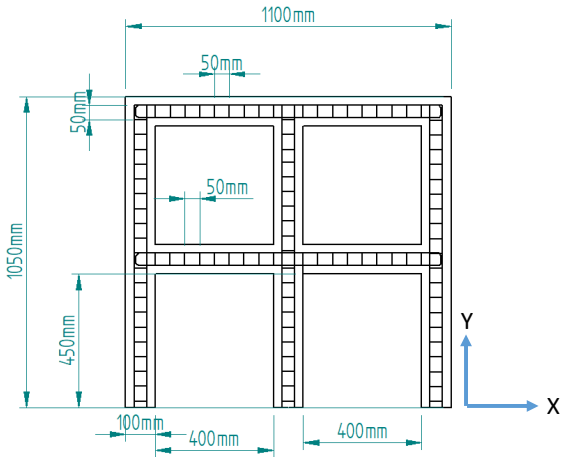

(a) Front view

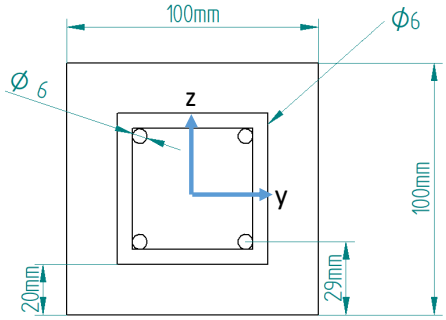

(b) Cross-section

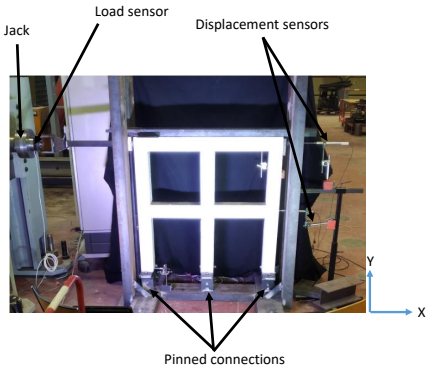

(c) Portal frame experimental set up

Figure 3: Geometry of the RC portal frame

(orange circles) representing the contribution of upper floors. $M_1 = M_2 = M_3 = 1148\ kg$. Therefore, $M_{tot} = M_1 + M_2 + M_3 = 3444.4\ kg$. Where M_{tot} is the total mass of the frame (self weight is neglected). The same concentrated masses will be simulated numerically when conducting pseudo-dynamic tests on the portal frames. As seen in figure 4b the structures are pinned at their three ends. It was chosen to use pinned ends rather than fixed ends since such type of connections are more commonly used in constructions (it is very hard to realize fixed connections in practice).

2.4 Multifiber beam model

The portal frame was devided into 3D Timoshenko beam elements, where each beam element is composed of two nodes. At each node there are 6 degrees of freedom: 3 rotations and 3 displacements. Each beam element is composed of 2 Gauss integration points and each integration point represents a cross section made of concrete and steel fibers (for the reinforcements). Concrete fibers are located at the section Gauss points. Using shape functions, displacement value can be calculated at any point of the beam element knowing displacement values at the

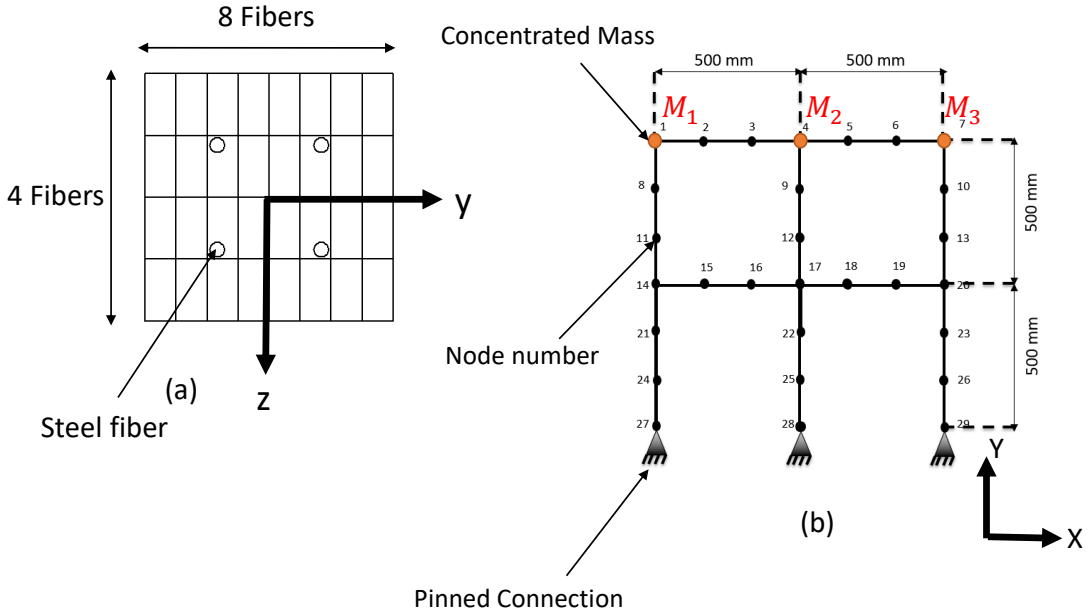

Figure 4: (a) Multifiber cross-section and (b) Finite element mesh and concentrated masses

nodes. Timoshenko kinematic then allows determining strain values at the different fiber elements with displacement values. Then, using a non-linear strain to stress relation stress is determined at the different fibers. Through integration over the cross section, force values at the Gauss points are determined. Figure 5 summarizes the principle of the multifiber beam model used for the portal frames ([10] and [7]). Where: K= Stiffness Matrix; a_s= Section compatibility Matrix; B= Gradient Metric; L= Length of the beam element; U= Nodal displacement; σ = Stress Matrix; P=Load Vector; ϵ= Strain Matrix. Figure 4a gives the multifiber reinforced concrete cross-section used for the concrete portal frames. Its is composed of 32 concrete fibers: 4 fibers in the z direction and 8 fibers in the y direction. 4 additional fibers are used to model steel longitudinal reinforcements (x axis).

2.5 Constitutive Laws

Strain and stress calculation details are given hereafter.

2.5.1 Constitutive laws for concrete

Strain decomposition Deformation at each concrete fiber is calculated in a way to take into account the influence of shrinkage, ceep, thermal deformation, and mechanical deformation. The total deformation at a fiber element is considered to be equal to the sum of all 4 contributions. Hence:

$$\epsilon_{tot} = \epsilon_{shrinkage} + \epsilon_{thermal} + \epsilon_{creep} + \epsilon_{mechanical} \tag{1}$$

Mechanical model Strain to stress relationship for concrete fibers is determined using a non-linear Mazars μ model [8]. This model is based on continuum mechanics. It relates deformation

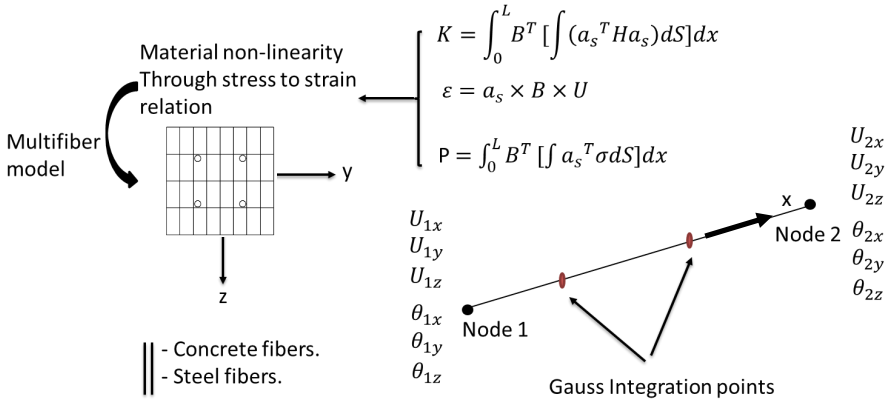

Figure 5: Principle of the multifiber beam model ([7] [10])

to stress using a damage variable D that can be calculated using a thermodynamics framework based on two variables Y_t and Y_c for concrete cracking and crushing.

$$\sigma = \Delta_0(1 - D) : \epsilon \tag{2}$$

$$Y = rY_t + (1 - r)Y_c \tag{3}$$

$$D = 1 - (1 - A)\frac{Y_0}{Y} - Ae^{-B(Y - Y_0)} \tag{4}$$

Where: Δ_0 = Stiffness Matrix; ϵ = Strain Matrix; σ = Stress Matrix; D = Damage; r = Triaxiality factor; A and B and constant parameters; Y_0 is the initial elastic treshold (takes into account compression and traction contributions). Thus, a 1D cyclic strain to stress relation is used at each concrete fiber as shown in Figure 6a. Where σ_{xx} stands for normal stress along the concrete fiber axis.

Creep model Since strain due to creep and to mechanical deformation are related to each other, an intermediate subsystem as shown in Figure 7 is solved. It is composed of 3 viscoelastic Kelving-Voigt models for creep [5] in series with a non-linear Mazars μ model for concrete [3]. Creep evolution follows a Briffaut model [5] where creep 1 is the primary creep (also known as the transient creep), creep 2 is the secondary creep (also called steady-state creep) and creep 3 is the tertiary creep and has an exponential evolution. Each creep model uses 2 viscoelastic constants τ and k_∞. $\tau_1 = 0.1\ day$; $\tau_2 = 1\ day$; $\tau_3 = 10\ days$ and $k_{1\infty} = 3 \times 10^{11}(\mu m/m)$; $k_{2\infty} = 9 \times 10^{10}(\mu m/m)$; $k_{3\infty} = 2.5 \times 10^{10}(\mu m/m)$. Those values were determined through calibration tests [3] .

Shrinkage and thermal deformations Shrinkage and thermal deformations are calculated independently using a THC (Thermo-hygro-chemo) model with COMSOL Software. The model is based on the work of Buffo-Lacarrière [4] and Mainguy [13]. In such model, the

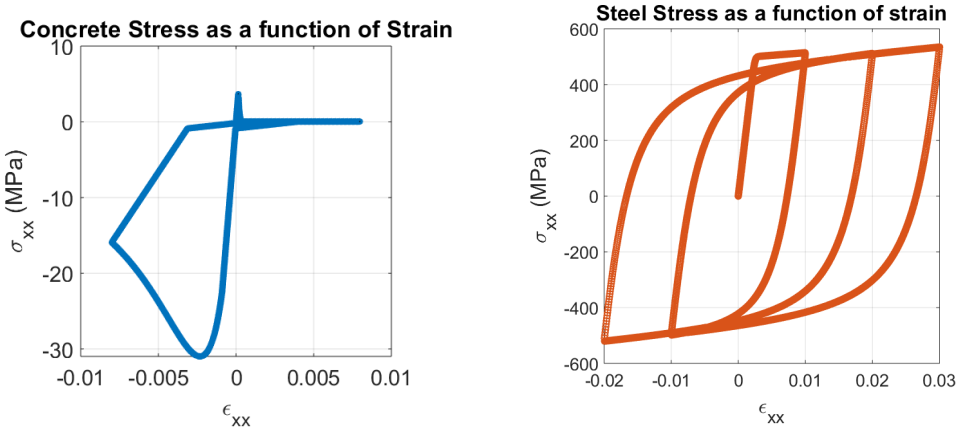

(a) Concrete Cyclic μ model [8] (b) Steel Cyclic model [9]

Figure 6: Material constitutive laws

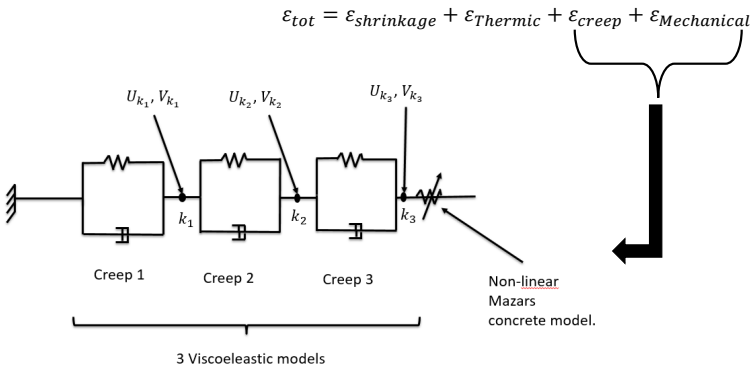

Figure 7: Strain calculation at a fiber element [3] [5]

degree of saturation of the mortar is calculated by solving three sets of differential equations based on conservation laws: liquid water, water vapour and wet air equilibrium equations. The evolution of the total porosity as well as the distribution of pores were taken into account when solving the equilibrium equations to account for early age effects. Using the equivalent pore pressure of cement based materials concept as explained by Coussy [14] shrinkage evolution is then calculated. As for thermal deformation, it was calculated by solving a heat transfer thermal conduction differential equation. All differential equations were solved using COMSOL software and model parameters were calibrated to account for the properties of concrete used in the portal frames.

2.5.2 Constitutive law for steel

For steel reinforcements, a non-linear 1D Menegotto cyclic model with strain hardening [9] is used as presented in Figure 6b. Here, σ_{xx} stands for normal stress along the steel fiber axis.

2.5.3 Material parameters

Table 1 gives concrete and steel parameters used in the numerical model of the portal frames.

Concrete parameters	Steel parameters
$E = 25\ GPa$	$E = 210\ GPa$
$A_t = 0.8$	$F_y = 500\ MPa$
$A_c = 1.62$	
$B_t = 20000$	
$B_c = 500$	
$f_t = 3.67\ MPa$	
$f_c = -10\ MPa$	
$\beta_1 = 0\ MPa$	
$\beta_2 = 0\ MPa$	

Table 1: Concrete and Steel reinforcements model parameters

Where: E= Elastic modulus; ν= Poisson ratio; Y_{01}= Initial damage treshold for traction; Y_{02}= Initial damage teshold for compression; A_t= 1st parameter govering the evolution of damage (traction); A_c = 1st parameter govering the evolution of damage (compression); B_t= 2nd parameter governing the evolution of damge (traction); B_c= 2nd parameter governing the evolution of damage (compression); β_1= anelastic parameter for traction; β_2= anelastic parameter for compression and F_y = Steel yield stress.

2.6 Input Data

Shrinkage and temperature evolutions calculated using COMSOL were implemented into the multifiber model by interpolation. Figure 8 gives shrinkage and temperature evolutions used as input datas of the numerical model (values at the concrete fibers).

3 Results

With the enhanced multifiber beam model presented in section 2, concrete damage was followed during the 28 first days of the life time of the two portal frame groups. A modal analysis and spectral analysis were performed in order to quantify the difference in response of both structures after their early age period. A static pushover and a non-linear dynamic analysis were also numerically conducted. Results of those simulations are presented in this section.

3.1 Early Age Damage Evolution

Damage evolution due to shrinkage, creep and thermal deformation was followed for the endogenous and non-endogenous portal frames during their early age period (0-28days). The following results were obtained: During step 1, damage at the different concrete fibers remained

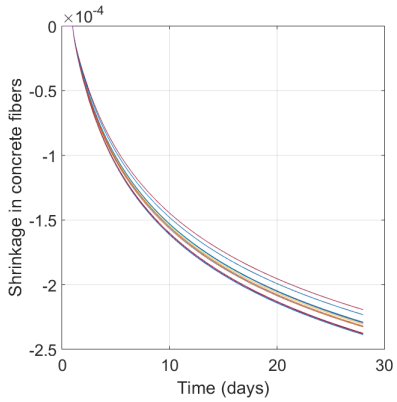

(a) Endogenous case Shrinkage

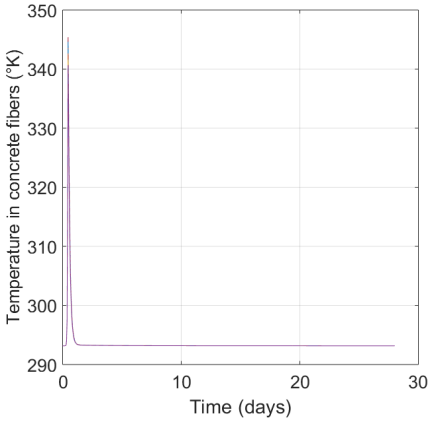

(b) Endogenous case Temperature

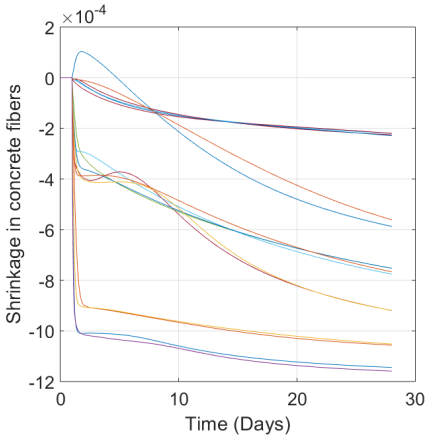

(c) Non-Endogenous case Shrinkage

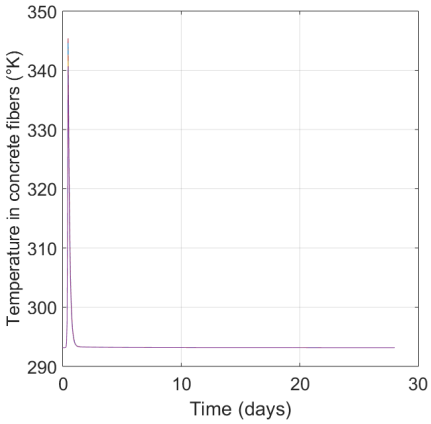

(d) Non-Endogenous case Temperature

Figure 8: Shrinkage and temperature evolutions (at the concrete fibers)

equal to 0 in the portal frame kept in endogenous conditions as shown in Figure 9a since stress value remained below the maximum allowable concrete tensile stress (Figure 9b). In the portal frame kept in non-endogenous conditions, damage increased during the early age period at the different concrete fibers (Figure 9c) since stress reached its maximum allowable value R_t of 3.7 MPa (Figure 9d). Concrete damage during the early age period is thus more important in the non-endogenous case than in the endogenous case because of shrinkage.

3.2 Modal Analysis

After 28 days (end of step 1 as shown in Figure 2), a modal analysis was performed on both groups. The 3 mode shapes are presented in Table 2. Natural frequencies were calculated after early age for both groups as shown in Table 3. Where f_1= First Natural frequency; f_2= Second Natural frequency and f_3= Third Natural frequency. For the endogenous portal frame, there is no decrease of the natural frequency after the first step since no damage occured. In the non endogenous case, an important damage happened during the first step due to shrinkage, which induced concrete to reach its maximum tensile stress value. A modal analysis performed after that first step showed a decrease (Table 2) of its first natural frequency of about 53% (f_1

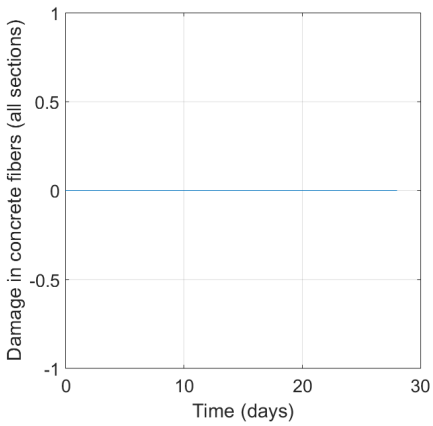

(a) Endogenous portal frame Damage

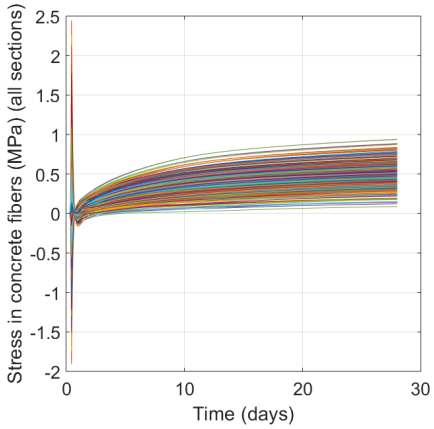

(b) Endogenous portal frame Stress

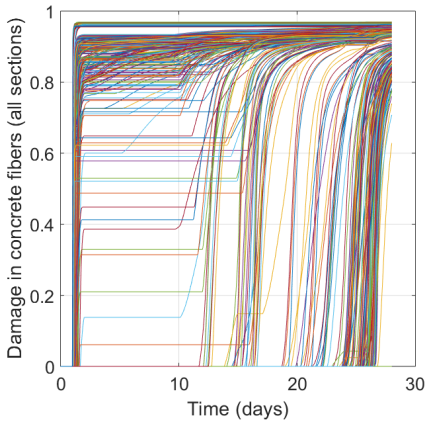

(c) Non-Endogenous portal frame Damage

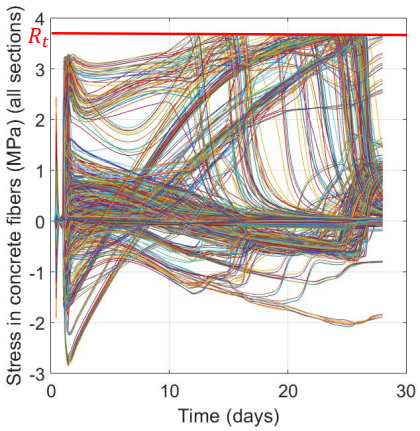

(d) Non-Endogenous portal frame Stress

Figure 9: Damage and normal stress (σ_{xx}) evolutions at early age in all portal frame concrete fibers (many fibers get damaged at early age)

decreased from 6.8 Hz to 3.2 Hz).

It should be noted that the behaviour of the portal frames will be mainly dictated by mode 1. Indeed, concentrated masses on top are very important compared to the self weight of the portal frame. Consequently, effective modal mass participation calculation shows that the total mass M_{tot} of the structure is almost equal to the effective modal mass participation of mode 1. Effective modal mass participation m_{eff_i} of mode i is calculated as follows:

$$m_{eff_i} = \frac{(\phi_i^T M \delta)^2}{\phi_i^T M \phi_i}; \tag{5}$$

Where: ϕ_i is the mode shape value at mode i; M is the structure mass matrix and δ is the projection vector. For instance the endogenous case gives the following results: $M_{tot} = m_{eff_1} + m_{eff_2} + m_{eff_3} \approx m_{eff_1} = 3444.4\ kg$. Thus, the structure behaves as a one degree of freedom system of mass M_{tot}.

Mode1	Mode2	Mode3
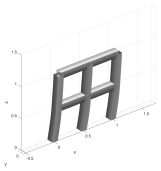	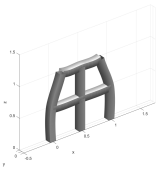	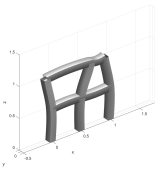
f_1	f_2	f_3

Table 2: Portal frame mode shapes

	Endogenous	Non-Endogenous
f_1 (Hz)	6.8	3.2
f_2 (Hz)	110.7	71.2
f_3 (Hz)	190.8	123.0

Table 3: Natural frequency values at the end of 28 days

3.3 Spectral Analysis

Modal analysis showed that there is a difference in behaviour between the portal frame that was kept in endogenous conditions and the one that was kept in non-endogenous conditions (change in frequency content). In order to further illustrate this difference, a spectral analysis was performed on the portal frames using a Eurocode (French annex) non-linear Time History (Figure 10a). The response spectrum obtained using this non-linear Time History is given in Figure 10b. Spectral Analysis conducted on the two types of portal frames using the Eurocode

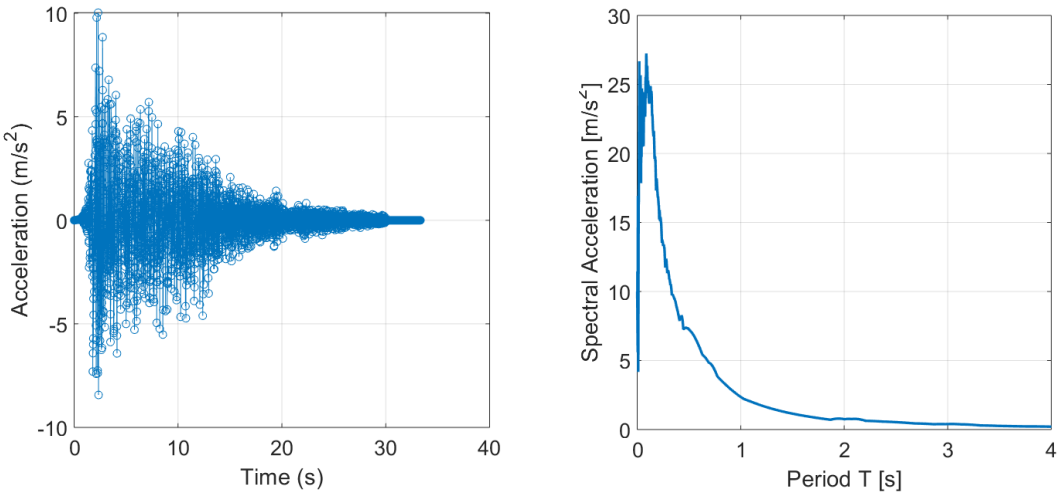

(a) Time History [12] (b) Pseudo-acceleration Response Spectrum

Figure 10: Eurocode input data for spectral analysis

accelerogram showed (Figure 11) that the maximum base shear in the endogenous case is equal to 78 kN while it is equal to 42 kN in the non-endogenous case (about 46% decrease). Maximum

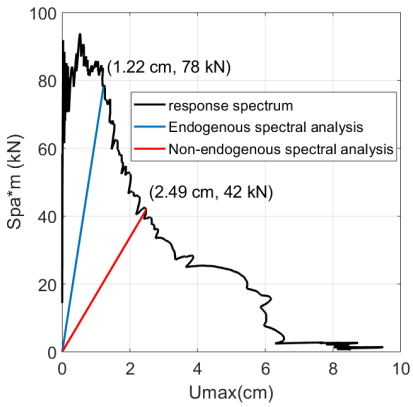

Figure 11: Spectral Analysis results

Base shear is calculated by summing up base shear values F_i^{max} at each mode i.

$$F_i^{max} = \frac{S_{pa} \times \phi_i^T M \delta}{\phi_i^T M \phi_i} M \phi_i; \tag{6}$$

Where: S_{pa} is the spectral acceleration of mode i; ϕ_i is the mode shape value at mode i; M is the structure mass Matrix and δ is the projection vector.

3.4 Static Pushover

A numerical pushover was performed on both groups after their early age period. An incremental displacement was imoposed at node 1 (Figure12b) until reaching the maximum capacity of structures. Load and displacement values at node 1 are calculated in order to plot pushover curves. Results are given in Figure 12a. It can be seen that the initial slope in the endogenous case is 53% higher than the one of the non-endogenous case, while their maximum capacity is similar and equals approximately 16 kN. Pushover results suggest that the behaviour of such structures when subjected to a moderate earthquake will be different while if they are subjected to a very devastating earthquake that cause them to reach their maximum capacity their behavior will be similar.

3.5 Dynamic Analysis

A moderate 0.13 g synthetic accelerogram of the city of Nice (Figure 13a) was applied numerically on the portal frames. Such signal was already used for experimental analysis in [11] and complies with French standards. Load as a function of displacement curves were plot (Figure 13b). Results show that there is a significant difference in behavior between the endogenous and non-endogenous cases. Dynamic curves have the same initial slope as spectral analysis curves, then their slope decreases due to stiffness decrease. Displacement and force evolutions over time are presented in Figures 13c and 13d. It can be seen that the maximum displacement in the non-endogenous case is 30 % higher than the endogenous case while the maximum force is 16 % higher in the non-endogenous case than in the endogenous case. The behaviour of the two portal frames groups is very similar (14) when they are subjected to a

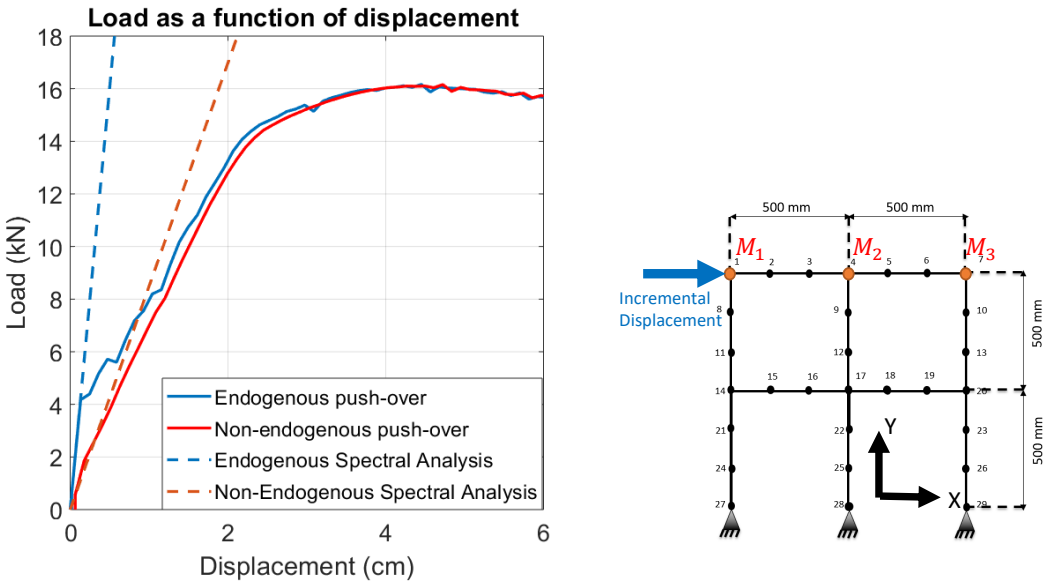

(a) Pushover results

(b) Pushover loading

Figure 12: Static numerical pushover loading (12b) and results (12a)

Eurocode devastating synthetic Time History [12] (French annex) as it causes them to reach their maximum capacity.

4 CONCLUSIONS AND PERSPECTIVES

Hence, numerical multifiber finite element models that allow assissing the behavior of RC structures under a seismic loading while accounting for early age damage were developed. Such models showed that the first natural frequency of a portal frame that was kept during its early age period in non-endogenous conditions, decreases by 53% after its first 28 days while it remains constant for a portal frame kept at early age in endogenous conditions. Under a non-linear moderate intensity accelerogram, portal frames kept in endogenous and non-endogenous conditions during their early age behave differently. It was noticed that the maximum displacement in the non-endogenous case is 30 % higher than the endogenous case whereas the maximum force is 16 % higher in the non-endogenous case than in the endogenous case. Pseudodynamic tests are undergoing on the RC structures. Experimental results will be compared to numerical ones in order to improve and validate the numerical model.

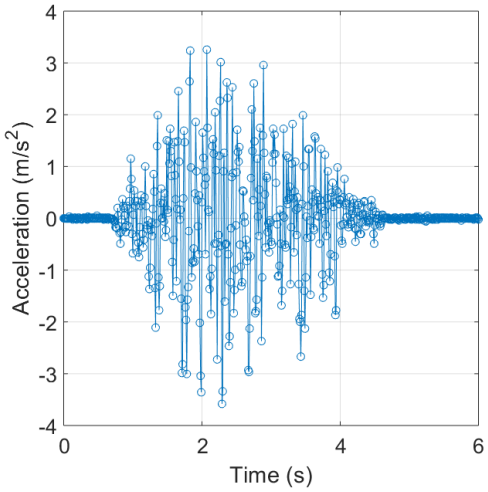

(a) 0.13 g accelerogram of Nice city ([11])

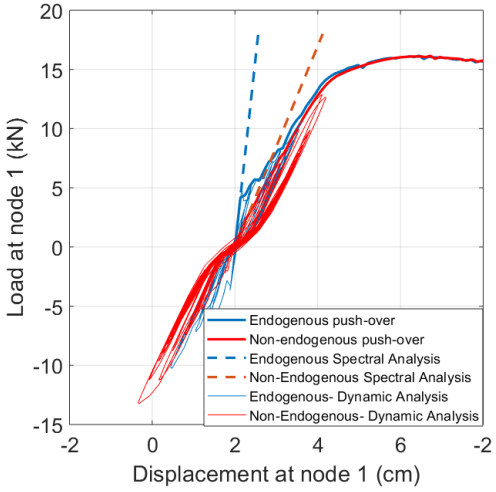

(b) Load Displacement curve

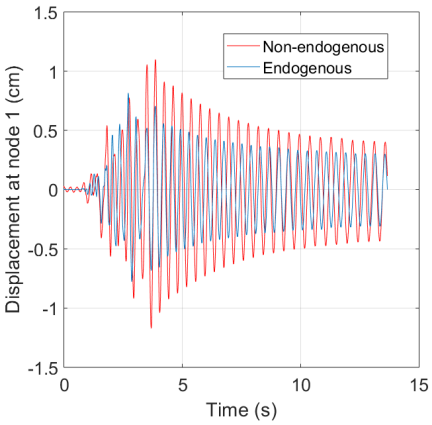

(c) Displacement over time

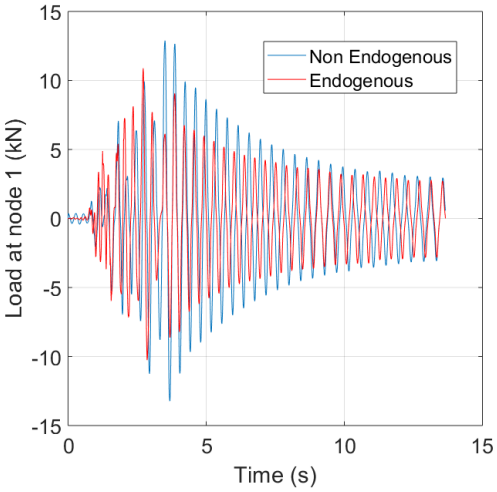

(d) Load over time

Figure 13: Dynamic analysis results using a non linear moderate intensity accelerogram

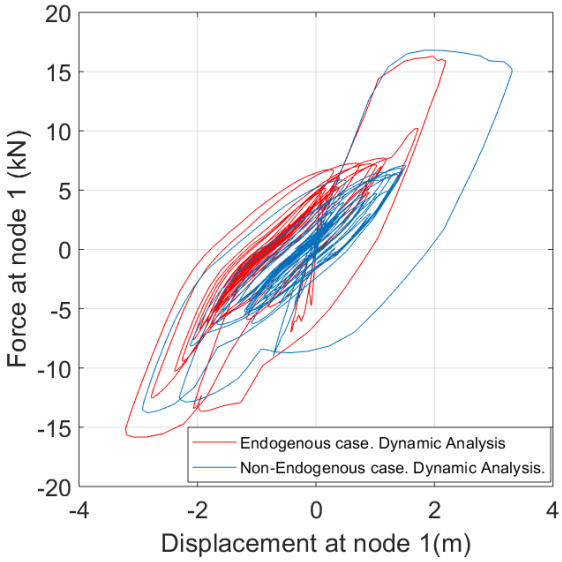

Figure 14: Dynamic results under Eurocode synthetic signal [12]

REFERENCES

[1] Caprani, Colin. *Genoa bridge collapse a sign of things to come if infrastructure maintenance ignored*, 2018.

[2] Portland Cement Association. *Types and causes of concrete deterioration*, Portland Cement Association: Skokie, IL, USA,2002.

[3] Mazars J., Grange S., Briffaut M. *Simplified modeling strategy for the thermomechanical analysis of massive reinforced structures at an early age.* Applied Science, MDPI, 2018.

[4] L. Buffo-Lacarrière. *Prévision et évaluation de la fissuration précoce des ouvrages en béton.* These de doctorat, Université de Toulouse France, 2007.

[5] M. Briffaut, F. Benboudjema, J.M. Torrenti, G. Nahas. *Numerical analysis of the thermal active restrained shrinkage ring test to study the early age behaviour of massive concrete structures.* Eng. Struct, 33, 1390–1401, 2011.

[6] Combescure, Pegon. *α-Operator splitting time integration technique for pseudodynamic testing error propagation analysis.*Soil Dynamics and Earthquake Engineering, 1997,vol.16, no 7-8, p. 427-44.

[7] Bitar Ibrahim, Stéphane Grange, Panagiotis Kotronis, and Nathan Benkemoun.. *A comparison of displacement-based Timoshenko multi-fiber beams finite element formulations and elasto-plastic applications.* European Journal of Environmental and Civil Engineering 22, no. 4: 464-490, 2018.

[8] Mazars, Jacky, François Hamon, and Stéphane Grange. *A new 3D damage model for concrete under monotonic, cyclic and dynamic loadings.* Materials and Structures 48, no. 11: 3779-3793, 2015.

[9] M. Menegotto. *Method of Analysis for Cyclically Loaded Reinforced Concrete Plane Frames Including Changes in Geometry and Nonelastic Behavior of Elements under Combined Normal Force and Bending.* In IABSE Symposium on Resistance and Ultimate Deformability of Structures Acted on by Well-Defined Repeated Loads, Final Report, Li. 1973.

[10] P. Kotronis, J. Mazars. *Simplified modelling strategies to simulate the dynamic behaviour of R/C walls.* J. Earthq. Eng , 9, 285–306, 2005.

[11] D. Combescure, T. Chaudat, Direction des Réacteurs Nucléaires. *Départe-ment de Mécanique et de Technologie, ICONS European program seismictests on R/C walls with uplift*. CAMUS IV specimen, ICONS project, Rapport,2000.

[12] CEN.Eurocode 8. *Design of Structures for Earthquake Resistance - Part 1: General Rules, Seismic Actions andRules for Buildings, EN 1998–1. European Committee for Standardization*. Bruxelles, Belgium, 2005.

[13] Mainguy, Marc. *Modèles de diffusion non linéaire en milieux poreux. Applications à la dissolution et au séchage des matériaux cimentaires.* PhD diss., Ecole Nationale des Ponts et Chaussées, 1999.

[14] Coussy, Olivier, Patrick Dangla, Thierry Lassabatère, and Véronique Baroghel-Bouny. *The equivalent pore pressure and the swelling and shrinkage of cement-based materials.* Materials and structures 37, no. 1 (2004): 15-20.

COMPDYN 2019
7th ECCOMAS Thematic Conference on
Computational Methods in Structural Dynamics and Earthquake Engineering
M. Papadrakakis, M. Fragiadakis (eds.)
Crete, Greece, 24–26 June 2019

NONLINEAR DYNAMIC RESPONSE AND PROGRESSIVE COLLAPSE OF RC FRAMED BUILDINGS UNDER MULTIPLE COLUMN-LOSS SCENARIOS

Martina Scalvenzi[1] **and Fulvio Parisi**[2]

[1] Department of Structures for Engineering and Architecture, University of Naples Federico II,
Via Claudio 21, 80125 Naples, Italy
email: {martina.scalvenzi,fulvio.parisi}@unina.it

Abstract

Progressive collapse consists in the spreading of local damage from element to element, which results in the collapse of the entire structure or a large part of it. To avoid progressive collapse, the structure should withstand events like fire, explosions, impact or the consequences of human error, without being damaged to an extent disproportionate to the original cause. In this study, nonlinear dynamic response of a reinforced concrete framed structure to multiple column-loss scenarios is investigated by means of fiber-based finite element capacity models and incremental-mass dynamic analysis. The influence of removal of two columns on the behavior of the structure is evaluated. The residual capacity of the structure was assessed under varying location and time of columns' removal. Two different multiple column-loss scenarios were explored, namely simultaneous and sequential removals. Analysis results allow the worst scenarios to be identified, as well as the sensitivity of progressive collapse resistance to be evaluated.

Keywords: Progressive collapse, Robustness, Reinforced concrete buildings, Column loss, Nonlinear dynamic analysis.

1 INTRODUCTION

Extreme events can produce a special type of structural failure that is named progressive collapse and is characterized by damage propagation from a portion of the structure to the whole structural system or a significant part of it. Such a type of systemic failure is referred to as disproportionate collapse when damage propagation produces a disproportion in size between the final and initial amounts of damage. Many structures have suffered progressive collapse, motivating a growing research on this topic in the last twenty years [1]. The Ronan Point apartment building in London, UK, which partially collapsed after a gas explosion, and the Murrah Federal Building in Oklahoma City, Oklahoma, which was destroyed by a bomb explosion, are two symbolic events that have contributed to increase the worldwide interest on progressive collapse. Nonetheless, a few studies have been carried out to assess the influence of multi-column loss on nonlinear dynamics and progressive collapse resistance of reinforced concrete (RC) building structures [2-4]. This work is aimed at investigating the capacity of RC framed buildings subjected to either simultaneous or sequential, sudden loss of couples of columns at the ground floor. The loss of multiple columns can be induced by several actions such as detonation of explosives at different locations and impact of objects dragged by floods or flow-type landslides.

2 METHODOLOGY AND CASE-STUDY STRUCTURE

The building under study is a RC framed structure investigated in previous studies (see e.g. [5]), from which a two-dimensional (2D) capacity model was extracted to carry out progressive collapse simulations. The structure was designed only to gravity loads, according to Eurocode 2 [6], and consists of five floor levels, five primary frames with six bays in the *x*-direction and seven secondary frames with four bays in the *y*-direction. Primary frames provide the main support to one-way slabs and one of those 2D framed systems is considered herein. The case-study structure is characterized by the same span length in both directions ($L_x = L_y = 5$ m) and the interstory height is 3 m at each floor. Column and beam cross sections are 400×400 mm^2 and 300×500 mm^2, respectively. Uniform longitudinal reinforcement consisting of 8 Ø18 was assigned to columns, while 6 Ø18 were used to reinforce beams. Transverse reinforcement is composed of Ø8 stirrups with spacing of 200 mm, both in beams and columns. Concrete and steel properties are listed in Table 1.

Material	Property	Value [MPa]
Concrete	f_{ck}	20
	f_{cd}	11.3
Steel	f_{yk}	450
	f_{yd}	391.3

Table 1: Material properties.

Design strengths of concrete and reinforcing steel were defined as $f_{cd} = 0.85f_{ck}/1.5$ and $f_{yd} = f_{yk}/1.15$, respectively, where f_{ck} and f_{yk} denote the characteristic values of cylinder concrete strength and yielding steel strength.

The structure was modeled through the FE code Seismostruct [7], in which the nonlinear capacity modeling of the structure was based on a spread plasticity approach with force-based fiber formulation. The use of fiber elements allows the flexural, arching and catenary behavioral modes of RC beams to be well simulated [6,8-10]. A force-based formulation was assumed to accurately simulate the deformed shape during progressive collapse analysis. Each

cross section was discretized in 200 fibers. A simple bilinear hysteretic model with isotropic strain hardening was assigned to reinforcing steel. The uniaxial uniform confinement model by Mander et al. [11] was used for concrete, explicitly accounting for tension softening and conservatively omitting strain rate effects in the simulations [12].

Nonlinear time history analysis (NLTHA) was carried out using a tangent stiffness-proportional Rayleigh damping and the Newton-Raphson algorithm with a displacement/rotation based convergence criterion to iteratively equilibrate loads.

The progressive collapse capacity of the structure was assessed through IDA, which is a series of NLTHAs performed with an incremental intensity of gravity loads. According to UFC guidelines [13], the following design load combination was used:

$$Q_{bd} = 1.2DL + 0.5LL \tag{1}$$

in which *DL* and *LL* indicate the dead load and live load, respectively. The former was assumed to be 3 kN/m^2, whereas the latter was set to 2 kN/m^2.

Different scenarios were identified, depending on the position of the removed column and its deactivation time. A special purpose, death element routine (i.e. activation/deactivation time option) was integrated in Seismostruct [7] to operate member removal. Columns were labeled as shown in Figure 1. As gravity loads on the structure were increased, the maximum load capacity, $Q_{b,max,}$ and the corresponding vertical drift, θ_{max}, were monitored in order to identify the worst column-removal scenarios. The vertical drift was defined as follows:

$$\theta = \tan^{-1}(D_v / L_b) \tag{2}$$

where L_b is the beam length and D_v denotes the downward displacement of the residual structure after column removal. That kind of displacement was monitored at the upper joint (control point) of one of the removed columns until system failure was reached.

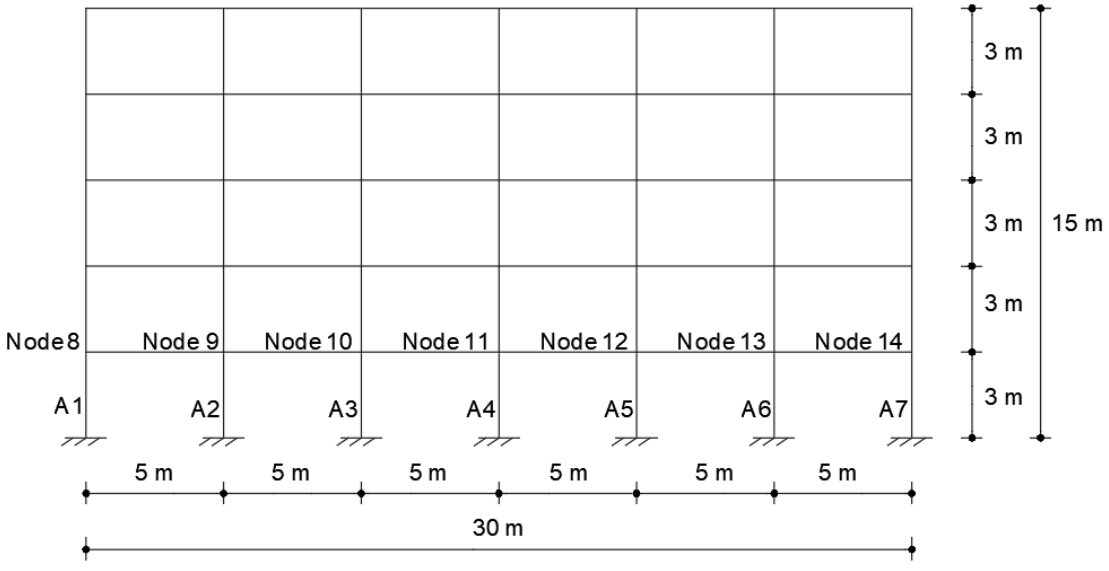

Figure 1: Labeling of columns removed at the ground floor and control points.

The methodology used to generate the multiple column-loss scenarios considered in this research is outlined in Figure 2. Two different strategies were used by varying the deactivation time of columns, which is here denoted as T_d. If two generic columns *i* and *j* are considered, the simultaneous removal was obtained by assigning them the same deactivation time,

i.e. $T_{di} = T_{dj} = 10^{-2}$ s. Conversely, the sequential removal was achieved by removing the generic column *i* (or *j*) at $T_{di} = 10^{-2}$ s and column *j* (or *i*) at either 10^{-1} s or 1 s.

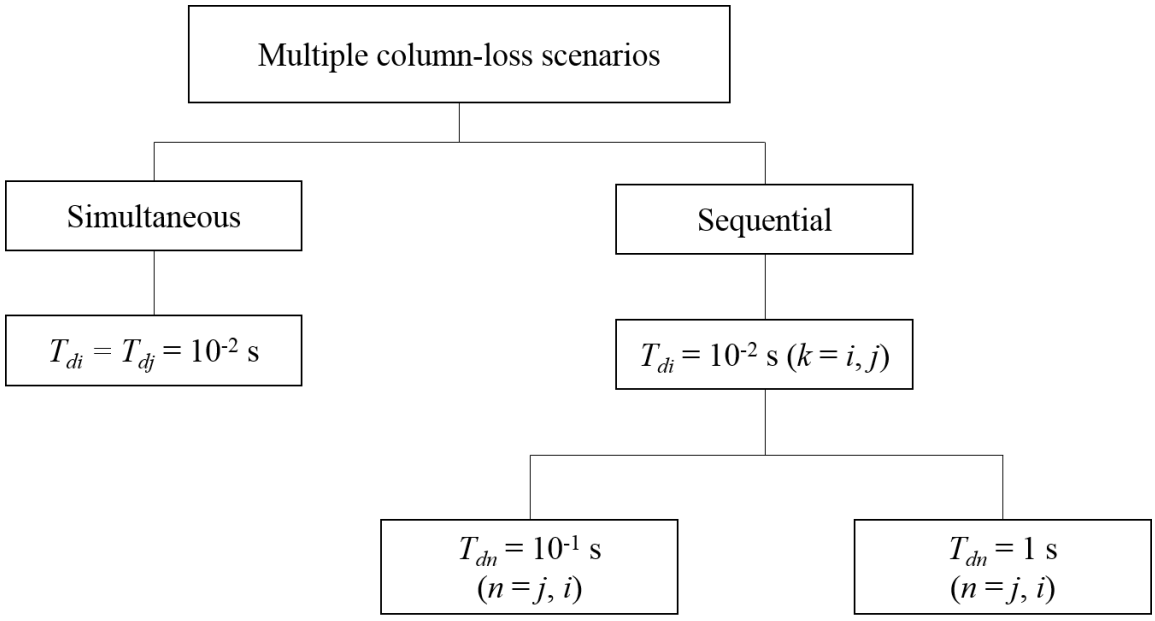

Figure 2: Framework for progressive collapse resistance assessment.

3 DISCUSSION OF RESULTS

3.1 Simultaneous removal of columns

In the first stage of research, the influence of simultaneous removal of columns on the progressive collapse capacity of the structure was evaluated. As previously mentioned, simultaneity was obtained by assigning the same deactivation time to couples of columns *i* and *j*, that is $T_{di} = T_{dj} = 10^{-2}$ s. Twelve multi-column removal scenarios were selected due to the symmetry of the structure and one hundred NLTHAs were carried out. Analysis results in terms of $\alpha_{max} = Q_{b,max}/Q_{bd}$, i.e. the percentage of design load associated with maximum load capacity, and corresponding vertical drift are listed in Table 2. The results show that the structure was able to withstand the highest percentage of design load in case of simultaneous removal of corner columns (scenario A1-A7) and when opposite columns adjacent to corner columns were simultaneously removed (scenario A2-A6). By contrast, when consecutive columns at a frame corner were removed, the capacity of the structure drastically reduced to 30% of design load. Table 2 also shows that, in the case of simultaneous removal of a corner column (A1) and any internal column (A2, A3, A4, A5, A6), the vertical drift is more sensitive to the control point than in the case of other scenarios that do not involve a corner column. To better understand this finding, IDA curves related to scenarios A1-A4 and A2-A4 are plotted in Figures 3a and b. The former scenario involved a corner column, while the latter did not. It is recalled that IDA curve is a dynamic capacity curve that provides the relationship between the gravity load intensity and a response parameter, namely the downward displacement of the control point in this case. Figure 3a shows that IDA curves associated with scenario A1-A4 are quite different in terms of displacement capacity, as the latter structural feature is sensitive to the control point (i.e. node 8 or 11). On the other hand, the curves related to scenario A2-

A4 (Fig. 3b) indicate a negligible variation in displacement capacity between the two control points (i.e. nodes 9 and 11).

Scenario	α_{max} [%]	θ_{max} [%]	
A1-A2	30	Node8	Node9
		11.67	10.57
A1-A3	136	Node8	Node10
		10.18	6.88
A1-A4	135	Node8	Node11
		9.76	6.38
A1-A5	136	Node8	Node12
		10.06	6.54
A1-A6	134	Node8	Node13
		9.30	6.3
A1-A7	140	Node8	Node14
		11.37	11.36
A2-A3	61	Node9	Node10
		9.82	9.84
A2-A4	127	Node9	Node11
		4.25	3.71
A2-A5	132	Node9	Node12
		5.65	5.08
A2-A6	140	Node9	Node13
		8.31	8.31
A3-A4	63	Node10	Node11
		11.07	11.07
A3-A5	138	Node10	Node12
		7.03	7.05

Table 2: Maximum load capacity and drift capacity under simultaneous column-removal scenarios.

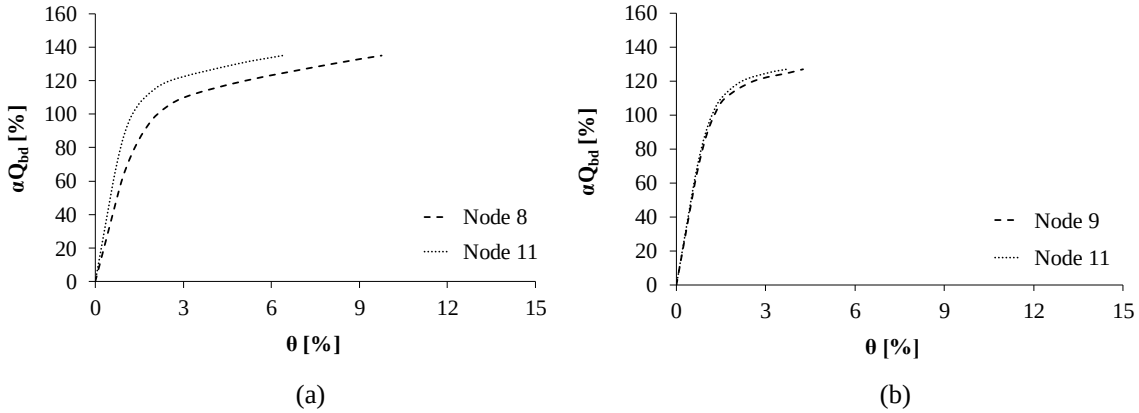

Figure 3: IDA curves corresponding to multi-column removal: (a) scenario A1-A4; (b) scenario A2-A4.

Since scenarios A1-A2 and A1-A7 are related to the minimum and maximum loadbearing capacity of the structure, respectively, their deformed shapes at ultimate conditions are shown in Figures 4a and b.

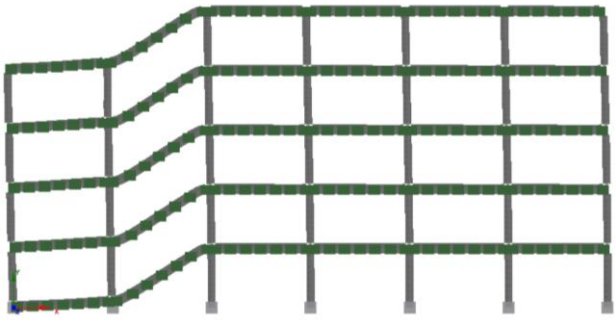

(a)

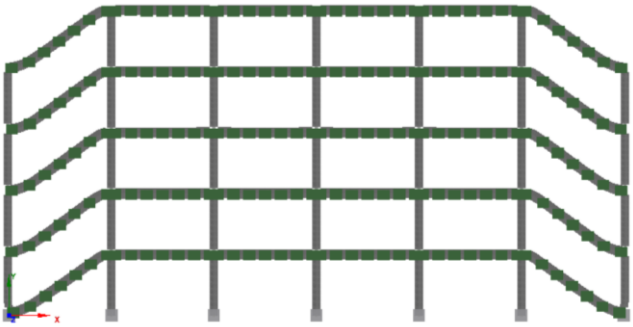

(b)

Figure 4: Collapse mechanisms under multi-column removal: (a) scenario A1-A2; (b) scenario A1-A7.

3.2 Sequential removal of columns

The consequences of column loss scenarios involving the notional (sudden) removal of column A1 were evaluated, because of their greater impact in simultaneous scenarios in terms of maximum load capacity and vertical drift of the structure.

According to the scheme in Figure 2, sequential column-removal scenarios were generated by assigning different deactivation times T_{di} and T_{dj} to each couple of columns i and j, as well as the possible loss sequences with $T_{di} < T_{dj}$ and vice versa. This approach led to 6 scenarios, each of them with 4 combinations of deactivation times (Table 3).

Table 4 outlines the maximum load capacity and maximum drift capacity associated with each scenario and couple of deactivation times, denoting maximum values in bold. It is evident that structural capacity under sequential removal scenarios reduces or does not change when the column is removed at 0.1 s, compared to the case of simultaneous removal. Conversely, the capacity of the structure increases when either a corner or internal column is removed at 1 s.

Scenario A1-A7 remains always the local damage condition that allows the highest load capacity of the structure. Even when central columns were removed at 0.1 s, load capacity reduced by 5%. In almost all scenarios, the removal of the second column at 1 s produced an increase in $Q_{b,max}$, nearly approaching the maximum value (α_{max} = 140%). Indeed, in scenarios A1-A3 and A1-A4, the removal of columns A1 and A4 at 1 s induced the attainment of α_{max} = 139%.

Scenario	Deactivation times
A1-A2	T_{d1} = 0.01 s, T_{d2} = 0.1 s
	T_{d1} = 0.01s, T_{d2} = 1s
	T_{d2} = 0.01s, T_{d1} = 0.1s
	T_{d2} =0.01s, T_{d1} = 1s
A1-A3	T_{d1} = 0.01s, T_{d3} = 0.1s
	T_{d1} = 0.01s, T_{d3} = 1s
	T_{d3} = 0.01s, T_{d1} = 0.1s
	T_{d3} = 0.01s, T_{d1} = 1s
A1-A4	T_{d1} = 0.01s, T_{d4} = 0.1s
	T_{d1} = 0.01s, T_{d4} = 1s
	T_{d4} = 0.01s, T_{d1} = 0.1s
	T_{d4} = 0.01s, T_{d1} = 1s
A1-A5	T_{d1} = 0.01s, T_{d5} = 0.1s
	T_{d1} = 0.01s, T_{d5} = 1s
	T_{d5} = 0.01s, T_{d1} = 0.1s
	T_{d5} = 0.01s, T_{d1} = 1s
A1-A6	T_{d1} = 0.01s, T_{d6} = 0.1s
	T_{d1} = 0.01s, T_{d6} = 1s
	T_{d6} = 0.01s, T_{d1} = 0.1s
	T_{d6} = 0.01s, T_{d1} = 1s
A1-A7	T_{d1} = 0.01s, T_{d7} = 0.1s
	T_{d1} = 0.01s, T_{d7} = 1s
	T_{d7} = 0.01s, T_{d1} = 0.1s
	T_{d7} = 0.01s, T_{d1} = 1s

Table 3: Sequential column-loss scenarios and deactivation times.

Table 4 also shows the vertical drift capacity of the structure for each sequential loss scenario. The highest value of θ_{max}, which is equal to 11.40%, was attained when considering scenario A1-A2, particularly in the combination where column A2 was removed at 0.01 s and column A1 was removed at 1 s. By contrast, scenario A1-A3 was found to be the worst case in terms of vertical drift capacity. Indeed, the lowest value of θ_{max}, that is 2.54%, was reached when columns A1 and A3 were removed at 0.01 s and 0.1 s, respectively. It is worth noting that such a drift capacity is very low compared to beams drifts observed in several experimental tests, as discussed in [1].

Deactivation times	α_{max} [%]	θ_{max} [%]	
Scenario A1-A2		Node8	Node 9
T_{d1} = 0.01s, T_{d2} = 0.01s	30	11.67	10.57
T_{d1} = 0.01s, T_{d2} = 0.1s	29	10.43	9.37
T_{d1} = 0.01s, T_{d2} = 1s	31	9.64	8.59
T_{d2} = 0.01s, T_{d1} = 0.1s	27	8.53	7.55
T_{d2} = 0.01s, T_{d1} = 1s	34	11.40	10.28
Scenario A1-A3		Node8	Node 10
T_{d1} = 0.01s, T_{d3} = 0.01s	136	10.18	6.88
T_{d1} = 0.01s, T_{d3} = 0.1s	119	4.91	2.54
T_{d1} = 0.01s, T_{d3} = 1s	138	10.88	6.01
T_{d3} = 0.01s, T_{d1} = 0.1s	136	10.08	6.85
T_{d3} = 0.01s, T_{d1} = 1s	139	8.96	7.61
Scenario A1-A4		Node8	Node 11
T_{d1} = 0.01s, T_{d4} = 0.01s	135	9.76	6.38
T_{d1} = 0.01s, T_{d4} = 0.1s	129	7.77	4.59
T_{d1} = 0.01s, T_{d4} = 1s	139	10.49	5.57
T_{d4} = 0.01s, T_{d1} = 0.1s	135	9.68	6.37
T_{d4} = 0.01s, T_{d1} = 1s	134	7.84	5.89
Scenario A1-A5		Node8	Node 12
T_{d1} = 0.01s, T_{d5} = 0.01s	136	9.69	6.20
T_{d1} = 0.01s, T_{d5} = 0.1s	134	9.31	5.81
T_{d1} = 0.01s, T_{d5} = 1s	135	9.63	5.03
T_{d5} = 0.01s, T_{d1} = 0.1s	129	7.67	4.34
T_{d5} = 0.01s, T_{d1} = 1s	136	8.11	6.43
Scenario A1-A6		Node8	Node 13
T_{d1} = 0.01s, T_{d6} = 0.01s	134	9.30	6.30
T_{d1} = 0.01s, T_{d6} = 0.1s	131	8.30	5.25
T_{d1} = 0.01s, T_{d6} = 1s	134	9.31	5.81
T_{d6} = 0.01s, T_{d1} = 0.1s	132	8.61	5.61
T_{d6} = 0.01s, T_{d1} = 1s	129	6.59	4.76
Scenario A1-A7		Node8	Node 14
T_{d1} = 0.01s, T_{d7} = 0.01s	140	11.37	11.36
T_{d1} = 0.01s, T_{d7} = 0.1s	135	9.44	9.31
T_{d1} = 0.01s, T_{d7} = 1s	140	11.44	8.49
T_{d7} = 0.01s, T_{d1} = 0.1s	135	9.34	9.45
T_{d7} = 0.01s, T_{d1} = 1s	140	8.29	10.98

Table 4: Maximum load capacity and drift capacity under sequential column-removal scenarios.

3.3 Comparison between simultaneous and sequential removal

Table 5 shows variations in maximum load capacity and vertical drift capacity from simultaneous to sequential column-removal scenarios.

Deactivation times	$\Delta Q_{b,max}$ [%]	$\Delta\theta_{max}$ [%]	
Scenario A1-A2		Node8	Node9
T_{d1} = 0.01s, T_{d2} = 0.01s	–	–	–
T_{d1} = 0.01s, T_{d2} = 0.1s	–3.33	–10.65	–11.34
T_{d1} = 0.01s, T_{d2} = 1s	+3.33	–17.36	–18.67
T_{d2} = 0.01s, T_{d1} = 0.1s	–10.00	–26.94	–28.56
T_{d2} = 0.01s, T_{d1} = 1s	**+13.33**	–2.27	–2.75
Scenario A1-A3		Node8	Node10
T_{d1} = 0.01s, T_{d3} = 0.01s	–	–	–
T_{d1} = 0.01s, T_{d3} = 0.1s	**–12.50**	–51.73	**–63.05**
T_{d1} = 0.01s, T_{d3} = 1s	+1.47	+6.90	–12.67
T_{d3} = 0.01s, T_{d1} = 0.1s	0.00	–0.94	–0.43
T_{d3} = 0.01s, T_{d1} = 1s	+2.21	–11.99	**+10.70**
Scenario A1-A4		Node8	Node11
T_{d1} = 0.01s, T_{d4} = 0.01s	–	–	–
T_{d1} = 0.01s, T_{d4} = 0.1s	–4.44	–20.43	–28.09
T_{d1} = 0.01s, T_{d4} = 1s	+2.96	+7.50	–12.75
T_{d4} = 0.01s, T_{d1} = 0.1s	0.00	–0.85	–0.24
T_{d4} = 0.01s, T_{d1} = 1s	–0.74	–19.68	–7.67
Scenario A1-A5		Node8	Node12
T_{d1} = 0.01s, T_{d5} = 0.01s	–	–	–
T_{d1} = 0.01s, T_{d5} = 0.1s	–1.47	–3.93	–6.28
T_{d1} = 0.01s, T_{d5} = 1s	–0.74	–0.64	–18.81
T_{d5} = 0.01s, T_{d1} = 0.1s	–5.15	–20.82	–29.97
T_{d5} = 0.01s, T_{d1} = 1s	0.00	–16.34	+3.76
Scenario A1-A6		Node8	Node13
T_{d1} = 0.01s, T_{d6} = 0.01s	–	–	–
T_{d1} = 0.01s, T_{d6} = 0.1s	–2.24	–2.24	–10.82
T_{d1} = 0.01s, T_{d6} = 1s	0.00	0.00	0.07
T_{d6} = 0.01s, T_{d1} = 0.1s	–1.49	–7.49	–10.93
T_{d6} = 0.01s, T_{d1} = 1s	–3.73	–29.13	–24.41
Scenario A1-A7		Node8	Node14
T_{d1} = 0.01s, T_{d7} = 0.01s	–	–	–
T_{d1} = 0.01s, T_{d7} = 0.1s	–3.57	–16.94	–18.05
T_{d1} = 0.01s, T_{d7} = 1s	0.00	0.59	–25.22
T_{d7} = 0.01s, T_{d1} = 0.1s	–3.57	–17.88	–16.83
T_{d7} = 0.01s, T_{d1} = 1s	0.00	–27.04	–3.30

Table 5: Variations in maximum load capacity and drift capacity from simultaneous to sequential scenarios.

If $T_{di} = T_{d1}$ = 0.01 s and T_{dj} = 0.1 s (with j = 2,….,7) are considered, the maximum load capacity reduces with variations ranging from –1.47% (scenario A1-A5) to –12.50% (scenario A1-A3). In scenarios with T_{dj} = 1 s, the maximum load capacity increased, except for scenarios A1-A6 and A1-A7 that produced the same capacity levels and scenario A1-A5 that induced a small capacity drop. The maximum increase, which was equal to 3.33%, was obtained for scenario A1-A2.

Sequential scenarios with T_{dj} = 0.01 s and varying T_{d1} produced the following outcomes:

- the load capacity reduced again in almost all cases when T_{d1} = 0.1 s;

- if T_{d1} = 1 s, the load capacity increased in scenario A1-A2 and A1-A3, while reducing or remaining the same in other scenarios.

The highest increase in maximum load capacity (i.e. +13.33%) was recorded for scenario A1-A2, which was characterized by T_{d2} = 0.01 s and T_{d1} = 1 s. The highest reduction in load capacity (i.e. –12.50%) occurred in scenario A1-A3, namely when the following deactivation times were assumed: T_{d1} = 0.01 s and T_{d3} = 0.1 s.

Scenario A1-A3 is also characterized by the maximum and minimum variations in vertical drift capacity, which were respectively found to be +10.70% and –63.05%. The analysis results outline that in most cases the maximum vertical drift reduced.

IDA curves were derived for each scenario, showing the sensitivity of maximum vertical drift to the percentage of design gravity load and deactivation times of removed columns. Figures 5a–d show the IDA curves related to scenario A1-A3, which turned out to be the most significant. Markers allow a quick identification of the difference between sequential scenarios (red and blue lines) and simultaneous scenarios (black lines).

In addition to IDA curves, displacement time histories associated with consecutive increments of gravity loads were obtained, particularly recording the structural response corresponding to the maximum load capacity. Figures 6a–d show the displacement time histories related to scenario A1-A3 and ultimate conditions (i.e. associated with $Q_{b,max}$).

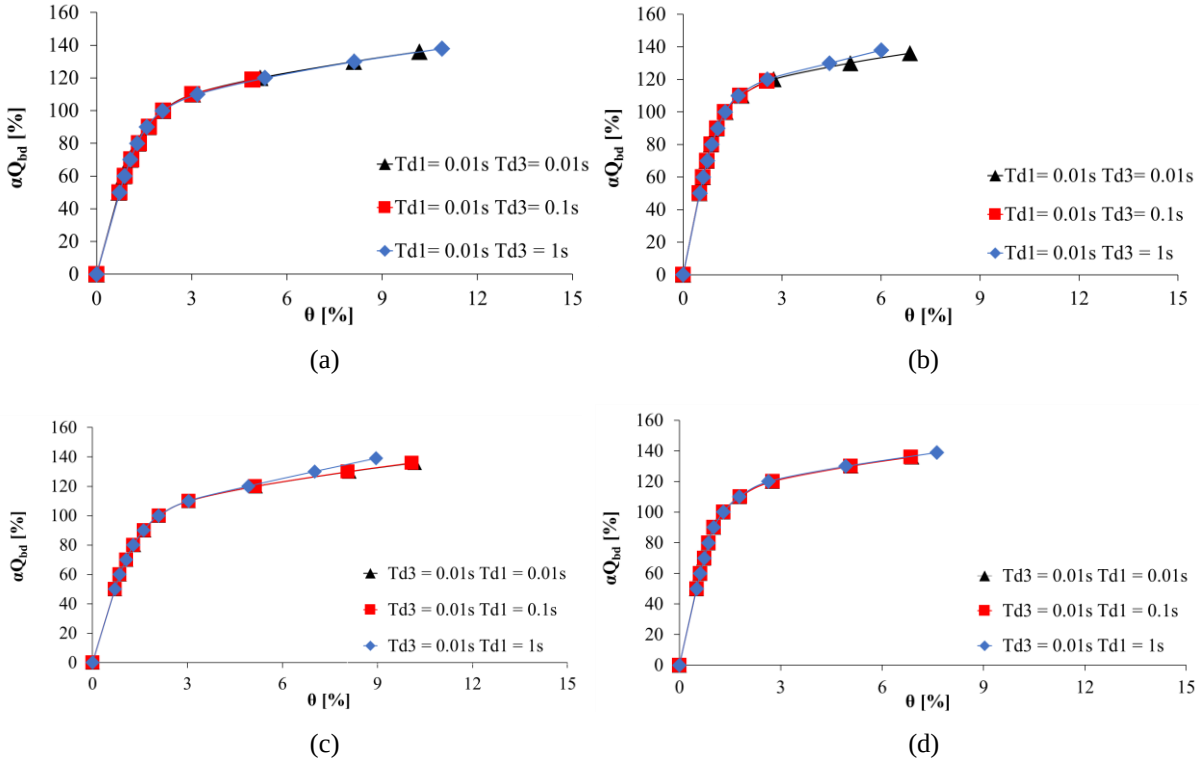

Figure 5: IDA curves related to scenario A1-A3: (a) T_{d1} = 0.01 s and control node 8; (b) T_{d1} = 0.01 s and control node 10; (c) T_{d3} = 0.01 s and control node 8; (d) T_{d3} = 0.01 s and control node 10.

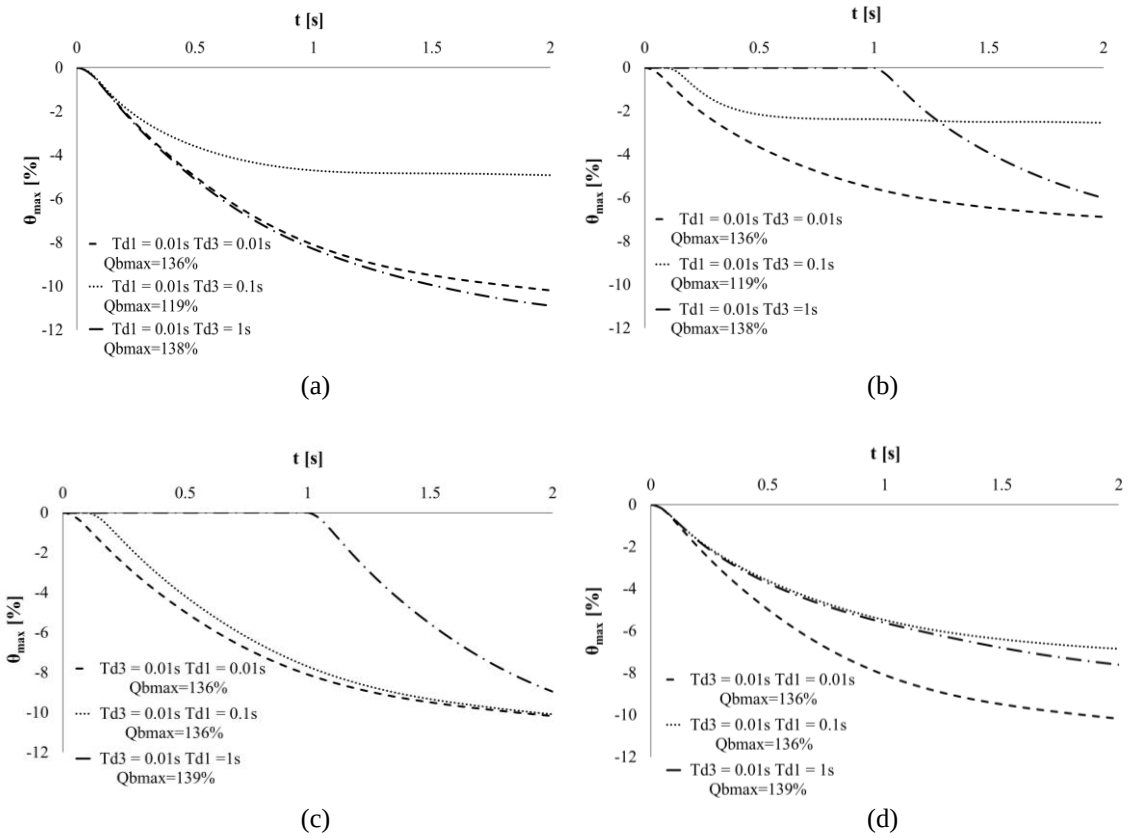

Figure 6: Displacement time histories at ultimate conditions related to scenario A1-A3: (a) T_{d1} = 0.01 s and control node 8; (b) T_{d1} = 0.01 s and control node 10; (c) T_{d3} = 0.01 s and control node 8; (d) T_{d3} = 0.01 s and control node 10.

4 CONCLUSIONS

In this study, two different cases of multiple columns loss, namely simultaneous and sequential scenarios, and their influence on a RC framed building were investigated. Scenarios were differentiated one each other by considering different couples of columns, deactivation times and removal sequences. Analysis results allow the following conclusions to be drawn:

- Simultaneous removal of two columns induced 140% and 30% of design gravity load as maximum and minimum load capacities, respectively.
- After simultaneous removal of columns, the maximum load capacity was reached when two corner columns (scenario A1-A7) and two opposite columns adjacent to corner columns (scenario A2-A6) were removed. Conversely, the minimum load capacity was found when two consecutive columns were removed.
- The maximum load capacity under sequential removal scenarios was lower than or equal to that associated with simultaneous scenarios when the second column was removed at a time instant 10 times higher than that of the first column removal. On the contrary, the load capacity increased again when the second column was removed at a time instant 100 times higher than that of the first column removal.

Further research is required to assess the progressive collapse resistance under simultaneous and sequential scenarios involving the loss of multiple columns located at different floor levels.

REFERENCES

[1] J. Adam, F. Parisi, J. Sagaseta, X. Lu. Research and practice on progressive collapse and robustness of building structures in the 21st century. *Engineering Structures*, **173**, 122-149, 2018.

[2] B. Iribarren, P. Berke, Ph. Bouillard, J. Vantomme, T.J. Massart. Investigation of the influence of design and material parameters in the progressive collapse analysis of RC structures. *Engineering Structures*, **33**, 2805-2820, 2011.

[3] J.L. Gross, W. McGuire. Progressive collapse resistant design. *Journal of Structural Engineering*, **109**, 1-15, 1983.

[4] K. Qian, B. Li, Z. Zhang. Influence of multicolumn removal on the behavior of RC floors. *Journal of Structural Engineering*, **142**(5), 2016.

[5] F. Parisi, M. Scalvenzi, E. Brunesi. Performance limit states for progressive collapse analysis of reinforced concrete framed buildings. *Structural Concrete*, **20**(1), 68-84, 2019.

[6] CEN. *Eurocode 2: Design of concrete structures — Part 1-1: General rules and rules for buildings, EN 1992-1-1*. Brussels, Belgium: Comité Européen de Normalisation, 2004.

[7] Seismosoft. *SeismoStruct — A computer program for static and dynamic nonlinear analysis of framed structures*, 2016.

[8] S.K. Kunnath, Y. Bao, S. El-Tawil. Advances in computational simulation of gravity-induced disproportionate collapse of RC frame buildings. *Journal of Structural Engineering*, **144**, 2018.

[9] E. Brunesi, F. Parisi. Progressive collapse fragility models of European reinforced concrete framed buildings based on pushdown analysis. *Engineering Structures*, **152**, 579-596, 2017.

[10] E. Brunesi, R. Nascimbene, F. Parisi, N. Augenti. Progressive collapse fragility of reinforced concrete framed structures through incremental dynamic analysis. *Engineering Structures*, **104**, 65-79, 2015.

[11] J.B. Mander, M.J.N. Priestley, R. Park. Theoretical stress-strain model for confined concrete. *Journal of Structural Engineering*, **114**(8), 1804-26, 1988.

[12] P.H. Bischoff, S.H. Perry. Compressive behaviour of concrete at high strain rates. *Materials and Structures*, **24**(6), 425-50, 1991.

[13] DoD. *Unified facilities criteria (UFC): Design of structures to resist progressive collapse*. Washington, DC: Department of Defence, 2013.

COMPDYN 2019
7th ECCOMAS Thematic Conference on
Computational Methods in Structural Dynamics and Earthquake Engineering
M. Papadrakakis, M. Fragiadakis (eds.)
Crete, Greece, 24–26 June 2019

USING STANDARD PDA TESTING TO ESTIMATE THE LATERAL CAPACITY OF CONCRETE PILES IN MEDIUM LOOSE TO DENSE SAND

Andrew G. Gouda [1], Mina Mikaeel [2], MarianneWilliam[3] Marina Shenoda[4]

[1] Teaching Assistant, Construction & Building Eng. Dept., Arab Academy for Science & Technology & Maritime Transport AASTMT
andrew.gouda@aast.edu
[2] Senior Geotechnical Engineer, P.E., Greenman-Pedersen, Inc., Lebanon, NJ, USA
mmikaeel@gpinet.com
[3] Teaching Assistant, School of Engineering, Engineering, Alexandria University
marianne.nagui90@gmail.com
[4] Senior student New Jersey Institute of technology(NJIT) , Newark NJ
mas287@njit.edu

Abstract

Driven piles used in the foundations of earthquake resistant structures are typically designed to sustain horizontal shear loads together with excessive axial loads. Moreover, it is frequent to use the equivalent static load analysis in piles design. However, in contrast to vertically loaded piles, laterally loaded piles behavior has different characteristics. Such characteristics include that the soil-pile interaction is more complex, as well as the demand that the soil-pile system must respond elastically.

As a result of that, it can be figured out that the lateral capacity of the pile depends on the soil properties, the geometrical and material properties of piles, such as the pile stiffness, embedded depth, and the horizontal allowable displacement. Furthermore, in-situ static and dynamic pile tests indicate that the lateral capacity of piles results from the comprehensive behavior of various factors described above. Based on such complexity of modeling the problem, it may be beneficial to use field tests results such as PDA tests and CAPWAP analysis to give a close estimate to the actual piles lateral capacity. Such results can act as proof testing, confirming that the expected capacities assumed in design are in fact available in the field.

Thus, based on accumulative results of PDA-CAPWAP tests in different types of soil for different types of piles and by modeling the soil pile-system and asymptotically loading laterally till critical displacements are achieved, a stochastic equation is derived to correlate the piles lateral capacities to available geotechnical information and PDA-CAPWAP tests. This is based on the assumption that the resistance to penetration can be divided into lateral and vertical components.

Keywords: Instructions, Structural Dynamics, Earthquake Engineering.

Andrew G. Gouda [1], Mina Mikaeel [2] MarianneWilliam[3] Marina Shenoda[4]

1 INTRODUCTION

There are many reasons why a geotechnical engineer would recommend a deep foundation over a shallow one, but some of the common reasons are very large design loads, a poor soil at shallow depth, or site constraints like property lines. There are different terms that are used to describe the different types of deep foundations including piles, drilled shafts, and caissons. Piles are generally driven into the ground in situ where other deep foundations or pile are typically put in place using excavation and drilling. The naming conventions may vary between engineering disciplines and firms.

Piles are designed to withstand lateral applied loads without undergoing a structural failure or exceeding deformation limits. The behavior of laterally loaded piles is complicated due to the nature of the pile-soil interaction, where the soil resistance at any point is a function of the pile's deflection at that point, while the pile deflection is a function of the soil's resistance. As such; the engineering parameters of the soil, the pile properties, and geometry are the main parameters determining the response of a laterally loaded free-head single pile. Laterally loaded piles are commonly analyzed using the well-known *P*-*Y*-method, in which the pile-soil stiffness is defined by nonlinear soil resistance (p) vs. lateral deflection (y) curves derived from field tests.[1]

However, the soil profile properties under any structure cannot be neglected in such an assessment since the soil underneath structures is undoubtedly the medium that transfers the seismic excitation to the structures foundations. The process in which the response of the soil influences the motion of the structure and the motion of the structure influences the response of the soil is termed as soil-structure interaction (SSI) [2]. Moreover, studying the soil formation in any region, one can recognize that the geological conditions, topographic characteristics and climatic conditions play a vital role in such soil formation. Thus, the soil is generally considered as a three-phase system (air, water and solid) causing significant changes in the system characteristics due to the interaction of these phases under applied dynamic or static loads [2]. Accordingly, determination of dynamic soil properties is a critical requirement in geotechnical-earthquake engineering problems.

2 PROBLEM DEFINITION

Pile foundations usually find resistance to lateral loads from (a) passive soil resistance on the face of the cap, (b) shear on the base of the cap, and (c) passive soil resistance against the pile shafts. The latter source is usually the only reliable one. Analysis of the problem yields deflections, rotations, moments, shears, and soil reactions as required for the structural design. Beam-on-elastic-foundation theory is adequate for analysis of the problem. Most piles are relatively flexible and may be analyzed as though infinitely long. Only short rigid piles are likely to require consideration of the lower boundary conditions in the analysis. Non-dimensional solutions are available for both constant and linearly increasing modulus-depth relationships. [3].

As Designers usually seek simpler methods for application in their design and assessments, it would be beneficial to obtain estimates of the lateral capacity from available soil properties and CAPWAP field tests results. Such estimates not only can help designers but rather can even help confirm to quality control engineers that the erected driven piles in-situ complies to specifications requirements. For efficiency, the expected behavior of different soil profiles under seismic effect needs to be verified in advance. This application is important as it affects

the design strategy of structures in general but mostly large and strategic ones including piles in their foundation systems.

3 LITERATURE REVIEW

Laterally loaded piles may be classified as active piles or passive piles, with regard to the loading transferring direction between the piles and the surrounding soils (De Beer, 1977). An active pile is principally loaded at its top, with the lateral load being transferred to the soil; such as piles acting as foundations for transmission towers, advertisement posts and offshore structures. A passive pile usually sustains lateral thrusts along its shaft arising from horizontal movement of the surrounding soil; such as piles in a moving slope or landslides. A variety of design and analysis methods have been developed for both active and passive piles. These methods range from relatively simplistic approaches that calculate the ultimate lateral capacity to relatively sophisticated methods involving advanced numerical analyses that estimate the pile deflections. First, the approaches for analyzing active piles are reviewed. They are subdivided into five sections: (1) pile flexibility and critical length; (2) failure modes; (3) limiting force or ultimate soil resistance profiles; (4) ultimate lateral capacity; and (5) load- deflection calculation of laterally loaded piles.

4 CASE STUDY

The lateral load resistance of pile foundations is critically important in the design of structures which may be subjected to earthquakes, high winds, wave action, and ship impacts. Because of the high cost and logistical difficulty of conducting lateral load tests on the pile. Several case studies on 28 driven pre-stressed concrete piles areas in Route 52 Causeway, New Jersey, United States of America (fig. 1)

As part of the site investigation, cone penetration tests were performed to characterize the subsurface conditions. The pile load testing program consisted of dynamic testing by means of the Pile Driving Analyzer (PDA), CAPWAP and full-scale static load tests. The results of the cone penetration tests, dynamic and static load tests, and pile driving records were analyzed to form a database of high quality, well-correlated data to inform the models. The results indicate that cone penetration tests can be used to accurately predict capacity and required embedment lengths for the tapered piles. PDA and CAPWAP testing measures acceleration and strain imparted to a pile during driving. These data are then used in CAPWAP to calculate pile capacity. The CAPWAP program runs a numerical simulation of load testing the pile. It compares calculated capacity to the acquired PDA data, iterating until it converges on the indicated pile capacity.

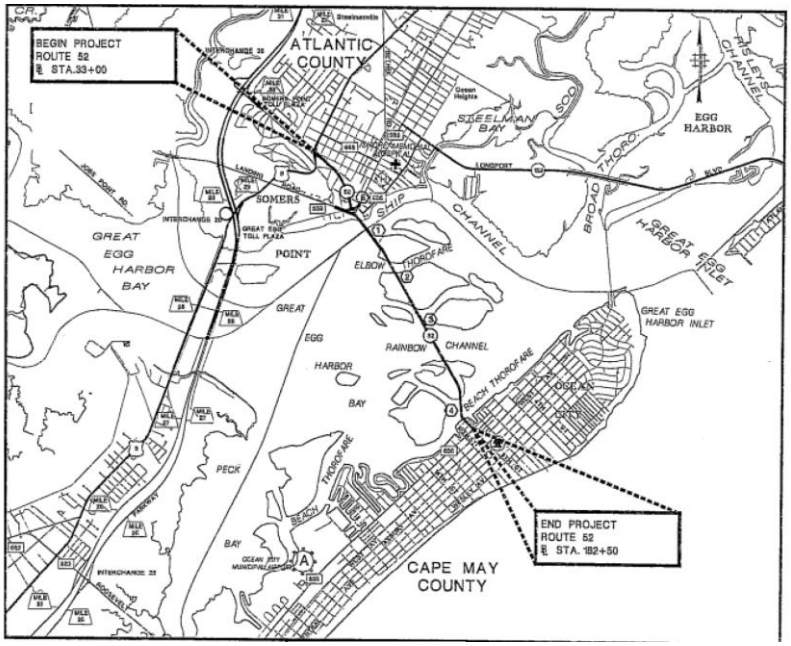

Figure 1

5 DATABASE

Data was collected from 28 PDA tests for the purposes of this study which driven piles were installed for bridge foundations. Typical records of pile driving (pile penetration rate and hammer stroke) were accompanied with dynamic measurements using a Pile Driving Analyzer (PDA) for both end of driving and beginning of restrike conditions. All piles were prestressed concrete piles driven with an impact hammer and is presented in Table 1. In the case of the square piles was calculated the equivalent diameter. According to AASHTO bridge design specifications [4], the resistance factor for driven piles is 0.65.

Table (1) Dimensions and allowable capacities of the concrete piles

no.	type	name	Dimensions		Mobilized axial Capacity	allowable axial Capacity
			side	pile length		
			m	m	KN	KN
1	Conc.	P 46 NB	0.76	28.04	9277.71	6030.51
2	Conc.	P56 NB	0.76	31.09	8232.02	5350.81
3	Conc.	P 63 sB	0.76	20.51	8294.32	5391.31
4	Conc.	P 64 sB	0.76	20.09	7626.86	4957.46
5	Conc.	P 67 NB	0.76	19.23	10025.27	6516.42
6	Conc.	P 67 sB	0.76	19.26	7675.80	4989.27
7	Conc.	P 57 NB	0.76	19.26	11760.67	7644.43
8	Conc.	P60sB	0.76	21.61	8605.80	5593.77
9	Conc.	P1NB	0.76	33.77	7595.71	4937.21
10	Conc.	n.ab	0.61	15.88	4133.81	2686.98

11	Conc.	P48 sB	0.76	26.21	12414.78	8069.61
12	Conc.	P58 nB	0.76	24.08	11346.84	7375.45
13	Conc.	P59 sB	0.76	24.08	12815.25	8329.92
14	Conc.	P 63 sB	0.76	20.51	8294.32	5391.31
15	Conc.	P42 n	0.76	33.38	8677.00	5640.05
16	Conc.	P46s	0.76	29.11	8779.34	5706.57
17	Conc.	P 48 n	0.76	26.97	11177.75	7265.54
18	Conc.	P 51 n	0.76	24.69	11791.81	7664.68
19	Conc.	P 56s	0.76	28.04	12325.78	8011.76
20	Conc.	P57s	0.76	22.25	12290.19	7988.62
21	Conc.	P 58s	0.76	24.84	12815.25	8329.92
22	Conc.	P 59n	0.76	15.54	11124.35	7230.83
23	Conc.	p 1s	0.76	33.53	6247.44	4060.83
24	Conc.	p 2s	0.76	33.53	8992.93	5845.40
25	Conc.	p 68s	0.76	19.72	10283.35	6684.18
26	Conc.	p60n	0.76	21.76	6238.54	4055.05
27	Conc.	p69s	0.76	21.06	10056.41	6536.67
28	Conc.	p65s	0.76	19.35	7693.60	5000.84

6 SOIL STRATIFICATION

The subsurface profile was characterized using a variety of methods to provide basic geotechnical data for use in subsequent computer analyses of the test results. Based on the results of the field and laboratory testing, but to simplify reading the soil properties of each layer, the soil profile shown in Table 2 was developed. The soil profile generally consists of two main layers first one was losses sand and the second layer was dense sand.

Table (2) Sample of soil Profile

Pile no.	sand			sand		
	Layer thickness	ɣ	ϕ	Layer thickness	ɣ	ϕ
	m	kN/m^3		m	kN/m^3	
1	18.90	20.16	32	54.86	21.73	41
2	18.59	20.63	34	48.77	21.57	40
3	13.72	20.50	33.5	27.43	21.28	38
4	13.72	21.02	36	48.77	21.00	40
5	13.72	20.44	35	48.77	20.47	40.5
6	13.72	20.98	36	48.77	20.69	41
7	10.36	19.95	32.5	30.48	20.69	38
8	14.63	21.10	37.5	35.05	19.84	39.1
9	26.82	21.30	38	50.29	21.51	40
10	11.58	20.20	35.1	36.58	19.84	39.1
11	15.24	19.84	31	36.58	21.57	40
12	18.29	20.16	32	33.53	20.79	35
13	11.58	20.63	34	30.48	21.57	40
14	13.72	20.60	33.5	27.43	20.28	38
15	18.29	17.95	27	35.05	21.26	38
16	18.29	20.16	32	35.05	21.73	41
17	18.29	19.84	31	32.00	21.57	40
18	13.72	18.58	28	32.00	21.73	41
19	12.80	20.63	34	32.00	21.73	41
20	16.76	20.00	32	32.00	21.57	40
21	18.29	20.16	32	32.00	20.79	35
22	12.19	20.63	34	32.00	21.57	40
23	13.11	21.08	35.5	39.62	20.60	39
24	9.00	21.51	38.5	40.00	21.70	41
25	10.00	20.20	32	50.00	18.90	36
26	14.02	20.80	37	28.96	20.70	39
27	12.34	20.30	34.5	27.43	20.30	39
28	14.33	20.42	35.5	30.48	20.40	38

7 METHODOLOGY

The present study focuses on determining the pile-head deflections. Typically, these values may often govern the design of laterally loaded piles. Therefore, an estimate of these values is of primary importance. In the present study, the LPile program was utilized to determine the pile-head deflections corresponding to the applied lateral load the pile head at the ground surface (i.e., lateral load applied at an eccentricity from the ground surface). The latter program has the capability to generate and take into account nonlinear values of flexural stiffness (EI). These values are generated internally by the program based on cracked/uncracked concrete behavior and user-specified pile dimensions, and material properties for reinforced concrete sections. LPile software can perform pushover analyses and analyze the pile behavior after a plastic hinge (yielding) develops. The soil-layers data structures can be entered conveniently with default values provided. Therefore, LPile may be advantageous over other applications for the subject handled in this research. However, future studies would use other techniques as finite element analysis for soil modeling in the studied problem for comparison.

By using (H. G. Poulos 1980) [5] method, a linear elastic soil response due to lateral pile movements was assumed. A critical length, *L*c, exists for a laterally-load pile, over which any increase in pile length has no influence on the ground line deflection δ. The critical pile length *L*c is a function of the relative stiffness of pile and soil nature (H. G. Poulos 1989). *L*c can be calculated from the following equations:

$$L_c = 4.44 \sqrt[4]{\frac{E_p I_p}{E_s}} \qquad (1)$$

Where: E_pI_p is the bending stiffness of pile, and E_s is the Young's modulus of soil.

8 FAILURE CRITERIA

There are many methods of analyzing the response of a laterally loaded pile. These methods can be categorized into the subgrade reaction approach and elastic continuum approach. Subgrade reaction approach has been initially proposed by Palmer & Thompson and subsequently further developed by Reese and Matlock (1956). Further advancements lead to the development of p-y curves and are commonly used to model the non-linear pile and soil behavior. These have been described by McClelland and Focht [6] and Davisson and Gill (1963), Often nonlinearity typifies the pile load-deflection behavior.

The p - y curve simply relates the unit soil resistance to pile deflection. Theoretically, it is normally assumed that the soil in the back and front of the pile will remain in contact with reference to the pile during lateral displacement. The slope of the *P-Y* curve at any deflection represents the tangent soil stiffness at that deflection. The ratio p/y at any deflection represents the secant soil stiffness corresponding to that deflection [7].

(H. Matlock 1970) developed the empirical expression to represent the p - y curve defined by the power function of deflection normalized by pile deflection at 50% of the ultimate soil reaction. In case of the sand layer (L. C. Reese 1974) [8] proposed the procedure in constructing the *p-y* curves for sand under static and cyclic lateral loadings. The method in developing the *p-y* curves involves the estimation of the initial modulus of subgrade reaction and ultimate soil resistance. Flexible driven piles embedded in a deposit of submerged, dense, fine sand (Cox *et al*., 1974). The characteristic shape of the *p-y* curve is highly nonlinear and can be described by three straight line portions and a parabolic curve as illustrated in Figure 2

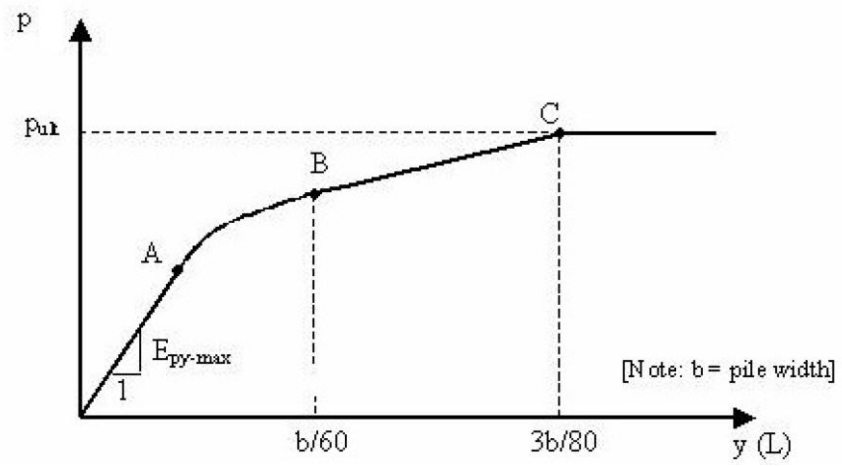

Figure 2

The method in developing the *p-y* curves involves the estimation of the initial modulus of subgrade reaction and ultimate soil resistance. The suggested values of initial modulus of subgrade reaction for different relative densities of sand are given by Reese *et al*. (1974). This initial straight-line portion of the curves (where *Es* is linearly with deflection) governs for only small deflections. Therefore, the initial slope of the *p-y* curve influences analyses for only very small load level, The ultimate soil resistance near the ground surface is developed based on equations for estimating the soil resistance where the ultimate resistance is assumed at pile deflection equal 3/80D where D is a pile diameter. the allowable lateral capacity of a pile is half of the load causing 3/80D of deflection (50% of the ultimate soil resistance)

9 ANALYSIS OF CASE STUDY

Predictive methods of pile behavior under lateral loading are widely ranging in complexity from simple and empirical methods to three-dimensional, non-linear finite element methods, modeling the pile-soil interaction with great detail. (S. L. Paikowsky 2007) [9] Reported that *P-Y* curves were most commonly used by geotechnical engineers in analyzing the behavior of laterally loaded piles in bridge design.

LPile[10] is a widely used computer software which specializes in the analysis of piles and drilled shafts under lateral load. The development for the commercial distribution of LPile by Dr. Lymon C. Reese began in 1985. However, it was preceded by general pile theory a methodology similarly used in the computer program COM624 developed for mainframe computers. The current version used in this work is LPile version 2015.8.03 which will be referred to as LPile throughout the remainder of this thesis. LPile computes deflection, shear, bending moment and soil response as a function of depth. The user interface allows for the consideration of various soil types as well as pile configurations. These features qualify their use in this study

In an LPile model, the soil around the pile is replaced with a series of nonlinear springs representing the soil resistance over a length, p, as a nonlinear function of pile deflection, y Figure (3). The pile is typically divided up into 50 to 100 nodal points, and p-y curves appropriate for the soil type and soil strength are computed at each node. In an iterative process, the lateral resistance at each node is adjusted until it is consistent with the deflection computed at that node based on the p-y curve defined for that node.

The basic differential equation governing the lateral load behavior of a pile in a soil profile is given by the equation[11]

$$EI\frac{d^4y}{dx^4} + Q\frac{d^2y}{dx^2} - p + W = 0$$

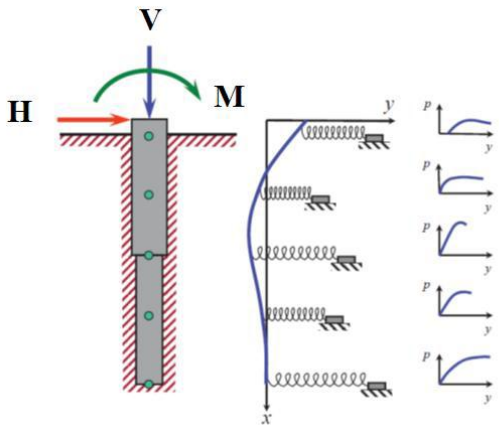

Figure 3

Where:

Q = axial thrust load in the pile

y = lateral deflection of the pile at a point x along the length of the pile,
p = soil reaction per unit length,
EI = flexural rigidity, and
W = distributed load along the length of the pile.

The first term governs the influence of pile flexural resistance; the second term deals with p-delta effects from the axial load on the pile as it deforms laterally, the third term accounts for the soil resistance along the length of the pile, and the last term accounts for the distributed load. The differential equation can only be solved by the application of boundary conditions at the top of the pile which defines applied load or moment, rotation or deflection.

10 RESULTS AND DISCUSSION

For the given pile and the given set of soil conditions, pile-head load versus deflection curves were generated by increasing the lateral load as shown in Figure (4) For the range of pile sizes and soil parameters used in this study, for laterally loaded pile, it was found that the depth below the critical length (L_c) of the pile remains unaffected by the lateral load. Most of the piles achieved complete bending with zero deflection at the pile tip.

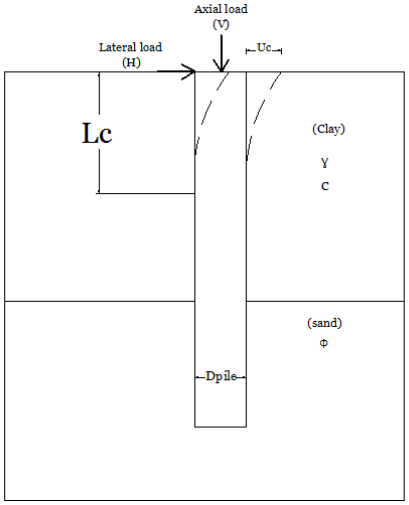

Figure 4

Calculation of lateral load capacity of pile using LPile

Lpile is capable of determining the flexural response of pile and load increased automatically. The passive resistance of soil is considered by the software and is indicated by it whenever it is exceeded. This principle has been considered taking into account the generated *P-Y* curves. In the present paper, the load acting at the pile head and the number of increments have been provided to reach the load. In Lpile software, an automatic load increment feature is available which is used to estimate
the lateral load capacity of the pile as shown in table 3

Table (4) the results of critical deflection and lateral capacity

Pile no.	**yc (critical def.)**	**(H) lateral capacity**		**yc (critical def.)**	**(H) lateral capacity**
	cm	KN		cm	KN
1	0.867	391.22	**15**	1.126	281.23
2	0.787	422.57	**16**	0.839	386.04
3	0.809	417.33	**17**	0.846	347.30
4	0.739	460.74	**18**	1.017	289.02
5	0.714	444.05	**19**	0.734	375.81

6	0.737	454.28	**20**	0.789	344.76
7	0.790	355.67	**21**	0.774	339.09
8	0.703	472.10	**22**	0.752	391.14
9	0.701	503.50	**23**	0.770	447.25
10	0.643	388.50	**24**	0.693	488.00
11	0.819	331.04	**25**	0.820	372.10
12	0.820	350.61	**26**	0.721	476.24
13	0.720	367.19	**27**	0.765	405.68
14	0.793	414.42	**28**	0.755	440.71

ESTIMATION OF LATERAL LOAD CAPACITY OF PILE

After the analysis of these results for 28 concrete pile in soil profile a trial was done to find a relation between the lateral load (H) versus the internal friction angle (Φ), as well as the relation with the unit weight (ɣ) of the soil where the pile-soil system is assumed to deflect along the critical length. Nearly linear relations were found in both cases, as shown in Figure (5), (6). In addition, the relationship between the lateral load capacity and axial load, therefore, it was tried to find a between the ratio (H/V) versus the axial vertical load (V) was investigated and found that (H/V) is inversely proportional to (V). The relationship is non-linear between (V), and (H/V) as shown in figure (7). Moreover, it is shown in Figure (7). That the lateral to vertical capacities ratio ranges from 4% to 11% of the axial capacity.

Figure 5 The relation between *H* in *kN* vs. the internal friction angle tan (*Φ*)

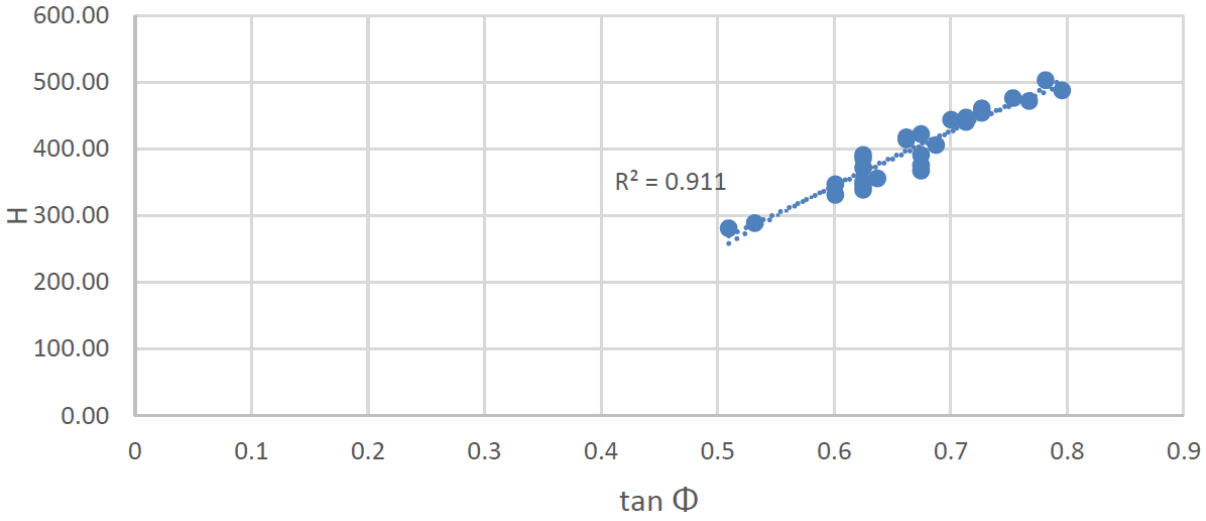

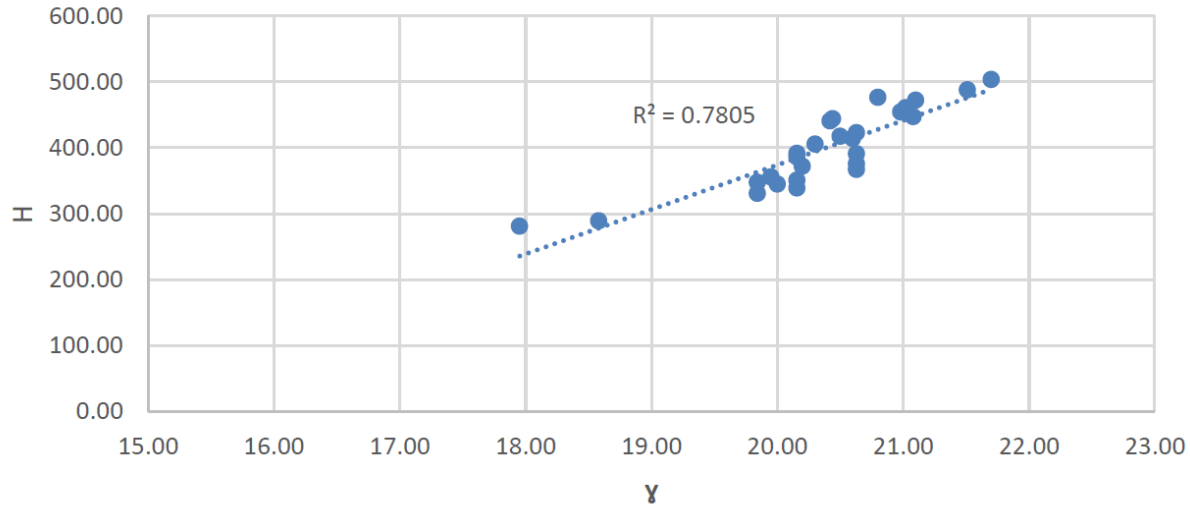

Figure 6 The relation between *H* in *kN* vs. the unit weight *ɣ* in *kN/m*³

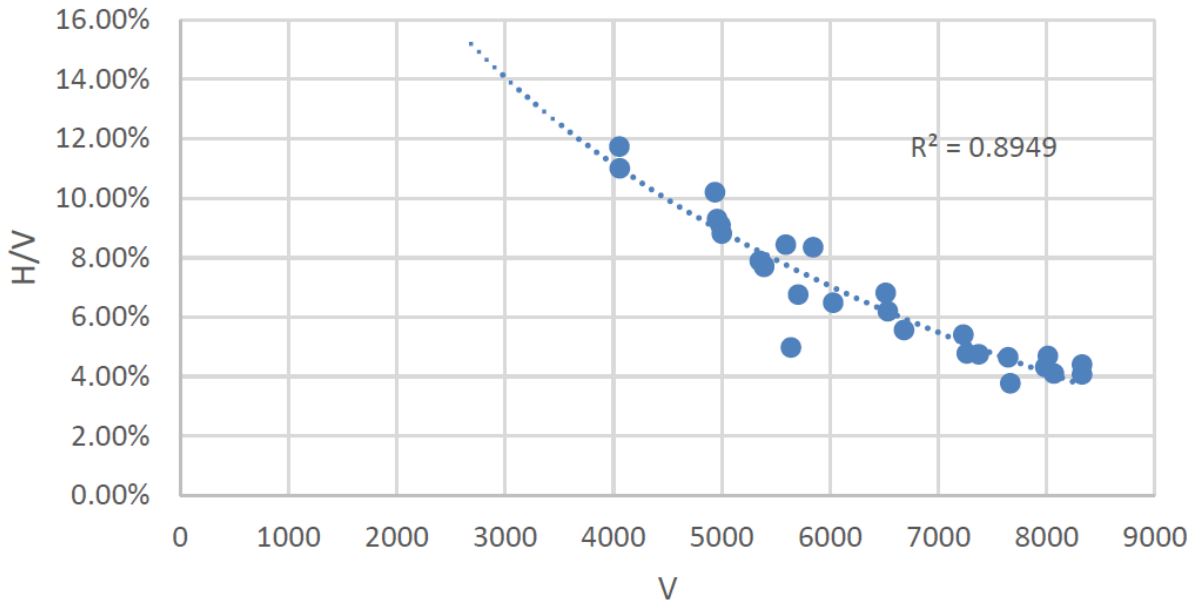

Figure 7 The relation between the ratio (*H/V*) vs. the axial load (*V*)

Based on the observed relations from Figures (5),(6),(7) one can distinguish that there are multiple parameters that affect the estimate of the lateral capacity such as the friction angle **(Φ)**, the unit weight, *ɣ*, and the vertical capacity, *V*. Moreover, studying the results as shown in Figure (7), one can realize that there is not one parameter that is solely sufficient to identify the lateral capacity. Thus, a multiple non-linear regression analysis by using SPSS program is applied to relate the cor-related parameters to the lateral capacity of piles. where founded that H = fn. (V, *Φ* ɣ). The latter analysis between the friction angle **(Φ)**, the soil unit weight (ɣ) and the axial load (V), is used to obtain a four-dimensional relationship between the above-mentioned parameters versus the lateral load capacity.

After finding correlated parameters to the lateral capacity of piles, we can draw a relation in two-dimensional between the H vs. V and H vs. Φ with constant values for other parameters in Figures (8),(9).

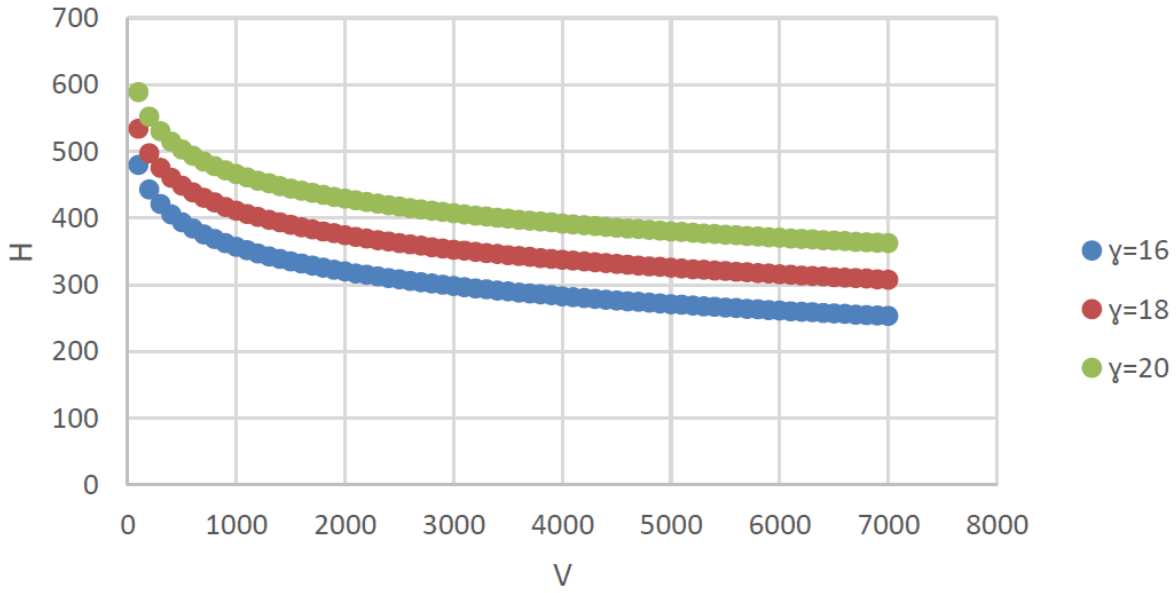

Figure 8 The relation between *H* in *kN* vs. *V* in *kN* at *(ϕ) =32*

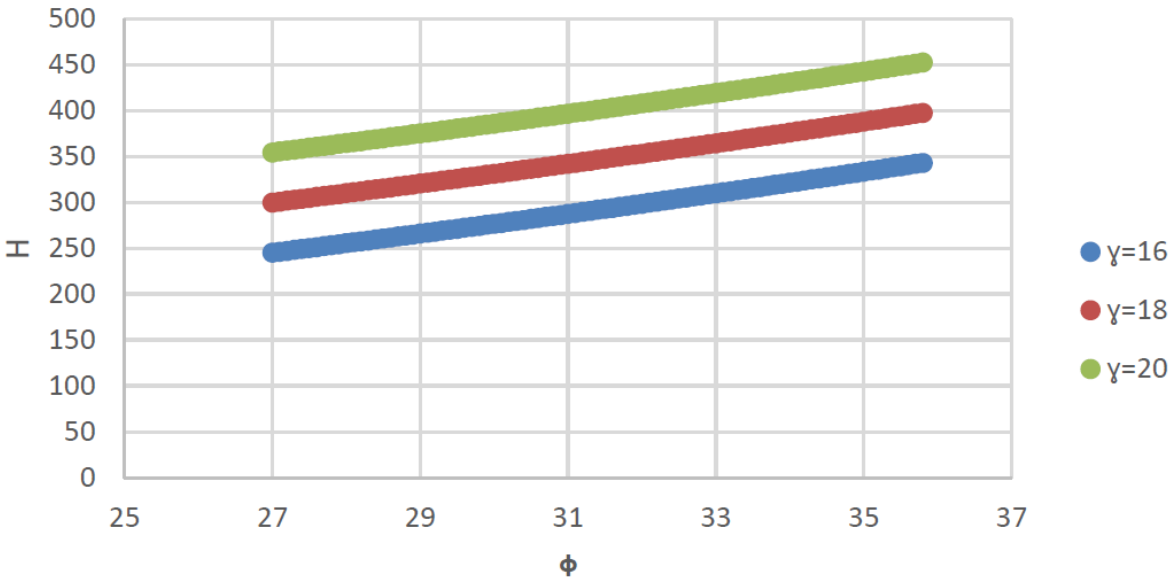

Figure 9 the relation between *H* in *kN* vs. *Φ* at *v* =3000 *kN*

Moreover, from the defined nonlinear multi parametric equation, by setting the unit weights to be in the range between 16 to 20 *kN*/*m*3, the space schematic is shown in Figure (10) is obtained. The latter schematic incorporates the full results from the CAPWAP tests and the available soil profiles properties for all piles to allow users to estimate a lateral capacity for any driven prestressed pile.

Furthermore, Figure (11) shows a three-dimensional surface that relates the soil properties and the CAPWAP results for the case of having a unit weight of 17 kN/m3 for the soil layers within the critical depth of the piles. Similarly, other three dimensional surfaces can be obtained for other unit weights of the soil within the critical depth of the pile along which the pile deflects. The lateral capacity for the driven piles can be obtained easily from such relations.

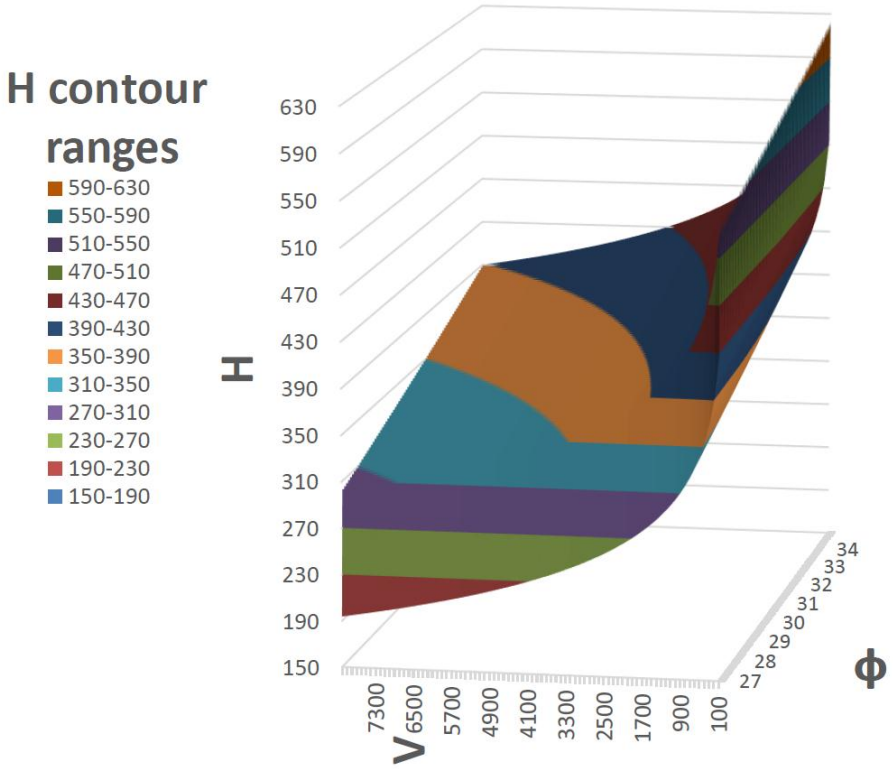

Figure 10 The relation between lateral capacity (*H*), vertical capacity (*V*) and friction angle (ϕ) for a unit weight (ɣ) from 16-20 kN/m^3

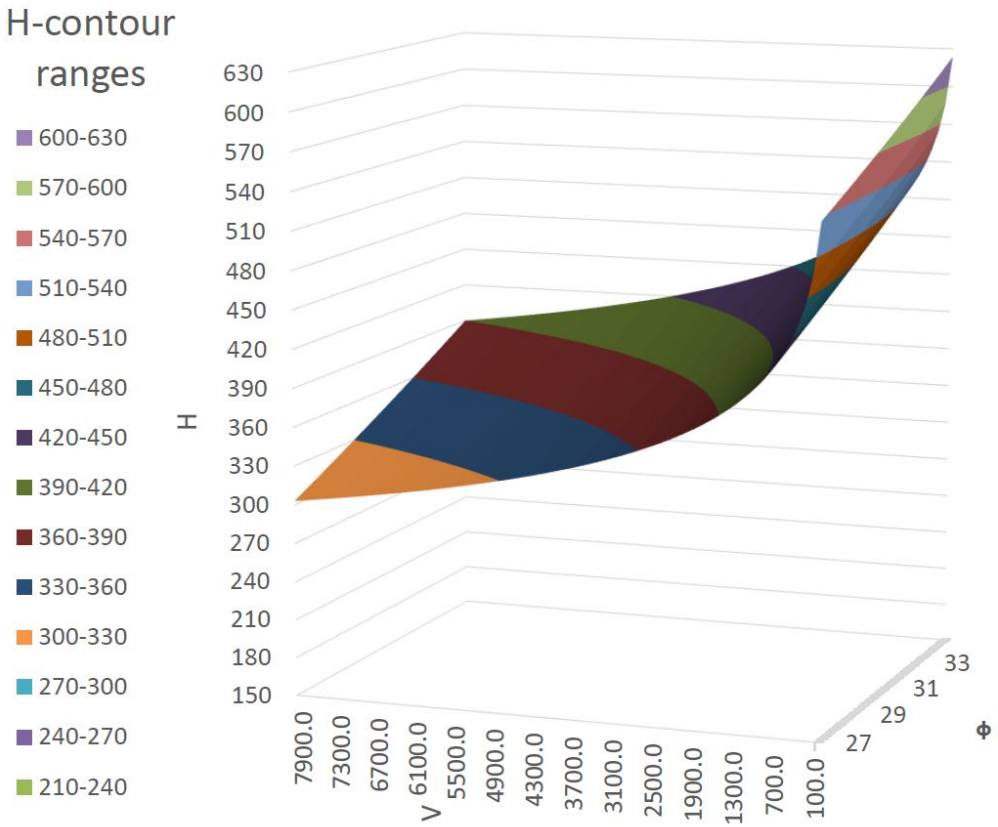

Figure 11 The relation between lateral load (H) & axial load (V) & and friction angle (ϕ) and a unit weight (ɣ)=17kN/m^3

11 CONCLUSIONS

As Designers usually seek simpler methods for applications in their design and assessments, it would be beneficial to help designers to obtain estimates of the piles lateral capacity from available soil properties and axial load. This study focused on piles behavior in soil profiles that are composed of soft stratum right below the surface, followed by stiff stratum underneath. The lateral capacity of the pile was found to depend mainly on three major parameters. These parameters include the angle of internal friction *(Φ)*, unit weight *(ɣ)* for the soil layers within the critical depth of the pile from the surface in which the pile is allowed to deflect, in addition to the vertical axial load capacity of piles *(V)*.

Based on the results of the present study, it was observed that:

- The lateral load capacity of the pile *(H)* is strongly affected by the properties of soil layers surrounding the critical length (L_c) in which the pile deflects laterally.

- The pile's lateral capacity *(H)* increases in a nearly linear relation to the soil cohesion *(c)* or tan *(Φ)* the angle of internal friction and unit weight *(ɣ)*.

- The relationship between the pile vertical axial load capacity *(V)* and the ratio *(H/V)* is a non-linear relation.

- For the studied case, the ratio *(H/V)* is ranging from 3.00% to 11.00%.

12 REFERENCES

1. Ayhan Gurbuza, Samuel G. Paikowsky (2009). *The Lateral Response of Single Free Headed Piles in Sandy Soils – Methods, Measurements, and Reliability*.

2. S.S. Kumar, A.M. Krishna, A. Dey (2013), *Parameters Influencing Dynamic Soil Properties, A Re-view Treatise. National Conference on Recent Advances in Civil Engineering.*

3. DAVISSON M. T. 1970. *Lateral Load Capacity of Piles, Department of Civil Engineering, University of Illinois, Urbana.*

4. FHWA-HRT-. 2006. *Federal Highway Administration Research and Technology 05-159* .

5. Poulos, H. G., and Davis, E. H. (1980*). Pile Foundation Analysis and Design. John Wiley and Sons, New York.*

6. McClelland, Bramlette, and John A. Focht, Jr., *"Soil Modulus of Laterally Loaded Piles," Transactions, American Society of Civil Engineers, Vol 123, 1958, pp 1049-1063*

7. Kramer, S. L. 1988. *Development of p-y curves fro analysis of laterally loaded piles in western.*

8. Reese, L. C., Cox, W. R., and Koop, F. D. 1974. *"Analysis of laterally loaded piles in sand," Proc. 6th Offshore Technology Conference, Paper 2080, Houston, Texas, 473-483.*

9. Paikowsky, S.G., Lu, Y. and A. Gurbuz. 2007. *"Prediction and Reliability of Pipe Piles response to Lateral Loading" ASCE,Denver 2007,GSP 158 Contemp.Issues in12-Deep Found., pp.1-12*

10. LPile. 2015. *for Windows, Data Format 6 (version 2015.8.03) through 2015-6-37.*

11. Isenhower, W. M. and Wang, S-T. 2015. *User's Manual for LPile 2015 (Using Data Format Version 8): A Program to Analyze Deep Foundations Under Lateral Loading.*

COMPDYN 2019
7th ECCOMAS Thematic Conference on
Computational Methods in Structural Dynamics and Earthquake Engineering
M. Papadrakakis, M. Fragiadakis (eds.)
Crete, Greece, 24–26 June 2019

DUCTILITY OF STEEL-FIBRE-REINFORCED RECYCLED LIGHTWEIGHT CONCRETE

Hasanain Al-Naimi, Ali Abbas

School of Architecture, Computing and Engineering
University of East London
E16 2RD, UK
{u1637128, abbas}@uel.ac.uk

Abstract

This work examines experimentally and numerically the influence of steel fibre reinforcement on lightweight aggregate concrete (LWAC). The replacement of conventional aggregates with recycled lightweight ones has several benefits such as reducing the mass of the structure leading to more economical designs (also beneficial under earthquake loading). The experimental project showed that it was possible to produce higher strength to weight ratio of LWAC compared to normal weight aggregate concrete (NWAC) as dry densities were approximately 700 Kg/m3 lower for identical characteristic compressive strengths between 40MPa and 30MPa. This could lead to savings in materials, construction and transportation costs making it especially useful and economical for long-span and seismic-resistant structures. Conversely, LWAC is noted for its highly brittle nature due to its associated weak aggregate interlock mechanism which can be typically compensated for by increasing shear reinforcement and dowel action by means of adding higher reinforcement ratios. Nonetheless, this creates several challenges in construction such as congestion of reinforcement in critical regions as well as increased dead loads which render LWAC use counterproductive. Thus, steel fibre reinforcement emerges as a promising solution where partial or total substitution of conventional transverse reinforcement could become a possibility. This project carries out examination of the effectiveness of hooked-end steel fibre reinforcement with fibre volume fractions of Vf = 1% and Vf = 2%. The experimental investigation includes the study of direct uniaxial compression and tension (unique pullout test) and indirect splitting and flexural tensile tests. Moreover, a nonlinear finite element study has been carried out using ABAQUS to model the experiments using CDP. Currently, there is no international standards or design guidelines for steel fibre reinforced lightweight concrete (SFRLC). This project will help address that and lead to sustainable and innovative seismic design solutions in the future.

Keywords: Recycled lightweight concrete, Hooked-end steel fibres, ABAQUS, Ductility, Flexural beam test, Pullout.

1 INTRODUCTION

Today, the use of structural lightweight aggregate concrete has become attractive especially as a precast material due to advantages which mainly involve the reduction in structural weight as compared to normal weight aggregate concrete. This in turn results in a decrease in the amount of reinforcement required, material transport costs and in the cross section of structural members especially columns, beams, walls and foundations which leads to reduced inertial and gravity loads and the catering for the growing need for taller and longer span structures. This is especially beneficial for seismic structures. In this sense, LWAC can grow to be competitive against NWC (Libre et al., 2011; Campione, 2014; Dias-Da-Costa, 2014; Mo et al., 2017). Although the price for lightweight concrete per m^3 can be higher than that of normal weight concrete, the overall cost of the structure due to the aforementioned savings can be substantially reduced with increased structural performance for an equivalent normal concrete structure. Kang and Kim (2010) report overall savings of 10% to 20%. Other advantages of lightweight concrete include reduction in carbon emissions and providing solutions to the lack of sufficient gravel and quarry resources foreseen in the imminent future (Gerritse, 1981).

Concrete in general and lightweight in particular is a brittle material which lacks material toughening mechanisms such as aggregate interlock. This makes LWAC susceptible to cracking and sudden brittle failure. To address the latter and enhance ductility, steel-bar reinforcement is usually incorporated in structural elements. However, due to the brittle nature of lightweight concrete this may become impractical and inherently counterproductive as a large number of reinforcement bars coupled with stirrups may increase the total weight of the structure and lead to difficulties in placing them within critical zones in concrete section during construction. Therefore, fibre reinforcement which has long proven its effectiveness in controlling and bridging tensile and shear cracks in the past for both lightweight and normal weight concretes can become an adequate solution (Gao et al., 1997; Balendran et al., 2002; Campione and La Mendola, 2004; Abbas et al., 2014a; Di Prisco, Colombo and Dozio, 2013; Grabois et al., 2016).

Steel fibre reinforced concrete is a composite material defined mainly by improved post cracking tensile behaviour due to the capability of fibres to bridge the crack faces preventing their propagation and widening into bigger cracks. This crack control mechanism leads to improved toughness, ductility and flexural and shear load carrying capacity (Swamy, Jones and Chiam, 1993; Kang and Kim, 2010; Di Prisco, Colombo and Dozio, 2013; Iqbal et al., 2015; Grabois et al., 2016). Unlike plain concrete, fibrous concrete can display tension softening or tension hardening depending on fibre dosage which leads to enhanced energy dissipation and ductility. Also, since cracking due to shrinkage is present naturally in concrete even prior to loading, fibres can be used to control cracking due to all types of shrinkage (Libre et al., 2011). The mechanical properties of SFRC are governed essentially by the bond strength between matrix and steel fibres, their dispersion, location, orientation, volume fraction and type (geometry and aspect ratio) (Concrete Society, 2007; Di Prisco, Colombo and Dozio, 2013).

Even though the advantages of the usage of fibrous concrete has been reported for over 40 years (Ritchie and Kayali, 1975), comprehensive studies on SFRLC (especially with modern fibres) is still largely scarce with most of the current work being merely theoretical and SFRC-based. It should also be noted that currently, there is no international standards or design guidelines for steel fibre reinforced lightweight concrete (SFRLC). This work will help pave the path for the latter.

This project suggests a comprehensive methodology to test lightweight fibrous concrete both on the meso- and micro-scale levels experimentally and numerically.

2 EXPERIMENTAL LABORATORY WORK

2.1 Experimental Programme

The experimental programme comprises tensile and compressive tests on lightweight and fibrous concretes. The aim is to study the influence of the incorporation of fibres into the lightweight mix on the mesoscale level (compression tests, direct fibre pullout tests) and macroscale level (flexural beam tests). The philosophy behind the experimental testing and its parameters can be seen in the table 1 below. As mentioned previously, the experimental programme will include a variety of specimen types. For uniaxial compression tests, both cylinders and cubes (3 per mix) are used and compared besides prisms to evaluate Modulus of Elasticity, Poisson's ratio, compressive ductility and to study the effect of fibres on short columns. For tensile tests, direct pullout cubes (2 per mix) will be tested to evaluate the direct tensile behaviour of plain and fibrous lightweight concrete while indirect tensile tests on splitting cylinders (3 per mix) and unnotched and notched beams will be carried out to study the material and flexural and shear behaviour of LWAC and SFRLC.

Mix	**Parameters**					**Aims**
	V_f (%)	**Fibre type**	**f_{ck} /$f_{ck,cube}$**	**Reinforcement layout**	**Stirrups spacing**	
1.1	0	N/A	LC30/33	2T12 @ Bot; 2T6 @ Top	R6 @120mm & 240mm	Study the behaviour of plain concrete
1.2	1	3D				Study the effect of increasing fibre dosage and potential replacement of stirrups with fibres in beams
1.3	2					
1.4	1	5D				Study the effect of the modern 5D fibres on the behaviour of concrete
1.5	0	3D	LC35/38			Study the effect of fibres on a different concrete strength
1.6	1					

Table 1: Summary of parameters used in experimental testing

The testing programme encompasses the study of 3 types of concrete strengths, 2 different steel fibres, 2 different fibre dosage V_f and 2 different steel cages. Steel fibres were either 3D or 5D. This was the case because hooked-end 3D fibres are currently the most commonly used in industry (Abdallah et al., 2018) and will be used as the base of experiments while modern hooked-end 5D fibres with more extensive hooks than the typical hooked-end 3D fibres are considered to be the strongest. Moreover, DRAMIX claim that this type of fibre is capable of replacing primary reinforcement in beams. Fibre dosages of 1% and 2% are chosen for testing. This is the case since most common structures such as tunnels and pavements require at least a dosage of V_f=1% for efficient crack control and thickness reduction (The concrete Society, 2007). Also, 2 different stirrups spacing was used. A spacing of 120mm is valid to EC2 shear design and the beam should thus fail in flexure while a spacing of 240mm is inadequate according to EC2 and the beam should thus fail in shear. The cross sections for the beams are shown in figure 1. Also, a relatively low reinforcement ratio in tension (ρ=0.0018)

was used to study the flexural effect of fibres on concrete beams. This was similar to the reinforcement ratio used by Kodur et al. (2019).

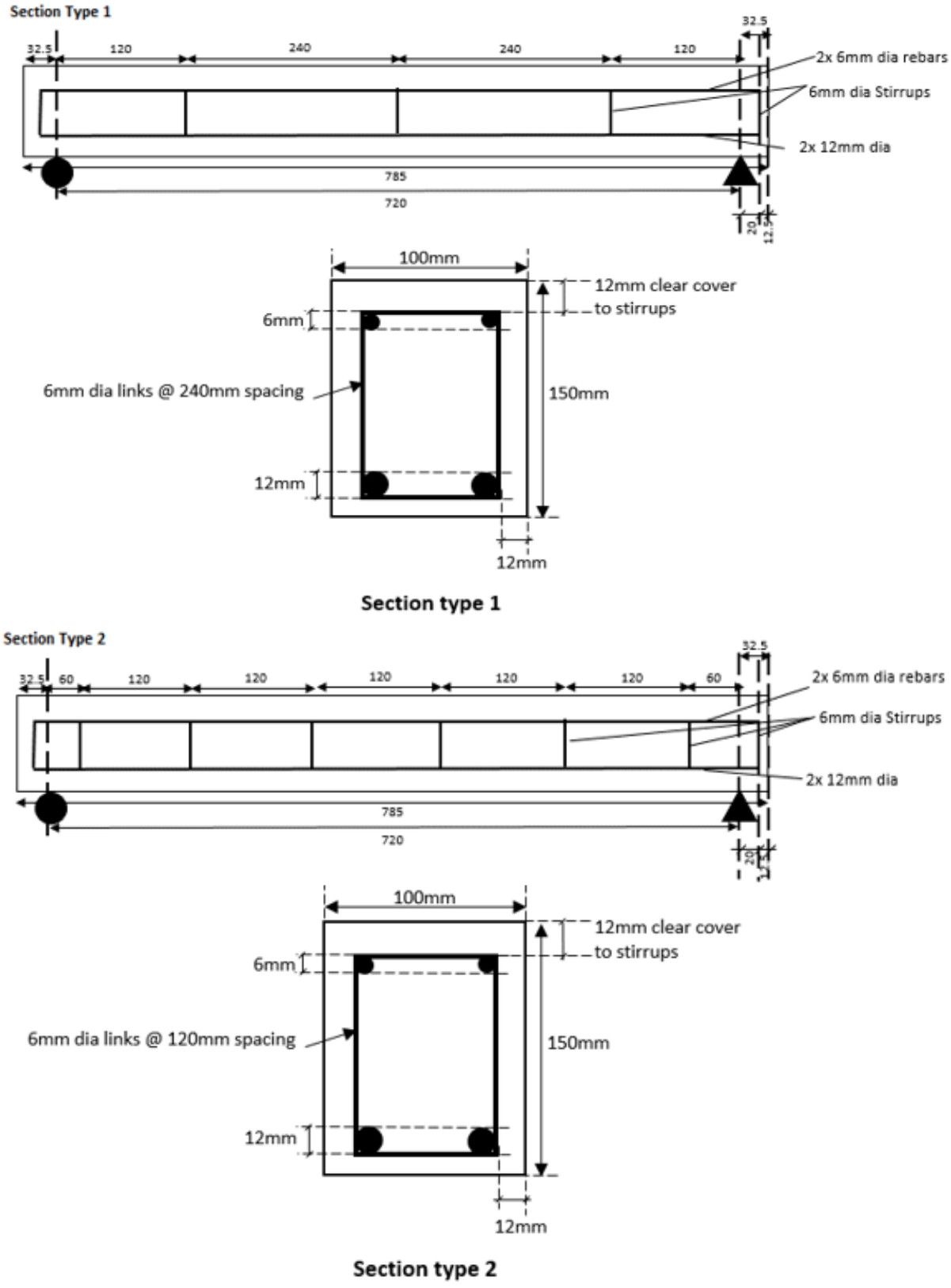

Figure 1: Longitudinal and cross-sectional sections for the beams tested

2.2 Experimental tests

The experiments include splitting tensile, the pullout test, compression cylinder and flexural beam tests. The Splitting tensile tests on cylinder specimens will be performed according to BS EN 12390-6. A direct uniaxial tensile fibre pull-out test was designed to study the effect of the embedded fibre onto the direct tensile stress-crack width of the concrete. Unlike Robins et al (2002) pullout test, the test is designed to have the fibre completely embedded in Lytag concrete. To ensure breakage of the specimen in tension at the monitored middle section, this section of the concrete was reduced to a diameter corresponding to the area a single DRAMIX fibre is predicted to occupy in the concrete. This area was determined using numerical and statistical models which depend mainly on fibre geometry and fibre volume fraction and take random distribution and dispersion of fibres into account (Krenchel et al., 1975; Romualdi and Mendel, 1964; Soroushian and Lee, 1990). Hence, this test can be regarded as a truer and more realistic pullout test than the classical pullout test with the fibre embedded on 1 side while the other end of the fibre is clamped by the machine (Abdallah et al., 2018). The pullout specimen is carefully placed in a tensile testing machine equipped with an in-built calibrated displacement transducer which will be used to measure the deformation histories of the effective section of the pullout specimens with a load cell where the two steel bars from each end are securely gripped in a way to disallow any superfluous slip. While one end is fixed, the other will be gradually pulled in tension at a displacement-controlled loading.
Due to their uniform stress distribution and adequate confinement, cylinders are the chosen specimens to test for compression and thus generate the complete compressive stress-strain behaviour for lightweight plain and fibrous concrete. A calibrated compressometer-extensometer steel ring designed according to ASTM C 469 and fitted with LVDT's is clamped onto the concrete cylinders. For the flexural beam tests the LVDTs were glued using high strength epoxy after the concrete surface in touch with the LVDT was ground in the mid-section at the front of the beam to enable the LVDTs to fully adhere onto the concrete. The LVDT's are connected to a computer software. For the purpose of estimating the vertical deflection accurately, a steel bar inspired by a technique similar to JSCE-SF4 recommendations was made. The beams are placed onto two frictionless steel supports. This was deemed adequate as the loading was symmetrical. A displacement controlled constant loading of 0.2mm/min was adopted using the hydraulic machine which has a load capacity of 500kN. It should be noted that the machine is also supplied with a calibrated displacement transducer.

3 NUMERICAL PROGRAMME

3.1 FEM approach

The 3D NLFEM analyses (Zienkiewicz and Taylor, 2005) will be carried out using the finite element package ABAQUS (Habbit et al., 2000). This software has proven its successful prediction of the behaviour of SFRC specimens and other composites in the past by using material relationships adopting a discrete crack approach (σ-ω) (Ngo and Scordelis, 1967) or smeared crack approach (σ-ε) (Rashid, 1968) to predict the tension stiffening behaviour post-crack and was used by a number of researchers (Tlemat, Pilakoutas and Neocleous, 2006; Mirza, 2008; Syed Mohsin, 2012; Abbas et al, 2014a, b). ABAQUS can address the tensile, compressive and shear behaviour of fibrous concrete to a great level of accuracy as well as determining the cracking patterns and failure mechanism in the presence of steel fibres and reinforcement. The methodology used in this work will not model fibres discretely. Instead, fibres will be modelled as part of the concrete matrix. This approach was opted for as modelling fibres discretely can be time consuming and will produce a purely FE based model, diffi-

cult to practically use by designers. In addition, fibrous concrete as a composite material involves the randomness of fibres inherently. This means that modelling fibres discreetly as realistic as it might be is also likely to completely miss the actual distribution and location of the fibres in a particular beam test especially for lower V_f and longer fibres. On the other hand, modelling fibres as part of the concrete matrix can offer an easier and simpler way to derive the behaviour of the material while also taking into consideration the random distribution and dispersion of fibres by introducing factors on the composite fibrous concrete stress-strain. The latter is derived from the uniaxial tensile pullout tests. However, the main disadvantage of the homogenous composite concrete modelling method is that local failures on the mesoscale level (such as fibre pullout) are not explicitly detected unlike in the discrete fibre 3D continuum modelling method (Zhang et al., 2018).

Concrete damaged plasticity (CDP) was calibrated and chosen to model the concrete specimens of the experiments. Previous papers (Syed Mohsin, 2012; Behinaein et al, 2018) claim that both brittle cracking (CBC) and damaged plasticity produced good results for their models. While this remains somewhat true, for the work carried out in this project CDP was deemed the more accurate and suitable tool to model reinforced and non-reinforced plain and fibrous concrete beams. This was the case as the experimental results for both tension as well as compressions tests can be used which makes CDP more realistic as compared to the crude CBC which assumes the behaviour of concrete to be completely elastic in compression. The other issue with CBC is that the performance of concrete is highly sensitive to the material shear behaviour which has to be calibrated. No material pure shear tests were carried out in this research. It should also be noted that convergence problems were very common for CBC and there was a need to use the Brittle failure criterion which might significantly affect the accuracy of the results.

The explicit dynamic solver in a quasi-static analysis is also adopted. The explicit dynamic analysis was found to be a more computationally efficient tool at solving the problems used in this project as compared with implicit solver which had a tendency to terminate.The experimental results from this thesis will be input into ABAQUS to model SFRLC structural beams. This project models the uniaxial pullout cubes and compression cylinders on ABAQUS first to calibrate both the behaviour of fibrous Lytag concrete in tension and compression. Then, these were used to model the flexural beam tests.

3.2 Calibration of material models

For concrete model using CDP a few important parameters need to be defined namely; Eccentricity, fb0/fc0 which is the ratio of initial equibiaxial compressive yield stress to initial uniaxial compressive yield stress, K is the viscosity parameter and the dilation angle. The latter was found to be the single most influencing parameter on the behaviour of concrete beams for explicit CDP analysis. The dilation angle was calibrated using uniaxial compression tests on cylinders where volumetric strains for both experimental and numerical results were compared in a manner inspired by Kupfer (1974) (Szczecina and Winnicki, 2016). Other factors were determined to have little to no influence on the behaviour of plain and lightweight fibrous concrete based on the calibration work from this research and previous work (Szczecina and Winnicki, 2016; Rodriguez et al., 2013; Jankowiak and Lodygowski, 2005; Hafezolghorani et al., 2017). The behaviour of concrete in uniaxial compression and tension was taken directly from the experiments. With regards to the behaviour of plain concrete in uniaxial tension, lightweight concrete would fail abruptly once the peak is reached. However, ABAQUS requires a tension softening curve to avoid computational errors and convergence problems. For this reason, a small displacement based on a calibrated fracture energy method calculated using fib model code 2010 was used.

With Regards to steel material model, a simple elastic-plastic stress-strain curve based on experiments is input.

4 RESULTS AND DISCUSSION

4.1 Experimental Results

Slump tests according to BS EN 12350-2 are carried out immediately after mixing the concrete to evaluate the consistency of the concrete and compare it to the consistency values recommended by Lytag. Table 2 below summarises the values of slump. Although consistent amongst each other, it can be seen that the values of slump highly exceed those recommended by Lytag (70 mm). This was also observed elsewhere (Lambert, 1982). In the latter, it was also explained that in a practical situation such as mixing on site, longer period of time lapses between mixing and placing allowing more of the free water to either evaporate or be absorbed by the lightweight aggregates.

It can be seen that the addition of fibres drastically reduces workability. At fibre dosage of V_f=2%, it was observed that the finishing process becomes challenging, the possibility for balling of fibres high and inhomogeneity of concrete likely. This further emphasizes that the design of mixes for fibre dosage should not exceed V_f=2% provided that no superplasticizers or water reducing agents are used.

Overall the wet density of concrete fell in the recommended range 1910-2000Kg/m^3. Theoretically the addition of steel fibres should increase the density of the concrete. However, it is clear from the table below that the higher the steel fibre dosage the less the density of the concrete. This was the case as hooked end fibres tend to create air voids within the concrete lattice. This finding is also consistent with Mo et al. (2017) observations for fibres with similar geometrical properties.

	Properties of mix		Slump (mm)			Wet Density Kg/m3
	W/C ratio	Fibre Type	Plain	V_f =1%	V_f = 2%	
Mix 1.1	0.49		169			2145
Mix 1.2	0.49	3D	168	60		2000
Mix 1.3	0.49	3D	147	55	26	1860
Mix 1.4	0.49	5D	150	50		1934
Mix 1.5	0.43	3D	170			2081
Mix 1.6	0.43		150	45		2002

Table 2: Slumps and Wet densities

Figure 2 depicts the average normal compressive stress-strain behaviour for the cylinders. The compressive strength values for the cylinders lied within the acceptable design values for both LC30 and LC35. Young's Modulus of Elasticity was measured to be 17.8, 17.3, 18.6 and 17.6 GPa for mix 1.1, 1.2, 1.3 and 1.4 respectively. These values are lower than Eurocode 2 table 3.1.11 recommendations, which suggest 22.1 and 22.8 GPa for both LC30 and LC35 respectively. Nonetheless, this is consistent with Lambert (1982) experiments on Lytag, which measured the modulus of Elasticity to be between 17.5 and 18 GPa for similar strengths de-

pending on curing conditions. The measured Poisson's ratio values ranged between 0.16 and 0.19 for all the specimens. These were consistent with Lambert (1982).
The behaviour of cylinders can be split into 3 stages. During stage A, both fibrous and plain Lytag lightweight concrete mixes experience a progressive load increase before macro cracking starts to take place in the middle section of the cylinder. This gradually reduces the tangent modulus of Elasticity and marks the start of stage B. As soon as a larger crack is formed, the cylinder specimens for plain Lytag concrete mixes 1.1 and 1.5 collapse in diagonal shear through the middle section. This is attributed to the absence of crack arresting and lateral confining mechanisms such as aggregate interlock. For fibrous lightweight concrete however, stage B illustrates a plateau-like behaviour. The macro cracking at the end of stage. At stage C, as extensive lateral cracking dominates the post peak behaviour of the cylinders, the compressive load finally begins to decline in a ductile manner for both lightweight fibrous mixes 1.3 and 1.6. The post-peak compressive ductility is measured by $(\varepsilon_{ult} - \varepsilon_{peak})/ \varepsilon_{peak}$ with ε_{ult} as the strain at 50% of the peak compressive strength. Cylinders with V_f=2% added a post peak ductility of about 7.7 whereas those with V_f=1% added a post peak ductility of about 3.5. Hence, as V_f dosage is doubled, the ductility provided doubles as well
It can be seen that fibre reinforcement has no effect on the elastic behaviour of the cylinders and merely gradually manifest as post peak softening depending on type and dosage of fibres. Therefore, compressive strength, modulus of Elasticity and Poisson's ratio remained unaffected with the addition of fibres to the lightweight concrete mix whereas post-peak ductility substantially increased. This finding is consistent with Li et al. (2018) which found that random SFRC has little to no effect on the modulus of Elasticity and slight favourable or unfavourable effect on compressive strength depending on the mixing process and the geometry of fibres.

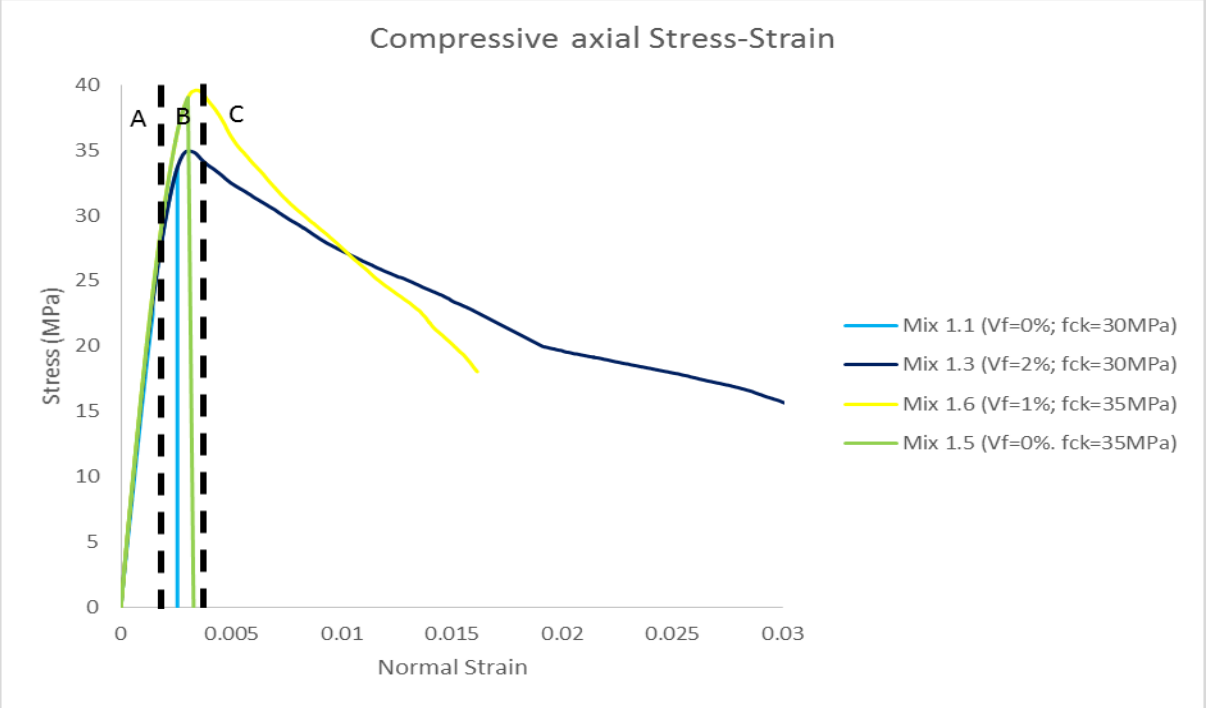

Figure 2: Compressive stress-strain behaviour for cylinders

Table 3 summarises the mean values of splitting tensile strength measured by crushing 3 cylinders per mix. It can be seen that plain lightweight concrete cylinders which included mix 1.1 and 1.5 produced splitting tensile strengths within 10% of Eurocode 2 table 11.3.1 recom-

mendations. LC30/33 cylinders reinforced with V_f=1% produced splitting tensile strengths equivalent to those of C40/44 while those reinforced with V_f=2% produced tensile strengths equivalent to those of C70/77. Also, LC35/38 cylinders reinforced with V_f=1% generated an equivalent strength of LC100. This shows that steel fibres are highly effective at upgrading the tensile resistance of lightweight concrete. Nonetheless, fibres may or may not be concentrated at the vicinity of the main crack to provide bridging reinforcement. Hence, it can be understood from the table below that some cylinders reinforced with V_f=1% (mix 1.2) showed a lower upgraded splitting tensile strength at 20% as compared to those reinforced with V_f=1% (mix 1.6) which was estimated to be at 47%. This can also be blamed for by the possibility of developing stronger bond between 3D fibres and LC35 which has lower W/C ratio than that between 3D and LC30. The latter and the random distribution and dispersion of fibres remain the two most important factors governing the behaviour of fibrous lightweight concrete. This will be investigated in the pullout test.

Mix	**$f_{lctm,\ Exp}$ (MPa)**	**$f_{lctm,\ EC2}$ (MPa)**	**Upgraded Strength due to fibres (%)**	**Equivalent EC2 Class**	**Std**
Mix 1.1 (LC30/33, Vf=0%)	2.67	2.64		LC30	0.12
Mix 1.2 (LC30/33, Vf=1%)	3.21	2.64	20.1	LC40	0.10
Mix 1.3 (LC30/33, Vf=2%)	4.20	2.64	57.3	LC70	0.12
Mix 1.4 (LC30/33, Vf=1%)	3.03	2.64	13.5	LC35	0.49
Mix 1.5 (LC35/38, Vf=0%)	3.19	2.91		LC40	0.47
Mix 1.6 (LC35/38, Vf=1%)	4.70	2.91	47.3	LC100	0.02

Table 3: Splitting tensile strength

The figure below depicts the uniaxial tensile pullout behaviour of plain and fibrous lightweight concrete with V_f=1%. Using the curve above the peak uniaxial tensile stress of plain lightweight concrete was calculated to be 2.16MPa based on the cylindrical volume of concrete through which the fibre is embedded. After reaching peak, the concrete stress drops immediately to 0 at 0.8mm slip which is expected for lightweight concrete due to the absence of strong aggregate interlock and any tension stiffening mechanism. The peak uniaxial tensile stress of lightweight concrete reinforced with a single 3D fibre equivalent to V_f=1% was calculated to be 2.35MPa and 2.88MPa at approximately 1.2mm and 1.8mm slips for both LC30 and LC35, respectively based on the cylindrical volume of concrete through which the fibres are embedded. As compared to mix 1.1, mix 1.2 saw an upgrade of 9% in maximum uniaxial tensile strength due to the presence of steel fibre. After reaching peak, fibre hook straightening followed by eventual frictional pullout which took place at approximately 19mm and 14mm slips for mix 1.2 and 1.6, respectively. For 5D fibres, the concrete again cracks at a load of 280N, however due to the extensive number of mechanical hooks and higher fibre tensile strength the load peaks at a higher load of 662N. This is equivalent to a uniaxial tensile stress of 5.86MPa which is 2.6 times greater than that of plain Lytag fibrous concrete. After that, hook straightening, and frictional pullout finally took place at a slip of around 26mm.

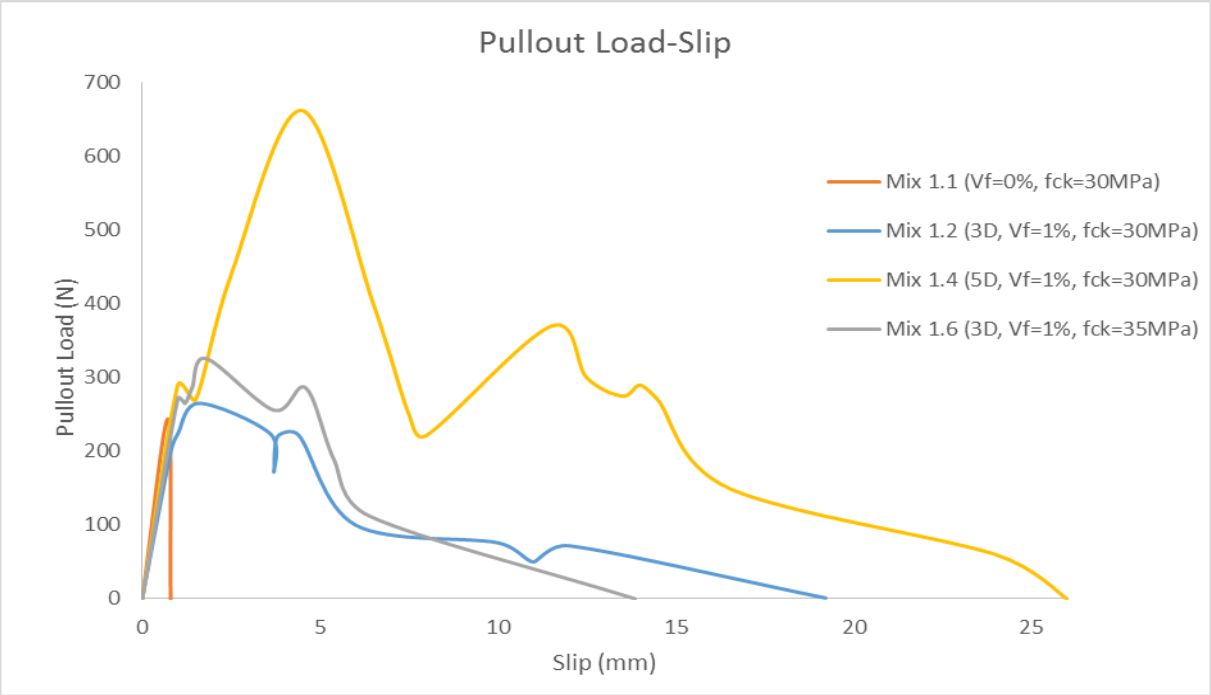

Figure 3: Pullout load-slip

Figure 4 below depicts the load-deflection curves for the 6 beams tested with different stirrup spacing and fibre dosages. All beams showed ductile behaviour as expected aside from mix 1.1 beam with inadequate spacing S=240mm and V_f=0% which failed in a brittle shear manner as predicted by Eurocode 2 shear design calculations. Hence, steel fibres are capable of altering the failure mode from shear to flexure. Using uniaxial tensile test results in combination with TR63 and Model Code 2010 flexural and shear design calculations for SFRC, it was possible to theoretically estimate the failure mode and the maximum load possible for the structural beams which agreed with the flexural beam tests results. It is observed that the ductility of the beams increases as spacing of stirrups and dosage of fibres increase. Ductility is calculated by dividing ultimate deflection at load 85% of the peak by the yield deflection at the load-deflection curve gradient before reaching peak. The ductility of fibrous beams are summarised in the table below. Relative ductility is the ductility of the beam being evaluated divided by the beam with the lowest ductility (failed in shear).

It can be seen from the table that the relative ductility for the beams with V_f=0%, S=120mm and that of V_f=1%, S=240mm are approximately identical with the latter having slightly higher ductility. A similar trend is seen for beams with V_f=1%, S=120mm and that of Vf=2%, S=240mm. This means that adding 1% of fibres is equivalent to halving the spacing of stirrups from S=240mm to S=120mm. The behaviour of beams with 2% fibre volume fraction is of an elastic plastic nature.

Beam	Ductility	Relative ductility
V_f=0%; S=240mm	1.57	1
V_f=0%; S=120mm	1.91	1.21
V_f=1%; S=240mm	1.99	1.26
V_f=1%; S=120mm	2.69	1.71
V_f=2%; S=240mm	2.83	1.80
V_f=2%; S=120mm	9.22	5.87

Table 4: Ductility and Relative Ductility of the beams

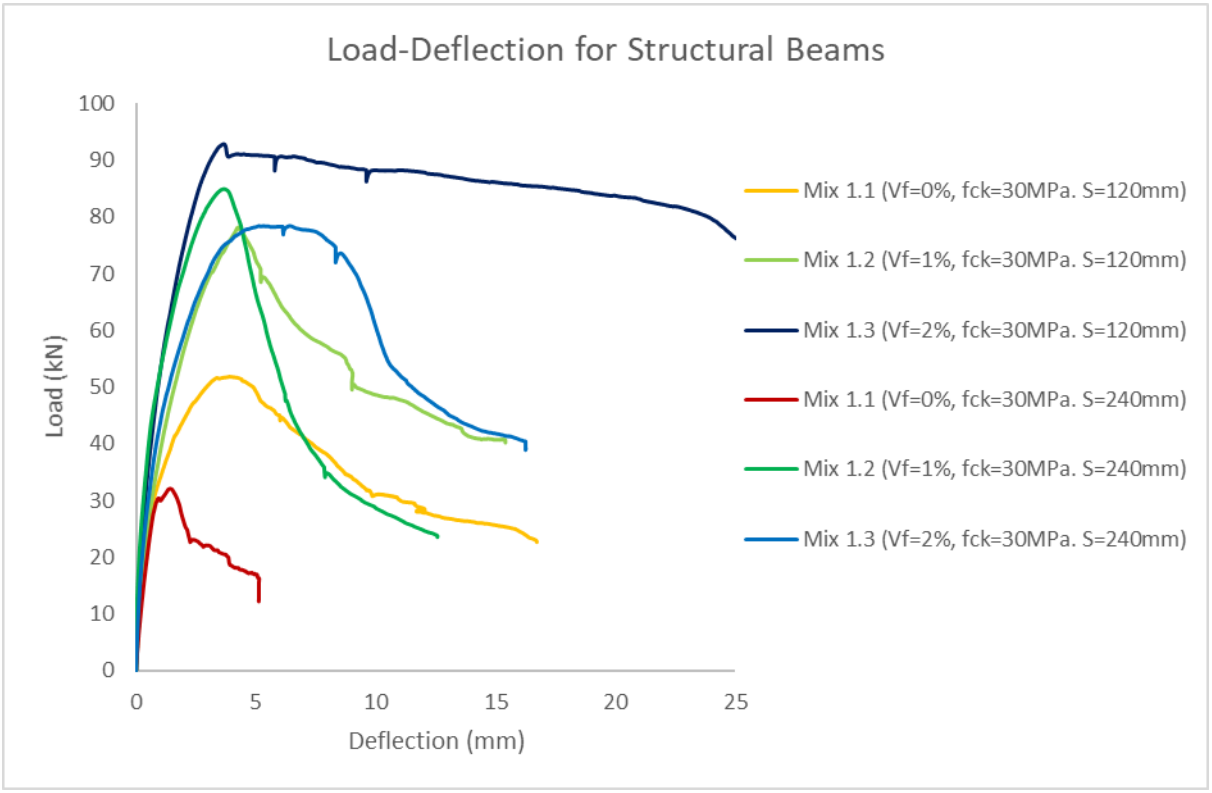

Figure 4: Load-deflection for flexural beam

4.2 Numerical Results

Figure 5 below depicts the pullout stress-displacement of plain concrete from ABAQUS in comparison with experimental fib model code derived curve. It is noticed that ABAQUS is capable of predicting with a reasonable approximation the uniaxial tensile stress-cracking displacement until the load drops to about 5% where an asymptote is seen to avoid numerical convergence errors.

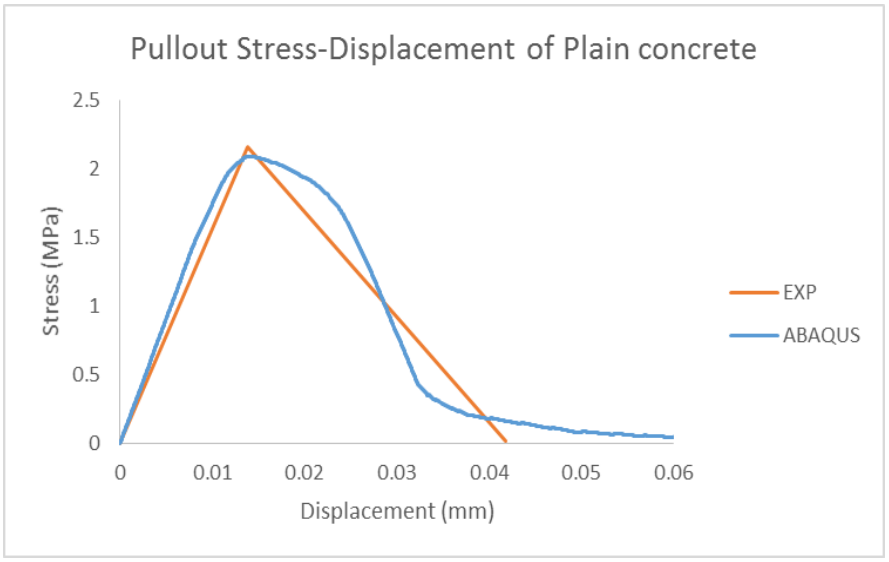

Figure 5: Derived Stress-Displacement using ABAQUS

For the compression cylinders, the ABAQUS and Experimental stress-strain behaviour is almost perfectly identical aside from 5% difference at the peak strength where the ABAQUS prediction is more conservative than the experimental solution. Figure 6 illustrates the latter relationship for plain lightweight concrete.

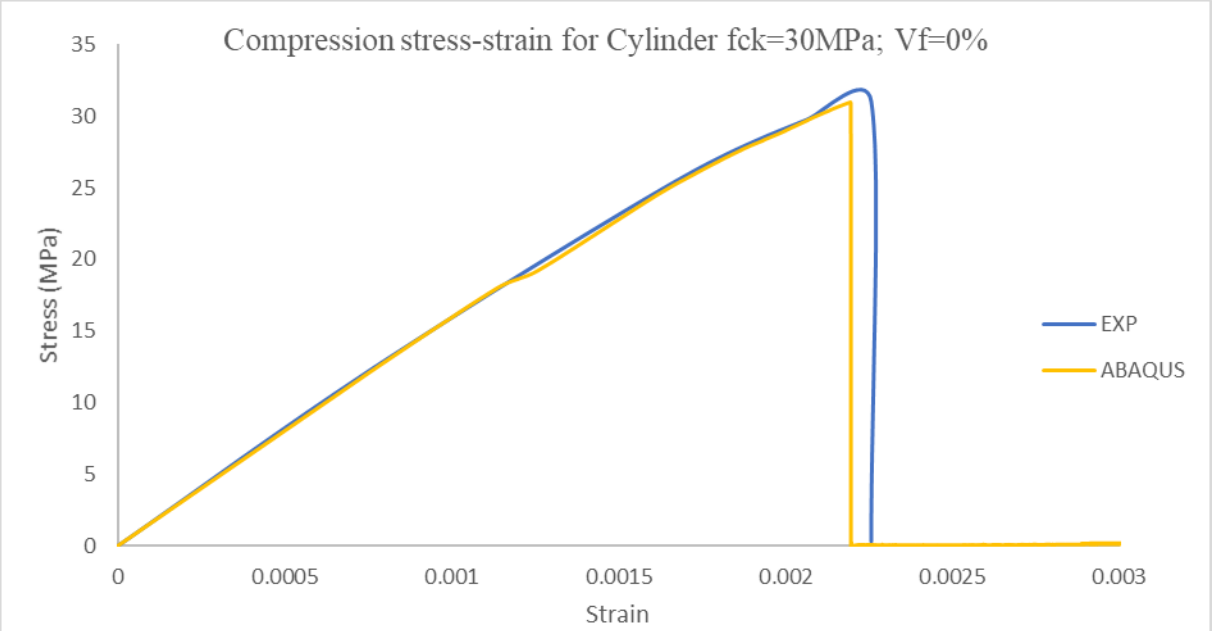

Figure 6: Compression stress-strain for ABQUS vs EXP

Figure 7 below show the cracking pattern for the reinforced beam with stirrup spacing S=120mm. The patterns are similar to experiments

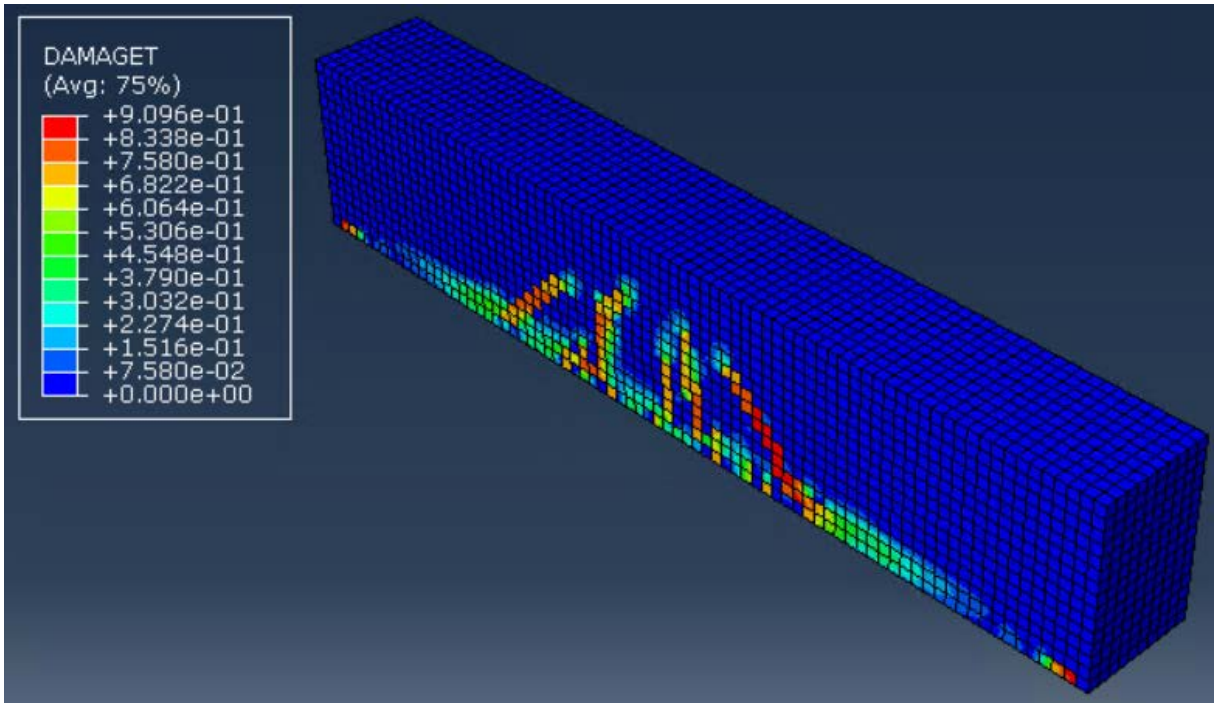

Figure 7: Development of flexural cracks for beam with S=120mm

Figure 8 below depicts the load-deflection relationship of the beam reinforced with S=120mm. It can be seen that the approach employed predicted accurate results.

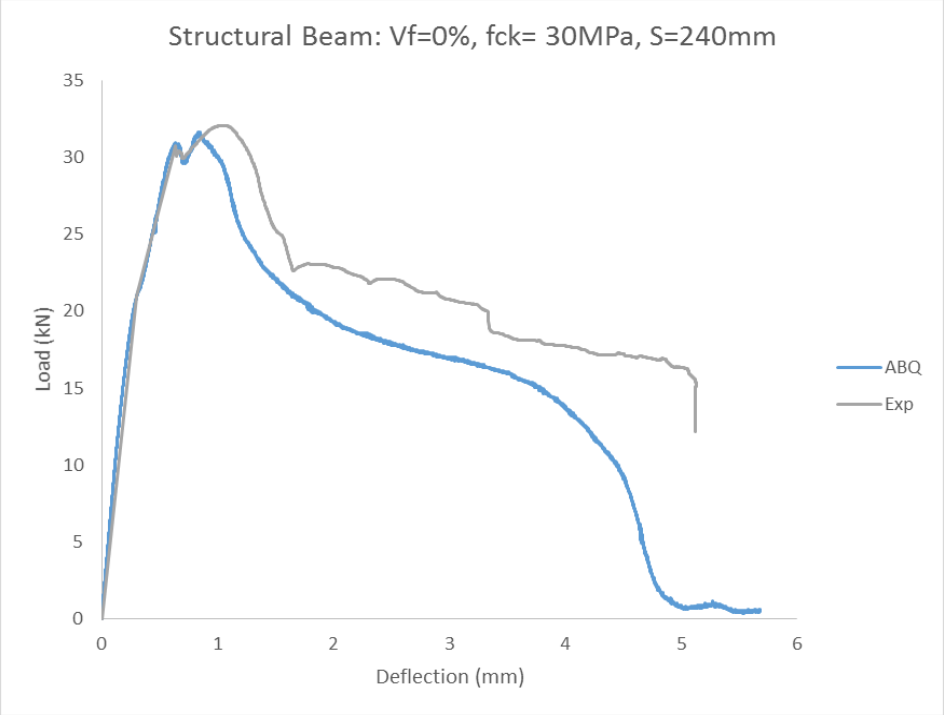

Figure 8: Load-deflection relationship of beam reinforced with S=240mm

5 CONCLUSIONS

- Density and workability are negatively influenced by the addition of steel fibres.
- Compression peak strengths are unaffected by fibres however post peak ductility is enhanced.
- Beam load carrying capacity and ductility are enhanced while mode of failure changes from shear to flexure as V_f increases. Fibres can adequately replace stirrups.
- The designed direct tensile test was successful at showing the behaviour of concrete and its bond with different fibres.
- The approach adopted for the numerical modelling shows good correlation between experimental and numerical results.

REFERENCES

[1] Abdallah Sadoon, David W.A Rees, Sayed Hamidreza Ghaffar and Mizi Fan. (2018). Understanding the effects of hooked-end steel fibre geometry on the uniaxial tensile behaviour of self-compacting concrete. *Construction and Building Materials*. 178, 484-494.

[2] ABAQUS Version 6.7 Documentation, 2007. [Online]. Available at http://www.engine.brown.edu:2080/v6.7/index.html.

[3] Abbas, A., Syed Mohsin, S. and Cotsovos, D. (2014a). Seismic response of steel fibre reinforced concrete beam–column joints. *Engineering Structures*, 59, pp.261-283.

[4] Abbas, A., Syed Mohsin, S., Cotsovos, D. and Ruiz-Teran, A. (2014b). Shear behaviour of steel-fibre-reinforced concrete simply supported beams. *Proceedings of the Institution of Civil Engineers - Structures and Buildings*, 167(9), pp.544-558.

[5] Balendran, R., Zhou, F., Nadeem, A. and Leung, A. (2002). Influence of steel fibres on strength and ductility of normal and lightweight high strength concrete. *Building and Environment*, 37(12), pp.1361-1367.

[6] Behinaein, Demetrios M. Cotsovos and Ali A. Abbas. (2018). Behaviour of steel-fibre-reinforced concrete beams under high-rate loading. *Computers and concrete*. 22 (3), 337-353.

[7] Campione, G. and La Mendola, L. (2004). Behavior in compression of lightweight fiber reinforced concrete confined with transverse steel reinforcement. *Cement and Concrete Composites*, 26(6), pp.645-656.

[8] Campione, G. (2014). Flexural and Shear Resistance of Steel Fiber–Reinforced Lightweight Concrete Beams. *Journal of Structural Engineering*, 140(4), p.04013103.

[9] Dias-da-Costa, D., Carmo, R., Graça-e-Costa, R., Valença, J. and Alfaiate, J. (2014). Longitudinal reinforcement ratio in lightweight aggregate concrete beams. *Engineering Structures*, 81, pp.219-229.

[10] Di Prisco, M., Colombo, M. and Dozio, D. (2013). Fibre-reinforced concrete in fib Model Code 2010: principles, models and test validation. *Structural Concrete*, 14(4), pp.342-361.

[11] Gao, J., Sun, W. and Morino, K. (1997). Mechanical properties of steel fiber-reinforced, high-strength, lightweight concrete. *Cement and Concrete Composites*, 19(4), pp.307-313

[12] Gerritse, A. (1981). Design considerations for reinforced lightweight concrete. *International Journal of Cement Composites and Lightweight Concrete*, 3(1), pp.57-69.

[13] Grabois, T., Cordeiro, G. and Filho, R. (2016). Fresh and hardened-state properties of self-compacting lightweight concrete reinforced with steel fibers. *Construction and Building Materials*, 104, pp.284-292.

[14] Hafezolghorani, Farzad Hejazi, Ramin Vaghei, Mohd Saleh Bin Jaafar and Keyhan Karimzade. (2017). Simplified Damage Plasticity Model for Concrete. *Structural Engineering International*. 1 (1), 68-78.

[15] Hibbitt, Karlsson and Sorensen Inc (2000) Abaqus User's Manual, Vol. II, Version 6.1, PP 11.5.1.1–11.5.1.14 (USA).

[16] Iqbal, S., Ali, A., Holschemacher, K. and Bier, T. (2015). Mechanical properties of steel fiber reinforced high strength lightweight self-compacting concrete (SHLSCC). *Construction and Building Materials*, 98, pp.325-333.

[17] Javier Rodríguez, Francisco Martínez, and Joaquín Martí. (2013). Concrete Constitutive Model, Calibration and Applications. *2013 SIMULIA Community Conference*. N/A (N/A), 1-1.

[18] Kang, T. and Kim, W. (2010). *Shear strength of steel fiber-reinforced lightweight concrete beams*. Oklahoma: Korea Concrete Institute, pp.1386-1392.

[19] Kang, T. and Kim, W. (2010). *Shear strength of steel fiber-reinforced lightweight concrete beams*. Oklahoma: Korea Concrete Institute, pp.1386-1392.

[20] Kodur Venkatesh, Roya SOlhmirzaei, Ankit Agrawal, Esam M Aziz and Parviz Soroushian. (2018). Analysis of flexural and shear resistance of ultra high performance fiber reinforced concrete beams without stirrups. *Engineering Structures*. 174, 873-884.

[21] Krenchel, H. Fiber spacing and specific fiber surface. In: Neville A M, ed. RILEM Symposium on Fiber Reinforced Cement and Concrete. London: The Construction Press, 1975, 69–79.

[22] Lambert, G, (1982) *Properties and behaviour of structural lightweight (Lytag-sand) concrete.* PhD thesis, University of Sheffield.
[23] Li Fang-Yuan, Cheng-Yuan Cao, Yun-Xuan Cui, and Pei-Feng Wu. (2018). Experimental Study of the Basic Mechanical Properties of Directionally Distributed Steel Fibre-Reinforced Concrete. *Advances in Materials Science and Engineering*. 2018 (1), 1-11.
[24] Libre, N., Shekarchi, M., Mahoutian, M. and Soroushian, P. (2011). Mechanical properties of hybrid fiber reinforced lightweight aggregate concrete made with natural pumice. *Construction and Building Materials*, 25(5), pp.2458-2464.
[25] Lyag (2011). Technical manual. London: Lytag ltd.
[26] Mo, K., Goh, S., Alengaram, U., Visintin, P. and Jumaat, M. (2017). Mechanical, toughness, bond and durability-related properties of lightweight concrete reinforced with steel fibres. *Materials and Structures*, 50(1).
[27] Mirza, O. (2008). *BEHAVIOUR AND DESIGN OF HEADED STUD SHEAR CONNECTORS IN COMPOSITE STEELCONCRETE BEAMS*. BEng (Hons). University of Western Sydney, Australia.
[28] Ngo, D. and Scordelis, A.C. (1967). "Finite Element Analysis of Reinforced Concrete Beams," Journal of ACI, Vol. 64, No. 3, pp. 152-163.
[29] Ritchie A., Kayali O. 1975. The effects of fiber reinforcement on lightweight aggregate concrete. In: Neville A (ed.), Proceedings of RILEM Symposium on Fiber Reinforced Cement and Concrete, The Construction Press Ltd, p. 247–56.
[30] Robins, P., Austin, S., and Jones, P., 2002. Pull-out Behaviour of Hooked Steel Fibres. Materials and Structures, RILEM, 35; p. 4343-442
[31] Romualdi, James P., and Mandel, James A., "Tensile Strength of Concrete Affected by Uniformly Distributed and Closely Spaced Short Length of Wire Reinforcement," AC1 JOURNAL, Proceedings V. 61, No. 6, June 1964, pp. 657-671.
[32] Soroushian and Lee. (1990). Tensile Strength of Steel Fiber Reinforced Concrete: Correlation with Some Measures of Fiber Spacing. *ACI materials journal*. 87 (6), 542-546.
[33] Swamy, N., Jones, R. and Chiam, A. (1993). Influence of Steel fibers on the Shear Resistance of Lightweight Concrete I-Beams. *ACI Structural Journal*, 90(1), pp.103-114.
[34] Syed Mohsin SM (2012) Behaviour of Fibre-reinforced Concrete Structures under Seismic Loading. PhD thesis, Imperial College London, London, UK.
[35] SZCZECINA and WINNICKI. (2016). SELECTED ASPECTS OF COMPUTER MODELING OF REINFORCED CONCRETE STRUCTURES. *ARCHIVES OF CIVIL ENGINEERING*. 62 (1), 51-64.
[36] The Concrete Society, 2007. Guidance for the Design of Steel-Fibre-Reinforced Concrete. Technical Report No. 63. Cement and Concrete Industry.
[37] Tlemat, H., Pilakoutas, K. and Neocleous, K. (2006). Stress-strain characteristic of SFRC using recycled fibres. *Materials and Structures*, pp.365-377.
[38] Tomasz JANKOWIAK, Tomasz LODYGOWSKI. (2005). IDENTIFICATION OF PARAMETERS OF CONCRETE DAMAGE PLASTICITY CONSTITUTIVE MODEL. *FOUNDATIONS OF CIVIL AND ENVIRONMENTAL ENGINEERING*. 6 (unknown), 53-69.
[39] Zhang, Y.J. Huang, Z.J. Yanga, S.L. Xua, X.W. Chen. (2018). A discrete-continuum coupled finite element modelling approach for fibre reinforced concrete. *Cement and Concrete Research.* 106 (2018), 130-143.
[40] Zienkiewicz OC and Taylor RL (2005) Vol. 2: The Finite Element Method for Solid and Structural Mechanics, 6th edn. Butterworth-Heinemann, Oxford, UK.

COMPDYN 2019
7th ECCOMAS Thematic Conference on
Computational Methods in Structural Dynamics and Earthquake Engineering
M. Papadrakakis, M. Fragiadakis (eds.)
Crete, Greece, 24–26 June 2019

ANALYSIS OF THE EXPERIMENTAL BEHAVIOR OF A BASED ISOLATED BUILDING DURING A RELEASE TEST

F.C. Ponzo[1], R. Ditommaso[1], D. Nigro[1], G. Oliveto[2], C. Iacovino[1, 3] and A. Mossucca[1]

[1] School of Engineering, University of Basilicata, Italy
Viale dell'Ateneo Lucano, 10
felice.ponzo@unibas.it, r.ditommaso@unibas.it, domenico.nigro@unibas.it, chiara.iacovino@unibas.it, antonello.mossucca@unibas.it

[2] Department of Civil Engineering and Architecture, University of Catania
Viale Andrea Doria, 6
giuseppe.oliveto@dica.unict.it

[3] Center of Integrated Geomorphology for the Mediterranean Area, Potenza, Italy
Via Francesco Baracca, 175
c.iacovino@cgiam.org

Abstract

In this article, the dynamic behavior of a base isolated structure located in Augusta City (Italy) is analyzed during ambient noise and during several release tests. On the 22th of May 2013, through different release tests, several accelerometers have been installed within the structure and on the surrounding soil in order to acquire the dynamic response of the structure and the effects of soil-structure interaction. During the experimental campaign, the dynamic behavior of the structure has been monitored before, during and after each test, comparing the dynamic characteristics in the different phases and evaluating possible damages on nonstructural elements. Particularly, the base-isolated structure has been characterized in terms of eigenfrequencies, equivalent viscous damping factor and mode shapes in ambient noise (considering the superstructure as a fixed-base structure) and during the release tests (monitoring the dynamic behavior of superstructure, base isolation system and underground floor). The aim of this article is to analyze the experimental behavior of the based isolated building and evaluate soil-structure effects in terms of energy released into the ground and maximum acceleration produced on the surrounding structures during the released tests.

Keywords: Base isolation, Full-scale tests, Dynamic identification, Non-linear dynamics.

1 INTRODUCTION

The loss of life and the enormous damages occurred in civil engineering structure disasters during the last decades have exposed the importance of preventative actions to mitigate the effects of structural failures. The serious damages and structural collapses are caused by high vulnerability of the existing buildings, designed and built without seismic details, but also by the frequency and intensity of earthquakes. Therefore, the evaluation of potential effects to structures in different permanent and/or accidental load scenarios is an important issue to be considered in rehabilitation decisions and emergency measure planning. Furthermore, there is the need to ensure more effective protection of existing constructions in regard to earthquakes, in order to mitigate the damages associated with these events. For this reason, it is very important to identify the real structural behavior, using Structural Health Monitoring (SHM) and dynamic identification techniques. Using this kind of approach, it is possible, using ambient and/or forced vibration and/or release test, to evaluate all the dynamic characteristics of a monitored structure: eigenfrequencies, equivalent viscous damping factors and mode shapes.

In this article, we analyzed the dynamic behavior of a base isolated structure during ambient noise and during several release tests; dynamic tests were performed applying an initial displacement to the structure using a special kind of jack. Release tests have already been carried out in Italy on base isolated buildings of TELECOM Ancona [1]-[3]. In that case it was applied to a shift of about 10 cm, through a complex system of synchronized cylinders with explosive charges in order to apply the instantaneous release. Other similar experiments have been carried out on the building of Rapolla in Potenza [4]-[6] and on some building of the University of Basilicata [7]. In the first case, the experiment was carried out on a building composed by two different interchangeable isolation systems. At Rapolla city, the initial displacement was applied by moving the structure just above the isolation system using the same mechanical set-up employed at the University of Basilicata. The device was redesigned to apply an initial displacements ranging from 0 to 20 cm. It consists of a three-hinged arch (two sets of trusses and three cylindrical shafts) vertically pulled on the middle hinge by means of a hydraulic jack equipped with a load cell. The release takes place when the three hinges reach the horizontal unstable alignment and the trusses detach from the middle hinge (central shaft).

In the second case, in order to characterize the real dynamic behavior of the headquarters of the Department of Mathematics of the University of Basilicata, an experimental campaign complete of a sequence of snap-back tests was performed. In this case many release tests were carried out by using a mechanical device purposely designed to give the initial displacement to the building and then produce free damped vibrations. In the summer of 2004 and in July of the same year another example of release tests were performed on two reinforced concrete building by base isolation in a small town of Solarino in Eastern Sicily. Dynamic tests were performed in the form of free vibrations after applying an initial displacement as close as possible to the design displacement [8]-[9]. Free vibration tests performed on base-isolated buildings have also been reported in literature.

A four-story building was built in 1992 in Santiago, Chile, on 8 HDRB and subjected to 5 free vibration tests under imposed displacements, ranging from a minimum of 6.1mm to a maximum of 19.5 mm, with corresponding deformations from 0.140 to 0.445. The main results were the measured periods of vibration and the equivalent damping ratio [10]. In literature there are also other examples of experimentation using snap-back test to estimate the behavior of different type of structures [11]-[13]. Several authors used accelerometric recordings of release tests also to analyze the problem of energy back-radiated from vibrating structures on both models [14] and real buildings [15]-[18]. Scientific literature provides several case studies that confirm the capability of fixed-base structures to modify the motion on the

surrounding area during an earthquake or a release test [19], on the contrary, with reference to the same soil-structure interaction mechanism, there are few case studies related to base-isolated structures.

For this reason, exploiting a series of release tests carried out on a base isolated structure in Augusta city (Italy), aim of this article is to test the seismic performance of the base isolation system, to compare the dynamic characteristics of the structure before, during and after each test (individuating possible damage on non-structural elements) and to evaluate soil-structure effects in terms of energy released into the ground and maximum acceleration produced on the surrounding structures during the released tests.

2 EXPERIMENTAL CAMPAIGN

During the experimental campaign carried out on the base isolated structure in Augusta city (Italy), a jack able to apply a maximum thrust force of about 200 tons has been applied. Following the test, the structure has shifted about 10 cm but without any damage, demonstrating the effectiveness of the isolation system. Figure 1a shows the tested structure and Figure 1b the device used to make the release test. The release test was carried out using a specially designed system able to impart to the building a prefixed initial displacement. Then, the structure was instantaneously released in a free-oscillating condition. The displacement impressed to the building during different release tests were prefixed taking into account the target maximum design displacement. The dynamic "snap-back" tests were carried out to verify the compliance of the isolation system to the expected behavior derived from the numerical analyses. In Figure 2 the plan of the building and the section A-A of structure are shown.

a) b)

Figure 1: a) Base isolated structure of Augusta; b) Thrust device of the release test.

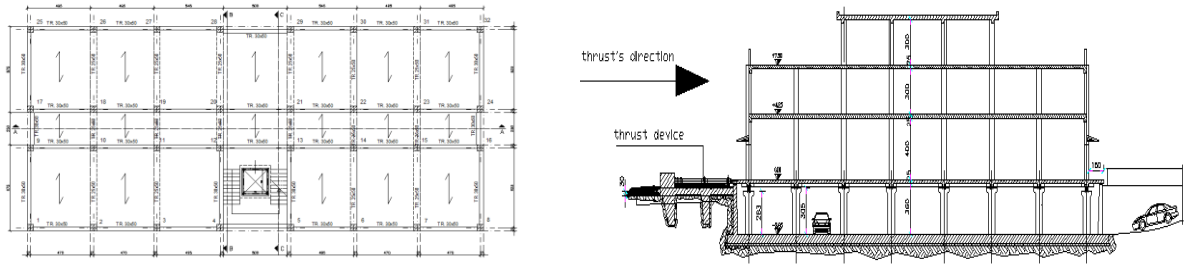

a) b)

Figure 2: a) Plan of the building; b) Section A-A of building.

The building, designed and constructed using the new Italian technical regulations, D.M. 14/01/2008 (NTC08), is characterized by a hybrid base isolation system composed by 16

High Damping Rubber Bearings and 20 low friction sliding Bearing [20]. The structure is made using reinforced concrete and characterized by three stories above the isolation plane and one story beneath it (Figure 2b). The ground floor is characterized by an inter-story height equal to 3.85 m respect to the basement, the first floor is characterized by an inter-story height equal to 4.25 m and finally the last level is characterized by an inter-story height equal to 3.25 m. The building has a rectangular shape with a length of 35.70 m, a width of 16 m and a maximum height above the ground at 10.50 m. The mass of the structure is equal to 2400 tons. The isolation plan runs along the top of the pillars of the basement story slightly above the ground level.

In order to evaluate the dynamic behavior and the soil-structure interaction effects, several accelerometers were installed within the structure and on the surrounding area (both in ambient vibration and during the release tests). Figure 3 shows the accelerometers position on the last floor of the structure while in Figure 4 the n°125-126 accelerometers installed on the top floor are detected.

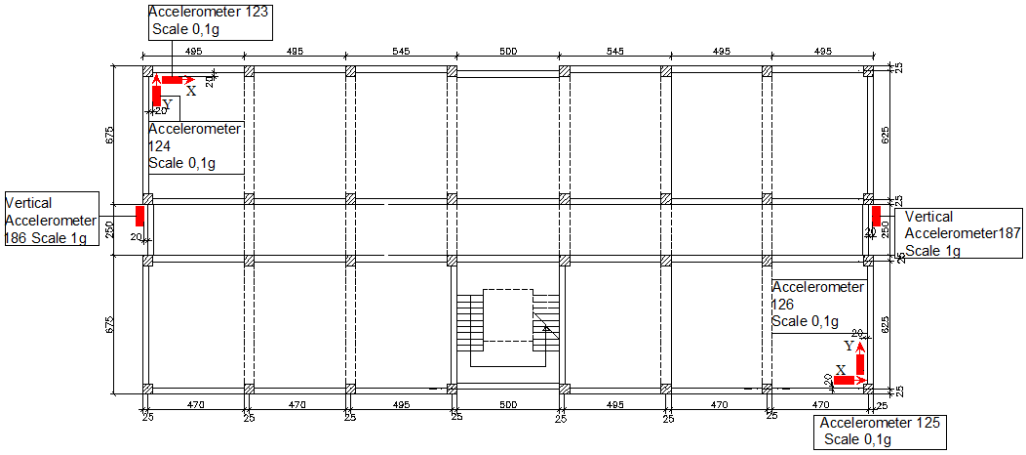

Figure 3: Accelerometers position on the last floor for the first configuration.

Figure 4: Accelerometers n° 125-126.

In order to assess the displacements of the structure appropriate transducers were installed in correspondence of the elevator shaft, of the pillars and on two corner of the structure, along the same diagonal, as shown in the following figures (from Figure 5 to Figure 7).

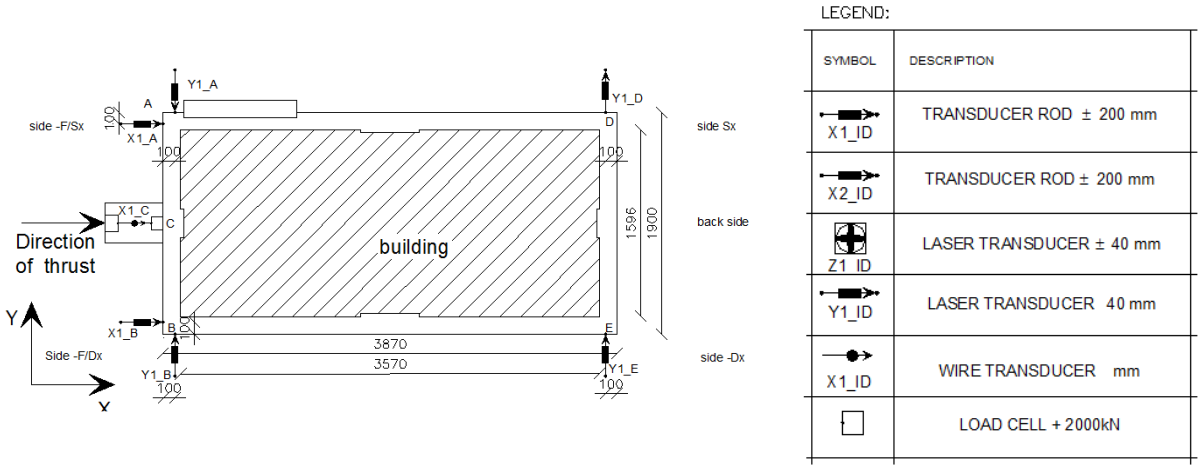

a) b)

Figure 5: a) Transducers position on the corner of the building; b) transducers characteristics.

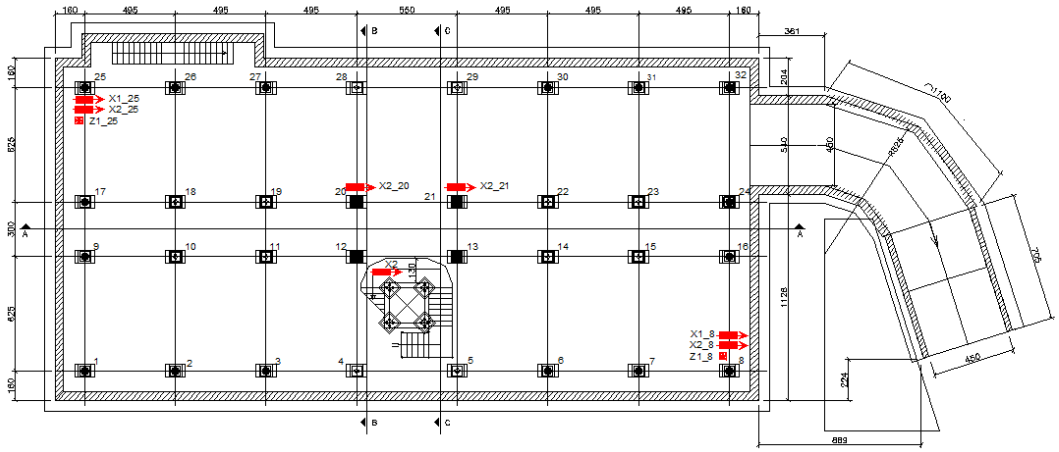

Figure 6: Transducers position along the rubber bearings 25 and 8, the sliding bearing 20, 21 and the sliding bearing of elevator shaft.

a) b)

Figure 7: a) Monitored displacement of the pillars and b) along the perimeter of the structure.

Figure 8 shows the recorded signals at each floor of test structure during an ambient noise (Figure 8a) and a release test (Figure 8b).

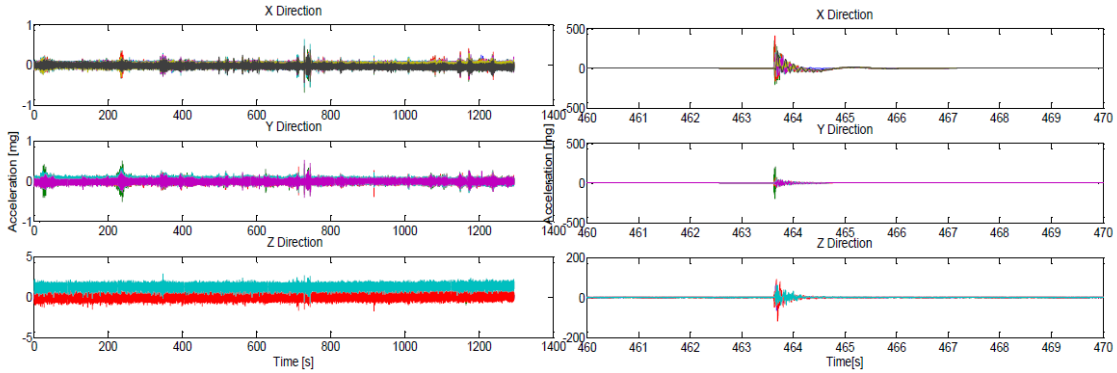

a) b)

Figure 8: a) Recorded signals at each floor of structure in ambient noise and b) in forced vibration.

3 STRUCTURAL DYNAMIC IDENTIFICATION DURING AMBIENT NOISE AND RELEASE TESTS

In order to assess the dynamic characteristics of the monitored structure, in the fixed base condition, the transfer functions have been calculated using seismic noise recordings retrieved from the accelerometers installed at each floor. Figure 9a shows the transfer function evaluated using the accelerometric recordings performed on the base and the top floor of the building. The mode shapes evaluated on the experimental data using time domain analyses are depicted in Figure 9b.

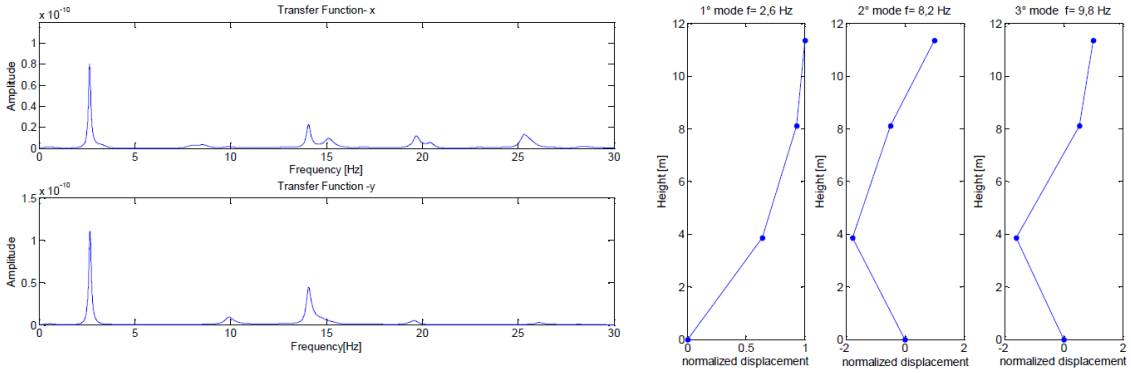

a) b)

Figure 9: a) Transfer function calculated using ambient noise and b) mode shapes.

In ambient noise condition, using the transfer function it has been possible to evaluate the main frequencies of the superstructure. The fundamental frequency of the superstructure is equal to 2.6Hz and, observing the related modal shape it seems to be a torsional mode. It is important to highlight that the dynamic characterization has been performed using ambient vibration test (characterized by very small amplitude), so also the contribution of non-structural elements is considered. The second mode (translational) is characterized by a frequency equal to 8.2 Hz and the third mode (translational) by a frequency equal to 9.8 Hz.

The accelerometric recording acquired on the top floor during release tests was analyzed using the Stockwell Transform [21], operating on the time-frequency domain, and transfer

function of the signal, operating on the frequency domain. From the time-frequency analyses (Figure 10) it was been possible to confirm the linear behavior of the superstructure and to detect the main eigenfrequencies.

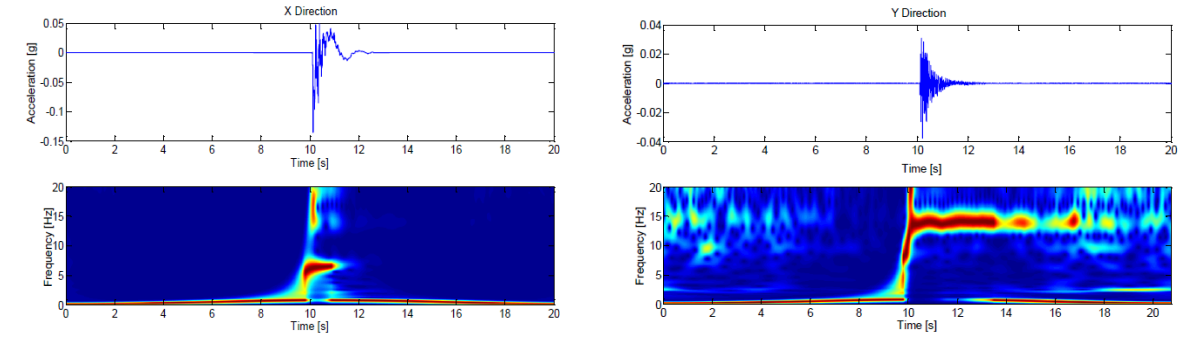

a) b)

Figure 10: a) Stockwell transform along x direction and b) y direction.

Using the Stockwell transform on the signal recorded on the superstructure and on the base isolation level it was been possible to evaluate the frequency of the base isolation system, equal to 0.73 Hz while the first detected frequency for the superstructure is equal to 2.6 Hz. Analyzing the data using the transfer function the same frequency for the base isolation system has been detected. Figure 11 shows these last results with the related modal shapes.

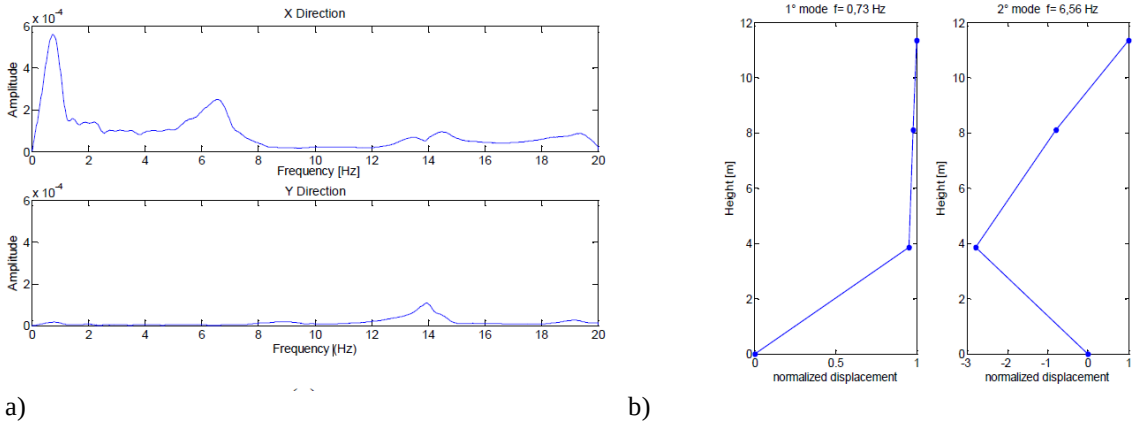

a) b)

Figure 11: a) Transfer Function evaluated on the accelerometric recordings during the release test and b) modal shapes of the structure for the main frequencies.

The values of the fundamental frequencies of superstructure evaluated in ambient noise and release test and the characteristics of the base isolation system are reported in Table 1 and Table 2.

FREQUENCIES OF SUPERSTRUCTURE	
1° roto-translational Y mode	2,6 Hz
2° translational X mode	8,2 Hz
3° translational Y mode	9,8 Hz

Table 1: Values of superstructure frequencies.

CHARACTERISTICS OF BASE ISOLATION SYSTEM	
1° translational X mode	0,73 Hz
Equivalent viscous damping factor	14,65%

Table 2: Characteristics of the base isolation system.

The evaluation of the equivalent viscous damping factor of the structure was carried out using the logarithm decrement method. Particularly, the accelerometric recordings related to the station installed to the last level have been considered for the equivalent viscous damping factor evaluation along the x direction (test direction). Figure 12 shows the kinematic parameter (acceleration, velocity and displacements) evaluated at each floor of the test building.

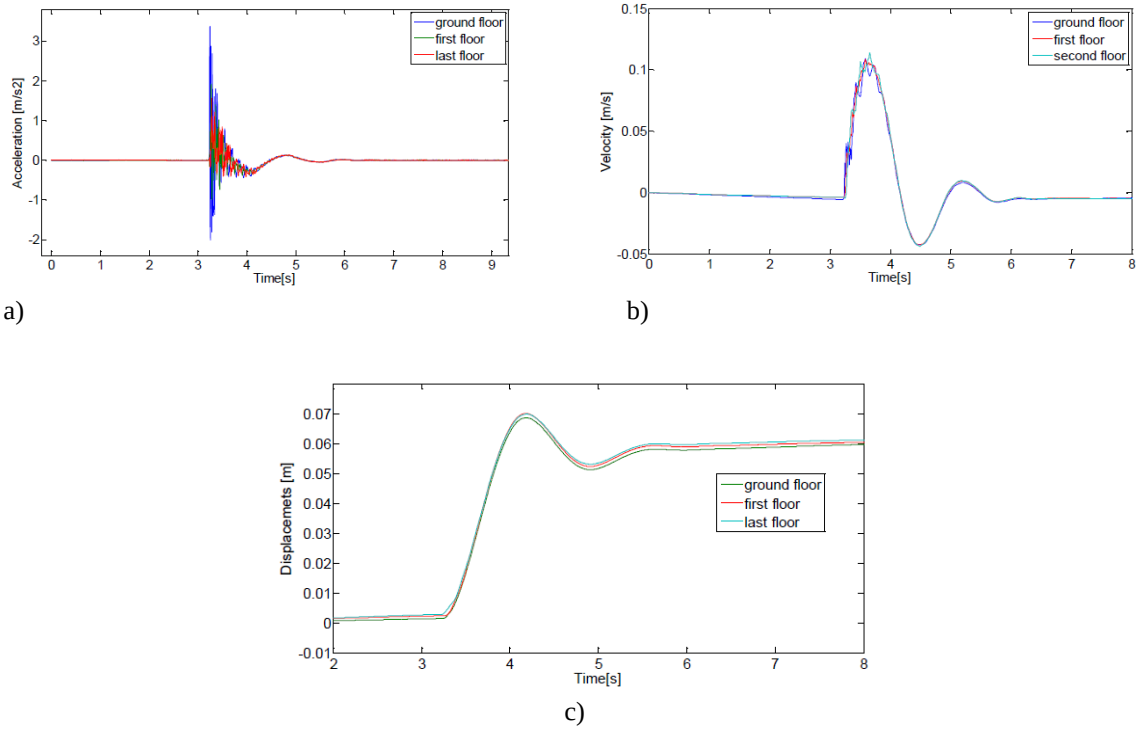

Figure 12: Kinematic parameters: a) acceleration, b) velocity and c) displacements.

Starting from the accelerometric recordings, a routine developed in MATLAB software was used to evaluate velocity and displacement. The main problem related to the determination of the displacement time-history starting from the accelerometric recordings, acquired during a release test, is related to the use of classical filter (standard approach) on impulsive signals. For this reason a special kind of filter was built using a routine implemented in MATLAB. Comparing the displacement time-history retrieved from the accelerometric recordings with those acquired using the displacement transducers it is possible to observe a very good agreement. On the contrary, using the standard approach the displacement retrieved from the accelerometric recordings is very different from those acquired from the transducers (Figure 13).

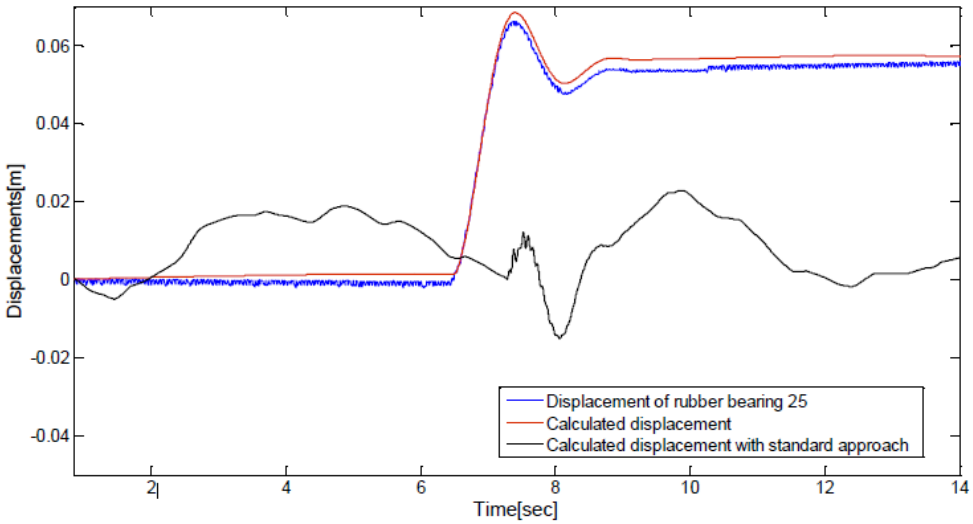

Figure 13: Comparison between the displacements evaluated using a MATLAB routine, the displacements acquired using a displacement transducer (on the rubber bearing n° 25) and the displacements obtained with standard methods.

4 CONCLUSIONS

This paper reports the preliminary results of the experimental campaign performed on a base isolated structure located in Augusta, providing information about the test and consideration on the seismic behavior of the structure. The release test allowed to simulate the maximum displacement occurred during a very strong earthquake on the area where the building is located. Taking the advantage of the release tests it has been possible to analyze and compare the experimental structural dynamic behavior during ambient vibration conditions (microtremors), and simulating the effects of weak and strong motion earthquakes. The maximum displacement reached during the experimental campaign is 10cm at the base isolation level. The dynamic behavior of the structure and of the base isolation system was monitored using several kind of instrumentation: cabled accelerometric stations, displacement transducers and wireless accelerometric station.

The analyses were performed both in ambient vibration and during the release test using transfer function and time-frequency analyses based on the S-Transform. In order to evaluate the displacement time-history, starting from the accelerometric recordings a special kind of filter has been designed. The results were compared with those acquired directly from the displacement transducers installed at the base isolation level.

The preliminary results obtained from the experimental campaign confirmed the high performance level of protection of the base isolation system installed on new buildings. Further studies are necessary to analyze the dynamic performance of the structure in more detail, to build a realistic numerical model (using model updating techniques) and to compare the experimental behavior with those predicted from linear and nonlinear numerical models.

REFERENCES

[1] F. Bettinali, M.Forni, M. Indirli, A. Martelli, P. Masoni, G. Bonacina, G. Pucci, G. Serino, M. Venturuzzo, G.C. Giuliani, On site dynamic tests of a large seismically isolated building. *International Meeting on Earthquake Protection of Buildings*, Ancona, 1991.

[2] F. Bettinali, M.Forni, A. Martelli, G. Pucci, Experimental and numerical analysis of isolated structures. *Earthquake Engineering*, Tenth World Conference, Balkema, Rotterdam, 1992.

[3] M.Forni, A. Martelli, B. Spadoni, E. Casalini, G. Bonacina, G. Pucci, G. Serino, Dynamic tests on seismically isolated structure mock – ups and validation of numerical models. *International Meet-ing on Earthquake Protection of Buildings*. Ancona, 1991.

[4] F. Braga, M. Laterza, R. Gigliotti, D. Nigro, Prove Di Rilascio Di Un Edificio Per Civile Abitazione Costruito nel Comune di Rapolla: sistema di isolamento isolatori elastomerici. *10° Convegno Nazionale L'ingegneria Sismica in Italia*, 2001.

[5] F. Braga, M. Laterza, Field testing of low-rise base isolated building. *Engineering Structures*, **26**, 1599–1610, 2004.

[6] F. Braga, M. Faggella, R. Gigliotti, M. Laterza, Nonlinear Dynamic Response of HDRB and Hybrid HDRB-Friction Sliders Base Isolation Systems. *Bulletin of Earthquake Engineering*, **3**(3), 333–353, 2005.

[7] A.R. Bixio, F. Braga, M. Dolce, D. Nigro, F.C. Ponzo, Prove dinamiche di rilascio di un edificio isolato alla base dell'Università di Potenza. 2001.

[8] A. Athanasiou, G. Oliveto, Modelling Hybrid base isolation system for free vibration simulation. *8th International Conference on Urban Earthquake Engineering* March 7-8, 2011.

[9] N.D. Oliveto, G. Scalia, G. Oliveto, Time domain identification of hybrid base isolation systems using free vibration tests. *Earthquake Engineering and Structural Dynamics*, **39**(9), 1015 – 1038, 2010.

[10] M. Moroni, M. Sarazzin, R. Boroschek, Experiments on a base-isolated building in Santiago, Chile. *Engineering Structures*, **20**(8), 720-725, 1998.

[11] M.J. Pender, T.B. Algie, R.P. Orense, L.M. Wotherspoon, Snap-back testing for estimation of nonlinear behaviour of shallow and pile foundations. *Proceedings of the Ninth Pacific Conference on Earthquake Engineering Building an Earthquake-Resilient Society*, Auckland, New Zealand, 2011.

[12] P. Chugh, S. Kumar, B. Valeti, M.M. Atif, R.K. Ranjan, Small Scale Modeling and testing of a 3-story steel momentframe building - with/without base isolation. 2011.

[13] M. Seki, M. Miyazaki Y. Tsuneki, K. Kataoka, A masonry school building retrofitted by base isolation. Technique, *Paper, 1118 12WCEE*, Auckland, New Zealand, 2000.

[14] P. Guéguen, P.Y. Bard, F.J. Chavez-Garcia, Site-city seismic interaction in Mexico City like environments: An analytic study. *Bull. Seism. Soc. Am.*, **92**, 794- 811, 2002.

[15] M. Mucciarelli, M.R. Gallipoli, F.C. Ponzo, M. Dolce, Seismic waves generated by oscillating building. *Soil Dyn. Earthq. Eng*., **23**, 255-262, 2003.

[16] M.R. Gallipoli, M. Mucciarelli, F.C. Ponzo, M. Dolce, E. D'Alema, M. Maistrello, Buildings as a Seismic Source: Analysis of a Release Test at Bagnoli, Italy. *Bulletin of the Seismological Society of America*, **96**(6), 1-8, 2006.

[17] R. Ditommaso, M.R. Gallipoli, M. Mucciarelli, F.C. Ponzo, Effect of vibrating building on "free field" ground motion: from the Bagnoli experiment to many buildings simula-

tion. *Proc. 4th Int. Conf. Earthq. Geot. Eng*., CD-Rom edition, Paper No. 1388. Springer, ISBN 978-1-4020-5893-6, 2007.

[18] R. Ditommaso, M.R. Gallipoli, M. Mucciarelli, F.C. Ponzo, Effect of a single vibrating building on free-field ground motion: numerical and experimental evidences. *Bulletin of Earthquake Engineering*, **8**(3), 693-703. DOI:10.1007/s10518-009-9134-5, 2010.

[19] R., Ditommaso, S., Parolai, M., Mucciarelli, S., Eggert, M., Sobiesiak, J.Zschau, Monitoring the response and the back-radiated energy of a building subjected to ambient vibration and impulsive action: the Falkenhof Tower (Potsdam,Germany). *Bulletin of Earthquake Engineering*, **8**(3), 705-722. DOI: 10.1007/s10518-009-9151-4, 2010.

[20] G. Oliveto, A. Athanasiou, M. Granata, Blind simulation of full scale free vibration tests on a three story base isolated building. *10th International Conference on Urban Earthquake Engineering*, March 1-2, 2013, Tokyo Institute of Technology, Tokyo, Japan.

[21] R.G. Stockwell, L. Mansinha, R.P. Lower, Localization of the complex spectrum: the S-transform. *IEEE Trans Signal Process*, **44**, 998-1011, 1996.

COMPDYN 2019
7th ECCOMAS Thematic Conference on
Computational Methods in Structural Dynamics and Earthquake Engineering
M. Papadrakakis, M. Fragiadakis (eds.)
Crete, Greece, 24–26 June 2019

NUMERICAL PERFORMANCE OF A NEW ALGORITHM FOR PERFORMING MODAL ANALYSIS OF FULL-SCALE REINFORCED CONCRETE STRUCTURES THAT ARE DISCRETIZED WITH THE HYMOD APPROACH.

Dewald Z. Gravett[1], Christos Mourlas [2], George Markou [1], and Manolis Papadrakakis [2]

[1] Department of Civil Engineering, University of Pretoria, South Africa
e-mail: u16004664@tuks.co.za; george.markou@up.ac.za

[2] Institute of Structural Analysis & Seismic Research, National Technical University of Athens, 9 Iroon Polytechniou Str.,Zografou Campus,GR-15780 Athens, Greece
e-mail: {mourlasch, mpapadra}@central.ntua.gr

Abstract

Nonlinear dynamic modeling of full-scale mid- and high-rise reinforced concrete structures through the use of the 3D detailed approach that foresees the use of hexahedral elements with embedded rebars is not yet feasible due to numerous reasons. The two main numerical problems that do not allow for this type of analysis to be performed, are the numerical instabilities that immerse when the opening and closing of cracks initiates during the dynamic analysis and the excessive computational demand that is required even when dealing with small numerical models. This work will present the computational response of a newly developed algorithm that is used herein to perform modal analysis of large-scale models. The under study algorithmic development is a part of a project that aims towards alleviating the prementioned numerical constraints in regard to performing nonlinear dynamic analysis of full-scale reinforced concrete structures. An extensive numerical investigation is presented that foresees the performance of modal analysis on different full-scale reinforced concrete structures that are discretized with the Hybrid Model (HYMOD) approach. Based on the numerical investigation findings, the developed algorithm was found to be computationally efficient offering a robust numerical tool for performing modal analysis of large-scale numerical models.

Keywords: Eigenvalue problem, hybrid modeling, large-scale numerical models, reinforced concrete, finite element method, 3D detailed modeling

1 INTRODUCTION

The development of a computationally efficient model for reinforced concrete (RC) structures that can produce accurate results in dynamic nonlinear modeling has been a critical issue for many researchers. It is difficult to simulate and capture the mechanical behavior of RC structures due to the complexity of the concrete material's behavior. Researchers usually simulate RC structures by using 1D and 2D numerical models, in order to decrease the computational cost of the analysis and avoid numerical instabilities when nonlinearities occur. Although, 3D numerical approaches produce objective results, they increase significantly the computational demand of the analysis. Therefore, a numerical tool that can alleviate numerical limitations and produce numerically robust solutions has to be developed.

The use of the detailed RC modeling approach is impractical for engineers due to the computational complexity of the derived models. One of the main numerical limitations when dealing with 3D detailed modeling through the use of solid elements with embedded rebars, is the high computational demand that arises during the nonlinear analysis. Additionally, many researchers try to increase the objectivity of their models by using higher order models and high integration rules, which can significantly increase the computational cost of the numerical analysis. Therefore, several researchers (Hartl [1], Spiliopoulos and Lykidis [2], Červenka and Papanikolaou [3], Papanikolaou and Kappos [4], Markou and Papadrakakis [5], Mourlas et al. [6,7]), used their proposed numerical models in order to study single RC structural members or relatively small structural configurations (i.e. 1-span RC frames).

Dynamic nonlinear analysis is still not an option when deploying the 3D detail approach, while this research work aims towards alleviating this obstacle. When analyzing any multistorey structure under dynamic loading conditions, the models' eigenmodes have to be computed, whereas this numerical problem can become computationally demanding when dealing with large-scale models. Therefore, decreasing the computational cost of this numerical procedure is of great importance. The results presented within this manuscript were developed by using the model presented by Mourlas et al. [8], where a 4-storey RC building was analyzed by using the 3D detailed modeling and the hybrid modeling (HYMOD) approach. The original model found in [8] was modified accordingly by adding more storeys and/or by increasing the model's plan view in order to construct the meshes that were analyzed herein. A modal analysis through the use of the developed models in order to compare the numerically obtained fundamental periods with those derived from different design codes is also performed and presented herein.

In order to overcome the numerical limitations derived from the high computational demand of the 3D detailed modeling, the HYMOD method is implemented in this research work as it was proposed by Markou and Papadrakakis [9], while the proposed modal algorithm [8] was programmatically optimized for the needs of this research work to be able to manage large-scale numerical problems. The HYMOD approach and its main assumptions are presented in the next section. Section 3 discusses the theory in regards to the numerical methodology that lies behind the calculation of the eigenvalues for large-scale models and section 4 presents the numerical results as they derived from the parametric investigation.

2 HYBRID MODELING

The HYMOD approach adopted in this work is based on the formulation presented by Markou and Papadrakakis [9], which was also extended in [8] in order to analyze large-scale RC structures submitted to cyclic loading conditions. Based on the proposed framework of Markou and Papadrakakis [9], the element types that are combined, are the isoparametric hexahedral element and the natural Beam-Column Flexibility-Based (NBCFB) fiber element. The

NBCFB element is a one dimensional element and the 8-noded isoparametric hexahedral element is a three dimensional element that consists of 24 degrees of freedom (dof). By using the HYMOD method, a mesh can be created that will combine the different in dimensionality elements managing to decrease the computational demand and at the same time maintain a sufficient level of accuracy [9].

The NBCFB element offers simplicity and accuracy, given it is computationally efficient, a numerical feature that makes it ideal for 1D concrete material modeling. Furthermore, the NBCFB element foresees that each concrete section is divided into fibres, where each fibre is assigned with a maximum tensile stress that is directly connected to the corresponding compressive strength of the material. Therefore, it has the ability to capture material nonlinearities that may occur at the section level.

As seen in Fig. 1, the coupling between the beam-column and hexahedral elements is achieved through kinematic constraints. The kinematic constraints are enforced at each hexahedral node that is located on the interface between the beam and the solid elements [9]. The kinematic connection is performed as follows:

$$\underset{(3x1)}{\boldsymbol{u}_i^{HEXA}} = \underset{(3x6)}{\boldsymbol{T}_{im}} \cdot \underset{(6x1)}{\boldsymbol{u}_m^{NBCFB}}, \tag{1}$$

with

$$\underset{(3x6)}{\boldsymbol{T}_{im}} = \begin{bmatrix} 1 & 0 & 0 & 0 & z_i - z_m & y_m - y_i \\ 0 & 1 & 0 & z_m - z_i & 0 & x_i - x_m \\ 0 & 0 & 1 & y_i - y_m & x_m - x_i & 0 \end{bmatrix} \tag{2}$$

where $\boldsymbol{u}_m^{NBCFB}$ and $\boldsymbol{u}_i^{HEXA}$ are the displacement vectors of the NBCFB node corresponding to 6 dofs and the hexahedral nodes (3 dofs per node) at the interface, respectively. The subscript *i* of the global coordinates x, y, z refer to the hexahedral node ID located at the interface section Ω_j^1, while subscript *m* refers to the NBCFB elemental node ID that controls the displacements (master node) of the interface section Ω_j^1 (Fig. 1). The connection matrix $\boldsymbol{T}_{im}$ is computed from the compatibility conditions of the NBCFB and hexahedral nodal coordinates.

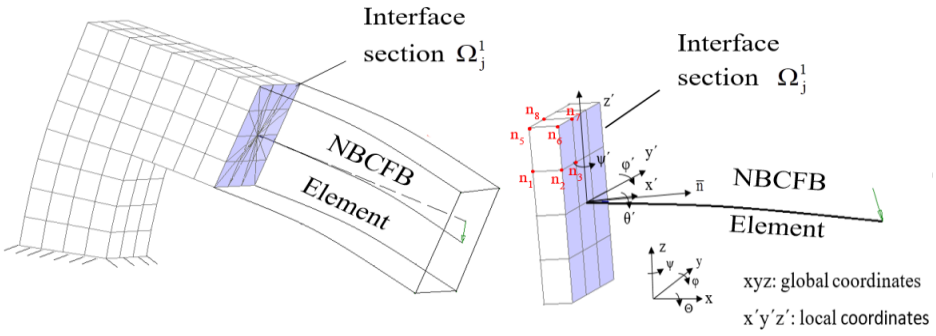

Figure 1: Hybrid model showing the interface between 1D and 3D elements [9].

It is noteworthy to state here that, the main limitation of layered or fibre elements is related to the fact that they cannot simulate the nonlinear response of structural members that undergo considerable shear deformations. One of the first attempts to overcome this limitation was that of Vecchio and Collins [10] who proposed a model with a dual-section analysis procedure discretizing the element into layers, where iterations are performed for each layer until the internal

equilibrium between adjacent sections was satisfied. Nevertheless, the beam-column finite element cannot overcome the modeling limitations when dealing with the simulation of real 3D structures that consist of shear walls and irregular geometry. Both approaches used in HYMOD modeling (beam-column and solid element) have their advantages and disadvantages that cannot be surpassed just by improving their numerical features and formulations, whereas their combination was found to be optimal in developing computationally efficient and numerically accurate models.

It must be noted at this point that, the length of the solid part is a crucial geometrical parameter that defines the length of the plastic hinge that is developed during the nonlinear analysis (see Fig. 1). Therefore, the value of this length is crucial for the overall accuracy of the nonlinear analysis. The numerical investigation conducted in [8, 9], showed that the length of the potential plastic hinge at the ends of the structural members should be equal to *h - 2h*, where *h* is the height of the member's section. This was also the values that were adopted in this research work.

3 MODAL ANALYSIS OF LARGE-SCALE MODELS

In this article, several models are developed and used to perform a modal analysis in order to calculate the natural frequencies and natural modes of their framing system, which provide an overview of the structures' dynamic response. Therefore, it is important to determine the eigenfrequencies of any RC structure so as to provide the structural engineer with the ability to understand the dynamic behavior of their designs, where they will be able to establish that periodic excitations will not cause resonance phenomena that may lead to the development of excessive stresses and strains. The eigenfrequencies depend on the geometry of the framing system and the material of the elements. Mass is also a controlling parameter when dealing with heavy or light structures, thus the investigation that will presented in the following section assumes the detailed representation of the frame's geometry and structural mass.

There are several solution methods for solving the eigenvalue problem that are describe by the following equation:

$$\mathbf{K}\boldsymbol{\varphi}_i = \lambda_i \mathbf{M}\boldsymbol{\varphi}_i \tag{1}$$

where, **K** is the stiffness matrix of the model, **M** is the mass matrix of the model, $\boldsymbol{\varphi}_i$ is a vector that contains the eigenvectors of the system and λ_i is the corresponding eigenvalue. The solution method used in this research work is called the subspace iteration algorithm [11]. This solution technique is indicated when dealing with large-scale structures since it calculates few eigenvalues and eigenvectors of a significantly demanding finite element system.

This solution algorithm finds an orthogonal basis of vectors in $\boldsymbol{E}_{K+1}$, calculating in one step the required eigenvectors when $\boldsymbol{E}_{K+1}$ converges to $\boldsymbol{E}_{\infty}$. The developed algorithm foresees the iteration used in the subspace iteration method, i.e., step 2 of the complete solution phase proposed by Bathe [11]. For k = 1, 2, …, iterate from $\boldsymbol{E}_k$ to $\boldsymbol{E}_{k+1}$:

$$\boldsymbol{K}\boldsymbol{X}_{k+1} = \boldsymbol{M}\boldsymbol{x}_k \tag{2}$$

then, find the projections of matrices **K** and **M** onto $\boldsymbol{E}_{k+1}$:

$$\boldsymbol{K}_{k+1} = \boldsymbol{X}_{k+1}^T \boldsymbol{K}\boldsymbol{X}_{k+1} \tag{3}$$

$$\boldsymbol{M}_{k+1} = \boldsymbol{X}_{k+1}^T \boldsymbol{M}\boldsymbol{X}_{k+1} \tag{4}$$

and solve for the eigensystem of the projected matrices:

$$\boldsymbol{K}_{k+1}\boldsymbol{Q}_{k+1} = \boldsymbol{M}_{k+1}\boldsymbol{Q}_{k+1}\boldsymbol{\Lambda}_{k+1} \tag{5}$$

Thereafter, find an improved approximation to the eigenvectors:

$$\boldsymbol{x}_{k+1} = \boldsymbol{X}_{k+1}\boldsymbol{Q}_{k+1} \tag{6}$$

and then provided that the vectors $\boldsymbol{x}_1$ are not orthogonal to one of the equilibrium eigenvectors, $\boldsymbol{\Lambda}_{k+1} \rightarrow \boldsymbol{\Lambda}$ and $\boldsymbol{X}_{k+1} \rightarrow \boldsymbol{\Phi}$ as k $\rightarrow \infty$.

It is important to note that the convergence of this method assumes that within the iteration procedure the vectors in $\boldsymbol{X}_{k+1}$ are ordered in such a way that the i^{th} diagonal element in $\boldsymbol{\Lambda}_{k+1}$ is always larger than the previous i-1 element, i=2, ..., p. This ensures that the i^{th} column in $\boldsymbol{X}_{k+1}$ converges linearly to $\boldsymbol{\Phi}_i$. Although this is an asymptotic convergence rate, it was found that the smallest eigenvalues converge fastest [11]. This numerical response was also verified in section 4 of this research work were all numerical analysis managed to converge for six or less internal iterations.

4 NUMERICAL IMPLEMENTATIONS

The models that formed part of the first parametric investigation were constructed by modifying the geometry of the initial model examined in [8], by adding or removing storeys. These models foresee the use of columns and drop beams only. The initial meshes that were examined herein foresaw the use of 2-,4-,6-,8-,10- and 20-storeys (as can be seen in Fig. 2a). The second group of models that were constructed for the computational efficiency investigation of the developed algorithm foresaw the use of a shear wall throughout the height of the two parallel frames. In this case, the same number of storeys were used as described above and as shown in Fig. 2b. The height per storey for all models was equal to 3 meters.

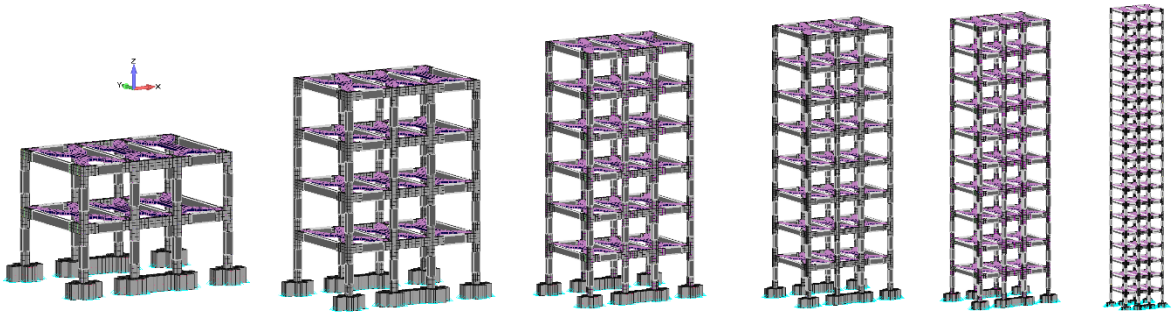

(a)

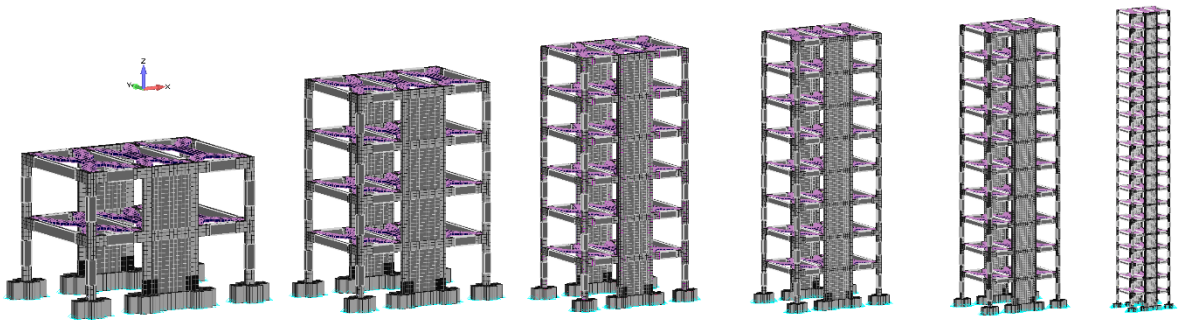

(b)

Figure 2: Initial models with 2, 4, 6, 8, 10 and 20 storeys. HYMOD meshes (a) without and (b) with shear walls (not to scale).

The eigenfrequencies obtained from the analysis of the 12 meshes shown in Fig. 2, were compared to the values derived from the codes of South African National Standard (SANS), Eurocode (EC), Cyprus and NEAK (New Greek Antiseismic Code).

The formulae for calculating the periods for the different under study codes are expressed by the following equations:

NEAK [12]:

$$T_{NEAK} = 0{,}09\frac{H}{\sqrt{L}}\sqrt{\frac{H}{H+pL}} \quad (7)$$

where, H is the total height of the building, L is the dimension of the building along the direction that the period is computed for, and ρ is the percentage of the summation of the shear wall areas positioned along the direction of the computed oscillation over the total of the vertical structural members' area.

Cyprus [13]:

$$T_{Cyprus} = \frac{N}{10} \quad (8)$$

where, N is the total number of storeys of the RC structure.

EC [14] and SANS [15]:

$$T_{EC} = C_T H^{0,75} \quad (9)$$

where, C_T = 0,085 for steel frames, C_T = 0,075 for RC moment – resisting frames and for eccentrically braced frames, C_T = 0,05 for all other buildings, while H is the total height of the building. Alternatively, for structures with concrete or masonry shear walls, the value of C_T may be taken as:

$$C_T = \frac{0{,}075}{\sqrt{A_c}} \quad (10)$$

where, $A_c = \Sigma\,[A_i(0{,}2 + (\frac{L_{wi}}{H})^2)]$, which is the total effective area of shear walls in the first storey of the building (subject to walls remaining relatively unchanged over the height of the building) in square meters [14].

Table 1 shows the eigenperiods, as they derived from the numerical analysis and the ones calculated according to the four under study design codes. It must be noted here that, the SANS and EC codes use the same formulae, given that South Africa adopted the Eurocode considerations in regards to the periods calculations, thus the results are shown as EC for brevity purposes. Additionally, all periods (T_1 and T_2) that were computed through the numerical models foresaw an oscillation along the y and x directions, respectively, thus referred here as T_y and T_x. The mode shape that foresees the rotation about the z-axis is referred to as T_z. As it can seen in Table 1, as the number of storeys increases, the magnitude of the first two periods is significantly increasing due to the corresponding height increase. This phenomenon is explained by the fact that the stiffness of the building is decreasing as its height increases, where the mass per storey remains constant.

Number of storeys	Height (m)	Numerical			NEAK		Cyprus	EC
		Ty (s)	Tx (s)	Tz (s)	Ty (s)	Tx (s)	Tx & Ty (s)	Tx & Ty (s)
2	6	0.23	0.18	0.12	0.22	0.18	0.2	0.29
4	12	0.44	0.36	0.16	0.43	0.36	0.4	0.48
6	18	0.59	0.5	0.2	0.65	0.54	0.6	0.66
8	24	0.74	0.64	0.24	0.86	0.72	0.8	0.81
10	30	0.94	0.87	0.31	1.08	0.90	1.0	0.96
20	60	1.99	1.93	0.64	2.16	1.81	2.0	NA

Table 1: Periods for all the initial models without shear walls. Numerical and design code results.

The initial models without shear walls for the cases of 2- and 20-storey models, can be seen in Figs. 3 and 4, respectively. In order to avoid a lengthy manuscript, the rest of the models are not shown herein. As it was stated above, the first two modes foresee the translational deformation along the y- and x-axis directions, for all models. Furthermore, the third mode for the cases of the shorted buildings was the rotation about the z-axis, while the multistorey buildings resulted additional translational modes that foresaw a sinusoidal deformation along the x- and y-axis prior to deriving the T_z deformed shape.

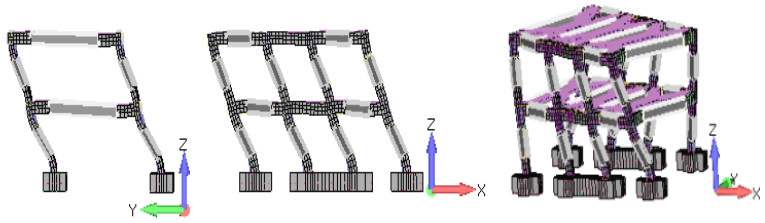

Figure 3: Initial 2-storey model without shear walls. Mode (Left) T_y, (Center) T_x and (Right) T_z.

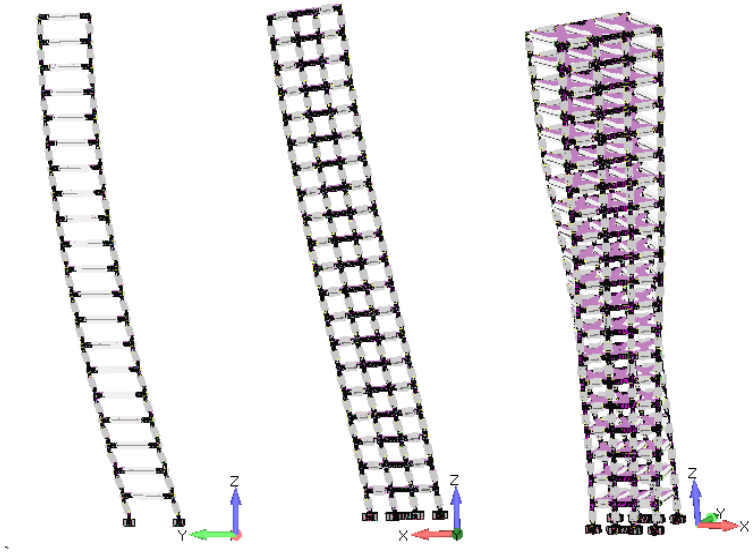

Figure 4: Original 20-storey model without shear walls. Mode (Left) T_y, (Center) T_x and (Right) T_z.

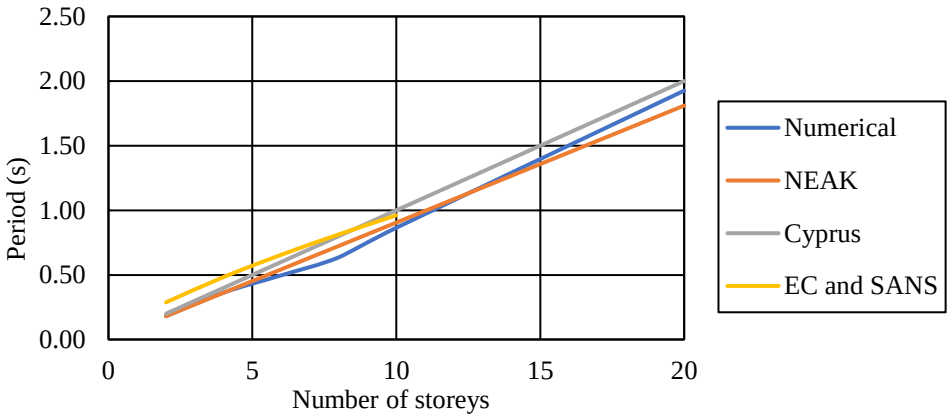

Figure 5: Relationship between period along the x-direction and number of storeys for the initial models without shear walls.

The numerical results are compared with the values of the periods derived from the formulas proposed by the four codes (Eqs 7-10) in Fig. 5 (see also Table 1). As it resulted from the

numerical investigation, the periods obtained from the design codes along the x-axis direction are on average in a good agreement with the numerical results for the case where shear walls are not included within the framing system of the structure. Base on Eurocode, the proposed formula can only be used for structures with heights equal or less than 40 m, therefore, the 20-storey case is not included within Table 1 and Fig. 5. It is also easy to observe that for the computed periods for the cases of the 2, 4 and 6 storey buildings, the codes illustrate a higher divergence from the numerical results, where for the higher storey models the difference decreases. The periods derived from the Cyprus code are the most accurate compared to the other three codes' results, deriving an average of a 1% divergence when compared to the numerical values of the computed periods along the y-axis direction. The NEAK follows with an average divergence of 7% and last Eurocode with 12%.

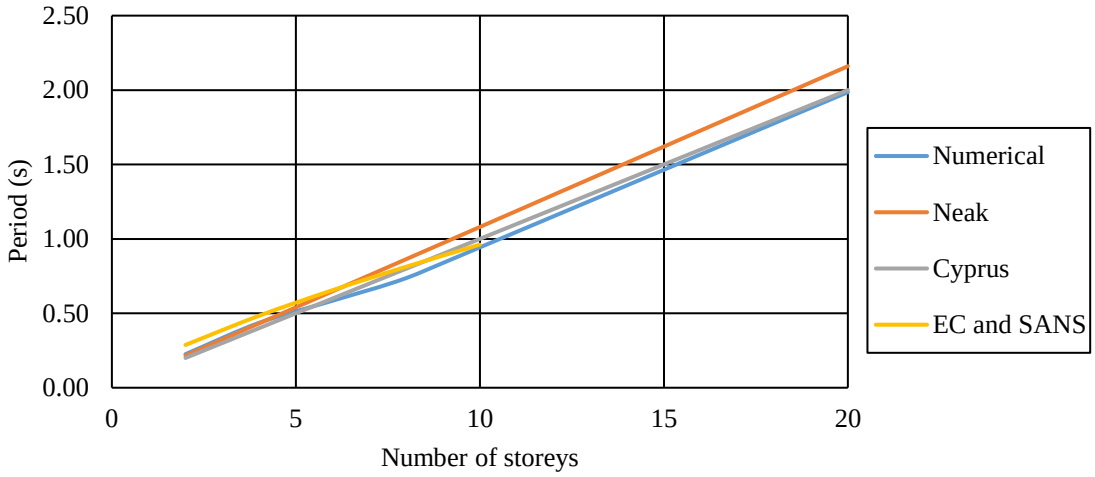

Figure 6: Relationship between period along the y-direction and number of storeys for the initial models without shear walls.

When the code formulae are used to compute the fundamental period along the x-axis direction, the computed periods were found to be close to the numerically obtained magnitudes, but with a higher average divergence. Fig. 6 shows the comparison between the numerical and design code formulae results for the case of the T_x period. Based on the analysis of the results presented in Table 1, the NEAK formulae was found to derive the lowest average divergence in comparison to the numerical results (3%), followed by the Cyprus code with 14%. Eurocode (and SANS) had the highest average divergence in this case, which reached a 32.7%, for the case of computing the T_x period (mode 2 for all numerical models).

Table 2 shows the computational time and finite element numerical details for each mesh according to the modal analyses performed in this work. It can be observed that for the case of the 20-storey model the maximum embedded rebar mesh generation time was 237.7 s, while the corresponding modal analysis for computing the first 12 eigenmodes was 11 minutes and 42 seconds. As it was expected, the computational demand of the numerical problem when the number of storeys is increased to 20, derives a more computationally demanding problem, for which the developed algorithm manages to maintain its computational efficiency and robustness. For this reason, the corresponding models with the shear walls were also analyzed in order to investigate the numerical response of the under study algorithmic implementation.

Number of storeys	Time for embedded rebar mesh gen. (s)	Number of embedded rebars	RAM requirement for the stiffness matrix (Mb)	Number of unknown equations	Time for Modal analysis (s)
2	6.0	8 672	51	16 716	2.9
4	19.8	14 546	276	32 028	33.6
6	40.9	20 376	389	47 052	39.1
8	73.4	26 228	676	62 220	80.4
10	106.6	32 080	1 000	77 388	156.0
20	237.7	61 340	4 000	153 228	702.9

Table 2: Computational performance and numerical details for the initial models without shear walls.

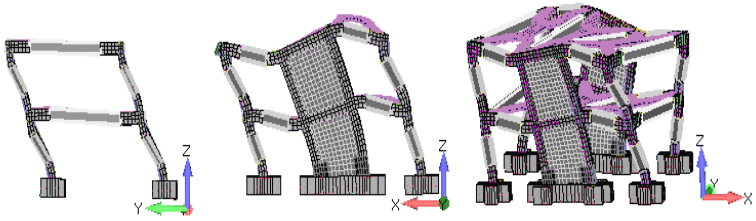

Figure 7: Initial 2-storey model with shear walls. Mode (Left) T_y, (Center) T_x and (Right) T_z.

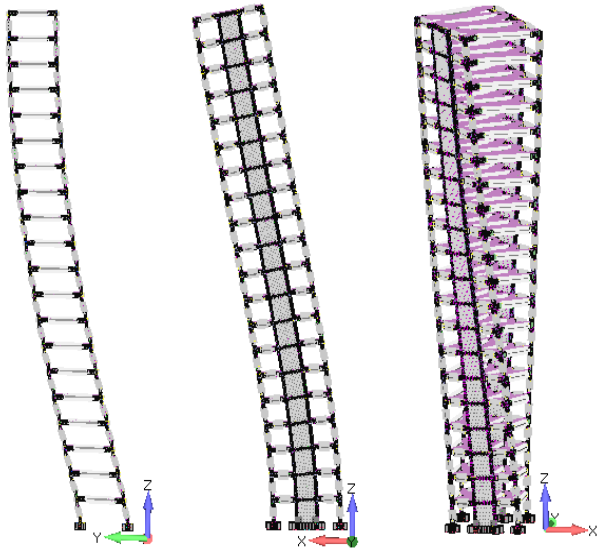

Figure 8: Initial 20-storey model with shear walls. Mode (Left) T_y, (Center) T_x and (Right) T_z.

Figs. 7 and 8 illustrate the deformed modal shapes of the 2- and 20-storey models, respectively, as they resulted from the numerical analysis. As it can be seen, the obtained results demonstrate a similar behavior in terms of deformation when compared with those derived from the models that did not assume for any shear walls (see Figs. 3 and 4). However, Table 3 shows that the values of the corresponding eigenperiods are smaller than the ones presented in Table 1 due to the increase of the stiffness of the models with the addition of the shear walls along the x-axis direction.

Number of storeys	Height (m)	Numerical		NEAK		Cyprus	EC	
		Ty (s)	Tx (s)	Ty (s)	Tx (s)	Tx & Ty (s)	Ty (s)	Tx (s)
2	6	0.193	0.115	0.216	0.123	0.2	0.288	0.363
4	12	0.377	0.187	0.432	0.288	0.4	0.484	0.790
6	18	0.558	0.323	0.648	0.461	0.6	0.655	1.145
8	24	0.729	0.481	0.864	0.637	0.8	0.813	1.458
10	30	0.914	0.673	1.08	0.815	1.0	0.961	1.745
20	60	1.914	1.857	2.16	1.713	2.0	NA	NA

Table 3: Periods for all the initial models with shear walls. Numerical and design code results.

According to the comparison of the modes depicted in Table 3, the SANS code and Eurocode show a significant divergence in term of values for the case of the T_x period, the global direction of the shear wall sections. Even though Eurocode has the provision of taking into account the effect of the shear walls' stiffness, it fails to predict a realistic period along the x-axis direction. This is attributed to Eq. 10, which derives a C_T variable that is larger than 0.075 given that the minimum computed value of $\sqrt{A_c}$ was equal to 0.55 for the case of the 20-storey and the maximum was equal to 0.79 for the case of the 2-storey. When this value is used to divide the 0.075 (initial C_T value) it results into a higher C_T magnitude, which is not realistic. The low $\sqrt{A_c}$ value is attributed to the fact that there are only two shear walls thus the summation of the $A_i(0{,}2 + (\frac{L_{wi}}{H})^2)$ equation for each shear wall does not result into a value that is larger than 1. Therefore, in this case, the T_x period value should be taken equal to the T_y for all models, which derives a more realistic period value. It is also easy to observe (see Table 3) that Eurocode (hence SANS code as well) fail to capture the period of the models along the stiffer x-axis direction.

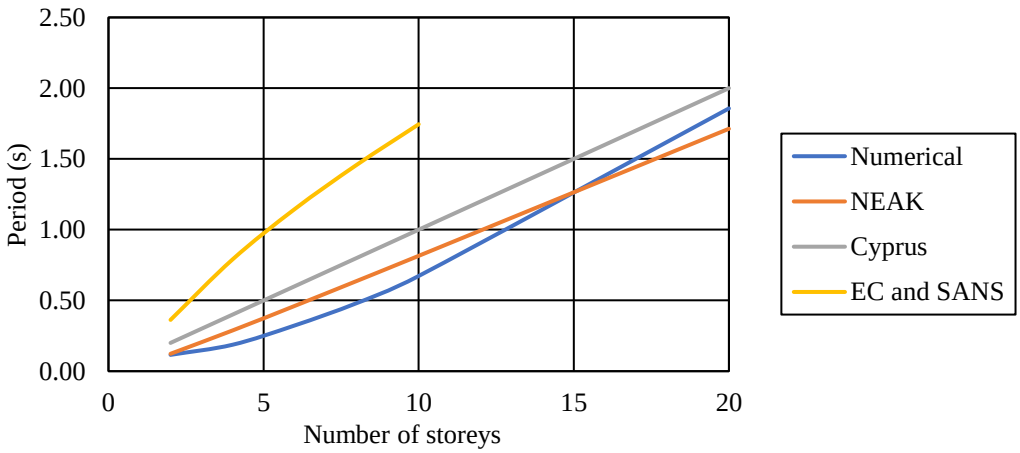

Figure 9: Relationship between period along the x-direction and number of storeys for the initial models with shear walls.

On the other hand, the formula proposed by NEAK code shows a better approximation when compared with the numerical values, with an average divergence of 25% for the values of T_x. The Cyprus code that uses the most simplified formula out of the four codes, basically ignores the presence of the shear walls thus fails to capture the effect of the relevant stiffness increase within the framing system. Therefore, the periods derived from the Cyprus code diverge from the numerical ones by an average value of 66%. It is obvious that the divergence of the T_y is

significantly smaller than the T_x because the shear walls have a minimal contribution to the overall stiffness of the structure along the y direction. The corresponding average divergences along the y-axis are 22%, 10% and 7% for the Eurocode, NEAK and Cyprus codes, respectively. The values of the periods of T_x and T_y calculated by using the different approaches, are plotted in Figs. 9 and 10.

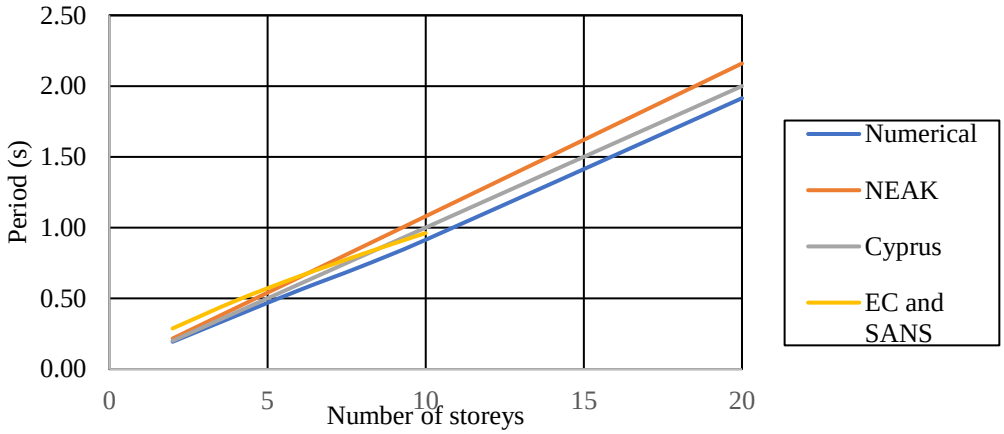

Figure 10: Relationship between period along the y-direction and number of storeys for the initial models with shear walls.

Number of storeys	Time for embedded rebar mesh gen. (s)	Number of embedded rebars	RAM requirement for the stiffness matrix (Mb)	Number of unknown equations	Time for Modal analysis (s)
2	11.4	11 804	109	23 412	4.6
4	21.1	20 398	335	44 460	25.9
6	46.0	29 196	840	65 508	78.7
8	77.7	37 696	1 000	86 556	175.5
10	121.4	46 836	2 000	107 604	336.6
20	468.7	90 936	8 000	212 844	2 214.6

Table 4: Computational performance and numerical details for the initial models with shear walls.

Table 4 shows the computational performance of the proposed algorithm when the models with the shear walls are analyzed. As it can be seen, the largest model required 8 Gb just for the stiffness matrix allocation, while consisted of 90,936 embedded rebar elements. The computational demand for computing the 12 modes for the case of the 20-storey model was approximately 37 minutes. Even though this is a relatively large model, the algorithm managed to finish the analysis in a reasonable computational time. For this reason, the initial models with shear walls were modified accordingly and they were increased along the x, y and z-directions in constructing larger models.

Therefore, the second phase of this numerical investigation foresaw the construction of models with high computational demand to examine the computational response of the developed algorithm and investigate the ability of the codes to predict the first two modes of realistic RC buildings. For the needs of this second investigation phase, three additional models were developed by assuming 8 shear walls placed along the x-axis direction. When constructing the models, the geometry of the initial models with shear walls presented above were modified by

enlarging the surface area of the initial model along both directions (x- and y-axis), where the dimension. Along the x-axis the size was doubled (17.386 m) and along the y direction it was tripled (18.255 m). The three models assumed 4-, 10- and 20- storeys, respectively.

The numerically derived eigen-shapes of the 4- and 20-storey models can be seen in the Figs. 11 and 12, respectively. In order to demonstrate the abilities of the code to generate and analyze the 368,773 embedded rebars found in the 20-storey modified model, Fig. 13 was developed where the deformed shape of the embedded rebar elements is shown for the case of the fourth modal shape. As it can be seen, the embedded rebar elements follow the deformed shape of the concrete domain.

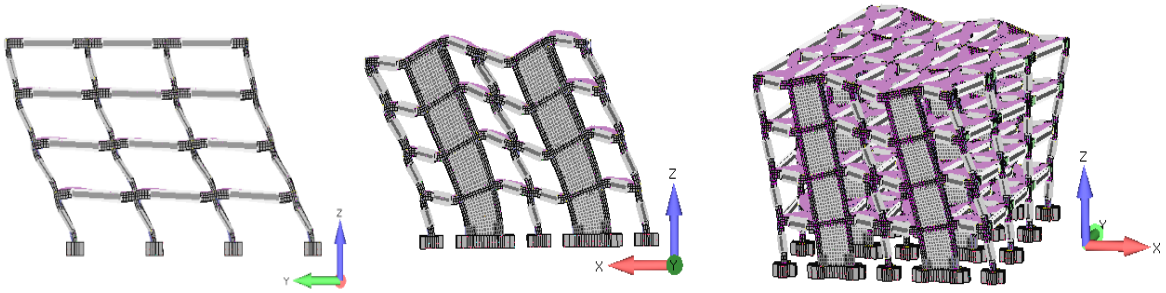

Figure 11: Modified 4-storey model with shear walls. Mode (Left) T_y, (Center) T_x and (Right) T_z.

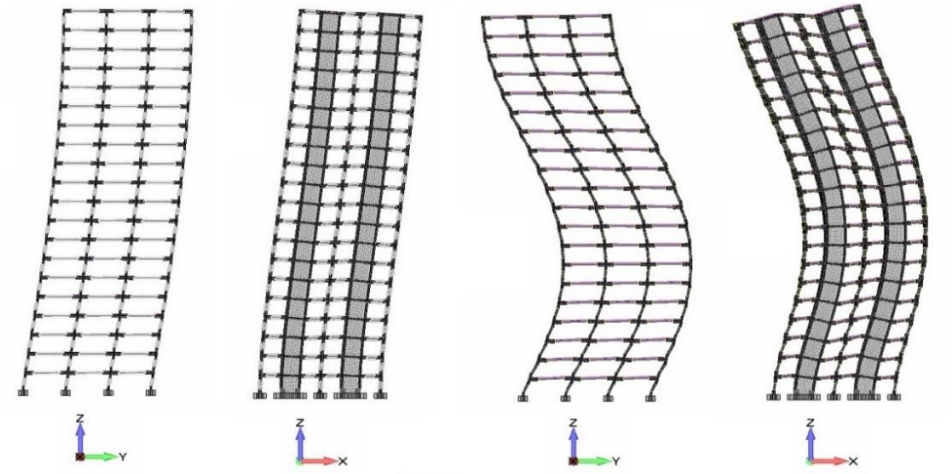

Figure 12: First four modes of the modified 20-storey model with shear walls.

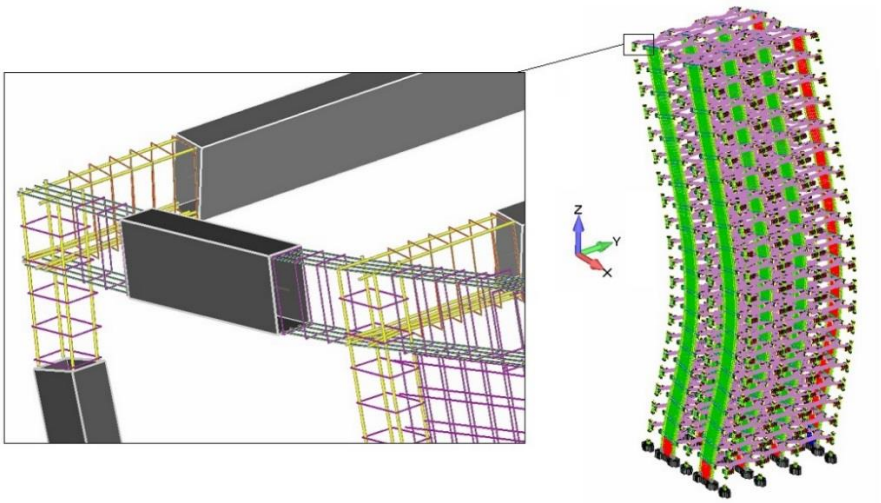

Figure 13: Deformed shape of the embedded rebar elements of the modified 20-storey model with shear walls. Mode 4.

The 20-storey model was identified as a large computationally demanding model given that the model, which was constructed by using the HYMOD approach took a full nine days to finish the analysis and used a total of 185 Gb RAM for the solution of the problem. Given that the computer that was used to perform all the analysis had a 4.2 GHz computational power standard pc with a 64 Gb RAM, the operating system used the compressed memory feature so as to handle this large numerical problem that significantly slowed down the computational procedure. This was the main reason why the computational demand was controlled from the procedure of compressing and uncompressing the RAM in order to handle this extremely large numerical problem. Table 5 shows the computational times for the modal analyses and the corresponding numerical problem size for each one of the modified model that was developed for the needs of this investigation.

Number of storeys	Number of virtual embedded rebars	RAM requirement for the stiffness matrix (Mb)	Number of FEM elements	Number of unknown equations	Time for Modal analysis (minutes)
4	82 514	3 000	59 062	198 840	473.7
10	191 802	18 000	140 364	484 032	13 822.2
20	368 773	87 000	275 288	959 352	9 days

Table 5: Computational performance and numerical details for the modified models with shear walls.

A 15-storey model was also constructed and analyzed, as seen in Fig. 14, so as to decrease the RAM requirements and investigate whether the RAM compression feature is significantly affecting the performance of the algorithm. This analysis required approximately 11 hours to complete demonstrating the significant effect of the RAM compressing feature that was noted in the case of the 20-storey model. The compression in memory extends the computational time by a large margin as illustrated herein. Fig. 14 shows the deformation modal shapes as they resulted from this last analysis for the case of the 15-storey RC building.

Tables 6 and 7 show the comparison between the periods computed numerically and through the use of the design formulae. Table 7 shows the error that each design formulae resulted in comparison to the numerically computed periods. It is evident that all design codes fail to provide with a realistic estimation of the mode value along the x- and/or y- directions.

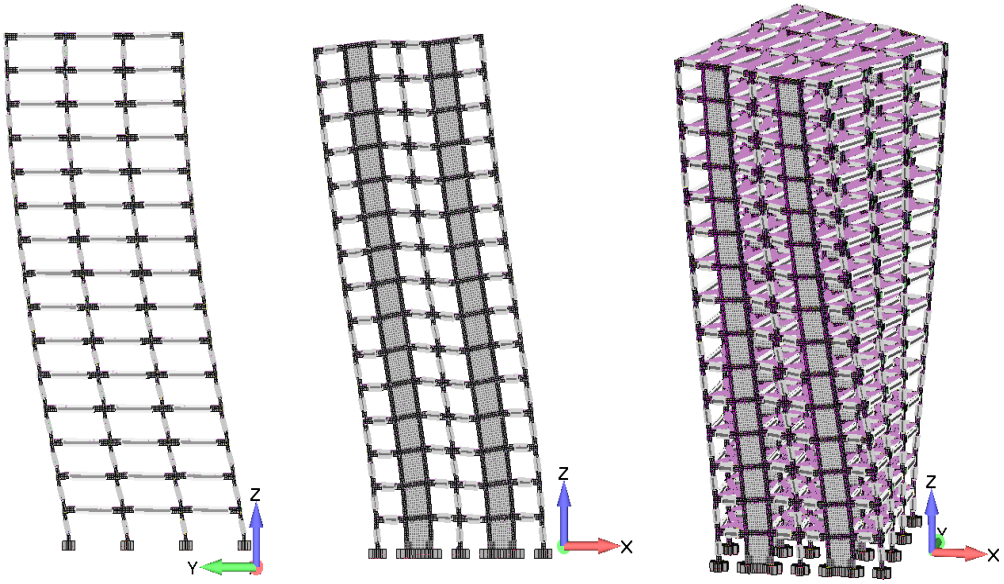

Figure 14: Modified 15-storey model with shear walls. Mode (Left) T_y, (Center) T_x and (Right) T_z.

Number of storeys	Height (m)	Numerical		NEAK		Cyprus	EC	
		Ty (s)	Tx (s)	Ty (s)	Tx (s)	Tx & Ty (s)	Tx (s)	Ty (s)
4	12	0.434	0.214	0.253	0.175	0.4	0.395	0.484
10	30	1.071	0.696	0.632	0.532	1.0	0.872	0.961
20	60	2.115	1.720	1.264	1.163	2.0	NA	NA

Table 6: Periods for all the modified models with shear walls. Numerical and design code results.

Number of storeys	Height (m)	Numerical		NEAK error		Cyprus error		EC error	
		Ty (s)	Tx (s)	Ty	Tx	Ty	Tx	Ty	Tx
4	12	0.434	0.214	41.8%	18.4%	7.9%	-86.8%	-11.3%	-84.5%
10	30	1.071	0.696	41.0%	23.5%	6.6%	-43.7%	10.2%	-25.3%
20	60	2.115	1.720	40.2%	32.4%	5.4%	-16.3%	NA	NA
			Average:	41.0%	24.8%	6.7%	-48.9%	-0.6%	-54.9%

Table 7: Design code formulae error in comparison to the numerical results.

The corresponding values of the periods T_x and T_y as they can be depicted in Tables 6 and 7 are illustrated in Figs. 15 and 16, to visually compare the period values as they resulted for the two global axis directions (x- and y-axis, respectively). As it can be easily observed from these figures, the only curve that manages to capture the numerical results with less than 10% error is the Cyprus code for the case of the T_y period. Based on the findings of this numerical investigation, it is recommended to use this approximate formula when dealing with framing systems or directions that do not consist of shear walls. In regards to the directions where the use of shear walls is foreseen; none of the codes was found to be effective, thus further research is required to develop objective formulae that will provide with more accurate period predictions in the case where the period is not computed by using finite element models.

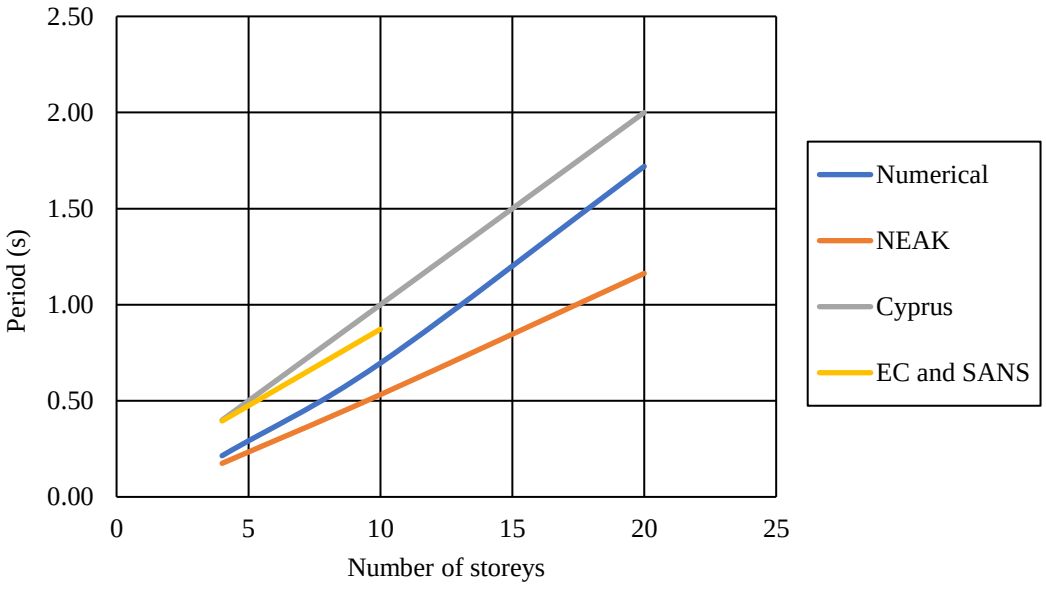

Figure 15: Relationship between period along the x-direction and number of storeys for the modified models with shear walls.

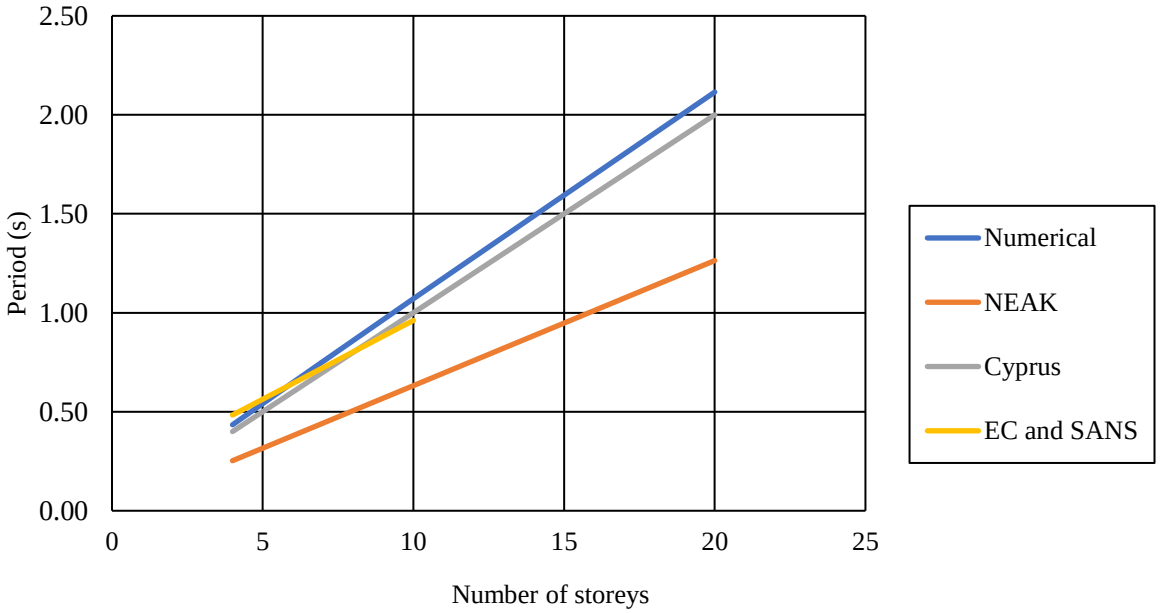

Figure 16: Relationship between period along the y-direction and number of storeys for the modified models with shear walls.

5 SOIL STRUCTURE INTERACTION

In order to model realistically the boundary conditions of any RC structural system, the soil structure interaction (SSI) phenomenon has to be taken into account. The effect of the SSI is crucial for the mechanical behavior of any structure [16]. In this article, a flexible soil is assumed and modeled by assuming a Young Modulus of elasticity E=65 MPa and the numerically obtained results were compared with the fixed base 4-storey model with shear walls. Fig. 17 shows the SSI model as it was developed for the needs of this initial parametric investigation. The objective was to develop an initial model to be tested prior to a more rigorous parametric investigation that will be performed in the near future. Based on the discretization of the soil domain, the model assumed that the length and width of the soil medium would be three times larger than the relevant dimensions of the RC structure along both the x- and y-axis.

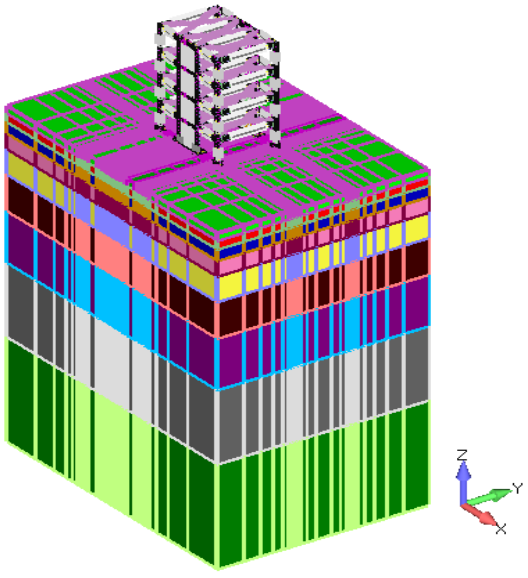

Figure 17: 4-storey model with shear walls and soil domain.

	Fixed Base Model		SSI (soft soil) Model E = 65 MPa		
Mode	***f*(Hz)**	**T(s)**	***f*(Hz)**	**T(s)**	**Dif. %**
1	2,656	0,3766	2,532	0,395	4,66%
2	5,349	0,1870	2,885	0,347	**46,07%**
3	7,508	0,1332	6,259	0,160	16,63%
4	7.983	0.1253	6.310	0.158	20.97%
5	8.626	0.1159	7.652	0.131	11.30%
6	8.734	0.1145	8.691	0.115	0.49%
7	8.767	0.1141	8.749	0.114	0.21%
8	8.791	0.1138	8.779	0.114	0.13%
9	10.478	0.0954	9.031	0.111	13.81%
10	10.599	0.0944	10.577	0.095	0.20%
11	10.636	0.0940	10.654	0.094	-0.17%
12	10.690	0.0935	10.667	0.094	0.21%

Table 8: Comparison between the fixed base and the SSI models. Computed modes and frequencies.

As it can be seen in Table 8, there is a significant difference between the fixed base model and the model with the flexible soil foundation (isolated footings). The maximum derived difference was found to result at mode 2 (46%), where the structure oscillates along the x-axis direction. Given that the shear walls are very stiff, it was found that their foundations rotated significantly due to the settlement of the soil, resulting into a significant stiffness decrease along this direction (global x-axis). Fig. 18 shows the first three modes as they resulted from the analysis, where the deformed shape of both the frame and the soil domain can be depicted. Further investigation will be performed as a continuation of this research work in order to study the effect of the SSI and the foundation system's effect on the modal response of different framing geometries. One of the main objectives of this future research work will be to establish a relation between the dimensions of the structure and the SSI effect when SSI considerations are accounted for, whereas propose improved formulae for the computation of the fundamental periods when the SSI effect is accounted for.

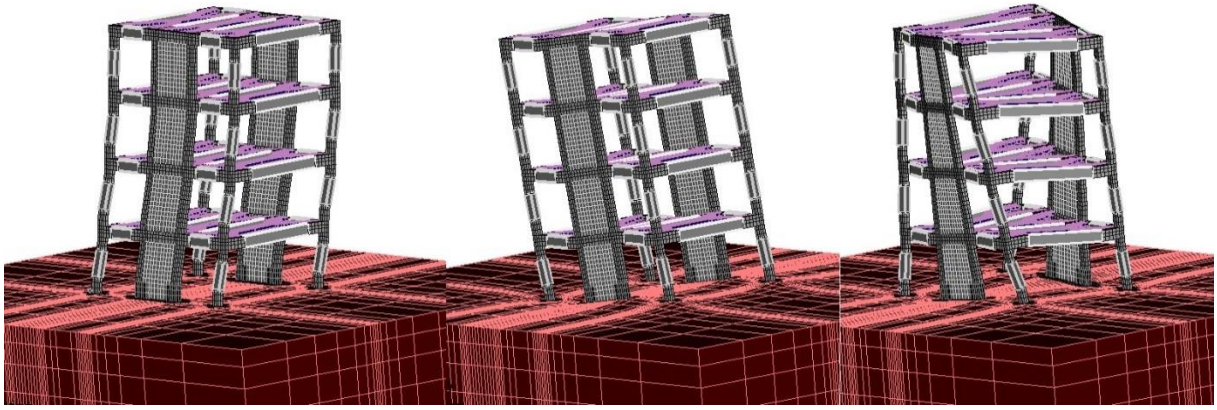

Figure 18: 4-storey model with shear walls and soil domain. Deformed shapes of modes 1, 2 and 3 (from left to right).

6 CONCLUSION

Based on the findings of this research work, it is evident that the HYMOD approach provides with computational efficiency and numerical accuracy when dealing with modal analysis of large-scale numerical problems. The HYMOD method manages to alleviate the computational limitations when analyzing large 3D models without losing the required accuracy of the numerical analysis. Therefore, this method is found to be suitable for modeling large-scale structures and will be used for the dynamic analysis or RC buildings in future research projects.

By conducting the analysis and interpreting the results in section 4, it can be concluded that the design codes yielded inaccurate results were Eurocode (EC) and the South African National Standard codes did not manage to satisfactorily predict the periods of the numerous models that were studied herein. These codes approximated the periods inaccurately, especially when dealing with frames that assumed shear walls. Eurocode, which is adopted by the South African code as well, needs to be scrutinized for improvements in order to take into account more efficiently the effect of the RC shear walls found within any RC frame geometry. On the other hand, the NEAK formula produced results that were found to be closer to the numerical analysis data, given its objective formulation that takes into account the ratio of the shear wall section areas along the under study direction. Nevertheless, the NEAK code equation should also be improved to approximate accurate results when dealing with RC structures with different geometries. The Cyprus code, which is now obsolete, proposed a simplified formula that does not take into account for the shear walls' contribution when computing the fundamental period. This makes the formula inadequate for computing the fundamental modes along directions that foresee the use of shear walls. Nevertheless, when shear walls are not present, it is a formula that provides with a good fundamental period approximation.

Further research foresees the use of the HYMOD approach to study the dynamic behavior of structures by performing modal analysis with SSI models. Based on the preliminary findings from the analysis of a model that also discretized the soil domain through the use of hexahedral elements, it was found that the periods can be significantly affected especially when the soil material characteristics assume for a soft soil and the structure uses a relatively flexible foundation system (i.e. isolated footing). It is also evident that the assumption of a fixed base structure is not a realistic approach in cases where structures are founded on flexible soils.

7 REFERENCES

[1] Hartl H. *Development of a continuum mechanics based tool for 3D FEA of RC Structures and application to problems of soil structure interaction*. Ph.D. thesis, Faculty of Civil Engineering, Graz Univ. of Technology, 2002.

[2] Spiliopoulos K V., Lykidis GC. *An efficient three-dimensional solid finite element dynamic analysis of reinforced concrete structures*. Earthquake Engineering & Structural Dynamics, Vol. **35**(2), pp. 137–57, 2006.

[3] Červenka J, Papanikolaou VK. *Three dimensional combined fracture–plastic material model for concrete*. International Journal of Plasticity, Vol. **24**(12), pp. 2192–220, 2008.

[4] Papanikolaou VK, Kappos AJ. *Numerical study of confinement effectiveness in solid and hollow reinforced concrete bridge piers: Methodology*. Computers & Structures, Vol. **87**(21–22), pp. 1427–39, 2009.

[5] Markou G, Papadrakakis M. *Computationally efficient 3D finite element modeling of RC structures*. Computers and Concrete, Vol. **12**(4), pp. 443–98, 2013.

[6] Mourlas Ch, Papadrakakis M, Markou G. *A computationally efficient model for the cyclic behavior of reinforced concrete structural members*. Engineering Structures, Vol. **141**, pp. 97–125, 2017.

[7] C. Mourlas, G. Markou, and M. Papadrakakis. *Accurate and computationally efficient nonlinear static and dynamic analysis of reinforced concrete structures considering damage factors*. Engineering Structures, Vol. **178**, pp. 258–285, Jan. 2019.

[8] G. Markou, C. Mourlas, H. Bark, and M. Papadrakakis. *Simplified HYMOD non-linear simulations of a full-scale multistory retrofitted RC structure that undergoes multiple cyclic excitations – An infill RC wall retrofitting study*. Engineering Structures, Vol. **176**, pp. 892–916, Dec. 2018.

[9] Markou G & Papadrakakis M. A simplified and efficient hybrid finite element model (HYMOD) for non-linear 3D simulation of RC structures. Eng Comput 2015;**32**(5).

[10] Vecchio, F.J. and Collins, M.P. (1986), *Modified compression-field theory for reinforced concrete elements subjected to shear, Journal of the American Concrete Institute*, Vol. **83** No. 2.

[11] Bathe KJ. *Solution Methods for Large Generalized Eigenvalue Problems in Structural Engineering*. Report UCSESM 71-20, Department of Civil Engineering, University of California, Berkeley: 1971.

[12] New Greek Seismic Code (NEAK), Athens. 2000.

[13] Cyprus earthquake resistant design code 1991, Cyprus.

[14] European Standard. Eurocode 8: Design of structures for earthquakes resistance. Part 1: General rules, seismic actions and rules for buildings, 1998.

[15] SABS Standards Division, South African National Standard (SANS), *Edition 1 Part 4: Seismic actions and general requirements for building*, 2009.

[16] Markou G, Sabouni R, Suleiman F, El-Chouli R. *Full-Scale Modeling of the Soil-Structure Interaction Problem Through the use of Hybrid Models (HYMOD)*. International Journal of Current Engineering and Technology, Vol. **5**(2), pp. 885–92, 2015.

COMPDYN 2019
7th ECCOMAS Thematic Conference on
Computational Methods in Structural Dynamics and Earthquake Engineering
M. Papadrakakis, M. Fragiadakis (eds.)
Crete, Greece, 24–26 June 2019

DEVELOPMENT OF SEISMIC RESPONSE ANALYSIS METHOD USING HIGH-FIDELITY MODEL FOR LARGE-SCALE REINFORCED CONCRETE STRUCTURES CONSIDERING SOIL-STRUCTURE INTERACTION

H. Motoyama[1] **and M. Hori**[2]

[1] IECMS, Kagawa University
Saiawi-cho 1-1, Takamatsu, 760-8521, Japan
e-mail: motoyama@cc.kagawa-u.ac.jp

[2] Earthquake Research Institute, The University of Tokyo
Yayoi 1-1-1, Bunkyo, Tokyo 113-0032, Japan
e-mail: hori@eri.u-tokyo.ac.jp

Abstract

In the seismic response analysis of large-scale reinforced concrete (RC) structures, such as nuclear power plant buildings, while considering the soil-structure interaction (SSI) using high-fidelity models, the application of high-performance computing (HPC) is indispensable owing to the number of the degrees of freedom (DOF). This study shows the development of a seismic response analysis method for large-scale RC structures with FEM utilizing HPC.
Herein, we implemented a previously proposed constitutive relation of concrete to the HPC-FEM program, FrontISTR. In the HPC-FEM program, conjugate gradient method is usually used as the solver algorithm that requires a positive-definiteness of the stiffness matrix. However, the constitutive relation of concrete expresses the material damage by stress-strain curve softening; hence one cannot assure that the stiffness matrix is positive-definite. Several techniques have been proposed to overcome this limitation. Herein, we adopted the method to calculate the stiffness matrix using elastic tensor of the material by comparing the speed of computation. We applied the developed software to a seismic response analysis of a nuclear power plant with surrounding ground, which is approximately 150 million-DOF problem. This paper shows the results and discusses the analysis performance.

Keywords: Seismic Response Analysis, Large-Scale Reinforced Concrete Structure, Soil-Structure Interaction, High Performance Computing, High-Fidelity Model.

1 INTRODUCTION

Lumped mass models are usually used in the seismic response analysis of reinforced concrete (RC) structures. Using such models for structures, which are sufficiently validated with experiments, is rational because of their low computational cost. Even in a nonlinear analysis, applying experimental results to the structural elements, which represent the members or groups of members, is not difficult.

Meanwhile, it is necessary to care to the applicability of the models. A method that can be applied to the analysis for a seismic load larger than the design load is needed because of the large earthquakes that happened in Japan in the recent years. In such cases, it is required to consider the models' applicability to such a load. High-fidelity models using solid elements should be applied when the applicability check is difficult. For considering the safety of nuclear power plant (NPP) buildings, it is meaningful to simulate the response for a seismic load larger than the design load using high-fidelity models due to their importance.

To apply the high-fidelity models is also useful to consider soil-structure interaction (SSI) precisely. In lumped mass models, a few spring elements are used for the soil-structure interaction even in the seismic response analysis of large-scale structures such as NPP buildings.

However, it is difficult for the existing finite element method (FEM) programs for the RC structures to deal with large-scale structures and surrounding ground using high-fidelity models because the number of the degrees of freedom is large. Therefore, applying a high-performance computing (HPC) technology is indispensable.

In HPC-FEM programs, the conjugate gradient (CG) method [1] is usually used as the fast solver algorithm that requires the positive-definite stiffness matrix. The CG method cannot be easily applied to a concrete material, whose strain-stress curve has a negative stiffness representing the fracture in the material. When using the concrete material in HPC-FEM programs, we need to focus on the combination of implementation of the concrete constitutive relation model and that of nonlinear analysis method. We have several possible combinations, and the faster one must be chosen.

Herein, we study the optimization of combination of the implementation of concrete constitutive relation model and that of nonlinear analysis method. A basic performance study is done using a small-scale RC structure. Finally, we apply the method to the seismic response analysis of NPP buildings considering the SSI and show the results and its performance.

2 PROBLEM IN DEVELOPMENT

We outline the problem to develop the HPC-FEM for RC structures. We explain the constitutive relation model of the concrete material used herein and its problems from the viewpoint of the stability of analysis and computational cost.

This study employs the constitutive relation model of the concrete material proposed by Maekawa et al. [2], and is one of the de-facto standards in Japan. The elasto-plastic fracture model is used before cracking occurs and the model switch to the cracked concrete model after cracking occurs, as shown in Figure 1.

This model can be utilized to solve two problems in HPC-FEM. One is the computational cost of the model itself and the other is the difficulty in assuring that the stiffness matrix is positive definite.

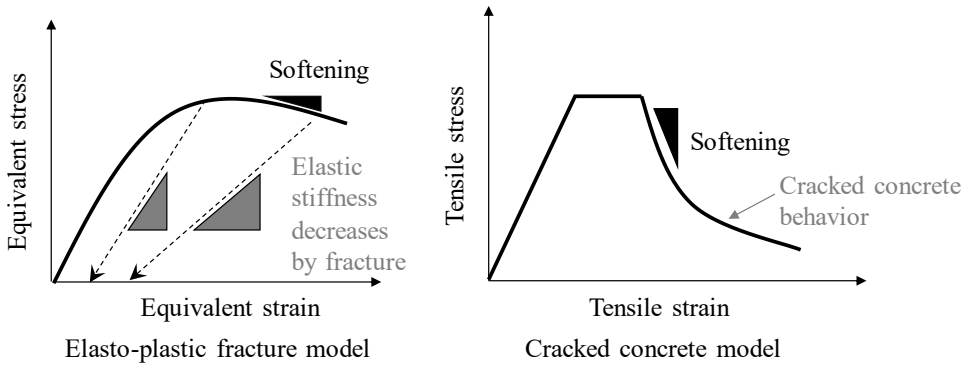

Figure 1: Concrete constitutive relation model.

Although it is relatively easy for HPC-FEM to achieve high scalability on computation about constitutive model in each element, saving the computational cost is still important because the number of elements or integration points is large. The original model has an inverse matrix computation that would acquire the elasto-plastic tensor, whose computational cost is high. In the study by Yamashita et al. [3], the original model was reconstructed to reduce this computational cost. The outline is shown below. Equation (1) presents the method of computing the elasto-plastic tensor $\mathbf{c}^{EP}$ in the original Maekawa model.

$$\mathbf{c}^{EP} = (\mathbf{c} + \nabla\mathbf{c}{:}\,\boldsymbol{\varepsilon}^{E})(\mathbf{I} + l)^{-1}, \tag{1}$$

where $\mathbf{c}$ is the elastic tensor, $\boldsymbol{\varepsilon}^{E}$ is elastic strain tensor, $\mathbf{I}$ is unit tensor, and l is the tensor that associates the elastic strain and plastic strain increments, which is a unique part of this model. Yamashita derived Equation (2) using the same constitutive relation with Maekawa as follows:

$$\mathbf{c}^{EP} = (\mathbf{c} + \nabla\mathbf{c}{:}\,\boldsymbol{\varepsilon}^{E})(\mathbf{I} - \mathbf{L}) \tag{2}$$

where $\mathbf{L}$ is the tensor that associate stain and plastic strain increments. Equation (2) avoids the inverse matrix computation. An implementation technique is shown in the authors' work [4].

Another problem in the constitutive model of concrete, which is a difficulty in assuring the positive-definite of the stiffness matrix, is still remained after reconstructing. We first studied the method that directly uses the elasto-plastic tensor shown in Equation (2) for calculating the stiffness matrix. In this method, the stiffness matrix is not assured as positive definite in the large strain area. However, in the seismic response analysis, the dynamic effect is added to the stiffness matrix. The dynamic stiffness matrix $\widehat{\mathbf{K}}$ is derived as $\widehat{\mathbf{K}} \approx 1/dt^2\ \mathbf{M} + \mathbf{K}$. Hence, a smaller *dt* will improve the condition of the stiffness matrix $\widehat{\mathbf{K}}$. In the first study, the authors tried to acquire computational stability by setting a smaller *dt*.

This method also has a problem, in which the stability and the elapsed time depend on targets. A decrease in the elapsed time with stability conservation becomes a limitation because of the large number of time steps. In other words, the method is necessary in which the stability of computation does not depend on *dt*. We focus on the method of the nonlinear analysis or the Newton method. New method uses an elastic tensor to calculate the stiffness matrix. In this method, the computation stability is expected to be assured even with a larger *dt*. On the contrary, the estimation of the increment of displacement is supposed to have a larger error introducing the increase in the number of the nonlinear steps. It is needed that the suitable nonlinear analysis method for the RC structures in HPC is selected by comparing the performances of existing method and the new one.

The proposed method is explained in the next chapter. The chapter after the next one presents the method application to the target problem and its performance.

3 NONLINEAR ANALYSIS METHOD FOR RC STRUCTURES

3.1 Trial method

This section explains the trial method of the nonlinear analysis. In consideration of convenience, we call this method as proposed method in this study.

Unlike the existing method explained in Section 2, the elastic tensor is used in the proposed method for calculating the stiffness matrix. This method can directly avoid dealing with the softening behavior that expresses a negative stiffness; hence, the positive definite of the stiffness matrix is assured. In the implementation, we need to ensure that the elastic stiffness is changed by the strain increase. This method is a kind of modified Newton method ignoring the change of elastic stiffness. Figure 2 depicts the method outline.

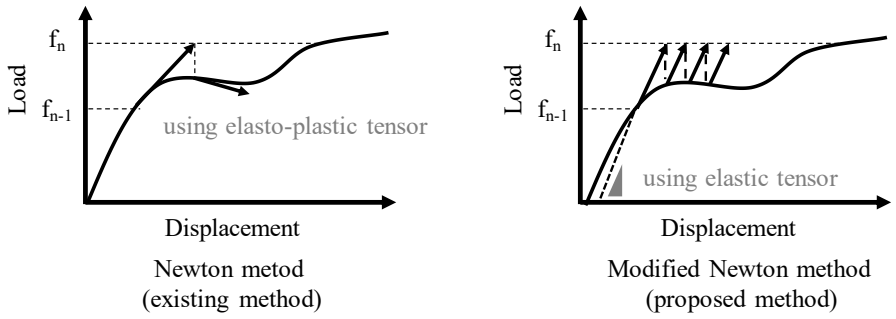

Figure 2: Outline of the nonlinear method.

3.2 Model for performance check

The cyclic loading test of the RC structure by Habasaki et al. [5] was used as the target. We constructed a simulation model and tried the response analysis. This target is constructed by four RC walls as a box structure. The thickness, width, and height of each wall was 75, 1500, and 1000 mm, respectively. The reinforced bars were 6 mm in diameter (D6), equivalent to SD345. The steel ratio in the wall was 1.2%. The material parameter in the simulation was set from the test literature.

Figure 3 exhibits the outline of the simulation model. The loading slab whose thickness was 200 mm was modeled on the walls as a rigid body. Figure 3 also shows the cross-section of the wall. The groups of reinforced bars were modeled by shell elements. The bottom face was fixed and the loading condition is set by displacement at the center of loading slab as the boundary conditions.

Figure 4 depicts an example result. The simulation result was compared with the loading test which is traced by the literature. Although the accurate estimation of the hysteresis curve needed additional study, the skeleton was estimated to be accurate enough. This result implied that this model can express the damage history of the structure. Hence, this simulation model is suitable for the test model of the performance check of the nonlinear analysis method for the RC structure.

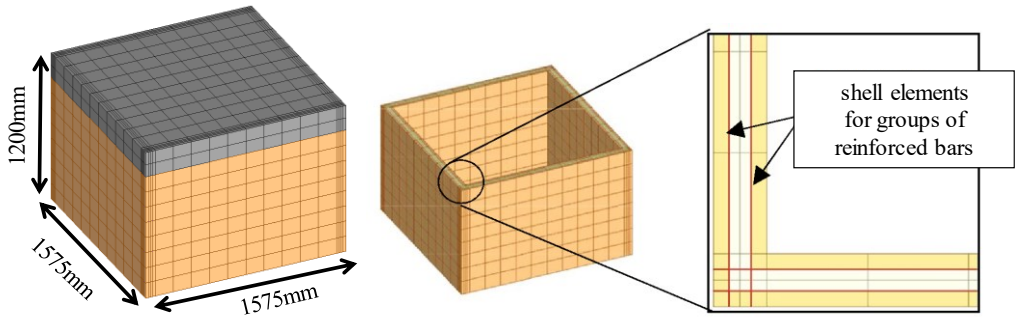

Figure 3: Outline of the simulation method.

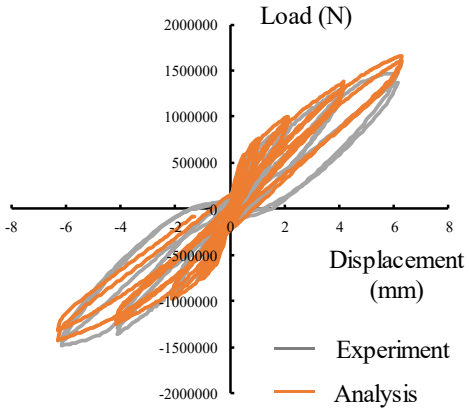

Figure 4: Example of the simulation result.

3.3 Performance check

The basic performance study of the nonlinear analysis for the RC structure was tested herein by comparing the elapsed time and number of analysis steps of the two mentioned methods above, existing method using the elasto-plastic tensor and proposed method using the elastic tensor. A monotonic loading simulation, in which the target displacement was 2 mm, was the target case. Considering the existing method, a dynamic simulation was applied with a loading time of 10 s. While applying the existing method, we tried three cases in which dt was different (i.e., $dt = 0.1, 0.01, 0.001$). The stiffness was fixed at each time step (the model was linearized), indicating no repeated calculation for convergence. Only $dt = 0.01$ was tried in the proposed method. In this method, the limitation of the maximum of the repeated calculation for convergence was five times. The force was carried over to the next step if the residual force was not converged.

Figure 5 shows the simulation results. In this trial, although a smaller time step improved stability of simulation, the existing method could not acquire the convergence of the CG method even in the case of $dt = 0.001$. On the contrary, the proposed method was stable for this target case.

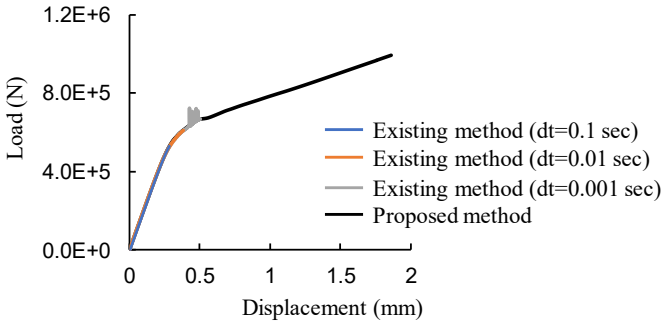

Figure 5: Result of the performance check simulation.

	Existing (dt=0.1)	Existing (dt=0.01)	Existing (dt=0.001)	Proposed (dt=0.01)
Number of analytical steps	100 (25)	1000 (304)	10000 (3278)	3485
Elapsed time of solver per one step	0.328 s	0.332 s	0.300 s	0.322 s
Number of CG steps per one step	898.5	894.5	786.4	800.9

Table 1: Comparison of the performances in each case.

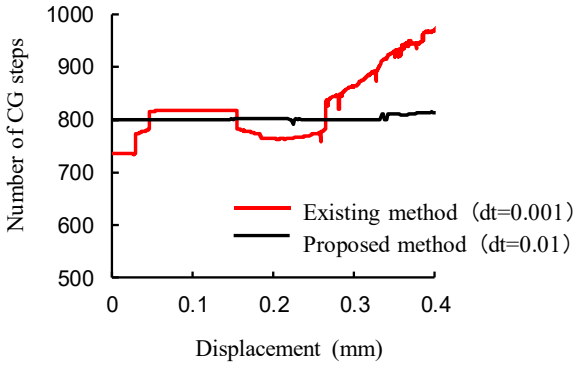

Figure 6: Number of CG steps at each step.

Table 1 lists the number of analytical steps and averaged elapsed time per one step. The number of analytical steps means the total number of calculation steps for the Newton method convergence, which is equal to the number of solver functions called. We also show the number of calculation steps for the CG method convergence per one step. The results of the existing method show the supposed number of analytical steps and the number of analytical steps before calculation stopped in round brackets.

We discuss using case dt = 0.001 as the existing method. Using the proposed method, the number of analytical steps was decreased by approximately one third in comparison with the existing method. Considering an increase of the elapsed time per one step, the performance of the proposed method is still high. By existing method, dt should be set smaller; hence, the difference in performance was larger than the results in Table 1.

Additionally, we compared the change of the number of CG steps depending on the progress of the loading step. Figure 6 shows the result. The x-axis denotes the loading displacement,

whereas the y-axis denotes the number of CG steps at each displacement. In the existing method, the number of CG steps increases at a larger displacement. In contrast, in the proposed method, the change of the number of CG steps is smaller because the change of stiffness by proposed method is smaller than that by existing method. In other words, the proposed method is suitable to the analysis for the RC structures using HPC.

The obtained results imply that the proposed method is a better method for the RC structures from the view of analytical stability and computation performance.

4 SEISMIC RESPONSE ANALYSIS OF NPP BUILDINGS

4.1 Target building

We tried the seismic response analysis of NPP buildings with a surrounding ground. Figure 7 illustrates the model outline. The surrounding ground size was 600 m × 800 m horizontally and 200 m vertically. This model was constructed by a real structure; hence, the size is omitted because of safety. Table 2 lists the computation scale.

The seismic wave was set compatible to the spectrum proposed by Kato et al. [6], whose duration time of the seismic wave was 22.08 s, boundary condition of the seismic load was set to the bottom and each side of the surrounding ground, each time step was 0.005 s, and the total number of time steps was 4,416.

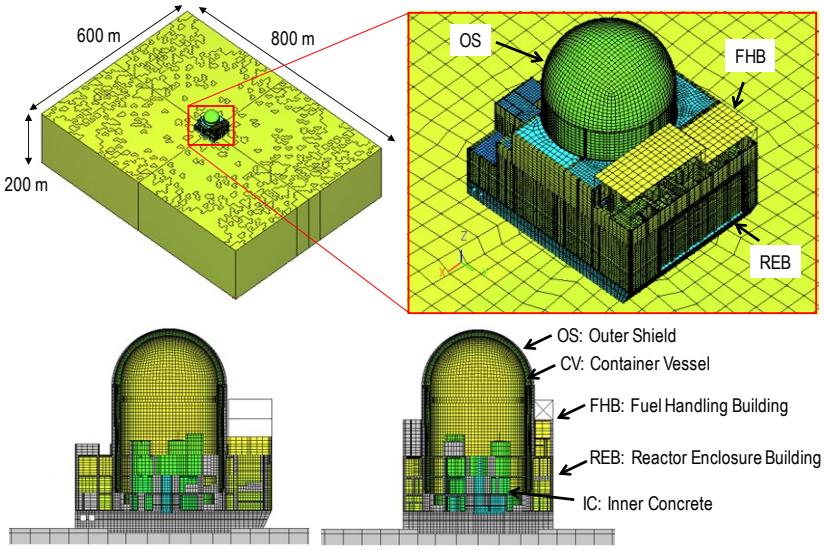

Figure 7: Outline of the model of the NPP buildings.

Node	Element	DOF
405,326	444,060	1,472,529

Table 2: Computation scale.

4.2 Results of the seismic response analysis

The elapsed time of this analysis was approximately 10 h using 64 cores. This is enough fast for the practical use. The proposed method herein utilized the HPC technique considering the nonlinearity of the concrete material.

Figure 8 presents the examples of the results. The crack distribution on the outer shield is shown as well as the shear strain distribution at the same time step. These results imply that we can analyze the deformation and the damage caused by the deformation with a high resolution.

Figure 9 exhibits the acceleration response and acceleration response spectrum. The target points are at the same level of the reactor enclosure building. These results show that the response has spatial distribution, which means that the accurate estimation of the seismic response needs such a high-fidelity model. The linear analysis results are also shown in this figure. The acceleration response spectrum changes at some frequency in comparison with the nonlinear analysis results. Considering fine nonlinearity might make the device design more rational.

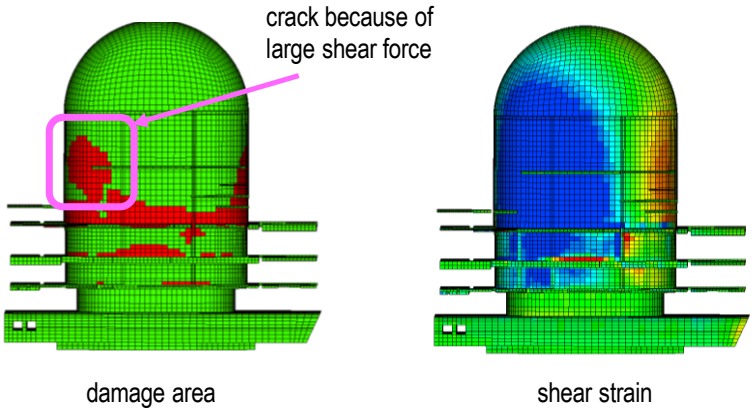

Figure 8: Distribution of the crack and shear strain on OS.

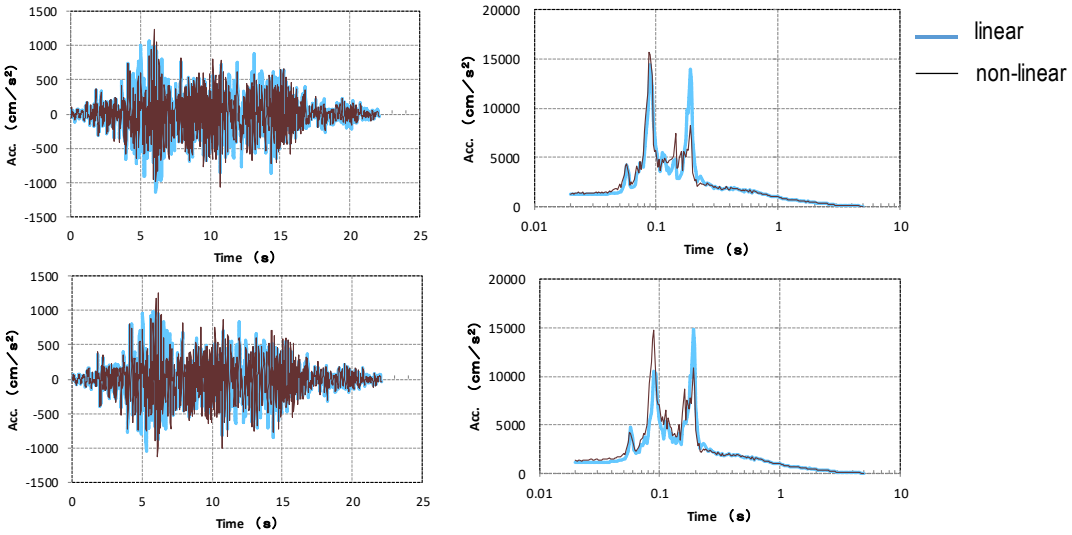

Figure 9: Acceleration and acceleration response spectrum.

5 CONCLUSIONS

Herein, we developed the nonlinear analysis method suitable for RC structures using HPC. The performance of the proposed method was checked by the loading test of a small RC structure. We applied the developed method to the seismic response analysis of the NPP buildings considering the soil-structure interaction. The results showed that the computation performance is high enough for practical use. We finally discussed the effectiveness of the analysis with a high-fidelity model.

ACKNOWLEDGEMENTS

This study is supported by commissioned projects from the Agency for Natural Resources and Energy, Ministry of Economy, Trade and Industry, Japan.

REFERENCES

[1] Hestenes, M. R. and Stiefel, E., Method of conjugate gradients for solving linear systems, *Journal of Research of the National Bureau of Standards,* Vol.49, No.6, 1952.

[2] Maekawa, K., Okamura, H. and Pimanmas, A., *Non-Linear Mechanics of Reinforced Concrete*. Taylor & Francis, 2003.

[3] Yamashita, T., Hori, M., Oguni, K., Okazawa, S., Maki T. and Takahashi Y., Reformulation of non-linear constitutive relations of concrete for large-scale finite element method analysis. *Journal of JSCE*, Vol.67, No.1, pp.145-154, 2011.

[4] Motoyama, H., Hori, M., Akiba, H. and Tanaka, S., Practicality verification of large-scale finite element method analysis using constitutive relations of concrete considering scalability. *Journal of JSCE*, Vol.73, No.2, pp.211-221, 2017.

[5] Habasaki, A., Kitada, Y., Torita, H. and Nishikawa, T., Restoring force characteristics of box type shear wall subjected to diagonal load, *Journal of structural and construction engineering,* 541, pp.129-136, 2001.

[6] Kato, K., Miyakoshi, K., Takemura, M., Inoue, D., Ueta K. and Dan, K., Earthquake ground motions by blind faults in the upper crust - categorization of earthquakes based on geological survey and examination of the upper level from strong motion records - *Journal of Japan Association for Earthquake Engineering*, Vol.4, No.4, pp.46-86, 2004.

COMPDYN 2019
7th ECCOMAS Thematic Conference on
Computational Methods in Structural Dynamics and Earthquake Engineering
M. Papadrakakis, M. Fragiadakis (eds.)
Crete, Greece, 24–26 June 2019

3D DETAILED MODELING OF REINFORCED CONCRETE FRAMES CONSIDERING ACCUMULATED DAMAGE DURING STATIC CYCLIC AND DYNAMIC ANALYSIS – NEW VALIDATION CASE STUDIES

Christos Mourlas [1], George Markou [2], and Manolis Papadrakakis [1]

[1] Institute of Structural Analysis & Seismic Research, National Technical University of Athens, 9 Iroon Polytechniou Str., Zografou Campus, GR-15780 Athens, Greece
e-mail: {mourlasch, mpapadra}@central.ntua.gr

[2] Department of Civil Engineering, University of Pretoria, South Africa
e-mail: george.markou@up.ac.za

Abstract

The study of the hysteretic behavior of reinforced concrete members that undergo static cyclic and dynamic loading conditions in cases where the loading level is close to their carrying capacity, is a challenging open research subject, which currently is being investigated by many researchers. The development of an objective and robust 3D constitutive modeling approach that will be able to account for the accumulated material damage and stiffness deterioration is of great importance in order to realistically describe the physical failure mechanisms thus numerically study the seismic performance of RC structures. The adopted concrete material model in this research work is based on the material model proposed by Markou and Papadrakakis, which was an extension of the Kotsovos and Pavlovic work. Furthermore, the use of two newly proposed damage factors that are computed through the use of the number of opening and closing of cracks during the nonlinear cyclic analysis, are further investigated and their ability in capturing the accumulated material damage in both steel and concrete is further discussed in this research work.

The numerical accuracy of the proposed method is validated by comparing the numerical results with the experimental data of two beam-column frame joints, a shear wall and a three-storey three-bay RC frame. According to the experimental setups, the RC joint and the shear wall specimens were tested under ultimate limit state cyclic loading, whereas the RC frame was tested under dynamic loading conditions. Based on the numerical findings, the proposed algorithm manages to capture the experimental results in an accurate manner and the numerical response of the understudy algorithmic implementation was found to exhibit computational robustness and efficiency.

Keywords: Nonlinear dynamic analysis, concrete material modeling, finite element method, damage factor, accumulated material damage

1 INTRODUCTION

Many numerical constitutive models have been proposed for the simulation of reinforced concrete (RC) structural members. Most of these approaches are based on uniaxial constitutive laws with strain softening and tension stiffening characteristics. The analysis of RC structural members under ultimate limit state conditions is characterized by heavy nonlinearity, which is mainly caused by the cracking of concrete and steel rapture. Mainly due to the complex behavior of concrete structures under cyclic and dynamic loading conditions, the numerical procedure becomes unstable causing the nonlinear solution procedure to diverge. Therefore, a realistic 3D approach that is characterized by simplicity and computational efficiency is an open research subject for Civil Engineering scientific community.

As a solution to this numerical modeling limitation, most researchers use uniaxial constitutive laws that can describe only certain aspects of concrete behavior. Many of these numerical approaches are based on elastoplasticity theories, thermodynamic laws and fracture mechanics. These models place emphasis on strain softening, tension stiffening characteristics and generally they foresee for numerous material parameters that describe the post cracking behavior of concrete. By adopting this approach, they introduce properties of concrete that are related to the triaxial behavior of concrete such as plasticity, concrete crushing and effect of confinement, but have no actual physical meaning nor interpretation. Additionally, most of these models are restricted to 2D analysis in order to capture the biaxial behavior of concrete structures that are subjected to monotonic loading conditions. This makes these numerical material models difficult to handle (lacking in objectivity) and not of practical interest given their limited applicability. Therefore, the necessity of a 3D constitutive material law that will not require additional material parameters that are not associated with the behavior of concrete at a material level is required.

Furthermore, the implementation of the pre-mentioned modeling methods is limited to examples of small practical interest (i.e. single structural members). Thus, it is important to formulate a constitutive model that will represent accurately the realistic mechanical behavior of concrete and offer the required computational efficiency allowing its implementation in full-scale structure nonlinear dynamic analysis.

The proposed approach described in [1, 2] and further investigated herein, emphasizes on the objectivity and the applicability of the proposed modeling method under nonlinear static cyclic and dynamic analysis of RC structures. In this research article, the proposed damage parameters for concrete and steel reinforcement that are proposed in [2], are further validated in capturing the accumulated material damage that is developed during cyclic and dynamic loading conditions, through the use of experimental data found in the international literature. The numerical accuracy and robustness of the proposed modeling method [2] is investigated by comparing the numerical results with the experimental data of two beam-column frame joints, a shear wall and a three-storey three-bay RC frame.

2 MATERIAL MODELING

2.1 Concrete Material Modeling and Damage Factor

The proposed numerical model adopted herein is based on the experimental findings of Kotsovos and Newman [3], which were derived from tests on specimens subjected to triaxial loading conditions, through the use of techniques capable of both inducing definable states of stress in the specimens and measuring reliably the deformational response of concrete [4]. Based on the experiment findings [4], the concrete material loses all of its carrying capacity

when the criterion of failure is satisfied, thus the adopted material model assumes that the cracked concrete will behave in a brittle manner. The expression of the strength envelope of concrete that was used during the nonlinear analysis in this research work is provided in Eq. 1 and it's based on the Willam and Warkne [5] formulae.

$$\tau_{0u} = \frac{2\tau_{0c}(\tau_{0c}^2 - \tau_{0e}^2)\cos\theta + \tau_{0c}(2\tau_{0e} - \tau_{0c})\sqrt{4(\tau_{0c}^2 - \tau_{0e}^2)\cos^2\theta + 5\tau_{0e}^2 - 4\tau_{0c}^2\tau_{0e}^2}}{4(\tau_{0c}^2 - \tau_{0e}^2)\cos^2\theta + (2\tau_{0e} - \tau_{0c})^2} \tag{1}$$

The concrete stress-strain relationships are expressed most conveniently by decomposing each state of strain and stress into hydrostatic and deviatoric components describing a realistic behavior of concrete under generalized three-dimensional states of stress. The constitutive relations take the following form:

$$\varepsilon_0 = \varepsilon_{0(h)} + \varepsilon_{0(d)} = (\sigma_0 + \sigma_{id}) / (3K_s) \tag{2}$$

$$\gamma_0 = \gamma_{0(d)} = \tau_0 / (2G_s) \tag{3}$$

where K_s and G_s are the secant forms of bulk and shear moduli, respectively. The secant forms of bulk, shear modulus and σ_{id} are expressed as functions of the current state [4] take into account the coupling effect of τ_0-$\varepsilon_{0(d)}$ (h and d stand for hydrostatic and deviatoric components, respectively). It must be also noted herein that, the model uses the smeared crack approach for simulating cracking, therefore, the model simulates the geometrical discontinuity by the assumption of displacement continuity and by modifying the material properties along the crack plane. This approach avoids the need of remeshing when cracks open and close during the cyclic analysis.

Furthermore, a new criterion of crack closing which was introduced in [1] is used that defines the crack closure in a numerical manner. The criterion has the following form:

$$\varepsilon_i \leq a \cdot \varepsilon_{cr} \tag{4}$$

where ε_i is the current strain in the i-direction normal to the crack plane and ε_{cr} is the strain that caused the crack formation. Parameter a is a reduction factor described by Eq. 5.

$$a = 1 - \frac{\varepsilon_{cr}}{\varepsilon_{\max}} = \frac{\varepsilon_{\max} - \varepsilon_{cr}}{\varepsilon_{\max}} \tag{5}$$

The maximum strain ε_{max} is determined through the iterative Newton-Raphson procedure. For more details in regards to the closing crack criterion one may refer to [5]. According to the solution strategy and the material modeling of concrete [2], when the criterion of crack-closure is satisfied at a Gauss Point (assuming that this point had prior to that only one crack formation), a part of the stiffness is lost along the crack plane at this Gauss Point to account for the damage accumulation due to the opening and closing of the under study crack. Therefore, the proposed damage factor [2] modifies the constitutive matrix of concrete accordingly to model the stiffness deterioration. The damage factor is denoted as D_C and describes the accumulated energy loss due to the number of times a crack has opened and closed. After a numerical investigation, the proposed damage factor was found to perform in a numerically optimum manner when it takes the form of Eq. 6:

$$D_c = e^{-(1-a)/f_{cc}} = e^{-\left(1-\left(1-\frac{\varepsilon_{cr}}{\varepsilon_{\max}}\right)\right)/f_{cc}} = e^{-\left(\frac{\varepsilon_{cr}}{\varepsilon_{\max}}\right)/f_{cc}} \tag{6}$$

where f_{cc} is the number a crack has closed during the cyclic loading history and it is updated in every iteration for every Gauss Point.

After the crack closure, the stresses are corrected by using the following expression:

$$\sigma^i = \sigma^{i-1} + C' \cdot \Delta\varepsilon^i \tag{7}$$

where *C'* is the modified constitutive matrix of concrete with the damaged material properties across the direction of the closed cracks. The constitutive matrix takes the following form:

$$\boldsymbol{C}_i^{'} = \begin{bmatrix} 0.25\cdot(1-D_c)\cdot(2G_t+\mu) & 0.25\cdot(1-D_c)\cdot\mu & 0.25\cdot(1-D_c)\cdot\mu & 0 & 0 & 0 \\ 0.25\cdot(1-D_c)\cdot\mu & 2G_t+\mu & \mu & 0 & 0 & 0 \\ 0.25\cdot(1-D_c)\cdot\mu & \mu & 2G_t+\mu & 0 & 0 & 0 \\ 0 & 0 & 0 & 0.125\cdot(1-D_c)\cdot\beta\cdot G_t & 0 & 0 \\ 0 & 0 & 0 & 0 & 0.125\cdot(1-D_c)\cdot\beta\cdot G_t & 0 \\ 0 & 0 & 0 & 0 & 0 & 0.125\cdot(1-D_c)\cdot\beta\cdot G_t \end{bmatrix} \tag{8}$$

where β is the concrete shear retention factor. Additionally, the material deterioration that occurs due to the opening and closing of cracks affects the bonding relation between the steel reinforcement and the damaged concrete domain that contains them. In order to take into account this loss of bonding, a modification of the steel stress-strain relation of Menegotto-Pinto [6] was proposed in [2]. Therefore, pinching characteristics that are caused by the loss of bonding between steel reinforcement and its surrounding concrete medium can be taken into account indirectly by reducing the stiffness contribution of the steel reinforcement [2]. In order to numerically establish such a connection, the average of all parameters *a* (Eq. 5) at the 8 Gauss Points within each concrete hexahedral element is computed and used to determine the overall level of damage of each concrete hexahedron found within the concrete mesh. Eq. 9 gives the expression through which the steel damage factor is computed through the use of the damage factor *a*.

$$D_s = \left[1 - a_{Element}\right] \tag{9}$$

where,

$$a_{Element} = \frac{\sum_{1}^{ncr} a_i}{ncr}, \; ncr \text{ is the number of cracked Gauss Points} \tag{10}$$

The material deterioration of the steel reinforcement is computed based on the following proposed formulae:

$$E_s^{'} = (1-D_s)E_s \tag{11}$$

where E_s' is the modified steel modulus of elasticity. As explained in [7], an alternative way of introducing the pinching effect through the stress-strain law of steel reinforcement, is by reducing the parameter *R* of the Menegotto-Pinto [6], which has the following form:

$$R = R_0 - \frac{a_1 \xi}{\alpha_2 + \xi} \tag{12}$$

where ξ is the strain difference between the current asymptote intersection point and the previous load reversal point with maximum or minimum strain, depending on whether the corresponding steel stress at reversal is positive or negative. R_0, a_1 and a_2 were assumed to be 20, 18.5 and 0.15, respectively, in this study. Therefore, by using the same reduction factor the parameter R' is calculated though the following expression:

$$R' = (1 - D_R)R \text{, where } D_R = D_s \tag{13}$$

In this case, the material deterioration is applied when the criterion $\sigma_s \cdot \varepsilon_s < 0$ is satisfied during the nonlinear analysis. This criterion describes the situations when crack closures and re-openings occur, where the pinching phenomena are present. The modified material model is shown in Fig. 1 for different damage levels.

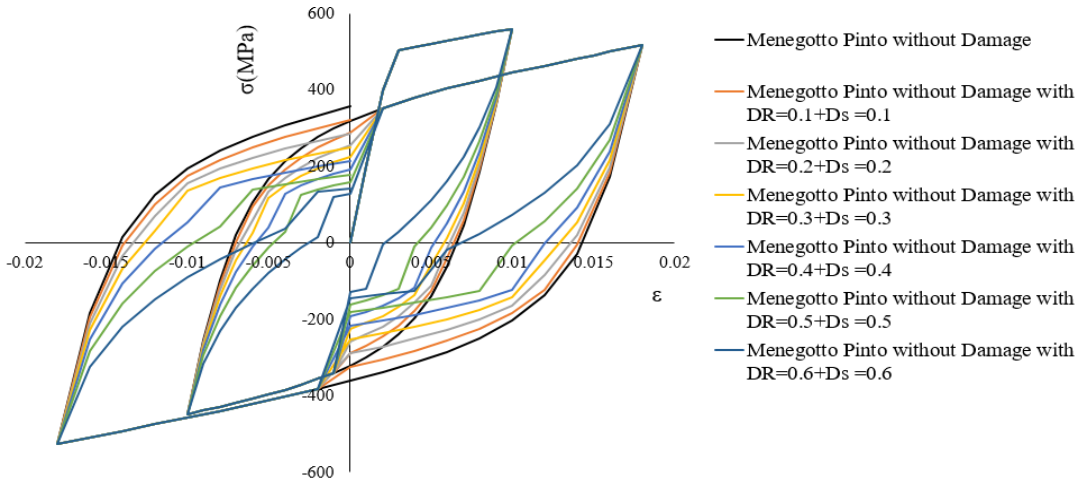

Figure 1: Menegotto-Pinto steel model by taking into account the accumulated damage due to opening/closure of cracks. Different damage levels. [7]

3 NUMERICAL IMPLEMENTATION

3.1 Beam-Column frame joints

Two beam-column joints shown in Fig. 2, were tested by Shiohara and Kusuhara [8] under static cyclic loading. The uniaxial compressive concrete strength was reported to be equal to f_c = 28.3 MPa and the yielding stress of the steel reinforcement was 456 MPa for the 13 mm in diameter rebars found in the beam section. The rebars placed within the column section, were reported to have a 357 MPa yielding stress [8]. The Young modulus of elasticity for the longitudinal reinforcement was reported to be equal to E_S = 176 GPa, where 6 mm stirrup reinforcement had a yielding stress of 326 MPa and a Young modulus of elasticity equal to 151 GPa.

The frame joint was subjected to different cyclic loading sets according to the experiment [8]. The loading history that was numerically applied in this work, is presented in the form of 15 cycles of imposed displacements as shown in Fig. 3 and as it was reported in [8].

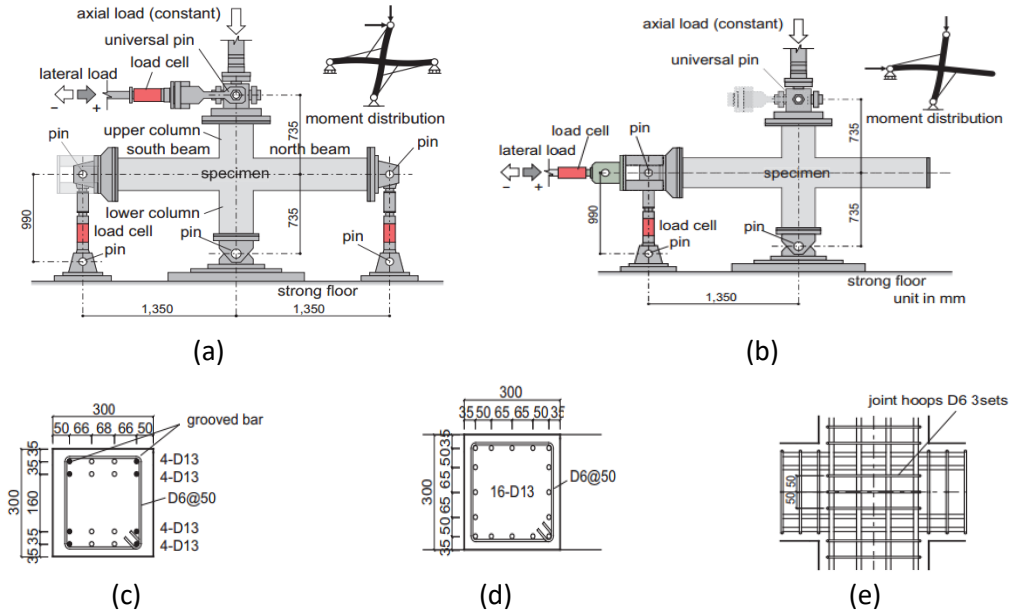

Figure 2: Beam-Column joints. Geometry of (a) A1 and (b) A3 specimens, and reinforcement details of the (c) beam, (d) column and (e) joint section. [8]

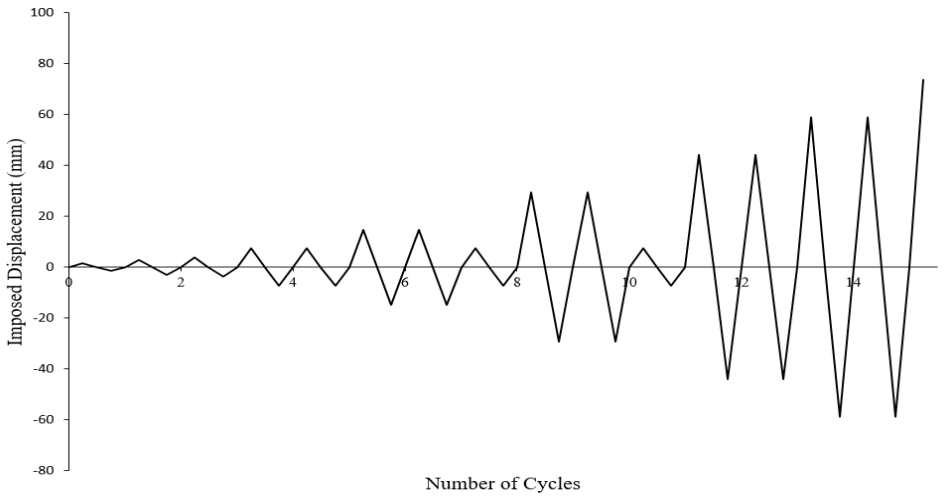

Figure 2: Beam-Column joints. Imposed displacement history.

For the modeling requirements, the concrete domain was discretized with 8-noded hexahedral finite elements and the steel reinforcement was discretized with beam-column finite elements. A total number of 128 concrete (23cm x 15cm x 15cm) and 888 steel Natural Beam-Column Flexibility-Based (NBCFB) finite elements were used to discretize the entire frame joint. Specimen A1 was simulated as an interior beam-column joint, while specimen A3 was developed to simulate the conditions of an exterior corner joint. The boundary conditions of the numerical model can be seen in Fig. 4, where the displacements were imposed at the top section of the column for specimen A1 and at the left edge of the beam for specimen A3 (according to the experimental setup described in [8]). A 216 kN compressive force was applied at the top section of the column for both specimens. Additionally, 8-noded hexahedral finite

elements were used at the support and at the sections where displacements are imposed to simulate the metallic plates, which were placed in order to avoid local failure.

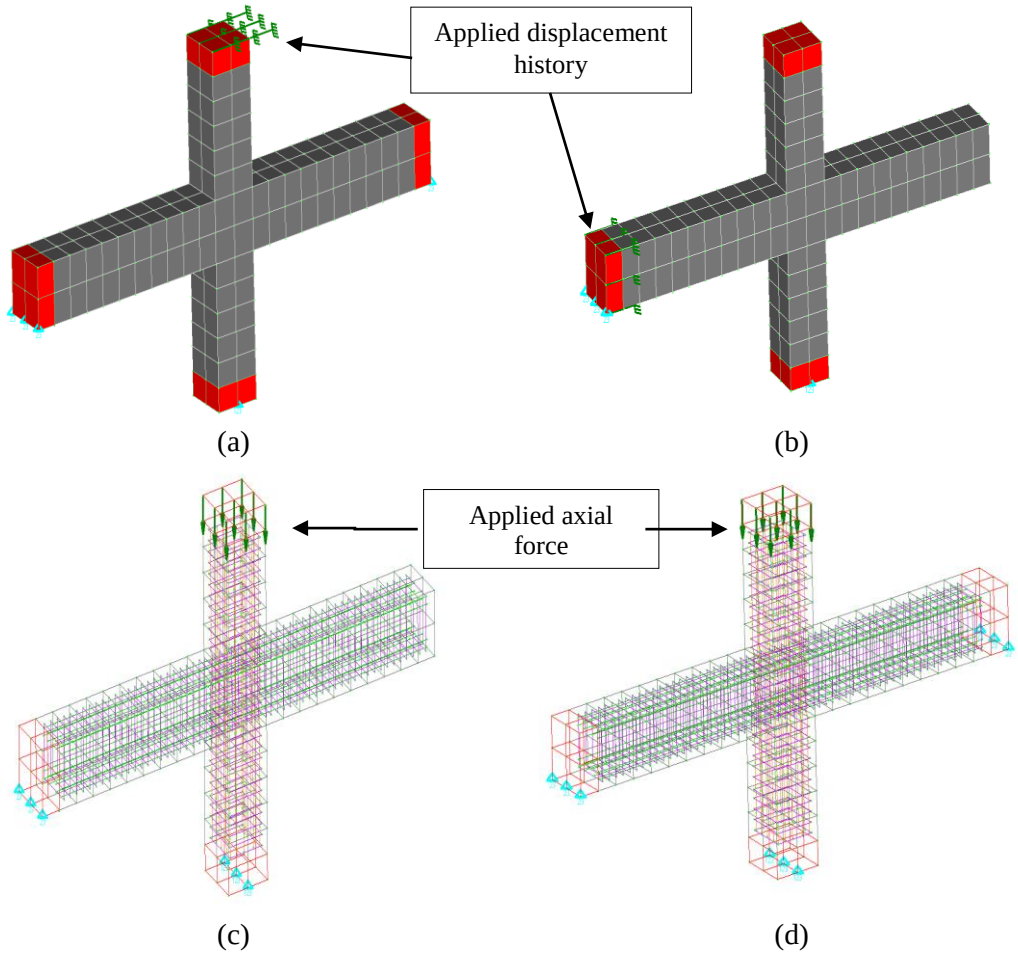

Figure 4: RC beam-column frame joint. Finite element concrete mesh with imposed displacements for specimens a) A1 and (b) A2. Steel reinforcement mesh and applied axial loads for specimens c) A1 and (d) A2.

The numerically computed force-displacement curves are compared with the corresponding experimental data in Fig. 5. As can be seen, the numerical results match very well with the experimental data, where the stiffness and the resulted load-carrying capacity of the specimen were predicted in an accurate manner. Furthermore, the numerical energy dissipation values were found to be close to the experimental ones. Fig. 6 also shows the force-displacement curves and the corresponding hysteretic behavior when the proposed damage factors for concrete and steel reinforcement are being activated and deactivated for the modeling of specimen A1. The numerical results show that the concrete damage factors manage to capture the stiffness and load-capacity degradation, whereas the pinching characteristics are captured through the use of the steel material damage factor (see Fig. 6b).

When modeling the A3 specimen, the pinching effect is observed to be smaller than the experimental one. This is probably attributed to the loss of bond, which resulted during the experimental test (Fig. 5) due to the slippage of the steel reinforcement. Nonetheless, the numerical model manages to capture the hysteretic behavior with an acceptable accuracy.

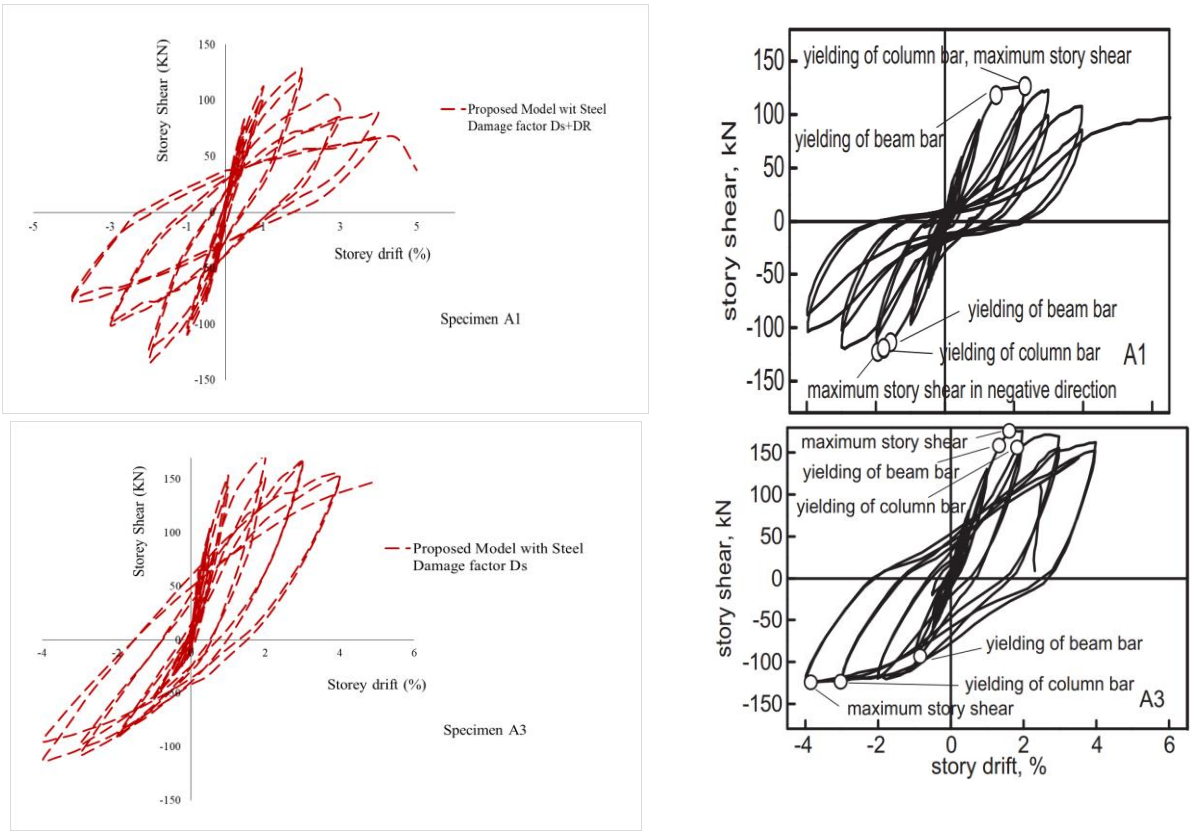

Figure 5: Beam-Column frame joint. Comparison between numerical (Left) and experimental results [8] (Right). Complete force-displacement history for specimens A1 (up) and A3 (down).

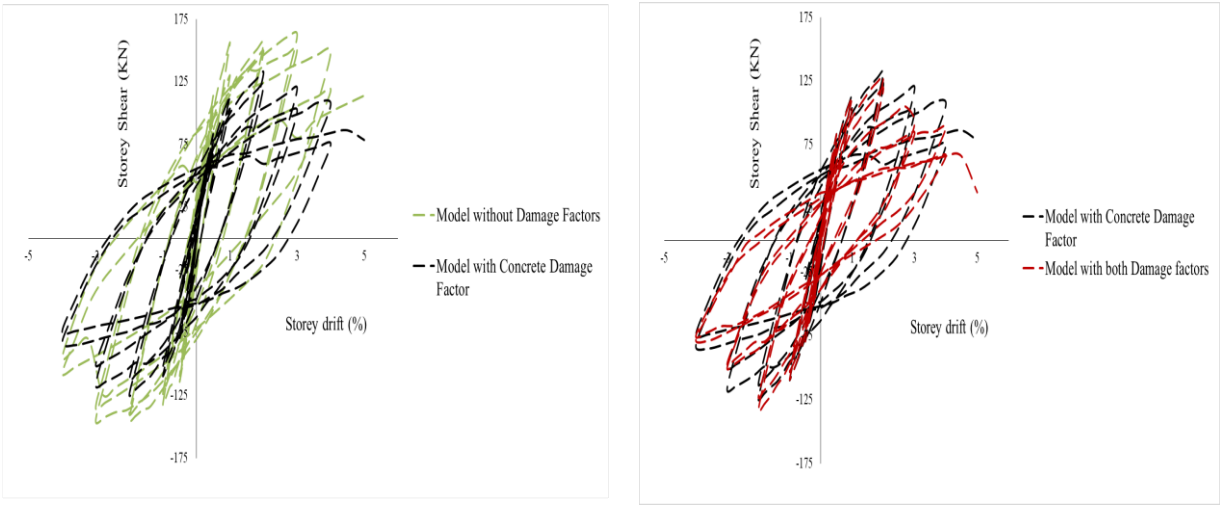

(a) (b)

Figure 6: Beam-Column frame joint. Comparison between numerical results that were obtained by activating and deactivate the two damage factors for specimen A1. Comparison between numerical results when a) Model assumes no damage factors and compared to the model that assumes only for the concrete damage factor. b) Model with concrete damage factor only and compared to the case with both damage factors activated.

Furthermore, as it resulted from the numerical investigation, the hysteretic loops of specimen A3 produce larger hysteretic loops when compared with that of specimen A1, a mechanical behavior that can be easily observed through Figs. 5 and 6. Based on the numerical findings obtained through the analysis of the two specimens, it can be concluded that the use

of both damage factor (D_C, D_S) play an important role in capturing the strength and stiffness deterioration of the RC specimens.

According to the numerically obtained results, Table 1 was developed to compare the numerically predicted maximum (negative and positive) storey shear forces with the corresponding experimental data. The comparison shows that the discrepancy between the numerical and the experimental data is lower than 10%.

Specimen		Maximum Storey Shear		Divergence from Experiment (%)
		Experimental (kN)	Numerical (kN)	
A1	(+)	126.6	127.84	0.98
	(-)	-122.8	-134.12	-9.21
A3	(+)	176.4	171.16	-2.97
	(-)	-124.5	-112.98	9.25

Table 1: Beam-Column frame joint. Comparison of the maximum storey shear between experimental and numerical results.

3.2 RC Shear wall SW4

The RC shear wall investigated by Pilakoutas and Elnashai [9], was also analyzed by using the proposed model. The shear wall was denoted as SW4 and it has a rectangular geometry with a 1.2 m height and a 0.6 m length, where its thickness was reported to be equal to 0.06 m, as showed in Fig. 7. The material properties and reinforcement details are given in Table 2, as they were reported in [9].

Region	Concrete		Horizontal Reinforcement		Vertical Reinforcement		Confining Reinforcement	
	f_c (MPa)	E_c (MPa)	ρ (%)	f_y (MPa)	ρ (%)	f_y (MPa)	ρ (%)	f_y (MPa)
Web	36.9	35240	0.39	545	0.5	545	-	-
Boundary	36.9	35240	0.79	545	6.86	470	0.43	545

Table 2: Material properties and reinforcement ratios of Shear wall SW4

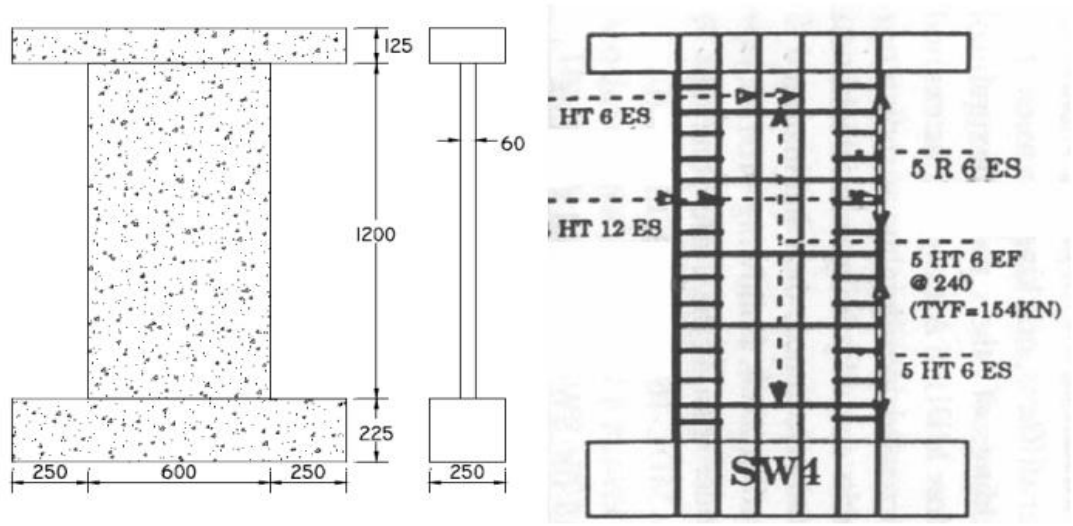

Figure 7: Geometric and reinforcement details of Shear wall SW4 [9].

The shear wall was subjected to different cyclic loading sets according to the experimental setup [9]. The loading history represents extreme conditions experienced during a severe earthquake and it was modeled as shown in Fig. 8. The concrete domain was discretized with 8-noded hexahedral finite elements and the steel reinforcement was discretized with NBCFB elements. A total number of 50 concrete (23cm x 15cm x 15cm) and 250 steel embedded rebar elements were used to discretize the entire shear wall as shown in Fig. 9. Additionally, rigid hexahedral elements were used to simulate the metallic plates near the boundaries in order to avoid local failure (red elements in Fig. 9).

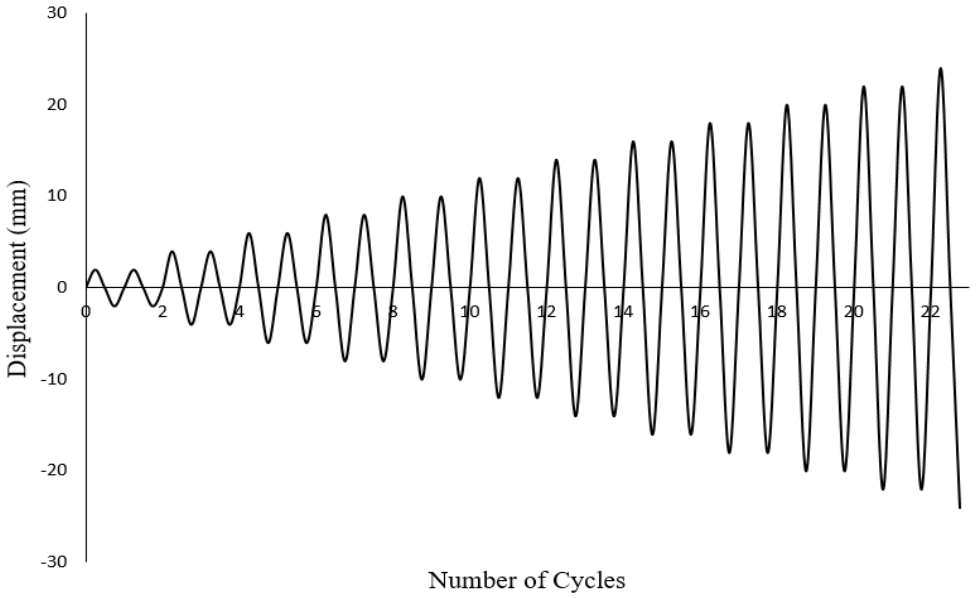

Figure 8: Loading history imposed at the top beam of specimen SW4.

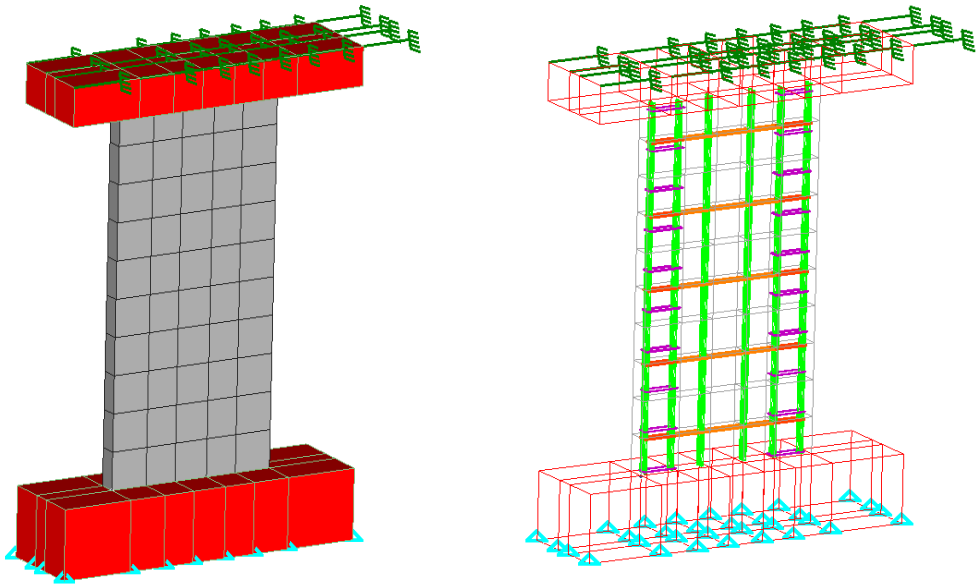

Figure 9: Shear wall SW4. 3D views of the finite element meshes of concrete and embedded rebar elements.

The numerically obtained curves are compared with the corresponding experimental data in Fig. 10. As can be seen, the numerical results match very well with the experimental data,

where the stiffness and the load-carrying capacity of the specimen were predicted in an accurate manner (less than 10% deviation from the experimental data). Furthermore, the numerical energy dissipation of the structure was found to be very close to the experimental one. In addition, the experimental results show a more flexible behavior in terms of structural response without significant pinching effect characteristics. The same mechanical behavior was captured from the numerical results that also did not indicate for any significant pinching behavior.

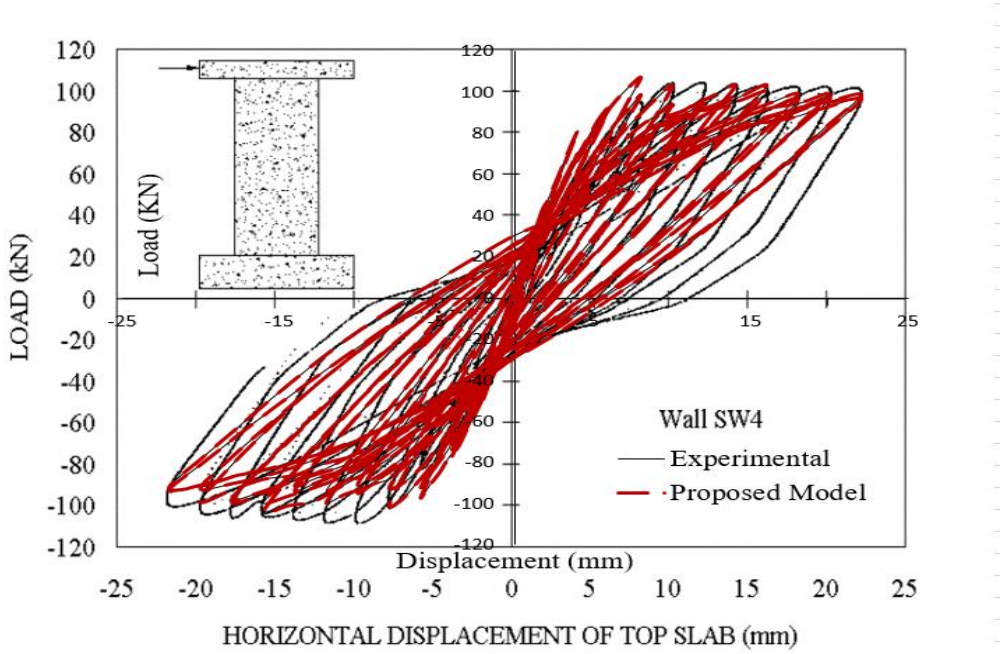

Figure 10: Shear Wall SW4. Comparison between numerical and experimental results in terms of the force-deflection curves.

3.3 Three-storey, Three-bay RC Frame Subjected to High Intensity Ground Motions

A three-storey, three-bay frame was designed, built and tested at the University of California, Berkeley [10] in order to study the collapse behavior of RC frames with light transverse reinforcement. The geometrical and reinforcement details of the specimen can be depicted in Fig. 11. The RC frame was subjected to a dynamic loading test. The cylindrical compressive strength of concrete that was used to construct the RC frame, was equal to f_c = 24.6 MPa, where the yielding stress of the longitudinal steel reinforcement was reported to be equal to f_y = 445 MPa. Additionally, the beam and column ties were 4.8 and 3.2 mm in diameter with a yielding strength of 558 and 655 MPa, respectively.

Two of the columns, as shown in Fig. 11, have been designed according to ACI 318-08 [11] and they were referred to as "ductile" columns with a longitudinal reinforcement ratio of ρ_l = 1.09% and a transverse reinforcement ratio of ρ_t = 1.1% at the end of the column members. The other two columns were referred to as "older type" columns, with longitudinal reinforcement ratio equal to ρ_l = 2.45% and a transverse reinforcement ratio of ρ_t = 0.15%. Furthermore, the beam's transverse reinforcement was also designed according to ACI 318-08 [11], while beam-column joint failure was not expected based on the design provisions of the frame.

Each beam span has been loaded with four packets of lead weights (6.67 kN per packet). The total load (load packets and weight of concrete frame) of the structure produced the equivalent amount of load in a typical office building. Additionally, the resulting gravity axial load on the first-storey interior columns was approximately $0.16A_g f_c$, while the axial load of the exterior loads was approximately of $0.08A_g f_c$ (where A_g is the column gross section area). Therefore, every beam span was considered that it had a uniformly distributed load of 16.67 kN/m, which was the load used to account for the mass contribution within the numerical model developed for the needs of this numerical investigation. The ground motion record from the 1985 Chilean earthquake at Valparaiso (Llolleo Station, Component 100) was chosen for this dynamic test. The motion was scaled up 4.06 times from its original acceleration amplitudes for the dynamic test and it is given in Fig. 12. In addition to that, the ground motion time scale was divided by a factor of $3^{0.5}$ to satisfy the amplitude requirements [10].

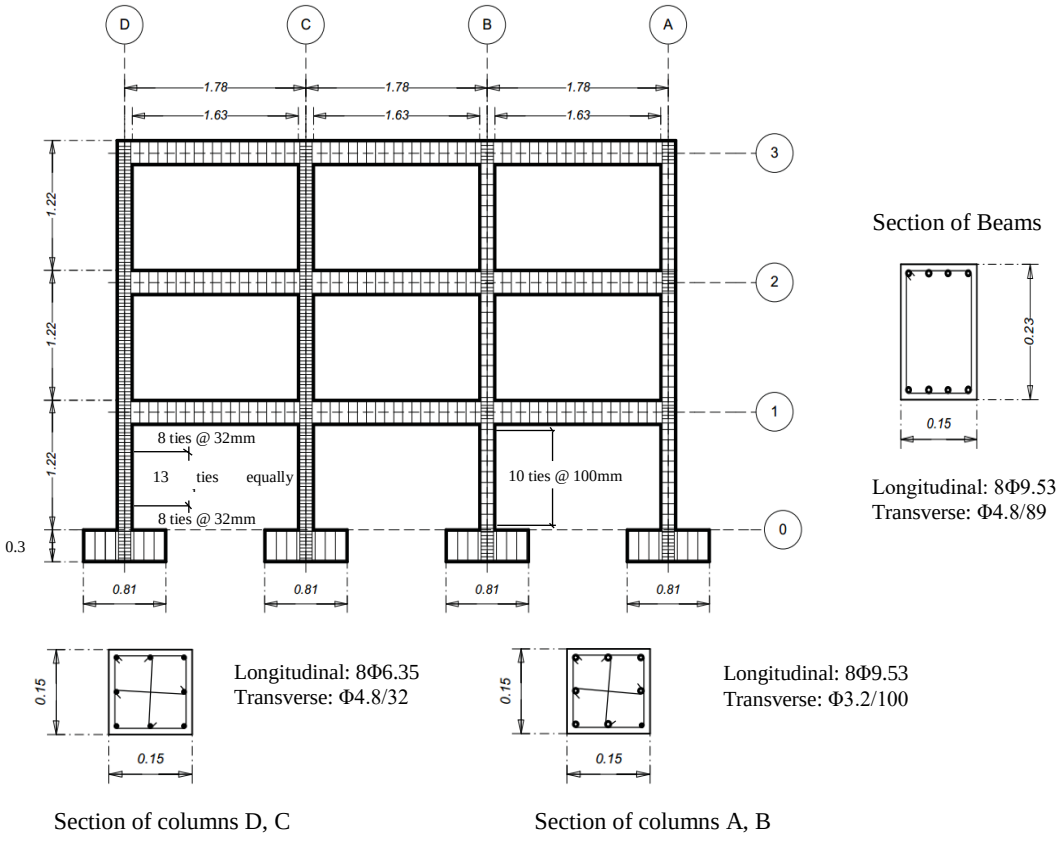

Figure 11: Three-storey, three-bay RC frame. Geometrical and reinforcement details. [10]

For the modeling requirements, the concrete mesh foresaw the use of 336 hexahedral elements and 4,554 steel embedded rebar NBCFB elements were used to model the reinforcement of the specimen, as shown in Fig. 13. Furthermore, 108 hexahedral elements are used (red elements, see Fig. 13) in order to account for the additional mass placed on the structure. In order to account for the exact applied load through the packets, the red hexahedral elements where assigned a mass density that would derive the corresponding load after it was multiplied by its volume. Finally, 60 hexahedral elements (blue elements, see Fig. 13) were used

for the support of the columns so as to simulate the boundary conditions of the specimen and to avoid any local failure at the area where the accelerogram was applied.

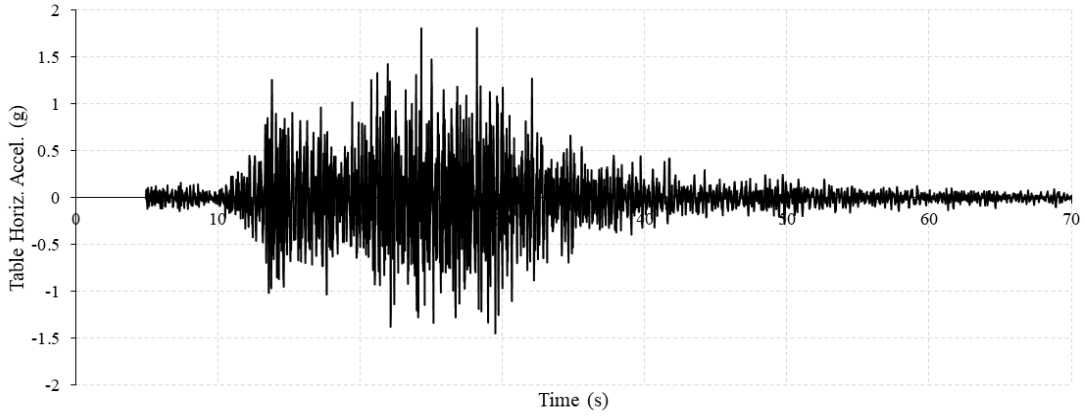

Figure 12: Three-storey, three-bay RC frame. Acceleration history used during the experiment [10].

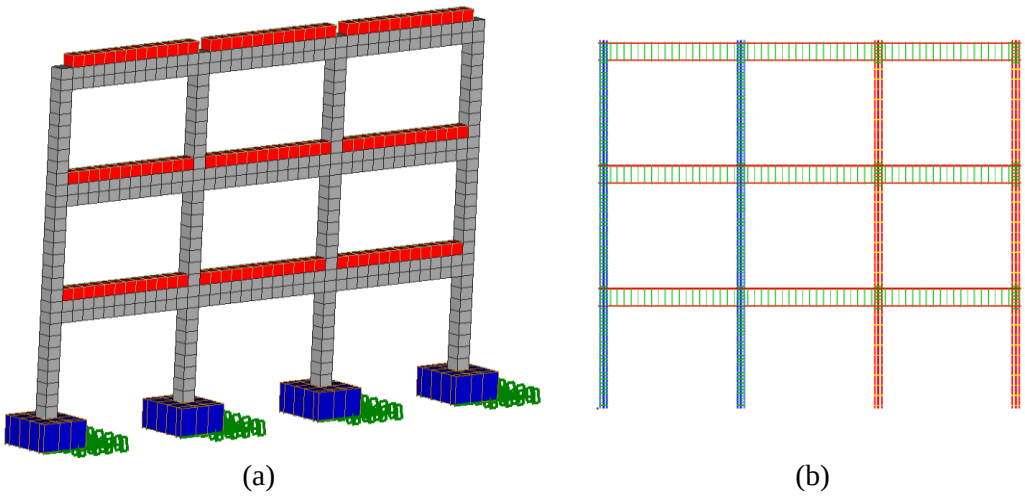

Figure 13: Three-storey, three-bay RC frame. 3D view of the finite element mesh of the (a) 8-noded hexahedral and (b) embedded rebar elements.

The natural periods for the first three modes were compared with the corresponding experimental ones and given herein in Table 3. The comparison shows that the natural periods that derived from the numerical model, were very close to the experimental ones, where the average computed error was equal to 8.7%.

Mode	Experimental period T (s)	Numerical period T (s)	Divergence from experimental (%)
First	0.30	0.30	0
Second	0.10	0.09	10
Third	0.069	0.08	15.94
		Average	8.65

Table 3: Three-storey, three-bay RC frame. Comparison between the numerically and the experimentally derived natural periods.

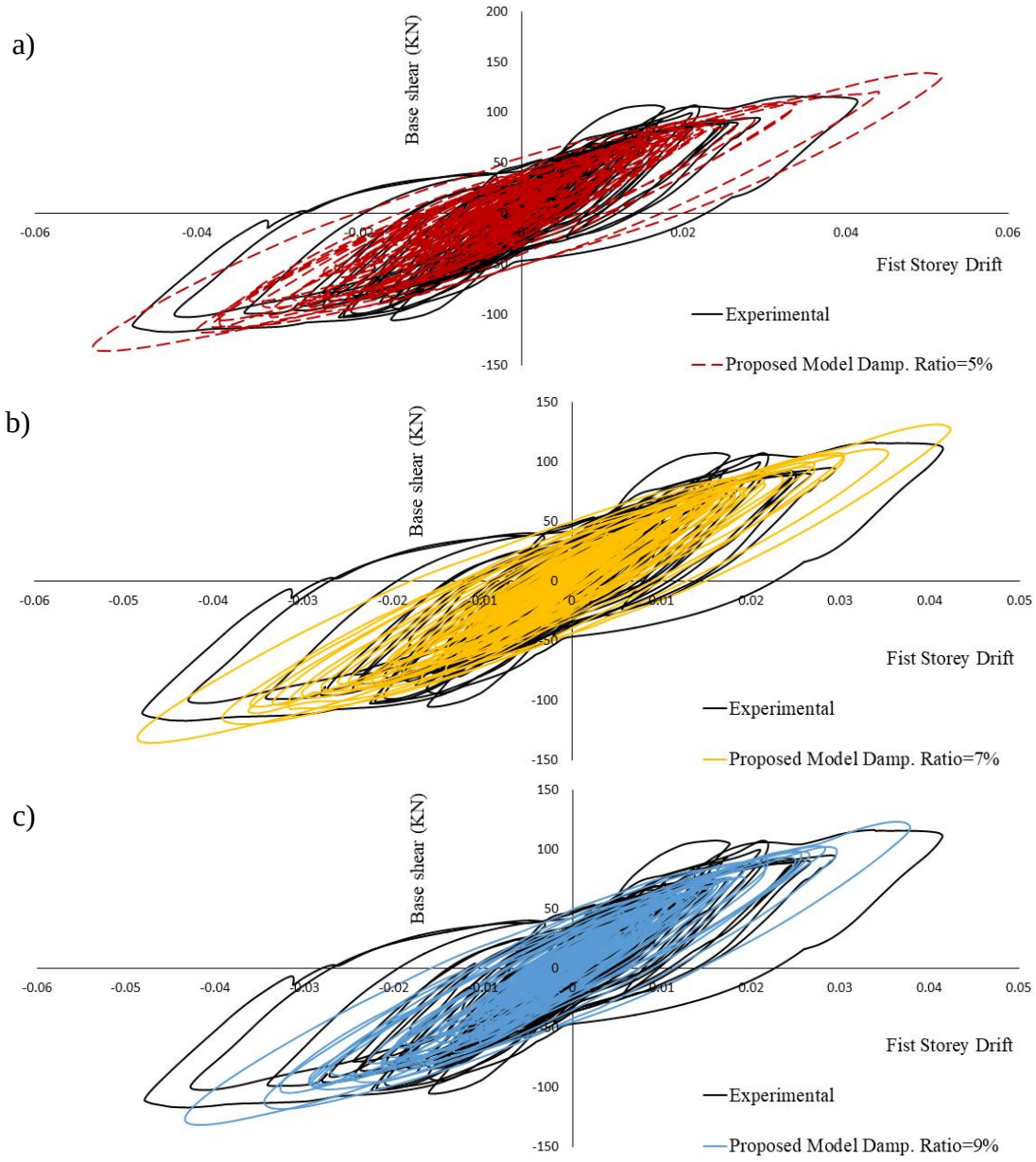

Figure 14: Three-storey, three-bay RC frame. Comparison between the numerical and experimental results of base shear-fist storey drift curves when using damping ratio equal to (a) 5%, (b) 7% and (c) 9%.

Fig. 14 shows the force-displacement curves comparison between the numerical and experimental data. For the needs of this numerical investigation, three different damping ratios were examined (9%, 7% and 5% damping). Based on the analysis of the computed curves, it was found that the two numerical models that adopt damping ratios equal to 7% and 9% produce more accurate results in comparison to the model with a 5% damping ratio. It is also easy to observe that the proposed modeling method manages to capture the overall dynamic response of the specimen, maintaining a good accuracy when compared with the experimental curves. It important to note at this point that, during the experiment, there was a steel frame that was post-tensioned to the shake table on each side of the concrete frame to restrain the out-of-plain movements. This frame could have had an impact on the stiffness of the specimen and on the damping mechanisms that were developed. This effect was not accounted for

during the numerical results and can explain the differences between the curves given in Fig. 14.

The required Newton-Raphson internal iterations per displacement increment are shown in Fig. 15 for the case where the damping ratio was set to 9% (similar results derived when the use of 5% and 7% damping ratios is adopted). It can be easily seen that all the displacement increments require a minimal number of iterations to achieve convergence, regardless the degree of nonlinear behavior of the model. As it can be seen, the required internal iterations per dynamic step during the solution procedure were limited to 1 to 2, underlining the numerical stability of the proposed modeling method [2]. The computational time for the nonlinear solution procedure is given in Table 4, which refers to the solution of 12,125 dynamic time increments. The total required time for solving the nonlinear dynamic problem was 658.5s with an average error of 1.1×10^{-5}. It is important to note herein that, the CPU used to perform all the analyses in this study had a 3.7 GHz computing power.

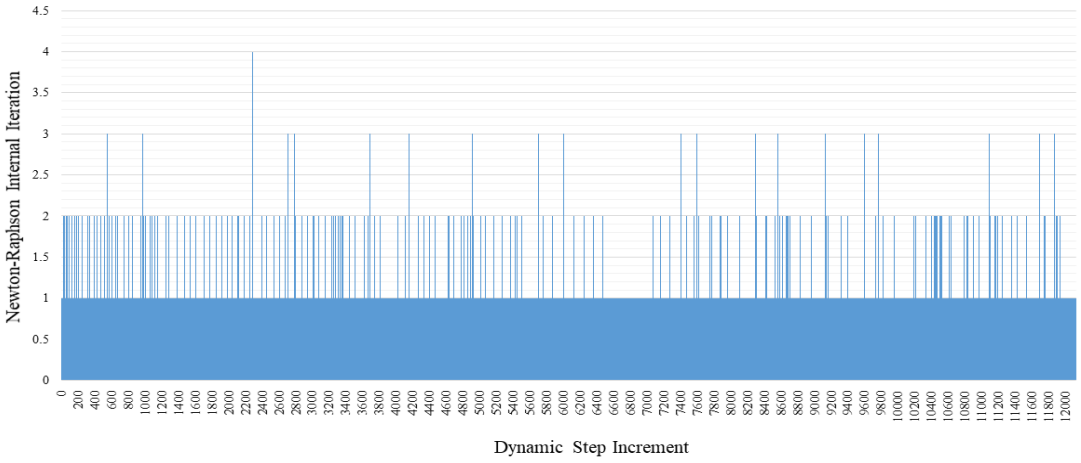

Figure 15: Three-storey, three-bay RC frame. Number of internal iterations per dynamic step increment.

Task	CPU Time (s)
Embedded rebar element mesh generation	0.24
Nonlinear incremental-iterative solution	658.22
Total Time	658.46

Table 4: Three-storey, three-bay RC frame. CPU time for different tasks of the nonlinear analysis.

4 CONCLUSIONS

In this research paper, a proposed 3D constitutive modeling approach is used for the analysis of RC structures that are subjected to limit states static cyclic and dynamic loading conditions. The concrete material constitutive model was found to describe a realistic behavior of concrete under generalized 3D states of stress. Based on the adopted modeling method of concrete, the cracking phenomenon was modeled through the smeared crack approach. The introduction of two damage parameters for concrete and steel reinforcement materials in order to take into account the accumulated damage during the nonlinear analysis was found to pro-

vide the analysis with objectivity and numerical accuracy when dealing with extreme nonlinearities.

Furthermore, the proposed numerical model managed to capture the mechanical behavior of two RC beam-column frame joints, a shear wall and a three-storey three-bay RC frame that was tested under extreme dynamic loading conditions. This validation study is an extension on the research work presented in [2] that reported similar findings.

Based on the numerical findings of the research work presented herein, for the case of the RC beam-column joints, the damage parameter for steel reinforcement was found to be able to take into account for the loss of bonding within the damaged concrete areas, where it manages to partially capture the pinching characteristics observed within the experimental hysteretic curves. For extreme pinching modeling through the use of the proposed modeling approach, one may refer to [7].

Finally, the thee-storey RC frame specimen was modeled for both modal and nonlinear dynamic analysis. According to the parametric investigation, the first three natural modes were captured with an overall deviation from the experimental data equal to 8.7%, a finding that highlights the ability of the developed algorithm in capturing the modes of a real structural system. Finally, the dynamic analysis of the RC frame that was designed to exhibit a brittle behavior was performed successfully through the use of different damping rations. The ability of the proposed modeling method in capturing the nonlinear dynamic response of the RC frame through the use of the exact material properties (as they were reported within the report [10]) demonstrates its computational superiority, indicating that it is a powerful tool when it comes to the modeling of RC structures.

REFERENCES

[1] Mourlas, C., Papadrakakis, M., Markou, G. *A computationally efficient model for the cyclic behavior of reinforced concrete structural members*. Engineering Structures, Vol. **141**, pp. 97–125, 2017.

[2] Mourlas, C., Markou, G., Papadrakakis, M. *Accurate and computationally efficient nonlinear static and dynamic analysis of reinforced concrete structures considering damage factors*. Engineering Structures, Vol. 178, pp. 258–85, 2019.

[3] Kotsovos, M.D., Newman J.B. *Behavior of Concrete Under Multiaxial Stress*. ACI Journal Proceedings, Vol. **74**(9), pp. 213–23, 1977.

[4] Kotsovos, M.D., Pavlovic, M. *Structural concrete : finite-element analysis for limit-state design.* T. Telford; 1995.

[5] Willam, K., Warnke, E.P. *Constitutive model for the triaxial behavior of concrete*. Seminar on concrete structures subjected to triaxial stresses, Instituto Sperimentale Modeli e Strutture, Bergamo, Paper III-1., 1974.

[6] Menegotto, M., Pinto, P.E. *Method of analysis for cyclically loaded reinforced concrete plane frames including changes in geometry and non-elastic behavior of elements under combined normal force and bending*. Proceedings, IABSE Symposium on Resistance and Ultimate Deformability of Structures Acted on by Well Defined Repeated Loads, Lisbon, Portugal, 15–22., 1973.

[7] Markou, G., Mourlas, C., Garcia, R., Pilakoutas, K., Papadrakakis, M., “Cyclic

Nonlinear Modeling of Severely Damaged and Retrofitted Reinforced Concrete Structures", COMPDYN 2019, 7th International Conference on Computational Methods in Structural Dynamics and Earthquake Engineering, 24-26 June 2019, Crete, Greece.

[8] Shiohara, H., Kusuhara, F. *Benchmark Test for Validation of Mathematical Models for Nonlinear and Cyclic Behaviour of R/C Beam–Column Joints.* Department of Architecture, School of Engineering, University of Tokyo: 2006.

[9] Elnashai, A.S., Pilakoutas, K., Ambraseys, N.N. *Experimental behaviour of reinforced concrete walls under earthquake loading.* Earthquake Engineering & Structural Dynamics, Vol. **19**(3), pp. 389–407, 1990.

[10] Ghannoum, W.M., Moehle, J.P. *Experimental Collapse of a Lightly Reinforced Concrete Frame Subjected to High Intensity Ground Motions*. 14th World Conference on Earthquake Engineering, vol. 12-01-0052, Beijing, China: 2008, p. 12–7.

[11] ACI Committee 318. *Building Code Requirements for Structural Concrete (ACI 318-95) and Commentary*. American Concrete Institute, Farmington Hills, MI: 1995.

COMPDYN 2019
7th ECCOMAS Thematic Conference on
Computational Methods in Structural Dynamics and Earthquake Engineering
M. Papadrakakis, M. Fragiadakis (eds.)
Crete, Greece, 24–26 June 2019

SEISMIC RELIABILITY OF RC BUILDINGS MADE WITH EAF CONCRETES

Mariano Angelo Zanini[1], Flora Faleschini[1,2], and Klajdi Toska[1]

[1] Dept. of Civil, Environmental and Architectural Engineering, University of Padua.
Via Marzolo 9, 35131 Padua, Italy
e-mail: marianoangelo.zanini@dicea.unipd.it
e-mail: lorenzo.hofer@dicea.unipd.it

[2] Dept. of Industrial Engineering, University of Padua.
Via Gradenigo 6, 35131 Padua, Italy
e-mail: flora.faleschini@dicea.unipd.it

Abstract

The development of sustainable concretes is becoming an emerging issue in civil construction sector. The use of recycled aggregates is one way to fulfill sustainability goals in concrete industry, and among others, Electric Arc Furnace (EAF) slag aggregates has been proven to be promising. Past research demonstrated a significant increase of mechanical properties of EAF concretes when compared with ones made with natural aggregates (NA); however, at the same time, their use implies also an increase of self-weight loads. The present study aims therefore to investigate the seismic reliability of reinforced concrete frame buildings made with EAF, and compare it with the same structural configurations built with NA mixes, in order to show how the change in mechanical properties and self-weight can impact the seismic response of the analyzed case-studies.

Keywords: EAF slag, reinforced concrete moment frames, seismic fragility, seismic reliability.

1 INTRODUCTION

Construction waste reduction is one of the main goals construction industry has to face in the upcoming years [1]. Recycling and reuse are seen as the main policies for waste reduction disposal and a lot of studies and research has been done on achieving this objective. Recycled Aggregates (RAs) production is one of the main uses of Construction and Demolition Waste (C&DW) and their use is allowed in most countries around the world [3-5]. Among RAs from C&DW, recently, other kind of waste, mostly originating from industrial processes, have been object of research to evaluate their possible use to produce RAs or so-called industrial aggregates. Only in Europe, nearly 2.7 billion tonnes of natural aggregates are consumed each year [2]. Previous research has shown that among all industrial waste or by-products, those coming from steelmaking industry, particularly electric arc furnace (EAF) slag, offer the best performance when used in structural concrete. Particularly has been observed that EAF slag use enhances both mechanical strength [6-10] (i.e compressive strength, tensile strength and elastic properties) and durability [11-13] of concrete mixtures when compared to ordinary ones. Another difference worth highlighting is heavy-weight metals presence in the EAF slag composition which gives EAF concrete mixtures a higher specific weight with respect to NA mixtures. [14-15] have demonstrated that reinforced concrete (RC) elements with EAF slag aggregates manifest better flexural and shear capacity with respect to ordinary RC when tested to monotonic loading under four-point bending. Columns under uniaxial compression has shown a similar ductility to that of NA mixtures [17] while a higher shear strength of exterior beam-column joint is observed [18]. Experiments of EAF concrete joints under cyclic loading have shown a gain with respect to NA ones in terms of ductility, dissipated energy and reduced cracking patter. The same results were obtained even for a joint made with a minor cement amount [18]. Bond properties, between reinforcement and concrete, are also improved when using EAF slag aggregates [16]. Other beam-column joint conditions (i.e strong beam – weak column and strong column – weak beam situations) have been numerically investigated [19].

EAF concrete has found different applications, especially in gravity structures that require shielding from radiations where its high specific weight and high strength can be better exploited [20]. However, no studies have been made to investigate the efficacy of EAF slag concrete when applied in elevation RC structures, particularly, in seismic regions where an important change of the building mass can lead to a variation of the vibration modes and fundamental periods, impacting so the seismic loads acting in the structure elements.

Therefore, the present study aims to investigate this topic, analyzing the seismic response of code conforming RC frame buildings designed with ordinary NA concretes then replaced with three different EAF concrete classes characterized by different aggregates replacement ratios. For the mechanical properties' definition of EAF concrete mixtures a dataset of experimental tests based on two previous research works of some of the authors [21-22] is used. Mean mechanical properties, ratios of variation and self-weight were extracted via statistical processing for three EAF concrete classes (C1, C2, A) with respect to a benchmark mixture realized with NAs. For the purpose, three RC frame structures with three, six and nine stories were designed according to the current Italian Code for Constructions [5] for a medium-to-high seismic hazard site. From these an overall of 12 models resulting from the combinations of 3 structural configurations and 4 concrete mixes, were created. Fragility functions were then computed from the seismic responses of the analyzed configurations under a set of non-linear time history analysis (NLTHAs) and a seismic reliability assessment was carried out for all 12 combinations, investigating the variation of structural safety margins related to the use EAF concrete mixtures in replacement to a conventional NA concrete.

2 EAF SLAG AND ITS USE AS AGGREGATE IN STRUCTURAL CONCRETE

EAF slag properties depend on several factors, such as the type of steel to be produced, scrap composition, slag cooling method and speed, and further weathering process. Its composition includes mainly iron, calcium, silicon and aluminum oxides [23]. Usually, before the raw product is ready to be used as a recycled aggregate, it must pass through a weathering protocol [23] to reduce the volumetric instability of the matrix. The main properties of the slag for two size fractions compared, with a dolomitic aggregate, are reported in Table 1.

	Apparent density (kg/m3)	Water absorption (%)	Porosity (%)	shape
EAF slag 0-4 mm	3800	1.0 – 1.5	2.0	Crushed
EAF slag 4-16 mm	3950	<1.0	0.5 – 2-7	Crushed
NA 0-4 mm	2760	1.0 1.5	< 2.0	Roundish
NA 4-16 mm	2790	<0.5	0.9 – 1.8	Roundish

Table 1: Physical properties of EAF slag compared to dolomitic aggregate (NA).

The properties of the concrete matrix with EAF slag aggregates depends on type and amount of substitution. Generally coarse aggregates improve mechanical properties, while fine fraction affect is minor [12]. Workability of EAF concrete is highly reduced by high porosity and the crushed shape that characterizes the slag. Another important variation is observed on the specific weight of EAF concrete. Compared to a conventional NA concrete, the use of EAF slag can increase the specific weight of the matrix up to 15-20%. While gain in mechanical properties depends on slag type and fraction size, it seems that specific weight increase is almost constant and is not affected by these factors. Elastic modulus is also improved when using EAF slag. This is mainly because concrete elastic modulus depends mainly on the aggregates elastic modulus. The overall property improvements are also due to the interfacial transition zone between EAF aggregate and cementitious matrix. If a bad quality cementitious matrix or a high water/cement ratio is employed property enhancements are less important.

3 RC FRAME CODE-CONFORMING ANALYZED CASE STUDIES

To analyze the seismic response of different buildings built with EAF concrete three moment frame RC structures with 3-, 6-, and 9- stories were considered. The structures are characterized by a rectangular shape with five spans in the longitudinal direction and three in the transversal one. Span length is equal to 5 m in both directions.

The structures were designed in accordance with the Italian Building Code [5] considering a moderate-to-high seismic hazard site (Municipality of Pordenone, Northeast Italy) and a low ductility class (Class B). Seismic actions were computed from a dynamic linear analysis while beams and columns were designed accordingly using a C25/30 conventional concrete class.

4 THEORETICAL BACKGROUND ON SEISMIC RELIABILITY ANALYSIS

The occurrence of main shock events at a given site is assumed to be a Homogenous Poisson Process for the Performance-Based Earthquake Engineering (PBEE) framework [24]. So, the process of events causing structural failure is also a HPP and its unique parameter, failure rate λ_f, can be used for computing the failure probability at any time. The failure rate depends on the seismicity of the site (hazard curve λ_{im}) and on the structural behavior (fragility curve $P[f|im]$) [25-29]. λ_f is computed by applying the Total Probability Theorem as:

$$\lambda_f = \int_{im} P[f|im] \cdot |d\lambda_{im}| \tag{1}$$

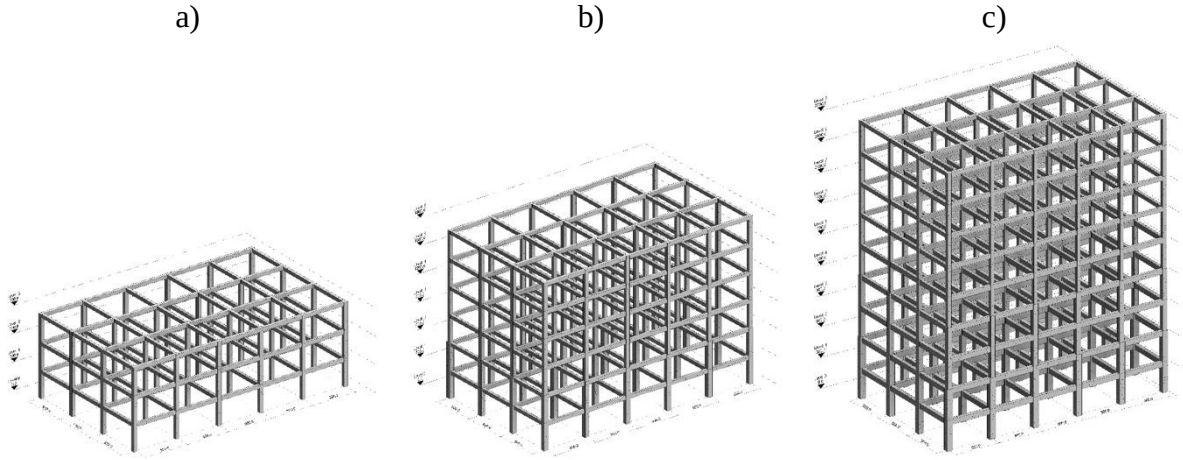

Figure 2: RC frame layouts analyzed: 3- (a), 6- (b) and 9-story (c) building archetypes.

4.1 Seismic hazard estimation

The so-called Probabilistic Seismic Hazard Analysis [30-31], for the computation of λ_{im} associates to each im value, the annual rate of events that exceed it at a given site. The seismicity of a given area di defined by three main components: the earthquake occurrence model, the spatial seismogenic model and the attenuation model. $|d\lambda_{\mathrm{im}}|$ represents the mean number of events per year with an intesity of exactly im and is obtained as:

$$|d\lambda_{\mathrm{im}}| = -\frac{d\lambda_{\mathrm{im}}}{d(im)} d(im) \tag{2}$$

On the other hand, $\lambda_{im}$is obtained via the following PSHA integral:

$$\lambda_{im} = \sum_{i=1}^{n_{SZ}} \nu_{m_{min,i}} \int_{m_{min,i}}^{m_{max,i}} \int_{r_{min,i}}^{r_{max,i}} P[IM > im|m,r] f_{M_i}(m) f_{R_i}(r)\, dm\, dr \tag{3}$$

where $\nu_{m_{min,i}}$ is the rate of occurrence of earthquakes greater than a suitable minimum magnitude $m_{min,i}$ of the i^{th} seismogenic zone *(SZ)*, $f_{M_i}(m)$ is the magnitude distribution for the i^{th} *SZ* and $f_{R_i}(r)$ is the distribution of the source i^{th}-to-site distance. Given a combination of magnitude m and distance r, $P[IM > im|m,r]$ is the probability to exceed im. The seismic hazard map for Italy is provided by the National Institute of Geology and Volcanology (INGV) [32]. To compute the failure rate a continuous hazard function is needed. Since INGV provides hazard data (values of the 16th, 50th and 84th percentile) only for nine return times, it is possible to fit the median values (i.e., the 50th percentile) with a quadratic function in the logarithmic space as:

$$\lambda(s) = k_0\, e^{(-k_1 \ln(s) - k_2 ln^2(s))} \tag{4}$$

In assessing seismic reliability, instead of the median hazard curve, it is more suitable to refer to the mean one which is possible to derive with the following equation:

$$\bar{\lambda}(s) = \lambda(s)\, e^{(\frac{1}{2}\beta_H^2)} \tag{5}$$

where β_H can be estimated as:

$$\beta_H = \frac{\ln(S_{84\%}) - \ln(S_{16\%})}{2} \quad (6)$$

4.2 Seismic fragility analysis

The fragility function ($P[f|im]$) represents the probability to reach and exceed a certain damage state given a specific intensity im. Several frameworks for fragility function estimation exits in literature, the most popular ones are the Incremental Dynamic analysis [33], the Cloud Analysis [34] and the Multi-Stripes Analysis [35].

In this work the Cloud Analysis method is adopted. The fragility parameters are estimated starting from a set of n natural ground motion records. The fragility function is computed as follows:

$$[f|im] = P\left[EDP > \overline{edp}|im\right] = 1 - P\left[EDP \leq \overline{edp}|im\right] = 1 - \Phi\left[\frac{ln(\overline{edp}) - ln(edp)}{\beta}\right] \quad (7)$$

$\overline{edp}$ is the median threshold value of the assumed structural limit state, and edp represents the median estimate of the demand that can be computed with a ln-linear regression model, as:

$$ln(edp) = a + b \cdot ln(im) \quad (8)$$

β is the standard deviation of the demand conditioned on im and can be estimated from the regression of the seismic demands as:

$$\beta_H = \frac{\ln(S_{84\%}) - \ln(S_{16\%})}{2} \quad (9)$$

5 SEISMIC RELIABILITY ASSESSENT OF THE ANALYZED EAF RC FRAME ARCHETYPES

NLTHAs were carried out with SeismoStruct software [36]. A diffused plasticity model, using a fiber section discretization, was adopted to consider material non-linearities. Unconfined and confined concrete was modeled via the Mander et al. [37] model whereas the Menegotto-Pinto [38] steel model was used for the non-linear behavior of rebars. EAF concrete characteristics are computed using the ratio coefficients in Table 2 and the reference concrete material (C25/30) characteristics.

	Class EAF-C1	Class EAF-C2	Class EAF-A
$\rho_{c,EAF} / \rho_{c,Ref}$	1.166	1.166	1.154
$f_{c,EAF} / f_{c,Ref}$	1.395	1.404	0.915
$f_{ct,EAF} / f_{ct,Ref}$	1.280	1.100	1.080
$E_{c,EAF} / E_{c,Ref}$	1.330	1.100	1.040

Table 2: Ratios between EAF and Reference concrete properties.

Fragility analysis is computed from a set of point data representing the Intensity Measure (IM) of a given seismic event and the corresponding non-linear response parameter (i.e Engineering Demand Parameter (EDP)). Since the Performance Based Earthquake Engineering was introduced, many researchers have tried to study IM and EDP parameters that best describe structure response under seismic excitation [39-41]. In the present paper, the chosen EDP parameter is the maximum interstory drift ratio (IDR) while the peak ground acceleration (PGA) is used as IM. In addition, four damage states: Slight, Moderate, Extensive and Complete, with corresponding EPD threshold of 0.4%, 0.8%, 1.5% and 3%, were defined.

Threshold values result similar to those proposed for ductile RC moment frame structures by [39] and were defined from non-linear static analysis. For the mid-rise and high-rise buildings, a reduction factor of respectively 2/3 and 1/2 as proposed by [42] was considered to account for higher mode effects and differences between average computed in a non-linear static analysis and maximum individual IDR from NLTHAs.

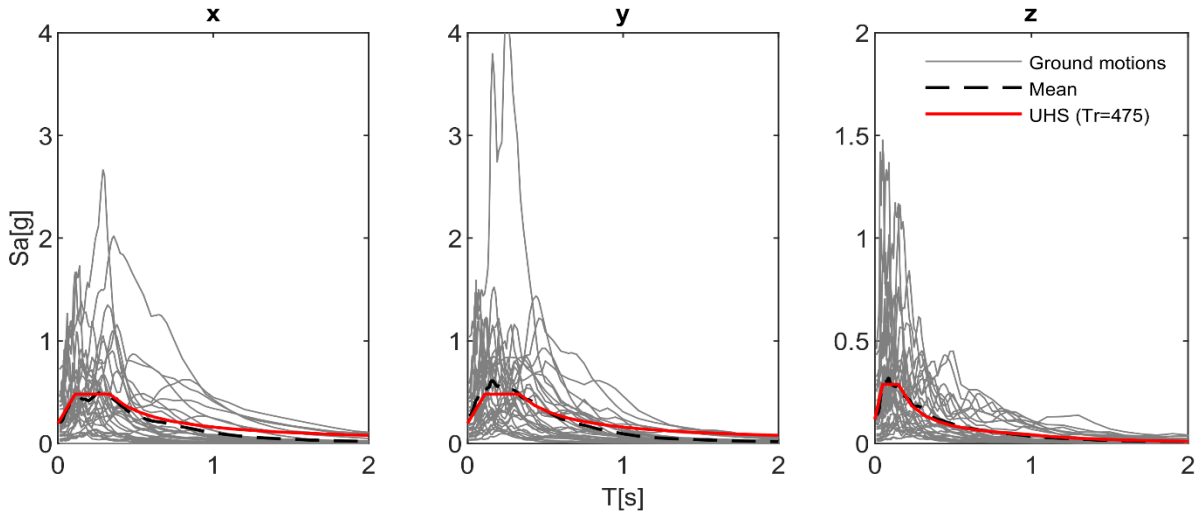

Figure 3: Selected seismic records: X- , Y- and Z- direction.

6 RESULTS AND DISCUSSION

For the NLTHAs a set of 30 natural unscaled ground motion records were adopted. In the seismic simulation all three components of the seismic wave, which spectral response is shown in figure 3, were considered. The structural response was then evaluated with respect to the four DSs previously defined, varying from Slight to Complete. Fragility functions were computed for each of the 12 cases, resulting from different geometrical and material combinations, using the Cloud Method described in Section 4.2.

Fragility curves for Slight, Moderate, Extensive and Complete damage are shown in Figure 4 in green, yellow, orange and red color respectively. Additionally, solid lines were used for frames realized with the reference concrete; instead, dotted, dashed and dash-dot lines were used for EAF-C1, EAF-C2 and EAF-A concretes, respectively.

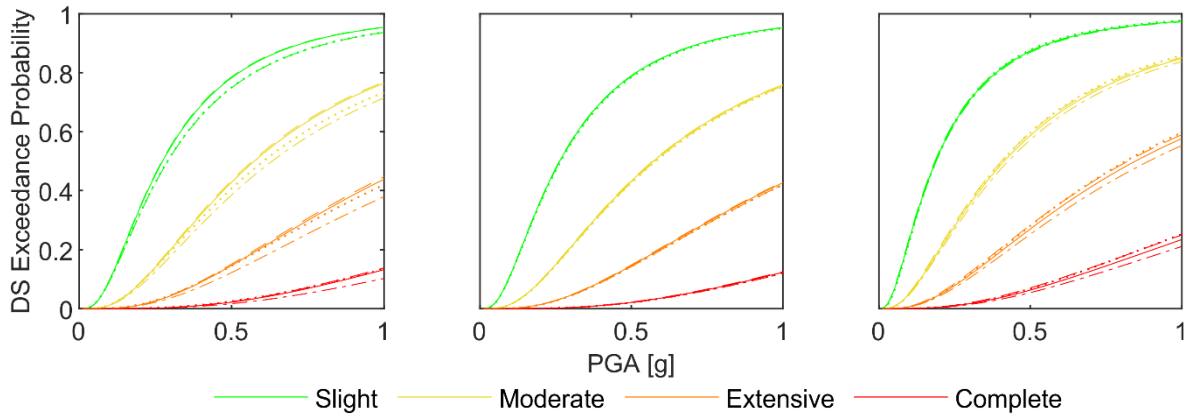

Figure 4: Slight, Moderate, Extensive and Complete DS fragility curves for 3- (a), 6- (b) and 9- (c) story RC frame archetypes (Solid - reference material (C25/30); Dotted - EAF-C1; Dashed - EAF-C2; Dash-dot – EAF-A).

A comparison of the seismic performance of structures built with the reference concrete and EAF concrete is given in Figure 4. It can be noted that the overall performance of EAF concrete structures is close to the performance of the reference material one. The 6- story model has shown almost the same response for all considered materials, proven by the overlapping fragility curves, while the 3- and 9- story curves tend to vary more when considering different materials. Comparing the fragility curves for the different geometrical configurations considered, is noted that 3- and 6- story buildings fragilities result similar for all DSs considered, while the 9 story building results more vulnerable under seismic solicitation with respect to the low- and mid-rise buildings.

Mean failure rates were also computed for all building frames (Table 3). When compared to the reference material the EAF concrete buildings report similar mean failure rate values. This confirms that in terms of safety margins with respect to seismic actions, buildings designed with ordinary concrete but built with EAF aggregates are exposed to almost the same risk as those realized with NAs ones. This highlights that NAs replacement with EAF aggregates, in the same structural system, has a small impact in terms of seismic reliability levels achieved. It is also observed that the mean failure rate for the 9-story building is almost twice the ones computed for the 3- and 6- story archetypes. This great difference may be affected by the reduced damage states EDP threshold adopted for the 9- story by considering it a high-rise building but it also points out that current code recommendations does not guarantee building design characterized by the same level of seismic reliability but often some differences can be observed, especially when comparing different rise buildings.

The construction of the three hypothesized models would require more than 2000 m^3 of concrete. In terms of environmental benefits, considering about 1700kg of NA/m^3 in a mix design for a reference concrete, nearly 3400 tons of NA could be saved if natural material would be fully replaced with EAF slag.

DS	Story	C25/30	C1-EAF	C2-EAF	A-EAF
Slight	3-	4.31E-03	4.28E-03	4.37E-03	4.22E-03
	6-	4.97E-03	4.91E-03	5.05E-03	4.94E-03
	9-	1.08E-02	1.02E-02	1.12E-02	1.08E-02
Moderate	3-	8.98E-04	9.23E-04	9.23E-04	8.27E-04
	6-	9.93E-04	9.77E-04	1.01E-03	9.76E-04
	9-	2.46E-03	2.39E-03	2.61E-03	2.34E-03
Extensive	3-	1.80E-04	1.93E-04	1.88E-04	1.55E-04
	6-	1.89E-04	1.85E-04	1.94E-04	1.83E-04
	9-	5.27E-04	5.30E-04	5.78E-04	4.80E-04
Complete	3-	2.43E-05	2.76E-05	2.58E-05	1.90E-05
	6-	2.36E-05	2.31E-05	2.45E-05	2.26E-05
	9-	7.71E-05	8.13E-05	8.80E-05	6.58E-05

Table 3: Comparison between mean failure rates derived for 3-, 6- and 9-story RC frame archetypes.

7 CONCLUSIONS

The main goal of this paper was to investigate the seismic performance of different code conforming RC-frame archetypes (3-, 6- and 9- stories) built with different substitution rates of NAs with EAF slag. The impact of EAG slag in weight and stiffness variation can change the

eigen values of the structure, therefore, seismic loads and global response of the building. A seismic reliability assessment was carried out and mean failure rates were computed for each combination of geometrical configuration and concrete type considered starting from the fragility functions derived with the cloud analysis for four DSs. Based on the results of the present study the following conclusions can be highlighted:

- Using materials that were proved to have higher mechanical strength than the reference one, might not improve the global seismic behavior of the structure.
- The seismic reliability analysis demonstrates that when replacing NAs of ordinary concrete with EAF ones the seismic safety levels achieved are comparable ti those of the same structural configuration built with ordinary concrete.
- For the low- and mid- rise buildings considered (3- and 6- stories) results showed a similar mean failure rate, while a significant variation was observed for the high-rise case (9- story). This marks out how current building codes may non ensure the same seismic reliability level for higher structures as for low- and mid- rise ones.

REFERENCES

[1] United Nations (2015) Resolution adopted by the General Assembly on 25 September 2015. 70/1. Transforming our world: the 2030 Agenda for Sustainable Development.

[2] European Aggregates Association (2017) Annual Review 2016-2017. (available online at: http://www.uepg.eu/uploads/Modules/Publications/uepg-ar2016-17_32pages_v10_18122017_pbp_ small.PDF).

[3] FHWA (1997) User Guidelines for Waste and Byproduct Materials in Pavement Construction. Federal Highway Administration Research and Technology Report no. FHWA-RD-97-148.

[4] EN 12620 (2008) Aggregates for concrete. Comité Européen de Normalisation, Brussels, Belgium.

[5] DM 17/01/2018 (2018) Aggiornamento delle Norme Tecniche per le Costruzioni, Roma, Italy. (in Italian).

[6] Pellegrino C., Gaddo V. (2009) Mechanical and durability characteristics of concrete containing EAF slag as aggregate. Cem Concr Compos 31(9): 663-671. doi: 10.1016/j.cemconcomp.2009.05.006.

[7] Arribas I., Santamaría A., Ruiz E., Ortega-López V., Manso J.M. (2015) Electric arc furnace slag and its use in hydraulic concrete. Constr Build Mater 90: 68-79. doi: 10.1016/j.conbuildmat.2015.05.003.

[8] Rondi L., Bregoli G., Sorlini S., Cominoli L., Collivignarelli C., Plizzari G. (2016) Concrete with EAF steel slag as aggregate: A comprehensive technical and environmental characterisation. Compos Part B 90: 195-202. doi: 10.1016/j.compositesb.2015.12.022.

[9] Liapis A., Anastasiou E.K., Papachristoforou M., Papayianni I. (2018) Feasibility Study and Criteria for EAF Slag Utilization in Concrete Products. J Sustain Metall 4(1): 68-76. doi: 10.1007/s40831-017-0152-2.

[10] Qasrawi H. (2014) The use of steel slag aggregate to enhance the mechanical properties of recycled aggregate concrete and retain the environment. Constr Build Mater 54: 298-304. doi: 10.1016/j.conbuildmat.2013.12.063.

[11] Faleschini F., Alejandro Fernández-Ruíz M., Zanini M.A., Brunelli K., Pellegrino C., Hernández-Montes E. (2015) High performance concrete with electric arc furnace slag as aggregate: mechanical and durability properties. Constr Build Mater 101, 113-121. doi: 10.1016/j.conbuildmat.2015.10.022

[12] Pellegrino C., Cavagnis P., Faleschini F., Brunelli K. (2012) Properties of concretes with black/oxidizing electric arc furnace slag aggregate. Cem Concr Compos 37: 232-240. doi: 10.1016/j.cemconcomp.2012.09.001.

[13] Ortega-López V., Fuente-Alonso J.A., Santamaría A., San-José J.T., Aragón Á. (2018) Durability studies on fiber-reinforced EAF slag concrete for pavements. Constr Build Mater 163: 471-481. doi: 10.1016/j.conbuildmat.2017.12.121.

[14] Pellegrino C., Faleschini F. (2013) Experimental behavior of reinforced concrete beams with electric arc furnace slag as recycled aggregate. ACI Mater. J. 110: 197-206.

[15] De Domenico D., Faleschini F., Pellegrino C., Ricciardi G. (2018) Structural behavior of RC beams containing EAF slag as recycled aggregate: Numerical versus experimental results. Constr Build Mater 171: 321-337. doi: 10.1016/j.conbuildmat.2018.03.128.

[16] Faleschini F., Santamaria A., Zanini M.A., San José J.-T., Pellegrino C. (2017) Bond between steel reinforcement bars and Electric Arc Furnace slag concrete. Mater Struct 50: 170. doi: 10.1617/s11527-017-1038-2.

[17] Lee J.-M., Lee Y.-J., Jung Y.-J., Park J.-H., Lee B.-S., Kim K.-H. (2018) Ductile capacity of reinforced concrete columns with electric arc furnace oxidizing slag aggregate. Constr Build Mater 162: 781-793. doi: 10.1016/j.conbuildmat.2017.12.045.

[18] Faleschini F., Hofer L., Zanini M.A., Dalla Benetta M., Pellegrino C. (2017) Experimental behavior of beam-column joints made with EAF concrete under cyclic loading. Eng Struct 139: 81-95. doi: 10.1016/j.engstruct.2017.02.038.

[19] Faleschini F., Bragolusi P., Zanini M.A., Zampieri P., Pellegrino C. (2017) Experimental and numerical investigation on the cyclic behavior of RC beam column joints with EAF slag concrete. Eng Struct 152: 335-347. doi: 10.1016/j.engstruct.2017.09.022.

[20] Pomaro B., Gramegna F., Cherubini R., De Nadal V., Salomoni V., Faleschini F. (2019) Gamma-ray shielding properties of heavyweight concrete with Electric Arc Furnace slag as aggregate: An experimental and numerical study. Constr Build Mater 200: 188-197.

[21] Pellegrino C., Faleschini F. (2016) Experimental Database of EAF Slag Use in Concrete. in: Sustainability Improvements in the Concrete Industry. Springer, Switzerland. doi: 10.1007/978-3-319-28540-5.

[22] Zanini M.A. (2019) Structural reliability of bridges realized with reinforced concretes with electric arc furnace slag aggregates. Eng Struct xx: yy-zz (accepted).

[23] Santamaria A., Faleschini F., Giacomello G., Brunelli K., San José J.T., Pellegrino C., Pasetto M. (2018) Dimensional stability of electric arc furnace slag in civil engineering applications. J Clean Prod 205: 599-609. doi: 10.1016/j.jclepro.2018.09.122.

[24] Cornell C.A., Krawinkler H. (2000) Progress and challenges in seismic performance assessment. PEER Centre News, 3(2): 1-3.

[25] Castaldo, P., Palazzo, B., Alfano, G., Palumbo, M.F. (2018) Seismic reliability-based ductility demand for hardening and softening structures isolated by friction pendulum bearings, Structural Control and Health Monitoring 25(11),e2256.

[26] Castaldo, P., De Iuliis, M. (2014) Effects of deep excavation on seismic vulnerability of existing reinforced concrete framed structures, Soil Dynamics and Earthquake Engineering 64, 102-112.

[27] Castaldo, P., Mancini, G., Palazzo, B. (2018) Seismic reliability-based robustness assessment of three-dimensional reinforced concrete systems equipped with single-concave sliding devices, Engineering Structures 163, 373-387.

[28] Castaldo, P., Ripani, M., Priore, R.L. (2018) Influence of soil conditions on the optimal sliding friction coefficient for isolated bridges, Soil Dynamics and Earthquake Engineering 111, 131-148.

[29] Castaldo, P., Palazzo, B., Perri, F. (2016) Fem simulations of a new hysteretic damper: The dissipative column, Ingegneria Sismica, 33(1), 34-45.

[30] Cornell C. (1968) Engineering seismic risk analysis. Bull Seismol Soc Am 58(5): 1583-1606.

[31] McGuire R.K. (1995) Probabilistic seismic hazard analysis and design earthquakes: closing the loop. Bull Seismol Soc Am 85(5): 1275-1284.

[32] INGV. Interactive Seismic Hazard Maps. Available at: http://esse1-gis.mi.ingv.it/s1_en.php (last access 04/03/2019).

[33] Vamvatsikos D., Cornell C.A. (2004) Applied incremental dynamic analysis. Earthquake Spectra, 20(2):523–553. doi: 10.1193/1.1737737.

[34] Jalayer F., Cornell C.A. Direct probabilistic seismic analysis: implementing non-linear dynamic assessments. Stanford University, 2003.

[35] Baker J.W. (2015) Efficient analytical fragility function fitting using dynamic structural analysis. Earthquake Spectra, 31(1): 579–599. doi: 10.1193/021113EQS025M.

[36] SeismoSoft (2013) SeismoStruct – a computer program for static and dynamic nonlinear analysis of frames structures. Available at: http://www.seismosoft.com.

[37] Mander J.B., Priestley M.J.N., Park R. (1988) Theoretical stress-strain model for confined concrete. Journal of Structural Engineering, 114(8): 1804-1826.

[38] Menegotto M., Pinto P.E. (1973) Method of analysis for cyclically loaded reinforced concrete plane frames including changes in geometry and non-elastic behavior of elements under combined normal force and bending. Proceedings IABSE Symposium of Resistance and Ultimate Deformability of Structures Acted on by Well Defined Repeated Loads, International Association of Bridge and Structural Engineering, Lisbon, Portugal, Vol. 13: 15-22.

[39] Whittaker A., Deierlein G. G., Hooper J., Merovich A. (2004) Engineering demand parameters for structural framing systems. Task 2.2 report for the ATC-58 project, Applied Technology Council (available from www.ATCouncil.org), Redwood City, California.

[40] Ghobarah, A. (2004) On drift limits associated with different damage levels. International workshop on Performance based design: concepts and implementations, 28 June- 1 July 2004.

[41] Stocchi A., Richard B. (2019) Sensitivity of engineering demand parameters as a function of structural typology and assessment method. Nuclear Eng Des 343: 151-165. doi: 10.1016/j.nucengdes.2019.01.006.

[42] FEMA (2012) Earthquake Model, Hazus-MH 2.1 Technical Manual. Federal Emergency Management Agency, Washington DC, US (available at: www.fema.gov/plan/prevent/hazus).

COMPDYN 2019
7th ECCOMAS Thematic Conference on
Computational Methods in Structural Dynamics and Earthquake Engineering
M. Papadrakakis, M. Fragiadakis (eds.)
Crete, Greece, 24–26 June 2019

SHAKING TABLE TESTS ON POST-INSTALLED TRADITIONAL AND DISSIPATIVE FASTENERS IN UNCRACKED AND CRACKED CONCRETE

Jonathan Ciurlanti[1], **Simona Bianchi**[1], **and Stefano Pampanin**[1]

[1] Sapienza University of Rome
Department of Structural and Geotechnical Engineering, Via Eudossiana 18, 00184, Rome, Italy
jonathan.ciurlanti@uniroma1.it,
simona.bianchi@uniroma1.it, stefano.pampanin@uniroma1.it

Abstract

In consideration of the increased community expectations towards the reduction of post-earthquake damage to non-structural elements, even for strong seismic events, and in the context of performance-based design, this paper focuses on the experimental investigation of the seismic behavior of fasteners and practical implementation to improve their performance.
In the last decade several laboratory tests have been carried out to better understand the seismic behavior of anchors and a new concept of low-damage solution has been proposed. This earthquake-resistant fastener, referred to as EQ-Rod, relies upon the use of supplemental damping to reduce the acceleration demand and consequently the force applied to the non-structural component placed on the floors of multi-storey reinforced concrete buildings.
Building on this original research, the paper presents a second experimental campaign carried out at the Structural Laboratory of the University of Rome "La Sapienza" to extend the investigation and propose solutions to a larger variety of fastening systems (expansion and chemical anchors) and focusing on the behavior in both un-cracked and cracked concrete.
A comprehensive set of uniaxial shaking table tests have been performed using a specific apparatus and considering a test matrix with spectra compatible accelerograms.
The experimental tests provided satisfactory confirmation of the beneficial effects of the concept of dissipative anchor rod to seismically protect the non-structural components and suggestions are provided to further improve the system.

Keywords: Non-structural system, Post-installed fastener, Earthquake-Resistant Rod, Shake table tests, Seismic Performance.

1 INTRODUCTION

Non-structural components are typically connected to reinforced concrete buildings using post-installed fasteners, which are usually preferred by designers for their flexibility, easy handling and large field of possible applications compared to cast-in-place anchors.

In the research field, the study of the seismic behaviour of this type of anchors is spreading, with the aim of better understanding through experimental and numerical investigations both the seismic performance of anchors and the effect onto the attached non-structural system. Following the higher community expectations towards the reduction of post-earthquake damage, economic losses and downtime, mainly due to non-structural systems, the study and improvement of the seismic behavior of post-installed anchors/fasteners is becoming fundamental.

Over the past few decades, large amount of work has been carried out to study the behaviour of different types of individual or groups of post-installed anchors, subjected to quasi-static and dynamic forces or displacement-controlled loading protocols, either in uncracked or cracked concrete [1, 2, 3, 4, 5]. In recent years, the dynamic behaviour of post-installed fasteners has been also investigated through shake table tests, including tests performed using tri-axial shake table excitations [6], or uniaxial shaking table tests on anchors installed in regions where cracking of the structure is expected due to the seismically induced demands [7].

In the current context of performance-based seismic design and with the aim of improving fastening techniques, a comprehensive experimental and numerical campaign has been carried out at the University of Canterbury to develop a new generation of post-installed fasteners referred to as EQ-Rod, able to reduce the damage onto the non-structural component under severe seismic events [8]. This type of fastener relies upon the use of supplemental damping, either viscous and/or hysteretic, added in series or in parallel to a traditional fastener to reduce the acceleration demand and consequently the force applied to the non-structural component and represents a first generation of low-damage system for this type of component (Figure 1).

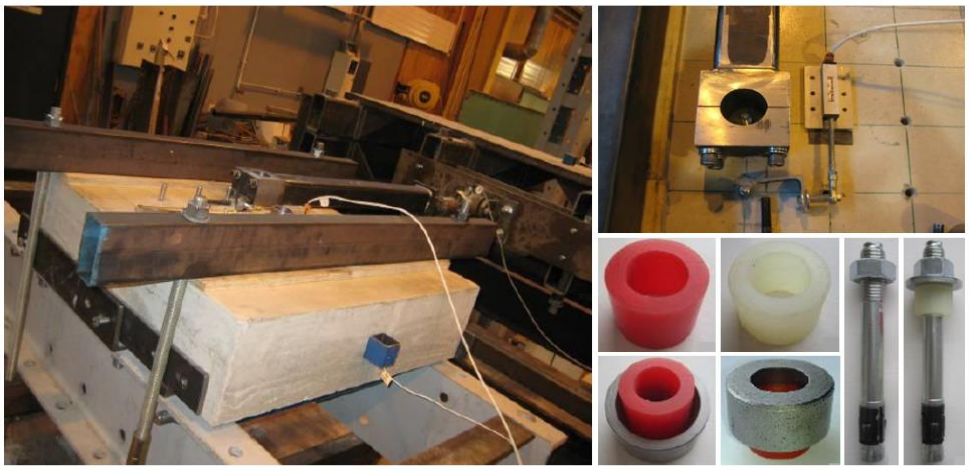

Figure 1: Shake-table test details on traditional and EQ-Rod fasteners (left and top-right) and configurations adopted for the supplemental damping devices (bottom-right) [8, 9].

Building on this original research, the paper presents the findings of a second experimental campaign carried out at the Structural Laboratory of the University of Rome “La Sapienza” with the aim of extending the previous investigation and propose solutions to a larger variety of fastening systems (traditional and low-damage expansion and chemical anchors), focusing on the behavior in both un-cracked and cracked concrete.

2 INNOVATIVE EARTHQUAKE-RESISTANT FASTENERS

Fasteners can be grouped in function of the way they transfer tension loads to the anchorage material [10]. Load-transfer mechanisms are typically identified as: 1) mechanical interlock, where the load is transferred by bearing the fastener onto the anchorage material; 2) friction, due to fasteners that have a geometry that generates an expansion force, which in turn produces a friction force between the anchor and the sides of the drilled hole; 3) bond, where the tension load is transferred to the anchorage material by a chemical interlock.

During an earthquake, a fastener may be subjected to tension, shear, combined tension-shear, and combined shear and bending cycling loading [10]. Referring to a non-structural component anchored to a reinforced concrete structure using a fastener, during the seismic motion the anchor loads develop due to the inertial response of the non-structural element to the acceleration of the building floor to which it is attached.

The seismic behaviour of the acceleration-sensitive non-structural component is typically described by floor acceleration response spectra, which provide the maximum associated acceleration as a function of the fundamental period of vibration of the element. The response spectra depend on the system viscous damping (non-structural component + connections), therefore by increasing the value of the damping the demands on the non-structural component can be reduced. Taking into account this concept and in order to achieve a significant reduction of the seismic demand and increase in performance, the idea of adding supplemental damping to the fasteners started to develop and a first innovative damage-resistant fastener was developed [8, 9], the so-called EQ-Rod fastener. An external supplemental damper is added to a traditional anchor, increasing the system damping, and this results in reducing the amplitude of the spectral response and the acceleration on the non-structural element under a given ground motion (Figure 2).

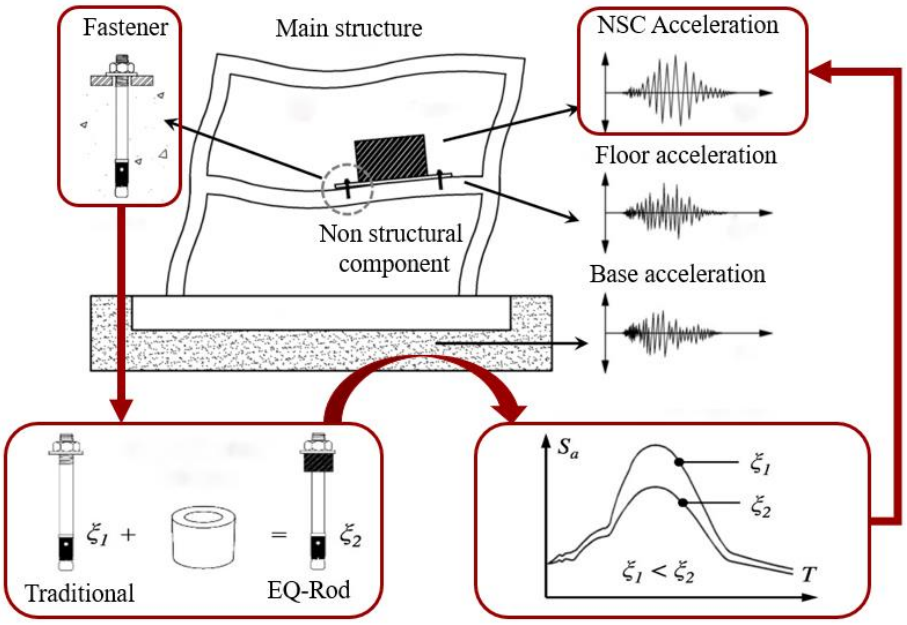

Figure 2: Effect of supplemental damping on fasteners in reducing the seismic demands of the attached non-structural component (modified after [8]).

3 RESEARCH MOTIVATION

Following on the first initial yet comprehensive experimental campaign on the EQ-Rod solution for post-installed fasteners, further investigations are needed to explore the beneficial

effects of the concept of dissipative anchor rod to seismically protect the non-structural components for a greater variety of fastening systems (expansion and chemical anchors) in both un-cracked and cracked concrete.

The shaking table tests carried in 2008 at the University of Canterbury focused on the response of expansion fasteners in uncracked concrete. As a follow-up it was considered important to extend the application of the low-damage solution to other types of anchors and system conditions. In fact, fasteners can be located in a crack that either forms during an earthquake or has formed at some prior time and the crack width can typically change over the duration of an earthquake, therefore investigations are also needed to apply the low-damage strategy in cracked concrete.

In such a context, a new low-damage prototype (EQ-Rod 2.0) has been proposed and a new Research and Development project has been carried out between the University of Rome "La Sapienza" (Research Leader), the University of Natural Resources and Life Sciences (Vienna, Austria), and Fischer (Fischerwerke Artur Fischer GmbH & Co. KG).

The paper describes the shaking table test setup, the testing protocol and the key results and findings of the experimental investigation carried out at Sapienza University

4 EXPERIMENTAL CAMPAIGN

Uniaxial shake table tests have been carried out at the Structural Engineering Laboratory of the University of Rome "La Sapienza" through a specific testing protocol capable of simulating the dynamic response of fasteners under seismic actions.

The experimental campaign involved different phases: 1) preparation of the ad-hoc test setup and monitoring system; 2) preliminary tests on different types of anchors to confirm the correct functioning of the whole testing apparatus, including fastener installation, loading protocol, control and acquisition system, post-processing of the results; 3) finally, further and comprehensive experimental tests have been performed according to a detailed test matrix on cracked and uncracked blocks.

Six different types of M12 anchors – i.e. two categories, expansion (FAZ II) and chemical (Superbond) anchors, in three configurations, traditional, EQ-Rod 2.0, traditional with mortar filling - have been tested under real recorded earthquake ground motions, through shear loads to the anchors, to investigate the anchor behaviour as well as the accelerations and displacements transferred to the attached non-structural component.

4.1 Test setup

The experimental Single-Degree of Freedom (SDOF) test setup comprises of three main parts: a concrete block representing the floor slab; a driving mass representing the attached non-structural element (NSE); the anchorage system. The shake table reproduces the selected input motion transmitted to the floor concrete block where the anchor rod is installed and connected through a lever arm to the driving mass, that is excited (Figure 3).

The 1.5m x 1.5m shake-table at the University of Rome "La Sapienza" is a uni-axial earthquake ground motion simulator (MOOG n. L081-324-011), consisting of guiding rails designed for a maximum stroke (travel) of ± 200 mm and a maximum payload capacity of 2 tons.

The concrete floor slab on which the anchor is installed is represented by a cracked or uncracked concrete block (80x80x30 cm, f_{ck}=20 MPa) rigidly attached to the shake table. Lateral sliding is prevented by steel angles fixed on the shake table in both directions.

A driving mass of 1046 kg, made by assembling steel plates, represents the non-structural mass attached to the anchor rod. The mass is located on low-friction linear rail guides (LLT of the SKF Group), fixed on an exterior steel frame, to allow the movement along the shaking

direction. These guides have precision-ground raceways and a carriage with four rows of balls in an X-arrangement, the dynamic coefficient of friction of the whole system is approximately μ_d=0.5% while the maximum acceleration guaranteed is 75 m/s^2.

A steel lever-arm connects the driving mass to the anchor and consists of L profiles of S355 steel seated to a steel plate where the load cell ends. The rigid lever arm spreads the inertia force from the driving mass to the fastener and the inertia force acts in the center of the attached element, therefore the vertical displacement of the anchor is not influenced by additional push and pull forces.

Finally, a steel plate with two different holes is located on the concrete block to install the fasteners. A larger hole, with a diameter of 24mm, is adopted for the EQ-Rod solutions, while the smaller one, with a diameter of 14mm, is adopted for the traditional anchors.

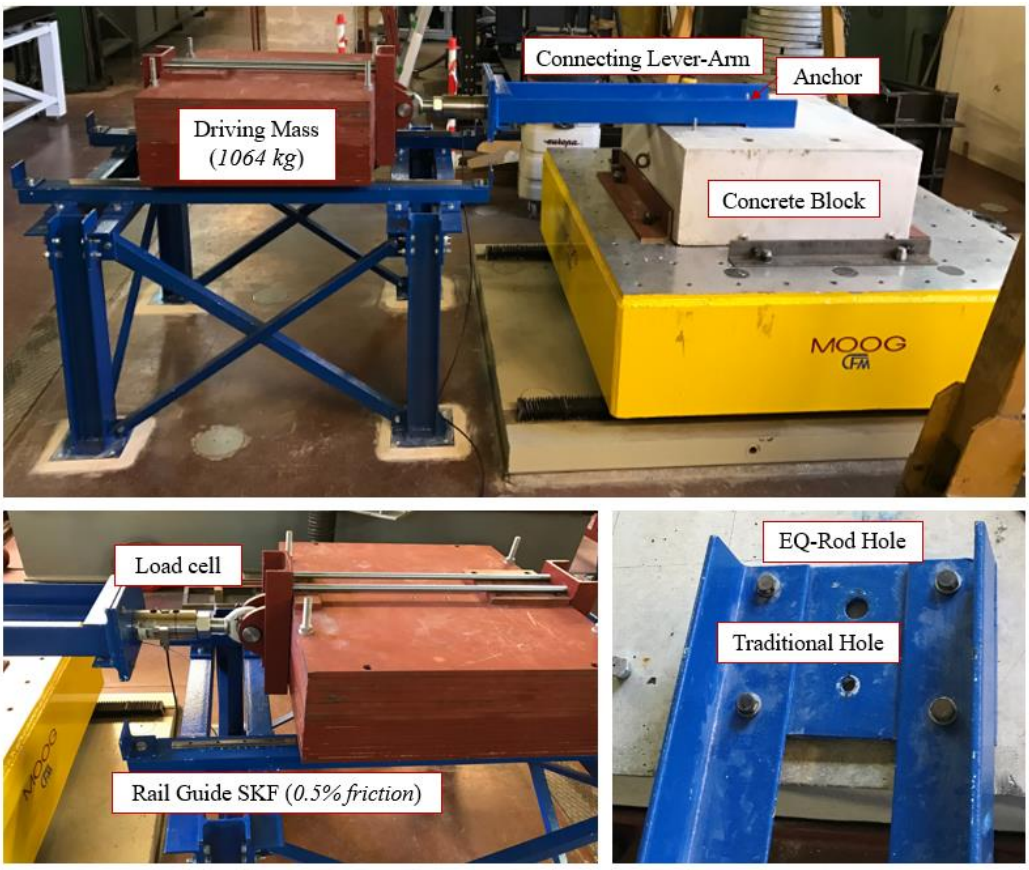

Figure 3: Details of shake-table test setup.

4.2 Test instrumentation

The load transferring to the anchor rod is measured by a load cell, with a maximum capacity of 200kN (tension and compression), installed between the driving mass and the steel lever-arm.

Three accelerometers attached to the driving mass, the concrete block and the shake table are used to monitor the system acceleration. The shake table acceleration is measured to compare the input record and the output signal of the table. The acceleration of the concrete block is needed to check that the connection between concrete block and shake table is effectively "rigid". The acceleration of the driving mass provides information on the effect of the fastener in the transfer of acceleration to the non-structural component.

Three LVDT transducers are used to measure the relative displacement between driving mass and concrete block. In particular, the vertical displacement of the anchor rod is monitored and the horizontal displacement of both the fastener and the steel plate is measured; the difference between these horizontal displacements provides information on the gap between steel plate and fastener.

4.3 Input motions

Different types of input signals have been considered for the experimental test campaign. Initially, sinusoidal inputs, either acceleration history with constant frequency and varying the amplitude (from 0.05 g to 0.5 g) or sweep signals with amplitude of 0.15g and 0.3g, a frequency range of 1-5Hz and a time-period of 10s, were considered to study the dynamic behaviour of the fasteners. Finally, the experimental tests were carried out using time-history earthquake inputs, selecting three Far Field and two Near Fault ground motions, properly scaled. The characteristics of the selected records can be found in Table 1, while the acceleration spectra of each record are shown in Figure 4.

Input name	Year	M_w	Record ID
Cape Mendocino	1992	7	EQ_1
Landers	1992	7.3	EQ_2
Friuli	1976	6	EQ_3
Kobe	1995	6.8	EQ_4
Christchurch	2011	6.3	EQ_5

Table 1: Main characteristics of the selected input earthquake records.

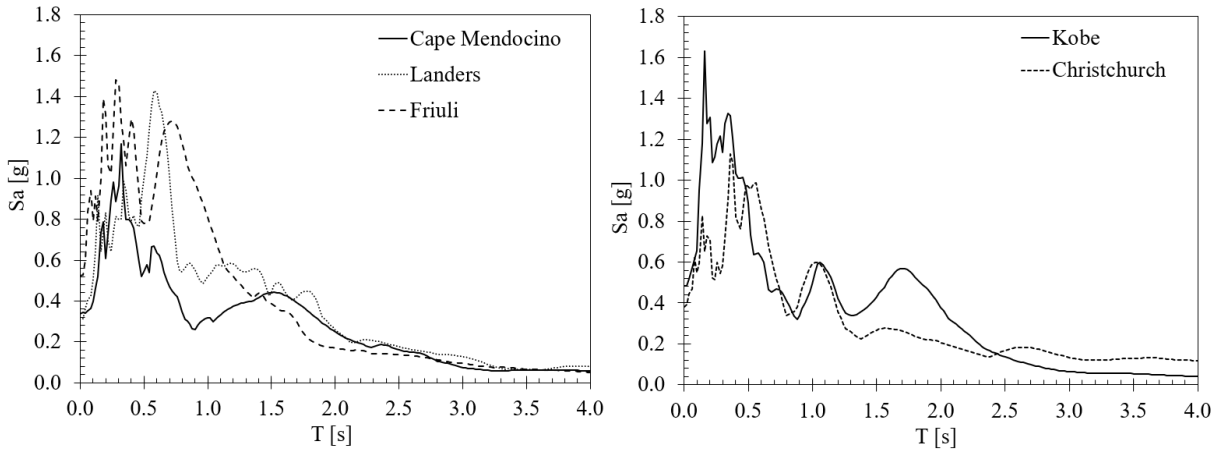

Figure 4: Acceleration response spectra for the Far Field (left) and Near Fault (right) input ground motions.

4.4 Testing protocol

The installation of anchors is a crucial phase for the experimental test. In fact, test results can be directly affected by the installation operation of the fasteners, therefore for each type of anchors the installation procedure has to be applied in a rigorous manner before performing the shaking table tests.

Each M12 fastener was installed into the concrete block following the procedure specified by the manufacturer. Regarding the concrete blocks, to study the seismic performance of anchor rods located along cracks parallel to the shaking direction, an appropriate apparatus was developed to generate these cracks (Figure 5): a bar with a sharp edge was positioned exactly

between two cotters inserted in the concrete block and the crack was opened by blowing onto both cotters on the left and on the right of the bar until the crack reaches 0.5 mm width.

Figure 5: Testing protocol for crack opening.

Therefore, the shaking table tests were performed following a specific test matrix that included three different expansion anchors (*FAZ II Traditional, FAZ II EQ-Rod and FAZ II Traditional with Mortar Filling*) and three different chemical anchors (*Superbond Traditional, Superbond EQ-Rod and Superbond Traditional with Mortar Filling*) anchored in uncracked and cracked concrete blocks. The configurations with mortar filling indicated the presence of mortar into the gap due to construction tolerances between steel plate and anchor.

Referring to the five input motions previously described and their simulated aftershocks (EQ_i-50), assumed as 50% of the input motion (amplitude-only reduction, same duration), for each type of expansion/chemical fastener the experimental test matrix in Table 2 was considered.

Test ID	Input motion	Type of fastener
1	EQ_1 + EQ_1-50	Traditional
2	EQ_1 + EQ_1-50	Traditional with Mortar Filling
3	EQ_1 + EQ_1-50	EQ-Rod
4	EQ_2 + EQ_2-50	Traditional
5	EQ_2 + EQ_2-50	Traditional with Mortar Filling
6	EQ_2 + EQ_2-50	EQ-Rod
7	EQ_3 + EQ_3-50	Traditional
8	EQ_3 + EQ_3-50	Traditional with Mortar Filling
9	EQ_3 + EQ_3-50	EQ-Rod
10	EQ_4 + EQ_4-50	Traditional
11	EQ_4 + EQ_4-50	Traditional with Mortar Filling
12	EQ_4 + EQ_4-50	EQ-Rod
13	EQ_5 + EQ_5-50	Traditional
14	EQ_5 + EQ_5-50	Traditional with Mortar Filling
15	EQ_5 + EQ_5-50	EQ-Rod

Table 2: Test matrix for the FAZII or Superbond type of fasteners.

The tests in Table 2 were performed three times on different anchors of the same typology to provide at least three responses for the same input motion and derive mean and standard deviation probabilistic results. In total, the test matrix of the experimental campaign consisted

of a total number of 360 shake table tests (input + aftershocks), 180 for uncracked concrete and 180 for cracked concrete.

5 EXPERIMENTAL RESULTS

The acceleration of the driving mass representing the non-structural system and the hysteretic behaviour (force-displacement relationship) of the fastener anchored in the concrete block fixed to the shake table have been determined from the experimental tests.

This paper presents only some of the main findings and discussions related to the obtained experimental tests on all the anchor types (Figure 6), while a more complete description of all the experimental data can be found in the Research Project report [11].

The efficacy of EQ-Rod prototypes in improving the seismic response of the system is determined as the capacity of reducing the acceleration demand onto the connected non-structural component (driving mass) when compared to the demand related to the application of traditional (expansion or chemical) fasteners.

Concerning the data processing, it is observed that the data obtained with the high-speed logger connected to the shake table was filtered using a low pass (6th order Butterworth filter) with a cut off frequency of 20Hz to reduce external noise.

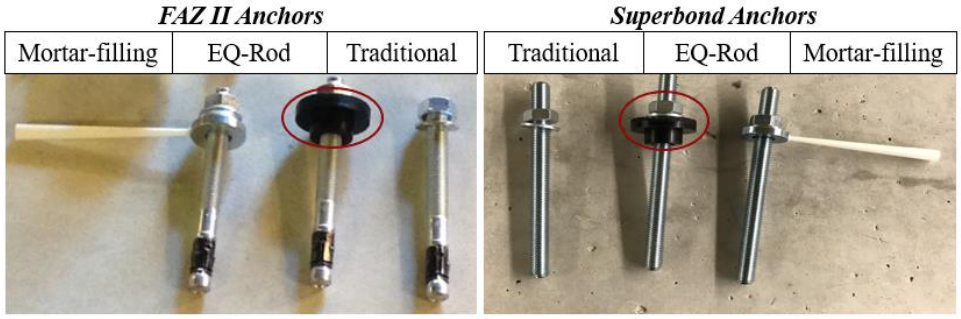

Figure 6: FAZ II and Superbond anchors.

5.1 Sinusoidal input test results

The preliminary experimental results from the sinusoidal input tests on uncracked concrete blocks are initially presented in terms of hysteretic loops for both Traditional anchor and EQ-Rod 2.0 considering either FAZ II or Superbond configurations (Figure 7).

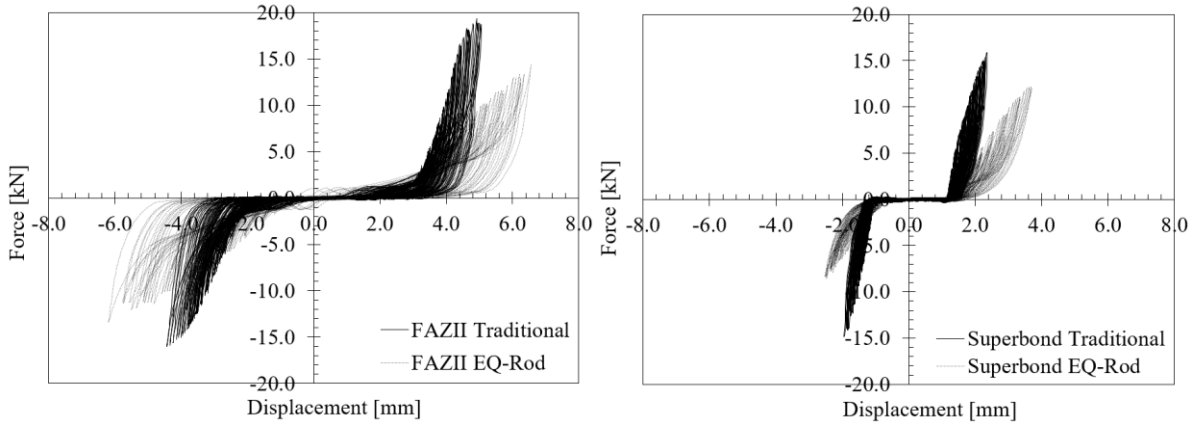

Figure 7: Comparison between FAZ II Traditional and FAZ II EQ-Rod (left) and Superbond Traditional and Superbond EQ-Rod (right) in terms of Hysteretic Loop for uncracked concrete.

The installation of each anchor followed the testing protocol, with the only difference that the application of the torque was reduced to 0 Nm - instead of 30Nm or 20 Nm - in order to simulate the complete loss of tightening torque due to long period.

Analyzing the maximum force values determined on the non-structural system, the results showed a reduction in the range of 15-25% for the EQ-Rod solution when compared to the FAZII traditional one, and 20-35% for EQ-Rod system when compared to the Superbond traditional anchor. These results were associated to the large hysteretic energy of the EQ-Rod system, thus to the greater displacements that it reached during most of the cycles.

5.2 Ground motion input test results

In accordance to the proposed test matrix, the shake table tests were carried out for all the proposed configurations in uncracked and cracked concrete. Test results in terms of force/displacement curves of the driving mass are shown for just one test of an input record (EQ_1) for all the three types of expansion anchors (Figure 8) and chemical anchors (Figure 9).

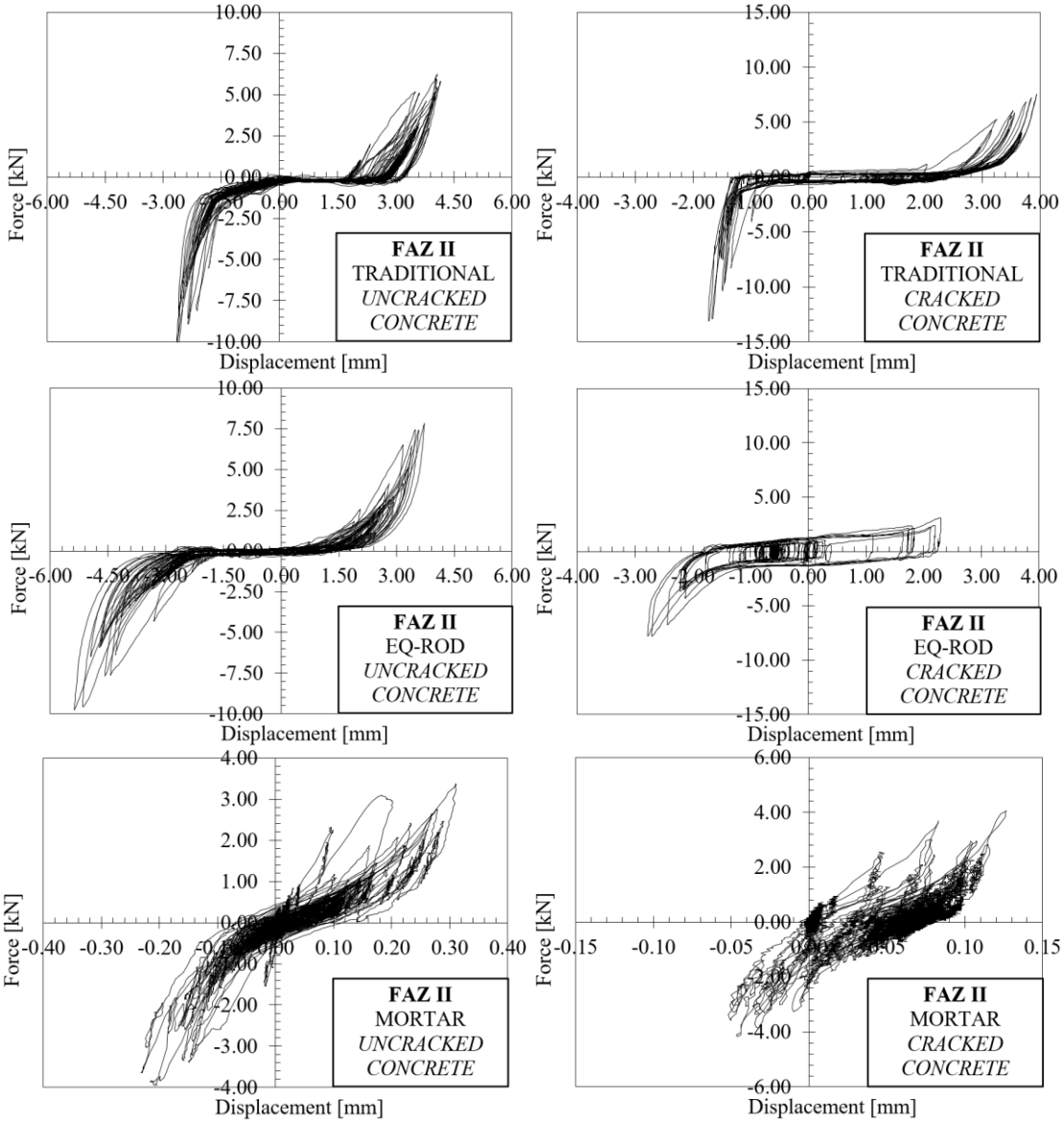

Figure 8: Force-displacement relationships for the FAZII Traditional, FAZII EQ-Rod, FAZII Traditional with Mortar Filling in uncracked and cracked concrete.

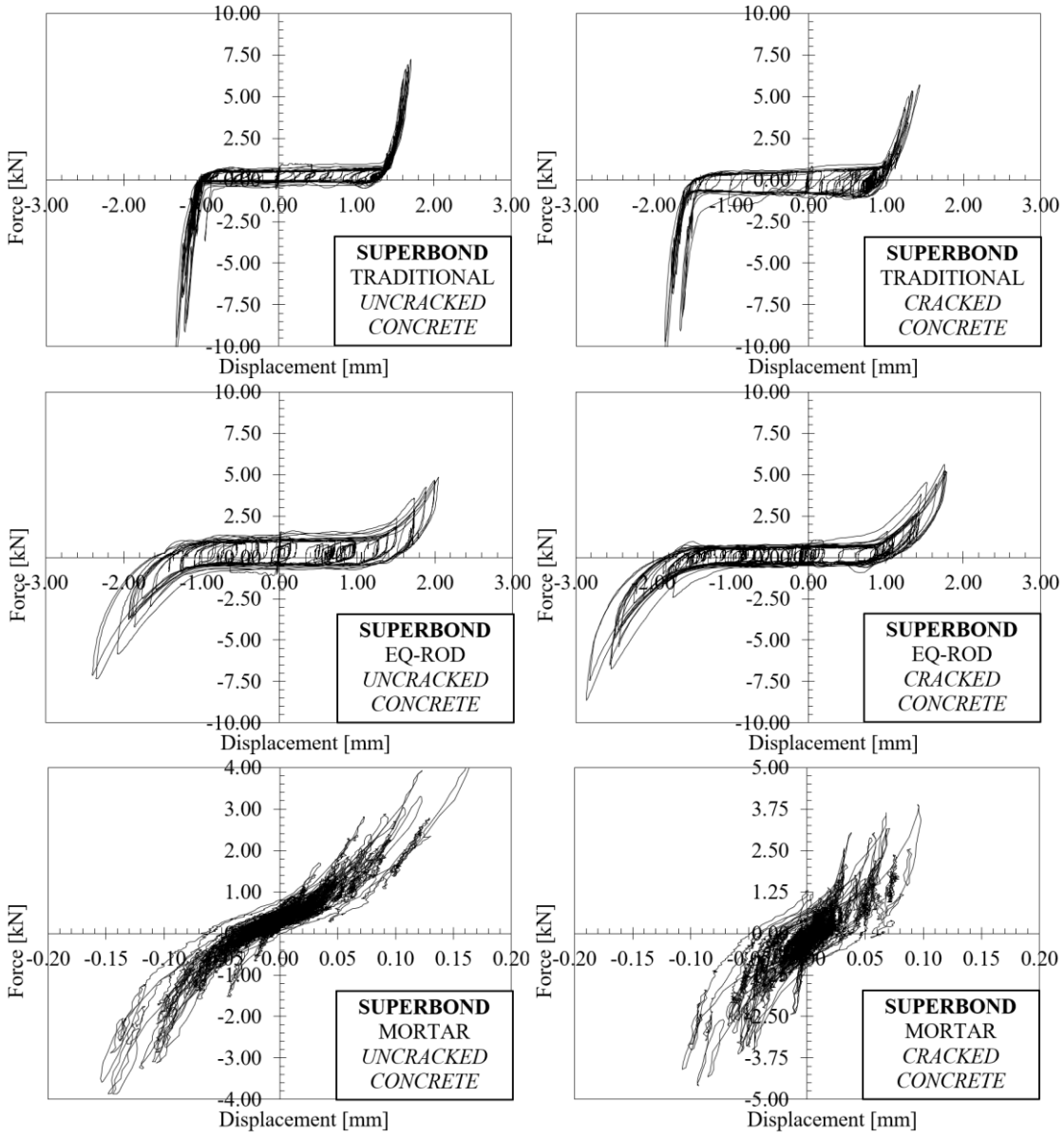

Figure 9: Force-displacement relationships for the Superbond Traditional, Superbond EQ-Rod, Superbond with Mortar Filling in uncracked and cracked concrete.

The experimental tests provided the following main results: 1) for the expansion anchors in uncracked concrete, the EQ-Rod system can provide a reduction in terms of driving mass forces and accelerations in the range of 10-15% for the input signals and of 15-30% for the aftershocks; 2) for the expansion anchors in cracked concrete the EQ-Rod reduction in terms of driving mass forces is in the range of 20-30%, while in terms of accelerations in the range of 25-40% for the input signals and 30-40% for both accelerations and forces considering the aftershocks; 3) for chemical anchors in uncracked concrete the EQ-Rod reduction is 10-25% in terms of forces and 20-30% in terms of accelerations when considering the input signals, while 30-40% for both demands when considering the aftershocks; 4) finally, for chemical anchors in cracked concrete, the EQ-Rod solution provided a reduction in terms of driving mass forces and accelerations in the range of 20-30% for the input signals and of 30-40% for the aftershocks.

The performance and benefits of EQ-Rod in cracked concrete appears in general superior to that in uncracked concrete. It should be noted that, in addition to the inherent isolation-dissipation mechanism, EQ-Rod anchor reaches larger displacements in cracked concrete and the overall system has thus lower frequencies (higher period) and attracts less forces as it moves towards the de-amplification part of the spectra.

Notwithstanding the efficiency of the proposed EQ-Rod configuration, test results also showed that a significant benefit in terms of response can be obtained by applying mortar filling, with a reduction of 40-60% for all the analyzed configurations in uncracked and cracked concrete. This high reduction is due to the lack of dynamic impact (pounding) due to the presence of gaps between steel plate/anchor and concrete/anchor. The anchor with mortar filling thus acts as a more rigid element, while EQ-Rod allows for a combination of isolation and dissipation. It appears that a combination of the two concepts (filling the gap and adding a tight-fit EQ-Rod dissipative system) would be able to provide the best and most reliable benefits.

6 CONCLUSIONS

With the aim of improving the seismic response of non-structural systems anchored to concrete structures a post-installed fastener with supplemental damping has been experimentally proposed and studied. The first prototype of this solution, referred to as EQ-Rod, was developed in 2008, while a new system, named EQ-Rod 2.0, is herein considered, conceived as an easily applicable solution useful for either expansion or chemical fasteners. The seismic performance of this system has been deeply studied through uni-directional shake table tests using specific testing protocols for both uncracked and cracked concrete.

Worth noting that due to the larger geometric tolerances between the EQ-rod and fastener rod (inner tolerance/gap) as well as due to the different material of the new EQ-Rod when compared to the initial prototype, during the tests the bearing stresses on the rubber material led sometimes to the yielding of the rubber damper with permanent deformations and amplifications of the dynamic effects and this in turns reduced the efficiency of the EQ-Rod system as a damping element under cumulative aftershocks.

However, the experimental results confirmed that the concept of adding damping to a fastener can be adopted to improve the seismic performance of the system, reducing both accelerations and forces onto the connected non-structural component. The proposed system can thus be considered as a damage-control solution for such applications.

The shake table test results provided evidence of the efficiency of the dissipative solution, yet further improvements of the system design are needed and recommended to fully exploit the novelty of the dissipative/isolation mechanism of the EQ-Rod and obtain a greater and robust reduction of the driving mass accelerations when compared to the traditional anchor (with or without mortar filling).

7 ACKNOWLEDGEMENTS

The research project has been funded by Fischerwerke Artur Fischer GmbH & Co. KG, whose support is gratefully acknowledged. Acknowledgements are also provided to Dr.-Ing. Quintana-Gallo for his technical support, particularly during the initial phases, based on his personal experimental test experience on EQ-Rod at the University of Canterbury. Special thanks go also to Dr.-Ing. Andreas Pürgstaller, supervised by Prof. Konrad Bergemeister, from the University of Natural Resources and Life Sciences Vienna, Austria for developing FEM analysis and initial quasi-static tests on the anchor prototype.

8 REFERENCES

[1] R. Eligehausen, Behavior, design and testing of anchors in cracked concrete. *ACI Structural Journal*, **130**, S123-175, 1991.

[2] R. Eligehausen and T. Balogh, Behavior of fasteners loaded in tension in cracked reinforced concrete. *ACI Structural Journal*, **92**, S35, 1995.

[3] P. Mahrenholtz and R. Eligehausen, Behavior of anchor groups installed in cracked concrete under simulated seismic actions. *Fracture Mechanics of Concrete and Concrete Structures - Assessment, Durability, Monitoring and Retrofitting of Concrete Structures*, B. H. Oh, et al. (eds), Korea Concrete Institute, Seoul, 2010.

[4] M. S. Hoehler, P. Mahrenholtz, R. Eligehausen, Behavior of Anchors in Concrete at Seismic-Relevant Loading Rates. *ACI Structural Journal*, **108**, 2, 238-247, 2011.

[5] E. Vintzéleou, and R. Eligehausen, Behaviour of Fasteners under Monotonic or Cyclic Shear Displacements, Anchors in Concrete – Design and Behavior. *ACI Special Publication*, SP 130-7, 181-204, 2012.

[6] A. Rieder, Seismic Response of Post-Installed Anchors in Concrete. *PhD Dissertation*, University of Natural Resources and Life Sciences, Vienna, Austria, 2009.

[7] P. Mahrenholtz, T.C. Hutchinson, and R. Eligehausen, Shake Table Tests on Suspended Nonstructural Components in Cyclically Cracked Concrete, *Journal of Structural Engineering*, **140**, 11, 2014.

[8] P. Quintana-Gallo, M. Moghaddasi, S. Pampanin, and K. Bergmeister, Shake table tests of post-installed fasteners in concrete with supplemental damping. ACI Structural Journal, **115**, 3, 595-606, 2018.

[9] S. Pampanin, M. Moghaddasi, P. Quintana-Gallo, A. Rieder, EQ-Rod a New Generation of Earthquake-Resistant Fasteners. *Report prepared for Fischerwerke Artur Fischer GmbH & Co. KG*, University of Canterbury, Christchurch, New Zealand, 2008.

[10] R. Eligehausen, R. Mallée, J.F. Silva, *Anchorage in Concrete Construction*, 1st Edition, Ernest and Sohn Publisher, Berlin, Germany, 2006.

[11] S. Pampanin, S. Bianchi, J. Ciurlanti, Shake table tests of post-installed anchors with supplemental damping (EQ-Rod 2.0). *Report prepared for Fischerwerke Artur Fischer GmbH & Co. KG*, Sapienza University of Rome, Rome, Italy, 2017.

COMPDYN 2019
7th ECCOMAS Thematic Conference on
Computational Methods in Structural Dynamics and Earthquake Engineering
M. Papadrakakis, M. Fragiadakis (eds.)
Crete, Greece, 24–26 June 2019

MODIFICATION OF FORCE BASED FIBER BEAM COLUMN ELEMENT FORMULATION TO CATER HIGHLY LOCALIZED NONLINEAR BEHAVIOR

Sameera S. Hippola[1], Chatura M. Rajapakse[2], Kushan K. Wijesundara[1] and Ranjith Dissanayake[1]

[1] Department of Civil Engineering,
University of Peradeniya,
Peradeniya, Sri Lanka
e-mail: samhipo@gmail.com, chaturarajapakse@gmail.com, kushanw@pdn.ac.lk,
ranjith@fulbrightmail.org

Abstract

Nonlinear static analysis of reinforced concrete frame structures is useful in pushover analyses for structural capacity computation. A popular method for nonlinear static analysis is by modelling with force-based fiber beam column elements, where equilibrium, compatibility and constitutive relationship are satisfied at structure level, element level and fiber level respectively. The existing formulation of the fiber beam column element consists of an iterative procedure at the element level to satisfy element compatibility, where the residual deformations of the sections are integrated to find the element residual deformation. Then the corrective force corresponding to element residual deformation is applied globally at the element level which is in turn distributed to the section level according to force interpolation functions. However, the existing formulation does not evaluate section level equilibrium directly where the section forces and deformations are calculated by minimizing element level residual deformations. This paper proposes a modification to this existing formulation by transferring equilibrium satisfaction to the section level. This modification allows the minimization of section unbalanced forces at the section level itself, rather than transferring unbalanced forces of the sections displaying high nonlinearity, to element level. This equilibrium satisfaction is done by adjusting the section deformation through an iterative procedure which yields the correct section stiffness and deformation for the corresponding section force increment. Section stiffness can be assembled to find corresponding structure stiffness which can be used to calculate structure resisting force. At structure level, the Newton Raphson iterative procedure is identical to that of the existing formulation. The study focuses on the reinforced concrete frame elements with only material nonlinearity where plane sections remain plane and normal to the longitudinal axis. Furthermore effects of bond slip and shear were not considered in this study. The proposed formulation was experimentally validated and was proved to be well suited to predict the nonlinear static response of rein-forced concrete structures exhibiting highly localized nonlinear behavior.

Keywords: RC frames, nonlinear static analysis, force based fiber beam column element

1 INTRODUCTION

Reinforced concrete structures exposed to severe earthquakes and winds can cause massive destruction of lives and property. Therefore accurate numerical simulation of reinforced concrete structures using nonlinear analysis is vital. The existing nonlinear analysis methods can be categorized in to three groups namely, lumped plasticity method, distributed plasticity method and modelling with three dimensional solid elements. In lumped plasticity method, plasticity is monitored at predetermined locations where nonlinear behavior is expected. This method requires expert knowledge to identify intended plastic hinges. Modelling with three dimensional solid elements can yield an accurate prediction but unfortunately that accuracy comes with a huge computational cost. The best compromise between accuracy of prediction and cost of computation is the line element with distributed plasticity, where plasticity is monitored at several integration points along the element. The line element with distributed plasticity can be modelled using either force based or displacement based finite element approaches. The displacement based finite element formulation is based on satisfying compatibility and constitutive relationship in strong form while satisfying equilibrium in weak form. In addition to that, the relationship between element nodal deformations and section deformations needs to be assumed. Therefore displacement based formulation requires discretization of frame elements, in the cases of material nonlinearity and/ or tapered sections which is computationally expensive. However, force based formulation do not require such refinement as the force interpolation functions which defines the relationship between nodal forces and section forces is exactly known. It is important to note that in force based formulation there are no additional assumptions except compatibility satisfaction in weak form. Accordingly researchers are inclined to use force based finite element formulation to model line elements with distributed plasticity. Reference [2] introduced a force based fiber element which was later improved in [9]. The main problem at that time was determining the element resisting forces corresponding to a given element nodal deformation. Reference [1] introduced an iterative procedure at element level to minimize element residual deformations to obtain element resisting forces corresponding to a given element nodal deformation. Later, [7] improved the method of stated in [1] which resulted in the force based fiber beam column element. This element is capable to predict the axial force – bending moment interaction of reinforced concrete structures and is widely used by structural Engineers [4]. The existing fiber beam column element formulation has two main nested iterative procedures at structure level and element level. When satisfying compatibility at element level, the residual deformation of the element is calculated using section residual deformations. Then the corrective force corresponding to element residual deformation is applied at the element level and is subsequently distributed to the section level according to force interpolation functions. However, if the nonlinear behavior is concentrated to a certain section, the corrective force applied at element level may fail to directly address the section which exhibits highly nonlinear behavior. Therefore in such cases satisfaction of element level compatibility becomes problematic. The novel formulation is proposed with the idea of correcting the section unbalanced forces at the section level itself rather than correcting integrated section residual deformations at element level. In the novel formulation, an iterative procedure is introduced at the section level to minimize section unbalanced forces and achieve section level equilibrium at the section level itself.

2 MODEL ASSUMPTIONS

The proposed formulation focuses on planar reinforced concrete structures which exhibit material nonlinearity. The present study do not account the effects of geometric nonlinearity.

The novel formulation is based on force based line element which has two nodes, each having three degrees of freedoms. Figure 1 illustrates the nodal forces and deformations of the force based frame element referring global (X, Y) coordinate system.

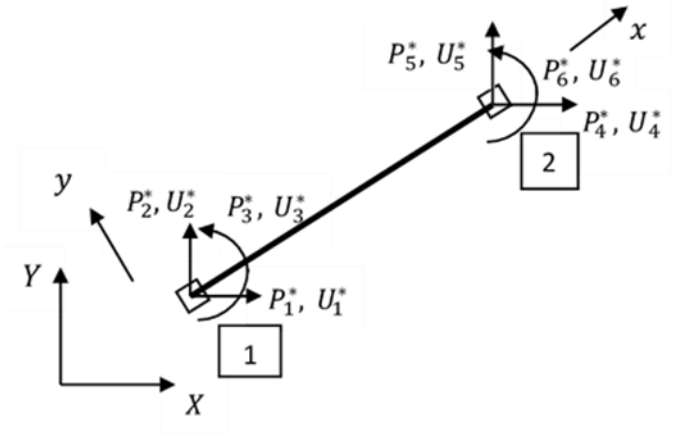

Figure 1: Nodal forces and deformations of the force based frame element referring global (X, Y) coordinate system

The element force vector and the deformation vector can be written as $\{P_1^* \; P_2^* \; P_3^* \; P_4^* \; P_5^* \; P_6^*\}^T$ and $\{U_1^* \; U_2^* \; U_3^* \; U_4^* \; U_5^* \; U_6^*\}^T$ respectively.

The frame element shown in Figure 1 has a singular stiffness matrix. Thus, the nodal forces, deformations and element stiffness are expressed referring local coordinate system (x, y) and the rigid body modes are removed to achieve a nonsingular stiffness matrix. This resulting basic system is illustrated in Figure 2 referring (x, y) local coordinate system.

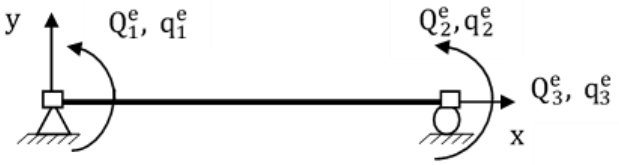

Figure 2: Nodal forces and deformations of the basic system referring local coordinate system (x, y)

Hereafter in this paper, the element force and deformation vectors refer to the force and deformations vectors of the basic system. Accordingly, the element force and deformation vectors can be written as $\{Q_1^e \; Q_2^e \; Q_3^e\}^T$ and $\{q_1^e \; q_2^e \; q_3^e\}^T$ respectively.

The element proposed, is a line element with distributed plasticity where the nonlinearity is monitored at selected number of gauss integration points. Each section at control stations are sufficiently divided in to several number of fibers where uniaxial material models are assigned to each fiber. The control stations and division of a section into fibers is illustrated in Figure 3.

The proposed formulation is based on the assumption that plane section remains plane and perpendicular to the longitudinal axis. This assumption allows to use a uniaxial material model for the relationship between fiber strain (ε_{fib}) and fiber stress (σ_{fib}). Accordingly, the section force vector can be written in terms of axial force ($N(x)$) and bending moment ($M(x)$) while section deformation vector can be written in terms of section curvature ($\kappa(x)$) and axial

strain of the centroid axis (ε_0) as illustrated in Figure 4. Section force and deformation vectors can be written as $\begin{pmatrix} N(x) \\ M(x) \end{pmatrix}$ and $\begin{pmatrix} \varepsilon 0 \\ \kappa(x) \end{pmatrix}$ respectively.

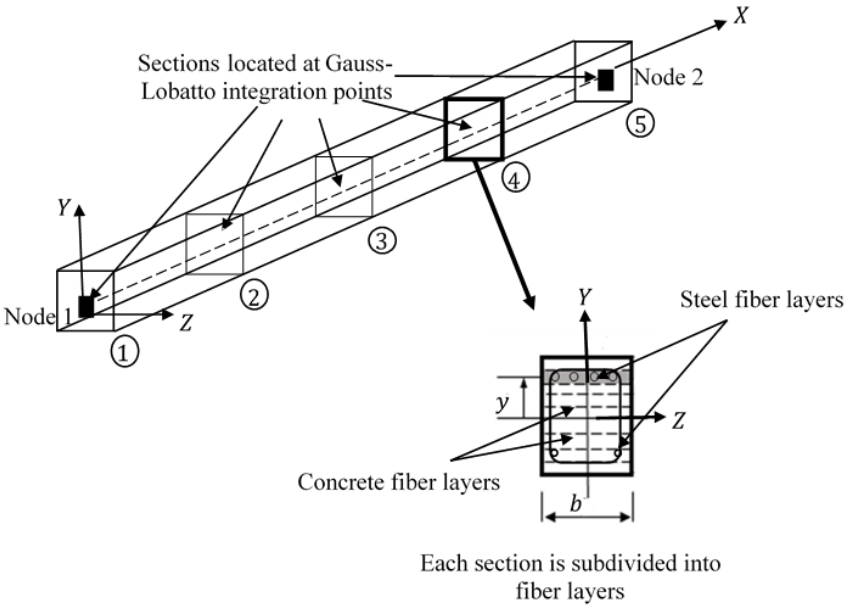

Figure 3: The integration points and division of a section into fibers of the force based frame element without rigid body modes

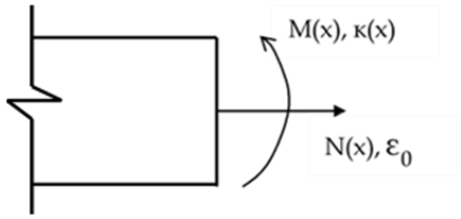

Figure 4: Section forces and deformations at a control station.

In addition, effect of bond slip and shear was not accounted in this study.

3 PROPOSED FORMULATION

The formulation is based on four hierarchical levels namely, structure level, element level, section level and fiber level where, the law of equilibrium is satisfied at both structure level and section level while constitutive relationship is fed at the fiber level. However, the compatibility of the structure is satisfied indirectly by the computation of the correct section deformation and section stiffness for a given section force increment by entertaining an iterative procedure at section level. In order to facilitate the satisfaction of equilibrium at structure and section levels, two nested iterative procedures are adapted at structure level and section level. It is important to note that there is no iterative procedure at element level as in the existing fiber beam column formulation.

The formulation was written utilizing the displacement control method of structure state determination where, displacement is applied to a specific degree of freedom using a series of steps. At each displacement step, the structure force and deformation increments are calculated by following the aforementioned iterative procedures. Once the calculation of structure

force and deformation vectors are completed for a series of steps, the load – deformation response of the reinforced concrete structure can be generated.

The computations at structure level are performed after applying boundary conditions and rearranging vectors and matrices by shifting the rows and columns representing displacement controlling degree of freedom to the end. Here, P2 and U2 represent the force and displacement at displacement controlling degree of freedom while F1 and U1 represent the forces and deformations of other degrees of freedom excluding the restrained ones. The structure stiffness matrix is condensed accordingly for the computations. O and R represent unbalanced forces and resisting forces while i represent the structure level iteration number.

At the start of a step, a displacement is applied on a certain degree of freedom. Based on this displacement increment, an initial estimate of structure force and deformation increment is computed linearizing around the structure stiffness matrix of the previous iteration as shown in (1).

$$\Delta\lambda^{i=1}\begin{Bmatrix}P_1\\P_2\end{Bmatrix}=\begin{bmatrix}K_{11} & K_{12}\\K_{21} & K_{22}\end{bmatrix}_{i=0}\begin{Bmatrix}\Delta U_1\\\Delta U_2\end{Bmatrix}^{i=1} \tag{1}$$

In the next stage, structure resisting force corresponding to the deformation increment estimate needs to be calculated as shown in (2).

$$\begin{Bmatrix}R_1\\R_2\end{Bmatrix}^{i=1}=\begin{bmatrix}K_{11} & K_{12}\\K_{21} & K_{22}\end{bmatrix}_{i=1}\Delta\begin{Bmatrix}U_1\\U_2\end{Bmatrix}^{i=1} \tag{2}$$

For this purpose, the updated structure stiffness matrix corresponding to the estimated structure force increment is computed using an iterative procedure at section level. Here, the correct section deformation and updated section stiffness matrix is generated corresponding to a section force increment by minimizing the force difference between section force and section resisting force.

Once the structure resisting force corresponding to the estimated displacement increment is computed, the difference between the estimated structure force and resisting force is evaluated using (3).

$$\begin{Bmatrix}O_1\\O_2\end{Bmatrix}^{i=1}=\Delta\lambda^{i=1}\begin{Bmatrix}P_1\\P_2\end{Bmatrix}-\begin{Bmatrix}R_1\\R_2\end{Bmatrix}^{i=1} \tag{3}$$

If the unbalanced force is significant, a corrective force and deformation vectors are calculated linearizing around the freshly calculated structure stiffness matrix as demonstrated in (4).

$$\begin{Bmatrix}\Delta U_1\\\Delta U_2\end{Bmatrix}^{i=2}=\begin{bmatrix}K_{11} & K_{12}\\K_{21} & K_{22}\end{bmatrix}_{i=1}^{-1}\begin{Bmatrix}O_1\\O_2\end{Bmatrix}^{i=1}+\begin{bmatrix}K_{11} & K_{12}\\K_{21} & K_{22}\end{bmatrix}_{i=1}^{-1}\Delta\lambda^{i=2}\begin{Bmatrix}P_1\\P_2\end{Bmatrix} \tag{4}$$

In the next phase, the structure stiffness matrix will be updated again for the calculated displacement correction, by delving to element, section and fiber levels and completing the section state determination process. Subsequently, structure resisting force corresponding to the structure deformation correction is computed as before. Then, structure force and resisting force is evaluated again. These nested iterative procedures are continued until structure unbalanced force comes under a prescribed tolerance value. This process will produce a correct structure force and displacement increment, corresponding to the applied displacement step.

Once this process is repeated for a series of displacement steps, the behavior of the structure can be predicted.

4 EXPERIMENTAL VALIDATION

4.1 Flexural cantilever wall

The experimental validation of the proposed novel formulation was done with the reinforced concrete cantilever wall RW2, experimented in [8] which was designed to behave in flexure mode. Figure 5 and Table 1 depicts the loading arrangement and details of the reinforced cantilever wall RW2. Figure 6 illustrates the cross section with reinforcement arrangement.

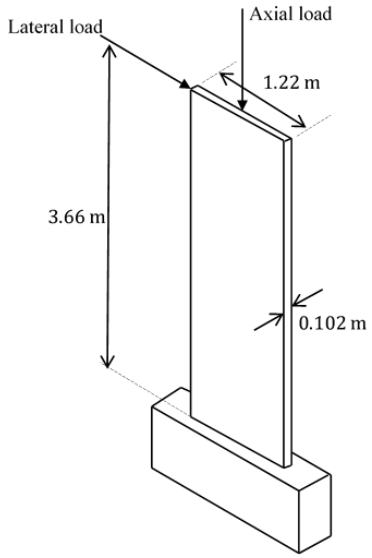

Figure 5: Loading arrangement and dimensions of RW2

Height (mm)	3660
Outer perimeter depth x width (mm x mm)	1220 x 102
Aspect ratio	3
Compressive axial load (kN)	240.41
Cube strength (MPa)	42.8
Yield strength of longitudinal reinforcement (MPa)	414

Table 1: Information about RW2

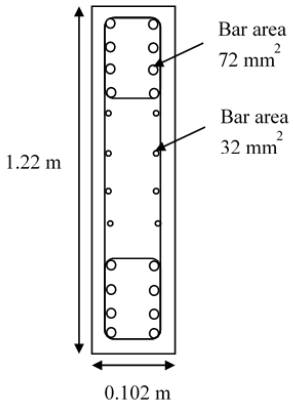

Figure 6: Details of the cross section

Input Parameter	Novel formulation	OpenSees model
Number of elements	1	1
Number of integration points	6	6
Number of fibers	20	20
Section level force tolerance (kN or kNm)	10^{-10}	-
Element level residual deformation tolerance (m)	-	10^{-20}
Structure level force tolerance (kN or kNm)	10^{-10}	10^{-10}

Table 2: Input parameters for numerical models

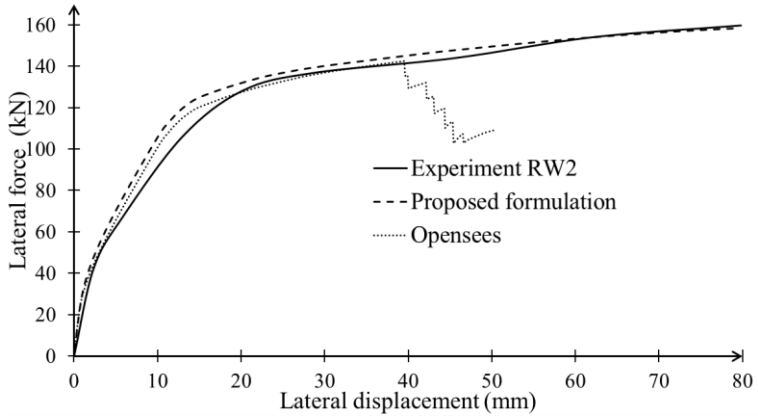

Figure 7: Load deformation responses of the RW2 cantilever wall obtained experimentally, using novel formulation and using OpenSees software

It is evident from Figure 7 that the prediction made by the proposed formulation is very close to the prediction made by experiment and OpenSees. The proposed novel formulation has been able to capture the tensile concrete cracking behavior, tensile steel yielding behavior and the ductility of the reinforced concrete wall.

In the load – deformation response predicted by the novel formulation, the initial slope is approximately constant until the tensile concrete fibers starts to crack around 13 kN load. Due to further cracking of concrete tensile fibers, a considerable drop of slope can be seen around 30 kN load. Due to this concrete tensile fiber cracking, the centroid axis shifts towards the compression zone. With the application of further displacement increments, cracking of concrete tensile fibers reaches a saturated level resulting a constant slope until tensile steel starts to

yield at 98 kN. The drop of tangent stiffness of the concrete constitutive model is reflected by the gradual reduction of slope in the load – deformation response. After yielding of tensile reinforcement, the stiffness of the beam drops to a very lower value and the strength remains approximately constant producing a larger ductility as shown in Figure 7. The comparison shown in Figure 7 also depicts that these nonlinear behaviors can be captured by the proposed novel formulation. Figures 8, 9, 10, 11, 12, 13, 14, 15 present the stress and strain distributions generated by the novel formulation, at different regions of the load - deformation curve. The section numbers referred in the figures correspond to the integration points shown in Figure 3.

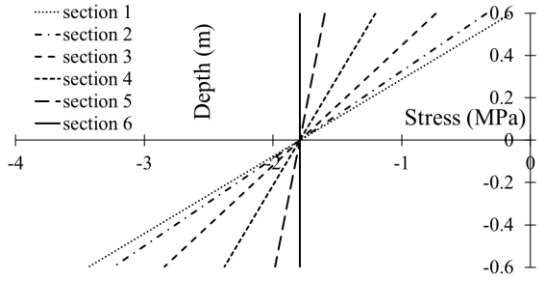

Figure 8: Stress distribution of the critical section at the end of 10 kN load

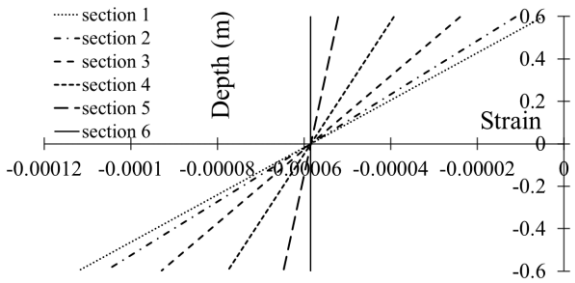

Figure 9: Strain distribution of the critical section at the end of 10 kN load

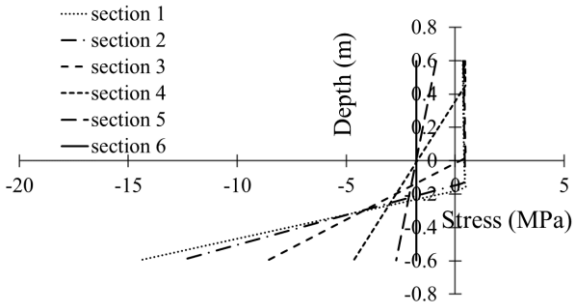

Figure 10: Stress distribution of the critical section at the end of 63 kN load

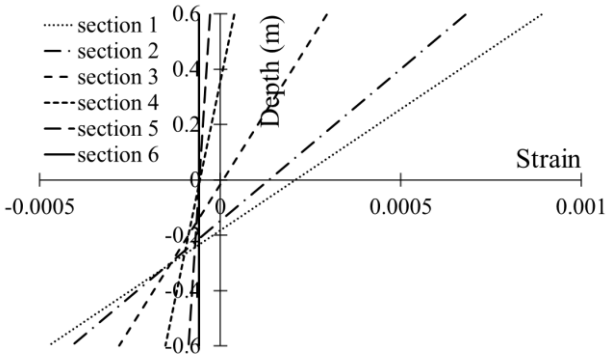

Figure 11: Strain distribution of the critical section at the end of 63 kN load

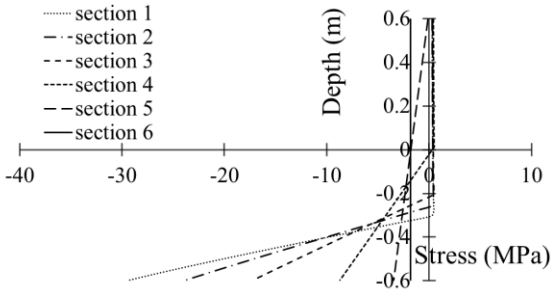

Figure 12: Stress distribution of the critical section at the end of 115 kN load

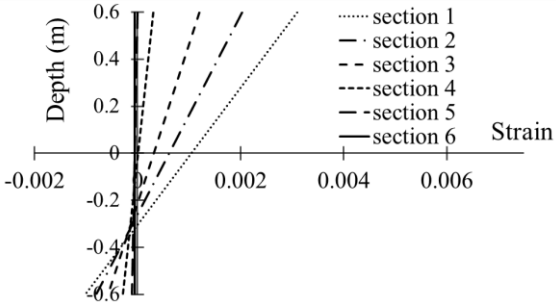

Figure 13: Strain distribution of the critical section at the end of 115 kN load

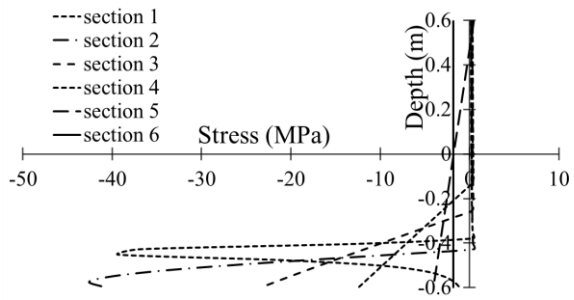

Figure 14: Stress distribution of the critical section at the end of 154 kN load

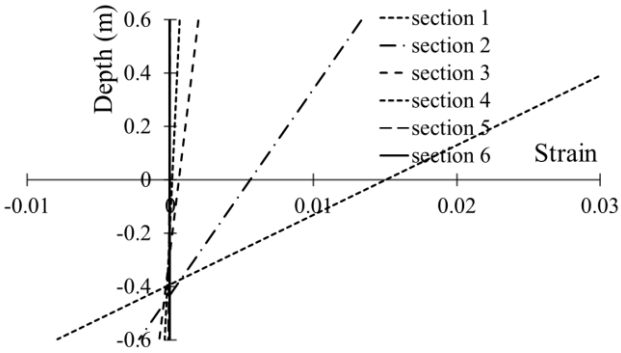

Figure 15: Strain distribution of the critical section at the end of 154 kN load

4.2 Shear dominant cantilever wall

The load-deformation response of a shear dominant reinforced cantilever wall (SW21), experiment by Lefas [3], was compared with that of numerical prediction from the proposed novel formulation. The loading arrangement, dimensions and reinforcement details of the cantilever wall are given in Figure 16. Table 3 lists out the physical parameters.

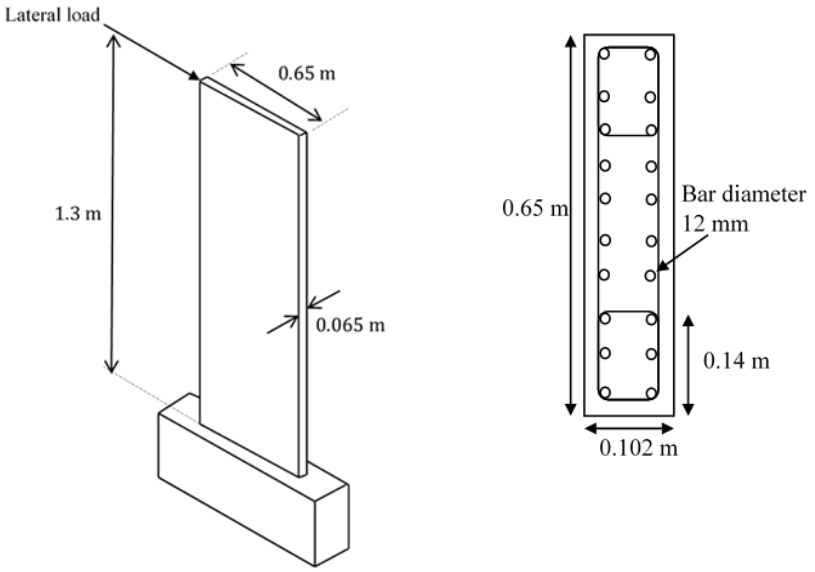

Figure 16: Loading arrangement, dimensions and reinforcement details of SW21

The load – deformation comparison of the experimental and numerical predictions given in Figure 17 displays a considerable deviation. The slope of the load – deformation curve of numerical prediction is quite high compared to that of experimental prediction. This behavior can be explained by the fact that the proposed formulation only accounts axial force – bending moment interaction. In the numerical prediction, a deformation corresponding to a certain force level consists of only flexural deformation component. However, in the real situation, the deformation should include the shear deformation component. Thus, the deformation in the experimental prediction is higher for the same force level. Thus, the proposed formulation cannot be recommended to predict the response of shear dominant reinforced concrete beams and walls. However, the proposed formulation can predict the flexural behavior accurately.

Height (mm)	1300
Outer perimeter Depth x width (mm x mm)	650 x 65
Aspect ratio	2
Compressive axial load (kN)	0
Cube strength (MPa)	42.8
Ratio of main flexural reinforcement to gross concrete area of edge element (%)	3.3
Yield strength of longitudinal reinforcement (MPa)	470
Ultimate strength of longitudinal reinforcement (MPa)	565

Table 3 Details of shear dominant reinforced concrete cantilever wall

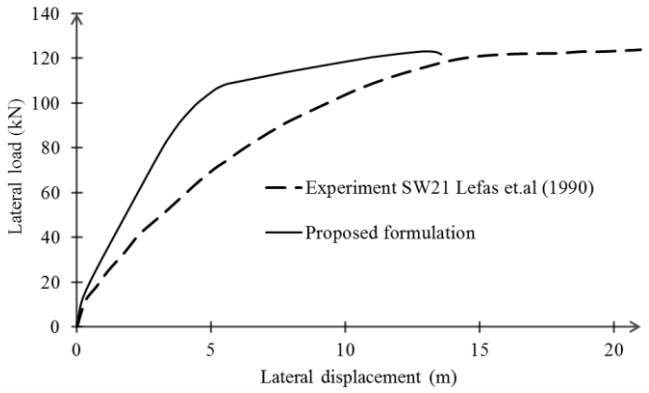

Figure 17: Load deformation response of shear dominant cantilever wall in the experiment and when using proposed formulation

5 SENSITIVITY ANALYSIS

A sensitivity analysis was performed on the proposed element using the reinforced concrete cantilever wall experimented [8]. The load deformation response was examined by changing number of fibers, number of integration points and step size. The force tolerances at structure level and section level was kept at 10^{-10}kN or kNm.

5.1 Number of fibers

Division of a section in to a sufficient number of uniaxial fibers is required to calculate section resisting forces corresponding to a given section deformation. In order to accurately predict the section resisting forces, number of fibers needs to be increased. However, drastic increase of number of fibers may cause an increase in the computational cost. Figure 18 demonstrates the variation of load-deformation curves with number of uniaxial fibers used in sections. In this comparison, number of integration points at each element was kept at six while the displacement step size was maintained at 0.1 mm. The load – deformation responses when the number of fibers 2, 4, 6, 8 shows a considerable deviation from that of having 50 fibers. The section height of RW2 is 1.22 m, thus the analysis should be carried out with higher number of concrete fibers.

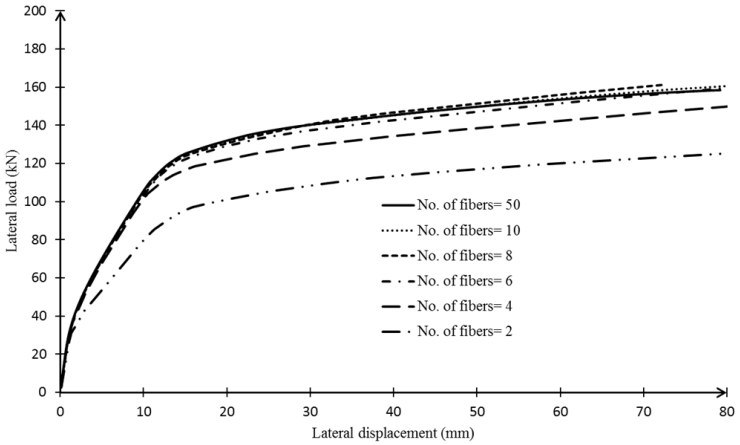

Figure18: Load deformation curves varying the number of fibers

5.2 Number of integration points

The proposed element utilizes Gauss-Lobatto integration scheme to find the element stiffness matrix from section stiffness matrix. Reference [7] describes that Gauss-Lobatto integration scheme is far more superior to the conventional Gauss integration due to the fact that the end sections are not monitored in Gauss integration. Reference [7] further suggest that if Gauss integration to be used, the order of integration needs to be increased. The load – deformation responses varying the number of integration points is plotted in Figure 19. These load – deformation curves were recorded while maintaining number of fibers at 50 and displacement step size at 0.1 mm. Figure 21 demonstrates that, in this problem, using 5 to 7 integration points per element provides a better monitoring of the plasticity along the element.

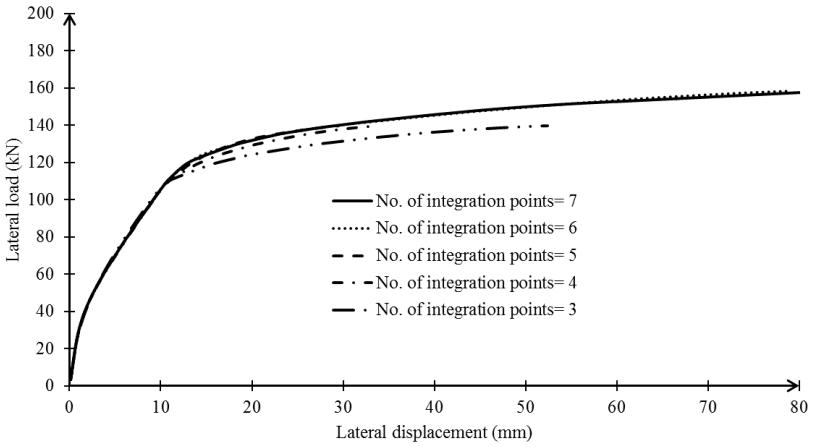

Figure 19: Load deformation curves varying number of integration points

5.3 Displacement step size

The load deformation responses varying the displacement step size is given in Figure 20. These load – deformation curves were obtained, maintaining number of fibers at fifty and number of integration points at six. The deviation of the load deformation curves exhibited in

the case of larger displacement steps, points out that in order to capture all nonlinear behaviors of reinforced concrete structures, the total displacement should be applied to the structure in sufficiently small displacement steps.

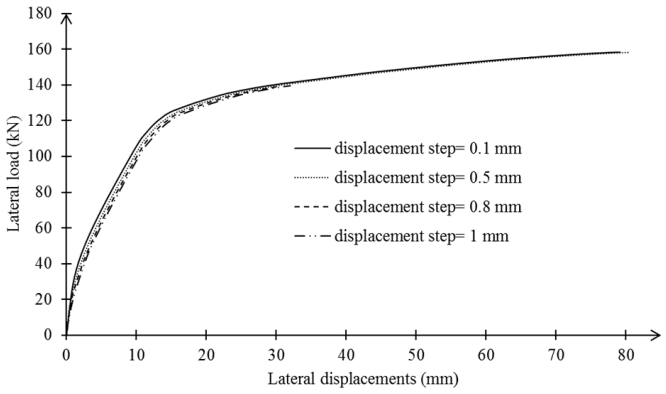

Figure 20: Load deformation curves varying displacement step size

6 CONCLUSIONS

This paper introduces a novel force based frame element with distributed plasticity which can predict the axial force – bending moment interaction. The existing force based fiber beam column element [6], [7] which can predict axial force – bending moment interaction, satisfies the equilibrium, compatibility and constitutive relationships at structure level element level and fiber level. However, section level equilibrium is not evaluated directly. Therefore the proposed formulation omits the compatibility satisfaction at element level and introduce an iterative procedure at section level to satisfy section level equilibrium. The novelties of the proposed formulation are introduction of section level iterative procedure to find correct section deformation and updated section stffness for a given force increment and the use of updated structure stiffness matrix to compute structure resisting force. The formulated element was validated with a well-recognized experimental reinforced cantilever wall RW2 [8]. The comparison of load – deformation response illustrated a very good agreement with the experimental response. The load – deformation response of reinforced cantilever wall was also predicted using OpenSees software, using equal number of elements, integration points, number of concrete fibers per section and tolerance values. The comparison proved that the proposed formulation has the capability to predict the load- deformation curve of RW2 to the level of the experimental curve where as the OpenSees prediction became unstable in the midway. Accordingly, the proposed novel formulation has the capability to predict the flexural response of reinforced concrete structures accurately in a stable manner.

ACKNOWLEDGMENT

This research was carried out with the aid of funding from Department of Civil Engineering, Faculty of Engineering, University of Peradeniya, Sri Lanka.

REFERENCES

[1] V. Ciampi and L. Carlesimo, “A nonlinear beam element for seismic analysis of structures”, Proceedings, 8th Euopean. Conference on earthquake engineering, Lisbon, 1986.

[2] S. Kaba and S. A. Mahin, ”Refined modeling of reinforced concrete columns for seismic analysis”, EERC Report 84/03, Earthquake Engineering Research Center, University of California, Berkeley, 1984

[3] I. D. Lefas, M. D. Kotsovos, N. N. Ambraseys, Behavior of Reinforced Concrete Structural walls: Strength, Deformation Characteristics, and Failure Mechanism, ACI Structural Journal 93 (1990) 23-31.

[4] G. Monti and E. Spacone, “Reinforced Concrete fiber beam element with bondslip.” Journal of structural engineering, 126(6), 654-661, 2000.

[5] S. Popovics, "A numerical approach to the complete stress strain curve for concrete," Cement and concrete research, 3(5), 583-599, 1973.

[6] E. Spacone, V. Ciampi and F. C Filippou, “Mixed formulation of nonlinear beam finite element.” Computers and Structures, 58, 71-83, 1996.

[7] E. Spacone, F. C Filippou and F.F Taucer, “Fiber beam-column model for non-linear analysis of R/C frames: Part I. Formulation”, Earthquake Engineering Structural Dynamics, 25(711-725), 1996a.

[8] J. H Thomsen and J.W Wallace, ‘‘Lateral load behavior of reinforced concrete columns constructed using high-strength materials,’’ ACI structural Journal, 91, 605–615, 1994.

[9] C. A. Zeris and S. A. Mahin, “Analysis of reinforced concrete beam-columns under uniaxial excitation”, Journal of Structural Engineering. ASCE 114 (ST9), 2657-2673, 1991.

COMPDYN 2019
7th ECCOMAS Thematic Conference on
Computational Methods in Structural Dynamics and Earthquake Engineering
M. Papadrakakis, M. Fragiadakis (eds.)
Crete, Greece, 24–26 June 2019

SEISMIC SHEAR AND MOMENT DEMANDS IN REINFORCED CONCRETE WALL BUILDINGS

Alejandro Morales[1], Paola Ceresa[2], and Matías Hube[3]

[1] School of Civil Engineering - Universidad de Valparaíso
222 General Cruz Street, Valparaíso, Chile
e-mail: alejandro.morales@uv.cl

[2] Seismic Hazard and Risk Analysis, Risk Engineering and Development RED
(formerly at the University School for Advanced Studies Pavia – IUSS Pavia)
Via Frank, 38, 27100 Pavia, Italia
paola.ceresa@redrisk.com

[3] Department of Structural and Geotechnical Engineering - Pontificia Universidad Católica de Chile
4860 Vicuña Mackenna Avenue, Santiago, Chile
mhube@ing.puc.cl

Abstract

This research aims to obtain envelopes of the moment and shear demands in reinforced concrete (RC) wall buildings subjected to ground motions. These envelopes are intended to be used for designing RC buildings. Three research buildings with non-rectangular walls designed according to Eurocode 8 are considered. The seismic performance of the buildings is evaluated from nonlinear response history analysis (NRHA) with increasing levels of ground motion intensity. The RC walls are simulated with a model with distributed inelasticity (MDI), which considers that the nonlinear behaviour can take place at any building level if the demand is larger than the wall yield capacity, while the flexural stiffness is a function of the moment demand of the wall. The design envelopes for moment and shear forces are obtained from the results of the NRHA, where the effects of higher modes are evidenced.

Keywords: Reinforced concrete, Walls, Seismic demands, Seismic behaviour.

1 INTRODUCTION

In high seismicity areas, RC structural walls are largely used as lateral-load resisting systems for mid- and high-rise buildings. RC walls are stiff and strong, easily incorporated into architectural layouts, and, when properly designed and detailed, perform satisfactorily when subjected to severe earthquakes. Structural walls can be configured in numerous ways within a building, with multiple walls resisting the demands in each principal direction. Rectangular sections are relatively easy to be designed, and have been extensively studied in the last years. Intersecting wall segments can be combined to create flanged or non-rectangular walls, including T-, C-, and L-shaped cross sections. RC walls are common in residential buildings and hotels and are usually located around stairs, elevators, corridors, and partitions between residential units [1].

Seismic moment and shear forces demand in walls of RC buildings have been studied mainly using a single wall as a representation of the entire building, where the interaction between different walls within buildings is not considered [2, 3]. Moreover, these studies assume that the nonlinear behaviour takes place at the base of the wall only. Therefore, elements with lumped plasticity and constant stiffness above the critical section have been used. The first problem of this approach is that a constant flexural stiffness is considered along the wall height. However, the flexural stiffness of the wall is a function of the moment demand which varies along the wall height. A second problem of such approach, that assumes an elastic response above the critical section, is that the bending moments in such regions are not bounded, while the bending moment at the base is bounded by the provided moment strength. Because certain design codes specify design envelopes for bending moments in RC wall buildings (e.g. Eurocode 8, NZS 3101, CSA A23.3), the assumption of elastic response and unbounded bending moments above the base of the walls may be an unrealistic situation under severe earthquakes.

The main objective of this research is to provide design recommendations for RC wall buildings. Specifically, design envelopes for moment and shear demands are proposed. The envelopes are obtained from an analytical study of three research buildings with non-rectangular RC walls.

2 RESEARCH BUILDINGS

The plan view of the research buildings is shown in Figure 1, where T-shaped and C-shaped RC walls are considered to resist lateral loads in both directions. The buildings have ten, twenty and thirty storeys and the inter-storey height is 3.0 m. The thickness of the walls of the three buildings varies between 0.3 m and 0.4 m, depending on the number of storeys.

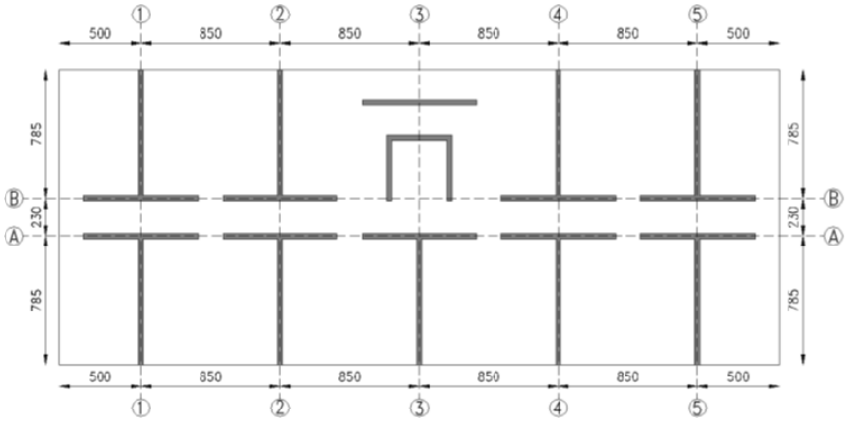

Figure 1: Plan view of the research buildings (dimensions in centimetres).

The buildings were designed according to Eurocode 8 (EC8) [4]. A type C soil (dense sand or gravel, or stiff clay) was used in conjunction with 0.4g design ground acceleration, considering a high seismicity area. The properties of concrete and reinforcement adopted for the seismic design are typical values used in engineering practice. The yield strength of the reinforcement (f_y) and characteristic compressive strength of the concrete (f'_c) are 500 MPa and 30 MPa, respectively.

Table 1 summarises the main design outputs of the three buildings, where T is the fundamental period of the buildings, q is the behaviour factor for uncoupled wall systems of high ductility class [4], W is the seismic weight, V is the design base shear of the building, ρ_L is the longitudinal reinforcement ratio, N_{ed} is the factored axial load in the walls, and A_g is the gross area of the walls. The value of ρ_L for the 30-storey building is lesser than that the 20-storey one because of the lower seismic demand induced by the larger period of the tall building.

N°-Storey	T [sec]	q	W [kN]	V/W	T-shaped wall		C-shaped wall	
					ρ_L [%]	$N_{ed}/A_g f'_c$	ρ_L [%]	$N_{ed}/A_g f'_c$
10-Storey	0.45	4.4	73412	0.19	0.5	0.06	0.6	0.05
20-Storey	1.12	4.4	156108	0.11	0.8	0.11	0.7	0.10
30-Storey	2.40	4.4	252851	0.08	0.7	0.15	0.4	0.16

Table 1: Design outputs.

3 ANALYTICAL MODELS OF BUILDINGS

The seismic performance of the research buildings is estimated from two-dimensional (2D) nonlinear response history analyses (NRHA) using the finite-element software RUAUMOKO 2D [5]. The walls and beams are modelled using beam elements with lumped flexural nonlinear behaviour and elastic shear behaviour.

Figure 2 shows the two-component beam element used to model the walls, where two members in parallel represent the behaviour of the element. The two members are elastic but one of them allows the formation of hinges at ends of the member [5]. The nonlinear behaviour is achieved assigning a hysteretic model to the flexural behaviour of the hinges.

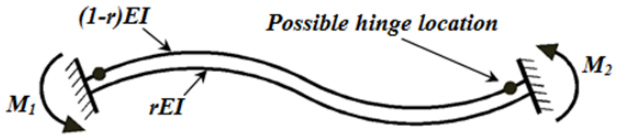

Figure 2: Two-component beam element, adapted from Carr [5].

In this study, the nonlinear moment-rotation relationship of the hinges of the two-component beam elements used to represent the RC walls is represented using the tri-linear SINA hysteretic model [6]. This hysteretic model is shown in Figure 3a and consists on a tri-linear backbone with stiffness changes at cracking (F_{cr}^+, F_{cr}^-) and yielding (F_y^+, F_y^-). The SINA hysteresis rule allows different behaviour in the two loading directions, allowing modelling the behaviour of asymmetric RC walls. Additionally, the pinching effect is considered through the definition of the crack closing moment (F_{cc}). The SINA model considers that F_{cc} is the same in both directions.

Using available experimental data of non-rectangular RC walls subjected to cyclic loads reported by Thomsen and Wallace [7] (named TW1, TW2), Sittipunt and Wood [8] (CLS, CMS), Beyer et al. [9] (TUA, TUB), and Brueggen [10] (NTW1, NTW2), the RC wall model

was calibrated achieving a good representation of the cyclic behaviour of the tested walls. For each specimen the tri-linear backbone was obtained directly from the moment-curvature relationship while the crack closing moment (F_{cc}) was defined through a trial and error procedure. The values of F_{cc} obtained for the specimens are shown in Figure 3b. The comparison between the experimental behaviour and the predicted response for two specimens is shown in Figure 4, where the proposed model is able to predict the cyclic response adequately in both loading directions.

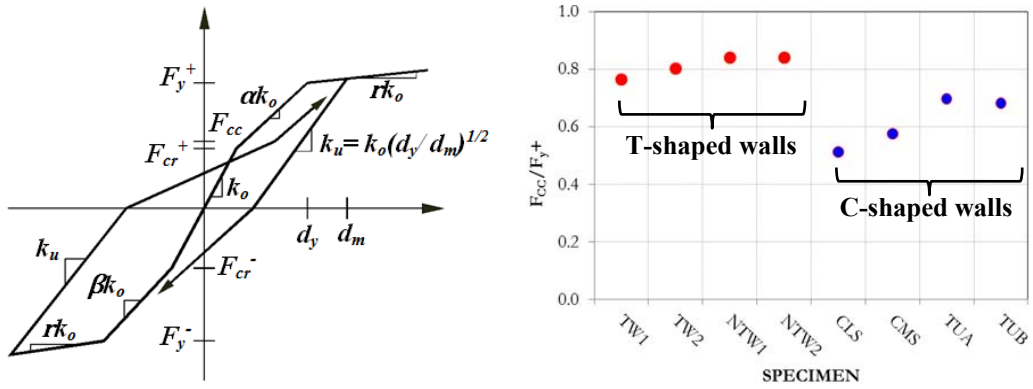

a) b)

Figure 3: a) Tri-linear SINA hysteretic model, adapted from Carr [5], and b) F_{cc} values used for the studied walls.

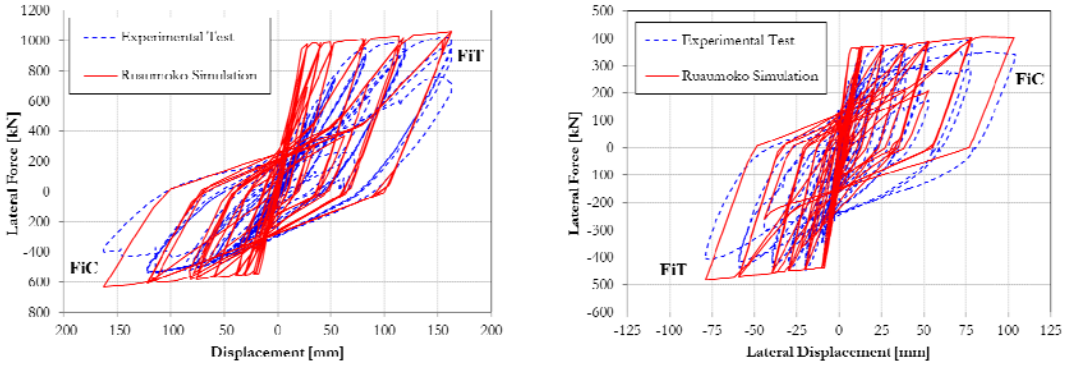

a) b)

Figure 4: Comparison between the analytical model and experimental results: a) T-shaped wall (NTW1) after Brueggen [10], and b) C-shaped wall (TUA) after Beyer et al. [9].

Figure 4 shows that the experimental yield displacements, mainly for flange in tension (FiT), are larger than the analytical values due to the gradual yielding of the tension reinforcement within the flanges, whereas the reinforcement closest to the webs yields first, and subsequently progressing out from the web–flange intersection as lateral displacement increases [11]. Even though the simulated values overestimate the elastic stiffness, the proposed model is considered adequate because the response of the studied walls is essentially inelastic.

3.1 Building Model

The two-dimensional model of the building is shown in Figure 5, where all the axes of the building are modelled simultaneously. The walls were modelled with two-components beam elements using the described tri-linear SINA hysteretic constitutive relationship that considers different strength and stiffness in opposite directions. The effective slabs, which connect the

two walls in each axis, were modelled using two-node beam elements considering the Takeda hysteretic rule. End offsets are considered in these elements to account for the wall widths.

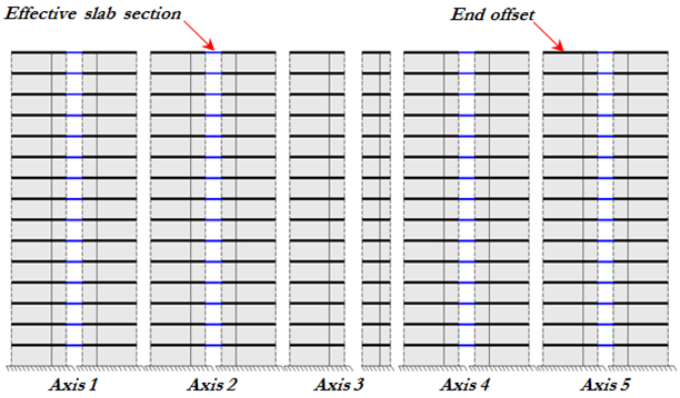

Figure 5: RUAUMOKO 2D structural model of studied buildings.

To model the RC walls, the approach used in this study is a model with distributed inelasticity (MDI), which considers that the nonlinear behaviour can take place anywhere in the wall if the moment demand is larger than the yield moment. The MDI of one wall is shown in Figure 6a, where four two-component beam elements are considered at each storey. This number of elements is considered adequate to represent satisfactorily the lateral displacement profile and flexural lateral stiffness of the walls. Since the inelastic behaviour is lumped in discrete points along the wall height (perfect hinge of two-component beam element), the proposed model in RUAUMOKO 2D was validated with a fibre beam model developed with SeismoStruct [12]. The comparison of a static pushover analysis of the T-shaped wall predicted with the two models in both loading directions is shown in Figure 6b. For the pushover analysis a concentrated load at the top of the wall was considered. The figure shows that the obtained behaviour with both models is similar for the two loading directions (flange in compression (FiC) and flange in tension (FiT)). Therefore, the proposed model with two-component beam elements is able to predict the behaviour of the wall adequately. A further development of the research will be the validation of the proposed MDI model with a fibre beam-column element able to capture the nonlinear shear behaviour of the wall [13, 14] and the multi-axial stress interaction under multi-axial loading conditions [15, 16].

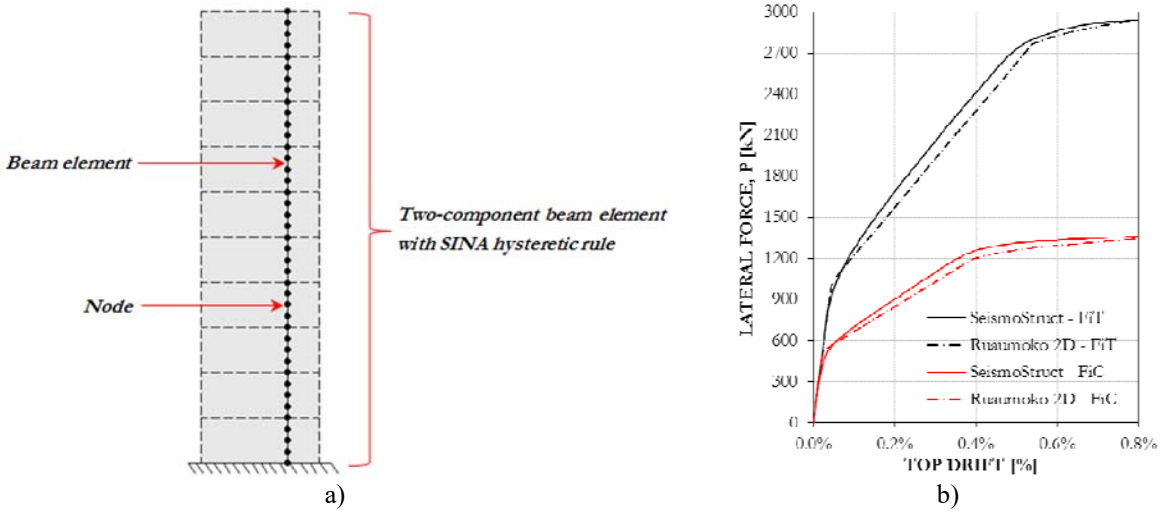

Figure 6: a) MDI and b) comparison of pushover analysis of the T-shaped wall using the proposed model with Ruamoko 2D and a fiber model with SeismoStruct.

4 CONSIDERED GROUND MOTIONS

To carry out the NRHA of the three buildings (Table 1) a set of seven artificial accelerograms were generated to be compatible with the design spectrum of EC8 [4]. Artificial records were selected because they matched the design spectrum for almost the full period range with a comparatively small error. The number of records was selected according to the prescriptions of the design codes (IBC, EC8, among others), which prescribe a minimum of seven spectrum-compatible records in order to obtain representative average results for design verification. The accelerograms were generated with SeismoArtif v2016 program [17]. Figure 7 compares the pseudo-acceleration and displacement spectra for 5% damping for each accelerogram with those of the EC8 design spectrum. Additionally, the figure shows the average response spectrum of the artificial accelerograms.

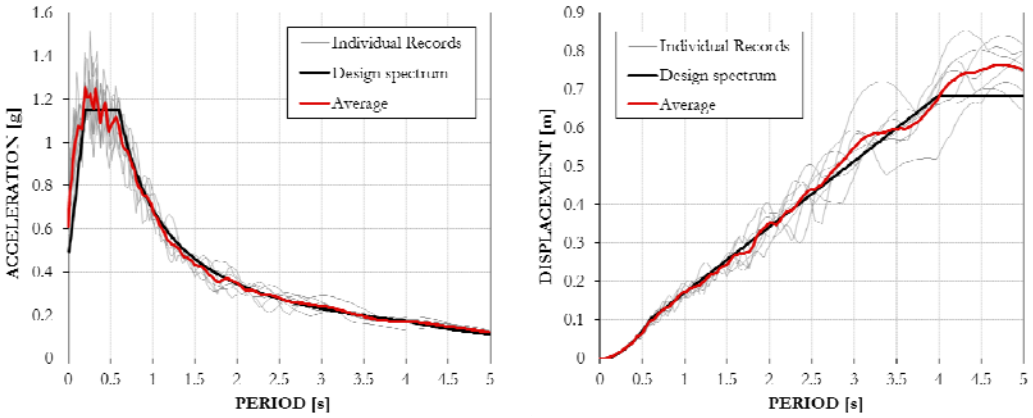

a) b)

Figure 7: EC8 design and artificial spectra used for NRHA: a) pseudo-acceleration and b) displacement.

5 RESULTS

The results obtained from NRHA are presented in this Section. The NRHAs were performed with RUAUMOKO 2D program using the seven records mentioned in the previous section. The records were scaled to 100% (IR=1.0), 150% (IR=1.5) and 200% (IR=2.0) of the design intensity to analyze the seismic behaviour of the buildings. The use of seven records for each analysis permits to obtain representative average values of the moments and shear forces.

From the nonlinear results of the buildings, moments and shear design envelopes are proposed for the walls of the studied buildings with the non-rectangular walls. Figure 8 shows the shape of the moment and shear envelopes and the parameters that define them (whose definition will be given later).

The proposed envelopes for capacity design are based on the Simplified Capacity Design model for rectangular cantilever RC walls developed by Priestley et al. [18]. This model was also used on T-shaped walls by Smyrou et al. [19]. However, the results obtained in this study present several differences with respect to the previous ones, as it is explained in the following sections.

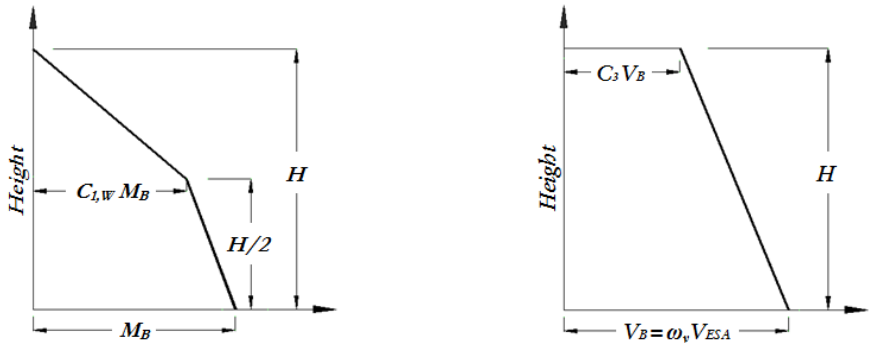

a) b)

Figure 8: Capacity design envelope for cantilever walls: a) moment and b) shear.

5.1 Superposition of the proposed envelopes and demands from NRHA

Figures 9, 10 and 11 show the maximum moment and shear demands from the NRHA, its average values and the proposed design envelopes (moment and shear forces). Due to the limited space, only some representative results are presented in this paper; however, more information is available elsewhere [20]. As expected, the figures shown different responses of the walls for the flange in tension (FiT) and flange in compression (FiC) directions, which is an important difference with respect to the responses of rectangular walls.

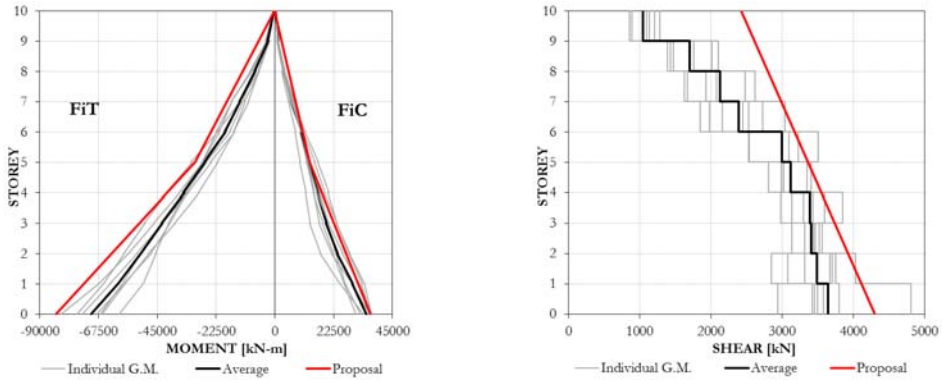

a) b)

Figure 9: T-shaped wall demands and design envelopes for 10-storey building (IR=1.0): a) moment and b) shear force.

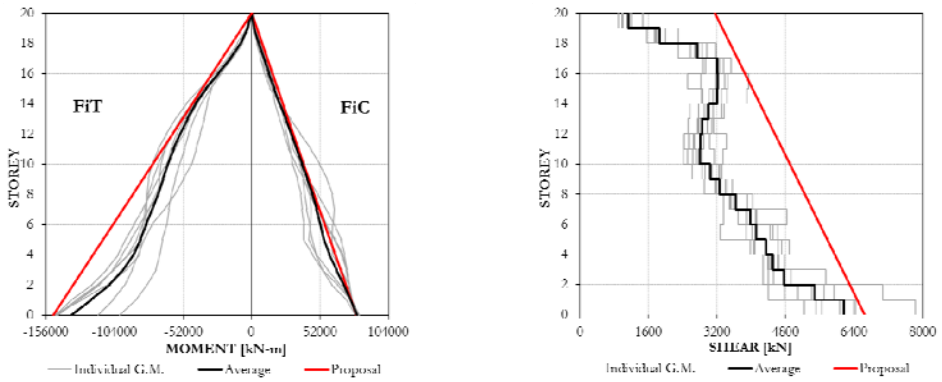

a) b)

Figure 10: T-shaped wall demands and design envelopes for 20-storey building (IR=1.5): a) moment and b) shear force.

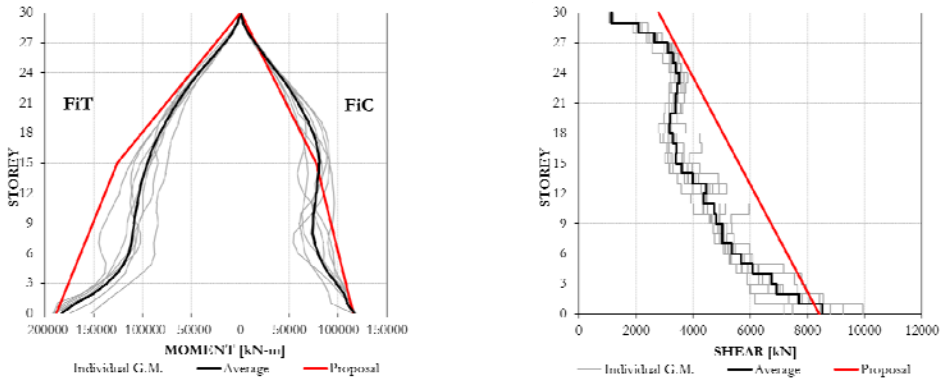

a) b)

Figure 11: T-shaped wall demands and design envelopes for 30-storey building (IR=2.0): a) moment and b) shear force.

5.2 Moment envelope

Figure 12 shows the values of the $C_{1,W}$ coefficient estimated for each record and each seismic intensity for the 10-storey building. This coefficient is the ratio of the mid-height moment to the overstrength base moment M_B (see Figure 8) that considers the overstrength conditions at the base hinge (strain hardening of reinforcement). The $C_{1,W}$ coefficients are similar for FiC and FiT for each intensity level; however, a large number of analyses is necessary to estimate the relationship between the storey numbers (or elastic period), the intensity ratio (IR) and the $C_{1,W}$ coefficient.

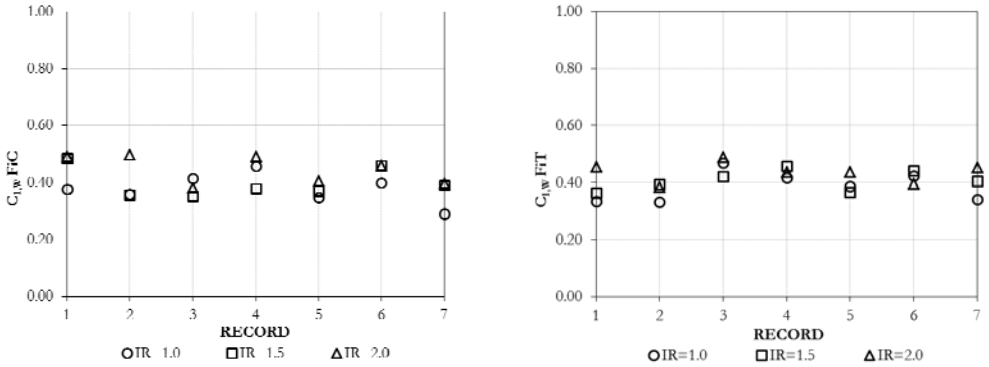

a) b)

Figure 12: Ratio of mid-height moment over base moment for T-shaped wall of 10-storey building with different intensity levels: (a) FiC, and (b) FiT.

The $C_{1,W}$ coefficients obtained for the three research buildings and three seismic intensity ratios (IR) are summarized in Table 2. The results obtained in this work show that the dynamic amplification in moment and shear profiles increases for higher intensity. The same tendency has been demonstrated in previous studies of RC wall buildings [3, 18, 19]. Therefore, the moment and shear force envelopes need to be related to the seismic intensity, which is characterized by the curvature ductility demand (μ_Φ) due its direct relationship with the seismic intensity.

N°-Storey	$C_{1,W\ FiC}$			$C_{1,W\ FiT}$		
	IR=1.0	IR=1.5	IR=2.0	IR=1.0	IR=1.5	IR=2.0
10-Storey	0.38	0.40	0.45	0.39	0.41	0.44
20-Storey	0.36	0.48	0.56	0.46	0.46	0.51
30-Storey	0.44	0.58	0.69	0.52	0.50	0.52

Table 2: Summary of $C_{1,W}$ coefficients.

From the $C_{1,W}$ values for FiC the following equation is proposed, which can also be conservatively be used for FiT.

$$C_{1,W} = m\,\mu_\Phi + b \tag{1}$$

where μ_Φ is the curvature ductility demand for FiC at the base of the walls, while the coefficient m and b are given by Equation 2 and Equation 3, respectively. These latter coefficients, estimated with a regression analysis, depend on the elastic periods of the buildings (T_e).

$$m = 0.022\,T_e + 0.006 \tag{2}$$

$$b = 0.03\,T_e + 0.33 \tag{3}$$

For the calibration and definition of previous equations, which define the moment and shear envelopes, the curvature ductility demand for FiC was used, even though the response of the T-shaped walls was different for FiT and FiC. For FiC both stiffness and yield curvature are lesser than for FiT. Therefore, due to the fact that larger nonlinear behaviour (or ductility demand) is expected if the flange acts in compression, the use of the curvature ductility demand for FiC is justified.

5.3 Shear envelope

NRHAs indicate that the shear force demand in the T-shaped walls is larger for the direction with FiT than for that with FiC because the moment strength and the stiffness of the wall is larger for the direction with FiC. Figure 13 shows the coefficient ω_v for the 10-storey building. This coefficient is the ratio of the maximum shear forces from NRHA at the base (V_B) to the shear forces from an equivalent static analysis (V_{ESA}), the capacity design base shear is calculated as the product of V_{ESA} at the base and ω_v (see Figure 8b). To estimate the base shear force of the wall (V_{ESA}) the provided moment strength at the base of the wall should be considered. Table 3 summarizes the maximum shear forces and the amplification factors (ω_v) for the three research buildings and three seismic intensity ratios (IR). The table shows that the values of ω_v depend on the seismic intensity, storey number, and the loading direction (FiC or FiT). Table 3 summarises the maximum average values for base shear forces from NRHA and equivalent static analysis, for T-shaped walls when flange acts in compression (FiC) and tension (FiT). Since the shear is resisted mostly by the web of the walls, identifying the loading direction is not relevant to the definition of the envelope, but the estimation of the ω_v factor should be consistent with the direction of analysis. In this study, the amplification factors ω_v were calculated with the shear forces for FiT. Table 3 shows that ω_v increases with the storey

numbers and with the seismic intensity. Therefore, this amplification factor increases with the elastic period (T_e) and curvature ductility demand (μ_Φ).

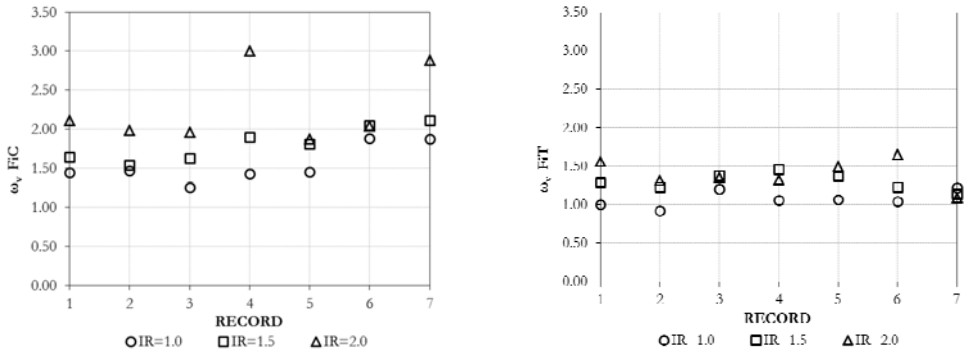

a) b)

Figure 13: Ratio between base shear from NRHA and ESA for T-shaped wall of 10-storey building with different intensity levels: (a) FiC, and (b) FiT.

N°-Storey	IR	Moment [kN-m]		Shear forces [kN]				ωv
		$M_{B\ FiC}$	$M_{B\ FiT}$	$V_{ESA\ FiC}$	$V_{ESA\ FiT}$	$V_{B\ FiC}$	$V_{B\ FiT}$	
10-Storey	1.0	34900	-70173	1685	3389	2579	-3641	1.07
	1.5	38609	-84406	1865	4076	3371	-5283	1.30
	2.0	41260	-87291	1993	4216	4482	-5903	1.40
20-Storey	1.0	65881	-105189	1624	2592	3402	-4226	1.64
	1.5	79981	-137129	1971	3380	4892	-5898	1.75
	2.0	83791	-149043	2065	3673	5672	-7804	2.12
30-Storey	1.0	90407	-128457	1494	2122	4776	-4387	2.06
	1.5	113071	-167429	1868	2766	5790	-7329	2.65
	2.0	116621	-183336	1927	3029	6824	-8060	2.68

Table 3: Summary of maximum shear forces and amplification factors.

From the ω_v values for FiT, the following equation is proposed.

$$\omega_v = 0.10\mu_\Phi + 0.5T_e + 0.70 \quad (4)$$

The ratio between the base shear and the top shear of the wall is given by:

$$C_3 = -0.08T_e + 0.60 \quad (5)$$

In previous equations, the curvature ductility demand for FiC and the elastic period of the building were used.

5.4 Comparison with previous studies

This section compares the proposed moment and shear design envelopes with those proposed by Priestley et al. [18] and Smyrou et al. [19]. Figure 14 compares the ratio of the mid-height moment over the base moment for the three research buildings. The model of Smyrou et al. is the most conservative for all the research buildings. On the other hand, for the 10-storey building, the ratios of the proposed model are similar to the ones of Priestley et al. approach. However, for taller buildings and larger ductility demands the aforementioned tendency changes and the values obtained from the proposed model are larger than those proposed by Priestley et al.

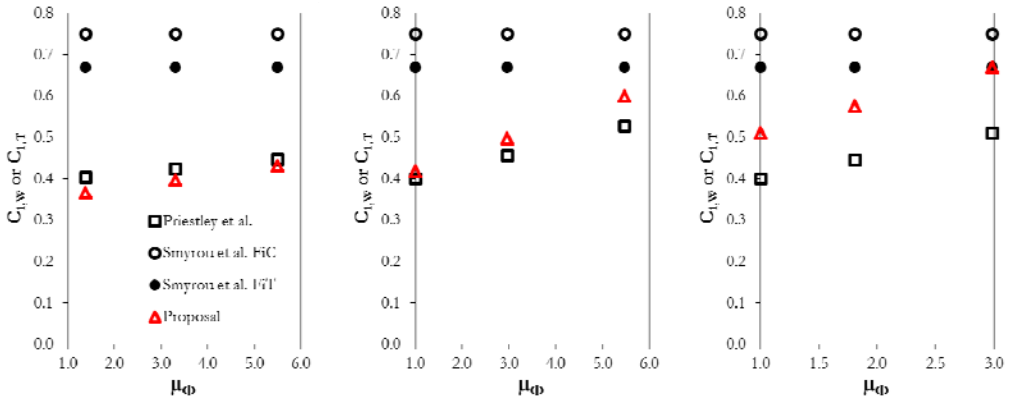

Figure 14: Ratios of mid-height moment over the base moment according to different approaches: a) 10-storey building, b) 20-storey building, and c) 30-storey building.

Figure 15 compares the dynamic amplification factors (ω_v) obtained from the proposed model with those presented by for Smyrou et al. and Priestley et al. for the three buildings. For the 10-storey building, the amplification factors of the proposed model are significantly larger than those of the other two models. For the 20- and 30-storey building, despite the differences between the models are lesser, the proposed approach is more conservative.

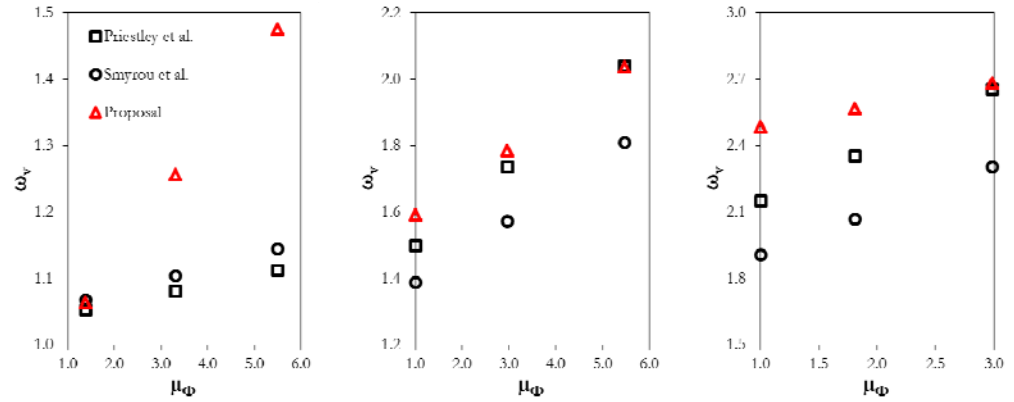

Figure 15: Dynamic amplification factors according to different approaches: a) 10-storey building, b) 20-storey building, and c) 30-storey building.

The discrepancies between the proposed model and the other two studied models can be explained by the different assumptions used in each of the cases. The periods of the studied

buildings are significantly smaller than those of the buildings studied by Priestley et al. and Smyrou et al. The larger periods of the buildings studied by Priestly et al. are related to the use of the direct displacement-based seismic design (DDBD) approach for designing their buildings. In this study, the EC8 design code was used, which resulted in buildings with shorter periods because of the drift limitation of the code. Another difference is that the flexural stiffness considered in this study varies along the height of the buildings due to the variation of the axial load in the walls (or moment strength) and also varies for FiC and FiT, whereas the flexural stiffness considered by Smyrou et al. and Priestley et al. was considered constant above the critical section.

Finally, in this study the whole building was modelled, which is expected to capture the interaction between walls [21].

6 CONCLUSIONS

In this work, three RC buildings with non-rectangular walls were designed according to Eurocode 8 and their seismic performance was assessed from nonlinear response history analysis (NRHA) for three different ground motion intensity levels. Walls were modelled with a model with distributed inelasticity (MDI) and the nonlinear behaviour was represented with a calibrated hysteretic rule. Capacity design envelopes for moment and shear of RC walls are proposed as a function of the building elastic period and the wall curvature ductility demand. These envelopes were defined and calibrated from the results of NRHA on T-shaped walls using a MDI. The proposed design envelopes have differences with respect to previous ones available in the literature. The differences are related to the use of non-rectangular walls in this study where strength and stiffness depend on the direction of loading. Additionally, this study considered the entire building in the analysis model, capturing the interaction and redistribution of strength between the walls within of building. The proposed envelopes are intended to be used for designing RC buildings.

7 ACKNOWLEDGMENTS

The first author acknowledges the support of the Becas Chile Programme (CONICYT) in form of PhD scholarship.

REFERENCES

[1] J. Moehle, *Seismic design of reinforced concrete buildings*. McGraw-Hill Education, New York, 2015.

[2] D. Pennucci, T.J. Sullivan, G.M. Calvi, Inelastic higher-mode response in reinforced concrete wall structures. *Earthquake Spectra*, **31**, 1493-1514, 2015.

[3] N. Priestley, A. Amaris, *Dynamic amplification of seismic moments and shear forces in cantilever walls. Research Report ROSE – 2002/01*. IUSS press, Pavia, Italy, 2002.

[4] CEN, *Eurocode 8 – Design of structures for earthquake resistance- Part 1: General rules, seismic actions and rules for buildings, EN 1998-1*. European Committee for Standardization, Brussels, Belgium, 2004.

[5] A.J. Carr, *Ruaumoko Manual – Volume 3: User manual for the 3-dimensional version Ruaumoko3D*. Department of Civil Engineering, University of Canterbury, Christchurch, New Zealand, 2012.

[6] M. Saiidi, M. Sozen, *Simple and complex model for nonlinear seismic response of reinforced concrete structures. A Report to the National Science Foundation*. Research Grant PFR 78-16318, 1979.

[7] J.H. Thomsen, J.W. Wallace, *Displacement-Based Design of RC Structural Walls: Experimental Studies of Walls with Rectangular and T-shaped Cross Sections. Report No.CU/CEE-95/96.* Department of Civil and Environmental Engineering, Clarkson University, 1995.

[8] C. Sittipunt, S. Wood, *Finite Element Analysis of Reinforced Concrete Shear Walls. A Report to the National Science Foundation*. Research Grant BCS 89-12992, 1993.

[9] K. Beyer, A. Dazio, M.J.N. Priestley, Quasi-static cyclic tests of two U-shaped reinforced concrete walls. *Journal of Earthquake Engineering*, **12**, 1023-1053, 2008.

[10] B.L. Brueggen, *Performance of T-shaped Reinforced Concrete Structural Walls under Multi-Directional Loading*. Ph.D Thesis, University of Minnesota, 2009.

[11] J.H. Thomsen, J.W. Wallace, Displacement-based design of slender reinforced concrete structural walls – experimental verification. *Journal of Structural Engineering*, *ASCE*, **130**, 618-630, 2004.

[12] Seismosoft, *SeismoStruct v6.5 – A computer program for static and dynamic nonlinear analysis of framed structures*. Available from http://www.seismosoft.com, 2013.

[13] A. Kagermanov, P. Ceresa, Physically Based Cyclic Tensile Model for RC Membrane Elements, *Journal of Structural Engineering, ASCE*, **142**(12), https://doi.org/10.1061/(ASCE)ST.1943-541X.0001590, 2016.

[14] A. Kagermanov, P. Ceresa, Fiber-Section Model with an Exact Shear Strain Profile for Two-Dimensional RC Frame Structures, *Journal of Structural Engineering, ASCE*, **143** (10), https://doi.org/10.1061/(ASCE)ST.1943-541X.0001839, 2017.

[15] A. Kagermanov, P. Ceresa, RC Fiber-Based Beam-Column Element with Flexure-Shear-Torsion Interaction. In: Hordijk D., Luković M. (eds) *High Tech Concrete: Where Technology and Engineering Meet*. Springer, Cham, https://doi.org/10.1007/978-3-319-59471-2_117, 2017.

[16] A. Kargermanov, P. Ceresa, 3D Fiber-based frame element with multiaxial stress interaction for RC structures, *Advances in Civil Engineering*, **2018**, https://doi.org/10.1155/2018/8596970, 2018.

[17] Seismosoft, *SeismoArtif v2016*. Available from http://www.seismosoft.com, 2016.

[18] M.J.N. Priestley, G.M. Calvi, M.J. Kowalsky, *Displacement-Based Seismic Design of Structures*. IUSS Press, Pavia, Italy, 2007.

[19] E. Smyrou, T.J. Sullivan, M.J.N. Priestley, G.M. Calvi, Dynamic Behaviour of T-shaped RC Walls Designed with Direct Displacement-based Design. *14th World Conference on Earthquake Engineering*, Beijing, China, 2008.

[20] J.A. Morales, *Seismic Shear and Moment Demands in RC Wall Buildings*. Ph.D Thesis, Istituto Universitario di Studi Superiori di Pavia (IUSS), 2018.

[21] K. Beyer, S. Simonini, R. Constantin, A. Rutenberg, Seismic shear distribution among interconnected cantilever walls of different lengths, *Earthquake Engineering & Structural Dynamics*, **12**, 1423-1441, 2014.

COMPDYN 2019
7th ECCOMAS Thematic Conference on
Computational Methods in Structural Dynamics and Earthquake Engineering
M. Papadrakakis, M. Fragiadakis (eds.)
Crete, Greece, 24-26 June 2019

A VEHICLE/TRACK CO-SIMULATION MODEL USING EASYDYN

Bryan Olivier, Olivier Verlinden, and Georges Kouroussis

Department of Theoretical Mechanics, Dynamics and Vibrations
Faculty of Engineering
University of Mons
Place du Parc 20, B-7000 Mons, Belgium
e-mail: [bryan.olivier, olivier.verlinden, georges.kouroussis]@umons.ac.be

Keywords: Railway, Dynamics, Solver-coupling, Co-Simulation

Abstract. *In the railway domain, studies have been undertaken on the attenuation of vibrations transmitted to the vehicle in order to improve the comfort of the passengers. However, a slight variation in the stiffness and damping characteristics of the train constitutive parts can considerably change the amount of energy transmitted to the soil in terms of vibrations. To predict those ground-borne vibrations generated by the vehicle moving along the track that could affect or disturb the surrounding environment, a relevant option would be to build a numerical model that simulates the passage of a vehicle on a track by coupling a multibody modeling of the train with a finite element modeling of the soil using co-simulation techniques. However the location where the model has to be split remains uncertain and then the border between the multibody and the finite element parts must be determined. The aim of this paper is to emphasize the possibility to perform co-simulation between two or more subsystems using an in-house C++ library package called EasyDyn. Using its co-simulation capabilities, the recoupling of a vehicle, that can be modeled using the minimal coordinates approach in multibody systems and a track modeled using a finite element representation of the rail and sleepers, will be discussed.*

1 INTRODUCTION

Nowadays virtual prototyping constitutes a truly useful tool that can provide decisive information about a specific problem. Indeed, in the railway domain, a modeling of a train passing over a soil can be used in order to estimate the ground-borne vibrations generated. Although single simulation were firstly adopted to predict the effect of a running train on the generated ground wave propagation [1, 2], recent research suggested to split the problem in order to take into account specific complex phenomena [3]. Theferore, Kouroussis et al. designed and validated a two-step model [4, 5, 6] that furnishes a sufficiently accurate prediction of the vibrations generated on the ground for different types of soil. This model uses a first step to estimate the forces applied on the soil through a fully coupled model of the vehicle, the track and a reduced coupled lumped masses (CLM) model of the soil [7]. While the first step uses a multibody representation of the vehicle and a finite element definition of the track, both two-dimensional, the second step involves a three-dimensional modeling of the soil including different layers if required. This soil modeling is performed into a dedicated finite element software which provides the different levels of vibrations for different distances from the track and also for different soil configurations.

In order to go further in the modeling of this vehicle/track/soil problem, it is interesting to investigate the possibilities offered by the co-simulation techniques that couple the problem during the time integration process. However this re-coupling involves a discussion on two different issues: the way the time integration of both subsystems is performed (co-simulation scheme) and the type of data (force or displacement) that are exchanged between each subsystem (co-simulation type). In order to compare efficiently the different co-simulated models, different types of tracks including a fixed soil will be studied. Indeed, depending on the split location and the co-simulation scheme chosen, the simulations can lead to drastically different results. Furthermore, depending on the split location, the number of coupling points and the stiffness and damping characteristics of the coupling link between both subsystems can significantly change the results obtained.

The aim of this work is to investigate the benefits and also the drawbacks of co-simulation techniques through a railway example using an in-house C++ library package called EasyDyn. After a brief description of the model used, the different split locations and coupling approaches will be discussed through the rail deflection results obtained.

2 EASYDYN FRAMEWORK

The EasyDyn framework [8] is an in-house set of tools initially dedicated to the time-integration of differential equations for teaching and research purposes. The framework programmed in C++ evolved in a library package able to simulate the behavior of multibody systems through the minimal coordinates approach. The workflow of the framework, illustrated in Figure 1, consists in:

- Defining the kinematics of bodies of the multibody system through their homogeneous transformation matrices $\mathbf{T_{0,i}}$ and their mass and inertial properties. This step is performed in a python environment that will, thanks to a python library called CaGEM (Computer Aided Generation of Motion), compute the different equations of motion symbolically. At the end of this step, a C++ file containing the kinematics is written.

- Defining applied forces and torques, through their wrench form $\mathbf{R_i}$ and $\mathbf{M_{G_i}}$, into the C++ file such that the multibody library (mbs) of EasyDyn can compute the equations of

motion into their residual form $\vec{\mathbf{f}}$.

- Time-integrating the equations of motion using the simulation (sim) library of EasyDyn.

Recently, co-simulation features were added to EasyDyn to allow it to communicate with other subsystems included in the same program or even with subsystems implemented in other software packages.

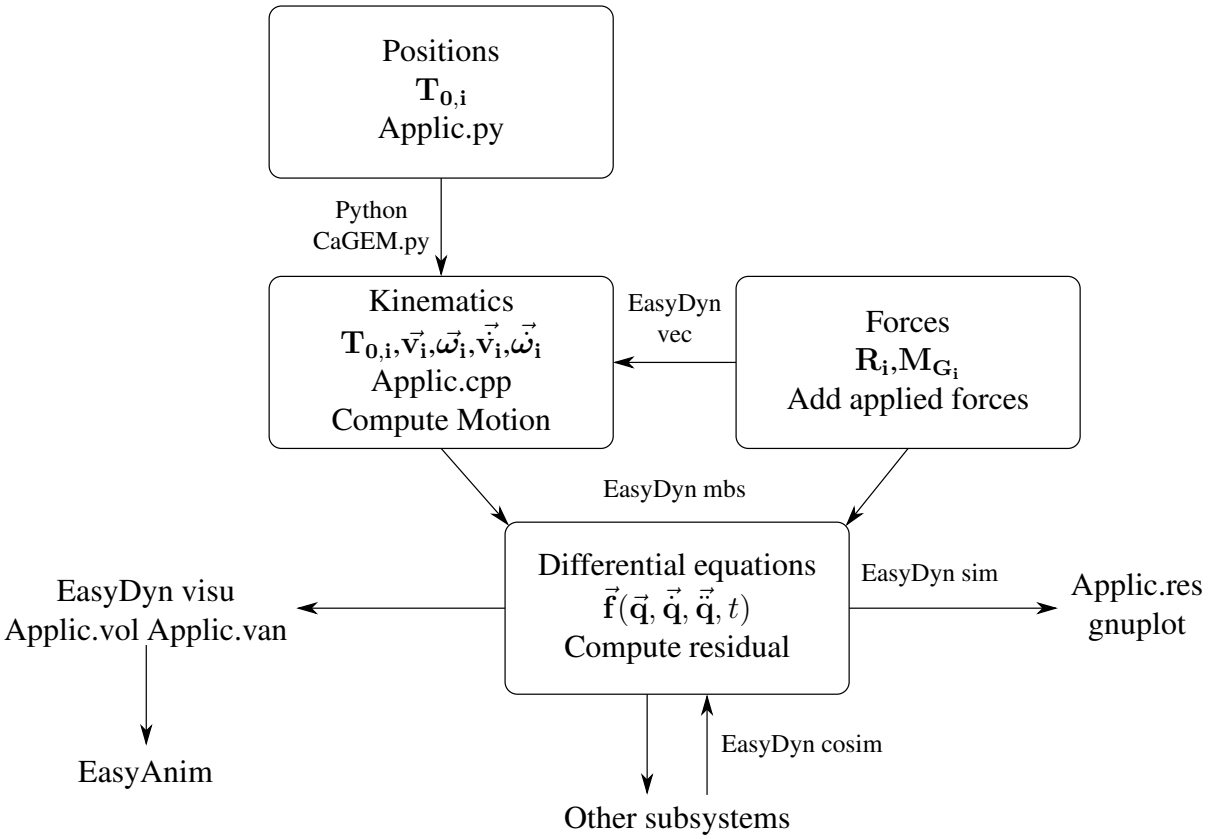

Figure 1: EasyDyn workflow

3 MODEL COMPOSITION

The model studied here (inspired by [9]) to test the co-simulation possibilities offered by EasyDyn is illustrated in Figure 2. It consists of a two-dimensional monolithic modeling of a wheel, on which a constant force $m_{tot}g$, equivalent to the static force applied by the whole vehicle, is applied. The wheel mass is tuned such that the maximal mass per wheelset is reached. The wheel is moving on a track at a v_0 speed and has a vertical degree of freedom q_0. Its contact with the rail is defined by a purely stiff and non-linear Hertz contact of stiffness K_{Hz}.

The track is composed of the rail which is described by its degrees of freedom $q_{r,j}$ related to the motions allowed by the Euler-Bernoulli definition of the rail beam elements. Each rail element possesses two nodes with two degrees of freedom each: one for the vertical translation and one for the rotation about the axis perpendicular to the plane containing the model.

The sleepers are described by their degrees of freedom $q_{s,i}$ that are only vertical. The soil is considered as a fixed reference.

The three parts that forms the monolithic model (vehicle, track and soil) are linked by different elastic elements. Besides the Hertz contact that links the vehicle and the rail, the railpads

(denoted by the subscript p) provides an elastic and damped link between the rail and the sleepers while the ballast (defined by subscript b) links the sleepers with the fixed soil.

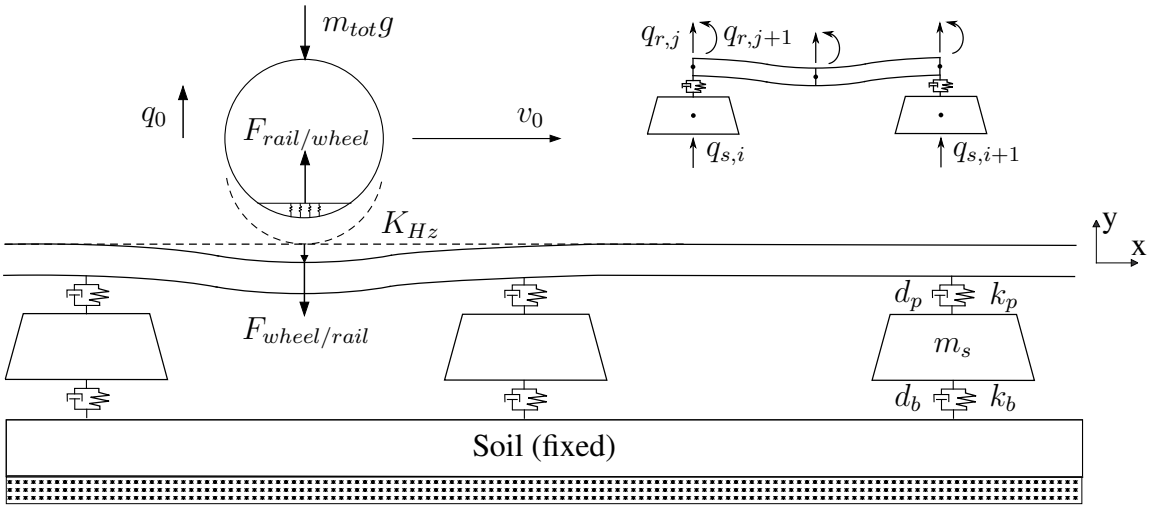

Figure 2: Monolithic modeling of a wheel passing over a flexible track.

The aforementioned monolithic modeling will be taken as a reference to compare the co-simulated results with. Furthermore, the co-simulated models will be very similar to the monolithic one since the only variable element will be the place in which the model will be split, all other parameters remaining identical.

4 SUBSYSTEMS DEFINITION AND INTERACTION

To define the subsystems from the monolithic reference, the only point that requires to be discussed is the split location. Once the subsystems are defined, it has to be decided the type of the data that each subsystem will send to the other one. Moreover, the order in which both subsystems are integrated must be defined.

4.1 Split locations

The co-simulation technique studied in this work consists of an applied-force coupling (see [10, 11]) of both subsystems. This means that the coupling will involve a force (computed or not in each subsystem) applied on both subsystems. Other co-simulation schemes exists such as the constraints coupling [12, 13, 14] but they involve algebraic equations that require specific time-integration schemes. Similar applied-force studies have been undertaken by Antunes et al. [15]. Nevertheless, the present work investigates the case of a flexible track and studies also different split locations and different types of data exchange.

Considering the applied-force methodology, the only way to split the monolithic modeling is through an elastic element that can be used to compute the applied force. The two possible locations are, for this example:

- **The wheel/rail contact:** it involves a relative asymmetry in the degrees of freedom distribution between the subsystems. Moreover, the contact is unique and purely stiff. The contact point is also moving horizontally when observed by the rail.
- **The rail/sleepers:** the asymmetry in the degrees of freedom distribution is minimized with respect to the previous case. Moreover, there exist as many exchange points as the

number of sleepers but in opposition to the wheel/rail case, those points do not move horizontally. Finally, the rail pads are stiff and also damped elements while the Hertz contact is only stiff.

Figure 3 and 4 show the wheel/rail split and rail/sleepers split respectively. The main variables are not changed between those Figures and Figure 2. In both Figures, the subsystem that contains the vehicle is always called Subsystem 1 (S_1) and the one that contains the sleepers, Subsystem 2 (S_2).

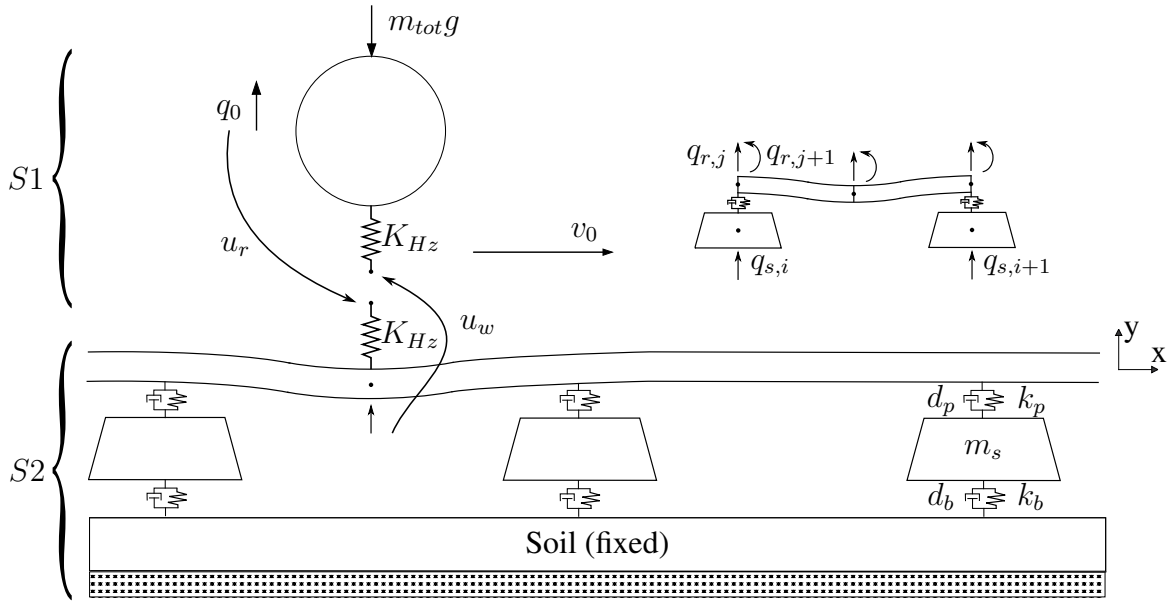

Figure 3: Coupling of wheel and track subsystems through a displacement/displacement method.

4.2 Type of data exchanged

Besides the cutting location, the type of data received by each subsystem (inputs u) must be defined. Indeed, the information going from one subsystem to the other one can take two forms: the displacement of the coupling point or a force applied on the coupling point. In the case of a displacement receiving, the velocity is also required if the element at which the cut is realized presents damping.

In the present work, two different cases will be investigated:

- Both subsystems S_1 and S_2 receive a displacement (called X-X case). Specifically in the case of the Rail/Sleepers cut, the velocity of the coupling points has also to be exchanged since the rail pads present damping characteristics. The X-X Wheel/Rail situation is illustrated in Figure 3.

- Subsystem S_1 receives a displacement and Subsystem S_2 receives a force (called X-T case). Again, a velocity must be sent by S_2 to S_1 in the case of the Rail/Sleepers cut due to the damping properties of the rail pads. The X-T coupling type for a Rail/Sleepers cut is illustrated in Figure 4.

It must be specified that, in the end, a force is always used (being re-computed or not) in the each subsystem. The major difference between the displacement and the force exchange is that

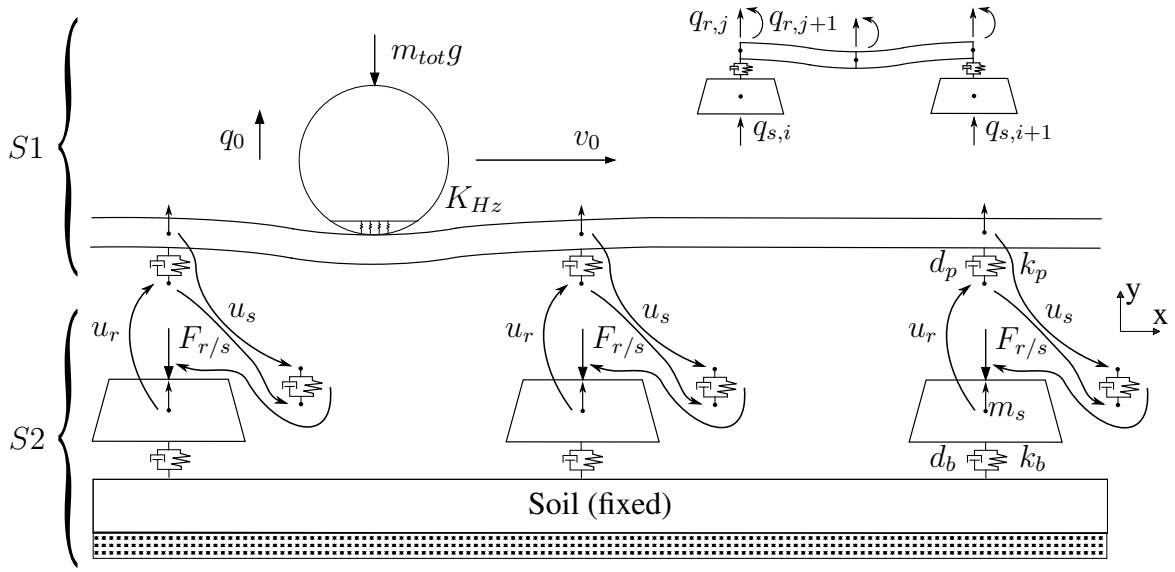

Figure 4: Coupling of wheel-rail and sleepers subsystems through a displacement/force method.

in the force case, the force is a constant until the next time step while this force is a function of the state variables of the subsystem in the displacement exchange.

4.3 Co-simulation schemes used

The co-simulation scheme defines the order in which both subsystems are time-integrated and then how the data are exchanged between them. There exist several types of co-simulation schemes such as explicit, semi-implicit and implicit schemes [10] but this work will focus on two explicit schemes [11]:

- A parallel scheme for which the inputs (coupling variables coming from the other subsystem) of each subsystem are extracted from the state variables of the other subsystem at the beginning of the time step. This means that each subsystem can be time-integrated without waiting for the other one to be integrated. This is called Jacobi scheme.

- A sequential scheme for which both subsystems are integrated sequentially since the inputs of the second subsystem will be computed using the states variables of the first subsystem integration. As for the Jacobi scheme, the inputs for first subsystem integration are computed from the state variables of the other subsystem but at the beginning of the timestep (then the values obtained at the previous time step integration). This is called the Gauß-Seidel scheme.

It has to be mentioned that the data are exchanged following a specific timestep called the macrotimestep while each subsystem can have its own timestep for its time-integration during a macrotimestep. Furthermore, this microtimestep can be different between both subsystems as far as the macrotimestep is common for both of them in order to have a consistent data exchange.

5 RESULTS

In order to demonstrate the co-simulation capabilities of EasyDyn and also the effect of co-simulation techniques on a railway problem, the different aforementioned methods were im-

plemented including the monolithic modeling. The different parameters, whose values are not changed between all the model representations, are expressed in Table 1. It must be mentioned that if the macrotimestep is specified in this table, the microtimestep of each subsystem is not given. This comes from the time integration scheme used that possesses an adaptive time-step. This scheme is identical for both subsystems and is a Newmark-β scheme tuned such that it does not produces numerical damping on the results ($\beta = 0.25$ and $\gamma = 0.5$).

Parameter	Symbol	Value	Unit
Total mass of the wheel	m_{tot}	11250	kg
Hertz contact stiffness	K_{Hz}	92.86	GN/m$^{\frac{3}{2}}$
Rail Young modulus	E	210	GPa
Rail geometrical moment of inertia	I	1987	cm^4
Mass of a sleeper	m_s	90.84	kg
Spacing between two sleepers	l	0.6	m
Area of rail cross section	A_r	63.8	cm^2
Rail density	ρ	7850	kg/m^3
Stiffness of rail pads	k_p	180	MN/m
Stiffness of the ballast	k_b	25.5	MN/m
Damping of rail pads	d_p	28	kNs/m
Damping of the ballast	d_b	40	kNs/m
Number of sleepers	N	50	-
Number of rail elements between sleepers	N_r	2	-
Vehicle speed	v_0	300	km/h
Vehicle initial position	x_0	2	m
Simulation macrotimestep	H	10^{-4}	s

Table 1: Values of the parameters involved in the model simulated.

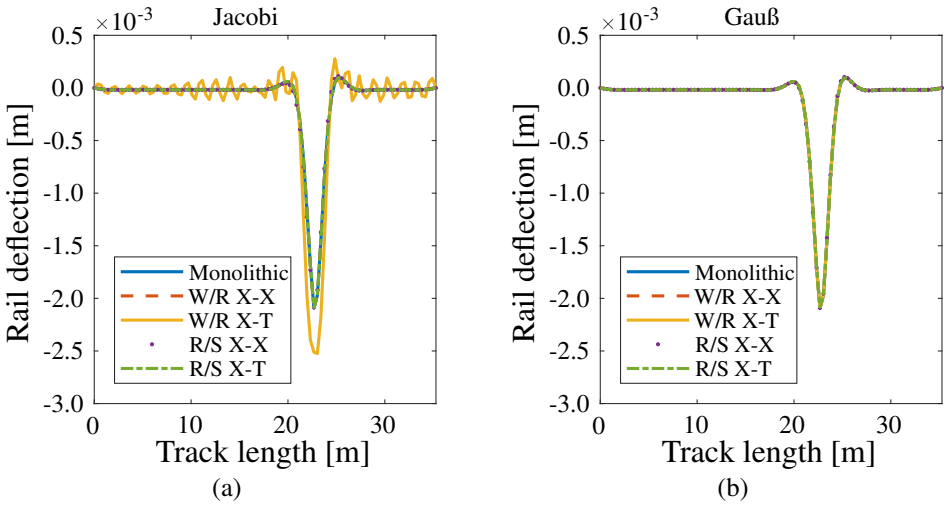

Figure 5: Rail deflexion at $t = 0.25$ s for Wheel/Rail and Rail/Sleepers coupling locations.

Generally speaking, the results obtained are compared through the rail deflection. Figures 5a and 5b illustrates the results obtained for the different coupling locations (W/R and R/S)

and also the different coupling types (X-X and X-T). It can be remarked that a large part of the solutions are slightly different from the monolithic reference. However, one solution involves an abnormal amplification of some specific modes: the Jacobi scheme with an X-T coupling at the wheel/rail contact level.

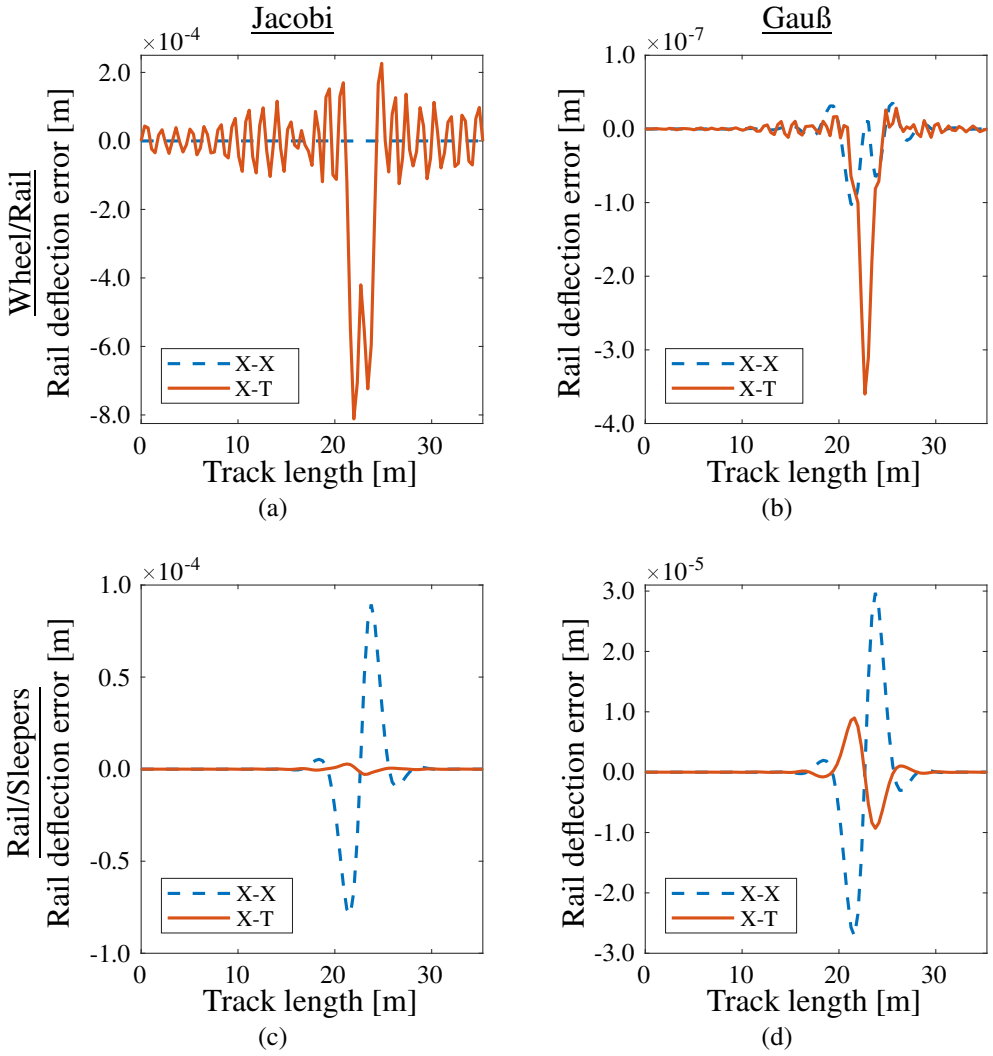

Figure 6: Rail deflexion error at $t = 0.25$ s for Wheel/Rail (top) and Rail/Sleepers (bottom) coupling locations, for Jacobi (left) and Gauß-Seidel (right) coupling approaches and X-X and X-T coupling types.

In order to distinguish the more accurate methods, Figure 6 proposes the rail deflection error defined as the subtraction of the rail deflection given by the monolithic modeling to the considered co-simulated solution. While the instability of the Jacobi X-T W/R is again clearly visible in Figure 6a, a similar but less amplified tendency is present in the corresponding Gauß-Seidel deflection curve in Figure 6b.

Furthermore, due to the classification between the different cases, the error encountered using a specific scheme can easily be observed between different cases. For example, since the Jacobi X-T W/R presents a huge amplification, the generated error remains the biggest found in all the cases. Also, it seems that changing to Gauß-Seidel from Jacobi in the X-X R/S case divides the error by almost 10.

6 CONCLUSIONS

Through a two-dimensional railway example, the capabilities of EasyDyn in co-simulation was highlighted and the effect of co-simulation techniques was studied and compared to the corresponding monolithic modeling. Several cases were developed in terms of coupling location (wheel/rail contact cut and rail pads cut), coupling type (displacement/displacement and displacement/force) and coupling approach (Jacobi and Gauß-Seidel).

Generally speaking, the parallel scheme (Jacobi) provides a less accurate rail deflection than the sequential Gauß-Seidel scheme for this specific railway example. This can be explained by the loss of accuracy in the parallel integration of both subsystems during a macrotimestep while the time-integration of the second subsystem in Gauß-Seidel scheme uses a more accurate version of its input variables thanks to the already performed integration of the first subsystem.

Furthermore, if the displacement/displacement coupling type seems to be more accurate in the wheel/rail coupling location case, the tendency is reversed in the rail/sleepers case. Meanwhile, even if the rail deflection seems more accurate in the wheel/rail coupling case (except for the Jacobi X-T case), the rail/sleepers case remains more stable. Additional studies could be carried out in order to detect if it comes from the lack of physical damping in the coupling element or if it comes from the fact that the coupling point is moving in the wheel/rail case.

Finally, this example was developed in order to determine the best coupling method that could be used to perform co-simulation on a more comprehensive model in order to evaluate the ground-borne vibrations in a 3D modeling of a soil. Indeed, it is currently possible to perform co-simulation between EasyDyn an another software containing a three-dimensional modeling of a soil. Based on the results obtained with the model treated in this work and thanks to the EasyDyn capabilities of co-simulation through network, actual co-simulation between a multibody modeling of a full vehicle and a finite element modeling of a soil will be investigated in further research.

REFERENCES

[1] D. Connolly, A. Giannopoulos, and M.C. Forde. Numerical modelling of ground borne vibrations from high speed rail lines on embankments. *Soil Dynamics and Earthquake Engineering*, 46:13–19, 2013.

[2] P. Galvín and J. Domínguez. Experimental and numerical analyses of vibrations induced by high-speed trains on the córdoba–málaga line. *Soil Dynamics and Earthquake Engineering*, 29(4):641–657, 2009.

[3] X. Song and Q. Li. Numerical and experimental study on noise reduction of concrete lrt bridges. *Science of the Total Environment*, 643:208–224, 2018.

[4] G. Kouroussis, S. Zhu, B. Olivier, D. Ainalis, and Zhai W. Urban railway ground vibrations induced by localized defects: using dynamic vibration absorbers as a mitigation solution. *Journal of Zhejiang University Science A*, 20(2):83–97, 2019.

[5] D. Connolly, B. Olivier, P. Galvín, G. Kouroussis, and A. Romero. A 2.5d time-frequency domain model for railway induced soil-building vibration due to railway defects. *Soil Dynamics and Earthquake Engineering*, 2019.

[6] G. Kouroussis and O. Verlinden. Prediction of railway ground vibrations: accuracy of a coupled lumped mass model for representing the track/soil interaction. *Soil Dynamics and Earthquake Engineering*, 69:220–226, 2015.

[7] G. Kouroussis, G. Gazetas, I. Anastasopoulos, C. Conti, and O. Verlinden. Discrete modelling of vertical track–soil coupling for vehicle–track dynamics. *Soil Dynamics and Earthquake Engineering*, 31(12):1711–1723, 2011.

[8] O. Verlinden, L. B. Fékih, and G. Kouroussis. Symbolic generation of the kinematics of multibody systems in easydyn: from mupad to xcas/giac. *Theoretical and Applied Mechanics Letters*, 3(1):013012, 2013.

[9] G. Kouroussis, O. Verlinden, and C. Conti. Influence of some vehicle and track parameters on the environmental vibrations induced by railway traffic. *Vehicle system dynamics*, 50(4):619–639, 2012.

[10] M. Busch. *Zur effizienten Kopplung von Simulationsprogrammen*. PhD thesis, Kassel University, 2012.

[11] B. Olivier, O. Verlinden, and G. Kouroussis. Stability and error analysis of applied-force co-simulation methods using mixed one-step integration schemes. In B. Schweizer, editor, *IUTAM Bookseries 35*, chapter 12, pages 1–12 in press (doi:10.1007/978–3–030–14883–6_12). Springer, 2019.

[12] B. Schweizer, D. Lu, and P. Li. Co-simulation method for solver coupling with algebraic constraints incorporating relaxation techniques. *Multibody System Dynamics*, 36(1):1–36, 2016.

[13] R. Schmoll and B. Schweizer. Co-simulation of multibody and hydraulic systems: comparison of different coupling approaches. In *Multibody Dynamics 2011, ECCOMAS Thematic Conference, Brussels, Belgium, 47 July*, pages 1–13, 2011.

[14] B. Schweizer, P. Li, and D. Lu. Implicit co-simulation methods: Stability and convergence analysis for solver coupling approaches with algebraic constraints. *ZAMM - Journal of Applied Mathematics and Mechanics*, 96(8):986–1012, 2016.

[15] P. Antunes, H. Magalhães, J. Ambrósio, J. Pombo, and J. Costa. A co-simulation approach to the wheel–rail contact with flexible railway track. *Multibody System Dynamics*, pages 1–28, 2018.

COMPDYN 2019
7th ECCOMAS Thematic Conference on
Computational Methods in Structural Dynamics and Earthquake Engineering
M. Papadrakakis, M. Fragiadakis (eds.)
Crete, Greece, 24–26 June 2019

MODELLING DAM-WATER DYNAMIC INTERACTION. NUMERICAL OPTIONS AND EXPERIMENTAL VALIDATION

José V. Lemos[1], **Jorge P. Gomes**[1] **and Sérgio Pereira**[2]

[1] National Laboratory for Civil Engineering (LNEC)
Av. do Brasil 101, 1700-066 Lisboa, Portugal
vlemos@lnec.pt; jgomes@lnec.pt

[2] Construct-ViBest, Faculty of Engineering (FEUP), University of Porto
Rua Dr. Roberto Frias, 4200-465 Porto, Portugal
pereira.sergio@fe.up.pt

Abstract

The safety evaluation of concrete arch dams requires validated numerical procedures capable of representing the dynamic interaction between the dam and the reservoir during a seismic event. The proposed numerical model employs a discrete element formulation, which is ultimately intended to represent the potential dynamic slip of discontinuities in the rock mass foundation. The present paper focuses on the dam-water interaction modelling, which is a key component of the dynamic response of concrete arch dams. A fluid element discretization of the reservoir domain was adopted, based on Cundall's mixed discretization technique, which provides a displacement formulation for time domain analysis. Simple validation tests confirmed the accuracy of the solution. The model was also applied to a case study involving a recently built arch dam in Northern Portugal. In situ measurements of the dam dynamic response were made by two methods: forced vibration tests, performed before and after filling the reservoir, and a continuous monitoring systems installed in the structure. These measurements provided extensive data that allowed the dynamic characterization of the concrete arch structure and the validation of the numerical model.

Keywords: Concrete dams, Dam-water interaction, Discrete elements.

1 INTRODUCTION

The safety evaluation of concrete arch dams built in regions of significant seismic hazard requires the simulation of their response under various levels of seismic action. The numerical models employed in those analyses have to be validated with experimental data, which is becoming more extensively available nowadays. There is a long experience in the development and application of finite element representations of dam-foundation-reservoir systems [1]. Direct finite element procedures involving nonlinear response history analysis have gained more attention recently, proving to be a highly performing tool [2].

Discrete element models are widely used in rock mechanics, namely in dam foundation analysis [3], given their ability to address the role of discontinuities and their complex nonlinear behavior. Some studies of dynamic slip on rock joints during earthquakes have been performed for arch dam foundations [4], in which the reservoir effect was modelled by the classical Westergaard's added mass technique. A more elaborate representation of the hydrodynamic interaction, involving the discretization of the water domain, is proposed in the present paper. The fluid elements are based on Cundall's mixed discretization technique [5], which is available in the discrete element code 3DEC [6]. The tests performed show that this formulation is capable of addressing the hydrodynamic interaction problem.

A research project involving a recently built arch dam in Northern Portugal is providing extensive data on the dynamic behavior of the structure. In situ measurements of the dam dynamic response were made by two methods: forced vibration tests, performed before and after filling the reservoir, and a continuous monitoring system that has been installed in the structure [7,8]. In the present paper, the results obtained with the proposed numerical model are compared with these field measurements, providing a test of its practical performance under essentially linear conditions, given the relatively low levels of vibration induced.

2 CUNDALL'S MIXED DISCRETIZATION TECHNIQUE

2.1 Fluid elements

The representation of the reservoir in the 3DEC model was achieved with a displacement formulation of fluid elements, as this approach provides a straightforward mechanical interaction with the dam upstream face and the foundation, using the standard contact logic.

The mixed discretization formulation was initially proposed by Marti & Cundall [5] for the accurate solution of plasticity problems with low order elements (or zones). The principle of the mixed discretization technique is to give the element more volumetric flexibility by proper adjustment of the first invariant of the element strain tensor. In the plane case, a 4-node plane element is formed by 2 overlays of 2 uniform-strain triangles. The volumetric strains and stresses are averaged in each overlay. A three-dimensional version of this formulation was subsequently implemented in the 8-node brick element available in the codes FLAC-3D [9] and 3DEC [6]. In this case, the 8-node brick element (or zone) is built by assembling 2 overlays of 5 uniform-strain tetrahedral elements each, as shown in Figure 1. The first invariant of the strain tensor of a particular tetrahedron is evaluated as the volumetric-average value over all tetrahedra in the brick element.

This formulation also allows the representation of the fluid behavior, so it can be used to derive fluid elements. Using the elastic bulk modulus, the same pressure results in the 5 tetrahedra of each overlay. The reduction of the number of deformation modes that this constraint enforces allows a stable numerical response even in the case of zero shear modulus, as it occurs in perfectly-plastic yielding or in a fluid. The main computational advantage of this ap-

proach is that it can be implemented in codes using explicit time stepping algorithms, such as FLAC-3D or 3DEC.

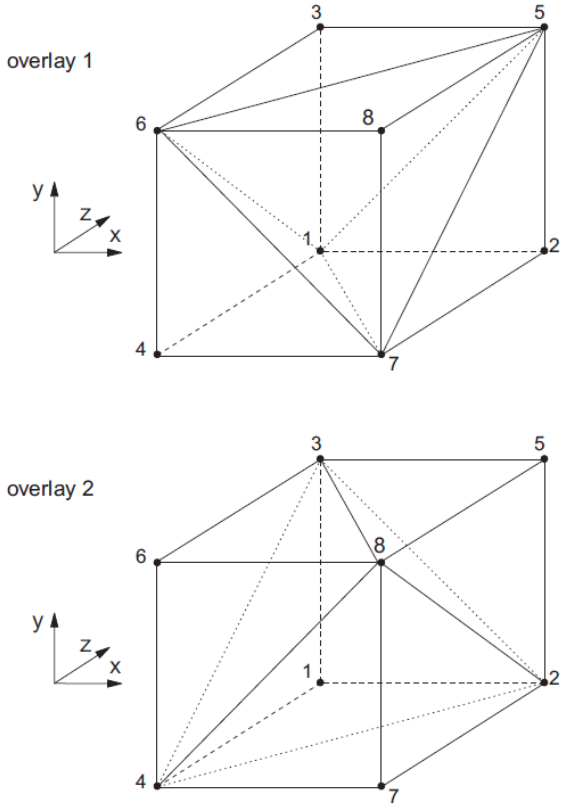

Figure 1: An 8-node element with 2 overlays of 5 tetrahedra in each overlay.

2.2 Application to dam-reservoir interaction problems

Tests of the 3DEC fluid elements based on the mixed discretization technique were performed by comparison with the classical Westergaard solution for a rigid dam with a vertical face. Figure 2 shows the numerical model of the reservoir, for the case of a 100 m high dam. The extension of the reservoir is 200 m, with absorbing boundaries based on a viscous formulation placed at the far end to allow energy radiation [6]. The acceleration was prescribed at the near end, and out of plane displacements were prevented along the two lateral boundaries. A time domain analysis was performed, which converged towards a steady-state solution. Figure 3 shows the pressure diagram along the height, comparing the analytical solution with the results of two fluid element models with different mesh sizes. The numerical results approach the analytical solution, as the element mesh is refined. A fair agreement is obtained with mesh A corresponding to elements with 10 m of dimension (shown in Figure 2), which improves as the element size is reduced to 2.5 m, in mesh B.

A series of tests of this type of fluid elements in transient conditions are presented by Andrian and Agresti [10], using a FLAC-3D model. These authors also performed an application of this model to the case of a gravity dam in Japan, for which field records of earthquake response are available.

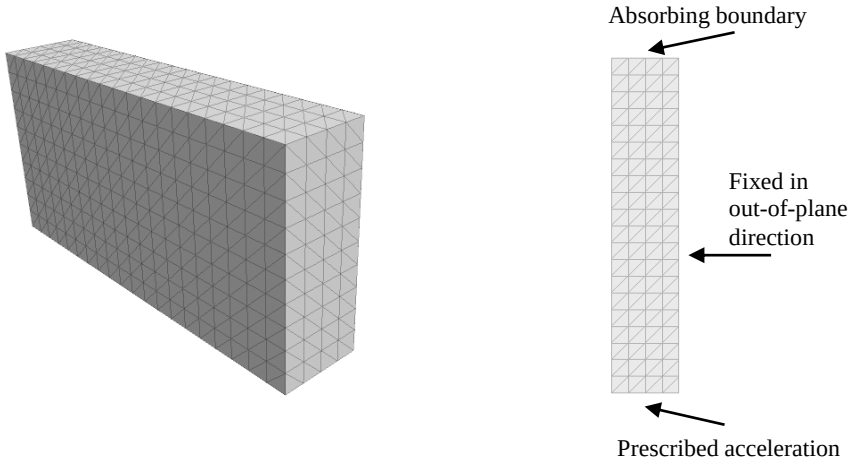

Figure 2: Model of fluid elements and boundary conditions for comparison with Westergaard formulation. Coarse mesh A (10 m elements).

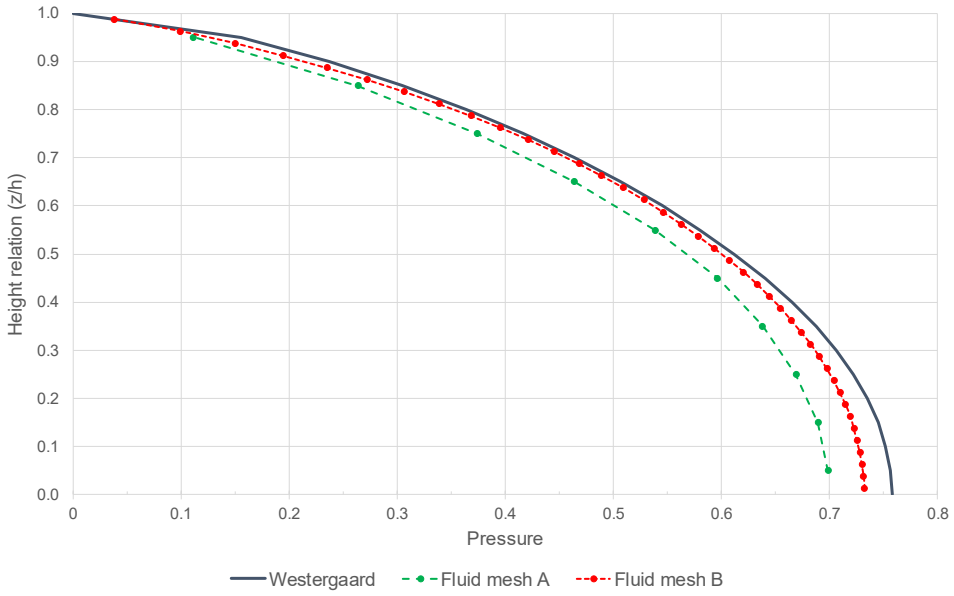

Figure 3: Comparison between the Westergaard formulation and fluid elements for mesh A (10 m elements), and mesh B (2.5 m elements)

3 CASE STUDY

3.1 Description of the dam

The Baixo Sabor hydroelectric project, owned by EDP, is located in Torre de Moncorvo, in the North of Portugal, over the lower reach of river Sabor, a right bank tributary of river Douro. The project includes an arch dam, upstream, and a gravity dam, downstream, to create the pool required for pumping. The main dam is a double curvature arch, with a maximum height of 123 m above the foundation (Figure 4). The crest, at elevation 236.00 m, has a 6.00 m thickness and a total length of 505 m. The arch is formed by 32 blocks, separated by vertical

contraction joints. At the upper central zone of the dam, a crest spillway is installed with 4 openings, equipped with radial gates.

Figure 4: View of Baixo Sabor arch dam and cross-section through the central cantilever

Forced vibration tests were performed for the dynamic characterization of the dam, before the reservoir filling [7], and with full reservoir. The dam is equipped with a seismic monitoring system to evaluate the behavior of the structure when subjected to seismic actions. In addition, a dynamic monitoring system, comprising 20 uniaxial accelerometers, has been installed to continuously characterize its dynamic response. Results obtained during the first six months of operation, which includes the reservoir-filling phase, have clearly shown the effect of the water level on the natural frequencies [8].

3.2 Numerical model

For interpreting the experimental results, a numerical representation of the dam was built with 3DEC [6], a discrete element code widely used in the field of rock mechanics. This code has been applied to the safety assessment of dams, considering the failure modes through the rock foundation, under static or dynamic loads, namely for Baixo Sabor dam [4]. The code allows the consideration of deformable blocks, which are discretized into an internal finite element mesh. For polyhedral rock blocks, tetrahedral elements are preferred, while to represent the concrete arch, 20-node brick elements can be employed. 3DEC has been employed in previous seismic analysis of arch dams considering the nonlinear behavior of the joints, but adopting added-masses to simulate the reservoir effect [11].

The dam model has 32 cantilever blocks separated by vertical contraction joints (Figure 5, where all element faces are approximated by triangular facets). The blocks of the dam cantilevers were discretized into 20-node brick elements, with 3 elements across the thickness. In the present study, focused on the hydrodynamic interaction, a simplified representation of the foundation rock mass was used. An elastic dam-rock interface was adopted, with a joint stiffness calculated to provide an approximate value of the rock mass deformability. Given the low intensity of the dynamic input, the dam contraction joints were assumed elastic. The dam-water and water-foundation interfaces were assigned a null shear stiffness, reproducing a frictionless behavior. At the far end of the reservoir a viscous boundary condition was applied to provide the energy radiation.

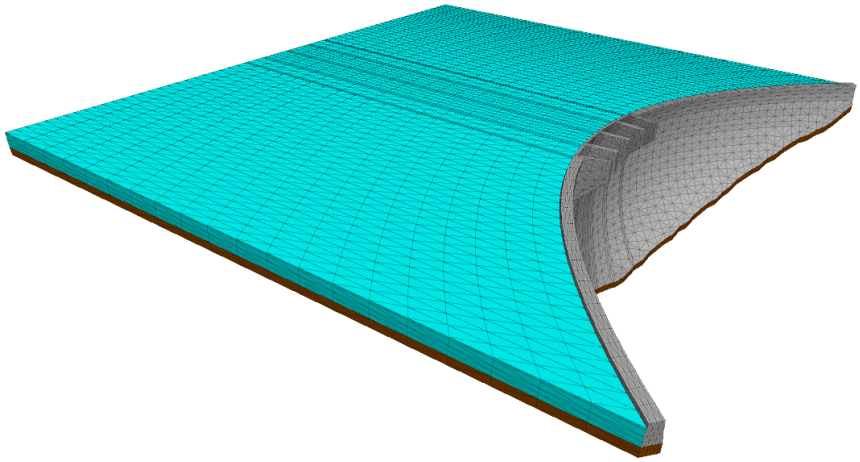

Figure 5: Numerical model of dam and reservoir.

The dam concrete Young's modulus was 36 GPa and the Poisson's ratio was 0.20, values consistent with in situ material tests. A joint normal stiffness of 50 GPa/m was assigned to the dam contraction joints, while a value of 12.5 GPa/m was used for the dam-rock interface. In both cases, the joint shear stiffness was taken as 0.42 of the normal stiffness. The water was assigned a bulk modulus of 2 GPa, and zero shear modulus; the water-dam and water-rock interfaces had a normal stiffness of 2 GPa/m, and zero shear stiffness.

3.3 Comparison of results

In order to determine the natural frequencies in the numerical model, time domain analyses were performed by applying a random excitation to the model, which was simulated by means of horizontal tractions distributed along the dam crest. The frequencies and modal shapes were then identified by standard software, from the response obtained at the locations in the dam that were also used in the experimental measurements.

A comparison of the numerical results with the experimental values is shown in Figure 6. The four lower modal frequencies and configurations, for a condition of full reservoir, are displayed. Regarding the experimental results, a good match had already been found between the forced vibration tests and the continuous monitoring data under ambient vibration conditions [8]. The measurements also agree quite well with the present numerical model using fluid elements, both in terms of frequency values and modal shapes. For this particular wide arch dam, the first mode is the symmetric configuration, while the second mode is anti-symmetric.

The classical Westergaard's added-mass approach is still often used in dam engineering, as it provides a relatively accurate solution with a low computational cost. Various authors have compared it with more elaborate models (e.g. [12]). In general, to have a better approximation, the values of the masses given by the analytical formula need to be scaled, with different scaling factors having been proposed for dams of various heights. In many cases, the full value overestimates the hydrodynamic interaction. The scaling procedure obviously implies the existence of field measurements, which are not available at design stage.

Forced vibration tests		Numerical model	
Freq, (Hz)	Modal configuration	Freq, (Hz)	Modal configuration
2.44	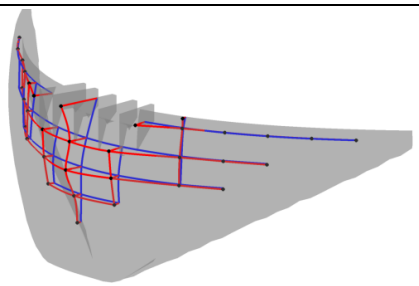	2.44	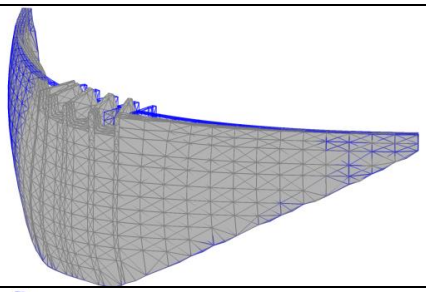
2.57	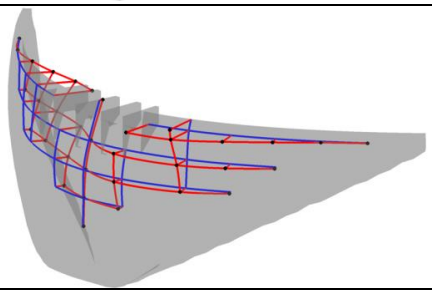	2.58	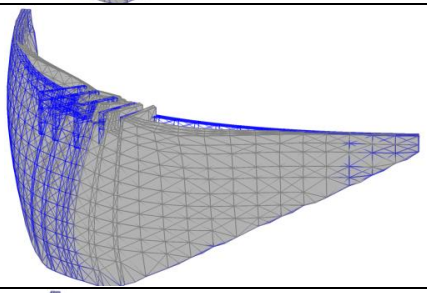
3.34	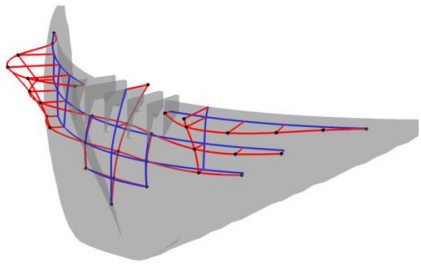	3.35	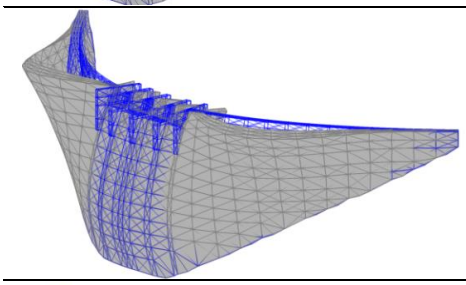
3.93	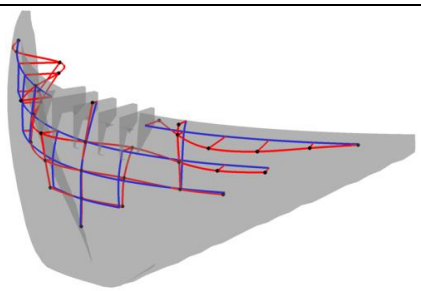	3.82	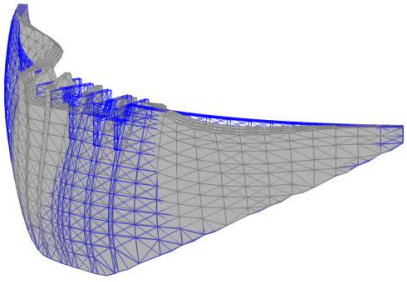

Figure 6: Comparison of experimental and numerical modal frequencies and configurations.

In the present study, the results of the fluid element model were also compared with the added-mass representation, using the same dam mesh. In order to match the first frequency, a scaling factor of 0.525 had to be applied to the added-masses. The comparison of frequencies is presented in Table 1. It may be seen that the fluid element results approximate better the measured field data. For example, the difference between the first two frequencies is overestimated with the added-mass solution. However, in many practical situations, the simpler added-mass model can still perform reasonably well in seismic analysis, provided a scaling factor can be determined by either experimental tests or by running a more elaborate numerical model of the reservoir.

Mode	Measured	Fluid elements	Added masses
1	2.44	2.44	2.44
2	2.57	2.58	2.67
3	3.34	3.35	3.56
4	3.93	3.82	4.03

Table 1: Natural frequencies measured in forced vibration tests and results of numerical models with fluid elements and scaled added masses.

4 CONCLUDING REMARKS

Various types of numerical representations have been proposed over the years for the dam-reservoir interaction under dynamic loads. The choice is often dictated by the particular aim of the study and by the formulations available in the code selected for the analysis. The present paper is framed within a discrete element environment, which provides appropriate representation of media with discontinuities. The particular model of the arch dam was focused on the assessment of the dam-water dynamic interaction. The only discontinuities were the dam contraction joints and the interfaces between dam, water and foundation, all of which could be assumed elastic for the low intensity of vibration that was measured in the field experiments. The fluid elements based on Cundall's mixed discretization technique showed a good performance in comparison with the measured data. In the future, this type of model is mainly intended for earthquake analysis, including the evaluation of potential movements in rock joints that may be induced by the seismic event.

ACKNOWLEDGEMENTS

This work was partially supported by: PTDC/ECM-EST/0805/2014|16761 – DAM_AGE - Advanced Online Dynamic Structural Health Monitoring of Concrete Dams, funded by FEDER funds through COMPETE2020 - Programa Operacional Competitividade e Internacionalização (POCI) – and by national funds through FCT - Fundação para a Ciência e a Tecnologia. The authors wish to thank EDP for permission to present the test results.

REFERENCES

[1] A.K. Chopra, Earthquake analysis of arch dams: factors to be considered. *Journal of Structural Engineering*, **138**(2), 205-214, 2012.

[2] A. Løkke, A.K. Chopra, Direct finite element method for nonlinear earthquake analysis of concrete dams: Simplification, modeling, and practical application. *Earthquake Engineering & Structural Dynamics*, **48**(1), 1-25, 2019.

[3] J.V. Lemos, Block modelling of rock masses. Concepts and application to dam foundations. *European Journal of Environmental and Civil Engineering*, **12**(7-8), 915-949, 2008.

[4] J.V. Lemos, Modelling the failure modes of dams' rock foundations. G. Barla ed. *MIR 2012 - Nuovi metodi di indagine, monitoraggio e modellazione degli amassi rocciosi*, Politecnico di Torino, 259-278, 2012.

[5] J. Marti, P.A. Cundall, Mixed discretization procedure for accurate solution of plasticity problems. *International Journal Numerical and Analytical Methods in Geomechanics*, **6**, 129-139, 1982.

[6] Itasca, *3DEC - Three-dimensional Distinct Element Code*. Version 5.2. Itasca Consulting Group, Minneapolis, USA, 2017.

[7] J.P. Gomes, J.V. Lemos, Characterization of the dynamic behavior of an arch dam by means of forced vibration tests. J.-J. Fry, N. Matsumoto eds. *Validation of Dynamic Analyses of Dams and Their Equipment: Edited Contributions to the International Symposium on the Qualification of Dynamic Analyses of Dams and their Equipments, 31 August-2 September 2016, Saint-Malo, France*, CRC Press, 2018.

[8] S. Pereira, F. Magalhães, J.P. Gomes, A. Cunha, J.V. Lemos, Dynamic monitoring of a concrete arch dam during the first filling of the reservoir. *Engineering Structures*, **174**, 548–560, 2018.

[9] Itasca, *FLAC-3D - Fast Lagrangian Analysis of Continua in 3 Dimensions Code*. Version 6.0. Itasca Consulting Group, Minneapolis, USA, 2017.

[10] F. Andrian, P. Agresti, Effects of radiative boundary conditions on seismic analyses of gravity dam. J.-J. Fry, N. Matsumoto eds. *Validation of Dynamic Analyses of Dams and Their Equipment: Edited Contributions to the International Symposium on the Qualification of Dynamic Analyses of Dams and their Equipments, 31 August-2 September 2016, Saint-Malo, France*, CRC Press, 2018.

[11] D. Silva Matos, J. Paixão, J.V. Lemos, N. Azevedo, Seismic Studies of Foz Tua and Fridão Dams. *15th World Conference on Earthquake Engineering*, Lisbon, SPES, 2012.

[12] M. Goldgruber, S. Shahriari, G. Zenz, Influence of damping and different interaction modelling on a high arch dam. C. Adam, R. Heuer, W. Lenhardt, C. Schranz eds. *Vienna Congress on Recent Advances in Earthquake Engineering and Structural Dynamics 2013 (VEESD 2013)*, Paper No. 559, Vienna, Austria, 2013.

COMPDYN 2019
7th ECCOMAS Thematic Conference on
Computational Methods in Structural Dynamics and Earthquake Engineering
M. Papadrakakis, M. Fragiadakis (eds.)
Crete, Greece, 24–26 June 2019

THE ROLE OF SOIL-STRUCTURE INTERACTION IN THE INTERPRETATION OF DYNAMIC TESTS ON THE "CHIARAVALLE VIADUCT"

Sandro Carbonari [1], **Francesca Dezi**[2], **Fabrizio Gara**[1]

[1] Università Politecnica delle Marche, DICEA
Via Brecce Bianche, 60128 Ancona, Italy
e-mail: {s.carbonari, f.gara}@univpm.it

[2] University of San Marino, DESD
Via Consiglio dei Sessanta, 99 47891 Dogana – Repubblica di San Marino
francesca.dezi@unirsm.sm

Abstract

The paper addresses the significance of soil-structure interaction on the dynamic behaviour of the "Chiaravalle viaduct", based on ambient vibration measurements and numerical simulations. The viaduct is located in Central Italy and is founded on piles in an eluvial-colluvial soil deposit. Experimental modal properties are evaluated by means of the operational modal analysis on accelerometric data from ambient excitation and the role of soil-structure interaction in the interpretation of tests is investigated by means of a refined finite element model of the viaduct. In the soil-structure interaction models the local site condition in correspondence of each bridge piers (resulting from geotechnical and geophysical investigations) are considered in the definition of the soil-foundations compliance. Comparison between the experimental and numerical results highlight the role of the pile-soil-pile interaction, the radiation problem, the pile cap embedment and the variability of the soil stratigraphy along the longitudinal direction of the viaduct in the interpretation of the experimental data.

Keywords: reinforced concrete viaduct; Soil-Structure Interaction; site response; dynamic identification; Operational Modal Analysis; finite element model.

1 INTRODUCTION

The high Italian seismicity in conjunction with the existing dense transport infrastructures require the seismic verification and upgrading of bridges to improve the overall earthquake resilience of communities. In this framework, system identification and structural health monitoring of structures have recently drawn attention for developing assessment tools and reducing uncertainties in the risk assessment procedures. Estimation of the dynamic properties of bridges using recorded vibration data allows the calibration of numerical models for the assessment of the structural safety and for the design of a seismic retrofit (e.g. [1-2]). The Ambient Vibration Test (AVT) is one of the most attractive methods for the evaluation of the dynamic properties of existing constructions in elastic range since it uses natural vibrations as input and foresee the use of small and portable instrumentation. It is generally common practice to perform AVTs, to get modal parameters through the Operational Modal Analysis (OMA) [3-4] and then to calibrate finite element models by changing the mechanical properties of materials, achieving the best fit of the model results with the experimental data. On the contrary, geometry of structural components is assumed in a deterministic way and the structure is assumed to be fixed at the base. However, it is well-known in the literature, from both numerical (e.g. [5-10]) and experimental studies (e.g. [11-12]), that Soil-Structure Interaction (SSI) may play an important role in the dynamic structural response, especially for medium or soft soil conditions and for existing bridges. Thus, numerical models developed to interpret results of vibrational measurements should include the soil-foundation compliance [13].

The objective of this work is to address the significance of soil-structure interaction in the interpretation of the vibrational tests performed on the Chiaravalle viaduct, for which detailed experimental campaigns and surveys on both the soil deposit and the superstructure were available. A 3D finite element model of the bridge is developed accounting for the soil-foundation compliance through Lumped Parameter Models (LPMs) [14], reproducing the dynamic impedances of soil-foundation systems. The latter are obtained with a refined 3D solid model accounting for the pile-soil-pile interaction, the radiation problem and the pile cap embedment. Modal parameters obtained from the OMA are compared with those derived from the numerical models of the bridge.

2 THE CHIARAVALLE VIADUCT

The Chiaravalle Viaduct in Central Italy connects the SS76 road to the Raffaello Sanzio airport (Figure 1a). The viaduct has a total length of 875 m and is constituted by 4 Kinematic Chains (KC#), separated by structural joints. The KCs are constituted by 27.5 m long simply supported girders connected over the piers through post-tensioned cables at the level of the concrete slab. The deck is 12.10 m wide and is constituted by three simply supported V-shaped r.c. beams underlying a 0.25 m thick concrete slab. The column bent piers are constituted by 2 circular columns with diameter of 1.4 m, with heights ranging between about 6÷12 m. Only one pier (P17 of KC2) is different, characterized by a single column with a rounded rectangular cross section (Figure 1a). The foundation of each pier is constituted by 6 r.c. piles of length 30 m and diameter 1 m, connected at the head by a rigid cap of dimensions 5 x 9 x 1.70 m (Figure 1b). During construction, 240 concrete samples were tested, so that results of samples, in conjunction with tests performed specifically for the retrofit design, allow to assume the mechanical parameters (mean compressive strength f_{cm} and elastic mean modulus E_{cm}) reported in Table 1.

From the geomorphological point of view, the viaduct is located in a wide almost flat area with low altitudes set at almost 17-20 m above the mean sea level. With reference to Figure 2a, the geological configuration of the site is constituted by three main formations: a Plio-

Pleistocene marine deposit, prevalently composed of Pleistocene marly, silty clays (AD4) underlying a recent continental covering soil that mainly consists of Quaternary (Pleistocene-Holocene) eluvial-colluvial (sandy and clayey silts, AD1) and Plio-Pleistocene alluvial (mainly sandy gravels with clayey silts lenses, AD2) deposits. Locally, above the Plio-Pleistocene clayey substratum, lenses of sands in clayey-silty matrix can be found (AD3). The area was investigated by means of Boreholes (B), laboratory tests (e.g. triaxial tests, oedometer test) and in-situ Standard Penetration Test (SPT) conducted up to a maximum depth of about 24 m. The geophysical characterization was performed through a Multichannel Analysis of Surface Waves (MASW) and Down Holes (DH). Locations of tests are shown in Figure 2a, b. Furthermore, two Piezometers (PZ) were used to monitor the ground-water level along the viaduct. Results of geotechnical and geophysical surveys leads to the mechanical and dynamic parameters reported in Table 2 for each lithotype.

3 AMBIENT VIBRATION TESTS

Ambient vibration measurements were performed to evaluate modal parameters of the viaduct in order to develop and validate a finite element model for the design of the bridge seismic upgrading.

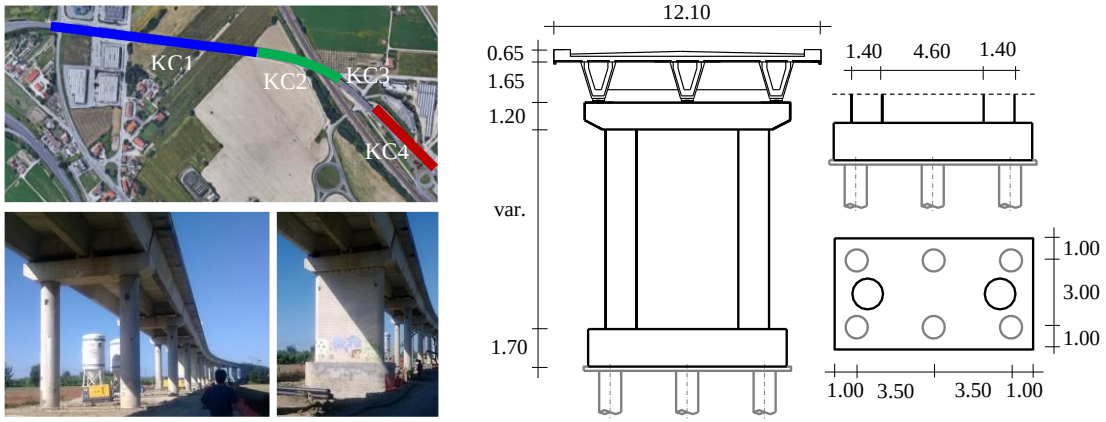

Figure 1. (a) Plan location of KCs and view of the viaduct, (b) dimensions of the viaduct cross section and foundations in [m].

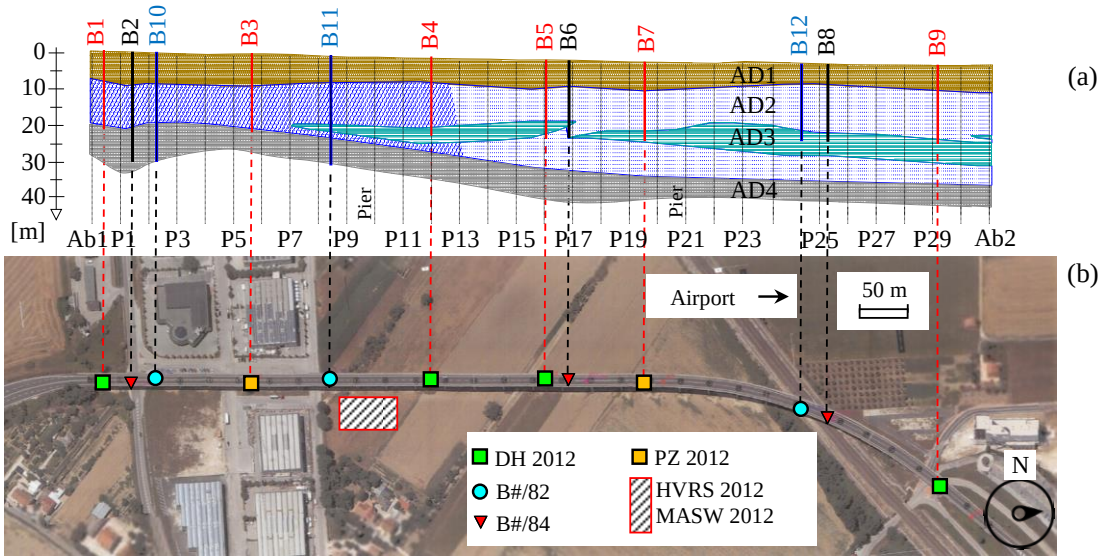

Figure 2. (a) Soil geological profile, (b) position of the test site and geotechnical surveys.

Structural element	Number of specimens	f_{cm} [MPa]	E_{cm} [MPa]
Columns	33	17.0	25796
Foundation piles	20	7.5	20181
Pile foundation caps	29	12.8	23691
Column caps	8	27.1	29670
Beams	10	40.7	33520

Table 1. Mechanical properties of concrete.

Soil	γ [kN/m³]	I_D [%]	c' [kPa]	c_u [kPa]	Φ' [°]	E_u [kPa]	E_{oed} [kPa]	V_s [m/s]	G_0 [kPa]
AD1	19.02	-	20	20	27	63000	8700	230	92000
AD2	19.60	63	-	-	39	42000	-	540	567000
AD3	20.00	-	7	35	27	15000	-	325	218000
AD4	20.00	-	30	400	26	70000	-	600	770000

I_D = density index; Vs = shear wave velocity; c' = drained cohesion
γ = unit weight of soil; G_0 = small strain shear modulus; c_u = undrained cohesion
Φ' = angle of internal friction; E_u = undrained modulus; E_{oed} = oedometric modulus

Table 2. Mechanical and dynamic parameters

AVTs are carried out with low noise unidirectional piezoelectric accelerometers connected to a 24-bit data acquisition system by means of coaxial cables and a portable PC for data storage. Each KC is monitored separately, and different sensor configurations are scheduled where necessary; KC3 was not investigated due to logistic problems. Tests for each KC were performed in different days during the same week of July 2014 in the same timeslot so that ambient effects on the estimated modal parameters can be considered negligible (e.g. [15-17]).

To capture the transverse dynamic behaviour of the bridge, unidirectional accelerometers are placed at each span support and oriented in the transverse direction. For each configuration, 1800 seconds long records sampled at a rate of 2048 Hz are acquired. All the recorded data are processed with standard signal processing techniques before performing the modal analyses. Finally, signals are down-sampled at 51.2 Hz to decrease the number of data and the SSI-Cov technique was used to identify the dynamic properties of the viaduct [3].

4 NUMERICAL MODELLING STRATEGY FOR THE AVTS INTERPRETATION

A refined 3D finite element model of the viaduct is developed to interpret results of AVTs. As for the superstructure, both deck and column bent piers are modelled with elastic frame elements considering the real position of the centroids through rigid links. Mechanical properties of the concrete are based on experimental results presented in Table 1. The deck bearings are modelled with elastic links of suitable stiffnesses. A Fixed Base model (FB) as well as a Compliant Base model (CB) of the viaduct, accounting for the soil-foundation dynamic stiffnesses are developed. In Figure 3a some pictorial views of the FB model are reported.

The CB model, addressing the SSI problem, is developed in the framework of the substructure approach, which allows analysing separately the soil-foundation and the superstructure systems. The analysis of the soil-foundation subdomain furnishes the frequency-dependent complex dynamic impedance matrix of the system that represents the behaviour of the superstructure restraints. Since software dedicated to structural modelling generally performs time domain analyses, the frequency dependent behaviour of the soil-foundation system is generally included through the use of LPMs constituted by assemblages of frequency independent springs, dashpots and masses. Parameters of the lumped system are calibrated to as-

sure the best match between its dynamic stiffness matrix and that of the actual soil-foundation system in a selected frequency range. The LPM presented by Carbonari et al. [14] is adopted to simulate the soil-foundation dynamic behaviour of each pier in the CB model (Figure 3b). Each LPM is characterized by 24 parameters and is able to reproduce the frequency dependent translational, rotational and coupled roto-translational dynamic behaviour of the pile foundations characterised by a double symmetric layout. The external node, representing the interface between the soil-foundation system and the superstructure, is located at the intersection of the two symmetry axes.

4.1 Soil-foundation modelling

The analysis of the soil-foundation system necessary to determine the relevant frequency-dependent impedance matrix is performed adopting a refined 3D solid model. Considering the 2D stratigraphic profile, characterised by an almost constant thicknesses of soil layers for the first 20 m, only one soil-foundation system, assumed to be representative for all the bridge, is modelled within the computer software ANSYS. 8-node brick elements are used to model a cylindrical soil portion with diameter D and height T satisfying conditions $D/d = 50$ and $T/d = 45$ (Figure 4) where d is the pile diameter. The soil is assumed to be a viscoelastic material and infinite elements are provided at boundaries to absorb the outgoing waves and satisfy the radiation condition. Piles are modelled with 2-node beam elements and their physical dimensions are considered by removing cylinders of soils. The beam-solid coupling is assured exploiting potentials of the software. The pile cap, which is assumed to be rigid, is simulated through the soil excavation and the introduction of a rigid constraint, with master node M, between soil-cap interfaces and the piles head. Meshing criteria aim at obtaining an as much as possible structured mesh and assuring a sufficient number of nodes per wavelength.

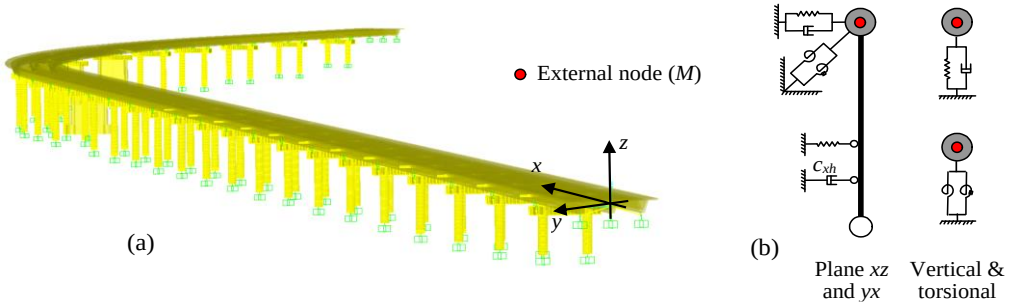

Figure 3. (a) Fixed base model (FB), (b) adopted LPM.

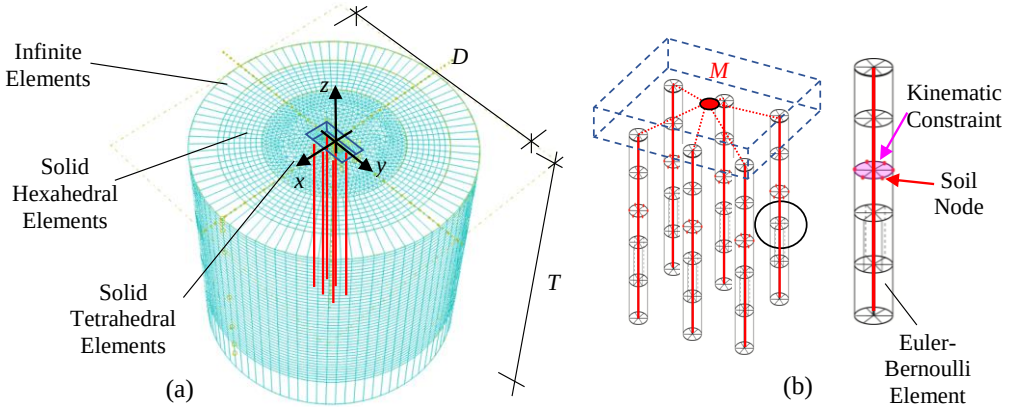

Figure 4. 3D solid finite element model of the soil-foundation system.

Some validation studies are preliminarily performed to define the mesh dimension, balancing results reliability with computational efforts; in particular, the mesh dimension is selected so as the propagation of waves with frequency up to 10 Hz are well captured. Components of the impedance matrix are obtained by imposing unit steady harmonic displacements at the fully restrained master node and evaluating the relevant reaction forces.

Figure 5 shows impedances obtained from the 3D solid model from which a change of the impedance functions slopes at 9.2 Hz is evident. The latter is due to the cut-off frequency of the deposit associated to the fundamental vibration mode of the first soil layer (lithotype DA1). However, as will be shown later, results of experimental tests (AVTs) revealed that the first three structural fundamental frequencies, which are expected to dominate the transverse dynamic response of the bridge, fall below 5 Hz. For this reason, parameters of LPMs are calibrated to reproduce the soil-foundation impedances in the frequency range 0-8 Hz. Impedances of the LPM are reported in Figure 5 with dotted lines. The lumped model is able to capture the dynamic behaviour of the comprehensive 3D solid model very well.

4.2 Experimental data and comparisons with numerical results

In this section results of AVTs are presented in terms of fundamental structural frequencies, modal damping ratios and mode shapes, providing comparisons with those obtained from the developed numerical models (FB and CB).

Figure 6a shows for each KC the normalised mean amplitude of transverse displacements measured above piers at the deck level, obtained from steady-state analysis of the CB model considering unit amplitude forces applied at the master node *M* of the LPMs implemented a the piers base to simulate the soil-foundation compliance. For each KC, the highest amplitude peaks are evident in correspondence of the relevant chain fundamental frequencies; in addition, the interaction of the *i*-th KC is revealed by the presence of lower response peaks also in the response of the other KCs. Three fundamental frequencies are highlighted in Figure 6a for each KC; these will be used to compare experimental and numerical mode shapes.

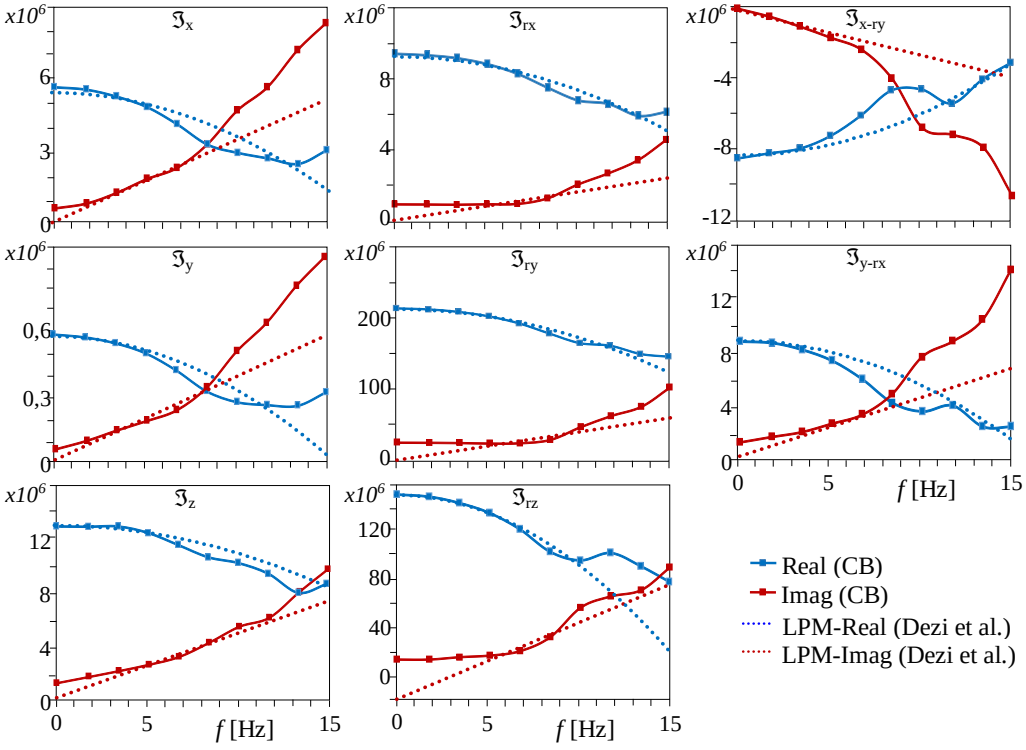

Figure 5. (a) Soil geological profile, (b) position of the test site and geotechnical surveys.

Figure 6b shows the stabilization diagrams obtained from the OMA (continuous lines are the average of PSD of sensors positioned on the KCs), used to identify the viaduct fundamental frequencies. It can be observed that the experimental response is consistent with the numerical one: peaks in the stabilization diagrams are almost aligned with the numerical ones for each KC, as highlighted by vertical dotted lines. Furthermore, also the measured relative amplitude of peaks at different frequencies is almost reproduced by the numerical model for all the KCs, with minor differences for the first peaks of KC1. Results from the FB model is not reported in Figure 6a since its response is sensibly different from the measured one. Results from this model is presented in terms of frequencies and mode shapes, obtained with a classical modal analysis.

Table 3 compares the selected three fundamental structural frequencies obtained from the AVTs and from the numerical models. With reference to experimental results, values of damping ratios are also reported for completeness. Frequencies resulting from the FB model are sensibly higher than the experimental ones; thus, the model appear not able to capture the actual viaduct dynamic behaviour. The CB model better reproduces the experimental data with relative errors always below 1% (excepting mode 3 of KC2).

Figure 7 compares the three transverse mode shapes previously selected for KC1, KC2 and KC4, obtained from the experimental tests and the numerical models, normalized with respect to its relevant maximum transverse displacement.

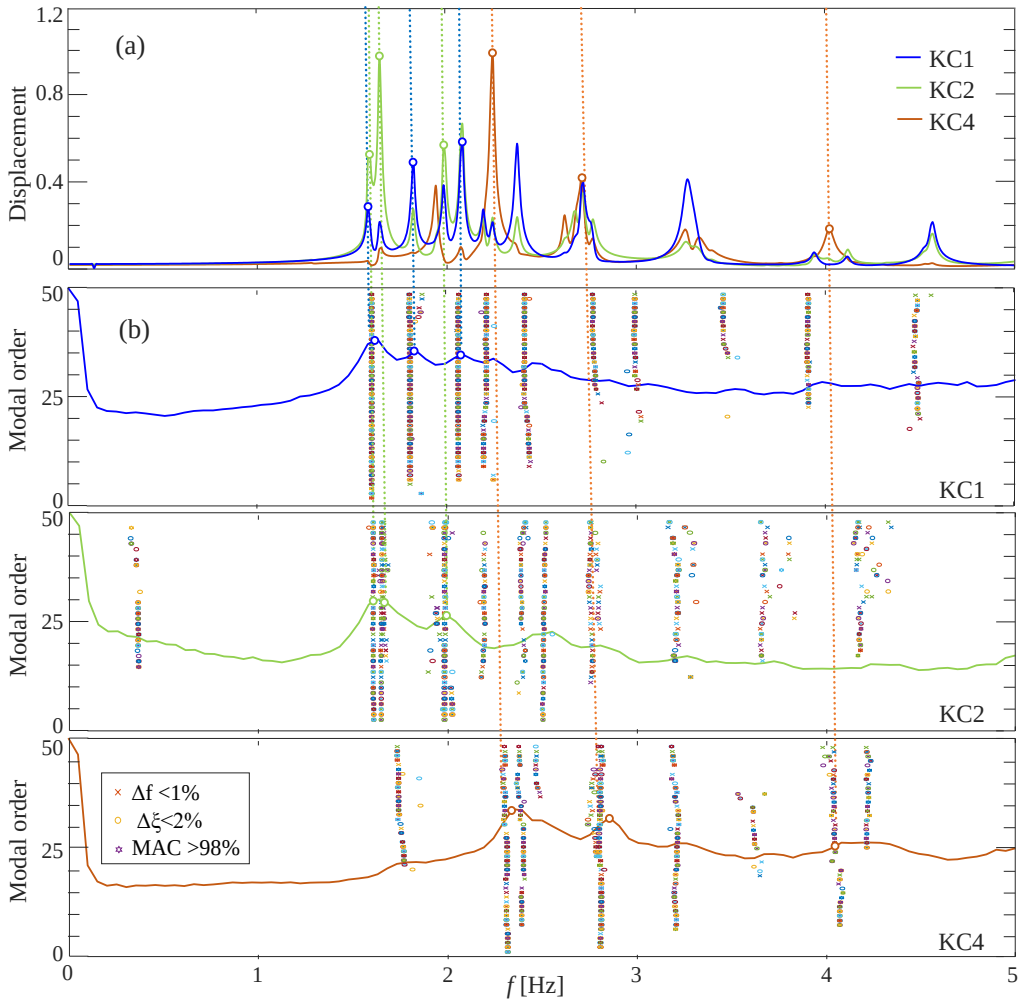

Figure 6. (a) Mean displacement amplitudes from the CB model, (b) stabilization diagrams.

KC#	Mode	OMA		CB		FB	
		f [Hz]	ξ (-)	*f* [Hz]	Δ*f* (%)	*f* [Hz]	Δ*f* (%)
1	1	**1.61**	0.57	1.60	-0.6	1.71	5.8
	2	**1.81**	1.91	1.83	1.1	1.87	3.2
	3	**2.05**	1.78	2.08	1.4	2.14	4.2
2	1	**1.58**	0.93	1.59	0.6	1.62	2.5
	2	**1.66**	0.43	1.66	0.0	1.71	2.9
	3	**1.98**	0.60	2.03	2.5	2.14	7.5
4	1	**2.26**	0.42	2.26	0.0	2.41	6.2
	2	**2.79**	0.27	2.79	0.0	2.84	1.8
	3	**4.04**	0.21	4.04	0.0	4.28	5.6

Table 3. Comparison of experimental and numerical fundamental frequencies.

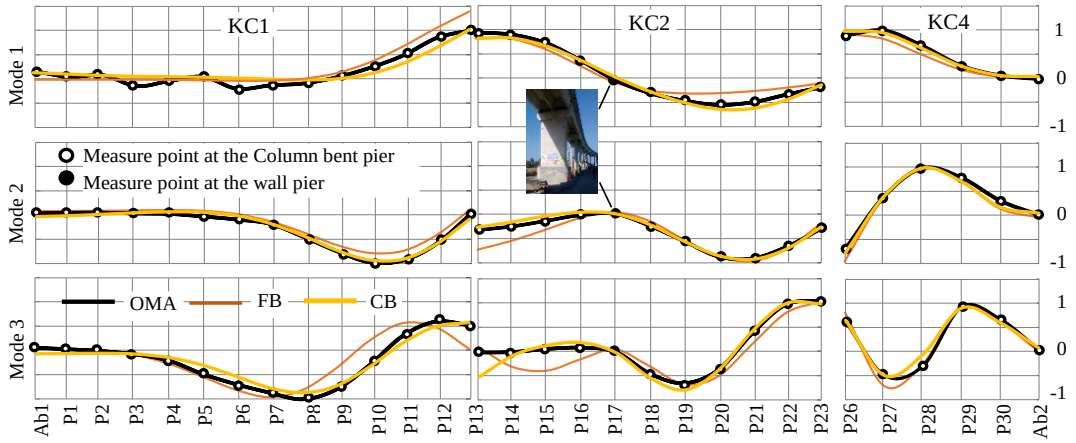

Figure 7. Comparison of numerical and experimental mode shapes.

Experimental data are reported with black lines while continuous lines are used for the numerical results. Experimental and numerical mode shapes from the CB model are practically superimposed while the FB model is not able to well interpret the experimental data.

5 CONCLUSIONS

The significance of soil-structure interaction in the interpretation of vibrational tests performed on bridges has been discussed in this work, with reference to a multi-span r.c. viaduct in Central Italy. A conventional fixed base, as well as a numerical model accounting for the soil-foundation compliance, are developed to interpret the experimental data. The soil-structure interaction is included through the sub-structure approach, simulating the frequency-dependent soil-foundation impedances through lumped parameter models. Models accuracy in reproducing the experimental modal parameters is evaluated on the basis of both fundamental frequencies and mode shapes. It is found that only a numerical model addressing the soil-structure interaction problem in a comprehensive way, i.e. including both the pile-soil-pile and pile-cap interactions, is able to interpret the experimental data.

The presented case study demonstrates that the common practice of calibrating and updating fixed base finite element models to fit experimental results from ambient vibration tests by only changing mechanical properties of materials should be prudently evaluated in the case of bridges, for which soil-structure interaction effects may significantly affects the structure dynamics, especially in the case of soft or medium soil deposits.

REFERENCES

[1] P. Omenzetter, S. Beskhyroun, F. Shabbir, G.W. Chen, X. Chen, S. Wang, A. Zha, Forced and ambient vibration testing of full scale bridges. A report submitted to Earthquake Commission Research Foundation (Project No. UNI/578), 2013.

[2] D. Zonta, B. Glisic, S. Adriaenssens, Value of information: impact of monitoring on decision-making. *Struct. Control Health Monit.* **21**: 1043–1056, 2014.

[3] Overschee, V., De Moor, B, *Subspace identification for linear systems*. Kluwer Academic Publishers, 1996.

[4] M. Dohler, E. Reynders, F. Magalhaes, et al., 2010. Pre- and Post - identification Merging for Multi-Setup OMA with Covariance-Driven SSI. *Dynamics of Bridges* **5**: 55-70, 2010.

[5] M.C. Capatti, G. Tropeano, M. Morici, S. Carbonari, F. Dezi, G. Leoni, F. Silvestri, Implications of non-synchronous excitation induced by nonlinear site amplification and soil-structure interaction on the seismic response of multi-span bridges founded on piles. *Bulletin of Earthq. Enging.* **15**(11): 4963-4995, 2017.

[6] S. Carbonari, M. Morici, F. Dezi, F. Gara, G. Leoni, Soil-structure interaction effects in single bridge piers founded on inclined pile groups. *Soil Dyn. and Earthq. Enging.* **92**: 52-67, 2017.

[7] F. Dezi, S. Carbonari, A. Tombari, G. Leoni, Soil-structure interaction in the seismic response of an isolated three-span motorway overcrossing founded on piles. *Soil Dyn. and Earthq. Enging.* **41**: 151-163, 2012.

[8] S. Carbonari, F. Dezi, G. Leoni, Seismic soil-structure interaction in multi-span bridges: application to a railway bridge. *Earthq. Enging. and Struct. Dyn.* **40**(11): 1219-1239, 2011.

[9] A.G. Sextos, K.D. Pitilakis, A.J. Kappos, Inelastic dynamic analysis of RC bridges accounting for spatial variability of ground motion, site effects and soil-structure interaction phenomena. Part 2: Parametric study. *Earthq. Enging. and Struct. Dyn.* **32**(4): 629-52, 2003.

[10] A.J. Kappos, G.D. Manolis, I.F. Moschonas, Seismic assessment and design of R/C bridges with irregular configuration, including SSI effects. *Intern. J. of Enging. Struct.* **24**(10): 1337–48, 2002.

[11] M.D. Trifunac, M.I. Todorovska, T.Y. Hao, Full-Scale experimental studies of soil-structure interaction. *2nd U.S. - Japan Workshop on Soil-Structure Interaction*, Tsukuba City, Japan, 2001.

[12] P. Faraonis, A. Sextos, E. Chatzi, V. Zabel, Model updating of a bridge-foundation - soil system based on ambient vibration data. *1st ECCOMAS Thematic Conference on International Conference on Uncertainty Quantification in Computational Sciences and Engineering, Papadrakakis M, Papadopoulos V, Stefanou G (eds.)* Crete Island, Greece, 25–27 May 2015.

[13] F. Gara, M. Regni, D. Roia, S. Carbonari, F. Dezi, Evidence of the soil-structure interaction and site response in continuous viaducts from ambient vibration tests. *Soil Dyn. and Earthq. Enging. Accepted for publication.*

[14] S. Carbonari, M. Morici, F. Dezi, G. Leoni, A Lumped Parameter Model for Time-Domain Iner-tial Soil-Structure Interaction Analysis of Structures on Pile Foundations. *Earthq. Enging. and Struct. Dyn.* **47**(11): 2147-2171, 2018.

[15] M. Regni, D. Arezzo, S. Carbonari, F. Gara, D. Zonta, Effect of Environmental Conditions on the Modal Response of a 10-Story Reinforced Concrete Tower. *Shock and Vibrations* Article ID 9476146, 2018.

[16] Y.L. Xu, B. Chen, C.L. Ng et al., Monitoring temperature effect on a long suspension bridge. *Struct. Control Health Monit*. **17**: 632-653, 2010.

[17] Y. Xia, B. Chen, S. Weng, Y.Q. Ni, Y.L. Xu, Temperature effect on vibration properties of civil structures: a literature review and case studies. *J. of Civil Struct. Health Monit.* **2**(1): 29-46, 2012.

COMPDYN 2019
7th ECCOMAS Thematic Conference on
Computational Methods in Structural Dynamics and Earthquake Engineering
M. Papadrakakis, M. Fragiadakis (eds.)
Crete, Greece, 24–26 June 2019

EFFECTS OF UNCERTAINTIES OF SOIL AND PILE MECHANICAL PROPERTIES ON THE DYNAMIC STIFFNESS OF SINGLE PILES IN HOMOGENOUS DEPOSITS

Lucia Minnucci[1], Francesca Dezi[2], Sandro Carbonari[1], Michele Morici[3], Fabrizio Gara[1], Graziano Leoni[3]

[1] Università Politecnica delle Marche, DICEA
Via Brecce Bianche, 60128 Ancona, Italy
e-mail: l.minnucci@pm.univpm.it, {s.carbonari, f.gara}@univpm.it

[2] University of San Marino, DESD
Via Consiglio dei Sessanta, 99 47891 Dogana – Repubblica di San Marino
francesca.dezi@unirsm.sm

[3] University of Camerino, SAAD
Viale della Rimembranza, 63100, Ascoli Piceno, Italy
{michele.morici, graziano.leoni}@unicam.it

Abstract

In the soil-structure interaction framework, among the results of the soil-foundation system analysis (kinematic analysis) the dynamic impedance functions represent the force-displacement relationships of the compliant restraint for the superstructure. The intrinsic variability of soil parameters and of design materials represents an uncertainty source which is necessary to include in the definition of the soil-foundation model, in order to predict the superstructure response adequately. The aim of this work is to evaluate effects of uncertainties on soil dynamic and mechanical properties on the impedance matrix of single piles in homogeneous soils, focusing on the sensitivity of the parameters. A Quasi Monte Carlo (QMC) simulation with sampling based on Sobol' sequence is performed starting from the probabilistic distribution of three main parameters characterizing the soil-piles response, i.e. the soil density, the shear waves velocity and the concrete elastic modulus of piles, available from the literature. The analyses are carried out through the numerical model developed by the Authors and a sensitivity study on the optimal number of simulations is performed, comparing the use of Quasi-random sampling with the classical Monte Carlo simulation technique. Moreover, results of sensitivity studies show the influence of variability of each considered mechanical parameter on the global response of the soil-foundation system.

Keywords: Probabilistic Analysis, Pile foundations, Soil-foundation impedance matrix, Soil-Structure Interaction Analysis, Quasi-random Simulation.

1 INTRODUCTION

It is known from the literature that Soil-Structure Interaction (SSI) has a not negligible impact on the structural response [1, 2]. To properly account for SSI in the structural design, the sub-structure approach can be employed under the assumption of a linear soil-foundation behaviour [3]. The method provides for the analysis of the structural system in two steps. The first one (kinematic interaction analysis) studies the soil-foundation system subjected to the Free-Field Motion (FFM) and provides (i) the dynamic impedance functions, which represent the force-displacement relationships of the compliant restraint for the superstructure, and (ii) the Foundation Input Motion (FIM), i.e. the actual motion experienced by the foundation because of the seismic waves propagating in the soil. The second step (inertial interaction analysis), allows to evaluate the actual superstructure response under the FIM with a compliant base characterized by the soil-foundation impedance matrix.

The soil-foundation geometrical and mechanical parameters largely affect results of the kinematic interaction analysis. Classically, deterministic values are adopted for the main quantities governing the kinematic interaction, basing on design statements, design drawings, field tests or expert engineering judgement. Even if the intrinsic variability of natural and construction materials has been widely studied in the literature, with both focus on the statistical characterization of soil mechanical properties [4, 5] and structural materials [6, 7], few works dealing with probabilistic approach for SSI are available [8-10] and, to the authors' knowledge, none of them address the problem of deep foundations. Since the kinematic interaction may produce not negligible effects on pile foundations [11, 12], a particular interest on the probabilistic characterization of such substructure behaviour arises.

This paper deals with the study of the impedance matrix of a single pile in homogenous soil with a probabilistic approach, suitably accounting for uncertainties related to the mechanical parameters of the soil-foundation system through statistic distributions available in the literature. The effects of the variability of the soil density, the shear wave velocity and the concrete elastic modulus on the dynamic impedance functions are investigated through the analytical model developed by the Authors [13], assuming no correlation between the aleatoric variables. Firstly, sensitivity analyses are performed to validate the sampling method: a comparison between Monte Carlo Simulations (MCSs) [14] and the adopted Sobol' Quasi Random Sampling (QRS) [15], which allows for a significant reduction of the number of samples and consequently of the computational effort, is shown. Then, trends of impedance functions in the frequency range of practical interest for seismic engineering is discussed. Finally, a second sensitivity analysis on the variable parameters highlights the different role of each one on the final output.

2 VARIABILITY OF SOIL AND FOUNDATION MECHANICAL PARAMETERS

In the sub-structure method, the impedance matrix defines the relationship between forces and displacements of the soil-foundation system that can be used in the inertial interaction analysis to simulate the foundation compliance. For a single pile of circular cross-section, the impedance matrix assumes the form

$$\mathfrak{I}(\omega)=\begin{bmatrix} \mathfrak{I}_x & 0 & 0 & 0 & \mathfrak{I}_{x-ry} & 0 \\ & \mathfrak{I}_y & 0 & \mathfrak{I}_{y-rx} & 0 & 0 \\ & & \mathfrak{I}_z & 0 & 0 & 0 \\ & & & \mathfrak{I}_{rx} & 0 & 0 \\ & sym & & & \mathfrak{I}_{ry} & 0 \\ & & & & & \mathfrak{I}_{rz} \end{bmatrix} \tag{1}$$

whose terms are complex-valued and express the harmonic forces to be applied at the pile head, where the degrees of freedom of the system are condensed according to the sub-structuring approach, to produce its uncoupled vibration.

Each term of the matrix depends on the mechanical and geometrical characteristics of the entire system. To investigate the effects of the variability of mechanical parameters on the impedance functions, three fundamental quantities are considered as independent aleatoric variables: the soil density ρ_s, the shear wave velocity V_s and the concrete elastic modulus E_p. The latter is evaluated basing on the variability of the concrete cylindrical compressive strength f_c. Mean values (μ), standard deviations (σ) and Coefficients of Variation (COV) of the variable parameters are chosen to represent a reinforced concrete foundation in homogeneous sand soil [5, 16] starting from values available in the literature [4, 7]. Regarding the other parameters affecting the definition of the impedance functions (i.e. soil and concrete Poisson's modulus, soil damping, concrete density), deterministic values are assumed since available works in the literature [8, 17] reveal that their variability is negligible as much as their effect on the impedance functions. Table 1 shows the statistical distributions and their relevant parameters for the three examined parameters, while Table 2 lists the deterministic values adopted for soil and concrete Poisson's modulus, soil and concrete damping and concrete density.

Uncertainties	Statistical Distribution	μ	σ	COV
Soil density ρ_s [t/m^3]	Normal	17.5	-	10
Shear wave velocity V_s [m/s]	Lognormal	400	σ_{ln} =0.39	-
Concrete elastic modulus E_p [MPa]	Lognormal	3E4	$\sigma_{ln\,(f_c)}$ =0.20	-

Table 1: Statistical distributions for ρ_s, V_s, f_c.

Mechanical parameters	value
Soil Poisson's Modulus v_s [-]	0.4
Concrete Poisson's Modulus v_p [-]	0.2
Soil Damping ξ_s [-]	0.05
Concrete Density ρ_p [t/m^3]	2.5

Table 2: Deterministic parameters.

3 CASE STUDY

In this paper, a single floating pile in a homogeneous deposit is considered, with L/d = 16, where L is the total length of the pile and d is its diameter. The analyses are performed through the analytical model proposed by the Authors in [13], in which the problem is formulated in the frequency domain, the pile is assumed to be a linear elastic Euler-Bernoulli beam, the soil is constituted by infinite independent horizontal layers, and the soil-pile interaction is included through Elastodynamic Greens' functions available in the literature. Figure 1 illustrates the case study and summarizes its geometrical and mechanical characteristics.

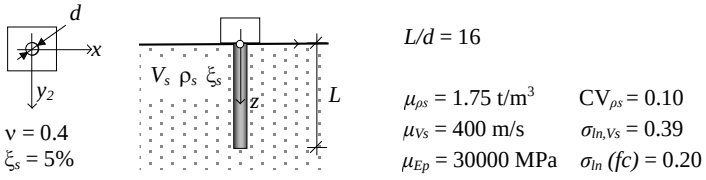

Figure 1: Case study.

4 GENERATION OF SAMPLES

The propagation of the uncertainties through the analytical model starts with a sampling procedure on the independent aleatoric variables according to their probability distributions. It is known that simple Monte Carlo sampling has a low efficiency since it requires a huge number of simulations to achieve a high precision in the results. Many different probabilistic approaches capable of reducing the required number of analyses without a loss in the accuracy of the final output are available in the literature, with many structural and seismic engineering applications (see the use of Latin Hypercube Sampling in [18], Importance Sampling [19] or Subset Simulation in [20, 21]). Among them, Quasi-Random Sampling (QRS) based on Sobol' sequence [15] is adopted in this paper. In the following sections, a brief recall on the QRS is provided, then a sensitivity analysis on the optimal number of simulations required is shown and commented to validate the adopted procedure in comparison with the standard Monte Carlo Simulation (MCS).

4.1 Quasi-Random Sampling (QRS)

Differently from the MCS, where samples are generated from a pseudo-random number source and result randomly distributed, in sense of being completely unpredictable, quasi-random samples derive from a particular algorithm in which the choice of the samples is steered to ensure a uniform cover of the sample space. Hence, quasi-random sampling techniques provide good results, since typical gaps or clusters of the MCS are avoided. Among the various quasi-random sequences available in the literature, Sobol' sequence can be used in sensitivity analysis [22], also for engineering applications [23]. More details about the efficiency of Sobol' sequence can be found in [24].

4.2 Comparison of Sobol' QRS and MCS

A preliminary study on the optimal number of required analyses is developed to validate the adopted sampling procedure, assuming results from the standard MCS as benchmark. The comparison is made on the basis of results of the sensitivity analyses.

Variance-based methods for sensitivity analysis [22] allow to study the influence of the input parameter uncertainties on the uncertainty of the final output, adopting variance as a measure of uncertainty. The first-order index, also called 'importance measure', represents the main effect contribution of each input factor to the variance of the output. Calling X_i the sample vector of the i-th input variable and Y_ω the output vector (one for each ω), the conditional expectation $E(Y_\omega | X_i)$ can be calculated by cutting the entire input variable domain into i slices and averaging the values of $(Y_\omega | X_i)$ within the same slice X_i. Thus, if the conditional expectation $E(Y_\omega | X_i)$ has a large variation across X_i, i.e. the variance of $E(Y_\omega | X_i)$, $V[E(Y_\omega | X_i)]$, is high, X_i is revealed to be important. The first-order sensitivity index $S_{i,\omega}$ for X_i is obtained dividing $V[E(Y_\omega | X_i)]$ for the unconditional variance $V(X_i)$:

$$S_{i,\omega} = \frac{V\left[E\left(Y_\omega \mid X_i\right)\right]}{V\left(X_i\right)} \tag{2}$$

Since the considered variable parameters have been assumed independent, the following condition holds

$$S_\omega = \sum_i S_{i,\omega} = 1 \tag{3}$$

where, for the present applications, i = 1, 2, 3 refers to the aleatoric parameters ρ_s, V_s and E_p. Values of S_ω greater than 1 suggests that a not sufficiently high number of samples have been considered. A comparison between MCS and Sobol' QRS is shown in Table 3 in terms of the mean value $\overline{S}$ of the sum of sensitivity indexes within the investigated frequency range, computed for different total numbers of processed analyses. It is worth noting that QRS performs much better than MCS. A reduction of the number of samples is gradually applied to reach an optimum on the minimum number of analyses to be performed with a maximum loss in precision equal to 1%. As a result, 10000 is chosen as the number of analyses to perform.

	Number of simulations			
	125000 (MCS)	25000 (QRS)	10000 (QRS)	5000 (QRS)
$\overline{S}$	1.164	1.002	1.006	1.012

Table 3: Evaluation of the sum of first-order sensitivity indexes.

5 RESULTS

5.1 Variability of impedance functions

Starting from previous considerations, 10000 analyses were executed on the soil-foundation model described in Chapters 2 and 3. The parameter distributions obtained through Sobol' QRS are illustrated in Figure 3 for the investigated aleatoric variables.

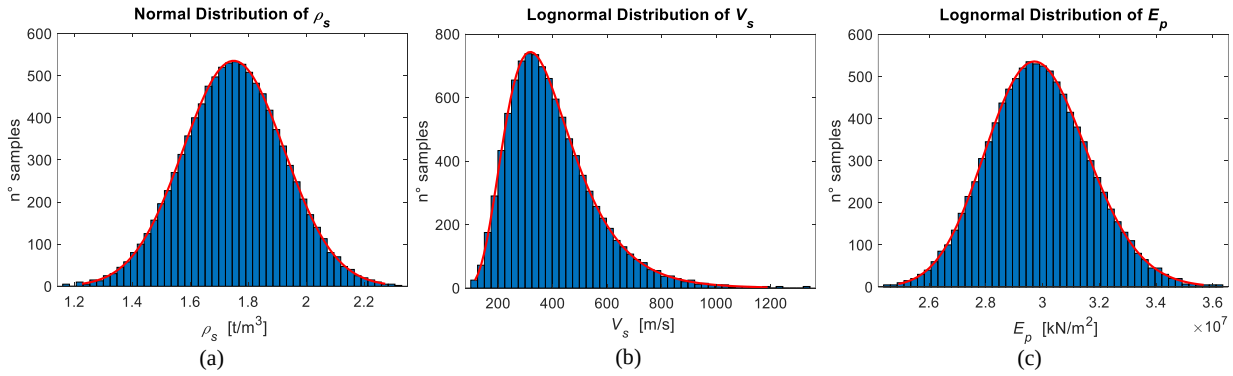

Figure 3: Sample distributions: (a) normal distribution of ρ_s, (b) lognormal distribution of V_s, (c) lognormal distribution of E_p

Boxplots in the following graphs show the statistic distribution of both real and imaginary components of the impedance functions in the frequency range 0-15 Hz, which may be considered of practical interest in earthquake engineering. In detail, the red dashed line represents the median trend of the response, the blue rectangular box encloses the 10th and the 90th percentile of the impedance at each frequency, black vertical dashed lines extend up to the 99th percentile of the output and red crosses represent the "outliers".

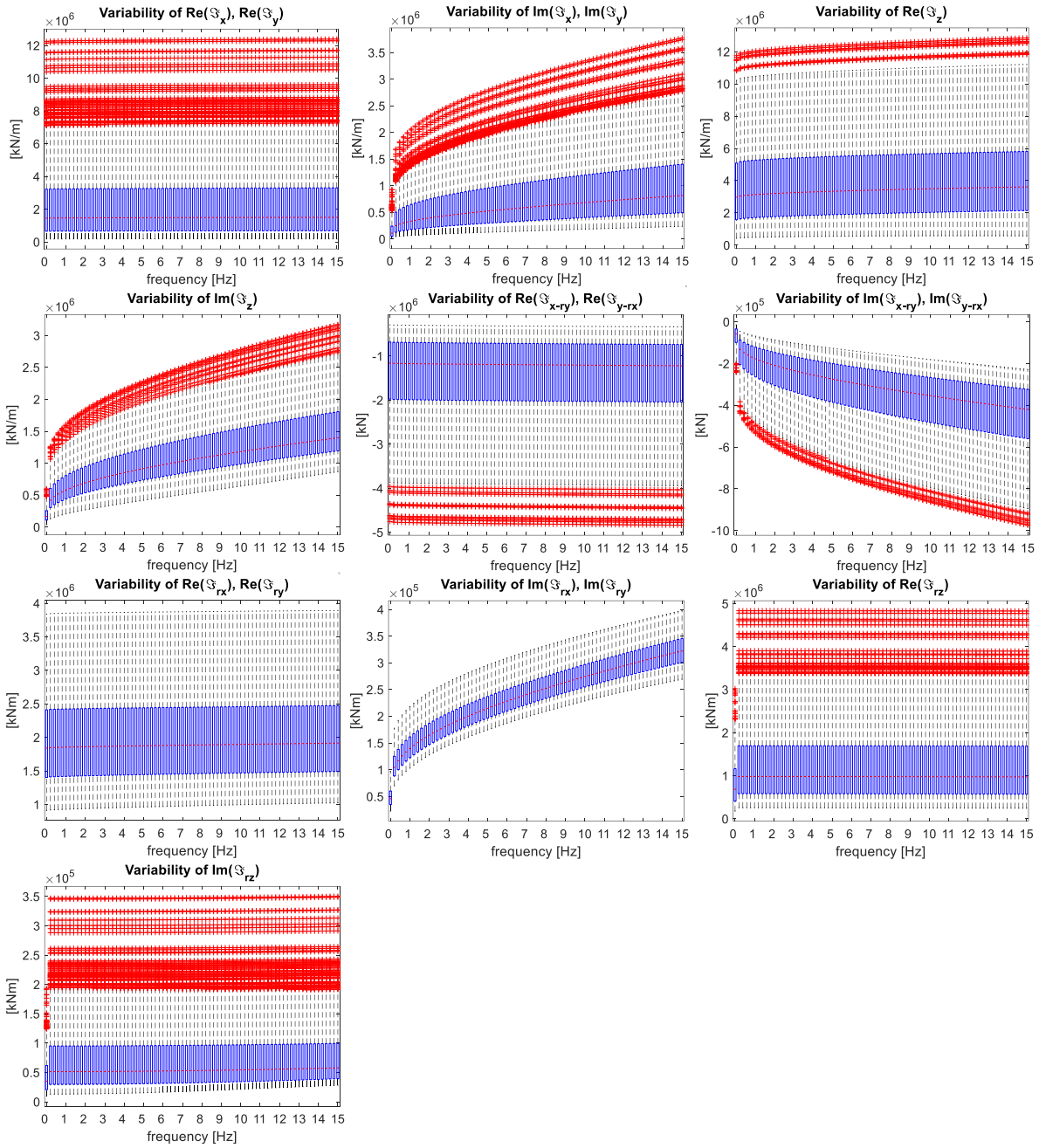

Figure 4: Impedance functions variability on the frequency range 0-15 Hz.

It is worth noting that the median trend well approximates the general one, while the ratio

$$r = \frac{\Im_{90th}}{\Im_{10th}} \tag{4}$$

between impedance values at 10th percentile and those at 90th can vary from 1.25 to 3, reflecting the great variability of the global response. Then, the variability of input parameters plays an important role in the definition of the soil-foundation response under the excitation produced by seismic waves, which should be properly addressed when the kinematic analysis is performed to reliably predict pile stress resultants, impedances and foundation input motion.

5.2 Sensitivity analysis on ρ_s, V_s and E_p

Sensitivity indexes are evaluated for each variable parameter. For sake of brevity, only sensitivity indexes of the real part of rotational impedance function $\Im_{rx}$ are illustrated in Figure 5. The graph shows the higher values on V_s, with S_{Vs} equal to 9 times S_{Ep} and over 10 times $S_{\rho s}$. Furthermore, a constant trend on the frequencies reveals that V_s is the most influential parameter for all the interest frequency domain. Similar results are obtained for other impedances functions. Hence, the response of the overall system is mainly governed by the variability of the shear wave velocity, while the soil density and the concrete elastic modulus have no predominant effect on the response in the frequency domain of interest.

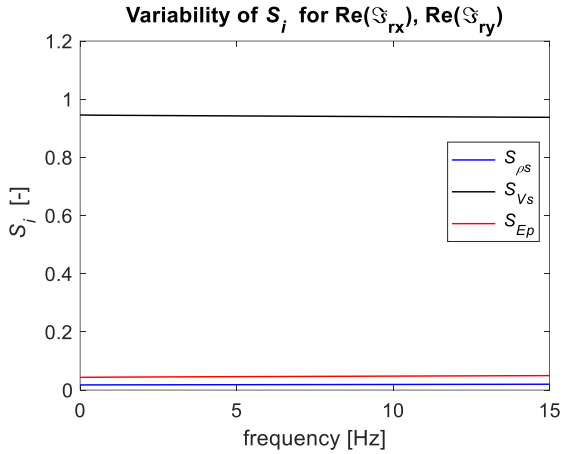

Figure 5: Sensitivity indexes of ρ_s, V_s and E_p; variability on the frequency range 0-15 Hz.

6 CONCLUSIONS

In this paper, first results of a research dealing with the effects of soil and foundation mechanical parameter uncertainties on soil-structure interaction analysis are addressed, focusing on the impedance functions of a single pile in a homogeneous soil deposit. Uncertainties are taken into account through statistical distributions of three fundamental parameters influencing the soil-pile system response, the soil density, the shear wave velocity and the elastic modulus of the pile concrete. The latter are assumed to be mutually independent. A Sobol's sequence Quasi-Random Sampling (QRS) technique is adopted to perform probabilistic analyses. A comparison between QRS and Monte Carlo Simulation (MCS) is discussed with the purpose of evaluating the optimal number of analyses to perform. The results of 10000 QRS analyses are shown and discussed, highlighting the not negligible role of uncertainties of the input parameters on the overall response. It appears that the variability of the input parameters should be included both in the kinematic analysis, where stresses on the foundation, features of the compliant base and foundation input motion are evaluated, and consequently in the inertial one, since the system "filters" the input experienced by the superstructure. Finally, sensitivity indexes of the three independent variables are calculated, addressing the soil shear wave velocity as the most influential parameter for the impedance variability. From the sensitivity analysis results, the primary influence of the shear wave velocity on the overall response allows to say that future applications may be developed considering the variability on V_s only, reducing the total computational effort without a significant loss in the result accuracy. Further studies are needed to investigate the role of uncertainties in the response of other kind of soil-substructure systems (for example, pile-group foundations), on both the impedance matrix and the FIM in order to characterize the kinematic interaction probabilistically.

REFERENCES

[1] A.M. Kaynia, E. Kausel. Dynamic stiffness and seismic response of sleeved piles. *Rep. R80-12*, MIT, Cambridge, Mass, 1982.

[2] R. Dobry, G. Gazetas. Simple Method for Dynamic Stiffness and Damping of Floating Pile Groups. *Geotechnique*, **38**(4), 557-574, 1988.

[3] J.P. Wolf. *Dynamic Soil-Structure Interaction*. Prentice-Hall, Inc., Englewood, N.J, 1985.

[4] A.L. Jones, S.L. Kramer, P. Arduino. *Estimation of uncertainty in geotechnical properties for performance-based earthquake engineering*. Technical Report 2002/16, Pacific Earthquake Engineering Research Center, PEER, Univ. of California at Berkeley, Berkeley, Calif., 2002.

[5] P.W. Mayne, M.R. Coop, S. Springman, A-B. Huang, J. Zornberg. State-of-the-Art Paper (SOA-1): GeoMaterial Behavior and Testing. *Proc. 17th Intl. Conf. Soil Mechanics & Geotechnical Engineering*, Vol. 4 (ICSMGE, Alexandria, Egypt), Millpress/IOS Press Rotterdam: 2777-2872, 2009.

[6] F.M. Bartlett, J.G. MacGregor. *Statistical analysis of the compressive strength of concrete in structures*. ACI Mater J, **93**(2),158-68, 1996.

[7] CNR. *Guide for the probabilistic assessment of the seismic safety of existing buildings. Report CNR-DT 212/2013*, CNR – Advisory Committee on Technical Recommentations for Construction, Rome, 2014.

[8] L.D. Lutes, S. Sarkani, S. Jin. Response variability of an SSI system with uncertain structural and soil properties. *Engineering Structures*, 22(6), 605-620, 2000.

[9] R. Cottereau, D. Clouteau, C. Soize, Construction of a probabilistic model for impedance matrices. *Computer Methods in Applied Mechanics and Engineering*, **196**(17–20), 2252-2268, 2007.

[10] M. Moghaddasi, M. Cubrinovski, J. G. Chase, S. Pampanin, A. Carr. Probabilistic evaluation of soil-foundation-structure interaction effects on seismic structural response. *Earthquake Engineering & Structural Dynamics*, **40**(2), 135-154, 2011.

[11] G. Mylonakis, G. Gazetas. Seismic soil-structure interaction: beneficial or detrimental? *Journal of Earthquake Engineering*, **4**, 277-301, 2000.

[12] S. Carbonari, F. Dezi, G. Leoni. Seismic soil-structure interaction in multi-span bridges: application to a railway bridge. *Earthquake Engineering & Structural Dynamics*, **40**(11), 1219-1239, 2011.

[13] F. Dezi, S. Carbonari, G. Leoni. A model for the 3D kinematic interaction analysis of pile groups in layered soils. *Earthquake Engineering & Structural Dynamics*, **38**(11), 1281-1305, 2009.

[14] R.Y. Rubinstein, D.P., Kroese. *Simulation and the Monte Carlo method*, Vol. 10, John Wiley & Sons, 2016.

[15] I.M. Sobol', V.I. Turchaninov, Yu.L. Levitan, B.V. Shukhman. *Quasirandom sequence generators.* Institute of Applied Mathematics, Russian Academy of Sciences, Moscow, 1992.

[16] S.W. Moon, T. Ku. Empirical estimation of soil unit weight and undrained shear strength from shear wave velocity measurements. *Proceedings, 5th International Conference on Geotechnical and Geophysical Site Characterization (ISC'5). Australian Geomechanics Society*, **2**, 1247-1252, 2016.

[17] S. Jin, L.D. Lutes, S. Sarkani. Response variability for a structure with soil–structure interactions and uncertain soil properties. *Probabilistic Engineering Mechanics*, **15**(2), 175-183, 2000.

[18] A. Olsson, G. Sandberg, O. Dahlblom. On Latin hypercube sampling for structural reliability analysis. *Structural safety*, **25**(1), 47-68, 2003.

[19] S. Engelund, R. Rackwitz. A benchmark study on importance sampling techniques in structural reliability. *Structural safety*, **12**(4), 255-276, 1993.

[20] S.K. Au, J.L. Beck. Estimation of small failure probabilities in high dimensions by subset simulation. *Probabilistic Engineering Mechanics*, **16**(4), 263-277, 2001.

[21] A. Dall'Asta, F. Scozzese, L. Ragni, E. Tubaldi. Effect of the damper property variability on the seismic reliability of linear systems equipped with viscous dampers. *Bulletin of Earthquake Engineering*, **15**(11), 5025-5053, 2017.

[22] A. Saltelli, M. Ratto, T. Andres, F. Campolongo, J. Cariboni, D. Gatelli, M. Saisana, S. Tarantola. *Global sensitivity analysis: the primer*. John Wiley & Sons, 2008.

[23] S. Burhenne, D. Jacob, G.P. Henze. Sampling based on Sobol'sequences for Monte Carlo techniques applied to building simulations. *Proceedings of the 12th Conference of International Building Performance Simulation Association*, Sydney, 2011.

[24] S. Kucherenko, D. Albrecht, A. Saltelli. Exploring multi-dimensional spaces: A comparison of Latin hypercube and quasi Monte Carlo sampling techniques. arXiv preprint arXiv:1505.02350, 2015.

COMPDYN 2019
7th ECCOMAS Thematic Conference on
Computational Methods in Structural Dynamics and Earthquake Engineering
M. Papadrakakis, M. Fragiadakis (eds.)
Crete, Greece, 24–26 June 2019

PARAMETRICAL DESIGN TRENDS FOR A HYPERBOLIC PARABOLOID SHAPED OVER A SQUARE PLAN: VERTICAL DISPLACEMENTS AND NATURAL PERIODS.

G.F. Giaccu[1] and A. Viskovic[2]
[1]Department of Architecture, Design and Urban Planning, University of Sassari,
Palazzo del PouSalit, Piazza Duomo 6, 07041 Alghero, Italy.
[2]Department of Engineering and Geology, G. D'Annunzio University,
viale Pindaro 42, 65127, Pescara
email: gf.giaccu@uniss.it, a.viskovic@unich.it

Abstract

Tensile structures are one of the most convenient solutions for covering large spans. For both temporary and permanent uses, they are optimal as sport arenas, meeting rooms or concert halls. However, codes and literature neglect these structures thus making it difficult to carry out preliminary designs for this structural typology in order to estimate the cost-benefit ratio compared to others. On the contrary, parametric equations used to preliminarily estimate the static and dynamic behavior of these structures are useful to designers. In order to give parametric information about some examples of these structures, this paper investigates the initial natural frequency and vertical displacements under dead and permeant loads of cable nets, with a hyperbolic paraboloid shape and square plan, depending on geometry. In total, two curvatures of a hyperbolic paraboloid surface and five different plan sizes are calculated with eight different cable tractions in order to give design trends. The trends are illustrated with an error bar resulting from the variation between different tractions considered for each geometry. The results are useful to preliminarily estimate the cost and the range of interference between wind and structure.

Keywords: Tensile structures, Cable net, modal analyses, design trends.

1 INTRODUCTION

Tensile structures for roofs are a particularly convenient way of covering large spans for both temporary or permanent conditions. Commonly, they were used for sport arenas but recent studies have shown that they can also be used for music halls ([1],[2]). Focusing the study on the cable net hyperbolic paraboloid roofs, the strength of these structural typologies is the roof lightness and its short thickness compared to the span. In addition, the absence of pillars except around the borders allows a multifunctional use of the indoor space. The limits are many but the most important are the wind action sensitivity and the gaps in technical codes.

The cable net tensile structure's sensitivity to wind action is well known. Many studies ([3]-[21]) have confirmed that the cable nets and membranes need to be designed by taking into account the dynamic instability given by the wind – structure interaction. This aspect is crucial because it affects the design of the roof and its reliability that closely depend on the geometry. In section 3 some basic information about the cable net design and calculus are given.

To investigate the wind – structure interaction, the roof needs to be designed statically and dynamically. Currently however, the design phase suffers from a gap in codes and literature which neglect this structural typology. In particular two aspects are neglected, the wind action estimation for the hyperbolic paraboloid roof and the geometrical parametrization of structural elements (i.e. cables and membrane). In order to estimate the wind action, tunnel tests are necessary during the preliminary phase of the project. A great number of examples of wind tunnel campaign tests are described in literature ([22]-[29]) However, all references are unique cases and thus are not standardized for various geometries. Some examples follow a parametric approach that is useful for replicating the study. This approach was followed by [31], [30] and [13]. In particular, [31] and [30] have carried out pressure coefficients maps (i.e. mean, maximum and minimum) on a total of 12 different plan geometries of hyperbolic paraboloid roofs. Recently[32]and [33] have analyzed the distribution of the peak factors on a hyperbolic paraboloid roof. These studies allow designers to estimate the wind action on the roof before carrying out expensive wind tunnel tests. Some of these studies synthetized the results achieved by the Codes of Practice for other geometries ([34] - [38]). However, the parametric results published in literature should be categorized by codes. [35] discussed some of the most important Codes of Practice ([39] - [48]). The shortcomings regard the generalization and parametrization of the aerodynamic coefficients to the widest number of geometries derived from the hyperbolic paraboloid. Similarly, very little information is given regarding the structural design of cable nets and membranes which makes it difficult to develop these structural systems at the expense of their dissemination.

Based on these gaps, this paper discusses through a parametrical approach the dynamics of cable nets with a square plan and hyperbolic paraboloid surface roof. The paper in particular investigates the dependence on the geometry of the first natural frequency and the vertical displacements under dead and permanent loads (i.e. 0.5 kN/m^2), known as the final construction condition. The first natural frequency (i.e. mode with biggest participating mass) was estimated taking into account masses given by structural and permanent loads and it was given considering the initial pretension of cables. It is known that the cables strain and stress vary significantly under snow or wind action. This study is only focused on the structural response under structural weight and permanent loads. For this reason, equations and figures, that illustrate structural response variation, are only referred to the structural weight and permanent loads. A comparison between ten geometries with two different hyperbolic paraboloid surfaces and five different plan sizes (i.e. 100, 80, 60, 40 and 20 meters), respectively are discussed. With the purpose to compare only cable net performances, the distance between load bearing and stabilizing cables are kept constant for all geometries and span length. For this reason, the curvature

of the roof with the smaller spans (i.e. 40 m or 20 m) is badly reproduced. However, the distance between cables can be proportionally varied as function of the span. In this research the cable net is only investigated. For this reason the border structures are restrained. In addition, the membrane in terms of roof stiffness is not considered so as to study only the cable net performances.

It is important to note that the study is focused on structures with medium and small spans in order to promote the dissemination about these kind of structures. The purpose is to use cables nets as an alternative to steel truss or wood structures for small and medium sport arenas. That's because they have an efficient cost-benefit ratio also for small span ([6], [7]). In addition, it is important to specify that the geometrical span range (i.e. from 100 to 20) was chosen as linear variation of the span in order to give a measure of the structural response variation as function of the span.

The aim is to give a range of the first natural frequency and vertical displacements for a preliminary structure design and to evaluate the cost-benefit. This last evaluation is possible because the vertical displacements depend on the cable traction and consequently on their section area. Section 2 describes the geometrical sample investigated while Section 3 gives some notions of the cable net calculation and information about the analyses carried out. Section 4 includes a short description of the analyses results.

2 THE GEOMETRICAL SAMPLE

The hyperbolic paraboloid surface equation is given by Eq(1). In the case of this research, the term *c* is equal to 1 (i.e. regular hyperbolic paraboloid). Consequently, the hyperbolic paraboloid cable net is made up of cables with the same curvature along one side. In Eq.(1), x, y and z are respectively the spatial variables; x_0, y_0 and z_0 are the coordinates of the origin of the axes while *a*, *b* and *c* are the geometric coefficients of the function. Parameter *c* was set equal to 1 making all the parabolas lying on the surface, parallel and of identical curvature ([6], [7]). Totally, the net is made up of two orders of cables, upward and downward, respectively. The upward cables are load bearing under gravitational loads, whereas the downward cables are stabilizing under gravitational loads. Under wind suction (i.e. upward action), the order is inverse. The global instability is usually due to the inversion of some cable curvatures caused by extreme wind or snow action; in the case of the cable net it is general due to the loss of the initial strain by cables.

$$\frac{(X-X_0)^2}{A^2} - \frac{(Y-Y_0)^2}{B^2} = \frac{(Z-Z_0)}{C} \quad ; 1/C = 1 \tag{1}$$

In this study, only the structural behavior under permanent loads is investigated. The aim is to compare different structural configurations in terms of weight, natural frequencies and difference in geometrical configurations between undeformed and deformed geometry under permeant loads.

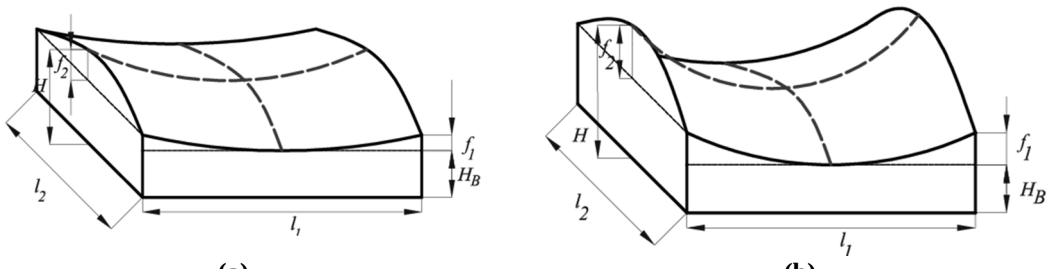

(a) **(b)**

Fig.1 Geometrical parameters (a) geometry (1), (b) geometry (2).

Fig.1 shows the geometrical parameters listed in Table 1 for investigated geometry (1) and (2) ([31]). The two couple parameters l_1, f_1 and l_2, f_2 are the upward and downward cable sags and spans, respectively. In this case, l_1 is equal to l_2. H is the sum of $f_1 + f_2 + H_B$ and it is equal to 1/10 (i.e. geometry (1)) and 1/6 (i.e. geometry (2)) of l_1. The geometry was chosen based on the geometrical parametrization, as function of the optimal structural performances of the net, given by [31]. The various curvatures of the hyperbolic paraboloid surface and the different values of the span, affect the static and dynamic behavior of the structures. In Table 1, N represents the number of cables along l_1 that is equal along l_2. The i quantities in Table 1 represent the distance between the cables.

Table 1 Geometrical sample

Geom-etry	model	l_1 [m]	l_2 [m]	f_1 [m]	f_2 [m]	H [m]	H_B [m]	i [m]	N
	1	100.00	100.00	3.33	6.67	10.00	13.33	2.00	51
	2	80.00	80.00	2.66	5.34	8.00	13.33	2.00	41
(1)	3	60.00	60.00	2.00	4.00	6.00	13.33	2.00	31
	4	40.00	40.00	1.33	2.67	4.00	13.33	2.00	21
	5	20.00	20.00	0.66	1.37	2.00	13.33	2.00	11
	1	100.00	100.00	5.55	11.11	16.66	13.33	2.00	51
	2	80.00	80.00	4.44	8.89	13.33	13.33	2.00	41
(2)	3	60.00	60.00	3.33	6.66	10.00	13.33	2.00	31
	4	40.00	40.00	2.22	4.44	6.66	13.33	2.00	21
	5	20.00	20.00	1.11	2.22	3.33	13.33	2.00	11

In Section 3, some base notions regarding the cable net theory are shortly given in order to clarify the static and dynamic response dependence on geometry.

It is important to note that in this study the ratio between f_1 and f_2 is equal to 0.5. This ratio was set based on [31], that gave a parametric study of geometries and suggested 0.5 as an optimal ratio in order to minimize the horizontal forces applied to the border structures.

3 METHOD OF ANALYSES

Hyperbolic paraboloid cable nets have a double curvature with different cable lengths and curvatures, and generally, different cable areas and pre-stresses. In addition, the shape plays a decisive role in the net deformation behavior under the action of external loads. The cable net deformation is given by vertical displacements of nodes. In fact, the two orders of cables are connected as shown in Fig.2 a. As discussed in Section 2, the two orders of cables become load-bearing or stabilizers depending on the direction of the acting load; the load-bearing cable is concave in the direction of the acting load. Therefore, in conditions of snow (i.e. gravitational) or wind (i.e. gravitational and suction), the two orders of cables may reverse their behavior. This inversion may be dangerous because it may lead to the instability of either the cable net or the border structures. It is worth noting that the theoretical geometry is only an initial condition and that the real geometry of the net is defined on the basis of the cable pre-stress under dead and permanent loads.

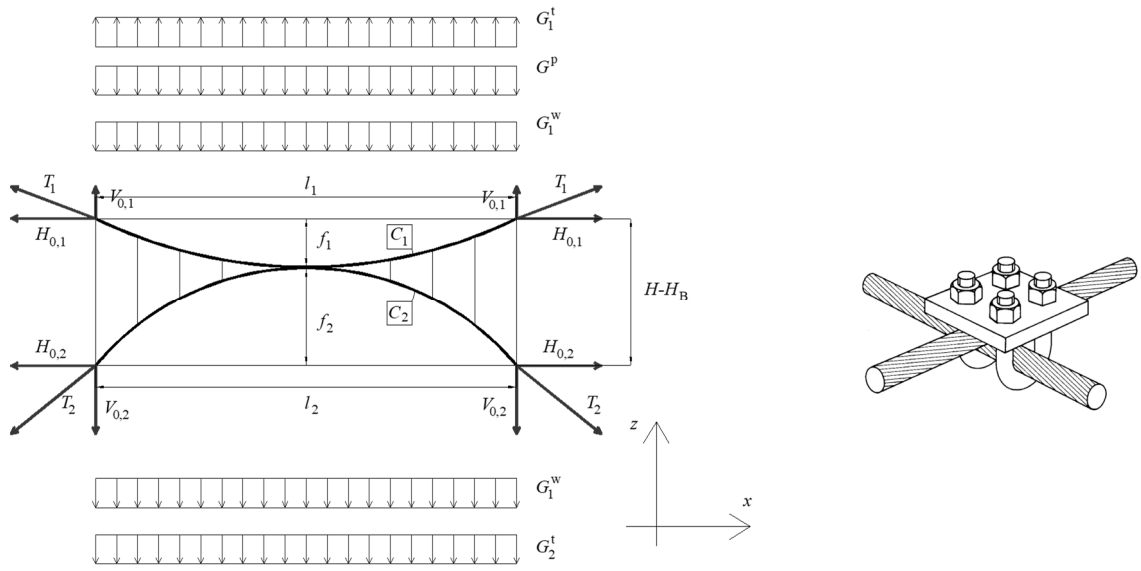

(a) **(b)**

Figure 2 The cable net model: the "Rope beam" model (a), the technological node detail (b).

The action given by loads and the pre-stress on the cables modify the theoretical geometry and the goal is to reduce the difference between theoretical and initial geometry. A small difference between the theoretical geometry and the deformed shape is important because, as it is known, the pressure coefficients evaluated in wind tunnel vary with the geometry. The theoretical fundamentals of the cable net calculation is its two-dimensional simplification model called "Rope beam" illustrated in Fig.2 a ([6], [7]). The equilibrium of the system forces in the mutual node ensures the forces' transmission between the two cables. The rope beam assumes the prefixed hypotheses listed in the following ([6], [7]). Vertical links in tension or in compression are treated as a continuous membrane between the two main cables. The horizontal displacements are neglected compared to the vertical ones which is due to the fact that the node connection permits the scroll between cables. The scroll results from the different strains of the two orders of cables (Fig.2 b). In order to preliminarily design the cable areas and strain, the rope beam model is used applying cable pretension as an equivalent distributed load. The system congruence is required only in the central span node. The mutual actions between cables are uniformly distributed as the external load, and consequently, load-bearing and stabilizing cable have a parabolic configuration also in elastic regime.

The stiffness coefficients are considered, respectively for the load-bearing cable (C_1) and stabilizing one (C_2) as expressed in Eq.(2) and Eq.(3), where k_1 and k_2 represent, respectively, the stiffness of the load-bearing cable C_1 and the stiffness of the stabilizing cable C_2, defined in Eqs.(4) and (5), while E is the Young Module of the cable steel assumed equal to 165000 Mpa and $A_{1,2}$are the cable areas.

As it is known, the yield stress of harmonic steel ranges from 1100 to 1700 Mpa, which is the limit under maximum loads (i.e. maximum wind and snow action). Consequently, under dead and permanent loads the cable stress should be smaller. It is worth noting that cables are made of ropes which are made of wires

$$\boldsymbol{C_1 = \frac{k_1}{k_1 + k_2}} \tag{2}$$

$$C_2 = \frac{k_2}{k_1 + k_2} \tag{3}$$

$$k_1 = \frac{EA_1}{l_1\left[1+\frac{8}{3}\left(\frac{f_1}{l_1}\right)^2-\frac{32}{5}\left(\frac{f_1}{l_1}\right)^4\right]} \quad (4)$$

$$k_2 = \frac{EA_2}{l_2\left[1+\frac{8}{3}\left(\frac{f_2}{l_2}\right)^2-\frac{32}{5}\left(\frac{f_2}{l_2}\right)^4\right]} \quad (5)$$

. The equivalent yield stress of the cable is not the same for a single wire. The initial stress (i.e. in traction) for cables is equal to 1150 Mpa to assume as maximum value under permanent loads. The applied load after construction and without snow and wind (Fig.2 a) corresponds to the sum of the cable weight (i.e. in the following dead loads, $G_{1,2}^{w}$), permanent loads (i.e. 0.5 kN/m^2, G^{p}) and initial pretension ($G_{1,2}^{t}$). Referring to Fig.2 a, the load balance is given by $+G^{p}$ (downward) $+G_1^{w}$ (downward) + G_1^{t} (upward) + G_2^{w} (downward) + G_2^{t} (downward) =0. Preliminarily, the cable weight was estimated based on the undeformed cable length, calculated according to Eqs. (6) and (7), referring to Fig.2 a (Majowiecki 1994).

$$\boldsymbol{L_{0,1,geom} = l_1 \cdot \left[1+\frac{8}{3}\cdot\left(\frac{f_1}{l_1}\right)^2-\frac{32}{5}\cdot\left(\frac{f_1}{l_1}\right)^4\right]} \quad (6)$$

$$L_{0,2,geom} = l_2 \cdot \left[1+\frac{8}{3}\cdot\left(\frac{f_2}{l_2}\right)^2-\frac{32}{5}\cdot\left(\frac{f_2}{l_2}\right)^4\right] \quad (7)$$

$L_{0,1,\mathrm{geom}}$ and $L_{0,2,\mathrm{geom}}$ are undeformed geometrical cable lengths ; the cable traction horizontal components$H_{0,1}$and$H_{0,2}$ are given by Eqs.(8) and (9) and they are assumed equal, ([6], [7]).The horizontal components depend on the cable geometry and it varies based on the different cable sags. If the sag of the two orders of cables are different, the cable traction (i.e. load bearing and stabilizing) has to be different. An iterative calculus procedure estimates the cable areas and strains in order to achieve the balance ([6], [7]).

Eqs. (8) and (9) link the geometry to the loads and consequently the cable traction to the geometry. Based on this, the initial traction into the cables gives the real geometrical configuration (i.e. f_1 and f_2) under dead and permeant loads (i.e. G). In this paper, in order to evaluate the geometry dependence on cable traction, five different values of T_1 are considered, 100 (A), 200 (B), 400 (C), 600 (D), 1000 (E), 2000 (F), 4000 (G) and 8000(H) kN respectively. It is important to specify that values bigger than 2000 kN are very big and they excessively overload the border structures.

$$\boldsymbol{H_{0,1} = \frac{G{l_1}^2}{8f_1} = \frac{T_1}{1+16\left(\frac{f_1}{l_1}\right)^2}} \quad (8)$$

$$H_{0,2} = \frac{G{l_2}^2}{8f_2} = \frac{T_2}{1+16\left(\frac{f_2}{l_2}\right)^2} \quad (9)$$

For this reason, it is suggested to balance these loads using stays. In this study, values of traction bigger than 2000 kN are used only to have a measure of the asymptotic trends of the displacements and first natural period. Consequently, having fixed the same exercise stress for both orders of cables, according to the Hook law (Eq.10), the initial cable elongation (ε)is defined equal for both orders of cables.

$$\begin{gathered}\boldsymbol{\sigma_1 = \sigma_2};\\ \sigma_1 = E \cdot \varepsilon_1;\ \sigma_2 = E \cdot \varepsilon_2\\ E \cdot \varepsilon_1 = E \cdot \varepsilon_2;\\ \varepsilon_1 = \varepsilon_2 = 0.0035\end{gathered} \tag{10}$$

$$\frac{\mathrm{T_1}}{1 + 16\left(\frac{f_1}{\mathrm{l_1}}\right)^2} = \frac{\mathrm{T_2}}{1 + 16\left(\frac{f_2}{\mathrm{l_2}}\right)^2} \tag{11}$$

$$\mathrm{T_2} = \frac{\mathrm{T_1}\left[1 + 16\left(\frac{f_2}{\mathrm{l_2}}\right)^2\right]}{1 + 16\left(\frac{f_1}{\mathrm{l_1}}\right)^2} = 1.05 \text{ or } 1.14\ \mathrm{T_1} \tag{12}$$

$$\begin{gathered}\mathrm{T_2} = E \cdot \varepsilon_2 \cdot A_2\\ \mathrm{T_1} = E \cdot \varepsilon_1 \cdot A_1\end{gathered} \tag{13}$$

$$A_2 = 1.05\ or\ 1.14\ A_1 \tag{14}$$

Consequently, assuming $H_{0,1} = H_{0,2}$, ratio T_2 / T_1 and A_2 / A_1 are geometrically calculated (Eqs. 11 to 13) and, for the case study considered, they are equal to 1.05 for geometry (1) and 1.14 for geometry (2). A_1 is assumed equal between geometry (1) and (2). The Based on Eq. (14) where the cable areas were evaluated. Table 2 lists the traction and areas of cables.

Table 2 Mechanical parameters after fixing the initial strength $\varepsilon_1 = \varepsilon_2 = 0{,}0035$.

Geometry	model	analysis	T_1 [kN]	T_2 [kN]	A_1 [m^2]	A_2 [m^2]
(1)	From 1 to 5	(A)	100.0	105.0	0.00017	0.00018
		(B)	200.0	210.0	0.00035	0.00037
		(C)	400.0	420.0	0.00070	0.00074
		(D)	600.0	630.0	0.00100	0.00105
		(E)	1000.0	1050.0	0.00170	0.00179
		(F)	2000.0	2100.0	0.00350	0.00368
		(G)	4000.0	4200.0	0.00700	0.00735
		(H)	8000.0	8400.0	0.01390	0.01460
(2)	From 1 to 5	(A)	100.0	114.0	0.00017	0.00019
		(B)	200.0	228.0	0.00035	0.00040
		(C)	400.0	456.0	0.00070	0.00080
		(D)	600.0	684.0	0.00100	0.00114
		(E)	1000.0	1140.0	0.00170	0.00194
		(F)	2000.0	2280.0	0.00350	0.00399
		(G)	4000.0	4560.0	0.00700	0.00798
		(H)	8000.0	9120.0	0.01390	0.01585

Static and modal analyses are carried out using TENSO, a non-commercial software that includes modules for simulating cable and beam finite element models and for the study of wind-structure interaction phenomena through the generation of wind speed time histories and simulation of various aeroelastic loads. The main cables are discretized as rectilinear cable segments. The global stiffness matrix is updated at each load step by assembly of the stiffness sub-matrices of the elements, updated to account for the strain found at the previous time step. In this way the software considers the geometric nonlinearity of the structure. The TENSO software first solves the static equilibrium of the structure under dead, gravity and construction loads (prior to the application of the wind loads) through nonlinear static analysis whereby two methods are simultaneously used: step-by-step incremental method and a "subsequent interaction" method with variable stiffness matrix (secant method). The secant method is a finite-

difference approximation of the Newton-Raphson's modified method for systems of nonlinear algebraic equations ([49], [50]). For geometry (1), the first three mode shapes are the same for traction T_1 greater than 1000 kN for each value of L_1. On the other hand, the first mode shape for T_1, smaller than 1000 kN, is similar to the second mode shape for traction greater than 1000 kN, while for geometry (2) it is the same. The first three modes are in descending order of participating mass. It is obvious that the cable areas and the plan sizes (i.e. l_1 and l_2) closely affect the weight of the cable net and consequently the masses of the structures, listed in Table 3 for L_1 equal to 100 m.

In this study the first natural frequency with the bigger participating mass is only considered to make a comparison between geometry (1) and (2). The fist mode is symmetric for T_1 smaller than 1000 kN and L_1 equal to 100, 80 and 60 for geometry (1), and equal to 100 and 80 m for geometry (2). The first mode is antisymmetric for traction bigger and equal to 1000 kN and L_1 smaller than 60 m for geometry (1) and 80 m for geometry (2). For sake of brevity Table 3 shows values for L_1=L_2=100 m.

Table 3 Geometry (1) and (2) modal analyses results (L_1 = L_2 =100 m)

analysis	M_i $[\frac{kg}{m^2}]$	Mode 1st	
		φ [Hz] Mode 1st	t [s]
(A)	5.23	0.0402	24.90
(B)	5.37	0.0462	21.66
(C)	5.64	0.0659	15.18
(D)	5.92	0.0794	12.59
(E)	6.46	0.1012	9.88
(F)	7.83	0.1342	7.45
(G)	10.57	0.1645	6.08
(H)	16.04	0.1890	5.29
(A)	5.23	0.0432	23.17
(B)	5.37	0.0570	17.54
(C)	5.65	0.0825	12.12
(D)	5.92	0.0981	10.19
(E)	6.47	0.1239	8.07
(F)	7.85	0.1629	6.14
(G)	10.60	0.1988	5.03
(H)	16.10	0.2278	4.39

All geometries listed in Table 1 are modelled with a FEM model. They were statically and dynamically calculated by TENSO in order to estimate the maximum (i.e. in the middle of the roof) vertical displacements and the first ten natural frequencies. Only the value of first natural frequency is discussed in this paper.

As previously described, the initial cable traction (i.e. T in Fig.2) affects the structural response because it modifies the cable net stiffness. In particular, the border anchorage structures and the vertical displacements under loads are closely affected by the traction (T). In order to investigate the dependence on cable traction of displacements and of the natural frequencies, a range of eight different initial tractions (i.e. cables pre-stress) are investigated.

Tables 3 gives a list of the first natural frequency and period of the structures (1) and (2), for l_1 = l_2 = 100 80 60 40 20] m), with the eight cable tractions (i.e. between 100 kN and 8000 kN). The tables also give the mass (M_i) for square meters for a generic node *i* of the net.

4 RESULTS

Static and model analyses results have shown that the vertical displacements under dead and permanent loads (i.e. 0.5 kN/m^2) varies nonlinearly as a function of load bearing cable traction (T_1). Figs 3a and b show the vertical displacement trend as function of T_1 for geometry (1) and (2), respectively. For geometry (1) vertical displacement δ(i.e. in the middle of the roof) tends towards very high values for small values of T_1. For the smallest values of T_1 (i.e. 100 kN), δranges from about 5/250 l_1 to 1.5/250 of l_1. On the contrary, for the biggest value T_1 (i.e. 8000 kN), $\delta$is almost constant for all plan sizes and it is equal nearly 1/250 l_1. Similarly, for geometry (2) vertical displacement δ (i.e. in the middle of the roof) tends towards very high values for small values of T_1. For the smallest values of T_1 (i.e. 100 kN), δranges from about 3/250 l_1 to 0.8/250 of l_1. On the contrary, for the biggest T_1value (i.e. 8000 kN), $\delta$is almost constant for all plan sizes and it is nearly 0.6/250 l_1 equal.

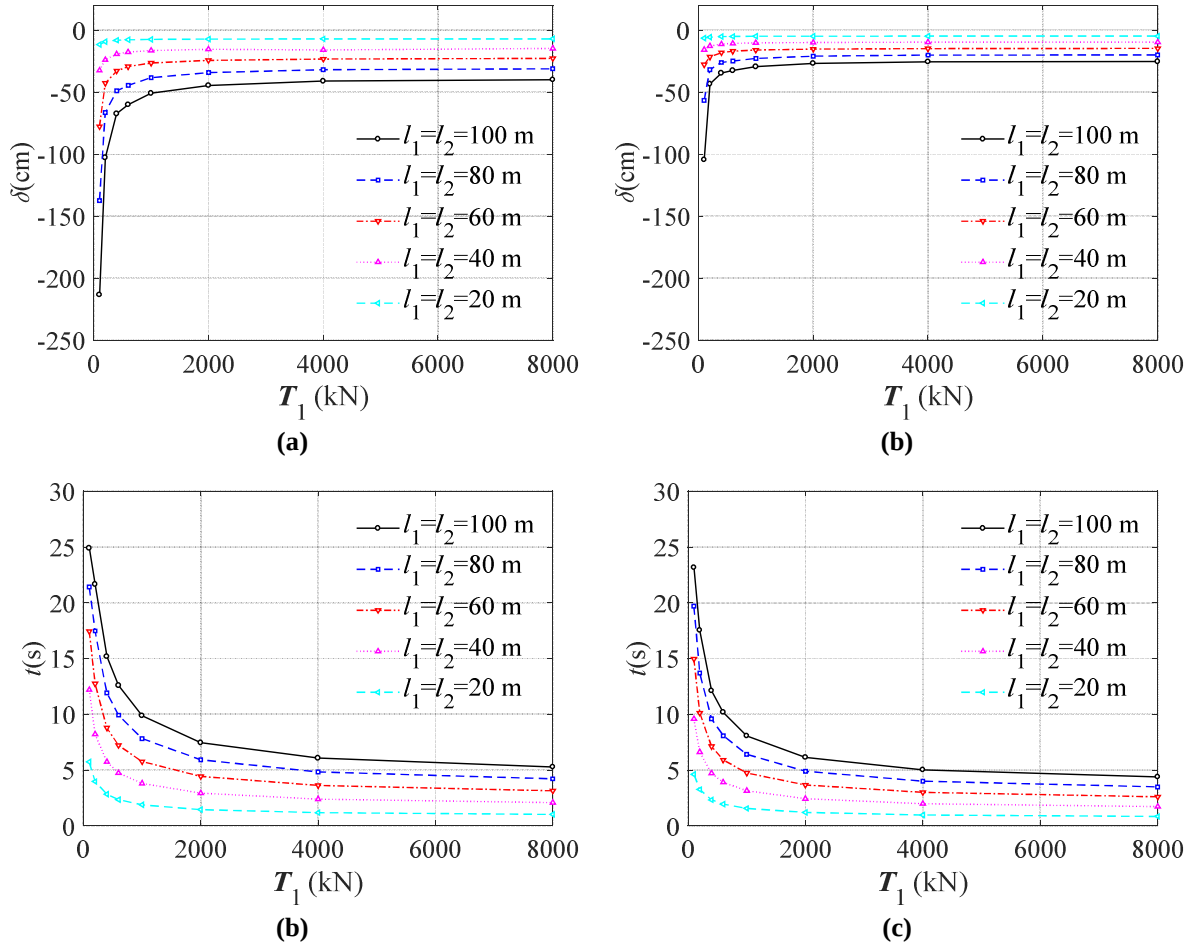

Fig.3 Vertical displacements under dead and permanent loads depending on cable traction, geometry

Fixed the cable stress limit due to the material yield stress, the T_1 variation depends on cable areas and consequently, the cable area variation gives the structural mass for square meter (M_i) variation. For the sake of brevity, Table 3 list the 1st natural frequency (ϕ) in Hz and period (t) in s values for all geometries (i.e. geometry (1) and (2) and conditions i.e. traction from (A) to (H)). Figs.3 c and d synthetized the values of t as function of T_1 for both geometry (1) and (2).M_i varies significantly between (A) and (H) traction condition and consequently, the 1st natural period varies too. However, it is quite constant for traction greater than 2000 kN. For geometry (1), the t values range from 24.90 s (i.e. l_1=100 m and T_1 = 100 kN) to about 1.03 s

(i.e. l_1=20 m and T_1=8000 kN). For geometry (2), the t values range from 23.17 s (i.e. l_1=100 m and T_1 = 100 kN) to about 0.85 s (i.e. l_1=20 m and T_1=8000 kN). As was expected, the first natural period of geometry (1) is slightly longer than geometry (2) and this is due to the larger radius of curvature of the hyperbolic parabolic surface for geometry (1) than geometry (2). The standard deviation of t ranges from 5.83 s (i.e. l_1=100 m) to 1.05 s (i.e. l_1=20 m) for geometry (1), whereas it ranges from 4.66 s (i.e. l_1=100 m) to 0.86 s (i.e. l_1=20 m) for geometry (2). The standard deviation decreases when the plan size decreases too.).

5 CONCLUSION

Design trends for the first natural period of a hyperbolic paraboloid cable net with a square plan depending on span length are given for two surfaces of the hyperbolic paraboloid. The H sum of the two orders of cable sags was divided by 10 (i.e. geometry (1)) and 6 (i.e. geometry (2)). For each geometry, the span length was varied between 100 m and 20 m. Static analyses were carried out with the aim to estimate the vertical displacements as function of the fixed cable traction in order to respect the material limits. The cable traction varied between 100 to 8000 kN. The structural mass variations due to the cable area variations gave different values of the first natural period for each geometry. Results showed that the first natural period varied very little for cable traction greater than 2000 kN and thus was described as a function of the cable span. The design trends showed that when the radius of curvature of the hyperbolic surfaces increases (i.e. geometry (1) radius is bigger than (2)), the first natural period slightly increases and it has greater values of standard deviation considering different cable tractions. The standard deviation increases when the span length increases too. The design trends are useful to designers in order to evaluate preliminarily the possibility of resonance due to wind – structure interaction. This knowledge, in the next development of the research, will be helpful to evaluate the structure reliability of existing roofs. The purpose is to design a retrofitting according the same scientific approaches followed for traditional structures as for examples structures made of reinforced concrete [51].

ACKNOWLEDGMENTS

The author thanks Dr. Fabio Rizzo of the Department of Engineering and Geology at G. D'Annunzio University, for his geometrical database, Professor Piero D'Asdia for the non-commercial TENSO software and implementation**.**

REFERENCES

[1]. Rizzo F., Zazzini P., 2017. Shape dependence of acoustic performances in buildings with a Hyperbolic Paraboloid cable net membrane roof. Journal of Acoustics Australia, 45 (2), 421–443.

[2]. Rizzo F., Zazzini P., 2016. Improving the acoustical properties of an elliptical plan space with a cable net membrane roof. Journal of Acoustics Australia, 44, 449-456, (11-16-2016) ISSN: 08146039, DOI: 10.1007/s40857-016-0072-5.

[3]. Vassilopoulou I, Gantes CJ., 2011. Nonlinear dynamic behavior of saddle form cable nets under uniform harmonic load. Engineering Structures 33(10), 2762–2771.

[4]. Vassilopoulou I, Gantes CJ., 2012. Vibration modes and natural frequencies of saddle form cable nets. ComputStruct. 88 (1–2), 105–19.

[5]. Vassilopoulou I, Petrini F, GantesCJ., 2017. Nonlinear dynamic behavior of cable nets subjected to wind loading. Structures 10, 170–83.

[6]. Majowiecki M., 1972. Tensostrutture, Inarcos, (313), http://www.majowiecki.com/studio/wp-content/uploads/2011/10/1972-Tensostrutture-INARCOS.pdf

[7]. Majowiecki M., 2004. Tensostrutture: Progetto e Verifica. EdizioniCrea, Massa, 1994.

[8]. Rizzo F., Sepe V., 2015. Static loads to simulate dynamic effects of wind on hyperbolic paraboloid roofs with square plan, Journal of Wind Engineering & Industrial Aerodynamics, 137, 46-57.

[9]. Daw D.J., Davenport A.G., 1989. Aerodynamic damping and stiffness of a semi-circular roof in turbulent wind. Journal of Wind Engineering and Industrial Aerodynamics, 32, 83-92.

[10]. Forster B.,1994. Cable and membrane roofs, a historical survey. Structural Engineering Review, 6,3-5.

[11]. Kassem M., Novak M., 1992. Wind-Induced response of hemispherical air-supported Structures. Journal of Wind Engineering and Industrial Aerodynamics 41(1-3),177-178.

[12]. Knudson W.C., 1991. Recent advances in the field of long span tension structures. Engineering Structures, 13(2), 174-193.

[13]. Letchford C.W., Killen G.P., 2002. Equivalent static wind loads for cantilevered grandstand roofs. Engineering Structures. 24(2), 207-217.

[14]. Letchford C.W., Denoon R.O., Johnson G., Mallam A., 2002. Dynamic characteristics of cantilever grandstand roofs. Engineering Structures, 24(8), 1085-1090.

[15]. Lewis W.J., (2003) Tension structures: form and behavior. Thomas Telford, London.

[16]. Pun, P.K.F. and Letchford C.W., 1993. Analysis of a tension membrane HYPAR roof subjected to fluctuating wind loads, 3rd Asia-Pacific symposium on Wind Engineering, Hong Kong, 13-15 December 1993, 741-746, University of Hong Kong.

[17]. Pun, P.K.F, 1993. Analysis of a tension membrane HYPAR subject to fluctuating wind loads, MEngSc Thesis, University of Queensland, Brisbane, October 1993.

[18]. Shen S., Yang, Q., 1999. Wind-induced response analysis and wind-resistant design of hyperbolic paraboloid cable net structures. International Journal of Space Structures, 14(1), 57-65.

[19]. Yang Q., Liu R., 2005. On Aerodynamic Stability of Membrane Structures. International Journal of Space Structures, 20(3), 181-188.

[20]. Yang Q., Wu Y. , Zhu W., 2010. Experimental study on interaction between membrane structures and wind environment. Earthquake Engineering and Engineering Vibration, 9(4), 523-532.

[21]. Dzwierzynska J., Prokopska A.,2018. Pre-Rationalized Parametric Designing of Roof Shells Formed by Repetitive Modules of Catalan Surfaces, Symmetry, 10(4), 105.

[22]. Biagini P., Borri C., Facchini L., 2007. Wind response of large roofs of stadiums and arena, Journal of Wind Engineering and Industrial Aerodynamics, 95, 9-11.

[23]. Dong X., Ye J.H., 2015. Development and verification of a flow model of conical vortices on saddle roofs. Journal of Engineering Mechanics, ASCE, 141(3).

[24]. Elashkar I., Novak M., 1983. Wind tunnel studies of cable roofs. Journal of Wind Engineering and Industrial Aerodynamics,13(1-3), 407-419.

[25]. Irwin H.P.A.H., Wardlaw R.L.A, 1979. Wind tunnel investigation of a retractable fabric roof for the Montreal Olympic stadium. In Proceedings of the 5th International Conference on Wind Engineering, Pergamon, 925-938.

[26]. Kawai H., Yoshie R, 1999. Wind-induced response of a large cantilevered roof. Journal of Wind Engineering and Industrial Aerodynamics. 83, 263-275.

[27]. Kawakita S., Bienkiewicz B., Cermak J.E., 1992. Aeroelastic model study of suspended cable roof. Fluid Mechanics and Wind Engineering Program, Department of Civil Engineering, Colorado State University, Fort Collins, Colorado USA.

[28]. Sykes D.M., 1994. Wind loading tests on models of two tension structures for EXPO'92, Seville. Journal of Wind Engineering and Industrial Aerodynamics, 52, 371-383.

[29]. Sun X., Wu Y., Yang Q., Shen S., 2008. Wind tunnel tests on the aeroelastic behaviors of tension structures. Proceedings of the VI International Colloquium on Bluff Bodies Aerodynamics & Applications, BBAA VI, Milan, Italy.

[30]. Rizzo F., 2012, Wind tunnel tests on hyperbolic paraboloid roofs with elliptical plane shapes, Engineering Structures, 45, 536–558.

[31]. Rizzo F., D'Asdia P., Lazzari M., Procino L., 2011. Wind action evaluation on tension roofs of hyperbolic paraboloid shape, Engineering Structures, 33 (2), 445-461.

[32]. Rizzo F., Barbato M., Sepe V., 2018. Peak factor statistics of wind effects for hyperbolic paraboloid roofs, Engineering Structures, 173, 313–330.

[33]. Liu M., Chen X., Yang Q., 2016. Characteristics of dynamic pressures on a saddle type roof in various boundary layer flows. Journal of Wind Engineering and Industrial Aerodynamics, 150, 1-14.

[34]. Rizzo F., D'Asdia P., Ricciardelli F., Bartoli G., 2012. Characterization of pressure coefficients on hyperbolic paraboloid roofs, Journal of Wind Engineering & Industrial Aerodynamics, 102, 61–71.

[35]. Rizzo F., Ricciardelli F., 2017. Design pressure coefficients for circular and elliptical plan structures with hyperbolic paraboloid roof, Journal of Engineering Structures, 139, 153-169.

[36]. Kimoto E., Kawamura S., 1986. Aerodynamic criteria of hanging roofs for structural Design. Proceeding of IASS Symposium, Osaka, 249-256.

[37]. Krishna P., Kumar K., Bhandari N.M., 2012. Wind Loads on Buildings and Structures. Indian Standard IS:875, Part 3, Proposed Draft & Commentary.

[38]. Killen G.P., Letchford C.W., 2001. A parametric study of wind loads on grandstand roofs, Engineering Structures, 23(6), 725-735.

[39]. AIJ (Architectural Institute of Japan), 2004. Recommendations for Loads on Buildings, Chapter 6: Wind Loads.

[40]. ASCE (American Society of Civil Engineering), 1999. Wind tunnel studies of buildings and structures.

[41]. ASCE (American Society of Civil Engineering), 2010. Minimum Design Loads for Buildings and Other Structures, ASCE 7:2010.

[42]. AS/NZS (Standards Australia / Standards New Zealand), 2011. Structural design actions; Part 2: Wind actions. AS/NZS 1170.2:2002.

[43]. Brito R. and Caracoglia L., 209. Extraction of flutter derivatives from small scale wind tunnel experiments. In: Proceedings of the 11th Americas Conference on Wind Engineering, American Association for Wind Engineering (AAWE), San Juan, Puerto Rico; 2009.

[44]. CEN (ComitéEuropéen de Normalization), 2005. Eurocode 1: Actions on structures - Part 1-4: General actions - Wind actions, EN-1991-1-4.

[45]. CNR (National Research Council of Italy), 2008. Guide for the Assessment of Wind Actions and Effects On Structures. CNR-DT 207/2008.

[46]. ISO (International Standards Organization), 2012. Wind action on structures - D.3 Wind tunnel testing procedures, 4354:2012(E).

[47]. NRC/CNRC (National Research Council / Conseil National de Recherches Canada), 2010. Commentary to the National Building Code of Canada, Commentary I: Wind Load and Effects.

[48]. SIA (Swiss Society of Engineers and Architects), 2003. Action on structures - Appendix C: Force and pressure factors for wind. SIA 261:2003.

[49]. Rizzo F., Caracoglia L., Montelpare S., 2018, Predicting the flutter speed of a pedestrian suspension bridge through examination of laboratory experimental errors, 172, 589-613.

[50]. Rizzo F., Caracoglia L., 2018. Examining wind tunnel errors in Scanlan derivatives and flutter speed of a closed-box, Journal of Wind and Structures, 26(4), 231-251.

[51]. Avossa A. M., Di Giacinto D., Malangone P., Rizzo F., 2018. Seismic Retrofit Of A Multi-Span Pre-stressed Concrete Girder Bridge With Friction Pendulum Devices, Shock and Vibration, 2018, Article ID 5679480.

COMPDYN 2019
7th ECCOMAS Thematic Conference on
Computational Methods in Structural Dynamics and Earthquake Engineering
M. Papadrakakis, M. Fragiadakis (eds.)
Crete, Greece, 24–26 June 2019

SEISMIC PERFORMANCE IMPROVEMENT OF STORAGE RACKS USING VISCOELASTIC DAMPERS

GwangHee Heo[1], **ChungGil Kim**[1], **YongSuk Kim**[2], **ChaeRin Park**[3], **ByeongChan Ko**[3]

[1] Civil Engineering Dept. Professor, Konyang University
e-mail : {heo, cg-kim}@konyang.ac.kr

[2] Medical IT Dept. Professor, Konyang University
e-mail : yongsuk@konyang.ac.kr

[3] Department of Disaster Safety Engineering Dept. Master's Candidate, Konyang University
e-mail : {cherish_7169, yunil-0}@naver.com

Abstract

The purpose of this study is to develop a damper to improve the seismic performance of storage racks, which are representative non-structural elements sustaining successive external loads, such as earthquakes. To evaluate the seismic performance of general storage racks, a shaking table test was conducted. As a result, the necessity of reinforcement of the general storage rack to prevent permanent deformation of the direction of passage was confirmed. In addition, the results of the member unit static experiment examining the function of the general storage rack proved the necessity of reinforcing a beam-column joint. To improve this performance, a viscoelastic damper was developed to strengthen the beam-column joint in the direction of passage. To verify the effect of improving the seismic performance of the developed viscoelastic damper, a shaking table test was conducted. The developed viscoelastic damper reduced not only the displacement in the time-domain when under an external load but also the damage of the storage racks due to permanent deformation.

Keywords: viscoelastic damper, storage racks, seismic performance, shaking table test, structural damage, permanent deformation

1 INTRODUCTION

Storage racks are representative nonstructural elements that are used to store and classify items from the point of origin to that of consumption. Multi-shelf storage racks are conventionally used as they are not only lightweight but can also support heavy loads. The number of shelves and the height of such storage racks tend to increase with the increase in volume of commodities that require efficient storage in a confined space. Typically, storage racks are simply assembled to immediately secure a space at a user's demand, and this assembly method implies structural instability [1]. The structural instability is an influential factor on the behavior characteristics of the storage rack under external loads, such as earthquakes, and this factor causes various damages. In addition, apart for some countries situated in earthquake fault zones, most other countries do not have any established standards for the installation and operation of storage racks. Therefore, the failure of a storage rack due to an external load is very likely to cause considerable damage

Seismic loads are representative of external loads that damage logistics facilities, including storage racks. The 1994 LA Northridge earthquake and the 1995 southern Hyogo earthquake caused financial damages of approximately US$ 40 billion and 9.7 trillion yen, respectively. Such enormous damages awakened people's interest in the seismic stability of storage racks, and new technologies for improving the seismic performance of storage racks started being developed. To date, various devices have been developed. Hydraulic damper, viscous elastic material damper, and base isolation system are devices that are commonly intended to enhance the seismic performance of storage racks. Fall prevention devices for objects stored have also been developed [2-5]. The majority of devices for enhancing the seismic performance of storage racks are based on either of the following two methods: In the first method, after large-scale storage rack sets form a single system through additional jigs, a large device is used to reduce the vibration of the storage rack. In the second method, after the operation of the existing storage rack is suspended, devices are installed on bottom surfaces and junction. These methods require the fabrication of additional jigs and have a high installation cost. Storage is also suspended while devices are being installed. As the use of small-scale storage facilities tends to increase, technical development needs to focus on ensuring the seismic safety of small storage racks.

This study was an attempt to develop a device that could solve the problems of existing devices and improve the seismic performance of small storage racks, thereby ensuring the safety of these racks under external loads. To develop such a device, the behavior characteristics of the existing storage racks were analyzed by conducting a test, in which seismic loads were applied. Based on the test result and the structural shape of the storage rack, the weak parts of the storage rack were identified. Then, a viscoelastic damper was developed to reinforce the identified weak parts and enhance the seismic performance of the storage rack. A static load test was also performed to evaluate the preliminary performance of the damper. Finally, a seismic load test for the storage rack, to which the proposed viscoelastic damper was applied, was conducted to experimentally verify the performance of the damper.

2 CONSTRUCTION AND BEHAVIOR CHARACTERISTICS OF THE BASIC STORAGE RACK

2.1 Construction

The storage rack is a nonstructural element of the logistics process used for efficiently storing objects either for a short or long period. As illustrated below, the storage rack simply consists of columns, beams, and bracings. Such a simple structure is easy to modify depending

on users' subjective judgments or situations. Specifically, the open down-aisle section is intended to prevent any interruption while objects are being loaded. In the cross-aisle direction, bracings are installed to supplement relatively smaller sections and ensure the structural stability of the storage rack. To secure a sufficient space for large objects, the simple hooked beam-to-column connection is applied, as shown in Figure 1.

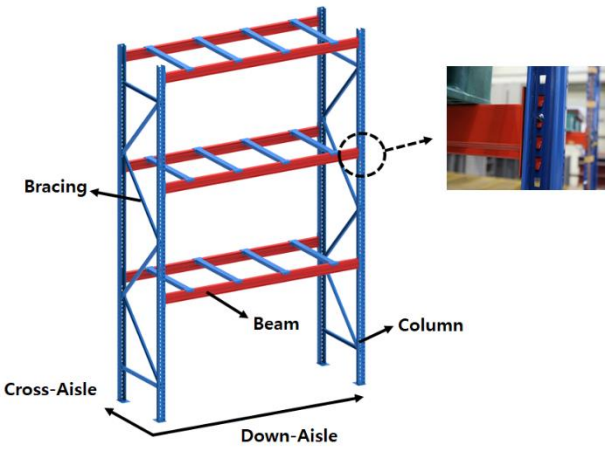

Figure 1: Construction of a storage rack

As there is no international standard for the specifications and dimensions of storage racks, majority of the storage racks are made-to-order to reflect the characteristics of each warehouse facility. Among the various storage racks, this study selected a three-shelf storage rack as the test object, which is widely used in mid- and small-sized logistics centers and warehouses in South Korea. The test object had a width of 2,785 mm, length of 1,000 mm, and height of 4,500 mm. M10 bolts were used for all the connections except the beam-to-column connections, for which M8 bolts were used along with hooks to prevent the separation of beams. Moreover, an additional load of 1.2 ton, which corresponds to 80% of the maximum designed load (1.5 ton), was installed on each shelf.

2.2 Behavior characteristics

To improve the seismic performance of storage racks, the behavior characteristics of the racks under external loads need to be accurately identified. To analyze the behavior characteristics of the storage rack under external loads, the dynamic characteristic analysis was conducted using the shaking table of the Seismic Simulation Test Center in South Korea. The shaking table test for analyzing dynamic characteristics was based on AC156 (Acceptance Criteria for Seismic Certification by Shake-table Testing of Nonstructural Components, 2010) proposed by ICC-ES, which is a representative testing method for nonstructural elements [6]. In accordance with the seismic response spectrum of KBC2016, the shaking table was assumed to be installed on normal rock soil in the seismic zone I. Table 1 presents the information of the seismic response spectrum [7].

Building Code	S_{DS}	z/h	Horizontal		damping
			$A_{FLX\text{-}H}$ (g)	$A_{RIG\text{-}H}$ (g)	
KBC2016	0.37	0	0.37	0.15	5%

Table 1: Shaking table test parameters

For the analysis of dynamic characteristics, the shaking table was vibrated by doubling the maximum acceleration (PGA = 0.3 g) of the seismic waveform created from the seismic spectrum information. The test was conducted only in two horizontal directions, and no vertical direction was considered.

The test results revealed that the 1st mode natural frequencies of the test object were 0.750 Hz in the longitudinal direction (x) and 2.375 Hz in the lateral direction (y). The test object was not overturned, inverted, or damaged. The bottom fixture was not separated, and the bolts did not show any crack or deformation. However, as shown in Figure 2 below, 84 mm and 7 mm performant deformations were observed in the longitudinal direction (x) and lateral direction (y), respectively.

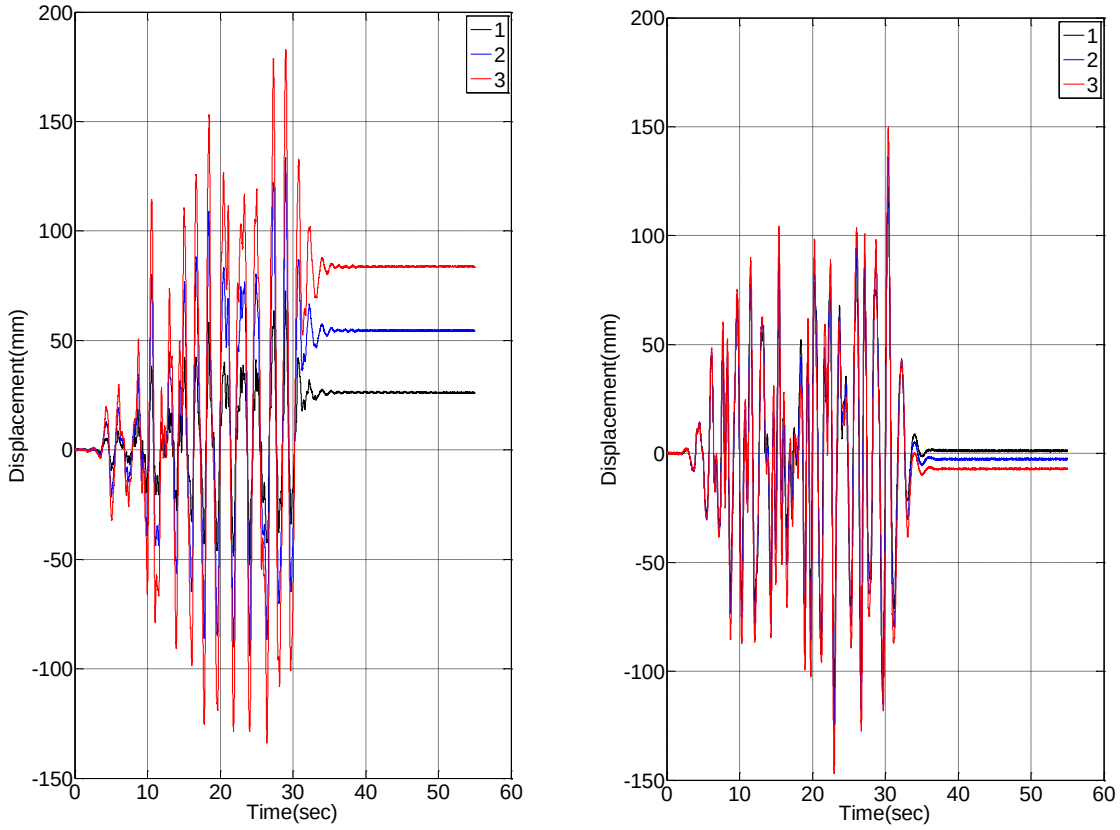

(a) longitudinal direction (x) (b) lateral direction (y)

Figure 2: Permanent deformation of storage racks

3 DEVELOPMENT OF VISCOELASTIC DAMPER FOR IMPROVING THE SEISMIC PERFORMANCE OF STORAGE RACKS

Based on the shaking table test results regarding the dynamic characteristics of the storage racks, a larger permanent deformation occurred in the longitudinal direction (x) than in the lateral direction (y). The reason for this phenomenon is the shape of the storage racks. Most components of a storage rack are connected through bolts. Conversely, the beam-to-column connection in the longitudinal direction (x) depends on a simple hook system. Unfortunately, this method cannot satisfy the longitudinal stiffness requirement. This study developed a damper that could enhance the seismic performance of a storage rack by reinforcing the beam-

to-column connection in the longitudinal direction (x). ISD-111 VE polymer produced by 3M was used for the damper. The down-aisle direction of a storage rack should not be an obstacle in loading or unloading objects to achieve the purpose of the rack. In this regard, three types of small triangular viscoelastic dampers were developed, as illustrated below.

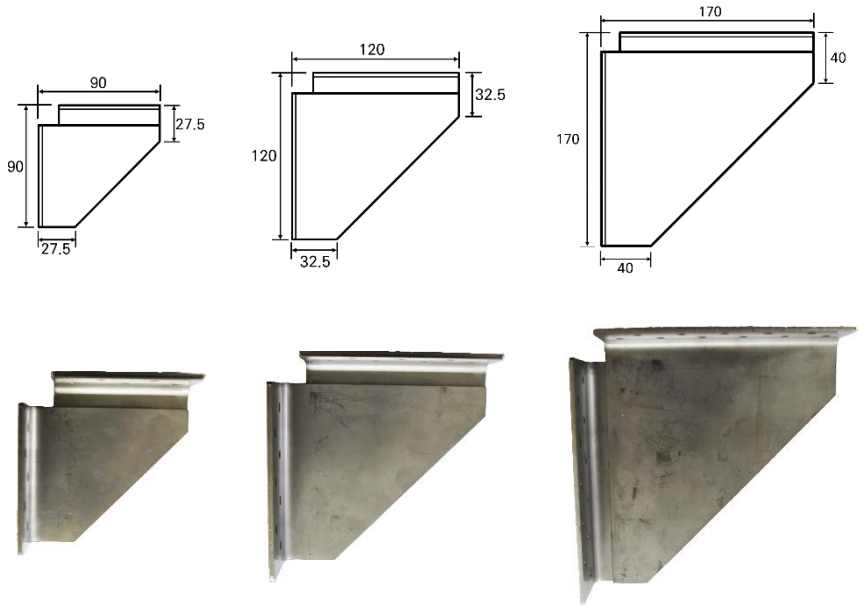

(a) 7 cm (b) 10 cm (c) 15 cm

Figure 3: Viscoelastic dampers for reinforcing the beam-to-column connection of storage racks

To verify the basic performance of the viscoelastic dampers, which were developed to improve the seismic performance of storage racks, a test was conducted using an actuator of the Advanced Construction Materials Testing Center in South Korea. In the performance test, the displacement condition varied (±2 mm, ±4 mm, ±6 mm) at 1 Hz. As the size of the viscoelastic damper increased, the control force was almost doubled. Additionally, the control force was proportional to the displacement. Figure 4 illustrates the force-displacement graphs obtained from the performance tests for the three dampers.

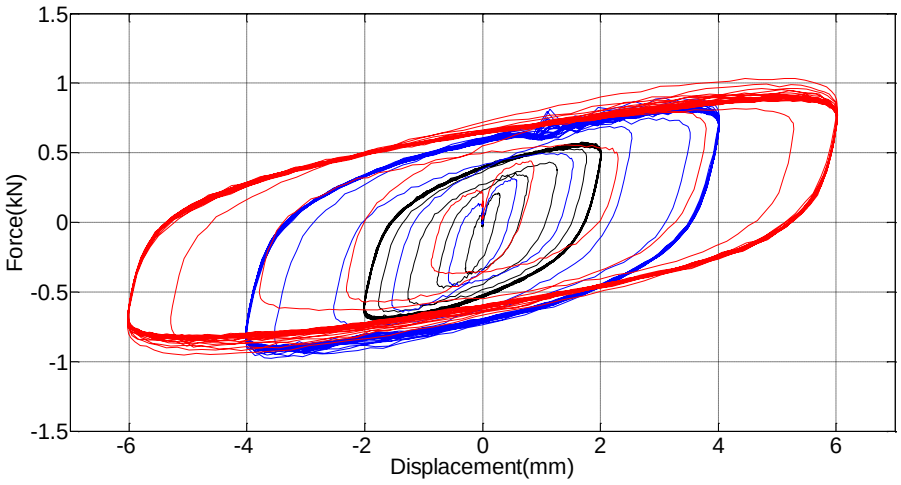

(a) 7 cm

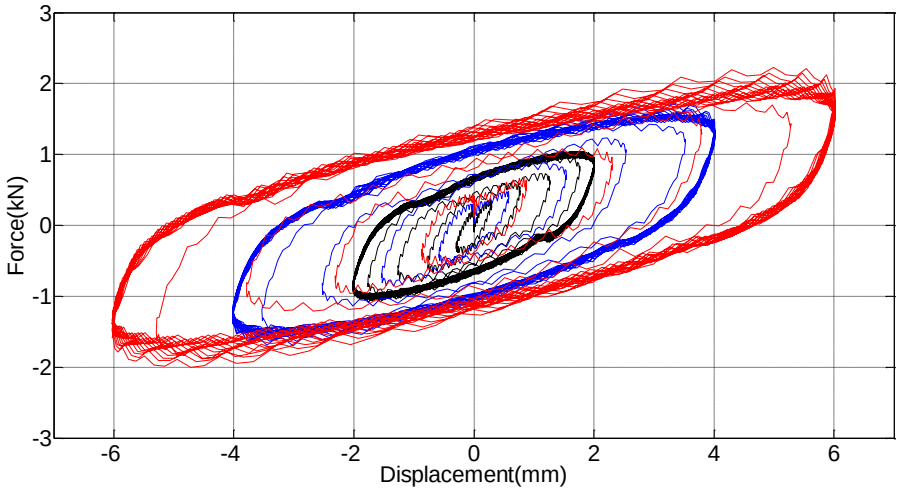

(b) 10 cm

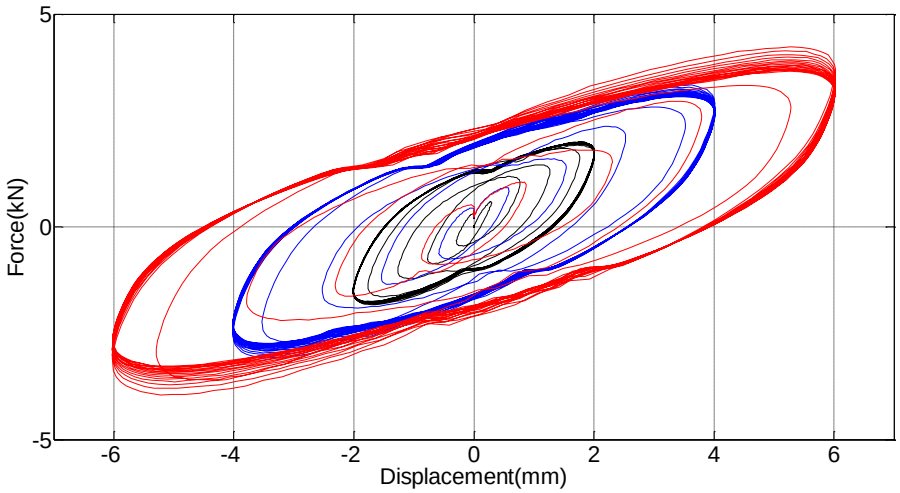

(c) 15 cm

Figure 4: Performance test results for viscoelastic dampers for reinforcing the beam-to-column connections of storage racks

4 ANALYSIS OF BEHAVIOR CHARACTERISTICS OF THE STORAGE RACKS WITH VISCOELASTIC DAMPERS

A shaking table test was performed to experimentally evaluate the performance of the viscoelastic dampers that were developed to reinforce the seismic performance of storage racks. The shaking table test was intended to identify the effect of reducing seismic loads and permanent deformation of the proposed dampers. For the test, three types of viscoelastic dampers were installed in each shelf of the basic storage rack, as shown below. The conditions of the dynamic characteristics test were applied to the shaking table test. Data obtained from the shaking table test were compared with the experimental data of the basic storage rack.

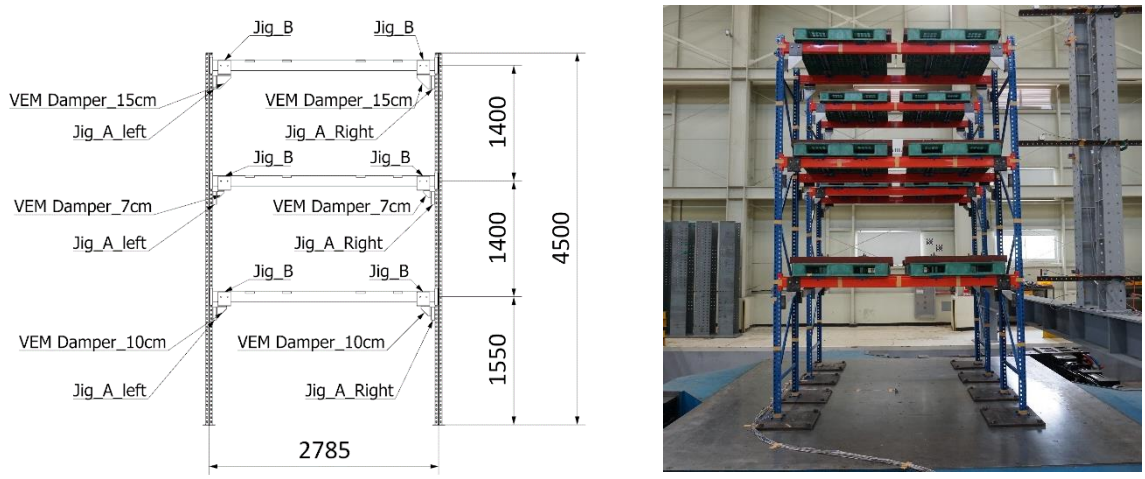

(a) Installation diagram of dampers (b) Storage rack with dampers

Figure 5: Test for reducing the seismic loads of the storage rack with viscoelastic dampers

Figure 6 depicts the displacement responses on each shelf, which were obtained from the basic storage rack and the storage rack with viscoelastic dampers. Table 2 presents the values of the maximum displacement and permanent deformation obtained from each test.

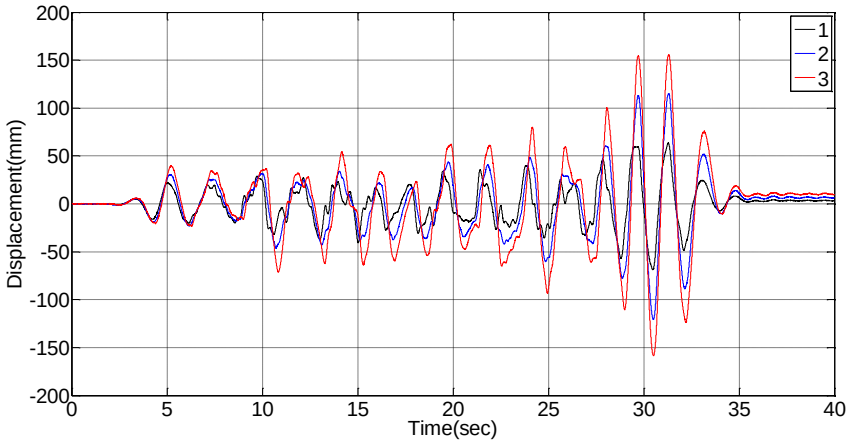

Figure 6: Shaking table test result (Displacement generated)

Experiment result	Maximum displacement (mm)			Permanent deformation (mm)		
	1st	2nd	3rd	1st	2nd	3rd
Basic storage racks	88	164	222	15.56	29.82	44.46
Storage racks using viscoelastic damper	67	121	162	3.72	6.69	10.78
Reduction rate (%)	23.9	26.2	27	76.1	77.6	75.8

Table 2: Maximum and permanent deformation of storage racks

As shown in the above figure and table, in comparison with the basic storage rack, the storage rack reinforced with the proposed viscoelastic dampers reduced the maximum displacement by 23.9% on the 1st shelf, 26.2% on the 2nd shelf, and 27% on the 3rd shelf. In addition, after the test, the permanent deformation, or residual displacement, improved by 76.1% on the 1st shelf, 77.6% on the 2nd shelf, and 75.8% on the 3rd shelf. Here, the maximum displacement is influential on the behavior characteristics of the stored objects, and the permanent deformation is related to the inversion of the storage racks.

5 CONCLUSIONS

The present study aimed to develop a damper to ensure the safety of storage racks. Although the demand for storage racks drastically increases due to the increase of logistics service, there is no standard concerning the design and operation of storage racks, and devices have not been sufficiently developed to enhance the safety of the racks under external loads, such as seismic loads. To develop an appropriate damper for storage racks, a shaking table test was conducted to analyze the behavior characteristics of the basic storage rack. Weak parts of the storage rack were identified based on the test result and the analysis result of the shape of the storage racks. Then, viscoelastic dampers were developed to ensure the safety of storage racks through the reinforcement of the identified weak parts. The performance of the developed dampers was evaluated by conducting the basic performance test. Finally, another shaking table test was also performed for the storage rack reinforced with the proposed viscoelastic dampers to experimentally evaluate the excellent performance of the dampers. The findings of this experimental study can be summarized as follows.

1) The test for analyzing the dynamic characteristics of the basic storage rack demonstrated that the permanent deformation was much larger in the down-aisle direction than in the cross-aisle direction. In addition, the analysis of the storage rack shape revealed that the hook system for the beam-to-column connections, which were installed in the down-aisle direction, was the most unsafe part of the storage rack. In other words, the reinforcement of the beam-to-column connections and the reduction of the down-aisle behaviors were of utmost importance to ensure the safety of storage racks.

2) Viscoelastic dampers were developed to reinforce the safety of storage racks. The dampers were designed to have a small triangular shape to minimize the interruption of loading or unloading objects. Three types of dampers with different sizes were developed. The test of the basic performance of the viscoelastic dampers showed that as the size of the damper increased, the control force was almost doubled.

3) A shaking table test was performed to check whether the storage rack with the developed viscoelastic dampers could reduce the seismic loads. The data obtained from the shaking table test were compared with the experimental data of the basic storage rack. In comparison with the basic storage rack, the storage rack with the viscoelastic dampers could reduce the maximum displacement by over 20% and the permanent deformation by approximately 76% or more on every shelf.

In conclusion, the viscoelastic dampers improved the stiffness of the beam-to-column connection, which was the weakest part, thereby demonstrating excellent performance of ensuring the safety of the storage rack under external loads. Moreover, because the dampers developed in this study were cheap and easy to install without any interruption of the operation of storage racks, they proved to be applicable to secure the safety of small storage racks.

ACKNOWLEDGMENTS

This work was supported by the Research Foundation of Korea funded by the Korea government (Grant no: 2016R1A2A1A05005499, 2016R1A6A3A11931945, and 2018R1A6A1A03025542). In addition, we would like to appreciate and acknowledge the National Research Foundation who made this research possible.

REFERENCES

[1] BSSC Storage Rack Project Task Group, Seismic considerations for steel storage racks located in areas accessible to the public. FEMA 460, Building Seismic Safety Council for the Federal Emergency Management Agency, Washington, D.C., 2005.

[2] M.C. Pollino, Y. Gao, R. Michael, *Seismic response and protection of steel storage rack palleted merchandise*, Proceedings of the 10th National Conference on Earthquake Engineering, Earthquake Engineering Research Institute, Anchorage, AK, 2014.

[3] Yuan Gao, *Seismic evaluation and performance enhancement of industrial storage racks*, Case Western Reserve University, January, 2013.

[4] Samin Sorourian, *Study of seismic control systems on the behaviour of industrial storage racks*, University of Technology Sydney, degree of Master of Engineering, 2014.

[5] R.J. Michael, J.A. Courtwright, E.B. Ferro, A. Filiatrault, P.S. Higgins, A. Wanitkorkul, *Development of a new base isolation system for seismic isolation of steel pallet storage racks*, Proceedings of the 9th US National and 10th Canadian Conference on Earthquake Engineering (9USN10CEE), 10p, Toronto, Ontario, Canada, July 26, 2010.

[6] ICC-ES, AC156, Acceptance Criteria for Seismic Certification by Shake-table Testing of Nonstructural Components. 2010.

[7] Korea Building Code. Architectural Institute of Korea, Ministry of Land, Transport and Maritime Affairs, 2016.

COMPDYN 2019
7th ECCOMAS Thematic Conference on
Computational Methods in Structural Dynamics and Earthquake Engineering
M. Papadrakakis, M. Fragiadakis (eds.)
Crete, Greece, 24–26 June 2019

FLOOR VIBRATION BEHAVIOR OF CAR PARK STRUCTURES – ASSESSMENT OF DIFFERENT STEEL CONCRETE SOLUTIONS

Riccardo ZANON[1]

[1] ArcelorMittal Global R&D
66 rue du Luxembourg, L-4009 Esch-sur-Alzette, Luxembourg
e-mail: Riccardo.zanon@arcelormittal.com

Abstract

This paper analyses the floor vibration behavior of typical car park structures made of steel - concrete composite decks. Two configurations are chosen amongst the most common on the European market and compared from the static and dynamic point of view. Beside a modal analysis made with different mass assumptions, time-history analysis are performed under realistic load cases with vehicle loading the deck at different speeds to test the realistic structural response.
The results show that standard steel-composite decks reasonably comply with acceptance criteria given in the literature. It is interesting to notice as different configurations with same static design may present significant differences in respect to the dynamic response.

Keywords: Floor vibration, dynamic acceptation criteria, steel-concrete composite structure, car park.

1 STEEL FRAMED CAR PARK STRUCTURES

1.1 Introduction and market overview

One of the major objectives of modern traffic planning is to reduce, as much as possible, the use of private transport in densely populated areas. Parking facilities located in the suburbs, having optimal connections with the public transport network (so called Park and Ride) are necessary prerequisites for this purpose. In this view open over ground car parks are gaining more and more relevance in dense urban areas as well as in medium cities, as the need towards improved mobility form is becoming more urgent.

Figure 1: External views of typical steel framed open car park structures.

Car Parks structure are therefore over ground or underground buildings providing parking facilities. From the Fire Safety Approach point of view, these buildings are classified either Open or Closed Car Parks – and this distinction has relevant consequences in the structural design. Open refers to the requirement that such buildings must provide sufficient natural ventilation through permanent openings along the façades so to exclude the occurrence of a generalized fire embracing the whole compartment. In this case only localized fire scenarios can be applied, which by mean of an adequate Natural Fire Safety approach lead to reasonable requirements for the fire design the structural elements [5]. The requirement to classify a Car Park as opens slightly different from country to country but is typically expressed as minimal ratio of permanent façade openings on built surface [2].

In most European countries this kind of buildings are realized by means of steel-framed structures when they are classified as open. This choice is based both on economical as well as on architectural aspects, since it is appreciated the possibility to avoid obstacles between parking lots which affect the functionality of the building. This leads to rather considerable main spans – usually from 16 up to 18 meters [7].

When the requirement concerning sufficient natural ventilation is not fulfilled, the Car Park is conversely classified as closed. This is typically the case for the car parks which are built under ground or below other buildings. One first important difference from the open overground car parks is that the structural grid is oven linked with constraint from the upper levels, from walls or stiffening systems as well as from the choice of the retaining walls. This fact in general limits the designer in the choice of an optimal structural grid and in the general case leads to significant shorter free spans (typically main spans about 8m, like the buildings on top) where the benefits of steel framed structures are less relevant.

Figure 2: Internal views of typical steel framed open car park structures.

The second reason is that Natural Fire Safety Concept is nowadays established in Europe for Open Car Parks which leads to unprotected steel structures therefore sparing the significant cost of fire protection. In the case of closed car parks the limited natural ventilation linked with the interactions with other structures makes the task more complicated. For this reason the conservative Prescriptive Fire Safety Approach based on ISO834 heating curve is adopted leading to severe requirements for 60, 90 or even 120 minutes. This prescriptive requirements may hardly affect the cost competitiveness of steel structures [5].

These two reasons are the main causes to explain why modern Open Car Parks are today a domain of steel framed structures, whereas conversely closed underground car parks remain the domain of traditional prestressed or reinforced concrete typology. In the scope of this paper will consider the first case, so standard steel framed car parks conceived for external building so in view of an optimized grid in view of architectural, functionality and structural requirements.

1.2 Floor vibration – Situation and scope of this paper

As every long-span slender floor, steel-concrete decks for car parks are exposed to the risk of vibration [1], [3], [8], [9], [10]. The complexity in the case of car parks is that two kind of loadings are present: human and vehicular. But beside this structural consideration, the experience shows that floor vibration is not an issue for car parks: in fact visitors are just shortly crossing by feet the lanes so floor vibration won't disturb them significantly, and once they are in the car they are well isolated from the floor vibrations. For this reason typically no serviceability requirements concerning deflection under live loads is imposed [3].

Nevertheless in some literature and design rules there are still some recommendation concerning the limit of eigenfrequencies, for example 3 Hz according [11]. Such prescriptive approach may in fact result in becoming the main design criteria and therefore affecting the competitiveness of the solution. Scope of this paper is to identify a realistic case study, define two different relevant structural configurations, and analyze their dynamic behavior under realistic assumptions in order to assess their dynamic behavior in view of human comfort criteria. With the help of this two representative examples we will furthermore evaluate whether such frequency limitation criteria are appropriate.

2 DEFINITION OF A GENERAL RELEVANT CASE STUDY

2.1 Geometrical layout

In the scope of this paper we will consider a standard layout of parking lots 5 x 2.5m with a central lane of 6m. This bay of 16.0m will be framed by steel construction, so we will consider a span for the secondary beam of 16.5m [5].

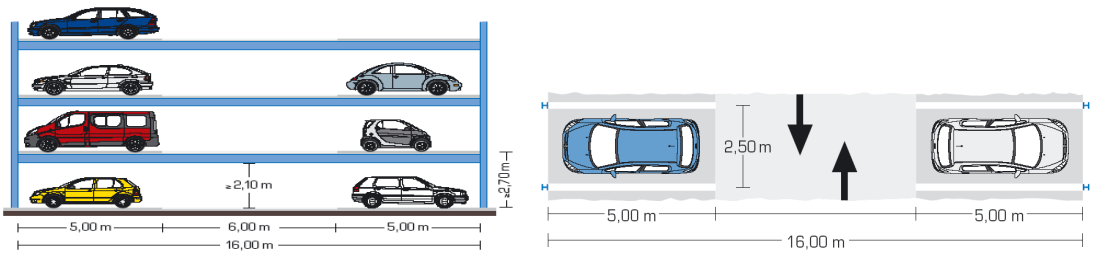

Figure 3: Standard geometrical layout

2.2 Structural deck - Configuration A and B

In the frame of this example we will consider a composite steel concrete structures according Eurocode 4 [6], as they are currently in use since decades for this kind of buildings. Secondary beams are stock hot rolled sections with headed studs welded on the top flange. The use of high steel strength S460 has become a standard for these elements since it permits to optimize the steel weight for strength design, whereas deformation under self-weight and permanent weight are compensated by adequate cambering (for this kind of structures typically in the range L / 100 … 120, where L is the span).

In the scope of this paper two different configurations will be considered and compared. Configuration A presents a shallow steel decking with depth 60mm (type Cofraplus 60 [13]) made composite with reinforced concrete depth of 70mm on top of the rib for a total depth of 130mm. The ribs have an center distance of 207mm. The decking is set on top of the beam flange and is pre-holed in correspondence of the headed stud location. The beam spacing which this slab system covers efficiently is 2.5m – corresponding to 1 parking lot. This typology corresponds to the classical steel-concrete composite floors in use since several decades.

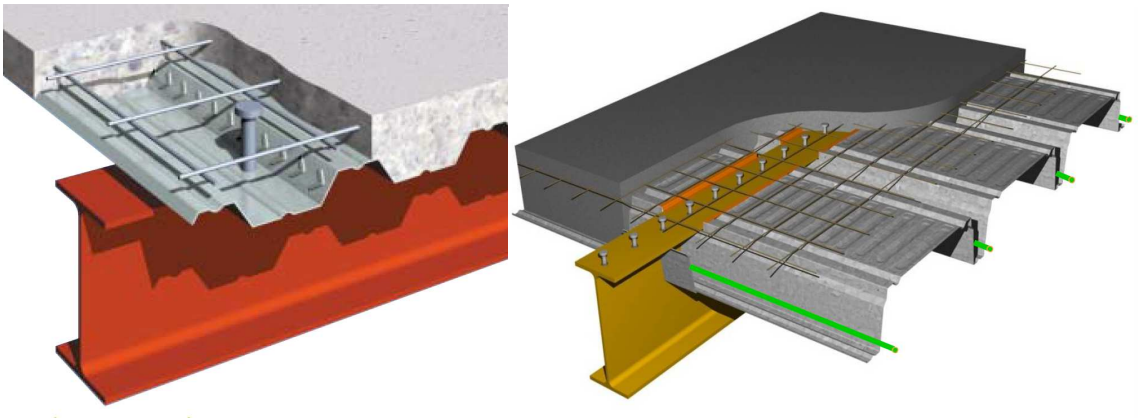

Figure 4: Configuration A (left), pre-holed shallow steel decking posed on top of the beam flange. Configuration B (right), deep steel decking set in the depth of the beam.

Configuration B is an alternative where the main aim is to cover 2 parking spaces instead of 1, which results in a beam spacing of 5.0m without propping in the construction stage. This is achieved with a deep steel decking of 220mm (type Cofraplus 220 [13]) with 90mm of reinforced concrete on top. The deep steel decking cannot be placed on the top of the flange due to their height, therefore they are integrated in the secondary beam height by fixing them on special supports welded onto it. These supports shoes where the ribs of the decks are supported are called wings. In the final phase, the steel-concrete floor behaves therefore as a ribbed deck, with a rib center distance of 750mm. This solution with 5m beam spacing has begun to spread in Europe in the ’90 thanks to the introduction of a successful decking – beam connection system and has afterwards evolved in the shape presented here.

In table 1 we present the principal data for each configuration presented. Configuration B has for sure the advantage to decrease the number of elements and is more efficient in steel consumption in the regular car parks bays. Configuration A is more flexible and requires usually less steel tonnage in the irregular part of the parking (slab ends, ramps, transition to staircases cores). Anyway as it can be seen the total steel consumption is comparable and both configurations are fit for use in this application; the choice between the two systems depends mainly on the designer and / or the steel contractors habits.

Configuration	A	B	
Span	16.50	16.50	[m]
Beam spacing	2.50	5.00	[m]
Secondary beam - cross section	IPE A 450	IPE A 550	[-]
Steel grade	S460M	S460M	[-]
Studs - Type and spacing	d22/100 - 207	d19/80 - 150	[-]
Steel decking type	Cofraplus60	Cofraplus220	[-]
Decking thickness	0.75	1.13	[mm]
Beam weight	26.88	18.42	[kg / m^2]
Studs weight	0.70	0.29	[kg / m^2]
Wings weight	-	0.98	[kg / m^2]
Connection plates / bolts weight	0.54	0.37	[kg / m^2]
Decking weight	8.53	15.14	[kg / m^2]
Total weight - sec. beams + decking	36.64	35.20	[kg / m^2]
Concrete utilization	0.095	0.127	[m^3 / m^2]

Table 1: Resume of main structural data for Configuration A and Configuration B

3 STRUCTURAL MODEL AND MODAL ANALYSIS

3.1 Base structural model

Self-weight and permanent loads are based on [4]. For the traffic loads we have considered §6.3.3 for garages and vehicle traffic areas, category F (Traffic and parking areas for light vehicles <30 kN gross vehicle weight and < 8 seats not including driver) [4] (see Table 2).

Configuration	A	B	
G : Self-weight	2.69	3.46	[kN / m^2]
P: Permanent loads	1.00	1.00	[kN / m^2]
Q_k: Design variable loads	2.50	2.50	[kN / m^2]
Q_{Real}: Realistic variable loads	1.25	1.25	[kN / m^2]

Table 2: Surface loads considered for design.

The design has been made according Eurocode 4 [4] for a simply supported standard composite beam. Freely available tools are available on the net for this kind of application (for example ABC edited by ArcelorMittal – CTICM [13]). As expected for this kind of structure, the value of the first frequency is between 2 and 3 Hz (see Table 3).

Configuration	A	B	
ULS utilization factor	95.6%	96.0%	[-]
Pre-cambering foreseen	140	180	[mm]
First frequency (G + P)	**2.71**	**2.27**	**[Hz]**

Table 3: Resume of most relevant design results.

3.2 Finite Element Model

A complex Finite Element Model has been built with the software SCIA Engineer [12]. For the scope of this study we have considered a portion of a car park structure with a bay of 20m (corresponding to 8 parking spaces, so 9 beams for configuration A and 5 for Configuration B) by 16.5m in the other direction (corresponding to the span of a simply supported beam). The slab is modeled with shell elements, whereas secondary beam and slab ribs re modeled by beam elements. It has been paid proper attention that in longitudinal direction (=beam direction) only the part of the slab above the dovetail is participating with the adequate offset. In transversal direction the ribs have been added as beam elements attached to the shell with an adequate offset. The model is linear concerning material and geometry.

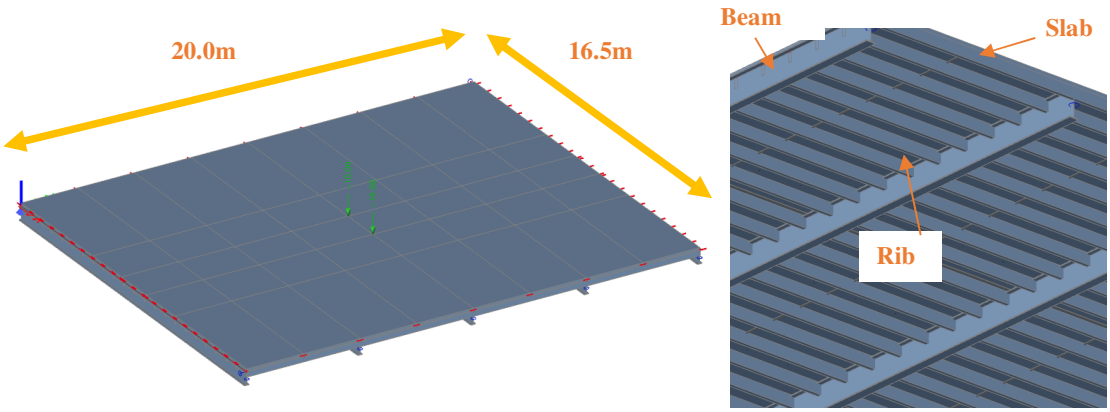

Figure 5: View of the FE structural model used for Configuration B.

3.3 Results of the modal analysis

The modal analysis is run with the model described above where the self-weight of the structure is given in table 2. It has been checked that for the load case self-weight and permanent loads (G+P), the first eigenfrequency calculated with the FEM software corresponds to the result of the analytical tool (compare Table 3 and table 4 for (G+P)).

When considering the mass linked with the presence of variable loads, only realistic configurations shall be considered. Therefore we have decided to consider a maximal value showed in table 2 but only in the parking lots where the presence of vehicles can expected. The realistic surface load corresponds to a vehicle of 1600 kg, which approximates the average vehicle weight in European countries, spread of a standard parking lot of 2.5m x 5m.

Configuration	A	B
G + P	**2.71**	**2.27**
G + P + Q_{Real} in every parking space	**2.56**	**2.18**
G + P + Q_{Real} in every parking space on one side of the lane	2.63	2.22
G + P + Q_{Real} in every second parking space	2.67	2.25
G + P + 0.8 * Q_{Real} in every parking space	2.59	2.20
G + P + 1.2 * Q_{Real} in every parking space	2.53	2.16

Table 4: First eigen frequency calculated for different load combinations.

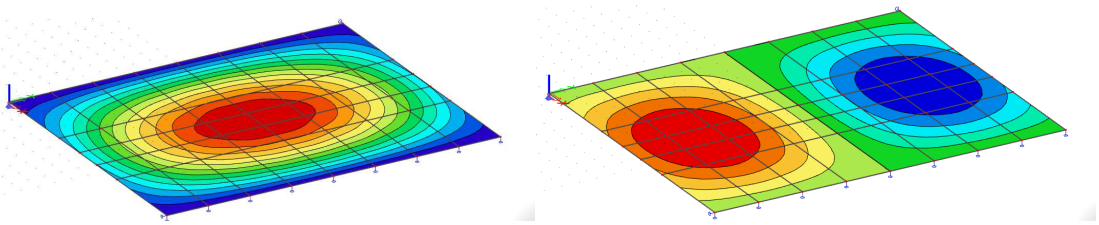

Figure 6: First two eigenmodes of the system

The eigenfrequencies have been afterwards calculated for each system with different combinations of parking lots being occupied (see load combinations in Table 4). In the scope of a sensitivity analysis, we have also evaluated the case of an exceeding of loading of +/- 20%, and as it can be seen the variation of the first eigenfrequency remains moderate as the main masses are still linked with the self-weight.

As it could be expected, all relevant modes, independently from the loading combinations showed before, are one-wave bending in the sense of the secondary beams (on the 16.5m length) and n-wave in transversal direction (mode 1: 1 wave which means all beams upwards or downwards together; mode 2: 2 wave in transversal direction, and so on).

It shall be noted that the first 4 modes are in a range of 1 Hz, which means that the transversal stiffness is relatibe small compared to the longitudinal one and it is rather easy to uncouple the bending modes of each secondary beam.

4 TIME-HISTORY ANALYSIS

4.1 Load model considered

For this study we have considered an axle load running in the middle of the central lane at a given speed. The load model is taken directly from [4] and is showed in Figure 7. The total load point load (Q_k in figure below) has been set equal to 20kN as the recommended upper boundary value.

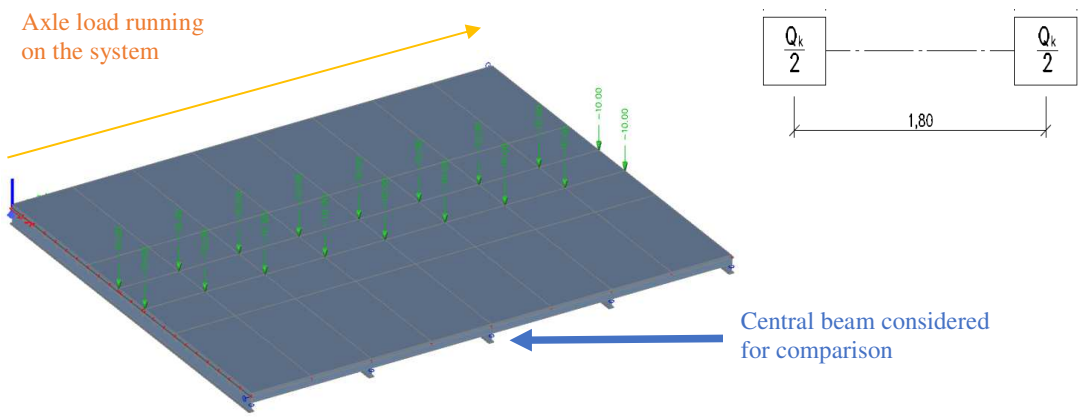

Figure 7: Loading model considered for the time-history analysis.

The load has been moving with different speeds chosen in the range from 18 km/h to 90km/h. The speeds exceeding 20…30 km/h in a parking are rather unprobeable event but are considered anyway as a term of comparison to establish an upper bound scenario.

In the meantime, the parking spaces have been considered full as per the previous simulation in order to achieve the lowest Eigen frequency that the system could possibly express. It has to be stressed that this corresponds to a very conservative approach, since an extreme vehicle load of 2tons (so quite unprobeable) is applied compactly on only single axle in a parking where are parking lots are full.

4.2 Analysis and damping ratio

The analysis has been run for each given speed for configuration A and B in a space of in a time step of 0.02s. The size of the mesh has been reduced to 0.25m so to achieve a good accuracy in the results. A damping ratio of 3% has been assumed in the analysis. This value is quite conservative as it applies, whereas a significant amount of the mass is given by the mass of the vehicles which provide a substantial higher damping ratio according to the literature [3], [11], [9].

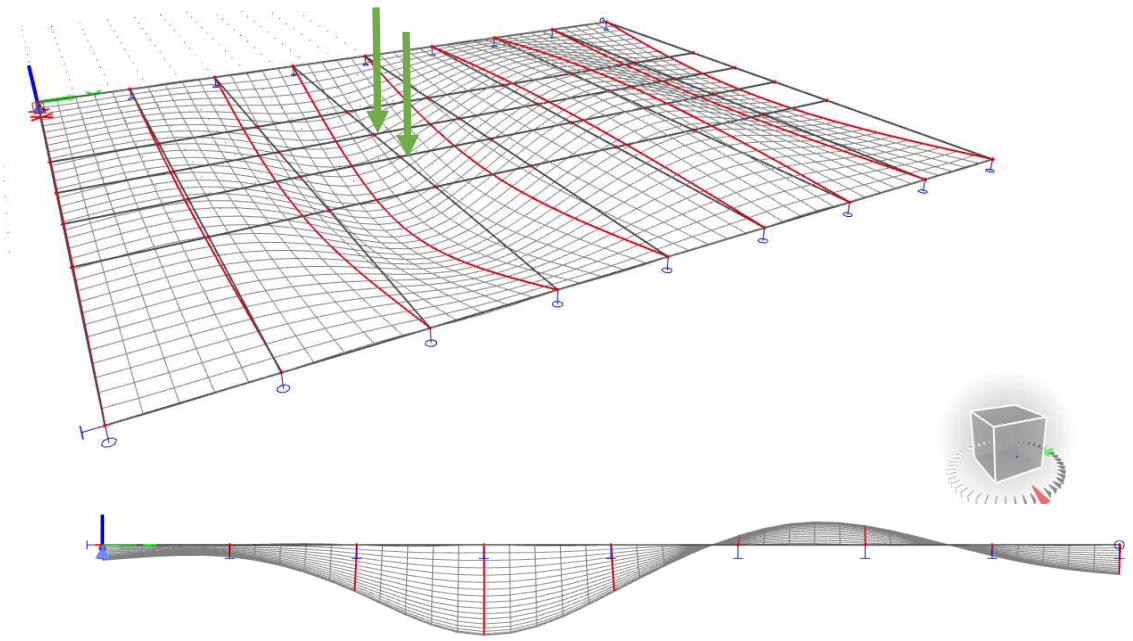

Figure 8: Example of displacement form achieved for a given load position in a dynamic analysis

4.3 Results - displacements

In figure 9 and 10 it is shoed the displacement curves of the midspan of the central beam in function of the time. The peak displacement corresponds to the moment where the vehicle is right above the central beam: this moment occurs in different time of analysis since the speed of the vehicle starting from the edge of the parking are different (the quicker the vehicle travels the sooner it will reach the central mid-span of the beam).

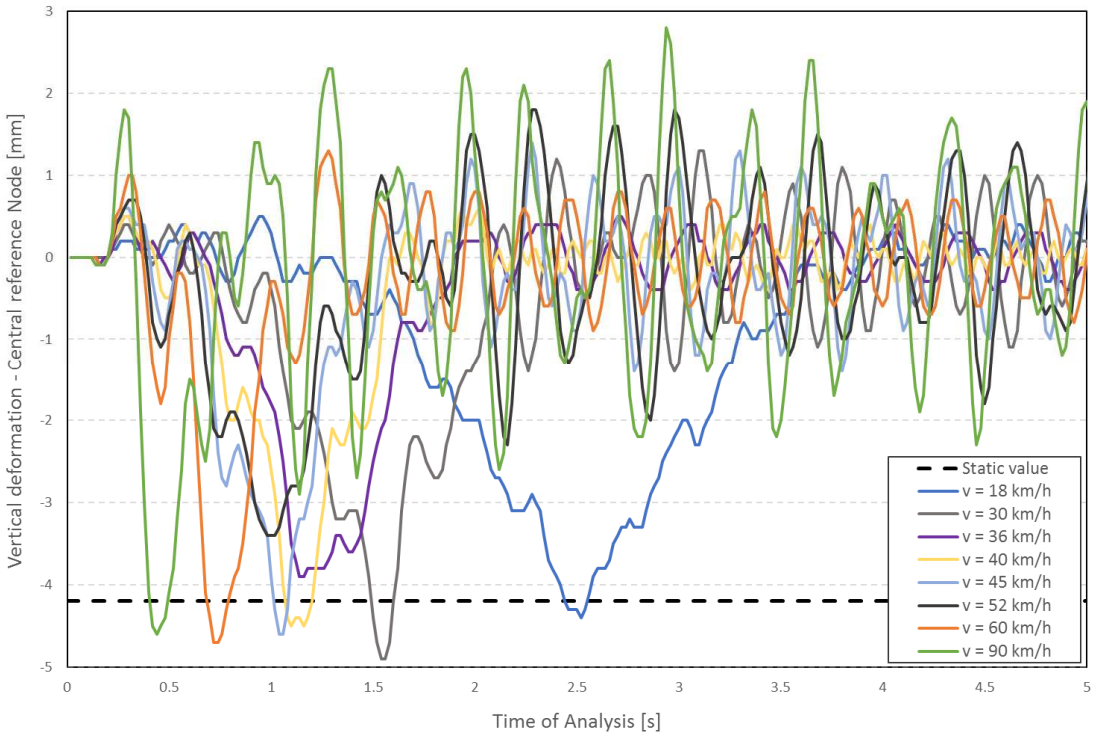

Figure 9: Configuration A – vertical deformation of central reference beam in function of different speeds.

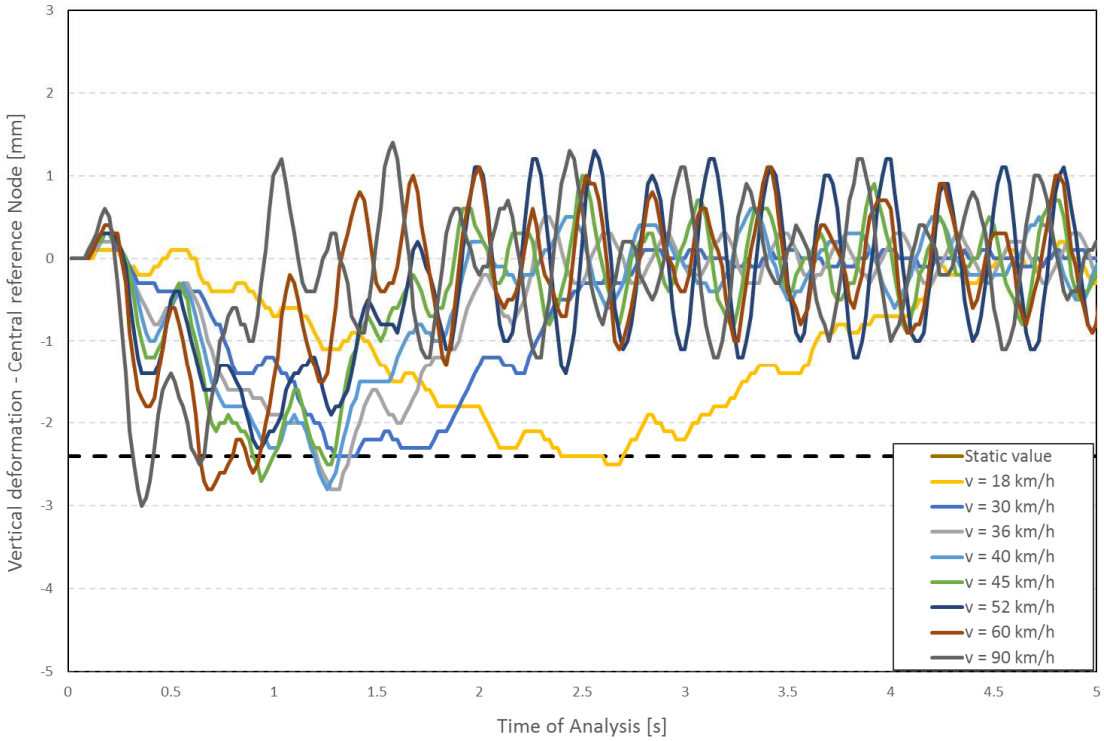

Figure 10: Configuration A – vertical deformation of central reference beam in function of different speeds.

Some key results are showed in the table below. It has to be stressed that despite configuration B presents an higher dynamic impact factor, nevertheless the displacement and the amplitude of the vibration is substantially lower (between 35% and 45%) than configuration A.

Configuration	A	B	
Static displacement	4.2	2.4	[mm]
Dynamic displacement	4.9mm	2.8	[mm]
Dynamic impact factor	1.17	1.25	[-]

Table 5: Dynamic impact factor concerning displacement.

4.4 Results - accelerations

In the assessment of the dynamic behavior of a floor the accelerations are far more important than the actual displacements. For the assessment of the floor vibration the guide [1], [11] will be followed. According the guidelines the root mean square acceleration has been calculated based on the calculated vertical values for each speed and each configuration. The results have been multiplied by two weighting factors, whereas the base curve for acceptance has been multiplied for a factor based on the type of structure considered.

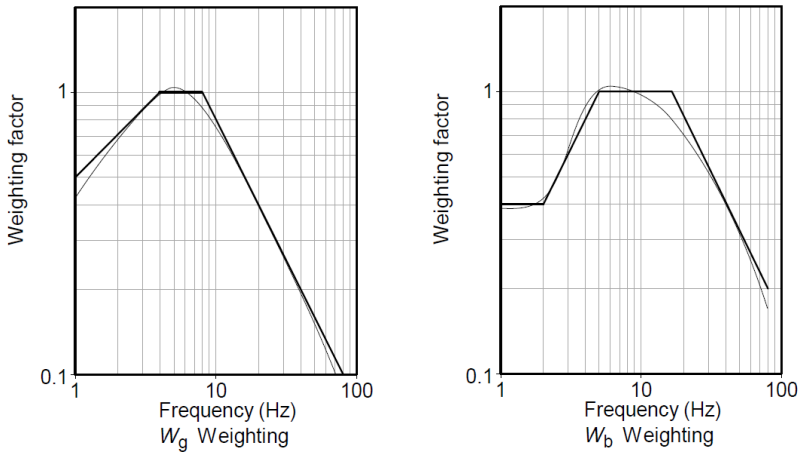

Figure 11: Weighting factors used as multiplier of the root mean square acceleration for each load case.

Configuration	A	B	
Wb	0.512	0.436	[-]
Wg	0.800	0.7382	[-]
Base curve multiplying factor	24	24	[-]

Table 6: Factors used based on BS 6472 [1] and [11]

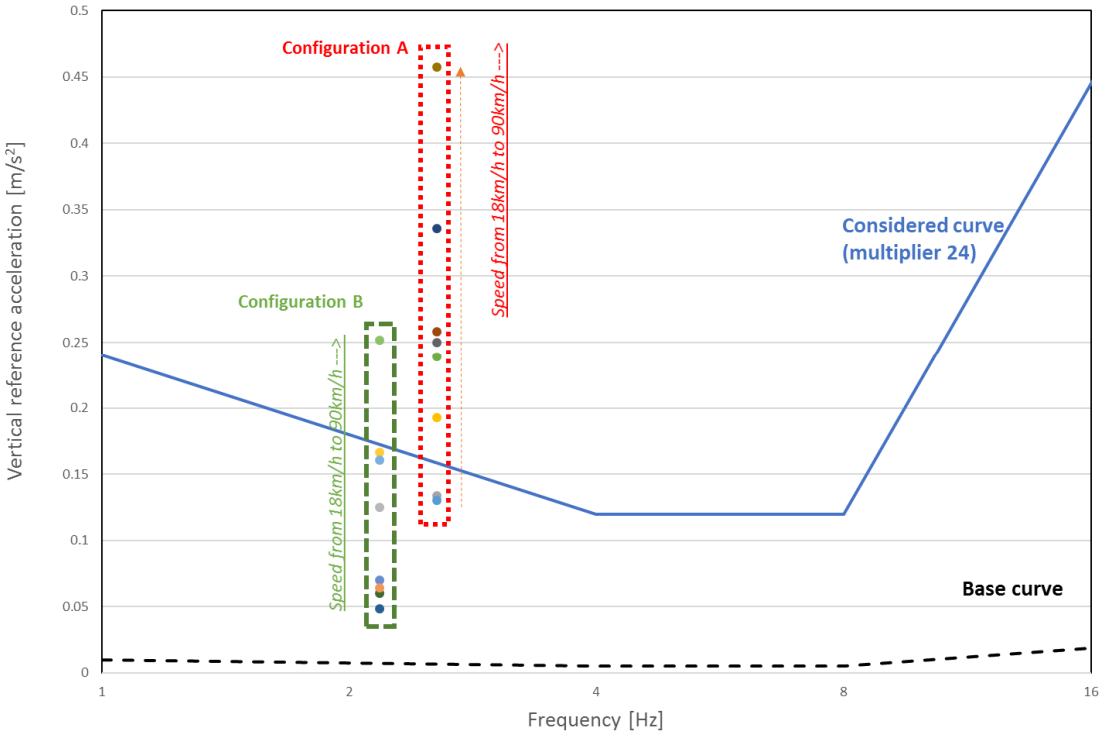

Figure 12: Vertical reference acceleration obtained for different speeds for Configuration A and B compared to the reference acceptance curve for floor vibration

4.5 Findings from the Time-history analysis

Figure 12 shows that several points lye below the considered acceptable floor vibration curve, whereas by increasing the speed the response of the system may result outside the conventional acceptance criteria. In order to express more clearly the results, the same points of Figure 12 have been replotted in Figure 13, but with the speed of the vehicle on the horizontal axis and the vertical reference acceleration in the vertical axis. The limits of the acceptance criteria have been set corresponding to the frequency of configuration A and configuration B.

Thanks to this representation we can clearly recognize that the acceptance criteria is satisfied for speed up to 22 km/h for Configuration A and up to 52 km/h for Configuration B, even under quite conservative assumptions that were taken to obtain these results. For vehicle speeds over this limit, the comfort acceptance criteria concerning criteria is not more guaranteed. Let's remind that current speed limitation criteria for cark parks are in the range of 20 km/h, so it can be considered that floor vibration disturbance can be excluded.

It is interest to remark that configuration B, despite having significantly lower eigenfrequencies, behaves consistently better than A under realistic traffic load. Even up to 60 km/h the vertical acceleration remains quite limited. This is mainly linked with the possibility of a larger transversal distribution under point loads. In this view it has to be stressed the importance of the continuity of the transversal ribs (there are systems with discontinuous slab ribs – in this case the dynamic behavior may be different due to a less efficient transversal distribution).

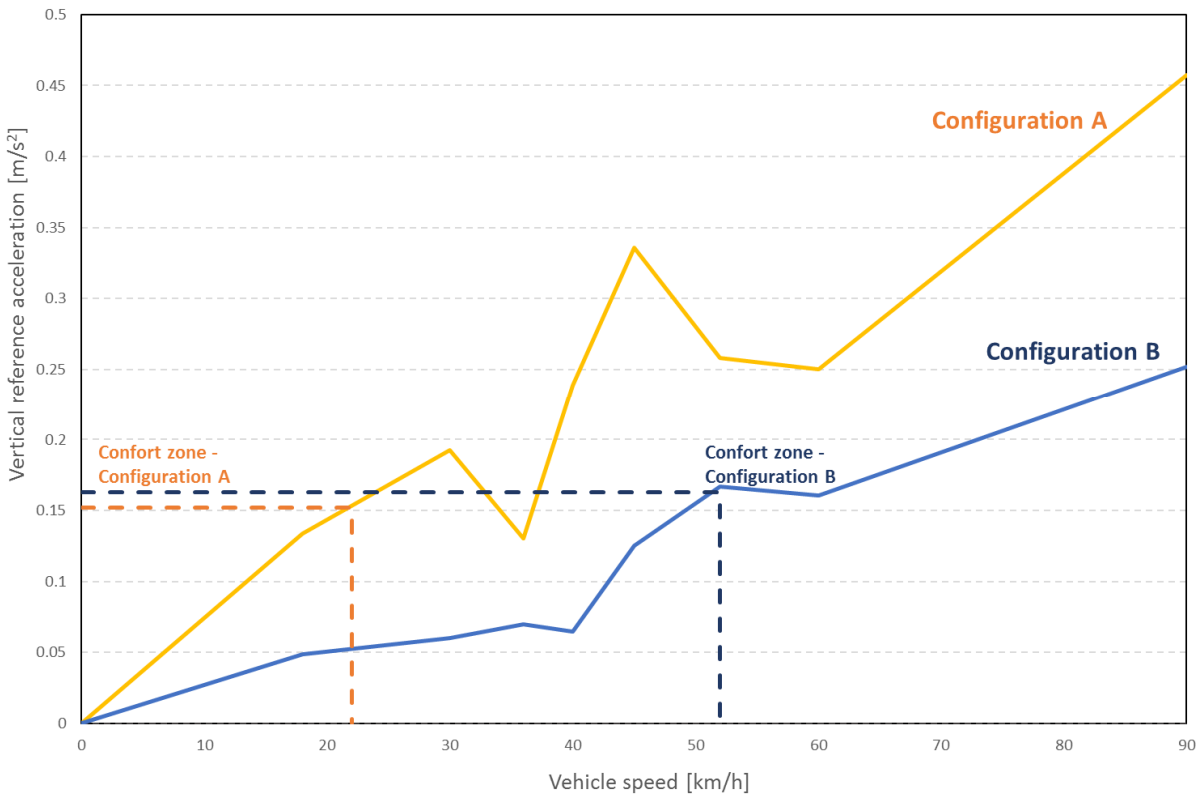

Figure 13: Vertical reference acceleration towards Vehicle speed

5 CONCLUSIONS

It is possible to resume the investigations showed in this paper in mainly three assessments:

- The two case studies considered, which are representative of the common solutions built nowadays, shows that steel-framed structures optimized for design strength behaves correctly also in serviceability limit states and more specifically regarding floor vibration. This shall confirm that no further serviceability criteria are needed.
- The first frequency is not a clear indicator for the dynamic performance of the system under traffic load, which is considered the more relevant for car park structure. Therefore imposing an arbitrary limit on this does not appear to be appropriate.
- For the loading considered and under same design assumptions, steel concrete composite structure with larger beam spacing (e.g. over two parking lots) and composite slabs with continuous ribs behave better from the dynamic point of view than comparable system with smaller beam spacing (e.g. over one parking lots). This is mainly due to a better load transversal distribution that in the case of localized loads (phenomena already known in bridge design).

REFERENCES

[1] BS 6472:1992 Guide to evaluation of human exposure to vibration in buildings (1 Hz to 80 Hz), British Standards Institution (1992).

[2] Technical Committee 3, Fire safety in open car parks – Modern fire Engineering ECCS Publication N° 75 (1993).

[3] Allen D.E., Pernica G., Control of Floor Vibration, Canadian Institute for Research in Construction (1998).

[4] EN 1991-1-1; Eurocode 1: Action on structures, Part 1-1: General actions – Densities, self-weight, imposed loads for buildings (2001).

[5] Cajot, L-G., Mathieu, J., Thomas, L., Les structure métalliques pour les parkings ouverts, La revue de Métallurgie CIT (2003).

[6] EN 1994-1-1; Eurocode 4: Design of composite steel and concrete structures, Part 1-1: General rules and rules for buildings (2005).

[7] Henley, S., The architecture of parking (2007), Thames & Hudson.

[8] ISO 10137 Bases for design of structures – Serviceability of buildingsagainst vibration-International Organisation for Standardization (2007).

[9] Oliver Hechler, Markus Feldmann, Christoph Heinemeyer, Flavio Galanti, Design Guide for Floor Vibrations, EUROSTEEL (2008).

[10] Hivoss – Human Induced Vibration of Steel Structures, Guidelines and background documentation for the design for human induced vibrations on pedestrian bridges and floors – Floor Vibrations, Guideline and Background documents (2008).

[11] Smith A.L, Hicks S J, Devine P J, Design of Floors for Vibration: A New Approach (2009).

[12] Advanced Professional Training – Dynamics, SCIA Engineer (2014).

[13] Website: www.constructalia.com

COMPDYN 2019
7th ECCOMAS Thematic Conference on
Computational Methods in Structural Dynamics and Earthquake Engineering
M. Papadrakakis, M. Fragiadakis (eds.)
Crete, Greece, 24–26 June 2019

PROBABILISTIC THEORY OF PLASTIC MECHANISM CONTROL: DESIGN AND SEISMIC ASSESSMENT

Alessandro Pisapia[1], Elide Nastri[1*]
[1] University of Salerno
Via Giovanni Paolo II, 132, 84084 Fisciano SA
e-mail: alpisapia@unisa.it, enastri@unisa.it

Abstract

This paper reports an application of the Probabilistic Theory of Plastic Mechanism Control (P-TPMC) to a steel Moment Resisting Frames (MRFs) assumed as a case study. The validation of the accuracy of the proposed design methodology is given through non-linear dynamic analyses. In particular, the aim of the non-linear dynamic analyses is to check the collapse mechanism developed by the structures designed by P-TPMC. In fact, it is expected that the percentage of structures exhibiting a collapse mechanism of global type completely developed or compatible with it agrees with the fixed probability given as design achievement of P-TPMC. In other words, if the probability of having a collapse mechanism different from the global one is the 10% the aim of the non-linear dynamic analysis is to check if at least the 90% of the analysis output is entirely in agreement with the global mechanism.
The analysis results are given in terms of the number of plastic hinges developed in columns and beams. Each mechanism showing a lower number of plastic hinges on beams and first storey column bases is considered as compatible with a global mechanism while if plastic hinge also appears on columns of other storeys the mechanism has been considered partial.
The most significant part of analyses leads to the development of a collapse mechanism of global type. In quantitative terms, the percentage of success in achieving a collapse mechanism of global type is about 91% thus confirming the reliability of the design exploiting the P-TPMC.

Keywords: Theory of Plastic Mechanism Control, collapse mechanisms, moment resisting frames, stochastic frames, probability of failure, series systems.

1 INTRODUCTION

Under severe earthquake excitation, structures need to assure an adequate local [1]-[6] and global ductility and high-energy dissipation [7]-[12]. For this reason, the structure needs to exhibit the collapse mechanism of global type, where the dissipative zones are at beams ends and at the base of columns of the first storey, avoiding the partial failure mechanism. Modern design codes [13],[14] provide simple rules to prevent unsatisfactory collapse mechanisms. In case of Moment Resisting Frames (MRFs), the use of the so-called beam-column hierarchy criterion is suggested, but it is widely demonstrated that it is only able to prevent soft storey mechanism and generally it does not assure the development of a mechanism of global type.
In nineties, Mazzolani and Piluso suggested a deterministic procedure, the so-called Theory of Plastic Mechanism Control (TPMC) [15]-[28] to design Moment Resisting Frames able to assure a collapse mechanism of global type after a seismic event. The design rules are based on the extension of the kinematic theorem of plastic collapse to the concept of mechanism equilibrium curve to take into account second order effects. Recently, an improvement of this procedure has been proposed by taking into account the influence of random material variability. A probabilistic analysis is proposed to define the proper value of an overstrength factor to be applied as a multiplying coefficient of the bending resistance of dissipative zones. This approach is called Probabilistic Theory of Plastic Mechanism Control (P-TPMC) [29]-[31].
In this paper, the effectiveness of the P-TPMC is investigated through non-linear dynamic analyses. First of all, the benchmark structure has been defined, and it has been designed given a fixed reliability performance goal. To this scope, an adequate overstrength coefficient is used to increase the beam strength. As higher this coefficient is as highest is the expected probability of having a collapse mechanism of global type. After that, the deterministic TPMC is applied to design the structures considering the assigned overstrength. To check if the collapse mechanism of global type is verified under real earthquake record, the benchmark structure has been modelled and analysed by SAP 2000. A series of 84 real earthquake record for different soils conditions have been used to excite the structure.
For each earthquake, the collapse mechanism achieved is evaluated. Naturally, when the collapse mechanism of global type occurs, it is a success of P-TPMC. Conversely, the failure in the design purpose is verified when the structures exhibit a collapse mechanism different from the global one. Finally, the probability of success in applying the TPMC is defined as the ratio between the number of times when the global mechanism is verified and the total number of analyses.

2 DESIGN OF MOMENT RESISTING FRAME ACCORDING TO P-TPMC

In this section, the design of steel moment resisting frame is presented according to the Probabilistic Theory of Plastic Mechanism Control [29]. The considered benchmark structure is characterized by 4 storeys (number of storeys: n_s), 5 bays (number of bays: n_b) The interstorey height is 3.50 m and the bay span is equal to 6.00 m. The considered steel grade is S275. Moreover, in this step the hypothesis on the soil characteristics are not provided because the design procedure is dependent on the horizontal action distribution only [17]. Therefore, the seismic actions are deterministically distributed according to the first vibration mode of the structure.

2.1 Definition of overstrength factor

In previous works [29], a probabilistic procedure is proposed to compute an overstrength factor to apply to the deterministic version of TPMC which considers the aleatoric uncertainty of material properties. This probabilistic approach is based on the application of the First Order Reliability Method (FORM), and the Ditlevsen Bounds applied for events located in series [32]-

[35] combined with Theory of Plastic Mechanism Control [16]-[31]. Moreover, the same authors provided a mathematical relationship for computing the overstrength factor depending on the number of beams:

$$\gamma_{ov} = -0.0192 n_b + 1.2036 \tag{1}$$

Eq.(1) is derived by a parametric analysis performed for steel grade S275 and for fixed reliability level equal to 90%, which represents the success probability of the TPMC in the development of collapse mechanism of global type. In this case, the overstrength factor to be applied to the deterministic procedure of TPMC is equal to 1.11. More details on the probabilistic approach applied to TPMC and on the parametric analysis carried out to define Eq.(1) are provided in [29].

2.2 Application of Theory of Plastic Mechanism Control

In this section the steps followed in designing the member sections of the examined frame are presented:

Step 1

Definition of the ultimate displacement δ_u, compatible with the ductility supply of the dissipative zones:

$$\delta_u = \theta_u h_{n_s} \tag{2}$$

where θ_u is the steel plastic rotation assumed equal to 0.04 rad, and h_{n_s} represents the total height of the structure. In this case, the ultimate displacement is 0.56 m.

Step 2

The beam sections are the same for all the bays, and they are designed for gravity loads whose values are $G_k = 15.00\ kN/m$ and $Q_k = 6.00\ kN/m$ for permanent and live load, respectively. Referring to the non-seismic load combination, the maximum gravity load acting on the beams is:

$$q_v = 1.35 G_k + 1.50 Q_k = 28.50\ kN/m \tag{3}$$

This value is assumed as a deterministic quantity. The selected beams are IPE 360.

Step 3

All the collapse mechanism equilibrium curves are identified for the studied frame:

$$\alpha = \alpha_0 - \gamma \delta_u \tag{4}$$

where α is a collapse multiplier of structures, α_0 represents the first order multiplier, γ is the slope of curve depending on the second-order effects and, finally, δ_u is the ultimate displacement of the structure. The definition of the column sections is carried out, amplifying the plastic modulus of beams with the overstrength factor γ_{ov} and applying the following design condition:

$$\alpha^{(g)} \leq \alpha^{(t)} => \alpha_0^{(g)} - \gamma^{(g)} \delta_u \leq \alpha_{0.i_m}^{(t)} - \gamma_{i_m}^{(t)} \delta_u \quad for\ t = 1,2,3\ and\ i_m = 1,2,\dots n_s \tag{5}$$

where "g" indicates the global mechanism while "t" represents a generic collapse mechanism different by the global type and i_m is the generic storey of the structure. It is important to underline that the Eq.(5) ensures that the curve of the global mechanism is located below those corresponding to all the other undesired mechanisms until the ultimate displacement δ_u [16],[17]. The column cross-sections are given in Figure 1.

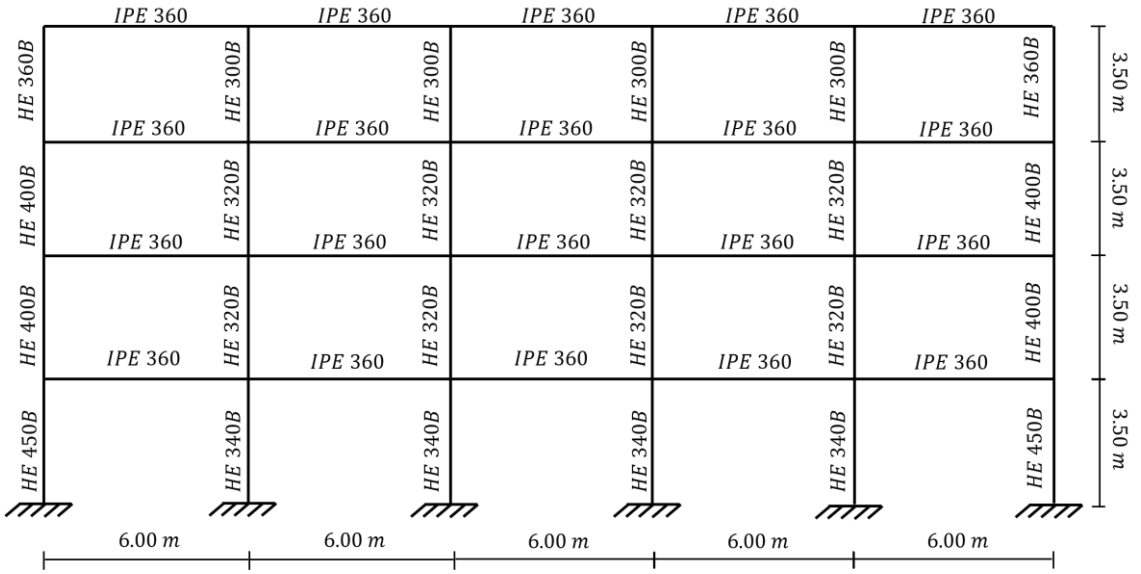

Figure 1: Case-study Frame.

3 VALIDATION BY MEANS NON-LINEAR DYNAMIC ANALYSIS

The aim of the non-linear dynamic analyses presented in this section is to check the collapse mechanism developed by the structures designed by P-TPMC [36]-[39]. In fact, it is expected that the percentage of structures exhibiting a collapse mechanism of global type completely developed or compatible with it agrees with the fixed probability given as design achievement of P-TPMC. In other words, if the probability of having a collapse mechanism different from the global one is the 10% the aim of the non-linear dynamic analysis is to check if at least the 90% of the analysis output is completely in agreement with the global mechanism. The same structure, reported in Figure 1, has been undergone to a set of 84 recorded accelerograms selected from OFEUS database [40]. In particular, 16 earthquake ground motions for soil A, 34 for soil B and 34 for soil C have been selected. Rayleigh formulation for a 5% damping has been assumed with the proportional factors computed with reference to the first and third mode of vibration (T_1=0.74 s and T_2=0.22 s). In Table 1 the analysed records (name, component, date, magnitude, soil, the ratio between PGA and gravity acceleration, length and magnitude) have been reported. The step recording is equal to 0.005 s for each signal. Each earthquake has been scaled to achieve the same level of spectral acceleration. The reference spectrum is Type 1 according to EC8 with a a_g/g equal to 0.35.

The scaling factor the earthquake has to be scaled with is different for each soil category, and it has been computed by multiplying the collapse mechanism multipliers reported in Table 2 with the spectral acceleration achieved in correspondence with the first period of vibration of the structure. In this way, the structure is expected to overcome the elastic phase.

The structure has been modelled and analysed in SAP 2000 [40]. The geometrical and mechanical model is given by beam-column element whose yielding has been taken in account by P-hinge properties.

Two rigid-plastic hinges are located at the member ends. Plastic hinge properties are defined in pure bending (M3 hinge) for beams while in case of columns they are defined to account for the interaction between bending and axial force (P-M3 hinges).

Both geometrical and mechanical non-linearities have been accounted for in the analysis phase [41].

Earthquake	Component	Date	SOIL	PGA/g	Length	Magnitude
	[-]	[-]	[-]	[-]	[s]	[-]
4101_17_08_1999	East-West	17/08/1999	A	0.039	119.99	7.6
ALT_23_11_1980	East-West	23/11/1980	A	0.057	66.485	6.9
ASG_06_05_1976	North-South	06/05/1976	A	0.028	17.045	6.4
BRC_15_09_1976	East-West	15/09/1976	A	0.026	24.22	6.0
BSC_23_11_1980	North-South	23/11/1980	A	0.096	76.21	6.9
CGL_26_09_1997	East-West	26/09/1997	A	0.020	29.175	6.0
CRD_15_09_1976	East-West	15/09/1976	A	0.012	31.195	6.0
KYPA_18_11_1997	Long-Transv	18/11/1997	A	0.017	27.8	6.4
LSS_06_04_2009	East-West	06/04/2009	A	0.010	105	6.1
LSS_24_08_2016	East-West	24/08/2016	A	0.023	80	6.0
LSS_30_10_2016	North-South	30/10/2016	A	0.053	69.9	6.5
MMP1_24_08_2016	North-South	24/08/2016	A	0.012	200	6.0
MMP1_30_08_2016	North-South	30/08/2016	A	0.022	130	6.5
MVB_30_10_2016	North-South	30/10/2016	A	0.008	140	6.5
SBC_30_10_2016	East-West	30/10/2016	A	0.007	89.085	6.5
SGR_23_11_1980	East-West	23/11/1980	A	0.017	14.495	6.9
AIGA_15_06_1995	Transversal	15/06/1995	B	0.052	39.79	6.5
AMATRICE_24_08_2016	East-West	24/08/2016	B	0.044	27.89	6.0
FORCA_30_10_2016	East-West	30/10/2016	B	0.055	76.24	6.5
AMATRICE_30_10_2016	East-West	30/10/2016	B	0.532	40.195	6.5
AQA_06_04_2009	East-West	06/04/2009	B	0.402	40	6.1
AQG_06_04_2009	North-South	06/04/2009	B	0.489	100	6.1
AQK_06_04_2009	East-West	06/04/2009	B	0.353	100	6.1
BRN_23_11_1980	North-South	23/11/1980	B	0.219	78.835	6.9
FRC_15_09_1976	North-South	15/09/1976	B	0.348	24.595	6.0
GEMONA_15_09_1976	East-West	15/09/1976	B	0.255	9.285	6.0
KAL1_18_11_1997	Long-Transv	18/11/1997	B	0.038	40.81	6.4
KOZ1_13_05_1995	Long-Transv	13/05/1995	B	0.216	29.385	6.6
L'AQUILA_06_04_2009	East-West	06/04/2009	B	0.656	100	6.1
MTL_26_09_1997	North-South	26/09/1997	B	0.116	29.05	6.0
MZ10_30_10_2016	North-South	30/10/2016	B	0.398	60.255	6.5
MZ27_30_10_2016	North-South	30/10/2016	B	0.206	148.835	6.5
MZ30_30_10_2016	North-South	30/10/2016	B	0.483	93.76	6.5
MZ63_30_10_2016	North-South	30/10/2016	B	0.384	75.29	6.5
NIS_04_03_1977	East-West	04/03/1977	B	0.043	43.41	7.5
NOR_24_08_2016	East-West	24/08/2016	B	0.202	39.95	6.0
NOR_30_10_2016	East-West	30/10/2016	B	0.049	50	6.5
NRC_24_08_2018	East-West	24/08/2018	B	0.374	40	6.0
PATRASSO_15-06_1995	Long-Transv	15/06/1995	B	0.090	39.52	6.5
PYR1_15_06_1995	Long-Transv	15/06/1995	B	0.056	33.895	6.5
STR_23_11_1980	East-West	23/11/1980	B	0.072	70.76	6.9
TDG_23_11_2018	North-South	23/11/2018	B	0.060	53.01	6.9
TIG_15_04_1979	East-West	15/04/1979	B	0.054	45.55	6.9
TK_01_05_2003	North-South	01/05/2003	B	0.519	64.73	6.3

TK_01_10_1995	East-West	01/10/1995	B	0.059	27.79	6.0
TK_13_03_1992	East-West	13/03/1992	B	0.082	16.875	6.6
TK_17_08_1999	North-South	17/08/1999	B	0.047	135.04	7.6
TK_27_06_1998	East-West	27/06/1998	B	0.128	22.3	6.2
TLM1_06_05_1976	North-South	06/05/1976	B	0.352	36.39	6.4
TRL_30_10_2016	North-South	30/10/2016	B	0.096	49.54	6.5
0105_27_06_1998	East-West	27/06/1998	C	0.277	29.215	6.2
0301_03_02_2002	North-South	03/02/2002	C	0.115	100.12	6.5
0302_01_10_1995	East-West	01/10/1995	C	0.044	27.995	6.0
1401_12_11_1999	East-West	12/11/1999	C	0.820	55.79	7.3
1404_17_08_1999	North-South	17/08/1999	C	0.140	55.4	7.6
1612_17_08_1999	East-West	17/08/1999	C	0.126	205.05	7.6
1801_06_06_2000	East-West	06/06/2000	C	0.064	82.54	6.0
4302_17-08_1999	East-West	17/08/1999	C	0.061	185.82	7.6
5903_17_08_1999	East-West	17/08/1999	C	0.103	85.465	7.6
8101_12_11_1999	East-West	12/11/1999	C	0.526	85.81	7.3
8101_17_08_1999	East-West	17/08/1999	C	0.375	27.09	7.6
AVZ_06_04_2009	East-West	06/04/2009	C	0.069	120	6.1
BUI_15_09_1976	East-West	15/09/1976	C	0.088	25.89	6.0
BVG_24_08_2016	East-West	24/08/2016	C	0.040	176.315	6.0
BVG_26_09_1997	North-South	26/09/1997	C	0.079	50.5	6.0
BVG_30_10_2016	North-South	30/10/2016	C	0.075	130	6.5
BVN_23_11_1980	North-South	23/11/1980	C	0.048	62.58	6.9
CNG_06_05_1976	East-West	06/05/1976	C	0.069	38.35	6.4
EDE1_21_12_1990	Long-Transv	21/12/1990	C	0.103	38.695	6.1
GBP_26_09_1997	East-West	26/09/1997	C	0.098	100.225	6.0
GBP_30_10_2016	North-South	30/10/2016	C	0.053	180	6.5
LEF1_17_01_1983	Transversal	17/01/1983	C	0.065	45.83	6.1
MDN_29_05_2012	North-South	29/05/2012	C	0.052	130	6.0
MRN_20_05_2012	North-South	20/05/2012	C	0.264	130.15	6.1
MRN_29_05_2012	North-South	29/05/2012	C	0.294	68.565	6.0
MZ04_30_10_2016	North-South	30/10/2016	C	0.808	92.915	6.5
MZ24_30_10_2016	East-West	30/10/2016	C	1.020	87.84	6.5
NAS_15_04_1978	North-South	15/04/1978	C	0.148	28.98	6.0
NVL_20_05_2012	North-South	20/05/2012	C	0.052	160.2	6.1
NVL_29_05_2012	East-West	29/05/2012	C	0.054	139.89	6.0
SNG_24_08_2016	North-South	24/08/2016	C	0.046	200	6.0
SNG_30_10_2016	East-West	30/10/2016	C	0.051	180	6.5
SRP_29_05_2012	East-West	29/05/2012	C	0.054	220.315	6.0
ZAK1_18_11_1997	Transversal	18/11/1997	C	0.132	65.44	6.4

Table 1.Characteristics of the earthquake records.

Soil		
A	B	C
1.68	1.21	1.04

Table 2.Collapse multiplier for different soils.

SOIL A				
Case	**Earthquakes**	**Collapse Mechanism**	**Number of plastic hinges**	
			beams	columns
1	4101_17_08_1999	global	30	2(only first storey)
2	ALT_23_11_1980	global	26	6(only first storey)
3	ASG_06_05_1976	global	31	6(only first storey)
4	BRC_15_09_1976	global	25	0
5	BSC_23_11_1980	global	30	6(only first storey)
6	CGL_26_09_1997	global	5	0
7	CRD_15_09_1976	global	30	6(only first storey)
8	KYPA_18_11_1997	global	22	0
9	LSS_06_04_2009	global	26	2(only first storey)
10	LSS_24_08_2016	global	13	0
11	LSS_30_10_2016	global	30	2(only first storey)
12	MMP1_24_08_2016	global	13	0
13	MMP1_30_08_2016	global	10	0
14	MVB_30_10_2016	global	19	0
15	SBC_30_10_2016	global	27	6(only first storey)
16	SGR_23_11_1980	global	31	6(only first storey)

Table 3. Results of non-linear dynamic analysis referred to soil A.

The analysis results are given in terms of the number of plastic hinges developed in columns and beams. The maximum number of plastic hinges able to develop at beam ends is 30 while only 6 plastic hinges at column bases should develop if the mechanism exhibited by the structure is compatible with the global one. Each mechanism showing a lower number of plastic hinges on beams and first storey column bases is considered as compatible with a global mechanism while if plastic hinge appears also on columns of other storeys the mechanism has been considered partial.

From Table 3 to Table 5 it is observed that the largest part of analyses lead to the development of a collapse mechanism of global type. In quantitative terms, the percentage of success in achieving a collapse mechanism of global type is about the 91% thus confirming the reliability of the design exploiting the P-TPMC.

SOIL B				
Case	**Earthquakes**	**Collapse Mechanism**	**Number of plastic hinges**	
			beams	columns
17	AIGA_15_06_1995	global	27	2(only first storey)
18	AMATRICE_24_08_2016	global	0	0
19	FORCA_30_10_2016	global	27	0
20	AMATRICE_30_10_2016	global	30	6(only first storey)
21	AQA_06_04_2009	global	14	0
22	AQG_06_04_2009	global	27	6(only first storey)
23	AQK_06_04_2009	global	27	0
24	BRN_23_11_1980	global	0	0
25	FRC_15_09_1976	global	0	0
26	GEMONA_15_09_1976	global	30	6(only first storey)
27	KAL1_18_11_1997	global	31	6(only first storey)
28	KOZ1_13_05_1995	global	0	0
29	L'AQUILA_06_04_2009	global	27	0

30	MTL_26_09_1997	global	27	0
31	MZ10_30_10_2016	global	30	2(only first storey)
32	MZ27_30_10_2016		32	10
33	MZ30_30_10_2016	global	30	2(only first storey)
34	MZ63_30_10_2016	global	30	0
35	NIS_04_03_1977	global	30	6(only first storey)
36	NOR_24_08_2016	global	31	6(only first storey)
37	NOR_30_10_2016		32	8
38	NRC_24_08_2018	global	31	6(only first storey)
39	PATRASSO_15-06_1995	global	31	6(only first storey)
40	PYR1_15_06_1995	global	30	6(only first storey)
41	STR_23_11_1980	global	30	6(only first storey)
42	TDG_23_11_2018	global	30	6(only first storey)
43	TIG_15_04_1979	global	18	0
44	TK_01_05_2003	global	20	0
45	TK_01_10_1995	global	31	6(only first storey)
46	TK_13_03_1992	global	1	0
47	TK_17_08_1999	global	31	6(only first storey)
48	TK_27_06_1998	global	24	0
49	TLM1_06_05_1976	global	31	6(only first storey)
50	TRL_30_10_2016	global	30	6(only first storey)

Table 4. Results of non-linear dynamic analysis referred to soil B.

SOIL C				
Case	**Earthquakes**	**Collapse Mechanism**	**Number of plastic hinges**	
			beams	columns
51	0105_27_06_1998	global	30	6(only first storey)
52	0301_03_02_2002	global	31	6(only first storey)
53	0302_01_10_1995	global	27	6(only first storey)
54	1401_12_11_1999	global	30	6(only first storey)
55	1404_17_08_1999	global	15	0
56	1612_17_08_1999	global	31	6(only first storey)
57	1801_06_06_2000	global	30	6(only first storey)
58	4302_17-08_1999	global	32	6(only first storey)
59	5903_17_08_1999		30	10
60	8101_12_11_1999	global	32	6(only first storey)
61	8101_17_08_1999	global	30	6(only first storey)
62	AVZ_06_04_2009	global	30	6(only first storey)
63	BUI_15_09_1976	global	27	0
64	BVG_24_08_2016	global	32	6(only first storey)
65	BVG_26_09_1997	global	31	6(only first storey)
66	BVG_30_10_2016	global	30	6(only first storey)
67	BVN_23_11_1980	global	27	0
68	CNG_06_05_1976	global	30	6(only first storey)
69	EDE1_21_12_1990	global	32	6(only first storey)
70	GBP_26_09_1997	global	30	6(only first storey)
71	GBP_30_10_2016	global	30	6(only first storey)
72	LEF1_17_01_1983	global	30	2(only first storey)
73	MDN_29_05_2012	global	31	6(only first storey)

74	MRN_20_05_2012	global	30	2(only first storey)
75	MRN_29_05_2012	global	30	0
76	MZ04_30_10_2016	global	31	0
77	MZ24_30_10_2016	global	27	2(only first storey)
78	NAS_15_04_1978	global	22	0
79	NVL_20_05_2012	global	2	
80	NVL_29_05_2012	global	19	0
81	SNG_24_08_2016	global	30	6(only first storey)
82	SNG_30_10_2016	global	30	2(only first storey)
83	SRP_29_05_2012	global	30	6(only first storey)
84	ZAK1_18_11_1997	global	4	0

Table 5. Results of non-linear dynamic analysis referred to soil C.

4 CONCLUSIONS

- In this paper an application of the Probabilistic Theory of Plastic Mechanism Control (P-TPMC) to a steel Moment Resisting Frames (MRFs) assumed as a case study is reported.
- Non-linear dynamic analyses on a base of 84 earhquake records have been performed to assess the accuracy of the design procedure proposed.
- The expected percentage of success is equal to 90%.
- The obtained percentage of success is 91% thus confirming the reliability of the proposed procedure.

REFERENCES

[1] R. Fusco, R. Montuori, E. Nastri, V. Piluso, "Critical analysis of ultimate rotation formula for R.C. columns subjected to cyclic loadings" *Engineering Structures*, **177**, pp. 160-174, (2018).

[2] K. Mitsui, M. Latour, G. Rizzano, A. Sato, V. Piluso, "Experimental and numerical analysis of the ultimate behaviour of square hollow sections under combined axial and bending loads" *Ingegneria Sismica*, **35** (2), pp. 5-22, (2018).

[3] F. Di Lauro, R. Montuori, E. Nastri,V. Piluso,"Partial safety factors and overstrength coefficient evaluation for the design of connections equipped with friction dampers" *Engineering Structures*, **178**, pp. 645-655, (2019).

[4] V. Piluso, A. Pisapia, E. Nastri, R. Montuori, "Ultimate resistance and rotation capacity of low yielding high hardening aluminium alloy beams under non-uniform bending" *Thin-Walled Structures*, **135**, pp. 123-136, (2019).

[5] P. Castaldo, E. Nastri, V. Piluso, "Ultimate behaviour of RHS temper T6 aluminium alloy beams subjected to non-uniform bending: Parametric analysis" *Thin-Walled Structures*, **115**, pp. 129-141, (2017).

[6] P. Castaldo, E. Nastri, V. Piluso, "FEM simulations and rotation capacity evaluation for RHS temper T4 aluminium alloy beams" *Composites Part B: Engineering*, **115**, pp. 124-137, (2017).

[7] L. Fiorino, V. Macillo, R. Landolfo, "Shake table tests of a full-scale two-story sheathing-braced cold-formed steel building" *Engineering Structures*, **151**, pp. 633–647, (2017).

[8] M. Latour, M. D'Aniello, M. Zimbru, G. Rizzano, V. Piluso, R. Landolfo,"Removable friction dampers for low-damage steel beam-to-column joints" *Soil Dynamics and Earthquake Engineering*, **115**, pp. 66-81, (2018).

[9] S. Costanzo, M. D'Aniello, R. Landolfo, "The influence of moment resisting beam-to-column connections on seismic behavior of chevron concentrically braced frames" *Soil Dynamics and Earthquake Engineering*, **113**, pp. 136-147, (2018).

[10] L. Fiorino, M.T. Terracciano, R. Landolfo, "Experimental investigation of seismic behaviour of low dissipative CFS strap-braced stud walls" *Journal of Constructional Steel Research,* Vol. **127**, pp. 92-107, (2016).

[11] V. Macillo, L. Fiorino, R. Landolfo, "Seismic response of CFS shear walls sheathed with nailed gypsum panels: Experimental tests" *Thin-Walled Structures*, Vol. **120**, pp. 161-171, (2017).

[12] V. Macillo, O. Iuorio, M.T. Terracciano, L. Fiorino, R. Landolfo, "Seismic response of Cfs strap-braced stud walls: Theoretical study" *Thin-Walled Structures*, Vol. **85**, pp. 301-312, (2014).

[13] CEN (2005) EN 1998-1-1: Eurocode 8 - Design of Structures for Earthquake Resistance. Part 1: General Rules, Seismic Actions and Rules for Buildings, Comite Europeen de Normalisation, CEN/TC 250.

[14] ANSI/AISC 341-10, "Seismic Provisions for Structural Steel Buildings", American Institute of Steel Construction, Chicago, IL, 2010.

[15] F.M. Mazzolani, V. Piluso, Plastic design of seismic resistant steel frames, *Earthquake Engineering and Structural Dynamics*, **26**, pp. 167-191, (1997).

[16] A. Longo, E. Nastri, V. Piluso, "Theory of plastic mechanism control: State-of-the-art", *Open Construction and Building Technology Journal*, **8**, Pages 262-278, (2014).

[17] V. Piluso, E. Nastri, R. Montuori, "Advances in Theory of Plastic Mechanism Control: Closed Form Solution for MR-Frames", *Earthquake Engineering and Structural Dynamics*, **44**, Issue 7, Pages 1035-1054, (2015).

[18] R. Montuori, E. Nastri, V. Piluso, "Theory of Plastic Mechanism Control for MRF-EBF dual systems: Closed form solution", Vol. **118**, *Engineering Structures*, Pages 287-306, (2016).

[19] V. Piluso, R. Montuori, E. Nastri, A. Paciello, "Seismic response of MRF-CBF dual systems equipped with low damage friction connections" *Journal of Constructional Steel Research*, **154**, pp. 263-277, (2019).

[20] E. Nastri, M. D'Aniello, M. Zimbru, S. Streppone, R. Landolfo, R. Montuori, V. Piluso, "Seismic response of steel Moment Resisting Frames equipped with friction beam-to-column joints" *Soil Dynamics and Earthquake Engineering*, **119**, pp. 144-157, (2019).

[21] G. Dell'Aglio, R. Montuori, E. Nastri, V. Piluso, "A critical review of plastic design approaches for failure mode control of steel moment resisting frames" *Ingegneria Sismica*, **34** (4), pp. 82-102, (2017).

[22] R. Montuori, E. Nastri, V. Piluso, "Influence of the bracing scheme on seismic performances of MRF-EBF dual systems" *Journal of Constructional Steel Research*, **132**, pp. 179-190, (2017).

[23] R. Montuori, E. Nastri, V. Piluso, M. Troisi, "Influence of connection typology on seismic response of MR-Frames with and without 'set-backs'" *Earthquake Engineering and Structural Dynamics*, **46** (1), pp. 5-25, (2017).

[24] R. Montuori, V. Sagarese, "The use of steel rbs to increase ductility of wooden beams" *Engineering Structures*, **169**, pp. 154-161, (2018).

[25] R. Montuori, E. Nastri, V. Piluso, "Theory of Plastic Mechanism Control for MRF-EBF dual systems: Closed form solution" *Engineering Structures*, **118**, pp. 287-306, (2016).

[26] E. Nastri, "Eccentrically braced frames designed for the energy dissipation optimization" *ECCOMAS Congress 2016 - Proceedings of the 7th European Congress on Computational Methods in Applied Sciences and Engineering*, **4**, pp. 8476-8491, (2016).

[27] A. Longo, R. Montuori, E. Nastri, V. Piluso, "On the use of HSS in seismic-resistant structures" *Journal of Constructional Steel Research*, **103**, pp. 1-12, (2014).

[28] R. Montuori, R. Muscati, "A general design procedure for failure mechanism control of reinforced concrete frames", *Engineering Structures*, **118**, pp. 137-155, (2016).

[29] V. Piluso, A. Pisapia, P. Castaldo, E. Nastri, "Probabilistic Theory of Plastic Mechanism Control for Steel Moment Resisting Frames" *Structural Safety*, **76**, pp. 95-107, (2019).

[30] P. Castaldo, E. Nastri, V. Piluso, A. Pisapia, "Stochastic Approach for Theory of Plastic Mechanism Control", *XXIII Conference AIMETA 2017*, September 4–7, 2017, Salerno, Italy.

[31] P. Castaldo, E. Nastri, V. Piluso, A. Pisapia, "Stochastic Theory of Plastic Mechanism Control: Parametric analysis", *XXIII Conference AIMETA 2017*, September 4–7, 2017, Salerno, Italy.

[32] O.V. Ditlevsen, "Narrow reliability bounds for structural systems", *Journal of Structural Mechanics*, **7**, No. 4, pp. 453-472, (1979).

[33] S. Krishnan, M. Muto, "Mechanism of collapse of Tall Steel Moment-Frame Buildings under Earthquake Excitation", *Journal of Structural Engineering*, ASCE, 138: 1361-1387, (2012).

[34] P.E. Pinto, R. Giannini, P. Franchin, "Seismic Reliability Analysis of Structures", IUSS Press, (2004).

[35] C.A. Cornell, "A Probability-Based Structural Code", *ACI-Journal*, **66**, 1969, pp. 974-985, (1969).

[36] R. Montuori, E. Nastri, V. Piluso,"Influence of the bracing scheme on seismic performances of MRF-EBF dual systems" *Journal of Constructional Steel Research*, **132**, pp. 179-190, (2017).

[37] R. Montuori, E. Nastri, V. Piluso,"Preliminary analysis on the influence of the link configuration on seismic performances of MRF-EBF dual systems designed by TPMC" *Ingegneria Sismica*, **33** (3), pp. 52-64, (2016).

[38] R. Montuori, E. Nastri, V. Piluso, M. Troisi, “Influence of the cyclic behaviour of beam-to-column connection on the seismic response of regular steel frames” *Ingegneria Sismica*, **33** (1-2), pp. 91-105, (2016).

[39] L. Mastrandrea, E. Nastri, V. Piluso, “Validation of a design procedure for failure mode control of EB-Frames: Push-over and IDA analyses” *Open Construction and Building Technology Journal*, **7**, pp. 193-207, (2013).

[40] L. Luzi, R. Puglia, E. Russo & ORFEUS WG5 “ Engineering Strong Motion Database, version 1.0. Istituto Nazionale di Geofisica e Vulcanologia*”, Observatories & Research Facilities for European Seismology*, (2016).

[41] R. Tartaglia, M. D'Aniello, G. Di Lorenzo, A. De Martino, “Influence of EC8 rules on p-delta effects on the design and response of steel MRF” *Ingegneria Sismica*, **35** (3), pp. 104-120, (2018).

[42] SAP2000 Design Manual version 14.0.

COMPDYN 2019
7th ECCOMAS Thematic Conference on
Computational Methods in Structural Dynamics and Earthquake Engineering
M. Papadrakakis, M. Fragiadakis (eds.)
Crete, Greece, 24–26 June 2019

DESIGN AND SEISMIC ASSESSMENT OF MRFs AND DUAL CBFs EQUIPPED WITH FRICTION DAMPERS.

Rosario Montuori[1], Vincenzo Piluso[1] and Simona Streppone[1]

[1] University of Salerno
Via Giovanni Paolo II, 132, 84084 Fisciano SA
e-mail: {r.montuori,v.piluso,sstreppone}@unisa.it

Abstract

In the present work, the design and the non-linear static analysis of innovative steel seismic-resistant perimeter systems are reported. In particular, Moment Resisting Frames (MRFs) and Dual-Concentrically Braced Frames (D-CBFs) were designed by using the Theory of Plastic Mechanism Control (TPMC). Eight structures, having the same geometric characteristics and the same seismic parameters of the site and the structure, were designed for each structural typology. The structures differ in the number of storeys, number of bays, bay length but they were designed for a Peak Ground Acceleration equal to 0.35g. The innovation consists in locating friction dampers of FREEDAM typology at the beam ends and at the intersection of chevron braces. The FREEDAM dampers can dissipate input seismic energy through the relative slippage between pads, of which they are made up. They preserve the main structural elements, such as beam ends and chevron braces, from damage. In the case of MRFs, FREEDAMs replace the traditional dissipative zones. In Dual CBFs, a share of FREEDAMs substitute the aforementioned dissipative zones and, besides, those located at the top of chevron braces, represent a supplement to the seismic energy dissipation. In this way, the structure remains intact even after severe earthquakes; meanwhile, the dampers can be easily substituted. Furthermore, the TPMC design procedure, based on the kinematic theorem of plastic collapse, allows all the dissipative zones are involved in the yielding, thus developing a collapse mechanism of global type. Thanks to the design procedure, it is sure the yielding occurs in the dissipative zones, where dampers are located, and not in any other parts of the structure.
The work aims to analyse and compare the two structural typologies both in terms of design results and in terms of seismic performance. It has been investigated which is the more convenient structural typology, keeping in mind the Eurocode 8 limitation on the interstorey drift. In addition, the design procedure has been validated using non-linear static analyses, such as pushover analyses. The designed structures have been finally compared also in terms of seismic performances.

Keywords: Plastic design, Connections, Friction Dampers, Moment Resisting Frames, Concentrically Braced Frames, FREEDAM Project.

INTRODUCTION

The use of friction devices is increasing all over the world because of their clear advantages. Adequately replacing the dissipative zones, or just added to the frames as an additional dissipative resource, they safeguard the main structural elements from damage with effectiveness and versatility [1]-[8].
The structural damage is essential to dissipate the earthquake input energy, but it is the main source of direct and indirect losses. Many researchers have focused their attention on the strategy of supplementary energy dissipation with the aim to reduce the structural damage under destructive seismic events. This strategy is based on the use of specific energy dissipation devices to be inserted between couples of points of the structural scheme for which high relative displacements or velocities are expected under the action of severe ground motions [9]-[12]. In the framework of passive control [13]-[17] dampers can completely substitute the dissipative zones, i.e. beam ends. To this purpose, beam-to-column connections can be equipped with friction dampers, which can be located either at the level of the two flanges or at the bottom flange level only. In this paper, reference is made to beam-to-column FREEDAM connections that have been widely tested at the Laboratory of Materials and Structures of University of Salerno in the framework of FREEDAM project.
In particular, two structural typologies are investigated in this paper, the first one refers to Moment Resisting Frames (MRFs) while the second one relates to Moment Resisting Frames-Concentrically Braced Frames dual systems (MRF-CBFs dual system). In fact, in many cases, MRFs could be highly oversized due to the need to respect serviceability requirements. This can be specially highlighted in structures where the primary beam is parallel to the secondary beams of the floor, i.e. when the beam sections are not deeply loaded. In such cases, indeed, to respect the serviceability limitations, could be useful adding chevron braces which can be dimensioned only to limit the lateral displacement. Furthermore, the braces intersection can be the natural location of an additional friction damper helping in the overall dissipation capacity of the structure. Given the above, the scope of the paper is highlighting the differences occurring between MRFs and Dual systems in terms of structural weight and seismic performances. Moreover, structures are designed according to the Theory of Plastic Mechanism Control [18]-[30], which assure that all dissipative zones are involved in yielding showing at the collapse a global mechanism. In particular, the design procedure adopted for designing MRFs and MRF-CBF dual systems is reported in a previous paper [20] and it is not herein reported for the sake of shortness. Both MRFs and Dual systems are also analysed by pushover analyses to highlight the difference between the two structural schemes investigated.

1 FREEDAM DAMPERS

The FREEDAM dampers are dissipative elements which can dissipate the input seismic energy using the slippage force arising between the pads constituting the device [17],[31]-[35]. In this work, the FREEDAM dampers are used in the field of both the substitution and the supplementary seismic design strategy. Indeed, a FREEDAM damper is located at the intersection of the chevron braces of MRF-CBF dual systems and in beam-to-column joints of MRF, respectively. The two different details are reported in Figure 1 and Figure 2 and are better described in the following. The main advantage of these connections is that their flexural resistance can be calibrated to transmit, as carefully as possible, the bending moments occurring under the seismic load combination, thus promoting the simultaneous activation of all the friction dampers. In particular, the dissipation is concentrated in the friction pads, located at the bottom flange level of beams, whose slippage is the basis of the energy dissipation process. The other elements

constituting the FREEDAM connections are designed to remain in elastic range as the column sections at each storey.

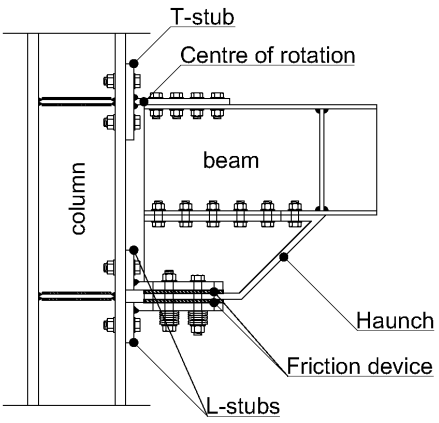

Figure 1: FREEDAM Beam-to-column connection

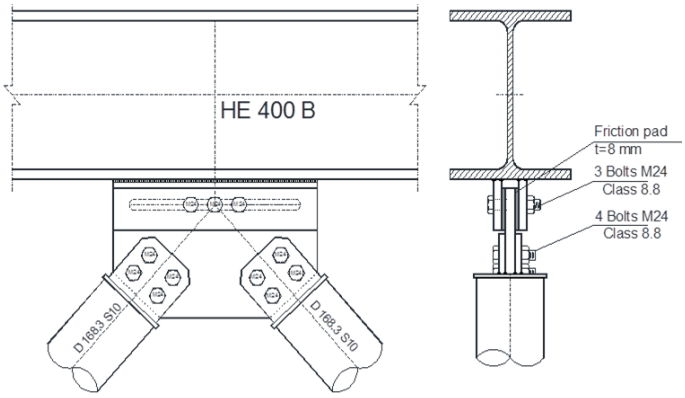

Figure 2: FREEDAM friction damper to the chevron brace

The FREEDAM beam-to-column joint is made up of an upper beam flange, connected to the column by means of a classical T-stub, in which the rotation centre of the joint is located. The friction damper is at the bottom flange level where slippage occurs due to the use of slotted holes, realised on the additional haunch. The friction pads are preloaded by means of high strength bolts [17],[31]-[35]. The FREEDAM damper located at the top of chevron braces is made up of a haunch composed by vertical steel plates with horizontally slotted holes. The only exception is the inner plate realised in Stainless Steel and bolted to the pre-stressed friction shims.

In order to design the joint [36]-[37], the two principles of capacity design are applied. According to the first one, the dissipative zones are designed using the maximum stress deriving from load combinations. Moreover, the second principle states that the non-dissipative zones have to be designed according to the maximum internal actions that dissipative ones can transmit in their full yielded and strain hardened conditions.

In the study cases herein reported, the FREEDAM beam-to-column dampers have been designed once the beams and columns had already been sized. This happens because the Serviceability Limit State checks are the most stringent requirements. The maximum value due to the seismic actions and to the vertical loads has to be chosen [19] to evaluate the flexural resistance of each joint. The former is evaluated using distribution along the storey height analogous to the seismic storey shear distribution, as suggested by Goel and Lee [38]. Hence, the slip force, F_{slip}, acting on the FREEDAM damper at j-th bay of k-th storey has to be evaluate by dividing the joint flexural resistance, $M_{f.Ed}$, by the lever arm, z:

$$F_{slip} = \frac{M_{f.Ed}}{z} \tag{1}$$

The lever arm is the sum of the beam depth, d_b, and of the haunch height, h_h.

Similarly, also the slip resistance of the friction dampers located in series with the chevron braces is distributed along the building height according to the seismic storey shear distribution [21], [39]-[42]. However, in this case, friction dampers are properly designed at first, while the remaining structural elements have been obtained as a result. For the non-dissipative zones, such as beams and diagonal, the second principle of capacity design is applied. In particular, for the beam, it has to be check that the capacity design value of bending moment is less than

the bending resistance of the beam. Moreover, as soon as the design resistance of such chevron braces dampers has been established, the braces can be designed by considering the maximum friction resistance which the dampers are able to transmit in their ultimate condition. The columns, also constituting the non-dissipative zones, will be derived from the TPMC design procedure.

2 THEORY OF PLASTIC MECHANISM CONTROL

The Theory of Plastic Mechanism Control (TPMC) is a design procedure based on the kinematic theorem of plastic collapse and extended to the concept of mechanism equilibrium curve:

$$\alpha = \alpha_0 - \gamma\delta \tag{2}$$

where, according to the theory of rigid-plastic analysis, α_0 is the first order collapse multiplier of horizontal forces, γ is the slope of the linearized mechanism equilibrium curve due to second-order effects and δ is the plastic top sway displacement. Differently, from the Eurocode 8 provisions [43]-[44], TPMC can directly and rigorously take into account the second-order effects. As illustrated in Figure 3, this theory states that the curve corresponding to the global mechanism has to be located under those corresponding to all the undesired mechanisms, until a design displacement δ_u, compatible with the local ductility supply [19], is achieved. Starting from the design of the dissipative zones, the TPMC design procedure provides the column sections by which a global collapse mechanism is assured.

More details about this design procedure applied can be found in [19] for steel MRFs and in [20] for MRF-CBF dual systems equipped with friction dampers.

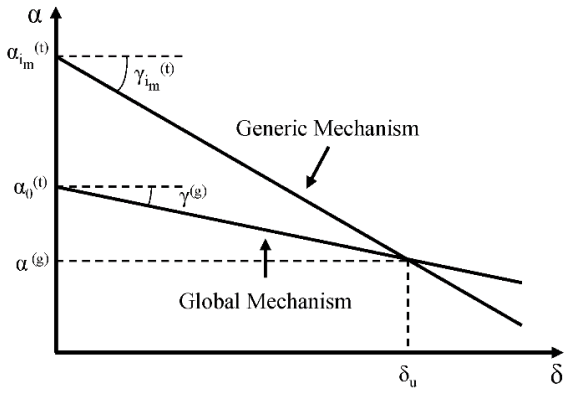

Figure 3: TPMC statement

3 DESIGNED CASE STUDIES

The plan configuration of the study case is reported in Figure 4. The material adopted for all the members is S355 steel grade (f_{yk}=355 MPa). The buildings are made up of a pinned internal part and of a perimeter seismic-resisting system. For this latter, two structural typologies have been designed: MRFs and MRF-CBFs dual systems, both equipped with FREEDAM dampers. In particular, for MRF-CBFs dual systems not only beam ends but also the intersection between diagonal is equipped with FREEDAM dampers. Eight structures for each typology have been resulted by varying the span length, the number of bays and the number of storeys. The values of the considered span length are 6 and 8 meters. The number of bays is 3 or 5 and the buildings consist of 3 and 6 floors. In elevation, all the buildings consist of a first-floor interstorey height equal to 4.5 m and of 3.5 m interstorey height for the other floors. Table 1 shows all the designed structures including the relative characteristics.

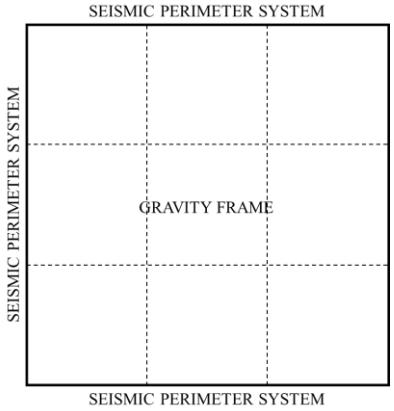

Figure 4: General plan configuration of the designed buildings.

Scheme name	Number of storeys	Number of spans	Span length [m]	Designed structural typology
Scheme 2	3	3	6	MRF MRF-CBF
Scheme 4	3	3	8	MRF MRF-CBF
Scheme 6	3	5	6	MRF MRF-CBF
Scheme 8	3	5	8	MRF MRF-CBF
Scheme 10	6	3	6	MRF MRF-CBF
Scheme 12	6	3	8	MRF MRF-CBF
Scheme 14	6	5	6	MRF MRF-CBF
Scheme 16	6	5	8	MRF MRF-CBF

Table 1: Report of the structures and their geometric features.

The permanent (G_k) and live (Q_k) loads have been chosen within a practical range and are reported in Table 2. This latter also includes the values of the combination coefficients for the variable actions ψ_2 and ψ_E used, respectively, for the quasi-permanent value of the variable actions and for determining the effects of the seismic design action.

Location	Type	Load [kN/m^2]	$\psi_{2,i}$	$\psi_{E,i}$
Roof	Permanent Variable	4.5 2	0.3	0.24
Intermedi-ate stories	Permanent Variable	4.5 2	0.3	0.15

Table 2: Characteristic values of loads

The structures have been subjected to the Lateral Force Method of analysis, according to Eurocode 8 [44], assuming a Peak Ground Acceleration (PGA) equal to 0.35g, a seismic response factor equal to 2.5, a behaviour factor equal to 6.5 for the design spectrum with a 2%

damping, a response spectrum Type 1 and soil Type C. In addition, the serviceability conditions have been checked, such as the interstorey drift has been kept under the limitation of 1% of the interstorey height, as the code [44] requires. It is important to underline that this kind of check significantly conditions the designing, being the most restrictive condition to comply with.

Table 3 sums up the results of the design, while Figure 5 shows the members size of Scheme 2 and allows to understand the column labels reported in Table 3.

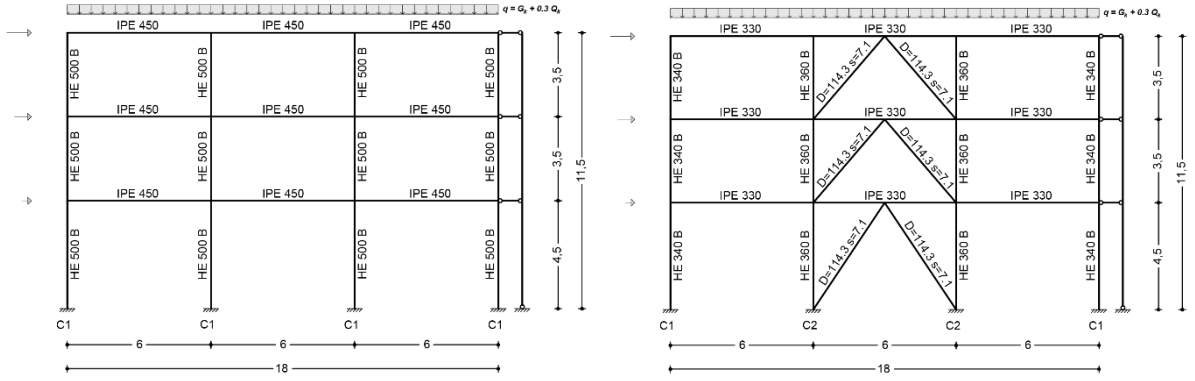

Figure 5: Scheme 2 designed structure.

	Scheme name	Storey	Beam section	C1 column section	C2 column section	Diagonal section
Scheme 2	MRF	1-3	IPE 450	HEB 500		
	MRF-CBF	1-3	IPE 330	HEB 360	HEB 340	D=114.3s=7.1
Scheme 4	MRF	1-3	IPE 550	HEB 650		
	MRF-CBF	1-3	IPE 400	HEB 500	HEB 500	D=139.7s=6.3
Scheme 6	MRF	1-3	IPE 500	HEB 600		
	MRF-CBF	1-3	IPE 400	HEB 450	HEB 500	D=139.7s=12.5
Scheme 8	MRF	1-3	IPE 600	HEM 650		
	MRF-CBF	1-3	IPE 550	HEM 450	HEM 500	D=219.1s=6.3
Scheme 10	MRF	1-4	IPE 450	HEB 600		
		5-6	IPE 450	HEB 550		
	MRF-CBF	1-3	IPE 400	HEB 500	HEB 500	D=114.3s=10
		4-6	IPE 400	HEB 340	HEB 360	D=114.3s=10
Scheme 12	MRF	1-4	IPE 550	HEM 700		
		5-6	IPE 550	HEM 600		
	MRF-CBF	1-3	IPE 500	HEM 550	HEM 600	D=139.7s=10
		4-6	IPE 500	HEM 400	HEM 400	D=139.7s=10
Scheme 14	MRF	1-4	IPE 500	HEM 650		
		5-6	IPE 500	HEM 550		
	MRF-CBF	1-3	IPE 500	HEM 550	HEM 700	D=139.7s=12.5
		4-6	IPE 500	HEM 400	HEM 400	D=139.7s=12.5
Scheme 16	MRF	1-4	IPE750x134	HD400x818		
		5-6	IPE750x134	HD400x744		
	MRF-CBF	1-3	IPE 500	HEM 800	HEM 900	D=168.3s=6.3
		4-6	IPE 500	HEM 650	HEM 650	D=168.3s=6.3

Table 3: Size of the members resulting from the design.

The MRF-CBF dual systems structures have shallower sections than the related ones designed as MRF. The difference in weight obtained between the two structural typologies has been evaluated. In general, it is possible to state that the use of MRF-CBF dual systems allows a moderate weight reduction of the structure, on average, which results in economic savings. In Table 4 the weights of designed structures and the weight loss in per cent are reported. These values are better shown in Figure 6.

Scheme	MRF weight [kg]	MRF-CBF weight [kg]	Weight loss % [-]
Scheme 2	12987.90	9724.29	25.13
Scheme 4	18137.81	14322.76	21.03
Scheme 6	23121.66	19606.11	15.20
Scheme 8	35415.03	32492.47	8.25
Scheme 10	27028.87	23825.81	11.85
Scheme 12	41731.93	39499.50	5.35
Scheme 14	55205.64	55661.29	-0.83
Scheme 16	138423.56	89653.51	35.23
		AVERAGE	15.15

Table 4: Comparison between the MRFs and MRF-CBFs weights

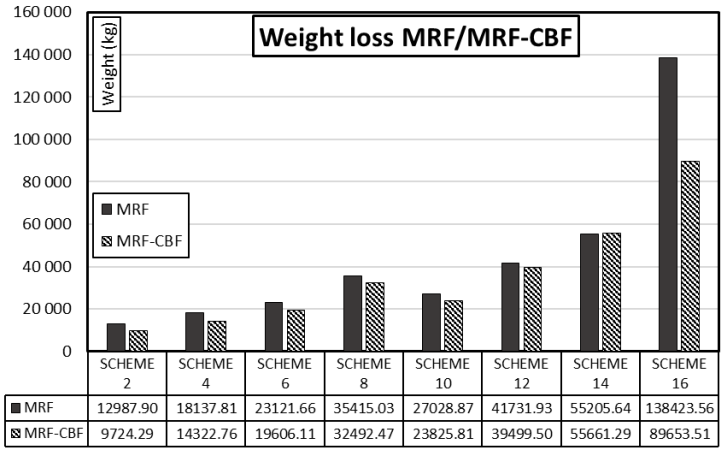

Figure 6: Comparison between the MRFs and MRF-CBFs weights

4 SEISMIC ASSESSMENT BY PUSHOVER ANALYSES

The designed structures have been subjected to pushover analyses employing SAP2000 [45].

All the structural elements constituting the structures, i.e. beams, columns and diagonal braces, have been modelled by means of beam-column elements. The non-linearities are located in plastic hinges ("P-hinge" elements), equipping the ends of the abovementioned elements. The plastic hinges put at the ends of diagonals and columns account the interaction between axial force and bending moment. The plastic hinges have been modelled in pure rigid-plastic bending, resulting from the product between the slippage resistance of the friction damper and the lever arm. For what concerns the FREEDAMs located at the chevron braces intersection, they have been modelled by means of a short beam-column element equipped with rigid plastic P-hinge properties in shear, whose threshold is calibrated to represent the slippage resistance of the friction damper. The slippage resistance of friction dampers accounts for the over-strength

due to the random variability of the friction coefficient and the uncertainties of the bolt preloading level. The elastic component of the structural behaviour is directly taken into account by the elasticity of the beam-column element.

In Figure 7, the pushover results are reported concerning the MRFs and MRF-CBF dual systems both equipped with FREEDAM connections. The softening branch of pushover curves is in perfect agreement with the global mechanism equilibrium curve for each structure. It means that all the structures develop a collapse mechanism of global type, i.e. all the dissipative zones are involved in yielding and the dissipation of the seismic energy is maximised.

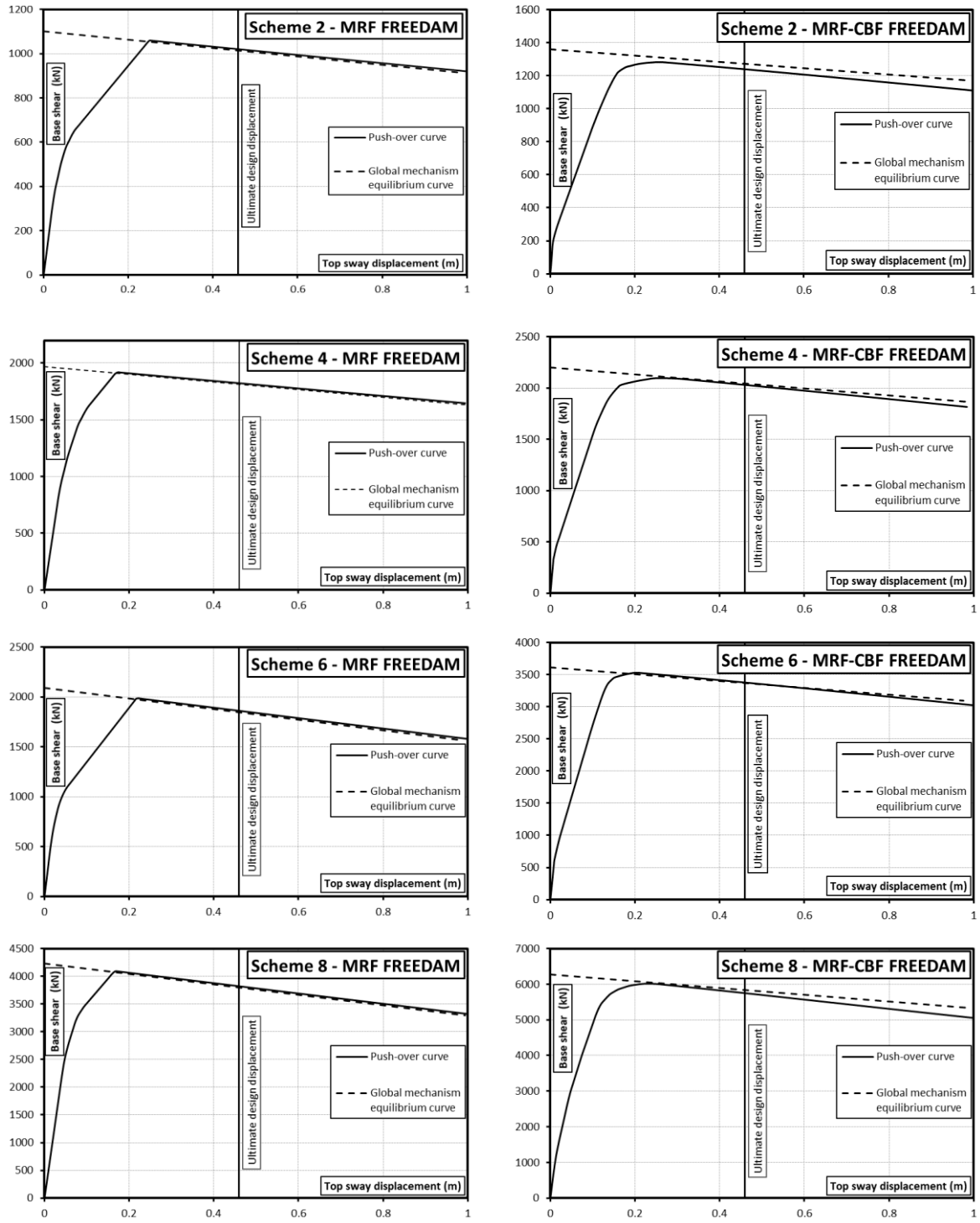

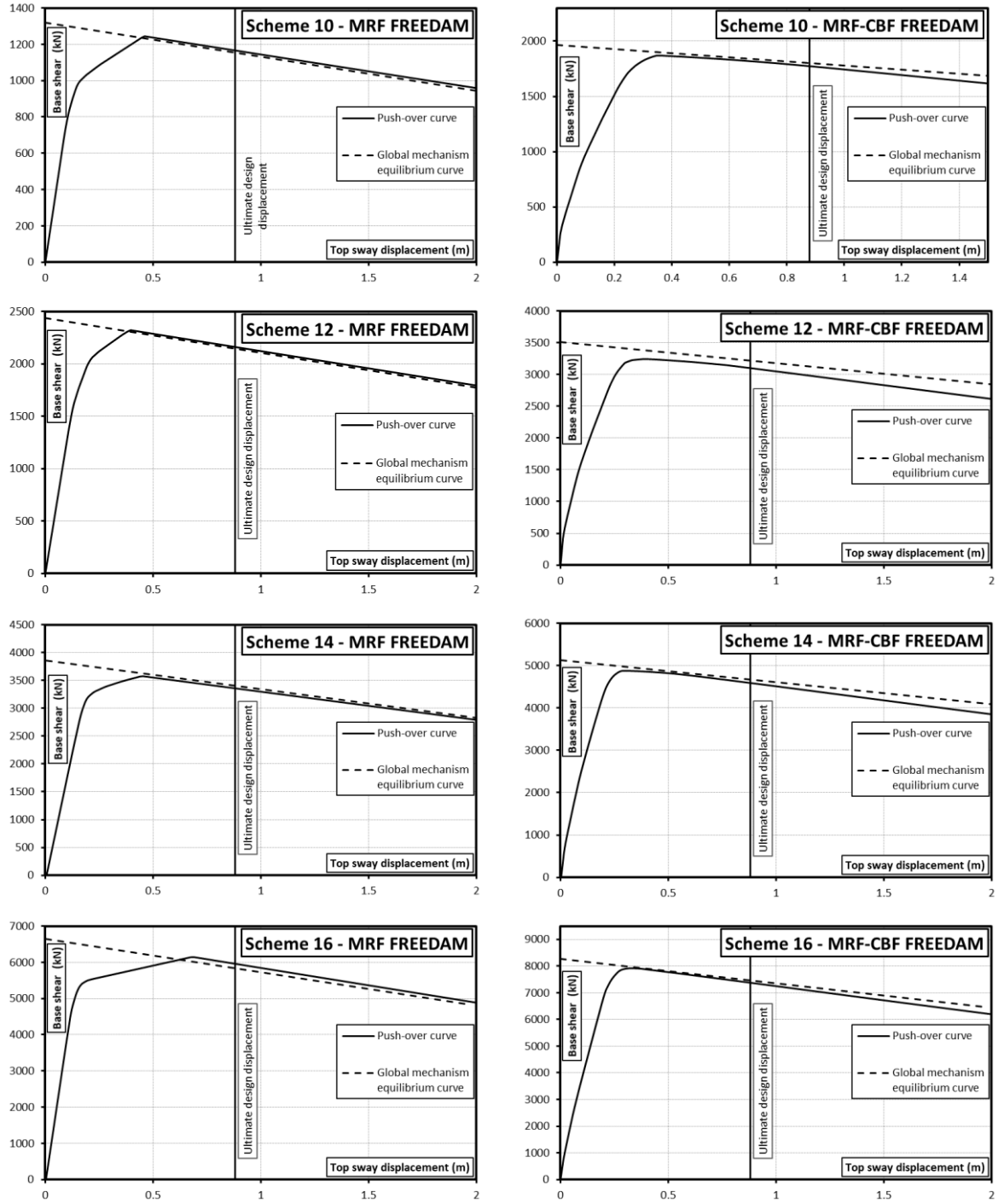

Figure 7: Pushover curves

5 CONCLUSIONS

- In this paper, many samples of steel structures designed according to the TPMC have been presented.
- MR-Frames and MRF-CBF dual systems equipped with FREEDAM dampers in beam-to-column joint and in the intersection of chevron braces have been considered. They have the same geometrical features and seismic parameters.

- In terms of weight, MRF-CBF dual systems show shallower sections if compared with MRFs. On average, the weight loss between the two different typologies is about 15.15%.
- Pushover analyses demonstrate that TPMC guarantees the development of a collapse mechanism of global type, thus engaging all the dissipative zones in yielding.
- Pushover curves show that the MRF-CBF dual systems, even if shallower, can achieve higher resistance than MRFs with lower displacement.
- Finally, in light of the considerations made so far, when the issue governing the design is the respect of serviceability limitation, the use of MRF-CBFs is more convenient if compared with MRFs because they allow obtaining lighter structures respecting the drift limitations and with higher seismic performances.

ACKNOWLEDGEMENTS

The research activity herein presented has been supported by the European Community by research grant RFSR-CT-2015-00022. The support of the European Commission within RFCS Research & Innovation is gratefully acknowledged.

REFERENCES

[1] L. Fiorino, V. Macillo, R. Landolfo, Shake table tests of a full-scale two-story sheathing-braced cold-formed steel building. *Engineering Structures*, **151**, pp. 633–647, 2017.

[2] N.M. Mirzai, R. Attarnejad, J.W. Hu, Enhancing the seismic performance of EBFs with vertical shear link using a new self-centering damper. *Ingegneria Sismica*, **35 (4)**, pp. 57-76, 2018.

[3] A. Campiche, S. Shakeel, V. Macillo, M.T. Terracciano, B. Bucciero, T. Pali, L. Fiorino, R. Landolfo, Seismic behaviour of sheathed CFS buildings: Shake table tests and numerical modelling. *Ingegneria Sismica*, **35 (2)**, pp. 106-123, 2018.

[4] E. Totter, A. Formisano, F. Crisafulli, F. Mazzolani, Seismic upgrading of RC structures with only beam connected Steel Plate Shear Walls. *Ingegneria Sismica*, **35 (2)**, pp. 91-105, 2018.

[5] G. De Matteis, G. Brando, F. Caldoso, F. D'Agostino, Seismic performance of dual steel frames with dissipative metal shear panels. *Ingegneria Sismica*, **35 (2)**, pp. 124-141, 2018.

[6] L. Fiorino, M.T. Terracciano, R. Landolfo, Experimental investigation of seismic behaviour of low dissipative CFS strap-braced stud walls. *Journal of Constructional Steel Research*, **127**, pp. 92-107, 2016.

[7] V. Macillo, L. Fiorino, R. Landolfo, Seismic response of CFS shear walls sheathed with nailed gypsum panels: Experimental tests. *Thin-Walled Structures*, **120**, pp. 161-171. 2017.

[8] V. Macillo, O. Iuorio, M.T. Terracciano, L. Fiorino, R. Landolfo, Seismic response of Cfs strap-braced stud walls: Theoretical study. *Thin-Walled Structures*, **85**, pp. 301-312, 2014.

[9] C. Christopoulos, A. Filiatrault, Principles of Passive Supplemental Damping and Seismic Isolation. *IUSS PRESS*, Pavia, 2006.

[10] T.T. Soong, Jr B.F. Spencer, Supplemental Energy Dissipation: State-of-the-Art and State-of-the-Practice, *Engineering Structures*, **24**, 243-259, 2002.

[11] I. Mualla, B.Belev, Seismic Response of Steel Frames Equipped with a New Friction Damper Device Under Earthquake Excitation2. *Engineering Structures*, **24**, 365-371, 3-2002.

[12] S. Oh, Y. Kim, H. Ryu, Seismic Performance of Steel Structures with slit dampers. *Engineering Structures*, **31**, 1997-2008, 2009.

[13] M. Latour, V. Piluso, G. Rizzano, Experimental behaviour of friction T-stub beam-to-column joints under cyclic loads. *Steel Construction*, **6**(1), 2013.

[14] H. Khoo, C. Clifton, J. Butterworth, G. MacRae, S. Gledhill, G. Sidwell, Development of the self-centering Sliding Hinge Joint with friction ring springs. *Journal of Constructional Steel Research*, **78**, 201-211, 2012a.

[15] H. Khoo, C. Clifton, J. Butterworth, G. Macrae, Experimental Study of Full-Scale Self-Centering Sliding Hinge Joint Connections with Friction Ring Springs. *Journal of Earthquake Engineering*, **17:7**, 972-997, 2013.

[16] J. Borzouie, G. Macrae, J.G. Chase, G. Rodgers, R. Xie, J.C. Golondrino, C. Clifton, Cyclic Performance of Asymmetric Friction Connections. *The Bridge and Structural Engineer*, **45**, 2015.

[17] M. Latour, V. Piluso, G. Rizzano, Experimental analysis of innovative dissipative bolted double split tee beam-to-column connections. *Steel Construction*, **4**, 53-64, 2011.

[18] A. Longo, E. Nastri, V. Piluso, Theory of plastic mechanism control: State-of-the-art, *Open Construction and Building Technology Journal*, **8**, Pages 262-278, 2014.

[19] V. Piluso, E. Nastri, R. Montuori, Advances in Theory of Plastic Mechanism Control: Closed Form Solution for MR-Frames, *Earthquake Engineering and Structural Dynamics*, **44**, Issue 7, Pages 1035-1054, 2015.

[20] V. Piluso, R. Montuori, E. Nastri, A. Paciello, Seismic response of MRF-CBF dual systems equipped with low damage friction connections. *Journal of Constructional Steel Research*, **154**, pp. 263-277, 2019.

[21] E. Nastri, M. D'Aniello, M. Zimbru, S. Streppone, R. Landolfo, R. Montuori, V. Piluso, Seismic response of steel Moment Resisting Frames equipped with friction beam-to-column joints. *Soil Dynamics and Earthquake Engineering*, **119**, pp. 144-157, 2019.

[22] R. Montuori, V. Sagarese, The use of steel rbs to increase ductility of wooden beams *Engineering Structures*, **169**, pp. 154-161, 2018.

[23] G. Dell'Aglio, R. Montuori, E. Nastri, V. Piluso, A critical review of plastic design approaches for failure mode control of steel moment resisting frames. *Ingegneria Sismica*, **34** (4), pp. 82-102, 2017.

[24] R. Montuori, E. Nastri, V. Piluso, Influence of the bracing scheme on seismic performances of MRF-EBF dual systems. *Journal of Constructional Steel Research*, **132**, pp. 179-190, 2017.

[25] R. Montuori, E. Nastri, V. Piluso, M. Troisi, Influence of connection typology on seismic response of MR-Frames with and without 'set-backs. *Earthquake Engineering and Structural Dynamics*, **46** (1), pp. 5-25, 2017.

[26] R. Montuori, E. Nastri, V. Piluso, Theory of Plastic Mechanism Control for MRF-EBF dual systems: Closed form solution. *Engineering Structures*, **118**, pp. 287-306, 2016.

[27] E. Nastri, Eccentrically braced frames designed for the energy dissipation optimization. *ECCOMAS Congress 2016 - Proceedings of the 7th European Congress on Computational Methods in Applied Sciences and Engineering*, **4**, pp. 8476-8491, 2016.

[28] A. Longo, R. Montuori, E. Nastri, V. Piluso, On the use of HSS in seismic-resistant structures. *Journal of Constructional Steel Research*, **103**, pp. 1-12, 2014.

[29] R. Montuori, R. Muscati, A general design procedure for failure mechanism control of reinforced concrete frames, *Engineering Structures*, **118**, pp. 137-155, 2016.

[30] V. Piluso, A. Pisapia, P. Castaldo, E. Nastri, Probabilistic Theory of Plastic Mechanism Control for Steel Moment Resisting Frames. *Structural Safety*, **76**, pp. 95-107, 2019.

[31] G. Ferrante Cavallaro, A. Francavilla, M. Latour, V. Piluso, G. Rizzano, Experimental behaviour of innovative thermal spray coating materials for FREEDAM joints. *Composites Part B: Engineering*, **115**, pp. 289-299, 2017.

[32] M. Latour, M. D'Aniello, M. Zimbru, G. Rizzano, V. Piluso, R. Landolfo, Removable friction dampers for low-damage steel beam-to-column joints. *Soil Dynamics and Earthquake Engineering*, **115**, pp. 66-81, 2018.

[33] M. Latour, G. Rizzano, A. Santiago, L. Simões da Silva, Experimental response of a low-yielding, self-centering, rocking column base joint with friction dampers. *Soil Dynamics and Earthquake Engineering*, **116**, pp. 580-592, 2019.

[34] G. Ferrante Cavallaro, A.B. Francavilla, M. Latour, V. Piluso, G. Rizzano, Cyclic response of low yielding connections using different friction materials. *Soil Dynamics and Earthquake Engineering*, **114**, pp. 404-423, 2018.

[35] M. Latour, V. Piluso, G. Rizzano, Experimental analysis of beam-to-column joints equipped with sprayed aluminium friction dampers. *Journal of Constructional Steel Research*, **146**, pp. 33-48, 2018.

[36] CEN. Eurocode 3: Design of steel structures - Part 1-8: Design of joints, 2005c.

[37] F. Di Lauro, R. Montuori, E. Nastri, V. Piluso, Partial safety factors and overstrength coefficient evaluation for the design of connections equipped with friction dampers. *Engineering Structures*, **178**, pp. 645-655, 2019.

[38] S.C. Goel, S-S Lee, Performance-Based Design of Steel Moment Frames using Target Drift and Yield Mechanism. *Research Report UMCEE 01-17*, December 2001.

[39] S. Costanzo, M. D'Aniello, R. Landolfo, Seismic design criteria for Chevron CBFs: European vs North American codes (Part-1). *Journal of Constructional Steel Research*, **135**, pp. 83-96, 2017.

[40] S. Costanzo, M. D'Aniello, R. Landolfo, Critical review of seismic design criteria for chevron concentrically braced frames: The role of the brace-intercepted beam. *Ingegneria Sismica*, **33 (1-2)**, pp. 72-89, 2016.

[41] M. D'Aniello, S. Costanzo, R. Landolfo, The influence of beam stiffness on seismic response of chevron concentric bracings. *Journal of Constructional Steel Research*, **112**, pp. 305-324, 2015.

[42] R. Montuori, E. Nastri, V. Piluso, S. Streppone, M. D'Aniello, M. Zimbru, R. Landolfo, Comparison between different design strategies for freedam frames: Push-overs and IDA analyses. *Open Construction and Building Technology Journal*, **12**, pp. 140-153, 2018.

[43] R. Tartaglia, M. D'Aniello, G. Di Lorenzo, A. De Martino, Influence of EC8 rules on p-delta effects on the design and response of steel MRF. *Ingegneria Sismica*, **35 (3)**, pp. 104-120, 2018.

[44] CEN. Eurocode 8: Design of structures for earthquake resistance - Part 1: General rules, seismic actions and rules for buildings, 2005a.

[45] CSI 2007. SAP 2000: Integrated Finite Element Analysis and Design of Structures. Analysis Reference. Computer and Structure Inc. University of California, Berkeley.

COMPDYN 2019
7th ECCOMAS Thematic Conference on
Computational Methods in Structural Dynamics and Earthquake Engineering
M. Papadrakakis, M. Fragiadakis (eds.)
Crete, Greece, 24–26 June 2019

VERIFICATION OF NUMERICAL LIQUEFACTION MODEL USING DYNAMIC CENTRIFUGE TEST

Jinsun Lee[1], Seongnam Kim[2], Jeonggon Ha[3], Moongyo Lee[4], and Dongsoo Kim[2]

[1] Dept. of civil and environmental engineering, Wonkwang Univ.
Iksan-daero 460, Iksan, South Korea
e-mail: blueguy@wku.ac.kr

[2] Civil and environmental engineering, KAIST
291 Daehak-ro, Yuseong-gu, Daejeon, South Korea
{seong8nam, dskim}@kaist.ac.kr

[3] Korea Institute of Nuclear Safety
62 Gwahak-ro, Yuseong-gu, Daejeon, South Korea
jgha87@kaist.ac.kr

[4] Korea Institute of Geoscience and Mineral Resources
124 Gwahak-ro, Yuseong-gu, Daejeon, South Korea
mglee@kigam.re.kr

Abstract

Numerical liquefaction model and analysis procedure are verified based on the dynamic centrifuge test results. The test was a part of the Liquefaction Experiments Analysis Project (LEAP). The model ground was formed inside of the rigid box by using the submerged Ottawa F65 sand with a relative density of 55% and 5 ° of surface inclination. A tapered sinusoidal wave with a frequency of 1 Hz was applied to the base of the model box. Numerical analyses were performed under two and three-dimensional condition in prototype scale. The soil is modeled to show hysteretic behavior before shear failure, and Mohr-Coulomb model is applied for shear failure criterion. Byrne's liquefaction model was applied to track the changes in pore pressure due to cyclic loading after static equilibrium. The numerical analyses performed in this study showed good agreement with the physical test results.

Keywords: Liquefaction, Numerical Analysis, Centrifuge Test, Finite Difference Method, Liquefaction Model.

1 INTRODUCTION

The liquefaction phenomenon occurs during the earthquake in the saturated silty to sandy ground began to be noticed after the 1964 Niigata and the Alaska earthquake. The Kobe earthquake, which occurred in 1995, is well known as the earthquake that clearly shows the extent of damage according to the application of liquefaction mitigation measures. The existing liquefaction assessment procedures have been focused on whether liquefaction occurs and how to select the mitigation method. However, in order to evaluate the seismic safety of the overall structure system, a reliable method to predict liquefaction, as well as post-liquefaction behavior, should be provided and applied to soil-structure interaction analysis. There are several types of the numerical soil constitutive model to account for the above liquefaction phenomenon. However, the reliability of the model is still questionable. Thus, there have been effort to verify the existing liquefaction model as well as the experimental technique. For this purpose, the Liquefaction Experiments Analysis Project (LEAP) -the UCD-2017 project was carried out by nine institutes from all over the world. The round-robin liquefaction test was conducted using the dynamic centrifuge test equipment of each institution for the given test conditions. The aim of the project is to evaluate the reliability of dynamic centrifuge test procedure and the numerical model. This paper aims to verify numerical liquefaction model and analysis procedure. The verification is made based on the dynamic centrifuge test results conducted at the KAIST Geocentrifuge center [1].

2 DYNAMIC CENTRIFUGE TEST

2.1 Centrifuge facility

A dynamic geotechnical centrifuge facility at KAIST was utilized to perform the tests for LEAP 2017. An electro-hydraulic earthquake simulator was mounted on the centrifuge with a platform radius of 5 m and maximum capacity of 240 g-tons. The main body of the centrifuge has the unique feature of an automatic balancing system and includes parts, such as fluid rotary joints, slip rings, and a fiber optic rotary, for general testing purposes [2]. The centrifuge test of KAIST was conducted with a gravitational acceleration of 40 g. Target excitations were applied using an earthquake simulator that adopted a dynamic self-balancing technique to eliminate a large portion of the undesired reaction forces and vibrations transmitted to the main body. The earthquake simulator was designed to operate at up to 100 g of centrifugal acceleration, and the base shaking acceleration can be exerted to the maximum value of 20 g at 40 g of centrifugal acceleration with the maximum payload of 700 kg. The dimensions of the slip table were 670 mm (length) × 670 mm (width).

2.2 Test model setup

The model ground was formed inside of the rigid box by using the submerged Ottawa F65 sand with a relative density of 55% and 5 ° of surface inclination. The grain size characteristics and properties of the soil are as follows: Gs = 2.665, D_{10} = 0.13 mm, D_{30} = 0.17 mm, D_{50}=0.20 mm and D_{60}=0.21 mm [3]. The sand layer was formed by dry pluviation through a sieve. The density of the soil model was determined by the size of the opening slot and the drop height, and a calibration test is necessary when the geometry is changed. After the sand was pluviated to the target elevation, an inclined guide of 5° was installed on the top of the box. The manufactured scraper was connected directly to the inclined guide and was carefully scraped according to the slope. The viscous fluid is used to saturate model soil layer and to simulate viscosity of water under the centrifugal force. The viscous fluid was a mixture of water and methylcellulose, and the target viscosity was set to 40 cSt as dictated by the scaling law defined by Garnier

[4]. A rigid box with a transparent window was manufactured with internal dimensions of 570 mm × 225 mm × 450 mm (length × width × depth). This will simulate 22.8 m × 4 m × 9 m box in prototype scale under centrifugal acceleration of 40 g. Saturation process was made with starting the box to be completely sealed from the external air. In order to replace air in void with viscous fluid, vacuum pressure was applied first then the void is filled with CO2 gas, repeatedly. Finally, the viscous fluid slowly dripped into the ground model. Okamura's method was used to measure the degree of saturation for the saturated model [5]. The degree of saturation 99.4% is achieved for a relative density of 55%. The responses of the soil model during the shaking were monitored using accelerometers along the direction of shaking and pore pressure transducers. The 18 surface markers were installed on the ground surface uniformly with a spacing of 2 m × 2 m in prototype scale. A high-speed camera was mounted at the centrifuge arm to measure the plane view lateral displacements of the surface markers during the shaking. Cone penetration test (CPT) was conducted under centrifugal force to evaluate the shear modulus changes of the sandy soil with confining pressure before and after the excitation motion was applied. A tapered sinusoidal wave with a frequency of 1 Hz was applied to the base of the model box (Figure 1). Figure 2 shows schematic diagram of the test setup.

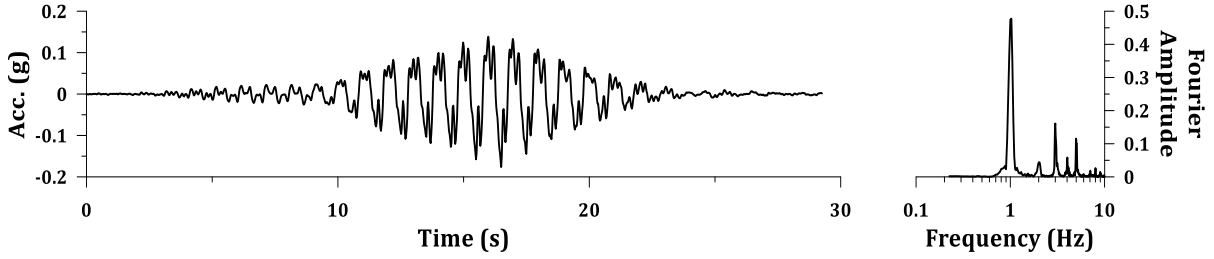

Figure 1 Applied excitation motions

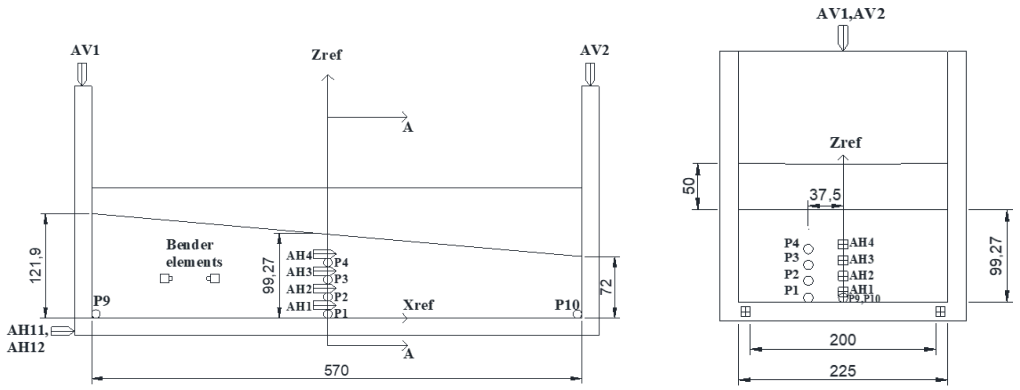

(a) Side view (b) Cross section view

Figure 2 : Schematic diagram of the model setup and the location of the transducers (AH : Accelerometer in horizontal direction, P : Pore pressure transducer)

3 NUMERICAL ANALYSIS

Numerical analysis was performed under two-dimensional plane strain condition and three-dimensional space in prototype scale. The finite difference analysis program, FLAC2D and 3D, is used for the analysis, respectively [6].

3.1 Numerical model and boundary condition

The numerical model is made in prototype scale. Fixed boundary condition for the bottom and side wall of the box is applied because the physical test model is made inside of the rigid box. The excitation motion recorded at the bottom of the box is applied at the bottom of the numerical model as well as along the side of the numerical model in forms of the acceleration. The minimum size of the finite difference element is 0.2 m and 0.5 m for two- and three-dimension model, respectively. The size of the element is determined to capture the response of the soil when the excitation motion propagates in upward direction. The numerical models used in this study are shown in Figure 3.

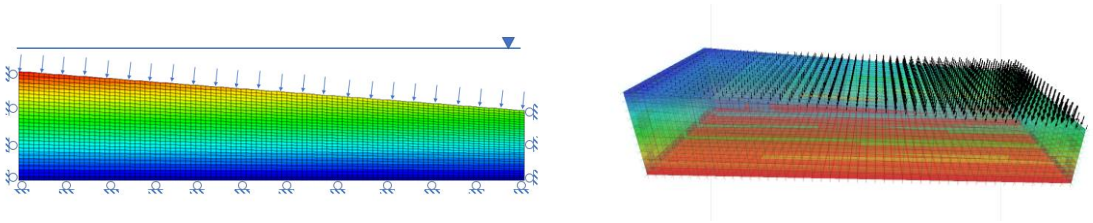

Two-dimension model (b) Three-dimension model

Figure 3: Numerical models

3.2 Soil properties and liquefaction model

The soil is modeled to show hysteretic behavior before shear failure, and the Mohr-Coulomb model is applied for shear failure criterion. The shear wave velocity of the soil is estimated from the CPT penetration results. Nonlinear stress-strain behavior of soil is modeled by using the hyperbolic model suggested by Hardin and Drnevich [7]. Byrne's liquefaction model was applied to track the changes in pore pressure due to cyclic loading after the static equilibrium [8]. The model parameters C_1, C_2, and C_3 for Byrne's model is derived from the relative density of the soil. The other parameters are referenced form the previous work done by Para [9]. The engineering properties used for the soil model is listed in Table 1.

The Max. Shear Modulus (kPa)	Dry Density (kg/m^3)	Porosity (%)	Cohesion (Pa)	Internal Friction Angle (°)	Dilation Angle (°)	Liquefaction Parameters		
						C_1	C_2	C_3
Eqn. (1)	1,592	40.1	300	24.6	0	0.215	0.930	1×10^{-5}

Table 1: Engineering properties of the soil model.

The static equilibrium is achieved under the Eulerian coordinate system. Static pore pressure distribution, hydrostatic pressure is applied, and the maximum shear modulus is re-distributed according to the effective confining pressure in Eq. (1).

$$V_s = 1.18 \times 10^4 exp\left(\frac{-0.125}{\bar{\sigma}_m + 1.19}\right) - 1.16 \times 10^4$$

$$G_{max} = \rho V_s^2 \tag{1}$$

Where, V_s is shear wave velocity in (m/s); $\bar{\sigma}_m$is mean effective stress in (Pa); G_{max} is the maximum shear modulus in (Pa), ρ is the saturated unit density of the soil (kg/m^3).

3.3 Dynamic analysis

The Lagrangian coordinate system is applied before dynamic analysis. The analysis is performed in undrained condition during the shaking. Thus, the fluid properties for the undrained condition; fluid modulus of 2×10^9 Pa and fluid tension of 1×10^{10} Pa are adopted for the analysis. Cyclic threshold shear strain and the minimum required number of timesteps for counting strain reversal were also considered by reflecting the characteristics of the explicit time integration method.

3.4 Analysis results

The numerical analysis results are directly compared with the physical test. Time histories for the horizontal acceleration and porewater pressure are compared. The residual displacement of the soil surface is also compared with the physical test results obtained from the high-speed camera images. Figure 4 shows comparison of the time histories. Both two- and three-dimensional numerical analysis show good agreement with the physical test results. The spikes shown in the pore water pressure histories of the physical test can occur after the excess pore pressure reaches the initial effective stress and is termed as the de-liquefaction shock [10]. It is shown that these spikes cannot be simulated by the numerical analyses.

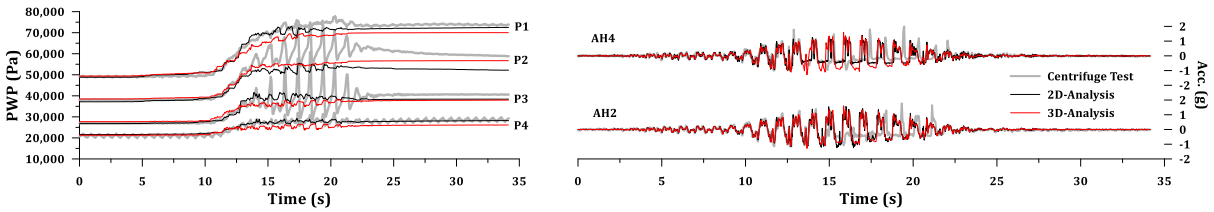

(a) Pore water pressure (b) Horizontal acceleration

Figure 4: Comparison of the time histories

Figure 5 shows horizontal displacement contour of the physical model after shaking. It was captured by the high-speed camera installed on the top of the model. The surface slope goes down to the right side of the image shown in the Figure 5. The permanent horizontal displacement ranges from 45 to 251 mm.

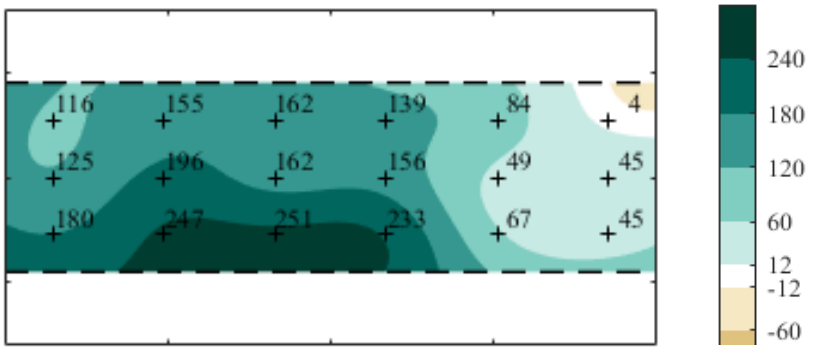

Figure 5: Horizontal displacement contour after shaking (from the centrifuge test, unit in mm)

Figure 6 and 7 shows horizontal displacement contour of the two- and three-dimensional numerical analysis after shaking, respectively. In the two-dimensional analysis, the residual displacement ranges from 50 to 140 mm. The maximum displacement occurs around the down side of the slope. However, in the tree-dimensional analysis, the residual displacement ranges from 70 to 180 mm and shows the maximum value around the upper side of the slope.

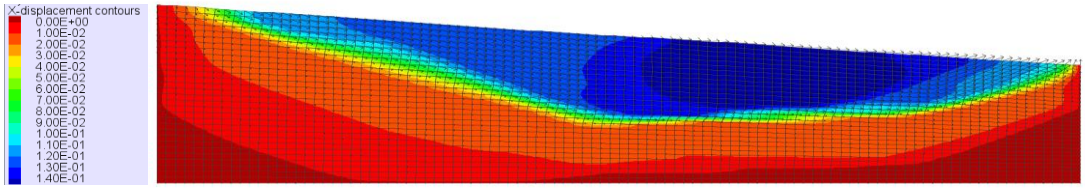

Figure 6: Horizontal displacement contour after shaking (Side view, from two-dimensional analysis, unit in m)

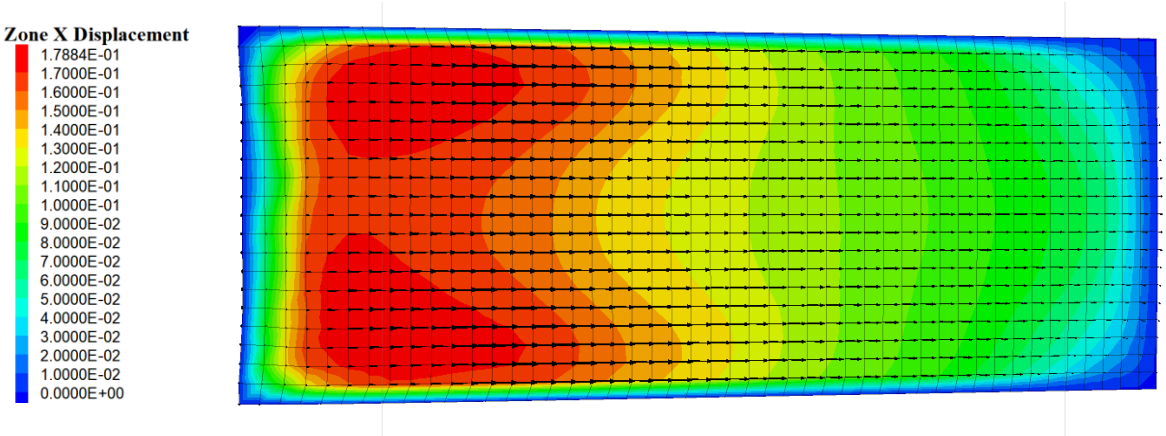

Figure 7: Horizontal displacement contour after shaking (Top view, from three-dimensional analysis, unit in m)

The amount of permanent horizontal displacement is similar with the physical test for the two types of the analysis. However, distribution of the permanent displacement is quite different because the two-dimensional plane strain analysis is unable to capture frictional effect acting on the side of the box.

4 CONCLUSION

- Numerical liquefaction model is verified with the dynamic centrifuge test results for two- and three-dimensional analysis.
- The numerical models show good agreement with the test results for the horizontal acceleration and pore water pressure histories
- Three-dimensional analysis yields more reasonable result for estimating permanent displacement distribution of the slope.

ACKNOWLEDGEMENT

This research was supported by a grant (NRF-2017R1D1A1A09000525) from the National Research Foundation of Korea.

REFERENCES

[1] D.S. Kim, N.R. Kim, Y.W. Choo, G.C. Cho, A newly developed state-of-the-art geotechnical centrifuge in Korea. *KSCE Journal of Civil Engineering*, **17**, 77-84, 2013.

[2] D.S. Kim, S.H. Lee, Y.W. Choo, J. Perdriat, Self-balanced earthquake simulator on centrifuge and dynamic performance verification. *KSCE Journal of Civil Engineering*, **17**, 651-661, 2013.

[3] B.L. Kutter, et al., LEAP-GWU-2015 experiment specifications, results, and comparisons. *Soil Dynamics and Earthquake Engineering*, **113**, 616-628, 2018.

[4] J. Garnier, et al., Catalogue of scaling laws and similitude questions in geotechnical centrifuge modelling. *International Journal of Physical Modelling in Geotechnics*, **7**, 1-23, 2007.

[5] M. Okamura, T. Inoue, Preparation of fully saturated models for liquefaction study. *International Journal of Physical Modelling in Geotechnics*, **12**, 39-46, 2012.

[6] Itasca Consulting Group, www.itascacg.com

[7] B.O Hardin, V.P. Drnevich, Shear modulus and damping in soils: Design equation and curves. *Journal of Soil Mechanics Foundation Engineering Division ASCE*, **98**(7), 667-691, 1972

[8] P.M. Byrne, A cyclic shear-volume coupling and pore-pressure model for sand. *Proceedings of Second International Conference on Recent Advances in Geotechnical Earthquake Engineering and Soil Dynamics*. St. Louis, Missouri, March. 1991.

[9] A.M. Parra, *Ottawa F-65 Sand Characterization*. Ph. D Dissertation. UC Davis, 2016.

[10] B.L. Kutter, D.W. Wilson, De-liquefaction shock waves. *In: Proceedings of the seventh US–Japan workshop on earthquake resistant design of lifeline facilities and countermeasures against soil liquefaction*, Seattle, USA, 1999.

COMPDYN 2019
7th ECCOMAS Thematic Conference on
Computational Methods in Structural Dynamics and Earthquake Engineering
M. Papadrakakis, M. Fragiadakis (eds.)
Crete, Greece, 24–26 June 2019

PSEUDO-STATIC RESPONSE OF PILED RAFTS FOR DIFFERENT PILE HEAD CONNECTIONS

Prasun Halder[1] **and Bappaditya Manna**[2]

[1] Research Scholar
Department of Civil Engineering, Indian Institute of Technology Delhi,
Hauz Khas, New Delhi, India-110016
e-mail: prasun.siliguri@gmail.com

[2] Associate Professor
Department of Civil Engineering, Indian Institute of Technology Delhi,
Hauz Khas, New Delhi, India-110016
e-mail: bmanna@civil.iitd.ac.in

Abstract

The connection condition of pile head with the raft i.e. rigid and hinged connection plays an important role in defining the behavior of piled raft system under seismic loads. In the present study, an attempt is made to understand the effect of different pile head connections on the response of piled rafts subjected to earthquake motions by using finite element-based program PLAXIS 3D. Here, the pseudo-static approach is used by substituting the real earthquake load with an equivalent static horizontal load on the foundation. This pseudo-static load is calculated by multiplying the applied vertical load with the seismic coefficient of a particular earthquake and applied at the raft level. A three-dimensional numerical model of piled raft, validated using a geotechnical centrifuge test data available in the literature, is used to study the response of piled raft for Uttarkashi (1991) and Sikkim (2011) earthquake pseudo-static loading conditions. Analyses results are presented in terms of pile-raft load sharing, normalized lateral displacement and bending moment of pile. Results show that piles in a piled raft foundation carry about 25% to 57% and raft carries about 43% to 75% of the pseudo-static load depending upon the pile head connection conditions. The lateral displacement is maximum at pile head portion for both the connections. For rigidly connected piles, the maximum bending moment occurs at the pile head whereas, piles with hinged connection show zero bending moment at top and maximum value at a certain depth from pile head.

Keywords: Piled Raft, Connection Condition, Pseudo-Static Analysis, Finite Element Model, Lateral Displacement, Bending Moment.

1 INTRODUCTION

Piled raft is widely recognized as an efficient foundation type for high-rise buildings due to its effectiveness in load sharing between the raft and piles under the action of vertical load. The settlement of the raft can be limited to acceptable value by incorporating the piles under the raft [1]. A number of design concepts and guidelines regarding piled raft foundations have been reported by various researchers [2, 3, 4, 5, 6] over the years. But in earthquake-prone areas, the safety of the piled raft foundation against earthquake forces should be ensured during the design process of the foundation. In this connection, one of the very popular and practical method is to analyze the seismic behavior piled raft by applying an equivalent static horizontal force at the foundation level. The connection condition of piles with the raft (rigid and hinged) plays an important role in defining the response of piled raft under seismic loading condition. Few numbers of literatures have been published regarding the lateral and cyclic loading tests on piled rafts [7, 8, 9, 10, 11]. However, the response of piled raft foundation with different pile head connections subjected to horizontal and seismic load in addition to vertical load has not been well explored till date due to intrinsic complexities related to pile-raft-soil interaction.

In this paper, the influence of different pile head connections i.e. rigid and hinged on the response of piled raft under pseudo-static load of Sikkim (2011) and Uttarkashi (1991) earthquakes is studied using finite element method. The responses of piled raft are presented in terms of pile-raft load sharing, lateral displacement and bending moment of piles.

2 FINITE ELEMENT MODEL AND PSEUDO-STATIC LOADING

The numerical modelling of the present study is done using finite element-based software PLAXIS 3D [12] which is an efficient tool to deal with soil-structure interaction problem. The schematic diagram of the 3D finite element (FE) model is presented in Figure 1.

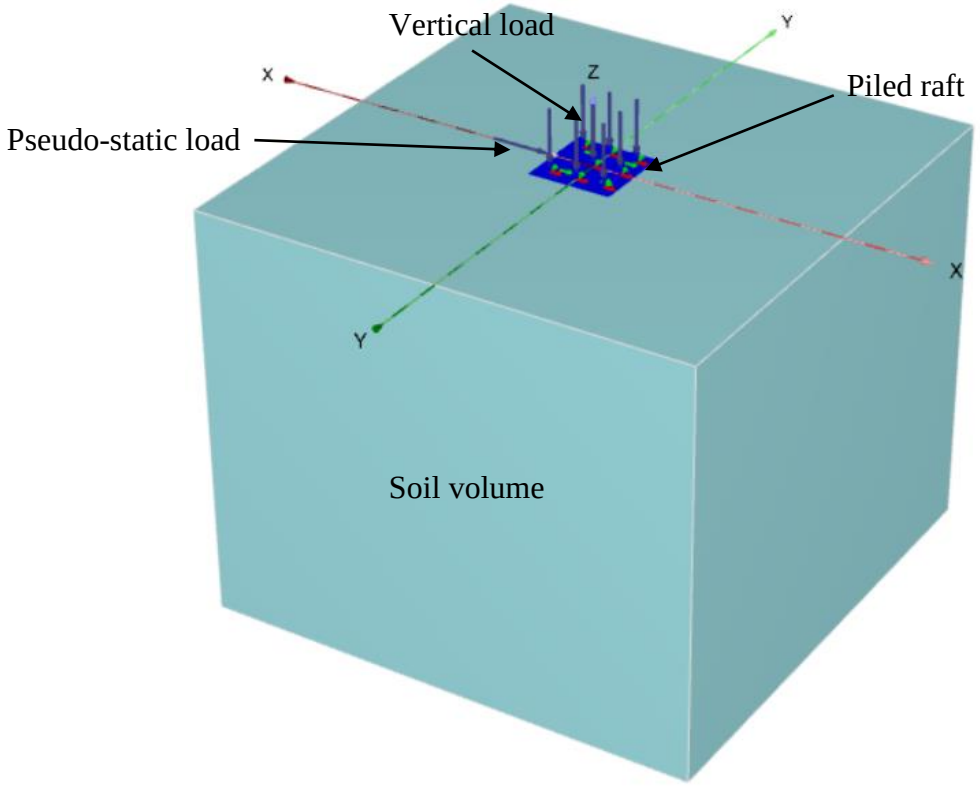

Figure 1: Finite element model of piled raft system.

Sides of the model are restricted to lateral movement and the base is restrained from both horizontal and vertical movements. The soil domain is created using the borehole option in PLAXIS 3D. The soil volume is modelled using 10-noded tetrahedral soil elements. The displacement of the soil particle due to externally applied load is calculated at the nodes of the soil element. Medium meshing scheme is selected for the present FE model.

The conventional linear elastic perfectly plastic Mohr-Coulomb model is used to simulate the behavior of the sand. This model requires fewer number of input parameters for the soil i.e. Young's modulus (E), Poisson's ratio (ν), Angle of internal friction (ϕ), cohesion (c). A 4 m square raft having 1 m thick-ness is modelled using a plate element. The embedded pile element option is used to model 4 no of 9 m long piles having 500 mm diameter (d). The piles are placed at 2 m center-to-center spacing under the raft. The raft and piles are considered to behave linear-elastically in this study. Rigid and hinged connections are considered between the pile heads and raft using the available options during the modelling of the piles. In PLXIS, the rigid connection indicates a case where the displacement and rotation of the pile head are both coupled with the displacement and rotation of the raft. On the other hand, hinged connection refers to a case where only the displacement of the pile head is directly coupled with that of the raft [12]. A vertical load of 5880 kN is applied on the piled raft model. The properties of sand, pile and raft used for the analysis are taken from [13] and presented in Table 1.

Properties	Soil	Pile	Raft
Elastic modulus, E (kN/m^2)	40×10^3	42×10^6	70×10^6
Friction angle, ϕ (Degree)	31	-	-
Cohesion (c)	1	-	-
Poisson's ratio, ν	0.3	0.2	0.35
Unit weight, γ (kN/m^3)	16.3	24	24

Table 1. Properties of soil, pile and raft used for analysis.

In the current study, the three-dimensional piled raft model is validated using the results presented in [13]. The vertical settlement of piled raft and the pile load proportion are compared with the reported values. Table 2 shows the comparison between the present FE analysis and the reported value in the literature.

Parameters	Settlement (mm)	Pile load proportion (%)
Present FE analysis	22.53	45.3
Kumar et al. [13]	21.0	47

Table 2. Comparison of results.

Here, the pile load proportion is calculated as the percentage of total applied vertical load carried by the piles only in a piled raft. From Table 2, it can be seen that the obtained results of the current FE analysis are in close agreement with that of the literature. The settlement of piled raft is over predicted by only 7.4% whereas, the pile load proportion is under predicted by only 3.6% in comparison to the reported values. Therefore, this validated 3D FE model is used to investigate the response of piled raft foundation for different pile head connections under pseudo-static loading condition.

The current study is carried out to investigate the response of piled raft system under the action of seismic load using the pseudo-static approach. In this method, the seismically induced load is replaced with equivalent static horizontal load to be acted at the level of the raft along with the application of vertical load. This particular horizontal load is known as pseudo-static load. This load is calculated by multiplying the applied vertical load with the seismic coefficient of a particular earthquake. The soil amplification effect is not considered in this approach. Figure 2 shows the time-acceleration histories of the earthquake input motions i.e. Sikkim (2011) and Uttarkashi (1991) used for the pseudo-static analysis. The peak ground accelerations (PGA) of the Sikkim (2011) and Uttarkashi (1991) earthquakes are 0.202g and 0.38g respectively. The equivalent static horizontal loads for Sikkim (2011) and Uttarkashi (1991) earthquakes are calculated as 1187.1 kN and 2234.4 kN respectively.

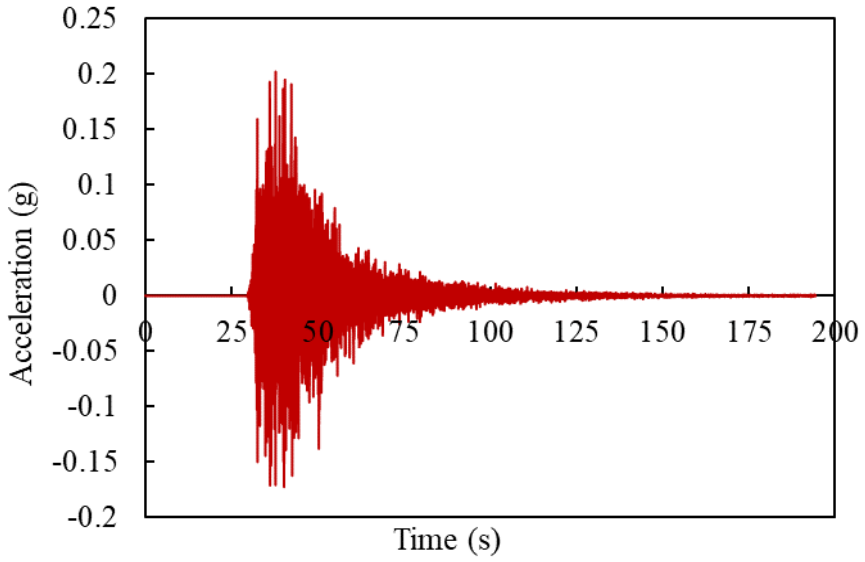

(a)

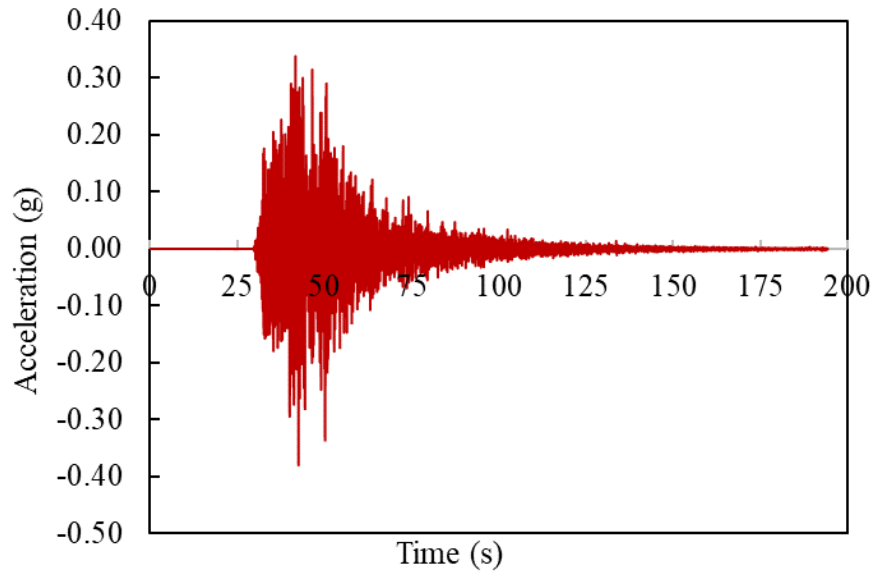

(b)

Figure 2: Time-acceleration history of earthquake events: (a) Sikkim (2011); (b) Uttarkashi (1991).

3 RESULTS AND DISCUSSION

This section highlights the results obtained from the finite element analysis. Emphasis is given on the load sharing between piles and raft as well as on the structural behavior of piles in a piled raft system for both rigid and hinged connections.

3.1 Load sharing between piles and raft

The proportion of load sharing between piles and raft is presented in the Table 3.

Pseudo-static Load	Rigid Connection		Hinged Connection	
	Pile load proportion (%)	Raft load proportion (%)	Pile load proportion (%)	Raft load proportion (%)
Sikkim (2011)-1187.1 kN	51.3	48.7	25.5	74.5
Uttarkashi (1991)-2234.4 kN	56.8	43.2	37.4	62.6

Table 3. Proportion of load shared between piles and raft.

From Table 3, it is evident that piles carry majority of the applied pseudo-static load as compared to the raft component in a piled raft system in case of rigid pile head connection. It is noteworthy that with the increase of the horizontal pseudo-static load, the piles share more load than the raft in a piled raft system. However, in case of hinged connection, the raft takes higher load than the piles. It can also be noted that the raft load proportion decreases with increasing pseudo-static load i.e. increasing PGA values of earthquake motions.

3.2 Lateral displacement of pile

Figure 3 shows the normalized lateral displacement (*U/d*) profile along the length of pile for rigidly connected piles with raft. Here, *U* is lateral displacement and *d* is diameter of pile.

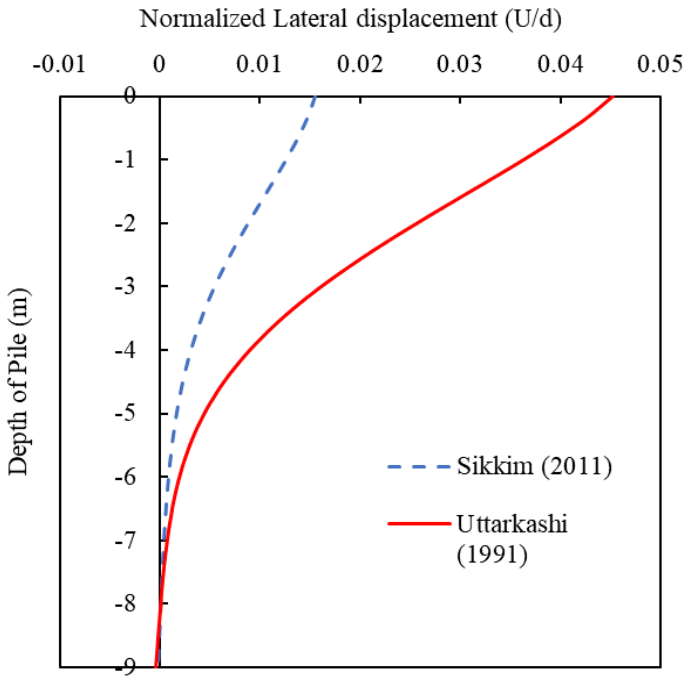

Figure 3: Variation of lateral displacement with depth of pile for rigid connection.

It can be noticed from Figure 3 that the lateral displacement is maximum at the pile head and becomes zero at pile tip. The normalized lateral displacements are found 0.016 and 0.045 for Sikkim (2011) and Uttarkashi (1991) earthquakes receptively. With higher magnitude of pseudo-static force, the lateral displacement also becomes larger. The lateral displacement (*U/d*) profile along the length of pile for hinged connection is shown in Figure 4.

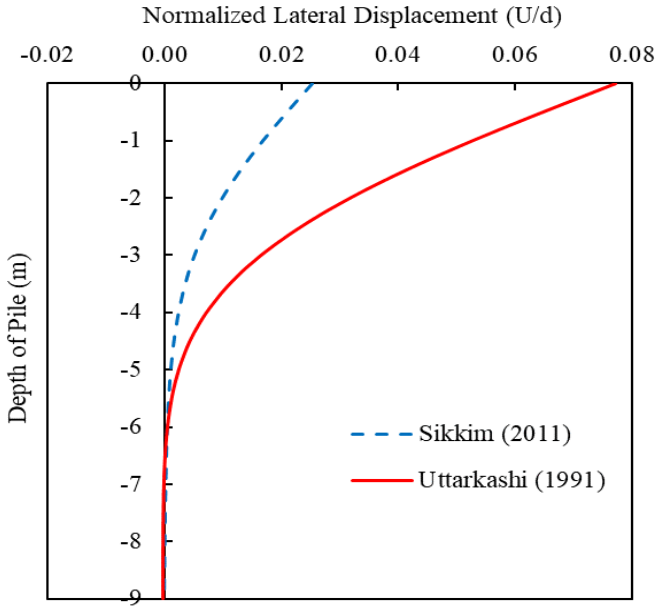

Figure 4: Variation of lateral displacement with depth of pile for hinged connection.

In this case the lateral displacement becomes higher than the rigid connection case. The normalized lateral displacements are found 0.025 and 0.078 for Sikkim (2011) and Uttarkashi (1991) earthquakes receptively.

3.3 Bending moment of pile

Figure 5 shows the bending moment distribution along the length of the pile for rigidly connected piles with the raft.

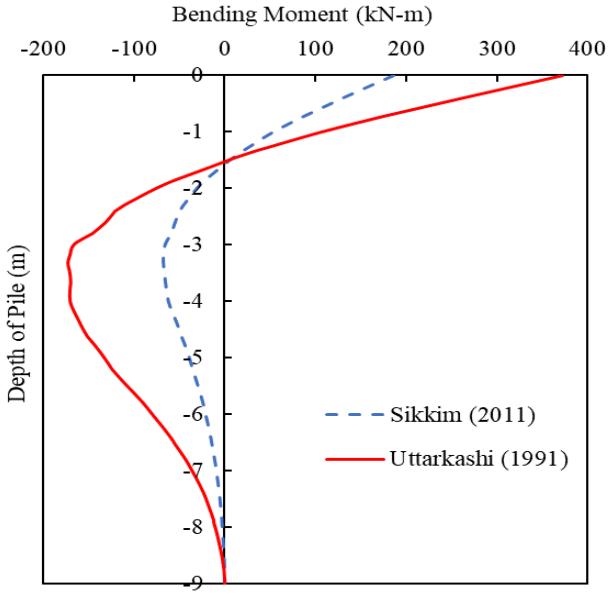

Figure 5: Variation of bending moment with depth of pile for rigid connection.

It can be observed from Figure 5 that the maximum bending moment occurs at the pile head due to fixed connection with the raft. It can also be noted that bending moment gets transformed from positive to negative along the pile length and finally comes to zero at pile tip. The maximum bending moments, as found from Figure 5, are 192 kN-m and 380 kN-m for Sikkim (2011) and Uttarkashi (1991) earthquakes respectively. Here also the bending moment increases with the increase of PGA of the earthquake motion. Figure 6 presents the bending moment profile for piles having hinged connection with the raft.

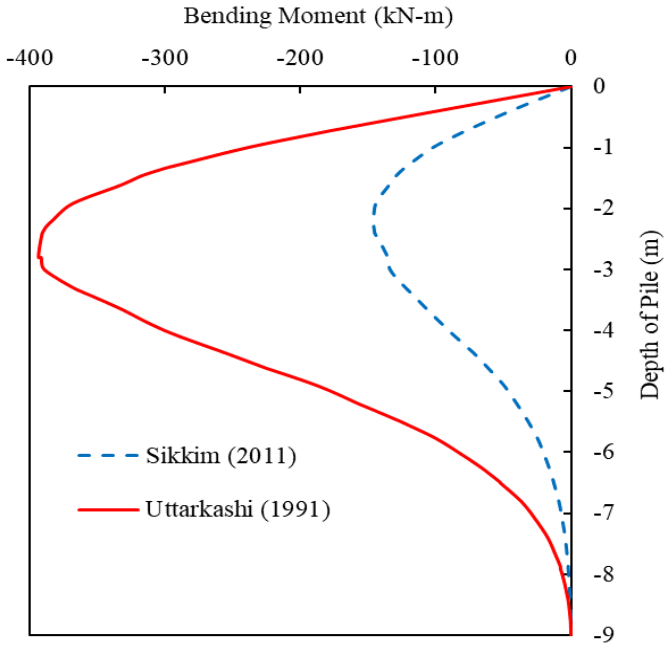

Figure 6: Variation of bending moment with depth of pile for hinged connection.

It is noticeable that for the hinged connection, the bending moment of pile starts from zero and attains the maximum value at the pile depth ranging from 2 m to 3 m and finally comes to zero again at the pile tip. The maximum bending moments, as noted from Figure 6, are 147 kN-m and 394 kN-m for Sikkim (2011) and Uttarkashi (1991) earthquakes respectively.

4 CONCLUSIONS

From the present study, the following can be concluded.

- The piles in a piled raft foundation are found to carry 25% to 57% and raft is found to share 43% to 75% of the pseudo-static load depending upon the pile head connection conditions.
- The load proportion of raft is found to decrease with increasing magnitude of pseudo-static load i.e. increasing PGA value of earthquake motions irrespective of the pile head connection condition.
- The lateral displacement is observed to have the maximum value at the pile head portion for both the connections.
- For rigidly connected piles, the maximum bending moment occurs at the pile head and the bending moment profile changes from positive to negative at a pile depth of 1.5m. However, piles with hinged connection exhibit zero bending moment at the pile head and maximum value at the pile depth ranging from 2m to 3m.

REFERENCES

[1] J.B. Burland, B.B. Broms, V.F.B. De Mello, Behavior of foundations and structures. *9th Inter-national Conference on Soil Mechanics*, Tokyo, **2**, 495-546, 1977.

[2] K. Horikoshi, M.F. Randolph, A contribution to optimum design of piled rafts. *Geotechnique*, **48(3)**, 301-317, 1998.

[3] H.G. Poulos, Piled raft foundations: Design and applications. *Geotechnique*, **51(2)**, 95-113, 2001.

[4] R. Katzenbach, U. Arslan, C. Moorman, *Pile raft foundation project in Germany*, Hemsley J.A. Editor, Thomas Telford, 323-392, 2000.

[5] K. Katzenbach, R. Katzenbach, H. Ramm, D. Choudhury, Combined pile-raft foundations – A sustainable foundation concept. *9th International Conference on Testing and Design Methods for Deep Foundations*, Kanazawa, Japan, **1**, 25-34, 2012.

[6] K. Katzenbach, D. Choudhury, ISSMGE Combined Pile-Raft Foundation Guideline. International Society for Soil Mechanics and Geotechnical Engineering, ISSN: 1436-6517, ISBN: 978-3-942068-06-2, 1-28, 2013.

[7] K. Horikoshi, T. Matsumoto, Y. Hashizume, T. Watanabe, H. Fukuyama, Performance of piled raft foundations subjected to static horizontal loads. *International Journal of Physical Modelling in Geotechnics*, **3(2)**, 37-50, 2003a.

[8] K. Horikoshi, T. Matsumoto, Y. Hashizume, T. Watanabe, H. Fukuyama, Performance of piled raft foundations subjected to dynamic loading. *International Journal of Physical Model-ling in Geotechnics*, **3(2)**, 51-62, 2003b.

[9] P. Kitiyodom, T. Matsumoto, A simplified analysis method for piled raft and pile groups foundations with batter piles. *International Journal of Numerical and Analytical Methods in Geo-mechanics*, **26**, 1349-1369, 2002.

[10] T. Matsumoto, K. Fukumara, P. Kitiyodom, K. Horikoshi, A. Oki, Experimental and analytical modelling study on behavior of model piled raft in sand subjected to horizontal and moment loading. *International Journal of Physical modelling in Geotechnics*, **4(3)**, 1-19, 2004.

[11] D. Choudhury, V.S. Phanikanth, S.Y. Mhaske, R.R. Phule, K. Chatterjee, Seismic liquefaction hazard and site response for design of piles in Mumbai city. *Indian Geotechnical Journal*, **45(1)**, 62-78, 2015.

[12] Plaxis AE, Netherland User Manual, PLAXIS 3D, 2015.

[13] A. Kumar, D. Choudhury, R. Katzenbach, Effect of earthquake on combined pile-raft foundation. *International Journal of Geomechanics*, **16(5)**, 04016013 (1-16), 2016.

COMPDYN 2019
7th ECCOMAS Thematic Conference on
Computational Methods in Structural Dynamics and Earthquake Engineering
M. Papadrakakis, M. Fragiadakis (eds.)
Crete, Greece, 24–26 June 2019

PREDICTION OF GROUND VIBRATION DUE TO RAILWAY TRAFFIC IN MRTS UNDERGROUND CUT AND COVER TUNNELS

Arnab Sur[1], **Bappaditya Manna**[2] **and Shiva Shankar Choudhary**[3]

[1] Research Scholar, [2] Associate Professor
Department of Civil Engineering, Indian Institute of Technology Delhi, New Delhi, India – 110016
e-mail: arnabsur2@gmail.com; bmanna@civil.iitd.ac.in

[2] Assistant Professor
Department of Civil Engineering, National Institute of Technology Patna, Bihar, India - 800005
e-mail: shv.snkr@gmail.com

Abstract

Underground railway tunnels are the most preferred option for Mass Rapid Transit Systems (MRTS). The circulation of trains inside underground tunnels generate noise and vibrations, which propagate through soil and reach building foundations to cause noise and vibration inside the building. Buildings susceptible to vibration damage such as heritage structures and sensitive buildings may show signs of distress like damage of architectural façade or widening of cracks in members. The ground-borne vibrations and noise due to underground trains sometimes cross the threshold value for human perception leading to inconvenience of residents.

Therefore in the present study, a two-stage coupled analysis is carried out to estimate ground-borne vibrations in the free field due to moving train for different soil stiffness, tunnel depths and train speeds. Two sub models are generated – (a) train-track sub-model and (b) tunnel-soil coupling sub-model. The first model estimates the dynamic force exerted by a moving train on track structure. In the second model the calculated dynamic force is applied at track locations of a 2D FE model generated in PLAXIS. The numerical models are validated using measured results available in the literature. The train data and tunnel dimensions are taken from the MRTS projects in Delhi, India.

It is found that the noise and vibration due to underground rail depends on distance and depth of tunnel, stiffness of soil and train speed. In some cases, the estimated vibration levels at ground cross the threshold limit to damage of sensitive buildings and therefore additional care should be taken when tunnel alignment is close to heritage or sensitive buildings. The conclusions obtained from this parametric study can be useful for practicing engineers for prediction of ground vibration due to railway traffic in MRTS underground cut and cover tunnels in Delhi.

Keywords: Ground vibration; Free field; Finite element; Railway traffic; Tunnel; Stiffness; Underground

1 INTRODUCTION

In metropolitan cities Mass Rapid Transit Systems (MRTS) are lifeline to the daily commuters. Underground railway tunnels are the most preferred option for such rapid transit systems. However, ground-borne vibrations due to underground railway traffic can disturb life and property of residents living in buildings in close proximity of underground tunnels. When trains move along underground tunnels vibrations are generated. The vibrations thus generated radiate away from the railway tunnel and may cause disturbances to the nearby residents. Structural damage of the sensitive buildings may also happen depending on vibration intensity at ground surface and building built quality. To address such problem study of vibration characteristics of underground tunnels certainly become an important research subject. Several research works have been carried out in this regard which are based on actual site measurements, numerical analysis or a combination of numerical and experimental results.

Analysis of train-induced vibrations and their propagation can be done with 2D as well as 3D models. The vibration source, i.e. the train is generally considered as an oscillating force. The propagation path between the source and the receiver is commonly modelled as a plane perpendicular to the tunnel. NGI (2004) and Lai et al. (2005) pointed out that the propagation between source and receiver is a true 3D problem when heterogeneities are included since the vibration propagates along the most beneficial path. Liu et al. (2014) developed analytical solution by using Navier's wave propagation theory in 3D elastic medium and found that frequency and vibration characteristics match with FEM solutions with acceptable error limits. Xu et al. (2015) made comparison of 2D and 3D prediction models for environmental vibrations induced by underground railway. It is found that with a suitable equivalent force, 2D prediction models can be used to assess environmental vibrations with considerable accuracy for engineering problems. However, 2D prediction models are not suitable for evaluating structures with sensitive instruments. Based on 2D finite difference model results, Nejati et al. (2012) found the most important factor influencing vibration is train axle weight, spacing of axles and speed of train.

Most of the studies available were carried out for a specific case and parametric studies involving different parameters are not available. This paper is targeted to cover a parametric study with varying soil stiffness, depths of tunnel and train speeds. The train and tunnel data are taken from the executed underground MRTS projects in Delhi. In the present study the soil is considered as isotropic and tunnel is considered on a straight alignment, hence, 2D FE model is used. A two-stage coupled analysis approach is followed to estimate ground-borne vibrations in the free field when the origin of vibration is moving train. Two sub models are generated – (a) train-track sub-model and (b) tunnel-soil coupling sub-model. The first model is an analytical model which estimates the dynamic force generated by the moving train on rail tracks. The second model is a numerical 2D model created using PLAXIS. In the second model the calculated dynamic force is applied at track locations on the tunnel base slab and wave propagation through ground is estimated.

2 MATHEMATICAL MODELS

Prediction of train-induced environmental vibration has to cope with the problem of complexity of the dynamic interaction between train, track and soil. Two mathematical sub-models are used to represent the problem.

2.1 Train-track sub-model

When a train moves on infinitely long rail then dynamic force is generated on the substructure which gets transmitted to the tunnel structure. This dynamic problem can be solved analytically by classical theory of beam on elastic foundation. In the present analysis the rail is considered as an infinitely long Euler – Bernoulli beam having constant cross section. The foundation material is represented as linearly elastic Winkler springs. Both beam and foundation are assumed to be isotropic and homogeneous. The differential equation of motion considering vertical equilibrium of forces on beam element is solved and closed form solution for the deflection due to moving load P is given by Kumari et al. (2012).

The load P is the wheel load of the train and spring constant k is obtained from a static FE analysis of tunnel section embedded in soil. Fig. 1 shows a time-displacement curve generated for train speed of 60 km/hr inside a rectangular cut and cover tunnel at 10 m depth (measured at tunnel axis) from ground having average standard penetration test (SPT) value of 20.

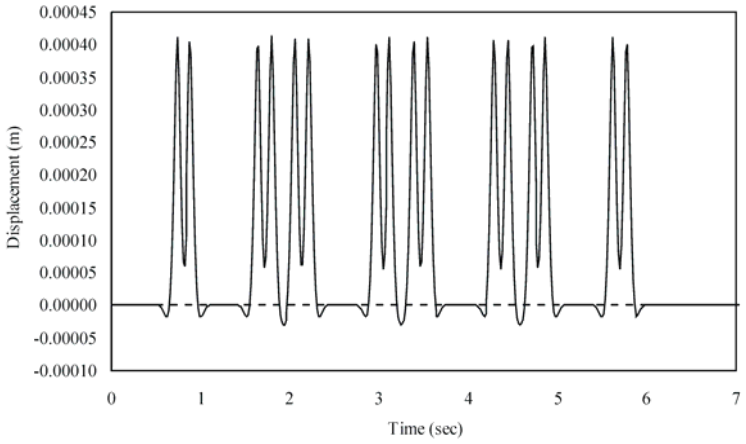

Figure 1: Time vs. Displacement plot for train speed of 60 km/hr

2.2 Tunnel-soil coupling sub-model

This is the second stage of analysis where calculated dynamic force from first stage analysis is applied on a 2D FE model generated in PLAXIS software. A plain strain analysis is done with 6 noded elements. Concrete is considered as an elastic material, soil is considered as mohr-coulomb elasto-plastic material. The dynamic modulus of soil layer is calculated by knowing shear wave velocity through that layer. The radiation damping and material damping are considered in the analysis. For material damping Rayleigh damping coefficients are calculated. The train details used in analyses are similar to metro rail corridors managed by Delhi Metro Rail Corporation (DMRC). Train speeds of 40 km/hr, 60 km/hr, 80 km/hr, 100 km/hr and 120 km/hr are considered for the study. Dimension and loading details of one passenger coach is shown in Fig. 2. The train is made up of four coaches. The track is considered as ballast-less direct fixation track. The section of rail considered is UIC60.

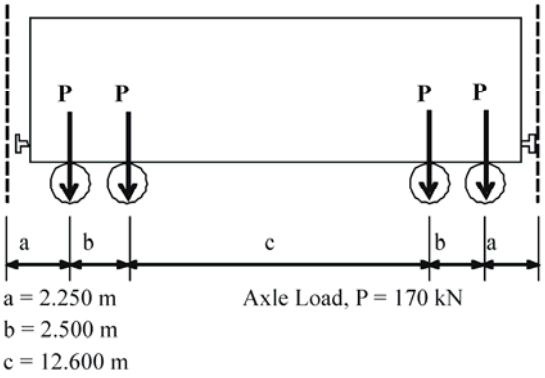

Figure 2: Details of a passenger coach used in analysis

3 INPUT PARAMETERS FOR ANALYSIS

Cut and cover tunnels have been used in several MRTS projects in Delhi, India. In this method excavation is done by earth retaining system like soldier pile wall, secant pile, sheet pile and diaphragm wall. Tunnel lining is then cast inside the excavation followed by back filling over the tunnel. The tunnel lining thickness is considered as 0.7m and internal clear dimension of tunnel is considered as 5.25 m x 5.75 m. Concrete grade for lining is considered as 35MPa.

3.1 Dynamic properties of soil

In this study the dynamic soil properties are co-related with Standard Penetration Test (SPT) results as this test is widely used and easy to perform with acceptable level of accuracy. Hanumantharao and Ramana (2008) had done microzonation of Delhi and given relationship between SPT values and dynamic soil properties. Based on their observation shear wave velocity has been calculated.

The wave propagation depends largely on the stiffness, density and Poisson's ratio of soil. The shear strength parameters are generally less significant unless a large strain which may cause plastic deformation is expected to happen. The dynamic problems are generally small strain problems, hence the shear strength parameters can be assumed to be same even if the SPT values are varied. To verify this, PLAXIS runs with different shear strength parameters are investigated and the results obtained show insignificant change in PPV. Therefore, variation in shear strength parameters is neglected in present study.

3.2 Soil damping

Geometric damping in soil is about 30% of critical damping and is taken care by assigning absorbent boundaries in the FE Model. The material damping of soil generally ranges from 0% to 10%. This damping behavior is considered in FE Model in terms of Rayleigh Damping Coefficients. Whitman and Richard (1967) suggested material damping in range of 0% to 10%. In the present study for "Delhi Silt" damping ratio of 5% is considered.

4 VALIDATION OF MATHEMATICAL MODELS

The validation of mathematical models with actual field measured data is important as the reliability and correctness of the whole study can be thus established. The two models are

used in this study – (a) train-track sub-model and (b) tunnel-soil coupling sub-model, both are validated with measured results from site.

4.1 Validation of train-track sub-model

The train-track sub model is validated with actual measurements from high-speed track of Beugnâtre site observed by Ferreira (2010). The substructure of the reference track consists of 35 cm thick ballast, 30 cm thick granular subballast and 60 cm thick form layer having Young's modulus of 150 MPa, 100 MPa and 80 MPa respectively. The track was resting on a subgrade having Young's modulus of 80 MPa. For a train speed of 300 km/hr, the measured and calculated time versus acceleration data are shown in Fig. 3. The measure time versus acceleration plot is similar to that of calculated and the peak values are satisfactorily comparable.

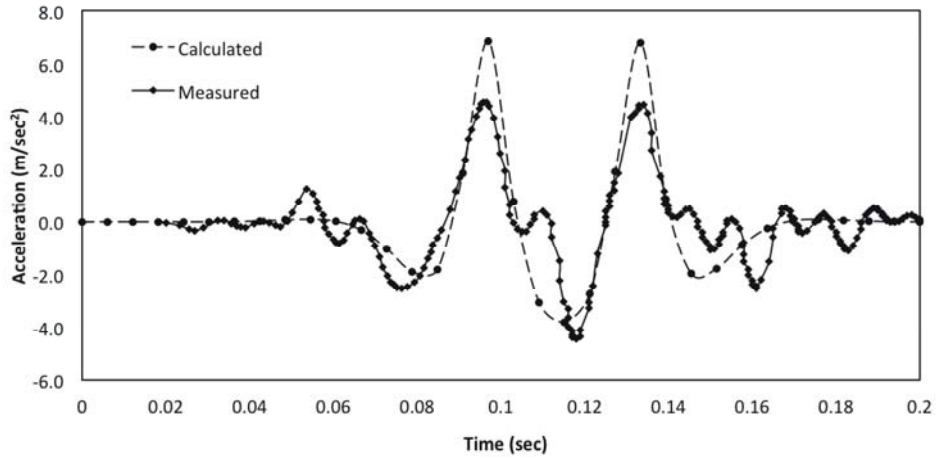

Figure 3: Time vs. acceleration data at Beugnâtre track section at 300 km/hr measured by Ferreira (2010) and as calculated in present study

4.2 Validation of tunnel-soil coupling sub-model

This model is validated with site measured data from metro tunnel on the line RER B at Cité Universitaire measured within the frame of the EC-Growth project CONVURT and reported by Chatterjee (2003). The metro tunnel was a shallow cut-and-cover tunnel in masonry structure. The depth of the tunnel was about 9.3 m below ground and the overall width of the tunnel was 11.9 m. The thicknesses of the top slab, bottom slab and side walls were 0.6 m, 0.4 m and 1.5 m respectively.

The FE model to represent tunnel-soil coupling behaviour is generated in PLAXIS software using actual tunnel and soil data. The time history of the vertical velocity as measured at sleeper position during passage of test train at speed of 80 km/hr is applied in the FE model at track location. The site measured time history of free field vertical velocity at 8 m distance from longitudinal axis of tunnel during passage of test train is compared with that calculated from FE model as shown in Fig. 4. It can be seen from Fig. 4 that the peak amplitude values of free field vibration from the site measurement and that calculated by FE model are fairly close.

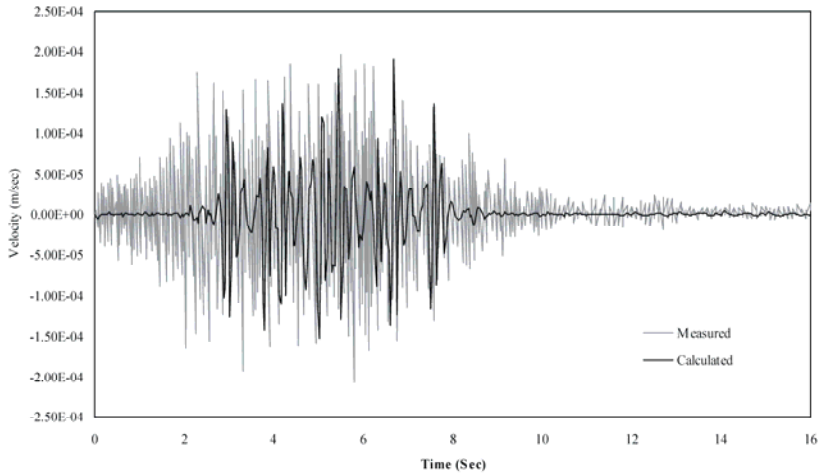

Figure 4: Time history of free field vertical velocity at 8m from longitudinal axis of tunnel during passage of test train at speed of 80 km/hr as observed by Chatterjee (2003) and as calculated in present study

5 ANALYSIS RESULTS

The dynamic effects of underground moving trains inside tunnels are studied in free field. The impacts of ground stiffness, tunnel depth and train velocity are studied. Based on free field vibration, researchers have established guidelines which give limits of vibration for structural safety.

5.1 Study on cut and cover tunnel

Cut and cover tunnel in rectangular box shape having tunnel lining thickness of 0.7m and internal clear dimension of tunnel 5.25 m x 5.75 m is considered in present study. Tunnel axis depths are considered as 10 m, 20 m and 30 m. The results are noted at 0 m, 10 m, 20 m and 30 m distances from tunnel axis at the ground level. From Fig. 5 it can be seen that vibration is maximum at the tunnel invert as the dynamic load from railway track is applied directly here. As the vibration travels through the lining and surrounding soil the magnitude of vibration attenuates due to damping.

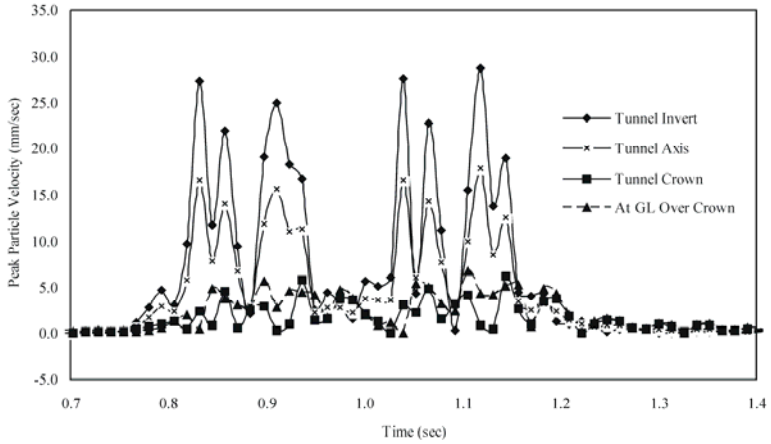

Figure 5: Time vs. peak particle velocity at tunnel invert, axis, crown and ground for train speed of 120 km/hr in 10 m deep tunnel in soil with SPT value of 20.

5.2 Dependency of vibration magnitude on different parameters

The ground-bone vibration due to underground moving train is found to depend of the following parameters – (a) Distance from tunnel, (b) Train speed, (c) Soil stiffness, (d) Depth of tunnel below ground. The vibration is also dependent Tunnel geometry and Lining stiffness.

Distance from tunnel

Time versus vertical velocity in free field are plotted for different distances from tunnel axis for a 10 m deep tunnel in soil having SPT value of 20 and for a train speed of 120 km/hr as shown in Fig. 6. It can be seen from the obtained results that the amplitude of vibration reduces drastically as the distance from the tunnel increases. A phase difference in vibration can also be noticed in the plot. With increase in distance from tunnel axis the vibration wave reaches there later than the nearer points. This happens as the wave travels through the soil with certain velocity depending on stiffness of soil.

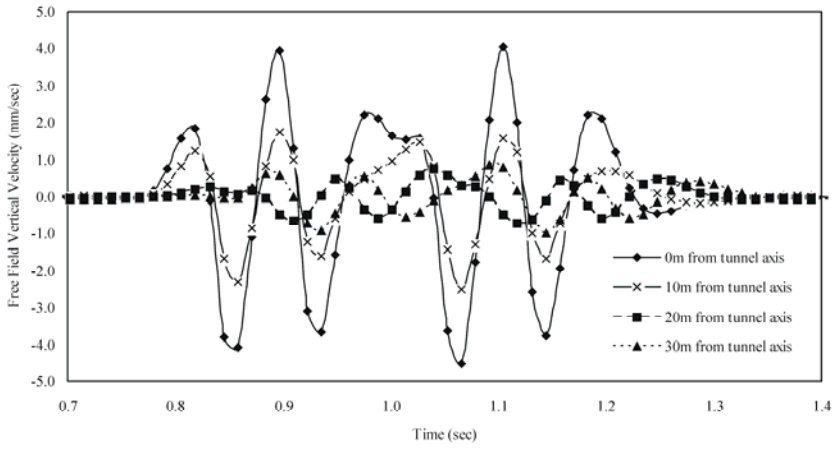

Figure 6: Time vs. vertical velocity in free field at different distances from tunnel axis for train speed of 120 km/hr in 10 m deep tunnel in soil with SPT value of 20

Train speed

To study variation of PPV as a function of distance from tunnel axis, a parametric study is done in which at a time only one parameter is varied keeping all other parameters constant to see the change in result. Fig. 7 shows PPV versus distance from tunnel axis for different train speeds when all other parameters are unchanged, such as tunnel depth of 10 m and soil stiffness corresponding to SPT value of 20.

It can be seen that with increase in train speed the observed PPV increases. At 40 km/hr speed the maximum PPV observed at ground at 0 m from tunnel center is just 1.0 mm/sec whereas when the train speed increase to 120 km/hr, the PPV at the same location increases to 4.5 mm/sec.

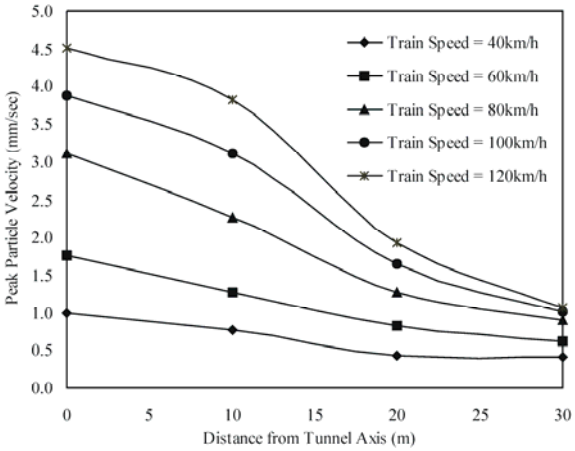

Figure 7: PPV vs. distance from tunnel axis for different train speeds for 10 m deep tunnel in soil with SPT value of 20

Soil stiffness

The shear wave velocity is a function of soil stiffness. As the soil stiffness increases the shear wave velocity also increases. A parametric study is done considering soil stiffness corresponding to SPT values of 20, 40, 60 and 80 while all other parameters are unchanged. From Fig. 8 which shows the change in PPV with ground stiffness, it can be seen that the vibration at ground increases in softer ground condition.

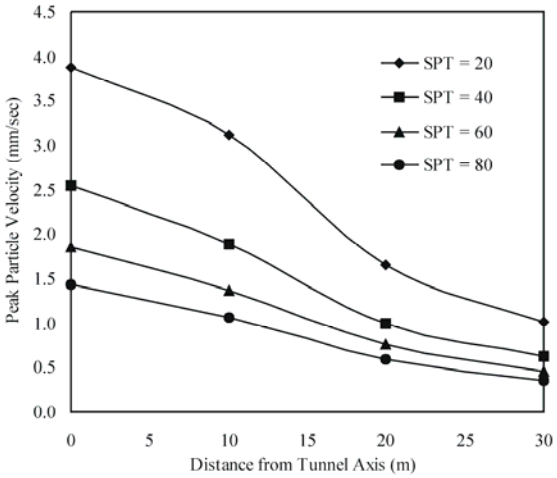

Figure 8: PPV vs. distance from tunnel axis for different soil stiffness for 10 m deep tunnel when train speed is 100 km/hr

Tunnel depth

The soil vibrations attenuate due to radiation damping and material damping with distance from the source of vibration. A parametric study is done considering tunnel depths of 10 m, 20 m and 30 m while all other parameters are kept unchanged. The increase in tunnel depth reduces the vibration at ground level. It can be seen from Fig. 9. With increase in tunnel depth the distance of source of vibration increases from the observation points at ground level. Due to attenuation of vibration when waves are propagating through the ground, the vibration amplitude reduces with increasing tunnel depth.

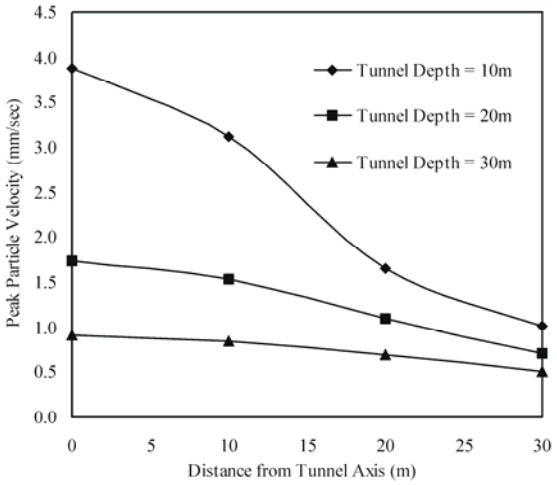

Figure 9: PPV vs. distance from tunnel axis for various depths of tunnel when train speed is 100 km/hr and soil has SPT value of 20

6 CONCLUSIONS

In the present scope of study vibration problem of underground moving train is studied. The tunnel dimensions are taken from MRTS Projects in Delhi, India. The present study includes the calculation for generated dynamic loads from moving trains, propagation of the wave through the tunnel lining and soil medium. A coupled analysis is followed in which two sub models are generated – (a) train-track sub-model and (b) tunnel-soil coupling sub-model. Both the mathematical models are validated with actual site measured values.

From this study it is noticed that the Free Field ground vibration depends on parameters – (a) Distance from tunnel, (b) Train speed, (c) Soil stiffness, (d) Depth of tunnel below ground. The ground vibration is found to be inversely proportional to distance from tunnel, soil stiffness and tunnel depth, while the vibration is directly proportional to the train speed. Buildings closer to the tunnel alignment are more susceptible to get damaged.

The tunnels in soils having SPT value higher than 40 generally do not exhibit any significant vibration. In case the soil is poor, then vibration can be reduced by either increasing the proposed depth of the tunnel or by reducing the design speed of the tunnel in the affected section.

REFERENCES

[1] C Hanumantharao, G V Ramana (2008), “Dynamic soil properties for microzonation of Delhi, India”, *J. Earth Syst. Sci. Vol. 117, S2, pp. 719–730.*

[2] Hamid Reza Nejati, Morteza Ahmadi and Hamid Hashemolhosseini (2012), "Neumerical analysis of ground surface vibration induced by underground train movement", *Tunnelling and Underground Space Technology*, *Vol. 29 pp. 1-9.*

[3] Kurzweil, L.G. (1979), “Ground-borne noise and vibration from underground rail systems”, *Journal of Sound and Vibration, Vol. 66(3), pp. 363–370.*

[4] Lai. C.G., Callerio, A., Faccioli, E. Morelli, V. and Romani, P. (2005), "Prediction of railway-induced ground vibrations in tunnels", *Journal of Vibration and Acoustics, Vol. 127, pp. 503-514.*

[5] Melke, J. (1988), "Noise and vibration from underground railway lines: proposal for a prediction procedure", *Journal of Sound and Vibration, Vol. 120(2), pp. 391–406.*

[6] NGI (2004), "New double tracked line Sandvika – Asker. Measures against structure borne noise", *Vol. 20041010-2. Oslo: Norges Geotekniske Institutt.*

[7] P. Chatterjee , G. Degrande , S. Jacobs, J. Charlier, P. Bouvet and D. Brassenx (2003), "Experimental results of free field and structural vibrations due to underground railway traffic", *Tenth International Congress on Sound and Vibrations, 7-10 July 2003, Stockholm, Sweden.*

[8] P. A. Ferreira (2010). "Modelling and prediction of the dynamic behaviour of railway infrastructures at very high speeds. " *Ph.D. thesis, IST-UTL, Lisbon, Portugal*.

[9] Paolo Panzeri, Alberto Bonaldi (2009), "An experimental numerical combined approach to forecast groundborne vibrations and noise due to trains in underground lines", *8th International Conference on Contact Mechanics and Wear of Rail/Wheel Systems (CM2009), Firenze, Italy, September 15-18, 2009.*

[10] Sunita Kumari, Pragyan P Sahoo and Dr. V A Swant (2012), "Dynamic Analysis of Railway track", *International Journal of Emerging Technology and Advanced Engineering.*

[11] Whitman and F. E. Richart, Jr. (1967), "Design Procedures for Dynamically Loaded Foundations," *JSMFD, ASCE, vol. 93, SM 6, Nov, pp. 169-193.*

[12] Qingyuan Xu, Zucai Xiao, Tao Liu, Ping Lou and Xuming Song (2015), "Comparison of 2D and 3D prediction models for environmental vibration induced by underground railway with two types of tracks", *Computers and Geotechnics, vol. 68, pp. 169-183.*

[13] Zeng-rong Liu, Guang-qin Cui and Xin Wang (2014). "Vibration Characteristics of a Tunnel Structure Based on Soil-Structure Interaction", *International Journal of Geomechanics, ASCE.*

COMPDYN 2019
7th ECCOMAS Thematic Conference on
Computational Methods in Structural Dynamics and Earthquake Engineering
M. Papadrakakis, M. Fragiadakis (eds.)
Crete, Greece, 24–26 June 2019

DYNAMIC ANALYSIS OF SINGLE BATTER PILE USING DIFFERENT SOIL MODELS

Rohit Ralli[1], **Bappaditya Manna**[2], **and Manoj Datta**[2]
[1]Research Scholar
Department of Civil Engineering, IIT Delhi, India
e-mail: rohit.iitd15@gmail.com
[2] *Associate Professor*
e-mail: bmanna@civil.iitd.ac.in
[3]*Professor*
e-mail: mdatta@civil.iitd.ac.in

Abstract

Modelling of dynamic soil-pile interaction behavior is very complex. Different soil models have been proposed to model the complex soil-pile behavior under dynamic loading. Applicability of different soil models for dynamic loading is very limited for batter piles. To study the dynamic response of batter pile, three different soil models are used; (i) Linear Model : This model that considers no slippage between the pile and soil; (ii) Nonlinear Model 1: This model that includes a cylindrical zone around the pile with less inner zone soil modulus than outer zone and neglects the inner weak zone soil mass to avoid the wave reflections between the inner zone and outer zone; (iii) Nonlinear Model 2: Nonlinear soil model that uses a nonreflective boundary formed between the inner zone and outer zone to account for the mass of soil in the cylindrical boundary zone.

In this present study the frequency dependent stiffness, damping and amplitude of soil-pile system under vertical vibrations are calculated using continuum approach by Novak with three soil models. A series of vertical field vibration tests were also conducted on a single batter driven pile (L/d =26) of inclination 10 degrees for different eccentric moments (0.449, 0.670, 1.664 and 1.830 Nm) with static load of 12 kN. The effectiveness of the soil models has been checked by comparing the test results with the analytical results obtained using three soil models. It has been observed that the frequency amplitude responses obtained from Nonlinear Model 1 for a precise range of boundary zone parameters are found close to the experimental results. So it can be concluded Nonlinear Model 1 predict the dynamic response of batter pile under vertical vibrations more accurately than Linear Model and Nonlinear Model 2.

Keywords: Batter piles; Soil models; Dynamic loading; Stiffness; Damping; Amplitude; Vertical vibration; Field vibration test; Boundary zone.

1. INTRODUCTION

Pile foundations are often used to support structures that are exposed to dynamic loads such as earthquakes, wind, wave and machine induced vibrating machines. They are used to large vertical or lateral or combined loads which may be static or dynamic in nature. In situations, where there are excessive lateral and vertical loads coming from the superstructure, batter piles in combination with vertical piles are used to increase the stiffness of soil-pile system.

For the evaluation of the dynamic response of pile foundation involves the calculation of stiffness and damping values of soil-pile system considering the actual soil conditions. Several researchers [1,2,3,4] contributed to formulate and postulate the continuum approach to analyse the dynamic response of pile foundation. The continuum approach was mainly given by Novak and Aboul-Ella [5] for deriving the complex stiffness of soil-pile system of single pile in layered medium [6]. Novak and Sheta [7] later contribute with the development of weak boundary zone around the pile with less shear modulus ratio and increase damping to account for the nonlinearity of the soil-pile system while neglecting the mass of the inner zone to prevent the spurious reflections between the inner and outer zone around the pile. Later Velestos and Doston [8] overcome the assumption given by Novak and Sheta [7] by introducing the mass of the inner zone. Han and Sabin [9] proposed a new model of boundary zone with nonreflection interface in which parabolic variation of the medium properties in assumed (the boundary zone has properties smoothly approaching those of outer zone). Based on this model Han [10] done a parametric study on boundary zone parameter under vertical vibration.

Extensive studies have been done by various researchers on the dynamic behavior of single vertical and group piles under machine induced vibrations. To investigate the dynamic behavior of vertical pile and pile groups and to understand the soil-pile interaction, various full scale and model-prototype tests were conducted by various researchers [11,12,13,14,15,16,17].

From the literature review it is understandable that both the analytical and experimental study on the batter pile under rotating machine induced vertical vibrations are rarely performed. Hence, in this paper with the help of the continuum approach by Novak for different soil stiffness models [6,7,9] are used to analyse the complex soil -pile stiffness of batter pile. To verify the applicability of the proposed model, dynamic forced vibration tests were performed in the field on a hollow steel pipe ($L/D = 26$) with angle of inclination of 10 degrees.

2. CONTINUUM APPROACH

The dynamic response of batter pile is governed by complex interaction phenomenon between the soil and the pile. This complex soil-pile interaction phenomenon can be modeled by using the complex impedance functions where the real and imaginary parameters represent the stiffness and damping of the soil-pile system. The stiffness and damping are calculated based on the assumption that the soil is perfectly bonded to the circumference of the pile and the behavior of the soil is governed by the law of viscoelasticity. The complex stiffness of vertical pile is calculated by using the methodology given by Novak and Aboul-Ella [5].

There is no analytical solution for the calculating the impedance function (stiffness and damping) of the battered pile but they can be established by using the observations made by Poulos and Madhav [20]. They theoretically investigated the static displacement of the battered pile by using the Mindlin's equation. They applied the axial loads (longitudinal direction) to the battered pile and found out that that axial displacements are almost unaffected by the batter of pile. Only 4 percent was the maximum effect for pile with batter angle up to 30 degrees. So, it can be concluded that the impedance function of the battered pile up to 30 degrees can be calculated using the impedance function by means of dynamic solution available for vertical piles [21]. , the complex stiffness of the batter pile-soil system can be calculated using the

stiffness along the local axes of the single vertical pile then transforms the stiffness into the local axes by multiplying the stiffness by a transformation matrix [21] which is given by

$$[K^1_{vb}] = [T]^T [K^1_w] [T] \quad (1)$$

where K^1_{vb} = complex dynamic stiffness of batter pile, [T] is the transformation matrix which depends on direction cosines and K^1_w is the complex stiffness of the vertical pile. With the stiffness and damping of the batter pile, the vertical response of the batter pile is calculated.

To account for the nonlinearity and slippage, the consideration of linear viscoelastic medium can be divided into an outer infinite zone and inner weak boundary zone with reduced shear modulus and higher soil damping as compared to the outer zone. Without any modification in theory, the soil reactions of the composite medium are introduced into the dynamic analysis of batter pile foundation. In this study, three different soil models are used to analyze the nonlinear behavior of batter pile foundation.

- Linear Model: In this model the dynamic complex stiffness function of the soil medium in calculated considering no slippage between the pile and the soil. The complex stiffness of the soil is derived using the solution of the equation of the motion of viscoelastic medium using the hysteric damping which is obtained from the solution of wave propagation of elastic medium [6].
- Nonlinear Model 1: In this model, Novak and Sheta [7] considered a cylindrical annulus of soft soil around the pile which has less shear modulus and high damping than the outer zone. The mass of the inner weak zone is considered as zero ($\rho = 0$) to avoid any wave reflection between the interface of inner and outer zone. This soil model with continuum approach is available in the computer software package DYNA 6 [18].
- Nonlinear Model 2: This model assumes the boundary zone has a nonzero mass and a smooth variation into the outer zone by introducing the parabolic variation function [9]. This type of soil model with continuum approach is programmed in a software named DYNAN [19].

3. EXPERIMENTAL INVESTIGATION

The test site was situated in between Block II and Block III at the Indian Institute of Technology Delhi, Hauz Khas, New Delhi, India. The soil properties were determined by laboratory and in situ tests. Standard penetration tests (SPT) were conducted in the field to determine the N values of soil layers. It is found that soil is predominately sandy silt up to depth 6.0 m. Piles were made of hollow steel pipes of outer diameter (d) 0.114 m and length (L) of 3 m. Initially, a borehole of 0.1 m diameter was made to reduce the resistance of pile driving. The pile was then driven into the ground by dropping of SPT hammer of weight 65 kg from a height of 0.3 m. During driving, the batter angle was maintained with the help of guide rod fixed at required batter angle. A steel plate of dimension 0.9 m $\times$ 0.9 m $\times$ 0.037 m was used as a pile cap which was connected rigidly with the pile. Forced vertical vibration tests were conducted on model single batter pile ($\beta = 10^o$). The dynamic forces are produced by Lazan type mechanical oscillator in the form of harmonic motion. Two counter rotating-mass are moved inside the oscillator to develop the dynamic forces on the pile. The amplitude of the dynamic force was controlled by adjusting the eccentricity (θ) of the rotating masses. The excitation force, $P(t)$, is given by

$$P(t) = m_e.e.\omega^2 \sin \omega t = (W_e/g).e.\omega^2 \sin \omega t \quad (2)$$

where, W_e and *me* are the weight and mass of eccentric rotating parts of the oscillator, respectively, *e* is the eccentric distance of the rotating masses, *g* is the acceleration due to gravity and ω is the circular frequency of vibration. The magnitude of the exciting force was changed by adjusting the angle of eccentric mass. The mechanical oscillator was connected by means of a flexible shaft with a DC motor and the speed of DC motor was controlled by a speed control unit. The oscillator was run slowly through a motor using speed control unit. Mild steel plates of size 0.5 m $\times$ 0.5 m $\times$ 0.022 m were placed on the pile cap to provide

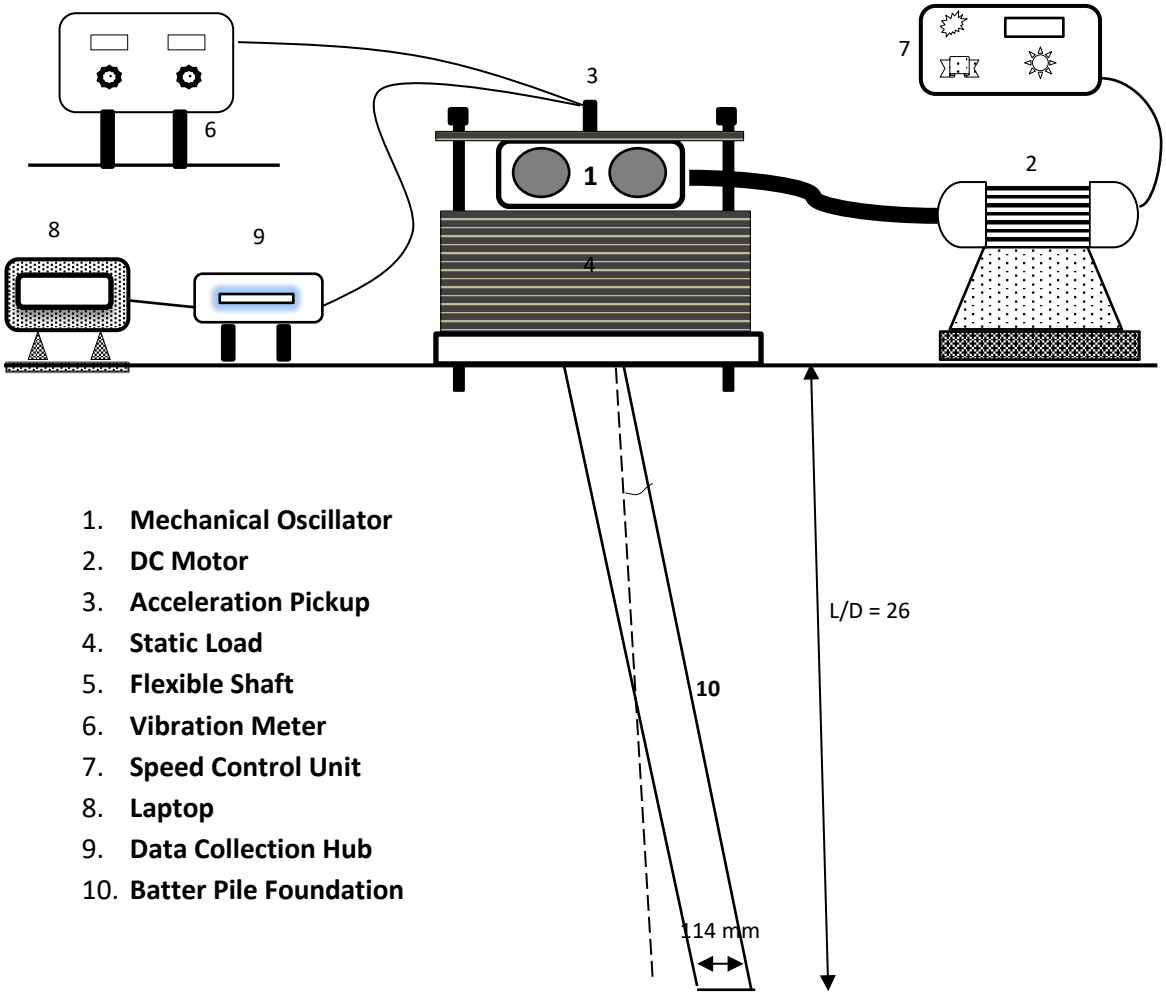

Figure 1: Schematic diagram of vertical vibration test setup in batter pile (L/D = 26, β = 10º)

desired static weight. Then the mechanical oscillator assembly was mounted on the top of the steel plates in such a way that the oscillator imposed a vertical harmonic excitation force on the pile foundation. The whole assembly was properly tightened with the pile cap using four bolts so that it could act as a single unit. The accelerometer was attached vertically on the top of the plate over the center of the pile cap. Tests were conducted for four different eccentric moments ($W_e.e$ = 0.449, 0.670, 1.664, and 1.830 N m) with the static load (*Ws*) of 12 kN. The complete vertical vibration test set up is shown in Fig. 3. The experimental frequency-amplitude response curve of single batter pile for different eccentric moment is shown in Fig.

2. It is observed from the dynamic test results that the measured frequency-amplitude response curve exhibits nonlinear behavior by showing decrement in resonant frequencies and disproportional increment in resonant amplitudes with the increase in excitation moments.

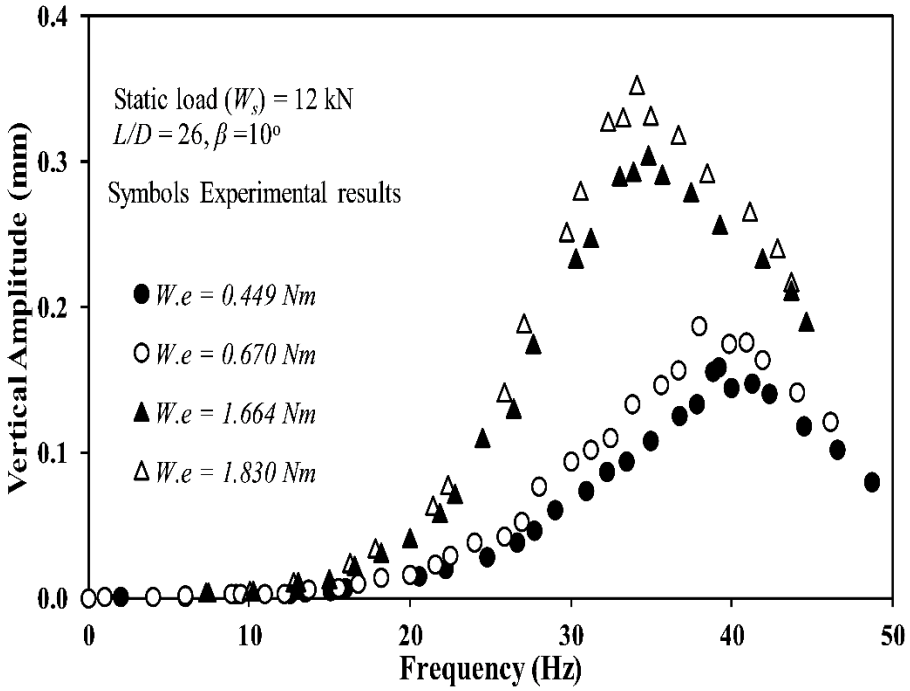

Figure 2: Experimental frequency versus vertical amplitude response of single batter pile

4. COMPARISON BETWEEN THE EXPERIMENTS AND THEORETICAL RESULTS

The test pile on the field has been analysed with all the soil models i.e. Linear Model, Nonlinear Model 1 and Nonlinear Model 2 to get the frequency-amplitude response of the batter pile-soil system. The soil material damping has been assumed 10 percent for the analysis. For different eccentric moments the weak boundary zone parameters were adjusted so that the nonlinear theoretical response curves match closely to dynamic field test data. For the current soil conditions and applied dynamic load, G_{ws}/G_s varied from 0.015 to 0.22, T_{ws}/R_i varied from 0.5 to 1, D_m varied from 0.2 to 0.35. The results obtained from the field experiments are compared with the theoretical analysis for eccentric force (*W.e =1.644 Nm*) as shown in Fig. 3.

- Linear Model: It can be well comprehended from the figure that the theoretical resonant frequency is higher and resonant amplitude are lower than the dynamic test result on the single batter pile (L/D = 26, β = 10°). This is due to the assumption that the soil is perfectly bonded to the pile and that the soil behaviour is primarily governed by laws of linear elasticity explicating no weak inner zone resulting in larger stiffness of batter pile-soil system which produces higher resonant frequency and lower resonant amplitude values.

- Nonlinear Model 1: From the comparison, it is observed that Nonlinear Model I show a well-defined match with the test results. Nonlinearity of batter pile foundation is also

exhibited from the figure with the increase in the resonant amplitude and decrease in the resonant frequency with the increase in excitation levels.

- Nonlinear Model 2: It can be observed that the Nonlinear model 2 produces high resonant frequency and high resonant amplitude when compared to dynamic test result.

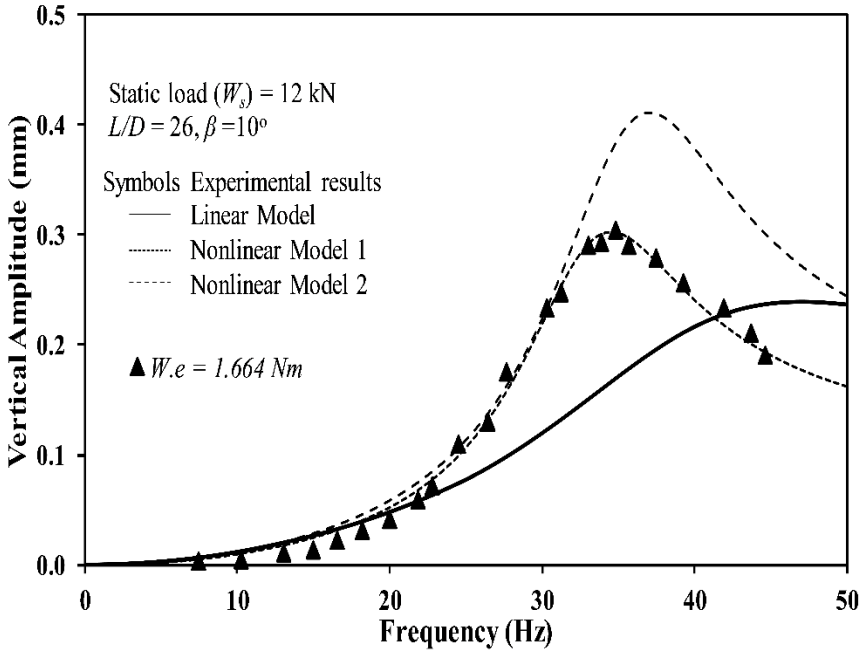

Figure 3: Comparison between the response curve obtained from vertical vibration test and Linear Model analysis

5. STIFFNESS AND DAMPING OF BATTER PILE

The vertical stiffness and damping of single batter pile ($L/d = 26, \beta = 10^o$) with frequency were determined using three models i.e. Linear model; Nonlinear model 1 and Nonlinear model 2 for all eccentric forces. The comparison of variation of stiffness and damping for different models are shown in Fig. 4a and Fig. 4b for eccentric force ($W.e = 1.664\ Nm$) respectively. It is found that Linear model highly overestimates both the stiffness and damping of single batter pile. It also shows that frequency dependent stiffness and damping of single batter pile **is** not varied with different eccentric moments showing a single stiffness and damping curves. In Nonlinear Model 1 the frequency dependent stiffness and damping values are decreased with increase of excitation force. This phenomenon occurs due to the development of weak boundary zone between pile and soil. For low frequency range, the stiffness values tend to remain linear showing the dynamic stiffness of batter pile close to static stiffness. However, the damping values of the batter pile increases rapidly as frequency approaches to zero due to the conversion of soil material damping to the frequency-dependent equivalent viscous damping. In Nonlinear model 2 the frequency dependent stiffness is

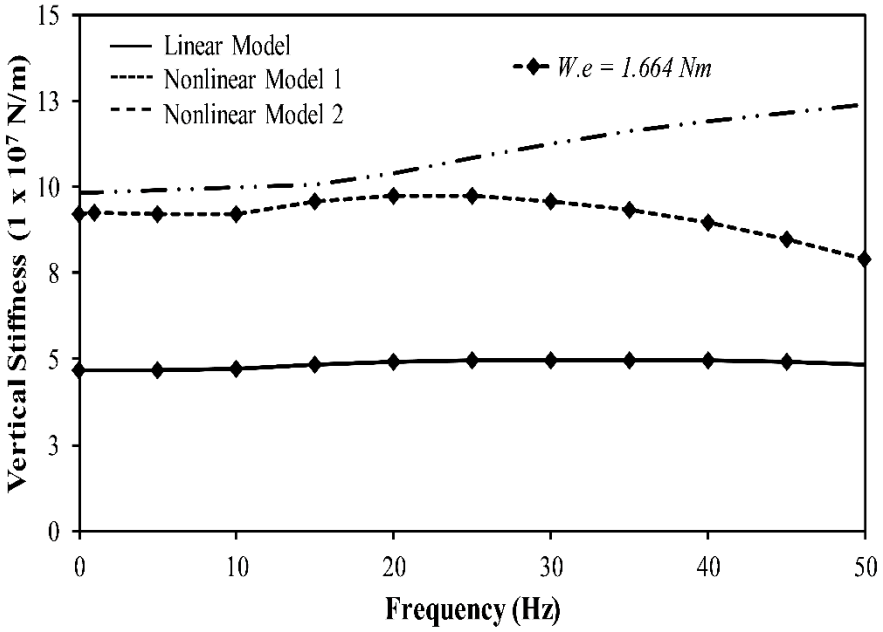

Figure 4a: Comparison of stiffness of soil-pile system obtained from Linear Model, Nonlinear Model 1 and Nonlinear Model 2b

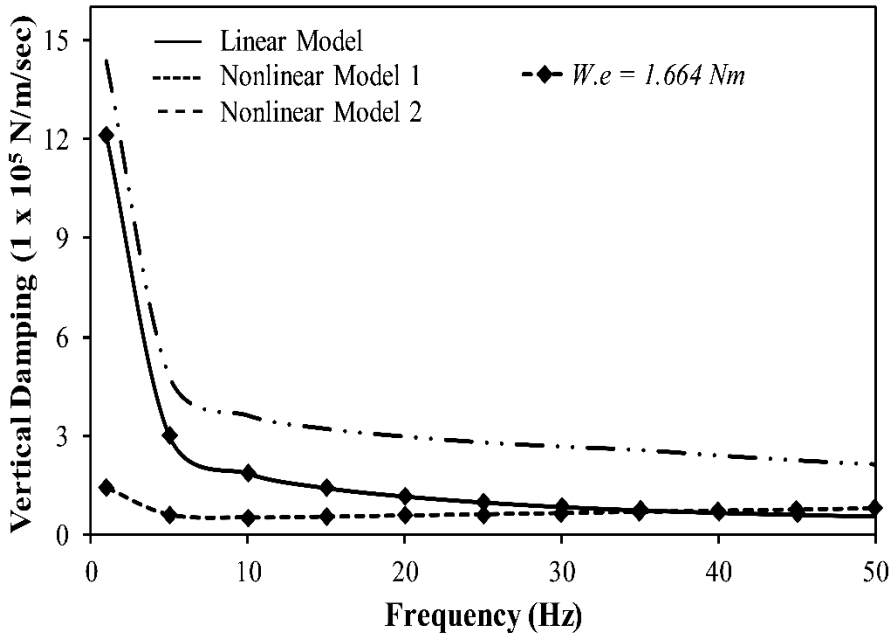

Figure 4b: Comparison of stiffness of soil-pile system obtained from Linear Model, Nonlinear Model 1 and Nonlinear Model 2b

decreased with the increase in the excitation force and the damping values tends to give a small change (overlapping) with the excitation force.

6. CONCLUSIONS

The main objective of the present study is to compare the different soil model i.e. Linear model; Nonlinear model 1 and Nonlinear model 2 to evaluate the frequency-amplitude response of the batter piles subjected to machine induced vertical vibrations. The study also includes the characterization of different soil model and variation of boundary zone parameters of the batter pile-soil system. A field vertical vibration test was also conducted on a on a single batter driven pile (L/d = 26) of inclination 10 degrees for different eccentric moments (0.449, 0.670, 1.664 and 1.830 Nm) with static load of 12 kN. On the basis of the dynamic test result, the effectiveness of different soil models is monitored. The major conclusions for the present study are as follows

- From both the dynamic test data and analysis results it is observed that the measured frequency-amplitude response curves for batter pile ($L/d = 26, \beta = 10^o$) shows marked nonlinearity which was manifested by the reduction in the resonant frequency and disproportional increment in resonant amplitudes with the increase in excitation intensity.
- Nonlinear Model 1 accurately predicts the response of the batter pile reasonably well as compared to Linear Model and Nonlinear Model 2 with dynamic test results.
- The stiffness and damping of the batter pile system are decreased for vertical mode of vibration with increase in excitation level. This reduction is primarily due to the development of weak boundary zone around the pile.
- The Nonlinear Model 1 is found capable of predicting the stiffness and damping value of single batter pile reasonably well for vertical mode of vibration with reasonable estimation of nonlinear parameters. On the other hand, the Linear Model and Nonlinear Model 2 was found to be unsatisfactory in this study.
- The nonlinear parameters like shear modulus reduction (G_m/G), damping factor (D_s), thickness ratio (t_m/R) and separation length plays a major role for actual nonlinear response of soil -pile system.

REFERENCES

1. Kobori T, Minai R, Baba K (1975) Dynamic interaction between an elastic cylinder and its surrounding visco-elastic halfspace. In: proceedings of the 25th japan national congress of applied mech, university of tokyo press, tokyo, japan, pp 215–226.
2. Nogami T, Novak M (1976) Soil–pile interaction in vertical vibration. Int J Earthq Eng Struct Dyn 5(3):277–293
3. Novak, m. 1974. Dynamic stiffness and damping of piles. Canadian geotechnical journal, 11(4): 574–598. Doi:10.1139/t74-059.
4. Tajimi H (1966) Earthquake or foundation structures. Report of the Faculty of Science and Engineering, Nihon University, Tokyo City, Japan, pp 1.1–3.5
5. Novak M, Aboul-Ella F (1978) Impedance functions of piles in layered media. J Eng Mech Div 104(3):643–661.

6. Novak M, Nagomi T, Aboul-Ella F (1978) Dynamic soil reaction for plain strain case. J Eng Mech Div ASCE 104(EM4):953–959
7. Novak M, Sheta M (1980) Approximate approach to contact problems of piles. In: O'Neill M (ed) Proceedings of the dynamic response of pile foundations: analytical aspects, New York, ASCE, pp 53–79
8. Veletsos AS, Dotson KW (1988) Vertical and torsional vibration of foundations in inhomogeneous media. J Geotech Geoenviron Eng ASCE 114(9):1002–1021.
9. Han YC, Sabin GCW (1995) Impedances for radially inhomogeneous viscoelastic soil media. J Eng Mech Div ASCE 121(9):939–947.
10. Han YC (1997) Dynamic vertical response of piles in nonlinear soil. J Geotech Geoenviron Eng ASCE 123(8):710–716.
11. Novak M, Grigg RF (1976) Dynamic experiments with small pile foundations. Can Geotech J 13(4):372–385
12. Novak, M., and El Sharnouby, B. (1984). "Evaluation of dynamic experiments on pile groups." Journal of geotechnical engineering, asce, 110 (6): 738-756.
13. Puri, V. K. And Prakash, S. (1992). "Observed and predicted response of piles under dynamic loads." In: piles under dynamic loads (gps 34), asce, 153-169.
14. Manna B, Baidya DK (2010) Dynamic nonlinear response of pile foundations under vertical vibration-theory versus experiment. Soil Dyn Earthq Eng 30:456–469
15. Elkasabgy, M., and El Naggar, M. H. (2013). "Dynamic response of vertically loaded helical and driven steel piles." Can. Geotech. J., 50: 521–535.
16. Biswas, S., Choudhary, S.S., Manna, B. (2013). Prediction of nonlinear characteristics of soil-pile system under vertical vibration. Geomechanics and engineering, an international journal. 5(3) - 2013,223 - 240,
17. Elkasabgy, M., and El Naggar, M. H. (2017). "Lateral vibration of helical and driven steel piles installed in clayey soil." Journal of geotechnical and geoenvironmental engineering, © asce, issn 1090-0241.
18. El Naggar, M.H., Novak, M., Sheta, M., El Hifnawi, L., and El Marsafawi, H. 2011. DYNA 6 –a computer program for calculation of foundation response to dynamic loads. Geotechnical Research Centre, The University of Western Ontario, London, Ont.
19. ENSOFT INC, (2004). DYNAN user's manual, Version 2.
20. Poulus H. G. and Madhav M. R. Analysis of the movement of battered piles. Proc. 1st australia-newzealand conf. Geomechanics, maelbourne, 1971, 1, 268-275.
21. Novak, M. 1980. Soil-pile interaction under dynamic loads. Institution of civil engineers, numerical methods in offshore piling, ice, london 1980, 59-68
22. Han Y, Novak M (1988) Dynamic behavior of single piles under strong harmonic excitation. Can geotech j 25:523–534
23. Vaziri H, Han Y (1992) Nonlinear vibration of pile groups under lateral loading. Can geotech j 29:702–710.

COMPDYN 2019
7th ECCOMAS Thematic Conference on
Computational Methods in Structural Dynamics and Earthquake Engineering
M. Papadrakakis, M. Fragiadakis (eds.)
Crete, Greece, 24–26 June 2019

DETERMINATION OF THE EFFECT OF VARIOUS MATERIALS PRESENT BELOW PILE TIP: NON-DESTRUCTIVE TESTING AND NUMERICAL STUDY

A. Yadav[1], K. Tandon[1], B. Manna[1], G. V. Ramana[1] and A. Ganguli[1]

[1] Indian Institute of Technology Delhi
Hauz Khas New Delhi - 110016
e-mail: anildv61@gmail.com, kavita.tandon2008@gmail.com, bmanna@civil.iitd.ac.in, gvramana@civil.iitd.ac.in, aganguli@civil.iitd.ac.in

Abstract

Non-destructive testing methods are an important aspect for the structural integrity and quality assurance of reinforced concrete pile foundations which are normally built on difficult soil conditions. Hence, the structural integrity of deep foundation requires definitive and economical test procedures that can be used shortly after construction to identify the anomalies, defects and the causes of imperfections in cast-in-situ concrete pile foundations.

In the present study, an attempt has been made to detect the effect of various materials present below the pile tip by non-destructive testing. To examine the various pile tip conditions related to the construction of RCC pile, two piles of diameter 150 mm and length 4 m are constructed with two different pile tip conditions: Case 1 – pile tip at natural soil and Case 2 - pile tip at stiff material of thickness 50 cm. The weathered quartzite rock is used at the pile bottom to obtain the required stiffness as of rock. The field tests are performed on two piles using Pile Integrity Tester (PIT) to determine time velocity response for both the pile tip conditions. In case of pile with stiff material at the pile tip it was observed that the resulting velocity of the reflective wave is negative. However, the resulting velocity of the reflective wave is found positive, as the stiffness of natural soil is less than concrete.

The experimental results obtained from the field tests are simulated and examined by axisymmetric Finite Element model using PLAXIS 2D (2015). The concrete pile is modelled as linear elastic whereas; soil is modelled as Mohr Coulomb model. The jointed rock model is used to simulate the behaviour of rock at the pile tip. The dynamic impact load is applied at the top of pile and the velocity amplitude graphs are plotted as a function of time. The results obtained from the numerical analysis are compared with the field tests. It is found that the field tests and numerical results are comparable and match with good agreement. From the present study it can be concluded that non-destructive testing like PIT is useful method to determine the stiffness of the various materials present below pile tip.

Keywords: Field Tests, Foundations, Non-destructive Testing, Pile Foundations.

1 INTRODUCTION

The quality control and quality assurance of deep foundations during the construction of cast in situ piles are an integral part of manufacturing process. As an essential requirement of engineering practice, the quality control of deep foundations is guaranteed by the acoustic methods to investigate the length and continuity of the deep foundations. Integrity testing is widely used to characterize the changes during the construction and installation of pre-cast and cast in situ piles. Hence, the structural integrity of deep foundation requires definitive and economical test procedures that can be used shortly after construction. The technological aspects of non-destructive testing (NDT) for dynamic pile integrity have seen substantial improvement in recent years. NDT of deep foundations is a complex method covering several different techniques to gain information about the integrity and quality of the deep foundation. Non-destructive testing of piles is used worldwide for various purposes e.g., quality control and quality assurance, verification of existing conditions, and quantification of dimensions. Various methods are available for checking the integrity of concrete piles after installation. Among the most widely used method, impulses or vibrations are applied to the pile and time velocity responses are measured. The commonly used testing methods such as, sonic methods, vibration methods, sonic logging techniques, etc., have been used in the last three decades in different parts of the world. The correct use of these techniques can greatly simplify and expedite investigation and be economical in addressing concerns or questions on pile conditions.

The concept of pile driving analyzer was used widely in the early 1990s. Goble and Likins [1], Teferra and Webster [2] and Likins et al. [3] used Pile Driving Analyzer for the evaluation of deep foundations workability. Hussein and Likins [4] assessed pile drivability quantitatively and evaluated the hammer-pile-soil system using Pile Driving Analyzer (PDA) based on pile force and velocity records under the impact force from a hammer. Sheahan and Hussein [5] dynamically tested 112 substructure units beneath a 5000 m long bridge. They performed dynamic pile tests to assess pile drivability and to verify design parameters for quality assurance of the structures. Morgano [6] determined the embedment depth of deep foundation using one dimensional wave propagation theory. Pile Integrity testing and Parallel Seismic testing methods were used to determine length of steel piles. Johnson and Rausche [7] used low strain integrity testing utilizing two acceleration signals. Rausche et al. [8] used non-destructive pulse echo method to determine the pile lengths under existing substructures and bridges. The method was successfully used for the evaluation of structural integrity of cast-in situ piles, drilled shafts, driven concrete and timber piles. Mullins and Winters [9] identified the presence of anomalies in both small scale and full-scale pile foundations using thermal integrity testing. Liang and Beim [10] studied numerically the effect of soil resistance distribution on the mobility and simulated the velocity and force curves for an impact force applied at the pile top surface for different soil resistance distributions. In the present study, an attempt has been made to examine the different material below the pile tip in the field using pile integrity tester. The experimental results obtained from the field tests were simulated and examined through an axisymmetric pile model fully embedded in a homogeneous soil using finite element software PLAXIS 2D [11]. The results obtained from experimental and analytical study are comparable and matches with good agreement.

2 EXPERIMENTAL STUDY

2.1 Methodology

Non-destructive testing methods used to analyze deep foundations and other structural members are either surface reflection or direct transmission methods. The most common and widely used surface reflection method include the impulse response test – pile integrity testing (PIT). The principle of integrity testing method is time-domain reflectometry of stress wave propagation through pile material acting as a one dimensional medium. In these tests, a hammer impact is used which generates compression waves at the surface of a concrete drilled shaft, pile or pier and reflected waves are received with a transducer (geophone or accelerometer) at the surface. The schematic diagram of PIT test set up is shown in Figure 1.

The generated wave travels down along the length of pile in axial direction. Downward traveling waves caused by the impulse and the reflected upward travelling waves are measured by an accelerometer held against the pile head. These reflections are stored in a small hand-held computer where they are integrated to yield a time versus velocity graph. The test equipment can amplify the signal exponentially with time to emphasis the signal reflected along the pile shaft and from the pile toe. Therefore, the effects of any signal attenuations are removed as it travels along the pile. The major components of the pile integrity testing used in the experiment are a hand-held hammer of diameter 38.1 mm, an accelerometer with high natural frequency (0.7 to 9000 Hz) and sensitivity (50 mV/g). A PIT-X tester with sampling speed of 64 kHz to record the results. The complete experimental setup with PIT equipment is shown in Figure 2.

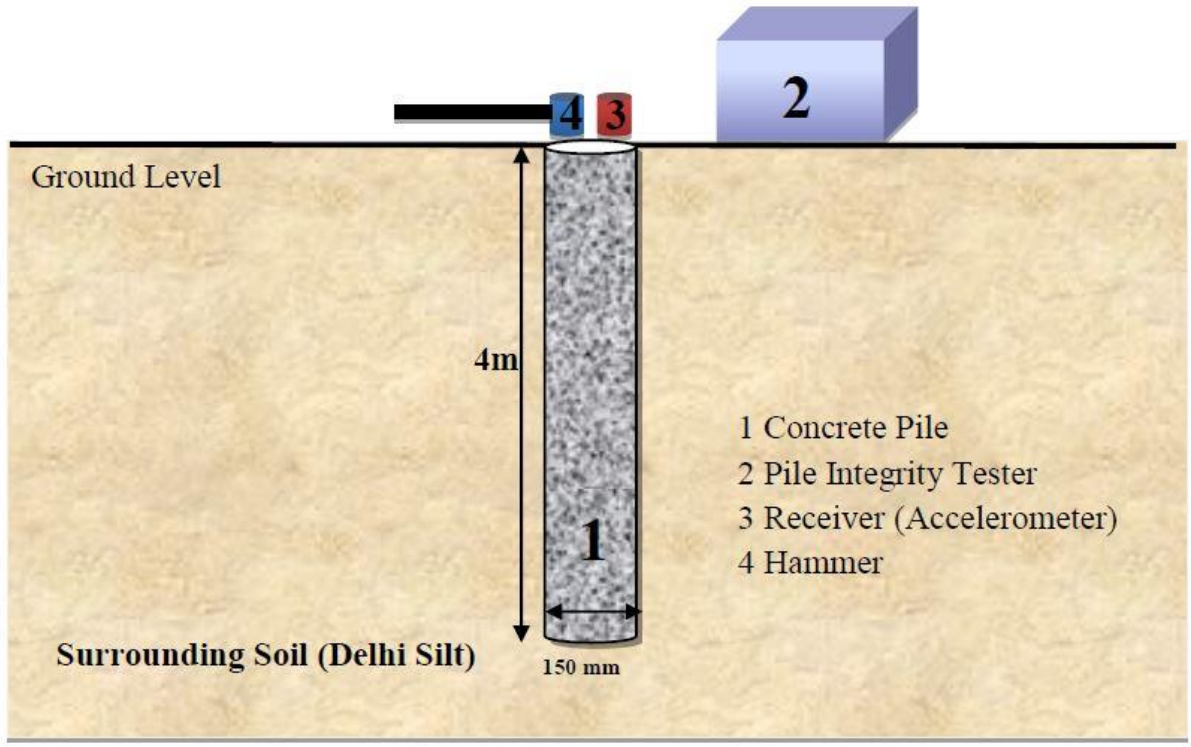

Figure 1 Schematic representation of Pile integrity test setup

Figure 2 Complete experimental setup with PIT equipment

2.2 Site Conditions

The tests are performed at the site located between Block II and III, at Indian Institute of Technology Delhi, New Delhi, India. The soil samples are collected and both laboratory and in situ tests are performed up to the depth of 5 m. It is found that the soil up to 5 m depth is predominantly sandy silt (silt = 58.8%, sand = 30.3%, clay = 10.9 %). The water table is not encountered up to the depth of exploration. The SPT test is also conducted in the field and corrected N value varies from 11 to 29.

2.3 Pile Construction

The piles are casted for two different pile tip conditions in the field. Two bore holes of diameter 150 mm and length 4 m are made with the help of hand auger. The boreholes are filled using M30 grade concrete with different arrangement at the pile tip and tested after 28 days of curing. Two different pile tip conditions are as follows:

a. Case 1 – Pile tip at natural soil
b. Case 2 – Pile tip at stiff material of thickness 50 cm. To obtain the required stiffness as of rock at the pile tip weathered Quartzite rock was put in the borehole.

3 NUMERICAL MODELLING

Numerical modeling for two different pile tip conditions is carried out using finite element software PLAXIS 2D. The pile is modelled using 15 node axisymmetric elements and the behaviour of pile is considered as linear elastic. The soil layers are modelled using Mohr-Coulomb model and behaviour of the soil is considered as drained. The soft toe below the pile tip is modelled using Mohr – Coulomb model but the behaviour is considered as drained. The quartzite rock used in the field is modelled using Jointed Rock Model. The rock properties for quartzite rock are taken from Rao K. S. et al. [12]. The properties of concrete, soil and rock considered in the analysis are tabulated in Table 1 and Table 2 respectively. The dynamic load is applied in the form of line load at the pile top surface. The absorbent boundaries are considered along the boundaries to avoid the spurious reflections. The mesh is generated with

very fine element distribution and the simulation is carried out for the actual field data. The velocity – time graphs obtained from PLAXIS 2D are compared with the PIT results obtained from the field tests.

Materials	Young's Modulus E (kN/m^2)	Poisson's Ratio, μ	Unit weight γ (kN/m$^{3)}$	Cohesion, c (kN/m^2)	Friction angle, ϕ (Degrees)
Pile	25.0×10^6	0.20	24.00	-	
Delhi silt	33.9×10^3	0.35	15.95	15	24

Table 1 Pile and Soil properties used in finite element modelling

Young's modulus for rock as a continuum, E_1 (GPa)	93.75
Poisson's ratio for rock as a continuum, μ_1	0.2
Young's modulus in Plane 1 (stratification) direction, E_2 (GPa)	63.75
Poisson's ratio in Plane 1 (stratification) direction, μ_2	0.18
Unit weight, γ (kN/m^3)	24.2
Cohesion, c (MPa)	0.372
Friction angle, ϕ (Degrees)	64.63

Table 2 Rock properties used in PLAXIS modeling

4 RESULTS AND DISCUSSIONS

4.1 Field Test Results

The typical time velocity graph of averaged signal response for pile tip at natural soil for Case 1 is shown in Figure 3 and for pile tip at stiff material of thickness 50 cm for Case 2 is shown in Figure 4. It can be seen from Figure 3 that the peak at toe is in the same direction as of impact peak due to the presence of natural soil. However, for Case 2 the peak at toe is observed in the opposite direction of impact peak as the material below the pile tip is stiffer than the pile material as observed from Figure 4.

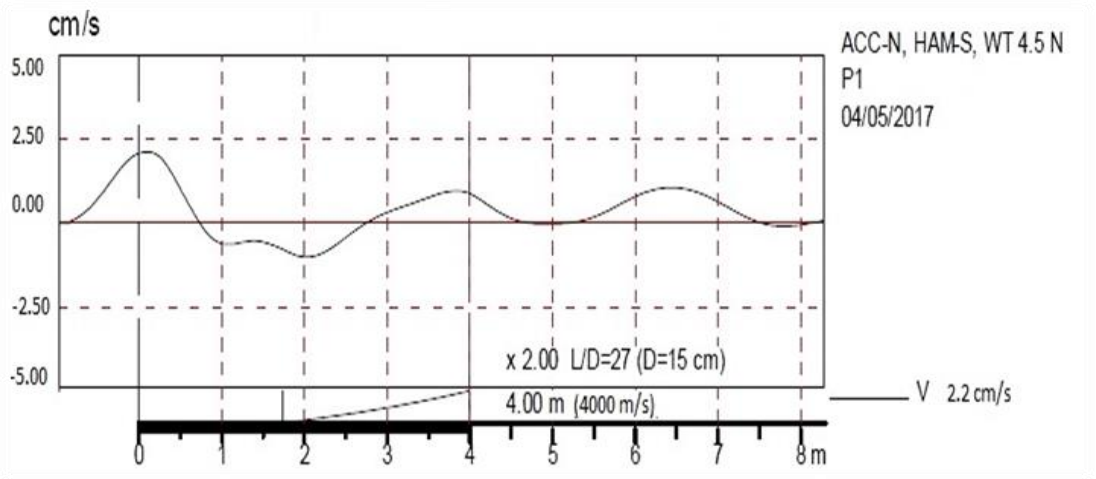

Figure 3 Signal response of Pile tip at natural soil (Case 1)

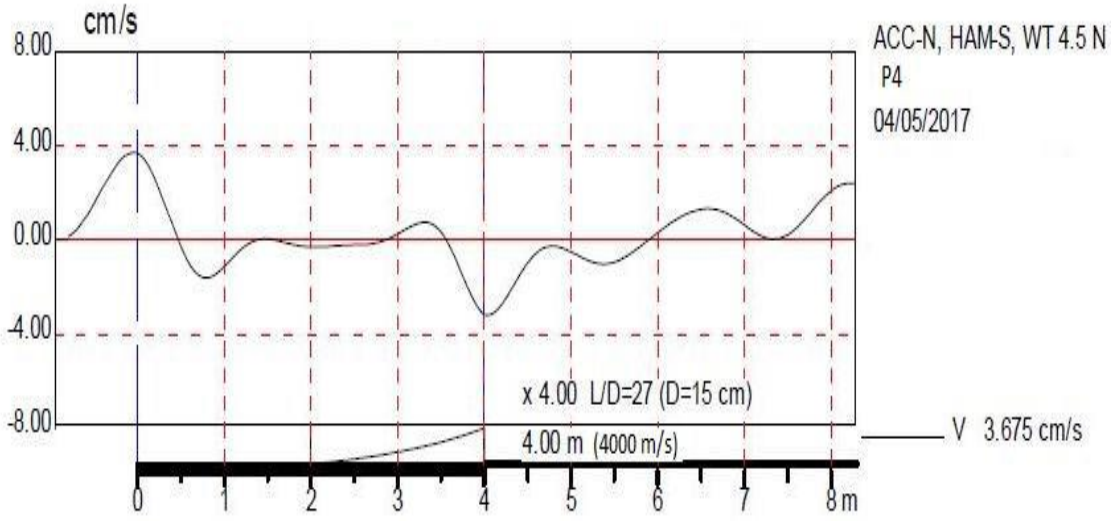

Figure 4 Signal response of Pile tip at stiff material of thickness 50 cm (Case 2)

4.2 Comparison of PIT and FE results

The field test results obtained from PIT are compared with finite element analysis results obtained using PLAXIS 2D. A typical comparison of time-velocity graph obtained from field test with FE analysis for Case 1 is shown in Figure 5. It can be seen from Figure 5 that time-velocity graphs obtained from the FE analysis matches with good agreement with the PIT results. It is also observed from Figure 5 that the toe reflection in case of PIT results is obtained prior to the PLAXIS result. This may be due to magnitude of the impact force and higher compression wave velocity in cast-in-situ pile than the velocity of the longitudinal wave considered in FE analysis.

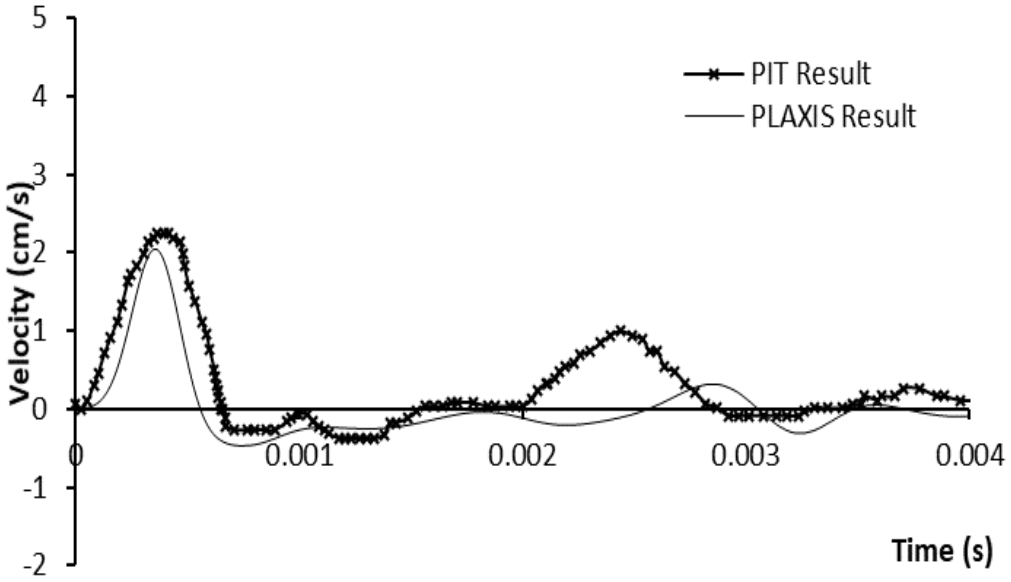

Figure 5 Comparison of PLAXIS results with PIT results for pile tip at natural soil

5 CONCLUSIONS

In the present study both field testing and finite element analysis were carried out to determine the various pile tip conditions. Based on the present study the following conclusions can be drawn:

- For Case 1 that the peak at toe is in the same direction as of the peak at the pile top surface whereas in Case 2 the peak at toe is in the opposite direction as the material below the pile tip is stiffer than the pile material.
- The time velocity graphs obtained from the FE analysis matches with good agreement with the PIT results whereas some differences occur due to the variation in the magnitude of impact force and the velocity of longitudinal wave in the pile.

6 REFERENCES

[1] G. G. Goble, G. E. Likins, On the Application of PDA Dynamic Pile Testing. *Proceedings of the Fifth International Conference on the Application of Stress-wave Theory to Pile*, Orlando FL, 263-273, 1996.

[2] W. Teferra, S. Webster, Pile Damage Assessments Using the Pile Driving Analyzer. *Proceedings of the Fifth International Conference on the Application of Stress-wave Theory to Piles*, Orlando FL, 980-990, 1996.

[3] G. E. Likins, F. Rausche, G. Thendean, M. Svinkin, CAPWAP Correlation Studies. *Proceedings of the Fifth International Conference on the Application of Stress-wave Theory to Piles*, Orlando FL, 447-464, 1996.

[4] M. H. Hussein, G. E. Likins, Deep Foundations Quality Control and Assurance Testing Methods. *Florida Engineering Society Journal*, 10-13, 2005.

[5] J. M. Sheahan, M. H. Hussein, Deep Foundations for a 5000 Meter Long Bridge. *Tenth Pan-American Conference on Soil Mechanics and Foundation Engineering* Guadalajara Mexico, 23-37, 1995.

[6] C. M. Morgano, Determining Embedment Depths of Deep Foundations Using Non-Destructive Methods. *Proceedings of the Fifth International Conference on the Application of Stress-wave Theory to Piles* Orlando FL, 734-747, 1996.

[7] M. Johnson, F. Rausche, Low Strain Testing of Piles Utilizing Two Acceleration Signals. *Proceedings of the Fifth International Conference on the Application of Stress-wave Theory to Piles*, Orlando FL, 859-869, 1996.

[8] F. Rausche, M. H. Hussein, M. Bixler, Non-Destructive Testing to Determine Unknown Pile Lengths under Existing Bridges. PDA, CAPWAP, CHA and PIT Workshops *Pile Dynamics Inc* Cleveland OH, 2002.

[9] G. Mullins, D. Winters, Infrared Thermal Integrity Testing Quality Assurance Test Method To Detect Drilled Shaft Defects WSDOT Project WA-RD, 770.1, 2011.

[10] L. Liang, J. W. Beim, Effect of Soil Resistance on the Low Strain Mobility Response of Piles Using Impulse Transient Response Method. *Proceedings of the Eighth International Conference on the Application of Stress-Wave Theory to Piles*, Lisbon Portugal,435-441, 2008.

[11] PLAXIS 2D 2015 PLAXIS user manual, Delft University of Technology PLAXIS The Netherlands.

[12] A. S. Gupta, K. S. Rao, Index properties of weathered rocs: inter-relationships and applicability. *Bulletin of Engineering Geology and the Environment.* **57**, 161-172, 1998.

COMPDYN 2019
7th ECCOMAS Thematic Conference on
Computational Methods in Structural Dynamics and Earthquake Engineering
M. Papadrakakis, M. Fragiadakis (eds.)
Crete, Greece, 24–26 June 2019

AN ENSEMBLE KALMAN FILTER APPROACH FOR ESTIMATING SITE SPECIFIC EARTHQUAKE RESPONSE

Wael G. Slika[1], **Farah I. Jaafar**[2]

[1] Beirut Arab University
Debbieh-Lebanon
w.slika@bau.edu.lb

[2]American University of Beirut
Beirut-Lebanon
fij01@mail.aub.edu

Abstract

Accurate local site response analysis allows for assessing the response of sites nearby an active seismic zone, and consequently modeling the expected earthquake behavior at the surface level. However, the modeling of this non-linear behavior is always accompanied with high uncertainty and variability that could lead to either an unsafe or a very conservative design. One way to overcome these challenges is by relying on site specific instrumentation techniques. In this study a sequential data assimilation technique is employed for real time calibration of the adopted soil model by relying on a measurement data array from different soil layers in the site of interest. The dynamic model parameters are updated in an optimal probabilistic framework using Ensemble Kalman Filter and therefore minimizing the mismatch between the measured and the predicted response of the site of interest. Due to complexities associated with inverting and updating a non-linear soil model, limited number of studies used monitoring techniques to calibrate a non-linear hysteretic soil model while incorporating different sources of uncertainties. Therefore, in this study monitored data are coupled with a non-linear dynamical model in a probabilistic setting to accurately simulate the vertical wave propagation through the soil layers of a given site. This study uses simulated vertical arrays measurements to assess the validity of the framework and to determine several practical concerns such as convergence and robustness of the presented non-linear scheme.

Keywords: Earthquake response, Ensemble Kalman Filter, Uncertainty Quantification, Geotechnical Earthquake.

1 INTRODUCTION

It's widely known among geotechnical engineers and researchers that the effect of strong motion earthquakes on man-made structures is largely dependent on the nature of the subsoil through which the shock waves pass [1]. Therefore, any analysis of the superstructures will require a prior knowledge on the soil properties. In getting the latter, a seismic site response analysis should be conducted through one of the following methods: frequency and time domain, equivalent linear and nonlinear analyses [2]. Depending on the numerical approach being used and the modeling of the nonlinear soil, the output of these methods may greatly vary. The nonlinear and time varying behavior of soil layers are detected using time domain methods, especially when subjected to strong ground motions [3]. Another simplified approach for site response analyses is the equivalent linear method in frequency domain which is known to be efficient and reduces computational time requirements of the site response analysis.

Although extensive efforts and advanced computational algorithms has been utilized in developing these soil response models, in practice the output of these algorithm is not always satisfactory. The main aim of geotechnical engineers is to investigate all the conditions under which predictable soil effects will be expected and to quantify uncertainties in the spatial and temporal characteristics of the predictive theoretical models [4]. However, the main hindering factor that faces practitioners and researcher is the ability to identify accurate soil parameters especially due to lack of extensive soil related data and expensive accurate experimental testing. Although some field methods are being used for evaluation of model parameters and evolution of prognosticative tools and design procedures, a high level of uncertainty and high expenses are involved [5]. As for the laboratory tests, many restrictions are applied due to the irritated samples and the complications in reproducing the site stratification and boundary conditions (Kramer 1996). Therefore, accurate implementation of soil response models is always limited to accurate identification of real site conditions. To overcome this issue, and in the light of recent advancements of geophysical instrumentations such as downhole, seismic cross hole, seismic CPT, steady state vibration and seismic reflection and refraction; application of system identification (SI) methods to dynamic soil behavior has been popular recently.

Constitutive model SI methods are divided into self-Learning simulations, parametric techniques and nonparametric techniques. The aim of SI methods is studying the behavior of existing systems, by recording input-output vibrations of soil in discrete time signals and utilizing inverse programming tools to identify or calibrate adopted system parameters. A broad range of simplified and advanced soil constitutive models have been employed in non-linear site response analysis. The aim of the prior SI techniques is to copy the observed earthquake excitation without prior knowledge on the soil parameters [5].

Parametric system identification methods enable the estimation of constitutive model parameters by solving the equation of motion [5]. Knowing that these parameters represent the characteristics of a given soil column, the prediction of its behavior under different loading conditions could be easily achieved [5]. However, the performance of the proposed framework is altered by the size of the state vector, which include the soil parameters. Therefore, a different algorithm should be adopted to account for multiple parameters in the constitutive model.

With attention to the numerous applications of system identification, some approaches that depend on time series are used to estimate the nonlinear behavior of the soil and to develop

the extended Kalman Filter algorithm and autoregressive-moving average models [7]. By coupling both, the proposed scheme and the recursive methods, an accurate estimation of the discrepancy in the approximated properties could be reached [7]. Irikura and Pavlenko suggested further idealization models to determine the stress-strain behavior of a nonlinear soil column [8,9]. Despite the simplicity of the aforementioned approach, the estimated characterizations of the soil from this linearization analysis can render significant errors due to the linearization of the highly nonlinear soil response analysis, especially when coupled with high amplitude earthquake records. Hence the model should be subjected to further calibration in order to be used in the required constitutive model [10]. Not to mention, a two dimensional site response analysis and soil-structure interaction require formulation of constitutive models and hysteretic rules for the soil profile [10].

Assimaki et al. proposed a waveform inversion algorithm, that depends on the number of parameters used, to estimate insitu soil behavior [10]. This dependency weakens the proposed algorithm, hence, a different approach should be conducted to estimate multiple parameters associated with a constitutive model. Tsai and Hashash (2007) extended the neural network based constitutive model developed by Ghaboussi [11] to include non-linear modeling of soil behavior from downhole arrays. Although this new approach was a huge jump from the known system identification methods, it was accompanied by a high level of uncertainties; mainly in the characterization of the dependency of the soil parameters. Hence, difficulties in convergence aroused, in addition to stability problems in the frame work.

To that end, this study develops a probabilistic framework for estimating dynamic soil properties using the Ensemble Kalman Filter (EnKF). Since EnKF is a non-intrusive filter, it propagates and updates the error statistics of the state vector efficiently and accurately as it does not require a linear approximation of the adopted model. The adopted data filtering technique can be easily coupled with available algorithms that simulate nonlinear soil behavior. In the study, the response of the soil is identified through the open source package, Opensees. The coupling of the non-intrusive filter, EnKF, with Opensees adds to the robustness of the framework and facilitates the application of soil identification techniques for practitioners and geotechnical engineers since the framework relies on open source and less-complicated tools. In this study a simulated vertical arrays measurements are employed to calibrate the state vector in a statistical setting. Several simulations are conducted with a main aim of investigating multiple practical concerns, such as convergence to true state and robustness of nonlinear soil identification.

2 OPENSEES

The Open System for Earthquake Engineering Simulation (OpenSees) is an open-source, object-oriented finite element software framework. The potentialities of OpenSees encompass modeling, analysis and structural reliability. Unique among software for earthquake engineering, OpenSees allows integration of models of structures and soils to investigate challenging problems in soil-structure-foundation interaction [14]. In this study Opensees is employed in the EnKF framework to integrate the dynamic response of soil layers forward in time. Details of the adopted soil modeling are presented in the next section.

2.1 Modeling features

A two-dimensional nonlinear model of the soil column was developed using OpenSees. The soil layers are modeled as four nodes plane-strain isoperimetric quadrilateral elements.

Each element node has 2 degrees of freedom. The soil material is behavior is modeled using the built-in material the "PressureDependendMultiYield" which is an elasto-plastic material. During static loading (gravity), the material behavior is linear elastic. Once dynamic loading phase is initiated, the stress-strain response is elastic-plastic. Assuming fully undrained conditions, a built-in "FluidSolidPorousMaterial" is defined to simulate the response of saturated porous media. At each layer, the nodes and coordinates are determined, and the dynamic soil properties; elastic modulus (E), bulk modulus (B), damping ratio (D), mass density (ρ), friction angle (Fang), phase angle (Pang) and Poisson's ratio (ν) are defined. The soil mass density (rho) is often estimated by a nearby subsurface sampling or using correlation methods. In this model it's important to realize that at low strain levels, the elastic theory is adopted, hence the response is linear. While at intermediate and high levels of strains (~10-2 to 5 percent), the response becomes non-linear and will experience plastic deformation continuously until failure.

3 SEQUENTIAL DATA ASSIMILATION

Sequential data assimilation techniques stem from the need to improve the model output. These techniques are based on "assimilating" observations into the model, whenever they are available; in order to correct the model, reduce parameter uncertainty and increase prediction creditability.

Among the known sequential data assimilation scheme, the Kalman filter is the best. It was developed by Kalman (1960), to solve linear problems by minimizing the mean square error between the guessed output and measurements whenever they are available. For nonlinear analysis, the extended Kalman Filter (EKF) is applied, which works by simply linearizing the predictions and measurements about their mean. The simplicity of the approach leads to an unbounded error variance where higher order moments are discarded.

To overcome this drawback, Evensen(1994b) came up with the Ensemble Kalman Filter. It states that if the dynamical model can be written in a stochastic differential equation, one can derive the Fokker-Plank equation for the time evolution of the probability density function, which contains all the information about the predicted error statistics using Monte-Carlo. Integrating an ensemble of state vector and forwarding it in time, will make the calculation of the mean and error covariance applicable. This new approach was well implemented by Slika and Nasr [15,16] in structural health monitoring applications.

3.1 Ensemble Kalman Filter

The EnKF proposed by Evensen (1994b) consists of 3 stages: the representation of error statistics using an ensemble of state vector, the alternative model for error statistics prediction, and a consistent analysis scheme. Different than the other Kalman filters, the EnKF executes multiple simulation independently, incorporates the new measurements and updates the multiple models simultaneously. After each update, the EnKF describes model parameters through mean and variance. For each time recursive process, the EnKF consists of a forecasting step based on the current state variables, and an assimilation step to update the state variables.

In this paper, the state vector (U) incorporates dynamic variables and soil parameters:

$$U=[V\ P]^T \tag{1}$$

where V consists of the displacement, velocity and acceleration at the top of each soil layer.

P is the model parameters that will be updated, at each available measurement, in the forward model. The soil density, elastic modulus friction angle and phase angle are to be updated at each iteration. A sensitivity analysis was performed to identify the correlation between the soil parameters and to determine the sensitivity of the model to a small change in those parameters.

The initial ensemble is chosen in a way that represent the statistical distribution of the initial guess of the state vector. U, the matrix holding the ensembles such that $U_i \in R^n$ as shown in (2). Where N is the number of ensemble members, and n is the size of the model state vector.

$$U = (U_1, U_2, \dots, U_N) \in R^{n \times N} \tag{2}$$

The ensemble mean is given by

$$\overline{U} = U1_N \tag{3}$$

Where $1_N \in R^{N \times N}$ is a matrix where each element is equal to equal to $1/N$.

The ensemble perturbation matrix could be defined as

$$U' = U - \overline{U} \tag{4}$$

The model error covariance matrix can be computed as follow

$$P_e = \frac{U'.(U')^T}{N-1} \tag{5}$$

As mentioned previously, the EnKF consists of a forecast step (U^f), calculated using the forward model in order to propagate the model state vector from time step (t-1) to time step (t), as shown below:

$$U^f_{t,i} = f\left(U^a_{t-1,i}\right) \qquad i = 1, \dots, N \tag{6}$$

Note that in this forward step, only dynamic parameters are updated to minimize the discrepancy between the measurements and the corresponding predictions.

Using observed measurements d, that are measured response from data array at the top of each of layer, we can define an N vectors of perturbed observations as

$$d_j = d + \epsilon_j, \qquad j = 1, \dots, N \tag{7}$$

Which can be stored in the columns of the following matrix

$$D = (d_1, d_2, \dots, d_N) \in R^{m \times N} \tag{8}$$

The ensemble perturbations are assumed to be unbiased and Gaussian, with a mean equal to zero, and can be stored in matrix such as

$$E=(\gamma_1,\gamma_{2,\ldots..},\gamma_N) \in R^{m\times N} \quad (9)$$

From which we can construct the ensemble representation of the measurement error covariance matrix

$$R_e = \frac{E.E^T}{N-1} \quad (10)$$

If the measurement errors are uncorrelated, R_e will be a diagonal matrix.

The update state is computed as follow

$$U^a_{t,i} = U^f_{t,i} + K_t(d_{t,i} - HU^f_{t,i}) \quad (11)$$

Where H is a matrix operator, depending on the number of observations, and whose elements are only ones or zeros.

$$H = [\mathbf{0} \mid \mathbf{I}] \quad (12)$$

Where I is an identity matrix.

The Kalman gain is given by

$$K_t = P_eH^T(HP_eH^T + R_e)^{-1} \quad (13)$$

When the ensemble size (N) is increased by adding random samples, Ktcwill converge toward the exact solution of eq. (11).

Therefore, at the end of time ti, the probability density function (PDF) of the state vector is known. At the end of time of ti+1, new measurements are available and the PDF up to ti+1 is regarded as the prior PDF. By using the assimilation step, the EnKF members are conditioned with these new measurements and the PDF turns into the posterior PDF. From this point of view, the solution provided by the EnKF is based on maximizing the posterior PDF of the state vector within the context of Bayesian inversion. It is equivalent to minimizing the variances of the posterior covariance matrix in probabilistic settings.

4 NUMERICAL APPLICATION AND ANALYSIS

The simulated behavior of the soil column is based on the discussed non-linear hysteretic model in opensees in the previous section. A distribution of the material parameters are assumed for each soil layer, based on conventional soil material as presented in table 1, and will be considered as the reference true parameters. The modeled deposit is subjected to the known Elcentro earthquake record at to the bottom of the soil column. The output of the computer simulation is the mechanical response at the top of each soil layer which constitutes of acceleration, velocity and displacement. A 5% perturbation error is added to the simulated output and will be assumed herein as the measured response from the accelerometers. The measured acceleration response at the top of each layer is presented in figure 1.

Layer	Soil Type	Modulus of Elasticity (kPa)	Density ton/m^3	Poisson ratio	Friction angle (degree)	Phase angle (degree)	Depth (m)
Layer 1 (bottom layer)	Dense Sand	E1=135000	2.1	0.35	40	16	4
Layer 2 (middle layer)	Medium Sand	E2=100000	2	0.32	37	20	3
Layer 3 (top layer)	Loose Sand	E3=750000	1.8	0.27	33	23	2

Table 1: True state parameters used for simulation of measured response

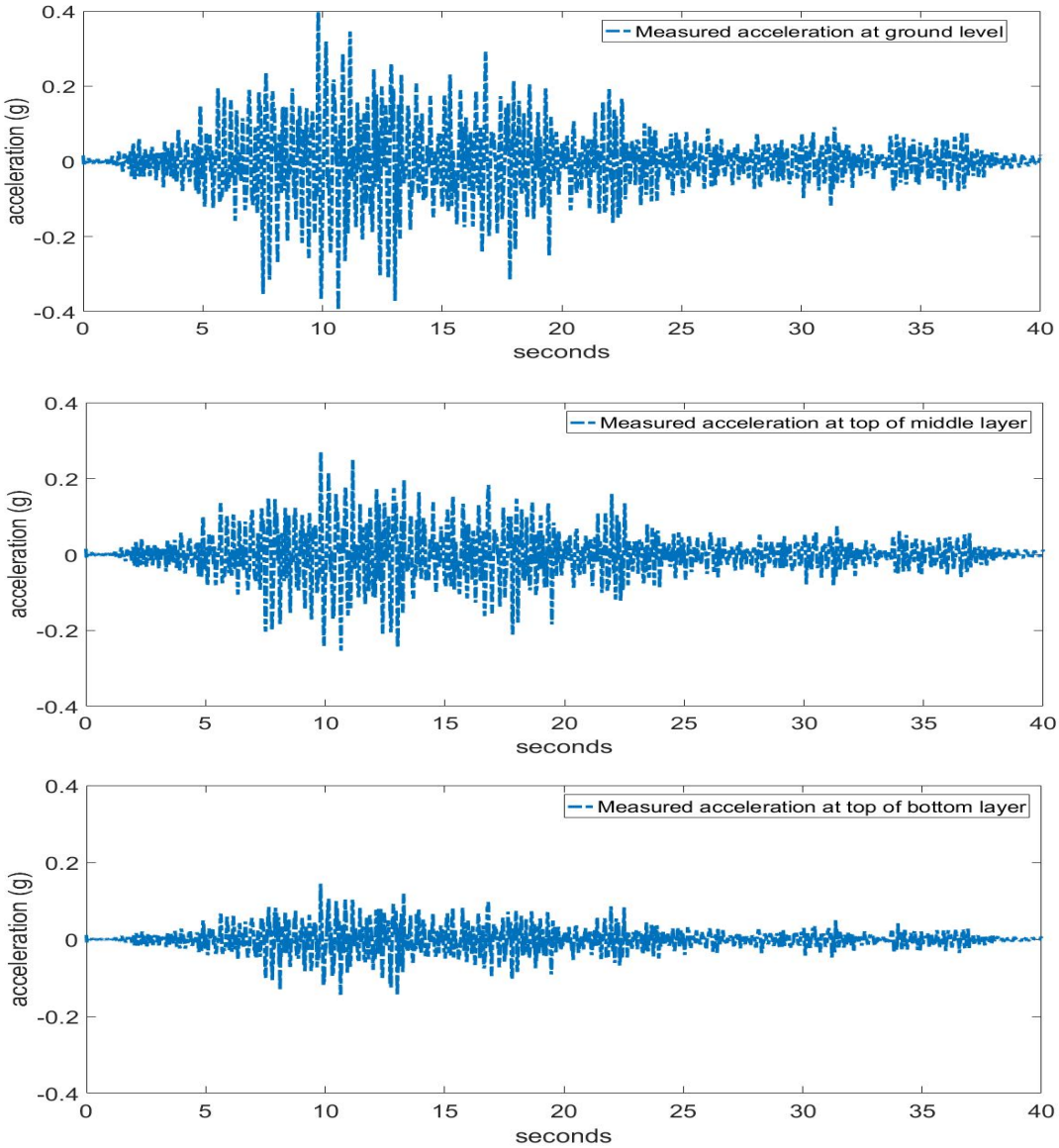

Figure 1: Measured acceleration response at the top of each layer

The main aim of the presented numerical application is to illustrate the accuracy of the suggested framework and perform sensitivity and convergence analysis. The accuracy of the framework is investigated by identifying the soil material properties starting from a probabilistic initial estimates of the soil parameters based on the "inaccurate initial knowledge". To assess the robustness and applicability of the framework different sensitivity analysis is conducted by varying several contributing factors such as, effect of initial guesses, update frequency and stability of solution as a function number of identified parameters.

4.1 Updated variable parameters

In general, a main problem in system identification is to deal with the large number of potentially necessary parameters which can lead to inefficient filtering and divergence from the optimal solution.

In nonlinear soil identification several parameters are necessary to parametrise the soil layers. However due to noisy and limited data over fitting is a common concern that requires adequate attention. A common approach to avoid divergence and handle inefficient filtering is to make the number of used parameters considerably less than the number of offered parameters. In this study, convergence analysis to optimal solution is investigated as a function of identified parameters. Four parameters are considered: Modulus of Elasticity E, soil density ρ, friction angle Fang, and phase angle Pang for each layer. In each simulation the state vector is assemble based on the assumed unknown/calibrated parameter. Summary of convergence analysis for the identified parameters is presented in table 2.

Number of Identified Parameters	Identified Parameters	Convergence of Solution
Four	E, ρ, Fang, Pang	Diverged from true state
Three	E, ρ, Fang	Diverged from true state
Three	E, ρ, Pang	Diverged from true state
Three	E, Pang, Fang	Diverged from true state
Two	E, ρ	Converged to true state
Two	E, Fang	Converged to true state
Two	ρ, Fang	Converged to true state

Table 2: Convergence of EnKF with number of identified parameters

As evident from the table above, in this nonlinear identification exercise with measurements only at the top of each layer, only two-parameters-identification guarantee a stable solution that can convergence to true state and avoids over fitting. Although capturing nonlinear response using two parameters can be a challenging task, in practice, several soil parameters are correlated and can be expressed as function of different soil types. Therefore, in practice, the number of parameters per soil layer is recommended to be limited to two guarantees efficient filtering from stability analysis point of view. In the remaining sections two parameters will be used for soil identification of each layer that are, E and ρ.

4.2 Stability of solution versus number of updates

To study the effect of the update on the accuracy of the EnKF framework, sensitivity analysis is performed to investigate the effect of the number of updates on the stability of the solution or its convergence to true state. All sources of uncertainties are incorporated in this exercise as presented in table 3.

EnKF Uncertainties	Mean	Standard deviation	Distribution
Initial estimate of E1	80,000 kPa	12% of mean value	lognormal
Initial estimate of E2	78,000 kPa	12% of mean value	lognormal
Initial estimate of E3	71,600 kPa	12% of mean value	lognormal
Initial estimate of ρ1	2.0 ton/m^3	8% of mean value	lognormal
Initial estimate of ρ2	1.8ton/m^3	8% of mean value	lognormal
Initial estimate of ρ3	1.8 ton/m^3	8% of mean value	lognormal
Model Uncertainty	0	7% of predicted mean	normal
Parametric Uncertainty	0	2% of predicted mean	normal
Measurement Error	0	3.5% of measured response	normal

Table 3 Quantified uncertainty in EnKF framework

Table 4 presents the recorded results for convergence of the calibrated parameters, E and ρ, to true state for each EnKF simulation. As evident from this table, the number of update is essential to capture the nonlinear characteristics of the soil response and guarantee convergence to true state. At higher update rate (more than 0.15 sec) the convergence to true state is not guaranteed, however at a lower update frequency, both identified parameters converged to the true state in less than 15sec. Therefore, small incremental updates are essential to guarantees convergence to the optimal solution in the neighborhood of the previous updated state, however when using less frequent updates. Divergence from true state can be attributed to the nature of the no-linear oscillating hysteretic problem that possess multiple potential local optimum solutions, therefore sequential updates shall be close enough to guide the state vector to optimum posterior solution or the true state.

Update frequency (sec)	Time needed to converge to true state
0.02	Converged after 6.5 sec
0.05	Converged after 9 sec
0.1	Converged after 15 sec
0.15	Diverged
0.2	Diverged
0.3	Diverged
0.5	Diverged

Table 4 Convergence of EnKF framework versus update frequency

To illustrate the convergence of the state vector, the identified parameters modus of elasticity E, and density ρ, are plotted versus true state values in figures 2 and 3, respectively, for an EnKF framework with 0.05 sec update frequency. These graphs confirm the convergence of all identified parameters to the true state when incorporating a frequent update strategy.

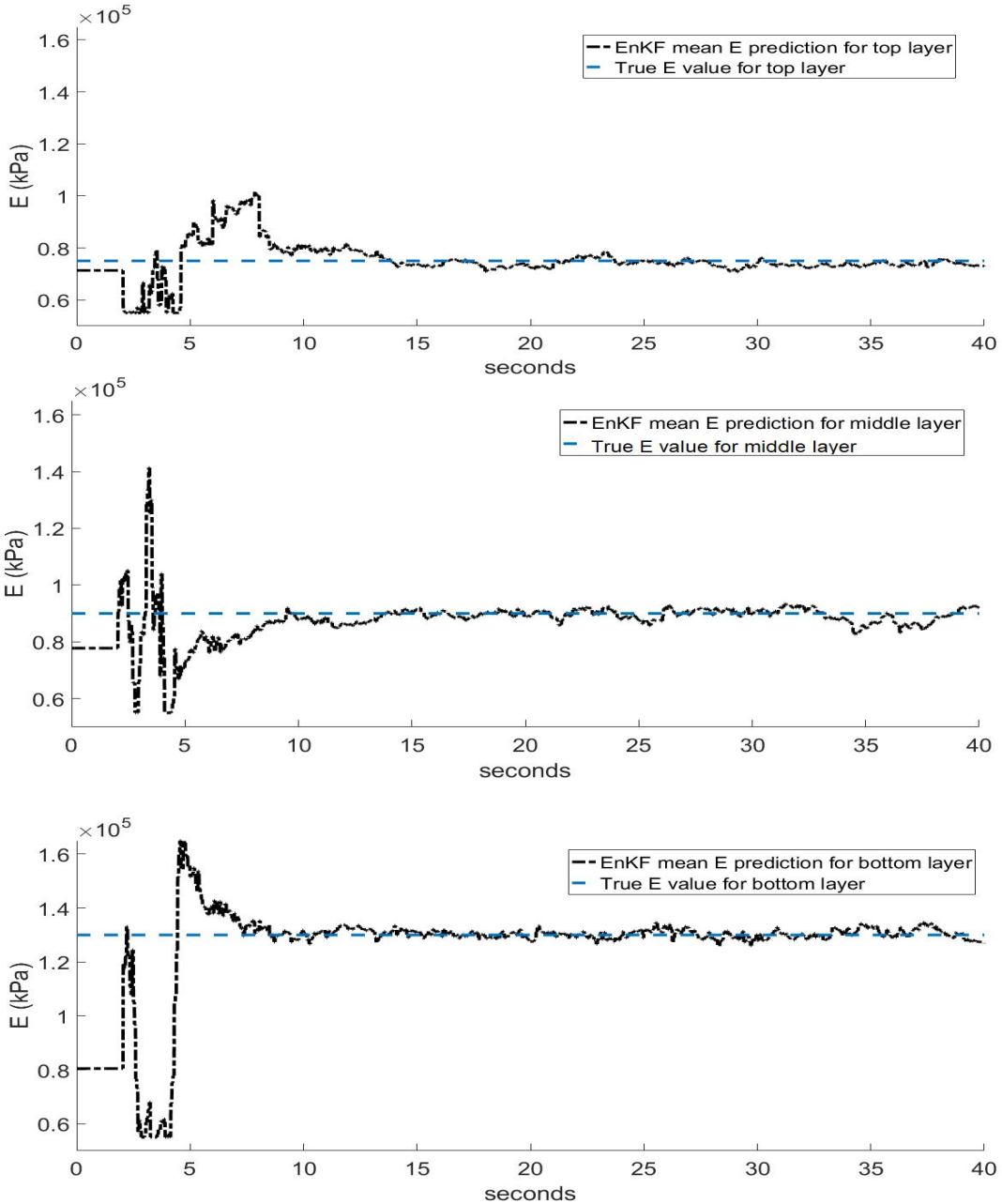

Figure 2: Identified mean modulus of elasticity for each soil layer

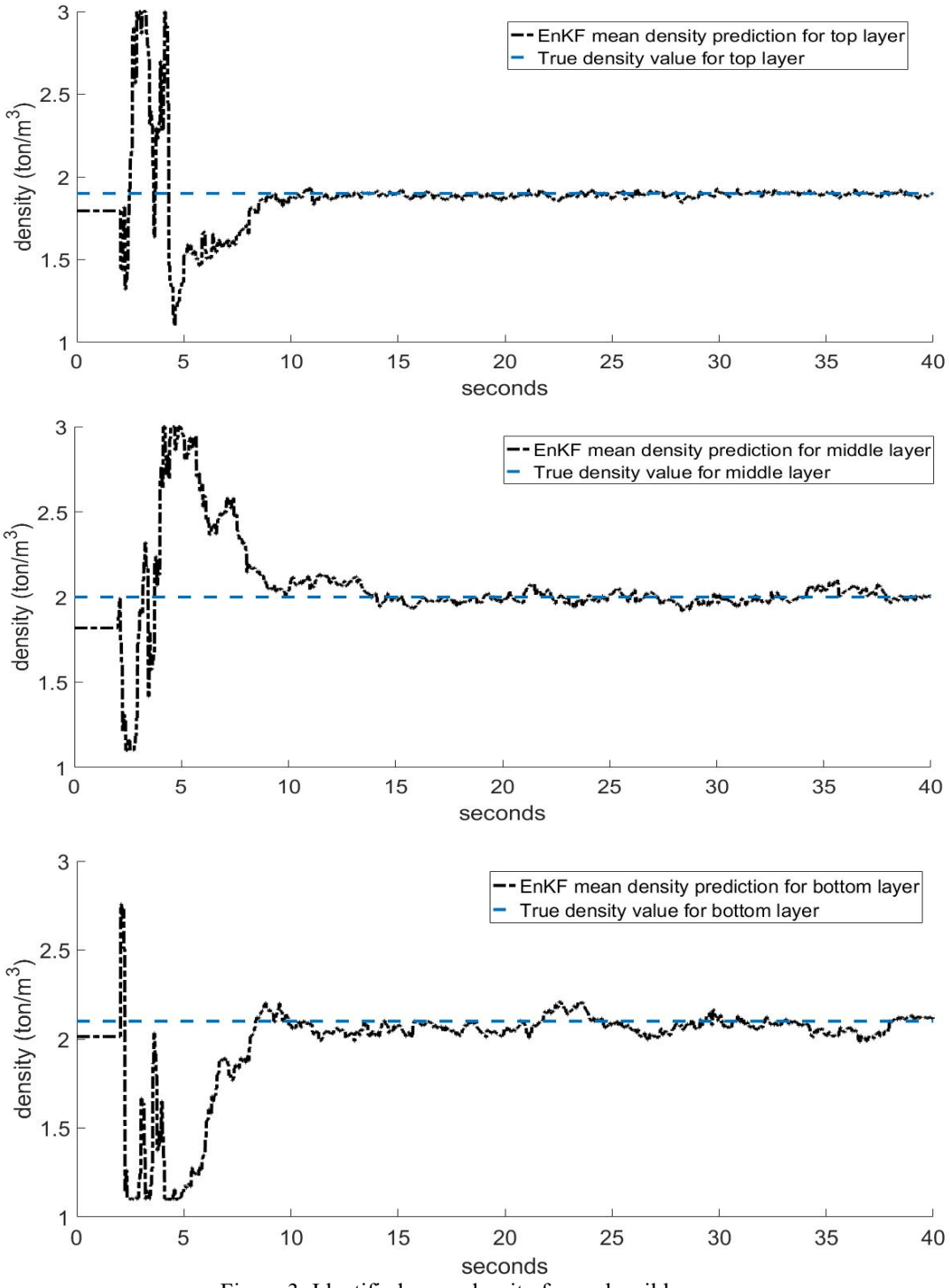

Figure 3: Identified mean density for each soil layer

4.3 Initial guess

To assess the robustness and capabilities of the presented framework to converge to the true state despite initial errors, random initial distribution for modulus of elasticity of soil and soil densities for each layers were integrated in the framework and convergence to true state were recorded in table 5. In this exercise, the update frequency is set to 0.05 sec, and the statistical uncertainties in the EnKF ate the same as assumed in table 2 except for initial mean estimate.

Mean Initial Guess set	Mean Modulus of Elasticity (kPa)	Mean Density ton/m^3	Time needed to converge
IG1	E1=110,000 E2=90,000 E3=85,000	ρ1=2.2 ρ2=2.1 ρ3=1.9	8 sec
IG2	E1=95,000 E2=95,000 E3=70,000	ρ1=2.3 ρ2=2.0 ρ3=1.7	10sec
IG3	E1=160,000 E2=120,000 E3=65,000	ρ1=2.25 ρ2=1.9 ρ3=1.65	12 sec

Table 5: Convergence of the EnKF starting from different initial guesses

As evident from table above, the presented scheme is robust and guarantees convergence within only 12 seconds even if the initial guess is far from true state by more than 30%. Therefore, the presented scheme is capable to converge to true state in some high uncertainty settings even when the soil column is subjected to a short earthquake records.

5 CONCLUSION AND REMARKS

This study presents the coupling of the widely the EnKF, with an open source soil response software package, the Opensees. The power of the suggested framework lies in its ability to identify nonlinear behavior in statistical settings based on an easy-to-implement and readily-available-tools for practitioners. Convergence analyses was conducted to investigate several concerns in nonlinear identification and to assess the robustness of the framework. Based on the presented study, several remarks were noted, (1) nonlinear identification should be mainly based on two-variable identification, (2) the frequency of update is essential for the success of a sequential nonlinear identification technique, (3) statistical nonlinear identification is successful with wide range of initial guesses even when coupled with short earthquake excitations.

REFERENCES

[1] Nzsee.org.nz. (2019). *Effect of soil properties on earthquake response*. Available at: http://www.nzsee.org.nz/db/Bulletin/Archive/04(1)0073.

[2] Hashash, Youssef M. A., and Park, Duhee. (2001). *Non-linear one-dimensional seismic ground motion propagation in the Mississippi embayment.* Engineering Geology, 62(1-3), 185-206.

[3] A. Mikami, T. Sawada and T. Ekawa, *Identification of non-linear and non-stationary soil properties during the 1995 Hyoguken-nanbu earthquake*, Soil Dynamics and Earthquake Engineering, vol. 23, pp. 279-286, 2003.

[4] Erdik, M. (1987, January 01). *Site Response Analysis*. Retrieved from https://link.springer.com/chapter/10.1007/978-94-017-3095-2_17

[5] C. Oskay and M. Zeghal, *A survey of geotechnical system identification techniques*, Soil Dynamics and Earthquake Engineering, vol. 31, no. 4, pp. 568-582, 2011.

[6] S. Glaser and L. Baise, *System identification estimation of soil properties at the Lotung site,* Soil Dynamics and Earthquake Engineering, vol. 19, pp. 521-531, 2000.

[7] S. Glaser and L. Baise, *System identification estimation of soil properties at the Lotung site*, Soil Dynamics and Earthquake Engineering, vol. 19, pp. 521-531, 2000.

[8] O. Pavlenko and K. Irikura, *Estimation of Nonlinear Time-dependent Soil Behavior in Strong Ground Motion Based on Vertical Array Data*, Pure and Applied Geophysics, vol. 160, no. 12, pp. 2365-2379, 2003.

[9] O. V. Pavlenko and K. Irikura, *Identification of the non-linear behaviour of liquefied and non-liquefied soils during the 1995 Kobe earthquake*, Geophysical Journal International, vol. 160, no. 2, pp. 539 - 553, 2005.

[10] D. Assimaki, W. Li and A. Kalos, *A Wavelet-based Seismogram Inversion Algorithm for the In Situ Characterization of Nonlinear Soil Behavior*, Pure and Applied Geophysics, vol. 168, no. 10, pp. 1669-1691, 2011.

[11] C.-C. Tsai and Y. M. Hashash, *A novel framework integrating downhole array data and site response analysis to extract dynamic soil behavior*, Soil Dynamics and Earthquake Engineering, vol. 28, no. 3, pp. 181 - 197,2008

[12] Y. Zheng, W. Mansheng, H. Liu, Y. Yao and Z. Xiyuan, *Time-domain identification of dynamic properties of layered soil by using extended Kalman filter and recorded seismic data*, Earthquake Engineering and Engineering Vibration, vol. 3, no. 2, pp. 237 - 247, 2004.

[13] H. Madsen and R. Cañizares, *Comparison of extended and ensemble Kalman filters for data assimilation in coastal area modelling*, International Journal for Numerical Methods in Fluids, vol. 31, no. 6, pp. 961 - 981, 1999.

[14] F. McKenna, G.L. Fenves and M.H. Scott, *Open system for earthquake engineering simulation.* University of California, Berkeley, CA, 2000.

[15] W. Slika and G. Saad. *An Ensemble Kalman Filter approach for service life prediction of reinforced concrete structures subject to chloride-induced corrosion,* Construction and Building Materials, vol 115, pp. 132-142, 2016.

[16] D. Nasr, W. Slika, and G. Saad. *Uncertainty quantification for structural health monitoring applications.* Smart Structures and Systems, vol. 22, no 4, pp. 399-411, 2018.

COMPDYN 2019
7th ECCOMAS Thematic Conference on
Computational Methods in Structural Dynamics and Earthquake Engineering
M. Papadrakakis, M. Fragiadakis (eds.)
Crete, Greece, 24–26 June 2019

THE SEISMIC RESPONSE OF NATURAL GAS PIPELINES BURIED IN DISCONTINUOUS PERMAFROST UNDER VERTICALLY PROPAGATING SHEAR WAVES: PARAMETRIC ANALYSIS

Daniel A. Pohoryles[1] , Luigi Di Sarno[2], Oh-Sung Kwon[3], Marianna Ercolino[4] and Anastasios Sextos[5]

[1] European Commission, Joint Research Centre (JRC), Ispra, Italy; University of Sannio, Italy
e-mail: daniel.pohoryles@ec.europa.eu

[2] University of Sannio, Italy and University of Liverpool, UK

[3] University of Toronto, Canada;

[4] University of Greenwich, UK;

[5] University of Bristol, UK;

Abstract

Buried natural gas pipelines are important infrastructure to connect areas of gas exploration to areas of use. In many parts of the world, pipelines cross seismic regions and varieties of soil strata, including regions of discontinuous permafrost in the Northern hemisphere. Initial studies find that the seismic response of soils can be strongly influenced by changes in underlying soil strata, hence potentially leading to greater seismic demands on buried infrastructure such as pipelines. Frozen soil deposits, in particular, can lead to a significant change in dynamic soil response to seismic excitation. To study the effect of crossing discontinuous permafrost zones on the seismic behaviour of buried natural gas pipelines, a combined modelling approach is proposed: (1) dynamic site response analysis to determine the load conditions and (2) quasi-static finite-element analysis on the pipeline and surrounding soil. In this paper, results from one-dimensional equivalent linear soil response analyses for a site of discontinuous permafrost is presented. Despite the frozen soil stratum lying at a depth of 40 m, the response of the soil at the depth of the buried pipeline is found to be significantly affected. A parametric numerical validation study on a finite element model of a typical buried natural gas pipeline is then presented to assess the influence of geometrical and mechanical parameters on the response of pipeline and surrounding soil by means of a series of incremental dynamic analyses. Outcomes of this study highlights the strong effect of the soil properties on the strain in buried pipelines.

Keywords: Pipelines, Seismic behaviour, Structural Dynamics, Earthquake Engineering, Frozen Soil, Discontinuous Permafrost.

1 INTRODUCTION

Long-distance buried pipelines often unavoidably cross terrain with different soil types as well as with variation of surface-level built-environment. For instance, the pipeline can cross highways or railways that may induce additional settlement under static loading [1]; moreover, they may also concern the boundaries between soil strata causing local stress concentrations under vertically propagating seismic waves [2].

The effect of local site conditions on the ground motions is a known phenomenon and ground response analyses are common practice in geotechnical earthquake engineering [3]. Changes in soil properties along the length of a pipeline are still considered to be an under-examined issue of importance. A variation in the seismic behaviour of soils and, hence, a variation in local stress in pipelines can be caused by discontinuous permafrost, which occurs in regions with mean annual soil surface temperature of -2 to -4°C, causing partial freezing of soil layers below ground. In the Northern Hemisphere, 24% of the ice-free land area is affected by permafrost, i.e. soil that continuously has a ground temperature below 0 °C for at least two consecutive years [4]. Still, its effect on the seismic site response for buried infrastructure has not yet been studied extensively, and in current design practice, it is ignored. As the exploration of natural resources in seismically active regions, such as Alaska, U.S., or Canada, that are also permafrost regions, is expanding, it is critical to further explore this topic [5].

Frozen soil deposits can lead to a significant change in dynamic soil response to seismic excitation. In particular, geotechnical properties, such as soil stiffness and shear wave velocities, increase in frozen soils. In a discontinuous permafrost zone, only some parts of the soil mass are in frozen conditions. This can lead to a stark contrast in soil response at their boundaries, in both lateral and vertical directions. The effect of permafrost on the ground response to transient ground motions has only sparked interest in the last decade. Some examples are given in northern Canada [6], Alaska [5], as well as in Tibetan regions of China [7], where critical infrastructure, such as railways or buried pipelines, cross seismically active zones and permafrost sites.

To study the effect of crossing discontinuous permafrost zones on the seismic behaviour of buried natural gas pipelines, a combined modelling approach is proposed: (1) dynamic site response analysis to determine the load conditions and (2) quasi-static finite-element analysis on the pipeline and surrounding soil.

In this paper, the results from one-dimensional equivalent linear analyses for soil strata in discontinuous permafrost at a site in Alaska are presented. Despite the frozen soil stratum lying at a depth of 40 m, the response of the soil at the assumed depth of the buried pipeline (5 m) is found to be significantly affected due to the large change in shear wave velocities in the frozen layer. This paper also presents the outcomes of a preliminary numerical validation study to define the influence of some geometrical and mechanical parameters on the response of pipeline and surrounding soil. A 3D finite element model of a typical buried natural gas pipeline is developed, including the soil surrounding it. By means of a series of incremental dynamic analyses (IDA), parameters, such as mesh size and geometry of the surrounding soil, are investigated to assess their effect on the response of the pipeline in soils with different geotechnical properties. Outcomes of this study highlight the significant effect of the surrounding soil properties on the strain in buried pipelines. Moreover, the study validates the use of both coarse mesh and smaller geometry of the surrounding soil to allow a computationally efficient model.

2 BACKGROUND

2.1 The effect of vertical components of ground motions

A majority of studies on the seismic resilience of buried steel pipelines considers seismic loading in the horizontal plane of the pipeline, be it in lateral or axial directions [8]. The effect of the vertical component of ground motions is not well-studied. Vertical loading is mainly considered in the case of static loading or permanent ground deformations caused by earthquakes, such as fault movements or landslides.

Lee [9] undertook a series of finite-element analyses on the combined vertical static (traffic and soil weight) and vertical seismic loading. The soil is modelled homogenously along its depth and length and traffic load is spread evenly across the surface of the soil and is not considered in the dynamic load. A number of different, albeit homogenous, soil conditions are investigated, as well as the effect of boundary conditions, corresponding to continuous and segmented pipelines. It is found that continuous pipelines behave better, and that sandy soils increase the stress in the pipelines compared to clay under static loading conditions, however only to a level that may lead to temporary serviceability issues. While no specific limit states are specified, under vertical seismic loading, it is found that for continuous boundary conditions, acceptable stress levels are obtained, while stress increases for segmented boundary conditions. A deeper analysis of the local effect of variation in soil type or built-environment is however needed.

Jeon [10] carried out incremental dynamic analyses (IDAs) to investigate the relative behaviour of buried pipelines designed to Korean and US guidelines under vertical seismic excitation. A two-dimensional model along the length of the pipeline is created, with the soil considered homogenous throughout. Maximum strains along the pipelines of up to 0.6% are observed. The range of peak ground accelerations (pga) in the study is limited to up to 1.2g and no internal pipeline pressure is assumed in the analysis.

2.2 Variations in vertical load conditions along pipelines

The effect of different vertical surface load conditions on buried high-pressure gas pipelines is the topic of a finite element study by Brückner et al [11], who applied a modular approach to look at traffic loading, water loading and railway crossings.

Manna and Duari [12] investigated the local effect of pipeline-road crossings in terms of cyclic traffic load and find that corrosion and damage is more likely underneath road-crossings. Zhou et al [1] assessed the uneven static loading conditions on a buried pipeline using finite element analysis. The authors determined that local stress concentrations in the pipeline are observed when a gas pipeline crosses a high-filling road, which may affect its operational safety. The effect of pipeline internal pressure, as well as pipeline wall-thickness are found to be significantly affecting local stress in pipeline elements under static vertical loading.

The combined effect of seismic and traffic loading has been studied by Kokavessis and Anagnostidis [2], which however focused on the soil-structure interaction in the case of soil-liquefaction.

2.3 Variations in soil conditions along pipelines

Changes in soil properties along the length of a pipeline are still considered to be an under-examined issue of importance. Local site conditions can significantly influence the response of soil to ground motions [3], [6]. A variation in soil properties may be a case of two horizontally

adjacent soil strata of different stiffness, but also the case of a pipeline crossing a soft alluvial valley [3].

In the case of pipelines crossing soil strata characterized by large temperature differences in soil layers, such as discontinuous permafrost regions, a multitude of potential issues have been studied in the literature, including uplift of the pipeline due to frozen soil around pipelines under static loading conditions [13], but also the effect of thawed layers in frozen soil on soil liquefaction [14].

However, also the dynamic properties of frozen soil are significantly different, for instance, the Young´s modulus of frozen soils can be magnitudes of 10s or 100s times larger than for the same soil in unfrozen state [4]. As ground temperatures can increase with depth below the permafrost, its stiffness will hence also decrease with depth. Similarly, the shear wave velocities are lower for unfrozen soil.

Wang et al [7] compiled wave velocities obtained from field tests along the Quinghai-Tibet railway in China for different soil types (silty clay, mudstone, marl, fine sandy soil) under frozen and unfrozen conditions. This zone is very seismically active and constitutes the largest area of permafrost at high elevations in the world. The data from ten boreholes was then used to carry out site response analyses and obtain ground motion acceleration spectra. Wave velocities are 1.2 - 1.6 times and 1.4 - 1.7 times larger in frozen soils for S-wave and P-waves, respectively.

Yang et al. [5] looked at another seismically active permafrost region, namely Alaska. One-dimensional equivalent linear analysis was carried out looking at the vertically propagating horizontal shear waves. The aim was to investigate the effect of permafrost on the seismic response of bridges in Alaska, hence looking at the response at ground level in soils with and without permafrost. Variations in permafrost depth, thickness as well as depth to bedrock were the main parameters studied.

The parametric study showed that a soil profile with a permafrost table at -20 m and the bedrock table at -66 m produces the largest surface response spectrum. This particular soil profile may produce a site response that is larger than anticipated by design codes. The authors hence concluded that the seismic design of structures should consider the presence of continuous permafrost, as it influences the site response significantly.

Dadfar et al [6] investigated the effects of discontinuous permafrost on the seismic behaviour of pipelines by modelling the 2D response of a pipeline that is crossing alternating regions of frozen and unfrozen soil. The frozen and unfrozen free-field responses in the horizontal direction of the soil are determined to be significantly different due to a large change in seismic shear wave velocities. The results from the soil free-field response study is then used as input motion along the length of the pipeline and compared to a uniform support excitation case. It is found that considering regions of frozen soils leads to a large induced moment and plastic deformation in the pipeline, which is not observed in the uniform case. Ovalisation is not found to be critical, but the pipeline is instead found to yield in bending.

In discontinuous permafrost, frozen soil deposits can lead to a significant change in soil response. In particular, the stiffness of the soil and shear wave velocities are increased in the frozen soil [15]. In a discontinuous permafrost zone, parts of the soil mass are frozen conditions while others are not. This can lead to a stark contrast in soil response at their boundaries, in both lateral and vertical directions, as frozen soils have different geotechnical properties and shear-wave velocities than unfrozen soils.

Dadfar et al [15] conducted a combined experimental and numerical study on the seismic site response of alternate blocks of frozen and unfrozen soil. Free-field spectral accelerations were

found to be larger for the frozen soil, but the increase is affected significantly by the spacing and geometry of the frozen soil blocks.

3 METHODOLOGY

An intensive study of available literature on modelling the effect of transient seismic ground motions on pipelines [3] found that the inertial soil-pipeline interaction is negligible and that the fully dynamic problem of buried pipelines can be split into a dynamic soil analysis and a quasi-static analysis of the pipeline behaviour.

In the case of vertical loading with variation in soil properties in the soil model, ovalisation of the pipeline cross-section, as well as bending failure of the pipeline are assumed the only potential failure mechanisms, the latter being less realistic due to the high ductility of steel pipelines used for natural gas transportation [8]. Excessive ovalisation of the cross-section can lead to loss of pipeline integrity or serviceability and is limited to 15% by most guidelines [6]. Buckling or fracture of the pipeline are only observed under axial loading [3].

It is hence proposed to use a similar two step approach to modelling as proposed by Psyrras and Sextos [3]. First, one-dimensional equivalent linear analysis on two different sets of soil strata, with and without permafrost layer at 40 m depth, is performed to obtain soil response spectra at different depths of the soil. Initial results from the ground response analysis step are presented in the next section, highlighting the effect of permafrost layers on the soil response at ground level.

Next, the pipeline and surrounding soil are modelled in a three-dimensional finite element model, with vertical displacement applied to the top of the soil, according to the obtained acceleration histories obtained from the ground response analysis. In this study, a parametric analysis on the various parameters affecting the finite element modelling of the pipeline-surrounding soil model is presented. The effects of different soil materials around the pipeline, different pipeline diameter and thickness of the pipeline-wall, as well as geometric parameters of the surrounding soil model, including mesh-size and depth of modelled soil stratum are assessed.

The results obtained in this study can then be used for future modelling of pipelines crossing two different soil strata, by applying two different loading histories along the length of the pipeline, obtained from ground response analyses.

4 GROUND RESPONSE ANALYSIS WITH AND WITHOUT PERMAFROST

In this section, an initial response analysis of potential vertical soil strata with and without permafrost layer is presented. Two soil profile are constructed for a site in Alaska [5], with the mechanical properties of the different layers provided in Table 1 and Table 2.

A one-dimensional equivalent linear analysis is then performed in the DEEPSOIL software [16], with two low velocity transition layers with thickness of 1.5 m assigned on the top and bottom of permafrost layer to account for the surface condition and the partially frozen layer between frozen and unfrozen soils.

Layer name	Thickness (m)	Unit weight (kN/m3)	Shear wave velocity (m/s)	Damping ratio (%)
Sandy Silt 1	14.00	20.00	200.00	0.48
Sandy Silt 2	23.00	20.00	300.00	0.48
Sandy Silt 3	14.00	20.00	400.00	0.48
Gravel	6.00	20.40	450.00	0.50
Weathered Rock (Clay)	9.00	20.40	550.00	2.60

Table 1. Soil characteristics for the stratum without permafrost

Layer name	Thickness (m)	Unit weight (kN/m3)	Shear wave velocity (m/s)	Damping ratio (%)
Sandy Silt 1	10.00	20.00	200.00	0.48
Sandy Silt 2	20.00	20.00	300.00	0.48
Sandy Silt 3	10.00	20.00	400.00	0.48
Frozen Soil	11.00	20.00	1500.00	2.20
Gravel	6.00	20.40	450.00	0.50
Weathered Rock (Clay)	9.00	20.40	550.00	2.60

Table 2. Soil characteristics for the stratum without permafrost

A dynamic analysis was performed using twelve earthquake records (Chi Chi, Coyote, Imperial Valley, Kocaeli, Loma Gilroy, Loma Gilroy (2), Mammoth Lake, Nahanni, Northridge, Northridge(2), Parkfield and Whittier Narrows). For details of the records, the reader is directed to the documentation of DEEPSOIL[16].

A comparison of the two soil profiles is hence made based on this analysis. In a first stage, the response of the soil at 5 m depth, i.e. in the first soil layer of sandy silt, is analysed. This corresponds to the buried depth of the pipeline assumed in the initial finite element analysis [9]. The results are hence compared for strain, acceleration and displacement for this depth in the presence or absence of a layer of frozen soil below.

Looking at soil acceleration at 5 m depth for soil with and without permafrost layer below, respectively, an increase between 2.7% and 22.0% with a mean of 9.2% (standard deviation = 0.08) is recorded over the twelve applied ground motions. This difference in soil acceleration at a boundary between two soil profiles could lead to a highly localised difference in demand on a buried pipeline. In Figure 1, an example of the effect of a permafrost layer at 40 m depth on the acceleration time history in the top soil layer for the Parkfield ground motion record is displayed. The figure highlights the effect on the peak acceleration in the top layer of soil due to the presence of permafrost.

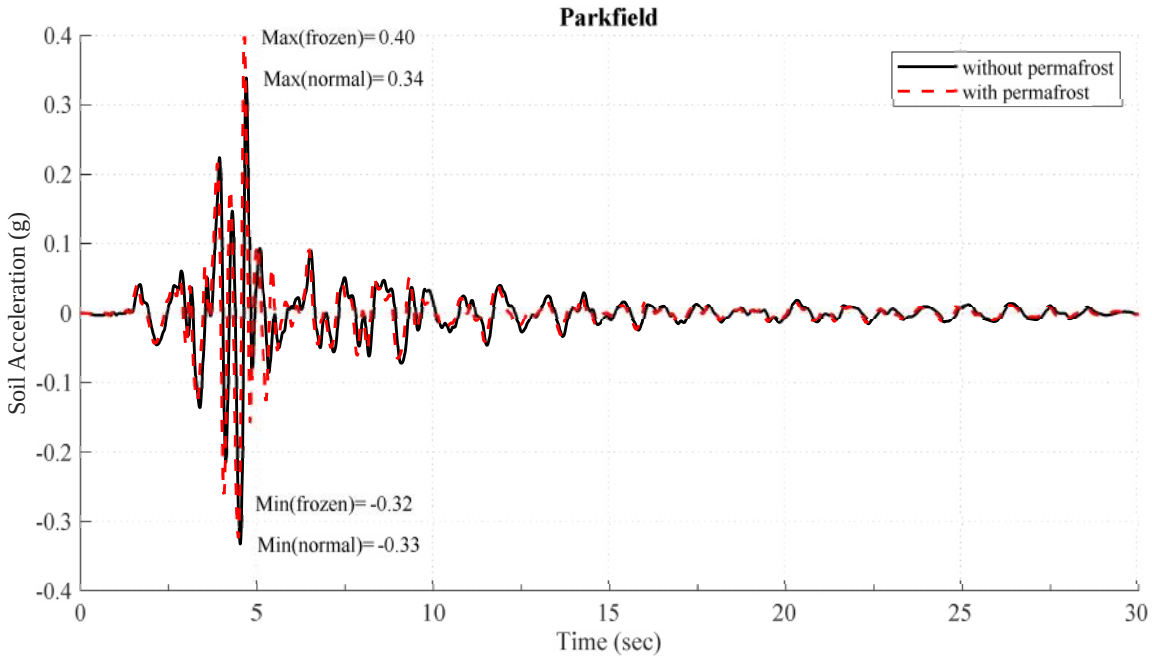

Figure 1. Acceleration - time history at 5m depth for both soil profiles for the Parkfield record

Obtained maximum strain in the top layer of soil and recorded peak ground acceleration for the soil strata are shown in Figure 2. It indicates that higher levels of strain are reached in the soil without permafrost in the strata below. It would hence seem that the presence of permafrost attenuates the strain in the top layer of soil. A similar trend, albeit with more dispersion, can be seen for the maximum soil displacements, shown in Figure 3.

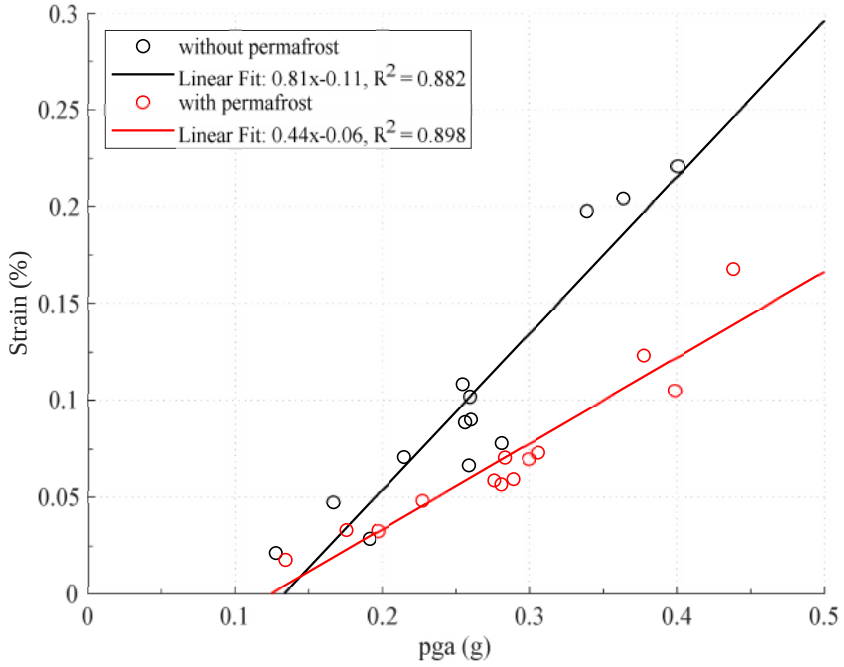

Figure 2. Strain in the first soil layer against pga for all records

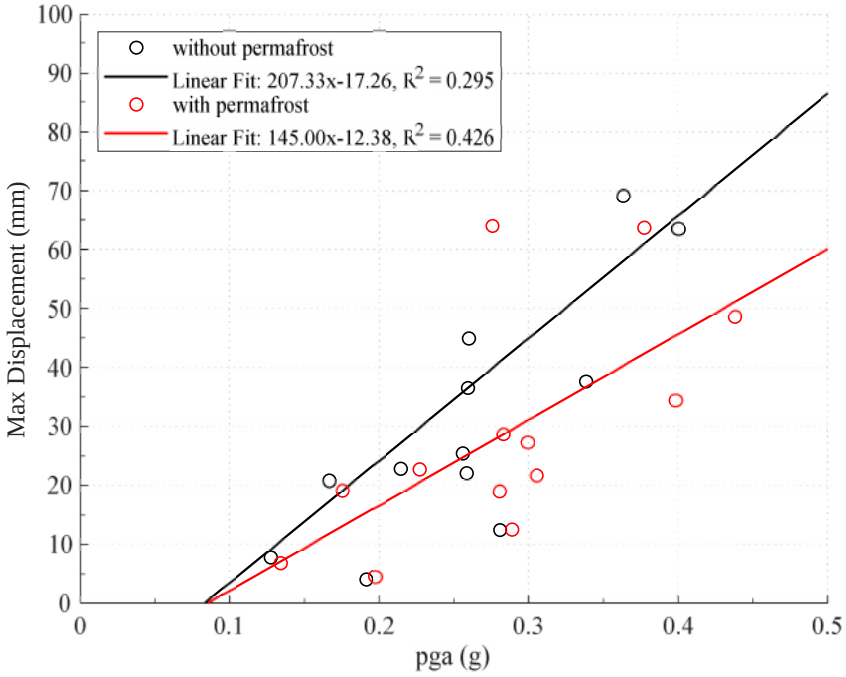

Figure 3. Maximum displacement in the first soil layer against pga for all records

To further investigate of the results, the maximum soil strain and displacement throughout the depth of the two soil profiles is analysed. The results displayed in Figure 4 highlight that in the frozen soil, due to the strong increase in stiffness, a very low maximum strain is obtained, compared to the unfrozen soil. This reduction in strain for the same ground motions is then transferred to the layers, leading to the attenuation in soil strain observed at 5 m depth.

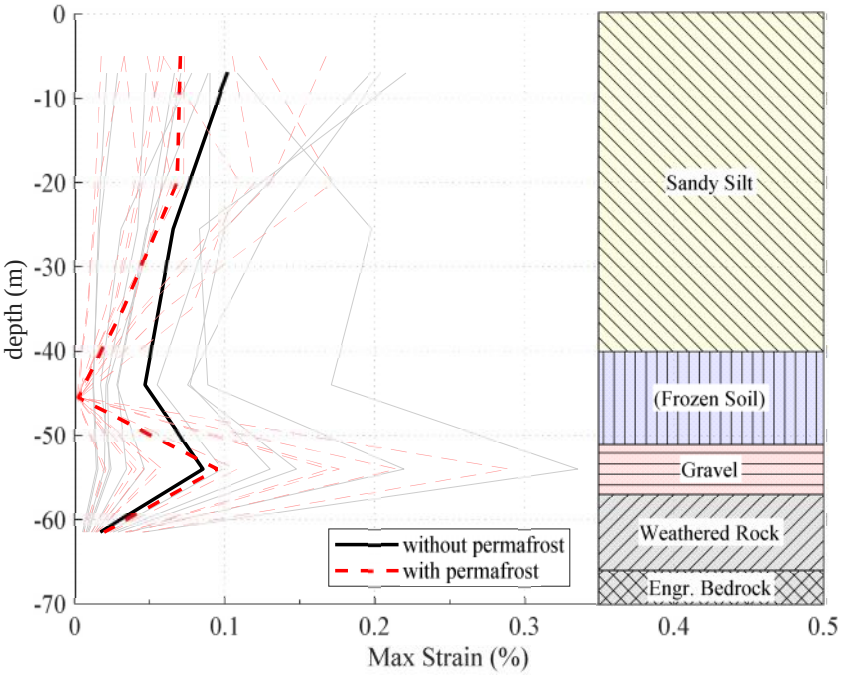

Figure 4. Maximum strain versus depth in the soil profile for all ground motions

For soil displacement, a similar observation can be made, with reduced values observed in the permafrost layer and the layers above it (Figure 5). In both cases, below the frozen soil

layer, the response of gravel and weathered bedrock are not affected by the presence of permafrost. In the top soil layer, i.e. where the pipeline is buried, a reduction of 21% in soil displacement and 31% in soil strain are observed on average for the profile including a layer of permafrost.

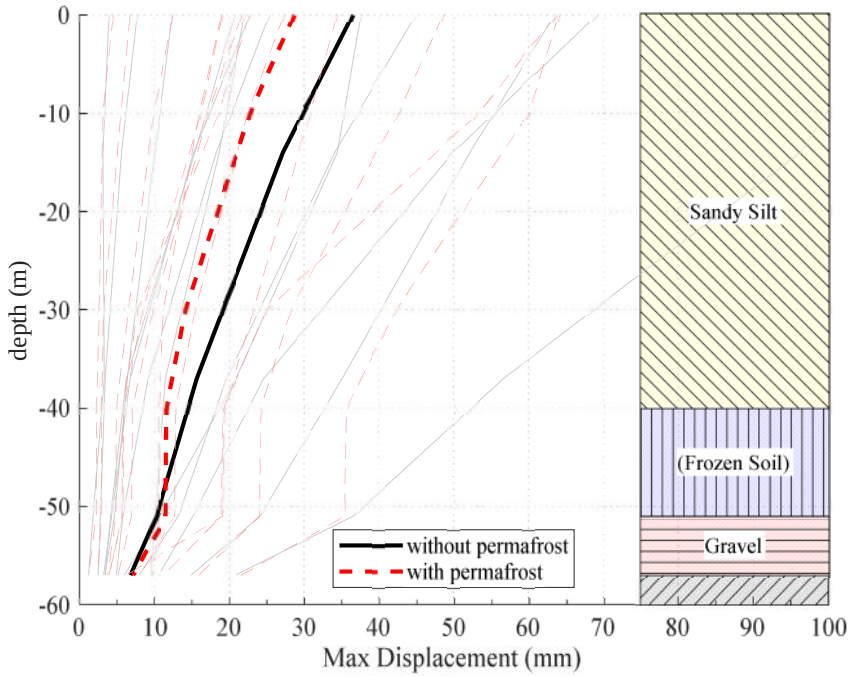

Figure 5. Maximum displacement versus depth in the soil profile for all ground motions

Overall, the results from this initial soil response study are in line with previous studies ([15], [17]) and highlight the difference in behaviour between the two soil profiles under the same earthquake loading. It is important to note, however, that the response is highly dependent on the selection of ground motions and that larger spectral acceleration will amplify this difference.

5 PARAMETRIC FINITE ELEMENT ANALYSIS

In the literature, finite element studies on the seismic behaviour of buried pipelines that assess the relative influence of modelling parameters are rare. Lee [9] undertook a parametric study concentrating on the influence of buried depth, mesh size and pipeline length. In this study, the influence of four model parameters (soil type, soil depth below pipeline, pipeline diameter and mesh size) are assessed individually. These parameters are summarised in Table 3 and are described in more detail in the following section.

Soil Type	Soil depth below pipeline, h' (m)	Pipeline diameter (m)	Mesh size (m)
Saturated sand / Silty sand	10 - 30	0.2 – 0.4	1 – 2 – 4

Table 3. Assessed parameters in the finite element model

A finite element model of a buried pipeline is created in ABAQUS [18]. The pipeline has a diameter of 0.4 m and a wall thickness of 10 mm for all models except for the parametric study of pipeline diameter for which a smaller diameter of 0.2 m and thickness of 5 mm are tested. For all models, this pipeline is buried at a depth of 5 m and has a length of 15 m. The soil surrounding the pipeline is modelled with a width of 10 m and a length of 15 m. The model dimensions are summarized and illustrated in Table 4 and Figure 6, respectively.

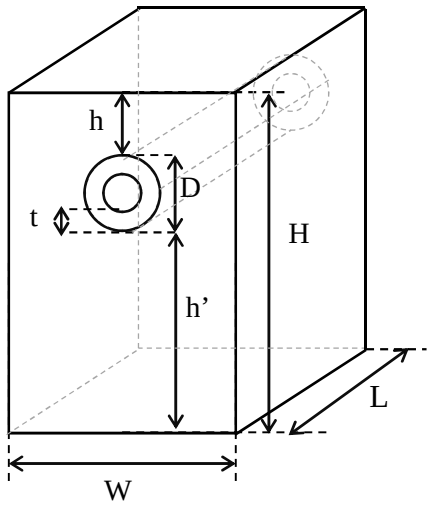

Figure 6. Finite element model dimensions

Dimension	Symbol	Value (m)
Length	L	15
Width	W	10
Total depth	H	15.4 – 35.4
Buried depth	h	5
Depth below	h'	10 – 30
Pipeline diameter	D	0.2 – 0.4
Pipeline wall thickness	t	5 – 10 (mm)

Table 4. Model dimensions summary

The material properties of the pipeline are constant in all models and represent a ductile steel pipeline. The elasto-plastic material properties [9] are shown in Table 5. To model the pipeline, second order reduced integration shell element with eight nodes (S8R) are chosen. The elements have a thickness corresponding to the pipeline wall thickness and a mesh size of 1 m for all models in the parametric study (Figure 7).

Mechanical property	Symbol	Value
Density (kg/m3)	ρ	7850
Young's modulus (GPa)	E	210.7
Poisson's ratio	ν	0.3
Shear modulus (GPa)	G	81.0
Yield strength (MPa)	f_y	490
Yield strain (%)	ε_y	0.23

Table 5. Pipeline elasto-plastic material properties

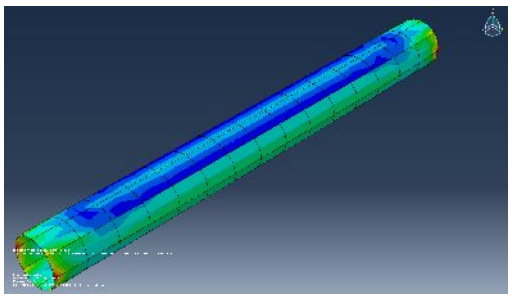

Figure 7. Pipeline finite element model and meshing.

The effect of two different soil types on the seismic performance of the pipeline is assessed. As shown in Table 6, a flexible silty sand material [5], as well as a stiffer saturated sandy material [9] are defined. The materials aim to reflect the material in the top layer of the soil strata defined in the ground response study, as well as a stiffer variant of it. The soil is considered as elasto-plastic material with Mohr-Coulomb plastic properties and is modelled using three-dimensional second order reduced integration brick elements with 20 nodes (C3D20R). The material properties for the soil types are summarised in Table 6.

Type of property	Mechanical property	Symbol	Saturated sandy soil	Silty sand
Elastic	Density (kg/m3)	ρ	2160	2160
	Young's modulus (MPa)	E	96.00	5.00
	Poisson's ratio	ν	0.25	0.35
Mohr-Coulomb	Friction angle (°)	φ	40.00	20.00
	Dilation angle (°)	ψ	2.00	2.00
Cohesion	Cohesive strength (kPa)	c	17.00	10.00

Table 6. Soil properties in finite element model

The influence of soil depth below the pipeline is assessed in the parametric study for a constant mesh size (4 m), for a pipeline buried at 5 m in sandy silt, for one earthquake record. The comparison is performed on two soil depths representative of values found in the literature. As shown in Figure 8, these correspond to 15 and 35 m total depth, for the shallow [9] and deep [10] soil models, respectively.

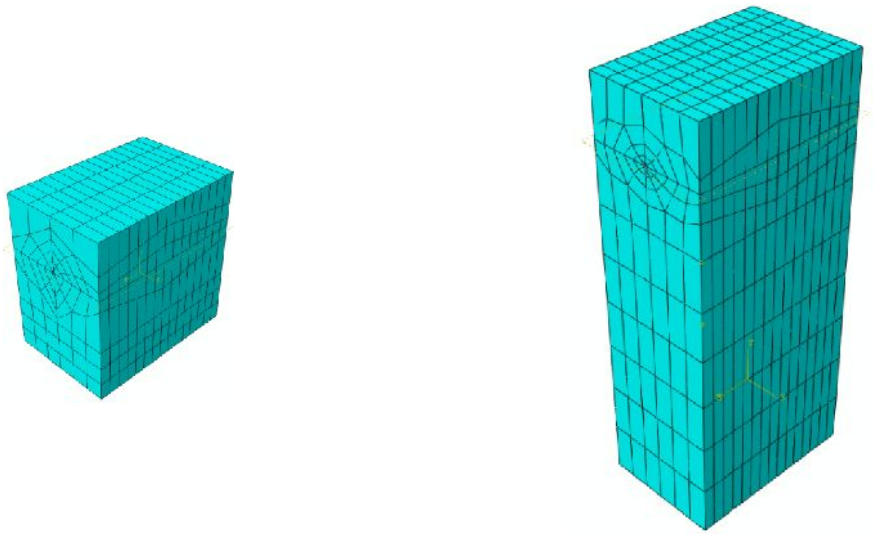

Shallow soil (15m total depth) Deep soil (35 m total depth)

Figure 8. Model geometry with different soil depths

While the mesh size of the pipeline is kept constant at 1 m, a mesh size sensitivity study for the soil surrounding it is conducted, testing the effect of mesh size varying from 1 m to 4 m. The mesh obtained for the three sizes, varying from fine to coarse, for the soil elements are shown for the deeper soil model in Figure 9.

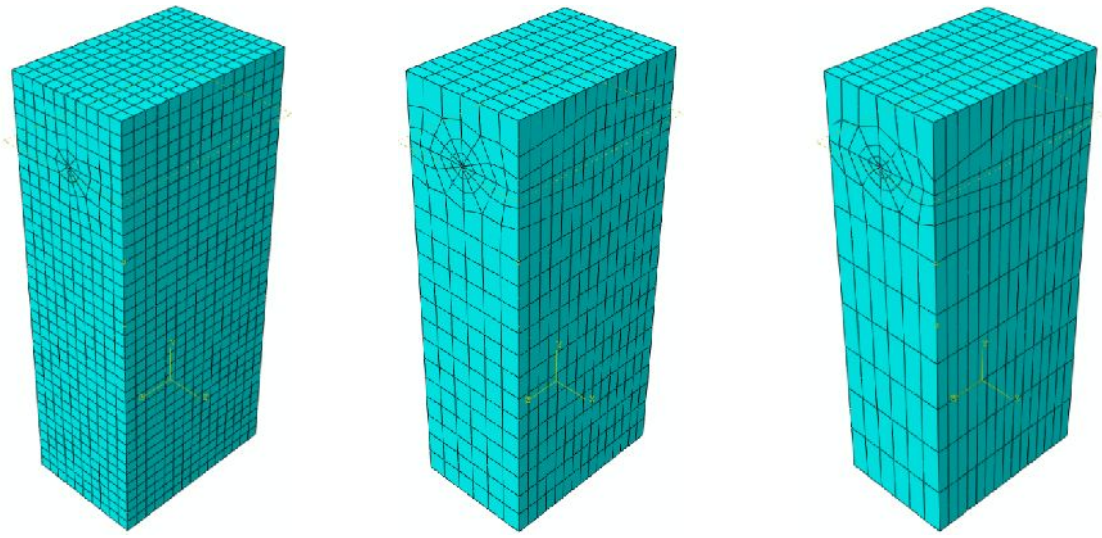

Fine mesh (1 m) Medium coarse (2 m) Coarse mesh (4 m)

Figure 9. Mesh sizes for sensitivity study

The boundary conditions for the model are shown in Figure 10. The base of the soil is fully restrained, while roller supports are put on the side faces (Y-Z planes) of the soil model. The ends (Y-X planes) of the pipeline are also modelled as rollers. The nodes at the interface between soil and pipeline are fully tied.

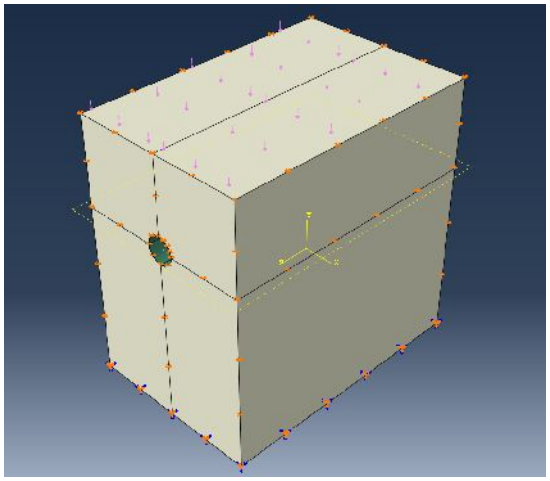

Figure 10. Boundary conditions in finite element model.

For the parametric analysis, an IDA is performed scaling the six sample records for values of pga up to 2.0 g. While this value of pga is large, it is consistent with other studies in the field (e.g.: [19]). The reader is reminded that the purpose of this initial study is the investigation of modelling parameters´ influence, rather than a vulnerability assessment of pipelines. The details of each analysis are reported within the sections focusing on the individual parameters. The seismic load is applied as body force in Abaqus [18]. Before applying the seismic load, a realistic static load is applied in the first step of the analysis. This includes the gravity load and an additional load due to traffic loading applied on the ground surface as a uniformly distributed pressure of 1100 kPa. This corresponds to a total load of 165 000 kN applied on the soil with dimensions of 10 by 15 m.

The seismic behaviour of the pipeline is then assessed by comparing the maximum absolute strain and stress in the longitudinal direction along the axis of the pipeline and the vertical displacement in the pipeline elements at midspan at each step in the IDA.

6 RESULTS

6.1 Mesh sensitivity

As an initial assessment, sensitivity to the mesh size is analysed using the larger diameter pipeline and saturated sandy soil properties. The deeper soil geometry is chosen as the difference in mesh size would be more pronounced for it. The pipeline material and pipeline element mesh size are kept constant. An IDA with pga intensities of 0.25 up to 2.0 g with a step size of 0.25 g are ran and the differences in results for the three mesh sizes are compared.

In particular, mean differences in terms of longitudinal strain ($\Delta\varepsilon$) and vertical displacement ($\Delta\delta$) to the fine mesh for the coarser mesh sizes are reported in Table 7. The differences to the fine meshed model in terms of strain are below 1.7% on average and around 1.0% in terms of displacement.

	Medium mesh	Coarse mesh
$\Delta\varepsilon$	1.68 %	0.21%
$\Delta\delta$	1.04%	1.09%

Table 7. Mesh size sensitivity in terms of strain and vertical displacement

These minor differences in results combined with the reduced computational time for the coarse mesh. On average, one step in the IDA for the coarse mesh size (ca. 1 h per run) is about four times lower than the fine mesh (ca. 4 h). The heavily reduced computational cost hence justifies the use of a 4 m mesh size.

6.2 Influence of pipeline diameter

As a parameter of pipeline geometry, the influence of the pipeline diameter is assessed. Two different diameters (0.4 m and 0.2 m) with different wall thicknesses (10 mm and 5 mm, respectively) are modelled. Note that for both geometries the diameter to thickness ratio (D/t) is kept constant at 40. The ground motions selected for the IDA are scaled with pga intensities ranging from 0.25 to 2.0 g with a step size of 0.25 g. For this comparison, the total soil depth used is 15 m (shallow soil) and the soil material corresponds to the saturated sandy soil.

The results for the applied ground motion records and the average are plotted in Figure 11. It can be observed that for the pipeline with larger diameter, the average longitudinal strain at mid-span is up to 10.8% higher. The average strain values obtained reach 0.13 % for the small diameter pipeline and 0.11% for the larger diameter. In both cases this is below the yield strain of 0.23%.

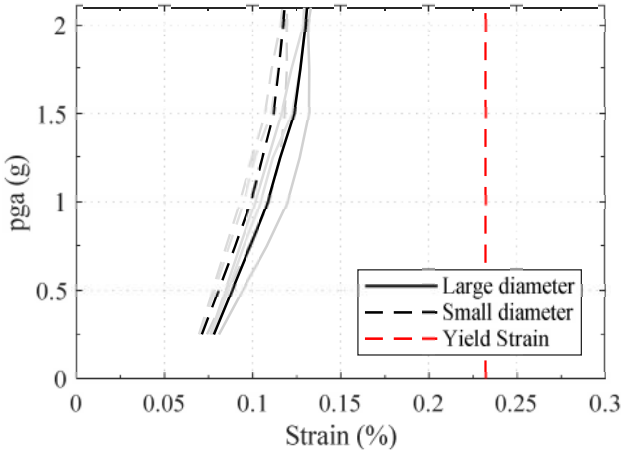

Figure 11. pga against strain comparing the influence of pipeline geometry.

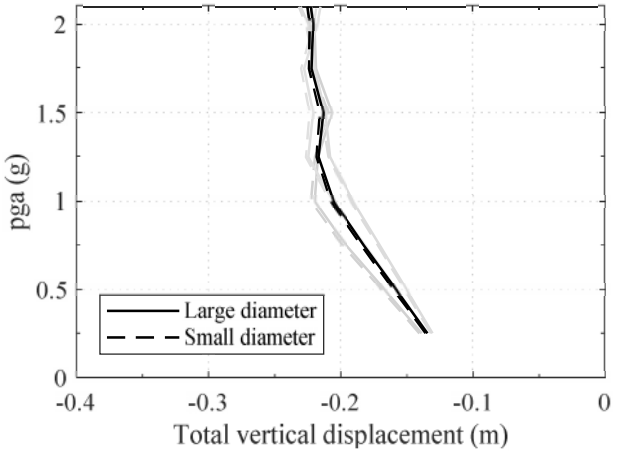

Figure 12. pga against total vertical displacement for two pipeline geometries.

In terms of maximum vertical displacement, for both relatively low values up to -0.22 m are obtained due to the stiffness of the soil (Figure 12). As it would be expected, the pipeline properties do not influence the response of the soil, instead it is expected that the soil geometry and properties, assessed in the next section, are critical parameters.

6.3 Influence of soil depth

Another important point in terms of computational cost is the total model size. This can be heavily reduced by reducing the depth of soil layers below the pipeline. In the literature for similar pipeline dimensions, 10 m to 30 m of soil below the pipeline can be found. To test the influence of this parameter, a constant mesh size of 4 m is selected. The silty soil material deposit of the site response analysis is chosen as soil material, as the influence of soil depth is expected to be highest for softer soils.

In terms of vertical displacement, large displacements for the deep soil model are observed, resulting from the significantly larger accumulated settlement under the imposed traffic load. Removing this contribution, an average difference of 14.2% is obtained between the two models, with the deeper soil presenting larger vertical displacements.

Looking at the maximum strain at mid span in Figure 13, on average there is a 20.2% higher strain in the bottom elements of the pipeline for the shallow soil model. The maximum values of strain obtained exceed the yield strain in the case of the shallow soil at 1.4 g of pga. For analysing the seismic behaviour and fragility of buried pipelines, using the shallower soil geometry seems hence appropriate as it gives more conservative results with higher strain, while simultaneously requiring less computational time (50 mins compared to 90 mins on average).

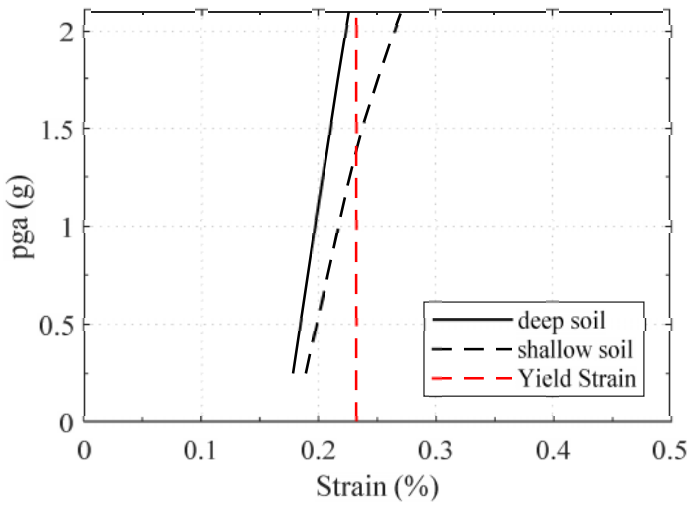

Figure 13. pga against strain comparing the influence of soil depth

6.4 Effect of soil material properties

As the model with shallow soil is deemed most appropriate and coarse mesh size is deemed appropriate for analysis, giving more conservative results and computational efficiency, the influence of material properties is also tested for the shallow geometry. The results for the same pipeline buried in soft silty soil are compared to the saturated sandy soil model.

As shown in Figure 14, the difference in strain is pronounced, with the pipeline reaching yield in the case of the soft silty sand only. The longitudinal strain is more than double the value for the pipeline buried in silty sand compared to saturated sandy soil at the extreme val-

ue of pga of 2.0 g. Strain is increased from maximum values of 0.12% to up to 0.27% in the silty sand (+125%).

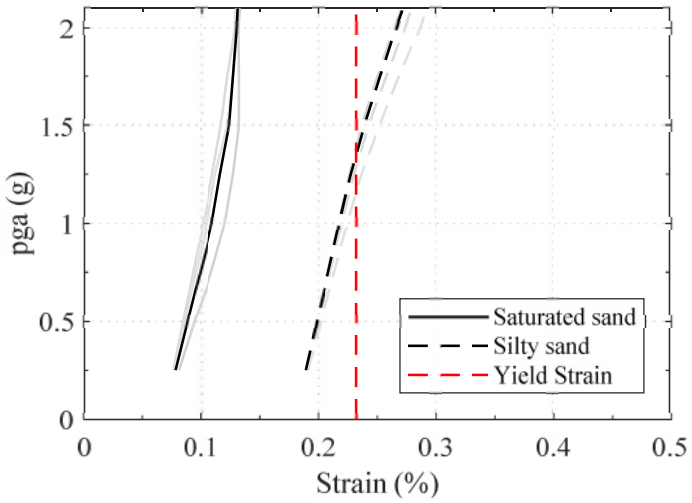

Figure 14. pga against strain comparing the influence of soil stiffness

This observation can be explained by the much larger vertical displacements observed for the softer soil. Even when the settlement under gravity loading is excluded (Figure 15), the vertical displacement is 81% lower for the saturated sand compared to soft silty sand.

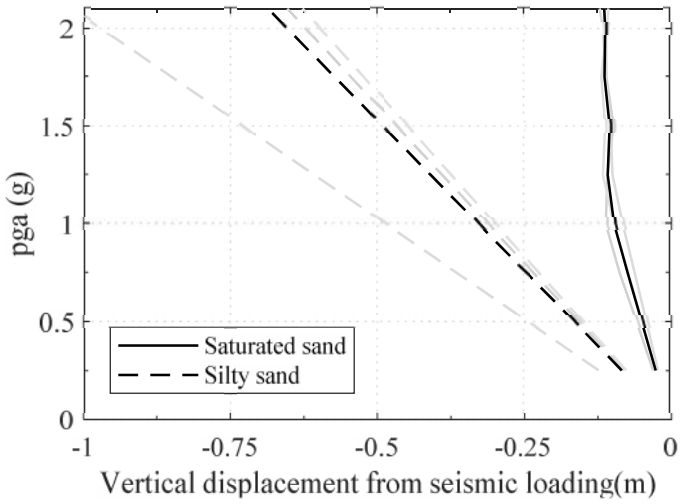

Figure 15. pga vs vertical displacement without gravity load contribution for the comparison of soil types.

Overall it can be concluded that the case of softer soils leads to higher values of strain. The sandy silt material deposit studied in the ground response study hence constitutes an important case study.

6.5 IDA of a pipeline buried in a layer of silty sand

After assessing the influence of different parameters on the behaviour of the model, an incremental dynamic analysis with six records scaled to pga values of 0.25 to 2.0 g in steps of 0.25g is undertaken for a pipeline buried in the soft silty material. This constitutes a case

study of a pipeline buried in a similar soil to the one at the location of ground response study. The effect of underlying permafrost is however not yet considered in this study.

The material properties for silty sand in Table 6 are used for the IDA. The model soil geometry is chosen to be of 15 m total depth (shallow soil), with 10 m of soil beneath pipeline and 5 m buried depth, similar to the model geometry used by Lee [9]. Based on the mesh size sensitivity analysis presented in the previous section, a 4 m mesh for the soil elements is deemed appropriate.

As shown in Figure 16, values of strain up 0.3% are reached, with an average of 0.27% at the highest pga of 2.0 g. On average, plastic strain is reached in the pipelines at a pga of 1.4 g. Plastic behaviour is hence observed for the pipeline after this level of pga, as shown in Figure 17.

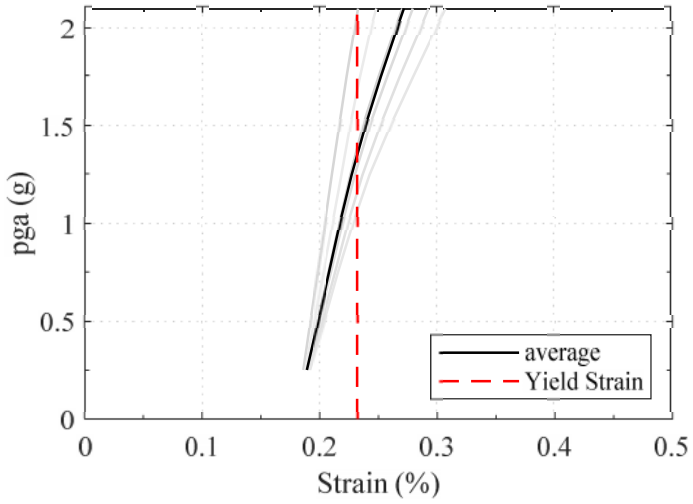

Figure 16. pga against strain for the case study pipeline buried in layer of silty sand

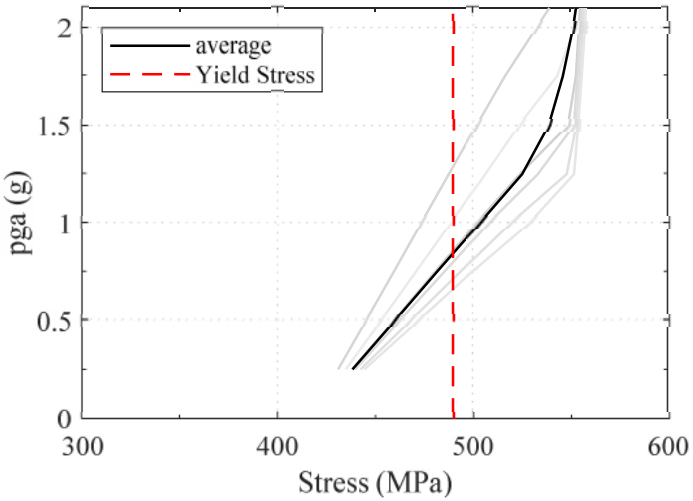

Figure 17. pga against strain for the case study pipeline buried in layer of silty sand

It is worth noting that the ground response study on the soil strata with and without underlying permafrost suggests a differential acceleration history along the length of the pipeline, which is not investigated here. Larger values of strain at the interface of the two soil strata

would be expected. In this case, which may lead to reaching yield at lower values of pga then the ones reported here. This constitutes an important factor to be analysed in future studies.

7 CONCLUSIONS

This paper discussed the modelling parameters of influence for buried natural gas pipelines crossing seismic regions with underlying irregular permafrost soil layers. An initial soil response study for a site in Alaska shows results in line with previous studies ([15], [17]). The study highlights the difference in behaviour between two soil profiles, with and without underlying permafrost, under the same earthquake records applied. The soil acceleration at 5 m depth is increased by up to 22%, resulting in a change in response of the buried pipeline. This is particularly remarkable given the depth of the permafrost layer, still influencing the relatively shallow depth of the buried pipeline. These findings are however not general and are highly dependent on the spectral accelerations of the selected ground motion at the natural frequencies of the soil strata.

A parametric finite element study is then conducted to assess the influence of various modelling parameters on the results of incremental dynamic analyses carried out on a model of the buried pipeline and the surrounding soil layer.

It is found that parameters such as mesh size and soil geometry selected to render the most computationally efficient models will render more conservative results. An increase in soil element mesh size from 1 m to 4 m is only found to affect the results in terms of maximum strain in the pipeline by 1.7%. A larger depth of surrounding soil in the model has a more pronounced effect, increasing the relative displacement in the pipeline soil layer by an average of 14.7%. The increased strain in the pipeline for the smaller soil depth, however, justifies the conservative use of the more computationally efficient parameters. The results are most influenced by the type of soil in which the pipeline is buried, as reduced stiffness of the soil will enhance the strain in the pipeline, with maximum strain results for a softer silty sand more than double of the ones obtained for a pipeline buried in a stiffer material.

The next steps of the study could hence bring interesting results when looking at the response of pipelines to vertically propagating waves at the boundary of two different soil profiles, such as the ones investigated in the ground response analysis. It is anticipated that the different soil response along the length of the pipeline would lead to higher strains in the pipeline than anticipated when only assessing the pipeline for the two soil strata individually, as it is usually done at the design stage.

REFERENCES

[1] X. Zhou, Z. Yang, and P. Han, Innovation design of long-distance pipelines buried under high-filling planned roads, *Natural Gas Industry B*, **2**, 2, 198–202, 2015.

[2] N. K. Kokavessis and G. S. Anagnostidis, Finite Element Modeling of Buried Pipelines Subjected to Seismic Loads: Soil Structure Interaction Using Contact Elements, presented at the ASME 2006 Pressure Vessels and Piping/ICPVT-11 Conference, Vancouver, BC, Canada, July 23, 2006, 119–125.

[3] N. K. Psyrras and A. G. Sextos, Safety of buried steel natural gas pipelines under earthquake-induced ground shaking: A review, *Soil Dynamics and Earthquake Engineering*, **106**, 254–277, 2018.

[4] N. A. Tsytovich, *Mechanics of Frozen Ground*. McGraw-Hill Inc.,US, October 1, 1975.

[5] Z. (Joey) Yang, U. Dutta, G. Xu, K. Hazirbaba, and E. E. Marx, Numerical analysis of permafrost effects on the seismic site response, *Soil Dynamics and Earthquake Engineering*, **31**, 3, 282–290, 2011.
[6] B. Dadfar, M. H. El Naggar, and M. Nastev, Seismic behavior of buried energy pipelines in northern permafrost regions, presented at the 6th International Conference on Earthquake Geotechnical Engineering, Christchurch, New Zealand, November 1, 2015.
[7] L. Wang, Z. Wu, J. Sun, X. Liu, and Z. Wang, Characteristics of ground motion at permafrost sites along the Qinghai-Tibet railway, *Soil Dynamics and Earthquake Engineering*, **29**, 6, 974–981, 2009.
[8] G. Tsinidis, L. Di Sarno, A. Sextos, and P. Furtner, A critical review on the vulnerability assessment of natural gas pipelines subjected to seismic wave propagation. Part 1: Fragility relations and implemented seismic intensity measures, *Tunnelling and Underground Space Technology*, **86**, 279–296, 2019.
[9] H. Lee, Finite element analysis of a buried pipeline, MSc, The University of Manchester, 2010.
[10] S.-S. Jeon, Seismic behavior of buried pipelines constructed by design criteria and construction specifications of both Korea and the US, *Natural Hazards and Earth System Science*, **13**, 9, 2271–2278, 2013.
[11] J. Brückner, C. Engel, U. Marewski, and M. Steiner, Numerical simulation of external loads on buried pipelines, *gas for energy*, 2, 2017.
[12] J. Manna and B. Duari, Effect of Vehicular Movement on Petroleum Pipelines at Road Crossing and Cathodic Protection, *International Journal of Engineering and Innovative Technology (IJEIT)*, **3**, 9, 188–192, 2014.
[13] J. F. (Derick) Nixon, Discrete ice lens theory for frost heave in soils, *Canadian Geotechnical Journal*, **28**, 6, 843–859, 1991.
[14] W. D. L. Finn, K. W. Lee, and R. N. Y. Yong, Liquefaction of Thawed Layers in Frozen Soil, *Journal of the Geotechnical Engineering Division*, **104**, 10, 1243–1255, 1978.
[15] B. Dadfar, M. H. El Naggar, and M. Nastev, Experimental and analytical study of seismic site response of discontinuous permafrost, *Canadian Geotechnical Journal*, **53**, 9, 1363–1375, 2016.
[16] Y. M. A. Hashash, M. I. Musgrove, J. A. Harmon, D. Groholski, C. A. Phillips, and D. Park, DEEPSOIL V6.1, User Manual, Board of Trustees of University of Illinois at Urbana-Champaign, Urbana, IL, 2016.
[17] Z. (Joey) Yang, B. Still, and X. Ge, Mechanical properties of seasonally frozen and permafrost soils at high strain rate, *Cold Regions Science and Technology*, **113**, 12–19, 2015.
[18] ABAQUS, Theory Manual Version 6.11. ABAQUS Inc., USA, 2011.
[19] D. H. Lee, B. H. Kim, S.-H. Jeong, J.-S. Jeon, and T.-H. Lee, Seismic fragility analysis of a buried gas pipeline based on nonlinear time-history analysis, *International Journal of Steel Structures*, **16**, 1, 231–242, 2016.

COMPDYN 2019
7th ECCOMAS Thematic Conference on
Computational Methods in Structural Dynamics and Earthquake Engineering
M. Papadrakakis, M. Fragiadakis (eds.)
Crete, Greece, 24–26 June 2019

NON-LINEAR DYNAMIC SEISMIC SLIDING MOVEMENT OF DRY SLOPES

Loukas C. Katsenis[1], Constantine A. Stamatopoulos[2] and Vassilis P. Panoskaltsis[3]

[1] Ph. D candidate, Department of Civil Engineering, Demokritos University of Thrace, Greece
e-mail: katsenisloukas@yahoo.gr

[2] Partner, Stamatopoulos and Associates Co; Instructor, Hellenic Open University; 5 Isavron str, Athens, 11471, Greece, e-mail: k.stam@saa-geotech.gr

[3] Professor, Department of Civil Engineering, Demokritos University of Thrace, Greece
e-mail: panoskaltsis@yahoo.com

Abstract

In earthquake analyses, usually the input seismic acceleration is applied at the underlying bedrock. Seismic displacement along a slip surface for given motion, depends on the dynamic response of the soil profile above the bedrock, both above and below the slip surface. In addition, the seismic displacement is affected by the rotation of the sliding mass with displacement towards a gentler configuration. Furthermore, the response of the soil profile is non-linear. Ordinary finite element methods cannot be applied in the cases where the seismic displacement along slip surfaces is larger than a few meters and no reliable cost-effective method simulating all the above effects was found in the bibliography. In the present work a new cost-effective method predicting the seismic displacement of dry slopes along a slip surface with constant shear resistance is proposed. For this purpose, state-of the-art equations modeling (a) the coupled dynamic response of soils with slippage, (b) the non-linear soil response at the dry soil medium and (c) the rotation of the sliding mass effect are combined in a unique manner. The new method implemented in an excel worksheet and applied at both the linear and non-linear cases.

Keywords: slopes, sliding-block model, dynamic response, seismic displacement, constitutive modeling, slip surface, coupled analyses, slopes.

1 INTRODUCTION

Simplified models predicting the seismic displacement of slopes [1, 2, 3] are less accurate than elaborate continuum numerical methods, but have the advantage of simplicity, which makes them usable by practicing engineers. In addition they are well-suited for extensive parametric analyses, often-needed in geotechnical earthquake engineering as soil properties and applied motions are often not known with certainty. Furthermore, they have the advantage that they can predict displacement of tens of centimeters along slip surfaces in a cost-effective numerically stable manner, something that ordinary finite element methods cannot achieve. Thus, development of simplified models predicting the seismic displacement of slopes, such as the one presented in this paper, is appropriate.

The "conventional" sliding-block model with a Mohr-Coulomb strength law [2] is the most commonly used simplified model predicting the seismic displacement of slopes for given earthquake motions [3]. As illustrated in Fig. 1a, a rigid block rests on an inclined plane. The resistance along the block-inclined plane boundary follows the Mohr-Coulomb law. Critical acceleration is the minimum horizontal acceleration which causes movement of the block. Every time where the applied horizontal acceleration is larger than the critical acceleration, the block slides. The total displacement is obtained by the addition of the partial slips. This model is used for the prediction of permanent seismic movement of slopes along a predefined slip surface, by appropriately selecting the equivalent critical and applied acceleration values of the rigid block [2, 3].

The "conventional" sliding-block model simulates the basic mechanism of the generation of seismic displacement along slip surfaces. However, it is not accurate in some cases, primarily because of (a) the dynamic response of the sliding mass and the soil profile below the sliding mass [4-7], (b) the degradation of the shear modulus along the soil profile with shear strain [6], (c) changes of the geometry of the sliding mass towards a gentler inclination [8-15], and (d) the loss of strength in the slip surface with permanent shear displacement [16,17].

Improvements have been proposed and applied in the conventional sliding-block model to simulate the effects (a)-(d), described above. In particular, regarding effect (a) above, Lin and Whitman [4] studied the dynamic response of both the sliding mass and the soil below using a lumped-mass linear system. As illustrated in Fig. 1b, only shear deformations are considered and the flexible parts of the actual system were represented by linear springs and dashpots. At one elevation, there is a sliding element, with a rigid massless plate just above it. This sliding element is rigid-plastic, and can slip in one direction only so as to simulate behavior of the conventional sliding-block model described above. On the other hand, as illustrated in Fig 1c, Rathje and Bray [5] used a generalized Single Degree of Freedom (SDOF) system with the mass and stiffness distributed along the height of the system above a sliding element. The analysis procedure proposed by Chopra and Zhang [18] who model the response of the sliding mass by considering only the fundamental vibration mode is used with a mode shape appropriate for a horizontal soil deposit.

The above formulations (a) are linear. It is well-known that soil behaves linearly only at very small shear strains, well below the typical shear strains exerted under severe earthquakes. Non-linear response has been predicted by different models, ranging form non-linear elastic to truly elasto-plastic. Elasto-plastic models which predict the response of soil at both small and large shear strains which occur under failure under general stress conditions have recently been proposed and validated [19, 20, 21]. Regarding effect (b) above, according to the definition of the problem, (i) the constitutive model must be in terms of shear stress, and not in terms of the principal stresses and (ii) along the soil profile, and not at slip element, failure does not occur and only the degradation of the shear modulus with shear strain must be mod-

eled under the dry case. Papadimitriou et al [19] proposed and validated a model simulating the pre-failure decrease of the shear modulus with shear strain.

The effect (c) above is the usual state in slides in the field, and is caused by the law of physical equilibrium where masses move towards a more stable configuration. It has been modeled in an approximate way by Stamatopoulos [8] using a chain sliding in different planes (Fig 1d), by a multi-block model [10, 13, 15], as well as by other methods [9, 11, 12, 14]. It is considerable when the seismic displacement larger than a few centimeters and when the slip surface is smaller than about 50 meters [13]. The empirical expression proposed by [8] simulating the decrease in the critical acceleration in terms of the shear displacement along the sliding mass was used in a previous dynamic sliding-block model by Jafarian and Lashgari [7].

The effect (d) above is important when considerable post-failure strain softening exists along slip surfaces, especially in saturated soils. It is beyond the present work to study it.

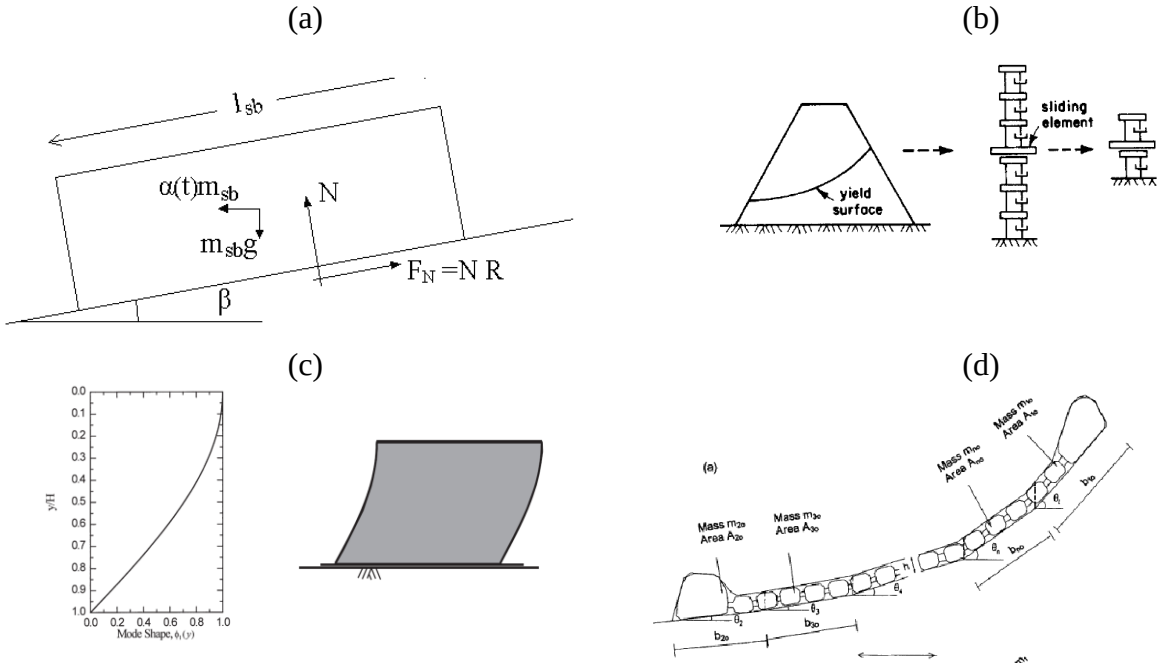

Figure 1: (a) A block sliding in an inclined plane (the "conventional" sliding-block model), (b) the discrete dynamic system considered by Lin and Whitman [4], (c) the continuous dynamic system considered by Rathje and Bray [5] and (d) the sliding system considered by Stamatopoulos [8] to simulate the effect of rotation of the sliding mass on the seismic displacement.

The purpose of the present work is to propose, derive and apply a cost-effective method predicting the seismic displacement along slip surfaces with constant shear resistance of dry slopes, by considering all the above effects (a)-(c) simultaneously. Regarding effect (a), only shear waves propagating vertically are considered. In earthquake analyses, usually the input seismic acceleration corresponds at the underlying bedrock. In addition, according to Eurocode [22] in seismic analysis the soil profile until 30m depth is considered. Furthermore, the slip surface usually is at a depth less than that of the bedrock, or the 30m depth limit of suggested by Eurocode. For these reasons, the actual dynamic soil response both above, and below the slip surface must be simulated. Thus, the applied formulation must be similar to that of Lin and Whitman [4]. Yet, unlike their formulation, the state-of-the art method predict-

ing the mass, stiffness and damping assuming the first node of a continuous mass system proposed by Rathje and Bray [5], described above, is used.

Regarding effect (b) above, an expression proposed by Papadimitriou et al [19] to simulate the pre-failure decrease of the shear modulus with shear strain in the soil profile will be used. The reason is that this relation has been validated against laboratory test results and requires a minimum number of parameters.

Regarding effect (c) above, similarly to the dynamic method of Jafarian and Lashgari [7], the empirical expression proposed by [8] is used to simulate the increase in the critical acceleration in terms of the shear displacement of the sliding mass. The reason is that this method simulates directly and cost-effectively the effect of rotation of the sliding mass in dynamic sliding-block analyses.

The paper first gives the proposed model predicting the non-linear sliding dynamic response of slopes. Following that, it discusses the proposed model and the constitutive equations associated with the model. Then, it describes the numerical implementation of the proposed model and applies it in order to illustrate the manner that different parameters affect the seismic displacement.

2 PROPOSED EQUATION SIMULATING THE NON-LINEAR SLIDING DYNAMIC RESPONSE OF SLOPES

2.1 Simulation of sliding dynamic response

As shown in Fig. 2a, the present work models a slope with a slip surface as a continuous dynamic system of height (h_1+h_2) separated by a horizontal slip element at height h_2 above its base. Only horizontal acceleration is applied at the base of the lower body and above and below the slip element different properties exist. Thus, the system is divided in two non-linear elastic bodies. The index "1" is used for the upper body and the index "2" is used for the lower body. The upper body and lower bodies have mass m_i, tangent shear modulus $G_{t\text{-}i}$, viscous material damping ratio λ_i, and density ρ_i where i takes the values 1 and 2 for bodies 1 and 2 respectively. The two bodies move a horizontal distance x_i, velocity x'_i and acceleration x''_i, where i takes the values 1 and 2 for bodies 1 and 2 respectively

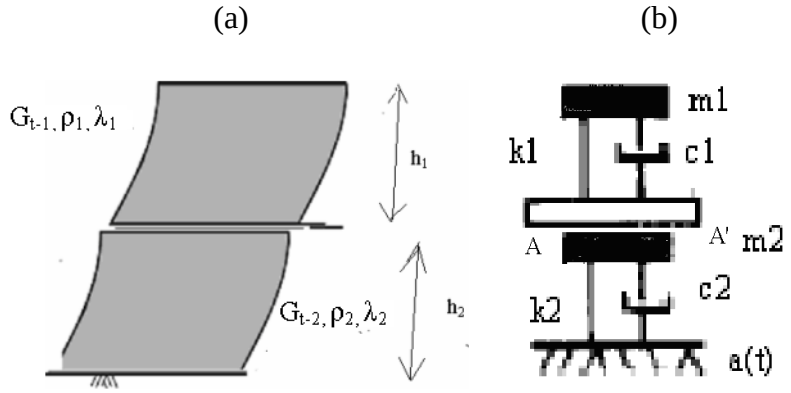

Figure 2: (a) Continuous system dynamic system considered in the present work, (c) the assumed discrete dynamic system approximation.

Fig. 2b gives the assumed equivalent discrete 2-body dynamic system with slip element approximation of the continuous system of Fig. 2a. If no slippage at the slip surface occurs, the equation of motion of the 2-body system of Fig 1b is:

$$m_1 x_1'' = m_{ef-1} \times a(t) + k_1(t)[x_1 - x_2] + c_1(t)[x_1' - x_2'] \tag{1a}$$

$$m_2 x_2'' = m_{ef-2} \times a(t) - k_1(t)[x_1 - x_2] - c_1(t)[x_1' - x_2'] - c_1(t)[x_1' - x_2'] + k_2(t)x_2 + c_2(t)x_2'$$

where

$$m_i = \frac{\rho_i \times h_i}{2} \tag{1b}$$

$$m_{ef-i} = \frac{2 \times \rho_t \times h_i}{\pi}$$

$$k_i(t) = \frac{\pi^2 \times m_i \times G_{t-i}(t)}{4 \times h_i^2 \times \rho_t}$$

$$c_i(t) = \frac{\pi \times m_i \times \lambda_i}{h_i} \sqrt{\frac{G_{t-i}(t)}{\rho_t}}$$

where a(t) is the applied acceleration in the base of the system in terms of time t, $k_i(t)$ and $c_i(t)$ are the viscous damping and spring stiffness coefficients of bodies 1 and 2, in terms of time t, m_i are the masses of bodies 1 and 2 and m_i are the equivalent masses of bodies 1 and 2 where the inertia acceleration is applied.

The above system can be expressed in matrix form as

$$\begin{bmatrix} m_1 & 0 \\ 0 & m_2 \end{bmatrix} \begin{bmatrix} x''_1 \\ x''_2 \end{bmatrix} = \begin{bmatrix} k_1(t) & -k_1(t) \\ -k_1(t) & k_1(t)+k_2(t) \end{bmatrix} \begin{bmatrix} x_1 \\ x_2 \end{bmatrix} + \begin{bmatrix} c_1(t) & -c_1(t) \\ -c_1(t) & c_1(t)+c_2(t) \end{bmatrix} \begin{bmatrix} x'_1 \\ x'_2 \end{bmatrix} - a(t) \begin{bmatrix} m_{ef-1} \\ m_{ef-2} \end{bmatrix} \tag{2}$$

Also, non-linear elasticity and the geometry of Fig. 2b predicts that for any incremental change in horizontal displacement of the two bodies (dx_1, dx_2) the corresponding incremental change in shear stress at time t ($d\tau_1$, $d\tau_2$) at the two bodies equals

$$d\tau_1 = G_{t-1}(t)\frac{dx_1 - dx_2}{h_1} \tag{3a}$$

$$d\tau_2 = G_{t-2}(t)\frac{dx_2}{h_2} \tag{3b}$$

Sliding at the slip element of Fig. 2b occurs when

$$-a_c(t) - \frac{m_{ef-1}}{m_1} x_1'' - a(t) > 0 \tag{4a}$$

where $a_c(t)$ is the horizontal acceleration for relative displacement of the slip element, in terms of time. In particular, the effect of rotation of the sliding mass above the slip surface is simulated by increasing the critical acceleration of the slip element with the distance moved along the slip element (u) as:

$$a_c(t) = a_{co} + 11\frac{u}{L} \tag{4b}$$

where a_{co} is the critical acceleration at u=0 and L is the slip length.

Sliding in only one direction is assumed and the governing equation of motion at the slip element is

$$u'' = -a_c(t) - \frac{m_{ef-1}}{m_1} x_1'' - a(t) = -a_c(t) - 0.64x_1'' - a(t) \qquad \text{for} \quad u' > 0 \qquad (5)$$

where u'' and u' is the relative acceleration and velocity along the slip element.

During sliding, the two bodies move separately. The equations of motion for the upper and lower masses become:

$$m_1 x_1'' + c_1(t)x_1' + k_1(t)x_1 = -m_{ef-1}[a(t) + u''(t)] \qquad (6)$$

$$m_2 x_2'' + c_2(t)x_2' + k_2(t)x_2 = -m_{ef-2}a(t) - u''(t)m_{ef-1} \qquad (7)$$

Sliding stops when the relative velocity of the slip element (u') becomes zero. Then, again equations (1) hold.

The above solution is, according to the terminology used by [4,5], is "coupled". On the other hand, in the approximate "decoupled" case, separation of the two bodies is not simulated and equations (6), (7) are not applied. Furthermore, for the rigid conventional sliding-block case, the above equations do not hold: sliding occurs when

$$-a_c(t) - a(t) > 0 \qquad (8a)$$

and the governing equation of motion at the slip element is

$$u'' = -a_c(t) - a(t) \qquad \text{for} \quad u' > 0 \qquad (8b)$$

It should be noted that in equations (7) the critical acceleration for relative motion is expressed in terms of $a_c(t)$, and thus the effect of rotation of the sliding mass above the slip surface is simulated by equation (3b).

2.2 Constitutive modeling of the soil profile in the non-linear case

For the non-linear case, at the soil profile bodies i (i=1,2), the tangent shear modulus G_{t-i} is estimated as:

$$G_{t-i}(t) = \frac{G_{o-i}}{T_i(t)} \qquad (9a)$$

where

$$G_{o-i} = Vs_i^{\,2}\rho_t \qquad (9b)$$

$$T_i(t) = 1 + \left(\frac{1}{a_i} - 1\right)\left|\frac{\tau_t(t) - \tau_{o-t}(t)}{b_i}\right| \qquad (9c)$$

where $G_{o\text{-}i}$ and Vs_i are the shear modulus and shear wave velocity respectively at very small shear strain, a_i and b_i are model parameters and $\tau_i(t)$ and $\tau_{o\text{-}i}(t)$ is the shear stress and the shear stress of the last stress reversal at time t of body i.

3 DISCUSSION OF THE PROPOSED EQUATIONS

Based on the discussion in section 1 above, equations (1b), (4a), (5) are identical to those used by Rathje and Bray [5] and the form of equations (1a), (6) and (7) is similar to those used by Lin and Whitman [4]. In addition, equation (4b) has been used by Jafarian and Lashgari [7].

The constitutive model equations (9) predicting shear modulus degradation along of the body above and below the slip element are similar to those proposed by Papadimitriou et al. [19], but adjusted for the dry simpler case. The state-of-art work by Vucetic and Dobry [23], indicates that the decrease of the shear modulus with the shear strain depends as a first approximation only on the Plastisity Index (PI) of the soil, as illustrated in Fig. 2a. In equations (8), the model parameters a_i specifies the Gs/Gmax ratio where the shear stress-degradation response is fitted, and the model parameter b_i fits the value of the actual response at a_i. A typical value of a_i for the problem considered is 0.5. Assuming ηa=0.5, for the simulation of Fig. 3a, β_i must vary in terms of only Go and PI. Assuming that ρ=2T/m^3, numerical simulations illustrated that typical values for sands are 1, 0.1, 0.02 for Vs = 100, 250, 500 m/s.

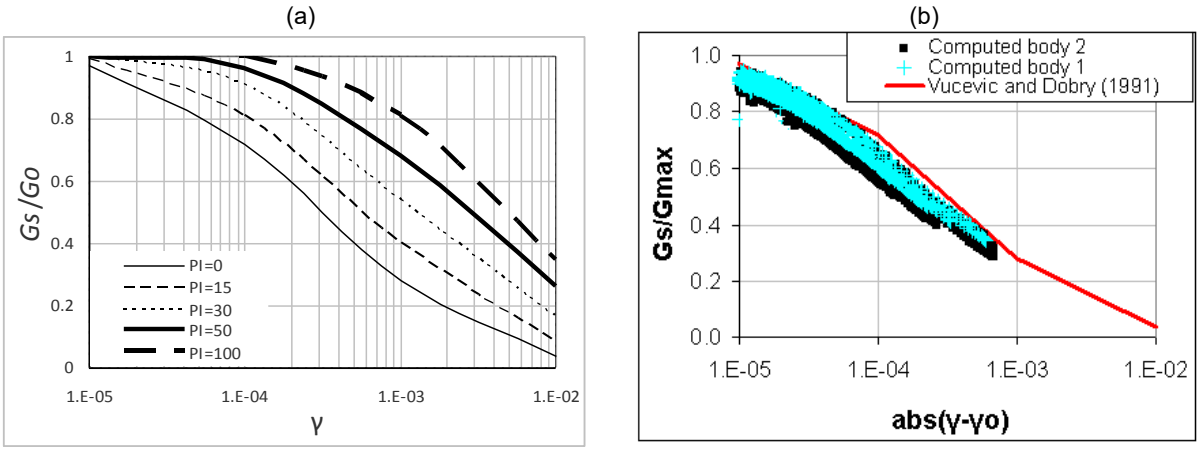

Figure 3: (a) State-of the art shear modulus degradation in terms of shear strain (γ) and Plasticity Index (PI) [23]. (b) simulation for this degradation for the case studied in section 4.1.

4 NUMERICAL IMPLEMENTATION AND APPLICATION

4.1 Numerical implementation

Equations (1)-(6), (8) and (9) simulating the non-linear dynamic response of a 2-body system with a slip element with constant strength were solved numerically using the Newmark method with its parameters β and γ taking the values of 0.25 and 0.50 respectively.

The linear case corresponds to a_1=a_2=1. For the linear case, input at the numerical code is the seismic acceleration history, the critical acceleration a_{co} and the variables h_i, Vs_i, ρ_i, λ_i. Output includes the acceleration time history of the two bodies for the coupled and decoupled cases and the acceleration, velocity and displacement history along the slip element for the coupled, decoupled and rigid cases. For the non-linear dry case, additionally, the val-

ues of the parameters a_i and b_i are needed. Additional output of the program in this case is (a) the tangent shear moduli of bodies 1 and 2 versus time, (b) the shear stress-strain response of the two bodies and the (c) the secant modulus degradation with shear strain of the two bodies.

Figures 4 and 3b give typical output results of the proposed method. The case of non-linear sandy soil with $h_1=h_2=15$m, $Vs_1=200$m/s, $Vs_2=300$m/s, $\rho_1=\rho_2=2$t/m^3, $\lambda_1=\lambda_2=0.15$, under the Aegion 1995 earthquake input motion and slip surface with $a_{c0}=0.5$m/s^2 and, L=100m and model parameters $a_1=\alpha_2=0.5$, $\beta_1=\beta_2=1$ is presented.

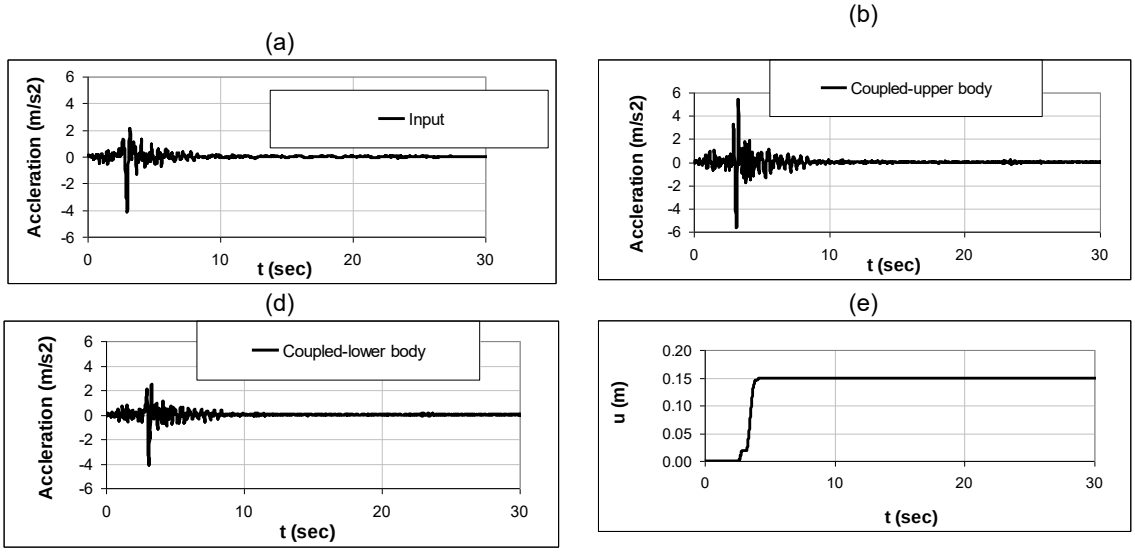

Figure 4: Typical results of the proposed method. The case of non-linear sandy soil with $h_1=h_2=15$m, $Vs_1=200$m/s, $Vs_2=300$m/s, $\rho_1=\rho_2=2$t/m^3, $\lambda_1=\lambda_2=0.15$, under the Aegion 1995 earthquake input motion and slip surface with $a_{c0}=0.5$m/s^2, L=100m and model parameters $a_1=\alpha_2=0.5$, $\beta_1=\beta_2=1$. (a) input acceleration history, (b),(c) acceleration histories of bodies 1 and 2, (d) seismic displacement along the slip surface versus time.

4.2 Example applications

Limited parametric analyses of the new model were performed to investigate critical factors affecting the final seismic displacement along the slip surface (u_f). In these analyses, the depth of rock (h_1+h_2) was taken as 30m, because this is the maximum depth which affects the results according to Eurocode [22]. In addition, for the density value, which does not affect considerably the dynamic soil response, the typical value of $\rho_1=\rho_2=2$t/m^3 was selected. Furthermore, the damping $\lambda_1=\lambda_2$ was taken as 15%, similarly to analyses by [5, 7]. Regarding the applied input motions, the Aegion 1995 earthquake input motion was used. Its characteristics are: Maximum acceleration (a_{max})=2.1(m/s^2), Predominant Period=0.42s, Mean Period (Tm)=0.62s, Magnitude (Ms)=6.1. It was selected because it is a typical European medium-magnitude motion.

In linear analyses, in order to define the proposed dynamic system, in addition to the parameters specified in the above paragraph, a_{co}, Vs_1, Vs_2, h_1 (or h_2) and L must be specified. The critical acceleration a_{co} was selected as 0.5m/s^2, because it corresponds for a rigid system to a seismic displacement of about 10cm, which is the tolerable displacement value for typical structures. Regarding the slip length L, first the case L=1000m was selected, because it corresponds to a large landslide where the effect of the rotation of the sliding mass does not play an important role. Then, the case of L=10m, because it corresponds to a landslide of very small slip length where the effect of the rotation of the sliding is critical even when the seismic displacement is a few centimeters. Similarly to the previous works [5, 7], the seismic displace-

ment is presented in terms of a_{co} and the Ts_1/Tm ratio, where Tm was defined above and Ts_1 is the fundamental period of the upper body of the system which slides, which equals

$$T_{S1} = \frac{4h_1}{Vs_i} \tag{10}$$

Figs 5a-c present the results of elastic parametric dynamic analyses described above. In particular, in Fig 4a the case with $Vs_2=Vs_1$ and $h_2=15$m is given. The rigid and decoupled case solutions, as well as the case of L=10m are given for comparison. In Fig 5b the case with $Vs_2=Vs_1$ and $h_2=1$m, 15m, 25m is presented. In Fig 5c the case with $Vs_2=150$, 300 or 500m/s and $h_1=h_2=15$m is presented. Fig. 6 presents the seismic displacement in terms of a_{co} for the case of $h_2=15$m, $Vs_1=Vs_2=200$m/s for L=1000m and L=10m for the Aegion 1995 earthquake. Fig. 6 also presents the seismic displacement in terms of L for $a_{co}=0.1$m/s^2 for the Aegion 1995 earthquake. In Fig. 6, in all cases the decoupled and rigid cases are also given for comparison.

The cases above do not simulate the decrease of shear modulus with shear strain, which is considerable, especially for sandy loose soils and high intensity input motions. Fig. 4d illustrates the effect of non-linearity of the soil profile on seismic displacement versus Ts_1/Tm for the case of Fig. 5d with $h_2=15$m, $Vs_1=Vs_2=$ 200m/s, $\rho_1=\rho_2=2$t/m^3, $\lambda_1=\lambda_2=0.15$, L=1000m, $a_1=\alpha_2=0.5$, $\beta_1=\beta_2=1$.

5 DISCUSSION

5.1 Interpretation

First the results of the linear analyses of section 4 are considered and the following can be observed:

(a) Regarding the response of u_f versus Ts_1/Tm, similarly to [5, 7]: (i) for $Ts_1/Tm=0$, u_f corresponds to the seismic displacement of the rigid case, (ii) as Ts_1/Tm increases, u_f increases until a peak value is reached, (iii) as Ts_1/Tm increases further, u_f decreases until if becomes zero and (iv), the coupled (and correct) solution gives u_f values less than the decoupled solution for most Ts_1/Tm values and, especially for Ts_1/Tm values, near unity.

(b) Regarding the effect of the stiffness soil layer below the slip surface, which has not been studied in detail by previous researchers, it changes significantly uf: For example Fig 5c illustrates that for $Vs_1=Vs_2$ and $Ts_1/Tm=1$, as h_2 varies, u_f changes from 0 to 0.20m and Fig 5b illustrates that for $h_1=h_2=15$m and $Ts_1/Tm=0.5$, as Vs_2 varies, u_f changes from 0.15 to 0.25m.

(c) Regarding the response of u_f versus a_{co}, similarly to [3] u_f decreases as aco increases, approximately, in a logarithmic manner. The dynamic response plays an important role for small seismic displacement and diminishes for very large seismic displacement (>1m).

Regarding the effect of rotation of the slip surface on u_f, similarly to [8], it is considerable for L values less than about 100m and uf values larger than about 0.1m.

Regarding the effects of non-linearity, Fig. 5d illustrates that the u_f versus Ts_1/Tm results are shifted to the left. This can be interpreted by the fact that as shear strain increases, the shear modulus decreases, and thus the effective Ts_1/Tm increases.

5.2 Possible applications and improvements/extensions

The parametric analyses illustrated that the proposed method simulates all critical factors affecting the seismic displacement of dry slopes, where the shear resistance along the slip surface does not change considerably with shear displacement. A typical case where this occurs

is the case of dry loose sandy soils. It would be interest to validate the model predictions against well-documented landslides on this type. Furthermore, the proposed method may be extended for the cases of (a) saturated soil profiles and (b) saturated surfaces which lose a considerable part their strength along the slip surface in terms of shear displacement, by implementing models predicting pore pressure build up (a) at the soil profile and (b) at the slip surface at the proposed method.

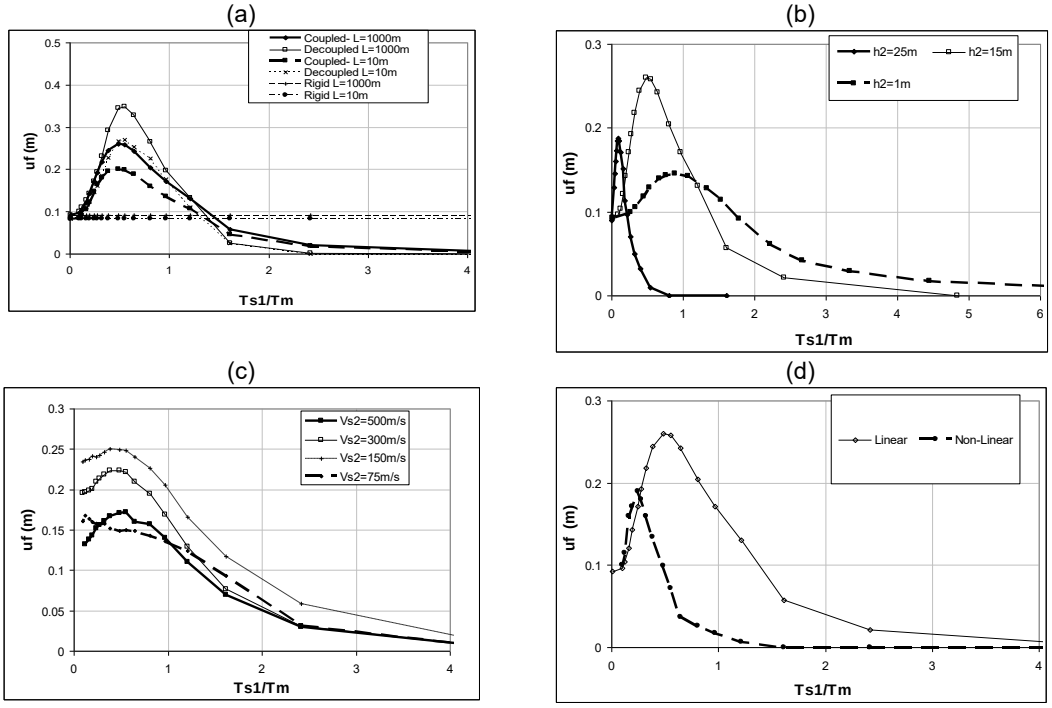

Figure 5: Results of dynamic parametric analyses The seismic displacement u_f for the coupled case versus Ts_1/T_m for the Aegion 1995 earthquake case with a_{co}=0.5m/s2, h_1+h_2=30m, $\rho_1=\rho_2$=2t/m3, $\lambda_1=\lambda_2$=0.15 for (a) elastic analyses if $Vs_2=Vs_1$ with h_2=15m and L=1000m and L=10m, (b) for elastic analyses if $Vs_2=Vs_1$, L=1000m, in terms of h_2 and (c) for elastic analyses if h_2=15m, in terms of Vs_2, L=1000m. (d) the linear and non-linear soil profile with $a_1=\alpha_2$=0.5, $\beta_1=\beta_2$=1 in the case of Fig. b, with h_2=15m. In (a) the rigid and decoupled cases are also given for comparison.

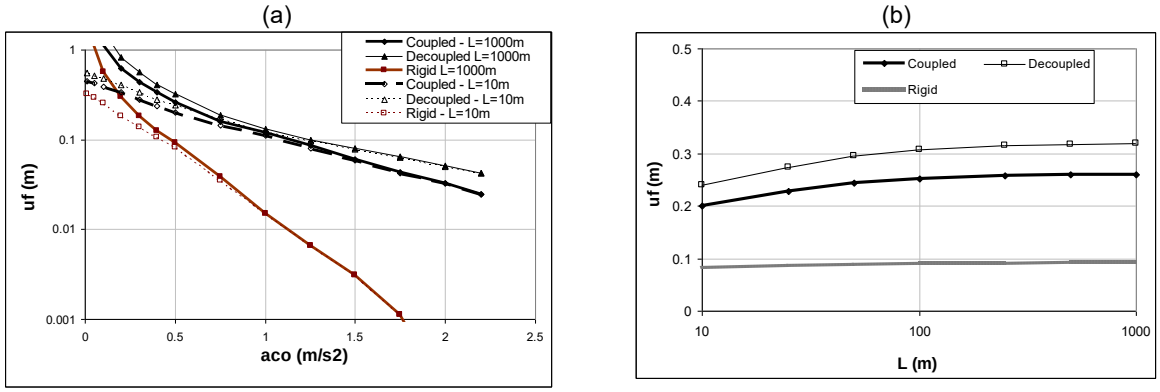

Figure 6: Results of dynamic parametric linear coupled, decoupled and rigid analyses. The seismic displacement u_f (a) in terms of a_{co} for L=1000m and L=10m and (b) in terms of L for a_{co}=0.5m/s^2.

6 CONCLUSIONS

- A new cost-effective method, given by equations (1)-(7) and (9), is proposed predicting the seismic sliding movement of dry slopes along slip surfaces with resistance that does not change considerably with shear displacement. The method models (a) the coupled dynamic response of soils both above and below the slip surface, (b) the rotation of the sliding mass effect and (c) the non-linear soil response at the soil medium, by combining previous work in a unique manner.
- The new method was solved numerically and applied at both the linear and non-linear cases. In the linear case the effects of the stiffness of the soil layer both above and below the slip surface on the seismic displacement are illustrated and interpreted. The effect of the rotation of the sliding mass is also illustrated. In the non-linear case, the effect of the shear modulus degradation in the soil profile was illustrated and interpreted.

REFERENCES

[1] Whitman R. V. (1993). Predicting earthquake-caused permanent deformations of earth structures, article on “Predictive Soil Mechanics”, Thomas Telford, London, 729-741

[2] Newmark, N. M. (1965). Effects of earthquakes on dams and embankments. Geotechnique, 55 (2), 139-159.

[3] Ambraseys N. and Menu J. (1998). Earthquake induced ground displacements, Earthquake engineering and structural dynamics, 16, 7, 985-1006.

[4] Lin J.-S., and Whitman, R.V. 1983. Decoupling Approximation to the evaluation of earthquake-induced plastic slip in earth dams. Earthquake Engineering and Structural Dynamics, 11: 667–678.

[5] Rathje E. M. and Bray J. D. An examination of simplified earthquake induced displacement procedures for earth structures. Can. Geotech. J. 36: 72–87 (1999)

[6] Rathje E. M. and Bray J. D. Nonlinear coupled seismic sliding analysis of earth structures. Journal of Geotechnical and Geoenvironmental Engineering 126 (11), 1002-1014 (2000)

[7] Jafarian Y. and Lashgari A. (2016). Simplified Procedure for Coupled Seismic Sliding Movement of Slopes Using Displacement-Based Critical Acceleration, International Journal of Geomechanics, Volume 16 Issue 4 - August 2016

[8] Stamatopoulos, C. A. Sliding System Predicting Large Permanent Co-Seismic Movements of Slopes. Earthquake Engineering and Structural Dynamics. 1996. Vol. 25, No, 10, 1075-1093.

[9] Stamatopoulos C. A., Velgaki E. and Sarma S. (2000). Sliding-block back analysis of earthquake-induced slides. Soils and foundations, The Japanese Geotechnical Society, Vol. 40, No. 6, Dec., pp 61-75.

[10] Sarma S.K. and Chlimitzas G. Co-seismic & post-seismic displacements of slopes, 15th ICSMGE TC4 Satellite Conference on "Lessons Learned from Recent Strong Earthquakes". 2001, 25 August, Istanbul, Turkey

[11] Stamatopoulos C. A., Velgaki E. Modaressi A., Lopez-Caballero F. (2006) Seismic displacement of gravity walls by a two-body model. Bulletin of Earthquake Engineering, Springer, Volume 4 Number 3, 295-318.

[12] Deng, J., Tsutsumi, Y, Kameya, H., Koseki, J. A Modified Procedure to Evaluate Earthquake-induced Displacement of Slopes Containing a Weak Layer. Soils and Foundations. 2010, 50, 3; 413-420

[13] Stamatopoulos C. A., Mavromihalis C, Sarma S. (2011). Correction for geometry changes during motion of sliding-block seismic displacement, ASCE, Journal of Geotechnical and Geoenvironmental Engineering, 137 (10), 926-938.

[14] Bandini V., G. Biondi, Cascone E., Rampello S.A (2015) GLE-based model for seismic displacement analysis of slopes including strength degradation and geometry rearrangement. Soil Dynamics and Earthquake Engineering 71. 128–142

[15] Stamatopoulos C. (2009). Constitutive modeling of earthquake-induced slides on clays along slip surfaces. Landslides. Volume 6, Number 3, 191-207.

[16] Stamatopoulos C. (2015). Constitutive and multi-block modeling of slides on saturated sands along slip surfaces, Soils and foundations, The Japanese Geotechnical Society, 55(4): 703–719

[17] Stamatopoulos C. A., Di B., Sidiropoulos P. , Stamatopoulou M. C. The seismic displacement of a block sliding on an inclined plane with resistance varying with the distance moved. Soil Dynamics and Earthquake Engineering, Volume 114, November 2018, Pages 69-84

[18] Chopra, A.K., and Zhang, L. 1991b. Earthquake-induced base sliding of concrete gravity dams. Journal of Structural Engineering, ASCE, 117(12): 3698–3719.

[19] Papadimitriou A., Bouckovalas G., Dafalias Y. (2001) Plasticity model for sand under small and large cyclic strains. Journal of Geotechnical and Geoenviromental Engineering, ASCE; Vol.127, No. 11, pp. 973-983.

[20] Lopez-Caballero Fernando, Arezou Modaressi-Farahmand Razavi, Hormoz Modaressi. Nonlinear numerical method for earthquake site response analysis I— elastoplastic cyclic model and parameter identification strategy. Bull Earthquake Eng (2007) 5:303–323

[21] Modaressi, A. and López-Caballero, F., Global Methodology for Soil Behavior Identification and its Application to the Study of Site Effects (2001). International Conferences on Recent Advances in Geotechnical Earthquake Engineering and Soil Dynamics. 7.

[22] European Standard (2003). Eurocode 8: Design of structures for earthquake resistance, Final Draft, prEN 1998-5, 2003, December.

[23] Vucetic M. And Dobry R. "Effect of soil plasticity on cyclic response, Journal of the Geotechnical Division, ASCE, 117 (1). 1991. Bolton M. D. (1986). The strength and dilatancy of sands. Geotecnique 36 (1), 65-78.

[24] Chopra A. K. 2012. Dynamics of Structures. (4th Edition). Prentice-hall International Series in Civil Engineering and Engineering MechanicsO.C. Zienkiewicz, R.C. Taylor, *The finite element method, Vol. I, 4th Edition*. McGraw Hill, 1989.

COMPDYN 2019
7th ECCOMAS Thematic Conference on
Computational Methods in Structural Dynamics and Earthquake Engineering
M. Papadrakakis, M. Fragiadakis (eds.)
Crete, Greece, 24–26 June 2019

PREDICTING THE GROUND MOVEMENT ABOVE A TUNNEL IN CHITTAGONG COASTAL AREA OF BANGLADESH UNDER SEISMIC LOADING

Mehedi Ansary[1], **MF Haque**[2]

[1] Professor, Department of Civil Engineering, BUET
Dhaka-1000
e-mail: ansary@ce.buet.ac.bd

[2] Graduate Student, Department of Civil Engineering, BUET
Dhaka-1000
e-mail: mfh.civil@gmail.com

Abstract

Settlement is the vital issue for analysis of a tunnel in any conditions of soils such as sand, clay etc. Many researches have been carried out to predict surface settlement above a tunnel but some technique needs further research to be established. In this paper, analysis of EPB-TBM (Earth Pressure Balanced Tunnel Boring Machine) tunnel has been considered along a straight line through homogeneous sand layer which has been observed in the Chittagong Coastal area, Bangladesh. Circular type tunnel is considered for analysis. Direct effect of seismic fault has been neglected. Phased construction method has been incorporated to analyze this event. Important parameters for surface settlement of tunnel are tunnel depth, tunnel diameter, tunnel construction technique, different relative densities of sand etc. In this paper, the variation of tunnel depth and tunnel diameter has been considered and analyzed. Analysis has been performed through finite element based software PLAXIS 3D. Surface settlement along transverse and longitudinal to the tunnel axis has been predicted. Variation of depth (distance between free surfaces to top surface of the tunnel), tunnel diameter and length (phased excavation) have been considered to evaluate surface settlement for static and dynamic cases in sands.

Keywords: Settlement, PLAXIS 3D, Sand, EPB – TBM, Seismic, etc.

1 INTRODUCTION

Developing of underground space, tunneling is the most important issue in civil engineering. Tunnel is being constructed to densely populated areas as well as for long transportation infrastructures. Construction of tunnel induces ground movements which may affect existing structures. Ground movement is related with damage rate of tunnel. Generally, damage rate of tunnels are lower than surface structures under seismic loading. To prevent damages of tunnels, accurate assessment is necessary to predict tunneling-induced ground movements. Ground movement above a tunnel in sand has been reported by Mair and Taylor (1997), Vorster et al. (2005), Marshall et al. (2012) etc. Tunneling effects on pipelines and buildings have been investigated in sand by several authors (Klar et al., 2007, 2015; Farrell et al., 2014; Giardina et al., 2015; Franza & Marshall, 2017; Ritter et al., 2017). Relative depth of tunnel (A_n/D_n) and diameter of tunnel (D_n) are main factor to handle ground movement above a tunnel in sand with proper construction technique and relative density. The goal of this paper is to predict ground movement above a tunnel in sand in Patenga, Chittagong, Bangladesh. In this paper, circular type tunnel has been considered which moves along a straight line in sand layer. Variable parameters in these paper are relative depth of tunnel, diameter of tunnel and tunnel length with constant relative density and construction method (EPB – TBM). Numerically, ground settlements are observed with the variation of variable parameters under static as well as seismic loading. Linear analysis has been performed to predict ground movement above a tunnel. Finally, appropriate placement of tunnel in sand layer has been performed through numerical analysis.

Figure 1: Under construction of tunnel at Potenga, Chittagong, Bangladesh

2 LOCAL GEOLOGY AND GEOTECHNICAL PARAMETERS

According to GSB (1990), the local geology consists of mainly beach and dune sand. This sand contains light to whitish-grey sand which is medium to fine, well sorted, and

subrounded; this also contains concretions, shell fragments, heavy minerals, and rare clasts which include small mud-flat deposits. Unconformably overlies Late Tertiary formations. Several bore logs have been carried out at the project site. A typical bore log has been presented in Figure 2. The soil profile mainly consists of softy silty clay up to a depth of 3 to 5 m, which is underlain by fine sand.

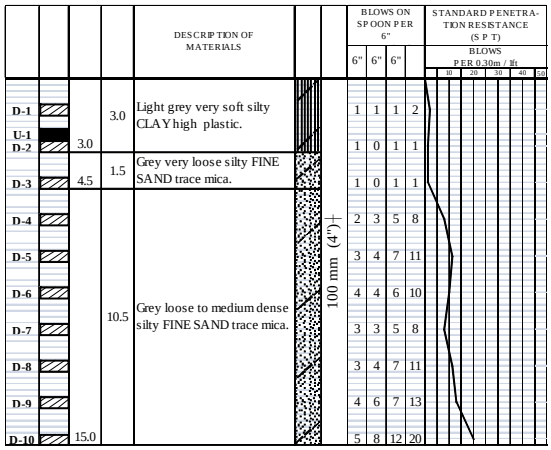

Figure 2: Typical borehole log at Potenga, Chittagong, Bangladesh

3 MODIFIED EMPIRICAL AND ANALYTICAL FORMULAS

Underground space technology such as tunneling has become very popular and demanding. In urban areas, people wants alternative mode of transportation for excellent facilities. Engineer must take note and gain high knowledge about tunneling technology. Protection needs of surface structures as well as underground facilities from ground movements due to construction of tunneling as well as seismic shaking after construction exist.

3.1 Modified Empirical Formula of Vertical Settlement

Vertical ground settlement is the major important issue during tunneling as well as seismic shaking and also long term behavior of tunnel. For practical purpose, important issue is the maximum settlement due to tunneling. The authors have modified Mair's (1993) maximum ground settlement formula with the consideration of 0.5 percent uniform volume loss (Mair and Taylor, 1997) for sand and 35 percent of *K* factor (Mair and Taylor, 1997) as shown below.

$$V_{(z),max.} = 0.0045 \frac{D^2}{(H - z)} \quad (1)$$

Where, *D, H, z,* $V_{(z),max.}$ are represented by inner diameter of tunnel (m), vertical distance (m) from free surface to tunnel center line, any vertical distance (m) from free surface and maximum vertical settlement (m). For surface settlement, z is equal to zero.

3.2 Modified Empirical Formula of Lateral Settlement

Lateral ground settlement affects surface structures and underground facilities similar to vertical settlement of ground. Maximum lateral settlement of ground has great role in professional field. O'Reilly and New (1981) gives an empirical formula to predict lateral surface settlement. The authors have modified this formula with the consideration of Atkinson and

Potts (1977) equation from the centrifuge tests for tunneling in dry sands which is shown below:

$$U_{(x),max.} = V_{(z),max.} \frac{A + D}{4(H - z)} \tag{2}$$

Maximum lateral ground settlement (m) and distance (m) from free surface to tunnel crown are expressed as $U_{(x),max.}$ and A in equation (2).

3.3 Modified Empirical Formula of Longitudinal Settlement

Most of tunneling analysis (Franza et al., 2018, Pescara et al., 2011, Franza and Marshall 2015) has been carried out based on plain strain consideration which has not included longitudinal settlement profile of tunnel. A few researches have been expressed in longitudinal settlement above a tunnel based on field observations. Attewell and Woodman (1982) gives an empirical relation to predict longitudinal ground settlement above a tunnel. Authors have modified this relation as shown below:

$$U_{(y),max.} = \frac{V_{(z),max.}}{(H - z)} \tag{3}$$

Where $U_{(y),max.}$ is expressed as maximum longitudinal ground settlement (m) and unit length consider along the longitudinal direction of tunnel due to plain strain consideration.

3.4 Modified Empirical Formula of Lateral Settlement Under Seismic Loading (USL)

A lot of seismic analysis has been performed for surface structures. A few data are available to express damage of tunnels after an earthquake before 1970's. Pescara, (2011) gives an empirical relation to predict lateral displacement above a tunnel under seismic shaking by using Eurocode 8. The authors have modified Pescara, (2011) formulae as shown below:

$$\Delta_{(x),max.} = f \frac{a_1 g S C k}{C_s} \left(C_d - (H - z)\right) \tag{4}$$

Where $\Delta_{(x),max.}$, a_1, g, S, C, k, C_d, f and C_s are represented as maximum lateral settlement (mm), seismic coefficient such as 0.15 (Bangladesh National Building Code (BNBC) 2006), gravitational acceleration (9.81m/s^2), soil factor (1.15) based on Eurocode 8 which equivalent to BNBC 2006, factor of ground motion (0.9) (Power et.al 1996), ratio of peak ground velocity to peak ground acceleration (142) (Power et.al 1996), total depth (27.5m) of upper layer and tunnel layer, modified factor (10) based on present author modified analytical formulae and apparent propagation velocity of S-wave: several authors [O'Rourke and Liu, 1999; Power et al., 1996; Paolucci and Pitilakis, 2007] have suggested values between 1 and 5 km/s.

3.5 Modified Analytical Formula of Vertical Settlement

Verruijt and Booker (1996) have showed a closed form general solutions for the calculation of the vertical ground settlement under uniform radial ground loss. Authors have modified these formula for long term as well as seismic loading. Long term ground deformation has been taken as 1mm based on observations by Rankin, (1988) and Loganathan et.al (1998). Maximum ground settlement for long term and seismic loading has been expressed by equations (5) and (6) which have been provided below, respectively.

$$V_{(z)max.} = -0.005R^2\left(\frac{z_1}{r_1^2}+\frac{z_2}{r_2^2}\right)+0.001R^2\left[\frac{z_1(-z_2^2)}{r_1^4}+\frac{z_2(-z_2^2)}{r_2^4}\right] + \frac{0.01R^2}{m}\left[\frac{(m+1)z_2}{r_2^2}+\frac{mz(-z_2^2)}{r_2^4}\right] - 0.002R^2H\left[\frac{-z_2^2}{r_2^4}+\frac{m}{m+1}\frac{2zz_2(-z_2^2)}{r_2^6}\right] \quad (5)$$

$$V_{(z)max.} = -0.005R^2\left(\frac{z_1}{r_1^2}+\frac{z_2}{r_2^2}\right)+\frac{0.01R^2}{m}\left[\frac{(m+1)z_2}{r_2^2}+\frac{mz(-z_2^2)}{r_2^4}\right] \quad (6)$$

Where, $z_1 = z - H$, $z_2 = z + H$, $r_1^2 = z_1^2$, $r_2^2 = z_2^2$, $R = D/2$, $m = 1/(1 - 2\upsilon)$, $k = \upsilon(1 - \upsilon)$. υ is the Poisson's ratio of soil. Long term ground deformation due to ovalization is equal to zero under seismic loading.

3.6 Modified Analytical Formula of Lateral Settlement

Verruijt and Booker (1996) have also showed a closed form general solutions for the calculation of the lateral ground settlement under uniform radial ground loss. Authors have also modified these formula based on Hunt (2004) and Zhou (2014) considering lateral distance from tunnel axis for long term and seismic loading which is shown below:

$$U_{(x),max.} = 0.00125R^2\left(\frac{(A+D)}{r_1^2}+\frac{(A+D)}{r_2^2}\right) - 0.0000625R^2\left[\frac{z_1((A+D)^2-16kz_1^2)}{r_1^4}+\frac{((A+D)^3-(A+D)16kz_2^2)}{4r_2^4}\right] + \frac{0.0025(A+D)R^2}{m}\left(\frac{1}{r_2^2}-\frac{2mzz_2}{r_2^4}\right) + \frac{0.001R^2(A+D)H}{(m+1)}\left[\frac{z_2}{r_2^4}+\frac{mz((A+D)^2-48z_2^2)}{16r_2^6}\right] \quad (7)$$

$$U_{(x),max.} = 0.00125R^2\left(\frac{(A+D)}{r_1^2}+\frac{(A+D)}{r_2^2}\right)+\frac{0.0025(A+D)R^2}{m}\left(\frac{1}{r_2^2}-\frac{2mzz_2}{r_2^4}\right) \quad (8)$$

Where, equation (7) represents as the maximum lateral settlement for long term loading and equation (8) represents as the maximum lateral settlement for seismic loading.

4 NUMERICAL ANALYSIS

Numerical analysis is necessary to evaluate behavior of underground structures under seismic loading. Material properties have been determined from two types of tri-axial tests such as consolidated drained and consolidated un-drained. Models have been created for analysis in software PLAXIS 3D based on the Potenga, Chittagong site conditions. Two types of parameters are used in this model such as fixed and variable. Fixed parameters are soil volume, material properties of soil and tunnel lining, borehole location etc. Variable parameters are tunnel length, diameter and relative depth. Mohr-Coulomb material model has been con-

sidered for soil and linear elastic model consider for tunnel lining in long and short term behavior. Non-porous drainage type has been considered for lining segment. Bulk unit weight of silty clay, fine sand and lining segments are 16.4 kN/m^3, 18.6 kN/m^3 and 24 kN/m^3 for long term behavior and for short term behavior these values are 17 kN/m^3, 19.03 kN/m^3. Saturated unit weight of short and long term behavior of sands, clays are 20 kN/m^3, 20 kN/m^3, 19 kN/m^3 and 18.90 kN/m^3. Modulus of elasticity of clay, sand and lining segments are 14.4 MPa, 26.1 MPa and 28 GPa for long term behavior and 22.5 MPa, 40.8 MPa for short term loading. Cohesion of clay has 30 kPa for both long as well as short term loading. Internal friction angle of sands and clays are 29^0, 23^0 for short term loading and 36^0, 23^0 for short term behavior. Dilatancy angle of sand is 6^0 for long term behavior only. Poisson's ratio of sands, precast segment and clays are 0.25, 0.20 and 0.31 for both cases. Face pressure, grouting pressure and jacking force of tunnel are 90 kN/m^2 with axial increment 14 kN/m^2/m, 100 kN/m^2 with axial increments of 20 kN/m^2/m and 600 kN/m^2. 0.5% uniform surface contraction has to be taken with axial increment of 0.05%.

In seismic analysis, free field boundary conditions have been taken along lateral direction because of seismic loading has to be applied in this direction. Software automatically considers other values which are necessary to analyze this model. Most of the earthquakes have a frequency range such as 8 to 12 Hz. Material damping has been considered as 5%. Length of Earth Pressure Balance Tunnel Boring Machine (EPB-TBM) considered is 12m. Maximum number of steps and maximum number of iteration are 250 and 60 in analysis for long and short term loading. Initial length of tunnel is 25m and tunnel advancement of 2m along its own axis is considered. Three stage of advancement of tunnel have been considered for analysis. Variable diameters of tunnel are 10.5m, 10.8m and 11.0m. Depths from free surface to top surface of tunnel are 4.5m, 5.5m, 6.5m, 7.5m, 8.5m. Thickness of pre-cast segment considered is 0.5m. The finite element model is shown in Figure 3.

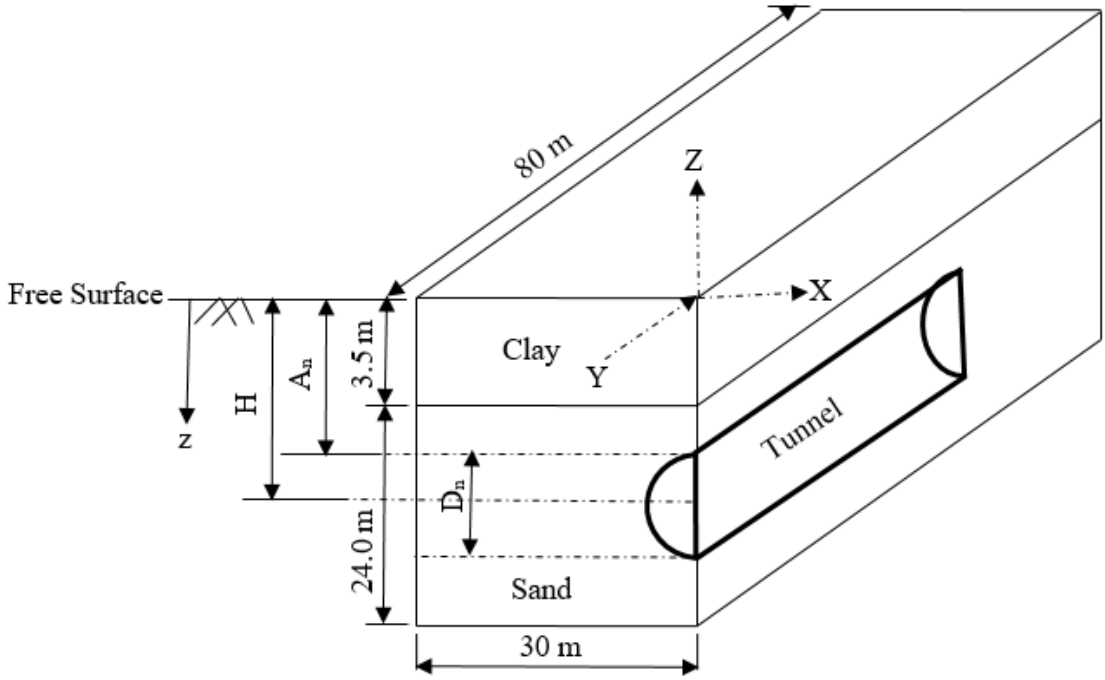

Figure 3: Finite element model based on Potenga soil conditions at Chittagong

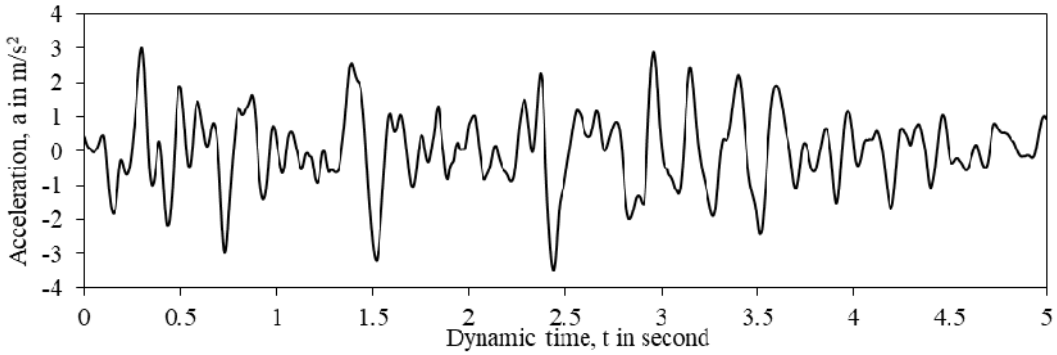

Figure 4: Seismic data at Potenga, Chittagong.

When model geometry, material properties and other relevant data are fully defined then model has to be divided into finite elements in order to perform finite element calculations. This type of composition of finite element method is called mesh. Fine mesh will be used to obtain accurate numerical results. Half portion of the tunnel has been considered because of symmetry. 10-node tetrahedrons soil element have been taken for analysis. Every phase consists of a particular loading or construction stage. Analysis phases are initial, plastic and seismic. In plastic phase of calculation, drained behavior has been taken and un-drained (A) option has been taken for seismic loading. Seismic data has been input in the software based on a real seismic event in Chittagong as shown in Figure 4. Plastic calculation is related with the elastic-plastic deformation analysis. In a normal plastic calculation, the stiffness matrix is based on the original un-deformed geometry. Loading can be defined in various sense during plastic calculation mode such as changing the load combination, stress state, weight, strength or stiffness of elements, activated by the changing the load and geometry configuration or pore pressure distribution by means of staged construction. For meshing, the number of cores is set to 256 for this model. Software performs seismic analysis after the completion of modeling and static analysis. Seismic analysis is the complex type of dynamic analysis which contains non-periodic loading history. The applied seismic load is the product of the input value of the defined seismic load and corresponding seismic load multiplier. Activation of the seismic load or seismic prescribed displacement, free field boundary conditions can be defined for a seismic analysis. Meshing of the model is presented in Figure 5. Meshing effect on model has been shown in Table 1.

Table 1: Meshing effect on model due to tunneling

Tunnel Length, y_1 (m)	Ratio, A_1/D_1	Maximum total vertical settlement, V_{zt} in mm		
		Coarse	Medium	Fine
27	0.4286	44.7	44.5	44.5

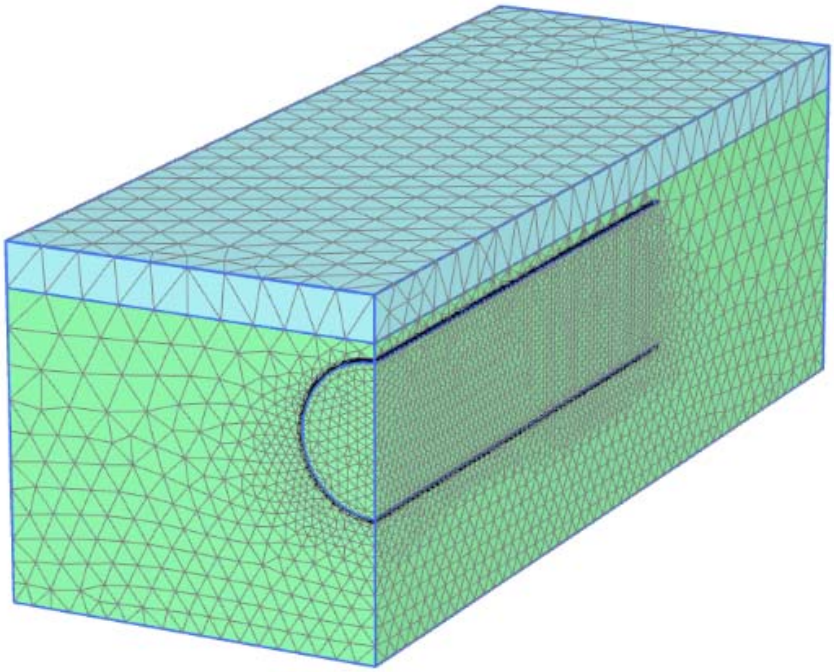

Figure 5: Un-deformed fine meshing of the research model

Seismic loadings are imposed for a short time but its impact upon the structures or soil is high. High frequency of seismic loading can easily pass through the small elements of these model. Fine meshing which yields best analysis is applied under seismic loading.

5 RESULTS AND DISCUSSIONS

Maximum surface settlement in vertical, lateral and longitudinal directions above a tunnel has been discussed here. Variation of surface acceleration in lateral direction is also presented. Seismic loading has been applied in the model for five seconds in lateral direction. Some terms used to express results are MEF-LTL (Modified Empirical Formulae Long Term Loading), MEF-SL (Modified Empirical Formulae Seismic Loading), MAF-LTL (Modified Analytical Formulae Long Term Loading), MAF-SL (Modified Analytical Formulae Seismic Loading) etc. Following parameters are varied: diameter – 10.5m (D_1), 10.8m (D_2), 11.0m (D_3), length – 27m (y_1), 29m (y_2), 31m (y_3) and relative depth – 4.5m (A_1), 5.5m (A_2), 6.5m (A_3), 7.5m (A_4), 8.5m (A_5).

5.1 Vertical Surface Settlement Above a Tunnel

Vertical surface settlement consists of stability of structures which stands on the ground surface. Vertical surface settlement depends on the variation of relative depth, tunnel length and tunnel diameter. These settlements are calculated based on previously mentioned equations and are shown in Figure 6. Three diameters represent almost similar results during seismic and long term loading based on modified formula. Results of modified analytical and empirical formulae are very close for long term loading. Settlement gradually decreases with the increase in relative depth based on author modified formulae. Minimum settlement is 30mm at A_5/D_1 location using MAF-SL formula.

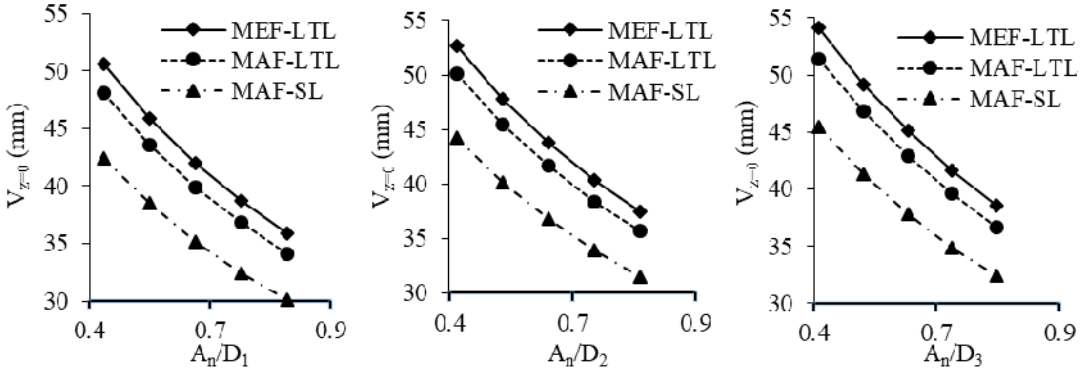

Figure 6: Vertical surface settlement for long term and seismic loading based on modified formulae.

Figure 7 and Figure 8 present the vertical surface settlement for long term and seismic loading based on numerical analysis using PLAXIS 3D. Uplift has been observed for each loading types, longitudinal length and diameter. Three construction stages of tunnel coincide at a point A_5 for long term loading which represents minimum settlement, apparently 7 mm at A_5/D_1 location. Third construction stage of tunnel fully represents uplift under seismic loading for three diameters. Minimum settlement is nearly 2 mm at A_5/D_1 location under seismic loading.

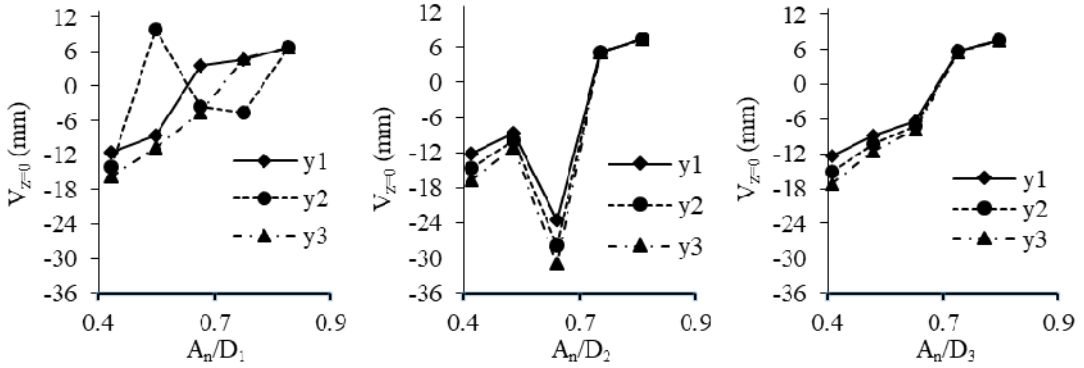

Figure 7: Vertical surface settlement for long term loading based on finite element method.

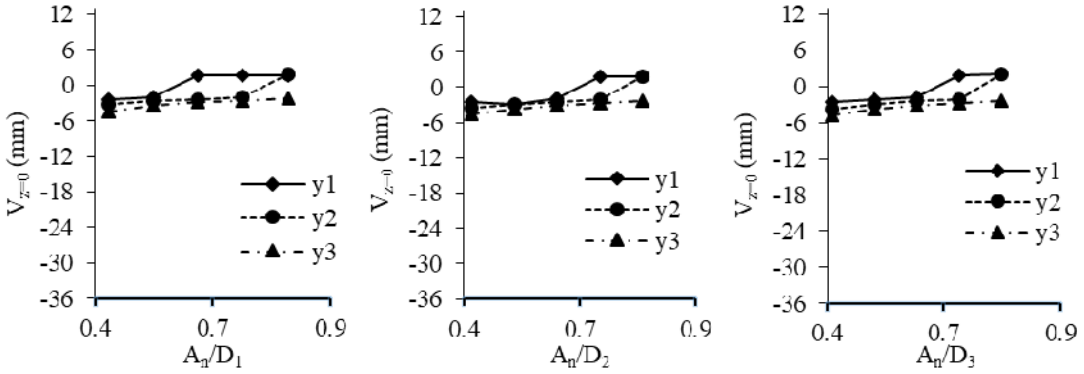

Figure 8: Vertical surface settlement for seismic loading based on finite element method.

5.2 Lateral Surface Displacement Above a Tunnel

Lateral surface settlement consists of lateral stability of super structures under long term (Figure 9) and under seismic (Figure 10) loading effect. Change of these settlements is made based on variation of depth of tunnel crown, length of tunnel and diameter of tunnel. Modified

and numerical methods have been used to calculate these settlements. At A_5 location, lateral settlement is nearly 9mm of diameter D_1 for long term loading based on modified formulae in Figure 9.

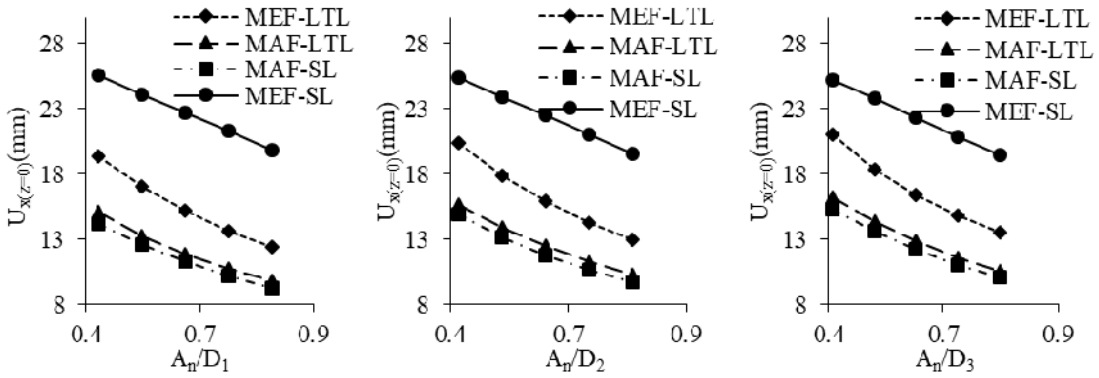

Figure 9: Lateral surface settlement for long term and seismic loading based on modified formulae.

At A_5 location, lateral settlement is nearly 3mm of diameter D_1 for long term loading based on finite element method in Figure 10. According to Figure 11, uplift is observed during seismic loading at A_5 location which indicates the minimum value.

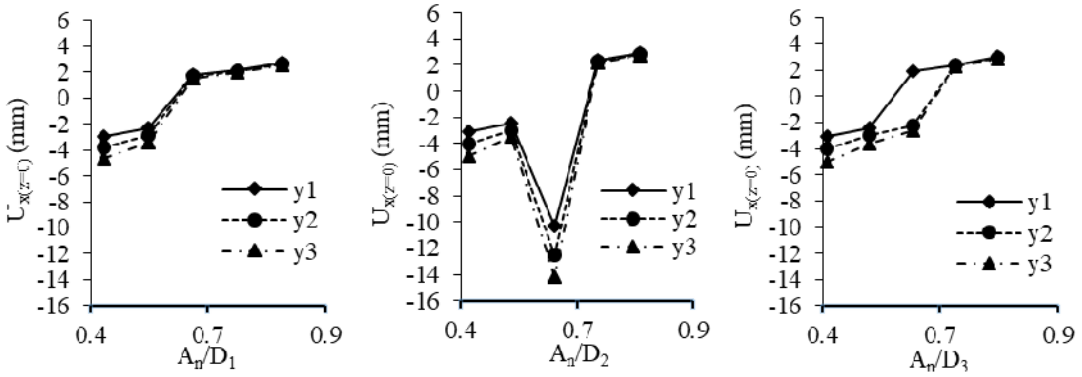

Figure 10: Lateral surface settlement for long term loading based on finite element method.

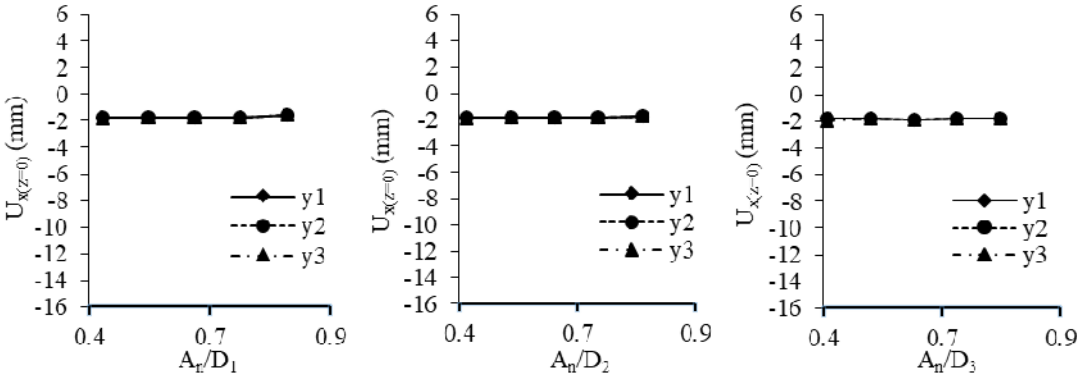

Figure 11: Lateral surface settlement for seismic loading based on finite element method.

5.3 Longitudinal Surface Displacement Above a Tunnel

Longitudinal ground movement along length of the tunnel can be seen in Figure 12. These settlement profile also express that the effect of phased construction of tunnel. Minimum val-

ue of settlement is 2.6mm due to extension at A_5/D_1 location based on author modified formulae as can be seen in Figure 12.

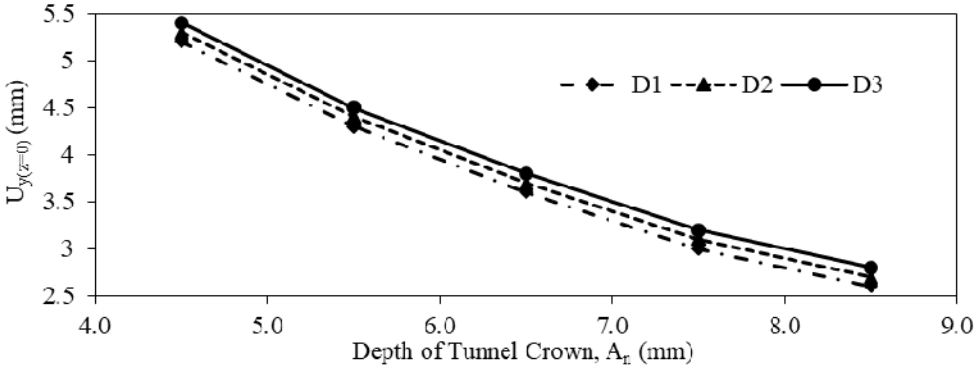

Figure 12: Longitudinal surface settlement for long term loading based on modified formulae.

Figures 13 and Figure 14 show negative value of settlement which indicates the contraction of ground due to tunneling and positive settlement express that the extension of tunnel along its length. Settlement gradually decreases with the increase of depth of tunnel crown for modified and numerical formulae. Minimum settlement is 3mm due to contraction at A_5/D_1 locations for long term loading based on numerical analysis. Longitudinal settlement is very low during seismic analysis which is nearly 0.3mm at A_5/D_1 location. Figure 15 shows longitudinal surface settlement profile based on finite element method PLAXIS 3D.

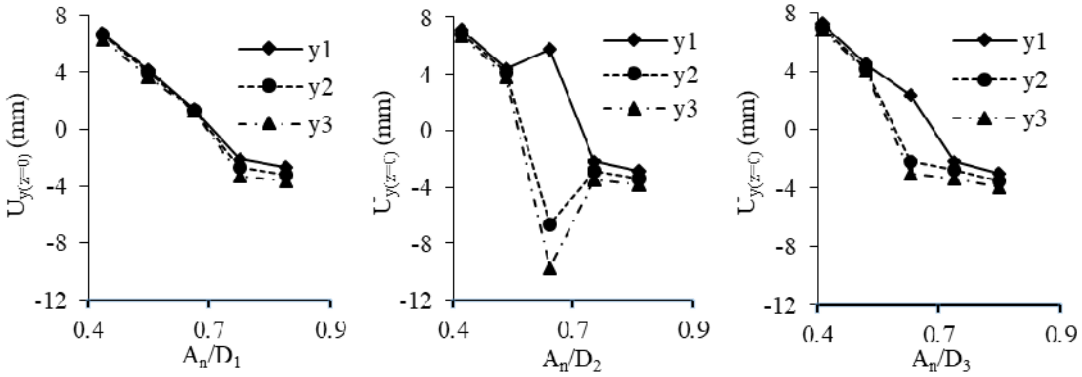

Figure 13: Longitudinal surface settlement for long term loading based on finite element method.

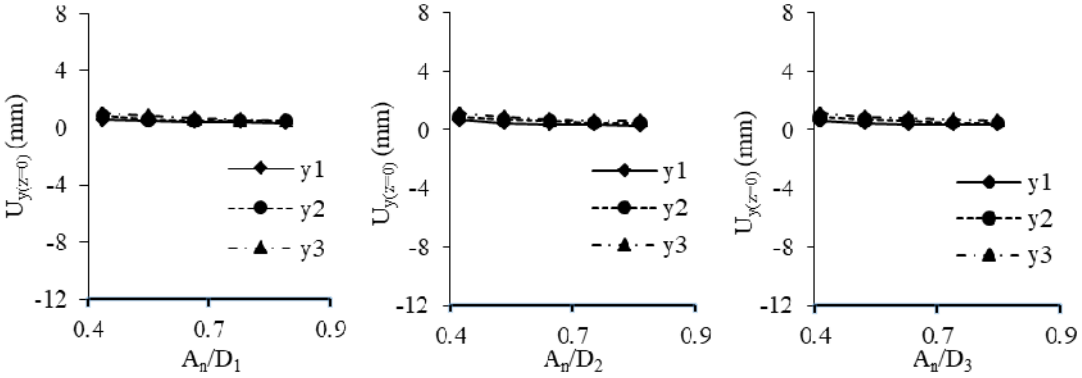

Figure 14: Longitudinal surface settlement for seismic loading based on finite element method.

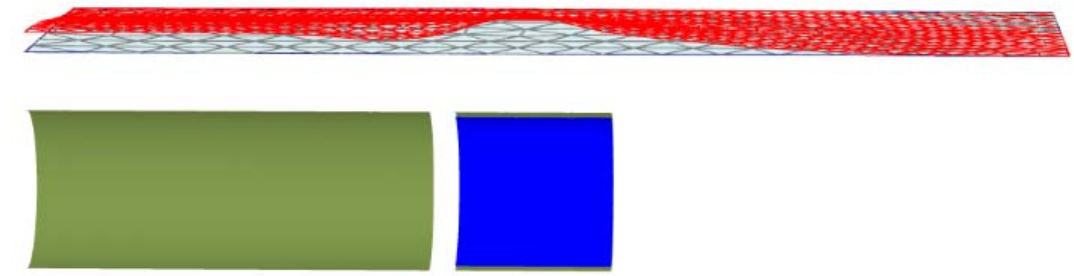

(a) Upward settlement due to tunneling

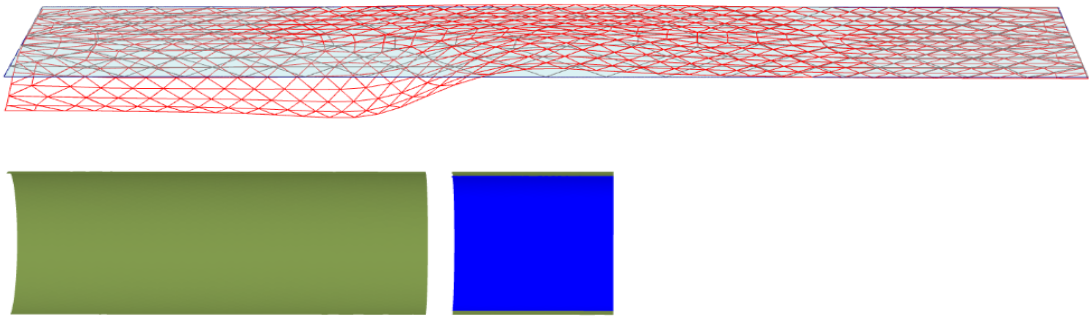

(b) Downward settlement due to tunneling

Figure 15: Longitudinal surface settlement profile based on finite element method.

5.4 Surface Accelerations Above a Tunnel Under Seismic Loading (USL)

Ground movement above a tunnel has been produced by surface acceleration. Lateral acceleration of tunnel is critical than other two directions. A lot of points are present on the surface. One point (-3, 15.5, -0.1) has been used here to express surface acceleration. Surface acceleration gradually decreases with the increase in depth of tunnel crown for diameter, D_1 as shown in Figure 16. Line A_5 shows the minimum acceleration for diameter, D_1 at 0.25s. The acceleration value is nearly 0.24 m/s^2. The value of acceleration for diameter, D_2 and D_3 is higher than diameter, D_1. Acceration values are -0.5 m/s^2 for diameter D_2 and nearly 0.8 m/s^2 for diameter D_3 at 0.25s.

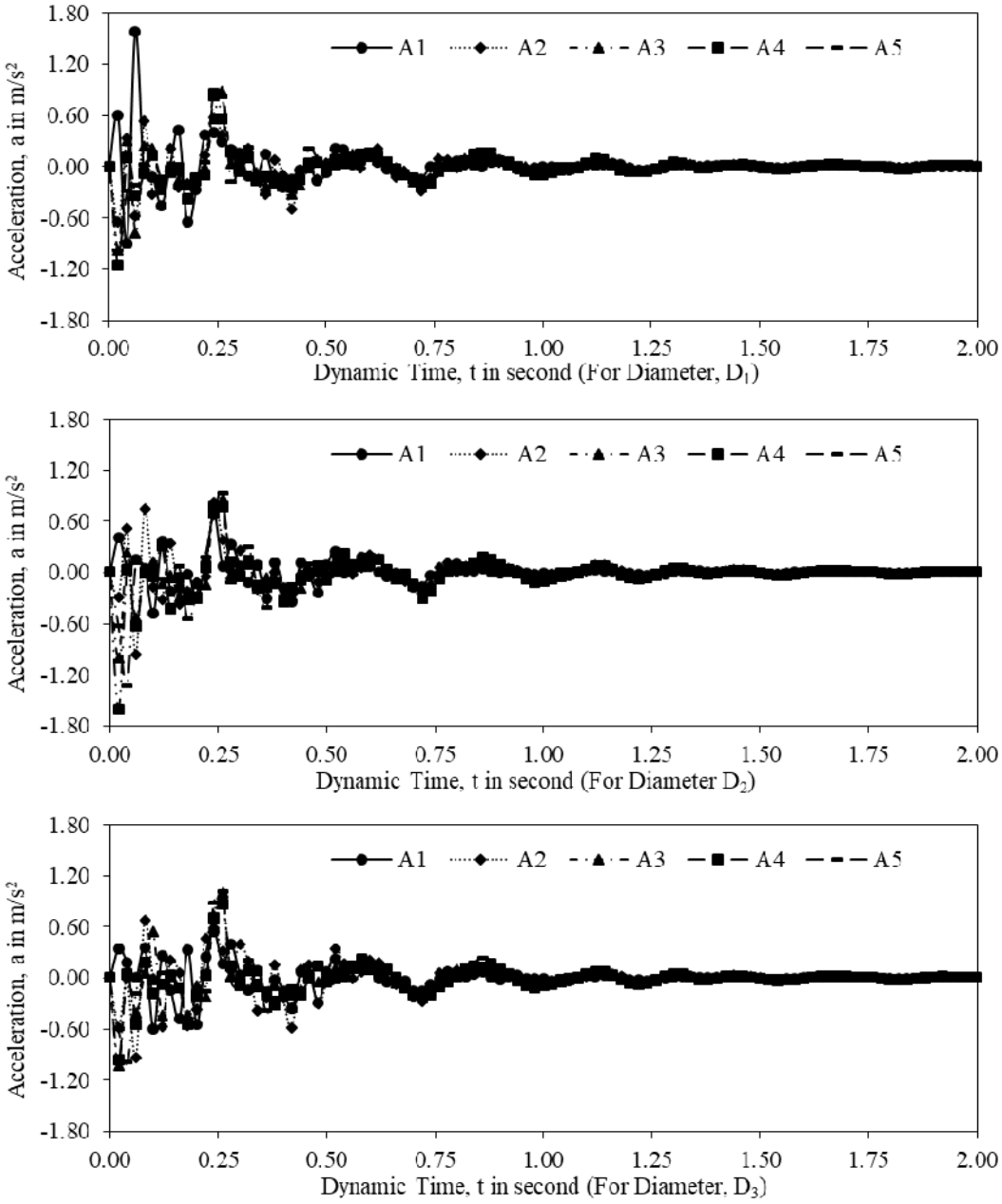

Figure 16: Lateral surface acceleration during seismic loading based on numerical analysis.

6 CONCLUSIONS

Movement of tunnel in homogeneous sand layer has been studied for ground structures in Chittagong coastal area. Upward surface settlement occur because of soft upper clay layer. Another reason of upward settlement is the shallow depth of tunnel placement. The results obtained from author modified empirical and analytical formula apparently match well. Surface settlement is more important than the total settlement for tunneling. Results of these research deals with maximum value. Minimum values of maximum vertical surface settlements are 7 mm for long term loading and 2 mm for seismic loading. Minimum values of maximum lateral surface settlements are 3 mm for long term as well as seismic loading and

9 mm for modified formulae. Similarly, minimum values of maximum longitudinal surface settlements are 3 mm due to contraction for long term loading and 0.3 mm for seismic loading. Settlement obtained from the author modified formula are greater or nearly equal to the finite element methods. Minimum value of acceleration is 0.24 m/s^2 under seismic loading. In these research, value of seismic loading is lower than the long term loading because of seismic source is located far away from the tunneling project. Two major conclusions are:

(1) Author modified formula may be used for practical purpose for all types of underground tunnel which passes through the sand layers.
(2) Suitable depth of the tunnel for this analysis is 8.5 m and suitable diameter is 10.5 m.

Future studies may be conducted such as replacement of homogeneous layer with the heterogeneous layers, considering strong seismic loading, inclination of tunnel, two or more tunnel, tunnel passes through the active seismic fault reason etc.

ACKNOWLEDGEMENTS

This work has been carried out in the Department of Civil Engineering, BUET. The authors gratefully acknowledge the support and facilities provided by BUET.

REFERENCES

[1] Mair, R. J. & Taylor, R. N. (1997). *Bored tunneling in the urban environment*. In 14th International conference on soil mechanics and foundation engineering, pages 2353–2385. 5, 10, 14, 169.

[2] Vorster, T. E., Klar, A., Soga, K., & Mair, R. J. (2005). *Estimating the e□ects of tunneling on existing pipelines*. Journal of Geotechnical and Geoenviromental Engineering, pages 1399–1410. 8, 22, 52, 65, 117.

[3] Marshall, A. M., Farrell, R., Klar, A. & Mair, R. (2012). *Tunnels in sands: the effect of size, depth and volume loss on greenfield displacements*. Géotechnique 62, No. 5, 385–399, https://doi.org/ 10.1680/geot.10.P.047.

[4] Klar, A., Vorster, T. E., Soga, K. & Mair, R. J. (2007). *Elastoplastic solution for soil–pipe–tunnel interaction*. J. Geotech. Geoenviron. Engng 133, No. 7, 782–792, https://doi.org/10.1061/(ASCE) 1090-0241(2007)133:7(782).

[5] Klar, A., Elkayam, I. & Marshall, A. M. (2015). *Design oriented linear-equivalent approach for evaluating the effect of tunneling on pipelines*. J. Geotech. Geoenviron. Engng 142, No. 1, 04015062, https://doi.org/10.1061/(ASCE)GT.1943-5606. 0001376.

[6] Farrell, R., Mair, R., Sciotti, A. & Pigorini, A. (2014). *Building response to tunnelling*. Soils Found. 54, No. 3, 269–279, https://doi.org/10.1016/j.sandf.2014.04.003.

[7] Giardina, G., DeJong, M. J. & Mair, R. J. (2015). *Interaction between surface structures and tunnelling in sand: centrifuge and computational modelling*. Tunnelling Underground Space Technol. 50, 465–478, https://doi.org/10.1016/j.tust.2015.07.016.

[8] Marshall, A. M. & Franza, A. (2017). Discussion of *"Observation of ground movement with existing pile groups due to tunneling in sand using centrifuge modelling"* by Ittichai Boonsiri and Jiro Takemura. Geotech. Geol. Engng 35, No. 1, 535–539, https://doi.org/10.1007/s10706-016-0083-x.

[9] Ritter, S., Giardina, G., DeJong, M. J. & Mair, R. J. (2017). *Influence of building characteristics on tunnelling-induced ground movements*. Géotechnique 67, No. 10, 926–937, https://doi.org/10.1680/jgeot.SIP17.P.138.

[10] GSB (1990). *Geological Map of Bangladesh*.

[11] Mair, R. J. (1993). *Developments in geotechnical engineering research: application to tunnels and deep excavations* Proc. Inst. Civil Engineers, Civil Engineering, Vol.93, 27-41.

[12] O'Reilly, M. P. & New, B. M. (1982). *Settlements above tunnels in the United Kingdom - their magnitude and prediction*. In Tunnelling 82, Papers Presented at the 3rd International Symposium, London, England, Brighton, England. Inst of Mining and Metallurgy. 13, 14, 22.

[13] Attewell, P. B. & Woodman, J. P. (1982). *Predicting the dynamics of ground settlement and its derivatives caused by tunnelling in soil*. Ground Engineering, Vol.15, No. 8, 13-22 and 36.

[14] Pescara, M., Gaspari G. M., & Repetto, L. (2011). *Design of underground structures under seismic conditions: a long deep tunnel and a metro tunnel*. Geodata Engineering SpA, Torino, Italy.

[15] Power, M. S., Rosidi, D. & Kaneshiro, J. (1996). *Strawman: screening, evaluation, and retrofit design of tunnels*. Report Draft. Vol. III, National Center for Earthquake Engineering Research, Buffalo, New York.

[16] O'rourke, M.J. & Liu, X. (1999). *Response of buried pipelines subject to Earthquake effects*. Monograph No.III, MCEER (Multidisciplinary Center for Earthquake Engineering Research) Publications, University at Buffalo, Red Jacket Quadrangle, Buffalo, NY 14261.

[17] Paolucci, R., Pitikalis, k. (2007). *Seismic risk assessment of underground structures under transient ground deformation*. In Pitikalis, K. (editor). Earthquake Geotechnical Engineering. Chapter 18, pp 433-459. SpringerVienna.

[18] Verruijt, A. & Booker, J. R. (1996). *Surface settlements due to deformation of a tunnel in an elastic half plane,* Geotechnique, Vol. 46, No. 4, 753-756.

[19] Rankin, W. J. (1988). "*Ground Movements Resulting from Urban Tunnelling: Predictions and Effects.*" Engineering Geology of Underground Movements Geological Society, 76-88.

[20] Loganathan, N. & Poulos, H. G. (1998). *Analytical Prediction For Tunnelling Induced Ground Movement In Clays*. Journal of Geotechnical and Geoenvironmental Engineering / September 1998.

[21] Hunt, D. (2004). *Predicting The Ground Movements Above Twin Tunnels Constructed In London Clay*. PhD Thesis. Department of Civil Engineering, School of Engineering, The University of Birmingham.

[22] Zhou, B. (2014). *Tunnelling-induced ground displacements in sand*. PhD thesis, University of Nottingham. millan Company, New York.

[23] Technical Manual for Design and Construction of Road Tunnels — Civil Elements. Publication No. FHWA-NHI-10-034. December 2009.

[24] EUROCODE 8. (2003). Design of Structures for Earthquake Resistance, Draft No. VI, European Committee for Standardization, Brussels.

[25] BNBC 2006. Bangladesh National Building Code – 2006.

[26] Franza, A., Marshall, A. M. & Zhou, B. (2018). *Greenfield tunnelling in sands: the effects of soil density and relative depth*. Géotechnique

[27] Franza A. and Marshall A.M. (2015). "Semi-analytical prediction of ground movements due to shallow tunnels in sand". Proceedings of the XVI ECSMGE, Geotechnical Engineering for Infrastructure and Development, ISBN 978-0-7277-6067-8, doi:10.1680/ecsmge.60678.

[28] Atkinson, J. H. and Potts, D. M. (1977). Stability of a shallow circular tunnel in cohesionless soil. G´eotechnique, 27(2):203–215. 12, 29, 85.

COMPDYN 2019
7th ECCOMAS Thematic Conference on
Computational Methods in Structural Dynamics and Earthquake Engineering
M. Papadrakakis, M. Fragiadakis (eds.)
Crete, Greece, 24–26 June 2019

SEISMIC SLIDING DISPLACEMENT OF SLOPES IN TERMS OF SOIL PROFILE TYPE

Loukas C. Kastenis[1], Constantine A. Stamatopoulos[2] , Vassilis P. Panoskaltsis[3] and Kyriaki T. Thomaidou[4]

[1] PhD candidate, Department of Civil Engineering, Demokritos University of Thrace, Greece
e-mail: katsenisloukas@yahoo.gr

[2] Partner, Stamatopoulos and Associates Co; Instructor, Hellenic Open University; 5 Isavron str, Athens, 11471, Greece, e-mail: k.stam@saa-geotech.gr

[3] Professor, Department of Civil Engineering, Demokritos University of Thrace, Greece
e-mail: panoskaltsis@yahoo.com

[4] Former student, Hellenic Open University; 1 Anixeos street, Veria, Greece,
e-mail: kyrithoma@hotmail.com

Abstract

In earthquake analyses, usually the seismic displacement along slip surfaces is estimated by the sliding-block model, where a rigid block rests on an inclined plane and every time that the applied horizontal acceleration is larger than the critical horizontal acceleration value for relative motion, the block slides. Different empirical expressions have been proposed predicting the seismic displacement of the sliding-block model, in terms of characteristics of the applied seismic motion and the critical horizontal acceleration for sliding. However, the seismic displacement along a slip surface depends on the dynamic characteristics of the soil profile both above and below the slip surface. Eurocode classifies the soil profiles into at least 4 distinct categories. The present work proposes empirical expressions relating the seismic displacement along slip surfaces in Greece, in terms of not only to characteristics of the acceleration history and the critical horizontal acceleration for sliding, but also to the soil type category according to Eurocode, as well as, the depth of the slip surface. For this purpose, extensive parametric analyses using a recently developed dynamic coupled numerical code which predicts the seismic displacement along slip surfaces at some of depth of elastic soil profiles. An extensive data base of seismic motions recorded in Greece is used and applied for typical soil profiles according to Eurocode with varying critical acceleration value and slip surface depth. The results are analyzed statistically and related to the conventional sliding-block permanent seismic displacement predictions.

Keywords: slopes, sliding-block model, dynamic response, seismic displacement, Greece, empirical equations.

SEISMIC SLIDING DISPLACEMENT OF SLOPES IN TERMS OF SOIL PROFILE TYPE

1 INTRODUCTION

Damage of natural and man-made slopes usually occurs as a result of excessive movement along slip surfaces. Engineers usually assess the seismic safety of slopes using the dynamic factor of safety calculated along slip surfaces by comparing the applied forces to the soil strength [1]. However, evaluations based on the dynamic factor of safety have the serious drawback that they do not consider the seismic displacement, which is directly related to damage [2].

The "conventional" sliding-block model [3] is the most commonly used simplified model predicting the seismic displacement of slopes for given earthquake motions [4]. A rigid block rests on an inclined plane. The resistance along the block-inclined plane boundary follows the Mohr-Coulomb law. Critical acceleration is defined as the minimum horizontal acceleration which causes movement of the block. Every time where the applied horizontal acceleration is larger than the critical acceleration, the block slides. The total displacement is obtained by the addition of the partial slips. It depends on the critical acceleration of the block and the applied seismic motion. This model is used for the prediction of permanent seismic movement of slopes along a predefined slip surface, by appropriately selecting the equivalent critical and applied acceleration values of the "conventional" sliding-block model [2, 3, 4].

Different empirical expressions have been proposed predicting the seismic displacement of the sliding-block model, in terms, primarily, of the ratio of the maximum acceleration of the applied seismic motion divided by the critical horizontal acceleration for sliding [4-9]. Some of these expressions use other than the maximum acceleration parameters of the seismic motion, such as the maximum velocity or the Arias Intensity, or parameters of the earthquake that produced the seismic motion, such as its earthquake magnitude or its earthquake fault distance [5, 9]. In addition, region-specific empirical expressions have been proposed predicting the seismic displacement of the sliding-block model, as different regions have different earthquake faults and geological profiles conditions, and thus potentially different applied seismic motions characteristics. Region-specific empirical expressions predicting the seismic displacement with the "conventional" sliding-block model for seismic motions in Greece has been proposed by [9].

The conventional sliding-block model described above assumes rigid motion and thus it does not consider the dynamic response of the soil both above and below the slip surface, which affects the seismic displacement along the slip surface. Based on results of simplified dynamic models, expressions have been proposed predicting the seismic displacement along the slip surface in terms of not only the critical acceleration for sliding and characteristics of the applied seismic motion described above, but also characteristics affecting the dynamic response of the sliding mass such as its height and shear wave velocity [10-12]. However, the seismic displacement along a slip surfaces depends not only on the dynamic characteristics of the sliding mass, but also on the dynamic characteristics of the soil profile below [13, 14]. On the other hand, recently, a new cost-effective method, is proposed predicting the seismic sliding movement of dry slopes in soil profiles along slip surfaces with resistance following the Mohr-Coulomb law. The method models the coupled dynamic response of soils both above and below the slip surface [13]. An advantage of this method is simplicity, which makes it ideal in performing dynamic parametric analyses.

Depending on the geographical locations, National Codes specify the characteristics of the design typical seismic motion, such as the maximum seismic acceleration [15]. This seismic

motion typically corresponds at bedrock sites. Furthermore, Eurocode [1] classifies the soil profiles into distinct categories, presumably exhibiting similar dynamic response. Based on the above, it is of interest for practicing engineers, to relate the seismic displacement along slip surfaces, not only to characteristics of the seismic motion and the critical horizontal acceleration for sliding, but also to the soil type category according to Eurocode, as well as, possibly, the depth of the slip surface.

The purpose of the present work is to propose empirical expressions relating the seismic displacement along slip surfaces in Greece, in terms of not only characteristics of the acceleration history and the critical horizontal acceleration for sliding, but also to the soil type category according to Eurocode, as well as, the depth of the slip surface. In particular, it proposes and validates equations correcting the predictions of the conventional sliding-block model for typical seismic motions of Greece in terms of the soil profile type according to Eurocode and the depth of the slip surface. For this purpose, the following are performed below: (a) ground profile types are described according to Eurocode, (b) a data base of seismic motions in Greece is collected, (c) typical ground profile types according to Eurocode are selected and numerical analyses are performed using the recently developed numerical code by [13], (d) based on the analyses performed and statistical analysis an empirical equation correcting the seismic displacement predictions of the sliding-block model based on the soil type category according to Eurocode, as well as the depth of the slip surface is derived and validated, (e) the results are discussed and an example practical application of the proposed expression for the prediction of the seismic displacement of an actual slope in Greece is given.

2 GROUND TYPES ACCORDING TO EUROCODE

Eurocode [1] defines ground types A-E, as given in table 1, based on observations by the earthquake engineering community that (a) only the first 30m depth of a soil profile play a critical role in the dynamic response, (b) for given soil type, the only soil property that affects the dynamic response is the shear wave velocity and (c) for similar dynamic response, a non-uniform soil profile with n layers may be simplified by an uniform one, with shear velocity Vs_{30}, defined as :

$$Vs_{30} = \frac{30\text{m}}{\sum_{i=1}^{n} \frac{h_i}{Vs_i}} \tag{1}$$

where h_i and Vs_i is the thickness in m and elastic shear wave velocity of layer i of the n layers of the soil profile.

Ground type	Description	Vs_{30} (m/s)
A	Rock or other rock-like geological formation	>800
B	Deposits of very dense or medium-dense sand, gravel or stiff clay	360-800
C	Deep deposits of dense or medium-dense sand, gravel or stiff clay	180-360
D	Deposits of loose-to-medium cohesionless soil or of soft-to-firm cohesive soil	<180
E	Soil profile consisting of a surface alluvium layer with Vs values of type C or D and thickness varying between 5-20m, underlain by type A soil	

Table 1: Ground type according to Eurocode [1].

3 DATA BASE OF SEISMIC MOTIONS IN GREECE

For the present work, real-time acceleration histories from the most significant recorded seismic events that took place in Greece between 1970 and 2014 were used as a database. Data were obtained from the Internet Site for European Strong-Motion Data (www.isesd.hi.is/). In addition, the seismic recording from the recent earthquake that occurred in Kefalonia on 03/02/2014 of size M≥6.10 [Argostoli, Lixuri, Chavriata], which were not included until recently in the European Strong-Motion Database (ESD) was used. In particular, the filtered acceleration time histories for the horizontal seismic component xx were obtained. The criteria used to select the Database are the magnitude of the earthquake and the maximum acceleration α max≥0.04g.. A total of 50 seismic motions were selected in this manner. Table A1 of the Appendix presents the number of the seismic motion, its name, its station, its date, and its magnitude (Mw). The time histories were analyzed with the seismosignal program [16] the to extract the spectral and temporal parameters. Table A2 of the Appendix presents for each seismic motion, its mean period, its predominant period, its peak acceleration and velocity value (a_{max} and V_{max}), its Arias intensity and its Epicentral distance.

4 NUMERICAL ANALYSES PERFORMED AND TYPICAL RESULTS

The analyses were performed using the coupled sliding dynamic model and associated numerical code proposed by Katsenis et al [13]. The model, illustrated in Fig. 1, considers the 1-dimensional dynamic response of a horizontal soil profile of depth (h_1+h_2) with a slip element at depth h_1. Different shear wave velocities (Vs_1, Vs_2), densities (ρ_1, ρ_2) and damping (λ_1, λ_2) may exist above and below the slip element. The resistance along the slip element is defined by the critical horizontal value at the initial configuration (a_{co}), for which relative movement in only one direction occurs. Thus, the horizontal slip element simulates the seismic displacement of the conventional sliding-block model. The model also simulates the rotation of the slip surface with displacement by adjusting the critical acceleration value (a_c) in terms of the accumulated seismic displacement. For seismic displacement less than about 1m, this effect diminishes when the length of the slip surface is larger than about 1000m. An option also exists where the model also simulates the non-linear shear stress-stain response of the soil profile. The numerical code associated with the numerical model above predicts the final seismic displacement along the slip element (u_f). Furthermore the numerical code predicts the corresponding seismic displacement for the given applied acceleration history and critical acceleration value that the conventional sliding-block model predicts ($u_{f\text{-}rigid}$).

In the present application, the elastic soil profile option of the model [13] was used. In addition a very long slip surface option (10000m) of the model [13] was used and thus a_{co}=a_c. According to Eurocode ground types of table 1, the soil profiles of table 2 were selected. The Vs_1,Vs_2 values correspond to the average ones of each soil profile of table 1, while the density value does not affect considerably the dynamic soil response and the typical value of ρ=2t/m^3 was selected. The damping was taken as λ_1=λ_2=15%, similarly to analyses by [5, 7, 13]. The critical acceleration value a_c was selected in such a way that computed final seismic displacement of the conventional sliding-block case ($u_{f\text{-}sl}$) varies from about 0.05m to about 0.5m. The reason is these are tolerable displacement values for typical structures.

At least five (5) a_c values were selected for each seismic motion and Vs_1,Vs_2 soil profile. For all these cases of soil profiles and a_c values, the 50 seismic motions described in section 2 above were applied and the seismic displacement (u_f) was computed. For comparison

reasons, the seismic displacement for a rigid block for the same applied motion and critical acceleration value ($u_{f\text{-}sb}$) was also estimated. Typical obtained result for seismic motions with high and low a_{max} values for the 4 seismic profiles considered are given in Fig. 2.

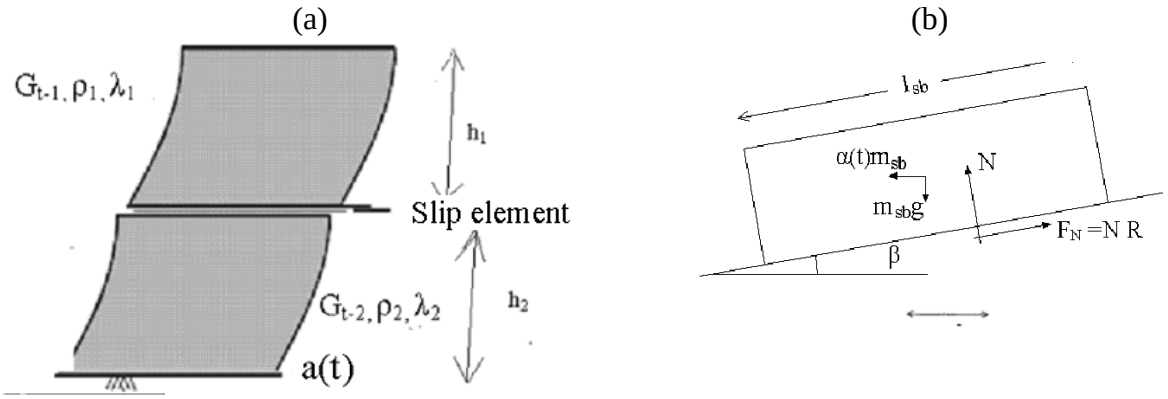

Fig. 1: (a) The dynamic system considered in the present work. The slip element simulates the response of the conventional sliding block model, given in (b).

Ground type	Vs (m/s)	h_1	h_1+h_2	$\rho_1=\rho_2$	$\lambda_1=\lambda_2$	a_{co}
S-B	$Vs_1=Vs_2=580$	5, 10, 20m	30m	2t/m3	0.15	In such a way that computed final seismic displacement along the slip surface (uf) varied from a few mm to tens of cm
S-C	$Vs_1=Vs_2=270$					
S-D	$Vs_1=Vs_2=100$					
S-E	Vs_1=200m/s, Vs_2=1000m/s					

Table 2: Soil profiles assumed in the analysis

5 EMPIRICAL EQUATION: FORM AND DERIVATION AND VALIDATION PROCEDURE

As described in the introduction section, different empirical expressions have been proposed predicting the seismic displacement of the conventional sliding-block model ($u_{f\text{-}rigid}$) in terms of factors such as a_c, a_{max}, Arias intensity, earthquake magnitude etc. In addition, some of these expressions are region-specific. As described above, as different regions have unique earthquake faults and geological profiles characteristic conditions, they have seismic motions of different characteristics and thus different empirical expressions predicting seismic displacement. Region-specific empirical expressions predicting ($u_{f\text{-}rigid}$) in Greece has been proposed by [9].

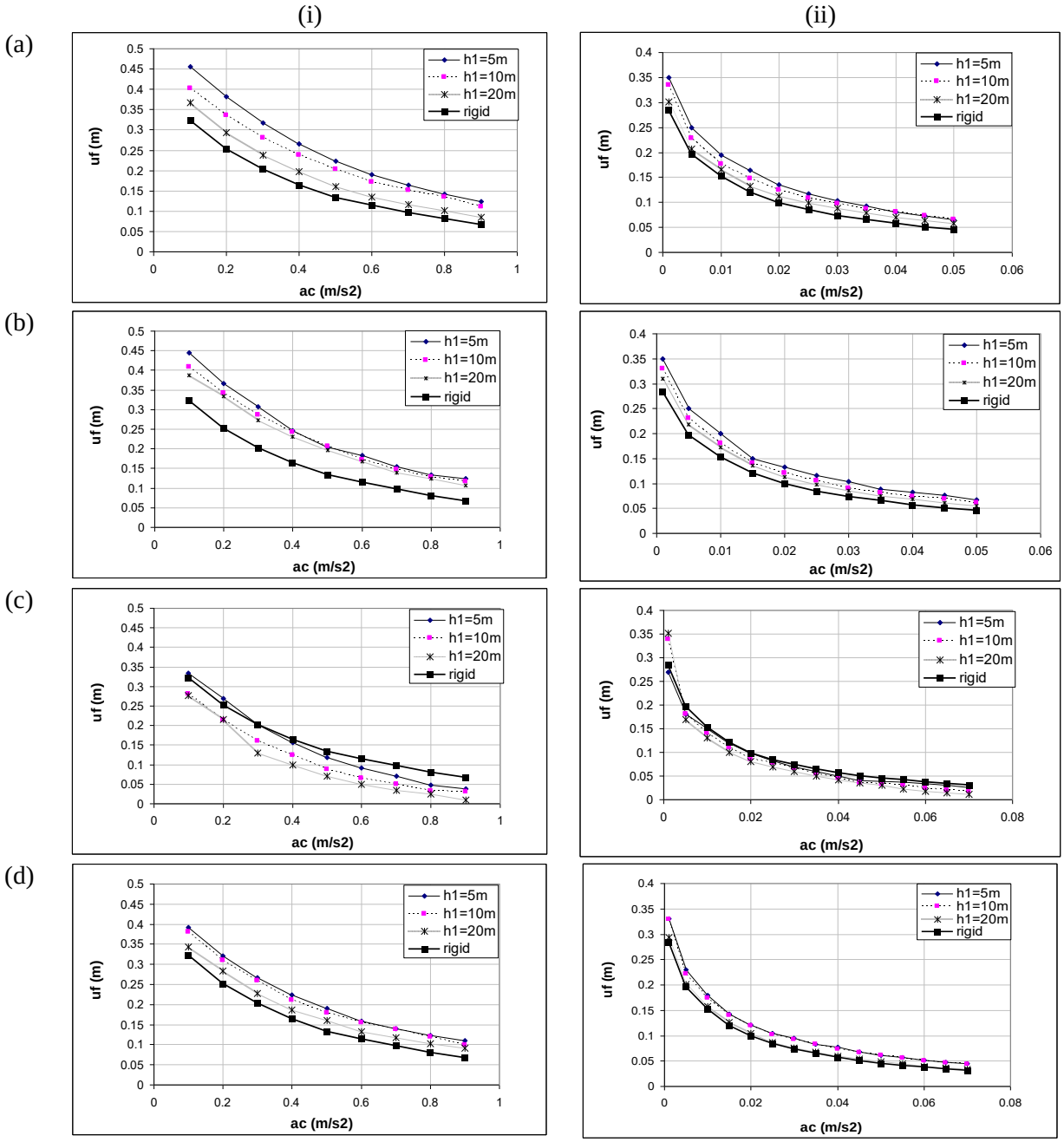

Fig. 2: Typical results for a seismic motion of high and low a_{max} value. Seismic displacement u_f in terms of the critical acceleration value for soil profiles (a) S-B, (b) S-C, (c) S-D, (d) S-E of table 2 for seismic motion (i) S3 and (b) S29 of table A1. The corresponding sliding-block displacement ($\mathbf{u_{f\text{-}rigid}}$) is given in all cases.

For this reason, in order, possibly to omit predicting the effect of factor such as a_c, a_{max}, Arias intensity, earthquake magnitude etc on u_f , we propose just to relate u_f on $u_{f\text{- rigid}}$, where $u_{f\text{- rigid}}$,is predicted with previously proposed equations and the u_f incorporates, additional the dynamic effects of the soil profile both above and below the slip surface. More specifically, we propose the following equation to predict $u_{f.}$:

$$u_f = R\, u_{f\text{-rigid}} \tag{2}$$

Thus,

$$R = u_f / u_{f\text{-rigid}} \tag{3}$$

It is of interest to establish the factors of the soil profile affecting the value of R based on the numerical analyses performed. Fig. 3 gives the ratio R in terms of ($u_{f\text{-rigid}}$) of soil profiles (a) S-B, (b) S-C, (c) S-D, (d) S-E of the analyses of Fig. 2. Preliminary inspections of the obtained results illustrates that R increases or decreases as a_c decreases, and at small a_c value it tends to 1. However, a_c for the design seismic displacement value varies a lot for different seismic motions. For example, according to Fig. 2, for the typical results for a seismic motion of high and low a_{max} value, a_c varies between 0.1-0.9g and 0.002-0.05g This variation is eliminated if the factor R is related to $u_{f\text{-rigid.}}$ Fig. 3 presents the ratio R in terms of ($u_{f\text{-rigid}}$) of soil profiles (a) S-B, (b) S-C, (c) S-D, (d) S-E of table 2 for seismic motion (i) S3 and (b) S29. It can be observed that: R increases or decreases as $u_{f\text{-sb}}$ increases, and at large $u_{f\text{-rigid}}$ value it tends to 1. Furthermore, from Fig 3 we observe that the response depends considerably on the soil type and the height of the depth of slip surface (h1): R takes a considerably less value for soil profile S-D than the other soil profiles and as h_1 increases, R generally decreases.

Based on the above we propose the following equation:

$$R = 1 + a1\, (0.1 / u_{f\text{-rigid}})^{a2} \tag{4}$$

where a1, a2 are model parameters. In particular, a1 gives the factor (R-1) at $u_{f\text{-rigid}}$=0.1m and a2 gives the manner that the factor R changes in terms of $u_{f\text{-sb}}$

Furthermore, based on the observations described above, we propose to relate the parameters a1, a2 of equation (4) with the soil profile type and h_1. For this purpose, the following procedure was followed:

- (a) First, the data base was divided in two parts, one to determine the model parameters (DB1), and the other to validate it (DB2). The data base DB1 is the odd number earthquakes and DB2 is the even number of earthquakes.

- (b) The model parameters n1 and n2 fitting best the results of the numerical analyses are obtained for each numerical analysis case of the data base DB1. Thus, 14 values for each seismic motion, and 12*25=300 in total. The best-fitting is performed under the conditions that the error has zero mean value and minimum standard deviation value. The error of the predictions is defined in the present work as

$$Er = 1 - \text{Predicted/Computed} \tag{5}$$

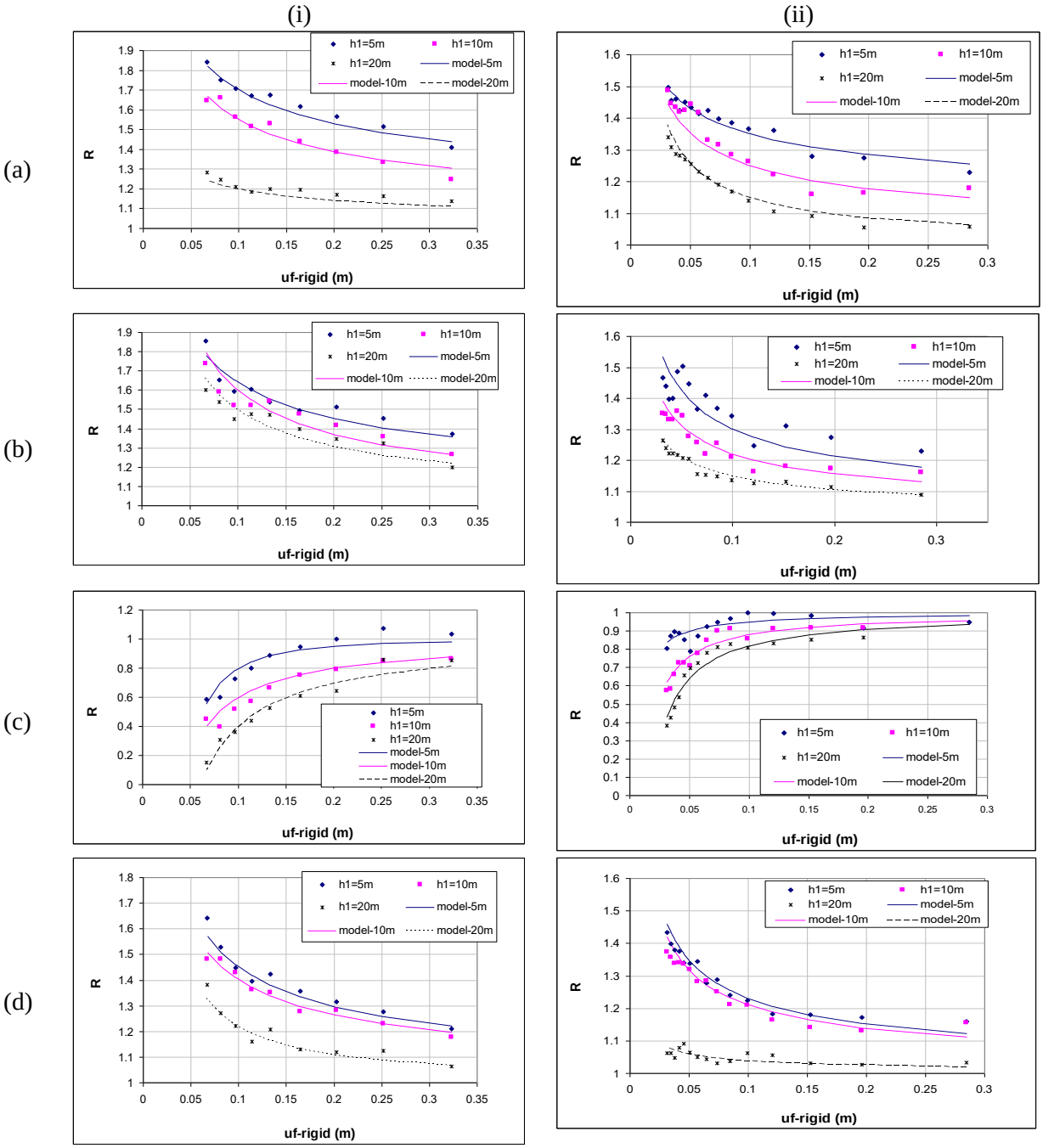

Fig. 3: Ratio R in terms of ($u_{f\text{-}rigid}$) of soil profiles (a) S-B, (b) S-C, (c) S-D, (d) S-E of the analyses of Fig. 2.

- (c) The obtained average parameters a1 and a2 for all earthquakes were statistically analyzed in terms of soil profile and h_1 value (12 cases) in order to derive the effect of soil profile and h_1 on them and propose the empirical expressions predicting R.

- (d) Once these empirical expressions were derived, the database DB2 described above was used to validate the proposed equation. The Error was measured in all 12 cases of the 25 input motions, thus in 12*25=300 cases in total and the mean and standard deviation of the error was established. If the mean and standard deviation values are close to zero, the error is small.

Furthermore, the obtained error for all earthquakes was obtained in terms of soil type and h1 (for 12 cases each time) in order to establish if the accuracy depends on soil type and h1.

6 EMPIRICAL EQUATION: PROPOSAL AND VALIDATION

Based on the procedure described in section 5, Fig. 4 gives the average factors (a) a1, (b) a2 in terms of h1 and the soil profile for the database DB1. It can be observed that, as a first approximation a1 depends on both the soil profile and h1, while a2 depends only on the soil profile. More specifically, regarding the effect of h1 on a1, Fig 5 plots the average factor $\{a1\text{-}a1_{10m}\}$, where $a1_{10m}$ is the a1 value when h1=10m, versus {h1-10m} in terms of the soil profile type. It can be observed that an approximately linear response is observed. Thus, equation (4) can be adjusted as

$$R= 1+ [n1 - n2 (h_1\text{-}10m)] (0.1/ u_{f\text{-}rigid})^{a2} \quad (6)$$

where n1, n2, a2 are parameters which depend on soil type. Finally, Table 3 gives the factors n1, n2, a2 according to Figs 4, 5.

Once the empirical equation (6) with the model parameters of table 3 was established using the database DB1, its error in the predictions of this equation was established using DB2. Considering all the data of DB2, the absolute value mean and standard deviation of the error (equation 5) were estimated as 0.05 and 0.05 respectively. As these values are close to zero, the error is small and acceptable. Furthermore, the obtained error for all earthquakes was obtained in terms of soil type and h_1 as given in table 4. It can be observed that accuracy is less in soil profile S-D.

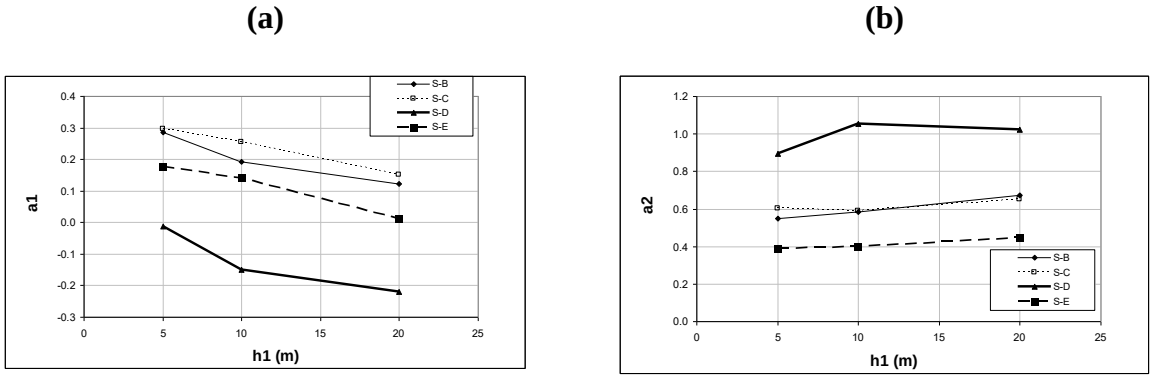

Fig. 4: The average factors (a) a1, (b) a2 in terms of the soil profile type and h1 for DB1.

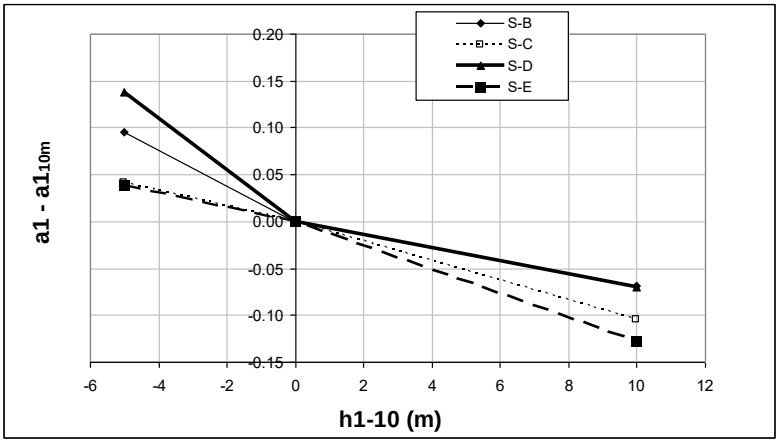

Fig. 5: The average factor a1-a1$_{10m}$ versus (h1-10m) in terms of the soil profile type

Soil type	n1	n2	a2
S-B	0.19	0.0093	0.6
S-C	0.26	0.0101	0.6
S-D	-0.15	0.0111	1.0
S-E	0.14	0.0118	0.4

Table 3: Parameters of equation (6) in terms of soil type

	Mean Value (Absolute value)			Standard Deviation		
Soil type	h1=5m	h1=10m	h1=5m	h1=5m	h1=10m	h1=5m
S-B	0.05	0.06	0.01	0.07	0.05	0.03
S-C	0.04	0.01	0.06	0.04	0.03	0.03
S-D	0.09	0.08	0.05	0.12	0.07	0.06
S-E	0.03	0.04	0.03	0.02	0.02	0.02

Table 4: Statistical analysis of the error in the predictions of equation (6) with the parameters of table 3 in terms of soil type and h_1

7 DISCUSSION AND EXAMPLE APPLICATION

The present work proposes the empirical expressions (2) and (6) with the parameters of table 3 relating the seismic displacement along slip surfaces in Greece, in terms of (a) the conventional sliding-block predictions, (b) soil type category according to Eurocode and (c) the depth of the slip surface. As an example application, we consider a site of soil category S-E where the slip surface is at average depth 5m and geotechnical and seismic analysis for bedrock seismic motion characteristics of the site gave ac=0.02g, and design earthquake of magnitude Mw=7.0 at distance R=2km. Equation (13) by [9] predicts an Arias Intensity Ia=17m/s and equation (21) by [9] predicts a corresponding maximum value of seismic displacement with "conventional" sliding-block model $u_{f\text{-}rigid}$=5.1cm. Application of the empirical expressions (6) with the parameters of table 4 would predict that when considering dynamic effects, R=1.26 and the seismic displacement u_f would increase to 6.4cm.

The proposed empirical expressions (2) and (6) assume elastic response of the soil profile and a slip surface with very large length. The proposed expression may be extended to include (a) non-linear response of the soil profile and (b) the effect of the rotation of the slip surface with shear displacement, which is considerable for slip surfaces of small length. Effect (a) may be simulated using for example shear modulus degradation expressions proposed by [17] and effect (b) may be simulated using for example the chain model proposed by [18] . In order to achieve this, numerical analyses of the method [13] should be used considering the above effects. Furthermore, the empirical expressions may be extended for regions other than Greece, by using data bases of seismic motions from these different regions.

8 CONCLUSIONS

- The present work proposes the empirical expressions (4) and (6) with the parameters of table 3 relating the seismic displacement along slip surfaces in Greece, in terms of (a) the conventional sliding-block predictions, (b) soil type category according to Eurocode and (c) the depth of the slip surface.
- These equations were obtained by extensive parametric analyses using a recently developed dynamic coupled numerical code which predicts the seismic displacement of an elastic soil profile along a slip surface at some depth. An extensive data base of seismic motions recorded in Greece was applied below typical soil layers according to Eurocode category type with slip surface at different depths and varying the resistance (as defined by the critical acceleration value) in such a way that computed final seismic displacement of the conventional sliding-block case varies from about 0.05m to 0.5m. The results were analyzed statistically.

REFERENCES

[1] European Standard (2003). Eurocode 8: Design of structures for earthquake resistance, Final Draft, prEN 1998-5, 2003, December.

[2] Whitman R. V. (1993). Predicting earthquake-caused permanent deformations of earth structures, article on "Predictive Soil Mechanics", Thomas Telford, London, 729-741

[3] Newmark, N. M. (1965). Effects of earthquakes on dams and embankments. Geotechnique, 55 (2), 139-159.

[4] Ambraseys N. and Menu J. (1998). Earthquake induced ground displacements, Earthquake engineering and structural dynamics, 16, 7, 985-1006.

[5] Ambraseys NN, Srbulov M (1994) Attenuation of earthquake-induced displacements. Journal of Earthquake Engineering and Structural Dynamics 23: 467–487

[6] Ambraseys Jibson R. W. Regression models for estimating coseismic landslide displacement

[7] Jibson R. W. Regression models for estimating coseismic landslide displacement Engineering Geology 91 (2007) 209–218.

[8] Rathje EM, Saygili G (2006) A vector hazard approach for Newmark sliding block analysis. Proc.Earthquake Geotech. Engrg. Workshop, University of Canterbury, Christchurch, New Zealand, Nov. 20–23

[9] Chousianitis K., Gaudio V., Kalogeras I, Ganas A. Predictive model of Arias intensity and Newmark displacement for regional scale evaluation of earthquake – induced landslide hazard in Greece , Soil Dynamics and Earthquake Engineering , 2014

[10] Bray J. D. and Travasarou T. (2007). Simplified Procedure for Estimating Earthquake-Induced Deviatoric Slope Displacements, Journal of Geotechnical and Geoenvironmental Engineering, 133 (4), 381-392.

[11] Rathje E. M. and Bray J. D. An examination of simplified earthquake induced displacement procedures for earth structures. Can. Geotech. J. 36: 72–87 (1999)

[12] Jafarian Y. and Lashgari A. (2016). Simplified Procedure for Coupled Seismic Sliding Movement of Slopes Using Displacement-Based Critical Acceleration, International Journal of Geomechanics, Volume 16 Issue 4 - August 2016

[13] Katsenis L, Stamatopoulos C. Panoskaltsis V (2019) Non-linear dynamic seismic sliding movement of dry slopes, COMPDYN 2019, 7th International Conference on Computational Methods in Structural Dynamics and Earthquake Engineering, 24-26 June 2019, Crete, Greece

[14] Lin J.-S., and Whitman, R.V. 1983. Decoupling Approximation to the evaluation of earthquake-induced plastic slip in earth dams. Earthquake Engineering and Structural Dynamics, 11: 667–678.

[15] Organization of antiseismic design and protection of Greece (OASP) (1999), Hellenic Seismic Code, September (in Greek).

[16] https://www.seismosoft.com/seismosignal

[17] Vucetic M. And Dobry R. "Effect of soil plasticity on cyclic response, Journal of the Geotechnical Division, ASCE, 117 (1). 1991. Bolton M. D. (1986). The strength and dilatancy of sands. Geotecnique 36 (1), 65-78.

[18] Stamatopoulos, C. A. Sliding System Predicting Large Permanent Co-Seismic Movements of Slopes. Earthquake Engineering and Structural Dynamics. 1996. Vol. 25, No, 10, 1075-1093.

Appendix

Table A1. Earthquakes applied

No	Name	Station	Year	M (Mw)
1	Off Cephallonia	Chavriata Chv1	03/02/14	6,10
2	Off Cephallonia	Lixouri Lxr1	03/02/14	6,10
3	Ionian	Lefkada-OTE Building	04/11/73	5,80
4	Pyrgos	Pyrgos-Agriculture Bank	26/03/93	5,40
5	Patras	Patra-San Dimitrios Church	14/07/93	5,60
6	Ano Liosia	Athens-Sepolia (Garage)	07/09/99	6,00
7	Alkion	Korinthos-OTE Building	24/02/81	6,60
8	Kalamata	Kalamata-Prefecture	13/09/86	5,90
9	Ano Liosia	Athens 3 (Kallithea District)	07/09/99	6,00
10	Alkion	Xilokastro-OTE Building	24/02/81	6,60
11	Kalamata	Kalamata-OTE Building	13/09/86	5,90
12	Kozani (aftershock)	Karpero-Town Hall	19/05/95	5,20
13	Off Cephallonia	Argostoli Arg2	03/02/14	6,10
14	Kefallinia (aftershock)	Argostoli-OTE Building	23/03/83	6,20
15	Kefallinia island	Argostoli-OTE Building	23/01/92	5,60
16	Ano Liosia	Athens-Sepolia (Metro Station)	07/09/99	6,00
17	Kozani	Kozani-Prefecture	13/05/95	6,50
18	Komilion	Lefkada-OTE Building	25/02/94	5,40
19	Aigion	Aigio-OTE Building	17/05/90	5,21
20	Patras	Patra-National Bank	14/07/93	5,60
21	Patras	Patra-OTE Building	14/07/93	5,60
22	Ierissos	Ierissos-Police Station	26/08/83	5,09
23	Heraklio	Heraklio-Prefecture	19/03/83	5,60
24	Etolia	Valsamata	18/05/88	5,30
25	Kefallinia island	Argostoli-OTE Building	23/06/92	5,09
26	Kefallinia island	Kefallinia	17/09/72	5,6
27	Kefallinia (aftershock)	Kefallinia	30/10/72	5,36
28	Kozani (aftershock)	Chromio-Community Building	15/05/95	5,20
29	Kyllini	Amaliada-OTE Building	16/10/88	5,90
30	Kyllini	Zakynthos-OTE Building	16/10/88	5,90
31	Ano Liosia	Athens 2 (Chalandri District)	07/09/99	6,00
32	Volvi	Thessaloniki-City Hotel	20/06/78	6,20
33	Arnaia	Poligiros-Prefecture	04/05/95	5,30
34	Preveza	Preveza-OTE Building	10/03/81	5,40
35	Mouzakaiika	Lefkada-OTE Building	13/06/93	5,30
36	Kozani (aftershock)	Chromio-Community Building	17/05/95	5,30
37	Komilion	Lefkada-Hospital	25/02/94	5,40
38	Ano Liosia	Athens-Sygrou-Fix	07/09/99	6,00
39	Strofades	Zakynthos-OTE Building	18/11/97	6,60
40	Alkion	Korinthos-OTE Building	25/02/81	6,30
41	Ano Liosia	Athens 4 (Kipseli)	07/09/99	6,00
42	Lefkada	Lefkada-OTE Building	27/05/81	5,30
43	Kalamata	Koroni-Town Hall	13/10/97	6,40
44	Volvi	Thessaloniki-City Hotel	04/07/78	5,41
45	Pyrgos	Amaliada-OTE Building	26/03/93	5,40
46	Kalamata (aftershock)	Kyparrisia-Agr. Bank	10/06/87	5,30
47	Ierissos	Ouranoupolis	26/08/83	5,10
48	Ano Liosia	Athens-Syntagma	07/09/99	6,00
49	Ierissos	Poligiros-Prefecture	26/08/83	5,10
50	Gulf of Corinth	Nafpaktos- OTE Building	04/11/93	5,30

Table A2. Characteristics of applied earthquakes

No	Mean Period	Predominant Period	a_{max} (m/s^2)	V_{max} (m/sec)	Arias intensity (m/sec)	Epicentral distance (km)
1	0,30729	0,16	7,3360	0,3215	2,76936	7,00
2	0,82566	0,9	6,545	0,7677306	2,75813	7,00
3	0,45012	0,34	5,1459	0,38516	0,89603	15,00
4	0,246	0,08	1,4244	0,06406	0,06707	10,00
5	0,24819	0,08	1,4992	0,07922	0,11386	9,00
6	0,22257	0,16	2,7592	0,21152	0,39398	14,00
7	0,4679	0,34	2,2566	0,14617	0,42166	20,00
8	0,46054	0,3	2,108	0,27389	0,41461	10,00
9	0,26487	0,08	2,6014	0,25544	0,22299	16,00
10	0,4544	0,22	2,8382	0,1593	0,60747	19,00
11	0,43318	0,22	2,3537	0,29092	0,38456	11,00
12	0,25146	0,14	2,601	0,10955	0,25406	16,00
13	0,13857	0,06	2,198	0,0488	0,15636	12,00
14	0,18438	0,1	1,788	0,09629	0,20986	9,00
15	0,21945	0,12	1,249	0,1062	0,07634	14,00
16	0,25703	0,16	2,1698	0,16418	0,17729	14,00
17	0,21054	0,16	2,0388	0,16501	0,19868	17,00
18	0,35851	0,18	1,71620	0,09177	0,12485	16,00
19	0,2101	0,14	1,14910	0,03693	0,02189	20,00
20	0,2754	0,2	1,37730	0,11783	0,09903	10,00
21	0,2702	0,14	1,13720	0,0423	0,09253	10,00
22	0,2295	0,12	1,22820	0,09927	0,05427	8,00
23	0,1989	0,16	0,75026	0,05918	0,0576	40,00
24	0,2261	0,22	1,62380	0,06671	0,09257	23,00
25	0,2124	0,18	1,71720	0,06517	0,09291	16,00
26	0,2016	0,12	1,19270	0,07615	0,0717	31,00
27	0,242	0,18	0,61381	0,05185	0,01451	19,00
28	0,1706	0,08	1,2951	0,06495	0,05646	9,00
29	0,2968	0,18	0,7845	0,08526	0,04902	36,00
30	0,3089	0,34	1,4789	0,07214	0,15926	14,00
31	0,2522	0,08	1,0685	0,07901	0,05804	20,00
32	0,329	0,20	1,3095	0,07733	0,12136	29,00
33	0,1528	0,10	1,4255	0,07613	0,0596	28,00
34	0,2328	0,20	1,4019	0,06422	0,17736	28,00
35	0,2159	0,16	0,4262	0,01477	0,00905	48,00
36	0,1945	0,16	1,2897	0,05671	0,05639	16,00
37	0,3595	0,32	1,2701	0,091	0,12521	15,00
38	0,4444	0,12	0,8329	0,06277	0,02688	19,00
39	0,3493	0,18	1,1944	0,08539	0,20123	38,00
40	0,6177	0,18	1,1714	0,10388	0,14958	25,00
41	0,294	0,3	1,1710	0,08864	0,06613	17,00
42	0,2086	0,16	1,1703	0,05143	0,04701	26,00
43	0,2677	0,12	1,1217	0,07781	0,12713	48,00
44	0,2761	0,2	1,12480	0,05836	0,04483	16,00
45	0,265	0,1	1,1214	0,16299	0,04209	24,00
46	0,2177	0,1	0,6611	0,03294	0,01229	17,00
47	0,1816	0,16	0,8164	0,03718	0,02224	15,00
48	0,3574	0,14	1,0872	0,06552	0,03649	18,00
49	0,1915	0,08	1,0500	0,07606	0,021	42,00
50	0,2863	0,12	0,6532	0,03156	0,03005	10,00

COMPDYN 2019
7th ECCOMAS Thematic Conference on
Computational Methods in Structural Dynamics and Earthquake Engineering
M. Papadrakakis, M. Fragiadakis (eds.)
Crete, Greece, 24–26 June 2019

EXPERIMENTAL AND NUMERICAL ASSESSMENT OF DYNAMICS OF HAILSTONE IMPACT ON COMPOSITE PLATES

Dimitris K. Siorikis[1], Christoforos S. Rekatsinas[1], Christos V. Nastos[1], Theodosis C. Theodosiou[1], Nikolaos A. Chrysochoidis[1], Andreas P. Christoforou[2], Ahmet S. Yigit[2], Dimitris A. Saravanos[1]

[1] Department of Mechanical Engineering and Aeronautics, University of Patras
Rion-Patras, Greece
e-mail: d.siorikis@upnet.gr

[2] Department of Mechanical Engineering, Kuwait University
Kuwait

Abstract

The dynamic response of composite structures under impact loading conditions is a complex problem which is attracting substantial attention. The case of hailstone impacts introduces additional challenges. Hence, the main goal of this paper is to present recent work towards the development of a computationally efficient impact model that combines a novel phenomenological viscoplastic contact law with a new time domain spectral shear plate finite element including nonlinear effects due to large displacements and rotations. The new viscoplastic contact law, which provides the coupling between the hailstone impactor and the target composite plate, is derived from analytical expressions and observations based on experiments and numerical results. The proposed model simulations are compared with a 3-D continuum explicit FEA model and experimental results from high-velocity spherical hailstone impacts on woven glass/epoxy composite plates, which are conducted in our impact facility. The results demonstrate the efficiency and accuracy of the proposed model.

Keywords: Composite Structures, Hailstone, High-velocity Impact, Time domain spectral elements, Contact Law

1 INTRODUCTION

Composite materials technology is of fundamental importance to current and future aircraft structures where high strength, high stiffness, and integration of multiple functionalities are essential to improve weight, fuel efficiency, CO_2 emissions and safety, and to reduce component complexity and manufacturing costs. However, an issue of particular concern is the vulnerability of composite structures to foreign object damage by small objects, such as hail and tool drop, which may result in unpredictable complex localized damage and a loss of post-impact residual strength [1, 2]

The impact behavior of composite structures is even more complicated at high velocity impacts, which is generally more detrimental to the integrity of composite structures [3], thus setting new challenges for constituent models, computational structural dynamic models and experimental studies. One case of high-velocity impact, which is the driver for the present research, encompasses hailstone impact on composite wing leading edge structures with integrated deicing heating layers, which may create localized, visible or barely visible damage in both composite and heating layers.

A major step in gaining an understanding of the impact problem is the accurate knowledge of impact/contact force. The most typical approach employs detailed 3-D continuum finite element models for the composite structure and the impactor, which results in computationally intense explicit time integration solutions. Though, hailstones are not common materials that can be easily modelled by the use of commercial finite element software. Various FE models that have been developed so far, which are based on material algorithms of Lagrangian FE, ALE or SPH [4–6], have given significantly different predictions [7,8].

In order to address these difficulties, a number of lumped-parameters models have been proposed [9]. This approach employs simplified models for the target structure usually assuming a single-layer laminate theory in the context of a global Ritz, or finite element discretization, and treats the impactor as a concentrated mass with one degree of freedom. The interaction between the impactor and target structure is based on a contact law in the form of force-indentation relationship [10].

The Hertz contact law, developed for perfectly elastic contact between compact bodies, was one of the first models used for impacts at low velocities. However, this model is not adequate for most impacts in practice, as some energy is dissipated due to plastic deformation, wave propagation, and other effects. As an alternative, an elastoplastic contact law was proposed [11] to account for energy losses due to local plastic deformation during impact. One drawback of this model is the fact that it does not account for energy loss duo to wave propagation. To encounter this problem, a number of contact models have been developed with the addition of a damping element, in order to account for energy dissipation during impact [12]. The Hunt-Crossley model gained popularity in recent years and has been used in number of studies [13]. However, the contact parameters are difficult to determine and are usually adjusted on experimental results [14].

This present study moves a step forward and aims to cover a void between numerical, analytical and simplified impact models for hailstone impact in composite structures. This is accomplished by integrating a viscoplastic modified Hunt-Crossley model with well defined parameters that are based on analytical solutions and physical observations, into a novel time domain spectral finite element for the structural dynamics of composite plate structures. In the following sections, the theoretical framework and governing equations of the developed impact model is outlined. The contact law is formulated and its performance is validated with measured data from impact tests on a rigid target [15], and subsequently simulated with 3-D solid explicit finite element models [4].The development and basic features of a time domain spectral finite

element (TDSFE) based on first order shear theory (FSDT) and geometric nonlinearities are presented. The proposed contact law and the TDSFE are integrated in the framework of an explicit time integration scheme, to provide the rapid impact simulation model. Numerical predictions of the model are presented and compared in terms of accuracy and computational speed, with results obtained by explicit 3-D FEA analysis models for impact cases on glass/epoxy plate, and also with experimental results from our impact facility.

2 VISCOPLASTIC CONTACT LAW FOR HAILSTONE

2.1 Ice Material Model

A 3-D continuum finite element model was constructed using the commercial code Abaqus/Explicit to gain deeper and broader insight into the experiments and to establish the capability to conduct virtual testing for various impactor's diameters and velocities. The model of the hailstone projectile and rigid target was built using a Lagrangian mesh. The ice was modeled with solid, reduced integration elements (C3D8R) and the element size was 1 mm. The material model, which was previously developed by Tippmann [4], incorporates a strain rate dependent elastic-plastic yield strength with element failure based on a tensile hydrostatic stress failure criterion (Table 1). The target was modeled as rigid (R3D4) and the contact between the target and the impactor was hard and frictionless (Figure 1).

Material Property	Value
Young's modulus, E (GPa)	9.38
Poisson ratio, ν	0.33
Density, ρ (kg/m^3)	836
Tensile failure pressure (MPa)	0.517
Quasi-static yield strength, σ_{yo} (MPa)	5.2
Rate dependent yield strength	See Table 2

Table 1: Summary of ice material model properties

Stress ratio (σ_y/σ_{y0})	Strain rate (s^{-1})
1	0
1.50	0.5
2.20	5
2.91	50
3.62	500
4.33	5000
5.04	50000
5.75	500000
5.96	1000000

Table 2: Strain rate dependent yield strength

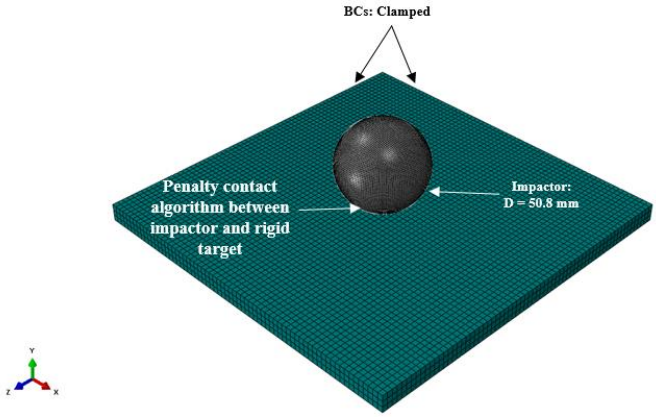

Figure 1: 3-D continuum FE model of hailstone and rigid target.

Simulations were conducted in Abaqus/Explicit and were compared to experimental tests of simulated hail ice impacts on a force measurement bar apparatus for four different velocities [15]. The simulated force-time history results during the ice impact event are in agreement with the experimental data, as shown in Figure 2, ensuring the validity of the ice material model for further virtual testing and physical observation.

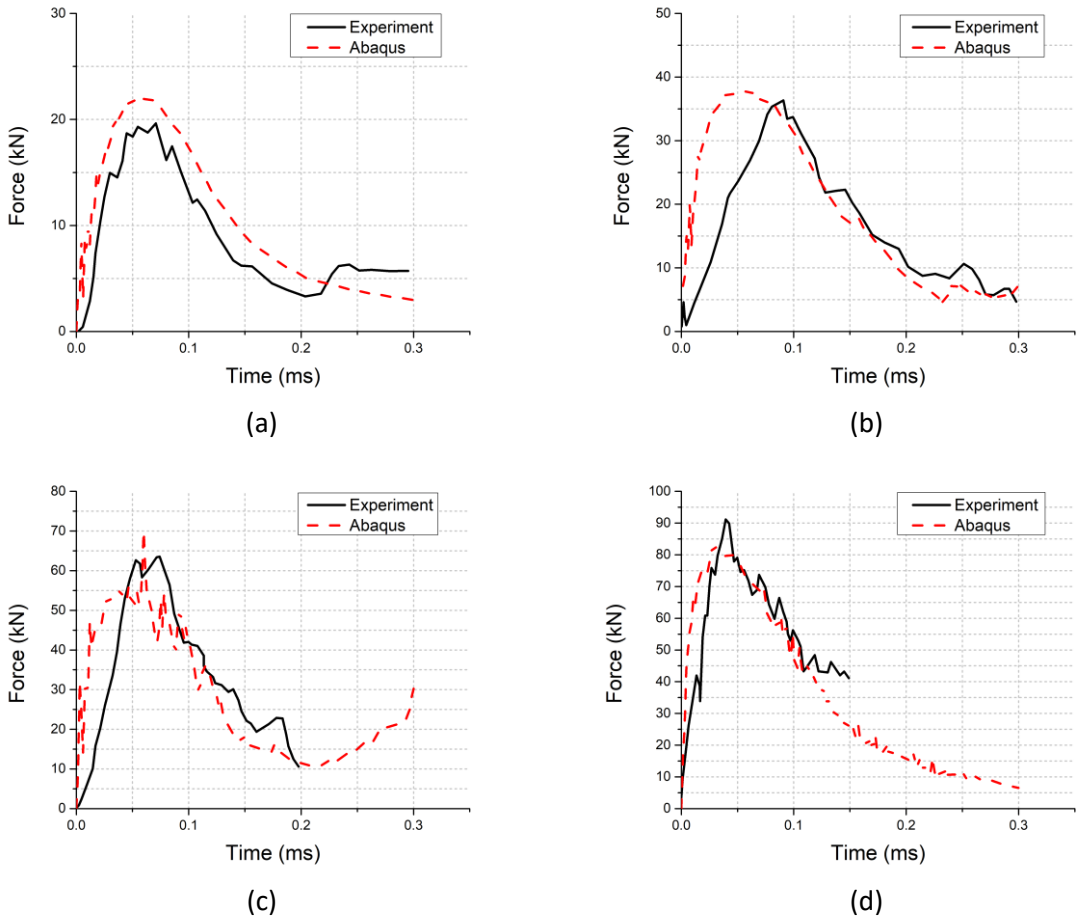

Figure 2: Force-time history for ice-impactor with diameter 50.8 mm at various impact velocities (a) v = 60.6 m/s, (b) v = 107.3 m/s, (c) v = 144.1 m/s, (d) v = 190 m/s.

In the following the Abaqus model simulations will be used as a calibrating virtual testing tool to capture the impact behavior of ice at high velocities using a simple lumped-parameter viscoplastic model.

2.2 Contact Law

Equations of Motion:

The impact between a deformable sphere having an initial velocity v_o with a flat rigid surface can be modeled as shown in Figure 3.

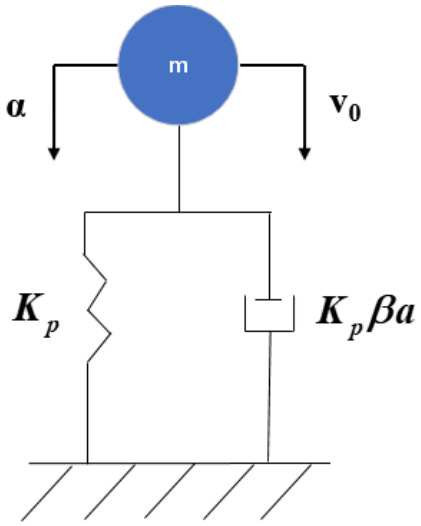

Figure 3: Sketch of the proposed viscoplastic model.

The motion of the sphere is described by,

$$m\ddot{a} = -F \tag{1}$$

where m is the mass of the hailstone, a is the displacement of the hailstone and F is the impact force to be obtained from a contact law given as,

$$F = K_p a(1+\beta\dot{a}) \tag{2}$$

The initial conditions are described as,

$$a(0) = 0, \dot{a}(0) = \dot{a}_0 = v_0 \tag{3}$$

Contact Stiffness (K_p):

In the above equation, K_p is the linear plastic contact stiffness determined by the properties of the contacting sphere and is calculated as,

$$K_p = 2\pi R p_0 \tag{4}$$

where the mean contact pressure is denoted as p_0 and the radius of the impactor as R. It has been shown that the mean contact pressure remains approximately constant when there is substantial damage (fully plastic flow) in the contact area [16], as shown in Figure 4.

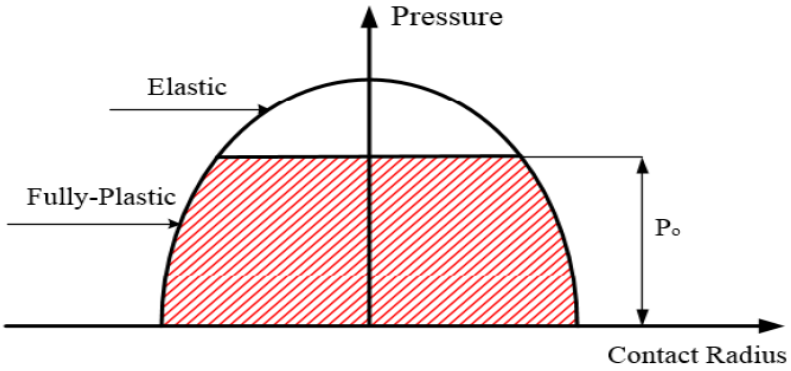

Figure 4: Contact pressure distribution.

The contact pressure is assumed to be equal with the tensile failure pressure of the ice, which is the failure threshold that the deviatoric stresses are set to zero and only hydrostatic stresses are allowed in the element. As shown in Figure 5, after impact, a constant pressure is applied in the elements that have failed (0.517 MPa), ensuring the hypothesis that the mean contact pressure remains approximately constant after failure. Using equation (4) the contact stiffness is calculated as 82.51 kN/m.

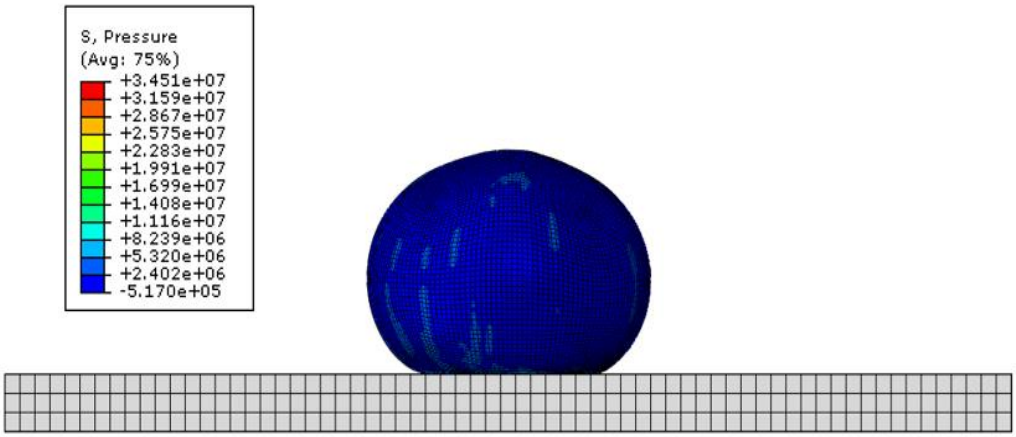

Figure 5: Pressure distribution of hailstone impact on rigid surface after failure.

Dissipation Parameter and Coefficient of Restitution:

Substituting the contact force into the equation of motion, it is easy to show that the impact problem is governed by the following differential equation given as,

$$m\ddot{a} + (K_p \beta a)\dot{a} + K_p a = 0 \tag{5}$$

which is similar to the well known Hunt-Crossley model [12]. Since the contact stiffness K_p is obtained from equation (4), the only parameter that needs to be determined in equation (5) is the dissipation parameter β. Traditionally, this has been done by matching the coefficient of restitution (COR) resulting from this model to the one obtained from experiments. In this study it will be accomplished by matching the COR obtained from Abaqus model simulations, which were shown to correlate well with the available experimental data (Figure 2).

The severity of impact can be assessed by the COR, as it expresses the energy loss in an impact event. Newton's definition for the COR is the easiest as it involves the ratio of the relative velocities of the impactor and the target after and before impact. It is simply given as:

$$COR = -\frac{\dot{a}_f}{\dot{a}_0} \tag{6}$$

Several expressions have been reported in the literature for the dissipation parameter and COR. In the present study, the simplified expression of Garib et al [17] is used, which assumes that at the end of the collision the contact force reduces to zero, but the final indentation velocity is not zero and results in the expression,

$$\beta = \frac{1}{COR\dot{a}_0} \tag{7}$$

It is well known from experiments that the COR is fairly constant for high velocity impact events in most materials (> 40 m/s). In the cases under study all the impact velocities are much higher. Using the Abaqus simulation results for an impact velocity v = 60.6 m/s the COR is estimated to be equal to 0.0078. Using equation (7) the dissipation parameter is obtained as β = 2.11 s/m. Thus, for the rest of the simulations at higher impact velocities, the dissipation parameter for each case is calculated from equation (7) using the same value of COR.

2.3 Time Domain Spectral Finite Element

Kinematic Assumptions:

The contact law described above was combined with a time domain spectral finite element (TDSFE), which was formulated using first order shear plate theory kinematic assumptions,

$$\begin{aligned} \mathbf{u}(\mathrm{x,y,z,t}) &= \mathrm{u}_0 + z\cdot\beta_x \\ \mathbf{v}(\mathrm{x,y,z,t}) &= \mathrm{v}_0 + z\cdot\beta_y \\ \mathbf{w}(\mathrm{x,y,z,t}) &= \mathrm{w}_0 \end{aligned} \tag{8}$$

where u_0 and v_0 denote the in-plane displacements, w_0 the normal displacement, β_x and β_y the in-plane rotations and z the thickness dimension of the plate.

Strain-displacement relation:

Composite structures under high-velocity impact loading exhibit geometrically nonlinear response. Therefore, the Green-Lagrange strains are assumed to have the following form:

$$\begin{aligned} \varepsilon_x &= \boldsymbol{u}_{,x} + \frac{1}{2}\boldsymbol{w}_{,x}^2 \\ \varepsilon_y &= \boldsymbol{v}_{,y} + \frac{1}{2}\boldsymbol{w}_{,y}^2 \\ \varepsilon_{xy} &= (\boldsymbol{u}_{,y} + \boldsymbol{v}_{,x}) + \boldsymbol{w}_{,x}\boldsymbol{w}_{,y} \\ \varepsilon_{yz} &= (\boldsymbol{u}_{,z} + \boldsymbol{w}_{,x}) \\ \varepsilon_{xz} &= (\boldsymbol{v}_{,z} + \boldsymbol{w}_{,y}) \\ \varepsilon_z &= 0 \end{aligned} \tag{9}$$

Finite Element Formulation:

The generalized equations presented in previous section are used as a foundation for developing a multi node plate finite element with C¬0 Lagrange shape functions. Exploitation of high order Lagrangian polynomial shape functions ensures the efficient spatial discretization in the plane of the plate. The nodes of the proposed element are located at Gauss-Lobatto-Legendre (GLL) integration points provided as solutions of the equation $\left(1-\xi_i^2\right)\cdot P_{p,\xi}\left(\xi_i\right)=0$ where $-1\le\xi,\eta\le 1$ is the local coordinate of the element.

Figure 6 shows an 81-node plate time domain spectral element (TDSFE), where the integration points are collocated with the element's nodes, as denoted earlier in the section. The generalized displacement degrees of freedom in the element, are approximated as,

$$\mathbf{U}_L(x,y,t)=\sum_{i=1}^{nodes}\mathbf{N}^i(x,y)\hat{\mathbf{U}}^i(t) \tag{10}$$

where over hat indicates nodal variables, superscript *i* denotes the respective node, and ***N*** is the in-plane shape function matrix.

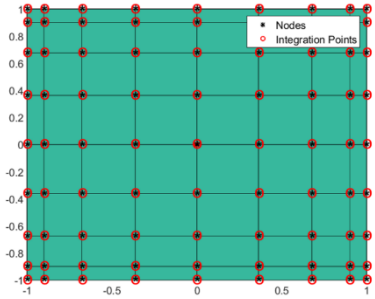

Figure 6: Outline of the developed 81-node plate TDSFE.

Validation of the Proposed Impact Model:

The capabilities of the proposed contact law combined with the TDSFE were tested for the impact case of a hailstone with diameter of 50.8 mm and velocity 60.6 m/s and the results provide an excellent approximation for both force-time history and force-displacement curve, as shown in Figure 7. As it will be demonstrated, below this case will be used as a calibration for the rest of the impact cases under study with excellent results.

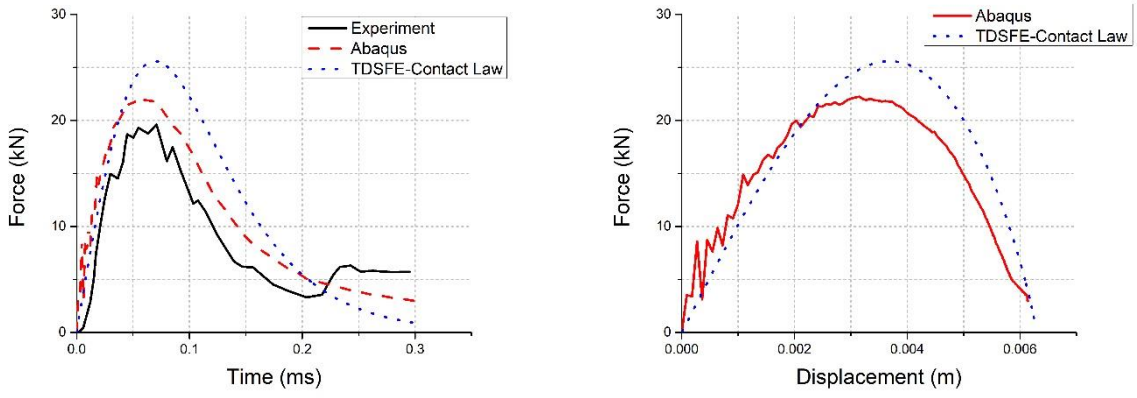

(a) (b)

Figure 7: Validation of the proposed impact model for hailstone impact on rigid target with D = 50.8 mm and v = 60.6 m/s. (a) Force-time curve, (b) Force-displacement curve.

2.4 Contact Law Evaluation for Various Velocities

The proposed impact model is evaluated for three higher impactor velocities with constant COR = 0.0078 which was obtained based on the case shown in Figure 7. As mentioned above, the dissipation parameter for each impactor velocity is calculated using equation (7). As it can be seen in Figure 8, the proposed method captures the impact response of hailstone impact on rigid target quite accurately, demonstrating the validity of the viscoplastic contact law.

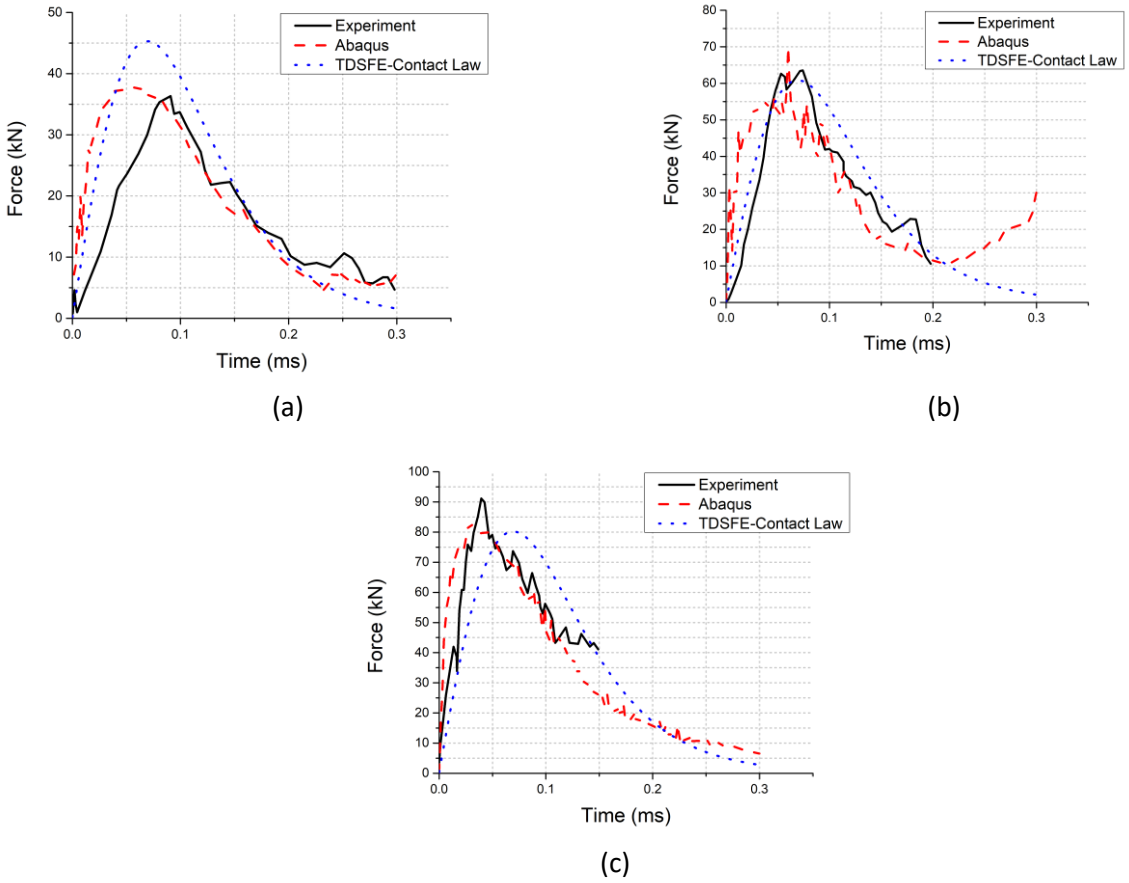

Figure 8: Contact law evaluation for hailstone impact on rigid target with D = 50.8 mm, (a) v = 107.3 m/s, (b) v = 144.1 m/s, (c) v = 190 m/s.

3 EXPERIMENTAL FACILITY

The laboratory is equipped with a functional Impact Test Bench (ITB), which mainly consists of three main parts: **i)** A pre-charged nitrogen gas gun. A sturdy gas gun (Figure 9) with a 10lit pressure vessel, 3m barrel and 60mm diameter bore is capable of launching any spherical projectile up to 50mm diameter and up to 972km/h (velocity was tested & verified for a 25mm diameter ice ball). The repeatability of impactor velocity and trajectory was thoroughly tested and calibrated for each impactor case (for different masses and velocities), in order to achieve accurate results which are further investigated by efficient micromechanical numerical models.

Figure 9: Impact Gas Gun

ii) Measurement devices and supporting apparatus. A high precision digital pressure gauge (Omega DPG1000DAR) for accurate measurements and repeatable impact velocities is located on the vessel. The entire impact event is captured by a high speed camera (Photron SA4) with typical 50k-100k fps capacity (Figure 10Figure 10a) and two chronographs (Chrony M-1) measure both the launching and the penetration velocity at each impact case (b). The impacted structure is monitored using SoA equipment. Strain gauge rosettes (LDT1-028K Piezosensors; high voltage capacity and high strain rate) are used for monitoring target's post-impact response. Sensor signals are captured using NI PXI 6070E at 10k samples/sec. A custom-made LabVIEW VI has also been developed to eliminate human error and ensure that all the apparatus is properly triggered at each impact experiment.

(a) (b)

Figure 10: Measurement devices and supporting apparatus. (a) High-speed camera. (b) Chronographs for measuring launching and penetration velocity.

iii) Non destructive testing apparatus. The lab has access to the Ultrapac II by Mistras Group (Figure 11a), which provides reliable C scans and is used for assesing pre- and post-impact condition of the impacted structures. The post-impact condition (i.e the size of the delaminated area) is schematically validated by micromechanical models. For complex composite structures such as sandwich panels and leading edges, an ultrasonic set-up of pitch-catch is conducted using the Olympus BondMaster 1000e+ (Figure 11b). The bond condition beneath the two probe tips (elements) will affect the characteristics of the acoustic energy that is transmitted between the two tips, hence the device is used for the investigation of delaminations and debondings.

(a) (b)

Figure 11: Non destructive testing apparatus. (a) Ultrapac II by Mistras Group. (b) Olympus Bondmaster.

The ITB was already employed by two Cleansky projects which were efficiently completed. The gas gun has been already employed to perform an adequate number of experiments, using both hailstone and steel projectiles of various diameters, per project requirements. As for the impacted targets, flat plates, thick sandwich plates and leading edges were mounted and successfully tested.

4 HAILSTONE IMPACT ON WOVEN GLASS/EPOXY COMPOSITE PLATES

Initially, virtual impact experiments on a rigid target were performed for hailstone of diameter of 25 mm and various velocities in the range 60.6-190 m/s, as in Section 2, in order to calculate the contact stiffness (40.6 kN/m) and the COR (0.007). After, a series of woven glass/epoxy plates (8 – Harness Satin weave), with properties listed in Table 3, were fabricated by a HexPly 1454/43%/664 with dimensions 300x300x1 mm^3 and lamination $[0/90]_s$. Autoclave processing was used to ensure efficiency and repeatability of the test method.

Material Property	Value
E_{11} (GPa)	23.126
E_{22} (GPa)	20.780
E_{33} (GPa)	12.431
$G_{13} = G_{23}$ (GPa)	2.779
G_{12} (GPa)	3.218
$V_{12} = V_{23}$	0.271
V_{12}	0.116
Density (kg/m^3)	1792
CPT (mm)	0.25
V_f (%)	41.5

Table 3: Mechanical Properties of Glass/Epoxy material.

The test plate was impacted by a hailstone of diameter of 25 mm and velocity of 165 m/s in our impact facility. In parallel, this impact case was modeled in Abaqus/Explicit. The composite plate was modeled with 3-D solid elements with reduced integration (C3D8R) and geometric nonlinearity was considered to capture large displacements and rotations. To ensure an adequate element size and number in the vicinity of contact region, an edge-biased technique was applied with the element size varying from 2 mm to 5 mm away from impact region. The results look very promising, ensuring the validity of the proposed impact model for hailstones of various diameters and velocities (Figure 12). The effect of geometric nonlinearity is shown to be crucial

for the accurate modelling of high-velocity impact on composite structures, as illustrated by the exact predictions of impact force and target displacement.

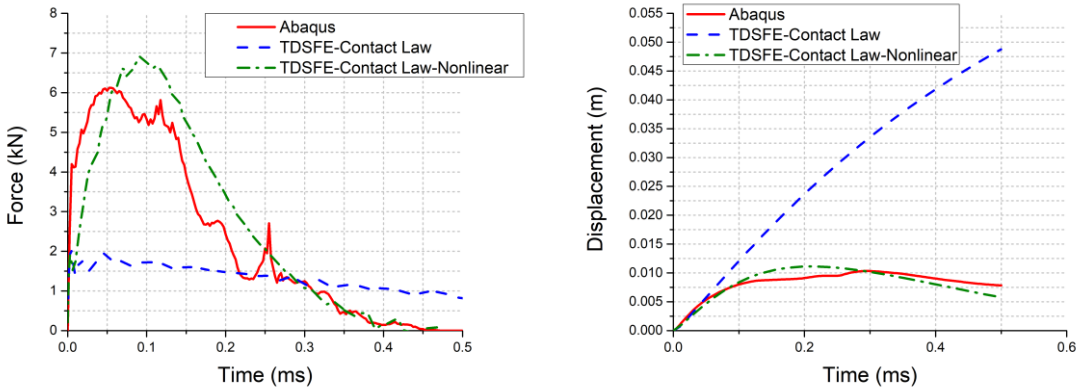

Figure 12: Hailstone impact on woven glass/epoxy laminated plate. (a) Force-history, (b) Target displace

Therefore, screenshots obtained from the high-speed camera illustrate wave excitations which were induced by hailstone impact. Qualitative comparisons of the developed impact model took place and their wavelength was clearly captured (Figure 13). Last but not least, the Abaqus 3-D model requires approximately 2.4 million DOFs, while the TDSFE requires approximately 26 thousands DOFs, accomplishing an over 98% reduction in the size of the required dynamic system.

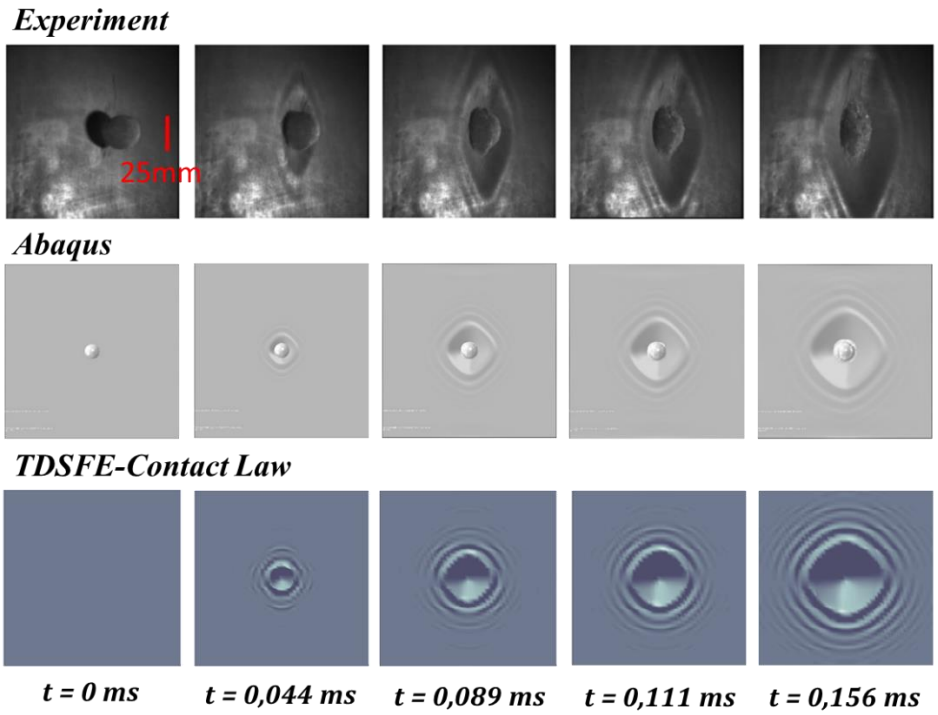

Figure 13: Numerical correlation of screenshots of impact on the glass/epoxy plate [0/90]s 300x300x1mm with 25mm hailstone at 165m/s.

5 CONCLUSIONS

A computationally efficient impact model has been presented, for the simulation of the hailstone impact response of composite laminates, combining a new visccoplastic contact law and a time domain plate spectral finite element with explicit time integration and geometric nonlinearity. The numerical evaluations illustrated very good agreement with experimental and 3-D solid element FEA results for hailstone impact on both rigid and deformable composite targets. In all cases, the impact force and displacement time response were predicted with good accuracy, while the computational efficiency and speed was drastically improved. Finally, it should be noted that the consideration of geometric nonlinearities contributed to the good predictions of impact response.

REFERENCES

[1] Abrate S. Impact on composite structures. Cabridge: Cambridge University Press; 1998.

[2] Cantwell WJ, Morton J. The impact resistance of composite materials - a review. Composites 1991;22:347–62. doi:10.1016/0010-4361(91)90549-V.

[3] Cantwell WJ, Morton J. Comparison of the low and high velocity impact response of cfrp. Composites 1989;20:545–51. doi:10.1016/0010-4361(89)90913-0.

[4] Tippmann JD, Kim H, Rhymer JD. Experimentally validated strain rate dependent material model for spherical ice impact simulation. Int J Impact Eng 2013;57:43–54. doi:10.1016/j.ijimpeng.2013.01.013.

[5] Juntikka R, Olsson R. Experimental and Modelling Study of Hail Impact on Composite Plates. ICCM-17 17th Int Conf Compos Mater 2009.

[6] Carney KS, Benson DJ, Dubois P, Lee R. A phenomenological high strain rate model with failure for ice 2006;43:7820–39. doi:10.1016/j.ijsolstr.2006.04.005.

[7] Sun J, Lam N, Zhang L, Ruan D, Gad E. Contact forces generated by hailstone impact. Int J Impact Eng 2015;84:145–58. doi:10.1016/J.IJIMPENG.2015.05.015.

[8] Anghileri M, Ã LLC, Invernizzi F, Mascheroni M. A survey of numerical models for hail impact analysis using explicit finite element codes 2005;31:929–44. doi:10.1016/j.ijimpeng.2004.06.009.

[9] Yigit AS, Christoforou AP. Limits of asymptotic solutions in low-velocity impact of composite plates. Compos Struct 2007;81:568–74. doi:10.1016/j.compstruct.2006.10.006.

[10] Siorikis DK, Rekatsinas CS, Christoforou AP, Saravanos DA. Experimental and numerical investigation of contact laws for the rapid simulation of low-energy impacts on laminated composite plates. Compos Struct 2017;168:646–56. doi:10.1016/j.compstruct.2017.02.049.

[11] Majeed MA, Yigit AS, Christoforou AP. Elastoplastic contact/impact of rigidly supported composites. Compos Part B Eng 2012;43:1244–51. doi:10.1016/j.compositesb.2011.08.053.

[12] Hunt K, Crossley F. Coefficient of restitution interpreted as damping in vibroimpact. J Appl Mech 1975;42:440e5.

[13] Zhang Y. Validation of Nonlinear Viscoelastic Contact Force Models for Low Speed Impact 2013;76:1–12. doi:10.1115/1.3112739.

[14] Yigit AS, Christoforou AP, Majeed MA. A nonlinear visco-elastoplastic impact model and the coefficient of restitution. Nonlinear Dyn 2011;66:509–21. doi:10.1007/s11071-010-9929-6.

[15] Kim H, Kedward KT. Modeling Hail Ice Impacts and Predicting Impact Damage Initiation in Composite Structures. AIAA J 2000;38:1278–88. doi:10.2514/2.1099.

[16] Kim H, Kedward KT. Modeling Hail Ice Impacts and Predicting Impact Damage Initiation in Composite Structures. AIAA J 2000;38:1278–88. doi:10.2514/2.1099.

[17] Stronge WJ. Impact mechanics. Cabridge: Cambridge University Press; 2000.

[18] Gharib M, Hurmuzlu Y. A New Contact Force Model for Low Coefficient of Restitution Impact. J Appl Mech 2012;79:064506. doi:10.1115/1.4006494.

COMPDYN 2019
7th ECCOMAS Thematic Conference on
Computational Methods in Structural Dynamics and Earthquake Engineering
M. Papadrakakis, M. Fragiadakis (eds.)
Crete, Greece, 24–26 June 2019

DYNAMIC IMPACT OF DEBRIS AVALANCHES ON STRUCTURES

Sabatino Cuomo[1], Sabrina Moretti[2], Stefano Petrosino[1], Stefano Aversa[2]

[1] Dept. of Civil Engineering, University of Salerno

Via Giovanni Paolo II, 132, 84084 Fisciano (Salerno), Italy

e-mail: scuomo@unisa.it; petrosino.stefano@gmail.com

[2] Dept. of Engineering, University of Naples "Parthenope"

Centro Direzionale, Isola C4, 80133 Napoli, Italy

e-mail: sabrina.moretti@uniparthenope.it; stefano.aversa@uniparthenope.it

Abstract

Flow-like landslides are largely studied because they cause damage to the structures and loss of life. In particular, debris avalanches propagate quickly along slopes for hundred meters. This work deals with the dynamic impact of debris avalanches against civil structures. The analyses are carried out through a numerical code implementing the Smoothed Particle Hydrodynamic (SPH) method that has reasonable computational time for the accurate evaluation of kinematical features of the debris avalanches such as heights, velocities and pore water pressures during the propagation stage. The dynamic impact is evaluated for different scenarios of landslides differently triggered inside the source areas. Distinct literature formulations are used to evaluate the impact pressure and its time variation. The numerical results outline the ranges of potential impact pressures on civil structures the threated to be impacted by a debris avalanche. A comparison is also made with critical values of impact pressures recorded in a similar context, and it is outlined the potential damage from such impact scenarios for the existing structures.

Keywords: SPH, structures, landslide, dynamic impact, flow.

1 INTRODUCTION

Flow-like landslides includes several natural phenomena which propagate along the slopes (debris avalanches) or drainage line (debris flows). They are extremely rapid and travel for hundreds of meters with increase of volume during the propagation stage [1]. The attention is here focused on the debris avalanches defined by [2] as "very rapid to extremely rapid shallow flow of partially or fully saturated debris on a steep slope, without confinement in an established channel". Several methods have been used to analyze the propagation of flow-like landslides, e.g. Finite Element Method [3], Finite Difference Method [4], Material Point Method [5]. The "GeoFlow SPH" model (SPH) is used in this paper as it is considered capable to provide a good compromise of accuracy and time efficiency [6-7]. The area of Cervinara (Southern Italy) is selected as case study inside the wider context of the pyroclastic soils originated from the explosive eruptions of the Vesuvius volcano. The slopes facing the municipality of Cervinara are very steep, 35 degrees on average, and are covered by pyroclastic deposits 2-3 m thick [8]. In December 1999 a number of shallow landslides were triggered due to heavy rainfall and propagated as flows. Among these, a debris avalanche turned into a channelized flow and caused 5 victims [9]. Other soil volumes could be potentially triggered and the landslides could reach the piedmont area where several civil structures exist.

The paper proposes some preliminary numerical analyses to outline the ranges of velocity (v) and height (h) of the debris avalanches potentially occurring at specific points of the study area (Fig. 1). Then, the mean impact pressure (p) values are computed by using distinct formulations available in the literature.

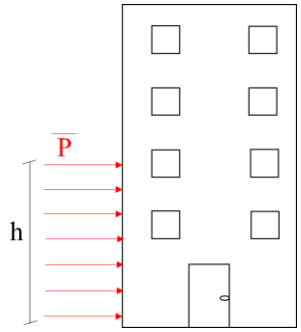

Figure 1: Schematic of the mean impact pressure (p) of a flow characterized by a velocity (v) and a height (h).

2 METHODS

The "GeoFlow_SPH" model proposed by [6] is here used to simulate the propagation pattern of a number of selected debris avalanches. This model is a depth-integrated hydromechanical coupled model that schematizes the propagating mass into a mixture of solid skeleton and pore water. It is based on a set of partial differential equations such as: i) the balance of mass of the mixture combined with the balance off the linear momentum of the pore water pressure; ii) the balance of the linear momentum of the mixture; iii) the rheological equation of the mixture; iv) the kinematical relations between velocity and deformation. The Smoothed Particle Hydrodynamics (SPH) numerical technique is particularly useful to ensure appropriate accuracy and reasonable computational times. More details are provided in [6-10] and [7]. The input data of the model are: the Digital Terrain Model (DTM) where the potential debris avalanches may propagate; the rheological features of the flows, here taken from [8]. Particularly, h_{trig} is the soil thickness in the triggering area; $tan\ \varphi_b$ is the base friction angle of the

flow propagating over the ground surface; h_w^{rel} is the height of the water table relative to the soil thickness in the triggering area; p_w^{rel} is the base pore water pressure divided by the soil liquefaction value; c_v is the soil consolidation coefficient; and E_r is the bed entrainment coefficient regulating the increase of landslide volume. Two set of rheological properties are referred, as taken from successful back-analyses of real debris avalanches occurred at locations not far from the study area, namely Monte Albino ("A" in Tab.1), and Monte Foresta ("F" Tab. 1).

Several potential triggering volumes are considered to propagate over the DTM (Fig. 2b). The peak impact force is calculated in correspondence of buildings (points B1, B2, B3, Fig. 2a) and streets (points S1, S2, Fig. 2a) starting from the height-velocity (*h*-*v*) pairs of the flow and using literature formulations.

Table 1. Sets of rheological properties used in the numerical modelling.

Rheology	φ'	tan φ'	h_w^{rel}	p_w^{rel}	c_v	E_r	Reference
A	19°	0.34	0.4	1.0	0.01	0.019	Cuomo et al. (2014)
F	22°	0.40	0.4	1.0	0.01	0.007	Cuomo et al. (2016)

Figure 2: a) Cervinara study area (Italy) and b) Digital Terrain Model (DTM) used.

The pressure induced by lateral forces could be very dangerous for structures as showed by [11]. Here, the pressure is considered applied on the structures as constant along the height as a simplification of real distribution during a natural phenomenon (Fig. 1). [12] proposed two formulations that depend on the impact mechanism: i) formation of a completely reflected wave; ii) formation of a vertical bulge; the last formulation depends on both height and velocity and is here considered (Eq. 3 in Tab. 2). [13] carried out real scale tests and laboratory tests to evaluate the impact pressure against rigid barriers and they evaluated the impact introducing an empirical coefficient *k* comprises between 1.5 and 5 (Eqs. 1 and 2, respectively in Tab. 2). Finally, [14] evaluate the impact force as the sum of a static component (height dependent) and a dynamic component (velocity dependent), (Eq. 4). The peak values of pressure versus height are compared with the maximum pressures applied to the structures as function of reinforced; the maximum pressure applied to the structures are taken by [11]. In particular, three reinforce level are considered taking into account a reinforced-concrete column: i)

strongly-reinforced; ii) medium-reinforced; iii) low-reinforced. It is possible to calculate the critical pressure that gives the ultimate bending moment inside the structures as function of flow height.

Table 2. Empirical equations used for estimation of impact pressure of the debris avalanche against structtures.

Name	Equation	Notes	References
Eq. 1	$p= k\rho_m v^2$	k=1.5	Canelli et al. (2012)
Eq. 2	$p= k\rho_m v^2$	k=5	Canelli et al. (2012)
Eq. 3	$p=(0.5g\rho_m h^2+\alpha h v^2\rho_m)/A$	α=1	Armanini et al. (2011)
Eq. 4	$p=0.5K_p\rho_m gh+5v^2\rho_m$	$Kp=\tan^2(\pi/4+\varphi/2)$	Gioffrè et al. (2017))

3 RESULTS AND DISCUSSION

The flow deposition heights are showed in Fig. 3 for both rheology A (Case A20) and rheology F (Case F20). The debris avalanches reach the structures in both cases and they are characterized by a maximum height equal to 1.5 m at the distal part of the flow deposit. The debris avalanche results in greater deposition height for the rheology "A" than for rheology "F" and the affected area is larger for the rheology "A" than rheology" F".

In Fig. 4 the heights and velocities computed in the control points are showed versus time. In correspondence of the structures (points B1 and B2) the flow deposits in both cases; while, the flow does not deposit in correspondence of the streets and the structure at point B3 where the flow height decreases until zero during the propagation stage.

The highest flow deposition height is equal to 6 m and is recorded for rheology A and in correspondence of point B2. The velocities increase quickly until a peak and then decreases down to zero in about 5 seconds. The maximum velocity is recorded in correspondence of the control point B3 for both rheologies (A and F) with the peak value is respectively equal to 16 m/s and 12 m/s. In correspondence of the street, the maximum height is simulated for rheology A and is equal to 3 m while the velocity is the lowest among all the control points and is equal to 1 m/s. The impact pressures are computed versus time considering different control points and rheologies in correspondence of the buildings (Fig. 5).

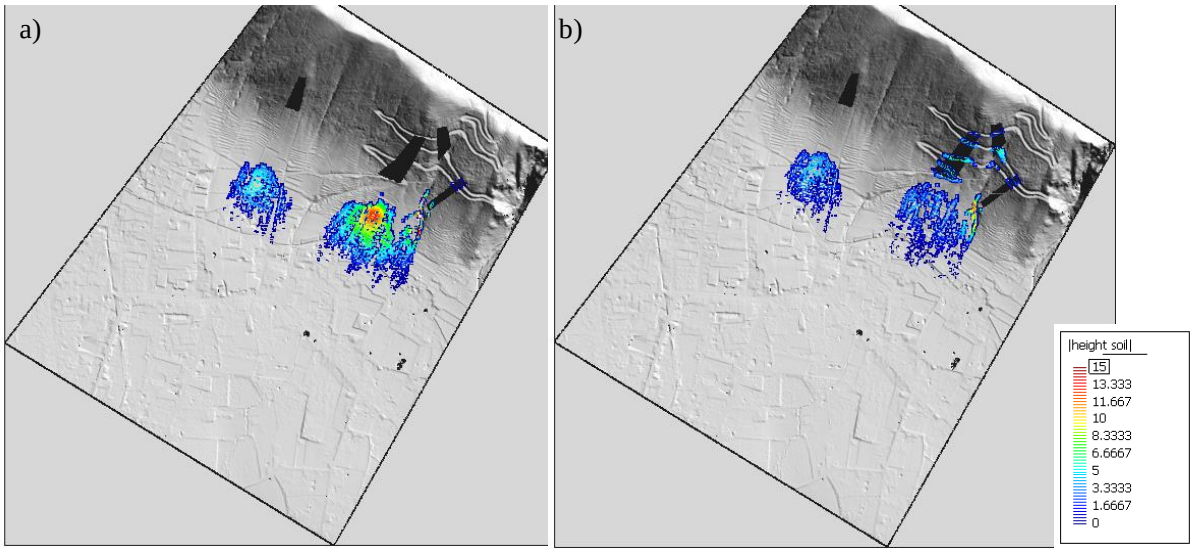

Figure 3: Deposition height of debris avalanche for: a) rheology A; b) rheology F.

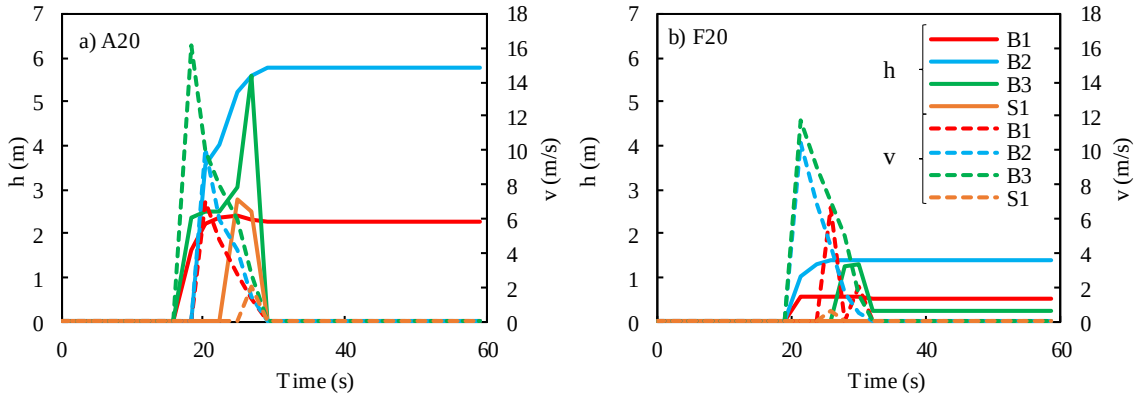

Figure 4: Heights (h) and velocity (v) versus time for a) rheology A and b) rheology F.

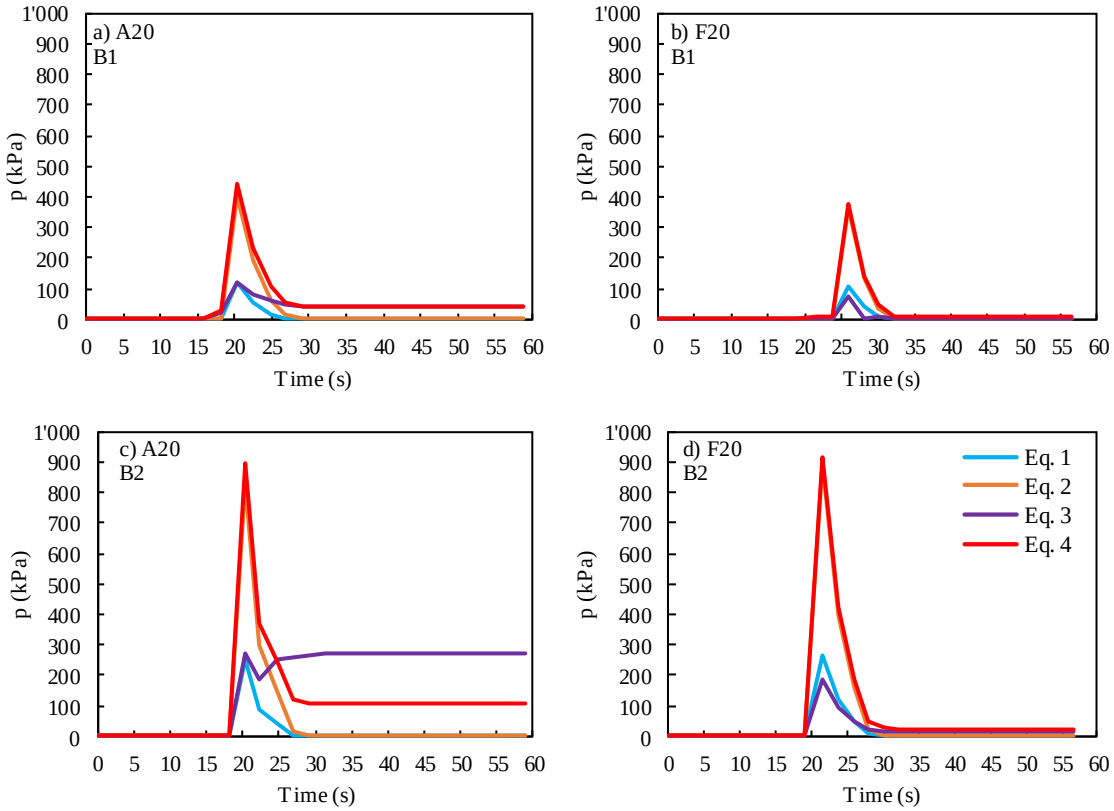

Figure 5: Maximum pressure (p) of the flow versus time in correspondence of the buildings (B1 and B2) for flow rheology A (Case A20, Fig. 5a, c) and rheology F (Case F20, Fig. 5b, d).

The impact pressure increases until a peak value (with the peak time at about 20 s) and then decreases. In general, the dynamic impulse of the pressure has duration less than 10 seconds in all the cases. The pressure decreases down to a constant value calculated through Eqs. 3-4, which are both dependent on height and velocity of the debris avalanche. The impact pressures are comparable for the Case A20 and Case F20. In particular, the maximum peak value is given by Eq. 4 and equal to 900 kPa and 2,000 kPa, respectively in correspondence of the points B2 and B3 (Fig. 6a) for case A20 and equal to 1,000 kPa in correspondence of the same point for case F20. The pressure calculated through the Eqs. 1 and 2 is comparable to the pressure calculated from Eq. 4 considering the maximum value of empirical coefficient k (equal to 5); at the same time, pressure computed through Eq. 1-2 are in agreement with the

pressure calculated through Eq. 3 considering the minimum value of *k* (equal to 1.5). The control point B3 has the highest value of pressure independent of the equation used for computing the pressure impact.

The case A20 presents the highest values of impact pressure in correspondence of the control point B3 (equal to 2,000 kPa) while the maximum impact pressures are comparable between the two rheologies considering the control points B1 and B2.

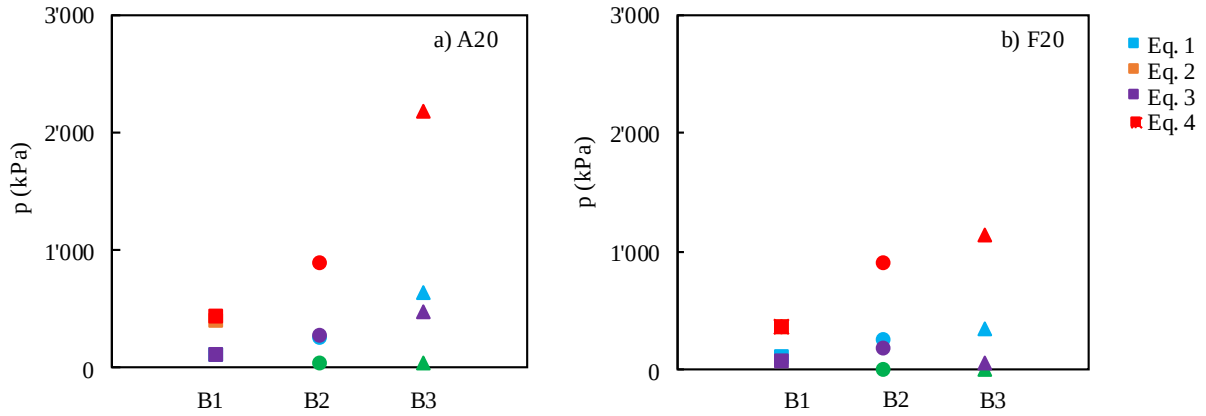

Figure 6: Peak pressure estimated in the different control points (B1, B2, and B3) for: a) flow rheology A; b) flow rheology F.

In Fig. 7, the pressure calculated through literature formulae is showed as function of the impact height and compared with the critical pressure of three levels of reinforced column reported in [11]. It is not possible to identify a critical value of impact pressure, but it is possible to individuate the trend of pressure as function of the impact height. In the case A20 (Fig. 7a), the pressures caused by the debris avalanches are lower than the critical pressure of the strongly-reinforced column for impact height less than 1 m; the medium-reinforced column and low-reinforced column can resist to the impact for values of impact height less than 0.8 m. The impact pressure increases when the impact height increase, then the structures should be not enough resistant for impact height more than 1 m. The strongly-reinforced column resists in correspondence of all control points considering the case F20 (Fig. 7b).

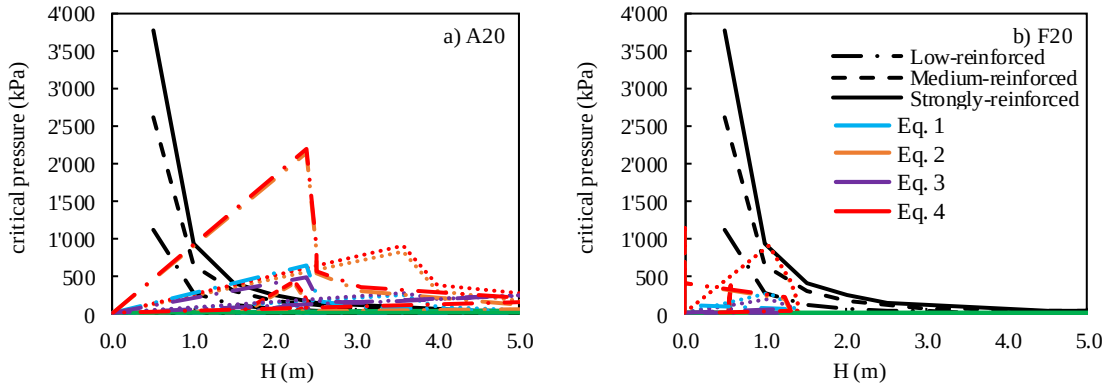

Figure 7: Black lines indicate the critical pressure computed for differently reinforced structures as a function the impact height (*H*) of a debris avalanche. Coloured lines indicated the flow pressure computed through different formulations (Eqs. 1-4) with reference to different control points such as B1 (dashed line), B2 (dots line), B3 (dashed dot line).

4 CONCLUSION

The paper deals with the dynamic phenomena of debris avalanche against structures during the propagation. Two different rheologies are taken into account and the area affected by different debris avalanches is studied; it is shown that the debris avalanches propagate until the urban zone. Then, the pairs of height-velocity are computed in several control points in correspondence of either building (B points) or streets (S points). During the propagation, the flow may produce two different scenarios: i) the height increases until a maximum value and then decreases until a constant value (there is a deposition of material); ii) the height increases until a maximum value and then decreases until a null value; while, the flow-velocities increases until a peak value and then decreases until null value. The impact pressure exerted against the structures is calculated considering distinct literature formulae and starting by the pairs height-velocity previously computed. The pressure versus time increases until the peak value and then decreases following two different trends: i) the flow impacted against the structures and a part of it deposited; in this case the deposition of material exerted a force also after the end of the propagation; ii) the flow propagate without deposition of material in the surrounding of the structure so that the force is null after the propagation of the flow. Finally, the range of maximum pressure are showed for each control point to give some indications to designer on the peak impact pressure due to an event such as a debris flow and take into account the several precautions for the aim taking into account that the peak pressure will be applied for several seconds.

A single critical value of flow pressure against the structure cannot be individuated because the critical pressure is dependent on the impact height. The pressures are plotted versus impact height and compared with the pressure that gives the ultimate bending moment taken by literature in relation to the impact height. The structures taken into account are able to resist to the debris avalanches for impact height less than 1 m in rheology A; while in rheology F, the strongly reinforced column is able to resist in al control points.

5 ACKNOWLEDGEMENTS

Prof. Manuel Pastor (Universidad Politecnica de Madrid, Spain) and co-workers are much acknowledged for having provided the “GeoFlow_SPH” code used for the numerical simulations. The authors wish to thank the Autorità di Bacino Liri-Garigliano e Volturno, which provided the data necessary to develop this work. This research was developed within the framework of different projects: i) Industrial Partnership PhD Course (Dottorato Industriale Regione Campania, Italia); ii) project FARB 2017 “Modellazione numerica e analisi inversa per frane tipo flusso” funded by the Italian Education and Research Ministry.

REFERENCES

[1] Cascini L, Cuomo S, Pastor M, Sorbino G, Piciullo L (2014) SPH run-out modelling of channelised landslides of the flow type. Geomorphology, 214, 502-513.

[2] Hungr O, Evans SG, Bovis MJ, Hutchinson JN (2001) A review of the classification of landslides of the flow type. Environmental & Engineering Geoscience, 7(3), 221-238.

[3] Quecedo, M., Pastor, M., Herreros, M. I., & Fernández Merodo, J. A. (2004). Numerical modelling of the propagation of fast landslides using the finite element method. International Journal for Numerical Methods in Engineering, 59(6), 755-794.

[4] McDougall, S., & Hungr, O. (2004). A model for the analysis of rapid landslide motion across three-dimensional terrain. Canadian Geotechnical Journal, 41(6), 1084-1097.

[5] Andersen, S., & Andersen, L. (2010). Modelling of landslides with the material-point method. Computational Geosciences, 14(1), 137-147.

[6] Pastor, M., Haddad, B., Sorbino, G., Cuomo, S., & Drempetic, V. (2009). A depth‐integrated, coupled SPH model for flow‐like landslides and related phenomena. International Journal for numerical and analytical methods in geomechanics, 33(2), 143-172.

[7] Cuomo S, Pastor M, Cascini L, Castorino GC (2014) Interplay of rheology and entrainment in debris avalanches: a numerical study. Canadian Geotechnical Journal, 51(11), 1318-1330.

[8] Cuomo, S., & Iervolino, A. (2016). Investigating the role of stratigraphy in large-area physically-based analysis of December 1999 Cervinara shallow landslides. Journal of Mountain Science, 13(1), 104-115.

[9] Cascini L., Cuomo S., De Santis A. (2011). Numerical modelling of the December 1999 Cervinara flow-like mass movements (Southern Italy). Proc. of 5th International Conference on Debris-Flow Hazards Mitigation: Mechanics, Prediction and Assessment. Italian Journal of Engineering Geology and Environment, 635-644.

[10] Cascini, L., Cuomo, S., Pastor, M., Sorbino, G., & Piciullo, L. (2014). SPH run-out modelling of channelised landslides of the flow type. Geomorphology, 214, 502-513.

[11] Zeng, C., Cui, P., Su, Z., Lei, Y., & Chen, R. (2015). Failure modes of reinforced concrete columns of buildings under debris flow impact. Landslides, 12(3), 561-571.

[12] Armanini A, Larcher, M, & Odorizzi, M (2011) Dynamic impact of a debris flow front against a vertical wall. In Proceedings of the 5th International Conference on Debris-Flow Hazards Mitigation: Mechanics, Prediction and Assessment, Padua, Italy, 1041-1049.

[13] Canelli L, Ferrero AM, Migliazza M, Segalini A (2012) Debris flow risk mitigation by the means of rigid and flexible barriers-experimental tests and impact analysis. Natural Hazards and Earth System Sciences, 12(5), 1693-1699.

[14] Gioffrè, D., Mandaglio, M. C., Di Prisco, C., & Moraci, N. (2017). Evaluation of rapid landslide impact forces against sheltering structures. Rivista Italiana di Geotenica, 3, 64-76.

COMPDYN 2019
7th ECCOMAS Thematic Conference on
Computational Methods in Structural Dynamics and Earthquake Engineering
M. Papadrakakis, M. Fragiadakis (eds.)
Crete, Greece, 24-–26 June 2019

CONTACT OF VISCOELASTIC SIPED TYRE TREAD BLOCKS ON GRAVEL ROAD

Arne Leenders[1], **Stephanie Kahms**[1], **Matthias Wangenheim**[1]

[1]Institute of Dynamics and Vibration Research
Appelstraße 11, 30167 Hannover
e-mail: {leenders,kahms,wangenheim}@ids.uni-hannover.de

Keywords: multi-body system, tyre tread block, self-contact, viscoelasticity, gravel road, linear complementarity problem, friction, model order reduction.

Abstract. *One focus of modelling the movement of vehicle tyres on the road is the contact of the tread with the road surface. The tread can consist of many blocks, that vary in form and length and can exhibit a siped structure to improve the traction of the tyre on the road, especially for winter tyres. The rotation of the tyre leads to periodical impacts of each tread block into the road surface, which is often uneven. The road can have loose gravel on it or can be covered with grit (icy roads). To simulate the dynamics of a tyre on a gravel road, we suppose to focus on a single tyre tread block. This block gets into frictional contact with the surface, the granular material and also with itself, when the block is siped and the individual lips touch each other. In our model these contact configurations are formulated as linear complementarity problems. The tyre tread is made of an elastomer material, which possesses viscoelastic behaviour.*
With our approach we can simulate the dynamics of a tyre tread block concerning displacement of the gravel, external and self-contact of the tread block's lips. The simulation can help to investigate contact phenomena of a rolling tread for different surfaces and materials.

1 Introduction

Viscoelastic components like tyre tread blocks show elastic as well as viscous properties. They have dissipative character and their deformations are time-dependent [6]. The material's properties vary in temperature and frequency. Many types of rheological models exist to describe viscoelastic behaviour. One of the most established ones are the standard linear solid model and its extension, the generalized Maxwell-Wiechert-model [2, 13, 14]. These models contain components of masses, springs and dashpots, whose parameters can be fitted by experimental measurements.

2 Approach

By extracting stiffness and mass matrices of a tyre tread block out of commercial FEM software and combining them with rheological models for viscoelasticity we get a viscoelastic system of the tread block. The gravel is modelled as an accumulation of single pebbles, that have individual degrees of freedom. The combination of the viscoelastic tread block and the gravel represents a multi-body system, see **figure 1**.

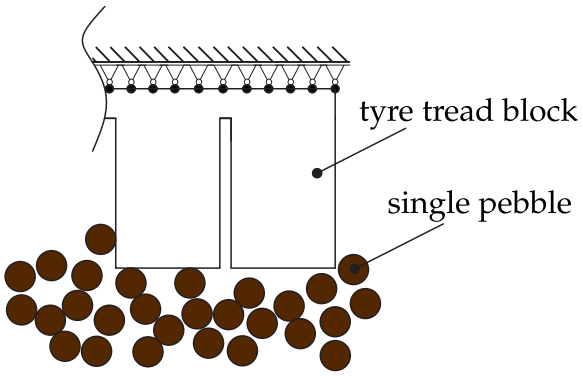

Figure 1: Multi-body system consisting of viscoelastic tread block and granular material

To lower the computational effort of solving the transient deformations of the viscoelastic system different model order reduction techniques can be applied. For our approach a reduction based method, called Craig-Bampton model order reduction, is implemented. This method retains important degrees of freedom (master dof), that are connected to boundaries of the system, where external forces or contact forces affect the structure [10]. The remaining slave dof are reduced and replaced by modal dof.
The occasional contact of the tyre tread into the road has to be considered. This kind of contact can be described by unilateral constraints. All constraints have to be fulfilled for every contact configuration. A mathematical way to solve the equations of motion with unilateral constraints simultaneously is the formulation as a linear complementarity problem (lcp) [8].

3 Mathematical description of viscoelastic multi-body system

The dynamical behaviour of a tyre tread block on gravel road is modelled as a multi-body system consisting of a viscoelastic tyre tread and rigid gravel. The granular material is modelled as rigid bodies as well as the road surface. The surface is modelled as rough and frictional. Including the unilateral contact forces a multi-body system in general can be expressed by:

$$\boldsymbol{M}\ddot{\boldsymbol{q}} + \boldsymbol{D}\dot{\boldsymbol{q}} + \boldsymbol{K}\boldsymbol{q} = \boldsymbol{F}_{\mathrm{ex}} + \boldsymbol{W}_{\mathrm{N}}\boldsymbol{F}_{\mathrm{N}} + \boldsymbol{W}_{\mathrm{T}}\boldsymbol{F}_{\mathrm{T}}\,. \tag{1}$$

The generalized holonomic degrees of freedom of the tread block and the gravel are contained in the vector $\boldsymbol{q}$, while $\boldsymbol{M}, \boldsymbol{D}, \boldsymbol{K}$ label the system's structural matrices of mass, damping and stiffness. The unilateral contact forces in normal and tangential direction $\boldsymbol{F}_{\mathrm{N}}, \boldsymbol{F}_{\mathrm{T}}$ are projected to the differential equations by the transformation matrices $\boldsymbol{W}_{\mathrm{N}}, \boldsymbol{W}_{\mathrm{T}}$. $\boldsymbol{F}_{\mathrm{ex}}$ represents the external forces acting onto the system.
For the viscoelastic standard linear solid model, see **figure 2**, the differential equations of second order yield without contact forces:

$$m\ddot{q} + kq + d_1\dot{y}_1 = F_{\mathrm{ex}}\,, \tag{2}$$

$$d_1\dot{y}_1 = k_1\left(q - y_1\right)\,. \tag{3}$$

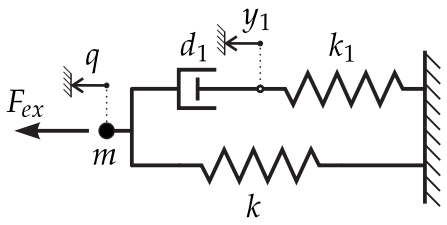

Figure 2: Standard linear solid model

The system of equations of motion can be solved numerically by schemes of time integration or event-based schemes. Time integration can provide faster and more robust solutions than event-based schemes and will be used in our approach [15, 1].
The combination of equations 2,3 would lead to a system of differential equations of third order. Differential equations with orders greater than two need multi-step time integration schemes. These methods use more than the last time step. Especially for contact situations with impacts that occur suddenly, one-step solvers are recommended because prior time steps, that are not affected by impacts, do not affect the results of the recent time step [4]. For this reason the time derivative of equation 3 is replaced by a backward difference quotient:

$$m\ddot{q}_{n+1} + kq_{n+1} + d_1\frac{y_{1,n+1} - y_{1,n}}{\Delta t} = F_{\mathrm{ex},n+1}\,, \tag{4}$$

$$d_1\frac{y_{1,n+1} - y_{1,n}}{\Delta t} = k_1\left(q_{n+1} - y_{1,n+1}\right)\,, \tag{5}$$

$$m\ddot{q}_{n+1} + kq_{n+1} + \underbrace{k_1\frac{d_1}{d_1 + k_1\Delta t}}_{k_{1,\mathrm{ers}}}\,q_{n+1}\,\underbrace{-k_1\frac{d_1}{d_1 + k_1\Delta t}y_{1,n}}_{F_{\mathrm{hist}}} = F_{\mathrm{ex},n+1}\,. \tag{6}$$

The term F_{hist} contains the historic restoring forces, that result from the viscoelastic material formulation.

4 Time-stepping scheme

The multi-body system (gravel and tread block) is solved by the *Newmark* time integration scheme [12]. This method is in particular used for dynamical problems. It contains two parameters β, γ, which control the numerical damping, stability and accuracy of the scheme. The

time-stepping equations are defined as:

$$\dot{\boldsymbol{q}}_{n+1}\left(\ddot{\boldsymbol{q}}_{n+1}\right) = \dot{\boldsymbol{q}}_n + \left[(1-\gamma)\,\ddot{\boldsymbol{q}}_n + \gamma\ddot{\boldsymbol{q}}_{n+1}\right]\Delta t\,, \tag{7}$$

$$\boldsymbol{q}_{n+1}\left(\ddot{\boldsymbol{q}}_{n+1}\right) = \boldsymbol{q}_n + \dot{\boldsymbol{q}}_n\Delta t + \left[\left(\frac{1}{2}-\beta\right)\ddot{\boldsymbol{q}}_n + \beta\ddot{\boldsymbol{q}}_{n+1}\right]\Delta t^2\,. \tag{8}$$

The *Newmark* parameters β, γ can be chosen in the range of $0 \leq \beta \leq \frac{1}{2}$, $0 \leq \gamma \leq 1$ [19]. The stability of the integration scheme is guaranteed for $\gamma \geq \frac{1}{2}\,, \beta \geq \frac{1}{4}\left(\gamma + \frac{1}{2}\right)^2$ [18]. The parameters control the stability and accuracy of the time integration and are chosen in the following as $\gamma = \frac{1}{2}, \beta = \frac{1}{4}$, which is called the Newmark scheme of constant average acceleration [19].

5 Unilateral external and self-contact

The contacts among the different parts of the multi-body system occur occasionally. In case of a contact unilateral constraints in the form of

$$\mathbf{0} \leq \boldsymbol{x} \perp \boldsymbol{z} \geq \mathbf{0} \tag{9}$$

have to be fulfilled simultaneously. A way to handle these constraints with the equations of motion of the dynamical system is the formulation as a linear complementarity problem, the combination of the equation system

$$\boldsymbol{A}\boldsymbol{x} + \boldsymbol{b} = \boldsymbol{z} \tag{10}$$

and the constraint conditions 9. With this kind of contact reaction it is possible to consider nonlinear mechanical effects like friction and impacts for multi-body contact situations with external and self-contact.
The constraints of the unilateral contact has to be divided into normal and tangential contact, see **figure 3**.

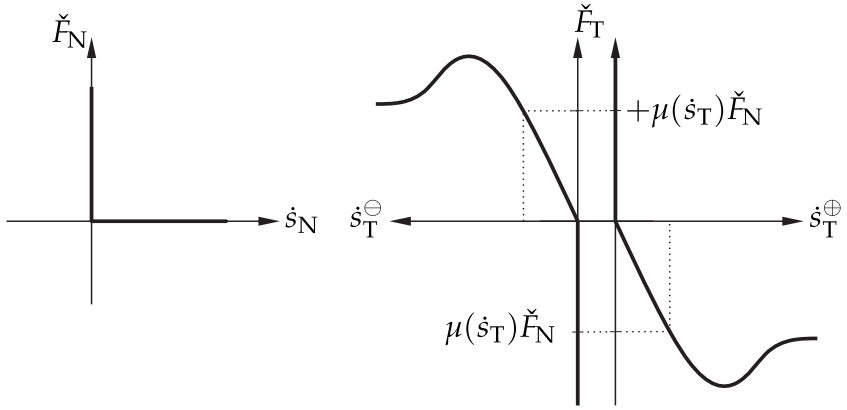

Figure 3: Complementarity conditions of normal and tangential unilateral contact

The normal contact constraint can be formulated by the complementarity condition

$$\mathbf{0} \leq \check{\boldsymbol{F}}_\mathrm{N} \perp \dot{\boldsymbol{s}}_\mathrm{N} \geq \mathbf{0}\,, \tag{11}$$

which means, that the relative velocity between both bodies $\dot{\boldsymbol{s}}_\mathrm{N}$ will be zero, if the contact normal force $\boldsymbol{F}_\mathrm{N}$ is greater than zero and vice versa [8]. Only one of both items can be greater

than zero. By separating the tangential relative velocity $\dot{\boldsymbol{s}}_\mathrm{T}$ into two nonnegative parts for each half space by

$$\dot{\boldsymbol{s}}_\mathrm{T} = \dot{\boldsymbol{s}}_\mathrm{T}^{\oplus} - \dot{\boldsymbol{s}}_\mathrm{T}^{\ominus}\,, \tag{12}$$

one can find complementarity conditions for the tangential unilateral contact in the same way with Coulomb's friction law and the matrix of friction coefficients $\underline{\underline{\boldsymbol{\mu}}}\,(\dot{\boldsymbol{s}}_\mathrm{T})$ [7]:

$$\begin{aligned} \mathbf{0} &\leq +\check{\boldsymbol{F}}_\mathrm{T} + \underline{\underline{\boldsymbol{\mu}}}\,(\dot{\boldsymbol{s}}_\mathrm{T})\,\check{\boldsymbol{F}}_\mathrm{N} \perp \dot{\boldsymbol{s}}_\mathrm{T}^{\oplus} \geq \mathbf{0}\,, \\ \mathbf{0} &\leq -\check{\boldsymbol{F}}_\mathrm{T} + \underline{\underline{\boldsymbol{\mu}}}\,(\dot{\boldsymbol{s}}_\mathrm{T})\,\check{\boldsymbol{F}}_\mathrm{N} \perp \dot{\boldsymbol{s}}_\mathrm{T}^{\ominus} \geq \mathbf{0}\,. \end{aligned} \tag{13}$$

The complementarity conditions and the equations of motion are defined by equations 1, 6, 11 and 13. To set up the entire lcp for contact configurations like impacts, we need an impact law and kinematic relations between the velocities $\dot{\boldsymbol{q}}$ and the gap functions $\dot{\boldsymbol{s}}$. We use Newton's impact law

$$\dot{\boldsymbol{s}}_\mathrm{N,e} = -\underline{\underline{\boldsymbol{\epsilon}}}_\mathrm{N}\dot{\boldsymbol{s}}_\mathrm{N,s}\,, \quad \dot{\boldsymbol{s}}_\mathrm{T,e} = -\underline{\underline{\boldsymbol{\epsilon}}}_\mathrm{T}\dot{\boldsymbol{s}}_\mathrm{T,s} \tag{14}$$

with the subscript 'e' denoting the end of an impact and 's' denoting the start. Because of the time integration the length of an impact is limited to the time step size. For the discretized form of equations 14 the velocities for Newton's impact law are the ones at the time step $n+1$ (end of impact) and time step n (start of impact).
The coefficients of restitution for the normal direction $\underline{\underline{\boldsymbol{\epsilon}}}_\mathrm{N}$ and tangential direction $\underline{\underline{\boldsymbol{\epsilon}}}_\mathrm{T}$ are chosen as zero. This leads to an energy loss for every impact of mass into another but this energy loss is small in contrast to the kinetic and deformation energy of the multi-body system [8, 16]. The advantage of coefficients of restitution being zero is the numerical solution of the contact configuration which is physically compatible. Coefficients greater than zero could lead to unrealistic 'flattering' of the tyre tread block's surface, which means that the masses in contact would oscillate inside the contact region because the contact forces and restoring structural forces of the tread block are accelerating the mass alternately.
The kinematic relations of the normal and tangential gap functions $\dot{\boldsymbol{s}}_\mathrm{N}, \dot{\boldsymbol{s}}_\mathrm{T}$ yield:

$$\dot{\boldsymbol{s}}_\mathrm{N} = \boldsymbol{W}_\mathrm{N}^\mathrm{T}\dot{\boldsymbol{q}} + \hat{\boldsymbol{w}}_\mathrm{N}\,, \quad \dot{\boldsymbol{s}}_\mathrm{T} = \boldsymbol{W}_\mathrm{T}^\mathrm{T}\dot{\boldsymbol{q}} + \hat{\boldsymbol{w}}_\mathrm{T}\,. \tag{15}$$

The items $\hat{\boldsymbol{w}}_\mathrm{N}, \hat{\boldsymbol{w}}_\mathrm{T}$ are the kinematic excitations of the masses within the multi-body system, e.g. due to cycloid movement of the tread block [8]. Using the equations of motion for the multi-body system on velocity level leads to

$$\int_{t_\mathrm{s}}^{t_\mathrm{e}} \left(\boldsymbol{M}\ddot{\boldsymbol{q}} - \boldsymbol{D}\dot{\boldsymbol{q}} - \boldsymbol{K}\boldsymbol{q} - \boldsymbol{W}_\mathrm{N}\boldsymbol{F}_\mathrm{N} - \boldsymbol{W}_\mathrm{T}\boldsymbol{F}_\mathrm{T}\right)\mathrm{d}t = \mathbf{0}\,, \tag{16}$$

$$\boldsymbol{M}\left(\dot{\boldsymbol{q}}_{\mathrm{n}+1} - \dot{\boldsymbol{q}}_\mathrm{n}\right) - \boldsymbol{D}\dot{\boldsymbol{q}}\Delta t - \boldsymbol{K}\boldsymbol{q}\Delta t - \boldsymbol{W}_\mathrm{N}\check{\boldsymbol{F}}_\mathrm{N} - \boldsymbol{W}_\mathrm{T}\check{\boldsymbol{F}}_\mathrm{T} = \mathbf{0}\,, \tag{17}$$

by integrating equation 1.
With the use of the definitions of the nonnegative impulses

$$\check{\boldsymbol{F}}_\mathrm{T}^{\oplus} = +\check{\boldsymbol{F}}_\mathrm{T} + \underline{\underline{\boldsymbol{\mu}}}\,(\dot{\boldsymbol{s}}_\mathrm{T})\,\check{\boldsymbol{F}}_\mathrm{N}\,, \tag{18}$$

$$\check{\boldsymbol{F}}_\mathrm{T}^{\ominus} = -\check{\boldsymbol{F}}_\mathrm{T} + \underline{\underline{\boldsymbol{\mu}}}\,(\dot{\boldsymbol{s}}_\mathrm{T})\,\check{\boldsymbol{F}}_\mathrm{N}\,, \tag{19}$$

and the summation of both equations

$$\check{\boldsymbol{F}}_\mathrm{T}^{\ominus} = 2\underline{\underline{\boldsymbol{\mu}}}\,(\dot{\boldsymbol{s}}_\mathrm{T})\,\check{\boldsymbol{F}}_\mathrm{N} - \check{\boldsymbol{F}}_\mathrm{T}^{\oplus}\,, \tag{20}$$

the entire complementarity conditions yield:

$$\mathbf{0} \leq \dot{\boldsymbol{s}}_{\mathrm{n+1}} = \begin{bmatrix} \dot{\boldsymbol{s}}_{\mathrm{N}} \\ \dot{\boldsymbol{s}}_{\mathrm{T}}^{\oplus} \\ \check{\boldsymbol{F}}_{\mathrm{T}}^{\ominus} \end{bmatrix} \perp \begin{bmatrix} \check{\boldsymbol{F}}_{\mathrm{N}} \\ \check{\boldsymbol{F}}_{\mathrm{T}}^{\oplus} \\ \dot{\boldsymbol{s}}_{\mathrm{T}}^{\ominus} \end{bmatrix} = \check{\boldsymbol{F}} \geq \mathbf{0}\,. \tag{21}$$

Combining equation 6, written in matrix form to include all masses of the multi-body system and containing the contact forces, with the Newmark equations 8 leads to:

$$\boldsymbol{M}\ddot{\boldsymbol{q}}_{\mathrm{n+1}} + \boldsymbol{K}\boldsymbol{q}_{\mathrm{n+1}} + \boldsymbol{K}_{\mathrm{1,ers}}\boldsymbol{q}_{\mathrm{n+1}} = \boldsymbol{F}_{\mathrm{ex,n+1}} + \boldsymbol{F}_{\mathrm{hist,n}} + \boldsymbol{W}_{\mathrm{N,n+1}}\boldsymbol{F}_{\mathrm{N,n+1}} + \boldsymbol{W}_{\mathrm{T,n+1}}\boldsymbol{F}_{\mathrm{T,n+1}}\,, \tag{22}$$

$$\begin{aligned} \underbrace{\left[\boldsymbol{M} + \left(\boldsymbol{K} + \boldsymbol{K}_{\mathrm{1,ers}}\right)\beta_{\mathrm{lcp}}\Delta t^2\right]}_{\boldsymbol{M}_{\mathrm{ers}}}\ddot{\boldsymbol{q}}_{\mathrm{n+1}} &= \boldsymbol{F}_{\mathrm{ex,n+1}} + \boldsymbol{F}_{\mathrm{hist,n}} + \boldsymbol{W}_{\mathrm{N,n+1}}\boldsymbol{F}_{\mathrm{N,n+1}} + \boldsymbol{W}_{\mathrm{T,n+1}}\boldsymbol{F}_{\mathrm{T,n+1}} \\ &\quad - \underbrace{\left(\boldsymbol{K} + \boldsymbol{K}_{\mathrm{1,ers}}\right)}_{\boldsymbol{K}_{\mathrm{ers}}} \underbrace{\left(\boldsymbol{q}_n + \dot{\boldsymbol{q}}_n\Delta t + \left(\frac{1}{2} - \beta_{\mathrm{lcp}}\right)\ddot{\boldsymbol{q}}_n\Delta t^2\right)}_{\boldsymbol{q}_{\mathrm{n,ers}}}\,, \end{aligned} \tag{23}$$

$$\begin{aligned} \dot{\boldsymbol{q}}_{n+1} = \underbrace{\dot{\boldsymbol{q}}_n + \left(1 - \gamma_{\mathrm{lcp}}\right)\Delta t\ddot{\boldsymbol{q}}_n}_{\dot{\boldsymbol{q}}_{\mathrm{n,ers}}} + \gamma_{\mathrm{lcp}}\Delta t\ddot{\boldsymbol{q}}_{n+1}\boldsymbol{M}_{\mathrm{ers}}^{-1}\Big[\boldsymbol{F}_{\mathrm{ex,n+1}} \ldots \\ + \boldsymbol{F}_{\mathrm{hist,n}} + \boldsymbol{W}_{\mathrm{N,n+1}}\boldsymbol{F}_{\mathrm{N,n+1}} + \boldsymbol{W}_{\mathrm{T,n+1}}\boldsymbol{F}_{\mathrm{T,n+1}} - \boldsymbol{K}_{\mathrm{ers}}\boldsymbol{q}_{\mathrm{n,ers}}\Big]\,. \end{aligned} \tag{24}$$

This additional Newmark parameters $\beta_{\mathrm{lcp}}, \gamma_{\mathrm{lcp}}$ only exist for the lcp. These parameters control the stability of the calculation. We choose $\beta_{\mathrm{lcp}} = 0.5$ and $\gamma_{\mathrm{lcp}} = 1$ to stabilize the calculation by introducing numerical damping. With the kinematic relations 15, the abbreviations 18-20 and the identities $\check{\boldsymbol{F}}_{\mathrm{N}} = \boldsymbol{F}_{\mathrm{N}}\Delta t\,, \check{\boldsymbol{F}}_{\mathrm{T}} = \boldsymbol{F}_{\mathrm{T}}\Delta t$ the final equation system yields:

$$\begin{aligned} \begin{bmatrix} \dot{\boldsymbol{s}}_{\mathrm{N}} \\ \dot{\boldsymbol{s}}_{\mathrm{T}}^{\oplus} \\ \check{\boldsymbol{F}}_{\mathrm{T}}^{\ominus} \end{bmatrix} &= \begin{bmatrix} \gamma_{\mathrm{lcp}}\boldsymbol{W}_{\mathrm{N}}^{\mathrm{T}}\boldsymbol{M}_{\mathrm{ers}}^{-1}\left(\boldsymbol{W}_{\mathrm{N}} - \boldsymbol{W}_{\mathrm{T}}\underline{\underline{\boldsymbol{\mu}}}\left(\dot{\boldsymbol{s}}_{\mathrm{T}}\right)\right) & \gamma_{\mathrm{lcp}}\boldsymbol{W}_{\mathrm{N}}^{\mathrm{T}}\boldsymbol{M}_{\mathrm{ers}}^{-1}\boldsymbol{W}_{\mathrm{T}} & \mathbf{0} \\ \gamma_{\mathrm{lcp}}\boldsymbol{W}_{\mathrm{T}}^{\mathrm{T}}\boldsymbol{M}_{\mathrm{ers}}^{-1}\left(\boldsymbol{W}_{\mathrm{N}} - \boldsymbol{W}_{\mathrm{T}}\underline{\underline{\boldsymbol{\mu}}}\left(\dot{\boldsymbol{s}}_{\mathrm{T}}\right)\right) & \gamma_{\mathrm{lcp}}\boldsymbol{W}_{\mathrm{T}}^{\mathrm{T}}\boldsymbol{M}_{\mathrm{ers}}^{-1}\boldsymbol{W}_{\mathrm{T}} & \boldsymbol{I} \\ 2\underline{\underline{\boldsymbol{\mu}}}\left(\dot{\boldsymbol{s}}_{\mathrm{T}}\right) & -\boldsymbol{I} & \mathbf{0} \end{bmatrix} \begin{bmatrix} \check{\boldsymbol{F}}_{\mathrm{N}} \\ \check{\boldsymbol{F}}_{\mathrm{T}}^{\oplus} \\ \dot{\boldsymbol{s}}_{\mathrm{T}}^{\ominus} \end{bmatrix} \ldots \\ &\quad + \begin{bmatrix} \boldsymbol{W}_{\mathrm{N}}^{\mathrm{T}}\left[\dot{\boldsymbol{q}}_{\mathrm{n,ers}} + \gamma_{\mathrm{lcp}}\Delta t\boldsymbol{M}_{\mathrm{ers}}^{-1}\left(\boldsymbol{F}_{\mathrm{ex,n+1}} + \boldsymbol{F}_{\mathrm{hist,n}} - \boldsymbol{K}_{\mathrm{ers}}\boldsymbol{q}_{\mathrm{n,ers}}\right)\right] + \hat{\boldsymbol{w}}_{\mathrm{N}} \\ \boldsymbol{W}_{\mathrm{T}}^{\mathrm{T}}\left[\dot{\boldsymbol{q}}_{\mathrm{n,ers}} + \gamma_{\mathrm{lcp}}\Delta t\boldsymbol{M}_{\mathrm{ers}}^{-1}\left(\boldsymbol{F}_{\mathrm{ex,n+1}} + \boldsymbol{F}_{\mathrm{hist,n}} - \boldsymbol{K}_{\mathrm{ers}}\boldsymbol{q}_{\mathrm{n,ers}}\right)\right] + \hat{\boldsymbol{w}}_{\mathrm{T}} \\ \mathbf{0} \end{bmatrix}\,. \end{aligned} \tag{25}$$

The most time-consuming task during the contact simulation is the contact detection because of the different detection routines for external and self-contact. Especially the identification of undercuts and beadings within the self-contact detection routine requires particular attention. All contacts, which are found within one time step, are sorted in the following particular order: Self-contacting masses (superscript 'self') of the viscoelastic block are taken into account first, then all contacts of the viscoelastic body (superscript 'visco') with gravel or the road and last all contacts among the solid bodies (superscript 'sb') are considered:

$$\boldsymbol{W}_{\mathrm{N/T}}^{\mathrm{T}} = \begin{bmatrix} \boldsymbol{W}_{\mathrm{N/T}}^{\mathrm{self}} & \boldsymbol{W}_{\mathrm{N/T}}^{\mathrm{visco}} & \boldsymbol{W}_{\mathrm{N/T}}^{\mathrm{sb}} \end{bmatrix}^{\mathrm{T}} \tag{26}$$

The viscoelastic tyre tread block is forced kinematically onto a cycloid, that is typical for a rolling movement of a tyre. The kinematic excitations of all masses of the viscoelastic body are cycloids with individual radii for all mass points. The solid bodies are not excited. For each contact pair the different material properties have to be considered. That means the coefficients of restitution and the friction coefficients can be set differently for each body pair. The final lcp 21,25 then is solved by the pivoting Lemke algorithm [11].

6 Model order reduction

The computational effort of the contact detection and solving the lcp can be high, because the contact configurations can change every time step and the amount of variables of the lcp varies. To lower the computation time, the *Craig-Bampton* model order reduction is implemented [3]. This method reduces the number of physical dof by selected nodes, that are important to describe the system's behaviour [9]. With an efficient choice of the dof the accuracy of the solution remains high [5, 17]. Every single pebble is modelled as a rigid body that only contains two translational and one rotational dof. Those dof can not be reduced. The tyre tread block is represented by a system of coupled nodes, that can be divided into surface nodes and inner nodes inside the tread block. The surface nodes, see **figure 4**, are partly affected by boundaries or contact to surrounding bodies.

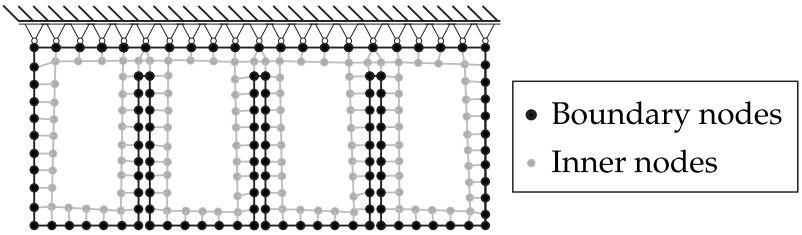

Figure 4: Definition of master and slave nodes for applying Craig-Bampton model order reduction

The surface nodes are defined here as the master nodes, whose dof are retained. The Craig-Bampton-reduction is a combined static-modal reduction. The inner nodes, defined as the slave nodes, are replaced by a selected number of modal dof of the inner system. Sorting the generalized holonomic coordinates, the vector $\boldsymbol{q}$ can be written as $\boldsymbol{q} = [\boldsymbol{q}_\mathrm{M}\ \boldsymbol{q}_\mathrm{S}]^\mathrm{T}$, where the subscripts 'M' and 'S' denote the master and slave coordinates. The equations of motion for the multibody system for the undamped case without contact then read as

$$\begin{bmatrix} \boldsymbol{M}_\mathrm{MM} & \boldsymbol{M}_\mathrm{MS} \\ \boldsymbol{M}_\mathrm{SM} & \boldsymbol{M}_\mathrm{SS} \end{bmatrix} \begin{bmatrix} \ddot{\boldsymbol{q}}_\mathrm{M} \\ \ddot{\boldsymbol{q}}_\mathrm{S} \end{bmatrix} + \begin{bmatrix} \boldsymbol{K}_\mathrm{MM} & \boldsymbol{K}_\mathrm{MS} \\ \boldsymbol{K}_\mathrm{SM} & \boldsymbol{K}_\mathrm{SS} \end{bmatrix} \begin{bmatrix} \boldsymbol{q}_\mathrm{M} \\ \boldsymbol{q}_\mathrm{S} \end{bmatrix} = \begin{bmatrix} \boldsymbol{F}_\mathrm{M} \\ \boldsymbol{F}_\mathrm{S} \end{bmatrix} . \tag{27}$$

The slave nodes are selected in a way, that they are not affected by external or contact forces. Therefore the inner forces yield $\boldsymbol{F}_\mathrm{S} = \boldsymbol{0}$, which leads to the dependency of the slave dof on the master dof in the static case:

$$\boldsymbol{q}_\mathrm{s} = -\boldsymbol{K}_\mathrm{ss}^{-1} \boldsymbol{K}_\mathrm{sm} \boldsymbol{q}_\mathrm{m} \, . \tag{28}$$

The additional expression of the slave dof by the modal coordinates $\boldsymbol{\eta}$ requires solving the eigenvalue problem of the inner system

$$\left(\boldsymbol{K}_\mathrm{SS} - \omega_j^2 \boldsymbol{M}_\mathrm{SS} \right) \boldsymbol{\phi}_{\mathrm{S},l} = 0 \quad \forall\ l = 1, 2, \ldots, n_\mathrm{max} \, , \tag{29}$$

which leads to the $n_{\max}$ linear independent eigenvectors, of which only a lower amount of $n_{\lim}$ selected eigenvectors is used. The eigenvectors are summarized by the modal matrix

$$\underbrace{\left[\boldsymbol{\phi}_{\mathrm{S},1}\,,\ldots,\boldsymbol{\phi}_{\mathrm{S},n_{\lim}}\right]}_{\boldsymbol{\Phi}_{\mathrm{S,mod}}}. \tag{30}$$

The transformation of the coordinates of the unreduced system $\boldsymbol{q} = \boldsymbol{T}_{\mathrm{CB}}\boldsymbol{q}_{\mathrm{red}}$ into the reduced vector $\boldsymbol{q}_{\mathrm{red}} = [\boldsymbol{q}_{\mathrm{M}}\ \boldsymbol{\eta}]^{\mathrm{T}}$ is done by the transformation matrix

$$\boldsymbol{T}_{\mathrm{CB}} = \begin{bmatrix} \boldsymbol{I} & \boldsymbol{0} \\ -\boldsymbol{K}_{\mathrm{SS}}^{-1}\boldsymbol{K}_{\mathrm{SM}} & \boldsymbol{\Phi}_{\mathrm{S,mod}} \end{bmatrix}. \tag{31}$$

The model order reduction then reads for the multi-body system with contact:

$$\boldsymbol{T}_{\mathrm{CB}}^{\mathrm{T}}\boldsymbol{M}\boldsymbol{T}_{\mathrm{CB}}\ddot{\boldsymbol{q}}_{\mathrm{red}} + \boldsymbol{T}_{\mathrm{CB}}^{\mathrm{T}}\boldsymbol{D}\boldsymbol{T}_{\mathrm{CB}}\dot{\boldsymbol{q}}_{\mathrm{red}} + \boldsymbol{T}_{\mathrm{CB}}^{\mathrm{T}}\boldsymbol{K}\boldsymbol{T}_{\mathrm{CB}}\boldsymbol{q}_{\mathrm{red}} = \boldsymbol{T}_{\mathrm{CB}}^{\mathrm{T}}\boldsymbol{F}_{\mathrm{ex}} + \boldsymbol{W}_{\mathrm{N}}\boldsymbol{T}_{\mathrm{CB}}^{\mathrm{T}}\boldsymbol{F}_{\mathrm{N}} + \boldsymbol{W}_{\mathrm{T}}\boldsymbol{T}_{\mathrm{CB}}^{\mathrm{T}}\boldsymbol{F}_{\mathrm{T}}. \tag{32}$$

7 Simulation of a tyre tread block on gravel road

The simulation of a tyre tread block on gravel road is performed for a cycloid movement of the tread with a rotation speed of $\omega = 3\,\mathrm{s}^{-1}$ and a belt diameter of the tyre of $d_{\mathrm{i}} = 650\,\mathrm{mm}$. The gravel is represented by a accumulation of 80 balls with varying diameter and weight. The time step size is chosen as $\Delta t = 1 \cdot 10^{-5}\,\mathrm{s}$. The siped tread structure has the following dimensions: length $20\,\mathrm{mm}$ and width $8\,\mathrm{mm}$. The temporal evaluation of the cycloid movement of the block is shown in **figure 6**. The surface masses of the viscoelastic block without contact are represented by blue markers, the ones in contact by red markers. The figures show that most of the gravel is displaced by the tread block. Some small stones are pressed on the road with the result that the lips of the tread block bend. After $t = 0.2\,\mathrm{s}$ the bending of the lips is high enough that self-contact of the block occurs. One single pebble is clamped between two block lips, when the tread moves upwards on the cycloid. The normalised contact forces, that are acting on each lip, are shown in **figure 5**. Within the first duration of $0.15\,\mathrm{s}$ the block has not yet

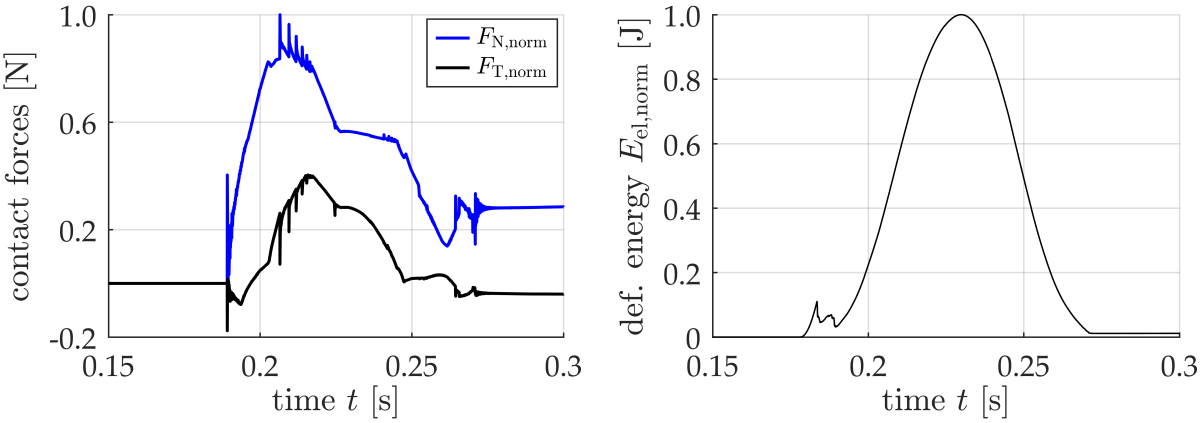

Figure 5: Contact forces acting on each lip, that clamps the pebble (left) and deformation energy of the viscoelastic tyre tread block (right)

come into contact with the gravel on the road. The contact forces rise, just as the block hits the gravel and the block's lips are bended by the clamped pebble, see **figure 6 (e)-(f)**. The pebbles

on the ground push the clamped one between the lips so the contact forces increase further and then decrease towards constant values, when the tread block leaves the contact area on the road. The pebble sticks between the lips and the contact forces oscillate because of further impulses due to other pebbles. The normalised elastic deformation energy, see **figure 5**, is greater than the oscillatory energy of the tread block. For this reason, the kinetic energy is left out here. The elastic deformation energy shows an initial rise and decrease, which is caused by the bending and rebound of the incoming block's lip at the initial contact with the gravel. The subsequent increase up to the maximum value occurs as the lips begin to bend due to the sticking pebble. The self-contact of the lips contributes to the elastic deformation energy. After leaving the contact area the energy decreases about a small value because of the viscoelastic material properties.

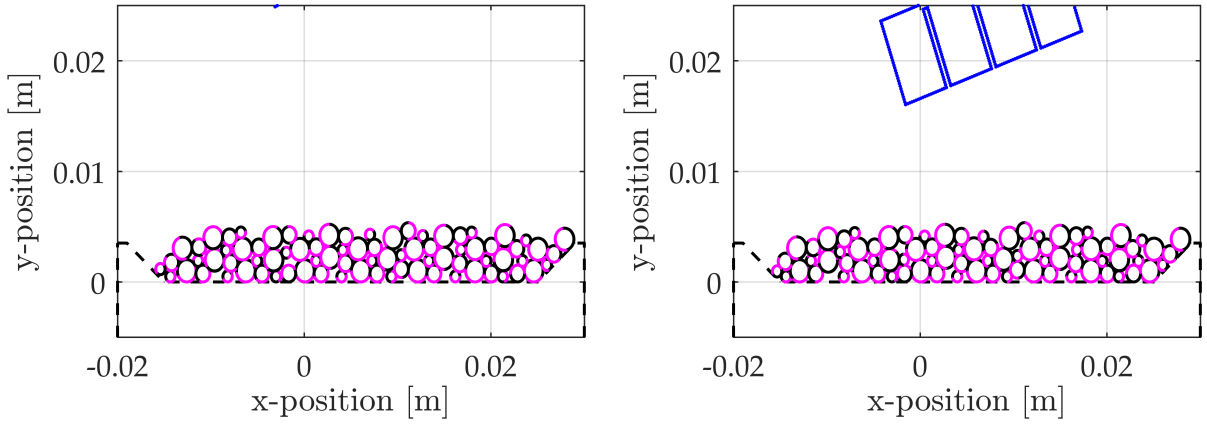

(a) $t = 0.094\,\mathrm{s}$ (b) $t = 0.12\,\mathrm{s}$

(c) $t = 0.16\,\mathrm{s}$ (d) $t = 0.17\,\mathrm{s}$

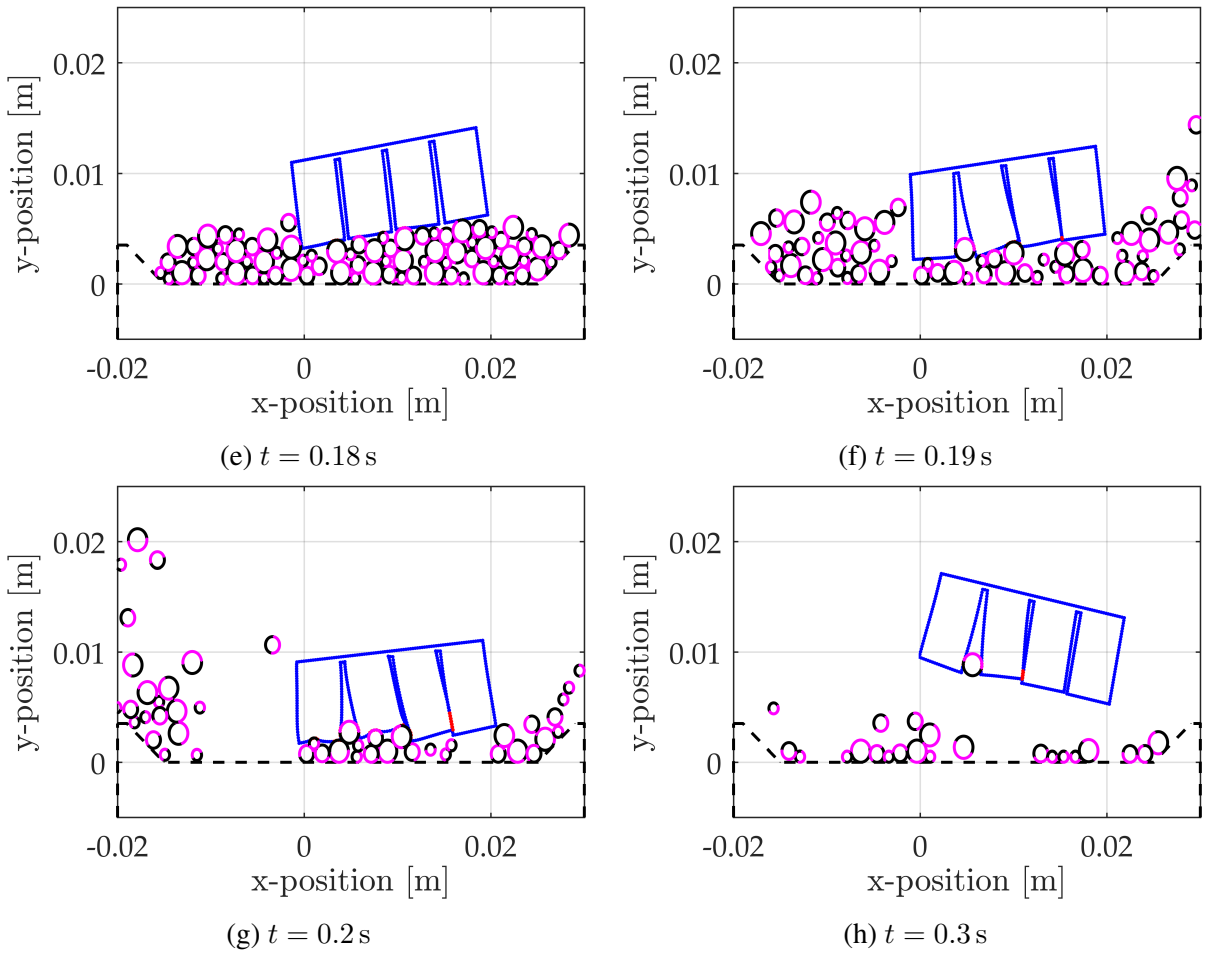

(e) $t = 0.18\,\mathrm{s}$ (f) $t = 0.19\,\mathrm{s}$

(g) $t = 0.2\,\mathrm{s}$ (h) $t = 0.3\,\mathrm{s}$

Figure 6: Temporal evaluation of the tyre tread block on gravel road: surface masses (blue), contact masses (red)

8 Conclusions

In this paper the frictional and impulsive multi-body contact of a viscoelastic tyre tread block on granular road is simulated. The unilateral contact configurations of the multi-body system, consisting of block and granular material, are considered by complementarity conditions. To lower the computational effort, the Craig-Bampton model order reduction is applied.
With our simulation it is possible to consider the transient deformations of a tyre tread block and the displacements of granular material for a cycloid movement of the block into the road. Both the displacement of the gravel by the moving tread block and the sticking of single pebbles between the block's lips can be simulated. Even self-contact of the lips can be shown.

REFERENCES

[1] ACARY, Vincent ; BROGLIATO, Bernard: *Lecture notes in applied and computational mechanics*. Bd. 35: *Numerical Methods for Nonsmooth Dynamical Systems: Applications in Mechanics and Electronics*. Berlin, Heidelberg : Springer-Verlag Berlin Heidelberg, 2008. http://dx.doi.org/10.1007/978-3-540-75392-6. http://dx.doi.org/10.1007/978-3-540-75392-6. – ISBN 978–3–540–75391–9

[2] ASSIE, A. E. ; ELTAHER, M. A. ; MAHMOUD, F. F.: Modeling of viscoelastic contact-impact problems. In: *Applied Mathematical Modelling* 34 (2010), Nr. 9, S. 2336–2352. http://dx.doi.org/10.1016/j.apm.2009.11.001. – DOI 10.1016/j.apm.2009.11.001. – ISSN 0307904X

[3] BAMPTON, Mervyn C. C. ; CRAIG, Roy R.: Coupling of substructures for dynamic analyses. In: *AIAA Journal* 6 (1968), Nr. 7, S. 1313–1319. http://dx.doi.org/10.2514/3.4741. – DOI 10.2514/3.4741. – ISSN 0001–1452

[4] BROGLIATO, Bernard: *Lecture Notes in Physics*. Bd. 551: *Impacts in Mechanical Systems: Analysis and Modelling*. Berlin and Heidelberg : Springer, 2000. http://dx.doi.org/10.1007/3-540-45501-9. http://dx.doi.org/10.1007/3-540-45501-9. – ISBN 3–540–67523–X

[5] CRAIG, Roy R. ; KURDILA, Andrew: *Fundamentals of structural dynamics*. 2. Auflage. Hoboken and N.J : John Wiley & Sons Inc., 2006. – ISBN 978–0–471–43044–5

[6] FLÜGGE, Wilhelm: *Viscoelasticity*. 2. Auflage. Berlin Heidelberg : Springer-Verlag, 1975. – ISBN 978–3–662–02278–8

[7] GLOCKER, Christoph: *Lecture notes in applied mechanics*. Bd. 1: *Set-Valued Force Laws: Dynamics of non-smooth systems*. 1. Auflage. Berlin Heidelberg : Springer-Verlag, 2001. – ISBN 978–3–642–53595–6

[8] GLOCKER, Christoph ; STUDER, Christian: Formulation and Preparation for Numerical Evaluation of Linear Complementarity Systems in Dynamics. In: *Multibody System Dynamics* 13 (2005), Nr. 4, S. 447–463. http://dx.doi.org/10.1007/s11044-005-2519-6. – DOI 10.1007/s11044–005–2519–6. – ISSN 1384–5640

[9] GUYAN, Robert J.: Reduction of stiffness and mass matrices. In: *AIAA Journal* 3 (1965), Nr. 2, S. 380. http://dx.doi.org/10.2514/3.2874. – DOI 10.2514/3.2874. – ISSN 0001–1452

[10] KUETHER, Robert J. ; TROYER, Kevin L.: Substructuring of Viscoelastic Subcomponents with Interface Reduction. Version: 2017. http://dx.doi.org/10.1007/978-3-319-54930-9{_}2. In: ALLEN, Matthew S. (Hrsg.) ; MAYES, Randall L. (Hrsg.) ; RIXEN, Daniel J. (Hrsg.): *Dynamics of Coupled Structures, Volume 4* Bd. 46. Cham : Springer International Publishing, 2017. – DOI 10.1007/978–3–319–54930–9_2. – ISBN 978–3–319–54929–3, S. 17–27

[11] LEMKE, Carlton E.: Some pivot schemes for the linear complementarity problem. Version: 1978. http://dx.doi.org/10.1007/BFb0120779. In: BALINSKI, Michel L. (Hrsg.) ; COTTLE, Richard W. (Hrsg.): *Complementarity and Fixed Point Problems*. Berlin Heidelberg : Springer-Verlag, 1978 (Mathematical Programming Studies). – DOI 10.1007/BFb0120779. – ISBN 978–3–642–00787–3, S. 15–35

[12] NEWMARK, Nathan M.: A Method of Computation for Structural Dynamics: Proceedings of the American Society of Civil Engineers, Vol. 85. In: *Journal of the Engineering Mechanics Division* 85 (1959), Nr. 3, S. 87–94

[13] PACHECO, Juliana E. L. ; BAVASTRI, Carlos A. ; PEREIRA, Jucélio T.: Viscoelastic Relaxation Modulus Characterization Using Prony Series. In: *Latin American Journal of Solids and Structures* 12 (2015), Nr. 2, S. 420–445. http://dx.doi.org/10.1590/1679-78251412. – DOI 10.1590/1679–78251412. – ISSN 1679–7825

[14] PÁLFI, László ; VÁRADI, Károly: Characterization and implementation of the viscoelastic properties of an EPDM rubber into FEA for energy loss prediction. In: *Periodica Polytechnica Mechanical Engineering* 54 (2010), Nr. 1, S. 35. http://dx.doi.org/10.3311/pp.me.2010-1.06. – DOI 10.3311/pp.me.2010–1.06. – ISSN 0324–6051

[15] STUDER, Christian ; PFEIFFER, Friedrich ; WRIGGERS, Peter: *Lecture notes in applied and computational mechanics*. Bd. 47: *Numerics of Unilateral Contacts and Friction: Modeling and Numerical Time Integration in Non-Smooth Dynamics*. Berlin and Heidelberg : Springer, 2009. http://dx.doi.org/10.1007/978-3-642-01100-9. http://dx.doi.org/10.1007/978-3-642-01100-9. – ISBN 978–3–642–01099–6

[16] TATZKO, Sebastian: Unilateral Impact and Contact of Elastic Structures Using Lagrangian Multipliers. In: AMERICAN SOCIETY OF MECHANICAL ENGINEERS (Hrsg.): *ASME 2011 International Mechanical Engineering Congress & Exposition*, 2011, S. 717–724

[17] WIJKER, Jaap J.: *Spacecraft structures*. 1. Auflage. Berlin Heidelberg : Springer-Verlag, 2008. – ISBN 978–3–540–75553–1

[18] WILSON, Edward L.: *Three dimensional static and dynamic analysis of structures: A physical approach with emphasis on earthquake engineering*. 3. Auflage. Berkeley, CA : Computers and Structures Inc., 2000. – ISBN 0–923907–00–9

[19] WRIGGERS, Peter: *Nonlinear finite element methods*. 1. Auflage. Berlin Heidelberg : Springer-Verlag, 2008. – ISBN 978–3–540–71000–4

COMPDYN 2019
7th ECCOMAS Thematic Conference on
Computational Methods in Structural Dynamics and Earthquake Engineering
M. Papadrakakis, M. Fragiadakis (eds.)
Crete, Greece, 24-26 June 2019

DYNAMIC MAGNIFICATION FACTORS FOR SNOW AVALANCHE IMPACT (WITH PILE-UP) ON WALLS AND PYLONS

Perry BARTELT*, Othmar BUSER, Marc CHRISTEN, Andrin CAVIEZEL

WSL Institute for Snow and Avalanche Research SLF, Davos Dorf, Switzerland
e-mail: bartelt@slf.ch

Keywords: Natural hazards, Snow Avalanche, Impact Loadings, Pile-up, Work-Energy Theorem, Dynamic Magnification Factors, Pylons, Walls.

Abstract. *Snow avalanches are a significant natural hazard in many mountainous regions throughout the world. Although long recognized that avalanche impact can easily destroy buildings and other infrastructure, design codes rarely, if at all, consider dynamic magnification factors. The underlying problem is that flowing snow at impact behaves both as a solid and as a fluid. The combination of solid and fluid behaviour makes it difficult to characterize the avalanche impact loading. The solid behaviour of flowing snow leads to pile-up regions of highly compacted snow in front of the structure. This dead-zone often adopts the form of a prismatic wedge with two distinct shear planes. The wedge serves to deflect avalanche snow around the impacted object. Because avalanche snow likewise exhibits fluid behaviour, the deflected snow can easily bypass the structure without stopping. In this paper we model the compaction, pile-up and deflection of avalanche snow around walls, pylons and trees. The work energy theorem is used to model the forces assocated with the compaction process and therefore pile-up phase. We show why the pile-up produces intensive, short duration loadings in the form of a triangular impulse. We quantify the duration time as a function of the pile-up geometry and compactive properties of the flowing snow. This allows us to both quantify the impact duration as well as select the appropriate form of the impulsive loading. If the eigenfrequency of the structure is known, dynamic magnification factors can be calculated for avalanche impact on a wide range of structure geometries, especially ski-lift masts, walls and power transmission towers.*

1 INTRODUCTION

In mountain environments snow avalanches pose a considerable threat to the built infrastructure [1, 2, 3, 4]. Structural engineers require calculation methods to relate avalanche speed to design loads in order to construct structures that can survive avalanche impact (Fig. 1). At present snow engineering practice applies the generic formula

$$p = \frac{1}{2} C_D \rho_\Phi V_\Phi^2 \tag{1}$$

to caluate the impact *pressure* p as a function of avalanche density ρ_Φ and velocity V_Φ^2 [5]. The pressure factor C_D accounts for avalanches impacting thin (C_D=1) and wide (C_D=2) structures. A more general equation to calculate the impact *force* $F(t)$ on a structure hit by a snow avalanche is,

$$F(t) = F_\Delta(t) + F_\Upsilon(t) + \oint_E f(s,t)\, ds. \tag{2}$$

Figure 1: On March 8, 2017 a snow avalanche destroyed several chalets at the Swiss village of Salvan, Canton Wallis. Impact pressures were higher than 30 kPa. The air-blast from the avalanche blew down several trees behind the buildings. The building on the right was completely destroyed. The picture appeared in the *Walliser Bote* on March 8, 2017.

This formula characterizes the three physical processes that must be considered at impact: (1) the shock loading $F_\Delta(t)$ caused by the solid, entirely plastic "pile-up" of snow mass in front of the structure, (2) the deflection force $F_\Upsilon(t)$ arising from the fluid movement of snow mass around the structure and (3) edge forces $f(s,t)$ which are produced when the deflected snow jams the on-coming avalanche mass at the exterior edges E of the structure. The line integral

is given by the fact that jamming forces $f(s,t)$ are defined per unit edge length. The upper limit of the integration is given by the flow height of the avalanche which defines the sum of the exposed edges of the structure. An important distinction between the two approaches is that first approach (Eq. 1) calculates a mean *pressure*, whereas the second approach (Eq. 2) predicts time-dependent *forces* that are assumed to be distributed unequally over the structure at impact.

By far the greatest challenge of developing methods to predict avalanche impact forces is due to the complex solid-fluid behaviour of avalanche snow. The piled-up snow typically forms a solid "deadzone" in the shape of a prismatic wedge (Fig. 2). (Hence there designation with the capital greek symbol Δ.) The wedge consists of highly compacted snow that serves to efficiently deflect the on-coming avalanche snow around the impacted object. That is, at impact both solid and fluid behaviour is evident. The solid material response is complicated further by the irreversible compactibility (or *Stauchen*) of avalanche snow. Bulk avalanche flow densities ρ_Φ range between (say) ρ_Φ = 150 kg/m^3 for a disperse flowing/powder avalanche to (say) ρ_Φ = 450 kg/m^3 for a dense wet snow avalanche [1]. Density measurements of piled-up snow in front of obstacles indicates that final compaction densities are over $\rho_\Delta \geq$ 500 kg/m^3 [6]. The dynamic, impulsive loading at impact results from the compaction of the avalanche snow from density ρ_Φ to density ρ_Δ. The time required to compact the snow to build the wedge therefore defines the duration of the impact loading and therefore the rate of energy dissipation and the impulsive (shock) response of the structure.

In this paper we develop a method to calculate how snow piles-up at impact allowing us to estimate the magnitude, form and duration of the impulsive loading $F_\Delta(t)$. This is a necessary prerequisite to determine the shock response (failure) of structures impacted by snow avalanches. We begin by considering forces for pile-up without deflection. This serves to introduce the application of the work-energy theorem to determine forces from the compaction of avalanche snow at impact. We then turn our attention to the more realistic problem of pile-up with deflection. This analysis allows us to determine dynamic magnification factors for simple structures such as cantilever-type constructions such as pylons and masts which are typical for ski-lifts and power transmission lines. We provide several example calculations. The first example considers an avalanche impacting trees, where the eigenfrequencies are low. The second example treats an avalanche impacting a circular ski-lift pylon, a common problem in avalanche mitigation.

2 PILE-UP WITHOUT DEFLECTION: FORCES F_Ξ

For the purpose of explanation we find the force F_Ξ where all avalanche mass piles-up completely at impact in front of the structure (Fig. 3). There is no deflection ($F_\Upsilon = 0$) or jamming ($f(s,t) = 0$). In this case the impact force $F(t) = F_\Xi$.

We consider a dense avalanche Φ with velocity V_Φ, height h_Φ and bulk density ρ_Φ impacting a rigid structure. The structure of width w is positioned at the position x=0; the positive x-direction defining the upstream direction of the pile-up. For simplicity we assume the avalanche strikes the structure with a mean depth-averaged velocity and density; that is, both variables are constant over the flow height defined in the z-direction, but can vary in the streamwise direction and therefore time. We do not consider the impact of the powder dust cloud Π. For now we assume that the height of the structure h is higher than the flow h_Φ i.e. there is no overtopping of the structure. The width of the flow is assumed to be larger than the width of the obstacle.

We describe the pile-up process by considering avalanche mass immediately before and after the pile-up (Fig. 3). All the incoming mass is piled-up. The avalanche is divided into "compacting" avalanche snow, the *knautschzone* (region Ξ, density not yet ρ_Ω, velocity not yet zero,

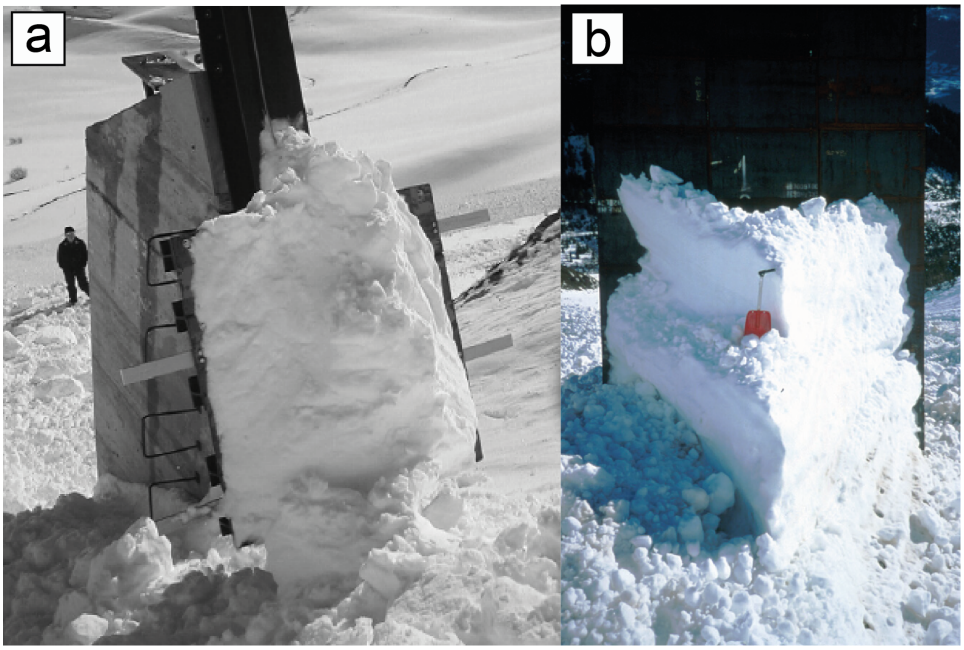

Figure 2: Examples of impact wedges. a) Pile-up at the measurement pylon at the French Col du Lautaret test site reported by [6]. Note the dihedral shape of a triangular prism. The width of the impact plane is 1 m. The reported compaction density was 540 kg/m^3; wedge angles ω_1=40° and ω_2=50°, impact pressures of 30 kPa, see [6] for details. b) Pile-up at the measurement wall at the Swiss Vallée de la Sionne test site [7]. The wall is 7m high and 3.5 m in width. The impact wall was designed to resist 500 kPa pressures. The depositions are from an wet snow avalanche recorded on December 12, 1998 with maximum recorded forces of 61 kN. Measured densities are 500 kg/m^3 at the wedge apex and 450 kg/m^3 at the wall. Photograph: M. Kern, SLF

time t) and "compacted" avalanche snow (region Ω, density ρ_Ω, no velocity, time $t + \Delta t$). Measurements of compacted snow density are rare. Thibert [6] measured a pile-up density ρ_Ω of 540 kg/m^3 in front of the instrumented pylon at the French Col du Lautaret test site.

The avalanche mass arriving at the obstacle M_Ξ and stopping within the time interval Δt is

$$M_\Xi = \rho_\Phi h_\Phi w \left[V_\Phi \Delta t \right]. \tag{3}$$

The corresponding change of kinetic energy ΔK_Ξ of the avalanche is therefore

$$\Delta K_\Xi = \frac{1}{2} M_\Xi(t) V_\Phi^2 = \frac{1}{2} \rho_\Phi h_\Phi w \left[V_\Phi^3 \Delta t \right]. \tag{4}$$

The length of the compacted, pile-up zone is denoted S_Ω, the height h_Ω. The pile-up height might be larger than or equal to the incoming avalanche height $h_\Omega \geq h_\Phi$. Because we do not have overtopping, we assume it remains smaller than the height of the obstacle $h_\Omega < h$. The length of the pile-up zone is growing at the rate $\dot{S}_\Omega$; it is given by conservation of mass,

$$\dot{S}_\Omega = \frac{\rho_\Phi(t) h_\Phi(t)}{\rho_\Omega h_\Omega} V_\Phi(t). \tag{5}$$

During the pile-up, the region Ξ of length $V_\Phi(t)\Delta t$ in the x-direction compacts, increasing the length of the compaction zone Ω (Fig. 3). The difference in the locations of the center-of-mass of the compacting zone Ξ and the piled-up mass Ω defines the braking distance $d_{\Xi \to \Omega}$ over which the incoming mass must stop,

$$d_{\Xi \to \Omega} = \frac{1}{2} \left[V_\Phi \Delta t - \dot{S}_\Omega \Delta t \right]. \tag{6}$$

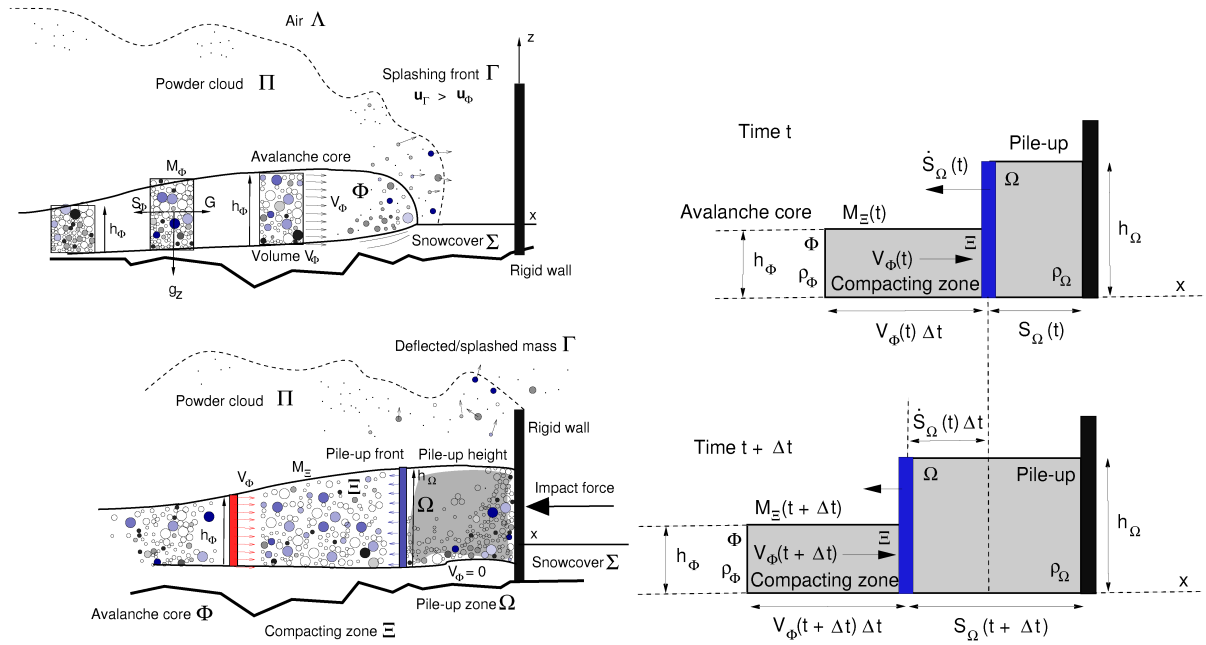

Figure 3: Avalanche impact with no deflection. The upstream zone is divided into three regions: the dense flowing avalanche Φ, the compacting region Ξ and the pile-up or accumulation zone Ω. The avalanche arrives at time t travelling with the velocity V_Φ, bulk density ρ_Φ and flow height h_Φ. Within the time interval Δt the *knautschzone* Ξ develops in front of the structure with length $V_\Phi \Delta t$. A pile-up zone Ω with length S_Ω forms. The pile-up zone is increasing at the speed $\dot{S}_\Omega$.

The mean force on the obstacle F_Ξ is found by equating the work-done by the braking and the change of kinetic avalanche energy in the compaction zone ΔK_Ξ,

$$F_\Xi d_{\Xi\to\Omega} = [p_\Xi h_\Omega w]\, d_{\Xi\to\Omega} = \Delta K_\Xi \tag{7}$$

or,

$$F_\Xi = \rho_\Phi h_\Phi w \frac{V_\Phi}{\left[V_\Phi - \dot{S}_\Omega\right]} V_\Phi^2 \tag{8}$$

The impact pressure p_Ξ is found assuming the force is applied uniformly over the impact area $h_\Omega w$. Therefore,

$$p_\Xi = \rho_\Phi \frac{h_\Phi}{h_\Omega} \frac{V_\Phi}{\left[V_\Phi - \dot{S}_\Omega\right]} V_\Phi^2 \tag{9}$$

and with the subsitution of the equation for mass conservation

$$p_\Xi = \rho_\Phi \frac{h_\Phi}{h_\Omega} \left[1 - \frac{\rho_\Phi h_\Phi}{\rho_\Omega h_\Omega}\right]^{-1} V_\Phi^2. \tag{10}$$

It is therefore possible to define an pressure factor C_D for the pile-up without deflection regime,

$$C_D^\Xi = 2\frac{h_\Phi}{h_\Omega} \left[1 - \frac{\rho_\Phi h_\Phi}{\rho_\Omega h_\Omega}\right]^{-1}. \tag{11}$$

Note that the pressure factor becomes infinite when $\rho_\Phi h_\Phi = \rho_\Omega h_\Omega$. These values of equivalent C_D are in agreement with measured values for all $\rho_\Omega > \rho_\Phi$, see Fig. 4b, and compare to

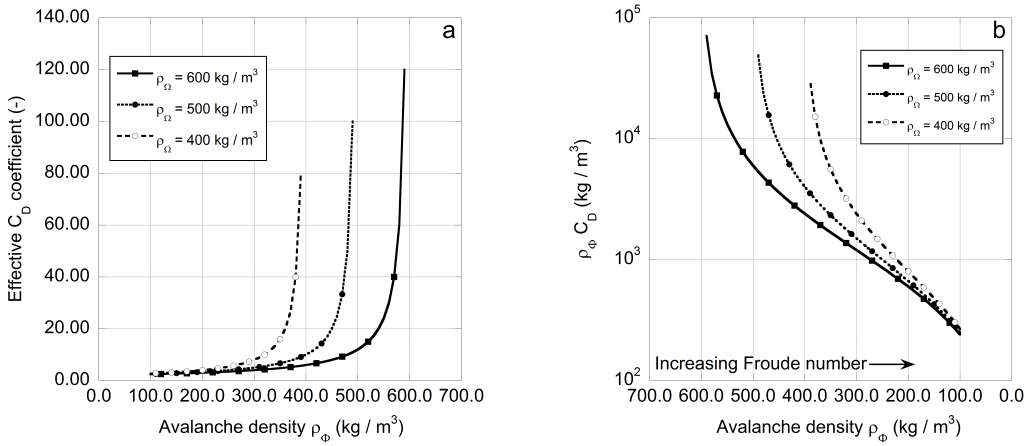

Figure 4: a) Effective C_D^{Ξ} coefficient (Eq. 11) for different incoming avalanche densities ρ_Φ and three compaction densities ρ_Ω. The flow height and pile-up heights are equal $h_\Phi = h_\Omega$. Large effective C_D coefficients result when $\rho_\Phi \approx \rho_\Omega$. In this case compacting (braking) distances are short and impact pressures are large. b) The calculated $\rho_\Phi C_D$ are in agreement with values derived from full scale measurements, e.g. [8]. For the sake of comparison to measured values we plot the calculated $\rho_\Phi C_D$ values with decreasing density to mimic increasing Froude numbers (higher Froude numbers correspond to lower flow densities). This produces the effect that effective pressure factors C_D are higher for lower flow velocities.

[8]. This result suggests that impact pressures of slow moving avalanches can be large if the density of the incoming avalanche is near the compaction density. Substitution of Eq. 1 into the work-energy theorem (Eq. 8) leads to

$$C_D^{\Xi} = \frac{V_\Phi \Delta t}{d_{\Xi \to \Omega}}. \tag{12}$$

The pressure factor is therefore the length of the *knautschzone* Ξ relative to the braking distance $d_{\Xi \to \Omega}$.

3 PILE-UP WITH DEFLECTION: FORCES F_Δ

We again consider a dense avalanche Φ impacting a rigid structure with velocity V_Φ, height h_Φ and bulk density ρ_Φ. This time, however, a prismatic wedge forms at the face of the structure and avalanche snow is deflected (Fig. 5). We assume symmetry (a head-on interaction with the structure). The structure of half width w_0 is positioned at x=0; the positive x direction defining the incoming avalanche direction; the y direction is defined along the width of the obstacle. The total width of the obstacle is therefore 2 w_0. We make the same avalanche flow assumptions as for the previous case.

In the time interval Δt the incoming mass of the avalanche core M_Φ is partitioned into two parts. The mass that is deflected M_Υ and the mass that is piled-up in a triangular wedge M_Δ

$$M_\Phi = \underbrace{\rho_\Phi h_\Phi w V_\Phi \Delta t}_{\textit{Incoming mass}} = \underbrace{M_\Upsilon}_{\textit{Deflected mass}} + \underbrace{M_\Delta}_{\textit{Wedge mass}}. \tag{13}$$

The mass piled-up on the wedge per unit width (y-direction) m_Δ is

$$m_\Delta(y) = \left(1 - \frac{y}{w}\right) \rho_\Delta h_\Delta \dot{S}_\Delta \Delta t. \tag{14}$$

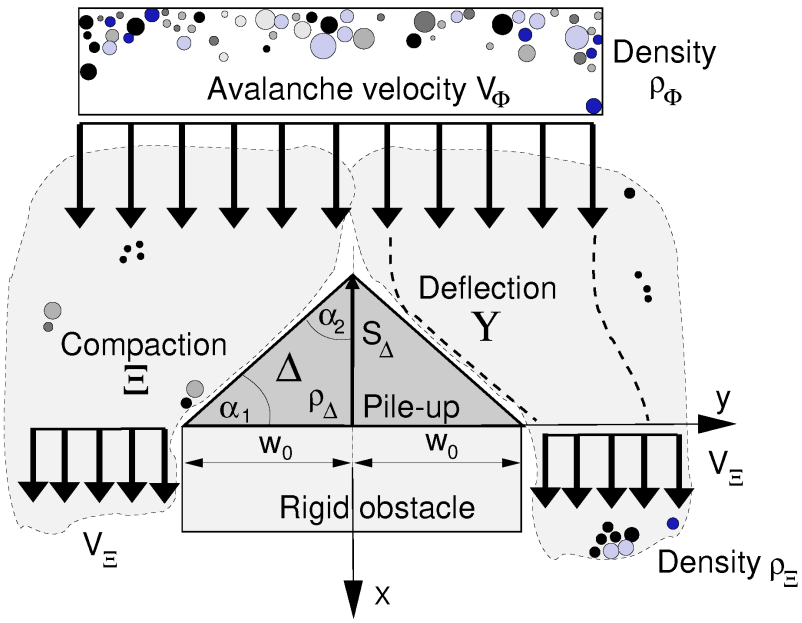

Figure 5: Definition of wedge-shaped pile-up with deflection plus compaction in front of the obstacle. The avalanche approaches the obstacle in the positive x-direction with velocity V_Φ. The bulk density of the flow is ρ_Φ. A pile-up wedge Δ is formed. The density of the piled-up snow is ρ_Δ. The length of the wedge in the flow (negative) x-direction is S_Δ. The speed the length of the triangular wedge grows is $\dot{S}_\Delta$. The wedge geometry is defined by the angle α_1 with α_2 = 90° - α_1.

where S_Δ is the length of the wedge in the x-direction at the location x=0, see Fig. 5. The speed the wedge is growing is therefore $\dot{S}_\Delta$. The total mass of the snow pile up is found by integration

$$M_\Delta = \int_0^w m_\Delta(y)dy = \frac{1}{2}\rho_\Delta h_\Delta w \dot{S}_\Delta \Delta t. \tag{15}$$

The loss of kinetic energy $k_\Delta(y)$ per unit length in the y-direction is

$$k_\Delta(y) = \frac{1}{2}m_\Delta(y)V_\Phi^2 = \frac{1}{2}\left(1 - \frac{y}{w}\right)\rho_\Delta h_\Delta \dot{S}_\Delta V_\Phi^2. \tag{16}$$

The kinetic energy is lost over the ”braking” distance

$$d_{\Phi\to\Delta}(y) = \frac{1}{2}\left[V_\Phi \Delta t - \left(1 - \frac{y}{w}\right)\dot{S}_\Delta \Delta t\right]. \tag{17}$$

From the work-energy theorem, the force per unit length f_Δ is applied

$$f_\Delta d_{\Phi\to\Delta} = k_\Delta. \tag{18}$$

Therefore,

$$f_\Delta = \frac{k_\Delta}{d_{\Phi\to\Delta}} = \frac{\left[\left(1 - \frac{y}{w}\right)\dot{S}_\Delta\right]}{\left[V_\Phi - \left(1 - \frac{y}{w}\right)\dot{S}_\Delta\right]}\rho_\Delta h_\Delta V_\Phi^2 \tag{19}$$

This value can be integrated over width of the triangle w (y-direction) to find the mean pile-up force F_Δ on the obstacle

$$F_\Delta = \int_0^w f_\Delta(y)dy = \left[\frac{V_\Phi}{\dot{S}_\Delta}\ln\left(\frac{V_\Phi}{V_\Phi - \dot{S}_\Delta}\right) - 1\right]\rho_\Delta h_\Delta w V_\Phi^2. \tag{20}$$

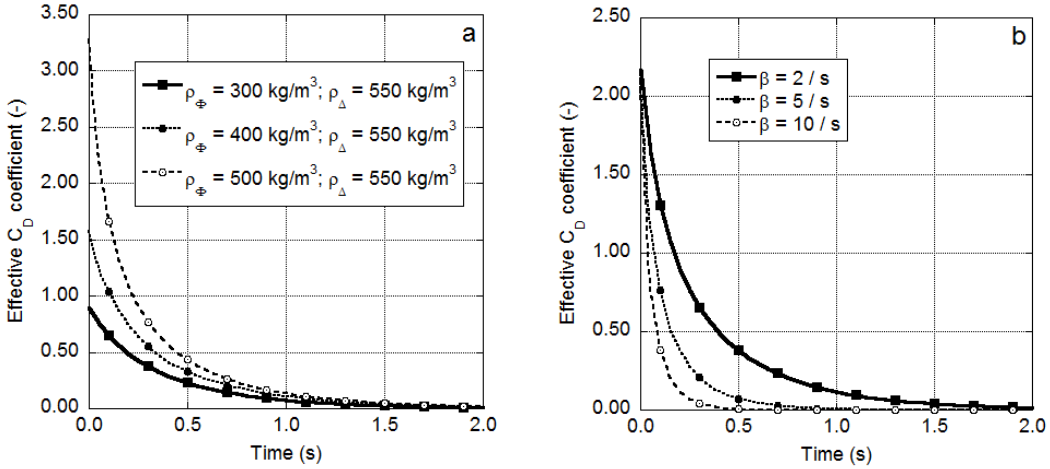

Figure 6: a) Effective C_D^{Δ} coefficient (Eq. 22) for different incoming avalanche densities ρ_Φ and three wedge pile-up densities ρ_Δ. The flow height and pile-up heights are equal $h_\Phi = h_\Omega$. Large effective C_D^{Δ} coefficients result when $\rho_\Phi \approx \rho_\Delta$. b) Effective C_D^{Δ} coefficient (Eq. 22) for different β values. Note that the pile-up times vary between 0.25s and 1.0s.

The pile-up pressure acting on the rigid obstacle is

$$p_\Delta = \frac{F_\Delta}{w h_\Delta} = \left[\frac{V_\Phi}{\dot{S}_\Delta} \ln\left(\frac{V_\Phi}{V_\Phi - \dot{S}_\Delta}\right) - 1\right] \rho_\Delta V_\Phi^2. \tag{21}$$

The pressure retains a V_Φ^2 dependency with the pre-multiplier serving as the pressure factor C_Δ,

$$C_D^{\Delta} = 2\left[\frac{V_\Phi}{\dot{S}_\Delta} \ln\left(\frac{V_\Phi}{V_\Phi - \dot{S}_\Delta}\right) - 1\right] \tag{22}$$

At present the model contains no constitutive parameters. The quantity $\dot{S}_\Delta$ controls the duration of the wedge formation and therefore the duration of the pile-up loading. We consider the growth of the wedge to be given by the relationship

$$\dot{S}_\Delta = \frac{\rho_\Phi}{\rho_\Delta} V_\Phi \exp\left(-\beta t\right). \tag{23}$$

The coefficient β (dimension 1/s) therefore describes the partitioning of the incoming mass into the deflected and piled-up mass. At a certain time, when the wedge is sharp enough, the growth of the wedge stops. Clearly other constitutive formulations can be postulated. The pressure factor C_D^{Δ} is a function of time, see Fig. 6.

4 RESULTS: DYNAMIC MAGNIFICATION FACTORS

The results of the preceeding section (Fig. 6) demonstrate that the impact pressure for pile-up p_Δ is well represented by a triangular impulse of the form

$$p_\Delta \approx p_\Delta(0)\left[1 - t/t_1\right] \tag{24}$$

where t_1 defines the duration time of the impulse. The dynamic magnification factor D for triangular impulse loadings are treated in standard structural dynamics texts, see [9]. Table

1 presents D values for various impulse length t_1/T ratios (T is the period of vibration of the impacted structure). Periods of vibration for steel pylons and trees can be found using Rayleigh's method treating the structure as a partially loaded cantilever beam [10]. At the ground the structures are fixed allowing no translational deformation or bending rotations. The flow height of the avalanche defines the region on the cantilever which is loaded at impact.

t_1/T	0.20	0.40	0.50	0.75	1.00	1.50	2.00
D	0.60	1.05	1.19	1.38	1.53	1.68	1.76

Table 1: Dynamic magnification factors for triangular impulse loadings, from [9].

The first practical result of our analysis is that pylon-type structures with eigenfrequencies of greater than 5Hz (approximately) should consider dynamic magnification factors in design and back analysis. Interestingly, mature spruce trees, typical for most mountain environments have eigenfrequencies of ω = 1Hz (and lower) [10, 11] and therefore long periods of vibration $T \approx 6$ s. From the results above we find pile-up loading intervals $0.25 \leq t_1 \leq 1.0$ s. The calculated impulse length ratios are between $0.04 \leq t_1/T \leq 0.17$. The dynamic magnification factors for trees are less than 1 meaning that $0.1 \leq D \leq 0.6$ (Table 1). This result indicates that trees are able to withstand short duration avalanche pile-up loadings, but are remain susceptible to longer duration air-blasts. This result would explain the extensive forest damage caused by powder avalanches and the fact that many trees can withstand the impact of fast moving avalanche cores, see Fig. 1.

For the next example problem we consider a circular ski-lift pylon made of steel with a height of H= 15m and diameter of d = 1m. The thickness of the steel section is 3cm. The pylon is struck by an avalanche with flow height h_Φ = 3m. For this loading, the calculated eigenfrequency of the pylon is approximately ω = 80 Hz, the period of vibration $T \approx 0.08$s. Calculated impulse length ratios are $t_1/T > 3$, indicating large dynamic magnification factors D = 1.76 (Table 1). Unlike trees, rigid steel structures appear to be more vulnerable to impulsive pile-up loadings.

Finally we consider the impact forces on wall depicted in Fig. 2b [7]. This wall has a total width of 3.5m. Measured maximum reaction forces on the right, center and left supports are 29kN, 61kN and 49kN respectively for a wet snow avalanche impacting the wall with a 4m flow height and velocity of 4.6m/s. The length of the pile-up wedge was found to be 2m. This pile-up height can be reproduced using a β=1.5/s. The calculated reaction forces from Eq. 20, assuming a direct hit, are 38kN, 63kN and 38kN.

5 CONCLUSIONS

In this paper we have applied the work-energy theorem to calculate the magnitude, form and duration of the impulse loading that results when mass is piled-up in the form of prismatic wedge. We consider two cases – pile-up without deflection (force F_Ξ) and pile-up with deflection (force F_Δ). The model assumes a single constitutive parameter (β) that defines the loading interval which can be compared to the vibration period of the impacted structure. Dynamic magnification factors can therefore be calculated and used in structural design. An interesting and unexpected result of our analysis is that trees appear to have low magnification factors $D \leq 0.5$, in comparison to rigid steel structures $D \geq 1.5$. This result would help explain the usefulness of forests in avalanche defense and the danger caused by avalanches to the built environment.

REFERENCES

[1] Bozhinskiy, A. N., and Losev, K. S. *The fundamentals of avalanche science*, Mitt. Eidgenöss. Inst. Schnee- Lawinenforsch., Davos. 280 p., 1998.

[2] Bertrand, D., Naaim, M., and Brun, M.: Physical vulnerability of reinforced concrete buildings impacted by snow avalanches, *Nat. Hazards Earth Syst. Sci.*, 10, 1531-1545, https://doi.org/10.5194/nhess-10-1531-2010, 2010.

[3] De Biagi, V., B. Chiaia, B. Frigo, Barbara, Impact of snow avalanche on buildings: Forces estimation from structural back-analyses, *Engineering Structures*, 92, 15-28, 2015.

[4] Ousset, I., D. Bertrand, M. Brun, E. Thibert, A. Limam, M. Naaim, Static and dynamic FE analysis of an RC protective structure dedicated to snow avalanche mitigation, *Cold Regions Science and Technology*, 112, 95-111, 2015.

[5] Salm, B. A. Burkard and H. Gubler, Berechnung von Fliesslawinen: Eine Anleitung für Praktiker mit Beispielen, Mitt. Eidgenöss. Inst. Schnee- Lawinenforsch., Davos. 30 p., 1990.

[6] Thibert, E., D. Baroudi, A. Limam, P. Berthet-Rambaud, Avalanche impact pressure on an instrumented structure, *Cold Regions Science and Technology*, 54(3), 206-215, 2008.

[7] Gruber U. and 7 others, Lawinendynamik-Versuchsgelände Vallee de la Sionne, Arbaz, Wallis Schulssbericht Winter 1998/1999, Interner Bericht Eidgenöss. Inst. Schnee- Lawinenforsch., Davos. 120 p., 2002.

[8] Sovilla, B., M. Schaer, M. Kern, P. Bartelt, Impact pressures and flow regimes in dense snow avalanches observed at the Vallee de la Sionne test site, *Journal of Geophysical Research-Earth Surface*, 113(F1),DOI: 10.1029/2006JF000688, 2008.

[9] Clough R.W and J. Penzien, *Dynamics of Structures*, McGraw-Hill Inc, New York, 634p, 1975.

[10] Bartelt, P., P. Bebi, T. Feistl, O. Buser, A. Caviezel, Dynamic magnification factors for tree blow-down by powder snow avalanche air blasts, *Natural Hazards and Earth System Sciences*, 18(3), 759-764, 2018a.

[11] Feistl, T., P. Bebi, M. Christen, S. Margreth, L. Diefenbach, P. Bartelt, Forest damage and snow avalanche flow regime, *Natural Hazards and Earth System Sciences*, 15(6), 1275-1288, DOI 10.5194/nhess-15-1275-2015.

COMPDYN 2019
7th ECCOMAS Thematic Conference on
Computational Methods in Structural Dynamics and Earthquake Engineering
M. Papadrakakis, M. Fragiadakis (eds.)
Crete, Greece, 24-26 June 2019

QUASI-STATIC CORRECTION OF MODALLY REDUCED ORDER MODELS FOR SYSTEM INVERSION IN STRUCTURAL DYNAMICS

K. Maes[1], F. Karlsson[2] and G. Lombaert[1]

[1]KU Leuven, Department of Civil Engineering
Kasteelpark Arenberg 40, 3001 Leuven, Belgium
e-mail: {kristof.maes,geert.lombaert}@kuleuven.be

[2]KTH Royal Institute of Technology, Division of Structural Engineering and Bridges
Brinellvägen 23, 114 28 Stockholm, Sweden
e-mail: freddie.karlsson@byv.kth.se

Keywords: System inversion, joint input-state estimation, joint input-state-parameter estimation, out-of-band modes, state-space model.

Abstract. *A wide variety of system inversion algorithms has been proposed in the literature, tackling the problem of force identification, parameter estimation, and state/response estimation. Recently, much focus has gone to recursive joint input-state estimation and joint input-state-parameter estimation, where the forces applied to the structure, the corresponding system states, and its parameters are simultaneously estimated in a recursive fashion. In order to reduce the computational load, these techniques are frequently used in combination with modally reduced order models. This paper shows that a model order reduction can lead to large estimation errors in the system inversion caused by disregarding the contribution of the so-called out-of-band modes. A recently developed computationally efficient quasi-static correction technique, which can be used in state-space modeling, is implemented and evaluated for both joint input-state estimation and joint input-state-parameter estimation. The evaluation is based on numerical simulations. It is shown that the quasi-static correction significantly reduces the estimation errors introduced by the model order reduction.*

1 INTRODUCTION

In civil and mechanical engineering, system inversion techniques are applied to observe the states, inputs, and parameters of a structure, based on data obtained from sensors (accelerometers, strain gauges, ...) and a model of the structure. Various techniques for force and state/response estimation have been proposed in the literature, tackling the problem in the frequency domain or the time domain [6, 14]. Recently, much focus has gone to recursive joint input-state estimation. Commonly adopted techniques are the Augmented Kalman filter (AKF) [8, 13], the so-called Gillijns and De Moor filter (GDF), proposed in [5] and further extended in [7], [12], and [9] and the Dual Kalman filter (DKF) [2]. Several extensions of these algorithms for joint input-state-parameter estimation have recently been developed, allowing for the tracking of uncertain parameters in addition the estimation of the inputs and system states. The AKF was extended by Naets et al. in [13], the GDF was extended by Wan et al. in [16], the smoothing variant of the GDF presented in [9] was extended by Maes et al. in [10], and the DKF algorithm was extended by Azam et al. in [1].

System inversion techniques are commonly used in combination with modally reduced order models to reduce the computational load. Indeed, the use of a full order finite element model for most applications results in large computation times. However, modal truncation can introduce large estimation errors in the system inversion. These errors are caused by disregarding the quasi-static contribution of the out-of-band modes within the frequency band of interest, which is mostly important near antiresonance and at very low frequencies, where the response of the structure is essentially quasi-static. A novel technique to account for the quasi-static contribution of the out-of-band modes was recently presented in [11]. As opposed to already existing quasi-static correction techniques [3, 4, 15], this technique can be used in state-space modeling, commonly adopted in system inversion.

This contribution presents a demonstration of the quasi-static correction technique presented in [11] for joint input-state estimation and joint input-state-parameter estimation. The demonstration is based on numerical simulations, hereby considering the case of a simply supported steel beam.

The outline of the paper is as follows. Section 2 briefly recapitulates the quasi-static correction technique presented in [11]. Next, Section 3 presents a demonstration of the correction technique for joint input-state estimation and joint input-state-parameter estimation. Finally, Section 4 concludes the work.

2 QUASI-STATIC CORRECTION IN STATE-SPACE MODELING

For a linear dynamic system described in modal coordinates, any displacement/strain $d(t) \in \mathbb{R}$ can be written as a sum of modal contributions:

$$d(t) = \sum_{m=1}^{\infty} \phi_{\mathrm{d}m} z_m(t) \tag{1}$$

with $\phi_{\mathrm{d}m} \in \mathbb{R}$ the mode shape component for a given mode m at the assumed output location and $z_m(t) \in \mathbb{R}$ the corresponding modal displacement. Under the assumption of proportional damping, the modal displacement $z_m(t)$ for a given mode m satisfies the following differential equation:

$$\ddot{z}_m(t) + 2\xi_m\omega_m\dot{z}_m(t) + \omega_m^2 z_m(t) = \boldsymbol{\phi}_m^{\mathrm{T}}\mathbf{S}_{\mathrm{p}}\mathbf{p}(t) \tag{2}$$

where $\omega_m \in \mathbb{R}$ and $\xi_m \in \mathbb{R}$, and $\boldsymbol{\phi}_m \in \mathbb{R}^{n_{\mathrm{dof}}}$ denote respectively the natural frequency, the modal damping ratio, and the mode shape vector corresponding to mode m, $\mathbf{S}_{\mathrm{p}} \in \mathbb{R}^{n_{\mathrm{dof}} \times n_{\mathrm{p}}}$ is

a selection matrix specifying the force locations, and $\mathbf{p}(t) \in \mathbb{R}^{n_\mathrm{p}}$ is the force vector with n_p components.

The quasi-static correction technique proposed in [11] assumes the following approximation:

$$d(t) \approx \sum_{m=1}^{n_\mathrm{m}} \phi_{\mathrm{d}m} z_m(t) + \sum_{n=1}^{n_\mathrm{p}} \phi'_{\mathrm{d}n} z'_n(t) \tag{3}$$

For the first n_m modes, the full dynamic contribution is accounted for. For the higher modes, the quasi-static correction required for each force component is obtained by a so-called dummy mode. The number of dummy modes equals the number of force components n_p. For every force component $p_n(t)$, the modal displacement $z'_n(t)$ corresponding to the dummy mode is obtained by solving the following differential equation:

$$\ddot{z}'_n(t) + 2\xi'_n\omega'_n\dot{z}'_n(t) + \omega'^2_n z'_n(t) = \phi'_{\mathrm{p}n} p_n(t) \tag{4}$$

where ω'_n and ξ'_n are respectively the natural frequency and modal damping ratio assigned to dummy mode n, which are both user defined parameters. The mode shape components $\phi'_{\mathrm{p}n}$ and $\phi'_{\mathrm{d}n}$ are determined such that the static response of the structure (at 0 Hz) is correctly represented by the modally reduced order model. The following expressions are obtained:

$$\phi'_{\mathrm{p}n} = \omega'_n \sqrt{\mathbf{S}_{\mathrm{p}_n}^\mathrm{T}\mathbf{K}^{-1}\mathbf{S}_{\mathrm{p}_n} - \sum_{m=1}^{n_\mathrm{m}} \frac{\mathbf{S}_{\mathrm{p}_n}^\mathrm{T}\boldsymbol{\phi}_m\boldsymbol{\phi}_m^\mathrm{T}\mathbf{S}_{\mathrm{p}_n}}{\omega_m^2}} \tag{5}$$

$$\phi'_{\mathrm{d}n} = \frac{\omega'^2_n}{\phi'_{\mathrm{p}n}} \left(\mathbf{S}_\mathrm{d}\mathbf{K}^{-1}\mathbf{S}_{\mathrm{p}_n} - \sum_{m=1}^{n_\mathrm{m}} \frac{\phi_{\mathrm{d}m}}{\omega_m^2}\boldsymbol{\phi}_m^\mathrm{T}\mathbf{S}_{\mathrm{p}_n} \right) \tag{6}$$

where $\mathbf{S}_{\mathrm{p}_n}$ contains the n-th column of the selection matrix $\mathbf{S}_\mathrm{p}$. Note that the expressions for the mode shape components in Eqs. (5) and (6) only require the first n_m mode shapes and natural frequencies.

In case of a single force ($n_\mathrm{p} = 1$), applying the Fourier transform to Eq. (3) and introducing the Fourier transform of Eqs. (2) and (4) allows calculating the transfer function $H''_{\mathrm{dp}}(\omega)$ of the approximating system obtained by introduction of the dummy mode. After extension to velocity and acceleration measurements, the following expression is obtained:

$$H''_{\mathrm{dp}}(\omega) = (i\omega)^q \left(\sum_{m=1}^{n_\mathrm{m}} \frac{\phi_{\mathrm{d}m}\phi_{\mathrm{p}m}}{-\omega^2 + 2i\xi_m\omega_m\omega + \omega_m^2} + \frac{\phi'_{\mathrm{d}1}\phi'_{\mathrm{p}1}}{-\omega^2 + 2i\xi'_1\omega'_1\omega + \omega'^2_1} \right) \tag{7}$$

where ω is the angular frequency in rad/s and q is an integer which equals 0 for displacements, 1 for velocities, and 2 for accelerations. The natural frequency ω'_n and modal damping ratio ξ'_n of every dummy mode have to be chosen such that the contribution of this mode to the transfer function $H''_{\mathrm{dp}}(\omega)$ is nearly constant in the frequency range of interest, hereby accounting for the quasi-static contribution of the out-of-band modes. The natural frequency ω'_n of the dummy modes should be chosen larger than the upper limit ω_u of the frequency band of interest, but smaller than the Nyquist frequency ω_N adopted for the time discretization. The damping ratio ξ'_n should be chosen sufficiently small to avoid a dynamic contribution of the dummy mode within the frequency band of interest. The reader is referred to [11] for an in-depth discussion on the choice of the natural frequency and modal damping ratio assigned to the dummy modes.

3 DEMONSTRATION

In this section, the quasi-static correction technique described in Section 2 is demonstrated for joint input-state estimation (Section 3.1) and joint input-state-parameter estimation (Section 3.2).

The structure considered in the demonstration is the simply supported steel beam shown in figure 1. The beam has a length of $1\ \mathrm{m}$ and a rectangular cross section of width $50.8\ \mathrm{mm}$ and height $25.4\ \mathrm{mm}$. The Young's modulus, Poisson's ratio, and material density are initially taken as $210\ \mathrm{GPa}$, 0.3, and $7750\ \mathrm{kg/m^3}$, respectively. Ideal hinges are assumed at both ends of the beam, only constraining the translation of the end nodes and not their rotation.

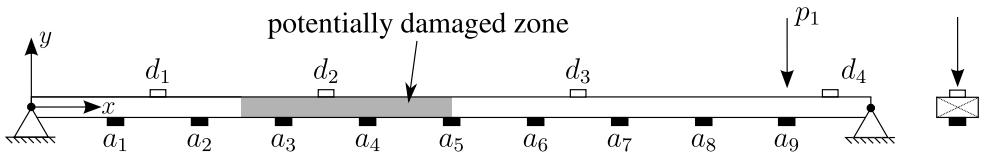

Figure 1: Side view (left) and front view (right) of a simply supported steel beam, indicating the force p_1 and the locations where the vertical response of the structure is calculated (a_i: acceleration i, d_i: displacement i).

A two-dimensional finite element (FE) model of the beam with 100 Euler-Bernoulli beam elements is constructed. Only bending in the vertical plane is considered. Shear deformation is not accounted for. The first four natural frequencies obtained from the beam model are 59.9 Hz, 239.6 Hz, 538.3 Hz, and 955.2 Hz. The corresponding bending mode shapes are shown in Fig. 2. A modal damping ratio of 0.25% is assumed for all modes.

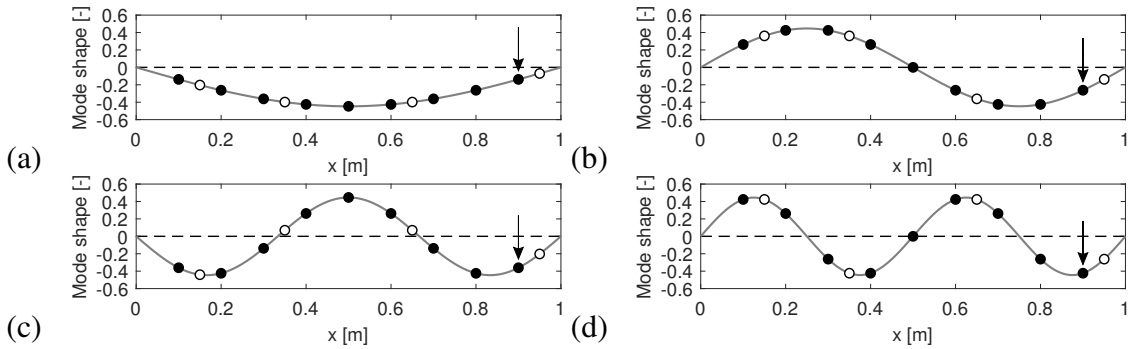

Figure 2: Mode shape along the neutral axis of the simply supported beam, for (a) mode 1, (b) mode 2, (c) mode 3, and (d) mode 4. The undeformed neutral axis is shown by a black dashed line. The markers indicate the output coordinates (black: acceleration, white: displacement). The arrow indicates the force location.

The excitation of the beam consists of a vertical impact force p_1, applied at a distance of $0.1\ \mathrm{m}$ from the right support. The impact force is a triangular pulse that increases linearly from zero at time $t = 0.1\ \mathrm{s}$ to $100\ \mathrm{N}$ at $t = 0.102\ \mathrm{s}$, before decreasing linearly to zero at $t = 0.104\ \mathrm{s}$, shown in Fig. 3. A subset of nine vertical accelerometers $a_1 - a_9$ and four vertical displacement sensors $d_1 - d_4$ is considered in the following analysis. The focus is put on the frequency band from 0 to 1000 Hz, which contains most of the dynamic response of the beam due to the impact loading.

Figure 4 compares the transfer function that relates displacement d_4 to the force p_1, (1) for the full order model (200 modes), (2) a modally reduced order model which includes the contribution of the first four modes, and (3) a modally reduced order model which includes the

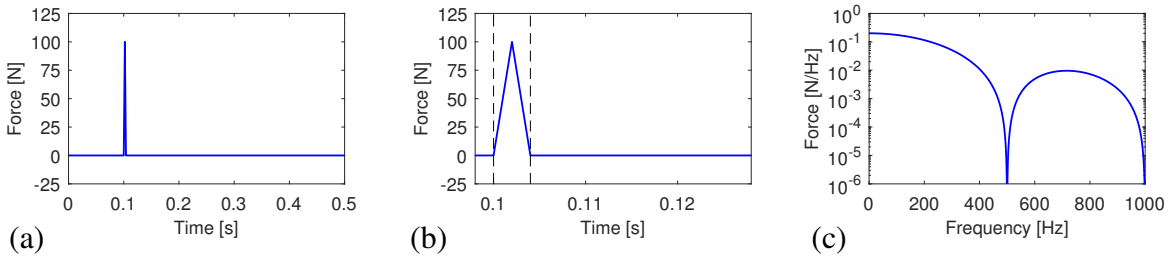

Figure 3: (a) Time history, (b) detail time history, and (c) frequency spectrum up to 1000 Hz of the applied impact force. The begin and end of the impact are indicated in (b) by a vertical dashed line.

full dynamic contribution of the first four modes and a single dummy mode to account for the quasi-static contribution of the out-of-band modes to the frequency band of interest. The natural frequency ω_1' and modal damping ratio ξ_1' of the dummy mode are assigned a value of 1800 Hz and 2%, respectively. For the selected parameter values, the contribution of the dummy mode to the transfer function $H''_{\mathrm{dp}}(\omega)$ is nearly constant within the frequency band of interest (0 to 1000 Hz). The three transfer functions nearly coincide at resonance, where a single mode dominates the response of the system. A large difference between the transfer function of the full order model and the modally reduced order model without dummy mode correction is observed near antiresonance, where higher modes that are omitted in the modal truncation significantly contribute to the system response. Within the frequency band of interest, the transfer function of the modally reduced order model with dummy mode correction nearly coincides with the transfer function of the full order model. For higher frequencies, the approximation deviates from the full-order model. Therefore, a model with dummy mode correction can only be used for calculations within a predefined frequency range.

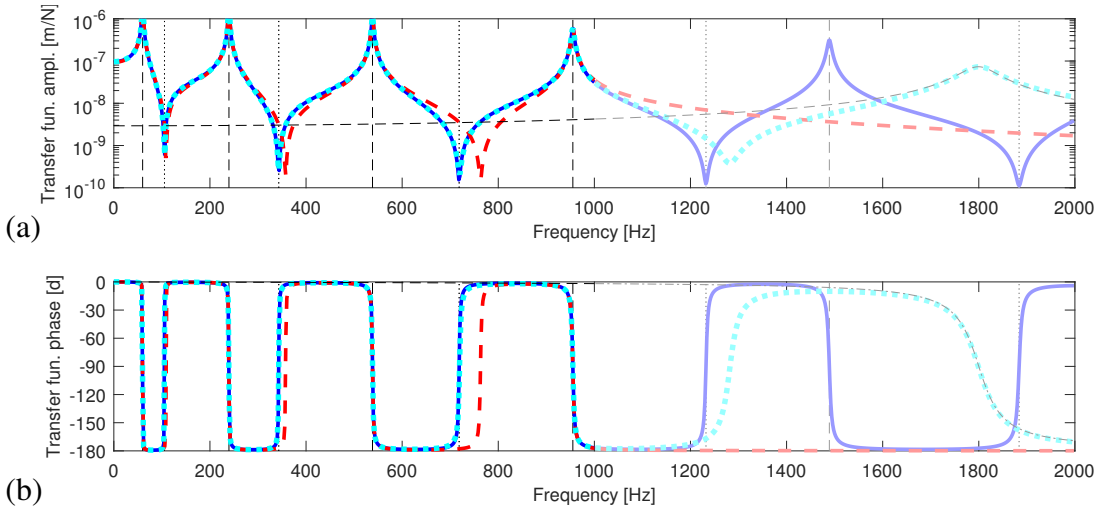

Figure 4: (a) Amplitude and (b) phase of transfer function of the full order model (200 modes, blue solid line), a modally reduced order model with 4 modes, without quasi-static correction (red dashed line), and a modally reduced order model with 4 modes, with dummy mode correction (cyan dotted line) that relates displacement d_4 to force p_1. The contribution of the dummy mode is indicated by a black dash-dotted line. The undamped natural frequencies are indicated by vertical dashed lines, the antiresonance frequencies of the full-order model by vertical dotted lines.

3.1 Joint input-state estimation

In this section, the recursive joint input-state estimation algorithm presented in [12] is applied to estimate the impact force p_1 applied to the simply supported steel beam. In the present example, a state-space model representing the dynamic behavior of the beam in the frequency range from 0 to 1000 Hz is constructed from the first four bending modes of the beam ($n_\mathrm{m} = 4$). The static contribution of the higher modes is accounted for by a single dummy mode ($n_\mathrm{p} = 1$), with a natural frequency and modal damping ratio of 1800 Hz and 2%, respectively (see also figure 4). The expressions for the system matrices are given in [11]. A sampling rate of 10 kHz is applied, using a first-order hold (FOH) assumption on the input in the time discretization of the model.

The input is reconstructed from displacement d_4 and acceleration a_9 (see Fig. 1). The response is obtained from a forward frequency domain calculation, hereby considering a full-order model that includes all modes of the structure. The signals obtained from the forward calculation are polluted with additive sensor noise, which is drawn independently from a normal distribution with a zero mean value and a standard deviation of 10^{-8} m for the displacements and 10^{-4} m/s^2 for the accelerations. In the application of the joint input-state estimation algorithm, the initial state vector estimate $\hat{\mathbf{x}}_{[0|-1]}$ and its corresponding error covariance matrix $\mathbf{P}_{\mathrm{x}[0|-1]}$ are both assigned zero values. The process noise covariance matrix $\mathbf{Q}$ and the process-measurement noise cross-correlation matrix $\mathbf{S}$ are both assumed zero, since no unmodeled forces or modeling errors are present. The matrix $\mathbf{R}$ accounts for measurement noise and is assumed diagonal, with the noise variance (diagonal values) corresponding to the actual measurement noise, i.e. 10^{-16} m^2 for the displacements and 10^{-8} m^2/s^4 for the accelerations.

Fig. 5 shows the force $\hat{p}_1$ estimated by the joint input-state estimation algorithm, using both the modally reduced order model without dummy mode correction and the model with dummy mode correction. In both cases, the estimated force is lowpass filtered with a cutoff frequency of 1000 Hz in order to retain only information within the frequency band of interest and to remove the dynamic contribution of the dummy mode at higher frequencies. A comparison of the estimated forces with the actual applied force shows how the introduction of the dummy mode allows to significantly reduce the force estimation errors. For both models, the triangular pulse is accurately reconstructed. For the model without quasi-static correction, however, the force time history right after the pulse is characterized by large oscillations, which are due to modeling errors that are mainly situated near the antiresonance frequencies (Fig. 5c). For the model with quasi-static correction, these oscillations are much less pronounced.

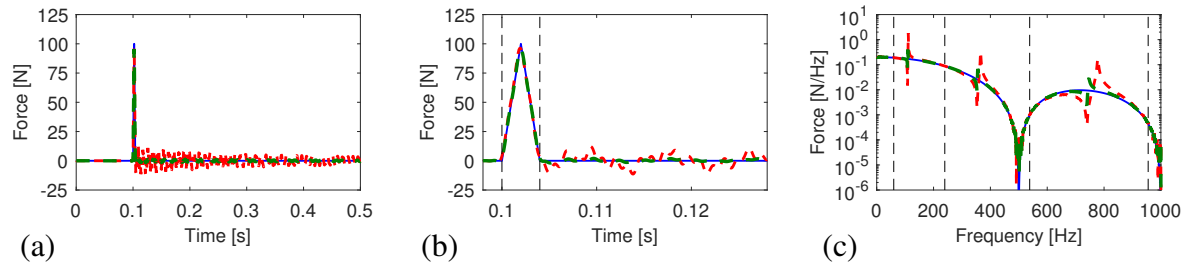

Figure 5: (a) Time history, (b) detail time history, and (c) frequency spectrum up to 1000 Hz of the estimated force $\hat{p}_1$ obtained from the joint input-state estimation algorithm using the model without dummy mode correction (red dashed line), using the model with dummy mode correction (green dashed line), and comparison to the applied force (blue solid line). The begin and end of the impact are indicated in (b) by a vertical dashed line. The undamped natural frequencies are indicated in (c) by vertical dashed lines.

3.2 Joint input-state-parameter estimation

In this section, the recursive joint input-state-parameter estimation algorithm presented in [10] is adopted for parameter estimation in presence of unknown inputs. Consider the case where the part of the simply supported steel beam situated at $L/4 < x < L/2$ is characterized by a reduced stiffness, for example due to corrosion. The reduction in stiffness is modeled as a local reduction of the Young's modulus from 210 GPa to 190 GPa, which corresponds to a reduction of 9.5%.

The dynamic system model is parameterized by a single parameter θ, which relates the Young's modulus E of the damaged section to the initial Young's modulus of the healthy structure ($E = \theta \times 210$ GPa). In the joint input-state-parameter estimation, the initial parameter value is assumed 1 (no damage). The target value of this parameter is 190 GPa$/210$ GPa $= 0.905$.

For demonstration purposes, a series of four impacts is considered. The time between two consecutive impacts is 0.5 s. The response applied in the joint input-state-parameter estimation consists of displacements d_1 and d_4 and accelerations a_2 and a_9 (see Fig. 1). Two additional sensors are added compared to the case of joint input-state estimation, as to obtain a system which is observable in terms of the unknown input and the unknown parameter. The reader is referred to [10] for a discussion on the sensor network design. As for the case of joint input-state estimation, two different models are considered in the system inversion. The first model is a modally reduced order model that includes the dynamic contribution of the first four bending modes without quasi-static mode correction. The second model is a modally reduced order model that includes the dynamic contribution of the same four bending modes with additionally the contribution of a single dummy mode. The same dummy mode parameters as those assumed in section 3.1 have been selected.

Although the smoothing algorithm presented [10] allows to adopt a delay in the estimation, this was deemed unnecessary in the present case, since a collocated acceleration measurement is used. Therefore, no delay is applied. In the application of the smoothing algorithm, the initial state $\hat{\mathbf{x}}_{[0|-1]}$ is assigned zero values for the modal displacements and velocities and a unit value is assigned for the parameter θ, corresponding to the original structure before damage. Due to the perturbation of the model in terms of the parameter θ, the corresponding model uncertainty should be reflected in the process noise covariance matrix $\mathbf{Q}$, through the choice of the parameter covariance matrix $\mathbf{Q}_\theta$. This matrix, which is in this case given by a scalar $\sigma^2_{Q_\theta}$, regularizes the parameter estimation. Indeed, $\sigma^2_{Q_\theta}$ is the variance characterizing the parameter variation over time. The choice of a large variance $\sigma^2_{Q_\theta}$ enables a large variation of the parameter between two time steps, leading to a potentially fast convergence of the parameter towards its actual value. Such choice, however, makes the parameter estimation more sensitive to noise and modeling errors (see also [10]). In this case, a parameter variance $\sigma^2_{Q_\theta} = 10^{-16}$ is adopted. The entries of the noise covariance matrices $\mathbf{Q}$ and $\mathbf{S}$ which correspond to process noise on the dynamic system states are assigned zero values. The measurement noise covariance matrix $\mathbf{R}$ is assumed identical to this assumed in section 3.1.

Fig. 6 shows the time history of the force $\hat{p}_1$ and the parameter $\hat{\theta}$ estimated by the joint input-state-parameter estimation algorithm and a comparison of the actual force and parameter values. During the first 0.1 seconds, i.e. before the first impact is applied, the structure is at rest and the algorithm does not get any information regarding the unknown structural parameter. This results in almost constant parameter estimates during this period, as observed from Fig. 6b. Some negligible oscillations of the parameter values are present, which are due to measurement

noise. As soon as the first impact is applied, the parameter estimate is characterized by a significant variation, where the parameter estimate first changes abruptly and drops below the target value 0.905 for both models, hereafter converging towards this target value. For the model without quasi-static correction, a much larger drop in the parameter value is observed than for the model with quasi-static correction. Once the parameter estimates have converged towards the true parameter value, one would expect that the parameter estimates stay close to the true parameter values, with small oscillations that are attributed to measurement noise. This is, however, not entirely true, due to the presence of modeling errors, which are inevitable. When the next impact is applied, the parameter estimate drops again, hereafter showing a convergence towards to the target parameter value. For the model without quasi-static correction, a larger variation of the parameter estimate following the impact is observed than for the model with quasi-static correction.

For each of the four impacts, the triangular pulse is accurately reconstructed for both models. This is in line with the findings of section 3.1, where it was found that the quasi-static correction is only of minor importance for the reconstruction of the triangular pulse. As for the case of joint input-state estimation, however, the force time history right after the pulse is characterized by large oscillations without quasi-static correction. Furthermore, it is worth noting that the first triangular pulse is also accurately identified, whereas this estimation relies on the wrong stiffness ($\theta = 1$). This is due to the fact that the response during a short pulse is mainly determined by the structural mass, which is correctly represented by the model, and only to a minor extent by the structural stiffness [3].

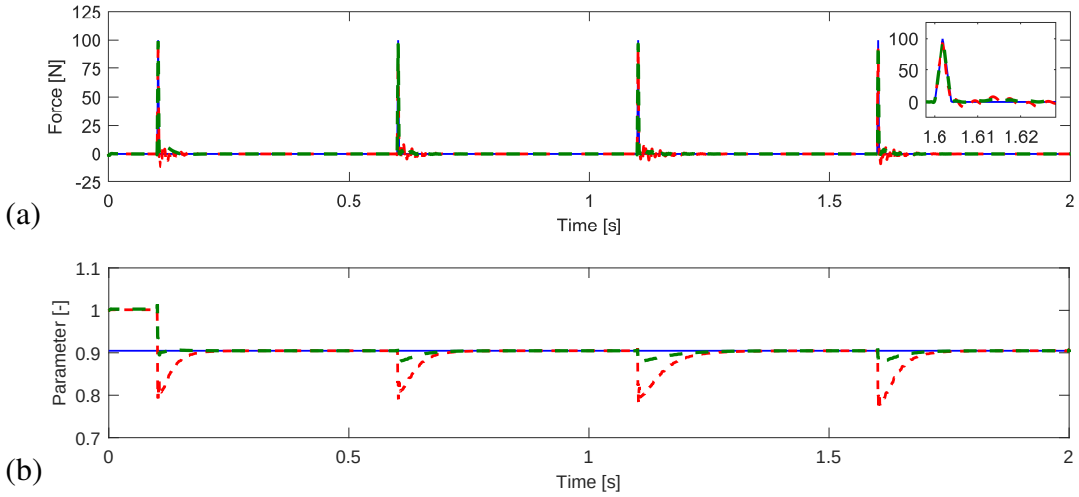

Figure 6: Time history of (a) the estimated force $\hat{p}_1$ and (b) the estimated parameter $\hat{\theta}$ obtained from the joint input-state-parameter estimation algorithm using the model without dummy mode correction (red dashed line), using the model with dummy mode correction (green dashed line), and comparison to the actual force and parameter values (blue solid line).

4 CONCLUSIONS

This paper evaluates the use of quasi-static correction of modally reduced order models for joint input-state estimation and joint input-state-parameter estimation in structural dynamics. Numerical simulations show that disregarding the contribution of so-called out-of-band modes can lead to significant errors in input and parameter estimation. Though not shown here, the same applies to state and response estimation. A recently developed quasi-static correction

technique is implemented and shown to be successful in reducing the modeling errors introduced by the model order reduction. This correction results in significantly smaller estimation errors in the system inversion.

ACKNOWLEDGEMENTS

Kristof Maes is a Postdoctoral Fellow of the Research Foundation Flanders (FWO), Belgium. The financial support of FWO is gratefully acknowledged.

REFERENCES

[1] S.E. Azam, V. Dertimanis, E. Chatzi, and C. Papadimitriou. Output-only schemes for joint input-state-parameter estimation of linear systems. In M. Papadrakakis, V. Papadopoulos, and V. Plevris, editors, *Proceedings of the 1st International Conference on Uncertainty Quantification in Computational Sciences and Engineering, UNCECOMP 2015*, Crete Island, Greece, May 2015.

[2] S.E. Azam, C. Papadimitriou, and E. Chatzi. A dual Kalman filter approach for state estimation via output-only acceleration measurements. *Mechanical Systems and Signal Processing*, 60–61:866–886, 2015.

[3] A.K. Chopra. *Dynamics of structures: theory and applications to earthquake engineering*. Prentice-Hall, Englewood Cliffs, New Jersey, 1995.

[4] A.K. Chopra and J.A. Gutierrez. Earthquake response analysis of multistorey buildings including foundation interaction. *Earthquake Engineering and Structural Dynamics*, 3:65–77, 1974.

[5] S. Gillijns and B. De Moor. Unbiased minimum-variance input and state estimation for linear discrete-time systems with direct feedthrough. *Automatica*, 43(5):934–937, 2007.

[6] M. Klinkov and C.-P. Fritzen. An updated comparison of the force reconstruction methods. *Key Engineering Materials*, 347:461–466, 2007.

[7] E. Lourens, C. Papadimitriou, S. Gillijns, E. Reynders, G. De Roeck, and G. Lombaert. Joint input-response estimation for structural systems based on reduced-order models and vibration data from a limited number of sensors. *Mechanical Systems and Signal Processing*, 29:310–327, 2012.

[8] E. Lourens, E. Reynders, G. De Roeck, G. Degrande, and G. Lombaert. An augmented Kalman filter for force identification in structural dynamics. *Mechanical Systems and Signal Processing*, 27:446–460, 2012.

[9] K. Maes, S. Gillijns, and G. Lombaert. A smoothing algorithm for joint input-state estimation in structural dynamics. *Mechanical Systems and Signal Processing*, 98:292–309, 2018.

[10] K. Maes, F. Karlsson, and G. Lombaert. Tracking of inputs, states and parameters of linear structural dynamic systems. *Mechanical Systems and Signal Processing*. Under review.

[11] K. Maes and G. Lombaert. The influence of out-of-band modes in system inversion. *Mechanical Systems and Signal Processing*, 115:173–187, 2019.

[12] K. Maes, A.W. Smyth, G. De Roeck, and G. Lombaert. Joint input-state estimation in structural dynamics. *Mechanical Systems and Signal Processing*, 70–71:445–466, 2016.

[13] F. Naets, J. Cuadrado, and W. Desmet. Stable force identification in structural dynamics using kalman filtering and dummy-measurements. *Mechanical Systems and Signal Processing*, 50–51:235–248, 2015.

[14] L.J.L. Nordström. *Input estimation in structural dynamics*. PhD thesis, Chalmers University of Technology, Sweden, 2005.

[15] B. Peeters, H. Van der Auweraer, P. Guillaume, and J. Leuridan. The PolyMAX frequency-domain method: a new standard for modal parameter estimation? *Shock and Vibration*, 11(3–4):395–409, 2004.

[16] Z. Wan, T. Wang, L. Li, and Z. Xu. A novel coupled state/input/parameter identification method for linear structural systems. *Shock and Vibration*, 2018(7691721), 2018.

COMPDYN 2019
7th ECCOMAS Thematic Conference on
Computational Methods in Structural Dynamics and Earthquake Engineering
M. Papadrakakis, M. Fragiadakis (eds.)
Crete, Greece, 24-26 June 2019

VISCOELASTIC BEAM DYNAMICS: THEORETICAL ANALYSIS ON DAMPING MECHANISMS (COMPDYN 2019)

E. Pierro[1]

[1]Scuola di Ingegneria (SI - UniBas), Universita' degli Studi della Basilicata
Via dell'Ateneo Lucano 10, 85100 Potenza - Italy
e-mail: elena.pierro@unibas.it

Keywords: Viscoelastic beam, beam dynamics, damping identification, damping control, linear systems.

Abstract. *Viscoelastic materials are widely utilized in different engineering areas, however it is still not so easy to properly assess their mechanical properties, in terms of viscoelastic - frequency dependent modulus. Standard experimental procedures are utilized in this direction (e.g. DMA - Dynamic mechanical analysis), but such techniques still present some complexities, and this is why possible alternative approaches would be desirable. For example, the experimental investigation of a viscoelastic beam dynamics would be challenging, especially for the intrinsic simplicity of this kind of test. In this direction, a deep understanding of damping mechanisms in viscoelastic beams results to be a quite important task to better predict their dynamics. With the aim to elucidate damping properties in such structures, in this paper an analytical study of the transversal vibrations of a viscoelastic beam is presented. By means of a dimensional analysis, some key parameters are presented, which depend on the material properties and the beam geometry. In this way, by properly tuning such disclosed parameters, e.g. the dimensionless beam length once the material is chosen, it is possible to enhance or suppress some resonant peaks, one at a time or more simultaneously. This is a remarkable possibility to efficiently control damping in these structures, and the results presented in this paper may help in elucidating experimental procedures for the characterization of viscoelastic materials.*

1 INTRODUCTION

Nowadays, in the common engineering applications, the vibrating structures are mostly characterized by composite materials, with superior damping and high energy absorbing properties. The viscoelastic mechanical response of such materials must be correctly considered during the design process of structural components, thus making of huge importance the full comprehension of phenomena involving viscoelastic energy dissipation [1, 2, 3, 4, 5]. Viscoelasticity plays a key role in many applications, such as: (i) rolling contacts [6, 7, 8], (ii) sliding contacts [9, 10, 11, 12], (iii) crack propagation [13, 14, 15], (iv) seals [1], (v) adhesives and biomimetic adhesives [2, 3, 4], (vi) viscoelastic dewetting transition [16]. Many theoretical studies on the dynamics of non-viscous damped oscillators, for both SDOF [21, 22], and MDOF [23, 24] systems, have been presented in literature. Also viscoelastic continuous systems have been theoretically and experimentally investigated in their dynamics, such as beams and plates [25, 26, 27]. However, most of these studies do not present a qualitative analysis of the dynamic characteristics of such systems, in terms of eigenvalues and their connection with the most representative physical parameters. Only in Ref. [28], a comprehensive analysis of a single degree-of-freedom non-viscously damped oscillator has been presented. Extending this kind of investigation to continuous systems would be of crucial concern when viscoelastic properties of materials must be properly established. In particular, it is quite common in the experimental assessments of the viscoelastic properties of these materials, to consider beam-like structures as standard geometries [18, 19, 20]. With the aim to shed light on the vibrational behaviour of such systems, in this paper a detailed study of the dynamics of a viscoelastic beam is presented. We recall that the viscoelastic materials are characterized by the most general stress-strain relation [29]

$$\sigma\left(x,t\right)=\int_{-\infty}^{t}d\tau G\left(t-\tau\right)\dot{\varepsilon}\left(x,\tau\right) \tag{1}$$

where $\dot{\varepsilon}(t)$ is time derivative of the strain, $\sigma(t)$ is the stress, $G\left(t-\tau\right)$ is the time-dependent relaxation function, which is related, in the Laplace domain, to the viscoelastic modulus $E\left(s\right)$ through the relation $E\left(s\right)=sG\left(s\right)$. Usually, a discrete version of $E\left(s\right)$ is utilized to characterize linear viscoelastic solids, which can be represented in the Laplace domain as

$$E\left(s\right)=E_{0}+\sum_{k}E_{k}\frac{s\tau_{k}}{1+s\tau_{k}} \tag{2}$$

where E_0 is the elastic modulus of the material at zero-frequency, τ_k and E_k are the relaxation time and the elastic modulus respectively of the generic spring-element in the generalized linear viscoelastic model [29]. The general trend of the viscoelastic modulus $E(\omega)$ is shown in Figure 1. It can be observed that at low frequencies the material is in the 'rubbery' region, indeed $\mathrm{Re}[E(\omega)]$ is relatively small and approximately constant (Figure 1-a), and the viscoelastic dissipations related to the imaginary part $\mathrm{Im}[E(\omega)]$ of the viscoelastic modulus becomes negligible (Figure 1-b). At very high frequencies the material is elastically very stiff (brittle-like). In this 'glassy' region $\mathrm{Re}[E(\omega)]$ is again nearly constant but much larger (generally by 3 to 4 orders of magnitude) than in the rubbery region. The intermediate frequency range (the so called 'transition' region) determines the energy dissipation, and can completely deviate the modal behaviour of a viscoelastic solid from the equivalent elastic one. Moreover, the transition region, and hence the functions $\mathrm{Re}[E(\omega)]$ and $\mathrm{Im}[E(\omega)]$, can be shifted towards higher or smaller frequencies by simply varying temperature, because of the viscoelastic modulus $E(\omega)$ dependence on temperature [29].

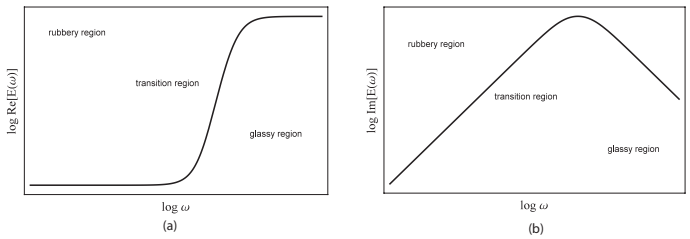

Figure 1: The real part (a) and the imaginary part (b) of the elastic modulus $E(\omega)$ of a generic viscoelastic material.

Of course, only the knowledge of the analytical vibrational response of a viscoelastic structure can provide the right parametric quantities, useful to accurately enlighten the relationship between the material properties and the modal contents. In this direction, the flexural vibrations of a viscoelastic beam is analytically studied in this paper, and by introducing some non-dimensional parameters, a qualitative analysis of the eigenvalues is presented. At first, an ideal viscoelastic material is considered, i.e. characterized by one single relaxation time. This kind of study, indeed, is useful for a first understanding of the physical parameters enclosed in the problem. Finally, some considerations are pointed out regarding the vibrational response of the beam in case of real viscoelastic materials.

2 BEAM DYNAMICS

In this section the analytical dynamic response of a viscoelastic beam with rectangular cross section is derived. Let be L, W, and H respectively the length, the width and the thickness of the beam, and let us assume that $L \gg W$, $L \gg H$. Assuming also that the displacement along the z-axis $|u(x,t)| \ll L$, the Bernoulli theory of transversal vibrations can be applied and therefore it is possible to neglect the influence of shear stress in the beam. It is worth noticing that this hypotesis does not limit the validity of the analysis, since the attention is paid to the first resonant peaks, which are not affected by shear deformations. Hence, the general equation of motion is [30]

$$J_{xz} \int_{-\infty}^{t} d\tau E(t-\tau) \frac{\partial^4 u(x,\tau)}{\partial x^4} + \mu \frac{\partial^2 u(x,t)}{\partial t^2} = f(x,t) \tag{3}$$

where $\mu = \rho A$, ρ is the bulk density of the material the cantilever is made of, A is the area of the cross section of the beam, i.e. $A = WH$, $J_{xz} = (1/12)WH^3$, and $f(x,t)$ is the generic forcing term. It must be highlighted that some additional terms could be considered in Eq.(3), representing different kind of damping contributes [31] (e.g. viscous damping and hysteresis damping). In the present study such terms are neglected, but it is important to underline that the results obtained in this paper are not affected by this assumption from a qualitative point of view. The forced solution of the above problem Eq.(3) can be found in the form of a series of the eigenfunction $\phi_n(x)$ of the following problem

$$J_{xz} \int_{-\infty}^{t} d\tau E(t-\tau) u_{xxxx}(x,\tau) + \mu u_{tt}(x,t) = 0 \tag{4}$$

($u_x(x,t) = \partial u(x,t)/\partial x$, $u_t(x,t) = \partial u(x,t)/\partial t$), with the opportune boundary conditions. In this study, the free-free boundary conditions are considered

$$\begin{aligned} u_{xx}(0,t) &= 0 \\ u_{xxx}(0,t) &= 0 \\ u_{xx}(L,t) &= 0 \\ u_{xxx}(L,t) &= 0 \end{aligned} \tag{5}$$

. By Laplace transforming the time-dependence in Eq.(4), and considering equal to zero the initial conditions, it is easy to show that the eigenfunctions $\phi(x,s)$ must satisfy the following equation

$$\phi_{xxxx}(x) - \beta_{eq}^4(s)\,\phi(x) = 0 \tag{6}$$

where it is defined

$$\beta_{eq}^4(s) = -\frac{\mu\, s^2}{J_{xz} E(s)} \tag{7}$$

. The boundary conditions then become

$$\begin{aligned} \phi_{xx}(0) &= 0 \\ \phi_{xxx}(0) &= 0 \\ \phi_{xx}(L) &= 0 \\ \phi_{xxx}(L) &= 0 \end{aligned} \tag{8}$$

The solution of the above Eq.(6) can be written in the form

$$\phi(x,s) = W_1 \cos[\beta_{eq}(s)\,x] + W_2 \sin[\beta_{eq}(s)\,x] + W_3 \cosh[\beta_{eq}(s)\,x] + W_4 \sinh[\beta_{eq}(s)\,x] \tag{9}$$

and by requiring that the determinant of the system matrix obtained from Eqs.(8) is zero, one obtains

$$[1 - \cos(\beta_{eq} L)\cosh(\beta_{eq} L)] = 0 \tag{10}$$

The solutions $\beta_n L = c_n$ of the above Eq.(10) are well known [30], and they are the same of the perfectly elastic case. In particular, from the following relation

$$-\frac{\mu\, s^2}{J_{xz} E(s)} = (\beta_n)^4 = \left(\frac{c_n}{L}\right)^4 \tag{11}$$

it is possible to calculate the complex conjugate eigenvalues s_n corresponding to the n_{th} mode, and the real poles s_k related to the material viscoelasticity (a detailed analysis of the eigenvalues will be shown in the next section). The values β_n allow to determine the eigenfunctions $\phi_n(x)$

$$\phi_n(x) = \cosh(\beta_n x) + \cos(\beta_n x) - \frac{\cosh(\beta_n L) - \cos(\beta_n L)}{\sinh(\beta_n L) - \sin(\beta_n L)}\left[\sinh(\beta_n x) + \sin(\beta_n x)\right] \tag{12}$$

which are equal to the eigenfunctions of the elastic case.

2.1 Response decomposition

The solution of Eq.(3) can be calculated, by considering (see Ref.[26]) the decomposition of the system response into the modes $\phi_n(x)$ of the beam

$$u(x,t) = \sum_{n=1}^{+\infty} \phi_n(x)\, q_n(t) \tag{13}$$

and by utilizing the orthogonality condition

$$\frac{1}{L}\int_0^L dx \phi_n(x)\, \phi_m(x) = \delta_{nm} \tag{14}$$

where δ_{nm} is Kronecker delta function. Indeed, by projecting the equation of motion on the function $\phi_m(x)$ of the basis, Eq.(3) becomes

$$\mu \ddot{q}_n(t) + J_{xz}\beta_n^4 \int_{-\infty}^{t} d\tau E(t-\tau)\, q_n(\tau) = f_n(t) \tag{15}$$

where $f_n(t) = \frac{1}{L}\int_0^L dx f(x,t)\, \phi_n(x)$ is the projected force term. In the Laplace domain, therefore, one has that Eq.(13) can be written

$$U(x,s) = \sum_{n=1}^{+\infty} \phi_n(x) \frac{F_n(x,s)}{\mu s^2 + J_{xz}\beta_n^4 E(s)} \tag{16}$$

3 VISCOELASTIC MODEL - SYSTEM EIGENVALUES

Let us consider an ideal viscoelastic material with a single relaxation time τ_1, whose elastic properties can be represented by the modulus

$$E(s) = E_0 + E_1 \frac{\tau_1 s}{1+\tau_1 s} \tag{17}$$

By substituting the previous complex function in Eq.(11), the characteristic equation for each n_{th} mode can be obtained

$$\tau_1 s^3 + s^2 + (E_0 + E_1)\tau_1 r_n s + r_n E_0 = 0 \tag{18}$$

where $r_n = (\beta_n)^4 J_{xz}/\mu$. Notice that the solutions of the cubic equation Eq.(18) can be i) one real root and two complex conjugate roots, ii) all roots real. This means that one eigenvalue is always related to an overdamped motion. When the other two eigenvalues are complex conjugate, they represent the oscillatory contribute of the n_{th} mode in the beam dynamics. Otherwise, in case of three real roots, the n_{th} mode is not oscillatory.

3.1 Dimensional analysis

With regards to the transverse motions of a narrow, homogenous beam with a bending stiffness $E_0 J_{xz}$ and density ρ, the value of the natural frequencies can be calculated using a simple formula which is always valid, regardless of the boundary conditions [32]:

$$\omega_n = \left(\frac{c_n}{L}\right)^2 \sqrt{\frac{E_0 J_{xz}}{\rho A}} \tag{19}$$

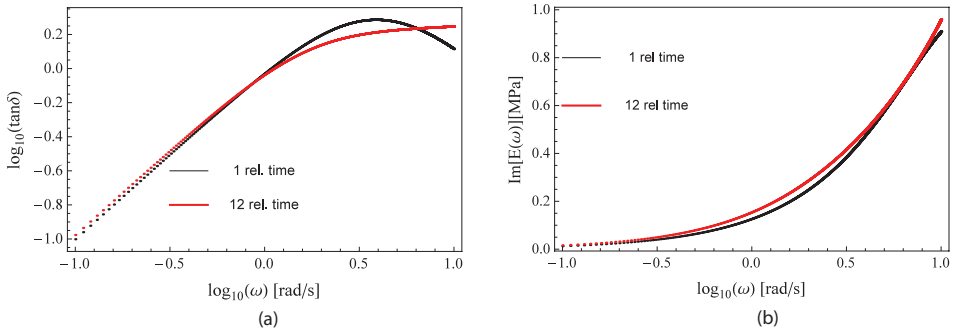

Figure 2: The function $\tan\delta = \mathrm{Im}[E(\omega)]/\mathrm{Re}[E(\omega)]$ (a) and the imaginary part of the viscoelastic modulus $E(\omega)$ (b), of a rubber like material [36]. Black curves are obtained, in a limited frequency range, by considering one single relaxation time. Red curves are the fitting results, with 12 relaxation times, in a wider frequency range, of experimental DMA described in Ref.[36].

where coefficient c_n depends on the specific boundary conditions. The first natural frequency, in particular, can be written as

$$\omega_1 = \alpha^2 \delta_1 \tag{20}$$

being $\delta_1 = (c_1^2/H)\sqrt{E_0/(12\rho)}$, and $\alpha = H/L$ the dimensionless beam length. The non-dimensional eigenvalue is now defined

$$\bar{s} = s/\delta_1 \tag{21}$$

and in particular one has, for the n_{th} mode, $\omega_n^2 = E_0\beta_n^4 J_{xz}/\mu = r_n E_0$ and $\delta_n = (c_n^2/H)\sqrt{E_0/(12\rho)}$.

By substituting Eq.(21) in Eq.(18), the following non-dimensional characteristic equation is obtained

$$\bar{s}^3 + \bar{s}^2\frac{1}{\theta_1} + (1+\gamma_1)\alpha^4\Delta_n^2\bar{s} + \frac{1}{\theta_1}\alpha^4\Delta_n^2 = 0 \tag{22}$$

where $\Delta_n = \delta_n/\delta_1$, and having defined the dimensional groups

$$\theta_1 = \delta_1\tau_1 \tag{23}$$

$$\gamma_1 = E_1/E_0 \tag{24}$$

. Eq.(22) can be then re-written as

$$\bar{s}^3 + \sum_{j=0}^{2} a_j^j \bar{s}^j = 0 \tag{25}$$

where $a_0 = (1/\theta_1)\alpha^4\Delta_n^2$, $a_1 = (1+\gamma_1)\alpha^4\Delta_n^2$, $a_2 = 1/\theta_1$.

By defining

$$Q = \frac{3a_1 - a_2^2}{9} \tag{26}$$

$$R = \frac{9a_2a_1 - 27a_0 - 2a_2^3}{54} \tag{27}$$

the discriminant of Eq.(25) is defined as $D = Q^3 + R^2$. In our case, the discriminant D, indicated as $D(n)$, is function of n, i.e. of the number of the n_{th} mode considered

$$D(n) = \frac{\alpha^4 \Delta_n^2 \left\{4 + \alpha^4 \Delta_n^2 \theta_1^2 \left[8 - \gamma_1 (20 + \gamma_1) + 4\alpha^2 (1 + \gamma_1)^3 \Delta_n^2 \theta_1^2\right]\right\}}{108 \theta_1^4} \tag{28}$$

This function $D(n)$ plays a key role in the understanding the nature of the roots of Eq.(25), as it will be widely discussed in Section of Results.

At last, the beam cross-section acceleration $A(x, s)$ in terms of the above defined non-dimensional groups is formulated, considering that $A(x, s) = s^2 U(x, s)$ (see Eq.(16))

$$A(x, \bar{s}) = F_0 \sum_{n=1}^{+\infty} \frac{\bar{s}^2 (1 + \theta_1 \bar{s}) \phi_n(x) \phi_n(x_f)}{\mu \theta_1 \left(\bar{s}^3 + \sum_{j=0}^{2} a_j \bar{s}^j\right)} \tag{29}$$

being $\phi_n(x)$ the eigenfunctions defined in Eq.(12), and being the forcing term impulsive.

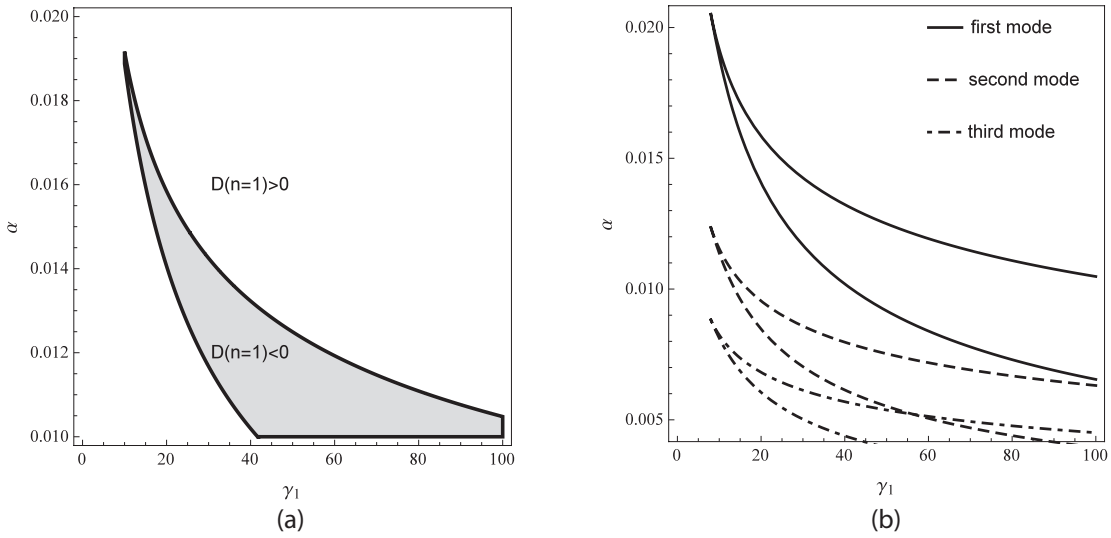

Figure 3: The region map for the first flexural mode of the beam $n = 1$, for $\theta_1 = \bar{\theta}_1$ (a). The shaded area indicates the parameter (α, γ_1) combinations which determine the suppression of the first peak. Similar region maps are shown, for the first three modes $n = 1, 2, 3$ (b). Interestingly, for several values of α and γ_1, some areas at $D(n) < 0$ are overlapped, determining the suppression of more peaks simultaneously.

4 RESULTS

In this section the main results of the presented analysis are discussed. The flexural vibrations of a viscoelastic beam with rectangular cross section and thickness $H = 1\,[\mathrm{cm}]$, which oscillates in the xz-plane are studied. The analysis starts from the characterization of a self-adhesive synthetic rubber found in literature [36]. The elastic modulus, experimentally obtained from DMA, has been fitted by Eq.2 with twelve relaxation times, in the frequency range $0 - 10^6\,[\mathrm{Hz}]$ [36]. A beam made of this material ($\rho = 1000\,[\mathrm{kg/m^3}]$), rectangular cross section with $H = 1\,[\mathrm{cm}]$ and $L = 50\,[\mathrm{cm}]$, has the first resonant peak in the frequency range $0 - 10\,[\mathrm{rad/s}]$. In order to evaluate the influence of the beam length on the first peak, the reduced frequency range $0 - 10\,[\mathrm{rad/s}]$ has been considered, in which the elastic modulus has been characterized

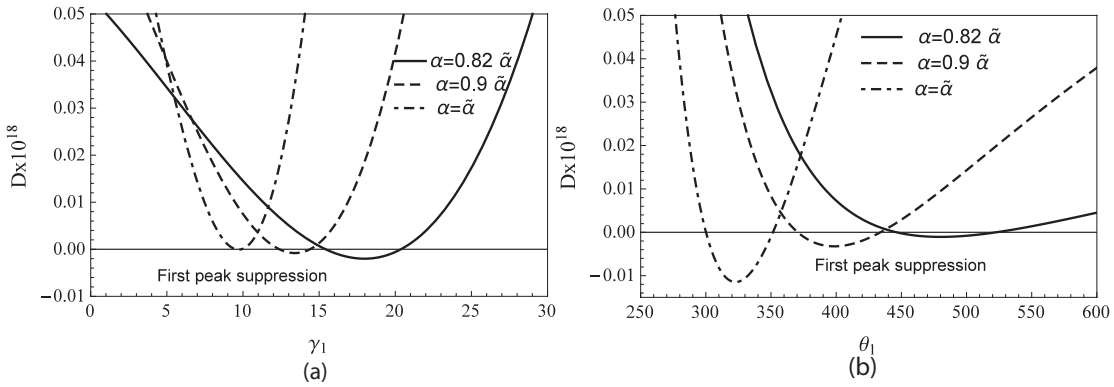

Figure 4: The discriminant $D\,(1)$ for the first mode $n = 1$, as a function of γ_1, for $\theta_1 = \bar{\theta}_1$ (a), and as a function of θ_1, for $\gamma_1 = \bar{\gamma}_1$ (b), for different values of α, i.e $\alpha = 0.82\tilde{\alpha}$ (solid line), $\alpha = 0.9\tilde{\alpha}$ (dashed line), $\alpha = \tilde{\alpha}$ (dot-dashed line).

by means of one single relaxation time. The parameters obtained by the fitting procedure, by means of (Eq.17), are $E_0 = 1.27 * 10^5$ [Pa], $E_1 = 2.018 * 10^6$ [Pa], $\tau_1 = 0.0628$ [s], from which one obtains $\bar{\gamma}_1 = E_1/E_0 = 15.9.$ and $\bar{\theta}_1 = \delta_1\tau_1 = 457.6$, being $\delta_1 = 7283$. It must be pointed out that the behaviour of the material is represented pretty well by this approximation in such limited frequency range, as one can observe in Figure 2, where it is shown the comparison between the original curve (red) and the reduced curve fitted by considering one relaxation time (black), in terms of the function $\tan\delta = \mathrm{Im}[E\,(\omega)]/\,\mathrm{Re}[E\,(\omega)]$ (Figure 2-a) and the imaginary part $\mathrm{Im}[E\,(\omega)]$ (Figure 2-b) of the viscoelastic modulus $E\,(\omega)$. Moving from this reference rubber like material, the two properties considered constant in the numerical calculations are $\rho = 1000$ [kg/m^3] and $E_0 = 1.27 * 10^5$ [Pa], so that the parameters δ_n are constant, and the other properties E_1 and τ_1 are taken varying in the analysis by means of γ_1 and θ_1. The only geometrical parameter which is considered varying in calculations, is the beam length L. In particular, the ratio $\alpha = H/L$ is changed maintaining H constant.

In must be observed that for each n_{th} mode, the three eigenvalues (solutions of Eq.(25)) can be calculated. The two complex conjugate eigenvalues represent the oscillatory counterpart of the beam n_{th} mode. The real eigenvalue gives rise to a pure dissipative contribute. However, when the discriminant $D\,(n)$, defined in Eq.(28), is negative $D\,(n) < 0$, all roots of Eq.(22) are real, and the n_{th} mode is not oscillatory. In Figure 3-a, a region map is shown, for the first flexural mode of the beam ($n = 1$), with $\theta_1 = \bar{\theta}_1$. The shaded area is obtained with the parameter values (α, γ_1) which give the condition $D\,(1) < 0$. Analogous maps, for the first three flexural modes of the beam, are represented by the correspondent curves in Figure 3-b, which are obtained by finding the two real solutions $\alpha = \alpha\,(\gamma_1)$ of the equation $D\,(n) = 0$, for $n = 1, 2, 3$. By properly combining the parameters (α, γ_1), different peaks can be suppressed simultaneously, since the areas which give the condition $D\,(n) < 0$ for different values of n are overlapped. In particular, this means that, once the material is prescribed, i.e. for given values of θ_1 and γ_1, the dynamics of the beam can be decisively modified by varying its length L. The sign of the discriminant $D\,(1)$, for the first mode, can be directly deduced by means of the curves plotted in Figure 4, where $D\,(1)$ is shown as a function of γ_1 (Figure 4-a), for $\theta_1 = \bar{\theta}_1$, and as a function of θ_1, for $\gamma_1 = \bar{\gamma}_1$ (Figure 4-b), for different values of α, i.e. $\alpha = 0.82\tilde{\alpha}$ (solid line), $\alpha = 0.9\tilde{\alpha}$ (dashed line), $\alpha = \tilde{\alpha}$ (dot-dashed line), where it has been considered the reference beam length equal to $\tilde{L} = 52[\mathrm{cm}]$. In Figure 5 the system response is represented, in terms of the acceleration modulus $|A\,(\bar{x}, \omega)|$ (see Eq.29), evaluated at the beam section $x = x_f = \bar{x} = 0.5L$,

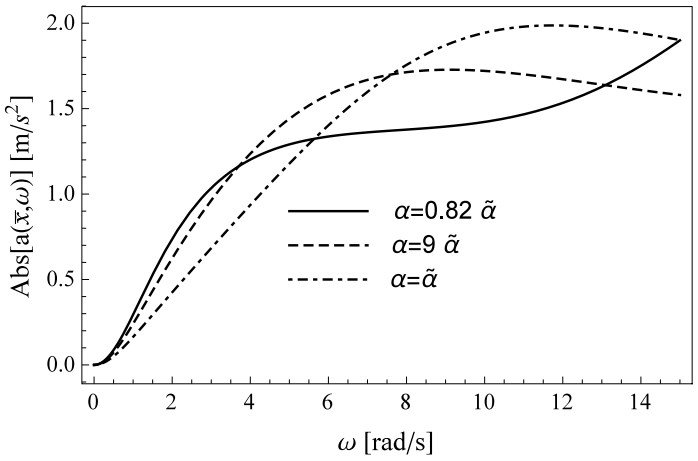

Figure 5: The acceleration modulus $|A(\bar{x},\omega)|$ of the viscoelastic beam with one relaxation time, in the section $x = x_f = \bar{x} = 0.5L$, for $\theta_1 = \bar{\theta}_1$, $\gamma_1 = \bar{\gamma}_1$, and for three different values of α, i.e. $\alpha = 0.82\tilde{\alpha}$ (solid line), $\alpha = 0.9\tilde{\alpha}$ (dashed line), $\alpha = \tilde{\alpha}$ (dot-dashed line). For $\alpha = 0.82\tilde{\alpha}$, being $D(1) < 0$, the first peak is suppressed.

for $\theta_1 = \bar{\theta}_1$ and $\gamma_1 = \bar{\gamma}_1$. Three different values of beam length L are considered, i.e. $\alpha = 0.82\tilde{\alpha}$ (solid line), $\alpha = 0.9\tilde{\alpha}$ (dashed line), $\alpha = \tilde{\alpha}$ (dot-dashed line), which give a damped first peak for $\alpha = 0.9\tilde{\alpha}$ and $\alpha = \tilde{\alpha}$, a suppressed first peak for $\alpha = 0.82\tilde{\alpha}$, being $D(1) < 0$ in the last case, as one can notice in Figure 4.

It is important to underline that, because of the intrinsic characteristics of viscoelastic materials [29], which see the viscoelastic modulus $E(\omega)$ depending on temperature, the above mentioned damping effect can be observed just modifying the surrounding temperature. Indeed, increasing or decreasing the working temperature, the functions $\mathrm{Re}[E(\omega)]$ and $\mathrm{Im}[E(\omega)]$ are shifted towards higher or smaller frequencies respectively, and consequently the material damping is differently spread in frequency, as well as the parameter θ_1 assumes different values.

However, once the material is prescribed, i.e. the viscoelastic modulus $E(\omega)$ is defined with the related parameters, θ_1 and γ_1, the dimensionless beam length α plays a crucial role in the possible overlapping of the first natural frequency ω_1 with the transition region. Moreover, in the hypothesis of linearity, such considerations can be extended to all the peaks, since the system can be decoupled and each vibration mode can be studied independently.

In conclusion, through the defined dimensionless parameters, it is possible to completely disclose the transversal vibrations of a viscoelastic beam. Suppressing certain peaks, by varying the beam length with α, or by changing the material properties (i.e. θ_1 and γ_1) for example by modifying the surrounding temperature, is an appealing chance for different applications. In particular, it is important to stress that, although the real viscoelastic materials present more than two relaxation times, the number of relaxation times to be considered in modelling the beam dynamics, does not represent a limit of our study. Indeed, it has been shown that it is always possible to divide the frequency spectrum under analysis in several intervals, thus allowing the decreasing of the predominant time relaxations number in such intervals. Moreover, by varying the beam length, it is possible to study a wide frequency range, by focusing the attention only to the first resonant peaks, so that the (Euler-Bernoulli) hypothesis still remains valid.

5 CONCLUSIONS

An analytical study of the transversal vibrations of a viscoelastic beam has been presented. The analytical solution has been obtained by means of modal superposition. In particular, the eigenvalues strongly depend on the material viscoelasticity, and they increase in number with the relaxation times of the viscoelastic modulus. A dimensional analysis has been performed, which has disclosed the fundamental parameters involved in the vibrational behaviour of the beam. Such parameters depend on both the material properties and the beam geometry. Some new characteristic maps related to the eigenvalues nature of the studied system have been provided, that can be drawn for each natural frequency of the beam. In comparison to the existing maps presented in literature for a sdof system, these maps may help in determining the parameter compounds needed to enhance or suppress certain frequency peaks, one at a time or more simultaneously, and the same approach can be exploited for any kind of mdof system. Results have shown that, by maintaining constant the thickness of the beam cross section, the dimensionless beam length can be utilized as key parameter to properly adjust the resonant peaks, once the material has been selected, thus becoming a powerful tool for many applications, from system damping control to materials characterization.

REFERENCES

[1] Bottiglione F., Carbone G., Mangialardi L., Mantriota G., Leakage Mechanism in Flat Seals, Journal of Applied Physics 106 (10), 104902, (2009).

[2] Carbone G., Pierro E., Gorb S., Origin of the superior adhesive performance of mushroom shaped microstructured surfaces, Soft Matter 7 (12), 5545-5552, DOI:10.1039/C0SM01482F, (2011).

[3] Carbone G., Pierro E., Sticky bio-inspired micropillars: Finding the best shape, SMALL, 8 (9), 1449-1454, (2012).

[4] Carbone G., Pierro E., Effect of interfacial air entrapment on the adhesion of bio-inspired mushroom-shaped micro-pillars, Soft Matter, 8 (30), 7904-7908, (2012).

[5] Carbone G., Pierro E., A review of adhesion mechanisms of mushroom-shaped microstructured adhesives, Meccanica, 48(8), 1819-1833, (2013).

[6] Persson B.N.J., Rolling friction for hard cylinder and sphere on viscoelastic solid, Eur. Phys. J. E 33, 327-333 (2010).

[7] Dumitru N. Olaru, Ciprian Stamate,Gheorghe Prisacaru, Rolling Friction in a Micro Tribosystem, Tribol Lett , 35:205–210, (2009).

[8] G. Carbone, C. Putignano, A novel methodology to predict sliding and rolling friction of viscoelastic materials: Theory and experiments, Journal of the Mechanics and Physics of Solids, Volume 61, Issue 8, pp. 1822-1834, (2013).

[9] Grosch K. A. , The Relation between the Friction and Visco-Elastic Properties of Rubber, Proceedings of the Royal Society of London. Series A, Mathematical and Physical,274-1356, pp. 21-39, (1963).

[10] Carbone G., Mangialardi L., Adhesion and friction of an elastic half-space in contact with a slightly wavy rigid surface, Journal of the Mechanics and Physics of Solids, 52 (6), 1267-1287, 2004.

[11] Carbone G., Lorenz B., Persson B.N.J. and Wohlers A., Contact mechanics and rubber friction for randomly rough surfaces with anisotropic statistical properties, The European Physiscal Journal E – Soft Matter, 29 (3), 275–284, (2009)

[12] Persson B.N.J.,Theory of rubber friction and contact mechanics, Journal of Chemical Physics,115, 3840 -3861(2001).

[13] Carbone G., Persson B.N.J., Hot cracks in rubber: origin of the giant toughness of rubber-like materials, Physical Review Letters, 95, 114301 (2005).

[14] Carbone G., Persson B.N.J.: "Crack motion in viscoelastic solids: The role of the flash temperature", the European Physical Journal E-Soft Matter 17 (3), 261 (2005).

[15] Persson BNJ; Albohr O; Heinrich G; et al., Crack propagation in rubber-like materials, JOURNAL OF PHYSICS-CONDENSED MATTER 17 (44), R1071-R1142, doi: 10.1088/0953-8984/17/44/R01, (2005)

[16] Carbone G., Persson B.N.J., Dewetting at Soft Viscoelastic Interfaces, The Journal of Chemical Physics, 121 (5): 2246-2252 (2004).

[17] Rasa A., Applying dynamic mechanical analysis to research and development for viscoelastic damping materials, Internoise 2014 - Melbourne, Australia - Novembre 16-19, 2014.

[18] Caracciolo R., Gasparetto A., Giovagnoni M., Measurement of the isotropic dynamic Young's modulus in a seismically excited cantilever beam using a laser sensor, Journal of Sound and Vibration 231(5), 1339-1353, (2000).

[19] Caracciolo R., Gasparetto A., Giovagnoni M., An experimental technique for complete dynamic characterization of a viscoelastic material, Journal of Sound and Vibration 272, 1013–1032, (2004).

[20] Cortes F. , Elejabarrieta M.J., Viscoelastic materials characterisation using the seismic response, Materials and Design, 28, 2054–2062, (2007).

[21] Muller P., Are the eigensolutions of a 1-d.o.f. system with viscoelastic damping oscillatory or not?, Journal of Sound and Vibration 285, 501–509, (2005).

[22] García-Barruetabeña J., Cortés F., Abete J. M., Influence of Nonviscous Modes on Transient Response of Lumped Parameter Systems With Exponential Damping, Journal of Vibration and Acoustics, 133, (2011).

[23] Adhikari S., Dynamics of Nonviscously Damped Linear Systems,J. Eng. Mech., 128:328-339, (2002).

[24] Lázaro M., Pérez-Aparicio L., Epstein M., A viscous approach based on oscillatory eigensolutions for viscoelastically damped vibrating systems, Mechanical Systems and Signal Processing, 40, 767–782, (2013).

[25] García-Barruetabeña J., Cortés F., Abete J. M., Dynamics of an exponentially damped solid rod: Analytic solution and finite element formulations, International Journal of Solids and Structures 49, 590–598, (2012).

[26] Inman D. J., Vibration analysis of viscoelastic beams by separation of variables and modal analysis, Mechanics Research Communications, Vo1.16(4), 213-218, (1989).

[27] Gupta A.K., Khanna A., Vibration of visco-elastic rectangular plate with linearly thickness variations in both directions, Journal of Sound and Vibration 30, 450–457, (2007).

[28] Adhikari S., Qualitative dynamic characteristics of a non-viscously damped oscillator, Proc. R. Soc. A, 461, 2269–2288, (2005).

[29] Christensen R. M., Theory of viscoelasticity,Academic Press, New York.

[30] Inman D. J., Engineering Vibrations, Prentice Hall, isbn: 0-13-518531-9, (1996).

[31] H. T. Banks and D. J. Inman , On Damping Mechanisms in Beams, J. Appl. Mech 58(3), 716-723, (1991).

[32] Thomson WT, Dahleh MD, "Theory of vibration with applications", 5th edn. Prentice Hall, Englewood Cliffs, (1997).

[33] Abramowitz, M., and Stegun, I. A., 1965, Handbook of Mathematical Functions, With Formulas, Graphs, and Mathematical Tables, Dover Publications, New York.

[34] Lazard D., "Quantifier elimination: Optimal solution for two classical examples". Journal of Symbolic Computation, 5: 261–266, (1988).

[35] Rees E. L., "Graphical Discussion of the Roots of a Quartic Equation", The American Mathematical Monthly, 29 (2): 51–55, (1922).

[36] L. Rouleau, R. Pirk, B. Pluymers, W. Desmet, "Characterization and Modeling of the Viscoelastic Behavior of a Self-Adhesive Rubber Using Dynamic Mechanical Analysis Tests, J. Aerosp. Technol. Manag., 7, 2, (2015).

COMPDYN 2019
7th ECCOMAS Thematic Conference on
Computational Methods in Structural Dynamics and Earthquake Engineering
M. Papadrakakis, M. Fragiadakis (eds.)
Crete, Greece, 24-–26 June 2019

MODEL UPDATING OF A MULTI-SPAN QUASI-PERIODIC ROADWAY VIADUCT BASED ON FREE WAVE CHARACTERISTICS

J. Zhang, K. Maes, G. De Roeck, G. Lombaert

KU Leuven, Department of Civil Engineering, Structural Mechanics Section
Kasteelpark Arenberg 40, 3001 Leuven, Belgium
e-mail: {jie.zhang, kristof.maes, guido.deroeck, geert.lombaert}@kuleuven.be

Keywords: Model updating, multi-span viaduct, periodic structures, free wave characteristics

Abstract. *The K032 viaduct of the A11 highway is a recently built multi-span viaduct in Bruges, Belgium. The viaduct is a typical quasi-periodic structure with, even at low frequencies, a high modal density. This leads to difficulties in distinguishing between these clustered modes in modal identification as well as the pairing of experimental and numerically predicted mode shapes in finite element model updating. Alternatively, for periodic structures, use can be made for structural identification of the so-called free wave characteristics. A model updating method based on free wave characteristics has recently been proposed for periodic structures. In this work, this method is applied to the K032 viaduct. Vibrational measurements were first conducted on the viaduct to identify the free wave characteristics. Next, the discrepancy between the calculated and identified free wave characteristics is minimized to update the finite element model of the viaduct. The model updating results are validated by comparing the measured frequency response functions and those calculated from the updated finite element model.*

1 INTRODUCTION

Vibration-based finite element model updating is widely used in civil engineering to calibrate numerical models with unknown or poorly known parameters [3, 4, 9]. It is usually performed by minimizing the discrepancy between the calculated and experimentally identified dynamic data, which are generally modal characteristics including natural frequencies and mode shapes. For repetitive structures, as often found in school and office buildings, multi-span bridges and parking buildings, mode clustering occurs with closely spaced natural frequencies and mode shapes with similar wavelength [10, 11]. This leads to difficulties in distinguishing between the modes in modal identification and consequently poses challenges in model updating where matching the measured and calculated modes is required. As alternatives, the use of free wave characteristics in the model updating of periodic structures has been explored in [11]. Free wave characteristics for periodic structures, including propagation constants and free waves, have been extensively studied by means of Floquet theory [1, 8]. In this work, the proposed model updating method is applied on the K032 viaduct (figure 1), a multi-span quasi-periodic viaduct in Bruges, where free waves were identified from vibration measurements and used to update the finite element model.

Figure 1: The K032 viaduct.

The K032 viaduct is introduced in section 2. The wave propagation theory is briefly introduced in Section 3. The measurement and the identification of the free waves of the viaduct are elaborated in Section 4. These measured free waves are used to update the finite element model of K032 in Section 5. Conclusions are given in Section 6.

2 The K032 viaduct

The K032 viaduct consists of two curved integral bridges K032L and K032R in parallel with each other. Each bridge has 23 spans, with most of the spans having a length of around 35 m. The total length of the viaduct is about 800 m. The two bridge are connected by a passway at the 19th and 20th span, allowing traffic to pass from one bridge to the other. Each bridge is composed of concrete girders with solid sections and concrete columns supported by pile foundations. The viaduct is divided into 5 zones, as shown in figure 2, with different material properties and cross section dimensions. Zones 2 and 3 are nearly periodic, giving the possibility for the analysis of free wave characteristics. The cross section dimensions of the deck and columns and the pile configuration of bridge K032R at sections A-A are shown in figures 3. The lateral view of K032R at zone 3 is shown in figure 4, where the lengths of columns and piles are given. Small variances are found on the lengths of columns and piles. At this zone, concrete grade C56/60 is used for the bridge deck and the columns, grade C35/45 is used for the piles and the pile caps.

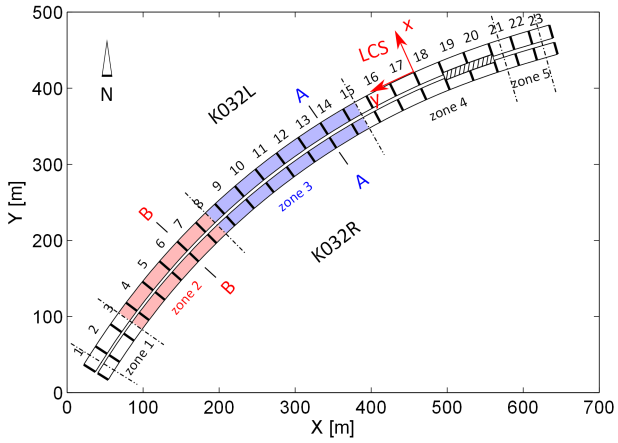

Figure 2: Top view of the viaduct.

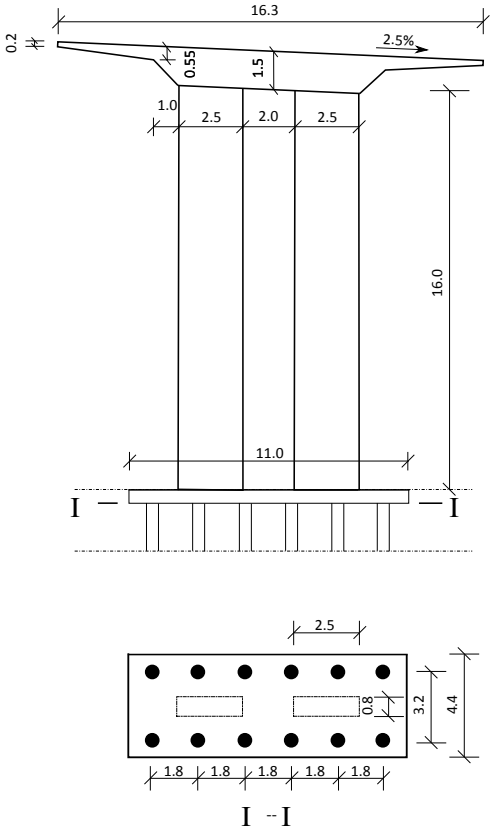

Figure 3: Dimensions [m] of the concrete deck and column at section A-A for K032R (top), pile configurations at sections I-I (below).

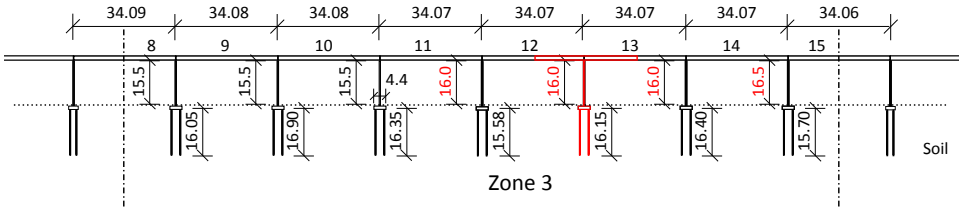

Figure 4: Lateral view of K032R in zone 3 with column eng pile lengths [m] and a repetitive unit (red).

3 Free wave characteristics

The calculation of the free wave characteristics is briefly recapitulated in this subsection for the case of multi-coupled one-dimensional infinite periodic structures. The procedure is applied for a repetitive unit of bridge K032R at zone 3 shown in figure 4. The finite element model of the deck and column of one unit is shown in figure 5. This unit is taken from the center of one span to the center of the next span. It is modeled in ANSYS using solid45 elements. The stiffness and mass matrices are extracted from ANSYS and coupled in MATLAB to the model of the pile foundation in StaBIL [2]. The piles are modeled using beam elements in StaBIL and the surrounding soil is modeled by static distributed springs with lateral ($k^{\mathrm{s}}_{\mathrm{lateral}}$), axial ($k^{\mathrm{s}}_{\mathrm{axial}}$) and end-bearing axial ($k^{\mathrm{s}}_{\mathrm{end}}$) stiffness. The pile cap is assumed to be rigid and the column base is fixed at the center of the cap. From the finite element model of the pile foundation, the static impedance matrix is calculated and coupled to the degrees of freedom which correspond to the support of columns.

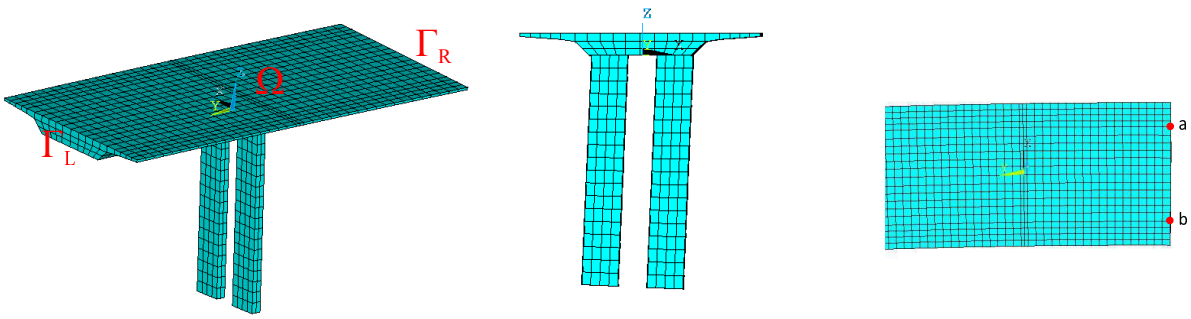

(a) 3D (b) Longitudinal view (c) Lateral view

Figure 5: The ANSYS model of one unit at zone 3.

The degrees of freedom (DOFs) of a repetitive unit are divided into two sets (figure 5a): the interface DOFs (at interfaces Γ_{L} and Γ_{R}) and the internal DOFs (in the internal domain Ω). Γ_{L} and Γ_{R} contain the DOFs that are coupled with the adjacent units on the left and right hand side, respectively. Ω contains the remaining internal DOFs that are not coupled with the adjacent units. The free wave characteristics are found by solving the free vibration problem of an infinitely long periodic structure without external forces, leading to the following condensed system of equation of motion considering the DOFs at Γ_{L} and Γ_{R} only.

$$\begin{bmatrix} \hat{\mathbf{F}}_{\mathrm{L}} \\ \hat{\mathbf{F}}_{\mathrm{R}} \end{bmatrix} = \begin{bmatrix} \mathbf{D}^{(\mathrm{c})}_{\mathrm{LL}} & \mathbf{D}^{(\mathrm{c})}_{\mathrm{LR}} \\ \mathbf{D}^{(\mathrm{c})}_{\mathrm{RL}} & \mathbf{D}^{(\mathrm{c})}_{\mathrm{RR}} \end{bmatrix} \begin{bmatrix} \hat{\mathbf{u}}_{\mathrm{L}} \\ \hat{\mathbf{u}}_{\mathrm{R}} \end{bmatrix} \tag{1}$$

where $\hat{\mathbf{F}}_{\mathrm{L}}$ and $\hat{\mathbf{F}}_{\mathrm{R}}$ are forces transfered at the interfaces, and $\mathbf{D}^{(\mathrm{c})}$ is the condensed dynamic stiffness matrix, $\hat{\mathbf{u}}_{\mathrm{L}}$ and $\hat{\mathbf{u}}_{\mathrm{R}}$ are the displacements at the interfaces.

According to the Floquet theory [1, 8], the displacements and forces at one unit are related to those of the next unit by a propagation constant μ as follows:

$$\hat{\mathbf{u}}_{\mathrm{L},r+1} = e^{\mu}\hat{\mathbf{u}}_{\mathrm{L},r} \tag{2a}$$

$$\hat{\mathbf{F}}_{\mathrm{L},r+1} = e^{\mu}\hat{\mathbf{F}}_{\mathrm{L},r} \tag{2b}$$

where the subscripts r and $r+1$ refer to unit r and the next unit $r+1$.

For compatibility and equilibrium to hold, the following equations are required:

$$\hat{\mathbf{u}}_{\mathrm{L},r+1} = \hat{\mathbf{u}}_{\mathrm{R},r} \tag{3a}$$

$$\hat{\mathbf{F}}_{\mathrm{L},r+1} = -\hat{\mathbf{F}}_{\mathrm{R},r} \tag{3b}$$

Introducing conditions (2a) and (2b) and the compatibility and equilibrium equations (3a) and (3b) in the equation of motion leads to the following quadratic eigenvalue problem:

$$[\mathbf{D}_{\mathrm{LR}}^{(\mathrm{c})} e^{2\mu} + (\mathbf{D}_{\mathrm{LL}}^{(\mathrm{c})} + \mathbf{D}_{\mathrm{RR}}^{(\mathrm{c})}) e^{\mu} + \mathbf{D}_{\mathrm{RL}}^{(\mathrm{c})}]\{\hat{\mathbf{u}}_{\mathrm{L}}\} = \mathbf{0} \tag{4}$$

The corresponding forces at the left interface Γ_{L} are calculated from $\hat{\mathbf{u}}_{\mathrm{L}}$:

$$\hat{\mathbf{F}}_{\mathrm{L}} = [\mathbf{D}_{\mathrm{LL}}^{(\mathrm{c})} + e^{\mu} \mathbf{D}_{\mathrm{LR}}^{(\mathrm{c})}]\{\hat{\mathbf{u}}_{\mathrm{L}}\} \tag{5}$$

By solving the eigenvalue problem (4), n_{c} pairs of free waves are obtained where n_{c} is the number of the coupling DOFs. Each pair contains one positive going and one identical but negative going free wave, characterized by a pair of negative and positive propagation constants. A propagation constant is a complex number with the real and imaginary part indicating the attenuation and the phase change of the corresponding wave across a unit cell, respectively. The k^{th} positive and negative going free wave characteristics are denoted as $[\mu_{\mathrm{p}k},\ \boldsymbol{\psi}_{\mathrm{p}k}]$ and $[\mu_{\mathrm{n}k},\ \boldsymbol{\psi}_{\mathrm{n}k}]$, respectively, where $\boldsymbol{\psi}$ is the displacement vector of dimension $n_{\mathrm{c}} \times 1$. Subscripts p and n represent the positive and negative going free waves, respectively. $\mu_{\mathrm{p}k}$ and $\mu_{\mathrm{n}k}$ are the propagation constants with $\mu_{\mathrm{p}k} = -\mu_{\mathrm{n}k}$ [7].

As an example, the free waves of K032R that can propagate at zone 3 at 40 Hz are calculated. Frequency independent hysteretic damping is added where the equation of motion becomes $(\mathbf{K} + i\eta\mathbf{K} - \omega^2\mathbf{M})\hat{\mathbf{u}} = \hat{\mathbf{F}}$ with η the hysteretic damping factor. η is initially taken as 0.02. The effective stiffness of the deck, column and piles are taken as $E_{\mathrm{deck}} = E_{\mathrm{column}} = 37$ GPa and $E_{\mathrm{pile}} = 34$ GPa. Three pairs of free waves with pronounced motion of the deck are plotted over several units in figure 6a-c. The first pair of free waves involves local bending of the deck, where the bending motion is approximately anti-symmetric around the longitudinal axis, while the second pair shows a local bending wave symmetric around the longitudinal axis. The third pair is a lateral wave with local bending of the deck. In figure 6d, a pair of longitudinal waves is plotted.

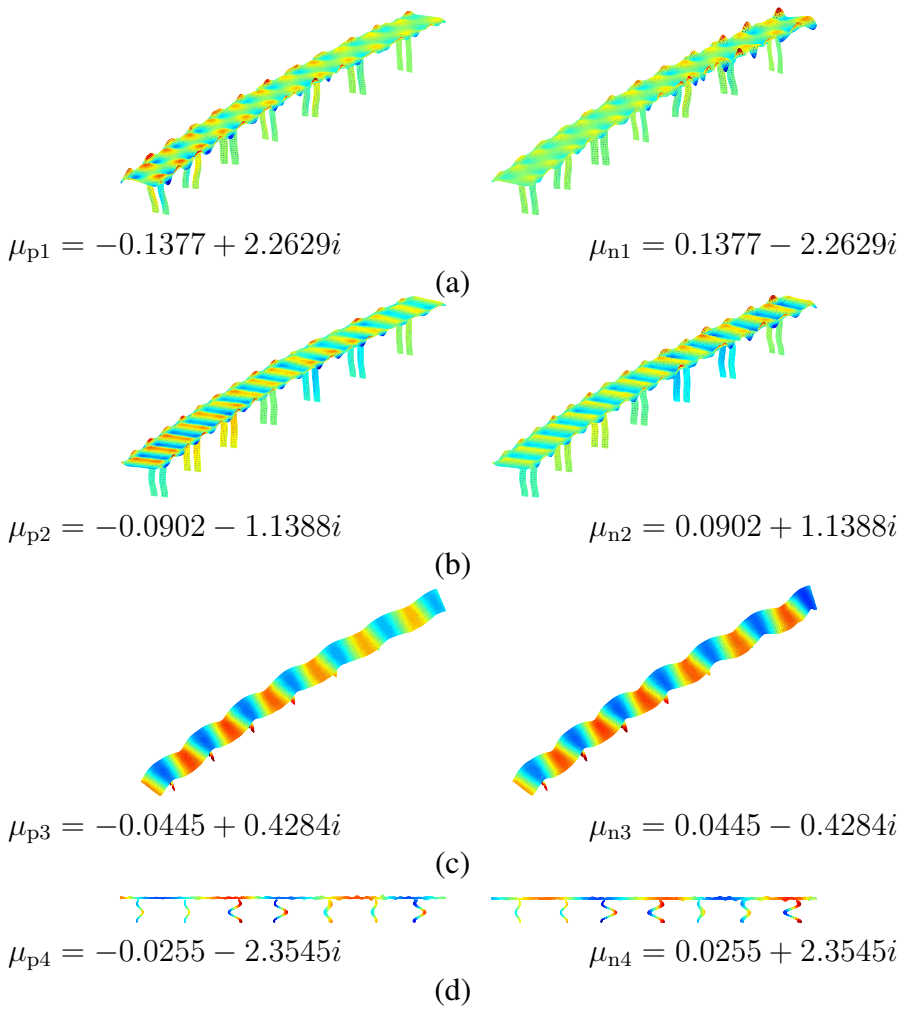

Figure 6: The calculated positive going (left) and the corresponding negative going (right) free waves at 40 Hz, (a)-(d): free wave pairs 1-4.

4 Free wave identification

First, the forced vibration of finite periodic structures is introduced based on the free wave analysis proposed by Mead [8]. Second, the inverse method of extracting the free waves from measured responses is briefly recapitulated [11]. This method is applied to K032R to identify the free wave characteristics, which will be used in the next section for model updating.

4.1 Forward problem

The forced vibration of periodic structures (forward problem) has been studied [6, 8] based on wave analysis. Mead [8] developed a method to calculate the forced harmonic motion of periodic structures by a linear superposition of all characteristic free waves. Figure 7 shows how the free waves propagate at zone 3 of K032R when the viaduct is excited at its right end. The negative going free waves are generated at the excitation point and propagate to the left though zone 3, the positive going free waves are reflected at the left end of zone 3 and propagate to the right. The responses at the left end of the first unit $\hat{\mathbf{u}}_1$ and second unit $\hat{\mathbf{u}}_2$ of zone 3 are

calculated as follows:

$$\hat{\mathbf{u}}_1 = \sum_{k=1}^{n_c} (\boldsymbol{\psi}_{pk}\alpha_{pk} + \lambda_{nk}^{-N}\boldsymbol{\psi}_{nk}\alpha_{nk}) = \sum_{k=1}^{n_c} (\boldsymbol{\psi}_{pk}\alpha_{pk} + \lambda_{pk}^{N}\boldsymbol{\psi}_{nk}\alpha_{nk}) \tag{6a}$$

$$\hat{\mathbf{u}}_2 = \sum_{k=1}^{n_c} (\lambda_{pk}\boldsymbol{\psi}_{pk}\alpha_{pk} + \lambda_{pk}^{(N-1)}\boldsymbol{\psi}_{nk}\alpha_{nk}) \tag{6b}$$

In equation (6a), $\boldsymbol{\psi}_{pk}\alpha_{pk}$ is the contribution of the k^{th} positive going free wave with α_{pk} the corresponding generalized coordinate, while $\lambda_{nk}^{-N}\boldsymbol{\psi}_{nk}\alpha_{nk}$ is the contribution of the k^{th} negative going free wave after propagation to the left through N units. In this case N is equal to 7. Since $e^{\mu_{pk}} = e^{-\mu_{nk}}$ and $\lambda_{pk} = \lambda_{nk}^{-1}$, the term $\lambda_{nk}^{-N}\boldsymbol{\psi}_{nk}\alpha_{nk}$ is re-written as $\lambda_{pk}^{N}\boldsymbol{\psi}_{nk}\alpha_{nk}$ in equation (6a). Similarly, the response $\hat{\mathbf{u}}_2$ is written in equation (6b). The responses at the other units can be obtained in the same way.

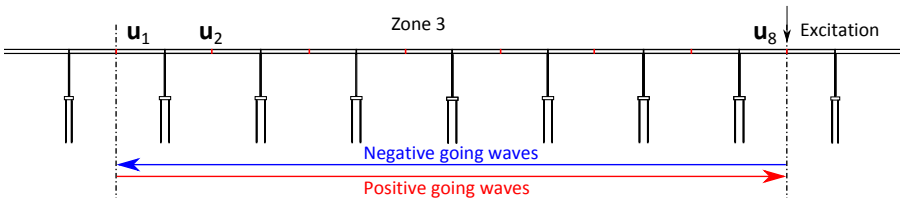

Figure 7: Waves propagating in zone 3 excited at its ends.

4.2 Inverse problem

The inverse problem, where the free waves are identified from measured responses, has been investigated by [5, 11]. It is briefly introduced in this subsection. The response at the left end of the first measured unit ($\bar{\mathbf{d}}_1$) is written in terms of the free wave contributions as follows:

$$\bar{\mathbf{d}}_1 = \mathbf{L}\hat{\mathbf{u}}_1 = \mathbf{L}\sum_{k=1}^{n_w} (\boldsymbol{\psi}_{pk}\alpha_{pk} + \lambda_{pk}^{N}\boldsymbol{\psi}_{nk}\alpha_{nk}) = \sum_{k=1}^{n_w} (\mathbf{x}_{pk} + \lambda_{pk}^{N}\mathbf{x}_{nk}) \tag{7}$$

where $\hat{\mathbf{d}}_1$ is the dynamic response at the measured DOFs at the left end of the first measured unit and $\mathbf{L}$ is a $n_m \times n_c$ selection matrix that selects the n_m measured DOFs from all n_c coupling DOFs. The vectors $\mathbf{x}_{pk} = \mathbf{L}\boldsymbol{\psi}_{pk}\alpha_{pk}$ and $\mathbf{x}_{nk} = \mathbf{L}\boldsymbol{\psi}_{nk}\alpha_{nk}$ are the k^{th} positive and negative going free wave component of size $n_m \times 1$ which need to be determined. The number of wave pairs that participate to the response is given by n_w.

Similarly, the measured response is obtained for the other units:

$$\begin{bmatrix} \sum_{k=1}^{n_w} (\mathbf{x}_{pk} + \lambda_{pk}^{N}\mathbf{x}_{nk}) \\ \sum_{k=1}^{n_w} (\lambda_{pk}\mathbf{x}_{pk} + \lambda_{pk}^{(N-1)}\mathbf{x}_{nk}) \\ \vdots \\ \sum_{k=1}^{n_w} (\lambda_{pk}^{N}\mathbf{x}_{pk} + \mathbf{x}_{nk}) \end{bmatrix} - \begin{bmatrix} \bar{\mathbf{d}}_1 \\ \bar{\mathbf{d}}_2 \\ \vdots \\ \bar{\mathbf{d}}_{(N+1)} \end{bmatrix} = \mathbf{0} \tag{8}$$

To solve this system of equations, Zhang et al. [11] have proposed a non-linear least-squares

method where the objective function is formulated as follows:

$$\mathbf{F}(\mathbf{x}_{\mathrm{p}k};\ \mathbf{x}_{\mathrm{n}k};\ \lambda_{\mathrm{p}k}) = \left\| \begin{bmatrix} \sum_{k=1}^{n_{\mathrm{w}}} (\mathbf{x}_{\mathrm{p}k} + \lambda_{\mathrm{p}k}^{N} \mathbf{x}_{\mathrm{n}k}) \\ \sum_{k=1}^{n_{\mathrm{w}}} (\lambda_{\mathrm{p}k} \mathbf{x}_{\mathrm{p}k} + \lambda_{\mathrm{p}k}^{(N-1)} \mathbf{x}_{\mathrm{n}k}) \\ \vdots \\ \sum_{k=1}^{n_{\mathrm{w}}} (\lambda_{\mathrm{p}k}^{N} \mathbf{x}_{\mathrm{p}k} + \mathbf{x}_{\mathrm{n}k}) \end{bmatrix} - \begin{bmatrix} \bar{\mathbf{d}}_1 \\ \bar{\mathbf{d}}_2 \\ \vdots \\ \bar{\mathbf{d}}_{(N+1)} \end{bmatrix} \right\|_2^2 \tag{9}$$

Data $\bar{\mathbf{d}} = [\bar{\mathbf{d}}_1; \bar{\mathbf{d}}_2; \cdots; \bar{\mathbf{d}}_{(N+1)}]$ can be directly measured (displacement, velocity or acceleration) responses or frequency response functions (FRFs). $\lambda_{\mathrm{p}k}$, $\mathbf{x}_{\mathrm{p}k}$ and $\mathbf{x}_{\mathrm{n}k}$ ($k = [1, 2, \cdots, n_{\mathrm{w}}]$) are the unknown free wave characteristics to be determined. The objective function is minimized to obtain the least-squares solution of the free wave characteristics:

$$[\mathbf{x}_{\mathrm{p}k};\ \mathbf{x}_{\mathrm{n}k};\ \lambda_{\mathrm{p}k}]^* = \min_{[\mathbf{x}_{\mathrm{p}k};\ \mathbf{x}_{\mathrm{n}k};\ \lambda_{\mathrm{p}k}]} \mathbf{F}(\mathbf{x}_{\mathrm{p}k};\ \mathbf{x}_{\mathrm{n}k};\ \lambda_{\mathrm{p}k}) \tag{10}$$

4.3 Free wave identification of K032

Measurements were conducted to identify the free waves of K032R. Twelve wireless recorders including 9 GeoSIG GMS-18 units and 3 GeoSIG GMSplus units were used. Each recorder measured the accelerations in 3 orthogonal directions x, y, and z, that are aligned with the LCS shown in figure 8. The GeoSIG GMSplus units have 3 additional channels, which were used to connected additional uni-axial accelerometers and the hammer. Repeated hammer impacts in the vertical direction z were applied at the right end of zone 3 to excite vertical bending or torsional free waves. In 2 setups, the locations in figure 8 are measured. The frequency response functions at the measured locations are calculated and used in the free wave identification.

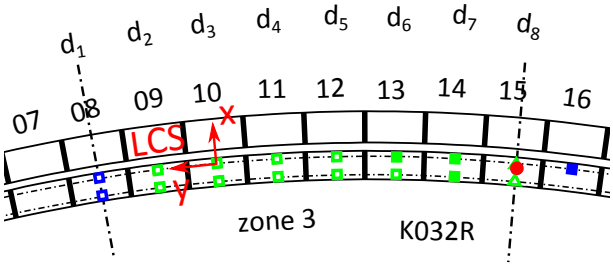

Figure 8: Sensor configurations for setup 1 (green) and setup 2 (blue) with the GeoSIG GMS-18 units (hollow squares), the GeoSIG GMSplus units (solid squares) and the uni-axial accelerometers (triangles) connected to the GeoSIG GMSplus units and the hammer excitation (circles).

One pair of stable torsional free waves is identified at each frequency in the range between 38 Hz and 44 Hz with an increment of 1 Hz. The negative going torsional free wave contributes most to the total response, while its positive going counterpart only has a small contribution. The stable torsional free wave pair identified here in fact corresponds to the local bending wave pair 1 computed from the preliminary FE model which was shown in figure 6a. The identified negative going free waves at the measured locations are shown in figure 10. The free waves calculated from the preliminary finite element model (Section 3) are also plotted over the measured locations. The corresponding propagation constants are listed in table 1. Discrepancies are found between the measured and predicted free wave characteristics. These discrepancies will be minimized to update the finite element model in the following section.

5 Model updating of the K032 viaduct

Deterministic model updating [9] is usually performed by minimizing a least-squares cost function quantifying the discrepancy between calculated and experimentally identified dynamic data. Based on the study in [11], free wave characteristics can be used as the data feature for the model updating of periodic structures. The eigenvalues $\lambda_{\mathrm{p}k}$ and $\lambda_{\mathrm{n}k}$, the positive and negative going free wave vectors $\boldsymbol{\psi}_{\mathrm{p}k}$ and $\boldsymbol{\psi}_{\mathrm{n}k}$, are used to construct the following least-squares cost function.

$$\mathbf{F}(\boldsymbol{\theta}_{\mathrm{M}},\omega)=\sum_{k=1}^{n_{\mathrm{w}}}a_k\frac{(\bar{\lambda}_{\mathrm{p}k}(\omega)-\lambda_{\mathrm{p}k}(\boldsymbol{\theta}_{\mathrm{M}},\omega))^2}{(\bar{\lambda}_{\mathrm{p}k}(\omega))^2}+\sum_{k=1}^{n_{\mathrm{w}}}b_k\frac{||\chi_{\mathrm{p}k}\bar{\boldsymbol{\psi}}_{\mathrm{p}k}(\omega)-\mathbf{L}\boldsymbol{\psi}_{\mathrm{p}k}(\boldsymbol{\theta}_{\mathrm{M}},\omega)||_2^2}{||\chi_{\mathrm{p}k}\bar{\boldsymbol{\psi}}_{\mathrm{p}k}(\omega)||_2^2}$$
$$+\sum_{k=1}^{n_{\mathrm{w}}}c_k\frac{(\bar{\lambda}_{\mathrm{n}k}(\omega)-\lambda_{\mathrm{n}k}(\boldsymbol{\theta}_{\mathrm{M}},\omega))^2}{(\bar{\lambda}_{\mathrm{n}k}(\omega))^2}+\sum_{k=1}^{n_{\mathrm{w}}}d_k\frac{||\chi_{\mathrm{n}k}\bar{\boldsymbol{\psi}}_{\mathrm{n}k}(\omega)-\mathbf{L}\boldsymbol{\psi}_{\mathrm{n}k}(\boldsymbol{\theta}_{\mathrm{M}},\omega)||_2^2}{||\chi_{\mathrm{n}k}\bar{\boldsymbol{\psi}}_{\mathrm{n}k}(\omega)||_2^2} \tag{11}$$

where n_{w} is the number of free wave pairs considered; ω is the considered frequency; $\bar{\lambda}_{\mathrm{p}k}(\omega)$, $\bar{\lambda}_{\mathrm{n}k}(\omega)$, $\bar{\boldsymbol{\psi}}_{\mathrm{p}k}(\omega)$ and $\bar{\boldsymbol{\psi}}_{\mathrm{p}k}(\omega)$ are the measured free wave characteristics at frequency ω, while $\lambda_{\mathrm{p}k}(\boldsymbol{\theta}_{\mathrm{M}},\omega)$, $\lambda_{\mathrm{n}k}(\boldsymbol{\theta}_{\mathrm{M}},\omega)$, $\boldsymbol{\psi}_{\mathrm{p}k}(\boldsymbol{\theta}_{\mathrm{M}},\omega)$ and $\boldsymbol{\psi}_{\mathrm{n}k}(\boldsymbol{\theta}_{\mathrm{M}},\omega)$ are the corresponding computed quantities; $\chi_{\mathrm{p}k}$ and $\chi_{\mathrm{n}k}$ are scaling factors which are introduced to obtain similar scaling of the free waves obtained from FE model and experiments. These scaling factors are calculated as $\chi_{\mathrm{p}k}=\dfrac{\bar{\boldsymbol{\psi}}_{\mathrm{p}k}^{\mathrm{H}}\mathbf{L}\boldsymbol{\psi}_{\mathrm{p}k}(\boldsymbol{\theta}_{\mathrm{M}})}{\|\bar{\boldsymbol{\psi}}_{\mathrm{p}k}\|_2^2}$ and $\chi_{\mathrm{n}k}=\dfrac{\bar{\boldsymbol{\psi}}_{\mathrm{n}k}^{\mathrm{H}}\mathbf{L}\boldsymbol{\psi}_{\mathrm{n}k}(\boldsymbol{\theta}_{\mathrm{M}})}{\|\bar{\boldsymbol{\psi}}_{\mathrm{n}k}\|_2^2}$. $\mathbf{L}$ is a selection matrix that selects the observed DOFs of the FE model; a_k, b_k, c_k and d_k are weighting factors, representing the importance of the corresponding terms.

When free wave characteristics at multiple frequencies are available, they can be considered simultaneously in the objective function:

$$\mathbf{F}(\boldsymbol{\theta}_{\mathrm{M}})=\sum_{j=1}^{n_{\mathrm{f}}}\mathbf{F}_j(\boldsymbol{\theta}_{\mathrm{M}},\omega_j) \tag{12}$$

where $\mathbf{F}_j(\boldsymbol{\theta}_{\mathrm{M}},\omega_j)$ contains the squared residuals at frequency ω_j and n_{f} is the number of frequencies considered. The cost function is minimized to obtain the model parameters:

$$\boldsymbol{\theta}_{\mathrm{M}}^{*}=\min_{\boldsymbol{\theta}_{\mathrm{M}}}\ \mathbf{F}(\boldsymbol{\theta}_{\mathrm{M}}) \tag{13}$$

For the updating of the preliminary unit model of the viaduct, 6 possible material related updating parameters are initially considered, including the effective stiffness of the concrete deck ($\theta_1 E_{\mathrm{deck}}$), the effective stiffness of the column ($\theta_2 E_{\mathrm{column}}$), the effective stiffness of the piles ($\theta_3 E_{\mathrm{pile}}$), the lateral stiffness provided by the soil ($\theta_4 k_{\mathrm{lateral}}^{)}$) and the axial and end bearing stiffness of the soil ($\theta_5 k_{\mathrm{axial,end}}^{\mathrm{s}}$) and the hysteretic damping factor ($\theta_6\eta$). The sensitivities of the free wave characteristics to these parameters have been studied. It is found that the free wave characteristics are more sensitive to the effective stiffness of the concrete deck ($\theta_1 E_{\mathrm{deck}}$) and the damping factor ($\theta_6\eta$) than to the other parameters. These two parameters are therefore considered in the updating with an initial value of 1. The identified negative going free waves are used in the updating. The weighting factors are taken as 1. The Levenberg-Marquardt algorithm is used to solve the least-squares problem. The residual of the objective function is shown in figure 9. The updated values of the parameters are $\theta_1 = 1.2408$ and $\theta_6 = 4.6430$. As expected, the effective stiffness of the deck is increased due to the pre-stressing of the steel

reinforcement. The updated propagation constants and free waves are shown in table 1 and in figure 10, respectively. A better agreement between the identified and updated free wave characteristics is obtained.

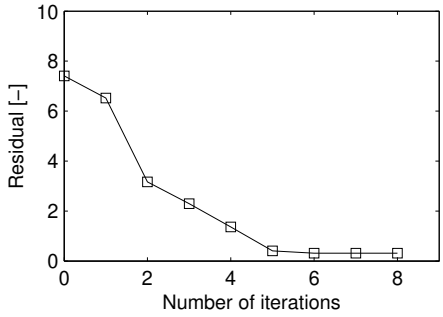

Figure 9: The residual of the objective function for the updating of the preliminary unit model.

Frequency	$\bar{\mu}_{\mathrm{N1}}$ [-]	μ_{N1} [-]	μ^*_{N1} [-]
38 Hz	$0.7330 + 2.0586i$	$0.1768 + 3.3010i$ (62.3%)	$0.7222 + 2.1786i$ (5.5%)
39 Hz	$0.6250 + 2.4098i$	$0.1378 + 3.6634i$ (54.0%)	$0.7235 + 2.5162i$ (5.8%)
40 Hz	$0.5591 + 2.8299i$	$0.1377 + 4.0203i$ (43.8%)	$0.7316 + 2.8446i$ (6.0%)
41 Hz	$0.6324 - 3.0734i$	$0.1488 - 1.9011i$ (40.4%)	$0.7479 - 3.1194i$ (4.0%)
42 Hz	$0.7350 - 2.8837i$	$0.2210 - 1.5083i$ (49.3%)	$0.7727 - 2.8127i$ (2.7%)
43 Hz	$0.6673 - 2.6902i$	$0.2926 - 1.4450i$ (46.9%)	$0.7973 - 2.5225i$ (7.7%)
44 Hz	$0.5653 - 2.3840i$	$0.1762 - 1.0256i$ (57.7%)	$0.8134 - 2.2329i$ (11.9%)

Table 1: The propagation constants of the negative going free waves identified from the experiment $\bar{\mu}_{\mathrm{N1}}$, calculated from the preliminary FE model μ_{N1} and the updated FE model μ^*_{N1}. The values between the brackets indicate the relative error between the identified and the calculated propagation constants.

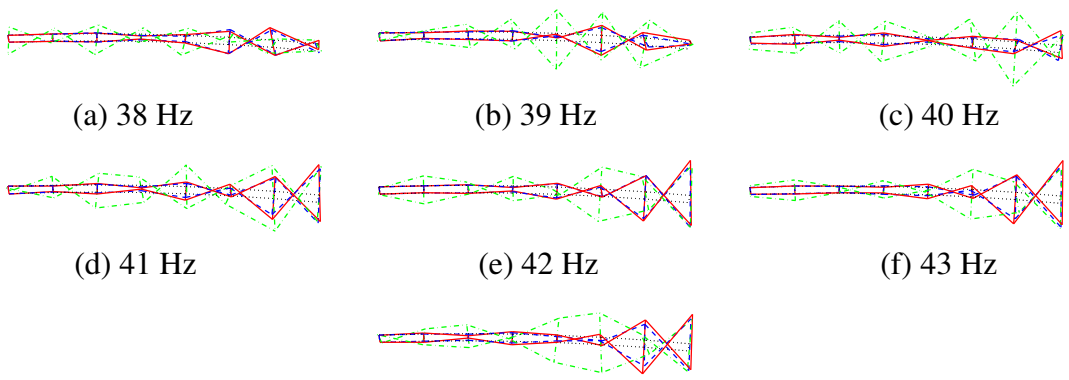

(a) 38 Hz (b) 39 Hz (c) 40 Hz

(d) 41 Hz (e) 42 Hz (f) 43 Hz

(g) 44 Hz

Figure 10: The negative going free waves identified from the measurements (solid lines), calculated from the preliminary (dot-dashed lines) and updated model (dashed lines); (a)-(g): at frequencies 38 Hz to 44 Hz.

In order to validate the updating results, the frequency response functions (FRFs) representing the acceleration responses are calculated using the preliminary and updated finite element model and compared to the measured ones. The measurement was conducted where the hammer excitation was applied at the left side end of zone 3 and the responses were measured at few bays, as shown in figure 11. The measured and calculated FRFs at bay 08, 09 and 10 in the frequency between 0 Hz and 45 Hz are shown in figure 12. The FRFs zoomed between 0 Hz and 10 Hz are plotted in figure 13. At the measurement location on bay 08 closest to the excitation, the updated model gives a good prediction of the FRF. It also gives a good prediction of the FRFs at the other measured locations below 9 Hz. However, the preliminary and updated solid models do not predict very well the response on bays 09 and 10 above 9 Hz when the free waves propagate across one unit and two units, respectively. It is also observed that the FRFs on bays 09 and 10 calculated from the updated solid model are generally smaller than those of the preliminary solid model. One reason is that the damping factor used in the updated model is larger than the one in the preliminary model. In general, damping of bridges is difficult to be represented in numerical models. It varies with the vibration frequencies, which is not considered in the modeling. The inaccurate modeling of damping may be one reason for the discrepancies between the measured and calculated FRFs. It is also noted that the estimation of the experimental FRFs might not be accurate especially for the locations measured far away from the excitation due to the influence of noise.

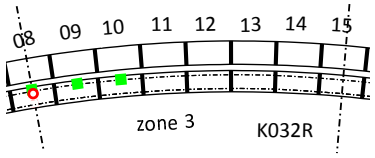

Figure 11: The excitation location (circle) and the measurement locations (squares) for the validation of the model updating results.

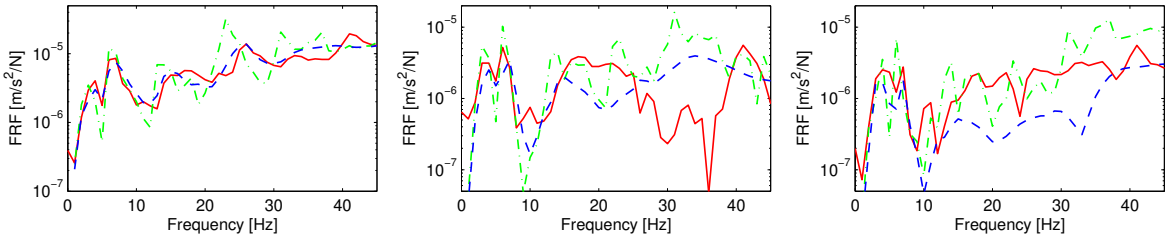

Figure 12: The frequency response function between 0 Hz and 45 Hz in z-direction measured from the experiment (solid lines), calculated from the preliminary (dot-dashed lines) and updated (dashed lines) solid model.

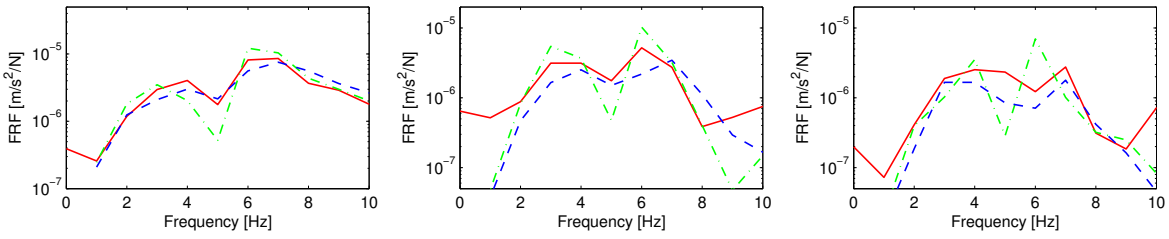

Figure 13: The frequency response function between 0 Hz and 10 Hz in z-direction measured from the experiment (solid lines), calculated from the preliminary (dot-dashed lines) and updated (dashed lines) solid model.

6 CONCLUSIONS

Following the method of free wave characteristics-based model updating for periodic structures, measurements have been conducted on the multi-span quasi-periodic viaduct. The free wave characteristics have been identified from the measurements and used to update the finite element model. It is found that the updated model leads to a much better prediction of the free wave characteristics that match well with the identified ones. It also gives generally good predictions on the frequency response functions. The feasibility of free wave characteristics-based model updating is validated though this case study.

ACKNOWLEDGEMENTS

The research presented in this paper has been performed within the framework of project OT/13/59 "Quantifying and reducing uncertainty in structural dynamics", funded by the Research Council of KU Leuven. The financial support of KU Leuven is gratefully acknowledged. The second, third and last author are members of the KU Leuven-BOF PFV/10/002 OPTEC-Optimization in Engineering Center. The authors would also like to thank Jeffrey Depauw and Dieter Van Boeckel of the THV KW A11 for providing access to the viaduct and their support in the practical organization of the measurements.

REFERENCES

[1] L. Brillouin. *Wave propagation in periodic structures: electric filters and crystal lattices*. MacGraw-Hill, New York, 1946.

[2] D. Dooms, G. De Roeck, G. Degrande, G. Lombaert, M. Schevenels, and S. François. StaBIL: A finite element toolbox for MATLAB. Technical Report BWM-2009-20, Department of Civil Engineering, KU Leuven, October 2009.

[3] M. Friswell and J. Mottershead. *Finite element model updating in structural dynamics*. Kluwer Academic Publishers, Dordrecht, The Netherlands, 1995.

[4] C.-P. Fritzen, D. Jennewein, and T. Kiefer. Damage detection based on model updating methods. *Mechanical Systems and Signal Processing*, 12(1):163–186, 1998.

[5] L. Junyi and D.S. Balint. An inverse method to determine the dispersion curves of periodic structures based on wave superposition. *Journal of Sound and Vibration*, 350:41–72, 2015.

[6] R.S. Langley. The response of two-dimensional periodic structures to point harmonic forcing. *Journal of Sound and Vibration*, 197(4):447–469, 1996.

[7] D.J. Mead. A general theory of harmonic wave propagation in linear periodic systems with multiple coupling. *Journal of Sound and Vibration*, 27(2):235–260, 1973.

[8] D.J. Mead. The forced vibration of one-dimensional multi-coupled periodic structures: An application to finite element analysis. *Journal of Sound and Vibration*, 319:282–304, 2009.

[9] E. Simoen, G. De Roeck, and G Lombaert. Dealing with uncertainty in model updating for damage assessment: A review. *Mechanical Systems and Signal Processing*, 56–57:123–149, 2015.

[10] J. Zhang, K. Maes, G. De Roeck, E. Reynders, C. Papadimitriou, and G. Lombaert. Optimal sensor placement for multi-setup modal analysis of structures. *Journal of Sound and Vibration*, 401:214–232, 2017.

[11] J. Zhang, E. Reynders, G. De Roeck, and G. Lombaert. Model updating of periodic structures based on free wave characteristics. *Journal of Sound and Vibration*, 442:281–307, 2018.

COMPDYN 2019
7th ECCOMAS Thematic Conference on
Computational Methods in Structural Dynamics and Earthquake Engineering
M. Papadrakakis, M. Fragiadakis (eds.)
Crete, Greece, 24-26 June 2019

INVERSE IDENTIFICATION OF BUFFETING AND SELF-EXCITED WIND LOADS ON THE HARDANGER BRIDGE FROM ACCELERATION DATA

Øyvind W. Petersen[1], Ole Øiseth[1], Torodd S. Nord[1] and E. Lourens[2]

[1] NTNU, Norwegian University of Science and Technology
7030 Trondheim, Norway
e-mail: {oyvind.w.petersen,ole.oiseth,torodd.nord}@ntnu.no

[2] Delft University of Technology
2628 CN Delft, The Netherlands
e-mail: e.lourens@tudelft.nl

Keywords: suspension bridge, structural monitoring, force identification, Kalman filter.

Abstract. *The traditional wind load assessment for long-span bridges rely on assumed models for the wind field and aerodynamic coefficients from wind tunnel tests, which usually introduces some uncertainties. It is therefore desired to develop tools that can utilize full-scale vibration response data from existing bridges in order to study the wind loading in detail for in-situ conditions. This paper presents a novel case study of inverse identification of dynamic wind loads on the 1310 m long Hardanger bridge, a suspension bridge equipped with a network of accelerometers. The identification method used is an extented Kalman-type filter for joint input, state, and parameter estimation. A system model considering the still-air modes in addition to a quasi-steady submodel for the self-excited forces of the bridge is presente. The coefficients for self-excited lift and pitching moment are considered unknown and are jointly estimated with the buffeting forces.*

1 INTRODUCTION

For very long and slender bridges, aerodynamic performance often becomes the critical factor in the design [1]. Hence, it is important to understand the dynamic response behavior under wind excitation. In this arena, it is commonly accepted that the theories behind buffeting forces due to turbulence [2] and self-excited forces induced by the motion of structure [3] are governing. In addition to this comes static wind pressures and vortex-shedding [4, 5], but these are not the focus of this contribution. The calculation of the buffeting and self-excited forces involves the use of aerodynamic coefficients or functions, which in today's practice often are obtained from series of wind tunnel tests. Alternatively, simulations based on computational fluid dynamics can be performed [6, 7], with the drawback of requiring immense computational power. The numerical and small-scale experiments involve some uncertainties and simplifications, and sometimes it can be beneficial to learn directly from existing bridges in their operating environment.

In recent years, the focus on structural health monitoring (SHM) have given engineers an abundance of full-scale data from long-span bridges. This full-scale data can be valuable since it contains information on the behavior of the bridge in the complex conditions that occur in reality. It is therefore desired to use such data to explore the ability for testing and validation of the models for the wind loading and aerodynamic interaction. This can be a difficult task since the application of advanced signal processing methods can encounter some trouble due to uncertain or non-idealized conditions, disturbances, and data from limited sensors.

One available tool to reduce the dynamic load uncertainties is the use of inverse force identification methodologies. Herein, the excitation forces are considered unknown and are estimated from limited output response measurements, typically accelerations. Although many techniques have recently been proposed in the literature [8–18], the application of these inverse methods are not well-explored for long-span bridges. There is therefore a need to test the available methods to get experience on the actual performance under realistic conditions.

In this work, the apply the input and state estimator in [8] to study the estimation of wind loads. This Kalman-type algorithm, which is an extended version of earlier algorithms [19, 20], allows for an extension to estimation of unknown system parameters. The method is tested for measurement data from a long-span suspension bridge. In the presented framework, the states are the modal responses, the unknown inputs are the buffeting forces and the uncertain parameters are quasi-steady coefficients related to the self-excitation of the bridge box girder under wind loading.

2 THEORY

2.1 Equations for the wind-induced dynamic response

This section derives a state-space formulation for the bridge dynamics, taking into account a quasi-steady form of self-excitation leading to aerodynamic stiffness and damping. We assume the following equations of motion in a FE-format for the response $\mathbf{u}(t) \in \mathbb{R}^{\mathrm{n_{DOF}}}$:

$$\mathbf{M}_0\ddot{\mathbf{u}}(t) + \mathbf{C}_0\dot{\mathbf{u}}(t) + \mathbf{K}_0\mathbf{u}(t) = \mathbf{f}_{\mathrm{b}}(t) + \mathbf{f}_{\mathrm{se}}(t) \tag{1}$$

where $\mathbf{f}_{\mathrm{b}}(t)$ are the buffeting forces and $(\cdot)_0$ denotes still-air properties. The self-excited forces $\mathbf{f}_{\mathrm{se}}(t)$ depend on the displacement and velocity motion of the structure, and is dealt with later in this section. A modal truncation ($\mathbf{u}(t) = \mathbf{\Phi}\mathbf{z}(t)$) yields the reduced-order representation for the

modal coordinate vector $\mathbf{z}(t) \in \mathbb{R}^{n_m}$:

$$\ddot{\mathbf{z}}(t) + 2\boldsymbol{\Xi}\boldsymbol{\Omega}\dot{\mathbf{z}}(t) + \boldsymbol{\Omega}^2\mathbf{z}(t) = \boldsymbol{\Phi}^{\mathrm{T}}\mathbf{f}_{\mathrm{b}}(t) + \boldsymbol{\Phi}^{\mathrm{T}}\mathbf{f}_{\mathrm{se}}(t) \tag{2}$$

$\boldsymbol{\Omega}$ and $\boldsymbol{\Xi} \in \mathbb{R}^{n_m}$ are diagonal matrices that contain the still-air natural frequencies and damping ratios. By introducing the modal state variable $\mathbf{x}(t) = [\mathbf{z}(t)^{\mathrm{T}} \quad \dot{\mathbf{z}}(t)^{\mathrm{T}}]^{\mathrm{T}} \in \mathbb{R}^{2n_m}$, Eq. 2 can be cast into state-space form. Furthermore, the force vector $\mathbf{f}_{\mathrm{se}}(t)$ is set equal to $\mathbf{H}_{\mathrm{se,d}}(t,\boldsymbol{\epsilon})\boldsymbol{\Phi}\mathbf{z}(t) + \mathbf{H}_{\mathrm{se,v}}(t,\boldsymbol{\epsilon})\boldsymbol{\Phi}\dot{\mathbf{z}}(t)$, a transformation that is explained later. The time-evolution of the system then becomes:

$$\dot{\mathbf{x}}(t) = \Bigg(\begin{bmatrix} \mathbf{0} & \mathbf{I} \\ -\boldsymbol{\Omega}^2 & -2\boldsymbol{\Xi}\boldsymbol{\Omega} \end{bmatrix} + \begin{bmatrix} \mathbf{0} & \mathbf{0} \\ \boldsymbol{\Phi}^{\mathrm{T}}\mathbf{H}_{\mathrm{se,d}}(t,\boldsymbol{\epsilon})\boldsymbol{\Phi} & \boldsymbol{\Phi}^{\mathrm{T}}\mathbf{H}_{\mathrm{se,v}}(t,\boldsymbol{\epsilon})\boldsymbol{\Phi} \end{bmatrix} \Bigg)\mathbf{x}(t) + \begin{bmatrix} \mathbf{0} \\ \mathbf{I} \end{bmatrix} \boldsymbol{\Phi}^{\mathrm{T}}\mathbf{f}_{\mathrm{b}}(t) \tag{3}$$

or in compact notation:

$$\dot{\mathbf{x}}(t) = \mathbf{A}_{\mathrm{c}}(t,\boldsymbol{\epsilon})\mathbf{x}(t) + \mathbf{B}_{\mathrm{c}}\boldsymbol{\Phi}^{\mathrm{T}}\mathbf{f}_{\mathrm{b}}(t) \tag{4}$$

It is noted this results in a system which is linear, but time variant. When considering acceleration and displacement measurements, the output vector become:

$$\mathbf{y}(t) = \mathbf{S}_{\mathrm{a}}\ddot{\mathbf{u}}(t) + \mathbf{S}_{\mathrm{d}}\mathbf{u}(t) = \mathbf{G}_{\mathrm{c}}(t,\boldsymbol{\epsilon})\mathbf{x}(t) + \mathbf{J}_{\mathrm{c}}\boldsymbol{\Phi}^{\mathrm{T}}\mathbf{f}_{\mathrm{b}}(t) \tag{5}$$

with corresponding matrices:

$$\mathbf{G}_{\mathrm{c}}(t,\boldsymbol{\epsilon}) = \mathbf{S}_{\mathrm{a}}\boldsymbol{\Phi}\begin{bmatrix} -\boldsymbol{\Omega}^2 & -2\boldsymbol{\Xi}\boldsymbol{\Omega} \end{bmatrix} + \begin{bmatrix} \mathbf{S}_{\mathrm{d}}\boldsymbol{\Phi} & \mathbf{0} \end{bmatrix} + \mathbf{S}_{\mathrm{a}}\boldsymbol{\Phi}\begin{bmatrix} \boldsymbol{\Phi}^{\mathrm{T}}\mathbf{H}_{\mathrm{se,d}}(t,\boldsymbol{\epsilon})\boldsymbol{\Phi} & \boldsymbol{\Phi}^{\mathrm{T}}\mathbf{H}_{\mathrm{se,v}}(t,\boldsymbol{\epsilon})\boldsymbol{\Phi} \end{bmatrix} \tag{6}$$

$$\mathbf{J}_{\mathrm{c}} = \mathbf{S}_{\mathrm{a}}\boldsymbol{\Phi} \tag{7}$$

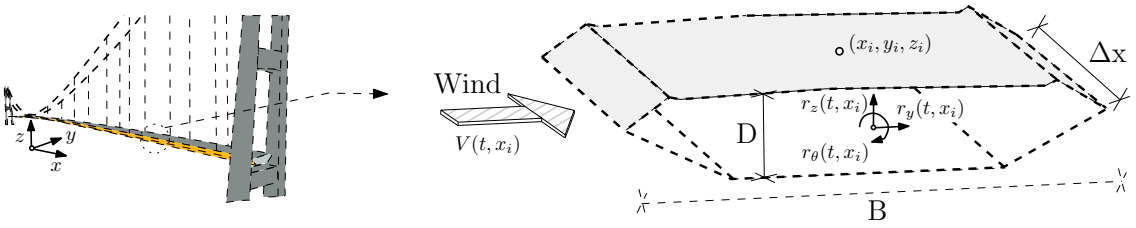

Figure 1: Suspension bridge and motion vectors of a segment of the box girder subjected to wind.

Next, the self-excited forces on the box girder are discussed. Although many model formulations are available [21], a simple memory-less model is adopted in this study for reasons of simplicity, implying the self-excited forces depend only on the structural displacement and velocity in the same time instant. Specifically, we employ a model called modified quasi-steady theory [22]. With reference to Fig. 1, the localized self-excited forces on a slice of the box girder with coordinate x_i are given in the form:

$$\begin{bmatrix} f_{\mathrm{se},y} \\ f_{\mathrm{se},z} \\ f_{\mathrm{se},\theta} \end{bmatrix} = \frac{1}{2}\rho V^2 B\Delta x\Bigg(\begin{bmatrix} p_4\frac{1}{B} & p_6\frac{1}{B} & p_3 \\ h_6\frac{1}{B} & h_4\frac{1}{B} & h_3 \\ a_6 & a_4 & a_3 B \end{bmatrix} \begin{bmatrix} r_y \\ r_z \\ r_\theta \end{bmatrix} + \begin{bmatrix} p_1\frac{1}{V} & p_5\frac{1}{V} & p_2\frac{B}{V} \\ h_5\frac{1}{V} & h_1\frac{1}{V} & h_2\frac{B}{V} \\ a_5\frac{B}{V} & a_1\frac{B}{V} & a_2\frac{B^2}{V} \end{bmatrix} \begin{bmatrix} \dot{r}_y \\ \dot{r}_z \\ \dot{r}_\theta \end{bmatrix} \Bigg) \tag{8}$$

or in compact notation:

$$\mathbf{f}_{\mathrm{se}}(t,x_i) = \mathbf{H}_{\mathrm{d}}(t,x_i,\boldsymbol{\epsilon})\mathbf{r}(t,x_i) + \mathbf{H}_{\mathrm{v}}(t,x_i,\boldsymbol{\epsilon})\dot{\mathbf{r}}(t,x_i) \tag{9}$$

where the parameter set $\boldsymbol{\epsilon} = [a_1 \dots a_6 \quad h_1 \dots h_6 \quad p_1 \dots p_6]^{\mathrm{T}}$ consist of 18 quasi-steady coefficients. This corresponds to modeling the well-established aerodynamic derivatives as functions proportional to $(\frac{B\omega}{V})^{-1}$ or $(\frac{B\omega}{V})^{-2}$ [22], where $\omega = 2\pi f$ is the angular frequency. In the presented framework, the mean wind velocity $V(t, x_i)$ is allowed to vary with time, although the notation V is used for brevity. The span is divided into M equally spaced nodal points with coordinates $\{x_1, \dots, x_M\}$. Using matrices $\mathbf{S}_i \in \mathbb{R}^{3\times \mathrm{n_{DOF}}}$ to select $\mathbf{r}(t, x_i)$ from the larger vector $\mathbf{u}(t)$, the vector $\mathbf{f}_{\mathrm{se}}(t)$ in Eq. 1 is now taken as the lumped sum of the contributions from all M nodes:

$$\begin{aligned}
\mathbf{f}_{\mathrm{se}}(t) = \sum_{i=1}^{M} \mathbf{S}_i^{\mathrm{T}} \mathbf{f}_{\mathrm{se}}(t, x_i) &= \sum_{i=1}^{M} \mathbf{S}_i^{\mathrm{T}} \big(\mathbf{H}_{\mathrm{d}}(t, x_i, \boldsymbol{\epsilon}) \mathbf{r}(t, x_i) + \mathbf{H}_{\mathrm{v}}(t, x_i, \boldsymbol{\epsilon}) \dot{\mathbf{r}}(t, x_i) \big) \\
&= \sum_{i=1}^{M} \mathbf{S}_i^{\mathrm{T}} \big(\mathbf{H}_{\mathrm{d}}(t, x_i, \boldsymbol{\epsilon}) \mathbf{S}_i \mathbf{u}(t) + \mathbf{H}_{\mathrm{v}}(t, x_i, \boldsymbol{\epsilon}) \mathbf{S}_i \dot{\mathbf{u}}(t) \big) \\
&= \sum_{i=1}^{M} \mathbf{S}_i^{\mathrm{T}} \mathbf{H}_{\mathrm{d}}(t, x_i, \boldsymbol{\epsilon}) \mathbf{S}_i \boldsymbol{\Phi} \mathbf{z}(t) + \sum_{i=1}^{M} \mathbf{S}_i^{\mathrm{T}} \mathbf{H}_{\mathrm{v}}(t, x_i, \boldsymbol{\epsilon}) \mathbf{S}_i \boldsymbol{\Phi} \dot{\mathbf{z}}(t) \\
&= \mathbf{H}_{\mathrm{se,d}}(t, \boldsymbol{\epsilon}) \boldsymbol{\Phi} \mathbf{z}(t) + \mathbf{H}_{\mathrm{se,v}}(t, \boldsymbol{\epsilon}) \boldsymbol{\Phi} \dot{\mathbf{z}}(t)
\end{aligned} \tag{10}$$

where the definitions of the (time and) parameter-dependent matrices $\mathbf{H}_{\mathrm{se,d}}(t, \boldsymbol{\epsilon})$ and $\mathbf{H}_{\mathrm{se,v}}(t, \boldsymbol{\epsilon}) \in \mathbb{R}^{\mathrm{n_{DOF}} \times \mathrm{n_{DOF}}}$ now are clear. A discretization in time ($t_k = k\Delta t$) of Eq. 4 and 5 now gives the following system equations:

$$\mathbf{x}_{k+1} = \mathbf{A}_{\mathrm{d}}(t_k, \boldsymbol{\epsilon}_k) \mathbf{x}_k + \mathbf{B}_{\mathrm{d}} \mathbf{p}_k \tag{11}$$

$$\mathbf{y}_k = \mathbf{G}_{\mathrm{d}}(t_k, \boldsymbol{\epsilon}_k) \mathbf{x}_k + \mathbf{J}_{\mathrm{d}} \mathbf{p}_k \tag{12}$$

where the substitution $\mathbf{p}_k = \boldsymbol{\Phi}^{\mathrm{T}} \mathbf{f}_{\mathrm{b}}(t_k)$ define the buffeting loads in the modal space. No parametric model is introduced for the buffeting loads or the turbulence. Provided that the wind velocity, the parameters, and the modal buffeting loads were known, the system output response could be straightforwardly solved from Eq. 11 and 12 for some given initial conditions. However, these are all, except the wind velocity, treated as unknown quantities; the estimation methodology is discussed in the next section.

2.2 Equations for the identification problem

The goal is to jointly estimate the inputs, states and the parameters for this system. The parameters are augmented into the state vector, resulting in the following final model of the dynamics:

$$\begin{bmatrix} \mathbf{x}_{k+1} \\ \boldsymbol{\epsilon}_{k+1} \end{bmatrix} = \begin{bmatrix} \mathbf{A}_{\mathrm{d}}(t_k, \boldsymbol{\epsilon}_k) & \mathbf{0} \\ \mathbf{0} & \mathbf{I} \end{bmatrix} \begin{bmatrix} \mathbf{x}_k \\ \boldsymbol{\epsilon}_k \end{bmatrix} + \begin{bmatrix} \mathbf{B}_{\mathrm{d}} \\ \mathbf{0} \end{bmatrix} \mathbf{p}_k + \begin{bmatrix} \mathbf{w}_k \\ \boldsymbol{\mu}_k \end{bmatrix} \tag{13}$$

$$\mathbf{y}_k = \begin{bmatrix} \mathbf{G}_{\mathrm{d}}(t_k, \boldsymbol{\epsilon}_k) & \mathbf{0} \end{bmatrix} \begin{bmatrix} \mathbf{x}_k \\ \boldsymbol{\epsilon}_k \end{bmatrix} + \mathbf{J}_{\mathrm{d}} \mathbf{p}_k + \mathbf{v}_k \tag{14}$$

According to principles from Kalman filtering, this model includes stochastic white noise on the modal states ($\mathbf{w}_k$) and on the measurements ($\mathbf{v}_k$), as well as a fictitious driving term for the parameters ($\boldsymbol{\mu}_k$). These vectors are all assumed mutually uncorrelated, zero-mean and with covariance relations:

$$\mathbb{E}[\mathbf{w}_k \mathbf{w}_l^{\mathrm{T}}] = \mathbf{Q}_{\mathrm{w}}\, \delta_{kl}, \quad \mathbb{E}[\mathbf{v}_k \mathbf{v}_l^{\mathrm{T}}] = \mathbf{R}\, \delta_{kl}, \quad \mathbb{E}[\boldsymbol{\mu}_k \boldsymbol{\mu}_l^{\mathrm{T}}] = \mathbf{Q}_{\mu}\, \delta_{kl} \tag{15}$$

Figure 2: The Hardanger bridge
(photo: Ø.W. Petersen/NTNU)

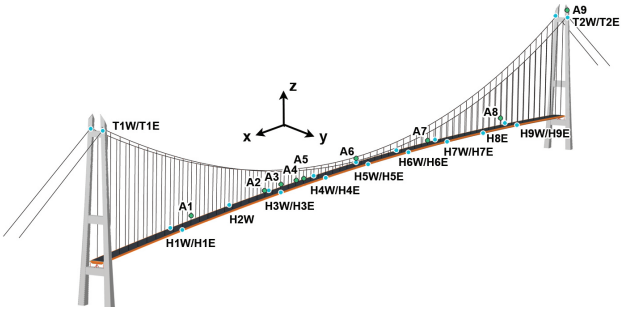

Figure 3: Positions of the installed anemometers (A) and accelerometers (H,T).

This is essentially a non-linear problem since the system matrices depends on the parameters in the augmented state. We apply a Kalman-type algorithm from [8], which is termed extended joint input-state (EJIS) estimation. This is an extension of previous algorithms [19, 20] that considers minimum-variance unbiased estimation in systems with unknown inputs.

Some necessary mathematical conditions for the estimation should be discussed. Firstly, $\text{rank}(\mathbf{J}_\text{d}) = \text{n}_\text{m}$ is required is order to identify all n_m modal forces [23]. This condition is fulfilled for the actual system model presented later in Section 3.1. As the system matrices changes with time, the observability should formally be checked according to the theory in reference [24], which is considered future work.

3 IMPLEMENTATION FOR THE HARDANGER BRIDGE

3.1 Data from the Hardanger bridge

The practical test of the methodology is applied to data from the Hardanger bridge, a suspension bridge shown in Fig. 2. In this study, the bridge is modelled with $\text{n}_\text{m} = 19$ vibration modes from a FE model [25, 26]. Fig. 4 shows the shape of the modes along the main span together with the natural frequencies and damping ratios, where the naming convention is according to the dominant motion of each mode: H1-H5 (horizontal), V1-V9 (vertical), T1-T2 (torsional), P1-P2 (pylon) and M1 (mixed). As discussed in [26, 27], the number of modes in the reduced-order model for long-span bridges (in inverse estimation) is mainly limited by the necessary criterion that $\text{rank}(\mathbf{J}_\text{d}) = \text{n}_\text{m}$; more acceleration sensors are needed to be able to identify more modal forces.

This bridge have 20 triaxial accelerometers for measuring the dynamic response, and eight anemometers that measures wind velocities in the main span [28], as shown in Fig. 3. The details of the sensors are given in references [26, 28].

A measurement data set with duration 60 min ($\Delta t = 0.1$ s) is studied. The direction of the wind is approximately normal to the bridge deck throughout this period. The span of the bridge is discretized into $M = 65$ points ($\Delta x \approx 20$ m). First, the mean wind velocity for the eight anemometer measurements is found by using 10 minute moving averages. Then, linear interpolation is used to estimate the field $V(x,t)$ between the anemometers, resulting in the time-spatial distribution in Fig. 5. Inhomogeneous features in the wind field is not uncommon for this bridge location [29], and in this case an apparent trend of higher velocities for one part of the bridge is observed. Although robust testing for (non-)stationarity of time series generally is difficult, the mean wind velocity could intuitively also be said to have weakly non-stationary features for this 60 minute period. This is not a direct problem, however, as no stationarity assumptions are imposed on the loading or dynamic behavior in the EJIS estimation.

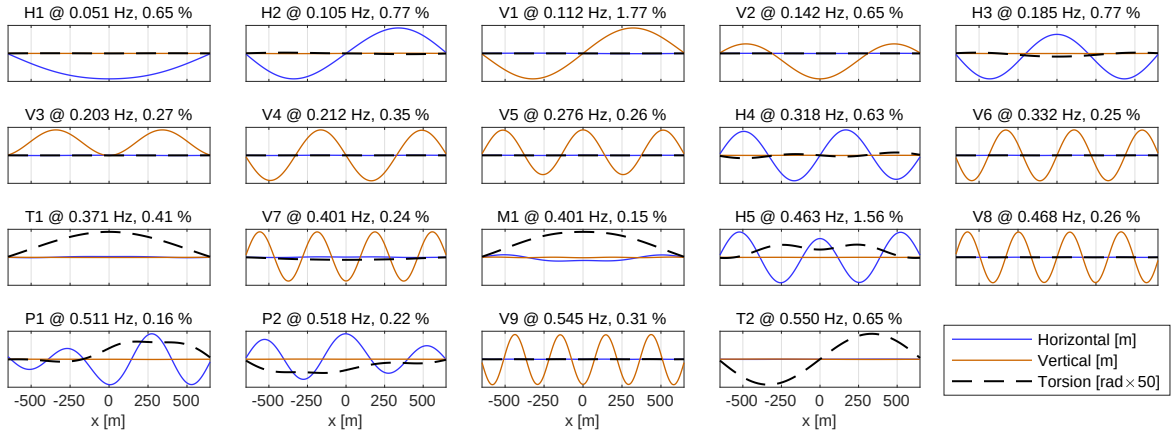

Figure 4: Horizontal, vertical and torsional deflection of the mode shapes along the main span.

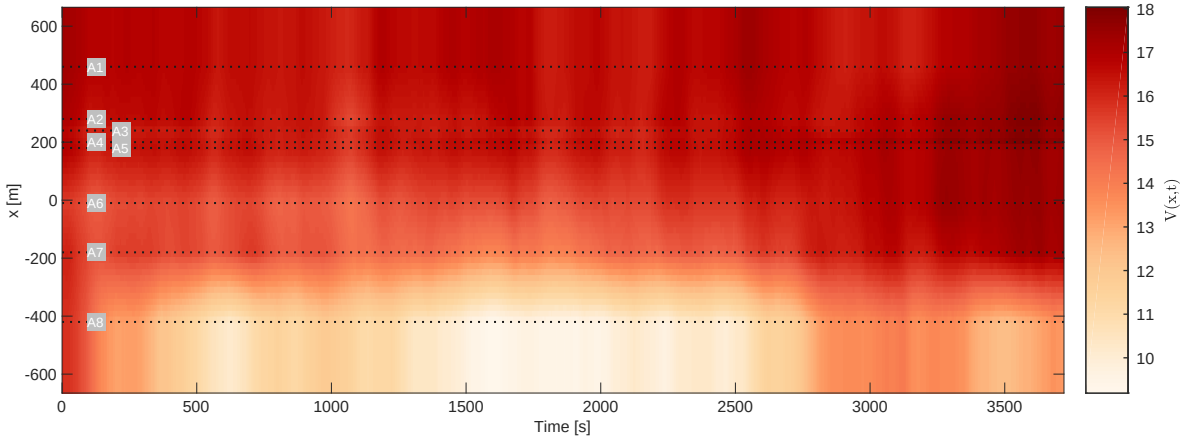

Figure 5: Estimated time-spatial distribution of the mean wind velocity along the main span. The horizontal lines indicate the positions of the anemometers A1-A8. Linear interpolation is used along the x-axis, with constant end values for extrapolation beyond A1 and A8.

Some pre-processing of the output response data is necessary. A low-pass filter is applied to mitigate the content above 0.6 Hz. A subset of the acceleration response data is shown in Fig. 6 for sensors in the quarter span. In addition to the acceleration data, displacements in the form of (offline) integrated accelerations are also included in the output vector to avoid instabilities in the estimation. This also involves high-passing the displacement data at 0.01 Hz.

3.2 Estimation of inputs, states and parameters

Some initial values for the unknown quantities are also needed for the first time step in the estimation. As the conditions at time t_0 are not practically determinable, the initial guess is set to $\mathbf{x}_0, \mathbf{p}_0 = \mathbf{0}$. For the parameters, the initial values ($\boldsymbol{\epsilon}_0$) are set to values given in Table 1, which are estimated from wind tunnel experiments [30]. The corresponding initial covariances are set to $\mathbf{P}_0^{\mathbf{x}} = \mathbf{I}$, $\mathbf{P}_0^{\boldsymbol{\mu}} = 10^{-2}\,\mathbf{I}$, $\mathbf{P}_0^{\mathbf{p}} = \mathbf{I}$.

After some trials, it was found that estimation of all 18 parameters lead to some unrealistic results. For this type of bridge, it is well-known that not all the self-excitation coefficients are

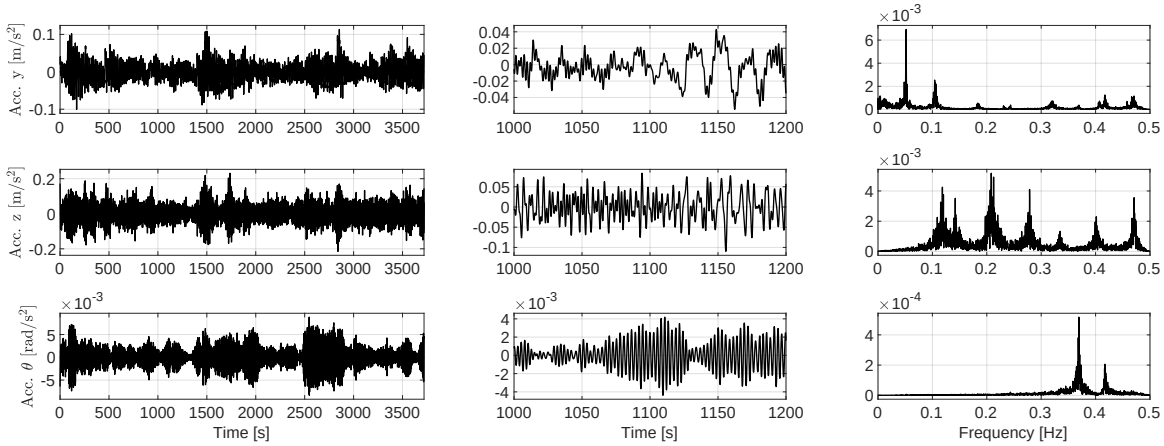

Figure 6: Acceleration response in the quarter span. The measurements have been transformed into the horizontal (y), vertical (z) and torsional (θ) motions of the box girder center to show the contributions of the different modes.

Quasi steady parameter					
$a_1 = -0.852,$	$a_2 = -0.312,$	$a_3 = 0.907,$	$a_4 = -0.048,$	$a_5 = -0.015,$	$a_6 = 0.007$
$h_1 = -2.870,$	$h_2 = -0.079,$	$h_3 = 3.062,$	$h_4 = -0.379,$	$h_5 = 0.813,$	$h_6 = -0.055$
$p_1 = -0.312,$	$p_2 = -0.051,$	$p_3 = -0.030,$	$p_4 = 0.004,$	$p_5 = -0.247,$	$p_6 = -0.024$

Table 1: Parameters values from wind tunnel testing of the bridge section.

equally important. It was therefore chosen to reduce the parameter set to the four coefficients a_1, a_2, h_1 and h_2 (i.e., the vertical-torsional coupled damping in Eq. 8). These are deemed the most important contributors for streamlined cross sections. The remaining 14 parameters were set to fixed values from Table 1.

An important aspect of the estimation is the choice of covariance matrices (Eq. 15). As noted in [10], the covariance magnitudes (noise levels) could influence the results quite considerably. $\mathbf{R} = 10^{-6}\,\mathbf{I}$ is used, a level which corresponds to $1-5\%$ of the output data standard deviations. For the process noise covariance, $\mathbf{Q}_{\mathrm{w}} = 10^{-1}\,\mathbf{I}$ is set. For the parameter covariance $\mathbf{Q}_{\mu} = c_{\mu}\,\mathbf{I}$, the two scalar values $c_{\mu} = 10^{-5}$, 10^{-7} are tested, which are much less than the expected parameter order.

The identified modal forces are shown in Fig. 7 in the frequency-domain by a fast Fourier transform (FFT) of the time series, where $c_{\mu} = 10^{-7}$ was used. Characteristic to ill-conditioned problems, identification of forces generally suffer from sensitivity in the solution to errors on the model or the output data. A known practical problem is that a few so-called cable-modes that could not be included in the state-space model in reality has a small contribution to the dynamic response in the box girder [27]. This leads to some unfortunate effects visible in Fig. 7, namely a spurious contribution around the frequencies 0.24, 0.37 and 0.41 Hz in the horizontal modes. Other than this, the modal loads appear to realistically resemble the frequency-domain characteristics of buffeting forces due to turbulence. A closer examination of the time-evolution of the modal loads in light of the wind data from the anemometers is deemed future work.

Next, the attention is shifted to the parameter estimation, as shown in Fig. 8. It is seen that for $c_{\mu} = 10^{-5}$, the dynamic response or loading tend to bleed into the parameter estimate, thus $c_{\mu} = 10^{-7}$ is deemed a more suitable choice. It is expected that the parameters should be quite constant, but small time-variations could happen for changes in environmental conditions such

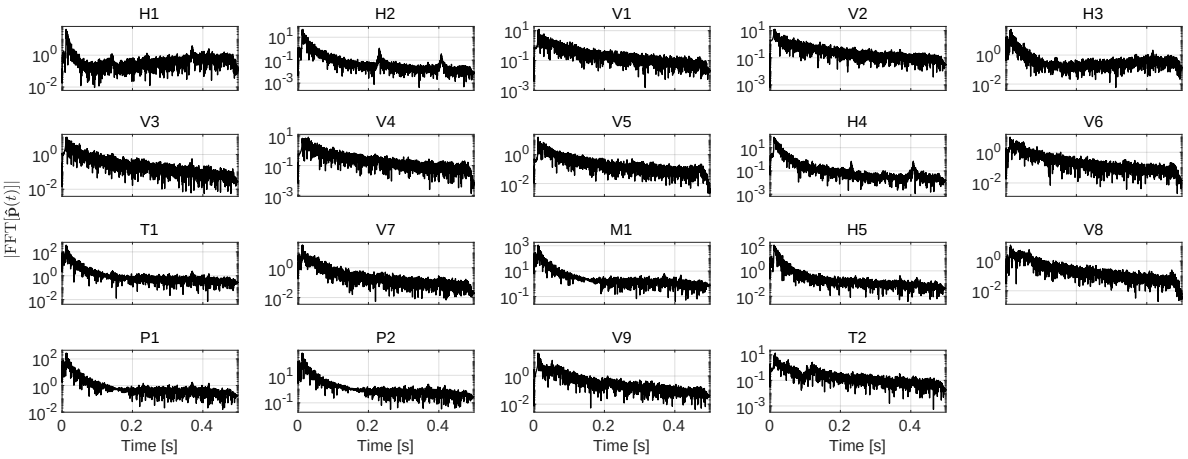

Figure 7: Estimated modal forces in the frequency-domain.

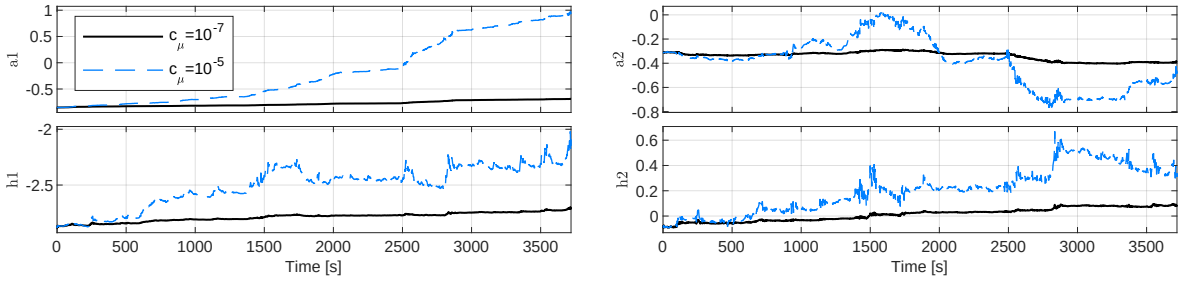

Figure 8: Estimated quasi-steady parameters.

as the wind yaw angle or mean the angle of attack. No formal convergence is achievable in the estimation, and the parameters tend to either stay at a relatively stable level or slowly change throughout the time period. A potential problem here is parameter magnitude differences, for which a shared c_μ-value introduces some compromise. As pointed out in [10], a correct parameter model is also necessary for convergence. The interpretation of the results should also factor in the individual parameter influence on the system dynamics. Generally, it is expected the most influential parameters for the system response are most accurately estimated, whereas parameters with a smaller influence could be more inaccurate since its deviations do not to the same degree affect the goodness of fit for the solution to the data. A sensitivity analysis could give some indications of the significance to trim out non-essential parameters.

3.3 Assessment of effective modal properties

A more intuitive way to assess the results is to study the effective natural frequencies and damping ratios of the system for the in-wind conditions. These can be solved from the eigenvalues of $\mathbf{A}_c(t, \boldsymbol{\epsilon})$, which are on the form $\lambda_j = -\xi_j\omega_j \pm i\omega_j\sqrt{1-\xi_j^2}$, $(\omega_j = 2\pi f_j)$. The modal properties will be time-varying since they are dependent on the mean wind velocity and the quasi-steady parameters, and Fig. 9 and 10 shows the evolution. Herein, it is the vertical and torsional modes that are most interesting, as changes in the horizontal modes mainly are driven by the assigned a priori values from Table 1.

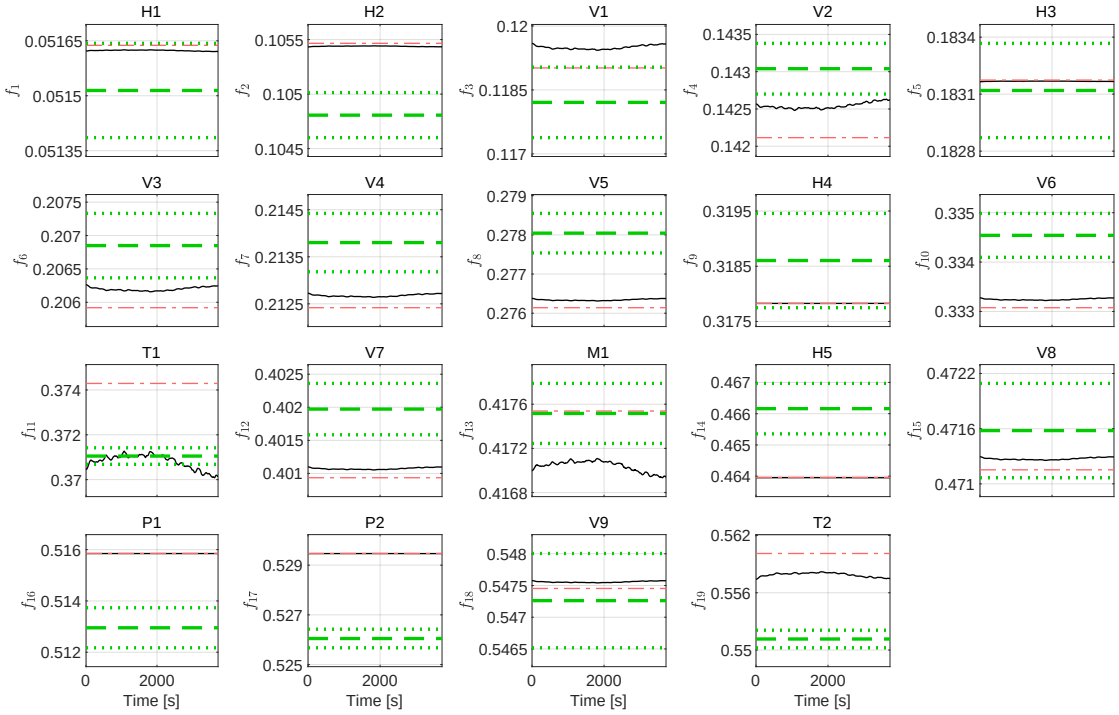

Figure 9: Evolution of natural frequencies (f in Hz) from the parameter estimation. The red lines denote the still-air modal properties, and the green lines denote modal properties from cov-SSI with an uncertainty interval of one standard deviation.

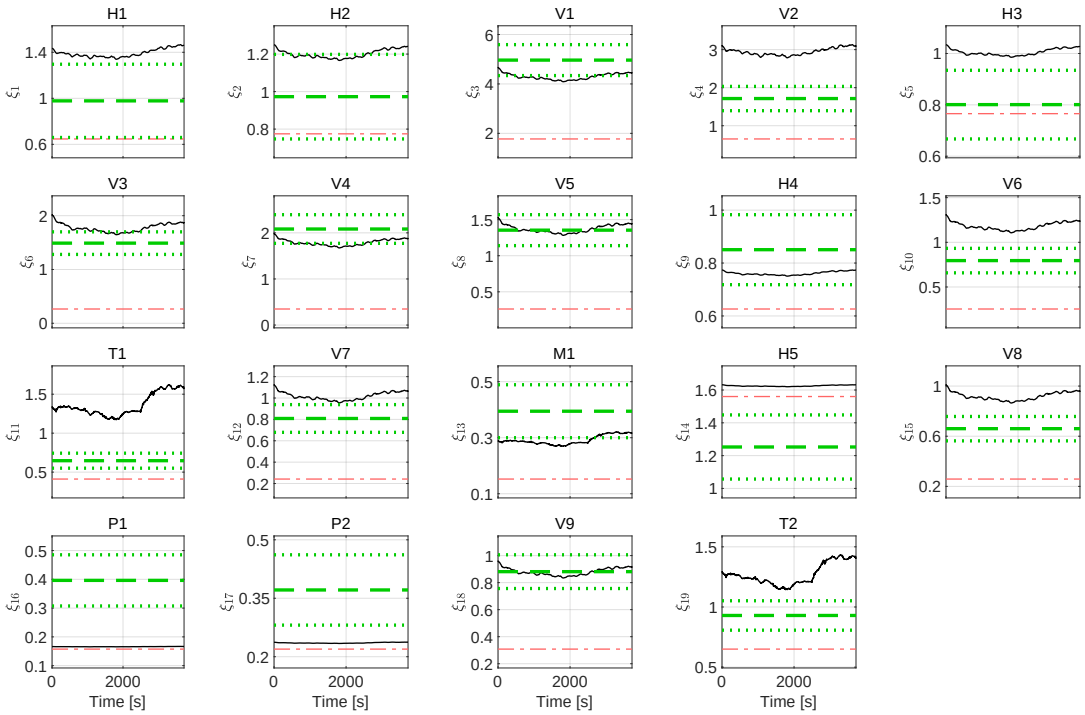

Figure 10: Evolution of damping ratios (ξ in %) from the parameter estimation. The red lines denote the still-air modal properties, and the green lines denote modal properties from cov-SSI with an uncertainty interval of one standard deviation.

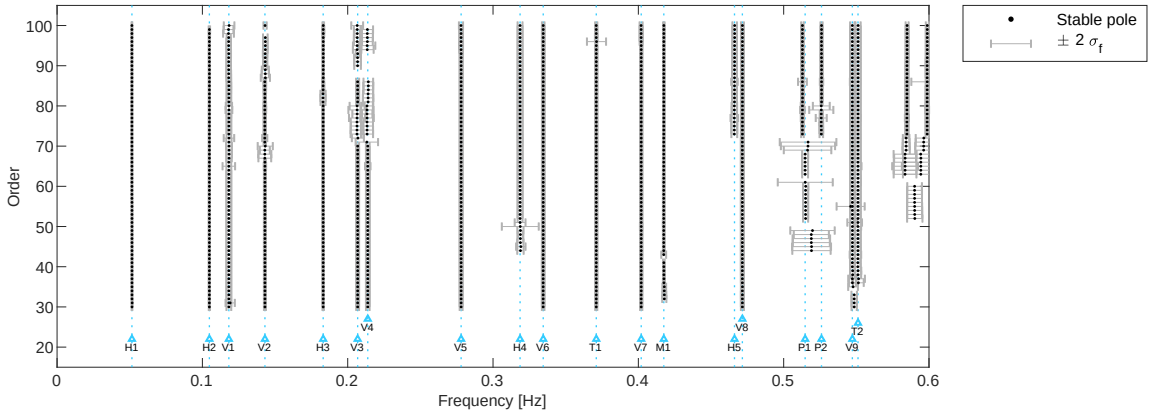

Figure 11: Stabilization diagram with uncertainty interval for the natural frequencies. Only poles with $\sigma_f/f < 0.02$ are shown. The vertical blue lines indicate the different modes.

As a reference solution, modal parameters with uncertainty bounds are identified using the tool covariance-driven stochastic subspace identification (cov-SSI) [31], supplemented by the fast implementation from [32]. Fig. 11 shows the poles and their frequency uncertainty range. These are also superimposed in Fig. 9 and 10. In general, the damping ratios for the vertical modes agree tend to agree between the inverse estimation and the cov-SSI. However, it does not for the torsional modes. The exact reason for this is hard to formalize, and these results could very well be case-dependent, as the performance of inverse estimation often highly depends on the sensor network as well as the quality of the system model. It is generally accepted that inverse estimation is difficult for systems with high-complexity dynamics, and the obtained results also support this notion.

The use of advanced computational methodology to full-scale bridge data always has some uncertainties that are difficult to eliminate. In this context, the following sources could be mentioned:

- Limited anemometer data leads to uncertainties in the interpolated wind field $V(x,t)$.
- A number of significant uncertainties can be related to the EJIS estimation itself. Herein, the Kalman-type algorithms always have an estimate uncertainty inherited from the white noise disturbance model. As shown, the noise covariance matrices influence to some degree the solution.
- Errors in the FE-based state-space model could give some incorrect estimates. Although the model is tuned [25], some temperature variations could affect the still-air natural frequencies and damping and thus also slightly the graphs in Fig. 9 and 10.
- The self-excitation of the cables could give some damping contributions. If the wind velocity at the elevation of the main cable was known, formulas similar to Eq. 8 could be included for the self-excitation of the main cable by letting its drag coefficient be an unknown parameter.
- Local traffic could give some small dynamic response contributions to the considered modes, although this would be small compared to strong winds.

4 CONCLUSIONS

The wind-induced dynamic response is an important but often uncertain aspect of long-span bridges due to uncertainties in the models for wind load prediction. This paper has presented a framework for state-space modelling of long-span bridges, taking into account the self-excited forces through a set of modified quasi-steady parameters. Using recently developed Kalman-type estimation schemes, this model can be applied for coupled input-state-parameter estimation to bridges with monitoring systems.

The methodology is tested to acceleration from the Hardanger bridge, which is modelled using 19 still-air vibration modes. Generally, the frequency-domain characteristics of the identified wind loads have features that resembles buffeting due to turbulence. Small errors on the state-space model, for example not including cable vibration modes, lead to some small but visible errors on the identified loads. A comparison with the wind measurement data could give better insight in the validity of the load estimates.

The parameter estimation for the self-excited damping works to some extent. Compared to the damping values from cov-SSI, the estimated parameters generally lead to similar effective damping for the vertical modes of the bridge deck, but not the torsional modes. Overall, the methodology show some promising results, but a robust application of inverse estimation to long-span bridges remains difficult.

REFERENCES

[1] A. Larsen. Aerodynamic aspects of the final design of the 1624 m suspension bridge across the Great Belt. *Journal of Wind Engineering and Industrial Aerodynamics*, 48 (2-3):261–285, 1993.

[2] R. Scanlan. The action of flexible bridges under wind, II: buffeting theory. *Journal of Sound and Vibration*, 60(2):201–211, 1978.

[3] R. Scanlan. The action of flexible bridges under wind, I: flutter theory. *Journal of Sound and Vibration*, 60(2):187–199, 1978.

[4] G. Diana, F. Resta, M. Belloli, and D. Rocchi. On the vortex shedding forcing on suspension bridge deck. *Journal of Wind Engineering and Industrial Aerodynamics*, 94(5): 341–363, 2006.

[5] T. Wu and A. Kareem. An overview of vortex-induced vibration (VIV) of bridge decks. *Frontiers of Structural and Civil Engineering*, 6(4):335–347, 2012.

[6] M. Sarwar, T. Ishihara, K. Shimada, Y. Yamasaki, and T. Ikeda. Prediction of aerodynamic characteristics of a box girder bridge section using the LES turbulence model. *Journal of Wind Engineering and Industrial Aerodynamics*, 96(10-11):1895–1911, 2008.

[7] T. A. Helgedagsrud, Y. Bazilevs, A. Korobenko, K. M. Mathisen, and O. A. Øiseth. Using ALE-VMS to compute aerodynamic derivatives of bridge sections. *Computers & Fluids*, 2018.

[8] Z. Wan, T. Wang, L. Li, and Z. Xu. A novel coupled state/input/parameter identification method for linear structural systems. *Shock and Vibration*, vol. 2018, 2018.

[9] F. Naets, J. Croes, and W. Desmet. An online coupled state/input/parameter estimation approach for structural dynamics. *Computer Methods in Applied Mechanics and Engineering*, 283:1167–1188, 2015.

[10] W. Song. Generalized minimum variance unbiased joint input-state estimation and its unscented scheme for dynamic systems with direct feedthrough. *Mechanical Systems and Signal Processing*, 99:886–920, 2018.

[11] S. E. Azam, V. Dertimanis, E. Chatzi, and C. Papadimitriou. Output-only schemes for joint input-state-parameter estimation of linear systems. In *Proceedings of the 1st ECCOMAS Thematic Conference on Uncertainty Quantification in Computational Sciences and Engineering (UNCECOMP 15)*, pages 497–510, 2015.

[12] Y. Ding, B. Zhao, B. Wu, X. Zhang, and L. Guo. Simultaneous identification of structural parameter and external excitation with an improved unscented kalman filter. *Advances in Structural Engineering*, 18(11):1981–1998, 2015.

[13] L. Liu, Y. Su, J. Zhu, and Y. Lei. Data fusion based EKF-UI for real-time simultaneous identification of structural systems and unknown external inputs. *Measurement*, 88:456–467, 2016.

[14] J. Chen and J. Li. Simultaneous identification of structural parameters and input time history from output-only measurements. *Computational Mechanics*, 33(5):365–374, 2004.

[15] B. Xu, J. He, R. Rovekamp, and S. J. Dyke. Structural parameters and dynamic loading identification from incomplete measurements: approach and validation. *Mechanical systems and signal processing*, 28:244–257, 2012.

[16] H. Sun and R. Betti. Simultaneous identification of structural parameters and dynamic input with incomplete output-only measurements. *Structural Control and Health Monitoring*, 21(6):868–889, 2014.

[17] Z. Lu and S. Law. Identification of system parameters and input force from output only. *Mechanical Systems and Signal Processing*, 21(5):2099–2111, 2007.

[18] V. Jayalakshmi and A. R. M. Rao. Simultaneous identification of damage and input dynamic force on the structure for structural health monitoring. *Structural and Multidisciplinary Optimization*, 55(6):2211–2238, 2017.

[19] E. Lourens, C. Papadimitriou, S. Gillijns, E. Reynders, G. De Roeck, and G. Lombaert. Joint input-response estimation for structural systems based on reduced-order models and vibration data from a limited number of sensors. *Mechanical Systems and Signal Processing*, 29:310–327, 2012.

[20] S. Gillijns and B. De Moor. Unbiased minimum-variance input and state estimation for linear discrete-time systems with direct feedthrough. *Automatica*, 43(5):934–937, 2007.

[21] I. Kavrakov and G. Morgenthal. A comparative assessment of aerodynamic models for buffeting and flutter of long-span bridges. *Engineering*, 3(6):823–838, 2017.

[22] O. Øiseth, A. Rönnquist, and R. Sigbjörnsson. Simplified prediction of wind-induced response and stability limit of slender long-span suspension bridges, based on modified quasi-steady theory: a case study. *Journal of Wind Engineering and Industrial Aerodynamics*, 98(12):730–741, 2010.

[23] K. Maes, E. Lourens, K. Van Nimmen, E. Reynders, G. De Roeck, and G. Lombaert. Design of sensor networks for instantaneous inversion of modally reduced order models in structural dynamics. *Mechanical Systems and Signal Processing*, 52:628–644, 2014.

[24] M. N. Chatzis, E. N. Chatzi, and A. W. Smyth. On the observability and identifiability of nonlinear structural and mechanical systems. *Structural Control and Health Monitoring*, 22(3):574–593, 2015.

[25] Ø. W. Petersen and O. Øiseth. Finite element model updating of a long span suspension bridge. In R. Rupakhety, S. Olafsson, and B. Bessason, editors, *Proceedings of the International Conference on Earthquake Engineering and Structural Dynamics*, pages 335–344. Springer International Publishing, 2019. ISBN 978-3-319-78187-7.

[26] Ø. W. Petersen, O. Øiseth, and E. Lourens. The use of inverse methods for response estimation of long-span suspension bridges with uncertain wind loading conditions. *Journal of Civil Structural Health Monitoring*, 9(1):21–36, 2019.

[27] Ø. W. Petersen, O. Øiseth, and E. Lourens. Investigation of dynamic wind loads on a long-span suspension bridge identified from measured acceleration data. *(submitted for journal publication)*, 2019.

[28] A. Fenerci, O. Øiseth, and A. Rønnquist. Long-term monitoring of wind field characteristics and dynamic response of a long-span suspension bridge in complex terrain. *Engineering Structures*, 147:269–284, 2017.

[29] T. M. Lystad, A. Fenerci, and O. Øiseth. Evaluation of mast measurements and wind tunnel terrain models to describe spatially variable wind field characteristics for long-span bridge design. *Journal of Wind Engineering and Industrial Aerodynamics*, 179:558–573, 2018.

[30] B. Siedziako, O. Øiseth, and A. Rønnquist. An enhanced forced vibration rig for wind tunnel testing of bridge deck section models in arbitrary motion. *Journal of Wind Engineering and Industrial Aerodynamics*, 164:152–163, 2017.

[31] E. Reynders, R. Pintelon, and G. De Roeck. Uncertainty bounds on modal parameters obtained from stochastic subspace identification. *Mechanical Systems and Signal Processing*, 22(4):948–969, 2008.

[32] M. Döhler and L. Mevel. Efficient multi-order uncertainty computation for stochastic subspace identification. *Mechanical Systems and Signal Processing*, 38(2):346–366, 2013.

COMPDYN 2019
7th ECCOMAS Thematic Conference on
Computational Methods in Structural Dynamics and Earthquake Engineering
M. Papadrakakis, M. Fragiadakis (eds.)
Crete, Greece, 24–26 June 2019

GEOMETRICALLY NONLINEAR ANALYSES OF TENSILE STRUCTURAL SYSTEMS: WIND-STRUCTURE INTERACTION.

Marco Di Giovanni[1], **Chiara Taddeo**[1].

[1] G. D'Annunzio University, School of Engineering, viale Pindaro 42, 65127, Pescara (Italy)
mardg2693@hotmail.it; chiarataddeo00@gmail.com

Abstract

Tensile structural systems as for example cables nets, suspended bridges or membranes usually have nonneglecting p-delta effects under wind action. Consequently, great displacements give a geometrically nonlinear structural behavior. In addition, the wind action is nonlinear spatially and time depending. This closely affect the dynamic interaction between loads and structure. For this reason, the calculation process needs to take into account the time-depending nonlinear response of the structure. Finally, the wind action can be critical for structural and it can induce global or local instability. Analyses has to be able to capture and to describe the instability response in term of displacements, in the case of cables net, or rotations, in the case of suspended bridges. The paper is focused on the wind – structure interaction analyses carried out by wind tunnel experiments. The wind action is generally given by wind tunnel experiments, and it is time depending. For roofs, it generally is given as pressure time histories measured by some pressure taps on the roof. The process from experiments to structural response is described using a case of study of cables net. The dynamic geometrically nonlinear analyses were performed using the TENSO non-commercial program, which can execute dynamic step-by-step integration of the nonlinear three-dimensional structure with geometric nonlinearities by the Newmark-Beta method with Rayleigh damping.

Keywords: Tensile structural systems, Non-Linear analyses, cables.

1 INTRODUCTION

Light structures, as for example tensile structures or suspended bridges, has a small ratio between structural weight and environmental or live loads. For this reason, differently from traditional reinforced concrete structures [1], they are sensitive to the snow action and in particular the wind action dynamics. The dynamic wind action can give local or global instability due to great displacements and/or rotations.

However, recently, these structural typologies are more common than it was in the past because they have a convenient cost/benefit ratio. For example, light roof are often used to cover sport arenas, meeting rooms or concert halls [2, 3]. The large use of tensile structural systems (i.e. roof or bridges) would require simplifications of calculation methods. In addition, guidelines in codes should be improved and increased.

Contrarily, codes neglects cables structures and very few information are given for unconventional shapes as for example hyperbolic paraboloid, that are commonly used for roof tensile structures, or the closed box sections similar to the Great Belt , that is commonly used for suspended bridges [4-13].

For these reasons, the most of these structures need experimental campaign in wind tunnel to be designed. Wind tunnel experiments on in-scale models investigates the structure aerodynamics (i.e. on rigid models) and aero-elasticity (i.e. on flexible models).

Aerodynamics tests are focused on pressure coefficients acquisition on the building surfaces or on the vortex shedding distribution around the buildings that is simulated as a rigid body [14-16]. Aeroelastic measurements are focused on the wind-structure dynamically interaction. In particular, for roofs, these measurements are focused on the aerodynamic damping and added masses estimation [17, 18]. For bridge, aeroelastic tests are focused on the flutter derivatives estimation [19-21].

Generally, the scientific literature proposes simplifications of experimental tests as for example simplified maps of pressure coefficients [22, 23] or parametrical studies of the structural dynamics [19]. However, the most of literature examples are focused on specific cases of study [24-38] that sometimes are not generalizable.

Some studies discuss the structural design of tensile structures following a more general view [39-44] even if they do not discuss the complete process to design a tensile structure, that start from the architecture and it continues through experiments to the structural calculation.

Non-linear analyses have to be processed using time-depending experimental data through software able to calculate the wind-structure interaction. The complexity of calculation is crucial for these kind of structures and it affects negatively their development and dissemination.

This paper aims to describe the process of applying wind tunnel measurements for non-linear structural analyses using a case of study. Only aerodynamics results are discussed here. The case of study is a cable net with hyperbolic paraboloid roof and rectangular plane.

2 STRUCTURAL REMARKS

In order to discuss geometrically non-linear analyses the case of cables net was used as examples. In particular, the hyperbolic paraboloid cables net was assumed as significant examples of cables systems.

Hyperbolic paraboloid cables net have a double curvature with two order of cables (i.e. upward and downward) that can have a different lengths and curvatures. Consequently, cables can have different areas and initial pre-stresses.

These two order of cables assume a different role under gravitational (i.e. downward) and suction (i.e. upward) loads. In fact, under gravitational loads (i.e. dead, permanent loads

and snow action), the upward cables are load bearing and the downward cables are stabilizing, under suction (i.e. wind action) is opposite. The local instability occurs if stabilizing cables reduce their sag until almost to be horizontal or if the load bearing cables exceeds the stress limit of material.

The function adopted to describe the hyperbolic paraboloid is expressed by Eq.(1), where x, y and z are respectively the spatial variables; x_0, y_0 and z_0 are the coordinates of the origin of the axes *a*, *b* and *c* are the geometric coefficients of the function. The *c* parameter was set equal to 1, making all the parabolas that lying on the surface, parallel and of identical curvature.

$$\frac{(X-x_0)^2}{a^2} - \frac{(Y-y_0)^2}{b^2} = \frac{(Z-Z_0)}{c} \quad \text{where } 1/c = 1 \tag{1}$$

It's important to precise that the initial geometry is only an initial condition and that the real geometry of the net, whiteout environmental or live loads, is defined on bases of the initial cables pre-stress, dead and permeant loads.

The environmental and live loads effect modifies again the geometry. The goal is to predict the structural geometry under extreme loads in order to exclude instability phenomena. For this reason the preliminary design of cables areas and initial pre-stress is crucial.

The pre-sizing process has the aim to estimate an initial pre-stress and areas in order to minimize the shape between un-loaded and loaded condition. This is important because the pressure coefficients evaluated in wind tunnel are measured on a fixed geometry that generally correspond to the un-loaded shape.

The cables net preliminary design can be carried out using the simplified two dimensional model named "Rope Beam" illustrated in Fig.(1). The model consist in two cables with opposite curvature connected only by vertically.

The prefixed assumptions are:

1) vertical links, in tension or in compression, are treated as a continuous membrane between the two main cables;

2) the horizontal displacements are neglected compared to the vertical ones; pretension is considered as an equivalent distributed load;

3) the system congruence is required only in the central span node;

4) the mutual actions between cables are uniformly distributed as the external load, and consequently, load-bearing and stabilizing cable have a parabolic configuration also in elastic regime [43, 44].

Eq.(2) and Eq.(3), define the load-bearing cable (C_1) and stabilizing cable (C_2) stiffness coefficients, K_{c_1} and K_{c_2}. k_1 and k_2 are the stiffness of the load-bearing cable C_1 and the stiffness of the stabilizing cable C_2, respectively, defined in Eqs.(4) and (5). A_1 and A_2, f_1 and f_2, L_1 and L_2 are area, sag and span values of the cable C_1 and C_2, respectively.

$$K_{c_1} = \frac{k_1}{k_1 + k_2} \tag{2}$$

$$K_{c_2} = \frac{k_2}{k_1 + k_2} \tag{3}$$

$$k_1 = \frac{EA_1}{l\left[1 + \frac{8}{3}\left(\frac{\bar{f}_1}{l}\right)^2 - \frac{32}{5}\left(\frac{\bar{f}_1}{l}\right)^4\right]} \tag{4}$$

$$k_2 = \frac{EA_2}{l\left[1 + \frac{8}{3}\left(\frac{\bar{f}_2}{l}\right)^2 - \frac{32}{5}\left(\frac{\bar{f}_2}{l}\right)^4\right]} \tag{5}$$

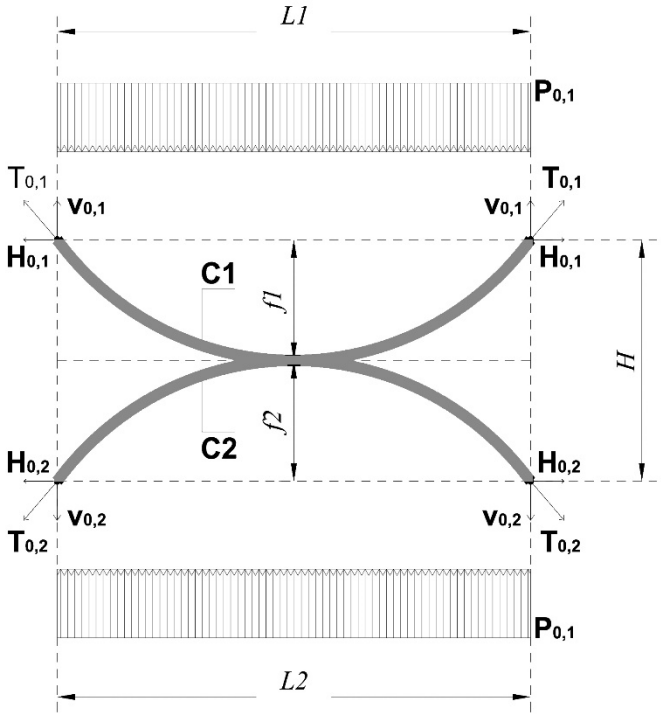

Fig.1: Rope beam, 2D structural system.

In Fig.1 $T_{0,1}$ and $T_{0,2}$ are the cables traction given by the initial pre-stress and $H_{0,1}$ and $H_{0,2}$ are their horizontal components. The horizontal components are generally much bigger than vertical ($V_{0,1}$ and $V_{0,2}$) because the curvature given by the sag/span ratio (i.e. *f1/L1* and *f2/L2*) is generally small. For this reason, cables nets need of very rigid support structures. In the preliminary design the initial pre-stress is approximated as an uniform distributed load applied on cables, upward for stabilizing cables (C2) and downward for load bearing cables (C1).

The design process almost takes into account the following load configuration:

1) Load condition 0, given by initial pre-stress only;

2) Load condition 1, given adding to condition 0 dead and permanent loads (i.e. gravitational);

3) Load condition 2, given adding to condition 1 the snow action (i.e. gravitational);

3) Load condition 3, given adding to condition 1 the wind action (i.e. upward action).

Cables areas $A_{0,1}$, $A_{0,2}$ and strain ($\epsilon_{0\ldots3,1}$, $\epsilon_{0\ldots3,2}$) are fixed iteratively matching results given by all loads conditions. In the following strain values for condition 2 are $\epsilon_{2,1}$, $\epsilon_{2,2}$ and for condition 3 $\epsilon_{3,1}$, $\epsilon_{3,2}$ for C1 and C2, respectively. The suffix "*i*" means a generic load condition, G_{p1} is the dead load, G_{p2} is the permanent load, S is the maximum snow action, W is the maximum wind suction. Like a start point the ratio $\frac{k_1}{k_2}$ between the cables stiffness is assumed equal to ΔP according Eq.(6).

$$\Delta P = \left[\frac{G_{p1} + G_{p1} + |W|}{G_{p1} + G_{p1} + S}\right] = \frac{\text{Load Condition (3)}}{\text{Load Condition (2)}} \tag{6}$$

The initial geometrical cables length $L_{0,1,geom}$ and $L_{0,2,geom}$ are given by Eqs.(7) and (8), as function of cables initial sag and span.

$$L_{0,1,geom} = L_1 \cdot \left[1 + \frac{8}{3} \cdot \left(\frac{f_1}{L_1}\right)^2 - \frac{32}{5} \cdot \left(\frac{f_1}{L_1}\right)^4\right] \quad (7)$$

$$L_{0,2,geom} = L_2 \cdot \left[1 + \frac{8}{3} \cdot \left(\frac{f_2}{L_2}\right)^2 - \frac{32}{5} \cdot \left(\frac{f_2}{L_2}\right)^4\right] \quad (8)$$

The initial cables internal traction $T_{0,1}$ and $T_{0,2}$ are given by Eqs.(9) and (10) and their horizontal component $H_{0,1}$ equal to $H_{0,2}$ are given by Eqs.(11) and (12).

$$T_{0,1} = H_{0,1}\sqrt{1 + 16\left(\frac{f_1}{L_1}\right)^2} \quad (9) \qquad T_{0,1} = H_{0,2}\sqrt{1 + 16\left(\frac{f_2}{L_2}\right)^2} \quad (10)$$

$$H_{0,1} = \frac{G_{p1}{L_1}^2}{8f_1} \quad (11) \qquad H_{0,2} = \frac{G_{p1}{L_2}^2}{8f_2} \quad (12)$$

The horizontal components $H_{i,1\ldots2}$ of traction for loads conditions 1, 2 and 3 varying as function of the cables traction and the deformed cables sag, according Eq.13. Cables are made of harmonic steel and the cables traction is in agreement with the Hook law.

$$H_{i,1} = \frac{T_{i,1}}{1 + 16\left(\frac{f_{i,1}}{L_1}\right)^2} \quad (13)$$

Step by step, cables stiffness vary as function of the deformed shape and cables strain given by loads. Eqs. (14) and (15) give the K_{C_1} and K_{C_2} expressions given by the balance between geometry deformation and applied loads ΔP.

$$K_{C_1} = \left\{\frac{\left[\frac{EA_1f_1^2}{L_1^4}\right]}{\left[\frac{EA_1f_1^2}{L_1^4}\right] + \left[\frac{E(A_2)f_2^2}{L_2^4}\right]}\right\} = \left\{\frac{1}{1 + \frac{\left[\frac{E(A_2)f_2^2}{L_2^4}\right]}{\left[\frac{EA_1f_1^2}{L_1^4}\right]}}\right\} = \left[\frac{1}{1 + \frac{1}{\Delta P}}\right] \quad (14)$$

$$K_{C_2} = \left\{\frac{\left[\frac{EA_2f_2^2}{L_2^4}\right]}{\left[\frac{EA_1f_1^2}{L_1^4}\right] + \left[\frac{E(A_2)f_2^2}{L_2^4}\right]}\right\} = \left\{\frac{1}{\frac{\left[\frac{EA_1f_1^2}{L_1^4}\right]}{\left[\frac{E(A_2)f_2^2}{L_2^4}\right]} + 1}\right\} = \left[\frac{1}{\Delta P + 1}\right] \quad (15)$$

Eq.(16) give the residue un-balance Δ that need to be iteratively minimized. As an example, Eq.(16) show the balance for condition 2.

$$\Delta = \left\{ P_{0,1} + \left[\frac{(G_{p1}+G_{p1}+S)}{\left(\frac{1}{K_{c_1}}\right)} - \frac{(G_{p1}+G_{p1})}{\left(\frac{1}{K_{c_1}}\right)} \right] \right\} - P_{2,1} = \left\{ \left[\left(\frac{8\varepsilon_{0,1} f_{0,1}}{L_1^2} \right) A_1 \right] - \left[\frac{(S)}{\left(\frac{1}{K_{c_1}}\right)} \right] \right\} - \left[\frac{8\varepsilon_{2,1} f_{2,1} A_1}{L_1^2} \right] = 0 \quad (16)$$

3 EXPERIMENTAL DATA ACQUISITION

Experimental data consist in pressure expressed in mmH_2O acquired by pressure transducers. A sampling frequency (F) and a time duration (T) of experiments are preliminary fixed based on the wind tunnel setup. Pressure series $p(P,t)$ are acquired using pressure taps distributed on the model. Teflon tubes measure pressure and send data to transducers. Transducers send electrical signals to the control system. Pressure coefficients $c_p(P,t)$ are calculated according to Eq.19. Results are pressure coefficients time histories with a number of time step equal to $T \cdot F$.

$$c_p(P,t) = \frac{p(P,t) - p_0}{\frac{1}{2}\rho V_m^2} \quad (19)$$

In Eq. 19, $p(P,t)$ is the measured pressure at point P of the roof surface, p_0 is the static pressure in the bare tunnel and ½ ρ V^2_m is the dynamic pressure measured by a pitot.

The pressure taps distribution is a crucial point of the experimental campaign. Each pressure tap represent a specific area of influence. It is obvious that a great number of pressure taps improve the aerodynamic study. However, the number of pressure taps depend on the wind tunnel setup.

The model surfaces were discretized in polygons surrounding each pressure taps. Generally, if the pressure taps distribution does not follow an orthogonal grid, Thiessen polygons are used to map surfaces. Thiessen polygons are polygons whose boundaries define the area that is closest to each point relative to all other points. The perpendicular bisectors of the lines between all points mathematically define them.

4 NON LINEAR ANALYSIS THROUGH EXPERIMENTAL DATA

For the case of cables net, the FE model is generally computed using cables elements and loads are applied on net nodes. It is important to precise that the wind tunnel pressure taps grid generally is different from the Finite Element (FE) structural models grid. Generally, the number of nodes in FE models are closely bigger than the number of pressure taps on wind tunnel models. This problem is far from negligible because it means that the numerical calculation is

affected by the experimental setup. In the case of cables net, there are two complementary approaches:

1) Experimental data sample given by pressure taps is numerically expanded make its size equal to the FE model nodes number.
2) Grid nodes (i.e. of the FE model) which are included in the same Thiessen polygon are loaded with the same experimental data.

If performed correctly, the first approach permits to obtain a more precise solution in term of lift and vertical displacements. However, the alteration of experimental data through numerical methods is not always correct. For the case of study discussed in the following, it was followed the second approach.

Cables net are non-linear structural systems and if the cables sag is between 1/10 and 1/6 of the cables span, the difference between the orthogonal direction and the vertical direction according the Cartesian System is neglected.

The wind action time history, $W(t)$, is calculated according to Eq.20.

$$W(t) = \left(\frac{1}{2}\rho V^2\right) c_p(P,t) Ai \tag{20}$$

In Eq.20 ρ is the air density assume equal to 1.25 kg/m^3, V is the wind speed in m/s, $c_p(P,t)$ is the pressure coefficient that varies on the roof and Ai is the surface of influence for the net node i-esimo.

Each node on his area of influence is loaded by a wind force time history to carry out non-linear analyses. The structural response is generally investigated estimating nodal vertical displacements time series [47].

The structural analysis program should be designed for static and dynamic analysis with step-by-step integration of nonlinear geometric three-dimensional structures. It has to contain cable and beam finite elements to permit the study of wind-structure interaction with generation of wind histories and simulation of aeroelastic phenomena [20, 48-51].

In this research, a not commercial software was used to carry out non-linear analyses though wind foresees time histories. It is named TENSO. Using TENSO, is possible to compute parabolic cables in two ways: in the first case, the cable can be divided in an appropriate number of elements that are rectilinear cable, in the second case elastic catenary configuration or parabolic cable can be used. The first case is applicable only with nodal loads. Possible applications of this methodology are suspension bridges with a distance between the hangers sufficiently small compared to the cable span length, and cables nets with a small spacing between cables compared to the maximum span length. For this kind of structures the global stiffness matrix is updated for each load step through the assembly of stiffness matrices of the elements varied according to the strain found in the previous step. In this way the software takes into account the geometric nonlinearity of the structure. As regards to the beam finite element, it is possible to choose among a beam with a uniform or a variable section. For each case it is possible to introduce prestressing actions or tractions as well as thermal loads. In particular, the beam finite element with variable section provides the calculation of ten coefficients in order to describe the area variation and the moment of inertia along the beam axis with a polynomial function. In order to evaluate the stiffness matrix, a numerical procedure based on the validity of the constitutive elastic low is used and six independent functions to describe the displacement field is used, too. At the beginning, the procedure computes the flexibility matrix of the element, applying a forces system and evaluating a displacement system using an algorithm that, step by step, computes the twelve conditions of kinematic compatibility and the balance evaluated in the previous step. The Gauss method is used for the numerical integration and Rayleigh

damping is implemented. In the case investigated a value of 5% of structural damping is used taking into account the membrane effect that increase the structural damping.

TENSO software simultaneously uses two solution methods to solve nonlinear analysis: the step by step incremental method and the interaction progressive method with the variable stiffness matrix as well as the secant method. The secant method can be thought of as a finite difference approximation of Newton's method. In TENSO, secant method is used as a check method that permits to stop the analysis with a unbalanced solution. Using the step by step incremental method, nonlinear problem can be transformed in a succession of linear problems. Each calculation step stores loads and strains history evaluated during the previous step. For each analysis step, a small enough part of load (ΔP) necessary to ensure that is possible to use the elasticity method is applied. However, this simple and classical approach presents the difficulty to evaluate the exact dimension of load step and so the exact step of analysis. A non-appropriate chosen range can cause an inexact solution. In order to solve it, TENSO uses the method with the variable stiffness matrix; this method is a vector version of the Newton-Raphson modified method about nonlinear equation systems. The Newton-Raphson procedure guarantees convergence if and only if the solution at any iteration is close to the exact solution. Therefore, even without a path-dependent nonlinearity, the incremental approach (i.e., for subsequent load steps) is sometimes required in order to obtain a solution corresponding to the final load level. If the displacements are large, the product between the stiffness matrix, evaluated on the basis of the solution of the previous step, and the displacements vector, give the internal force vector, not equilibrate with the external forces vector according to Eq.(21). In Eq.(21) K is the stiffness matrix, δ is the displacements vector, $\widetilde{P}$ is the external forces vector.

The difference between these two forces vectors (i.e. internal and external) represents the imbalance force vector, according to Eq. (22). R is the residual vector and P is the internal forces vector. Subsequently, R is applied as an external load modifying the displacement vector with a residual value of displacements $\Delta\delta$, according to Eq.(23).

$$[K]_{k+1}\{\delta\}_{k+1} = \{\tilde{P}\}_{k+1} \tag{21}$$

$$[R]_{k+1} = [\{P\} - \{\tilde{P}\}_{k+1}] \neq 0 \tag{22}$$

$$\{\Delta\delta\}_{k+1} = [K]_{k+1}^{-1}\{R\}_{k+1} \tag{23}$$

In order to solve nonlinear dynamic analyses, TENSO uses the Newmark-beta method, a numerical integration method used to solve differential equations. It is used in finite element analysis to model dynamic systems. In order to illustrate the use of this family of numerical integration methods, the solution of a linear dynamic system have to be firstly considered. In 1962 Newmark's method in matrix notation was formulated, stiffness and mass proportional damping was added, and the need for iteration by introducing the direct solution of equations at each time step was eliminated. The time dimension is represented by a set of discrete points each a time increment apart. The system is solved at each of these points in time using as data the solution at a previous time. The procedure follows these subsequent phases: reading of initial boundary conditions; assembly of the stiffness matrix, setting β and γ, Newmark method parameters that control the stability and the accuracy of the integration procedure. They are equal to ¼ and ½ respectively; assembly of the vector forces; step by step calculation with iterative process and convergence check. For each integration step, a check of the solution precision is done in order to evaluate if it is necessary to modify the integration step dimension. Generally, a more precise solution needs a very small integration step and so a higher computational work. Unbalanced loads are evaluated according to the Newmark's algorithm, as the difference between the reactions and the applied external loads. In TENSO, a correction

of this algorithm is implemented: the precision of solution is evaluated as a ratio between unbalanced loads and applied external loads for each unconstrained degree of freedom. At each integration step, unbalanced loads are added to the next load step, in order to obtain an optimal solution, [20].

5 CASE OF STUDY

The geometry discussed here as case of study is illustrated in Fig.2. Globally, it is 40 m wide and 80 m long, with a maximum height of 21.3 m. A Hyperbolic paraboloid roof made of a cable net and membrane covers the rectangular plane.

The l_1, f_1, l_2 and f_2 parameters are the upward and downward parabola sags and spans, respectively; H is the biggest height of the roof and was estimated at 1/10 of l_1 [16].

Data used to estimate the wind action on the roof, are given by aerodynamic tests carried out on a scaled model in the CRIACIV open circuit (Interuniversity Research Center on Building Aerodynamics and Wind Engineering) wind tunnel boundary layer. The CRIACIV test chamber size is 2.4 x 1.6 meters [16]. The model sizes are summarized in Table 1.

Table 1 Wind tunnel model sizes

model	l_1 [mm]	l_2 [mm]	f_1 [mm]	f_2 [mm]	H [mm]
1	400	800	27	53	213

The pressure series were acquired at a sample frequency equal to about 252 Hz for a period of nearly 30 s (i.e. 7504 time steps). The scaled wooden model was instrumented with Teflon 1.5 mm diameter tubes to acquire pressures. Totally, 95 pressure taps were located on the roof and sixteen wind angles were acquired. The cables net was dimensioned taking into account the local peaks factors distribution on the roof [46].

With the purpose of estimating the roof geometry variation when under wind action, structural analyses were performed on a FE model of cable net.

The wind forces time histories were calculated using [16] wind tunnel tests campaign and Eqs. (19) and (20). Following the second approach listed in Section 4, each node included in the same pressure tap area of influence was loaded using the same pressure coefficients time histories. Fig.2a shows the geometrical configuration of the building assumed as case of study and Fig.2b shows a FE model view. It is important to precise that the model took into account only the cable net and that it neglected the membrane (i.e. non-structural element).

The numerical model contains 861 nodes spaced according a 2 x 2 m square grid. The first ten natural frequencies estimated by modal analyses are between 0.25 to 0.43 Hz. Figs.2c and 2d show the first two modal shapes.

Fig.3 shows an example of forces time history (i.e. input), F, and an example of displacements time history (i.e. output), δv. In Fig.3, Negative values of F mean suction (i.e. upward) values, negative values of displacements mean gravitational (i.e. downward) displacements.

The time series applied in input were expanded with an initial ramp. The time length was 1800 s and it was calculated based the geometrical scale of the wind tunnel model size. The wind tunnel model geometrical scale was equal to 1/100. The tests were performed at a mean wind speed of 16.7 m/s at a height of 10 cm that in a 1:100 scale would be the standard reference height. Assuming that the prototype mean wind speed at 10 m of height is U = 27 m/s (design value for most of the Italian territory), then there results a velocity scale λ_v = 0.62,

which corresponds to a time scale $\lambda_t = 0.0162$. Therefore, the 30 s model scale acquisition time corresponds to a full scale time of approximately 1800 s [23].

Totally, 861 time history with 7504 time steps were applied on the model for a time equal to 1800 s.

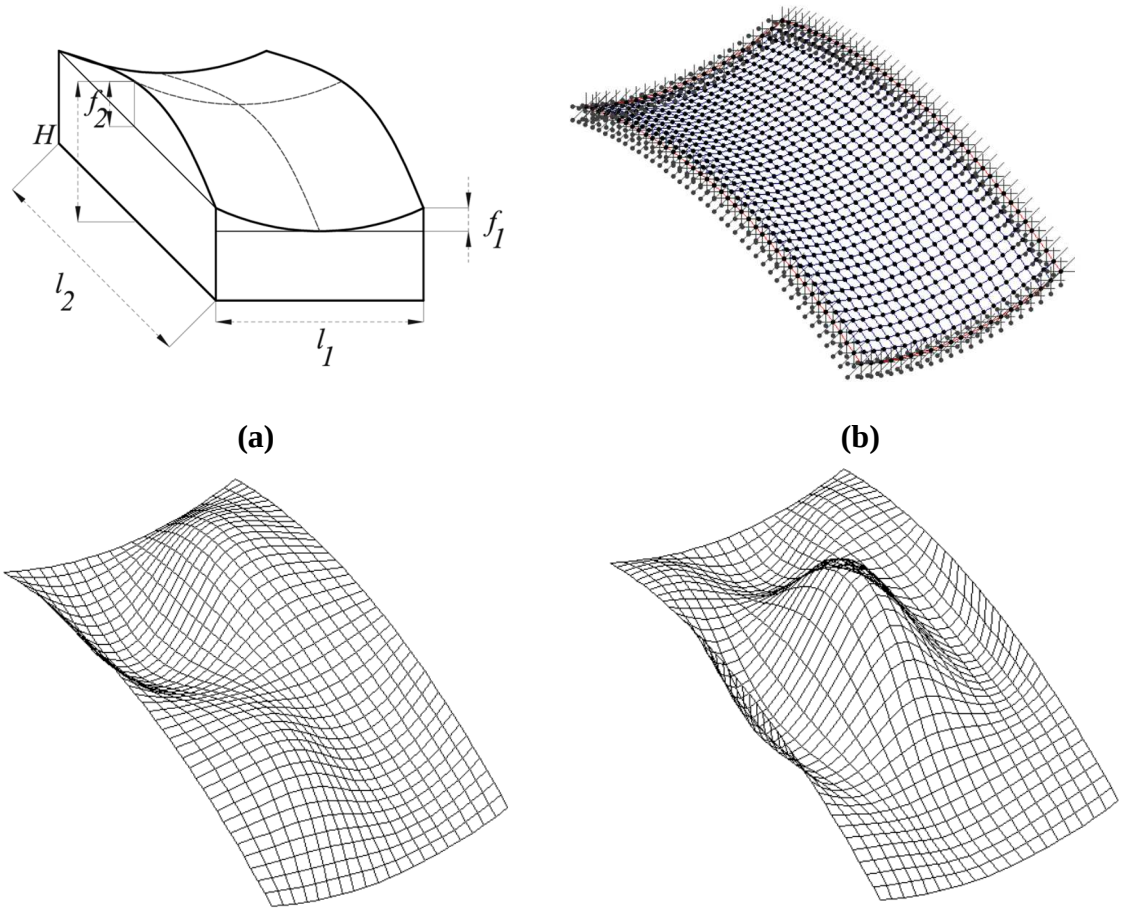

(a) **(b)**

Frequency = 0.25 Hz **Frequency = 0.27 Hz**

(c) **(d)**

Fig. 2 Case of study: geometrical configuration (a), FE model view (b), the first two modal shapes (c) and (d), respectively.

The non-linear analyses results give vertical displacements and cables stresses time series. Both of these results need to be post-processed in order to estimate their statistics as mean, maximum and minimum values, standard deviation end local peaks.

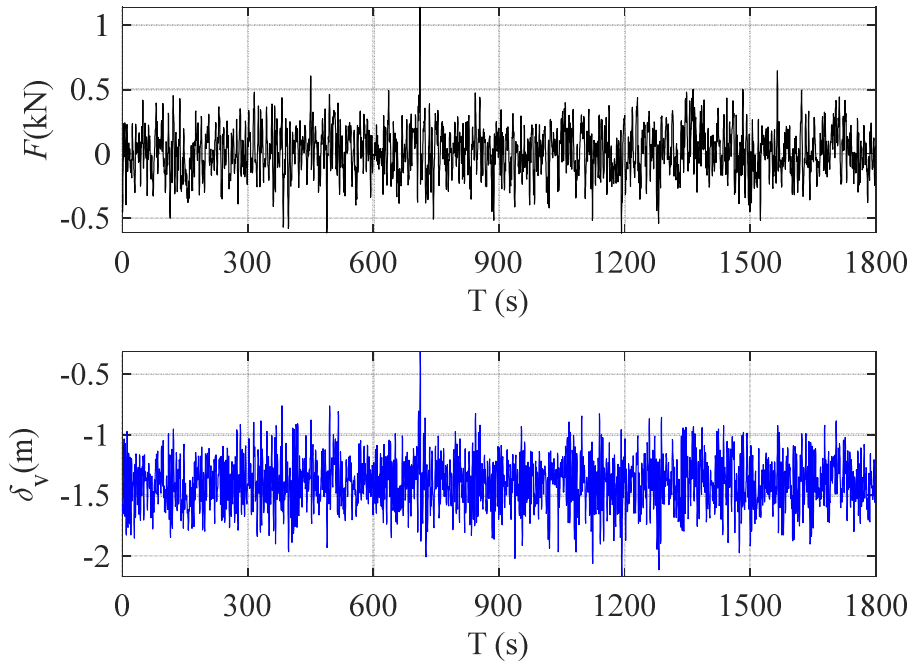

Fig.3 Wind force (*F*) and vertical displacements (δv) time history in node #320 middle point)

6 CONCLUSION

The paper discussed the non-linear analyses of cables net carried out trough wind tunnel experimental data. The process of calculation was described discussing the cables net structural behavior, the wind tunnel data acquisition and the non-linear time history analyses on FE model. The paper give comments about the dynamic geometrically non-linear analyses of cables systems and their computing using a calculus software.

7 ACKNOWLEDGMENTS

The authors thanks Professor Fabio Rizzo of the Department of Engineering and Geology at G. D'Annunzio University, for his geometrical database, Professor Piero D'Asdia for the non-commercial TENSO software and implementation, and finally Professor Luca Caracoglia of the Department of Civil and Environmental Engineering at Northeastern University for his studies and teachings.

REFERENCES

[1] Avossa A. M., Di Giacinto D., Malangone P., Rizzo F., 2018. Seismic Retrofit Of A Multi-Span Prestressed Concrete Girder Bridge With Friction Pendulum Devices, Shock and Vibration, 2018, Article ID 5679480.

[2] Rizzo F., Zazzini P., 2017. Shape dependence of acoustic performances in buildings with a Hyperbolic Paraboloid cable net membrane roof. Journal of Acoustics Australia, 45 (2), 421–443.

[3] Rizzo F., Zazzini P., 2016. Improving the acoustical properties of an elliptical plan space with a cable net membrane roof. Journal of Acoustics Australia, 44, 449-456, (11-16-2016) ISSN: 08146039, DOI: 10.1007/s40857-016-0072-5.

[4] AIJ (Architectural Institute of Japan), 2004. Recommendations for Loads on Buildings, Chapter 6: Wind Loads.

[5] ASCE (American Society of Civil Engineering), 1999. Wind tunnel studies of buildings and structures.

[6] ASCE (American Society of Civil Engineering), 2010. Minimum Design Loads for Buildings and Other Structures, ASCE 7:2010.

[7] AS/NZS (Standards Australia / Standards New Zealand), 2011. Structural design actions; Part 2: Wind actions. AS/NZS 1170.2:2002.

[8] CEN (ComitéEuropéen de Normalization), 2005. Eurocode 1: Actions on structures - Part 1-4: General actions - Wind actions, EN-1991-1-4.

[9] CNR (National Research Council of Italy), 2008. Guide for the Assessment of Wind Actions and Effects On Structures. CNR-DT 207/2008.

[10] NRC/CNRC (National Research Council / Conseil National de Recherches Canada), 2010. Commentary to the National Building Code of Canada, Commentary I: Wind Load and Effects.

[11] ISO (International Standards Organization), 2012. Wind action on structures - D.3 Wind tunnel testing procedures, 4354:2012(E).

[12] Krishna P., Kumar K., Bhandari N.M., 2012. Wind Loads on Buildings and Structures. Indian Standard IS:875, Part 3, Proposed Draft & Commentary.

[13] SIA (Swiss Society of Engineers and Architects), 2003. Action on structures - Appendix C: Force and pressure factors for wind. SIA 261:2003.

[14] Biagini P., Borri C., Facchini L., 2007. Wind response of large roofs of stadiums and arena, Journal of Wind Engineering and Industrial Aerodynamics, 95, 9-11.

[15] Rizzo F., 2012, Wind tunnel tests on hyperbolic paraboloid roofs with elliptical plane shapes, Engineering Structures, 45, 536–558.

[16] Rizzo F., D'Asdia P., Lazzari M., Procino L., 2011. Wind action evaluation on tension roofs of hyperbolic paraboloid shape, Engineering Structures, 33 (2), 445-461.

[17] Sun X., Wu Y., Yang Q., Shen S., 2008. Wind tunnel tests on the aeroelastic behaviors of tension structures. Proceedings of the VI International Colloquium on Bluff Bodies Aerodynamics & Applications, BBAA VI, Milan, Italy.

[18] Yang Q., Wu Y. , Zhu W., 2010. Experimental study on interaction between membrane structures and wind environment. Earthquake Engineering and Engineering Vibration, 9(4), 523-532.

[19] Rizzo F., Caracoglia L., Montelpare S., 2018, Predicting the flutter speed of a pedestrian suspension bridge through examination of laboratory experimental errors, 172, 589-613.

[20] Rizzo F., Caracoglia L., 2018. Examining wind tunnel errors in Scanlan derivatives and flutter speed of a closed-box, Journal of Wind and Structures, 26(4), 231-251.

[21] Brito R. and Caracoglia L., 209. Extraction of flutter derivatives from small scale wind tunnel experiments. In: Proceedings of the 11th Americas Conference on Wind Engineering, American Association for Wind Engineering (AAWE), San Juan, Puerto Rico; 2009.

[22] Rizzo F., D'Asdia P., Ricciardelli F., Bartoli G., 2012. Characterization of pressure coefficients on hyperbolic paraboloid roofs, Journal of Wind Engineering & Industrial Aerodynamics, 102, 61–71.

[23] Rizzo F., Ricciardelli F., 2017. Design pressure coefficients for circular and elliptical plan structures with hyperbolic paraboloid roof, Journal of Engineering Structures, 139, 153-169.

[24] Daw D.J., Davenport A.G., 1989. Aerodynamic damping and stiffness of a semi-circular roof in turbulent wind. Journal of Wind Engineering and Industrial Aerodynamics, 32, 83-92.

[25] Dzwierzynska J., Prokopska A.,2018. Pre-Rationalized Parametric Designing of Roof Shells Formed by Repetitive Modules of Catalan Surfaces, Symmetry, 10(4), 105.

[26] Kassem M., Novak M., 1992. Wind-Induced response of hemispherical air-supported Structures. Journal of Wind Engineering and Industrial Aerodynamics 41(1-3),177-178.

[27] Dong X., Ye J.H., 2015. Development and verification of a flow model of conical vortices on saddle roofs. Journal of Engineering Mechanics, ASCE, 141(3).

[28] Kawai H., Yoshie R, 1999. Wind-induced response of a large cantilevered roof. Journal of Wind Engineering and Industrial Aerodynamics. 83, 263-275.

[29] Kawakita S., Bienkiewicz B., Cermak J.E., 1992. Aeroelastic model study of suspended cable roof. Fluid Mechanics and Wind Engineering Program, Department of Civil Engineering, Colorado State University, Fort Collins, Colorado USA.

[30] Killen G.P., Letchford C.W., 2001. A parametric study of wind loads on grandstand roofs, Engineering Structures, 23(6), 725-735.

[31] Irwin H.P.A.H., Wardlaw R.L.A, 1979. Wind tunnel investigation of a retractable fabric roof for the Montreal Olympic stadium. In Proceedings of the 5th International Conference on Wind Engineering, Pergamon, 925-938.

[32] Letchford C.W., Killen G.P., 2002. Equivalent static wind loads for cantilevered grandstand roofs. Engineering Structures. 24(2), 207-217.

[33] Letchford C.W., Denoon R.O., Johnson G., Mallam A., 2002. Dynamic characteristics of cantilever grandstand roofs. Engineering Structures, 24(8), 1085-1090.

[34] Lewis W.J., (2003) Tension structures: form and behavior. Thomas Telford, London.

[35] Liu M., Chen X., Yang Q., 2016. Characteristics of dynamic pressures on a saddle type roof in various boundary layer flows. Journal of Wind Engineering and Industrial Aerodynamics, 150, 1-14.

[36] Pun, P.K.F. and Letchford C.W., 1993. Analysis of a tension membrane HYPAR roof subjected to fluctuating wind loads, 3rd Asia-Pacific symposium on Wind Engineering, Hong Kong, 13-15 December 1993, 741-746, University of Hong Kong.

[37] Pun, P.K.F, 1993. Analysis of a tension membrane HYPAR subject to fluctuating wind loads, MEngSc Thesis, University of Queensland, Brisbane, October 1993.

[38] Sykes D.M., 1994. Wind loading tests on models of two tension structures for EXPO'92, Seville. Journal of Wind Engineering and Industrial Aerodynamics, 52, 371-383.

[39] Kimoto E., Kawamura S., 1986. Aerodynamic criteria of hanging roofs for structural Design. Proceeding of IASS Symposium, Osaka, 249-256.

[40] Knudson W.C., 1991. Recent advances in the field of long span tension structures. Engineering Structures, 13(2), 174-193.

[41] Elashkar I., Novak M., 1983. Wind tunnel studies of cable roofs. Journal of Wind Engineering and Industrial Aerodynamics,13(1-3), 407-419.

[42] Forster B.,1994. Cable and membrane roofs, a historical survey. Structural Engineering Review, 6,3-5.

[43] Majowiecki M., 1972. Tensostrutture, Inarcos, (313), http://www.majowiecki.com/studio/wp-content/uploads/2011/10/1972-Tensostrutture-INARCOS.pdf

[44] Majowiecki M., 2004. Tensostrutture: Progetto e Verifica. EdizioniCrea, Massa, 1994.

[45] Yang Q., Liu R., 2005. On Aerodynamic Stability of Membrane Structures. International Journal of Space Structures, 20(3), 181-188.

[46] Rizzo F., Barbato M., Sepe V., 2018. Peak factor statistics of wind effects for hyperbolic paraboloid roofs, Engineering Structures, 173, 313–330.

[47] Rizzo F., Sepe V., 2015. Static loads to simulate dynamic effects of wind on hyperbolic paraboloid roofs with square plan, Journal of Wind Engineering & Industrial Aerodynamics, 137, 46-57.

[48] Shen S., Yang, Q., 1999. Wind-induced response analysis and wind-resistant design of hyperbolic paraboloid cable net structures. International Journal of Space Structures, 14(1), 57-65.

[49] Vassilopoulou I, Gantes CJ., 2011. Nonlinear dynamic behavior of saddle form cable nets under uniform harmonic load. Engineering Structures 33(10), 2762–2771.

[50] Vassilopoulou I, Gantes CJ., 2012. Vibration modes and natural frequencies of saddle form cable nets. ComputStruct. 88 (1–2), 105–19.

[51] Vassilopoulou I, Petrini F, GantesCJ., 2017. Nonlinear dynamic behavior of cable nets subjected to wind loading. Structures 10, 170–83.

COMPDYN 2019
7th ECCOMAS Thematic Conference on
Computational Methods in Structural Dynamics and Earthquake Engineering
M. Papadrakakis, M. Fragiadakis (eds.)
Crete, Greece, 24-–26 June 2019

COMPLEX MODAL DERIVATIVES FOR MODEL REDUCTION OF NONCLASSICALLY DAMPED, GEOMETRICALLY NONLINEAR STRUCTURES

Christian H. Meyer[1], **Fabian M. Gruber**[1], **and Daniel J. Rixen**[1]

[1]Technische Universität München, Chair of Applied Mechanics
Boltzmannstr. 15
e-mail: {christian.meyer, fabian.gruber, rixen}@tum.de

Keywords: Nonlinear Model Reduction, Damped Systems, Structural Dynamics, Complex Eigenmodes, Modal Derivatives, Large Deflection.

Abstract. *Finite element simulations of structures that undergo large deformations can imply high computation costs due to the nonlinearity of the resulting equations of motion and high numbers of degrees of freedom. Model reduction can encounter this burden by approximating the nodal displacements as a linear combination of some basis vectors and applying a Galerkin projection. The main challenge for this step is a proper selection of basis vectors that are able to capture the deformation states of the system.*

A prevalent selection of basis vectors for geometrically nonlinear systems is the combination of modes of the linearized system and so called modal derivatives. The modal derivatives describe the change of the modes when the system is perturbed and thus contain nonlinear information. However, modal derivatives are only defined for modes that are real. This makes this approach unusable for systems that have complex eigenmodes, such as nonclassically damped systems, i.e., systems with the damping matrix not fulfilling the Caughey condition.

This contribution shows how modal derivatives can be defined for nonclassically damped systems by extending the concept of modal derivatives to complex eigenmodes and how this can be used to build a reduction basis for geometrically nonlinear, nonclassically damped systems. A simple beam test case demonstrates that this approach can improve the accuracy of the reduced system slightly compared to the use of eigenmodes and modal derivatives of the underlying undamped system.

1 INTRODUCTION

One can find many applications in engineering that contain structural parts that undergo large deformations during operation, such as MEMS [14], wind turbine blades [15] or spring leafs for truck suspension [16]. Finite element analysis of such structures leads to the equations of motion

$$\boldsymbol{M}\ddot{\boldsymbol{u}}(t) + \boldsymbol{C}\dot{\boldsymbol{u}}(t) + \boldsymbol{f}(\boldsymbol{u}(t)) = \boldsymbol{F}^{\mathrm{ext}}(t)\,, \tag{1}$$

where $\boldsymbol{u} \in \mathbb{R}^N$ describes the displacements of the nodes of the finite element mesh, $\boldsymbol{M} \in \mathbb{R}^{N\times N}$ is the mass matrix, $\boldsymbol{C} \in \mathbb{R}^{N\times N}$ is the linear viscous damping matrix and $\boldsymbol{F}^{\mathrm{ext}} \in \mathbb{R}^N$ describes the external loads. N is the number of degrees of freedom. The term $\boldsymbol{f}(\boldsymbol{u})$ is the restoring force that is nonlinear for systems that undergo large deformations.

Due to a large number of degrees of freedom, which is typical for real world applications, and the nonlinearity of the restoring force term, simulation times can become very large. That makes design studies, in which the equation of motion must be solved several times, a tedious task. This burden can be faced by model reduction.

Model reduction in structural dynamics has been the focus of research for many years. Some techniques such as the Craig-Bampton method [3] or modal truncation have emerged to a standard and are implemented in many software packages. All these methods rely on the approximation of the displacement vector $\boldsymbol{u} \approx \boldsymbol{V}\boldsymbol{q}$ by a linear combination of some basis vectors that are column-wise stacked into a reduction matrix $\boldsymbol{V}$. The reduction is then carried out by a Galerkin projection onto the subspace that is spanned by the basis vectors. Different reduction methods only differ in how a proper reduction matrix is determined.

Most prominent reduction techniques use system properties of the undamped system for building the reduction matrix, such as the normal modes of the undamped system. This gives rise to the question if these techniques are also able to reduce systems that do not satisfy the Caughey conditions, i.e., systems whose eigenvalues are not equal to those of the underlying undamped system. This concern has been investigated in literature, too. Different methods for reduction of such systems as substructures can be found in [1, 2, 8, 4, 6].

These techniques can reduce linear systems, but they cannot be applied to geometrically nonlinear systems described by equation (1). Model reduction for this kind must overcome two additional issues: First, the reduction basis $\boldsymbol{V}$ must provide a subspace capturing large deformation states. Second, the evaluation of the nonlinear restoring force term must be accelerated. The reason for the second issue becomes clear by viewing the reduced equations of motion

$$\boldsymbol{V}^{\mathsf{T}}\boldsymbol{M}\boldsymbol{V}\ddot{\boldsymbol{q}}(t) + \boldsymbol{V}^{\mathsf{T}}\boldsymbol{C}\boldsymbol{V}\dot{\boldsymbol{q}}(t) + \boldsymbol{V}^{\mathsf{T}}\boldsymbol{f}(\boldsymbol{V}\boldsymbol{q}(t)) = \boldsymbol{V}^{\mathsf{T}}\boldsymbol{F}^{\mathrm{ext}}(t)\,. \tag{2}$$

The last term on the left hand side cannot be precomputed beforehand but must be evaluated in the full element domain. The acceleration of its evaluation is crucial to reduce computation time and can be gained by applying so called hyperreduction methods [16].

The first issue, namely the generation of a reduction basis, can be solved by two different classes of methods: The first class is 'simulation-based', which means that the basis is generated by data from full dynamic simulations of the high dimensional model. The most prominent example for this class is the Proper Orthogonal Decomposition [12, 10]. The second class is 'simulation-free'. These methods compute basis vectors from system properties. A common approach is to take the eigenmodes of the linearized system and augment them by modal derivatives [9]. Modal derivatives are the directional derivatives of the eigenmodes with respect to the displacements in the direction of the eigenmodes themselves. The use of these vectors as reduction basis for nonlinear systems is shown for example in [17, 18, 19].

The modal derivatives approach is able to include nonlinear information into the reduction basis without the need for dynamic simulations of the full high dimensional model. This makes this approach much more comfortable compared to the simulation-based methods. However, in contrast to methods for linear systems, there are no simulation-free basis generation techniques for geometrically nonlinear systems that consider damping properties. Available methods either do not consider damping or are limited to classically damped systems satisfying the Caughey condition, such as Rayleigh damping. But one can find many systems that do not satisfy this constraint in engineering. Thus, the question arises if available techniques can handle nonclassically damped systems or if better bases can be found by using the system's damping properties.

This contribution extends the modal derivative approach to complex eigenmodes which have been shown to be good candidates for nonclassic damped linear systems (cf. [7]). It is shown how a reduction basis for geometrically nonlinear systems can be built up from these vectors. A case study of a locally damped cantilever beam shows that their performance is slightly better than that of basis vectors computed from the properties of the underlying undamped system.

The remainder of this paper is organized as follows: First, the classic approach, i.e., the modal derivatives neglecting the damping properties of the system, is recapped in section 2. Section 3 summarizes the defintion of complex modes for the linearized equations of motion. Section 4 formulates a modal derivative for the complex modes with respect to the displacements $\boldsymbol{u}$. Section 5 shows how bases can be built by using the complex modes and modal derivatives. A case study demonstrates the new basis' performance in comparison to bases that neglect the damping properties of the system. This is illustrated in section 6. The results are summarized in section 7.

2 MODAL DERIVATIVES FOR UNDAMPED SYSTEMS

The equation

$$\boldsymbol{M}\ddot{\boldsymbol{u}}(t) + \boldsymbol{C}\dot{\boldsymbol{u}}(t) + \boldsymbol{K}\,\Delta\boldsymbol{u}(t) = \boldsymbol{F}^{\text{ext}}(t) - \boldsymbol{f}(\bar{\boldsymbol{u}}) \tag{3}$$

describes the linearization of equation (1) around $\boldsymbol{u} = \bar{\boldsymbol{u}}$ with the tangential stiffness matrix

$$\boldsymbol{K} = \left.\frac{\partial \boldsymbol{f}(\boldsymbol{u})}{\partial \boldsymbol{u}}\right|_{\boldsymbol{u}=\bar{\boldsymbol{u}}} . \tag{4}$$

In classic approaches, it is assumed that damping can either be neglected or the damping matrix satisfies the Caughey condition. The eigenmodes $\boldsymbol{\phi}_i$ can then be computed by solving the eigenproblem

$$(\boldsymbol{K}(\bar{\boldsymbol{u}}) - \omega_i^2\,\boldsymbol{M})\boldsymbol{\phi}_i = \boldsymbol{0}\,. \tag{5}$$

The modal derivatives that are used for reduction bases for nonlinear systems are defined by

$$\partial_{\boldsymbol{\phi}_j}\boldsymbol{\phi}_i = \lim_{h\to 0}\frac{\boldsymbol{\phi}_i(\bar{\boldsymbol{u}} + h\,\boldsymbol{\phi}_j) - \boldsymbol{\phi}_i(\bar{\boldsymbol{u}})}{h} \tag{6}$$

which is the directional derivative of a mode $\boldsymbol{\phi}_i$ with respect to the displacements in the direction of a mode ϕ_j. This derivative is not zero because the tangential stiffness matrix of the eigenproblem (5) is dependent on $\bar{\boldsymbol{u}}$ for geometrically nonlinear systems according to equation (4). There are several options to compute the derivative numerically. An extensive overview over different methods is given in [11].

3 COMPLEX MODAL DERIVATIVES FOR DAMPED SYSTEMS

Equation (3) can be transformed to implicit state-space form

$$\boldsymbol{E}\,\dot{\boldsymbol{x}} = \boldsymbol{A}\,\boldsymbol{x} + \boldsymbol{B} \tag{7}$$

with

$$\boldsymbol{x} = \begin{bmatrix} \Delta\boldsymbol{u} \\ \dot{\boldsymbol{u}} \end{bmatrix}, \qquad \boldsymbol{E} = \begin{bmatrix} \boldsymbol{C} & \boldsymbol{M} \\ \boldsymbol{M} & \boldsymbol{0} \end{bmatrix}, \qquad \boldsymbol{A} = \begin{bmatrix} -\boldsymbol{K}(\bar{\boldsymbol{u}}) & \boldsymbol{0} \\ \boldsymbol{0} & \boldsymbol{M} \end{bmatrix}, \qquad \boldsymbol{B} = \begin{bmatrix} \boldsymbol{F}^{\text{ext}} \\ \boldsymbol{0} \end{bmatrix}. \tag{8}$$

The damping matrix $\boldsymbol{C}$ is assumed to be symmetric but does not necessarily satisfy the Caughey condition. This constraint is often satisfied in practice except for systems with gyroscopic effects.

The eigenvectors of the generalized eigenvalue problem

$$(\boldsymbol{A} - \boldsymbol{\lambda}_i\,\boldsymbol{E})\;\boldsymbol{r}_i = \boldsymbol{0} \tag{9}$$

describe the complex mode shapes. The eigenvalues λ_i and eigenvectors $\boldsymbol{r}_i$ occur in complex conjugate pairs or are real (see for instance [5]). We normalize the eigenvectors such that

$$\boldsymbol{r}_i^{\mathsf{T}}\boldsymbol{E}\boldsymbol{r}_i = 1\,, \qquad \boldsymbol{r}_i^{\mathsf{T}}\boldsymbol{A}\boldsymbol{r}_i = \boldsymbol{\lambda}_i\,. \tag{10}$$

4 COMPLEX MODAL DERIVATIVES

The motivation is to extend the modal derivative approach from section 2 to complex modes that take the damping properties into account. Thus, we search for the directional derivative

$$\partial_{\boldsymbol{v}_j}\boldsymbol{r}_i = \lim_{h\to 0}\frac{\boldsymbol{r}_i(\bar{\boldsymbol{x}} + h\,\boldsymbol{v}_j) - \boldsymbol{r}_i(\bar{\boldsymbol{x}})}{h}\,. \tag{11}$$

with $\bar{\boldsymbol{x}} = [\bar{\boldsymbol{u}},\ \boldsymbol{0}]^{\mathsf{T}}$. There are several methods to compute the derivatives as outlined in [11]. One of these methods is Nelson's method [13]. This procedure will be transferred to the state-space eigenvalue problem (9) in this section. First, we apply a directional derivative to the eigenproblem (9)

$$\partial_{\boldsymbol{v}_j}(\boldsymbol{A}(\bar{\boldsymbol{x}}) - \lambda_i\,\boldsymbol{E})\boldsymbol{r}_i = \boldsymbol{0}\,. \tag{12}$$

The dependency on $\bar{\boldsymbol{x}}$ is omitted from now on for the sake of simplicity. The product rule leads to

$$(\boldsymbol{A} - \lambda_i\boldsymbol{E})\cdot\partial_{\boldsymbol{v}_j}(\boldsymbol{r}_i) + \partial_{\boldsymbol{v}_j}(\boldsymbol{A})\cdot\boldsymbol{r}_i - \partial_{\boldsymbol{v}_j}(\lambda_i)\cdot\boldsymbol{E}\boldsymbol{r}_i - \lambda_i\cdot\partial_{\boldsymbol{v}_j}(\boldsymbol{E})\,\boldsymbol{r}_i = \boldsymbol{0}\,. \tag{13}$$

The matrix $\boldsymbol{E}$ does not depend on the stiffness matrix and thus does not depend on $\bar{\boldsymbol{x}}$. Therefore, the last term cancels and one gets

$$(\boldsymbol{A} - \lambda_i\boldsymbol{E})\;\partial_{\boldsymbol{v}}\boldsymbol{r}_i = -\partial_{\boldsymbol{v}}(\boldsymbol{A})\,\boldsymbol{r}_i + \partial_{\boldsymbol{v}}(\lambda_i)\,\boldsymbol{E}\boldsymbol{r}_i\,. \tag{14}$$

The term $\partial_{\boldsymbol{v}}(\lambda_i)$ is unknown and needs to be expressed by other terms. We use the same trick as in Nelson's method and premultiply equation (14) by $\boldsymbol{r}_i^{\mathsf{T}}$ which leads to

$$\boldsymbol{r}_i^{\mathsf{T}}(\boldsymbol{A} - \lambda_i\boldsymbol{E})\,\partial_{\boldsymbol{v}}(\boldsymbol{r}_i) = -\boldsymbol{r}_i^{\mathsf{T}}\partial_{\boldsymbol{v}}(\boldsymbol{A})\,\boldsymbol{r}_i + \partial_{\boldsymbol{v}}(\lambda_i)\,\boldsymbol{r}_i^{\mathsf{T}}\boldsymbol{E}\boldsymbol{r}_i\,. \tag{15}$$

The left hand side vanishes because it satisfies the eigenproblem (9) due to the symmetry of $\boldsymbol{A}$ and $\boldsymbol{E}$. The equation simplifies to

$$\partial_{\boldsymbol{v}}(\lambda_i) = \boldsymbol{r}_i^{\mathsf{T}}\partial_{\boldsymbol{v}}(\boldsymbol{A})\,\boldsymbol{r}_i \tag{16}$$

due to the normalization condition $\boldsymbol{r}_i^\mathsf{T}\boldsymbol{E}\boldsymbol{r}_i = 1$. Inserting this into (14) gives

$$(\boldsymbol{A} - \lambda_i \boldsymbol{E})\, \partial_{\boldsymbol{v}}(\boldsymbol{r}_i) = \underbrace{-\partial_{\boldsymbol{v}}(\boldsymbol{A})\, \boldsymbol{r}_i + \left(\boldsymbol{r}_i^\mathsf{T} \partial_{\boldsymbol{v}}(\boldsymbol{A}) \boldsymbol{r}_i\right)\, \boldsymbol{E}\boldsymbol{r}_i}_{\boldsymbol{g}} \,. \tag{17}$$

This equation cannot be solved at hand because $(\boldsymbol{A} - \lambda_i \boldsymbol{E})$ is singular. The general solution

$$\partial_{\boldsymbol{v}}(\boldsymbol{r}_i) = \boldsymbol{\vartheta} + c\, \boldsymbol{r}_i \tag{18}$$

consists of a particular part $\boldsymbol{\vartheta}$ and a homogeneous part $c\,\boldsymbol{r}_i$ with an arbitrary scalar factor c. Similar to [13], a particular part is determined by setting one coordinate of $\boldsymbol{\vartheta}$ to zero. The system is then partitioned into

$$\left(\begin{bmatrix} \boldsymbol{A}_{11} & \boldsymbol{0} \\ \boldsymbol{0} & 1 \end{bmatrix} - \lambda_i \begin{bmatrix} \boldsymbol{E}_{11} & \boldsymbol{0} \\ \boldsymbol{0} & 0 \end{bmatrix} \right) \begin{bmatrix} \boldsymbol{\vartheta}_1 \\ \vartheta_2 \end{bmatrix} = \begin{bmatrix} \boldsymbol{g}_1 \\ 0 \end{bmatrix} \tag{19}$$

where the index 2 denotes the coordinate which is set to zero, the index 1 denotes the remaining coordinates and $\boldsymbol{g}$ is the right hand side from equation (17).

The homogeneous part is determined by using the normalization condition

$$\partial_{\boldsymbol{v}} \left(\boldsymbol{r}_i^\mathsf{T} \boldsymbol{E} \boldsymbol{r}_i\right) = 0 \qquad \Rightarrow \qquad \partial_{\boldsymbol{v}}(\boldsymbol{r}_i^\mathsf{T})\, \boldsymbol{E}\boldsymbol{r}_i = 0 \tag{20}$$

where we assumed $\boldsymbol{E}$ is symmetric and independent on $\bar{\boldsymbol{x}}$. The scaling factor c is then found by

$$(\boldsymbol{\vartheta} + c\, \boldsymbol{r}_i)^\mathsf{T} \boldsymbol{E} \boldsymbol{r}_i = 0 \qquad \Rightarrow \qquad c = -\boldsymbol{\vartheta}^\mathsf{T} \boldsymbol{E} \boldsymbol{r}_i \,. \tag{21}$$

5 BUILDING THE REDUCTION BASIS

The classic approach for building simulation-free reduction bases for geometrically nonlinear systems is to build up the basis from two parts

$$\boldsymbol{V} = [\boldsymbol{V}_{\text{lin}}\, \boldsymbol{V}_{\text{nl}}] \,, \quad \boldsymbol{V} \in \mathbb{R}^{N \times n} \,. \tag{22}$$

The first part $\boldsymbol{V}_{\text{lin}}$ contains modes $\boldsymbol{\phi}$ of the undamped system (eq. (5)), the second part $\boldsymbol{V}_{\text{nl}}$ contains their modal derivatives (eq. (6)). All vectors are orthogonalized to gain better numerical conditions.

We propose a new basis for damped systems by transferring this strategy to complex modes: The linear part $\boldsymbol{V}_{\text{lin}}$ is built by information from the complex modes $\boldsymbol{r}_i$ of the damped system. A complex mode $\boldsymbol{r}_i$ can be partitioned in

$$\boldsymbol{r}_i = \begin{bmatrix} \boldsymbol{d}_i \\ \boldsymbol{e}_i \end{bmatrix} \tag{23}$$

where the upper part describes displacements and the lower part velocities as defined in equation (7). The desired reduction basis $\boldsymbol{V}$ must suit to the dimension of the second order system (1) making the Galerkin projection described by (2) applicable. For this reason we use only the upper portion $\boldsymbol{d}_i$ of the eigenvectors $\boldsymbol{r}_i$. We propose

$$\boldsymbol{V}_{\text{lin}} = [\text{Re}(\boldsymbol{d}_1)\;\; \text{Im}(\boldsymbol{d}_1)\;\; \text{Re}(\boldsymbol{d}_2)\;\; \text{Im}(\boldsymbol{d}_2)\;\; \ldots\;\; \text{Im}(\boldsymbol{d}_m)] \tag{24}$$

as linear part. It contains the real and imaginary parts of the displacement portion of the first m complex modes belonging to the linearized system. The nonlinear part

$$\boldsymbol{V}_{\mathrm{nl}} = [\, \cdots \ \mathrm{Re}(\partial_{\boldsymbol{r}_j} \boldsymbol{d}_i) \ \mathrm{Im}(\partial_{\boldsymbol{r}_j} \boldsymbol{d}_i) \ \cdots \,] \quad \text{for } i,j \in \{1,\dots,m\} \tag{25}$$

consists of the real and imaginary parts of the complex modal derivatives. Again only the displacement portion $\boldsymbol{d}$ is contained. The derivatives $\partial_{\boldsymbol{v}} \boldsymbol{A}$ that appear during the computation of the complex modal derivatives, such as in equation (17), are computed via central differences. The relation

$$\partial_{\boldsymbol{v}} \boldsymbol{A} = \frac{\partial \boldsymbol{A}}{\partial \bar{\boldsymbol{x}}} \cdot \boldsymbol{v} = \frac{\partial \boldsymbol{A}}{\partial \bar{\boldsymbol{x}}} \cdot \mathrm{Re}(\boldsymbol{v}) + \mathrm{i}\, \frac{\partial \boldsymbol{A}}{\partial \bar{\boldsymbol{x}}} \cdot \mathrm{Im}(\boldsymbol{v}) \tag{26}$$

gives the central difference scheme

$$\partial_{\boldsymbol{v}} \boldsymbol{A} = \frac{\boldsymbol{A}(\bar{\boldsymbol{x}} + h \cdot \mathrm{Re}(\boldsymbol{v})) - \boldsymbol{A}(\bar{\boldsymbol{x}} - h \cdot \mathrm{Re}(\boldsymbol{v}))}{2h} + \mathrm{i}\, \frac{\boldsymbol{A}(\bar{\boldsymbol{x}} + h \cdot \mathrm{Im}(\boldsymbol{v})) - \boldsymbol{A}(\bar{\boldsymbol{x}} - h \cdot \mathrm{Im}(\boldsymbol{v}))}{2h}\,. \tag{27}$$

The full reduction basis

$$\boldsymbol{V} = [\boldsymbol{V}_{\mathrm{lin}}\ \boldsymbol{V}_{\mathrm{nl}}] \tag{28}$$

is stacked together from the linear and nonlinear part. All vectors are orthogonalized to each other by using a singular value decomposition. Vectors that are almost linear dependend are removed by truncating vectors belonging to small singular values. After orthogonalization the full reduction matrix $\boldsymbol{V}$ has the dimension $N \times n$.

6 CASE STUDY

The performance of the proposed reduction basis is tested by means of a case study. Figure 1 shows the finite element model of a cantilever beam that is used for this purpose. The beam is fixed on the left and excited through a harmonic excitation on the tip. The amplitude of the excitation force is chosen so that the beam undergoes large deflection. The beam is slightly damped by a Rayleigh damping. Additionally, a linear viscous damper is applied at a variable position x_d. We consider two positions x_d, namely $30.0\,\mathrm{mm}$ and $50.0\,\mathrm{mm}$. The system has $N = 7,184$ degrees of freedom. The eigenvalues of the linearized system are listed in Table 1.

Three reduction bases are compared against each other. First, the new proposed reduction basis is generated. Four complex modes ($m = 4$) are used to build the reduction basis, namely $1, 2, 3$ and 5. Mode number 4 is not included because it is the complex conjugate pair to the third mode. Thus, its real and imaginary part is linear dependend and does not contribute new information. All complex modal derivatives to the chosen modes are computed. Their real and

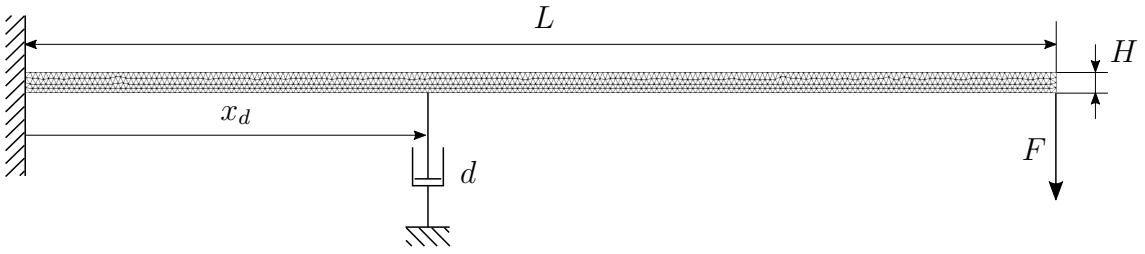

Figure 1: Cantilever Beam for Case Study. Parameters: $L = 100\,\mathrm{mm}$, $H = 2\,\mathrm{mm}$, thickness in 3rd dimension $= 10\,\mathrm{mm}$, $\varrho = 0.94\,\mathrm{g/cm^3}$, Rayleigh Damping: $0.001 \cdot \boldsymbol{M} + 0.001 \cdot \boldsymbol{K}(\boldsymbol{0})$, viscous damper constant $d = 2,700\,\mathrm{g/s}$, St.-Venant-Kirchhoff material model with Young's modulus $E = 50\,\mathrm{MPa}$, Poisson's ratio $\nu = 0.49$, harmonic excitation force $F = \hat{F} \cdot (\sin(80.0\,\mathrm{rad/s} \cdot t) + \sin(29.2\,\mathrm{rad/s} \cdot t) + \sin(18.0\,\mathrm{rad/s} \cdot t))$

No.	$x_d = 30.0\,\mathrm{mm}$	$x_d = 50.0\,\mathrm{mm}$
1	-0.001+0.000i	-2.265+0.000i
2	-2.264+0.000i	-0.000+0.000i
3	-0.002-0.008i	-0.001+0.013i
4	-0.002+0.008i	-0.001-0.013i
5	-0.003-0.052i	-0.001-0.082i
6	-0.003+0.052i	-0.001+0.082i
7	-0.003-0.147i	-0.009+0.118i
8	-0.003+0.147i	-0.009-0.118i
9	-0.004-0.256i	-0.001-0.262i
10	-0.004+0.256i	-0.001+0.262i

Table 1: First 10 complex eigenvalues of the linearized eigenvalue problem of the full cantilever beam model in $\mathrm{rad}/(10^{-4}\,\mathrm{s})$.

imaginary parts are stacked into the reduction matrix as described by equation (25). This results in 8 basis vectors for the linear part and 32 for the nonlinear part. However, after orthogonalization some vectors are removed because they show approximately linear dependence. This is done by truncating vectors belonging to singular values smaller than 10^{-9} times the largest singular value. This leads to a smaller dimension n than expected, namely $n = 31$.

Second, two classic reduction bases are computed for comparison. The first part $\boldsymbol{V}_{\mathrm{lin}}$ consists of undamped modes according to eq. (5), the second part $\boldsymbol{V}_{\mathrm{nl}}$ contains their modal derivatives according to eq. (6). They neglect the damping properties of the system. One of these bases contains the same number of modes ($m = 4$) and all modal derivatives. After orthogonalization and truncation using the same tolerance as above, the basis' dimension is $n = 14$. The other classic reduction basis contains $m = 7$ modes and their modal derivatives. This leads to a dimension of $n = 35$ after orthogonalization which is comparable to the dimension of the first basis. All linearization points $\bar{\boldsymbol{x}}$ and $\bar{\boldsymbol{u}}$ are chosen to be zero for all bases. This linearization point describes the static rest position of the beam.

Figures 2 and 3 show the tip displacements of the full simulations over time and their error generated by the reduced systems. The plotted error describes the absolute error Δu_{tip} normalized by $|u_{\mathrm{tip}}|_{\max}$ which is the maximum tip displacement over time. It can be seen that the new proposed basis performs better than the classic bases for $x_d = 30.0\,\mathrm{mm}$. It also performs better for $x_d = 50.0\,\mathrm{mm}$ compared to the classic basis computed with the same number of modes. However, the error is approximately the same as for a classic basis with almost same number of basis vectors. When using the same dimension for the basis, the new proposed method does not enhance the accuracy for this case.

7 CONCLUSION

Model reduction for geometrically nonlinear systems is used to reduce computation times for design studies. A crucial part for successful reduction is a proper chosen reduction basis. The basis can either be computed simulation-based by relying on training sets from full dynamic simulations or can be computed by simulation-free methods that are much more comfortable. So far, available simulation-free methods do not take the system's damping properties into account or at least assume a viscous damping matrix that satisfies the Caughey condition. The fact, that damping can drastically change the dynamic behavior of a system, motivates to develop

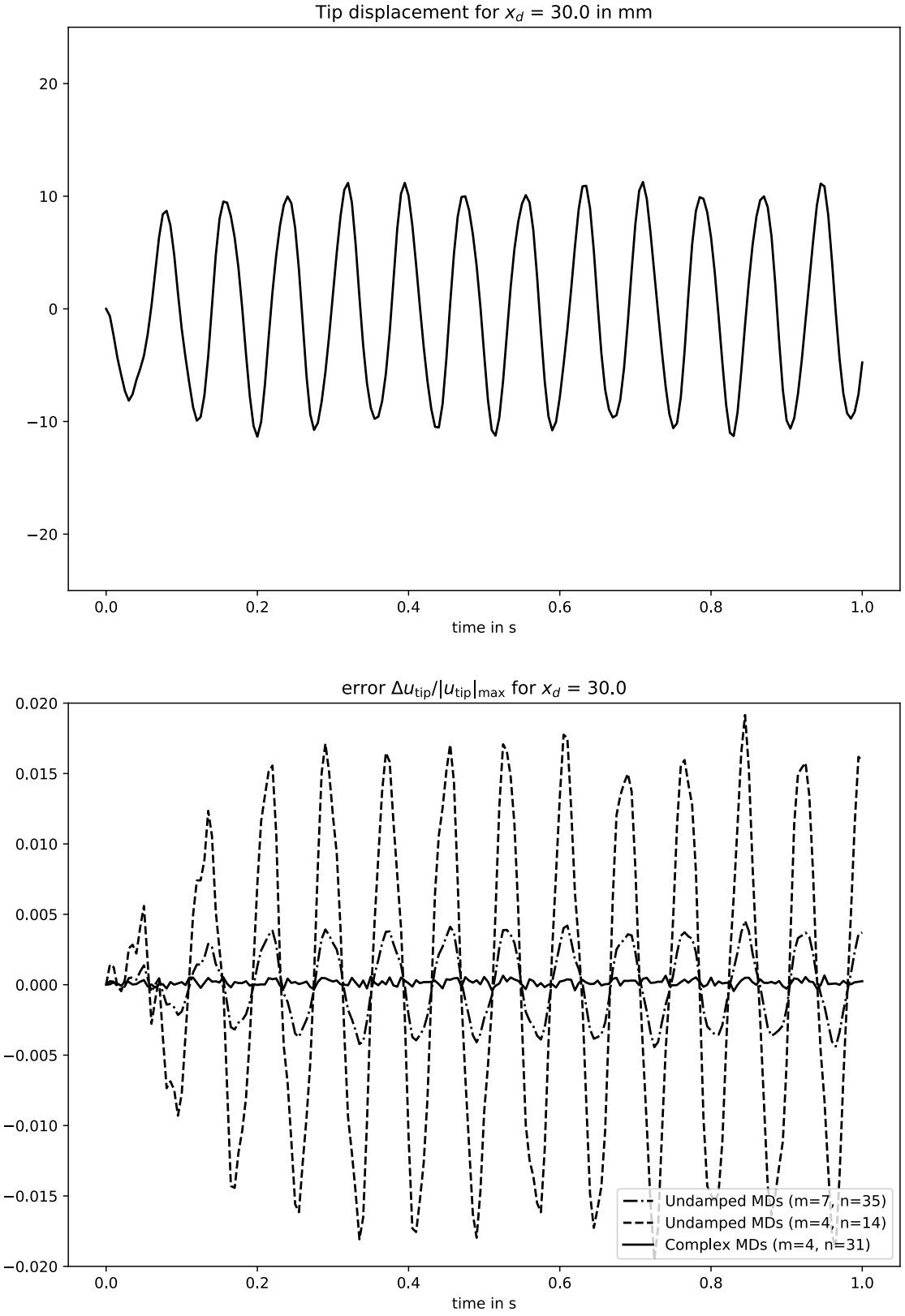

Figure 2: Tip displacement and error.

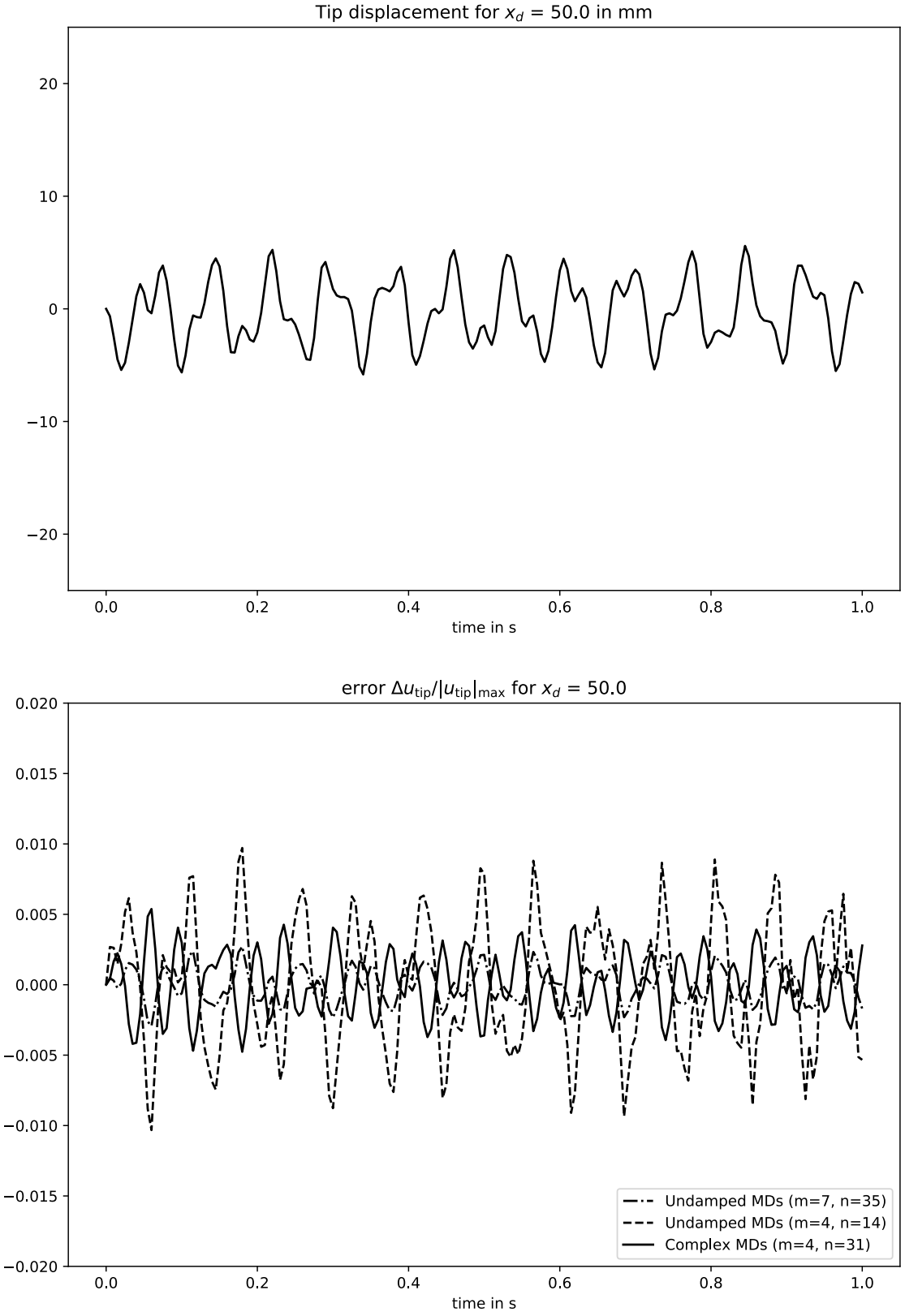

Figure 3: Tip displacement and error.

simulation-free bases that take the damping properties into consideration.

This contribution provides a simulation-free basis that is based on complex modes of the damped linearized system. The idea of modal derivatives is transferred to the complex modes formulation. Nelson's method is applied to derive modal derivatives for the complex modes. A reduction basis is built by using the real and imaginary parts of the modes and their modal derivatives. A case study on a cantilever beam is carried out to evaluate the performance of the new proposed basis. The results show a slight improvement compared to classic bases. But this improvement is small. The higher computation costs associated with the new basis do not outweigh its improvement. Further case studies are necessary to evaluate if there are systems where the improvements are greater and their use more reasonable or if the new basis fails for specific systems.

REFERENCES

[1] J.-G. Béliveau, Y. Soucy, Damping synthesis using complex substructure modes and a hermitian system representation. *AIAA Journal*, **23** (12), 1952–1956, 1985.

[2] R.R. Jr. Craig, Z. Ni, Component mode synthesis for model order reduction of nonclassically damped systems. *Journal of Guidance, Control, and Dynamics*, **12** (4), 577–584, 1989.

[3] R.R. Craig, M.C.C. Bampton, Coupling of substructures for dynamic analyses. *AIAA Journal*, **6** (7) 1313–1319, 1968.

[4] A. De Kraker, D.H. Van Campen, Rubin's CMS reduction method for general state-space models. *Computers and Structures*, **58** (3) 597–606, 1996.

[5] M. Géradin, D. Rixen, Mechanical Vibrations. Theory and Application to Structural Dynamics, 3rd edition, Wiley & Sons, 2015.

[6] F.M. Gruber, D.J. Rixen, Dual Craig-Bampton component mode synthesis method for model order reduction of nonclassically damped linear systems. *Mechanical Systems and Signal Processing*, **111**, 678–698, 2018.

[7] Fabian M. Gruber, Daniel J. Rixen, Comparison of Craig-Bampton Approaches for Systems with Arbitrary Viscous Damping in Dynamic Substructuring. *Dynamics of Coupled Structures*, **4**, 35–49, 2018.

[8] T.K. Hasselman, A. Kaplan, Dynamic analysis of large systems by complex mode synthesis. *Journal of Dynamic Systems, Measurement and Control, Transactions of the ASME*, **96** (3), 327–333, 1974.

[9] S.R. Idelsohn, A. Cardona, A reduction method for nonlinear structural dynamic analysis. *Computer Methods in Applied Mechanics and Engineering*, **49** (3), 253–279, 1985.

[10] G. Kerschen et al., The method of proper orthogonal decomposition for dynamical characterization and order reduction of mechanical systems: An overview. *Nonlinear Dynamics*, **41** (1-3), 147–169, 2005.

[11] F. van Keulen, R.T. Haftka, N.H. Kim, Review of options for structural design sensitivity analysis. Part 1: Linear systems. *Computer Methods in Applied Mechanics and Engineering*, **194** (30-33 SPEC. ISS.), 3213–3243, 2005.

[12] P. Krysl, S. Lall, J.E. Marsden, Dimensional model reduction in non-linear finite element dynamics of solids and structures. *International Journal for Numerical Methods in Engineering*, **51** (4), 479–504, 2001.

[13] R.B. Nelson, Simplified calculation of eigenvector derivatives. *AIAA Journal*, **14** (9), 1201–1205, 1976.

[14] M. Putnik et al., Simulation methods for generating reduced order models of MEMS sensors with geometric nonlinear drive motion. *IEEE International Symposium on Inertial Sensors and Systems (INERTIAL)* 1–4, 2018.

[15] M.M. Rezaei et al., Development of a reduced order model for nonlinear analysis of the wind turbine blade dynamics. *Renewable Energy*, **76**, 264–282, 2015.

[16] J.B. Rutzmoser, Model Order Reduction for Nonlinear Structural Dynamics. *Dissertation*. Technische Universität München, Munich, Germany, 2018.

[17] P.M.A. Slaats, J. de Jongh, A.A.H.J. Sauren, Model reduction tools for nonlinear structural dynamics. *Computers and Structures*, **54** (6), 1155–1171, 1995.

[18] P. Tiso, D.J. Rixen, Reduction methods for MEMS nonlinear dynamic analysis. *Nonlinear Modeling and Applications*, **2**, Conference Proceedings of the Society for Experimental Mechanics Series, 2011.

[19] O. Weeger, U. Wever, B. Simeon, On the use of modal derivatives for nonlinear model order reduction. *International Journal for Numerical Methods in Engineering*, **108** (13), 1579–1602, 2016.

COMPDYN 2019
7th ECCOMAS Thematic Conference on
Computational Methods in Structural Dynamics and Earthquake Engineering
M. Papadrakakis, M. Fragiadakis (eds.)
Crete, Greece, 24–26June 2019

MODELING NON-LINEARITY ON CABLE STAYED MASTS OF TENSILE FABRIC STRUCTURES.

F. Rizzo[1] and A. Viskovic[1]
[1]Department of Engineering and Geology, G. D'Annunzio University,
viale Pindaro 42, 65127, Pescara
email: fabio.rizzo@unich.it, a.viskovic@unich.it

Abstract

Tensile membrane structures are part of a unique technology that gives designers the capability to experiment new forms and new solutions to conventional design problems. These structures are extremely efficient for long span application and allows considerable savings in the foundations and supporting structure costs. Cable stayed masts are integral part of this structure typology and consists of a inclined elements supported by several layers of pre-tensioned cables. Generally their dynamic loading is not a concern in the design of tensile structures, nevertheless in case of massive shafts, their dynamics can play a fundamental role for global behaviour of the structure. Therefore pre-tensioning force on supporting cables system is an important issue since the internal force distribution, significantly affects their structural dynamic behaviour. A non-linear cable model, combined with the taut-cable theory has been employed to simulate the non-linearity conditions in the stays and cables, by using a restoring-force equivalent spring model to replicate the behaviour of each cable. In the present paper a simplified based displacement technique is utilized to examine the non-linear dynamics of the system. The proposed approach, based on energetic method Equivalent Linearization method (ELM), shows a robust simplified technique capable to linearize the non-linear system, taking into account of slackening effects of pre-tensioned stays. It is concluded that performance coefficient and linearized frequency, may possibly be used as useful indicators for designing pre-tensioned cable stayed masts where a suitable selection of the initial pre-tensioning force can effectively improve dynamic performance of the system.

Keywords: Tensile fabric structures, cable stayed masts; cable response, non-linear effects.

1 INTRODUCTION

Guyed masts are tall structures whose function is to support tensile fabric structures. Pre-tensioning has a beneficial effect on these structures, since it increases the stiffness of the system and improves their dynamic performances [1, 2], on the other hand, a high level of pre-stressing can lead to undesirable yielding of the cables of fabric structures or to high compression strengths on the mast which can lead to buckling of the system.

A suitable configuration of the pre-tensioning force in the cable system can be considered an important issue since the internal force distribution, emerging from the interaction with mast, significantly affects the structural dynamic behavior of the tensile structure [2-5]. The study of the structural optimization of these systems has recently received attention by the researches. Innovative approaches to study the dynamics and the modal response of frames and similar structures are considered in recent papers [6-8]. Furthermore new approach to evaluate the equivalent dynamic stiffness these structures is examined in a recent work [9].

In past years, the several authors have been investigating the dynamics of similar systems, installed on cable-stayed bridges [10-15], furthermore a similar approach suitable for simulating slackening on Pre-Tensioned-Cable Cross-Braced Structures is been recently devel-

oped [16, 17]. This paper proposes, capitalizing from the recent works on non-linear cable dynamics, a new approach to analyze, in pre-tensioned cable stayed masts, the non-linear behavior of the cables, which could lead to a complete loss in the pre-tensioning force imparted to the cables (cable-less structure). A new "linearized solution" is presented to directly simulate the non linear behavior *i* o in the stays on the dynamics of the structural system. Even though other similar approaches have been considered to study the nonlinear dynamics, (e.g. [18, 19]), the proposed method is simple and may be considered attractive for practical engineering design.

2 BACKGROUND

A generalized configuration of cable mast is studied in the present paper, as a typical prototype example of pre-tensioned cable stayed masts configuration present in many existing tensile structures. The structure is modeled as lumped-mass system connected to the rest of the tensile structure through an equivalent cable which simulate the interaction with the fabric structure. Figure 1 illustrates the model geometry, employed for the free vibration dynamics. In the considered case, a 2D plane model has been considered, accounting for a symmetric in-plane configuration of the stays. Constitutive equation of non linear spring (Figure 1c) illustrate a simplified constitutive model of the reaction of a tensile fabric structure around the equilibrium shape. It must be noted that the configuration is general and the proposed preliminary model could easily be extended to a more complex systems (different constitutive models). A set of various lumped masses are utilized in the model to simulate both the main mast mass and additional equivalent masses to simulate the presence of the fabric structure. In the present stage the axial stiffness of the primary structure and dynamic mast-cable interactions are not considered. The mass of the mast has been considered uniformly distributed along its elevation with density ρ_j and is been simulated through a lumped mass discretization of each element $m_j=m=\rho_j \Delta H$. Each lumped mass is associated with a transverse horizontal degree of freedom (x_j). In order to perform a parametric study, generalized mass properties of the prototype system in Fig. 1 are expressed as function of the constant distributed mass m of the antenna, with $\mu_k=M_k/m$ being the mass ratio of the *i-th* fabric structure and $\xi_k=H_k/H$ the dimensionless geometric constants designating the mass position with H being the total height of the mast.

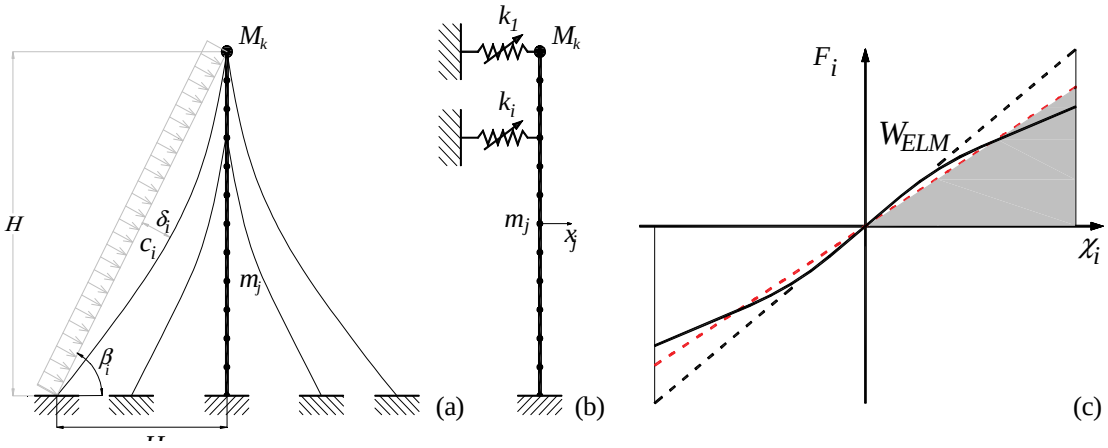

Fig.1 (a) Cable stayed mast, simulated as a lumped-mass model (descriptive example) (b) Lumped mass model with non-linear springs (c) Constitutive equation of non-linear springs and corresponding work performed by: linearized spring (red line) (WELM).

Generalized stiffness properties of the structure are defined through the diameter ratio $\delta_d=d/H$ where d represents the characteristic size of an equivalent constant circular cross-section with area $A_c=\pi(d^2/4)$ and moment of inertia $I=\rho_g^2 A_c$, being ρ_g is the radius of gyration of the cross-section defined as $\zeta=\rho_g/d$. Axial stiffness of the cables are defined as function of their normalized area $\eta_{s,i}=A_{s,i}/A_c$ where $A_{s,i}$ is the cross-sectional area of the *i-th* cable, horizontal normalized distance between the mast and the connection of the *i-th* cable to the ground is been defined by the parameter κ_i. The presence of the fabric pre-tensioned system are definedin the *i-th* cable, through the parameter $v_i=q_i c_i/T_i$.

In the case of linear (or linearized) dynamic free vibration of the system in Fig. 1, the lumped-mass dynamic equilibrium equations can be solved by setting $\mathrm{Re}\left|\mathbf{\Phi}e^{i\omega t}\right|$, with $\mathbf{\Phi}$ generalized amplitude vector and ω a generic unknown pulsation. A homogeneous algebraic system of equations can be consequently derived, after proper manipulation, as $[\mathbf{S}-\omega^2=\mathbf{0}\ \mathbf{I}]\mathbf{\Phi}$ with $\mathbf{S}$ being a N_{dof} by N_{dof} matrix and $\mathbf{\Phi}$ a vector containing vibration amplitudes A_j. More details on the derivation of the system and corresponding equilibrium equations are provided in Section 3.

3 DESCRIPTION OF THE LINEAR MODEL FOR DYNAMIC EQUILIBRIUM

The dynamic equilibrium equation at each mass level, described by each mass element (Fig. 1), accounts for the effects of the inertial force related to M or m_j and the effects of the generalized restoring force effect F due to the stiffness effect of the main shaft and to the axial stiffness of the cables connected to the mast. The global dynamic equilibrium of the system can be expressed through the following

$$\mathbf{M}\ddot{\mathbf{x}}+\mathbf{K}\mathbf{x}=\mathbf{0} \tag{1}$$

with $\ddot{\mathbf{x}}=d^2\mathbf{x}/dt^2$ for $j=1,...,N_{dof}$ where N_{dof} is the total number of DOFs. The presence of the unilateral internal force effect is not discussed at this point but is introduced in the next section. A dynamic system is obtained from Eq. (1), conveniently rewritten in matrix form for the *j-th* mass m_j as function of a non-dimensional time $\tau=\omega_0 t$, non-dimensional displacements $\chi_j=x_j/H$ and non dimensional acceleration, $\mathrm{d}^2\chi_j/\mathrm{d}t^2=\omega_0^2\left(\mathrm{d}^2\chi_j/\mathrm{d}\tau^2\right)=\omega_0^2\chi_j''$.

$$\omega_0^2 M_1\mathbf{M}_N\boldsymbol{\chi}''+k_1\mathbf{K}_N\boldsymbol{\chi}=\mathbf{0} \tag{2}$$

The quantity $\omega_0=(k_{ref}/m_{ref})^{0.5}$ is a reference pulsation of a 1DOF system with mass $m_{ref}=m$, and stiffness $k_{ref}=3EI/H^3$ being E and I respectively elastic modulus and moment of inertia of the mast cross section. In Eq. (2) $\mathbf{M}_N$ is a dimensionless mass matrix and $\mathbf{K}_N$ is a normalized stiffness matrix. Eq. (2) can be further simplified as

$$\mathbf{M}_N\boldsymbol{\chi}''+\mathbf{K}_N\boldsymbol{\chi}=\mathbf{0} \tag{3}$$

The linear discrete eigen-value/eigen-vector problem is derived by postulating that the free-vibration solution of the differential system (3) is converted to an algebraic homogeneous matrix system, which can be numerically solved to determine the frequencies α and the non-trivial modes $\mathbf{\Phi}$ from$[-\alpha^2\mathbf{M}_N+\mathbf{K}_N]\mathbf{\Phi}=\mathbf{0}$. As shown in previous works [11, 20], the ELM can be used to derive an approximate solution in the case of non-linear restoring effects in a cable-cross-tie system.

The ELM (Equivalent Linearization Method) is an energy approach requiring the derivation of the work performed by an equivalent linearized spring element (W_{ELM}) and the actual

work performed by the non-linear component of the spring (W_{SLK}), related to each mass $m_j$or M_k of the system in Fig. 1.

In this preliminary step, the presence of the pre-tensioned tensile fabric structure apparatus, is simulated through the equivalent uniformly distributed load q which act on the mast stays, load q simulates the presence of the fabric pre-tensioning apparatus, which at the present stage can be considered uniformly distributed as shown in Fig. 1a. The static configuration of the *i-th* cable can be written as:

$$y_i(\chi) = \frac{q_i}{2T_i}\left(c_i \cdot \chi - \chi^2\right) \tag{4}$$

Where the sag δ_i of the cable can be written as:

$$\delta_i = \frac{q_i \cdot c_i^2}{8T_i} \tag{5}$$

And T_i is the *i-th* axial component of the equilibrium tension of the main cable.

The pre-tensioning parameter represents the initial deformation pre-assigned to the *i-th* pair of stays $\varepsilon_{0,j}$. The work performed by the linearized and non linear pair of stays experiencing slackening ("SLK"), depends on the (still) unknown frequency α. The work becomes espressed in terms of the dimensionless time τ becomes for both cases:

$$W_{ELM,j} = \frac{2\alpha}{\pi}\int_0^{\pi/(2\alpha)} \left\{\chi_j'(\tau)\cdot\chi_j(\tau)\cdot k_{N,ELM,j}\right\} \mathrm{d}\tau \;,\; W_{SLK,j} = \frac{2\alpha}{\pi}\int_0^{\pi/(2\alpha)} \left\{\chi_j'(\tau)\cdot\chi_j(\tau)\cdot k_{N,j}(\chi_j)\right\} \mathrm{d}\tau \tag{6,7}$$

Where the stiffness of the spring of the *j-th* pair of cables corresponding to the lumped mass m_j,or M_j in the model (Fig. 1); it is defined as a function of the dimensionless displacement χ_j .

After imposing $W_{ELM,j}=W_{SLK,j}$ and postulating $A_{E,j}\approx A_j$ (e.g. [12, 15]), the equivalent frequency can be expressed as a function of the equivalent linearized dimensional stiffness of the spring model with slackening of the pair of cables can be determined as

$$k_{N,ELM,j}(\lambda, \varepsilon_{0,j}) = k_{N,j}(W_{ELM,j}, W_{SLK,j}) \tag{8}$$

Were $A_j(\lambda)$ represents the amplitude of the considered eigenvector at the *j-th* mass re-scaled in terms of a reference dimensionless maximum amplitude $A_{max}=\lambda$.

The nonlinear behavior of the tho pair of cables, lead to a "fictitious" reduction of the equivalent spring stiffness $0<k_{N,ELM,j}<k_{N,j}$. In order to quantify the level of "malfunctioning" of the considered pair of stays, a relative "performance coefficient" ΔK can be defined. The ΔK quantity expresses the ratio between the reduced stiffness of the non-linear cable, due to slackening, and the total stiffness which tends to a perfectly linear behavior:

$$\Delta \mathrm{K}_j(\lambda, \varepsilon_{0,j}) = \frac{k_{N,ELM,j}(\lambda, \varepsilon_{0,j})}{k_{N,j}} \tag{9}$$

The quantity ΔK_j does not depend on the frequency α; it is a positive real number be which varies between 0 and 1. The upper and lower limits of ΔK_j refer to two different specific conditions. The upper limit (ΔK_j=1.0) correspond with a approximately linear behavior; the pre-tensioning parameter $\varepsilon_{0,j}$ is sufficiently large to avoid slackening of the of the considered pair of cables for the the considered vibration amplitude λ, ensuring linear response at the pre-selected mode (Full-Stiffness System). The lower limit (ΔK_j=0.0) for the pre-tensioning parameter $\varepsilon_{0,j}$=0, corresponds to the case of cable less structure with and to a practically absence of stiffening effects due to the stays.. The ELM generalized equivalent eigen-value/eigen-vector problem can be formulated in compact matrix form as $\mathbf{Q}(\lambda,\varepsilon_{0,j})\mathbf{\Psi}=\mathbf{0}$,; the linearized eigen-vector $\mathbf{\Psi}=[A_{E,1}, A_{E,2}...A_{E,n}]$ ($\mathbf{\Psi}\neq\mathbf{\Phi}$) collects the modal amplitudes in the case of ELM. Results obtained by ELM were verified through a direct integration approach of the discrete dynamic equations by imposing, mode by mode, suitable boundary conditions in terms of displacement.

4 PARAMETRIC STUDY BY ELM

A special case, derived from the cable stayed mast illustrated in Fig. 1, is investigated; distributed masses are considered as constant $m_j=m=\rho_j \Delta H$ and $M_j=\mu_j m$ (μ_1= 7.7) simulates the masses of the fabric structure of the fabric structure located in in ξ_1=1, ξ_2=0.9 as shown in Fig.1. Presence of the load q was simulated through the non-dimensional parameter $\nu_1=\nu_2$=0.01. Stiffness and geometrical properties of the mast are the described by δ_d=0.002, ζ= 1.0854 with the normalized area of each cable $\eta_{s,i}=\eta_s$=0.00225, $\kappa_1=\kappa_2$=0.8. A parametric study was carried out to examine the effect of internal pre-tensioning force in the cables of the system; the first three of the in-plane modes of the system were analyzed. The presence of non-linearity in the pair of cables produces a reduction in their performance coefficient ΔK and consequently of the equivalent frequency α_E, these parameters are function of the pre-tensioning level $\varepsilon_{0,i}$ imparted to the *i-th* pair of stays and of the vibration parameter λ>0. The numerical results by ELM are presented as a function of the level of the pre-tensioning force $\varepsilon_{0,i}$. The structural response is non-linear due to the alternate slackening in the cables. Various levels of amplitude λ were selected to evaluate different vibration regimes: moderate vibration (λ=0.002, corresponding to 0.2% lateral drift), large vibration (λ=0.004 and λ=0.005) and unrealistically large vibration (λ=0.010).

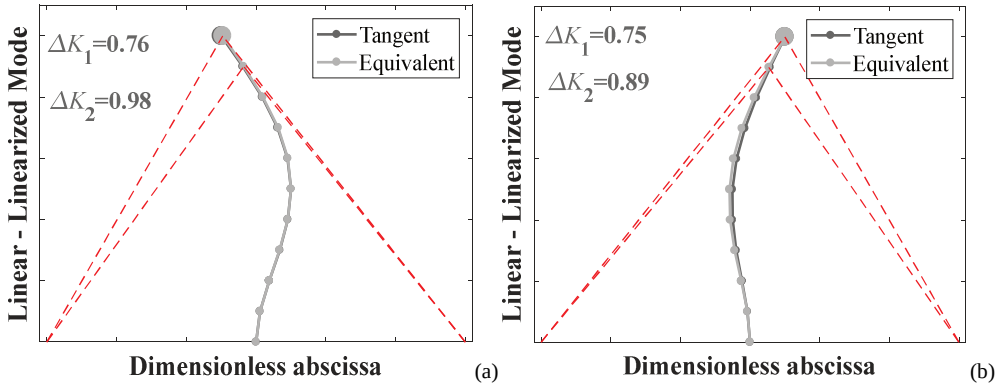

Fig. 2 Comparison between linear and linearized mode shapes for the LM system system depicted in Fig.1with amplitude parameter λ=0.005, experiencing alternate slackening in the *two* pair of cables with pre-tensioning level (a) $\varepsilon_{0,1}=\varepsilon_{0,2}$=0.0005 for the first mode, (b) $\varepsilon_{0,1}=\varepsilon_{0,2}$=0.0005 for the second mode.

In Fig. 2 is illustrated a comparison between linear and linearized mode shapes of the structural system for the first two modes relative to an amplitude λ=0.005, a low level of pre-

tensioning force ($\varepsilon_{0,i}$=0.0005) is been assigned (mode by mode) to both pair of cables identified by the index i (i=1,2); Fig. 3 shows performance coefficients of the two pair of stays of the system illustrated in Fig.1a, in the case of slackening occurring in the first pair (i=1) and linear behavior for the second pair(i=2) and

Has to be noted that for both cases, for the same amplitude λ=0.005, a low pre-tensioning level $\varepsilon_{0,i}$=0.005 can ensure a linear behavior.

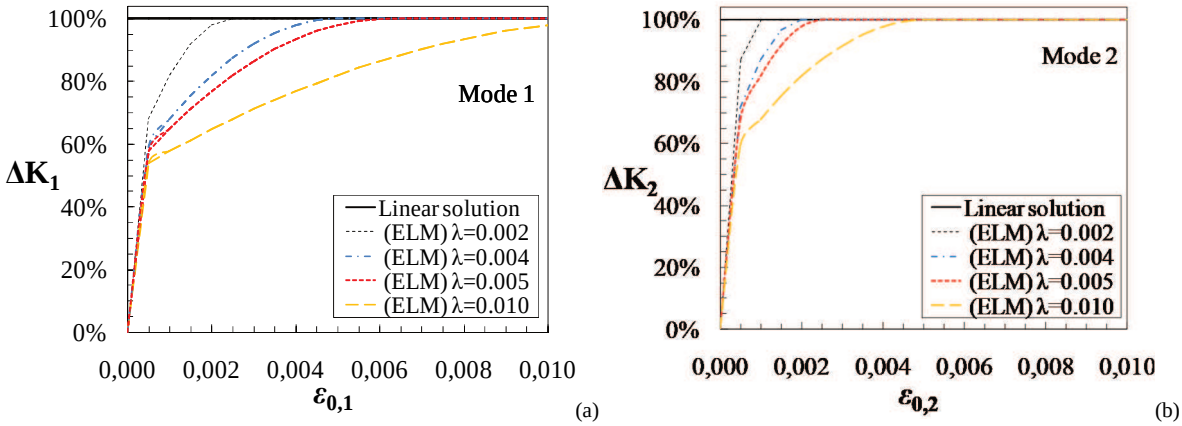

Fig. 3 Performance coefficient ΔK_i of the LM system, as a function of the pre-tensioning level of the *i-th* pair of cables $\varepsilon_{0,i}$ and vibration amplitude parameter λ with slackening in the cables simulated at: (a) first cable for the first mode, (b) second cable for the second mode .

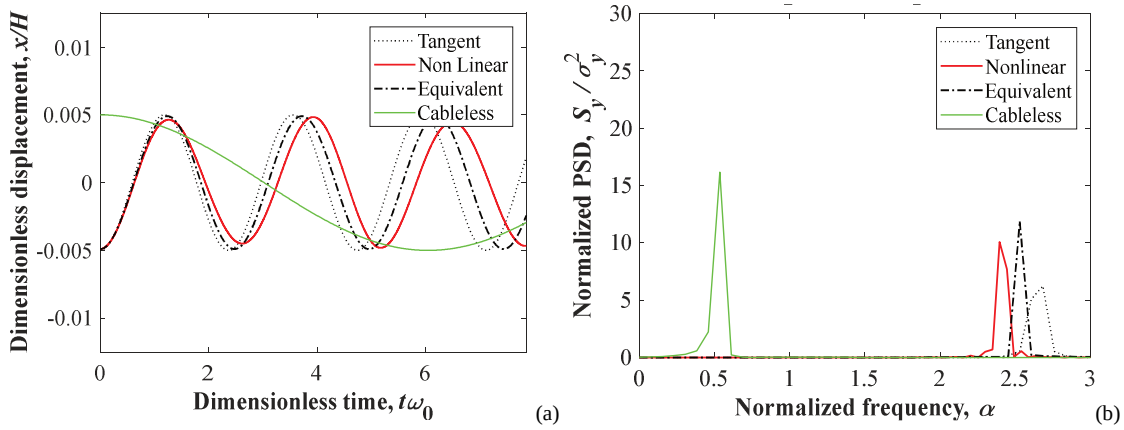

Fig. 4 Time history analysis for the first-mode vibrations of the system for an amplitude parameter λ=0.005, $\varepsilon_{0,1}$=0.0005 and linear behavior in the remaining cables: (a) time history of the horizontal in-plane displacements at the top obtained by direct integration approach , (b) power spectral density of the displacements at the top.

In Fig.3 is shown the parametric study conducted for the first two modes of the mast, performance coefficient ΔK_i is illustrated as function of the pre-tensioning level $\varepsilon_{0,i}$ of the *i-th* stay, results are shown for different values of the amplitude parameter λ, Fig.4a shows that for a chosen amplitude (λ=0.005) the first mode reaches the linear behavior (ΔK_1=1) for a pre-tensioning level $\varepsilon_{0,1}$ =0.006, on the other hand second mode requires a lower pre-tensioning level of the second stay ($\varepsilon_{0,2}$ =0.002). Figure 4 presents the results obtained through a direct integration approach, linearized frequency α_E is shown in comparison with α_{NL} (peak frequency of the non-linear system) for the pre-tensioning parameter $\varepsilon_{0,1}$=$\varepsilon_{0,2}$=0.0005.

5 DISCUSSION AND CONCLUSIONS

The present paper examined a generalized model of pre-tensioned-cable stayed mast of tensile fabric structure, with non-linear dynamic behavior caused by the slackening in the stays. The effects were analyzed by varying the pre-tension imparted to the cables. The ELM was used to study a simplified model of the system, which simulates the dynamic response. A performance coefficient was introduced to describe the dynamic behavior of each pair cables. If no slackening occurs and linear behavior is present in the cables, the performance coefficient is equal to one. On the other hand a performance coefficient smaller than one means the presence of slackening in the supporting cables. The performance coefficient can reach a lower limit of 0 in case of total absence of pre-tensioning force in the cables. The performance coefficient depends on the considered mode, on the level of pre-tensioning force assigned to the cables and on the initial conditions (reference vibration amplitude λ). Performance coefficient could be considered as helpful designing tool for setting a suitable pre-tensioning level in the cables. A concept of linearized frequency is been introduced aimed to characterize the dynamic non-linear behavior of the considered system.

ACKNOWLEDGMENTS

The author thanks, Professor Piero D'Asdia for the non-commercial TENSO software and implementation**.**

REFERENCES

[1] T.C.o.T.F. Structures, Tensile Fabric Structures, Design, Analysis and Construction, ASCE American Society of Civil Engineers, 1801 Alexander Bell Drive, Reston, Virginia, 20191-4400, 2013.
[2] M. Seidel, Tensile Surface Structures, A practical Guide to Cable and Membrane Construction, Ernest & Sohn, Wissenschaften GmbH &Co. KG, Berlin, Germany, 2009.
[3] R.-F. Fung, L.-Y. Lu, S.-C. Huang., Dynamic modeling and vibration analysis of flexible cable-stayed beam structure, Journal of Sound and Vibration 254(4) (2002) 717-726.
[4] V. Gattulli, M. Lepidi, Nonlinear interactions in the planar dynamics of cable-stayed beam, International Journal of Solids and Structures 40 (2003) 4729–4748.
[5] Rizzo, F.; Barbato, M.; Sepe, V. Peak factor statistics of wind effects for hyperbolic paraboloid roofs. Eng. Struct. 2018, 173, 313–330.
[6] M. Gioffrè, N. Cavalagli, V. Gusella, Movable guyed masts affected by wind loads: Buckling and stochastic response, Structural Control and Health Monitoring 15 (2008) 299–314.
[7] I. Venanzi, A.L. Materazzi, L. Ierimonti, Robust and reliable optimization of wind-excitedcable-stayed masts, Journal of Wind Engineering and Industrial Aerodynamics 147 (2015) 368-379.
[8] G.F. Giaccu, L. Caracoglia, Wind-load fragility analysis of monopole towers by Layered Stochastic-Approximation-Monte-Carlo method, Engineering Structures 174 (2018) 462-477
[9] S. Ali Ghafari Oskoei, G. McClure, A novel approach to evaluate the equivalent dynamic stiffness of guy clusters in telecommunication masts under ground excitation, Engineering Structures 33 (2011) 1764–1772.
[10] G.F. Giaccu, L. Caracoglia, B. Barbiellini, Higher-order moments of eigenvalue and eigenvector distributions for the nonlinear stochastic dynamics of cable networks, Procedia Engineering 2017 pp. 637-642.

[11] L. Caracoglia, G.F. Giaccu, B. Barbiellini, Estimating the standard deviation of eigenvalue distributions for the nonlinear free-vibration stochastic dynamics of cable networks, Meccanica (2016) 1-15.
[12] G.F. Giaccu, L. Caracoglia, B. Barbiellini, Modeling unilateral response in the cross-ties of a cable network: deterministic vibration, Journal of Sound and Vibration 333(19) (2014) 4427–4443.
[13]Rizzo, F.; Caracoglia, L.; Montelpare, S. Predicting the flutter speed of a pedestrian suspension bridge through examination of laboratory experimental errors. Eng. Struct. 2018, 172, 589–613.
[14] Rizzo, F.; Caracoglia, L. Examining wind tunnel errors in Scanlan derivatives and flutter speed of a closed-box. J. Wind Struct. 2018, 26, 231–251.
[15] G.F. Giaccu, L. Caracoglia, Effects of modeling nonlinearity in cross-ties on the dynamics of simplified in-plane cable networks, Structural Control and Health Monitoring (2011) DOI:10.1002/stc.435.
[16] G. Giaccu, L. Caracoglia, A Displacement-Based Approach for Determining Non-Linear Effects on Pre-Tensioned-Cable Cross-Braced Structures, Journal of Sound and Vibration accepted for publication (2016).
[17] G.F. Giaccu, An equivalent stiffness approach for modeling non-linearity in the dynamics of pre-tensioned cable-stayed masts, in: P. Engineering (Ed.) 2017 pp. 631-636.
[18] A.H. Nayfeh, D.T. Mook, Nonlinear oscillations, John Wiley and Sons, Hoboken, New Jersey, USA, 1995.
[19] W. Lacarbonara, G. Rega, A.H. Nayfeh, Resonant non-linear normal modes. Part I: analytical treatment for structural one dimensional systems, International Journal of Non-Linear Mechanics 38(6) (2002) 851-872.
[20] G.F. Giaccu, L. Caracoglia, Generalized power-law stiffness model for nonlinear dynamics of in-plane cable networks, Journal of Sound and Vibration 332(8) (2013) 1961-1981.

COMPDYN 2019
7th ECCOMAS Thematic Conference on
Computational Methods in Structural Dynamics and Earthquake Engineering
M. Papadrakakis, M. Fragiadakis (eds.)
Crete, Greece, 24-26 June 2019

TIME-HISTORY AND PUSHOVER ANALYSES OF ASYMMETRIC STRUCTURES USING AN EFFICIENT NON-LINEAR REINFORCED CONCRETE MODEL ACCOUNTING FOR CRACKING

LHERMINIER Olivier[1,2], HUGUET Miquel[2], NEDJAR Boumediene[1], ERLICHER Silvano[2], ARGOUL Pierre[1]

[1] IFSTTAR-MAST-EMGCU
14-20 Bd Newton, Cité Descartes, 77477 Marne-la-Valle Cedex 2
e-mail: olivier.lherminier@ifsttar.fr, pierre.argoul@ifsttar.fr, boumediene.nedjar@ifsttar.fr

[2] EGIS
4 rue Dolorès Ibarruri, 93188 Montreuil Cedex
e-mail: silvano.erlicher@egis.fr, miquel.huguet-aguilera@egis.fr

Keywords: Reinforced concrete, Cracking, Damage, Off-plane bending and shearing, Seismic margin assessment, Post-earthquake state, Non-linear constitutive model, Finite elements.

Abstract. *Non-linear calculation results can be significantly different when considering monotone or cyclic analyses. The crack opening and re-closing phenomena are quite difficult to represent with non-linear constitutive models using finite elements methods. The comparison between seismic time-history and pushover analyses is performed in this paper using GLRC_HEGIS non-linear global model for reinforced concrete mono-layer shell elements. It takes into account four different dissipative phenomena: concrete cracking, concrete damage, steel-concrete slip and steel yielding, by means of an analytical multi-scale analysis. This stress-resultant model is formulated for cyclic calculations in the framework of the thermodynamics of irreversible processes, in order to allow efficient numerical computations of earthquake engineering applications of RC buildings. This paper explores the validity range of this constitutive law through cyclic time-history analyses (that consider the crack opening and re-closing phenomena) and monotone pushover static analyses on asymmetric structures of CASH and SMART benchmarks. Pushover analysis is a nonlinear static procedure for evaluating the seismic margin of buildings accounting for their non-linear behavior. The pushover method used in this paper is the so-called Enhanced Direct Vectorial Addition (E-DVA) which defines the load pattern for the pushover analysis as a linear combination of load patterns proportional to the mode shapes. As this method is based on the application of a static force field with constant shape and increasing amplitude, only monotone non-linear phenomena are taken into account. The pushover and time-history analyses are performed (i) on the CASH benchmark model representing a multi-storey shear wall of a real nuclear power plant building structure and (ii) on the SMART benchmark mock-up representing a typical RC building of a nuclear facility. Several numerical comparisons are made at both global and Gauss points levels and are focused on the global mechanical behaviour and the computation of crack opening.*

1 Introduction

In many applications, RC structural analysis is usually realized by design offices using Finite Element (FE) models accounting for a structural linear elastic behaviour. However, in some cases (e.g. nuclear buildings), structural verifications have to be performed under extreme seismic solicitations; in this case, a non-linear behaviour is needed for RC cyclic calculations. Moreover, from a structural and earthquake-resistant point of view, when the bracing system of a structure essentially consists in shells connected to each other and to the slabs by heavily armed chaining, the contribution of RC slabs and walls have to be well represented.

The non-linear behaviour at the global scale of a RC element can be defined by the apparition and the evolution of different non-linear physical phenomena that dissipate energy. In this paper, the RC walls and slabs of the analyzed structures are modelled by GLRC_HEGIS [1] constitutive model. This thermodynamic admissible law accounts for four non-linear mechanisms: concrete cracking, concrete damage (or stiffness reduction), steel-concrete relative slip and steel yielding. It allows an efficient global modelling using a mono-layer shell FE, since the multiscale analysis has been performed analytically and the model implementation only accounts for the formulation at the global scale (macro-scale). A lot of information is available at the end of a FE calculation with GLRC_HEGIS since many results of interest (as crack width, steel plastic strain...) are internal variables of the model. More details about this constitutive model are presented in chapter 2.

In this paper, the seismic action is taken into account by two different methods: nonlinear time-history and nonlinear pseudo-static pushover analyses. The basic (or classical) version of the pushover method is based on three main assumptions: (i) the structure has a plane of symmetry; (ii) there is a single horizontal earthquake component, parallel to the plane of symmetry; (iii) the dynamic behavior is governed by a dominant mode of vibration (with high effective mass). Therefore, the basic pushover analysis cannot be applied for the assessment of global torsion, local effects or influence of high frequency modes, and asymmetric buildings cannot be analyzed. For that reason, in this paper the Enhanced Direct Vectorial Approach (E-DVA) [2] is used to take into account many modes of irregular buildings under a multi-component earthquake. The load pattern for the pushover analysis is defined as a linear combination of modal load patterns using the modal weighting factors (called α-factors), which are calculated using the elliptical response envelopes. The details of this pushover method are presented in chapter 3.

These two seismic nonlinear methods (time-history and pushover analysis) are compared with each other by application to two different structures in chapter 4. First, a four-story framed in-plane irregular asymmetric wall extracted from the CASH benchmark is analyzed in section 4.1. Then, the three-story RC building of SMART benchmark is considered in section 4.2, accounting for the nonlinear behavior of its RC walls and slabs. Comparisons are done at the global (force, displacements) and local (crack width, steel yielding...) scales to analyze the pertinence and the interest of each of these two different nonlinear methods for seismic structural analysis.

2 Constitutive model: GLRC_HEGIS law for RC walls and slabs

An efficient and realistic material cyclic constitutive model is necessary for the comparison between the different seismic calculation approaches. Since the applications in chapter 4 are RC structures composed by walls and slabs, the GLRC_HEGIS model [1] is used for the material modelling. As shown in [3], this model is adapted to nonlinear seismic applications.

The model is implemented in the FE software Code_Aster [4] and allows an efficient global modelling and computation since it is implemented in mono-layer shell FE, accounting for an equivalent "reinforced concrete material". In order to obtain a stress-resultant model accounting for many nonlinear cyclic local phenomena which are at the origin of the nonlinear global behavior of RC elements, an analytical multi-scale analysis has been performed in [1]. Therefore, there is no need of time-costly numerical multi-scale analysis at each Gauss point and at each load step. The resulting model is formulated in the framework of the Thermodynamics of Irreversible Processes; the detailed formulation can be found in [5]. The four different local nonlinear cyclic mechanisms taken into account by GLRC_HEGIS are the following ones:

- Concrete cracking is the development of concrete displacement discontinuities (or macro-cracks) caused by tensile stresses. At each Gauss point, a constant average stabilized crack pattern characterized by the crack spacing s_r (obtained with Vecchio and Collins [6] formula) and orientation θ_r (perpendicular to the principal tensile strength) appears when tensile forces reach the concrete tensile strength f_{ct}. After this cracking onset, these two parameters remain known and constant (fixed crack model), where only the normal (crack width) w_n and tangential w_t crack displacements evolve with the applied force by following the retained bridging stress and aggregate interlock local laws respectively. Four family of cracks are considered: for each layer (top and bottom) of the RC shells, the typical crack pattern of RC walls submitted to cyclic in-plane shear loading can be reproduced by two family of cracks characterized by two different crack orientations.

- Concrete damage is assumed to be associated with the onset and development of homogeneous diffuse micro-cracking, which results in a concrete stiffness reduction. This degradation of concrete stiffness only takes place at high strain levels, above the limit value in tension f_{ct}/E_c. Therefore, concrete damage is supposed to be associated to compressive concrete behaviour. GLRC_HEGIS considers concrete damage as isotropic and it is introduced as an internal damage variable d scalar (two values, defined for both top and bottom layers of the RC shell), positive, non-decreasing in time and which can evolve only at high stress states.

- Relative slip between concrete and steel bars originates bond stresses for each x and y and top and bottom steel reinforcement layers. As stresses are transmitted from steel to concrete between consecutive cracks, this phenomena is at the origin of the tension stiffening effect. GLRC_HEGIS model uses an inelastic steel-concrete slip variable to limit the average tension stiffening effect to values given by the codes like [7].

- Steel reinforcement yielding is supposed to be concentrated at the crack crossings due to the steel-concrete stress transfer by bond. GLRC_HEGIS model considers that reinforcement bars only carry longitudinal forces and that the constitutive law is elastic-perfectly plastic characterized by a constant threshold equal to the steel yielding stress f_{sy}.

3 Pushover method: the Enhanced Direct Vectorial Approach (E-DVA)

The pushover analysis is a seismic nonlinear calculation method based on the application of a static force field with constant pattern and increasing amplitude on a nonlinear structural model. In the basic versions, the pattern of the applied load is generally chosen as proportional to the deformed shape of the dominant vibration mode for a given earthquake component. Other conventional patterns are constant or triangular, or more complex when choosing the vector of the CQC (Complete Quadratic Combination) of the pseudo-accelerations for a given earthquake component. Some adaptive approaches exist, where the load pattern is updated to account for the effects of the non-linear phenomena.

As presented in section 1, the basic version of the pushover analysis does not reproduce accurately the seismic behavior of no-perfectly regular and no-perfectly symmetric structures. For that reason and for the numerical comparisons of this paper, more advanced pushover methods are needed in order to account for interesting and conclusive results. When doing a pushover analysis, the loading pattern selection is likely more critical than the accurate determination of the target displacement.

Several generalizations of the basic pushover analysis have been proposed in the past years, in particular by Chopra and co-workers [8, 9, 10, 11], Fajfar and co-workers [13, 12, 14] and Penelis and Papanikolaou [15]. Some of these approaches take into account the possible multi-modal structural behavior, but all assume that the earthquake is mono-component. The Direct Vectorial Addition (DVA) (Kunnath [16], Lopez-Menjivar [17]) extends the pushover method to the case of multi-component earthquake by application of a load pattern obtained by a linear combination on the modes and earthquake directions.

The E-DVA pushover method is used in this work. It is based on the DVA approach and a rigorous definition of the weighting factors (α-factors) is provided, based on the notion of response envelopes of Menun and Der Kiureghian ([18]). This definition for the load pattern was first proposed by Erlicher et al. [20], which allows imposing an a priori chosen response of the structure. The pertinence of this pushover approach when comparing to time-history non linear analysis has been shown in [21]-[22].

3.1 The load pattern as a linear combination of modes

On the global axes (x, y, z) of the FE model of a structure, the mass $\underline{\underline{M}}$ (assumed diagonal) and the stiffness matrix $\underline{\underline{K}}$ are defined. It is supposed that the seismic input may have 1, 2 or 3 translational components, whose corresponding ground accelerations are named $a_{g,x}(t)$, $a_{g,y}(t)$ and $a_{g,z}(t)$, which act in the directions given by the influence vectors $\underline{\Delta_k}$ corresponding to the translation in the $k = x, y, z$ direction.

The non-adaptative pushover analysis are defined by a nodal force vector $\underline{q}_{pushover}(t)$ with constant shape and increasing amplitude:

$$\underline{q}_{pushover}(t) = c(t)\underline{Q} \tag{1}$$

where $c(t)$ is a scalar increasing pseudo-time function and $\underline{Q}$ is the constant vector defining the pattern of the nodal force field (a displacement-driven is also equivalently possible). The E-DVA approach defines this load pattern as:

$$\underline{Q} = \sum_{k=1}^{n_{ec}} \sum_{i=1}^{n} \alpha_{i,k} \underline{\underline{M}} \cdot \underline{A}_{max,i,k} \tag{2}$$

where $\alpha_{max,i,k}$ is the linear combination factor and $\underline{A}_{max,i,k}$ is the maximum pseudo-acceleration vector for the for the n retained modes i and n_{ec} earthquake directions k:

$$\underline{A}_{max,i,k} = (2\pi f_i)^2 S_{d,k}(f_i, \xi_i)\gamma_{i,k}\underline{\Phi}_i \tag{3}$$

where $S_{d,k}(f,\xi)$ is the response spectrum, f_i ,ξ_i and $\underline{\Phi}_i$ are respectively the modal frequency, damping ratio and deformed shape of mode i, and $\gamma_{i,k}$ is the participation factor of mode i with respect to earthquake direction k.

3.2 Different pushover analyses for different load cases

It can be shown that any response vector any any time $\underline{f}(t)$ (vector containing forces and/or displacements and/or stresses...) can be written as a linear combination of modal responses with the weighting factors $\alpha_{i,k}(t)$ [20]. Actually, only some response vectors are of interest when comparing to time-history analyses, those that maximize the value of parameters of interest, e.g. that maximum force in the x direction at the basis of a building or the maximum displacement in the y direction of a point of the roof. These response vectors corresponding to the load cases that maximize the interest parameters can be obtained using the notion of elliptical responses, as done in [21].

Once the response vector $\underline{f}(t)$ is known, the vector of modal combination $\underline{\alpha}$ is calculated following Erlicher et al. [20]:

$$\underline{\alpha} = \underline{\underline{\tilde{H}}} \cdot \underline{\underline{R}}_f \cdot \underline{\underline{X}}_f^{-1} \cdot \underline{f} \tag{4}$$

where $\underline{\underline{\tilde{H}}}$ is the modal coefficient correlation matrix, $\underline{\underline{R}}_f$ is the modal response vector matrix and $\underline{\underline{X}}_f = \underline{\underline{R}}_f^T \cdot \underline{\underline{\tilde{H}}} \cdot \underline{\underline{R}}_f$ is the matrix which defines the elliptical domain of the concomitant values of $\underline{f}$ by:

$$\underline{f}^T \cdot \underline{\underline{X}}_f^{-1} \cdot \underline{f} \leq 1 \tag{5}$$

Finally, in Erlicher et al. [24] a method is proposed to choose several dominant modes to reach the searched response. As the total value of the response vector is $\underline{f} = \underline{\underline{R}}_f^T \cdot \underline{\alpha}$, the value of the parameter of interest of the response vector is compared to the cumulative contribution of each mode (and earthquake direction) by means of the sum of the products between α_{ik} and the corresponding line of $\underline{\underline{R}}_f$, for the column corresponding to the parameter of interest.

3.3 The equivalent seismic spectrum for multi-direction earthquakes

A difficulty exists when trying to define the response spectrum for an earthquake acting in the direction of the earthquake $\underline{t}$, which is identified as the direction of the resultant of the load pattern $\underline{Q}$. By considering the deformed shape $\underline{U}$ under $\underline{Q}$ load $\underline{U} = \underline{\underline{K}}^{-1} \cdot \underline{Q}$, the participation factor of $\underline{U}$ in the $\underline{t}$ direction can be defined. In this direction, the structure vibrates with an equivalent frequency f^* and damping ratio ξ^*.

For a single-component earthquake, the maximum displacement can be easily calculated from the corresponding spectrum. For example, for single-component earthquake in direction $k = x$, one has $\gamma_{U,t} = \gamma_{U,x}$ and the response spectrum is $S_{d,x}(f^*, \xi^*)$. Analogous formulas can be written for earthquake components y and z. Based on the assumption of non-correlation between accelerograms in the x, y and z directions, the SRSS combination is used to define s_{max} for a multi-component earthquake:

$$S_{d,t}(f^*, \xi^*) := \frac{1}{|\gamma_{U,t}|}\sqrt{(\gamma_{U,x}S_{d,x}(f^*,\xi^*))^2 + (\gamma_{U,y}S_{d,y}(f^*,\xi^*))^2 + (\gamma_{U,z}S_{d,z}(f^*,\xi^*))^2} \tag{6}$$

4 Numerical Applications

4.1 Irregular wall from CASH : Benchmark on the beyond design seismic capacity of reinforced concrete shear walls

CASH is an international benchmark organised by the OEDC-NEA (Nuclear Energy Agency). The main purpose is to evaluate the accuracy of tools and prediction methods used in civil engineering for the estimation of the seismic capacity of shear reinforced concrete walls in "beyond design" seismic situation (important seismic excitation). The benchmark study focuses on two different multi-storey shear walls representative of a real NPP building structure. The results presented in the article are those obtained for the irregular structure (Figure 1-b) and the following post-treatment results are not those presented to the benchmark but are only examined for the purpose this article.

4.1.1 Model description

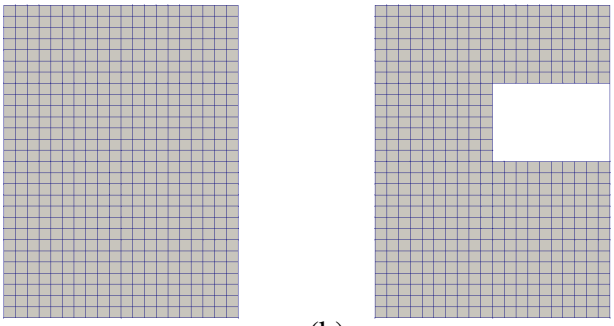

(a) (b)

Figure 1: CASH Finite Element models on Code_Aster

The structure represents the facade of a building with four floors, the studies are done in the plane (2D) of the wall. The height of the structure is 16m for 12m width and 0.40m thick. Slabs and out-of-plane walls are represented by beams and columns with strong depths. In-plane walls are modelled with shell elements using the GLRC_HEGIS global constitutive law and beams and columns are modelled with multifiber beams elements using the MAZARS constitutive law [23] for concrete fibers and an elastic-plastic model (with kinematic hardening) for steel fibers.

4.1.2 Modal and spectral analyses

The purpose of this section is to evaluate the linear response of the considered irregular structure for a given pseudo-acceleration spectrum. First, the modal analysis is performed and the corresponding spectral values are calculated.

The results of the modal analysis performed on the FE model are summarized in Table 1. The 5 retained modes account for 99% of the total mass for x and z directions.

4.1.3 Pushover analysis

The objective of this analysis is to evaluate the non-linear response of the wall under an increasing horizontal load proportional to a specific profile. The E-DVA method procedure described in [24] is applied step by step.

Modes	**Frequency [Hz]**	**Effective mass in X [kg]**	**Effective mass in Z [kg]**	$S_{a,X}$ $[m/s^2]$	**Damping factor [%]**
1	4.21	1730	0	4.06	2.00
2	14.1	422.0	0	2.37	1.36
3	24.1	0	21.80	1.91	1.54
4	24.8	0	373.0	1.79	1.75
5	26.2	68.80	0	1.71	1.95

Table 1: Five first modes calculated for the irregular CASH specimen

(a) Based on the modal basis above, response-spectrum analysis and CQC coefficients are used to determine the response matrix of the six efforts $\underline{f} = [F_x, F_y, F_z, M_{xx}, M_{yy}, M_{zz}]^T$ at the basis of the structure, for the spectra of Figure 1(c):

(b) The response matrix $\underline{\underline{X}}_f$ of Eq.(5) defining the ellipse of the maximum seismic efforts F_x, F_z is obtained from the first and the third rows and columns of the matrix.

(c) The choice of the loading direction is done here in the plan X-Z in the directions of the global coordinate system +X and -X to maximize the global forces $+F_x$ and $-F_x$.

(d) The corresponding $\underline{\alpha}$-vectors are computed using Eq. (4)

Direction	**+Fx**	**-Fx**
F_X (kN)	7571	-7571
f^* (Hz)	4.92	4.92
$\xi^*(\%)$	2.0	2.0
$\gamma_{U,X}(m^{-1})$	237	237
$[\underline{U}]_{j,X}$ (mm)	5.42	-5.42
	0.00	0.00
	-0.550	0.550

Table 2: Equivalent SDOF parameters for the considered load cases

Direction	**+Fx**		**-Fx**	
	Modes	Contribution	Modes	Contribution
	1	(90.4%)	1	(90.4%)
	2	(9.25%)	2	(9.25%)
	4	(0.302%)	4	(0.302%)
	3	(0.0%)	3	(0.0%)
	5	(0.0%)	5	(0.0%)
$\tilde{ik}_{max}$	1 mode is sufficient		1 mode is sufficient	

Table 3: Number of modes and corresponding percentage of the total response needed

(e) The procedure is applied to determine the dominant modes: based on the $\alpha_{i,k}$ factors calculated at step (d),the products $\alpha_{i,X}\underline{F}_{i,X}^T$ are computed for the two load cases. The cumulative sum of the products according to the order defined in Table 3 is normalized according

to the maximum response (second row of Table 2). For instance, when taking $C_d = 0.90$ as suggested in [25] at chapter 4.3.1(b), the first ik_{max} modes are dominant since their contribution to the response $F = \underline{f}^T \cdot \underline{b}$ is 90% of the total response. Table 3 shows that only the first mode is needed to fulfill this condition.

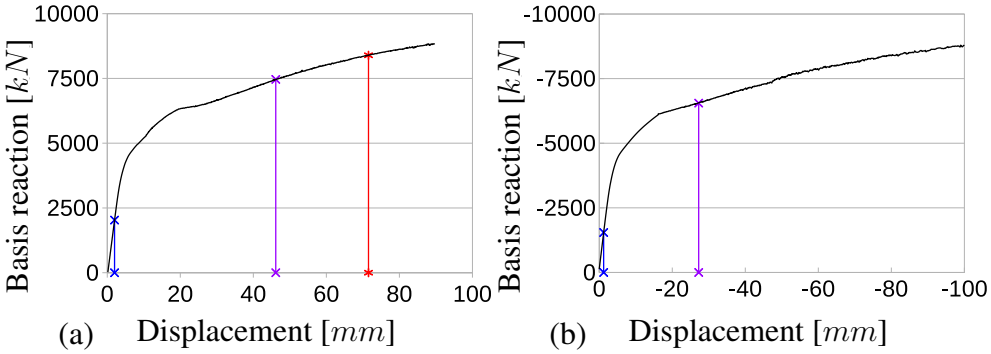

Figure 2: Pushover curve (Force-Displacement) for (a) +Fx and (b) -Fx load cases

The application of incremental unidirectional loading for pushover analysis gives global force-displacement curves which can be analyzed to distinguish the evolution of the activated non-linear phenomena. First, in Figure 2, a linear segment describe the non-cracked phase (before the blue line), then there is creation of several cracks. When the crack pattern is stabilized, the crack width increase and the steel reinforcement can yield (purple line) and finally a "tension-stiffening" effect can be observed. As shown in Figure 2, the concrete ultimate limit in compression is reached for a displacement of +72 mm (red line) and corresponds to a strain level of $\epsilon_u = 3.5‰$. It can be explained by the fact that the concrete developed too many micro-cracks in compression and can't bear more stress. The structure only reach its ultimate capacity in compression in the direction +Fx.

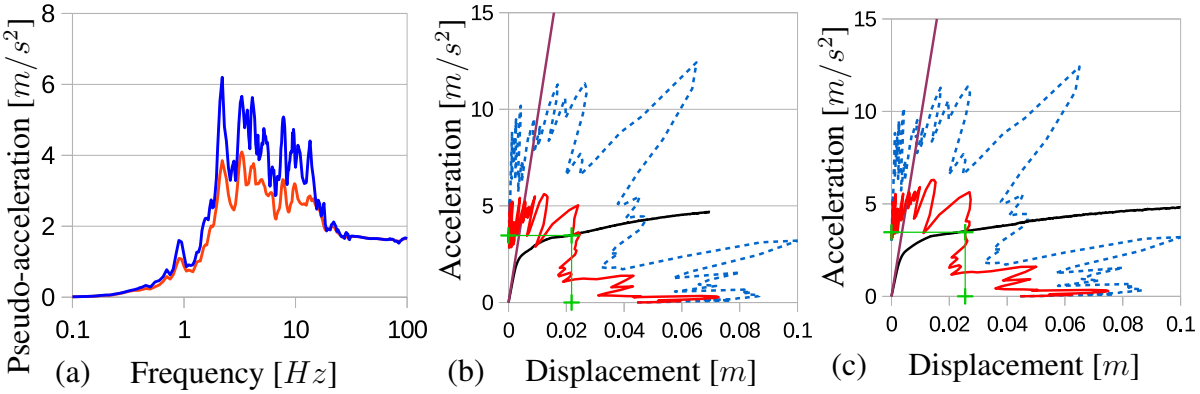

Figure 3: (a) Spectra and graphical results in the ADRS plane for the cases (b) +Fx (c) -Fx

Then, the coordinates of each target point are determined at the intersection of the capacity spectrum with the Acceleration Displacement Response Spectrum (ADRS) given by Eq. (6). The damping ratio $\tilde{\xi}^*$ of ADRS after iteration accounts for the hysteretic damping (Figure 3). The target point coordinates are shown in Table 4, with F_X and V_X corresponding to the obtained target global reaction and displacement of the structure, respectively.

Direction	+Fx	-Fx
$S_a(m/s^2)$	2.78	2.81
$S_d(mm)$	7.79	8.08
$\tilde{\xi}^*(\%)$	12.6	8.80
F_x(kN)	5257	-5272
V_x(mm)	10.18	-10.25

Table 4: Obtained target points for the considered load cases

4.1.4 Time history analysis

To evaluate the non-linear response of the irregular specimen under a horizontal seismic loading, a accelerogram whose spectrum corresponds to the one used in the pushover analysis is imposed to the structure. The chosen seismic input data is scaled to a $PGA = 0.16g$ intensity earthquake.

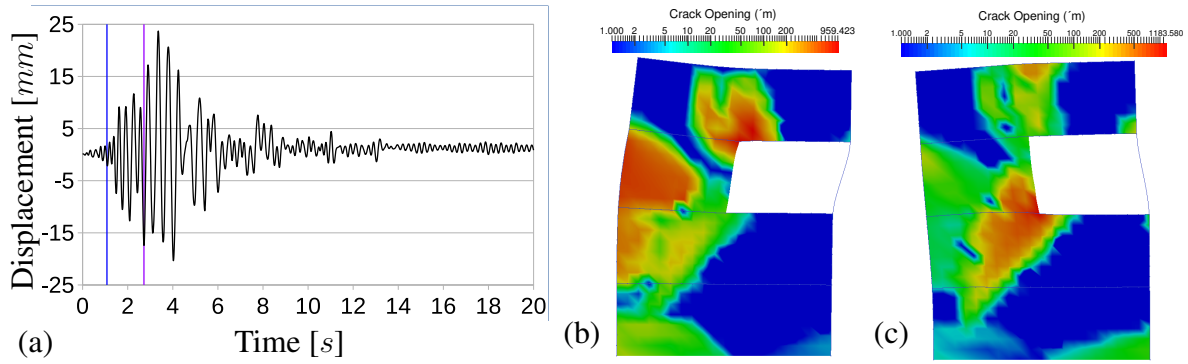

Figure 4: (a) Time-history roof displacement and obtained crack opening at (b) maximal displacement +Vx and (c) maximal displacement -Vx

The graphical results are shown in Figure 4 (a). Two non-linear indicators are given : the first concrete crack (blue line) and the first steel reinforcement yielding (purple line). The crack pattern at the maximal displacements in both directions are shown in Figure 4 (b) and (c).

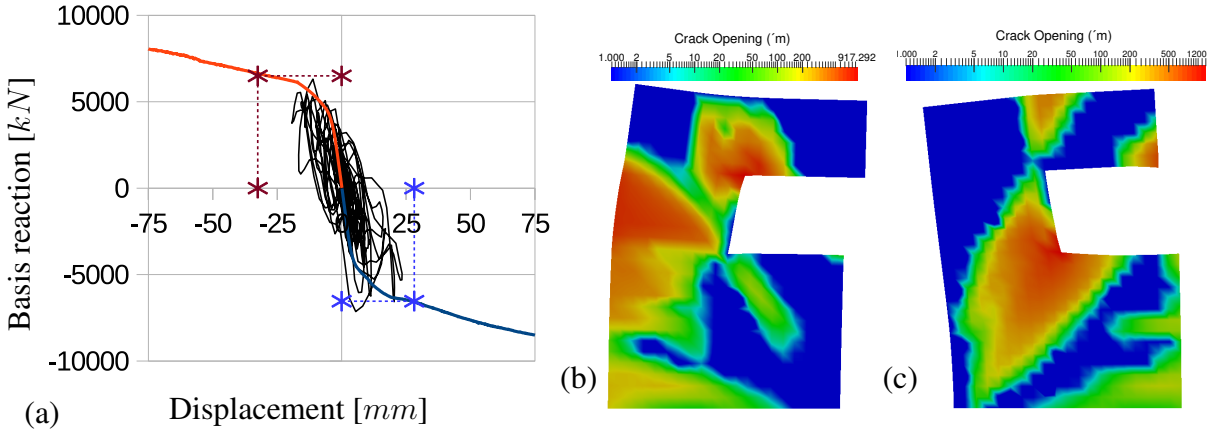

Figure 5: (a) Comparison of the capacity curves and obtained crack opening during the pushover analyses at (b) target point +Vx and (c) target point -Vx

4.1.5 Comparison between time history and pushover analyses

The graphical comparison of Figure 5 (a) shows that the dynamic results (black lines) are mostly inside the envelope area defined by the obtained target points (red and blue) and that the calculated forces that are presented in Table 4 are well estimated by the pushover (Figure 5 (a)) compared to the time-history results. The pushover results given by the E-DVA approach provide a suitable and accurate envelope of the maximum roof displacements and global forces at the basis of the building.

In order to compare the obtained crack pattern, the crack opening values using GLRC_HEGIS are plotted at the pushover target point. The results of Figure 5 (b) and (c) show that the crack patterns obtained by the pushover analyses are very close of the one obtained by time-history analysis showed in Figure 4 (b) and (c).

4.2 SMART: Seismic design and best-estimate Methods Assessment for Reinforced concrete buildings subjected to Torsion and non-linear effects

The experimental program SMART [26] was supported by the French companies Commissariat l′Energie Atomique et aux Energies Alternatives (CEA) and Electricite de France (EDF) and partially by the International Atomic Energy Agency (IAEA). The goals of the benchmark are to compare and to validate the used methods to evaluate the seismic responses of reinforced concrete structures under a seismic loading that induce 3D effects such as torsion and out-of-plane shear and to check the accuracy of prediction approaches of advanced calculation methods used in earthquake engineering.

4.2.1 Model description

The program concerns a $1/4$ scale mock-up of a representative asymmetric RC multi-storey building in nuclear power plants. The experimental moke-up was tested under seismic loadings applied by the shaking table with 6 degrees of freedom AZALE at CEA Saclay. The tested structure corresponds to SMART 2013 international benchmarks [26], but the foundation conditions are not respected in this article and all the comparisons to experimental results are out-of-scope of this paper. The structure shown in Figure 6(a) represents a asymmetric 3 storey reinforced

(a) 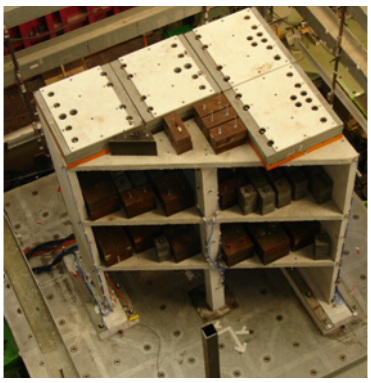 (b) 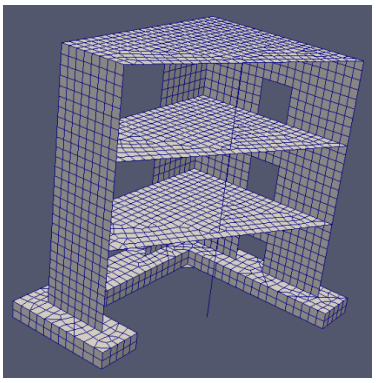

Figure 6: SMART (a) experimental moke-up and (b) used FE model on Code_Aster

concrete building and consists of RC slabs, walls, beams and columns. In the FE model of Figure 6(b), only the two first types of structural elements are modelled with the developed GLRC_HEGIS constitutive model, while beams and columns are modelled with a linear elastic

law. Therefore, all the non-linearities are originated by the nonlinear response of the developed model. The full building is 3.650 m height for 3.100 m width, walls are 10 cm thick and beams and columns are 15 cm and 20 cm thick respectively. In order to check the performances of the constitutive law GLRC_HEGIS, several studies were carried in parallel of the benchmark to compare the obtained results in the same way than those of the previous numerical application. Therefore, the shaking table was not taken into account here to save computation time but the benchmark will be fully conducted in a second time and the shaking table will be added.

For preliminary studies carried on the SMART building, several sets of seismic input data were generated. There particularity is that they all were generated from a unique aimed spectrum. Therefore, spectral, pushover and time-history results can be compared between each seismic input sets. The obtained pseudo-acceleration spectra were compared to only keep those which don't exceed a 10% error from the aimed spectrum, see Figure 7. All the generated accelerograms are different but the modes of the structure can be excited in a comparable way. The seismic intensity of the aimed spectrum is given by PGA$= 2.45m/s^2$.

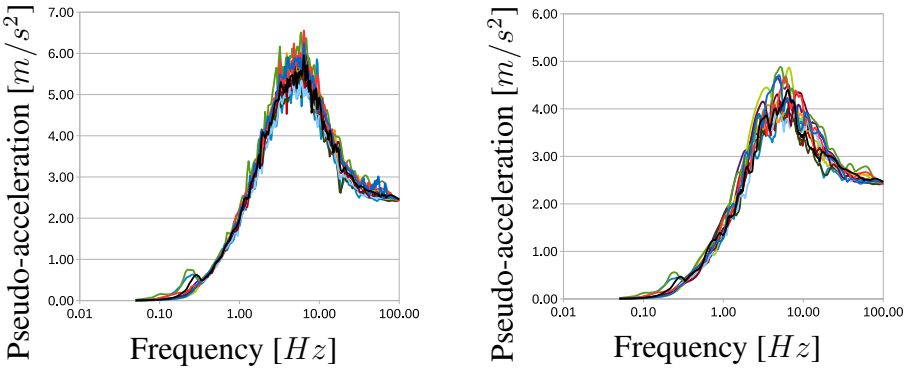

(a) Spectra at 5% damping

(b) Spectra at 10% damping

Figure 7: Chosen spectra associated to the seismic pseudo-acceleration inputs for the preliminary SMART studies

4.2.2 Modal and spectral analyses

First, the modal analysis is performed and the corresponding spectral values are calculated. The nine first modes are calculated for the structure. The results of the modal analysis performed on the FE model are summarized in Table 5. The 9 retained modes account for 83% of the total mass for x and y directions. The presented pushover method allows to choose along these modes which really need to be considered.

4.2.3 Pushover analysis

The E-DVA method procedure previously applied in section 4.1.3 is also applied to this 3D structure. The pushover directions are chosen here following 8 horizontal directions given by the Newmark combinations, as explained in [2].

Then, the coordinates of each target point are determined at the intersection of the capacity spectrum with the ADRS spectrum given by Eq. (6). The damping ratio $\tilde{\xi}^*$ of ADRS spectra

Modes	**Frequency [Hz]**	**Effective mass in X [%]**	**Effective mass in Y [%]**	$S_{a,X}$ $[m/s^2]$	$S_{a,Y}$ $[m/s^2]$	**Damping factor [%]**
1	8.47	52.6	8.19	6.77	6.77	2.81
2	15.2	15.9	52.8	6.41	5.80	2.97
3	29.8	13.2	7.48	3.78	4.10	4.49
4	30.8	0.53	2.19	3.58	4.06	4.60
5	32.5	0.05	0.39	3.45	4.04	4.81
6	32.7	0.00	1.58	3.42	4.01	4.84
7	35.5	0.56	0.46	2.79	3.74	5.17
8	35.6	1.63	1.08	2.74	3.75	5.19
9	37.1	0.31	0.00	2.57	3.86	5.37

Table 5: Nine first modes of the SMART FE model

θ	$12.9°$	$51.9°$	$122°$	$168°$
F_θ (kN)	222	197	198	225
F_x (kN)	216	121	106	-219
F_y (kN)	49.6	155	-167	48.6
f^* (Hz)	9.06	12.3	9.32	8.79
$\xi^*(\%)$	2.94	3.39	3.45	3.05
$\gamma_{U,t}(m^{-1})$	496.1	1044	560.5	453.3
	2.01	0.919	1.30	-2.20
$[\underline{U}]_{j,t}$ (mm)	-0.548	0.210	-1.05	0.959
	-0.059	0.001	-0.080	0.086

Table 6: Equivalent SDOF parameters for the considered load cases

$12.9°$		$51.9°$		$122°$		$168°$	
Modes		Modes		Modes		Modes	
1	(54.1%)	2	(87.5%)	2	(22.9%)	1	(78.7%)
2	(37.9%)	1	(5.97%)	1	(54.0%)	2	(5.93%)
3	(5.68%)	10	(4.83%)	3	(14.4%)	3	(12.4%)
10	(1.45%)	6	(0.794%)	10	(3.22%)	8	(1.08%)
8	(0.399%)	4	(0.519%)	4	(2.22%)	10	(0.492%)
4 modes are sufficient		4 modes are sufficient		7 modes are sufficient		6 modes are sufficient	

Table 7: Number of modes and corresponding percentage of the total response needed

after iteration accounts for the hysteretic damping (Figure 8). The target point coordinates are shown in Table 8, with F_t and V_t corresponding to the obtained target global reaction and displacement of the structure in the considered direction t.

4.2.4 Time history analysis

To evaluate the non-linear response of the irregular specimen under a horizontal seismic loading, accelerograms whose spectra correspond to those of Figure 7 used in the pushover analysis are imposed to the structure. The seismic input data are all scaled to a $PGA = 2.45m/s^2$ intensity earthquake. For the sake of brevity, only two time-history results are showed here.

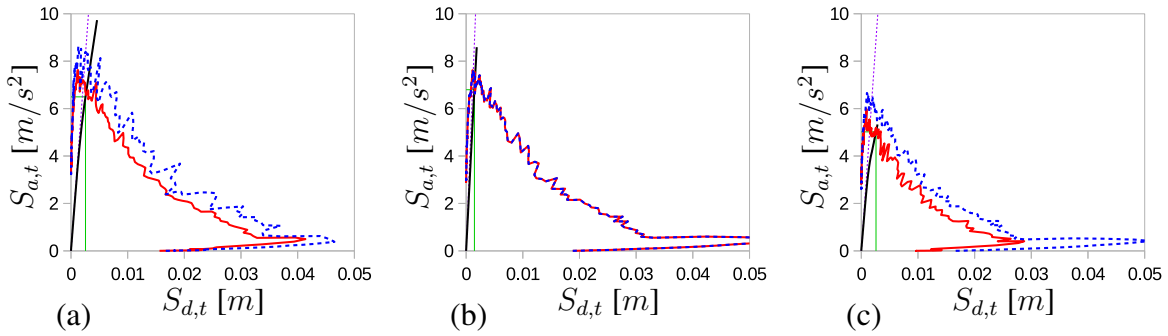

Figure 8: Capacity curves vs. spectrum in the ADRS plane for three of the load cases

Direction	12.9°	51.9°	122°	168°	−167°	−128°	−57.6°	−12.5°
$S_a(m/s^2)$	6.50	6.80	5.02	5.26	6.84	6.68	5.69	6.06
$S_d(mm)$	0.256	0.146	0.260	0.211	0.273	0.149	0.215	0.267
F_t(kN)	357	395	428	374	359	383	410	363
V_t(mm)	8.14	7.92	7.89	8.03	8.38	8.02	8.34	8.08
$\tilde{\xi}^*(\%)$	3.37	3.39	7.11	2.41	3.56	3.39	4.12	4.33

Table 8: Obtained target points for the considered load cases

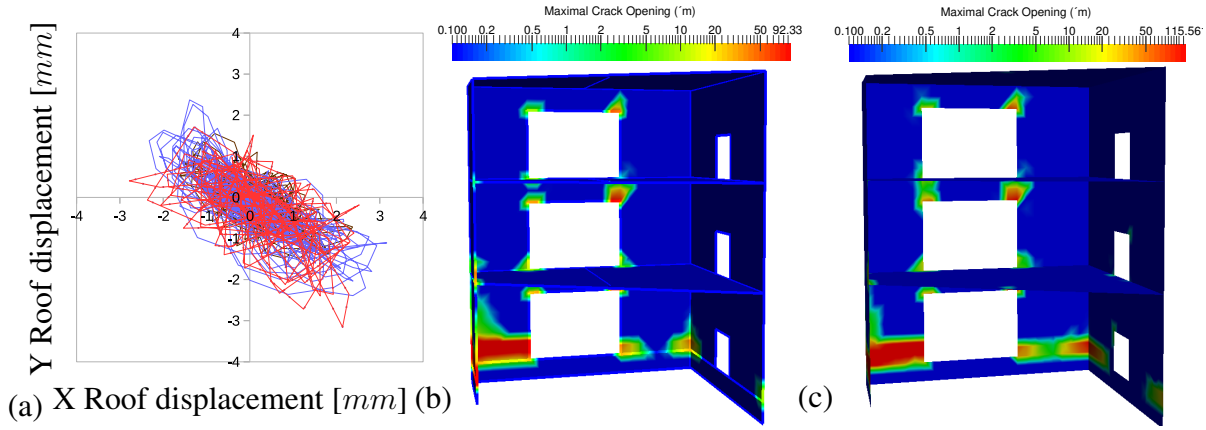

Figure 9: (a) Time-history roof displacement and maximal obtained crack opening during (b) a first seismic input and (c) a second one

The roof displacements shown in Figure 9 (a) are characteristic of an asymmetric structure with a dominant torsion mode. In Figures 9 (b) and (c), the maximal values of the crack opening during two whole earthquakes are plotted and represent the obtained crack patterns. When analyzing the results, it can be observed that the cracks are localized near the openings. The structure is heavily cracked at its left basis corner and steel reinforcement yielded.

4.2.5 Comparison between time history and pushover analyses

In order to compare the obtain results, the pushover results are plotted at their target point steps. The graphical comparison of Figure 10-a shows that the dynamic results obtained by all performed time-history analyses are mostly inside the envelope area defined by the obtained target points. The results show that the calculated forces that are presented in Table 7 are well

estimated (Figure 10-a). The pushover results given by the E-DVA approach provide a suitable and accurate envelope of the maximal global forces at the basis of the building.

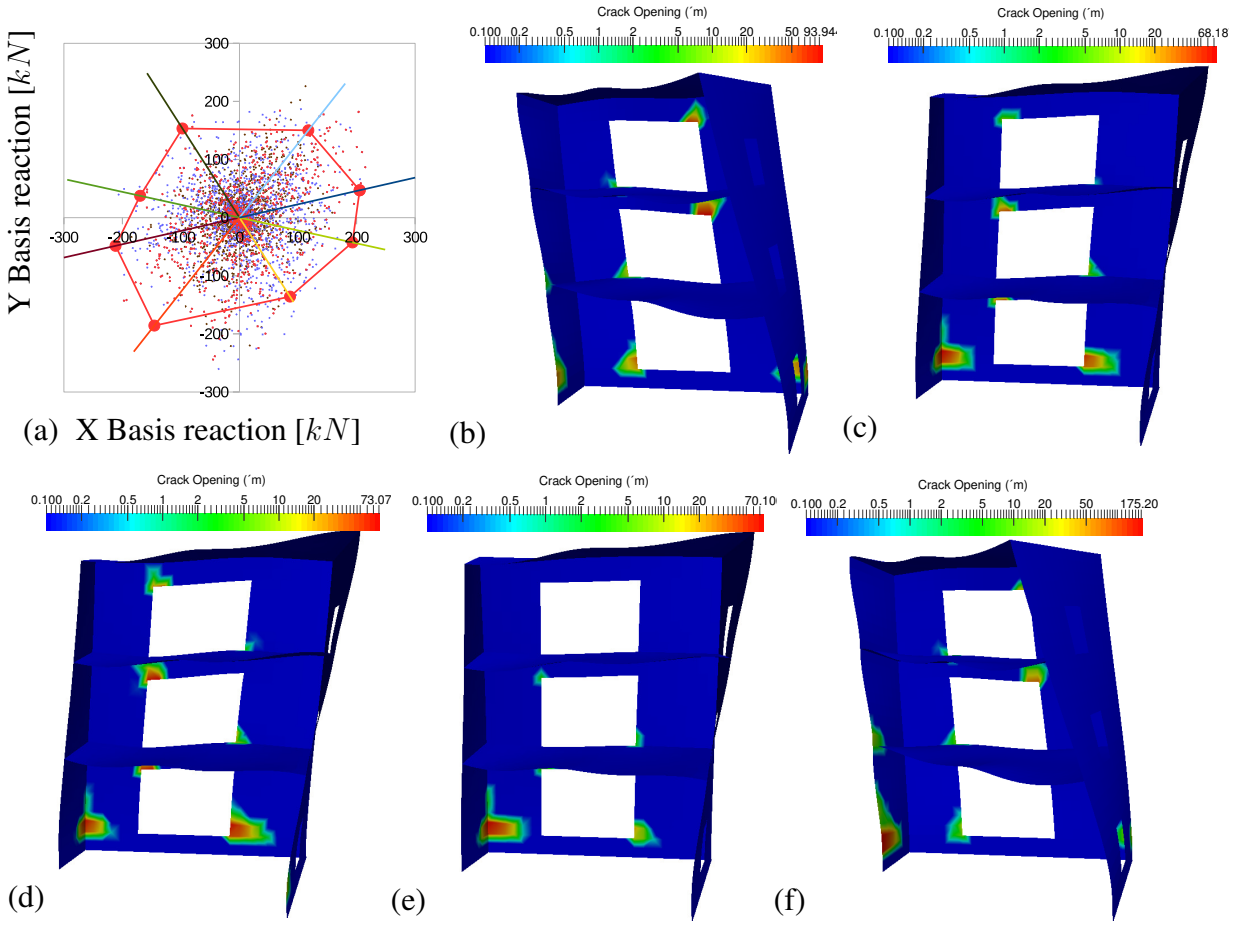

Figure 10: (a) Comparison of the capacity curves and obtained crack opening during the pushover analyses at (b) target point $12.9°$, (c) target point $168°$, (d) target point $-167°$, (e) target point $-57.6°$ and (f) target point $-12.5°$

The crack patterns obtained the pushover analyses (Figure 10-b-c-d-e-f) show that the crack opening are well estimated near the openings compared to the two time history crack opening pattern showed in Figure 9-b-c. As the time history analysis is a cyclic loading, the phenomena of cracking and reclosing cannot be reproduced by monotonic pushovers therefore several pushovers are needed to reproduce the crack pattern. The maximum obtained crack opening values obtained with the pushover analyses (Figures 10) give a quite accurate localization and value of the maximal crack opening obtained by time-history analyses (Figures 9). However, the severally cracked left basis corner due to the torsion behaviour of the structure cannot be fully predicted by pushover analyses that maximize basis reactions but it can be interesting in another study to perform multi-modal and multi-component pushover analyses that maximize the torsion (global torsion moment of the building M_{zz}).

5 Conclusions

The GLRC_HEGIS [1] model for RC plates (walls and slabs) is implemented for shell finite elements in Code_Aster [4] software and is applied to incremental static pushover and transient dynamic structural analyses corresponding to the same seismic intensity level. The structures which have been studied in this paper consisting of RC walls and slabs and the possibilities offered by this thermodynamic admissible law accounting for non-linear mechanisms have been used to compare available crack patterns at the end of a FE calculation since many results of interest (as crack width, steel plastic strain...) are internal variables of the with GLRC_HEGIS constitutive model.

In this paper, the seismic action has been taken into account by two different methods: non-linear time-history and nonlinear pseudo-static pushover analysis. In this paper the Enhanced Direct Vectorial Approach (E-DVA) [2] is used to take into account many modes of irregular buildings under a multi-component earthquake. The load pattern for the pushover analysis has been defined as a linear combination of modal load patterns using the modal weighting factors (called α-factors), which have been calculated using the elliptical response envelopes. The results obtained by time-history and pushover analyses have been compared.

First, a four-story framed in-plane irregular asymmetric wall extracted from the CASH benchmark has been analyzed in section 4.1. Then, the three-story RC building of SMART benchmark has been considered in section 4.2, accounting for the nonlinear behavior of its RC walls and slabs. Comparison between obtained results shows a relatively good fitting both at the local (e.g. crack width) and global (structural behavior) scales. The capabilities of the model to show the evolution of variables (crack width, steel reinforcement plastic strain, energy dissipation...) fields at every load step, and to estimate in a relatively accurate manner the RC section strength, have been also demonstrated. Comparisons have shown that forces and displacements can be estimated by pushover analyses and that time-history analyses have given a lot of local results (crack width, steel yielding...) that show the interest of each of these two different nonlinear methods for seismic structural analysis.

REFERENCES

[1] M. Huguet, S. Erlicher, P. Kotronis, F. Voldoire, Stress resultant nonlinear constitutive model for cracked reinforced concrete panels. *Engineering Fracture Mechanics*, **176**, 375–405, 2017.

[2] O. Lherminier, S. Erlicher and M. Huguet, Multi-modal pushover analysis for a multi-component earthquake: an operative method inspired by the Direct Vectorial Approach, *Proceedings of the 16th European Conference on Earthquake Engineering*, Thessaloniki, Greece, 2018.

[3] M. Huguet, M. Bourahla, S. Erlicher, P. Kotronis, GLRC_HEGIS global constitutive model for RC walls and slabs for seismic nonlinear structural analyses, *Proceedings of the 16th European Conference on Earthquake Engineering*, Thessaloniki, Greece, 2018.

[4] Electricité de France, Open source on www.code-aster.org. Finite element $Code\_Aster$, *Analysis of Structures and Thermomechanics for Studies and Research*, 1989–2017.

[5] M. Huguet, A homogenized nonlinear stress resultant constitutive model for cracked reinforced concrete panels *Ph.D. Thesis Report, Ecole Centrale Nantes / Egis*, 2016.

[6] F.J. Vecchio, M.P. Collins, The modified compression-field theory for reinforced concrete elements subjected to shear, *ACI Journal* **83:2**, 219–231, 1986.

[7] Comité Européen de Normalisation, *EuroCode 2 - 2004 Design of concrete structures: Part 1-1*, 2005.

[8] A.K. Chopra, R.K. Goel, Capacity-demand-diagram methods based on inelastic design spectrum, *Earthquake Spectra*, **15:4**, 1999.

[9] A.K. Chopra, R.K. Goel, A modal pushover analysis procedure for estimating seismic demands for buildings, *Earthquake Engineering and Structural Dynamics*, **31**, 561–582, 2002.

[10] A.K. Chopra, R.K. Goel, A modal pushover analysis procedure to estimate seismic demands for unsymmetric-plan buildings, *Earthquake Engineering & Structural Dynamics*, **33**, 903–927, 2004.

[11] R.K. Goel, A.K. Chopra, Evaluation of modal and FEMA pushover analyses: SAC buildings, *Earthquake Spectra*, **20:1**, 225–254, 2004.

[12] P. Fajfar, D. Marusic and I. Perus, The extension of the N2 method to asymmetric buildings, *Symposium on Earthquake Engineering Challenges and Trends, honoring Prof. Luis Esteva, J. J. Prez-Gaviln (Ed.)*, Univ. Nacional Aut. Mexico, ISBN: 970-32-3699-5, 2006.

[13] P. Faifar, A nonlinear analysis method for performance-based seismic design, *Earthquake Spectra*, **16:3**, 573–592, 2000.

[14] P. Fajfar, D. Marusic and I. Perus, Torsional effects in the pushover-based seismic analysis of buildings, *Journal of Earthquake Engineering*, **9:6**, 831–854, 2008.

[15] G.G. Penelis and V.K. Papanikolaou, Nonlinear static and dynamic behavior of a 16-story torsionally sensitive building designed according to Eurocodes, *Journal of Earthquake Engineering*, **14**, 706–725, 2010.

[16] S.K. Kunnath, Identification of modal combination for nonlinear static analysis of building structures, *Computer-Aided Civil and Infrastructure Engineering*, **19**, 246–259, 2004.

[17] M.A. Lopez-Menjivar, Verification of a displacement based adaptive pushover method for assessment of 2-D reinforced concrete buildings, PhD Thesis, European School for Advanced Studies in Reduction of Seismic Risk (ROSE School), University of Pavia, Italy, 2004.

[18] C. Menun and A. Der Kiureghian, Envelopes for seismic response vectors. I: Theory, *Journal of Structural Engineering*, **126:4**, 467–473, 2000.

[19] B. Gupta and S.K. Kunnath, Adaptive spectra-based pushover procedure for seismic evaluation of structures, *Earthquake Spectra*, **16:2**, 367–392, 2000.

[20] S. Erlicher, Q.S. Nguyen and F. Martin, Seismic design by the response spectrum method: a new interpretation of elliptical response envelopes and a novel equivalent static method based on probable linear combinations of modes, *Nuclear Engineering and Design*, **276**, 277–294, 2014.

[21] S. Erlicher and M. Huguet, A new approach for multi-modal pushover analysis under a multi-component earthquake, *Technological Innovations in Nuclear Civil Engineering*, Paris, France, 2016.

[22] M. Huguet, O. Lherminier and S. Erlicher, The E-DVA pushover method for multi-modal pushover analysis with multi-component earthquake: analysis of two irregular buildings, *Technological Innovations in Nuclear Civil Engineering*, Paris-Saclay, France, 2018.

[23] www.code-aster.org/V2/doc/default/fr/man_r/r7/r7.01.08.pdf, Code_Aster.

[24] S. Erlicher, 0. Lherminier and M. Huguet, The E-DVA method: a new approach for multi-modal pushover analysis under multi-component earthquake, *Nuclear Engineering and Design*, submitted and under acceptation, 2019.

[25] ASCE-4-16, Seismic analysis of safety-related nuclear structure, *ASCE Standard*, Reston, Virginia, US, 2017.

[26] B. Richard, S. Cherubini, F. Voldoire, P.E. Charbonnel, T. Chaudat, S. Abouri, N. Bonfils, SMART 2013: Experimental and numerical assessment of the dynamic behavior by shaking table tests of an asymmetrical reinforced concrete structure subjected to high intensity ground motions, *Engineering Structures*, 109:99-116, 2016.

COMPDYN 2019
7th ECCOMAS Thematic Conference on
Computational Methods in Structural Dynamics and Earthquake Engineering
M. Papadrakakis, M. Fragiadakis (eds.)
Crete, Greece, 24–26 June 2019

A SIMPLE MODEL FOR INVESTIGATING THE NON-LINEAR DYNAMIC BEHAVIOR OF ELASTIC SYSTEMS SUBJECTED TO STICK-SLIP MOTION

S. Bennati[1], R. Barsotti[2], and G. Migliaccio[3]

[1] University of Pisa, s.bennati@ing.unipi.it

[2] University of Pisa, r.barsotti@ing.unipi.it

[3] University of Pisa, giovanni.migliaccio.it@gmail.com

Abstract

The stick-slip phenomenon is the typical jerking motion that may occur when two objects are forced to slide with friction over each other. There are several situations in which this motion can be observed in practice, for example, between the components of different kinds of seismic protection systems, like the slabs of some friction dampers or the sliding elements of some base isolation systems. These kinds of systems are generally designed to work in a smooth, flawless manner. However, it cannot be excluded that in particular situations undesired jerking motions might develop. Similar situations are widespread in all areas of engineering and may result in complex dynamic behavior, even when only a small number of degrees of freedom are involved. A well-known simple scheme for problems of this kind consists of a rigid block connected elastically to one support while its base is in contact with a second, moving rough surface. This model, despite its apparent simplicity, can provide useful indications on the main features of many physical systems. This contribution illustrates an analytical study conducted to better understand the non-linear dynamic behavior of such systems, with the objective of identifying conditions that may disrupt their proper functioning. In particular, the equations of motion are solved analytically, the sticking and sliding phases are studied, the influence on the solution of the system's main parameters is investigated, and some typical long-term system responses are discussed. Lastly, some results obtained by means of a specifically developed numerical procedure are illustrated.

Keywords: Non-linear dynamics, stick-slip motion, friction dampers, seismic isolators.

1 INTRODUCTION

Dynamic systems containing components that slide with friction over others are widespread in many engineering applications. Systems in which friction forces play a significant role are encountered in mechanical, aerospace and automotive engineering, for instance in brakes, wiper blades, and so on. In civil engineering, several examples can be found by looking at the damping devices and base-isolation devices developed to protect buildings from earthquakes. In this regard, several devices exploiting friction have been effectively proposed and used as a means for increasing a building's capacity to dissipate energy or isolating it from the oscillating ground.

Systems of this kind are generally designed to work in a smooth, steady manner. However, it cannot be excluded that in particular conditions undesired jerking motions may develop. Over the years, several studies have been conducted to better understand the dynamic behavior of systems in which two components are forced to slide with friction over each other, the objective being to identify any conditions that may disrupt their proper functioning, and to optimize their performance. Generally speaking, the body of literature on the topic may be subdivided into two main categories. The first category is represented by numerical studies, performed by means of finite element models [6]. The second approach, to which this paper belongs, applies simplified models which regard the system as a mechanical system endowed with a small number of degrees of freedom [4].

Over the last century particular attention has been devoted to the single degree-of-freedom (DoF) system subjected to elastic and friction forces. The first studies on systems of this kind are contained in the work by Den Hartog [7], after which similar problems have been considered by other researchers [9-16]. Although the full list of contributions is too lengthy to cite here, we recall the relevant works by Parnes [8], Hong [9], Shaw [10], Butikov [11], and Andreaus and Casini [12].

The present work addresses the dynamic response of a simple model composed of a rigid block connected elastically to a first rigid support while in frictional contact with a moving second rigid support. The paper is organized as follows. The mechanical model is introduced in Section 2. A description of the different types of motion that the considered system may undergo is provided in Section 3. Subsequently, we focus attention on some limit cycles – continuous sticking or sliding – that the system may undergo (Section 4). In particular, we show that it is possible to foresee some features of the system's long-term response, provided its mechanical parameters are known. In this regard, some reference maps are illustrated, which provide useful indications on possible long-term system responses. Finally, in Section 5, some results from an application example are shown.

2 THE MECHANICAL MODEL

The mechanical problem addressed here concerns the motion of a structure that is connected elastically to a moving support, while its base can slide over a moving rough surface (Figure 1). The single degree-of-freedom system is composed of a rigid block with mass m attached to a spring with elastic constant k. The other end of the spring is connected to point A, which may move according to a prescribed law, $x_A(t)$. The block is restrained so as to remain in contact with a rough rigid support whose reference point B moves according to the prescribed motion law, $x_B(t)$. The friction force acting on the block is F_a; the position of the block's center of gravity, G, with respect to a suitable (inertial) reference frame, is $x(t)$. The equation of motion reduces simply to

$$m\ddot{x} + k(x - x_A) = F_a \tag{1}$$

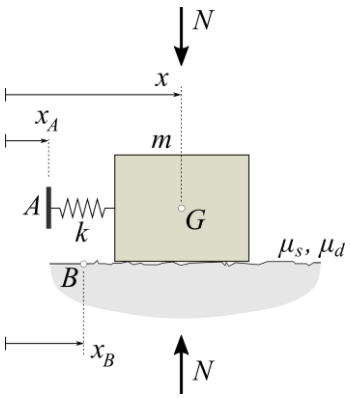

Figure 1: A schematic representation of a rigid body (mass m) connected elastically to a rigid support A (spring constant k) and with friction to a rigid support B (static and kinematic friction forces F_s and F_k)

The friction force, F_a, which the support exerts on the block when the relative velocity between the two is not zero is given by the following relation:

$$F_a = -\mathrm{sgn}(\dot{x}_{rel})F_k \tag{2}$$

where $\dot{x}_{rel} = \dot{x} - \dot{x}_B$ is the relative velocity between the block and support, and $sgn(\dot{x}_{rel})$ is the sign of the relative velocity; moreover, when the relative velocity between the block and the support is zero:

$$|F_a| \le F_s \tag{3}$$

A well-known property of such systems is that at the beginning of a sticking phase it will take some short time to actually establish a contact condition (see, for example, the studies by Sampson [13]). Hence, the standard version of Coulomb's law is modified as follows:

- in any *sliding phase* the friction force is equal to the kinematic value (2);
- at the *beginning of a sticking phase* the friction force cannot exceed the kinematic value ($|F_a| \le F_k$);
- at any time *within a sticking phase* the friction force cannot exceed the static value ($|F_a| \le F_s$).

In the following we will consider the special case in which point A is kept fixed (i.e., x_A = constant), while B moves according to the law $x_B = A_b sin(\omega_b t)$, where A_b and ω_b are the amplitude and angular frequency, respectively.

3 STICKING AND SLIDING PHASES

In the general case, the motion of the system may involve a sequence of sticking phases, during which the block follows the motion of the underlying moving support, and sliding phases, during which the mass moves with respect to the base support. As the friction force is non-smooth, the equation of motion has to be solved separately in each of the two phases, and the time lapse between one phase and the other has to be determined.

A sticking phase following a sliding phase will begin if both the block and the support have the same velocity, and if the magnitude of the friction force on the block does not exceed the kinematic value, F_k. Vice versa, a sliding phase following a sticking phase may begin if and only if the magnitude of the friction force on the block reaches the maximum static value, and a friction force greater than F_s would be required to keep the block sticking to the support.

3.1 The sticking phase

The law of motion for the block during the sticking phase reduces to

$$x(t) = A_b \sin(\omega_b t) + C \tag{4}$$

The sticking phase will persist until the magnitude of the friction force reaches the maximum static value, F_s. After some algebraic manipulation, such condition can be expressed as

$$|\alpha| + |\lambda| \le 1 \tag{5}$$

where $\alpha = a(1-\Omega^2)$, $a = A_b / x_s$, $x_s = F_s / k$, $\Omega = \omega_b / \omega$, $\omega = \sqrt{k/m}$, and $\lambda = C / x_s$.

Condition (5) enables distinguishing the α, λ pairs corresponding to systems that may be in a sticking condition up to a certain time, as well as those which cannot initially be in a sticking condition. Figure 2 (left) shows the partition of the α, λ plane produced by condition (5).

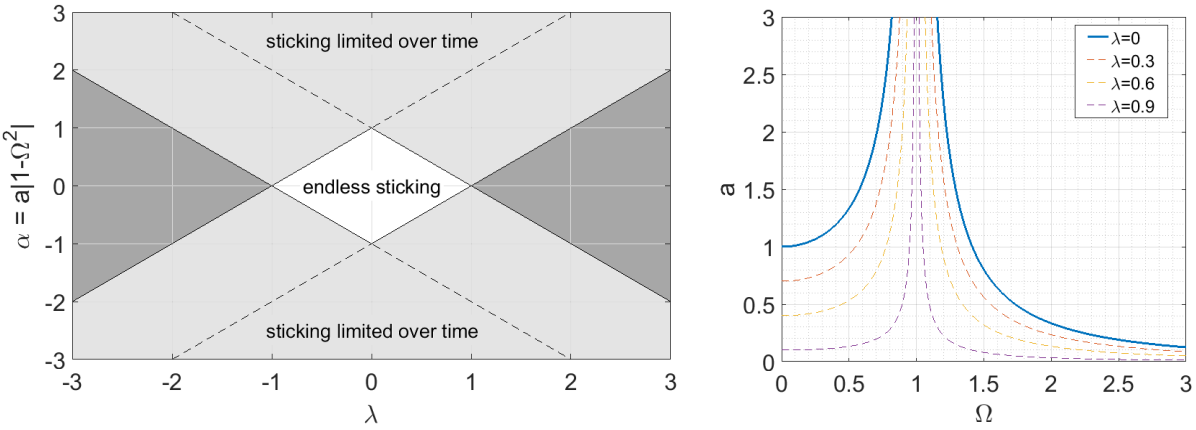

Figure 2: Sticking regions in the α, λ plane (left), and a, Ω plane (right)

Condition (5) can be recast in an alternative form in order to determine the set of values a, λ, Ω, corresponding to systems that may undergo a sticking phase. Such alternative condition can be expressed as:

$$a \le \frac{1-|\lambda|}{|1-\Omega^2|} = f(\Omega, \lambda) \tag{6}$$

The interesting feature of the curve $a = f(\Omega,0)$ is that it enables distinguishing the systems for which endless sticking motion is impossible regardless of the initial conditions (region above the thick curve on the right of Figure 2), from those systems for which such motion is possible.

We conclude this section by observing that it is possible to determine *a priori* the time, t_{SL}, at which a sticking phase will end. A simple, though nonlinear equation, not displayed for the sake of brevity, enables determining t_{SL} for a given system from the very start of the sticking phase.

3.2 The sliding phase

Let us assume that the block is sliding at a certain instant. The block's equation of motion in the sliding phase reads

$$m\ddot{x} + kx = \pm F_k \tag{7}$$

where the sign depends on that of the relative velocity during the sliding phase. Integration of equation (7) yields the law of motion

$$x(t) = c_1 \cos(\omega t) + c_2 \sin(\omega t) \pm x_k \tag{8}$$

where $x_k = \eta x_s$ and $\eta = F_k / F_s$.

The necessary condition for a sliding phase to stop at time t_{ST} is that the relative velocity between the block and the surface become zero. According to the rules introduced in section 2, a sticking phase may actually begin at t_{ST} only if the following condition holds

$$\left| -a\Omega^2 \sin(\omega_b t_{ST}) + x(t_{ST}) / x_s \right| \le \eta \tag{9}$$

Condition (9) ensures that the magnitude of the friction force on the block at the beginning of a sticking phase does not exceed the kinematic friction, F_k. If such inequality is not satisfied, the friction force would be greater than F_k and a sticking phase could not actually begin.

4 LIMIT CYCLES

Limit cycles are periodic solutions to the equation of motion characterized by a balance between the energy dissipated by and that supplied to the mass-spring system. Different possible limit cycles may be observed for systems like those considered here [9,13], depending on the values chosen for the system's initial conditions and mechanical parameters a, Ω, and η.

In broad terms, the limit cycles that a system may reach after a transient phase can be subdivided into three main categories, in which the block:

1) slides indefinitely,
2) sticks indefinitely,
3) periodically alternates sliding and sticking phases.

In this section, we concentrate our attention on limit cycles corresponding to pure sticking and on some kind of limit cycles corresponding to pure sliding.

4.1 Sticking limit cycles

If condition (5) is fulfilled, it is straightforward to conclude that periodic solutions to the equation of motion characterized by continuous sticking to the surface become possible. All these periodic solutions may be expressed in the form

$$x / x_s = a \sin(\omega_b t) + \lambda \tag{10}$$

where the parameter λ represents the dimensionless relative initial position between the block and point B.

4.2 Sliding limit cycles

In this section we study particular sliding limit cycles, in which the block undergoes a periodic motion and slides over the moving support, B, without ever sticking to it. In addition, we restrict the analysis to motion satisfying the following constraints:

$$\begin{aligned} x(0) &= x(T_b / 2) = x(T_b) = 0 \\ \dot{x}_{rel}(0) &= \dot{x}_{rel}(T_b / 2) = \dot{x}_{rel}(T_b) = 0 \end{aligned} \tag{11}$$

Moreover, as an additional condition, we assume that the component of the friction force in the direction of the x axis has a prescribed sign (for example, $+F_k$) over one half of the period and the opposite sign over the other half-period (*relative velocity sign condition*).

By imposing that the velocity of B be equal to that of the block at the beginning of any half-period, and by requiring that the friction force have a specified sign during a half-period and the opposite sign during the subsequent one, we obtain an inequality that must be verified for the validity of the considered limit cycle motion. After some manipulations, such inequality can be expressed as:

$$a > \eta g(\Omega) \tag{12}$$

where

$$g(\Omega) = \sqrt{\frac{M_\Omega^2}{\Omega^4} + \frac{1}{\Omega^2}\tan^2\left(\frac{\pi}{2\Omega}\right)} \tag{13}$$

$$M_\Omega = \max\left\{1; \sup_{z\in(0,1)} \left|h_\Omega(z)\right|\right\}, \quad \text{for a given } \Omega \tag{14}$$

$$h_\Omega(z) = \frac{\Omega}{\sin(\pi z)}\left[\tan\left(\frac{\pi}{2\Omega}\right)\left(\cos\left(\frac{\pi z}{\Omega}\right) - \cos(\pi z)\right) - \sin\left(\frac{\pi z}{\Omega}\right)\right] \tag{15}$$

4.3 The influence of the system parameters on its long-term response

The motion of the single degree-of-freedom system considered in this paper is fully determined if the values of its mechanical parameters, a, Ω, η, and initial conditions are given. Moreover, it is reasonable to believe that it should be possible to forecast some features of the system's long-term response regardless of its initial conditions. For example, if a, Ω and η satisfy inequality (5), the system will undergo continuous sticking, otherwise at least one sliding phase will take place.

Inequalities (5) and (12) enable making some predictions on the system's long-term response, provided the system parameters, a, Ω, η, are assigned. For example, if such parameters satisfy inequality (5), *i.e.*, if the corresponding point belongs to the dashed area below the blue curve in Figure 3, the system will undergo continuous sticking. Instead, if condition $a>f(\Omega,0)$ is verified, an endless sticking motion is not possible, regardless of the initial condition. In addition, for a given η, if condition (12) is not verified, *i.e.* if the corresponding point is below the red curve in Figure 3, the system cannot undergo the limit slipping motion defined in section 4.2. Instead, if a system verifies the assumptions discussed in section 4.2, and its parameters comply with the discussed constraint (12), then such a system may actually undergo the periodic limit motion discussed in section 4.2.

That said, it is worth noting that the illustrated study of the long-term response of systems like those considered in this paper is not conclusive. Further studies are needed and will be discussed in future works to carry out an exhaustive or, at least, wider examination of the possible limit cycles and the corresponding conditions of existence. Nevertheless, the results illustrated in this work are promising, and the introduced reference maps already furnish important information.

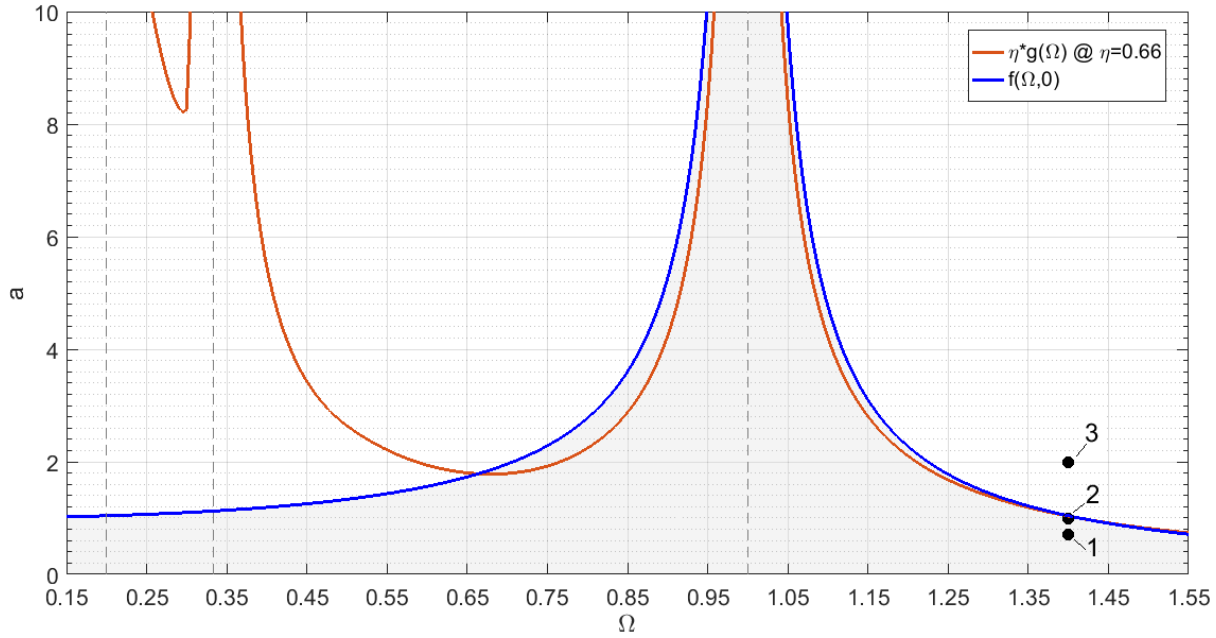

Figure 3: Reference map summarizing the limit cycles constraints

5 AN APPLICATION EXAMPLE

In the literature, several works propose numerical or semi-analytical solutions to equations of motion like those considered here [11,14,15]. The solution strategy we follow is of the semi-analytical type. It consists of piecewise solution of the equations of motion by identifying, *a priori*, the transition time (if any) from a slip to a stick phase, or vice versa

The following section illustrates the results obtained by applying the developed method to a particular system, whose parameters (e.g., mass, elastic constant, and friction actions) have been chosen so as to be representative of a small-sized building fitted with a seismic protection system. Different values of a and Ω, as well as different initial conditions, have been considered.

5.1 Simulation results

Many simulations have been performed, starting with different initial conditions, and for different values of the system parameters a and Ω. Three typical results are illustrated in the following (see Figures 4-6). The simulations have been performed by assuming a system mass of m = 6000 kg, elastic constant k = 30 kN/m, and values of the static and kinematic friction forces F_s = 240 kN and F_k = 168 kN, respectively.

The first example, in Figure 4, illustrates the results of a simulation in which the system (corresponding to point 1 in Figure 3), after an initial sliding phase, tends towards a sticking limit cycle. In the second example in Figure 5, the system (point 3 in Figure 3) is sliding right from the beginning and, after a certain period of time, tends towards a sliding limit cycle. Finally, the third example, in Figure 6, illustrates a case in which the system (point 2 in Figure 3) is sliding in an irregular fashion in the first part of the simulation and then, after a certain moment in time, tends towards a limit cycle characterized by alternating phases of sliding and sticking.

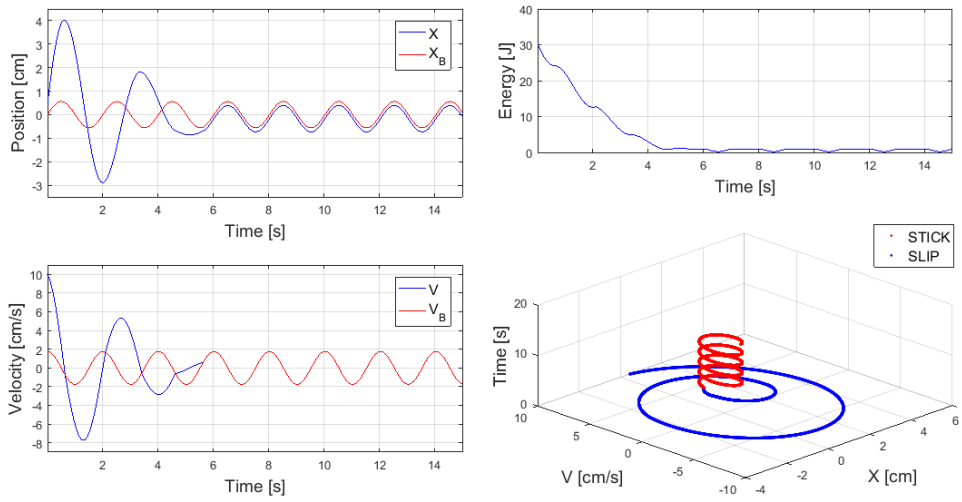

Figure 4: Sticking limit cycle (a =0.7, Ω=1.4) - positions and velocities (left), energy and trajectory (right)

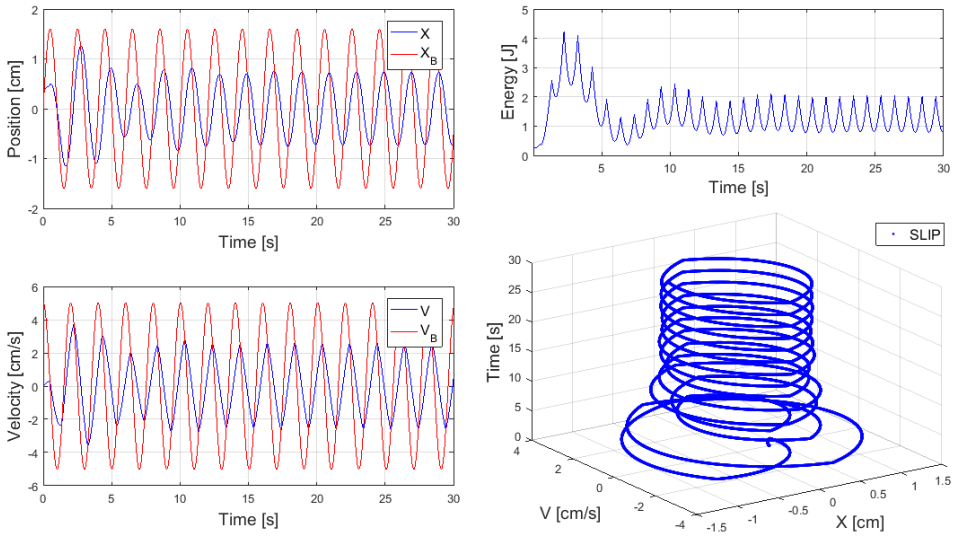

Figure 5: Sliding limit cycle (a =2.0, Ω=1.4) - positions and velocities (left), energy and trajectory (right)

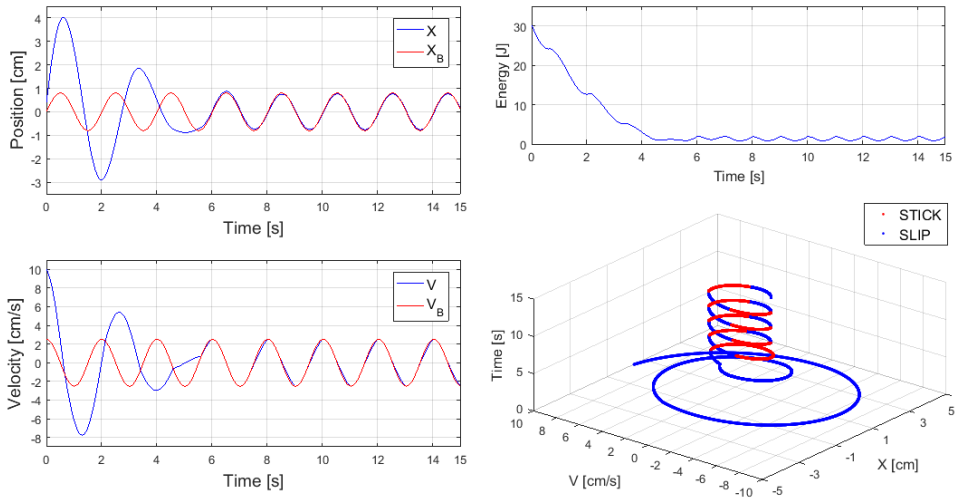

Figure 6: Stick-Slip limit cycle (a =1.0, Ω=1.4) - positions and velocities (left), energy and trajectory (right)

6 CONCLUSIONS

The present paper has addressed the dynamic response of a rigid block connected elastically to a support while in frictional contact with a rough support which is moving according to a sinusoidal law. Such a basic model has been chosen as a benchmark case to investigate the main features of dynamic systems undergoing stick-slip motion, such as seismic protection systems, wiper blades and brakes.

The contact force between the block and the support has been described by Coulomb's law, which has been suitably modified to account for the short time usually needed to restore static contact conditions after a sliding phase.

The nonlinear equation of motion for the block has been solved piecewise analytically in both the sticking and sliding phases, and the instants at which the system passes from one phase to another have been evaluated precisely. The study highlighted the effects on the system dynamics of three dimensionless parameters: the ratio Ω between the oscillation frequency of the moving support and the system's natural frequency; the ratio η between the kinematic and static friction coefficient; and the ratio a between the oscillation amplitude of the moving support and a reference length. In particular, the conditions for existence of some limit cycles have been discussed. According to the results obtained, it is possible to foresee some features of the long-term response of a system for which parameters Ω, a and η are known. The regions in the Ω, a plane corresponding to systems that may undergo continuous sticking or particular periodic sliding have been determined.

The proposed approach seems to provide a better understanding of the main features of the dynamic response of systems ruled by friction. The results obtained should prove to be useful for developing design criteria aimed at avoiding undesired jerking motion between such systems' components, with the final objective of optimizing their performance.

REFERENCES

[1] A. Chopra, *Dynamics of Structures: Theory and Applications to Earthquake Engineering, 2nd Edition*. Prentice Hall, Inc, Upper Saddle River, NJ, 2003.

[2] C. Grigorian, E. Popov, *Energy dissipation with slotted bolted connections, UCB/EERC-94/02*, California University, Richmond, Earthquake Engineering Research Centre, 1994.

[3] P. Castaldo, B. Palazzo, P. Della Vecchia, Seismic reliability of base-isolated structures with friction pendulum bearings, *Engineering Structures*, 95, 80-93, 2015.

[4] A.V. Bhaskararao, R.S. Jangid, Seismic analysis of structures connected with friction dampers, *Engineering Structures*, 28, 690-703, 2006.

[5] O. Ozbulut, M. Bitaraf, S. Hurlebaus, Adaptive control of base-isolated structures against near-field earthquakes using variable friction dampers, *Engineering Structures*, 33, 3143-3154, 2011.

[6] I. Kavvadias, L. Vasiliadis, Finite Element Modeling of Single and Multi-Spherical Friction Pendulum Bearings, *6th Thematic Conference on Computational Methods in Structural Dynamics and Earthquake Engineering*, Rhodes Island, Greece, June 15-17, 2017.

[7] J. Den Hartog, Forced Vibrations with Combined Coulomb and Viscous Friction, *Trans. ASME*, Vol. 53, pp. 107-115, 1931.

[8] R. Parnes, Response of an Oscillator to a Ground Motion with Coulomb Friction Slippage, *Journal of Sound and Vibration*, Vol. 94, no. 4, pp. 469-482, 1984.

[9] H.K. Hong, C.-S. Liu, Non-Sticking Oscillation Formulae for Coulomb Friction Under Harmonic Loading, *Journal of Sound and Vibration*, Vol. 244, pp. 883-898, July 2001.

[10] S.W. Shaw, On the dynamic response of a system with dry friction, *Journal of Sound and Vibration*, Vol. 108, no. 2, pp. 305-325, 1986.

[11] E.I. Butikov, Spring pendulum with dry and viscous damping, *Communications in Nonlinear Science and Numerical Simulation*, Vol. 20, no. 1, pp. 298-315, 2015.

[12] V. Andreaus, P. Casini, Dynamics of Friction Oscillators Excited by a Moving Base and/or Driving Force, *Journal of Sound and Vibration*, Vol. 245, n. 4, pp. 685-699, 2001.

[13] J. Sampson, F. Morgan, D.W. Reed, M. Muskat, Friction behavior during the slip portion of the stick-slip process, *Journal of Applied Physics*, Vol. 14, n. 12, pp. 689-700, 1943.

[14] R.I. Leine, D.H. Van Campen, A. De Kraker, Stick-slip vibrations induced by alternate friction models, *Nonlinear Dynamics*, Vol. 16, pp. 41-54, 1998.

[15] G.J. Stein, R. Zahoranský, P. Múčka, On dry friction modelling and simulation in kinematically excited oscillatory systems, *Journal of Sound and Vibration*, Vol. 311, pp. 74-96, March 2008.

[16] G. Licskó, G. Csernák, On the chaotic behaviour of a simple dry-friction oscillator, *Mathematics and Computers in Simulation*, Vol. 95, pp. 55-62, 2014.

COMPDYN 2019
7th ECCOMAS Thematic Conference on
Computational Methods in Structural Dynamics and Earthquake Engineering
M. Papadrakakis, M. Fragiadakis (eds.)
Crete, Greece, 24–26 June 2019

FREQUENCY ANALYSIS OF NONLINEAR SHEAR WALL MODEL UNDER SEISMIC LOADING

P. Rosko[1], **A. Beko**[2]

[1] Vienna University of Technology
Karlsplatz 13, 1040 Vienna, Austria
e-mail: peter.rosko@tuwien.ac.at

[2] FCP
Marxergasse 1, 1030 Vienna, Austria
e-mail: beko@fcp.at

Abstract

The paper deals with dynamic analysis of reinforced shear wall under seismic loading. The shear walls of Kashiwazaki-Kariwa nuclear power plant structures reported no significant structural damage during 2007 Chuetsu earthquake despite of the fact, that the response spectra exceeded the design spectra of bearing structures. That was the reason for research of applied shear wall. The IRIS research project on industrial safety assessment and management included the cyclic testing of full-scale reinforced concrete walls. The results of the laboratory tests were used to analyze the nonlinear behavior of reinforced concrete wall under seismic excitation. The hysteresis (force-displacement relation) has been used for numerical SDOF model design. The calibrated model was used for earthquake simulations. Data of a set of strong motion records with different amplitudes, acceleration/velocity ratios and frequency content was selected to model excitation. The frequency analysis of the response signal was carried out with wavelet transformation. The frequency content at a certain time during the earthquake excitation was obtained. The responses of inelastic structure for different excitations were compared and analyzed in frequency domain.

Keywords: Shear Wall, FE Model, Structural Dynamics, Earthquake Engineering.

1 INTRODUCTION

Even though most of the surprises that earthquakes bring us are negative, examples on the positive note do exist. The 2007 Chūetsu offshore earthquake had an epicenter just 19km from the location of the Kashiwazaki-Kariwa nuclear power plant built in the 1980's. The earthquake shook the plant beyond design basis. The response spectra of the Chūetsu earthquake surpassed the design spectra for the investigated structures. The earthquake-proofing no significant structural damage was reported [1]. The power plant was shut down due to technological damage only. This was the incentive to delve deeper into the dynamic behavior of shear walls which are the structural elements that provide the necessary integrity to nuclear structures. It was also the reason to include base research in the form of shear wall testing in the IRIS research project on industrial safety assessment and management [2].

2 EXPERIMENTAL TESTING

The novel experimental testing was carried out (reported in Bekö et al. [3]). During cyclic testing (Fig. 1) of full-scale reinforced concrete low-rise shear wall specimen the pure shear was simulated. The obtained data was analyzed and well-defined hysteresis curve (Fig.2) was obtained.

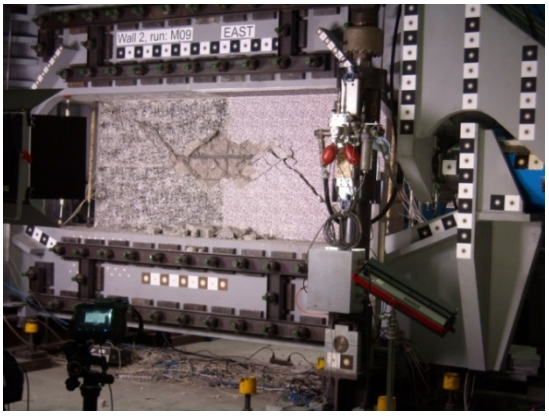

Figure 1: Reinforced concrete shear wall test.

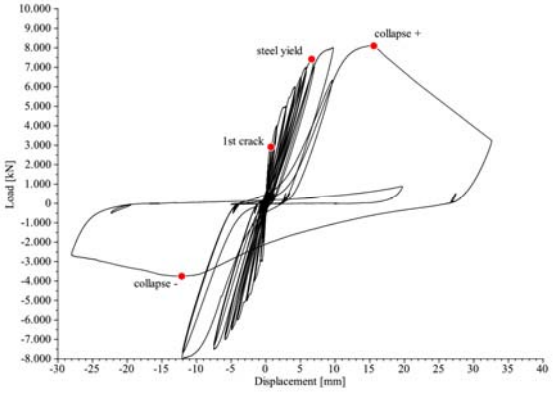

Figure 2: Test hysteresis (force vs displacement).

3 MODELING

A nonlinear mathematical model was created which is capable of simulating the hysteresis of the tested shear walls. The analytical model is a single DOF model of the Takeda family. Litton's [4] simplification of the Takeda model [5] was used as a base for the development of a dedicated model with stiffness degradation and pinching. The model is piecewise linear hysteresis model with a quadrilateral backbone curve and unsymmetrical positive and negative quadrants. Two separate sets of governing parameters were adopted for the positive and negative quadrants each with four variables $\alpha, \beta, \gamma, \delta$. The governing equations of the model are defined as follows (for definition of the symbols see Fig. 3)

- unloading stiffness $k_u = k_0 \left(\frac{u_{max}}{u_y}\right)^{-\alpha}$ (1)

- reloading point $Y = [u^+, f^+]$; $u^+ = \frac{u_{max}}{u_y} - \beta \frac{u_{max} - u_y}{u_y}$, $f^+ = f_y + k_t\left(u^+ - u_y\right)$ (2)

- pinching stiffness $k_s = \frac{f_{max}}{u_{max}-u_q}\left(\frac{u_{min}}{u_y}\right)^{-\gamma}$ (3)

- pinching point $P = [u_P, f_P]$; $u_P = \frac{-k_s u_q + k_u u_{0c}}{k_u - k_s}\delta$, $f_P = k_s(u_P - u_q)$ (4)

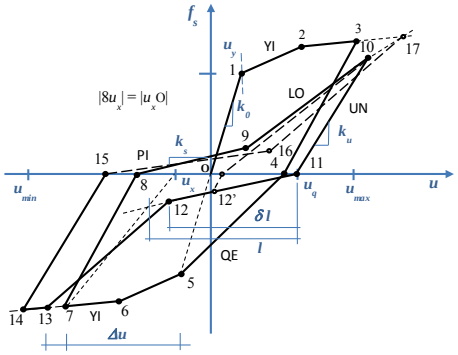

Figure 3: Takeda-Litton`s model

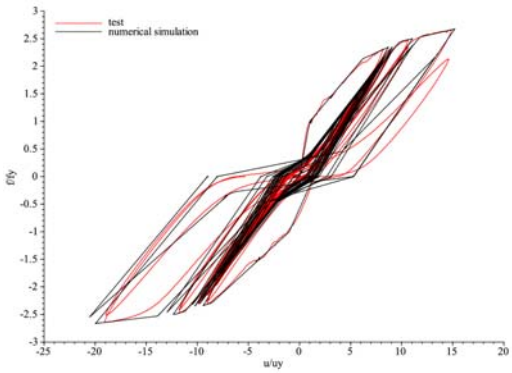

Figure 4: Test (red) and simulation (black) hysteresis

The verification of the model is shown in Fig. 4. The numerical investigations were hinged on an analytic model developed on the basis of laboratory tests. The model was used to analyze the nonlinear behavior of a single RC shear wall under seismic excitation. Various aspects of this behavior were studied using this model.

4 TIME-FREQUENCY ANALYSIS

The calibrated model was used for earthquake simulations of an imaginary shear wall that is analogous to the test. Nonlinear response spectra were derived for a selected set of earthquakes. The earthquake selection was based on the following considerations. It was required to have a selection of strong motions with different A/V (maximum acceleration to maximum velocity) ratios. At the same time we wanted to have different frequency content, varying duration and overall amplitudes of the ground motions. This has led to a set of well-studied earthquakes summarized in in Table 1.

Earthquake	Date	Mw	Site	E.Dist	A (g)	V(m/s)	A/V
Central Honshu Japan	Feb. 26 1971	5.5	Yoneyama Bridge	27	0.151	0.060	2.52
San Fernando California	Feb. 9 1971	6.4	Pacomia Dam	4	1.076	0.577	1.87
Imperial Valley California	May 18 1940	6.6	El Centro	8	0.348	0.343	1.02
Montenegro Yugoslavia	Apr. 15 1979	7.0	Albatros Hotel, Ulcinj	17	0.171	0.194	0.88
Bam Earthquake, Iran	Dec. 6 2003	6.5	Bam	10	0.799	1.242	0.64
Mexico Earthquake	Sep. 19 1985	8.1	Zihuatenejo, Guerrero Ar.	135	0.103	0.318	0.32

Table 1: Selected earthquake records.

To shed light into the workings of the inelastic structure its seismic response is compared to that of an elastic model. For analyzing the structural behavior over time a specific type of wavelet analysis was employed. Fundamentally, the wavelet analysis is defined as a correlation method, wherein one can define the wavelet transform trough a correlation coefficient

$$a(t) = \int_{-\infty}^{\infty} s(\tau) w^*(\tau - t) d\tau \tag{5}$$

where $w^*(t)$ is the complex conjugate to $w(t)$. If the signal $s(t)$ correlates with the wavelet $w(t)$ well the coefficient a(t) will be large; otherwise it will be small. The only requirement on the wavelet is that it be localized at a specific point of time. The harmonic wavelet developed by Newland [6] is one that is compact in the frequency domain. It has a simple structure of the form

$$W_{m,n} = \begin{cases} \dfrac{1}{(n-m)2\pi} & \text{for} \quad m2\pi \leq \omega \leq n2\pi \\ 0 & \text{elsewhere} \end{cases} \tag{6}$$

where *m* and *n* are real but not necessarily integer. As one can see easily the value of the wavelet function is nonzero and constant only in a frequency band specified by *m, n.* The result of the procedure above is a time series corresponding to each frequency band. This time representation of a selected band is a representation of information and energy within this band. The wavelet is applied to the data in the Fourier domain which then is inversely transformed to the time domain. The harmonic wavelet transform was applied to the response of the models.

The goal of this assessment was to understand how the nonlinearity of the wall influenced its response and possibly affects its bearing capacity in an event of an earthquake. To do this, structures of different eigenfrequencies were taken for each earthquake record in such a way that the response of the model to the specific strong motion in terms of displacements is close to the defining limits of the model. That is to say, the model with the chosen natural frequency under the corresponding ground motion yields a displacement response that nears the maximum displacement values reached in the tests. This takes the model well into the nonlinear range without exceeding physically feasible boundaries. Our application of the harmonic wavelet transform produces time-frequency plots which, for the responses to the six ground motions, are given below. The figures clearly show case how the frequency response of the nonlinear structure changes over time as well as with respected to its linear counterpart. Once the structure is taken beyond its elastic limit the frequency of vibration changes significantly. The frequency drop can be sudden as in the case of El Centro or Montenegro earthquakes or more gradual like for the Honshu and Mexico earthquakes.

Harmonic wavelet transforms of the displacement responses of the elastic (left) and inelastic (right) models including time history plots of displacements for six earthquakes: Honshu, San Fernando, El Centro, Montenegro, Bam, Mexico are presented in Fig. 5-16.

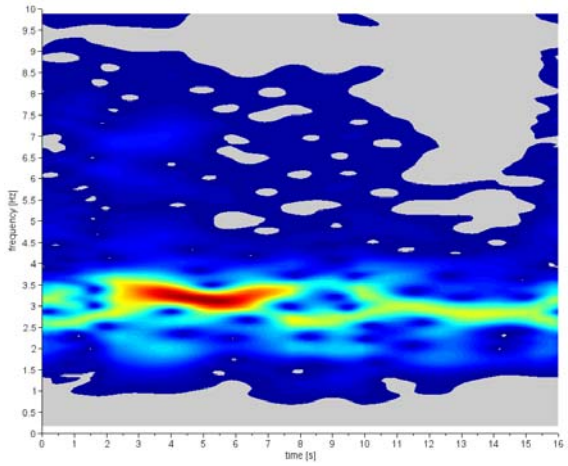

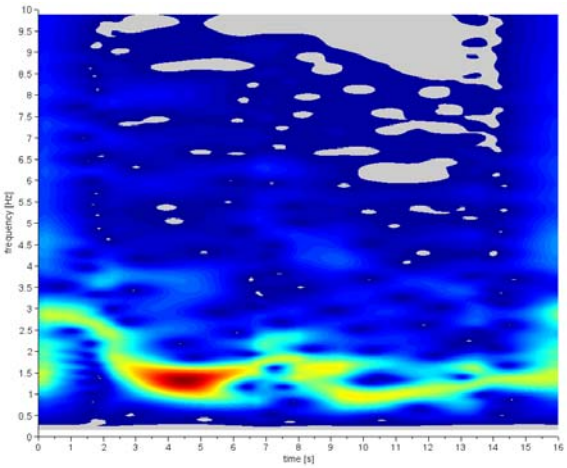

Honshu 1971

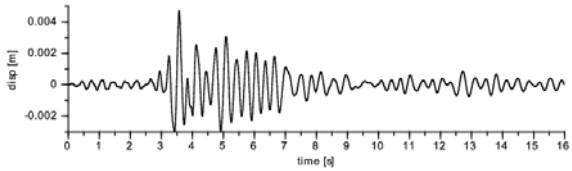

Figure 5: Honshu earthquake 1971: Displacement response of elastic model, its wavelet transform.

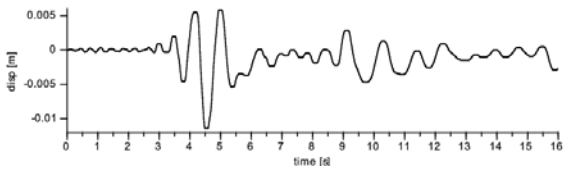

Figure 6: Honshu earthquake 1971: Displacement response of inelastic model, its wavelet transform.

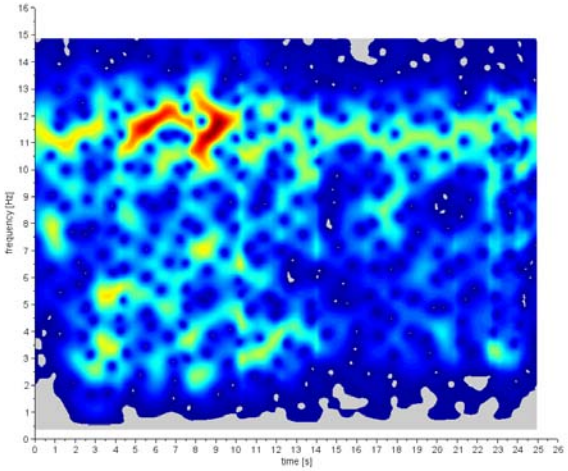

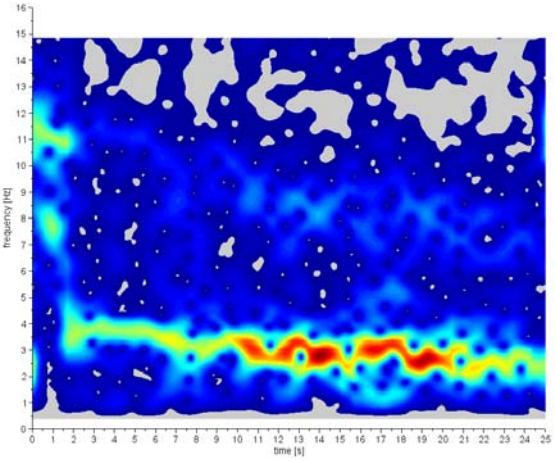

San Fernando 1971

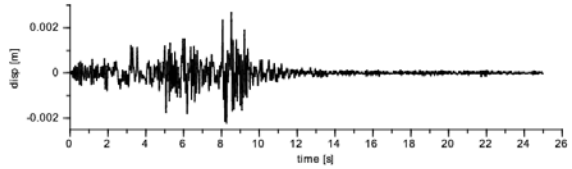

Figure 7: San Fernando earthquake 1971: Displacement response of elastic model, its wavelet transform.

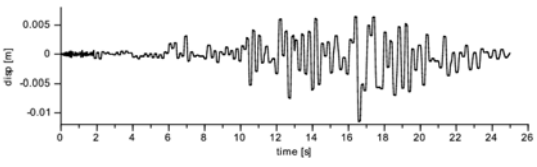

Figure 8: San Fernando earthquake 1971: Displacement response of inelastic model, its wavelet transform

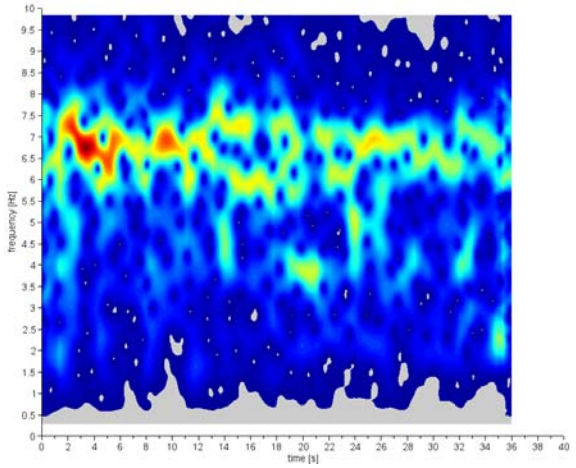

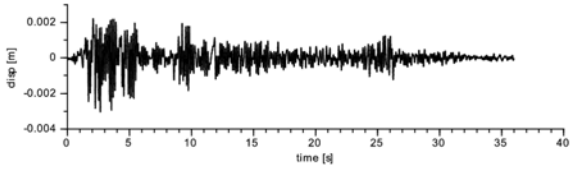

Figure 9: El Centro earthquake 1940: Displacement response of elastic model, its wavelet transform.

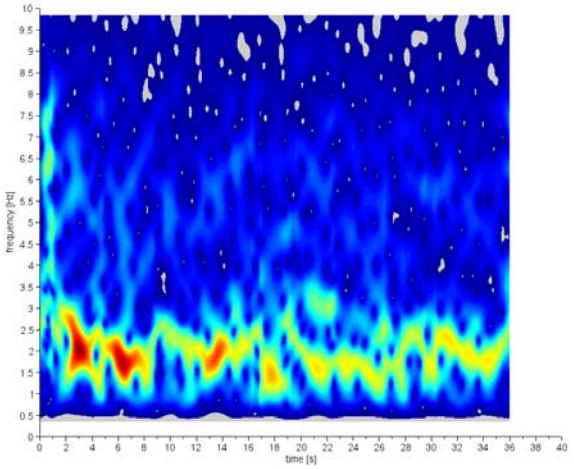

El Centro 1940

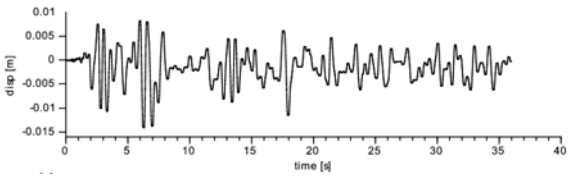

Figure 10: El Centro earthquake 1940: Displacement response of inelastic model, its wavelet transform.

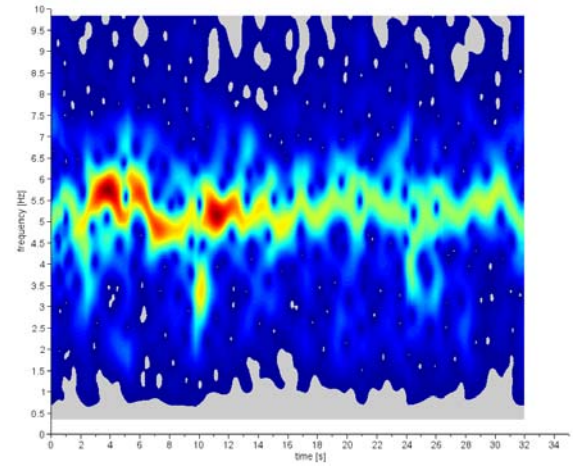

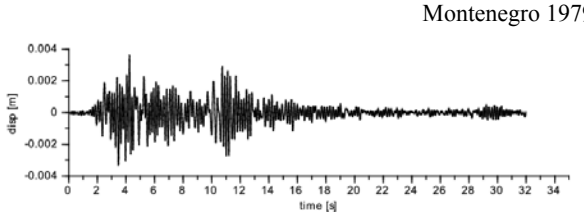

Figure 11: Montenegro earthquake 1979: Displacement response of elastic model, its wavelet transform.

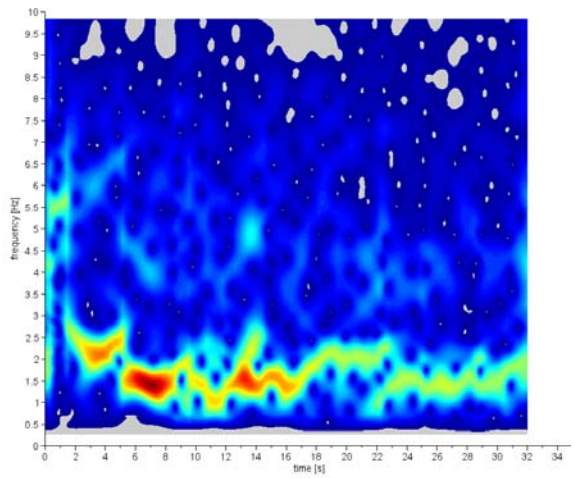

Montenegro 1979

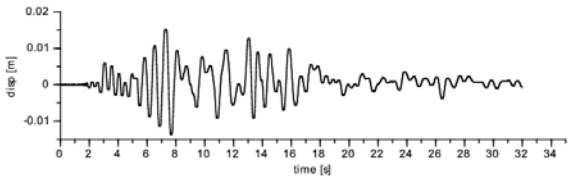

Figure 12: Montenegro earthquake 1979: Displacement response of inelastic model, its wavelet transform

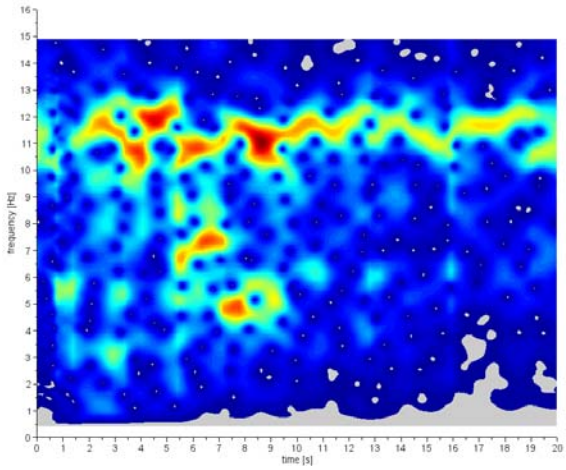

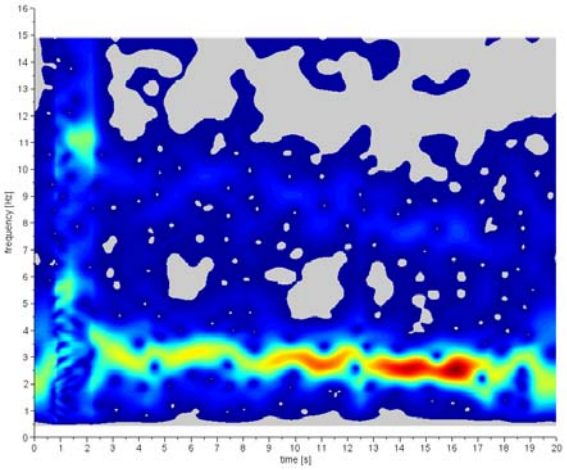

Bam 2003

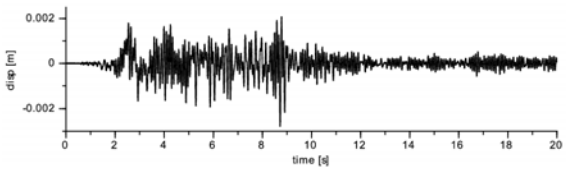

Figure 13: Bam earthquake 2003: Displacement response of elastic model, its wavelet transform.

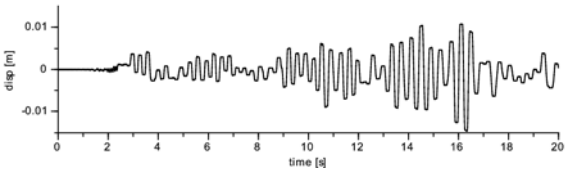

Figure 14: Bam earthquake 2003: Displacement response of inelastic model, its wavelet transform.

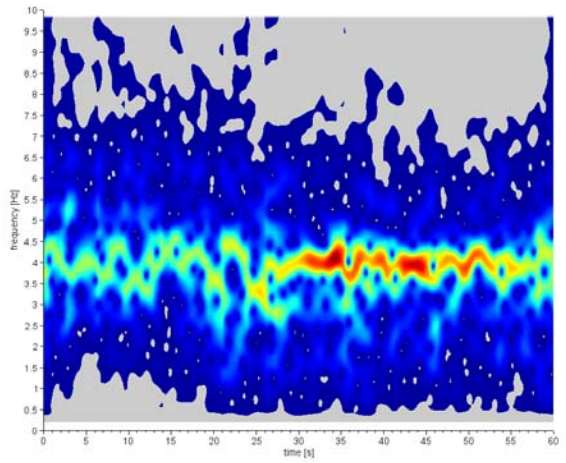

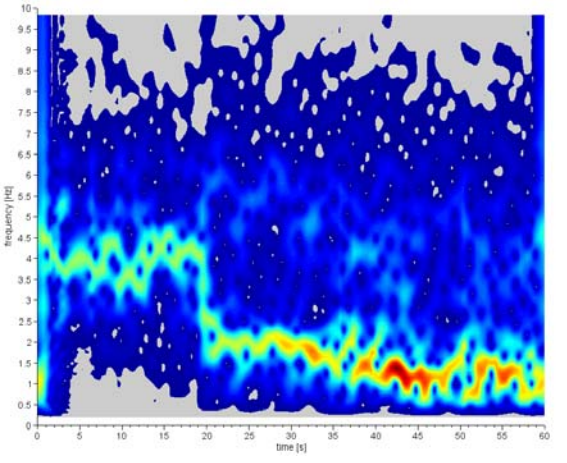

Mexico 1985

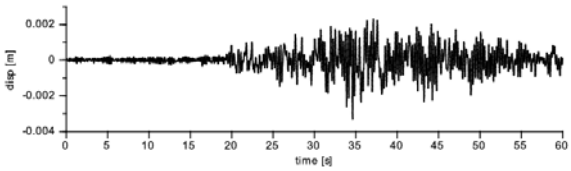

Figure 15: Mexico earthquake 1985: Displacement response of elastic model, its wavelet transform.

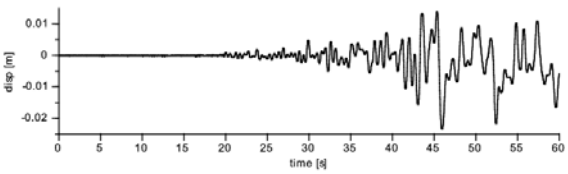

Figure 16: Mexico earthquake 1985: Displacement response of inelastic model, its wavelet transform.

5 NONLINEAR VS CODE BASED RESPONSE SPECTRA

To investigate possible design margins from yet another perspective we have chosen to look at nonlinear responses more specifically. The goal was to examine if the code based response spectra can be exceeded by elastic response spectra for cases when the nonlinear model still performs within the physical limits of the specimen for it was calibrated to. For the normative response spectra the ones defined in Eurocode 8 were selected. In light of this, to increase the number of European earthquakes in the set, for the scope of this assessment the accelerogram of the Friuli earthquake was added to the ones specified in Table e. Three distinct hypothetical cases were analyzed with initial periods $T_{01} = 0.083s$, $T_{02} = 0.11s$ and $T_{03} = 0.225s$. These periods are in relation to the initial stiffness, i.e. before cracking, of the inelastic model. All models were taken through the same procedure. For each earthquake a scaling factor was found that pushes the inelastic model to its "elastic" limit. The elastic limit of the model was selected as the point which marks the start of the yielding of the reinforcement in the physical system. This was the point of 5.4mm and 6943kN. It is noted that the point of elasticity was taken such, as it is the most correct choice for practical purposes.

Earthquake	Model 1 $T_{01} = 0.083s$	Model 2 $T_{02} = 0.11s$	Model 3 $T_{03} = 0.225s$	Model 0 $T_0 = 0.027s$
Honshu 1971	3.44	3.17	1.33	57.5
San Fernando 1971	0.71	0.38	0.09	7.9
El Centro 1940	2.00	1.12	0.28	23.0
Montenegro 1979	3.12	1.61	0.43	47.5
Bam 2003	0.63	0.34	0.19	9.1
Mexico 1985	7.11	4.05	0.64	76.0
Friuli 1976	2.31	1.14	0.29	21.5

Table 2: Example Scaling factors for earthquake accelerograms that take the model to its elastic limit.

Elastic response spectra derived from scaled accelerograms were compared to design response spectra from EC8 for model 1, model 2 and model 3 in Fig. 17-19.

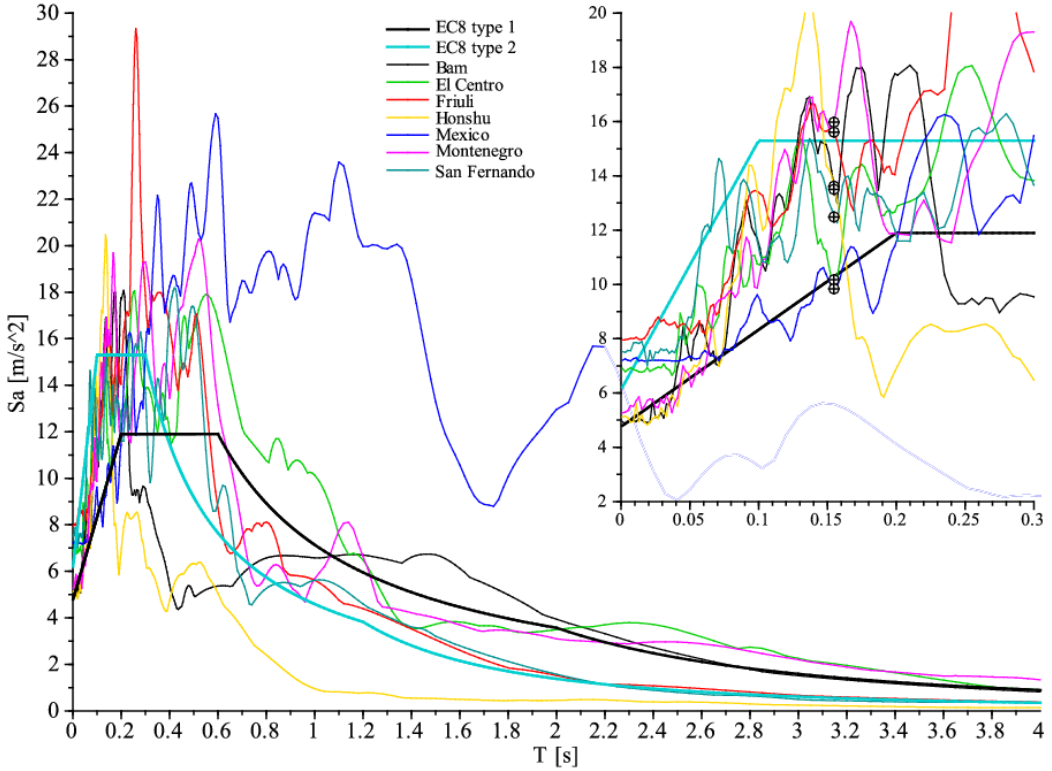

Figure 17: Elastic response spectra derived from scaled accelerograms compared to design response spectra from EC8 for model 1.

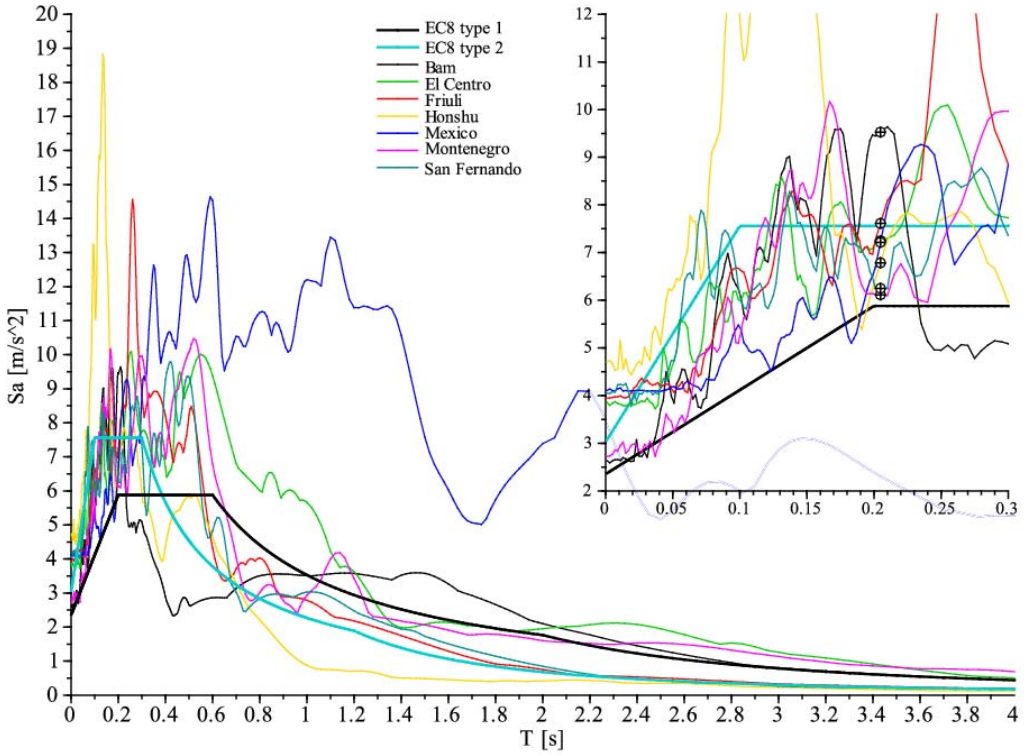

Figure 18: Elastic response spectra derived from scaled accelerograms compared to design response spectra from EC8 for model 2.

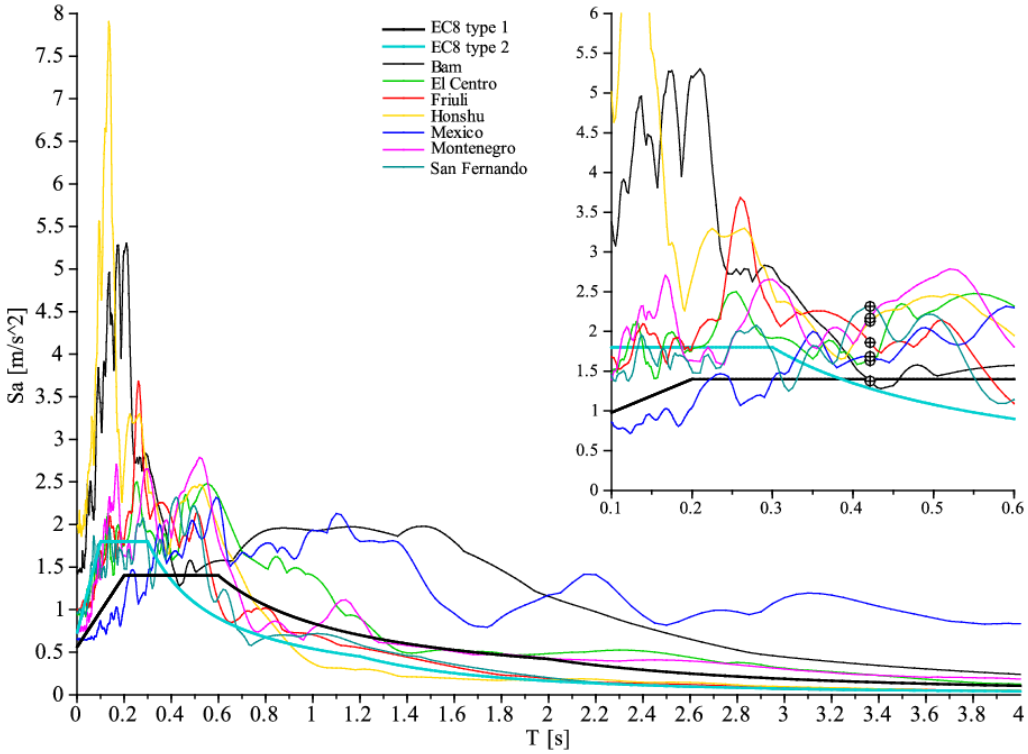

Figure 19: Elastic response spectra derived from scaled accelerograms compared to design response spectra from EC8 for model 3.

To define the imagined design capacity of the wall the value of 8.0MN, derived from testing, was assumed. To simulate design of the wall to this resistance the design response spectra needed to be scaled in such a way that at the design period they yield a design seismic force of 8.0 MN. This was simply achieved by an appropriate choice of base ground acceleration a_g for the type 1 response spectrum from EN 1998. Type 2 response spectrum was also plotted for reference. Viewing the results it is very evident that the model earthquake response spectra do reach above the design spectra. In some cases, especially for low periods, the overshoot is significant. Still when considering the differences at the design period (marked with dots in the subplots) many of the model response spectra lie above the design spectrum. In these cases it is not considered substantial, possibly with some exceptions. The interpretation of the results is that the linear response spectrum computed for a scaled excitation, which takes the nonlinear model to its elastic limit, yields forces that are higher than those defined by the code based design spectrum. Thus a reinforce concrete structure, namely a shear wall, to the extent it is represented by the mathematical model, can bear within its linear limits, dynamic forces higher than designed for based on a selected code, EN 1998 in this case.

6 CONCLUSIONS

- Based in the test data a mathematical hysteretic model was developed based on Litton's modification of the original Takeda model. This is a single degree of freedom nonlinear material model with the feature of pinching included. The model is tuned by two sets of four steering parameters for the two opposite quadrants. Upon the observation that the model would require different steering parameters for small and large displacement a functional relation was introduced for them. With such a refined model a good agreement with test data was reached.

- The behavior of a massive shear wall, represented by the mathematical model was analyzed for different selected earthquake records. The harmonic wavelet transform was applied to unravel the frequency response of the modelled structure over the time of excitation. The frequency shift could be evidently shown with the point of transition to inelastic yielding visible. For this analysis models of different natural frequencies were chosen for each earthquake record, so that they are driven by the excitation close to the maximum displacement value of the test specimen the model was based on. This was needed to study the inelastic behavior during an earthquake.
- The presented investigations were triggered by the need to explain seemingly unexpected phenomena observed in the wake of some earthquakes in nuclear power plants. And although nuclear facilities are designed to very strict criteria and substantial margins, there are indications of intrinsic margins beyond the intended ones due to disparities between the physics involved and the simplifications in the design procedures. It comes as no surprise that the accepted design procedures applicable in cases of massive shear walls were shown to be conservative.

REFERENCES

[1] K. Okano, *USGS Earthquake Science Center seminar*. http://earthquake.usgs.gov/regional/nca/seminars/2009-04-27/ [23 June 2014].

[2] A. Bekő, P. Rosko, Testing of stiff shear walls. In H. Wenzel, editor. *Industrial safety and life cycle engineering*. VCE ZT GmbH, Vienna, 2013.

[3] A. Bekő, P. Rosko, H. Wenzel, P. Pegon, D. Markovic, F. J. Molina, RC shear walls: Full-scale cyclic test, insights and derived analytical model, *Engineering Structure,* **102**, 120-131, 2015.

[4] R.W. Litton, A contribution to the analysis of concrete structures under seismic loading. PhD dissertation, Department of Civil Engineering, University of California, Berkeley CA, 1975.

[5] T. Takeda, M.A. Sozen, N.N. Nielsen, Reinforced concrete response to simulated earthquakes. *Journal of the Structural Division* ASCE, **96**(12), 2557-73, 1970 .

[6] D.E. Newland, Harmonic and Musical Wavelets. *Proceedings of the Royal Society*, **444**:605-620, The Royal Society, London, 1994.

[7] T. Strutz, *Bilddatenkompression.* Springer Vieweg, 2009.

[8] C. W. De Silva (ed.), *Vibration and Shock – Handbook*. Taylor & Francis, 2005.

COMPDYN 2019
7th ECCOMAS Thematic Conference on
Computational Methods in Structural Dynamics and Earthquake Engineering
M. Papadrakakis, M. Fragiadakis (eds.)
Crete, Greece, 24–26 June 2019

FLUTTER INSTABILITY CALCULATION FOR SUSPENDED BRIDGES USING GEOMETRICALLY NONLINEAR ANALYSES.

Chiara Taddeo[1],**Marco Di Giovanni**[1].
[1] G. D'Annunzio University, School of Engineering
viale Pindaro 42, 65127, Pescara (Italy)
mardg2693@hotmail.it; chiarataddeo00@gmail.com

Abstract

The paper investigates the modelling and calculation of the flutter instability condition due to the wind – structure interaction in the case of suspended bridges. In particular, the paper is focused on FEM (Finite Element Model) analyses on three dimensional models that compute the flutter instability. Geometric non-linear flutter instability analyses were carried out using a research and design software program (TENSO), which enables non-linear dynamic analysis of wind-structure interaction. All the bridge structure is modelled. In particular, the bridge deck model was simplified by a beam model located in the deck section's center of gravity and two massless rigid links to simulate the connection of the deck to the hangers and cables. The cables are represented by rectilinear cables element. The critical flutter speed was estimated using quasi-static approximation of the unsteady wind loads calculated by aerodynamic coefficients (i.e. lift, drag and moment coefficients) estimated by aerodynamic forces (i.e. lift, drag and moment) directly measured by wind tunnel tests. The executed analyses are by dynamic step-by-step integration of the nonlinear three-dimensional structure with geometric nonlinearities. The global stiffness matrix is updated at each load step by assembly of the stiffness sub-matrices of the elements, updated to account for the strain found at the previous time step, taking into account the geometric nonlinearity of the structure.

Firstly, the calculation provides for the static equilibrium of the structure under dead, gravity and construction loads by nonlinear static analysis. It was computed simultaneously using two methods: step-by-step incremental method and a "subsequent interaction" method with variable stiffness matrix (secant method). The secant method is a finite-difference approximation of the Newton-Raphson's modified method for systems of nonlinear algebraic equations. The solution under gravity loads is subsequently used as the initial step of the dynamic wind load analysis. The Newmark-Beta method with Rayleigh damping is used for numerical integration of the dynamic equations. Wind loads on the bridge deck are time dependent and they are simulated by applying the aerodynamic coefficients as a function of the time-dependent angle of attack at a given mean wind speed U. Displacements and rotations of the bridge deck at progressively increasing values of U, are estimated. The velocity at incipient flutter is fixed when the reference deck vibration amplitude exceeds ±5°. Details of the analyses results and calculation are given for an example of suspended foot bridges. Vertical displacements (δ) and rotations of the deck about the longitudinal bridge axis (αx) in normalized format (i.e. upward deck displacements are positive and counterclockwise rotations are positive) are discussed.

Keywords: Non-Linear analyses, Suspended bridge, flutter instability.

1 INTRODUCTION

The main suspended bridge structural model is a system made of a deck hanging by cables that are supported by pillars (i.e. bridge's towers).

Differently from traditional concrete bridges ([1]), suspended bridges are cables structures with a geometrical non-linear behavior and they are sensitive to the wind action ([2]). In addition, they have a small ratio between self-weight and length-span and this increases they vulnerability to dynamical action as for example the wind action. In particular, extreme peaks of wind force affect the structure reliability [3] and they have to be investigated in wind tunnel ([4], [5][6][7][8][9]). Alternatively, the wind-structure interaction can be analyzed by computational fluid dynamics simulations (CFD) and fluid and structure simulations (FSI). These approaches are common in the field of building construction and structural engineering and they are mostly used to investigate multihazard effects, as for example in the field of the sound propagation ([11], [12]), earthquake and tsunami effects or pedestrian-induced lateral vibrations ([13], [14], [15], [16]). However, the big Reynolds number (i.e. as in the case of civil big structures) makes it difficult to apply.

A suspended bridge design needs of two different experimental campaigns: aerodynamic and aeroealstic experiments ([17]).

Aerodynamic tests mostly aim to estimate the wind action around the bridge deck. The deck shape and its aerodynamics has a crucial role for bridge stability ([18], [19]). Generally, deck shape is regular and its aerodynamics is not discussed by codes ([20], [21], [22]). As for most shapes does not discussed by codes ([23]-[[27]), experimental tests in wind tunnel are necessary in order to estimate the pressure coefficients and the aerodynamic forces coefficients. The pressure coefficients are used to estimate the local pressure given by wind on the deck; the aerodynamic coefficients are used to calculate the flutter critical speed (i.e. quasi-static method) and to size the anchorages structures dimensions ([28][28]).

Aeroelastic tests aim to measure the wind-structure interaction dynamically. In particular, the goal is to calculate the flutter derivatives of the bridge section model. The flutter derivatives are used to estimate the flutter critical speed ([29]-[34]). In addition, aeroelastic tests permit to calculate the aerodynamic damping of the bridge.

Aerodynamic tests results give time histories of pressure coefficients or aerodynamic coefficients (i.e. Lift, Drag and Moment). Both results depend on the wind angle of attack. They are not wind-speed depending. Contrarily, aeroelastic tests results give speed-depending flutter derivatives.

Similarly to other cables structural systems, as for example cables nets ([35]-[38]) the experimental results in term of wind action are applied on Finite Element Method (i.e. FEM) models in the form of forces time histories. Time histories are applied on the structure nodes. In this phase, the different modeling approach followed for numerical model (i.e. FEM model) and experimental model (i.e. aerodynamic and aeroelastic tests model) represent one of the most severe problems in the wind-structure interaction study. For bridges, this is particularly relevant because the experimental model is commonly very simplified. It is often the case that numerical model is computed by a smaller grid mesh than experimental model. In this case, numerical methods to expand the experimental results are often used.

This paper discusses the wind-bridge interaction using aerodynamic tests results in term of aerodynamic coefficients though three dimension FEM non-linear analyses [39]. One of the three pedestrian suspended bridges ([40], [41]) discussed in [42] and [43] is used as case of study and experimental data and structural parameters are used for non-linear geometrically analyses. Analyses are pushed as far as the flutter instability and the flutter critical speed was estimated.

2 THEORETICAL FUNDAMENTALS OF WIND-STRUCTURE INTERACTION MODELLING

The critical flutter speed was estimated using two different approaches. The first is a two-mode (2-DOF) generalized numerical model of the deck motion in the frequency domain and flutter derivatives were considered to more correctly examine bridge aeroelasticity. The second consists in nonlinear dynamic analysis by three-dimensional finite element models and quasi-static approximation of the unsteady wind loads (i.e. lift, drag and moment derived from the wind tunnel tests) were employed.

The first approach is applying if aeroelastic tests results (i.e. flutter derivatives) are available. The dynamic response of a long-span bridge due to wind excitation can be modeled through the multi-mode approach in the frequency domain ([42]). The dynamic component of the wind loading, causing deck vibration, can be represented by superposition of turbulence-induced (aerodynamic) forces and motion-induced (aeroelastic) forces. Self-excited forces, acting on a unit-length section of the deck are defined as lift (L_h), drag (D_p) and moment (M_α). These forces are commonly based on a first-order linear expansion of the h vertical displacement and α torsional rotation of the generic deck cross section, ([33]). This model is strictly valid for simple-harmonic vibration of the deck and it is usually acceptable for small-amplitude random vibration. The aeroelastic lift and moment forces of the generic cross section, per unit deck span (or longitudinal model length), were determined as reported in Eqs. (1) and (2).

$$L_h = \frac{1}{2}\rho U^2 B\left[KH_1^*(K)\frac{\dot{h}}{U} + KH_2^*(K)\frac{B\dot{\alpha}}{U} + K^2H_3^*(K)\alpha + K^2H_4^*\frac{h}{U}\right] \tag{1}$$

$$M_\alpha = \frac{1}{2}\rho U^2 B^2\left[KA_1^*(K)\frac{\dot{h}}{U} + KA_2^*(K)\frac{B\dot{\alpha}}{U} + K^2A_3^*(K)\alpha + K^2A_4^*\frac{h}{U}\right] \tag{2}$$

In Eqs(1) and (2), ρ is the air density, U the mean wind speed perpendicular to the bridge (or model) longitudinal axis, B is the deck width; the "over-dot" symbol denotes derivation with respect to time t. The quantities H_i^* and A_i^* (with i=1,…,4) are the "flutter derivatives" (Scanlan and Tomko, 1971). These functions are experimentally found in wind tunnel by testing a section model of the full-scale girder at a reduced scale. The flutter derivatives depend on the reduced frequency $K=\omega B/U$ or, equivalently, reduced velocity $U_r=U/(nB)=2\pi/K$, with ω being the angular vibration frequency of the deck in rad/s and $n=\omega/(2\pi)$ the frequency in Hz.

The dynamic equilibrium equations of the 2-DOF system which is tested in the wind tunnel, reproduce the vertical (h) and torsional (α) aeroelastic vibration of a representative finite-length section of the full-scale bridge deck. The lift force L_h and overturning moment M_α per unit length of the deck are measured over the span length ℓ of the experimental model.

The vibration of the apparatus tested in wind tunnel, is given by Eqs(3) and (4) ([33], [34]).

$$M\left(\ddot{h} + \ddot{\alpha}\frac{S}{M} + 2\zeta_h\omega_h\dot{h} + \omega_h^2 h\right) = L_h\ell \tag{3}$$

$$I_\alpha\left(\ddot{\alpha} + \ddot{h}\frac{S}{I_\alpha} + 2\zeta_\alpha\omega_\alpha\dot{\alpha} + \omega_\alpha^2\alpha\right) = M_\alpha\ell \tag{4}$$

In Eqs. (3) and (4) M is the total mass of the model over the length ℓ, which also accounts for the mass of the moving components of the experimental rig; I_α is the total mass moment of

inertia; S is the static mass unbalance about the elastic axis, equal to the product of mass M and the distance (with appropriate sign) between the elastic center (center of stiffness) and the center of mass; ℓ is the longitudinal length of the model; ω_h and ω_α are the angular frequencies of vibration corresponding to the two DOFs; ζ_h and ζ_α are the corresponding structural damping ratios. The damping ratios coefficients replicate unavoidable dissipation mechanisms in the wind tunnel setup, which cannot be eliminated. The careful selection of the model's frequencies is also an important issue in the design of the experimental apparatus to ensure the successful measurement of the flutter derivatives.

According this theory, the solution to the flutter problem is based on the iterative procedure described by [34] simulating a 2DOF dynamical system with mass, inertia, damping ratios and flutter derivatives corresponding to the actual setup. The free-vibration method ([33]) is used for the extraction of the flutter derivatives, [44]

The second approach, discussed in detail in section 4, consists in Nonlinear dynamic flutter analysis, that are carried out using the aerodynamic coefficients in accordance with the reference force system.

3 EXPERIMENTAL MEASUREMENTS

Experimental tests results given by [42] are discussed here in order to explain the entire process of flutter analyses. Aerodynamic tests were carried out to estimate the deck loads of a pedestrian bridge with closed-box bridge deck (structural properties are described later in a subsequent section). It is important to note that, in this study, the deck guardrail was neglected because it was assumed that it was made of cables and, therefore, would not affect the aerodynamics and the aeroelastic response.

Aerodynamic tests were carried out using rigid wind tunnel models with the same dimensions. The tests were designed to minimize any potential discrepancies induced by geometric scaling differences. The models were made of wood. The geometry of the experimental models is illustrated in Fig. 1.

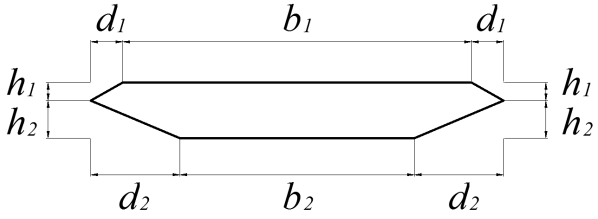

Figure 1 Section deck size.

Dimensions in Fig. 1 respectively are: $\boldsymbol{h_1}$ is equal to 530 mm at prototype scale and 13 mm at model scale; $\boldsymbol{h_2}$ is equal to 1110 mm at prototype scale and 27 mm at model scale**;** $\boldsymbol{d_1}$ is equal to 860 mm at prototype scale and 21 mm at model scale; $\boldsymbol{b_1}$ is equal to 1025 at prototype scale and 25 mm at model scale; $\boldsymbol{d_2}$ is equal to 2620 at prototype scale and 64 mm at model scale; $\boldsymbol{b_2}$ is equal to 6770 at prototype scale and 165 mm at model scale ([4], [42]).

Figure 2 experimental tests.

Measurements were carried out in the wind tunnel of the Marche Polytechnic University (Ancona, Italy). The wind tunnel is a closed-circuit facility. The cross-sectional dimensions of the main test chamber are about 1.8 m by 1.8 m. The main test section has three main test subsections: the first one is used for aerodynamic tests requiring uniform velocity distribution and low turbulence level. The second one is used to test aerodynamic interference between slender bodies. The last one is the environmental section where atmospheric boundary layer flows can be reproduced for general studies on buildings and structures. The wind tunnel is equipped with a motor/fan having a constant rotational speed (975 rpm) and 16 blades with adjustable pitch. The mean wind speeds range between 6 m/s and 40 m/s. Preliminary flow measurements, using a Constant Temperature Hot Wire Anemometer, showed a deviation less than 2.5% from the reference value of the mean flow speed and longitudinal turbulence intensity less than 0.3% across more than 90% of the test cross section. A compact heat exchanger was used to control temperature fluctuations within the range of ±1 [°C]. Fig. 2 presents a picture of a typical setup of the chamber with the experimental model. Measurements were carried out at a flow speeds equal to 14.8 m/s.

The purpose of these tests was to measure the Drag (D), Lift (L) and Torsional Moment (M) of the deck per unit span for the three geometries. The average values of drag, lift and torsional moment coefficients per unit span, respectively C_D, C_L and C_M, were evaluated according to Eq. 5 below. Fig.3 shows an example of the Lift aerodynamic force coefficient trend as function of the angle of attack ([42]).

In Eq. 5 U is equal to 14.5 m/s, ρ is equal to 1.18 kg/m^3 and, referring to Table 1, B is the reference width equal to $2d_1+b_1$= 298 mm. The model was placed vertically, as visible from Fig. 3, and the reference system for the calculation of the aerodynamic forces is given in Fig. 3. Twenty-one values of attack angle (α) were considered in the interval between -10° and +10°. Positive angles are “nose up” in relation to the approaching flow.

$$C_D = \frac{D}{\frac{1}{2}\rho U^2 B} \quad , \qquad C_L = \frac{L}{\frac{1}{2}\rho U^2 B}, \qquad C_M = \frac{M}{\frac{1}{2}\rho U^2 B^2} \tag{5}$$

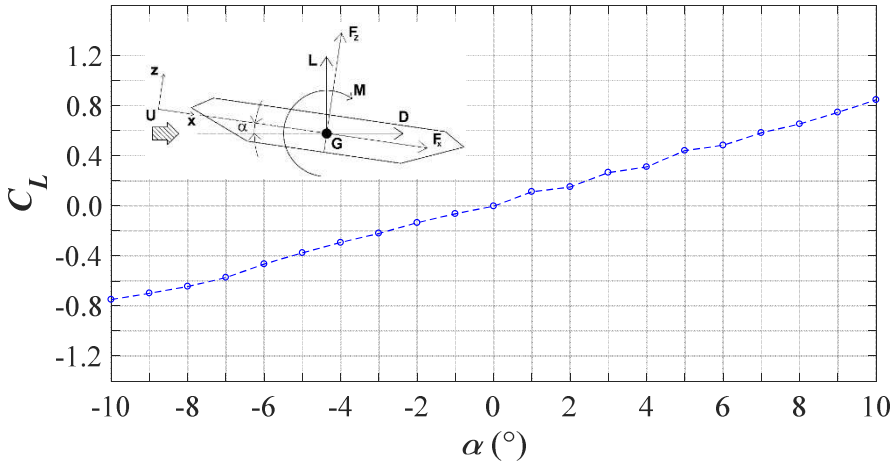

Figure 3 Example of Lift coefficient trend.

4 WIND-STRUCTURE INTERACTION CALCULATION

Nonlinear dynamic flutter analysis discussed here was carried out using the aerodynamic coefficients and were performed using the TENSO nonlinear geometrical analysis program, which can execute dynamic step-by-step integration of the nonlinear three-dimensional structure with geometric nonlinearities. Tenso is not a commercial software.

The software used includes modules for simulating cable and beam finite element models and for the study of wind-structure interaction phenomena with generation of wind speed time histories and simulation of various aeroelastic loads. The main cables are discretized as rectilinear cable segments.

The global stiffness matrix is updated at each load step by assembly of the stiffness submatrices of the elements, updated to account for the strain found at the previous time step. In this way the software considers the geometric nonlinearity of the structure. This software first solves for the static equilibrium of the structure under dead, gravity and construction loads (prior to the application of the wind loads) by nonlinear static analysis; two methods are simultaneously used: step-by-step incremental method and a "subsequent interaction" method with variable stiffness matrix (secant method). In TENSO, secant method is used as a check method that permits to stop the analysis with a unbalanced solution. Nonlinear problem can be transformed in a succession of linear problems. Each calculation step stores loads and strains history evaluated during the previous step. For each analysis step, a small enough part of load (ΔP) necessary to ensure that is possible to use the elasticity method is applied. A non-appropriate chosen range can cause an inexact solution. In order to solve it, this software uses a vector version of the Newton-Raphson modified method about nonlinear equation systems with the variable stiffness matrix. The Newton-Raphson procedure [42] guarantees convergence if and only if the solution at any iteration is close to the exact solution. Therefore, even without a path-dependent nonlinearity, the incremental approach (i.e., for subsequent load steps) is sometimes required in order to obtain a solution corresponding to the final load level. If the displacements

are large, the product between the stiffness matrix, evaluated on the basis of the solution of the previous step, and the displacements vector, give the internal force vector, not equilibrate with the external forces vector according to Eq.(6). In Eq.(6) K is the stiffness matrix, δ is the displacements vector, $\widetilde{P}$ is the external forces vector.

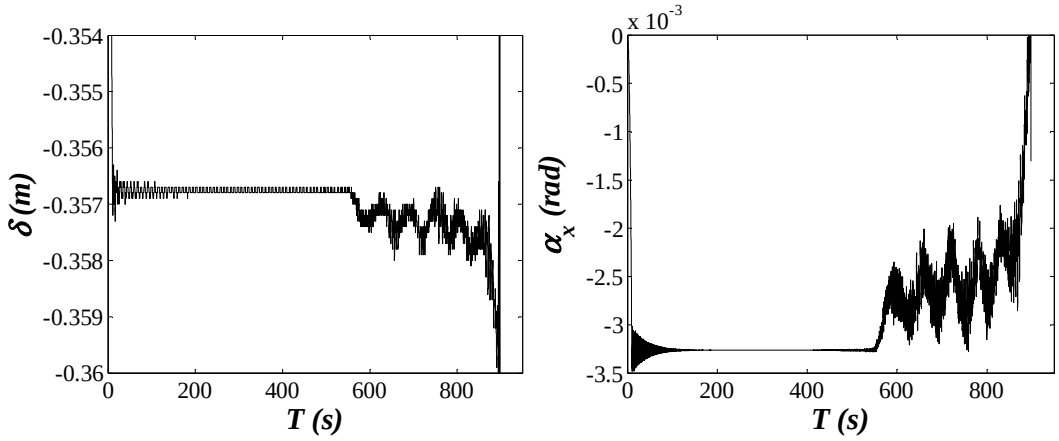

Figure 4 Flutter instability given by FEM analyses:

The difference between these two forces vectors (i.e. internal and external) represents the imbalance force vector, according to Eq. (7). R is the residual vector and P is the internal forces vector. Subsequently, R is applied as an external load modifying the displacement vector with a residual value of displacements $\Delta\delta$, according to Eq.(8).

$$[K]_{k+1}\{\delta\}_{k+1} = \{\tilde{P}\}_{k+1} \tag{6}$$

$$[R]_{k+1} = [\{P\} - \{\tilde{P}\}_{k+1}] \neq 0 \tag{7}$$

$$\{\Delta\delta\}_{k+1} = [K]_{k+1}^{-1}\{R\}_{k+1} \tag{8}$$

Wind loads on the bridge deck are time dependent; they are simulated by applying the aerodynamic coefficients (CD, CL and CM) as a function of the time-dependent angle of attack and by setting the appropriate values of dynamic wind pressure at a given mean wind speed U (at deck level). The program evaluates displacements and rotations of the bridge deck at progressively increasing values of U, and records the velocity at incipient flutter when the reference deck vibration amplitude exceeds ±5° [42]. Fig. 4 illustrates an example of time histories exhibiting flutter instability in terms of vertical deck displacement (δ) and rotation (α), for the middle-span section (i.e. upward displacements are positive and counter clockwise rotation are positive).

The critical flutter speed estimated was equal to 79.8 m/s. This value corresponds to global the instability illustrated in Fig.4.

5 CONCLUSIONS

This paper discusses the wind-structure interaction modeling for suspended bridges. The geometrical non-linear analyses operation using wind tunnel experiments was commented and the flutter instability analyses calculation was described on a case of study. The procedure to apply

wind tunnel experiments results on FEM models of suspended bridges was commented by explaining the functioning. The paper aims to inspire readers to deepen the wind-structure interaction analyses on cables structural systems.

ACKNOWLEDGMENTS

The authors thanks Professor Fabio Rizzo of the Department of Engineering and Geology at G. D'Annunzio University, for his experimental data, Professor Piero D'Asdia for the non-commercial TENSO software and implementation, Professor Luca Caracoglia of the Department of Civil and Environmental Engineering at Northeastern University for his studies and teachings and, finally, Professor Sergio Montelpare for wind tunnel experiments.

REFERENCES

[1] Avossa, A.M.; Di Giacinto, D.; Malangone, P.; Rizzo, F. Seismic Retrofit of a Multi-Span Prestressed Concrete Girder Bridge with Friction Pendulum Devices. Shock Vib. 2018, doi:10.1155/2018/5679480.

[2] Knudson, W.C. Recent advances in the field of long span tension structures. Eng. Struct. 1991, 13, 174–193.

[3] Rizzo, F.; Barbato, M.; Sepe, V. Peak factor statistics of wind effects for hyperbolic paraboloid roofs. Eng. Struct. 2018, 173, 313–330.

[4] Rizzo, F.; Caracoglia, L. Examining wind tunnel errors in Scanlan derivatives and flutter speed of a closed-box. J. Wind Struct. 2018, 26, 231–251.

[5] Argentini T, Belloli M, Fossati F, Rocchi D, Villani M. Experimental and numerical analysis of the dynamic response of cable-stayed bridge: vortex induced vibrations and buffeting effects. In: Proceedings of the 13th International Conference on Wind Engineering. IAWE, Amsterdam, Netherlands; 2011.

[6] Argentini T, Diana G, Larsen A, Pagani A, Portentoso M, Somaschini C, Yamasaki Y. Comparisons between wind tunnel tests on a full aeroelastic model and numerical results of the Izmit bay bridge. In: Proceedings of the 6th European African Conference on Wind Engineering, Cambridge UK; 2013.

[7] Argentini T, Pagani A, Rocchi D, Zasso A. Monte Carlo analysis of total damping and flutter speed of a long span bridge: Effects of structural and aerodynamic uncertainties. Journal of Wind Engineering and Industrial Aerodynamics 2014;128:90-104.

[8] Mannini C, Bartoli G. A probabilistic approach to bridge deck flutter. In: Proceedings of the Twelfth International Conference on Wind Engineering (ICWE12), Cairns, Australia; 2007.

[9] Mannini C, Bartoli G. The problem of uncertainty in the measurement of aerodynamic derivatives. In: Safety, Reliability and Risk of Structures, Infrastructures and Engineering Systems, Proceedings 10th International Conference on Structural Safety and Reliability, Osaka, Japan; 2010: p. 824–31.

[10] Bartoli G, Mannini C. Reliability of bridge deck flutter derivative measurement in wind tunnel tests. In: Proceedings of ICOSSAR 2005 Conference; 2005.

[11] Rizzo, F.; Zazzini, P. Improving the acoustical properties of an elliptical plan space with a cable net membrane roof. J. Acoust. Aust. 2016, 44, 449–456, doi:10.1007/s40857-016-0072-5.

[12] Rizzo, F.; Zazzini, P. Shape dependence of acoustic performances in buildings with a Hyperbolic Paraboloid cable net membrane roof. J. Acoust. Aust. 2017, 45, 421–443.

[13] Ingólfsson ET. Pedestrian-induced lateral vibrations of footbridges: Experimental studies and probabilistic modelling", Ph.D. Thesis, Department of Civil Engineering Technical University of Denmark; 2011.

[14] Ingólfsson ET, Georgakis CT, Jönsson J. Pedestrian-induced lateral vibrations of footbridges: A literature review. Engineering Structures 2012; 45:21-52.

[15] Rehmanjee Y H. Lateral Vibration of Pedestrian Bridges. MS Thesis. Boston, Massachusetts, USA: Massachusetts Institute of Technology, Department of Civil and Environmental Engineering; 2000.

[16] Roberts T. M., 2005. “Lateral Pedestrian Excitation of Footbridges”, Journal of Bridge Engineering,

[17] Singh L. Experimental determination of aeroelastic and aerodynamic parameters of long-span bridges. PhD Dissertation. Baltimore, Maryland, USA: Johns Hopkins University; 1997.

[18] Belloli M, Fossati F, Giappino S, Muggiasca S. Vortex induced vibrations of a bridge deck: Dynamic response and surface pressure distribution. Journal of Wind Engineering & Industrial Aerodynamics 2014;133:160-68.

[19] Buljac A, Kozmar H, Pospíšil S, Macháček M, Král R. Dynamic stability of the Golden Gate Bridge deteriorated by roadway wind barriers". In: Proceedings of the 8th International Symposium BBAA VIII, Northeastern University, paper ID 109 (electronic proceedings); 2016.

[20] ASCE (American Society of Civil Engineering). Wind Tunnel Studies of Buildings and Structures; Manuals of Practice (MOP); Isyumov, N., Ed.; ASCE: Reston, VA, USA, 1999; Volume 67.

[21] ASCE (American Society of Civil Engineering). Minimum Design Loads for Buildings and Other Structures; ASCE: Reston, VA, USA, 2010; Volume 7.

[22] CEN (Comité Européen de Normalization). Eurocode 1: Actions on Structures—Part 1–4: General actions—Wind Actions; EN-1991-1-4; CEN: European Union, 2005.

[23] Rizzo, F.; Ricciardelli, F. Design pressure coefficients for circular and elliptical plan structures with hyperbolic paraboloid roof. J. Eng. Struct. 2017, 139, 153–169.

[24] Rizzo F., 2012, Wind tunnel tests on hyperbolic paraboloid roofs with elliptical plane shapes, Engineering Structures, 45, 536–558.

[25] Rizzo F., D’Asdia P., Ricciardelli F., Bartoli G., 2012. Characterization of pressure coefficients on hyperbolic paraboloid roofs, Journal of Wind Engineering & Industrial Aerodynamics, 102, 61–71.

[26] Rizzo F., D’Asdia P., Lazzari M., Procino L., 2011. Wind action evaluation on tension roofs of hyperbolic paraboloid shape, Engineering Structures, 33 (2), 445-461.

[27] Biagini, P.; Borri, C.; Facchini, L. Wind response of large roofs of stadiums and arena. J. Wind Eng. Ind. Aerodyn. 2007, 95, 9–11.

[28] Zasso A, Stoyanoff S, Diana G, Vullo E, Khazem D, Serzan K et al. Validation analyses of integrated procedures for evaluation of stability, buffeting response and wind loads on the Messina bridge. Journal of Wind Engineering and Industrial Aerodynamics 2013;122:50–9.

[29] Brito, R.; Caracoglia, L. Extraction of flutter derivatives from small scale wind tunnel experiments. In Proceedings of the 11th Americas Conference on Wind Engineering, American Association for Wind Engineering (AAWE), San Juan, Puerto Rico; 22–26 June 2009.

[30] Scanlan, RH, Jones NP, Singh L. Inter-relations among flutter derivatives. Journal of Wind Engineering and Industrial Aerodynamics 1997;69-71:829-37.

[31] Jones NP, Scanlan RH. Theory and full-bridge modeling of wind response of cable-supported bridges. Journal of Bridge Engineering, ASCE, 2001; (6):365-75.

[32] Scanlan, RH, Jones NP. Aeroelastic analysis of cable-stayed bridges. Journal of Structural Engineering, ASCE 1990;116(2):279-97.

[33] Scanlan RH, Tomko JJ. Airfoil and bridge deck flutter derivatives". Journal of Engineering Mechanics, ASCE 1971;97(EM6):1717-37.

[34] Simiu E Scanlan RH. Wind Effects on Structures: Fundamentals and Applications to Design, 3rd edition. New York, USA: John Wiley and Sons; 1996.

[35] Rizzo, F.; Sepe, V. Static loads to simulate dynamic effects of wind on hyperbolic paraboloid roofs with square plan. J. Wind Eng. Ind. Aerodyn. 2015, 137, 46–57.

[36] Vassilopoulou, I.; Gantes, C.J. Nonlinear dynamic behavior of saddle form cable nets under uniform harmonic load. Eng. Struct. 2011, 33, 2762–2771.

[37] Vassilopoulou, I.; Gantes, C.J. Vibration modes and natural frequencies of saddle form cable nets. Comput. Struct. 2012, 88, 105–119.

[38] Shen, S.; Yang, Q. Wind-induced response analysis and wind-resistant design of hyperbolic paraboloid cable net structures. Int. J. Space Struct. 1999, 14, 57–65.

[39] Gordon S. Critical analysis of the first Severn Bridge. In: Proceedings of Bridge Engineering 2 Conference, Bath, United Kingdom; 2010.

[40] Ricciardelli F, Hangan H. Pressure distribution and aerodynamic forces on stationary box bridge sections". Wind and Structures 2001;4:399-412.

[41] Ricciardelli F, de Grenet ET, Hangan H. Pressure distribution, aerodynamic forces and dynamic response of box bridge sections. Journal of Wind Engineering & Industrial Aerodynamics 2002;90(10):1135-50.

[42] Rizzo, F.; Caracoglia, L.; Montelpare, S. Predicting the flutter speed of a pedestrian suspension bridge through examination of laboratory experimental errors. Eng. Struct. 2018, 172, 589–613.

[43] Speziale F. Aerodynamic and aeroelastic response of streamlined single box sections for long-span bridge decks. PhD Dissertation. Pescara, Italy: University of Pescara; 2015.

[44] Sarkar PP, Caracoglia L, Haan FL, Sato H, Murakoshi J. Comparative and sensitivity study of flutter derivatives of selected bridge deck sections. Part 1: Analysis of inter-laboratory experimental data. Engineering Structures 2009;31(1):158-69.

COMPDYN 2019
7th ECCOMAS Thematic Conference on
Computational Methods in Structural Dynamics and Earthquake Engineering
M. Papadrakakis, M. Fragiadakis (eds.)
Crete, Greece, 24-26 June 2019

MODELING DYNAMIC LOADING RATE EFFECTS IN CONCRETE SPECIMENS AND CRACK BRANCHING AT A WEAK INTERFACE IN A PMMA PLATE USING PERIDYNAMICS

Pablo Castillo[1,2], Vitor Leitão[1] and Ferdinando Auricchio[2]

[1]CERIS, Instituto Superior Técnico, Universidade de Lisboa
Av. Rovisco Pais 1, 1049-001, Lisboa, Portugal
e-mail: {vitor.leitao,pablo.usyaopin}@tecnico.ulisboa.pt

[2] Università degli Studi di Pavia
Via Ferrata 3, 27100 Pavia, Italy
e-mail: {auricchio, pablo.castillousyaop01}@unipv.it

Keywords: Peridynamics, Crack Branching, Concrete Damage, PMMA Interface Failure

Abstract. *The present work demonstrates the use of peridynamic equations to capture dynamic crack patterns observed during experimental tests performed in concrete and polymethylmethacrylate (PMMA) materials. In the first part of the work, two concrete specimen configuration, namely a compact tension and a L-specimen, are modeled at different dynamic loading rates. In the second part the effect of having a weaker interface in between a PMMA plate is simulated and compared, with the case of not having an interface at all. In both, it is observed that simulation provides good agreement with experimental results.*

1 INTRODUCTION

Peridynamics (PD) is a reformulation of classical elasticity where stress and strain partial derivatives are substituted by force and displacement integral equations. The fact of not having to differentiate displacement to get strains (as in classical mechanics where a continuous displacement field is assumed, therefore allowing for strains to be derived from the displacement as long as there are no discontinuities) allows PD to be naturally suited to model discontinuities.

Silling [11] in 1999 introduced peridynamics for the first time. This initial version, nowadays termed "Bond Based Peridynamics" (BB-PD), combined with a simple damage model [14], based on a critical bond stretch parameter, has successfully been used in high impact dynamic applications to predict complex crack patterns and fragmentation observed in quasi-brittle materials. Even today BB-PD still accounts for over 90% of all work developed in the PD field [13]. However, the original BB-PD suffers from the limitation of only being able to model materials with a Poisson ratio $\nu = 1/4$ for 3D, 2D plane strain, and $\nu = 1/3$ for 2D plane stress cases [4].

To overcome this limitation, Silling in 2007 [12] introduced the "State Based Peridynamics" (SB-PD) with two variants: ordinary (OSB-PD) and non-ordinary (NOSB-PD), the difference between the two being the force vector direction with respect to the bond deformation vector, which in the OSB-PD are parallel and in NOSB-PD are not.

SB-PD offers the advantage of modeling different Poisson ratios. In fact BB-PD may be viewed as a subset of OSB-PD [3], and through NOSB-PD it even allows to incorporate classical mechanics materials into PD formulation [18]. For the latter case, many works have tried to incorporate classical damage models too. Some works have apparently succeded, but it is still an open question when it comes to distributing the damage from the global particles to the individual bonds and then re-calculating an approximation of the deformation gradient.

On the other hand, the critical stretch damage model has shown to naturally capture cracks by first breaking individual bonds that eventually propagate into damage and therefore originate cracks.

The following work analyses three examples using the critical stretch damage model within an OSB-PD formulation. On the first part a brief introduction will be given to the OSB-PD material employed and of the critical stretch damage model. Afterwards it wil be shown how a 2D plane stress formulation may adequately capture the main crack patterns observed in two different concrete specimen configuration experiments. Following, the same method will be employed to capture crack branching at a weak interface in a PMMA plate subject to an impact stress wave.

1.1 State Based Peridynamic Theory

The SB-PD equation of motion is expressed as eq. (1):

$$\rho(\mathbf{x})\ddot{\mathbf{u}}(\mathbf{x},t) = \int_{\mathcal{H}_\mathbf{x}} \underline{\mathbf{T}}\big[\mathbf{x},t\big]\big\langle \mathbf{q}-\mathbf{x}\big\rangle - \underline{\mathbf{T}}\big[\mathbf{q},t\big]\big\langle \mathbf{x}-\mathbf{q}\big\rangle dV_\mathbf{q} + \mathbf{b}(\mathbf{x}) \tag{1}$$

where $\big\langle\cdot\big\rangle$ notation indicates the bond in which the force state $\underline{\mathbf{T}}$ is acting on. Following figure (1) $\mathcal{H}_\mathbf{x}$ is defined as a spherical neighbourhood of radius δ centered in $\mathbf{x}$, such that particles $\mathbf{q}$ inside it will have an influence over $\mathbf{x}$ through a bond force. δ is also refered as the particle's horizon and in our simulations it will assume a constant value. The quantities ρ, $\ddot{\mathbf{u}}$, dV and $\mathbf{b}$ represent the particle's density, acceleration, volume and body force correspondigly.

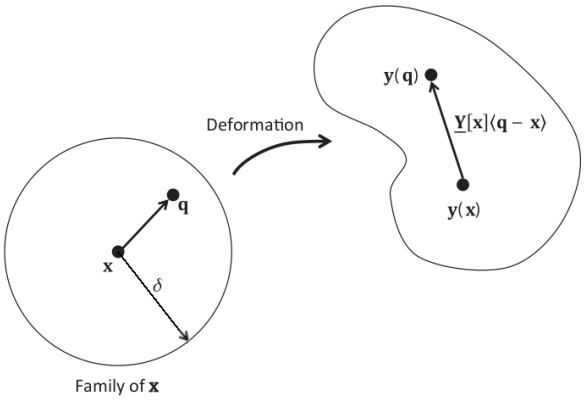

Figure 1: Deformation Map. (Adapted from [13])

In eq. (1), $\underline{\mathbf{T}}$ contains a constitutive model $\hat{\underline{\mathbf{T}}}(\underline{\mathbf{Y}})$ which depends on a deformation state $\underline{\mathbf{Y}}$. By employing a Fréchet derivative of a PD strain energy density $\hat{W}$, with respect to the deformation state, the expression in eq. (2) arises:

$$\underline{\mathbf{T}} = \hat{\underline{\mathbf{T}}}(\underline{\mathbf{Y}}) = \hat{W}_{\underline{\mathbf{Y}}} = \underline{t}\frac{\underline{\mathbf{Y}}}{\sqrt{\underline{\mathbf{Y}} \cdot \underline{\mathbf{Y}}}} = \underline{t}\underline{\mathbf{M}} \tag{2}$$

From eq. (2), $\underline{t}$ is a bond force and $\underline{\mathbf{M}}$ is a unit vector with direction of the deformed bond $\underline{\mathbf{Y}}\langle\xi\rangle = \mathbf{y}(\mathbf{q}) - \mathbf{y}(\mathbf{x})$. For completion, the bond initial configuration $\underline{\mathbf{X}}\langle\xi\rangle = \mathbf{q} - \mathbf{x}$, together with the deformed bond define the bond extension as (3).

$$\underline{e} = \underline{y} - \underline{x}, \qquad \underline{y} = |\underline{\mathbf{Y}}|, \qquad \underline{x} = |\underline{\mathbf{X}}| \tag{3}$$

By employing $\hat{W}$ from [12] for the 3D case, and from [3] for the 2D plane stress/strain conditions, and equating under the same deformations both strain energy densities: PD and classical mechanics $\hat{W}_{PD} = \hat{W}_{CCM}$, the bond force in (2) may be expressed as following:

$$\underline{t} = \begin{cases} \dfrac{3K\theta}{m}\underline{wx} + \dfrac{15\mu}{m}\underline{we^d} & \text{3D,} \\ \dfrac{4K\mu}{3K+4\mu}\dfrac{\theta}{m}\underline{wx} + \dfrac{8\mu}{m}\underline{we^d} & \text{pl. stress,} \\ \dfrac{4(3K-\mu)}{9}\dfrac{\theta}{m}\underline{wx} + \dfrac{8\mu}{m}\underline{we^d} & \text{pl. strain} \end{cases} \tag{4}$$

Quantities K and μ are the bulk and shear modulus correspondingly, $\underline{w}$ is an influence function which in our simulations takes the constant value 1, m, θ, and $\underline{e^d}$ are the weighted volume, dilatation and deviatoric bond extension defined as follows:

$$m = \int_{\mathcal{H}_{\mathbf{x}}} (\underline{wx}) \cdot \underline{x}\, dV_{\mathbf{q}} \tag{5}$$
$$\theta = \frac{3}{m} \int_{\mathcal{H}_{\mathbf{x}}} (\underline{\omega x}) \cdot \underline{e}\, dV_{\mathbf{q}}$$
$$\underline{e^d} = \underline{e} - \frac{\theta \underline{x}}{3}$$

1.2 Damage in Peridynamics

The simplest way to introduce damage in PD is through bond breaking as described in [14]. Following previous notation, the bond stretch is computed as $s = e/\underline{x}$.

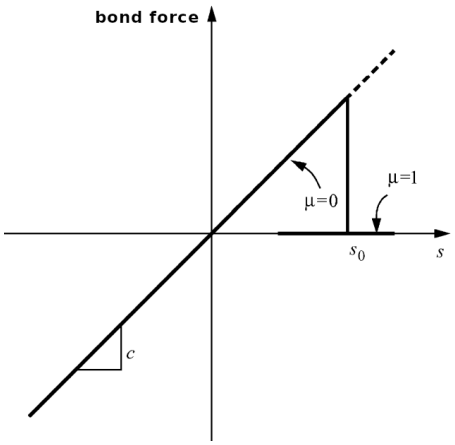

Figure 2: Critical Stretch Damage Model (Adapted from [14])

When s gets bigger than a critical bond stretch s_0 (figure 2), the bond becomes damaged:

$$\mu(\xi) = \begin{cases} 1 & \text{if} \quad s > s_0 \\ 0 & \text{otherwise,} \end{cases} \tag{6}$$

and the particle's damage is evaluated as the rate of broken bonds divided by the particle's total bond number:

$$d(\mathbf{x}) = \frac{\int_{\mathcal{H}_{\mathbf{x}}} \mu(\xi) dV q}{\int_{\mathcal{H}_{\mathbf{x}}} dV q} \tag{7}$$

s_0 is calibrated with the material's fracture energy release rate G_F. Following the procedure in [13] and after setting $\nu = 1/4$ for 3D and plane strain and $\nu = 1/3$ for plane stress conditions, the critical stretch expressions in (8) for the critical stretch are obtained:

$$s_0 = \begin{cases} \sqrt{\dfrac{5G_F}{6E\delta}} & \text{3D,} \\ \sqrt{\dfrac{8\pi G_F}{9E\delta}} & \text{pl. stress,} \\ \sqrt{\dfrac{5\pi G_F}{6E\delta}} & \text{pl. strain} \end{cases} \tag{8}$$

2 COMPACT TENSION TEST

In this example the experiments performed in [7] are simulated for a concrete specimen subjected to different dynamic loading rates. The specimen geometry and its initial hexagonal (for 3D) configuration are displayed in figure (3) on the left and right hand side correspondingly. It should be noted that PD deals with particles, not elements. However for simplicity is convenient to start by defining a pseudo-mesh, in this case of hexagons. For each hexagon a particle is assigned to the hexagon's centroid containing the total volume of the hexagon. For this simulation a non-uniform distribution of particles resulted, having an average distance between each particle of $\Delta x \approx 1\,mm$.

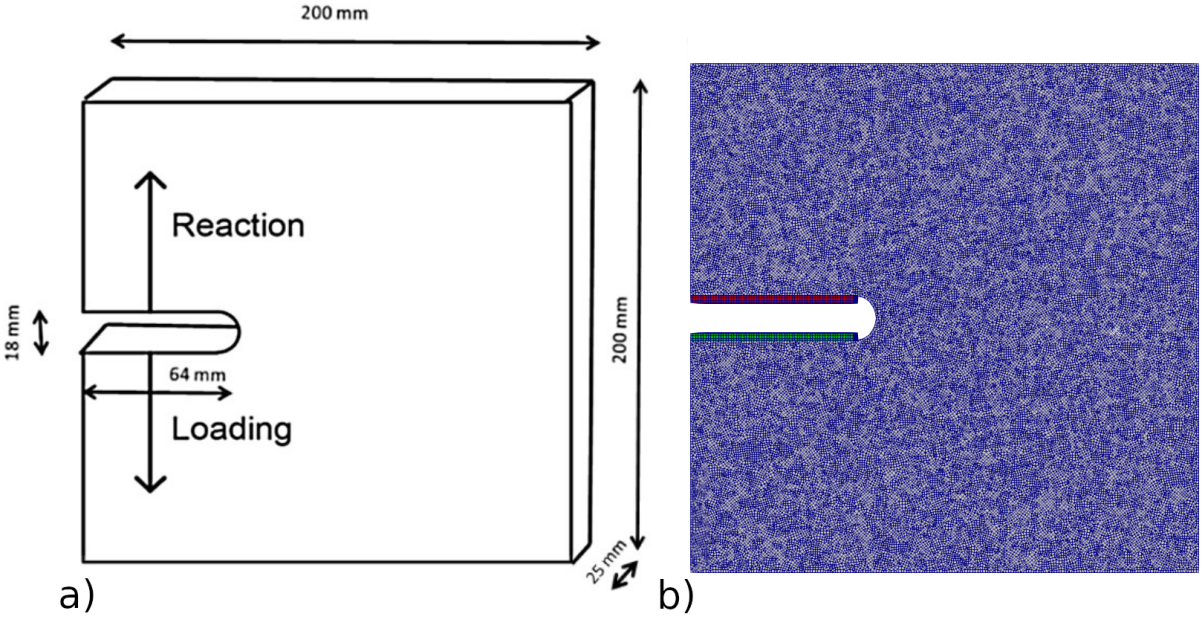

Figure 3: Compact Tension Specimen. a) Geometry (Reprinted from [2]), b) Initial Hexagonal Discretization

In red and green colors may also be observed two additional material blocks added to the geometry corresponding to the reaction (fixed position) and loading boundary conditions (BC). These two extra material blocks have δ width added size and are required because in PD (as in any other non-local theory), the existence of a "traditional" BC does not emerge as in the local theory [11].

The initial mesh was generated with GMSH and converted into EXODUS II format [15] using a local MATLAB script plus the MAT2EXO tool from SEACAS library. For performing PD calculations, the open source program PERIDIGM [8],[5] was employed, and modified to include 2D support and accordingly, the plane stress/strain material model mentioned before.

All results are output in another EXODUS II file that may be visualized using PARAVIEW. For the 3D case the file contains only particles with their respective computed properties. As for 2D, the mesh generator and Delaunay triangulator TRIANGLE [10] was implemmented to the PERIDIGM code to link particles to triangular elements. This helps to better visualize surface results and employ other PARAVIEW's available tools.

A velocity-Verlet time integration scheme was employed. Such scheme computes current velocities and displacements based on previous time step accelerations. All variables are stored explicitly and a small enough constant integration time step is selected. Such parameter is chosen to be 0.7 times the maximum stable time step Δt_{crit} determined as:

$$\Delta t_{crit} = \begin{cases} \sqrt{\dfrac{2\rho}{\sum_q dV_q C_q}} & \text{3D,} \\ \dfrac{h}{c} & \text{2D} \end{cases} \tag{9}$$

The expression in (9) for 3D was intrinsically developed in [14]. The summation implies an iteration over all neighbourhood $\mathbf{q}$ of material particle $\mathbf{x}$. dV is the particle's volume and C is the effective micromodulus constant computed as $C = 18k/\underline{x}\pi\delta^4$. The parameters ρ and k (material density and bulk modulus, respectively) and $\underline{x}$ (the undeformed bond length) were previously defined in eq. (3).

The expression for 2D follows the classical Courant Friedrichs-Lewy (CFL) approach, where h is the minimum undeformed bond length in all domain particles and c is the material wave speed computed as $c = \sqrt{k/\rho}$.

Table (1) lists the material and discretization parameters used in the simulations.

Parameter	Value
Elastic Modulus E	$36.00\,GPa$
Poisson's Ratio ν	0.18
Material Density ρ	$2400\,kg/m^3$
Block Horizon δ	$3.002\,mm$
Fracture Energy G_F	$65.00\,J/m^2$
Critical Stretch s_0	0.00130 / 0.00078 *@3D / pl.stress*
Time Step dt	$1.7495 \times 10^{-7}\,s$ / $1.3076 \times 10^{-7}\,s$ *@3D / pl.stress*
Number of Particles	$1,273,125$ / $50,925$ *@3D / pl.stress*

Table 1: Compact Tension Material and Discretization Parameters

Figure (4) shows the obtained damage results for the specimen, subject to four different increasing velocity loading rates: $v = 0.3,\ 1.4,\ 3.3$ and $4.0\,m/s$. For comparison, results obtained from [2] using a a two-scale FEM damage model were also included. For the PD case, plane stress and 3D simulations results compare quite well. One single main crack is observed when the velocity is lower than $3.3m/s$, but multiple crack branching starts to develop as the velocity increases. Regarding the maximum computed force, the plane stress material seems to overestimate it more than the 3D. However, except for the a) ($v = 0.3\,m/s$) case, simulations are observed to be close to the registered value. In general good agreement is observed between results in [2], the current PD simulation and the experimental ones.

3 L-SPECIMEN TEST

In this section the concrete L-Specimen in [6] is analyzed with the current approach. The simulated results compare quite well with the experimental ones. Figure (5) displays on the left side the geometry dimensions and simulation setup, whereas on the right the initial hexagonal mesh is displayed.

The loading point is modeled using an external block (in red) of size ($30 \times \delta\, mm$), whereas the blocked part is fixed in all directions on the same block. Table (2) displays the material and discretization parameters employed. Same as in the previous case, a non-uniform distribution of particles with an average particle distance $\Delta x \approx 2.33\,mm$ is employed.

Parameter	Value
Elastic Modulus E	$32.20\,GPa$
Poisson's Ratio ν	0.18
Material Density ρ	$2210\,kg/m^3$
Block Horizon δ	$7.002\,mm$
Fracture Energy G_F	$58.00\,J/m^2$
Critical Stretch s_0	$0.0004630\,/\,0.00084$ *@3D / pl.stress*
Time Step dt	$4.1492 \times 10^{-7}\,s\,/\,2.8120 \times 10^{-7}\,s$ *@3D / pl.stress*
Number of Particles	$939,834\,/\,44,757$ *@3D / pl.stress*

Table 2: L-Specimen Material and Discretization Parameters

The specimen is dynamically loaded with increasing velocity rates. Both crack patterns and registered forces for each rate are illustrated in figures (6, 7). When available, simulations performed by [2] are also included for comparison.

From PD results, it is observed that as velocity increases, the crack becomes more aligned with the applied loading direction. This behaviour was also observed during the experimental tests.

Regarding material models, both plane stress and 3D seem to provide close results between each other, either in crack pattern or maximum registered force.

One single main crack is observed for small loading rates, where as multiple branching is developed when the rate is increased, particularly for the last case, in which a crack developed near the loading area and another started next to the fixed boundary condition. Close agreement was also observed with simulation results obtained in [2], with a difference in the fracture energy, for which a lower value ($G_F = 40J/m^2$) than the one used in [6] is employed.

4 WEAK INTERFACE IN A PMMA PLATE

The case analyzed in this section intends to simulate the experiments performed in [16], whereby a PMMA plate glued in the middle, thus having a weaker interface than the monolithic case, kinks and branches an upcoming crack in two smaller symmetric daughter cracks.

Figure (8) ([17]) illustrates the original experiment, where a long AL 7075-T6 aluminum Hopkinson pressure bar of dimensions ($L = 1830\,mm$, $\phi = 25.4\,mm$), whose "wedge" shape end is in direct contact with the PMMA plate. A striker of the same material as the bar, and dimensions ($L = 305\,mm$, $\phi = 25.4\,mm$) hits it and induces a stress wave with time duration ($t_s \approx 120\mu s$). The wave travels through the bar and exerts a contact force on the "free" supported specimen. In the experiment free boundary conditions are achieved by applying a putty layer on top and bottom of the plate. Therefore in the simulations no other boundary conditions but the applied contact force were considered.

The plate dimensions are illustrated in figure (9). The monolithic case represents a single PMMA block material, where as the bilayered case is composed of two blocks of the same material and a layer of adhesive "Weldon 16" of thickness $0.025\,mm$ and $0.100\,mm$ representing the "strong" and "weak" interface correspondingly. However, in the following approach the interface thickness is not directly input, but rather modeled by weakening the bonds that cross from one region to the other. The way to perform this was by reducing the critical stretch parameter [1] and again, this was added to PERIDIGM.

Although it is possible to use PERIDIGM to completely simulate in 3D the whole experiment, this task would require a quite high computational time. Therefore the approached followed here was to split the simulation into two stages. On the first part, ABAQUS (FEM) was employed to fully model in 3D, the stress wave propagation through the long bar up to the contact with the specimen (no fracture was considered at this point), thus this stage being purely elastic. On the second part the computed contact force was input into PERIDIGM, using the 2D plane stress model to capture fracture (fracture stage). Following, the mentioned procedure in presented in sequential order.

4.1 Elastic Stage

Table (3) presents material and discretization parameters employed for the analysis, whereas fig. (10) illustrates the corresponding mesh. The simulation was carried out using a contact "surface to surface" condition type with a fully explicit time discretization. The total computed time was $1000\,\mu s$ with a time step $dt = 2.7042 \times 10^{-8}\,s$.

According to [9] the bar's propagated stress wave may be obtained as eq. (10), in which $v = 15\,m/s$ is the striker velocity and ρ, E are the bar's density and elastic modulus respectively. The pulse time length τ is twice the wave's transit time on the striker bar: eq. (11), where $L_s = 0.305\,m$ is the striker length and $c \approx 5051.33\,m/s$ is the wave's speed on aluminum medium. Combined, the generated input pulse specified into ABAQUS is represented in eq. (12).

$$\sigma = \frac{v\sqrt{\rho E}}{2} \approx 106.5\,MPa \tag{10}$$

Parameter	Value	
	AL 7075-76 Bar	PMMA Plate
Elastic Modulus E	$71.70\,GPa$	$5.00\,GPa$
Poisson's Ratio ν	0.33	0.34
Material Density ρ	$2810\,kg/m^3$	$1010\,kg/m^3$
Element length dx	$1.50\,mm$	$0.80\,mm$
Number of Elements	$1,289,945$	$599,104$

Table 3: Bilayer Plate: Elastic Stage performed in ABAQUS. Material and Discretization Parameters

$$\tau = 2\frac{L_s}{c} \approx 120.76\,\mu s \tag{11}$$

$$\sigma = \begin{cases} 106.5\,MPa & \text{if} \quad t < 120.76\,\mu s \\ 0 & \text{otherwise} \end{cases} \tag{12}$$

From ABAQUS, a graph of Time vs Contact Force - Area in fig. (11), indicates that contact may be considered constant along the wedge surface area of the specimen, where as the force may be approximated using a polynomial function. Such approximation (based on time) is obtained with the polifit function from MATLAB for a high polynomial degree, and imported into PERIDIGM as a body force. The result is illustrated in fig. (12), where the displacement on a single same point, from both ABAQUS and PERIDIGM (this latter one in 2D) are measured and compared. PD solution is offset by $\approx 280\mu s$ which is the time in takes for the stress wave to travel through the long bar and reach the specimen. Both displacements seem to agree well enough for the corresponding applied body force.

4.2 Fracture Stage

This section will present the obtained results during fracture of the PMMA bilayer plate. Such computations were performed based on the previous calculated contact force when imported into PERIDIGM and assuming a PD-plane stress condition. Table (4) displays the material and discretization parameters employed, and figure (13) illustrates the initial PD-plane stress quadrangular mesh, later converted into particles. On it, two extra blocks of size $(17.15 \times 2\delta\,mm)$ for the boundary conditions were added. On the mesh they appear overlapped, but in the simulation were specified not to interact. Remaining blocks behave as usual with the exception of the damage properties on the interface when the case applies. The total computed time was $230\,\mu s$ with a time step $dt = 3.1398 \times 10^{-11}\,s$.

The objective is to model the following three scenarios: a single monolithic type, where no interface is present; a weaker; and a stronger interface type. The adopted procedure was the following:

- Start modeling the monolithic type. Since no interface is required an initial critical stretch, just enough to avoid branching and ensure a monothonic mode I advancing crack was selected. Such parameter was found to be $s_0 = 0.0235$.

Parameter	Value
Elastic Modulus E	$5.00\,GPa$
Poisson's Ratio ν	0.34
Material Density ρ	$1010\,kg/m^3$
Block Horizon δ	$1.07\,mm$
Number of Particles	$394,432$

Table 4: Bilayer Plate: Fracture Stage Material and Discretization Parameters

- Model the weak and strong interface cases by choosing smaller critical stretchs correspondingly. The range ($s_0 = \{0.0116 - 0.0164\}$) was selected for such purpose and the corresponding results are illustrated in fig.(14).

From the results it is observed that small enough s_0 values on the interface perturb an upcoming mode I type crack. When s_0 is smaller than a specific range ($s_0 = \{0.0126 - 0.0156\}$), the crack propagates into two symmetric daugther cracks that remain trapped inside the interface, whereas if s_0 is bigger that the mentioned range, the crack propagates monotonically throughout the whole specimen without feeling the interface effect. Only inside the range, the crack got trapped and could also escape by branching in two inclined angled cracks. This same behaviour was observed in [16].

The two extremes s_0 of the mentioned range were identified correspondingly as "weak" and "strong" interfaces with $\approx 53\%$ and $\approx 66\%$ of virgin PMMA material. Surprisingly, similar percentage ratios were also obtained in [16] when characterizing the PMMA interface material crack initiation toughness.

A comparison of experimental and PD results is presented in figs. (15,16). From the results, both strong and weak interfaces present very similar crack bifurcation angles ($28°$). The principal difference was observed in the propagated crack length inside the interface, which for the strong scenario, was shorter ($\approx 1\,mm$) than the weak one ($\approx 3.5\,mm$). This behaviour was also observed during experiments, however numerical results seem to underestimate it. Regarding the monolithic case, a monothonic advancing crack front was attained as expected.

5 CONCLUSIONS

This work demonstrated the use of PD equations combined with a bond breaking damage rule (critical stretch) for simulating damage in concrete and PMMA specimen materials subject to high dynamic loading rates. Observed results display excellent crack path agreement between numerical and experimental tests.

For the compact tension and the L-Specimen, full 3D simulations were also carried out and compared with plane stress material model. The results matched very well both in damage and maximum registered force, suggesting the use of the plane stress model (when applicable), as a good alternative to speed up computational results.

By assigning lower critical stretch thresholds on specified regions inside a domain, PD was able to capture expected perturbations imposed when having a weaker interface over an advancing crack front. Other possible approaches may have included reducing the elastic modulus,

fully simulate in 3D the experiment and having contact evaluated using a PD model. Nevertheless, the assumed simplifications still managed to provide a good insight into the simulation of damage in PMMA.

REFERENCES

[1] A. AgwaiI, I. Guven, and E. Madenci. Predicting crack propagation with peridynamics: a comparative study. *International Journal of Fracture*, **171**:65–78, 2011.

[2] M. K. Atiezo, W. Chen, and C. Dascalu. Simulation of loading rate effects on dynamic brittle failure of concrete structures using a two-scale damage model. *Springer Nature Singapore Pte Ltd*, 91–98, 2019.

[3] J. T. Foster. *Handbook of Peridynamic Modeling*, chapter Constitutive Modeling in Peridynamics, pages 143–173. CRC Press, 2017.

[4] D. Huang, G. Lu, and P. Qiao. An improved peridynamic approach for quasi-static elastic deformation and brittle fracture analysis. *International Journal of Mechanical Sciences*, **94-95**:111–122, 2015.

[5] D. J. Littlewood. Roadmap for peridynamic software implementation. techreport SAND2015-9013, Sandia National Laboratories, 2015.

[6] J. Obolt, N. Bede, A. Sharma, and U. Mayer. Dynamic fracture of concrete l-specimen: Experimental and numerical study. *Engineering Fracture Mechanics*, **148**:27–41, 2015.

[7] J. Obolt, J. Bonjak, and E. Sola. Dynamic fracture of concrete compact tension specimen: Experimental and numerical study. *International Journal of Solids and Structures*, **50**:4270–4278, 2013.

[8] M. L. Parks, D. J. Littlewood, J.A. Mitchell, and S.A. Silling. Peridigm users guide v1.0.0. techreport SAND2012-7800, Sandia National Laboratories, 2012.

[9] K. Ravi-Chandar. *Dynamic Fracture*, chapter Methods of Generating Dynamic Loading, pages 81–93. Elsevier, 2004.

[10] J. R. Shewchuk. Triangle: Engineering a 2d quality mesh generator and delaunay triangulator. In M. C. Lin and D. Manocha, editors, *Applied Computational Geometry: Towards Geometric Engineering*, volume 1148 of *Lecture Notes in Computer Science*, pages 203–222. Springer-Verlag, May 1996. From the First ACM Workshop on Applied Computational Geometry.

[11] S. Silling. Reformulation of elasticity theory for discontinuities and long-range forces. *Journal of the Mechanics and Physics of Solids*, **48**:175–209, 1999.

[12] S. Silling, M. Epton, O. Weckner, J. Xu, and E. Askari. Peridynamic states and constitutive modeling. *Journal of Elasticity*, **88**:151–184, 2007.

[13] S.A. Silling. *Handbook of Peridynamic Modeling*, chapter Introduction to Peridynamics, pages 25–60. CRC Press, 2017.

[14] S.A. Silling and E. Askari. A meshfree method based on the peridynamic model of solid mechanics. *Computers and Structures*, **83**:1526–1535, 2005.

[15] G. D. Sjaardema, L. A. Schoof, and V. R. Yarberry. Exodus ii: A finite element data model. techreport SAND92-2137, Sandia National Laboratories, 1995.

[16] B. M. Sundaram and H. V. Tippur. Dynamic crack growth normal to an interface in bi-layered materials: An experimental study using digital gradient sensing technique. *Experimental Mechanics*, **56**:37–57, May 2016.

[17] B. M. Sundaram and H. V. Tippur. Dynamics of crack penetration vs. branching at a weak interface: An experimental study. *Journal of the Mechanics and Physics of Solids*, **96**:312–332, July 2016.

[18] T. L. Warren, S. A. Silling, A. Askari, O. Weckner, M.l A. Epton, and J. Xu. A non-ordinary state-based peridynamic method to model solid material deformation and fracture. *International Journal of Solids and Structures*, **46**:1186–1195, 2009.

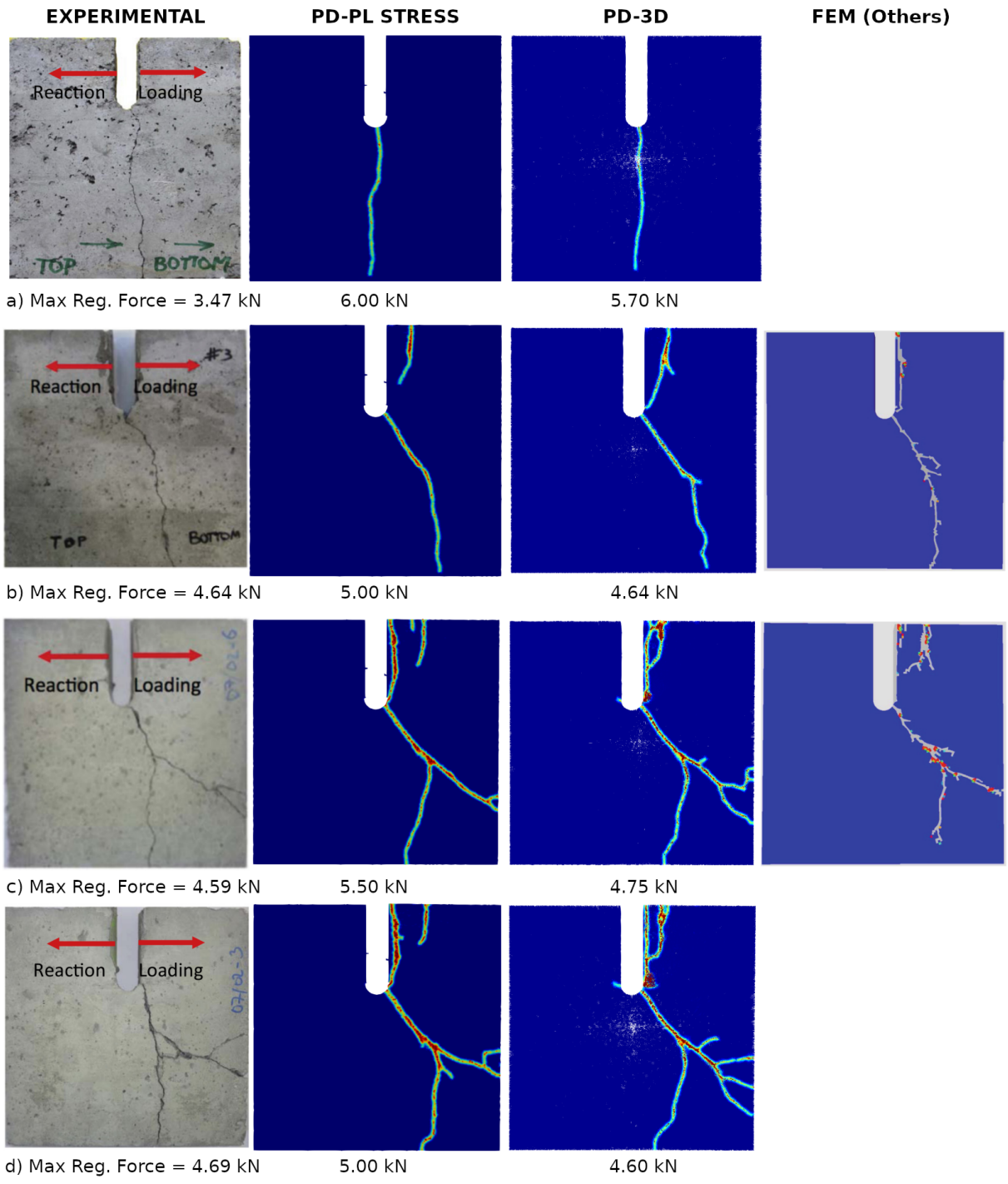

Figure 4: Compact Tension Damage Results. (Experimental illustrations reprinted from [7]; FEM reprinted from [2]); a) $v = 0.3m/s$, b) $v = 1.4m/s$, c) $v = 3.3m/s$, d) $v = 4.0m/s$

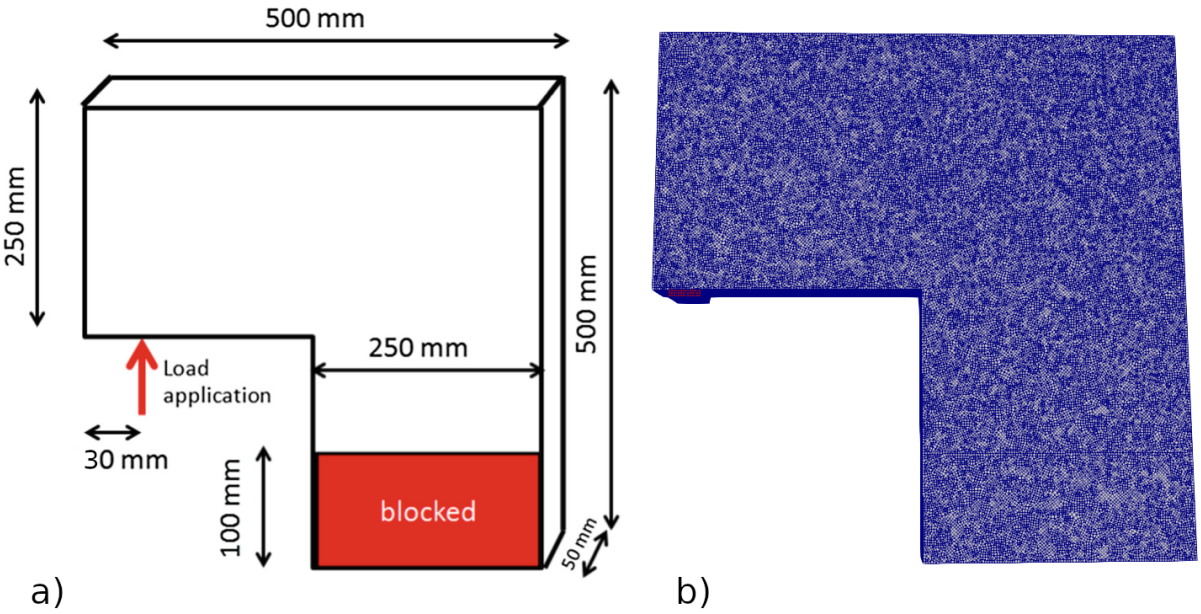

Figure 5: L-Specimen. a) Geometry (Adapted from [2]), b) Initial Hexagonal Discretization

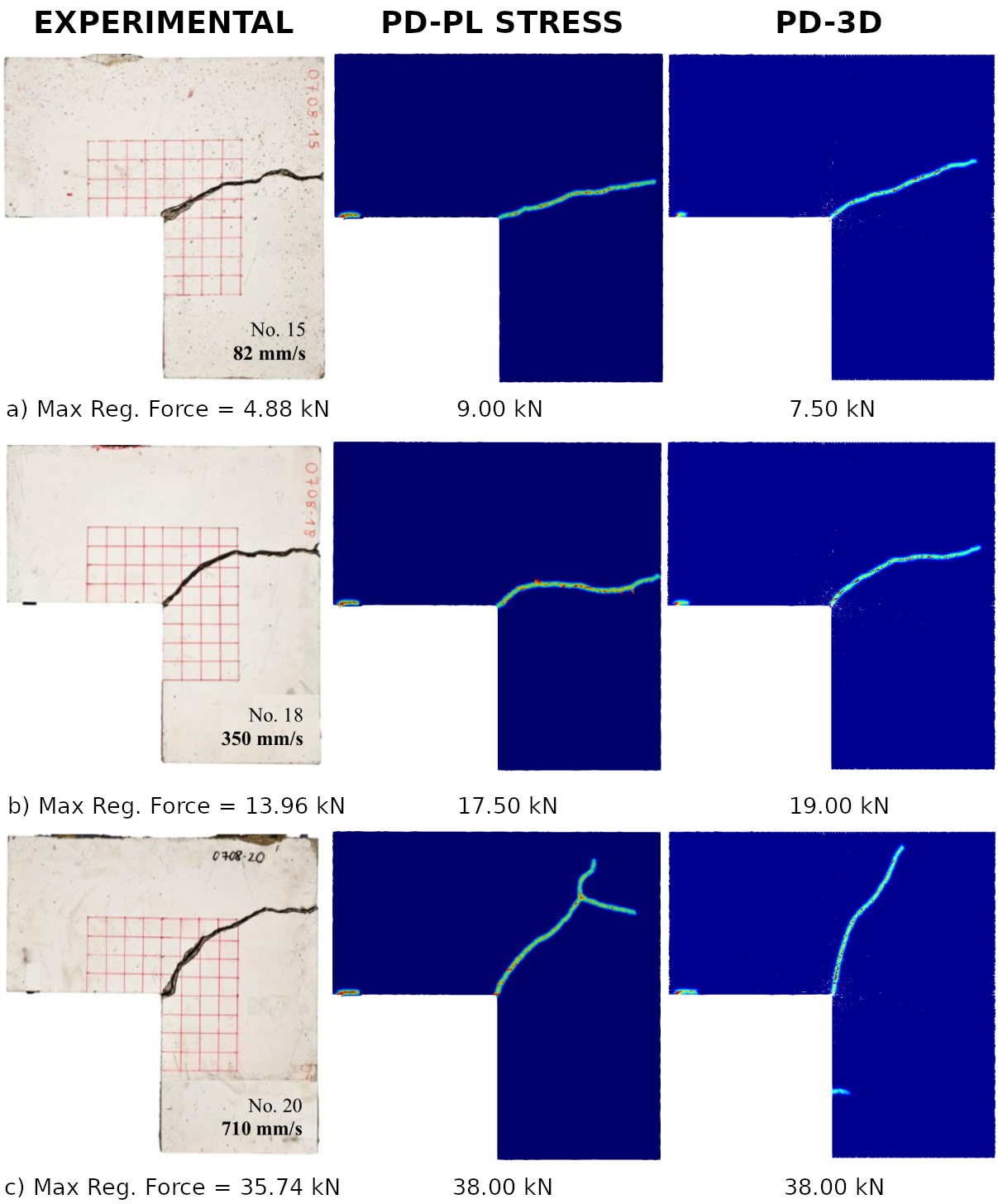

Figure 6: L-Specimen Results part I. (Experimental illustrations reprinted from [6]); a) $v = 0.082m/s$, b) $v = 0.350m/s$, c) $v = 0.710m/s$

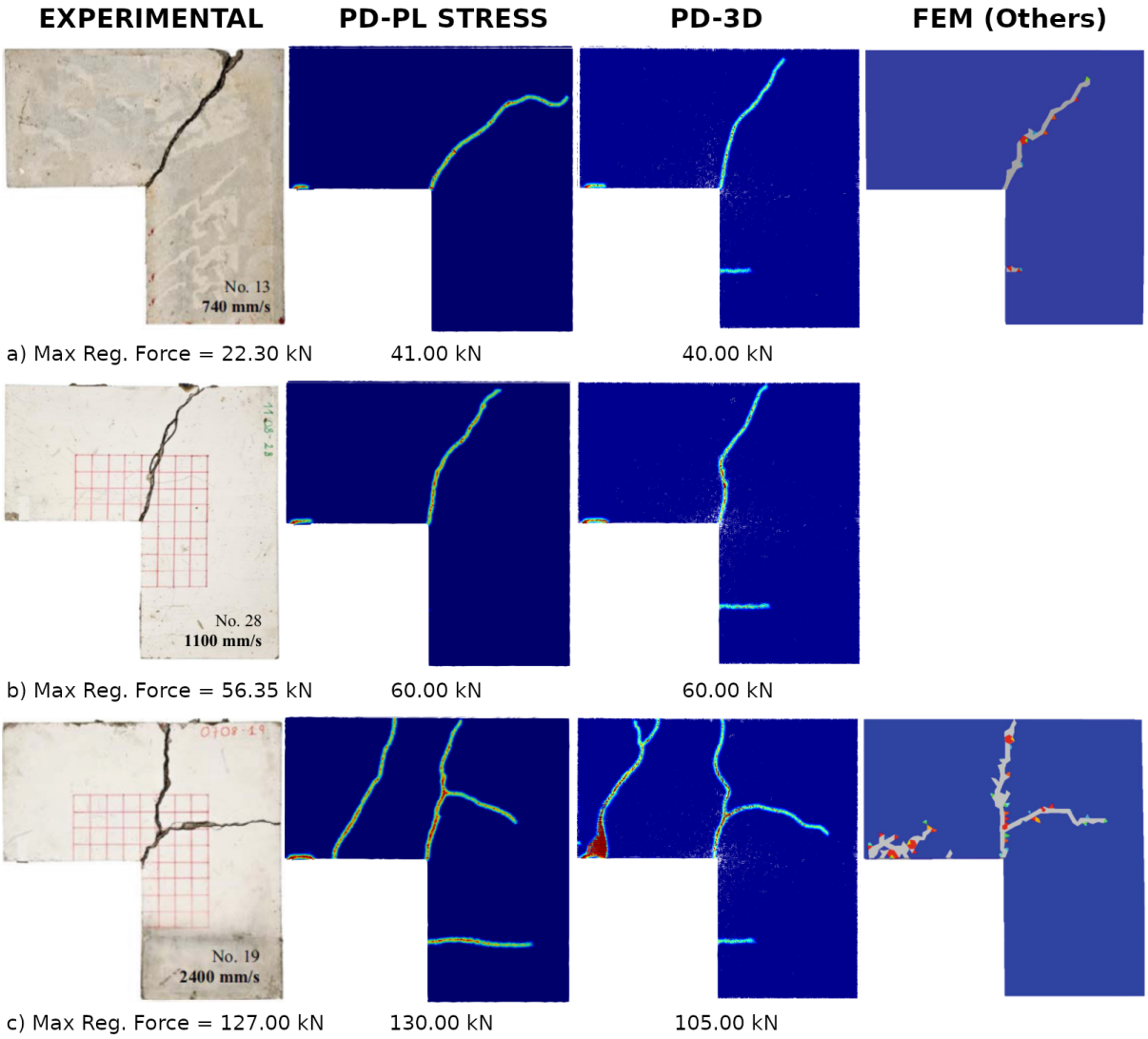

Figure 7: L-Specimen Results part II. (Experimental illustrations reprinted from [6]; FEM reprinted from [2]); a) $v = 0.740m/s$, b) $v = 1.100m/s$, c) $v = 2.400m/s$

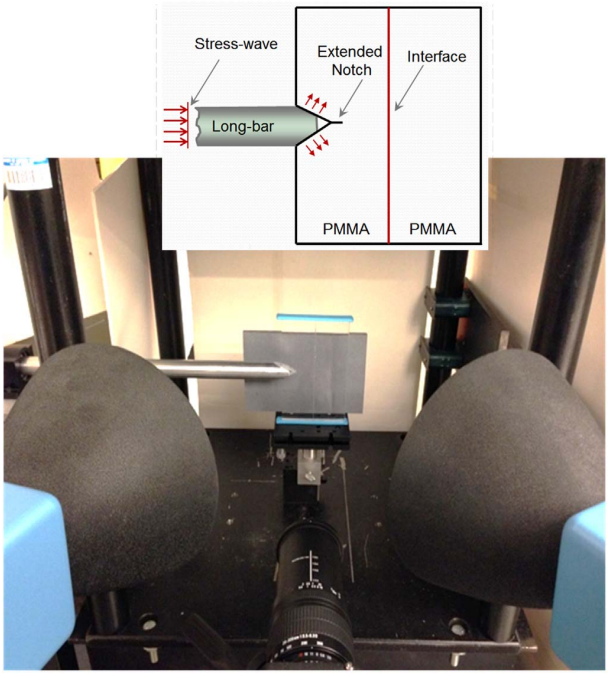

Figure 8: PMMA Plate Hopkinson Bar Test (Reprinted from [17])

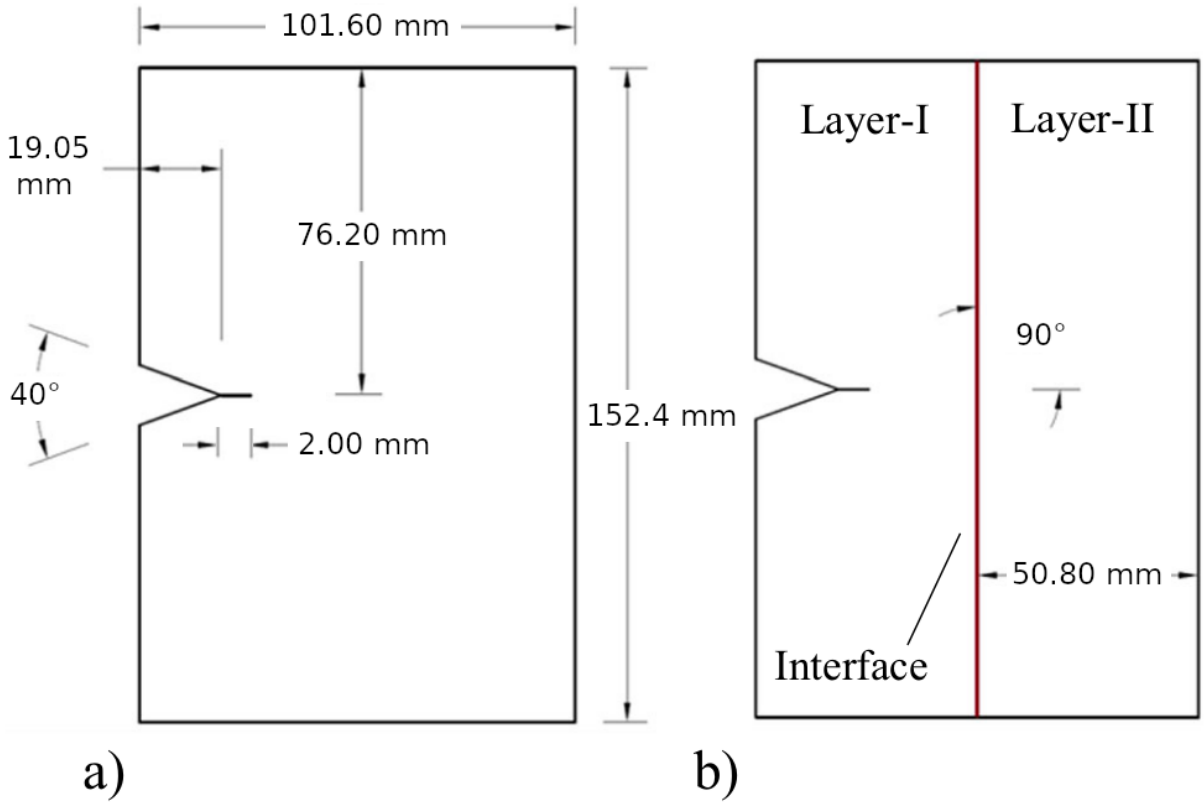

Figure 9: PMMA Plate Geometry of Thickness = $8.60\,mm$ (Adapted from [16]): a) Monolithic, b) Bilayer

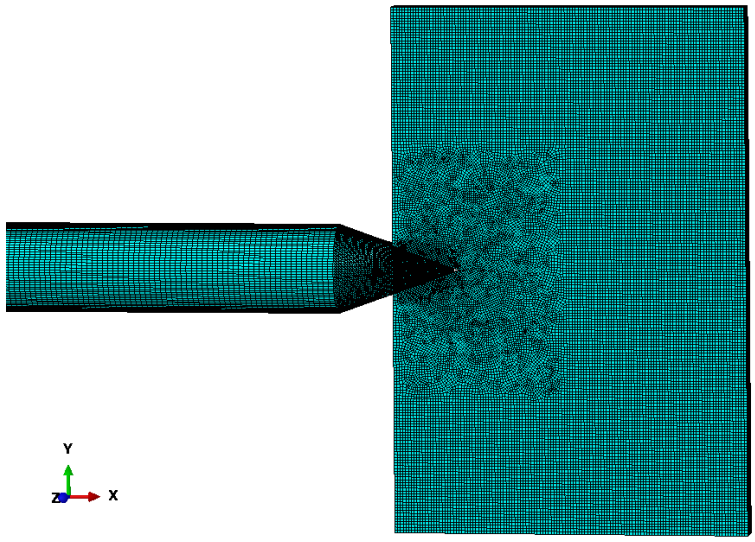

Figure 10: Aluminum Bar and PMMA plate FEM (ABAQUS) Discretization

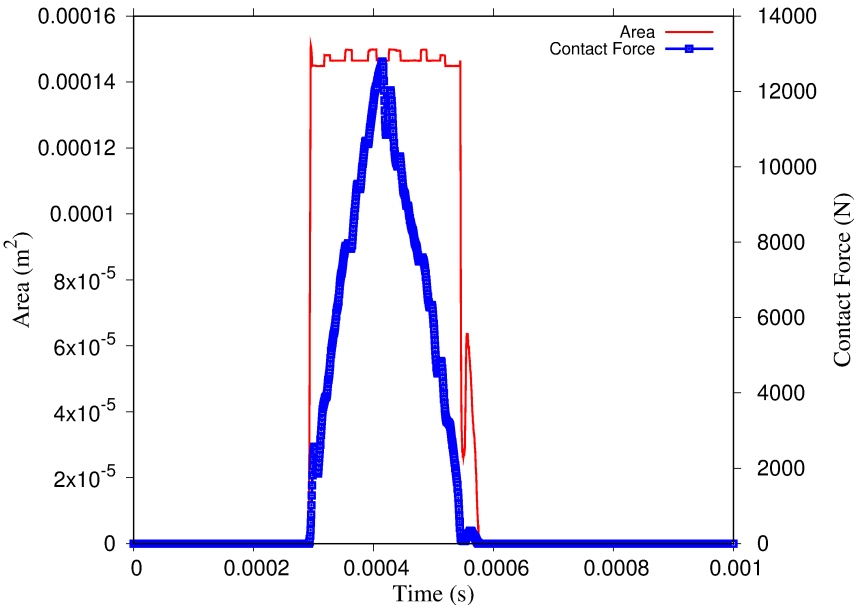

Figure 11: PMMA Plate ABAQUS Contact Force and Area

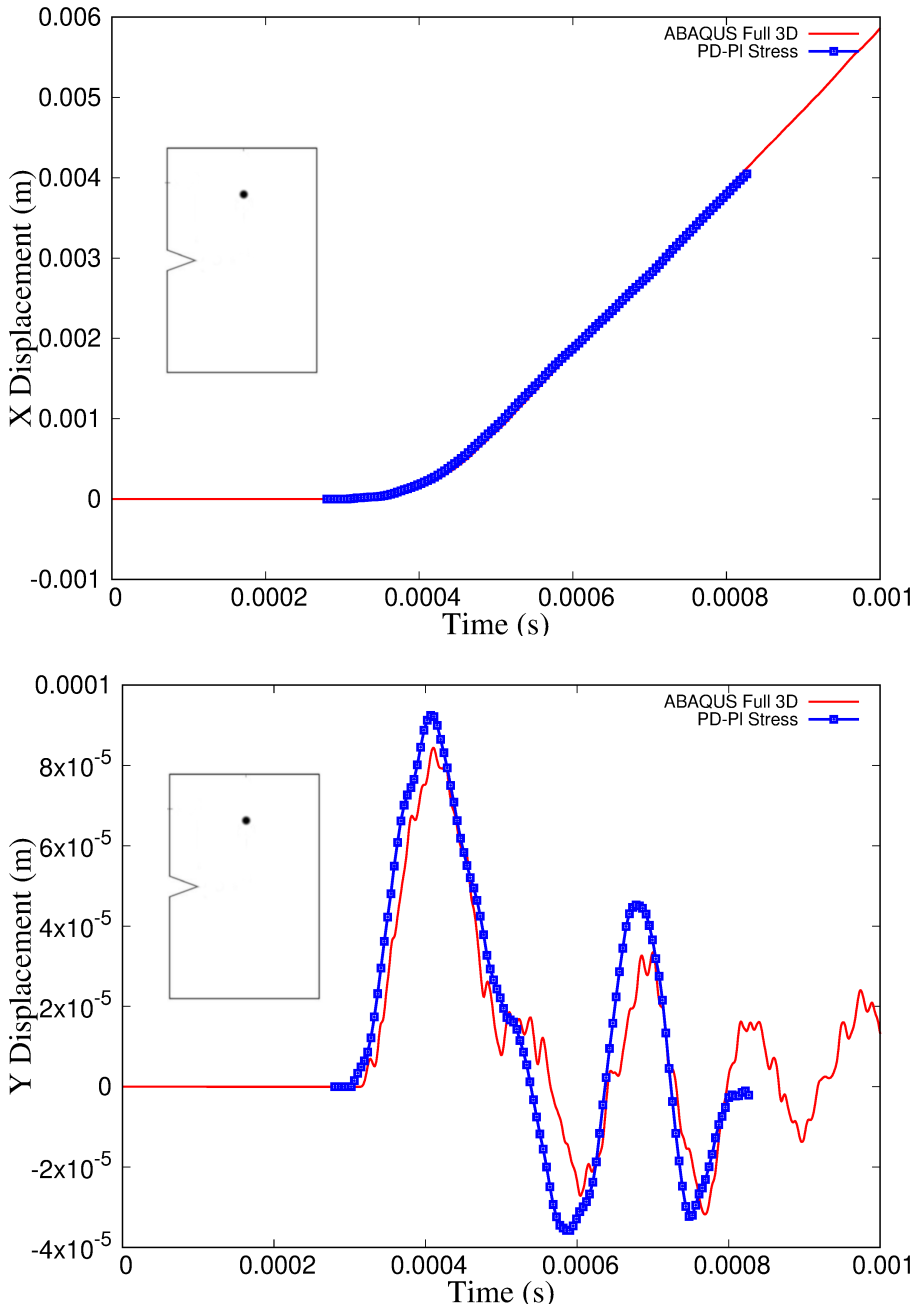

Figure 12: PMMA Plate ABAQUS-3D and PD-PI Stress Displacement Comparison for the same point (PD solution is offset $\approx 280\mu s$)

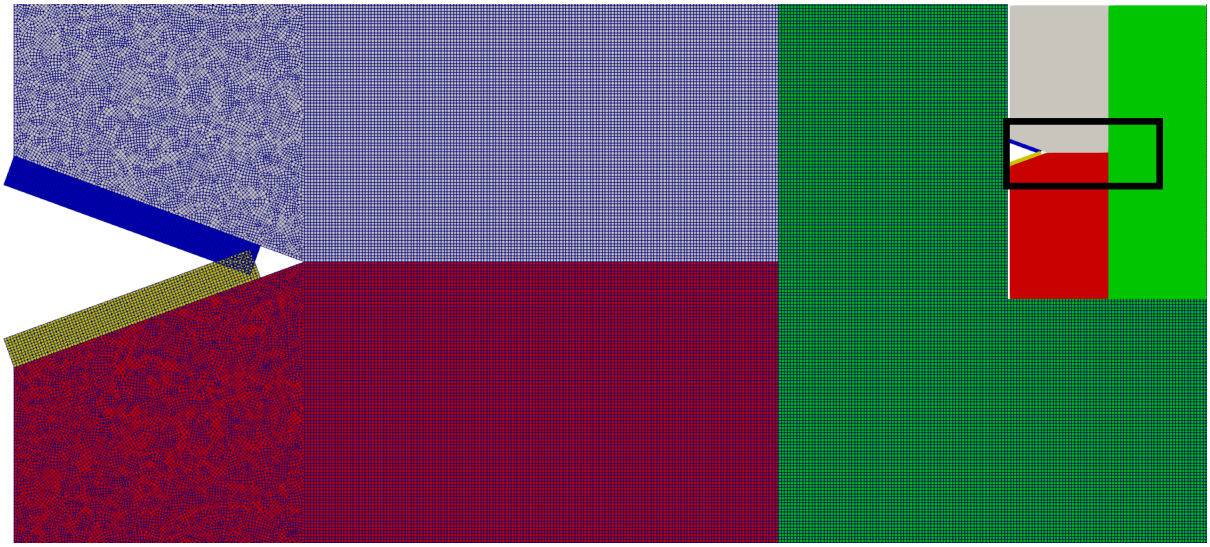

Figure 13: PMMA Plate Initial Quadrangular Mesh. Zoomed area corresponding to rectangular selection shown in black

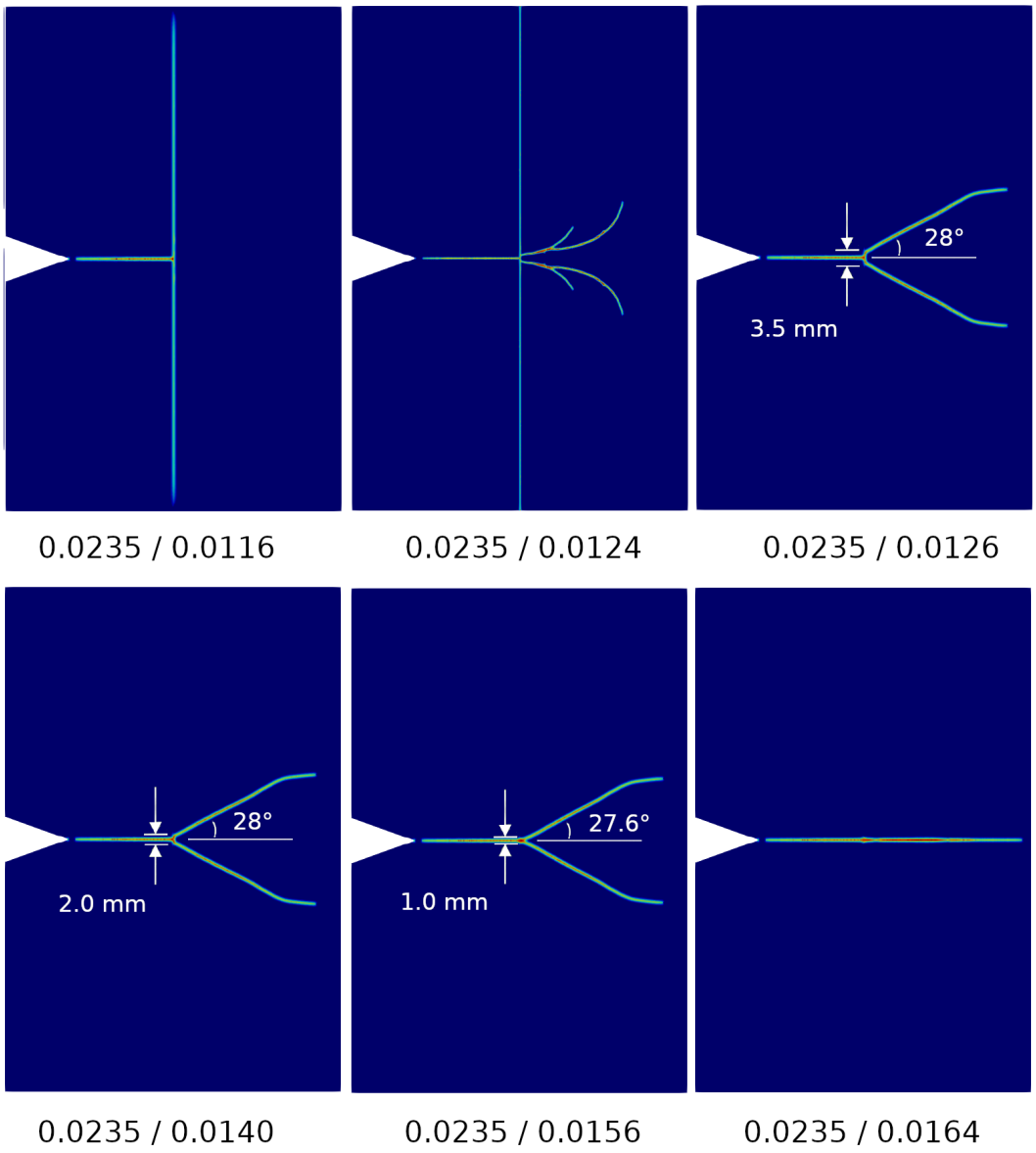

Figure 14: PMMA Plate Damage Results for the range $s_0 = \{0.0116 - 0.0164\}$

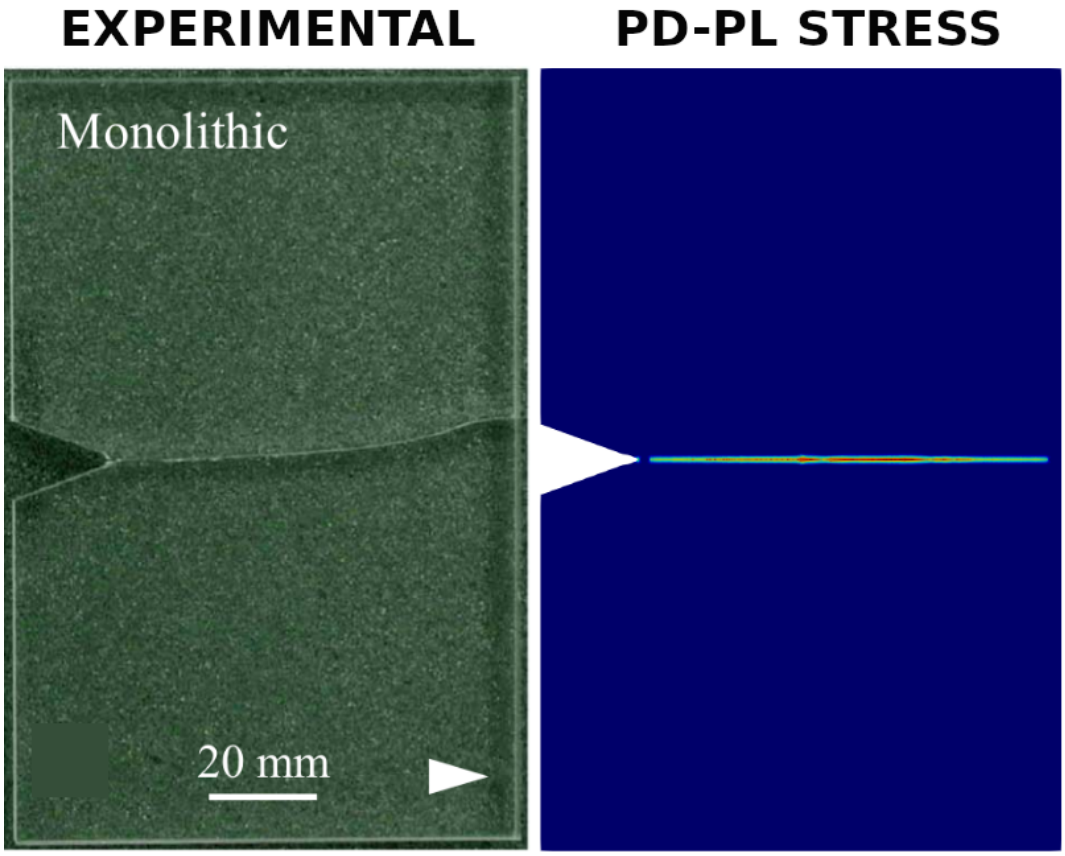

Figure 15: PMMA Plate Damage Results (Experimental reprinted from [17]): Monolithic Case $s_0 = 0.0235$

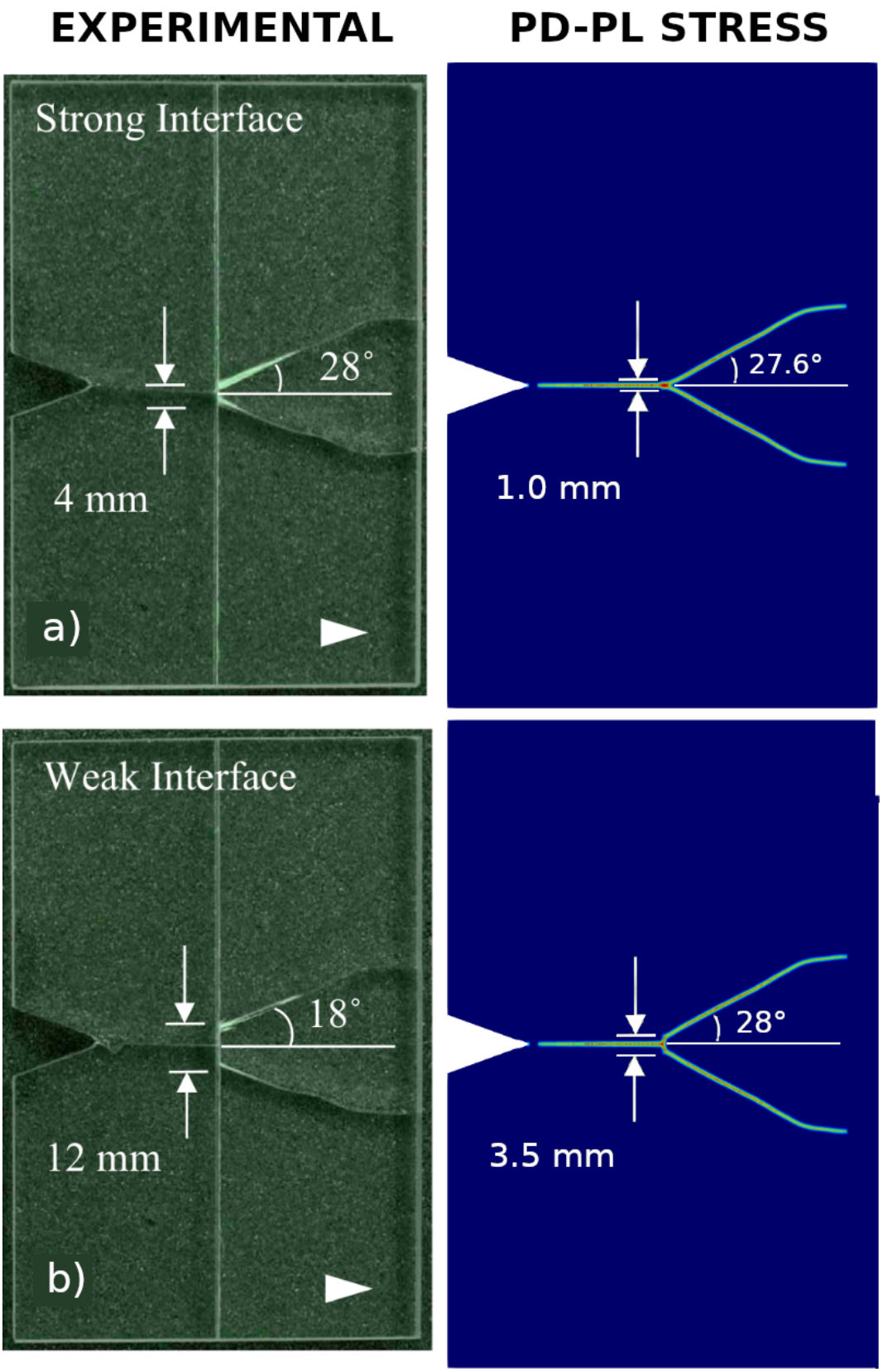

Figure 16: PMMA Plate Damage Results (Experimental reprinted from [17]): a) Strong Interface $s_0 = 0.0235 \,/\, 0.0156$, b) Weak Interface $s_0 = 0.0235 \,/\, 0.0126$

COMPDYN 2019
7th ECCOMAS Thematic Conference on
Computational Methods in Structural Dynamics and Earthquake Engineering
M. Papadrakakis, M. Fragiadakis (eds.)
Crete, Greece, 24-–26 June 2019

WAVE FINITE ELEMENT METHOD FOR COMPUTING THE DYNAMIC RESPONSE OF RAILWAY TRANSITION ZONES SUBJECTED TO MOVING LOADS

B. CLAUDET[1], T. HOANG[1], D. DUHAMEL[1], G. FORET[1], J-L. POCHET[2] and F. SABATIER[2]

[1]Laboratoire Navier, UMR 8205, Ecole des Ponts ParisTech
IFFSTTAR, CNRS, UPE, Champs-sur-Marne, France
e-mail: {benjamin.claudet, tien.hoang, denis.duhamel, gilles.foret}@enpc.fr

[2] Eurotunnel
BP69, 62904 Coquelles Cedex, France
e-mail: {franncis.sabatier, jean-luc.pochet}@eurotunnel.com

Keywords: Wave Finite Element, Transition zones, Railway, Dynamics, Moving loads

Abstract. *The dynamics of a railway track on transition zones is the subject of numerous analytical and numerical researches. This article presents a new development of the wave finite element method for such a structure in order to reduce the calculation time. We consider a transition zone which is between two half infinite periodic tracks (which could be of different types, e.g. a zone between ballasted and non-ballasted tracks) and train loads are represented by concentrated moving loads. We applied WFE for each half periodic track to obtain the relationship that links the responses of the boundary zone of each periodic part with the help of the wave analysis. Then, this relationship is combined with the dynamic equation of the zone to get the global dynamic equation of the whole railway track. This technique permits to reduce the degrees of freedom (DoF) of the track to those of the transition zone. Numerical studies show the influence of the geometrical and mechanical parameters of the transition zone on the mechanical response of the track with a transition zone compared to a uniform track.*

1 Introduction

Mechanical behaviour of railway tracks have been studied for a long time. The most common model considers the track as an infinitely long beam resting on equally spaced identical supports. The dynamics of the track under some known loads can be solved analytically by modelling each support by a mass-springs-dampers system and the rail by an Euler beam [1–4] or a Timoshenko beam [5]. Metrikine and Popp [6] also modelled the support and the ballast - for ballasted tracks - as continuous media. All these studies used the Floquet's theorem which takes into account the spatial periodicity of the structure. In the case of transition zones, the structure is not periodic so the Floquet's theorem can't be used.

The high speed transition zone between a ballast to ballastless track situated in Chauconin (France) had been damaged by train traffic. These damages include hanging sleepers. Consequently, the train speed in this zone has been reduced from $320\,\mathrm{km}\cdot\mathrm{h}^{-1}$ to $230\,\mathrm{km}\cdot\mathrm{h}^{-1}$. This transition zone is the subject of both experimental and numerical studies [7, 8]. Fortunato *et al*. [9] also pointed out hanging sleepers which are due to the deformation of the lowest vertical stiffness part in transition zones. Wang [10] gave a review of studies dealing with transition zones in the railway domain. The problems encountered points out a need to better understand transition zones dynamics.

A default or a damage also breaks the track periodicity even if this default is very localised. Hoang *et al*. [11] studied the mechanical behaviour of such a track considering a constant moving load on a periodically supported beam. Considering a "sufficiently large" computation domain, Hoang *et al*. gave a digital method to compute this dynamic behaviour. Kouroussis *et al*. [12] proposed a two steps method for a numerical computation of the rail-support-train system response and applied it to some common defaults.

Dividing the structure into substructures and considering the equilibrium relationship in a substructure, Germonpré *et al*. [13] studied the free wave modes in a substructure and then computed the whole structure dynamics. By separating left going and right going modes, Germonpré *et al*. [14] applied this method to a transition zone including a train-track-soil coupling. Arlaud [15] developed a similar method excepted that it fixed the wave-number instead of fixing the frequency. Then, a mode reduction was performed in order to increase the calculation efficiency.

Like the method developed by Germonpré *et al*. [13], the wave finite element (WFE) method is a computational method for periodic structures and waveguides. In the WFE method, for each frequency, the equilibrium relationship in one pattern of the structure is transformed into a recurrence relationship. Free wave modes of the recurrence operator calculation is described in [16]. Hoang *et al*. improved this method by adding the possibility to take into account a load which may be applied to any pattern of the structure [17] and used it for computation of railway tracks dynamics [18].

In this article, a transition zone is defined as a zone between two semi-infinite periodic structures which can be different or not. This can represent either a zone passing from ballast to ballastless track or a damaged zone between two healthy identical zones. After this introduction, the classical WFE method is presented. The third part of this article presents new developments enabling the computation of transition zones mechanical behaviour. The forth part gives two examples of results of this method on the mechanical behaviour: effects of a damaged zone in an infinite periodic healthy track and effects of a variation in the support spacing. Then, the conclusions of this work are given in the last part.

2 WFE Method: Homogeneous Periodic Structure

In this part an homogeneous periodic structure is considered. It is assumed that all the loads applied to the structure are known. The dynamic equation of one pattern (a substructure) at a given angular frequency ω is given by the equation (1), where $\mathbf{q}$ is the vector containing the degrees of freedom of one substructure and $\mathbf{F}$ the vector containing the external loads applied on this substructure.

$$\mathbf{D}_{tot}\mathbf{q} = \mathbf{F} \tag{1}$$

The dynamic stiffness matrix (DSM) $\mathbf{D}_{tot}$ can be calculated using the finite element method with $\mathbf{D}_{tot} = \mathbf{K} + j\omega\mathbf{C} - \omega^2\mathbf{M}$ where $\mathbf{K}$ is the static stiffness matrix, $\mathbf{M}$ the mass matrix and $\mathbf{C}$ the damping matrix. Then, (1) can be rewritten separating the nodes of the left and right boundaries, and the inner nodes of the substructure respectively denoted with the subscripts $_{L,R}$ and $_I$. Hence, the relationship (2) is obtained.

$$\begin{bmatrix} \tilde{\mathbf{D}}_{II} & \tilde{\mathbf{D}}_{IL} & \tilde{\mathbf{D}}_{IR} \\ \tilde{\mathbf{D}}_{LI} & \tilde{\mathbf{D}}_{LL} & \tilde{\mathbf{D}}_{LR} \\ \tilde{\mathbf{D}}_{RI} & \tilde{\mathbf{D}}_{RL} & \tilde{\mathbf{D}}_{RR} \end{bmatrix} \begin{bmatrix} \mathbf{q}_I \\ \mathbf{q}_L \\ \mathbf{q}_R \end{bmatrix} = \begin{bmatrix} \mathbf{F}_I \\ \mathbf{F}_L \\ \mathbf{F}_R \end{bmatrix} \tag{2}$$

As shown in [18], this relation leads to the recurrence equation (3) where the superscript $^{(n)}$ denotes for the n^{th} substructure.

$$\mathbf{u}^{(n+1)} = \mathbf{S}\mathbf{u}^{(n)} + \mathbf{b}^{(n)} \tag{3}$$

where

$$\mathbf{u}^{(n)} = \begin{bmatrix} \mathbf{q}_L^{(n)} \\ -\mathbf{F}_L^{(n)} \end{bmatrix}, \quad \mathbf{b}^{(n)} = \begin{bmatrix} \mathbf{D}_{qI}\mathbf{F}_I^{(n)} \\ \mathbf{D}_{fI}\mathbf{F}_I^{(n)} - \mathbf{F}_{\partial R}^{(n)} \end{bmatrix}$$

$\mathbf{F}_{\partial R}^{(n)}$ is the external load applied at the right boundary of the n^{th} substructure and $\mathbf{S}, \mathbf{D}_{qI}$ and $\mathbf{D}_{fI}$ definitions are given in [18].

That leads to the equation system (4):

$$\begin{cases} \mathbf{u}^{(n)} = \mathbf{S}^n\mathbf{u}^{(0)} + \displaystyle\sum_{k=1}^{n} \mathbf{S}^{n-k}\mathbf{b}^{(k-1)} \\ \mathbf{u}^{(-n)} = \mathbf{S}^{-n}\mathbf{u}^{(0)} - \displaystyle\sum_{k=1}^{n} \mathbf{S}^{-n+k-1}\mathbf{b}^{(-k)} \end{cases} \tag{4}$$

To compute the power of the $\mathbf{S}$ matrix, the eigenvalues and eigenvectors $\{\mu_j, \phi_j\}_j$ of the $\mathbf{S}$ matrix are computed by a $\mathbf{S} + \mathbf{S}^{-1}$ transformation. The eigenvalues come in pair $\left(\mu_j, \mu_j^\star\right)$ with $\|\mu_j\| \leqslant 1$ and $\mu_j^\star = \frac{1}{\mu_j}$ [16]. The corresponding eigenvectors are noted $\left(\phi_j, \phi_j^\star\right)$. Let the eigenbasis $\{\mathbf{\Phi}\, \mathbf{\Phi}^\star\}$ be defined as: $\mathbf{\Phi} = [\phi_1 \dots \phi_n]$ and $\mathbf{\Phi}^\star = [\phi_1^\star \dots \phi_n^\star]$. Where the subscript "$_q$" (respectively "$_F$") denotes for the components of this basis corresponding to the degrees of freedom (DoF)[1] (resp. the loads), leading to (5).

$$\mathbf{\Phi} = \begin{bmatrix} \mathbf{\Phi}_q \\ \mathbf{\Phi}_F \end{bmatrix} \quad \mathbf{\Phi}^\star = \begin{bmatrix} \mathbf{\Phi}_q^\star \\ \mathbf{\Phi}_F^\star \end{bmatrix} \tag{5}$$

[1] Usually displacements/rotations

In (6), $\mathbf{u}^{(n)}$ and $\mathbf{b}^{(n)}$ are written in this wave basis:

$$\begin{aligned}\mathbf{u}^{(n)} &= \mathbf{\Phi}\mathbf{Q}^{(n)} - \mathbf{\Phi}^{\star}\mathbf{Q}^{\star(n)} \\ \mathbf{b}^{(n)} &= \mathbf{\Phi}\mathbf{Q}_E^{(n)} - \mathbf{\Phi}^{\star}\mathbf{Q}_E^{\star(n)}\end{aligned} \tag{6}$$

Hoang *et al.* proved [18]:

$$\begin{aligned}\mathbf{Q}_E^{(k)} &= \left[\left(\boldsymbol{\mu}\mathbf{\Phi}_q^{\star T}\mathbf{D}_{LI} + \mathbf{\Phi}_q^{\star T}\mathbf{D}_{RI}\right)\mathbf{F}_I^{(k)} - \mathbf{\Phi}_q^{\star T}\mathbf{F}_{\partial R}^{(k)}\right] \\ \mathbf{Q}_E^{\star(k)} &= \left[\left(\boldsymbol{\mu}^{\star}\mathbf{\Phi}_q^{T}\mathbf{D}_{LI} + \mathbf{\Phi}_q^{T}\mathbf{D}_{RI}\right)\mathbf{F}_I^{(k)} - \mathbf{\Phi}_q^{T}\mathbf{F}_{\partial R}^{(k)}\right]\end{aligned} \tag{7}$$

3 Transition Zone between Two Semi-infinite Zones

In this part, a transition zone between two infinite periodic zones (see figure 1) is considered. For railways the transition zone can for instance be a zone between a ballasted track and a concrete slab track. These two types of track have different stiffness. Therefore, $\mathbf{S}$ can be different in each zone and some formulas from the previous part are no longer valid.

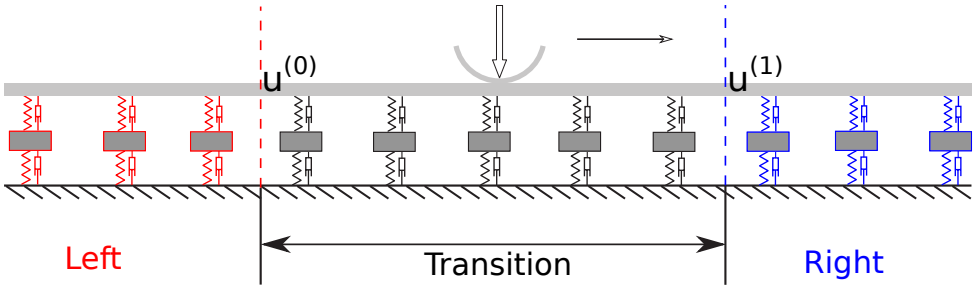

Figure 1: Transition zone between two semi-infinite periodic railway tracks.

In the transition zone the equilibrium relationship is:

$$\mathbb{D}_{H,trans}\begin{bmatrix}\mathbf{q}_I \\ \mathbf{q}_L \\ \mathbf{q}_R\end{bmatrix} = \begin{bmatrix}\mathbf{F}_I \\ \mathbf{F}_L \\ \mathbf{F}_R\end{bmatrix} \tag{8}$$

Where $\mathbb{D}_{H,trans}$ is the dynamic stiffness matrix (DSM) of the transition zone.

The equilibrium relationships for one pattern in the left and right zones were written in the same way replacing $\mathbb{D}_{H,trans}$ by the DSM of the corresponding zone. So, applying the same method as in the previous part, propagation equations (9) were obtained (instead of (3)) - with "$_R$" subscript denoting for the right zone and "$_L$" subscript the left zone.

$$\begin{cases}\forall n \geqslant 1,\ \mathbf{u}_R^{(n+1)} = \mathbf{S}_R\mathbf{u}^{(n)} + \mathbf{b}^{(n)} \\ \forall n \leqslant 0,\ \mathbf{u}_L^{(n-1)} = \mathbf{S}_L^{-1}\mathbf{u}^{(n)} - \mathbf{S}_L^{-1}\mathbf{b}^{(n-1)}\end{cases} \tag{9}$$

With $\mathbf{u}^{(0)}$ corresponding to the left boundary of the transition zone, and $\mathbf{u}^{(1)}$ to the left boundary of the right zone (see figure 1).

3.1 Decomposition in the Right Zone and in the Left Zone

Thus, for the right zone the recurrence relationship is:

$$\forall n \geqslant 1,\ \mathbf{u}^{(n)} = \mathbf{S}_R^{n-1}\mathbf{u}^{(1)} + \sum_{k=2}^{n} \mathbf{S}_R^{n-k}\mathbf{b}^{(k-1)} \tag{10}$$

Let $\mathbf{u}_R = \mathbf{u}^{(1)}$. As in the first part, $\mathbf{u}_R$ was rewritten in the eigenbasis $\{\mathbf{Q}_R, \mathbf{Q}_R^\star\}$ of $\mathbf{S}_R$ associated with the eigenvalues $\{\boldsymbol{\mu}_R, \boldsymbol{\mu}_R^\star\}$ where $\|\mu_{R,j}\| \leqslant 1$ and $\|\mu_{R,j}^\star\| \geqslant 1$. That led to the wave decomposition (11) for $\mathbf{u}_R$ and (12) for $\mathbf{u}^{(n)}$ and $\mathbf{b}^{(n)}$:

$$\mathbf{u}_R = \boldsymbol{\Phi}_R\mathbf{Q}_R - \boldsymbol{\Phi}_R^\star\mathbf{Q}_R^\star \tag{11}$$

$$\forall n \geqslant 1, \begin{cases} \mathbf{u}^{(n)} = \boldsymbol{\Phi}_R\mathbf{Q}^{(n)} - \boldsymbol{\Phi}_R^\star\mathbf{Q}^{\star(n)} \\ \mathbf{b}^{(n)} = \boldsymbol{\Phi}_R\mathbf{Q}_E^{(n)} - \boldsymbol{\Phi}_R^\star\mathbf{Q}_E^{\star(n)} \end{cases} \tag{12}$$

Using (10) with (11) and (12) led to:

$$\begin{aligned} \mathbf{u}^{(n)} &= \boldsymbol{\Phi}_R\mathbf{Q}^{(n)} - \boldsymbol{\Phi}_R^\star\mathbf{Q}^{\star(n)} \\ &= \boldsymbol{\Phi}_R\boldsymbol{\mu}_R^{n-1}\left(\mathbf{Q}_R + \sum_{k=2}^{n}\boldsymbol{\mu}_R^{\star k-1}\mathbf{Q}_E^{(k-1)}\right) - \boldsymbol{\Phi}_R^\star\boldsymbol{\mu}_R^{\star n-1}\left(\mathbf{Q}_R^\star + \sum_{k=2}^{n}\boldsymbol{\mu}_R^{k-1}\mathbf{Q}_E^{(k-1)}\right) \end{aligned} \tag{13}$$

$\|\boldsymbol{\mu}_R^\star\| > 1$, so taking the limit $n \to +\infty$ led to $\mathbf{Q}_R^\star = -\sum_{k=2}^{+\infty}\boldsymbol{\mu}_R^{k-1}\mathbf{Q}_E^{(k-1)}$ because DoF and loads can't be infinite. (13) then became (14).

$$\begin{cases} \mathbf{q}_R = \boldsymbol{\Phi}_{R,q}\mathbf{Q}_R + \boldsymbol{\Phi}_{R,q}^\star\displaystyle\sum_{k=1}^{\infty}\boldsymbol{\mu}_R^k\mathbf{Q}_E^{\star(k)} \\ \mathbf{F}_R - \mathbf{F}_{\partial R} = \boldsymbol{\Phi}_{R,F}\mathbf{Q}_R + \boldsymbol{\Phi}_{R,F}^\star\displaystyle\sum_{k=1}^{\infty}\boldsymbol{\mu}_R^k\mathbf{Q}_E^{\star(k)} \end{cases} \tag{14}$$

With the same reasoning on the left part of the structure, the relationship (15) was proved.

$$\begin{cases} \mathbf{q}_L = \boldsymbol{\Phi}_{L,q}\displaystyle\sum_{k=1}^{\infty}\boldsymbol{\mu}_L^{k-1}\mathbf{Q}_E^{(-k)} - \boldsymbol{\Phi}_{L,q}^\star\mathbf{Q}_L^\star \\ -\mathbf{F}_L = \boldsymbol{\Phi}_{L,F}\displaystyle\sum_{k=1}^{\infty}\boldsymbol{\mu}_L^{k-1}\mathbf{Q}_E^{(-k)} - \boldsymbol{\Phi}_{L,F}^\star\mathbf{Q}_L^\star \end{cases} \tag{15}$$

Finally, by substituting (14) and (15) into (8), (16) was obtained:

$$\begin{aligned} &\mathbb{D}_{H,trans}\begin{bmatrix} \mathbf{q}_I \\ -\boldsymbol{\Phi}_{L,q}^\star\mathbf{Q}_L^\star \\ \boldsymbol{\Phi}_{R,q}\mathbf{Q}_R \end{bmatrix} + \mathbb{D}_{H,trans}\begin{bmatrix} \mathbf{0} \\ \boldsymbol{\Phi}_{L,q}\sum_{k=1}^{\infty}\boldsymbol{\mu}_L^{k-1}\mathbf{Q}_E^{(-k)} \\ \boldsymbol{\Phi}_{R,q}^\star\sum_{k=1}^{\infty}\boldsymbol{\mu}_R^k\mathbf{Q}_E^{\star(k)} \end{bmatrix} = \\ &\qquad\begin{bmatrix} \mathbf{0} \\ \boldsymbol{\Phi}_{L,F}^\star\mathbf{Q}_L^\star \\ \boldsymbol{\Phi}_{R,F}\mathbf{Q}_R \end{bmatrix} + \begin{bmatrix} \mathbf{F}_I \\ -\boldsymbol{\Phi}_{L,F}\sum_{k=1}^{\infty}\boldsymbol{\mu}_L^{k-1}\mathbf{Q}_E^{(-k)} \\ \mathbf{F}_{\partial R} + \boldsymbol{\Phi}_{R,F}^\star\sum_{k=1}^{\infty}\boldsymbol{\mu}_R^k\mathbf{Q}_E^{\star(k)} \end{bmatrix} \end{aligned} \tag{16}$$

Which was rewritten as follows:

$$\left(\mathbb{D}_{H,trans}\mathbb{C}_q - \mathbb{C}_F\right)\tilde{\mathbf{q}} = \tilde{\mathbf{F}} \tag{17}$$

where

$$\begin{aligned}
\tilde{\mathbf{q}} &= \begin{bmatrix}\mathbf{q}_I \\ \mathbf{Q}_L^\star \\ \mathbf{Q}_R\end{bmatrix},\ \mathbb{C}_q = \begin{bmatrix}\mathbf{I} & \mathbf{0} & \mathbf{0} \\ \mathbf{0} & -\mathbf{\Phi}_{L,q}^\star & \mathbf{0} \\ \mathbf{0} & \mathbf{0} & \mathbf{\Phi}_{R,q}\end{bmatrix},\ \mathbb{C}_F = \begin{bmatrix}\mathbf{0} & \mathbf{0} & \mathbf{0} \\ \mathbf{0} & \mathbf{\Phi}_{L,F}^\star & \mathbf{0} \\ \mathbf{0} & \mathbf{0} & \mathbf{\Phi}_{R,F}\end{bmatrix} \\
\tilde{\mathbf{F}} &= \begin{bmatrix}\mathbf{F}_I \\ -\mathbf{\Phi}_{L,F}\sum_{k=1}^{\infty}\boldsymbol{\mu}_L^{k-1}\mathbf{Q}_E^{(-k)} \\ \mathbf{F}_{\partial R} + \mathbf{\Phi}_{R,F}^\star\sum_{k=1}^{\infty}\boldsymbol{\mu}_R^{k}\mathbf{Q}_E^{\star(k)}\end{bmatrix} - \mathbb{D}_H\begin{bmatrix}\mathbf{0} \\ \mathbf{\Phi}_{L,q}\sum_{k=1}^{\infty}\boldsymbol{\mu}_L^{k-1}\mathbf{Q}_E^{(-k)} \\ \mathbf{\Phi}_{R,q}^\star\sum_{k=1}^{\infty}\boldsymbol{\mu}_R^{k}\mathbf{Q}_E^{\star(k)}\end{bmatrix}
\end{aligned} \tag{18}$$

In the case of a constant moving load[2], $\mathbf{Q}_E^{\star(k)}$ and $\mathbf{Q}_E^{(-k)}$ follow:

$$\forall k \geqslant 1, \begin{cases}\mathbf{Q}_E^{\star(k)} = e^{-i(k-1)\frac{\omega L}{v}}\mathbf{Q}_E^{\star(1)} \\ \mathbf{Q}_E^{(-k)} = e^{i(k-1)\frac{\omega L}{v}}\mathbf{Q}_E^{(-1)}\end{cases} \tag{19}$$

That led to (20):

$$\begin{cases}\displaystyle\sum_{k=1}^{\infty}\boldsymbol{\mu}_L^{k-1}\mathbf{Q}_E^{(-k)} = \frac{1}{1-\boldsymbol{\mu}_L e^{i\frac{\omega L}{v}}}\mathbf{Q}_E^{(-1)} \\ \displaystyle\sum_{k=1}^{\infty}\boldsymbol{\mu}_R^{k}\mathbf{Q}_E^{\star(k)} = \frac{\boldsymbol{\mu}_R}{1-\boldsymbol{\mu}_R e^{-i\frac{\omega L}{v}}}\mathbf{Q}_E^{\star(1)}\end{cases} \tag{20}$$

With $\mathbf{Q}_E^{\star(k)}$ and $\mathbf{Q}_E^{(k)}$ given by (7).

Then, $\tilde{\mathbf{q}}$ can be computed by inverting the linear equation (17). This computation gives the DoF of each node in the transition zone ($\mathbf{q}_I$) and at its boundaries ($\mathbf{q}_L$ and $\mathbf{q}_R$ calculated with (15) and (14)). The DoF in the other zones can be calculated using the classical WFE method (*ie.* using (10) for the right zone and a similar formula for the left zone).

4 Examples

In this part, the track considered is a ballastless track in which each support contains two elastic floors: one under rail rubber pad and one under sleeper rubber pad. The support was modelled as a mass (the sleeper) between two damper-spring systems (the pads). B21 elements from ABAQUS were used to get the beam DSM and the supports dynamic stiffness were added to the corresponding terms to obtain the DSM of each substructure. The beam cell length was $1\,\mathrm{cm}$. In the results presented here, the spatial period choosen for the computation was of the same length $L = 3\,\mathrm{m}$ for each zone (five sleepers per period). The right, left and transition zones are represented in the figure 1. To simplify results understanding, only a single load moving at a constant speed was applied. Table 1 gives the rail and supports mechanical characteristics and the load characteristics.

4.1 Periodically Supported Beam with a Broken Support

We considered a periodically supported beam resting on identical supports which means that the right and left zones were identical. To model a broken support, we assumed that this support had no influence on the structure stiffness. This is equivalent to a lack of one support. This broken support was located in the middle of the transition zone ($x = 0\,\mathrm{m}$).

[2](19) remains true if the load is repeated with a spatial period equal to the length of one substructure.

Content	Notation	Value	Unit
Rail linear mass	ρS	60	$\mathrm{kg \cdot m^{-1}}$
Load speed	v	38	$\mathrm{m \cdot s^{-1}}$
Load applied	Q	100	kN
Rail stiffness	EI	6.38	$\mathrm{MN \cdot m^{2}}$
Sleeper mass	m	100	kg
Sleeper spacing	l	0.6	m
Under rail pad stiffness	k_1	192	$\mathrm{MN \cdot m^{-1}}$
Under rail pad damping coefficient	η_1	1.97	$\mathrm{MN \cdot s \cdot m^{-1}}$
Under sleeper pad stiffness	k_2	26.4	$\mathrm{MN \cdot m^{-1}}$
Under sleeper pad damping coefficient	η_2	0.17	$\mathrm{MN \cdot s \cdot m^{-1}}$

Table 1: Parameters of the load and railway track considered.

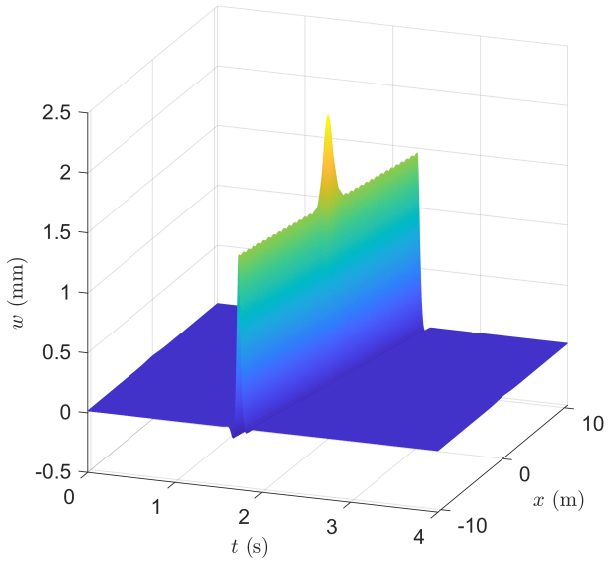

(a) Rail deflection against time and position.

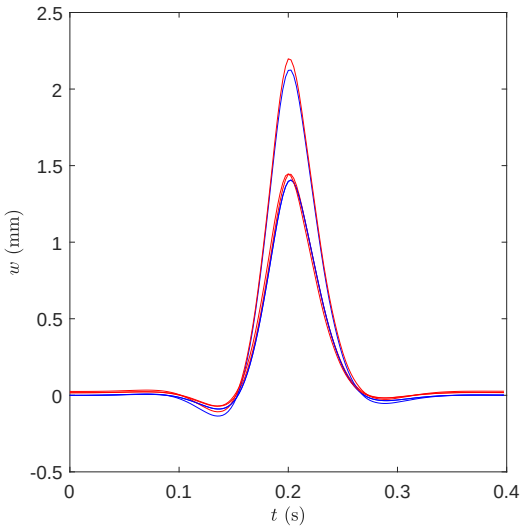

(b) Rail deflection against time for three different sleepers. WFE results (red curves) and results obtained with the method of [11] (blue curves).

Figure 2: Rail deflection for a track with a broken support.

Figure 2 shows the track deflection due to the load for this type of track. On the left side (figure 2a) the deflection is plotted against time and position. As the WFE method works in the frequency domain, an inverse Fourier transform was necessary to obtain temporal values. At each position, the maximum of the deflection corresponds to the time when the load is over this position. Consequently, the line of the maxima represents the load trajectory. As expected, the deflection is maximum for the broken support. On the right part of this figure (figure 2b), the deflection obtained by the WFE method (red curves) is compared with the one obtained with [11] method (blue curves, 21 supports modelled, 80 iterations). In this graph the deflection is plotted against time for three supports: the broken one ($x = 0\,\mathrm{m}$) and two suports at $x = \pm 6\,\mathrm{m}$. These results show a good agreement which validated the WFE method for computing track deflection in damaged zones.

4.2 Variation of the Support Spacing

In this example, the influence of a variation in the support spacing on the track behaviour was evaluated. In the left zone, the distance between two consecutive sleepers was $l_L = 0{,}3\,\mathrm{m}$ whereas in right and transition zones, this distance was $l_R = l_T = 0{,}6\,\mathrm{m}$. All the other parameters remained identical to the values given in the table 1.

The computed deflection of this track is given in figure 3. Once again, in the left part of the figure (figure 3a), the deflection is plotted against time and position. There were two times more support in the left zone, thus, as expected, this zone seems approximately two times stiffer. The right part of the figure (figure 3a) gives the deflection at the frequency $5\,\mathrm{Hz}$. The results are compared with analytical results obtained with an equivalent periodically supported Timoshenko beams with supports spacing equal to the one of the left or right zones (formula from [5]). Analytical formulas and WFE results are in close agreement for points sufficiently far from the transition. Whereas the transition is steep, the rail needs several meters to pass from one mechanical behaviour to the other one. This transition does not show overcharged support.

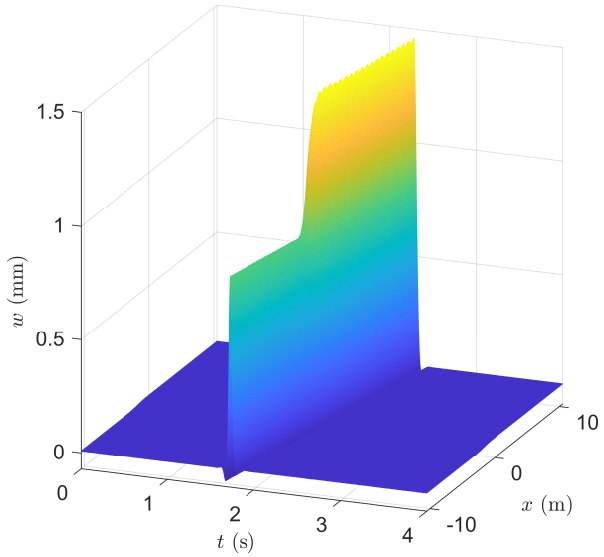

(a) Rail deflection against time and position.

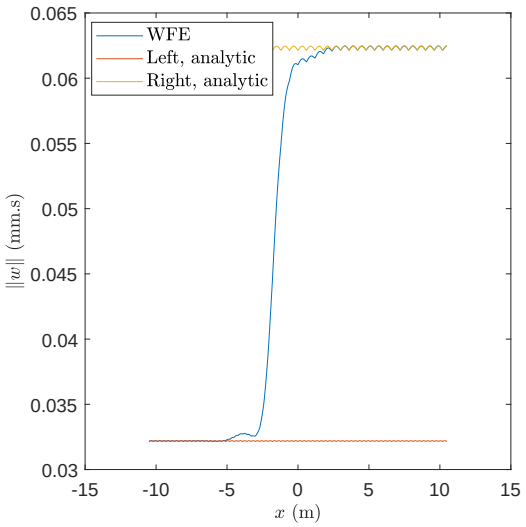

(b) Rail deflection in the frequency domain (at $5\,\mathrm{Hz}$) against position. WFE results compared with analytical results obtained for an infinite track.

Figure 3: Rail deflection for a variation in the support spacing.

5 Conclusion

The Wave Finite Element method is very efficient to compute infinite periodic structures mechanical behaviour under charges compared to classical finite element methods (see [18]). This article presented new developments to apply this method to transition zones between two semi-infinite periodic structures. Railway examples of application were presented and show a strong agreement with other semi-analytical methods or analytical laws. This method can also provide information on the damping of waves which can propagate over a given structure.

REFERENCES

[1] P.M. Belotserkovskiy. On The Oscillation of infinite periodic beams subjected to a moving concentrated force. *Journal of Sound and Vibration*, 193(3):705–712, jun 1996.

[2] A. Nordborg. Vertical Rail Vibrations: Parametric Excitation. *ACUSTICA· acta acustica*, 84:289–300, 1998.

[3] G. Bonnet and R. Lassoued. Response of a Periodically Supported Beam To a Moving Load From the Superposition of Bloch Waves. In *7th European Conference on Structural Dynamics Eurodyn*, Southampton, 2008.

[4] T. Hoang, D. Duhamel, G. Foret, H.P. P. Yin, P. Joyez, and R. Caby. Calculation of force distribution for a periodically supported beam subjected to moving loads. *Journal of Sound and Vibration*, 388:327–338, feb 2017.

[5] T. Hoang, D. Duhamel, and G. Foret. Dynamical response of a Timoshenko beams on periodical nonlinear supports subjected to moving forces. *Engineering Structures*, 176:673–680, dec 2018.

[6] A.V. Metrikine and K. Popp. Vibration of a periodically supported beam on an elastic half-space. *European Journal of Mechanics - A/Solids*, 18(4):679–701, jul 1999.

[7] E. Arlaud, S. Costa D'aguiar, and E. Balmes. Receptance of railway tracks at low frequency: Numerical and experimental approaches. *Transportation Geotechnics*, 9:1–16, 2016.

[8] S. Costa D'Aguiar, E. Arlaud, R. Potvin, E. Laurans, and C. Funfschilling. Railway Transitional Zones: A Case History from Ballasted to Ballastless Track. *International Journal of Railway Technology*, 3:37–61, 2014.

[9] E. Fortunato, A. Paixão, and R. Calçada. Railway Track Transition Zones: Design, Construction, Monitoring and Numerical Modelling. *International Journal of Railway Technology*, 2(4):33–58, 2013.

[10] H. Wang and V. L. Markine. Methodology for the comprehensive analysis of railway transition zones. *Computers and Geotechnics*, 99:64–79, jul 2018.

[11] T. Hoang, D. Duhamel, G. Foret, H.P. Yin, G. Cumunel, P. Joyez, and R. Caby. Response of a Periodically Supported Beam on a Non-Uniform Viscoelastic Foundation subject to Moving Loads. In J. Pombo, editor, *Proceedings of the Third International Conference on Railway Technology: Research, Development and Maintenance*, number April, Stirlingshire, Scotland, 2016. Civil-Comp Press.

[12] G. Kouroussis, D. P. Connolly, G. Alexandrou, and K. Vogiatzis. Railway ground vibrations induced by wheel and rail singular defects. *Vehicle System Dynamics*, 53(10):1500–1519, oct 2015.

[13] M. Germonpré, G. Degrande, and G. Lombaert. A track model for the prediction of ground-borne vibrations due to parametric excitation. *Procedia Engineering*, 199:2663–2668, jan 2017.

[14] M. Germonpré, G. Degrande, and G. Lombaert. Periodic track model for the prediction of railway induced vibration due to parametric excitation. *Transportation Geotechnics*, 17:98–108, dec 2018.

[15] E. Arlaud. *Modèles dynamiques réduits de milieux périodiques par morceaux : application aux voies ferroviaires*. PhD thesis, École Nationale Supérieure d'Arts et Métiers, 2016.

[16] J. M. Mencik and D. Duhamel. A wave-based model reduction technique for the description of the dynamic behavior of periodic structures involving arbitrary-shaped substructures and large-sized finite element models. *Finite Elements in Analysis and Design*, 101:1–14, 2015.

[17] T. Hoang, D. Duhamel, G. Foret, and Computing Methods. Wave finite element method for vibration of periodic structures subjected to external loads. In *6th European Conference on Computational Mechanics (ECCM 6)*, number June, pages 11–15, 2018.

[18] T. Hoang, D. Duhamel, G. Foret, J.L. Pochet, and F. Sabatier. Wave finite element method for the dynamic analysis of railway tracks. In *13th World Congress on Computational Mechanics (WCCM XIII) 2nd Pan American Congress on Computational Mechanics (PANACM II)*, New York City, NY, USA, 2018.

COMPDYN 2019
7th ECCOMAS Thematic Conference on
Computational Methods in Structural Dynamics and Earthquake Engineering
M. Papadrakakis, M. Fragiadakis (eds.)
Crete, Greece, 24-26 June 2019

COMPUTATION OF AXISYMMETRIC VIBRATION TRANSMISSION USING A WELL-CONDITIONED SYSTEM FOR ELASTIC LAYERS OVER A HALF–SPACE

Andrew T. Peplow[1], Lars V. Andersen[2], and Peter Persson[3]

[1]Department of Natural Sciences and Public Health, Zayed University
P.O. Box 144534, Abu Dhabi, United Arab Emirates
e-mail: andrew.peplow@zu.ac.ae

[2] Department of Engineering, Aarhus University
8000 Aarhus C, Denmark
e-mail: lva@eng.au.dk

[3] 3Department of Construction Sciences, Lund University
P.O. Box 118, SE-221 00 Lund, Sweden
e-mail: peter.persson@construction.lth.se

Keywords: Elastic wave propagation, axisymmetric, dynamic stiffness matrix.

Abstract. *In the context of range-independent solid media, we propose a well-conditioned dynamic stiffness matrix for an elastic layer sitting over an elastic half-space. This formulation overcomes the well-known problem of numerical ill-conditioning when solving the system of equations for deep-layered strata. The methodology involves the exact solutions of transformed ordinary differential equations in the wavenumber domain, namely a projection method based on the transformed equations with respect to the depth coordinate. By re-arranging the transformed equations, the solutions remain numerically well-conditioned for all layer depths. The inverse transforms are achieved with a numerical quadrature method and the results presented include actual displacement fields in the near-field of the load in plane-strain and three-dimensional axisymmetric cases. Verification against finite element method (FEM) calculations demonstrates the performance and complexity of the two approaches.*

1 INTRODUCTION

A three-dimensional axisymmetric model is considered which demonstrates the effect of a harmonic finite rigid disk-load over various layered strata. The results derived by Fourier transformation are valid for any frequency and, more importantly, for any depth of the layer. In principle, following the well-known traditional methods, [1], we could use displacement-continuity and traction-equilibrium boundary conditions at the bottom and top of a layer with equations at the ground surface to generate equations for six subsequent unknowns of stress and displacement. However, this direct approach leads to formidable numerical problems. The reason for this work is that if traditional expressions for the characteristic wave functions, such as $\cosh$ or $\sinh$, are employed, these can have a dramatic effect on the numerical evaluation of solutions. Problems arise due to the cancellation or division of either very small or very large numbers. To overcome this, Karasalo [2] derived a well-conditioned propagator matrix for radially symmetric problems. Recent advances in propagator-matrix techniques have proved successful, [3] and [4]; but we derive a simple and robust technique. In this work, then, we construct a single stiffness matrix for the physical layer for plane-strain problems which conveniently avoids these difficulties. We therefore deduce a new global dynamic stiffness matrix for functions that do not cause numerical problems on a desktop PC.

Although not developed in this work, solutions to characteristic equations, such as dispersion equations, which establish wave propagation parameters, can now be determined more efficiently. Similar work in this area for dynamic problems where the load is stationary has been presented in [6] or for general moving-load problems in [7]. In this work we show how we are able to solve *large* (read: deep) problems, due to the reduced number of equations.

2 VIBRATION TRANSMISSION

The model considered is shown in Figure 1(a). A rigid disk load has a radius $b > 0$, with respect to the r-axis. It rests on homogeneous, isotropic, axisymmetric elastic layers, with material properties E (Young's modulus), ρ (density) and ν (Poisson's ratio). A harmonic vertical load acts uniformly over the disk. A submerged elastic layer (the concrete block) of finite depth, $H > 0$, of homogeneous and isotropic material then overlies a half-space of flexible material. The block is considered as a finite-width disk, radius $L > 0$, or as having infinite width, which is a similar problem to one studied in [8].

2.1 Geometry

The problem is solved semi-analytically by a numerical quadrature method suited for oscillatory integrands and, for verification and parametric analysis, by COMSOL 5.2 Solid Structures analysis. For the benefit of the reader, Fig. 1(b) includes an illustration of a typical mesh for the problem in the axisymmetric case. The model has $37,454$ degrees of freedom (d.o.f.), $4,064$ domain elements, and 611 boundary elements with cubic shape functions. In this example, the perfectly matched layer (PML) region surrounds the solution zone at $R = 75.0$ m, and receiver positions of interest are at $R_1 = 4.0$ m, $R_2 = 16.0$ m, and $R_3 = 32.0$ m.

2.2 Theoretical background

Much of the analysis necessary for the derivation of the dynamic stiffness matrix has been presented in references [9] and [10], so this will only be briefly summarized. For plane strain, the behaviour of the isotropic elastic material is described by Navier's elastodynamic equations,

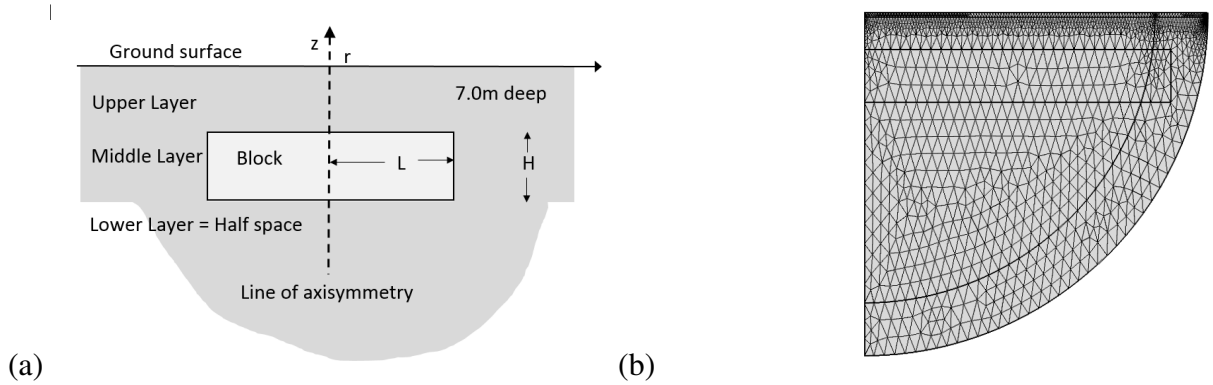

Figure 1: The schema for the two approaches: (a) For the semi–analytical domain, block has radius $L \to \infty$; (b) Axisymmetry model from COMSOL 5.2 showing the block of finite radius $L = 70$ m penetrating the PML region within the finite element mesh.

[9]. In the absence of body forces, these can be written as:

$$(\lambda+\mu)\frac{\partial e}{\partial z^2} \;+\; \mu\left(\frac{\partial^2 u}{\partial r^2}+\frac{1}{r}\frac{\partial u}{\partial r}-\frac{u}{r^2}+\frac{\partial^2 u}{\partial z^2}\right) \;=\; \rho\frac{\partial^2 u}{\partial t^2}, \tag{1}$$

$$(\lambda+\mu)\frac{\partial e}{\partial z} \;+\; \mu\left(\frac{\partial^2 w}{\partial r^2}+\frac{1}{r}\frac{\partial w}{\partial r}+\frac{\partial^2 w}{\partial z^2}\right) \;=\; \rho\frac{\partial^2 w}{\partial t^2}, \tag{2}$$

where u, w are the components of the displacement in the r and z directions and e is the volume strain, and λ, μ are complex Lamé constants assuming a constant loss-factor damping model. The quantities c_1 and c_2 are, respectively, the P and S wave speeds, given by:

$$c_1^2=\frac{\lambda+2\mu}{\rho}=\frac{E(1-\nu)}{\rho(1+\nu)(1-2\nu)}, \quad c_2^2=\frac{\mu}{\rho}=\frac{E}{2\rho(1+\nu)}. \tag{3}$$

and the boundary conditions for this problem are a uniform rigid disk-load of width b acting over the surface and at, for the example given here, at $z = H_1$, $z = (H_1 + H_2)$ continuity of displacement and equilibrium of traction between the mid-layer and the upper and lower media. Equations (2) may be solved by introducing potentials ϕ and H such that

$$u \;=\; \frac{1}{r}\frac{\partial \phi}{\partial r} \;-\; \frac{\partial H}{\partial z} \quad \text{and} \quad w \;=\; \frac{\partial \phi}{\partial z} \;+\; \frac{1}{r}\frac{\partial H}{\partial r}. \tag{4}$$

Also, assuming harmonic time-dependence $\mathrm{e}^{\mathrm{i}\omega t}$ and axial symmetry of the problem, this suggests seeking solutions in the form of Hankel integrals. For this purpose, the following Hankel transforms are introduced, assuming ζ is the transform variable:

$$\overline{U} \;=\; \int_0^\infty u\, r J_1(\zeta r)\, dr \quad \text{and} \quad \overline{W} \;=\; \int_0^\infty w\, r J_0(\zeta r)\, dr, \tag{5}$$

Taking the Hankel transform of the frequency version of equations (1) and (2) leads to a coupled set of ordinary differential equations.

$$\mu\frac{d^2\overline{U}}{\partial z^2}+\left[(\lambda+2\mu)\zeta^2-\rho\omega^2\right]\overline{U}-(\lambda+\mu)\zeta\frac{d\overline{W}}{\partial z} \;=\; 0, \tag{6}$$

$$(\lambda+2\mu)\frac{d^2\overline{W}}{\partial z^2}-\left[\mu\zeta^2-\rho\omega^2\right]\overline{W}-(\lambda+\mu)\zeta\frac{d\overline{U}}{\partial z} \;=\; P\, r J_0(\zeta r). \tag{7}$$

Soil	Upper–layer and half–space Soft soil–type	Embedded block Concrete
E (Pa)	2.69×10^8	204×10^8
ρ (kg m^{-3})	1550	2450
ν	0.257	0.179
c_R (m s^{-1})	242	1706
c_2 (m s^{-1})	263	1879
c_1 (m s^{-1})	459	3005

Table 1: Material properties

It is common practice to write solutions to the ensuing ordinary differential equations over a finite-length domain, $z \in [0, D]$ in terms of $\cosh$ and $\sinh$ functions. For computational purposes, this choice of characteristic functions is not convenient for problems involving spatial domains chosen to be extremely deep. Hence, we propose the general solutions may be written as a *scaled formulation*:

$$\begin{aligned} \overline{\phi} &= A_1\, \mathrm{e}^{-\alpha_1 z} + A_2\, \mathrm{e}^{\alpha_1 (z-D)}, \quad 0 \le z \le D \\ \overline{H} &= B_1\, \mathrm{e}^{-\alpha_2 z} + B_2\, \mathrm{e}^{\alpha_2 (z-D)}, \quad 0 \le z \le D. \end{aligned} \tag{8}$$

$$\alpha_1^2 = \zeta^2 - k_1^2 \quad \text{and} \quad \alpha_2^2 = \zeta^2 - k_2^2.$$

The reasons for choosing the scaled exponential characteristic functions over the hyperbolic functions is clear. Essentially, this choice ensures the characteristic functions do not grow unbounded with depth. Substituting the values $z = 0$ and $z = D$ into the equations (8) yields the first matrix equation

$$\{\overline{u}\} = [C]\,\{A\}\,. \tag{9}$$

where $\overline{u} = [\mathrm{i}\overline{w}_0,\ \overline{u}_0,\ \mathrm{i}\overline{w}_D,\ \overline{u}_D]^T$ and the 4×4 complex-valued matrix $[C]$ is given by

$$[C] = \begin{bmatrix} -\mathrm{i}\alpha_1 & \mathrm{i}\alpha_1 \mathrm{e}^{-\alpha_1 D} & -\zeta & -\zeta \mathrm{e}^{-\alpha_2 D} \\ \mathrm{i}\zeta & \mathrm{i}\zeta \mathrm{e}^{-\alpha_1 H} & \alpha_2 & -\alpha_2 \mathrm{e}^{-\alpha_2 D} \\ -\mathrm{i}\alpha_1 \mathrm{e}^{-\alpha_1 D} & \mathrm{i}\alpha_1 & -\zeta \mathrm{e}^{-\alpha_2 D} & -\zeta \\ \mathrm{i}\zeta \mathrm{e}^{-\alpha_1 D} & \mathrm{i}\zeta & \alpha_2 \mathrm{e}^{-\alpha_2 D} & -\alpha_2 \end{bmatrix}. \tag{10}$$

Now, further developing the system of equations, we get

$$\{\overline{\sigma}\} = [S]\,\{A\}\,, \tag{11}$$

$$[S] = \begin{bmatrix} -\mathrm{i}\alpha_1^2\beta + \mathrm{i}\lambda\zeta^2 & (-\mathrm{i}\alpha_1^2\beta + \mathrm{i}\lambda\zeta^2)\, g_1 & -2\mu\zeta\alpha_2 & 2\mu\zeta\alpha_2\zeta g_2 \\ 2\mathrm{i}\mu\zeta\alpha_1 & -2\mathrm{i}\mu\zeta\alpha_1\zeta g_1 & \mu\,(\alpha_2^2 + \zeta^2) & \mu\,(\alpha_2^2 + \zeta^2)\, g_2 \\ \mathrm{i}\,(\alpha_1^2\beta - \lambda\zeta^2)\, g_1 & \mathrm{i}\,(\alpha_1^2\beta - \lambda\zeta^2) & 2\mu\zeta\alpha_2 g_2 & -2\mu\zeta\alpha_2 \\ -2\mathrm{i}\mu\zeta\alpha_1 g_1 & 2\mathrm{i}\mu\zeta\alpha_1 & -\mu\,(\alpha_2^2 + \zeta^2)\, g_2 & -\mu\,(\alpha_2^2 + \zeta^2) \end{bmatrix} \tag{12}$$

with $\beta = \lambda + 2\mu$, $g_i = \mathrm{e}^{-\alpha_i D}, i = 1, 2$, and $\overline{\sigma} = [-\mathrm{i}\overline{\sigma}_0,\ -\overline{\tau}_0,\ \mathrm{i}\overline{\sigma}_D,\ \overline{\tau}_D]^T$. We now combine equations (9) and (11), to arrive at a single matrix expression which expresses the displacements and stresses at the surface and the interface in the wavenumber domain:

$$[T]\,\{\overline{u}\} = \{\overline{\sigma}\}\,. \tag{13}$$

where $[T] = [S][C]^{-1}$. The entries of the matrix $[T]$ are provided in the work of Peplow, [5]. Specifically, $[T]$ is the dynamic stiffness matrix for a single elastic layer, valid for any layer-depth $D > 0$. To include the half-space, we utilize the matrix equations presented in [10], which leads to a matrix system:

$$[P] = \frac{1}{DET}\begin{bmatrix} (\lambda+2\mu)\alpha_2 k_1^2 & 2\mu\zeta(\alpha_1\alpha_2-\zeta^2)+(\lambda+2\mu)\zeta k_1^2 \\ 2\mu\zeta(\alpha_1\alpha_2-\zeta^2)+\mu\zeta k_2^2 & \mu\alpha_1 k_2^2 \end{bmatrix}\begin{bmatrix} \mathrm{i}\overline{w}_D \\ \overline{u}_D \end{bmatrix} = \begin{bmatrix} \mathrm{i}\overline{\sigma}_D \\ \overline{\tau}_D \end{bmatrix} \quad (14)$$

where $DET = 1/(\alpha_1\alpha_2 - \zeta^2)$ and it is understood the soil parameters are related to the half-space below the upper layer.

Equations can now be combined to give a single matrix equation for an elastic layer over an elastic half-space, involving the *scaled* stiffness matrix for the elastic layer $[T_{ij}]$ and the matrix for the half-space $[P_{ij}]$. The general matrix form for any global domain becomes a 4×4 complex valued matrix:

$$[T]_G = \left[\begin{array}{cc:cc} T & T & T & T \\ T & T & T & T \\ \hdashline T & T & T\text{-}P & T\text{-}P \\ T & T & T\text{-}P & T\text{-}P \end{array}\right] \quad (15)$$

It is straightforward then to generalise this technique to n elastic layers over a half-space, where the size of the dynamic stiffness matrix will become a single complex-valued $2(n+1)\times2(n+1)$ matrix. On our case we have essentially two layers on a half-space ($n = 2$), which results in a 6×6 system.

3 NUMERICAL COMPUTATIONS

Generally, for non-dimensional wavenumbers $k_s h \geq 13$, where k_s is the shear wavenumber, the conventional approach "breaks down". That is, for depths greater than around two shear wavelengths, $h \geq 2\lambda_s$, a numerical bottleneck problem arises when solving the linear system of algebraic equations. Equally, for high frequencies, computations can become ill-conditioned. The choice of projected method permits a stable numerical evaluation for entries in the stiffness matrix for all soil types, frequencies and layer depths. This avoids numerical round-off errors.

It was found that numerical inversion of the Hankel transforms worked well with a cut-off at $R = 20\,\mathrm{m}^{-1}$ with $2,000$ sample points spaced logarithmically in the interval $\zeta \in [10^{-4}, R]$. Fast numerical Hankel methods, similar to Fast Fourier Transform (FFT), which are freely available, were not used in this work since our interest is in a few receiver positions.

4 RESULTS

Soil parameters used are presented in Table 1, that is two sets of soil characteristics which represent different conditions, soil and concrete. The response has been calculated for a disk-load with $b = 1.0$ m and subjected to a uniform unit load, $P = 1$ N. Calculation times for 100 frequency points on an i3-chip desktop took around 3.0 minutes in total. Integration was not particularly slow due to the modes associated to the deep bedrock stratum. Numerical integration is possible for all deep models and it is recommended to include an underlying half-space for computational and realistic modelling purposes, since bedrock models will include many modes.

Nonetheless the results presented are calculated using the Clenshaw–Curtis numerical quadrature method. The related ground parameters are shown in Table 1. The configuration is an elastic

circular block layer embedded 7.0 m deep within a half-space. To verify results of the simple model, we compare with a numerical scheme provided by COMSOL 5.2, see Fig. 1(b).

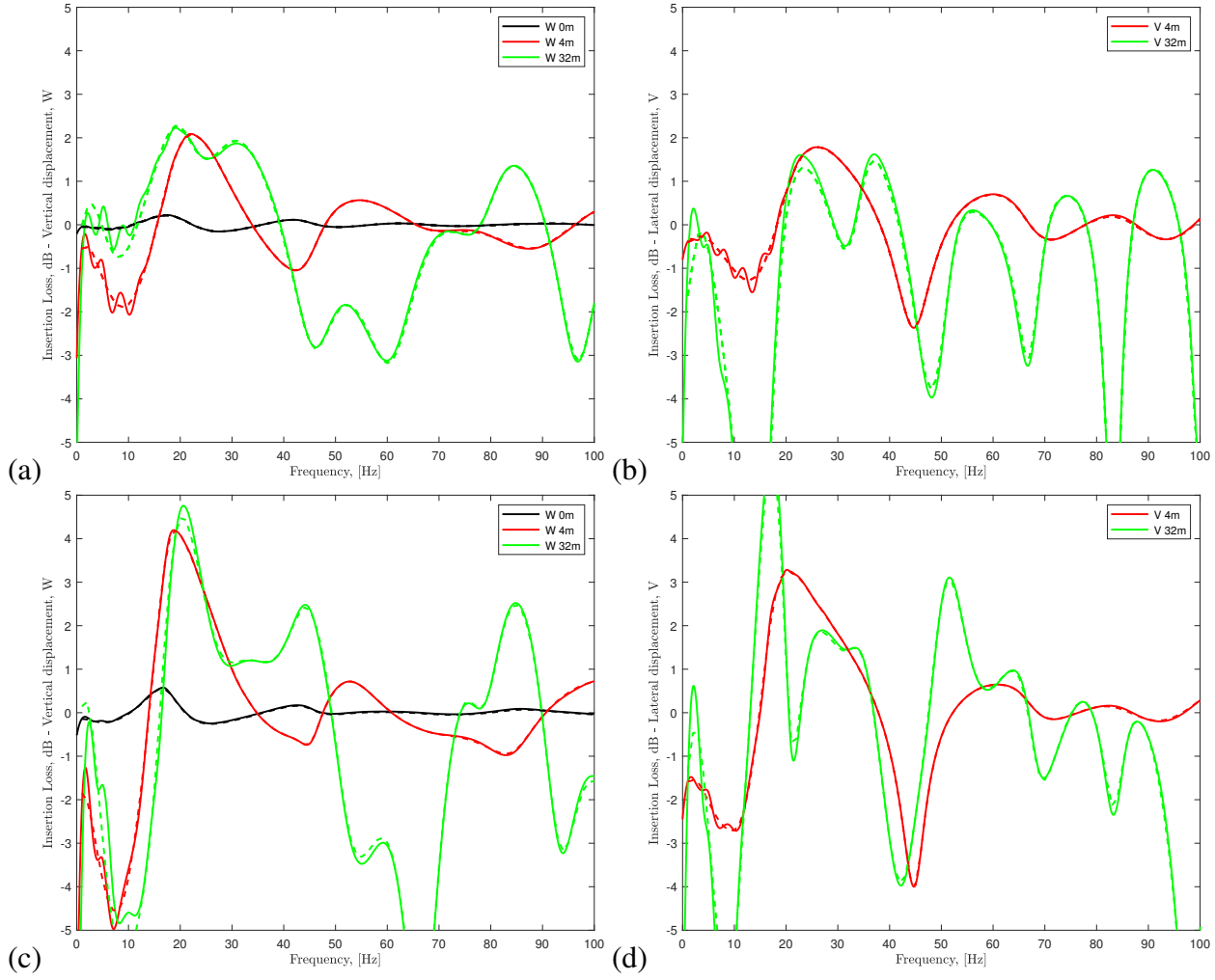

Figure 2: Verification of the method compared to a PML version in COMSOL 5.2 for: (a) and (b) 0.5 m deep embedded concrete block; and (b) and (c) a 2.0 m embedded block.

Our approach, as a possible measure for mitigating vibration, is based on the impeding behaviour of a soil layer over a bedrock. It occurs if the excitation frequency is below the lowest eigenfrequency of the layer. Since it is not convenient to develop real bedrock layers below buildings, where the length of the block in Fig. 1 tends to infinity, for example, we may use a stiff finite-length obstacle as an artificial bedrock instead. The results correspond to the possible positive effect for replacing bedrock by a feasible concrete block. For a bedrock layer at depth, $H = 7.0$ m, the first eigenfrequency related to shear waves is around 10 Hz. We only show two examples where the rigid bedrock is approximated by a concrete block, 0.5 m thick, with various lengths and evaluated at three receiver positions.

Figures 3(a) and (b) correspond to amplitude increase or decrease, against the half-space response, as the thin 0.5 m concrete block increases width from $L = 2.0$ m, to $L = 4.0$ m to $L = 12.0$ m with respect to the receiver position 4.0 m from the load-centre. For both vertical and longitudinal motion we observe a characteristic dip in insertion loss below the cut-on frequency with a slight insertion loss up to 2 dB performance in the interval 20 Hz to

40 Hz. A concrete block of length 12.0 m appears to approximate well as a substitute for an infinite layer. Figures 3(c) and (d) correspond to amplitude increase or decrease as the thin 0.5 m concrete block increases width from $L = 8.0$ m, $L = 16.0$ m to $L = 24.0$ m with respect to the receiver position 16.0 m from the load–centre. Here, the complex interactions below cut-on are evident, again a possible 2 dB insertion loss between 20 Hz and 40 Hz seems possible. Figures 3(e) and (f) correspond to amplitude increase or decrease as the thin 0.5 m concrete block increases width from $L = 24.0$ m, $L = 32.0$ m to $L = 40.0$ m with respect to the receiver position 32.0 m from the load-centre. As the receiver position increases its distance from the load, the concrete block, substituting a rigid layer foundation, also requires greater length Again the possible effectiveness as a mitigation device reduces to below 40 Hz.

5 CONCLUSIONS

An axisymmetric three-dimensional model has been developed for investigating the propagation of surface vibration over arbitrary-depth elastic layers. The model consists of an elastic, isotropic and homogeneous layer which overlies a half-space. A well-conditioned dynamic stiffness matrix has been developed for this model, which is derived by considering a different set of characteristic functions.

We have shown that by including a bedrock foundation buried under a surface load this can have a positive effect in reducing vibration across the surface of the ground, in certain frequency bands. However, below the *cut–on* frequency, in which travelling waves cannot propagate, the effectiveness is difficult to assess.

Rather than turning to large-scale finite element models we have shown that it is possible to draw conclusions for vibration reduction assessments from an alternative general semi-analytical model. In future work we shall extend the semi-analytical model illustrated in this work from the axisymmetric case to general three-dimensional models.

6 ACKNOWLEDGEMENTS

The third author gratefully acknowledges the financial support from the Swedish Governmental Agency for Innovation Systems (Vinnova), grant ref.no. 2018-04159, as well as from the City of Helsingborg through the call Plattformen.

REFERENCES

[1] D.V. Jones, M. Petyt, Ground vibration in the vicinity of a strip load: an elastic layer on an elastic half–space. *Journal of Sound and Vibration*, **161**, 1–18, 1993.

[2] I. Karasalo, Exact finite elements for wave propagation in range–independent fluid–solid media. *Journal of Sound and Vibration*, **172**, 671–688, 1994.

[3] J.F. Lu, R.F. Shen, M.Q. Sh, Reflection-transmission matrix method for the consolidation of a multilayered saturated soil. *International Journal for Numerical and Analytical Methods in Geomechanics*, **40**, 1594–1622, 2016.

[4] C.H. Chapman, Yet another elastic plane-wave, layer-matrix algorithm. *Geophysical Journal International*, **154**, 212–223, 2003.

[5] A.T. Peplow, Surface ground vibration from a stripload acting over elastic layers: A uniform approach. *Soil Dynamics and Earthquake Engineering*, **116**, 289–292, 2019.

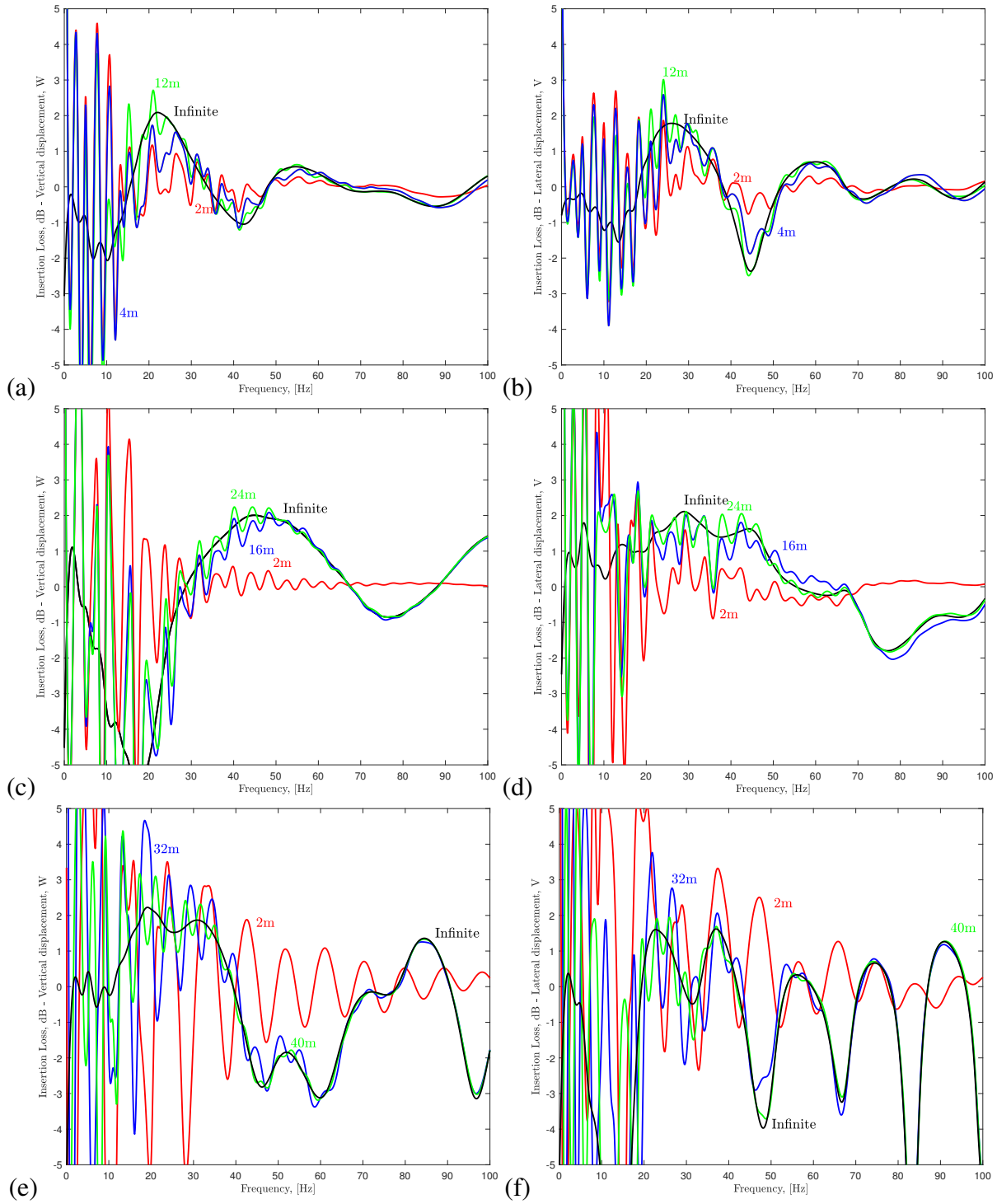

Figure 3: Convergence of insertion loss for various finite-radius embedded concrete blocks: (a), (b) at receiver 4.0 m from load-centre; (c), (d) at 16.0 m from load-centre; and (e), (f) at 32.0 m from load-centre. Also shown results from the simple model for an infinite radius disk.

[6] C.L. Liu, Z.Y. Ai, Vertical harmonic vibration of piled raft foundations in layered soils. *International Journal for Numerical and Analytical Methods in Geomechanics*, **41**, 1711–1723, 2017.

[7] H. Sun, Y. Cai, C. Xu, Three-dimensional steady-state response of a railway system on layered half-space soil medium subjected to a moving train. *International Journal for Numerical and Analytical Methods in Geomechanics*, **33**, 529–550, 2009.

[8] A.T. Peplow, M. Petyt, C.J.C. Jones, Surface vibration propagation over a layered half–space with an inclusion. *Applied Acoustics*, **56**, 283–296, 1999.

[9] W.M. Ewing, W.S Jardetzky, F. Press, *Elastic waves in layered media*, McGraw–Hill, New York, 1957.

[10] D.V. Jones, M. Petyt, Ground vibration in the vicinity of a strip load: A two–dimensional half–space model. *Journal of Sound and Vibration*, **147**, 155–166, 1991.

COMPDYN 2019
7th ECCOMAS Thematic Conference on
Computational Methods in Structural Dynamics and Earthquake Engineering
M. Papadrakakis, M. Fragiadakis (eds.)
Crete, Greece, 24-–26 June 2019

EFFICIENT PROPORTIONAL DAMPING MODEL FOR SIMULATING SEISMIC RESPONSE OF LARGE-SCALE STRUCTURES

Chin-Long Lee[1]

[1]University of Canterbury
Department of Civil and Natural Resources Engineering
69 Creyke Road, Christchurch 8041, New Zealand
e-mail: chin-long.lee@canterbury.ac.nz

Keywords: Proportional Damping Model, Constant Modal Damping Ratio, Sparse Matrix, Large Number of Degrees of Freedom, Computational Efficiency.

Abstract. *An efficient proportional viscous damping model is proposed to simulate energy dissipation in a large-scale structure due to components not already accounted for by hysteretic material models. The proposed model overcomes the limitations of existing models, e.g. Rayleigh model, Caughey model, Wilson-Penzien model, and a generalized proportional model, that are either inflexible in matching a damping ratio curve in the structural frequency domain, or computationally expensive for response history analysis due to a fully populated damping matrix, or both. The proposed model allows a smooth function without large oscillation to match damping ratios across a wide range of frequencies. The damping matrix of this model can be implemented exactly as a sparse block matrix without using an approximate version, leading to very fast computation for response history analysis. The larger the number of degrees of freedom, the more computationally efficient is the proposed model compared to existing models that result in a fully populated damping matrix. Several case studies are reported to showcase the superior performance of the proposed model against existing models in terms of accuracy and computational efficiency.*

1 INTRODUCTION

In a typical seismic analysis of a large-scale structure, proportional viscous damping models are popularly used to simulate damping. They are particularly preferred to other non-proportional or non-viscous damping models in the consideration of computational cost and calibration against measured damping ratios.

Popular models usually considered include Rayleigh model [1], Caughey model [2; 3], and Wilson-Penzien model [4]. A generalized proportional model has recently been proposed [5] but is not as popular.

In the following, the advantages and disadvantages of these models will be reviewed, focusing on the accuracy in matching a user-defined damping ratio curve in the structural frequency domain, and the computational efficiency in computing displacement solutions from time step to time step in a response history analysis.

In terms of accuracy for matching a curve, the Rayleigh model, with only two terms, could only match modal damping ratios for two modes. For other modes, the damping ratios follow the curve controlled by these two modes. The Rayleigh model is, therefore, very inaccurate in matching a curve for a structure with more than two modes. The Caughey model allows the modal damping ratio to be matched at a lot more modes. Unfortunately, the curve often oscillates drastically, with some parts potentially fall into a negative region. The matrix for determining the coefficients also becomes ill-conditioned when more terms are considered. The coefficients would eventually become sensitive to round-off errors. The Wilson-Penzien model directly matches a damping ratio at each mode. However, it requires a costly computation of eigendecomposition to determine structural frequencies and mode shapes. To reduce this cost, only the frequencies and mode shapes for some lower modes are calculated. Consequently, most higher modes become undamped. A stiffness proportional term could be added to avoid undamped higher modes [6], but the corresponding damping ratios are forced to follow this linear curve. The generalized proportional damping model generates the damping ratio with general functions including square root, trigonometric, hyperbolic, or exponential functions. Compared to the previous models, it is much more flexible in matching an arbitrary damping ratio curve.

In terms of computational cost, it is important to note that the computational cost is directly related to the number of nonzero elements in the damping coefficient matrix $\mathbf{C}$. The sparser the $\mathbf{C}$ matrix, the lower the computational cost. The Rayleigh model forms the $\mathbf{C}$ matrix with a mass proportional term and a stiffness proportional term. Since it gives a $\mathbf{C}$ as sparse as the stiffness matrix, it is computationally very efficient. The Caughey model forms the $\mathbf{C}$ matrix with each term written as $\mathbf{M}\alpha_l(\mathbf{M}^{-1}\mathbf{K})^l$, where l is an integer, $\mathbf{M}$ the mass matrix, and $\mathbf{K}$ the stiffness matrix. Its $\mathbf{C}$ matrix is often dense and even fully populated. It also requires $\mathbf{M}$ to be invertible, which is, unfortunately, rare for large-scale structures based on lumped masses. The Wilson-Penzien model forms the $\mathbf{C}$ matrix by superposition of modal damping matrices. The resultant $\mathbf{C}$ matrix is generally fully populated for the degrees of freedom (DOFs) with mass inertias, even if only a few modes are included. The generalized proportional damping model forms the $\mathbf{C}$ matrix using general functions of $\mathbf{M}^{-1}\mathbf{K}$, $\mathbf{K}^{-1}\mathbf{M}$, $\mathbf{K}\mathbf{M}^{-1}$, or $\mathbf{M}\mathbf{K}^{-1}$. Its $\mathbf{C}$ matrix is likely fully populated. In addition, it is not always computationally friendly for computing functions of matrices, and the cost is likely in the same order of computing eigendecomposition. It also requires either $\mathbf{M}$ or $\mathbf{K}$ to be invertible, making it undesirable for lumped mass

systems commonly used for large-scale structures.

As discussed above, the existing models are not only very inflexible in matching damping ratios but also very costly for computing structural response due to a fully populated $\mathbf{C}$ matrix, or both.

In addressing the above limitations, the author has recently proposed a proportional viscous damping model [7]. This model has the following advantages over existing models:

- Damping ratios can be matched for any number of modes,
- The damping ratios at the zero and infinite frequencies are zero, avoiding spurious damping forces on DOFs without mass inertia [8] and unrealistic damping forces during rigid body motions, and
- The resultant damping ratio curve is smooth without large oscillation and is accurate for a constant damping ratio across a wide range of frequencies.

This model is further discussed in this paper in terms of computer implementation, which is not yet reported in the last paper [7]. The focus will be placed on the sparsity of the resultant damping $\mathbf{C}$ matrix and its computational efficiency for computing solutions, particularly for a large-scale structure with a large number of DOFs. Several examples will be used to showcase its advantages compared to other damping models. Due to space limitation, only key results will be presented in this paper to demonstrate the computational efficiency of the proposed model. Detailed discussions on the formulas and computer implementations of the proposed model have been submitted to a journal and will soon be made available to keen readers.

2 PROPOSED DAMPING MODEL IN FREQUENCY DOMAIN

The proposed model [7] generates a curve of modal damping ratio ζ in the domain of structural circular frequencies ω by a sum of multiple basis functions $N(\omega)$. Each basis function is a bump-like function given in Eq. (1) and plotted in Fig. 1.

$$N(\omega;\omega_p) = \frac{2\omega_p\omega}{\omega_p^2+\omega^2} \tag{1}$$

The parameter ω_p is the frequency at the peak of the function, serving as the parameter

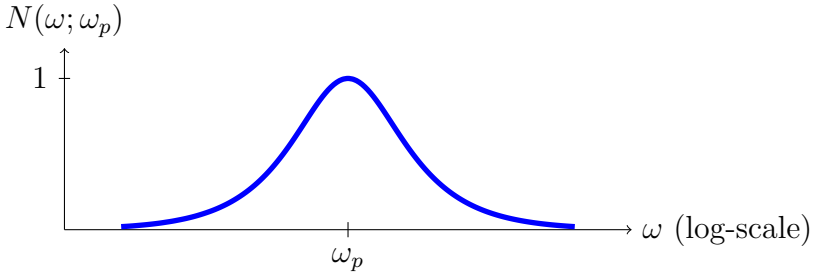

Fig. 1: Basis function of proposed damping model in frequency domain.

controlling the location of the peak.

The basis function is non-negative, has only one unit peak at frequency ω_p, is symmetric about the line where $\omega = \omega_p$ on the logarithmic scale, has a constant bandwidth independent of ω_p on the logarithmic scale, approaches asymptotically to zero at the two

extreme limits of frequencies, i.e. $\omega = 0$ and $\omega = \infty$, is a zero function when $\omega_p = 0$ or $\omega_p = \infty$, is independent from functions with different ω_p, and is symmetric with respect to ω_p and ω, i.e. $N(\omega;\omega_p) = N(\omega_p;\omega)$.

With n_b number of basis functions an arbitrary modal damping ratio curve could be generated with the following equation.

$$\zeta(\omega) = \sum_{j=1}^{n_b} N(\omega;\omega_{p_j})\zeta_{p_j} \tag{2}$$

where ζ_{p_j} is the ζ-coordinate of the peak for the j^{th} basis function. For example, suppose a constant damping ratio of 5% is matched for frequencies between 0.1 Hz and 10 Hz, three basis functions could be used to generate this curve. The values of ω_p's and ζ_p's can be obtained by using a least squares curve fitting method. The resultant damping ratio curve is shown in Fig. 2. The figure shows that the damping ratio curve matches the constant

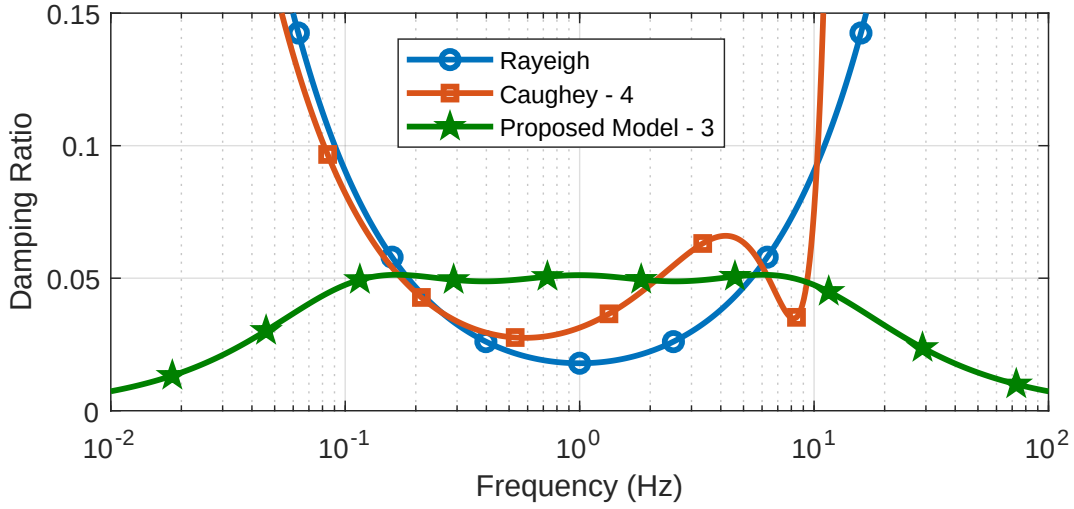

Fig. 2: Damping ratio curves generated using Rayleigh, Caughey and proposed damping models.

damping ratio within the frequency interval of [0.1 Hz, 10 Hz] with high accuracy. There is oscillation within the interval but the relative error is within 2 to 3%, and the error reaches 5% only at the ends of the interval. This error is considered negligible, as can be shown in an example later. If so desired, more basis functions could be added to further reduce the error. Outside the interval, the damping ratio decreases asymptotically to zero on the logarithmic scale. For comparison, the curves obtained using the Rayleigh and the Caughey models (4 terms) are also plotted for comparison. They were also obtained using a least squares curve fitting method. Their curves have much larger errors that are evidently unacceptable.

3 MATRIX FORM, SPARSITY AND COMPUTATIONAL EFFICIENCY

The proposed model has the damping coefficient matrix $\mathbf{C}$ shown in the following when one basis function is used.

$$\mathbf{C} = \mathbf{M_C} - \mathbf{M_C}\left(\mathbf{K_C} + \mathbf{M_C}\right)^{-1}\mathbf{M_C} \tag{3}$$

where $\mathbf{M_C}$ and $\mathbf{K_C}$ are defined as

$$\mathbf{M_C} = 4\zeta_p\omega_p\mathbf{M}, \quad \mathbf{K_C} = \frac{4\zeta_p}{\omega_p}\mathbf{K} \tag{4}$$

It is, nonetheless, fully populated. However, unlike other models, this form can be expanded into a larger block matrix $\mathbf{C_X}$ of size $2n \times 2n$, where n is the number of DOFs, shown in the following for one basis function

$$\mathbf{C_X} = \begin{bmatrix} \mathbf{M_C} & -\mathbf{M_C} \\ -\mathbf{M_C} & \mathbf{K_C} + \mathbf{M_C} \end{bmatrix} \tag{5}$$

This matrix $\mathbf{C_X}$, an expanded matrix form of $\mathbf{C}$, has the number of DOFs doubled. The first block row corresponds to the usual displacement DOFs, and the second block row corresponds to a new set of DOFs being introduced. When multiple basis functions are used, the matrix will be expanded further with more block rows. Although the size of $\mathbf{C_X}$ is larger than $\mathbf{C}$, it is much sparser, as explained below using an example to compare $\mathbf{C}$ and $\mathbf{C_X}$.

Consider a two-dimensional simply-supported beam. Suppose it is discretized into 101 beam elements with 100 free transverse DOFs and 100 free rotational DOFs. The axial DOFs are ignored. The mass of the beam is lumped at the nodes and the mass inertias are only considered for transverse DOFs. As a result, $\mathbf{M}$ is diagonal and $\mathbf{K}$ is banded. Note, although a simple structure is used in this comparison, the ensuing conclusions will be the same should this structure be much more complex like multi-span bridges or multi-story multi-bay buildings.

Fig. 3 shows the sparsity patterns of the two matrices $\mathbf{C}$ and $\mathbf{C_X}$ for this chimney using a MatLab™ function `spy` that shows a dot at the corresponding row and column indices for each nonzero in the matrices. In this example, four basis functions are used to form the damping matrices, covering the frequency interval of [0.1 Hz, 10 Hz]. The size of $\mathbf{C_X}$ is 1000×1000 because each basis function requires a new set of 200 DOFs to be introduced.

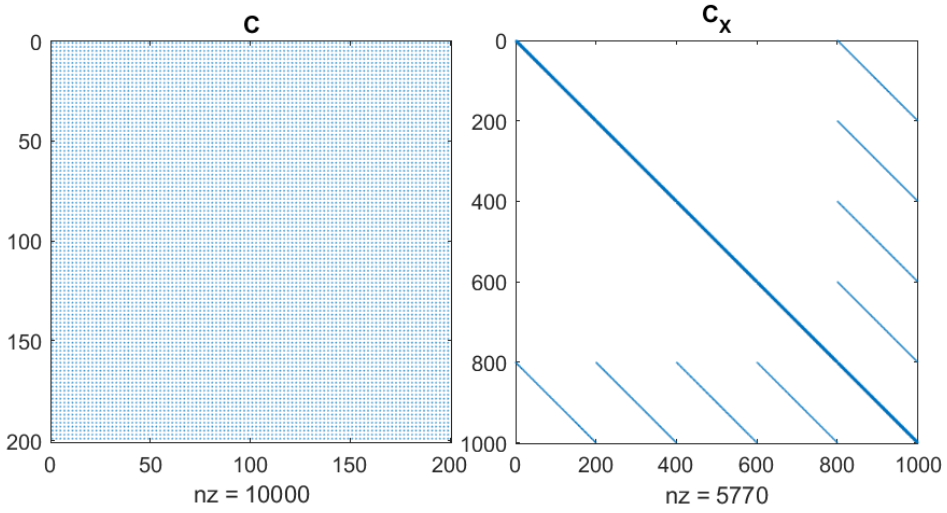

Fig. 3: Comparison of sparsity patterns of $\mathbf{C}$ (left) and $\mathbf{C_X}$ (right).

This example shows that, although $\mathbf{C_X}$ is much larger in size than $\mathbf{C}$, it is much sparser. In fact, the ratio, denoted as r, between the numbers of nonzeros in $\mathbf{C_X}$ and of nonzeros in $\mathbf{C}$ is inversely proportional to the number of DOFs n.

$$r \overset{\text{def}}{=} \frac{nnz(\mathbf{C_X})}{nnz(\mathbf{C})} = O(1/n) \tag{6}$$

In other words, the larger the number of DOFs, the fewer are the nonzeros in $\mathbf{C_X}$ compared to a fully populated $\mathbf{C}$ of other damping models. This ratio of comparison also applies to the time required to compute the displacement solutions using the effective tangent stiffness based on $\mathbf{C_X}$ and $\mathbf{C}$. Fig. 4 shows the ratio r for number of nonzeros and the elapsed time required estimated using MatLab functions `tic` and `toc`, with increasing number of DOFs. The solution process is based on MatLab's backslash (\) operation, i.e. `mldivide`, which has been optimised for each matrix type. The computer used was a personal desktop computer. Note, the solutions using $\mathbf{C_X}$ and $\mathbf{C}$ are practically identical with negligible differences due to round-off errors.

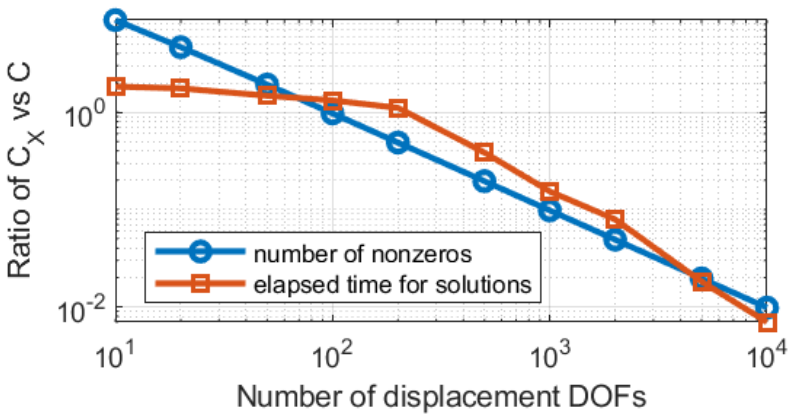

Fig. 4: Ratio of $\mathbf{C_X}$ vs $\mathbf{C}$ for number of nonzeros and elapsed time for computing solutions.

Fig. 4 shows that the ratio r for the number of nonzeros and the elapsed time for computing solutions in this example is indeed inversely proportional to the number of DOFs. The increase in efficiency is at least 100 times when n is larger than 10,000. This example clearly shows the remarkable performance of the proposed model with the expanded representation of the damping matrix, i.e. $\mathbf{C_X}$, in terms of memory storage and computational efficiency. Nevertheless, when n is small, it may be better to use the original matrix representation of damping matrix, i.e. $\mathbf{C}$.

4 EXAMPLE OF RESPONSE HISTORY ANALYSIS

In this example, the accuracy of the proposed model is compared against the Wilson-Penzien model in response history analysis. The structure considered is a two-dimensional 1-bay 5-story steel frame with fixed based. The story height is 2.5 m and the bay width is 3 m. All the beams are 610UB125kg/m and all the columns are 310UC158kg/m. They are modelled using concentrated plastic hinge element with N-M interactions incorporated. The yield strength of the materials is 300 MPa. Masses are lumped at nodes. Only horizontal mass inertias are considered. Vertical and rotational mass inertias are ignored. Each mass is 15300 kg. The five fundamental frequencies of the structure are 1.9 Hz, 6.0

Hz, 10.9 Hz, 15.3 Hz, and 18.6 Hz. The damping ratio is 5% for the first three modes. For the proposed model, two basis functions are used such that the relative error within the frequency interval covering the first three modes is about 2%. The damping ratios using the Wilson-Penzien model and the proposed model are shown in Fig. 5. The damping ratios at structural frequencies are highlighted with markers. The damping matrix remains

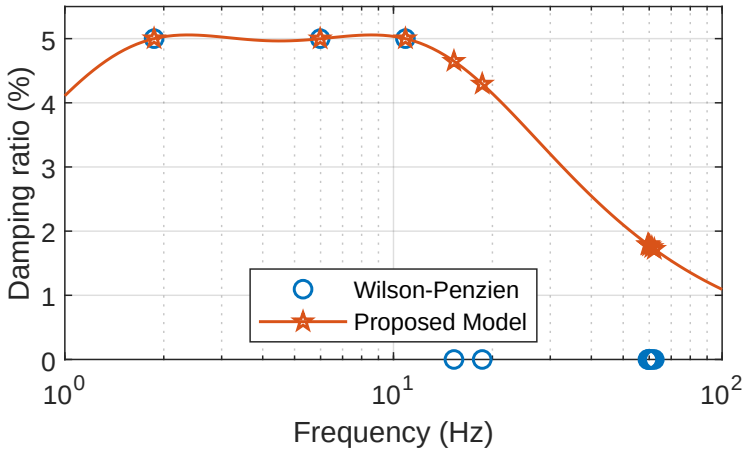

Fig. 5: Damping ratios using Wilson-Penzien and proposed damping models.

constant throughout the analysis, as suggested by Chopra [8]. The ground motion is the North-South component of the 1940 El Centro earthquake with its PGA scaled to 1 g.

The roof displacement time histories are shown in Fig. 6. The comparison shows that

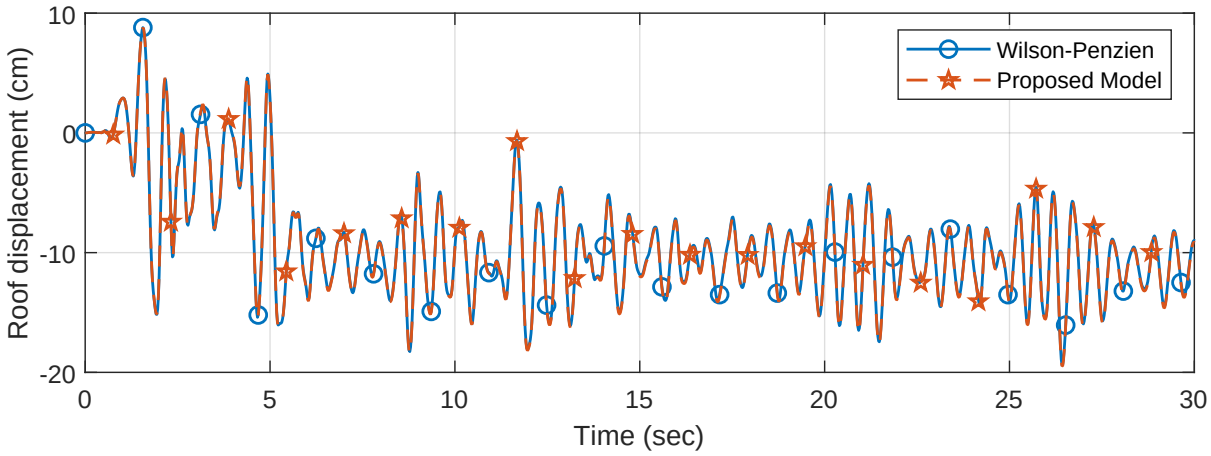

Fig. 6: Roof displacement time histories using Wilson-Penzien and proposed damping models.

both models give almost identical roof displacement time histories. It proves that the proposed model is as accurate as the Wilson-Penzien model for this structure where the lowest three modes dominate the roof displacement response.

5 CONCLUSIONS

A proportional viscous damping model has recently been proposed. It generates a damping ratio curve with multiple bump-like basis functions controlled by frequency and

damping ratio at the peak of each basis function. It is accurate for matching a constant damping ratio typically used in the earthquake engineering community for a response history analysis of large-scale structures.

In this paper, the matrix form of this model has been introduced, and its computer implementation has been discussed, with its computational efficiency emphasized. It has its damping matrix in a special form that can be expanded into a sparse block matrix. Although the expanded block matrix is much larger than the original damping matrix, it is much sparser. The computation of solution using this block matrix is, therefore, much faster compared to a fully populated damping matrix of existing models. The ratio of nonzeros between the block matrix and the original matrix is inversely proportional to the number of degrees of freedom. The larger the number of degrees of freedom, the faster the computation. The proposed model is, therefore, suitable for a structure with a large number of degrees of freedom. Some case studies have been reported to showcase the performance of the proposed model against existing models in terms of accuracy and computational efficiency.

6 ACKNOWLEDGEMENTS

The author thanks Prof. Athol Carr of the University of Canterbury, Christchurch, for many helpful discussions on the problems and challenges of existing damping models.

REFERENCES

[1] J. W. S. B. Rayleigh. *The theory of sound*, vol. 2. Macmillan, 1896.

[2] T. Caughey. Classical normal modes in damped linear dynamic systems. *Journal of Applied Mechanics*, **27**(2), 269–271, 1960.

[3] T. Caughey and M. E. O'Kelly. Classical normal modes in damped linear dynamic systems. *Journal of Applied Mechanics*, **32**(3), 583–588, 1965.

[4] E. Wilson and J. Penzien. Evaluation of orthogonal damping matrices. *International Journal for Numerical Methods in Engineering*, **4**(1), 5–10, 1972.

[5] S. Adhikari. Damping modelling using generalized proportional damping. *Journal of Sound and Vibration*, **293**(1-2), 156–170, 2006.

[6] R. Clough and J. Penzien. *Dynamics of structures*. Computers and Structures, Inc, Berkeley, Calif, 2003.

[7] C.-L. Lee. A novel damping model for earthquake induced structural response simulation. In *2019 Pacific Conference on Earthquake Engineering*. Auckland, New Zealand, 4–6 Apr 2019.

[8] A. K. Chopra and F. McKenna. Modeling viscous damping in nonlinear response history analysis of buildings for earthquake excitation. *Earthquake Engineering & Structural Dynamics*, **45**(2), 193–211, 2016.

COMPDYN 2019
7th ECCOMAS Thematic Conference on
Computational Methods in Structural Dynamics and Earthquake Engineering
M. Papadrakakis, M. Fragiadakis (eds.)
Crete, Greece, 24-–26 June 2019

DYNAMIC ANALYSIS OF A REINFORCED CONCRETE SHEAR WALL BUILDING USING A NOVEL FINITE ELEMENT

T. L. Chang[1], C.-L. Lee[1], A. J. Carr[1], and R. P. Dhakal[1]

[1]Department of Civil and Natural Resources Engineering, University of Canterbury, Christchurch, NZ, 8041.
tlcfem@gmail.com, chin-long.lee@canterbury.ac.nz, athol.carr@canterbury.ac.nz, rajesh.dhakal@canterbury.ac.nz

Keywords: drilling element, RC shear wall, nonlinear dynamic analysis

Abstract. *To simulate reinforced concrete shear walls under seismic loads, a new finite element called GCMQ (generalized conforming mixed quadrilateral) developed based on the three-field Hu-Washizu variational principle is adopted in this paper for the nonlinear time history analysis of a reinforced concrete shear wall multistory building. Unlike other well-known 1D wall elements, GCMQ is a 2D membrane element that exhibits very good performance in terms of coarse mesh accuracy. It takes into consideration the nonlinear distribution of both strain and stress across the wall width, which is difficult to achieve with 1D elements that often adopt 'plane sections remain plane' assumption. Two shear wall examples are analysed in this paper. With a smeared approach adopted for reinforcement and a proper material model for concrete, GCMQ can simulate accurate global response with a coarse mesh grid. For time efficient analysis, one element per storey could also be adopted. GCMQ provides a more versatile solution to wall simulation and could be a useful tool in future analysis and design of wall structures.*

1 INTRODUCTION

Unlike slender structural members such as beams and columns that could be idealised as 1D finite elements, modelling reinforced concrete shear walls is in general a difficult task due to the conflict between efficiency and accuracy of numerical analyses. Classic finite elements such as four-node isoparametric quadrilateral element (Q4) can, of course, be adopted to develop fine models for static analysis. However, such an approach is not practicable when it comes to nonlinear time history analysis due to the large amount of computational power required, particularly with very dense mesh grids. On the other hand, recently proposed 1D macroscopic elements, such as MVLEM [1] and its variants, including SFI-MVLEM [2], are typically formulated based on spring systems. Although they are relatively more efficient, those elements lack proper justifications in terms of representing the physical problem from continuum mechanics perspective. As a result, the error of analysis could be significantly large and convergence to theoretical solutions may not be guaranteed.

To ease the problem, as well as to achieve a better balance between analysis efficiency and accuracy, a mixed membrane element called GCMQ (generalized conforming mixed quadrilateral) is proposed recently [3]. This paper evaluates the performance of GCMQ in the context of nonlinear time history analysis. Two examples are presented to showcase both linear elastic and inelastic performance. The formulation of GCMQ is briefly discussed first, followed by a summary of material models used. The performance in simulating two cantilever walls is then investigated. The numerical results indicate that GCMQ is a good element for future nonlinear response history analysis of shear wall structures.

2 THE GCMQ ELEMENT

The GCMQ element is a mixed four-node quadrilateral with in-plane drilling degrees of freedom. It is formulated in a three field framework based on a modified Hu-Washizu variational theorem. The displacement field is split into two components by using additive decomposition. An illustration of such a procedure can be seen in Fig. 1. The distortion $\mathbf{u}_d$ is generated purely by the drilling degrees of freedom.

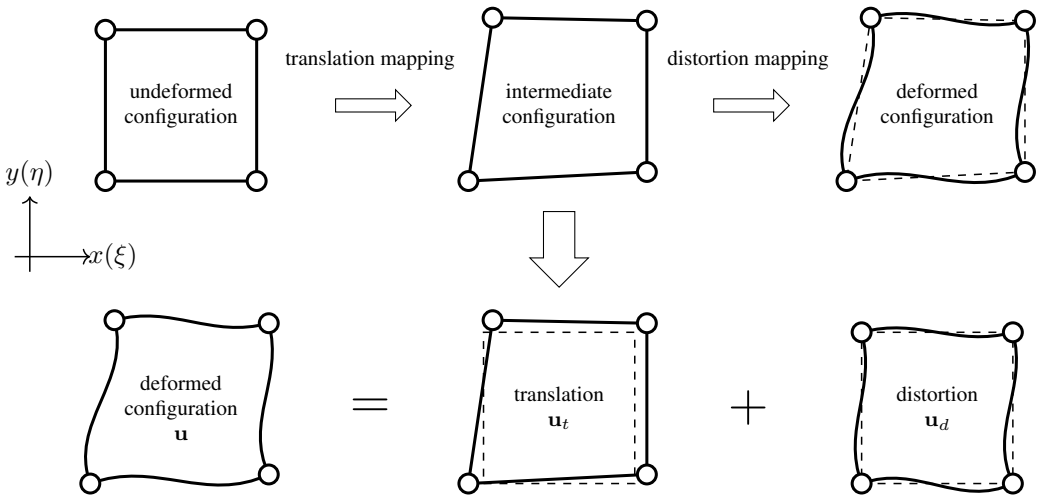

Figure 1: Deformation decomposition.

Another feature of GCMQ that is worth mentioning is the fully interpolated stress field which is complete up to second order. It also satisfies the stress equilibrium. Various stress patterns

could be described, some of which are shown in Fig. 2. Although such a stress field does not possess inter-element continuity, it is considered to be sufficient for elements without edge loadings.

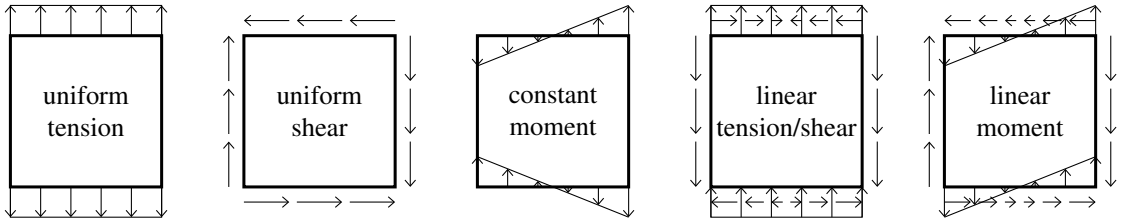

Figure 2: Stress patterns of selected terms.

For numerical integration, compared to other elements, more choices are provided in GCMQ. Three different schemes are proposed. They are:

1. GCMQ-I: five-point scheme, four at element edge centres, one at element centre.
2. GCMQ-L: nine-point Lobatto scheme, eight on edges, one at element centre.
3. GCMQ-G: nine-point Gauss scheme, all nine points located inside element.

All three schemes are tested in this paper. For different types of analysis, different schemes may be recommended due to their different performance and efficiency. Details are presented in the following sections.

3 MATERIAL MODELS

For linear analyses, an isotropic elastic material model is used. For idealised inelastic analyses, a bilinear isotropic hardening model with the J2 yield criterion and associative plasticity is adopted for the ease of obtaining a converged solution. The corresponding material parameters are chosen to be close to that of concrete.

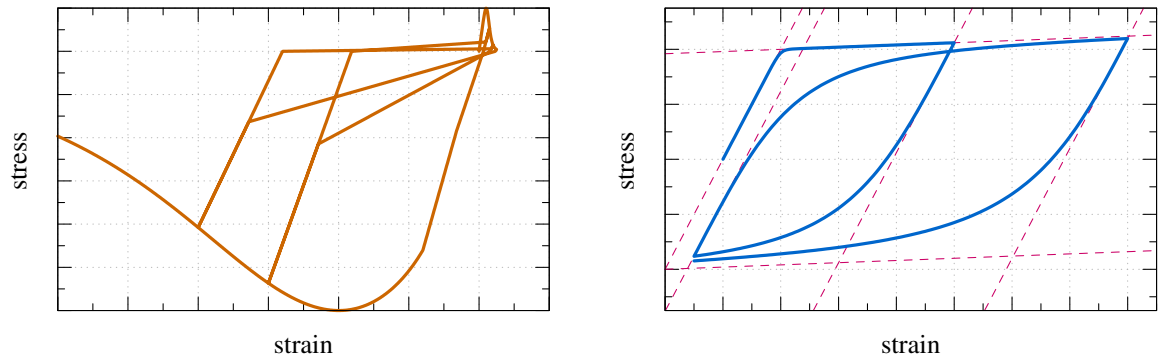

(a) concrete model (b) steel model

Figure 3: Schematic sketches of the material models used in analyses.

For a more realistic concrete model, a fix crack planar concrete model that incorporates a Rankine type square initial yield surface is used. The formulation resembles the one presented

by Crisfield and Wills [4]. Similar formulations can be seen elsewhere. For simplicity, no coupling effect between two crack directions are considered. For each direction, the uniaxial concrete model uses Tsai's equation [5] as the backbone and a simple linear hysteresis rule. An illustrative example is depicted in Fig. 3a. It shall be noted that the parameters are tweaked for a clearer plot and do not represent a real concrete behaviour. The shear response is assumed to be bilinear elastic with a shear retention factor to account for dowel action, aggregate locking, etc. Such a concrete model is simple and in most cases convergence can be achieved with little computational effect. Nevertheless, other more complex material models [6, 7] can also be used.

Reinforcement is implemented in a smeared approach. In this work, all reinforcements are assumed to be uniformly distributed and they do not necessarily represent the real rebar layout. An alternative could be the combination of both concentrated and smeared reinforcement. The Menegotto-Pinto steel model [8] is used to simulate the behaviour of reinforcement. A representative example is shown in Fig. 3b.

4 WALL EXAMPLES

Two different wall examples are presented for different purposes. A summary is shown in Table 1. For both examples, no vertical load is considered for simplicity and only horizontal point mass is applied. The Rayleigh damping model is used.

Table 1: Summary of wall examples.

	type	material	excitation	purpose
Example 1	cantilever	homogeneous	long impulse	performance baseline in both elastic and inelastic cases
Example 2	cantilever	reinforced concrete	El Centro (NS)	general performance with RC material

4.1 Example 1 — A cantilever beam

The first example is a simple cantilever wall with isotropic material models, which is illustrated in Fig. 4. A critical damping of $5\,\%$ is applied to the first two modes via Rayleigh

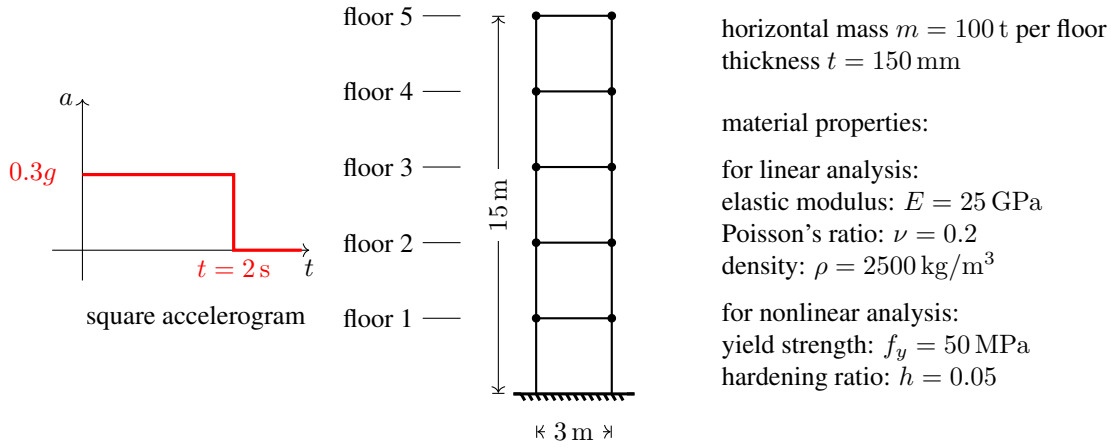

Figure 4: An idealised wall specimen

damping model. A long impulse with a constant acceleration of $0.3g$ is used as excitation with

the duration (2 s) twice the first period. The main purpose of such a choice is to suppress high frequency response as much as possible so that the comparison and analysis of results would become clearer.

4.1.1 Natural period

Before presenting natural frequencies/periods, various formulations of mass matrix $\mathbf{M}$ are first discussed. Several approaches are available:

1. Full rank consistent formulation derived from nodal displacement shape function,
2. Diagonalised (lumped) consistent mass matrix.The off diagonal terms are omitted while the main diagonal terms are scaled,
3. Rank deficient consistent mass matrix with drilling components omitted. This mass matrix is identical to the one of Q4, with additional zero rows and columns at drilling DoFs, and
4. Lumped version of the rank deficient consistent mass matrix.

The modal analysis is performed with the above four mass matrices. The first four frequencies are listed in Table 2. Numerical investigations show neither two lumped formulations nor two consistent matrices show significant difference. Hence only two categories are shown in the table. With a coarse mesh grid, GCMQ is able to predict the periods of lower modes with good accuracy, this could be validated by the result of a beam model. Compared to beam and Q4 elements, GCMQ is softer and produces smaller frequencies. Furthermore, consistent formulations give slightly higher frequencies than lumped versions. Also, since Gauss scheme has a higher integration accuracy, GCMQ-G predicts a more accurate fourth frequency than that of the other two schemes. In conclusion, all four mass formulations could be used in practical analysis. The lumped versions can be adopted for a smaller matrix storage.

Table 2: first four natural frequencies

	1×5 coarse mesh					4×20 fine mesh			
f_1 (cycles/second)	GCMQ-I	GCMQ-L	GCMQ-G	Q4	Beam	GCMQ-I	GCMQ-L	GCMQ-G	Q4
consistent	1.02	1.02	1.02	1.22	1.03	1.01	1.01	1.01	1.03
lumped	1.02	1.02	1.02			1.01	1.01	1.01	
f_2	GCMQ-I	GCMQ-L	GCMQ-G	Q4	Beam	GCMQ-I	GCMQ-L	GCMQ-G	Q4
consistent	6.16	6.16	6.16	7.11	6.57	5.83	5.83	5.83	5.93
lumped	6.13	6.13	6.13			5.83	5.83	5.82	
f_3	GCMQ-I	GCMQ-L	GCMQ-G	Q4	Beam	GCMQ-I	GCMQ-L	GCMQ-G	Q4
consistent	15.92	15.92	15.92	17.50	18.59	14.22	14.22	14.21	14.51
lumped	15.79	15.79	15.79			14.21	14.21	14.20	
f_4	GCMQ-I	GCMQ-L	GCMQ-G	Q4	Beam	GCMQ-I	GCMQ-L	GCMQ-G	Q4
consistent	27.13	27.12	24.74	28.39	35.94	22.97	22.96	22.94	23.47
lumped	26.83	26.83	24.59			22.95	22.95	22.93	

4.1.2 Dynamic analysis

The consistent mass matrix is used in the following examples. Fig. 5 shows the linear displacement history of Example 1 using linear elastic material model. According to Fig. 5a,

GCMQ and beam models give very close response. However, with the same mesh grid, Q4 model is stiffer and results in quite a different response. It can be spotted that with mesh refinement, Q4 model can converge to the same solution to that of GCMQ and beam models. It could be concluded that GCMQ element could be used with very coarse mesh grids to predict accurate response.

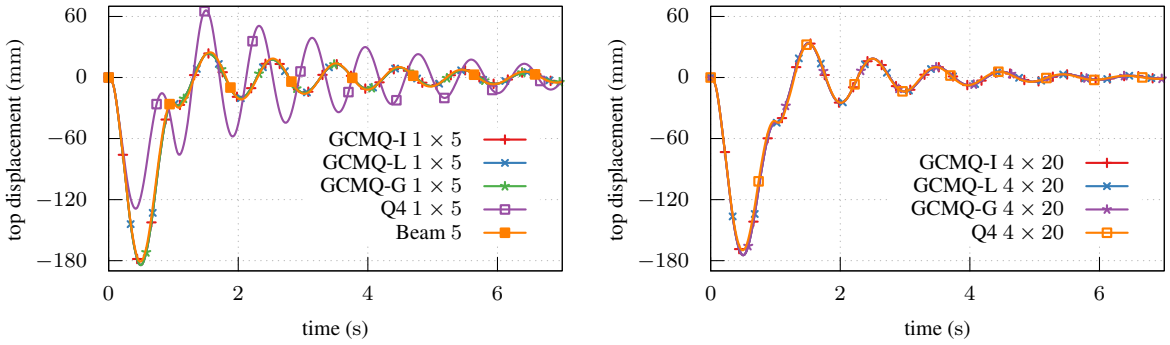

(a) coarse mesh (b) mesh refinement

Figure 5: linear displacement history due to long impulse

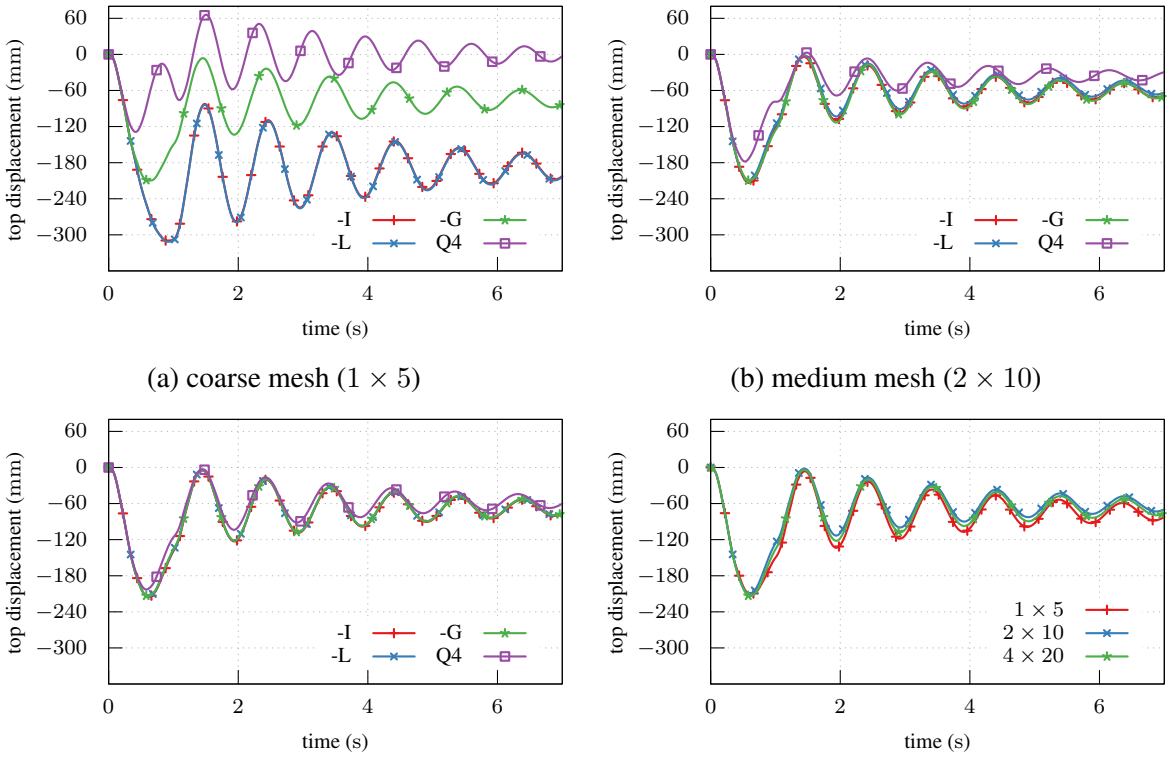

(a) coarse mesh (1 × 5) (b) medium mesh (2 × 10)

(c) fine mesh (4 × 20) (d) mesh refinement of GCMQ-G

Figure 6: nonlinear displacement history due to long impulse

The nonlinear displacement history is shown in Fig. 6. In this particular example, the model using five Q4 elements (with four quadrature points well inside the element) cannot develop any plasticity. Hence, as can be seen in Fig. 6a, there is no residual displacement generated by Q4

model. In the meantime, the GCMQ elements produce distinctive response. Due to that most integration points are located on element edges, GCMQ-I and GCMQ-L exaggerate plasticity development. As a result, the peak and residual displacements are large than that of GCMQ-G. However, with a 2×10 or denser mesh grid, the difference between three versions is negligible. Another important fact can be observed from Fig. 6d, that is, for inelastic applications, GCMQ-G has a very low initial error bound and the difference between three mesh grids are exceptionally small. With 5 elements, GCMQ-G could predict more accurate result than using 80 Q4 elements. It indicates that GCMQ-G could be used in practical simulations with the most coarse mesh grid.

4.2 Example 2 — A RC shear wall

This wall model is taken from Taylor's work [9] and is depicted in Fig. 7. The first two natural periods computed are $2.49\,\mathrm{s}$ and $0.45\,\mathrm{s}$, which are close to the values ($2.46\,\mathrm{s}$ and $0.42\,\mathrm{s}$) reported in the original literature. Taylor [9] adopted $10\,\%$ damping on the first two modes. It shall be emphasised that such a value is considered too large for RC shear walls. However, given that the Rayleigh damping model has its own issues in inelastic analysis [10, 11], here the authors have no intention of matching the damping ratio with a more realistic value. Meanwhile, the gross reinforcement ratio can be computed as $8\,\%$ for the bottom four floors. This value appears unrealistically large for such a wall section and may violate modern design practice. But as an illustrative example, no correction would be made, so that comparison with the original literature is possible. Another issue may be clarified is the relatively low strength of both concrete and steel, $21\,\mathrm{MPa}$ and $280\,\mathrm{MPa}$ respectively. These values are typical of 1970s. Nowadays, higher performance material would be used. The total mass w of the system is $56\,\mathrm{MN}$. The model is analysed with ten GCMQ-G elements (one per storey).

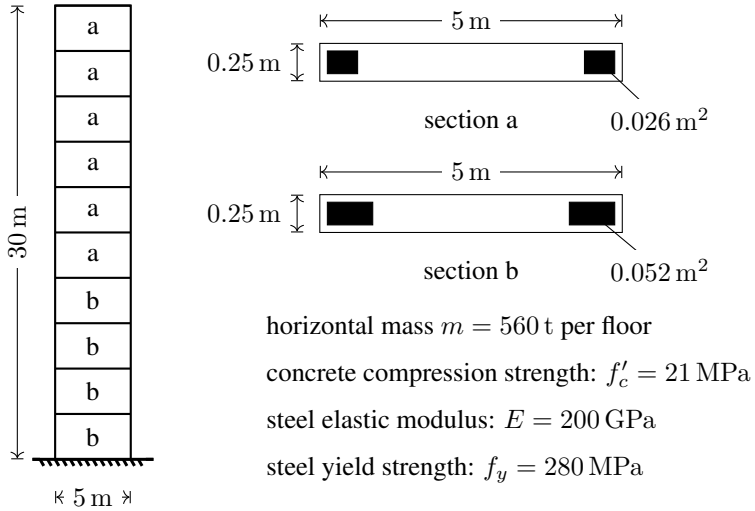

Figure 7: A reinforced concrete shear wall specimen

Fig. 8 shows the nonlinear displacement history for all floors. Clearly, it is dominated by the first vibration mode. The asymmetric behaviour of concrete leads to a one-sided displacement dominated history, which significantly differs from the linear response. The maximum displacement predicted is around $300\,\mathrm{mm}$, which is equivalent to $1\,\%$ drift. The residual drift is around $0.1\,\%$ due to the presence of a large amount of reinforcement.

The roof displacement against base shear/moment is plotted in Fig. 9. Although simple hysteresis rules are defined in concrete and steel material models, no explicit pattern can be found to relate material behaviour with global response of structure. This is because the roof displacement is mainly affected by the first vibration mode while the base shear has contributions from all modes of free vibration.

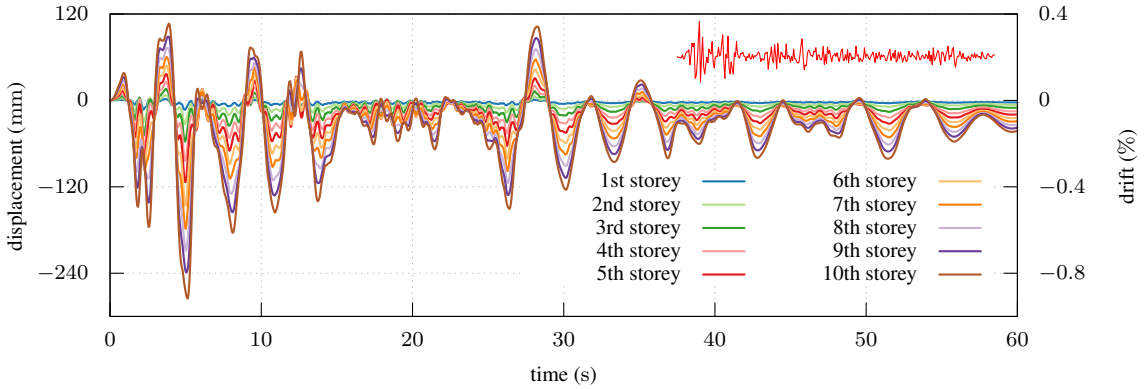

Figure 8: Nonlinear displacement history of Example 2.

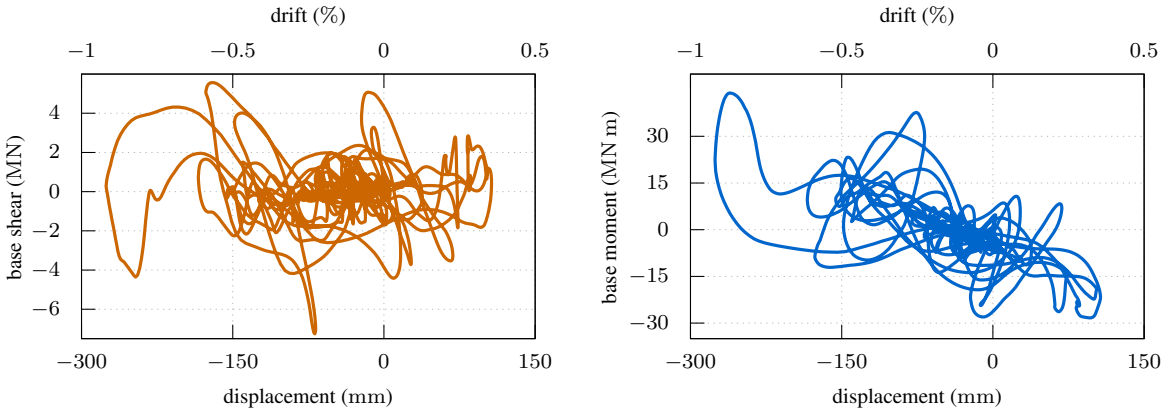

(a) base shear (b) base moment

Figure 9: Nonlinear hysteresis of Example 2.

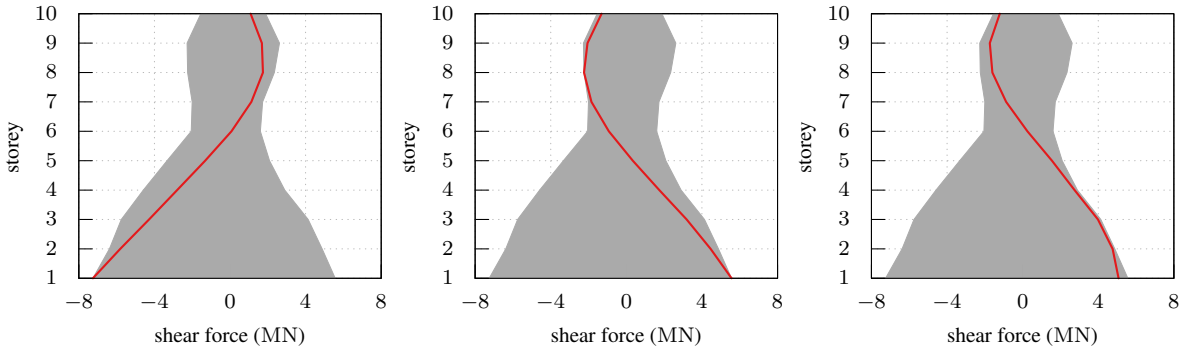

(a) $t_1 = 2.173\,\mathrm{s}$ (b) $t_2 = 2.634\,\mathrm{s}$ (c) $t_3 = 12.285\,\mathrm{s}$

Figure 10: Distribution of shear forces with envelops of Example 2.

The distributions of storey shear forces at three distinct time points are plotted in Fig. 10 with their envelopes. Between sixth to seventh floor, shear force changes its sign, indicating that the maximum moment occurs here. Fig. 11 and Fig. 12 show the absolute acceleration and shear force history respectively for each storey. From the plots, it is clear to see the eighth storey experiences significantly smaller acceleration, indicating that the second mode is dominant in terms of acceleration.

5 CONCLUDING REMARKS

This paper presents evaluations of GCMQ in nonlinear dynamic analysis. As a guideline, the following recommendations are made for the use of GCMQ.

- For linear elastic analysis, all three versions of GCMQ converge to the same response with the most coarse mesh configuration (one element per storey). Since GCMQ-I could reduce the analysis time by about $30\,\%$, it is thus recommended.
- For inelastic analysis, GCMQ-G has a lower initial error bound, which results in an excellent response with the coarse mesh grid.
- For any mesh grids denser than one element per storey, the difference among all three versions of GCMQ is negligible. In such a case, to improve efficiency, GCMQ-I is recommended. Nevertheless, material objectivity shall be handled carefully to obtain mesh independent results.

The novel GCMQ element shows great potential in terms of coarse mesh accuracy. As it is formulated based on continuum mechanics theories, the convergence is guaranteed with mesh refinement. Compared to other wall elements, GCMQ is considered a better analysis tool for future simulations of wall structures. The GCMQ element has been implemented in `suanPan` [12], which is available online[1].

ACKNOWLEDGEMENT

The authors would like to acknowledge the financial support with grant number E6953 provided by the Earthquake Commission (EQC)[2].

References

[1] A. Vulcano, V. V. Bertero and V. Colotti. Analytical modeling of R/C structural walls. In *Proceedings of Ninth World Conference on Earthquake Engineering*, 1988.

[2] K. Kolozvari. *Analytical Modeling of Cyclic Shear-flexure Interaction in Reinforced Concrete Structural Walls*. phdthesis, University of California, Los Angeles, 2013.

[3] T. L. Chang, C.-L. Lee, A. J. Carr, R. P. Dhakal and S. Pampanin. A new drilling quadrilateral membrane element with high coarse-mesh accuracy using a modified Hu-Washizu principle. *International Journal for Numerical Methods in Engineering*, mar 2019. doi: 10.1002/nme.6066.

[1] https://github.com/TLCFEM/suanPan

[2] https://www.eqc.govt.nz/

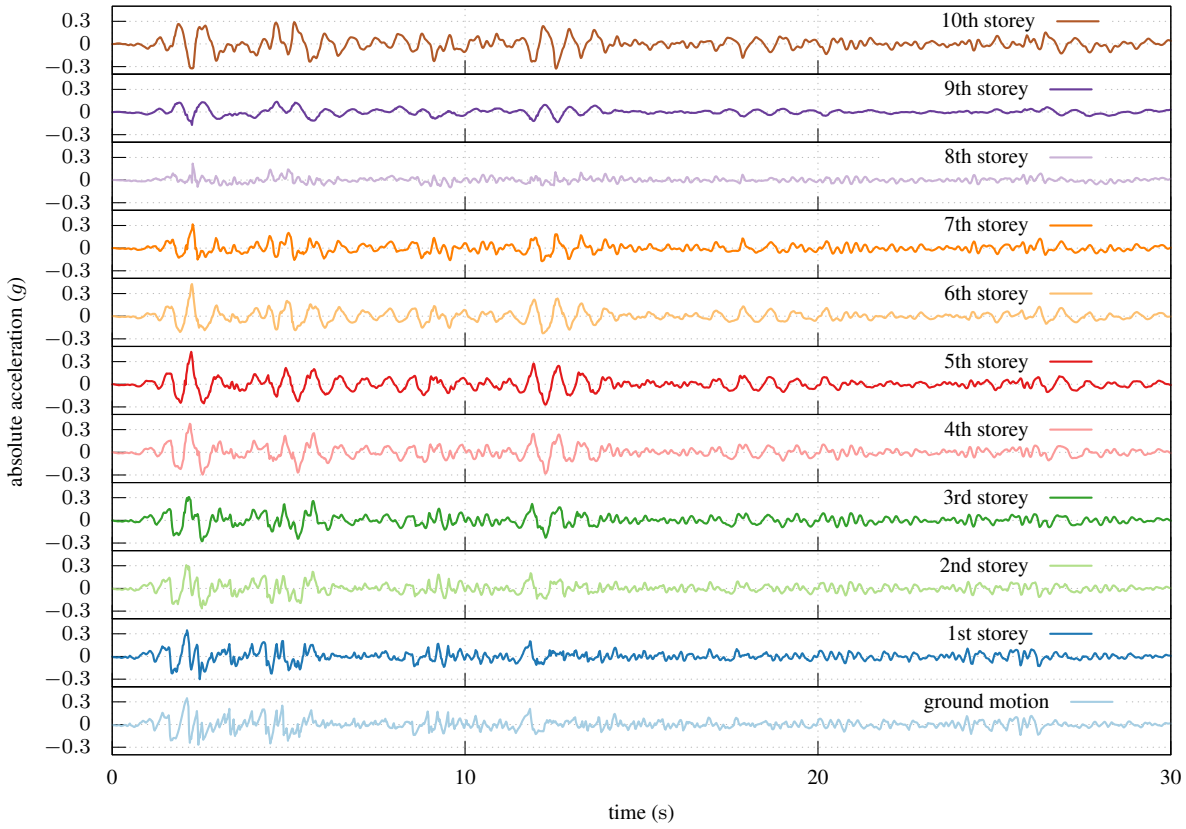

Figure 11: Nonlinear acceleration history of Example 2.

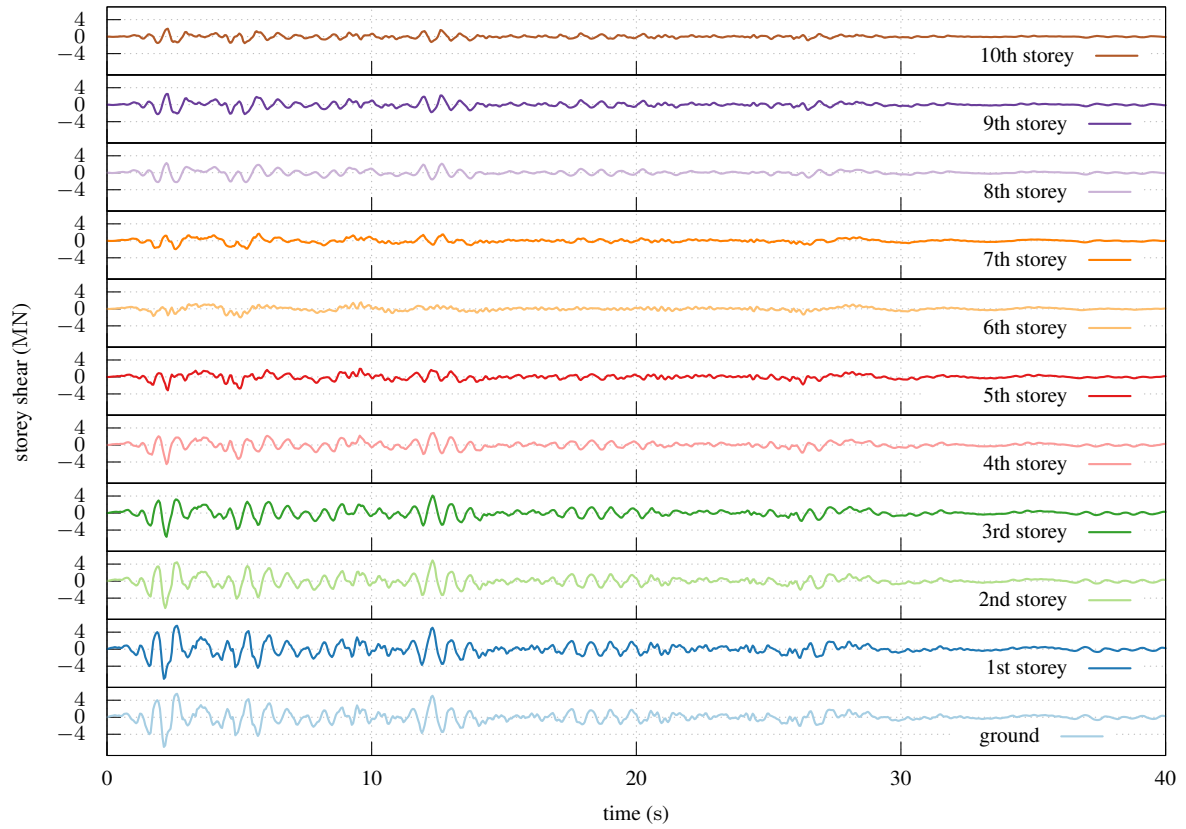

Figure 12: Nonlinear shear history of Example 2.

[4] M. A. Crisfield and J. Wills. Analysis of R/C panels using different concrete models. *Journal of Engineering Mechanics*, **115**(3), 578–597, Mar. 1989. doi:10.1061/(asce)0733-9399(1989)115:3(578).

[5] W. T. Tsai. Uniaxial compressional stress-strain relation of concrete. *Journal of Structural Engineering*, **114**(9), 2133–2136, Sep. 1988. doi:10.1061/(asce)0733-9445(1988)114:9(2133).

[6] J. Lee and G. L. Fenves. Plastic-damage model for cyclic loading of concrete structures. *Journal of Engineering Mechanics*, **124**(8), 892–900, Aug. 1998. doi:10.1061/(asce)0733-9399(1998)124:8(892).

[7] P. Grassl, D. Xenos, U. Nyström, R. Rempling and K. Gylltoft. CDPM2: A damage-plasticity approach to modelling the failure of concrete. *International Journal of Solids and Structures*, **50**(24), 3805–3816, Nov. 2013. doi:10.1016/j.ijsolstr.2013.07.008.

[8] M. Menegotto and P. E. Pinto. Method of analysis for cyclically loaded R.C. plane frames including changes in geometry and non-elastic behaviour of elements under combined normal force and bending, 1973. doi:10.5169/seals-13741.

[9] R. G. Taylor. *The Nonlinear Seismic Resposne of Tall Shear Wall Structures*. phdthesis, University of Canterbury, 1977.

[10] A. J. Carr. Damping models for inelastic analysis. In *Asia-Pacific Vibration Conference*, 1997.

[11] A. K. Chopra and F. McKenna. Modeling viscous damping in nonlinear response history analysis of buildings for earthquake excitation. *Earthquake Engineering & Structural Dynamics*, **45**(2), 193–211, Sep. 2015. doi:10.1002/eqe.2622.

[12] T. L. Chang. suanPan — an open source, parallel and heterogeneous finite element analysis framework, Jun. 2018. doi:10.5281/zenodo.2556012.

COMPDYN 2019
7th ECCOMAS Thematic Conference on
Computational Methods in Structural Dynamics and Earthquake Engineering
M. Papadrakakis, M. Fragiadakis (eds.)
Crete, Greece, 24-26 June 2019

A DUAL FORMULATION OF CYCLIC SYMMETRY: APPLICATION IN FREE VIBRATION ANALYSIS

Guilherme Jenovencio[1], **Daniel J. Rixen**[1]

[1] Technische Universitaet Muenchen, Chair of Applied Mechanics
Boltzmannstrasse 17 85748 Garching

e-mail: {jenovencio,rixen}@tum.de

Keywords: Cyclic Symmetry, Dual Formulation, Free Vibration, Projected Arnoldi Algorithm, Preconditioner.

Abstract. *In this work, the cyclic symmetry boundary condition between sectors of a rotationally periodic structure are reformulated and the compatibility condition is imposed by means of Lagrange multipliers. In the augmented system, the constraint matrix carries the dependence on the nodal diameters (ND) whereas stiffness and mass matrices do not vary with ND. The Dual assembly formulation is exploited in the computation of eigenvectors and eigenvalues using a Preconditioned Projected Arnoldi Algorithm. The complex constraint matrix is used to build a projection operator, which imposes the compatibility constraint between the left and right side of the periodic geometry. Because the complex constraint matrix has orthogonal rows, the projector operator is easily assembled without the need of matrix inversion. The explicit factorization of the projected stiffness matrix is not required since Preconditioned Conjugated Gradient algorithm is used to solve the linear system during the inverse Arnoldi iteration step. Consequently, all ND share the same preconditioner reducing the global cost of eigenpairs computation, especially when multiple ND solutions are required. Five different preconditioners are tested to evaluate the numerical scalability of the linear solution: Identity, Projected Incomplete Chosleky, Projected Cholesky, Incomplete Cholesky and Cholesky. The Preconditioned Projected Arnoldi Algorithm is implemented in Python using the Scipy library which provides a wrapper for the Implicity Restarted Arnoldi method implemented in ARPACK. The projection and preconditioner steps are carried-out by Scipy sparse linear operator. The method is applied in 2D and 3D finite element models. The preconditioners studied can dramatically reduce the number of iterations when compared to CG without preconditioning. The full Cholesky preconditioner is on average 8 times faster than the identity precondicioner in the 2D, whereas it is approximately 16 faster in the 3D case. The factorizing is performed only once, and its computational cost can be divided among the different NDs, which makes the method especially advantageous for geometries with a large number of sectors.*

1 INTRODUCTION

Free vibration analysis plays an important role in understanding the dynamics of structures. It provides the natural frequencies which must be identified in order to avoid catastrophic failures due to resonances. Moreover, eigenmodes can be used to reduce the number of degrees of freedom by using Reduced Order Models (ROM) such as Craig-Bampton [1], Dual-Craig-Bampton [2], Rubin [3], among others. Despite its advantages, full eigenanalysis is very costly, which means that in many cases only the modes related to the lowest frequencies are relevant for practical problems. Therefore, Lanczos [4], and implicit restarted Arnoldi algorithms [5] are often used as eigensolvers due to their efficiency. The major cost of the algorithms mentioned lies in the inverse iteration, where the solution of a linear system is required.

When structures such as turbines, propellers, and gears are analysed, the property of rotational periodic symmetry is often utilized, reducing the computational cost of the linear system as well as the memory required to store the system matrices. Figure 1 shows a cyclic structure with the highlighted reference sector used for analyzing the whole geometry. In such cases, a Discrete Fourier Transform is applied in the equation of motion and in the compatibility condition between neighbors, which reformulates the problem in terms of harmonic indices. The speed-up is achieved by means of a harmonic decoupling among sectors when imposing the periodic condition by eliminating the constrained degrees of freedom, namely, primal assembly. In the work developed in[6], the cyclic symmetry is imposed by complex constraints relating the left to the right side. Considering a periodic structure composed of N sectors, which has θ as the sector angle, the classical cyclic boundary condition creates approximately $N/2$ different systems of equation to be solved independently. The number of variables is not changed by the harmonic transformation, because the transformed system has complex degrees of freedom. Therefore, the cyclic symmetry should not be understood as a reduction technique, since it is only a transformation operation. However, the decoupling provided by the harmonic decomposition results in the ability of solving independent problems for a given set of harmonic indices, also known as Nodal Diameter (ND). If cyclic symmetry is considered for ROM, not only a subset of modes must be selected but also a subset of nodal diameters. This is usually done by analyzing the possible excitations, using the Campbell diagram or SAFE diagram, see [7].

In this paper, the primal and dual assembly of cyclic constraints are presented using a substructuring framework and applied to the computation of the eigen-pairs of a cyclic structure. In the dual formulation, the cyclic constraints are described with a complex constraint matrix thereby rendering the system matrices, namely stiffness, and mass, unaffected. Due to the hybrid nature of the eigen-value problem in the dual formulation (displacements and Lagrange multipliers), the conventional eigen-solvers are not suitable. Therefore, a modified version of Projected Arnoldi algorithm is employed to efficiently solve the dual cyclic formulation. The novel approach introduces a preconditioning step in the inverse iteration of the Arnoldi process, which uses the reference sector without constraints. Five different preconditioners are tested to evaluate the numerical scalability of the linear solution, namely: Identity, Projected Incomplete Chosleky, Projected Cholesky, Incomplete Cholesky and Cholesky.

In the remaining sections the classical cyclic symmetry is formally introduced and the dual formulation is presented. The projected Arnoldi method is described, eigen-analysis is performed using the complex cyclic constraints and its projection operator. Three different Finite element test-cases are presented in order to show the application of the new formulation.

2 Classical Cyclic Symmetry Formulation

In this section, the classical theory behind cyclic symmetry boundary condition is summarized. Let us consider a geometry composed of N identical sectors, as shown in the Figure 1. If each sector has its own local coordinate system and no mistuning is considered, the equation of motion together with the compatibility constraint can be written as:

$$\begin{aligned} M\ddot{u}^s + Ku^s &= f^s + g^s \qquad s = 1, ..., N \\ Tu_l^s &= u_r^{s+1} \\ Tg_l^s &= -g_r^{s+1} \end{aligned} \tag{1}$$

where M and K are the mass and stiffness matrices respectively, f is the external force vector, g is the connecting forces among neighbors, and superscript s represents the index of a sector. The second expression in (1) represents the compatibility condition among sectors, where T is a rotation matrix, and the subscripts l and r represent the interface dofs of the left and right respectively.

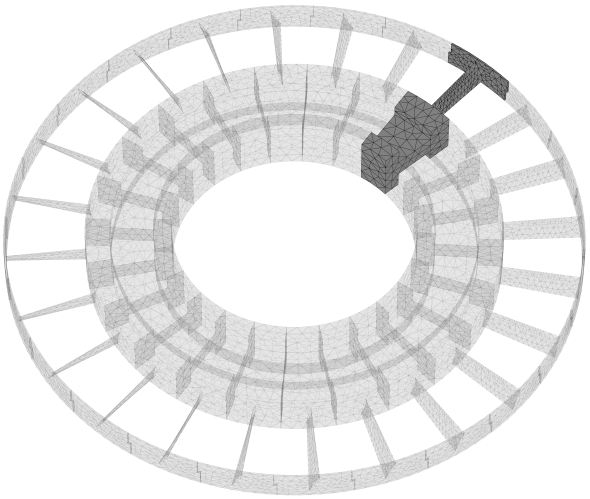

Figure 1: Cyclic Structure and the highlighted reference sector.

It is important to notice that given the choice of local coordinate system, the stiffness and mass matrices are the same for all sectors, however the transformation matrix T is required to define a proper compatibility condition. Applying a Discrete Fourier Transform in space $\{\mathcal{F} : u^s \rightarrow u^n \quad | \quad \sum_{s=1}^{N} u^s e^{-jn\theta s}\}$ in (1) and rewriting the displacement solution, interface force and external forces in terms of Fourier Series:

$$\begin{aligned} u^s &= \frac{1}{\bar{N}} \sum_{n=0}^{\bar{N}} u^n e^{jn\theta s} \\ g^s &= \frac{1}{\bar{N}} \sum_{n=0}^{\bar{N}} g^n e^{jn\theta s} \\ f^s &= \frac{1}{\bar{N}} \sum_{n=0}^{\bar{N}} f^n e^{jn\theta s} \end{aligned} \tag{2}$$

where $j = \sqrt{-1}$ is the imaginary unit, $\theta = \frac{2\pi}{N}$ is the sector angle, n is the nodal diameter index, and $\bar{N}$ is the largest nodal diameter index such that:

$$\begin{aligned} \bar{N} &= \frac{N}{2} - 1 \quad \text{if } N \text{ is even} \\ \bar{N} &= \frac{N-1}{2} \quad \text{if } N \text{ is odd} \end{aligned} \tag{3}$$

equation (1) becomes (4).

$$\begin{aligned} M\ddot{u}^n + Ku^n &= f^n + g^n \qquad n = 1, ..., \bar{N} \\ Tu_l^n &= u_r^{n+1} = u_r^n e^{jn\theta} \\ Tg_l^n &= -g_r^{n+1} = -g_r^n e^{jn\theta} \end{aligned} \tag{4}$$

If a permutation matrix is applied in the displacement degrees of freedom of a sector such that one defines a block vector $u = [u_r, u_l, u_i]$, where the indices r, l and i are the right, left and interior dofs respectively, equation (4) can be rewritten using block matrices:

$$\begin{bmatrix} M_{rr} & M_{rl} & M_{ri} \\ M_{lr} & M_{ll} & M_{li} \\ M_{ir} & M_{il} & M_{ii} \end{bmatrix} \begin{bmatrix} \ddot{u}_r^n \\ \ddot{u}_l^n \\ \ddot{u}_i^n \end{bmatrix} + \begin{bmatrix} K_{rr} & K_{rl} & K_{ri} \\ K_{lr} & K_{ll} & K_{li} \\ K_{ir} & K_{il} & K_{ii} \end{bmatrix} \begin{bmatrix} u_r^n \\ u_l^n \\ u_i^n \end{bmatrix} = \begin{bmatrix} f_r^n \\ f_l^n \\ f_i^n \end{bmatrix} + \begin{bmatrix} g_r^n \\ g_l^n \\ g_i^n \end{bmatrix} \tag{5}$$

Classically, the left degrees of freedom are removed by replacing the harmonic compatibility presented in equation (4) into equation (5):

$$\begin{bmatrix} M_{rr} + TM_{ll}T^T + e^{jn\theta}M_{rl}T^T + e^{-jn\theta}TM_{lr} & M_{ri} + e^{-jn\theta}TM_{li} \\ M_{ir} + e^{jn\theta}M_{il}T^T & M_{ii} \end{bmatrix} \begin{bmatrix} \ddot{u}_r^n \\ \ddot{u}_i^n \end{bmatrix} + \begin{bmatrix} K_{rr} + TK_{ll}T^T + e^{jn\theta}K_{rl}T^T + e^{-jn\theta}TK_{lr} & K_{ri} + e^{-jn\theta}TK_{li} \\ K_{ir} + e^{jn\theta}K_{il}T^T & K_{ii} \end{bmatrix} \begin{bmatrix} u_r^n \\ u_i^n \end{bmatrix} = \begin{bmatrix} f_r^n + e^{-jn\theta}Tf_l^n \\ f_i \end{bmatrix} \tag{6}$$

Equation (6) is the constrained equation of motion, which contains only the right and interior degrees of freedom. Using the property $TT^T = I$, the elimination process can be carried out by defining a complex matrix L_n which lies in the null space of the constraints.

$$L_n = \begin{bmatrix} I & 0 \\ e^{jn\theta}T^T & 0 \\ 0 & I \end{bmatrix} \tag{7}$$

Therefore, the primal assembly of cyclic symmetry can be written using a substructuring framework as presented in [8]:

$$M_n\ddot{u}_{\text{primal}}^n + K_n u_{\text{primal}}^n = L_n^H f^n \qquad n = 1, ..., \bar{N} \tag{8}$$

where $M_n \equiv (L_n^H M L_n)$ and $K_n \equiv (L_n^H K L_n)$, and the superscript H represents the adjoint matrix. It can be readily verified that (8) leads to the form (6).

For free vibration problems, one sets $f^n = 0$ and $u_{\text{primal}}^n = \phi_{\text{primal}}^n e^{\omega t}$, which leads to the generalized eigenvalue problem:

$$[K_n - \omega^2 M_n]\phi_{\text{primal}}^n = 0 \qquad n = 1, ..., \bar{N} \tag{9}$$

where the subscript n represents the dependency on the nodal diameter, ϕ^n_{primal} is a complex eigenvector, and K_n and M_n are Hermitian matrices. If the full set of eigenvector is required, all nodal diameter indices in (9) must be evaluated.

3 Dual Cyclic Symmetry Formulation

The classical treatment of cyclic symmetry formulation modifies the system operator, namely stiffness and mass matrices, by means of the primal assembly operator L_n as shown above. This results in a set of unique variables defined as u_{primal}. In this section, the dual formulation of (4) is presented. First, let us define two Boolean operators to extract 'left' and 'right' dofs as classical FETI methods [9].

$$\begin{aligned} u_l &= B_l u \\ u_r &= B_r u \end{aligned} \tag{10}$$

For the re-arranged displacement vector $u = [u_r, u_l, u_i]$ the Boolean operators are defined by $B_r = [I\ 0\ 0]$ and $B_l = [0\ I\ 0]$. Rewritting the compatibility constraint in (4) by using the Boolean definition in (10):

$$C_n u = [B_r - e^{-jn\theta} T B_l] u = 0 \tag{11}$$

where C_n is a linear complex cyclic constraint operator. It is easy to show that $L_n^H C_n^H = 0$. Therefore, a Lagrange multiplier must be introduced in the equation of motion in order to satisfy the compatibility constraint, such that:

$$\begin{aligned} M\ddot{u}^n + Ku^n &= f^n - C_n^H \lambda^n \qquad n = 1, ..., \bar{N} \\ C_n u^n &= 0 \end{aligned} \tag{12}$$

Or in matrix notation:

$$\begin{bmatrix} M & 0 \\ 0 & 0 \end{bmatrix} \begin{bmatrix} \ddot{u}^n \\ \lambda^n \end{bmatrix} + \begin{bmatrix} K & C_n^H \\ C_n & 0 \end{bmatrix} \begin{bmatrix} u^n \\ \lambda^n \end{bmatrix} = \begin{bmatrix} f^n \\ 0 \end{bmatrix} \qquad n = 1, ..., \bar{N} \tag{13}$$

where C_n^H is the adjoint matrix of the cyclic constraint operator.

The above expression is the dual assembly formulation for cyclic symmetry boundary condition. This equation contains not only displacement dofs but also Lagrange multipliers to enforced continuity among sectors. Clearly, this results in a system which contains more unknowns than the formulation in (8), however the stiffness and mass matrices do not depend on the nodal diameter n. Therefore, this property can be exploited using dual Schur complement solvers such as described in [10]. A similar technique for cyclic problems was already applied in the work developed in [11]. However, in [11] the Lagrange multipliers are connected to sectors as substructures, whereas in this work, λ^n is defined in the harmonic space. The novel approach can be seen as a decoupling of the interface displacement and forces generated among neighboring sectors. Besides that, the formulation gives the explicit harmonic gap, namely $C_n u^n$, which can be useful when the interface connection between sector is nonlinear.

3.1 Projected Arnoldi for Cyclic Symmetry Modal Analysis

The free vibration analysis of the system (13) results in the following hybrid generalized eigenvalue problem:

$$\begin{bmatrix} K & C_n^H \\ C_n & 0 \end{bmatrix} \begin{bmatrix} \phi'_u \\ \phi_\lambda \end{bmatrix} = \omega^2 \begin{bmatrix} M & 0 \\ 0 & 0 \end{bmatrix} \begin{bmatrix} \phi'_{u_1} \\ \phi_\lambda \end{bmatrix} \tag{14}$$

The dimension of the above problem is n_c+n_{dofs}, where n_c is the number of cyclic symmetry constraints, and n_{dofs} is the total number of dofs in the reference sector. The eigenpair solutions $(\omega_i, [\phi'_{u_i}, \phi_{\lambda_i}])$ have the form:

$$\left(\omega_1^u, \begin{bmatrix} \phi'_{u_1} \\ \phi_{\lambda_1} \end{bmatrix}\right), ..., \left(\omega_{n_{dofs}}^u, \begin{bmatrix} \phi'_{u_{n_{dofs}}} \\ \phi_{\lambda_{n_{dofs}}} \end{bmatrix}\right), \left(+\infty, \begin{bmatrix} 0 \\ \phi_{\lambda_{(n_{dofs}+1)}} \end{bmatrix}\right), ..., \left(+\infty, \begin{bmatrix} 0 \\ \phi_{\lambda_{(n_{dofs}+nc)}} \end{bmatrix}\right) \tag{15}$$

Note that, the eigenvector ϕ'_{u_i} lies in the null space of the complex cyclic symmetry constraint $C_n\phi'_{u_i} = 0$. In [12] some techniques are presented to solve the constrained eigenvalue problem presented in (14) , but it does not explore the structure of the problem to accelerate the inverse iteration of the eigen-solver. In order to solve the eigenvalue problem efficiently and profit from the independence of stiffness and mass matrices of the nodal diameter n, a constrained Krylov subspace is built based on the complex cyclic constraint operator, see [13]. The Krylov matrix for the generalized eigenvalue problem without constraints is defined as:

$$V_m = [b,\ Db,\ D^2b,\ ...\ ,\ D^{m-1}b] \tag{16}$$

where $D \equiv (K-\sigma M)^{-1}M$, which is the inverse shift operator such that $D : \mathbb{R}^n \to \mathbb{R}^n$, $b \in \mathbb{R}^n$. When a constraint $h(b) = 0$ such that $h : \mathbb{R}^n \to \mathbb{R}^{n_c}$ is defined, a Krylov basis vector b' must lie in the set of admissible vectors, mathematically $\Omega = \{b' \in \mathbb{R}^n \mid h(b') = 0\}$ as represented in Figure 2. Thus, the constrained Krylov matrix has the form:

$$V_m^c = [b',\ (Db')',\ (D^2b')',\ ...\ ,\ (D^{m-1}b')'] \tag{17}$$

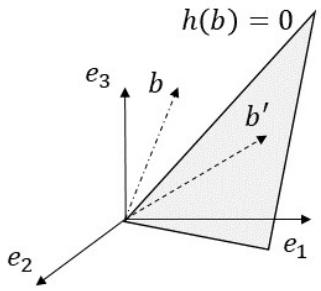

Figure 2: Vectors b and b' to build constrained Krylov subspace.

In the case of cyclic symmetry, one has a linear constraint, defined by $C_nu = 0$. One can write a projection operation P_n into the $Null(C_n)$ such that $P_n : b \to b'$, where the constraint $C_nb' = 0$ always holds. The projection matrix is explicitly written as:

$$P_n = I - C_n^H(C_nC_n^H)^{-1}C_n \tag{18}$$

where the subscript n refers to the nodal diameter dependency in the constraint matrix C_n. It is easy to show that $(C_n C_n^H)^{-1} = \frac{1}{2} I$, therefore the projection matrix can be written without matrix inversion as shown below:

$$P_n = \begin{bmatrix} I & 0 & 0 \\ 0 & I & 0 \\ 0 & 0 & I \end{bmatrix} - \frac{1}{2} \begin{bmatrix} I & -e^{-jn\theta} T & 0 \\ -e^{jn\theta} T^T & I & 0 \\ 0 & 0 & 0 \end{bmatrix} \tag{19}$$

The generalized constrained eigenvalue problem (14) can be rewritten as:

$$K\phi'_u + C_n^H \phi_\lambda = \omega^2 M \phi'_u \tag{20}$$

where ϕ'_u is a vector which respects the cyclic symmetry constraint. If one projects equation (20) in the feasible space using P_n^H and uses the relation $\phi'_u = P_n \phi_u$ one finally derives the projected eigenvalue problem:

$$P_n^H K P_n \phi_u = \omega^2 P_n^H M P_n \phi_u \tag{21}$$

where $\phi_u \in R^n$. Therefore a projected Arnoldi algorithm can be used to build the constrained orthonormal Krylov bases vectors. The projected Arnoldi method is exploited in [14] for updating eigenvalues in nonlinear dynamic problems. The procedure is summarized in Algorithm 1.

Algorithm 1 Projected Arnoldi Iteration

• **Parameters:** K, M, P_n and n_{int}.

1: **Initialization**
Compute $M_n^P = P_n^H M P_n$ and $K_n^P = P_n^H K P_n$
Start with an arbitrary vector ϕ_u^0 and $\beta_0 = 0$

2: **First step iteration**
Compute a projected unitary vector $v_n^1 = \frac{M_n^P \phi_u^0}{||\phi_u^0||_{M_n^P}}$
Solve the static-like problem $K_n^P \hat{\phi}_u^1 = v_n^1$
Compute $\alpha_1 = \hat{\phi}_u^{1T} v_n^1$
Compute a new orthogonal constrained Krylov vector ${\phi_u}^1 = \hat{\phi}_u^1 - \alpha^1 v_n^1$

3: **For** $j = 2, ..., n_{int}$
compute $\beta_j = ||\phi_u^{(j-1)}||_{M_n^P}$
if $\beta_j \neq 0$ then compute $v_n^j = M_n^P \phi_u^{(j-1)} / \beta_j$
Solve the static like problem $K_n^P \hat{\phi}_u^j = v_n^j$
Compute $\alpha_j = \hat{\phi}_u^{jT} v_n^j$
Compute a new constrained Krylov vector $\phi^{j+1} = \hat{\phi}_u^j - \alpha^j v_n^j - \beta_j v_n^{(j-1)}$

The bottleneck of Algorithm (1) is the solution of the singular linear system $K_n^P \hat{\phi}_u^j = v_n^j$. In this work, the linear system is solved by a Preconditioned Conjugate Gradient (PCG) algorithm. The preconditioner $\bar{K}_n^P$ is an estimation of the generalized pseudoinverse of $(K_n^P)^{-1}$. A set of preconditioners are constructed such that, they can be reutilized for all nodal diameters. In this paper, 5 different preconditioners are studied:

- Identity : I
- Incomplete Cholesky : $\hat{K}^{-1}$

- Complete Cholesky : K^{-1}
- Projected Incomplete Cholesky : $P_n\hat{K}^{-1}P_n$
- Projected Cholesky : $P_nK^{-1}P_n$

4 Application Examples

The Preconditioned Projected Arnoldi Algorithm is implemented in Python using the Scipy [15] sparse linear algebra library, which provides a wrapper for the Implicity Restarted Arnoldi (IRA) method implemented in ARPACK. The projection and preconditioner steps are carried-out by Scipy sparse linear operator. Three examples are considered to illustrate the algorithm proposed by this paper. In all cases, structural steel property is used ($E = 210GPa$, $\nu = 0.3$ and $= 7500Kg/m^3$). The PCG tolerance is set to 1.0^{-10} and maximum Arnoldi iterations n_{int} is set to 10 times the number of eigenpairs required. For all test-cases, the first 20 modes are computed for all possible nodal diameters.

The first example, named case A, consists of a 2D mesh, with plane stress triangle elements with 1m of thickness. The number of displacement dofs of the reference sector is 266, number of cyclic constraints is 14, and the whole geometry consists of 8 sectors. Table 1 shows for all nodal diameters the number of average iterations took by the PCG depending on the choice of the preconditioner. The average iterations is measured by the number of linear operator calls divided by the predefined number of modes to be computed by the IRA algorithm. Consequently, the average is measuring the overall performance of the eigensolver and not only the PCG performance. Figure 3 shows the first three modal families for nodal diameter 0,1 and 2.

Preconditioner	I	$\hat{K}^{-1}$	K^{-1}	$P_n\hat{K}^{-1}P_n$	$P_nK^{-1}P_n$
$n = 0$	165.64	42.77	18.95	42.26	18.42
$n = 1$	163.33	45.31	20	45.41	20.00
$n = 2$	162.48	46.30	20	46.13	19.97
$n = 3$	161.77	47.36	19.99	47.30	19.98

Table 1: Average PCG iterations per mode for case A.

Preconditioner	I	$\hat{K}^{-1}$	K^{-1}	$P_n\hat{K}^{-1}P_n$	$P_nK^{-1}P_n$
$n = 0$	491.08	95.35	29.92	94.89	29.95
$n = 1$	485.56	166.56	33.65	167.02	33.54
$n = 2$	481.02	175.24	33.78	174.62	33.76
$n = 3$	474.08	201.08	34.29	201.59	34.27

Table 2: Average PCG iterations per mode for case B.

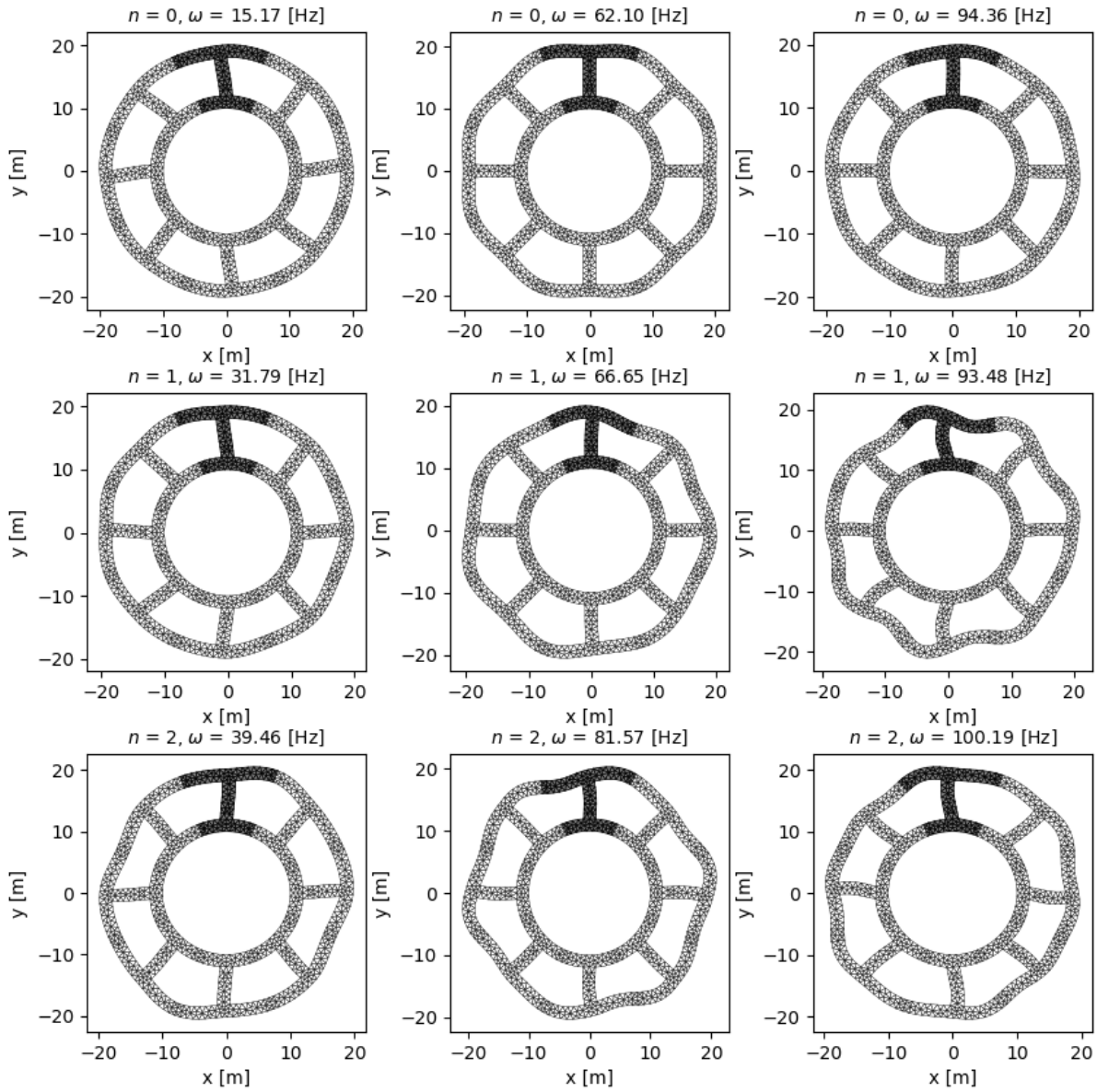

Figure 3: Mode shapes for case A.

The two remaining test cases, B and C, are both 3D Finite Element Models with 1596 and 1467 degrees of freedom respectively. Case B has a simple geometry composed by 8 sector, with 86 cyclic constraints, and the mesh contains only linear hexa elements. Figure 4 shows the first three modes for three nodal diameters and Table 2 summarizes the number of average iterations per mode using the five preconditioners. Case C is composed by tetra elements, 153 cyclic constraints, and it has a more realistic geometry with 24 sector, which resembles a blade-disk geometry. Figure 5 shows the first 3 modes for nodal diameter 0,1, and 2 for the case C. Table 3 presents the number of iteration by the PCG solver. It is clear that for all cases, the projection operation in the preconditioners, $P_n^H K^{-1} P_n$ and $P_n^H \hat{K}^{-1} P_n$ does not increase the performance of the PCG algorithm. Therefore, they must be avoid due to the additional computational cost. For case A and B, the precondition performance is almost constant with the

nodal diameters, whereas in the case C it is possible to see some discrepancies. For instance, the nodal diameter 1 and 4 converged with less than 81 iteration whereas $n = 2$ and $n = 3$ took more than 350 iterations to converge. This behavior can possibly be explained by the differences between free vibration modes without and with cyclic symmetry. If the complex cyclic symmetry constraint does not affect much the free vibration of the reference sector, then K^{-1} will be a good estimation of $(P_n^H K P_n)^{-1}$. Physically, this means that the projected and free modes are almost identical. This fact shows that finding efficient preconditioners for all nodal diameter indices remains a challenge. However, it might be possible to define a family of preconditioners which a more suitable for specific subsets of ND.

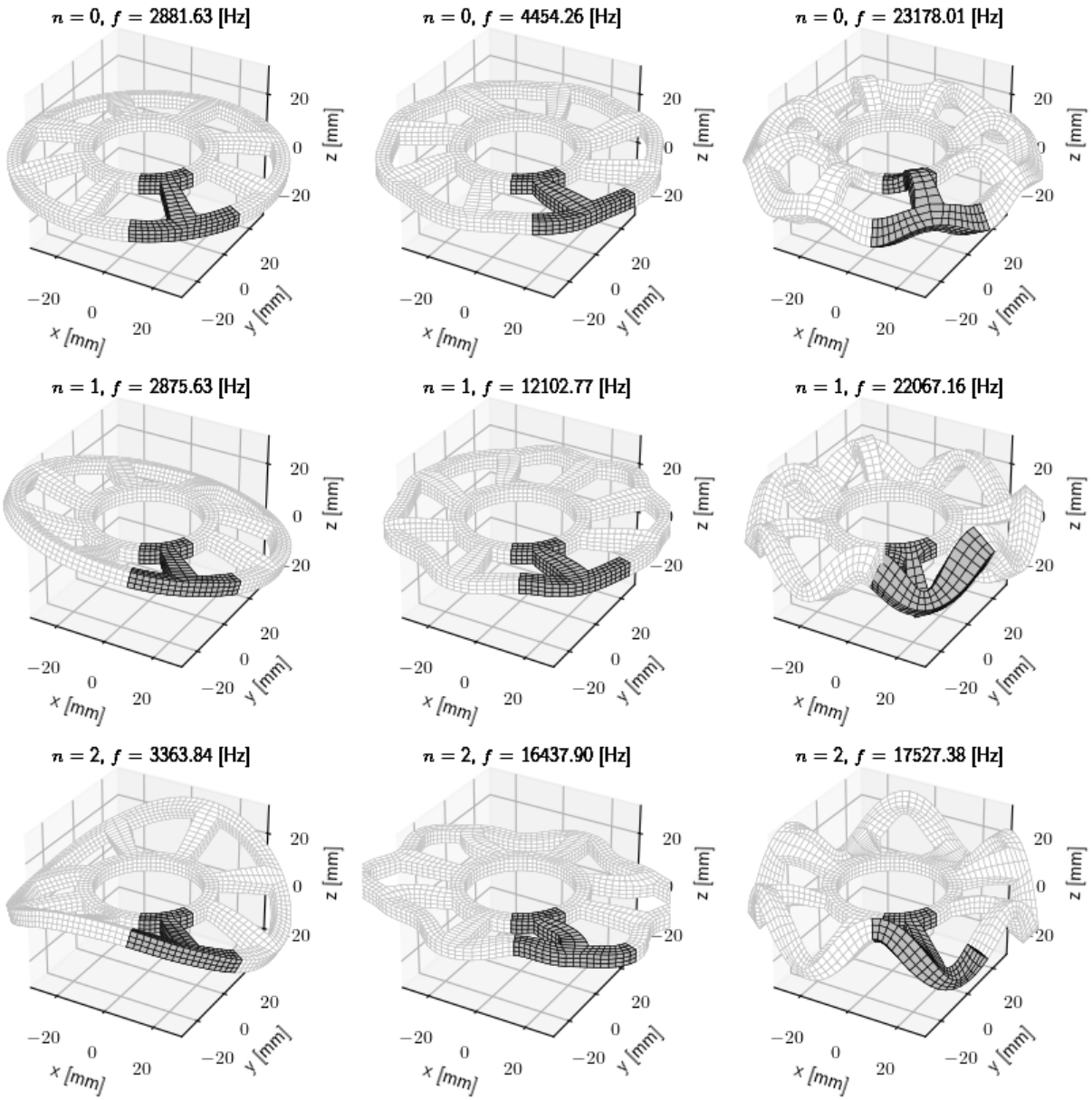

Figure 4: Mode shapes for case B.

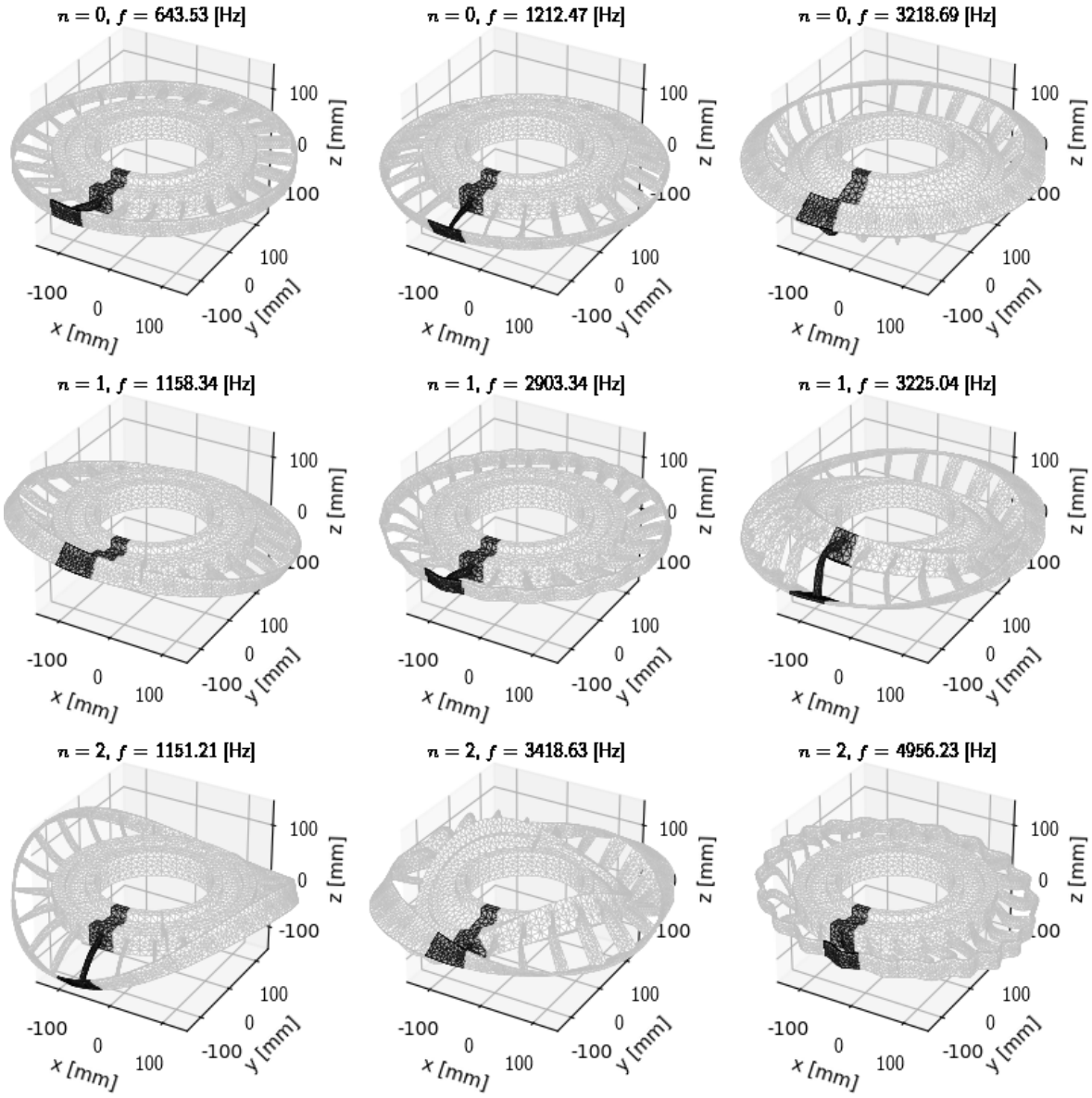

Figure 5: Mode shapes for case C.

Preconditioner	I	$\hat{K}^{-1}$	K^{-1}	$P_n\hat{K}^{-1}P_n$	$P_nK^{-1}P_n$
$n=0$	1676.8	568.3	526.4	568.0	526.4
$n=1$	1438.3	354.6	68.6	354.9	300.2
$n=2$	1421.8	409.1	352.2	360.1	303.5
$n=3$	1610.8	137.8	356.8	367.1	76.1
$n=4$	1371.3	142.7	80.3	142.0	310.4
$n=5$	1344.0	156.5	81.8	155.3	81.7
$n=6$	1323.4	162.4	86.4	163.4	86.7
$n=7$	1307.1	170.9	89.3	171.1	89.4
$n=8$	1295.0	178.3	91.0	178.6	90.7
$n=9$	1286.1	176.8	90.9	176.8	90.3
$n=10$	1272.0	182.5	92.8	181.7	92.8
$n=11$	1268.7	184.4	93.0	182.5	92.9
$n=12$	1266.9	179.9	92.6	180.7	92.7

Table 3: Average PCG iterations per mode for case C.

5 CONCLUSIONS

The cyclic symmetry constraints are presented using a substructuring framework, where primal and dual systems are formulated. These two approaches can be exploited and lead to different eigen-solvers strategies. The primal assembly formulation modifies the reference sector stiffness and mass matrices, which fully decouples the cyclic sectors by means of the unique set of primal variables. The $\bar{N}$ harmonic problems may be solved independently, but the similarity between the harmonic systems and the reference sector is usually not explored. On the other hand, the dual assembly formulation leads to a singular hybrid system of equations with the displacements and the Lagrange multipliers. In this case, the reference sector matrices, K and M are retained unchanged, whereas the complex cyclic constraint depends on the nodal diameter. Despite the singularity, the structure of the dual formulation allows to build a projected generalized eigenvalue problem. Using this technique, one can utilize the stiffness matrix of the reference sector, with some variations, as an efficient preconditioner. A total of five preconditioners namely, Identity (I), Incomplete Cholesky (IC), Complete Cholesky (CC), Projected Incomplete Cholesky (PIC) and Projected Cholesky (PC) were implemented and tested. The projected versions, PCI and PC, added unnecessary computational cost since they do not reduce the number of iterations when compared to IC and CC. The Cholesky preconditioner performed very well, where speed-ups could be seen in all developed test-cases when compared to pure CG (identity preconditioner). In the 2D case, the complete Cholesky is around 8 times faster than the identity preconditioner, whereas in the 3D case varies from 3 to 17 faster depending on the ND index. This suggests that finding suitable preconditioner for all nodal diameters spectrum is very challenging. Besides that, it is important to notice that, the incomplete Cholesky reveals an algorithmic trade-off with a less costly factorization, but more iterations in the PCG. In the future, it is intended to compare the eigen-solvers' computational efficiency for primal and dual formulation with respect to the number of eigen-pairs required. Furthermore, the projected Arnoldi algorithm will be extended to deal with blade-disk mistuning and quasi-cyclic geometries.

ACKNOWLEDGMENTS

This project has received funding from the European Union's Horizon 2020 research and innovation program under the Marie Sklodowska-Curie grant agreement No 721865.

REFERENCES

[1] M. C. C. Bampton and R. R. Craig, Jr. Coupling of substructures for dynamic analyses. *AIAA Journal*, 6(7):1313–1319, 1968.

[2] Daniel J Rixen. A dual craig–bampton method for dynamic substructuring. *Journal of Computational and applied mathematics*, 168(1-2):383–391, 2004.

[3] S Rubin. Improved component-mode representation for structural dynamic analysis. *AIAA journal*, 13(8):995–1006, 1975.

[4] Roger G Grimes, John G Lewis, and Horst D Simon. A shifted block lanczos algorithm for solving sparse symmetric generalized eigenproblems. *SIAM Journal on Matrix Analysis and Applications*, 15(1):228–272, 1994.

[5] Joost Rommes. Arnoldi and jacobi-davidson methods for generalized eigenvalue problems $Ax = \lambda Bx$ with singular B. *Mathematics of Computation*, 77(262):995–1015, 2008.

[6] D L Thomas. Dynamics of rotationally periodic structures. *Internatinal Journal for Numerical Methods in Engineering*, 4:81–102, 1979.

[7] Marari P Singh, John J Vargo, Donald M Schiffer, James D Dello, et al. Safe diagram-a design and reliability tool for turbine blading. In *Proceedings of the 17th Turbomachinery Symposium*. Texas A&M University. Turbomachinery Laboratories, 1988.

[8] D De Klerk, D J Rixen, and S N Voormeeren. General Framework for Dynamic Substructuring: History, Review, and Classification of Techniques.

[9] Charbel Farhat. A method of finite element tearing and interconnecting and its parallel solution algorithm. *International Journal For Numerical Methods In Engineering*, 32:1205–1227, 1991.

[10] Daniel J Rixen. Dual schur complement method for semi-definite problems. *Contemporary Mathematics*, 218(1):341–348, 1998.

[11] D Rixen and RF Lohman. Efficient computation of eigenmodes of quasi-cyclic structures. In *Proceedings of the IMAC-XXIII conference and exposition on structural dynamics*, pages 1–13, 2005.

[12] Walter Gander, Gene H Golub, and Urs von Matt. A constrained eigenvalue problem. *Linear Algebra and its applications*, 114:815–839, 1989.

[13] Richard B Lehoucq and Danny C Sorensen. Deflation techniques for an implicitly restarted arnoldi iteration. *SIAM Journal on Matrix Analysis and Applications*, 17(4):789–821, 1996.

[14] Dan Yang and Venkataramana Ajjarapu. Critical eigenvalues tracing for power system analysis via continuation of invariant subspaces and projected arnoldi method. In *2007 IEEE Power Engineering Society General Meeting*, pages 1–9. IEEE, 2007.

[15] Eric Jones, Travis Oliphant, Pearu Peterson, et al. SciPy: Open source scientific tools for Python, 2001 – http://www.scipy.org/.

COMPDYN 2019
7th ECCOMAS Thematic Conference on
Computational Methods in Structural Dynamics and Earthquake Engineering
M. Papadrakakis, M. Fragiadakis (eds.)
Crete, Greece, 24-26 June 2019

APPLICATION OF THE WAVE FINITE ELEMENTS FOR CALCULATING DYNAMIC RESPONSES OF 2D STRUCTURES OF ARBITRARY SHAPES SUBJECTED TO EXTERNAL LOADS

Tien Hoang[1], **Denis Duhamel**[1], **and Gilles Foret**[1]

[1]Laboratoire Navier
UMR 8205, Ecole des Ponts ParisTech, IFSTTAR, CNRS, UPE
6-8 av. Blaise Pascal, Cite Descartes, 77420 Champs-sur-Marne, France
e-mail: {tien.hoang, denis.duhamel, gilles.foret}@enpc.fr

Keywords: Wave Finite Element, Dynamic, Vibration, Periodic structure, Waveguide

Abstract. *The wave finite element method (WFE) has been developed originally for one dimensional periodic structures with advantage in calculation time. However, this method cannot apply easily for 2D structures of arbitrary shape. This communication presents a new technique of WFE to calculate the dynamic responses of such a structure subjected to external loads. The structure is decomposed into rectangular domains which can be considered as periodic structures subjected to external loads and nodal reaction forces at the domains boundaries. Then, by using the WFE for theses domains, we can obtain a relation between the external loads, the DOF and the nodal reaction forces at the boundaries of the domains. Finally, by combining this relation with the dynamic equation of the rest of the structure, we obtain an equation of the whole structure to compute its response. This technique permits to reduce all the DOF of the rectangular domains of the structure. Examples showing the efficiency of the method are presented.*

1 INTRODUCTION

The wave finite element method has been developped originally for the wave propagation along one-dimensional periodic elastic structures [1]. From the finite element method for a period of the structure, we can obtain a relation (a transform) between the left and right boundaries of the period. This relation leads to a wave base which is obtain from the eignenvectors of the transform. Then, the response at the boundary of a period can be decomposed in this base to compute with different approaches [2]. Recently, this method has been applied for many different problem of periodic structures [3, 4, 5, 6, 7, 8, 9, 10]. For 2D structures, WFE has been developed by using superelements which are rectangular subdomains[11]. By considering each rectangular domain as a periodic structure, this technique permits to obtain the wave decompositions of the domain responses and to combine in the global dynamic equation. However, this technique cannot be applied easily when the structure is subjected to complex external loads or density loads.

In this article, we present another technique of WFE using superelements for 2D structures subjected to external loads. Let's consider a 2D structure containing a rectangular domain $\mathcal{P}$ with rectangular elements as shown in Figure 1 and the rest domain is denoted by $\mathcal{R}$. The domain $\mathcal{P}$ is subjected to external density force $\mathbf{F}_E$ and the reaction force $\mathbf{F}_\partial$ of the domain $\mathcal{R}$ at the common boundary of the two domains. We will use the wave finite element method to obtain a relation between the forces $\mathbf{F}_E, \mathbf{F}_\partial$ and the DOF at the boundary of the two domains $\mathbf{q}_\partial$.

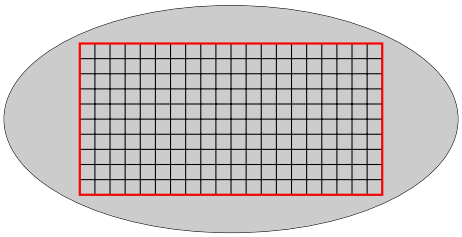

Figure 1: Structure including a rectangular domain $\mathcal{P}$ and the rest $\mathcal{R}$

The rectangular domain $\mathcal{P}$ is a periodic structure of N periods where each one is a column of elements with only nodes on the left and right boundaries as shown in Figure 2. The nodes of $\mathcal{P}$ are denoted by each column (n) with $0 \leq n \leq N$. From the dynamic equation of each

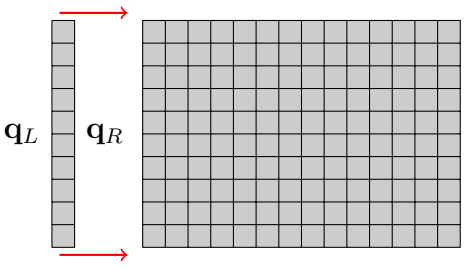

Figure 2: A periodic structure subjected to external loads

column, we get the relation $\mathbf{u}_R = \mathbf{S}\mathbf{u}_L$ with $\mathbf{u}_*$ is the column vector of DOF $\mathbf{q}_*$ and nodal loads $\mathbf{F}_*$. Moreover, the right boundary of the column (n) is also the left boundary of the column $(n+1)$ and we have

$$\mathbf{F}_L^{(n+1)} + \mathbf{F}_R^{(n)} = -\mathbf{F}_B^{(n)}$$

where $\mathbf{F}_B^{(n)}$ are the loads applying on the common boundary of (n) and $(n+1)$. Then, by using the wave analysis approach of the wave finite element method [12], we can obtain the wave bases $\mathbf{\Phi}, \mathbf{\Phi}^\star$ with eigenvalues $\boldsymbol{\mu}$ of the transform $\mathbf{S}$. The wave decomposition of the response can be written as follows

$$\mathbf{q}^{(n)} = \mathbf{\Phi}_q \boldsymbol{\mu}^n \mathbf{Q} - \mathbf{\Phi}_q^\star \boldsymbol{\mu}^{N-n} \mathbf{Q}^\star + \mathbf{\Phi}_q \sum_{k=1}^{n} \boldsymbol{\mu}^{n-k} \mathbf{Q}_B^{(k)} + \mathbf{\Phi}_q^\star \sum_{k=n+1}^{N} \boldsymbol{\mu}^{k-n} \mathbf{Q}_B^{\star(k)} \tag{1}$$

where $\mathbf{Q}, \mathbf{Q}^\star$ are the wave amplitudes of the left and right ends of the domain and $\mathbf{Q}_B, \mathbf{Q}_B^\star$ are the wave amplitude of the external loads which are calculated by

$$\begin{aligned} \mathbf{Q}_B^{(k)} &= \mathbf{\Phi}_q^{\star T} \mathbf{F}_B^{(k)} \\ \mathbf{Q}_B^{\star(k)} &= \mathbf{\Phi}_q^{T} \mathbf{F}_B^{(k)} \end{aligned} \tag{2}$$

where $\mathbf{F}_B^{(k)}$ is nodal loads on the right boundary of the period. Thus, we have

$$\mathbf{q}^{(n)} = \mathbf{\Phi}_q \boldsymbol{\mu}^n \mathbf{Q} - \mathbf{\Phi}_q^\star \boldsymbol{\mu}^{N-n} \mathbf{Q}^\star + \mathbf{\Phi}_q \sum_{k=1}^{n} \boldsymbol{\mu}^{n-k} \mathbf{\Phi}_q^{\star T} \mathbf{F}_B^{(k)} + \mathbf{\Phi}_q^\star \sum_{k=n+1}^{N} \boldsymbol{\mu}^{k-n} \mathbf{\Phi}_q^{T} \mathbf{F}_B^{(k)} \tag{3}$$

Equation (3) presents the response of the rectangular domain in function of the external loads applying on this domain and the wave ampltudes at the left and right ends of the domain.

2 FORMULATIONS

2.1 Wave analysis of rectangular domains

Now we will decompose the nodal loads $\mathbf{F}_B^{(k)}$ in function of the external loads and the reaction force of the domain $\mathcal{R}$. For $0 < n < N$, we can write

$$\mathbf{F}_B^{(n)} = \mathbf{F}_E^{(n)} + \tilde{\mathbf{F}}^{(n)} \tag{4}$$

where $\mathbf{F}_E^{(n)}$ are external loads at the column n and $\tilde{\mathbf{F}}^{(n)}$ is the reaction force of the domain $\mathcal{R}$ applying on the periodic domain which is almost zeros except the two nodes at the common boundary of the column n and the domain $\mathcal{R}$.

For the left boundary ∂L of the periodic domain $\mathcal{P}$, we have

$$\mathbf{F}^{(0)} = -\mathbf{F}_L^{(1)} = \mathbf{F}_E^{(0)} + \mathbf{F}_{\partial L} \tag{5}$$

where $\mathbf{F}_{\partial L}$ is the reaction of $\mathcal{R}$ at ∂L.

For the right boundary ∂R of the periodic domain $\mathcal{P}$, we need to find out the expression of the reaction force $\mathbf{F}_{\partial R}$ in function of $\mathbf{F}^{(N)}$ which is the nodal load of the left boundary of period $(N+1)$ (see Figure 3). We have

$$\begin{aligned} \mathbf{F}^{(N)} &= -\mathbf{F}_L^{(N+1)} = -\left(\mathbf{F}_{\partial R} - \dot{\mathbf{F}}^{(N)}\right) \\ \mathbf{F}_B^{(N)} &= \mathbf{F}_E^{(N)} + \dot{\mathbf{F}}^{(N)} \end{aligned} \tag{6}$$

where $\dot{\mathbf{F}}^{(N)}$ is the reaction forces of at the upper and lower node of ∂R. By combining equations in (6), we obtain

$$\mathbf{F}_B^{(N)} - \mathbf{F}^{(N)} = \mathbf{F}_E^{(N)} + \mathbf{F}_{\partial R} \tag{7}$$

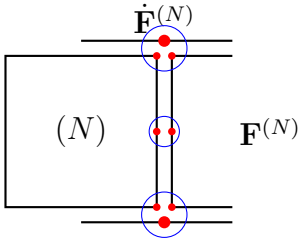

Figure 3: Nodal loads at the column (N) (right boundary of $\mathcal{P}$)

In addition, we obtain the following results from the definition of the wave amplitude [12]

$$\begin{aligned}\mathbf{Q} &= \mathbf{\Phi}^{\star T}\mathbf{J}\mathbf{u}^{(0)} = \mathbf{\Phi}_q^{\star T}\mathbf{F}^{(0)} - \mathbf{\Phi}_F^{\star T}\mathbf{q}^{(0)} \\ \mathbf{Q}^{\star} &= \mathbf{\Phi}^{T}\mathbf{J}\mathbf{u}^{(N)} = \mathbf{\Phi}_q^{T}\mathbf{F}^{(N)} - \mathbf{\Phi}_F^{T}\mathbf{q}^{(N)}\end{aligned} \tag{8}$$

Therefore, by combining equations (3), (4), (5), (7), and (8), we obtain

$$\begin{aligned}\mathbf{q}^{(n)} =& -\mathbf{\Phi}_q\boldsymbol{\mu}^{n}\mathbf{\Phi}_F^{\star T}\mathbf{q}^{(0)} + \mathbf{\Phi}_q^{\star}\boldsymbol{\mu}^{N-n}\mathbf{\Phi}_F^{T}\mathbf{q}^{(N)} \\ &+ \mathbf{\Phi}_q\sum_{k=0}^{n}\boldsymbol{\mu}^{n-k}\mathbf{\Phi}_q^{\star T}\left(\mathbf{F}_E^{(k)} + \tilde{\mathbf{F}}^{(k)}\right) + \mathbf{\Phi}_q^{\star}\sum_{k=n+1}^{N}\boldsymbol{\mu}^{k-n}\mathbf{\Phi}_q^{T}\left(\mathbf{F}_E^{(k)} + \tilde{\mathbf{F}}^{(k)}\right)\end{aligned} \tag{9}$$

where $\tilde{\mathbf{F}}^{(0)} = \mathbf{F}_{\partial L}$ and $\tilde{\mathbf{F}}^{(N)} = \mathbf{F}_{\partial R}$. We can rewrite the aforementioned equation in matrix form as follows

$$\begin{aligned}&\begin{bmatrix} \mathbf{I}+\mathbf{\Phi}_q\mathbf{\Phi}_F^{\star T} & 0 & 0 & 0 & -\mathbf{\Phi}_q^{\star}\boldsymbol{\mu}^{N}\mathbf{\Phi}_F^{T} \\ \vdots & \ddots & \vdots & \vdots & \vdots \\ \mathbf{\Phi}_q\boldsymbol{\mu}^{n}\mathbf{\Phi}_F^{\star T} & 0 & \mathbf{I} & 0 & -\mathbf{\Phi}_q^{\star}\boldsymbol{\mu}^{N-n}\mathbf{\Phi}_F^{T} \\ \vdots & \vdots & \vdots & \ddots & \vdots \\ \mathbf{\Phi}_q\boldsymbol{\mu}^{N}\mathbf{\Phi}_F^{\star T} & 0 & 0 & 0 & \mathbf{I}-\mathbf{\Phi}_q^{\star}\mathbf{\Phi}_F^{T} \end{bmatrix}\begin{bmatrix} \mathbf{q}^{(0)} \\ \vdots \\ \mathbf{q}^{(n)} \\ \vdots \\ \mathbf{q}^{(N)} \end{bmatrix} \\ =& \begin{bmatrix} \mathbf{\Phi}_q\mathbf{\Phi}_q^{\star T} & \cdots & \mathbf{\Phi}_q^{\star}\boldsymbol{\mu}^{n}\mathbf{\Phi}_q^{T} & \cdots & \mathbf{\Phi}_q^{\star}\boldsymbol{\mu}^{N}\mathbf{\Phi}_q^{T} \\ \vdots & \ddots & \vdots & \vdots & \vdots \\ \mathbf{\Phi}_q\boldsymbol{\mu}^{n}\mathbf{\Phi}_q^{\star T} & \cdots & \mathbf{\Phi}_q\mathbf{\Phi}_q^{\star T} & \cdots & \mathbf{\Phi}_q^{\star}\boldsymbol{\mu}^{N-n}\mathbf{\Phi}_q^{T} \\ \vdots & \vdots & \vdots & \ddots & \\ \mathbf{\Phi}_q\boldsymbol{\mu}^{N}\mathbf{\Phi}_q^{\star T} & \cdots & \mathbf{\Phi}_q\boldsymbol{\mu}^{N-n}\mathbf{\Phi}_q^{\star T} & \cdots & \mathbf{\Phi}_q\mathbf{\Phi}_q^{\star T} \end{bmatrix}\begin{bmatrix} \mathbf{F}_E^{(0)} + \mathbf{F}_{\partial L} \\ \vdots \\ \mathbf{F}_E^{(n)} + \tilde{\mathbf{F}}_{\partial n} \\ \vdots \\ \mathbf{F}_E^{(N)} + \mathbf{F}_{\partial R} \end{bmatrix}\end{aligned} \tag{10}$$

Equation (10) is a relation between the DOF and nodal loads of the whole domain. Moreover, the matrix on the right side of equation (10) is a block Toeplitz matrix [13, 14].

2.2 Assembly of boundary nodes

We are interested in the boundary nodes of the domain. The left and right boundaries are $\mathbf{q}^{(0)}$ and $\mathbf{q}^{(N)}$. Otherwise, the up and down boundaries at the column n (noted by ∂n) are the first and the last nodes of the column and we can define a matrix $\mathbf{L}$ so that:

$$\mathbf{q}_{\partial n} = \mathbf{L}\mathbf{q}^{(n)}, \quad \mathbf{F}_{\partial n} = \mathbf{L}\tilde{\mathbf{F}}^{(n)} \quad 0 < n < N \tag{11}$$

If we note

$$\tilde{\mathbf{\Phi}}_q = \mathbf{L}\mathbf{\Phi}_q, \quad \tilde{\mathbf{\Phi}}_q^{\star} = \mathbf{L}\mathbf{\Phi}_q^{\star} \tag{12}$$

Equation (10) become

$$\begin{bmatrix} \mathbf{I}+\boldsymbol{\Phi}_q\boldsymbol{\Phi}_F^{\star T} & 0 & 0 & 0 & -\boldsymbol{\Phi}_q^{\star}\boldsymbol{\mu}^N\boldsymbol{\Phi}_F^T \\ \vdots & \ddots & \vdots & \vdots & \vdots \\ \tilde{\boldsymbol{\Phi}}_q\boldsymbol{\mu}^n\boldsymbol{\Phi}_F^{\star T} & 0 & \tilde{\mathbf{I}} & 0 & -\tilde{\boldsymbol{\Phi}}_q^{\star}\boldsymbol{\mu}^{N-n}\boldsymbol{\Phi}_F^T \\ \vdots & \vdots & \vdots & \ddots & \vdots \\ \boldsymbol{\Phi}_q\boldsymbol{\mu}^N\boldsymbol{\Phi}_F^{\star T} & 0 & 0 & 0 & \mathbf{I}-\boldsymbol{\Phi}_q^{\star}\boldsymbol{\Phi}_F^T \end{bmatrix} \begin{bmatrix} \mathbf{q}_{\partial L} \\ \vdots \\ \mathbf{q}_{\partial n} \\ \vdots \\ \mathbf{q}_{\partial R} \end{bmatrix}$$

$$= \begin{bmatrix} \boldsymbol{\Phi}_q\boldsymbol{\Phi}_q^{\star T} & \cdots & \boldsymbol{\Phi}_q^{\star}\boldsymbol{\mu}^n\tilde{\boldsymbol{\Phi}}_q^T & \cdots & \boldsymbol{\Phi}_q^{\star}\boldsymbol{\mu}^N\boldsymbol{\Phi}_q^T \\ \vdots & \ddots & \vdots & \vdots & \vdots \\ \tilde{\boldsymbol{\Phi}}_q\boldsymbol{\mu}^n\boldsymbol{\Phi}_q^{\star T} & \cdots & \tilde{\boldsymbol{\Phi}}_q\tilde{\boldsymbol{\Phi}}_q^{\star T} & \cdots & \tilde{\boldsymbol{\Phi}}_q^{\star}\boldsymbol{\mu}^{N-n}\boldsymbol{\Phi}_q^T \\ \vdots & \vdots & \vdots & \ddots & \\ \boldsymbol{\Phi}_q\boldsymbol{\mu}^N\boldsymbol{\Phi}_q^{\star T} & \cdots & \boldsymbol{\Phi}_q\boldsymbol{\mu}^{N-n}\tilde{\boldsymbol{\Phi}}_q^{\star T} & \cdots & \boldsymbol{\Phi}_q\boldsymbol{\Phi}_q^{\star T} \end{bmatrix} \begin{bmatrix} \mathbf{F}_{\partial L} \\ \vdots \\ \mathbf{F}_{\partial n} \\ \vdots \\ \mathbf{F}_{\partial R} \end{bmatrix}$$

$$+ \begin{bmatrix} \boldsymbol{\Phi}_q\boldsymbol{\Phi}_q^{\star T} & \cdots & \boldsymbol{\Phi}_q^{\star}\boldsymbol{\mu}^n\boldsymbol{\Phi}_q^T & \cdots & \boldsymbol{\Phi}_q^{\star}\boldsymbol{\mu}^N\boldsymbol{\Phi}_q^T \\ \vdots & \ddots & \vdots & \vdots & \vdots \\ \tilde{\boldsymbol{\Phi}}_q\boldsymbol{\mu}^n\boldsymbol{\Phi}_q^{\star T} & \cdots & \tilde{\boldsymbol{\Phi}}_q\boldsymbol{\Phi}_q^{\star T} & \cdots & \tilde{\boldsymbol{\Phi}}_q^{\star}\boldsymbol{\mu}^{N-n}\boldsymbol{\Phi}_q^T \\ \vdots & \vdots & \vdots & \ddots & \\ \boldsymbol{\Phi}_q\boldsymbol{\mu}^N\boldsymbol{\Phi}_q^{\star T} & \cdots & \boldsymbol{\Phi}_q\boldsymbol{\mu}^{N-n}\boldsymbol{\Phi}_q^{\star T} & \cdots & \boldsymbol{\Phi}_q\boldsymbol{\Phi}_q^{\star T} \end{bmatrix} \begin{bmatrix} \mathbf{F}_E^{(0)} \\ \vdots \\ \mathbf{F}_E^{(n)} \\ \vdots \\ \mathbf{F}_E^{(N)} \end{bmatrix} \tag{13}$$

where $\tilde{\mathbf{I}} = \mathbf{L}\mathbf{I}\mathbf{L}^T$ which is also an identity matrix. We can rewrite the aforementioned equation as follows

$$\mathbb{A}\mathbf{q}_{\partial} = \mathbb{B}\mathbf{F}_{\partial} + \mathbb{C}\mathbf{F}_E \tag{14}$$

where $\mathbb{A}, \mathbb{B}, \mathbb{C}$ are defined corresponding to the matrices in equation (13).

2.3 Assembly of the whole structure

For the domain $\mathcal{R}$, we have

$$\begin{bmatrix} \mathbf{D}_{\partial\partial}^{\star} & \mathbf{D}_{\partial I}^{\star} & \mathbf{D}_{\partial B}^{\star} \\ \mathbf{D}_{I\partial}^{\star} & \mathbf{D}_{II}^{\star} & \mathbf{D}_{IB}^{\star} \\ \mathbf{D}_{B\partial}^{\star} & \mathbf{D}_{BI}^{\star} & \mathbf{D}_{BB}^{\star} \end{bmatrix} \begin{bmatrix} \mathbf{q}_{\partial} \\ \mathbf{q}_I \\ \mathbf{q}_0 \end{bmatrix} = \begin{bmatrix} \mathbf{F}_{\partial} \\ \mathbf{F}_0^{\star} \\ \mathbf{F}_B^{\star} \end{bmatrix} \tag{15}$$

where $\mathbf{q}_0, \mathbf{F}_0^{\star}$ are given by the boundary condition and the loads of the domain $\mathcal{R}$. From the aformentioned equation, we obtain

$$\begin{bmatrix} \mathbf{D}_{\partial\partial}^{\star} & \mathbf{D}_{\partial I}^{\star} \\ \mathbf{D}_{I\partial}^{\star} & \mathbf{D}_{II}^{\star} \end{bmatrix} \begin{bmatrix} \mathbf{q}_{\partial} \\ \mathbf{q}_I \end{bmatrix} = \begin{bmatrix} \mathbf{F}_{\partial} \\ \mathbf{F}_0^{\star} \end{bmatrix} - \begin{bmatrix} \mathbf{D}_{\partial B}^{\star}\mathbf{q}_0 \\ \mathbf{D}_{IB}^{\star}\mathbf{q}_0 \end{bmatrix} \tag{16}$$

Equations (14) and (16) decribe the relations between $\mathbf{q}_{\partial}$ and $\mathbf{F}_{\partial}$ with the external loads and the boundary conditions of the whole structure. We can have different methods to combine these two equations which cost different calculation times. It is possible to reduce the cost by using the properties of the Toeplizt block matrix $\mathbb{B}, \mathbb{C}$ [14]. However, this article is limited to a simple method by substituting equation (14) into equation (16) and we obtain

$$\begin{bmatrix} \mathbf{D}_{\partial\partial}^{\star} - \mathbb{B}^{-1}\mathbb{A} & \mathbf{D}_{\partial I}^{\star} \\ \mathbf{D}_{I\partial}^{\star} & \mathbf{D}_{II}^{\star} \end{bmatrix} \begin{bmatrix} \mathbf{q}_{\partial} \\ \mathbf{q}_I \end{bmatrix} = \begin{bmatrix} -\mathbb{B}^{-1}\mathbb{C}\mathbf{F}_E \\ \mathbf{F}_0^{\star} \end{bmatrix} - \begin{bmatrix} \mathbf{D}_{\partial B}^{\star}\mathbf{q}_0 \\ \mathbf{D}_{IB}^{\star}\mathbf{q}_0 \end{bmatrix} \tag{17}$$

Equation (17) permits to calculate the response of the domain $\mathcal{R}$. This technique permits to get the final expression of the dynamic stiffness matrix (DSM) of the whole structure by modifying only the diagonal block of DSM of $\mathcal{R}$ corresponding to the rectangular domain boundary.

When the structure has severalrectangular domains, we can use the same technique for each diagonal block to get the final DSM. For structures with connected rectangular domains, we need to combine these domains as superelements before replacing into the DSM.

3 EXAMPLE

Let's consider a 2D elipse of axes 6mx3m which contain a rectangular of size 4mx2m as shown in Figure 4. The mesh is created by using 1586 elements S4 of thickness 0.1m. The stiffness and mass matrices are generated by Abaqus and other calculations have been performed with Matlab. Figure 5 shows the results obtained by the finite element method (for the whole

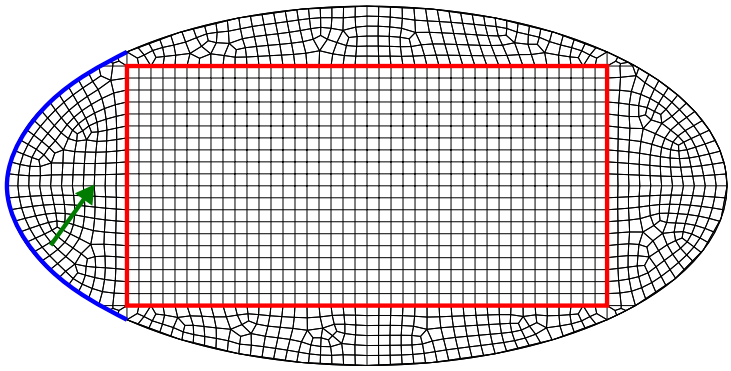

Figure 4: Example of 2D structure with a rectanglar domain (red), a fixed boundary (blue) and a load (green)

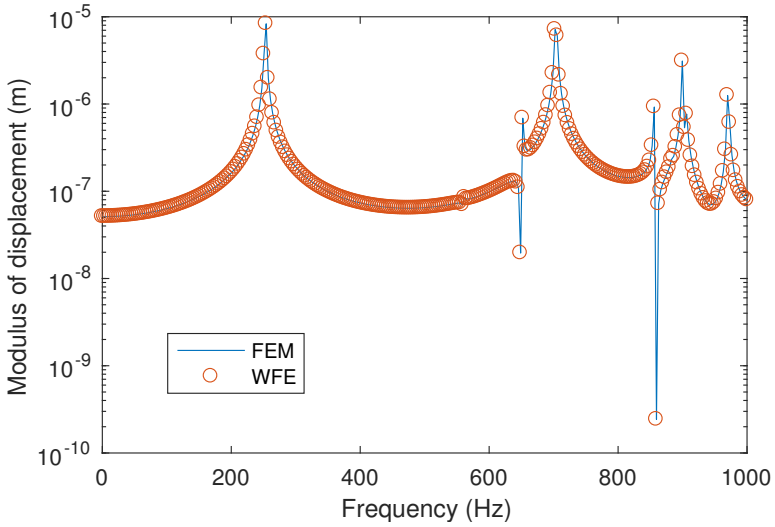

Figure 5: Response of one node calculated by the finite element method and the new method

structure) and the new method. The two results agrees well. Althought the new method can

reduce the number of DOF (from 3322 to 1840), the WFE cannot reduce the calculation time in comparing with FEM (5.4s vs 20.9s). One reason is that the calculation of Toeplitz matrices (which are full matrices) have not been optimized.

4 CONCLUSIONS

This article introduces a new technique for coupling the finite element method and the wave finite element method by using superelements. For a 2D structure of arbtrary shapes, we define superelements as rectangular domains. Each superelement is a periodic structure where we can apply WFE. We obtain then a relation between the DOF at the superelement boundary and the external nodal loads via Toeplitz matrices. The technique permits to reduce the number of DOF but it needs to optimize the calculation of Toeplitz matrices in order to reduce the calculation time.

REFERENCES

[1] D. Mead, A general theory of harmonic wave propagation in linear periodic systems with multiple coupling, *Journal of Sound and Vibration* , **27**, 235 – 260, 1973.

[2] D. Duhamel, B. R. Mace, M. J. Brennan, Finite element analysis of the vibrations of waveguides and periodic structures, *Journal of Sound and Vibration*, **294**, 205–220, 2006.

[3] Y. Waki, B. Mace, M. Brennan, Free and forced vibrations of a tyre using a wave finite element approach, *Journal of Sound and Vibration*, **323**, 737 – 756, 2009.

[4] W. Zhou, M. Ichchou, Wave propagation in mechanical waveguide with curved members using wave finite element solution, *Computer Methods in Applied Mechanics and Engineering*, **199**, 2099 – 2109, 2010.

[5] M. Ichchou, J.-M. Mencik, W. Zhou, Wave finite elements for low and mid-frequency description of coupled structures with damage, *Computer Methods in Applied Mechanics and Engineering*, **198**, 1311 – 1326, 2009.

[6] B. Lossouarn, M. Aucejo, J.-F. Deu, Electromechanical wave finite element method for interconnected piezoelectric waveguides, Computers & Structures, **199**, 46 – 56, 2018.

[7] A. Kessentini, M. Taktak, M. B. Souf, O. Bareille, M. Ichchou, M. Haddar, Computation of the scattering matrix of guided acoustical propagation by the wave finite element approach, *Applied Acoustics*, **108**, 92 – 100, 2016.

[8] J.-M. Mencik, A wave finite element approach for the analysis of periodic structures with cyclic symmetry in dynamic substructuring, *Journal of Sound and Vibration*, **431**, 441 – 457, 2018.

[9] T. Gras, M.-A. Hamdi, M. B. Tahar, O. Tanneau, L. Beaubatie, On a coupling between the finite element (fe) and the wave finite element (wfe) method to study the effect of a local heterogeneity within a railway track, *Journal of Sound and Vibration*, **429**, 45 – 62, 2018.

[10] J.-M. Mencik, D. Duhamel, A wave finite element-based approach for the modeling of periodic structures with local perturbations, *Finite Elements in Analysis and Design*, **121**, 40–51, 2016.

[11] J. M. Mencik, D. Duhamel, A wave-based model reduction technique for the description of the dynamic behavior of periodic structures involving arbitrary-shaped substructures and large-sized finite element models, *Finite Elements in Analysis and Design*, **101**, 1–14, 2015.

[12] T. Hoang, D. Duhamel, G. Foret, Wave finite element method for vibration of periodic structures subjected to external loads, *6th European Conference on Computational Mechanics (ECCM 6)*, Glasgow, UK, June 2018.

[13] A. Bottcher, S.M. Grudsky, Toeplitz Matrices - Asymptotic Linear Algebra and Functional Analysis, *Hindustan Book Agency*, 2000.

[14] W. F. Trench, Inversion of Toeplitz band matrices, *Mathematics of Computation*, **28**, 1089–1095, 1974.

COMPDYN 2019
7th ECCOMAS Thematic Conference on
Computational Methods in Structural Dynamics and Earthquake Engineering
M. Papadrakakis, M. Fragiadakis (eds.)
Crete, Greece, 24–26 June 2019

BIBLIOGRAPHIC REVIEW OF ITALIAN REGULATIONS FROM 1900 TO THE PRESENT FOR THE SIMULATED DESIGN OF ITALIAN RAILWAY BRIDGES

Antonella Di Meo[1], Barbara Borzi[2], Davide Bellotti[2], and Francesco Bruno[2]

[1] European Centre for Training and Research in Earthquake Engineering (*Eucentre*)
Via Adolfo Ferrata, 1, 27100, Pavia (Italy)
e-mail: antonella.dimeo@eucentre.it

[2] European Centre for Training and Research in Earthquake Engineering (*Eucentre*)
Via Adolfo Ferrata, 1, 27100, Pavia (Italy)
{barbara.borzi, davide.bellotti, francesco bruno}@ eucentre.it

Abstract

The many catastrophic earthquakes that occurred in Italy in the last fourty years underline how Italy is one of the European countries at the highest seismic risk. For this reason, the vulnerability of infrastructures needs to be investigated. This paper considers the railway network as a case study with a focus on railway bridges, which are neuralgic nodes of the whole system. The most common types of railway bridges in Italy are masonry arch bridges and girder bridges with either a continuous deck or a simply supported deck. Here, we specifically analyze railway girder bridges.

Eucentre evaluates the seismic vulnerability of railway bridges through the definition of fragility curves. Fragility curves result from analytical procedures that determine the seismic behaviour of structures according to the structural typology as well as the level of knowledge of the bridge. One step of these procedures is the simulated design, which aims at reducing the number of variables in the process and requires the knowledge of the regulatory limits used at the time of the design. This paper presents those regulatory limits that concern: (i) loads, (ii) materials resistance, (iii) longitudinal and transversal reinforcement percentages for reinforced concrete bridges, and (iv) bearings. These limits derive from a detailed bibliographic study on Italian regulations, concerning the design of railway bridges from the beginning of 1900 to the present.

Keywords: Railway Bridges, Italian Regulation, Simulated Design, Seismic Vulnerability.

1 INTRODUCTION

The Italian railway network is made up of about 17000 km of rail lines that are in operation and are largely developed in medium-to-high seismic hazard zones. Important elements of this network are viaducts. The most common types of railway bridges in Italy are masonry arch bridges and girder bridges with either a continuous deck or simply supported deck. In this paper, only the railway girder bridges are analyzed, a brief description of which is also given in relation to the deck material.

The seismic vulnerability of railway bridges is generally assessed through fragility curves. Fragility curves can be obtained through different methods, such as analytical methods that involve the mechanical modeling of the structure.

For the seismic behaviour of the modeled structure to be plausible, the characteristics of materials, the amount of reinforcement, and the types of bearings used in the modeling need to be as close as possible to the actual conditions of the bridge. This information is included in the project documents which are usually not available. To solve this problem, the simulated design of the structure is carried out using the limits imposed by the regulations in force at the time of design.

To this end, this paper provides a brief bibliographic review of the regulations used for the construction of reinforced concrete railway bridges from the beginning of the last century to the present day. The first Italian regulation available on the design of reinforced concrete railway bridges dates back to 1995. For this reason, the provisions on the reinforcement of piers as well as on the mechanical characteristics of materials derive from the regulations issued in Italy starting from 1907 concerning the construction of public reinforced concrete structures. For mobile loads, instead, specific technical standards have been considered starting from 1946.

The definition of the permanent load depends on the composition of the superstructure. For this purpose, this paper also provides the weights of the railway track and ballast, as well as the weight of noise barriers suggested by the latest technical specifications issued by the Italian State Railways ([1], [2], [3]).

Finally, this paper gives a brief bibliographic review of the standards on the types of bearings for railway girder bridges from 1972 onwards. It is very important to identify the geometrical and mechanical characteristics of these devices so that their actual function can be taken into account during their simulated design. A wrong modeling of bearings could affect the actual seismic response of a bridge because it changes the way in which mechanisms of the pier-bearing system are activated.

2 RAILWAY GIRDER BRIDGES

One of a widely used bridge typology in the Italian railway network is represented by girder bridges. The deck can consist of reinforced concrete, prestressed reinforced concrete, or steel, and generally lies on unreinforced concrete, reinforced concrete, or masonry piers. The deck can be simply supported or continuous, thus giving rise to an isostatic or hyperstatic static scheme, respectively. Between the deck and the vertical structure of the bridge are the bearings, the choice of which depends mainly on the type of deck and the type of constraint to be obtained.

In case of a reinforced concrete deck, the method of construction depends mainly on the length of the individual spans as well as on the total length of the bridge. Specifically, the deck can be made of: (i) a slab, (ii) steel girders embedded in concrete, and (iii) reinforced concrete plate girder. The bridge with slab deck is the simplest system used in rail transport, but only when the spans do not exceed 4 m. On the contrary, the deck with steel girders em-

bedded in concrete or reinforced concrete plate girder is used when, for orographic reasons, the deck cannot be very thick. In particular, the deck with steel girders embedded in concrete is no longer than either 13 m, in the case of "double T" beams, or 20 m, in the case of "double T" beams with wide wings. In presence of a deck with reinforced concrete plate girder, instead, the girders also have the function of parapet and can reach heights of also 3.5 m. The deck is continuous and supports the railway superstructure.

In addition to reinforced concrete, the deck can be realized with prestressed reinforced concrete beams. This deck can reach a length that ranges 35 m and 50 m and is generally made of isolated or box beams. When the beam has a box cross-section, the common practice provides for the use of a box for each track. In this case, the beams are connected among each other with cross-beams (which are prestressed, too) to guarantee the beams cooperation in the usual load conditions (e.g. the passage of a train) so that fatigue phenomena can be reduced. Nowadays, the prestressed reinforced concrete deck is really common on both ordinary and high-speed railway lines.

Another type of deck is the steel deck, which has been widely used in the past; nowadays, however, it is mainly used for long span bridges with reduced height or to replace pre-existing steel girders. Because of the high cost of construction and maintenance, steel decks have mostly been replaced by either the prestressed reinforced concrete decks for medium-to-long span bridges, or reinforced concrete and mixed structure decks for bridges with shorter spans. The most common railway steel bridges are made of straight girders lying on masonry or reinforced concrete piers. In the case of bridges with more than one span, however, it is preferable to create non-continuous decks on which the track can be either direct lying or ballasted. Depending on the length of the deck, the direct-laying girders can be twin-girders (for spans between 10-25 m), plate girders (for spans between 30-40 m), or truss girders (for spans between 35-100 m). For what concerns bridges with railway tracks lying on the ballast, they generally have a deck with steel-concrete composite girders. In this case, the beams can be "double T" or box section collaborating with the concrete slab and reach a length of about 20-25 m. To guarantee the interaction between all the girders of the deck, cross-beams are also used, especially in the presence of live loads.

3 ITALIAN REGULATIONS FROM 1900 TO NOWADAYS FOR RAILWAY GIRDER BRIDGES

3.1 Resistance of Materials

The first recommendations about the construction of reinforced concrete structures were issued in Italy with the Royal Decree 10/01/1907 [4]. This decree provided the first indications about the maximum strength to be considered in the structural calculation for both concrete and reinforcement. In particular, this standard stated that the compressive strength of concrete at 28 days of hardening $\sigma_{r,28}$ must not be less than 150 kg/cm^2, the fifth part of which corresponds to the simple compressive safety load of the concrete to be used in the calculation. Concerning the reinforcement, the regulation allowed the use of smooth steel rebars with a tensile strength between 36 kg/mm^2 and 45 kg/mm^2. The safety tensile and shear loads, instead, should not exceed 1000 kg/cm^2 and 800 kg/cm^2, respectively. For the reinforcement, the decree introduced a further limitation, namely the quality coefficient, which is obtained by multiplying the unit failure load per mm^2 by the percentage elongation. This coefficient, which should not exceed 900, was then replaced by the percentage of elongation at maximum tensile strength of the reinforcement in the Royal Decree issued on 4/09/1927 [5]. With the exception of this introduction, the Royal Decree 4/09/1927 [5] has not made substantial changes compared to what was already established by the previous decree [4]. In fact, the de-

cree only reduced and slightly increased the values of the safety concrete load (30 kg/m^2 and 40 kg/m^2 for 2nd and 1st quality concretes) as well as the tensile and shear steel ones (1200 kg/cm^2 and 960 kg/cm^2). As a result, the tensile strength of the steel changed slightly, i.e. 3800-5000 kg/cm^2, corresponding to a minimum elongation of 27% and 21%, respectively.

With the Royal Decree 23/05/1932 [6], the classification of concretes had been improved and divided into Portland, blast furnace, pozzolanic, and aluminous. Portland, blast furnace, and pozzolanic concretes could be of normal or high strength (see Table 1). The mechanical characteristics of steel, instead, did not change compared to what was already indicated in the Royal Decree 4/09/1927 [5].

Mechanical characteristics of concrete	Portland, blast furnace, pozzolanic concrete		Aluminous concrete
	Normal strength	High strength	
Crushing strength [kg/cm^2]	450	600	650
Compressive safety load [kg/cm^2]	40*-50**	50	65
Maximum tangential strength without reinforcement [kg/cm^2]	2	4	4
Maximum tangential strength with reinforcement [kg/cm^2]	14	16	16

*for structures under simple pressure; **for bent structures with a thickness not less than 10 cm.

Table 1: Mechanical characteristics of portland, blast furnace, pozzolanic, and aluminous concretes in the Royal Decree 23/05/1932 [6].

The Circular 17/05/1937 [7] introduced the use of medium carbon steel, only in absence of homogeneous steel. In terms of mechanical characteristics, the medium carbon steel had an ultimate tensile strength between 5000 kg/cm^2 and 6500 kg/cm^2 to which percentages of elongation corresponded to 21% and 14%, respectively. The safety load of the steel increased from 1200 kg/cm^2 to 1600 kg/cm^2.

In 1939 a new Royal Decree [8] was issued to regulate the construction of structures made of unreinforced or reinforced concrete. In this decree, the compressive strength of concrete at 28 days of hardening $\sigma_{r,28}$ had to be at least three times the safety load $\sigma_{c,a}$ adopted in the structural calculations, but never less than 120 kg/cm^2 and 160 kg/cm^2 for normal-strength concrete and high-strength or aluminous concrete, respectively. Regarding the reinforcement, the Royal Decree 16/11/1939 [8] introduced high carbon steel, which allowed to adopt smaller rebar sizes due to its high specific resistance [9].

Table 2 reports the mechanical properties of the three types of steel permitted by the Royal Decree 16/11/1939 [8].

Mechanical characteristics of steel	Mild Steel	Medium carbon steel	High carbon steel
Yield characteristic strength [kg/cm^2]	≥2300	≥2700	≥3100
Ultimate characteristic strength [kg/cm^2]	4200-5000	5000-6000	6000-7000
Elongation [%]	≥20	≥16	≥14
Safety load [kg/cm^2]	≤1400	≤2000	≤2000

Table 2: Mechanical characteristics of steels in the Royal Decree 16/11/1939 [8].

The Royal Decree 16/11/1939 [8] has remained in force until the first years of 1970s as a consequence of a regulatory gap due to the Second World War and the following period of

reconstruction. Between 1939 and the early 1970s, however, a series of circulars have been issued, among which it is necessary to mention the Circular 23/05/1957 [10]. This circular not only introduced a new denomination for smooth steel rebars, i.e. AQ42, AQ50 and AQ60, equivalent respectively to the mild, medium carbon, and high carbon steel of Table 2, but also introduced first indications on ribbed steel rebars [9]. The ribbed steel rebars were allowed in special cases, such as shaped or bent rebars, and with a minimum elongation percentage of 12%.

A substantial change with respect to the previous regulations occurred with the Ministerial Decree 30/05/1972 [11] which has laid the foundations of modern legislation. It introduced a classification of ribbed steel rebars as well as a calculation method at the limit states, which replaced the permissible stresses approach. This change defined the transition from a deterministic to a statistical calculation system due to the introduction of the characteristic value. As a consequence, the yield strength and the ultimate strength were not intended anymore as an average value but as the strength that had only a 5% probability of being lowered by the effective resistance [9]. The Ministerial Decree of 30/05/1972 [11] distinguished six classes of concrete by a number that expressed the characteristic cubic resistance at 28 days of hardening R'_{bk}, from which it was possible to obtain the mechanical characteristics of the concrete (e.g. compressive strength, tensile strength, etc.). For what concerns the reinforcement, smooth steels were divided in only two classes (i.e. Fe B 22 and Fe B 32), and the ribbed steel rebars into three classes (i.e. A 38, A 41, and Fe B 44) (see Table 3).

Mechanical characteristics of steel	Smooth steel rebars		Ribbed steel rebars		
	Fe B 22	Fe B 32	A 38	A 41	Fe B 44
Yield characteristic strength [kg/cm^2]	≥ 2200	≥ 3200	≥ 3800	≥ 4100	≥ 4400
Ultimate characteristic strength [kg/cm^2]	≥ 3400	≥ 5000	≥ 4600	≥ 5000	≥ 5500
Elongation [%]	≥ 24	≥ 23	≥ 14	≥ 14	≥ 12
Safety load [kg/cm^2]	1200	1600	2200	2400	2600

Table 3: Mechanical characteristics of smooth steel rebars and ribbed steel rebars in the Ministerial Decree of 30/05/1972 [11].

After 1972, other decrees were issued about the construction of reinforced concrete structures, but they have not considerably changed the provisions of the Ministerial Decree 30/05/1972 [11] in terms of mechanical characteristic of materials. This is evident in Table 4 and Table 5, which report the mechanical characteristics of the rebars defined in the latest standards on the construction of railway bridges, issued by Italian State Railways ([1], [2], [3]). The only significant difference between the Circular n. I/SC/PS-OW2298 1997 [1] and the newest Technical Specifications by Italian State Railways ([2], [3]) is the mechanical characteristics of ribbed steel rebars (see Table 5). As stated in the Italian Seismic Codes (NTC08) [12], the use of smooth steel rebars is definitely prohibited. Concerning concrete properties, no substantial changes were made.

Mechanical characteristics of steel	Smooth steel rebars		Ribbed steel rebars	
	Fe B 22k	Fe B 32k	Fe B 38k	Fe B 44k
Yield characteristic strength [kg/cm^2]	≥ 2150	≥ 3150	≥ 3750	≥ 4300
Ultimate characteristic strength [kg/cm^2]	≥ 3350	≥ 4900	≥ 4500	≥ 5400
Elongation [%]	≥ 24	≥ 23	≥ 14	≥ 12

Table 4: Mechanical characteristics of smooth steel rebars and ribbed steel rebars in the Circular n. I/SC/PS-OW2298 and following update of 1997 [1].

Mechanical characteristics of steel	B450C
Yield characteristic strength [kg/cm^2]	≥ 4500
Ultimate characteristic strength [kg/cm^2]	≥ 5400
Elongation [%]	≥ 7.5

Table 5: Mechanical characteristics of ribbed steel rebars in the newest technical specifications by Italian State Railways ([2], [3]).

3.2 Definition of loads

3.2.1 Permanent loads

The permanent loads are obtained from the structural and non-structural loads, to which the hydraulic and lateral earth pressures are added too, if existing.

The permanent structural loads are evaluated on the basis of the geometric characteristics of the elements constituting the deck of the bridge (i.e. girders, cross-beams, and slab) and the specific weights of the materials with which they are made. The latter are regulated by the codes in force at the time of the structure design.

The non-structural load, instead, is obtained by adding the weight of all non-structural elements composing the superstructure, that are mainly: (i) the railway track, (ii) the ballast, (iii) the waterproofing, and (iv) the noise barriers.

A railway track is defined as the totality of rails, sleepers, and fasteners.

The first rails were entirely made of cast iron, were very short, and mounted on large stone blocks drowned in the ground. Due to the fragility of cast iron, it was later replaced by iron, which is, however, subjected to wear. The solution to the problem of wear was the “double headed rail”, which was mounted through hardwood wedges into special fixing plates, fixed in turn on wooden sleepers. When the upper table was worn out, the rail was inverted so that the lower table was ready to be used. As this process was complex and expensive, other solutions were developed, such as the “Vignoles rail” (named by the engineer who invented it), which has a “double-T” profile with a wider lower table than the upper one. Advances in material science led to the replacement of iron with steel: steel performs better than iron and deforms less at high speeds. The intended use of the tracks defines the type of steel used for the rails, their dimensions and, consequently, the weight and maximum permissible speed of the vehicles. The higher the linear weight of the rail, the higher are its performances. Initially, the rails had a weight of 18-25 kg/m or 27 kg/m. Later on, rails with a weight of 36 kg/m and 46-48 kg/m became very common for secondary and main railways, respectively.

Since the 1960s, during the maintenance of existing railway systems, Italian State Railways replaced the old rails with “Vignoles” types UIC 50 and UIC 60. In Italy, the code that describes the “Vignoles” type rails is UNI-3134 [13] which doesn't differ much from the Eu-

ropean and UIC (i.e. Union Internationale des Chemins de fer) regulations. Table 6 shows the weight of rails in kg/ml according to UNI-3141 [13].

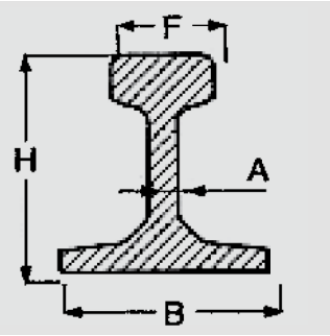

Type	Weight [kg/m]	H [mm]	F [mm]	B [mm]	A [mm]
21	21.373	100	50	80	10
27	27.350	120	50	95	11
30	30.152	125	56	100	12
36	36.188	130	60	100	14
46	46.786	145	63.5/67.2	135	14
50	49.850	148	65.2/70	135	14
60	60.34	172	70.6/74.3	150	16.5

Table 6: Weight and geometrical properties of rails in kg/m according to UNI-3141 [13].

The sleepers, instead, can be made of wood or prestressed reinforced concrete.

Wooden sleepers are the oldest and still widespread. For reasons of cost, of supply as well as of a reduced service life due to adverse weather conditions, in the past wooden sleepers were replaced by iron ones. Nowadays, especially on high-speed rails, prestressed concrete mono-block or twin-block sleepers are used. The twin-block sleepers differ from the mono-block types because they consist of two parallelepiped prestressed concrete elements connected to each other by a steel bar.

Table 7 shows the geometric characteristics and the sleeper's weight in kilogram. To calculate the weight per meter, it is necessary to refer to the module, i.e. the number of sleepers that are in 6 m of track length. The module depends on the class of the railway line, and consequently on the maximum load and speed of the train, and can be:

- *Module 6/10*, i.e. 10 sleepers in 6 m (used for tracks belonging to the main rail network suitable for the highest speeds, for 18 t/axle in case of isolated axles, and for more than 18 t in case of locomotive axles);
- *Module 6/9*, i.e. 9 sleepers in 6 m (used for complementary rail network as well as for crossing or priority rails suitable for lower speeds, for 18 t/axis in case of isolated axles, and for more than 18 t in case of locomotive axles); and
- *Module 6/8*, i.e. 8 sleepers in 6 m (used for tracks belonging to the secondary rail network as well as for all other rails suitable for even lower speeds and 16 t/axis in case of isolated axles).

To connect the sleepers to the rails, and often to ensure electrical insulation, the used fasteners can be of different types; their weight has little impact on the non-structural load.

Type of sleeper	Length [mm]	Depth [mm]	Thickness [mm]	Weight [kg]
Wood	2600	260	160	80 – 100
Prestressed concrete mono-block	2300 - 2600	300	180 – 230	250 – 370
Prestressed concrete twin-block	2300	300	220	245

Table 7: Geometric characteristic of the sleepers.

The railway tracks generally lay on a layer of ballast; the latter can be replaced by a concrete plate in very special cases, such as viaducts with an isostatic structure and length span

not exceeding 30 m. The ballast is a layer of crushed stone with a thickness that can be about 50 cm or 35 cm, depending on whether the importance of the rail network is primary or secondary. The stone material has an internal friction angle of not less than 45° and an apparent volumetric mass of not less than 1.5 t/m^3.

Between the deck and the ballast exists a waterproofing layer consisting of two sheaths, one at the top and one at the bottom, and a protective layer of bituminous conglomerate about 5 cm thick. The membranes at the top and the bottom of the waterproofing layer have a thickness of about 5 mm and 3 mm, respectively, and a weight of 4 kg/m^2 and 3-3.5 kg/m^2, respectively. The bituminous conglomerate generally weighs 80-90 kg/cm^2.

Finally, the superstructure is also composed of noise barriers, the weight of which is usually taken from the manufacturer's data sheets.

Table 8 shows the weight and height to be considered for the design of the noise barriers provided by: (i) the Circular n. I/SC/PS-OW2298 1997 [1], (ii) the Technical Specification "RFI DTC INC PO SP IFS 001 A" 2011 [2], (iii) and the Manual for the Design of Civil Structures "RFI DTC SI PS MA IFS 001 A" 2016 [3].

Regulation	Weight [kN/m^2]	Height from the slab floor [m]
Circular 13/01/1997 [1]	2,0	4,0
Technical Specification "RFI-DTC-INC-PO-SP-IFS-001-A" 2011 [2]	4,0	4,0
Manual for the design of civil Structures "RFI DTC SI PS MA IFS 001 A 2016 [3]	4,0	4,0

Table 8: Prescriptions for noise barriers ([1], [2], [3]).

In the case of a superstructure consisting of ballast, railway track, and waterproofing (including the bituminous conglomerate), the non-structural load can be simply calculated by considering a total volume weight of 18 kN/m^3. This volume weight is applied over the entire average width between the paraballast walls, for an average height between the top rail and the extrados of the deck equal to 0.80 m. For bridges in curved railway sections, , the weight of the ballast used to create the superelevation must be added to the conventional weight indicated above, which is evaluated with its actual geometric distribution and with a volume weight of 20 kN/m^3 ([1], [2], [3]).

3.2.2 Train Live Loads

The simulated design of railway bridges requires an estimate of the train live loads used in the planning step according to the year of structure design.

For reinforced concrete bridges, the first regulation on this topic was issued in 1946, when Circular 30/10/1946 [14] introduced a formula for the evaluation of a dynamic increase coefficient φ to be used for reinforced concrete bridges:

$$\varphi = \frac{0.4}{1+0.2L} + \frac{0.6}{1+4P/S}, \tag{1}$$

in which L is the theoretical load capacity of the beam, P the overload, and S the permanent load. For the concrete structures design before the Circular n. I/SC/PS-OW2298 1997 [1], the increase in load due to the passage of trains was carried out by increasing the values of

overloading by 25%. This criterion derived from some regulations concerning the construction of concrete structures that were issued before 1945.

From 1945 until the following year, instead, the design of reinforced concrete bridges was carried out by using the dynamic increase coefficient φ defined in the Circular 15/07/1945 [15] for steel bridges: its value depended on both the design speed V and the theoretical capacity L of the structural element to be designed. Specifically, if rail joints were absent or only welded, the dynamic increase coefficient φ was assumed to be maximally of 40% to be associated to the elements of limited theoretical capacity L. This value was subsequently increased to 50% as well as the maximum design speed V_{max} that became equal to 100 km/h. As a consequence, the dynamic increase coefficient φ never exceeded 50%. Concerning the train live loads, Circular 15/07/1945 [15] defined two types of load in relation to the presumed railway traffic, i.e. "Type A" and "Type B" (see Figure 1). Alternatively, for the calculation of longitudinal ties, cross-beams, and structural elements with a low theoretical load capacity, the standard allowed the use of an isolated axle of 30 t and 25 t, instead of the train live loads "Type A" and "Type B", respectively.

Before the Circular 15/07/1945 [15], other regulations defining the train live loads were issued in Italy, but we did not consider them here as they concerned exclusively iron and masonry railway bridges, which were in the past much more common than the ones made of reinforced concrete. In Figure 2 we report only the train live loads used to design railway bridges before 1916, when the Italian State Railways was founded.

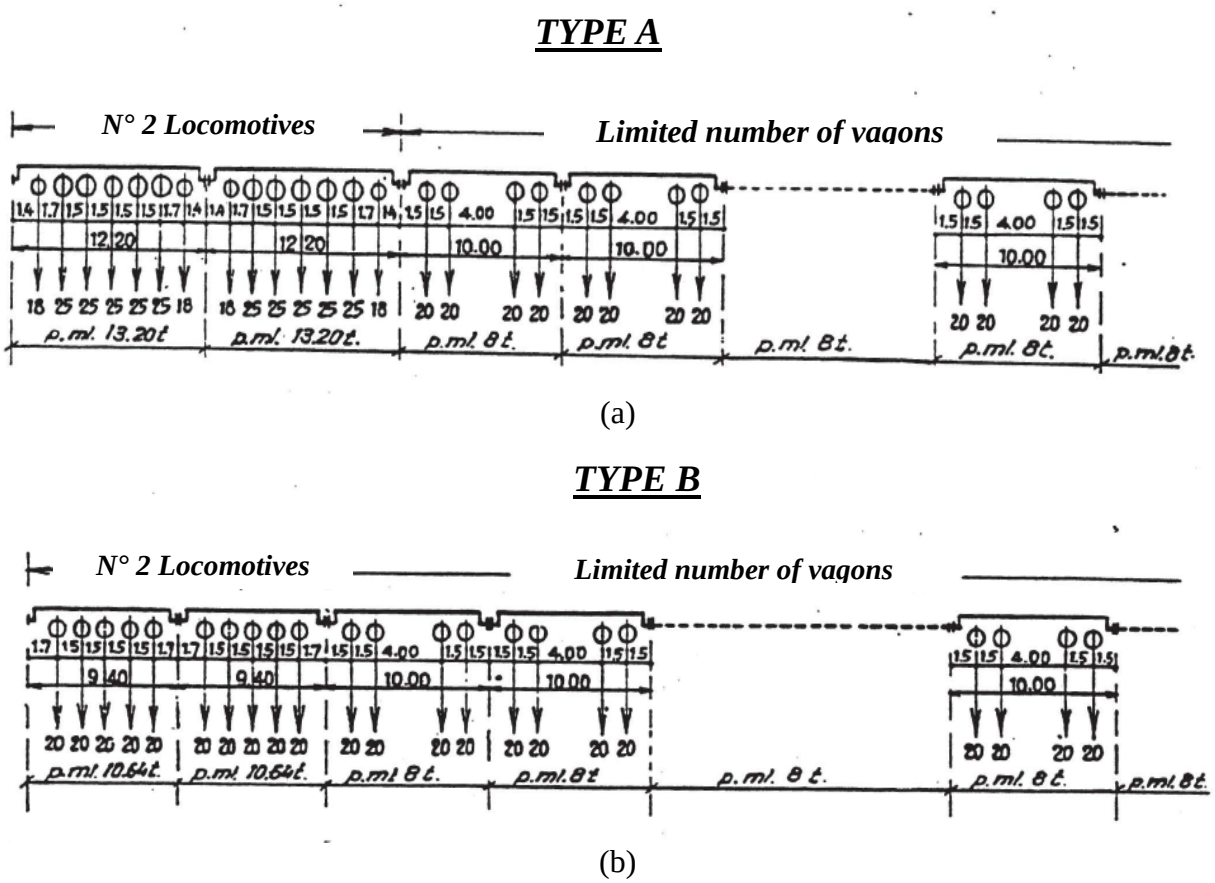

Figure 1: (a) "Type A" and (b) "Type B" train live loads, used for the design of railway bridges according to Circular 15/07/1945 [15].

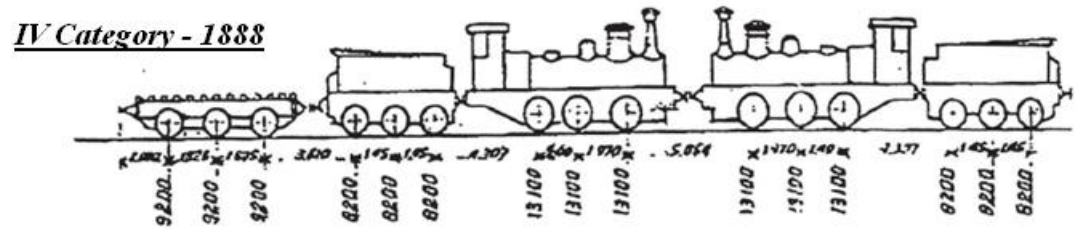

(a)

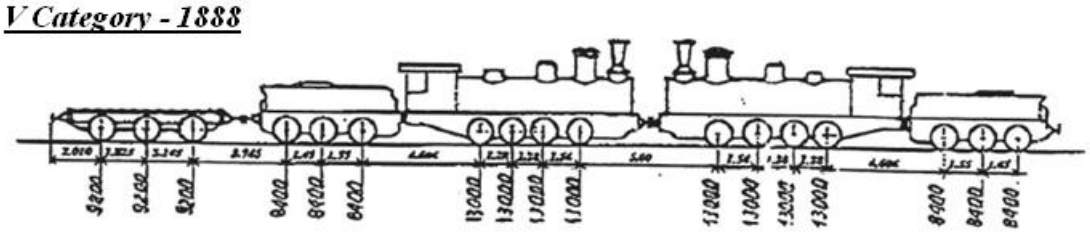

(b)

Figure 2: (a) “Category IV” and (b) “Category V” train live loads, used to design railway bridges before the standard issued in 1916.

The provisions of the Circular 15/07/1945 [15] have remained valid until 1995, when the Circular n. I/SC/PS-OW2298 *"Overloads for the calculation of railway bridges - Instructions for design, execution and testing"* were issued, and then updated in 1997 [1]. This Circular incorporated the instructions from the Eurocodes and introduced two new models of train live load that replaced the previous ones. The new models of train live loads were:

- for normal railway traffic “LM71”;
- for heavy railway traffic “SW”, which was available in two different configurations “SW1” and “SW2”.

The characteristic values attributed to the load models had to be multiplied by an adaptation coefficient α, which varied according to the category of the railway bridge to be designed (see Table 9). Bridges could belong to two different railway categories, i.e. “ Category A” and “Category B”. In particular, bridges in “Category A” applied to railways on which heaviest trains circulated or should be able to circulate; on the contrary, bridges in “Category B” applied to the secondary railways of normal gauge, not included in “Category A”.

Load model	Adaption coefficient α	
	Category A	Category B
LM71	1.1	0.83
SW/0	1.1	0.83
SW/2	1.0	0.83

Table 9: Adaptation coefficient α depending on the load model and the bridge category defined in Circular n. I/SC/PS-OW2298 " and its following update [1].

As it can be seen from Figure 3a, contrary to the provisions of the previous regulations, the train live load was represented by both axial and distributed loads.

In particular, the load model for normal traffic “LM71” consisted of four axles Q_{vk} of 250 kN, placed at a distance of 1.60 m from one another, and of a distributed load q_{vk} of 80 kN/m in both directions, starting from 0.8 m from the end axles Q_{vk} till an unlimited length. In addi-

tion, for this load model an eccentricity of the load towards the track axis was contemplated, depending on the gauge *s*, to take into account the displacement of loads.

The load model for the heavy traffic "SW" (see Figure 3b), instead, was characterized by two distinct configurations, as shown in Table 10.

Finally, for some particular controls, the Circular introduced a special train live load called "Unloading Train", represented by an uniformly distributed load equal to 12.5 kN/m.

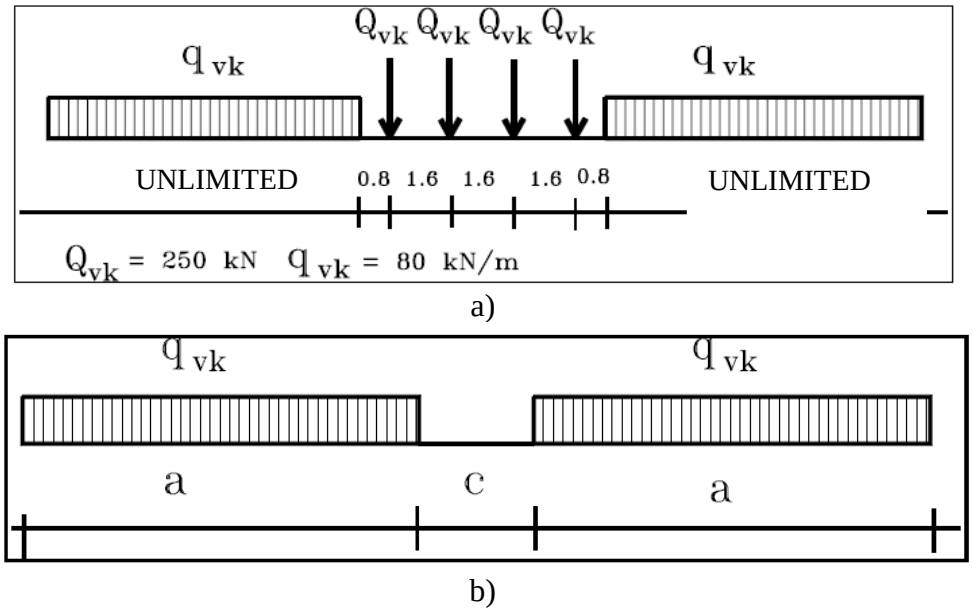

Figure 3: a) Load model for normal railway traffic "LM71" and b) Load model for heavy railway traffic "SW" defined in the Circular n. I/SC/PS-OW2298 and following update in 1997 [1].

Load model	Q_{vk} [kN/m]	a [m]	c [m]
SW/0	133	15.0	5.3
SW/2	150	25.0	7.0

Table 10: Load model for heavy railway traffic "SW" defined in the Circular n. I/SC/PS-OW2298 and following update in 1997 [1].

The Circular n. I/SC/PS-OW2298 1997 [1] further introduced two different dynamic increase coefficients φ in relation to the state of maintenance of the railway line which could be standard or reduced. These coefficients had to be applied to the theoretical load models "LM71" and "SW" in case of a static analysis, to take into account the movement effects and any imperfections of the rail, the wheels, and the suspension system. The Circular n. I/SC/PS-OW2298 1997 [1] also contemplated real dynamic increase coefficients φ_{real} to be multiplied to load models representing a real train. Real train load models are used in particular conditions of analysis (or for the design of specific bridge typologies) and are made of concentrated loads, variously spaced, that schematize the succession of the axes of convoys actually or potentially circulating; each of them was characterized by a maximum speed and a certain overall length [3].

Finally, the latest "RFI DTC INC PO SP IFS 001 A" 2011 [2] and "RFI DTC SI PS MA IFS 001 A" 2016 [3] assume the same load models defined in the Circular n. I/SC/PS-OW2298 1997 [1]. The only differences are: (i) the adaptation coefficient α, which herein depends only on the load model (see Table 11), (ii) the calculation of the real dynamic coefficient φ_{real}, and (iii) the value corresponding to the unloading train, which became 10.0 kN/m.

Load model	Adaption coefficient α
LM71	1.1
SW/0	1.1
SW/2	1.0

Table 11: Adaptation coefficient α depending on the load model defined in "RFI DTC INC PO SP IFS 001 A" 2011 [2] and in "RFI DTC SI PS MA IFS 001 A" 2016 [3].

3.3 Longitudinal and transverse reinforcement

In the seismic assessment of existing reinforced concrete bridges through analytical methods, the amount of longitudinal and transverse reinforcement in the piers needs to be known. This information is usually given in construction plans, but not often available. To fill this gap, the amount of the reinforcement can be derived from the appropriate code that was in use at the time of the structure design.

Table 12 reports the minimum values of both longitudinal and transverse reinforcement defined from the Royal Decree 16th November 1939 [8] to the Ministerial Decree 4th 1992 [16]. The Royal Decree 10th January 1907 [4] is excluded since it does not contain any information on the reinforcement to be placed in the reinforce concrete structural vertical elements. Instead, we deal separately with the Circular n. I/SC/PS-OW2298 1997 [1], the Technical Specification "RFI DTC INC PO SP IFS 001 A" 2011 [2], and the Manual for the Design of Civil Structures "RFI DTC SI PS MA IFS 001 A" 2016 [3] because they are regulations issued directly by Italian State Railways.

In particular, for all viaducts built in territories seismically classified in 1st category (S=12, where *S* represents the seismicity level), 2nd category (S=9), 3rd category (S=6), the Circular n. I/SC/PS-OW2298 1997 [1] defined the minimum quantity of longitudinal reinforcement as 0.6%A_{eff}, where A_{eff} is the area of the effective concrete cross-section. This limit changed to 0.4%A_{eff} for all viaducts designed in the 4th seismic zone category (i.e. not classified zone), with the exception of the Sardinia region. In addition, the longitudinal rebars had not to be more than 300 mm apart. The diameter of the stirrups and transverse ligatures, instead, had not to be less than 8 mm and was obtained according to relationships that depended on the cross-section type of the pier, i.e. whether they were rectangular or circular, in both cases solid or hollow. Furthermore, in piers with a solid or hollow circular cross-section the use of spirals was not permitted anymore and were replaced by circular stirrups. To increase the level of ductility of the structure, the distance *s* between the stirrups had to be more than 10 times the minimum diameter of the vertical rebars.

The Technical Specification "RFI DTC INC PO SP IFS 001 A" 2011 [2] and the Manual for the Design of Civil Structures "RFI DTC SI PS MA IFS 001 A" 2016 [3] resumed with the established values from the Circular n. I/SC/PS-OW2298 1997 [1]. Regardless of the seismic category for which the viaduct was designed, both Technical Specification and Manual for the Design of Civil Structures ([2], [3]) fix a minimum longitudinal reinforcement value of 0.6%A_{eff}. As established in the Circular n. I/SC/PS-OW2298 1997 [1], the longitudinal rebars should be connected by stirrups, which should have a diameter greater than 8 mm, but a pitch neither greater than 10 times the diameter of the longitudinal bars they connect nor 1/5 of the diameter of the section core inside them. In addition, piers with hollow section should have at least 6 ties per square meter connecting the longitudinal reinforcements. Finally, the limitations to define the diameter of pier stirrups provided by the Circular n. I/SC/PS-OW2298 1997 [1] were also present in the Technical Specification [2] and the Manual for the Design of Civil Structures [3]. The only difference was that such limitations only applied if the bridge design required the use of a structure factor *q* equal or less than 1.5.

Code	Longitudinal reinforcement	Transversal reinforcement
R.M.D. 16/11/1939 [8]	$A_s \geq 0.8\ \% A_c$ ($A_c \leq 2000$ cm^2) $A_s \geq 0.5\ \% A_c$ ($A_c \geq 8000$ cm^2) $0.8\%A_c < A_s < 0.5\%A_c$ ($2000\text{cm}^2 < A_c < 8000\text{cm}^2$)	$p \leq \min(1/2L_{min}, 10\phi_l)$
M.D. 30/05/1972 [11]	$0.6\ \%A_c \leq A_s \leq 5\ \%A_c$ $A_s \geq 0.3\ \% A_{eff}$ $\phi_l \geq 12$ mm	$p \leq \min(15\phi_{l,min}; 25\text{cm})$ $\phi_t \geq 6$ mm
M.D. 30/05/1974 [17] M.D. 16/06/1976 [18]	$A_s \geq 0.6\%A_c$ $0.3\%A_{eff} \leq A_s \leq 5\%A_{eff}$ $\phi_l \geq 12$ mm	$p \leq \min(15\phi_{l,min}; 25\text{cm})$ $\phi_t \geq 6$ mm
M.D. 26/03/1980 [19] M.D. 01/04/1983 [20] M.D. 27/07/1985 [21] M.D. 14/02/1992 [16]	$A_s \geq 0.8\%\ A_c$ $0.3\%A_{eff} \leq A_s \leq 6\%A_{eff}$ $\phi_l \geq 12$ mm	$p \leq \min(15\phi_{l,min}; 25\text{ cm})$ $\phi_t \geq \max(6\text{mm}; 1/4\phi_{l,max})$

A_s=Total steel area in a reinforced concrete pier cross-section; A_c=Concrete area strictly necessary for the axial load; ϕ_l=Diameter of the longitudinal steel in the pier cross-section; A_{eff}=Effective concrete cross-section; p=Stirrups pitch; ϕ_t=Stirrups diameter; L_{min}=Smallest size of the pier cross-section; $\phi_{l,min}$, $\phi_{l,max}$ =Smallest and biggest diameter of the longitudinal steel in the pier cross-section.

Table 12: Longitudinal and transverse reinforcement of reinforced concrete piers from the Royal Ministerial Decree 16th November 1939 [8] to Ministerial Decree 4th February 1992 [16].

3.4 Bearings

Another necessary specification for the seismic verification of existing bridges relates to the actual function of supports in the structural response. The structural response cannot properly model the reality in case of inadequate modelling of support devices.

To this end, this section contains a brief description of the state of the art of bearings available in the Italian regulations from 1972 to the present.

The Technical Instructions CNR 10018/72 [22] provided guidance for the calculation, acceptance, and installation of elastomeric bearings, which could also be reinforced. To design this type of bearing required to define: (i) the normal force due to vertical loads acting on the support surface, (ii) the horizontal force due to permanent loads and thermal variations, and (iii) the horizontal force depending only on accidental loads and maximum rotation expected in the beam plane. Considering the most unfavorable combinations of the above mentioned loads and deformations, it was possible to calculate: (i) the normal tension due to the vertical load, (ii) the tangential tensions produced by the vertical load, the horizontal loads and the rotation, and (iii) the shortening and the elastic sliding due to the vertical load and the horizontal forces, respectively. These stress values were then used to carry out strength, sliding, and stability analyses in case of elastomeric bearings. In case of reinforced elastomeric devices, the verification of reinforcement was added to the analyses [23].

In 1985, Technical Instructions CNR 10018/72 [22] was updated. Specifically, in addition to elastomeric devices, the Technical Instructions CNR 10018/85 [24] allowed also the use of confined elastomeric disc bearings as well as PTFE slide bearings (PTFE stands for polytetrafluoroethylene, commonly known as teflon).

The confined elastomeric disc bearings allow rotations around any horizontal axis due to the deformability of an unreinforced rubber disc, confined within a steel monolithic base.

PTFE slide bearings, on the other hand, use sliding surfaces that consist of a layer of PTFE sliding on a surface with a flat, cylindrical, or spherical shape and that is usually made of stainless steel or aluminum alloy. To increase the load resistance, teflon is often combined with other materials (e.g. graphite, glass fibers, etc.), which can bring its load resistance up to

1000 daN/cm^2. Although they have mostly good properties, the negative characteristic of these bearings is that they deplete due to their highly viscous behavior, especially if subjected to reciprocal translations [25].

In 1987 the Technical Instructions CNR 10018 instructions were updated again: in this case the changes mainly concerned the level of the maximum horizontal forces that the supports could transmit to the structure [26]. In particular, bearings with metal plates solidified with reinforced concrete structures with cement or epoxy malt could transfer shear stresses of no more than 25% of the normal concurrent action. For supports with ribbed steel plates as well as with appropriate cavities or prominences, this limit could be increased by up to 35%. For shear stresses exceeding the above limits, mechanical connections had to be used (e.g. pins, clamps, etc.), especially in presence of bridges located in zones of high seismic hazard or when potentially exposed to significant dynamic actions [23].

In 1996, the Technical Instructions FS 44/B [27] were issued and incorporated all the innovations introduced by the Decree of the Ministry of Public Works 16.1.96 [28] in case of under-track structures designed in zones of high seismic hazard.

In 1998, the Technical Instructions CNR 10018 were improved again [29]. An important change compared to the latest version of the instructions, i.e. CNR 10018/85 [24], was that the use of natural rubber or neoprene devices was prohibited in favor of reinforced elastomeric bearings. Initially, natural rubber or neoprene devices were considered a valid alternative to steel devices, characterized by phenomena such as slippage (for cylindrical steel devices) or corrosion (both punctual and uniform). However, they were abolished because they showed several problems, such as deterioration due to atmospheric agents, hardening of the rubber, sliding of the support, as well as phenomena of fatigue and creep. These negative aspects were greatly reduced in reinforced elastomeric devices, which were capable of withstanding simultaneous loads and displacements in any direction and of restoring the undeformed configuration after the permitted displacements. Moreover, being immersed in the rubber, the steel of the reinforced elastomeric bearings is preserved from the phenomenon of corrosion. The only phenomenon that can cause the collapse of such devices is the delamination between elastomer and steel, which, depending on the entity, can cause the total or partial loss of compressive strength without additional deformation. Finally, for the design and verification of the elastomeric devices, the Technical Instructions CNR 10018/85 [24] considered the actions to which they are subjected as well as the permitted displacements, both of which had to be calculated using a three-dimensional analysis of the structure.

In addition to the different types of bearings already described in the previous versions, the Technical Instructions CNR 10018/98 [29] provided new information on bridge bearings made entirely of steel. The functioning of the steel devices is based on the physical rolling phenomenon of two or more steel surfaces in contact with each other.

In 2002 the Technical Instructions FS 44/E were issued [30] that initially defined and described in detail which bearings had to be used for railway bridges, also according to the type of movement allowed in the plane. In particular, the bearings could be fixed or movable. If they are fixed, all the translations are prevented, otherwise translations in one or more directions of the plane are allowed. The Technical Instruction FS 44/E [30] also stated that all bearings had to be capable of rotation in accordance with the values given in the instruction itself and that, if bearings were required to transmit high horizontal forces, it might be convenient to use seismic restraints (fixed or movable).

Finally, the recommendations defined in the Technical Instructions FS 44/E [30] were also included in the Technical Specification "RFI DTC INC PO SP IFS 005 A" 2011 [2], and then later replaced by the Manual for the Design of civil Structures “RFI DTC SI PS MA IFS 001 A” 2016 [3]. The latter provides the requirements for the calculation, construction, installation,

and control of bearings used for railway bridges in accordance with the New Technical Regulations [12], and following the Ministerial Circular 2 February 2009 no. 617 [31].

4 CONCLUSIONS

This paper gave a bibliographic review about the regulations on the design of railway girder bridges, issued in Italy from 1900 to the present.

In particular, the paper intended to report the main changes that have occurred at the regulatory level on the construction of reinforced concrete railway bridges, especially in terms of mechanical characteristics of materials, loads, longitudinal and transverse reinforcements, as well as bearings.

The first Italian regulation on the design of reinforced concrete railway girder bridges that is publicly available dates back to 1995. The provisions on the reinforcement of piers and on the mechanical characteristics of materials derived from regulations that had been issued in Italy starting from 1907. For mobile loads and bearings, technical standards specifically issued for railway bridges had been taken into account from 1946 until 1972.

The definition of the permanent load depends on the composition of the superstructure. For this purpose, this paper also provided information about the weights of the railway track and ballast, as well as the weight of noise barriers.

The bibliographic review of the Italian regulations given in this paper provides a collection of data that is necessary for the simulated design of railway reinforced concrete girder bridges in Italy using analytical methods. The presented data depend on the year of design and the type of railway bridge and eventually define the likely seismic behavior of these structures.

REFERENCES

[1] Circolare 13.01.1997, *Testo aggiornato della istruzione n° i/sc/ps-om/2298 del 2 Giugno 1995 completo delle relative integrazioni: Sovraccarichi per il calcolo dei ponti ferroviari – Istruzioni per la progettazione, l'esecuzione e il collaudo*. Ferrovie dello Stato, 1997. (in Italian)

[2] RFI DTC INC PO SP IFS 001 A, *Specifica per la progettazione e l'esecuzione dei ponti ferroviari e di altre opere minori sotto binario*. Ferrovie dello Stato, 2011. (in Italian)

[3] RFI DTC SI PS MA IFS 001 A, *Manuale di progettazione delle opere civili. Parte II – Sezione 2 – Ponti e Strutture*. Ferrovie dello Stato, 2016. (in Italian)

[4] D.M. 10 Gennaio 1907 (Gazz. Uff. del 2 febbraio 1907 n°28), *Prescrizioni normali per l'esecuzione di opere in cemento armato.* (in Italian)

[5] R.D.L. 4 settembre 1927, n°1981 (Gazz. Uff. del 11 novembre 1927 n°261), *Nuove norme tecniche per l'accettazione degli agglomerati idraulici e l'esecuzione delle opere in conglomerato cementizio semplice ed armato*. (in Italian)

[6] R.D.L. 23 maggio 1932, n°832 (Gazz. Uff. del 23 luglio 1932 n°169); Quest'ultimo convertito in legge con modificazioni con la Legge 22 dicembre 1932, n°1830 (Gazz. Uff. del 26 gennaio 1933 n°21), *Norme per l'accettazione degli agglomerati idraulici e per l'esecuzione delle opere in conglomerato cementizio*. (in Italian)

[7] Circolare 17 maggio 1937 n°2202, *Impiego dell'acciaio semiduro nelle costruzioni in conglomerato cementizio armato*. (in Italian)

[8] R.D.L. 16 Novembre 1939 – XVIII n°2229, *Norme per l'esecuzione delle opere in conglomerato cementizio semplice o armato*. (in Italian)

[9] G.M. Verderame, P. Ricci, M. Esposito, and F.C. Sansiviero, Le caratteristiche meccaniche degli acciai impiegati nelle strutture in c.a. realizzate dal 1950 al 1980. *Atti del XXVI Convegno Nazionale AICAP "Le prospettive di sviluppo delle opere in calcestruzzo strutturale nel terzo millennio"*, Paper 54, Padua, Italy, May 19-21, 2011. (in Italian)

[10] Circolare 23 maggio 1957 n°1472, *Armature delle strutture in cemento armato*. (in Italian)

[11] D.M. 30 Maggio 1972 (Suppl. Ord. Gazz. Uff. del 22 luglio 1972 n°190), *Norme tecniche alle quali devono uniformarsi le costruzioni in conglomerato cementizio, normale e precompresso ed a struttura metallica.* (in Italian)

[12] D.M. 14 Gennaio 2008 (Gazz. Uff. del 4 febbraio 2008 n° 29), *Norme Tecniche per le Costruzioni (NTC)*. (in Italian).

[13] UNI 3141, *Rotaie per linee ferroviarie - Tipi, dimensioni e tolleranze*. 1991. (in Italian)

[14] Circolare N°125 del 30.10.1946, *Ponti ferroviari in conglomerato cementizio armato – Azione dinamica.* Ferrovie dello Stato, 1946. (in Italian)

[15] Circolare N°54 del 15.07.1945, *Nuovi sovraccarichi per il calcolo dei ponti metallici*. Ferrovie dello Stato, 1945. (in Italian)

[16] D.M. 4 Febbraio 1992 (Suppl. Ord. Gazz. Uff. del 5 febbraio 1996 n°19), *Norme tecniche per l'esecuzione delle opere in cemento armato normale e precompresso e per le strutture metalliche*. (in Italian)

[17] D.M. 30 Maggio 1974 (Suppl. Ord. Gazz. Uff. del 29 luglio 1974 n°198), *Norme tecniche per la esecuzione delle opere in cemento armato normale e precompresso e per le strutture metalliche*. (in Italian)

[18] D.M. 16 Giugno 1976 (Gazz. Uff. del 14 agosto 1976 n°214), *Norme tecniche per la esecuzione delle opere in cemento armato normale e precompresso e per le strutture metalliche*. (in Italian)

[19] D.M. 26 Marzo 1980 (Suppl. Ord. Gazz. Uff. del 28 giugno 1980 n°176), *Norme tecniche per la esecuzione delle opere in cemento armato normale e precompresso e per le strutture metalliche.* (in Italian)

[20] D.M. 1 Aprile 1983 (Gazz. Uff. del 7 maggio 1983 n°124), *Norme tecniche per la esecuzione delle opere in cemento armato normale e precompresso e per le strutture metalliche*. (in Italian)

[21] D.M. 27 Luglio 1985 (Suppl. Ord. Gazz. Uff. del 17 maggio 1986 n°113), *Norme Tecniche per l'esecuzione delle opere in cemento armato normale e precompresso e per le strutture metalliche*. (in Italian)

[22] CNR-UNI 10018/72, *Istruzioni per il calcolo e l'impiego di apparecchi di appoggio in gomma nelle costruzioni*. Consiglio Nazionale delle Ricerche, 1972. (in Italian)

[23] ANAS, *I quaderni tecnici per la salvaguardia delle infrastrutture – Volume II. Quaderno tecnico n°7: Interventi locali sugli appoggi*. 2016. (in Italian)

[24] CNR-UNI 10011/85, *Costruzioni in acciaio – Istruzioni per il calcolo, l'esecuzione, il collaudo e la manutenzione*. Consiglio Nazionale delle Ricerche, 1985. (in Italian)

[25] Mayer L., *Impianti ferroviari - Volume I.* CIFI Editore, 2005. (in Italian)

[26] CNR-UNI 10018/87, *Apparecchi di appoggio in gomma e PTFE nelle costruzioni. Istruzioni per il calcolo e l'impiego*. Consiglio Nazionale delle Ricerche, 1987. (in Italian)

[27] Istruzione Tecnica 44/B, *Istruzioni tecniche per manufatti sotto binario da costruire in zona sismica*. Ferrovie dello Stato, 1996. (in Italian)

[28] D.M. 16 gennaio 1996, *Norme tecniche relative ai criteri generali per la verifica delle costruzioni e dei carichi e sovraccarichi*. (in Italian)

[29] CNR-UNI 10018/98, *Apparecchi di appoggio per le costruzioni. Istruzioni l'impiego.* Consiglio Nazionale delle Ricerche, 1999. (in Italian)

[30] Istruzione Tecnica 44/E, *Istruzione tecnica per il calcolo, l'esecuzione, il collaudo e la posa in opera dei dispositivi di vincolo e dei coprigiunti negli impalcati ferroviari e nei cavalcavia*. Ferrovie dello Stato, 2002. (in Italian)

[31] Circolare del 2 febbraio 2009, n. 617, *Istruzioni per l'applicazione delle Nuove Norme Tecniche per le Costruzioni*. (in Italian)

COMPDYN 2019
7th ECCOMAS Thematic Conference on
Computational Methods in Structural Dynamics and Earthquake Engineering
M. Papadrakakis, M. Fragiadakis (eds.)
Crete, Greece, 24–26 June 2019

FRAGILITY CURVES FOR LARGE-SCALE ASSESSMENT OF RC RAILWAY BRIDGES

Davide Bellotti[1], **Antonino Famà**[2], **Antonella Di Meo**[2], **and Barbara Borzi**[2]

[1] European Centre for Training and Research in Earthquake Engineering (EUCENTRE)
Via Ferrata, 1, 27100 Pavia, Italy
davide.bellotti@eucentre.it

[2] European Centre for Training and Research in Earthquake Engineering (EUCENTRE)
Via Ferrata, 1, 27100 Pavia, Italy
{antonino.fama, antonella.dimeo, barbara.borzi}@eucentre.it

Abstract

The aim of this work is to present an application developed by Eucentre (EUropean CENtre for Training and Research in Earthquake engineering) to define fragility curves for RC railway bridges in the framework of large scale vulnerability assessment.
The application creates a digital model of the analyzed structure automatically assembling the representative objects which constitute the bridge, such as decks or piers, and the mutual relationships that each object has with the others. Then, the application generates a sequence of nodes and beams, placed on a horizontal plane corresponding to the added planimetric layout and, given the bridge coordinates, defines the site reference seismic hazard.
The obtained digital model allows to convert the structure individual components' description into a useful and functional finite element model. After selecting a certain number of return periods corresponding to the reference seismic action, the application generates several spectrum-compatible accelerograms to perform nonlinear time history analysis. Nonlinear dynamic analyses are preferred to others to better detect the seismic behaviour of bridges whose vulnerability is herein evaluated through the definition of fragility curves. In case of partial level of knowledge, the finite element model cannot be defined. Hence, ad hoc simplified mechanic-based methodologies have been developed.
Two levels of capacity for the seismic verification are considered: one regarding the functionality (damage limit state) and the other regarding the bridge safety (collapse limit state).
These limit states, considered in the fragility curves derivation, essentially concern the piers' deformation and resistance capacity (ductile and brittle failures) and the girders' loss of support.

Keywords: Fragility curves, Railway bridges, Seismic vulnerability.

1 INTRODUCTION

This work deals with the description of the development of an application for the determination of fragility curves for large-scale assessment of reinforced railway bridges.

Several studies on seismic risk assessment of infrastructures have been done in the past on Italian infrastructures which mainly concerned the seismic assessment of highway and road bridges [2][4][16][19][20]. Hence the need to deepen the seismic assess of railway bridges through a methodology that allows a large-scale study of the seismic vulnerability of such structures through the construction of fragility curves. The goal of the work is to create a tool able to generate the numerical model of a bridge through the execution of numerous non-linear time-history analyzes to derive the bridge-specific fragility curves.

The application performs the structural calculations using OpenSEES [17] finite element analysis program and generates a digital model of the analyzed structure, automatically constructing the representative objects of its parts, such as the deck, the piers and mutual relationships that each object has with the others. This digital model makes it possible to convert the description of the individual components of the bridge into a useful and functional finite element model in order to carry out the simulations for the calculation of fragility curves.

The aim of the work is to provide specific fragility curves for individual railway bridges of which complete data are known. The study of the methods of analysis of the seismic vulnerability of railway bridges object started by studying the structural typologies prevalently widespread in Italy. Among all the typologies, girder bridges were taken into account.

Girder bridges are generally formed by a deck constituted by multiple beams which can be simply supported or continuous, in such a way as to have an isostatic or hyperstatic structural scheme. Due to static and seismic loading, beams are subject to shear and bending forces. In girder bridges, the deck it's supported by unreinforced or reinforced concrete piers and can be constituted by reinforced concrete, prestressed reinforced concrete or steel.

Between the deck and the vertical structure of the bridge there are the support devices, the choice of which depends mainly on the type of deck and the type of constraint required. In the case of a reinforced concrete deck, the adopted construction technologies are dependent mainly on the total length of the bridge and the individual bays.

For spans over 4 m the simplest system used in the railway infrastructures consists of girder deck and upper flange. The beams can have a double "T" or a box section and reach a length of about 20-25 m. Cross beams are used to guarantee the collaboration between all the beams of the deck: generally they have a height equal to that of the concrete ribs to which they are connected both in the head and in intermediate positions.

In addition to ordinary reinforced concrete, the deck can be made of prestressed concrete beams. This type of deck allows to cover spans between 35 and 50 m and is used both in ordinary and high speed railway rail.

Another type are the steel decking bridges which have been widely used in the past; nowadays, however, these decks are mainly used for large-span bridges with reduced height or to replace pre-existing metal girders.

Regarding decks with ballast presence, they are usually with a box or a mixed structure, or composed of double "T" or box beams with a concrete flange slab.

2 MODELING

The application divides the bridge into three areas: super-structure, connections and sub-structures, where for connection area is intended all that is in between the super-structure and

the sub-structures. These three areas are treated and processed in sequence because the geometric construction of the bridge is from top to bottom and the underlying parts depend on those above them.

The elements constituting the super-structure are organized in a rigid hierarchy: the bridge tracking is composed by decks, which are composed by one or more bays, divided into bay segments. It is assumed that at the beginning and at the end of each bay there is a sub-structure (pier or abutment). It is not necessary to specify either the planimetric position or the orientation of these sub-structures, since it can be automatically deduced from the terminal position of bays (the latter derives from the planimetric layout already known at the modeling of the sub-structures). The spans' division into segments is useful for several reasons: to change the structural section within a single bay; to insert internal releases (such as Gerber saddles); to follow a plan curve layout; to obtain a discretization of the masses along the span to capture the dynamic response of super-structure modes.

The application allows the maximum flexibility of definition of the super-structure: it allows, in fact, to alternate both supported and continuous decks as well as to alternate straight or curved (mixed pattern), even within the same bay.

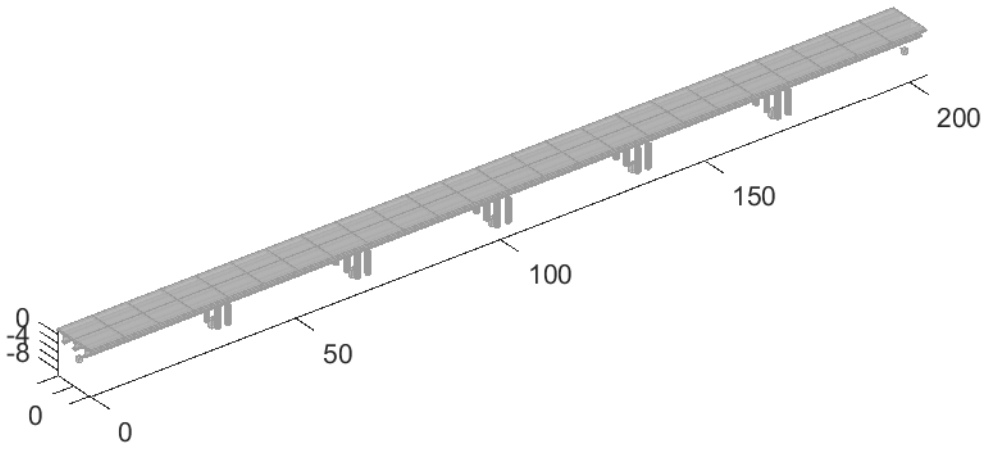

Figure 1: Extruded view of a modeled bridge.

Each railway line of the bridge is modeled with an elastic single-line model consisting of only finished beam elements (Figure 1).

For the geometric construction of the path, the application automatically calculates the planimetric angle that is tangent to the path in each node of the superstructure. This procedure allows to define an intrinsic reference in the same point (horizontal axes tangent and orthogonal to the bridge direction, plus the vertical axis) that is automatically assigned as a natural reference also for the connecting elements and for the substructures. In other words, substructures are naturally and automatically rotated in their local reference to follow the trend of a curvilinear path.

The connection between the superstructure and the substructure is made by two objects: connections and supports. The connection has the function of rigidly transferring the load transmitted by the end node of a span to the extrados of the substructure. This transfer is regulated by two geometric quantities: one horizontal (ΔL) and one vertical (ΔZ). The latter consists of two quantities: the distance of the center of gravity of the section measured by the deck intrados (ΔZ_G) and the distance between the extrados of the pier cap and the intrados of the deck (ΔZ_C). The ΔL and ΔZ_C values are input data, the ΔZ_G value is calculated automatically by the appli-

cation. In a real bridge, the value ΔL represents the distance between the alignment of the supports and the end of the deck, while ΔZ_C is usually the vertical encumbrance of the bearings plus the supports (Figure 2).

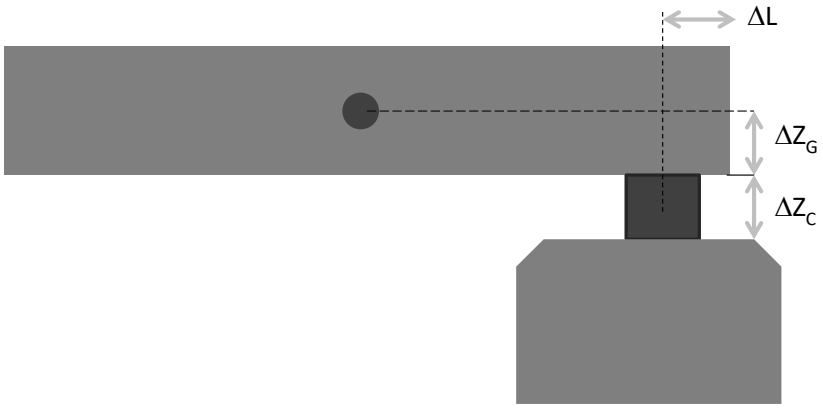

Figure 2: Deck and bearing geometry.

Figure 3 represents a simple substructure (single pier); in the case of portal, frame or multiple-frame piers, different assumptions are made for the connection between the nodes of the pier and the lower ones of the supports.

In both articulated and simplest cases, it is always assumed that the axis of the substructure is placed in the center of gravity of the master nodes of the respective connections that converge to it.

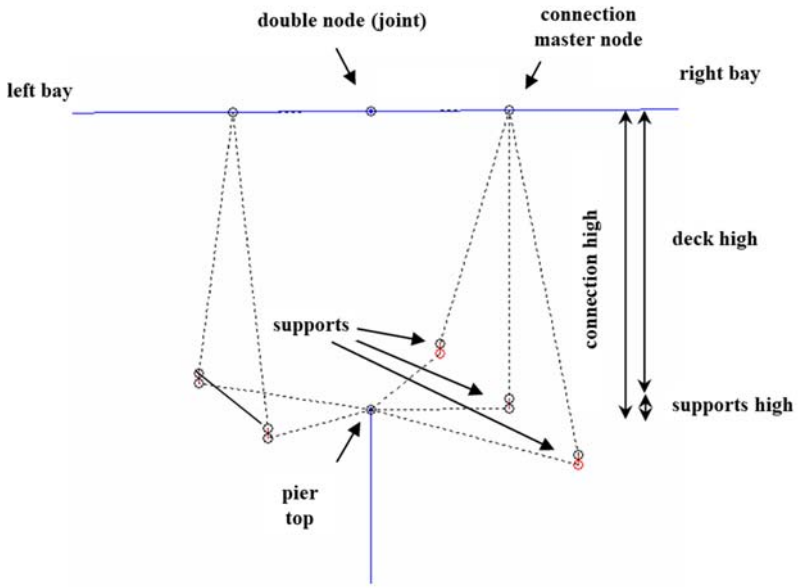

Figure 3: Connection modeling scheme.

The element used for modeling the piers is the BeamWithHinges element of the OpenSEES library [17]. It is formulated with an optimized integration scheme along its development that employs non-linear fiber sections at the ends and elastic sections in the central part. The model

considers a non linear behaviour that occurs in piers and supports. This limit is imposed by the need to automatically manage numerous non-linear finite element time-history analyses.

To define the concrete material, the application employs a very small set of parameters.

For the definition of elastic properties it is necessary to specify the Young's modulus, the Poisson's module and the unit weight.

For the definition of the non-linear properties, it is assumed a nonlinear stress-strain law (the application uses OpenSEES's Concrete01 material [17]) for which, in addition to the weight density, four values need to be specified: the concrete compressive strength at 28 days, the concrete strain at maximum strength, the concrete crushing strength and the concrete strain at crushing strength.

It is assumed that the mechanical properties of the concrete follow a lognormal distribution. For each numerical simulation different sampled values are adopted.

For example, the case of the concrete compressive strength is illustrated:

$$f_{co\ simulation,i} = f_{co} \times \varepsilon_{f_{co},i} \tag{1}$$

where:

$$\varepsilon_{f_{co}} \sim LN\left(0, \beta_{f_{co}}\right) \tag{2}$$

where β_{fco} parameter is the standard deviation of the logarithmic distribution assumed for the peak resistance of the concrete.

Similar to concrete, the application uses a very small set of parameters to define the steel material. Also in this case, for the definition of the elastic properties, it is necessary to specify the Young's modulus, the Poisson's modulus and the unit weight.

For the definition of the non-linear properties, the application uses OpenSEES's Steel01 material [17] with uniaxial bilinear steel material object with kinematic hardening for which it is necessary to specify the yield stress and the hardening in addition to the unit weight and the Young's modulus. Also in this case, the mechanical properties follow a lognormal distribution defined in the same way as concrete.

2.1 Supports

The first support devices used for reinforced concrete bridges, with a span less than 18 meters, were those made of two lead sheets of one centimeter each, between which was interposed or a steel sheet thick one millimeter (fixed type support) or two steel sheets with graphite contact faces (mobile type support).

Nowadays, steel support devices are spherical, hinged or pendulum type and are used in the presence of steel decks or high reactions transmitted by the deck.

The support constraints of girder bridges vary according to the type of deck. They can be classified in relation to the physical principle used (i.e. rolling, deformation, and sliding), to the degrees of freedom (i.e. fixed supports and mobile bearings) to the transmission of the load (i.e. punctual, linear, and superficial) and to the material they are made (i.e. steel, aluminum, natural or synthetic rubbers).

For the support devices, the application foresees that the constitutive law of the two degrees of freedom associated with horizontal translations is specified, since the remaining DOF are either completely rigid (vertical or rotational DOF) or completely flexible (rotational DOF).

The types of support that have been implemented in the program have been chosen according to the most common types of support in Italian railway bridges and are summarized in Table 1.

Type of support	Description
Fixed	the translational DOF and all the rotational DOF are fixed
Spherical hinge	both the DOF (in plan) are fixed and all the rotational DOF are free
Cylindrical hinge	both the DOF (in plan) are fixed and a single free rotational DOF
Mobile	both DOF (in plan) are free
Unidirectional longitudinal	the longitudinal DOF (in the local reference) is free, the transverse one is fixed
Unidirectional transversal	the transverse DOF (in the local reference) is free, the longitudinal one is fixed
Anisotropic elastoplastic	the two DOF have two elastic perfectly plastic constitutive laws decoupled
Isotropic elastoplastic	the two DOF have isotropic elastic perfectly plastic constitutive law
Friction	the two DOF have a friction isotropic constitutive law

Table 1: Typologies of supports.

With reference to the OpenSees calculation engine [17], the finite elements used for each type of support are constituted by TwoNodeLink finite elements: depending on the type of constraint and on the degrees of freedom, materials that represent a linear or fixed DOF are assigned. In the case of anisotropic elastic a ElastomericBearing finite element is used in the two direction, while in isotropic only one typology is defined. In the case of friction support a FlatSliderBearing finite element is used.

2.2 Definition of loads

The weights and permanent loads are calculated directly in the hypothesis of standard configurations provided by the application for super-structures and sub-structures. For what concerns super-structures, the application allows two different ways to define the contribution due to the dead load. The first is the direct specification of total weight per meter of deck: this condition makes it possible to generalize the application to all those configurations that are explicitly provided for. The second is the specification of the weight only of the carried permanent loads, assigning to the application the automatic calculation of the weight contribution of the structural section of the deck.

The determination of the carried permanent loads referring to the ballast, the railway track and the waterproofing has been carried out assuming a volume weight equal to 18 kN/m^3 applied over the entire average width between the ballast retaining walls for a medium height between rail level and deck extrados of 0.80 m, as indicated in § 5.2.2.1.1 of DM2018 [11]. In particular, the ballast load was defined per unit length of longitudinal development of the bridge (in kN/m), considering an average width of the ballast equal to 4.90m.

In addition to its own weights and permanent vertical loads and masses, the application allows to apply a portion of the vertical loads and masses associated with the transit of the train. The loads used in the application are those in § 5.2.2.2.1 of the Italian DM2018 [11] code by

means of different load models representing the different types of rail traffic: normal and heavy. Three types of load can be considered: LM71, SW/0 and SW/2. The loads' values have to be multiplied by an adaptation coefficient "α", variable according to the type of infrastructure, and by a coefficient φ, which takes into account the dynamic nature of the trains transit.

In order to evaluate the overloads associated with the transit of trains and the part of them to be used for seismic checks, the value of the q_{tr} load per unit of length was assumed equal to:

$$q_{tr} = q_{eq,tr} \cdot \alpha \cdot \varphi \tag{3}$$

where α and φ are respectively the adaptation coefficient and the dynamic coefficient described above, while $q_{eq,tr}$ represents the equivalent uniformly distributed load per unit of length defined as a function of load models LM71, SW/0 and SW/2.

The loads associated to the transit of trains are applied to the bridge as loads per unit of longitudinal development length (in kN/m) and assumed ones equal to $\psi_2 \cdot q_{tr}$.

In the seismic vulnerability calculations the condition that involves the presence of the overloads and the masses associated with the transit of the train convoys is assumed by adopting ψ_2 equal to 0.2 according to § 5.2.2.8 of the Italian DM2018 [11].

3 DEFINITION OF LIMIT STATES

The limit states considered in the calculation of fragility curves vary in relation to structural elements and are:

1) for piers: the ductile and fragile mechanisms. The ductile mechanisms depend on the total chord rotation amount while the fragile ones depend on the element shear.

2) for decks: the loss of support mechanism towards the supports or the pier cap, controlled by the relative excursion of the support devices.

3) for supports bearings the achievement of the maximum capacity in terms of resistance.

For all the limit states considered, two levels of capacity are foreseen during the verification: one related to the necessity to carry out repair interventions (damage limit state) and the other concerning the safety of the bridge (collapse limit state). An exception to this rule is the fragile shear mechanism on the piers, for which only the collapse limit state is defined. The operation limit state is, instead, linked to the deformations limit defined in relation to the train's safe transitability of the bridge and the limits imposed are not connected with the damage to the structures.

The expressions of capacity used for the calculation of the mechanisms inherent to the piers are those reported in DM2018 [11] and described in §3.1.

These capacities are to be understood different according to the two directions of the cross section of the pier. When verifying the overall limit state of the section, it is assumed that the risk indicator ρ, understood as the ratio between demand and capacity, is obtained, for each time step, by the SRSS combination of the results of the checks on the two main flexion plans. As an alternative to the SRSS combination rule, the rule for combining the directional maximum is used, for example in the loss of support verification. With reference to the three mechanisms examined ("θ" ductile mechanism, "V" fragile mechanism, "d" loss support mechanism), is obtained:

$$\begin{aligned}
\rho_{\theta,x} &= \frac{\theta_{demand,x}}{\theta_{capacity,x}} \quad \rho_{V,x} = \frac{V_{demand,x}}{V_{capacity,x}} \quad \rho_{d,x,SL} = \frac{d_{demand,x}}{d_{capacity,x,SL}} \\
\rho_{\theta,y} &= \frac{\theta_{demand,y}}{\theta_{capacity,y}} \quad \rho_{V,y} = \frac{V_{demand,y}}{V_{capacity,y}} \quad \rho_{d,y,SL} = \frac{d_{demand,y}}{d_{capacity,y,SL}} \\
\rho_{\theta} &= \sqrt{\rho_{\theta,x}^2 + \rho_{\theta,y}^2} \quad \rho_{V} = \sqrt{\rho_{V,x}^2 + \rho_{V,y}^2} \quad \rho_{d,SL} = max\left(\rho_{d,x,SL}, \rho_{d,y,SL}\right)
\end{aligned} \tag{4}$$

The application optionally allows to replace the directional combination rule related to the SRSS shear with the most usual rule that uses the directional maximum:

$$\rho_V = max\left(\rho_{V,x}, \rho_{V,y}\right) \tag{5}$$

The loss-of-support mechanism of decks, although rare, is very dangerous in bridges and occurs when there is an excess of relative excursion between the super-structure and the sub-structure. This eventuality can occur either on alignments of mobile bearings, when they don't guarantee an appropriate restraining retention or they collapse, or on alignments of fixed bearings when they collapse.

The loss of support can have a different degree of severity if referring to the support or pier cap. In the first case, the span falls from its natural seat but does not collapse because supported by the pier cap while, in the second case, the falls of the deck from the pier cap implies the partial collapse of the bridge. This substantial differentiation is maintained during the verification by associating the fall from the support to the damage limit state and the fall from the pier cap to the collapse limit state.

Finally, the assumptions regarding the definition of the limit states concerning the bridge as a whole and not just its components (piers and supports) are illustrated. As already highlighted, each of the controlled mechanisms on the components is a main mechanism, i.e. the achievement of the corresponding limit state on the component implies the achievement of the same limit state on the bridge. This hypothesis is known in the theory of systems as a series arrangement of the components and, although it is the simplest hypothesis that can be formulated, it is quite adherent to the physical reality of bridges, especially in the collapse limit state. It is normal, in fact, to assume a collapsed bridge when one of its piers or girders has collapsed.

3.1 Ductile and brittle mechanisms

The capacities, in terms of total yield and ultimate rotation, are given by the expressions:

$$\theta_y = \phi_y \frac{L_V}{3\nu} \tag{6}$$

$$\theta_u = \theta_y + \left(\phi_u - \phi_y\right) L_{pl} \left(1 - \frac{L_{pl}}{2L_V}\right) \tag{7}$$

where the length of plastic hinge was evaluated as:

$$L_{pl} = 0.1L_V + 0.17h + 0.24\frac{d_{bL} f_y}{\sqrt{f_c}} \tag{8}$$

where φ_y and φ_u are the yield and the ultimate curvatures; h is the height of the section, d_{bL} is the diameter of the longitudinal bars; f_y and f_c are the strengths of the materials; L_V is the shear span at member end and is equal to M/V. L_V can be approximated to L (for single beam and frame piers) and to L/2 (for frame piers) in the longitudinal and transversal direction, respectively.

These capacity expressions are evaluated separately for longitudinal and transverse direction of the base section of each pier.

The application provides for the adoption of different expressions for the shear capacity (resistance): the expressions in the DM2018 [11] (attached to the Circular § C8.8.5.5 [9]), the expressions referable to Priestley-Kowalski [21]or those present in the Eurocode 8 part 3[6].

The shear capacity V_u is always calculated according to the expression:

$$V_u = V_c + V_s + V_N \tag{9}$$

where V_C, V_S and V_N are the contributions of concrete, stirrups and normal stress.

3.2 Loss of support

The amount of demand for determining the risk related to the loss of support mechanism is the relative excursion between super-structure and sub-structures for each alignment of supports, equal to the average deformation of the bearings of each alignment.

This excursion is verified both in the longitudinal direction (parallel to the bridge axis) and in the transversal direction, since the two directions can have different capacity limits. In particular, these capacities must be specified in each alignment, as well as for the two main directions, also for both the verified limit states (SLD and SLC): $d_{SLD,longitudinal}$, $d_{SLC,longitudinal}$, $d_{SLD,transverse}$, $d_{SLC,transverse}$.

Normally, it is assumed, as a capacity to the damage limit state, the limit that implies the non-damage of the devices and in any case the fall from any supports, and as limit of the collapse limit state, the limit of fall from the pier cap which implies collapse.

In the absence of input data, the application estimates the capacities for the loss of support mechanism based on the geometrical data of the bridge. In this case, it is advisable to carefully evaluate the engineering consistency of these quantities. As an example, Figure 4 reports a typical case for the loss of support of the span from the pier cap in the longitudinal direction; in this case the application simply estimates a capacity equal to b/2-e according to Figure 4.

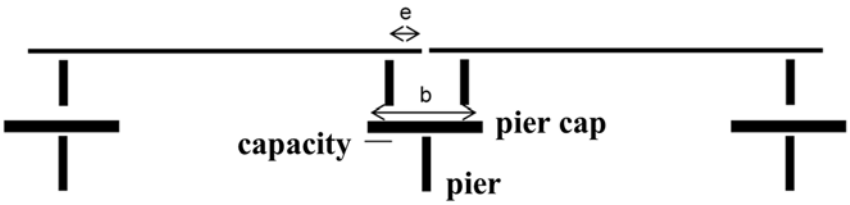

Figure 4: Scheme for the loss of support in the longitudinal direction.

4 GENERATION OF FRAGILITY CURVES

For girder bridges the application generates fragility curves, defined by cumulative probability distributions that allow to estimate the probability of reaching or exceeding a given level of damage for a given severity of ground shaking, for each boundary state analyzed through the following steps. The bridge is modeled for non-linear analyzes in the time domain.

The seismicity of the national zonation site is acquired, i.e. on the basis of the seismic hazard related to the site of the bridge as well as of the local amplification effects due to the soil. Then it is possible to select n periods of return of the seismic action and calculate the corresponding elastic response spectra (n ~ 9). The maximum number of selectable return periods is 9 in line with national technical standards (DM2018 [11]). Spectrum compatible signals (m ~ 10) are generated on the basis of the elastic projections for each return period.

Simulations are performed and the application proceeds with the extraction of the time history of the variables and the quantity of demand (N, V, θ for piers and d for supports), where N is the normal stress acting on the elements, V is the shear and d is the excursion of the supports.

Subsequently the capacity vectors are calculated for each verified limit state, generally dependent on the time history of the variables (θ_{SO}, V_{SLC}, θ_{SLD}, θ_{SLC}, d_{SLD}, d_{SLC}). At this point, risk indicators (ρ) are calculated as the ratio between demand and capacity for each limit state verified for each component of the bridge. Each risk indicator depends on five indices: the period of return of the seismic action (i1); the analyzed signal (i2); the time step of the signal (i3); the component of the bridge (pier or support) (i4) in hypothesis of state limit of damage (SLD) and collapse (SLC), while monitoring only the displacement at the top of the piers in hypothesis of operation limit state (SLO); the verified direction (i5), indicating more simply X or Y. At this point a directional combination of the risk indicators is made according to whether they are piers or supports. The Y risk indicators of the system are calculated from the component indicators (envelope of the mechanisms). Subsequently, the normal fit log of the Y risk indicators is performed with respect to the signals analyzed and the calculation of the probability of exceeding the verified limit state, conditioned to the return period (point of the fragility curve).

Figure 5 shows the risk indicators for the damage limit state (sx) and the collapse limit state (dx), and at the bottom the relative fragility curves for a specific bridge analyzed.

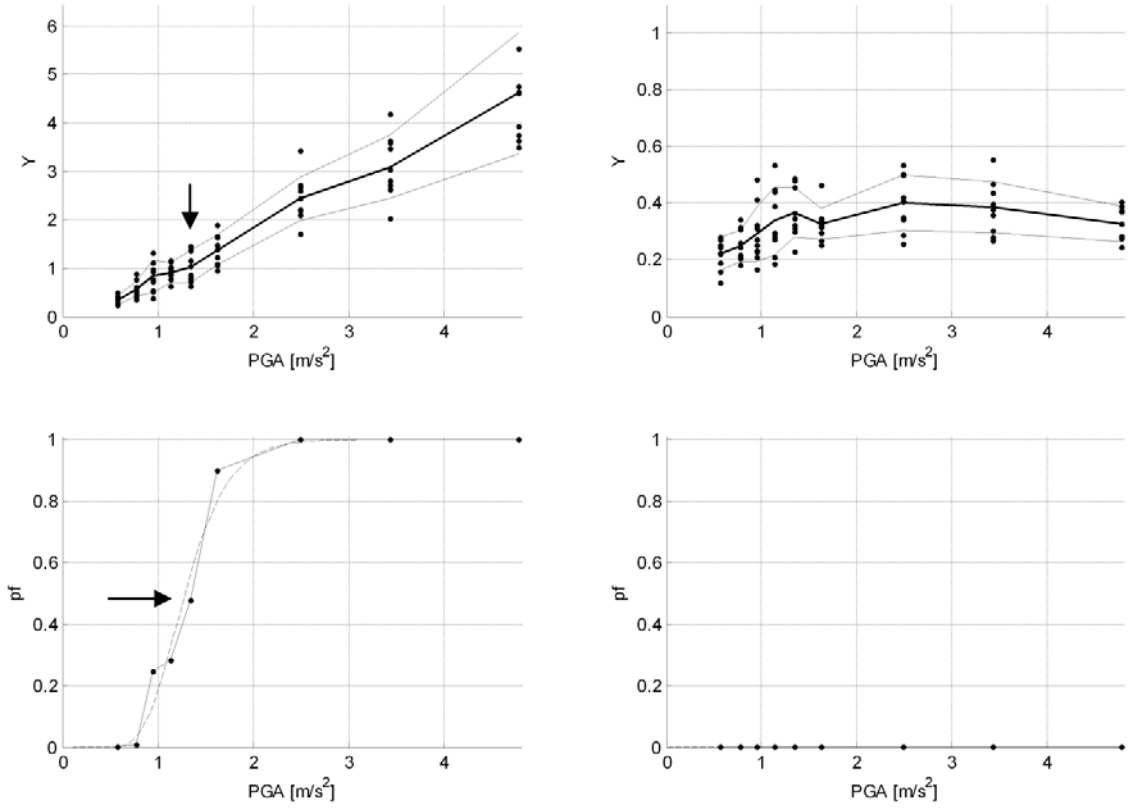

Figure 5: Risk indicator and fragility curve example.

For the calculation of the fragility curves shown in Figure 5, nine return periods of the reference input motion were adopted, and for each of them 10 simulations were carried out.

The application provides a report for each of the four phases of analysis: data acquisition, static analysis, seismic input, and dynamic analysis.

5 CONCLUSIONS

The paper deals with the development of an application for the automatic calculation of fragility curves of railway bridges in the hypothesis of complete knowledge of the bridge. The main hypotheses adopted in the structural modeling of bridges are illustrated.

The FEM analyzes are carried out in the time domain with partially degrading hysteretic constitutive laws, using the OpenSEES [17] code: a description is given of the main analytical options used in the calculation models. The application automatically manages numerous non-linear finite element time-history analyses after carrying out the static analysis and calculating the curvature moment relationship of each pier.

For each simulation, the input motion is obtained from a pair of artificial spectral-compatible accelerograms generated by the application and applied to the structure fixed at the base in two horizontal and orthogonal directions. The adopted reference spectra are those contained in the current national code (DM2018 [11]).

The limit states considered in the calculation of the fragility curves essentially concern the deformation and resistance capacity of the piers (ductile and fragile mechanisms) as well as the loss of support of the deck towards the supports (bearing device or pier cap), due to the excessive horizontal excursion induced by seismic motion. These limit states are defined and checked for the individual components of the bridge (piers and supports); since these components are all main elements of the bridge, the achievement of a limit state on a component automatically determines the achievement of the same limit state on the bridge (system in series).

The procedure for calculating fragility curves is described with particular reference to the articulated use of risk indicators. These indicators are instantaneous quantities defined as the relationship between the seismic demand and the capacity of the components for each verified limit state. Their elaboration allows the production of fragility curves.

ACNOWLEDGMENTS

This research has been funded by the project “783298 – INFRA-NAT – UCPM-2017-PP-AG - Increased Resilience of Critical Infrastructure to Natural and Human-Induced Hazards”, funded by DG-ECHO – European Union Civil Protection.

REFERENCES

[1] S. Akkar, J. J. Bommer, Empirical equations for the prediction of PGA, PGV, and spectral accelerations in Europe, the Mediterranean Region, and the Middle East. *Seismological Research Letters 81*, 195–206, 2010.

[2] B. Borzi, P. Ceresa, P. Franchin, F. Noto, G. M. Calvi, P. E. Pinto, Seismic Vulnerability of the Italian Roadway Bridge Stock. *Earthquake Spectra: November 2015, Vol. 31*, No. 4, pp. 2137-2161, 2015

[3] G. M. Calvi, A displacement-based approach for vulnerability evaluation of classes of buildings. *Journal of Earthquake Engineering, 3(3)*, 411-438, 1999

[4] G. M. Calvi, P. E. Pinto, P. Franchin, R. Marnetto, The highway network in the area struck by the event. *Progettazione Sismica 1*, IUSSPress, Pavia, Italy, 2010

[5] G. M. Calvi, P. E. Pinto, P. Franchin, Seismic design practice in Italy, in *Bridge Engineering Handbook, Second Edition* (W.-F. Chen and L. Duan, Eds.), CRC Press, Boca Raton, FL, ISBN 9781439852187, 2013

[6] CEN Eurocode 8: Earthquake resistance design of structures Part 3: Assessment and retrofitting of buildings, EN 1998-3:2005, 2005

[7] G. Chellini, L. Nardini, W. Salvatore (2011) Dynamical identification and modelling of steel–concrete composite high-speed railway bridges. *Structure and Infrastructure Engineering,* 7:11, 823-841, 2011

[8] Circolare applicativa delle NTC2008 (2009), "Circolare del Ministero delle Infrastrutture e dei Trasporti 2 febbraio 2009, n. 617 recante Istruzioni per l'applicazione delle Nuove norme tecniche per le costruzioni di cui al Decreto Ministeriale 14 gennaio 2008", pubblicata sul supplemento ordinario n. 27 della Gazzetta ufficiale n. 47 del 26 febbraio 2009.

[9] Circolare applicativa delle NTC2018 (2019), "Circolare del Ministero delle Infrastrutture e dei Trasporti 21 gennaio 2019, n. 7 recante Istruzioni per l'applicazione dell'«Aggiornamento delle "Norme tecniche per le costruzioni"» di cui al decreto ministeriale 17 gennaio 2018.", pubblicata sul supplemento ordinario n. 5 della Gazzetta ufficiale n. 35 del 11 febbraio 2019.

[10] D.M. 14/01/2008. Norme Tecniche per le Costruzioni. Gazzetta Ufficiale, n. 29 del 14/02/2008, Supplemento ordinario n.30, 2008.

[11] D.M. 17/01/2018. Norme Tecniche per le Costruzioni. Gazzetta Ufficiale, n. 42 del 20/02/2018, Supplemento ordinario n.8, 2018.

[12] C.B. Haselton, A. Liel, G.G. Deierlein, B.S. Dean, J.H. Chou, Seismic collapse safety of reinforced concrete buildings, I: Assessment of ductile moment frames. *ASCE Journal of Structural Engineering 137*, 481–491, 2011.

[13] F. Jalayer, P. Franchin, P.E. Pinto, A scalar damage measure for seismic reliability analysis of RC frames. *Earthquake Engineering & Structural Dynamics, Vol.36(13)*, 2059-2079, Wiley, 2007.

[14] G. Lupoi, P. Franchin, A. Lupoi, P.E. Pinto, Seismic Fragility Analysis of Structural Systems, Journal of Engineering Mechanics. *Vol.132, ASCE*, 2006.

[15] G. Magliulo, V. Capozzi, G. Fabbrocino, G. Manfredi, Neoprene-concrete friction relationships for seismic assessment of existing precast buildings. *Eng Struct, 33(2)*, 532-538, 2011

[16] C. Modena, G. Tecchio, C. Pellegrino, F. Da Porto, M. Donà, P. Zampieri, M. A. Zanini, Reinforced concrete and masonry arch bridges in seismic areas: typical deficiencies and retrofitting strategies. *Structure and Infrastructure Engineering, 11:4*, 415-442, 2015.

[17] OpenSees – Open System for Earthquake Engineering Simulation Pacific Earthquake Engineering Research Center – University of Berkeley, CA

[18] P. E. Pinto, R. Giannini, P. Franchin, *Seismic reliability analysis of structures*. IUSSpress, Pavia, 2004

[19] P.E. Pinto, P. Franchin, A. Lupoi, *Valutazione e consolidamento dei ponti esistenti in zona sismica*. IUSSpress, Pavia, 2009

[20] P.E. Pinto, P. Franchin, Issues in the upgrade of Italian highway structures. *Journal of Earthquake Engineering 14*, 1221–1252, 2010.

[21] M.J.N. Priestley, G.M. Calvi, M. Kowalsky, *Displacement Based Seismic Design of Structures*. IUSS Press, Pavia, 2007

[22] M.H. Scott, G.L. Fenves, Plastic Hinge Integration Methods for Force-Based Beam-Column Elements. *Journal of Structural Engineering, ASCE, 132(2)*:244-252, 2006

[23] A.G. Sextos, K.D. Pitilakis, A.J. Kappos, Inelastic dynamic analysis of RC bridges accounting for spatial variability of ground motion, site effects and soil–structure interaction phenomena. Part 1: Methodology and analytical tools. *Earthquake Engineering & Structural Dynamics 32*, 607–627, 2003a.

[24] A.G. Sextos, K.D. Pitilakis, A.J. Kappos, Inelastic dynamic analysis of RC bridges accounting for spatial variability of ground motion, site effects and soil-structure interaction phenomena. Part 2: Parametric study. *Earthquake Engineering & Structural Dynamics 32*, 629–652, 2003b.

[25] D. Vamvatsikos, C.A. Cornell, Incremental dynamic analysis. *Earthquake Engineering & Structural Dynamics 31*, 491–514, 2002.

COMPDYN 2019
7th ECCOMAS Thematic Conference on
Computational Methods in Structural Dynamics and Earthquake Engineering
M. Papadrakakis, M. Fragiadakis (eds.)
Crete, Greece, 24-–26 June 2019

A SIMPLE PROCEDURE FOR EMBEDDING SEISMIC LOADS IN FOUNDATION SUPERELEMENTS FOR COMBINED WIND, WAVE AND SEISMIC ANALYSIS OF OFFSHORE WIND TURBINE STRUCTURES

Martin B. Nielsen[1*], **Emrah Sahin**[1]

[1]Ramboll Offshore Wind
Hannemanns Allé 53, DK-2300 Copenhagen, Denmark.
[*]e-mail: mbni@ramboll.com

Keywords: Offshore wind turbines, earthquakes, superelements.

Abstract. *A simple approach for integrating loads associated with seismic excitation of offshore wind turbine structures into foundation superelements is presented. This allows the load calculation process for combined wind, wave and seismic loads typically conducted in collaboration between the foundation and the wind turbine designers to be performed similarly to the conventional sequential procedure used for combined wind and wave loads. It is illustrated how a time-varying seismic acceleration field can be converted into ground displacement time series that can be used to excite the integrated wind turbine structure through a superelement representation of the foundation. In contrast to the conventional approach where an acceleration field is applied to a local frame of reference, the present approach operates in an absolute reference frame such that the kinematic variables – displacements, velocities and accelerations – include the overall rigid body contribution from the prescribed ground motion. It is shown that the proposed method exactly matches the results from the conventional approach based on an acceleration field applied to a local frame of reference in absence of damping/or with deformation proportional damping only. Furthermore, it is illustrated for a more realistic example of a jacket-founded multi-MW turbine model including a both mass and stiffness proportional damping matrix that both methods still yield very similar results.*

1 INTRODUCTION

A key aspect in design and analysis of offshore wind turbine structures in seismically active regions such as the rapidly growing new markets in Southern Europe, East Asia and Western United States is to properly account for the loading associated with earthquakes. While the governing standards for offshore wind structures such as DNVGL-ST-0126, [1] are highly developed for design load cases combining wind and hydrodynamic loads, less detailed guidelines are available for earthquake design and reference is instead made to EN 1998-5, [2] or ISO 19901-2, [3] for detailed design criteria. However, these are mainly developed for building structures or offshore oil & gas platforms, respectively, and not particularly suited for slender offshore wind structures as also highlighted in e.g. [4, 5]. Nor do they consider the practical issue that the design responsibility of the combined wind turbine and foundation structure typically is split between the wind turbine and the foundation designers, such that each has their own structural analysis model in different special purpose software packages.

In contrast to hydrodynamic loads where the fluid-structure interaction is often ignored for small structural deformations, the nature of earthquake-induced inertia loads requires the seismic analysis to be conducted on an integrated model representing the combined dynamic behavior of the substructure, here defined as the foundation including piles or buckets below mudline, and the superstructure, i.e. the tower and rotor-nacelle-assembly (RNA). The traditional approach adopted for modeling seismic loads is to apply a uniform acceleration field representing the ground motion to the integrated structure, [6, 7], whereby the kinematic results – displacements, velocities and accelerations – refer to a local accelerated frame of reference, [8]. However, due the split of responsibilities, no unified model accounting for combined seismic and wind and wave loads exist. Instead, the aero-servo-elastic analysis conducted by the turbine designer is performed on a superstructure model with a so-called superelement representation of the substructure serving as boundary condition, [9, 10]. Therefore, application of a simultaneous acceleration field to both the substructure by the foundation designer before model reduction and to the superstructure in the aero-elastic model by the turbine designer is complicated due to the fact that commonly used software packages in the industry do not accommodate the necessary modeling or validation features across the split interface. To circumvent this issue in practice, a simplified design approach is to perform the seismic analysis on a separate model in either time of frequency domain and superimpose static wind/wave loads e.g. corresponding to a 1-year return period, see [7]. However, neglecting the lack of correlation between the extrema for each of the environmental load contribution significantly increases the conservatism inherent in the design.

In this paper a practical solution to the above described problem is presented. It is illustrated how a time-varying seismic acceleration field can be converted into ground displacements that can be used to excite the integrated structure solely through the foundation, thereby permitting the loads to be embedded into a superelement representation hereof. In contrast to the conventional approach where an acceleration field is used to accelerate the structure in a local frame of reference, the present approach operates in absolute frame of reference such that the kinematic results include the overall contribution from the ground motion. An overview of the conventional procedure for foundation design is given in section 2, while the theoretical framework for extension to seismic analysis and the validation hereof by means of representative numerical examples are presented in sections 3 and 4, respectively.

2 DESIGN PROCESS FOR OFFSHORE WIND TURBINE FOUNDATIONS

As mentioned in the introduction, it is common practice to split the responsibility between the wind turbine and the foundation designers such that the former is responsible for the superstructure as well as the coupled aero-elastic simulations, while the latter performs the detailed design of the substructure. For this purpose, it is convenient to exchange the computer model of the substructure along with associated loads in a condensed form typically referred to as a superelement that can be included in the aero-elastic software used by the wind turbine designer. This sequential approach serves two purposes: It significantly reduces the computational effort needed to perform the integrated aero-elastic analysis, and it provides a clear split between the responsibilities of the wind turbine and the foundation designers, see e.g. [11] for further details.

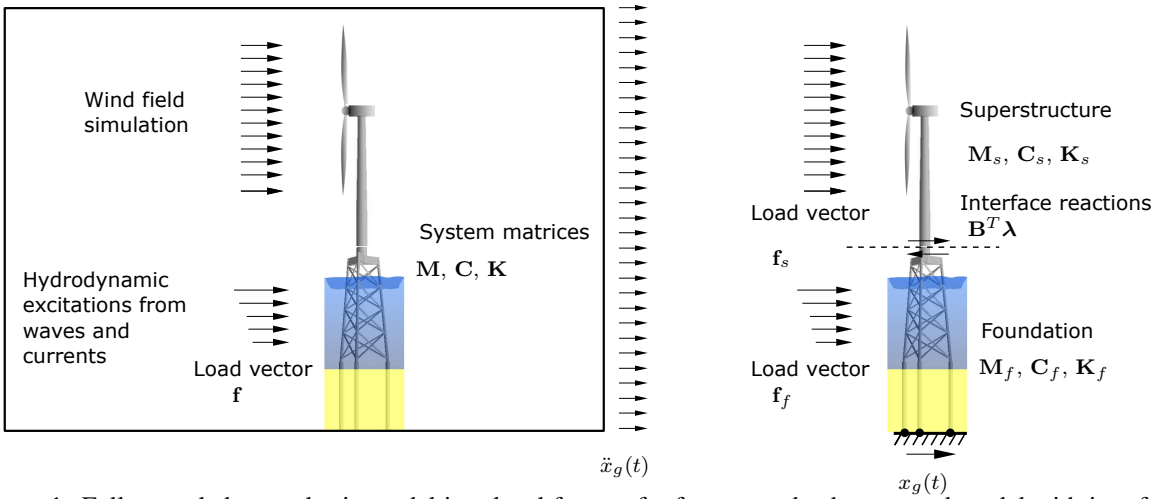

Figure 1: Fully coupled aero-elastic model in a local frame of reference and substructured model with interface section forces $\mathbf{B}^T\boldsymbol{\lambda}$ in a global frame of reference.

The details of the procedure can be summarized in the following three steps:

- Foundation model: The foundation designer prepares a detailed computer model of the foundation that closely represents the geometry, relevant structural details, local joint flexibility and pile-soil interaction as well as the excitations acting directly on the foundation such as gravity, buoyancy, wave/current loads.

- Aero-elastic simulation: A superelement representation of the detailed foundation model and the associated load time series is prepared – typically according to the Craig-Bampton reduction method, [10] – and delivered to the wind turbine designer, who performs coupled aero-elastic simulations of the full wind turbine model subject to combined wind and other environmental loadings from the previous step.

- Recovery-run: The foundation designer performs a dynamic time domain analysis where dynamic section force time series, extracted at the tower-bottom from the integrated aero-elastic analysis, are applied on a foundation-only model along with correlated permanent and environmental loads. Hereby, the response of the full (non-reduced) foundation structure is recovered and can be used as basis for detailed design of individual members and joints.

The approach has been adopted by the industry for a wide range of detailed designs of offshore foundations and has further been validated within the scientific community e.g. in [11, 12].

3 DESIGN PROCESS FOR SEISMICALLY-INDUCED LOADS

3.1 Equations of motion in local frame

Consider a discretized system representing an offshore wind turbine model including tower, RNA and foundation to be used for aero-elastic analysis as illustrated in Fig. 1a. The full model is described in terms of the mass matrix $\mathbf{M}$, the damping matrix $\mathbf{C}$ and the stiffness matrix $\mathbf{K}$, while the associated degrees of freedom (DoF) – typically accommodating both translations and rotations with respect to a local frame of reference – are stored in the vector $\mathbf{u}$.

A seismic event acting on such a system is often modeled as a time-varying base motion $x_g(t)$, which may be interpreted as a forced translation of the reference frame in which the structure is defined, such that absolute displacement may be expressed, as

$$\mathbf{x} \,=\, \mathbf{u} \,+\, \mathbf{r}x_g(t)\,. \tag{1}$$

The vector $\mathbf{r}$ is introduced as an influence vector that picks out the relevant degrees of freedom, i.e. of the form $[\,1,0,0,0,0,0,1,0,\ldots]^T$ for translations in the x-direction.

Lagrange's equations provide a classic and fairly general method for deriving the equations of motion for a mechanical system. For motion in the local frame of reference these can be expressed in terms of the variable $\mathbf{u}$ and its time derivative $\dot{\mathbf{u}}$ in the form

$$\frac{d}{dt}\left(\frac{\partial L}{\partial \dot{\mathbf{u}}^T}\right) \,-\, \frac{\partial L}{\partial \mathbf{u}^T} \,=\, \mathbf{f}(t) \,-\, \mathbf{C}\dot{\mathbf{u}}\,, \tag{2}$$

where L denotes the *Lagrangian*:

$$L \,=\, T \,-\, G\,, \tag{3}$$

in terms of the kinetic energy T and the elastic potential G. See e.g [13] for further details. The right-hand side of (2) holds the time-varying external force vector $\mathbf{f}(t)$ representing direct external loads on the structure such as wind, waves and gravity as well as the dissipative forces $\mathbf{C}\dot{\mathbf{u}}$ associated with local viscous damping.

The kinetic energy T for the integrated system expressed in terms of absolute velocities $\dot{\mathbf{x}}$ yields

$$T \,=\, \tfrac{1}{2}\dot{\mathbf{x}}^T\mathbf{M}\dot{\mathbf{x}}\,. \tag{4}$$

The mass matrix $\mathbf{M}$ is here constant as it refers to initial local geometry, hence the first term in Lagrange's equations follow as the time-derivative of the expression

$$\frac{\partial L}{\partial \dot{\mathbf{u}}^T} \,=\, \mathbf{M}\dot{\mathbf{x}} \,=\, \mathbf{M}[\dot{\mathbf{u}} \,+\, \mathbf{r}\dot{x}_g(t)]\,, \tag{5}$$

while the second term defines the internal forces

$$\frac{\partial G}{\partial \mathbf{u}^T} \,=\, \mathbf{K}\mathbf{u}\,. \tag{6}$$

In this context, the procedure is illustrated for a linear system, i.e. without a time- or state-dependent stiffness matrix $\mathbf{K}$, however, the extension to general systems accounting for both material and geometrical non-linearities is straightforward. The internal forces are expressed solely in terms of the local displacements $\mathbf{u}$ since the contribution from the base displacements $\mathbf{r}x_g(t)$ merely results in a rigid body translation of the local frame, and thus does not contribute to the elastic energy.

Upon substitution of (5) and (6) into Lagrange's equations (2), the dynamic equations of motion are obtained in the form

$$\mathbf{M}\ddot{\mathbf{u}} + \mathbf{C}\dot{\mathbf{u}} + \mathbf{K}\mathbf{u} = \mathbf{f} - \mathbf{M}\mathbf{r}\ddot{x}_g(t)\,. \tag{7}$$

This corresponds to the classical format adopted for seismic analysis where the inertia loads on the right hand side appear as a uniform acceleration field that has to be applied simultaneously to the substructure and the superstructure. However, as mentioned introductory, this does not fit within the framework for the split approach used in practice.

By substitution of the relative displacements $\mathbf{u}$ defined as the difference between the absolute displacements $\mathbf{x}$ and the ground motion $x_g(t)$ via the relation (1), the equations of motion (7) can be recast into a format in terms of absolute displacements $\mathbf{x}$, as

$$\mathbf{M}\ddot{\mathbf{x}} + \mathbf{C}\dot{\mathbf{x}} + \mathbf{K}\mathbf{x} = \mathbf{f} + \mathbf{K}\mathbf{r}x_g(t)\,. \tag{8}$$

It is here assumed that the damping forces are associated with local deformation only such that no dissipation occurs for rigid body motion, whereby $\mathbf{C}\dot{\mathbf{x}} = \mathbf{C}\dot{\mathbf{u}}$. A similar argument is valid for the term $\mathbf{K}\mathbf{r}x_g(t)$ representing loads associated with seismic excitation – now expressed in terms of base displacements $x_g(t)$ – which would also vanish for an unsupported structure. However, when support conditions are imposed e.g. via a rigid spring k at mudline, a translation of the base of x_g would require an elastic force of the form kx_g to be applied locally on the foundation. It is illustrated explicitly in the following section how this enters as a term appearing solely in the equations associated with the foundation, and thus can be embedded in a superelement representation of the substructure.

3.2 Split approach in absolute frame

For sake of argument it is now assumed that the system degrees of freedom $\mathbf{x}$ are divided into DoF associated with the superstructure $\mathbf{x}_s$ and the foundation $\mathbf{x}_f$, respectively, as illustrated in Fig. 1b:

$$\mathbf{x}^T = [\,\mathbf{x}_s^T,\, \mathbf{x}_f^T]\,, \tag{9}$$

where the matrices with subscripts s and f refer to the superstructure and foundation, respectively. Similarly, the system mass, stiffness and damping matrices for the combined system may be expressed in the block-diagonal format,

$$\mathbf{M} = \begin{bmatrix} \mathbf{M}_s & \\ & \mathbf{M}_f \end{bmatrix}, \quad \mathbf{K} = \begin{bmatrix} \mathbf{K}_s & \\ & \mathbf{K}_f \end{bmatrix}, \quad \mathbf{C} = \begin{bmatrix} \mathbf{C}_s & \\ & \mathbf{C}_f \end{bmatrix}. \tag{10}$$

The associated load vector combining wind loads on the superstructure $\mathbf{f}_s$ and foundation loads $\mathbf{f}_f$ also takes the form

$$\mathbf{f}^T = [\,\mathbf{f}_s^T,\, \mathbf{f}_f^T]\,. \tag{11}$$

In this format the two substructures are uncoupled. However, a necessary condition when linking the wind turbine tower to the foundation is that the common interface DoF shared between the two substructures are equal, i.e.

$$x_i^s - x_j^f = 0\,. \tag{12}$$

This is commonly known as the compatibility condition, which may be enforced via a homogeneous constraint equation formally expressed as

$$\mathbf{B}\mathbf{x} = [\,\mathbf{B}_s \quad \mathbf{B}_f\,] \begin{bmatrix} \mathbf{x}_s \\ \mathbf{x}_f \end{bmatrix} = \mathbf{0}\,, \tag{13}$$

where $\mathbf{B}$ is a Boolean matrix that operates solely on the interface degrees of freedom.

It is here convenient to introduce the link between the local and global reference frames in a similar format. Since the absolute displacements of the base components in the vector $\mathbf{x}_f$ associated with the supported DoF must equal the time varying base excitations $x_g(t)$, this can be expressed as

$$\mathbf{D}_f(\mathbf{x}_f - \mathbf{r}x_g) \,=\, \mathbf{0}\,, \tag{14}$$

with $\mathbf{D}_f$ being a Boolean matrix that picks out the supported DoF in the foundation only. Similarly to the derivation of the classical format for the coupled equations of motion (7) presented in the previous section, the equivalent format for the partitioned system can be derived via Lagrange's equations (2) based on the augmented Lagrangian

$$L \,=\, T \,-\, G \,+\, (\mathbf{B}\mathbf{x})^T\boldsymbol{\lambda} \,+\, [\mathbf{D}_f(\mathbf{x}_f \,-\, \mathbf{r}x_g)]^T\boldsymbol{\Lambda}\,, \tag{15}$$

where the constraint equations (13) and (14) are included via Lagrange multipliers collected in the vectors $\boldsymbol{\lambda}$ and $\boldsymbol{\Lambda}$, respectively. The kinetic energy T and the elastic energy G of the system can still be expressed in the form (4) via the partitioned system matrices and vector described by (9) and (10), respectively.

While the interpretation of the energy terms in (15) is rather straightforward, the two latter terms represent the vanishing work done by the homogeneous constraints (13) and (14), hence these can be added without changing the Lagrangian of the system. In this context, the Lagrange multipliers λ serve as generalized reaction forces needed to enforce the compatibility condition at the interface, and thus directly represent the internal forces at interface that are interchanged between the superstructure s and the foundation f. Similarly, the Lagrange multipliers Λ represent the forces required for imposing the base motion to the integrated system through the foundation.

By substitution of the augmented Lagrangian (15) into Lagrange's equation (2) and differentiation, the coupled dynamic equations follow as

$$\mathbf{M}\ddot{\mathbf{x}} \,+\, \mathbf{C}\dot{\mathbf{x}} \,+\, \mathbf{K}\mathbf{x} \,=\, \mathbf{f} \,+\, \mathbf{B}^T\boldsymbol{\lambda} \,+\, \mathbf{D}^T\boldsymbol{\Lambda}\,. \tag{16}$$

Together with the compatibility equation (13) and the support constraint condition (14), these constitute the coupled equations of motion equivalent to (8). When the partition (9) is introduced, the equations of motion take the form:

$$\mathbf{M}_s\ddot{\mathbf{x}}_s \,+\, \mathbf{C}_s\dot{\mathbf{x}}_s \,+\, \mathbf{K}_s\mathbf{x}_s \;\;=\, \mathbf{f}_s \,+\, \mathbf{B}_s^T\boldsymbol{\lambda}\,, \tag{17a}$$

$$\mathbf{M}_f\ddot{\mathbf{x}}_f \,+\, \mathbf{C}_f\dot{\mathbf{x}}_f \,+\, \mathbf{K}_f\mathbf{x}_f \,=\, \mathbf{f}_f \,+\, \mathbf{B}_f^T\boldsymbol{\lambda} \,+\, \mathbf{D}_f^T\boldsymbol{\Lambda}\,, \tag{17b}$$

$$\mathbf{B}\mathbf{x} \,=\, \mathbf{0}\,, \tag{17c}$$

$$\mathbf{D}_f(\mathbf{x}_f - \mathbf{r}x_g) \,=\, \mathbf{0}\,, \tag{17d}$$

where the first two equations are the dynamic equations for the superstructure and the foundation, respectively. This form is often referred to as the *dual* format, i.e. in which the equations of motion are augmented by the compatibility equations (13) and (14), see [14] for further details. It is noted that the base excitation forces only appear explicitly in the foundation equations of motion (17b), yet their influence will be reflected in the response of the entire structure similar to the case when the seismic loading is applied as a uniform acceleration field as described in (7). The advantage is that the seismic loads only have to be applied to the foundation, and thus may be embedded in a superelement representation hereof as explained in the following section.

3.3 System reduction compatibility

As outlined in section 2 it is common practice that the aero-elastic simulations of the integrated structure are performed by the turbine designer, which amounts to solving the full set of equations (17). In these simulations, the foundation part (17b) is typically represented in the form of a superelement based on either the Guyan-Irons or the Craig-Bampton reduction techniques [9, 10]. Common for these (and other methods) are that they permit the full set of DoF contained in the vector $\mathbf{x}$ – conveniently divided into interface (or boundary) DoF $\mathbf{x}_b$ and internal Dof $\mathbf{x}_i$ – to be expressed solely in terms of a generalized boundary DoF vector $\tilde{\mathbf{x}}$, as

$$\mathbf{x} = \mathbf{T}\tilde{\mathbf{x}} \,. \tag{18}$$

The reduction basis $\mathbf{T}$ is typically formed by a combination of static constraint modes and dynamic pseudo modes improving the description of the internal flexibility. By substitution of (18) into (17b) and pre-multiplication with the reduction basis $\mathbf{T}^T$, the reduced system matrices $\tilde{\mathbf{M}}$, $\tilde{\mathbf{C}}$ and $\tilde{\mathbf{K}}$ and associated load vector $\tilde{\mathbf{f}}_f$ constituting the superelement are identified as

$$\begin{aligned} \tilde{\mathbf{M}} = \mathbf{T}^T\mathbf{M}\mathbf{T} \quad , \quad \tilde{\mathbf{C}} = \mathbf{T}^T\mathbf{C}\mathbf{T} \quad , \quad \tilde{\mathbf{K}} = \mathbf{T}^T\mathbf{K}\mathbf{T} \,, \\ \tilde{\mathbf{f}}_f = \mathbf{T}^T(\mathbf{f}_f + \mathbf{D}_f^T\boldsymbol{\Lambda}) \,. \end{aligned} \tag{19}$$

The actual foundation equations of motion solved in the integrated aero-elastic simulations instead of (17b), hereby yields

$$\tilde{\mathbf{M}}_f\ddot{\tilde{\mathbf{x}}}_f + \tilde{\mathbf{C}}_f\dot{\tilde{\mathbf{x}}}_f + \tilde{\mathbf{K}}_f\tilde{\mathbf{x}}_f = \tilde{\mathbf{f}}_f + \mathbf{T}^T(\mathbf{B}_f^T\boldsymbol{\lambda}) \,, \tag{20}$$

such that the external loads representing the effect of the base excitation have been embedded in the reduced load vector $\tilde{\mathbf{f}}_f$, and thus constitutes a part of the superelement that is typically prepared by the foundation designer.

3.4 PRACTICAL DESIGN PROCEDURE

Based on the theoretical framework developed in sections 3.1–3.3, an approach applicable for integrated load calculations combining seismic, wind and wave loads is illustrated in Fig. 2.

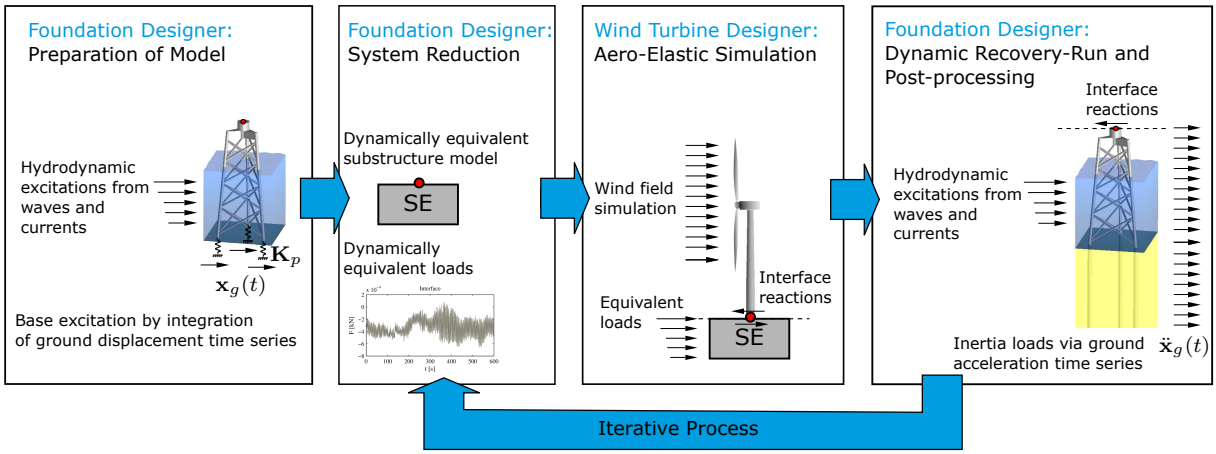

Figure 2: Flow chart for load calculation including seismic loads.

First, a detailed model of the substructure in line with the first step in section 2 is established. However, the combined simultaneously occurring actions now also include earthquake-induced

loads applied as time series. The substructure as well as the associated load time series are then condensed into a superelement in line with (19) via the Craig-Bampton system reduction approach, [10], and provided to the turbine designer, who performs the aero-elastic simulation.

A key aspect is that the pile-soil interaction in general exhibits a non-linear relationship. However, the superelement approach is by default linear hence the pile-soil interaction curves are linearized based on either the initial tangent stiffness or a secant stiffness associated with a representative deformation level. In essence this allows the pile supports to be represented by a 6×6 stiffness matrix in the form,

$$\mathbf{K}_p \;=\; \begin{bmatrix} k_{xx} & & & & & \\ & k_{yy} & & & sym & \\ & & k_{zz} & & & \\ & k_{x'y'} & & k_{x'x'} & & \\ k_{y'x'} & & & & k_{x'x'} & \\ & & & & & k_{z'z'} \end{bmatrix}, \tag{21}$$

where the subscripts x, y, z refer to directions for translational stiffnesses, while x', y', z' refer to directions for rotational stiffnesses. This is conveniently implemented in the structural model as general stiffness elements linking the foundation structure to fixed support node(s) on which ground displacements can be imposed, as illustrated in the first step in Fig. 2. Hereby the forces associated with base excitation of the support node(s) as described in section 2 can be embedded in the superelement permitting the aero-elastic simulations to be performed in the conventional way.

It should be noted that earthquake motion typically is measured in terms of acceleration time series $\ddot{x}_g(t)$, however, the associated displacement records are readily available by integrating the accelerations twice, which under the assumption of homogeneous initial conditions follow as

$$x_g(t) \;=\; \int\int \ddot{x}_g(t)\, dt\, dt\,, \quad x_0 = \dot{x}_0 = 0\,. \tag{22}$$

For an arbitrary acceleration record, direct integration may lead to a so-called baseline drift such that the obtained displacement (and velocity) time series do not represent the physical behavior. However, several methods for baseline correction exist, yet this is outside the scope of the present paper. A review discussing this particular issue can e.g. be found in [15].

The last step in Fig. 2 illustrating the recovery-run can finally be performed either based on the original foundation model subject to displacement-controlled base excitation in an absolute frame of reference and with the linearized pile-soil interaction represented via generalized stiffness elements or based on a foundation model where the piles are modeled explicitly and the structure is excited by a uniform acceleration field in a local frame of reference. As illustrated in the previous section, the two methods are equivalent, however, the latter approach has the advantage that the performance of the piles can be assessed directly during the recovery-run.

4 NUMERICAL EXAMPLES

This section presents two numerical examples. The first example illustrates the basics of the approach in the absence of viscous damping via a simplified monopile structure clamped at mudline. The second example considers a more realistic jacket structure subject to combined earthquake and wave loads. A comparison of the results obtained via the conventional approach based on a uniform acceleration field and the approach where seismic loads associated with base motion are embedded in a superelement representation of the foundations is presented for

combined mass and stiffness proportional damping. Simulations are performed as dynamic time domain analysis in Ramboll's in-house offshore structural analysis program package (ROSAP). These are in general conducted with a time step of 0.02 s using the generalized-α method with a high frequency spectral radius limit $\lambda_\infty = 0.8$, [16].

4.1 Monopile

In this example a simplified monopile model as illustrated in Fig. 3 is considered.

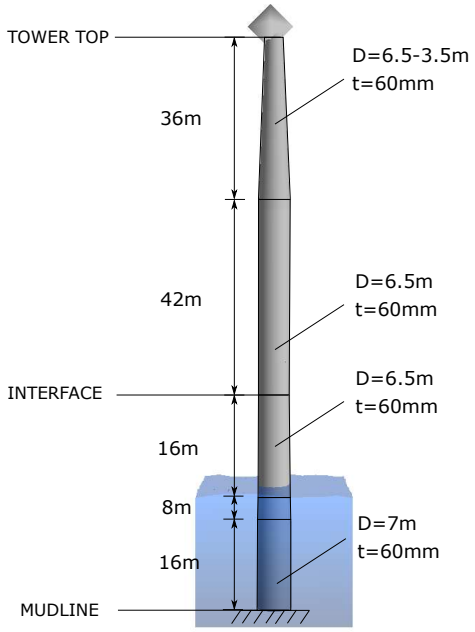

Figure 3: Simplified monopile geometry.

The monopile model is without a transition piece and directly connected to the tower e.g. by means of a bolted flange connection at the interface level. The outer diameter varies from 7.0 m at mudline to 6.5 m at interface level. The diameter transition is introduced via a conical section defined by a cone angle of approximately $1.8°$ and a length of 8 m, and the total length of the foundation is 40 m. The monopile is located on a generic site with a water depth of 25 m with respect to mean sea level (MSL). It supports a 78 m long tower structure with a diameter varying from 6.5 m at the interface level to 3.5 m at tower top. For simplicity purposes, a wall thickness of 60 mm is used for all members of the integrated structure and neither secondary steel structures nor marine growths and corrosion allowances have been included on the foundation. The monopile is clamped at mudline as illustrated in Fig. 3 and generic tower internals and RNA properties have been adopted to ensure representative dynamic properties for the integrated model. For the present case, the natural frequencies associated with the first and second global bending modes are around 0.32 Hz and 1.80 Hz, respectively. For simplicity no structural damping is included.

The external loads are here limited to a strong seismic loading in the global x-direction based on the historically measured accelerogram for El Centro 1940 (NW), which has been scaled to a peak ground acceleration of $0.51g$. Three different models are considered:

ACC: An integrated model where the seismic loads are applied as a uniform acceleration field according to (7).

DISP: An integrated model where the seismic loads are imposed as ground displacements through the clamped support node according to (8).

SE: A reduced model where the monopile is represented as a superelement with inherent seismic loads according to the procedure outlined in section 3.4.

As a validation of the approach presented throughout this paper, results for the relative lateral displacement $\mathbf{u}_x$ in the loading direction at tower top as well as the governing design load component – overturning moment at interface – have been extracted for each of the three different configurations as shown in Fig. 4. A perfect match is found for all cases, however, it should be noticed that while internal forces – like the overturning moment depicted here – are invariant to rigid body motion, the tower top displacement $\mathbf{x}_x$ extracted from the models DISP and SE refer to absolute frame of reference and thus have to be corrected for the base displacements $x_g(t)$ according to (1).

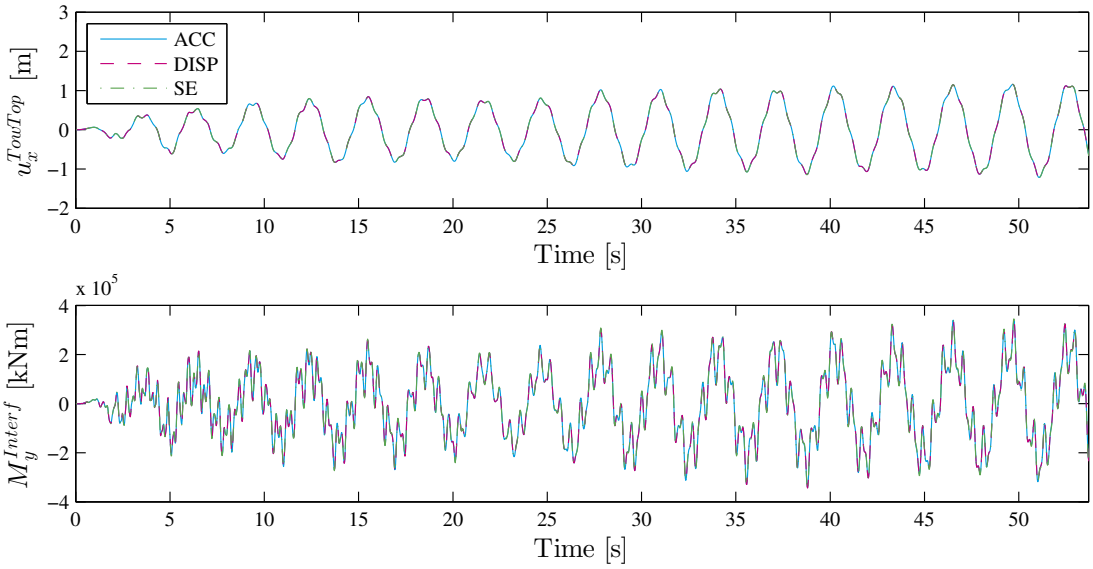

Figure 4: Lateral displacement in x-direction at tower top and overturning moment around y-axis at interface for monopile model.

4.2 Jacket

As a more realistic example for validating the presented approach, a generic, yet realistic 3-legged pile-jacket model supporting an 8-9 MW offshore wind turbine, is used as illustrated in Figure 5. The governing structural parameters for the jacket are summarized in Table 1. The jacket structure is located on a generic site with a water depth of 40 m and soil conditions represented by medium sand with a friction angle of $\phi = 35^o$. Pile-soil interaction is included in the foundation model, yet linearized based on the initial slope.

The structure is excited by the same seismic load time series based on a scaled El Centro accelerogram as described for the monopile example in section 4.1. This is combined with aligned waves in the global x-direction. The hydrodynamic loading is calculated according to Morison's equation where the wave kinematics for the irregular sea-state is modelled via the JONSWAP-spectrum according to [1]. Relevant metocean data are given in Table 1. Both added mass, contained mass and 100 mm marine growth are taken into account.

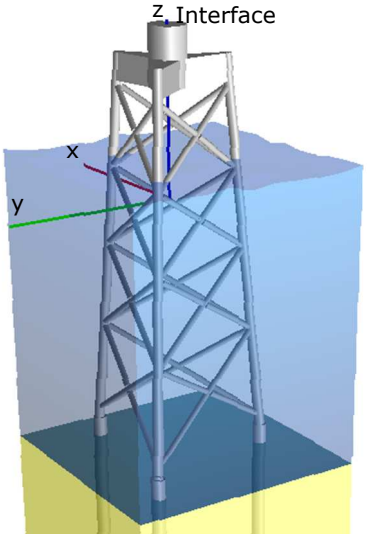

Figure 5: Jacket geometry.

Table 1: Generic jacket and loading parameters.

Geometry		Site conditions	
Parameter	Value	Parameter	Value
Footprint	25.0 m	Water depth	40.0 m
Topprint	16.0 m	Spectrum	JONSWAP
Leg diameter	1620 mm	Sign. wave height	10.0 m
Leg thickness	40 mm	Peak period	11.0 s
Brace diameter	1016 mm	Wave direction	x-dir
Brace thickness	25 mm	Accelerogram	El Centro
Tubular joint Chord thickness	70 mm	PGA	$0.51g$
		EQ direction	x-dir

In contrast with the previous example, structural damping is included via the Rayleigh approach of the form:

$$\mathbf{C} = \alpha\mathbf{M} + \beta\mathbf{K}$$

The Rayleigh parameters α and β have been calculated to provide damping ratios of 0.5% and 1.0% of critical for the first and second global bending modes, respectively. For the present structure, the associated frequencies are 0.28 Hz and 1.16 Hz, respectively.

Results for three different configurations – equivalent to the definitions of ACC, DISP and SE described in section 4.1 – are presented in Fig. 6. A very good match is obtained for cases DISP and SE to within the accuracy of the superelement, while minor differences are observed with respect to ACC.

As discussed in section 3.1, the transition from the equations of motion (7) in relative components $\mathbf{u}$ to the equations of motion (8) in absolute components $\mathbf{x}$ does not introduce any approximation for pure deformation/stiffness proportional damping. Contrary, introduction of mass proportional damping would lead to the term $\alpha\mathbf{M}\mathbf{r}\dot{x}_g(t)$ on the right-hand-side, which is not included in the present simulations. However, since the mass proportional contribution to the damping ζ decreases with the angular frequency ω_j, i.e. $\zeta \propto \alpha/(2\omega_j)$, this typically only has an influence on the dynamic response of the first vibration mode. Therefore, the difference is most pronounced for the lateral displacement at the tower top, where the lowermost mode has

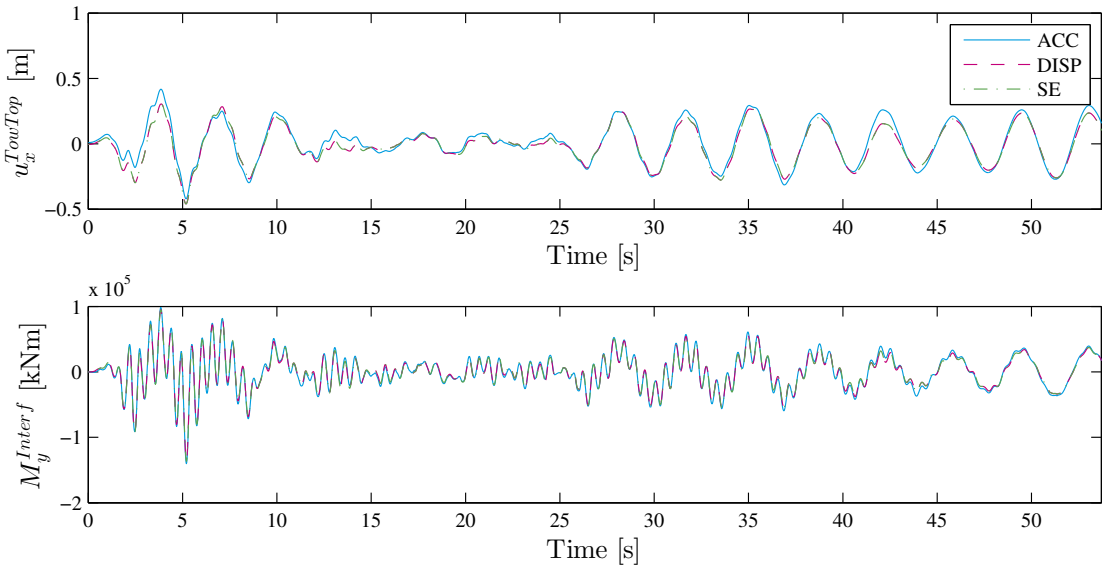

Figure 6: Lateral displacement in x-direction at tower top and overturning moment around y-axis at interface for jacket model including Rayleigh damping.

the largest modal displacement, while the effect is less significant at the interface, as illustrated by the overturning moment. Furthermore, it should be noted that the important contribution from aerodynamic damping has not been included here, hence the minor discrepancy associated with the mass proportional part of the damping will not have any significant impact on the design in practice.

5 CONCLUSIONS

A procedure for embedding earthquake-induced loads on an offshore wind turbine structure into a superelement representation of the foundation is presented. This permits the load calculation process, typically performed collaboratively by the foundation and the wind turbine designers, to be conducted via the conventional approach used for combined wind and wave loads. Rather than representing the seismic excitation by an uniformly distributed time-varying acceleration field applied to the full structure in a local frame of reference, base displacements – obtained by integrating the acceleration time series – are imposed through the supports of the foundation such that the measured kinematics includes the rigid-body motion of the local frame. It is illustrated explicitly by presenting the equations of motion for the coupled system in the so-called dual format how the loads required for exciting the structure solely enter the equations of motion associated with the substructure, and thereby can be embedded in the condensed load vector constituting a part of the superelement representation of the foundation. Since the internal forces forming the basis for design of the individual members are invariant to the rigid body motion, the present method yields equivalent results as the traditional approach where loads are introduced in the form of an acceleration field. This has successfully been validated by two representative examples considering multi-MW wind turbines founded on a simplified monopile and a generic, yet representative jacket, respectively.

REFERENCES

[1] DNVGL-ST-0126, Support Structure for Wind Turbines. DNVGL, 2018.

[2] EN 1998-5, Eurocode 8: Design of Structures for Earthquake Resistance Part 5: Foundations, Retaining Structures and Geotechnical Aspects. European Commitee for Standardization, 2004.

[3] ISO 19902-1, Petroleum and Natural Gas Industries — Specific Requirements for Offshore Structures — Part 2: Seismic Design Procedures and Criteria. International Standard, 2017.

[4] E. Katsants, S. Thöns, C.T. Georgakis, Wind turbines and seismic hazard: A state-of-the-art review. *Wind Energy*, **19**, 2113–2133, 2016.

[5] A.M. Kaynia, Seismic considerations in design of offshore wind turbines. *Soil Dynamics and Earthquake Engineering*, 2018 (In Press).

[6] D. Witcher, Seismic analysis of wind turbines in time domain. *Wind Energy*, **8**, 81–91, 2005.

[7] R.A. Kjørlaug, A.M. Kaynia, A. Elgamel, Seismic response of wind turbines due to earthquake and wind loading. A. Cunha, E. Caetano, P. Ribeiro, G. Müller eds. *9th International Conference on Structural Dynamics, EURODYN 2014*, Porto, Portugal, 30 June - 2 July, 2014.

[8] R.W. Clough, J. Penzien, *Dynamics of Structures, 2nd Edition*. McGraw-Hill, 1993.

[9] R. Guyan, Reduction of stiffness and mass matrices. *AIAA Journal*, **3**, 380, 1965.

[10] R. Craig, M. Bampton, Coupling of substructures for dynamic analysis. *AIAA Journal*, **6**, 1313–1319, 1968.

[11] P.L.C. van der Valk, et al. Dynamic models for load calculation procedures of offshore wind turbine support structures: Overview, assessment and outlook. *Journal of Computational and Nonlinear Dynamics* **10**, 041013, 2015.

[12] M.B. Nielsen, J.F. Jensen, D. Augustyn, R.P Pedersen. Efficient response recovery procedures for detailed design of jacket foundations, *6th International Conference on Structural Engineering, Mechanics and Computation (SEMC2016)*, Cape Town, South Africa, 5–7 September, 2016.

[13] M. Geradin, D. Rixen, *Mechanical Vibrations - Theory and Application to Structural Dynamics, 2nd Edition*. Wiley, 1997.

[14] D. de Klerk, D.J. Rixen, S.N. Voormeeren, General framework for dynamic substructuring: History, review, and classification techniques. *AIAA Journal*, **46**, 1169–1181, 2008.

[15] H. Guorui, L. Tao, Review on baseline correction of strong-motion accelerogram. *International Journal of Science, technology and Society*, **3**, 309–314, 2015.

[16] J. Chung, G.M. Hulbert, A time integration algorithm for structural dynamics with improved numerical dissipation: The generalized-α method . *Journal of Applied Mechianics*, **60**, 371–375, 1993.

COMPDYN 2019
7th ECCOMAS Thematic Conference on
Computational Methods in Structural Dynamics and Earthquake Engineering
M. Papadrakakis, M. Fragiadakis (eds.)
Crete, Greece, 24-–26 June 2019

ANCILLARY COMPUTATIONAL TOOLS FOR THE ANALYSIS OF STRUCTURAL SYSTEMS

Stavros Kasinos[1], Alessandro Palmeri[2], and Mariateresa Lombardo[2]

[1]Imperial College London
Department of Aeronautics, SW7 2AZ, London, UK
e-mail: s.kasinos@imperial.ac.uk

[2] Loughborough University
School of Architecture, Building and Civil Engineering, LE11 1AG, Loughborough, UK
e-mail: {a.palmeri, m.lombardo}@lboro.ac.uk

Keywords: API, nonlinear oscillators, SAP2000, software development, structural analysis.

Abstract. *Ancillary software tools are developed for the analysis and response quantification of structural systems in a systematic and automated fashion. The open application programming interface (OAPI) of the structural analysis software SAP2000 is exploited for this purpose and a procedure is presented for the analysis of linear systems in conjunction with MATLAB, featuring model updating, analysis execution and extraction of the results. This is facilitated by the development of ancillary functions that complement and extend existing capabilities of the OAPI. Standalone solvers are next presented for the dynamic response evaluation of bilinear hysteretic, rigid-plastic, and rocking oscillators with arbitrary excitation force. The dynamical systems considered, are indicative of distinct nonlinear behaviour and representative of a wide spectrum of structures of engineering interest. The features at the current development stage are finally showcased on the response-surface-based reliability analysis of a truss structure and the response quantification of stochastically driven nonlinear secondary oscillators. The ancillary tools developed allow convenient simplifications in the modelling and analysis process, error tractability, and can assist learning on the subject of structural dynamics. They may find application in parametric and stochastic analysis and form the basis for the development of additional modules.*

1 INTRODUCTION

In engineering practice, the analysis and design of structural systems is conventionally carried out with the aid of commercial structural analysis software. These are usually treated as black boxes with models of varying degrees of complexity that have to be extensively and often iteratively run in parallel by different design teams. Although such software are reliable in the functionalities they offer, they are usually limited by the exclusion of state-of-the-art advanced analysis features that become available within the academic community. Nevertheless, they benefit from the use of general-purpose solvers which comes at the expense of prohibitively time-consuming runs as well as strenuous pre- and post-processing tasks.

In an attempt to circumvent these limitations, the vast majority of software packages offer complementary open application programming interfaces (OAPI) that permit the development of custom engineering applications. In the case of the structural analysis software SAP2000 [1], for instance, this is solely left to the discretion of the user which encounters limited support and guidelines. Despite the apparent value, only a handful of the contributions available in the literature take advantage of the OAPI [2] and at present, none of these assistant simulation-based tools is designed to be extended by the structural engineering research community.

In this paper, we present ancillary computational tools for the analysis and response quantification of structural systems in a systematic and automated fashion. In a first stage, an overview of the SAP2000 OAPI is provided, and a procedure is presented for the analysis of linear systems in conjunction with MATLAB [3], featuring model updating, analysis execution and extraction of the results. This is facilitated by the use of ancillary functions that are developed to complement and extend existing capabilities of the SAP2000 OAPI. In a second stage, standalone solvers are presented for the dynamic response evaluation of bilinear hysteretic, rigid-plastic and free-standing rocking oscillators in presence of a general-type of excitation. The dynamical systems considered, are indicative of distinct nonlinear behaviour and representative of a wide spectrum of primary as well as secondary structures of engineering interest. Finally, the features at the current development stage are showcased on two examples: *i*) the response-surface-based reliability analysis of a truss structure facilitated through the use of the SAP2000 OAPI; and *ii*) the use and interoperability of the standalone solvers developed with SAP2000 for the response quantification of nonlinear cascaded secondary oscillators due to stochastic excitation. Basis of this contribution are the preliminary investigations carried out in [4, 5].

The proposed procedure, suited for both the industrial and research communities, allows convenient simplifications in the modelling and analysis process, error tractability, extendibility and can assist learning on the subject of structural dynamics in graduate and post-graduate level. It is particularly useful for parametric, stochastic analysis and optimisation and will form the basis for the development of additional modules.

2 ANCILLARY TOOLS FOR STRUCTURAL ANALYSIS WITH SAP2000

2.1 SAP2000 Open Application Programming interface

The Open Application Programming Interface (OAPI) of SAP2000 is a programming tool that permits coupling of SAP2000 with third-party software, thus providing a path for two-way exchange of model information, for automating the processes required for the construction, analysis, and design of structural models with SAP2000 as well as retrieval of customised results (Figure 1). Numerous programming languages can be used for this purpose, including Visual Basic for Applications (VBA), Visual Basic, Visual C#, Visual Fortran, Visual C++, MATLAB and Python.

Initiation of the link process requires pre-existing installation of the SAP2000 software and the integrated development environment (IDE). The procedure then requires initialisation of the IDE-SAP2000 assembly and sequential run of a set of predefined functions, each corresponding to one task within SAP2000, closely resembling the point-and-click procedure followed during conventional use of the SAP2000 software. It is noted that the syntax of each function depends on the choice of the IDE, and that not all the functionalities of SAP2000 are supported by the OAPI. The *CSi OAPI Documentation.chm* file, however, provides a list of the supported functions along with the syntax and description of the arguments it handles, as well as basic example code for each programming language supported.

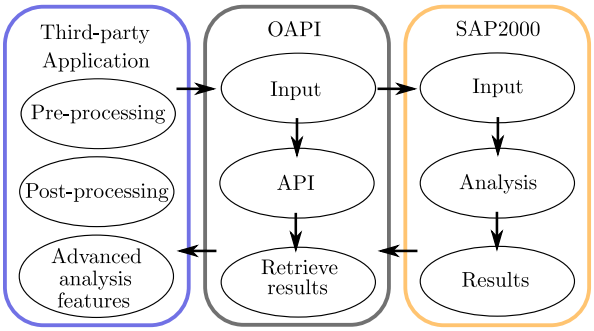

Figure 1: Schematic of the SAP2000 OAPI.

2.2 Using the SAP2000 OAPI for the analysis of linear systems

A procedure is presented in the following for automated analysis of linear structural systems with SAP2000 and MATLAB. The procedure is decomposed in the following main steps:

A: Construct the structural model in SAP2000. This typically consists of model generation, definitions as well as assignments. Preparing the model through the IDE is in most cases permissible, however, it can be cumbersome and it is therefore avoided.

B: Initialise the MATLAB-SAP2000 link. The function ***fx_intlSAP.m*** has been prepared for this purpose which requires an input directory of the pre-existing SAP2000 model. It is worth noting that the analyst is encouraged to use the $.sdb$ model file rather than importing the $.\$2k$ one. Use of the latter was found problematic in models with general frame sections.

C: Update the model. A new iteration of the model is obtained by updating the model input parameters via the OAPI. For a structure whose joint loads are to be varied, for instance, the function ***fx_JntLF.m*** has been prepared for assigning loads to point objects.

To proceed further, distinction is made on whether the analysis can be carried out externally. If the finite element model remains unchanged for each model iteration, then the analysis can be performed directly in MATLAB. This can be advantageous, as it provides the analyst with control and flexibility, limiting strenuous pre- and post-processing tasks.

D1: Analyse the structure in MATLAB. This is facilitated by the use of the function ***fx_getMK.m*** which has been prepared to construct the mass matrix and the global stiffness matrix by exporting and ordering these from the SAP2000 model. It is noted that this functionality further complements the existing capabilities of the OAPI.

D2: Analyse the structure in SAP2000. The function ***fx_runSAP.m*** runs the analysis in SAP2000. The load cases to run and the analysis options used are those configured in step **A**.

E: Retrieve analysis results. To reduce transferring times, the analyst is encouraged (in step **A**), to define a group containing the joints where the response is to be measured. The function ***fx_getJD*** can then be used to extract the diplacement response envelope, time history or the last step, for the joints of this group. This function has been constructed by piecing together various contributions from the *CSi OAPI Documentation.chm* file. Similar functions can be constructed to retrieve velocity or acceleration results.

F: Unlock model and break the MATLAB-SAP2000 link. If further analyses are to be carried out, the SAP2000 model is unlocked via the existing function ***SetModelIsLocked*** and the procedure is repeated from step **C**. When no more analyses are required, the MATLAB-SAP2000 link is interrupted through the function ***fx_closeSAP.m***.

Use of the functions presented in the previous has been tested with SAP2000 v.20 [1]. They extend, facilitate and simplify the existing capabilities of the SAP2000 OAPI, offering efficiency and readability, thus encouraging future developments for other IDEs. The proposed procedure, aimed at parametric, stochastic and optimisation analysis, provides recommendations to the user and has been successfully employed in our previous investigations on the dynamic analysis of composite beam structures [5] as well as the dynamic analysis of steel frames [4]. It will be demonstrated next through two illustrative examples.

3 SOLVERS FOR BILINEAR, RIGID-PLASTIC AND ROCKING OSCILLATORS

In this section, solvers are presented for the dynamic response evaluation of bilinear hysteretic, rigid-plastic and free-standing rocking oscillators, due to a general-type of excitation. The dynamical systems considered herein are indicative of distinct nonlinear behaviour, representative of a wide spectrum of primary and secondary structures of engineering interest.

3.1 Governing equations

3.1.1 Bilinear oscillator

The case of a bilinear oscillator is first considered, as depicted in Figure 2(a), whose vibration is ruled by:

$$\ddot{u}_{\mathrm{s}}(t) = -2\,\zeta_{\mathrm{s}}\,\omega_{\mathrm{s}}\,\dot{u}_{\mathrm{s}}(t) - \frac{f_{\mathrm{b}}\left(u_{\mathrm{s}}(t),\dot{u}_{\mathrm{s}}(t)\right)}{m_{\mathrm{s}}} - \ddot{\xi}(t)\,, \tag{1}$$

in which $\ddot{\xi}(t)$ is the horizontal base acceleration, where the overdot denotes differentiation with respect to time; $u_{\mathrm{s}}(t)$ is the unidirectional displacement, relative to the ground; ζ_{s} and $\omega_{\mathrm{s}} = \sqrt{k_{\mathrm{s}}/m_{\mathrm{s}}}$ are the viscous damping ratio and circular frequency, k_{s} and m_{s} being the elastic stiffness and mass, respectively.

In the above, f_{b} represents the bilinear restoring force (Figure 2(d)), given by:

$$f_{\mathrm{b}}\left(u_{\mathrm{s}}(t),\dot{u}_{\mathrm{s}}(t)\right) = \psi\,\omega_{\mathrm{s}}^2\,m_{\mathrm{s}}\,u_{\mathrm{s}}(t) + a_{\mathrm{s}}\,m_{\mathrm{s}}\,(1-\psi_{\mathrm{s}})\,z_{\mathrm{s}}(t)\,, \tag{2}$$

where ψ, in the range $0 \leqslant \psi \leqslant 1$, is the post-to-pre-yield stiffness ratio; a_{s} is the specific strength of the system; and $z_{\mathrm{s}}(t)$ is an auxiliary state variable satisfying $|z_{\mathrm{s}}(t)| \leq 1$, ruled by:

$$\dot{z}_{\mathrm{s}}(t) = \frac{\dot{u}_{\mathrm{s}}(t)\,\omega_{\mathrm{s}}^2}{a_{\mathrm{s}}}\left[1 - H\left(\dot{u}_{\mathrm{s}}(t)\right)H\left(z_{\mathrm{s}}(t)-1\right) - H\left(-\dot{u}_{\mathrm{s}}(t)\right)H\left(-z_{\mathrm{s}}(t)-1\right)\right]\,, \tag{3}$$

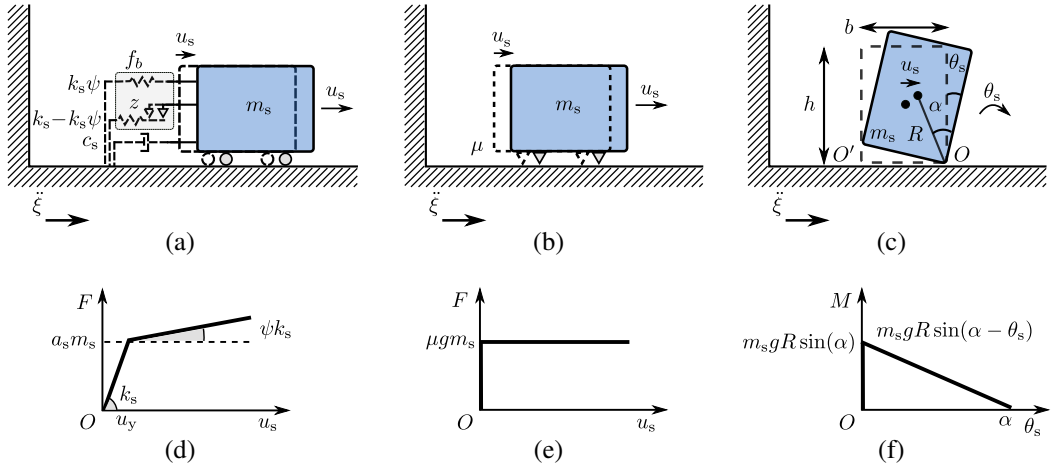

Figure 2: Bilinear (a), sliding (b) and rocking (c) oscillators and corresponding free-body diagrams (d, e, f).

where $H(\bullet)$ denotes the Heaviside unit step function, such that $H(x) = +1$ if $x \geq 0$ and $H(x) = 0$ if $x < 0$.

Setting $\psi = 0$ in Eq. (2) results to an elastic-perfectly-plastic oscillator; alternatively, setting $\psi = 1$ results to a linear one, with $f_{\mathrm{b}}(t) = \omega_{\mathrm{s}}^2 \, m_{\mathrm{s}} \, u_{\mathrm{s}}(t)$.

3.1.2 Sliding block

The rigid-perfectly plastic oscillator is considered next (Figure 2(b)). The system exhibits infinite pre-yielding stiffness and infinite ductility, and no motion during the sticking phase (i.e. $u_{\mathrm{s}} = \dot{u}_{\mathrm{s}} = 0$). During the sliding motion regime (i.e. $\dot{u}_{\mathrm{s}}(t) \neq 0$) its vibration is governed by:

$$\ddot{u}_{\mathrm{s}}(t) = -\frac{f_{\mathrm{s}}(\dot{u}_{\mathrm{s}}(t))}{m_{\mathrm{s}}} - \ddot{\xi}(t)\,, \tag{4}$$

where f_s is the associated restoring force (Figure 2(e)) and can be regarded as the limiting case of Eq. (2), when $\psi = 0$ and $\omega_{\mathrm{s}} \to +\infty$, given by:

$$f_{\mathrm{s}}(\dot{u}_{\mathrm{s}}(t)) = a_{\mathrm{s}} \, m_{\mathrm{s}} \, \mathrm{sgn}(\dot{u}_{\mathrm{s}}(t))\,; \quad |\dot{u}_{\mathrm{s}}(t)| > 0\,, \tag{5}$$

in which $\mathrm{sgn}(\bullet)$ is the signum function (i.e. $\mathrm{sgn}(x) = +1$ if $x > 0$, $\mathrm{sgn}(x) = -1$ if $x < 0$, and $\mathrm{sgn}(x) = 0$ if $x = 0$), and the specific strength is given by $a_{\mathrm{s}} = \mu \, g$, μ being the coefficient of sliding friction assuming horizontal contact surface and g the acceleration due to gravity.

The condition of initiation for sliding motion is $\left|\ddot{\xi}(t)\right| = a_{\mathrm{s}}$. Following initiation, an instantaneous stop or a full stop can occur in the system once the velocity drops to zero. In the former case, the motion will reverse or it will continue in the same direction, while in the latter case the system will remain at rest until the initiation condition is meet again.

3.1.3 Rocking block

The case of a rectangular free-standing block exhibiting pure rocking motion, is finally considered. In this regard, the coefficient of sliding friction is assumed to be sufficiently large (i.e. $\mu \to +\infty$), and the block oscillates about its centres of rotation O and O', as illustrated in Figure 2(c).

The equation governing the response during the rocking regime of motion is given by:

$$\ddot{\theta}_{\mathrm{s}}(t) = -p^2 \left[\sin\left(\alpha \,\mathrm{sgn}\left(\theta_{\mathrm{s}}(t)\right) - \theta_{\mathrm{s}}(t)\right) + \frac{1}{g} \cos\left(\alpha \,\mathrm{sgn}\left(\theta_{\mathrm{s}}(t)\right) - \theta_{\mathrm{s}}(t)\right) \ddot{\xi}(t) \right] , \tag{6}$$

where $\theta_{\mathrm{s}}(t)$ is the response rotation of the block; $\alpha = \tan^{-1}(b/h)$ is the slenderness angle, being a function of the width b and height h; $p = \sqrt{3\,g/(4\,R)}$ is a geometrical parameter, where R is half the block's diagonal.

As shown in Figure 2(f), the block initially possess infinite rotational stiffness until the applied moment about one of the pivot points O and O' reaches the value $|M_{\mathrm{s}}| = m_{\mathrm{s}}\, g\, R \sin(\alpha)$, and a softening branch initiates, reaching $M_{\mathrm{s}} = 0$ at the tipping condition $|\theta_{\mathrm{s}}| = \alpha$.

The initiation condition for Eq. (6) is $\left|\ddot{\xi}(t)\right| = g\,\tan(\alpha)$. Following initiation, a change in the sign of the rotation $\theta_{\mathrm{s}}(t)$ will correspond to an impact and (assuming that the block does not bounce back) the pivot point will switch from O to O' (or vice versa). It is assumed that the post-impact rotational velocity, $\dot{\theta}_{\mathrm{s}}^{+}$, is a fraction of the velocity prior to impact, $\dot{\theta}_{\mathrm{s}}^{-}$, that is: $\dot{\theta}_{\mathrm{s}}^{+} = \varepsilon\, \dot{\theta}_{\mathrm{s}}^{-}$, where ε is the coefficient of restitution, with $0 < \varepsilon \leq \varepsilon_{\max} < 1$, $\varepsilon_{\max} = 1 - 3\sin^2(\alpha)/2$ being the maximum value allowed.

3.2 Solvers for nonlinear dynamic response quantification

The dynamical systems considered in the previous are of piecewise linear form and therefore a highly efficient numerical procedure can be employed for quantifying the response. Specifically, each regime of motion is separately considered, and the solution is developed by interpolating the excitation over each time interval. Accordingly, recurrence formulae are derived for the response state vector of each system from exact solution of the associated equation of motion. To this end, the only requirement is that the time step is sufficiently small to closely approximate the excitation. The overall time history is finally constructed by piecing together the individual segments. Details on the methodology and the resulting expressions are provided in [6].

The solutions presented in [6] have been implemented in C++ along with an iterative procedure based on the bisection method [7] to identify state events (i.e. transition points of piecewise solutions such as the initiation and change in the regime of motion) and break down the solution in parts which have been later pieced together.

In order to confirm the validity of the solvers the solution has been compared to a MATLAB [3] implementation that has been prototyped using build-in Ordinary Differential Equation solvers. Specifically, ODE45 has been used, which is based on an explicit fourth- and fifth-order Runge-Kutta formulation. The implementation has been performed with consistent initial conditions and by setting MATLAB's odeset parameter values AbsTol = RelTol = 10^{-8} and Refine = 4, which refer to relative and absolute solution tolerances and interpolation output, respectively. The option 'Events' has been invoked to approximately identify state events.

The resulting standalone executables ***B1.exe***, ***S1.exe*** and ***R1.exe*** corresponding to the bilinear, rigid-plastic and rocking oscillators, respectively, accept their input arguments and export their results in standard fixed-length txt files which can be further processed by third-party software. Details on accessing the solvers along with their user instructions are provided in § 5.

They facilitate accurate and efficient dynamic analysis of the systems under consideration in presence of a general-type of base excitation and may find application in the stochastic analysis and optimisation of structural systems.

Table 1: Input random variable definition.

Variable	Distribution	Mean	CoV
E_1, E_2 $[\mathrm{N/m^2}]$	Lognormal	2.1×10^{11}	0.10
A_1 $[\mathrm{m^2}]$	Lognormal	2.0×10^{-3}	0.10
A_2 $[\mathrm{m^2}]$	Lognormal	1.0×10^{-3}	0.10
$f_1 - f_6$ $[\mathrm{N}]$	Gumbel	5.0×10^{4}	0.15

4 ILLUSTRATIVE EXAMPLES

Two examples are presented in the following for the analysis of structural systems with the ancillary tools developed. In the first example, the linear static analysis of a truss structure is facilitated through the use of the SAP2000 OAPI, with the purpose of quantifying the response statistics due to system uncertainties. The second example demonstrates the use and interoperability of the solvers presented in the previous with SAP2000, for the response quantification of nonlinear cascaded secondary oscillators in presence of stochastic excitation.

4.1 Example 1: Reliability analysis of a truss structure

4.1.1 Problem statement

The case of a truss structure is considered [8, 9], comprising of 11 horizontal and 12 diagonal members, as depicted in Figure 3. A finite element (FE) model is constructed in SAP2000 using 23 bar elements. The model is characterised by the input random variable vector $\mathbf{X} = \{E_1, E_2, A_1, A_2, f_1, \ldots, f_6\}$, consisting of a set of $n = 10$ independent random variables, where E_1, E_2 denote the Young's moduli and A_1, A_2 the cross sectional areas, of the horizontal and diagonal members, respectively, and $f_1 - f_6$ are applied loads, whose probabilistic definition is summarised in Table 1.

Requirement for this problem is the quantification of the response statistics of the midspan deflection u and the probability of failure $P_f = \mathrm{Prob}\left[g(\mathbf{X}) < 0\right]$, $g(\mathbf{X})$ being the limit state function, defined as:

$$g(\mathbf{X}) = u_{\max} - |u(\mathbf{X})| \leq 0\,, \tag{7}$$

where $u_{\max} = 0.11$ is the maximum permissible value of u.

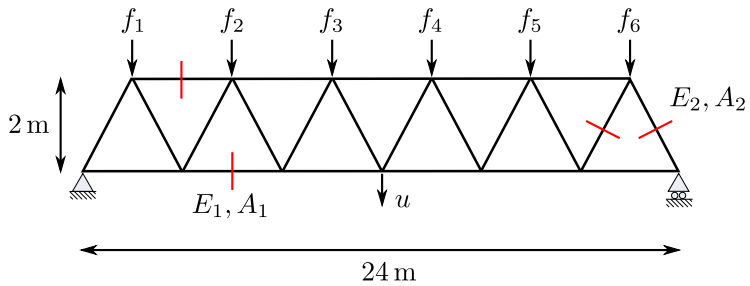

Figure 3: Truss structure [8].

4.1.2 Response surface-based metamodel

Owing to the presence of system uncertainties, the stiffness matrix is a random variable and therefore analysis is required within SAP2000. As $g(\mathbf{X})$ is algorithmically known, a response surface (RS) metamodel is constructed with the purpose of limiting the number of FE runs. Provided the fitted surface is an adequate approximation of the true response function, the analysis will be approximately equivalent to the one of the actual system.

In doing this, $g(\mathbf{X})$ is approximated with a quadratic polynomial of the form:

$$\tilde{g}(\mathbf{X}) = \alpha_0 + \sum_{i=1}^{n} \alpha_i x_i + \sum_{i=1}^{n} \alpha_{i,i} x_i^2 + \sum_{i=1}^{n-1} \sum_{j>i}^{n} \alpha_{i,j} x_i x_j \,, \tag{8}$$

where α_i, $\alpha_{i,i}$ and $\alpha_{i,j}$ are a set of $s = 1 + (n^2 + 3\,n)/2 = 66$ coefficients to be identified, conveniently collected in the vector:

$$\boldsymbol{\alpha} = \begin{bmatrix} \alpha_0 & \alpha_1 & \cdots & \alpha_n & \alpha_{1,1} & \cdots & \alpha_{n,n} & \alpha_{1,2} & \cdots & \alpha_{n-1,n} \end{bmatrix}^\top . \tag{9}$$

The values of the coefficients are determined via a set of sample points from the true limit state function, $g(\mathbf{X})$. In doing this, a circumscribed central composite design is adopted, widely used for fitting a second-order RS. This requires r FE runs with SAP2000 for evaluation of $g(\mathbf{X})$ symmetrically around the mean values of the random variables i.e. $x_i^{\pm} = \mu_i \pm h\,\sigma_i$, where $h = 0.95$ controls the size of the sampling domain. It is worth noting here that, if the shape of the true limit state function is not linear or quadratic the choice of h can significantly affect the accuracy of the approximation.

On minimising the error,

$$\varepsilon(\boldsymbol{\alpha}) = \sum_{k=1}^{r} \left(g(\mathbf{x}_k) - \tilde{g}(\mathbf{x}_k) \right)^2 , \tag{10}$$

with respect to $\boldsymbol{\alpha}$, the solution is given by,

$$\boldsymbol{\alpha} = \left(\mathbf{V}^\top \cdot \mathbf{V} \right)^{-1} \cdot \mathbf{V}^\top \cdot \mathbf{y} \,, \tag{11}$$

where $\mathbf{y}$ is a vector whose generic component is $g(\mathbf{x}_k)$, for the set of fitting points $\mathbf{x}_k, k = 1, \ldots, r$, and $\mathbf{V}$ is a matrix of size $(r \times s)$ collecting the associated polynomial terms:

$$\mathbf{V} = \begin{bmatrix} 1 & x_{1,1} & \cdots & x_{n,1} & x_{1,1}^2 & \cdots & x_{n,1}^2 & x_{1,1}x_{2,1} & \cdots & x_{n-1,1}x_{n,1} \\ \vdots & \vdots & \vdots & \vdots & \vdots & \vdots & \vdots & \vdots & \vdots & \vdots \\ 1 & x_{1,r} & \cdots & x_{n,r} & x_{1,r}^2 & \cdots & x_{n,r}^2 & x_{1,r}x_{2,r} & \cdots & x_{n-1,r}x_{n,r} \end{bmatrix} . \tag{12}$$

Analysis is finally performed using the fitted surface $\tilde{g} = \tilde{\mathbf{V}} \cdot \boldsymbol{\alpha}$, where $\tilde{\mathbf{V}}$, of size $(N \times s)$, retains a similar form as in Eq. (12) and is populated using N realisations of the vector of random variables.

4.1.3 Response quantification

The response probability density function (PDF) of u and the probability of failure P_f have been quantified using the RS model ($r = 178$ FE runs have been used with SAP2000) and have been compared to the reference FE solution. The results for both the RS and reference solution

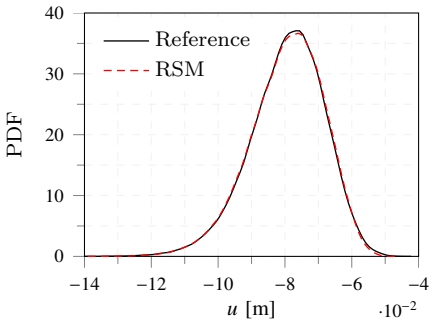

Figure 4: Response probability density function.

were obtained via crude Monte Carlo simulation with $N = 1 \times 10^6$ realisations. Analysis with SAP2000 was facilitated by use of the OAPI.

Figure 4 shows that the RS closely approximates the response PDF of u. Specifically, the calculated values of the first three statistical moments are in excellent agreement with the reference values reported in [9]. Further, the calculated $P_f = 0.00814$ is in good agreement with the reference FE solution $P_f^{\text{ref}} = 0.00898$.

4.2 Example 2: Stochastic response quantification of nonlinear cascaded secondary oscillators to white-noise and filtered-white noise process

4.2.1 Problem statement

The case of a multi-degree-of-freedom primary system [6] is next considered, comprising of a planar 5-storey single-bay moment-resisting frame, as depicted in Figure 5. A linear model of the structure is constructed using SAP2000. Floors are assumed rigid in their own plane, and the self-weight and super-dead load are the two sources of mass, lumped at the floor level. The total number of DoFs is $n_{\text{p}} = 75$ (i.e. 15 DoFs per storey, 2 finite elements are used for each frame element) and the fundamental circular frequency in the direction of interest x is $\omega_{\text{p}} = 14.76\,\text{rad/s}$, corresponding to a participation of 84% of the modal mass.

The structure is subjected to the unidirectional action of a horizontal ground acceleration, successively modelled as white noise and filtered white noise processes, commonly used in earthquake engineering applications. The latter is characterised by the well-known Kanai-

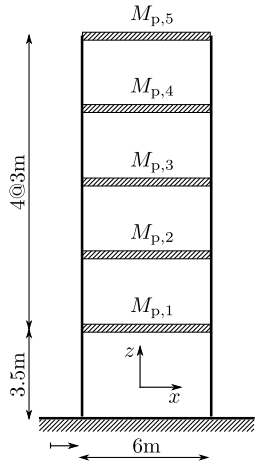

Figure 5: Primary structure [6].

Tajimi [10, 11] spectral density function:

$$S_{\ddot{\xi}}(\omega) = S_0 \cdot \frac{1 + 4\,\zeta_g^2\,(\omega/\omega_g)^2}{\left(1 - (\omega/\omega_g)^2\right)^2 + 4\,\zeta_g^2\,(\omega/\omega_g)^2}\,; \quad -\infty < \omega < \infty\,, \tag{13}$$

where S_0 represents a constant power spectral density level due to white noise, and the parameters ω_g and ζ_g denote the characteristic frequency and damping ratio of the soil layer, respectively. The filter represented by the second term in Eq. (13), thus attenuates the frequency content for $\omega > \omega_g$ as $\omega \to \infty$, and amplifies the frequencies in the vicinity of $\omega = \omega_g$. Neglecting the presence of the filter results to white noise modelling of the excitation, which implies infinite power of the resulting process, an unphysical yet mathematically convenient idealisation.

A secondary system is attached to the primary structure, at roof level, and is successively modelled as (i) linear, (ii) bilinear and (iii) sliding SDoF oscillator in cascade (see: § 3.1). Neglecting the feedback action of the secondary oscillator onto the primary one is in fact admissible provided the oscillator is sufficiently light and it does not vibrate close to or is in tune with the primary structure [6].

Requirement for this problem is the quantification of the full probabilistic structure of the response of each secondary system, due to white noise and filtered white noise modelling of the earthquake excitation.

4.2.2 Response quantification

Due to the linearity and deterministic form of the primary system considered, the analysis is carried out externally after extracting the mass and stiffness matrices from the SAP2000 model (see: § 2), thus avoiding strenuous pre- and post-processing tasks required by the Monte Carlo simulations. Further, owing to the cascade approximation, the analysis is independently carried out for the primary structure by means of classical modal analysis, retaining only a single mode of vibration. Such an approximation is permissible due to the high participation of modal mass.

A suite of 5000 synthetic ground motions are first generated through the summation of cosines with amplitudes and frequencies characterised by the power spectrum under consideration, and uniformly distributed over the interval $[0, 2\pi]$ [12]. In doing this, the frequency

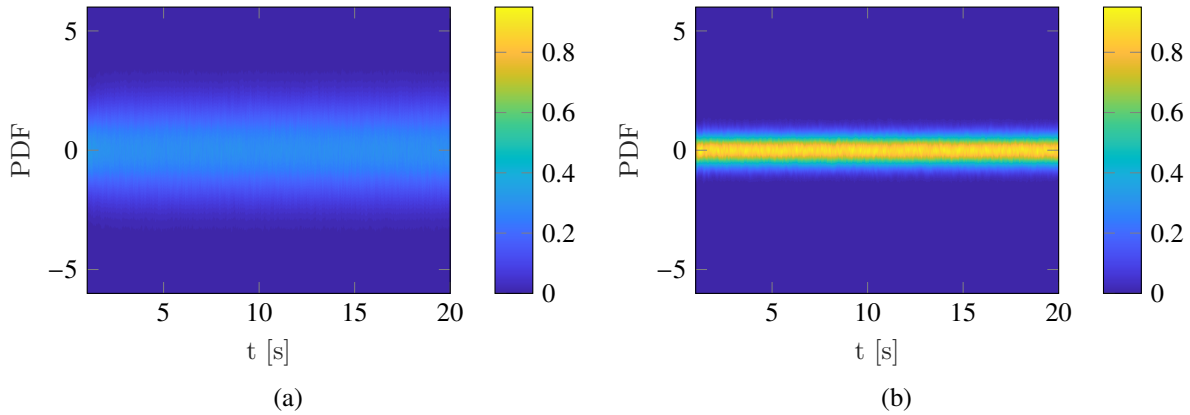

Figure 6: Response PDF of the absolute acceleration of the primary structure ($\omega_\mathrm{p} = 14.76\,\mathrm{rad/s}$, $\zeta_\mathrm{p} = 0.05$) due to: (a) white noise ($S_0 = 0.00214\,\mathrm{m^2/s^3}$); and (b) filtered white noise ($S_0 = 0.00214\,\mathrm{m^2/s^3}$, $\omega_g = 5\,\mathrm{rad/s}$, $\zeta_g = 0.2$) base excitation evaluated through 5000 Monte Carlo realisations.

interval $[0, \tilde{\omega}]$ is considered, where $\tilde{\omega} = 100$ is an upper cut-off frequency, beyond which the spectral density is regarded negligible. Furthermore, a soft soil is assumed with parameters $S_0 = 0.00214\,\mathrm{m}^2/\mathrm{s}^3$, $\omega_g = 5\,\mathrm{rad/s}$ and $\zeta_g = 0.2$ [13]. The resulting generated ground motions of variance $\sigma^2_{\ddot{u}_\xi} = 0.428$ and $\sigma^2_{\ddot{u}_\xi} = 0.097$, corresponding to white noise and filtered white noise, respectively, closely approximating the variance of the power spectrum.

The absolute acceleration response time history of the primary structure is then numerically determined at roof level. Figure 6 shows the evolution of the resulting stationary response PDF for $t \geq 1$, quantified through the kernel nonparametric probability density esimate, for the two forms of excitation under consideration.

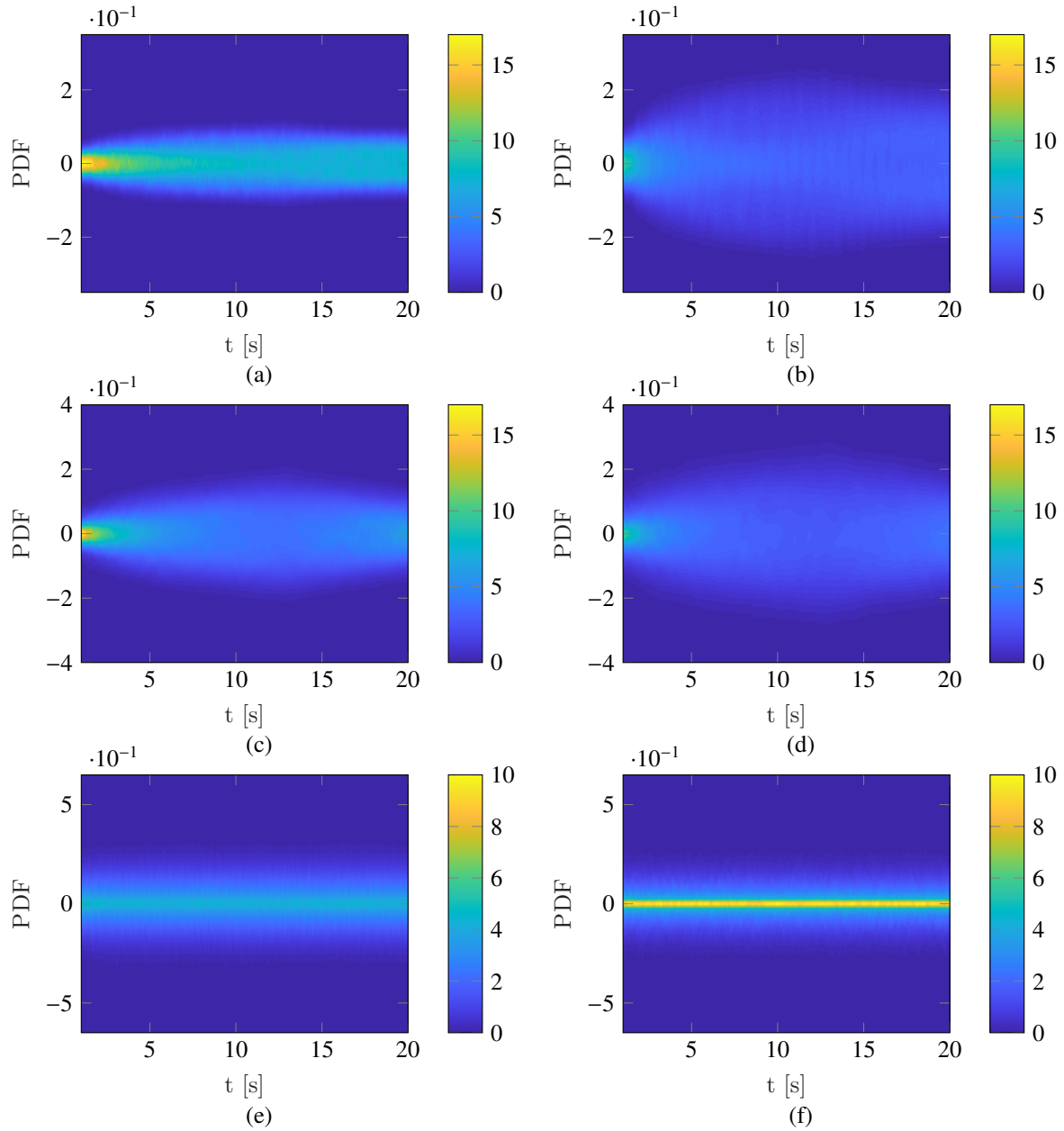

Figure 7: Response PDF of the (a, b) linear ($\omega_\mathrm{s} = 4.43\,\mathrm{rad/s}$, $\zeta_\mathrm{s} = 0.02$, $\psi = 1$), (c, d) bilinear ($\omega_\mathrm{s} = 4.43\,\mathrm{rad/s}$, $\zeta_\mathrm{s} = 0.02$, $a_\mathrm{s} = 0.3$, $\psi = 0.01$) and (e, f) sliding ($\mu = 0.02$) secondary oscillators, due to white noise (left) and filtered white noise (right) base excitation ($S_0 = 0.00214\,\mathrm{m}^2/\mathrm{s}^3$, $\omega_g = 5\,\mathrm{rad/s}$, $\zeta_g = 0.2$) evaluated through 5000 Monte Carlo realisations.

The analysis of the three secondary systems under consideration is carried out next. We circumvent the prohibitively time-consuming runs typically encountered in conventional analysis of such strongly-nonlinear systems by exploiting the solvers presented in § 3. In doing this, each response time history of the primary structure is successively used as input to the associated solver which is treated as black box model. For the linear and bilinear system, the parameters considered are $\psi = 1$ and $a_{\mathrm{s}} = 0.3$, $\psi = 0.01$, respectively, as well as $\omega_{\mathrm{s}} = 0.3$, $\omega_{\mathrm{p}} = 4.43\,\mathrm{rad/s}$ and $\zeta_{\mathrm{s}} = 0.02$. For the sliding system a friction coefficient of $\mu = 0.02$ is assumed.

Figures 7(a) - 7(d) plot the evolution of the displacement response PDF for the linear and bilinear secondary oscillators for $t \geq 1$. The velocity response PDF of the sliding oscillator is plotted in Figures 7(e) - 7(f). The results are quantified through the 5000 Monte Carlo realisations, and are presented for the two forms of excitation considered.

5 CONCLUSIONS

Assistant computational tools have been developed for the analysis and response quantification of structural systems in a systematic and automated fashion.

The open application programming interface (OAPI) of the commercial structural analysis software SAP2000 has been exploited and a procedure has been presented for the analysis of linear systems in conjunction with MATLAB, featuring model updating, analysis execution and extraction of the results. In-house ancillary functions have been developed for this purpose, that complement and extend existing capabilities of the OAPI.

Standalone solvers have been presented for the dynamic response analysis of bilinear hysteretic, rigid-plastic, and rocking oscillators subjected to an arbitrary excitation force. Such dynamical systems, are indicative of distinct nonlinear behaviour and representative of a wide spectrum of primary as well as secondary structures of engineering interest. The solvers developed herein can be used in a black-box type approach with third-party software.

The features at the current development stage have been showcased on the response-surface-based reliability analysis of a truss structure, facilitated through the use of the SAP2000 OAPI, and the response quantification of stochastically driven nonlinear secondary oscillators. The second application further demonstrates interoperability of the solvers with SAP2000.

The tools developed are available, along with user instructions, at this link. They allow convenient simplifications in the modelling and analysis process, error tractability, and can assist learning on the subject of structural dynamics. They may find application in parametric and stochastic analysis and form the basis for the development of additional modules.

References

[1] Computers and Structures. SAP2000. *Release 20.0.0*, 2013.

[2] A. Sextos and G. Balafas. Using the new SAP2000 open application programming interface to develop an interactive front-end for the modal pushover analysis of bridges. *International Conference on Computational Methods in Structural Dynamics and Earthquake Engineering*, 2011.

[3] The MathWorks Inc. MATLAB. *Release 8.2*, 2013.

[4] S. Kasinos, A. Palmeri, S. Maheshwari and M. Lombardo. Dynamic analysis of steel frames with uncertain semi-rigid connections. *International Conference on Structural Safety & Reliability*, 2017.

[5] S. Kasinos, A. Palmeri and M. Lombardo. Using the vibration envelope as a damage-sensitive feature in composite beam structures. *Structures*, **1**, 67–75, 2015.

[6] S. Kasinos. *Seismic response analysis of linear and nonlinear secondary structures*. PhD thesis, 2018.

[7] K. Atkinson. *An introduction to numerical analysis*. John Wiley & Sons, 2008.

[8] S. Lee and B. Kwak. Response surface augmented moment method for efficient reliability analysis. *Structural Safety*, **28**, 261–272, 2006.

[9] G. Blatman, B. Sudret and M. Berveiller. Quasi-random numbers in stochastic finite element analysis. *18 ème Congrès Français de Mécanique*, 2007.

[10] K. Kanai. An empirical formula for the spectrum of strong earthquake motions. *Bulletin of the Earthquake Research Institute, University of Tokyo, Japan*, **39**, 1961.

[11] H. Tajimi. A statistical method of determining the maximum response of a building structure during an earthquake. *Proceedings of the 2nd World Conference in Earthquake Engineering*, 1960.

[12] M. Shinozuka and G. Deodatis. Simulation of stochastic processes by spectral representation. *Applied Mechanics Reviews*, **44**, 191–204, 1991.

[13] K. Haciefendioglu and F. Birinci. Stochastic dynamic response of masonry minarets subjected to random blast and earthquake-induced ground motions. *Structural Design of Tall and Special Buildings*, **20**, 669–678, 2011.

COMPDYN 2019
7th ECCOMAS Thematic Conference on
Computational Methods in Structural Dynamics and Earthquake Engineering
M. Papadrakakis, M. Fragiadakis (eds.)
Crete, Greece, 24-26 June 2019

IMPLEMENTATION ASPECTS OF A SHELL FINITE ELEMENT IN STRUCTURAL ANALYSIS AND DESIGN CODE FOR DYNAMIC PROBLEMS

Christos Karakostas[1], Konstantinos Morfidis[1], Fotios Karaoulanis[1*] and Emmanuil Babukas[2]

[1]ITSAK-EPPO
Dasylliou Str., Elaiones Pylaias, Thessaloniki, Greece GR55535
e-mail: christos@itsak.gr, kmorfidis@itsak.gr, fotios.karaoulanis@gmail.com

[2] TOL - Technical Software House
60 Karterou Str., Heraklion, Greece GR71201
e-mail: man@tol.com.gr

Keywords: structural dynamics, shell element, MITC4, mass matrix, cantilever, eigenfrequencies.

Abstract. *In the framework of a EU-funded research project for the enhancement of the cooperation between academic institutions and private firms, the research team is currently enhancing the capabilities of an existing commercial code for the seismic design of buildings. Among the various tasks, a major one is the implementation of shell finite elements in the existing code, to be used, among others, for linear and nonlinear dynamic analyses of structural systems. In the present research effort, we present various aspects of the implementation process, starting from the criteria used for the selection of a suitable finite element among those proposed in the literature, the issues raised and the validation procedures used during the numerical implementation of the underlying theoretical aspects pertaining to dynamic analysis issues, and finally the incorporation of the numerical model into the existing code. In the present paper the four-node MITC4 shell element is presented. The MITC element formulation is based on the idea of degenerating a 3D solid finite element into a shell element by using special shape functions that are related to the Reissner-Mindlin kinematic assumption, and by introducing a zero stress assumption for the out of plane normal stress. To overcome the shear locking problem, a mixed interpolation of tensorial components is used resulting in an overall simple and transparent formulation, which gives the element a good predictive capability without containing spurious zero energy modes. The element is implemented into an existing commercial finite element code and several implementation aspects are discussed. The implementation is then tested against a selected problem in structural dynamics and its overall performance is assessed.*

1 INTRODUCTION

Four main approaches to applying finite element methods to shell structures can be found in the literature:

1. Shells are seen as an assembly of *flat elements* [1]. Coupling of membrane and bending effects due to curvature of the shell is inherently absent (except perhaps of the cases of composite laminated materials, see [2]). This approach is known to suffer from discontinuous bending moments between elements, while achieving convergence only for fine meshes [3].

2. *Axisymetric shells*, which refer to curved shell elements that exhibit symmetry about an axis of rotation [2]. These elements suffer from difficulties in describing complex geometries and/or complex loads, in achieving inter-element compatibility and from spurious effects as transverse shear and membrane locking.

3. *Solid shell elements*, which form a class of finite element models intermediate between conventional shell and solid models [4]. The inclusion of additional degrees of freedom renders this approach computationally ineffective. Furthermore, shear and membrane locking, trapezoidal locking caused by the deviation of the midplane from rectangular shape and thickness locking due to coupling of Poisson's ratio of the inplane and transverse normal stresses, make the element formulation a challenging task.

4. *Degenerated shell elements*, *i.e.* elements that are derived by degenerating a 3D solid element into a shell surface element. These are originating from the work of Ahmad, Irons and Zienkiewicz in 1970 [5] which still constitutes the basis for modern finite element analysis of shell structures. It has been shown [6] that there is a practical coincidence between degenerated shell elements and those based on standard Reissner-Mindlin/Naghdi type shell theory. This favours using the former for practical purposes as their formulation is generally simpler.

In the framework of a EU-funded research project for the enhancement of the cooperation between academic institutions and private firms, the research team is currently enhancing the capabilities of an existing commercial code for the seismic design of buildings. Among the various tasks, a major one is the implementation of shell finite elements in the existing code, to be used, among others, for linear and nonlinear dynamic analyses of structural systems. The MITC4 element [7, 8] has been selected for this purpose, which belongs to the class of the degenerated shell elements, presented above. The element formulation and a validation example is presented in what follows.

2 ELEMENT FORMULATION

Assuming small displacements/deformations, the *geometry* of the element is given as (see Figure 1):

$$x_i = \sum_{k=1}^{4} h_k x_i^k + \frac{r_3}{2} \sum_{k=1}^{4} a_k h_k V_{ni}^k \tag{1}$$

where x_i the Cartesian coordinates of any point in the element, x_i^k the Cartesian coordinates of nodal point k, V_{ni}^k the components of the so-called *director* vector $\boldsymbol{V}_n^k$, which is not required to be normal to the element's midsurface, a_k the thickness of the element at nodal point k measured

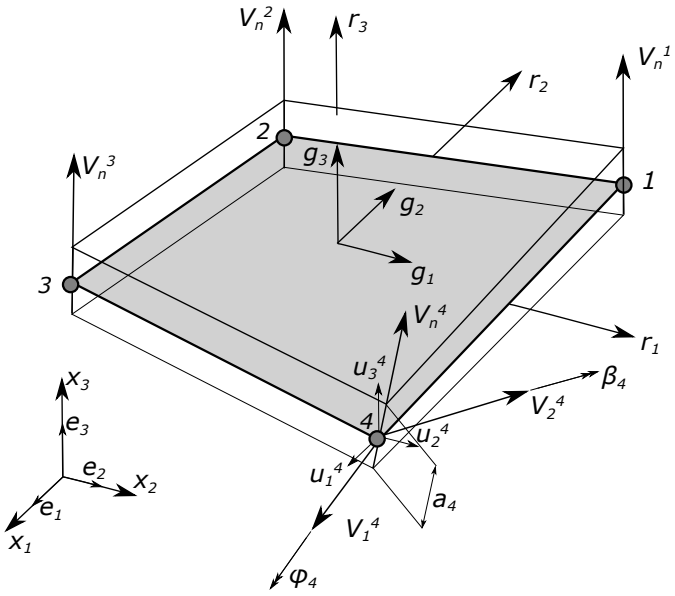

Figure 1: Element description

along the director vector and $h_k(r_1, r_2)$ the two-dimensional Lagrange interpolation functions in the $r_1 - r_2$ coordinate system (natural) corresponding to node k. For the MITC4 element h_k functions are defined as:

$$h_1 = \frac{1}{2}(1+r_1)(1+r_2) \qquad h_2 = \frac{1}{2}(1-r_1)(1+r_2) \tag{2}$$
$$h_3 = \frac{1}{2}(1-r_1)(1-r_2) \qquad h_4 = \frac{1}{2}(1+r_1)(1-r_2)$$

The *displacements* u_i of a point of the shell element with natural coordinates r_i $(i = 1, 2, 3)$ is given to the Cartesian coordinate system as:

$$u_i = \sum_{k=1}^{4} h_k u_i^k + \frac{r_3}{2} \sum_{k=1}^{4} a_k h_k \left(-V_{2i}^k \alpha_k + V_{1i}^k \beta_k\right) \tag{3}$$

where V_{1i}^k and V_{2i}^k the components of the vectors $\boldsymbol{V}_1^k$, $\boldsymbol{V}_2^k$ at point k (see Figure 1) defined as:

$$\boldsymbol{V}_1^k = \frac{\boldsymbol{e}_2 \times \boldsymbol{V}_n^k}{|\boldsymbol{e}_2 \times \boldsymbol{V}_n^k|}, \quad \boldsymbol{V}_2^k = \boldsymbol{V}_n^k \times \boldsymbol{V}_1^k \tag{4}$$

while α_k and β_k are the rotations in element k associated with vectors V_{1i}^k and V_{2i}^k respectively. Furthermore, $\boldsymbol{e}_2$ is the basis vector of Cartesian coordinate system, which is replaced by $\boldsymbol{e}_3$ in case that is collinear to the the director vector $\boldsymbol{V}_n^k$.

The strains are related to the displacement derivatives which are given as [8]:

$$\begin{bmatrix} \dfrac{\partial u_i}{\partial x} \\ \dfrac{\partial u_i}{\partial y} \\ \dfrac{\partial u_I}{\partial z} \end{bmatrix} = \sum_{k=1}^{4} \begin{bmatrix} \dfrac{\partial h_k}{\partial x} & g_{1x}^k G_x^k & g_{2x}^k G_x^k \\ \dfrac{\partial h_k}{\partial y} & g_{1x}^k G_y^k & g_{2x}^k G_y^k \\ \dfrac{\partial h_k}{\partial z} & g_{1x}^k G_z^k & g_{2x}^k G_z^k \end{bmatrix} \begin{bmatrix} \boldsymbol{u}_{ik} \\ \alpha_k \\ \beta_k \end{bmatrix} \tag{5}$$

where:

$$\frac{\partial h_k}{\partial x} = J_{11}^{-1}\frac{\partial h_k}{\partial r_1} + J_{12}^{-1}\frac{\partial h_k}{\partial r_2}, \quad G_x^k = r_3\left(J_{11}^{-1}\frac{\partial h_k}{\partial r_1} + J_{12}^{-1}\frac{\partial h_k}{\partial r_2}\right) + J_{13}^{-1}h_k \tag{6}$$

where J_{ij}^{-1} is the element (i,j) of $\mathbf{J}^{-1}$, $\mathbf{J}$ being the Jacobian matrix of the transformation between the Cartesian and the natural coordinate systems:

$$\mathbf{J} = \frac{\partial \boldsymbol{x}}{\partial \boldsymbol{r}} \tag{7}$$

Finally, the constitutive equation needs to be modified in order to enforce the *zero normal force condition* [9], which assuming its *reduced* form as

$$\tilde{\boldsymbol{\sigma}} = \tilde{\mathbf{C}}\tilde{\boldsymbol{\varepsilon}} \tag{8}$$

with

$$\tilde{\boldsymbol{\sigma}} = \left[\begin{array}{ccccc} \sigma_{xx} & \sigma_{yy} & \sigma_{xy} & \sigma_{yz} & \sigma_{zx} \end{array}\right], \quad \tilde{\boldsymbol{\varepsilon}} = \left[\begin{array}{ccccc} \varepsilon_{xx} & \varepsilon_{yy} & \varepsilon_{xy} & \varepsilon_{yz} & \varepsilon_{zx} \end{array}\right] \tag{9}$$

yields for the isotropic elasticity case:

$$\tilde{\mathbf{C}} = \frac{E}{(1-\nu)^2}\begin{bmatrix} 1 & \nu & 0 & 0 & 0 \\ & 1 & \nu & 0 & 0 \\ & & \dfrac{1-\nu}{2} & 0 & 0 \\ & & & \dfrac{1-\nu}{2} & 0 \\ & & & & \dfrac{1-\nu}{2} \end{bmatrix} \tag{10}$$

The above description should suffice to build up the element's stiffness matrix. However, a problem originating by the generation of the strains using the above linear displacement interpolation is the so-called element *locking* (*i.e.* the calculated displacements are orders of magnitude smaller than what they expected to be) when the element is thin. This can be explained by the fact that when using linear interpolations it is impossible for the transverse shear strains to vanish at all points in the element, when the element is subjected to a constant bending moment.

To solve this deficiency, various approaches have been proposed, as for example the use of selective and reduced integration [9]. The approach used in the MITC4 element formulation is to introduce separate interpolations for the shear strain components. In the natural coordinate system of the element the strain tensor is written as [10]:

$$\boldsymbol{\varepsilon} = \tilde{\varepsilon}_{ij}\boldsymbol{g}^i \otimes \boldsymbol{g}^j \tag{11}$$

where $\tilde{\varepsilon}_{ij}$ is the covariant components of the strain tensor measured in the natural coordinate system and $\boldsymbol{g}^i$ the contravariant base vector. In the MITC4 formulation the following strain interpolations are selected:

- The "in-layer" strain components ($\tilde{\varepsilon}_{11}$, $\tilde{\varepsilon}_{22}$, $\tilde{\varepsilon}_{12}$) are directly calculated from the displacement/rotation interpolations.

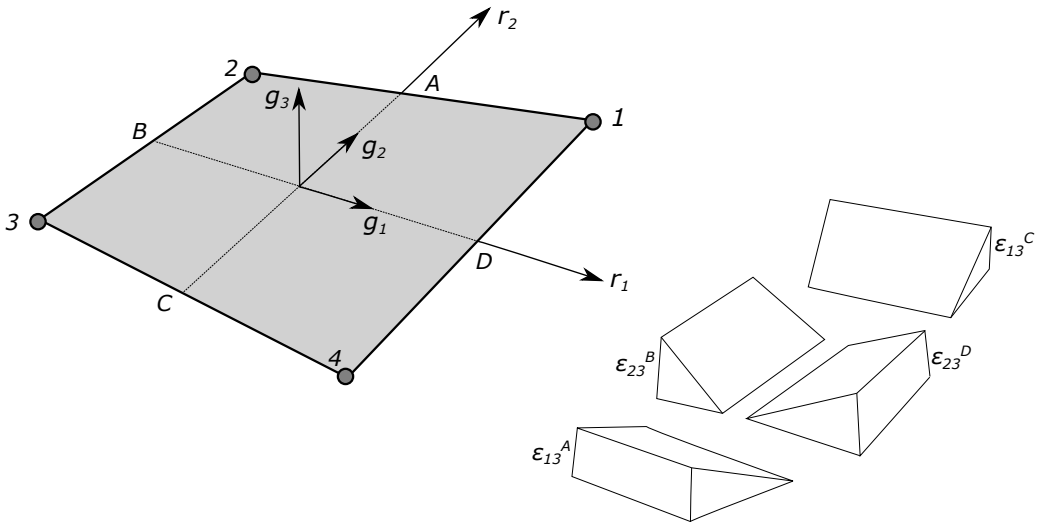

Figure 2: Strain interpolation

- The transverse shear strains ($\tilde{\varepsilon}_{13}$, $\tilde{\varepsilon}_{23}$) are interpolated using the following functions:

$$\tilde{\varepsilon}_{13}\frac{1}{2}(1+r_2)\tilde{\varepsilon}^A_{13}+\frac{1}{2}(1-r_2)\tilde{\varepsilon}^C_{13}, \quad \tilde{\varepsilon}_{23}\frac{1}{2}(1+r_1)\tilde{\varepsilon}^D_{13}+\frac{1}{2}(1-r_1)\tilde{\varepsilon}^B_{13} \tag{12}$$

  where $\tilde{\varepsilon}^A_{13}$, $\tilde{\varepsilon}^C_{13}$, $\tilde{\varepsilon}^D_{23}$ and $\tilde{\varepsilon}^B_{23}$, are the strain components at points A, C, B and D, evaluated from the displacement interpolations.

A lumped mass matrix based on the row summing approach of the consistent matrix [1] of the translational only masses is utilized within the context of this work. The consistent matrix is evaluated form the integral:

$$\mathbf{M}=\int_\Omega \mathbf{N}^T\rho\mathbf{N}d\Omega \tag{13}$$

where ρ the density and $\mathbf{N}$ the shape function matrix which follows directly from the kinematic assumptions defined above.

3 IMPLEMENTATION ASPECTS

The above formulation has been implemented in the Python programming language. Python's elegant syntax and dynamic typing, together with its interpreted nature, make it an ideal language for scripting and rapid application development [11].

An object oriented approach was followed, where five main classes have been defined:

- A `Node` class, which holds the coordinates and the local to global mapping vector of a finite element node and is responsible for storing the displacements, the reactions and the corresponding entries from the eigenvectors.

- A `Material` class, which is subclassed to `Isotropic` and `Orthotropic` classes, both of which hold the material properties and are responsible for the generation of the elasticity matrix $\mathbf{C}$.

- A `Section` class, which holds the `Material` and the thickness at a given point.

- A `GaussPoint` class, which holds a `Section`, the abscissae and the weights of the Gaussian quadrature and is responsible for updating the stresses, given a stress increment.

- The `MITC4` class, which contains the above and provides the functionality described in the previous section.

For the inclusion in the commercial code which is written in FORTRAN 2008, the above data structures will be ported as derived data types.

4 NUMERICAL VALIDATION

A cantilever beam serves as an initial validation example, which will be presented next. Assume a beam of length 10 (units: SI), defined by 1×1 uniform cross-section. The material is characterized by a Young's modulus $E = 3 \times 10^7$, a Poisson's ratio $\nu = 0.2$ and a density $\rho = 2500$. For the finite element model, the beam is divided into 100 elements.

The exact fundamental frequencies for the corresponding Euler-Bernoulli beam can be easily retrieved from literature as (see eg. [12])

$$\omega = (\beta l)^2 \sqrt{\frac{EI}{\rho A l^4}} \tag{14}$$

where I is the second moment of area and βl equals to 1.875104, 4.694091 and 7.854757 for the three first frequencies respectively.

The first eight eigenmodes and the corresponding eigenfrequencies are shown in Figure 3. A comparison between the numerical and the exact eigenfrequencies are given in the following table for the six (bending only) eigenmodes which the theory predicts. The difference in the two directions reflects the difference is the shell orientation: out-of-plane bending (first) *vs.* in-plane bending (second).

Exact (Euler-Bernoulli) [Hz]	MITC4 [Hz]	Difference [%]
0.1770	0.1761	-0.49
	0.1798	1.58
1.1090	1.0630	-4.33
	1.0840	-2.30
3.1052	2.7410	-13.29
	2.8240	-9.96

Table 1: Comparison between the exact (Euler-Bernoulli) and the MITC4 eigenfrequencies for the cantilever problem.

5 CONCLUSIONS

In the framework of a EU-funded research project for the enhancement of the cooperation between academic institutions and private firms, the research team is currently enhancing the capabilities of an existing commercial code for the seismic design of buildings. Among the various tasks, a major one is the implementation of shell finite elements in the existing code, to be used, among others, for linear and nonlinear dynamic analyses of structural systems.

The MITC4 shell element has been selected for this task. This element is based on the idea of degenerating a 3D solid finite element into a shell element by using special shape functions

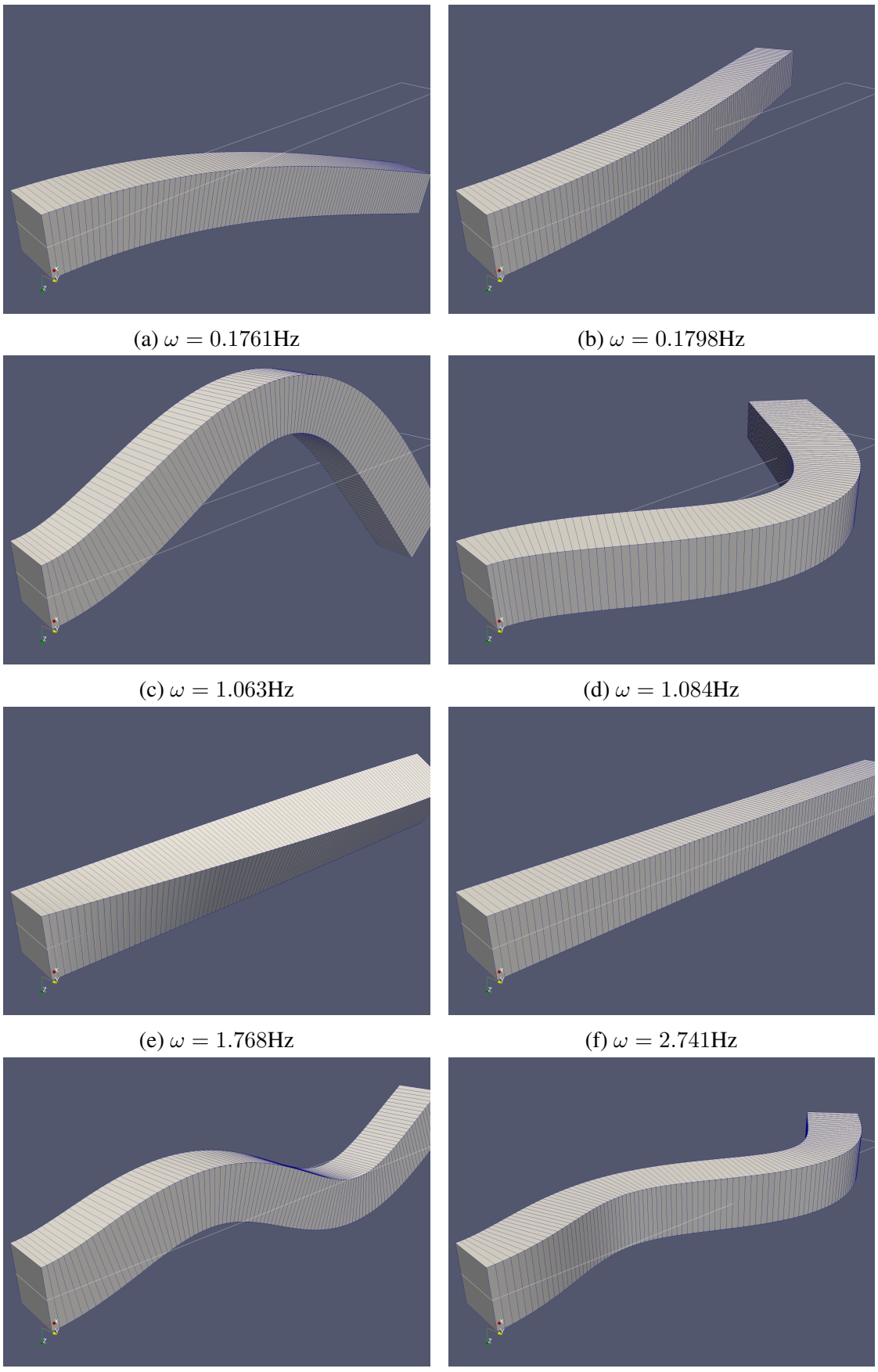

(a) $\omega = 0.1761$Hz (b) $\omega = 0.1798$Hz

(c) $\omega = 1.063$Hz (d) $\omega = 1.084$Hz

(e) $\omega = 1.768$Hz (f) $\omega = 2.741$Hz

(g) $\omega = 2.824$Hz (h) $\omega = 2.876$Hz

Figure 3: The first eight eigenmodes and the corresponding eigenfrequencies

that are related to the Reissner-Mindlin kinematic assumption, and by introducing a zero stress assumption for the out of plane normal stress. To overcome the shear locking problem, a mixed interpolation of tensorial components is used resulting in an overall simple and transparent formulation, which gives the element a good predictive capability without containing spurious zero energy modes.

The formulation of the element is briefly presented in this work and then the element is validated using against a simple dynamical problem referring to a cantilever beam.

6 ACKNOWLEDGMENT

This research has been cofinanced by the European Regional Development Fund of the European Union and Greek national funds through the Operational Program Competitiveness, Entrepreneurship and Innovation, under the call RESEARCH CREATE INNOVATE (project code: T1EDK-01800).

REFERENCES

[1] O.C. Zienkiewicz, R.L. Taylor, *The Finite Element Method for Solid and Structural Mechanics*, Sixth edition, Elsevier Butterworth-Heinemann, 2005.

[2] Oñate, E. *Structural analysis with the finite element method. Linear statics: volume 2: beams, plates and shells*. Springer Science and Business Media, 2013.

[3] A.N. Palazotto, *Nonlinear analysis of shell structures*. American Institute of Aeronautics and Astronautics, 1992.

[4] C.A. Felippa An 8-Node ANS Solid-Shell Element. *Report to Sandia National Laboratories, Albuquerque, NM*, 2001.

[5] S. Ahmad, B.M. Irons, O. C. Zienkiewicz, Analysis of thick and thin shell structures by curved finite elements *International Journal for Numerical Methods in Engineering* **23**, 419–451, 1970.

[6] Buechter N. Ramm, E. *Comparison of shell theory and degeneration*, In Nonlinear Analysis of Shells using Finite Elements, CISM, Udine, Italy, June 1991.

[7] E.N. Dvorkin, K.J. Bathe, A continuum mechanics based four-node shell element for general non-linear analysis *Engineering computations* **11**, 77–88, 1984.

[8] K.J. Bathe, *Finite element procedures*. 2006.

[9] T.J.R. Hughes, *The finite element method: linear static and dynamic finite element analysis*. Dover Publications, 2000.

[10] E.N. Dvorkin, Nonlinear analysis of shells using the MITC formulation *Archives of Computational Methods in Engineering* **2**, 1–50, 1995.

[11] The Python Tutorial, `https://docs.python.org/3/tutorial/`, 24 03 2019.

[12] Rao S.S. Mechanical Vibrations Pearson Education, Inc. 2011.

COMPDYN 2019
7th ECCOMAS Thematic Conference on
Computational Methods in Structural Dynamics and Earthquake Engineering
M. Papadrakakis, M. Fragiadakis (eds.)
Crete, Greece, 24-–26 June 2019

MULTIVARIATE PADÉ APPROXIMANTS FOR FINITE ELEMENT SOLUTIONS WITH COMPLEX PARAMETRIC DEPENDENCE

Romain Rumpler [1], **Raúl Rodríguez Sánchez** [2], **Peter Göransson** [1]

[1] MWL/Centre for ECO2 Vehicle Design, Department of Aeronautical and Vehicle Engineering,
KTH Royal Institute of Technology, Stockholm, Sweden
e-mail: rumpler@kth.se, pege@kth.se

[2] Chair of Structural Mechanics, Technical University of Munich, Arcisstraße,
Munich, 80333, Germany
e-mail: raul.rodriguez@tum.de

Keywords: Reduced Order Model, Padé Approximants, Fast Frequency Sweeps, Finite Element Method.

Abstract. *Most engineering applications involving solutions by numerical methods are dependent on several parameters, whose impact on the solution may significantly vary from one to the other. At times an evaluation of these multivariate solutions may be required at the expense of a prohibitively high computational cost. In the present work, a multivariate finite element approach is proposed, allowing for a fast evaluation of parametric responses. It is based on the construction of a reduced basis spanning a subspace able to capture rough variations of the response. The method consists in an extension of the Well-Conditioned Asymptotic Waveform Evaluation (WCAWE) to multivariate problems, by an appropriate choice of derivative sequences, and a selection of the most relevant basis components. It is validated and demonstrated for its potential on a semi-industrial sized 3D application involving coupled poroelastic and internal acoustic domains.*

1 INTRODUCTION

In order to limit the high computational burden associated with the evaluation of multivariate Finite Element (FE) solutions, an approach based on a Reduced-Order-Model (ROM), derived after a univariate moment-matching method, is proposed. This univariate method, namely the Well-Conditioned Asymptotic Waveform Evaluation (WCAWE) method, proposed by Slone *et al*. [1], is shown to allow for a robust generation of basis components with good convergence properties of the associated reduced systems [1–3]. It relies on a sequence of successive derivatives of the system of interest, leading to multiple Right-Hand-Side (RHS) problems to be solved sequentially, with intermediate orthonormalization steps and correction terms ensuring the robustness of the procedure and the good conditioning of the resulting transformation matrix. This univariate basis generation procedure may be extended to a multivariate procedure. However, the cost associated with the orthonormalization and correction steps, may lead to a computationally prohibitive cost, particularly as the dimension of the variable space increases [3]. Additionally, not all cross-derivative terms may contribute significantly to the convergence of the ROM, and it may be critical to be able to reduce them to a minimum. In this contribution, an effort is made to bring the WCAWE to multivariate problems, starting with a bivariate illustration, and attempting to limit the transformation bases to a minimum in view of higher dimensionality applications. The foundation for a multi-interval strategy is also presented in view of the reconstruction of wide parametric ranges. The approach is shown to benefit from the superior robustness of the WCAWE compared to the so-called component-wise Padé approximants [3–6], previously used to derive the Nested Padé approximant method [7, 8].

In the following Section, reminders are made about the WCAWE, the details of its procedure, and the proposed extension to multivariate problems. Then, the basis for a multi-interval strategy relying on error estimation following contours of convergence intervals is introduced. Finally, the accuracy and potential of the method are presented on a 3D poro-acoustic problem.

2 The WCAWE, a moment-matching, projection-based ROM

2.1 Generic multivariate problem and associated transformation

The starting point of the WCAWE-based parametric sweep is given by a linear system of the following form,

$$\mathbf{Z}(\mathbf{x})\mathbf{U}(\mathbf{x}) = \mathbf{F}(\mathbf{x}), \tag{1}$$

where $\mathbf{x}$ may be a vector of N_x independent variables corresponding to the parametric problem of interest, e.g. including the angular frequency ω, material parameters, ... For the original univariate case [1], the vector reduces to a scalar such that $\mathbf{x} = [x]$. In an FE problem, $\mathbf{Z}(\mathbf{x})$, $\mathbf{U}(\mathbf{x})$, and $\mathbf{F}(\mathbf{x})$ respectively represent the system matrix of the discretized problem, the solution vector and the vector of externally applied loads.

The projection-based approach, allowing to solve for a reduced set of equations associated with Eq. (1), relies on the construction of a transformation basis emerging from successive derivatives of the solution vector in Eq. (1) at a specific point $\mathbf{x}_0$ in the parameter space. The WCAWE algorithm provides a robust generation of this sequence of successive derivatives, overcoming the inherently ill-conditioned transformation matrix emerging from the direct approach used in the component-wise Padé approximants [3, 4], also used for the generation of Nested Padé approximants [7, 8]. The resulting well-conditioned transformation matrix $\mathbf{V}_\mathrm{N}$, consisting of N orthonormalized basis vectors, allows for a robust, non-stagnating convergence upon increasing the size of the subspace spanned. The associated approximation of the solution

in Eq. (1), to the order N, is such that

$$\widehat{\mathbf{U}}_{\mathrm{N}}(\mathbf{x}) = \mathbf{V}_{\mathrm{N}}\, \boldsymbol{\alpha}(\mathbf{x}) \approx \mathbf{U}(\mathbf{x}), \tag{2}$$

$\boldsymbol{\alpha}$ being a vector of N generalized coordinates. This transformation leads to a reduced system corresponding to Eq. (1), solving for the generalized coordinates in $\boldsymbol{\alpha}(\mathbf{x})$,

$$\mathbf{V}_{\mathrm{N}}{}^{T}\mathbf{Z}(\mathbf{x})\mathbf{V}_{\mathrm{N}}\boldsymbol{\alpha}(\mathbf{x}) = \mathbf{V}_{\mathrm{N}}{}^{T}\mathbf{F}(\mathbf{x}). \tag{3}$$

2.2 A multivariate WCAWE basis generation procedure

A generic expression of the multivariate WCAWE algorithm, as proposed in this contribution, may be given in $\mathbf{x} = \mathbf{x}_0$ by the following multiple right-hand-side procedure,

$$\begin{cases}
\mathbf{Z}^{(0)}\overline{\mathbf{v}}_1 = \mathbf{F}^{(0)} \\
\qquad Normalization\ \ \overline{\mathbf{v}}_1 \longrightarrow \mathbf{v}_1 \\
\mathbf{Z}^{(0)}\overline{\mathbf{v}}_2 = \mathbf{F}^{(1)}\mathbf{e}_1^T\mathbf{P}_{\mathbf{Q_1}}(2,1)\mathbf{e}_1 - \mathbf{Z}^{(1)}\mathbf{v}_1 \\
\qquad Othonormalization\ \ \overline{\mathbf{v}}_2 \longrightarrow \mathbf{v}_2 \\
\qquad \vdots \\
\mathbf{Z}^{(0)}\overline{\mathbf{v}}_n = \left(\displaystyle\sum_{j=1}^{(n-1)} \left(\mathbf{F}^{(n)}\mathbf{e}_1^T\mathbf{P}_{\mathbf{Q_1}}(n,j)\mathbf{e}_{n-j} \right) - \mathbf{Z}^{(1)}\mathbf{v}_{n-1} \right. \\
\qquad\qquad \left. - \displaystyle\sum_{j=2}^{(n-1)} \left(\mathbf{Z}^{(j)}\mathbf{v}_{n-j}\mathbf{P}_{\mathbf{Q_2}}(n,j)\mathbf{e}_{n-j} \right) \right) \\
\qquad Othonormalization\ \ \overline{\mathbf{v}}_n \longrightarrow \mathbf{v}_n \\
\qquad \vdots \\
\mathbf{Z}^{(0)}\overline{\mathbf{v}}_{\mathrm{N}} = \left(\displaystyle\sum_{j=1}^{(\mathrm{N}-1)} \left(\mathbf{F}^{(\mathrm{N})}\mathbf{e}_1^T\mathbf{P}_{\mathbf{Q_1}}(\mathrm{N},j)\mathbf{e}_{\mathrm{N}-j} \right) - \mathbf{Z}^{(1)}\mathbf{v}_{\mathrm{N}-1} \right. \\
\qquad\qquad \left. - \displaystyle\sum_{j=2}^{(\mathrm{N}-1)} \left(\mathbf{Z}^{(j)}\mathbf{v}_{\mathrm{N}-j}\mathbf{P}_{\mathbf{Q_2}}(\mathrm{N},j)\mathbf{e}_{\mathrm{N}-j} \right) \right) \\
\qquad Othonormalization\ \ \overline{\mathbf{v}}_{\mathrm{N}} \longrightarrow \mathbf{v}_{\mathrm{N}}
\end{cases} \tag{4}$$

where a modified Gram-Schmidt orthonormalization step is performed between each vector generation by the multiple RHS systems in Eq. (4), and where

- $\mathbf{Z}^{(k)}$ stands for the differentiation of the system matrix $\mathbf{Z}$, in $\mathbf{x} = \mathbf{x}_0$, to the "cumulative" order k, regardless of the distribution of the differentiation between the independent variables x_i. In other words, given the notation $\partial_{x_j}^{i_j}(\cdot)$ for the partial derivative with respect to x_j at order i_j, and the convention $\partial_{x_j}^{0}(\cdot) = (\cdot)$, then $\mathbf{Z}^{(k)}$ results from the partial derivative orders summation such that

$$\mathbf{Z}^{\left(\sum_{j=1}^{\mathrm{N}_x} i_j\right)} = \left(\prod_{j=1}^{\mathrm{N}_x} \partial_{x_j}^{i_j} \right) \mathbf{Z}, \tag{5}$$

  with the aforementioned convention implying that $\mathbf{Z}^{(0)} = \mathbf{Z}$.

- $\mathbf{e}_k$ is a unitary standard basis vector associated with the k^{th} component of the solution vector,
- $\overline{\mathbf{v}}_k$ is the non-orthonormalized vector generated in the k^{th} iteration of the procedure,
- $\mathbf{v}_k$ is the basis vector orthonormalized against $\mathbf{v}_{k-1}$, generated after the k^{th} iteration of the procedure,
- $\mathbf{P}_{\mathbf{Q}_\omega}(\alpha,\beta)$, $\omega = 1, 2$, corresponds to the RHS correction terms, chosen to be associated with the modified Gram-Schmidt orthonormalisation process [1].

The orthonormalized and non-orthonormalized bases, $\mathbf{V}_\text{N}$ and $\overline{\mathbf{V}}_\text{N}$ respectively, are related by

$$\mathbf{V}_\text{N} = \overline{\mathbf{V}}_\text{N}\mathbf{Q}^{-1}, \tag{6}$$

where $\mathbf{Q}$ is an N $\times$ N upper triangular, nonsingular matrix containing the modified Gram-Schmidt coefficients. More precisely, column k of $\mathbf{Q}$ contains the successive coefficients resulting from the projection of partially orthonormalized $\overline{\mathbf{v}}_k$ on the orthnormalized vectors $\mathbf{v}_j$, $j < k$, and Q_{kk} corresponds to the norm of $\mathbf{v}_k$ before its normalization. The correction terms $\mathbf{P}_{\mathbf{Q}_\omega}(\alpha,\beta)$, $\omega = 1, 2$, are given by the following product of block matrices extracted from $\mathbf{Q}$,

$$\mathbf{P}_{\mathbf{Q}_\omega}(\alpha,\beta) = \prod_{t=\omega}^{\beta} \mathbf{Q}^{-1}_{[t:\alpha-\beta+t-1,t:\alpha-\beta+t-1]} \tag{7}$$

Further discussions on the choice of the RHS correction coefficients other than associated with the Gram-Schmidt coefficients, may be found in Ref. [1].

The approximated solution is evaluated at all DOFs from the generalized coordinates vector $\boldsymbol{\alpha}$, after Eq. (2).

Adapting the WCAWE algorithm from univariate problems to multivariate ones lies in the generation of sequences of RHS vectors, emerging from sequences of iteratively differentiated matrices $\mathbf{Z}^{(k)}$. The choice adopted here is to generate such sequences independently, thus generating a set of N_V bases $\left\{\mathbf{V}_\text{N}^1, \cdots, \mathbf{V}_\text{N}^{\text{N}_\text{V}}\right\}$ associated with N_V sequences of iteratively differentiated matrices $\mathbf{Z}^{(k)}$. These bases, in principle all of the same size N, each consist of orthonormalized basis vectors, but these are naturally not mutually orthonormalized from one to the next basis. These are not even guaranteed to produce linearly independent subsets of vectors upon merging these bases. A simple way to ensure this, as well as to reduce the basis to a minimum number of basis vectors is to proceed to a compression, or a component selection, via a Singular Value Decomposition (SVD) of the merged set of bases. Either way, the initial step consists in an SVD of the merged basis after concatenation, $\mathbf{V}_\text{N}^\text{mer} = \left[\mathbf{V}_\text{N}^1 \cdots \mathbf{V}_\text{N}^{\text{N}_\text{V}}\right]$, resulting in

$$\mathbf{V}_\text{N}^\text{mer} = \sum_{i=1}^{\text{N}_\text{mer}} \sigma_i \mathbf{w}_i^\text{l} \mathbf{w}_i^{\text{r}T}, \tag{8}$$

where N_mer corresponds to the total number of basis vectors in $\mathbf{V}_\text{N}^\text{mer}$, *i.e.* $\text{N}_\text{mer} = \text{N} \cdot \text{N}_\text{V}$; σ_i, $\mathbf{w}_i^\text{l}$, and $\mathbf{w}_i^\text{r}$ correspond to the singular values, left and right singular vectors respectively.

From the SVD, either the (left) singular vectors associated with the highest singular values are selected as the components of the reduced merged basis, or the compression of the merged basis associated with the highest singular values is performed from the selected left singular vectors, right singular vectors and their corresponding singular values. Here the former approach

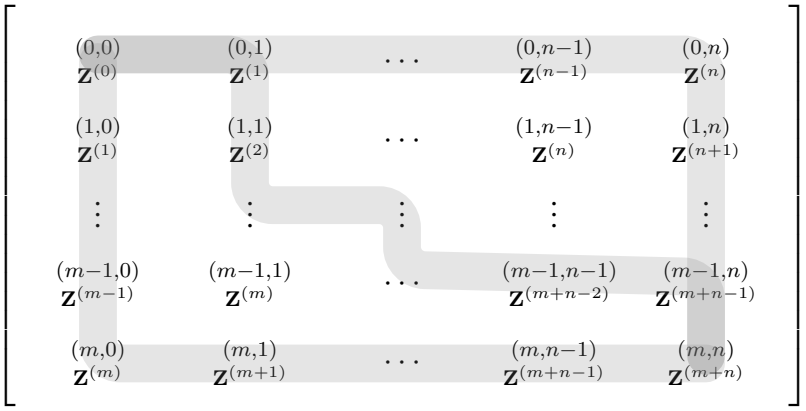

Figure 1: Illustration of three possible bivariate derivation paths for the system matrix $\mathbf{Z}$ up to the "cumulated order" $(m+n)$.

is used, such that assuming a descending-ordered sequence of singular values $(\sigma_1 \cdots \sigma_{\mathrm{N_{mer}}})$, the reduced, merged basis $\mathbf{V}^*$ is

$$\mathbf{V}^* = \left\{ \mathbf{w}_i^{\mathrm{l}} \mid i \in (1, \mathrm{N_{mer}}) \wedge \sigma_i \geq \sigma_{\mathrm{thresh}} \right\}, \tag{9}$$

where σ_{thresh} corresponds to the empirically chosen threshold value for the selection of the singular values resulting from the decomposition in Eq. (8).

The resulting reduced basis $\mathbf{V}^*$, consisting of $\mathrm{N_{V^*}}$ vectors, is then used in place of the univariate transformations corresponding to Eq. (2) and Eq. (3), in order to solve a reduced set of equations at most involving $\mathrm{N_{mer}}$ DOFs.

2.3 Sequences of multivariate differentiation

The sequential WCAWE procedure above depends on the generation of sequences of differentiated system matrices to successive "cumulated multivariate orders" k, i.e. $\mathbf{Z}^{(k)}$. The choice of these sequences is addressed empirically in this contribution, and illustrated for the case of bivariate problems. For the bivariate case, the cumulated differentiation orders and the associated differentiation paths may be represented in a matrix form, see Fig. 1.

The matrix sequences obtained from these differentiation paths of the system matrix subsequently feed the procedure presented in Eq. (4).

The rationale behind choosing a limited number of derivation paths is connected to the potential inefficiency resulting from the attempt to calculate all multivariate derivatives for a given set of maximum orders. Preliminary tests based on the methodology introduced in the previous section rapidly confirm the emergence of quasi-linearly dependent basis vectors associated with different differentiation orders from distinct sequences. In practice, it is estimated that a number of sequences of the order of the dimensionality of the multivariate problem may be sufficient in order to provide good convergence properties of the ROM. For instance, 2 sequences may be sufficient for a bivariate problem. Note that this observation addresses in part the issue of dimensionality and the associated efficiency of the approach: the number of successive derivatives necessary grows linearly with the dimensionality as opposed to an exponential growth if all cross-derivatives are calculated in a fully multivariate approach.

3 Multi-interval, multivariate WCAWE approach

In practice, the size of the reduction basis may be limited due to the increase of the computational cost of the procedure in Eq. (4) [3]. This implies that there may be a tradeoff between increasing the order of approximation, reflected in the size of the basis for a given reference point, and a multi-interval strategy. In order to proceed with an approximation based on multiple intervals, an error estimator is first necessary.

3.1 Error estimation

A Cauchy-type of convergence test is chosen in order to estimate the accuracy of the approximation without having to calculate the full solution. Provided an approximated output (scalar) quantity of interest, to the order N, in point $\mathbf{x}$, of the form

$$\widehat{S}_{\mathrm{N}}(\mathbf{x}) = 10\ \log\left(\frac{\widehat{U}_{\mathrm{N}}(\mathbf{x})^2}{U_{\mathrm{ref}}(\mathbf{x})^2}\right), \tag{10}$$

the convergence is estimated in a given point $\mathbf{x}$ with the Cauchy convergence test associated with the relative error $\epsilon^{(\mathrm{N})}(\mathbf{x}) = \widehat{S}_{(\mathrm{N}+2)}(\mathbf{x}) - \widehat{S}_{(\mathrm{N})}(\mathbf{x})$, such that

$$\epsilon^{(\mathrm{N})}(\mathbf{x}) \leq \epsilon_{\max}, \quad \forall \mathbf{x} \in [\mathbf{x}_{\min}, \mathbf{x}_{\max}]\,. \tag{11}$$

Note that the convergence test involves the solutions associated with several orders of difference. Two orders of difference is suggested here for examples associated with bivariate problems; more may be required for higher dimensionality. Despite a slight reduction of the convergence range achieved, a sufficiently enriched basis reduces the possibility of an erroneous estimate to occur, and leads to a conservative measure of the actual approximation error.

A Cauchy-type of convergence test however requires an evaluation of two solutions in each point of interest. It is consequently necessary to limit the number of evaluations of the relative error for each interval in order to limit the extra cost associated with the error estimation.

3.2 Contour-following and multi-interval strategy

In order to reduce the number of points at which the error estimation needs to be made, a contour-following strategy is implemented. Starting from the reference point for each interval, an isocontour is determined (Moore-Neighbour Tracing algorithm), associated with the max error $\epsilon_{\max}$ in Eq. (11). This contour subsequently allows to fit a regular shape (e.g. a rectangle for a bivariate problem) providing a simplified measure of the interval of convergence. The successive dimensions of the intervals of convergence may further be used in order to anticipate the choice of subsequent reference points for approximation of the solution on neighbour intervals.

There are several simple strategies possible in order to fill an entire parametric solution space with smaller intervals of convergence. One may iteratively choose reference points in direct connection with the range of convergence of the previously calculated intervals, as adopted for instance in Ref. [8]. Another possibility is to successively choose the reference points such that they are the furthest away from any boundary of the parametric space or the converged contours.

4 Application: poro-acoustic parametric sweep

The proposed multivariate approach is tested on an average-sized problem consisting of the interior cavity of a passenger train, treated with a 15-cm layer of sound absorbing porous material on the top surface. A time-harmonic point source is defined at a corner of the cavity, and

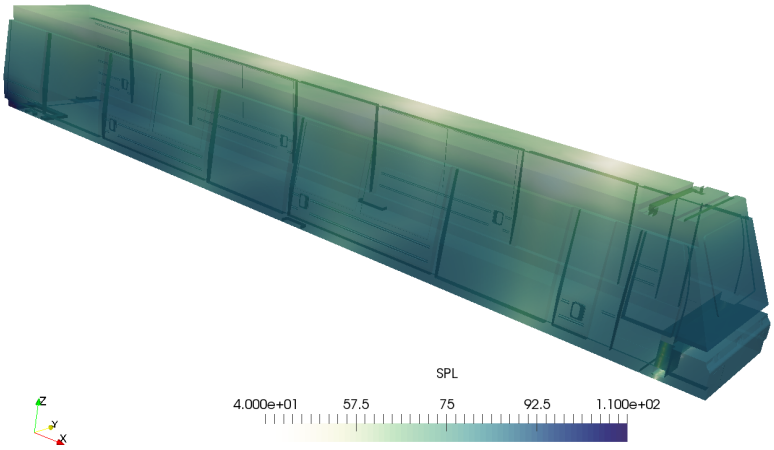

Figure 2: Sound pressure level of the damped solution at 63 Hz, $\Phi = 25000$ N.s.m^{-4}, scale $40 - 110$ dB.

parametric sweeps with respect to both the frequency and the static airflow resistivity of the porous layer are performed. All boundary walls are considered as rigid walls, except from the porous boundary. The porous boundary is modelled by an equivalent fluid formulation, consisting of a modified Helmholtz equation where the equivalent speed of sound is complex and frequency-dependent, given by

$$\tilde{c_{\mathrm{p}}} = \frac{c_0}{\sqrt{\dfrac{1 - i\Phi}{\rho_0 \omega}}}, \tag{12}$$

where $\tilde{(\cdot)}$ denotes a complex-valued quantity, $\rho_0 = 1.21$ kg.m^{-3} is the ambient density of the air saturating the pores and $c_0 = 343$ m.s^{-1} the speed of sound in the air. $\omega = 2\pi f$ is the angular frequency associated with the time-harmonic excitation, and Φ is the static flow resistivity, associated with the viscous dissipation in the porous material.

After a standard expression of the problem in its weak form and subsequent discretization by a Galerkin method, the finite element problem has the general form

$$\left(\mathbf{K_a} - \frac{\omega^2}{c_0^2} \mathbf{M_a} + \mathbf{K_p} - \frac{\omega^2}{\tilde{c_{\mathrm{p}}}^2} \mathbf{M_p} \right) \tilde{\mathbf{U}} = \mathbf{F}, \tag{13}$$

where $\square_{\mathbf{a}}$ correspond to air cavity global matrices, and $\square_{\mathbf{p}}$ to porous global matrices. $\tilde{\mathbf{U}}$ is the vector of nodal unknowns (acoustic pressure fluctuation here). The right-hand-side vector $\mathbf{F}$, associated with the time-harmonic acoustic excitation is in practice only non-zero at a few DOFs. The FE problem in Eq. (13) is evidently of the form of the generic problem in Eq. (1), thus suitable for the multivariate approach proposed. The discretized problem consists of around 300000 acoustic pressure DOFs.

Fig. 2 illustrates the solution at a given point of the parametric sweep, for a frequency of 63 Hz, and a flow resistivity of 25000 N.s.m^{-4}.

The reference solution for the bivariate parametric sweep, where $f \in [50, 150]$ Hz and $\Phi \in [3000, 50000]$ N.s.m^{-4}, at a point in the cavity, is plotted in Fig. 3.

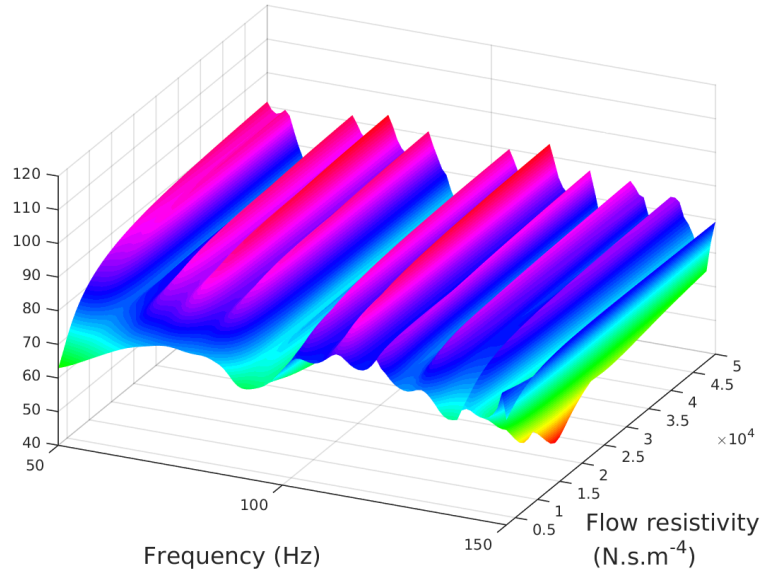

Figure 3: Reference solution. Sound pressure level at a point in the acoustic cavity, parametric solution, in dB.

The multivariate WCAWE procedure proposed here is applied for an approximated solution based on one reference point in the parametric space for the construction of the transformation basis.

Two configurations are tested regarding the number of sequences necessary in order to produce the reduced merged basis $\mathbf{V}^*$ of Eq. (9). The first configuration includes 3 sequences: the 2 ”outer” sequences, and one ”diagonal” sequence, as presented in Fig. 1. Given that in this configuration, some components added by the third sequence are not selected by the SVD, and that the increased size of the reduced basis $\mathbf{V}^*$ does not noticeably improve the accuracy of the approximation, the second configuration includes only the two ”outer” sequences. The singular value threshold σ_{thresh}, used for the selection of the main components for the reduced basis $\mathbf{V}^*$, is chosen to be such that $\sigma_{\text{thresh}} = \sigma_{\text{max}} \cdot 10^{-15}$, where σ_{max} corresponds to the largest singular value in the decomposition of Eq. (8).

In Fig. 4, the convergence of the approximated bivariate solution is illustrated for three different orders of approximation, for a reduced basis $\mathbf{V}^*$ based on the two ”outer” sequences.

Given the smooth variation of the solution with respect to the static flow resistivity, it is natural that a lower order of approximation is required than for the frequency. In this illustration, the order of differentiation for the static flow resistivity is set to 9. Three increasing orders of differentiation are plotted for the frequency, from order 19 to order 55. The degree of accuracy reached for the latter case, although using one point only at $f = 88$ Hz and $\Phi = 25000$ N.s.m^{-4} for the construction of the basis, highlights the potential of the method.

Table 1 provides a brief comparison of the size of the bases obtained from the proposed procedure when 2 or 3 sequences of differentiation are used prior to the SVD. A combination of the facts that some vectors added by the 3rd sequence are filtered out by the SVD, while all vectors emerging from the combination of the 2 ”outer” sequences are kept, indicates that a 2-sequence approach may be sufficient for the bivariate case. In particular, no improvement of

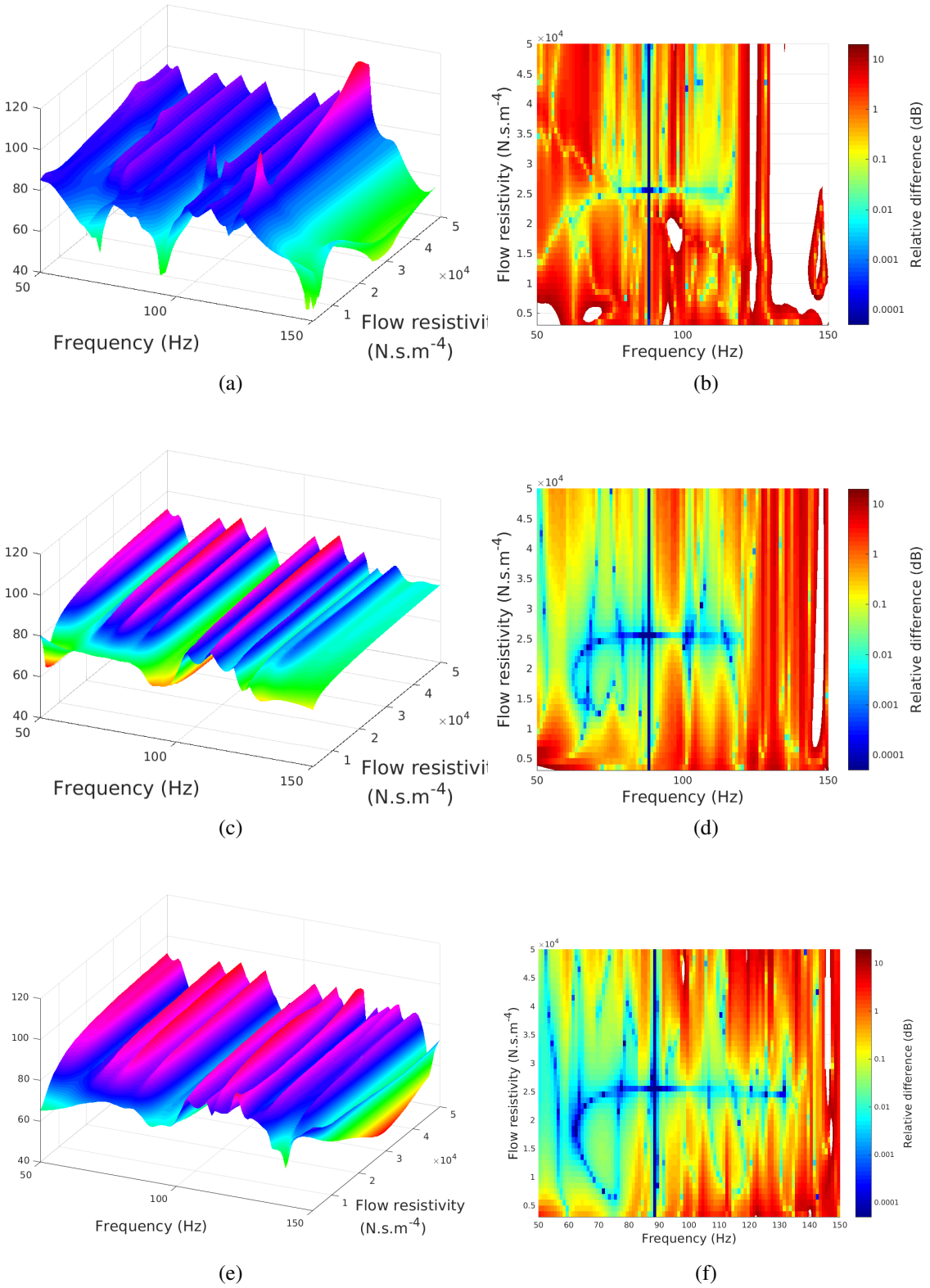

Figure 4: Convergence of the one-point WCAWE-approximated solution. SPL at a single point, in dB. Reference parametric point for the WCAWE basis procedure: $f = 88$ Hz and $\Phi = 25000$ N.s.m^{-4}. (a)-(b) Derivative orders 19/9 for frequency/resistivity; (c)-(d) Derivative orders 31/9 for frequency/resistivity; (e)-(f) Derivative orders 55/9 for frequency/resistivity. Approximation (left) and relative difference to the reference solution (right).

	N vec/basis	N_{mer}	N_{V^*}
2-sequence	29 (9+19+1)	56 (29+27)	56
3-sequence	29 (9+19+1)	83 (29+27+27)	79
2-sequence	41 (9+31+1)	80 (41+39)	80
3-sequence	41 (9+31+1)	119 (41+39+39)	112
2-sequence	65 (9+55+1)	128 (65+63)	128

Table 1: Overview of the size of the reduced basis $\mathbf{V}^*$ emerging from the 2- and 3-sequence procedure associated with the results in Fig.4.

convergence and accuracy was observed by adding the third sequence, thus indicating a minor contribution from the basis vectors emerging from this additional sequence. This also reflects a conservative threshold value for σ_{thresh}. Finally, the fact that no basis vector is filtered out by the SVD, when all vectors emerging from the combination of the 2 "outer" sequences are kept, implies that the SVD is in this case not associated with a selection of the basis components, but rather with a re-orthogonalization of the reduced basis $\mathbf{V}^*$.

Limiting the expansion to derivative orders 20/12 for the frequency and flow resistivity, respectively, Fig. 5 illustrates the contour-following, filling and shape-fitting approach in order to define sub-intervals of convergence. The error estimation is calculated along the contours only, in Figs. 5a and 5c, assuming a monotonous increase of the relative error inside the contours around the reference point of expansion, and a tolerance of $\epsilon_{\text{max}} = 0.02$ dB. These contours may subsequently be fitted, as plotted in grey in Figs. 5b and 5d, with a regular shape connected to the shape of the parametric space, i.e. a rectangle for this bivariate example.

A first attempt for a multi-interval approximation of the full bivariate parametric space is plotted in Figs. 6. This approach is based on a surface-fitting matching the surface area of the estimated contour, augmented by an overestimation factor, here set to 1.5. This over-estimation factor is justified by the slow increase of the error beyond the convergence contours, provided that the error tolerance is low enough (here 0.02 dB). The first reference point, associated with the first interval in Fig. 6a, is chosen following a preliminary step testing the convergence range associated with a reference point in the center of the parametric space. Then, subsequent intervals are chosen based on the dimensions of the last 2 calculated intervals, in the closest neighbourhood possible to the last calculated interval. When the parametric space has been entirely covered, the algorithm attempts to bridge the largest gaps, based on the dimension of the smallest interval of convergence. Fig. 6b shows in white the estimated range of convergence after 3 intervals (starting from the low frequency and low flow resistivity ranges). Fig. 6c shows the estimated range of convergence after 9 intervals, after which the entire parametric range is "covered". Finally, Fig. 6d plots the estimated range of convergence after the largest gaps have been added extra reference points, including 16 intervals in total. This implies the calculation of 16 multiple RHS problems consisting of 33 RHS vectors in order to build the complete set of reduced bases, to be contrasted with the full solution to be calculated at $101 \times 48 = 4848$ points for the reference solution.

The proposed approach is currently being tested for its robustness with respect to a wide range of problems, starting, as done here, with bi-parametric problems.

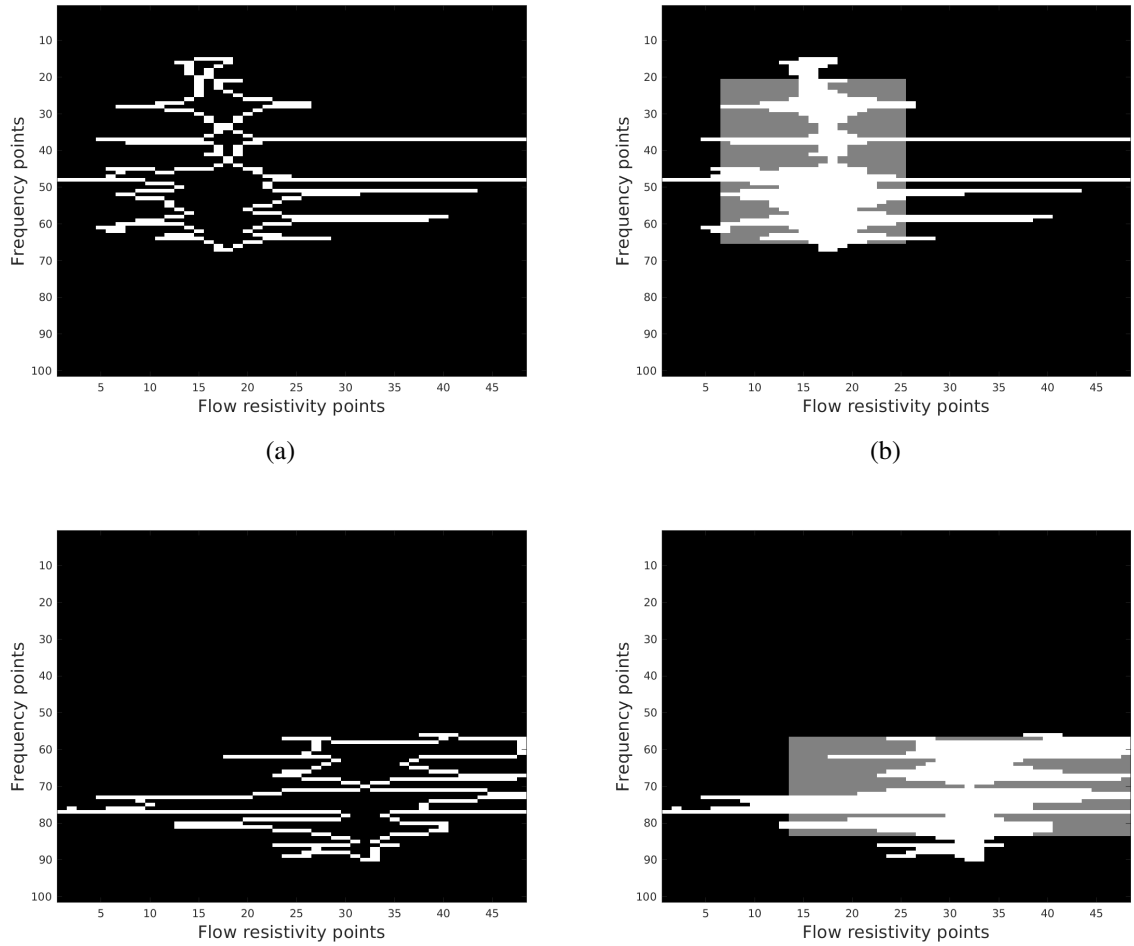

Figure 5: Illustration of the contour-following and shape fitting strategy for a single interval associated with the poro-acoustic bivariate problem. (a) and (c) Isocontour following of the max relative error; (b) and (d) Isocontour filling and fitting with a regular shape (rectangle).

5 CONCLUSIONS

In this contribution, a multivariate approach based on the Well-Conditioned Asymptotic Waveform Evaluation algorithm is proposed. It relies on the generation of basis vectors emerging from sequences of incrementally differentiated system matrices at parametric points of expansion. These sequences, efficiently generated by a multiple right-hand-side type of problem, are subsequently merged and further reduced via a singular value decomposition.

The convergence of the approach is illustrated on a bivariate poro-acoustic application of about 300000 degrees of freedom. The limitation to a reduced set of sequences is promising in the scope of using the proposed approach for higher dimensionality. An extension to a multi-interval approximation strategy, based on the efficient use of error estimator is also tested and currently under further developments in connection with its robustness.

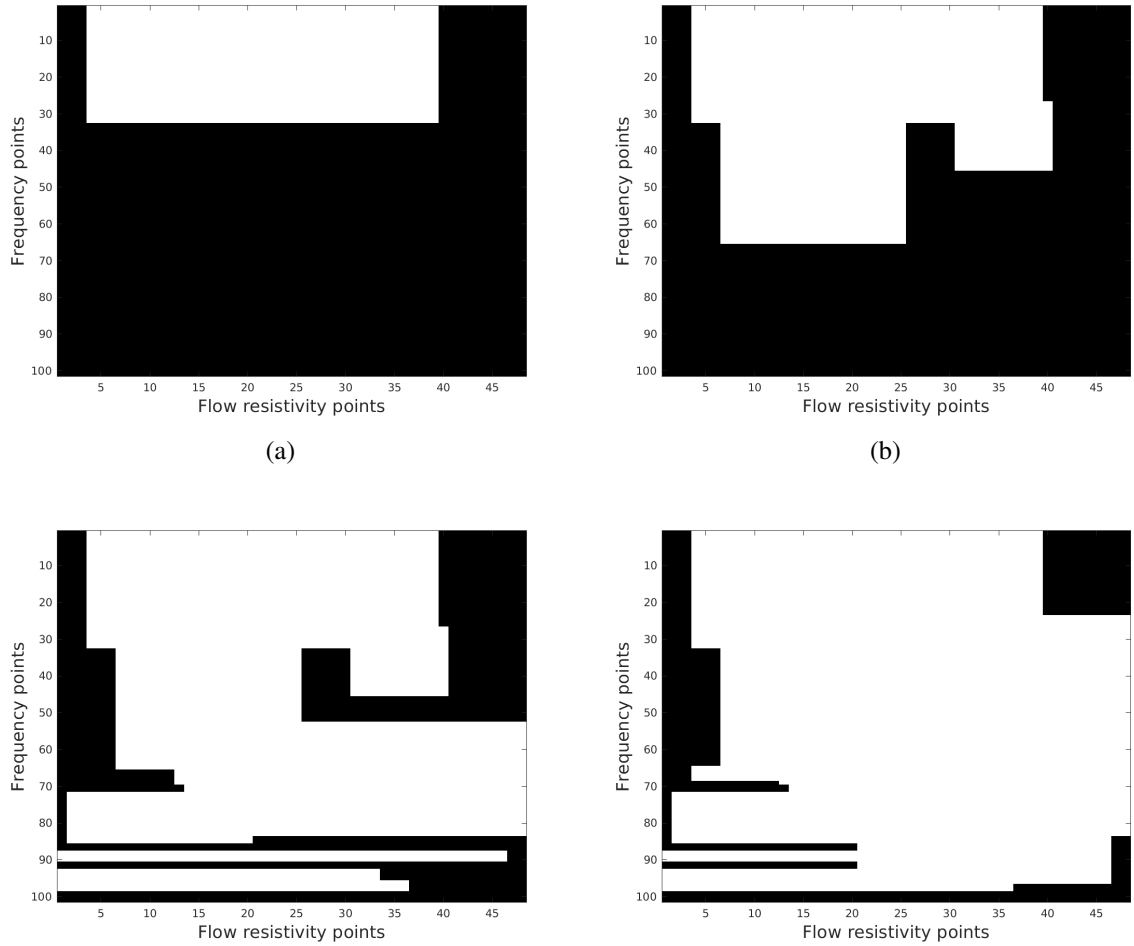

Figure 6: Convergence of a multi-interval approach for bases with fixed derivative orders 20/12, with a tolerance of $\epsilon_{\max} = 0.02$ dB. (a): 1 convergence interval, (b): 3 convergence intervals, (c): 9 convergence intervals, (d): 16 convergence intervals.

ACKNOWLEDGEMENTS

The financial support from the Swedish Research Council (Vetenskapsrådet VR Grant 2015-04925 for the first author) and the Centre for ECO2 Vehicle Design (VINNOVA Grant 2016-05195) are gratefully acknowledged.

REFERENCES

[1] R. D. Slone, R. Lee, and J.-F. Lee. Well-conditioned asymptotic waveform evaluation for finite elements. *IEEE Transactions on Antennas and Propagation*, 51(9):2442–2447, 2003.

[2] M. S. Lenzi, S. Lefteriu, H. Beriot, and W. Desmet. A fast frequency sweep approach using Padé approximations for solving Helmholtz finite element models. *Journal of Sound and Vibration*, 332(8):1897–1917, 2013.

[3] R. Rumpler, and P. Göransson. An assessment of two popular Padé-based approaches for fast frequency sweeps of time-harmonic finite element problems. *Proceedings of Meetings on Acoustics*, 30(1):022003, 2017. DOI: 10.1121/2.0000649

[4] G.A. Baker and P.R. Graves-Morris. *Padé approximants*, volume 59. Cambridge University Press, 1996.

[5] R. Djellouli, C. Farhat, and R. Tezaur. A fast method for solving acoustic scattering problems in frequency bands. *Journal of Computational Physics*, 168(2):412–432, 2001.

[6] R. Rumpler, P. Göransson, and J.-F. Deü. A finite element approach combining a reduced-order system, padé approximants, and an adaptive frequency windowing for fast multi-frequency solution of poro-acoustic problems. *International Journal for Numerical Methods in Engineering*, 97(10):759–784, 2014.

[7] P. Guillaume. Nested multivariate padé approximants. *Journal of computational and applied mathematics*, 82(1):149–158, 1997.

[8] R. Rumpler, P. Göransson, and H.J. Rice. An adaptive strategy for the bivariate solution of finite element problems using multivariate nested Padé approximants. *International Journal for Numerical Methods in Engineering*, 100(9):689–710, 2014.

[9] R. Rumpler. Padé approximants and the modal connection: towards increased robustness for fast parametric sweeps. *International Journal for Numerical Methods in Engineering*, 113(1):65–81, 2018.

COMPDYN 2019
7th ECCOMAS Thematic Conference on
Computational Methods in Structural Dynamics and Earthquake Engineering
M. Papadrakakis, M. Fragiadakis (eds.)
Crete, Greece, 24–26 June 2019

THE STUDY ON INSTABILITY OF DIFFERENT KERNELS IN SOLID DYNAMIC PROBLEMS BY SMOOTHED PARTICLE HYDRODYNAMICS

Meng Shuangs[1], Hassan Frissane[1], Lorenzo Taddei[1], Nadhir Lebaal[1] and Sebastien Roth[1]

[1] Laboratoire ICB, site UTBM, UMR 6303/Univ. Bourgogne Franche-Comte, UTBM
90010 BELFROT Cedex, France
e-mail: shuangshuang.meng@utbm.fr

Abstract

As the earliest meshless method, Smoothed Particles Hydrodynamics (SPH) has been applied in solid dynamics because of its great potentials in simulating extremely large deformations. However, the numerical instability of SPH is still a severe problem, especially tensile instability and pairing instability can lead to some unphysical cracks when the solid material is stretched or compressed. At present, no method exists to completely avoid these instabilities, although a few corrections like Artificial Viscosity, Artificial Stress, CSPH or the Godunov-type SPH have been proposed. The base of SPH formulation uses a kernel function for numerical approximations. Some literatures demonstrate mathematically that the types of the kernel function directly influences the stability of SPH method. In this paper, we study the stability of SPH with the different kinds of kernel functions including traditional types and several new ones proposed recently. Combined with some corrected techniques, the suitability of these kernels in SPH method is discussed in solid dynamic problems like bending deformation in elastic beam and elastic-plastic deformation in impact problems.

Keywords: Smoothed particle Hydrodynamics, Tensile instability, Kernel functions, Elastic-plastic deformation

1 INTRODUCTION

Smoothed particle hydrodynamics (SPH) is a numerical method proposed initially by (Gingold &Monaghan 1977) [1], which discretizes a continuum and has been used to solve a wide array of partial differential equations [5][9]. As a typical meshfree method, it was initially used in simulating astrophysical and cosmological problems [2], and then was developed quickly to be applied in computational fluid dynamics [3-5], electromagnetics [6], explosive process[7]. Considering the characteristic of SPH which models the governing equations by a group of particles and is more flexible to simulate the material's large deformations, lots of researchers expanded its applications into solid dynamics [8][9]. It has been effectively applied in impact problems [10], metal forming [11] and biomechanics [12] in recent years.

Different versions and corrections of SPH method are still developed to reduce some numerical instabilities especially when simulating solid dynamics [13-14]. Artificial viscosity was proposed in [15] to mainly remove the numerical oscillation, which has been used in all the SPH versions. Because this technique can generate unphysical dissipation by adding an "artificial pressure" into the momentum and energy equations, it easily makes the system over-dissipative. Amit Shaw et. [16] discussed it detailly and introduced a modified method based on original artificial viscosity terms. Corrected SPH (CSPH) is developed to make the SPH procedure more stable and especially for boundary inconsistency [18] by corrected kernels. In the overview paper by M.Rothlin et. [9] in 2018, two kind of Corrected SPHs were discussed, the first was proposed by Randles and Libersky [20] which reproduces a linear function by a correction tensor for the kernel estimate. The other was based on Taylor expansion to correct kernel introduced by Chen, Beraum and Jih [21]. In this paper, the latter approach is used because it provides higher order derivatives in SPH formulation than the other. Artificial stress term was developed by Monaghan and Gray [22] to remove tensile instability in elastic dynamics. It is implemented by adding a strong repulsive force only when particles become too close to each other, resulting in a more stable simulation for elastic problems. These techniques based on standard SPH like Artificial viscosity, Corrected SPHs and Artificial stress all are developed to achieve more stability of SPH. New SPH versions are still being developed, with an aim of improving the stability like Godunov SPH [23-24] and Tatal Lagrangian SPH [25-26].

In spite of these modifications, SPH still shows the pairing instability when simulating extreme tensile and compressive behaviors [17-18], which are considered as a severe barrier to develop the SPH application in solid mechanics. J.W.Swegle et. [27] studied the stability analysis of standard SPH in 1994 and firstly proposed the important concept of "tensile instability" which means particles severe clumping phenomenon in stretch sections of material. The result of this study is that the instability of SPH method has close relevance with the second derivative of kernel function. In addition, Walter Dehnen and Hossam Aly [28] also investigated the relations between the instability of SPH method and kernel functions and it proposed that the pairing instability can emerge in both stretch and compressive parts of materials, not just tensile instability in solid dynamics. Besides, this study also concluded that the Wendland kernels are more effective than traditional B-splines, but just based on the mathematical deductions. Therefore, the type of kernel plays a significant role in SPH instability. The hyperbolic-shape kernel [29] and double-cosine kernel [30] were proposed by Xiufeng Yang et. and proved that these kernels are more suitable to remove the tensile instability. But these new types of kernel are just tested for flows and for the elastic-plastic problems, there are few research to discuss it. Therefore, a study is necessary to investigate the performances of SPH with different kernels.

The structure of this paper includes five sections. Section 2 introduces the SPH formulation

and its implementation in elastic-plastic problems. Then, some corrected techniques are demonstrated including the discussion between SPH kernels with numerical instabilities in section 3. After, two examples are provided to investigate the performances of SPH with different kernels in section 4 and the conclusion is in section 5.

2 SPH METHOD APPLIED IN SOLID MECHANICS

SPH is a typical meshfree numerical method based on particles discretization, which mainly consists of two processes, kernel approximation and particles discretization. It has a great advantage in simulations with large deformation in dynamics. This section shows the implementation procedure of SPH method in elastic-plastic formulations.

2.1 SPH formulations

The first major process in SPH formulation is kernel approximation, which approximates the field variables and their derivatives by using the kernel function W. Therefore, kernel function in follow formulas is an important concept and its type has much weight for SPH performance. The kernel approximation can be shown by follow equations,

$$\langle f(x)\rangle = \int_{\Omega} f(x')W(x-x',h)\mathrm{d}x' \tag{1}$$

$$\langle \nabla\cdot f(x)\rangle = \int_{\Omega} f(x')\cdot\nabla W(x-x',h)\mathrm{d}x' \tag{2}$$

Where, h is the smooth length determining the size of nearby domain also called influence domain. Its value depends on the kernel function. Then, to discretize the above integral functions into the particles summations in its influence domain is called particles approximation.

$$\langle f(x_i)\rangle = \sum_{j=1}^{N}\frac{m_j}{\rho_j} f(x_j)W(x_i-x_j,h) \tag{3}$$

$$\langle \nabla\cdot f(x_i)\rangle = \rho_i\left[\sum_{j=1}^{N} m_j\left[\frac{f(x_i)}{\rho_i^2}+\frac{f(x_j)}{\rho_j^2}\right]\cdot\nabla W(x_i-x_j,h)\right] \tag{4}$$

2.2 Governing equations in solid elastic-plastic body and its SPH formulas

The conservation equations for solid mechanics are shown by

$$\frac{\mathrm{d}\rho_i}{\mathrm{d}t} = -\rho\frac{\partial v_i^{\alpha}}{\partial x_i^{\alpha}} = \sum_{j=1}^{N} m_j(v_i^{\alpha}-v_j^{\alpha})\cdot\frac{\partial W_{ij}}{\partial x_i^{\alpha}} \tag{5}$$

$$\frac{\mathrm{d}v_i^{\alpha}}{\mathrm{d}t} = \frac{1}{\rho}\frac{\partial\sigma_i^{\alpha\beta}}{\partial x_i^{\beta}} + f^{\alpha} = \sum_{j=1}^{N} m_j\left(\frac{\sigma_i^{\alpha\beta}}{\rho_i^2}+\frac{\sigma_j^{\alpha\beta}}{\rho_j^2}\right)\cdot\frac{\partial W_{ij}}{\partial x_i^{\beta}} + f^{\alpha} \tag{6}$$

$$\frac{\mathrm{d}e_i^{\alpha}}{\mathrm{d}t} = -\frac{\sigma_i^{\alpha\beta}}{\rho}\frac{\partial v_i^{\alpha}}{\partial x_i^{\beta}} = -\frac{1}{2}\sum_{j=1}^{N} m_j(v_i^{\alpha}-v_j^{\alpha})\left(\frac{\sigma_i^{\alpha\beta}}{\rho_i^2}+\frac{\sigma_j^{\alpha\beta}}{\rho_j^2}\right)\cdot\frac{\partial W_{ij}}{\partial x_i^{\beta}} \tag{7}$$

Where, for every particle i, the physical informations like mass m_i, density ρ_i, and internal energy e_i are carried. v_i is the component of the velocity vector and $\sigma_i^{\alpha\beta}$ is the stress tensor

and x_i is the Cartesian component of the position vector. The stress tensor in Eq.(6) and (7) can be written by

$$\sigma^{\alpha\beta} = P\delta^{\alpha\beta} - S^{\alpha\beta} \tag{8}$$

Where, P is pressure and $S^{\alpha\beta}$ is the deviatoric stress. In this paper, for elastic problem, calculating the pressure by a simple constitutive equation,

$$P = K(\frac{\rho}{\rho_0} - 1) \tag{9}$$

Where, K is the bulk modulus and ρ_0 is initial density. For the elastic-plastic problems, the Mie-Gruneisen equation is used,

$$P = (1 - \frac{1}{2}\Gamma\eta)P_H + \Gamma\rho e \tag{10}$$

Where,

$$P_H = \begin{cases} a_0\eta + b_0\eta^2 + c_0\eta^3 & \eta > 0 \\ a_0\eta^3 & \eta < 0 \end{cases} \tag{11}$$

$$\eta = \left(\frac{\rho}{\rho_0} \text{-} 1 \right) \tag{12}$$

$$a_0 = \rho_0 C^2,\ b_0 = a_0[1 + 2(S-1)],\ c_0 = a_0[2(S-1) + 3(S-1)^2] \tag{13}$$

Here, S and C, respectively, is the linear shock-velocity and the particle-velocity parameters to describe the Hugoniot fit and Γ is the Gruneisen parameter.

The deviatoric stress tensor $S^{\alpha\beta}$ can be calculated by its derivative,

$$\frac{\mathrm{d}S^{\alpha\beta}}{\mathrm{dt}} = 2\mu(\dot{\varepsilon}^{\alpha\beta} - \frac{1}{3}\delta^{\alpha\beta}\dot{\varepsilon}^{\gamma\gamma}) + S^{\alpha\gamma}R^{\beta\gamma} + S^{\beta\gamma}R^{\alpha\gamma} \tag{14}$$

$$\dot{\varepsilon}^{\alpha\beta} = \frac{1}{2}(\frac{\partial v^\alpha}{\partial x^\beta} + \frac{\partial v^\beta}{\partial x^\alpha}) \tag{15}$$

$$R^{\alpha\beta} = \frac{1}{2}(\frac{\partial v^\alpha}{\partial x^\beta} - \frac{\partial v^\beta}{\partial x^\alpha}) \tag{16}$$

Comined with the SPH formulations, the equations Eq.(14)-(16) can be described as summation forms of particles as follow,

$$\left(\frac{\partial v^\alpha}{\partial x^\beta}\right)_i = -\sum_{j=1}^{j=N} \frac{m_j}{\rho_j}(v_i^\alpha - v_j^\alpha)\frac{\partial W_{ij}}{\partial x_i^\beta} \tag{17}$$

In this paper, perfectly-plastic behaviors of the solid material are considered and Von Mises yield criterion is applied. The second stress invariant $J_2 = 0.5S^{\alpha\beta}S^{\alpha\beta}$ is checked and σ_y is the uniaxial yield stress. In every time step, if $\sqrt{J_2}$ exceeds the yield stress $\sigma_y/\sqrt{3}$, the individual stress components are given new values $S_{\text{new}}^{\alpha\beta} = fS^{\alpha\beta}$, where

$$f = \min\left\{\frac{\sigma_y}{\sqrt{3J_2}},\quad 1\right\} \tag{18}$$

The plastic strain $\varepsilon_p^{\alpha\beta}$ can be calculated by the increment form

$$\Delta\varepsilon_p^{\alpha\beta} = \frac{1-f}{2\mu} S^{\alpha\beta} \tag{19}$$

And here, the equivalent strain ε_e is defined as $\varepsilon_e = \sqrt{0.5\varepsilon^{\alpha\beta}\varepsilon^{\alpha\beta}}$, which includes both elastic and plastic deformation and it is an important variable to evaluate the material behavior and would be used in examples in this paper.

2.3 Time integration

In this paper, the predictor-corrector Leap-Frog (LF) scheme is applied in SPH time integration. Denoted the time step Δt, and the predictor step is

$$v_{n+1/2} = v_n + \Delta t \cdot \dot{v}_n \tag{20}$$

$$r_{n+1/2} = r_n + \Delta t \cdot v_n + 0.5\left(\Delta t\right)^2 \cdot \dot{v}_n \tag{21}$$

Where, r presents the value of particle's position which is not corrected. For the velocity v, the corrector step is shown by

$$v_{n+1} = v_{n+1/2} + 0.5 \cdot \Delta t \cdot (\dot{v}_{n+1/2} - \dot{v}_n) \tag{22}$$

Here, $\dot{v}_{n+1/2}$ is calculated using the predicted values. And the density ρ, energy e and deviatoric stress S are calculated by the same steps with velocity v. In that scheme, the time step is decided by below equation

$$\Delta t \approx 0.2\frac{h}{c_i + \left|v_i\right|_{\max}} \tag{23}$$

3 THE INSTABILITY PROBLEMS OF SPH FOR SOLID MECHANICS

In this section, standard SPH corrections are explained and implemented in our numerical code. Then, the discussion about the role of kernels in instability problems of SPH method is presented. Different kernels are also discussed and listed in table 3.1 for the investigation in mechanical tests in next section.

3.1 Artificial viscosity & Artificial stress

The artificial viscosity is widely used to remove the numerical oscillation in SPH method and it is also helpful to reduce the tensile instability when SPH simulates the solid problems. In this section, the basic form is introduced in Eq.(24).

$$\Pi_{ij} = \begin{cases} \dfrac{-\alpha_\Pi c_{ij}\phi_{ij} + \beta_\Pi \phi_{ij}^2}{\rho_{ij}}, & \vec{v}_{ij}\cdot\vec{x}_{ij} < 0 \\ 0, & \vec{v}_{ij}\cdot\vec{x}_{ij} < 0 \end{cases} \tag{24}$$

$$\phi_{ij} = \frac{h_{ij}\vec{v}_{ij} \cdot \vec{x}_{ij}}{\left|\vec{x}_{ij}\right|^2 + \left(\kappa h_{ij}\right)^2} \tag{25}$$

Where, $\vec{v}_{ij} = \vec{v}_i - \vec{v}_j$, $\vec{x}_{ij} = \vec{x}_i - \vec{x}_j$, $\rho_{ij} = \left(\rho_i + \rho_j\right)/2$, $h_{ij} = \left(h_i + h_j\right)/2$, $c_{ij} = \left(c_i + c_j\right)/2$ and c is the sound speed, which are explained well in [15]. κ is the constant and its value is 0.1 in this paper. And $\left(\alpha_\Pi,\ \beta_\Pi\right)$ is also a group of constant values. This term is added to momentum and energy conservations,

$$\frac{\mathrm{d}v_i^\alpha}{\mathrm{d}t} = \sum_{j=1}^{N} m_j \left(\frac{\sigma_i^{\alpha\beta}}{\rho_i^2} + \frac{\sigma_j^{\alpha\beta}}{\rho_j^2} - \Pi_{ij}\delta^{\alpha\beta} \right) \cdot \frac{\partial W_{ij}}{\partial x_i^\beta} + f^\alpha \tag{26}$$

However, the artificial viscosity adds an unphysical dissipation of energy into conservations. Then, choosing suitable parameters $\left(\alpha_\Pi,\ \beta_\Pi\right)$ is important to get satisfied results.

Artificial stress provides artificial repulsive forces to stress tensor specially in order to solve the tensile instability, adding the artificial stress terms $\mathbb{R}_{ij}^{\alpha\beta} = (R_i^{\alpha\beta} + R_j^{\alpha\beta}) \cdot f^n$ to the momentum and energy conservations as follow,

$$\frac{\mathrm{d}v_i^\alpha}{\mathrm{d}t} = \sum_{j=1}^{N} m_j \left(\frac{\sigma_i^{\alpha\beta}}{\rho_i^2} + \frac{\sigma_j^{\alpha\beta}}{\rho_j^2} - \Pi_{ij}\delta^{\alpha\beta} + \mathbb{R}_{ij}^{\alpha\beta} \right) \cdot \frac{\partial W_{ij}}{\partial x_i^\beta} + f^\alpha \tag{27}$$

Here, for 2-D problems just show the form of R_i^{xx} term when $\alpha = x$ and $\beta = x$,

$$R_i^{xx} = c^2 \bar{R}_i^{xx} + s^2 \bar{R}_i^{yy} \tag{28}$$

And, when the value of $\bar{\sigma}_i^{xx}$ is positive,

$$\bar{R}_i^{xx} = -\varsigma \frac{\bar{\sigma}_i^{xx}}{\rho^2} \tag{29}$$

Otherwise, $R_i^{xx} = 0$. In above equations, R_i^{xx} is the component of the artificial stress in the original coordinates and $\bar{R}_i^{xx}$ is new component of the stress tensor in a rotated frame and c denotes $\cos\theta_i$ and s denotes $\sin\theta_i$ (θ_i is the rotation angle which makes the stress tensor is diagonal). ς is a constant that controls the weight of artificial stress. f^n is defined as follow,

$$f_{ij}^n = \left(\frac{W(r_{ij})}{W(dx)} \right)^n \tag{30}$$

Where, r_{ij} is the distance of two particles and dx is the initial particle spacing. Constant value n is suggested as 4 in [22].

In this paper, XSPH correction is also used to update the velocity by an average of the particle velocities in every time step, like

$$\tilde{v}_i = v_i + \tilde{\varsigma} \sum_{j=1}^{N} \frac{m_j}{\bar{\rho}_{ij}} (v_j - v_i) W_{ij}, \qquad \bar{\rho}_{ij} = \frac{1}{2}(\rho_i + \rho_j) \tag{31}$$

It is suggested to be applied in tension problems simulated by SPH method in [9]. Corrected SPH (CSPH) proposed by Chen, Beraum and Jih [21] is also applied in our SPH code to simulate the examples in the section 4.

3.2 The role of kernel in SPH method

Illustrated in section 2, kernel function is an important concept in the SPH formulation, which directly determines the pattern to interpolate, and also defines the size of the influence area of a particle. As a kernel function, it needs satisfy three basic conditions like,

1. It must be normalized，

$$\int W(x-x',h)dx' = 1 \tag{32}$$

Obviously, kernel is the function with the distance between particles and h. h is the parameter called smoothing length determining the size of influence domain of a particle.

2. It has the characteristic of compact supportness, which means

$$if\ |x-x'| \le \kappa h,\ W(x-x') \ge 0\ \ else\ \ W(x-x') = 0 \tag{33}$$

Where, the combination between smoothing length h and a scale factor κ determines the spread of the specified smoothing function.

3. It should satisfy the Dirac delta function condition as $h \to 0$,

$$\lim_{h\to 0} W(x-x',h) = \delta(x-x') \tag{34}$$

Except for above three conditions, SPH kernel also should be an even function and need enough smooth. Otherwise, kernel function also can be written into the follow form,

$$W(x-x',h) = \alpha_d K(q),\ q = |x-x'|/h,\ d = 1,2,3 \tag{35}$$

Where, α_d is the dimension-dependent normalization constant for particular kernel functions.

Based on above conditions, one can construct any function as the kernel function in SPH algorithm, and M.B. Liu et. provide a systematic method to build kernels in [19]. However, specific kernel functions still have different performances for SPH instability and accuracy. Swegle et al. in [27] discussed the relation between SPH instability and kernel functions. They not only firstly proposed the concept of “tensile instability”, but also gives a conclusion about a sufficient condition for the unstable growth in SPH algorithm,

$$W''T > 0 \tag{36}$$

Where, W'' is the second derivative of the kernel W and determined by the slope of W'. T is stress state, which is negative in compression and positive in tension. According to this theory, some articles proposed new types of kernels for specific problems, for example Yang X et. in [29] introduced that using a hyperbolic shaped kernel function which possesses non-negative second derivatives can remove the tensile instability in viscous liquid drop problems. A new kernel called double cosine kernel function was also proposed in [30] which has smoother second derivative to obtain a better accuracy for SPH with applications in free surface flows.

Dehnen W et. in [28] proved that Wendland function is more effective to remove SPH clumping instability especially when increasing the number of neighbour particles. Besides, the kernel Fourier transform was found to have a strong relevance with SPH instability and an explanation in terms of the SPH density estimator was provided. K. Szewc et. used Wendland function as SPH kernel to simulate the incompressive flows and acquired better results compared with using traditional kernel functions based B-spline series [34].

Index	Name of Kernel	Function (α_d is the dimension-dependent)
Type-1	Cubic spline [35]	$W(r,h)=\alpha^d\begin{cases}1-\frac{3}{2}q^2+\frac{3}{4}q^3 & q<1\\ (2-q)^3 & 1\ll q<2\\ 0 & q\gg 2\end{cases}$
Type-2	Gauss [35]	$W(r,h)=\alpha^d e^{-q^2}\quad 0<q\ll 3$
Type-3	Quintic [35]	$W(r,h)=\alpha^d\begin{cases}(3-q)^5-6(2-q)^5+15(1-q)^5 & q<1\\ (3-q)^5-6(2-q)^5 & 1\ll q<2\\ (3-q)^5 & 2\ll q\ll 3\\ 0 & 3<d\end{cases}$
Type-4	Wendland [28]	$W(r,h)=\alpha^d\begin{cases}(1-0.5q)^4(2q+1) & 1\ll q<2\\ 0 & 2\ll q\end{cases}$
Type-5	Double cosine [30]	$W(r,h)=\alpha^d\begin{cases}4\cos\left(\frac{\pi}{k}q\right)+\cos\left(\frac{2\pi}{k}q\right)+3 & 0\ll q\ll k\\ 0 & k<q\end{cases}$
Type-6	Hyperbolic shaped [29]	$W(r,h)=\alpha^d\begin{cases}q^3-6q+6 & 0\ll q<1\\ (2-q)^3 & 1\ll q<2\\ 0 & 2\ll q\end{cases}$

Table 3.1 : A list for six types of kernel functions in SPH algorithm

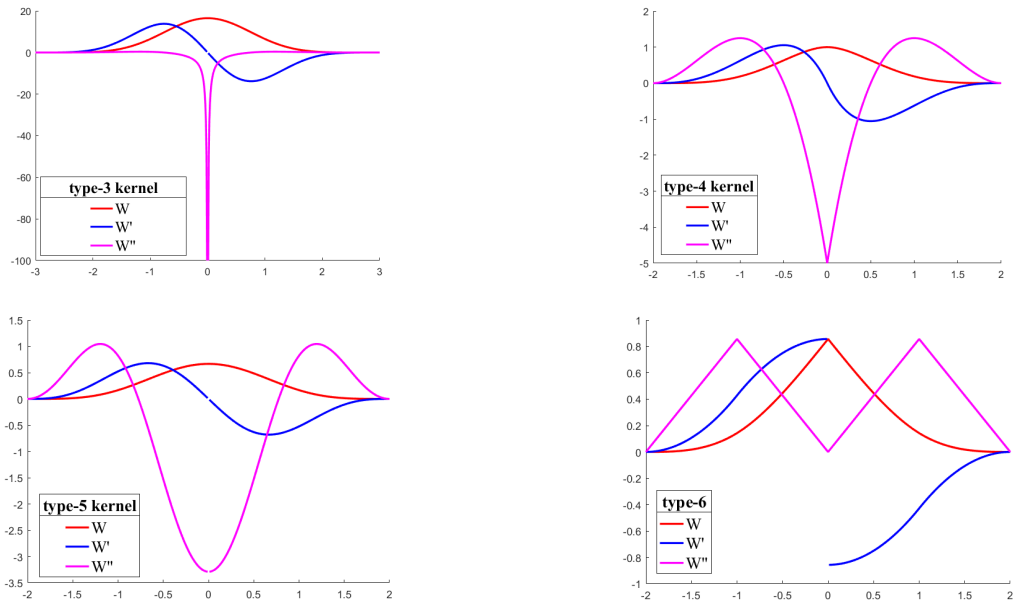

Figure 3.1 the curves of kernels in 1-D.

However, up to now, in the applications of SPH method simulating solid dynamics, the traditional kernels like the Gaussian function and B-spine functions are still mainly used. Table 3.1 lists six types of kernels including classic ones (type-1 to type-3) and some (type-4 to type-6) recently proposed for particular problems. Figure 3.1 shows four kernel curves including their

second derivatives. This paper aims to investigate the effect of these different kernel functions for dynamic problems with large deformations by the examples in next section.

4 EXAMPLES

This section shows two examples to investigate the different performances of different kernels listed in table 3.1. The first is the bending deformation of a cantilever beam with tip dynamic load simulated by CSPH method. It would demonstrate that different kernels have great influences on pairing instability and even unphysical cracks in elastic dynamics. The other is a 2-D Taylor rod impact problem which is considered frequently to investigate the performance of SPH in simulating material plastic behaviors.

4.1 Elastic bending beam

In this sample, the plane stress assumption is applied for the slender beam, therefore the physical three-dimensional solid problems can be degraded to two-dimensional problems. The geometrical dimensions of the beam structure are shown in figure 4.1, where the length $L=100\text{mm}$, the width $t=10\text{mm}$ and the beam thickness is fixed to 1mm. The left edge of the beam is fixed and the other edge is free and has a concentrated load given by acceleration a. The value of the load a is the quadratic function with time, starting from 0 to the maximum value a_{max} at time $T_1=1.5\text{ms}$ and after this time point keep the maximum load until the end of the simulation $T_{total}=3.0\text{ms}$. All the material parameters are shown in table 4.1 and the related parameters in CSPH are shown in table 4.2. The same tests are also studied by Liu Lin in his thesis [32].

Figure 4.1: the beam model and the left is fixed.

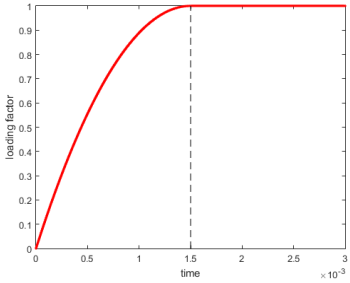

Figure 4.2: the dynamical loading.

Material	Young's modulus	Poisson's ratio	density	Sound speed
Steel	210 GPa	0.3	$7800\,\text{kg}/\text{m}^3$	5960 m/s

Table 4.1: material parameters.

Test	dx (mm)	Δt (s)	h	AV (α_Π, β_Π)	AS (ς)	XSPH $(\tilde{\varsigma})$
A	1	1.0e-7	$1.2\,dx$	0.1/0.1	0.5	0.5
B	1	1.0e-7	$1.4\,dx$	0.5/0.8	0.9	0.5

Table 4.2: the parameters in CSPH， AV is artificial viscosity and AS is artificial stress

This example consists of two tests denoted "Test A" and "Test B" distinguished by maximum loading. In Test A, when the maximum loading force $F_{max}=1750\text{N}$, the beam deflec-

tion can be regarded as a linear change with load and can be estimated by the static solution reported by Timoshenko [33] with $W_{analytical} = FL^3/3EI + 6FL/5GA = 33.59\text{mm}$. The average errors e_{av} with different kernels are listed in table 4.3, ranging from 2.25% to 17.62%. This results demonstrate that the types of kernel have a large influence on SPH accuracy. Except for type-5 kernel, other several kernels all make the simulating accuracy lower that 10%. Figure 4.3 shows the distribution of beam deflection, in which the simulation (a) by our codes (CSPH with type-1 kernel) is very close to the one obtained by [32] using Total Lagrangian SPH in figure 4.3 (b).

Types of kernel	Type-1	Type-2	Type-3	Type-4	Type-5	Type-6
Errors (e_{av})	2.55%	8.11%	7.96%	9.58%	17.62%	8.86%

Table 4.3: Errors in test A and e_{av} is calculated by $e_{av} = \frac{1}{T}\sum_{t=1.5\text{ms}}^{t=3.0\text{ms}} \frac{|W_t - W_{analytical}|}{W_{analytical}}$,

T is the number of time steps from $t = 1.5\text{ms}$ to $t = 3.0\text{ms}$.

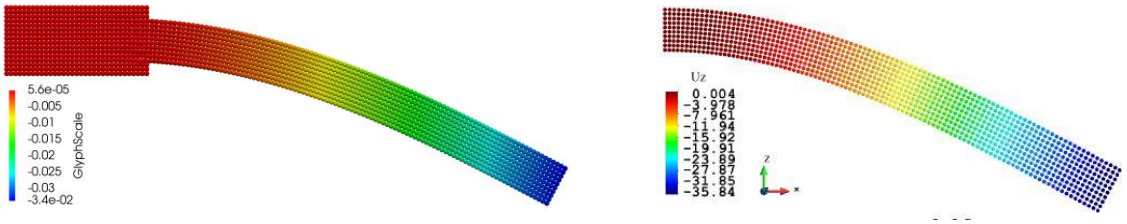

(a) (b)

Figure 4.3 the deflection distributions: (a) is simulated result by our code with type-1 kernel and (b) is simulated by Total Lagrangian SPH in [32]. the unity is mm in (b) and the unity is m in (a).

Test B gives a_{max} a larger value to make loading force $F_{max} = 17.5\text{kN}$ (the same loading process in figure 4.2), and in this case, the beam deflection W_c is non-linear related with loading force, and its analysical deflection is $W_{analysical} = 81.1\text{mm}$ according to Timoshenko [33] and Liu [32].

When the beam bends to nearly maximum deflection $W_{\max}$, different numerical instabilities happen when using different kernels as shown in figure 4.4. Obviously, when using the type-2 and type-3 kernel, the non-physical cracks emerge, which directly lead to wrong simulations. When applying type-5 kernel, the particles clump severely and cause the pairing instability in compressive part of the beam. The pairing instability also occurs in the case with type-1 kernel. Although the slightly tensile instability still exists in the fixed end of the beam with type-4 and type-6 kernel, it is not very severe especially using type-4 kernel and its average errors e_{av} is 4.89%. It is also observed that in figure 4.5, the simulation by SPH with type-4 kernel is in accordance with the results of both SPH code in [32] and FEM method in [32].

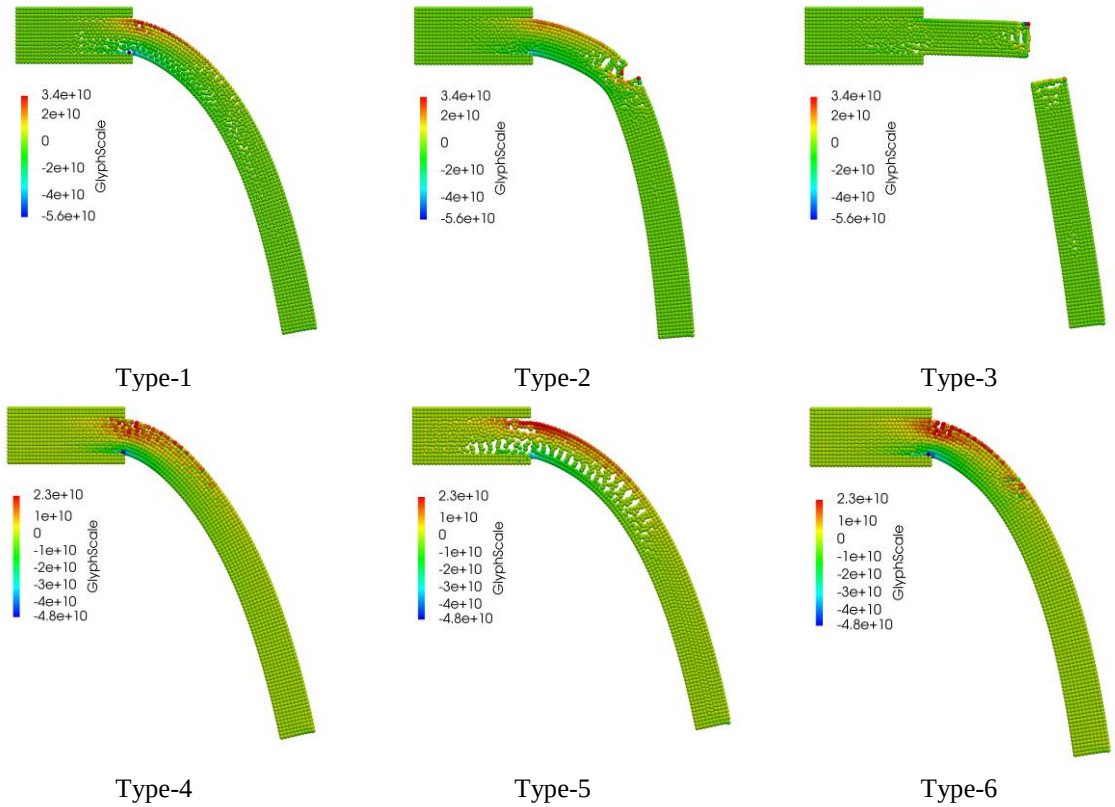

Figure 4.4: Distributions of σ_{xx} at the maximum deflection with 6 kernels.

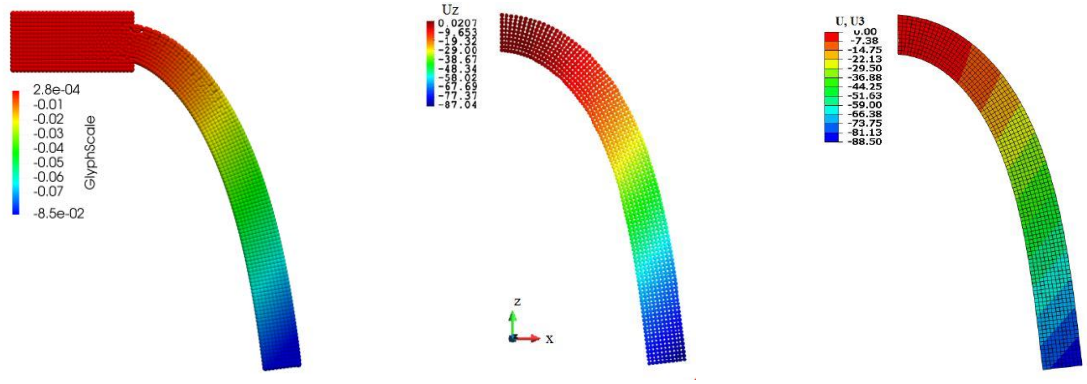

Figure 4.5 the distributions of deflections: (a) is simulated result by our code with type-4 kernel, (b) is simulated by Total Lagrangian SPH and (c) is FEM simulating in [32]. the unity is mm in both (b) and (c), the unity is m in (a).

Therefore, in this bending test, the conclusion is that types of kernel don't have much influences on clumping instability for small bending deflections but for large deflection problems they have obviously different performances. For the bending problem, the materials will experience both compression and stretch at the same time and both the tensile instability in large stress domain and paring instability in compressive domain are possible to occur. This test also shows that type-4 kernel has a more satisfied simulation compared with other kernels.

4.2 Plastic compressive

As a second test, a 2-D Taylor rod impact problem is simulated by standard SPH with artificial viscosity aiming to investigate the influences of different kernels. Figure 4.6 shows the 2D model of an iron rod which impacts a rigid surface. The values of all the parameters are set equal to those used by Libersky and Petschek [31]. The results can be compared with simulations conducted with the EPIC-2 code provided in [31]. For impact problem, Mie-Gruneisen EOS is used and its parameters are shown in table 4.4.

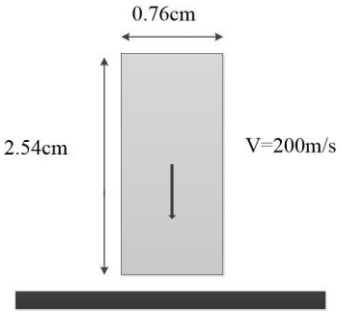

Figure 4.6: Model geometric of rob

Parameter	Values
Young's modulus	208GPa
Shear modulus	80GPa
Yield stress	600MPa
C	3630m/s
S	1.80
Γ	1.80

Table 4.4: Parameters in rob impact

In this simulation, the rod is discretized by $25\times81=2025$ particles. The initial space dx of particles is 1.058mm and the smoothing length $h=1.5dx$. The computational time is 50μm from the beginning of the contact between the rod and the rigid surface.

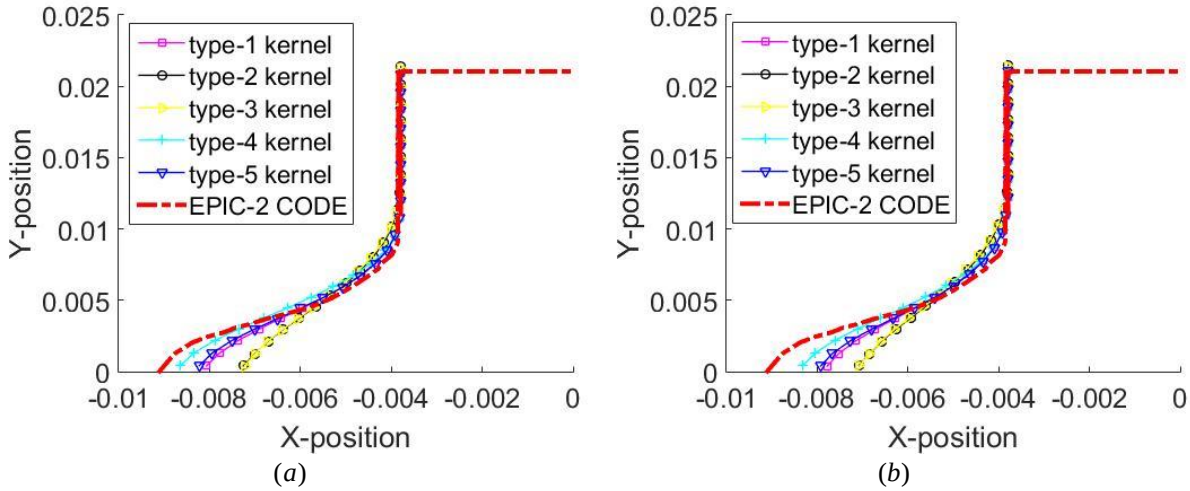

(*a*) (*b*)

Figure 4.7: the shapes of rod at the impact end.
The artificial viscosity coefficient $(\alpha_{\Pi},\ \beta_{\Pi})$=(0.05, 0.05) in (*a*) and $(\alpha_{\Pi},\ \beta_{\Pi})$=(0.5, 0.5) in (*b*).

Figure 4.7 compares the rod shapes at the end impact at $50\mu m$ by SPH with different kernels, in which (*a*) and (*b*) used two different group coefficients in artificial viscosity. From these results, it is observed obviously that the simulation using kernel type-4 is the closest to the result provided by EPIC-2 code, which is taken as a reference [31]. The result obtained with the type-6 kernel is obviously wrong because of severe numerical instability, showing that type-6 kernel is not smooth enough to provide correct results. Figure 4.8 illustrates the

bad distribution of the equivalent strain of the structure using type-6 kernel. By contrast, Figure 4.9 presents a very smooth distribution of equivalent strain in 2-D rod using type-4 kernel , which is also in agreement with the physical phenomenon.

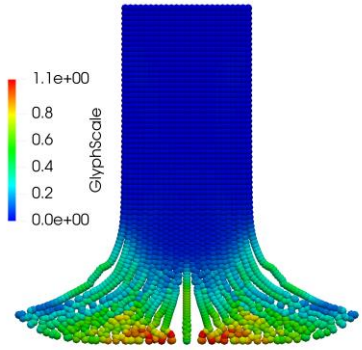

Figure 4.8: the distribution of equivalent strain with type-6 kernel

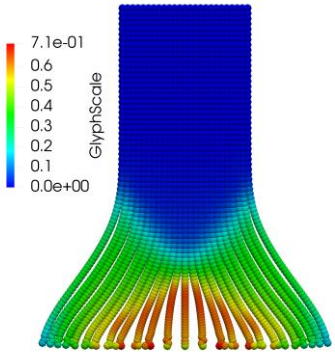

Figure 4.9: the distribution of equivalent strain with type-4 kernel

5 CONCLUSION

In this paper, the implementation of SPH method in dynamics is introduced and two examples including elastic and plastic dynamical deformations are tested to observe the influences of different types of kernels on instability of SPH simulations. The first example by a cantilever beam with tip dynamic load demonstrates that the different types of kernel directly affect the instability especially the tensile and pairing instability. The second test about rod impact with severe plastic deformations also shows that choosing the suitable kernels can improve effectively the accuracy of SPH simulations.

Kernel type-1 to type-3 are widely used in the scientific literature and they are also regarded as traditional kernels in SPH method. Type-4 to type-6 are proposed recently and applied in SPH in order to simulate different problems like flows or soils. But from our investigations, types-5 and type-6 do not have good performance in elastic-plastic problem. So, aiming to different fields, the kernel also has different suitability. Finally, the paper provides interesting step for the choice of a suitable kernel function to be used in SPH formulation for solid dynamic problems.

REFERENCES

[1] Gingold, Robert A., and Joseph J. Monaghan. "Smoothed particle hydrodynamics: theory and application to non-spherical stars." *Monthly notices of the royal astronomical society* 181.3, 375-389, 1977.

[2] Monaghan, Joe J. "Smoothed particle hydrodynamics." *Annual review of astronomy and astrophysics* 30.1,543-574, 1992.

[3] Monaghan, Joe J. "Simulating free surface flows with SPH." *Journal of computational physics* 110.2, 399-406, 1994.

[4] Wang, Zhi-Bin, et al. "An overview of smoothed particle hydrodynamics for simulating multiphase flow." *Applied Mathematical Modelling* 40.23-24, 9625-9655, 2016.

[5] Shadloo, M. S., G. Oger, and David Le Touzé. "Smoothed particle hydrodynamics method for fluid flows, towards industrial applications: Motivations, current state, and challenges." *Computers & Fluids* 136, 11-34, 2016.

[6] Ala, Guido, et al. "A smoothed particle interpolation scheme for transient electromagnetic simulation." *IEEE Transactions on Magnetics* 42.4, 647-650, 2006.

[7] Liu, M. B., et al. "Computer simulation of high explosive explosion using smoothed particle hydrodynamics methodology." *Computers & Fluids* 32.3, 305-322, 2003.

[8] Monaghan, Joseph J. "Smoothed particle hydrodynamics and its diverse applications." *Annual Review of Fluid Mechanics* 44, 323-346, 2012.

[9] Röthlin, Matthias, Hagen Klippel, and Konrad Wegener. "Meshless Methods for Large Deformation Elastodynamics." *arXiv preprint arXiv* 1807.01117, 2018.

[10] Libersky, Larry D., et al. "Recent improvements in SPH modeling of hypervelocity impact." *International Journal of Impact Engineering* 20.6-10, 525-532, 1997.

[11] Bonet, J., and Sd Kulasegaram. "Correction and stabilization of smooth particle hydrodynamics methods with applications in metal forming simulations." *International journal for numerical methods in engineering* 47.6, 1189-1214, 2000.

[12] Zhang, L. W., A. S. Ademiloye, and K. M. Liew. "Meshfree and Particle Methods in Biomechanics: Prospects and Challenges." *Archives of Computational Methods in Engineering:* 1-30, 2018.

[13] Liu, M. B., and G. R. Liu. "Smoothed particle hydrodynamics (SPH): an overview and recent developments." *Archives of computational methods in engineering* 17.1,25-76, 2010.

[14] Gui-rong, Liu, ed. Smoothed particle hydrodynamics: a meshfree particle method. *World Scientific*, 2003.

[15] Monaghan, J. J. "On the problem of penetration in particle methods." *Journal of Computational physics* 82, 1-15, 1989.

[16] Shaw, Amit, and Stephen R. Reid. "Heuristic acceleration correction algorithm for use in SPH computations in impact mechanics." *Computer Methods in Applied Mechanics and Engineering* 198.49-52 , 3962-3974, 2009.

[17] Belytschko T, Guo Y, Kam Liu W, et al. A unified stability analysis of meshless particle methods[J]. *International Journal for Numerical Methods in Engineering*, 48(9), 1359-1400, 2000.

[18] Monaghan J J. SPH without a tensile instability[J]. *Journal of computational physics*, 159(2), 290-311, 2000.

[19] Liu, M. B., G. R. Liu, and K. Y. Lam. "Constructing smoothing functions in smoothed particle hydrodynamics with applications." *Journal of Computational and applied Mathematics* 155.2, 263-284, 2003.

[20] P. Randles and L. Libersky, “Smoothed particle hydrodynamics: some recent improvements and applications,” *Computer methods in applied mechanics and engineering*, vol. 139, no. 1, pp. 375–408, 1996.

[21] J. Chen, J. Beraun, and C. Jih, “An improvement for tensile instability in smoothed particle hydrodynamics,” *Computational Mechanics*, vol. 23, no. 4, pp. 279–287, 1999.

[22] Gray J P, Monaghan J J, Swift R P. SPH elastic dynamics[J]. *Computer methods in applied mechanics and engineering*, , 190(49-50), 6641-6662, 2001.

[23] Sugiura K, Inutsuka S. An extension of Godunov SPH: Application to negative pressure media[J]. *Journal of Computational Physics*, 308, 171-197, 2016.

[24] Sugiura K, Inutsuka S. An extension of Godunov SPH II: Application to elastic dynamics[J]. *Journal of Computational Physics*, 333, 78-103, 2017.

[25] Vignjevic R, Reveles J R, Campbell J. SPH in a total Lagrangian formalism[J]. *CMC-Tech Science Press-*, 4(3), 181, 2006.

[26] Zhang A, Ming F, Cao X. Total Lagrangian particle method for the large-deformation analyses of solids and curved shells[J]. *Acta Mechanica*, 225(1), 253-275, 2014.

[27] Swegle J W, Hicks D L, Attaway S W. Smoothed particle hydrodynamics stability analysis[J]. *Journal of computational physics*, 116(1), 123-134, 1995.

[28] Dehnen W, Aly H. Improving convergence in smoothed particle hydrodynamics simulations without pairing instability[J]. *Monthly Notices of the Royal Astronomical Society*, 425(2), 1068-1082, 2012.

[29] Yang X, Liu M, Peng S. Smoothed particle hydrodynamics modeling of viscous liquid drop without tensile instability[J]. *Computers & Fluids*, 92: 199-208, 2014.

[30] Yang X F, Peng S L, Liu M B. A new kernel function for SPH with applications to free surface flows[J]. *Applied Mathematical Modelling*, 38(15-16), 3822-3833, 2014.

[31] Libersky, Larry D., and Albert G. Petschek. "Smooth particle hydrodynamics with strength of materials." *Advances in the free-Lagrange method including contributions on adaptive gridding and the smooth particle hydrodynamics method*. Springer, Berlin, Heidelberg, 248-257, 1991.

[32] Lin J. Nonlinear transient analysis of isotropic and composite shell structures under dynamic loading by SPH method[D]. Université de Technologie de Compiègne, 2014.

[33] Timoshenko S.P., Gere J.M., "Mechanics of materials", D. Van Nostrand Company, New York, ISBN-13: 9780442226374, 1972.

[34] Szewc, Kamil, Jacek Pozorski, and J‐P. Minier. "Analysis of the incompressibility constraint in the smoothed particle hydrodynamics method." *International Journal for Numerical Methods in Engineering* 92.4 , 343-369, 2012.

[35] Gui-rong, Liu, ed. Smoothed particle hydrodynamics: a meshfree particle method. *World Scientific*, 2003.

COMPDYN 2019
7th ECCOMAS Thematic Conference on
Computational Methods in Structural Dynamics and Earthquake Engineering
M. Papadrakakis, M. Fragiadakis (eds.)
Crete, Greece, 24–26 June 2019

POD-BASED NEW REDUCTION PROCESS CONSIDERING THE INTERFACE FOR DUAL FORMULATION OF DYNAMIC SUBSTRUCTURING

Sunyoung Im[1], Euiyoung Kim[2], Jonggeon Lee[1] and Maenghyo Cho[1]

[1] Multiscale Mechanical Design Division, Department of Mechanical and Aerospace Engineering, Seoul National University, Gwanak-ro 1, Gwanak-gu, Seoul 151-744, Republic of Korea
e-mail: {imsunyoung, feelsgood88, mhcho}@snu.ac.kr

[2] Korea Institute of Machinery & Materials, Gajeongbuk-ro 156, Yuseong-gu, Daejeon, Republic of Korea
eyoungkim@kimm.re.kr

Abstract

This study presents a new reduction process where the proper orthogonal decomposition method is applied to the dual formulation of dynamic substructuring. Dual formulation is significant as it is effectively solving problems and solving ill-conditioned problems on parallel processing computers. Dual formulation uses the Lagrange multiplier method to couple substructures. In the proposed approach, substructures are reduced under constraint conditions with the Lagrange multiplier method. Each domain is divided into internal and interface parts, and the two parts are treated separately during the reduction process. The interface part is preserved without further reduction (i.e., the internal reduction method) or reduced to a different ratio from the internal part (i.e., the internal and interface reduction method). After the substructures are reduced, the Lagrange multipliers are applied to the preserved or reduced interface parts. Because the Boolean matrices that preserve the constraint conditions are not reduced but newly constructed, the stability and accuracy of the reduced system are guaranteed. The proposed methods are verified for a large-scale linear structure and a hyperelastic structure considering material and geometrical nonlinearities.

Keywords: Dynamic substructuring, Lagrange multiplier method, reduced-order model, Proper orthogonal decomposition (POD), Internal and interface reduction method (IIRM), Internal reduction method (IRM).

1 INTRODUCTION

Domain decomposition method has been studied to solve large-scale problems that cannot be solved by the limits of computational resources. Dynamic substructuring, a kind of domain decomposition technique, divides a dynamic system into several subdomains and shares only interface to solve the subpart level. Depending on how substructures are assembled, dynamic substructures are expressed in a primal or dual manner. Dual formulation of dynamic substructures employs Lagrange multipliers and Boolean matrices to impose constraint conditions on subdomain interfaces.

Large-scale model can be solved by domain decomposition, but there is still a problem that requires a lot of time to analyze especially the dynamic problems. So, the proper orthogonal decomposition (POD) method has been used to reduce the dynamic substructuring. Conventional methods of POD application to dual formulation of dynamic substructuring do not consider interfacial degrees of freedom or constraint conditions. In conventional approaches, the Lagrange multiplier method is first applied to substructures, and the coupled system is subsequently reduced. Reduction bases are constructed for each subdomain. However, this reduced order model (ROM) sometimes diverges. This is because the internal and interface parts are reduced as a single unit, and Boolean matrices that connect the interfaces are also reduced during the reduction process.

This study proposes reversal of the order of reduction processes. In the proposed method, the reduction bases of each domain is divided into internal and interface parts. Then, the two part can be handled separately in ROM. The interface part can be preserved without reduction or reduced to a different ratio than the internal part. After reducing the substructures, the Lagrange multipliers are applied to the preserved or reduced interface parts. This means that the Boolean matrices are not reduced but are newly constructed.

2 DUAL FORMULATION OF DYNAMIC SUBSTRUCTURING

There are two type of formulations in dynamic substructuring depending on how the set of interface degrees of freedom is defined. A primal formulation defines the interface degrees of freedom only once. On the other hand, a dual formulation presents the interface degrees of freedom multiple times, as many as the number of substructures connected to the interface. For example, if an interface with degrees of freedom is connected to n number of substructures, the total degrees of freedom are retained in the primal formulation, but the total degrees of freedom are increased by $n\times(m-1)$ in the dual formulation.

Another difference between the primal formulation and the dual formulation is that the primal formulation selects the displacements at the interface as unknown while the dual formulation selects the force at the interface as unknown. The dual formulation uses the Lagrange multiplier method for assembling structures. Boolean matrices giving compatibility conditions and Lagrange multiplier vectors corresponding unknown interface forces are included in the system matrix.

Dual formulation of dynamic substructuring is expressed in matrix notations as follows:

$$\begin{bmatrix} \mathbf{M} & \mathbf{0} \\ \mathbf{0} & \mathbf{0} \end{bmatrix} \begin{bmatrix} \ddot{\mathbf{u}} \\ \boldsymbol{\lambda} \end{bmatrix} + \begin{bmatrix} \mathbf{K} & \mathbf{B}^{\mathrm{T}} \\ \mathbf{B} & \mathbf{0} \end{bmatrix} \begin{bmatrix} \mathbf{u} \\ \boldsymbol{\lambda} \end{bmatrix} = \begin{bmatrix} \mathbf{f} \\ \mathbf{0} \end{bmatrix} \tag{1}$$

where

$$\mathbf{M}=\begin{bmatrix}\mathbf{M}_1 & \mathbf{0} & \mathbf{0}\\ \mathbf{0} & \ddots & \mathbf{0}\\ \mathbf{0} & \mathbf{0} & \mathbf{M}_S\end{bmatrix},\quad \mathbf{K}=\begin{bmatrix}\mathbf{K}_1 & \mathbf{0} & \mathbf{0}\\ \mathbf{0} & \ddots & \mathbf{0}\\ \mathbf{0} & \mathbf{0} & \mathbf{K}_S\end{bmatrix}$$

$$\mathbf{u}=\begin{bmatrix}\mathbf{u}_1\\ \vdots\\ \mathbf{u}_S\end{bmatrix},\quad \ddot{\mathbf{u}}=\begin{bmatrix}\ddot{\mathbf{u}}_1\\ \vdots\\ \ddot{\mathbf{u}}_S\end{bmatrix},\quad \mathbf{f}=\begin{bmatrix}\mathbf{f}_1\\ \vdots\\ \mathbf{f}_S\end{bmatrix}$$

B is a signed Boolean matrix operating on the interface degrees of freedom. Let $u^{(a)}$ and $u^{(b)}$ refer to the same interface degrees of freedom, but belong to different substructure. This expression states any coupled interface degrees of freedom $u^{(a)}$ and $u^{(b)}$ must have the same displacement, i.e., $u^{(a)}-u^{(b)}=0$.

3 PROPER ORTHOGONAL DECOMPOSITION-BASED REDUCTION OF DYNAMIC SUBSTRUCTURING

While the modal reduction method obtains the reduction mode from the system matrix, Proper orthogonal decomposition (POD) method extracts the reduction mode by singular value decomposition of response data. In dynamic systems, large singular values give major characteristics of the system, while small singular values correspond to small perturbations to the overall system dynamics. Transformation matrix is constructed by choosing r dominant proper orthogonal modes corresponding large singular values. Using the transformation matrix, the original coordinates $\mathbf{X}$ can be reduced to the generalized coordinates $\mathbf{X}^{\mathbf{R}}$.

$$\mathbf{X}\approx\mathbf{T}\mathbf{X}^{\mathrm{R}} \tag{2}$$

Where $\mathbf{X}\in\mathbb{R}^{n\times1}, \mathbf{X}^{\mathrm{R}}\in\mathbb{R}^{r\times1}$ and $\mathbf{T}\in\mathbb{R}^{n\times r}\left(n\gg r\right)$.

First, the conventional method that reduces the dynamic substructures using POD is explained in Section 3.1. Then, the proposed method that considering interface degrees of freedom is introduced in Section 3.2 and Section 3.3.

3.1 Conventional method : One-unit Reduction

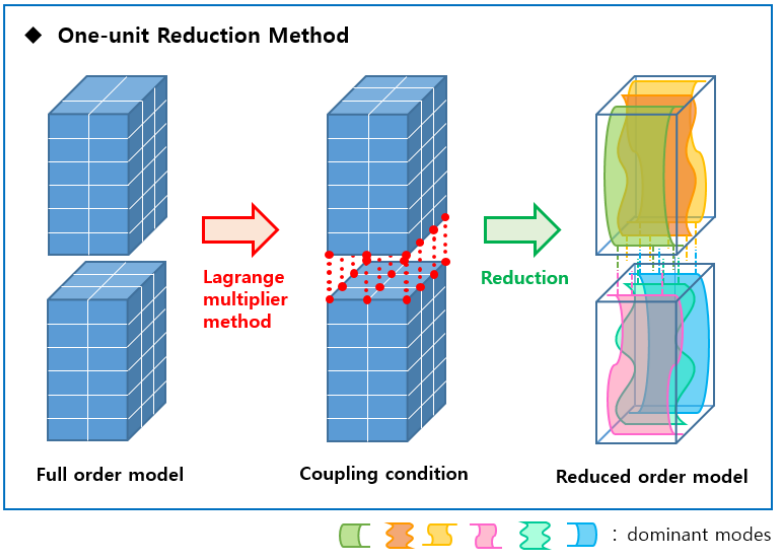

Figure 1: Conventional one-unit reduction method.

Figure.1 shows the conventional method to reduce the substructures in dual formulation. The two separated subdomains are first coupled by the Lagrange multiplier method and then reduced. Each subdomain is reduced by different modes. The interfaces and Boolean matrices for Lagrange multiplier method are also reduced by different modes, so the coupling condition cannot but be weakened.

3.2 Proposed method 1: Internal reduction

Internal reduction method reduces only internal degrees of freedom of substructures. In the subsystem equation, it is necessary to distinguish between the internal degrees of freedom and the interface degrees of freedom.

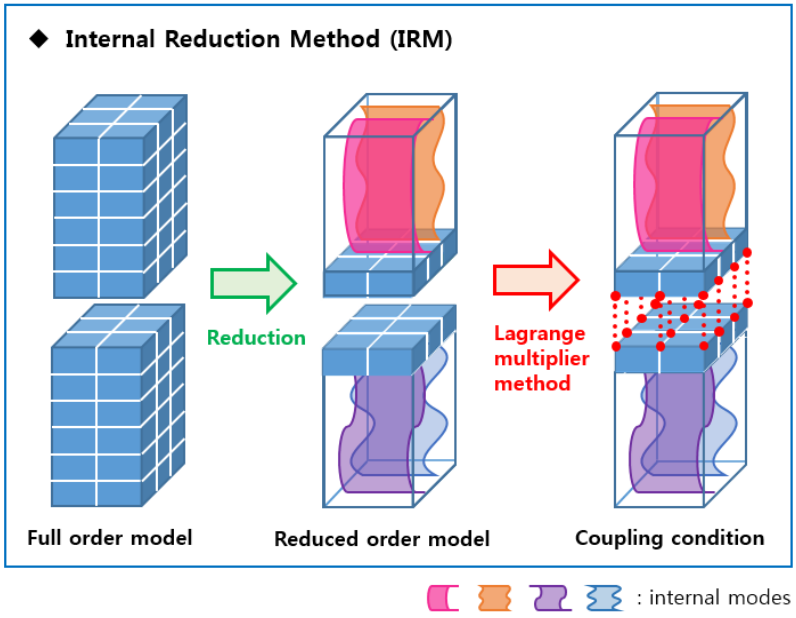

Figure 2: Proposed internal reduction method.

Figure. 2 shows the process of the proposed internal reduction method (IRM). In this method, only the internal part of each subdomain is reduced each different plane, and the Lagrange multiplier method is applied to the remaining interface part. In ROM, the coupling condition is highly robust and the interface responses can be considered well. However, since the interface degrees of freedom is not reduced, the overall calculation efficiency is lowered.

3.3 Proposed method 2: Internal and interface reduction

Internal & interface reduction method (IIRM) has been studied to overcome the limitation of internal reduction while maintaining constraint condition strong. IIRM also imposes constraint condition after reducing the subsystem. IIRM differs from IRM in that it reduces the interface degrees of freedom.

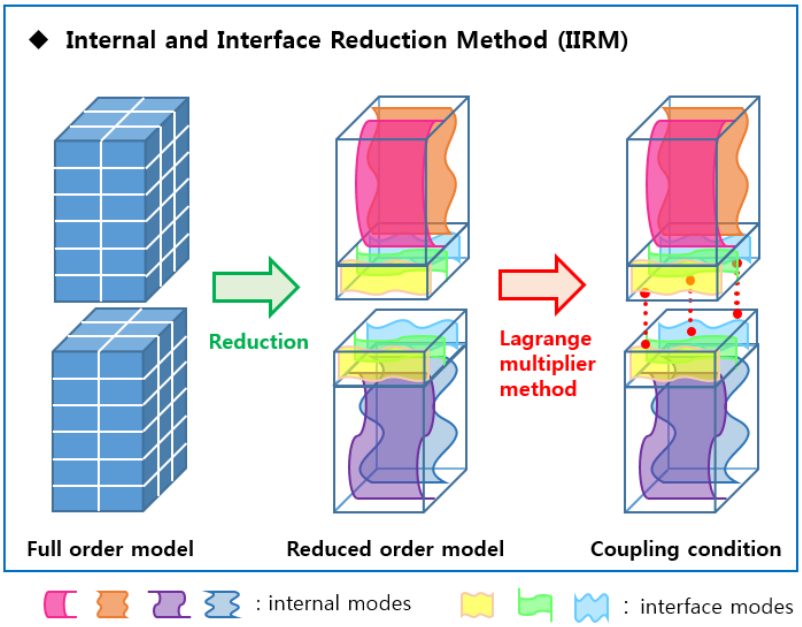

Figure 3: Proposed internal and interface reduction method.

Figure. 3 shows the process of the proposed IIRM. In this method, the internal part of each subdomain is reduced by different modes. Note that the interfaces of the subdomain are reduced by same dominant modes. By adjusting the reduction ratio differently from the internals, the interface degrees of freedom can be reduced in consideration of the interface response sufficiently. Coupling condition is imposed by applying the Lagrange multiplier method to the reduced interface. This method enables efficient computation while maintaining a strong constraint condition like internal reduction method.

4 NUMERICAL EXAMPLES

4.1 Wing model

A 3D wing model consisting of 6 substructures is dynamically analyzed with the three reduction methods in Fig. 4. The undivided wing model is a large scale structure with 72,438 degrees of freedom. The number of degrees of freedom corresponding to each subdomain listed in Table. 1. One interface consists of 678 degrees of freedom. Subdomain 1 and 6 have one interface while the other subdomains have two interface corresponding to 1356 degrees of freedom. As it is calculated in the dual formulation, the sum of the degrees of freedom of the subdomains is 678×5 more than the original degrees of freedom.

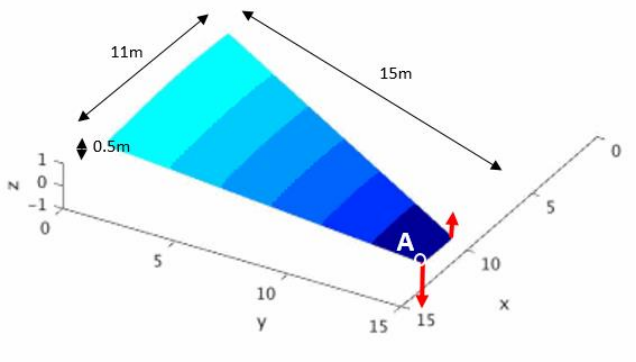

Figure 4: Wing model

The two concentrated forces are applied in opposite directions at different magnitudes, the wing model becomes not only up and down but also twisted. The thickness of the design variable is divided into 4 zones. With the thickness variation of both side skins and spars as 0.01/0.02/0.03/0.04 and of rips as 0.005/0.01/0.015/0.02, sampling analyses are performed 256 times. The sampling data set is subjected to singular value decomposition to construct the transformation matrix reducing full system matrix. The analysis results of ROM are compared to that of FOM with the randomly selected thickness.

(i : internal / b : interface)

Subdomain	1		2		3		4		5		6	
DOFs	14238		12318		12318		12318		12318		12318	
Internal/interface	i	b	i	b	i	b	i	b	i	b	i	b
DOFs	13560	678	10962	1356	10962	1356	10962	1356	10962	1356	11640	678

Table 1: Number of degrees of freedom corresponding to each subdomain

1) Conventional method : One-unit Reduction

Subdomain	1	2	3	4	5	6
POMs	400	500	500	500	500	400

2) Proposed method 1 : Internal Reduction

Subdomain	1		2		3		4		5		6	
POMs	978		1656		1656		1656		1656		978	
Internal/interface	i	b	i	b	i	b	i	b	i	b	i	b
POMs	300	678	300	1356	300	1356	300	1356	300	1356	300	678

3) Proposed method 2 : Internal & Interface Reduction

Subdomain	1		2		3		4		5		6	
POMs	400		500		500		500		500		400	
Internal/interface	i	b	i	b	i	b	i	b	i	b	i	b
POMs	300	100	300	200	300	200	300	200	300	200	300	100

Table 2: Number of used proper orthogonal modes corresponding to each subdomain

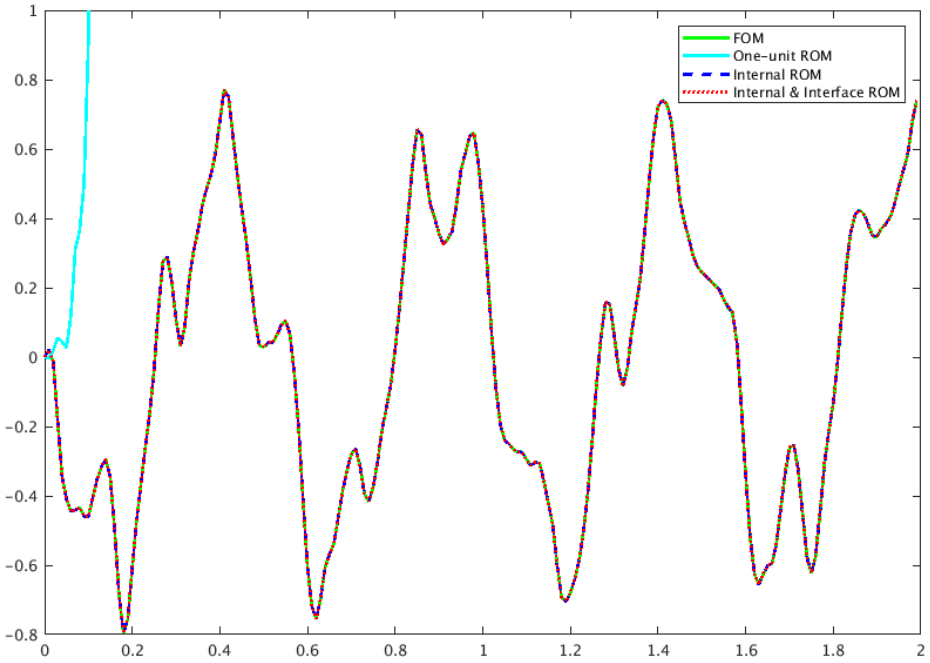

Figure 5: Z-direction displacement of point A

Figure. 5 shows that the analysis results of internal ROM and internal & interface ROM are accurate, whereas the analysis results of one-unit ROM are divergent. Even though the size of the internal & interface ROM is the same as the size of the one-unit ROM, it can be seen that IIROM is more stable than one-unit reduction method. In the case of IMR, there is a limit to reducing the ROM size as it does not reduce the interface.

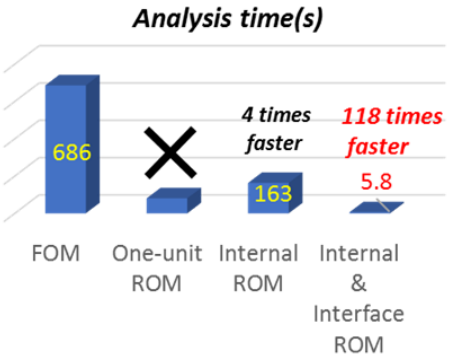

Figure 6: Analysis time

Figure. 6 shows the analysis time of full order model (FOM), one-unit ROM, internal ROM and internal & interface ROM. The time it takes to calculate the FOM is 11.4 minutes (686 seconds). It takes about 77 seconds to calculate the one-unit ROM, but it does not make sense because the result does not converge. The calculation time of the internal ROM and the internal & interface ROM takes about 163 seconds and about 5.8 seconds, respectively. Compared to the computing speed of FOM, it is 118 times faster to calculate the internal & interface ROM, while the internal ROM is 4 times faster.

4.2 Hyperelastic cubic with hole model

A hyperelastic cubic model with hole is dynamically analyzed with the two proposed reduction methods in Fig. 8. As this cubic model is Noe-Hookean model, the material nonlinearity and geometric nonlinearity are considered during the analysis. The undivided cubic model has 3,729 degrees of freedom. This model is divided two substructures which have 1,947 and 2,112 degrees of freedom. The interface consists of 380 degrees of freedom.

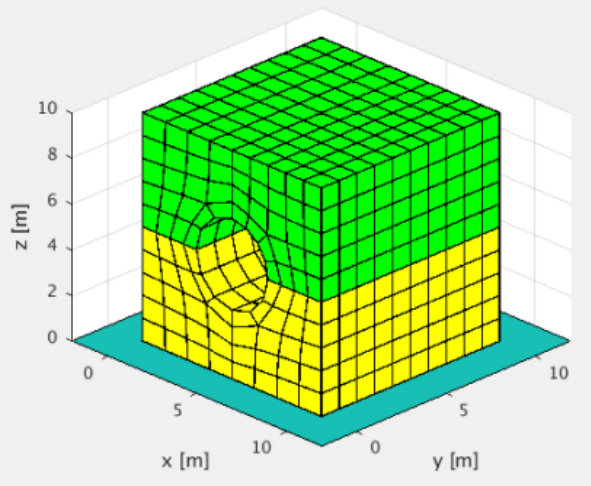

Figure 8: Hyperelastic cubic with hole model

Dynamic analysis is performed with the distributed load which pull up the cubic. Sampling analyzes were performed with the Neo-Hookean's material constants (λ, μ) set to values of (1e9, 5e8), (1e9, 1e9), (2e9, 5e8), and (2e9, 1e9) as design variables.

1) Proposed method 1 : IRM

Subdomain	1		2	
POMs	360		360	
Internal/interface	i	b	i	B
POMs /DOFs	30	330	30	330

2) Proposed method 2 : IIRM

Subdomain	1		2	
POMs	90		90	
Internal/interface	i	b	i	b
POMs	30	60	30	60

Table 3: Number of used proper orthogonal modes corresponding to each subdomain

This hyperelastic cubic model is reduced by IRM and IIRM as described in Table 3. ROMs of IRM and IIROM are computed in the error range of 1e-8. Comparing the results of two ROM, the size of the IIROM is one fourth of the size of the IROM, whereas the analysis time of the IIRM is almost the same as that of the IRM. IIRM took about 49.6 seconds to compute and about 50.6 seconds to IRM. This is because the time taken to construct the tangent stiffness during each iteration, which is a feature of the nonlinear analysis, is a large part. From this Neo-Hookean example, we can confirm that the two proposed reduction methods are convergent and robust in the nonlinear problem. However, in order to obtain the efficiency of the analysis time, the proposed method is not sufficient and it seems necessary to link it with other methods to reduce the time required to construct the system matrix.

5 CONCLUSIONS

This study suggests to impose the constraint conditions using the Lagrange multiplier method after reducing the dynamic substructures by POD method. This is the reversed order of general approaches. A substructure consists of the constrained interface part and the other internal part. By dividing the coordinate in the reduced system into internal part and interface part, the interface part can be fully preserved (proposed method 1) or reduced to a different ratio from the internal part (proposed method 2). Then, the Lagrange multiplier method can be directly applied the interface part of ROM. As Boolean matrices and the Lagrange multipliers are created for ROM without being reduced, the stability and accuracy of the analysis of the ROM is enhanced.

ACKNOWLEDGMENT

This work was supported by the National Research Foundation (NRF) of Korea funded by the Korea government (MSIP) (Grant No. 2012R1A3A2048841).

REFERENCES

[1] Klerk, D. D., Rixen, D. J., & Voormeeren, S. N., General framework for dynamic substructuring: history, review and classification of techniques. *AIAA journal*, *46*(5), 1169-1181, 2008.

[2] Corigliano, A., Dossi, M., & Mariani, S., Model order reduction and domain decomposition strategies for the solution of the dynamic elastic–plastic structural problem. *Computer Methods in Applied Mechanics and Engineering*, *290*, 127-155, 2015.

[3] Markovic, D., Park, K. C., & Ibrahimbegovic, A., Reduction of substructural interface degrees of freedom in flexibility-based component mode synthesis. *International journal for numerical methods in engineering*, *70*(2), 163-180, 2007.

COMPDYN 2019
7th ECCOMAS Thematic Conference on
Computational Methods in Structural Dynamics and Earthquake Engineering
M. Papadrakakis, M. Fragiadakis (eds.)
Crete, Greece, 24–26 June 2019

BLIND-TEST NUMERICAL SIMULATION OF SHAKE-TABLE TESTS ON THREE-LEAF MASONRY WALLS: AN APPLICATION OF LIA BLOCK_3D

R. Gagliardo[1], L. Cascini[2], F. Portioli[2] and R. Landolfo[2]

[1] Dept. of Structures for Engineering and Architecture, University of Naples "Federico II"
via Forno Vecchio 36, 80134 Naples, Italy
e-mail: raffaele.gagliardo@unina.it

[2] Dept. of Structures for Engineering and Architecture, University of Naples "Federico II"
via Forno Vecchio 36, 80134 Naples, Italy
{lucrezia.cascini, fportiol, landolfo}@unina.it

Abstract

These simulations deal with the application of LiABlock_3D, a rapid computational tool developed by the Authors [1], for limit analysis of masonry structures subjected to point live loads, seismic induced lateral loads and moving supports. The software was previously validated against several experimental tests available in the scientific literature mainly concerning small scale specimens of masonry walls subjected to lateral loads and settlement. The three-leaf masonry walls of the numerical contest will be represented as 3D assemblages of rigid blocks interacting at no-tension, frictional contact interfaces. LiABlock_3D will provide as outputs the computed collapse load and the plot of the corresponding failure mechanism.

Keywords: Micro-modeling approach; rigid block limit analysis; blind-test numerical prediction; collapse mechanism analysis.

1 INTRODUCTION

The seismic assessment of masonry structures has been receiving much attention in literature [2-5]. How to model the stone assemblage is a still open challenge. Several modeling approaches are available in literature in order to assess the seismic behavior of masonry structures [6]. Among these, simplified micro-modeling approach is one of the most used, thanks to the simplicity of the procedure compared to more complex approaches. According to this approach, the masonry brickwork is arranged as an assemblage of rigid blocks, considering a homogeneous material with no mechanical distinction between mortar and bricks. Failure gains through the contact interfaces.

In this framework, the paper is devoted to the application of "simplified micro-modeling" approach for the seismic-analysis of masonry structures. The proposed method starts with the generation of the geometrical model using simple CAD tools and continues with the analysis implemented in a novel software developed at the University of Naples "Federico II". The software, named LiABlock_3D, allows to analyze collections of polyhedral rigid blocks in contact via frictional surfaces, under the assumptions of infinite compressive strength and zero tensile strength. The formulation is part of the limit equilibrium analysis with the goal to predict the local and global failure modes of blocky structures. This kind of numerical formulation has the benefits of very quick calculation, without the need of a lot of input data. The high flexibility of the proposed formulation concerns also the loading conditions, where different loading axes and distributions can be assigned to the model. LiABlock_3D involves opening and sliding failure conditions under the assumptions of zero tension strength and frictional contact interfaces with infinite compressive strength.

In this study, LiaBlock_3D is applied to the blind-test prediction of experimental shake-table tests on a small-scale masonry walls in order to evaluate the software reliability in the prediction of seismic-induced collapse mechanisms.

The paper is organized as follows. Sections 2 deals with the micro-modeling approach and the numerical formulation for the rigid block limit analysis in LiABlock_3D. In Section 3 the application to two shake-table tests on three-leaf masonry walls is discussed in terms of failure modes and load factors promoting collapse.

2 MICRO-MODELING APPROACH AND NUMERICAL FORMULATION

2.1 Micro-modeling approach

The masonry structure performance under lateral seismic load can be assess according to three modeling approaches at least.

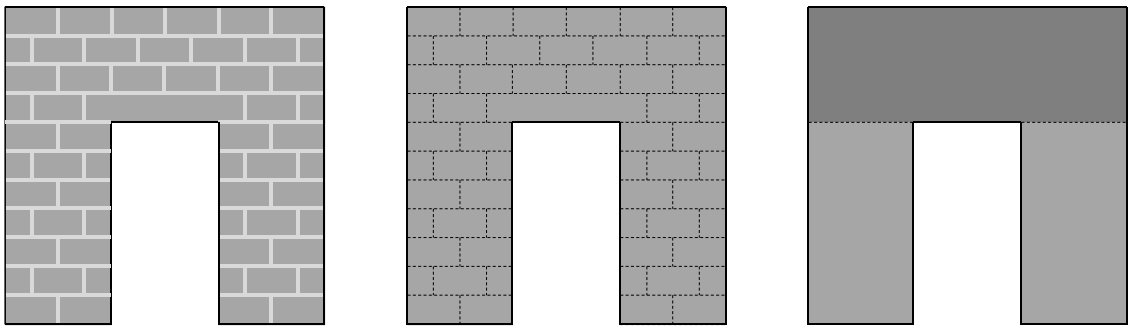

Figure 1: Modeling approaches for masonry structures: a) detailed micro-modeling; b) simplified micro-modeling; c) macro-modeling.

The most complex approach is a "detailed micro-model": this approach, particularly suitable for the finite element analysis, considers the separation between the mortar and bricks and requires two different constitutive laws. It is closer to the real masonry behavior but has the disadvantage of the slowness of calculation [7,8]. The "simplified micro-modeling" approach represents a good alternative where the mortar contribution is neglected, and the contact interfaces play an essential role in the failure modes definition. This approach perfectly commits to the rigid block model analysis [9]. Finally, the "macro-modeling" approach does not consider the real masonry texture but makes use of homogenization criteria for the material, considering average properties [10,11].

In this paper a simplified micro-modeling approach is used to create the geometry. According to the proposed approach the geometrical model is made of a collection of rigid block types generated in AutoCAD through the "Block Editor Menu". The block types are labeled with attributes which refer to the Cartesian coordinates of the vertexes of the block, its centroid and volume and the contact interfaces.

The full model is finally obtained by simply assembling the several block types in the CAD model space. The output of the modeling approach is represented by an Excel spreadsheet which contains the block type along the rows and the attributes in the columns. More details about the block generation and the output data extraction are provided in [1].

2.2 Numerical formulation implemented in LiABlock_3D

The modeling approach presented in the previous paragraph aims to the generation of a numerical model for the analysis in LiABlock_3D. This is a new tool, developed in MATLAB® environment, for the rigid block limit equilibrium analysis of masonry block assemblage. LiABlock_3D is equipped with a simple Graphical User Interface (GUI) where is possible to set the mechanical properties of the masonry and the loading and boundary conditions. A concave contact formulation is adopted to simulate the interaction between the blocks along the contact interfaces. In such a formulation, the internal forces are associated to the contact points located in the corner of the surfaces. These forces are the normal force n_k and the shear forces t_{1k} and t_{2k}.

LiABlock_3D solves an optimization linear programming problem based on the lower bound theorem of the limit analysis. The problem is described by the following formulation:

$$\begin{aligned} &max \quad \alpha \\ &s.t. \quad A \cdot x = f_D + \alpha \cdot f_L, \\ &\quad -n_k \le 0, \\ &\quad \sqrt{t_{1k}^2 + t_{2k}^2} - \mu \cdot n_k \le 0, \\ &\quad \mathrm{k} = 1, 2, ..., \mathrm{c}. \end{aligned} \tag{1}$$

Where c is the number of contacts. This formulation aims to calculate the maximum value of the load factor α subject to three constraints. The first equation constraint states the equilibrium condition: A is the contact equilibrium matrix, x is the vector of the static variables at contact point (t_{1k}, t_{2k} and n_k). The second member of the equation introduces the loading conditions since each rigid block is loaded by an external load f_i applied to its centroid and expressed as the sum of the dead load f_{Di} and of the live load f_{Li}, increased by the scalar multiplier α. The two inequalities constraints describe the failure conditions, involving both opening and sliding at contact points. The activation of a failure mode closely depends on the value of the friction coefficient μ.

LiABlock_3D returns the collapse mechanism and the value of the load factor promoting failure. The software contemplates both associative and non-associative flow plasticity rules. For the non-associative solution, the software implements an iterative procedure where the cohesion values for each iteration is calculated based on the normal forces of the previous iteration, starting from the value obtained in the associative solution. In order to achieve a comprehensive result, crushing and cracking failure condition should be considered [12].

3 APPLICATION TO EXPERIMENTAL CASE STUDIES

3.1 Test set-up

The case studies comprise two experimental shake-table tests developed at the University of Chieti-Pescara "Gabriele D'Annunzio" on two small-scale masonry walls. This study presents a blind-test prediction on three-leaf masonry walls made of two panels outside and an internal filling. The panels are 140 mm width and are made of stone blocks with dimensions 350 x 140 x 140 mm and mortar joints of 15 mm thickness. The internal filling is 170 mm width. The first case study is a simple wall and the second is a T-wall (Figure 4). The specimen is provided of a steel frame on the top for the application of a 6 tons additional mass. In the case of the T-wall, only in-plane load was contemplated (Figure 4b). Figure 4 shows the geometry and loading condition for the two case studies.

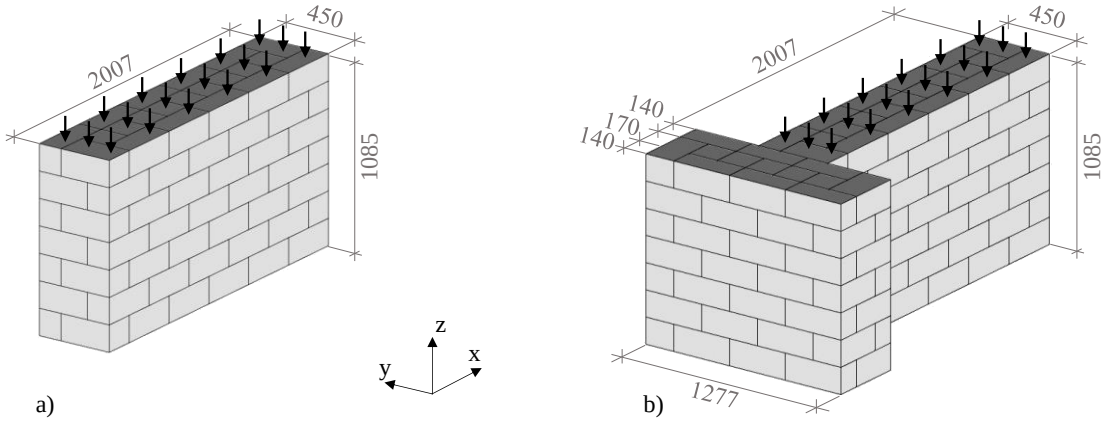

Figure 4: Experimental case studies geometry and loading condition: a) simple wall; b) T-wall.

Experimental campaign was carried on in order to obtain the mechanical properties of both mortar and stones. The shear tests return the value of the stone's properties involved in the sliding failure: the cohesion c, the friction coefficient μ and the sliding shear strength f_{vk0} was measured as 0.11 MPa, 0.21 and 0.091 MPa respectively. The Gazli earthquake record was selected as seismic input in the experimental tests. The Gazli earthquake dates to the 17th of May in 1976, with a magnitude equal to 6.8. Both horizontal and vertical acceleration component will be considered during the shake-table test.

3.2 Rigid block limit analysis using micro-modeling approach

The numerical models were generated through the proposed micro-modeling approach and then analyzed in LiABlock_3D. The block size follows the experimental data with a difference: seeing as how the formulation is not considering the mortar contribution, the brick size was increased in order to cover the mortar joints. Ad hoc blocks were generated to model the internal filling. The first case study (Figure 4a) is made of 150 rigid blocks (b) and 1812 contact points (c). The second case study (Figure 4b) is made of 241 rigid blocks and 2988 con-

tact points. With respect to mechanical parameters, the weight per unit volume was set equal to 24 kN/m^3 (average value for the selected stone type, *pietra di Pacentro*), the friction coefficient was set in the range between 0.4 (the value suggested by the Italian code [13]) and 0.6, and the cohesion was set equal to 0.00.

Both loading directions along the x-axis was analyzed in order to simulate the cyclic behavior of the seismic input considered in the experimental shake-table tests. Figure 5, Table 1 and Table 2 summarize the numerical outcomes obtained by LiABlock_3D software. Figure 5 shows the collapse mechanisms activated when a lateral live load is applied along the x-axis in both directions and a value of coefficient friction equal to 0.40 is used. The prevalent failure condition is the sliding at the contact points, except for the mechanism showed in figure 5b, where the model exhibits the overturning of the side wall. Table 1 and 2 contains the output of the analysis in LiaBlock_3D. The numerical analyses were carried out on a 3.50 GHz Intel Xeon Processor E5-1650 with 16.0 GB of RAM.

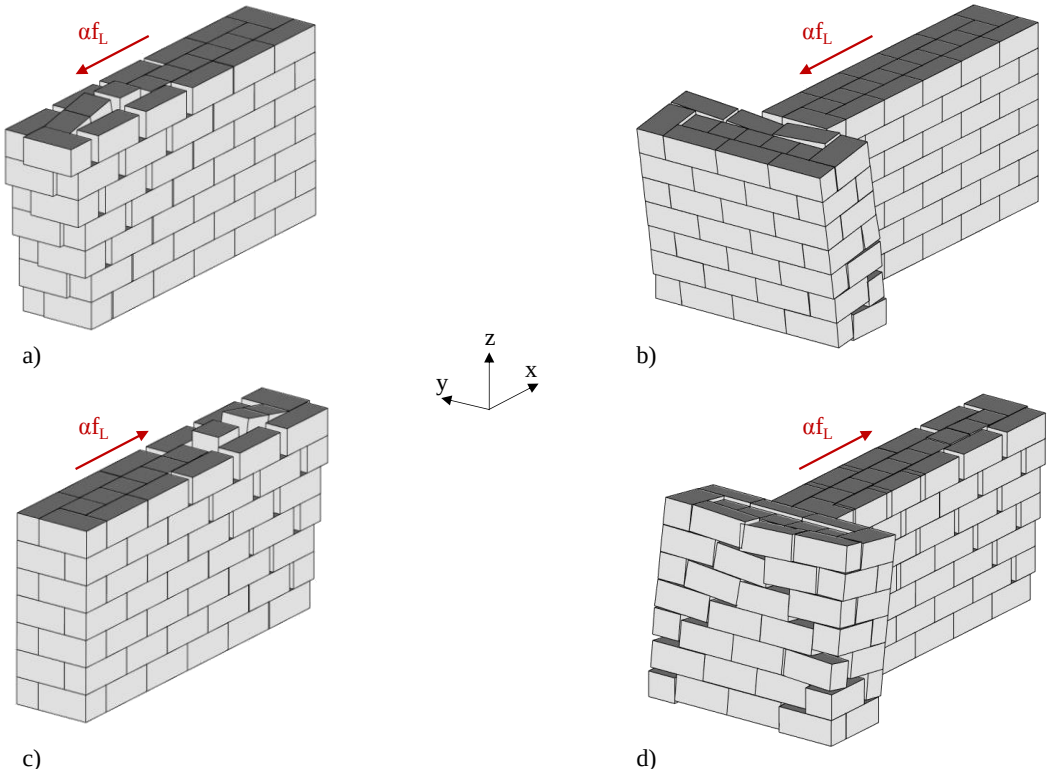

Figure 5: Collapse mechanism induced by live load applied along x-axis in both directions: (a)(c) simple wall; (b)(d) T-wall.

Model size (b x c)	ρ [kN/m^3]	c [N/mm^2]	Load directions	μ [-]	Numerical Solution		
					α [-]	αf$_L$ [N]	CPU Time [s]
150 x 1812	24	0.00	positive x-axis	0.40	0.38	31103.48	1.31
				0.50	0.45	37478.94	1.57
				0.60	0.56	46423.97	0.20
			negative x-axis	0.40	0.38	31068.96	1.36
				0.50	0.45	37478.94	1.58
				0.60	0.56	46423.97	0.30

Table 1: The case study of the simple wall: output by LiABlock_3D.

Model size (b x c)	ρ [kN/m^3]	c [N/mm^2]	Load directions	μ [-]	Numerical Solution		
					α [-]	αf_L [N]	CPU Time [s]
241 x 2988	24	0.00	positive x-axis	0.40	0.35	13522.47	2.83
				0.50	0.42	16405.84	2.76
				0.60	0.50	19229.06	1.92
			negative x-axis	0.40	0.27	10504.92	2.15
				0.50	0.29	11270.83	2.61
				0.60	0.31	12027.33	1.63

Table 2: The case study of the T-wall: output by LiABlock_3D.

Figure 6 shows the sensitivity analysis to the friction coefficient for both simple wall and T-wall specimens in terms of collapse load factor versus iteration number. As above mentioned, three values of friction coefficient were selected. Higher values of friction coefficient return higher value of the load factor and of the corresponding shear force at collapse.

The numerical analysis showed that the collapse could be expected for a load applied along both directions of the x-axis based on the shake-table shaking and the failure could occur with the overturning of the side wall along the negative direction or with the sliding in the opposite directions. The value of the acceleration promoting collapse in the experimental test should be derived by the value of the collapse load factor and the value of the behavior factor. Following the assessment method of force-based approach, the estimated peak ground acceleration (PGA) at collapse should be in the range between 0.8g and 1.0g, considering a behavior factor equal to 2.

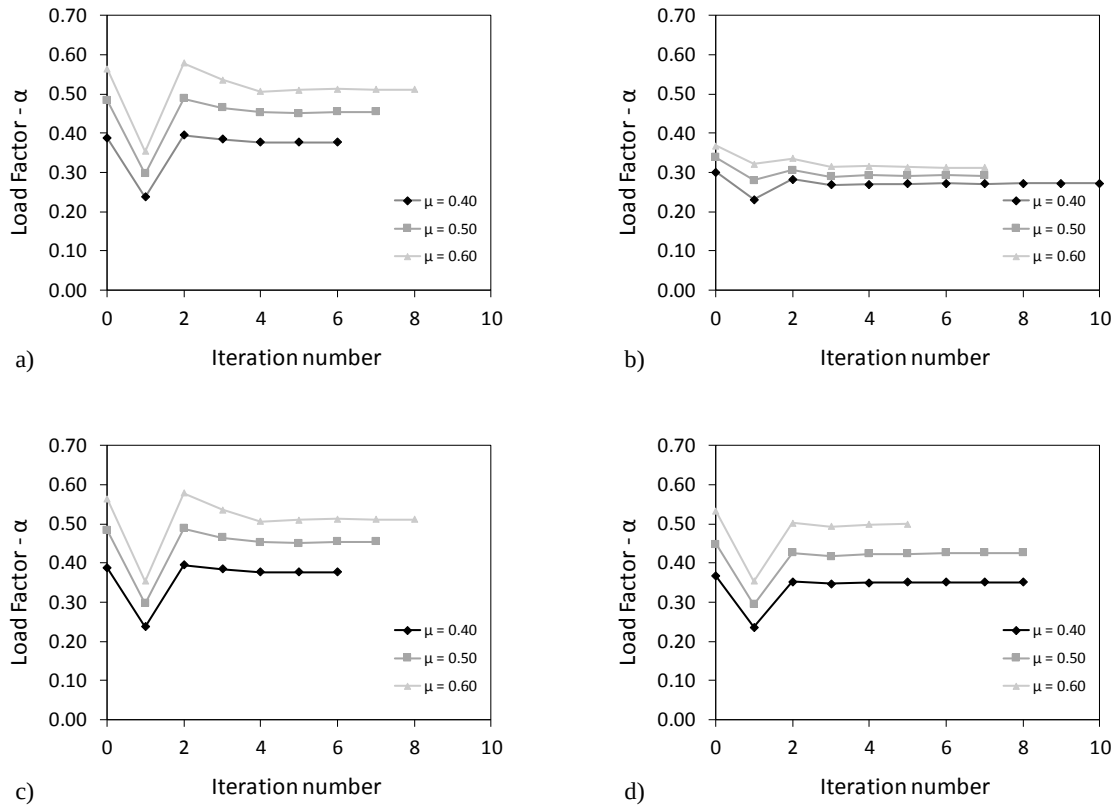

Figure 6: Collapse load factor vs iteration number for both simple wall (a)(c) and T-wall (b)(d) numerical simulation considering live loads applied along both negative (a)(b) and positive (c)(d) x-axis.

4 CONCLUSIONS

A procedure based on micro-modeling approach for the assessment of collapse mechanisms induced by seismic load was presented in this study. The approach is applied to the field of the blind-test numerical prediction. The numerical model is generated in AutoCAD model space, where each block is drawn and labeled with the attributes required for the numerical analysis. The software LiABlock_3D is used for the numerical analysis. It is a novel tool developed at the University of Naples "Federico II" based on the limit equilibrium analysis formulation and mathematical linear programming. LiABlock_3D can predict the local and global failure mechanisms and the value of the load factor for the mechanism activation considering different loading and boundary conditions.

Two blind shake-table tests on small-scale masonry walls represent the case studies with the goal of evaluating the ability of the proposed formulation in the failure mode prediction. The tests were designed by the University of Chieti-Pescara "Gabriele D'Annunzio".

The numerical simulations in LiABlock_3D tried to reproduce the shake-table loading condition. The software returned the failure modes and the load factor for the two case studies, proving the flexibility of the formulation and the high speed of calculation. The comparison between experimental and numerical outcomes is not yet available because the tests have not yet been carried out.

ACKNOWLEDGMENTS

The financial support of PRIN 2015 Programme by the Ministry of Education, University and Research (MIUR) is gratefully acknowledged for funding the research project "Protecting the Cultural Heritage from water-soil interaction related threats" (Prot. No. 2015EAM9S5), which is the main framework of the study presented in this article.

REFERENCES

[1] L. Cascini, R. Gagliardo, F. Portioli, LiABlock_3D: A Software Tool for Collapse Mechanism Analysis of Historic Masonry Structures, *International Journal of Architectural Heritage*, article in press, 2018.

[2] S. Lagomarsino, On the vulnerability assessment of monumental buildings, *Bulletin of Earthquake Engineering*, **4**, 445–463, 2006.

[3] S. Galassi, N. Ruggieri, G. Tempesta, A Novel Numerical Tool for Seismic Vulnerability Analysis of Ruins in Archaeological Sites, *International Journal of Architectural Heritage*, article in press, 2018.

[4] G. Brando, G. De Matteis, E. Spacone, Predictive model for the seismic vulnerability assessment of small historic centres: Application to the inner Abruzzi Region in Italy, *Engineering Structures,* **153**, 81-96, 2017.

[5] P. Zampieri, N. Simoncello, C. Pellegrino, Seismic capacity of masonry arches with irregular abutments and arch thickness, *Construction and Building Materials*, **201**, 789-806, 2019.

[6] P. Roca, M. Cervera, G. Gariup, L. Pelà, Structural Analysis of Masonry Historical Constructions. Classical and Advanced Approaches, *Archives of Computational Methods in Engineering*, **17**, 299-325, 2010.

[7] V. Sarhosis, J.V. Lemos, A detailed micro-modelling approach for the structural analysis of masonry assemblages, *Computers & Structures*, **206**, 66-81, 2018.

[8] A. M. D'Altri, S. de Miranda, G. Castellazzi, V. Sahrosis, A 3D detailed micro-model for the in-plane and out-of-plane numerical analysis of masonry panels, *Computers & Structures*, **206**, 18-30, 2018.

[9] M. Angelillo, A. Fortunato, A. Gesualdo, A. Iannuzzo, G. Zuccaro, Rigid block models for masonry structures, *International Journal of Masonry Research and Innovation*, **3**, 349-368, 2018.

[10] R. Marques, P.B. Lourenço, Possibilities and comparison of structural component models for the seismic assessment of modern unreinforced masonry buildings, *Computers & Structures*, **89**, 2079-2091, 2011.

[11] B. Pantò, I. Caliò, P.B. Lourenço, A 3D discrete macro-element for modelling the out-of-plane behaviour of infilled frame structures, *Engineering Structures*, **175**, 371-385, 2018.

[12] F. Portioli, L. Cascini, M. D'Aniello, R. Landolfo, A rigid block model with cracking units for limit analysis of masonry walls subject to in-plane loads, *Civil-Comp Proceedings*, **99**, 2012.

[13] DM 17.01.2018. Norme tecniche per le costruzioni. Rome: Italian Ministry of Infrastructure and Transportation; 2018 [in Italian].

COMPDYN 2019
7th ECCOMAS Thematic Conference on
Computational Methods in Structural Dynamics and Earthquake Engineering
M. Papadrakakis, M. Fragiadakis (eds.)
Crete, Greece, 24-26 June 2019

NONLINEAR PROGRAMMING APPROACH TO A SHEAR-DEFORMABLE HYBRID BEAM ELEMENT FOR LARGE DISPLACEMENT ANALYSIS

Charilaos M. Lyritsakis, Charalampos P. Andriotis, Konstantinos G. Papakonstantinou

The Pennsylvania State University
University Park, PA, 16802
e-mail: czl279@psu.edu
{cxa5246,kpapakon}@psu.edu

Keywords: geometrically exact beam theory, fiber elements, shear deformable beam , nonlinear programming, hybrid finite element

Abstract. *In the present work, a hybrid beam element based on exact kinematics is developed, accounting for arbitrarily large displacements and rotations, as well as shear deformable cross sections. At selected quadrature points, fiber discretization of the cross sections facilitates efficient computation of the stress resultants for any uniaxial material law. The numerical approximation is carried out through the lens of nonlinear programming, where the enengy functional of the system is treated as the objective function and the exact strain-displacement relations form the set of kinematic constraints. The only interpolated field is curvature, whereas the centerline axial and shear strains, along with the displacement measures at the element edges, are determined by enforcing compatibility through the use of any preferable constrained optimization algorithm. The solution satisfying the necessary optimality conditions is determined by the stationary point of the Lagrangian. A set of numerical examples demonstrates the accuracy and performance of the proposed element against analytical or approximate solutions available in the literature.*

1 INTRODUCTION

Problems frequently encountered by the engineering community over the last decades were concerned with structural systems whose response involved large displacements, rotations and strains on one hand, and inelastic behavior on the other. Such problems, in cases where the subject matter involved rod-like structures, necessitated the advancement of the classical Euler-Bernoulli theory, where displacements, rotations and strains were typically kept in the small range.

In the geometrically nonlinear case, the deformed geometry of the beam can be drastically different from the undeformed one, resulting in a rather involved description of beam kinematics. In general, there are two approaches in describing the kinematics of beams. The first one is the so-called continuum-based approach [1], which is employed for the derivation of the classical beam theory [2] and where all vectorial components are obtained from the three-dimensional theory of solids, with additional assumptions imposed on cross-section kinematics. The second approach, which is followed in this work, is concerned with the description of a material curve - an assemblage of material points representing the beam centroid - embedded in E^2 (or E^3 in the 3D case). The analysis of the curve by means of differential geometry of curves leads to the notion of intrinsic parameterization or one-dimensional formulation of beams, where spatial quantities can be expressed as functions of only one parameter. In the study of beams, this parameter is taken to be the arc-length of the beam. This in turn leads to the so-called arc-length parameterization of the beam with respect to a reference configuration. This approach was adopted in early works by Reissner [3, 4] and, next, Simo [5], Simo and Vu-Quoc [6] and can be traced back to Kirchhoff and his treatment of inextensible elastic rods. In these formulations, often termed as geometrically exact, the thickness of the rod is taken into consideration by attaching two vectors at each point on the material curve that would translate and rotate with the points, thus defining the properties of curvature and torsion at these points.

Approaches where strain measures are recast as primary field variables are often termed strain or deformation-based and were explored by Planinc et al. [7] for the planar case of the geometrically exact beam in order to properly account for the effect of local instabilites on the tangent stiffness matrix due to plastification, when global stability considerations are also present. It was later extended to the 2D dynamic case by Gams et al. [8] and to the three-dimensional case by Zupan and Saje [9] as a means to cope with the strain objectivity issue arising from the interpolation of the rotation vector [10]. Interpolation of strain measures is also encountered in mixed formulations, where more than one fields are interpolated and the underlying functional is augmented by additional terms to be satisfied in the weak sense [11]. Several other works with geometrically exact formulations in various settings can be found in the literature. Approaches based on mixed, hybrid, flexibility- and displacement-based considerations can be indicatively seen in [12, 13, 14, 15].

The present work is an extension of the geometrically exact hybrid formulation presented in [16] in order to account for the effect of shear deformation at the section level. As opposed to deriving the system equations from the Galerkin form after appropriate discretization, in the aforementioned work the problem is originally recast in a nonlinear programming framework, where the total potential energy functional (TPE) is augmented via Lagrange multipliers that enforce satisfaction of the exact kinematic conditions. The resulting functional is then approximated by employing a Gauss-Legendre quadrature rule, which yields the objective function to be minimized. Another interesting feature of this particular approach is that the primary variables in the element interior contributing to the elastic strain energy are the generalized

strain measures of the centroid, which are sought at quadrature points. Displacement measures, namely, the translations along the coordinate axes and the rotation of the cross sections, occur only at the nodes of the element and are associated with the external work. Kinematic consistency between the rotational measures of displacement and strain is enforced by using a Lagrange interpolation scheme to approximate the curvatures over the entire element domain. We should note that quadrature points coincide with the Lagrange interpolation points. In the remainder a succinct presentation of the formulation is presented, along with numerical investigations based on benchmark nonlinear problems studied in the literature, verifying the accuracy and efficiency of the suggested approach.

2 KINEMATICS AND TOTAL POTENTIAL ENERGY

We now proceed with the derivation of the kinematic equations that serve as constraints for the optimization problem. Let us consider two dimensional Euclidian space E^2 and a fixed Cartesian coordinate system $(X_1,\ X_2)$ with unit basis vectors $\{\mathbf{E_i}\}$, $i = 1,\ 2$ and a material curve of length L which represents the centroid of the beam embedded in that space. We will assume that the beam is initially straight, aligned with the coordinate axis X_1 and in an unstressed state. We also define the arc-length parameterization of the material curve $s \in I = [0,\ L] \rightarrow \mathbf{r} \in \mathbf{R}^2$, where s is the distance of a material point on the line of centroids in the reference configuration. The position vector of any material point on the centroid in any configuration can be written as:

$$\mathbf{r}(s) = (s + u(s))\mathbf{E}_1 + w(s)\mathbf{E}_2 \tag{1}$$

where u and w are the displacements of the material point along the coordinate axes X_1 and X_2 respectively.

Beam Kinematics

According to [3] the strain-displacement relations, assuming small axial strain of the beam centroid, are:

$$u' = (1+\epsilon)\cos\phi - \gamma\sin\phi - 1 \tag{2}$$

$$w' = (1+\epsilon)\sin\phi + \gamma\cos\phi \tag{3}$$

$$\phi' = \kappa \tag{4}$$

where $\epsilon,\ \gamma$ and κ are the axial, shear and bending strains of the line of centroids respectively, ϕ is the tangent angle to the material curve in the current configuration and derivatives with respect to the s are denoted by $(\,)'$. Integrating (2)-(4) over I yields:

$$\begin{aligned} u(L) - u(0) &= \int_0^L (1+\epsilon)\cos\phi - \gamma\sin\phi\, ds - L \\ w(L) - w(0) &= \int_0^L (1+\epsilon)\sin\phi + \gamma\cos\phi\, ds \\ \phi(L) - \phi(0) &= \int_0^L \kappa\, ds \end{aligned} \tag{5}$$

The integral form of the kinematic equations in (5) is utilized to impose the constraints on the nonlinear program.

Total Potential Energy

The total potential energy functional of the beam under a set of point loads $\mathbf{P} = [\,\mathbf{P}_1\ \mathbf{P}_2]^T$, with $\mathbf{P}_i$ the point loads at the element edge nodes, can be expressed in the reference configuration as:

$$\Pi(\epsilon,\ \gamma,\ \kappa,\ \mathbf{d}) = \int_0^L W(\epsilon,\ \gamma,\ \kappa)\ ds - \mathbf{P}^T\mathbf{d} \tag{6}$$

where W is the strain energy per unit length of the beam centroid. The displacement degrees of freedoms at the two edge nodes are collectively represented in vector $\mathbf{d}$ as:

$$\mathbf{d} = \begin{bmatrix} d_1 & d_2 & d_3 & d_4 & d_5 & d_6 \end{bmatrix}^T \tag{7}$$

with:

$$\begin{aligned} d_1 = u(0),\ d_2 = w(0),\ d_3 = \phi(0), \\ d_4 = u(L),\ d_5 = w(L),\ d_6 = \phi(L) \end{aligned}$$

The stress resultants on a section are associated with the strain energy as follows:

$$N = \frac{\partial W}{\partial \epsilon} \quad , \quad Q = \frac{\partial W}{\partial \gamma} \quad , \quad M = \frac{\partial W}{\partial \kappa} \tag{8}$$

The stress resultants defined in (8) can be numerically computed using appropriate fiber discretization at the cross section level. Thereby, any nonlinear constitutive law may be incorporated in beam element formulations to capture the effects of distributed elastoplastic behavior or damage [17, 18, 19].

3 NONLINEAR PROGRAMMING PROBLEM STATEMENT

In this section we formulate the equations pertaining to the description of our hybrid element as a nonlinear program.

Element Objective Function

The discrete form of the TPE in (6) is given by applying Gauss-Legendre quadrature to approximate the integral for one element:

$$f(\mathbf{x}) = \sum_{i=1}^{n} c_i W(\epsilon_i,\ \gamma_i,\ \kappa_i)\ - \mathbf{P}^T\mathbf{d} \tag{9}$$

where c_i are the weights of the quadrature, n the number of quadrature points and $\mathbf{x},\ \mathbf{d}$ and $\mathbf{y}_i$ are defined as:

$$\mathbf{x} = \begin{bmatrix} \mathbf{y}_1^T & \mathbf{y}_2^T & \dots & \mathbf{y}_n^T & \mathbf{d}^T \end{bmatrix}^T \tag{10}$$

with $\mathbf{y}_i = \begin{bmatrix} \epsilon_i & \gamma_i & \kappa_i \end{bmatrix}^T$

Element Constrains

The first set of constraints derived from the approximation of kinematic relations (5) is given as:

$$\mathbf{C}_{eq}^{A} = \begin{bmatrix} d_4 - d_1 - \sum_{i=1}^{n} c_i[(1+\epsilon_i)\cos\phi_i - \gamma_i \sin\phi_i] + L \\ d_5 - d_2 - \sum_{i=1}^{n} c_i[(1+\epsilon_i)\sin\phi_i + \gamma_i \cos\phi_i] \\ d_6 - d_3 - \sum_{i=1}^{n} c_i \kappa_i \end{bmatrix} = \mathbf{0} \tag{11}$$

In accordance with [16] we then interpolate the curvature field with Lagrange polynomials in order to obtain the rotations ϕ_i at the quadrature points:

$$\phi_i = d_3 + \sum_{j=1}^{n} \Theta_{ij} \kappa_j \tag{12}$$

$$\mathbf{\Theta} = L \begin{bmatrix} \xi_1 & \frac{\xi_1^2}{2} & \dots & \frac{\xi_1^n}{n} \\ \vdots & \vdots & \ddots & \vdots \\ \xi_n & \frac{\xi_n^2}{2} & \dots & \frac{\xi_n^n}{n} \end{bmatrix} \mathbf{G}^{-1}, \;\; \mathbf{G} = \begin{bmatrix} 1 & \xi_1 & \dots & \xi_1^{n-1} \\ \vdots & \vdots & \ddots & \vdots \\ 1 & \xi_n & \dots & \xi_n^{n-1} \end{bmatrix} \tag{13}$$

where $\xi = \frac{x}{L}$ and $\mathbf{G}$ is the Vandermonde matrix.

Notice that the first two equations of (11) are *nonlinear equality* constraints, while the third, along with the n equations of (12) are *linear equality* constraints. It is convenient to recast all constraints in one vector as follows:

$$\mathbf{C}_{eq} = \begin{bmatrix} \mathbf{C}_{eq}^{A} \\ \\ \mathbf{C}_{eq}^{B} \end{bmatrix} = \mathbf{0} \tag{14}$$

where

$$\mathbf{C}_{eq}^{B} = \begin{bmatrix} \phi_1 - d_3 - \sum_{j=1}^{n} \Theta_{1j} \kappa_j \\ \vdots \\ \phi_n - d_3 - \sum_{j=1}^{n} \Theta_{nj} \kappa_j \end{bmatrix} \tag{15}$$

Element Lagrangian Function

We now introduce a vector $\boldsymbol{\lambda}$ of the Lagrange multipliers and augment the TPE (6), constructing the Lagrangian of the optimization problem as:

$$f(\mathbf{x},\ \boldsymbol{\lambda}) = \sum_{i=1}^{n} c_i W(\epsilon_i,\ \gamma_i,\ \kappa_i)\ - \mathbf{P}^T \mathbf{d} + \boldsymbol{\lambda}^T \mathbf{C}_{eq} \tag{16}$$

Stationary points are provided by satisfying Karush-Kuhn-Tucker [20] optimality conditions for the Lagrangian function of (16).

4 NUMERICAL EXAMPLES

In the following examples we examine the performance of the proposed formulation and compare it with other well-known works in the literature. We first explore the accuracy when the shear stiffness is reduced and then we test against different loading cases. For each example, only one element with five quadrature points is used.

Table 1: Cantilever with constant transverse load at free end.

	w			u		
GA_s	Numerical	Analytical	Present	Numerical	Analytical	Present
$5 \cdot 10^{20}$	0.30172077	0.301720774	0.30172432	0.05643324	0.056433236	0.05643126
$5 \cdot 10^{2}$	0.31781387	0.317813874	0.31781567	0.06131566	0.061315658	0.06131317
$5 \cdot 10^{1}$	0.46541330	0.465413303	0.46541543	0.10328492	0.103284917	0.10328294
$1 \cdot 10^{2}$	1.16709588	1.167095878	1.16709542	0.25213661	0.252136606	0.25213357
$5 \cdot 10^{0}$	2.10408747	2.104087473	2.10409063	0.37612140	0.376121399	0.37612451

Problem data: $EA = 10^{21},\ EI = 10,\ L = 1$. Numerical data in [21], analytical in [22].

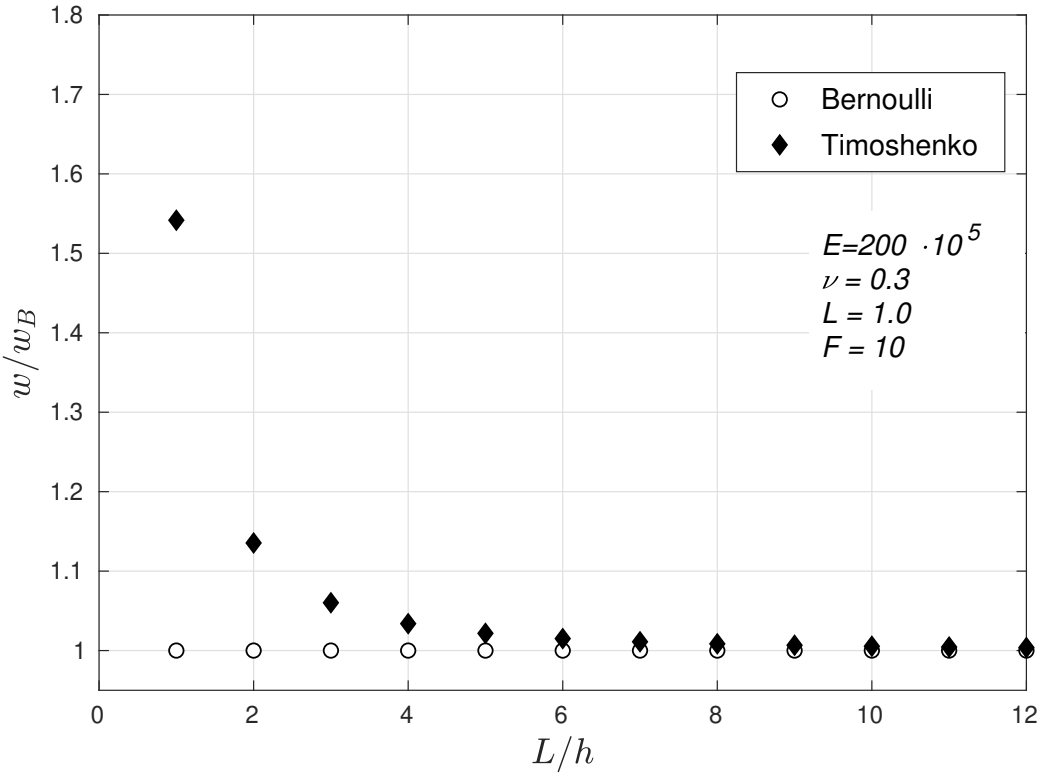

Figure 1: Timoshenko compared to Bernoulli solutions for different levels of slenderness.

Example 1 - Effect of shear deformation in cantilever deflection

In this example we explore the effect of shear flexibility on the tip deflection of a cantilever. A constant point transverse force $P = 10$ units is applied at the free end and, then, several analyses are performed by varying the shear stiffness coefficient, GA_s. Numerical and analytical results obtained by Batista in [21] and [22], respectively, are compared with the present formulation and are illustrated in Table 1.

Fig. 1 demonstrates the effect shear deformations have when not neglected, compared to the Bernoulli solutions, by varying the ratio L/h, with h being the height of the cross section and L the length of the beam. The applied load is F, ν is the Poisson's ratio and w_B is the deflection when shear flexibility is neglected. As can be seen from the results, when $L = 2h$, transverse

displacements due to shear deformation are increased by rougly 13%.

Example 2 - Cantilever with transverse point load at its tip

This problem has been analyzed in [23, 24], whereas Mattiasson [25] provided solutions by solving the elliptic integrals of the problem of large deflections of beams. Moreover, the problem was also examined in [26] using a co-rotational transformation for the Timoshenko beam, whereas Nanakorn [27] used 3 elements and a total tagrangian formulation.

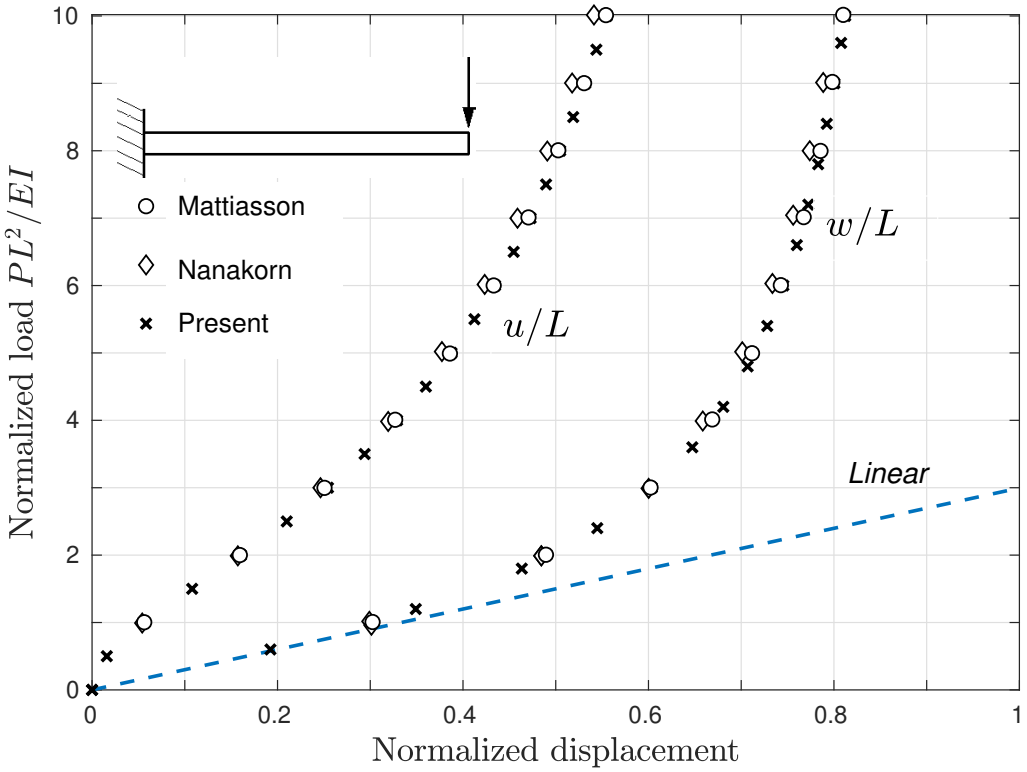

Figure 2: Cantilever with point transverse load at its free end.

Table 2: Cantilever with transverse load at its free end.

	w/L		u/L	
PL^2/EI	Mattiasson	Present	Mattiasson	Present
2.0	0.49346	0.49347	0.16064	0.16063
4.0	0.66996	0.67001	0.32894	0.32892
6.0	0.74457	0.74465	0.43459	0.43457
8.0	0.78498	0.78509	0.50483	0.50481
10.0	0.81061	0.81073	0.55500	0.55498

Problem data: $EI = 1000$ lb/in^2, $L = 100$in, $P = 1$lb, $N = 20$ steps.
Results in Mattiasson [25].

Figure 2 illustrates the performance of the element when compared against the analytical and numerical solutions - mentioned above - and Table 2 demonstrates the accuracy up to six decimal points when compared to the analytical solutions for a sample of loading levels. The dotted line indicates the linear response.

Example 3 - Cantilever with point moment at its free end

This example tests the capabilities of our developed model capturing the response of an inextensional beam subjected to a point moment, forcing a curl into a complete circle. As mentioned previously, in all examples we only used one element with five quadrature points for our analysis. Bathe and Bolourchi [28] using five and twenty elements and an updated lagrangian procedure showed accuracy up to 90 degrees. In subsequent works, Simo & Vu-Quoc [6] (five elements), Rankin & Brogan [29] (ten elements) and Crisfield [30] (five elements) duplicated the exact solution. In the second and third works a corotational formulation was employed. The mechanical and geometric properties for this problem are $I = 0.01042\text{in}^4$, $L = 100\text{in}$, $A = 0.5\text{in}^2$, $E = 1.2 \times 10^4\text{psi}$.

In Fig. 3 our solution is compared with the one using twenty elements. As mentioned earlier, with the element proposed by Bathe & Bolourchi [28], which is based on large-displacement and large-rotation assumptions, the response starts to diverge from the exact solution at an angle of 90 degrees rotation, irrespectively of the mesh density. Our proposed formulation is instead able to capture the response for the whole loading scenario (360 degrees), as can be seen from the line that represents the normalized displacement $\phi/2\pi$.

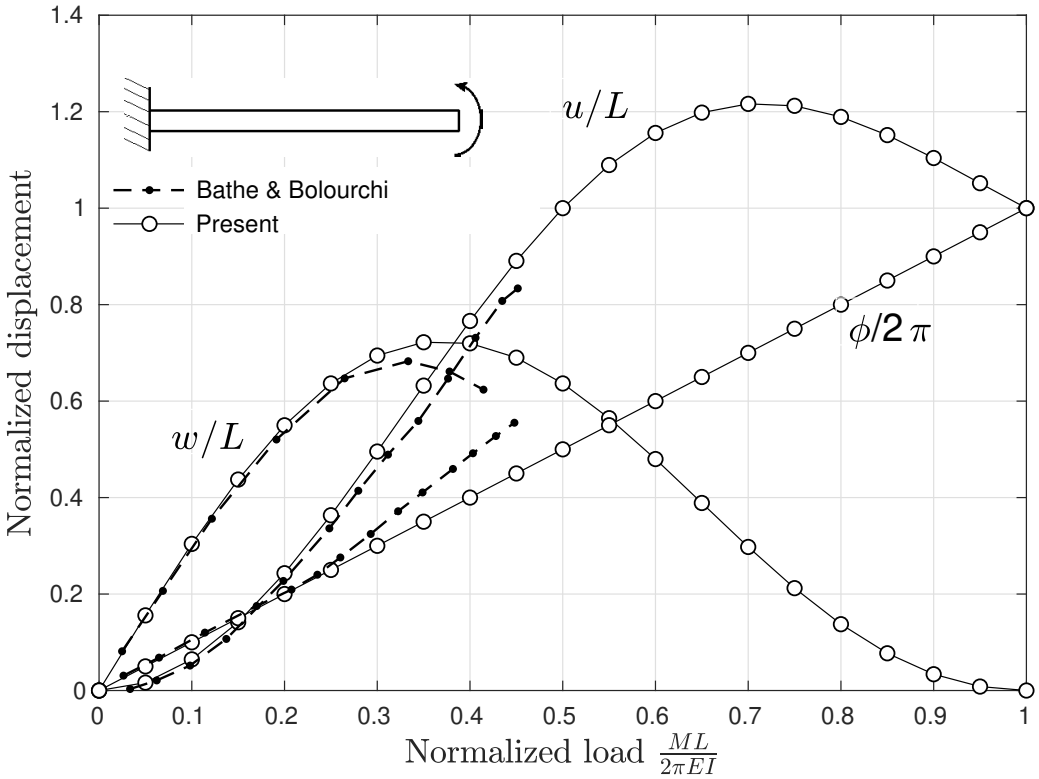

Figure 3: Cantilever with point moment at its free end.

Example 4 - Cantilever beam with eccentric compressive point load

We consider a cantilever beam of length $L = 100$, cross section thickness $b = 1$ and elastic modulus $E = 12$, with the load parameter $\lambda = P/P_{cr}$ is increased up to 4.0. The critical load for the cantilever is $P_{cr} = 0.25\pi^2 EI/L^2$. Wood & Zienkiewicz [31] used five continuum-based elements that allow for shear deformation and employed a total Lagrangian formulation. The results are illustrated in Fig. 4. Analytical solutions to the problem, provided in [23, 32] where it is assumed no axial or shear deformation occurs, show negligible discrepancy compared to the ones proposed here and in [31]. It should be noted that the eccentricity is $\epsilon = b/2$. The configurations for each load step for Examples 2,3 and 4 are depicted in Fig. 5, from left to right.

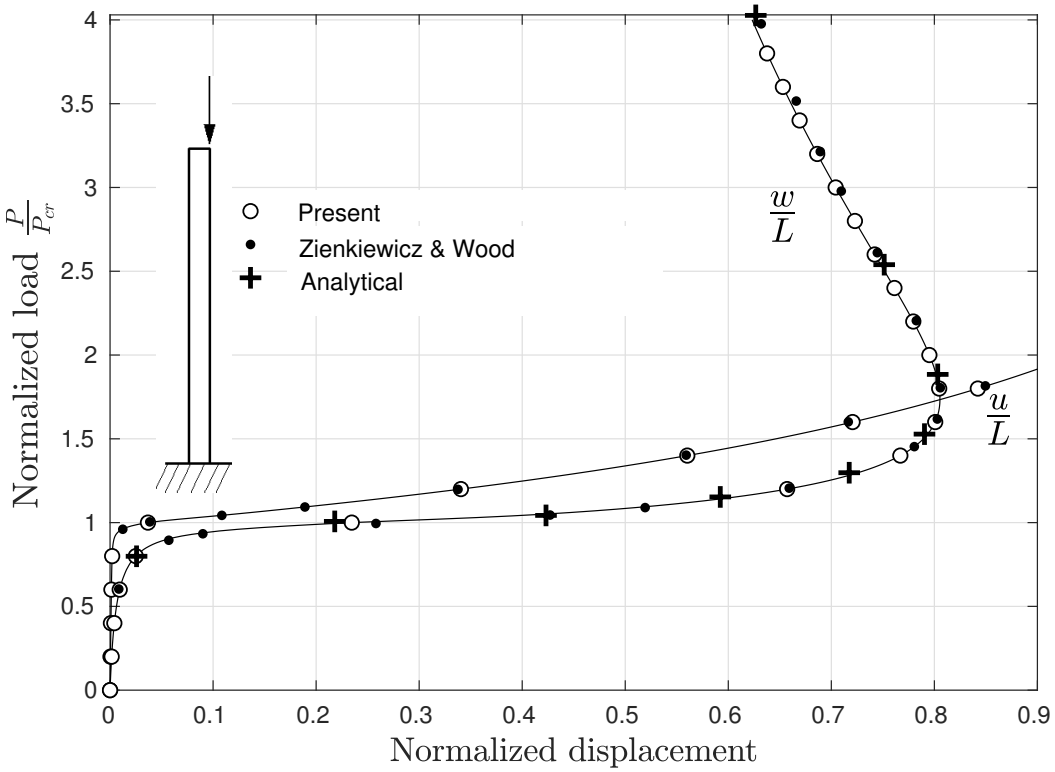

Figure 4: Cantilever with eccentric axial load at its free end.

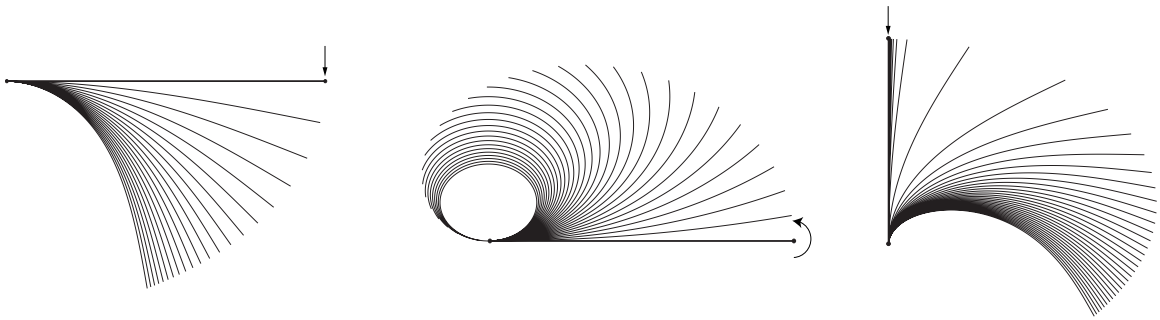

Figure 5: Configurations at each step for examples 2, 3 and 4 (left to right).

5 CONCLUSIONS

An extension to the geometrically exact hybrid element derived in [16] is presented herein that accounts for shear deformations. The system of equilibrium equations is originally derived within a nonlinear programming framework, where the total potential energy functional is discretized and then augmented by the exact kinematic constraints of the physical problem, also in discretized form, and solved by determining the stationary point of the Lagrangian. The suggested nonlinear programming hybrid formulation is capable of capturing the response of the benchmark problems with accuracy, using only one element, which is a desirable feature for framed structure applications. Ongoing work explores a variety of different approaches as far as the optimization algorithms are concerned, which is something the proposed formulation supports and enables, the extension of the material yield rule to account for the interaction of shear and axial stresses, as well as the extension to spatial and dynamic formulations.

Acknowledgements

This material is based upon work supported by the National Science Foundation under Grant No. 1634575. The authors gratefully acknowledge this support.

REFERENCES

[1] T. Belytschko, L. Schwer, and M.J. Klein. Large displacement, transient analysis of space frames. *International Journal for Numerical Methods in Engineering*, **11**(1):65–84, 1977.

[2] T.J.R. Hughes. *The finite element method: linear static and dynamic finite element analysis*. Dover, 2000.

[3] E. Reissner. On one-dimensional finite-strain beam theory: The plane problem. *Zeitschrift für Angewandte Mathematik und Physik ZAMP*, **23**(5):795–804, 1972.

[4] E. Reissner. On one-dimensional large-displacement finite-strain beam theory. *Studies in applied mathematics*, **52**(2):87–95, 1973.

[5] J.C. Simo. A finite strain beam formulation. The three-dimensional dynamic problem. Part I. *Computer Methods in Applied Mechanics and Engineering*, **49**(1):55–70, 1985.

[6] J.C. Simo and L. Vu-Quoc. A three-dimensional finite-strain rod model. Part II: Computational aspects. *Computer Methods in Applied Mechanics and Engineering*, 58(1):79–116, 1986.

[7] I. Planinc, M. Saje, and B. Cas. On the local stability condition in the planar beam finite element. *Structural Engineering and Mechanics*, **12**(5):507–526, 2001.

[8] M. Gams, M. Saje, S. Srpčič, and I. Planinc. Finite element dynamic analysis of geometrically exact planar beams. *Computers & Structures*, **85**(17-18):1409–1419, 2007.

[9] D. Zupan and M. Saje. Finite-element formulation of geometrically exact three-dimensional beam theories based on interpolation of strain measures. *Computer Methods in Applied Mechanics and Engineering*, **192**(49-50):5209–5248, 2003.

[10] M.A. Crisfield and G. Jelenić. Objectivity of strain measures in the geometrically exact three-dimensional beam theory and its finite-element implementation. *Proceedings of the Royal Society of London. Series A: Mathematical, Physical and Engineering Sciences*, **455**(1983):1125–1147, 1999.

[11] C.A. Felippa. A survey of parametrized variational principles and applications to computational mechanics. *Computer Methods in Applied Mechanics and Engineering*, **113**(1-2):109–139, 1994.

[12] M.V. Sivaselvan and A.M. Reinhorn. Collapse analysis: large inelastic deformations analysis of planar frames. *Journal of Structural Engineering*, **128**(12):1575–1583, 2002.

[13] H.A.F.A. Santos, P.M. Pimenta, and J.P.M. Almeida. A hybrid-mixed finite element formulation for the geometrically exact analysis of three-dimensional framed structures. *Computational Mechanics*, **48**(5):591, 2011.

[14] N.D. Oliveto and M.V. Sivaselvan. 3D finite-deformation beam model with viscous damping: Computational aspects and applications. *Journal of Engineering Mechanics*, **141**(1):04014103, 2014.

[15] M. Salehi and P. Sideris. A finite-strain gradient-inelastic beam theory and a corresponding force-based frame element formulation. *International Journal for Numerical Methods in Engineering*, **116**(6):380–411, 2018.

[16] C.P. Andriotis, K.G. Papakonstantinou, and V.K. Koumousis. Nonlinear programming hybrid beam-column element formulation for large-displacement elastic and inelastic analysis. *Journal of Engineering Mechanics*, **144**(10):04018096, 2018.

[17] E. Spacone, F.C. Filippou, and F.F. Taucer. Fibre beam–column model for non-linear analysis of R/C frames: Part I. Formulation. *Earthquake Engineering & Structural Dynamics*, **25**(7):711–725, 1996.

[18] P. Uriz, F.C. Filippou, and S.A. Mahin. Model for cyclic inelastic buckling of steel braces. *Journal of Structural Engineering*, **134**(4):619–628, 2008.

[19] C. Andriotis, I. Gkimousis, and V. Koumousis. Modeling reinforced concrete structures using smooth plasticity and damage models. *Journal of Structural Engineering*, **142**(2):04015105, 2015.

[20] J. Nocedal and S. Wright. *Numerical Optimization*. Springer Science & Business Media, 2006.

[21] M. Batista and F. Kosel. Cantilever beam equilibrium configurations. *International Journal of Solids and Structures*, **42**(16-17):4663–4672, 2005.

[22] M. Batista. A closed-form solution for Reissner planar finite-strain beam using Jacobi elliptic functions. *International Journal of Solids and Structures*, **87**:153–166, 2016.

[23] R. Frisch-Fay. *Flexible bars*. Butterworths, 1962.

[24] K.E. Bisshopp and D.C. Drucker. Large deflection of cantilever beams. *Quarterly of Applied Mathematics*, **3**(3):272–275, 1945.

[25] K. Mattiasson. Numerical results from large deflection beam and frame problems analysed by means of elliptic integrals. *International Journal for Numerical Methods in Engineering*, **17**(1):145–153, 1981.

[26] N.D. Kien. A Timoshenko beam element for large displacement analysis of planar beams and frames. *International Journal of Structural Stability and Dynamics*, **12**(06):1250048, 2012.

[27] P. Nanakorn and L.N. Vu. A 2D field-consistent beam element for large displacement analysis using the total Lagrangian formulation. *Finite Elements in Analysis and Design*, **42**(14-15):1240–1247, 2006.

[28] Klaus-Jürgen Bathe and S. Bolourchi. Large displacement analysis of three-dimensional beam structures. *International Journal for Numerical Methods in Engineering*, **14**(7):961–986, 1979.

[29] C.C. Rankin and F.A. Brogan. An element independent corotational procedure for the treatment of large rotations. *Journal of Pressure Vessel Technology*, **108**(2):165–174, 1986.

[30] M.A. Crisfield. A consistent co-rotational formulation for non-linear, three-dimensional, beam-elements. *Computer Methods in Applied Mechanics and Engineering*, **81**(2):131–150, 1990.

[31] R.D. Wood and O.C. Zienkiewicz. Geometrically nonlinear finite element analysis of beams, frames, arches and axisymmetric shells. *Computers & Structures*, **7**(6):725–735, 1977.

[32] S.P. Timoshenko and J.M. Gere. *Theory of elastic stability*. Dover, 2009.

COMPDYN 2019
7th ECCOMAS Thematic Conference on
Computational Methods in Structural Dynamics and Earthquake Engineering
M. Papadrakakis, M. Fragiadakis (eds.)
Crete, Greece, 24-–26 June 2019

A MACRO-ELEMENT FORMULATION FOR THE RESPONSE OF INELASTIC ROCKING BODIES DURING CYCLIC LOADING

Evangelos Avgenakis and Ioannis N. Psycharis

School of Civil Engineering, National Technical University of Athens
Heroon Polytechniou 9, 15780 Zografou, Greece
e-mail: {vavgen,ipsych}@central.ntua.gr

Keywords: Rocking, Macro-element, Nonlinear analysis, Inelastic response, Resilient structures

Abstract. *In this paper, a macroelement for the prediction of the response of inelastic rocking bodies is proposed, which can be used in cyclic loading simulations. The ideas presented for the elastic rocking element formulation in previous works by the authors are extended here to the inelastic material case. Thus, apart from the deformability along the height of the body, the proposed macroelement also takes into account the inelastic deformations near the rocking interface, which is considered crucial for the accurate determination of the rocking response of deformable rocking bodies. Due to the partial loading of the rocking interface, nonlinear stress distributions develop across the rocking interface, which produce additional displacements to those predicted by the technical theory of bending. Taking these and the additional plastic displacements due to material nonlinearity into account, the correct stress distribution is determined based on the target displacements. The pushover curves derived with the proposed macroelement for characteristic problems are presented, while comparison is made against experimental results from the literature, showing satisfactory accuracy.*

1 INTRODUCTION

The complex mechanics of the motion of rocking bodies and structural members have attracted attention from the scientific community in recent years. The rocking motion occurs when a member is unrestrained or at least partially restrained at its base, so that tensile stresses cannot be transmitted, as considered in classical structural mechanics. Given that the imposed forces are large enough, the rocking body detaches from the ground and rotates about one of its corners. The vertical force acts as the restoring force that tends to bring the body back to its original equilibrium position.

Numerous studies have been presented regarding the analytical response of solitary rocking members or rocking members included in various configurations ([1], [2], [3], [4], [5], [6], [7], [8], among others). However, the base of the rocking body is assumed to be rigid in most of these studies, an assumption which does not hold for rocking members included in usual structural configurations, which experience large deformations.

Masonry and precast shear wall members, partially connected at their base, are also expected to rock during a strong seismic event. Analytical and experimental results, as well as design methodologies for such configurations have been presented by several authors ([9], [10], [11], [12], among others). The generalization of their application is difficult though, since such methodologies are usually based on several assumptions regarding the stress distributions and member deformations near the base and the interaction between rocking and deformability and, in many cases, the aforementioned elements of the proposed methodologies are calibrated using experimental or numerical results of specific examined configurations.

Few computational models have been proposed, which can be incorporated in a general finite element framework, in order to include rocking members in actual structural models ([13], [14], [15], [16], [17], [18], among others). The main drawback of such approaches is that either the interface between the rocking body and its base is considered rigid or that the deformability of the rocking body near the contact area is only approximately taken into account.

A macroelement formulation for elastic rocking members, addressing the previous remarks, has been proposed by the authors [19], which is able to take into account deformability both along the height of the members, as well as near the contact with the base. This macroelement is used for the ends of the rocking member, where nonlinear stress distributions are expected to develop (Fig. 1). The macroelement is based on the theory of elasticity, without making excess assumptions, and can be used to predict the static response of solitary rocking bodies, as well as rocking members included in structures (e.g. shear walls) in a consistent manner.

This formulation is extended in this paper in order to take material nonlinearity into account, since rocking members are expected to yield during strong seismic events. The monotonic case has been addressed in [20], but cyclic loading, which is examined herewith, is much more complex and needs a different treatment.

2 PROBLEM STATEMENT

The macroelement used for each rocking end of the column shown in Fig. 1 can be used in the context of any finite element framework. As described in [19], the use of a natural coordinate system of a simply supported beam, where the rigid body motion has been removed (Fig. 2b), is more convenient than the original local element configuration (Fig. 2a). The conversion between the two coordinate systems can be found e.g. in [19].

The material of the rocking body is assumed to be elastic-perfectly plastic with Young's modulus E, Poisson's ratio ν and yield stress σ_y, while the same modulus of elasticity is

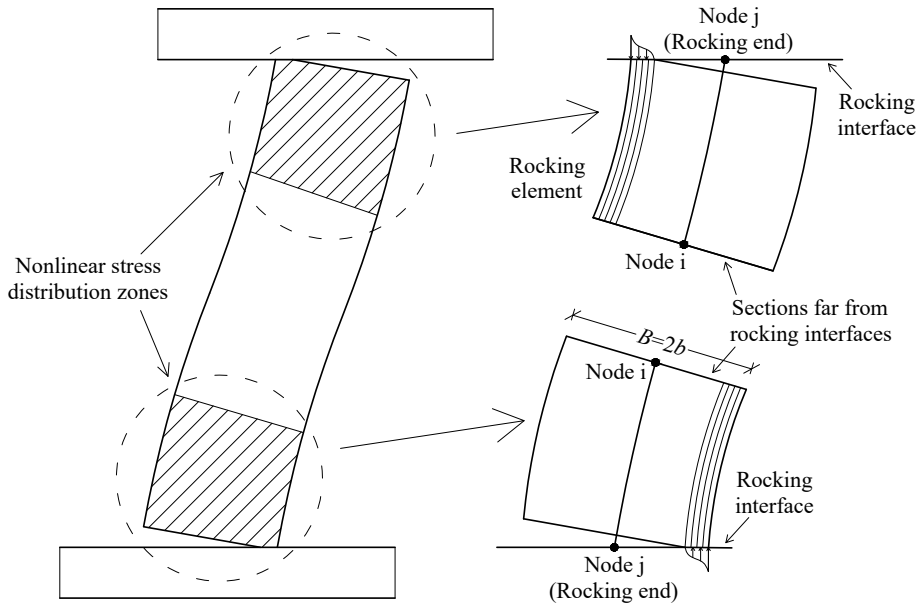

Figure 1: Use of the macroelement for the member segments near the rocking ends, where nonlinear stress distributions develop. Two rocking macroelements are used for the rocking column shown, one for each rocking end. Node j of each element refers to the corresponding rocking end. The fibers corresponding to the contact region of each element are shaded.

assumed during unloading. As usual practice in beam-column elements, material yielding is assumed only for the normal stresses, due to the increased difficulty of implementing another yielding criterion combining all stresses.

Due to the partial loading of the rocking interface, the stress distribution across this interface is nonlinear [21]. However, the technical theory of bending used in usual structural analyses cannot predict such response, meaning that this theory cannot be used for rocking members. As extensively described in [19], the following approach, based on the more general theory of elasticity, is used instead, which is considered an invaluable tool for the accurate prediction of deformable rocking bodies.

The displacements produced by the nonlinear stress distribution on the rocking interface can be examined by decomposing it into two distributions: (i) A stress distribution according to the technical theory of bending for the given rocking end resultant forces and (ii) Self-equilibrating distributions, which influence the local displacements but do not produce resultant forces and moments (Fig. 3).

The self-equilibrating stresses developing near the contact area have no resultant forces and moment, so according to the Saint-Venant principle their effect far from the contact area is negligible. This means that the displacement distribution across member sections far from the contact area is almost linear across the element, as predicted by the technical theory of bending (Fig 1). Furthermore, the additional displacements induced to the rocking body across the rocking interface by the self-equilibrating stresses can be calculated as those corresponding to a semi-infinite strip (Fig. 4), since this problem is much more easily solved. The semi-infinite strip examined is loaded with self-equilibrating normal and shear stresses across its end ($x = 0, -1 \leq y \leq 1$) and is stress-free at its sides ($y = \pm 1$). The results for the semi-infinite strip loaded with self-equilibrating normal and shear stresses can be easily translated into ones referring to the rocking body, as it will be shown in the ensuing.

Although the theory of elasticity used to solve the aforementioned semi-infinite strip problem

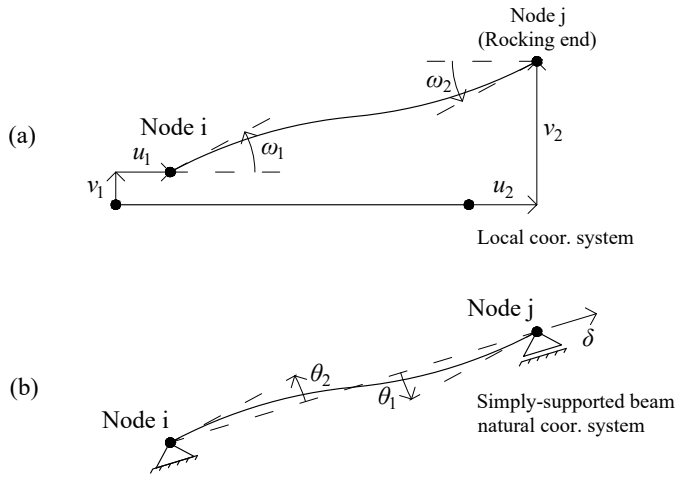

Figure 2: (a) Local member displacements, required by the general finite element framework and (b) Natural member displacements used by the element formulation

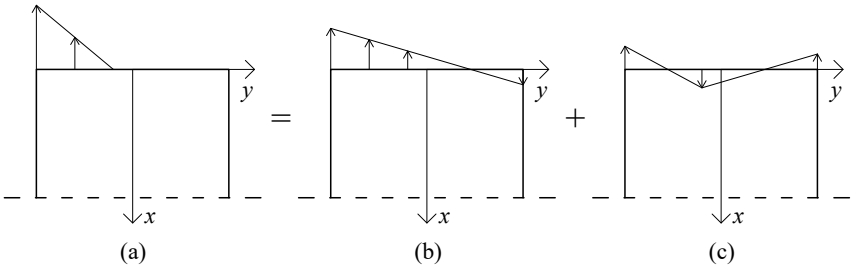

Figure 3: Decomposition of (a) the partial loading at the contact surface into (b) stresses according to the technical theory of bending and (c) self-equilibrating stresses

can only be rigorously applied to elastic bodies, it would be useful to use it appropriately also for inelastic ones. To this end, the following assumptions are made: (i) The inelastic behavior defined previously for the inelastic material is considered as is for the rocking interface. (ii) The stress distributions on the rocking interface produce elastic displacements, $[u_{\text{el}}]$, which are calculated according to the elastic theory of the semi-infinite strip. (iii) Fibers with inelastic behavior on the rocking interface are assumed to also develop plastic displacements, $[u_a]$, in addition to the aforementioned elastic ones, which are compressive ($u_a < 0$), while fibers that do not belong to the contact region develop gaps with the rocking interface, $[u_a]$, with $u_a > 0$ (Fig. 5).

Since the assumption of the linear strain distribution across the contact area cannot be applied

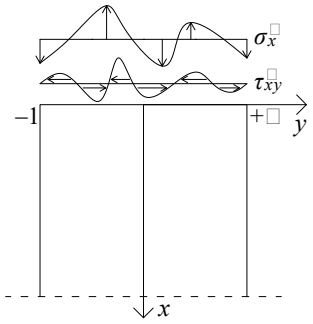

Figure 4: Semi-infinite strip

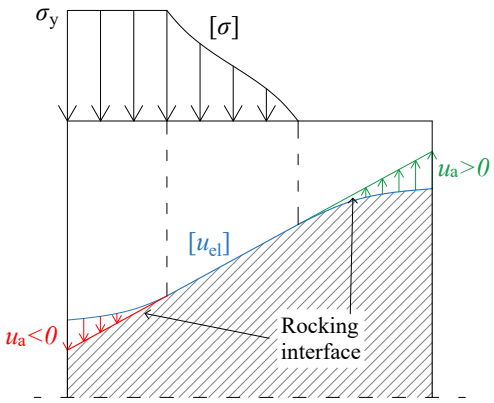

Figure 5: Normal stress distribution $[\sigma]$ acting on a rocking body. Elastic displacements due to this load, u_{el}, develop across the whole section (in blue), compressive additional displacements u_a develop across the yielded area (in red) and positive additional displacements u_a form between the rocking interface and the rocking body (in green). The shaded area corresponds to the deformed rocking body. Only deformations parallel to the loading are shown for clarity.

for cyclic loading due to arising inconsistencies between the plastic displacements and plastic strains, a different approach is presented in the following. For a given linear displacement distribution across the rocking end, $u_l(y)$, which corresponds to the planar rocking interface (Fig. 5), the real stress distribution at the rocking interface has to be determined, so that, for the produced elastic displacements, $u_{\text{el}}(y)$, the following conditions hold:

- $u_{\text{el}}(y) + u_{\text{pl}}(y) = u_l(y)$ for regions with $\sigma_y < \sigma(y) < 0$
- $u_{\text{el}}(y) + u_{\text{pl}}(y) \leq u_l(y)$ for regions with $\sigma(y) = 0$
- $u_{\text{el}}(y) + u_{\text{pl}}(y) \geq u_l(y)$ for regions with $\sigma(y) = \sigma_y$

where σ_y is the stress yield limit, $\sigma(y)$ is the normal stress at the fiber located at y and $u_{pl}(y)$ is the existing plastic displacement at this fiber, produced during previous cycles.

The additional displacements $u_a(y) = u_l(y) - u_{\text{el}}(y) - u_{\text{pl}}(y)$, needed in order the displacements match the given linear displacement distribution $[u_l]$, correspond to (i) the additional plastic elongations for the inelastic regions, where $u_a(y) < 0$, and (ii) the gap length between the body and the rocking base for the stress-free regions, where $u_a(y) > 0$ (Fig. 5). Therefore, for each fiber at location y, the unknown is either the normal stress, $\sigma(y)$ or the additional displacement, $u_a(y)$.

A number of control points, $\mathbf{Y}_w$, is chosen across the rocking interface, with normalized coordinates $-1 \leq y_w \leq 1$. Each of these points has an elastic stress, σ, or more conveniently an elastic strain, $\epsilon = \sigma/E$, and an additional displacement, u_a, normalized with respect to the semi-width of the member section, b. As previously described, these quantities are not independent of each other, since only one of them is unknown for each point y_w. Although quantities ϵ and u_a are not directly comparable with each other, a new dimensionless variable $w = \epsilon + u_a$ is introduced for algorithmic reasons, which is able to represent the whole allowable range of ϵ and u_a values at each fiber as follows:

$$\epsilon = \begin{cases} 0, \text{ if } w > 0 \\ w, \text{ if } \epsilon_y < w \leq 0 \\ \epsilon_y, \text{ if } w \leq \epsilon_y \end{cases} \tag{1}$$

and

$$u_a = \begin{cases} w, \text{ if } w > 0 \\ 0, \text{ if } \epsilon_y \leq w \leq 0 \\ w - \epsilon_y, \text{ if } w \leq \epsilon_y \end{cases} \tag{2}$$

where $\epsilon_y = \sigma_y / E$.

3 APPROXIMATE DETERMINATION OF REGION BOUNDARIES

By assigning a value of elastic strain, ϵ, or additional normalized displacement, u_a, at each control point across the rocking end, the corresponding strain and additional displacement distributions across the rocking end are created. However, by connecting the points of the aforementioned distribution with linear segments, regions are created that develop both elastic strains and additional displacements, which violates the assumptions taken into account, described above, unless specific points between the respective control points are chosen, corresponding to region boundaries with different behavior, where the additional displacements become zero and the elastic strains become either zero or equal to the yield strain.

This is why an approximate determination of the region boundaries is applied. Due to space reasons, the proof of the methodology is not given here, but can be found in [22]. The necessary region boundaries and correct strain and additional displacement distributions inside each interval are calculated as follows:

1. Calculate w' at the region boundaries:

$$w' = \begin{cases} w, \text{ if } w > 0 \\ w \dfrac{dy}{\pi}, \text{ if } \epsilon_y < w \leq 0 \\ w + \epsilon_y \left(\dfrac{dy}{\pi} - 1 \right), \text{ if } w \leq \epsilon_y \end{cases} \tag{3}$$

   where dy is the distance between the control points.

2. Draw the line connecting the aforementioned values.

3. Calculate the differences between all the linear segments of the plastic displacement distribution with the line connecting the plastic displacement values at the interval boundaries.

4. Add the opposite of the aforementioned deviant distribution to the line of step 2.

5. Determine the region boundaries from the points of the crossings of this curve with the horizontal lines corresponding to $w' = \epsilon'_y = \epsilon_y (dy/\pi)$ and $w' = 0$.

6. The regions between the aforementioned horizontal lines correspond to the correct modified strain or additional displacement distributions. The additional loads due to the nonlinearity of the strain distribution are calculated as the difference between the modified strain distribution, divided with (dy/π), from the line connecting the strain values at the interval boundaries.

4 CALCULATION OF DISPLACEMENTS

Convergence of the algorithm is achieved when the sum of the elastic, the additional and the plastic displacements equals the given target linear displacement distribution. This equality is checked explicitly only at the control points, $\mathbf{Y}_w$ and implicitly when region boundary points are formed between them, with the procedure described in the previous section.

Vector $\mathbf{U}_a$, calculated using Eq. (2), contains the additional displacements at the control points, while $\mathbf{U}_{pl}$ contains the plastic displacements induced at the control points from previous steps. The contribution of the elastic displacements induced by the loading is the most difficult to calculate and originates from three sources: The resultant forces at the rocking interface, the self-equilibrating normal stresses and the self-equilibrating shear stresses.

4.1 Displacements due to the resultant forces

Given the vectors $\mathbf{E}_s$ and $\mathbf{Y}_s$ of length n_s, containing the values of the elastic strain distribution at the respective coordinates, including those between the control points, the normalized axial force and the normalized moment at the rocking end are given by:

$$N_n = \frac{1}{2}\sum_{i=1}^{n_s-1}(y_{i+1}-y_i)(e_{i+1}-e_i) \tag{4}$$

$$M_n = \frac{1}{6}\sum_{i=1}^{n_s-1}(y_{i+1}-y_i)(2e_iy_i+e_iy_{i+1}+e_{i+1}y_i+2e_{i+1}y_{i+1}) \tag{5}$$

where e_i and y_i are the elements of vectors $\mathbf{E}_s$ and $\mathbf{Y}_s$ at entry i.

The displacement vector at the rocking end due to the resultant forces contribution, $\mathbf{u}_r = [\delta_r, \theta_{1r}]^T$, can be proven [22] that is given by the following equation:

$$\mathbf{u}_r = \begin{bmatrix} f_{r,11} & 0 \\ 0 & f_{r,22} - \dfrac{f_{r,23}\cdot f_{r,32}}{f_{r,33}} \end{bmatrix} \begin{Bmatrix} N_n \\ M_n \end{Bmatrix} + \begin{Bmatrix} 0 \\ \dfrac{f_{r,23}}{f_{r,33}}\theta_2 \end{Bmatrix} \tag{6}$$

where θ_2 is the given rotation at the end i of the element, $f_{r,11} = L/2$, $f_{r,22} = (3L)/(4b)$, $f_{r,23} = L^2/(4b^2) - a(1+\nu)$, $f_{r,32} = -(3L)/(4b)$ and $f_{r,33} = -L^2/(2b^2) - a(1+\nu)$.

4.2 Displacements due to the self-equilibrating shear stresses

If y_{cl} and y_{cr} are the boundaries of the compression zone, as determined by the approximate calculation of the region boundaries, since an equivalent parabolic shear stress distribution is considered between them, the maximum shear stress, normalized with respect to the modulus of elasticity, E, is:

$$t = \frac{3\,Q_n}{2\,(y_{cr}-y_{cl})} \tag{7}$$

where

$$Q_n = \frac{\theta_2 - f_{r,32}M_n}{f_{r,33}} \tag{8}$$

For given shear stress distribution boundaries, the displacements $\mathbf{u}_{tn} = [\delta_{tn}, \theta_{tn}]^T$ of the rocking end induced by a parabolic distribution with $t = 1$ can be calculated using the formulas

found in [22]. For the value of t calculated with Eq. (7), the respective vector containing the displacement parameters due to the self-equilibrating shear stresses is:

$$\mathbf{u}_t = t\ \mathbf{u}_{tn} \tag{9}$$

4.3 Displacements due to the self-equilibrating normal stresses

The contribution of the self-equilibrating normal stresses is the most cumbersome to calculate and is described in [22]. The procedure involves decomposing the normal stress distribution into triangular and trapezoidal normal loads. Afterwards, formulas for the calculation of the induced displacements due to these individual load shapes are employed, which result in a vector $\mathbf{U}_e$.

4.4 Target displacements

If $\mathbf{u}_n = [\delta, \theta_1, \theta_2]^T$ is the vector containing the element displacements in the natural coordinate system, namely the axial elongation, the chord rotation at the rocking end and the chord rotation at the other end, then a new vector $\mathbf{u}_{\text{tar}} = [\delta, \theta_1]^T$ is formed, which contains the two first elements of $\mathbf{u}_n$. These values describe the target linear displacement distribution of the rocking end, which must match the displacements produced by all the aforementioned contributions.

4.5 Combination of the control point displacements

The difference between the resultant and the target displacement vectors is finally defined as:

$$\mathbf{U}_d = \mathbf{U}_e + \mathbf{U}_a + \mathbf{U}_{pl} + \mathbf{C}\ \mathbf{u}_t + \mathbf{C}\ \mathbf{B}\ \mathbf{u}_r - \mathbf{C}\ \mathbf{B}\ \mathbf{u}_{\text{tar}} \tag{10}$$

with

$$\mathbf{C} = \begin{bmatrix} 1 & y_{w1} \\ 1 & y_{w2} \\ & \cdots \\ 1 & y_{w,n_w} \end{bmatrix} \tag{11}$$

and

$$\mathbf{B} = \begin{bmatrix} 1/b & 0 \\ 0 & 1 \end{bmatrix} \tag{12}$$

The algorithm converges if the norm of $\mathbf{U}_d$ is less than a convergence limit defined by the user. Usually, an iteration procedure is needed, in which a better estimation of $\mathbf{W}$ is derived in each step so that $\mathbf{U}_d$ fulfills the convergence criterion. After convergence is achieved, the forces and the respective stiffness matrix in the natural coordinate system are calculated as follows:

The produced forces in the natural coordinate system, $\mathbf{F}_n$, are calculated as:

$$\mathbf{F}_n = bdE \begin{bmatrix} 1 & 0 & 0 \\ 0 & b & 0 \\ 0 & -b & -L \end{bmatrix} \mathbf{F}_{nn} \tag{13}$$

where $\mathbf{F}_{nn} = [N_n, M_n, Q_n]^T$ is the vector containing the normalized rocking end forces.

The stiffness matrix in the natural coordinate system is derived as:

$$\mathbf{K}_n = \frac{D\mathbf{F}_n}{D\mathbf{u}_n} = \frac{\partial \mathbf{F}_n}{\partial \mathbf{u}_n} + \frac{\partial \mathbf{F}_n}{\partial \mathbf{W}} \frac{\partial \mathbf{W}}{\partial \mathbf{u}_n} \tag{14}$$

with

$$\frac{\partial \mathbf{W}}{\partial \mathbf{u}_n} = -\left(\frac{\partial \mathbf{U}_d}{\partial \mathbf{W}}\right)^{-1} \frac{\partial \mathbf{U}_d}{\partial \mathbf{u}_n} \tag{15}$$

5 EXAMPLES

5.1 Rocking body with constant vertical force

A free-standing rocking body with a constant vertical force on its top side (Fig. 6a) is examined first. The rocking body has height $H = 4$ m, width $B = 1$ m and thickness $d = 1$ m, modulus of elasticity $E = 30$ GPa and yield stress $\sigma_y = 20$ MPa and is loaded on its top with a vertical force $N = -2500$ kN. The whole body is modeled with one proposed macroelement with its rocking end at the bottom.

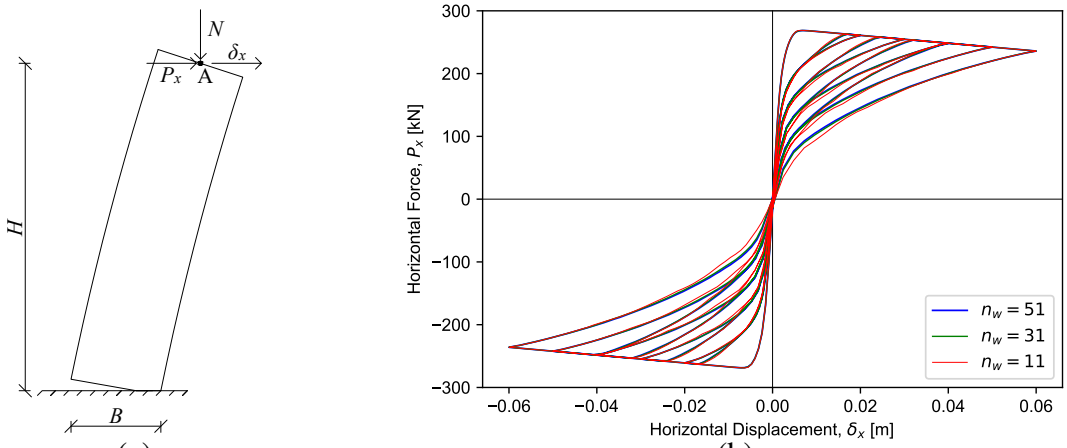

Figure 6: (a) Rocking body with constant vertical force model; (b) Rocking body with constant vertical force: Horizontal displacement versus applied horizontal force curves for various number of control points, n_w, used.

In Fig. 6b, the loading - unloading curves (applied horizontal force, P_x, versus horizontal displacement, δ_x) are shown for varying number of control points, n_w, used in the analysis. It can be seen that even the model with only 11 control points (red line) produces results that are very close to more dense control point configurations, meaning that the proposed algorithm can capture well the real deformation and stress distribution between control points.

In Fig. 7, the stress (blue curves) and plastic displacements (red curves) of the element at several steps during loading - unloading of the first half-cycle are presented. It can be seen that gradually the element yields, starting to develop plastic displacements, before reaching the maximum displacement of the quarter-cycle, where the stress distribution becomes almost rectangular.

It is interesting to note that the element continues to yield while returning to its original position, with the stresses gradually moving towards the center of the element, before becoming elastic again, i.e. the contact region does not decompress immediately during motion reversal. This means that the formation of plastic displacements does not stop at the maximum displacement, but continues during unloading at regions a little further from the base edge.

5.2 Restrained rocking concrete wall

A tendon restrained rocking concrete wall is discussed here and more specifically the model SRW_B examined in [23]. In brief, the rocking wall has height $H = 2.86$ m, width $B = 0.8$ m and thickness $d = 0.125$ m and is restrained with three prestressed tendons located at the center and about 0.2 m from the center. Regarding the material properties, concrete strength

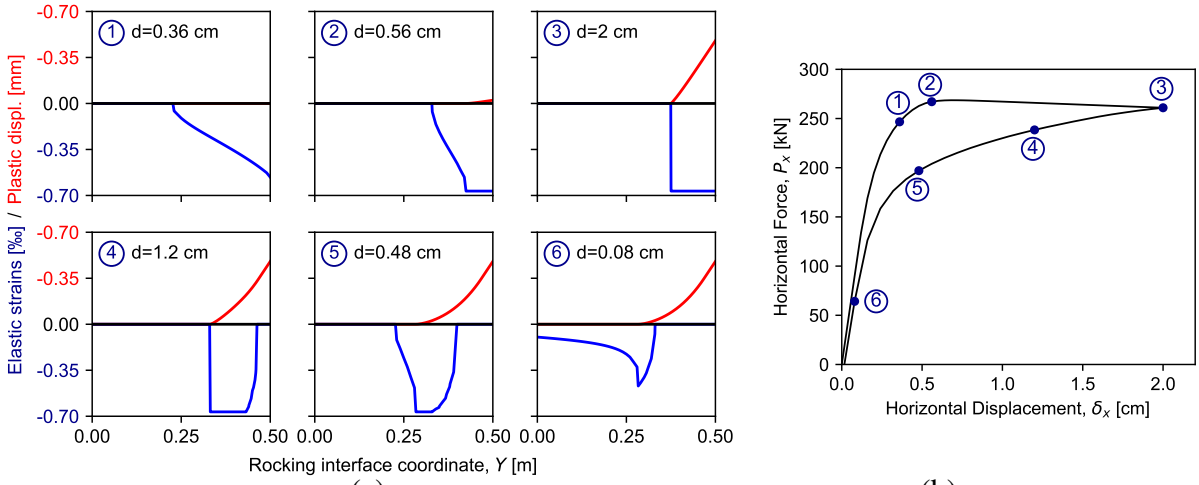

(a) (b)

Figure 7: (a) Stresses (blue curves) and plastic displacements (red curves) developing on the rocking interface before the end of the first half-cycle, where yielding occurs. The right half of the element section is shown. (b) Corresponding points on the loading - unloading curve.

is f_c = 35.0 MPa, its modulus of elasticity is assumed $E_c = 4700\sqrt{f_c}$ = 27.8 GPa, while the tendons have stiffness EA_t = 28529.0 kN/m and initial prestress 96.1 kN, which is reduced to 89.1 kN due to prestress losses equal to 7.3%. As mentioned in the paper, the prestress is further reduced with respect to the expected value as the lateral displacement increases, approximately following the simplified analysis by [24]. For this reason, in the present analysis the tendon stiffness was calibrated so that the sum of the tendon forces at the maximum lateral displacement matches the one measured at the experiment (about 440 kN). Additional weight is added on top of the wall equal to 31.35 kN, while the self-weight of the wall equals 7.15 kN.

The loading - unloading curves produced by the macroelement model is shown in Fig. 8, while the red line shows the envelope of the experimental response at the last cycle [23]. It can be seen that the results obtained with the proposed algorithm match well the experimental backbone curve. Comparing the results with those in [23], a notable discrepancy between the results can be seen during unloading for large displacements, where the experimental curve does not pass close to (0,0) as in the numerical analysis and contrary to what one would expect for typical rocking systems. This can be attributed to several reasons according to [23], such as prestress loss, debris underneath the wall or damage near the wall toes.

Although the bilinear material model assumed for the macroelement cannot account for the precise material response, such as that of concrete, the main characteristics of the cyclic response can be adequately predicted. Thus, the proposed macroelement can be used for a quick and adequately accurate estimation of the response of structural systems with rocking members.

6 CONCLUSION

In this paper, a macroelement able to predict the rocking response of inelastic members under cyclic loading is formulated. The usual assumption of linear strain distributions according to the technical theory of bending does not hold, due to the nonlinearity created by the partial loading of the rocking interface. However, since the contact region of the rocking interface remains planar, the proposed formulation involves checking the displacements instead of the strains at the control points of the discretized rocking interface.

In the regions of the rocking interface that remain elastic, the aforementioned displacements

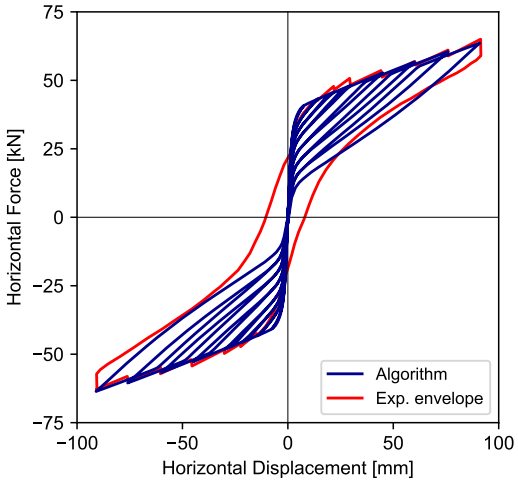

Figure 8: SRW_B response according to the proposed algorithm. The red line shows the envelope of the experimental response at the last cycle [23].

are caused by the contribution of the resultant forces, which is calculated according to the technical theory of bending, and the contribution of the self-equilibrating normal and shear stresses. Additionally, plastic displacements develop in inelastic regions, while the gap between the body and the rocking interface in non-contact regions is also taken into account.

The proposed macroelement formulation can be used to predict the response of rocking bodies included in structural configurations. The results show that the algorithm can predict the localization of the stress and plastic displacement distributions as the body rocks from one side to the other. In addition, comparison of the results produced for a typical rocking member configuration found in literature with the corresponding experimental data shows that the proposed algorithm can predict the cyclic response of yielding rocking bodies quite accurately, given the uncertainties of the experimental setups.

References

[1] G. W. Housner, "The behavior of inverted pendulum structures during earthquakes," *Bulletin of the seismological society of America*, vol. 53, no. 2, pp. 403–417, 1963.

[2] I. N. Psycharis and P. C. Jennings, "Rocking of slender rigid bodies allowed to uplift," *Earthquake Engineering & Structural Dynamics*, vol. 11, no. 1, pp. 57–76, 1983.

[3] A. K. Chopra and S. C.-S. Yim, "Simplified earthquake analysis of structures with foundation uplift," *Journal of Structural Engineering*, vol. 111, no. 4, pp. 906–930, 1985.

[4] N. Makris and D. Konstantinidis, "The rocking spectrum and the limitations of practical design methodologies," *Earthquake engineering & structural dynamics*, vol. 32, no. 2, pp. 265–289, 2003.

[5] E. G. Dimitrakopoulos and M. J. DeJong, "Revisiting the rocking block: closed-form solutions and similarity laws," in *Proceedings of the Royal Society of London A: Mathematical, Physical and Engineering Sciences*, vol. 468, pp. 2294–2318, The Royal Society, 2012.

[6] S. Acikgoz and M. J. DeJong, "The interaction of elasticity and rocking in flexible structures allowed to uplift," *Earthquake Engineering & Structural Dynamics*, vol. 41, no. 15, pp. 2177–2194, 2012.

[7] N. Makris and M. F. Vassiliou, "Planar rocking response and stability analysis of an array of free-standing columns capped with a freely supported rigid beam," *Earthquake Engineering & Structural Dynamics*, vol. 42, no. 3, pp. 431–449, 2013.

[8] A. I. Giouvanidis and E. G. Dimitrakopoulos, "Nonsmooth dynamic analysis of sticking impacts in rocking structures," *Bulletin of Earthquake Engineering*, vol. 15, no. 5, pp. 2273–2304, 2017.

[9] N. M. Priestley, S. Sritharan, J. R. Conley, and S. Pampanin, "Preliminary results and conclusions from the PRESSS five-story precast concrete test building," *PCI journal*, vol. 44, no. 6, pp. 42–67, 1999.

[10] S. Lagomarsino, "Seismic assessment of rocking masonry structures," *Bulletin of earthquake engineering*, vol. 13, no. 1, pp. 97–128, 2015.
[11] D. Kalliontzis and A. Schultz, "Improved estimation of the reverse-cyclic behavior of fully-grouted masonry shear walls with unbonded post-tensioning," *Engineering Structures*, vol. 145, pp. 83–96, 2017.
[12] Y. C. Kurama, S. Sritharan, R. B. Fleischman, J. I. Restrepo, R. S. Henry, N. M. Cleland, S. Ghosh, and P. Bonelli, "Seismic-resistant precast concrete structures: state of the art," 2018.
[13] H. Roh and A. M. Reinhorn, "Analytical modeling of rocking elements," *Engineering Structures*, vol. 31, no. 5, pp. 1179–1189, 2009.
[14] C. B. Barthes, *Design of Earthquake Resistant Bridges Using Rocking Columns*. PhD thesis, University of California, Berkeley, California, United States, 2012.
[15] A. Penna, S. Lagomarsino, and A. Galasco, "A nonlinear macroelement model for the seismic analysis of masonry buildings," *Earthquake Engineering & Structural Dynamics*, vol. 43, no. 2, pp. 159–179, 2014.
[16] M. F. Vassiliou, K. R. Mackie, and B. Stojadinović, "Dynamic response analysis of solitary flexible rocking bodies: modeling and behavior under pulse-like ground excitation," *Earthquake Engineering & Structural Dynamics*, vol. 43, no. 10, pp. 1463–1481, 2014.
[17] M. F. Vassiliou, K. R. Mackie, and B. Stojadinović, "A finite element model for seismic response analysis of deformable rocking frames," *Earthquake Engineering & Structural Dynamics*, 2016.
[18] S. Bracchi, A. Galasco, and A. Penna, "An improved macroelement model accounting for energy dissipation in in-plane flexural behavior of masonry walls," in *Proceedings of the 16th world conference on earthquake engineering, Santiago, Chile*, pp. 9–13, 2017.
[19] E. Avgenakis and I. N. Psycharis, "Modeling of rocking elastic flexible bodies under static loading considering the nonlinear stress distribution at their base," *Journal of Structural Engineering*, vol. 143, no. 7, p. 04017051, 2017.
[20] E. Avgenakis and I. N. Psycharis, "A new computational approach for the rocking response of deformable bodies considering material nonlinearity," in *Proc., 6th ECCOMAS thematic conference COMPDYN, Rhodes, Greece, June 2017*, 2017.
[21] E. Avgenakis and I. N. Psycharis, "Analytical expressions for the nonlinear displacement distribution of the semi-infinite strip - application to deformable rocking bodies," *International Journal of Solids and Structures*, 2019, Under review.
[22] E. Avgenakis and I. N. Psycharis, "Modeling of inelastic rocking bodies under cyclic loading," *Journal of Engineering Mechanics*, 2019, Under review.
[23] K. Twigden, S. Sritharan, and R. Henry, "Cyclic testing of unbonded post-tensioned concrete wall systems with and without supplemental damping," *Engineering Structures*, vol. 140, pp. 406–420, 2017.
[24] S. Aaleti and S. Sritharan, "A simplified analysis method for characterizing unbonded post-tensioned precast wall systems," *Engineering Structures*, vol. 31, no. 12, pp. 2966–2975, 2009.

COMPDYN 2019
7th ECCOMAS Thematic Conference on
Computational Methods in Structural Dynamics and Earthquake Engineering
M. Papadrakakis, M. Fragiadakis (eds.)
Crete, Greece, 24-26 June 2019

A PSEUDO THREE-DIMENSIONAL MULTI-SLICE NUMERICAL MODEL TO SIMULATE WIND-INDUCED VIBRATION OF THIN-WALLED ROOF SYSTEMS

Samir Chawdhury[1] **and Guido Morgenthal**[2]

[1] PhD Candidate, Faculty of Civil Engineering, Chair of Modelling and Simulation of Structures,
Bauhaus University Weimar, Marienstrae 13, 99423 Weimar, Germany
e-mail: samir.chawdhury@uni-weimar.de

[2] Professor, Faculty of Civil Engineering, Chair of Modelling and Simulation of Structures,
Bauhaus University Weimar, Marienstrae 13, 99423 Weimar, Germany
e-mail: guido.morgenthal@uni-weimar.de

Keywords: Wind–Induced Vibration, Pseudo 3D Multi-Slice Algorithm, Partitioned Approach, Vortex Methods, Thin-walled Roof System.

Abstract. *The paper presents a partitioned extension of vortex particle methods (VPM) in the context of pseudo three-dimensional (3D) multi-slice model to simulate wind-induced vibration of thin structural elements like membrane roof system. The fluid dynamics is analysed by using a pseudo-3D VPM. The immersed boundary methods are used to simulate the complex flow around deformable boundaries. The structural analysis is carried out using the superposition of the linear uncoupled vibration modes because of its efficiency to handle small displacement problems. Finite element model is used to extract the natural vibration modes of the structure. The equation of motion is solved at the mid-surface of thin element. At each time step, the pressures on the surface panels on each slice are projected to the structural nodes. Once the structural analysis is performed for a time step, the new positions and velocity of the surface panels are calculated from the nodal structural solution to update the boundary conditions. For the validation of the coupled solver, it has been utilized here to identify the critical wind speed at which an inverted cantilever plate exhibits large amplitude flapping. In contrast to a conventional flag configuration, a flag with a free leading edge and clamped trailing edge, an inverted cantilever flag shows unstable large amplitude vibration in axial flow. The identified critical wind speed is found to be in very good range when compared with the literature. This mentioned benchmark case is analysed using the coupled solver considering different number of slices, and the identification of the critical wind speed is found satisfactory for all cases. The solver is used further to simulate a skewed inverted cantilever, which is modified over the reference system, in order to simulate the differential displacement along the slices since the vortex induced forces varies along the slices. Finally, the dynamic response of a cantilever roof system which is fixed at the base and hinged in two sides is analysed under different incoming wind speeds.*

1 INTRODUCTION

Fluid-structure interaction (FSI) problems are frequently encountered in many areas of civil, mechanical, aerospace and biomechanical engineering, such as the aeroelastic analysis of long-span bridges, tall buildings, and lightweight structures, the stability analysis of airplane wings, the flow-induced vibration of marine risers and floating platforms, the hemodynamics and blood vessel dynamics [1, 2, 3]. In recent years, the use of membrane and umbrella-type has gained increasing popularity [4]. They are extremely light-weight and the flexible nature makes them prone to destructive aeroelastic effects. The numerical methods to solve FSI problems can be classified as monolithic and partitioned. The monolithic method is the direct approach to solve the complete nonlinear algebraic equations, and hence, it is highly robust and unconditionally stable [5]. The partitioned approach, in contrast, offers software modularity and allows synthesizing independent computational schemes for fluid and structure subsystems. Moreover, the recent advancements and reduction in computational costs for modelling of both fluid and solid structures have made the partitioned schemes more popular for simulating FSI problems [6, 7]. The partitioned approaches can be classified into two types: the loose coupling approach and the strong coupling approach depending on the satisfaction of the coupling conditions. The Arbitrary Lagrangian Eulerian (ALE) approach and Immersed Boundary (IB) methods are two general approaches for simulating flow around deformable boundaries.

This paper presents a partitioned new extension of vortex particle methods (VPM) in the context of pseudo three-dimensional (3D) multi-slice numerical model to simulate FSI of thin structural elements such as the thin membrane type roofs. The partitioned methods are often used in FSI simulations for their flexibility of using different existing solvers for fluid and structure models. Here, the pseudo-3D vortex particle method (VPM) is used for analysing the fluid dynamics [8, 9, 10, 11, 12]. A two-dimensional (2D) fully coupled FSI model was presented in [13] for simulating non-linear aeroelastic instabilities. The presented method is a further extension in 3D. The difference between the existing and currently implemented pseudo-3D VPM is presented schematically in Fig. 1. The immersed boundary methods are used to simulate the complex flow around deformable boundaries. The structural analysis is carried out using the superposition of the linear uncoupled vibration modes because of its efficiency to handle small displacement problems of large system. A finite element solver is used to model and extract the natural vibration modes of the thin-walled structural systems. The equation of motion is formulated and solved at the mid-surface of the thin element. At each time step, the pressures on the surface panels on each slice are calculated in the flow solver. An in-house python code is developed to project the surface pressure to the structural nodes. The projected nodal forces from each slice are applied to the structural nodes in the global coordinate system. Once the structural analysis is performed for a time step using the Newmark-Beta method, the new positions of the surface panels are calculated from the nodal displacements. The panel velocities are calculated from the nodal velocities in order to update the velocity boundary conditions in the flow solver.

For the validation of the coupled solver, it has been utilized here to identify the critical wind speed at which an inverted cantilever plate exhibits large amplitude flapping [17, 18]. In contrast to a conventional flag configuration, a flag with a free leading edge and clamped trailing edge, an inverted cantilever flag shows unstable large amplitude vibration in axial flow. It has been observed as vortex-induced vibration (VIV) in literature. This mentioned benchmark case is analysed using the coupled solver considering different number of slices, and the identification of the critical wind speed is found satisfactory for all cases. The solver is used further to

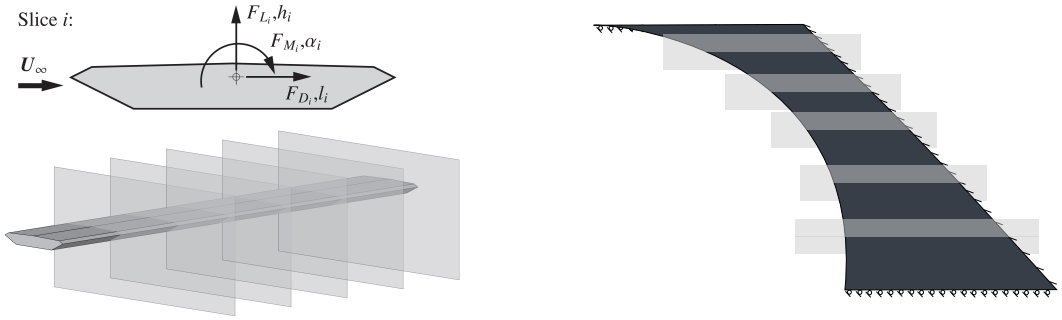

(a) (b)

Figure 1: Schematic representation of the difference between existing and new pseudo 3D VPM-based coupled solver: (a) existing pseudo 3D model analyses flexible line-like structures such as the long-span bridges. The structural dynamic calculations are performed by using the forces from 2D simulation slices with rigid cross sections. On the other hand, the newly extended VPM model (b) analyses thin-walled surface-type flexible element such as membrane roof systems considering the deformable geometry at the level of 2D simulation slices.

simulate a skewed inverted cantilever, which is modified over the reference system, in order to simulate the differential displacement along the slices since the vortex induces forces varies along the slices. Finally, the dynamic response of a cantilever roof system which is fixed at the base and hinged in two sides is analysed under different incoming wind speeds.

2 A PSEUDO-3D ALGORITHM FOR FLUID–STRUCTURE INTERACTION

2.1 Fluid solver

The flow solver uses simplified vorticity description of fundamental Navier–Stokes (NS) equations. For incompressible flow of a viscous fluid, the vorticity transport equation for 2D flow in a bounded domain $\mathcal{D}$ can be expressed as follows:

$$\frac{\partial \omega}{\partial t} + (\boldsymbol{u} \cdot \nabla)\,\omega = \nu \nabla^{\mathbf{2}} \omega. \tag{1}$$

where the vorticity $\boldsymbol{\omega}$ is the curl of velocity field $\boldsymbol{u}(\boldsymbol{x}, t)$ such that $\boldsymbol{\omega} = \nabla \times \boldsymbol{u}$, and ν is the kinematic viscosity. For inviscid flow Eq. (1) can be rewritten in substantial derivative notation such that $\mathrm{D}\omega/\mathrm{D}t = 0$. It allows the use of grid-less numerical scheme and discretization of particle elements in Lagrangian manner. The velocity field can be expressed in terms of stream function $\boldsymbol{\Psi}$ such that $\boldsymbol{u} = \nabla \times \boldsymbol{\Psi} + U_\infty$, and curl of it results in Poisson equation $\nabla^2 \boldsymbol{\Psi} = -\omega$. Greens functions are used to obtain the velocity distribution from vorticity field by solving the Poisson equation. By taking curl of $\boldsymbol{\Psi}$, the velocity field of a point in fluid domain $\mathcal{D}$ is computed using Biot-Savart relation

$$\boldsymbol{u}(\boldsymbol{x}_p) = \boldsymbol{U}_\infty - \frac{1}{2\pi} \int_{\mathcal{D}} \frac{\omega(\boldsymbol{x_0}) \times (\boldsymbol{x_0} - \boldsymbol{x_p})}{|\boldsymbol{x}_0 - \boldsymbol{x}_p|^2}\, \mathrm{d}\mathcal{D}_0. \tag{2}$$

The 2D vortex method is based on the discretization of the vorticity field by a finite sum of N_p Lagrangian particles located at $\boldsymbol{x}_p(t)$ as follows:

$$\omega(\boldsymbol{x}, t) = \sum_{p=1}^{N_p} \delta(\boldsymbol{x} - \boldsymbol{x}_p(t)) \Gamma_p, \tag{3}$$

where $\omega(\boldsymbol{x}, t)$ is the vorticity at position $\boldsymbol{x}$ and time t, δ is the Dirac delta function, Γ_p is the strength of pth particle, and $\boldsymbol{x}_p(t)$ is the position. The use of Eq. (3) in Eq. (2) yields

$$\boldsymbol{u}(\boldsymbol{x}_p) = \boldsymbol{U}_\infty - \frac{1}{2\pi}\sum_{p=1}^{N_p} \frac{e_z \times (\boldsymbol{x}_p - \boldsymbol{x})}{|\boldsymbol{x}_p - \boldsymbol{x}|^2}\Gamma_p = \boldsymbol{U}_\infty - \sum_{p=1}^{N_p} \boldsymbol{K}(\boldsymbol{x}_p - \boldsymbol{x})\Gamma_p, \tag{4}$$

where $\boldsymbol{K}$ is the velocity kernel. In the present implementation of the fluid solver, a hybrid particlemesh Vortex-In-Cell algorithm is used for smooth projection of the vorticity carried by the particles onto a regular mesh. The immersed interface techniques utilize fast Fourier transforms (FFT) on the regular mesh and enforce the appropriate boundary conditions on immersed interfaces to solve the Poisson equation efficiently. A Particle–Particle Particle–Mesh (P^3M) algorithm is employed to resolve sub-grid scales using an influence matrix technique in the presence of immersed interfaces. The solver uses the stochastic Random Walk Method for modelling the diffusion of the flow.

In order to perform pseudo-3D simulation with deformable bodies, the kinematic velocity boundary condition is enforced at each 2D simulation slice by applying boundary element technique. At the solid surface, the boundary condition $u\left(x_B\right) \cdot n_B = 0$ is enforced such that the surface is impermeable where n_B is the unit normal vector. The geometry of immersed bodies is discretized assuming piecewise linear panels of approximately uniform length. This creates a polygon of N_l panels of lengths Δ_{s_i}. The surface vorticity is discretized as sheets of linearly varying vorticity along the panels. The bound vortices are obtained from equation $M_i\gamma_0 = b$, in which M_i is the influence matrix that contains the influence coefficients in order to describe the mutual induction of the vortex sheets while the right-hand side (b) contains all external influences such as the induced velocities on the panels from the free stream contribution. The influence matrix is constant for non-deforming bodies undergoing solid body motion. However, the influence matrix for deforming bodies should be recalculated based on the updated surface geometry. The surface vorticity found by solving this system is assigned to the control points on the boundary and subsequently released into the flow. The section forces for aerodynamic analysis can be calculated by integrating pressures on the surface panels. More details about the solver can be found in [8, 9] while its specific implementations can be found in [10, 14, 15, 13, 16].

2.2 Structural equations

The superposition of generalized vibration modes is a powerful technique for performing dynamic response analyses of linear structures. It can reduce the computational time significantly. A system with few degrees of freedom (DOFs) can be solved using full system. However, for large systems, especially when the displacements are linear it is usually advantageous to transform the equation of motion to a smaller set of equations by expressing the displacements in terms of the first few natural vibration modes ϕ_n of the undamped system. The basic assumption in mode superposition is that the nodal displacements of the system are approximated by a linear combination of the first j eigenmodes such that

$$\boldsymbol{d}(t) = \sum_{n=1}^{j} \phi_n \boldsymbol{q}_n(t), \tag{5}$$

Here, $\boldsymbol{q}_n(t)$ are the modal amplitudes. The equation of motion related to time dependent forces can be expressed in modal coordinates as follows

$$\mathbf{M}\phi_j\ddot{d}_j + \mathbf{C}\phi_j\dot{d}_j + \mathbf{K}\phi_j d_j = f_{ext}\left(t\right), \tag{6}$$

pre-multiplying with ϕ_j^{T} gives

$$\phi_j^{\mathrm{T}}\mathbf{M}\phi_j\ddot{d}_j + \phi_j^{\mathrm{T}}C\phi_j\dot{d}_j + \phi_j^{\mathrm{T}}\mathbf{K}\phi_j d_j = \phi_j^{\mathrm{T}} f_{ext}\,(t)\,, \tag{7}$$

where ω_j is the modal circular natural frequency, ξ_j is the modal damping ratio, ϕ_j is the mode shape, the subscript j is the mode number and f_L is the lift force vector, respectively. The equation of motion can be written as following

$$\tilde{\mathbf{M}}\ddot{d} + \tilde{\mathbf{C}}\dot{d} + \tilde{\mathbf{K}}d = \tilde{\mathbf{P}}(t), \tag{8}$$

where

$$\tilde{\mathbf{M}} = \phi^{\mathrm{T}}\mathbf{M}\phi \qquad \tilde{\mathbf{C}} = \phi^{\mathrm{T}}\mathbf{C}\phi \qquad \tilde{\mathbf{K}} = \phi^{\mathrm{T}}\mathbf{K}\phi \qquad \tilde{\mathbf{P}(\mathbf{t})} = \phi^{\mathrm{T}} f_{ext}\,(t) \tag{9}$$

with $\tilde{\mathbf{M}}$, $\tilde{\mathbf{C}}$, and $\tilde{\mathbf{K}}$ being diagonal matrices. In dynamic analysis, it is a common choice to provide the relative damping for each mode directly since it allows the calculation of the response using the superposition of uncoupled modal responses. The use of modal damping ratios gives a more control to assign a higher damping value if, for physical reasons, they are expected to be strongly damped. The damping of a multi degrees of freedom (MDOF) system with N DOFs the damping matrix can be expressed in terms of the modal damping ratios ξ_n with $(n = 1, \ldots, N)$. In principle, the procedure can be explained by considering the complete diagonal matrix of generalized damping coefficients, given by pre- and post-multiplying the damping matrix by the mode shape matrix:

$$\tilde{\mathbf{C}} = \phi^{\mathrm{T}}\mathbf{C}\phi = diag(2\xi_1\omega_1 M_1, ..., 2\xi_n\omega_n M_n) \tag{10}$$

For classically damped systems, the square matrix $\tilde{\mathbf{C}}$ is diagonal. A numerical time integration scheme can be used to solve the system under external forces in the time domain. The implicit Newmark time integration with is used with the average acceleration method (γ = 0.5; β = 0.25), which is well known "unconditionally stable condition" irrespective of time step for linear problems. The structural element is considered linear according to the constitutive law.

2.3 Projection of the surface loads to the structural nodes at each 2D slice

The equation of motion of the 3D thin-walled system is formulated and solved at the mid-surface of the thin element. At each simulation slice of the multi-slice analysis, it is necessary to map the fluid pressure on the boundary panels to the structural nodes (Fig. 2). Moreover, to update the boundary conditions at the interface, it is also necessary to map the displacement and velocity of structural nodes from the mid-surface to boundary nodes. It is challenging to calculate the loads on the structure nodes imparted by fluid stresses at the fluid–structure interface. It is because at every point on the boundary panels there is a unique normal vector that points toward the fluid side of the interface, namely the positive wall normal vector. In other words, the fluid pressures acting toward the fluid side of the interface are positive. For such a case, it is readily apparent that at each FE node at the mid-surface in the local coordinate system (LCS) of the structure, it has both positive and negative wall normal vectors pointing toward the fluid side of the interface. Here, the FE nodes and elements are used to calculate and project the surface loads to the structural nodes. At first, the elements and the surface panels are defined as vectors as shown in Fig. 2. Importantly, the surface panels of each immersed body in presented VPM solver have always been defined in anticlockwise orientation. The definition of FE has no restriction about the direction. An iterative search is perform over the surface panels of an immersed body to find a corresponding element, at which the panel pressures of the interface

should be projected. The projection of the panel pressures on FE nodes is performed in LCS. The angle between the vectors of the surface panel and the corresponding element decides the position of the panel, which means above or below, corresponding to element in LCS. The same direction of the panel vector and element vector indicates the position of the panel below the element, and vice-versa. When the projection of the loads for each panel to the FE nodes are made, the force vector is transformed into the global coordinate system.

2.4 Fluid–structure coupling

The fluid and structural equations are coupled with each other through the coupling of boundary conditions at fluid–structure interface Σ to satisfy the continuity of displacement $\mathbf{d}$, velocity $\mathbf{v}$ and equilibrium of stresses such that

$$\mathbf{d}_\mathbf{s}^\mathbf{\Sigma} = \mathbf{d}_\mathbf{f}^\mathbf{\Sigma}, \quad \mathbf{v}_\mathbf{s}^\mathbf{\Sigma} = \mathbf{v}_\mathbf{f}^\mathbf{\Sigma}, \quad \mathbf{f}_\mathbf{s}^\mathbf{\Sigma} = \sigma_\mathbf{f}^\mathbf{\Sigma}.\mathbf{n}. \tag{11}$$

Here, no-penetration, velocity boundary condition, and traction condition are satisfied at the fluid–structure interface to couple VPM and nonlinear structural dynamics solver. The pressures on the solid bodies are computed from the vorticity flux. The presented partitioned solver is based on loosely coupled iteration which is displayed schematically in Fig. 3. For FSI problems of large mass ratio ($\rho_s \gg \rho_f$), the added mass effect of the fluid is not significant and the

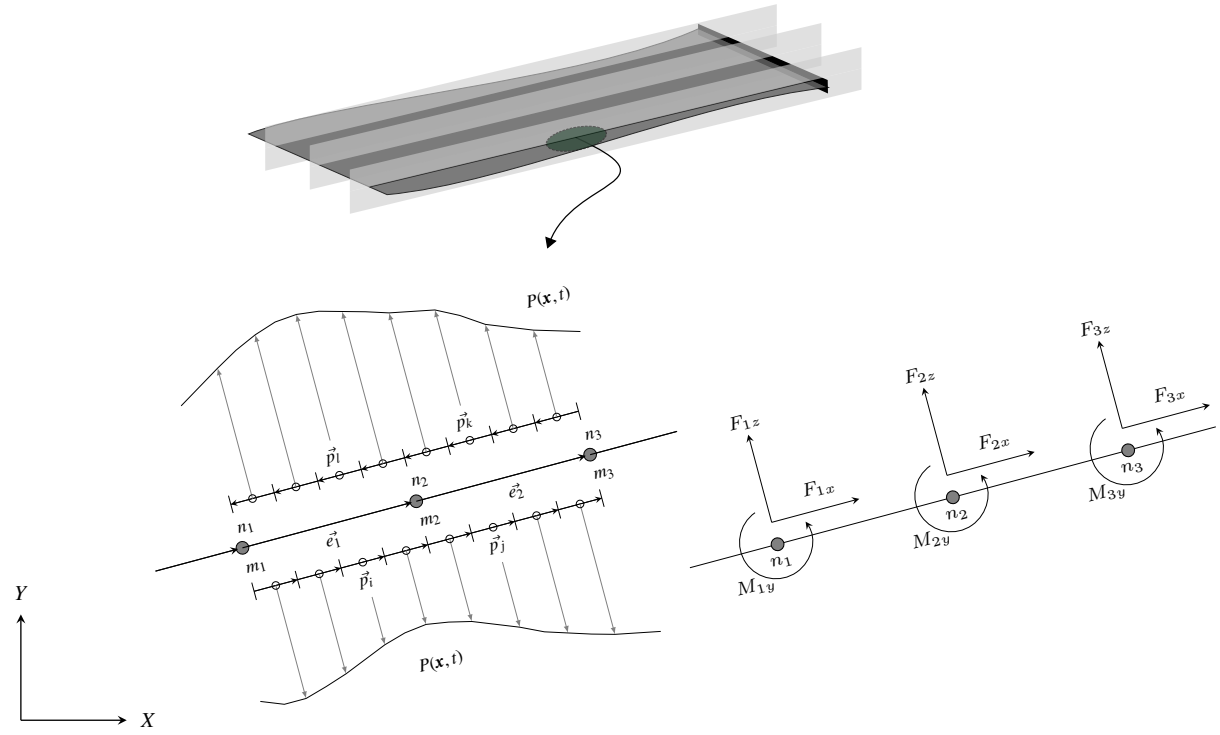

Figure 2: A partial and schematic presentation of thin-wall immersed body in fluid flow. The finite element (FE) formulation is used at the mid-surface to model the structural motion. The vectors of elements and the surface panels are presented as $\vec{e}$ and $\vec{p}$, respectively. Here, the filled circles (•) represents the FE nodes, numbered as n_i, at which the surface loads has to be projected. The unfilled circles (○) shows the nodes associated with the immersed boundary or surface panels. In local coordinate of an element at mid-surface, the direction or the angle between element and panel vectors are used to identify the position of the panel with respect to the element. The projection of the surface loads from the boundary panels is performed to the FE nodes in local coordinate (x-y) and then transformed into global coordinate (X-Y).

problem can be solved with staggered partitioned scheme such as in case of aeroelasticity. Assuming that the displacements and velocities of the solid structure $\mathbf{d_s}$, $\mathbf{v_s}$ are known at time step t_i, and the boundary conditions are projected accordingly. For time step t_{i+1}, the flow solver VPM recalculate and distribute the surface vorticity based on the updated boundary conditions. It computes the pressure distribution on the surface panels which are then interpolated at the FE nodes as nodal forces $\mathbf{f_s}$ for time step t_{i+1}. After achieving the nodal solution from the structure solver, the panel displacements and velocities are calculated and projected back to the interface for updating boundary conditions. This update of information to the flow solver is performed only at the global time step of the coupled simulation.

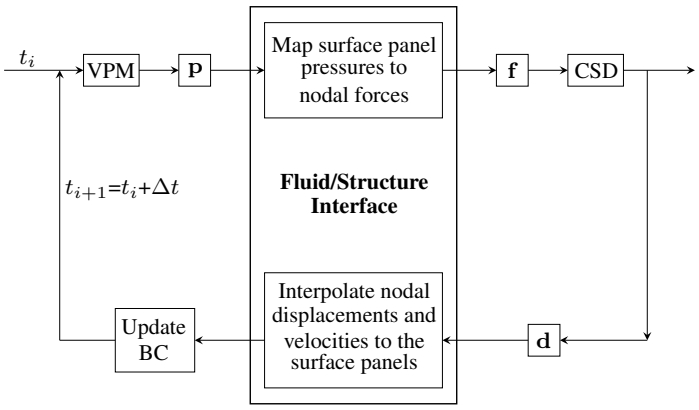

Figure 3: Schematic representation of the coupled numerical algorithm: At each time step, the pressure ($\mathbf{p}$) on the surface panels, which is calculated from the flow solver VPM, is mapped to the nodal force vector ($\mathbf{f}$) for finite element method (FEM) applied at the mid-surface. The panel displacements and velocities are calculated from the nodal displacements in order to update the boundary conditions.

3 FLAPPING MECHANISMS OF INVERTED CANTILEVER PLATES

In contrast to a cantilever plate in conventional flag configuration, the inverted flag or cantilever with a free leading edge and a clamped trailing edge displays large-amplitude flapping over a finite band of wind speeds [17]. Extensive studies on several influential parameters were performed in [18] to establish the flapping mechanism of an inverted cantilever plate. The schematic configuration of an inverted cantilever in axial flow is shown in Fig. 4(a). The typical flapping pattern is shown in Fig. 4(b). The simulation of the inverted cantilever in the context of multi-slice coupled model is shown schematically in Fig. 4(c). It is a non-linear large displacement problem. Though the presented model is based on linear analysis, the validation of the solver is performed in terms of identification of the wind speed at which large amplitude flapping initiates.

3.1 Validation of multi-slice model on a reference inverted cantilever

3.1.1 Flapping regions

The flow-induced vibration of elastic inverted cantilevers has drawn significant attention because of its complicated coupling mechanisms. The flapping of inverted cantilever was identified in [18] as two quasi-steady regimes, which are the straight mode and fully deflected mode, and a limit-cycle flapping mode with large amplitude that appears in between two quasi-steady regimes (Fig. 4(b)). The stability of inverted flags were explained in [18] in terms of two non-

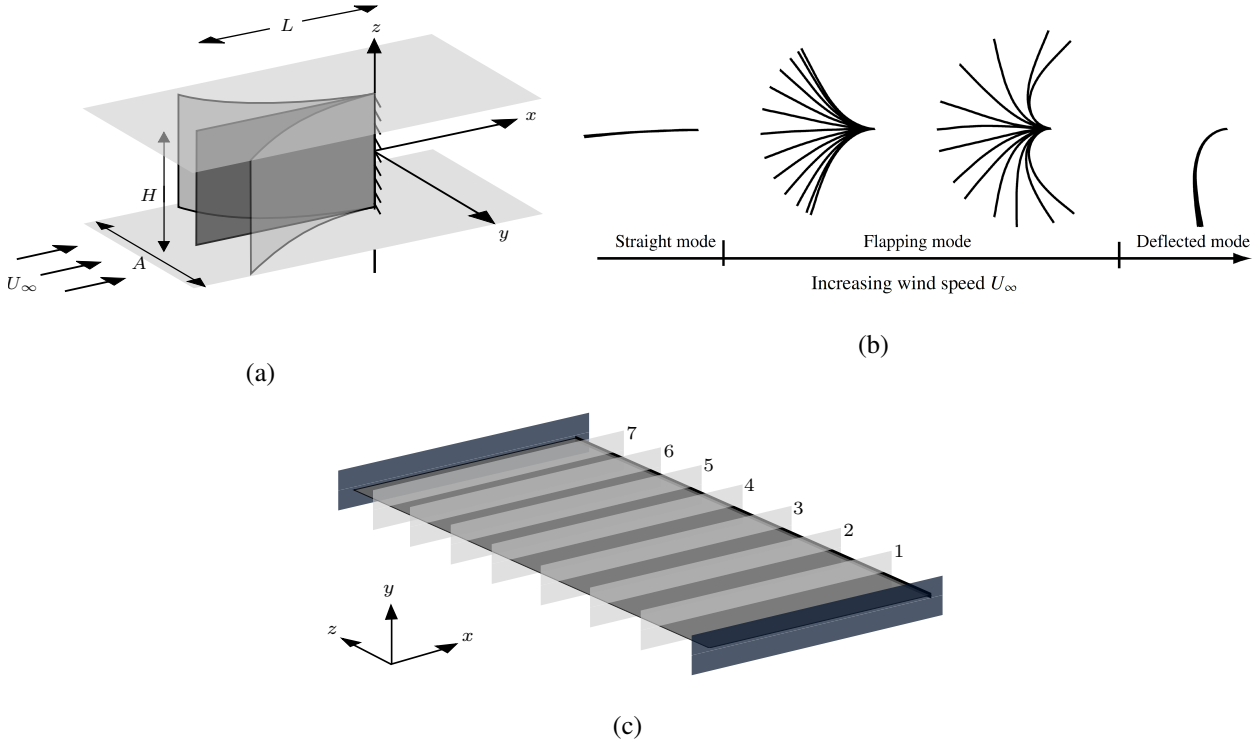

Figure 4: Pseudo 3D simulation of a cantilever plate in inverted flag configuration: (a) Schematic of an inverted cantilever plate (length L × height H). A is the peak-to-peak amplitude in y-direction. The presented coupled numerical model ignores the edge-effects of the cantilever plate, and it is visualized here by the confinement of the cantilever system in between the walls. The characteristic regions of dynamic motion of an inverted cantilever are shown in (b). The schematic multi-slice arrangement of the system for the coupled solver is shown in (c).

dimensional dynamic parameters:

$$\mu = \frac{\rho_f L}{\rho_s h}, \tag{12}$$

$$\kappa = \frac{\rho U_\infty^2 L^3}{D}, \tag{13}$$

where μ and κ specifies the mass ratio and dimensionless flow speed, respectively. The eigenvalue analysis was performed for infinite aspect ratio showed that the stability of an inverted cantilever is lost at zero frequency when $\kappa = 1.85$. The bifurcation of the inverted flag at zero frequency indicates its independence on μ. The flapping mechanism of the inverted flag was established as a vortex-induced vibration (VIV). The aspect ratio was shown to be an influential parameter. A plate with a small aspect ratio in a steady flow allows to generate edge vortices along and across the flow direction which reduces the overall lift. Therefore the bifurcation is primarily affected by the aspect ratio. However, the influences diminish with the increase in aspect ratio and converge to a bifurcation point $\kappa = 1.85$ for an infinite aspect ratio.

3.1.2 Pseudo 3D multi-slice simulation

Variations in cross section are common in civil structures. The fully coupled 3D simulations are computationally very expensive, in particular when it is necessary to resolve the flow around complex structural geometries with small details such as hand rails, guide vanes and wind shields in the case of bridges. The aerodynamic analysis of line-like thin-walled structure

is proposed to be represented as several 2D simulation slices along the structure. The in-plane forces and displacements are coupled to a 3D dynamic representation of the structure in terms of superposition of the natural vibration modes.

In the following, the dynamics of a reference inverted cantilever plate which was studied in [18] has been investigated numerically using the presented multi-slice coupled model. It is a very simple type of line-like thin-walled system. However, it is particularly chosen because of its complex aeroelastic interaction and large-amplitude flapping. The physical and geometrical properties of the plate are listed in Table 1. The coupled simulation is performed using 7 slices, as shown in Fig. 4(c). For the structural solver, the cantilever system is modelled first using a finite element solver in order to obtained the undamped natural vibration modes. The cantilever plate is discretized into 102 shell elements along the length while 8 elements along the width. The natural vibration modes and corresponding frequencies of the modelled system are shown in Fig. 5. Within the flow solver at each simulation slice, the non-dimensional size of the boundary elements is chosen such that $\Delta_s/h = 3.8462$ which results in 206 panels. The instantaneous number of particles in the flow domain for each slice is estimated approximately between 65,000 and 75,000. During the coupled analysis, at each simulation slice the panel pressures are integrated to the structural nodes. Each slice is assigned an effective width based on the selection of the slice locations. Finally, the inverted cantilever plate is simulated under different wind speeds. No edge-effects are considered in the analysis. Concerning edge-effects, the consideration of a 2D plate with infinite aspect ratio is analogous to the consideration of finite plate confined between the side walls (Fig. 4(a)).

The tip displacement of the cantilever at the middle slice (slice number 4) are displayed in Fig. 6 for both dimensional and non-dimensional incoming flow speeds. The time histories of the tip displacements for all the slices are found relatively same. There has been very negligible differential displacement in between the slices. The bifurcation is observed immediately after non-dimensional flow speed $\kappa = 1.85$. This is an agreement with the results from [18] since the present model doesn't consider the effect of vortices from the edges across the flow direction. This result indicates that the bifurcation of small aspect ratio is still possible at $\kappa = 1.85$ if the sides of the plates are perfectly isolated. The response frequencies of the cantilever for the periodic motion follows the frequency of the vortex shedding, which is found approximately to be 6.5 Hz. It is almost the half of the first natural frequency of the system. Similar fundamental behaviour was observed in [18]. The visualization of the vorticity field in all the slices for different vibration phases of the cantilever plate are shown in Fig. 7(a, b). This particular test case has been analysed considering different number of slices such as 1, 2, and 4. It requires the change of the effective width of the slices accordingly. Furthermore, several analyses are performed considering 2 to 4 number of vibration modes. The critical wind speed at which the large amplitude flapping initiates is always identified around 2.45 m/s for the studied case.

Table 1: The physical parameters of the reference inverted cantilever plate.

Solid	density	ρ_s	(kg m^{-3})	1200
	elastic modulus	E	(GPa)	2.4
	plate thickness	h	(mm)	0.13
	plate length	L	(cm)	5.1
	plate width	B	(cm)	6.4
	Poisson ratio	ν	(-)	0.38
Fluid	density	ρ_f	(kg m^{-3})	1.2
	kinematic viscosity	ν_f	(m^2 s^{-1})	1.54×10^{-5}

The model is presented for small displacement FSI problem, and therefore, it is not reliable to study the post-critical behaviour of the system using the present model. It requires a model that accounts the geometrical nonlinearity, such as in [13]. However, the presented model is very good regarding the identification of the critical flapping wind speed and shows its applicability for small displacement FSI problems. Moreover, the model is found computationally very efficient. Simulations are performed separately one after another using a computer having Linux

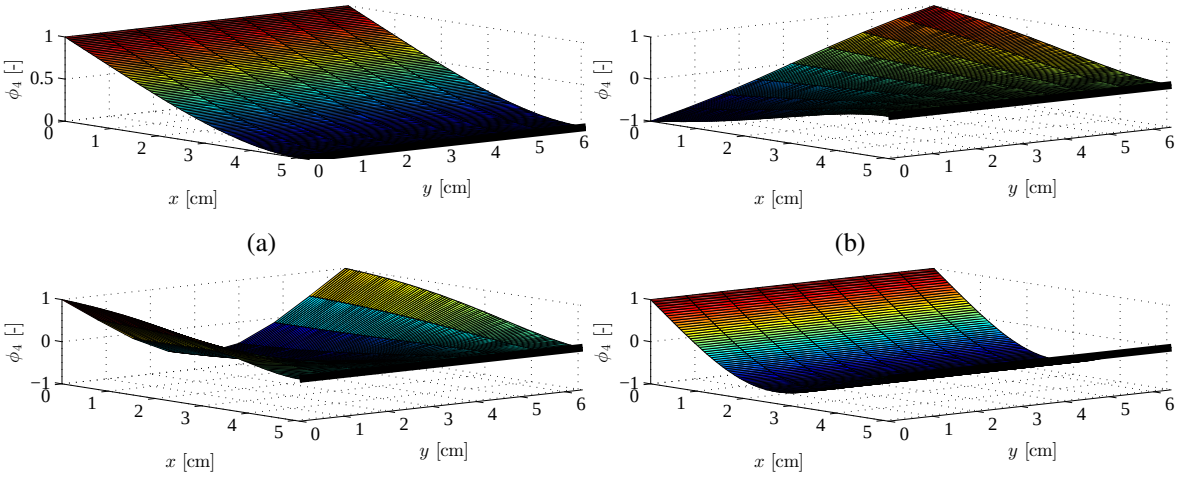

Figure 5: Normalized natural vibration modes and frequencies of the reference inverted cantilever plate model: (a) f_1 = 11.53 Hz, (b) f_2 = 26.22 Hz, (c) f_3 = 62.77 Hz, and (d) f_4 = 72.24 Hz.

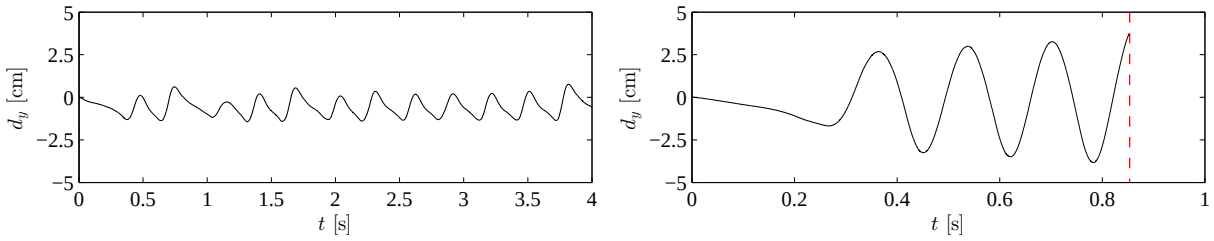

(a) U_∞ = 2.35 m/s, κ = 1.71 (b) U_∞ = 2.45 m/s, κ = 1.86

Figure 6: The tip displacement of the inverted cantilever plate at the central simulation slice under different dimensional and non-dimensional wind flows. The critical wind speed is identified as 2.45 m/s at which the large amplitude vibration initiates. The red dotted lines in (b) shows the initiation of divergent amplitude.

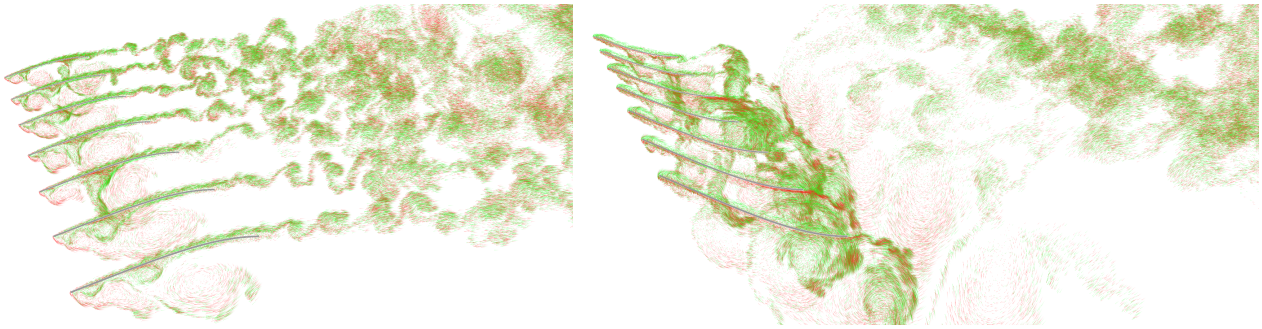

(a) (b)

Figure 7: The vortex street around the the cantilever plate at different slices due to the free stream flow.

operating system, 32 open-MP multithread Cores, 3.5GHz processor, 64 GB RAM. The 7-slice simulation for 20,000 steps took approximately around 12 hours only.

3.2 Multi-slice simulation of a skewed inverted cantilever plate

In the following, a skewed inverted cantilever plate is simulated under the axial wind using the multi-slice numerical model. It is expected that a differential motion between the slices should occur. The physical properties of the skewed inverted cantilever plate are chosen according to Table 1. The length of the plate is changed at top and bottom in order to make it skewed (L_{top} = 4.284 cm, L_{bottom} = 5.916 cm). The dimensions and multi-slice representation of the skewed inverted are shown in Fig. 8. The coupled simulation is performed using 7 slices as before. The cantilever system is modelled again using 102 and 8 shell elements along the length and width, respectively. The natural vibration modes and corresponding frequencies of the modelled system are shown in Fig. 9. Within the flow solver at each simulation slice 206 panels are used which means the size of the boundary elements Δ_s is different in slices. In such case, the simulation time step is normally considered either equal to the minimum average panel length for a slice over free stream flow ($\overline{\Delta}_{s(min)}/U_\infty$) or smaller. The displacement time histories of the cantilever tip for different slices are compared in Fig. 10. The differential displacement is clearly observed at different slices. The critical wind speed for initiation of large amplitude is identified 2.45 m/s as before.

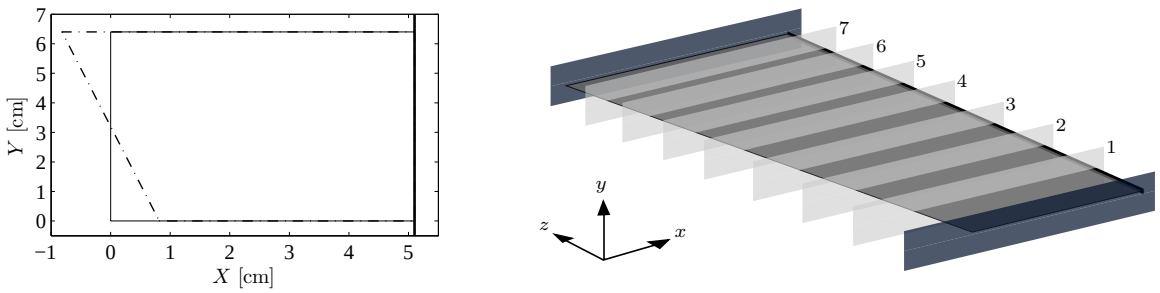

(a) (b)

Figure 8: Multi-slice simulation of a skewed inverted cantilever: (a) the modification over the reference inverted cantilever (—) to have an skewed inverted cantilever (– · –). (b) The multi-slice schematic representation of the skewed inverted cantilever.

4 MULTI-SLICE SIMULATION OF A THIN ROOF SYSTEM

Membrane roof systems are a good example of extremely light-weight and highly optimized constructions. Due to the constant stress state over the thickness, the material strength is optimally used. In the last years, the use of membranes in structural engineering became more and more common such as the Allianz Arena in Munich. Structural umbrella-type roofs have become popular for providing shelter whilst maintaining the feeling of open air. Their lightweight and flexible nature makes them prone to destructive aeroelastic effects. In this section, a thin-walled roof system is modelled and the responses are analysed under laminar wind flows. A Schematic configuration of a roof system under free stream wind U_∞ is shown in Fig. 11. The roof is considered curved in a parabolic way. The physical properties those are considered in this study for the roof system are presented in Table 2.

The coupled simulation is performed using 19 slices. The roof system is modelled using 80 and 20 shell elements along the length and width, respectively. The beam elements are used

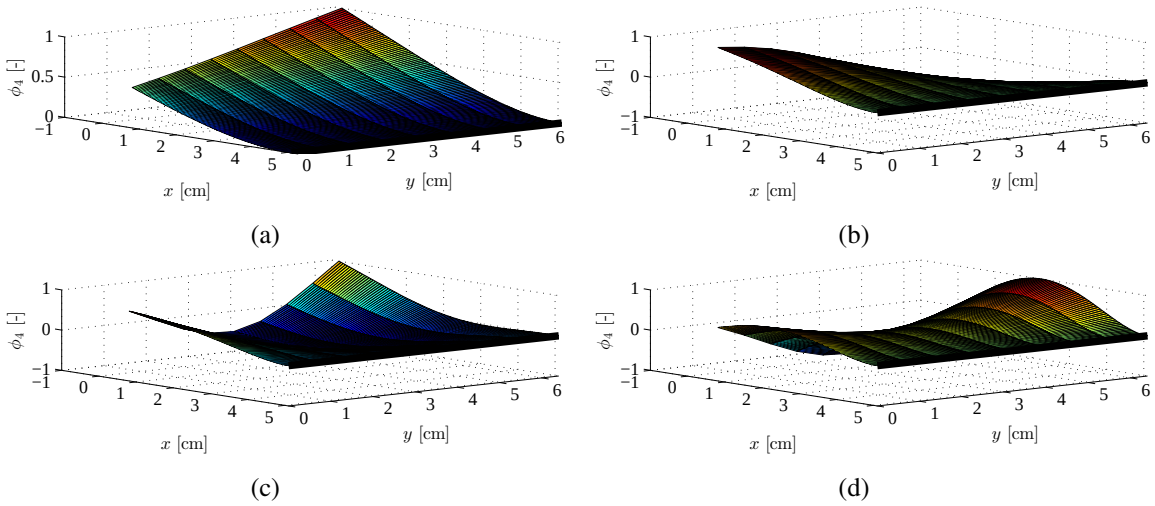

Figure 9: Normalized natural vibration modes and frequencies of the skewed inverted cantilever plate model: (a) f_1 = 11.12 Hz, (b) f_2 = 26.91 Hz, (c) f_3 = 62.21 Hz, and (d) f_4 = 66.69 Hz.

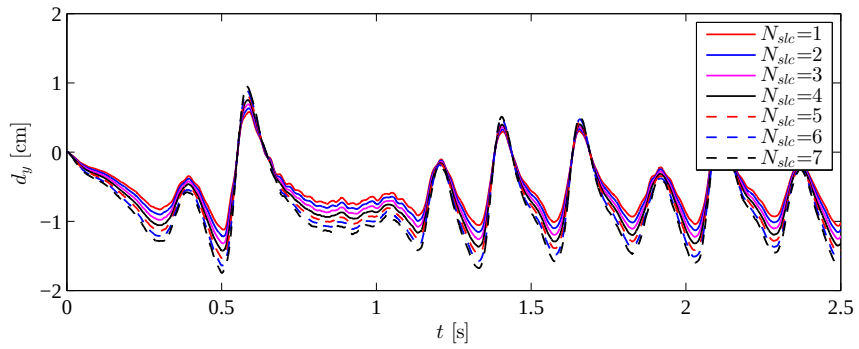

(a) U_∞ = 2.35 m/s

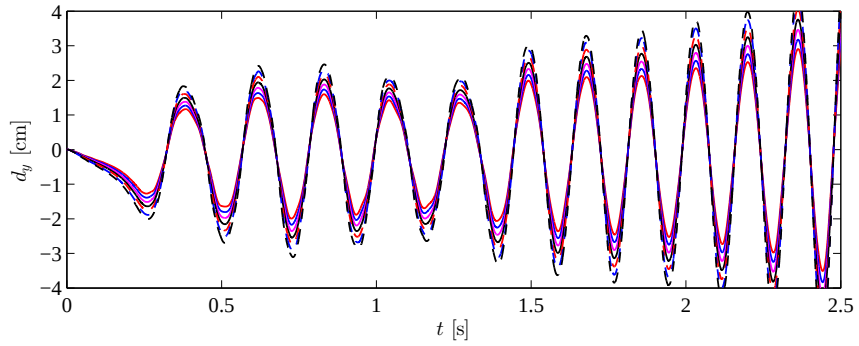

(b) U_∞ = 2.45 m/s

Figure 10: Multi-slice simulation of a skewed inverted cantilever: the time histories of tip displacements at different slices under different incoming wind flow.

as stiffeners regularly along the length and width of the roof. The natural vibration modes and corresponding frequencies of the modelled system are shown in Fig. 12. Within the flow solver at each simulation slice 162 panels are used which means the size of the boundary elements Δ_s is different in slices. As mentioned earlier for such cases, the simulation time step is considered either equal to the minimum average panel length for a slice over free stream flow ($\overline{\Delta_s}_{(min)}/U_\infty$) or smaller. The simulation of the roof system is under wind speed of 30 and 50 m/s. The

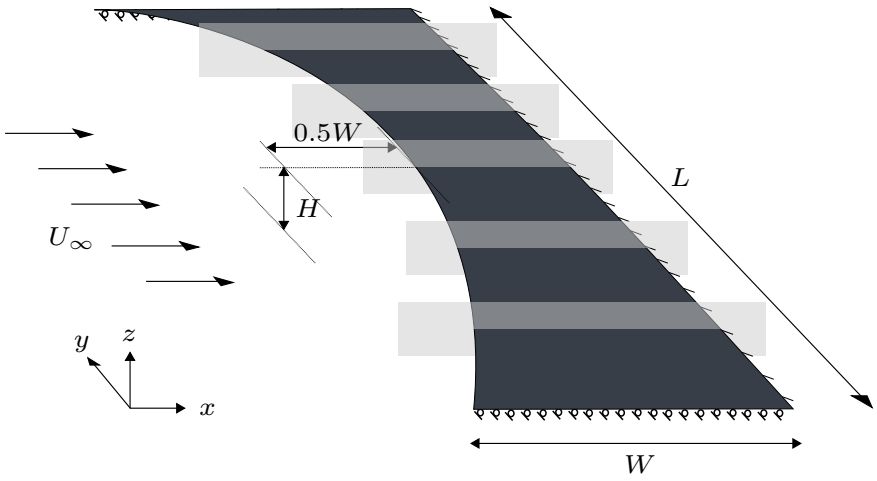

Figure 11: Schematic configuration of a roof system under free stream wind U_∞. The roof is considered curved in a parabolic way; the length, width and height are expressed as L, W, and H, respectively. The isometric view shows that the width of the system is reduced by half at the centre along the length. In this study, the fully coupled simulation of the system is performed in multi-slice sense which is by performing several 2D simulation slices that are interconnected by their natural vibration modes.

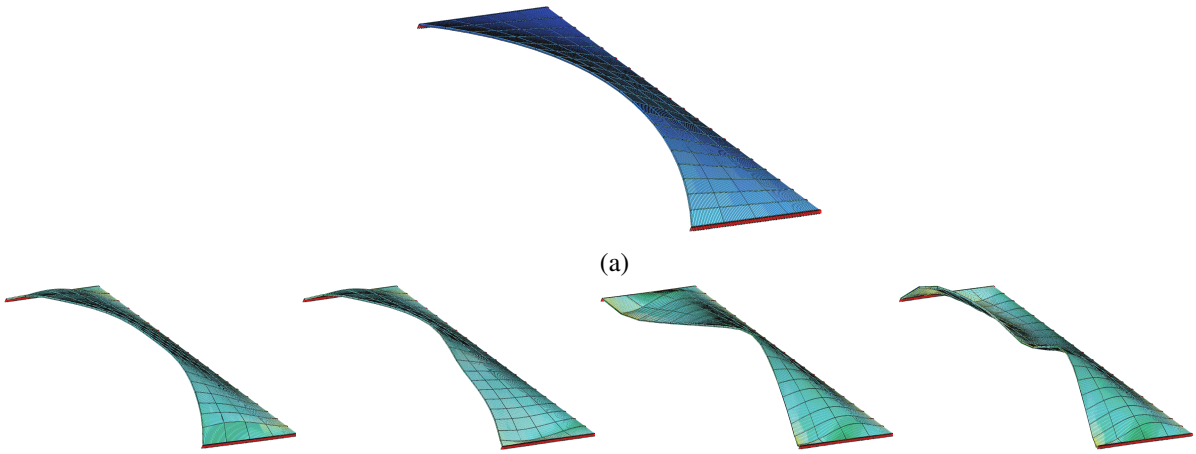

Figure 12: The modelled roof system and its natural vibration modes and frequencies: (a) the system, (b) f_1 = 8.97 Hz, (c) f_2 = 9.33 Hz, (d) f_3 = 15.21 Hz, and (e) f_4 = 16.44 Hz.

Table 2: The physical parameters considered for the cantilever roof system.

Solid	density	ρ_s	(kg m^{-3})	7950
	elastic modulus	E	(GPa)	180
	roof thickness	h	(mm)	4
	roof length	L	(m)	10
	roof width	W	(m)	2
	roof height	H	(m)	0.4
	Poisson ratio	ν	(-)	0.3
Fluid	air density	ρ_f	(kg m^{-3})	1.2
	kinematic viscosity	ν_f	(m^2 s^{-1})	1.5×10^{-5}

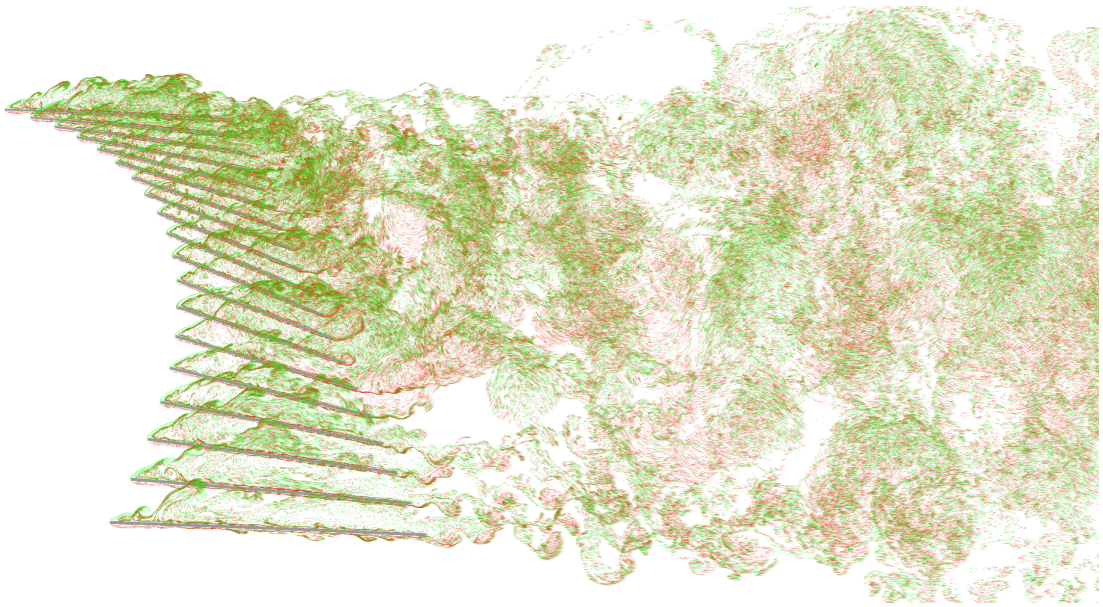

Figure 13: Instantaneous particle map for the Pseudo-3D roof system under laminar flow of 30 m/s.

corresponding simulation time steps are chosen 0.000754 s and 0.000452 s. The number of simulation time steps are 20,000 and 18,000, respectively. The instantaneous vorticity around the roof system at different simulation slices are shown in Fig. 13. The displacement time histories of the tip of the roof system at different slices are compared in Fig. 14 and Fig. 15, respectively under the wind speed of 30 and 50 m/s. The real time computation of such large scale analysis with the presented numerical model took only around 18 hours and 20 hours, respectively. As for future scope, the interest exists to study the influence of bluff vertical plate at the tip of the roof on aeroelastic response. The influence of incoming turbulence is also of particular study interest.

5 CONCLUSION

The paper has presented a partitioned extension of vortex particle methods (VPM) in the context of pseudo three-dimensional (3D) multi-slice numerical model which allows to simulate aeroelastic behaviour of thin structural elements, such as thin cantilevers and membrane roof system. A pseudo-3D VPM has been used to simulate the dynamics of the fluids. The complex flow around deformable boundaries has been analysed with the help of immersed boundary methods. The finite element model has been used to model the structural system. The linear uncoupled vibration modes are obtained for the structural dynamic solver because of its efficiency to handle small displacement problems. The equation of motion has been solved at the mid-surface of thin structural element. The projection of the surface pressures to the structural nodes at each 2D simulation slice has been explained. The validation of the solver has been performed by analysing the dynamics of an inverted cantilever in axial flow. The identified critical wind speed has been found to be in very good range when compared with the literature. A skewed inverted cantilever, which is modified over the reference system, has been analysed in order to simulate the differential displacement along the slices since the vortex induced forces varies along the slices. Finally, the dynamic response of a cantilever roof system which is fixed at the base and hinged in two sides has been analysed under incoming wind speeds of 30 and 50 m/s. The displacement time histories has been presented corresponding to the slices. The solver has been found computationally very efficient in terms of solving such large scale problem. The

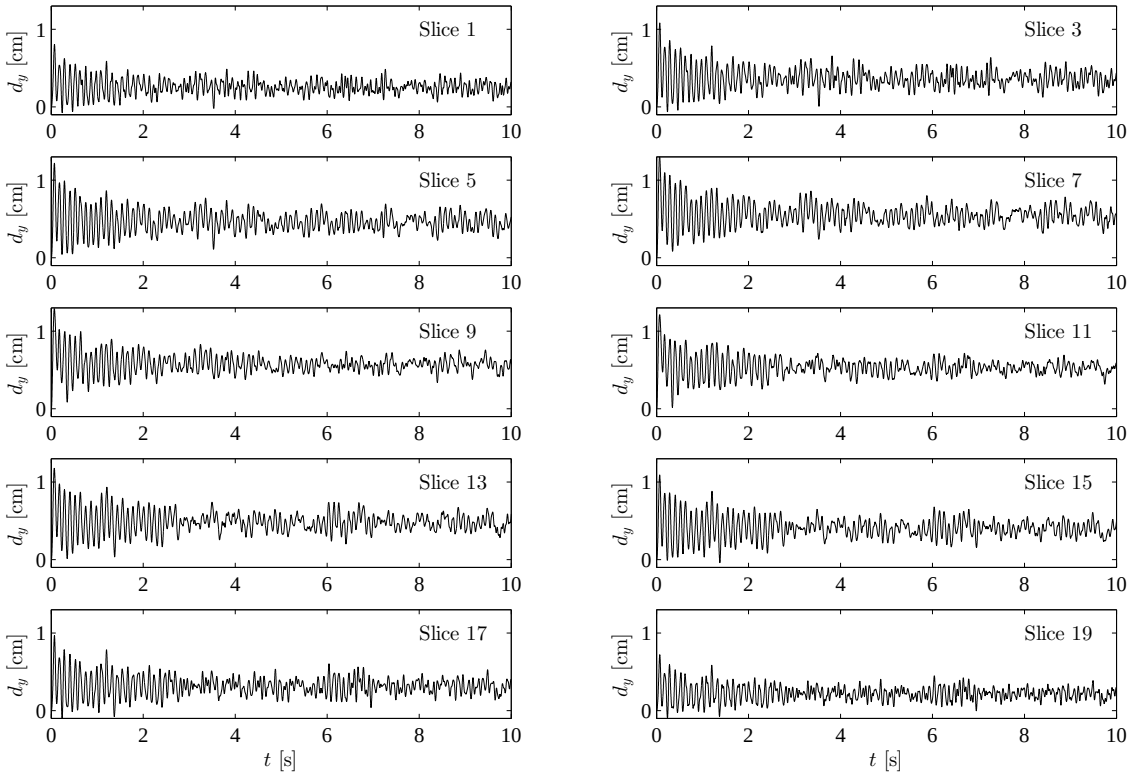

Figure 14: Tip displacement of the roof system at different slices under wind speed of 30 m/s.

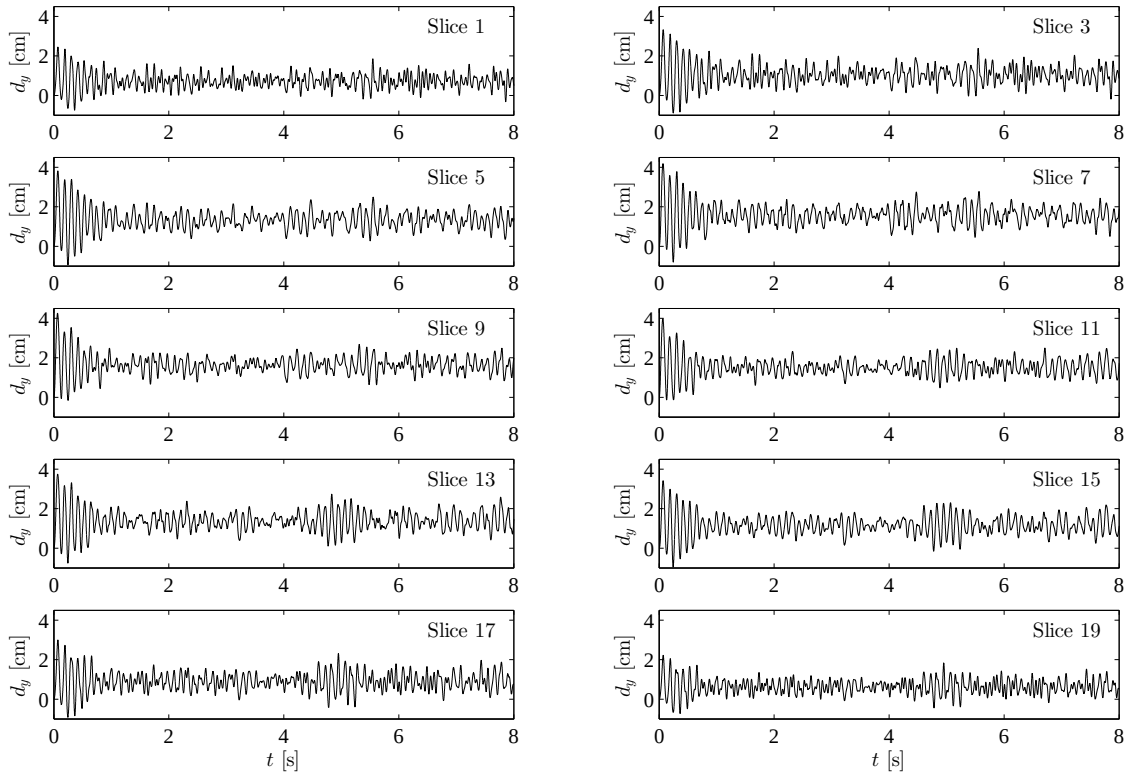

Figure 15: Tip displacement of the roof system at different slices under wind speed of 50 m/s.

influence of incoming turbulence on the dynamics of roof system is of particular study interest for future. The thin-walled circular tower system under vortex-induced vibration can be studied also.

REFERENCES

[1] M. Bathe, R. Kamm, A fluid-structure interaction finite element analysis of pulsatile blood flow through a compliant stenotic artery. *Journal of Biomechanical Engineering* **121**, 361–369, 1999.

[2] Y. Bazilevs, V.M. Calo, Y. Zhang, T.J. Hughes. Isogeometric fluidstructure interaction analysis with applications to arterial blood flow. *Computational Mechanics* , **38**, 310–322, 2006.

[3] J. Hron, S. Turek, A monolithic fem/multigrid solver for an ale formulation of fluid-structure interaction with applications in biomechanics, in: *Fluid-structure interaction*, Springer, 146–170, 2006.

[4] A. Michalski, B. Gawenat, P. Gelenne, E. Haug, Computational wind engineering of large umbrella structures. *Journal of Wind Engineering and Industrial Aerodynamics*, **144**, 96–107, 2015.

[5] B. Hübner, E. Walhorn, D. Dinkier, Strongly coupled analysis of fluid-structure interaction using space-time finite elements., in: *2nd European Conference on Computational Mechanics*, 546–547, 2001.

[6] W. Dettmer, D. Perić, A computational framework for fluid–structure interaction: finite element formulation and applications. *Computer Methods in Applied Mechanics and Engineering*, **195**, 5754–5779, 2006.

[7] A. Gilmanov, T.B. Le, F. Sotiropoulos, A numerical approach for simulating fluid structure interaction of flexible thin shells undergoing arbitrarily large deformations in complex domains. *Journal of Computational Physics*, **300**, 814–843, 2015.

[8] G. Morgenthal, Aerodynamic analysis of structures using high-resolution vortex particle methods. *PhD thesis, University of Cambridge*, 2002.

[9] G. Morgenthal, J.H. Walther, An immersed interface method for the vortex-in-cell algorithm. *Computers & structures*, **85**, 712–726, 2007.

[10] G. Morgenthal, A.S. Corriols, B. Bendig, A GPU-accelerated pseudo-3D vortex method for aerodynamic analysis. *Journal of Wind Engineering and Industrial Aerodynamics*, **125**, 69–80, 2014.

[11] I. Kavrakov, G. Morgenthal, A synergistic study of a CFD and semi-analytical models for aeroelastic analysis of bridges in turbulent wind conditions. *Journal of Fluids and Structures*, **82**, 59–85, 2018.

[12] K.I. Tolba, G. Morgenthal, Parallel scalability and efficiency of vortex particle method for aeroelasticity analysis of bluff bodies. *Computational Particle Mechanics*, 1–14, 2018.

[13] S. Chawdhury, G. Morgenthal, Numerical simulations of aeroelastic instabilities to optimize the performance of flutter-based electromagnetic energy harvesters. *Journal of Intelligent Material Systems and Structures*, **29(4)**, 479–495, 2018.

[14] D. Milani, G. Morgenthal, Methods for controlling the local spatial and temporal resolution of vortex particle simulations of bluff body aerodynamics problems. *Computers & Fluids*, **166**, 225–242, 2018.

[15] S. Chawdhury, G. Morgenthal, Flow reproduction using vortex particle methods for simulating wake buffeting response of bluff structures. *Journal of Wind Engineering and Industrial Aerodynamics*, **151**, 122–136, 2016.

[16] S. Chawdhury, D. Milani, G. Morgenthal, Modeling of pulsating incoming flow using vortex particle methods to investigate the performance of flutter-based energy harvesters. *Computers & Structures*, **209**, 130–149, 2018.

[17] D. Kim, J. Cossé, C.H. Cerdeira, M. Gharib, Flapping dynamics of an inverted flag. *Journal of Fluid Mechanics*, **736**, 2013.

[18] J.E. Sader, J. Cossé, D. Kim, B. Fan, and M. Gharib, Large-amplitude flapping of an inverted flag in a uniform steady flow – a vortex-induced vibration. *Journal of Fluid Mechanics*, **793**, 524–555, 2016.

COMPDYN 2019
7th ECCOMAS Thematic Conference on
Computational Methods in Structural Dynamics and Earthquake Engineering
M. Papadrakakis, M. Fragiadakis (eds.)
Crete, Greece, 24–26 June 2019

NONLINEAR DYNAMIC RESPONSES OF HIGHWAY BRIDGES EXPOSED TO PARTICULAR SEISMIC EVENTS CONSIDERING VEHICLE-BRIDGE INTERACTIONS

Sudanna Borjigin[1], Chul-Woo Kim[2], Kai-Chun Chang[2] and Kunitomo Sugiura[2]

[1] CORE Institute of Technology Corporation
Osaka JA Building 4F, 1 Chome 2-5 Nishitenma, Kita-ku, Osaka-shi, Osaka- Fu 530-0047, Japan
s.borjigin@coreit.co.jp

[2] Department of Civil and Earth Resources Engineering, Graduate School of Engineering
Kyoto University
Kyotodaigaku-katsura, Nishikyo-ku, Kyoto 615-8540, Japan
{kim.chulwoo.5u, chang.kaichun.4z, sugiura.kunitomo.4n}@kyoto-u.ac.jp

Abstract

The highway bridge design code in most countries does not consider the live load in seismic design of highway bridges. However, traffic jams on urban highway bridges occur with high probability, and the inertial effect of passing vehicles due to earthquakes thus could not be negligible in the context of seismic design of bridges when vehicle's weight is large enough compared with the dead load of bridges. It is therefore of engineers' interest to conduct a seismic analysis of bridges considering the vehicle dynamics effect on the seismic behavior of the bridge. Earthquakes occur unexpectedly and recently more and more strong motions were recorded, which are important for seismic engineering. This paper investigates nonlinear dynamic responses of a highway bridge considering vehicle‑bridge interactions (VBI) subjected to particular large earthquakes: Tohoku earthquake in 2011 and Kumamoto earthquake in 2016. Observations showed that, compared with those of disregarding vehicles, VBI changed the bridge displacement responses, plastic deformations, relative displacements of bearings and acceleration responses of the bridge but to different tendency and degree under different ground motions. The results revealed the importance of vehicle dynamic effect on seismic responses of bridges and view point that the current assumption of ignorance of vehicle effect in seismic design of highway bridges might be non-conservative.

Keywords: Bridge Non-linear Behavior, Moving Vehicle, Particular Earthquakes, Seismic Analysis, Vehicle‑bridge Interaction.

1 INTRODUCTION

Earthquakes occur randomly and such strong motion records are important for seismic design. On March 11, 2011, the 2011 off the Pacific Coast of Tohoku Earthquake (hereafter, the "Tohoku Earthquake") occurred in Japan. The magnitude was reported as being 9.0, the highest magnitude ever recorded in Japan. It was the most powerful earthquake ever recorded to have hit Japan, and the scale of the Tohoku Earthquake stands out in comparison even with some of the most destructive past earthquakes. It caused enormous damage due to the ground motion and the tsunami it triggered. About 200 highway bridges and numerous railway bridges were damaged, e.g., elevated bridges of the Tohoku Shinkansen. The Tohoku Earthquake was an inter-plate earthquake, occurring on the boundary between the Pacific plate and the Continental plate. The observed ground motions had a typical characteristic of a long duration because of the large scale of the fault plane, or the large number of waveforms observed, which was higher than massive earthquakes in the past. This phenomenon caused severe liquefaction effects for the ground in the Tokyo Bay area. Liquefaction resulted in much of the destruction associated with this earthquake, such as sand/mud boiling, ground cracking, depressions of pavement, ground settlement, leaning buildings and the exposure of underground pipes. The Kumamoto earthquake in 2016 consists of two strong ground motions and a series of smaller foreshocks and aftershocks. The first large ground motion hit the area on April 14, 2016, which was categorized into the foreshock before the larger ground motion on April 16, 2016. Such earthquakes caused strong response and significant damage to bridges. It was mentioned that this type of repeated strong motions has not been taken into account in conventional seismic design practices [1]. The repeated strong motions increase damage in all types of structures significantly. Service on the Shinkansen was suspended after a train derailed due to the earthquake. Thus, more research is needed to estimate and prevent the damage caused by such strong earthquakes.

Heavy traffic jams on urban highway bridges occur frequently and encountering an earthquake in urban areas of earthquake prone regions becomes more possible. The dynamic effect of vehicles could not be negligible in the context of seismic design of bridges. It is necessary to review the seismic performance of bridges, considering traffic loading. However, very few studies have specifically examined the vehicle effect on bridge seismic responses.

In seismic design of monorail bridges the effect of the train load is considered as additional mass [2]. He et al. [3] investigated the seismic responses of Shinkansen viaducts for high-speed trains under moderate earthquakes. Their results show that the train can act as a damper for the bridge. A study by Zeng and Dimitrakopoulos [4] studied a horizontally curved railway bridge subjected to train crossings and moderate ground motions of different periods. Results verified the favorable damping effect that the running vehicles have on the deck vibration. The study by Kim et al. [2] showed that consideration of the monorail train as additional mass rather than a dynamic system in numerical modeling overestimated the effect of the train load on seismic performance of monorail bridges. Kim and Kawatani [5] concluded that a train acts as a damper and tends to decrease acceleration response under a particular earthquake compared with the system which consider train as an additional mass.

In contrast to the railway system, the highway bridge design code of Japan Road Association does not consider the live load in seismic design of highway bridges due to the low probability of simultaneously encountering critical vehicle load and earthquake. A study by Sugiyama et al. [6] showed that the dynamic effect of the vehicles was more dominant in the transverse direction and that the vehicle loading tended to reduce the bridge response. A study addressing this matter was done by Kameda et al. [7], which concluded that seismic responses of the bridge increase or decrease depending on the phase difference between the bridge and

the vehicle. Kameda et al. [8] stated that the vehicles tended to amplify the bridge response when the vehicles and bridge were in phase and tended to decrease the response when they were out of phase. Another study by Kim et al. [9] concluded that the seismic response of the highway bridge subject to moderate earthquakes increased when the vehicle was considered as mass; and decreased when the vehicle was simulated as dynamic system. Kawatani et al. [10] demonstrated that heavy vehicles reduced the seismic response of bridges under a moderate ground motion with lower frequency characteristics; but slightly amplified the seismic response of the bridge under higher frequency ground motions. Borjigin et al. [11] proposed a seismic response analysis framework incorporating vehicle–bridge interactions (VBI) with nonlinear dynamic analysis, and the effects of vehicle dynamics on seismic responses of a highway bridge was clarified and the seismic performance of the bridge was checked.

As reviewed above, most studies were related to moderate earthquakes that caused linear behavior of bridges, and some studies discussed the seismic responses of bridges considering effect of vehicle dynamics under limited number of modified ground motions. It is therefore necessary to proceed with a seismic analysis of bridges considering vehicle effect, and describe the non-behavior of bridges for strong ground shakings of different levels. This study was conducted to investigate non-linear dynamic analysis incorporating vehicle–bridge interactions (VBI) subjected to particular earthquakes to clarify the effect of vehicles on the seismic responses of an urban highway viaduct. To investigate the seismic responses of the bridge under particular earthquakes, two strong ground motions recorded on-site with different frequency components are adopted for analysis. A numerical method, Recursive Substructure Method, was utilized, which integrates a commercial FEA package, ABAQUS®, into the authors' in-house VBI-solving programs developed with MATLAB®.

2 ANALYTICAL MODELS

2.1 Vehicle model

The vehicle model of a truck consists of a rigid body with single axle. The mass of the vehicle model is 25.0 ton. The vehicle model has five degree of freedoms (DOFs) considering transversal, longitudinal, vertical, pitching, and rolling motions as shown in Figure 1. The properties are shown in Table 1. The length of truck is 7 m. The natural frequency of longitudinal motion of the vehicle model is about 2.052 Hz. The slip or turning over of vehicles on the bridge during the earthquakes was not considered in this study.

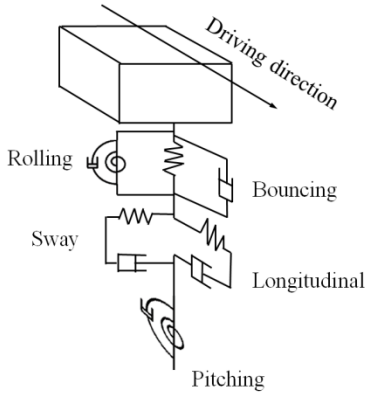

Figure 1: Vehicle model of 5DOF. (reproduced from [11])

	Natural frequency	Spring constant	Damping coefficient
Transversal & longitudinal	2.052 Hz	4.156×10^6 N/m	4.284×10^4 N·s/m
Vertical	3.477 Hz	1.193×10^7 N/m	5.871×10^4 N·s/m
Pitching	2.697 Hz	2.326×10^7 N·m/rad	1.505×10^5 N·m·s/rad
Rolling	1.739 Hz	9.665×10^6 N·m/rad	4.756×10^4 N·m·s/rad

Table 1: Properties of 5DOF vehicle model. (reproduced from [11])

2.2 Bridge model

The target bridge was designed in 2009 according to the design specifications for the Japan highway bridges. The bridge model (Figure 2) used in this study was a 3-span continuous non-composite steel plate girder bridge with two vehicle lanes. The superstructure of the bridge model contains an orthotropic plate supported by five girders. The girders, reinforced concrete (RC) piers and abutments were modelled with beam elements and the plate was modeled with shell elements. The properties of cross section and mechanical properties are given in Table 2 and Table 3. Rayleigh damping was adopted [12].

Strong earthquakes may cause non-linear behaviors of bridges. The failure mode of this bridge was predicted to be in the longitudinal direction. The bridge included isolation bearings of bi-linear force-displacement relationship on each abutment and pier (Table 4) which moved in the longitudinal direction, and plastic hinges of tri-linear moment-rotation relationships on the piers base (Table 5) which rotated along the transversal axis. The abutments were made of concrete and performed linear behavior, while the piers were made of reinforced concrete and performed non-linear behavior.

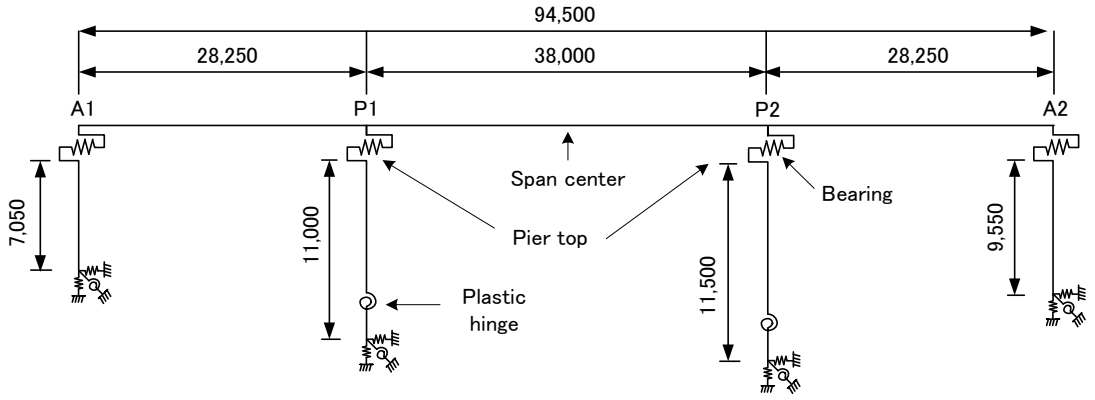

Figure 2: Analytical model of bridge (unit: mm). (reproduced from [11])

Component		Section area A (m^2)	Second moment of area Iz (m^4)	Ix (m^4)	Torsional constant J (m^4)
Girder		0.658	0.363	4.65820	0.0075
Abutment 1 (A1)	Column	33.375	17.383	495.700	61.260
	Footing*	10000	10000	10000	10000
Pier 1 (P1)	Bent cap*	10000	10000	10000	10000
	Column	12	4.41870	36	12.643457
	Plastic zone	12	10000	10000	10000
	Footing*	10000	10000	10000	10000
Pier 1 (P2)	Bent cap*	10000	10000	10000	10000
	Column	12	4.41870	36	12.643457
	Plastic zone	12	10000	10000	10000
	Footing*	10000	10000	10000	10000
Abutment 2 (A2)	Column	33.375	17.383	495.700	61.260
	Footing*	10000	10000	10000	10000

Note. * The unrealistic value 10000 was assigned herein simply for providing a relatively large rigidity.

Table 2: Properties of cross section main components. (reproduced from [11])

	Young's modulus E (N/m^2)	Shear modulus G (N/m^2)	Density (kg/m^3)
Girder	2.0×10^{11}	7.7×10^{10}	7857
Pier	2.5×10^{10}	—	2500

Table 3: Mechanical properties of the bridge model. (reproduced from [11])

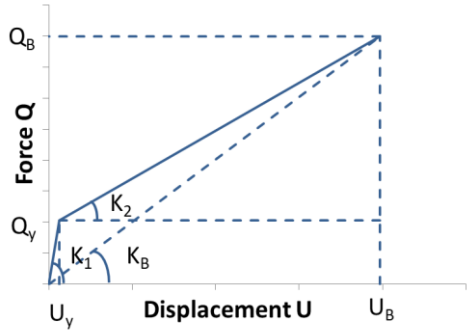

	A1	P1	P2	A2
K_1(kN/m)	16304.2	38371	38233	16373.8
K_2 (kN/m)	1545.6	3645.0	3632.2	1551.8
Q_y (kN)	102.39	214.88	213.34	102.66
Q_B (kN)	399.33	718.98	708.84	404.22
U_y (m)	0.006	0.006	0.006	0.006
U_B (m)	0.198	0.144	0.142	0.201
K_B(kN/m)	2013.03	4996.36	4992.75	2014.85

Note. K_1 denotes the initial stiffness, K_2 the post yielding stiffness, K_B the equivalent stiffness, and (U_y, Q_y) and (U_B, Q_B) indicates initial yielding point (yielding shear deformation and force) and ultimate point (yielding ultimate shear deformation and force) respectively.

Table 4: Properties of bearings. (reproduced from [11])

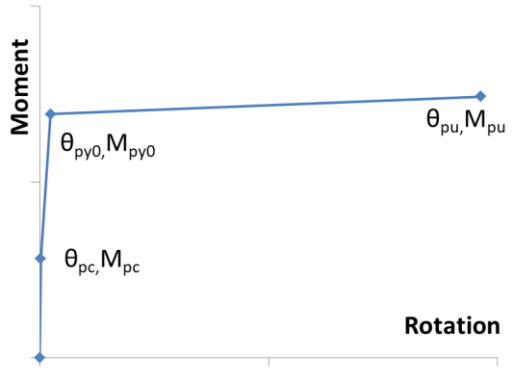

	P1	P2
M_{pc} (kN·m)	11297.8	11377.3
M_{py0} (kN·m)	27749.3	27928.4
M_{pu} (kN·m)	29725.7	29838.9
θ_{pc} (rad)	0.000103	0.000103
θ_{py0} (rad)	0.001192	0.001198
θ_{pu} (rad)	0.048174	0.047547

Note. Initial cracking moment M_{pc} and its corresponding rotational angle θ_{pc} specifies the initial cracking point and elastic limit, the yielding moment M_{py0} and rotation angle θ_{py0} specifies the yielding point, the ultimate moment M_{pu} and rotation angle θ_{pu} specifies the ultimate point.

Table 5: Properties of plastic hinge. (reproduced from [11])

The road condition was considered to be good in this study. The roadway profile generated based on ISO standard [13] is shown in Figure 3. Usually effects of vehicle vibrations actuated during moving on a bridge by road roughness are relatively small compared with seismic load effects. However, before an earthquake bridge vibration is mainly excited by vehicle vibrations, and the bridge vibration due to moving vehicles can be applied as initial conditions in the dynamic analysis of bridges during earthquakes. Before seismic responses, the responses by vehicles only should be identified. Therefore, this study considers the road roughness in the analysis [9].

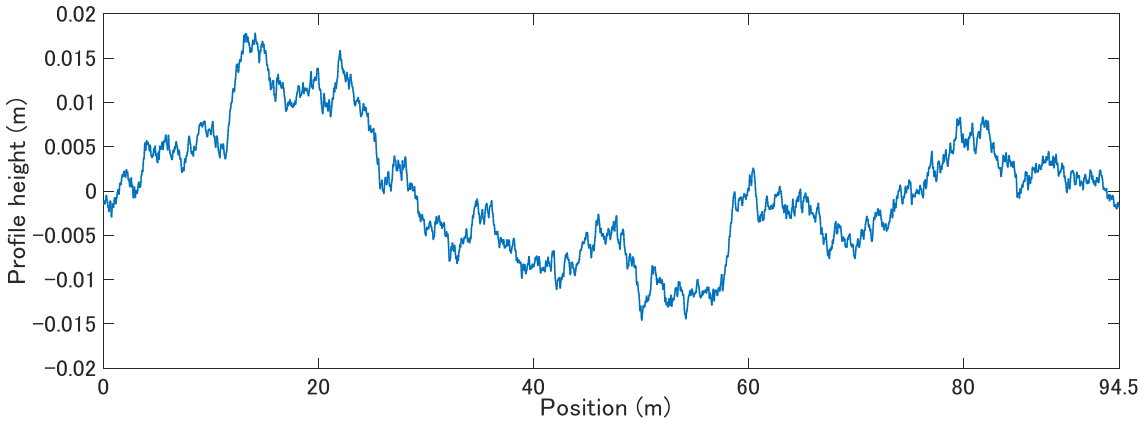

Figure 3: Road roughness profile. (reproduced from [11])

Since the vehicle position on the bridge varies with time, the natural frequency of bridge with vehicles standing at different loading locations were examined through eigenvalue analysis of the vehicle-bridge interactive system. There were five vehicles equally spaced on each lane and totally ten vehicles were considered in the VBI system. The natural frequency of the first longitudinal mode of the bridge without vehicle was 1.82 Hz. Position 1 (see Table 6) is a special condition with 2 vehicles exactly standing on the top of two piers on each lane. As shown in Table 6, the first mode is piers' longitudinal bending and rubber bearings' deformation mode. Two longitudinal modes and frequencies of the vehicle-bridge interactive sys-

tem corresponds to the first longitudinal mode: vehicles in-phase (vehicles move in the same direction as the bridge's movement) and out-of-phase (vehicles move in the opposite direction of the bridge's movement) with the bridge, with the frequency of 1.43 Hz and 2.02 Hz, respectively. Position 2 (Table 6) is one vehicle standing on the top of left abutment on each lane, while Position 3 (Table 6) is one vehicle standing on the top of right abutment on each lane and symmetrical with Position 2. For this reason, the discussion with position 3 scenario is omitted in following sections. With position 2 and 3, frequency of vehicles in-phase mode is 1.17 Hz and that of out-of-phase mode is 1.89 Hz. Position 4 (Table 6) is a random position different from the above 3 ones. Frequency of vehicles in-phase mode is 1.35 Hz and that of out-of-phase mode is 1.97 Hz.

It can be found that the bridge has varied fundamental natural frequencies as the vehicles were moving on the bridge. Due to the presence of vehicles, the frequency of the bridge may be changed to be larger or smaller than that of bridge alone, e.g. at position 1 the frequency of vehicles in-phase mode is 1.43 Hz that is smaller than the natural frequency of the first mode of bridge alone 1.82 Hz, while frequency of out-of-phase mode is 2.02 Hz, which is larger than the natural frequency of the first mode of bridge alone 1.82 Hz. Such frequency variation may significantly cause change in seismic responses of the bridge, as discussed below.

Bridge without vehicle	Bridge with 10 vehicles (position 1)	Bridge with 10 vehicles (position 2,3)	Bridge with 10 vehicles (position 4)
	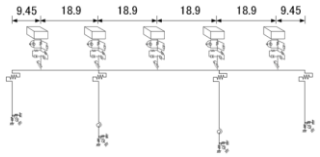	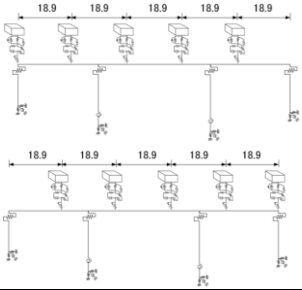	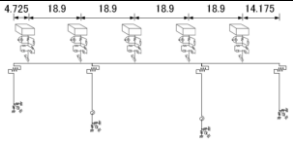
1.82 Hz 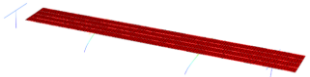	vehicles in phase with the bridge 1.43 Hz 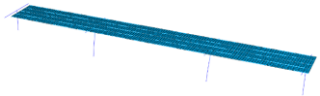 vehicles out of phase with the bridge 2.02 Hz 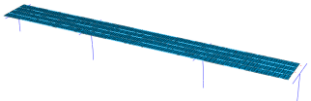	vehicles in phase with the bridge 1.17 Hz 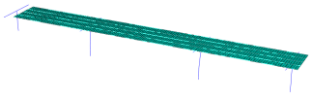 vehicles out of phase with the bridge 1.89 Hz 	vehicles in phase with the bridge 1.35 Hz  vehicles out of phase with the bridge 1.97 Hz 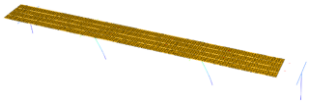

Table 6: Comparison of natural frequencies and mode shapes of the bridge based on equivalent stiffness without vehicle and with vehicles standing on different positions. (reproduced from [11])

2.3 Moving vehicle configuration

To investigate the effect of moving vehicles on the seismic response of the highway viaduct, the following scenario was considered. Figure 4 shows the moving pattern of heavy vehicles. It was assumed that the earthquake happened when the bridge was fully loaded with

moving vehicles. In other words, only the seismic response of the bridge fully loaded by moving vehicles is discussed in this study. All vehicles are assumed to travel with the constant speed of 2.7 m/s (9.72 km/h). The spacing between adjacent vehicles is 18.9 m. Comparing the responses in this scenario with another scenario, disregarding vehicular loadings, can be useful to elucidate the effects of continuously moving vehicles.

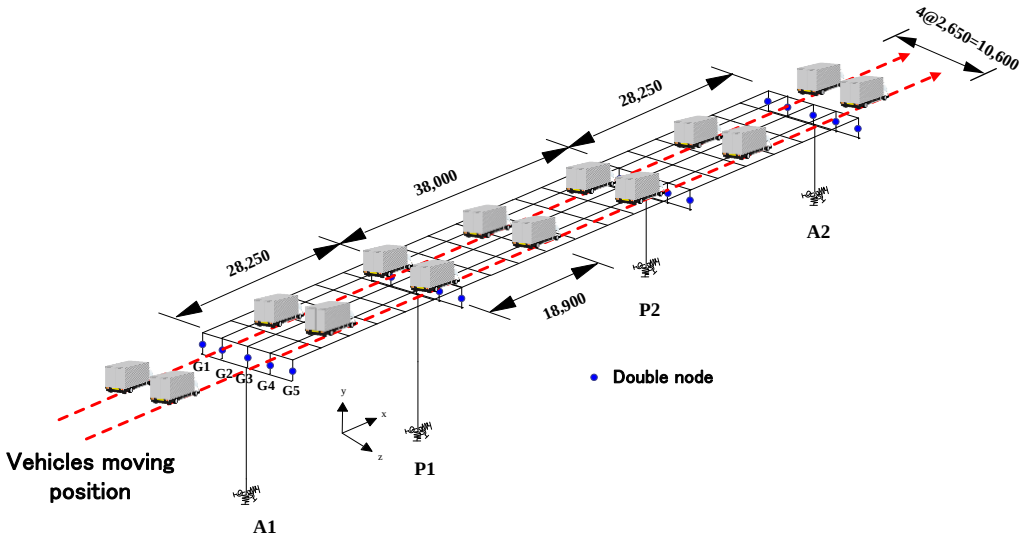

Figure 4: The bridge model with continuously moving vehicles. (reproduced from [11])

3 GROUND MOTIONS

Two particular ground motions were considered herein: 2011 Tohoku earthquake and 2016 Kumamoto earthquake. Their characteristics are given as follows.

3.1 Tohoku earthquake

The strong ground motion records of Tohoku earthquake clearly showed that this earthquake generated ground motions with multiple pulses and longer duration, compared to the 1995 Kobe Earthquake lasting about 20 seconds. Figure 5 shows the time history of Kaihoku Bridge, Ishinomaki EW component, a modified ground motion of Level 2 Type I recommended by JRA [14] used herein, which was obtained from the recorded ground motion in the Tohoku earthquake at the measurement station of Kaihoku Bridge, Ishinomaki. The designation of EW indicates data channels of East-West direction. The Level 2 ground motion indicates the extreme design ground motion with low occurrence probability such as Kobe earthquake in 1995 and Type I indicates inter-plate earthquakes. For the highway bridge adopted in this analysis, the ground condition is classified as Group I soil in the design code, which is defined as dense to stiff soil having a natural period of 0.16 – 0.6 s in the surface ground.

As shown in Figure 5, the ground motion contains two attacks with a spacing of about 50 seconds and lasts for about 240 seconds. The first attack has smaller peak value of acceleration (5.12 m/s^2) than the second attack does (7.95 m/s^2). The figure shows a drastic change in amplitude and spike-like phases, which all corresponds to the characteristics of the records on the liquefied ground. The sampling frequency is 100 Hz.

Figure 6 shows the acceleragram, Fourier amplitude spectrum and pseudo acceleration response spectrum (damping ratio h = 0.05) of the modified ground motion. The modified

ground motion was obtained by fitting its response spectrum to the target response spectrum. Periods (and frequencies) in the legend of response spectrum and Fourier amplitude spectrum are natural periods (frequencies) of vehicle's longitudinal mode, the first natural periods (frequencies) of the bridge's longitudinal modes disregarding vehicles and regarding vehicles as dynamic system (at Position 1, 2 and 4) respectively.

For computation efficiency, a shorter ground motion (referred to as GM1 hereafter) was extracted from the 20th to 140th second of the full record and then applied to the aforementioned VBI model. The ground motion was applied in the longitudinal direction because the piers' bending resistance is weakest in this direction according to the formal design.

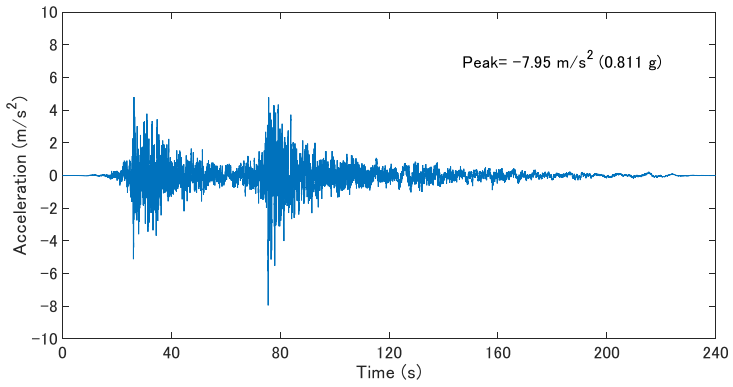

Figure 5: Kaihoku Bridge, Ishinomaki EW component (GM1).

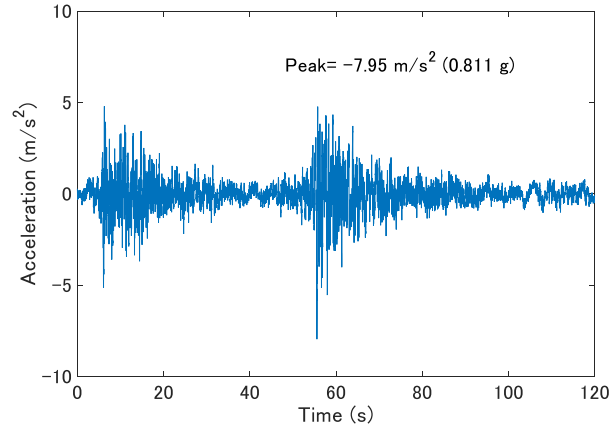

(a)

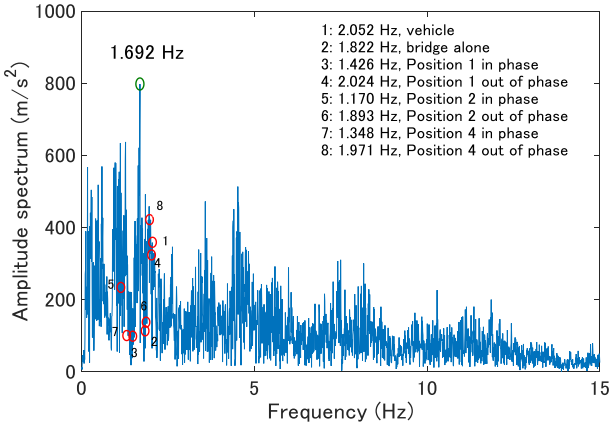

(b)

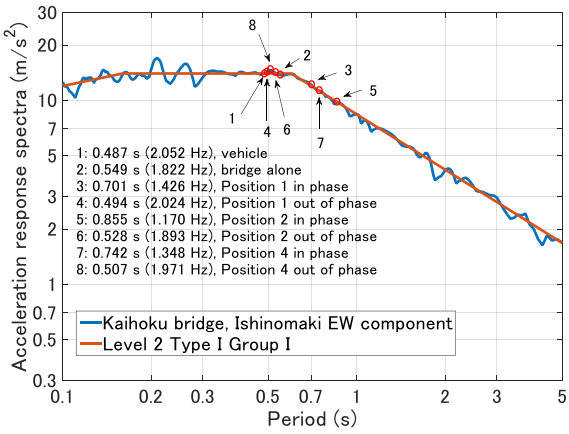

(c)

Figure 6: Accelerogram, response spectrum and Fourier spectrum of strong shaking interval (20 s ~ 140 s) of Kaihoku Bridge EW component (GM1): (a) accelerogram, (b) Fourier amplitude spectrum, (c) pseudo acceleration response spectrum.

3.2 Kumamoto earthquake

Figure 7 shows the acceleration time histories of the NS and EW components of the ground motion recorded at Mashiki town (referred to as GM2 hereafter) [15]. The strong mo-

tion record above the heavily damaged Mashiki residential area recorded over 1.0g in the EW direction. The designations of EW and NS in the figures, respectively, indicate data channels of East-West, North-South directions. The maximum acceleration is 6.53 m/s^2 in the NS component and 11.57 m/s^2 in the EW component. In the seismic analysis, EW component was applied to the longitudinal direction and NS was applied to the transverse direction of the bridge structure.

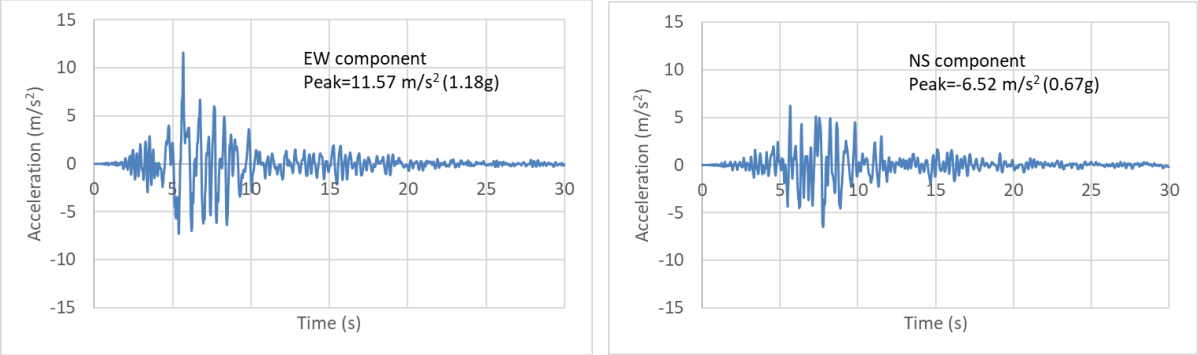

Figure 7: Accelerogram of Mashiki town EW component and NS component (GM2).

4 NUMERICAL METHOD

The equation of motion for a vehicle is written as [16] [17]

$$\boldsymbol{M}_v\ddot{\boldsymbol{u}} + \boldsymbol{C}_v(\dot{\boldsymbol{u}} - \dot{\boldsymbol{y}}_c) + \boldsymbol{K}_v(\boldsymbol{u} - \boldsymbol{y}_c) = \boldsymbol{0} \tag{1}$$

where $\boldsymbol{M}_v$, $\boldsymbol{C}_v$, and $\boldsymbol{K}_v$ respectively denote the mass, damping, and stiffness matrices of the vehicle, and where $\boldsymbol{u}$ represents the vector of vehicle's displacements and rotations at its degrees of freedom. A dot denotes the derivative with respect to time. $\boldsymbol{y}_c$ is the wheel displacement vector at the contact point. It is the summation of bridge displacement $\boldsymbol{w}_c$ and roughness $\boldsymbol{r}_c$ at that point.

The equation of motion for the bridge model is written as

$$\boldsymbol{M}_b\ddot{\boldsymbol{v}} + \boldsymbol{C}_b\dot{\boldsymbol{v}} + \boldsymbol{K}_b\boldsymbol{v} = \boldsymbol{f}_{seis} + \boldsymbol{f}_{vb} \tag{2}$$

where $\boldsymbol{M}_b$, $\boldsymbol{C}_b$ and $\boldsymbol{K}_b$ respectively stand for the mass, damping, and stiffness matrices of the bridge, and where $\boldsymbol{v}$ represents the vector of bridge's displacements and rotations at its degrees of freedom. Also, $\boldsymbol{f}_{seis}$ is the seismic loading. The force exerted by vehicle to bridge $\boldsymbol{f}_{vb}$ is the summation of vehicle weight, spring forces, and damping forces.

The two equations of motion (1) and (2) above are solved in a direct time integration manner to solve them at a certain time step $t+\Delta t$ (Δt is a finite small time increment) using the solution in previous time step t and the approximations for the derivatives. Newmark β-method [26] is adopted to solve equations of the equations of the vehicle and bridge system. The value of 0.25 is adopted for β to obtain stable and accurate solutions.

The Recursive Substructure Method (RSM) [11] was utilized to simulate the dynamic responses of bridges and moving vehicles under particular earthquake [18] [19]. It integrates the conventional nonlinear dynamic analysis in ABAQUS into the authors' in-house VBI-solving programs developed with MATLAB. The bridge Finite Element model is built in ABAQUS, and nonlinear dynamic analysis of bridge is conducted in ABAQUS. The vehicle model is built and the roughness profile is constructed in MATLAB. MATLAB controls the recursive ABAQUS executions and to perform time integrations in VBI problem. The time step of simulations was 0.01 s, being the same as the sampling period of the ground motion record.

5 SEISMIC RESPONSES OF HIGHWAY BRIDGE

5.1 Displacement responses of pier top and relative displacement of bearing

The shear force-displacement hysteresis loops of bearing, the longitudinal displacement responses of pier top and the moment-rotation hysteresis loops at pier base of P1 under GM1 are depicted in Figures 8-10 as typical example, and those of A1, P2 and A2 are omitted here for simplicity. As shown in Figure 9, the maximum displacement of pier top P1 under GM1 is about 0.04 m during first attack, and nonlinear behavior happened that caused a drift in the response of approximately 0.01 m. There is very little difference between the results with and without vehicle during the first attack. However, during the following second attack, which is like a strong aftershock of the first attack, the maximum displacement of the bridge appears and the displacement responses under second attack have larger amplitudes than those during first attack. From this phenomenon the larger residual displacement can be predicted. It is noteworthy that significant difference between two scenarios disregarding and regarding vehicles in the second attack could be found and the moving vehicles tend to reduce the displacement responses of the bridge, which indicates the presence of vehicles mitigates the variation tendency of the displacement response of the bridge while subjected to multi-attacks ground motions.

The relative displacements of bearings considering VBI under GM1 were slightly changed from those disregarding vehicles as indicated in Figure 8 and Table 7. The maximum relative displacements decreased by 0.6% for A1, by 3.8% for P1 and by 0.8% for P2, but increased by 2.4% at A2. The reason may be added damping and mass damper effect due to vehicle on the bridge. Another reason may be that the vehicle-bridge out-of-phase modes were excited by the ground motion and the vehicle's suspension system would suffer a larger deformation and dissipate more energy that was supposed to be dissipated by the rubber bearings. For example, the natural frequency of the vehicle-bridge out-of-phase mode in the Position 4 scenario is 1.971 Hz and it might be excited by the ground motion as indicated in Figure 6(b), and the out-of-phase mode might be excited by the ground motion. It can be said that the current seismic design disregarding vehicle dynamics was conservative if the rubber bearings were of concern.

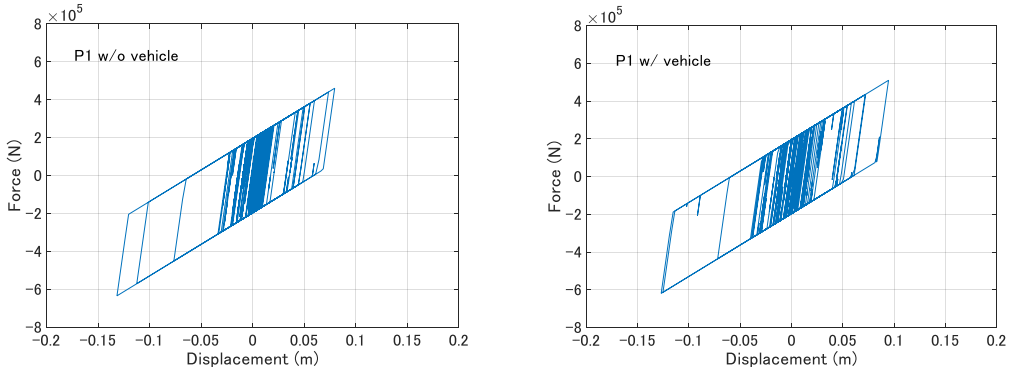

Figure 8: Hysteresis loop of bearing at P1 pier top under GM1, disregarding moving vehicles (left) and considering moving vehicle (right).

		Displacement	Reduction ratio * %
A1	w/o	0.164	0.6
	w/	0.163	
P1	w/o	0.132	3.8
	w/	0.127	
P2	w/o	0.126	0.8
	w/	0.125	
A2	w/o	0.168	-2.4
	w/	0.172	

Note. *reduction ratio is defined as the average displacement reduction from the w/o-vehicles case to the w/-vehicles case divided by the average displacement in the w/o-vehicles case.

Table 7: Maximum relative displacement of bearing under GM1 (unit: m).

The maximum longitudinal displacements of span center under GM1 were reduced when the moving vehicles presented by 1.8% as indicated in Table 8. Span center displacement is the summation of pier top displacement and bearing's relative displacement. Referring to Table 7 and 8, the span center maximum displacements and the bearing's maximum relative displacements are at a similar level (0.12 – 0.17 m), while the span center maximum displacements and the pier top maximum displacements (only about 0.06 m from Figure 9) are not. It indicates that the span center maximum displacements were more dominated by bearings' maximum relative displacements. As mentioned above, when the vehicles were considered on the bridge system, two modes appeared relevant to the first longitudinal mode of the bridge alone: vehicle-bridge in-phase and out-of-phase modes. Although the out-of-phase modes were excited by the ground motions to a similar level with the original bridge-alone mode was (see the pseudo acceleration response spectrum in Figure 6(c)), the phase-difference between vehicles and bridge might help bearings absorb energy and therefore reduce the bearings' relative displacements as well as the span center displacements.

The maximum displacements of pier tops were generally reduced when the moving vehicles presented (see Figure 9), and so were the residual displacements of pier tops as well as span center. Such ground motion caused the maximum displacement up to about 0.066 m and the residual displacement about 0.03 m at pier tops. But if vehicle-bridge interaction was considered, the reduction for maximum displacements was up to 19% and for residual displacement responses was 36%. The maximum displacement decreased by 13.8% at P1 pier top and 19.3% at P2 pier top; the residual displacement decreased by 31.6% at P1 pier top, 35.9% at P2 pier top, and 21.4% at span center, when vehicle–bridge interaction was considered. It could be concluded that the vehicles have a significant positive effect on the bridge's nonlinear displacement responses. When the moving vehicles were considered, the maximum rotation of the plastic hinge at pier base was smaller than those without vehicle under the ground motion (see the moment-rotation hysteresis loops in Figure 10), indicating that the bridge suffered from weaker plastic deformations. Table 9 quantifies the reduction of the maximum rotation: 37.5% at P1 pier base and 39.3% at P2 pier base. This trend is in line with that of the maximum longitudinal displacement of the pier tops, because pier top displacements and pier base rotations are related to each other acknowledging the fact that pier top displacements were majorly caused by pier-base rotations and pier deformations. The reason for the reduction in these responses can be pier base rotation and pier deformation's complex combination with out-of-phase motion of the system.

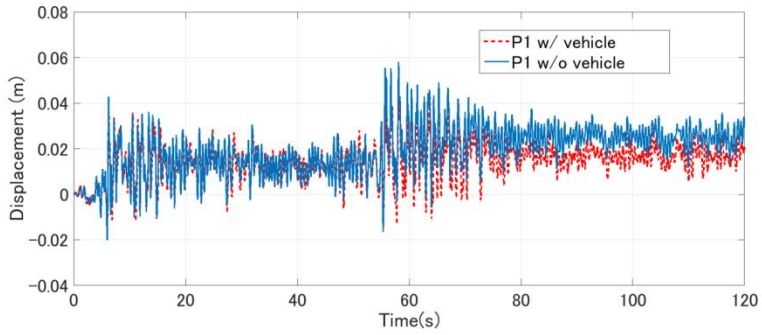

Figure 9: Longitudinal displacement responses of the pier top P1 under GM1.

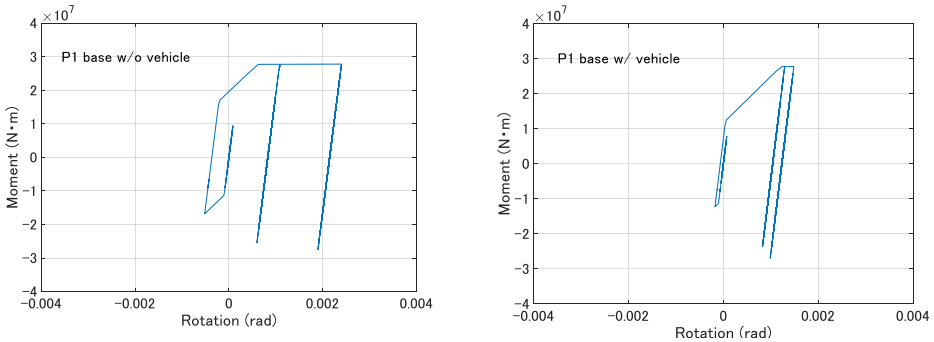

Figure 10: Hysteresis loop of plastic hinge at pier P1 base under GM1, disregarding moving vehicles (left) and considering moving vehicle (right).

Pier		Maximum displacement	Reduction ratio * %	Permanent dis-placement	Reduction ratio * %
Span center	w/o	0.166	1.8	0.014	21.4
	w/	0.163		0.011	
P1	w/o	0.058	13.8	0.025	31.6
	w/	0.050		0.017	
P2	w/o	0.066	19.3	0.031	35.9
	w/	0.053		0.020	

Note. *reduction ratio is defined as the average displacement reduction from the w/o-vehicles case to the w/-vehicles case divided by the average displacement in the w/o-vehicles case.

Table 8: Displacement responses of the bridge under GM1 (unit: m).

Pier		Rotation	Reduction ratio* %
P1	w/o	0.0024	37.5
	w/	0.0015	
P2	w/o	0.0028	39.3
	w/	0.0017	

Note. * reduction ratio is defined as the average rotation reduction from the w/o-vehicles case to the w/-vehicles case divided by the average rotation in the w/o-vehicles case.

Table 9: Maximum rotation of plastic hinge at pier base under GM1 (rad).

The hysteresis loop of bearing at P1 pier top and the longitudinal displacement responses of pier top under GM2 are depicted in Figures 11 and 12 as typical example, and those of A1, P2, A2 and the moment-rotation hysteresis loops at pier base are omitted here for simplicity. The maximum relative displacements of bearings considering VBI under GM2 increased up to 10% at A1, P1 and P2, but decreased slightly at A2 as indicated in Table 10. The maximum longitudinal displacements of pier tops were slightly reduced and the maximum displacement of span center was amplified a little, when the moving vehicles presented as shown in Table 11. The residual displacements of observation points were amplified by considering vehicle-bridge interaction up to 17% compared with those without considering vehicle-bridge interaction. Under strong ground motion GM2, the consideration of vehicle dynamics might yield larger longitudinal displacement and maximum relative displacement of bearing than those with bridge alone. The maximum rotation of the plastic hinge at pier base was reduced about 10% under moving vehicles compared with those with bridge alone subjected to GM2.

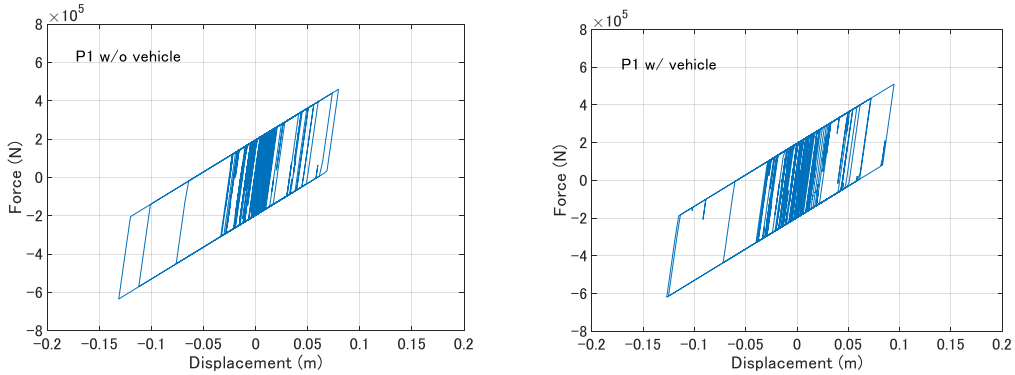

Figure 11: Hysteresis loop of bearing at P1 pier top under GM2, disregarding moving vehicles (left) and considering moving vehicle (right).

		Displacement	Reduction ratio * %
A1	w/o	0.403	-2.5
	w/	0.413	
P1	w/o	0.255	-9.4
	w/	0.279	
P2	w/o	0.240	-10.8
	w/	0.266	
A2	w/o	0.408	0.2
	w/	0.407	

Note. *reduction ratio is defined as the average displacement reduction from the w/o-vehicles case to the w/-vehicles case divided by the average displacement in the w/o-vehicles case.

Table 10: Maximum relative displacement of bearing under GM2 (unit: m).

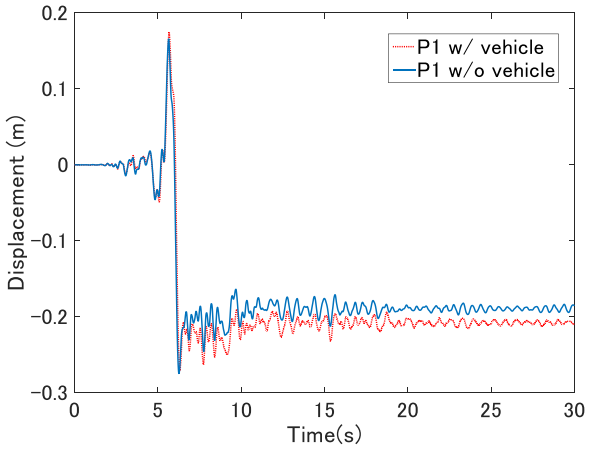

Figure 12: Longitudinal displacement responses of the pier top P1 under GM2.

Pier		Maximum displacement	Reduction ratio *%	Permanent displacement	Reduction ratio *%
Span center	w/o	-0.408	-1.0	-0.123	-17.1
	w/	-0.412		-0.144	
P1	w/o	-0.275	1.5	-0.189	-10.1
	w/	-0.271		-0.208	
P2	w/o	-0.285	1.4	-0.185	-8.6
	w/	-0.281		-0.201	

Note. *reduction ratio is defined as the average displacement reduction from the w/o-vehicles case to the w/-vehicles case divided by the average displacement in the w/o-vehicles case.

Table 11: Longitudinal displacement responses of the bridge under GM2 (unit: m).

Pier		Rotation	Reduction ratio*%
P1	w/o	-0.026298	10.1
	w/	-0.023652	
P2	w/o	-0.026038	9.7
	w/	-0.023504	

Note. * reduction ratio is defined as the average rotation reduction from the w/o-vehicles case to the w/-vehicles case divided by the average rotation in the w/o-vehicles case.

Table 12: Maximum rotation of plastic hinge at pier base under GM2 (unit: rad).

In general, in case of fully loaded traffic condition under strong earthquakes, ignoring vehicle effects would be on the non-conservative side. The vehicles had a significant negative effect on the bridge's nonlinear displacement responses.

5.2 Acceleration responses

Figure 13 shows the time history of the longitudinal acceleration observed at P1 pier top for example. The peak and RMS values of longitudinal acceleration responses of observation points are summarized in Figure 14.

From the peak and RMS values of longitudinal acceleration responses at span center and pier tops shown in Fig. 12, it is readily apparent that vehicles reduced the peak at span center and RMS values at span center and pier tops compared with that of disregarding vehicles, even if the peak values of acceleration responses at pier tops were amplified. The reduction in bridge acceleration could be explained by the relationship between the bridge's fundamental frequency and the response spectra of ground motions. The in-phase modes of the system were excited by the ground motions to cause the seismic responses of the bridge to a level lower than the original bridge-alone modes was. For example, in the pseudo acceleration response spectrum of the ground motion (Figure 6(c)), the spectral acceleration corresponding to the natural period (0.742 s, i.e. 1.348 Hz to the natural frequency) of the vehicle-bridge in-phase mode in Position 4 scenario, is smaller than that corresponding to the natural period (0.549 s, i.e. 1.822 Hz) of the bridge alone. The additional vehicle dynamics might move the system's fundamental period to a more favorable part of the spectrum where the spectral accelerations are less than the conventional case disregarding vehicle. Another reason may be the vehicles act as mass-spring-damper systems on the bridge. The natural period (0.549 s, i.e. 1.822 Hz) of the bridge alone and the longitudinal natural period (0.487 s, i.e. 2.052 Hz) of the vehicle are indicated in pseudo acceleration responses spectra of the ground motion in Fig. 6(c) and the vehicle and bridge would be excited by the ground motions. The vehicle resonated out of phase with the bridge motion and caused a phase difference in the bridge structural response, which affects the acceleration responses in way of a damper-like action.

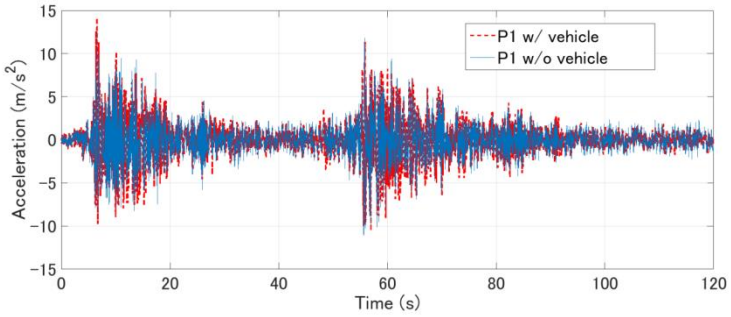

Figure 13: The time history of longitudinal acceleration responses of the bridge at pier top of P1 under GM1.

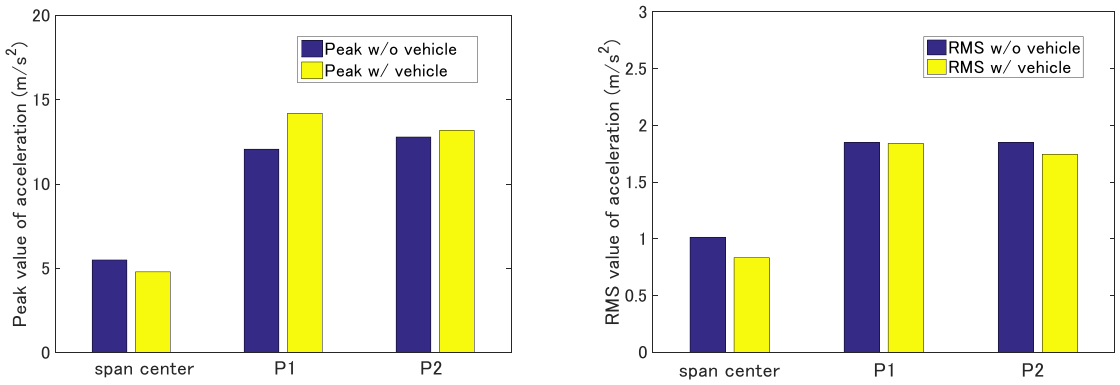

Figure 14: Peak (left) and RMS values (right) of longitudinal acceleration response of the bridge under GM1.

Figure 15 shows the time history of longitudinal acceleration responses of P1 pier top under GM2 as a typical example. Figure 16 shows the peak and RMS values of longitudinal acceleration responses of P1, P2 pier top and span center under GM2. As expected, they presented differently between the cases of regarding and disregarding moving vehicles. From the time histories, peak value and RMS values of longitudinal acceleration responses of observations points, it can be known that the longitudinal acceleration responses of the bridge generally decreased when the vehicles were considered in comparison with those when the vehicles were not considered. The observations presented herein showed that ignoring vehicle effects might be conservative when the acceleration responses were of concern.

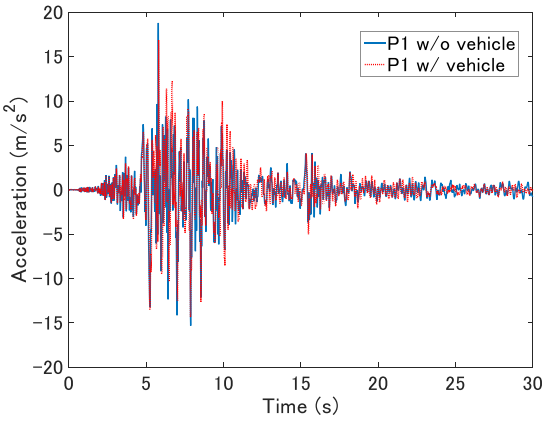

Figure 15: The time history of longitudinal acceleration response of P1 pier top under GM2.

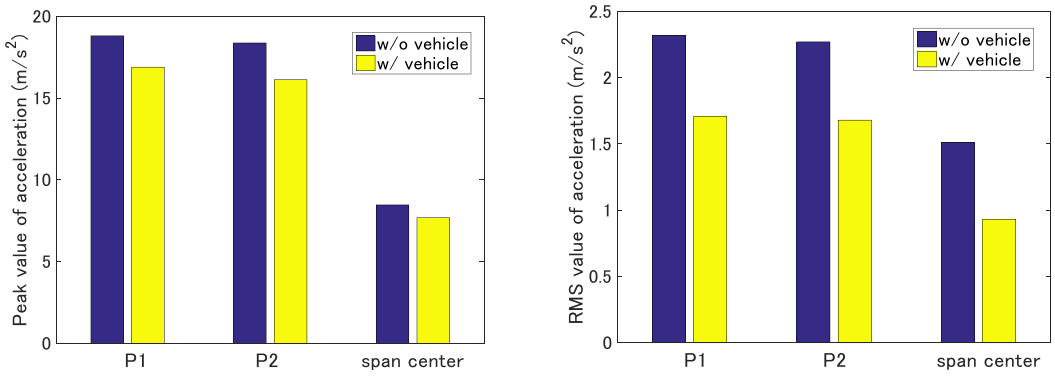

Figure 16: Peak (left) and RMS values (right) of longitudinal acceleration response of the bridge under GM2.

6 CONCLUSIONS

- In the longitudinal displacement, the presence of moving vehicles tends to reduce the maximum displacement and the permanent displacement under ground motion of Tohoku earthquake; reduce the maximum displacement and amplify the permanent displacement under ground motion of Kumamoto earthquake.
- In the bearing's relative displacement, the presence of moving vehicles tends to reduce the maximum displacement under ground motion of Tohoku earthquake, and amplify under ground motion of Kumamoto earthquake.

- The presence of moving vehicles reduced the RMS values of acceleration responses slightly even if increased the peak values of acceleration responses of bridge under ground motion of Tohoku earthquake;
- The results emphasized the need and importance of considering vehicle-bridge interaction as well as different ground motions in seismic design of bridges.
- The current assumption of ignorance of vehicle effect in seismic design of highway bridges might be non-conservative.

REFERENCES

[1] Japan Academic Network of Disaster Reduction, materials distributed in the press conference: http://janet-dr.com/11_saigaiji/160415kyushu_kaiken/160418all.pdf (retrieved: 04/22/2016).

[2] C.W. Kim, M. Kawatani, T. Kanbara, N. Nishimura, Seismic behavior of steel monorail bridges under train load during strong earthquakes. *Journal of Earthquake and Tsunami* , **7** (2), 1350006-1-1350006-17, 2013. DOI: 10.1142/S1793431113500061.

[3] H. Xia, M. Kawatani, T. Hayashikawa, T. Matsumoto, Numerical analysis on seismic response of Shinkansen bridge-train interaction system under moderate earthquakes. *Earthquake Engineering and Engineering Vibration,* **10** (1), 85-97, 2011. DOI: 10.1007/s11803-011-0049-1.

[4] Q. Zeng, E.G. Dimitrakopoulos, Seismic response analysis of an interacting curved bridge-train system under frequent earthquakes. *Earthquake Engineering & Structural Dynamics*, 45, 1129-1148, 2016. DOI: 10.1002/eqe.2699.

[5] C.W. Kim, M. Kawatani, Effect of train dynamics on seismic response of steel monorail bridges under moderate ground motion. *Earthquake Engineering & Structural Dynamics,* **35** (10), 1225-1245, 2006. DOI: 10.1002/eqe.580.

[6] I. Sugiyama, H. Kameda, N. Sasaki, S. Kawakita, Dynamic structure vehicle interaction of highway bridges and its implication to seismic design. *Proceedings of the 6th U.S.–Japan Bridge Engineering Workshop*, 379-392, Lake Tahoe, NV, 379-392May 7-8, 1990.

[7] H. Kameda, Y. Murono, A. Nanjou, N. Sasaki, Earthquake response of highway bridges under bridge-vehicle system. *Journal of Structural Mechanics and Earthquake Engineering JSCE (Doboku Gakkai Ronbushuu A)*, **626** (I-48), 93-106, 1999. (in Japanese)

[8] H. Kameda, H. Kita, H. Morikawa, Seismic load of highway bridges under dynamic effect of vehicle loading. *Journal of Structural Engineering,* 36 A, 791-801, 1990. (in Japanese)

[9] C.W. Kim, M. Kawatani, S. Konaka, R. Kitaura, Seismic responses of a highway viaduct considering vehicles of design live load as dynamic system during moderate earthquakes. *Structure and Infrastructure Engineering*, **7**(7-8), 523-534, 2011.DOI: 10.1080/15732479.2010.493339.

[10] M. Kawatani, C.W. Kim, K. Iwashita, K. Yasui, Seismic Responses of Highway Viaducts Incorporating Bridge-Vehicle Interaction. *Journal of JSCE A*, **64** (4), 678-691, 2008. (in Japanese)

[11] S. Borjigin, C.W. Kim, K.C. Chang, K. Sugiura, Nonlinear dynamic response analysis of vehicle–bridge interactive system under strong earthquakes. *Engineering Structures*, 176, 500-521, 2018. https://doi.org/10.1016/j.engstruct.2018.09.014

[12] R.W. Clough, J. Penzien, *Dynamics of Structures*. New York, McGraw Hill, 2003.

[13] ISO 8608: Mechanical vibration—Road surface profiles—reporting of measured data. *International Organization for Standardization*, 1995(E).

[14] *Design specification of highway bridges. Part V: Seismic design*. Japan Road Association, Japan, 2012.

[15] Earth Science and Disaster Prevention (NIED). (Available from: http://www.kyoshin.bosai.go.jp/kyoshin/) accessed on [24 August 2016].

[16] C.W. Kim, M. Kawatani, K.B. Kim, Three-dimensional dynamic analysis for bridge-vehicle interaction with roadway roughness. *Computer and Structures*,**83**,1627-1645, 2005. DOI:10.1016/j. compstruc. 2004.12.004.

[17] A. Gonzalez, Vehicle–bridge dynamic interaction using finite element modelling. *Finite Element Analysis, Moratal*, D. (Ed.), ISBN: 978-953-307-123-7, InTech, 2010. DOI: 10.5772/10235.

[18] S. Borjigin, C.W. Kim, K.C. Chang, K. Sugiura, Numerical investigations on dynamic responses of a highway bridge under moving vehicles subject to strong earthquakes. *Proceedings of JSCE Annual Conference*, Sendai, Japan, September 7-9, 2016.

[19] L.M. Anggraini, S. Borjigin, C.W. Kim, K. Sugiura, Seismic response analysis of urban highway viaducts under multiple vehicles subjected to strong earthquakes. *16th World Conference on Earthquake Engineering*, Santiago Chile, January 9-13, 2017.

COMPDYN 2019
7th ECCOMAS Thematic Conference on
Computational Methods in Structural Dynamics and Earthquake Engineering
M. Papadrakakis, M. Fragiadakis (eds.)
Crete, Greece, 24-–26 June 2019

NUMERICAL AND EXPERIMENTAL ASSESSMENT OF TUNED LIQUID DAMPERS EFFICIENCY FOR STRUCTURAL RESPONSE REDUCTION OF TALL BUILDINGS UNDER EARTHQUAKE EXCITATION

Alberto Stella[1], Steven Decelle[2], Mauro Dal Zovo[2], Roberto Scotta[2], and Lorenzo De Stefani[2]

[1]IUAV University of Venice
Dorsoduro 2206, 30123 Venezia, Italy
alberto.stella@iuav.it

[2] University of Padova
Department of Civil, Environmental and Architectural Engineering
Via Marzolo 9, 35131 Padova, Italy
roberto.scotta@dicea.unipd.it, lorenzo.destefani@dicea.unipd.it

Keywords: Tuned liquid dampers, Equivalent mechanical model, Non-linear modeling, Experimental analysis, Earthquake engineering.

Abstract. *The behavior of tuned liquid dampers subjected to random base motion has been investigated extensively. However, their efficiency in reducing the dynamic response of structures under earthquake excitation is still not completely understood. A non-linear modeling strategy based on Yu's model was implemented to perform numerical analyses on a 21-story building subjected to seismic base excitation. Three tank shapes were investigated: a rectangular tank, a vertical cylindrical tank, and a horizontal cylindrical innovative TLD. An experimental campaign has been conducted on a scaled physical model in order to calibrate the numerical model and validate its results. The effects of the dampers were evaluated in terms of structural relative displacements and absolute accelerations. Dampers efficiency in reducing the structural response was evaluated for different mass ratios. The non-linear numerical model showed good capability in reproducing experimental results for the rectangular tank. Some limitation has been evidenced for the other tank shapes, suggesting the use of different numerical techniques or the development of specific non-linear mechanical models. Results obtained from experimental and numerical analyses show that reduction of peak response during earthquake excitation is often limited and dependent on ground motion history. However, TLDs where found to be effective in reducing structural response when the structure experience free vibration motion.*

1 INTRODUCTION

Tall buildings can experience large displacements when excited by wind or earthquakes. Various methods for vibration control of tall buildings have been developed through the years. One of such methods is the use of the tuned mass damper (TMD) which is a mass connected to the main structure. The TMD-structure connection is designed so that the vibration frequency of the TMD is tuned to one of the structural frequencies. The purpose of such device is to diminish the structural response by oscillating out of phase with the structure and to dissipate energy. There have been various applications of TMDs [1] and in many of the cases they occupy a large amount of space in the structure, sometimes even whole floors. One particular variation of the TMD is the tuned liquid damper (TLD) which was first studied by Fujino et Al. [2] and Sun et Al. [3]. A TLD is a container partially filled with a liquid. It is similar to the TMD in the sense that the contained liquid acts as the mass of a TMD. The sloshing of the liquid inside the container can dissipate energy in many different ways compared to a solid mass. It is thus necessary to model the dynamics of the contained fluid in depth, in order to be able to predict the behavior of the TLD. In this context, Sun et Al. [4] proposed a non-linear model based on shallow water wave theory which considered wave breaking. Reed and Al. [5] and Yu et Al. [6] studied the behavior of tuned liquid dampers under large amplitude excitation and developed a non-linear mechanical model with stiffness and damping parameters which are dependent on the TLD base excitation amplitude. Kareem et Al. [7] developed a numerical model which is capable to simulate the slamming phenomenon and can predict the pressure peaks on tank walls due to this effect. Tanks with non-horizontal bottoms, such as conical or spherical, were investigated by Casciati et Al. [8] and Gardarrson et Al. [9]. Particular emphasis in the study of curved bottom TLDs was given by the works of Tait and Deng [10] and Bandyopadhyay et Al. [11]. In particular, Tait and Deng [10] showed that the horizontal cylinder TLD is more robust and offers greater performance in the reduction of structural response due to harmonic load, compared with rectangular and vertical cylinder TLD. Bandyopadhyay et Al. [11] developed a boundary element method (BEM) to estimate the sloshing frequency of parabolic shaped bottom TLDs. The main sloshing frequency of a horizontal cylinder TLD is less dependent on the liquid height with respect to other tank shapes, so it is less sensitive to detuning problems due to variations in the water depth. The capability of tuned liquid dampers in reducing structural response of buildings under earthquake excitation was investigated by Banerji et Al. [12], who used a numerical method based on shallow water wave theory to solve the water motion in the TLD. Further relevant studies include the work of Novo et Al. [13], who investigated the reduction response provided by TLDs installed on a 9-floors concrete building. A new experimental testing technique called Real-Time Hybrid Simulation (RTHS) was successfully employed by Lee et Al. [14] and Wang et Al. [15] to study multi-degree-of-freedom (MDOF) structures with installed TLDs. This approach recalls the hardware-in-the-loop method used by Yalla [16] and allows to perform experimental dynamic shaking table tests on complex MDOF systems by physically representing only a part of them. The other part is represented and solved numerically in real time. This technique allows to avoid building large and heavy structural models and to test tuned liquid dampers at the full scale. In any case, to do this, there is the need for a shaking table which can carry the weight of the full-scale water tank.

In the present work we experimentally investigate the effect of tuned liquid dampers on the response of a 21-floor concrete building. The structure was modeled as a single-degree-of-freedom (SDOF) system and the TLDs were represented with plexiglass and glass containers filled with water. Three tank shapes have been investigated: a rectangular tank, a vertical cylin-

drical tank and a horizontal cylindrical tank. The performance of the TLDs was determined in terms of reduction of peak response for relative displacements and absolute accelerations. Then, a non-linear mechanical model was implemented following the formulation proposed by Yu et Al. [6]. The model was validated on experimental results and tested with a recorded ground motion, for different values of mass ratio.
The paper is organized as follows. The second section presents a description of the case study. In the third section of the paper the experimental setup and results are presented. The fourth section deals with the numerical modeling of the TLD-structure system and the numerical analysis results. In the fifth section main conclusions are summarized and further developments are proposed.

2 CASE STUDY DESCRIPTION

The case study presented in this work is a 21-floor concrete building located in Baku, Azerbaijan. The building is composed by two adjacent blocks, as indicated in figure 1, separated by a $16cm$ wide joint. Resistance for horizontal seismic actions is provided by columns and shear walls. The plan dimensions of the east block are 22x20m while those of the west block are 22x32m. The maximum height of the building is $68m$. In this study we analyzed the ability of a TLD installation to reduce the maximum displacement experienced by the east block during a seismic event. The possibility of limiting the peak displacements of the blocks appears desirable, in order to limit damage due to pounding between the two structures. In the following of the paper we will refer to the east block as "the building" or "the structure", as it was taken as the block where TLD system is to be installed. Modal analysis of the structure provides a first mode which has a period $T_p = 4.06s$, a modal participation factor $\Gamma_p = 50.175\%$ and a participating mass $M_p = 3104t$. The total mass of the structure is $9783.22t$. In this study, we modeled the structure as a single-degree-of-freedom (SDOF) system, with mass, stiffness and damping properties equal to those of the first vibration mode of the real building. Damping ratio was assumed equal to $\xi = 2\%$ and stiffness is equal to $K_p = 7416kN/m$.

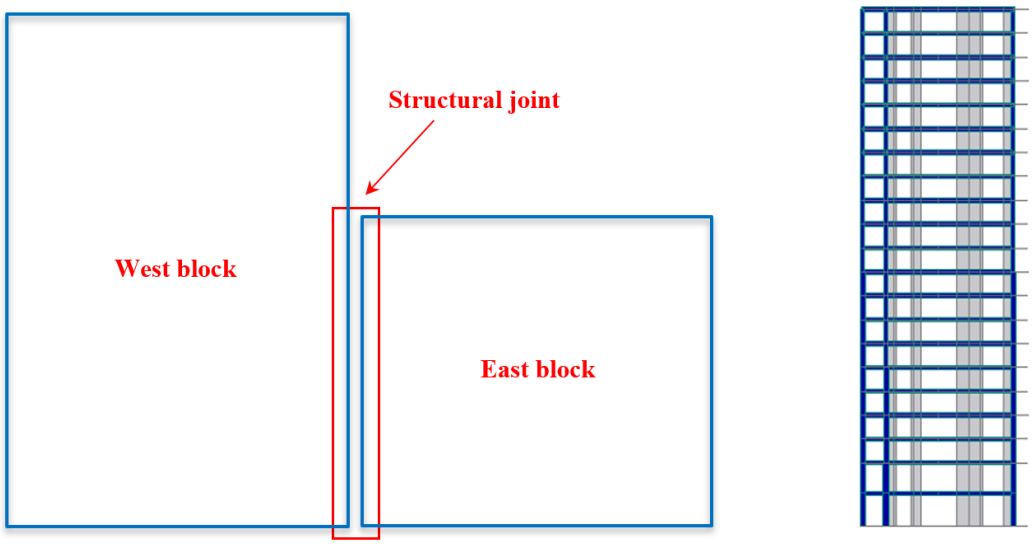

(a) (b)

Figure 1: a) Plain view of the case study building, b) East block structure.

3 EXPERIMENTAL TESTS

3.1 Scale model for TLD-structure interaction

In order to conduct experimental tests, the SDOF structure was represented with a scaled reverse pendulum physical model, composed of a wooden table supported by two rectangular aluminum plates fixed to a wooden base, as shown in figure 2. The mass of the system was represented by the upper wooden table and by the mass of the container, while the stiffness was provided by the flexural stiffness of the two steel plates. The shear-type lateral deformation of the two steel plates presents an equivalent stiffness $k_m = 890N/mm$ and a damping ratio $\xi_m = 0.007$. Since the damping ratio for the experimental model is out of scale, numerical comparisons have been made using the experimental value ξ_m for time history analyses. Three different tank shapes have been investigated, namely rectangular, vertical cylindrical and horizontal cylindrical. Due to the restriction given by the available tank dimensions and load bearing capacity of shaking table, the three physical models which represent the prototype have different scale ratios and the number of the installed TLDs was different for every tank shape. The consequence is that the mass ratio μ, calculated as the ratio between total liquid mass and total mass of the structure, was different for every tank shape.

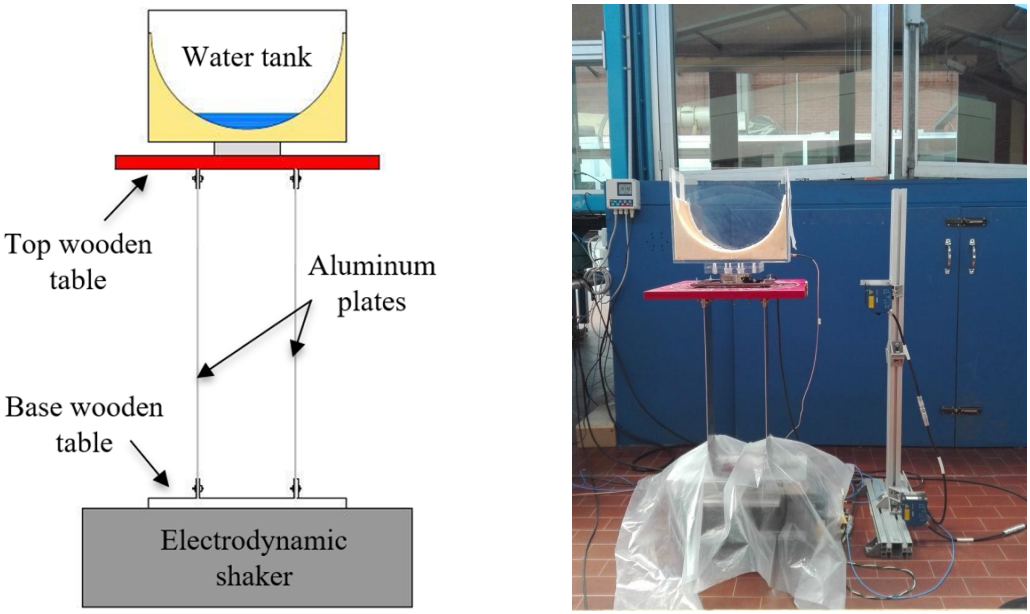

(a) (b)

Figure 2: a) Sketch of the experimental setup, b) Horizontal TLD-structure system.

Water depths were chosen in order to tune the TLD to the structure. Linear sloshing formulations, as reported by Ibrahim [17], were employed to calculate sloshing frequencies for rectangular and vertical cylindrical tanks. Horizontal cylinder sloshing frequency has been evaluated using the formulation proposed by McIver [18]. The rectangular tank dimensions were 150x$150mm$; the vertical cylinder has a radius of $67mm$ and the horizontal cylinder radius was $145mm$. Since the liquid density and the gravity acceleration were the same for the prototype and the experimental model, the length scale ratio allows to determine scale ratios for all the other variables.

Tank shape	$h[m]$	$m_w[kg]$	$m_s[kg]$	$m_s^{tot}[kg]$	$\mu[\%]$	$f_w[Hz]$	λ	n
Rectagular	0.024	0.540	10.013	31.765	1.7	1.554	39.6	5
Vertical cylinder	0.023	0.324	6.384	20.250	1.6	1.954	62.5	2
Horizontal cylinder	0.032	0.596	7.730	24.833	2.4	1.333	51	3

Table 1: Parameters of the three experimental models.

In table 1 the values of liquid height h, total liquid mass m_w (assumed equal to the convective mass), structural mass of the SDOF system m_s, scaled total structural mass m_s^{tot}, mass ratio μ, sloshing frequency f_w, number of required TLDs n and length scale ratio λ are reported.

3.2 Response reduction for artificial ground motion

The three TLD-structure systems were tested with an artificially generated accelerogram. The design acceleration response spectrum was chosen according to Akhundov et Al. [19] and is presented in figure 3. The original design spectrum was scaled along the time axes using the scale ratio for the vertical cylinder model, in order to obtain the scaled response spectrum for the experimental model.

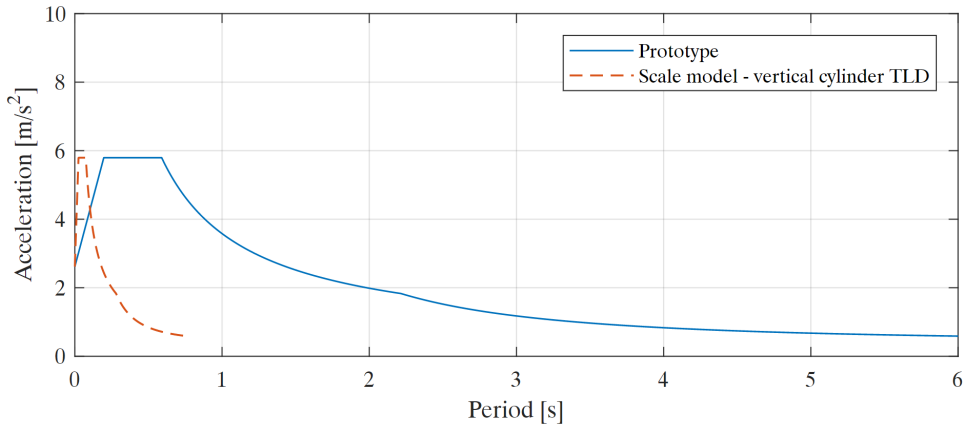

(a)

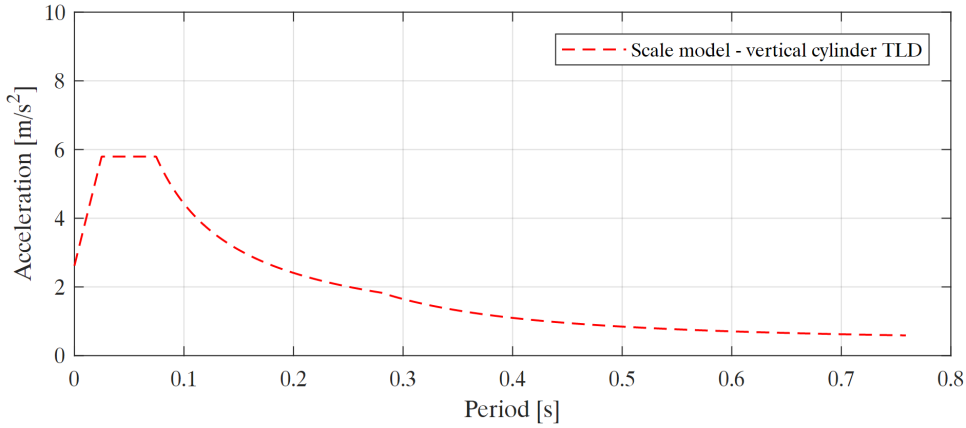

(b)

Figure 3: a) Original and scaled response spectra, b) Spectrum for vertical cylinder model.

A ground motion compatible with the scaled spectrum was generated using the software SIMQKE-I developed by Gasparini and Vanmarcke [20]. The generated accelerogram was scaled along the time axes in order to obtain ground motions for the rectangular and horizontal cylinder setups. After that, the three ground motions were scaled along the acceleration axes to obtain acceleration time histories with different values of peak ground acceleration (PGA). Three values of PGA were used, namely, $2.5m/s^2$, $3.5m/s^2$, $4.5m/s^2$.

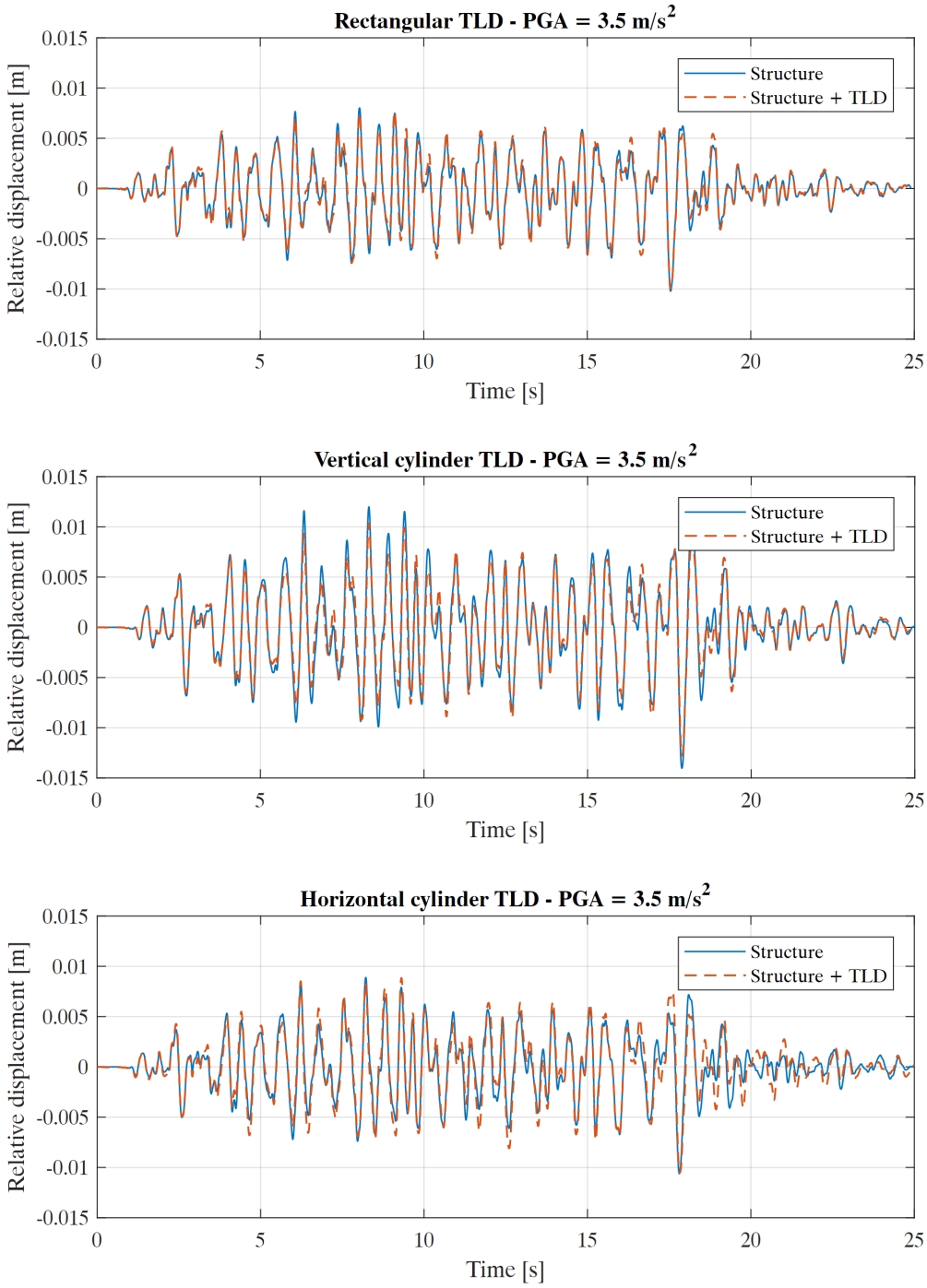

Figure 4: Example of relative displacements time histories for the three experimental models.

The ground motion inputs were applied by a long stroke electrodynamic shaker, controlled by a Labview routine. Acceleration and displacement were measured at the base and at the top of the structure, by means of capacitive accelerometers and laser displacement transducers. Measured data were filtered using a lowpass filter with a cutoff frequency equal to $20Hz$ for displacements and $25Hz$ for accelerations. Relative structural displacements are directly related to the shear force acting on the structural elements, and they also are responsible for pounding between adjacent structures when the buildings experience the same base motion. Moreover, absolute acceleration at the top of the structure generates seismic force on appendages and non-structural elements at the top floor of the building. For the previous reasons, the evaluation of TLD efficiency was measured in terms of reduction of relative displacement and absolute accelerations at the top of the structure. An example of time history comparison of relative displacement response for the three TLD-structure systems are presented in figure 4 for the case of $PGA = 3.5m/s^2$. For this comparison, vertical cylinder and horizontal cylinder response have been scaled at the same scale of the rectangular TLD, in order to have comparable time and displacement measures.

It can be seen that the design procedure adopted for the experimental setups has led to different maximum displacements for the different scale ratio sets. For further studies it will be important to consider the same scale ratio set for every tank shape. In figure 5 experimentally measured reduction of peak response (RPR) are presented for the three tank shapes. The RPRs for relative displacements and absolute accelerations have been defined as:

$$R_d = \frac{\max\{|d_r^{(s)}|\} - \max\{|d_r^{(s+TLD)}|\}}{\max\{|d_r^{(s)}|\}} \qquad R_a = \frac{\max\{|a_r^{(s)}|\} - \max\{|a_r^{(s+TLD)}|\}}{\max\{|a_r^{(s)}|\}}$$

Results evidence that RPR for relative displacement varies in the range of $-2\% \div 13\%$ and RPR for absolute acceleration ranges between 2.5% and 19%.

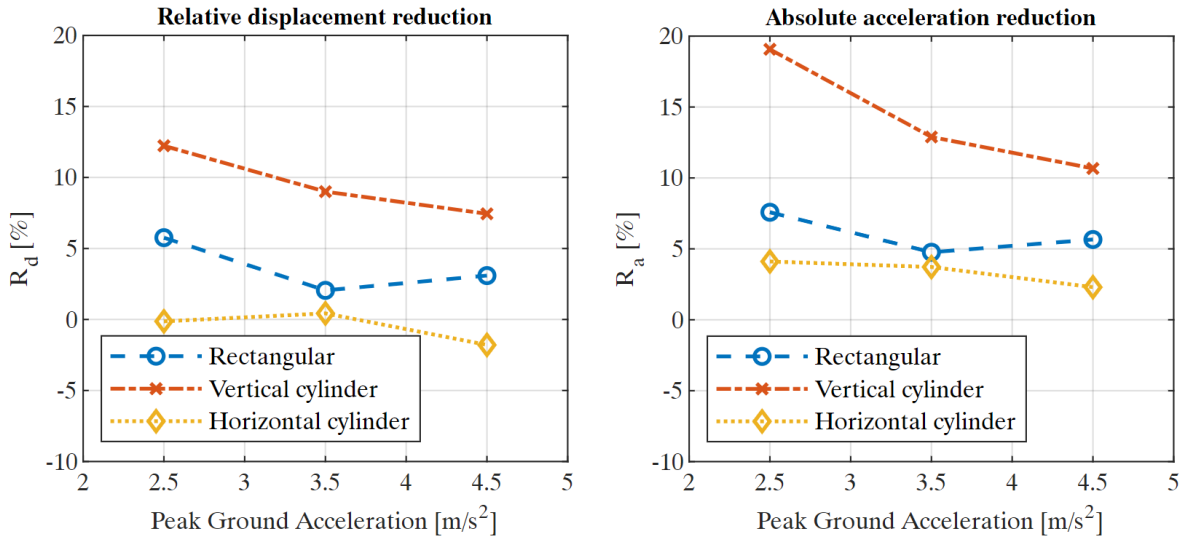

Figure 5: Reduction of peak response in terms of relative displacements and absolute accelerations for the three experimental models.

It is hard to identify a trend which is confirmed for all the tank shapes. In fact, since the ground motions for the different $PGAs$ have the same peaks distribution in time but different acceleration values, the displacement histories experienced by the base of the structure are significantly different. For this reason, the comparison of peak reductions for different $PGAs$ doesn't necessarily provide a trend, as in the case of the rectangular tank.

4 NUMERICAL MODELLING AND RESULTS

4.1 Non-linear mechanical model

In order to perform numerical time history analysis, a non-linear mechanical model was implemented to describe the TLD behavior. The formulation developed by Reed et Al. [5] and Yu et Al. [6] provides an equivalent mechanical model called "Non-linear Stiffness and Damping model" (NSD) in which stiffness and damping parameters of the TLD vary with amplitude excitation at the base of the water tank. The model was originally developed for a rectangular TLD and it was calibrated by matching the numerical energy dissipation curves to their corresponding experimental counterparts which were determined under harmonic base excitation. Say A is the amplitude of the harmonic motion experienced by the tank. The non-dimensional base excitation Λ can be expressed as:

$$\Lambda = \frac{A}{L}$$

where L is the length of the rectangular tank. The amplitude dependent damping ratio can be expressed as:

$$\xi_{NSD} = 0.52 \cdot \Lambda^{0.35}$$

The stiffness of the equivalent system k_{NSD} can be defined as the product of the linear modeling stiffness k_l (obtained from the linear sloshing frequency of the rectangular tank) and an amplitude dependent stiffness coefficient κ, defined as:

$$\begin{aligned} \kappa &= 1.075 \cdot \Lambda^{0.007} \qquad & \Lambda \leq 0.003 \\ \kappa &= 2.52 \cdot \Lambda^{0.25} \qquad & \Lambda > 0.003 \end{aligned}$$

In order to use the NSD model for a tank shape different from the rectangular one, it is necessary to treat the tank as it would be a rectangular tank, by calculating its equivalent length and width such that the water mass, water height and sloshing frequency would be the same as those of the rectangular tank. In figure 6 the time history of relative displacement for the experimental model with the rectangular TLD and $PGA = 2.5m/s^2$ is presented. It can be seen that, while the linear model overestimates the response in several parts, the non-linear mechanical model shows a good capability in reproducing the structural response.

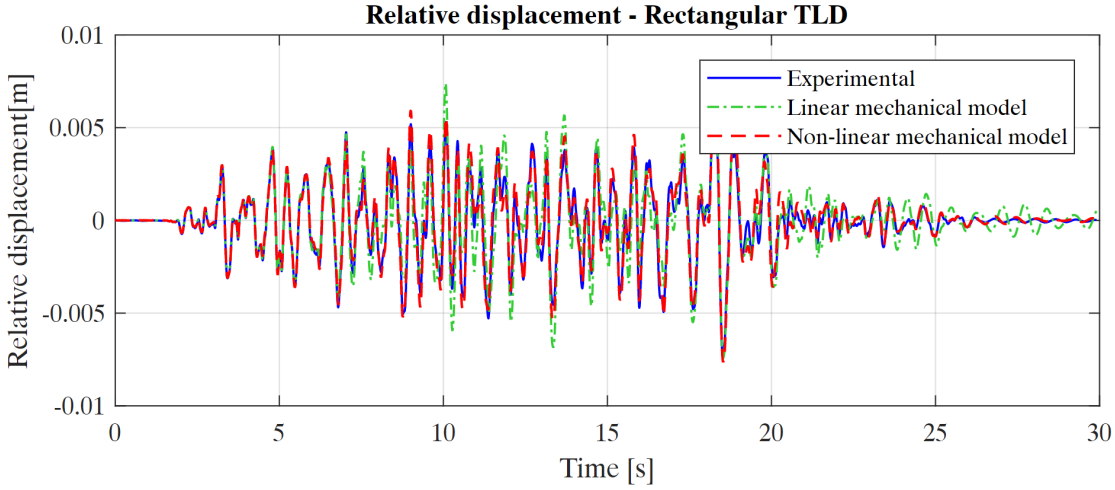

(a)

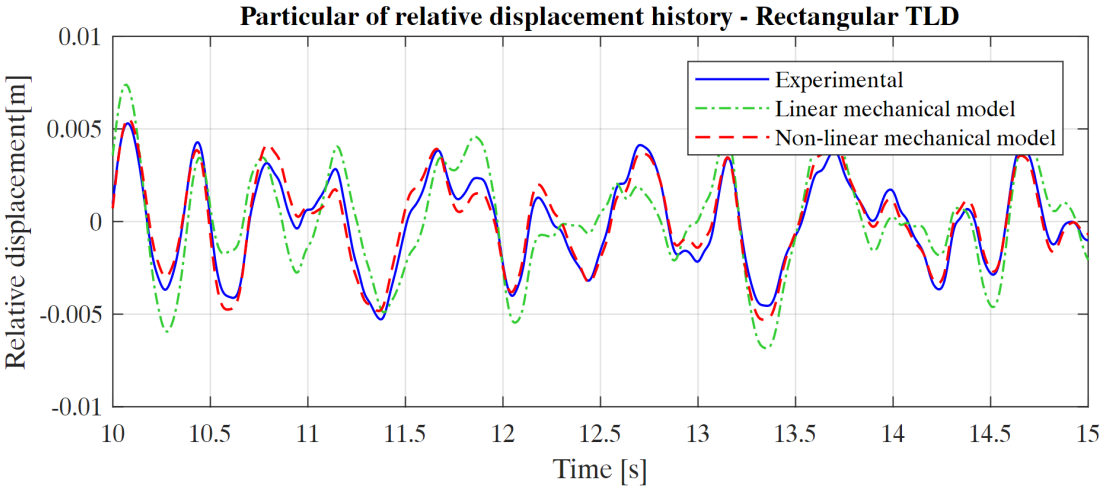

(b)

Figure 6: Comparison of experimental and numerical relative displacement history for rectangular TLD for the case with $PGA = 2.5m/s^2$ a) Complete time history, b) Range between $10s$ and $15s$.

In order to quantify the accuracy of numerical models, a measure of the error done by the numerical model over the whole response time history was defined as:

$$e = \frac{RMS_{num} - RMS_{exp}}{RMS_{exp}} \cdot 100 \quad [\%]$$

where RMS_{exp} and RMS_{num} are the root mean squares of the experimental and numerical relative displacement time history respectively. In table 2 the values of the error e are showed for every experimental test. It can be seen that the non-linear model performs well for the rectangular tank shape, while larger errors can be found for the vertical cylindrical and horizontal cylindrical tank shapes. For the rectangular and the vertical cylindrical TLD both the linear and the non-linear model overestimate the experimental results. For the horizontal cylindrical TLD the linear model provides displacement values which are greater than those experimentally mea-

sured. On the other side, non-linear model behaves in the opposite manner. These differences in error values can be addressed to the dissipation mechanisms of the water mass that occur in the rectangular tank, compared with those of the other tank shapes. A better accuracy in the modeling of non-rectangular shape TLDs can be achieved by using different approaches such as other numerical methods or ad hoc developed non-linear mechanical models.

Errors [%] for $\mathbf{PGA = 2.5 m/s^2}$

	Rectangular	Vertical cylinder	Horizontal cylinder
Linear model	5.1	10.6	3.9
Non-linear model	4.0	14.1	-6.5

Errors [%] for $\mathbf{PGA = 3.5 m/s^2}$

	Rectangular	Vertical cylinder	Horizontal cylinder
Linear model	7.3	14.8	4.0
Non-linear model	3.6	24.6	-5.7

Errors [%] for $\mathbf{PGA = 4.5 m/s^2}$

	Rectangular	Vertical cylinder	Horizontal cylinder
Linear model	9.5	35.0	4.6
Non-linear model	2.9	21.9	-5.8

Table 2: Numerical models percentage errors for relative displacements time histories.

4.2 Analyses with recorded ground motion

In order to test the numerical model with a recorded accelerogram the Kobe ground motion was selected and scaled in order to have a PGA equal to $0.5g = 4.903 m/s^2$. Only the rectangular TLD was used and the non-linear numerical model was employed. Figure 7 illustrates the applied ground motion.

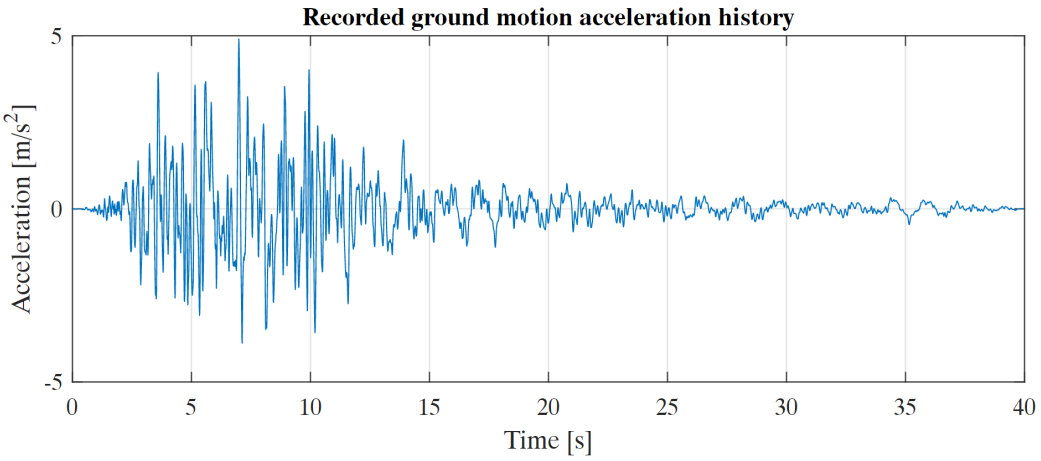

Figure 7: Kobe earthquake ground motion acceleration history used for the numerical analysis.

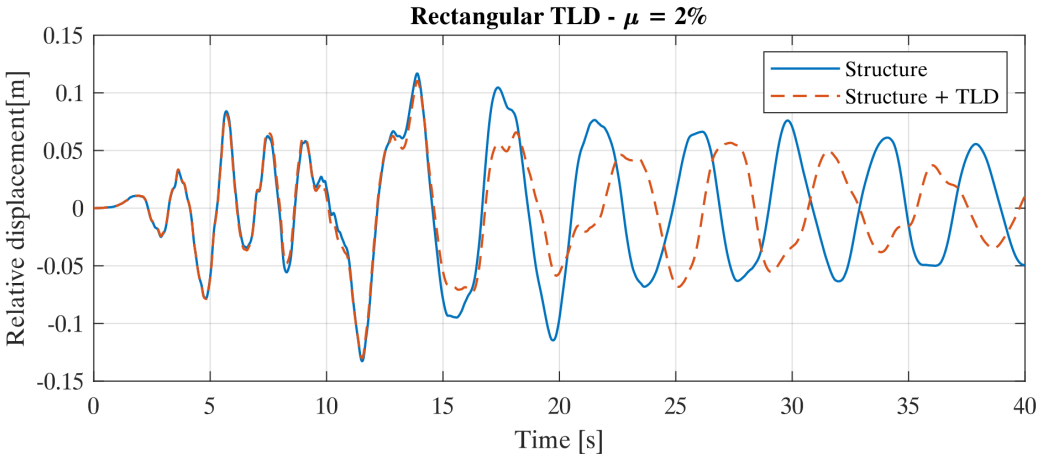

Figure 8: Numerical results for the rectangular TLD-structure system under Kobe earthquake.

The numerical analysis was conducted at the prototype scale and five TLDs were employed, with length $L = 6m$, width $b = 7m$ and water depth $h = 0.95m$. The mass ratio was equal to 2%. The relative displacement response is represented in figure 8. The reduction of the peaks in relative displacement and absolute acceleration responses are $R_d = 1.67\%$ and $R_a = 4.9\%$ respectively. A greater reduction in relative displacements is observed in the part of the response where the structure is in free vibration (i.e. the part of the response history after $15s$) as recognized by Fujino et Al. [2]. Figure 9 depicts the variation of RPR with the mass ratio, for relative displacements and absolute accelerations. It can be seen that, while the absolute acceleration reduction increases with the mass ratio, for the relative displacement there is an optimum value, after which the performance of the TLD decreases. However, it is important to underline that these graphs have been evaluated for the present structure and for the Kobe ground motion. The peak reduction (for response peaks which occur during the forced part of the history, i.e. when the particular part of the solution is prevailing) is strongly dependent on the ground motion and even when it exists, the reduction is often nearly negligible.

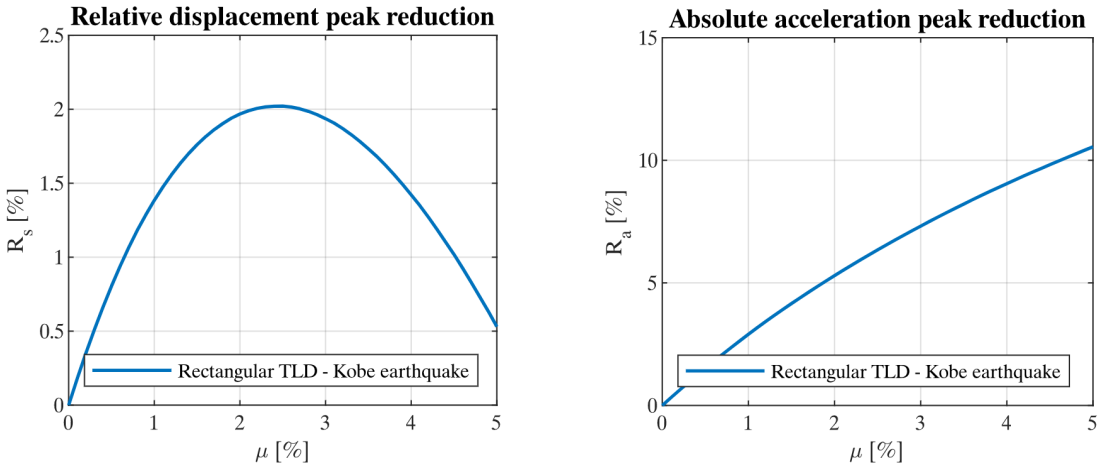

Figure 9: Relative displacement and absolute acceleration peak reduction variation with mass ratio for structure subjected to the Kobe earthquake for rectangular TLD.

5 CONCLUSIONS

This work investigated the seismic response of a tall building with tuned liquid dampers of different shapes installed. Three different scale models of the TLD-structure system were designed, built and tested with an artificially generated accelerogram applied at the base of the model by an electrodynamic shaker. Time histories of relative displacement and absolute acceleration of the structure were compared, for the structure only and for TLD-structure system. Results show that reductions of peak response are in the range of $0 \div 20\%$. However, in some cases, an increase in peak response was found. Numerical analyses showed that the non-linear mechanical model proposed by Yu et Al. [6] is suitable for performing time history analysis with seismic base excitation. The model can be employed for every tank geometry, by converting it into an equivalent rectangular tank, with the same liquid height, liquid mass and sloshing frequency. This approach yields good results when the sloshing motion and the energy dissipation curves for the tank are similar to those of a rectangular tank. For the horizontal cylindrical TLD a better modeling strategy could be obtained by using, for instance, a pendulum mechanical model, a specifically developed non-linear mechanical model, or a different numerical technique. Numerical analyses with a recorded ground motion showed that a TLD installation can effectively reduce the structural motion only when the structure experience a free vibration motion. TLDs are consequently not the best choice as a retrofit, in case the seismic response mitigation is necessary for a tall building. However, the capability of limiting the structural response during harmonic motions can be particularly useful for reducing the response of non-structural elements in resonance conditions. In fact, when the building vibrates with its own period, a secondary element can experience resonant conditions if both the secondary element and the building have similar vibration frequencies. In this case, a TLD installation above the secondary element can be very effective in reducing its peak response.

ACKNOWLEDGEMENTS

Part of the experimental campaign was conducted using the facilities of the CRIACIV boundary layer wind tunnel laboratory. The authors would thank Prof. Gianni Bartoli and Dr. Tommaso Massai from University of Florence for their very useful ideas and suggestions.

REFERENCES

[1] M.G. Soto, H. Adeli, Tuned Mass Dampers. *Archives of Computational Methods in Engineering*, **20**, 419–431, 2013.

[2] Y. Fujino, B.M. Pacheco, P. Chaiseri, L.M. Sun, Parametric studies on tuned liquid damper (TLD) using circular containers by free-oscillation experiments. *Structural Engineering and Earthquake Engineering*, **5(2)**, 381–391, 1988.

[3] L.M. Sun, Y. Fujino, B.M. Pacheco, M. Isobe, Nonlinear waves and dynamic pressures in rectangular tuned liquid damper (TLD): Simulation and experimental verification. *Structural Engineering and Earthquake Engineering*, **6(2)**, 251–262, 1989.

[4] L.M. Sun, Y. Fujino, A semi-analytical model for tuned liquid damper (TLD) with wave breaking. *Journal of Fluids and Structures*, **8(5)**, 471–488, 1994.

[5] D. Reed, J.K. Yu, H. Yeh, S.M. Gardarrson, Investigation of tuned liquid dampers under large amplitude excitation. *Journal of Engineering Mechanics*, **124(4)**, 405–413, 1998.

[6] J.K. Yu, T. Wakahara, D. Reed, A non-linear numerical model for the tuned liquid damper. *Earthquake Engineering and Structural Dynamics*, **28(6)**, 671–686, 1999.

[7] A. Kareem, S. Yalla, M. McCollough, Sloshing-Slamming Dynamics - S^2 - Analogy for Tuned Liquid Dampers. *Vibro-Impact Dynamics of Ocean Systems*, Springer-Verlag, Berlin, 123–133, 2009.

[8] F. Casciati, A. De Stefano, E. Matta, Simulating a conical tuned liquid damper. *Simulation Modelling Practice and Theory*, **11**, 353–370, 2003.

[9] S.M. Gardarrson, H. Yeh, D. Reed, Behavior of Sloped-Bottom Tuned Liquid Dampers. *Journal of Engineering Mechanics*, **127(3)**, 266–271, 2001.

[10] M.J. Tait, X. Deng, The performance of structure-tuned liquid damper systems with different tank geometries. *Structural Control and Health Monitoring*, **17**, 254–277, 2010.

[11] R. Banyopadhyay, S. Maiti, A Ghosh, A Chatterjee, Overhead water tank shapes with depth-independent sloshing frequencies for use as TLDs in buildings. *Structural Control and Health Monitoring*, **25(1)**, 2018.

[12] P. Banerji, M. Murudi, A.H. Shah, N. Popplewell, Tuned liquid dampers for controlling earthquake response of structures. *Earthquake Engineering and Structural Dynamics*, **29**, 587–602, 2000.

[13] T. Novo, H. Varum, F. Teixeira-Dias, H. Rodrigues, M. Falcao Silva, A. Campos Costa, L. Guerreiro, Tuned liquid dampers simulation for earthquake control response of buildings. *Bulletin of Earthquake Engineering*, **12**, 1007–1024, 2014.

[14] S.K. Lee, E.C. Park, K.W. Min, S.H. Lee, L. Chung, J.H. Park, Real-time hybrid shaking table testing method for the performance evaluation of a tuned liquid damper controlling seismic response of building structures. *Journal of Sounds and Vibrations*, **302**, 596–612, 2007.

[15] J.T. Wang, Y.Gui, F. Zhu, F. Jin, M.X. Zhou, Real-Time Hybrid Simulation of multy-story structures installed with tuned liquid dampers. *Structural Control and Health Monitoring*, **23**, 1015–1031, 2016.

[16] S. Yalla, Tuned liquid dampers for mitigation of structural response: Theoretical development and experimental verification. *PhD Thesis*, Department of Civil Engineering and Geological Science, University of Notre Dame, Indiana, 2001.

[17] R.A. Ibrahim, *Liquid Sloshing Dynamics: Theory and applications*. Cambridge University Press, 2005.

[18] P. McIver, Sloshing frequencies for cylindrical and spherical container filled to an arbitrary depth. *Journal of Fluid Mechanics*, **201**, 243–257, 1989.

[19] A. Akhundov, T. Mammadli, E. Garaveliyev, Q. Yethirmishli, G. Tanircan, *Seismic Hazard Assessment for Azerbaijan*. The NATO Science for Peace and Security Programme, 2010.

[20] D. Gasparini, E.H. Vanmarcke, *SIMQKE: A program for artificial motion generation*, Department of Civil Engineering, Massachusetts Institute of Technology, Cambridge (MA), 1976.

COMPDYN 2019
7th ECCOMAS Thematic Conference on
Computational Methods in Structural Dynamics and Earthquake Engineering
M. Papadrakakis, M. Fragiadakis (eds.)
Crete, Greece, 24–26 June 2019

PENDULUM VIBRATION ABSORBERS WITH SPATIALLY-VARYING TANGENTIAL FRICTION: MODELLING AND DESIGN

Emiliano Matta[1]

[1] Politecnico di Torino, Department of Architecture and Design
Viale Mattioli 39, 10125 Turin, Italy
e-mail: emiliano.matta@polito.it

Abstract

Passive vibration absorbers are widely used in structural control. They usually consist in a single-degree-of-freedom appendage of the main structure, tuned to a selected structural target mode by means of frequency and damping optimization. A classical configuration is the pendulum type, whose mass is bilaterally constrained along a curved trajectory and is typically connected to the structure through viscous dashpots. Although the principle is well known, the search for improved arrangements is still under way. In recent years this investigation has inspired a new type of bidirectional pendulum absorber (BPA), consisting of a mass moving along an optimal three-dimensional (3D) concave-up surface. For the BPA, the surface principal curvatures are conceived to ensure a bidirectional tuning to both principal modes of the structure, while damping is provided either by horizontal viscous dashpots or by vertical friction dampers between the BPA and the structure. In this paper, a BPA variant is proposed, in which damping is produced by the variable tangential friction force developing between the pendulum mass and the 3D surface, because of a spatially-varying friction coefficient. In fact, a friction coefficient pattern is proposed that varies along the pendulum surface proportionally to the modulus of the surface gradient. With this assumption, the absorber dissipative model proves nonlinear homogeneous at low response amplitudes. The resulting homogeneous BPA (HBPA) has a fundamental advantage over conventional friction-type absorbers, in that its equivalent damping ratio is independent of the amplitude of oscillations, i.e. its optimal performance is independent of the excitation level. At the same time, the HBPA is more compact and simpler than viscously damped BPAs, not requiring the installation of dampers. This paper presents the analytical modelling framework of the HBPA and a method for its optimal design. Numerical simulations under wind and earthquake loads are reported to compare the HBPA with classical viscously damped BPAs. Finally, the HBPA proves a promising alternative to existing pendulum absorbers, and the homogeneous tangential friction proves an effective way to realize amplitude-independent damping in structural systems.

Keywords: Amplitude-independent Damping, Homogeneous Friction, Pendulum Nonlinear Dynamics, Structural Control, Vibration Resonant Absorbers.

1 INTRODUCTION

Passive vibration absorbers are widely used in controlling civil engineering structures. Currently, they consist of single-degree-of-freedom (SDOF) appendages, tuned to the target structural mode through frequency and damping optimization [1-5]. One classical scheme is the pendulum absorber (PA), that exploits gravity to produce the restoring force, and consists of a damped mass moving along an arched trajectory. A PA can be conceived either as a hanging pendulum, suspended through cables or bars, or a supported pendulum, rolling or sliding on a physical track. In recent years, supported PAs have found several applications, because of their compactness, durability and versatility. Classical examples are the ball pendulum [6], the rolling and sliding pendulums [7], and the rocking pendulum.

Despite the numerous implementations reported in the literature and realized in practice, the research for novel arrangements is still ongoing, resulting in several new configurations, including the unbalanced rolling PA [8], the multiple-ball PA [9], and several types of track nonlinear energy sinks [10]. Among the others, this research has recently inspired the proposal of the so-called bidirectional pendulum absorber (BPA), made of a mass moving along an optimal three-dimensional (3D) concave surface, whose principal curvatures are chosen to ensure a bidirectional tuning to both principal modes of the main structure. The BPA has been proposed in two variants, respectively belonging to the supported pendulum and to the hanging pendulum types. The first variant is represented by the rolling-pendulum absorber proposed in [11]. Its 3D surface is manufactured as a double 3D rolling-pendulum bearing, comprising two equal concavities between which a rolling ball is interposed. Modifying the shape of the two concavities and the ball radius generates any possible 3D surface. The second variant is represented by the hanging-pendulum absorber proposed in [12]. Its 3D surface is realized through a Y-shaped configuration of the suspending cables. Modifying the length of the cables realizes any possible toroidal surface. In the first variant, energy dissipation is provided by horizontal viscous dampers, in the second variant it is provided by a vertical friction damper. In this latter case, the orthogonality between the damper and the 3D surface ensures an amplitude-independent equivalent damping, which should make the two variants approximately equivalent in terms of vibration suppression capability.

In this work, a further alternative of BPA is presented, in which damping is produced by the variable tangential friction developing between the pendulum mass and the 3D surface, as a result of a spatially-varying friction coefficient law [13, 14]. Namely, the friction coefficient is assumed to vary along the surface in proportion to the modulus of the surface gradient. This ensures a dissipative model which is nonlinear homogeneous at low response amplitudes [15]. Such a homogeneous BPA (HBPA) demonstrates superior to conventional friction ball absorbers (characterized by a constant friction coefficient), since its equivalent damping ratio proves amplitude independent, so that its performance does not vary with the excitation level. On the other hand, compared with the said existing BPAs ([11] and [12]), the HBPA is more compact, because it does not require the installation of additional dashpots. In the HBPA, friction is generated either by rolling [16] or by sliding, depending on the chosen type of pendulum. Friction can be spatially varied by changing the surface roughness or the material or the thickness of the surface coating, either continuously or discretely.

This paper describes the analytical model of the HBPA and presents an optimal methodology for its design. Simulations of single- and multi-story buildings under wind and seismic loads are reported, showing the pros and cons of the HBPA with respect to conventional viscously damped BPAs (VBPA) [17]. The results reveal that the HBPA is a promising alternative to conventional VBPAs, and that the homogeneous tangential friction is an effective solution to design mechanical systems having amplitude-independent damping.

2 GENERAL DESCRIPTION AND MODELING OF THE HBPA

2.1 Problem description

A BPA incorporating both viscous damping and tangential friction is shown in Fig. 1.

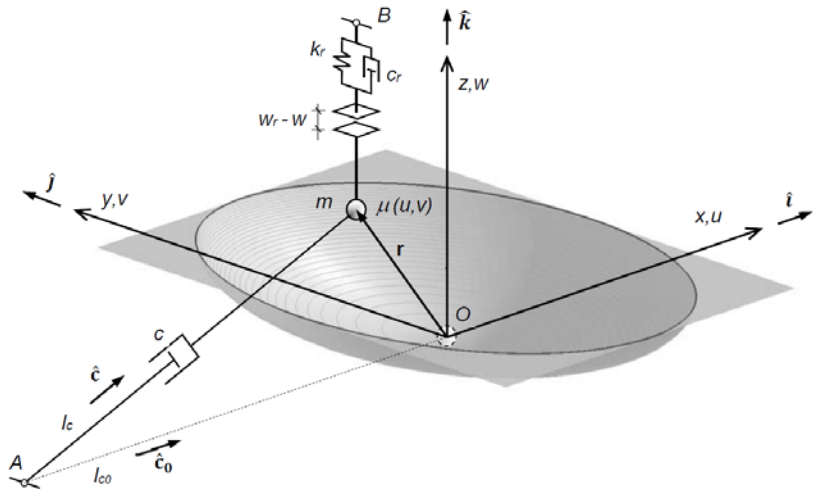

Figure 1: Schematic drawing of the BPA model.

Its model comprises a point mass m subject to gravity g and constrained to move along a 3D surface, connected to the structure at its minimum in O. The motion of m along the surface is opposed by: (i) the viscous damper linking m to the structure in A; (ii) the friction force acting on the surface; and (iii) the restrainer linking m to the structure in B. If structural rotations are negligible, the surface and the structural supports in A and B merely translate as the support in O. Denoting with u, v and w the coordinates of m w.r.t. the local reference system xyz fixed in O, and with $w = w(u,v) = w(\mathbf{q})$ the pendulum surface equation, the relative displacement of the HBPA w.r.t. the structure is $\mathbf{r} = [u,v,w]^T = [\mathbf{q}^T, w(\mathbf{q})]^T$, where u and v are the two independent coordinates, w is the dependent coordinate, and $\mathbf{q} = [u,v]^T$ is the HBPA degree-of-freedom vector. The structural support acceleration vector is $\mathbf{a} = [a_x, a_y, a_z]^T = [\mathbf{a}_h^T, a_z]^T$, and the BPA relative velocity vector is derived as $\dot{\mathbf{r}} = (\partial \mathbf{r}/\partial \mathbf{q})\dot{\mathbf{q}} = \mathbf{J}\dot{\mathbf{q}}$, where $\mathbf{J} = \partial \mathbf{r}/\partial \mathbf{q} = [\mathbf{I}, \nabla w]^T$ is the Jacobian matrix of the kinematic transformation and $\nabla w = \partial w/\partial \mathbf{q}$ is the surface gradient.

2.2 The dissipative model

The model in Fig. 1 accounts for three different dissipative mechanisms: (i) one or more viscous dashpot; (ii) the tangential friction; and (iii) the fail-safe restrainer.

Assuming for brevity a single viscous dashpot with damping coefficient c, undeformed length l_{c0}, deformed length l_c, and undeformed and deformed coaxial versors $\hat{\mathbf{c}}_0$ and $\hat{\mathbf{c}}$, and denoting by $s_c = l_c - l_{c0}$ its axial elongation, the corresponding viscous force vector acting on m is $\mathbf{f}_c = -f_c \hat{\mathbf{c}}$, where $f_c = c\dot{s}_c$ and $\dot{s}_c = \hat{\mathbf{c}}^T \dot{\mathbf{r}} = \hat{\mathbf{c}}^T \mathbf{J}\dot{\mathbf{q}}$.

Assuming a dry friction coefficient varying along the pendulum surface according to an assigned law $\mu = \mu(u,v) = \mu(\mathbf{q})$, and denoting by N the modulus of the normal contact reaction force $\mathbf{N}$, the friction force can be expressed as $\mathbf{f}_\mu = -f_\mu \hat{\mathbf{t}}$, where $\hat{\mathbf{t}} = \dot{\mathbf{r}}/\|\dot{\mathbf{r}}\| = \mathbf{J}\dot{\mathbf{q}}/\sqrt{\dot{\mathbf{q}}^T \mathbf{J}^T \mathbf{J}\dot{\mathbf{q}}}$ is the tangent versor, and

$$f_\mu = \mu(\mathbf{q}) N \tag{1}$$

In particular, the focus is here on a special friction pattern, where the friction coefficient varies along the pendulum surface proportionally to the surface gradient vector, according to:

$$\mu(\mathbf{q}) = \mu_0 \left\| \nabla w \right\| \tag{2}$$

where μ_0 is a proportionality factor, called the friction ratio. As shown later, Eq. (2) ensures a homogeneous first-order model.

Assuming a restrainer with stiffness k_r, damping coefficient c_r and initial clearance w_r, the restrainer force vector is $\mathbf{f}_r = -f_r \hat{\mathbf{k}}$, where $f_r = 0$ if $w \le w_r$ and $f_r = k_r(w - w_r) + c_r \dot{w}$ if $w > w_r$, with $\dot{w} = \nabla w^T \dot{\mathbf{q}}$.

The total dissipative force applied to m by the three mechanisms is therefore $\mathbf{f}_d = \mathbf{f}_c + \mathbf{f}_\mu + \mathbf{f}_r$. Denoting by $\mathbf{w} = -mg\hat{\mathbf{k}}$ the weight of m, and by $\boldsymbol{\lambda}_d = m(\mathbf{a} + \ddot{\mathbf{r}})$ the dynamic interaction force between the BPA and its support, the dynamic equilibrium of m reads $\mathbf{w} + \mathbf{N} + \mathbf{f}_d = \boldsymbol{\lambda}_d$, which finally provides N in Eq. (1) as the modulus of the vector $\mathbf{N} = \boldsymbol{\lambda}_d - \mathbf{w} - \mathbf{f}_d$.

2.3 The nonlinear three-dimensional model of the BPA

The BPA dynamic equation can be obtained by applying the Euler-Lagrange equation to the mass m:

$$\frac{d}{dt}\left(\frac{\partial T}{\partial \dot{\mathbf{q}}}\right) - \frac{\partial T}{\partial \mathbf{q}} + \frac{\partial V_g}{\partial \mathbf{q}} + \mathbf{Q}_i + \mathbf{Q}_e = \mathbf{0} \tag{3}$$

where $T = m\dot{\mathbf{r}}^T\dot{\mathbf{r}}/2$ is the kinetic energy of m; V_g=mgw is its gravitational potential energy; $\mathbf{Q}_i$ = $-\mathbf{J}^T\mathbf{f}_d$ is the generalized internal force due to the total dissipative force $\mathbf{f}_d$; and $\mathbf{Q}_e = m\mathbf{J}^T\mathbf{a}$ is the generalized external force due to the support acceleration. Deriving the first three terms of Eq. (3), and denoting by $\mathbf{M}^q = m\mathbf{J}^T\mathbf{J}$ the BPA generalized mass matrix, the BPA fully nonlinear 3D model is finally obtained as

$$\mathbf{M}^q\ddot{\mathbf{q}} + \mathbf{Q}_i + mg\nabla w = -m\mathbf{J}^T\mathbf{a} - \left(\dot{\mathbf{M}}^q\dot{\mathbf{q}} - \frac{\partial T}{\partial \mathbf{q}}\right) \tag{4}$$

In Eq. (4), the dissipative term on the left-hand side can be expressed as

$$\mathbf{Q}_i = -\mathbf{J}^T\mathbf{f}_d = f_c\mathbf{J}^T\hat{\mathbf{c}} + f_\mu\mathbf{J}^T\hat{\mathbf{t}} + f_r\mathbf{J}^T\hat{\mathbf{k}} \tag{5}$$

where

$$f_c\mathbf{J}^T\hat{\mathbf{c}} = c\left(\mathbf{J}^T\hat{\mathbf{c}}\hat{\mathbf{c}}^T\mathbf{J}\right)\dot{\mathbf{q}} \tag{6}$$

$$f_\mu\mathbf{J}^T\hat{\mathbf{t}} = \mu(\mathbf{q})N\mathbf{J}^T\mathbf{J}\dot{\mathbf{q}} / \sqrt{\dot{\mathbf{q}}^T\mathbf{J}^T\mathbf{J}\dot{\mathbf{q}}} \tag{7}$$

$$f_r\mathbf{J}^T\hat{\mathbf{k}} = f_r\nabla w \tag{8}$$

are the generalized viscous, friction and restrainer force vectors, respectively.

2.4 The nonlinear three-dimensional model of the BPA-MDOF system

The dynamic equation of a linear multi-degree-of-freedom (MDOF) structure coupled with the BPA and subjected to external forces and ground accelerations is

$$\mathbf{M}_s\ddot{\mathbf{q}}_s + \mathbf{C}_s\dot{\mathbf{q}}_s + \mathbf{K}_s\mathbf{q}_s + \mathbf{L}^T\boldsymbol{\lambda}_d = \mathbf{f}_s - \mathbf{M}_s\mathbf{R}_s\ddot{\mathbf{r}}_g \tag{9}$$

where $\mathbf{q}_s$ is the vector of structural DOFs; $\mathbf{M}_s$, $\mathbf{C}_s$ and $\mathbf{K}_s$ are the structural matrices of mass, damping and stiffness; $\mathbf{f}_s$ is the vector of external forces; $\ddot{\mathbf{r}}_g$ is the vector of ground accelerations; $\mathbf{L}$ and $\mathbf{R}_s$ are kinematic and topological matrices. Combining Eqs. (4) and (9), the fully nonlinear coupled dynamic equation can be finally expressed as

$$\begin{aligned}&\begin{bmatrix}\mathbf{M}_s+m\mathbf{L}^T\mathbf{L} & m\mathbf{L}^T\mathbf{J}\\ m\mathbf{J}^T\mathbf{L} & \mathbf{M}^q\end{bmatrix}\begin{bmatrix}\ddot{\mathbf{q}}_s\\ \ddot{\mathbf{q}}\end{bmatrix}+\begin{bmatrix}\mathbf{C}_s & \mathbf{0}\\ \mathbf{0} & \mathbf{0}\end{bmatrix}\begin{bmatrix}\dot{\mathbf{q}}_s\\ \dot{\mathbf{q}}\end{bmatrix}+\begin{bmatrix}\mathbf{K}_s & \mathbf{0}\\ \mathbf{0} & \mathbf{0}\end{bmatrix}\begin{bmatrix}\mathbf{q}_s\\ \mathbf{q}\end{bmatrix}+\\ &+\begin{bmatrix}\mathbf{0}\\ \mathbf{Q}_i\end{bmatrix}=\begin{bmatrix}\mathbf{f}_s\\ \mathbf{0}\end{bmatrix}-\begin{bmatrix}\mathbf{M}_s+m\mathbf{L}^T\mathbf{L}\\ m\mathbf{J}^T\mathbf{L}\end{bmatrix}\mathbf{R}_s\ddot{\mathbf{r}}_g-\begin{bmatrix}m\mathbf{L}^T\mathbf{J}\dot{\mathbf{q}}\\ \dot{\mathbf{M}}^q\dot{\mathbf{q}}-\dfrac{\partial T}{\partial\mathbf{q}}\end{bmatrix}.\end{aligned} \tag{10}$$

2.5 The first-order approximated model

Some fundamental properties of the BPA can be demonstrated by considering its response at low amplitudes. By developing in Taylor series Eqs. (4) to (8), and by truncating higher-order terms, the first-order 3D model of the BPA is obtained as

$$m\ddot{\mathbf{q}}+\mathbf{C}\dot{\mathbf{q}}+N_0\mathbf{K}_w\mathbf{q}+\mu_0N_0\|\mathbf{K}_w\mathbf{q}\|\dot{\mathbf{q}}/\|\dot{\mathbf{q}}\|=-m\mathbf{a}_h \tag{11}$$

where: $\mathbf{C}$ is the BPA viscous damping matrix, given by

$$\mathbf{C}=c\begin{bmatrix}\hat{c}_{0x}^2 & \hat{c}_{0x}\hat{c}_{0y}\\ \hat{c}_{0x}\hat{c}_{0y} & \hat{c}_{0y}^2\end{bmatrix} \tag{12}$$

if the viscous damper is set parallel to the xy plane; $N_0 = N/(mg) = 1+a_z/g$ is the normalized normal component of the reaction force; $\mathbf{a}_h = [a_x, a_y]^T$ is the vector of horizontal accelerations at the support; and $\mathbf{K}_w$ is the equivalent pendular stiffness matrix, given by:

$$\mathbf{K}_w=\begin{bmatrix}k_{wx} & 0\\ 0 & k_{wy}\end{bmatrix}=mg\begin{bmatrix}1/L_x & 0\\ 0 & 1/L_y\end{bmatrix}=mg\mathbf{H}_w \tag{13}$$

where $\mathbf{H}_w$ is the Hessian matrix of $w(\mathbf{q})$ in $\mathbf{0}$, and L_x and L_y are the pendulum lengths along x and y.

Accordingly, the first-order 3D model of the BPA-structure coupled system is

$$\begin{aligned}&\begin{bmatrix}\mathbf{M}_s+m\mathbf{L}_h^T\mathbf{L}_h & m\mathbf{L}_h^T\\ m\mathbf{L}_h & m\mathbf{I}\end{bmatrix}\begin{bmatrix}\ddot{\mathbf{q}}_s\\ \ddot{\mathbf{q}}\end{bmatrix}+\begin{bmatrix}\mathbf{C}_s & \mathbf{0}\\ \mathbf{0} & \mathbf{C}+\mu_0N_0\|\mathbf{K}_w\mathbf{q}\|/\|\dot{\mathbf{q}}\|\end{bmatrix}\begin{bmatrix}\dot{\mathbf{q}}_s\\ \dot{\mathbf{q}}\end{bmatrix}+\\ &+\begin{bmatrix}\mathbf{K}_s & \mathbf{0}\\ \mathbf{0} & N_0\mathbf{K}_w\end{bmatrix}\begin{bmatrix}\mathbf{q}_s\\ \mathbf{q}\end{bmatrix}=\begin{bmatrix}\mathbf{f}_s\\ \mathbf{0}\end{bmatrix}-\begin{bmatrix}\mathbf{M}_s+m\mathbf{L}_h^T\mathbf{L}_h\\ m\mathbf{L}_h\end{bmatrix}\mathbf{R}_s\ddot{\mathbf{r}}_g,\end{aligned} \tag{14}$$

where $\mathbf{L}_h$ is the vector containing the first two columns of $\mathbf{L}$.

Based on Eq. (11), the following observations can be formulated:

1) the inertia force $m\ddot{\mathbf{q}}$ and the restoring force $N_0\mathbf{K}_w\mathbf{q}$ are linear and uncoupled along x and y; this holds for the viscous force $\mathbf{C}\dot{\mathbf{q}}$, provided that all viscous dampers are aligned with the coordinate axes;
2) the friction force has modulus $\mu_0N_0\|\mathbf{K}_w\mathbf{q}\|$ and has direction and sign of the tangent versor $\dot{\mathbf{q}}/\|\dot{\mathbf{q}}\|$; because its modulus, direction and sign are nonlinear and coupled, the friction force is a nonlinear coupled function of $\mathbf{q}$ and $\dot{\mathbf{q}}$;
3) because its modulus increases proportionally with $\mathbf{q}$ and does not depend on $\dot{\mathbf{q}}$, the friction force is a homogeneous function of $\mathbf{q}$ and $\dot{\mathbf{q}}$; Eq. (11) is therefore homogeneous and

its solution is proportional to $\mathbf{a}_h$, which definitely makes the HBPA a first-order nonlinear but homogeneous system.

2.6 The simplified two-dimensional model

The 3D first-order models in Eqs. (11) and (14) can be further simplified for design purposes, assuming that: (i) the motion occurs in a vertical coordinate plane, e.g. the *xz* plane, so the model becomes two-dimensional (2D); (ii) in the *xz* plane the structural target frequency is far from the other ones, so the MDOF structure can be reduced to a 1DOF mode-generalized system; (iii) the vertical acceleration input a_z is negligible, so $N_0 = 1$. Under these conditions, Eqs. (11) and (14) become respectively

$$m\ddot{u} + c_x\dot{u} + k_{wx}[1 + \mu_0 \text{sign}(u\dot{u})]u = -ma_x \tag{15}$$

$$\begin{bmatrix} m_{sx}+m & m \\ m & m \end{bmatrix}\begin{bmatrix} \ddot{u}_s \\ \ddot{u} \end{bmatrix} + \begin{bmatrix} c_{sx} & 0 \\ 0 & c_x \end{bmatrix}\begin{bmatrix} \dot{u}_s \\ \dot{u} \end{bmatrix} + \\ + \begin{bmatrix} k_{sx} & 0 \\ 0 & k_{wx}[1+\mu_0 \text{sign}(u\dot{u})] \end{bmatrix}\begin{bmatrix} u_s \\ u \end{bmatrix} = \begin{bmatrix} f_{sx} \\ 0 \end{bmatrix} - \begin{bmatrix} m_{sx}+m \\ m \end{bmatrix}\ddot{u}_g, \tag{16}$$

where u_s is the horizontal displacement of the structure w.r.t. the ground; m_{sx}, c_{sx} and k_{sx} are the generalized mass, damping and stiffness of the structure along *x*; and c_x is the BPA viscous damping coefficient along *x*.

Eqs. (15) and (16) can be finally recast in modal form as

$$\ddot{u} + 2\varsigma_x\omega_x\dot{u} + \omega_x^2[1 + \mu_0 \text{sign}(u\dot{u})]u = -a_x \tag{17}$$

$$\begin{bmatrix} 1+m_{Rx} & m_{Rx} \\ 1 & 1 \end{bmatrix}\begin{bmatrix} \ddot{u}_s \\ \ddot{u} \end{bmatrix} + 2\omega_{sx}\begin{bmatrix} \varsigma_{sx} & 0 \\ 0 & \varsigma_x\omega_{Rx} \end{bmatrix}\begin{bmatrix} \dot{u}_s \\ \dot{u} \end{bmatrix} + \\ + \omega_{sx}^2\begin{bmatrix} 1 & 0 \\ 0 & \omega_{Rx}^2[1+\mu_0 \text{sign}(u\dot{u})] \end{bmatrix}\begin{bmatrix} u_s \\ u \end{bmatrix} = \begin{bmatrix} \bar{f}_{sx} \\ 0 \end{bmatrix} - \begin{bmatrix} 1+m_{Rx} \\ 1 \end{bmatrix}\ddot{u}_g, \tag{18}$$

where $m_{Rx} = m/m_{sx}$ is the BPA mass ratio along *x*; $\omega_{sx} = \sqrt{k_{sx}/m_s}$ and $\omega_x = \sqrt{g/L_x}$ are the structure and BPA circular frequencies along *x*; $\omega_{Rx} = \omega_x/\omega_{sx}$ is the BPA frequency ratio along *x*; and $\varsigma_{sx} = c_{sx}/(2\omega_{sx}m_{sx})$ and $\varsigma_x = c_x/(2\omega_x m)$ are the structure and BPA viscous damping ratios along *x*.

3 THE DESIGN PROCEDURE

A design methodology is here presented for a BPA of either viscous type (VBPA) or homogeneous friction type (HBPA). Their models can be obtained from those derived in Section II, by respectively annulling the friction or the viscous terms. The methodology comprises two steps: (1) a 2D first-order optimization; and (2) a 3D second-order completion.

3.1 The two-dimensional first-order optimization

According to the simplified 2D model in Eq. (18), which admits an uncoupled motion along *x* and *y*, and assuming the structure known, both the VBPA and the HBPA are completely determined, in each direction, by three dimensionless design parameters: m_{Rx}, ω_{Rx} and ς_x for the VBPA, and m_{Rx}, ω_{Rx} and μ_0 for the HBPA. If the mass ratio m_{Rx} is fixed based on cost-benefit expectations, the two remaining free parameters can be obtained by solving an H_∞ design problem [18], i.e. by minimizing the H_∞ norm of a significant input-output transfer function (TF) of the structure-BPA system. Denoting by ω the circular frequency of the excitation in-

put, two possible TFs are here considered for each BPA type: the force-to-displacement transfer function $T_f(\omega)$ (significant for wind load applications), and the ground acceleration-to-displacement transfer function $T_g(\omega)$ (significant for seismic load applications). Denoting as the response ratio R_x the ratio between the controlled and the uncontrolled H_∞ norm of those TFs, optimization can be formalized as follows, respectively for a wind-oriented VBPA:

$$R_{xopt} = \min_{\omega_{Rx},\varsigma_x} R_x = \min_{\omega_{Rx},\varsigma_x} \max_{\omega} \left(\left| T_f(\omega) \right|^{con} \Big/ \left\| T_f \right\|_\infty^{unc} \right) \tag{19}$$

for a seismic-oriented VBPA:

$$R_{xopt} = \min_{\omega_{Rx},\varsigma_x} R_x = \min_{\omega_{Rx},\varsigma_x} \max_{\omega} \left(\left| T_g(\omega) \right|^{con} \Big/ \left\| T_g \right\|_\infty^{unc} \right) \tag{20}$$

for a wind-oriented HBPA:

$$R_{xopt} = \min_{\omega_{Rx},\mu_0} R_x = \min_{\omega_{Rx},\mu_0} \max_{\omega} \left(\left| T_f(\omega) \right|^{con} \Big/ \left\| T_f \right\|_\infty^{unc} \right) \tag{21}$$

and for a seismic-oriented HBPA:

$$R_{xopt} = \min_{\omega_{Rx},\mu_0} R_x = \min_{\omega_{Rx},\mu_0} \max_{\omega} \left(\left| T_g(\omega) \right|^{con} \Big/ \left\| T_g \right\|_\infty^{unc} \right) \tag{22}$$

Eqs. (19) and (20) give the optimal VBPA parameters ω_{Rxopt} and ς_{xopt}, respectively for wind and seismic control. Eqs. (21) and (22) give the optimal HBPA parameters ω_{Rxopt} and μ_{0opt}, respectively for wind and seismic control.

The min.max. problems in Eqs. (19) to (22) are here numerically solved using a branch & bound search algorithm analogue to the one used in [5], followed by a nonlinear least-square solver for improved local convergence. The computation of the VBPA TF in Eqs. (19) and (20) is straightforward, based on classical closed-form expressions available for linear mechanical models, whereas the computation of the HBPA TF in Eqs. (21) and (22) needs simulating the system response time-history at each input frequency until stabilization of the response amplitude.

Assuming a structural damping ratio $\zeta_{sx} = 2\%$, the optimization results are reported in Fig. 2 for the VBPA (dashed lines) and the HBPA (continuous lines), as a function of the mass ratio m_{Rx}. The wind-oriented optimization is reported on the left (subfigures a, c and e), while the seismic-oriented optimization is reported on the right (subfigures b, d and f). Subfigures a and b show the optimal frequency ratio; subfigures c and d show the optimal damping ratio (for the VBPA) and the optimal friction ratio (for the HBPA), this latter normalized to π; and subfigures e and f show the optimal response ratios. Whereas the results obtained for the VBPA are well known (see for instance [19]) and do not deserve specific comments, the results obtained for the HBPA reveal that the optimal HBPA slightly improves the VBPA performance, especially for large values of m_{Rx}. To achieve this, ω_{Rxopt} is always larger for the HBPA than for the VBPA, except for very small mass ratios, when the optimal frequency ratio converges to unity for both types. On the other hand, μ_{0opt} converges to $\pi \cdot \varsigma_{xopt}$ for small mass ratios, but tends to be increasingly smaller than $\pi \cdot \varsigma_{xopt}$ as the mass ratio increases. The same trends are appreciated for the wind-oriented and the seismic-oriented design types.

Assuming that the structural target modes have the same damping ratio and the same generalized mass in the two horizontal directions, the results obtained above hold along x and y, and the x subscript can be dropped for brevity. Together with the mass ratio m_R and with the structural parameters, the resulting optimal dimensionless parameters ω_{Ropt}, ς_{opt} and μ_{0opt} allow the computation of all BPA dimensional parameters involved in the low amplitude domain, i.e. the BPA mass m, the BPA circular frequencies ω_x and ω_y, the BPA pendulum

lengths L_x and L_y, the VBPA damping coefficients c_x and c_y, and the HBPA friction pattern around the origin, this latter given around by

$$\mu(\mathbf{q}) = \mu_{0opt}\|\nabla w\| \approx \mu_{0opt}\sqrt{u^2/L_x^2 + v^2/L_y^2} \tag{23}$$

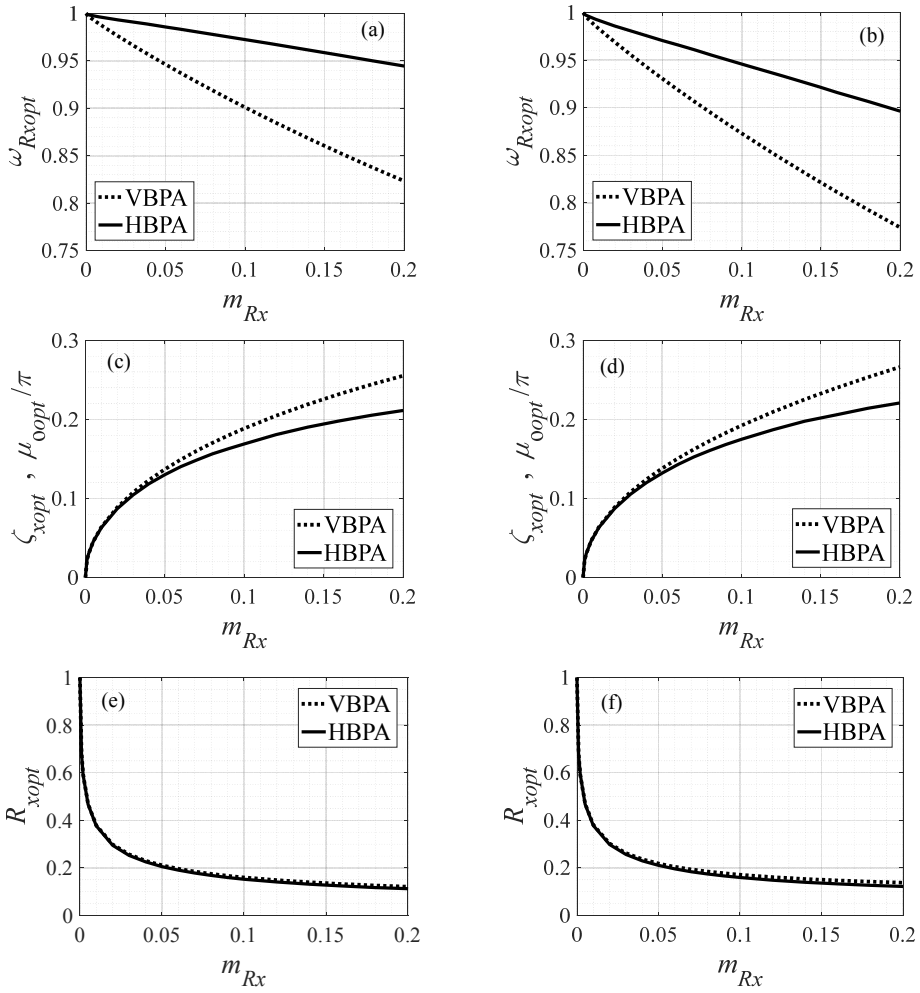

Figure 2: H_∞ optimal design of a VBPA (dotted lines) and a HBPA (continuous lines), as a function of m_{Rx}, for ζ_{sx} = 2%. Left: wind-oriented design. Right: seismic-oriented design. First row: optimal frequency ratios. Second row: optimal viscous/friction damping ratios. Third row: optimal response ratios.

3.2 The three-dimensional second-order completion

The subsequent completion step provides the BPA parameters which, involved only in the large-displacement domain, are excluded from the previous optimization step. These parameters include the pendulum shape (and consequently the friction pattern) far from the origin, the length and number of viscous dashpots, and the restrainer properties.

By providing L_x and L_y, the optimization step determines the pendulum shape around the origin. Far from it, however, different shapes correspond to the same pair of L_x and L_y. Among the possible choices are, for example, the ellipsoid, the torus or the elliptic paraboloid. If the ellipsoid is chosen, infinite ways of assigning its semi-axes b_x, b_y and b_z exist, all providing the desired L_x and L_y pair. Then, by imposing that $b_z = \sqrt{b_x b_y}$, only one admissible

ellipsoid exists, of semi-axes $b_x = \sqrt[4]{L_x^3 L_y}$, $b_y = \sqrt[4]{L_x L_y^3}$ and $b_z = \sqrt{L_x L_y}$. This choice is systematically assumed in the sequel.

With this assumption, the friction pattern defined by Eq. (2) becomes:

$$\mu(\mathbf{q}) = \mu_{0opt} \sqrt{\left(\frac{u^2}{L_x^2} + \frac{v^2}{L_y^2} \right) \Big/ \left(1 - \frac{u^2}{b_x^2} - \frac{v^2}{b_y^2} \right)} \tag{24}$$

where $\mu(\mathbf{q})$ tends to zero around the origin, tends to infinite at the ellipsoid equator, and describes iso-friction curves intersecting the level curves, as shown in Fig. 3 for an ellipsoid having $L_y/L_x = 2$, truncated at $w_r = b_z/2$. Both Figs. 3 (a) and (b) represent nine level curves, uniformly spaced between 0 and w_r, and nine iso-friction curves, uniformly spaced between 0 and 2 μ_{0opt}.

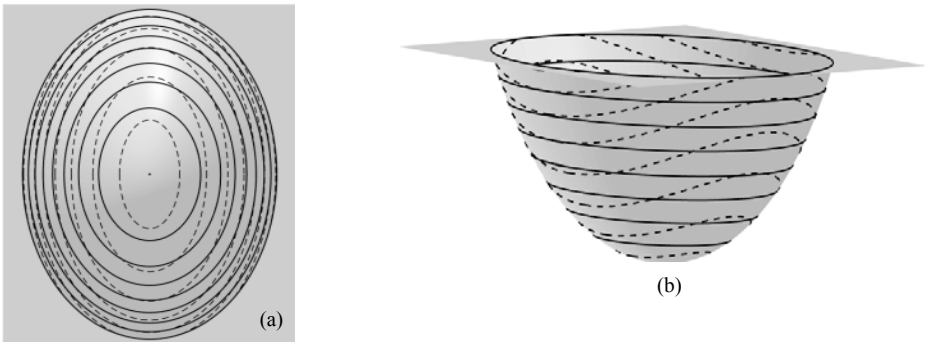

Figure 3: Level curves (continuous) and iso-friction curves (dashed) if $L_y/L_x = 2$: (a) planar view; (b) axonometric view (with the z dimension doubled for clarity).

Regarding the design of the viscous dampers, the optimization step provides the optimal values of c_x and c_y, in the assumption of a single damper for every direction. If more dampers are used in the same direction, the optimal damping coefficient must be subdivided among them. The length of the viscous dampers does not enter the optimization step. In the sequel, two dampers will be systematically assumed in each direction, each having length $l_{c0} = b_z = \sqrt{L_x L_y}$.

Finally, the restrainer too does not enter the optimization step. Its mechanical properties can be assigned to simulate a dissipative impact. In the remaining of this paper, its stiffness is systematically chosen as $k_r = m\omega_r^2$, where $\omega_r = 20\sqrt{\omega_x \omega_y}$; its damping is assigned as $c_r = 2\varsigma_r \omega_r m$, where $\varsigma_r = -\ln e_r \Big/ \sqrt{\pi^2 + \ln^2 e_r}$ and $e_r = 0.5$ (elastic restitution coefficient); its clearance is assigned as $w_r = b_z/2$.

4 TWO-DIMENSIONAL SIMULATIONS OF THE FIRST-ORDER MODEL

The optimal VBPA and the optimal HBPA are here compared at low amplitudes, by assuming the first-order 2D models expressed by Eqs. (16) or (18). The structure is a 2% damped SDOF system.

4.1 White noise force excitation

Optimized according to the wind-oriented design procedure described in Section 3, the VBPA and the HBPA are compared by subjecting the SDOF structure to a stationary Gaussi-

an zero-mean white-noise force $\bar{f}_{sx}$. For the uncontrolled and for the VBPA-controlled structure (linear cases), the system stationary root-mean-square (rms) response is computed solving the Lyapunov equation [18]. For the HBPA-controlled structure, the rms response is computed through Monte Carlo simulations, using 100 realizations of the input process. Each realization has lasts $3600T_{sx}$, with a sampling time of $0.01T_{sx}$, T_{sx} being the structural period.

The BPA performance is evaluated in terms of the rms structural displacement, rms(u_s), and the rms BPA relative displacement (stroke), rms(u). Two performance indices are considered, computed dividing the controlled value of the rms responses by the uncontrolled value of the rms structural displacement: the displacement response ratios R_{dx} = rms(u_s)$_{con}$/ rms(u_s)$_{unc}$, and the stroke response ratio R_{sx} = rms(u)$_{con}$/ rms(u_s)$_{unc}$.

The two response ratios are shown in Fig. 4, where they appear nearly identical for the two BPA types. The substantial equivalence already observed under a harmonic force input in Fig. 2 (e) is therefore confirmed under a white-noise force input. Expectedly, the absorber results more effective in H_∞ terms than against a white-noise input (i.e. in H_2 terms).

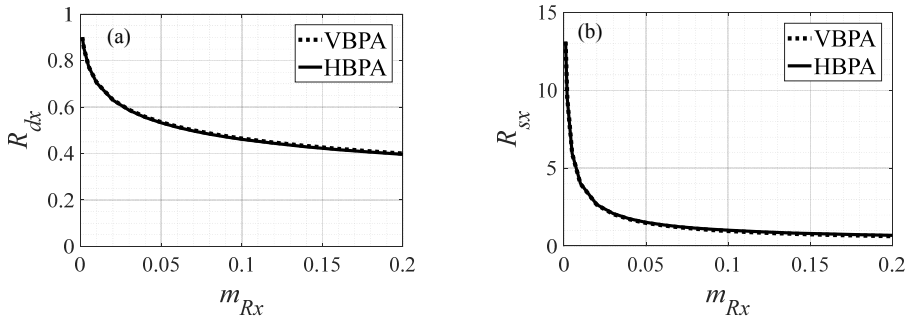

Figure 4: 2D first-order model. VBPA and HBPA response ratios under a unidirectional white-noise force input.

4.2 Natural seismic records

Optimized according to the seismic-oriented design procedure, the evaluation of the VBPA and the HBPA under a white-noise ground acceleration $\ddot{u}_g$ leads to very similar results to those presented in Fig. 4, which are therefore neglected here for brevity.

More interestingly, the structure (with or without BPA) is here subjected to an ensemble of 338 near-field real seismic records, and its period T_{sx} is varied from 0.1 s to 6.0 s, to obtain uncontrolled and controlled spectra. For each interesting response quantity, i.e. the maximum structural displacement $u_{s,max}$ and the maximum BPA stroke u_{max}, the 338 spectra are condensed into their rms spectrum. Dividing, at each period, the controlled rms response spectra by the uncontrolled structural displacement response spectrum, two rms response ratio spectra are obtained, respectively expressed in terms of structural displacement (R_{dx} = rms($u_{s,max}$)$_{con}$/ rms($u_{s,max}$)$_{unc}$), and of BPA stroke (R_{sx} = rms(u_{max})$_{con}$/ rms($u_{s,max}$)$_{unc}$). Results are presented in Fig. 5 for three mass ratios (m_{Rx} = 1%, 3% and 10%). Again, the VBPA and the HBPA exhibit very similar performances, both in terms of structural displacement and absorber strokes.

5 THREE-DIMENSIONAL SIMULATIONS OF THE FIRST-ORDER MODEL

This section broadens the analysis to 3D models, still operating at low amplitudes, according to (14). The equations of motion are still linear and uncoupled for the VBPA but nonlinear and coupled for the HBPA. The structure is a 2%-damped system having 1 DOF in each direction.

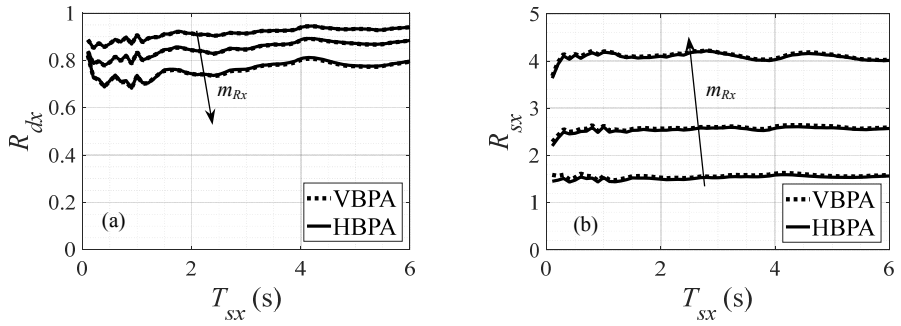

Figure 5: 2D first-order model. VBPA and HBPA response ratio spectra under a unidirectional seismic input, for m_{Rx} = 1%, 3%, 10%.

5.1 White noise force excitation

The structure, with T_{sx} = 1 s and T_{sy}/T_{sx} varying from 1 (axial-symmetry) to 2, is excited by two independent white-noise force input components f_{sx} and f_{sy}, having the same rms value $f_{sx0} = f_{sy0}$. The mass ratio $m_R = m_{Rx} = m_{Ry}$ is alternatively 1%, 3%, or 10%. The BPA performance is evaluated by considering the average response to 100 realizations of the input process, each one lasting 600 s with a sampling time of 0.01 s. The performance is expressed by the following two bidirectional response ratios: $R_d = \sqrt{R_{dx}R_{dy}}$ and $R_s = \sqrt{R_{sx}R_{sy}}$, which extend to 3D the 2D response ratios introduced in Section 4.1.

Results are shown in Fig. 6, where R_d and R_s are plotted as a function of T_{sy}/T_{sx}. The VBPA performance appears constant with T_{sy}/T_{sx}. The HBPA performance appears approximately constant with T_{sy}/T_{sx}, and quite similar to the VBPA performance, with only slightly larger structural displacements and moderately smaller BPA strokes.

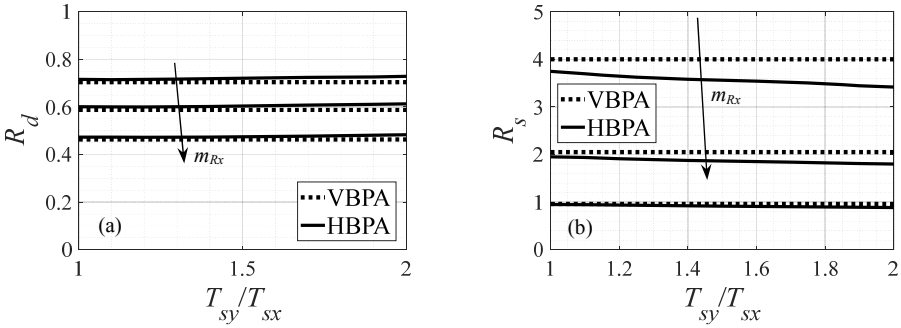

Figure 6: 3D first-order model under a bidirectional white-noise force input. VBPA and HBPA response ratios as a function of T_{sy}/T_{sx}, for m_{Rx} = 1%, 3%, 10%.

5.2 Natural seismic records

The bidirectional performance of the VBPA and of the HBPA is here assessed adopting the same ensemble of seismic records used in Section 4.2. Spectra are computed in terms of 3D rms response ratios, obtained by averaging the corresponding 2D rms response ratios along x and y, according to: $R_d = \sqrt{R_{dx}R_{dy}}$ and $R_s = \sqrt{R_{sx}R_{sy}}$. Fig. 7 shows R_d and R_s evaluated under the assumption that T_{sy}/T_{sx} = 1, for $T_{sx} = T_{sy}$ ranging from 0.5 to 4.0 s, and for m_R alternatively 1%, 3%, or 10%. As in Fig. 6, it appears that under bidirectional excitation, because of friction coupling, the nearly perfect coincidence between the VBPA and the HBPA response is lost. Friction damping implies a slightly larger structural response, and a slightly smaller stroke. The extent of this reduction is however quite limited.

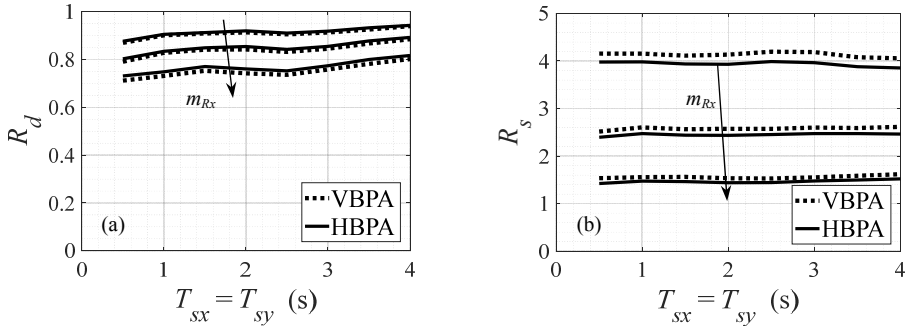

Figure 7: 3D first-order model. VBPA and HBPA response ratio spectra under a bidirectional seismic input, for $T_{sy}/T_{sx} = 1$ and $m_{Rx} = 1\%, 3\%, 10\%$.

6 TWO-DIMENSIONAL SIMULATIONS OF THE FULLY NONLINEAR MODEL

To show the influence of the excitation intensity on the BPA performance, the optimal VBPA and the optimal HBPA are here compared in the large-displacement domain, by assuming fully nonlinear 2D models. The structure is once again a 2% damped SDOF system.

6.1 White noise force excitation

A structure controlled through a wind-optimal BPA having $m_{Rx} = 3\%$ is simulated under a unidirectional white-noise force input of rms amplitude $\bar{f}_{sx0}$, duration 600 s and sampling time 0.01 s. The response ratios R_{dx} and R_{sx} are shown in Fig. 8 for the two types of BPA as a function of $\bar{f}_{sx0}$ ranging from 0 to 5 N/kg.

For $\bar{f}_{sx0} = 0$, the results are those already obtained in Fig. 4 for first-order models. As $\bar{f}_{sx0}$ increases, the effectiveness in mitigating the structural displacement diminishes, as typical of pendulum devices, and the absorber stroke decreases, as a result of bumping and loss of tuning. The effectiveness reduction appears delayed for the HBPA with respect to the VBPA, because of its amplitude-increasing dissipation capabilities.

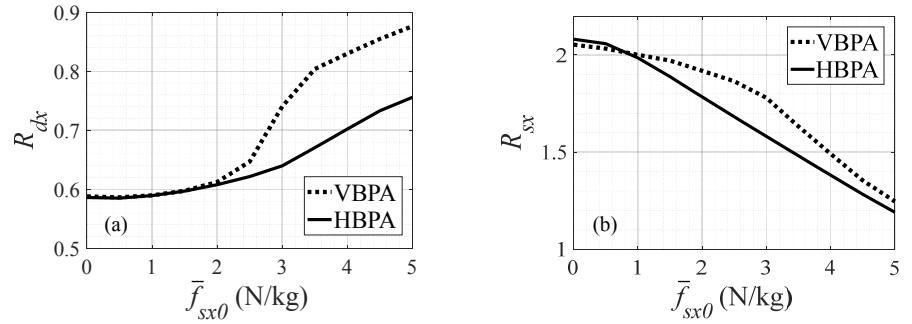

Figure 8: 2D fully nonlinear model. VBPA and HBPA response ratios under a unidirectional white-noise force input, as a function of the input level and for $m_{Rx} = 3\%$.

6.2 Natural seismic records

A structure controlled through a seismic-optimal BPA having $m_{Rx} = 3\%$ is simulated under the ensemble of real records already used in previous sections, for increasing seismic intensities. Denoting by I the intensity ratio, i.e. the dimensionless factor adopted to scale the entire ensemble of records, Fig. 9 reports R_{dx} and R_{sx} as a function of I, for the two BPA types and

for two possible periods of the structure, namely T_{sx} = 0.5 s (top subfigures) and T_{sx} = 4.0 s (bottom subfigures).

For I = 0, the results are those already obtained in Fig. 5 for first-order models. As I increases, both R_{dx} and R_{sx} decrease, as already observed in Section 6.1 under force excitation. However, significant variations are solely observed for T_{sx} = 0.5 s, because of the limited stroke capacity of small-period pendulums. In this case, the HBPA appears again superior to the VBPA, because of the increasing damping provided by the proposed friction pattern.

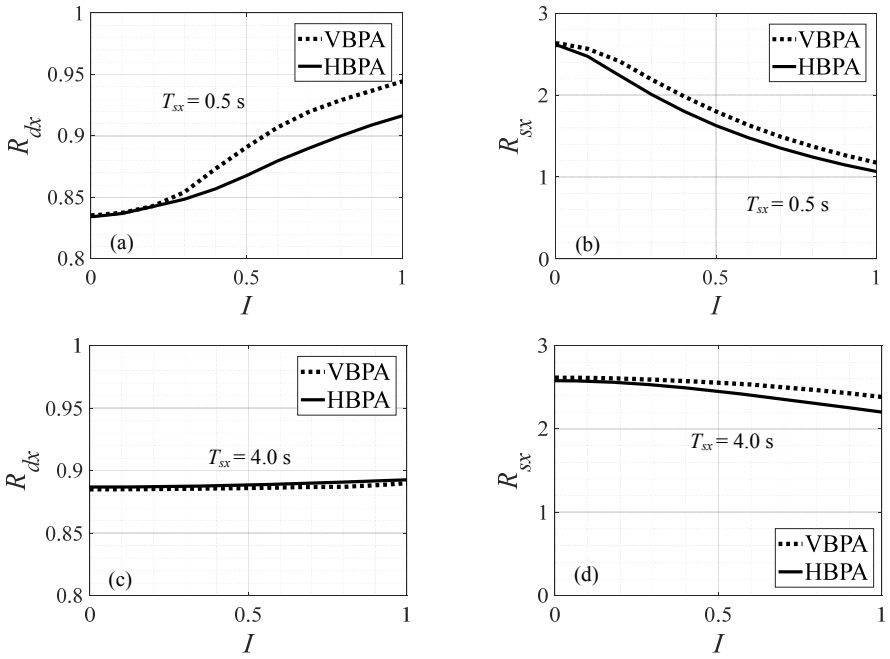

Figure 9: 2D fully nonlinear model. VBPA and HBPA response ratio spectra under a unidirectional seismic input, as a function of I and for m_{Rx} = 3%. Top figures: T_{sx} = 0.5 s; bottom figures: T_{sx} = 4.0 s.

7 THREE-DIMENSIONAL SIMULATIONS OF THE FULLY NONLINEAR MODEL

7.1 White noise force excitation

The optimal BPAs are mounted on a 2%-damped structure having 1 DOF in each direction, with $T_{sx} = T_{sy}$ = 1 s. The structure is excited by a bidirectional white-noise force input, having identical rms amplitude in the two directions, $\bar{f}_{sx0} = \bar{f}_{sy0}$, duration of 600 s, and sampling time of 0.01 s. Simulations are conducted for $\bar{f}_{sx0} = \bar{f}_{sy0}$ ranging from 0 to 5 N/kg, and results are shown in Fig. 10. The performance loss trends already observed for a unidirectional input in Fig. 8 are confirmed. Again, the HBPA performance is similar to the VBPA performance at low intensities, and better for large ones.

7.2 Natural seismic records

Table 1 reports the response ratios obtained by subjecting the controlled structure to the bidirectional seismic records included in the selected ensemble, for m_R = 3% and for the intensity ratio increasing from 0 to 0.5 to 1.0. Two cases are considered, with the first structural period T_{sx} being fixed at 1.0 s and the second structural period T_{sy} equaling either 1.0 s or 1.5 s. Table 1 confirms that under a bidirectional shaking the VBPA is preferable if second-order effects are negligible (I = 0), and the HBPA is preferable if they are not.

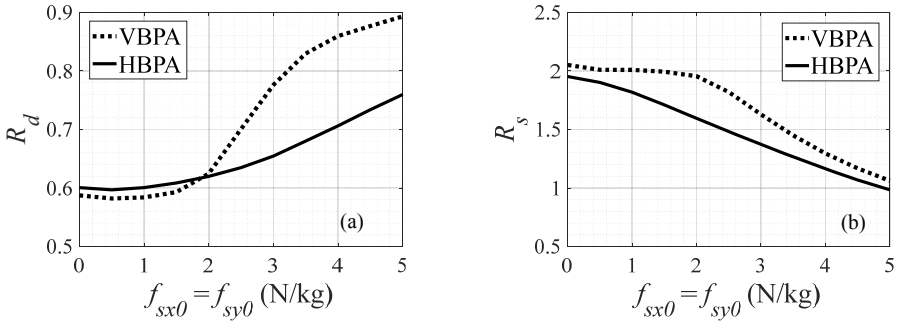

Figure 10: 3D fully nonlinear model. VBPA and HBPA response ratios under a bidirectional white-noise force input, as a function of the input level and for m_{Rx} = 3%. T_{sx} = T_{sy} = 1.0 s.

		R_d		R_s	
	I	VBPA	HBPA	VBPA	HBPA
T_{sx} = 1.0 s T_{sy} = 1.0 s	0.0	0.83	0.84	2.60	2.47
	0.5	0.90	0.88	1.81	1.52
	1.0	0.95	0.92	1.16	1.00
T_{sx} = 1.0 s T_{sy} = 1.5 s	0.0	0.84	0.85	2.58	2.35
	0.5	0.88	0.87	2.00	1.64
	1.0	0.94	0.91	1.38	1.15

Table 1: 3D fully nonlinear model under seismic input. RMS response ratios for different periods and intensities (m_R = 3%).

8 CASE STUDY: MDOF BUILDING UNDER WIND LOAD

An MDOF high-rise building structure subjected to wind loads is here simulated with or without a BPA atop, using the fully nonlinear model expressed by Eq. (10). The BPA is either of the VBPA or of the HBPA type, in both cases optimized according to the wind-oriented design procedure exposed in Section 3.

The structure is 168 m tall, with a 25 m x 25 m square section. Its shape, mass and stiffness are drawn from [20], but scaled to augment the building sensitivity to the across-wind component. Modelled as a 10-elements cantilever beam, the structure has a flexural stiffness which in the *y* direction is 1.21 times smaller than in the *x* direction. The natural periods along *y* are thus 1.10 times larger than along *x*. Along *x*, the first three periods are 4.00 s, 1.23 s, and 0.52 s, with participating modal masses of 45.3%, 21.8%, and 11.1%. Damping is 2% in every mode.

The BPA mass is 1% the total building mass, corresponding to an effective mass ratio of 6.45% according to Warburton [1]. By applying the design procedure presented in Section 3, the VBPA and the HBPA parameters are exposed in Table 2.

	ω_R	ς	μ_0	L_x	L_y	b_x	b_y	b_z	l_{c0}	w_r
	(-)	(-)	(-)	(m)	(m)	(m)	(m)	(m)	(m)	(m)
VBPA	0.93	0.15	-	4.57	5.53	4.79	5.27	5.03	5.03	2.51
HBPA	0.98	-	0.45	4.12	4.99	4.32	4.76	4.53	-	2.27

Table 2: BPA design parameters on the tall building.

Simulations are conducted under a moderate-to-high wind flow, blowing for 1 hour either along x or along y. Deterministic wind load time-histories are determined as the realization of a stationary, spatially nonhomogeneous, stochastic process, comprising both along-wind and across-wind components, acting simultaneously on the structure. Along- and across-wind components are derived according to classical wind load spectra ([21], [22]).

Results are presented in Table 3 only for the wind blowing in the x direction. Four cases are compared, corresponding to: (1) the uncontrolled structure; (2) the linear VBPA; (3) the (geometrically nonlinear) VBPA; and (4) the HBPA. For each case, several response quantities are investigated, including: (i) the maximum modulus of the top story displacement, $r_{N,max}$; (ii) the maximum modulus of the BPA stroke, r_{max}; (iii) the maximum friction damping ratio activated by the HBPA, μ_{max}; (iv) the rms of the modulus of the top story displacement, $r_{N,rms}$; (v) the rms of the modulus of the BPA stroke, r_{rms}; and the mean value of the instantaneous power dissipated by the structure, $W_{s,mean}$.

Case	$r_{N,max}$ (cm)	r_{max} (cm)	μ_{max} (-)	$r_{N,rms}$ (cm)	r_{rms} (cm)	$W_{s,mean}$ (kW)
Uncontrolled	79.4	0.0	-	27.3	0.0	31.1
Linear VBPA	39.6	110	-	13.7	37.5	8.12
VBPA	39.7	109	-	13.8	37.4	8.17
HBPA	38.4	107	0.10	13.7	37.8	8.63

Table 3: Building responses for wind blowing along x.

Table 3 reveals that:

1) With respect to the uncontrolled structure, the linear VBPA achieves a significant response reduction: 50% in $r_{N,max}$ and in $r_{N,rms}$, and 74% in $W_{s,mean}$.
2) The VBPA, accounting for geometrical nonlinearities, gives nearly identical results. The absorber strokes are relatively small and the restrainer is far from being activated, which makes the first-order model accurate enough.
3) The HBPA performance is also very similar to the VBPA performance. The greatest differences are in $W_{s,mean}$, which is 6% larger for the HBPA, and in $r_{N,max}$, which is 3% larger for the VBPA. The maximum friction coefficient met by the HBPA during motion is 0.10.

It can be concluded that the three controlled cases are substantially equivalent.

9 CONCLUSION

Main conclusions of this study can be formulated as follows:

1) The HBPA is shown to be roughly equivalent to the VBPA, especially when responding to a unidirectional excitation at low response amplitudes.
2) Both BPA types undergo a performance loss if the stroke demand exceeds their stroke capacity, as it often occurs in rigid structures under large input intensities. This drawback is partially compensated for the HBPA by its larger dissipation capacity at large displacements. Despite such loss, in all examined simulations both types still ensure a significant vibration mitigation effect.

REFERENCES

[1] G. B. Warburton, Optimum absorber parameters for various combinations of response and excitation parameters, *Earth. Eng. Struct. Dyn.*, **10**, 381-401, 1982.

[2] D. Wang, T.K.T. Tse, Y. Zhou, Q. Li, Structural performance and cost analysis of wind-induced vibration control schemes for a real super-tall building, *Struct. Infrastruct. Eng.*, **11**(8), 990-1011, 2015.

[3] E. Matta, Seismic effectiveness of tuned mass dampers in a life-cycle cost perspective, *Earthq. Struct.*, **9**(1), 73-91, 2015.

[4] R. Greco, G.C. Marano, A. Fiore, Performance-cost optimization of tuned mass damper under low-moderate seismic actions, *Struct. Des. Tall Spec. Build*., **25**(18), 1103-1122, 2016.

[5] E. Matta, Lifecycle cost optimization of tuned mass dampers for the seismic improvement of inelastic structures, *Earthq. Eng. Struct. Dyn*., **47**, 714‑737, 2017.

[6] J. Náprstek, C. Fischer, M. Pirner, and O. Fischer, Non-linear model of a ball vibration absorber, *Comput. Meth. Applied Sciences*, **30**, 381-396, 2013.

[7] V. P. Legeza, Rolling of a heavy ball in a spherical recess of a translationally moving body, *Int. Appl. Mech.*, **38**(6), 758-764, 2002.

[8] M. Bransch, Unbalanced oil filled sphere as rolling pendulum on a flat surface to damp horizontal structural vibrations, *J. Sound Vibr.*, **368**, 22-35, 2016.

[9] J. Chen, and C. T. Georgakis, Tuned rolling-ball dampers for vibration control in wind turbines, *J. Sound Vibr.*, **332**, 5271-5282, 2013.

[10] X. Lu, Z. Liu, Z. Lu, Optimization design and experimental verification of track nonlinear energy sink for vibration control under seismic excitation, *Struct. Control Health Monit.*, **24**(12), e2033, 2017.

[11] E. Matta, A. De Stefano, and B. F. Spencer Jr, A new passive rolling-pendulum vibration absorber using a non-axial-symmetrical guide to achieve bidirectional tuning, *Earthq. Eng. Struct. Dyn.*, **38**, 1729-1750, 2009.

[12] J. L. Almazan, J. C. De la Llera, J. A. Inaudi, D. Lopez-Garcia, and L. E. Izquierdo. A Bidirectional and homogeneous tuned mass damper: a new device for passive control of vibrations, *Eng. Struct.*, **29**, 1548-1560, 2007.

[13] E. Matta, A novel bidirectional pendulum tuned mass damper using variable homogeneous friction to achieve amplitude-independent control, *Earthquake Engng. Struct. Dyn.* 2019, 1-25, https://doi.org/10.1002/eqe.3153.

[14] E. Matta, Modeling and design of bidirectional pendulum tuned mass dampers using axial or tangential homogeneous friction damping, *Mech. Syst. Signal Proc. 116*, 392-414, 2019.

[15] J. Inaudi, and J. Kelly, Mass damper using friction-dissipating devices, *J. Eng. Mech*., **121**, 142-149, 1995.

[16] A. Fiore, G.C. Marano, M.N. Natale, Theoretical prediction of the dynamic behavior of rolling-ball rubber-layer isolation systems, *Struct. Control Health. Monit*., **23**, 1150‑1167, 2016.

[17] R. Greco, G.C. Marano, Identification of parameters of Maxwell and Kelvin-Voigt generalized models for fluid viscous dampers, *J. Vibr. Control*, **21**(2), 260–274, 2015.

[18] J. B. Burl, *Linear Optimal Control*. Menlo Park, CA: Addison-Wesley, Longman, 1999.

[19] A. Y. T. Leung, and H. Zhang, Particle swarm optimization of tuned mass dampers, *Eng. Struct.*, **31**, 715-728, 2009.

[20] Y. L. Xu, B. Samali, and K. C. S. Kwok, Control of along-wind response of structures by mass and liquid dampers, *J. Eng. Mech.*, 118(1), 20-39, 1992.

[21] A. G. Davenport, The spectrum of horizontal gustiness near the ground in high winds, *Q. J. R. Meteorol. Soc.*, **87**, 194-211, 1961.

[22] B. J. Vickery, and A. W. Clarke, Lift or across-wind response of tapered stacks, *J. Struct. Div. ASCE*, **98**, 1-20, 1972.

COMPDYN 2019
7th ECCOMAS Thematic Conference on
Computational Methods in Structural Dynamics and Earthquake Engineering
M. Papadrakakis, M. Fragiadakis (eds.)
Crete, Greece, 24–26 June 2019

EFFECT OF CHANGING THE COEFFICIENT OF RESTITUTION OF A SINGLE-SIDED VIBRO-IMPACT NONLINEAR ENERGY SINK IN A TWO-STORY STRUCTURE

Adnan S. Saeed[1] **and Mohammad A. AL-Shudeifat**[1]

[1] Aerospace Engineering, Khalifa University of Science and Technology
Abu Dhabi, UAE
e-mail: {adnan.saeed,mohd.shudeifat}@ku.ac.ae

Abstract

In many applications of structural dynamics, it is desirable to transfer energy from a primary system using a dynamic absorber to protect the structure from destructive vibration amplitudes. Nonlinear Energy Sinks (NESs) are local attachments used to rapidly and passively dissipate energy from a primary structure in a phenomenon known as Targeted Energy Transfer (TET). Consequently, many types of NESs, which incorporate an essential nonlinear property, have been proposed, designed and tested in the literature. Based on numerical and experimental investigations of these types, Single-Sided Vibro-Impact (SSVI) NESs, where impacts, usually between the top floor of the primary structure and the NES, are utilized to further dissipate energy, proved to be the most efficient for TET in small- and large-scale structures. In literature, researchers have mostly considered steel-to-steel impacts which correspond to a coefficient of restitution of approximately 0.7. In this work, the effect of changing this coefficient of restitution is analyzed and investigated in a two-story physical primary structure. The coupled systems are optimized to achieve the maximum energy transfer and dissipation by measuring the normalized weighted-averaged effective modal damping criteria. It is found that lowering the coefficient of restitution increases the capability of the SSVI NES to transfer and dissipate initial energy induced into a primary structure for a wide range of impulsive excitations.

Keywords: Nonlinear Energy Sink, Targeted Energy Transfer, Vibration Mitigation, Shock Mitigation.

1 INTRODUCTION

Structures are subject to destructive vibration amplitudes from impacts, collisions, earthquakes or wind. Hence, it is desirable to protect the structure by transferring energy to a dynamic absorber in a process known as passive targeted energy transfer (TET). It has recently gained increasing interest in many applications of structural dynamics where a small essentially nonlinear lightweight attachment called nonlinear energy sink (NES) is usually added to the primary structure to enable passive energy transfer for wide range of frequencies through single or cascades of resonance captures. Recently, various NES designs have been numerically, analytically and experimentally investigated to achieve high percentages of energy transfer and dissipation. Depending on the way the nonlinearity is added, these NESs can be categorized into several types such as stiffness-based NESs, impact-based NESs, rotary NESs, and magnet-based NESs. The translational stiffness-based NESs employ an essentially nonlinear (usually cubic) stiffness coupling element to attach the NES mass to a floor in the primary structure [1]. Several enhancements have been proposed to this type where the addition of a linear or nonlinear damping elements [2], additional nonlinearly coupled mass [2-3], additional lateral stiffness elements [4] and negative, unsymmetrical or variable nonlinear stiffness components [5-10] are analyzed for increasing the efficiency of the energy transfer and dissipation. Impact-based NESs employ a linearly coupled NES mass in addition to rigid barriers in the motion domain of the NES to engage in non-smooth impacts that integrate the essential nonlinear property required for cascades of resonance captures. There are two main types of impact-based NESs: (i) double-sided vibro-impact (DSVI) NESs in which two rigid barriers are placed symmetrically from the initial position of the NES mass [11-14] and (ii) single-sided vibro-impact (SSVI) NESs, which are the topic of this paper, realized by removing one of the rigid barriers to allow the NES mass gain considerable momentum during the non-impact phase [15-19]. Rotary-based NESs incorporate an inertially coupled NES mass through a rigid arm rotating about a vertical axis perpendicular to the direction of motion of the primary structure [20-21]. Similarly, this type of NES has been further enhanced by employing an elastic arm instead of the rigid arm [22] or by adding a rigid barrier to incorporate non-smooth impacts with the associated floor of the primary structure [23]. Finally, the magnet-based NES mass is coupled to the associated floor of the primary structure through a nonlinear symmetric or asymmetric coupling magnetic force [24-25]. Out of all the NES types, the SSVI NESs have been proven numerically and experimentally to be the most efficient for energy dissipation and shock mitigation. Hence, the focus of this paper is to investigate further enhancements to the SSVI NESs to improve its capability of engaging in rapid passive and nearly irreversible TET.

During an impact in the SSVI NESs, the coefficient of restitution, a material property depending solely on the materials which get in contact, is defined as the ratio of the magnitude of restitutive impulse to deformative impulse. Most current works related to impact-based NESs consider steel-to-steel impacts which correspond to a coefficient of restitution of 0.7. The aim of this article is to investigate the effect of changing the coefficient of restitution on the performance of SSVI NES when attached to the top floor of a physical two-story linear primary structure excited by an impulsive loading. The paper presents the system description and governing equations, a discussion of the numerical optimization process followed by results and concluded remarks.

2 SYSTEM DESCRIPTION AND NUMERICAL OPTIMIZATION

The physical small-scale two-story structure analyzed in [15,22-23] is considered here where a SSVI NES is attached to the top floor as shown in Fig. 1. The mass, damping and

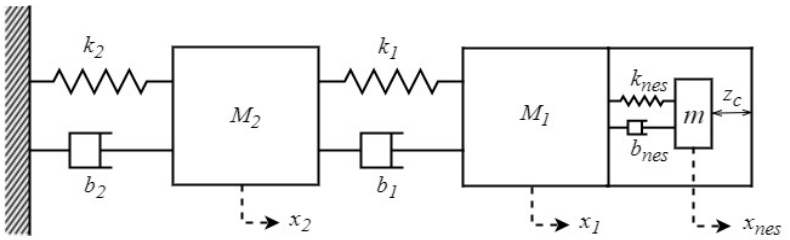

Figure 1: Illustration of 2 DOF primary system with SSVI NES on top floor.

stiffness matrices of the primary structure represented by $\mathbf{M}$, $\mathbf{C}$ and $\mathbf{K}$ identified by the modal analysis of the physical fixture for the system are given as

$$\mathbf{M} = \begin{bmatrix} 24.3 & 0 \\ 0 & 24.2 \end{bmatrix} \text{kg},$$
$$\mathbf{C} = \begin{bmatrix} 1.216 & -0.295 \\ -0.295 & 0.968 \end{bmatrix} \text{N}\cdot\text{s/m}, \tag{1}$$
$$\mathbf{K} = \begin{bmatrix} 15040 & -8220 \\ -8220 & 8220 \end{bmatrix} \text{N/m}$$

Upon updating the mass, damping and stiffness matrices of the whole structure due to the addition of the NES, the governing equations of motion are derived using Newtonian dynamics and numerically integrated using Runge-Kutta formulations. However, the numerical integration is continued until the impact condition for the SSVI NES given by $x_{nes} - x_1 > z_c$ is satisfied where x_{nes} and x_1 are the displacement of the NES mass and the top floor respectively and z_c is the clearance as shown in Fig. 1. After calculating the precise time of the impact, the velocities of the top floor and the SSVI NES after the impact are calculated based on the conservation of momentum and the coefficient of restitution r_c principles as

$$\dot{x}_1^+ = \frac{m\dot{x}_{nes}^- + M_1\dot{x}_1^- - mr_c(\dot{x}_1^- - \dot{x}_{nes}^-)}{m + M_1}$$
$$\dot{x}_{nes}^+ = \dot{x}_1^+ + r_c(\dot{x}_1^- - \dot{x}_{nes}^-) \tag{2}$$

where M_1 and m are the masses of the top floor and NES respectively and the superscripts $+$ and $-$ indicate the velocities after and before the impacts respectively. Accordingly, there are three sources of energy transfer and dissipation in the coupled system. The first is due to the linear damping element, represented by b_{nes} in Fig. 1, coupling the NES mass to the top floor of the structure. The second element is the kinetic energy lost during the inelastic impacts that occur when the NES collides with the rigid barrier attached to the top floor. The third is due to the non-smooth interference from the vibro-impacts which alters the global dynamic response of the structure causing energy to be transferred within its structural modes. Transferring energy from low-frequency high-energy destructive fundamental mode to high-frequency low-energy mode is another element of TET.

One way to quantify the performance of the coupled system for achieving efficient TET is by measuring the enhancement in the damping of the respective effective modal oscillators. This is quantified by the time-independent averaged effective modal damping measures $\lambda_{eff,i}$ expressed as

$$\lambda_{eff,i} = \frac{\dot{q}_i(T_0)^2 - \dot{q}_i(T_f)^2 + \omega_i^2\left(q_i(T_0)^2 - q_i(T_f)^2\right)}{2\int_{T_0}^{T_f} \dot{q}_i^2 dt} = \frac{E_i(T_0) - E_i(T_f)}{\int_{T_0}^{T_f} \dot{q}_i^2 dt} \quad (3)$$

where $\dot{q}_i$ is the modal velocity of the i-th mode, T_0 and T_f are the initial and final simulation times, E_i is the instantaneous energy and ω_i^2 is the effective modal stiffness. Because the modal response of a linear primary structure without the NES leads to no energy transfer within its modes, the nominal modal damping λ_i of the i-th structural mode are obtained from Eq. (3). The nonlinear interaction of the NES causes the energy dissipated by any mode plus its instantaneous energy to not sum up to its initial induced energy due to energy exchange between the structural modes and therefore the energy in each mode is not reserved. The ratio of the time-independent average effective damping measures $\lambda_{eff,i}$ to the nominal modal damping λ_i of the NES-free system is defined as the normalized weighted-averaged effective damping measures $\hat{\lambda}_{eff,i} = \lambda_{eff,i} \big/ \lambda_i$. If $\hat{\lambda}_{eff,i} < 1$, then energy is transferred into the i-th mode and it eventually dissipates more energy than its initial energy and vice versa.

The SSVI NES parameters: r_c, k_{nes} and b_{nes} are tuned in order to investigate the effect of changing the coefficient of restitution on achieving efficient and rapid transfer and dissipation of energy. The simulation time is set to 5 seconds to ensure efficient and rapid TET, the clearance z_c is fixed to $0.02m$ to ensure non-smooth vibro-impacts will occur and the NES mass ($m = 2.5kg \approx 0.05(M_1 + M_2)$) is assumed to be nonparasitic (i.e. do not add mass to the primary structure). Figure 2 shows the normalized weighted-averaged effective damping measures of mode 1 for varying NES parameters for an impulsive excitation induced by identical initial velocity of $0.25m/s$ equally to both floors of the primary structure. Generally, it is noticed that a relatively weak stiffness coupling and strong damping coupling elements are required for the SSVI NES to transfer significant amount of energy from the first fundamental mode to be dissipated the NES damping, inelastic impacts or higher structural modes for all values of the coefficient of restitution. Further, it is observed that the shape of the contour plots is reserved for varying coefficient of restitution values, however, the maximum achievable effective damping measure $\hat{\lambda}_{eff,1}$, indicated by the black crosses, occurs at higher damping values for higher coefficients of restitution values. This outcome can be understood from the fact that at high value of r_c, the energy dissipated by the inelastic collisions is decreased and therefore higher damping values are required to maximize the effective damping measure $\hat{\lambda}_{eff,1}$. Moreover, it is also concluded that low values of the coefficient of restitution enable wider range of stiffness and damping values to transfer and dissipate energy from the fundamental mode of the primary structure as observed from the size of high values of $\hat{\lambda}_{eff,1}$ (red color) in Fig. 2.

3 RESULTS AND DISCUSSION

The results of the numerical optimization are summarized in Fig. 3(a) which shows the maximum achievable normalized weighted-averaged effective mode 1 damping measures $\hat{\lambda}_{eff,1}$ by an optimized system at each specific value of the coefficient of restitution r_c for a clearance of $z_c = 0.02m$ and an impulsive loading through an identical initial velocity of $0.25m/s$ in

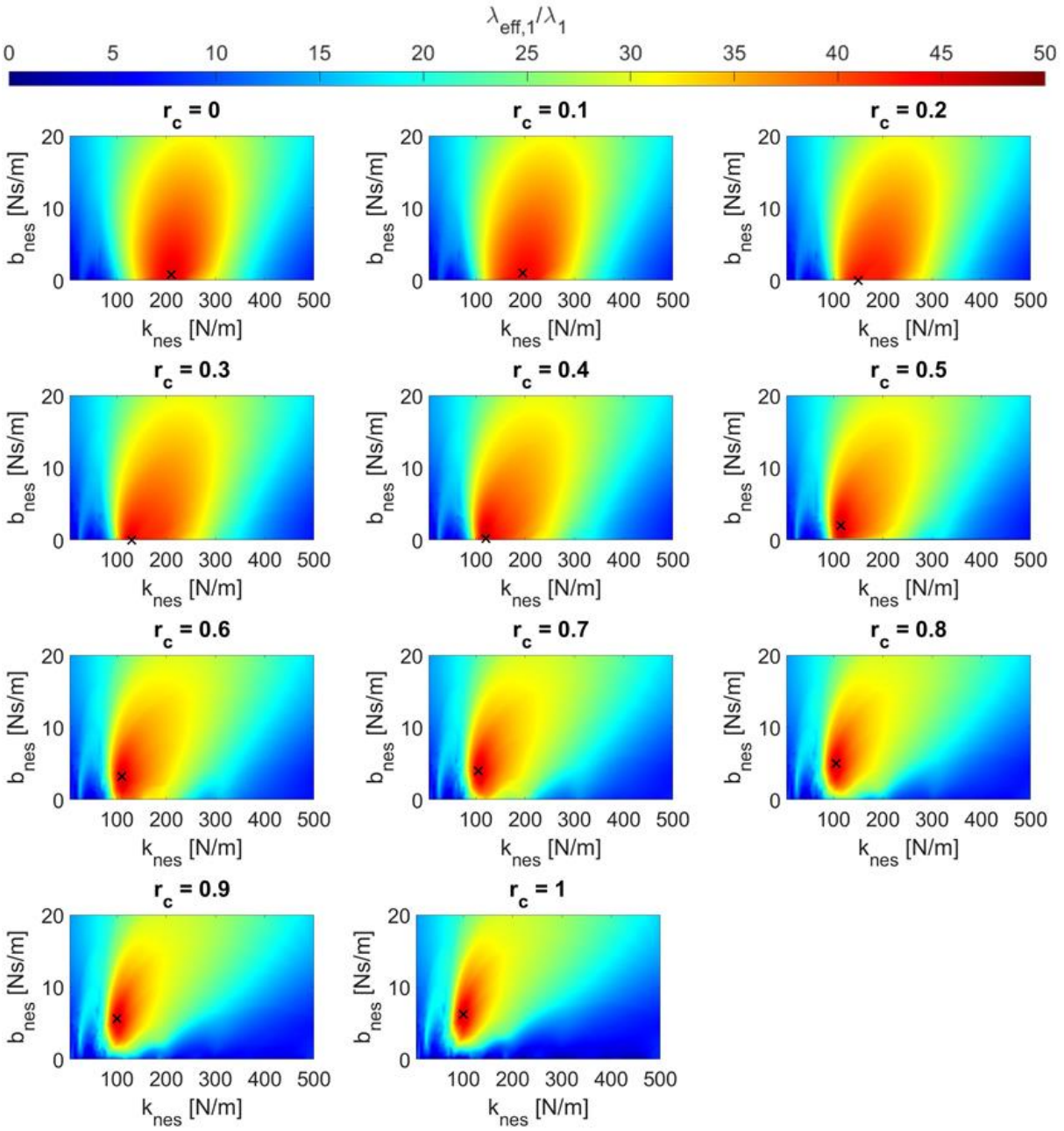

Figure 2: Contour plots of the normalized weighted-averaged effective damping measures for varying stiffness k_{nes}, damping b_{nes} and coefficient of restitution r_c for the two-story primary structure; identical initial velocity 0.25 m/s is considered for each floor, and black crosses indicate optimal system parameters.

duced equally to all floors of the primary structure. First, it is noticed that the optimized coupled systems for all values of r_c result in normalized weighted-averaged effective mode 1 damping measures $\hat{\lambda}_{eff,1}$ that are greater than unity. This indicates that in all cases, energy is being transferred from the high energy low frequency mode 1 to the NES itself or the second structural mode having lower energy and higher frequency. Consequently, this indicates that highly efficient TET has occurred by forcing energy to be transferred through single or cascades of resonance captures in a rapid and nearly irreversible way. In addition, the goal of this paper is to investigate if changing the coefficient of restitution from its typical value of 0.7 which corresponds to steel-to-steel impacts will enhance the energy transfer and dissipation

by resulting in higher values of $\hat{\lambda}_{eff,1}$. Fig. 3(a) shows that the maximum normalized weighted-averaged effective mode 1 damping measure is 46.2 achievable with a coefficient of restitution of 0.4 where the optimized SSVI NES parameters are $k_{nes} = 120N/m$ and $b_{nes} = 0.1078Ns/m$ compared to $\hat{\lambda}_{eff,1} = 45.7$ achievable with a coefficient of restitution of 0.7 where the optimized SSVI NES parameters are $k_{nes} = 106N/m$ and $b_{nes} = 4.0723Ns/m$. Additionally, the performance of the optimized NESs at $r_c = 0.4$ and $r_c = 0.7$ are compared in Fig. 3(b) for varying initial impulsive energies induced equally to all floors. Both system reach their optimum at around $1.4Nm$ which corresponds to the optimization initial energy. However, the new system with coefficient of restitution of 0.4 shows higher normalized weighted-averaged effective mode 1 damping measures $\hat{\lambda}_{eff,1}$ for a wide range of initial impulsive energies indicating that better energy transfer and dissipation is achievable at lower values of the coefficient of restitution.

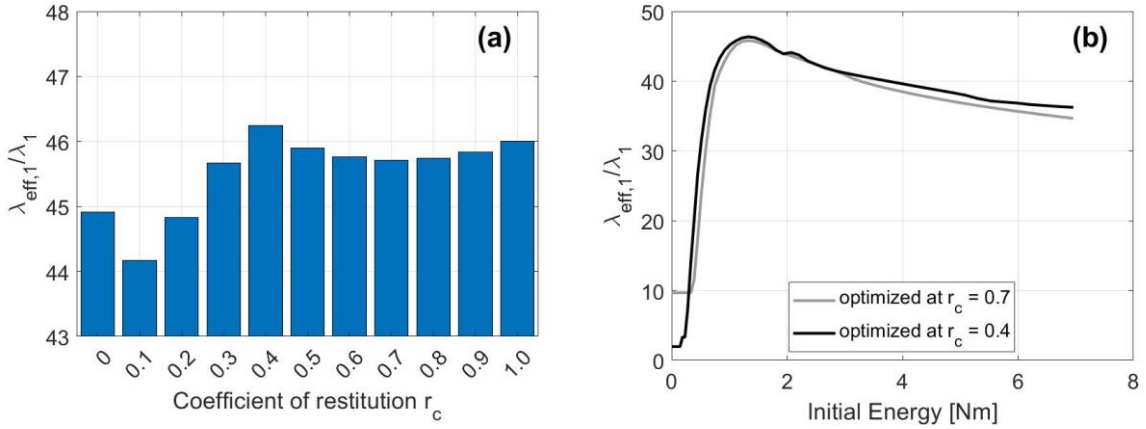

Figure 3: (a) bar chart showing the maximum achievable $\hat{\lambda}_{eff,1}$ at varying values of the coefficient of restitution r_c for the two-story primary structure with identical initial velocity $0.25m/s$ is considered for each floor and a fixed clearance of $0.02m$ (b) normalized weighted-averaged effective damping of the fundamental mode $\hat{\lambda}_{eff,1}$ of the two-story primary structure as function of the applied impulsive energy

4 CONCLUDED REMARKS

Many dynamical structures undergo continuous vibrations induced by shock or seismic excitations resulting from impacts, collisions, wind, earthquake, or fluid-structure interaction. Consequently, integrating dynamic vibration absorbers is becoming a high priority and essential requirement in many engineering applications. Nonlinear energy sinks (NESs) are the most efficient and robust attachments to act as rapid and passive device to transfer and dissipate energy from primary structure. Hence, this paper investigated further improvements to the currently most efficient nonlinear energy sink (NES), the single-sided vibro-impact (SSVI) NES by studying the effect of the coefficient of restitution, which is a ratio of restitutive to deformative impulses during impact, on its capability to irreversibly transfer induced impulsive energy out of the fundamental highly energetic mode. Currently, the coefficient of restitution used in most analytical, numerical and experimental analysis of impact-based NESs is 0.7 which corresponds to the typical steel-to-steel impacts. However, it is found in this paper that reducing the coefficient of restitution to 0.4 enhances the normalized weighted-averaged

effective damping measure of the fundamental mode of a two-story linear physical primary structure. The results are obtained for a simulation time of 5 seconds and using an NES mass of 5% of the whole structure indicating that rapid targeted energy transfer (TET) can occur with using a small mass of NES. The enhanced performance is obtained for a wide range of initial impulsive energies indicating the robustness of the proposed modification. Although the overall enhancement is not highly significant, this paper proves that lowering the coefficient of restitution leads to better shock and vibration mitigation and it is expected that using a large-scale structure will result in highly significant enhancement in the performance of SSVI NES by lowering the coefficient of restitution.

REFERENCES

[1] A.F. Vakakis, O.V. Gendelman, L.A. Bergman, D.M. McFarland, G. Kerschen, Y.S. Lee, *Nonlinear targeted energy transfer in mechanical and structural Systems*, Springer Verlag, 2008.

[2] T.P. Sapsis, D.D. Quinn, A.F. Vakakis, L. A. Bergman, Effective stiffening and damping enhancement of structures with strongly nonlinear local attachments. *Journal of Vibration and Acoust*ics, **134**(1), 011-016, 2012.

[3] O.V. Gendelman, T. Sapsis, A.F. Vakakis, L.A. Bergman, Enhanced passive targeted energy transfer in strongly nonlinear mechanical oscillators, *Journal of Sound Vibration*, **330**(1), 522–551, 2011.

[4] A.S. Saeed, M.A. AL-Shudeifat, Vibration suppression in two-dimensional oscillation dynamical systems, *Proceedings of the ASME 2018 International Mechanical Engineering Congress and Exposition (IMECE)*, Pittsburgh, PA, November 9-15, 2018.

[5] M.A. AL-Shudeifat, Nonlinear energy sinks with nontraditional kinds of nonlinear restoring forces, *Journal of Vibration and Acoustics*, **139**(2), 024503, 2017.

[6] A.F. Vakakis, M.A. AL-Shudeifat, M.A. Hasan, Interactions of propagating waves in a one-dimensional chain of linear oscillators with a strongly nonlinear local attachment, *Meccanica*, **49**(10), 2375-2397, 2014.

[7] M.A. AL-Shudeifat, Highly efficient nonlinear energy sink, *Nonlinear Dynamics*, **76**(4), 1905–1920, 2014.

[8] G. Habib, F. Romeo, The tuned bistable nonlinear energy sink, *Nonlinear Dynamics*, **89**(1), 179-196, 2017.

[9] M.A. AL-Shudeifat, A.S. Saeed, Frequency-energy dependence of the bistable nonlinear energy sink," *Proceedings of the ASME 2017 International Design Engineering Technical Conferences and Computers and Information in Engineering Conference (IDETC-CIE)*, Cleveland, OH, August 6-9, 2017.

[10] M.A. AL-Shudeifat, A.S. Saeed, Analytical treatment for bistable nonlinearly coupled oscillator," *Proceedings of the ASME 2017 International Design Engineering Technical Conferences and Computers and Information in Engineering Conference (IDETC-CIE)*, Cleveland, OH, August 6-9, 2017.

[11] O.V. Gendelman, Analytic treatment of a system with a vibro-impact nonlinear energy sink, *Journal of Sound Vibration*, **331**(21), 4599–4608, 2012.

[12] T. Li, S. Seguy, A. Berlioz, Dynamics of cubic and vibro-impact nonlinear energy sink: analytical, numerical, and experimental analysis, *Journal of Vibration and Acoustics*, **138**(3), 031010, 2016.

[13] O. V. Gendelman, A. Alloni, Dynamics of forced system with vibro-impact energy sink, *Journal of Sound Vibration*, **358**(1), 301–314, 2015.

[14] T. Li, S. Seguy, A. Berlioz, On the dynamics around targeted energy transfer for vibro-impact nonlinear energy sink, *Nonlinear Dynamics*, **87**(3), 1453-1466, 2017.

[15] M.A. Al-Shudeifat, N. Wierschem, D.D. Quinn, A.F. Vakakis, L.A. Bergman, B.F. Spencer, Numerical and experimental investigation of a highly effective single-sided vibro-impact non-

linear energy sink for shock mitigation, *International Journal of Nonlinear Mechanics*, **52**(1), 96–109, 2013.
[16] M.A. AL-Shudeifat, A.F. Vakakis, L.A. Bergman, Shock mitigation by means of low-to high frequency nonlinear targeted energy transfers in a largescale structure, *Journal of Computational and Nonlinear Dynamics*, **11**(2), 021006, 2016.
[17] N.E. Wierschem, S.A. Hubbard, J. Luo, L.A. Fahnestock, B.F. Spencer, D.M. McFarland, D.D. Quinn, A.F. Vakakis, L.A. Bergman, Response attenuation in a large-scale structure subjected to blast excitation utilizing a system of essentially nonlinear vibration absorbers, *Journal of Sound Vibration*, **389**(1), 52-72., 2017.
[18] W. Li, N.E. Wierschem, X. Li, T. Yang, On the energy transfer mechanism of the single-sided vibro-impact nonlinear energy sink, *Journal of Sound Vibration*, **437**(1), 166-179, 2018.
[19] J. Luo, N.E. Wierschem, S.A. Hubbard, L.A. Fahnestock, D.D. Quinn, D.M. McFarland, D.F. Spencer, A.F. Vakakis, L.A. Bergman, Large-scale experimental evaluation and numerical simulation of a system of nonlinear energy sinks for seismic mitigation, *Engineering Structures*, **77**(1), 34–48, 2014.
[20] G. Sigalov, O. Gendelman, M.A. Al-Shudeifat, L. Manevitch, A.F. Vakakis, L.A. Bergman, Resonance captures and targeted energy transfers in an inertially-coupled rotational nonlinear energy sink, *Nonlinear Dynamics*, **69**(4), 1693–1704, 2012.
[21] O. Gendelman, G. Sigalov, L. Manevitch, M. Mane, A.F. Vakakis, L.A. Bergman, Dynamics of an eccentric rotational nonlinear energy sink, *Journal of Applied Mechanics*, **79**(1), 011012, 2012.
[22] M.A. Al-Shudeifat, A.S. Saeed, Enhanced rotating nonlinear energy sink. *Proceedings of the ASME 2016 International Design Engineering Technical Conferences and Computers and Information in Engineering Conference (IDETC-CIE)*, Charlotte, NC, August 21-24, 2016.
[23] A.S. Saeed, M.A. AL-Shudeifat, A new type of NES: rotary vibro-impact, *Proceedings of the ASME 2017 International Design Engineering Technical Conferences and Computers and Information in Engineering Conference (IDETC-CIE)*, Cleveland, OH, August 6-9, 2017.
[24] D. Kremer, K. Liu, A nonlinear energy sink with an energy harvester: transient responses, *Journal of Sound Vibration*, **333**(20), 4859-4880, 2014.
[25] M.A. AL-Shudeifat, Asymmetric magnet-based nonlinear energy sink, *Journal of Computational and Nonlinear Dynamics*, **10**(1), 014502, 2015.

COMPDYN 2019
7th ECCOMAS Thematic Conference on
Computational Methods in Structural Dynamics and Earthquake Engineering
M. Papadrakakis, M. Fragiadakis (eds.)
Crete, Greece, 24–26 June 2019

SHORT- VERSUS LONG-TERM READINESS AND DISSIPATIVE CAPABILITY OF MR DAMPERS FOR STRUCTURAL CONTROL

Mariacristina Spizzuoco

Department of Structures for Engineering and Architecture, University of Naples Federico II
via Claudio n. 21 – 80125, Naples, Italy
spizzuoc@unina.it

Abstract

The proposed work is based on an experimental activity aimed at comparing the long-term behavior of control devices based on the use of magneterheological (MR) fluids for seismic protection of framed structures. They have been tested three times in ten years: first in 2008, then in 2013 after five years of inactivity, and finally in 2017 after further four years of quiescence. The results of the three campaigns of passive and promptness experimental tests, in terms of force-displacement loops, electrical delay of the electromagnetic circuit, dissipated energy and maximum reacting force. The evolution of the response of such dampers due to inactivity over the time is assessed and discussed, aiming at recognize those phenomena are most probably responsible of a MR fluid deterioration (namely oxidation of iron particles, their sedimentation, fluid thickening, seal wearing), finally trying to give practical suggestions to the designers of smart control systems who should take this issues into account when dealing with the above kind of devices.

Keywords: magnetorheological damper, MR fluid, ageing effects.

1 INTRODUCTION

Magnetorheological (MR) fluids are suspensions of ferromagnetic particles in a carrier oil fluid, with several types of additives; their rheological properties change rapidly, stably, and repeatedly when a magnetic field is applied. The particles, whose diameters range from 1 to 10 μm, align themselves along magnetic fluxes with the external magnetic field, and these clusters generate resistances against the orthogonal flow. The change in the yield stresses that occur due to the intensity of the external magnetic field, is much larger than the effect of the Newtonian viscosity of the base oil.

Actually, this possibility of modulating in real time the damping properties of devices based on MR fluids, represents one of the most promising way to manufacture a semi-active control system for civil structures. Aiming at avoiding structural resonance and maximize energy dissipation, the stiffness and/or damping of MR fluid devices can be varied in real time according to proper control algorithms which require real time acquisition of the external excitation and/or the structural response.

The most commonly applied model of a MR fluid is the simple and effective Bingham model [1]: it is characterized by a variable rigid-plastic component connected in parallel to a Newtonian viscosity element.

The rheological properties of the controllable MR fluids are influenced by the density and concentration of particles, size of particle, carrier fluid's features, type of additives, applied magnetic field, temperature, etc. Recent studies were addressed to the calibration of the above factors in order to improve the mechanical behavior and durability of the MR fluid [2].

In some real situations, MR devices work frequently: this is the case when they are applied for suspensions on vehicles and trains, for brakes, for vibration control of cable-stayed bridges subjected to wind, etc. On the contrary, in earthquake engineering applications, MR devices might be called to give a few seconds long effective response after years of quiescence. The authors [3], after a ten years long campaign, present and discuss the most important experimental results aimed to show the evolution over time of response promptness, dissipating capability, and force reaction of MR dampers.

In the following, a literature review is reported of the scientific research on the "ageing effects" of MR fluids due to long inactivity (i.e. those commonly occurring in case of seismic applications), rather than to fatigue or long-term use.

Two large scale prototype MR dampers, produced by the German firm Maurer Söhne for seismic applications, have been experimentally investigated during the above mentioned ten years long observation time period. The proposed paper tries to draw some conclusions on the possible causes of the small observed changes in the mechanical response over time.

It is worth to point out that the authors' research is addressed only to understand if and how the overall mechanical response of a MR fluid-based seismic dissipative device, at its macro scale, may change in time.

2 AGEING ISSUES OF MR DAMPERS

An MR fluid is a suspension of carbonyl magnetizable particles in a carrier liquid fluid. Various additives are present in the composition to improve the settling rate, reduce oxidation, etc. A literature review of the last twenty years of research on MR fluid are summarized here, by focusing on the main durability issues of MR dampers: many researchers have addressed their efforts to make up a mixture able to represent a satisfactory compromise among different and sometimes conflicting objectives: temperature stability, lower viscosity, lower settling, higher force, prevention of particle oxidation, etc.

A critical issue is represented by the low viscosity of the fluid, being the ratio of maximum (on-state) yield stress to minimum (off-state) viscous stress the responsible of the MR fluid ability to be controllable [1, 4].

Another important choice in the design of a MR fluid is the ratio of particles' weight to carrier fluid's weight (generally 0.1 – 0.5): it is chosen by trading-off its influence on the viscosity (off-state) and its effect on the maximum yield stress of the MR fluid (on-state).

A further issue is the influence of temperature [5], that doesn't affect the magnetically-induced (on-state) force but only the off-state force. If the temperature is in the range 0~100°C, the viscosity is relatively stable and would slightly decline as temperature rises: it is due to the fact that the thermal motion of molecules of carrier fluid is a little higher with temperature, and both attraction and internal friction decline; consequently, the shear stress produced by shear deformation slightly decreases, and as a result, the viscosity declines. In the range −40~0°C, the carrier fluid of MR fluid is solidified and settled, and as a result, large viscosity appears. Once the temperature is higher than 100°C, the carrier fluid would be volatilized and the additives would be decomposed, which make the viscosity gradually increase: some additives may cause irreversible thickening of MR fluid, which influences the chaining of the material in the applied magnetic field, resulting in the reduction of the shear stress and uncontrollability of the variation of the shear stress, the reduction of the transmission stability, and even the failure of transmission.

Long-term modifications of their behavior are a fundamental issue in Earthquake Engineering, because seismic dampers are generally dormant for most of their life, up to the occurring of an earthquake.

According to the literature, durability issues of MR dampers [6, 7, 8] are mainly associated to a) particle sedimentation, b) fluid thickening, c) particle oxidation and d) seal wearing:

a) Particle sedimentation

Magnetic particles are denser than the carrier fluid, so that long-term storage generates particle sedimentation and as such mixing processes might be required [9, 10]. This corresponds to an unexpected response of the fluid to the applied magnetic field.

b) Fluid thickening

Due to the fragmentation of the brittle oxide layer on the surface of the magnetic particles, the fluid can become thicker in time. This phenomenon causes an increase of the off-state viscosity and of the reacting force of the device. The coating of magnetic particles with a protective surface layer can be a solution to enhance the durability of MR fluids from this point of view [11, 12].

c) Particle oxidation

The MR fluid is characterized by a modification of its compositional properties, due to the absorption of carbon dioxide and the corresponding corrosion. This effect gets worse in case of higher shear rate and increasing temperature, that produce stronger collision of iron particles [13, 14]. The oxidation of particles determines a lower magnetization of iron oxides with respect to elemental iron and, consequently, to reduced mechanical performances of MR fluids. Surface protection agents and anti-oxidants can be added to the formulation in order to reduce or eliminate the process.

d) Seal wearing

Seal design and selection of proper seal material are a critical issue for MR devices. Iyengar and Alexandris [15] tested the wear resistance of five polyurethanes–based seal materials, in combination with four types of fluid lubricant, and investigated different abilities to resist wear. Then, Wiehe and Maas [16] made durability tests and showed the suitability of two seal types in terms of wear resistance for long-term usage.

According to previous studies, particle sedimentation in the absence of magnetic field represents the most severe problem for MR fluids, due to large difference of the densities between magnetic particles and carrier fluid. The non-uniform distribution of micro-particles can interfere with MR effect when the magnetic field is applied and hence MR fluid performance may be degraded. This is mainly the case of seismic MR devices where particles are subjected to only gravitational force for long time while not being functional.

Two strategies to reduce sedimentation are the adoption of fluid stabilizers additives or particle coating [17, 18], but high care should be taken in choosing fluid stabilizing additives so that they do not adversely affect the off-state viscosity [19]. The coating process is complicated and involves surface treatment and addition of monomer or stabilizer. Rahim et al. [17] studied the use of nano-particles additives of Al and Cu, simultaneously, to enhance the thermal conductivity and reduce the sedimentation rate of MR fluids. They proposed a procedure to find optimal components of the additives to achieve both the enhancement of the thermal conductivity and the reduction of the sedimentation rate, simultaneously.

The experimental tests showed in the following were conducted under virtually identical environmental conditions, so that a study about temperature effect on the mechanical response of the MR dampers is out of the scope of the work [20]. On the other hand, the authors have demonstrated the short-term readiness and efficacy of the investigated MR dampers through experimental dynamic characterization tests and also shaking table seismic tests on a scaled frame structure [21].

3 TEN YEARS AGEING EXPERIMENTAL CAMPAIGN ON PROTOTYPE MR DAMPERS

Dynamic characterization experimental tests of two prototype MR dampers were done in July 2017 and their results have been compared with those obtained for the same devices when they were tested in February 2008 and March 2013. The same experimental set-up were assumed, in similar environmental conditions. During both time periods, i.e. from 2008 to 2013 and from 2013 to 2017, the devices have been stored in a horizontal position. Then, they have been much slowly displayed to the testing machine for the 2013 and 2017 tests, in order to avoid the shaking of the MR fluid inside. This kind of storage just corresponds to the real inactivity condition of the dampers when they are installed horizontally inside a building at a certain floor level (i.e., under indoor environmental conditions), to seismically protect the structure. The comparison between the results processed from the three experimental testing periods, gave important information on how the devices' mechanical behavior changed after two long periods of rest. The authors tried to associate the variations of the mechanical behavior to the most probable physical modifications in MR fluids.

Figure 1 shows one of the prototypes full-scale MR dampers which were studied during a wide experimental campaign performed in 2008 and in 2013 [3], and were finally experimentally tested in July 2017. The intensity of the feeding current is in the range 0÷3 A and the maximum force, that can be developed at the maximum current intensity, is of about 30 kN. In order to assess the variations in their mechanical behavior due to the time elapsed with non-operating devices, harmonic and constant velocity displacements time-histories have been imposed between the ends of the devices.

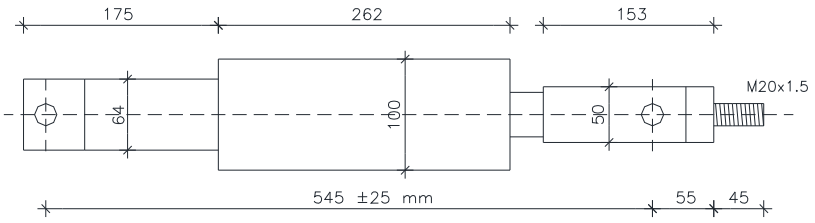

Figure 1: Photo and dimensions (in mm) of the prototype MR damper.

In order to be able to compare the results obtained by the tests performed during three different time periods, in July 2017, the same previous experimental setup has been used and some tests carried out in 2008 and 2013 have been performed again. Table 1 shows the list of tests: for each of them, made of 10 cycles, the type of test and the assumed parameters are reported. The promptness of each MR damper has been evaluated by performing the following tests: at first a harmonic displacement test at 1.5 Hz frequency and 20 mm amplitude; then, four constant velocity tests at 0.1 m/s velocity, 10 mm amplitude and 2 seconds pauses before inverting the sign of the velocity. These constant velocity tests were performed at different current values i=1.0; 2.0; 2.5; 3.0 A. Besides, for MR device 1, seven further passive tests were carried out by applying a harmonic displacement time-history at 1.5 Hz, 20 mm amplitude and different current intensities.

MR #	Type of test	Test No.	i [A]	f / v [Hz / ms^{-1}]	d [mm]
2	promptness	1	2.0	1.5 Hz	20
2	promptness	2	1.0	0.1 m/s	10
2	promptness	3	2.0	0.1 m/s	10
2	promptness	4	2.5	0.1 m/s	10
2	promptness	5	3.0	0.1 m/s	10
1	passive	1	2.7	1.5 Hz	20
1	passive	2	1.8	1.5 Hz	20
1	passive	3	0.9	1.5 Hz	20
1	passive	4	0.0	1.5 Hz	20
1	passive	5	2.7	1.5 Hz	20
1	passive	6	2.7	1.5 Hz	20
1	passive	7	2.7	1.5 Hz	20
1	promptness	8	2.0	1.5 Hz	20
1	promptness	9	1.0	0.1 m/s	10
1	promptness	10	2.0	0.1 m/s	10
1	promptness	11	2.5	0.1 m/s	10
1	promptness	12	3.0	0.1 m/s	10

Table 1: List of tests performed on MR dampers in 2017.

As shown in Table 1, both the MR dampers were subjected to five promptness tests. Their aim was to measure the time delays previously defined within the SA control chain. The change of dampers' behavior were commanded for each zero crossing of the displacement laws (i.e. in the instants in which x=0 occurred during constant velocity tests No. 2 to 5 on MR #2 and No. 9 to 12 on MR #1) or of the velocity curves (i.e. in the instants in which $\dot{x}$=0 occurred during harmonic displacement test No. 1 on MR #2 and No. 8 on MR #1). The electrical delay τ_e of the electromagnetic circuit, which spans from the instant when the current inside the coils starts to rise or to fall, to the stabilization of the current into the damper at its nominal value with a tolerance of 5%, has been measured at a certain number of on→off and off→on switches for each performed test. The minimum and maximum values of the electri-

cal delays τ_e measured in 2017 at on→off and off→on switches, are represented by the black filled circles in Figures 2(a) and 2(b), respectively. For each current intensity, they are compared to the minimum and maximum values measured in 2008, represented by the blank circles in the same Figures. The 2017 response delays fall within the 2008 relating ranges, in almost all the cases: they are within 2-6 ms for the on→off phases, 2-9 ms for the off→on phases.

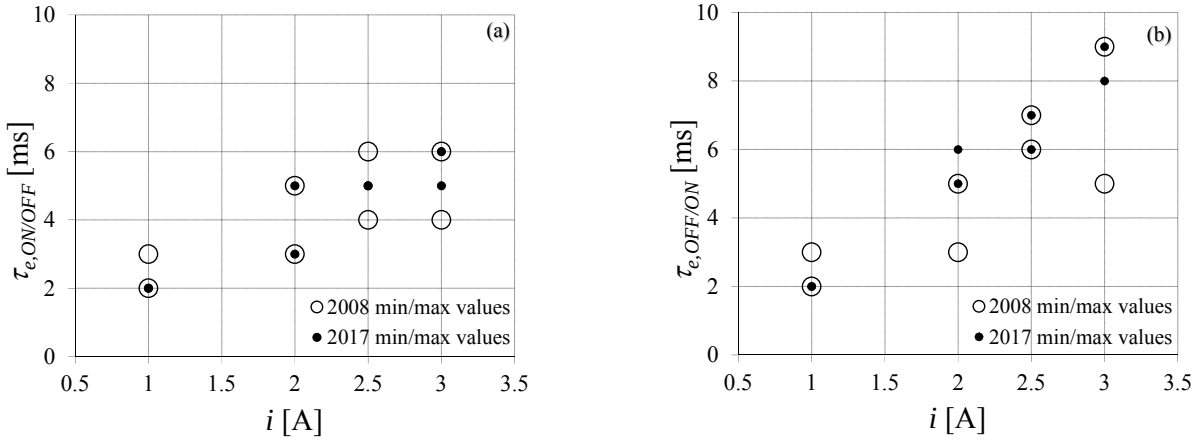

Figure 2: Minimum and maximum values of τ_e measured in 2008 and in 2017 for different levels of current.

Figures 3 and 4 show the most relevant results, in terms of force-displacement loops, of passive tests 1, 2, 4, 5 made on MR damper #1. An elongation of the damper is assumed as positive value of displacement, while a positive value of force indicates the device is in tension. Passive tests 3, 6, 7 are not discussed for the sake of brevity, because the results agree with those described in the following.

Figure 3(a) shows the first force-displacement cycle imposed in 2017 to MR damper #1 at a 2.7 A feeding current (test No. 1), after 4 years of rest. It is compared with the first cycle of the first test performed in 2013 after 5 years of inactivity, and with the first cycle of the same test done in 2008 after a certain number of tests. In the test of 2008 the device almost immediately reached the 27 kN yielding force, while an irregular trend is recognized in the reacting force measured in both 2017 and 2013, but that one recorded in 2017 is more irregular than the one of 2013. For some instant of the 2017 first loop, the maximum damper force is larger than four and nine years before. As already observed after the 2013 experimental tests, the mechanical behavior observed during the 2017 first cycle, performed after 4 years from the last activity, is most probably due to some phenomena occurring in MR fluid: sedimentation of the particles, presence of air bubbles and an increase of the fluid viscosity.

When the motion of the device piston operates a re-mixing of the fluid in its cylinder, the probable air is eliminated, the probable increase of fluid viscosity is recovered, and the recorded irregularities disappear from the following cycles. Figure 3(b) reports the second cycles of the same tests considered in Figure 3(a). It clearly shows that the 2017 second loop globally has a shape very similar to those recorded in 2008 and 2013, but the forces measured in 2017 are slightly lower than the forces of 2008 and 2013. The last part of the considered tests (10^{th} cycle) is in Figure 3(c) and makes in evidence that the 2017 forces become more and more less than those recorded in the 2017 first cycle. It is quite evident the typical Bingham behavior (i.e., friction and viscous components connected in parallel), but the decrease of the 2017 damping forces is probably due to the phenomenon of particle oxidation responsible of a decreasing of fluid's yielding stress, instead of a loss of MR fluid's viscosity.

Therefore, the experimental data explain that particle sedimentation have determined the most significant modifications during the first cycle, but the damper is able to recover after about one cycle through the mixing activity made by the piston within the fluid. Then, the mechanical response of the MR dampers exhibited after the 1st test is similar to that observed during the 10th cycle of the latter.

Figure 4 shows the first cycle of tests No. 4, 2 and 5 on MR #1 performed at 0.0, 1.8 and 2.7 A, respectively: they demonstrate that the viscous behavior in 2017 is quite equal to that in 2008 and 2013 (Figure 4(a)), so that the decay in 2017 damper force, with respect to 2008 and 2013, is depending on the current level. The amount of maximum force reduction is higher with increasing currents and it can be attributed to oxidation of particles which produces a not reversible decline of the MR fluids' mechanical performance, due to the lower magnetization of iron oxides.

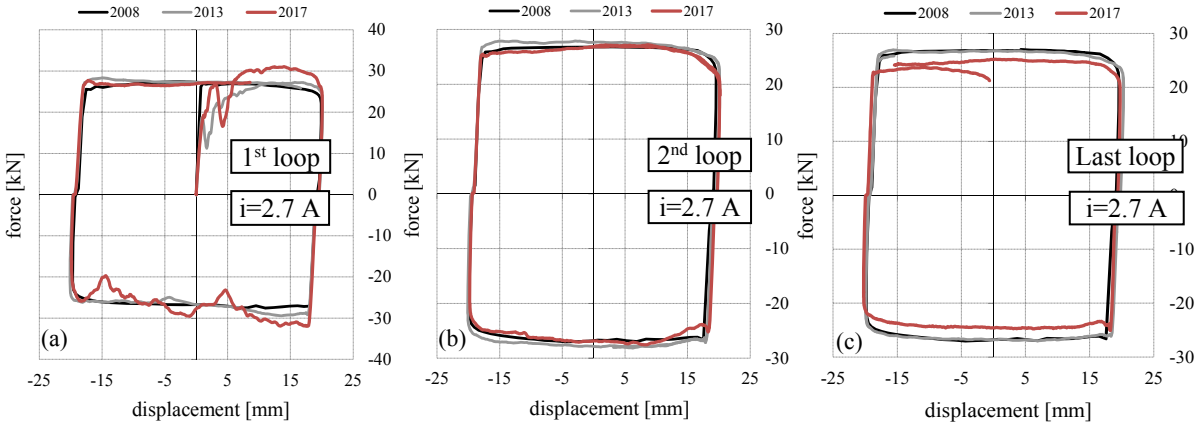

Figure 3: Comparison of force-displacement cycles (1.5 Hz, 20 mm) recorded in 2008, 2013 and 2017 at 2.7 A. Plots (a), (b) and (c) refer to the first, second and 10th loop, respectively.

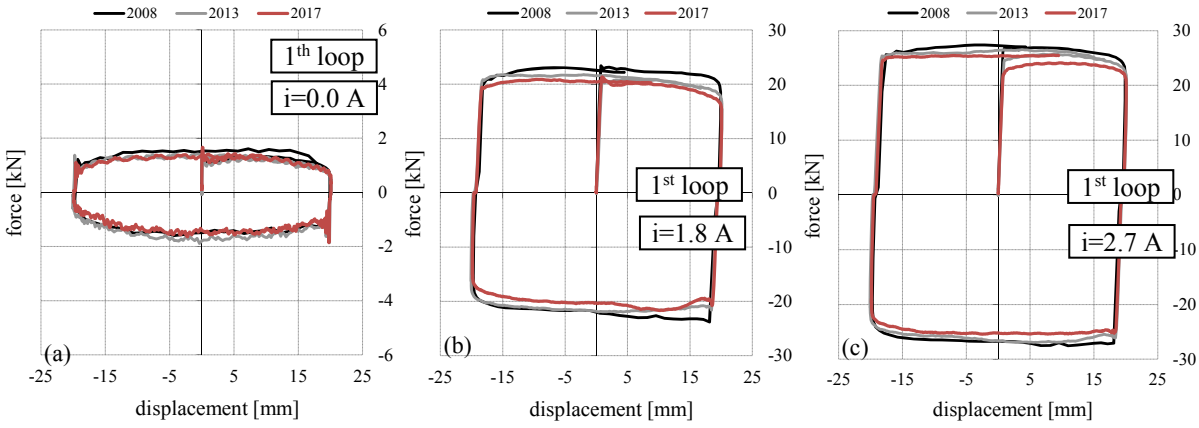

Figure 4: Comparison of force-displacement cycles (1.5 Hz, 20 mm) obtained in 2008, 2013 and 2017 for different levels of current (0.0, 1.8, 2.7 A).

The behavior of MR dampers, in terms of control forces and dissipated energy, is further analysed in the harmonic displacement tests of 2008, 2013, 2017 at 1.5 Hz frequency and 20 mm amplitude. Clearly, the first cycle performed in 2013 and 2017 after long time of device's inactivity were not considered due to the temporary irregularities described above. Figure 5(a) reports the value of maximum damper force at four levels of current intensity: from 2008 to 2013, a percentage reduction of approximately 2% has been found at i = 2.7 A, while an increment of about 4% has been computed at i = 0.0 A; from 2013 to 2017, a reduction of about

5% and 8% has been determined at the two above extreme currents. For the same harmonic tests, Figure 5(b) shows the energy dissipated in one displacement cycle, computed as mean of the of about 1% energy values related to three consecutive loops: from 2008 to 2013, a percentage increment has been calculated at i = 2.7, while a reduction of about 5% has been found at i = 0.0 A; from 2013 to 2017, a reduction of about 4% and 10% has been evaluated at the two extreme current levels.

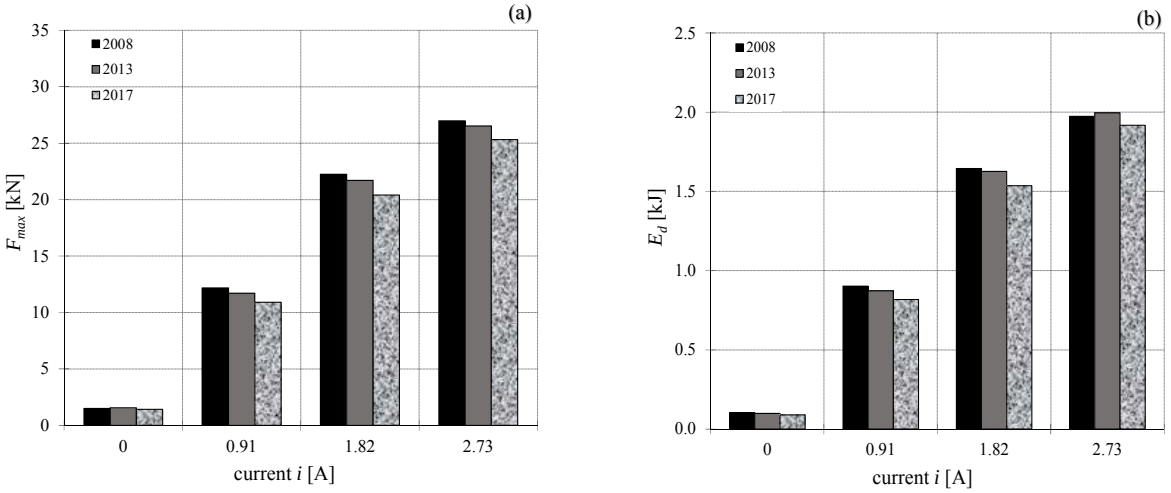

Figure 5: Maximum device force (a) and energy dissipated in one loop (b), for the tests at 1.5 Hz and 20 mm performed in 2008, 2013 and 2017 at currents 0.0, 0.9, 1.8, 2.7 A.

Table 2 reports the percentage of performance decay from 2008 to 2013, from 2013 to 2017, and finally from 2008 to 2013. In case of no current (0 A), the maximum reacting force is reduced by about 5%, while for current intensities 0.9 and 1.8 A the effect due to probable particle oxidation leads to less reacting forces of about 8-10% with respect to 10 years before. However, at current 2.7 A, the performance decay is less (6%) because the higher intensity of the magnetic field makes the device less sensitive to the oxidation of ferro-based particles. The average decay, over the four current levels, is 7%.

On the other hand, on the right side of Table 2 are summarized the results in terms dissipated energy: its decay in 10 years, is almost inversely proportional to current, i.e. from -14% at 0.0 A to -3% at 2.7 A.

	Response time	Maximum reacting force					Dissipated energy				
		0.0 A	0.9 A	1.8 A	2.7 A	*mean*	0.0 A	0.9 A	1.8 A	2.7 A	*mean*
2008 → 2013	Practically unchanged	4%	-4%	-2%	-2%	*-1%*	-5%	-3%	-1%	1%	*-2%*
2013 → 2017		-8%	-7%	-6 %	-5%	*-6%*	-10%	-6%	-6%	-4%	*-6%*
2008 → 2017		**-5%**	**-10%**	**-8%**	**-6%**	***-7%***	**-14%**	**-9%**	**-7%**	**-3%**	***-8%***

Table 1: Ageing effects due to inactivity (minus sign means a decrement).

4 CONCLUSIONS

The authors describe the results of an experimental activity designed to assess the long-term behavior of two prototype MR dampers after many years of rest. Four different phenomena have been found in literature as responsible of deterioration of MR fluids: sedimentation of particles within the fluid, their oxidation, thickening of the fluid and seal wearing. The oxidation phenomenon seems to be the most significant in compromising the effectiveness of a MR device over time. It is worth to point out that the seal wearing was never an issue for the

authors because no fluid leakage has been ever observed in the studied prototype MR devices. The first force-displacement cycle performed after the quiescence was quite irregular due to particles sedimentation and possible air bubble inside the fluid. This issue quickly reversed, both in the 2013 and 2017 years, after the first half of the first cycle. The effects of fluid's thickening on the mechanical response were not detected, as this typically becomes more evident when MR fluids are subjected to long-term high shear stress, rather than inactivity.

As conclusive consideration, it is possible to draw that in the worst case the performance decay caused by 10-years ageing effects is about 10%. It is acceptable, because it's within the limits of the uncertainties generally involved in structural analysis. It is worth to point out that the above conclusions are referred to a type of MR damper and fluid and can't be considered surely valid for all other cases.

REFERENCES

[1] J.D. Carlson, M.R. Jolly, MR fluid, foam and elastomer devices. *Journal of Mechatronics*, **10**(4-5), 555-569, 2000.

[2] J.D. Carlson, Critical factors for MR fluids in vehicle systems. *International Journal of Vehicle Design*, **33**(1–3), 207-217, 2003.

[3] N. Caterino, B.M. Azmoodeh, A. Occhiuzzi, Medium to long term behavior of MR dampers for structural control. *Smart Materials and Structures*, **23**, 117005, 2014.

[4] X. Zhang, W. Li, X.L. Gong, Study on magnetorheological shear thickening fluid. *Smart Materials and Structures*, **17**(1), 0150511-6, 2008.

[5] S. Chen, J. Huang, K. Jian, D. Jun, Analysis of Influence of temperature on magnetorheological fluid and transmission performance. *Advances in Materials Science and Engineering*, **5**, 1-7, 2015, DOI: 10.1155/2015/583076.

[6] J. Roupec, P. Berka, I. Mazurek, Z. Strecker, M. Kubik, O. Machacek, A.T. Andani, A novel method for measurement of MR fluid sedimentation and its experimental verification. *Smart Materials and Structures*, **26**, 107001, 2017.

[7] S.A. Wahid, I. Ismail, S. Aid, M.S.A. Rahim, Magneto-rheological defects and failures: A review. *Materials Science and Engineering*, **114**, 012101, 2016.

[8] B.K. Kumbhar, S.R. Patil, S.M. Sawant, Synthesis and characterization of magnetorheological (MR) fluids for MR brake application. *Engineering Science and Technology, an International Journal*, **18**(3), 432-438, 2015.

[9] T. Kikuchi, T. Kumagae, I. Abe, A. Inoue, Particle sedimentation in magnetorheological fluid and its effect. *IEEE International Conference on Advanced Intelligent Mechatronics (AIM),* Munich, Germany, July 3-7, 2017.

[10] K. Shah, D.X. Phu, M.S. Seong, R.V. Upadhyay, S.B. Choi, A low sedimentation magnetorheological fluid based on plate-like iron particles, and verification using a damper test. *Smart Material and Structures*, **23**(2), 027001, 2014.

[11] J.C. Ulicny, C.A. Hayden, P.M. Hanley, D.F. Eckel, Magnetorheological fluid durability test-Organics analysis. *Journal of Material Science Engineering*, **464**(1-2) 269-273, 2007a.

[12] J.C. Ulicny, M.P. Balogh, N.M. Potter, R.A. Waldo, Magnetorheological fluid durability test–Iron analysis, *Journal of Material Science Engineering*, **443**(1-2), 16-24, 2007b.

[13] J. Roupec, I. Mazurek, Z. Strecker, M. Klapka, The behavior of the MR fluid during durability test. *13th conference on Electrorheological Fluids and Magnetorheological Suspensions (ERMR2012), Journal of Physics: conference series*, **412**(1), 012024, 2013.

[14] J. Goldasz, B. Sapinski, Insight into magnetorheological shock absorbers, Chapter 2, 13-23, Springer, 2015, ISBN: 978-3-319-13232-7.

[15] V.R. Iyengar, A.A. Alexandris, Wear testing of seals in magneto-rheological fluids. *Journal of Tribology Transactions*, **47**(1), 23-28, 2004.

[16] A. Wiehe, J. Maas, Large-scale test bench for the durability analysis of magnetorheological fluids. *Journal of Intelligent Material Systems and Structures*, **24**(12), 1433-1444, 2012.

[17] M.S.A. Rahim, I. Ismail, S.B. Choi, W.H. Azmi, S.N. Aqida, Thermal conductivity enhancement and sedimentation reduction of magnetorheological fluids with nano-sized Cu and Al additives. *Smart Materials and Structures*, **26**, 115009, 2017.

[18] M. Kciuk, S. Kciuk, R. Turczyn, Magnetorheological characterization of carbonyl iron based suspension. *Journal of Achievements in Material and Manufacturing Engineering*, **33**(2), 135-141, 2009.

[19] J.D. Carlson, What makes a good MR fluid? *8th International Conference on Electrorheological (ER) Fluids and Magneto-rheological (MR) Suspensions*, Nice, France, July 9-13, 2000.

[20] N. Caterino, M. Spizzuoco, A. Occhiuzzi, Ageing effects due to inactivity for magnetorheological seismic dampers: a 10-years experimental investigation. *Smart Materials and Structures*, **27**(6), 067001, 2018, ISSN: 1361-665X (on line), 0964-1726 (print), DOI: 10.1088/1361-665X/aabd4a.

[21] N. Caterino, M. Spizzuoco, A. Occhiuzzi, Shaking table testing of a steel frame structure equipped with semi-active MR dampers: comparison of control algorithms. *Smart Structures and Systems*, Techno-Press, **15**(4), 963-995, 2015, ISSN: 1738-1584 (print), 1738-1991 (online), DOI: 10.12989/sss.2015.15.4.963.

COMPDYN 2019
7th ECCOMAS Thematic Conference on
Computational Methods in Structural Dynamics and Earthquake Engineering
M. Papadrakakis, M. Fragiadakis (eds.)
Crete, Greece, 24–26 June 2019

A COMPARATIVE ANALYSIS BETWEEN THE SPANISH AND PORTUGUESE SEISMIC CODES. APPLICATION TO A BORDER RC PRIMARY SCHOOL

M.V. Requena-Garcia-Cruz[1], A. Morales-Esteban[2], M.L. Segovia-Verjel[1], E. Romero-Sánchez[1], J. de-Miguel-Rodríguez[1] and J.M.C. Estêvão[2]

[1] Department of Building Structures and Geotechnical Engineering, University of Seville, Spain
Av. Reina Mercedes, 2, 41012, Seville, Spain
{mrequena1, ame, marisasegovia, eromero13, jdemiguel}@us.es

[2] Department of Civil Engineering, ISE, University of Algarve, Faro, Portugal
Campus da Penha, 8005-139, Faro, Portugal
jestevao@ualg.pt

Abstract

The Iberian Peninsula is close to the Eurasia-Africa plate boundary resulting in a considerable seismic hazard. In fact, the southwestern Iberian Peninsula is affected by far away earthquakes of long-return period with large-very large magnitude. A project named PERSISTAH (Projetos de Escolas Resilientes aos SISmos no Território do Algarve e de Huelva, in Portuguese) aims to cooperatively assess the seismic vulnerability of primary schools located in the Algarve (Portugal) and Huelva (Spain). Primary schools have been selected due to the considerable amount of similar buildings and their seismic vulnerability. In Portugal, the Decreto Lei 235/83 (RSAEEP) is mandatory while in Spain, the mandatory code is the Seismic Building Code (NCSE-02). In both countries, the Eurocode-8 (EC-8) is recommended. Despite the fact that both regions would be equally affected by an earthquake, both seismic codes are significantly different. This research compares the seismic action of Ayamonte (Huelva) and Vila Real de Santo António (Portugal). Both towns are very close and located at both sides of the border. Moreover, they share the same geology. This analysis has been applied considering a RC primary school building located in Huelva. To do so, the performance-based method has been used. The seismic action and the damage levels are compared and analysed. The results have shown considerable differences in the seismic actions designation, in the performance point values and in the damage levels. The values considered in the Portuguese code are significantly more unfavourable. An agreement between codes should be made for border regions.

Keywords: Performance-based method, seismic code, seismic behaviour, nonlinear analysis, Iberian Peninsula, reinforced concrete building.

1 INTRODUCTION

The Iberian Peninsula (IP) is close to the Eurasia-Africa plate boundary. This results in a considerable seismic hazard for the southern IP. In fact, the southwestern IP is affected by far away earthquakes of long-return period and large-very large magnitude [1]. Buildings in this area have been severely damaged in the past by relevant events such as the 1344, 1531, 1722, 1755, 1859 and 1909 earthquakes [2].

A project named PERSISTAH (*Projetos de Escolas Resilientes aos SISmos no Território do Algarve e de Huelva*, in Portuguese) aims to cooperatively assess the seismic vulnerability of primary schools located in the Algarve (Portugal) and Huelva (Spain) [3]. Primary schools have been selected due to their vulnerability [4], to the amount of buildings sharing a similar configuration and to the seismic hazard of the region. Moreover, a major part of them was constructed in the 1970s. That is, no seismic considerations were taken into account in their design or, if considered, the requirements were not very restrictive.

Despite the fact that both regions would be equally affected by an earthquake, the seismic codes of Portugal and Spain are significantly different [5]. In Portugal, the *Decreto Lei 235/83* (RSAEEP) [6] is mandatory. Whereas in Spain, the Seismic Building Code (NCSE02) [7] must be fulfilled. In both countries, the Eurocode-8 (EC8) [8] is recommended. The most outstanding difference between codes is the seismic action level. Some other specifications such as the ductility requirements and the limit states are very similar.

The European Union promoted a homogenization of the design rules for earthquake resistant structures through the EC8 [9]. However, the determination of the basic parameters such as the seismic action must be provided by the National Annexes. Moreover, the seismic hazard analyses implemented in these seismic codes are outdated. In fact, as pointed out in [10], further research must be performed on the definition of the ground motions including attenuation laws and scenario features.

A few studies are focused on the seismic codes provisions analysis. In [9], the authors performed a comparative study of the seismic hazard assessments in European national seismic codes. They obtained considerable differences in each seismic code. Hence, they concluded that inter-country cooperation would improve the earthquake catalogue and the criteria defining the seismogenic zones. In [11], the seismic design criteria and ground motion selection methods from five different world regions were compared. They demonstrated that despite the incentive for harmonization, obvious differences could be mainly found on the response spectra definitions.

In this context, this research compares the seismic action of Ayamonte (Huelva) and Vila Real de Santo António (Portugal). Both towns are very close and located at both sides of the border. Moreover, they share the same geology. This analysis has been applied considering a reinforced concrete (RC) primary school building located in Huelva. *To* do so, a comprehensive analysis of the seismic action level provisions of each code has been performed. The performance-based method has been used and nonlinear static analyses have been carried out. The seismic action and the damage levels are compared and analysed.

2 METHOD

2.1 Seismic action specific provisions.

In this section, a comprehensive analysis of the seismic action level provisions of each code has been performed. As in [9], Table 1 summarizes the principal parameters analysed and their correspondent values.

Parameter	Decreto Lei RSAEEP	ECEC-88	NCSE-02	Spanish update	EC8 Spanish annex	EC8 Portuguese annex
Date	1983	1998	2002	2012	2010	2010
Earthquake scale	Magnitude	-	Intensity	Magnitude	-	-
Earthquake estimation	Historical Attenuation laws Gumbel III	-	Historical	Historical Attenuation laws	-	-
Attenuation function	Acceleration	-	Macroseismic	Acceleration	-	-
Hazard assessment	Poissonian Gumbel I	-	Poissonian	Poissonian	-	-
Hazard descriptor	PGA	$a_g=a_{gR}\cdot\gamma_I$	$a_c=S\cdot\rho\cdot a_b$	PGA	$a_{gR}=0.8\cdot a_b$	a_{gR}
Importance factor	-	$\gamma_I=1$	$\rho=1$	$\rho=1$	$\gamma_I=1.3$	$\gamma_{I\text{-}T1}=1.45$ $\gamma_{I\text{-}T2}=1.25$
Type of spectrum	Type 1 and 2	Type 1 and 2	Type 1	Type 1	Type 1 and 2	Type 1 and 2
Non-collapse	T_{NCR}=1000yrs	T_{NCR}=475 yrs P_{NCR}=10%	T_{NCR}=500 yrs P_{NCR}=2 ‰	T_{NCR}=475 yrs P_{NCR}=10%	T_{NCR}=475 yrs P_{NCR}=10%	T_{NCR}=475 yrs P_{NCR}=10%
Damage level	-	T_{DLR}=95 yrs P_{DLR}=10%	T_{DLR}=95 yrs P_{DLR}=10%	T_{DLR}=95 yrs P_{DLR}=10%	T_{DLR}=95 yrs P_{DLR}=10%	T_{DLR}=95 yrs P_{DLR}=10%
Hazard value	-	-	Ayamonte a_c=1.597 m/s^2 a_g=1.428 m/s^2	Ayamonte a_c=1.763 m/s^2 a_g=1.5 m/s^2	-	Vila Real $a_{g\text{-}T1}$=2.2 m/s^2 $a_{g\text{-}T2}$=2.1 m/s^2

Table 1: summary of the basic seismic action designation parameters of each code.

In the case of Spain, the imperative seismic code is the NCSE-02 while the EC-8 is recommended. This code provides only requirements to prevent buildings collapse. Therefore, only static analyses are allowed and no damage thresholds are considered. The seismic hazard map followed a similar approach to the 1994 version of the code. The calculation was performed in terms of the European Macroseismic Scale (EMS-98) intensity scale based on a poissonian approach. The data came from the Spanish Geographic Institute, "*Instituto Geográfico Nacional*, National Geographical Institute of Spain (NGIS)". A logarithmical correlation was implemented to determine the horizontal acceleration using the EMS scale. The spectrum is defined according to the *C* and *K* coefficients. The *K* coefficient takes into account the different contribution of the Gibraltar-Azores zone to the seismic hazard. The *C* coefficient considers the influence of the soil. The return period (*T*) and the exceedance probability (*P*) differ from the rest of the codes. The hazard is described by the seismic acceleration (a_c), which is calculated as the product of the soil amplification coefficient (*S*), the importance factor (ρ) and the basic acceleration value (a_b). The coefficient *S* is used to calibrate the value of a_b since it is expressed for soil-type II.

In 2012, an update of the Spanish seismic hazard maps was performed [12]. Its use is recommended but it is not mandatory. This catalogue carried out a revision of earthquakes of other catalogues and specific studies. In addition, a homogenization process to convert all the events into moment magnitude (M_w) by applying different relations was performed. A total amount of 6999 events were implemented, ranging from M_w 3.5-8.5 and depth 0-65 km. A Probabilistic Seismic Hazard Analysis (PSHA) was implemented following a Poisson distribution to determine the probability of exceedance. *T* and *P* were considered similar to the EC8 values. The hazard was expressed as PGA on soil-type I.

In the Portuguese code RSAEEP (1983), the earthquake estimation implemented historical events, attenuation laws and the Gumbel III extreme distribution. The hazard assessment took into account a Poissonian approach as well as a Gumbel I distribution. As established by [10], the process of seismic occurrence was based on the Seismic Catalogue of the Iberian Peninsu-

la taking into account a 2000 years-period of observation. The return period was considerably superior to the other codes. The response spectra were tabulated for each of the four seismic zones and the influence of the soil was taken into account by means of the α-coefficient.

Regarding the EC-8 provisions, a different approach is used to determine the response spectrum. Depending on the soil type, different values of fundamental periods are designated. The hazard is described as the design ground acceleration on Type A-ground (a_g). This is equal to the reference peak ground acceleration (a_{gR}) multiplied by the importance factor (γ_I). The values to be ascribed to a_{gR} can be found in the National annexes. In the Spanish annex, the a_b must be reduced a 80% to obtain the a_{gR} since the a_b is expressed for the soil type II. Regarding the Portuguese annex, no reduction must be performed. Moreover, different values of the γ_I-factor are established in each Annex for the schools' buildings (i.e. 1.3 in the Spanish Annex and 1.45 and 1.25 in the Portuguese Annex, when considering the response spectrum Type 1 and 2, respectively).

The EC-8 and the Portuguese code establish different response spectra types. According to the EC-8 designation, Type 1 (T1) is used if the earthquakes that contribute most to the seismic hazard are far-earthquakes of moderate-high magnitude (M_w>5.5). Type 2 (T2) spectrum is implemented if the earthquakes are near-earthquakes of magnitude not larger than M_w<5.5. Nevertheless, the NCSE-02 considers only the far-earthquake scenario.

Concerning the return periods and the probability of exceedance, they remained the same in the case of the EC-8 and the National Annexes for the non-collapse (NCR) and the damage level cases (DLR). However, in the case of the NCSE-02, the *T* and the *P* for the non-collapse case are different as well as the return period of the Portuguese code.

The response spectra determined according to each seismic code provisions for the border region of Vila Real de Santo António - Ayamonte are shown in Figure 1. The following codes have been considered: the Portuguese *Decreto Lei*; the NCSE-02 response spectrum considering Ayamonte and the values obtained by the 2012 update; and the EC-8 response spectrum considering these former values and the Portuguese seismic action provisions for Vila Real established in the National Annex and in [13].

The soil type selected has been type III or C in the case of the National codes and European provisions, respectively. It should be noted that considerable differences could be found on the hazard value comparing the seismic codes. These values differ up to a 60%.

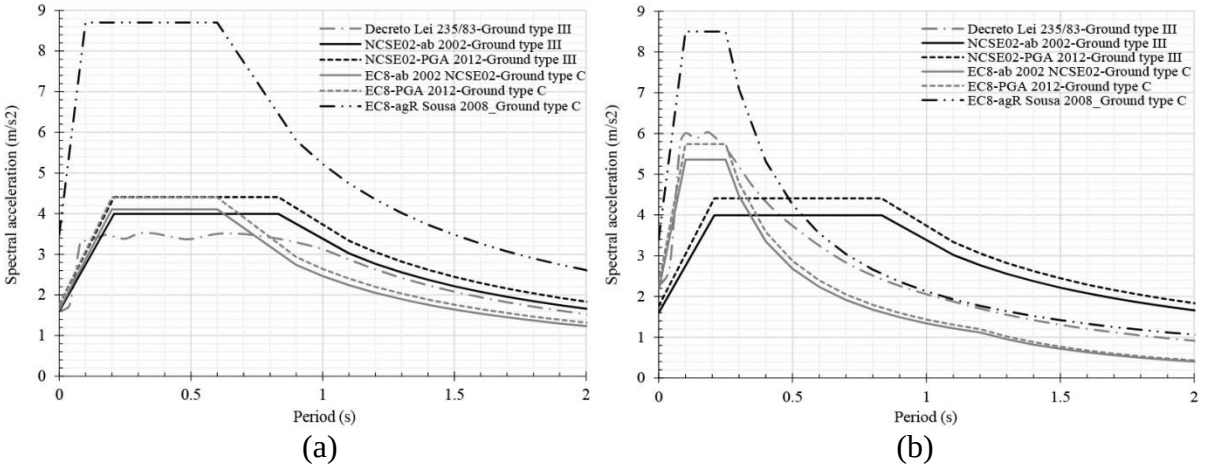

Figure 1: comparison of response spectra of each seismic code considered for a far-earthquake scenario (Type 1) (a) and a near-earthquake scenario (Type 2) (b).

2.2 Building's configurations.

A typical RC primary school has been selected. This is located in Ayamonte (Spain). However, this has been analysed as if it was located in Vila Real de Santo António (Portugal) and in Ayamonte (Spain). These two towns are placed at each side of the border between both countries (Figure 2a). Hence, buildings in this area share the same geology and the seismic hazard should be similar. The building is composed of two storeys and it was constructed during the 1970s. Therefore, basic seismic requirements were considered during its design. The plan and the elevation of the building have been depicted in (Figure 2b).

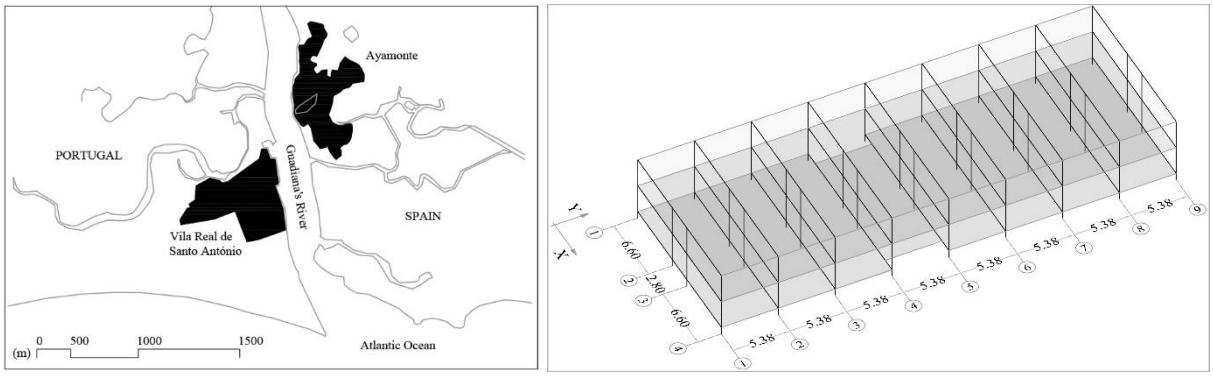

(a) (b)

Figure 2: towns location (a) and building's configuration (b).

The building is composed of RC wide-beams, columns and ribbed slabs. The frames in the X direction are the load bearing frames. Load beams are designed as 60x30 cm, they have 5Ø16 mm of longitudinal rebar and Ø6 mm each 20 cm of transversal rebar. Tie beams are of 30x30 cm, they have 4Ø12 mm of longitudinal rebar and Ø6 mm each 20 cm of transversal rebar. Columns are of 30x30 cm, they have 4Ø12 mm of longitudinal rebar and Ø6 mm each 15 cm of transversal rebar. The RC compressive strength (f_{ck}) is 17.5 MPa while the steel yield stress (F_y) is 420 MPa. The modulus of elasticity (E_c) are 25,000 MPa and 200,000 MPa, for the RC and the steel, respectively.

The gravitational loads considered in the analysis have been the self-weight of the elements and the permanent and variables loads. The first is automatically considered by the computer software used in the analysis. The dead loads are the sum of the weight of the ribbed slabs, the internal partitions, the ceiling and the ceramic flooring, which is in total 5.5 kPa. The variable load designated, corresponding to classrooms, is 3 kPa. This value is the same in both the Spanish and the Portuguese codes.

2.3 Performance-based method.

The building's performance analysis depends on the capacity and the demand [14]. According to these parameters, it can be obtained the so-called performance point of a building (displacement vs. basal shear force). The performance point is determined by the intersection of the capacity curve of the building and the inelastic response spectrum. This intersection can be performed by two methods: the capacity-demand spectrum method from the ACT-40 [15] and the N2-method [16].

In this work, the N2-method has been taken into account, which is the procedure implemented in the EC-8 to determine the target displacement. The construction of the theoretical bilinear curve has been carried out according to [17]. Different performance points have been obtained for each response spectrum defined in the previous section. These have expressed for

a multi-degree-of-freedom (MDOF) system. Also, the non-collapse safety condition required $d_u^*/d_t^*>1$ according to the EC-8 has been analysed and obtained for a single-degree-of-freedom (SDOF) system.

2.4 Nonlinear static analyses.

Although more accurate results can be obtained by means of dynamic analyses, they require high computational efforts and time to model the structures [18]. Since this study aims to compare the general seismic performance of a building according to different seismic actions, nonlinear static analyses have been carried out (pushover analyses). They have been performed to determine the capacity curves in the two orthogonal directions of the building (X and Y) by means of the SAP2000 v.19 software [19].

Two loads pattern have been considered as indicated in the EC-8. First, a triangular pattern based on lateral forces proportional to the height and the mass of each storey has been applied (mass). Then, a load patter proportional to the displacement produced by the first mode of vibration has been considered (mode). Numerous works can be found on the simulation of the nonlinear behaviour of RC [20]. In the SAP2000 software, RC frames nonlinear behaviour is simulated by means of the plastic hinges. Plastic hinges are added to all the RC frames. Two types of plastic hinges can be determined: default and manual. Manual plastic hinges determination takes considerable amount of time and the results do not differ from those obtained by the default designation [20]. Therefore, in this work, default plastic hinges have been defined according to the ASCE-41-13 [21] as implemented in [20]. PM2M3 plastic hinges have been added to columns whereas M3 hinges have been included in the beams. They have been included at both ends of the frames as established in the EC-8.

2.5 Damage level provisions.

The fragility curves define the probability of reaching a damage state. In this work, these curves have been determined according to the RISK-UE lognormal distribution [22]. The damage probability for each state (no-damage, slight, moderate, severe and collapse) has been determined. In addition, a useful index named the mean damage grade has been obtained according to [23]. This index represents the most likely damage state that will suffer the structure according to the seismic action. This value will range from 0 to 4.

3 RESULTS

This section presents the results obtained from the analyses carried out. Four capacity curves have been obtained, which are depicted in Figure 3. These have been named as AS (Ayamonte School) followed by the direction studied (X or Y) and the load pattern (proportional to the mass or to the first mode of vibration). Similar curves have been determined for each load pattern in both directions of the building. Therefore, the most unfavourable curves will be taken into account when obtaining the rest of the results (i.e. AS_X_mode and AS_Y_mode).

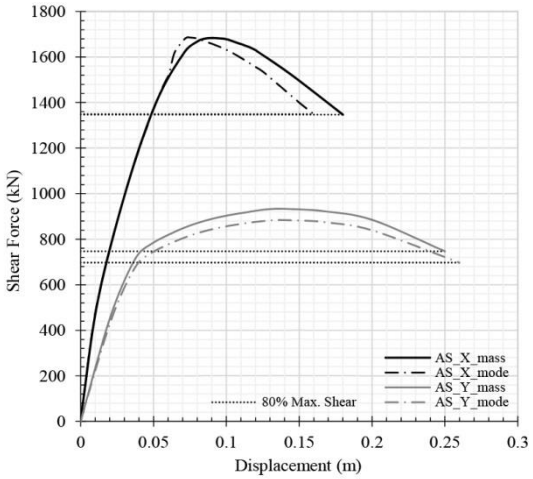

Figure 3: capacity curves in the X and the Y direction of the building.

Once the pushover curves have been obtained, the performance points for the MDOF system have been determined for each response spectrum considered. The performance points are plotted in Figure 4.

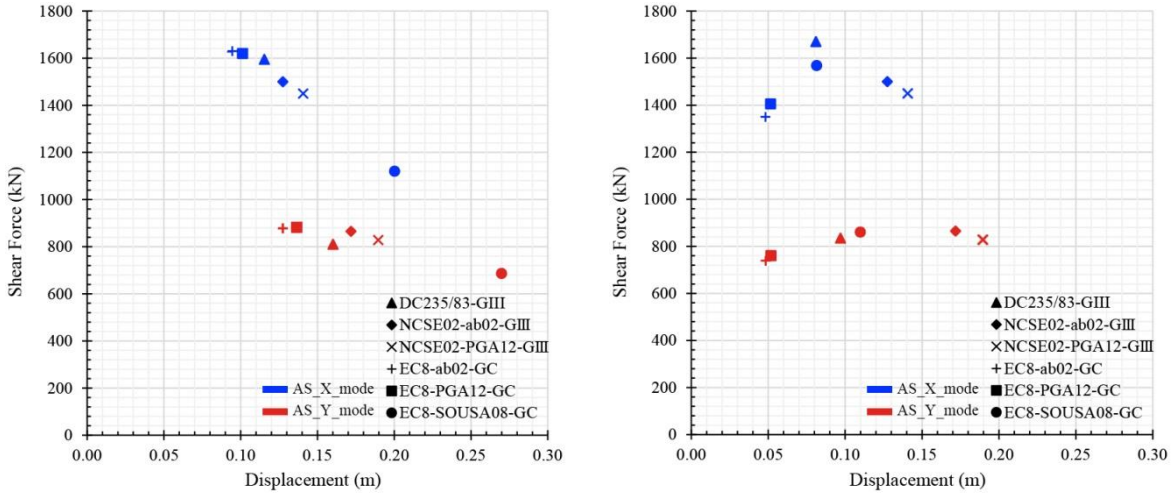

(a) (b)

Figure 4: performance points obtained for each unfavorable load pattern considering Type 1 (a) and Type 2 (b) response spectra.

In Figure 5, the damage level probability is shown for each capacity curve selected. Only the results concerning the Type 1 response spectrum have been shown owing to the worse results obtained.

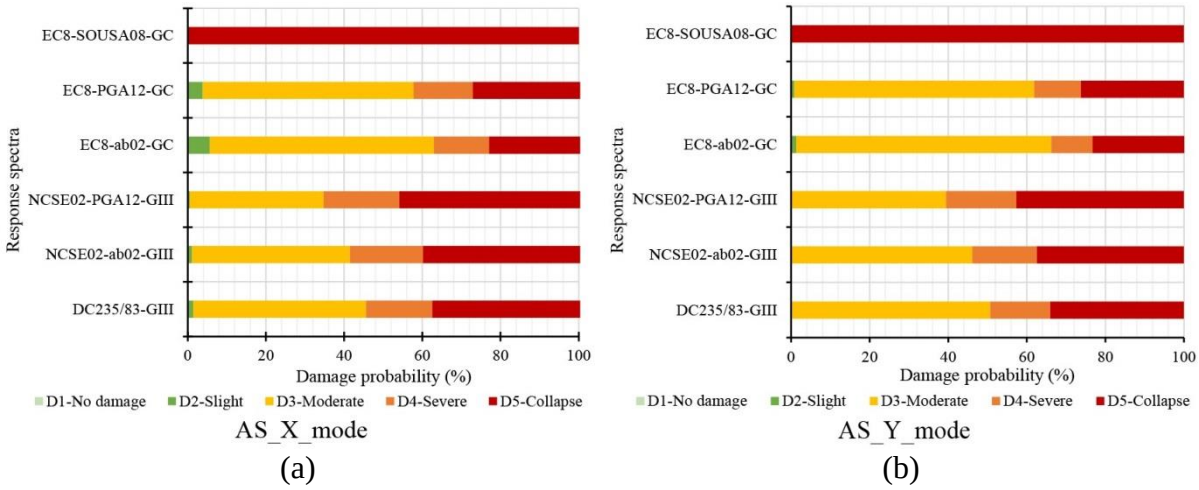

Figure 5: damage level probability for the capacity curves in the X (a) and Y (b) direction considering a load pattern based on the first vibration mode.

In Figure 6, the mean damage index is depicted for each capacity curve selected considering both types of response spectra.

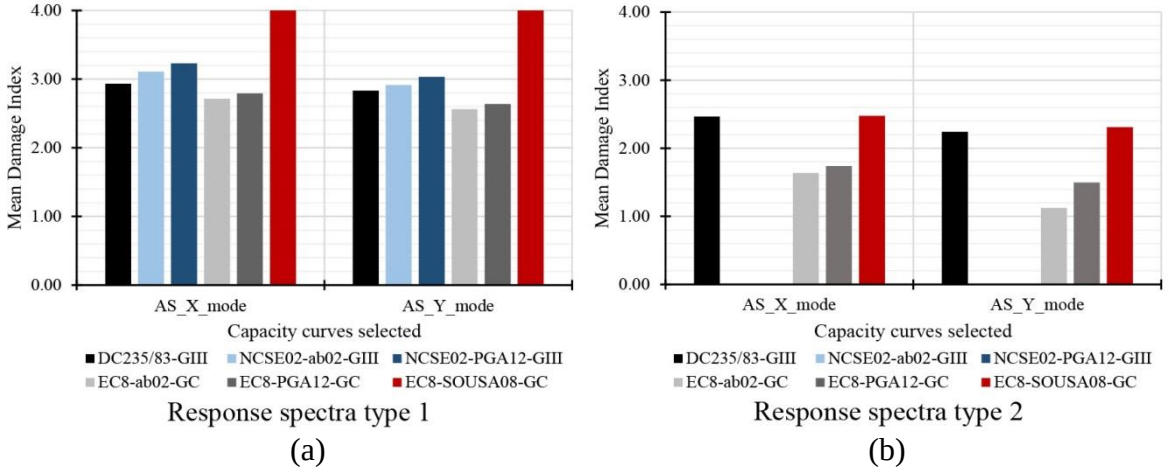

Figure 6: mean damage index for each capacity curve considering Type 1 (a) and Type 2 (b) response spectra.

Table 2 summarizes the SDOF ultimate displacements (d_u*) and the inelastic target displacements (d_t*) for the most unfavorable capacity curves considering each response spectrum.

Response spectrum	Type	Data	AS_X_mode	AS_Y_mode
Original building ultimate displacement		du*(m)	0.160	0.260
DC235/83-GIII	Type 1	dt*(m)	0.098	0.135
		du*/dt*	1.637	1.920
	Type 2	dt*(m)	0.069	0.082
		du*/dt*	2.332	3.171
NCSE02-ab02-GIII	Type 1	dt*(m)	0.108	0.145
		du*/dt*	1.482	1.789
	Type 2	dt*(m)	-	-
		du*/dt*	-	-
NCSE02-PGA12-GIII	Type 1	dt*(m)	0.119	0.160
		du*/dt*	1.343	1.622
	Type 2	dt*(m)	-	-

		du*/dt*	-	-
EC-8-ab02-GC	Type 1	dt*(m)	0.080	0.108
		du*/dt*	1.999	2.413
	Type 2	dt*(m)	0.041	0.041
		du*/dt*	3.923	6.363
EC-8-PGA12-GC	Type 1	dt*(m)	0.086	0.115
		du*/dt*	1.865	2.252
	Type 2	dt*(m)	0.044	0.044
		du*/dt*	3.661	5.939
EC-8-SOUSA08-GC	Type 1	dt*(m)	0.170	0.228
		du*/dt*	0.943	1.139
	Type 2	dt*(m)	0.069	0.093
		du*/dt*	2.317	2.798

Table 2: SDOF ultimate and target displacements for each capacity curve and corresponding ratios of d_u*/d_t*.

4 ANALYSIS OF RESULTS

The analysis of the specific provisions established in each seismic code has revealed considerable differences regarding the seismic action level designation. This is mainly due to the seismic hazard assessment of each code. The NCSE-02 considers a poissonian approach. This represents the probability of occurrence of an event in a time or spatial framework. The Portuguese seismic hazard assessment is based on a Gumbel distribution. Contrary to the poissonian approach, this represents a distribution of maximum values of events. This results in higher values of ground acceleration in the case of Portugal since only maximum values are considered in its hazard assessment.

Moreover, the importance factor of school buildings varies its value for each code. The values in each code can differ from each other up to a 30%. This also leads to higher values of ground acceleration in the Portuguese codes.

The nonlinear static analyses have resulted in similar capacity curves obtained for each load pattern considered in the X and Y direction. The most unfavourable curves have been those proportional to the first vibration mode of the structure. The MDOF performance point values obtained for the X direction have been considerably higher than those obtained for the Y direction. Differences of up to 200% can be found comparing both types of response spectra. Furthermore, the performance points have considerably differed from each response spectrum type. The displacement obtained for the Type 2-spectra have been lower than those obtained for the Type 1.

Regarding the damage level probability, lower values of damage have been obtained in the X direction of the building. This is due to the higher structural capacity of the building in this direction. Considering the response spectra, higher values of damage have been obtained for the response spectra designed according to the NCSE-02.

In the case of the mean damage level, the damage state D3-severe damage (value of 3) has been exceeded by the models that considered the NCSE-02 response spectrum. However, the worst value has been obtained for the consideration of the Portuguese seismic values. In the case of the Type 2 response spectra, the D3 limit has not been reached.

Regarding the safety requirement d_u*/dt*>1, higher ratio values have been obtained for the Type 2 response spectra. Moreover, higher values of this ratio have been obtained for the Y direction. This is due to the higher ductility that the building presents in this direction.

It should be highlighted that in the case of the Type 1-response spectra, the worst performance point has been obtained for the EC-8-designed spectrum considering the Portuguese seismic action values. Moreover, the target displacement has been higher than the ultimate displacement. Consequently, this resulted in the collapse of the structure as the damage prob-

ability has shown. Furthermore, the EC-8 safety requirement $d_u^*/dt^*>1$ has not been accomplished.

5 CONCLUSIONS

The Algarve-Huelva is located at the southwestern Iberian Peninsula, close to the Eurasia-Africa plate boundary. This results in a considerable seismic hazard. In fact, this region is affected by far away earthquakes of long-return period with large-very large magnitude. Despite the fact that both regions would be equally affected by an earthquake, the mandatory seismic codes of each country are significantly different. In this work, the seismic action of Ayamonte (Huelva) and Vila Real de Santo António (Portugal) have been compared. Both towns are very close and located at both sides of the border. Moreover, they share the same geology. This analysis has been applied considering a RC primary school building located in Huelva. Primary school buildings have been selected to be analysed owing to the considerable amount of similar buildings and the seismic vulnerability of this typology.

Nonlinear static analyses have been carried out to determine the performance point and the damage level of the building considering different response spectra definitions: the Portuguese *Decreto Lei*; the NCSE-02 response spectrum considering the Ayamonte seismic hazard values and those obtained by the update of 2012; and the EC-8 response spectrum considering these former values and the Portuguese seismic action provisions for Vila Real established in the National Annex and in [13].

This work has concluded that considerable differences can be found on each seismic code provision particularly in the definition of the response spectra. This is due to the seismic hazard approaches followed in each code (i.e. average event distribution in the Spanish code and maximum values distribution in the Portuguese code). Moreover, the impact factor that amplifies the ground acceleration value differs from each other. Despite the fact that the EC-8 was proposed as a homogenization tool, the seismic action is obtained from the National Annexes whose values considerably differ from each other. Therefore, although the buildings are close and share a similar geology, different values of ground acceleration are obtained when considering the different codes.

The nonlinear static analyses have shown that the worst seismic performance is obtained when considering the Portuguese seismic action updated. In fact, the EC-8 safety requirement has not been accomplished for this seismic action. This is due to the unfavourable values considered in the Portuguese code. Moreover, higher values of damage have been obtained when considering the NCSE-02 response spectrum. This is due to the reduction of the Ayamonte ground acceleration value established in the 2012 Spanish update. This study leads to the conclusion that safety provisions may not be fulfilled if a less restrictive seismic code is taken into account. Therefore, as pointed out in numerous works, an agreement between codes should be made for border regions.

ACKNOWLEDGEMENTS

This work has been supported by the INTERREG-POCTEP Spain-Portugal programme and the European Regional Development Fund through the 0313_PERSISTAH_5_P project and the VI-PPI of the University of Seville by the granting of a scholarship. The grant provided by the *Instituto Universitario de Arquitectura y Ciencias de la Construcción* is acknowledged.

REFERENCES

[1] J.L. Amaro-Mellado., A. Morales-Esteban., F. Martínez-Álvarez. Mapping of seismic parameters of the Iberian Peninsula by means of a geographic information system. *Central European Journal of Operations Research*, 2017.

[2] L. Sá., A. Morales-Esteban., P. Durand Neyra. The 1531 earthquake revisited : loss estimation in a historical perspective. *Bulletin of Earthquake Engineering*, **16**, 4533–59, 2018.

[3] J. Estêvão., M. Ferreira., A. Morales-Esteban., F. Martínez-Álvarez., L. Fazendeiro Sá., M.V. Requena-García-Cruz., M.L. Segovia-Verjel., C. Oliveira. Earthquake resilient schools in Algarve (Portugal) and Huelva (Spain), *16th European Conference on Earthquake engineering*, 2018, Thessaloniki.

[4] U. Hancilar., E. Çaktı., M. Erdik., G.E. Franco., G. Deodatis. Earthquake vulnerability of school buildings: Probabilistic structural fragility analyses. *Soil Dynamics and Earthquake Engineering*, **67**, 169–78, 2014.

[5] J.M.C. Estêvão., M.A. Ferreira., A. Braga., A. Carreira., V. Barreto., M. V Requena-García-Cruz., M.L. Segovia-Verjel., E. Romero-Sánchez., J. de Miguel., A. Morales-Esteban., L. Fazendeiro Sá., C. Sousa Oliveira. Projetos de escolas resilientes aos sismos no território do Algarve e de Huelva (PERSISTAH), *11º CONGRESSO NACIONAL DE SISMOLOGIA E ENGENHARIA SÍSMICA*, 2019.

[6] Imprensa Nacional-Casa da Moeda. Regulamento de segurança e acções para estruturas de edifícios e pontes. Decreto-Lei nº 235/83, de 31 de Maio, 1983.

[7] Spanish Ministry of Public Works [Ministerio de Fomento de España]. Spanish Seismic Code [Norma de Construcción Sismorresistente: Parte general y edificación (NCSE-02)], Spain, 2002.

[8] European Union. Eurocode 8: Design of structures for earthquake resistance. Part 1: General rules, seismic actions and rules for buildings, Brussels, 2004.

[9] J. García-Mayordomo., E. Faccioli., R. Paolucci. Comparative Study of the Seismic Hazard Assessments in European National Seismic Codes, 2004.

[10] C.S. Oliveira., A. Campos-Costa., M.L. Sousa. Definition of seismic action in the context of EC8. Topics for discussion, *12th World Conference on Earthquake Engineering*, 2000.

[11] M.M. Hachem., N.J. Mathias., Y.Y. Wang., P. Fajfar., K. c. Tsai., J.M. Ingham. An international comparison of ground motion selection criteria for seismic design, *Proceedings of Joint IABSE-fib Conference on codes in structural engineering: Developments and Needs for International Practice*, 2010, Dubrovnik, Croatia, pp.237–50.

[12] Spanish Ministry of Public Works [Ministerio de Fomento de España]. Update of the seismic hazard maps [Actualización de mapas de peligrosidad sísmica de España], Spain, 2012.

[13] A. Campos Costa., M.L. Sousa., A. Carvalho. SEISMIC ZONATION FOR PORTUGUESE NATIONAL ANNEX OF EUROCODE 8.

[14] R. Maio., J.M.C. Estêvão., T.M. Ferreira., R. Vicente. The seismic performance of stone masonry buildings in Faial island and the relevance of implementing effective

seismic strengthening policies. *Engineering Structures*, **141**, 41–58, 2017.

[15] Applied Technology Council (ATC). ATC-40: Seismic evaluation and retrofit of concrete buildings, California, 1996.

[16] P. Fajfar. Capacity spectrum method based on inelastic demand spectra. *Earthquake Engineering and Structural Dynamics*, **28**, 979–93, 1999.

[17] J. Estêvão., Estêvão., J.M. C. Feasibility of Using Neural Networks to Obtain Simplified Capacity Curves for Seismic Assessment. *Buildings*, **8**, 151, 2018.

[18] A.. Mwafy., A.. Elnashai. Static pushover versus dynamic collapse analysis of RC buildings. *Engineering Structures*, **23**, 407–24, 2001.

[19] Computers and Structures INC. "SAP2000 v.19".: <http://www.csiespana.com/software/2/sap2000>, cited 21 February, 2018.

[20] M. Inel., H.B. Ozmen. Effects of plastic hinge properties in nonlinear analysis of reinforced concrete buildings. *Engineering Structures*, **28**, 1494–502, 2006.

[21] American Society of Civil Engineers. ASCE/SEI 41-13: Seismic evaluation and retrofit of existing buildings, Reston, United States, 2014.

[22] Z. V. Milutinovic., Goran S. Trendafiloski. An advanced approach to earthquake risk scenarios with applications to different European towns. Vulnerability assessment of lifelines and essential facilities (WP06): basic methodological handbook. 71, 2003.

[23] Y.F. Vargas., L.G. Pujades., A.H. Barbat., J.E. Hurtado. Capacity, fragility and damage in reinforced concrete buildings: A probabilistic approach. *Bulletin of Earthquake Engineering*, **11**, 2007–32, 2013.

COMPDYN 2019
7th ECCOMAS Thematic Conference on
Computational Methods in Structural Dynamics and Earthquake Engineering
M. Papadrakakis, M. Fragiadakis (eds.)
Crete, Greece, 24–26 June 2019

CONSTANT-DUCTILITY RESIDUAL DISPLACEMENT RATIOS

M. Orlacchio[1], G. Baltzopoulos[1], and I. Iervolino[1]

[1]Università degli Studi di Napoli Federico II
Via Claudio 21, 80125 Naples, Italy
e-mail: {mabel.orlacchio, georgios.baltzopoulos, iunio.iervolino}@unina.it

Abstract

This paper presents a predictive model for evaluating the central tendency and related record-to-record variability for the residual displacements of simple inelastic oscillators under seismic excitation. For this study, yielding single-degree-of-freedom systems were considered, with bilinear backbones and non-degrading hysteretic rule characterized by peak-oriented reloading stiffness. Systems with natural periods belonging to the 0.3 s to 2.0 s range and exhibiting post-yield hardening ratios ranging from 0 to 10%, were analyzed via incremental dynamic analysis to obtain the residual displacements as a function of the ductility demand. A set of fifty acceleration records was used for the dynamic analysis, coming from medium-to-large magnitude events, recorded at the closest distance to the rupture surface ranging from 3.5 km to 43.7 km on firm soil or rock and devoid of apparent directivity effects of interest for seismic response. The model fitted on these results, consists of two regression equations: one equation for the period elongation given ductility demand and another for the residual displacement ratio given period elongation and ductility demand.
In this context, the residual displacement ratio is defined as residual-to-peak inelastic displacement. Thus, the model allows to assess the joint conditional distribution of period elongation and residual displacement at fixed ductility levels. These results could be useful for seismic reliability assessment for structures accumulating damage, for example during seismic sequences, where the seismic fragility of a structure damaged during a mainshock earthquake comes into play for risk calculations during the ensuing aftershock sequence.

Keywords: residual displacements; sequence-based seismic reliability; state-dependent seismic fragility.

1 INTRODUCTION

Within the Performance-Based Earthquake Engineering (PBEE; [1]) paradigm, the probabilistic assessment of a structure's residual displacement is of interest, in addition to the peak (transient) deformation demand, because the former can be useful in modelling the performance of structures during a seismic sequence, when these structures have been already damaged by the mainshock earthquake. In fact, the residual displacement is a response parameter closely related with the remaining capacity of mainshock-damaged structures to withstand aftershock sequences [2,3]. In this context, the residual deformation was established over the last years as a useful index of the severity of inelastic response, complementary to maximum transient response. Moreover, its amplitude can be used to determine the technical and economic feasibility of repairing seismic damages because of the difficulty to reverse permanent displacements [4]. Thus, several previous studies were focused on individuating the parameters that primarily affect residual displacement, and a few investigations also presented simple predictive equations for residual displacements.

Some early observations about residual displacement demands were provided by Mahin and Bertero [5] who found that the permanent displacements of elastoplastic systems averaged more than forty-percent of the peak inelastic displacement demand with high level of variability (coefficients of variation associated with residual displacements close to unity).

An early residual displacement predictive procedure was provided by MacRae and Kawashima [6]. They studied residual deformation demands of bilinear single-degree-of-freedom (SDOF) systems with several values of post-yield stiffness ratio, under three ductility demands. They pointed out the influence of post-yield stiffness ratio on the amplitude of residual displacements introducing a method for estimating the average value of residual displacements only dependent on the post-yield hardening ratio and the ductility demand, without identifying a clear trend with the structural period of natural vibration. Moreover, they proposed residual displacement response spectra for bilinear oscillators with varying post-yield hardening ratio [7]. The dependence of residual displacements amplitude on ductility demand and mainly on post yielding stiffness was also confirmed by Borzi et al. [8].

Subsequently, Pampanin et al. [9] studied residual displacements normalized by peak inelastic displacement demand of four equivalent SDOF systems representative of reinforced concrete (RC) frame buildings. They considered three hysteretic models (evolutionary and non-evolutionary) and different post-yielding stiffness ratios. These authors observed that the residual deformation demand depended on the type of hysteresis, seismic intensity and post-yield stiffness ratio.

Ruiz-Garcia and Miranda [4,10] studied the influence of several factors on the residual displacement ratio C_r, which they defined as the ratio of residual-to-maximum elastic displacement. These factors included period of natural vibration, lateral strength ratio, site conditions, earthquake magnitude, distance to the source, post-yield stiffness ratio and unloading stiffness. In that investigation residual displacement ratios were computed for elastoplastic, bilinear SDOF systems with kinematic strain hardening and for SDOF systems with three stiffness-degrading hysteretic models. They observed C_r to strongly depend on the lateral strength and on period of natural vibrations mainly for periods shorter than about 1.0 s. They also highlighted that residual displacements ratios exhibit record-to-record variability that should also be accounted for. Moreover, a simplified equation to estimate the central tendency of residual displacement demands for elastoplastic systems was suggested in [4], as function of two independent variables, period of natural vibration and strength ratio.

A detailed study about the influence of the hysteretic law on residual displacements was performed by Liossatou and Fardis [11]. They used hysteretic models which represent the cyclic degradation of stiffness and strength that is typical of RC structures. The scatter in residual displacements was also quantified providing at different periods of natural vibration.

The objective of this study is to present a predictive model for the central tendency and related record-to-record variability of residual displacements for SDOF bilinear systems with non-degrading hysteretic rule, characterized by peak-oriented reloading stiffness. To this end, the constant-ductility residual displacement ratio is investigated, defined as the absolute value of the ratio of residual to peak transient displacement, $C_\mu = \left|\delta_{res}/\delta_{\max}\right|$, where δ_{res} and $\delta_{\max}$ preserve their sign. This ratio is calculated for various combinations of input motion, natural vibration period and post-yielding hardening ratio. In all cases, ductility demand μ (defined as the ratio of maximum response to yield displacement of the intact system, $\mu = \delta_{\max}/\delta_y$) is held constant by appropriately scaling the input motion. Because it is typical to define the damage state of a structure based on crossing maximum transient displacement thresholds (e.g., [12,13]), this constant-ductility approach could be useful in the context of simplified estimation of state-dependent seismic fragility [2,3,14]. The main result of the study is a predictive equation for C_μ, derived via two-stage regression [15].

The article is structured as follows: first the analysis methodology is outlined describing the properties of the analyzed systems and the organization of the analyses used to collect the data set. The next two sections are dedicated to the detailed description of the predictive model development, presenting first the model for residual displacement and secondly the model for period elongation. Finally, the evaluation of the predictive model effectiveness is presented along with some evaluation and discussion of the obtained results.

2. ANALYSIS METHODOLOGY

In order to collect the required data on which to base the predictive model, yielding single-degree-of-freedom systems with bilinear backbone and modified Ibarra-Medina-Krawinkler (IMK) hysteretic model [16] were analyzed. Figure 1a shows an example of bilinear backbone and hysteresis in dimensionless $\{R, \mu\}$ coordinates, where $R = Sa(T)/Sa(T)_y$ is the strength ratio, defined as the ratio of spectral acceleration intensity to its value causing yield or, equivalently, the ratio of the elastic force over the yield base shear of the system, and μ is the ductility demand. The backbone starts elastically and presents a following hardening segment with a slope α_h, representing the ratio of post-yield stiffness to elastic stiffness, which ends at the capping point ductility μ_c where the loss of strength begins. Figure 1a reports a descending branch too, defined by the post-capping slope α_c, the ratio of the negative post-capping stiffness to elastic stiffness, and the fracture ductility, μ_f, point corresponding to complete loss of strength. This latter branch was defined exclusively for keeping track of the capping points in the damaged post-shock state, whilst only considering target ductility demands lower than the capping ductility during the execution of nonlinear dynamic time-history analyses. Figure 1b shows the modified IMK hysteretic model with peak-oriented response (presented in detail in [17]). This hysteretic model is characterized by peak-oriented reloading stiffness; therefore, the direction of the loading path targets the maximum displacement on the opposite side once the horizontal axis is intersected in each reloading cycle. Although the model can include cyclic deterioration modes, in this study it was implemented without considering any degradation rules for strength and unloading stiffness.

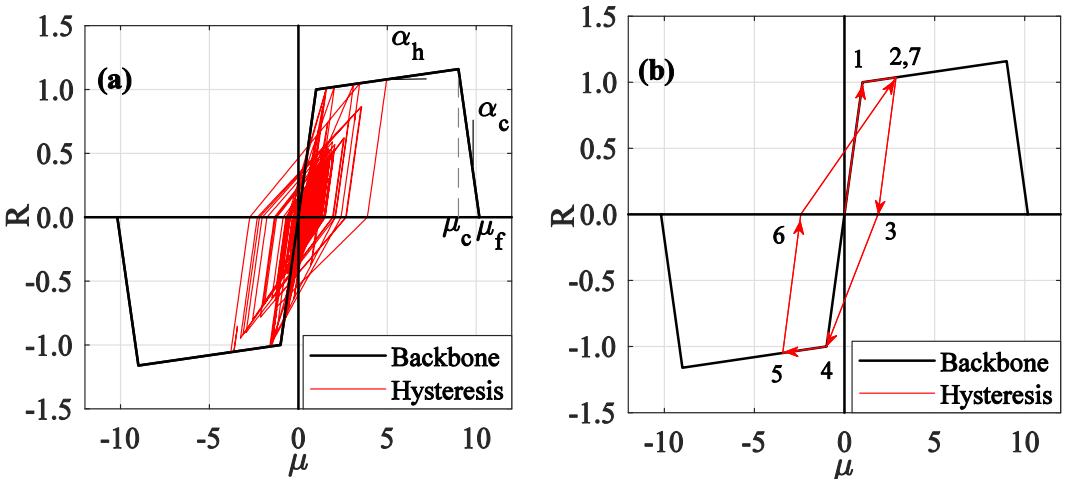

Figure 1: Backbone curve and non-degrading Modified Ibarra Medina Krawinkler (IMK) peak-oriented hysteretic model in dimensionless $\{R, \mu\}$ coordinates: backbone curve with defining parameters and an example of hysteresis for the case with $T = 1.0s$, $\alpha_h = 2.0\%$ and $\mu = 5.0$ (**a**); representation of IMK hysteretic model with peak-oriented response (**b**).

The residual displacements of the SDOF systems were computed using a set of analyses organized in two different phases. The first phase consists in the execution of *incremental dynamic analysis* (IDA) [18] fixing the target ductility μ, which defines the damage state reached by the structure during the earthquake. In this phase, the SDOFs are subjected to a suite of fifty earthquake ground motions selected from within the NESS dataset [19]. These ground motions were recorded on firm soil at a closest distance to the rupture surface (R_{RUP}) ranging from 3.5 km to 43.7 km and coming from seismic events with moment magnitude belonging to the 6.1-7.6 range. Furthermore, the selected records exhibit PGA ranging from 0.053 g to 1.43 g and are devoid of apparent directivity effects. IDA involves performing a set of nonlinear dynamic analyses using each record scaled in amplitude to increasing levels of intensity, represented by an intensity measure (IM), to reach or pass the limit of engineering demand parameter (EDP), the structural response corresponding to the level of ductility demand for each damage state. Thereby a scale factor (SF) for each accelerogram is evaluated to bring the response of the structural model to a fixed damaging level. The second phase consists in obtaining multiple realizations of the SDOF structure in post-mainshock damage state by performing non-linear dynamic analysis, using the records scaled by the SF calculated in the previous phase. Subsequently a *static pushover analysis* up to the collapse is performed for each realization, in both positive and negative direction of the load.

The performed analyses differ in the assumed values of ductility demand μ, period of natural vibration T and post-yield hardening ratios α_h of SDOF systems. Ductility demand assumed the following values $\mu = \{1.5, 2.0, 3.0, 4.0, 5.0, 6.0, 7.0, 8.0, 9.0\}$. The analyzed oscillators had a fixed backbone as shown in Figure 1. In detail, the bilinear backbone was defined assuming period, in seconds, $T = \{0.3, 0.6, 0.9, 1.0, 1.2, 1.5, 1.8, 2.0\}$, and hardening stiffness assuming the following percentage values with respect to the initial (elastic) one $\alpha_h = \{0.0, 0.5, 1.0, 2.0, 3.0, 4.0, 5.0, 10.0\}$. Setting the elastic stiffness and the period of natural vibration, the mass of the system for each single case was consequently computed. A viscous damping ratio $\xi = 5.0\%$ was used and kept constant throughout the time-history analyses.

The analyses were performed in order to study the variation of the backbone-defining parameters, following seismic damage. Large inelastic deformations during strong ground shaking leads SDOF systems with modified IMK hysteretic model to have residual displacements and elongation of natural vibration periods. The residual displacement at a certain ductility demand depends on the hysteretic characteristics of the system and it determines the remaining ductility capacity of the post-mainshock structure. The period elongation is caused by the reduction of the peak-oriented reloading stiffness which evolves according to the modified IMK hysteretic model reported in Figure 1b. Therefore, the structure from the natural vibration period T , in intact conditions, reaches by effect of the mainshock an elongated period T_{elon}. This elongated period is calculated from the post-shock reloading stiffness at the end of the dynamic analysis, k_{ps} as $T_{elon} = 2 \cdot \pi \cdot \sqrt{m/k_{ps}}$. Figure 2 shows the effects of seismic damage on the structural backbone for an analyzed case, where k_{ps} is evident from the slope of the pushover at the end of the excitation . In particular, Figure 2a shows the initial and post-mainshock backbones of a single SDOF system, highlighting the residual displacement and the elastic stiffness variation of the SDOF structure in its post-mainshock damage state, whereas in Figure 2b, the post-mainshock-damage-state realizations of the same SDOF structure under four accelerograms of the fifty-record set are shown, revealing the record-to-record variability.

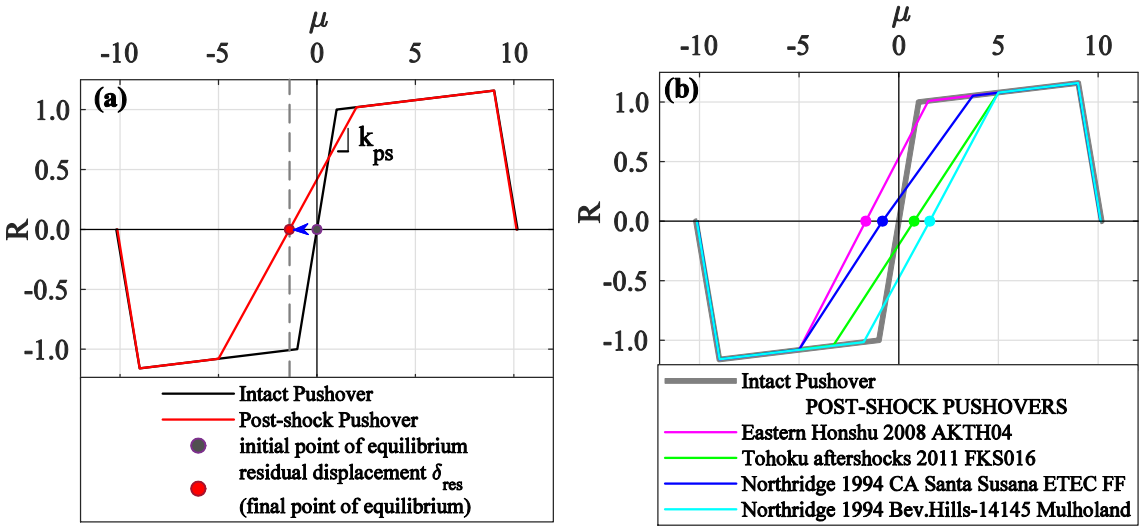

Figure 2: Examples of an SDOF structure's monotonic pushover (backbone) curve before and after the seismic damage in $\{R, \mu\}$ coordinates. Intact-structure backbone (dark line) and post-mainshock backbone (red line with pre-yield stiffness k_{ps} ,intersecting the zero-force horizontal axis at δ_{res}) for a generic analyzed case (**a**); post-mainshock backbones and residual displacements of an SDOF system with $T = 1.0s$ and $\alpha_h = 2.0\%$, evaluated for four different records scaled to cause ductility demand $\mu = 5.0$ (**b**).

3. PREDICTIVE MODEL FOR THE RESIDUAL DISPLACEMENT

During the investigation a total of 28800 elongated periods T_{elon} and constant-ductility residual displacement ratios C_μ were computed for peak-oriented bilinear systems, corresponding to fifty acceleration time histories, eight periods of natural vibration, nine levels of ductility demand and eight post-yield hardening ratios, and then processed to obtain the

predictive model. The highest C_μ value encountered among these results was 0.52. In subsequent elaborations, it was found useful to express these results in terms of the relation between the ratio of residual to peak transient displacement $\delta_{res}/\delta_{\max}$ (preserving the sign of both δ_{res} and $\delta_{\max}$ so that the ratio becomes negative when the two are in opposite directions) and $\ln(\Delta T/T)$, where $\Delta T = T_{elon} - T$ denotes the difference between the elongated post-mainshock period and the initial period. It was observed that $\delta_{res}/\delta_{\max}$ exhibits persistently high negative linear correlation with $\ln(\Delta T/T)$ for varying T, μ and α_h. In particular, values of the correlation coefficient between $\ln(\Delta T/T)$ and $\delta_{res}/\delta_{\max}$, ρ (see for example [20]), range from -0.50 to -0.99 with $\rho \le -0.7$ for the majority of analyzed cases (with $-0.5 < \rho < -0.7$ only in a few cases characterized by high ductility demands, $\mu \ge 7.0$, and long periods of natural vibration, $T \ge 1.8s$).

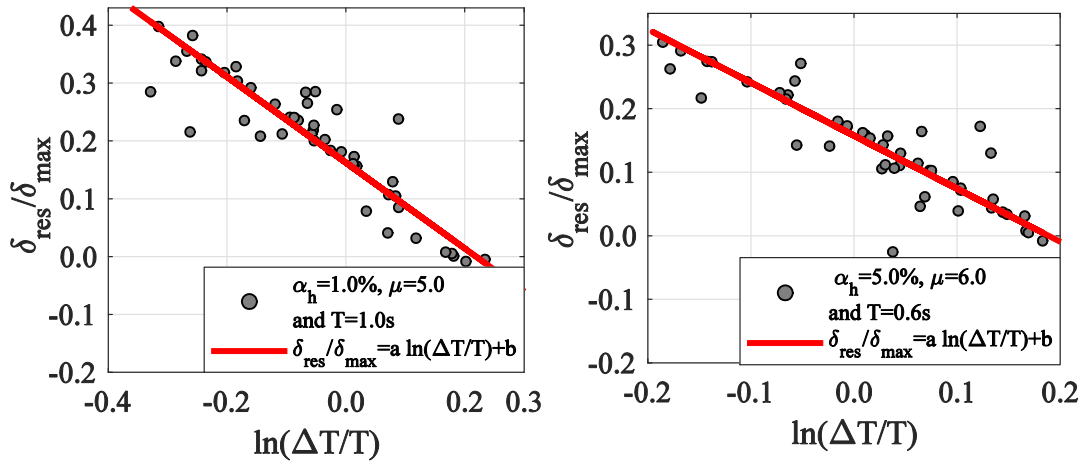

Figure 3: Examples of regression of $\delta_{res}/\delta_{\max}$ against $\ln(\Delta T/T)$ highlighting their (negative) linear correlation. Case of SDOF system with $\alpha_h = 1.0\%$, $T = 1.0s$ and $\mu = 5.0$ (left); case of SDOF system with $\alpha_h = 5.0\%$, $T = 0.6s$ and $\mu = 6.0$ (right).

This linear trend, examples of which are shown in Figure 3, motivates the adoption of a linear model for C_μ, whose slope and intercept are functions of the ductility demand μ and the post-yield hardening ratio α_h. The proposed model is given by Equation (1):

$$C_\mu = \left| \left[\beta_1 + \beta_2 \cdot (\mu - 1) + \beta_3 \cdot (\alpha_h + 1) \cdot (\mu - 1)^2 \right] \cdot \ln\left(\frac{\Delta T}{T} \right) + (\beta_4 + \beta_5 \cdot \alpha_h) \cdot (\mu - 1) + \beta_6 + \varepsilon \cdot \sigma_{C_\mu} \right| \quad (1)$$

where ε is the standard Normal variable and the parameters β_i, $i = \{1,2,...,6\}$ are coefficients estimated by means of robust regression of $\delta_{res}/\delta_{\max}$ against $\ln(\Delta T/T)$, μ, α_h using iteratively re-weighted least squares with bisquare weighting [20]. The standard deviation of the regression residual, σ_{C_μ}, was found to be non-constant, varying with T, μ and α_h (yet the residual can be assumed homoscedastic with $\ln(\Delta T/T)$ conditional on fixed values of the other independent

variables). Thus, σ_{C_μ} was also modelled analytically to account for this dependence (to follow). It should be mentioned that despite the perceived dependence of σ_{C_μ} on the oscillator's initial vibration period T, such dependence was not included in the expectation function of C_μ. In fact, according to the executed F-test [20] the null hypothesis that the slope of an additional linear term of T is zero, could not be rejected at the 5% significance level. Table 1 provides the parameter estimates for β_i appearing in Equation (1).

β_1	β_2	β_3	β_4	β_5	β_6
-0.1124	-0.1867	0.0094	0.1308	-0.6385	-0.3361

Table 1. Coefficient estimates in Equation (1).

Figure 4 shows the model for the mean of the constant-ductility residual displacement ratio for the cases with post-yield hardening ratio equal to 0.0% and 10.0%.

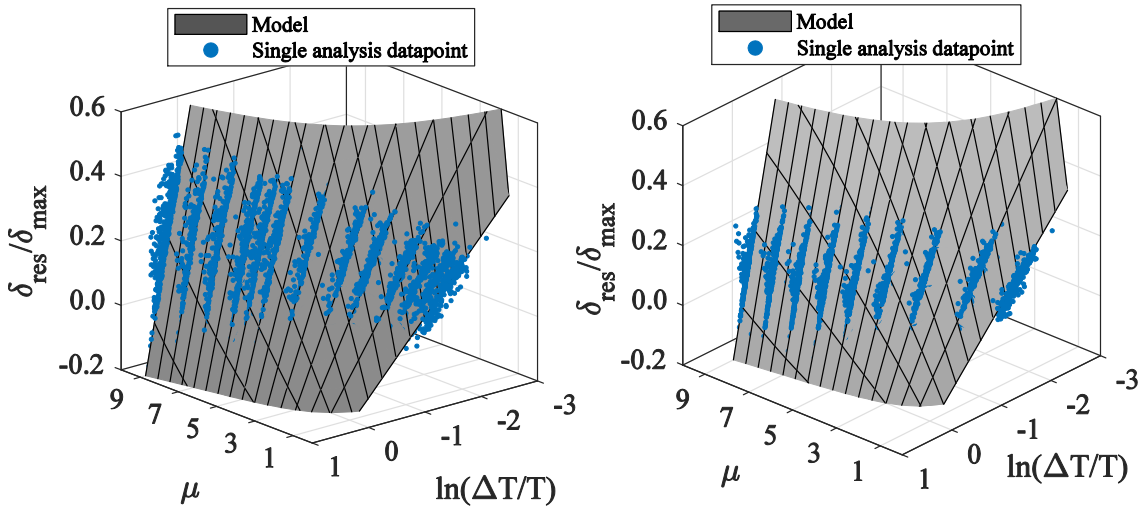

Figure 4: Central tendency of the model for the residual displacements. Case with $\alpha_h = 0.0\%$ (left); case with $\alpha_h = 10.0\%$ (right).

As already mentioned, non-constant variance of the residuals was dealt with by modelling σ_{C_μ} by means of least-squares curve-fitting of an analytical expression, with parameters γ_i, $i = \{1,2,...,7\}$, to the regression residuals for the various T, μ and α_h values, given in Equation (2):

$$\sigma_{C_\mu} = \begin{cases} \gamma_1 \cdot (\mu - 1) + \gamma_2 \cdot T \text{ , when } \alpha_h = 0 \\ \gamma_3 \cdot (\alpha_h + 1) \cdot (\mu - 1) + \gamma_4 \cdot T + \gamma_5 \cdot (\mu - 1)^2 + \gamma_6 \cdot (\mu - 1) \cdot T \cdot \alpha_h + \gamma_7 \cdot \alpha_h \text{ , when } \alpha_h > 0 \end{cases} \quad (2)$$

Due to the peculiar nature of increased response dispersion, as the post-yield stiffness of the systems goes to zero (due to the drifting effect observed for elastoplastic oscillators; e.g., [21]), Equation (2) provides separate equations for σ_{C_μ} in case of $\alpha_h = 0$ and $\alpha_h > 0$. Table 2 provides the fitted parameter values of γ_i for Equation (2).

γ_1	γ_2	γ_3	γ_4	γ_5	γ_6	γ_7
0.0090	0.0182	0.0402	0.0080	-0.0035	0.0535	0.4413

Table 2. Coefficient estimates of σ_{C_μ} in Equation (2).

Figure 5 shows the two model of standard deviation σ_{C_μ} in case of post-yield hardening ratio equal to 0.0% in Figure 5a and equal to 3.0 % in Figure 5b.

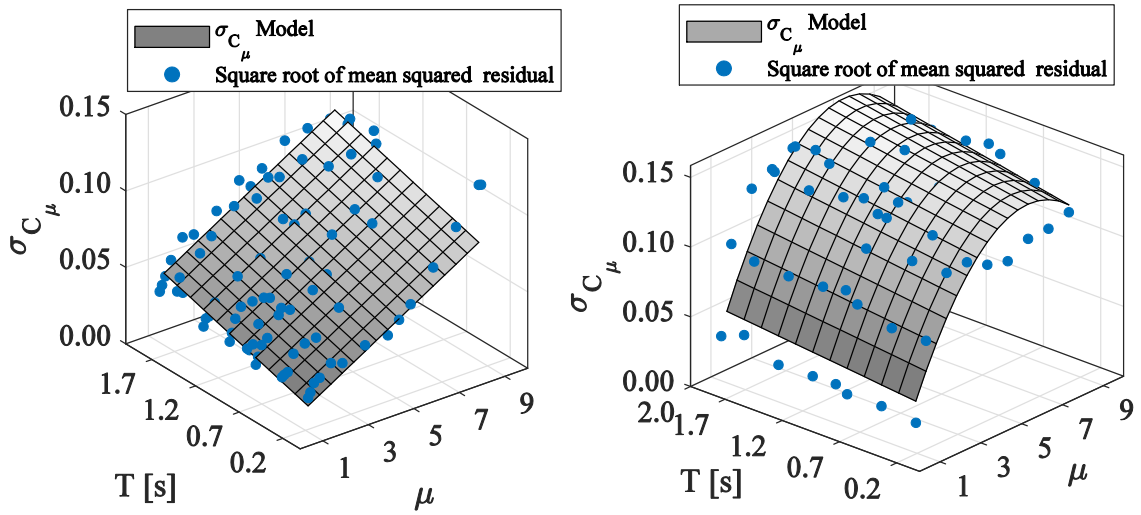

Figure 5: Models of standard deviation σ_{C_μ}. Case with $\alpha_h = 0.0\%$ (left); case with $\alpha_h = 3.0\%$ (right).

4. REGRESSION MODEL FOR PERIOD ELONGATION

The regression model for mean constant-ductility residual displacement ratios, given by Equation (1), is conditional on $\ln(\Delta T/T)$, which is also a random variable due to record-to-record variability. However, the results indicate that, given μ, α_h and T, $\ln(\Delta T/T)$ is conditionally independent of C_μ. Thus, in order to complete the predictive equation for residual displacements, an additional separate model for period elongation is needed to provide the conditional distribution of $\ln(\Delta T/T)$. The model for period elongation provides the period of the damaged structure T_{elon} at a fixed damage state represented by μ, given initial characteristics of the structure T and α_h. The analyses results were studied plotting in log-space the $\Delta T/T$ versus the ductility demand $(\mu-1)$, and assessing the dependence on independent variables T and α_h. The data showed a linear trend in log-space to each pair of T and α_h, therefore the model was realized fitting a straight line by ordinary least squares regression. The central tendency of $(\Delta T/T)$ resulted independent of the period of natural vibration T itself, whereas was strongly dependent on the post-yield hardening ratios α_h. Thus, the regression model proposed for period elongation uses only α_h and μ as predictor variables. A linear model was assumed, as reported in the following equation:

$$\ln\left(\frac{\Delta T}{T}\right)=\left(\theta_1\cdot\alpha_h+\theta_2\right)\cdot\ln\left(\mu-1\right)+\theta_3\cdot\alpha_h+\theta_4+\varepsilon\cdot\sigma_{\ln(\Delta T/T)}\ , \tag{3}$$

where ε was already defined as the standard Normal variable and $\sigma_{\ln(\Delta T/T)}$ represents the standard deviation of the regression residual, which was, also in this case, non-constant. It should be noted that, despite the Gaussian assumption for ε, for this type of hysteretic model and given μ and α_h, $\Delta T/T$ cannot exceed the value $\left(\Delta T/T\right)_{\max}$ given by Equation (4):

$$\left(\frac{\Delta T}{T}\right)_{\max}=\sqrt{\frac{2\mu-1+\alpha_h\cdot\left(\mu-1\right)}{1+\alpha_h\cdot\left(\mu-1\right)}}-1 \tag{4}$$

As reported in Equation (3), the slope and the intercept of the model for period elongation are only dependent on α_h. The coefficients $\theta_i, i=\{1,2,3,4\}$, were evaluated by curve fitting of the single regressions results performed for each value of α_h. A weighted regression, on account of the non-constant variance, was not deemed necessary because the ratio of the maximum to the minimum value of the mean squared error of the residuals did not exceed 1.5, as suggested in [15]. In Table 3 the values of the coefficients which characterize Equation (3) are reported.

θ_1	θ_2	θ_3	θ_4
-0.906	0.867	-1.163	-1.276

Table 3. Coefficient estimates of Equation (3).

Figure 6 shows the model fitted against the analysis results of SDOFs with α_h equal to 1.0% and T varying in the entire range considered, as well as a 3D graph of the model for period elongation, highlighting the dependence of its central tendency on α_h and μ.

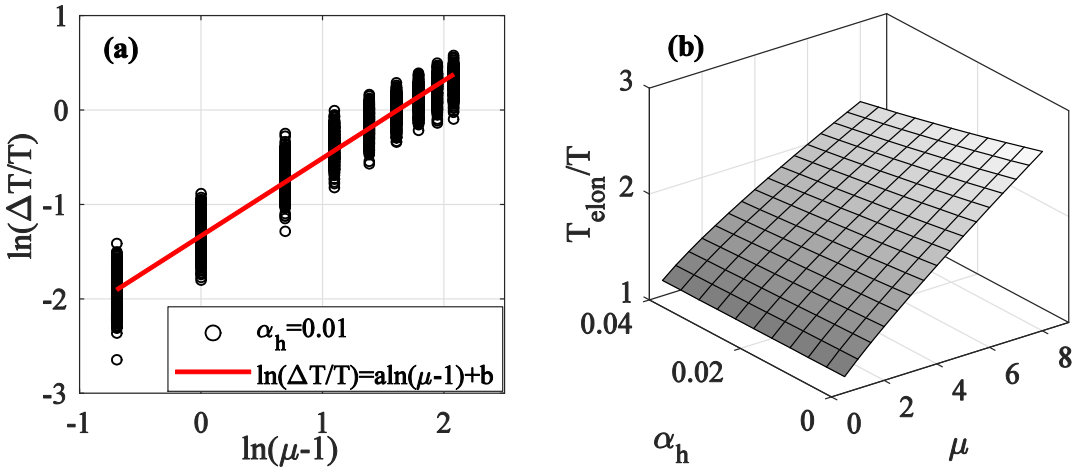

Figure 6: Central tendency of model for period elongation. Regression example of the form $\ln\left(\Delta T/T\right)=a\cdot\ln(\mu-1)+b$ used to define the model for period elongation evaluated in the case of post-yield hardening ratios α_h equal to 1.0% (**a**); Model for period elongation (**b**).

Finally, an analytical expression was proposed, to express the dependence of $\sigma_{\ln(\Delta T/T)}$ with the intact structure's period T and the hardening slope α_h, given by Equation (5) :

$$\sigma_{\ln(\Delta T/T)} = \xi_1 \cdot T + \xi_2 + \xi_3 \cdot \alpha_h + \xi_4 \cdot T^2 \tag{5}$$

Table 4 provides the values of the parameters ξ_i, $i = \{1,2,3,4\}$, appearing in Equation (5), estimated from curve-fitting against the regression residuals.

ξ_1	ξ_2	ξ_3	ξ_4
0.0472	0.1444	-0.1993	-0.0151

Table 4. Coefficient estimates for Equation (5).

Figure 7 shows the model of the standard deviation $\sigma_{\ln(\Delta T/T)}$ as a function of the hardening slope α_h and the period of natural vibration T.

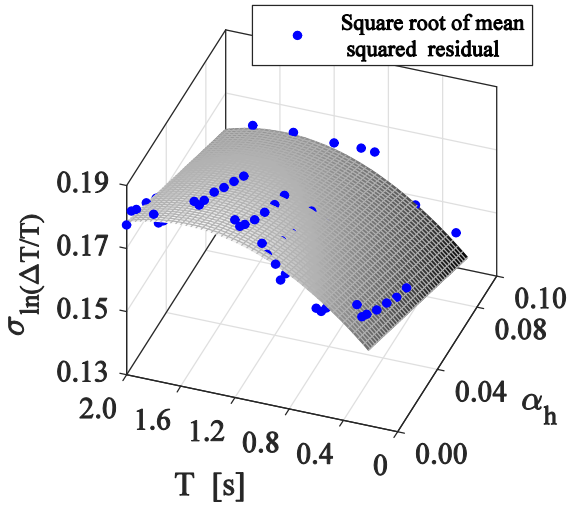

Figure 7: Model of standard deviation $\sigma_{\ln(\Delta T/T)}$.

5. PUTTING THE TWO COMPONENTS OF THE MODEL TOGETHER

Having completely defined both models, for period elongation and residual displacement, and recalling that period elongation was found conditionally independent of the residual displacement, it is possible to estimate the joint conditional distribution of the two random variables, given the ductility demand μ, the period T and the hardening slope α_h of the initial structure. Due to the fact that in Equation (1) C_μ is given by the absolute value of a regression model for $\delta_{res}/\delta_{\max}$, it is convenient to visualize its conditional joint distribution with relative period elongation T_{elon}/T by means of a Monte-Carlo sampling scheme. This entails fixing the values of T, α_h and μ, calculating the mean and standard deviation of $\ln(\Delta T/T)$ conditional to these values from Equations (3) and (5) and then extracting a random sample of $\ln(\Delta T/T)$ values from a normal distribution with that mean and $\sigma_{\ln(\Delta T/T)}$, truncated according to Equation

(4). Subsequently, the conditional mean and standard deviation of the ratio $\delta_{res}/\delta_{\max}$ is obtained for each sampled value of $\ln(\Delta T/T)$, from Equations (1) and (2), and a $\delta_{res}/\delta_{\max}$ value is randomly sampled from the corresponding normal distribution, truncated between -1 and 1. This amounts to random sampling of $\{\ln(\Delta T/T), \delta_{res}/\delta_{\max}\}$ from their joint conditional distribution. Finally, C_μ values are obtained by taking the absolute value of $\delta_{res}/\delta_{\max}$. An example of such a representation is reported in Figure 8a, that was constructed by sampling one thousand value-pairs from the joint distribution of $\delta_{res}/\delta_{\max}$ and $\ln(\Delta T/T)$. A representation of the marginal density of C_μ and its mean is also reported in Figure 8b, estimated during the same procedure.

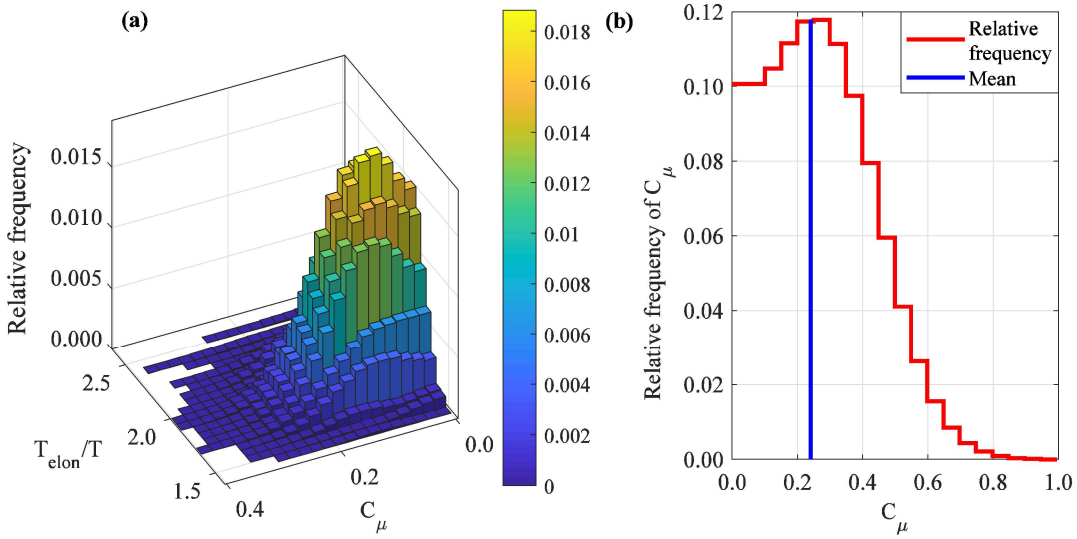

Figure 8. Sampling-based representation of the joint relative frequency of period elongation and residual displacement ratio (**a**), relative frequency of C_μ (**b**), for the case of ductility demand $\mu = 5.0$, post-yield hardening ratio $\alpha_h = 2.0\%$ and period of the initial structure $T = 0.9s$.

6. MODEL VALIDATION

To validate the predictive model a set of analyses for blind-testing the goodness-of-fit was performed. These analyses were organized in three groups: the first group was executed fixing the mass of SDOF systems and varying the elastic stiffness to achieve the required periods of natural vibration, whilst the analyses performed for the model evaluation, fixed the elastic stiffness and varied the mass to the same effect. The second group of analyses was executed levels of ductility demand and values of post-yield hardening ratio different from the ones used for fitting development the predictive model. The last group was performed using a different set of fifty records for IDA. To evaluate the accuracy of the predictive models in estimating elongated periods and residual displacements, the root mean square error (RMSE [20]) was computed for each group of analyses, according to Equation (6) .

$$RMSE = \sqrt{\frac{\sum_{i=1}^{n}(y_i - \bar{y})^2}{n}} \quad (6),$$

where $\bar{y}$ is the generic model of either $\ln(\Delta T/T)$ or C_μ, y_i is the data point from the i-th analysis and n is the total number of analyses run.

These RMSE values were employed to assess the goodness-of-fit for Equations (1),(3) in estimating mean C_μ and $\ln(\Delta T/T)$. In detail, the root mean square error measure was computed for the three groups of test data, comparing the results with the error evaluated on the entire data set used for fitting development the predictive model. Table 5 provides $RMSE_{\ln(\Delta T/T)}$ for the first and the second group of analyses defined by different values of μ and T.

Constant mass				Independent variable values (α_h, μ) not used in fitting the model			
T	μ	α_h	$RMSE_{\ln(\Delta T/T)}$	T	μ	α_h	$RMSE_{\ln(\Delta T/T)}$
0.3	4.0	0.02	0.024	0.3	4.3	0.07	0.020
0.6	4.0	0.02	0.016	0.6	4.3	0.07	0.013
2.00	4.0	0.02	0.008	2.00	4.3	0.07	0.002

Table 5. Values of $RMSE_{\ln(\Delta T/T)}$ for the first and the second group of validation analyses.

Table 6. provides $RMSE_{\ln(\Delta T/T)}$ for the third group of analyses executed fixing the ductility demand, the hardening slope and employing a new set of fifty acceleration records recorded on firm soil or rock and devoid of apparent directivity effects.

Using a different set of records			
T	μ	α_h	$RMSE_{\ln(\Delta T/T)}$
0.3	5.0	0.04	0.010
0.6	5.0	0.04	0.003
2.00	5.0	0.04	0.016
0.3	8.0	0.05	0.048
0.6	8.0	0.05	0.002
2.00	8.0	0.05	0.006

Table 6. Values of $RMSE_{\ln(\Delta T/T)}$ for the third group of validation analyses.

The values of $RMSE_{\ln(\Delta T/T)}$ previously reported are very close to the value evaluated on the data set used for fitting development the predictive model which is 0.024.

To evaluate the accuracy of the predictive model in estimating residual displacement, the error measure RMSE was computed for the three groups of test data. In particular, it was evaluated for C_μ as provided by the Equation (6). The values of RMSE for the three group of analyses are reported in Table 7 and Table 8. The values of $RMSE_{C_\mu}$ previously reported are very close to the value estimated on the data set used for fitting development the predictive model which is 0.056.

Constant mass				Independent variable values (α_h, μ) not used in fitting the model			
T	μ	α_h	$RMSE_{C_\mu}$	T	μ	α_h	$RMSE_{C_\mu}$
0.3	4.0	0.02	0.029	0.3	4.3	0.07	0.025
0.6	4.0	0.02	0.040	0.6	4.3	0.07	0.030
2.00	4.0	0.02	0.065	2.00	4.3	0.07	0.077

Table 7. Values of $RMSE_{C_\mu}$ for the first and second group of validation analyses.

Using a different set of records			
T	μ	α_h	$RMSE_{C_\mu}$
0.3	5.0	0.04	0.063
0.6	5.0	0.04	0.045
2.00	5.0	0.04	0.050
0.3	8.0	0.05	0.085
0.6	8.0	0.05	0.065
2.00	8.0	0.05	0.087

Table 8. Values of $RMSE_{C_\mu}$ for the third group of validation analyses.

7. DISCUSSION AND CONCLUSIONS

The main purpose of this study was to present a predictive model for the central tendency and related record-to-record variability of residual displacements for bilinear single-degree-of-freedom systems (SDOF). To this end, a probabilistic model for the constant-ductility residual displacement ratio, C_μ, was introduced. The residual displacement ratio, defined as the absolute-value ratio of residual to peak transient displacement, was calculated for various combinations of input motion, natural vibration period and post-yielding hardening ratio, via nonlinear dynamic analysis designed to hold the ductility demand μ constant, by appropriately scaling the input motion. Thus, SDOF systems with non-degrading, peak-oriented hysteretic response, according to the modified *Ibarra-Medina-Krawinkler* model, were analyzed subjected to a set of fifty earthquake ground motions recorded on firm site conditions. From the data obtained during the dynamic analyses, it was observed that the residual displacement demand did not exceed 52% of the peak inelastic displacement demand and is mainly affected on post-yield hardening ratio. In fact, the SDOF systems with higher post-yield stiffness ratio exhibit smaller residual displacement ratios on average, in agreement with previous studies.

The two-part predictive model was derived via two-stage regression: the first-stage regression model provides a prediction for the post-shock elongated period and the second one accounts for the residual displacement of the system conditional to its elongated period. It was found that central tendency of constant-ductility residual displacement ratios depends on the ductility demand, the post-yield hardening ratio and ratio of post-shock elongated period to the initial period of natural vibration, while the non-constant variance of the residual displacement ratio mainly depends on the post-yield hardening slope of the structure in its initial (undamaged) condition. It was also found that the period elongation has a central tendency that only depends on post-yield hardening ratio and ductility demand, whereas the corresponding variance also exhibits some dependence on the structural period of natural vibration. Finally, it should be mentioned that the complete model proposed, allows to estimate the joint conditional

distribution of the two random variables: residual displacement and period elongation, given ductility, period and hardening slope.

ACKNOWLEDGEMENTS

The work presented in this paper was developed within the activities of ReLUIS (*Rete di Laboratori Universitari di Ingegneria Sismica*) during the 2014-2018 research program, financed by the Department of Civil Protection (*Dipartimento della Protezione Civile* - DPC).

REFERENCES

[1] C.A. Cornell, H. Krawinkler, Progress and Challenges in Seismic Performance Assessment. *PEER Center News*, **3**, 1–4, 2000.

[2] P. Bazzurro, C.A. Cornell, C. Menun, M. Motahari, Guidelines for seismic assessment of damaged buildings. *Proceedings of the 13th World Conference on Earthquake Engineering,* Vancouver, Canada, August 1-6, 2004.

[3] N. Luco, P. Bazzurro, C. A. Cornell, Dynamic Versus Static Computation Of The Residual Capacity Of A Mainshock-damaged Building To Withstand An Aftershock. *Proceedings of the 13th World Conference on Earthquake Engineering,* Vancouver, Canada, August 1-6, 2004.

[4] J. Ruiz-García, E. Miranda, Residual displacement ratios for assessment of existing structures. *Earthquake Engineering and Structural Dynamics*, **35**, 315–336, 2006.

[5] S. Mahin, V. V. Bertero, An Evaluation of Inelatic Seismic Design Spectra. *Journal of Structural Engineering (ASCE)*, **107**, 1777–1795, 1981.

[6] G.A. Macrae, K. Kawashima, Post-earthquake residual displacements of bilinear oscillators. *Earthquake Engineering and Structural Dynamics*, **26**, 701–716, 1997.

[7] B.K. Kawashima, M. Asce, G.A. Macrae, Residual displacement response spectrum. *Journal of Structural Engineering*, 523–530, 1998.

[8] B. Borzi, G. M. Calvi, A. S. Elnashai, E. Faccioli, J. J. Bommer, Inelastic spectra for displacement-based seismic design. *Soil Dynamics and Earthquake Engineering*, **21**, 47–61, 2001.

[9] S. Pampanin, C. Christopoulos, M.J. Nigel Priestley, Performance-based seismic response of frame structures including residual deformations. Part II: Multi-degree of freedom systems. *Journal of Earthquake Engineering*, **7**, 119–147, 2003.

[10] J. Ruiz-García, E. Miranda, Performance-based assessment of existing structures accounting for residual dispalcements. Stanford University, Stanford, CA, 2004.

[11] E. Liossatou, M. N. Fardis, Residual displacements of RC structures as SDOF systems. *Earthquake Engineering and Structural Dynamics*, **44**, 713–734, 2015.

[12] G. Baltzopoulos, R. Baraschino, I. Iervolino, D. Vamvatsikos, SPO2FRAG: software for seismic fragility assessment based on static pushover. *Bulletin of Earthquake Engineering*, **15**, 2017.

[13] I. Iervolino, A. Spillatura, P. Bazzurro, Seismic Reliability of Code-Conforming Italian Buildings. *Journal of Earthquake Engineering*, **22,** 5-27, 2018.

[14] M. Raghunandan, A. Liel, N. Luco, Aftershock collapse vulnerability assessment of reinforced concrete frame structures. *Earthquake Engineering and Structural Dynamics*, **44**, 419–439, 2015.

[15] T. P. Ryan, *Modern Regression Methods, 2th Edition*. A. John Wiley & Sons,1945.

[16] L. F. Ibarra, R. A. Medina, H. Krawinkler, Hysteretic models that incorporate strength and stiffness deterioration. *Earthquake Engineering and Structural Dynamics*, **34**, 1489–1511, 2005.

[17] D. Lignos, Sidesway collapse of deteriorating structural systems under seismic excitations. *PhD Thesis*, **53**,1689–1699, 2013.
[18] D. Vamvatsikos, C. Allin Cornell, Incremental dynamic analysis. *Earthquake Engineering and Structural Dynamics*, **31**, 491–514, 2002.
[19] F. Pacor, C. Felicetta, G. Lanzano, S. Sgobba, R. Puglia, M. D'Amico, *et al.*, NESS v1.0: A worldwide collection of strong-motion data to investigate near source effects. *Seismological Research Letters*, 2018.
[20] N. R. Draper, H. Smith, *Applied regression analysis*, *3th Edition*. New York. John Wiley & Sons, 1998.
[21] R. Bouc, D. Boussaa, Drifting response of hysteretic oscillators to stochastic excitation , **37**, 1397–1406, 2002.

COMPDYN 2019
7th ECCOMAS Thematic Conference on
Computational Methods in Structural Dynamics and Earthquake Engineering
M. Papadrakakis, M. Fragiadakis (eds.)
Crete, Greece, 24–26 June 2019

SEISMIC RELIABILITY-BASED DESIGN OF SOFTENING STRUCTURES EQUIPPED WITH DOUBLE SLIDING DEVICES

Paolo Castaldo[1] **and Gaetano Alfano**[2]

[1] Department of Structural, Geotechnical and Building Engineering (DISEG), Politecnico di Torino, Turin, Italy
corso Duca degli Abuzzi 24, 10129 Torino, ITALY
e-mail: paolo.castaldo@polito.it

[2] Department of Structural, Geotechnical and Building Engineering (DISEG), Politecnico di Torino, Turin, Italy
corso Duca degli Abuzzi 24, 10129 Torino, ITALY
e-mail: gae.alfano@gmail.com

Abstract

This study deals with seismic reliability-based design (SRBD) relationships in terms of behavior factors and displacement demands for softening structures equipped with double friction pendulum system (DFPS) bearings. An equivalent 3dof system having a softening post-yield slope is adopted to describe the superstructure behavior, whereas velocity-dependent laws are assumed to model the responses of the two surfaces of the DFPS. The yielding characteristics of the superstructures are defined for increasing behavior factors in compliance with the seismic hazard of L'Aquila site (Italy) and with NTC18 assuming a lifetime of 50 years. Considering several natural seismic records and building properties under the hypothesis of modelling the friction coefficients of the two surfaces of the DFPS as random variables, incremental dynamic analyses are performed to evaluate the seismic fragility and the seismic reliability of these systems. Finally, seismic reliability is assessed and seismic reliability-based design (SRBD) curves for the two surfaces of the double sliding devices are described.

Keywords: behavior factor, ductility demand, friction pendulum bearing, post-yield softening stiffness, seismic isolation, seismic reliability.

1 INTRODUCTION

A very effective technique for the seismic isolation[1] of building frames and infrastructure is represented by the sliding pendulum bearings [2]-[3] examined by several literature studies (e.g., [4]-[7]). Probabilistic analyses and reliability-based analyses have also been presented by [8]-[9] as well as reliability analysis and reliability-based optimization of base-isolated systems including the main uncertainties have been performed by [10]-[14]. A non-dimensionalization of the motion equations governing the dynamic response of equivalent two-degree-of-freedom (2dof) models equipped with friction pendulum system (FPS) isolators has been proposed by [15]. In the hypothesis that the friction coefficient and the earthquake main characteristics are the relevant random variables, seismic reliability analyses of a 3D base-isolated r.c. system have been developed in Castaldo et al. [16] and Palazzo et al. [17] to propose a method useful to design the isolator dimensions in plan. The life-cycle cost analysis (LCCA) of a r.c. 3D structure isolated by FPS bearings has been examined by [18] to evaluate the dependence on increasing isolation degrees. The approach for a seismic reliability-based design (SRBD) of elastic systems isolated by FPS has been generalized in Castaldo et al. [19] for a wide range of structural properties. A robustness analysis in reliability terms of a r.c. 3D building frame isolated by FPS devices in presented in [20] proposing the failure scenarios if a malfunction affects a seismic device together with the design solution. The literature studies of [21] and [22] proposed, respectively, the optimal values of the friction coefficient, on the one hand, as a function of the system properties and of the soil condition in order to minimize the superstructure response and, on the other, as a function of the ground motion characteristics by means of the ratio PGA/PGV (peak ground acceleration/velocity). In [23], a robust design optimization (RDO) of base isolation system considering random system parameters characterizing the structure, isolator and ground motion model, is performed by minimizing the weighted sum of the expected value of the maximum root mean square acceleration of the structure as well its standard deviation. In [24], an optimal design of frictional devices is proposed by applying a Pareto-type optimization approach.

The seismic performance of bridges or structures isolated with FPS or DFPS has been investigated in [25]-[31]. Specifically, [28]-[30]provide useful relationships, according also to experimental results, for the evaluation of the seismic response of structures isolated by DFPS together with the equations governing the dynamic behaviour of these devices. The principal benefit of the DFPS bearing is its capacity to accommodate substantially larger displacements compared to a traditional FP bearing of identical plan dimensions as discussed in [28]. In [26] and [31], the seismic performance of isolated bridge and liquid storage tanks are respectively investigated, considering different combinations of radii of curvature and friction coefficients.

As for the design of base-isolated systems under strong earthquake events, seismic code provisions [32]-[36] are based on low values of the strength reduction factor [32]-[36] or behavior factor [33]-[34] to ensure a safety level against the non linear dynamic amplification phenomenon (partial resonance) [37]. Precisely, NTC18 [34], Eurocode 8 [33] and the Japanese building code [35] provide a maximum behavior factor value of 1.5, without explicitly distinguishing between the ductility and overstrength factor terms, ASCE 7 [32] prescribes a value equal to 0.375 times the one for corresponding fixed-base systems and no larger than 2. In this context, Vassiliou et al. [38] obtained that the displacement ductility demand of the inelastic base-isolated structure is 3 times the strength reduction factor confirming that, for base-isolated structures, it is not possible to adopt the formulas relating the strength reduction factor R and the displacement ductility demand μ of Newmark and Hall [39] and of Miranda and Bertero [40]. Then, seismic reliability-based relationships between the ductility-dependent strength reduction factors and the displacement ductility demand, respectively, for

equivalent perfectly elastoplastic and softening structural systems equipped with FPS depending on the structural properties have been proposed in [41],[42].

Inspired by [41],[42], this study proposes reliability-based design regressions relating the behavior factors and the displacement ductility demands for softening structural systems (sensitive or not sensitive to the $P-\Delta$ effects) equipped with double friction pendulum system (DFPS) devices and considering a high seismic hazard site like L'Aquila (Italy). By means of an equivalent 3dof system, different elastic and inelastic structural system properties are investigated. Specifically, the yielding characteristics of the softening superstructures are designed in compliance with the life safety limit state and with the seismic hazard of L'Aquila site (Italy) assuming a lifetime of 50 years and increasing behavior factors [32]-[35]. The model developed by [4] is used to describe the non-linear velocity-dependent behavior of the two surfaces of the DFPS. The study is also based on the hypothesis of assuming the both friction coefficients of the two surfaces of the DFPS and the characteristics of the records as the relevant random variables. In detail, appropriate Gaussian probability density functions (PDFs) are adopted to characterize the aleatory uncertainties of the both sliding friction coefficients and, by means of the Latin Hypercube Sampling (LHS) method [43]-[45], the input data have been generated.

Then, several incremental dynamic analyses (IDAs) are performed for increasing seismic intensity levels in compliance with the site seismic hazard to derive the seismic fragility curves related to the different degrees of freedom of the equivalent (3dof) system. Finally, by means of the convolution integral between the fragility curves and the seismic hazard curves of L'Aquila site (Italy), in the hypothesis of a design life of 50 years for the equivalent base-isolated systems, the corresponding reliability curves are derived.

2 EQUATIONS OF MOTION FOR NON-LINEAR SOFTENING STRUCTURAL SYSTEMS WITH DOUBLE CONCAVE SLIDING BEARINGS

The equivalent model, herein employed and depicted in Fig. 1, is a 3dof system with a dof representative of the superstructure behaviour and two dofs representative of the responses of the two surfaces of the DFPS. The model takes into account the inelastic softening response of the superstructure and non-linear behaviours of the two surfaces of the DFPS [28].

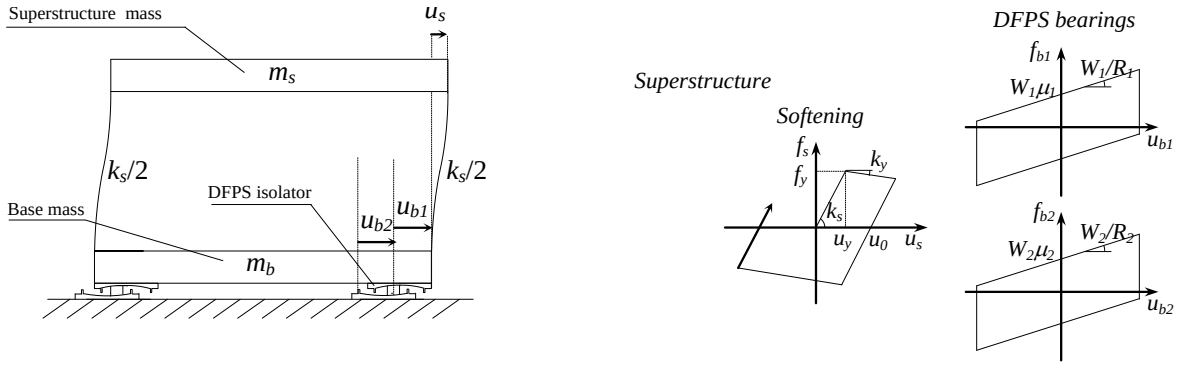

Figure1: 3dof model of an inelastic softening building frame isolated with DFPS.

Regarding the free body diagram of the DFPS, the bearing restoring force, considering only the horizontal component of the displacement on each surface, is:

$$f_{b,1} = \frac{W_1}{R_1} u_{b,1} + \mu_{d,1} W_1 \operatorname{sgn}\left(\dot{u}_{b,1}\right)$$
$$f_{b,2} = \frac{W_2}{R_2} u_{b,2} + \mu_{d,2} W_2 \operatorname{sgn}\left(\dot{u}_{b,2}\right) \quad (1)$$

where $W_1 = \left(m_b + m_s\right) g$ is the weight on the upper surface (surface 1) of the bearing, $W_2 = \left(m_b + m_s + m_d\right) g$ is the weight on the lower surface (surface 2) of the bearing, g is the gravity constant, R_1 and R_2 are the radii of curvature of the two surfaces of the device, $u_{b,1}$ denotes the displacement of the surface 1 with respect to the slider, $u_{b,2}$ represents the slider displacement with respect to the ground as well as $\mu_{d,1}$ and $\mu_{d,2}$ are the sliding friction coefficients of the two surfaces and sgn is the signum function of the sliding velocity for each surface. In this study, the upper surface (surface 1) is characterized by higher values of the friction coefficient and of the radius of curvature. Specifically, $\mu_{d,1}$ is selected as $4\mu_{d,2}$ and $R_1=2R_2$ [28]-[31]. The force of the bearing coincides with the force of each surface response $f_b = f_{b,1} = f_{b,2}$. For each surface, the friction coefficient is given as a function of the sliding velocity [4]-[6]:

$$\mu_{d,i} = f_{\max,\mathrm{i}} - \left(f_{\max,\mathrm{i}} - f_{\min,\mathrm{i}}\right) \exp\left(-\alpha \dot{u}_{b,i}\right) \quad \text{for } i = 1,2 \quad (2)$$

where $f_{\max,\mathrm{i}}$ and $f_{\min,\mathrm{i}}$ are, respectively, the friction coefficients at high and very low sliding velocities of the i-th surface, α is a constant set equal to 30 as well as the ratio $f_{\max,\mathrm{i}} / f_{\min,\mathrm{i}}$ equal to 3 for each surface [15]-[21],[41].

A bilinear constitutive law describes the inelastic softening behaviour of the superstructure, which responses in elastic phase if Eqn.(3) is satisfied and the restoring force $f_{s,i}$ is expressed by Eqn.(4):

$$\left|u_{s,i} - u_{0,i-1}\right| < y\left(u_{s,i}\right) \quad (3)$$

$$f_{s,i}\left(u_{s,i}\right) = k_s \left(u_{s,i} - u_{0,i-1}\right) \quad (4)$$

where $f_{s,i}$ is the restoring force at time instant i, $u_{s,i}$ is the superstructure deformation at the same instant, $u_{0,i-1}$ is the maximum plastic excursion at time instant $(i-1)$ and k_s is the elastic stiffness of the superstructure. The function $y(u_{s,i})$ is the yielding condition in function of the displacement and is non-univocally defined due to the translation of the elastic domain [46]. Defining u_y as the yield displacement, whose yield force is f_y, S denotes the ratio between the softening post-yield and the elastic stiffness [47]-[48], evaluated as:

$$S = \frac{k_y}{k_s} \quad (5)$$

The superstructure response is plastic if Eqn.(6) is satisfied and the restoring force applies according to Eqn.(7):

$$\left|u_{s,i} - u_{0,i-1}\right| \geq y(u_{s,i}) \quad (6)$$

$$f_{s,i}\left(u_s\right) = k_s (u_{s,i} - y(u_{s,i})) \operatorname{sgn}(u_{s,i} - u_{0,i-1}) \quad (7)$$

Therefore, the equations which describe the response of an inelastic 3dof system, isolated by DFPS devices, to the seismic input $\ddot{u}_g(t)$, without any viscous property for the DFPS, are:

$$\begin{aligned}
&m_s\ddot{u}_s + (m_s+m_b)\ddot{u}_{b,1} + (m_s+m_b+m_d)\ddot{u}_{b,2} + \frac{W_2}{R_2}u_{b,2} + W_2\mu_2\,\mathrm{sgn}\left(\dot{u}_{b,2}\right) = -(m_s+m_b+m_d)\ddot{u}_g \\
&m_s\ddot{u}_s + (m_s+m_b)\ddot{u}_{b,1} + (m_s+m_b)\ddot{u}_{b,2} + (m_s+m_b)\frac{g}{R_1}u_{b,1} + (m_s+m_b)g\mu_1\,\mathrm{sgn}\left(\dot{u}_{b,1}\right) = -(m_s+m_b)\ddot{u}_g \\
&m_s\ddot{u}_s + m_s\ddot{u}_{b,1} + m_s\ddot{u}_{b,2} + c_s\dot{u}_s + f_{s,i}(u_s) = -m_s\ddot{u}_g
\end{aligned} \tag{8}$$

where m_s, m_b and m_d are respectively the mass of the superstructure, of the isolation level and of the slider, c_s is the viscous damping factor of the superstructure. Dividing Eqn.(8a) by $m_s+m_b+m_d$ as well as Eqn.(8b) by m_b+m_s and Eqn.(8c) by m_s, defining the mass ratios as $\gamma_s = m_s/(m_s+m_b+m_d)$, $\gamma_b = m_b/(m_s+m_b+m_d)$ and $\gamma_d = m_d/(m_s+m_b+m_d)$ [49], the isolation $\omega_{b,i} = \sqrt{g/R_i}$ and structural $\omega_s = \sqrt{k_s/m_s}$ circular frequency, the structural damping ratio $\xi_s = c_s/2m_s\omega_s$, the non-dimensional equations apply:

$$\begin{aligned}
&\gamma_s\ddot{u}_s + (\gamma_s+\gamma_b)\ddot{u}_{b,1} + \ddot{u}_{b,2} + \omega_{b,2}^2 u_{b,2} + g\mu_2\,\mathrm{sgn}\left(\dot{u}_{b,2}\right) = -\ddot{u}_g \\
&\gamma_s\ddot{u}_s + (\gamma_s+\gamma_b)\ddot{u}_{b,1} + (\gamma_s+\gamma_b)\ddot{u}_{b,2} + (\gamma_s+\gamma_b)\omega_{b,1}^2 u_{b,1} + (\gamma_s+\gamma_b)g\mu_1\,\mathrm{sgn}\left(\dot{u}_{b,1}\right) = -(\gamma_s+\gamma_b)\ddot{u}_g \\
&\ddot{u}_s + \ddot{u}_{b,1} + \ddot{u}_{b,2} + 2\omega_s\xi_s\dot{u}_s + a_s(u_s) = -\ddot{u}_g
\end{aligned} \tag{9}$$

where $a_s(u_s) = f_s(u_s)/m_s$ is the dimensionless force of the superstructure that depends, respectively, on the stiffness k_s in the elastic phase and on the yielding condition in the plastic phase. Note that the elastic isolation period of vibration varies if the sliding movement occurs along surface 1 or surface 2 or along the both surfaces simultaneously [30]. Specifically, if the sliding movement is developed along only a surface, the isolation period depends only on the radius of curvature of the spherical surface R_i (i.e., typically the radius of the surface with the lower friction coefficient) and the bearing behaves like a simple FPS [19], whereas when the both surfaces are involved, the isolation effective period applies [30]:

$$T_b = 2\pi\sqrt{\frac{R_1+R_2}{g}} \tag{10}$$

The change of the vibration period shows the adaptive behavior to the seismic intensity that characterizes these devices [28]-[30]. It follows that the ratio between the variable isolation period and structural period of vibration, which defines the seismic isolation degree [52] cannot be a constant during an earthquake event. Moreover, when the both surfaces slide simultaneously the restoring force of the DFPS device can be evaluated as $\mu_e W_1$ neglecting the mass of the slider [28], where μ_e is the effective sliding coefficient given by:

$$\mu_e = \frac{\mu_{d,1}R_1 + \mu_{d,2}R_2}{R_1+R_2} \tag{11}$$

2.1 Inelastic properties of the superstructure

The inelastic behavior of the superstructure is assumed as an equivalent single dof system [50]-[51] having a softening post-yield stiffness. The behavior factor, *q*, and displacement ductility, μ, are defined, respectively, as:

$$q = \frac{f_{s,el}}{f_y} = \frac{u_{s,el}}{u_y} \tag{12}$$

$$\mu = \frac{u_{\mathrm{s,max}}}{u_y} \tag{13}$$

where $f_{s,el}$ and $u_{s,el}$ are, respectively, the peak elastic response values required to the superstructure, whereas $u_{\mathrm{s,max}} = \left|u_s(t)\right|_{\max}$ is the peak inelastic displacement during a ground motion.

For a softening systems (sensitive to the $P-\Delta$ effects), the behaviour factor *q* represents only the ductility-dependent strength reduction factor due the absolute absence of the overstrength capacities. It follows that the parameter *q* is consistent with both the code provisions [32]-[36] assuming a unitary overstrength factor, and with the one discussed in [41],[42].

3 UNCERTAINTIES RELEVANT TO THE PERFORMANCE ASSESSMENT

For the seismic reliability assessment of a building frame, within the structural performance (SP) evaluation method [53]-[55], specific correlations between the SP levels [56] and appropriate exceeding probabilities during its design life [57]-[58] as well as the relevant (aleatory and/or epistemic) uncertainties with the corresponding PDFs have to be defined. According to the PEER-like modular approach [59] and performance-based earthquake engineering (PBEE) approach [60]-[61], distinguishing the aleatory uncertainties related to the seismic input intensity from those corresponding to the characteristics of the record by means of an intensity measure (IM), this work evaluates and quantifies the seismic reliability of softening systems equipped with DFPS, located in L'Aquila site (Italy), assuming also the friction coefficients as other relevant random variables. Other aleatory uncertainties are not modelled since their effects can be neglected as discussed in [41],[62]. The epistemic uncertainties are not considered in this study.

Specifically, a Gaussian PDF truncated on both sides to 2% and 6% with a mean equal to 4% for the upper surface ($\mu_{d,1}$) and a Gaussian PDF truncated on both sides to 0.5% and 1.5% with a mean of 1% for the lower surface ($\mu_{d,2}$) are used to model, respectively, the sliding friction coefficients at large velocities of the two surfaces of the DFPS bearings [41]-[42]. These values are in compliance with [28]-[31] and chosen in order to obtain a mean value of the effective friction coefficient equal to 3% and, so to allow a comparison with the FPS analysed in [41]-[42]. Then, using the LHS technique [43]-[45], 15 sampled couples of the friction coefficients at large velocities are defined.

As for the uncertainty on the characteristics of the seismic records (record to record variability), according to PBEE approach [60]-[61] and similarly to [41]-[42], the spectral displacement $S_D(\xi_b, T_b)$, related to the equivalent effective period $T_b = 2\pi/\omega_b$ (Eq.(10)) and to damping ratio ξ_b [19],[41] is chosen as *IM* [64]-[66]. Considering ξ_b equal to zero [15],[41],[67], the corresponding IM is hereinafter denoted as $S_D(T_b)$ in the range from 0 m to 0.45 m according to the seismic hazard of L'Aquila site (Italy) [34]. The record-to-record variability is taken into account by means of 30 ground motion records, corresponding to 19 different earthquake events, selected form different national and international databases. A detailed description may be found in [41].

4 INCREMENTAL DINAMIC ANALYSES: RESULTS AND COMPARISON

The performance of systems isolated with DFPS is evaluated through incremental dynamic analyses (IDAs), considering several structural parameters combination and L'Aquila (Italy) as the reference site.

4.1 Design of the elastic and inelastic properties of the structural systems

An extended parametric analysis is carried out considering the following deterministic parameters: isolation degree I_d, varying between 2, 4, 6 and 8 with respect to the equivalent effective isolated period; the equivalent effective isolation period T_b, varying between 3s, 4s, 5s and 6s; the mass ratio γ_s, assumed equal to 0.6 and 0.8 with γ_d equal to 0.001 and so γ_b equal to 0.399 and 0.199; the behaviour factor q, ranging from 1.1 to 2, with a step of 0.1, according to the codes [32]-[35], and the post-yield softening stiffness ratio *S*, set equal to 0.03 [47]-[51]. It follows that 384 equivalent 3dof systems, with isolation damping ratio ξ_b and superstructure damping ratio ξ_s respectively equal to 0% and 2%, are properly defined. These abovementioned 384 equivalent 3dof systems derive from 32 different 3dof systems (with the different values of I_d, of T_b and of the mass ratio) by modifying the behavior factor In the hypothesis of $\mu_{d,1}$ and $\mu_{d,2}$ equal to 4% and 1%, respectively, and a ratio equal to 2 between R_1 and R_2 [28]-[31], the yielding characteristics of 32 3dof elastic systems, necessary to perform IDAs, are evaluated considering the average elastic responses to the 30 seismic inputs scaled to the *IM* value of the life safety limit state for L'Aquila site (Italy): the $IM = S_D(T_b)$ applies 0.311 m for T_b=3, 4, 5 s and 0.26 m for T_b =6 s (NTC18 [34]). In this way, the average values in terms of both yield strength $f_{y,\text{average}}$ and displacement $u_{y,\text{average}}$ of the superstructure have been computed in Matlab-Simulink [72] and, the yielding properties are finally defined for each value of *q*, according to Eqn.(14):

$$u_{y,average} = \frac{f_{y,average}}{k_s} = \frac{f_{s,el,average}}{k_s q} = \frac{u_{s,el,average}}{q} \tag{14}$$

4.2 Incremental dynamic analysis (IDA) curves

This section describes the responses of the 384 equivalent 3dof softening systems having different properties (i.e., I_d, T_b, γ_s, q, *S*) combined with the 15 sampled couples of the friction coefficients, to the 30 seismic inputs scaled to the different $IM = S_D(T_b)$, ranging from 0 m to 0.45 m. A total number of 450 numerical analyses has been performed for each *IM* level and parameter combination. The isolated non-linear softening systems are modelled in Matlab-Simulink [72], by employing the Runge-Kutta-Fehlberg integration algorithm to solve the coupled equations (Eqn.(9)) and determine the responses of each degree of freedom. For each structural system with a softening behaviour, the collapse condition assumed within the numerical analysis is reached when the response of the superstructure is equal to zero. The results of the non-linear IDAs have made it possible to estimate the collapsed system cases as well as the superstructure and isolation response parameters, expressed, respectively, in terms of displacement ductility demand μ and of displacements for the DFPS (i.e., peak value for each surface or peak value of their sum computed at each time instant). These response parameters are assumed as the engineering demand parameters (EDPs) and their peak values have been fitted with lognormal distribution [15],[16]-[21],[41],[60],[67], by estimating the sample

lognormal mean, $\mu_{\ln}(EDP)$, and the sample lognormal standard deviation $\sigma_{\ln}(EDP)$, or dispersion $\beta(EDP)$, through the maximum likelihood estimation technique, to determine the 50th, 84th and 16th percentile of each lognormal PDF [15]. Note that other uncertainties [73]-[78] as well as the influence of the infills [79]-[82] are not considered in this study.

Figures 2-6 show the IDA results related to softening structures. Only the results corresponding to some parameters (I_d =2 and 8, T_b =3s and 6s and mainly related to γ_s equal to 0.6) are reported due to space constraints.

Fig.s 2-3 show the IDA results regarding the isolation level EDP $u_{b,\max}$, which is the peak value of the sum of $u_{b,1}$ and $u_{b,2}$ in each time instant. This response parameter is important to design the elements and components at the isolation level and to estimate the maximum displacement of the isolation system. Therefore, the displacement $u_{b,\max}$ shown in Fig.s 2-3 is the maximum displacement recorded during the non-linear dynamic analysis, and generally is not concomitant with the maximum displacement recorded at each single surface.

Fig. 2 depicts the response of the EDP with a mass ratio equal to 0.8, whereas Fig. 3 and 4 illustrate the responses of the surface 1 and 2, respectively, with a mass ratio of 0.6. As for the isolation level EDP , the lognormal mean decreases by decreasing Tb (Fig. 2) and also for lower Id due to the lower values of the superstructure elastic stiffness.

As regards the softening superstructure, the statistics of the μ strongly increase for higher q (Fig.s 5-6).

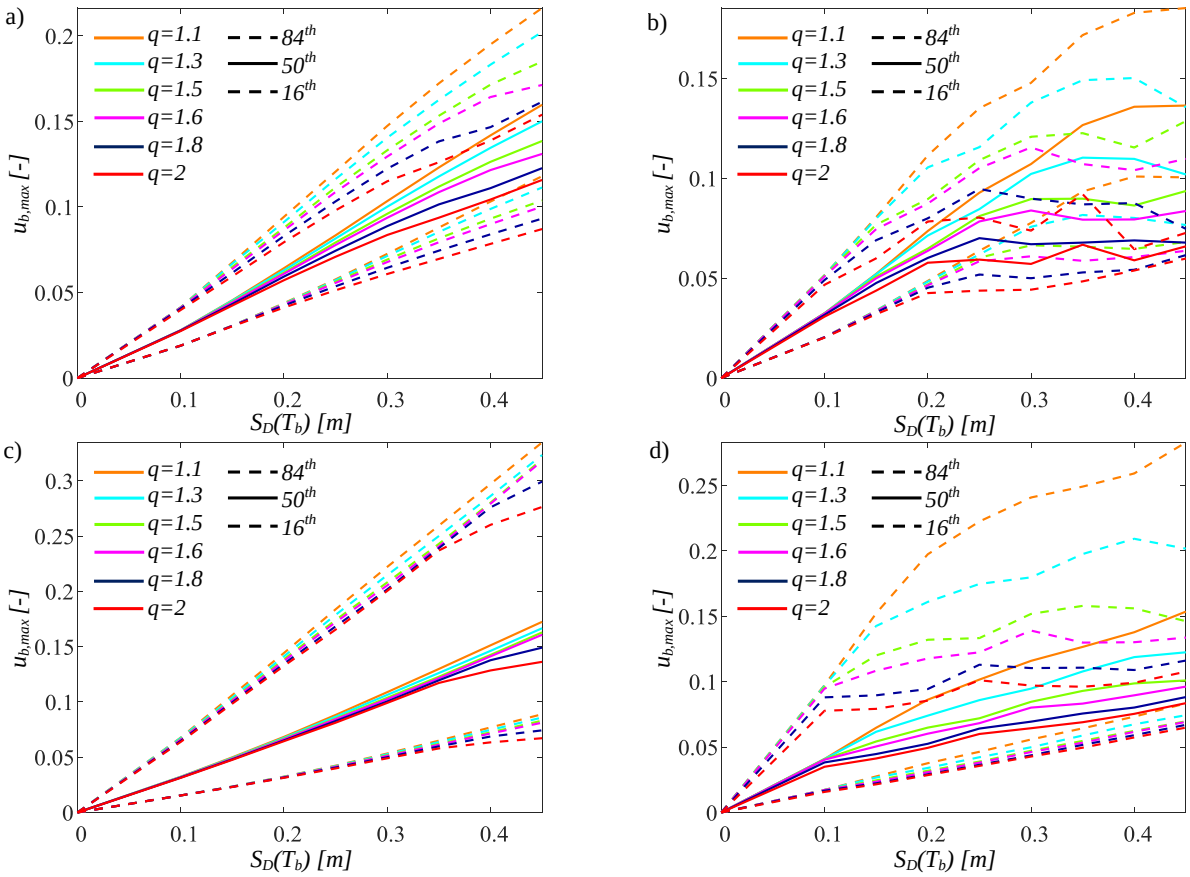

Figure 2: IDA curves of the isolation level with γ_s =0.8 for I_d=2, T_b=3 s, S=0.03 (a), I_d=2, T_b=6 s, S=0.03 (b), I_d=8, T_b=3 s, S=0.03 (c), I_d=8, T_b=6 s, S=0.03 (d).

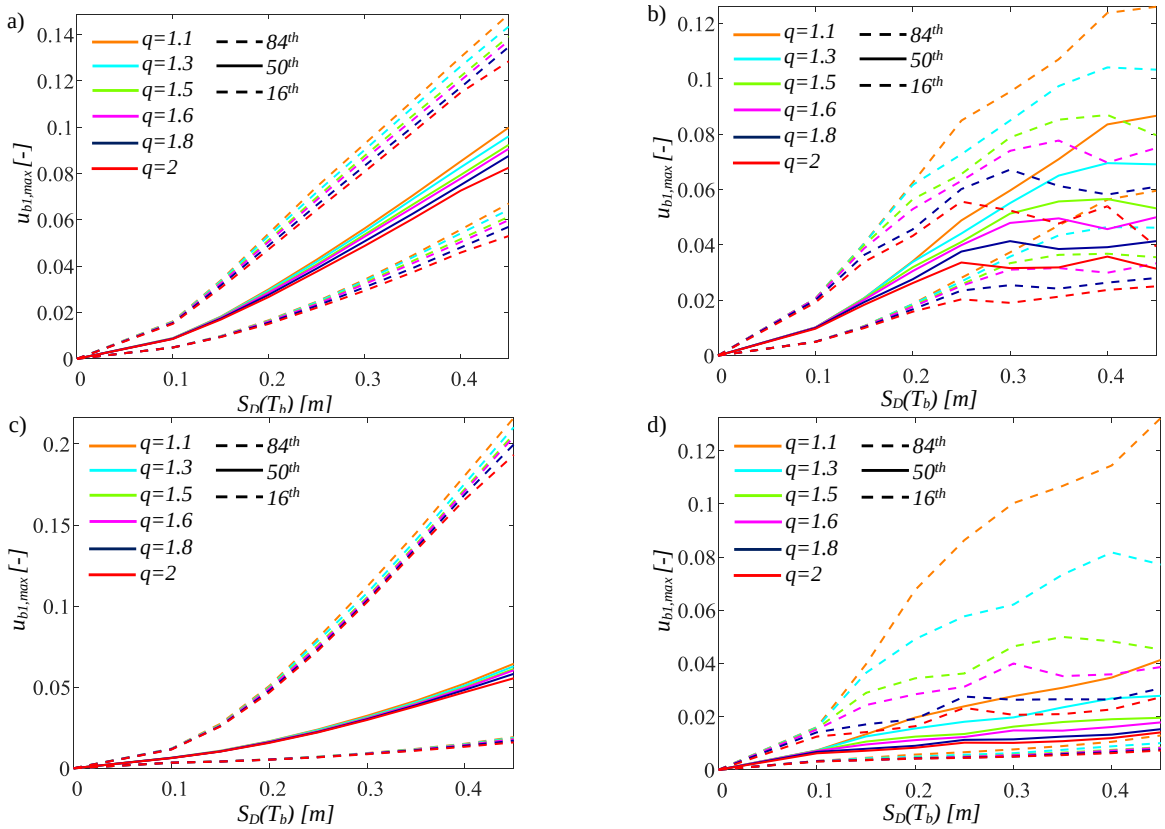

Figure 3: IDA curves of the sliding surface 1 with γ_s=0.6 for I_d=2, T_b=3 s, S=0.03 (a), I_d=2, T_b=6 s, S=0.03 (b), I_d=8, T_b=3 s, S=0.03 (c), I_d=8, T_b=6 s, S=0.03 (d).

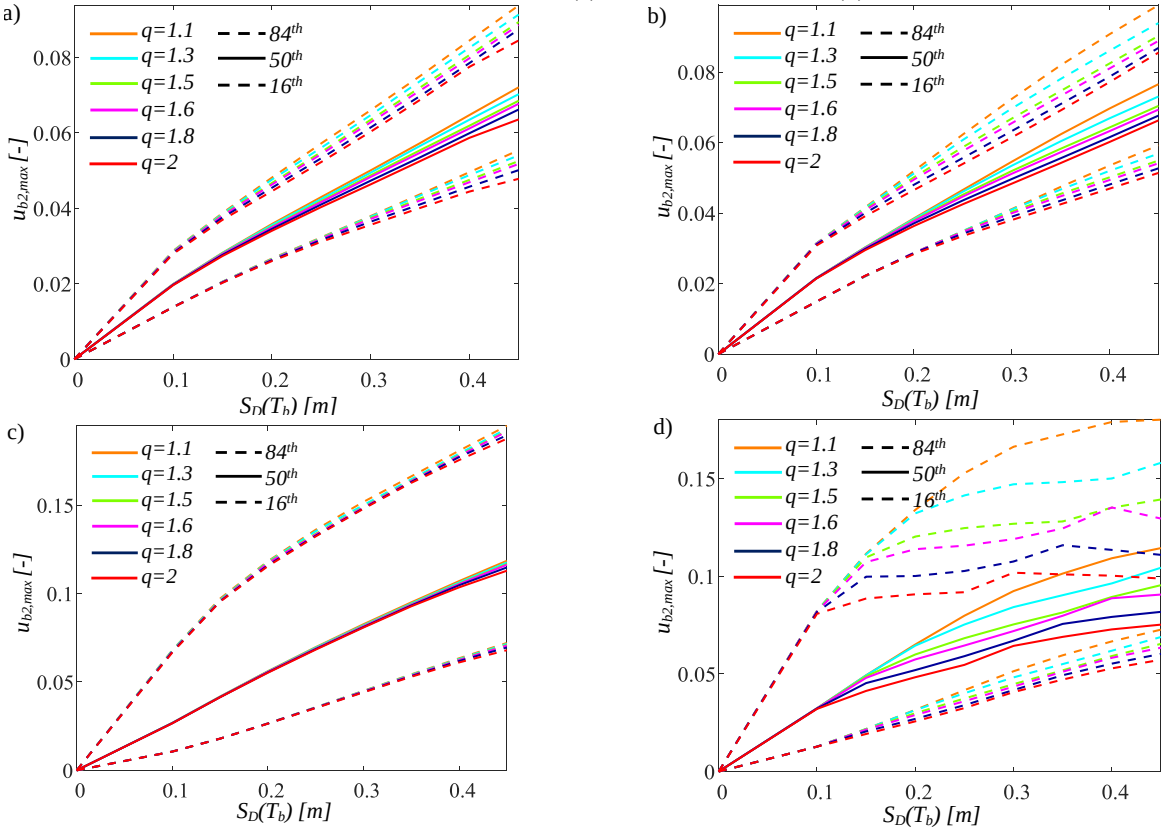

Figure 4: IDA curves of the sliding surface 2 with γ_s=0.6 for I_d=2, T_b=3 s, S=0.03 (a), I_d=2, T_b=6 s, S=0.03 (b), I_d=8, T_b=3 s, S=0.03 (c), I_d=8, T_b=6 s, S=0.03 (d).

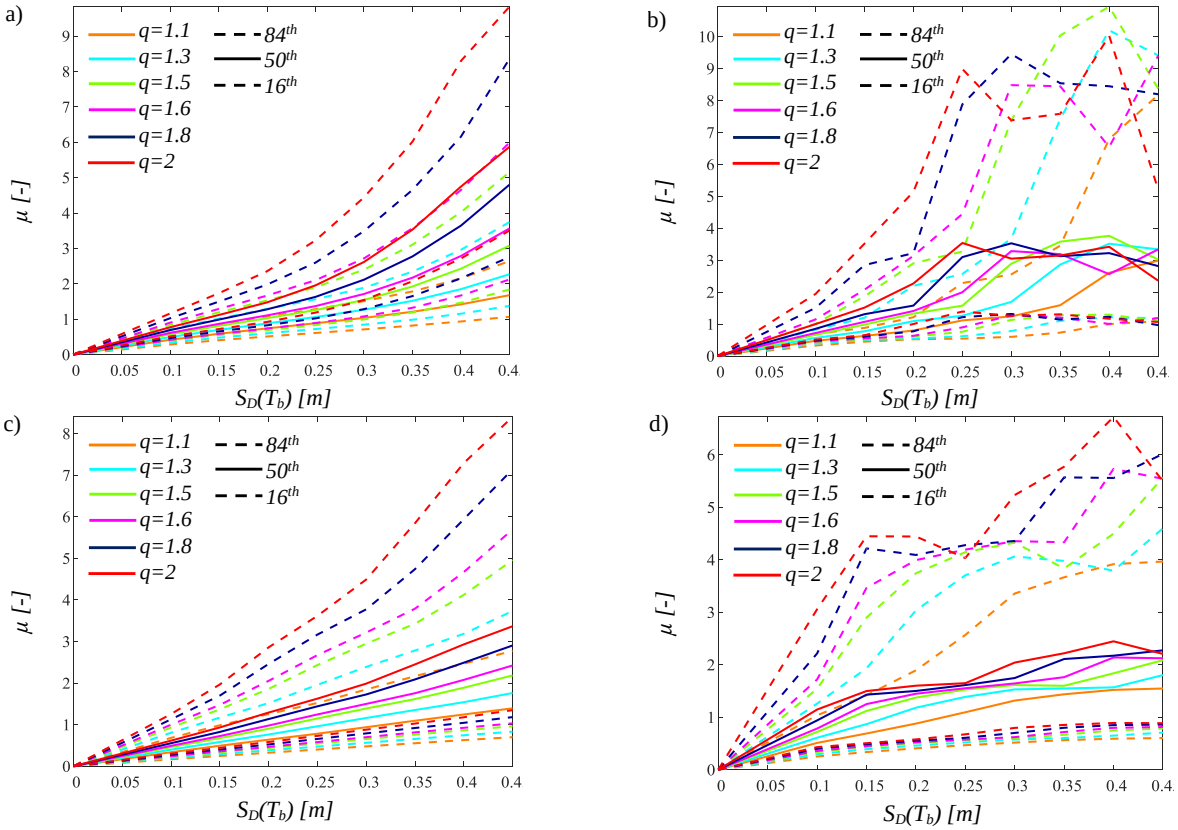

Figure 5: IDA curves of the superstructure with γ_s=0.6 for I_d=2, T_b=3 s, S=0.03 (a), I_d=2, T_b=6 s, S=0.03 (b), I_d=8, T_b=3 s, S=0.03 (c), I_d=8, T_b=6 s, S=0.03 (d).

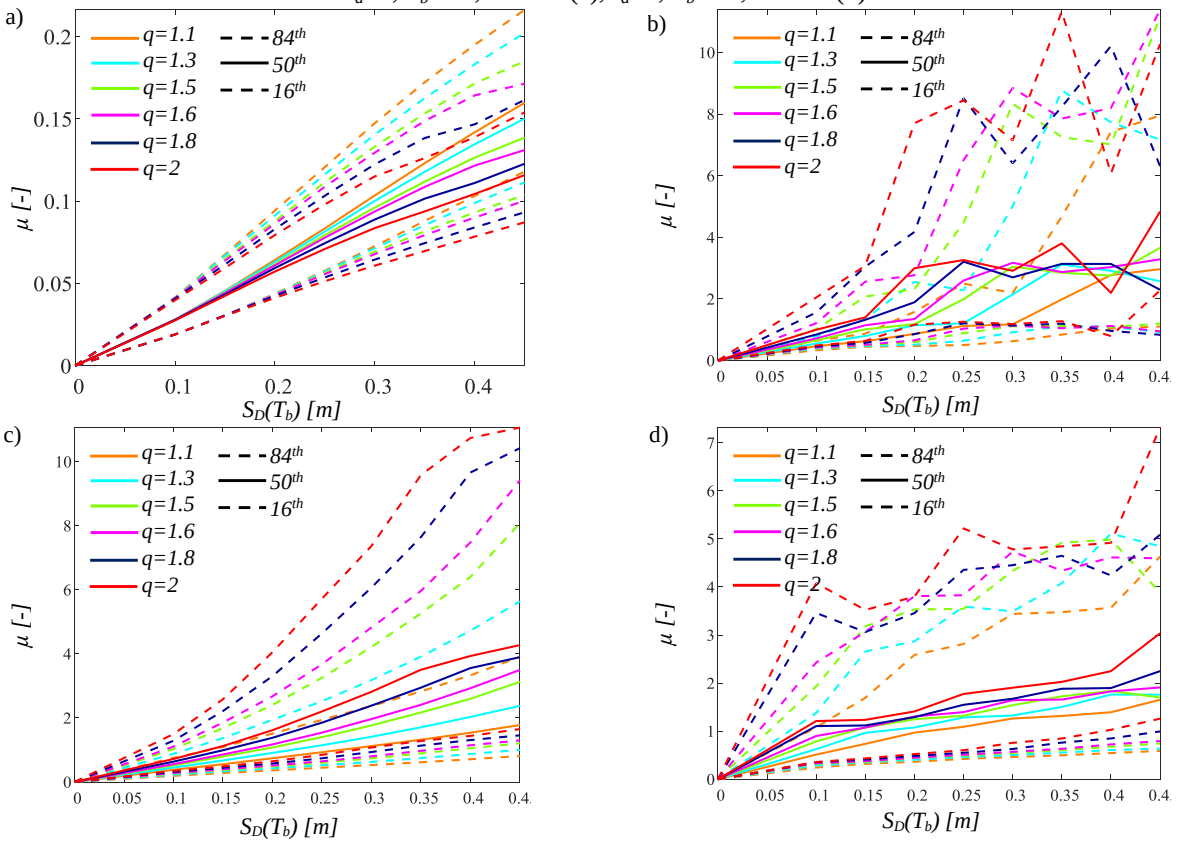

Figure 6: IDA curves of the superstructure with γ_s=0.8 for I_d=2, T_b=3 s, S=0.03 (a), I_d=2, T_b=6 s, S=0.03 (b), I_d=8, T_b=3 s, S=0.03 (c), I_d=8, T_b=6 s, S=0.03 (d).

It is worthy to note that the 50th, 84th and 16th percentiles illustrated in Figures 2-6 have been evaluated without considering the failure cases. From the IDA curves corresponding to the softening systems, it is possible to observe a number of dynamic collapses which increase in quite all the parameter combinations for increasing *IM* levels. The influence of the data related to the dynamic collapses has computed within the seismic fragility assessment as discussed later. Similarly, the influence of the other structural properties (i.e., γ, q and S) on both the DFPS and on the softening superstructures are properly discussed in the next section.

5 SEISMIC FRAGILITY CURVES

Defined the limit states, respectively, in terms of the radii in plan for the two surfaces of the DFPS device, $r_1[m]$ and $r_2[m]$, and of the displacement ductility for the superstructure, μ *[-]*, the seismic fragility, representative of the probabilities P_f exceeding the different limit states at each level of the *IM*, is evaluated. Tables 1-2 report, respectively, the failure probabilities in 50 years [54],[55] with the corresponding *LS* thresholds, related to the *LS*s provided by the codes [33]-[34]: the failure probability in 50 years [18],[54],[55] corresponding to the collapse *LS* [34] for the DFPS; whereas, the failure probability in 50 years [18],[54],[55] corresponding to the life safety *LS* [34] for the superstructure in compliance with the design. The limit state thresholds of Table 1 are also used to assess the fragility in terms of the overall displacement demand to the DFPS. For the both *LS*s, several thresholds are considered with the aim to provide reliable *LS* thresholds for these systems. For each parameter combination (384 equivalent 3dof systems), the probabilities P_f exceeding the different *LSs* at each *IM* level, are numerically computed and then fitted through lognormal distributions [19] with a R-square value higher than 0.8. For the softening systems, the number of both the collapse and not-collapse cases has been considered to estimate the seismic fragility for each parameter combination at each *IM* level by means of the total probability theorem [83], as follows:

$$P_{SL}(IM = im) = (1 - F_{EDP|IM=im}(LS_{EDP})) \cdot \frac{N_{not-collapse}}{N} + 1 \cdot \left(1 - \frac{N_{not-collapse}}{N}\right) \qquad (15)$$

where N is the total number of analyses at each *IM* level, and $N_{not-collapse}$ is the number of numerical simulations without any collapse. The first term of the sum in Eq.(15) represents the probability exceeding a *LS* corresponding to not-collapsing cases [83].

	$LS_{r,1}$	$LS_{r,2}$	$LS_{r,3}$	$LS_{r,4}$	$LS_{r,5}$	$LS_{r,6}$	$LS_{r,7}$	$LS_{r,8}$	$LS_{r,9}$	$LS_{r,10}$
r_i *[m] for i =1,2*	0.05	0.1	0.15	0.2	0.25	0.3	0.35	0.4	0.45	0.5
p_f*(50 years)=1.5·10*$^{-3}$										

Table 1: Limit state thresholds for the two surfaces of the DFPS with the associated exceeding probability.

	$LS_{\mu,1}$	$LS_{\mu,2}$	$LS_{\mu,3}$	$LS_{\mu,4}$	$LS_{\mu,5}$	$LS_{\mu,6}$	$LS_{\mu,7}$	$LS_{\mu,8}$	$LS_{\mu,9}$	$LS_{\mu,10}$
μ *[-]*	1	2	3	4	5	6	7	8	9	10
pf (50 years)=2.2·10^{-2}										

Table 2: Limit state thresholds for the superstructure with the associated exceeding probability.

Fig.s 7-9 depict the fragility curves (i.e., the exceeding probabilities P_f (complementary distribution functions (CCDFs))) versus the *IM* for softening structures. Precisely, the curves corresponding to the different structural properties of interest and related only to some *LS* thresholds ($LS_{r,4}$ and $LS_{\mu,3}$) and to I_d=8 and T_b=3s, are represented. Generally, the seismic fragility of each degree of freedom decreases for increasing the corresponding *LS* threshold.

Fig.s 7-8 illustrate the fragility curves regarding the response of two surfaces of DFPS. For the all limit states, the exceeding probabilities slightly increase for decreasing γ_s. Then, especially for high limit state thresholds, the fragility decreases by decreasing T_b, I_d and increasing q. Note that the probability exceeding a limit state is quite low for the single surface, with a lower probability for the surface 2 characterized by a lower friction coefficient with a lower radius of curvature, in compliance with the IDA results.

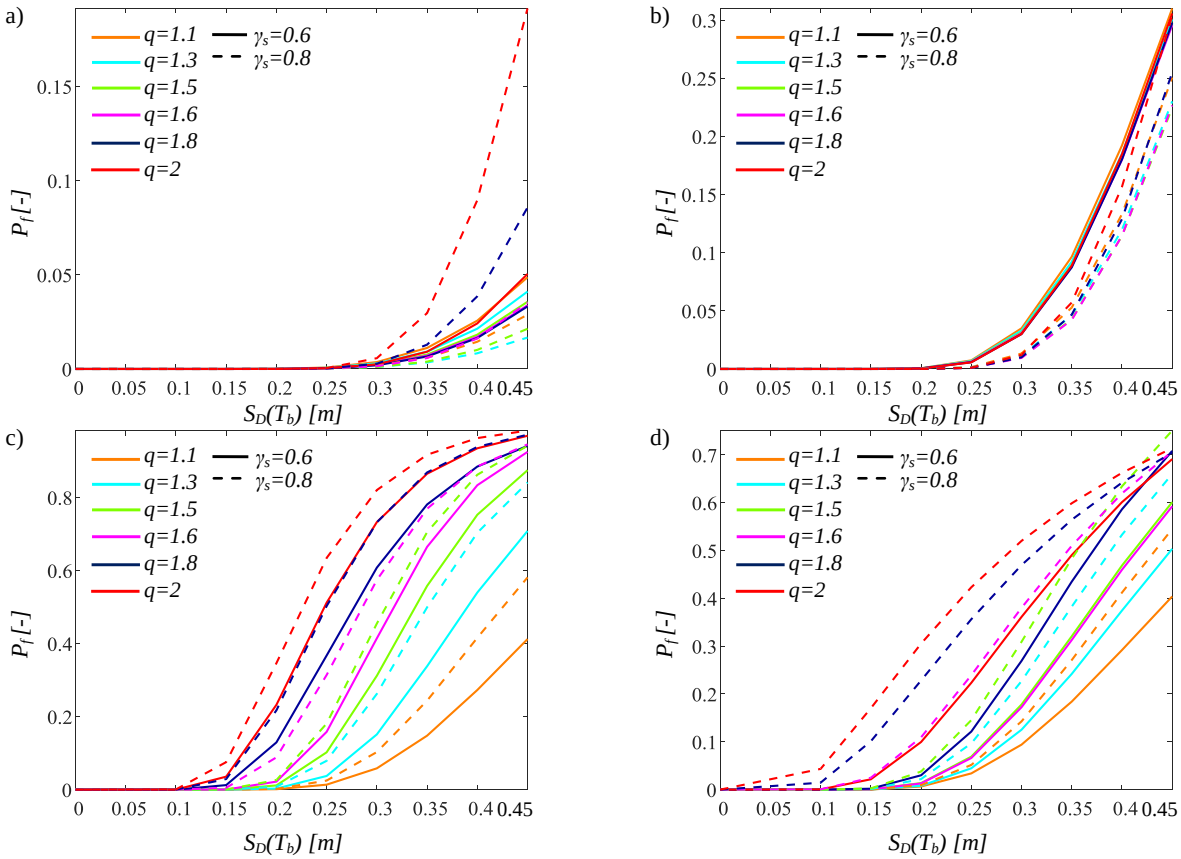

Figure 7: Seismic fragility curves of the sliding surface 1 related to $LS_{r,4}$=0.2 m, for I_d=2, T_b=3 s, S=0.03 (a), I_d=2 and T_b=6 s, S=0.03 (b), I_d=8 and T_b=3 s, S=0.03 (c), I_d=8 and T_b=6 s, S=0.03 (d).

The fragility curves of the nonlinear softening superstructures are shown in Fig. 9. The exceeding probabilities are slightly higher as γ_s increases but highly increase for increasing values of q. Conversely, higher values of T_b for fixed I_d lead to a decrease of the seismic fragility because an increase of the period T_s means an increase of the correlated yielding displacement as well as lower values of T_b for fixed I_d lead to higher values of the seismic fragility. In fact, the coupling between I_d and T_b is a very important parameter because it defines T_s and the corresponding yielding displacement.

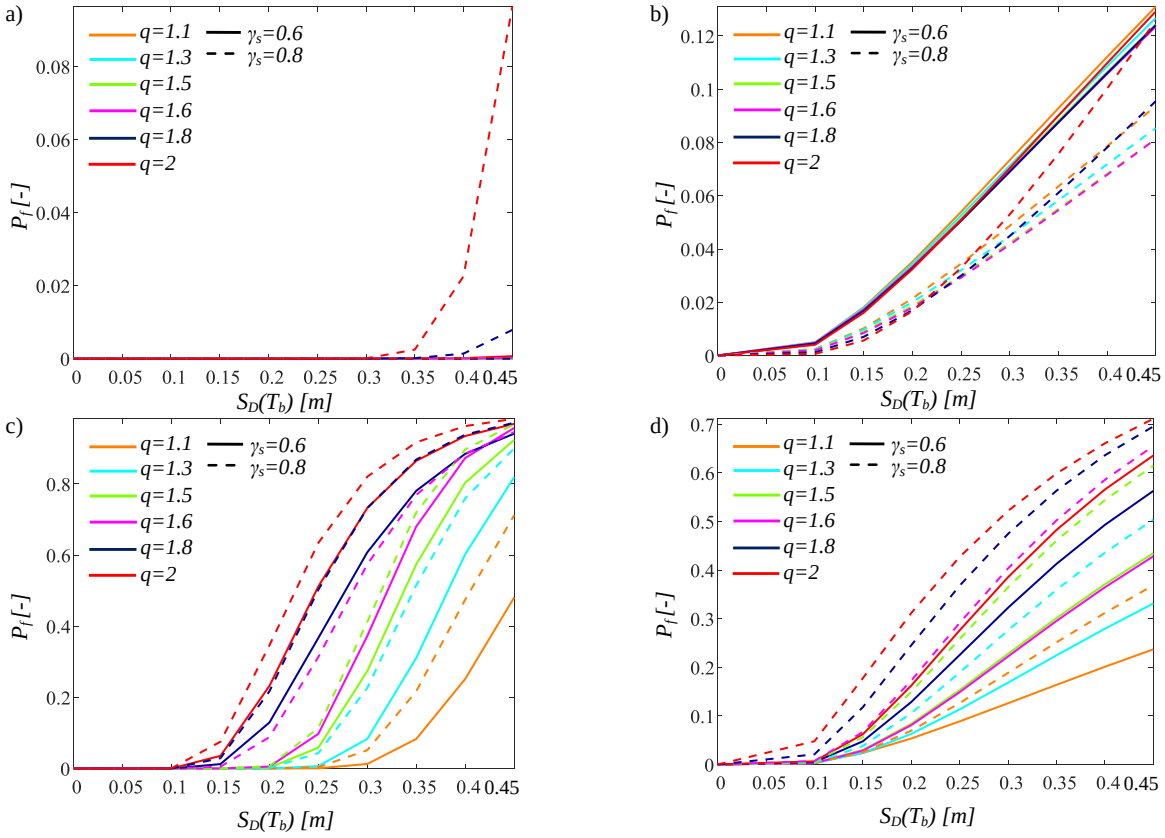

Figure 8: Seismic fragility curves of the sliding surface 2 related to $LS_{r,4}$=0.2 m, for I_d=2, T_b=3 s, S=0.03 (a), I_d=2 and T_b=6 s, S=0.03 (b), I_d=8 and T_b=3 s, S=0.03 (c), I_d=8 and T_b=6 s, S=0.03 (d).

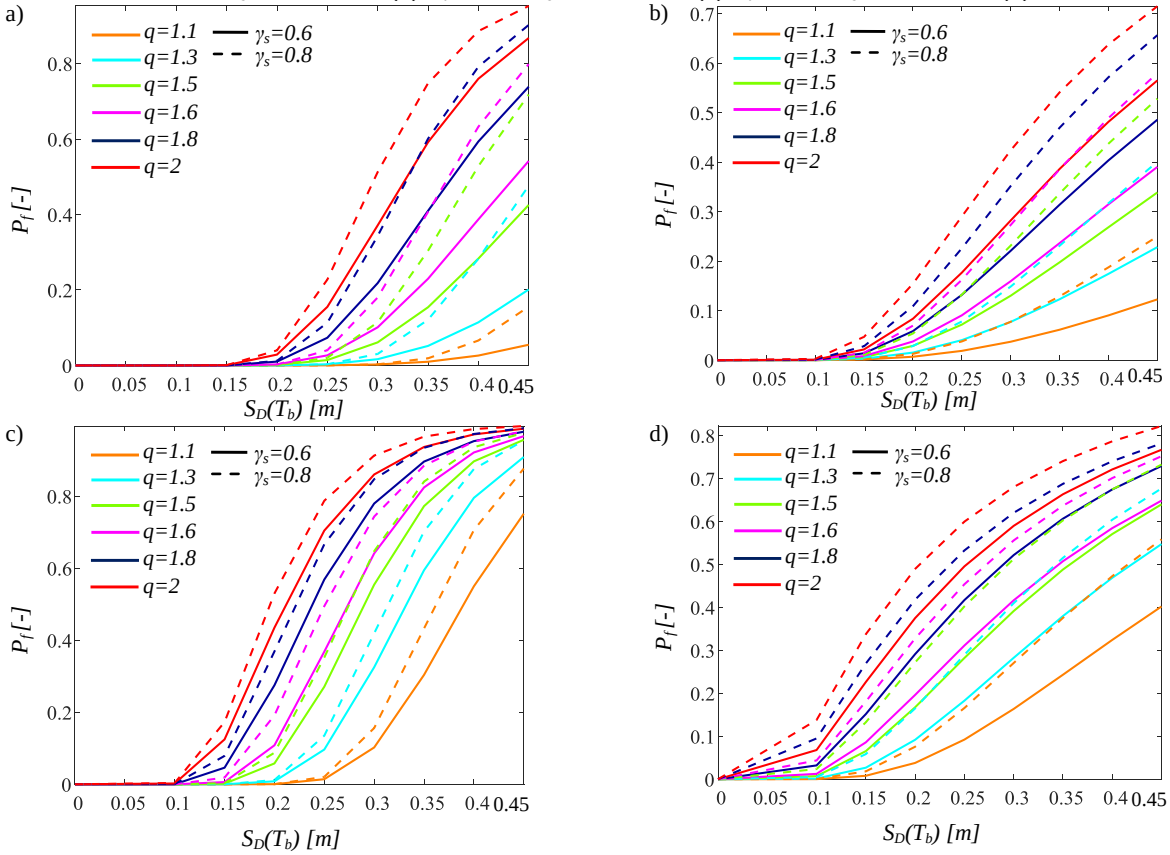

Figure 9: Seismic fragility curves of the superstructure related to $LS_{\mu,3}$=3, for I_d=2, T_b=3 s, S=0.03 (a), I_d=2 and T_b=6 s, S=0.03 (b), I_d=8 and T_b=3 s, S=0.03 (c), I_d=8 and T_b=6 s, S=0.03 (d).

Therefore, as also discussed in [41]-[42], in the case of systems with low T_s, the ensuing dynamic amplification can cause disproportioned superstructure responses and, so a high seismic fragility derives.

The post-yield softening stiffness ratio S strongly and negatively influences the superstructure seismic fragility leading to a very high displacement ductility demand. Comparing the results with the outcomes of [42], for the softening systems higher values of T_b lead to a higher probability exceeding a limit state, especially for the superstructure. This important difference is due to the lower effectiveness the DFPS in comparison to the FPS because at low *IM* and at the beginning of each seismic record, the sliding occurs along only one surface having lower friction coefficient with the consequence that both the energy dissipated and the actual equivalent isolation period are lower.

6 SEISMIC PERFORMANCE OF INELASTIC STRUCTURES WITH DFPS

The convolution integral between the previously achieved seismic fragility curves and the seismic hazard curves expressed in terms of the same *IM*, $S_D(T_b)$, related to the reference site (L'Aquila (Italy)), allows the evaluation of the mean annual rates exceeding the limit states for each parameter combination. Then, by using a Poisson distribution, the seismic reliability of the all softening structures isolated by DFPS in the time frame of interest (e.g., 50 years) have been computed.

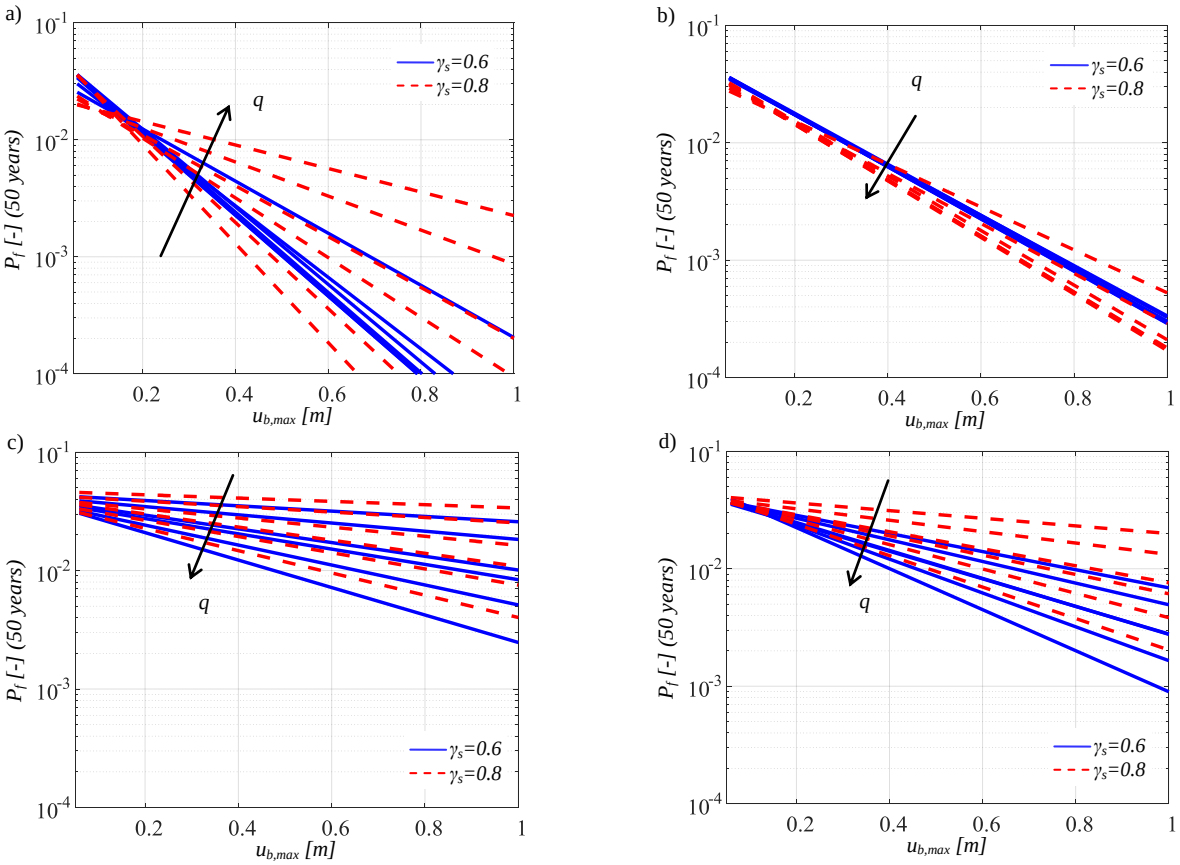

Figure 10: Seismic reliability curves of the isolation level related to I_d=2, T_b=3 s, S=0.03 (a), I_d=2 and T_b=6 s, S=0.03 (b), I_d=8 and T_b=3 s, S=0.03 (c), I_d=8 and T_b=6 s, S=0.03 (d). The arrow denotes the increasing direction of q.

In this work, the seismic hazard of L'Aquila site (Italy), soil class B, with geographic coordinates 42°38'49''N and 13°42'25''E, has been considered, as widely described in [41].

As for the DFPS devices, the seismic reliability evaluation makes it possible to define SRBD curves to design the dimensions in plan of each surface of these devices and the overall dimension of the isolation level as a function of the expected reliability level and of the structural properties.

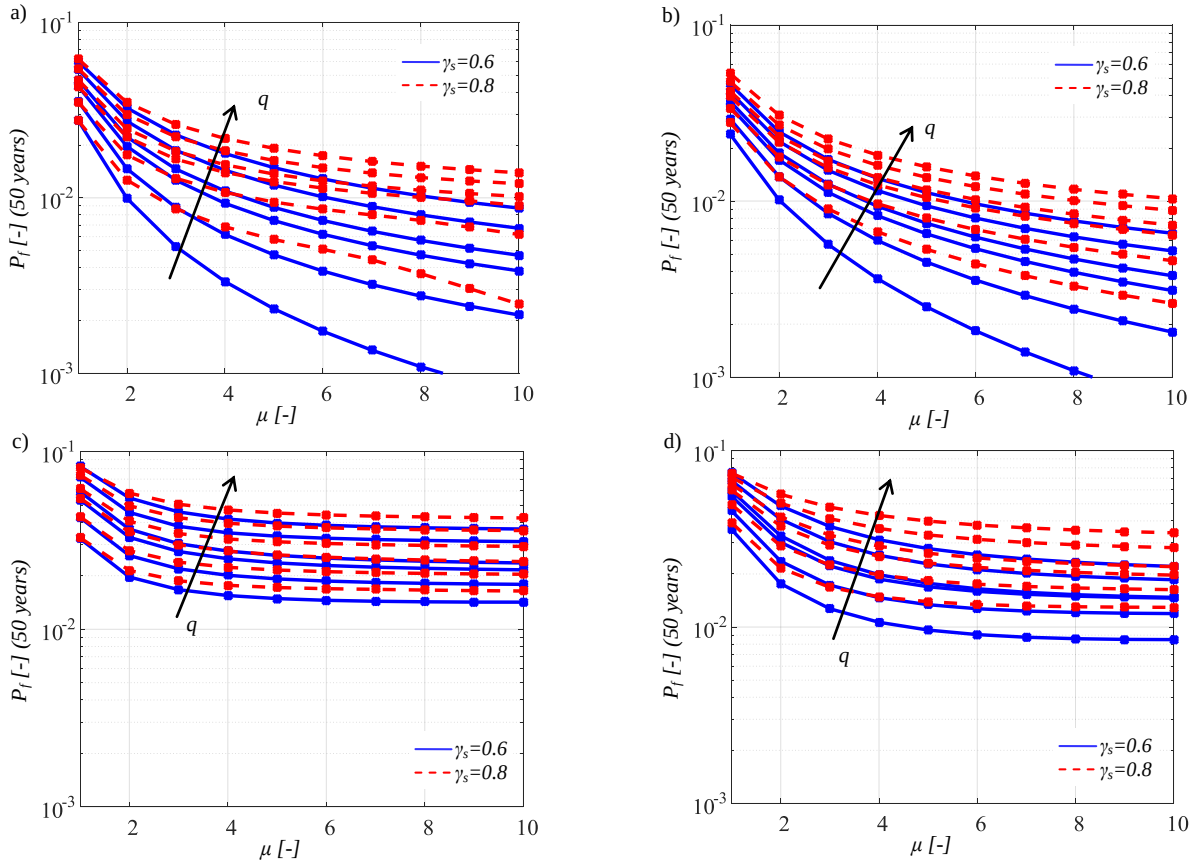

Figure 11: Seismic reliability curves of the superstructure level related to I_d=2, T_b=3 s, S=0.03 (a), I_d=2 and T_b=6 s, S=0.03 (b), I_d=8 and T_b=3 s, S=0.03 (c), I_d=8 and T_b=6 s, S=0.03 (d). The arrow denotes the increasing direction of q.

Fig. 10 depicts the linear regressions, representative of the seismic reliability of the overall dimension of the isolation level, in the semi-logarithmic space for softening systems. The value of R-square is higher than 0.8 demonstrating the robustness and the effectiveness of the kind of the regressions selected within the different statistic approaches [84]-[89]. The exceeding probability of $P_f = 1.5 \cdot 10^{-3}$ can be assured for a global dimension larger than 1 m, in the case of low I_d and γ_s, depending on the behaviour factors. The overall dimension of the isolation level estimated with the above described curves, can also be useful to define the radius in plan of each surface of the DFPS. In fact, SRBD curves of each surface, evaluated and not represented due to space constrains, highlighted that around 1/3 of the global dimension can be attributed to the surface 2 (having a lower friction coefficient with a lower radius of curvature) and 2/3 to the surface 1 for low T_b, whereas for high T_b, these ratios become 1/4 and 3/4, respectively. This aspect is a very important design feature because if high displacements are required to the isolation level, especially for softening systems, they are divided between the two sliding surfaces reducing the geometric encumbrance of the itself device and of the structural elements directly connected as also highlighted in [28]-[30].

Fig. 11 shows the results, representative of the SP curves of the softening superstructure in 50 years, in the logarithmic scale for the different *LS* thresholds in terms of μ and for the dif-

ferent structural properties. The seismic reliability of the superstructure increases for low values of γ_s, I_d, q and for high values of T_b. Comparing the results with the outcomes achieved by [42], the seismic reliability of systems equipped with DFPS, with different friction coefficients for the two surfaces, is slightly lower respect the systems equipped with simple FPS due to the reasons previously explained for the fragility assessment.

7 CONCLUSIONS

This study describes the seismic reliability-based performance of softening structural systems equipped with double concave sliding devices isolators on varying the elastic and inelastic building properties, seismic intensity levels with the hypothesis of the friction coefficients and of the characteristics of the seismic records assumed as the relevant random variables. By means of an equivalent 3dof system with a non-linear velocity-dependent model for the two surfaces of the DFPS, incremental dynamic analyses are carried out considering several natural seismic records, the seismic hazard of L'Aquila site (Italy), increasing behavior factors and different post-yield stiffness ratios. Then, the seismic fragility curves are derived for the softening superstructure and for the isolation level taking also into account the dynamic failure cases. After that, assuming a design life of 50 years, seismic reliability-based design (SRBD) curves are proposed useful to design the radii in plan of the two surfaces as well as the maximum demand to the DFPS. The results have highlighted the negative effects of the post-yield stiffness as well as the possibility to reduce the encumbrance of the devices and of the structural elements directly connected because the seismic demand is divided on the two surfaces. This aspect is a very important design feature of the DFPS representing an its advantage.

REFERENCES

[1] Christopoulos C, Filiatrault A. *Principles of Passive Supplemental Damping and Seismic Isolation*. IUSS Press: Pavia, Italy, 2006.

[2] Zayas VA, Low SS, Mahin SA. A simple pendulum technique for achieving seismic isolation. *Earthquake Spectra* 1990; 6:317–33.

[3] Su L, Ahmadi G, Tadjbakhsh IG. Comparative study of base isolation systems. *Journal of Engineering Mechanic* 1989; 115:1976–92.

[4] Mokha A, Constantino MC, Reinhorn AM. Teflon Bearings in Base Isolation. I: *Testing. J. Struct. Eng. 1990;* 116(2): 438-454.

[5] Constantinou MC, Mokha A, Reinhorn AM. Teflon Bearings in Base Isolation. II: *Modeling. J. Struct. Eng.* 1990; 116(2):455-474.

[6] Constantinou MC, Whittaker AS, Kalpakidis Y, Fenz DM, Warn GP. *Performance of Seismic Isolation Hardware Under Service and Seismic Loading. Technical Report*, 2007.

[7] Almazàn JL, De la Llera JC. Physical model for dynamic analysis of structures with FPS isolators. Earthquake Engineering and Structural Dynamics 2003; 32:1157–1184.

[8] Ayyub BM, McCuen RH. *Probability, statistics, and reliability for engineers. 2nd ed.* NY: CRC Press; 2002.

[9] Lin YK, Cai GQ. *Probabilistic structural dynamics—advanced theory and applications*. NY: McGraw-Hill; 1995.

[10] Chen J, Liu W, Peng Y, Li J. Stochastic seismic response and reliability analysis of base-isolated structures. *J Earthquake* Eng 2007;11:903–24.

[11] Alhan C, Gavin HP. Reliability of base isolation for the protection of critical equipment from earthquake hazards. *Eng Struct* 2005;27:1435–49.

[12] Han R., Li Y., van de Lindt J., Seismic risk of base isolated non-ductile reinforced concrete buildings considering uncertainties and mainshock–aftershock sequences, *Structural Safety*, 50, 39-56, 2014.

[13] Zou XK, Wang Q, Li G, Chan CM. Integrated reliability-based seismic drift design optimization of base-isolated concrete buildings. *J Struct Eng* 2010;136:1282–95.

[14] Mishra SK, Roy BK, Chakraborty S. Reliability-based-design-optimization of base isolated buildings considering stochastic system parameters subjected to random earthquakes. *Int J Mech Sci* 2013;75:123–33.

[15] Castaldo, P, Tubaldi, E. Influence of FPS bearing properties on the seismic performance of base-isolated structures. *Earthquake Engineering and Struct. Dynamics*, 44;15: 2817–2836, 2015.

[16] Castaldo P, Palazzo B, Della Vecchia P. Seismic reliability of base-isolated structures with friction pendulum bearings. *Engineering Structures* 2015;95:80-93.

[17] Palazzo B, Castaldo P, Della Vecchia P. Seismic reliability analysis of base-isolated structures with friction pendulum system, *2014 IEEE Workshop on Environmental, Energy and Structural Monitoring Systems Proc.s*, Napoli, September 17-18, 2014.

[18] Castaldo P., Palazzo B., Della Vecchia P., "Life-cycle cost and seismic reliability analysis of 3D systems equipped with FPS for different isolation degrees*", Engineering Structures*, 125;349–363, http://dx.doi.org/10.1016/j.engstruct.2016.06.056, 2016.

[19] Castaldo P., Amendola G., Palazzo B.,"Seismic fragility and reliability of structures isolated by friction pendulum devices: Seismic reliability-based design (SRBD)", *Earthquake Engineering and Structural Dynamics*, 46(3); 425–446, DOI: 10.1002/eqe.2798, 2017.

[20] Castaldo P, Mancini G, Palazzo B., Seismic reliability-based robustness assessment of three-dimensional reinforced concrete systems equipped with single-concave sliding devices. *Engineering Structures* 163:373-387. https://doi.org/10.1016/j.engstruct.2018.02.067, 2018

[21] Castaldo P., Ripani M., "Optimal design of friction pendulum system properties for isolated structures considering different soil conditions", *Soil Dynamics and Earthquake Engineering*, 2016, 90:74–87, DOI: 10.1016/j.soildyn.2016.08.025.

[22] Castaldo, P., Tubaldi, E., Influence of ground motion characteristics on the optimal single concave sliding bearing properties for base-isolated structures. *Soil Dynamics and Earthquake Engineering*, 104: 346–364, 2018.

[23] Roy B.K., Chakraborty S., Robust optimum design of base isolation system in seismic vibration control of structures under random system parameters, *Structural Safety*, 55: 49-59, 2015.

[24] Bucher C. Probability-based optimal design of friction-based seismic isolation devices, *Structural Safety*, 31(6): 500-507, 2009.

[25] Castaldo, P., Lo Priore, R. Seismic performance assessment of isolated bridges for different limit states, *J Civil Struct Health Monit* 8(1): 17–32, 2018.

[26] Kim Y.S., Yun C.B. Seismic response characteristics of bridges using double concave friction pendulum bearings with tri-linear behavior. *Engin. Struct. 29* (2007) 3082-3093, 2007.

[27] Castaldo P, Ripani M, Lo Piore R Influence of soil conditions on the optimal sliding friction coefficient for isolated bridges. *Soil Dynamics and Earthquake Engineering* 111:131–148, https://doi.org/10.1016/j.soildyn.2018.04.056, 2018.

[28] Fenz D.M, Constantinou M.C., Behaviour of the double concave friction pendulum bearing. *Earthquake Engineering and Structural Dynamics*, 2006; 35:1403-1424, 2006.

[29] Constantinou M.C., *Friction pendulum double concave bearings, technical report.* University of Buffalo NY, October 29, 2004.

[30] Tsai C.S., Chiang T.C., Chen B.J., Experimental evaluation of piecewise exact solution for predicting seismic responses of spherical sliding type isolated structures. *Earthquake Engineeering and Structural Dynamics* 2005;34:1027-1046 DOI: 10.1002/equ.430.

[31] Soni D.P., Mistry B.B., Panchal V.R., Double variable frequency pendulum isolator for seismic isolation of liquid storage tanks. *Nuclear Engineering and Design*, Volume 241, issue 3, march 2011:700-713.

[32] Structural Engineering Institute. Minimum design loads for buildings and other structures (Vol. 7, No. 5). *Amer Society of Civil Engineers*, 2010.

[33] European Committee for Standardization. *Eurocode 8-Design of Structures for Earthquake Resistance. Part 1: General Rules, Seismic Actions and Rules for Buildings,* Brussels, 2004.

[34] NTC18. *Norme tecniche per le costruzioni*. Gazzetta Ufficiale del 20.02.18, DM 17.01.18, Ministero delle Infrastrutture.

[35] Japanese Ministry of Land, Infrastructure and Transport, *Notification No. 2009–2000, Tech. Standard for Structural Specif.s and Calculation of Seismically Isolated Buildings* 2000.

[36] *Quantification of Building Seismic Performance Factors*, *FEMA P695* / June 2009.

[37] Occhiuzzi, A, Veneziano, D.and Van Dyck, J. (1994) *Seismic design of base isolated structures*, Savidis (Ed.), Balkema, Rotterdam, NL.

[38] Vassiliou M.F., Tsiavos A., Stojadinović B. Dynamics of inelastic base-isolated structures subjected to analytical pulse ground motions. *Eart. Eng. and Str. Dyn.* 2013; 42:2043–2060.

[39] Newmark NM, Hall WJ. *Seismic design criteria for nuclear reactor facilities, Report 46, Building Practices for Disaster Mitigation*, National Bureau of Standards, 1973.

[40] Miranda E, Bertero VV. Evaluation of strength reduction factors for earthquake-resistant design. *Earthquake Spectra* 1994; 10:357–379.

[41] Castaldo P., Palazzo B., Ferrentino T., "Seismic reliability-based ductility demand evaluation for inelastic base-isolated structures with friction pendulum devices", *Earthquake Engineering and Structural Dynamics*, 46(8): 1245-1266, DOI: 10.1002/eqe.2854, 2017.

[42] Castaldo P., Palazzo B., Alfano G., Palumbo M.F., "Seismic reliability-based ductility demand for hardening and softening structures isolated by friction pendulum bearings", *Structural Control and Health Monitoring*, 25(11),e2256, 2018.

[43] Mckey MD, Conover WJ, Beckman RJ. A comparison of three methods for selecting values of input variables in the analysis from a computer code. *Technometrics* 1979;21:239-45.

[44] Vořechovský M, Novák D. Correlation control in small-sample Monte Carlo type simulations I: a simulated annealing approach. *Probabilistic Engineering Mechanics* ;24(3):452–62, 2009.

[45] Celarec D, Dolšek M. The impact of modelling uncertainties on the seismic performance assessment of reinforced concrete frame buildings. *Engineering Structures*;52:340–354, 2013.

[46] Hong H-K, Liu C-S Internal symmetry in bilinear elastoplasticity, *International Journal of Non-Linear Mechanics*, 34:279–288, 1999.

[47] Hatzigeorgiou GD. Ductility demand spectra for multiple near- and far-fault earthquakes. *Soil Dynamics and Earthquake Engineering*;30 170-183, 2010.

[48] Hatzigeorgiou GD, Papagiannopoulos GA, Beskos DE. Evaluation of maximum seismic displacements of SDOF systems form their residual deformation. *Engineering Structures 2011;33 3422-3431.*

[49] Naeim F, Kelly JM. *Design of Seismic Isolated Structures: From Theory to Practice.* John Wiley & Sons, Inc.; 1999.

[50] Gupta A, Krawinkler H. Seismic demands for performance evaluation of steel moment resisting frame structures. *The John A. Blume Earth. Eng. Center report No. 132*, June 1999.

[51] Adam C, Ibarra LF, Krawinkler H. Evaluation of P-Delta effects in non-deteriorating MDOF structures from equivalent SDOF systems. *13th Word Conference on Earthquake Engineering, Vancouver, B.C., Canada* 2004, Paper No. 3407, 2004.

[52] Palazzo B. Seismic Behavior of base-isolated Buildings. *Proc. International Meeting on earthquake Protection of Buildings, Ancona*, 1991.

[53] Collins KR, Stojadinovic B. Limit states for performance-based design. *12WCEE*, 2000.

[54] Bertero RD, Bertero VV. Performance-based seismic engineering: the need for a reliable conceptual comprehensive approach. *Earthquake Engineering and Structural Dynamics 2002*;31:627–652 (DOI: 10.1002/eqe.146), 2002.

[55] Aoki Y, Ohashi Y, Fujitani H, Saito T, Kanda J, Emoto T, Kohno M. Target seismic performance levels in structural design for buildings. *12WCEE*, 2000.

[56] SEAOC Vision 2000 Committee. *Performance-based seismic engineering. Report prepared by Structural Engineers Association of California,* Sacramento, CA., 1995.

[57] CEN – *European Committee for Standardization. Eurocode 0: Basis of Structural Design. Final draft*. Brussels, 2006.

[58] Saito T, Kanda J, Kani N. Seismic reliability estimate of building structures designed according to the current Japanese design code. *Proc.s of the Str. Eng.s World Congress*, 1998.

[59] Cornell CA, Krawinkler H. *Progress and challenges in seismic performance assessment*. PEER Center News 2000;4(1):1-3

[60] Aslani H, Miranda E. Probability-based seismic response analysis. *Engineering Structures 2005*; 27(8): 1151-1163, 2005.

[61] Porter KA. An overview of PEER's performance-based earthquake engineering methodology. *Proceedings, Proceedings of the 9th International Conference on Application of Statistics and Probability in Civil Engineering (ICASP9)*, San Francisco, California, 2003; 973-980.

[62] Kulkarni JA, Jangid RS. Effects of superstructure flexibility on the response of base-isolated structures. *Shock and Vibration* 2003;26:1-13, 2003.

[63] http://www.fipindustriale.it/

[64] Shome N, Cornell CA, Bazzurro P, Carballo JE. Earthquake, records, and nonlinear responses. *Earthquake Spectra*; 14(3): 469-500, 1998.

[65] Luco N, Cornell CA. Structure-specific scalar intensity measures for near-source and ordinary earthquake ground motions. *Earthquake Spectra*; 23(2): 357-92, 2007.

[66] Pinto PE, Giannini R, Franchin P. *Seismic Reliability Analysis of Structures*, IUSS Press, Pavia, Italy, 2003.

[67] Ryan KL, Chopra AK., Estimation of Seismic Demands on Isolators Based on Nonlinear Analysis. *J. Struct. Eng.*, 130(3), 392–402, 2004.

[68] PEER, Pacific Earthquake Engineering Research Center http://peer.berkeley.edu/

[69] ITACA, Italian Accelerometric Archive http://itaca.mi.ingv.it/ItacaNet/itaca10_links.htm

[70] ISESD, Internet-Site for European Strong-Motion Data http://www.isesd.hi.is/ESD_Local/frameset.htm

[71] Vamvatsikos D, Cornell CA. Incremental dynamic analysis. Earthquake *Engineering and Structural Dynamics 2002*; 31(3): 491–514, 2002.

[72] Math Works Inc. MATLAB-High Performance Numeric Computation and Visualization Software. User's Guide. Natick: MA, USA, 1997.

[73] Castaldo P, Gino D, Carbone VI, Mancini G. Framework for definition of design formulations from empirical and semi-empirical resistance models, Structural Concrete, 19(4), 980-987, 2018 https://doi.org/10.1002/suco.201800083.

[74] Castaldo, P., De Iuliis, M. (2014) Effects of deep excavation on seismic vulnerability of existing reinforced concrete framed structures, Soil Dynamics and Earthquake Engineering 64, 102-112.

[75] Castaldo, P., Palazzo, B., Perri, F. (2016) Fem simulations of a new hysteretic damper: The dissipative column, Ingegneria Sismica, 33(1), 34-45.

[76] Castaldo, P., Calvello, M., Palazzo, B. (2013) Probabilistic analysis of excavation-induced damages to existing structures, Computers and Geotechnics, 53, 17-30.

[77] Castaldo P, Gino D, Bertagnoli G, Mancini G. Partial safety factor for resistance model uncertainties in 2D non-linear finite element analysis of reinforced concrete structures, Engineering Structures, 176(2018), 746-762.

[78] Castaldo, P., Jalayer, F., Palazzo, B. (2018) Probabilistic assessment of groundwater leakage in diaphragm wall joints for deep excavations, Tunnelling and Underground Space Technology 71, 531-543.

[79] Cavaleri L, Di Trapani F, Macaluso G, Papia M (2012) Reliability of code proposed models for assessment of masonry elastic moduli. Ing Sismica 29(1):38–59.

[80] Campione, G., Cavaleri, L., Di Trapani, F. and Ferrotto, M.F. (2017), "Frictional effects on structural behavior of no-endconnected steel-jacketed RC columns: Experimental results and new approaches to model numerical and analytical response", J. Struct. Eng., ASCE, 143(8), 04017070.

[81] Campione G, Cavaleri L, Di Trapani F, Macaluso G, Scaduto G (2016) Biaxial deformation and ductility domains for engineered rectangular RC cross-sections: a parametric study highlighting the positive roles of axial load, geometry and materials. Eng Struct 107(15):116–134

[82] Di Trapani, F., Bertagnoli, G., Ferrotto, M.F., Gino, D. Empirical equations for the direct definition of stress-strain laws for fiber-section-based macromodeling of infilled frames 2018. Journal of Engineering Mechanics 144(11),04018101.

[83] Bazzurro P, Cornell CA, Shome N, Carballo JE: Three proposals for characterizing MDOF nonlinear seismic response. *J. of Str.Engineering*, 124(11), 1281-1289, 1998.

[84] Garzillo, Carmine; Troisi, Roberta (2015) Le decisioni dell'EMA nel campo delle medicine umane. pp.85-133. In *EMA e le relazioni con le Big Pharma - I profili organizzativi della filiera del farmaco* - ISBN:9788892102279 - G. Giappichelli

[85] Nese, Annamaria; Troisi, Roberta (2018) Corruption among mayors: evidence from Italian Court of Cassation judgments. DOI:10.1007/s12117-018-9349-4. pp.1-26. In *TRENDS IN ORGANIZED CRIME* - ISSN:1084-4791 vol. agosto 2018

[86] Troisi, Roberta; Golzio, Luigi Enrico (2016). Legal studies and organization theory: a possible cooperation. pp.1-23. In *Manageable cooperation? - ISBN:0024667498 - European Academy of Management, Convegno: 16th EURAM Conference*, Paris, 1-4 June (ISSN 2466-7498).

[87] Troisi, Roberta; Guida, Vittorio (2018). Is the Appointee Procedure a Real Selection or a Mere Political Exchange? The Case of the Italian Health-Care Chief Executive Officers. DOI:10.5947/jeod.2018.008. pp.19-38. In *JOURNAL OF ENTREPRENEURIAL AND ORGANIZATIONAL DIVERSITY* - ISSN:2281-8642 vol. 7 (2).

[88] Troisi Roberta (2012). Le risorse umane nelle BCC: lavoro e motivazioni al lavoro. pp.399-417. In Progetto aree bianche. Il sistema del credito cooperativo in Campania - ISBN:8865580526 vol. 1.

[89] Golzio Luigi Enrico; Troisi Roberta (2013). 'The value of interdisciplinary research: a model of interdisciplinarity between legal research and research in organizations". pp.23-38. In *JOURNAL FOR DEVELOPMENT AND LEADERSHIP* , vol. 2.

COMPDYN 2019
7th ECCOMAS Thematic Conference on
Computational Methods in Structural Dynamics and Earthquake Engineering
M. Papadrakakis, M. Fragiadakis (eds.)
Crete, Greece, 24–26 June 2019

OPTIMAL SLIDING FRICTION COEFFICIENT FOR ISOLATED BRIDGES IN DIFFERENT SOIL CONDITIONS

P. Castaldo[1], M. Ripani[2], and R. Lo Priore[3]

[1] Department of Structural, Geotechnical and Building Engineering (DISEG)
Politecnico di Torino, Turin, Italy
e-mail: paolo.castaldo@polito.it

[2] Universidad de Buenos Aires. Consejo Nacional de lnvestigaciones Científicas y Técnicas (CONICET). Instituto de Tecnologías y Ciencias de la Ingeniería "Hilario Fernández Long" (INTECIN). Facultad de Ingeniería
Buenos Aires, Argentina
mripani@fi.uba.ar

[3] Department of Civil Engineering, University of Salerno
Fisciano, SA, Italy
r.lopriore@hotmail.it

Abstract

The work evaluates the optimal properties of friction pendulum system (FPS) bearings for the seismic protection of bridge piers under earthquake excitations having different frequency characteristics representative of different soil conditions in order to reduce the seismic vulnerability of infrastructures. A two-degree-of-freedom model is adopted to describe, respectively, the response of the infinitely rigid deck isolated by the FPS devices and the elastic behavior of the pier. By means of a non-dimensional formulation of the motion equations, a wide parametric analysis for several structural parameters is carried out. Seismic excitations, modelled as time-modulated filtered Gaussian white noise random processes having different intensities and frequency contents, are considered. Specifically, the filter parameters, which control the frequency contents, are properly calibrated to reproduce stiff, medium and soft soil conditions, respectively. Finally, the optimum values of the sliding friction coefficient able to minimize the pier displacements with respect to the ground are derived as a function of the structural properties, of the seismic input intensity and of the soil condition.

Keywords: Bridge, Seismic Isolation, Soil Condition, Performance, Optimal friction coefficient.

1 INTRODUCTION

Seismic isolation of bridges makes it possible to uncouple the deck from the horizontal components of the earthquake motion, leading to a substantial reduction of the deck acceleration and, consequently, of the forces transmitted to the pier [1]-[4]. In the last years, friction pendulum system (FPS) devices have often been preferred to other isolators for their capability of providing an isolation period independent of the mass of the supported structure, their capacity to assure high dissipation and recentering, and their longevity and durability properties [5]-[12]. In [13], with reference to an equivalent two-degree-of-freedom (2dof) model for base-isolated building frames, a non-dimensionalization of the motion equation considering different isolator and system properties has been proposed. Contextually, other studies have been focused on the seismic response of bridge isolated with sliding pendulum isolators highlighting the advantages [14]-[15]. Moreover, other works have been more oriented to develop design approaches for the isolators and to identify the optimal isolator properties. In this context, the seismic reliability-based design (SRBD) approach has been proposed and widely discussed in [16]-[22] as a new methodology useful to provide design solutions for seismic devices taking into account the main uncertainties relevant to the problem. Jangid [23], assuming a stochastic model of the earthquake ground motion, considered the seismic performance of a bridge equipped with FPS devices, characterized by a Coulomb behavior, illustrating that there exists an optimal value of the friction coefficient for which the pier base shear and deck acceleration can be minimized. Other works (e.g., [24]-[26],[27]) concerning isolated bridges have also demonstrated that soft soil condition leads to a higher demand in terms of displacements and shear forces by negatively influencing the isolated systems. In [28], the optimal values of the friction coefficient taking into account the influence of the ground motion characteristics by means of the ratio between the Peak Ground Acceleration (PGA) and the Peak Ground Velocity (PGV) have been proposed.

This work investigates the influence of soil characteristics in terms of frequency content on the seismic performance of bridges isolated with FPS isolators to define the optimal sliding friction coefficients. The two-degree-of-freedom model, as employed in [14],[29] is used for this purpose as an equivalent model representative of the dynamic behaviour of a single-column bent viaduct to describe, respectively, the seismic response of the infinitely rigid deck isolated by the FPS devices and of the elastic behavior of the pier. In compliance with the non-dimensionalization of the motion equations presented for base-isolated building frames in [13], in this study, a non-dimensionalization of the motion equations for isolated bridges is proposed in order to carry out a wide parametric analysis considering different values of the structural properties and three different sets of artificial ground motion records. These latter ones are modelled as non-stationary stochastic processes and generated through the power spectral density method [30], with different frequency contents corresponding to stiff, medium and soft soil conditions [31], respectively. Specifically, for each set of the random excitations, numerical simulations are executed to estimate the influence of the characteristic system and isolator properties on the response parameters relevant to the structural performance. Then, the optimal values of the sliding friction coefficient, able to minimize the pier displacements relative to the ground, are defined as a function of the structural parameters, of the seismic input intensity and of the soil condition.

2 NON-DIMENSIONAL MOTION EQUATIONS FOR ISOLATED BRIDGES

Assuming an equivalent 2dof model, the motion equations governing the response of a bridge equipped with single concave FPS devices (Figure 1), subjected to the seismic input $\ddot{u}_g(t)$, apply:

$$\begin{aligned} &m_d\ddot{u}_d(t)+m_d\ddot{u}_p(t)+c_d\dot{u}_d(t)+f_b(t)=-m_d\ddot{u}_g(t) \\ &m_p\ddot{u}_p(t)-c_d\dot{u}_d(t)+c_p\dot{u}_p(t)+k_pu_p(t)-f_b(t)=-m_p\ddot{u}_g(t) \end{aligned} \quad (1a,b)$$

where u_d denotes the displacement of the deck relative to pier, u_p the pier displacement relative to the ground, m_d and m_p respectively the mass of the deck and of the pier bridge, k_p and c_p respectively the pier stiffness and inherent viscous damping coefficient, c_d the bearing viscous damping factor, t the time instant, the dot differentiation over time, and $f_b(t)$ indicates the FPS force, that can be evaluated as:

$$f_b(t)=k_du_d(t)+\mu(\dot{u}_d)m_dg\,\mathrm{sgn}(\dot{u}_d) \quad (2)$$

where $k_d=W/R=m_dg/R$, g is the gravity constant, R is the radius of curvature of the FPS, $\mu(\dot{u}_d(t))$ the sliding friction coefficient, which depends on the bearing slip velocity $\dot{u}_d(t)$, and *sgn*(·) denotes the sign function. It follows that, similarly to base-isolated structures [13], the fundamental vibration period of an isolated bridge, $T_d=2\pi\sqrt{R/g}$, corresponding to the pendulum component, is independent of the deck mass and related only to the radius of curvature *R*.

According to [8]-[10], the sliding friction coefficient of teflon-steel interfaces can be expressed as:

$$\mu(\dot{u}_d)=f_{\max}-Df\cdot\exp(-\alpha|\dot{u}_d|) \quad (3)$$

where $f_{\max}$ and $f_{\min}=f_{\max}-Df$ represent, respectively, the maximum value of sliding friction coefficient attained at large velocities and the value at zero velocity. In this study, it is considered that $f_{\max}=3f_{\min}$ with the exponent α equal to 30 [13]. Considering the maximum value of the sliding friction coefficient, the effective stiffness of the FPS bearings $k_{eff}=W(1/R+f_{\max}/u_d)$ as well as the corresponding effective isolated period $T_{\mathrm{d},eff}$ [32],[33] (Fig. 1) can be computed depending on the displacement demand. Note that Eqn.(1) does not consider the effects of the higher modes due to flexibility of the pier and is verified if only the horizontal component of the bearing displacement is considered [18] (i.e., high radii of curvature *R*). Furthermore, the equivalent 2dof model [14],[29] can be assumed representative of the dynamic behaviour of a single-column bent viaduct as long as the bridge is straight and consists of a large number of equal spans, of piers with equal height/stiffness and considering a superstructure (deck) that can be assumed to move as a rigid body [34].

Let us introduce the time scale $\tau=t\omega_d$ in which $\omega_d=\sqrt{k_d/m_d}$ is the fundamental circular frequency of the isolated system with infinitely rigid superstructure, and the seismic intensity scale a_0, expressed as $\ddot{u}_g(t)=a_0\ell(\tau)$ where $\ell(\tau)$ is a non-dimensional function of time describing the seismic input time-history, the following non-dimensional equations can be obtained and herein proposed for isolated bridges:

$$\begin{aligned} &\ddot{\psi}_d(\tau)+\ddot{\psi}_p(\tau)+2\xi_d\dot{\psi}_d(\tau)+\psi_d(\tau)=-\ell(\tau)-\frac{\mu(\dot{u}_d)g}{a_0}\mathrm{sgn}(\dot{\psi}_d) \\ &\ddot{\psi}_p(\tau)-\frac{1}{\lambda}\left[2\xi_d\dot{\psi}_d(\tau)+\psi_d(\tau)+\frac{\mu(\dot{u}_d)g}{a_0}\mathrm{sgn}(\dot{\psi}_d)\right]+2\xi_p\frac{\omega_p}{\omega_d}\dot{\psi}_p(\tau)-\frac{\omega_p^2}{\omega_d^2}\psi_p(\tau)=-\ell(\tau) \end{aligned} \quad (4a,b)$$

where $\omega_p = \sqrt{k_p / m_p}$ and $\xi_p = c_p / 2m_p\omega_p$ represent respectively the circular frequency and damping factor of the pier bridge; $\omega_d = \sqrt{k_d / m_d} = \sqrt{g / R}$ and $\xi_d = c_d / 2m_d\omega_d$ are respectively the circular frequency and the isolator damping factor of the FPS isolator; $\lambda = m_p / m_d$ [14],[29],[32] the mass ratio. The non-dimensional parameters $\psi_d = \dfrac{u_d\omega_d^2}{a_0}$ and $\psi_p = \dfrac{u_p\omega_d^2}{a_0}$ describe the dynamic response of the deck and the pier, respectively. From Eqn.(4), it is possible to observe that the five non-dimensional Π terms [13],[35]-[36] that govern the system non-dimensional response are:

$$\Pi_\omega = \frac{\omega_p}{\omega_d}\,,\ \Pi_\lambda = \lambda\,,\ \Pi_\mu\left(\dot{\psi}_d\right) = \frac{\mu\left(\dot{u}_d\right)g}{a_0}\,,\ \Pi_{\xi_d} = \xi_d\,,\ \Pi_{\xi_p} = \xi_p \qquad \text{(5a,b,c,d,e)}$$

where Π_ω represents the isolation degree [32],[37], Π_λ is the mass ratio as previously defined, Π_{ξ_p} and Π_{ξ_d} are related to the inherent viscous damping of the pier and the isolator, respectively, Π_μ denotes the isolator strength which depends on both the friction coefficient $\mu\left(\dot{u}_d\right)$ and the seismic intensity. Since the sliding friction coefficient is a velocity-dependent parameter, Π_μ is considered as follows [13]:

$$\Pi_\mu^* = \frac{f_{\max}\,g}{a_0} \qquad (6)$$

From Eqn.s(4)-(6), note that only the non-dimensional terms Π_{ξ_d}, Π_{ξ_p}, Π_ω, Π_λ, Π_μ^*, the function $\ell(\tau)$, describing the frequency content and time-modulation of the seismic input, and the time scale parameter ω_d influence the non-dimensional seismic response of the bridge system isolated by FPS.

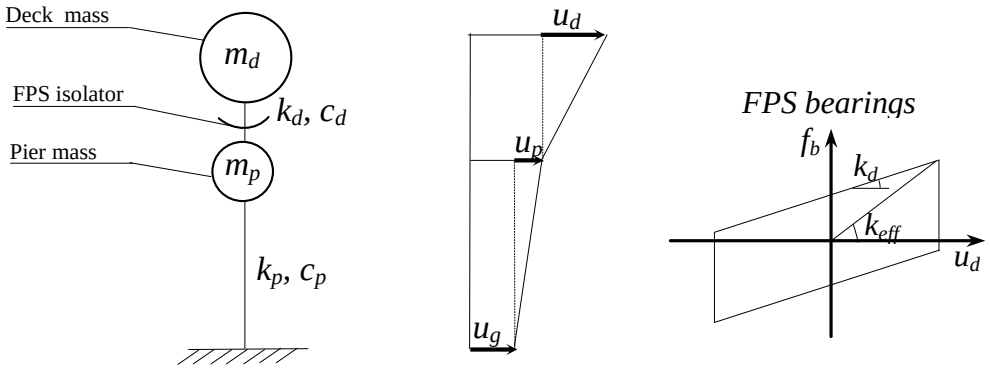

Figure 1: 2dof model of a bridge isolated by FPS bearings.

3 UNCERTAINTIES RELATED TO THE SEISMIC INPUT

This section describes the stochastic model employed for the generation of the artificial ground motions in order to reproduce the uncertainty in terms of frequency characteristics for different soil conditions as well as the uncertainty corresponding to the seismic intensity.

3.1 Random excitations

The "record-to-record" variability in terms of the dynamic characteristics of different seismic inputs related to stiff, medium and soft soil conditions, respectively, is herein described by means of three corresponding wide groups of artificial records having different frequency contents. These artificial inputs are modelled as time-modulated filtered Gaussian white noise random processes [30],[38] within the power spectral density (PSD) method [39] by adopting the Kanai-Tajimi model [40]-[41], modified by Clough and Penzien [42],[26],[43]-[53], as follows:

$$S_f(\omega) = \frac{\omega_g^4 + 4\xi_g^2\omega_g^2\omega^2}{(\omega_g^2 - \omega^2) + 4\xi_g^2\omega_g^2\omega^2} \cdot \frac{\omega^4}{(\omega_f^2 - \omega^2) + 4\xi_f^2\omega_f^2\omega^2} S_0 \qquad (7)$$

in which S_0 is the amplitude of the bedrock excitation spectrum, modeled as a white noise process; ω_f and ξ_f are the Clough-Penzien filter parameters assumed as deterministic values, set equal to $\omega_f = 1.6$ (rad/s) and $\xi_f = 0.6$; ω is the circular frequency, assumed varying in the range 0 and 50 rad/s; ω_g and ξ_g represent the fundamental circular frequency and damping factor of the soil, respectively, assumed as uniformly distributed independent random variables with appropriate ranges of variation [31],[54] as follows: ω_g varies in the range 5π-9π rad/s (high frequency/short period) with ξ_g =0.6-1 for stiff soil condition, ω_g is assumed ranging between 3π rad/s and 5π rad/s (intermediate frequency/ period) with ξ_g =0.4-0.6 for medium soil condition, and, finally, ω_g ranges from π to 3π (low frequency/high period) with ξ_g =0.2-0.4 for soft soil condition. Specific sampling techniques [47]-[52] are used to sample the data. Assuming the same duration [55],[56] equal to 31.25 s, longer than 25s as provided from [57], the Shinozuka-Sato function [58] is adopted as time-modulating function in order to define non-stationary stochastic processes for each set corresponding to each soil condition. Specifically, 100 artificial (non-stationary stochastic processes) records, generated through the Spectral Representation Method [30] and reflecting the wide uncertainty in terms of frequency content for each soil type [31],[54],[59] are defined for each soil condition.

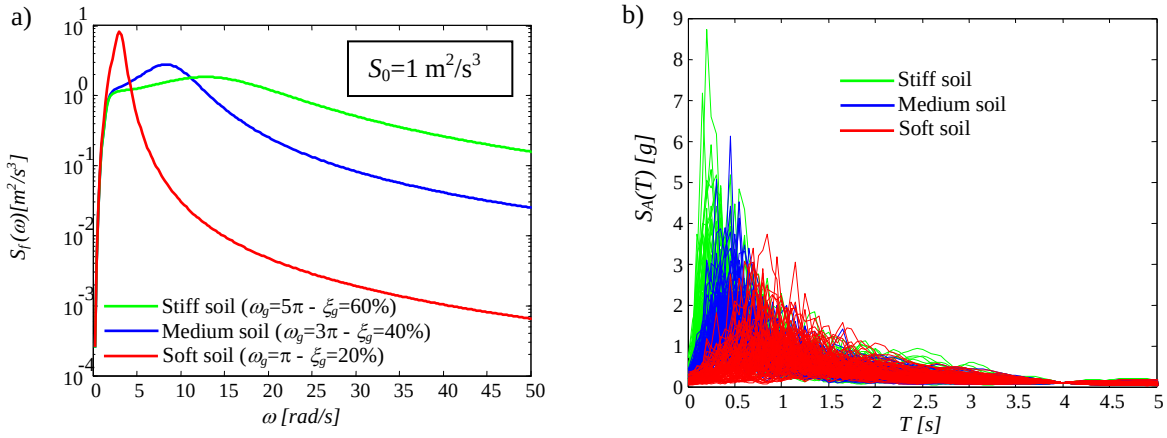

Figure 2: PSD functions corresponding to stiff, medium and soft soil conditions (a); Pseudo-acceleration response spectra for the 300 records scaled to the common seismic intensity measure $S_A(T)$ = 0.1 g, for T=4s (b).

Note also that, for each set of artificial records a high number of random excitations is defined in order to highly reduce the standard errors of the statistics of the response parameters [18]. As an example, Fig.s 2(a)-(b) show, respectively, the sampled PSD functions and the elastic pseudo-acceleration response spectra of the 300 artificial records, scaled to the common *IM* value $S_A(T)$ = 0.1g, for a period T = 4s.

3.2 Intensity measure

In order to take into account the uncertainty related to the seismic intensity, the intensity scale factor, a_0, of Eqn.(4), represents the seismic intensity measure (*IM)* in the context of the performance-based earthquake engineering (PBEE) [60],[61]. In this study, the abovementioned *IM* is denoted by the spectral pseudo-acceleration, $S_A\left(T_d,\xi_d\right)$, corresponding to the isolated period of the bridge $T_d = 2\pi/\omega_d$ with the damping ratio $\Pi_{\xi_d} = \xi_d$. Note that, in the analyses herein developed, the damping ratio ξ_d is set equal to zero [13],[23],[63] and the corresponding *IM* is hereinafter denoted as $S_A\left(T_d\right)$.

4 PARAMETRIC STUDY

This section describes the results of the parametric study carried out on the system of Figure 1 to evaluate the seismic performance of bridge isolated with FPS bearings for different structural properties and soil conditions. The first subsection describes the response parameters relevant to the seismic performance, whereas the final subsection illustrates the parametric study results. More details may be found in [62].

4.1 Non-dimensional response parameters relevant to the seismic performance assessment

The following response parameters relevant to the seismic performance assessment of isolated bridges are considered: the peak deck displacement relative to the pier $u_{\mathrm{d,max}}$, the peak pier displacement $u_{\mathrm{p,max}}$. These latter ones can be defined in non-dimensional form, as expressed in Eqn. (4), as:

$$\psi_{u_d} = \frac{u_{\mathrm{d,max}}\omega_d^2}{S_A\left(T_d\right)} = \frac{u_{\mathrm{d,max}}}{S_d\left(T_d\right)} \;,\; \psi_{u_p} = \frac{u_{\mathrm{p,max}}\omega_d^2}{S_A\left(T_d\right)} = \frac{u_{\mathrm{p,max}}}{S_d\left(T_d\right)} \tag{8a,b,c,d}$$

For each soil condition (i.e., set of the 100 ground motion records), Eqn. (4) is repeatedly solved computing a set of samples for each response parameter. As also described in [13]-[22],[63]-[64], the response parameters are modeled in probabilistic terms by means of a lognormal distribution. Specifically, the generic response parameter *D* (i.e., the extreme values ψ_{u_d}, ψ_{u_p} of Eq. (4)) can be fitted by a lognormal distribution estimating the sample geometric mean, $GM\left(D\right)$, and the sample lognormal standard deviation $\sigma_{\ln}\left(D\right)$, or dispersion $\beta\left(D\right)$, defined, respectively:

$$GM\left(D\right) = \sqrt[N]{d_1 \cdot \ldots \cdot d_N} \tag{9}$$

$$\beta\left(D\right) = \sigma_{\ln}\left(D\right) = \sqrt{\frac{\left(\ln d_1 - \ln\left[GM\left(D\right)\right]\right)^2 + \ldots\ldots + \left(\ln d_N - \ln\left[GM\left(D\right)\right]\right)^2}{N-1}} \tag{10}$$

in which d_i is the *i*-th sample value of *D*, and *N* represents the total number of samples. The *k*th percentile of the generic response parameter *D* can be evaluated as:

$$d_k = GM(D)\exp[f(k)\beta(D)] \tag{11}$$

where $f(k)$ is a function that assumes the following values $f(50)=0$, $f(84)=1$ and $f(16)=-1$ [65], for the 50th, 16th and 84th percentile, respectively.

4.2 Parametric study results for each soil condition

In this section, the results of the parametric study developed using the proposed non-dimensionalization, for the different structural properties and for each set of 100 records, are illustrated and discussed. According to several studies [1]-[2],[4],[14]-[15],[29],[66]-[70], the parameters $\Pi_{\xi_d}=\xi_d$ and $\Pi_{\xi_p}=\xi_p$ are assumed respectively equal to 0% and 5%, the isolation period T_d varies in the range between 2s and 4s, the pier period T_p ranges from 0.05s to 0.2s, $\Pi_\lambda=\lambda$ varies between 0.1 and 0.2, Π_μ^* ranges between 0 (no friction) and 2 (very high friction) [13]. Other uncertainties [71]-[76] are not considered. Indeed, a high value for the upper bound of Π_μ^* is considered in order to take also into account the very low values of the *IM* at high isolated periods (i.e., T_d=4s) depending on the seismic hazard [57]. For each parameter combination, the differential motion equations, i.e., Eqn. (4), have been repeatedly solved adopting the Bogacki-Shampine integration algorithm available in Matlab-Simulink [77]. After that, for each normalized response parameter, the geometric mean, *GM*, and the dispersion, β, have been evaluated through Eqns. (9) and (10) and are plotted in Figs. 5-12 for each soil type. Each figure contains several meshes, corresponding to the different Π_λ. The results for deck and pier displacements related to the all pier periods are reported.

Figs. 5-8 plot the results concerning the normalized deck displacement ψ_{u_d}, related to different pier period values. $GM\left(\psi_{u_d}\right)$ is quite perfectly equal to unit for $\Pi_\mu^*=0$ and T_p = 0.05 because of the very reduced influence of the pier behaviour. For $\Pi_\mu^*\neq 0$, and $GM\left(\psi_{u_d}\right)$ increases slightly for increasing T_d because of the period elongation. Obviously, $GM\left(\psi_{u_d}\right)$ decreases significantly as Π_μ^* increases while it is not heavily influenced by Π_λ. For soft soil condition and low Π_μ^* values, the decrease of $GM\left(\psi_{u_d}\right)$ for increasing Π_μ^* is more gradual, while, for high Π_μ^* values $GM\left(\psi_{u_d}\right)$ increases in the case of stiff soil, especially, for high T_p values due to the pier influence. The dispersion $\beta\left(\psi_{u_d}\right)$ for high T_d increases for increasing values of Π_μ^*, as a result of the reduction of the efficiency of the *IM* employed in the study for each soil condition. Moreover, with reference to soft soils, the values of $\beta\left(\psi_{u_d}\right)$ also result to be the highest for low or high values of both T_d and Π_μ^*. Obviously, in the reference situation corresponding to $\Pi_\mu^*=0$ and T_p=0.05s, the dispersion is zero for all the values of T_d and of Π_λ considered and for all the soil conditions. The mass ratio Π_λ does not affect significantly the response dispersion, especially in the case of high T_p values.

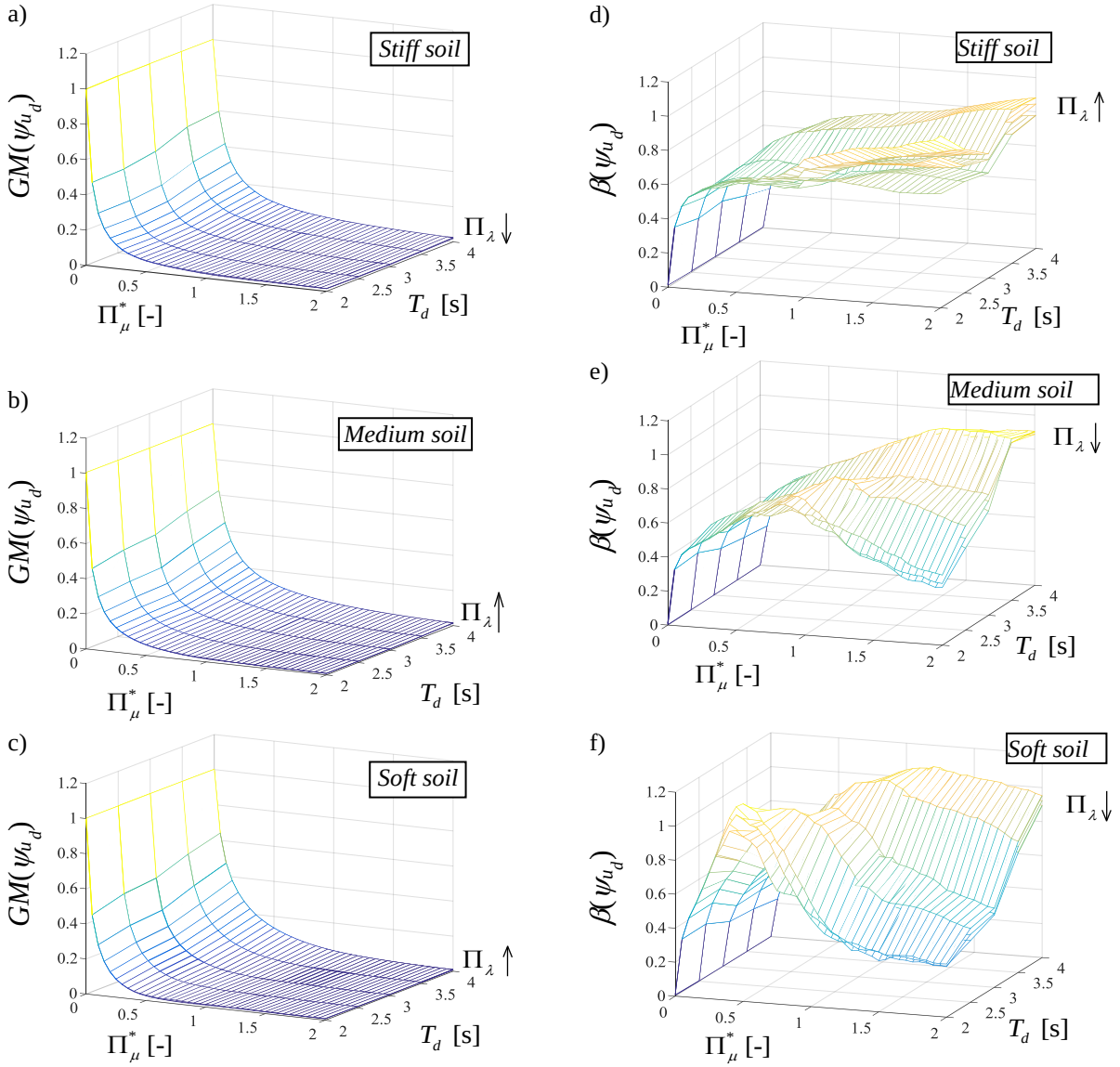

Figure 5: Normalized deck displacement vs. Π^*_μ and T_d for T_p =0.05s and each soil condition: median value (a,b,c) and dispersion (d,e,f) for different values of Π_λ. The arrow denotes the increasing direction of Π_λ.

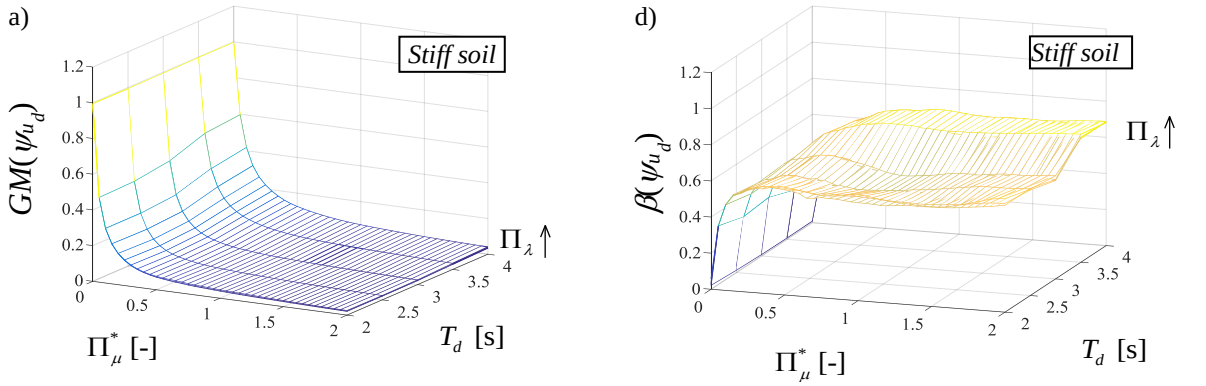

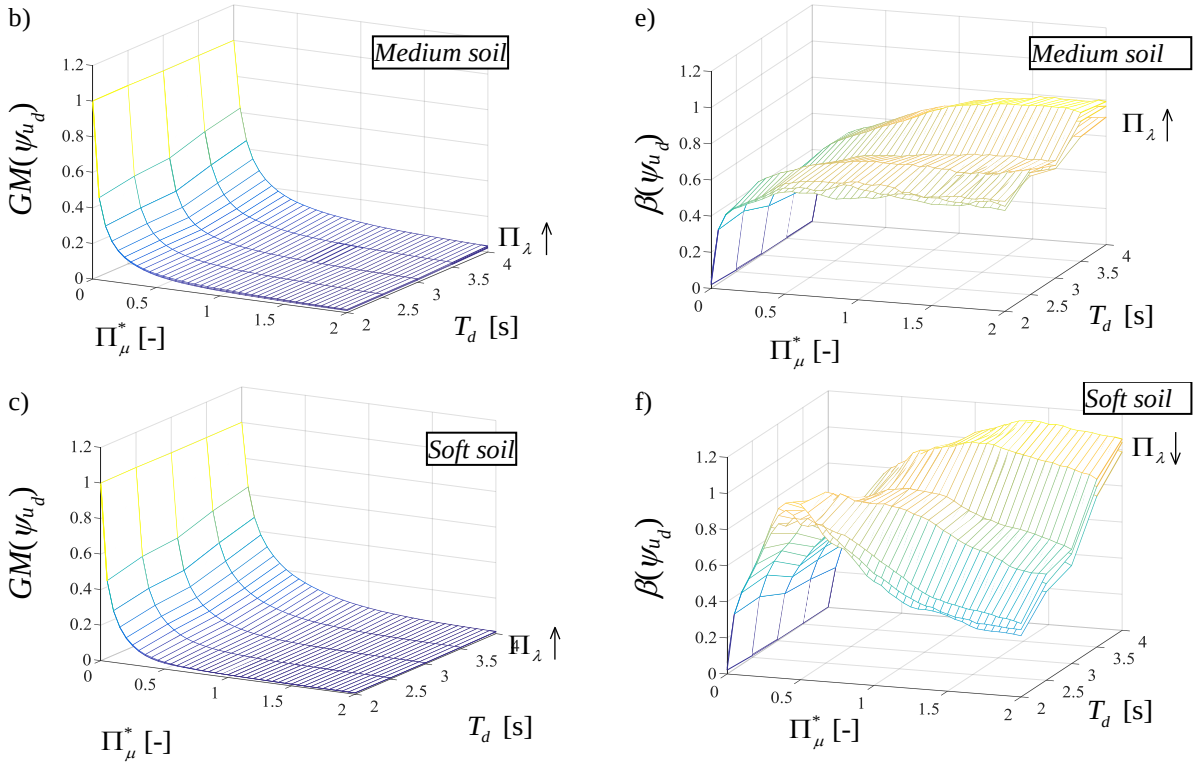

Figure 6: Normalized deck displacement vs. Π^*_μ and T_d for T_p =0.1s and each soil type: median value (a,b,c) and dispersion (d,e,f) for different values of Π_λ. The arrow denotes the increasing direction of Π_λ.

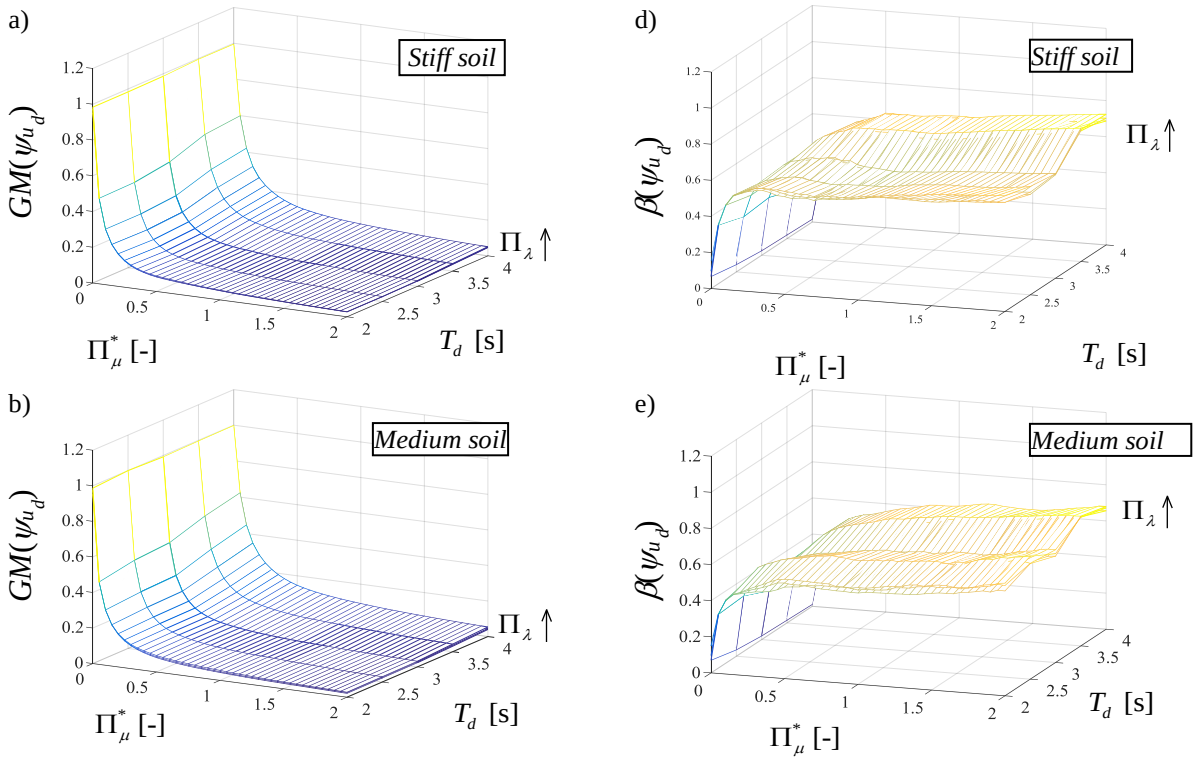

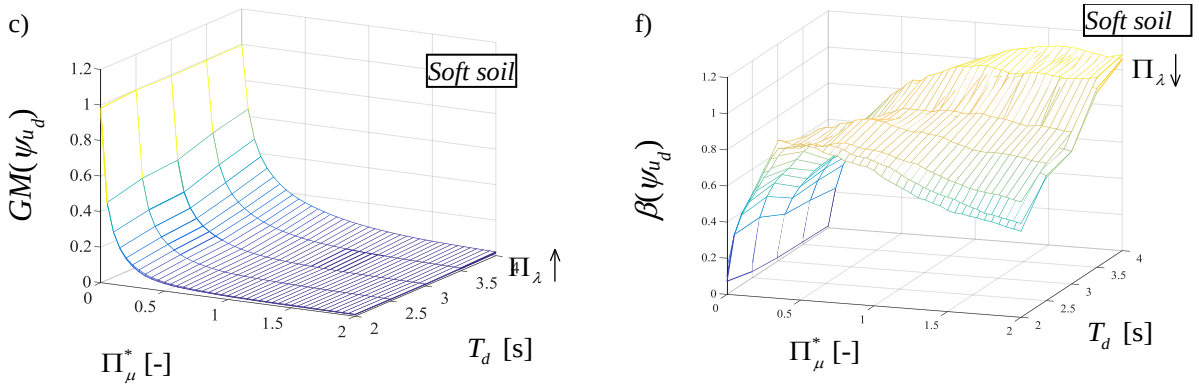

Figure 7: Normalized deck displacement vs. Π^*_μ and T_d for T_p =0.15s and each soil type: median value (a,b,c) and dispersion (d,e,f) for different values of Π_λ. The arrow denotes the increasing direction of Π_λ.

The above described peak values of both $GM\left(\psi_{u_d}\right)$ and $\beta\left(\psi_{u_d}\right)$ in the case of soft soil condition are high due to the resonance effects which mainly affect the effective frequency charactering the dynamic behaviour of the frictional bearings and the dominant frequency of the corresponding random excitations.

Figs. 8-12 show the response statistics of the normalized pier displacements ψ_{u_p}. $GM\left(\psi_{u_p}\right)$ decreases for increasing values of T_d and of Π_λ as well as for decreasing values of T_p, whereas it first decreases and then increases for increasing values of Π^*_μ. Thus, this means that there exists an optimal value of the normalized friction coefficient Π^*_μ such that the pier displacement is minimized for each soil condition. This optimal value is in the range between 0.1 and 0.3 and depends on the values of T_p, T_d, Π_λ and on the soil condition. Differently to the case of base-isolated systems, there is not a particular and specific trend of the optimal friction coefficients from stiff to soft soil condition, as discussed later in detail. There is a further increase in the value of $GM\left(\psi_{u_p}\right)$ from soft soil to stiff soil due to resonance effects, especially, for lower values of T_d. The values of the dispersion $\beta\left(\psi_{u_p}\right)$ are very low for low Π^*_μ values due to the high efficiency of the *IM* used in this work, and attain their peak for values of Π^*_μ close to the optimal ones. The other system parameters have a reduced influence on $\beta\left(\psi_{u_p}\right)$ compared to the influence of Π^*_μ. For the soft soil condition, the dispersion $\beta\left(\psi_{u_p}\right)$ strongly increases for increasing values of Π^*_μ for low isolation period and for higher pier periods because of the resonance effects which mainly affect the effective frequency of the frictional bearings and the dominant frequency of the corresponding random excitations.

As observed in similar studies [13],[23],[78]-[81], the existence of an optimal value of the friction coefficient derives from a combination of different effects. Indeed, an increase of the sliding friction coefficient leads to higher isolator strengths (and thus higher values of the equivalent stiffness, with a lowering of the corresponding effective fundamental vibration period (Fig.1)) and higher forces towards the deck. This also leads to an increase in the forces transmitted to the pier bridge due to inertial effect, relative to deck mass, on the pier.

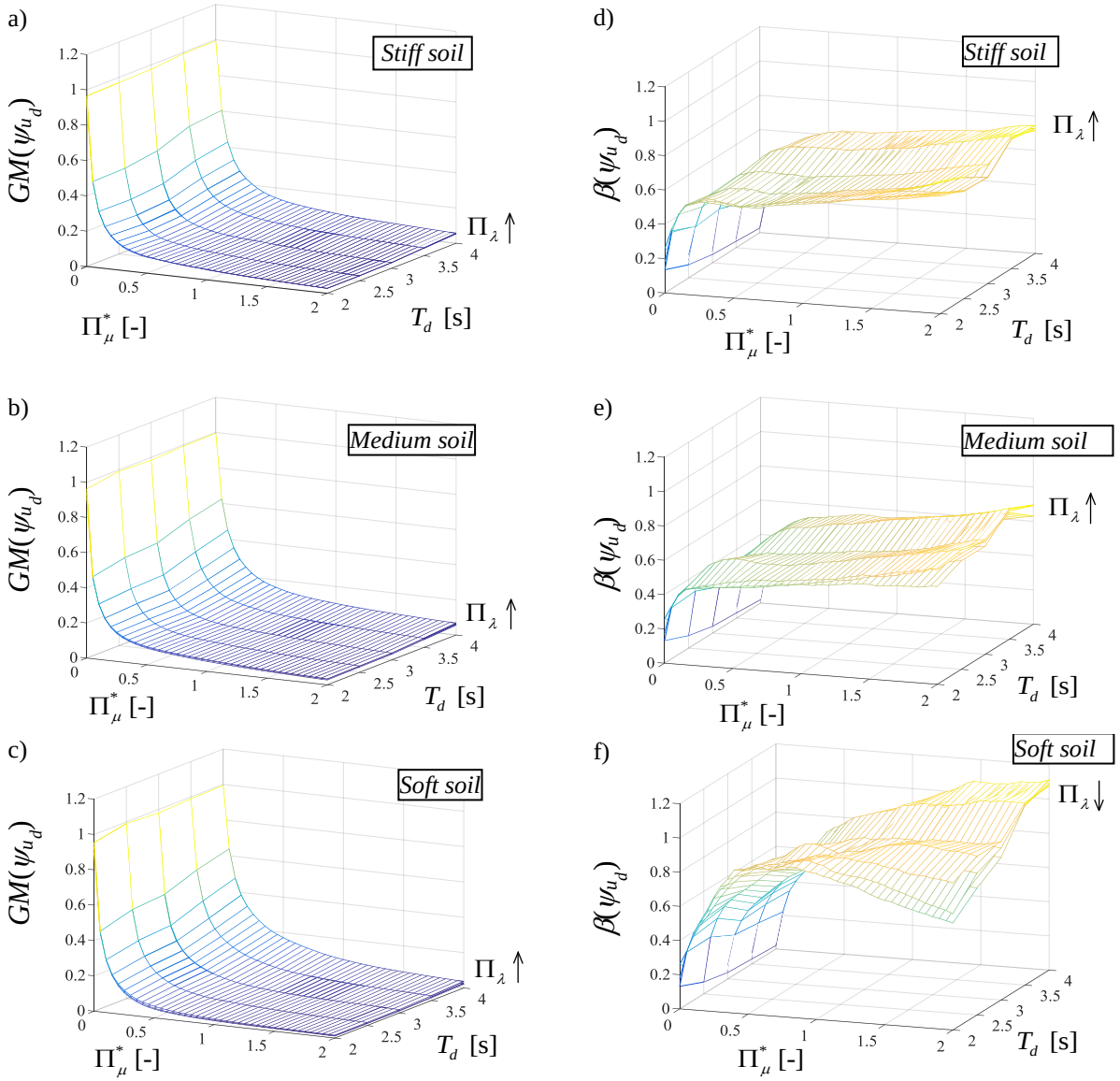

Figure 8: Normalized deck displacement vs. Π^*_μ and T_d for T_p =0.2s and each soil type: median value (a,b,c) and dispersion (d,e,f) for different values of Π_λ. The arrow denotes the increasing direction of Π_λ.

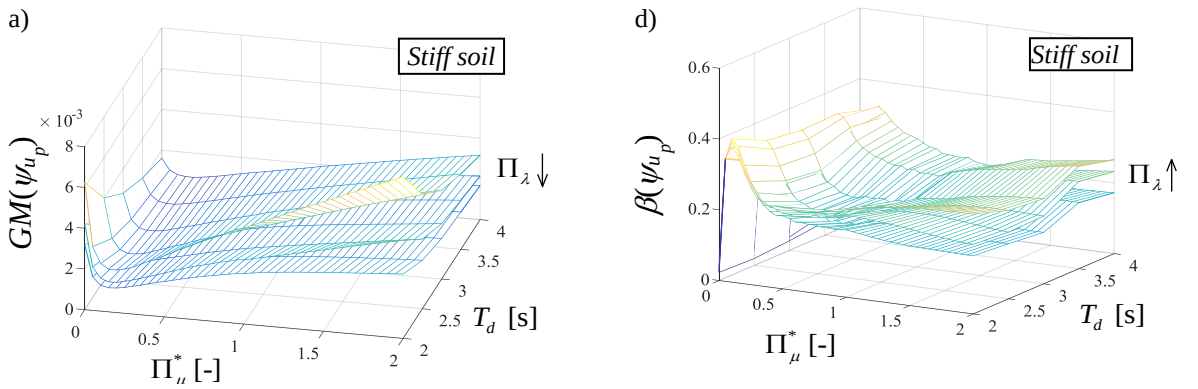

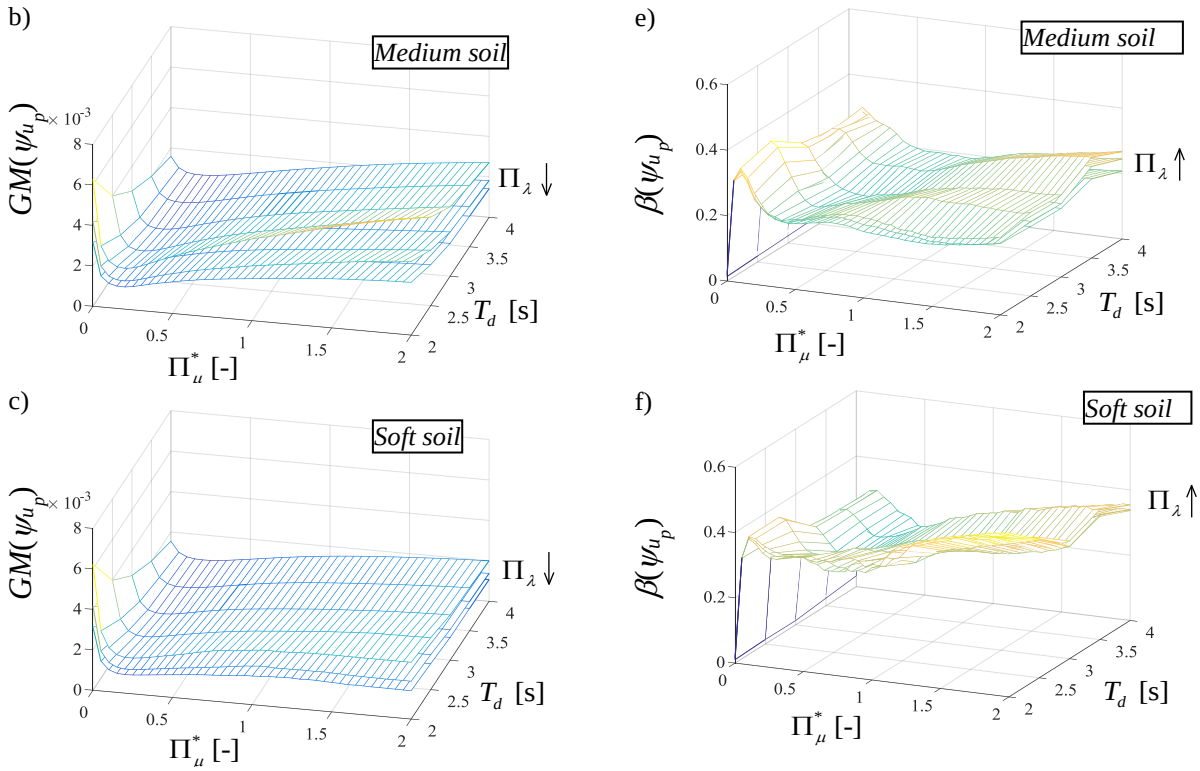

Figure 9: Normalized pier displacement vs. Π^*_μ and T_d for T_p =0.05s and each soil condition: median value (a,b,c) and dispersion (d,e,f) for different values of Π_λ. The arrow denotes the increasing direction of Π_λ.

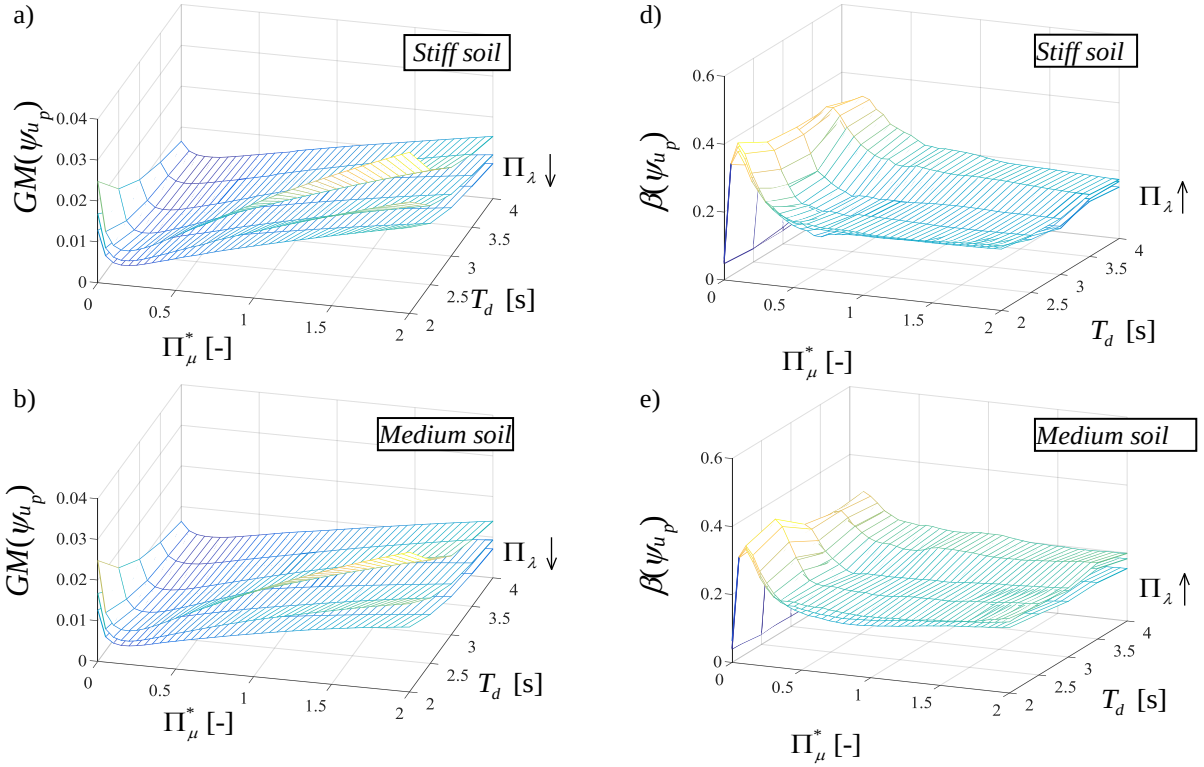

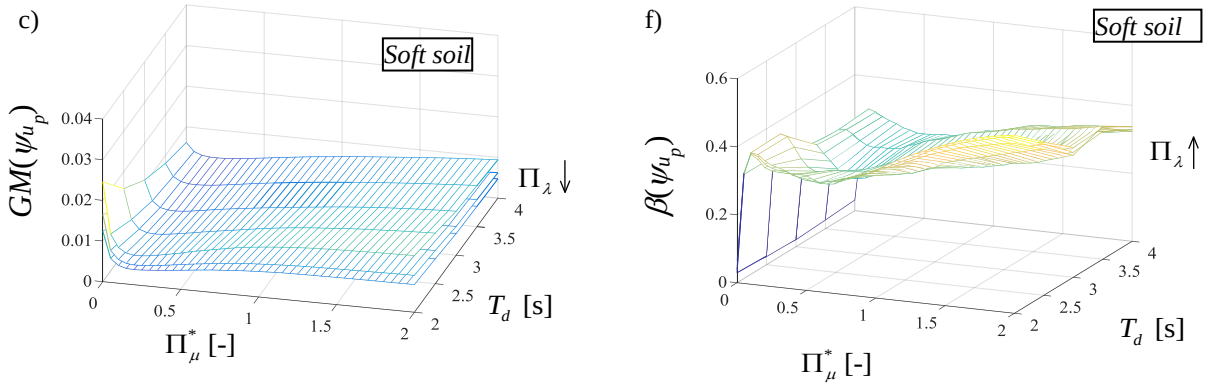

Figure 10: Normalized pier displacement vs. Π^*_μ and T_d for T_p =0.1s and each soil condition: median value (a,b,c) and dispersion (d,e,f) for different values of Π_λ. The arrow denotes the increasing direction of Π_λ.

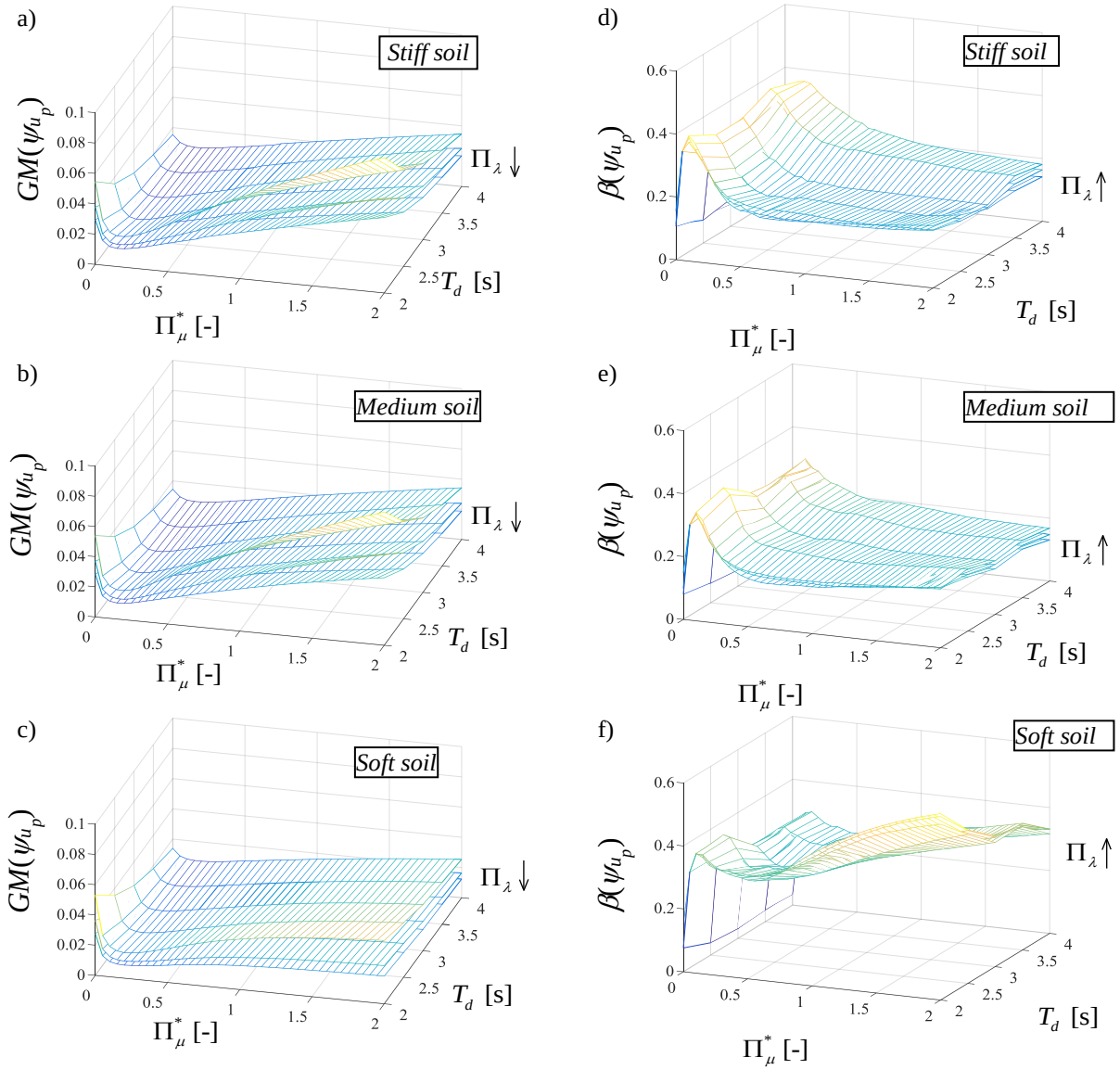

Figure 11: Normalized pier displacement vs. Π^*_μ and T_d for T_p =0.15s and each soil condition: median value (a,b,c) and dispersion (d,e,f) for different values of Π_λ. The arrow denotes the increasing direction of Π_λ.

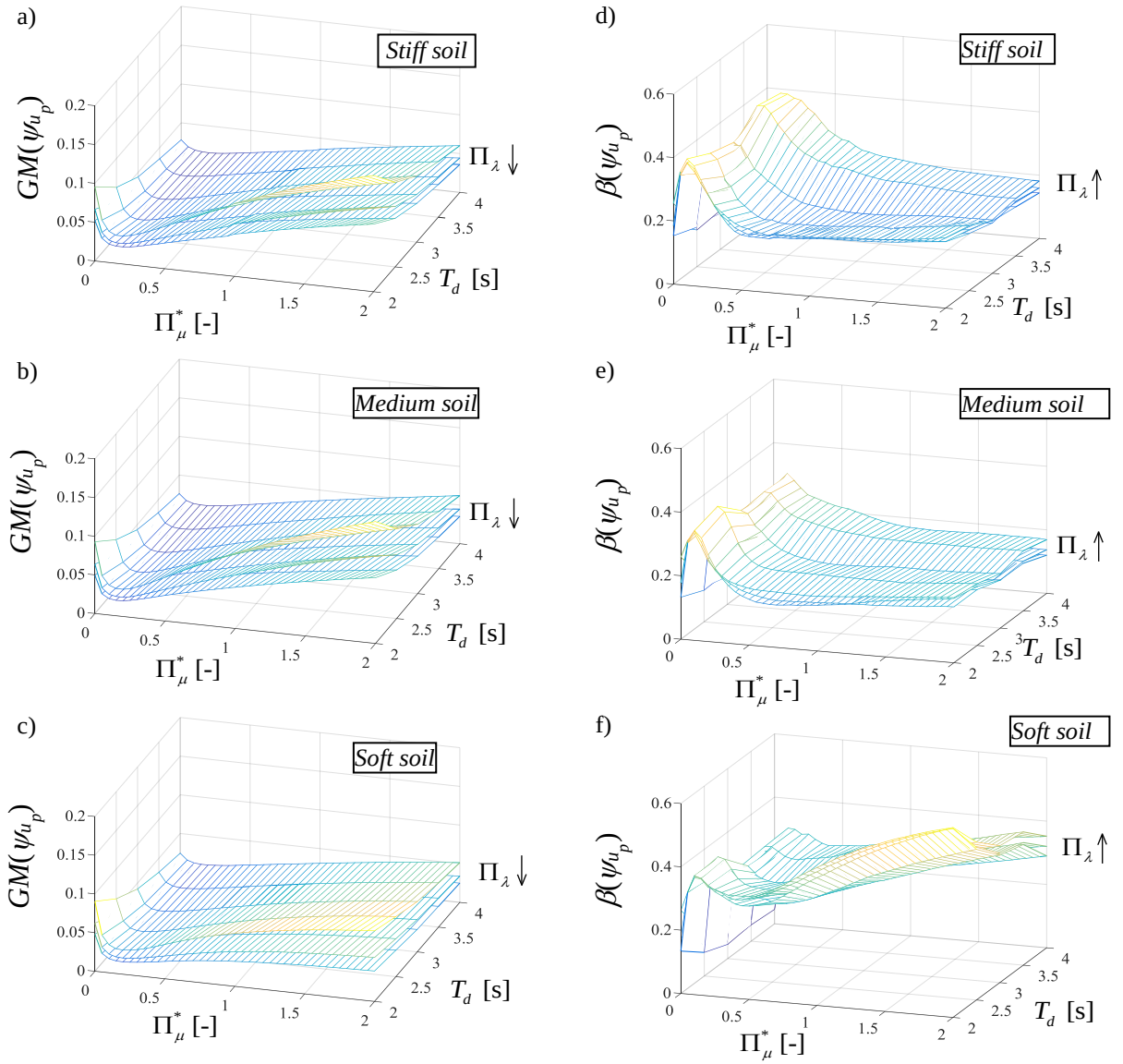

Figure 12: Normalized pier displacement vs. Π^*_μ and T_d for T_p =0.2s and each soil condition: median value (a,b,c) and dispersion (d,e,f) for different values of Π_λ. The arrow denotes the increasing direction of Π_λ.

However, the forces transmitted to the substructure also depend on the bearing displacements, which decrease as the friction coefficient increases. An increase of the forces transmitted to the substructure generally increases the substructure displacements. Contextually, another effect is the increase in terms of energy dissipation (equivalent damping), which reduces the substructure displacements. The balance between these effects defines the optimal friction coefficient of the FPS devices.

5 OPTIMAL SLIDING FRICTION COEFFICIENTS FOR ISOLATED BRIDGES DEPENDING ON SOIL CONDITIONS

From the results defined in the previous section, for each parameter combination (i.e., Π_λ, T_d and T_p) and soil condition, the optimal values of the normalized sliding friction coef-

ficient, $\Pi^*_{\mu,\text{opt}}$, that minimize the median (50$^{\text{th}}$ percentile) normalized pier displacements ψ_{u_p} have been computed and are illustrated in Fig. 13. Minimizing the pier displacements relative to the ground represents a notable design requisite for the safety of bridges in order to assure an adequate seismic protection. In fact, an inelastic response of the pier can lead to a disproportionately large displacement response that could also be amplified in the case of the resonance effects. Figure 13 shows the variation of $\Pi^*_{\mu,\text{opt}}$ with Π_λ and T_p for T_d = 2s (Figure 13a,b,c) and T_d = 4s (Figure 13d,e,f), for the three soil conditions.

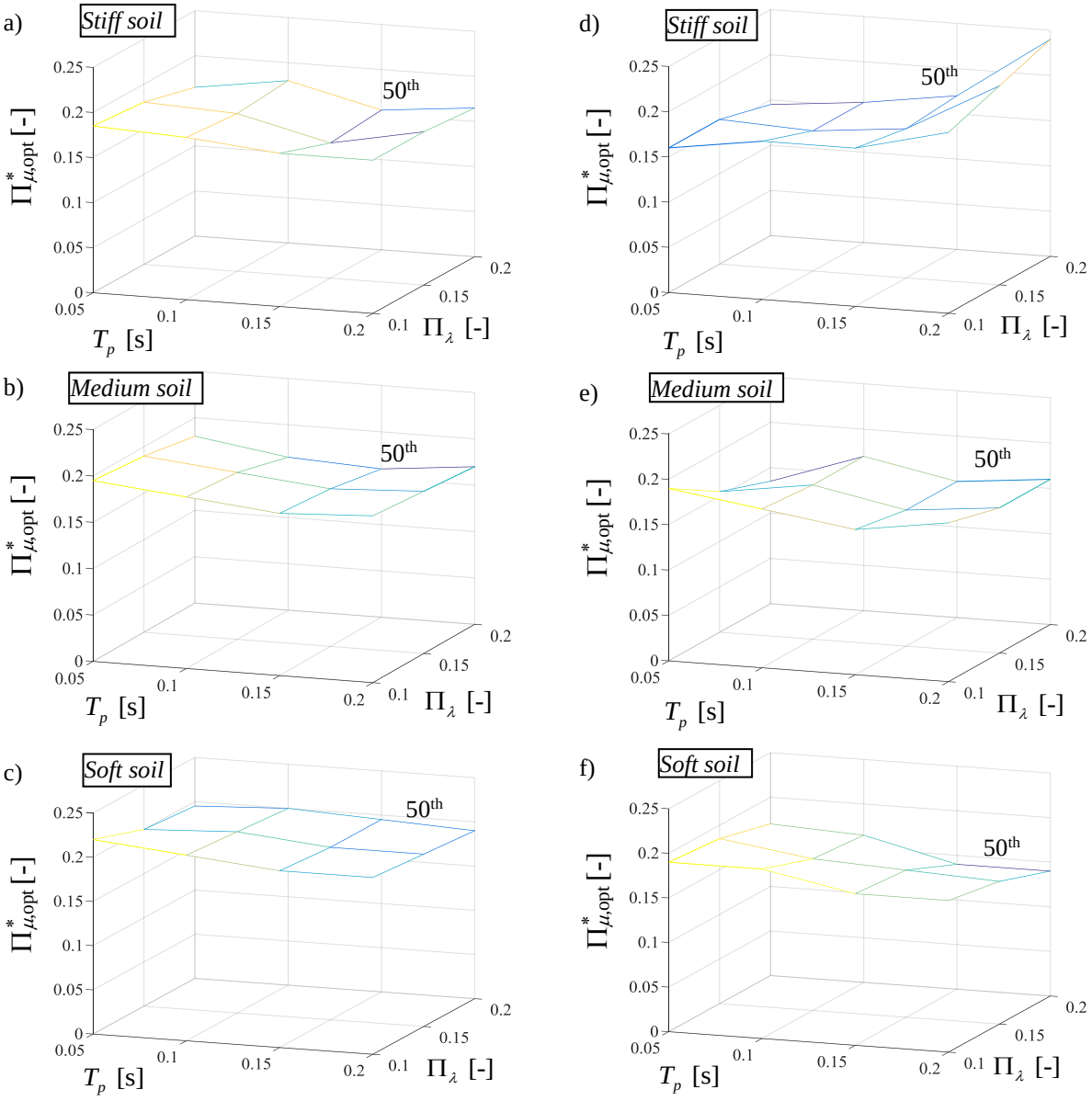

Figure 13: Optimal values of normalized friction that minimize the 50$^{\text{th}}$ percentile of the normalized pier displacements vs. Π_λ and T_p for each soil type and for T_d =2s (a,b,c) and T_d =4s (d,e,f).

According to [23], the optimal values of the (normalized) sliding friction coefficient slightly increase for decreasing T_d, especially for low T_p and for each soil condition. It is also observed that, for low T_d, $\Pi^*_{\mu,\text{opt}}$ generally decreases by increasing Π_λ and T_p. This trend is reversed with increasing of T_d and soil stiffness, when it is necessary to dissipate more energy, due to the resonance effects.

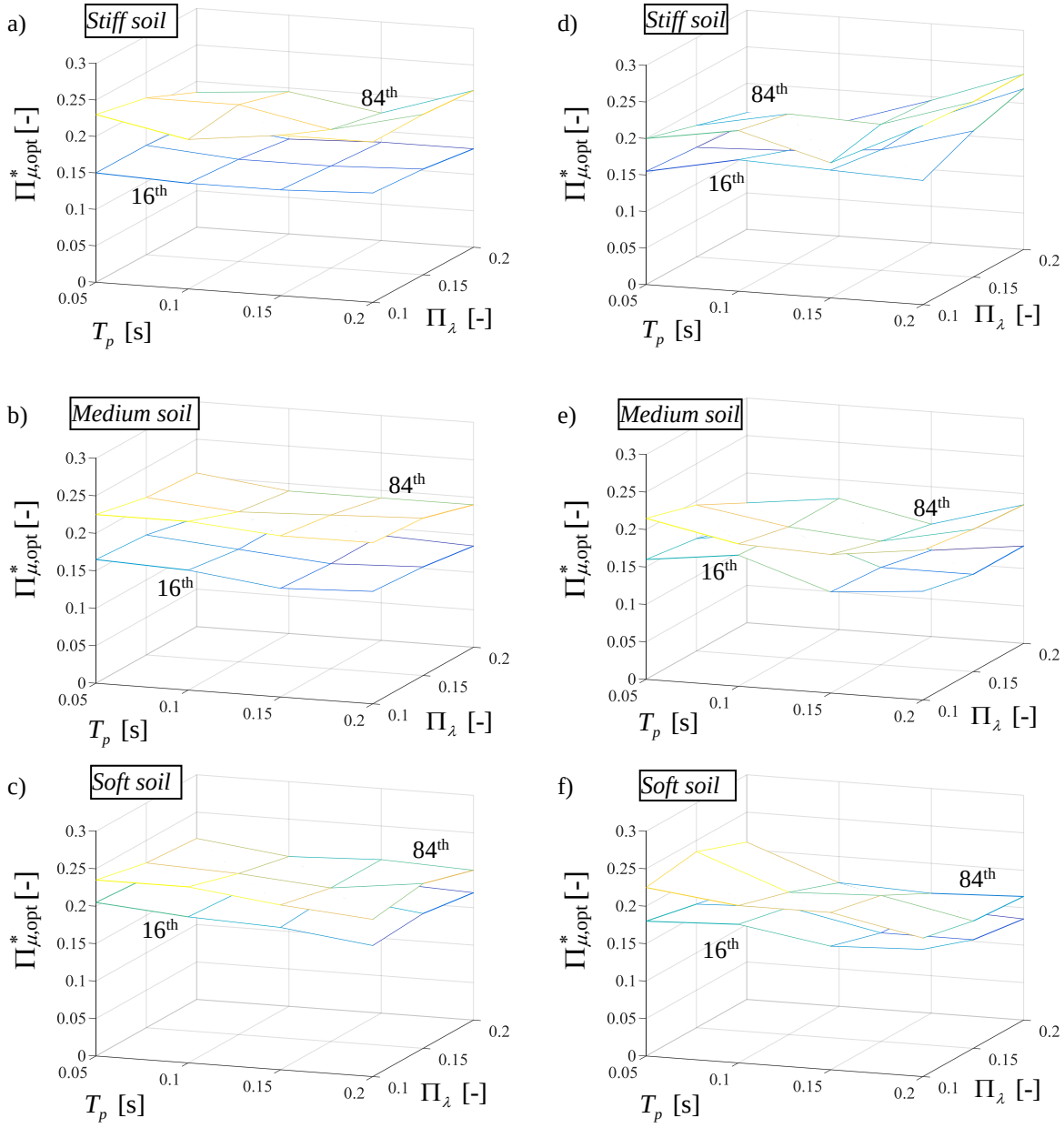

Figure 14: Optimal values of normalized friction that minimize the 84th and 16th percentiles of the normalized pier displacements vs. Π_λ and T_p for each soil type and for T_d =2s (a,b,c) and T_d =4s (d,e,f).

As previously discussed, it is also possible to observe that higher values of the optimum friction coefficient are required, especially for low isolated periods, for soft soil condition in order to reduce the bearing displacements and, consequently, the forces transmitted to the pier

as well as to increase the energy dissipation (equivalent damping). A reversal of this trend occurs for high values of both the isolation period and pier period, when it is necessary to dissipate more seismic energy input due to the resonance effect that affects the pier for stiff soil condition. In order to assure a high safety level, it might be of interest to define the values of $\Pi^*_{\mu,\text{opt}}$ that minimize others response percentiles [63]. Fig. 14 shows the optimal values of normalized friction that minimize the 84$^{\text{th}}$ and 16$^{\text{th}}$ percentiles of the normalized pier response for the different values of Π_λ, T_p, T_d = 2s (Fig. 14a,b,c), T_d = 4s (Fig. 14d,e,f) and for the three soil conditions. The trend is similar to the case of the 50$^{\text{th}}$ percentile. Regression expressions as statistics equations [82]-[87] to estimate the optimal friction coefficient may be found in [62].

6 CONCLUSIONS

This paper describes the seismic performance of elastic bridge pier equipped with friction pendulum system (FPS) bearings in order to define the optimal isolator friction properties as a function of the structural properties and of the soil characteristics in terms of frequency content, corresponding to stiff, medium and soft soils, respectively. Assuming an equivalent two-degree-of-freedom model, representative, respectively, of the dynamic behaviour of a single-column bent viaduct, describing a continuous and infinitely rigid deck with an elastic pier, and the velocity-dependent FPS isolator behaviour, a non-dimensionalization of the motion equations is herein proposed. For each soil type, the uncertainty in the seismic inputs is taken into account by means of a set of 100 artificial non-stationary stochastic records, obtained through the power spectral density method, with different frequency content. By means of the proposed non-dimensionalization, a wide parametric analysis is developed for several isolator and pier properties, and for different soil conditions, by monitoring the response parameters of interest.

With reference to the deck response, the geometric mean of the normalized deck displacement increases slightly for increasing isolation period because of period elongation and it decreases significantly as normalized friction increases while it is not heavily influenced by the mass ratio. The dispersion for high isolation period increases for increasing values of normalized friction. The mass ratio does not affect significantly the response dispersion, especially for high pier periods. There are resonance effects for soft soil condition and low normalized friction values, and for stiff soil condition and high normalized friction values, particularly, for higher values of the pier period.

With reference to the pier response, the geometric mean of the normalized displacement decreases for increasing values of isolation period and of mass ratio as well as for decreasing values of pier period, whereas it first decreases and then increases for increasing values of normalized friction. Thus, there exists an optimal value of normalized friction coefficient such that the pier displacement is minimized for each soil condition. This optimal value varies in the range between 0.1 and 0.3 depending on the system parameters and the soil type. The values of the dispersion are generally very low. The other system parameters have a reduced influence on the dispersion compared to the influence of the normalized friction. There are resonance effects for the stiff soil condition with increasing normalized friction values, particularly, for higher values of pier period and lower isolation period values.

REFERENCES

[1] P. Tsopelas, M. C. Constantinou, S. Okamoto, S. Fujii, D. Ozaki. Experimental study of bridge seismic sliding isolation systems. *Engineering Str.*, Vol. 18, No. 4, pp. 301-310, 1996.

[2] R.S. Jangid. Seismic Response of Isolated Bridges. *J. Bridge Eng*., 2004, 9(2): 156-166.

[3] A. Ghobarah and H. M. Ali. Seismic performance of highway bridges. *Eng. Struct.* 1988, Vol. 10, July.

[4] N.P. Tongaonkar, R.S. Jangid. Seismic response of isolated bridges with soil–structure interaction. *Soil Dynamics and Earthquake Engineering* 23 (2003) 287–302.

[5] Su L, Ahmadi G, Tadjbakhsh IG. Comparative study of base isolation systems. *Journal of Engineering Mechanic* 1989; **115**(9):1976–92.

[6] Zayas VA, Low SS, Mahin SA. A simple pendulum technique for achieving seismic isolation. *Earthquake Spectra* 1990; **6**(2):317–33.

[7] Mosqueda G, Whittaker AS, Fenves GL. Characterization and modeling of Friction Pendulum bearings subjected to multiple components of excitation. *J. of Str. Eng.* 2004; **130**(3):433-442.

[8] Mokha A, Constantinou MC, Reinhorn AM. Teflon Bearings in Base Isolation. I: Testing. *Journal of Structural Engineering* 1990; **116**(2):438-454.

[9] Constantinou MC, Mokha A, Reinhorn AM. Teflon Bearings in Base Isolation. II: Modeling. *Journal of Structural Engineering* 1990; **116**(2):455-474.

[10] Constantinou MC, Whittaker AS, Kalpakidis Y, Fenz DM, Warn GP. Performance of Seismic Isolation Hardware Under Service and Seismic Loading. *Technical Report* MCEER-07-0012, 2007.

[11] Almazàn JL, De la Llera JC. Physical model for dynamic analysis of structures with FPS isolators. *Earth. Engineering and Structural Dynamics* 2003;**32**(8):1157–1184.

[12] Landi, L, Grazi G, and Diotallevi P P. Comparison of different models for friction pendulum isolators in structures subjected to horizontal and vertical ground motions, *Soil Dynamics and Earthquake Engineering* 2016;**81**:75-83.

[13] Castaldo, P, Tubaldi, E. Influence of FPS bearing properties on the seismic performance of base-isolated structures. *Earthquake Engineering and Structural Dynamics* 2015;**44**(15):2817–2836.

[14] Young-Suk Kim, Chung-Bang Yun. Seismic response characteristics of bridges using double concave friction pendulum bearings with tri-linear behaviour. *Eng. Str.*, 2007, 29:3082–3093.

[15] Murat Eröz, Reginald DesRoches. Bridge seismic response as a function of the Friction Pendulum System (FPS) modeling assumptions. *Eng. Str.*, 2008, 30: 3204–3212.

[16] Castaldo P, Palazzo B, Della Vecchia P. Seismic reliability of base-isolated structures with friction pendulum bearings. *Engineering Structures* 2015;**95**:80-93.

[17] Castaldo P., Palazzo B., Della Vecchia P. Life-cycle cost and seismic reliability analysis of 3D systems equipped with FPS for different isolation degrees, *Engineering Structures*, 2016;**125**:349–363, http://dx.doi.org/10.1016/j.engstruct.2016.06.056.

[18] Castaldo P., Amendola G., Palazzo B. Seismic fragility and reliability of structures isolated by friction pendulum devices: Seismic reliability-based design (SRBD), *Earthquake Engineering and Structural Dynamics*, 2017; 46(3); 425–446, DOI: 10.1002/eqe.2798.

[19] Castaldo P., Palazzo B., Ferrentino T., (2016) "Seismic reliability-based ductility demand evaluation for inelastic base-isolated structures with friction pendulum devices", *Earthquake Engineering and Structural Dynamics*, DOI: 10.1002/eqe.2854.

[20] Castaldo, P., Mancini, G., Palazzo, B. (2018) Seismic reliability-based robustness assessment of three-dimensional reinforced concrete systems equipped with single-concave sliding devices, Engineering Structures 163, 373-387.

[21] Castaldo, P., Palazzo, B., Alfano, G., Palumbo, M.F. (2018) Seismic reliability-based ductility demand for hardening and softening structures isolated by friction pendulum bearings, Structural Control and Health Monitoring 25(11),e2256.

[22] Palazzo B, Castaldo P, Della Vecchia P. Seismic reliability analysis of base-isolated structures with friction pendulum system, 2014 IEEE Workshop on Environmental, Energy and Structural Monitoring Systems Proceedings, Napoli, September 17-18, 2014.

[23] Jangid RS. Optimum friction pendulum system for near-fault motions. *Engineering Structures* 2005;**27**(3):349-359.

[24] Dicleli, M., & Buddaram, S. Effect of isolator and ground motion characteristics on the performance of seismic-isolated bridges. *Earthquake Engineering and Structural Dynamics* 2006;**35**(2):233-250.

[25] Safak, E., Frankel, A. Effects of ground motion characteristics on the response of base-isolated structures. *11th World Conference on Earthquake Engineering 1996* (paper no. 1430).

[26] Saritaş, F, Hasgür Z. Dynamic Behavior of an Isolated Bridge Pier under Earthquake Effects for Different Soil layers and Support Conditions, *Digest* 2014, 1733-1756.

[27] Wai-Fah Chen and Lian Duan. Bridge Engineering Handbook - Second edition. Seismic design. *Taylor & Francis Group*. 2014.

[28] Castaldo, P., Tubaldi, E. (2018). Influence of ground motion characteristics on the optimal single concave sliding bearing properties for base-isolated structures. Soil Dynamics and Earthquake Engineering, 104: 346–364.

[29] Masoud Malekzadeh, Touraj Taghikhany. Multi-Stage Performance of Seismically Isolated Bridge Using Triple Pendulum Bearings. *Advances in Str. Engineering* Vol. 15 No. 7, 2012.

[30] Shinozuka M., Deodatis G. Simulation of stochastic processes by spectral representation. *Applied Mechanics Reviews* 1991;**44**(4):191-203.

[31] Pinto P, Giannini R, Franchin P. Seismic Reliability Analysis of Structures. *Iuss Press* 2004.

[32] Kelly JM. *Earthquake-Resistant Design with Rubber*. 2nd ed. Berlin and New York: Springer-Verlag; 1997.

[33] Building Seismic Safety Council. NEHRP Recommended Provisions: Design Examples FEMA 451 - Washington, D.C., August 2006.

[34] Priestley, M.J.N., Seible, F., Calvi, G.M., Seismic design and retrofit of bridges. *Wiley*,1996.

[35] Karavasilis TL, Seo CY, Makris N. Dimensional Response Analysis of Bilinear Systems Subjected to Non-pulse like Earthquake Ground Motions. *Journal of Structural Engineering* 2011;**137**(5):600-606.

[36] Barbato M, and Tubaldi E. A probabilistic performance-based approach for mitigating the seismic pounding risk between adjacent buildings. *Earthquake Engineering & Structural Dynamics* 2013;**42**(8):1203-1219.

[37] Palazzo B. Seismic Behavior of base-isolated Buildings. Proceedings of the International Meeting on earthquake Protection of Buildings, Ancona, 1991.

[38] Pradlwarter H. J., SchuiRler G. I., Dorka U. Reliability of MDOF-systems with hysteretic devices. *Engineering Structures*, 1998;**20**(8):685-691.

[39] Tung ATY, Wang JN, Kiremidjian A, Kavazanjian E. Statistical parameters of AM and PSD functions for the generation of site-specific strong ground motions. Proceedings *of the 10th World Conference on Earthquake Engineering*, Madrid, Spain, 1992;**2**:867-872.

[40] Kanai K. Semiempirical formula for the seismic characteristics of the ground. *Bulletin of earthquake research institute* 1957;**35**:309-325.

[41] Tajimi H. A statistical method of determining the maximum response of a building structure during an earthquake. *Proc., 2nd World Conf. on earthquake Engineering* 1960;**II**:781-798.

[42] Clough R.W., Penzien J.: Dynamics of Structures, 2nd edn. McGraw-Hill, New York; 1993.

[43] Zentner I., Allain F., Humbert N., Caudron M. Generation of spectrum compatible ground motion and its use in regulatory and performance-based seismic analysis. *Proceedings of the 9th Internat. Conf. on Str. Dyn.s*, EURODYN 2014 Porto, Portugal, 30 June - 2 July 2014.

[44] Peng Y., Chen J., Li J. Nonlinear Response of Structures Subjected to Stochastic Excitations via Probability Density Evolution Method. *Advances in Structural Engineering*, 2014;**17**(6):801-816.

[45] Li, C., Liu, Y. Ground Motion Dominant Frequency Effect On The Design Of Multiple Tuned Mass Dampers. *Journal of Earthquake Engineering*, 2004;**8**(1):89-105.

[46] Lopez-Garcia, D., Soong T.T. Assessment of the separation necessary to prevent seismic pounding between linear structural systems. *Prob. Engineering Mechanics*, 2009;**24**:210-223.

[47] Castaldo P, Gino D, Carbone VI, Mancini G. Framework for definition of design formulations from empirical and semi-empirical resistance models, Structural Concrete, 19(4), 980-987, 2018 https://doi.org/10.1002/suco.201800083.

[48] Castaldo, P., De Iuliis, M. (2014) Effects of deep excavation on seismic vulnerability of existing reinforced concrete framed structures, Soil Dynamics and Earthquake Engineering 64, 102-112.

[49] Castaldo, P., Palazzo, B., Perri, F. (2016) Fem simulations of a new hysteretic damper: The dissipative column, Ingegneria Sismica, 33(1), 34-45.

[50] Castaldo, P., Calvello, M., Palazzo, B. (2013) Probabilistic analysis of excavation-induced damages to existing structures, Computers and Geotechnics, 53, 17-30.

[51] Castaldo P, Gino D, Bertagnoli G, Mancini G. Partial safety factor for resistance model uncertainties in 2D non-linear finite element analysis of reinforced concrete structures, Engineering Structures, 176(2018), 746-762.

[52] Castaldo, P., Jalayer, F., Palazzo, B. (2018) Probabilistic assessment of groundwater leakage in diaphragm wall joints for deep excavations, Tunnelling and Underground Space Technology 71, 531-543.

[53] Tubaldi, E., Barbato, M., Ghazizadeh S. A probabilistic performance-based risk assessment approach for seismic pounding with efficient application to linear systems. *Structural Safety* 2012;36-37:14–22.

[54] Talaslidis D.G., Manolis G.D., Paraskevopoulos E.A., Panagiotopoulos C.G. Risk analysis of industrial structures with hazardous materials under seismic input, 13th World Conference on Earthquake Engineering, Vancouver, B.C., Canada, August 1-6, 2004.

[55] Hancock J, Bommer JJ. A state-of-knowledge review of the influence of strong- motion duration on structural damage. *Earthquake Spectra* 2006;**22**(3):827-845.

[56] Hancock J, Bommer JJ. Using spectral matched records to explore the influence of strong-motion duration on inelastic structural response. *Soil Dynamics and Earthquake Engineering* 2007;**27**:291-299.

[57] NTC08. Norme tecniche per le costruzioni. Gazzetta Ufficiale del 04.02.08, DM 14.01.08, Ministero delle Infrastrutture.

[58] Shinozuka M, Sato Y. Simulation of nonstationary random process. *J. Engrg. Mech. Div.* 1967;**93**(1):11-40.

[59] Armouti, N.S. Response of structures to synthetic earthquakes. *Emerging Technologies in Structural Engineering. Proc. of the 9th Arab Structural Engineering Conf.*, Nov. 29 – Dec. 1, 2003, Abu Dhabi, UAE, 331-340.

[60] Aslani H, Miranda E. Probability-based seismic response analysis. *Engineering Structures* 2005;**27**(8):1151-1163.

[61] Porter KA. An overview of PEER's performance-based earthquake engineering methodology. Proceedings, *Proceedings of the 9th International Conference on Application of Statistics and Probability in Civil Engineering* (*ICASP9*), San Francisco, California, 2003.

[62] Castaldo, P., Ripani, M., Priore, R.L. (2018) Influence of soil conditions on the optimal sliding friction coefficient for isolated bridges, Soil Dynamics and Earthquake Engineering 111, 131-148.

[63] Ryan K, Chopra A. Estimation of Seismic Demands on Isolators Based on Nonlinear Analysis. *Journal of Structural Engineering* 2004;**130**(3):392-402.

[64] Karavasilis T, Seo C. Seismic structural and non-structural performance evaluation of highly damped self-centering and conventional systems. *Eng. Structures* 2011,**33**(8):2248-2258.

[65] Ang AHS, Tang WH. Probability Concepts in Engineering-Emphasis on Applications to Civil and Environmental Engineering. John Wiley & Sons, New York, USA; 2007.

[66] Yen-Po Wang, Lap-Loi Chung, Wei-Hsin Liao. Seismic response analysis of bridges isolated with friction pendulum bearings. *Earth.Eng.& Str. Dyn.*, 1998; 27, 1069-1093.

[67] M.C. Kunde, R.S. Jangid. Seismic behavior of isolated bridges: A-state-of-the-art review. *Electronic Journal of Structural Engineering,* 3 (2003).

[68] Evan m. Lapointe. An investigation of the principles and practices of seismic isolation in bridge structures. *Department of Civil and Environmental Engineering*; 2004.

[69] Michael D. Symans, Steven W. Kelly. Fuzzy logic control of bridge structures using intelligent semi-active seismic isolation systems. *Earth. Engng. Struct. Dyn*. 28, 37-60, (1999).

[70] Jangid R.S. Stochastic response of bridges seismically isolated by friction pendulum system. J. Bridfe Eng., 2008, 13(4): 319-330.

[71] Di Lauro, F., Montuori, R., Nastri, E., Piluso, V. (2019) Partial safety factors and overstrength coefficient evaluation for the design of connections equipped with friction dampers, Engineering Structures, 178, pp. 645-655.

[72] Fusco, R., Montuori, R., Nastri, E., Piluso, V. Critical analysis of ultimate rotation formula for R.C. columns subjected to cyclic loadings (2018) Engineering Structures, 177, pp. 160-174.

[73] Dell'Aglio, G., Montuori, R., Nastri, E., Piluso, V. A critical review of plastic design approaches for failure mode control of steel moment resisting frames (2017) Ingegneria Sismica, 34 (4), pp. 82-102.

[74] Nastri, E., Vergato, M., Latour, M. Performance evaluation of a seismic retrofitted R.C. precast industrial building (2017) Earthquake and Structures, 12 (1), pp. 13-21.

[75] Piluso, V., Montuori, R., Nastri, E., Paciello, A. Seismic response of MRF-CBF dual systems equipped with low damage friction connections (2019) Journal of Constructional Steel Research, 154, pp. 263-277.

[76] Dell'Aglio, G., Montuori, R., Nastri, E., Piluso, V. Consideration of second-order effects on plastic design of steel moment resisting frames (2019) Bulletin of Earthquake Engineering.

[77] Math Works Inc. MATLAB-High Performance Numeric Computation and Visualization Software. User's Guide. Natick: MA, USA; 1997.

[78] Chung LL, Kao PS, Yang CY, Wu LY, Chen HM. Optimal frictional coefficient of structural isolation system. *Journal of Vibration and Control* 2013, Early view. DOI: 10.1177/1077546313487938.

[79] Iemura H, Taghikhany T, Jain S. Optimum design of resilient sliding isolation system for seismic protection of equipments. *Bulletin of Eart. Engineering* 2007;**5**(1):85-103.

[80] Bucher C. Probability-based optimization of friction-based seismic isolation devices. *Structural Safety* 2009;**31**(6):500-507.

[81] Fallah, N., Zamiri G. Multi-objective optimal design of sliding base isolation using genetic algorithm. *Scientia Iranica A*, 2013;**20**(1):87–96.

[82] Garzillo, Carmine; Troisi, Roberta (2015) Le decisioni dell'EMA nel campo delle medicine umane. pp.85-133. In *EMA e le relazioni con le Big Pharma - I profili organizzativi della filiera del farmaco* - ISBN:9788892102279 - G. Giappichelli

[83] Nese, Annamaria; Troisi, Roberta (2018) Corruption among mayors: evidence from Italian Court of Cassation judgments. DOI:10.1007/s12117-018-9349-4. pp.1-26. In *TRENDS IN ORGANIZED CRIME* - ISSN:1084-4791 vol. agosto 2018

[84] Troisi, Roberta; Golzio, Luigi Enrico (2016). Legal studies and organization theory: a possible cooperation. pp.1-23. In *Manageable cooperation? - ISBN:0024667498 - European Academy of Management, Convegno: 16th EURAM Conference*, Paris, 1-4 June (ISSN 2466-7498).

[85] Troisi, Roberta; Guida, Vittorio (2018). Is the Appointee Procedure a Real Selection or a Mere Political Exchange? The Case of the Italian Health-Care Chief Executive Officers. DOI:10.5947/jeod.2018.008. pp.19-38. In *JOURNAL OF ENTREPRENEURIAL AND ORGANIZATIONAL DIVERSITY* - ISSN:2281-8642 vol. 7 (2).

[86] Troisi Roberta (2012). Le risorse umane nelle BCC: lavoro e motivazioni al lavoro. pp.399-417. In Progetto aree bianche. Il sistema del credito cooperativo in Campania - ISBN:8865580526 vol. 1.

[87] Golzio Luigi Enrico; Troisi Roberta (2013). 'The value of interdisciplinary research: a model of interdisciplinarity between legal research and research in organizations". pp.23-38. In *JOURNAL FOR DEVELOPMENT AND LEADERSHIP* , vol. 2.

COMPDYN 2019
7th ECCOMAS Thematic Conference on
Computational Methods in Structural Dynamics and Earthquake Engineering
M. Papadrakakis, M. Fragiadakis (eds.)
Crete, Greece, 24–26 June 2019

DAMAGE DETECTION OF MASONRY STRUCTURES UNDER SHAKING TABLE TESTS THROUGH RELATIVE DISPLACEMENTS BY 3D OPTICAL MARKERS

Ivan Roselli[1], Vincenzo Fioriti[1], Gerardo De Canio[1], Michela Rossi[2], Chiara Calderini[2], and Sergio Lagomarsino[2]

[1] Department for Sustainability, ENEA
Via Anguillarese 301, 00123 Rome, Italy
{ivan.roselli, vincenzo.fioriti, gerardo.decanio}@enea.it

[2] Department of Civil, Chemical and Environmental Engineering, University of Genoa
Via Montallegro 1, 16145 Genoa, Italy
michela.rossi@dicca.unige.it, {chiara.calderini, sergio.lagomarsino}@unige.it

Abstract

Large-scale seismic experimental facilities play a relevant role and provide essential contribution to the performance-based earthquake engineering. In such a context, recent advances in experimental data acquisition methodologies in large laboratories can open new perspective to the evaluation of structural performance of tested mockups under seismic load. In particular, the application of 3D motion capture systems to shaking table testing provides a unique tool for recording relative displacements of a large number of measurement points. The analysis of 3D relative displacements during dynamic tests allows to evaluate the structure deformations and to monitor the cracks formation and evolution, which can lead to the formulation of damage indices. Also, the failure mechanism could be easily visualized and analyzed by monitoring the cumulative relative displacements between markers. In addition, in-plane and out-of-plane deformations of walls could be monitored during each seismic test, providing accurate information on the torsional and bending effects. A case study is presented about a full-scale model of a masonry cross vault of the mosque of Dey, Algiers, tested at the ENEA Casaccia shaking table. The cross vault was subjected to a seismic sequence based on the 21-May-2003 earthquake recorded at Keddara station. The results obtained through the processing of the data from 67 markers located on the vault showed the potentialities of the methodology.

Keywords: Damage Detection, Shaking Table Tests, 3D Motion Capture, Deformations, Crack, Masonry Structures.

1 INTRODUCTION

In the general context of performance-based earthquake engineering (PBEE), as developed by the Pacific Earthquake Engineering Research [1], several steps are considered in order to achieve the complete methodology. One of these steps is the damage analysis, in which a damage measure (DM) representing a damage state of a structural or non-structural element is associated with one or more engineering demand parameters (EDPs). As a final step, the loss analysis of constructions that have undergone a seismic event, enables to estimate repair costs, repair duration (downtime), and human losses. For the damage assessment of structures through numerical analyses (e.g. FEM etc.) many parameters and indices have been developed and validated by correlation with damage observed on-the-field, e.g. by comparison with the damage grades, as defined by reference guidelines and regulations, such as the European Macroseismic Scale EMS-98 [2], widely adopted by national standards, such as the Italian regulation [3].

Even if numerical methods are nowadays consolidated and widely used for structural and damage analyses, the study of damage occurrence/evolution and seismic performance of structures must be considered a more general objective that still needs laboratory experimentation and data collection. In this direction, the damage assessment in full-scale shaking table tests through non-destructive tests (NDTs) and measurements of the dynamic behavior of tested mock-ups have a remarkable importance [4].

The present paper focuses on pointing out a methodology for the construction of a simplified damage index based on the application of 3D motion capture systems to shaking table testing. This kind of measurement systems represent a unique tool for recording relative displacements of a large number of measurement points through simple markers located on the tested mock-up [5]. Analyzing the 3D relative displacements between markers during dynamic tests, the deformations and the cracks can be detected and measured, opening to the possibility of formulating damage indices from experimental seismic experiments.

The methodology is illustrated and applied to a case study representative of a typical full-scale historic masonry mock-up of a cross vault of the mosque of Dey, Algiers. The 67 markers located on the vault mock-up were processed and damage indices computed, showing the potentialities of the methodology.

2 DAMAGE INDICES

A variety of damage indices (DIs) can be built on the base of different kinds of properties (structural or dynamic) and at different scale (local or global), as described in the literature [6]. Also fatigue effects may be taken into account, defining cumulative indices [7]. In general, damage indices are typically normalized on a scale of 0 to 1, where zero represents the undamaged state and unity represents the final collapse state of the structure. Most of such indices have been built and consolidated through extensive theoretical and experimental studies on reinforced concrete buildings, which are very common construction typology in many parts of the world. On the other hand, reinforced concrete structures are designed with somewhat simple schemes and have a more homogeneous and controllable behavior in comparison to historic masonry constructions. Moreover, they commonly present large cracking damage before the most common hysteretic one. Thus, the definition of proper and effective DIs for historic masonry structures is a very complex topic [8].

Damage indices can be used to describe the condition of a structure after an earthquake by relating its values with the level of damage states. To this purpose, correlations between DIs and Macroseismic Scale EMS-98 grades have been proposed. The one illustrated in Table 1 developed for reinforced concrete buildings in Croatia [9] is one of the most recent examples.

DI value	Description of structural damage	Damage grade (EMS-98)
$0 < DI \leqslant 0.3$	Insignificant	1°
$0.3 < DI \leqslant 0.5$	Moderate	2°
$0.5 < DI \leqslant 0.8$	Severe	3°
$0.8 < DI \leqslant 1.0$	Heavy	4°
$DI > 1.0$	Collapse	5°

Table 1: Correlation between DI values and EMS-98 damage grades [9].

Specific approaches for historic masonry buildings, such as ancient churches, have been developed by [10], in which the role of damage and collapse mechanisms, as well as the characteristics of the different macroelements, are taken into account. The following subsections will focus on the most used DIs to assess the overall damage degree of a structure subjected to shaking table tests.

2.1 Damage indices based on deformations and energy

Many indices were developed since the years 1980s by a variety of authors as deformation-based indices starting from simply attempting to extend the ductility concept to repeated loading [7]. Other authors focused on the energy absorption during hysteretic loops as a measure of damage [7]. In fact, more complete models were developed as combined indices of both concepts. This is the case of one of the most widely used damage index that was proposed in 1984 by [11] as a linear combination of the maximum displacement and the dissipated energy. It can be formulated as follows:

$$I_D = \frac{d_m}{d_u} + \beta_e \frac{\int \mathrm{d}E}{F_y d_u} \tag{1}$$

where d_u is the ultimate displacement at monotonic loading, d_m is the maximum displacement corresponding to the point of maximum capacity, β_e is the parameter representing the cyclic loading, dE is the incremental dissipated hysteretic energy and F_y is the longitudinal reinforcement yielding force. On the one hand, the simplicity and the calibration of the above model through a large amount of experimental observations of damage make I_D a very consolidated index. On the other hand, a major problem is the determination of d_u and, especially, of β_e. In particular, empirical studies and related regression equations in the literature yielded quite small values of β_e, so that the energy term provides a limited contribution, often negligible with respect to the deformation term [7].

The above indices are usually calculated for each structural macroelement or floor in multistory buildings (local indices), then a weighted average value is computed to estimate the global damage. Weighting systems are often based on subjective assessments and criteria, e.g. through considerations on the different collapse mechanisms and the relevance of heavy localized damage. The contribution of local energy absorption to the overall damage state as a more objective criteria for weights determination was also proposed by several authors [7].

2.2 Global damage indices based on stiffness reduction

Damage indices based on the dynamic properties of a building are widely accepted as the main indicators of the global state of health of the overall structure [12]. They are usually built as a function of the modal parameters of the structure. In particular, they calculate the change in the fundamental frequency (or frequency shift), on the basis of the consolidated observation that damage processes induce a measureable decrease of the system's stiffness. A common formulation of this type is the following:

$$DI_f = 1 - \frac{f_d^2}{f_0^2} \tag{2}$$

where f_0 is the initial fundamental frequency of the undamaged structure and f_d is the fundamental frequency of the damaged structure. Several methods of modal analysis, such as the Experimental Modal Analysis (EMA) based on the computation of the Frequency Response Function (FRF), or other modal identification methods [13], can be used to estimate the modal frequencies of the studied structure.

2.3 Construction of a global damage index based on markers displacements

A global damage index based on the 3D displacements of markers recorded by a motion capture system [14] during shaking table tests is explored in the following. In fact, the energy absorption in shaking table tests is of difficult assessment. However, its contribution is generally limited, if not negligible, in comparison to the plastic deformation term. Therefore, it is here explored the possibility of providing rough indication through a simplified index based uniquely on measured displacements. A general model for the index was assumed as:

$$DI_m = f(\Sigma\Delta\delta, a, b) \tag{3}$$

where f is a function of the cumulative residual relative displacements $\Sigma\Delta\delta$ between markers at the end of each seismic test, as an estimate of accumulated plastic deformations, while a and b are empirical coefficients to be determined through correlation with experimental results of a consolidated global damage index. In the following, the DI_f described in the previous subsection will be taken as reference index for such correlation. The function f can be determined *a priori* or it can be chosen among several functions by best correlation criteria. In the following, the application of the method is illustrate with a case study. Obviously, the larger amount of experimental cases are used for statistical correlation, the more representative and consolidated is to be considered the constructed index.

3 CASE STUDY

3.1 Shaking table tests

As a case study, the shaking table tests executed on a mock-up representing one of the 10 cross vaults of the Mosque of Dey were considered. The tested cross vault is shown in Figure 1(a). It is one brick layer in thickness and its dimensions are 350 x 360 cm^2 square plan, with a total height of 565 cm. More structural details on the Mosque of Dey can be found in [15-16]. The structural properties and characteristics of the tested mock-up are described in detailed in [17]. The mock-up was initially tested with two steel longitudinal bars linking transversal walls, functioning as tie-rods. Successively, the two ties were removed to verify the specimen resistance up to collapse.

The historic Algerian masonry reproduced for the vault is a poor masonry made up of baked clay bricks of size 3.5 x 12 x 25 cm^3 with weak 2.5-cm-thick joints.

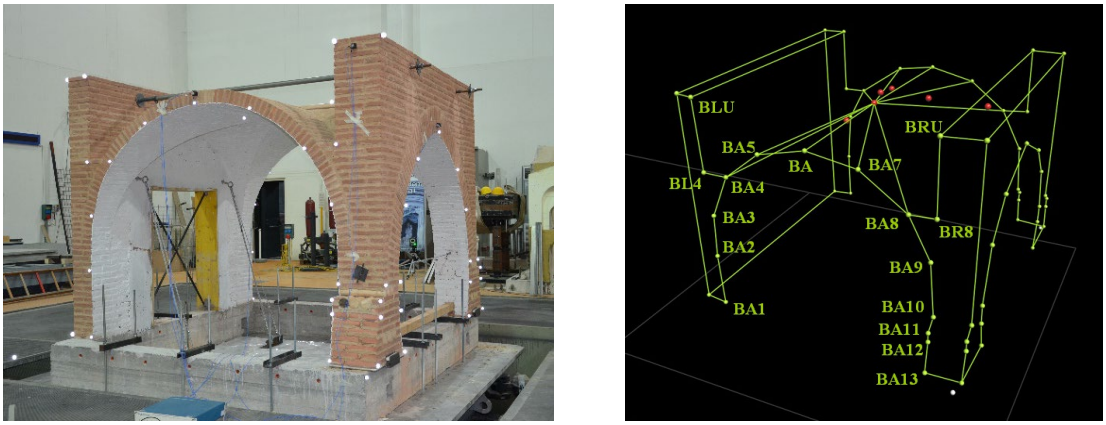

(a) (b)

Figure 1: Tested specimen with markers in white (a) and 3D markers reconstruction (b).

Characterization tests on seven mortar samples extracted from buildings of the Citadel of Algiers, dating back to the same period of construction of the mosque, indicated that clay, finely bricks, gravel, sand, lime, and pozzolana in varying proportions are the main components. The bricks were assembled according to ancient master builders' technique, similar to local historical cross vaults. Figure 1 shows the positions of the 67 retro-reflecting markers tracked by a 3D motion capture system based on a constellation of high-frequency and high-resolution cameras located around the shaking table [18]. In Figure 1(a) the markers appear white, as they reflect the photo camera flash light. The 3D reconstruction of markers positions is achieved through geometrical triangulation algorithms by the acquisition software and mock-up wireframe is displayed by connecting markers, as illustrated in Figure 1(b). The system overall accuracy is in the order of 0.01-0.1 mm in terms of RMS error of markers position [19]. Markers motion data were acquired at 200 Hz of sampling frequency.

Seismic sequence on shaking table was based on the NS component of the ground motion recorded at Keddara station during the 21-May-2003 earthquake occurred in the province of Boumerdes and the eastern part of Algiers with 6.8 Magnitude [20]. The seismic signal was normalized to the site of the Citadel of Algiers according to the uniform hazard response spectrum (UHRS) method and was applied in the direction transversal to the tie-rods. The seismic sequence started with a test at 0.05 g of nominal peak ground acceleration (PGA). Succeeding tests were performed increasing the PGA of 0.05 g at each step. Also low-intensity white-noise tests were performed for the dynamic identification of the mock-up.

4 RESULTS

In Table 2 the results obtained with the different regression models utilized for the construction of the damage index DI_m are shown.

DI_m model	Regression eq.	R^2
$a \log(\Sigma\Delta\delta) + b$	$0.17 \log x + 0.78$	0.942
$a(\Sigma\Delta\delta) + b$	$0.58 x + 0.26$	0.908
$a(\Sigma\Delta\delta)^b$	$0.78 x^{0.159}$	0.832
$a e^{b(\Sigma\Delta\delta)}$	$0.25 e^{1.29 x}$	0.754

Table 2: Different models utilized for construction of damage index DI_m and corresponding correlation coefficients R^2 with stiffness damage index DI_f.

After regression analysis with the stiffness damage index DI_f as defined in eq. 2, as a reference damage estimator, the correlation coefficients R^2 was considered to assess the effectiveness of each proposed model. The best results were found with the logarithmic model, which showed very high correlation (R^2 of 0.942) with DI_f. It must be noted that all regression models gave quite good correlations (R^2 higher than 0.75), even if the contribution of energy absorption was neglected. On the other hand, most of the experimental points in Figure 2 are concentrated at low levels of damage (DI < 0.3). Consequently, the found regression equation is not be considered highly representative of all possible damage states of the structure. In fact, the mock-up suddenly collapsed with little warning, hardly visible to the naked eye, at test with 0.25 g of PGA, corresponding to 0.318 g of peak table acceleration (PTA), showing a quite fragile behavior. However, the methodology seemed effective to catch the behavior of the tested structure and easily applicable to further experiments to increase the model representativeness for different collapse mechanism and structural typologies.

In Figure 3 the in-plane relative displacements between top and bottom of the façade before and during collapse at test at 0.25 g of PGA are shown. Final collapse was activated at time equal to about 10 s of the time history with the catastrophic out-of-plane overturning of the façade and the consequent development of a four-hinge mechanism of the vault.

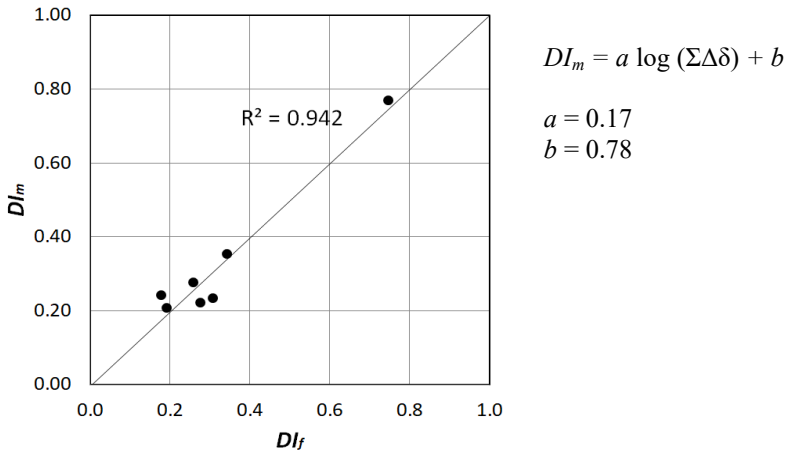

Figure 2: Best empirical correlation between DI_f (formulated according to eq. 2) and DI_m.

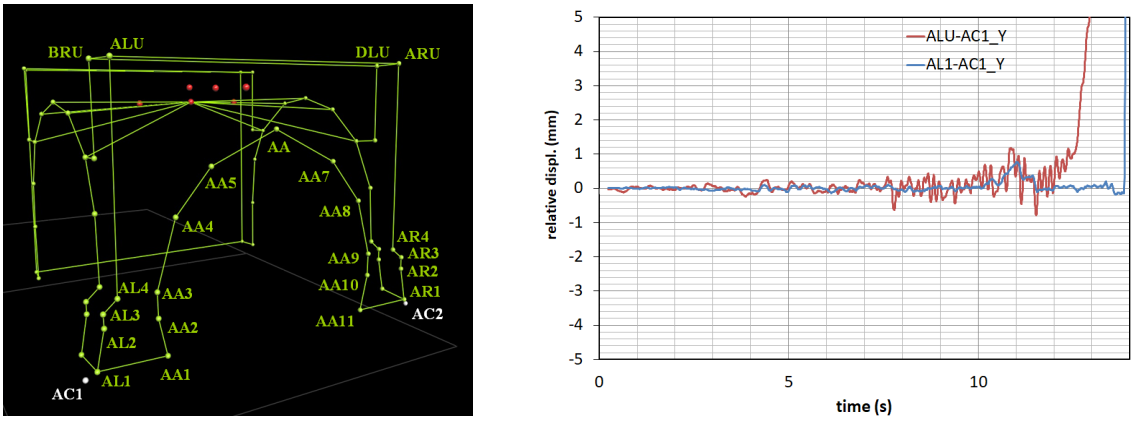

(a) (b)

Figure 4: Markers of mock-up façade (a). In-plane relative displacements between top (ALU) and bottom (AC1) of the façade left corner during seismic test at 0.25 g of PGA.

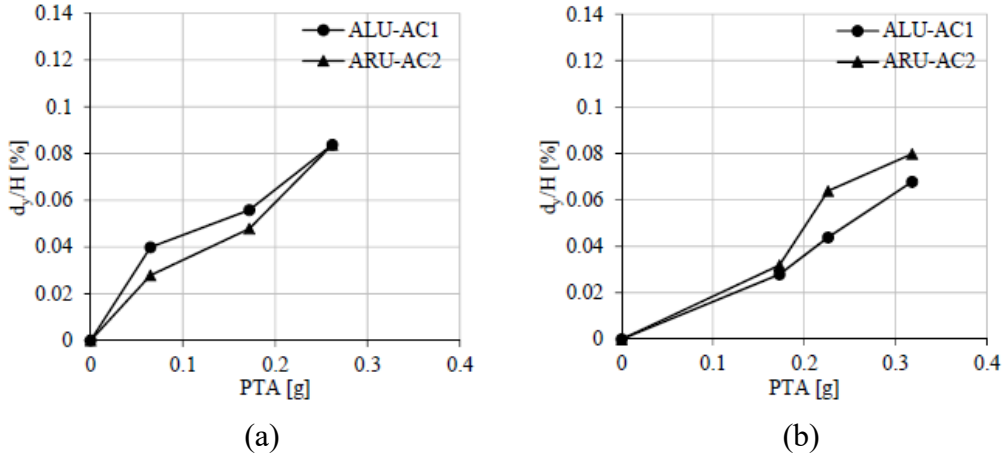

Figure 4: Comparison of in-plane shear deformation (d_y/H) between left (ALU-AC1) and right (ACU-AC2) corners of the façade during seismic sequence with ties (a) and without ties (b).

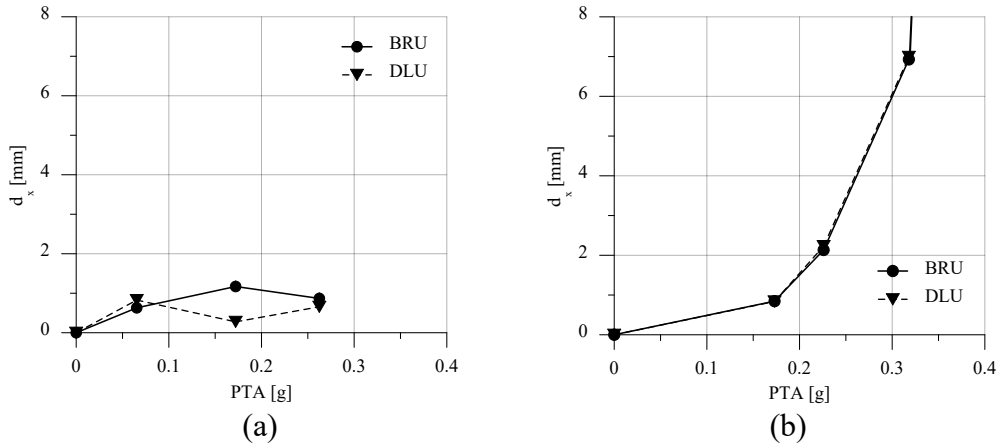

Figure 5: Maximum displacements d_x in direction of tie-rods achieved by the markers on top of mock-up façade on the left and right corners (BRU and DLU respectively) with ties (a) and without ties (b).

Through the monitoring of the markers motion, it was possible to detect even the initial deformations that occurred at the first steps of the seismic sequence, as depicted in the graphs of Figure 4 and 5. In particular, in Figure 4, the torsional effects are evidenced by the comparison between the behavior of the left and the right corners on the façade. While out-of-plane displacements on top of the left and right corners of the mock-up façade are compared in Figure 5.

5 CONCLUSIONS

A methodology was explored for the detection of damage occurrence and its evolution in historic masonry mock-ups tested on shaking table. In particular, the construction of a simplified damage index based on the displacements measured through a 3D motion capture systems to be utilized in shaking table testing was proposed. The attempt is to take advantage of the potentiality of such measurement systems to track the displacements of a large number of markers that can be easily and cheaply located on the tested mock-ups. The displacement-based index was determined among a series of regression models through the best-correlation criterion with a consolidated global damage index, based on the change in modal frequencies.

The application to the case study showed the potentialities of the methodology. The best regression model showed very high correlation. In fact, even the other models gave quite

good correlations (R^2 higher than 0.75), despite the contribution of energy absorption was neglected. It must be also noted that further experiments are needed to consolidate the model, as the case study provided results concentrated at low levels of damage (DI < 0.3), making the found regression equation not highly representative of all possible damage states. This because the studied masonry mock-up collapsed with quite fragile behavior, rapidly passing from low-damage to final failure.

Moreover, comparing the displacements of different markers in the same direction, in-plane and out-of-plane deformations of walls were monitored to assess the torsional and bending effects. This allowed to follow the evolution of the failure mechanism, which provided valuable information to assess the dynamic behavior of the structure.

REFERENCES

[1] K.A. Porter, An overview of PEER's performance-based earthquake engineering methodology. *9th International Conference on Applications of Statistics and Probability in Civil Engineering*. San Francisco, USA, 2003.

[2] G. Grünthal, European Macroseismic Scale 1998 (EMS-98). *Cahiers du Centre Européen de Géodynamique et de Séismologie.* 1998, 15, Helfent-Betrange (Luxembourg).

[3] OPCM Regulation n. 28, 9 June 2017, "Modifiche all'ordinanza n. 19, 7 aprile 2017, recante 'Misure per il ripristino con miglioramento sismico e la ricostruzione di immobili ad uso abitativo gravemente danneggiati o distrutti dagli eventi sismici verificatisi a far data dal 24 agosto 2016'. *Gazzetta Ufficiale*, **143**, 22 June 2017 (*in Italian*).

[4] M.R. Polimeno, I. Roselli, V. Luprano, M. Mongelli, A. Tatì, G. De Canio, A non-destructive testing methodology for damage assessment of reinforced concrete buildings after seismic events. *Engineering Structures*, **163**, 122-136, 2018.

[5] I. Roselli, V. Fioriti, M. Mongelli, A. Colucci, G. De Canio, Machine Vision-Based Application to Structural Analysis in Seismic Testing by Shaking Table. *Optoelectronics in Machine Vision-Based Theories and Applications*, IGI Global ed., 2018.

[6] R. Sinha, R. Shiradhonkar, Seismic damage index for classification of structural damage–closing the loop. *15th World Conference on Earthquake Engineering (15WCEE)*, Lisbon, Portugal, September 24-28, 2012.

[7] M.S. Williams, R.G. Sexsmith, Seismic Damage Indices for Concrete Structures: A State-of-the-Art Review. *Earthquake Spectra,* **11**(2), 319-349, 1995.

[8] F. Parisi, N. Augenti, Earthquake damages to cultural heritage constructions and simplified assessment of artworks. *Engineering Failure Analysis,* **34**, 735-760, 2013.

[9] M. Hadzima-Nyarko, *Contribution to the research of seismic vulnerability of RC buildings*. PhD Thesis, Faculty of Civil Engineering, University J. J. Strossmayer, Osijek, (in Croatian), 2011.

[10] S. Lagomarsino, A. Brencich, F. Bussolino, A. Moretti, L.C. Pagnini, S. Podestà, A new methodology for damage assessment on churches: first considerations on the mechanisms activated by the earthquake (in Italian). *Ingegneria Sismica,* **3**, 70-82, 1997.

[11] Y.J. Park, A.H.S. Ang, Y.K. Wen, Seismic damage analysis and damage-limiting design of RC buildings, *Structural Research Series*, **516**, University of Illinois: Urbana, USA, 1984.

[12] E. DiPasquale, J.W. Ju, A. Askar, A.S. Çakmak, Relation between Global Damage Indices and Local Stiffness Degradation. *Journal of Structural Engineering,* **116**(5), 1440-1456, 1990.

[13] I. Roselli, V. Fioriti, M. Mongelli, I. Bellagamba, G. De Canio, Mutual validation between different modal analysis techniques for dynamic identification of the so-called Temple of Minerva Medica, Rome. *IOP Conf. Series: Materials Science and Engineering,* **364**, 012004, 2018.

[14] G. De Canio, G. de Felice, S. De Santis, A. Giocoli, M. Mongelli, F. Paolacci, I. Roselli, Passive 3D motion optical data in shaking table tests of a SRG-reinforced masonry wall. *Earthquakes and Structures*, **40**(1), 53-71, 2016.

[15] A. Abdessemed-Foufa, Visual screening for a potential evaluation of seismic vulnerability of historical building: Palace of the Dey (Citadel of Algiers). *WIT Transactions on The Built Environment, ed. WIT Press,* **123***,* 119-123, 2012.

[16] A. Abdessemed Foufa, Y. Terki, D. Benouar, Case study: Local seismic culture in vernacular architecture in Algeria. *Seismic Retrofitting: Learning from Vernacular Architecture*, Correia M. R., Lourenco P.B. and Varum H. (eds.), CRC Press, 101-102, 2015.

[17] I. Roselli, G. De Canio, M. Rossi, C. Calderini, S. Lagomarsino, Relative displacements of 3D optical markers for deformations and crack monitoring of a masonry structure under shaking table tests. *International Journal of Computational Methods and Experimental Measurements (in press),* 2019.

[18] Vicon documentation, https://docs.vicon.com/display/CamDocs. Accessed on: 23 Jan. 2019.

[19] I. Roselli, M. Mongelli, A. Tatì, G. De Canio, Analysis of 3D motion data from shaking table tests on a scaled model of Hagia Irene, Istanbul. *Key Engineering Materials*, **624**, 66-73, 2015.

[20] A.M. Khellafi, Z. Harichane, H. Afra, A. Sadouki, A Case Study of Accelerometric Records Analysis of May 21st, 2003, Boumerdes (Algeria) Earthquake. *International Journal of Geotechnical Earthquake Engineering (IJGEE),* **4**(2), 34-52, 2013.

COMPDYN 2019
7th ECCOMAS Thematic Conference on
Computational Methods in Structural Dynamics and Earthquake Engineering
M. Papadrakakis, M. Fragiadakis (eds.)
Crete, Greece, 24–26 June 2019

MULTI-PERFORMANCE DESIGN OF DISSIPATIVE BRACING SYSTEMS THROUGH INTERVENTION COST OPTIMIZATION

Laguardia R.[1], Gigliotti R.[1], Braga F.[1]

[1] Sapienza University of Rome
Via Eudossiana,18 00184 Rome
e-mail: {raffaele.laguardia, rosario.gigliotti, franco.braga}@uniroma1.it

Abstract

In recent years, the need of retrofit interventions on existing buildings is increasing, also due to the high economic losses recorded after the recent seismic events. The intervention techniques based on stiffening and energy dissipation are one of the most widespread among the several available. Despite the great diffusion of this kind of interventions, there are still no clear and shared rules about design principles and, above all, about the performance objectives to be followed within the design. In particular, there is a lack of design approaches based on optimization of intervention costs and cost-benefit assessment. This paper concerns the optimal design of dissipative braces for seismic retrofitting of existing reinforced concrete buildings in the context of a multi performance design problem. Topological and dimensional optimization of the braces is achieved by minimizing the real intervention cost through an innovative formulation of the objective function. The procedure is based on elastic linear analyses, keeping in count the inelastic behavior of dissipative devices and concrete frame through linear equivalent schemes. The reliability of such linearized schemes is discussed by a comparison with structural response obtained with Non-Linear dynamic analyses on a case study structure. Further, it will be shown how the procedure allows, besides the design of the braces characteristics, a critical assessment and choice of the performance levels in order to optimize the cost benefit ratio of the intervention, thus showing its effectiveness as decision-making tool for seismic risk mitigation.

Keywords: Bracing; Energy Dissipation; Optimization; Retrofit; Multiperformance.

1 INTRODUCTION

Nowadays, the seismic protection of existing buildings is one of the most relevant topics in earthquake engineering. The recent seismic events that hit many countries all over the world (Umbria-Marche 1997, Italy; L'Aquila 2009, Italy; Christchurch 2011, New Zealand; Tohoku 2011, Japan; Emilia 2012, Italy; Centro Italia 2016, Italy) have highlighted the weaknesses of existing building heritage, causing many casualties and very high economic losses [1]–[3]. For many years politics, economists and the whole scientific community have not appropriately considered the problem of the enormous costs of reconstruction due to seismic events that have been very high [4] [5]. In the recent years, the need of a seismic risk mitigation strategy has emerged. In order to gain this goal, decision making tools are needed to obtain adequate seismic protection with the least financial investments possible.
To this aim, the existing design methodologies are often inappropriate because don't keep in count the financial aspects of a retrofit interventions [6]. Therefore, new methodologies based on seismic risk assessments are substituting traditional performance based approaches [7]–[10].
The risk-based methodologies allow to evaluate the economic losses of an asset throughout its nominal life by correlating seismic hazard, structural response and damages. The aim of retrofit interventions is to mitigate the damages and consequent economic losses by modifying the structural response. The intervention will be profitable if its cost is commensurate with the gain obtained in terms of damage reduction, in other words in the presence of an advantageous cost-benefit ratio. In this moment, there is a lack of methodologies capable of performing a cost-benefit assessment for retrofit interventions.
Among the several intervention techniques available, the most interesting in order to find an optimal cost/benefit ratio are the ones based on stiffening and energy dissipation [11]–[15]. The main advantage of this techniques is their potential low invasiveness and their broad adaptability to different performance requests.
Many design process and methodologies are available in the international literature for dissipative bracing design, some of them pursue an optimality criterion (e.g. minimum interstory drift, minimum base shear, maximum energy dissipation) [16]–[23], while others allow to find the brace characteristic and disposition just by guaranteeing some performance requirements through simplified procedures [24]–[28]. The design procedures based on an optimality criterion are commonly based on complex models that explicitly keep in count the nonlinear effects, while the simplified procedures are commonly based on the use of single degree of freedom (SDOF) equivalent models. Among the procedure previously cited, only few of them foreseen a multiperformance approach and, moreover, none of them foresee a risk-based design for retrofit intervention, even in the case the cost intervention is explicitly kept in count [20]–[22].
In this paper is adopted the optimization procedure proposed in [29], that allow a multiperformance design of braces by minimizing the intervention cost and by constraining the interstory drift ratio (IDR). The structural performance is assessed through linear analyses by adopting a model with a linearized behaviour of both existing frame and dissipative elastoplastic device. On the case study presented herein, will be shown how this procedure allows a dimensional and topological optimization of the braces by minimizing the intervention costs. Furthermore, a comparison between the intervention costs obtained for several performance requests is shown, in order to evidence the effectiveness of this procedure as a decision-making tool.

2 STRUCTURAL BEHAVIOUR AND MODELLING

The optimization procedure adopted herein is based on elastic linear analyses. The structural model keeps in count the non-linear behaviour of existing frame and dissipative braces through properly developed linearization schemes. The linearized secant stiffness of the frame is calculated on the basis of the maximum ductility demand expected on structural elements, while the braces behaviour is linearized within the procedure on the base of calculated local displacement demands. The global stiffness matrix is then assembled by adding to the un-braced frame stiffness matrix, the contribution of each brace assessed within the procedure. Similarly, the energy dissipated by each brace is assessed within the procedure and added to the energy dissipated by the frame in order to compute a global equivalent damping ratio for the braced building and reduce the seismic forces.

2.1 Existing frame

The existing frame behaviour is assumed as bilinear, as it is shown in Figure 1. The secant stiffness K_0 is calculated in correspondence of the final desired displacement of the braced structure, u_d, which can be determined on the base of the drift profile used as a constraint in the optimization procedure. Once known such final displacement, a reasonable estimate of the secant linear stiffness of each structural element can be determined on the base of expected global ductility demand through the following expressions [30]:

$$I_{ieq} = \frac{I_i}{\mu} \tag{1}$$

$$\mu = \frac{u_d}{u_y} \tag{2}$$

where: I_{ieq} is the equivalent inertia of the i-th section, I_i is the inertia of the i-th section, μ is the global ductility demand, u_d is the final displacement and u_y is the yielding displacement of the frame.

In correspondence of the final desired displacement, u_d, the energy dissipated by the frame is assessed through the following expression:

$$E_0 = 0.33 \times 4 \times \left(F_y u_d - F_y u_y \right) \tag{3}$$

where: F_y and u_y are the yielding force and the yielding displacement of the existing frame, respectively.

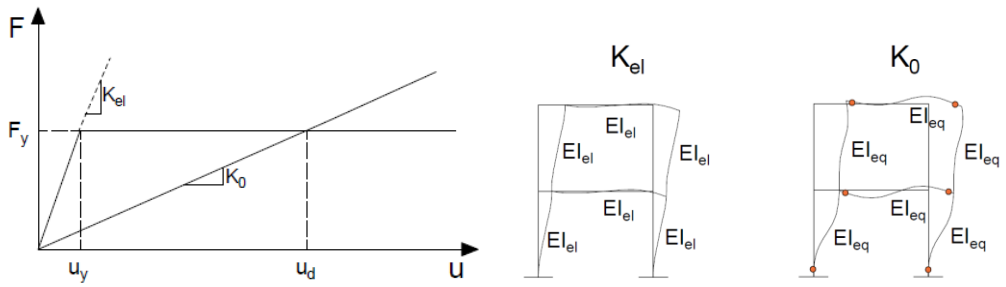

Figure 1: Existing frame behaviour, elastic stiffness K_{el} and equivalent secant stiffness K_0.

2.2 Dissipative brace

The dissipative brace is composed by a series disposition of an elastic steel truss and an elastoplastic dissipative device. The global bilinear behaviour of the brace is linearized in correspondence of its maximum displacement, u_u. Differently than for the existing frame, the linearization process of the brace is performed within the optimization procedure on the base of calculated local displacement of each brace. Given the force-displacement relationship of Figure 2, the linear secant stiffness of each brace and the associated dissipated energy can be calculated as follows:

$$K_i^B = F_{ui}^B / u_{ui}^B \tag{4}$$

$$E_i^B = 4 \times \left(F_{yi}^B u_{ui}^B - F_{ui}^B u_{yi}^B \right) \tag{5}$$

where: K_i^B, E_i^B F_{yi}^B, u_{yi}^B, F_{ui}^B, u_{yi}^B are the equivalent stiffness, the energy dissipated, the yielding force, the yielding displacement, the ultimate force and the ultimate displacement of the i-th brace, respectively.

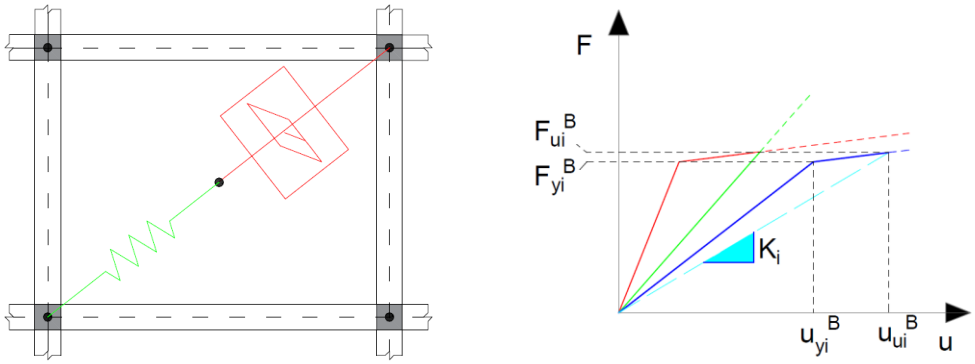

Figure 2: Brace assemblage and force-displacement relationship adopted for the brace (blue line), the steel truss (green line) and the dissipative device (red line).

2.3 Braced structure

In Figure 3 it is shown the sketch of the assembling procedure of stiffness and dissipated energies within the procedure. The global stiffness matrix of the braced structure is assembled by simply adding the contribution of the existing frame, K_0, and the contributions of each brace, represented through an influence matrix ΔK_i, using the following expression:

$$\mathbf{K} = \mathbf{K}_0 + \sum_i \Delta \mathbf{K}_i \tag{6}$$

Similarly, the total energy dissipated by the braced structure, E, is assembled as follows:

$$E_D = E_0 + \sum_i E_i^B \tag{7}$$

By using the total energy dissipated obtained through Eq.7, the equivalent damping ratio of the system can be assessed as follows:

$$\zeta_{eq} = \frac{1}{4\pi} \frac{E_D}{E_p} + \zeta_v \tag{8}$$

where E_p is the elastic energy of the braced structure and ζ_v is the added viscous damping.

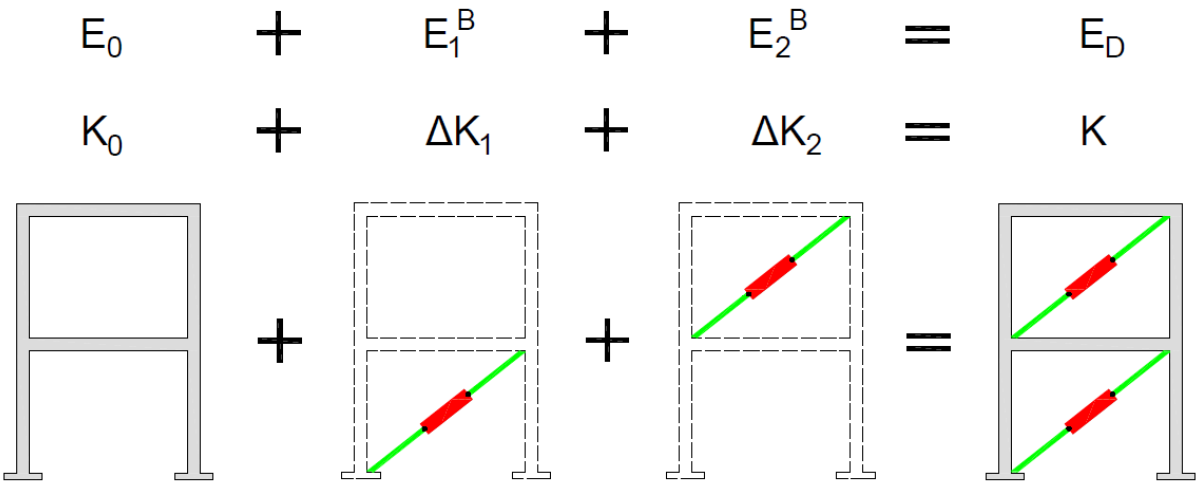

Figure 3: Assembling of stiffness and dissipated energies within the procedure.

3 OPTIMIZATION PROCEDURE

The optimization procedure is asked to provide the dimensional and topological characteristics of the dissipative braces. With this aim and given the brace characteristics exposed in section §2.2, the unknowns of the optimization problem, namely the independent variables, are defined as follows:

$$\mathbf{x} = \left[\mathbf{A^A} \quad \mathbf{F_y^D} \quad \mathbf{u_y^D} \right] \tag{9}$$

where: $\mathbf{A^A}$ is a vector whose generic component A_i^A is the area of the i-th steel truss, $\mathbf{F_y^D}$ is a vector whose generic component F_{yi}^D is the yielding force of the i-th dissipative device and $\mathbf{u_y^D}$ is a vector whose generic component u_{yi}^D is the yielding displacement of the i-th dissipative device.

The objective function of the optimization procedure can be defined, as follows:

$$O.F.(\mathbf{x}) = \sum_{i=1}^{n} (C_i^S(A_i^A) + C_i^D\left(F_{yi}^D\right) + C_i^M(A_i^A) + \sum_{r=1}^{n_p} C_r^F(\mathbf{x}) \tag{10}$$

where: C_i^S is the cost function of the steel elements, C_i^D is the cost function for the dissipative devices, C_i^M is the cost function for the masonry works, C_i^F is the cost function for the foundation system interventions.

A detailed description of Eq. 10 may be found in [29]. The constraints of the procedure are expressed in terms of interstory drift ratio and can be formalized as follows:

$$\mathbf{h_u}(\mathbf{x}) = \mathbf{IDR}(\mathbf{x}) - \mathbf{IDR}^{Lim} \tag{11}$$

where: $\mathbf{h_u}$ is the vector of constraints, **IDR** is the vector containing the interstory drift ratio obtained from structural response and $\mathbf{IDR}^{Lim}$ is the vector of maximum interstory drift ratio desired.

The optimization procedure can consequently be defined as follows:

$$\begin{aligned} &\min \quad O.F.(\mathbf{x}) \\ &\begin{cases} \mathbf{h_u}(\mathbf{x}) = \mathbf{IDR}(\mathbf{x}) - \mathbf{IDR}^{Lim} \le 0 \end{cases} \end{aligned} \tag{12}$$

4 NUMERICAL EXAMPLE

The procedure has been applied to a case study which represent the typical Italian reinforced concrete building realized in the absence of seismic provisions. It has six floors with a height of 3m, three spans with a length of 5m. The considered floor mass is 112.5kNs^2/m. The beams have a 30x50cm section, external columns have a 30x30cm section and central columns are tapered along the building height: a 30x60cm has been considered for the first three floors while a 30x30cm section has been considered for the other three floors. Braces are located in the central span of the building with a diagonal disposition, as shown in Figure 4.

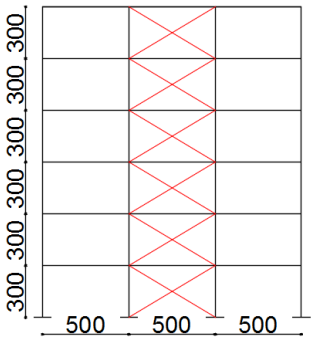

Figure 4: Case study structure and brace initial arrangement.

The optimization problem aims to find the optimal size and disposition of braces in order to obtain the desired interstory drift ratio for different action levels. The considered action levels are related to the Italian site of Reggio Calabria (LAT 38.11, LON 15.66) for the return periods (T_r) of 30, 101, 475 and 975 years, soil C and T1 site conditions as defined in the italian seismic code [31]. For each of these action levels the acceptance criteria for interstory drift ratio are defined as 0.1%, 0.4%, 0.7% and 1%, respectively. By considering these action levels and acceptance criteria, the optimization problem of Eq. (12) is extended to a multi-performance problem that can be posed as follows:

$$\begin{aligned} &\min \quad O.F.(\mathbf{x}) \\ &\begin{cases} \mathbf{h}_{u-30}(\mathbf{x}) = \mathbf{IDR}_{30}(\mathbf{x}) - \mathbf{IDR}_{30}^{Lim} \le 0 \\ \mathbf{h}_{u-101}(\mathbf{x}) = \mathbf{IDR}_{101}(\mathbf{x}) - \mathbf{IDR}_{101}^{Lim} \le 0 \\ \mathbf{h}_{u-475}(\mathbf{x}) = \mathbf{IDR}_{475}(\mathbf{x}) - \mathbf{IDR}_{475}^{Lim} \le 0 \\ \mathbf{h}_{u-975}(\mathbf{x}) = \mathbf{IDR}_{975}(\mathbf{x}) - \mathbf{IDR}_{975}^{Lim} \le 0 \end{cases} \end{aligned} \tag{13}$$

Where $\mathbf{h}_{u\text{-}j}$ is the vector of constraints for the j-th hazard level, $\mathbf{IDR}_j$ is the vector of IDR obtained for the j-th hazard level and $\mathbf{IDR}_j^{Lim}$ is the vector of acceptance criteria adopted for the j-th hazard level.

The results of the optimization problem are shown in Figure 5. Brace stiffness and strength reduces along the height with the exception of the fourth floor where the braces are sensibly stiffer than the floor below in order to balance the stiffness reduction due to the column tapering. In Figure 6a are shown the interstory drift ratio obtained with the elastic linear analyses performed within procedure, as it can be seen the drift are very regular along the height, with the exception of the last floor for events with low rate of occurrence. Furthermore, it should

be observed that the IDR for T_r=101yrs are quite lower than the maximum drift allowed (i.e. IDR_{101}^{Lim}=0.4%). In order to verify the reliability of the linearization procedure, several Non-linear-dynamic analyses are performed in the software Opensees [32] by considering the ductile flexural behaviour and by using the set of natural ground motions described in [33]. Despite of several modeling possibilities of fragile and degradation phenomena [34]–[38], it has been chosen to perform analyses with a model coherent with the one adopted within the procedure that does not take into account such phenomena, further information about modeling assumptions may be found in [29] and [39]. The average interstory drift ratio obtained through NL time history analyses are in good agreement with the one obtained through the procedure, proving the reliability of linearization schemes adopted. Furthermore, a parametric study has been performed solving several single-performance problems accepted through the optimization problem herein proposed by adopting different maximum IDR. In Figure 7 is shown the variation of the intervention cost with the maximum IDR accepted. It can be noticed that maintaining the structure in the elastic field (i.e. IDR <0.4%) considerably increases the costs of intervention, while admitting slight plasticization (i.e. IDR> 0.7%) allows to contain costs considerably, as well as using a multi-performance approach analogous to the one described above (i.e. MP in Figure 7). The intervention cost thus evaluated, if compared with the expected annual losses due to the achievement of the requested performances, can therefore be used to evaluate which performance configuration guarantees the optimal cost-benefit ratio.

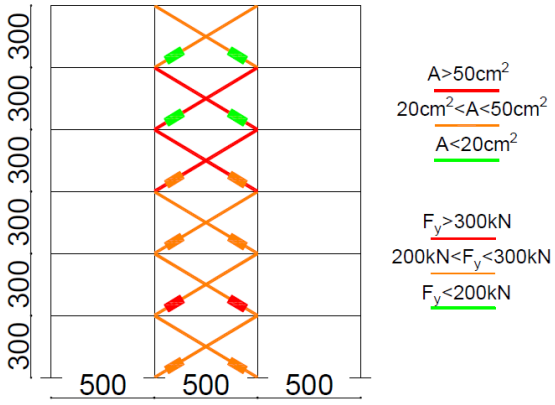

Figure 5: Brace characteristics and arrangement of the optimal solution.

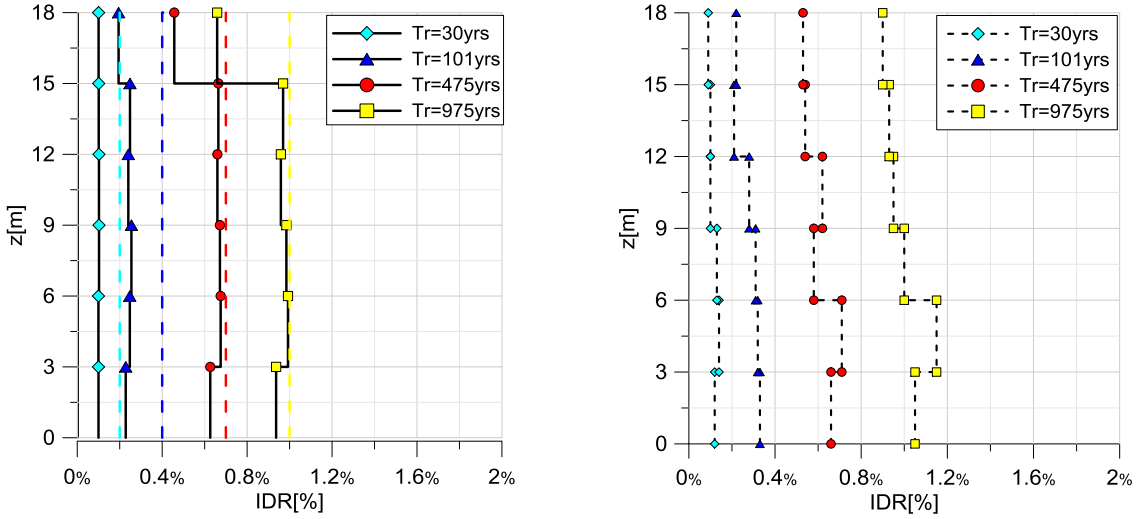

(a) (b)

Figure 6: Structural response of the braced structure: IDR obtained through elastic linear analyses within the procedure (solid lines) and IDR^{Lim} imposed as constraints (dashed lines) (a); average IDR obtained through NL time history analyses.

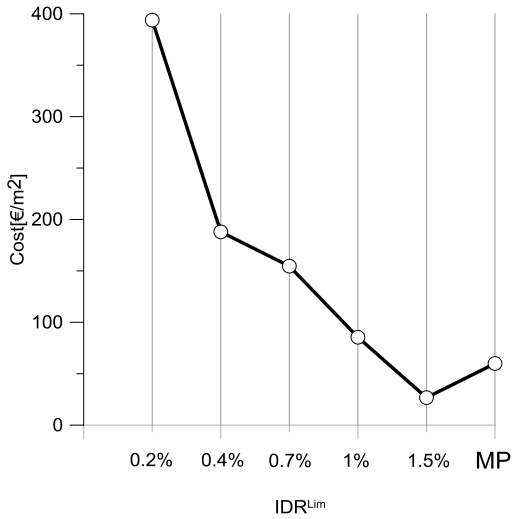

Figure 7: Total intervention cost for different maximum IDR.

5 CONCLUSIONS

In this paper is presented an optimization procedure which allows the design of bracing systems by minimizing the intervention costs through a multi-performance approach. In order to keep in count the nonlinear behaviour of frame and braces, equivalent linearization schemes are adopted. The analyses on the case study have shown how the braces designed through this procedure allow a regularization of the building behaviour along the height and the achievement of the desired performance requirements for all the considered action levels. The results obtained with NL analyses are in good agreement with the one obtained with linear analyses performed within the procedure, showing how the linearization schemes are reliable in order to describe the structural behaviour even when marked non-linear behaviour is expected. This procedure is therefore able to solve a complex multi-performance problem by linear analysis, with the great advantage of limiting the computational times and without the need to adopt complex structural models with explicit modeling of nonlinearities, thus showing itself as a

useful design tool. Furthermore, the comparison of results in terms of intervention costs, once given several performance requirements, show the effectiveness of the procedure as a fast and reliable tool to estimate the intervention cost and choice the performance requirements to optimize cost-benefit ratio too.

[1] W. Y. Kam, S. Pampanin, K. Elwood, Seismic performance of reinforced concrete buildings in the 22 February Christchurch (Lyttelton) earthquake. *Bulletin of the New Zealand Society for Earthquake Engineering* , **44** , 239–278 , 2011.

[2] D. F. D'Ayala, S. Paganoni, Assessment and analysis of damage in L'Aquila historic city centre after 6th April 2009. *Bulletin of Earthquake Engineering* , **9** , 81–104 , 2011.

[3] B. Khazai, J. E. Daniell, F. Wenzel, The March 2011 Japan Earthquake. *TATuP – Journal of Technology Assessment in Theory and Practice* , **20** , 22–33 , 2011.

[4] M. Di Ludovico, A. Prota, C. Moroni, G. Manfredi, M. Dolce, Reconstruction process of damaged residential buildings outside historical centres after the L'Aquila earthquake: part II—"heavy damage" reconstruction. *Bulletin of Earthquake Engineering* , **15** , 693–729 , 2017.

[5] M. Di Ludovico, A. Prota, C. Moroni, G. Manfredi, M. Dolce, Reconstruction process of damaged residential buildings outside historical centres after the L'Aquila earthquake: part I—"'light damage'" reconstruction. *Bulletin of Earthquake Engineering* , **15** , 667–692 , 2017.

[6] R.O. Hamburger, A vision for performance based earthquake engineering. Unpublished white paper.

[7] Moehle J., G. G. Deierlein, A framework methodology for performance-based earthquake engineering. *13th World Conference on Earthquake Engineering*, Vancouver , Canada, 1-6 August, 2004.

[8] A. Whittaker, R. Hamburger, M. Mahoney, Performance-based engineering of buildings for extreme events. *AISC-SINY Symposium on Resisting Blast and Progressive Collapse*, New York, USA, 4-5 December, 2003.

[9] F. Braga, F. Morelli, W. Salvatore, A Macroseismic Approach for the Evaluation of Seismic Risk. J. Kruis, Y. Tsompanakis, B. Topping, Eds., *Fifteenth International Conference on Civil, Structural and Environmental Engineering Computing*, 1–12.

[10] Applied Technology Council, *FEMA P-58-1 Seismic Performance Assessment of Buildings – Methodology*. Washington D.C.: Federal Emergency Management Agency (FEMA), 2012.

[11] A. Dall'Asta, G. Leoni, F. Morelli, W. Salvatore, A. Zona, An innovative seismic-resistant steel frame with reinforced concrete infill walls. *Engineering Structures* , **141** , 144–158 , 2017.

[12] A. Braconi, F. Morelli, W. Salvatore, Development, design and experimental validation of a steel self-centering device (SSCD) for seismic protection of buildings. *Bulletin of Earthquake Engineering* , **10** , 1915–1941 , 2012.

[13] A. Filiatrault, S. Cherry, Seismic design spectra for friction damped structures. *Journal of Structural Engineering* , **116** , 1334–1355 , 1990.

[14] C. Christopoulos, R. Tremblay, H.-J. Kim, M. Lacerte, Self-Centering Energy Dissipative Bracing System for the Seismic Resistance of Structures: Development and Validation. *Journal of Structural Engineering* , **134** , 96–107 , 2008.

[15] M. D. Symans *et al.*, Energy Dissipation Systems for Seismic Applications : Current Practice and Recent Developments. *Journal of Structural Engineering*, **134** , 3–21 , 2008.

[16] F. Braga, P. D'Anzi, Steel braces with energy absorbing devices: a design method to retrofit reinforced concrete existing buildings. *Italian-French Symposium on Strengthening and Repair of Structures in Seismic Area*, Nice, France, 1994.

[17] V. Ciampi, M. De Angelis, F. Paolacci, Design of yielding or friction-based dissipative bracings for seismic protection of buildings. *Engineering Structures* , **17** , 381–391 , 1995.

[18] I. Takewaki, Optimal damper placement for minimum transfer functions. *Earthquake Engineering and Structural Dynamics* , **26** , 1113–1124 , 1997.

[19] R. Levy, E. Marianchik, A. Rutenberg, F. Segal, Seismic design methodology for friction damped braced frames. *Earthquake Engineering & Structural Dynamics* , **29** 1569–1585 , 2000.

[20] O. Lavan, G. F. Dargush, Multi-Objective Evolutionary Seismic Design with Passive Energy Dissipation Systems Multi-Objective Evolutionary Seismic Design with Passive Energy Dissipation Systems. *Journal of Earthquake Engineering* , **13**, 758–790, 2009.

[21] N. Pollini, O. Lavan, O. Amir, Towards realistic minimum-cost optimization of viscous fluid dampers for seismic retrofitting. *Bulletin of Earthquake Engineering* , **14** , 971–998 , 2016.

[22] N. Pollini, O. Lavan, O. Amir, Minimum-cost optimization of nonlinear fluid viscous dampers and their supporting members for seismic retrofitting. *Earthquake Engineering & Structural Dynamics* , **46** , 1941–1961 , 2017.

[23] O. Lavan, P. J. Wilkinson, Efficient Seismic Design of 3D Asymmetric and Setback RC Frame Buildings for Drift and Strain Limitation. *Journal of Structural Engineering* , **143** , 1–12 , 2017.

[24] J. A. Inaudi, J. M. Kelly, C. W. S. To, Statistical linearization method in the preliminary design of structures with energy dissipating devices. *ATC 17-1 Seminar on seismic isolation, passive energy dissipation, and active control*, San Francisco , California, 11-12 March, 1993.

[25] Y. Fu, S. Cherry, Design of friction damped structures using lateral force procedure. *Earthquake Engineering and Structural Dynamics* , 989–1010 , 2000.

[26] A. S. Whittaker, M. C. Constantinou, O. M. Ramirez, M. W. Johnson, C. Z. Chrysostomou, Equivalent Lateral Force and Modal Analysis Procedures of the 2000 NEHRP Provisions for Buildings with Damping Systems. *Earthquake Spectra* , **19** , 959–980 , 2003.

[27] F. Mazza, A. Vulcano, Equivalent viscous damping for displacement-based seismic design of hysteretic damped braces for retrofitting framed buildings. *Bulletin of Earthquake Engineering* , **12** , 2797–2819 , 2014.

[28] J. Wen, W. Guo, C. Christopoulos, Performance spectra based method for the seismic design of structures equipped with passive supplemental damping systems. *Earthquake Engineering & Structural Dynamics* , **42**, 935–952 , 2013.

[29] F. Braga, R. Gigliotti, R. Laguardia, Intervention cost optimization of bracing systems with multiperformance criteria. *Engineering Structures* , **182** , 2019.

[30] M. J. N. Priestley, Performance based seismic design. *12th World Conference on Earthquake Engineering (WCEE)*, Auckland, New Zealand, 30 January-4 February, 2000.

[31] NTC 2008, Decreto Ministeriale 14/1/2008 - Norme tecniche per le costruzioni. Italian Ministry of Infrastructures and Transportations, Gazzetta Ufficiale n.30 4/2/2008.

[32] S. Mazzoni, F. McKenna, M. H. Scott, G. L. Fenves, OpenSees command language manual. *Pacific Earthquake Engineering Research (PEER) Center* , 451 , 2007.

[33] F. Morelli, R. Laguardia, M. Faggella, A. Piscini, R. Gigliotti, W. Salvatore, Ground motions and scaling techniques for 3D performance based seismic assessment of an industrial steel structure. *Bulletin of Earthquake Engineering* , **16** , 2018.

[34] M. Laterza, M. D'Amato, R. Gigliotti, Modeling of gravity-designed RC sub-assemblages subjected to lateral loads. *Engineering Structures* , **130** , 242–260 , 2017.

[35] M. Laterza, M. D'Amato, F. Braga, R. Gigliotti, Extension to rectangular section of an analytical model for concrete confined by steel stirrups and/or FRP jackets. *Composite Structures* , **176** , 910–922 , 2017.

[36] A. F. Mohammad, M. Faggella, R. Gigliotti, E. Spacone, Seismic performance of older R/C frame structures accounting for infills-induced shear failure of columns. *Engineering Structures* , **122** , 1–13 , 2016.

[37] S. Caprili, F. Mattei, R. Gigliotti, W. Salvatore, Modified cyclic steel law including bond-slip for analysis of RC structures with plain bars. *Earthquakes and Structures* , **14** , 187–201 , 2018.

[38] F. Romano, M. Faggella, R. Gigliotti, M. Zucconi, B. Ferracuti, Comparative seismic loss analysis of an existing non-ductile RC building based on element fragility functions proposals. *Engineering Structures* , **177** , 707–723 , 2018.

[39] R. Laguardia, R. Gigliotti,F. Braga, Optimal design of dissipative braces for seismic retrofitting through a multi- performance procedure. *ANIDIS 2017 "L'Ingegneria sismica in Italia*", Pistoia, Italia, 17-23 September, 2017.

COMPDYN 2019
7th ECCOMAS Thematic Conference on
Computational Methods in Structural Dynamics and Earthquake Engineering
M. Papadrakakis, M. Fragiadakis (eds.)
Crete, Greece, 24–26 June 2019

ON THE IMPORTANCE OF BRACE CONNECTION MODELLING FOR SEISMIC PERFORMANCE ASSESSMENT OF STEEL CBFS

A. Silva[1], **J.M. Castro**[2], **and R. Monteiro**[1]

[1] Scuola Universitaria Superiore IUSS Pavia
Piazza della Vittoria, 15, 27100 Pavia PV, Italy
e-mail: {antonio.moutinho, ricardo.monteiro}@iusspavia.it

[2] Faculty of Engineering, University of Porto
Rua Dr. Roberto Frias, s/n, 4200-465 Porto, Portugal
miguel.castro@fe.up.pt

Abstract

The main objective of this paper is to assess the effect of different modelling approaches of brace-to-frame gusset plate connections for seismic performance assessment of steel concentrically-braced frames (CBFs). Two scenarios are considered, namely: i) simplified simulation of braces through a centreline-to-centreline pinned-ended idealization; ii) explicit simulation of brace-to-frame gusset connections. A suite of building archetypes, with different bracing configurations and building heights, are used to show the effect of the aforementioned modelling variants on different metrics of seismic performance (e.g. lateral deformations, collapse risk, economic losses). Across the group of metrics considered, it is shown that the non-consideration of brace-to-frame connections may entail biased characterizations of seismic performance.

Keywords: concentrically-braced steel frames, brace gusset connections, OpenSees, seismic performance.

1 INTRODUCTION

Seismic performance assessment of buildings may be conducted through simplified numerical models based on several modelling assumptions. Such assumptions, however, may or not entail less accurate estimates of seismic performance. In the context of steel concentrically-braced frames (CBFs), more simplified strategies, in which diagonals are simulated using their centreline-to-centreline length coupled with fully-pinned boundary conditions, have been adopted in the literature [2]. On the other hand, more refined numerical models may be associated with explicit simulation of the brace-to-frame gusset plate connections [1], in which the gusset geometry plays a primordial role on the rigidification of portions of the beams and columns intersected by the gusset plate connection, as well as the physical length and boundary conditions of the bracing diagonals. As one may infer, this modelling approach requires the complete definition of the plate characteristics through a seismic design process, which may not be easily achievable for large building populations. Furthermore, it is unclear in the literature whether or not the two modelling approaches entail relevant differences in seismic performance characterizations across different bracing configurations and metrics of seismic performance (e.g. collapse risk, earthquake-induced economic losses). Based on the aforementioned aspects, this research study evaluates the implications of non-explicit simulation of brace-to-frame connections across different metrics of performance. This is achieved by resorting to a suite of archetype buildings seismically designed to Part 1 of Eurocode 8 (EC8-1) [3], using different bracing configurations and building heights.

2 ARCHETYPE BUILDING POPULATION

In order to assess the implications of numerical modelling refinement of brace-to-frame gusset connections, a comprehensive group of CBF archetypes was defined and seismically designed to EC8-1. According to EC8-1, several bracing configurations can be adopted for steel CBF buildings (see Figure 1). Depending on the bracing type, different design approaches are prescribed by the code. The code also differentiates the upper-bound reference value of the behaviour factor, q, which, for the medium ductility class (DCM), is set equal to 4 and 2 for non-chevron and chevron CBFs, respectively.

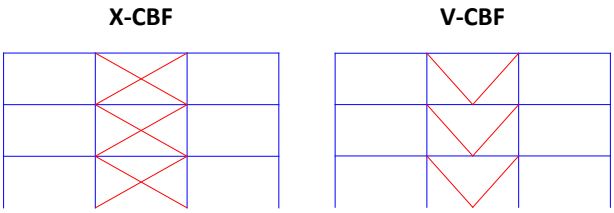

Figure 1: Considered concentric bracing configurations.

For this research study, the CBF typologies shown in Figure 1 were considered and Lagos, a moderate-seismicity location in Portugal was adopted to design a set of archetype buildings to EC8-1. The elastic response spectrum specified by the code for this location is shown in Figure 3. A single plan layout was adopted (see Figure 2), with a regular grid of 6m spans across both the longitudinal and transversal directions. The lateral load-resisting system (LLRS) in the longitudinal direction is composed by the two external frames, as highlighted in red in Figure 2. The internal longitudinal frame was assumed to provide no lateral resistance, serving only as a gravity-carrying system. Furthermore, the transversal and longitudinal LLRSs were assumed to be independent from each other, and only the latter was focus of attention herein. For all designs, the relevant tributary areas for gravity loads and seismic

masses were computed. The same level of distributed gravity loads was adopted for all designs, as summarized in Table 1.

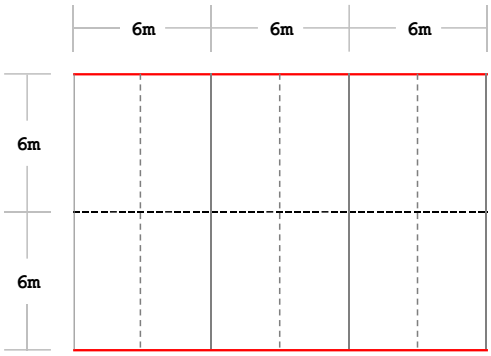

Figure 2. Plan view of the building configuration adopted.

Floor	Load type	Load [kN/m^2]
Top	Dead	4.75
	Live	1.00
Other	Dead	5.75
	Live	2.00

Table 1. Distributed gravity loads.

In elevation, archetypes of 3, 5 and 8 storeys were considered, with a bottom-storey height of 4.5m, and the remaining storey heights of 3.5m. In total, fifteen archetype steel CBF buildings were adopted in this study.

3 NUMERICAL MODELS AND GROUND MOTION RECORDS

To what regards the simulation of steel CBFs subjected to earthquakes, Karamanci and Lignos [4] have recently proposed a numerical modelling approach for the seismic performance assessment of steel CBFs using OpenSees [5]. With this approach, concentrated plasticity rotational springs simulating the inelastic response of both beams and columns are adopted [6]. For the braces, the model employs displacement-based distributed plasticity elements with an initial global imperfection, with material-level considerations regarding the effects of low-cycle fatigue. Brace-to-frame connections are also explicitly simulated, by resorting to the recommendations of Hsiao et al. [1]. According to the authors, the numerical length of the diagonals should reflect the physical dimensions of the members, and the out-of-plane response of the gusset plate is accounted for through inelastic rotational springs. The connection of these springs to the beams and/or columns is attained through rigid elements whose dimensions should consistent with the geometry of the gusset plate. In the absence of any gusset plate, the response of the beam-column shear tab connection should be considered at its physical location. Mohsenzadeh and Wiebe [7] have recently demonstrated that simulating these shear tabs by resorting to fully-pinned connections leads to identical seismic responses to those obtained with explicit connection simulation. All numerical modelling aspects detailed before were adopted for the research study detailed in this paper, under the reference (REF) modelling variant. In the case of the simulation of beam-to-column shear tab connections, a fully-pinned connection was considered [7]. All CBFs were modelled as fixed at the base, and global second-order (P-Δ) effects were explicitly considered. A 2-% Rayleigh damping was adopted by assigning a damping coefficient of 2% [8] to the first and one of the last significant modes of the structure, the latter taken as the number of storeys[9]. The stiffness component of the damping model was computed only for the elastic elements of the model, thus avoiding large artificial damping forces [4][7]. The gravity framing system was explicitly simulated following the recommendations available in the literature [4][7].

As one may infer from the description discussed before, the complexity of the REF models can be considered high. Brace-to-frame connections are explicitly simulated, which requires

complete definition of its geometry via a strenuous seismic design process. It should be noted, however, that whether or not more simplified approaches (e.g. fully-pinned boundary conditions for the diagonals) entail unrealistic estimates of seismic performance has not yet been thoroughly investigated. Even though Hsiao et al. [1] have demonstrated the importance of explicit simulation of gusset connections through cyclic force-deformation responses of single-span, single bay SD CBFs, a similar sensitivity study focusing on more macro-level metrics of performance (e.g. collapse risk, earthquake-induced economic losses) is mostly absent in the literature. With the aforementioned limitations in mind, a modification to the REF approach was evaluated. This modelling variant, hereafter referred as VAR, reflects a more simplified approach in which diagonal centreline-to-centreline lengths coupled with fully-pinned boundary conditions are adopted [2]. By modifying the reference model, the locations of the rotational springs of beams and columns were shifted to the physical location of beam-column connections (i.e. panel-zone boundaries).

As previously reported, all archetypes were assumed to be located in the city of Lagos, a moderate-seismicity region located in mainland Portugal. Probabilistic Seismic Hazard Analysis (PSHA) was performed for the site in question, using the open source software OpenQuake [10] and the seismic hazard model of SHARE [11]. Additional hazard sources and ground motion prediction equations were also adopted, as proposed by Silva et al. [12]. The hazard curves obtained in this process, in terms of the relationship between the first-period spectral accelerations, Sa(T1) and the annual rate of exceedance, λ, are summarized in Figure 3 for a select number of periods. Disaggregation of the seismic hazard [13] on magnitude, distance and ε was performed, which served as the basis for the ground motion record selection scheme and was used in conjunction with the average shear wave velocity for the first 30 meters of soil, vs,30. For this location, a suite of 30 ground motion records was selected and scaled so that the 2%-damped median spectrum of the suite matched the prescribed response spectrum of EC8-1 for a 10% in 50 years hazard level, considering a wide range of periods of interest. This approach, which is similar to the one adopted in FEMA P695 [14], was attained with the SelEQ [15]. As shown in Figure 3, a fairly accurate correlation between the mean/median spectrum of the selected ground motions and the code-specified response spectrum was achieved.

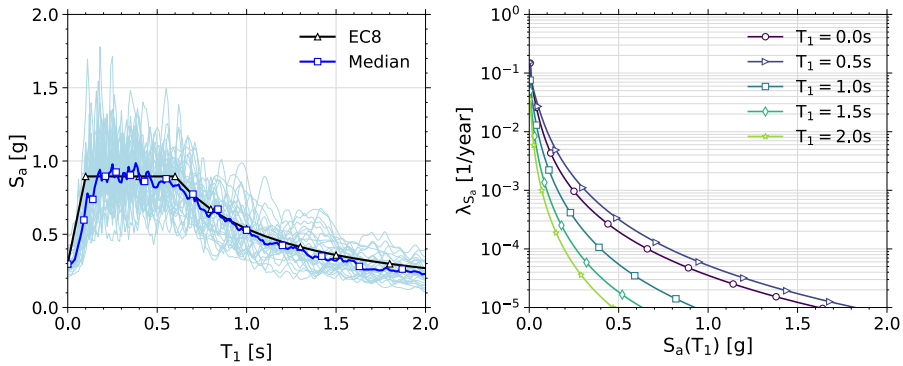

Figure 3: Code-specified and median ground motion response spectrum (left) and seismic hazard curves (right) for Lagos.

4 COMPARISON OF FUNDAMENTAL PERIODS AND SEISMIC DEMANDS

As a result of the application of the modelling procedures detailed before, one major implication of interest relates to the fundamental period, T_1, associated with the archetypes considered in this study, as per Figure 4. Furthermore, the different modelling approaches should

also influence the seismic demand imposed to the building, as summarized in Figure 4 via the spectral acceleration demands associated with the T_1, $S_a(T_1)$, of each model.

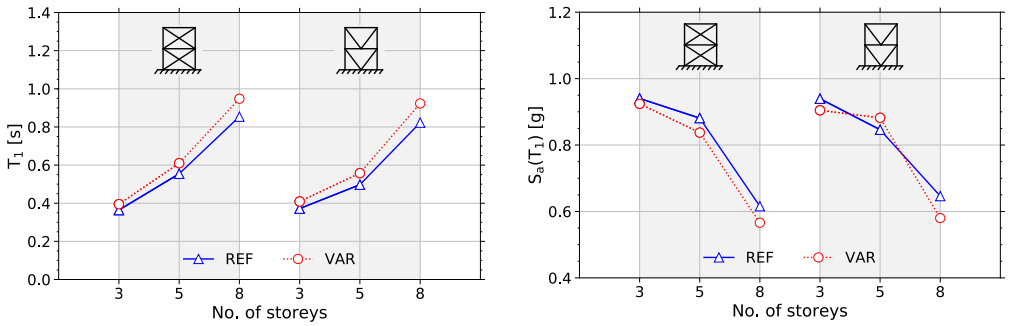

Figure 4: Comparison of fundamental periods (left) and first-period spectral demands (right).

Analysis of the results summarized in Figure 4 allows concluding about the relevant effect of non-explicit modelling of brace-to-frame gusset plates (VAR), namely by comparison to the reference models (REF). This is due to the fact that diagonal members are simulated through centreline-to-centreline lengths, which entails higher brace slenderness levels throughout the suite of diagonals. In turn, the lateral stiffness of the CBF reduces, and the period of vibration increases. These differences are carried to the seismic demands imposed to the archetypes, as denoted by the results of Figure 4. According to the comparison of first-period spectral demands, an important effect of a more simplified consideration of the brace-to-frame connections (VAR) can be observed. With a more simplified modelling approach, differences of $S_a(T_1)$ against the reference model remained roughly between -10% and +5%, being typically larger in amplitude for the taller archetypes.

5 LATERAL DEFORMATIONS AT THE EC8 LIMIT STATE INTENSITIES

The first performance metric evaluated in this study pertains the levels of lateral deformations observed across several seismic intensities of interest within the framework of Eurocode 8. These correspond to design and/or assessment limit states established in Part 1 [3] and Part 3 [16] of EC8. For each of these limit state intensities, every archetype was subjected to the same ground motion suite scaled to the respective intensity of interest. For each archetype, the results were then assessed via the mean response across all 30 records. Figure 5 shows the observed inter-storey drift ratios (i.e. ratio of inter-storey displacements and storey height), ISDRs, for the 5-storey archetypes at the ULS limit state intensity (return period of 475 years). In the figure, the two modelling considered in this study (REF and VAR) are represented.

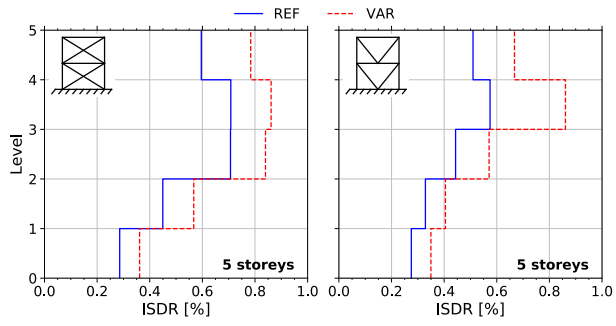

Figure 5: Comparison of ISDRs at the ULS limit state intensity for a 5-storey X-CBF and V-CBF.

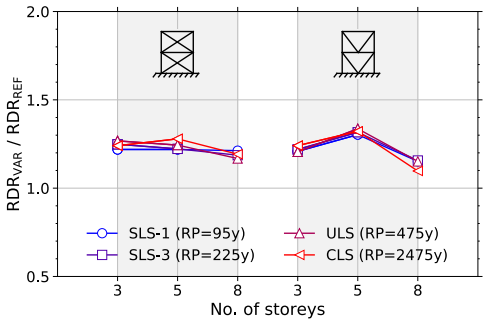

Figure 6: Comparison of roof drift ratios (RDRs) at the EC8 limit state intensities.

As shown in Figure 5, the ISDRs associated with VAR models were larger than those obtained with the REF models at all storeys. This observation was found across all archetypes and limit state intensities, as summarized in Figure 6. In the figure, the roof drift ratio, RDR, taken as the ratio between the lateral displacement of the uppermost floor level and the building height is shown. The results are presented as a direct comparison of the RDRs between those associated with the REF and VAR modelling variants. From the figure, it can be clearly observed that brace simulation through a pinned-ended centreline-to-centreline approach (VAR) may entail significantly higher lateral deformations levels in comparison to a more refined approach (REF). This occurred despite VAR models having lower first-period acceleration demands (see Figure 4). This observation clearly reveals the importance of explicit consideration of brace-to-frame gusset plates to evaluate the seismic response and performance of CBF buildings. The use of more simplified models that do not consider the influence of the dimensions and flexibility of the brace-to-frame gusset plates should be avoided, particularly if deformation-based seismic performance characterizations are adopted.

6 EARTHQUAKE-INDUCED RISK

The second performance metric evaluated in this study pertains the seismic collapse risk associated with the suite of archetypes. This was attained by subjecting building archetypes to Incremental Dynamic Analysis (IDA) [17]. The mean annual frequency of collapse, λ_c, was employed to interpret the collapse risk by integration of the collapse fragility curve and the seismic hazard at the site [18]. The ground motion record suite detailed in Section 3 of this paper was employed for the IDA process. Every time-history analysis was extended by 5 seconds of free vibration time, and the residual deformations of each storey were computed by averaging the lateral deformations of the CBF within this free vibration time. To what concerns the intensity measure (IM) adopted in this assessment, the 2%-damped spectral acceleration at the fundamental period, $S_a(T_1,2\%)$, was adopted. The resulting IDA curve was interpreted to pinpoint the exceedance of the collapse limit state, assumed as the instance associated with either a reduction to less than 20% of the initial slope of the IDA curve or an ISDR above 10% [19]. A collapse fragility curve was then constructed by fitting a lognormal cumulative distribution function, defined by a median value, θ, and a lognormal standard deviation, β. The results obtained in this assessment are summarized in Figure 7, in terms of the probability of collapse within a 50-year timeframe, $P_{c,50}$, across all archetypes and numerical modelling variants.

As shown in Figure 7, VAR models generally produced relevant disparities in relation to the reference modelling approach. This important observation highlights the fact that simulating the braces through a more simplified centreline-to-centreline pinned-ended approach may entail erroneous estimates of collapse performance when compared with results obtained with more refined modelling approaches (REF). It is thus recommended that explicit modelling considerations regarding the brace-to-frame gusset plates should be adopted, regardless of bracing configuration or number of storeys.

The last seismic performance metric employed in this research study concerns the expected annual losses (EALs) associated with the archetype population under assessment. These were computed following the building-specific storey-based loss estimation methodology proposed by Ramirez et al [21], considering the effect of demolition-related losses [22]. In order to compute the demolition-related losses, the probability of demolition given a residual ISDR, P(D|RISDR), was assumed to follow a lognormal distribution with a median of 1.85% and a logarithmic standard deviation of 0.3 [23]. To what pertains the repair losses, the structural damage fragility curves proposed in HAZUS [24] for high-code steel braced frames were used, in conjunction with the repair cost ratios proposed in HAZUS for multifamily dwellings. Fi-

nally, the component category weights were re-scaled to better reflect structural-to-non-structural content distributions in Portugal, namely: i) drift-sensitive structural components, 25%; ii) drift-sensitive non-structural contents, 55%; and iii) acceleration-sensitive non-structural components, 20%. The results obtained in this process are summarized in Figure 8, in terms of the total EALs across all archetypes and modelling variants.

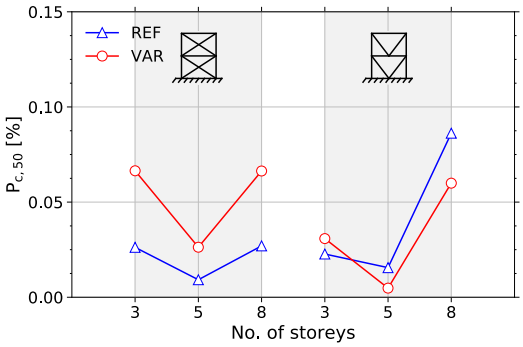

Figure 7: Comparison of collapse risk.

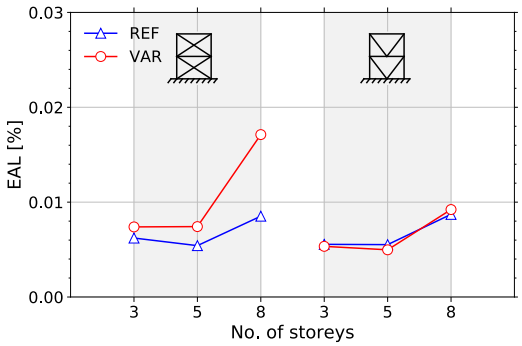

Figure 8: Comparison of expected annual losses.

A number of important conclusions can be inferred from Figure 8. Firstly, the EAL levels associated with the considered CBF archetypes, regardless of the modelling variant employed, were relatively low. In similar fashion to the collapse risk results discussed previously, the low seismic losses shown herein are directly correlated to the seismic hazard associated with Lagos. To what regards the results associated with VAR models, once again clear differences against the results obtained with the REF models were obtained. These finding once again demonstrate the importance of explicit modelling of brace-to-frame gusset plates for seismic performance assessment of steel CBFs.

7 CONCLUSIONS AND FUTURE WORK

In this paper, the sensitivity of seismic performance assessment results to the modelling refinement of brace-to-frame connections on steel CBFs was evaluated. In this context, two modelling variants were applied to a population of EC8-compliant archetypes, of various bracing configurations and building heights, namely: i) REF, in which the gusset plates are explicitly seismically designed and simulated [4]; ii) VAR, in which diagonals are simulated through a centreline-to-centreline length with fully-pinned boundary conditions, therefore neglecting the physical presence of the connection of the brace to the beams and columns [2]. A number of seismic performance metrics were considered as a comparison measure between the results obtained with each modelling variant. From the limited scope of the results obtained, a number of aspects merit discussion.

Firstly, VAR models produced more flexible CBFs in relation to equivalent REF models. This relates to a lower physical brace length compared to a centreline-to-centreline member length, in conjunction with the actual rotational flexibility of the connection. Consequentially, a non-negligible effect on the seismic demand imposed to the structure was also observed. Secondly, through an assessment of lateral deformations at the EC8 limit state intensities (i.e. return periods between 95 to 2475 years), VAR models generally produced unrealistic deformations in relation to the reference results. This observation tended to apply also to earthquake-induced collapse risk and expected annual losses. It is thus recommended that the use of more simplified models that do not consider the influence of the dimensions and flexibility of the brace-to-frame gusset plates should be avoided.

In the authors' opinion, the results shown in this paper demonstrate the relevant implications of non-explicit simulation of brace-to-frame gusset connections in the context of seismic performance assessment of steel CBF buildings. It is important to assess a wider building population to confirm the main findings detailed herein. Furthermore, the possibility of more simplified and expedited processes for the sizing of brace-to-frame gusset plates should be focus of research in the near future. This need is mainly due to the impracticality of explicit seismic design of brace-to-frame connections for large building populations. These aspects are presently being addressed in ongoing research work by the authors of this paper.

REFERENCES

[1] Hsiao, P-C., Lehman, D.E., Roeder, C.W., improved analytical model for special concentrically braced frames, Journal of Constructional Steel Research, 73:80-94, 2012.

[2] D'Aniello, M., La Manna Ambrosino, G., Portioli, F., Landolfo, R., Modelling aspects of the seismic response of steel concentric braced frames, Steel and Composite Structures, 15(5):539-566, 2013.

[3] CEN, EN 1998-1 Eurocode 8: Design of structures for earthquake resistance. Part 1, General rules, seismic actions and rules for buildings. European Committee for Standardization, Brussels, Belgium, 2004.

[4] Karamanci, E., Lignos, D.G., Computational approach for collapse assessment of concentrically braced frames in seismic regions, Journal of Structural Engineering, 140(8):A4014019, 2014.

[5] PEER, OpenSees: Open system for earthquake engineering simulation, Pacific Earthquake Engineering Research Center, University of California, Berkeley, California, 2006.

[6] Lignos, D.G., Krawinkler, H., Deterioration modeling of steel components in support of collapse prediction of steel moment frames under earthquake loading, Journal of Structural Engineering, 137(11):1291-1302, 2011.

[7] Mohsenzadeh, V. Wiebe, L., Effect of beam-column connection fixity and gravity framing on the seismic collapse risk of special concentrically braced frames, Soil Dynamics and Earthquake Engineering, 115:685-697, 2018.

[8] Bernal, D., Döhler, M., Kojidi, S.M., Kwan, K., Liu, Y., First mode damping ratios for buildings, Earthquake Spectra, 31(1):367-381, 2015.

[9] Carr, A.J., Damping models for inelastic structures, Proceedings of Asia Pacific vibration conference, 1997.

[10] Pagani, M., Monelli, D., Weatherill, G., Danciu, L., Crowley, H., Silva, V., Hanshaw, P., Butler, L., Nastasi, M., Panzeri, L., Simionato, M., Viganò, D., OpenQuake Engine: An Open Hazard (and Risk) Software for the Global Earthquake Model, Seismological Research Letters, 2014, 85(3):692–702.

[11] Woessner, J., Danciu, L., Giardini, D., Crowley, H., Cotton, F., Grünthal, G., Valensise, G., Arvidsson, R., Basili, R., Demircioglu, M.N., Hiemer, S., Meletti, C., Musson, R.W., Rovida, A.N., Sesetyan, K., Stucchi, M., The SHARE consortium, The 2013 European

Seismic Hazard Model: key components and results, Bulletin of Earthquake Engineering, 2015, 13(12):3553–3596.

[12] Silva, V., Crowley, H., Varum, H., Seismic risk assessment for mainland Portugal, Bulletin of Earthquake Engineering, 2015, 13:429–457.

[13] Bazurro, P., Cornell, C.A., Disaggregation of Seismic Hazard, Bulletin of the Seismological Society of America, 1999, 89(2):501–520.

[14] FEMA, FEMA P695: Quantification of building seismic performance factors, Federal Emergency Management Agency (FEMA), Washington, D.C., USA, 2009.

[15] Macedo, L., Castro, J.M., SelEQ: An advanced ground motion record selection and scaling framework. Advances in Engineering Software, 2017, 14:32–47.

[16] CEN, EN 1998-3 Eurocode 8: Design of structures for earthquake resistance. Part 3, Assessment and retrofitting of buildings. European Committee for Standardization, Brussels, Belgium, 2005.

[17] Vamvatsikos, D., Cornell, C.A., Incremental dynamic analysis. Earthquake Engineering & Structural Dynamics, 2002, 31(3):491–514.

[18] Eads, L., Miranda, E., Krawinkler, H., Lignos, D.G., An efficient method for estimating the collapse risk of structures in seismic regions. Earthquake Engineering & Structural Dynamics, 2013, 42(1): 25-41.

[19] Federal Emergency Management Agency, FEMA 350, Recommended seismic design criteria for new steel moment-frame buildings SAC Joint Venture, Sacramento, California, 2000.

[20] ASCE. Minimum design loads for buildings and other structures, ASCE/SEI 7-10. American Society of Civil Engineers: Reston, VA, 2010.

[21] Ramirez, C.M., Mitrasi-Reiser, J, Haselton, C.B., Spear, A.D., Steiner, J., Deierlein, G.G., Miranda, E., Expected earthquake damage and repair costs in reinforced concrete frame buildings. Earthquake Engineering and Structural Dynamics, 2012, 41(11), 1455-1475.

[22] Ramirez, C.M., Miranda, E., Significance of residual drifts in building earthquake loss estimation. Earthquake Engineering and Structural Dynamics, 2012, 41(11), 1477-1493.

[23] Jayaram, N., Shome, N., Rahnama, M., Development of earthquake vulnerability functions for tall buildings, Earthquake Engineering and Structural Dynamics, 2012, 41(11): 1495-1514.

[24] FEMA, HAZUS - Earthquake loss estimation methodology, Federal Emergency Management Agency, Washington, DC, 1999.

[25] Beck, J.L, Porter, K.A., Shaikhutdinov, R.V., Simplified estimation of seismic life-cycle costs, ASCE Library, 2004, 229–237.

COMPDYN 2019
7th ECCOMAS Thematic Conference on
Computational Methods in Structural Dynamics and Earthquake Engineering
M. Papadrakakis, M. Fragiadakis (eds.)
Crete, Greece, 24–26 June 2019

RELATIONSHIP BETWEEN RESPONSE MODIFICATION COEFFICIENT AND DISPLACEMENT AMPLIFICATION FACTOR FOR DIFFERENT SEISMIC LEVELS AND SITE CLASSES

Bulent Erkmen[1]

[1] Ozyegin University, Department of Civil Engineering
Istanbul-Turkey
e-mail: Bulent.erkmen@ozyegin.edu.tr

Abstract

Modern seismic design provisions allow structural systems to be designed for reduced forces, which are typically much smaller than the corresponding elastic design loads. This reduction in seismic loads is done by using response modification coefficient. The maximum deflection or drift of structural systems is typically predicted by scaling deflections corresponding to this reduced force on elastic line by displacement amplification factor. The values of these two seismic design factors, which are independent of seismic level and site (soil) class for a given type of structure, are mostly based on accumulated experience from past earthquakes and engineering judgment.

In this study, a large number of five story parking garage structures were designed with a range of response modification factors for two seismic levels and for different site classes. The seismic performance of the structures was determined by performing nonlinear time history analysis with several recorded earthquake records on corresponding site classes. The computed maximum drift values were used to develop relationship between response modification coefficient and corresponding deflection amplification factor for each site class and seismic level. The results show that these two seismic design parameters are related but seismic level and site classes does not have significant effects on the relationship.

Keywords: Response Modification Coefficient, Displacement Amplification Factor, Ductility, Seismic Design.

1 INTRODUCTION

Seismic design of a structural system to remain elastic or free of damage during a severe earthquake loading requires the structure to be designed to resists very large dynamic loads. Such a design approach results in significantly expensive and massive structures. Therefore, moderns seismic design provisions allow structures to be designed for much smaller loads then those required to maintain the structure elastic. This reduction is done by using reduction factor known as response modification coefficient (R), which solely depends on building seismic force-resisting system. The R coefficient was first introduced in 1978 by Applied Technology Council [1]. In the mid-1980s, researcher at the University of California at Berkeley performed a number of experiments to construct draft formulas for R as a function of reserve strength, ductility, and damping [2]. Relationships for R coefficient as a function of different parameters such as ductility, structure fundamental period, post-yielding stiffness, and soil characteristic were proposed by Newmark and Hall [3], Riddell et al. [4], Miranda [5], Nasar and Krawinkler [6], Vidic et al. [7], and Uang [8]. However, although value of R accounts for structural damping, ductility, over-strength, and redundancy, the code assigned values are mainly based on engineering judgment and seismic performance of structural systems in previous earthquakes [1, 8].

Because the reduced seismic forces are used in design, the computed lateral displacements from elastic analysis corresponding to design loads are amplified in order to estimate the actual nonlinear and inelastic lateral displacements that develop during design earthquake. This is done usually by using displacement amplification factor C_d. *Figure 1* show effects of these two seismic design factors on seismic design. The value of R as given in ASCE/SEI 7-16 [9] is between 1.5 an 8, where a value of 1.0 correspond to elastic structure, and those for C_d are between 1.0 and 6.5.

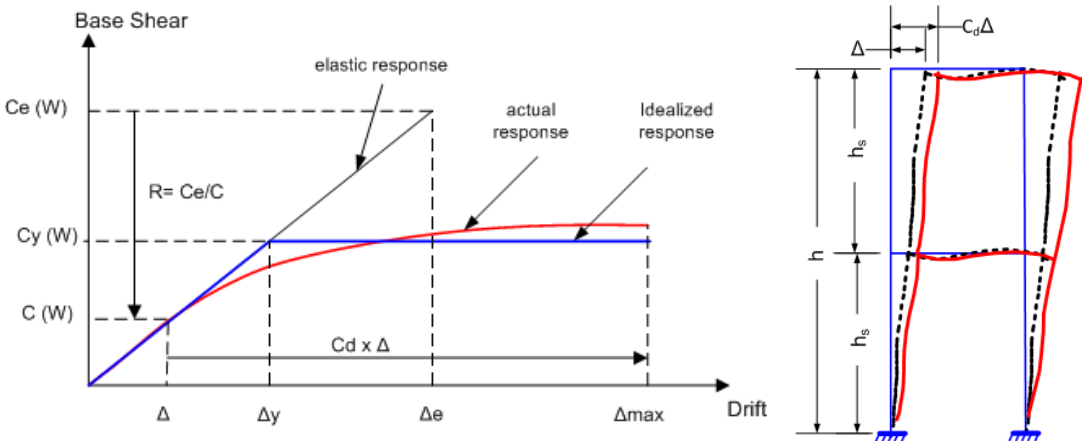

Figure 1: Design spectra and seismic design parameters.

Although it is well known that both R and C_d are interrelated, there is a limited number of studies investigating this relationship. The Uniform Building Code, which uses R_w as force reduction coefficient, assigns $3R_w/8$ for C_d factor [8]. The Commentary of the SEAOC Recommended Lateral Force Requirements, which is the basis for UBC seismic design provisions, states that C_d can be as high as R_w [8].

A review of national building codes indicates that the ratios of R and C_d vary considerably from one code to another. The objective of this study is to determine the relationship between

these two seismic design parameters including effects of site classes and seismic levels. For this purpose, a large number of prototype parking garage structures were designed using *R* values from 4.0 to 8.0 with 0.5 increments. In total, two seismic levels (high and low) and four site classes were considered. For each site class, six actual earthquake time-acceleration data recorded on the same site class were used to preform nonlinear time history analysis of the prototype buildings. The computed deflections were used to establish relationship between seismic design parameters for each seismic level and site class.

2 PROTOTYPE STRUCTURE

A precast parking garage structure was selected as the prototype structure. The structure was designed as five story to include higher modes effects on results. The structure was designed for two seismic levels mainly 0.4*g* (low) and 0.8*g* (high) for spectral response acceleration per ASCE/SEI 7-16. For building location, five site classes (i.e., A, B, C, D, and E) defined in ASCE/SEI 7-16 were considered. However, site classes A and B were considered as a single site class (AB) since the corresponding design spectra and design requirements were not much different. The plan and elevation views of the building are given in *Figure 2*. Each story was 3.2 m high with a roof of 1-m high from top of the spandrels. The floor plan is typical for parking garage structures, and it features four unbonded post tensioned precast (PTT) shear walls as the only seismic force-resisting system in the N-S direction. Two lines of "light bearing walls" were used as seismic force resisting system in E-W direction. In this study, building seismic performance only in N-S direction was considered.

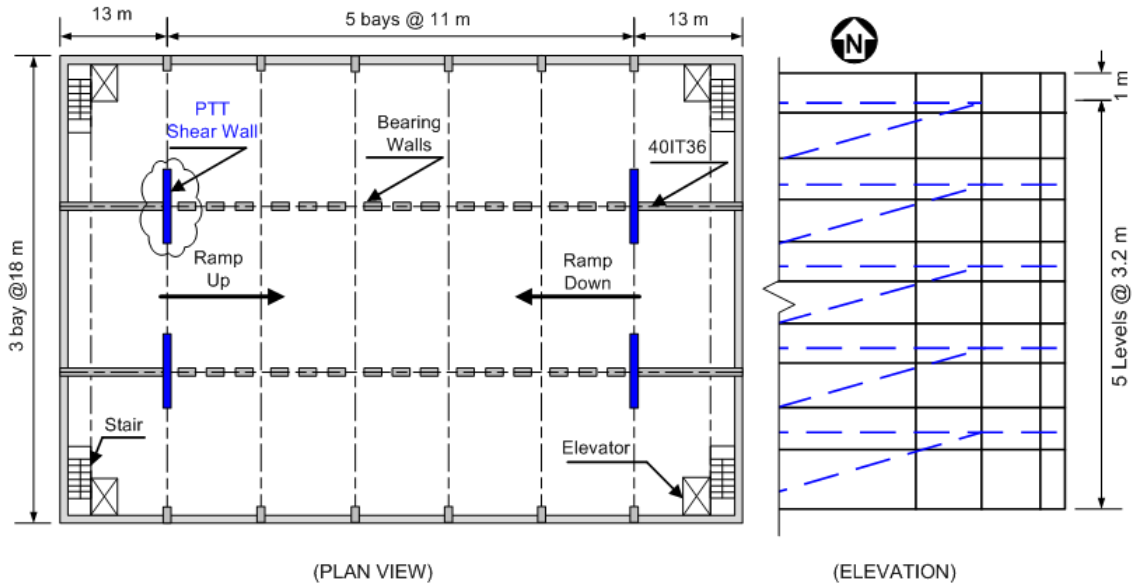

Figure 2: Plan and elevation views of prototype parking structure.

The unbonded post-tensioned precast shear walls are jointed construction, and they do not possess disadvantages of monolithic shear walls as shown by the PRESSS (PREcast Seismic Structural Systems) Research Program [10]. In such seismic force-resisting systems, concrete wall units remain almost undamaged due to lack of bond between post-tensioned tendons and concrete. The walls designed based on this design philosophy also known as jointed construction resist lateral loads by opening and closing of joints between precast members without causing significant damage to structural members. Unbonded precast concrete shear walls have been studied both experimentally and analytical by a number of researchers including Kurama et al. [11]., Shultz et al. [12], and Erkmen et al. [13].

The cross-section and elevation of prototype walls are given in *Figure 3*. Each wall has five precast wall panels with a horizontal joint at each floor level. The selected wall dimensions were based on site class and seismic level. The number and location of unbonded tendons were selected to ensure that each wall has the desired lateral strength level. Building overstrength was assumed to be unity. The amount and location of interlocking spirals (confining reinforcement) was determined based on design recommendations per ACI ITG-5.1-07 [14] and ACI ITG-5.2-09 [15].

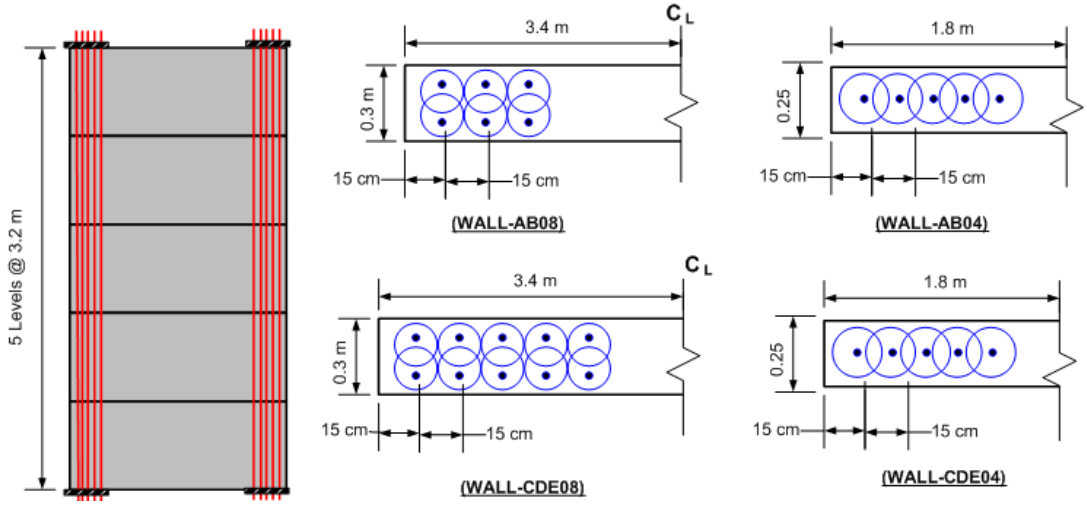

Figure 3: Plan and elevation views of prototype PTT walls.

2.1 Analytical Model and Verification

Nonlinear response-history analysis results of the porotype building were used to determine maximum lateral deflection of the building. Such nonlinear dynamic analyses shall utilize a structural mathematical model, which is capable of capturing nonlinear hysteretic behavior of structure [9]. The computational model was developed and verified using DRAIN-2DX program, which is a general-purpose computer program for both linear and nonlinear static and dynamic analysis of plane structures [16].

The computational model was verified using experimental test results given by Schultz et al [12]. The test PTT wall, which is given in *Figure 4*, was a 2/3-scale representation of the lowest two stories of a prototype precast concrete shear wall in a six-story office building. The wall featured six unbonded post-tensioned tendons and typical construction materials. The wall was tested under quasi-static cyclic loading and subjected to a combination of vertical and in-plane lateral loads history.

The main features of the developed analytical model are given in *Figure 4*, and a detailed description of the model and its verification are given by Erkmen et al [13]. The experimental and computed analytical responses given in *Figure 5* show no significant differences between the measured and computed stiffness, load capacity, and absorbed energy capacities of the wall.

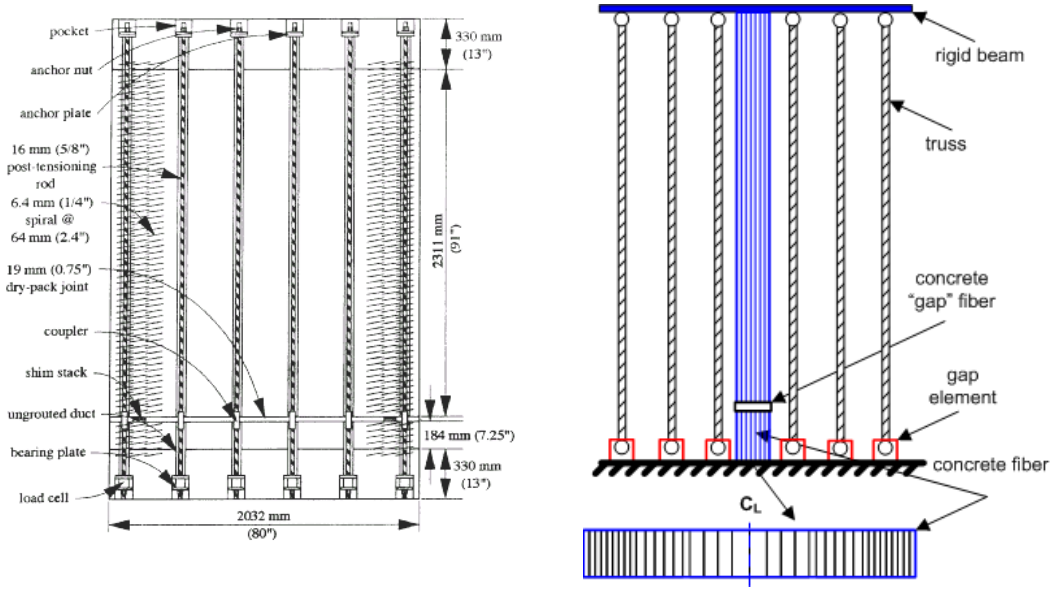

(a) (b)

Figure 4: Experimentally tested PTT wall (a) dimensions and (b) analytical model.

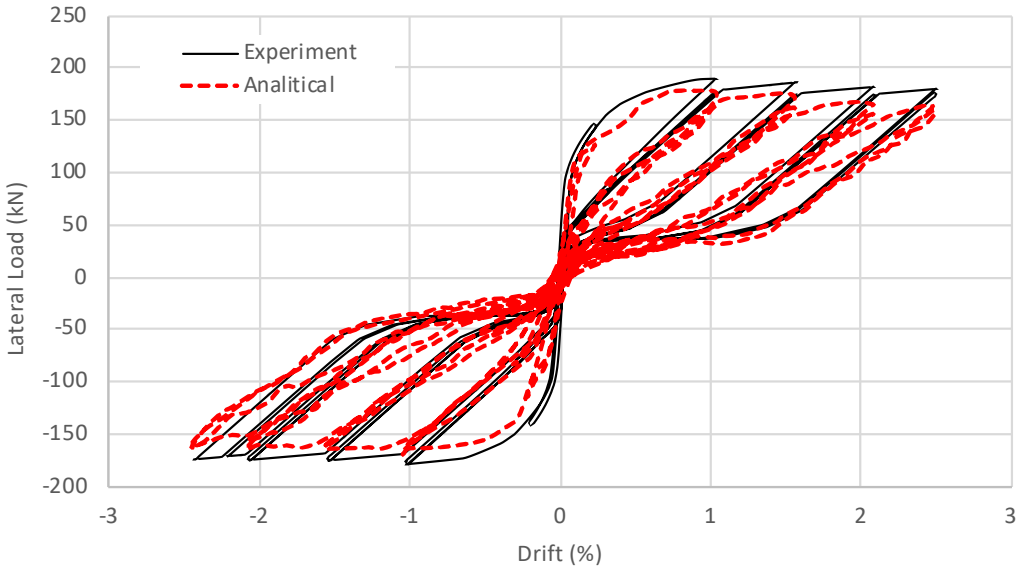

Figure 5: Experimental analytical force-displacement response of test PTT wall.

2.2 Selection and Scaling of Ground Motions

Six strong ground motion records were selected for each ASCE/SEI 7-16 Site Class A and B, C, D, and E. The ground motions records were obtained from the Pacific Earthquake Engineering Research (PEER) Center NGA-West2 database. A summary of all selected ground motions is given in *Table 1*. The ground motions records were selected giving preference to station site class, spectral shape over the period range of interest, free-field records, magnitude, and closest distance to the rupture plane.

No.	Motion, Year	Site Class	Station	Comp.	Mag.	Dist. km
EQAB1	Mendocino, 1992	AB	C. Mendocino	Cap.-Cpm000	7.1	8.5
EQAB2	Chi-Chi, 1999		HWA056	Coyotelk-G01230	7.6	48.8
EQAB3	Chi-Chi, 1999		ILA063	Chichi-Ila063N	7.6	71.6
EQAB4	Landers, 1992		12206 Silent Valley	Landers-Sil090	7.3	51.7
EQAB5	Northridge, 1994		24207 Pacoima Dam	Northr-Pul104	6.7	8.0
EQAB6	Northridge, 1994		90017 W. Ave.	Northr-Won095	6.7	22.7
EQC1	Northridge, 1994	C	90015 LA.Chalon Rd	Northr-Chl070	6.7	23.7
EQC2	Kern County, 1979		1095 T. L. School	Kern-Taf111	7.4	41.0
EQC3	Imp. Valley, 1979		6604 Cerro Prieto	I..H-CPE237	6.5	26.5
EQC4	Loma Prieta, 1989		57064 F. M. S. Jose	Lomap-Fre000	6.9	43.0
EQC5	Chi-Chi, 1999		CHY079	Chichi-Chy079N	7.6	55
EQC6	Kocaeli, 1999		Arcelik	Kocaeli-Arc090	7.4	17
EQD1	Erzincan, 1992	D	Erzincan	Erzincan-Erz-EW	6.7	4.4
EQD2	Chi-Chi, 1999		TCU072	Chichi-Tcu072-N	7.6	7.1
EQD3	I. Valley-02, 1940		El Centro A #9	Impvall.I-I-Elc270	7.0	6.1
EQD4	Northridge-0, 1994		Roscoe Blvd	North-Ro3090	6.7	10.1
EQD5	Big Bear-01, 1992		San B.E& Hosp.	Bigbear-Hos180	6.5	35.2
EQD6	S. Hills-02,1987		Imp. Co. Cent	Super.B-B-Icc000	6.5	18.2
EQE1	Kocaeli, 1999	E	Ambarli	Kocaeli-Ats090	7.5	69.6
EQE2	Chi-Chi, 1999		Chy002	Chichi-Chy002-N	7.6	25.0
EQE3	Chi-Chi, 1999		Chy025	Chichi-Chy025-N	7.6	19.1
EQE4	Chi-Chi, 1999		Tcu056	Chichi-Tcu056-N	7.6	19.5
EQE5	Loma Prietra, 1989		Treasure Island	Lomap-Tri000	6.9	77.4
EQE6	Taiwan, 1999		Tcu040	Chichi-Tcu040-N	7.6	22.1

Note: Mag. is moment magnitude, Dist. is distance to rupture plane.

Table 1: Summary of ground motion records used for dynamic analysis

The ground motions were scaled to match design spectrum based on ASCE/SEI 7-16 recommendations [9]. The ground motions were scaled using a constant scale factor to all acceleration ordinates of the motions such that the average value of the response spectra for the suite of all motions considered is not less than the design response spectrum for the site over the period range $0.2T$ to $1.5T$, where T is the natural period of the structure in its fundamental mode. The upper limit on the period is intended to account for period elongation due to inelastic actions and gap opening of the wall at its horizontal joints, and lower limit is intended to capture higher modes of response. The ASCE/SEI 7-16 design response spectrum for each site class at high seismic level (spectral response acceleration of $0.8g$) and scaled earthquake response acceleration spectra are given in *Figure 6*. The same approach was employed to scale the selected ground motions to low seismic level, which is $0.4g$.

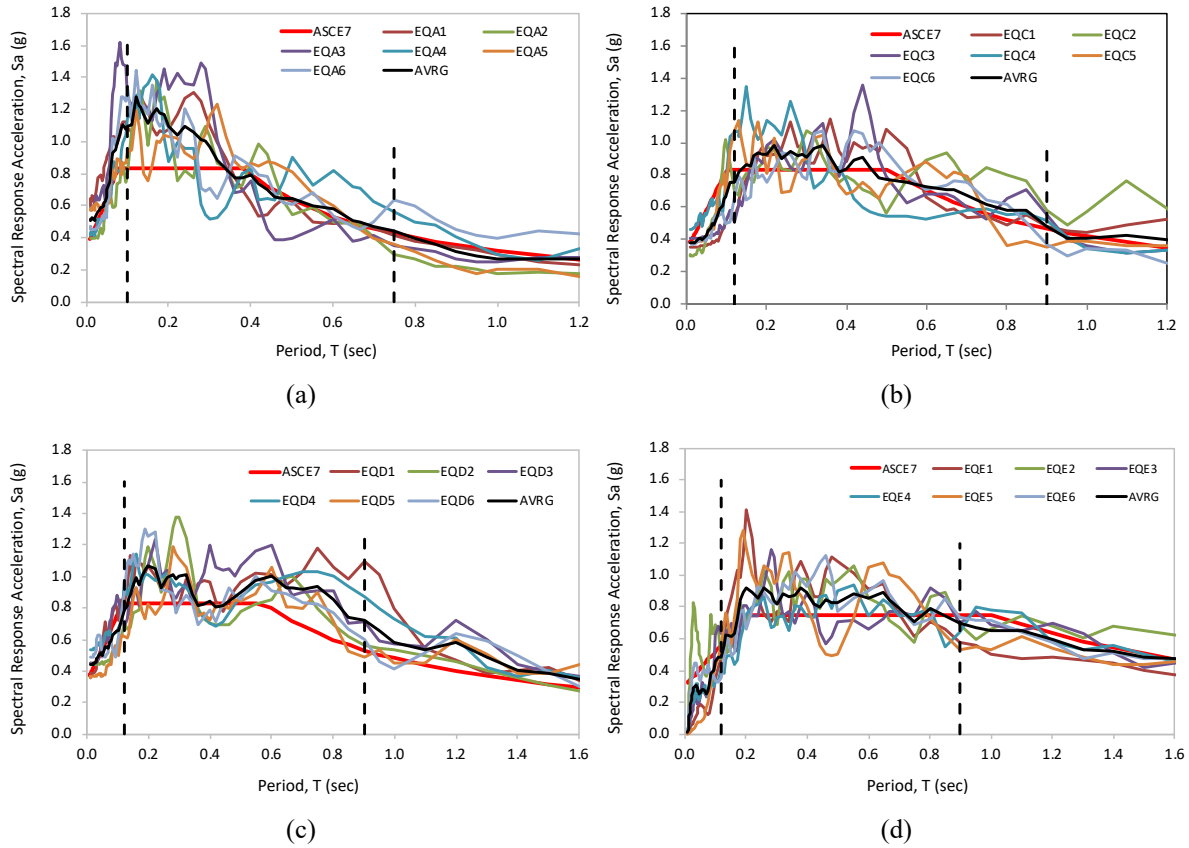

Figure 6: ASCE7 Design and spectral acceleration spectrum of selected ground motions at 0.8*g*

3 RESULTS AND DISCUSSIONS

The displacement amplification factor C_d was computed for the prototype buildings on the basis of computed building peak drift values using nonlinear time history analysis with the scaled ground motions. The C_d value was computed as the ratio of maximum drift to building drift corresponding to its design level lateral force. However, because the overstrength is neglected in the developed analytical models, the design level approximately corresponds to structure yielding. The computed C_d values for each site class and R value are given in *Figure 7* and *Figure 8* for seismic levels 0.4*g* and 0.8*g*, respectively. The results show that C_d value for prototype building increases with the increasing R value of the building. Large R values requires structural systems to be more ductile. Therefore, this observation is consistent with typical code values such as ASCE/SEI 7-16, where C_d value increases with increasing R value.

Figure 9 shows the computed average C_d value for each site class for both seismic levels. The average results show that structures located on sites with high seismic levels typically need to be designed with higher ductility capacities (larger C_d). However, the effects of seismic level and site class on C_d are not significant and probably can be ignored for design purposes. The only exception is Site Class E, which indicates that relatively larger C_d values are required as the site seismic level increases. However, because the structures designed with R values larger than 4.5 with high seismic level and 6.0 for low seismic levels failed (defined as maximum drift more than 2.5%), this observation is based on a limited number of structures. Finally, the average C_d values show that a C_d value that is equal to R value is conservative and reasonable for design purposes.

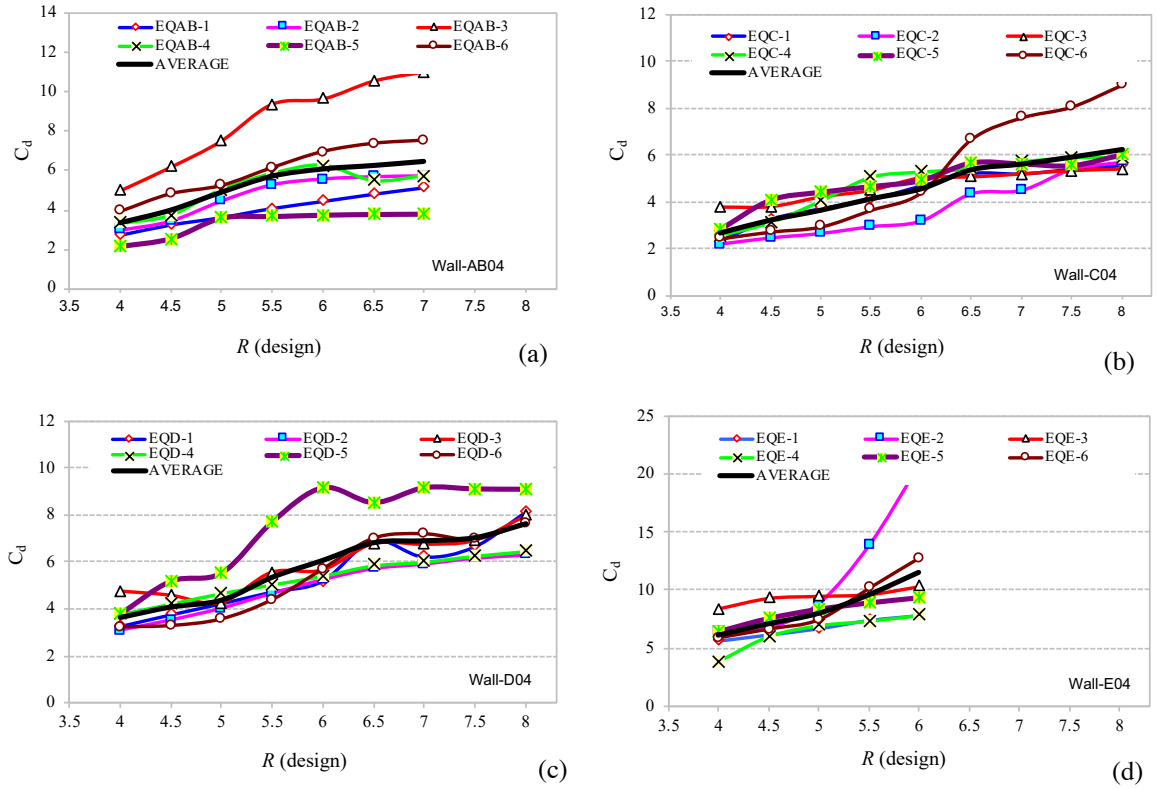

Figure 7: Computed C_d and R relationship at 0.4g for site class (a) AB, (b) C, (c) D, and (d) E

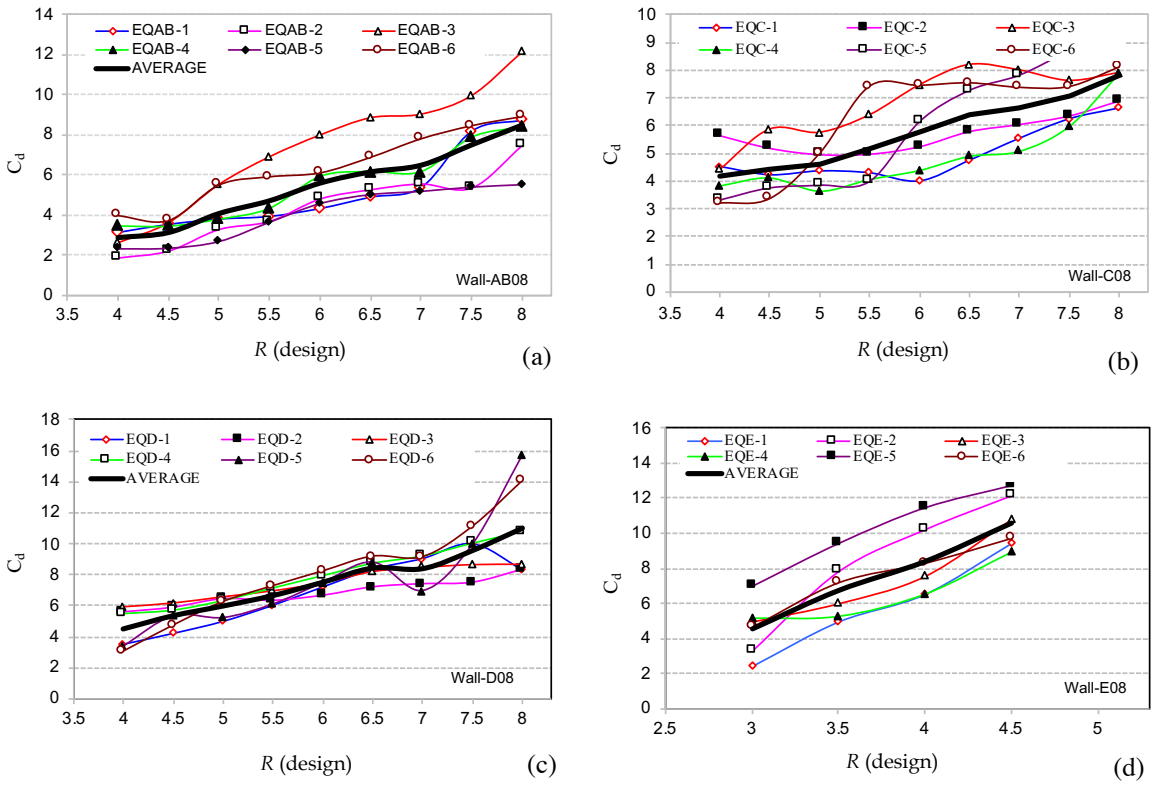

Figure 8: Computed C_d and R relationship at 0.8g for site class (a) AB, (b) C, (c) D, and (d) E

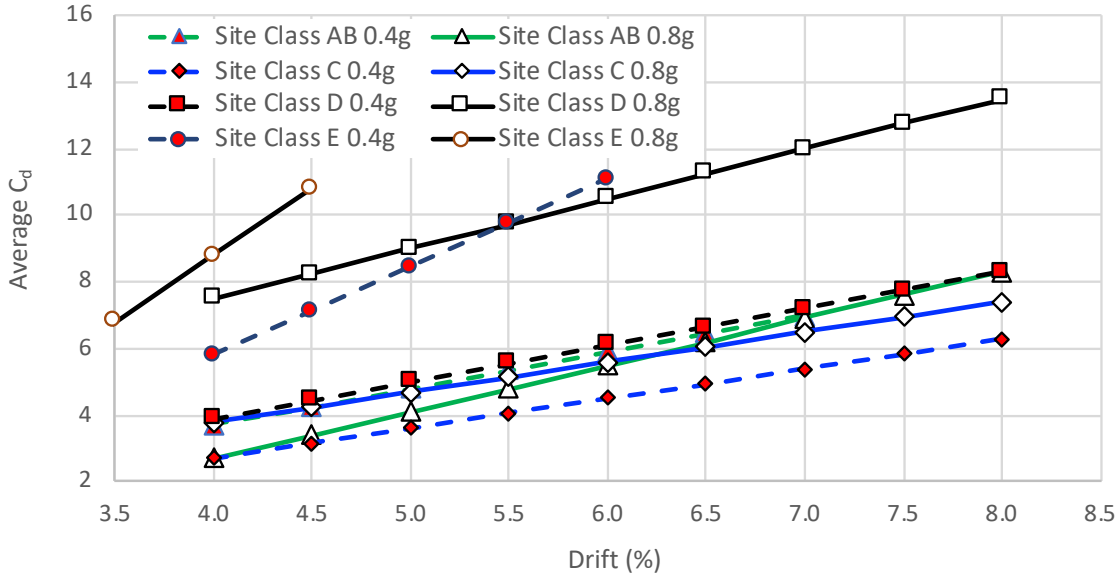

Figure 9: Average C_d and R relationship

4 CONCLUSIONS

A large number of prototype parking garage structures were designed for two seismic levels and several site classes. The structures were designed for values of response modification coefficient R ranging from 4.0 to 8.0. In total 24 recorded ground motions were used to perform nonlinear time history analysis of the designed structures. The computed maximum drifts were used to compute the required minimum displacement amplification factor C_d to ensure that structure does not collapse. Based on results presented the following main conclusions are made:

1. The seismic design parameters R and C_d are interrelated. For structures with larger R values the demand for C_d or ductility is also high.
2. Although demand for C_d increases as the site class become softer, the effects of site class are negligible for Site Class A, B, C, and D. However, structures located on Site Class E seems to have a requirement for larger values of C_d than those located on other site classes.
3. Increasing site seismic level increases the requirement for minimum value of C_d or building ductility, but the increase is typically not significant and can be ignored.
4. A value of C_d that is equal to building R value seems to be a reasonable design approach that envelope C_d requirements for structures presented in this study.

REFERENCES

[1] Applied Technology Council (ATC). Tentative provisions for the development of seismic regulations for buildings (ATC-3-06 Report). Redwood City, California, 1978.

[2] S. Wood, J. Wigth, and J. Moehle. *The 1985 Chile earthquake, observations on earthquake-resistant construction in Vina del Mar*. Civil Engineering Studies, Structural Research Series No 532, University of Illinois, Urbana, 1987.

[3] N.M. Newmark and W. J. Hall. *Seismic design criteria for nuclear reactor facilities* (*Tech. Rep. 46*). Building Practices for Disaster Mitigation, National Bureau of Standards, U.S. Department of Commerce, 1973

[4] R. Riddell, P. Hidalgo, and E. Cruz. Response modification factors for earthquake resistant design of short period structures. *Earthquake Spectra*, 5, 571-590, 1989.

[5] E. Miranda. Site-dependent strength reduction factors. *Journal of Structural Engineering*, 119, 1993.

[6] A. A. Nassar and H. Krawinkler. *Seismic demands for SDOF and MDOF systems* (Tech. Rep.95). The John A. Blume Earthquake Engineering Center, Stanford University, California, 1991.

[7] T. Vidic, P. Fajfar, and M. Fischinger. Consistent inelastic design spectra: strength and displacement. *Earthquake Engineering and Structural Dynamics*, 23, 507-521, 1994.

[8] U. Chia-Ming. Establishing R (or Rw) and Cd factors for building seismic provisions. Journal of Structural Engineering, **117**, 1991.

[9] American Society of Civil Engineers, *Minimum design loads for buildings and other structures* (ASCE/SEI 7-16). Reston, Virginia, 2016.

[10] M. J. N. Priestly, S. Sritharan, J. R. Conley, and S. Pampanin. Preliminary results and conclusions from PRESSS five-story precast concrete test building. *PCI Journal*, **44**, 1999.

[11] Y. Kurama, R. Sause, S. Pessiki, and L. W. L. Lateral load behavior and seismic design of unbonded post-tensioned precast concrete walls. *ACI Structural Journal,* **96**, 1994.

[12] A. E. Schultz, G. Cheok, and R. Magana. Performance of precast concrete shear walls. *Proc., 6th U.S. Nat. Conf. on Earth. Engineering*, EERI, Oakland, CA, 1998.

[13] B. Erkmen and A. E. Schultz. Self-centering behaviour of unbonded, post-tensioned precast concrete shear walls. *Journal of Earthquake Engineering*, **13**, 2009.

[14] ACI Innovation Task Group 5. A*cceptance criteria for special unbonded post-tensioned precast structural walls based on validation testing and commentary* (*ACI ITG-5.1-07*). Farmington Hills, MI, 2008.

[15] ACI Innovation Task Group 5. *Acceptance criteria for special unbonded post-tensioned precast structural walls based on validation testing and commentary (ACI ITG-5.1-07)*. Farmington Hills, MI, 2008.

[16] V. Prakash and G. Powell. *DRAIN-2DX Base Program Description and User Guide; Version 1.10*, Rep. No. UCB/SEMM-93/17, Dept. of Civil Engineering, University of California, Berkeley, 1993.

COMPDYN 2019
7th ECCOMAS Thematic Conference on
Computational Methods in Structural Dynamics and Earthquake Engineering
M. Papadrakakis, M. Fragiadakis (eds.)
Crete, Greece, 24–26 June 2019

IMPROVING THE ACCURACY OF THE SAC/FEMA APPROACH

Amirhossein Orumiyehei[1], **Timothy J. Sulivan**[2]

[1] University of Canterbury
20 Kirkwood Ave, Upper Riccarton, Christchurch 8041
e-mail: amir.orumiyehei@pg.canterbury.ac.nz

[2] University of Canterbury
20 Kirkwood Ave, Upper Riccarton, Christchurch 8041
timothy.sullivan@canterbury.ac.nz

Abstract

The development of simplified probabilistic performance assessment methods has opened up the possibility for risk targeted seismic design guidelines. As an example, international codes such as Eurocode 8 and ASCE7-10 have proposed simplified risk targeted seismic design objectives. The SAC/FEMA approach might be considered as one of the basic means of achieving such probabilistic performance objectives. However, this methodology is typically applied assuming that the equal displacement rule is a valid means of relating changes in intensity to changes in deformation demands, which can limit its accuracy. To address this, the results of a robust campaign of nonlinear time history analyses of a wide range of single degree of freedom systems are used to establish new intensity-displacement relationships and thereby improve the accuracy of the SAC/FEMA approach. In order to illustrate how the proposed relationships can be used in practice, the paper finishes by assessing the annual probability of exceeding the ultimate limit state for a 1-storey steel eccentrically braced system and a 1-storey rocking frame system. The results demonstrate that the refined approach is a practical and reasonably accurate means of obtaining probabilistic measures of seismic performance.

Keywords: Structural Performance, Probabilistic, Limit State, Exceedance, Assessment.

1 INTRODUCTION

The dynamic interaction between community expectations and earthquake engineering developments has seen the emergence of performance based earthquake engineering (PBEE). The PBEE framework new emerged innovation attempts to increase the level of safety not only by quantifying risk to people lives against the seismic events, but also by communicating the likely damage and business interruption. The required increase in structural performance confidence has been found to be provided by accounting for uncertainties in demand and capacity which has brought to light the necessity of simplified probabilistic design and assessment methods. In response to this, different methodologies have appeared to simplify both earthquake engineering aspects, structural demand/capacity assessment [1-4], and hazard function estimation [1, 5, 6].

The SAC/FEMA framework [1] is considered to be one of the pioneering approaches in the evolution of PBEE methodologies. This approach measures the structural performance by combining the probability of exceeding a target limit state with the associated hazard function, as shown by Eq. (1).

$$P_{LS} = \int P[C < D]|dH_D(d)| \tag{1}$$

Where P_{LS} is the annual probability of exceeding limit state, $P[C<D]$ is the cumulative distribution function (*CDF*) expressing the probability of exceedance of limit state at each shaking level, and $H_D(d)$ is the hazard function which defines the relation between shaking intensity and annual rate of exceedance.

There are several methods available in the literature to generate the fragility function, $P[C<D]$. Incremental dynamic analysis (IDA) [7] or multi stripe analyses (MSA) [8] are common procedures by which engineers compute the probability of exceeding a limit state. However, the annual probability of exceedance has not become a convenient tool to measure the structural performance comparing different alternatives in the phase of design or assessment due to complexity and required time. This is considered to be one of the benefits of the SAC/FEMA framework.

The SAC/FEMA framework establishes a solution in closed form to evaluate integral illustrated by Eq. (1), shown by Eq. (2) to Eq. (5). As is indicated by Eq. (2), annual probability of exceeding a limit state, here is called annual probability of failure (APOE), is computed by multiplication of annual rate of exceedance associated failure mechanism spectral acceleration (Sa) and three coefficients, C_H, C_f, and C_x. It has been assumed that the epistemic uncertainties hidden in ground motion prediction equations is accounted for adopting the mean of the hazard function values instead of median, and hence, C_H is a factor to convert the median to a mean value accounting for the epistemic uncertainty involved in ground motion prediction equations; C_f is the factor to account for the aleatory uncertainties in demand and capacity; and C_X is takes into account the confidence level. In this paper C_x and C_H are taken equal to one by targeting 50% confidence level and using median hazard value.

$$P_{LS} = H(S_a)C_H C_f C_x \tag{2}$$

$$C_f = \exp\left(\frac{k^2}{2b^2}(\beta_{DR}^2 + \beta_{CR}^2)\right) \tag{3}$$

$$\theta = aS_a(T_1)^b \tag{4}$$

$$H(S_a) = k_0(S_a)^{-k} \tag{5}$$

Where, *Sa,c* is the spectral acceleration associated with the failure mechanism displacement capacity; *H(Sa,c)* is the hazard function; β_{DR} and β_{CR} are the dispersion associated with demand and capacity distribution; Θ is the drift ratio; *a* and *b* are the coefficients corresponding to the IM-EDP relation; and k_0 and *k* are the first order fit hazard function coefficients.

This approach is based on few a assumptions which make the whole framework run in a simplistic way. However, they introduce some level of errors and cause some limitations as well, as has been identified by others [5, 9]. First, it presumes that the variation in the structural demands due to variability in shaking intensities could be approximately represented by Eq. (4), which is in line with the so-called empirical 'equal displacement rule' (EDR) [10]. Hence, one may employ Eq. (6) to estimate the spectral acceleration which causes target displacement demand associated with a specific limit state failure mechanism.

$$S_a = (\frac{\theta}{a})^{\frac{1}{b}} \tag{6}$$

Where the parameters have been defined before.

In this paper, new 'b' values are proposed, and the accuracy of the IM-EDP relation, Eq. (4) and Eq. (6), is investigated using the newly proposed 'b' values and 'b=1'. For that purpose, first, the IM-EDP relation is investigated for a wide range of SDOF systems; and updated 'a' and 'b' values are established. Consequently, to examine the accuracy of predicting the causal IM associated with the limit state failure, MSA are conducted for two case study buildings located in Christchurch and Wellington New Zealand, and the median of spectral accelerations distribution obtained for different limit states failure are compared with those obtained by applying Eq. (6) adopting the updated 'b' values. Furthermore, the precision of the APOE predicted by the SAC/FEMA framework is evaluated comparing that achieved with those from MSA results.

2 METHODOLOGY

In order to examine the relationship between intensity and demand, results of nonlinear time history analyses (NTHA) reported in [11] are assessed. The results include a wide range of single degree of freedom (SDOF) systems with periods of 0.1s, 0.2s, 0.3s, 0.4s, 0.5s, 0.6s, 0.8, 1.0s, 1.5s, 2.0s, 2.5s, 3.0s, 3.5s, 4.0s; and yield coefficients (defined as base shear at yield divided by system weight) of 0.025, 0.05, 0.075, 0.10, 0.125, 0.15, 0.20, 0.30, 0.40, 0.50 using 4284 ground motions available in the PEER database. Further, the hysteretic models adopted shown in Figure 1 include the Bilinear hysteretic model, which represents steel structures and base isolated systems, and the Flag-shaped model representing rocking frames fitted with energy dissipating devices. Moreover, for both hysteretic models the strain hardening ratio is assumed 0.05 compatible with general practice, and 5% tangent stiffness damping is adopted for each analysis.

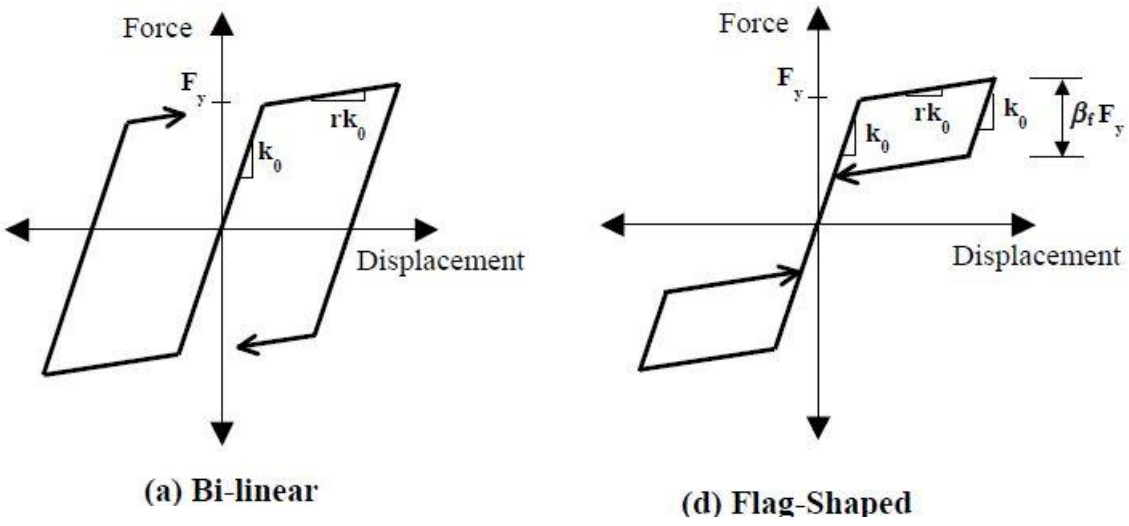

Figure 1. The adopted hysteretic models for single degree of freedom systems (a) Bilinear, (b) Flag-shaped [11]

2.1 Regression fit parameters of the IM-EDP relationship

To estimate the 'a' and 'b' coefficients corresponding to Eq. (6), a nonlinear regression analysis is carried out in MATLAB [12] using the obtained results from the cloud analyses [11] associated with each SDOF system. Figure 2 illustrates typical cloud analysis results corresponding to a SODF system with 0.5s period and the Flag-Shape hysteretic model.

On may expect to achieve similar results regardless of the binning approach associated with nonlinear regression analysis. This implies that the final coefficients derived by regression analysis will be identical no matter if Eq. (4) or Eq. (6) has been adopted as the model function. However, in this work it turned out that this statement will remain valid if a sufficient number of analyses have been conducted. The errors corresponding to each function model adopted in the nonlinear regression analysis are illustrated in Figure 3 and Figure 4.

The error distribution clarifies if the used model function can represent the data distribution without introducing any bias, and the validity of this assumption is assessed if the regression associated errors follows a normal distribution. As such for the conducted regression analyses, the distribution of the errors has been found. Figure 3 presents the error distribution associated with the results displayed in Figure 2. According to Figure 3, it is perceived that Eq. (6) efficiently represents the model function adopted in nonlinear regression analysis without generating any bias, hence, the found 'b' values are considered reliable. Figure 4, on the other hand, illustrates that Eq. (4) may not be used as the model function as the error is not distributed uniformly with *Sa* values increasing along the horizontal axis.

2.2 Proposed relationship between IM-EDP

Table 1 lists the median of the obtained 'b' values obtained for a range of different yield strength coefficients associated with each SDOF period. Examination of the new 'b' values reported by Table 1 illustrates three points. First, the listed dispersion by Table 1 is relatively small which implies that the proposed 'b' values change little with change of yield coefficient. Second, flag-shape systems have larger 'b' values in comparison with the Bi-linear systems for all periods as one may expect beforehand. This is in line with the amount of energy that is

dissipated by each hysteresis rule as elaborated by Figure 1 indicating that the nonlinear displacement demand will be less if more energy is dissipated by hysteresis loops. Third, the suggested 'b' values reduce with increasing period for both hysteresis rules.

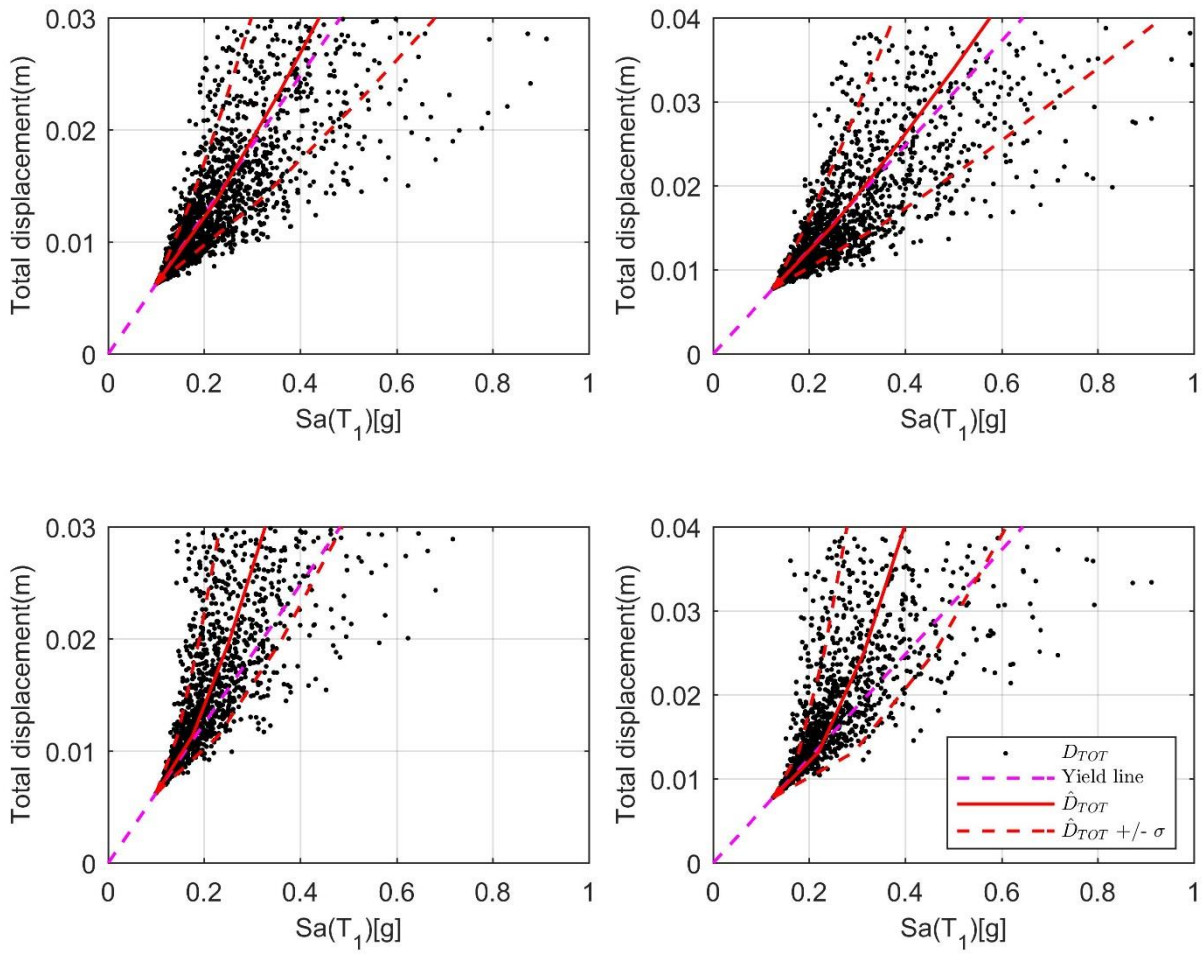

Figure 2. The NTHA results associated with 0.5s SDOF system Bi-linear Cy =0.10 (top-left) and Cy =0.125 (top-right); Flag-shape Cy=0.1 (bottom-left) Cy=0.125 (bottom right) (from [16])

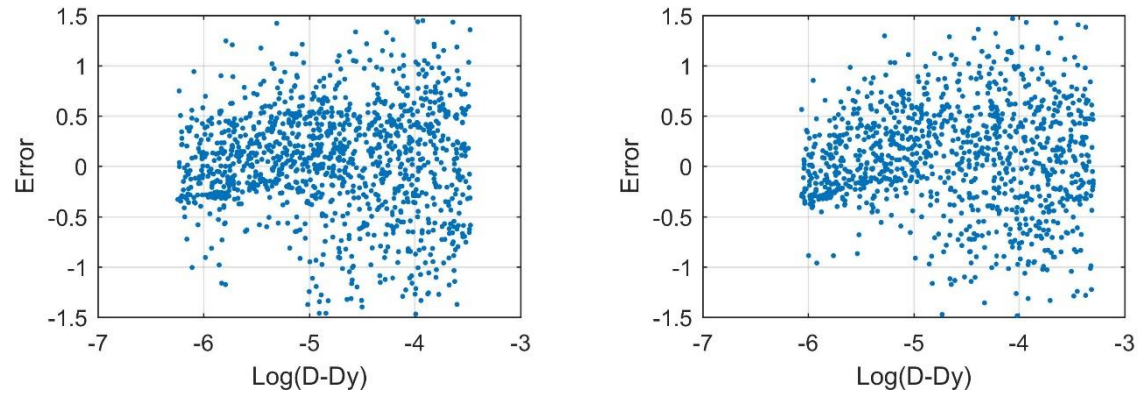

Figure 3. The error distribution associated with horizontal binning approach for SDOF with period of 0.5s and Flag-shape hysteretic model (left: Cy=0.10; right: Cy=0.125) (from [16])

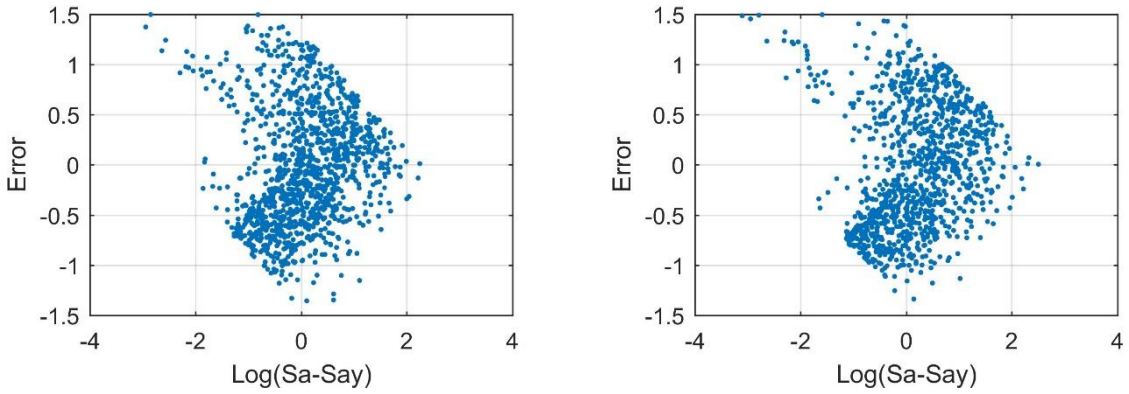

Figure 4. The error distribution associated with vertical binning approach for SDOF with period of 0.5s and Flag-shape hysteretic model (left: Cy=0.10; right: Cy=0.125) (from [16])

Table 1. The proposed 'b' values associated with different periods and hysteretic models from [16]

Period	Bilinear		Flag-shape	
T(s)	$\hat{b}$	β_b	$\hat{b}$	β_b
0.1	1.25	0.05	1.43	0.06
0.2	1.14	0.02	1.21	0.02
0.3	1.11	0.02	1.17	0.02
0.4	1.10	0.03	1.16	0.03
0.5	1.08	0.01	1.14	0.01
0.6	1.06	0.01	1.11	0.02
0.8	1.05	0.01	1.10	0.01
1.0	1.04	0.02	1.09	0.02
1.5	1.03	0.01	1.07	0.01
2.0	1.03	0.01	1.08	0.02
2.5	1.03	0.01	1.08	0.01
3.0	1.04	0.02	1.09	0.02
3.5	1.05	0.03	1.10	0.03
4.0	1.03	0.02	1.09	0.03

$\hat{b}$ Indicates the median associated with lognormal distribution;
β_b represents the associated dispersion

3 HIGHLIGHTING IMPACT OF USING THE NEWLY PROPOSED IM-EDP RELATIONSHIP

The proposed 'b' values reported in Table 1 should be applicable regardless of ductility range, as one may deduce from Figure 2 and Figure 3. Further, comparing the accuracy of the predicted *Sa* values for the same limit state for different site locations reveals how independent the results are due to site variation. Thus, to illustrate the benefits of the proposed 'b' values for different ductility ranges and site locations, two different case study buildings are modeled and analyzed in Ruaumoko [13]. Multi stripe analyses are carried out using the selected ground

motions for Christchurch and Wellington from [14]. Consequently, Eq. (6) employs the updated 'b' values, and the accuracy of predicted Sa causing limit state failure is gauged. Furthermore, APOE is computed and compared for each case study building according to the MSA results and SAC/FEMA approach.

3.1 Case study buildings

A 1-storey warehouse building and parking lot building are considered to be assessed as the case study buildings with two site locations being Christchurch and Wellington in New Zealand. The height and span used to represent these buildings are 3.5m and 6m respectively. The lateral resisting systems of the buildings are an eccentric braced frame (EBF) and a rocking reinforced concrete frame (RF), respectively. Figure 5 illustrates the schematic shape and dimensions of each case study building.

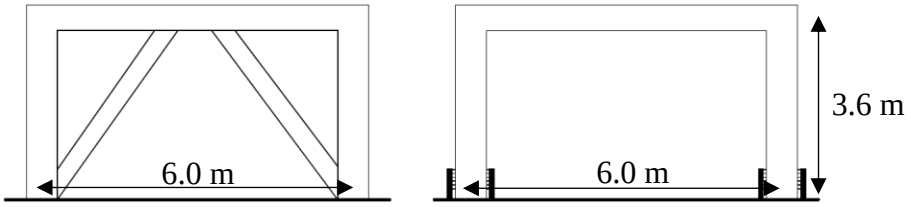

Figure 5. The case study building (left) EBF system (right) rocking RC frame;

3.2 MULTI STRIPE ANALYSES

In order to evaluate the structural performance, MSA is conducted, and hence NTHA are carried out using different sets of selected ground motions compatible with conditional spectra at different rates of exceedance [8]. Hence, the selected ground motions conditioned on a period of 0.5s for Christchurch and Wellington [14] are used. Figure 6, as an example, shows the spectral acceleration response for the selected 40 ground motions associated with the 475y return period and corresponding hazard curve. Moreover, Figure 7 presents the structural response at different hazard levels using the hazard consistent set of selected ground motions for the Christchurch case study buildings as an example.

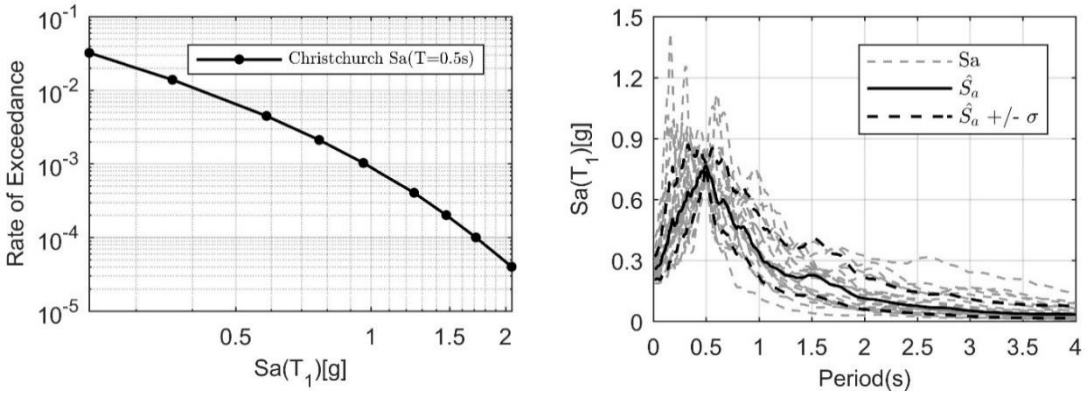

Figure 6. (left) The 0.5s spectral acceleration hazard curve associated with the Christchurch 500y return period (right) the selected ground motions corresponding to design base hazard level

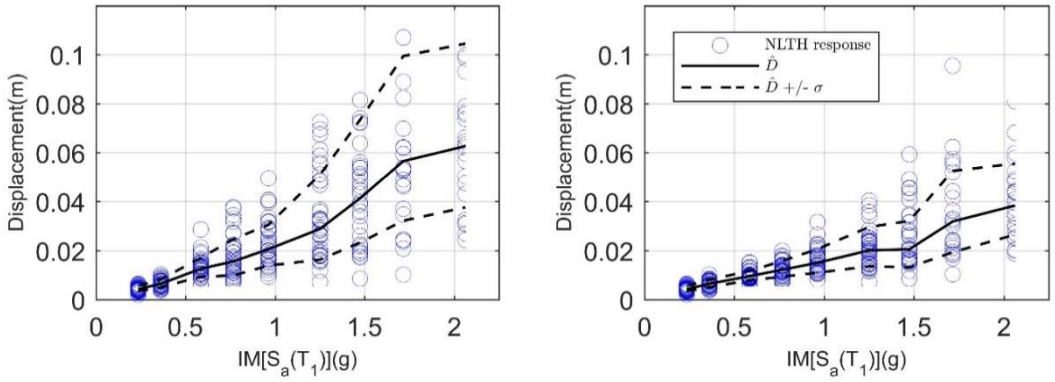

Figure 7. The multi strip analyses results (left) rocking frame (right) eccentric braced frame located in Christchurch

Table 2 compares the median intensity for different limit states obtained applying Eq. (6), adopting 'b=1', and also 'b' values reported in Table 1. It is observed that the proposed values of 'b' provide more accurate predictions of the spectral acceleration for both case study buildings with low sensitivity regarding site location. It is also noticed that the Christchurch EBF case study building second limit state Sa prediction accuracy is slightly low although the Sa associated with first and third limit state has been successfully predicted. Figure 7 examination clarifies that the median IM-EDP variation would slightly change if a larger number of ground motions could be adopted for MSA, and consequently a better estimation of IM-EDP relation would be achieved.

Table 2. The predicted spectral acceleration associated with different limit states and case study buildings

Location	Approach	EBF			RF		
		1%	2%	3.5%	1%	2%	3.5%
CHCH	Eq. (2)	0.58	1.10	1.82	0.53	0.9	1.37
	MSA	0.63	1.30	1.90	0.54	0.98	1.40
	'b'=1	0.57	1.15	2.01	0.56	1.13	1.97
WELL	Eq. (2)	0.58	1.10	1.82	0.53	0.9	1.37
	MSA	0.58	1.12	1.74	0.54	0.92	1.31
	'b'=1	0.57	1.15	2.01	0.56	1.13	1.97

The probability of exceeding limit state is required to compute the system APOE, as illustrated by Eq. (1). Using the obtained MSA results for each building and corresponding limit state a fragility curve is fitted using an optimization algorithm proposed by Baker [15]. Figure 8, and Figure 9, depict the fragility curves associated with different limit states for the EBF and RF systems located in Christchurch and Wellington, respectively.

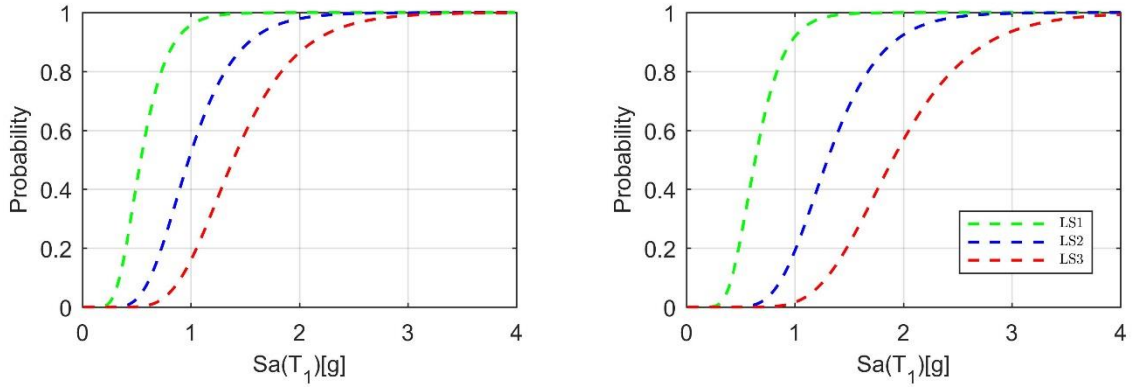

Figure 8.The achieved fragility curves corresponding to (left) rocking frame and (right) eccentric braced frame located in Christchurch

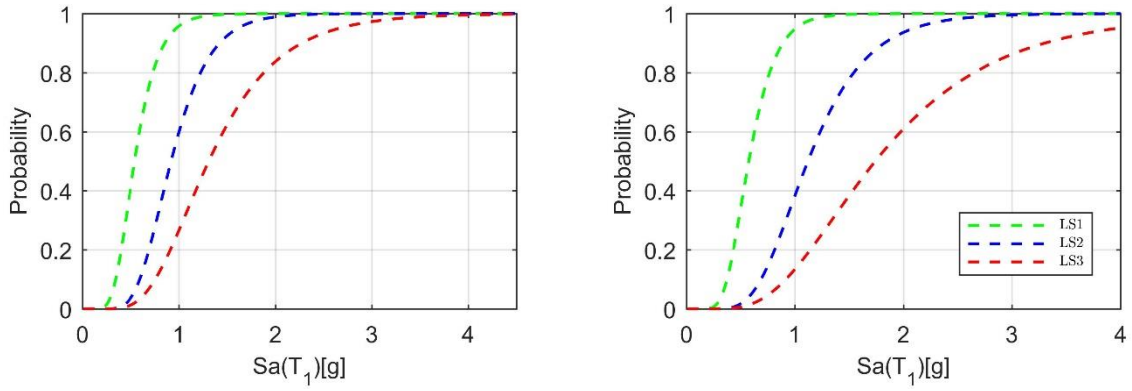

Figure 9. The achieved fragility curves corresponding to (left) rocking frame and (right) eccentric braced frame located in Wellington

4 COMPUTATION OF THE ANNUAL PROBABILITY OF EXCEEDANCE LIMIT STATE (APOE)

The APOE is computed combining each fragility curve with the corresponding hazard curve. The computed APOE following the aforementioned procedure is compared later with that found applying the simplified SAC/FEMA approach. The APOE is computed based on the achieved results in the previous section. This will provide a benchmark to assess the accuracy of the SAC/FEMA approach in two different cases: (a) assuming 'b=1' and (b) proposed 'b' values within Eq. (6).

The APOE computation approach via the MSA results is referred to here as the rigorous method. Following the rigorous approach, the generated fragility curves for each case study building are combined with the associated hazard curve adopting a numerical solution to evaluate Eq. (1), and the obtained APOE is reported in Table 3. It is detected that the APOE associated with Wellington case study building is larger than Christchurch, which is in line with difference between the two site locations' associated hazard. Further, the achieved APOE is larger for the RF case study building as the Flag-shape system dissipates less energy than the Bilinear system.

Table 3. The achieved APOE based on MSA results associated with different limit states and site locations

LS	Ductility	CHCH-EBF	CHCH-RF	WELL-EBF	WELL-RF
Drift	μ	$APOE_{LS}$	$APOE_{LS}$	$APOE_{LS}$	$APOE_{LS}$
3.50%	5.1	1.00E-04	4.50E-04	1.00E-03	1.50E-03
2.00%	2.9	5.30E-04	1.50E-03	1.90E-03	2.50E-03
1.00%	1.5	4.80E-03	7.20E-03	4.90E-03	5.40E-03

4.1 SAC/FEMA Approach

The SAC/FEMA methodology [1] is applied here to assess the performance of each case study building. The framework approximates the hazard curve using first order power law fit, adopting Eq. (5), as is illustrated by Figure 10. Further, the proposed closed form solution is applied to compute the system APOE regarding each limit state. This framework aggregates the probability of exceeding limit state with hazard function as presented by Eq. (2).

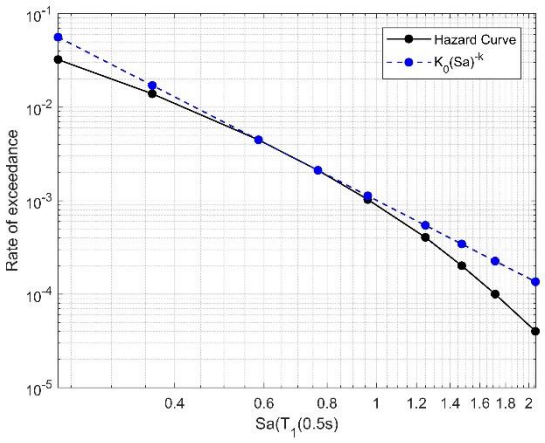

Figure 10. The hazard curve associated with Christchurch 0.5s, and the best fit curve using power law function

The proposed ‘b’ value affects the SAC/FEAM results in two different ways. First, more accurate prediction of the displacement demand is achieved through new IM-EDP relation, as was presented by Table 2. Second, a better estimation of C_f coefficient is yielded as elaborated by Eq. (3). Thus, the role of ‘b’ value on the uncertainty effect estimation in SAC/FEMA approach is investigated. To this end, the APOE is calculated for the buildings adopting simplified SAC/FEMA approach in two different cases. First, adopting Eq. (6) assuming ‘b’ equal 1; and second using the proposed ‘b’ values. Furthermore, to have a fair comparison, the MSA suggested dispersion and associated spectral acceleration values are adopted for the simplified method. Table 4 lists the parameters values used in the simplified method to quantify the APOE for each case study building and the target limit state. Table 5 presents the APOE found from the simplified methods adopting the aforementioned two cases assumptions.

Table 4. The adopted parameters to assess SDOF (T=0.5s) performance at different limit states

Location	LS (Drift)	Bilinear				Flag-shape			
		S_{at}[g]	H(Sat)	k	β_D	S_{at}[g]	H(Sat)	k	β_D
CHCH	3.5%	1.90	6.0e-5	5.00	0.30	1.40	2.5e-4	4.23	0.33
	2.0%	1.30	3.4e-4	4.23	0.30	0.98	9.6e-4	3.56	0.35
	1.0%	0.63	3.6e-3	2.78	0.32	0.54	5.4e-3	2.35	0.35
WELL	3.5%	1.73	7.6e-4	2.31	0.50	1.31	1.3e-3	1.68	0.43
	2.0%	1.12	1.7e-3	1.68	0.38	0.92	2.3e-3	1.33	034
	1.0%	0.58	4.3e-3	1.33	0.34	0.54	4.7e-3	1.38	0.36

Table 5. Estimated annual probability of exceedance applying rigorous and simplified method

Location	LS (Drift)	EBF				RF			
		'b'=1		'b'=1.08		'b'=1		'b'=1.14	
		C_f	$APOE_{LS}$	C_f	$APOE_{LS}$	C_f	$APOE_{LS}$	C_f	$APOE_{LS}$
CHCH	3.5%	2.86	1.7e-4	2.46	1.5e-4	2.65	7.0e-4	2.12	5.3e-4
	2.0%	2.21	7.5e-4	1.97	6.7e-4	2.17	2.1e-3	1.82	1.8e-3
	1.0%	1.52	5.5e-3	1.42	5.1e-3	1.40	7.6e-3	1.30	7.0e-3
WELL	3.5%	1.95	1.5e-3	1.77	1.3e-3	1.30	1.7e-3	1.22	1.6e-3
	2.0%	1.23	2.0e-3	1.19	2.1e-3	1.11	2.5e-3	1.08	2.5e-3
	1.0%	1.11	4.9e-3	1.09	4.8e-3	1.13	5.3e-3	1.10	5.2e-3

Table 6 compares the results achieved from MSA, and SAC/FEMA framework based on two different proposed 'b' values as elaborated in previous section for each site location. It is detected that the accuracy of the SAC/FEMA approach has improved for all limit states and both structural systems. Furthermore, the accuracy improvement seems stable although the site location varies. The accuracy improvement of SAC/FEMA in both levels, IM-EDP and APOE estimation, have been achieved remembering the estimated intensity measure associated with exceeding different limit states displayed in Table 2.

Table 6 Comparing the computed APoELS associated with different limit states and structural system (CHCH represents Christchurhc, and WELL represents Wellington)

Location	LS Drift	Eccentric Braced Frame			Rocking Frame		
		MSA	'b'=1	Eq.(2)	MSA	'b'=1	Eq.(2)
		$APOE_{LS}$	$APOE_{LS}$	$APOE_{LS}$	$APOE_{LS}$	$APOE_{LS}$	$APOE_{LS}$
CHCH	3.50%	1.0e-4	1.7e-4	1.5e-4	4.5e-4	7.0e-4	5.3e-4
	2.00%	5.3e-4	7.5e-4	6.7e-4	1.5e-3	2.1e-3	1.8e-3
	1.00%	4.8e-3	5.5e-3	5.1e-3	7.2e-3	7.6e-3	7.0e-3
WELL	3.50%	1.0e-3	1.5e-3	1.3e-3	1.5e-3	1.7e-3	1.6e-3
	2.00%	1.9e-3	2.0e-3	2.1e-3	2.5e-3	2.5e-3	2.5e-3
	1.00%	4.9e-3	4.9e-3	4.8e-3	5.4e-3	5.3e-3	5.2e-3

5 CONLUSION

This paper improves the accuracy of the SAC/FEAM approach by refining the IM-EDP relationship and uncertainty estimation through updated 'b' values. The accuracy of Eq. (6) assuming *'b'* equal to one has been trialed for an extended range of SDOF systems with a range of versatile fundamental periods and hysteretic rules. Through this study, it becomes evident that assuming *'b'* equal to one might be deemed reasonable for displacement demand estimate of SDOF systems with period ranging between 1.5s and 3.0s and the Bilinear hysteretic model. However, it is not expected to generate an accurate performance prediction for the other period ranges and hysteretic rules. Consequently, it is concluded that the updated IM-EDP relationship is able to differentiate the expected performance for different structural systems, and also is applicable for different site locations. Further, the study shows that for simple case study buildings the estimated APOE is of comparable accuracy with that achieved from a more rigorous MSA approach. This implies that the improved SAC/FEMA framework could provide a reliable tool to quantify the structural performance. Further study is recommended to examine the uncertainty in capacity, and its effect on structural performance assessment.

ACKNOWLEDGEMENT

This project was partially supported by the New Zealand Natural Hazard Research Platform Project. It is also partially supported by QuakeCore.

REFERENCES

[1] Cornell, C.A., et al., *Probabilistic basis for 2000 SAC federal emergency management agency steel moment frame guidelines.* Journal of structural engineering, 2002. **128**(4): p. 526-533.

[2] Priestley, M., G. Calvi, and M. Kowalsky. *Direct displacement-based seismic design of structures*. in *2007 NZSEE conference*. 2007.

[3] Fajfar, P., *A nonlinear analysis method for performance-based seismic design.* Earthquake spectra, 2000. **16**(3): p. 573-592.

[4] Dolšek, M. and P. Fajfar. *IN2-A simple alternative for IDA*. in *Proceedings of the 13th world conference on earthquake engineering, Vancouver, Canada, paper*. 2004.

[5] Bradley, B.A., et al., *Improved seismic hazard model with application to probabilistic seismic demand analysis.* Earthquake engineering & structural dynamics, 2007. **36**(14): p. 2211-2225.

[6] Vamvatsikos, D., *Derivation of new SAC/FEMA performance evaluation solutions with second‐order hazard approximation.* Earthquake Engineering & Structural Dynamics, 2013. **42**(8): p. 1171-1188.

[7] Vamvatsikos, D. and C.A. Cornell, *Incremental dynamic analysis.* Earthquake Engineering & Structural Dynamics, 2002. **31**(3): p. 491-514.

[8] Jalayer, F. and C. Cornell, *Alternative non‐linear demand estimation methods for probability‐based seismic assessments.* Earthquake Engineering & Structural Dynamics, 2009. **38**(8): p. 951-972.

[9] Vamvatsikos, D., *Accurate application and second-order improvement of SAC/FEMA probabilistic formats for seismic performance assessment.* Journal of Structural Engineering, 2012. **140**(2): p. 04013058.

[10] Veletsos, A. and N.M. Newmark. *Effect of inelastic behavior on the response of simple systems to earthquake motions*. 1960. Department of Civil Engineering, University of Illinois.
[11] Stafford, P.J., T.J. Sullivan, and D. Pennucci, *Empirical correlation between inelastic and elastic spectral displacement demands.* Earthquake Spectra, 2016. **32**(3): p. 1419-1448.
[12] MathWorks, I., *MATLAB: the language of technical computing. Desktop tools and development environment, version 7*. Vol. 9. 2005: MathWorks.
[13] Carr, A., *RUAUMOKO, Software for inelastic dynamic analysis.* Department of Civil Engineering, University of Canterbury, New Zealand, 2000.
[14] Yeow, T., et al., *Seismic performance of steel friction connections considering direct-repair costs.* Bulletin of Earthquake Engineering, 2018: p. 1-31.
[15] Baker, J.W., *Efficient analytical fragility function fitting using dynamic structural analysis.* Earthquake Spectra, 2015. **31**(1): p. 579-599.
[16] Orumiyehei, A, Sullivan, T.J., *Developing the SAC-FEMA approach for the seismic assessment of structural systems*. Journal of Earthquake Engineering, under review.

COMPDYN 2019
7th ECCOMAS Thematic Conference on
Computational Methods in Structural Dynamics and Earthquake Engineering
M. Papadrakakis, M. Fragiadakis (eds.)
Crete, Greece, 24–26 June 2019

A PERFORMANCE-BASED HYBRID FORCE-DISPLACEMENT SEISMIC DESIGN METHOD FOR REINFORCED CONCRETE STRUCTURES

Chao Pian[1], Edmond V. Muho[1*], Jiang Qian[1], Dimitri E. Beskos[1,2]

[1]Department of Disaster Mitigation for Structures, College of Civil Engineering
Tongji University
Shanghai 200092, People's Republic of China
edmondmuho@tongji.edu.cn, 1510216@tongji.edu.cn, jqian@tongji.edu.cn

[2]Department of Civil Engineering
University of Patras
26504 Patras, Greece
dimisof@hotmail.com

Abstract

A performance-based hybrid force-displacement (HFD) seismic design method is proposed for three types of reinforced concrete structures, i.e., moment resisting frames, frame with infills and wall-frame dual systems. HFD is a force-based method which controls with high accuracy both structural and non-structural deformation limits, since, both limits are input variables for the initiation of the design. This is accomplished by constructing explicit empirical expressions for a behavior (strength reduction) factor, which incorporates target non-structural and structural deformation metrics such as inter-storey drift ratio and member plastic rotation. Use of this factor in conjunction with an elastic acceleration spectrum can produce designs in one-step, by just conducting a strength checking, since the deformation restrictions are automatically satisfied. Those expressions for the behavior factor in terms of target deformation metrics, number of storeys, column to beam strength ratios, beam to column and column-to-wall stiffness ratios, respectively, are derived through extensive parametrical studies involving non-linear dynamic analysis of the above appropriately modeled structures under 100 ground motions scaled for different deformation targets. The proposed HFD method is demonstrated and validated with realistic design examples, which show its advantages over the force-based design method of the European seismic design code, Eurocode 8.

Keywords Performance-based seismic design, HFD seismic design, Reinforced concrete structures, Moment resisting frames, Infilled moment resisting frames, Wall-frame dual systems

1 INTRODUCTION

The force-based seismic design (FBD) method has been adopted by almost all current codes or standards, e.g., EC8 [1] or FEMA-450 [2]. The FBD accomplishes the design in two steps, firstly by strength checking under the design forces and secondly by deformation checking at the end of the design process. Displacements are determined by the equal displacement rule which usually underestimates them [3-5]. Moreover, the assumption of a reduced by 50% member gross stiffness to account for cracking, which is usually made in all codes, e.g., EC8[1], results to smaller and hence unconservative displacements compared to the more accurate one coming from the secant stiffness to yield assumption [6, 7].

During the last 25 years or so, a new seismic design philosophy called performance-based design (PBD) has emerged, with the goal of achieving a desired structural performance at various seismic action levels [7-9]. Displacements are intimately related to damage, and hence, displacements rather than forces control the damage or performance of a structure during the earthquake, which indicates that displacements are better design parameters than forces.

Contrary to the FBD, displacement-based design (DBD) methods and in particular the direct DBD [7] which employs displacements as the basic design parameters, can effectively control the damage by determining the required strength and stiffness so that displacement restrictions are satisfied [6]. This is done by using a target value of deformation as an input variable in the design procedure to effectively control damage and determine the necessary stiffness with the aid of a displacement design spectrum with high values of damping. Furthermore, the direct DBD does not require an assumption about the member stiffness, since it uses the well-defined and more appropriate secant stiffness to yield. However, the direct DBD method presents some shortcomings: a) it is based on a substitute single degree of freedom (SDOF) representation of the building which lowers the modeling accuracy, b) it imposes limits only on drift demands which are mainly capable to measure non-structural damage and not appropriate for structural damage, c) engineers are not familiar with the displacement design spectrum used by this method and d) almost all the current commercial structural design software packages have implemented the FBD method rather than the DBD method. Other types of DBD methods can be found in the works of Chopra and Goel [10] and Panagiotakos and Fardis [11]. Moreover, one can refer to [12] where eight DBD methods are studied and their limitations are identified through their application to realistic design examples.

Recently, the hybrid force/displacement (HFD) seismic design method, which follows the PBD philosophy, has been developed for steel plane and space frames by Karavasilis at al [13] and Tzimas et al. [14,15]. This method appropriately combines advantages and eliminates or reduces disadvantages of both FBD and DBD seismic design methods. Thus, the HFD 1) is essentially a force-based seismic design method working with acceleration response/design spectra, thereby retaining familiar concepts to engineers and compatibility with all commercial structural design software packages and 2) utilizes a behavior (strength reduction) factor, which is deformation-dependent and takes into account structural and non-structural deformation limits. Thus, the design process is accomplished in only one step (strength check), since the second step (deformation check), in contrast to the FBD method, is automatically satisfied. Besides, the HFD method does not employ a substitute SDOF structure and does not require the use of displacement response/design spectra as is the case with the direct DBD method.

In this work, the HFD method is extended to the seismic design of reinforced concrete (RC) plane structural systems, i.e., moment resisting frames (MRFs), infilled MRFs (I-MRFs) and wall-frame dual systems (WFDS), in an effort to provide an alternative seismic design method for these

three types of RC structures under the framework of performance-based design. The main tool in this method is a behavior (strength reduction) factor q, which depends on the geometrical and material characteristics of the structure as well as on the structural (member plastic rotation θ_{pl}) and non-structural (interstorey drift ratio IDR) deformation, the soil class and the performance level.

For the purpose of this work, 19 RC-MRFs, 19 WFDS and 19 I-MRF with a wide range of dynamic and mechanical characteristics are studied. The frames are designed on the basis of EC8 [1] and EC2 [16] and analysed through Non-Linear-Time-History/Incremental Dynamic Analysis (NLTH/IDA). A total number of 100 ordinary (far-fault) ground motions (25 for each soil type A, B, C, D as categorized by EC8[1]), appropriately scaled to capture different deformation targets, are used to study the response of the above RC structures. In the proposed HFD method, displacements are not affected by the code-based assumption of the reduced by 50% stiffness as they are in the case of the FBD. This is because the HFD method is constructed based on member stiffness equal to secant stiffness to yield.

In conclusion, a response databank is obtained with the execution of more than 65000 NLTH/IDA analyses and four empirical relations, linking the behavior factor to structural and non-structural deformation limits, are constructed through nonlinear regression analyses. These are the following: a) an expression that estimates the roof displacement at the first yield ($u_{r,y}$), b) a relation that connects the design roof displacement ductility ($\mu_{r,d}$) with the behavior (strength reduction) factor (q), c) a relation that correlates the maximum inter-storey drift ratio (IDR) with the roof displacement (u_r) and d) a relation that connects the maximum plastic rotation (θ_{pl}) with the roof ductility (μ_r). Some parameters regarding structural characteristics, such as the number of storeys and the column-to-beam strength ratios, beam-to-column and wall-to-column stiffness ratios, respectively, and the thickness and elastic modulus of infilled wall panels are also correlated with these relations. By applying the proposed empirical expressions in the framework of the HFD method, one can easily conduct performance-based seismic design for RC-MRFs, I-MRFs and WFDSs in one step involving only strength checking since deformation requirements are automatically satisfied by using a deformation dependent behavior factor.

A comparison of the proposed HFD method with the FBD method adopted in EC8 [1] is made on the basis of realistic design examples. The results of non-linear dynamic analyses demonstrate the advantages of the HFD seismic design method over the FBD method of EC8 [1].

2 THE HFD SEISMIC DESIGN METHOD

Having in mind the stepwise design framework of the HFD method for plane steel MRFs in [14], one can extend it here to RC-MRFs, I-MRFs and WFDSs as follows:

Step 1: Selection of performance objectives. The target performance metrics, i.e., IDR and θ_{pl} for the in-plane non-structural and structural damage, respectively, are selected according to the desired performance objectives and structural system. The performance levels are assumed here to be the immediate occupancy (IO) under the frequently occurred earthquake (FOE), the life safety (LS) under the design basis earthquake (DBE) and the collapse prevention (CP) under the maximum considered earthquake (MCE). The target values used to describe these performance levels for RC-MRFs, I-MRFs and WFDSs are shown in Table 1 [17-19]. For I-MRFs, the in-plane damage of infilled walls mainly controls their design, thus, only the maximum inter-storey drift ratio (IDR) is used here as the target performance metric.

RC-MRF and WFDS						IMRF		
IO		LS		CP		IO	LS	CP
IDR	θ_{pl}	IDR	θ_{pl}	IDR	θ_{pl}	IDR	IDR	IDR
1%	0.01	2%	0.02	4%	0.025	0.4%	0.8%	1.5%

Table 1: Representative performance-based target deformation values for RC-MRF, I-MRF and WFDS.

Step 2: Initial design of structures and estimation of input variables. RC structures are initially designed according to the EC8[1] and EC2[16] under the FOE with a behavior factor q =1. An initial estimation of some characteristic variables is done during this step. These variables are the column-to-beam strength ratio α, the beam-to-column and column-to-wall stiffness ratio ρ and γ, respectively, defined as

$$a = M_{RC,1,av}/M_{RB,av}$$
$$\rho = \frac{\Sigma(I/L)_b}{\Sigma(I/L)_c} \quad (1)$$
$$\gamma = \frac{\Sigma(I_c)}{\Sigma(I_w)}$$

where $M_{\mathrm{RC,1av}}$ is the average of the plastic moments of resistance for the first storey columns, $M_{\mathrm{RB,av}}$ is the average of the plastic moments of resistance for all beams of all storeys, I is the second moment of inertia at the storey closer to the middle height of the frame and L is the corresponding length (column c, beam b or wall w).

Step 3: Calculation of the behavior factor, q. The behavior factor q is calculated through a two-step process: 1) the target performance metrics (IDR, θ_{pl}) are transformed to the corresponding values of target roof ductility μ_r using a proposed expression and 2) the behavior factor q is determined by a proposed expression in terms of the design roof displacement ductility $\mu_{\mathrm{r,d}}$. The derivation of those expressions will be illustrated in detail in the next section.

Step 4: Iterative design of the structure. The structure is designed using the calculated behavior factor q in conjunction with the elastic design acceleration spectra of EC8 [1]. Thus, the values of α, ρ, γ, $\mu_{r,d}$ and q are updated. The iterative design procedure is continued until the updated behavior factor q do not significantly change from the previous one.

3 DERIVATION OF THE PROPOSED EMPIRICAL EXPRESSIONS

In order to develop the above mentioned empirical expressions of the HFD method, 19 RC-MRF, 19 I-MRFs and 19 WFDSs were designed according to EC8 [1] and EC2 [16] and analyzed through NLTH/IDA analyses under 100 ordinary (far-fault) ground motions selected from PEER [20] and scaled in such a way as to capture the desired deformation or performance levels. Thus, a response databank was obtained from which the proposed empirical expressions were derived through non-linear regression analyses. The details of the derivation procedure are illustrated through the following sections:

3.1 Design and modeling of RC structures

3.1.1 Design of RC structures

19 RC-MRFs, 19 I-MRFs and 19 WFDSs with a number of stories ranging from 2 to 20 were designed according to the EC8 [1] and EC2 [16] with the help of SAP2000 [21] and MATLAB

[22]. All the structures were designed based on a three-dimensional (3-D) model with regular arrangement of structural elements in both plan and elevation, i.e., three (or four for WFDS) bays of 6 m length in both horizontal directions, and a storey height of 3 m. The live load (Q) was assumed to be 2 kN/m^2, while the dead loads (G) were directly calculated by SAP2000 [20] according to the material properties and structural geometry. The additional dead load from the infill wall panels was assumed to be 10.5 kN/m and was distributed on beams. The material properties selected for the design of the RC frames were C25/30 for concrete and S500 for reinforcing steel. The concrete weight density was taken as 23.5 kN/m^3 and Young's modulus of the steel as 200 GPa. Material safety factors of 1.50 and 1.15 were used for the concrete and steel reinforcement, respectively. The seismic loads (E) were produced by the design spectrum of EC8 [1] with a peak ground acceleration a_g = 0.30g (where g denotes the acceleration of gravity, 9.81 m/sec^2), soil type B and behavior factor q = 3.9 for the RC-MRFs and I-MRFs and q = 3.6 for the WFDS, as suggested by EC8 [1] for medium ductility class (DCM). The combinations of loads used for the design were 1.35G+1.5Q and ±E +G+0.3Q for static and dynamic design loads, respectively. The middle two-dimensional (2-D) frames were isolated from the three-dimensional (3-D) frames by appropriately distributing the loads in order both models to have the same fundamental periods and modeled in Ruaumoko 2-D [23] software for conducting NLTH analyses. A typical 3-storey RC-MRF, I-MRF and WFDS are shown in Fig.1.

3.1.2 Modeling of beams, columns, walls and infills

In Ruaumoko 2D [23] software, all structural elements were modeled using a one component (Giberson) beam-element with concentrated hinges described by the modified Takeda hysteresis rule [23] at their both ends. Walls were modeled by a beam-column element with rigid zones at the floor level, plastic hinges at member ends and with uncoupled shear-moment behavior as suggested by [24]. The interaction between axial force and yield moment was taken into account for both columns and walls. The stiffness deterioration was considered for all members incorporating the modified Takeda hysteresis model, as shown in Fig. 2.a.

The ductility-based backbone curve model of Ruaumoko 2D [23], shown in Fig. 2.b, in conjunction with the empirical backbone curve of the moment M versus rotation θ given by [24] are used to model the strength degradation of a member. In Fig. 2.b, DUCT1 refers to the value of ductility where the strength degradation starts to occur and DUCT2 refers to the ductility at the end of the strength degradation [23] assuming here to be at M/M_y= 0.2. In order to consider the development of cracks in flexural structural members, the secant stiffness to yield is used as the effective member stiffness, i.e., $EI_{eff} = M_y/\phi_y$, where M_y is the yield moment and ϕ_y is the corresponding curvature at yielding.

The masonry infill panel of each bay of the I-MRFs is modeled as two equivalent pin-jointed compression diagonal struts that cross each other and placed concentrically across the diagonals of the frame, forming a concentrically braced frame system. The strut thickness t is the same as the infill wall, while its width, w is given as

$$w = dk\frac{c}{z}\frac{1}{(\lambda^*)^\beta} \tag{2}$$

where d is the diagonal length of the infill panel and c, k, z, λ^* and β are parameters referring to the mechanical and geometrical properties of the infill panel and the surrounding RC frame members and can be found in [25,26]. The envelope of the force – deformation relationship for the

equivalent diagonal strut is the one suggested by Panagiotakos and Fardis [27]. The geometrical and material properties of the infill panels used in this study are shown in Table 2, where the subscript 12 denotes the diagonal direction.

More details, regarding the design and modeling of the structures studied herein can be found in the work of Muho et al. [28, 29].

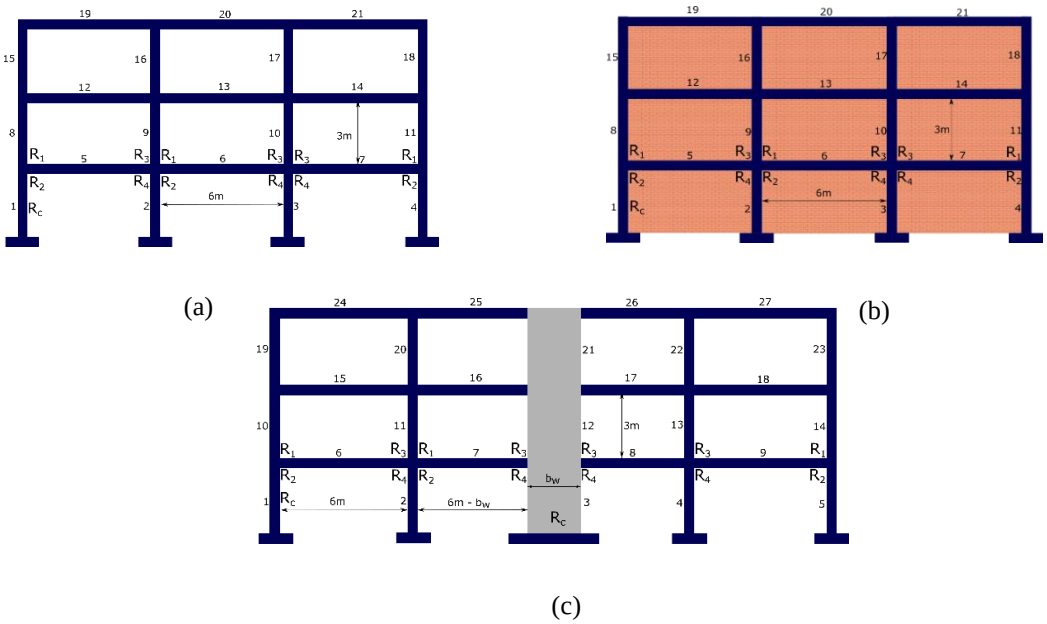

Figure 1: A representative 3-storey (a) RC-MRF, (b) I-MRF and (c) WFDS.

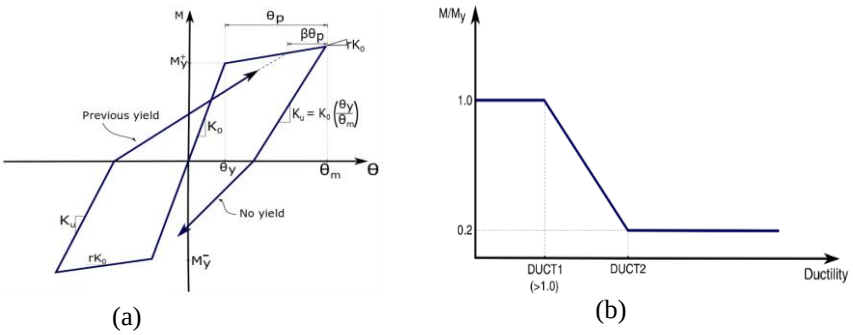

Figure 2: Modeling of stiffness and strength degradation: (a) Takeda hysteresis rule for moment M versus rotation θ and (b) Strength degradation model in terms of ductility and (c) Infill panel equivalent strut force-displacement relationship.

Items of geometrical and material properties	Values
Thickness	9cm/18cm
Compression strength f_c	2.5MPa
Shear strength f_v	0.3MPa
Modulus of elasticity at horizontal direction (E_1)	1375MPa/2000MPa
Modulus of elasticity at vertical direction (E_2)	3000MPa/2000MPa
Poisson ratio (v_{12})	0.15
Shear modulus (G_{12})	1300MPa/870MPa

Table 2: Geometrical and material properties of I-MRFs infill panels.

4 PROPOSED EMPIRICAL EXPRESSIONS

The proposed empirical expressions were derived through nonlinear regression analyses using the Levenberg-Marquardt algorithm of Matlab [22] in conjunction with the response databank. These relations apply only to frames with fundamental period T, column-to-beam strength ratio α, beam-to-column stiffness ratio ρ, column-to-wall stiffness ratio γ, thickness of the infill panel t and the infill modulus of elasticity at horizontal E_1 and vertical E_2 direction inside the range of these parameters defined by the frames used in this study and reading as follows: $0.549 \leqslant T \leqslant 4.414$, $1.142 \leqslant \alpha \leqslant 6.656$ and $0.151 \leqslant \rho \leqslant 0.887$ for RC-MRFs, $0.62 \leqslant T \leqslant 3.73$, $1.531 \leqslant \alpha \leqslant 8.927$ and $0.070 \leqslant \gamma \leqslant 0.451$ for WFDS and $0.23 \leqslant T \leqslant 1.79$, $1.279 \leqslant \alpha \leqslant 6.623$, $1.000 \leqslant E2/E1 \leqslant 2.182$ and $90mm \leqslant t \leqslant 180mm$ for I-MRFs.

4.1 Estimation of yield roof displacement $u_{r,y}$

The yield roof displacement, $u_{r,y}$ corresponds to the formation of the first plastic hinge in the frame. For RC-MRFs, I-MRFs and WFDSs, it can be estimated by the following proposed empirical expressions

$$\text{RC-MRF: } u_{r,y} = 0.04 \cdot n_s^{0.51} \cdot \rho^{0.08} \tag{3}$$

$$\text{I-MRF: } u_{r,y} = 0.018 \cdot n_s^{0.66} \cdot t^{0.28} \cdot \left(\frac{E_2}{E_1}\right)^{-0.61} \tag{4}$$

$$\text{WFDS: } u_{r,y} = 0.042 \cdot n_s^{0.36} \tag{5}$$

, respectively, where n_s is the number of stories, β is the beam-to-column stiffness ration, t is the thickness of the infill panel (in m), and E_1 and E_2 are the modulus of elasticity of infill walls along the horizontal and vertical direction, respectively. The mean, median and standard deviation of the ratio $u_{r,y,exact}/u_{r,y,app}$ are equal to 1.00, 0.98, 0.45, respectively for RC-MRFs, 1.00, 1.02, 0.30, respectively, for WFDSs and 0.98, 0.91, 0.89, respectively, for I-MRFs.

4.2 Estimation of q as a function of $\mu_{r,d}$

By analyzing the response databank of MRF, it was found that the structural characteristics and soil types have no significant effect on the relationship between the design roof ductility $\mu_{r,d}$ and the behavior factor q. The $\mu_{r,d}$ is equal to $\min(\mu_{r,IDR},\ \mu_{r,\Theta})$ with $\mu_{r,IDR}$ and $\mu_{r,\theta}$ computed as shown in the following subsections. Thus, the empirical q - $\mu_{r,d}$ relation for RC-MRFs as derived through regression analysis has the form

$$\begin{aligned} q &= 1 + 1.23\left(\mu_{r,d}^{1.07} - 1\right) \quad \mu_{r,d} \leq 3 \\ q &= 1 + 2.29\left(\mu_{r,d}^{0.75} - 1\right) \quad \mu_{r,d} > 3 \end{aligned} \tag{6}$$

estimates the q factor as a function of the maximum roof ductility μ_r with the mean, median and standard deviation of the ratio q_{exact}/q_{app} equal to 1.00, 0.97 and 0.21, respectively.

The empirical q - $\mu_{r,d}$ relation for WFDSs as derived through regression analysis has the form

$$\begin{aligned} q &= 1 + 0.83 \cdot \left(\mu_{r,d}^{1.32} - 1\right) \quad \mu_{r,d} < 3 \\ q &= 1 + 1.67 \cdot \left(\mu_{r,d}^{0.88} - 1\right) \quad \mu_{r,d} \geq 3 \end{aligned} \tag{7}$$

with the mean, median and standard deviation of the ratio q_{exact}/q_{app} equal to 1.00, 0.99, 0.21, respectively.

By analyzing the response databank of I-MRFs, the number of stories n_s was found to have a significant effect on the $q - \mu_{r,d}$ relation. Thus, the empirical equation obtained through regression analysis has the form

$$q = 1 + 1.21 \cdot \left(\mu_{r,d}^{0.73} - 1\right) \cdot n_s^{0.25} \tag{8}$$

with the correlation coefficient of exact and approximate values, the mean, median and standard deviation of the ratio q_{exact}/q_{app} equal to 0.83, 1.00, 0.97, 0.30, respectively.

4.3 Estimation of $\mu_{r,IDR}$ as a function of IDR

According to Karavasilis et al. [13], the roof displacement u_r for steel MRFs is indirectly connected with the maximum inter-storey drift ratio IDRby the expression $\beta = u_{r,IDR}/(H * IDR)$, where H is the total height of the structure and β is determined by regression analysis. Then the maximum roof displacement ductility is calculated by $\mu_{r,IDR} = u_{r,IDR}/u_{r,y}$ with $u_{r,IDR} = \beta\, H \times IDR$ and $u_{r,y}$ given by Eqs (3) and (5).

A study of the present response databank for RC-MRF and WFDS indicates that β can be expressed in the form

$$\text{RC-MRF: } \beta = 1 - 0.17 \cdot (n_s - 1)^{0.75} \cdot \rho^{0.07} \cdot \alpha^{-0.40} \tag{9}$$

$$\text{WFDS: } \beta = 1 - 0.18 \cdot (n_s - 1)^{0.61} \cdot \gamma^{0.36} \cdot \alpha^{-0.31} \tag{10}$$

, respectively, where the mean, median and standard deviation of the ratio $\beta_{exact}/\beta_{app}$ are equal to 1.00, 1.02, 0.33, respectively, for RC-MRF and 1.00, 1.03, 0.24, respectively, for WFDS.

For I-MRFs, the design roof displacement ductility $\mu_{r,d}$ was chosen to be directly related to the IDR, since it was found to have better correlation and smaller deviation than for the case through β as previously done for RC-MRF and WFDS. Thus, $\mu_{r,d}$ was found to be of the form

$$\mu_{r,d} = 1 + 1.75 \cdot n_s^{0.16} \cdot (1000 \cdot IDR)^{1.55} \cdot \left(\frac{E_2}{E_1}\right)^{0.88} \tag{11}$$

The mean, median and standard deviation of the ratio $\mu_{r,IDR,exact}/\mu_{r,IDR,app}$ resulted to be equal to 1.00, 1.00, 0.21, respectively.

4.4 Estimation of $\mu_{r,\theta}$ as a function of θ_{pl}

By analyzing the databank of RC-MRFs and WFDSs, the relation between the maximum roof displacement ductility $\mu_{r,max}$ and the maximum plastic rotation θ_{pl} was found to depend on the number of stories n_s and the column-to-beam strength ratio α. Thus, the empirical equation which represents the relation $\mu_{r,\theta}$ - θ_{pl} for RC-MRFs and WFDSs resulted to be of the form

$$\text{RC-MRF: } \mu_{r,\theta} = 1 + 0.12 \left(1000 \cdot \theta_{pl}\right)^{0.98} \cdot n_s^{-0.29} \cdot \alpha^{0.45} \tag{12}$$

$$\text{WFDS: } \quad \mu_{r,\theta} = 1 + 0.04 \cdot \left(1000 \cdot \theta_{pl}\right)^{1.19} \cdot n_s^{0.04} \cdot \alpha^{0.32} \tag{13}$$

, respectively, with the mean, median, and standard deviation of ratio $\mu_{r,exact}/\mu_{r,app}$ equal to 1.00, 0.97 and 0.29, respectively, for RC-MRF and 1.00, 1.00, 0.16, respectively, for WFDSs. Both Eqs. (12), (13) satisfy the physical constraint $\mu_r = 1$ for $\theta_{pl} = 0$ and serves to directly determine the roof displacement ductility μ_r given a maximum plastic rotation θ_{pl}, or vice versa.

For the case of I-MRFs the damage is controlled by the IDR and thus there is no need for establishing a corresponding μ_r - θ_{pl} relation.

5 NUMERICAL EXAMPLES

5.1 Design of RC-MRF

5.1.1 A ten-storey designed for LS under DBE and comparison with EC8

Two 10-storey RC-MRFs (Frames A and B) were designed for the LS level according to the proposed HFD method and the EC8 [1] design method, respectively, for α_g= 0.3g and soil class B. Both frames were designed assuming a 50% member gross stiffness reduction. Their sectional dimensions and reinforcement ratios are listed in Tables 3 and 4, where only sectional information for the first two and the last two storeys of the frames are provided due to space limitations.

The proposed HFD method was used to seismically design a ten-storey RC frame (Frame A) for soil class B, PGA_{DBE} = 0.3g and target values of 2% IDR and 0.02 θ_{pl}, which correspond to the LS level. The initial sectional dimensions and reinforcement ratios, shown in Table 3 (iteration 1), were obtained from only strength requirements under the FOE with peak ground acceleration assumed to be equal to 0.5×PGA_{DBE} = 0.15g and behavior factor q = 1.

According to Eq. (1), the values of ρ and α of the frame were equal to 0.41 and 2.45, respectively, while $u_{r,y}$ was found to be 0.121m from Eq. (3). These values serve as the initial estimation of the input variables of HFD in Step (2) of Section 2. Using IDR = 2.0%, n_s = 10, ρ = 0.41, α = 2.45 and u_{ry} = 0.121m, one can determine with the aid of Eq. (9) $\mu_{r,IDR}$=2.10. On the other hand, use of Eq. (12) with θ_{pl} = 0.02, n_s = 10 and α = 2.45 yields $\mu_{r,\theta}$ = 2.74. Thus, the design target roof displacement ductility is equal to min ($\mu_{r,IDR}$, $\mu_{r,\theta}$) = 2.09.

The behavior factor q was found from Eq. (6) to be equal to 2.5 and Frame A was designed again with spectrum analysis, ground acceleration PGA_{DBE}=0.3g and q=2.5. This led to a base shear of 531.7 kN and new sections and reinforcement as shown in Table 3 (iteration 2). The behavior factor did not change a lot until the second iteration. Thus, the design with respect to LS level is finalized.

The initial strength-based design (with q = 3.9) results, shown in the first part (design step 1) of Table 4 for Frame B designed according to EC8 [1], show maximum values for IDR and θ equal to 1.1% and 0.37, which are larger than their limit values of 1% and 0.2, respectively. Thus, an iterative design process led to the second part, not shown in Table 4 (design step 2), where IDR and the stability coefficient θ values resulted to be equal to 0.9% and 0.2, respectively, i.e., within their limit values. However, because the maximum value of θ equals 0.2, the design seismic actions were multiplied by 1/(1−q) = 1.25 to account for second order effects in accordance with EC8 [1]. This led to larger reinforcement ratios in the third part (design step 3) of Table 4. From the above procedure, it can be seen that in order to design a structure to comply both with the strength and deformation limits, many iterations need to be done.

Iter.	$u_{r,y}$(m)	ρ	α	$\mu_{r,IDR}$	$\mu_{r,\theta}$	u_r(m)	a_g(g)	q	Column	h(cm)	R_c(%)	Beam	h(cm)	R_1^*(%)	R_2(%)	R_3^*(%)	R_4(%)
1	0.121	0.41	2.45	2.09	2.74	0.253	0.15	1	1	50	1.09	5	40	1.82	1.64	1.82	1.67
									2	55	1.78	6	40	1.82	1.64	1.82	1.64
									8	50	1.09	12	40	2.04	1.91	2.03	1.89
									9	55	1.08	13	40	2.03	1.89	2.03	1.89
									57	35	1.88	61	40	1.13	0.98	1.07	0.94
									58	40	1.93	62	40	1.16	1.05	1.16	1.05
									64	35	1.88	68	40	0.58	0.58	0.70	0.58
									65	40	1.41	69	40	0.70	0.58	0.70	0.58
2	0.123	0.51	2.60	2.08	2.78	0.255	0.3	2.5	1	50	1.09	5	40	1.53	1.34	1.53	1.40
									2	55	1.08	6	40	1.47	1.34	1.47	1.34
									8	50	1.09	12	40	1.70	1.56	1.69	1.54
									9	55	1.08	13	40	1.69	1.54	1.69	1.54
									57	35	1.88	61	40	0.84	0.70	0.82	0.70
									58	40	1.41	62	40	0.87	0.82	0.87	0.82
									64	35	1.88	68	40	0.58	0.58	0.58	0.58
									65	40	1.41	69	40	0.58	0.58	0.58	0.58

Table 3: Sectional dimensions and reinforcement ratios of each iteration for Frame A.

In order to evaluate the applicability of the proposed HFD method to the design of a ten-storey frame, nonlinear dynamic analyses of the Frames A and B under 25 accelerograms compatible to EC8 [1] elastic spectrum for the FOE (IO) and DBE (LS) were conducted. Table 5 shows NLTH analysis deformation results and the corresponding estimated values by the two design methods as well as the deformation limits values of FEMA [17] for IO and LS levels.

Design steps	IDR(%)	θ	a_g(g)	q	Column	h(cm)	R_c(%)	Beam	h(cm)	R_1^*(%)	R_2(%)	R_3^*(%)	R_4(%)
1. Initial strength-based design	1.1	0.37	0.3	3.9	1	50	1.09	5	40	1.45	1.31	1.45	1.29
					2	55	1.08	6	40	1.45	1.29	1.45	1.29
					8	50	1.09	12	40	1.67	1.53	1.64	1.53
					9	55	1.08	13	40	1.64	1.53	1.64	1.53
					57	35	1.88	61	40	0.82	0.58	0.82	0.70
					58	40	1.41	62	40	0.82	0.70	0.82	0.70
					64	35	1.88	68	40	0.58	0.58	0.58	0.58
					65	40	1.41	69	40	0.58	0.58	0.58	0.58
3.Second order effects (Final Sectional and deformation Information)	0.9	0.20	0.38	3.9	1	55	1.08	5	50	1.11	0.92	1.09	0.88
					2	60	1.12	6	50	1.09	0.88	1.09	0.88
					8	50	1.09	12	50	1.29	1.10	1.28	1.09
					9	55	1.08	13	50	1.28	1.09	1.28	1.09
					57	35	1.68	61	40	0.94	0.82	0.98	0.84
					58	40	1.41	62	40	0.98	0.84	0.98	0.84
					64	35	1.68	68	40	0.58	0.58	0.58	0.58
					65	40	1.26	69	40	0.58	0.58	0.58	0.58

Table 4: Sectional dimensions and reinforcement ratios of Frame B.

HFD (Frame A)				
Response Values	FOE (IO level)		DBE (LS level)	
	NLTH	Estimation HFD	NLTH	Estimation HFD
IDR (%)	1.10	1.18	2.02	2.00
θ_{pl}	0.001	0.002	0.013	0.012
EC8 (Frame B)				
Response Values	FOE (IO level)		DBE (LS level)	
	NLTH	Estimation EC8	NLTH	Estimation EC8
IDR (%)	1.13	0.92	2.19	1.84
θ_{pl}	0.002	-	0.014	-

Table 5: Non-linear dynamic analysis deformation results for Frames A and B and comparison with estimated values by the HFD and EC8 methods; NLTH stands for nonlinear time history analysis.

On the basis of the response values of Table 5 the following observations can be made:

1) Even though IDR estimates of Frame B (designed by EC8 [1]) computed by the equal displacement rule do not exceed the limits of 1% and 2% for the IO and LS levels, respectively, the realistic IDR values obtained by NLTH analyses are non-safe sided and exceed the above limit values by 13% and 10%, respectively.
2) IDR estimates of Frame A (designed by HFD) are almost the same with the realistic IDR values obtained by NLTH analyses for both IO and LS levels and the IDR estimate for the LS level does not exceed the limit values of 2%. The IDR value for the IO level though exceeds the limit value of 1% by 10%. However, this result presents no problem since Frame A was designed by HFD method only for LS level and not for both LS and IO level as it is the case of Frame B designed by the EC8 [1] method. In a performance-based design framework, use of the HFD method considers more than one performance level and satisfies all deformation requirements for those levels. In Section 5.1.2 where the HFD method is used in a performance-based design framework with three performance levels to design again the ten-storey frame of this example, one can observe that all deformation requirements are satisfied for all three levels, including the IO level.
3) Estimates of θ_{pl} values for Frame A are almost the same with the realistic θ_{pl} values obtained by NLTH analyses and also do not exceed the limit values of 0.01 and 0.02 for both the IO and LS levels, respectively. Considering Frame B, only one of its beams is exceeding the allowable θ_{pl} value of LS by 4%. Estimates of θ_{pl} values cannot be made by the EC8 [1], and for this reason, there are no corresponding θ_{pl} values in Table 5.

Furthermore, from the procedural viewpoint, one can observe that the number of iterations during the HFD-based design was small, i.e., only two, as shown in Table 5. This fast convergence process is an advantage of the HFD method over the EC8 [1] method, which usually requires many iterations for its deformation check.

5.1.2 A performance-based seismic design

In this section, the ten-storey RC-MRF (Frame A) was re-designed by the HFD method for the three performance levels of Table 1. The peak ground acceleration for the DBE (PGA_{DBE}), was equal to 0.3g. The peak ground acceleration for the FOE and MCE are equal to $0.5\times PGA_{DBE}$ = 0.15g and $1.5\times PGA_{DBE}$ = 0.45g, respectively. The FOE, DBE, and MCE are expressed through the elastic displacement and pseudo-acceleration design spectra of EC8 [1] for soil class B and damping ratio equal to 5% (Fig.3).

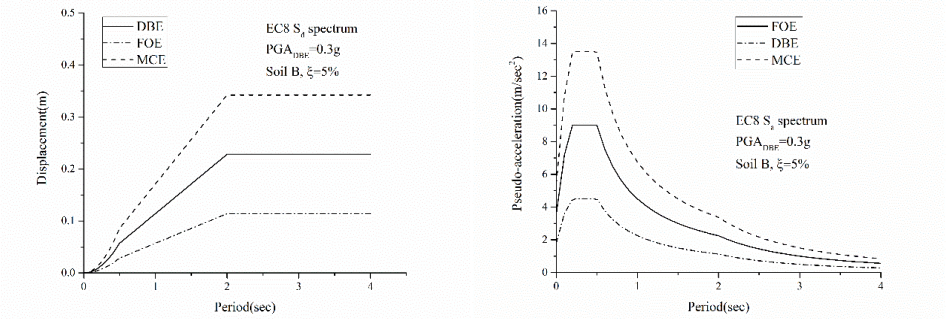

(a) (b)

Figure 3: (a) Elastic displacement design spectrum and (b) elastic pseudo-acceleration design spectrum, defined by EC8 [1].

The design for the three performance levels starts with the LS level. The seismic design of the ten-storey frame for the LS level by the HFD method has been presented in detail in section 5.1.1 (Frame A). The q factor of the frame under the FOE is easily obtained as (PGA_{FOE}/ PGA_{DBE})*q_{DBE}=0.5*2.5 ≈ 1.3, where the value of q_{DBE} = 2.5 is from iteration 2 of Table 3. Substituting this value of q=1.3 into Eqs. (6), (9) and (12), the response of the frame under the FOE can be obtained, i.e., $u_{r,d}$ = 0.151m, IDR=1.20% and θ_{pl} = 0.002, indicating that the limit value of IDR=1% for the IO level (Table 1) is exceeded. Correspondingly, $u_{r,d}$, IDR and θ_{pl} of the frame under the MCE are, 0.369m, 2.89%, and 0.022, respectively, which satisfy the CP level limits (Table 1). Therefore, the IO performance level controls the design of the frame. The design procedure for the IO performance level is summarized in Table 6, by taking the final sections of the LS level as the initially assumed sections. The behavior factor would not change a lot until the second iteration. Thus, the design with respect to IO level is finalized.

Iter.	$u_{r,y}$(m)	ρ	α	$\mu_{r,IDR}$	$\mu_{r,\theta}$	u_r(m)	a_g(g)	q	Column	h(cm)	R_c(%)	Beam	h(cm)	R_1^*(%)	R_2(%)	R_3^*(%)	R_4(%)
1	0.123	0.51	2.60	1.05	1.90	0.128	-	-	1	50	1.09	5	40	1.53	1.34	1.53	1.40
									2	55	1.08	6	40	1.47	1.34	1.47	1.34
									8	50	1.09	12	40	1.70	1.56	1.69	1.54
									9	55	1.08	13	40	1.69	1.54	1.69	1.54
									57	35	1.88	61	40	0.84	0.70	0.82	0.70
									58	40	1.41	62	40	0.87	0.82	0.87	0.82
									64	35	1.88	68	40	0.58	0.58	0.58	0.58
									65	40	1.41	69	40	0.58	0.58	0.58	0.58
2	0.121	0.41	2.50	1.06	1.88	0.127	0.15	1.1	1	50	1.09	5	40	1.54	1.42	1.56	1.42
									2	55	1.08	6	40	1.54	1.41	1.54	1.41
									8	50	1.09	12	40	1.76	1.64	1.73	1.64
									9	55	1.08	13	40	1.73	1.64	1.73	1.64
									57	35	1.88	61	40	0.94	0.82	0.94	0.82
									58	40	1.43	62	40	0.98	0.84	0.98	0.84
									64	35	1.88	68	40	0.58	0.58	0.58	0.58
									65	40	1.41	69	40	0.58	0.58	0.58	0.58
3	-	-	-	-	-	-	-	1.1	-	-	-	-	-	-	-	-	-

Table 6: Sectional dimensions and reinforcement ratios of each iteration for Frame A designed by HFD for three performance levels.

HFD (Frame A) designed for 3 performance levels									
Response Values	FOE (IO level)			DBE (LS level)			MCE (CP level)		
	NLTH	Estimation HFD	Limit value FEMA	NLTH	Estimation HFD	Limit value FEMA	NLTH	Estimation HFD	Limit value FEMA
IDR (%)	1.01	1.00	1.00	1.95	1.81	2.00	2.65	2.53	4.00
θ_{pl}	0.000	0.001	0.010	0.011	0.010	0.020	0.021	0.019	0.025

Table 7: Nonlinear dynamic analysis results of Frame A designed by HFD for three performance levels and comparison with limit values.

5.2 A WFDS designed for three performance levels

In this section, a four-storey WFDS named Frame C is designed by the proposed method for the three performance levels of Table 1. The PGA for the FOE (IO level), the DBE (LS level) and the MCE (CP level), over the PGA of DBE are 0.5, 1 and 1.5, respectively [9], where the PGA at DBE was selected to be 0.30g. The design is initiated with the LS level. The sectional dimensions, reinforcement ratios and relative design parameters for Frames C designed for LS level are summarized in Table 8.

The q factor under the MCE is easily obtained as $(PGA_{MCE}/PGA_{DBE}) * q_{DBE} = 1.5 * 3.6 = 5.4$, where $q_{DBE} = 3.6$ is given in Table 8. With $q_{MCE} = 5.4$ known, the roof ductility $\mu_{r,d}$ is found from Eq. (7) to be equal to 4.18. By substituting this value of $\mu_{r,d} = 4.18$ into Eq. (10) and Eq. (13), the maximum values of IDR and θ_{pl} are estimated to be equal to 3.55% and 0.030, respectively. Thus, the CP level limit value of $\theta_{pl} = 0.025$ according to Table 1, is exceeded, which indicates that the CP level controls the design of Frame C. The design procedure for the CP level is summarized in Table 9 by assuming the initial sections to be the same as those of the LS level shown in Table 8. The design with respect to the CP level is finalized within two iterations and it complies with all three performance levels, i.e., IO, LS and CP.

Iter.	$u_{r,y}$(m)	γ	α	$\mu_{r,IDR}$	$\mu_{r,\theta}$	u_r(m)	a_g(g)	q	Column	h(cm)	R_c	Beam	h(cm)	R_1^*	R_2	R_3^*	R_4
1	0.069	0.19	3.02	2.87	3.13	0.198	0.15	1.0	1	45	1.19%	6	40	1.36%	0.81%	1.39%	0.82%
									2	50	1.00%	7	40	1.42%	0.66%	1.13%	0.86%
									10	45	1.02%	15	40	1.51%	0.66%	1.13%	0.89%
									11	50	1.00%	16	40	1.55%	0.72%	1.24%	0.94%
									19	45	1.00%	24	40	1.37%	0.60%	1.01%	0.82%
									20	50	1.00%	25	40	1.42%	0.64%	1.13%	0.86%
									28	40	1.51%	33	40	0.78%	0.37%	0.84%	0.63%
									29	45	1.19%	34	40	1.06%	0.51%	0.87%	0.72%
									Wall	h(cm)	b(cm)	R_w					
									3	120	30	3.17%					
									12	120	30	0.57%					
									21	120	30	0.65%					
									30	120	30	0.42%					
Iter.	$u_{r,y}$(m)	γ	α	$\mu_{r,IDR}$	$\mu_{r,\theta}$	u_r(m)	a_g(g)	q	Column	h(cm)	R_c	Beam	h(cm)	R_1^*	R_2	R_3^*	R_4
2	0.069	0.16	2.42	2.99	2.98	0.206	0.3	3.6	1	35	1.16%	6	40	0.62%	0.44%	0.82%	0.54%
									2	40	1.00%	7	40	0.84%	0.66%	1.13%	0.59%
									10	35	1.16%	15	40	0.75%	0.66%	1.13%	0.57%
									11	40	1.17%	16	40	0.92%	0.72%	1.24%	0.65%
									19	35	1.16%	24	40	0.71%	0.60%	1.01%	0.54%
									20	40	1.17%	25	40	0.81%	0.64%	1.13%	0.61%
									28	35	1.49%	33	40	0.33%	0.37%	0.84%	0.50%
									29	40	1.00%	34	40	0.62%	0.51%	0.87%	0.50%
									Wall	h(cm)	b(cm)	R_w					
									3	120	30	1.20%					
									12	120	30	0.33%					
									21	120	30	0.33%					
									30	120	30	0.33%					
3								3.7									

Table 8: Sectional dimensions and reinforcement ratios of each iteration of Frame C designed for LS.

Iter.	$u_{r,y}$(m)	γ	α	$\mu_{r,IDR}$	$\mu_{r,\theta}$	u_r(m)	a_g(g)	q	Column	h(cm)	R_c	Beam	h(cm)	R_1^*	R_2	R_3^*	R_4
2	0.069	0.23	2.62	5.87	3.65	0.253	0.45	4.7	1	40	1.00%	6	40	0.81%	0.54%	0.91%	0.57%
									2	45	1.00%	7	40	0.89%	0.66%	1.13%	0.59%
									10	40	1.02%	15	40	0.94%	0.66%	1.13%	0.63%
									11	45	1.00%	16	40	1.01%	0.72%	1.24%	0.65%
									19	40	1.00%	24	40	0.85%	0.60%	1.01%	0.57%
									20	45	1.00%	25	40	0.88%	0.64%	1.13%	0.59%
									28	35	1.49%	33	40	0.44%	0.37%	0.84%	0.50%
									29	40	1.00%	34	40	0.67%	0.51%	0.87%	0.50%
									Wall	h(cm)	b(cm)	R_w					
									3	120	30	1.67%					
									12	120	30	0.33%					
									21	120	30	0.33%					
									30	120	30	0.33%					
3								4.8									

Table 9: Sectional dimensions and reinforcement of each iteration for Frame C designed for three performance levels

The response results for IDR and θ_{pl} and their comparison with the corresponding limit values from Table 1 and the estimated values by the HFD method are shown in Table 10. From this table, one can observe that both IDR and θ_{pl} are below the corresponding limit values of all three

performance levels. Besides, the estimated values are almost the same as the "exact" values obtained from NLTH analyses. Thus, the proposed HFD method can be successfully used for the performance-based seismic design of WFDSs.

	IO				LS				CP			
	NLTH	Limit	Estimation	Check	NLTH	Limit	Estimation	Check	NLTH	Limit	Estimation	Check
IDR(%)	0.86	1	0.92	OK	1.69	2	1.64	OK	2.43	4	2.49	OK
θ_{pl}	0.000	0.01	0.004	OK	0.009	0.02	0.015	OK	0.019	0.025	0.025	OK

Table 10: Nonlinear time history (NLTH) analysis results of Frame C designed by HFD for three performance levels and comparison with limit values.

5.3 An I-MRFs designed for three performance levels

Next, a four-storey I-MRF Frame D is designed for three performance levels as the WFDS of the previous section but with the corresponding target IDR values of Table 1 for I-MRFs.

The design is initiated with the LS level. The sectional dimensions, reinforcement ratios and relative design parameters for Frames D designed for LS level are summarized in Table 11, where only the final sectional information for the first two and the last two storeys are provided due to space limitations.

E_1(MPa)	E_2(MPa)	$\mu_{r,IDR}$	a_g(g)	q	Column	h(cm)	R_c	Beam	h(cm)	R_1^*	R_2	R_3^*	R_4
1375	3000	3.4	0.3	3.5	1	50	1.64%	5	50	1.48%	1.29%	1.49%	1.29%
					2	55	1.63%	6	50	1.46%	1.27%	1.46%	1.27%
					8	50	1.14%	12	50	1.49%	1.29%	1.49%	1.29%
					9	55	1.44%	13	50	1.46%	1.27%	1.46%	1.27%
					15	45	1.23%	19	45	1.34%	1.13%	1.34%	1.15%
					16	50	1.32%	20	45	1.34%	1.13%	1.34%	1.13%
					22	45	1.10%	26	45	0.67%	0.51%	0.77%	0.58%
					23	50	1.09%	27	45	0.72%	0.58%	0.72%	0.58%

Table 11: Sectional dimensions and reinforcement ratios of Frame D.

For the CP level, the q factor under the MCE is easily obtained as $(PGA_{MCE}/PGA_{DBE}) * q_{DBE} = 1.5 * 3.5 = 5.25$, with $q_{DBE} = 3.5$ as shown in Table 11. With $q_{MCE} = 5.25$ known, the roof ductility $\mu_{r,d}$ is found from Eq. (8) equal to 5.53. By substituting this value of $\mu_{r,d} = 5.53$ into Eq. (11), the maximum value of IDR = 1.19 is estimated, which satisfies the CP level limit value of IDR = 1.5% according to Table 1. Thus, here the LS level controls the design of Frame D and the final sectional dimensions and reinforcement ratios which satisfy all three performance levels are the same as the ones of the LS level (Table 11).

Finally, the response results from NLTH analyses under the 25 ground motions compatible to EC8 [1] elastic spectrum for the IO, LS, and CP levels and the response predictions according to the proposed equations are shown in Table 12. From that table, one can observe that the "exact" IDRs obtained from NLTH analyses are below the corresponding limit values of all three performance levels. Besides, the estimated values are almost the same as the realistic ones. Thus, the proposed HFD method can be successfully used for the performance-based seismic design of I-MRFs.

	IO				LS				CP			
	NLTH	Limit	Estimation	Check	NLTH	Limit	Estimation	Check	NLTH	Limit	Estimation	Check
IDR(%)	0.26	0.40	0.34	OK	0.71	0.80	0.80	OK	1.12	1.5	1.19	OK

Table 12: Nonlinear time history (NLTH) analysis results of Frame D for three performance levels and comparison with limit values.

6 CONCLUSIONS

Based on the results of previous sections, the following conclusions can be stated:

1. The hybrid force/displacement (HFD) seismic design method for RC structures has been successfully developed through extensive parametrical studies involving non-linear-time-history/incremental dynamic analyses of 19 RC-MRFs, 19 I-MRFs and 19 WFDSs under 100 seismic motions.
2. The HFD appropriately combines advantages of both force-based and displacement-based seismic design methods. It is a force-based design method working with acceleration response/design spectra and a deformation-dependent behavior (strength reduction) factor and it performs design in one step involving only strength checking.
3. The proposed empirical expressions can estimate the yield roof displacement, the roof displacement ductility as a function of IDR and θ_{pl} and the behavior (strength reduction) factor as a function of the roof displacement ductility.
4. The HFD method was proven, through numerical examples, to accurately estimate and control both structural and non-structural damage and hence to be successfully used as a full performance-based seismic design method, while, at least at the present time, this is not the case with the EC8 method.

ACKNOWLEDGMENTS

This research investigation has been supported by the National Key Research and Development Program of China (Grant No.2017YFC1500701) and the State Key Laboratory of Disaster Reduction in Civil Engineering (Grant No. SLDRCE15-B-06).

REFRENSES

[1] EC8, Eurocode 8 Part 1, *Design of structures for earthquake resistance, general rules, seismic actions and rules for buildings*. European Standard EN 1998-1, European Committee for Standardization (CEN), Brussels, 2004.

[2] FEMA-450, *The 2003 NEHRP Recommended Provisions for New Buildings and Other Structures*. Part 1: Provisions, Federal Emergency Management Agency, Washington D.C., 2003.

[3] Gupta, A. and H. Krawinkler, *Estimation of seismic drift demands for frame structures*. Earthquake Engineering & Structural Dynamics, 2000; 29(9): 1287-1305.

[4] Krawinkler, H. and R.A. Medina, *Evaluation of drift demands for the seismic performance assessment of frames*. Journal of Structural Engineering, 2005; 131(7): 1003-1013.

[5] Karavasilis, T.L., N. Bazeos, and D.E. Beskos, *Drift and ductility estimates in regular steel MRF subjected to ordinary ground motions: A design-oriented approach*. Earthquake Spectra, 2008. 24(2): 431-451.

[6] M. N. Fardis, E. Carvalho, A. Elnashai, E. Faccioli, and P. Pinto, *Designers' guide to EN 1998-1 and EN 1998-5 Eurocode 8: Design of structures for earthquake resistance*. Thomas Telford, London, 2005.

[7] Priestley, M.J.N., Calvi, G.M. and Kowalsky, M.J., *Direct Displacement-Based Design*, IUSS Press, Pavia, Italy, 2007.

[8] Bozorgnia Y. and Bertero, V.V., *Earthquake Engineering: From Engineering Seismology to Performance-Based Engineering*, Boca Raton, FL, USA, CRC Press, 2004.

[9] SEAOC. Vision 2000, *A Framework for Performance-Based Seismic Engineering*, Structural Engineers Association of California, Sacramento, California, 1995.

[10] Chopra, A.K. and Goel, R.K., *Direct displacement-based design: use of inelastic vs elastic*

design spectra, Earthquake Spectra, 2001;17(1):47-63.
[11] Panagiotakos, T. and Fardis, M.N., *A displacement-based seismic design procedure for RC buildings and comparison with EC8*. Earthquake Engineering & Structural Dynamics, 2001; 30(10): 1439-1462.
[12] Sullivan, T.J., Calvi, G.M., Priestley, M.J.N. and Kowalsky, M.J., *The limitations and performances of different displacement based design methods*. Journal of Earthquake Engineering, 2003; 7(1): 201-241.
[13] Karavasilis, T.L., Bazeos, N. and Beskos, D.E., *A hybrid force/displacement seismic design method for plane steel frames, in Behavior of Steel Structures in Seismic Areas*, Mazzolani, F. and Wada, A., editors, Proceedings of STESSA Conference, Yokohama, Japan, Taylor & Francis, 2006, pp. 39-44.
[14] Tzimas, A.S., Karavasilis, T.L., Bazeos, N. and Beskos, D.E., *A hybrid force/displacement seismic design method for steel building frames*. Engineering Structures, 2013; 56: 1452-1463.
[15] Tzimas, A.S., Karavasilis, T.L., Bazeos, N. and Beskos, D.E., *Extension of the hybrid force/displacement (HFD) seismic design method to 3D steel moment-resisting frame buildings*. Engineering Structures, 2017; 147: 486-504.
[16] Eurocode 2 (EC2), *Design of Concrete Structures, Part 1.1: General Rules for Buildings*, European Standard EN 1992-1-1, European Committee for Standardization (CEN), Brussels, 2004.
[17] FEMA-356, *Prestandard and Commentary for the Seismic Rehabilitation of Buildings*, Federal Emergency Management Agency, Washington D.C., 2000.
[18] Ghobarah A., *On drift limits associated with different damage levels*. In: Fajfar P, Krawinkler H, editors. Proceeding of the international workshop on performancebased seismic design: concepts and implementation, Bled, Slovenia [PEER Report2004/05]. Berkley: University of California; 2004, p. 321–32.
[19] Morandi P., Hak S. and Magenes G., *Performance-based interpretation of in-plane cyclic tests on RC frames with strong masonry infills*. Engineering Structures 2018;156:503–21.
[20] PEER, Pacific Earthquake Engineering Research Centre, Strong ground motion database, 2013.04
[21] SAP2000 *Structural Analysis Program*, Computers and Structures, Inc., California, USA." https://www.csiamerica.com/products/sap2000, 2016.
[22] MATLAB, *The Language of Technical Computing*, Version 2009a, The MathWorks, Inc., Natick, Mass., USA, 2009.
[23] A. J. Carr, Ruaumoko Manual, *Theory and User Guide to Associated Programs*. Department of Engineering, University of Canterbury, Christchurch, New Zealand, 2006.
[24] ATC72-1, *Modeling and Acceptance Criteria for Seismic Design and Analysis of Tall Buildings*. Redwood City, CA: Applied Technology Council, 2010.
[25] Cavaleri L., Di Trapani F., *Cyclic response of masonry infilled RC frames: experimental results and simplified modeling*. Soil Dynamics and Earthquake Engineering,2014;65:224–42.
[26] Cavaleri L., Papia M., Macaluso G., Di Trapani F., Colajanni P., *Definition of diagonal Poisson's ratio and elastic modulus for infill masonry walls*. Materials and structures, 2014;47:239–62.
[27] Panagiotakos T.B., Fardis M.N.. *Seismic response of infilled RC frames structures*. In:Proceedings of 11th World Conference on Earthquake Engineering; 1996, p. 238
[28] Muho E.V., Papagiannopoulos G.A. and Beskos D.E., *Deformation dependent equivalent modal damping ratios for the performance-based seismic design of plane R/C structures*. Soil Dynamics and Earthquake Engineering, 2019 (accepted).
[29] Muho E.V., Qian J. and Beskos D.E., *Modal behavior factors for the performance-based seismic design of R/C wall-frame dual systems and infilled-MRFs*. Soil Dynamics and Earthquake Engineering, 2019 (accepted).

COMPDYN 2019
7th ECCOMAS Thematic Conference on
Computational Methods in Structural Dynamics and Earthquake Engineering
M. Papadrakakis, M. Fragiadakis (eds.)
Crete, Greece, 24–26 June 2019

A COST-EFFECTIVE RETROFITTING TECHNIQUE FOR URM BUILDINGS BASED ON STEEL ENCIRCLEMENTS IN OPENINGS: A CASE STUDY

M.L. Segovia-Verjel[1], E. Justo-Moscardó[1], A. Morales-Esteban[1], M.V. Requena-García-Cruz[1], E. Romero-Sánchez[1], J. de-Miguel-Rodríguez[1], J.M.C. Estêvão[2]

[1]Department of Building Structures and Geotechnical Engineering, University of Seville, Spain
Av. Reina Mercedes, 2, 41012, Seville, Spain
{marisasegovia, ejem, ame, mrequena1, eromero13, jdemiguel}@us.es

[2]Department of Civil Engineering, ISE, University of Algarve, Faro, Portugal
Campus da Penha, 8005-139, Faro, Portugal
e-mail: jestevao@ualg.pt

Abstract

A project named PERSISTAH is being developed to study the seismic vulnerability of primary schools in Huelva (Spain) and the Algarve (Portugal). This area has a moderate seismicity but this is affected by a nearby area where earthquakes of large magnitude (Mw≥6) and long-return periods happen.
The seismic vulnerability of URM (UnReinforced Masonry) buildings has been observed and analysed in the last decades. The seismic retrofitting of these buildings is required in order to improve their seismic behaviour. Many retrofitting techniques have been developed for that purpose, most of them very complicated and expensive. Therefore, these are not appropriate to retrofit a large number of buildings. This is especially relevant in areas of moderate seismicity where the cost-efficiency ratio must be carefully considered.
The aim of this paper has been to develop a simple, effective and affordable technique to retrofit these buildings. These buildings are characterised by numerous openings which causes a great weakness in the URM walls. Then, a technique that consists in installing a steel encirclement or a grille in the openings of the walls has been proposed. This is a specific retrofitting technique for URM walls since this technique substantially improves the seismic capacity of these structures.
To test the technique a case study is proposed. The building under study is a primary school located in Huelva and built in 1961. Results have shown that the capacity of the building is notably increased. Also, the performance point and the damage level of the structure are decreased.

Keywords: URM buildings, retrofitting technique, Performance-based method, seismic behaviour, nonlinear analysis.

1 INTRODUCTION

The south of the Iberian Peninsula (IP) has a moderate seismicity. This area is close to the borders of the Eurasian and African plates where many active faults exist. Specifically, the southwestern IP is affected by several faults such as the Gibraltar-Azores, the San Vicente Cape and the Horseshoe faults. These faults have originated in the past some important earthquakes like the Lisbon earthquake in 1755 (Mw=8.5) and the 1969 earthquake (Mw=8) [1][2].

The seismic risk in this area is being assessed in a project named PERSISTAH (*Projetos de Escolas Resilientes aos SISmos no Território do Algarve e de Huelva*, in Portuguese). This project is being developed collaboratively by the University of Algarve and the University of Seville due to the similar seismic hazard of both regions. The aim of this project is to minimize the disaster risk of school buildings in the regions of Andalucia (Spain) and Algarve (Portugal). In the PERSISTAH framework, a total amount of 281 schools will be evaluated in both regions. Most of them were built without any consideration of the seismic actions.

Approximately half of the school building stock have URM structures with load-bearing walls. URM buildings are especially prone to damage due to seismic actions. Its vulnerability has been observed and analysed in the last decades by many authors. Some studies have developed different methods to assess the seismic vulnerability of existing buildings. Usually, methods based on the capacity spectrum are used to characterize the vulnerability and fragility of the buildings [3]. The seismic performance analysis results show the damage level that a building would suffer in case of an earthquake. Moreover, it allows to identify the structural characteristics that reduce the vulnerability of the buildings. In some studies, the damage estimated for a specific structure pertaining to a given typology is considered as representative for the whole group of structures belonging to the aforementioned structural typology [4], as is the aim of the PERSISTAH project. These studies have concluded that a seismic retrofitting of the structure would be required in order to improve their seismic behaviour.

The most common retrofitting strategies used for masonry buildings are (a) reinforcement of connections (wall to wall, wall to floor or wall to roof), (b) transforming flexible floors into rigid diaphragms, (c) improving the out-of-plane behaviour through tied rods or ring beams, and (d) reinforcement of masonry panels. These techniques have been applied in numerous studies and they have resulted effective [5] [6] [7] [8]. The case study building has good connections and rigid floors, which makes the reinforcement of panels the most suitable reinforcement technique to improve its behaviour. The reinforcement of panels has been implemented by means of the addition of diverse materials: reinforced concrete, steel, fibre polymer, polypropylene, mortar renders or injections. These techniques are often complex to perform, non-reversible and expensive. Since the aim of the PERSISTAH project is to retrofit a large number of buildings, these techniques are not the best option.

The school buildings are characterised by numerous openings, which cause a substantial weakness in the URM walls in case of an earthquake. In fact, none of these buildings have been designed considering seismic loads, since they were built prior to any seismic code or with emerging and permissive codes. Therefore, they may not be capable of resisting these actions without being damaged. This work aims to study a simple, effective and inexpensive technique to retrofit these buildings, which consists in installing steel encirclements in the openings of the walls.

A recent paper has experimentally studied this technique by means of cyclically testing an specimen to failure [9]. The authors have concluded that the encirclements led to a significant increase in strength and in-plane deformation capacity, as well as in cumulative dissipated energy at collapse. Comparing a retrofitted wall to a solid masonry wall (without openings), they have stablished that the results were very similar, especially in terms of peak strength.

To test this reinforcement technique a case study was conducted. The building is a primary school building located in Huelva (Spain) and built in 1961. It is an E-shaped, two storied building, with clay brick URM load-bearing walls and ribbed floor slabs.

A seismic performance-based assessment based on the N2 method was carried out (section 2.2). Then, a damage assessment was performed (section 2.3). Next, six different variants of the reinforcement technique (encirclements) were studied. Three of them consist solely on adding an L-profile to the window border, and the other three include also different types of grilles covering the window surface (section 2.4). The results of the retrofitted building assessment are shown in section 3 and analysed in section 4. Finally, the conclusions are outlined in section 5.

2 METHOD

2.1 Case study

The building under study is a two-storied school building located in Huelva (Spain) and built in 1961. The plan has an E-shape with 45 m by 21 m as larger dimensions. The building is composed of the intersection of four lineal blocks. One of them is wider, with an entrance gallery, staircases and two classrooms. The other three blocks are narrower, only equipped with classrooms.

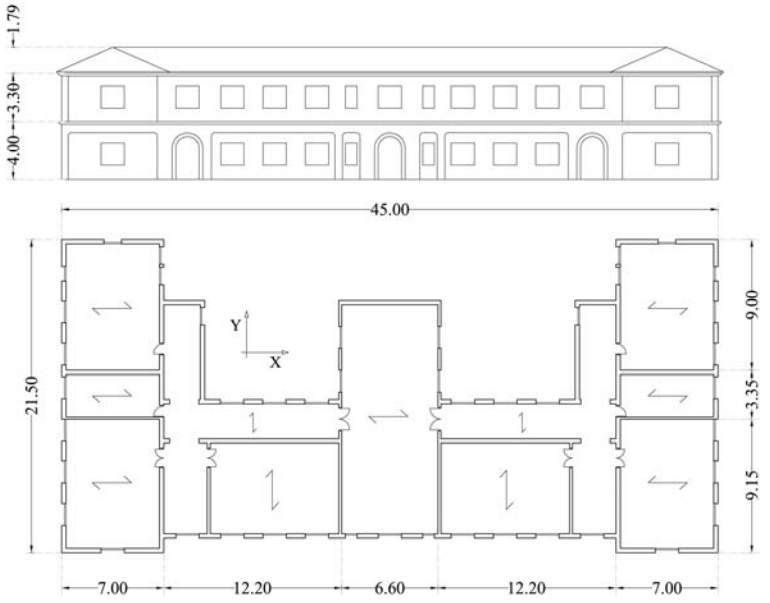

Figure 1: Architectural plans. Base floor (superior). Façade (inferior).

The structural system of the building consists of URM walls of clay brick and cement mortar. The walls have a thickness of 25 cm and a reinforced concrete ring beam on their top level. The floor structure is made up of ribbed floor slabs 25 cm thick. The foundation is a concrete beam on strip footings. The building has a sloping roof with tiles.

The load values used in the analysis were obtained from the Spanish building code [10]. For structural analyses, the dead load assigned to the ground and first floor was 5.3 kN/m^2 (including floor slabs, pavement and partition walls), and 6.3 kN/m^2 to the roof floor (including floor slab, and construction elements of the gable roof). The live load assigned to the school floors was 3 kN/m^2 (public use), and 1 kN/m^2 in case of the roof floor (maintenance).

The mechanical properties of masonry elements are typically available in the literature when these pertain to historical buildings. However, the mechanical properties of modern masonry elements are less likely to be found, as is the case of this building.

On one hand, these properties have been calculated using formulations from current codes as Eurocode 6 [11], and UIC Code 778-3 [12]. On the other hand, the data of the mechanical properties of brick clay and mortar have been obtained from project documents of similar construction dates (Table 1).

Mechanical properties	Value
Compressive strength (f_m) (MPa)	5
Shear strength (t_0) (MPa)	0.24
Young´s modulus (E) (MPa)	3,500
Shear modulus (G) (MPa)	875
Weight density (W) (kN/m^3)	15

Table 1: mechanical properties adopted for the brick masonry walls.

2.2 Seismic performance-based assessment

The URM structures have a non-linear behaviour due to their low tensile strength. Consequently, non-linear analyses must be used to evaluate them. [13]. In order to assess the seismic performance of buildings by means of nonlinear static analyses, the European code EC8-3 [14] recommends the N2 method. This method combines the pushover analysis with the demand spectrum. The displacement capacity of the structure and the seismic demand displacement must be intersected to obtain the performance point, which is the base parameter of the global seismic assessment [15]. The pushover analysis is a static non-linear analysis that consist of applying a horizontal incremental load until the collapse of the structure is reached. The result of this analysis is a capacity curve that represent the base shear with respect to the horizontal displacement of the control node, which is located on the top of the structure.

The masonry wall structure was modelled with the Equivalent Frame Model [16], using the Tremuri software [17]. In this model, the URM walls are divided in macro-elements to form an equivalent frame. The model is composed of piers and spandrel elements assembled through rigid nodes. The formulation used to model the elements is defined from the dissipative mechanism observed in real masonry structures affected by seismic actions. This model considers the possibility of flexural-rocking, shear-sliding and diagonal-cracking shear failure modes, allowing to simulate the non-linear in-plane behaviour of URM walls with acceptable accuracy [18].

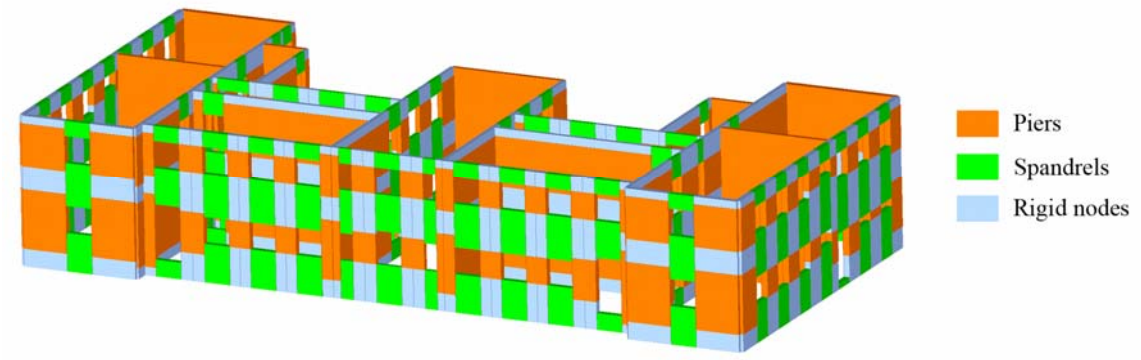

Figure 2: Three-dimensional view of the case study building model in Tremuri.

The seismic demand is defined in terms of a response spectrum, obtained from the EC8-1[19] and the Spanish annex [20]. The seismic action in Huelva is defined by the reference peak ground acceleration (a_{gR}) whose value is 0.12g according to the Spanish update of the seismic hazard maps [21]. Other parameters used to obtain the response spectrum are the importance factor and the soil coefficient. The importance factor depends on the use of the building. School buildings have an importance of class III, so the corresponding importance factor is 1.3. Regarding the soil coefficient, the type of soil has been defined from a geotechnical study performed in a near location. This study established that the soil is composed by a layer of silt-sand with medium-low compactness. According to the dynamic penetration test (DPSH) performed, the type of soil was determined as B, thus the corresponding soil coefficient is 1.2.

2.3 Damage assessment

The seismic performance of the reinforced buildings may be compared in terms of fragility curves. These curves describe the probability of reaching a given state of damage in a defined seismic scenario. The curves are defined by a lognormal function (Eq. 1) that expresses the probability of reaching or exceeding a defined damage state, given the spectral displacement.

$$P[d_s|S_d] = \Phi\left[\frac{1}{\beta_{ds}}\right]\ln\left(\frac{S_d}{\overline{S}_{d,ds}}\right) \quad (1)$$

Where S_d is the spectral displacement; d_s is the damage state; Φ is the standard normal cumulative distribution function; β_{ds} is the standard deviation of the natural logarithm of spectral displacement for damage state *ds;* and $\overline{S}_{d,ds}$ is the median value of spectral displacement at which a building reaches the threshold of damage state d_s.

The damage states considered according to the RISK-EU project (Eq. 2) are: slight damage ($S_{d,1}$), moderate damage ($S_{d,2}$), severe damage ($S_{d,3}$) and complete damage ($S_{d,4}$). The damage limit states were obtained from the idealised bilinear capacity curves. These states were defined by the yielding and ultimate displacements, as it is proposed in [22].

$$\begin{aligned} S_{d,1} &= 0.7\ S_{dy} \\ S_{d,2} &= 1.5\ S_{dy} \\ S_{d,3} &= 0.5\ (S_{dy} + S_{du}) \\ S_{d,4} &= S_{du} \end{aligned} \quad (2)$$

Then, the damage states probabilities were obtained by intersecting the fragility curves and the target displacements. Finally, the damage index (DI) or the mean damage value were calculated to represent the global expected damage in the structure with each reinforcement technique. The DI may be obtained from Eq. 3 [23]:

$$DI = \sum_{i=0}^{n} i \times P(d_{s_i}) \quad (3)$$

where n is the number of damage states, and $P(d_{si})$ is the probability that a damage state i occurs. The DI values range between 0 (no structural damage) and 4 (complete damage).

2.4 Strengthening technique

School buildings are usually characterised by numerous openings in the external walls. The presence of openings weakens the building under seismic action. Therefore, the reinforcement strategy chosen consisted in strengthening the openings, installing a steel encirclement in the building windows. A steel profile was fixed in the outer perimeter of the windows, with the possibility of adding a grille covering the whole surface of the window. The doors were not reinforced due to the difficulty of fixing the lower profile under the flooring. In any case, there are not as many doors as windows in these buildings. The advantages of this technique are that it is non-intrusive, easy to install (and remove) and cost-effective.

Six types of reinforcement were tested. The first three types consist on the installation of L-profiles of sizes L100.10, L150.10 and L200.15, respectively, on the windows perimeter (Figure 4a). The last three types are window grilles. Grille 1 includes an L100.10 profile in the perimeter and horizontal tubular profiles of 60x40 mm covering the windows surface (Figure 4b). Grille 2 combines a perimeter steel plate of 45x5 mm, horizontal 12 mm bars and two diagonal 12 mm bars (Figure 4c). Finally, Grille 3 was designed as the combination of a perimeter steel plate of 45x5 mm and seven diagonals 10 mm bars in both directions (Figure 4d).

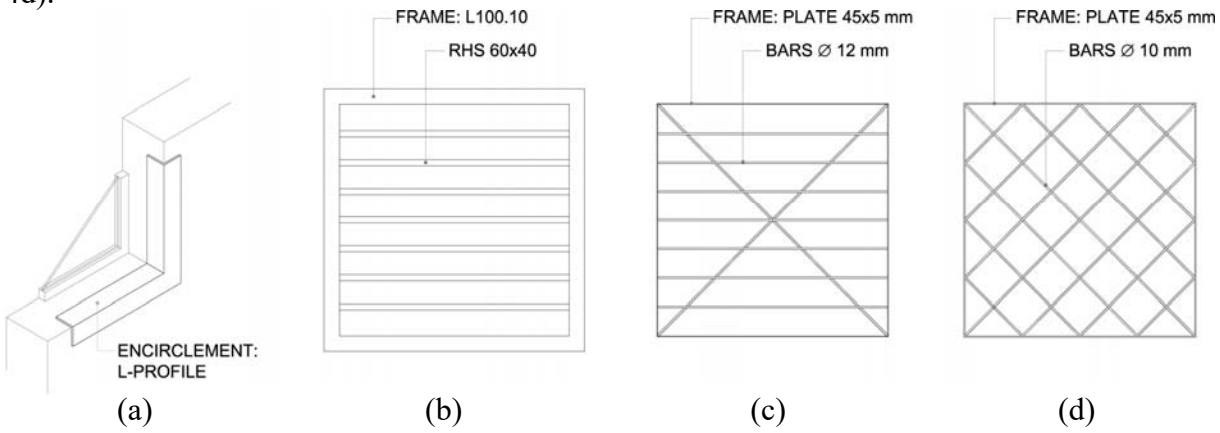

Figure 4: Reinforcements types: encirclements with L-profile (a), Grille 1 (b), Grille 2 (c) and Grille 3 (d).

The type of steel used in all reinforcements is S275JR steel both for profiles and bars. Their installation includes removing the windowsill, setting the encirclements or grilles (fixed with mechanical anchoring), and placing the windowsill back again. All six types of reinforcements integrate well with the architecture of the building.

The encirclements can be modelled in the Tremuri software, just setting this option in the window definitions. By contrast, the grilles are not included in the reinforcement library, but they can be simulated using an encirclement with equivalent rigidity. This equivalent encirclement was obtained applying a constant horizontal load to the grille and finding a profile which provided the same displacements.

3 RESULTS

3.1 Unretrofitted building

The results obtained from the seismic performance-based assessment of the unretrofitted building are presented hereafter. To obtain the capacity curves, a pushover analysis was performed in the two main orthogonal directions of the building (+X, -X, +Y and –Y), considering two lateral load patterns (uniform and triangular). Moreover, the existence or absence of an accidental eccentricity of 5% of the maximum size of the building (positive or negative)

was considered. A total of 24 different analyses were carried out and the worst-case combination for each direction was selected.

In Figure 3, it can be observed that the capacity curves in both directions X and Y are quite similar in terms of capacity. Regarding the ductility, defined by the ratio between ultimate and yielding displacements, the building presents a larger ductility in the X direction.

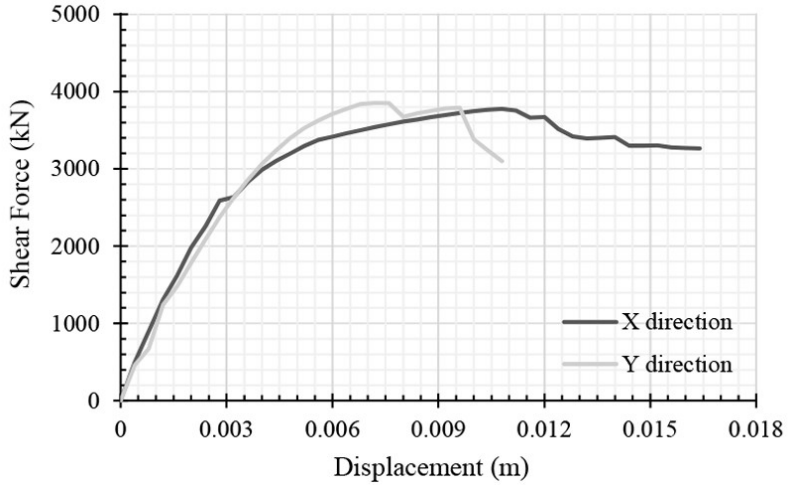

Figure 3: Capacity curves of the reference building in both directions X and Y.

After that, the performance points were calculated according to the N2 method. The main parameters used in the analysis are defined in the following paragraphs. Their values are summarized in Table 2.

	Γ	T^*(s)	μ	F_y^*/m^*(g)	q^*	$\mathbf{d_u^*/ d_t^*}$
X direction	1.20	0.24	3.34	2.47	1.72	**0.99**
Y direction	1.29	0.23	3.28	2.59	1.64	**0.70**

Table 2: Parameters and results of the analysis of the reference building.

Γ is the transformation factor, required to convert the parameters of the Multi Degree of Freedom (MDOF) system into an equivalent Single Degree of Freedom (SDOF) system and vice versa.

T^* is the period of the idealized equivalent SDOF system

μ is the ductility, the ratio between ultimate and yielding displacements.

F_y^*/m^* is the limited structural strength, the ratio between the ultimate strength and the mass of an equivalent SDOF system.

q^* is the ratio between the acceleration of the structure with unlimited elastic behaviour ($S_e(T^*)$) and the limited structural strength (F_y^*/m^*).

The results of the analysis, in terms of the ratio between ultimate displacement (d_u^*) and target displacement in the equivalent SDOF system (d_t^*) are also shown in table 2.

The ultimate limit state (ULS) safety verification according to the EC8-3 consist in checking that the ratio d_u^*/ d_t^* is higher than 1. It can be observed that this condition is not satisfied either in X or Y direction, although the results in Y are significantly worse. Non-compliance of the safety conditions indicated that the building required to be retrofitted.

3.2 Retrofitted building

Figure 5 shows the results of the pushover analysis in terms of capacity curves in X and Y directions for the retrofitted building (with all six types of reinforcements) and the unretrofitted building (reference building).

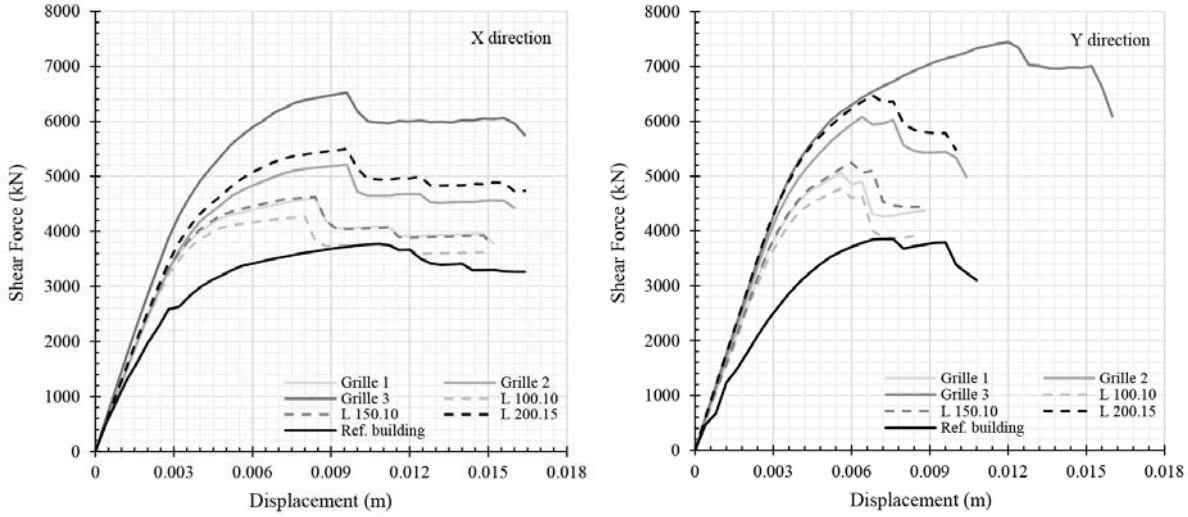

Figure 5: Capacity curves for each reinforcement technique, X direction (left) and Y direction (right).

As mentioned in the previous section, the performance points were obtained intersecting the capacity curves and the seismic displacement demand, as established in the N2 method. In Figure 6, the performance points of the reference and the reinforced buildings are shown.

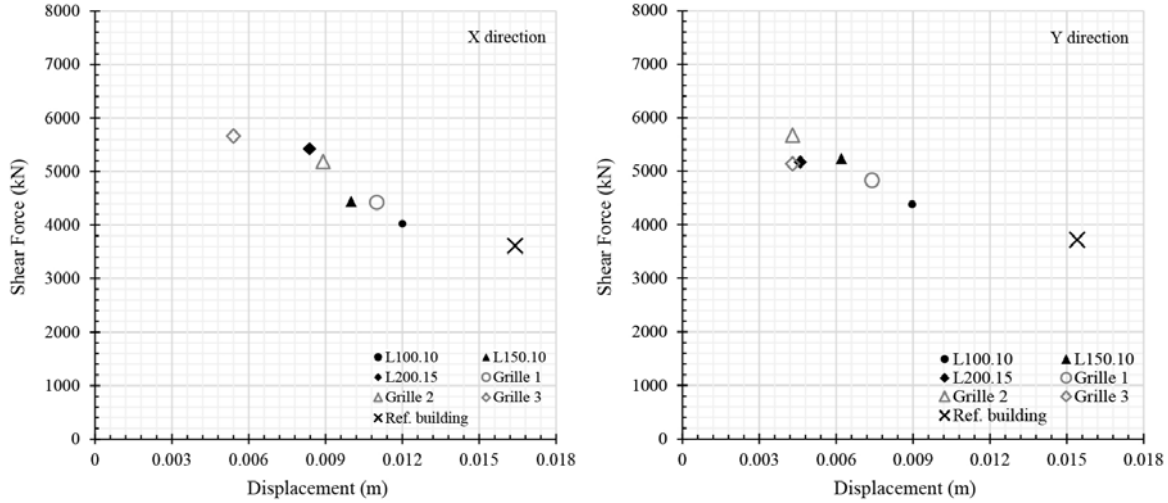

Figure 6: Performance point for each reinforcement technique in X (left) and Y direction (right).

In Table 3, the results of the N2 method are summarized. They are the target displacements (dt), obtained for the elastic response spectra defined in EC8-1; the yielding (dy) and ultimate (du) displacements. The ductility (μ) of each reinforcement type was calculated as the ratio d_u^*/d_y^*. Finally, the ratio d_u^*/d_t^*, that allowed to verify the ULS safety according to the EC8-3 was obtained.

		d_t^*	d_y^*	d_u^*	μ	$\mathbf{d_u^*/ d_t^*}$
X direction	Ref. building	1.37	0.40	1.36	3.40	**0.99**
	L100.10	1.00	0.31	1.23	3.97	1.23
	L150.10	0.90	0.34	1.26	3.71	1.40
	L200.15	0.69	0.41	1.35	3.29	1.96
	Grille 1	0.92	0.35	1.26	3.60	1.37
	Grille 2	0.76	0.42	1.32	3.14	1.74
	Grille 3	0.44	0.35	1.34	3.83	3.05
Y direction	Ref. building	1.19	0.36	0.83	2.31	**0.70**
	L100.10	0.69	0.28	0.65	2.32	**0.94**
	L150.10	0.48	0.33	0.67	2.03	1.40
	L200.15	0.34	0.30	0.75	2.50	2.21
	Grille 1	0.57	0.30	0.67	2.23	1.18
	Grille 2	0.32	0.28	0.79	2.82	2.47
	Grille 3	0.32	0.29	1.20	4.14	3.75

Table 3: Results obtained for each reinforced building through the N2 method (displacements in cm).

The fragility curves were derived from the capacity curves. Intersecting the fragility curves with the target displacements allowed to determine the damage states probabilities (table 4). Finally, the DI for each reinforcement condition was calculated. The results are shown in Figure 7.

		0 No damage	1 Slight damage	2 Moderate damage	3 Severe damage	4 Complete damage
X direction	Ref. building	0	0.29	9.88	39.56	50.25
	L100.10	0	0.53	15.37	45.77	38.31
	L150.10	0	1.65	21.68	45.31	31.37
	L200.15	0.2	15.3	34.18	33.91	16.37
	Grille 1	0	1.65	21.07	44.87	32.43
	Grille 2	0.04	9.26	31.37	38.05	21.26
	Grille 3	12.97	41.38	23.64	16.02	5.96
Y direction	Ref. building	0	0.34	5.83	24.8	69.01
	L100.10	0	2.391	13.32	29.74	54.01
	L150.10	0.32	17.48	20.91	27.9	33.37
	L200.15	13.48	41.49	13.84	13.48	14.68
	Grille 1	0.12	12.97	21.38	30.31	35.2
	Grille 2	18.38	41.73	13.55	15.09	11.23
	Grille 3	49.4	30.25	7.82	8.24	4.27

Table 4: Damage states probabilities for each retrofitting technique.

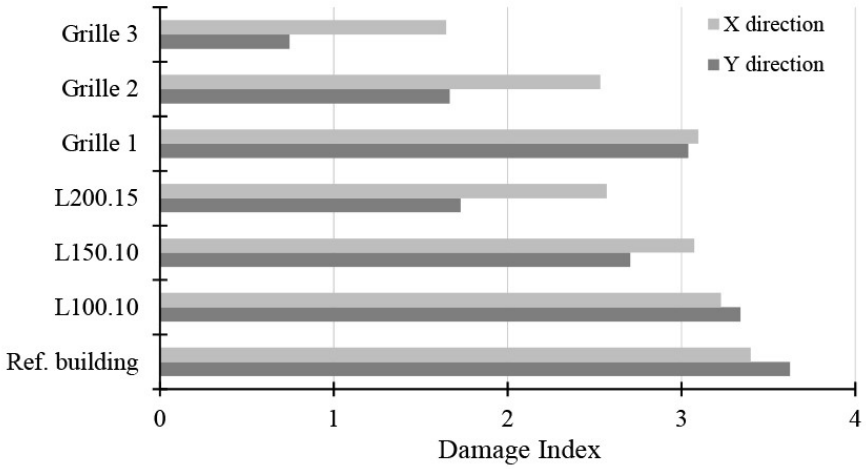

Figure 7: Damage index for the reference building and with each retrofitting technique.

4 ANALYSIS OF RESULTS

The results in terms of capacity curves show that both the encirclements alone and the window grilles were effective in both X and Y directions. Observing the curves, it can be noticed that all reinforcements provide a noticeable increase in both strength and rigidity.

For the unretrofitted condition, the building capacity was similar in X and Y directions, although in X the ultimate displacement of the structure was higher, indicating higher ductility in X. This may be due to the fact that the piers in the X direction walls are slenderer than those in the Y direction walls. Slenderer piers lead to a predominant flexural response, with higher values of drift. Otherwise, thick piers (predominant in the Y direction) tend to produce shear failure and lower values of drift. The same results were obtained experimentally in [24] and similar conclusions were reported in [6].

Even though all retrofitting techniques improve capacity, the enhancement is greater in Y than in X in all cases. In X direction, the maximum shear force increased between 11% (L100.10 encirclements) and 57% (Grille 3). In Y direction, the enhancement ranged between 24% (profile L100.10) and almost 100%, in the case of Grille 3.

Figure 6 shows the performance point of the reference building and the six reinforcement cases. In all cases, in line with their capacity improvement, the reinforced buildings presented a great decrease of the displacements as compared to the reference building. This reduction was from 25% to 69% along the X axis, and from 38% to 69% along the Y axis.

Table 3 presents the results of the N2 analysis in terms of the target d_t^*, ultimate d_u^* and yielding displacements d_y^*. Observing the ductility values, it can be noted that in most cases the retrofitting produced only a slight improvement in both directions. Even in some cases (e.g., L150.10 in Y), the ductility decreased when the reinforcement was applied. In general, the building presented a less ductile behaviour in the Y direction, but here once again the Grille 3 reinforcement proved very effective, producing an increase of 80% in ductility over the reference building. Regarding the ULS safety verification, it can be checked that every retrofitting case except L100.10 (Y direction) satisfied the condition $d_u^*/d_t^*>1$. The improvement ranged from 38 to 76% in the X direction. In the Y direction, the gain was in most cases up to 100% or 200%. A 400% was even reached in case of the Grille 3.

In Figure 7, the DI for the different reinforcement techniques can be compared. On one hand, it can be observed that adding the L100.10 encirclement produced a minimal decrease of DI in both axis and did not changed significantly the building´s behaviour. Adding Grille 1 produced a slight improvement in behaviour with a small reduction of the DI, down to severe

damage. On the other hand, the addition of L150.10 profiles provided a significant reduction of damage in Y direction, although the gain was minimal in X direction. Furthermore, applying the L200.15 encirclement or the Grille 2 led to significant improvements in both directions, especially in Y, where the DI was reduced below to moderate damage. Finally, the Grille 3 is the reinforcement that produced the best results. In this last case, the DI was reduced below moderate damage in the X direction and below slight damage in the Y direction.

In terms of DI, the behaviour of the unretrofitted building was slightly better in the X direction. Nevertheless, all reinforcements provided higher enhancements in the Y direction with the exception of the L100.10 case. This can be explained observing the building geometry. Firstly, there is symmetry in the plan building in the Y axis but not in the X axis. Moreover, despite the fact that there are similar number of openings in both directions, they are distributed uniformly in the Y direction, but not in the X direction, which increase the lack of symmetry in this direction. Thus, the vulnerability in the Y direction is mainly caused by the presence of openings in the walls, and can be substantially reduced with these retrofitting techniques. On the contrary, in the X direction, the vulnerability of the building is produced by many factors, including lack of symmetry and the irregular distribution of openings. As a consequence, the reinforcement of openings in the X walls is not as much effective as in the Y walls.

5 CONCLUSIONS

This work is framed in the PERSISTAH project, which aims to analyse the seismic vulnerability of primary school buildings located in the region Algarve-Huelva. In the present paper, the seismic vulnerability of a URM primary school building located in Huelva was assessed. The main goal was to develop a simple, effective and affordable technique to retrofit a large number of buildings. The seismic performance of the building with different retrofitting techniques was assessed using the N2 method, as recommended by the EC8-3. Nonlinear static analyses were performed to obtain the capacity curves of the building including the retrofitting techniques. Moreover, the fragility curves were determined to obtain the probability of reaching or exceeding each damage state. Finally, the DI for each retrofitting technique model was obtained and compared.

The results showed that the unretrofitted building presented a high seismic vulnerability and did not satisfy the EC8-3 ULS verification. Therefore, to avoid future damage in the event of an earthquake, a retrofitting technique based on reinforcing the wall openings was proposed. Six different reinforcement scenarios were tested, three of them with encirclements and the other three with grilles. The results showed that the seismic behaviour of the building improved considerably when the reinforcements were applied. In particular, a noticeable increase in capacity and an important decrease in the performance point values were observed. Regarding the EC8 ULS safety verification, the results showed that all retrofitting techniques have been effective, except in the case of the encirclement with L100.10 profile.

In terms of damage level reduction, it can be concluded that, in general, all reinforcement techniques improved the seismic behaviour of the building. On one hand, the encirclements led to enhance the seismic performance of the building, provided that the profile size is appropriate. As for the grilles, the results have shown that adding grilles composed by horizontal tubular profiles did not enhance significantly the damage level of the structure. On the contrary, including the diagonal bars has proved much more effective. Furthermore, it was found that a higher number of diagonal bars produced a higher improvement in the damage level. Consequently, the Grille 3 reinforcement, in which all bars are placed in a diagonal pattern, resulted the most suitable design. In this case, the architectural integration is better due to the use of a plate in the perimeter, instead of an L-profile. Moreover, the reinforcement of Grille 3

has the best cost-benefit ratio since the plates and bars included require less steel than the encirclements with L profiles. Furthermore, this has resulted to be the most optimal and efficient retrofitting technique to improve the seismic behaviour of the URM primary school buildings studied in Huelva and the Algarve.

ACKNOWLEDGEMENTS

This work has been supported by the INTERREG-POCTEP Spain-Portugal programme and the European Regional Development Fund through the 0313_PERSISTAH_5_P project.

REFERENCES

[1] D.K. Chester., O.K. Chester. The impact of eighteenth century earthquakes on the Algarve region, southern Portugal. *Geographical Journal*, **176**, 350–70, 2010.

[2] R. Bartolome., E. Gràcia., D. Stich., S. Martínez-Loriente., D. Klaeschen., F. de Lis Mancilla., C. Lo Iacono., J.J. Dañobeitia., N. Zitellini. Evidence for active strike-slip faulting along the Eurasia-Africa convergence zone: Implications for seismic hazard in the southwest Iberian margin. *Geology*, **40**, 495–8, 2012.

[3] A.H. Barbat., L.G. Pujades., N. Lantada. Performance of buildings under earthquakes in Barcelona, Spain. *Computer-Aided Civil and Infrastructure Engineering*, **21**, 573–93, 2006.

[4] A.H. Barbat., S. Lagomarsino., L.G. Pujades. Vulnerability assessment of dwelling buildings. In Assessing and managing earthquake risk, eds., C. S. Oliveira, A. Roca, and X. Goula. *Dordrecht, The Netherlands: Springer*, 115–134, 2006.

[5] R. Maio., J.M.C. Estêvão., T.M. Ferreira., R. Vicente. The seismic performance of stone masonry buildings in Faial island and the relevance of implementing effective seismic strengthening policies. *Engineering Structures*, **141**, 41–58, 2017.

[6] H.A. Meireles., R. Bento. Seismic assessment and retrofitting of Pombalino buildings by fragility curves. *15th World Conference on Earthquake Engineering, Lisbon Portugal*, 1–10, 2012.

[7] J. Ortega., G. Vasconcelos., H. Rodrigues., M. Correia. Assessment of the efficiency of traditional earthquake resistant techniques for vernacular architecture. *Engineering Structures*, **173**, 1–27, 2018.

[8] S. Diz., A. Costa., A.A. Costa. Efficiency of strengthening techniques assessed for existing masonry buildings. *Engineering Structures*, **101**, 205–15, 2015.

[9] J.M. Proença., A.S. Gago., A. Vilas Boas. Structural window frame for in-plane seismic strengthening of masonry wall buildings. *International Journal of Architectural Heritage*, **13**, 98–113, 2019.

[10] Gobierno de España. DB SE- AE Seguridad Estructural, Acciones en la Edificación. *Boletín Oficial del Estado*, 1–42, 2009.

[11] European Union. Eurocode-6: Design of masonry structures. Part 1-1: General rules for reinforced and unreinforced masonry structures, Brussels, 2005.

[12] Recommandations pour l'Evaluation de la Capacite Portante des Ponts-Voutes Existants en Maconnerie et Beton. Paris: Union Internationales des Chemins de Fer., France, 1995.

[13] S. Lagomarsino., S. Cattari. Seismic Performance of Historical Masonry Structures Through Pushover and Nonlinear Dynamic Analyses. *Perspectives on European Earthquake Engineering and Seismology. Vol. 39*. pp.265–92 (2015).

[14] European Union. Eurocode-8: Design of structures for earthquake resistance. Part 3: Assessment and retrofitting of buildings, Brussels, 2005.

[15] P. Fajfar., P. Gašperšič. The N2 method for the seismic damage analysis of RC buildings. *Earthquake Engineering & Structural Dynamics*, **25**, 31–46, 1996.

[16] A. Penna., S. Lagomarsino., A. Galasco. A nonlinear macroelement model for the seismic analysis of masonry buildings. *Earthquake Engineering & Structural Dynamics*, **43**, 159–79, 2014.

[17] A. Galasco., S. Lagomarsino., A. Penna. TREMURI Program: Seismic Analyser of 3D Masonry Buildings. *University of Genoa*, 2002.

[18] S. Lagomarsino., A. Penna., A. Galasco., S. Cattari. TREMURI program: An equivalent frame model for the nonlinear seismic analysis of masonry buildings. 2013.

[19] European Union. Eurocode 8: Design of structures for earthquake resistance. Part 1: General rules, seismic actions and rules for buildings, Brussels, 2004.

[20] Spanish Ministry of Public Works [Ministerio de Fomento de España]. Spanish annex to Eurocode-8 [Anexo español al Eurocódigo 8], Madrid, 1998.

[21] Spanish Ministry of Public Works [Ministerio de Fomento de España]. Update of the seismic hazard maps [Actualización de mapas de peligrosidad sísmica de España], Spain, 2012.

[22] S. Lagomarsino., S. Giovinazzi. Macroseismic and mechanical models for the vulnerability and damage assessment of current buildings. *Bulletin of Earthquake Engineering*, **4**, 415–43, 2006.

[23] R. Gonzalez-Drigo., A. Avila-Haro., A.H. Barbat., L.G. Pujades., Y.F. Vargas., S. Lagomarsino., S. Cattari. Modernist unreinforced masonry (URM) buildings of barcelona: Seismic vulnerability and risk assessment. *International Journal of Architectural Heritage*, **9**, 214–30, 2015.

[24] A. Penna., S. Lagomarsino., A. Galasco. A nonlinear macroelement model for the seismic analysis of masonry buildings. *Earthquake Engineering & Structural Dynamics*, **43**, 159–79, 2014.

COMPDYN 2019
7th ECCOMAS Thematic Conference on
Computational Methods in Structural Dynamics and Earthquake Engineering
M. Papadrakakis, M. Fragiadakis (eds.)
Crete, Greece, 24–26 June 2019

USING DIRECT ECONOMIC LOSSES AND COLLAPSE RISK FOR SEISMIC DESIGN OF RC BUILDINGS

Davit Shahnazaryan[1], Gerard J. O'Reilly[1], Ricardo Monteiro[1]

[1] Scuola Universitaria Superiore IUSS Pavia
Palazzo del Broletto, Piazza della Vittoria 15, Pavia 27100, Italy
e-mail: {davit.shahnazaryan,gerard.oreilly,ricardo.monteiro}@iusspavia.it

Abstract

In recent years, the consideration of earthquake-induced expected annual loss (EAL) has become a topic of great interest within the earthquake engineering community. Since the introduction of performance-based earthquake engineering (PBEE) in the 1990s, the principal goal of seismic design has been the verification of limit states in addition to the use of meaningful metrics of seismic performance that respond to the diverse needs and objectives of owner-users and society. However, the need for more focus on the control of earthquake-induced losses at a design stage is also of importance and interest. One possible solution for this gap may be to use a conceptual design framework that employs EAL as a design metric, serving as a first design step to identify suitable typologies and geometrical layouts. The objective of such an approach, which would require very little building information at the design outset, is to identify a number of feasible building typologies, in terms of lateral force resisting system, and associated structural geometries. This study implemented such a novel EAL-based design methodology, recently proposed, for a reinforced concrete (RC) frame as a parametric case study within the European context. A sensitivity study on the use of storey loss functions was also done to identify their compatibility with and impact on the framework at different performance limit states. Furthermore, effectively controlling the structure's ultimate limit state whilst also arriving at practical design solutions was seen to be an issue that requires further development. An alternative method to control collapse risk during design whilst also maintaining control on the EAL of the structure was therefore identified. As such, a conceptual design framework that focuses on both the economic losses and life safety in a direct and quantifiable manner has been identified to further implement the principles of PBEE in design practice.

Keywords: Performance-Based Earthquake Engineering; Conceptual Design; Reinforced Concrete; Expected Annual Loss; Storey Loss Functions.

1 INTRODUCTION

Current seismic design guidelines have a two-fold performance objective: the protection of human lives and the limitation of earthquake-induced damage. Hence, it is important to limit the likelihood of structural collapse, which is obtained by providing sufficient strength and ductility, in addition to proper detailing and capacity design, ensuring a controlled and stable ductile mechanism during strong seismic shaking. Additionally, damage limitation can be controlled during more frequent events. Neglecting damage control at a design stage can have severe consequences during an earthquake as both structural and non-structural damage, in conjunction with the interruption of building use, may entail disproportionally high economical losses compared to the costs of the structure itself. These aspects partially form what has become known as the Pacific Earthquake Engineering Research (PEER) PBEE methodology initially outlined by Cornell and Krawinkler [1]. This PBEE methodology [2,3] is an approach to quantify the performance of a given structural system. It utilises a fully probabilistic framework, employing methodologies with a solid scientific basis to improve seismic risk decision-making and expresses the levels of performance in terms of metrics meaningful to stakeholders and building owners. New guidelines like FEMA P58 [4] were developed, which allow the performance of existing buildings to be quantified in terms of metrics like expected annual loss (EAL) and mean annual frequency of collapse (MAFC). However, due to its iterative and cumbersome nature, more simplified options to take EAL into account have been sought.

O'Reilly and Calvi [5] recently proposed a novel conceptual seismic design (CSD) framework that employs EAL as a design metric and requires very little building information at the design onset. The framework encompasses the idea that designers may start with the definition of a required or limiting value of EAL and arrive at a number of feasible structural solutions without the need for any detailed design calculations or numerical analysis. Initially, the building performance definition is transformed into a design solution space using a number of simplifying assumptions. Subsequently, with a suitable structural response backbone, a number of feasible building typologies and associated structural geometries are identified. It is important to note that the methodology forms a stepping stone prior to further member detailing and robust design verifications, such as that outlined in FEMA P58.

This study aims to describe a detailed implementation of the CSD framework [5] and provide further insight by means of a parametric study. Serviceability limit state parameters are initially varied to see their effect on the design EAL and an alteration of the design solution space. A study on the use of storey loss functions (SLFs) is then carried out for their modification to overcome their incompatibility with the CSD framework at the ultimate limit state, in view of it not affecting the EAL. Finally, an approach to consider target collapse safety to define prospective structure's dynamic and strength characteristics is discussed, which could potentially solve the issues identified during the sensitivity study on SLFs.

2 CONCEPTUAL SEISMIC DESIGN

In order to implement the CSD framework shown in Figure 1, some simplifying assumptions are needed initially. First, SLFs are used to convert expected loss ratios (ELRs) to design peak storey drift (PSD) and peak floor acceleration (PFA). Three limit states were utilised: fully operational limit state (OLS); serviceability limit state (SLS); and ultimate limit state (ULS). Two limit state intensities, SLS and ULS, are considered to characterise the structure's elastic and ductile non-linear behaviour, respectively. The OLS performance point

describes the point when direct monetary losses begin to accumulate due to building damage, which can be thought of as an initial threshold akin to the excess amount on an insurance policy. The ULS performance point describes the point of building's full monetary replacement cost (Figure 3).

Current codes define the seismic design problem primarily in terms of ensuring life safety of its occupants. Therefore, mitigation of collapse is of primary importance and ensuring satisfactory performance at frequent levels of shaking is also checked. These are termed as '*no-collapse requirement*' and '*damage limitation requirement*' in the current version of Eurocode 8 (EC8) [6] and are suggested to correspond to ground shaking return periods of 475 and 95 years, respectively, with possible modifications to account for building importance class. New Zealand's NZS1170 [7] defines two limit states: serviceability and ultimate similar to EC8 and prescribes design return periods of 25 and 500 years, respectively, once again with the possibility of modification for different importance classes. The recently revised design code in the US, ASCE 7-16 [8], outlines a slightly modified approach where the building is designed using input as a fraction of the maximum considered event (MCE). The seismic hazard is determined from a series of maps outlining risk-targeted spectral values, which are found for a target risk of structural collapse of 1% in 50 years (~5,000 year return period). It uses a generic structural fragility curve along with some other adjustments following an approach outlined by Luco *et al.* [9] but has recently been noted by Vamvatsikos [10] to perhaps not be the most ideal approach. In this study, these general recommendations provided above for the definition of limit state return period will be followed for the case study application in Section 3 and parametric studies in Section 4.1.

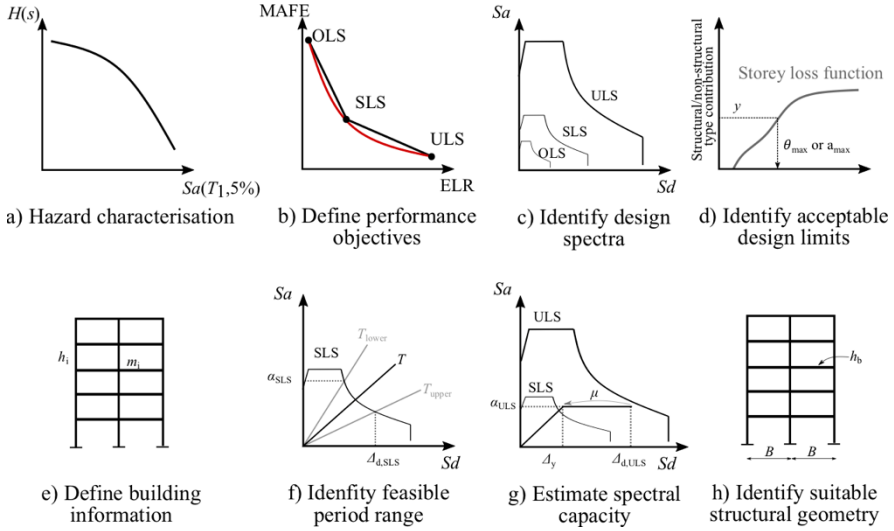

Figure 1: Overview of CSD framework for RC frames [5].

The CSD framework [5] is separated into two distinct parts: the identification of performance requirements, and the identification of feasible structural solutions. An overview of the framework for an RC frame is described in Figure 1. The first part includes: a) the site hazard initially identified with a uniform hazard spectra (UHS) for different return periods; b) performance objectives are set to establish the design loss curve characterised by an expected loss ratio (ELR, y), and corresponding mean annual frequency of exceedance (MAFE, λ), for each limit state. The loss curve is then integrated for the definition of design EAL, which has to be met by the subsequent obtainment of design solutions (Figure 3); c) using the MAFE for each limit state and the return periods of the UHS to be designed for, design spectra are identified; d) with the identification of design spectra, SLFs are used to relate expected monetary

losses to design parameters like the maximum PSD, θ_{max}, and maximum PFA, a_{max}, along the height of the building. The vertical axis in Figure 1(d) represents the ELR, y, contribution from PSD or PFA sensitive structural or non-structural elements.

The second part includes the following steps: e) minimal building information is needed, such as the number of storeys, n, seismic mass, m_i, and storey heights, h_i; f) at SLS, θ_{max} and a_{max} are converted to spectral displacement and acceleration limits, $\Delta_{d,SLS}$ and α_{SLS}, respectively. These are then used to identify the feasible initial secant to yield period range, where the initial period, T_1, of the sought structure must lie; g) knowing the design displacement at ULS, $\Delta_{d,ULS}$, and the required ductility, μ, the bilinear backbone curve is identified; h) and finally a suitable structural geometry from the established yield displacement, Δ_y, knowing that the yield displacement is a function of structural geometry and material properties. In the case of RC frames, the bay width, B, and the beam height, h_b, are computed. Overall, the framework works as an initial screening for suitable design before detailing and verification of the structure.

3 CASE STUDY APPLICATION

The CSD framework summarised in the previous section was used for a case study application herein. The goal of the study was to define certain performance objectives and come up with a set of design solutions in terms of bilinear backbone behaviour and required structural dimensions. No detailed verification analysis of these designs was carried out. Reasonable assumptions were made during the design process, since some information was not readily available. Minimal building information was necessary to implement the CSD framework. For the case study building discussed herein, a four-storey building with a floor area of 200m^2, seismic floor loading of 8kPa and roof loading of 7kPa was considered. The storey height was taken as 3.5m. The target EAL for the case study RC frame was predefined as 0.7%. With the already identified building performance requirements and minimal global characteristics of the possible building, a number of feasible design solutions were identified.

3.1 Identify site hazard

For the first step, the site hazard curve, H, was identified. Peak ground acceleration (PGA) was adopted along with EC8's type 1 design spectrum and soil type C was assumed. A higher fidelity second-order hazard model [11] was adopted instead of the first-order model initially utilised by O'Reilly and Calvi [5] to give a more accurate representation of the hazard, as described by Equation 1:

$$H(s) = k_0 \exp\left(-k_2 \ln^2 s - k_1 \ln s\right) \tag{1}$$

where the coefficients k_o, k_1 and k_2 were found to be 4.61E-05, 2.384 and 0.169, respectively, via a least-squares regression of the SHARE model [12] for a site in L'Aquila, Italy; and $H(s)$ is the hazard function representing the MAFE of a certain IM value s equal to PGA (Figure 2).

3.2 Define building performance objectives

Design performance objectives for the case study building are identified in Table 1. The values of return period, T_R, and ELR are decided. Then $H=1/T_R$ is used to determine the MAFE from Equation 2:

$$\lambda = \sqrt{p} k_0^{1-p} \left[H\left(\hat{s}\right)^p \right] \exp\left(\frac{1}{2} p k_1^2 \beta_s^2 \right)$$
$$p = \frac{1}{1 + 2k_2 \beta_s^2} \tag{2}$$

where $\hat{s}$ is the median value of s for a given limit state exceedance. Through the integration of the refined loss curve of Figure 3 and Equation 3, the EAL is computed and verified against the target one.

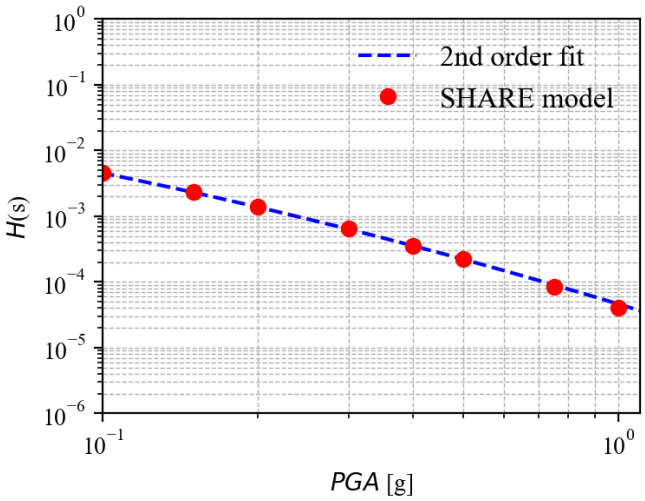

Figure 2: Second-order fit of a hazard curve for *PGA* at L'Aquila.

	OLS	SLS	ULS	Source
y	1%	25%	100%	User choice
T_R [years]	10	225	1600	User choice
H	1.00E-01	4.44E-03	6.25E-04	$=1/T_R$
β	0.1	0.2	0.3	Eurocode 8
λ	1.00E-01	4.65E-03	7.31E-04	Equation 2
EAL		0.64%		Equation 3
PGA [g]	0.01	0.10	0.28	Equation 1

Table 1: Design performance objectives defined by an ELR at each limit state, necessary to compute their respective MAFE and the design intensities.

Dispersions, β_s, were assumed based on those recommended in Appendix F of the recent draft of the revised Eurocode 8 [6] and are therefore deemed to be suitable for the present scope of illustration. In Figure 3, the EAL may be computed as the area beneath the approximate loss curve and is shaded in red. It is important to pay careful consideration since while the difference in area between the approximate and refined loss curve may appear insignificant, this is a result of the log scale of the vertical axis in Figure 3. However, it is possible to have an area between the two curves resulting in an EAL overestimation of up to 50% when compared to the refined curve. This can be overcome by using a closed-form expression with the same functional form of the refined loss curve as suggested by O'Reilly and Calvi [5]:

$$\lambda = c_0 \exp\left[-c_1 \ln y - c_2 \ln^2 y \right] \tag{3}$$

where the coefficients c_0, c_1 and c_2 can be fitted to pass through the three limit state points shown in Figure 3. The EAL was then evaluated as the area beneath this closed-form expression and is expected to be more representative of the actual EAL using more refined analysis. The ELR's were taken as y_{OLS}=1%, y_{SLS}=25% and y_{ULS}=100%, for the case study building. The values for the OLS and ULS limit states were based on the same consideration by O'Reilly and Calvi [5] whereby the OLS point is intended to represent the point at which the losses begin to accumulate and ULS when the losses reach the value of the building. The SLS point was chosen here and the sensitivity of the EAL to this value will be discussed in Section 4.1. The design EAL was established as the area under the refined curve, which was obtained as 0.64%, less than the target EAL (0.7%).

From each of these design limit state return periods, the design PGA was identified by inverting the hazard model in Equation 1 in terms of PGA. In the revised Eurocode 8, the 1600-year return period for the ULS corresponds to the significant damage limit state, so it was assumed to represent the complete replacement of the structure. In case of different design codes being used with differing minimum design requirements, such as NZS1170 or ASCE 7-16, the design return period of 2500 years is required at ULS, which may need to be accommodated as well.

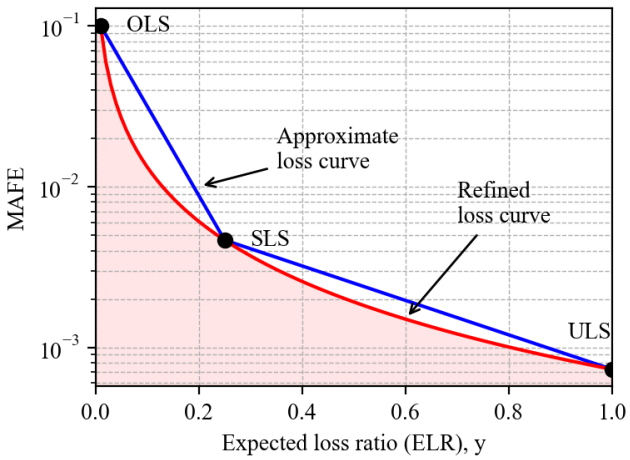

Figure 3: Approximate and refined loss curves, used to establish the design EAL shaded in red.

3.3 Identify structural design parameters

In order to convert the design loss ratios at both SLS and ULS into structural design parameters, storey loss functions (SLFs) were utilised and adopted from the literature [13]. Office occupancy was assumed and, for simplicity, only the typical SLFs were adopted (Figure 4). Considering the SLFs, the current formulation of CSD is not entirely compatible with their use when ELR is equal to 100% at ULS, since these functions' formulations tend to asymptotically increase towards large structural demand values of 15% storey drift (Figure 4), which are not realistic in design. To address this, a limiting value of 2% for PSD was adopted here, based on a sensitivity study presented in Section 4.2. Furthermore, some future developments to address this aspect relating to ULS performance are also envisaged in Section 4.3.

To link the ELR at each limit state to a structural demand parameter via the SLFs, as illustrated in Figure 4, the relative weights or contributions of the different component groups to expected loss, *Y*, were required. The ELR at each limit state is described by Equation 4:

$$y_{S,PSD} + y_{NS,PSD} + y_{NS,PFA} = y \tag{4}$$

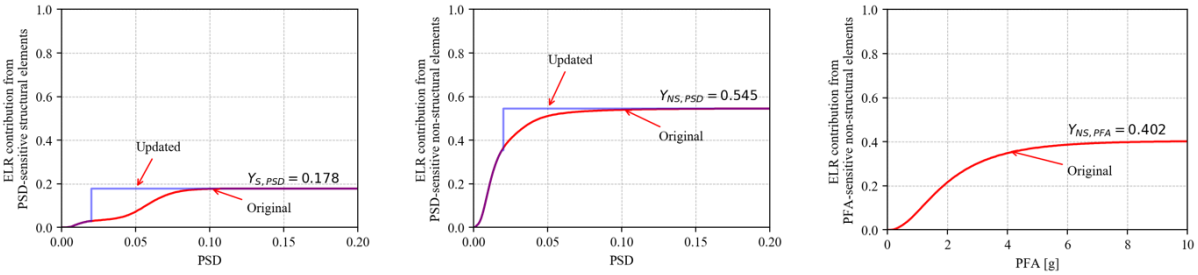

(a) PSD-sensitive structural elements

(b) PSD-sensitive non-structural elements

(c) PFA-sensitive non-structural elements

Figure 4: SLFs adopted from [13].

which is the sum of all sources of loss resulting from PSD-sensitive structural ($y_{S,PSD}$) and non-structural ($y_{NS,PSD}$) elements and PFA-sensitive non-structural ($y_{NS,PFA}$) loss contributions given in Figure 4. From Equation 4, the following expressions in Equation 5 can be written:

$$\begin{aligned} y_{S,PSD} &= yY_{S,PSD} \\ y_{NS,PSD} &= yY_{NS,PSD} \\ y_{NS,PFA} &= yY_{NS,PFA} \end{aligned} \tag{5}$$

meaning that the individual values of the damageable element group loss was computed as a product of the target ELR, y, and its relative weighting, Y, shown in Figure 4. By entering the vertical axis in Figure 4, these returned two values of θ_{max} and one value of a_{max} not to be exceeded in order to maintain that level of expected loss for that limit state. Taking the more critical of the two θ_{max} values at SLS, which will almost always be the non-structural-based value, the design demand parameters were established and are illustrated in Figure 5 and listed in Table 2.

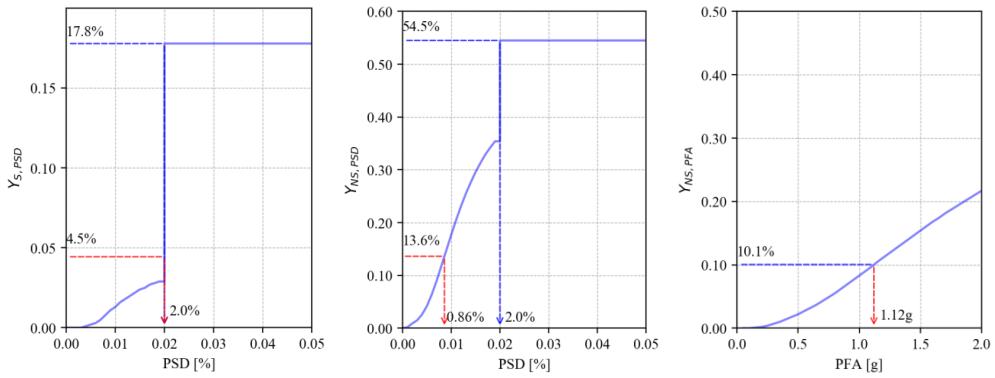

Figure 5: Illustration of the SLFs, and the identification of the design parameters for the SLS (red) and ULS (blue).

Structural demand parameter	SLS	ULS
PSD	0.86%	2.00%
PFA	1.12g	-

Table 2: Summary of structural design parameters for both limit states.

3.4 Compute spectral values

The identified values of θ_{max} and a_{max} at the SLS then needed to be converted to design spectral accelerations and displacements, $\Delta_{d,SLS}$ and α_{SLS}, respectively, as per Figure 1 (d). An equivalent single degree of freedom (SDOF) system is then employed in CSD to characterise a first-mode dominated multi-degree of freedom (MDOF) system. This is similar to the approach adopted in displacement based design (DDBD) [14] where the displacement of the equivalent SDOF system is given by Equations 6 and 7:

$$\Delta_d = \frac{\sum_{i=1}^{n} m_i \Delta_i^2}{\sum_{i=1}^{n} m_i \Delta_i} \tag{6}$$

$$\Delta_i = \omega_\theta \theta_{max} H_i \left(\frac{4H_n - H_i}{4H_n - H_1} \right) \tag{7}$$

where n is the number of storeys, m_i is the mass, Δ_i is the displaced shape at storey level i, ω_θ is the higher mode reduction factor and H_i is the i^{th} storey's elevation above the base. Detailed calculations are given in [5]. Unlike the PSD profile, PFA cannot be assumed to be first mode dominated, however, since the process of identifying a spectral acceleration, *Sa* for various building solutions assumes that the structure remains in the elastic range of response, some simplifications can be made. Combining the first few modes using square-root-sum-of-the-squares (SRSS) gives the PFA profile along the height, a_i, with a maximum value of a_{max}. For the case study building of RC frame with 4 storeys, the PFA may be approximated by a single coefficient γ defined as in Equation 8:

$$\alpha_{SLS} \approx \gamma a_{max} = 0.6 a_{max} \tag{8}$$

Initial parametric studies on the elastic modal properties of structures suggested that values of γ for low rise structures of 4 storeys of RC frame typology be around 0.6. Future research should look to improve this conversion, or at least refine this coefficient for different typologies of different number of storeys. For the purposes of CSD discussed here, they were deemed reasonable.

Table 3 lists the spectral acceleration and displacement for the case study building.

θ_{max} [%]	$\Delta_{d,SLS}$ [m]	a_{max} [g]	γ	α_{SLS} [g]
0.86	0.074	1.12	0.60	0.67

Table 3: Conversion of θ_{max} and a_{max} to spectral values at the SLS.

3.5 Quantify feasible initial secant to yield period range for SLS

The range of feasible initial secant to yield periods was identified using the equivalent SDOF spectral limits as presented in Table 3, which are illustrated in Figure 6, and the upper period bound, T_{upper}, for the RC frame in discussion was found to be 1.74 seconds. No lower period bound, T_{lower}, was identified, which is due to the fact that 0.67g of spectral acceleration is too high with respect to the maximum value of the spectrum at SLS (Figure 6). These bounds basically imply that the structure may be as stiff as needed since the SLS spectrum does not have enough spectral acceleration to exceed the PFA limits, while its flexibility will

be limited so that it does not undergo into excessive PSD. Hence, the period range is quite large, meaning that many potential design solutions could be accommodated. The damping was assumed as 5% for the case study RC frame.

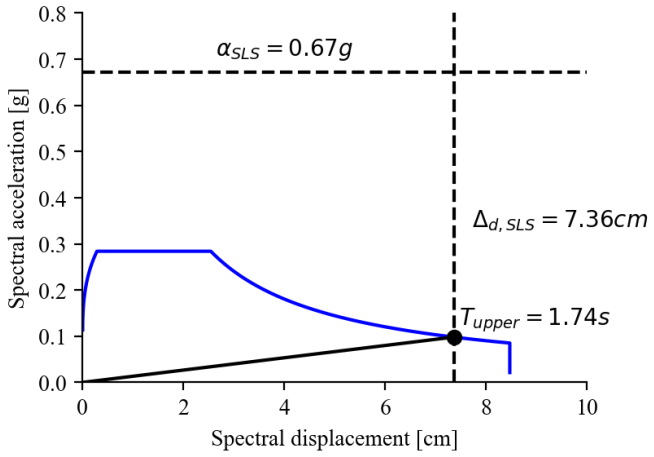

Figure 6: Identification of permissible initial secant to yield period range based on PFA and PSD limits for the SLS.

3.6 Establish required system strength and ductility

At the ULS, where the goal is to limit excessive PSD and provide a margin of safety against collapse during strong shaking, the effects of system non-linearity need to be accounted for. Figure 7 presents the permissible period range identified within the points 1 and 2, the trialled value of lateral strength capacity and the design solution space shaded in grey. It is important to note that for the case study building, point 2 is not representative since essentially there is no limit to the lower bound of the period range.

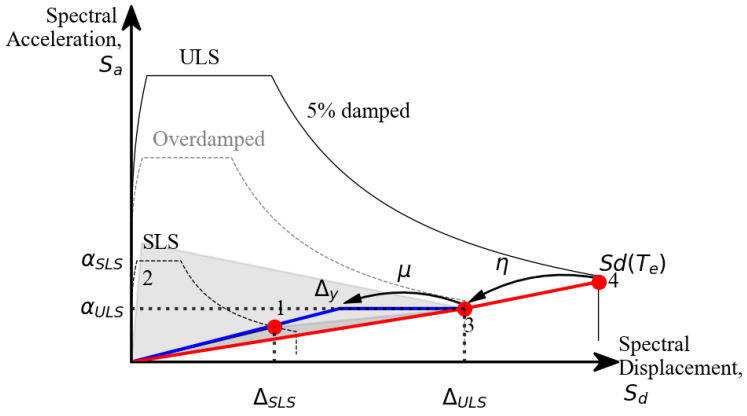

Figure 7: Identification of design solution space shaded in grey considering the permissible period range and the trialled value of lateral strength capacity (adapted from [5]).

For the given ULS spectrum and target design displacement, $\Delta_{d,ULS}$, a suitable SDOF system behaviour needed to be established. As noted by O'Reilly and Calvi [5], one way of doing this for the ULS, whilst still maintaining control over the initial period, is to simply trial a value of lateral strength. Then, by computing how much spectral reduction capacity would be required via non-linear behaviour, the structure's required ductility demand could be computed. This approach simply reworks the general DDBD approach, as the design displacement

and ULS spectrum are known but differs since the lateral strength is trialled and a compatible structural geometry is found (via the required yield displacement). DDBD, on the other hand, functions by commencing with a fixed structural geometry (meaning the yield displacement is known) and for the required ductility with respect to the design displacement and ULS spectrum, the lateral strength is found.

In this example, the approach described in [5] is followed but potential developments are described in Section 4.3. To account for the amplification in the structure's spectral capacity via non-linear behaviour of the structure, the effective period, T_e, passing from the origin through point 3 to point 4 was considered. In other words, the relation between linear and non-linear behaviour was found via a displacement modification factor (DMF) to the elastic design spectrum. As stated earlier, the design maximum PSD at ULS was 2.0% which gave a design displacement at ULS, $\Delta_{d,ULS}$, of 0.171m. Given $\Delta_{d,ULS}$ and the spectral displacement of the elastic response spectrum at T_e, $Sd(T_e)$, the required DMF, η, was determined from Equation 9.

$$\eta = \frac{\Delta_{d,ULS}}{Sd\left(T_e\right)} \tag{9}$$

Priestley *et al.* [14] outlined various expressions for different structural systems characterised by different hysteretic models representative of different structural systems and the one for RC frames was utilised here. From this relation, the required ductility, μ, was found by knowing the required spectral modification factor, η.

3.7 Compute structure backbone behaviour

With the knowledge of permissible period range, the design displacement, the lateral strength and the required structural ductility, the structure's backbone behaviour that respects these conditions was defined. The minimum required ductility already identified was then used to work back to find the yield displacement of the system, Δ_y, as per Equation 10.

$$\Delta_y = \frac{\Delta_{d,ULS}}{\mu} \tag{10}$$

The final bilinear backbone of the structural system was identified and is illustrated in Figure 8, where it was assumed that the second-order geometry effects, or P-Delta effects, were balanced out by the post-yield hardening of the structure to result in an elastic-perfectly plastic system.

The final values of yield displacement and lateral capacity are listed in Table 4. The base shear coefficient, *C*, is reasonable but the required initial period of the RC frame of 4 storeys is quite high to satisfy the design constraints. However, it is important to note that given a large range of allowable initial periods as identified earlier, a stiffer structure would have been obtained and this design scenario presented here was one of the many possibilities. This is a reflection of the current constraints imposed by the CSD at the ULS, where the advantage of being able to identify structural layouts is hampered by the fact that it tends to result in very flexible systems, as was the case in this example. Further consideration of the ULS performance that moves away from a single intensity-based verification of one PSD level (i.e. 2% PSD at 1600 years) should be pursued to arrive at a more risk-consistent approach to collapse safety. This would bring both CSD approach to a reasonable point whereby the losses via EAL and collapse safety are handled in a comprehensive manner. This was a limitation of CSD noted by O'Reilly and Calvi [5] and will be discussed further in Section 4.3

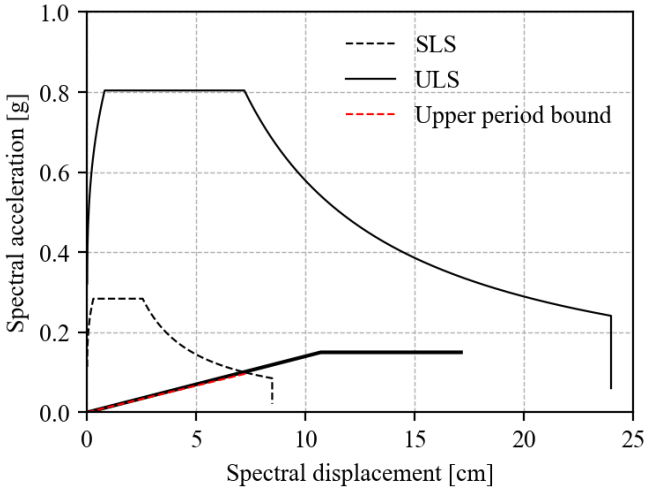

Figure 8: Required backbone response for the case study building design solution, where the period limits show how the design conditions have been respected.

a_{ULS} [g]	$\Delta_{d,ULS}$ [cm]	T_e [s]	$Sd(T_e)$ [cm]	$\eta_{required}$	Δ_y [cm]	$\mu_{provided}$	T_1 [s]	V_b [kN]	C
0.15	17.1	2.14	24.0	0.71	10.7	1.60	1.69	811	0.13

Table 4: Identification of structural system parameters to respect the design constraints, which fall within the design solution space

3.8 Identify structure layout

The final step of the design process was the identification of required geometry for the RC frame. In order to make use of the identified backbone leading to an acceptable building performance, defined in terms of expected loss, two parameters were required: the lateral strength and the yield displacement. As the lateral strength is a function of the member strengths, it can be easily adjusted by modifying the dissipative zone capacities. Structural geometry and material properties were required to establish the yield displacement. As the yield displacement was already known, the final dimensions and material properties of the structural system were identified as they are independent of the lateral strength [15].

For an RC frame with a ductile beam-sway mechanism, the yield drift, θ_y, has been shown by Priestley *et al.* [14] to be:

$$\theta_y = \frac{0.5\varepsilon_y B}{h_b} \tag{11}$$

where B is the bay width of the frame and h_b is the beam section height. Assuming a reinforcement of yield strength 350MPa and 200GPa of Young's modulus and a beam height of 0.5m, a bay width of around 6m would be required. Knowing the lateral load resisting system, structural geometry and the design base shear for the system, the structure can be detailed by providing enough capacity to ensure a ductile and stable mechanism. The resulting structural system would be representative of the backbone identified in Figure 8 and should satisfy the performance goals initially defined in terms of EAL described in Section 3.2.

4 DISCUSSION

Using the design framework summarised in Section 2 and implemented in a case study application in Section 3, additional studies on essential characteristics of the CSD framework were conducted. The goal was to understand whether the methodology could be improved in relation to the definition of the ULS performance and the sensitivity of the EAL to the SLFs. As before, the RC bare frame with office occupancy described in Section 3 was the reference design used for comparison throughout the discussion.

4.1 Influence of SLS parameters

One of the first studies regarding the definition of the performance objectives listed in Table 1 was on the sensitivity of the design EAL to the choices made regarding the return period of ground shaking, T_R, and the level of ELR at the SLS. The same values of y and T_R assumed for the OLS and ULS in Table 1 were maintained and the EAL was computed for numerous combinations of y_{SLS} and $T_{R,SLS}$. A summary of these design scenarios is presented in Figure 9. In essence, the hazard curve relates PGA (right axis) to T_R (left axis), and the SLF relates θ_{max} (top axis) to ELR (bottom axis). By increasing the y_{SLS} and $T_{R,SLS}$, the EAL, represented in green shades, will essentially stay constant. While, if the y_{SLS} is increased only or $T_{R,SLS}$ is decreased only, then the EAL will increase. Figure 9 then also shows the design solutions depending on $T_{R,SLS}$ and y_{SLS}. Only the upper bound results are shown, since the design indicated no lower period bound. The empty solution space represents an area where the solutions are beyond practicality, e.g. having high base shear coefficient, C, or high required bay width, B.

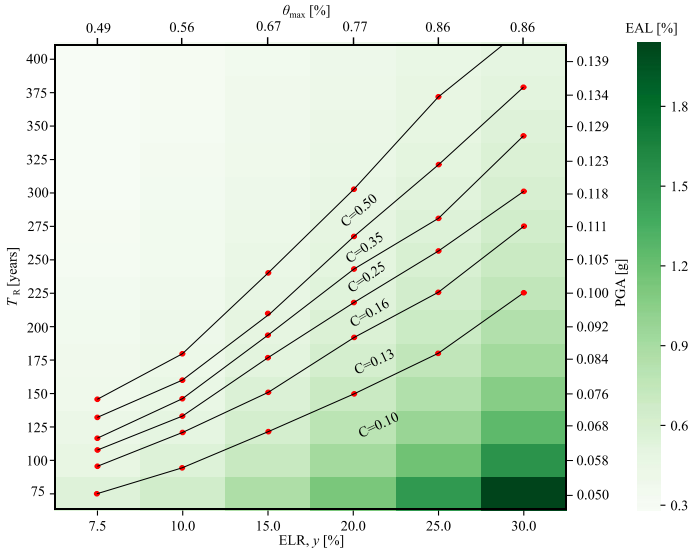

Figure 9: Impact of varying y_{SLS} and $T_{R,SLS}$ on the design EAL.

The study carried out on the variation of SLS parameters, showed high sensitivity of EAL to the SLS parameters. Additionally, the lower period range limit will be highly dependent on the *PGA* and subsequently $T_{R,SLS,}$ while the upper period range limit will be highly dependent on the θ_{max} and subsequently y_{SLS}. The curves defining C represent structures with an initial period equal to the upper period range limit and conditions imposed by each pair of $T_{R,SLS}$ and y_{SLS} below the curves can be satisfied by a structure with C equal to the curve value. Hence, the curves depend on an upper period range limit. Higher y_{SLS} and lower $T_{R,SLS}$ imply higher upper period range limit. For the study, the y_{SLS} was kept constant, while the $T_{R,SLS}$ was in-

creased sequentially, leading to a decreasing upper period range limit further constraining the design solution space, which resulted in the curves defining *C* boundaries.

4.2 Sensitivity study on SLFs

When using the SLFs as per Figure 4, the PSD at ULS for ELR=100% will be in the order of θ_{max}=10 to 20%. This value of θ_{max} may make sense purely from a monetary loss accumulation point of view, but is clearly unfeasible from a collapse performance perspective. To implement the CSD with these SLFs, a decision was made to limit θ_{max} to a certain limit similar to what ASCE 7-16 [8] prescribes to provide a level of life safety against collapse in their designs. This approach of utilising SLFs for the definition of the SLS design parameters but simply limiting the PSD to 2% at the ULS was adopted in the case study described in Section 3. The goal of the sensitivity study described here is to understand what impact this decision actually has on the design EAL. The SLF for PFA sensitive non-structural elements was not modified as the CSD methodology does not utilise the PFA at ULS.

Figure 10 shows the steps of the sensitivity study for the modification of SLFs for the CSD methodology. Initially, an original EAL was calculated through the employment of the SLF curves of the PSD-sensitive structural and non-structural elements adopted from Ramirez and Miranda [13]. Then a cut-off vertical line (in blue) representing a PSD value was gradually lowered, where the cut-off line describes a value of the PSD above which the ELR is assumed 100% times the respective weight of the element, Y_{PSD}. With each version of SLF, a corresponding EAL value was computed and then compared to the original one. The procedure was repeated until the error, ε_{EAL}, increased beyond 0.2% and the final updated SLF with the corresponding PSD cut-off line was used in the CSD presented herein.

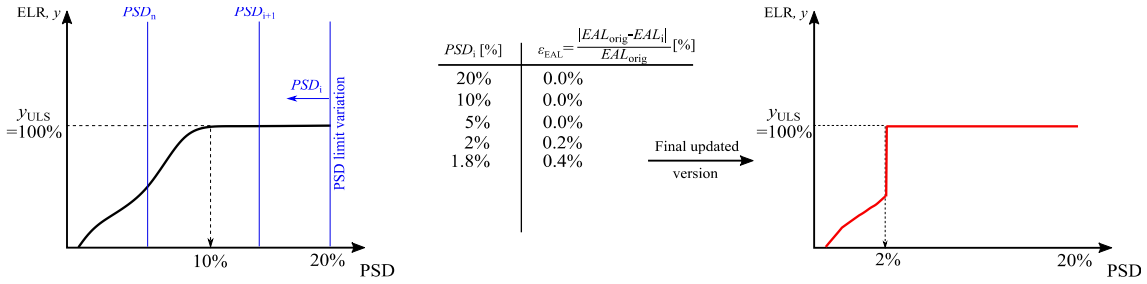

Figure 10: Sensitivity study on the modification of SLFs for the CSD methodology by the variation of PSD until EAL error, ε_{EAL}, is beyond 0.2%

The preliminary limit value obtained through the sensitivity study was 2% for PSD. By using the original and updated curves shown in Figure 4, the EAL variation error was found to be below 0.2%. Hence, the inclusion of such a limitation of PSD when utilising SLFs at ULS does not significantly impact the design EAL. Therefore, it can be concluded that the limitation of the PSD to 2% at ULS similar to what is done in the US with ASCE 7-16 [8], for example, with the aim for designing for collapse safety does not have any major impact on the design EAL that has been focused on up until now in CSD. Should the nature of determining the performance goals in CSD change from utilising EAL solely for the definition of the SLS limits and establishing an initial period range and then other possible criteria related to strength or ductility be utilised to protect against collapse, these two performance definitions will not have any major interaction with other and can be treated quite separately.

4.3 Consideration of collapse performance in design

As shown in the previous section, SLS and ULS performance can be handled with separate criteria without any major interference between them. With regards to collapse safety, MAFC, λ_c, may be used and a potential procedure to incorporate this in the CSD framework is described in Figure 11. The reasons for this are also illustrated in Figure 11(a) and are as follows. At ULS, a situation may occur where $\Delta_{d,ULS}$ is equal, or very close, to $Sd(T_e)$, meaning that the required DMF and consequently the ductility, μ, will be limited or equal to 1 (red point in Figure 11(a)). This will essentially result in designs with very long periods and limited ductility demand. Consequently, a high bay width will be required to provide a yield displacement equal to the required one. An alternative would be to neglect the condition of DMF equality, as also briefly discussed in O'Reilly and Calvi [5], and provide the structure with ductility higher than 1 (in blue in Figure 11(a)), which would then result in a lower bay width.

Alternatively, this could also be achieved by using MAFC to design for collapse safety in a more risk-consistent manner, as described a follows. An SDOF with period T that falls within the already identified period range [T_{lower}, T_{upper}] and an anticipated ductility capacity μ is considered. Knowing the yield lateral spectral acceleration, Sa_y, the dynamic performance of a trialled SDOF up to complete collapse can be quantified via SPO2IDA tool [16], as shown in Figure 11(b). Knowing the collapse fragility and the hazard curve, these may be integrated to get the MAFC, λ_c, where the collapse fragility defined in terms of R (Figure 11(b)) is transformed to spectral acceleration Sa by using a transformation factor, Γ, to a collapse fragility of the actual MDOF system (Figure 11(c)). By setting a target collapse safety to be respected by the resulting design, the base shear coefficient can be found for a given ductility, μ, and initial period, T_1. By varying T_1, a satisfactory base shear coefficient curve can be plotted in Sa versus Sd and the feasible structural solutions may be found (Figure 11(d)). It is noted that this approach is not too dissimilar to the yield frequency spectrum method [17] but here just the collapse behaviour is focused on, in addition to maintaining a degree of control on the EAL via the initial period range.

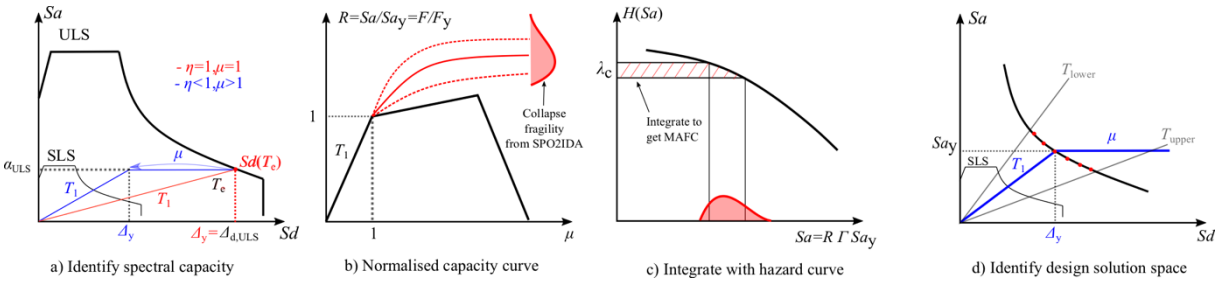

Figure 11: Potential development of the CSD framework to incorporate MAFC as a design variable.

The red dots in Figure 11(d) represent several of the numerous feasible design solutions within the period range that satisfy the collapse safety criterion. This approach would help to avoid the issue of SLFs identified in the previous section and overcome the difficulties explained in Section 3.6.

5 CONCLUSIONS

A novel CSD framework utilising EAL was used to identify feasible structural solutions aligning with the conceptual objectives of performance-based design. The general procedure with a case study application for an RC moment resisting frame was presented herein for its illustration. A number of assumptions were made: first, SLFs were used to convert ELRs to design PSD and PFA. At the ULS, where a collapse prevention requirement has to be met, the

PSD was cut-off at 2% and corresponds to the requirement brought forth by ASCE 7-16 [8]. Two limit state intensities, SLS and ULS, were utilised to characterise the structure's initial elastic and ductile non-linear behaviour. At SLS, design PSD and PFA were used to define a permissible initial secant to yield period range. Subsequently, with the choice of lateral strength and the knowledge of required system ductility, the yield displacement of the system was computed. Finally, the design solution space was identified and a potential bilinear backbone identified. Based on the characteristics identified, the required dimensions of the structure were identified as part of the first phase of design.

Moreover, some sensitivity studies were carried out to further investigate some particular aspects of the CSD framework. Several notes could be made based on these studies:

- High sensitivity of EAL and period range limits to the SLS parameters, as: 1) increasing ELR or decreasing T_R results in an increase of the EAL; and 2) decreasing T_R and increasing ELR will lead to an increase of the upper period range limit, meaning that care must be taken when establishing these points in design;
- Limiting PSD to 2% (similar to what is done in ASCE 7-16 with the aim to design for collapse safety) and modifying SLFs corresponded to an error in EAL of only 0.2%, demonstrating that it does not have any major impact on the design EAL;
- To avoid observed difficulties of implementing the CSD framework at ULS, an alternative approach was pondered. This does away with the issue where the required DMF and the ductility could potentially lead to large bay widths to satisfy the yield displacement requirement. The alternative approach foresees that the ULS is no longer considered, but rather a target MAFC, which is satisfied by a system with base shear coefficient, C, for a given ductility, μ, and an initial period, T, which must lie with the period range identified for SLS.

Within future developments, the CSD framework will be improved to include the current approach for SLS, where the elastic properties of the structure are chosen to satisfy the target EAL, while a simplified collapse analysis is used to satisfy a target MAFC.

6 ACKNOWLEDGEMENTS

The work presented in this paper has been developed within the framework of the project "Dipartimenti di Eccellenza", funded by the Italian Ministry of Education, University and Research at IUSS Pavia. The first author would like to acknowledge the financial support provided through the doctoral programme at IUSS Pavia.

REFERENCES

[1] Cornell CA, Krawinkler H. Progress and challenges in seismic performance assessment. PEER Cent News 2003:3(2): 1-2.

[2] SEAOC. Vision 2000: Performance-based seismic engineering of buildings 1995.

[3] Porter KA. An Overview of PEER's Performance-Based Earthquake Engineering Methodology. 9th Int Conf Appl Stat Probab Civ Eng 2003;273:973–80. doi:10.1.1.538.4550.

[4] Federal Emergency Management Agency. Seismic Performance Assessment of Buildings - methodology. Fema P-58-1 2012;1:278.

[5] O'Reilly GJ, Calvi GM. Conceptual seismic design in performance-based earthquake engineering. Earthq Eng Struct Dyn 2018:1–20. doi:10.1002/eqe.3141.

[6] EN 1998-1:2018. Design of structures for earthquake resistance (Draft) – Part 1: General rules, seismic actions and rules for buildings. Brussels: 2018.

[7] NZS 1170.5:2004. Structural design actions part 5: Earthquake actions. Wellington, New Zealand: 2004.

[8] ASCE 7-16. Minimum design loads for buildings and other structures. Reston, VA, USA: 2014. doi:10.1126/science.69.1782.217-a.

[9] Luco N, Ellingwood BR, Hamburger RO, Hooper JD, Kimball JK, Kircher CA. Risk-Targeted versus Current Seismic Design Maps for the Conterminous United States. Struct Eng Assoc Calif 2007 Conv Proc 2007:1–13.

[10] Vamvatsikos D. Performance-Based Seismic Design In Real Life : The Good, The Bad And The Ugly. Anidis 2017:17–24.

[11] Vamvatsikos D. Derivation of new SAC/FEMA performance evaluation solutions with second-order hazard approximation. Earthq Eng Struct Dyn 2013;42:1171–88. doi:10.1002/eqe.2265.

[12] Musson RW, Valensise G, Rovida AN, Woessner J, Cotton F, Hiemer S, et al. The 2013 European Seismic Hazard Model: key components and results. Bull Earthq Eng 2015;13:3553–96. doi:10.1007/s10518-015-9795-1.

[13] Ramirez CM, Miranda E. Building specific loss estimation methods & tools for simplified performance based earthquake engineering. 2009.

[14] Priestley MJN, Calvi GM, Kowalsky MJ. Displacement based seismic design of structures. Pavia, Italy: IUSS Press; 2007.

[15] Priestley MJN. Myths and Fallacies in Earthquake Engineering , Revisited. Pavia, Italy: IUSS Press; 2003.

[16] Vamvatsikos D, Cornell CA. Direct estimation of the seismic demand and capacity of MDOF systems through Incremental Dynamic Analysis of an SDOF approximation. J Struct Eng 2005;131:589–99.

[17] Vamvatsikos D, Aschheim MA. Performance-based seismic design via yield frequency spectra ‡. Earthq Eng Struct Dyn 2016;45:1759–78. doi:10.1002/eqe.2727.

COMPDYN 2019
7th ECCOMAS Thematic Conference on
Computational Methods in Structural Dynamics and Earthquake Engineering
M. Papadrakakis, M. Fragiadakis (eds.)
Crete, Greece, 24–26 June 2019

SELECTION OF EARTHQUAKE RECORDS FOR EFFICIENT DAMAGE ASSESSMENT

Kristina Strukar[1], Mario Jeleč[2], and Tanja Kalman Šipoš [2]

[1] Josip Juraj Strossmayer University of Osijek
Faculty of Civil Engineering and Architecture Osijek
Vladimira Preloga 3, HR 31000 Osijek, Republic of Croatia
e-mail: kstrukar@gfos.hr

[2] Josip Juraj Strossmayer University of Osijek
Faculty of Civil Engineering and Architecture Osijek
Vladimira Preloga 3, HR 31000 Osijek, Republic of Croatia
e-mail: mjelec@gfos.hr, tkalman@gfos.hr

Abstract

Earthquake engineering analyses are unavoidable to obtain response of buildings to earthquakes in order to ensure for structure to withstand a given level of ground shaking and to maintain a desired level of performance. Main reasons are vagueness and uncertainties related to the ground motion and structural modeling parameters in the available data such as location, size and resulting shaking intensity of future earthquakes. The selection of appropriate seismic input is known to be a critical step while performing this kind of analysis in order to estimate seismic performance in the basis of the hazard at the site where the structure is located. Selection of recorded ground motions are in most cases based on geophysical parameters, ground motion intensity measures, and spectral matching. In this paper seismic analysis will be performed for four-story reinforced concrete ISPRA frame structure designed according to Eurocode 8 (EC8) by selecting 30 different earthquake scenario for each EC8 target spectrums in order to evaluate average maximum inter-story drift ratio. Time history analysis for every earthquake record was obtained. As a result, Inter-story Drift Ratios (IDR) as a main damage measure were presented in order to make comparison with defined performance levels of reinforced concrete bare frames.

Keywords: seismic damage assessment, earthquake records, spectral matching

1 INTRODUCTION

The seismic damage assessment is found to be a very complex problem when analyzing reinforced concrete structures. Main reasons are vagueness and uncertainties related to the ground motion and structural modeling parameters in the available data such as location, size and resulting shaking intensity of future earthquakes [1].

In order to ensure for structure to withstand a given level of ground shaking and to maintain a desired level of performance, earthquake engineering analyses are unavoidable to obtain response of buildings to earthquakes. Response of buildings stands for complex, three dimensional and nonlinear dynamic problems, thus nonlinear dynamic analysis is unavoidable. It is also known as the most accurate method to evaluate the behavior of structures during an earthquake in both probabilistic assessment and design [2].

The selection of appropriate seismic input is known to be a critical step while performing this kind of analysis in order to estimate seismic performance in the basis of the hazard at the site where the structure is located. The current best practice in record selection is reviewed for the case of the probabilistic seismic risk analysis and for the code-based design [3]. In order to quantify former uncertainties and to combine them to produce an explicit description of the distribution of future shaking that may occur at the site, Probabilistic Seismic Hazard Analysis (PSHA) needs to be conducted [4]. This seismic analysis combines different magnitudes (M) and distances (R) with predictions of resulting ground motion intensity, and thus seismic hazard at the site can be computed [5]. Ground motion selection utilizes probabilistic seismic hazard disaggregation, as a key tool for all of the following ground motion selection approaches. The goal of this procedure is to accurately estimate the response of a structure at a specified ground motion intensity, as measured by spectral acceleration at the first-mode period of the structure, $S_a(T_1)$ [6]. It is also necessary to obtain time series that are representative of the strong shaking that a particular location may experience in the future during an earthquake. Ground motions should be selected from a database of previously recorded motions [7].

For probabilistic seismic risk assessment, record selection should be regarded as a reference case. In the case of code-based seismic assessment, there is an issue in selection of the real recordings set compatible with a code-specified spectrum, whose spectra are generally non-smooth. The structural response estimates were seen to be highly dependent on the type of ground motions that can be used for the seismic structural analysis as well on the methods utilized or selection and scaling of the records. Ground motions can be divided on 1) artificial waveforms; 2) simulated accelerograms; 3) natural records [8].

Selection of recorded ground motions are in most cases based on 1) geophysical parameters magnitude (M), source-to-site distance (R), and epsilon (e); 2) ground motion intensity measures; and 3) spectral matching, which will be the main focus in this paper. Brief review on selection of recorded ground accelerations based on spectral matching for different target spectrum EC8 spectrum, Uniform Hazard Spectrum (UHS) and Conditional Mean Spectrum (CMS) will be presented. Further, seismic analysis will be performed for four-story reinforced concrete frame structure designed according to EC8 – ISPRA frame by selecting 30 different earthquake scenarios according to spectral matching in order to evaluate average maximum inter-story drift ratio. The aim is to compare obtained results from seismic analysis for each earthquake scenario in order to observe the difference of performance levels achieved by EC8 target spectrum.

2 SELECTION OF RECORDED GROUND ACCELERATIONS – A BRIEF REVIEW

Calculating ground motions based on earthquake scenarios is an invaluable tool for evaluating direct and indirect losses from specific credible earthquakes. Hazard evaluation of earthquake ground motion in most cases is done with deterministic or probabilistic approach which

would be the two representative methods for seismic hazard assessments nowadays. Both approaches need to transform the seismic event to ground motion.

Deterministic Seismic Hazard Analysis (DSHA) is an analysis that considers a worst-case scenario in terms of earthquake size and location and it is basically governed by the seismic source that has the highest threat to the site with the largest motion estimated [9]. Contrary to DSHA, if probabilistic seismic hazard analysis (PSHA) has been used, which was the first formalized by Cornell [10], then the controlling earthquake scenarios need to be obtained by disaggregation [8]. PSHA combines the probabilities of all earthquake scenarios with different magnitudes (M), source-to-site distances (R) and epsilon (ε), the number of standard deviations from the median ground motion as predicted by an attenuation equation with predictions of resulting ground motion intensity, in order to compute seismic hazard at a site. PSHA also incorporates uncertainties in ground motion predictions. To quantify ground motion in PSHA, traditionally peak ground acceleration (PGA) was used. However, today the preferred parameter is Response Spectral Acceleration (Sa) which gives the maximum acceleration experienced by a damped, single-degree-of-freedom oscillator [11]. To identify the distribution of earthquake scenario that contribute to exceedance of a given spectral acceleration (Sa), current ground motion selection is utilized by probabilistic seismic hazard disaggregation [5].

Selection of recorded ground motions can be based on 1) geophysical parameters Magnitude (M) and Distance (R); 2) ground motion intensity measures; 3) spectral matching; etc. The main focus will be on spectral matching which is the most commonly proposed earthquake record selection method by seismic codes and, as such, can be utilized in the framework of both force-based and performance based design [12]. Spectrum matched records are artificially generated time histories of ground motion acceleration, or other relevant parameter, whose response spectral shapes are matched to a predetermined target spectrum and used as input to dynamic analysis [13]. While selecting ground motion records, main aim is to select representative records of the ground motion at the site of interest and at the consistent source-to site distance. Also there will generally be a requirement to ensure that the records of ground motion conform to some specified level of agreement with the ordinates of the design response spectrum, whether records are selected by performing searches in terms of response spectral ordinates or in terms of seismological and geophysical parameters [8]. If structural response is to be estimated by selecting ground motions to match a target response spectrum, typical response spectrum associated with the specified large amplitude S_a value at a single period must be defined [14].

In the part 1 of **design code Eurocode 8** [15] following criteria are established for the selection and scaling of ground motion records in the context of demand-based assessments of buildings: 1) the mean of the zero period spectral response acceleration values calculated from the individual time histories should not be smaller than the value of $a_g S$ for the site under study, a_g being the design ground acceleration on rock and S the soil parameter; and 2) in the range of period between 0.2 T_1 and 2.0 T_1, where T_1 is the fundamental period of the structure in the direction where the record will be applied, no value of the mean 5% damping elastic spectrum, calculated from all time histories, should be less than 90% of the corresponding value of the 5% damping elastic response spectrum [3], [8].

In Eurocode 8 [15] after the elastic response spectrum, seismic input for the time-history analysis is defined. Two spectral shapes are defined, Type 1 and Type 2, where the latter applies if the earthquake contributing most to the seismic hazard has surface waves magnitude not greater than 5.5. Contrary, the former type should be used. In EC8, for the structural assessment any form of accelerograms is allowed to be used. Regardless they are natural, artificial or simulated, the main criterion that the set of accelerograms should satisfy is 2) [16].

For the past two decades, the **Uniform Hazard Spectrum** (UHS) has been used as the target spectrum in the design practice. It is computed by PSHA and constructed by selecting a frequency of exceedance for the hazard, developing the spectral acceleration at each period and plotting spectral acceleration versus period [14]. It is suggested to select seven records which are compatible with the dominant earthquake scenario at the site of interest and that scenario is represented with the magnitude (M) and the distance (R) which are key parameters obtained by disaggregation analysis [17]. In order to match the design level of the UHS, the selected records need to be scaled when it is necessary.

Baker and Cornell [6] concluded that the UHS represents nearly impossible earthquake scenario because the rate of observing a high positive ε in all periods is much lower than the rate of observing a high ε in any single period. Although the UHS is frequent target spectrum in structural dynamic analysis, it does not represent a spectrum caused by a single earthquake at a given site and thus leads to a conservative spectrum in higher hazard levels.

Conditional Mean Spectrum (CMS) has been proposed by Baker [18] as an alternative to the Uniform Hazard Spectrum (UHS) that can be used as a target spectrum in ground motion record selection. CMS provides the expected (mean) response spectrum, conditioned on occurrence of a target spectral acceleration value at the period of interest. After it is computed, CMS can be used for selection of ground motion records. With CMS spectral shape associated with the target spectral shape *Sa(T*)* is obtained. Thus ground motions that match Sa(T*) can be treated as representative of ground motions that naturally have the target Sa(T*) value. The period ranges over which the CMS should be matched must be identified to find ground motions matching a target CMS, and this period range may include the periods of higher modes of vibration as well as longer periods that are seen to affect a nonlinear structure whose first-mode period has effectively lengthened.

3 DESCRIPTION OF EXPERIMENTAL AND NUMERICAL MODEL

3.1 Experimental model

Experimental full scale model presented in Figure 1 on which seismic analysis will be performed, is a four-storey frame structure designed according to previous version of Eurocode 2 [19] and Eurocode 8 [11]. Structure is in total 12.5 m high. Structure has three frames and thus two bays in both X and Y direction. Raster of bays in X direction are 4 and 6 m, and raster of both bays in Y direction is 5 m in which direction load was applied. Materials used in construction were concrete C25/30 and the B500 Tempcore reinforcing steel with characteristic yield strength of 500 MPa.

Columns were reinforced with ϕ8-ϕ12 mm bar. The total reinforcement ratio varied from 1% to 1.9%. Longitudinal reinforcement diameter in columns carried from ϕ16 at upper storeys and ϕ20 or ϕ25 in the bottom and in some cases in the first storey. In the critical regions of columns were used stirrups ϕ10/10. For the longitudinal reinforcement in beams were used bars ϕ14 in combination with bar ϕ12. More than half longitudinal reinforcement in the beams is placed at the bottom of the beam.

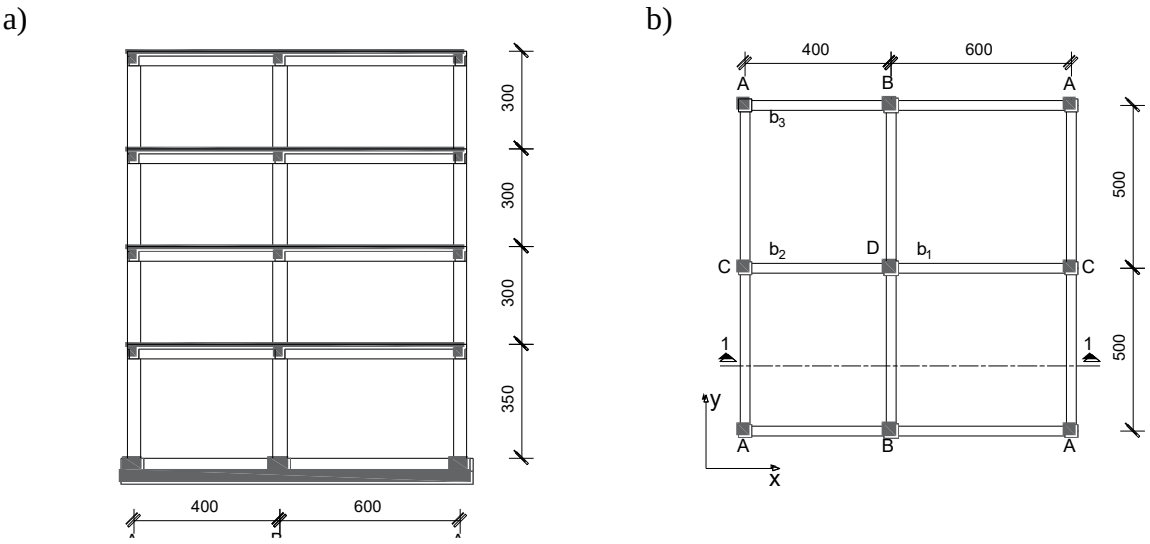

Figure 1: The four-storey reinforced concrete structure [20].

Since reinforced concrete beams and the slab are usually constructed at the same time, they act as a monolithic section. Therefore, in the seismic assessment, a contribution of slab to the stiffness and strength of beam has to be considered. In the Eurocode 8 [15] is prescribed that slab reinforcement parallel to the beam and within the effective flange width should be assumed in the design process to contribute to the beam flexural capacities, if it is anchored beyond the beam section at the face of the joint. In the Eurocode 2 [19] the values of effective width of beams for all limit states are suggested and are based on the distance l_0 between points of zero moments. It should be calculated according to next equatinos:

$$b_{eff} = \sum b_{eff,i} + b_w \leq b \tag{1}$$

$$b_{eff,i} = min \begin{cases} 0.2 \cdot b_i + 0.1 \cdot l_0 \\ 0.2 \cdot l_0 \end{cases} \tag{2}$$

$$b_{eff,i} \leq b_i \tag{3}$$

where $b_{eff}$is the beam's effective width, b_w is the width of the beam, b_i is the one half of the distance between the beams and l_0 is the distance between the zero moment points. In the seismic analysis the distance l_0 should be taken as $l_b/2$. Transversal beam spans should be taken as l_b and in Table 1 are given calculated effective widths of beams considered in analysis.

Beam	**Shape of beam**	$\boldsymbol{b_w}$ $[\boldsymbol{cm}]$	$\boldsymbol{b_{eff,1}}$ $[\boldsymbol{cm}]$	$\boldsymbol{b_{eff,2}}$ $[\boldsymbol{cm}]$	$\boldsymbol{b_{eff}}$ $[\boldsymbol{cm}]$
B1, B3, B4, B6	L	30	50	-	80
B2, B5	T	30	50	50	130
B7, B11	L	30	40	-	70
B8, B12	L	30	60	-	90
B9	T	30	40	40	110
B10	T	30	60	60	150

Table 1: The effective width of beams considered in analysis [20]

Except effective width of beams, critical region length, or plastic hinges length were determined according to Eurocode 8 [15]. As structure was designed for ductility class high (DCH)

and the behavior factor q = 5, the critical region length for beams were determined according to equation (4), and for columns according to (5):

$$L_p = 1.5\, h_w \tag{4}$$

$$L_p = max \begin{cases} 1.5\, h_c \\ 1.5\, b_c \\ 0.6 \\ L_c/6 \end{cases} \tag{5}$$

Values of concentrated masses were obtained from the self-weight of the structure, the permanent load of 2 kN/m^2 which presented floor finishing and partitions, and the live load also of 2 kN/m^2. In Table 2 are presented concentrated masses as point loads on each column and for every storey.

Column	Storey 1 m [t]	Storey 2 m [t]	Storey 3 m [t]	Storey 4 m [t]
1, 7	7.61	7.51	7.51	6.90
2, 8	11.23	11.13	11.13	10.52
3, 9	5.80	5.70	5.70	5.09
4	11.40	11.30	11.30	10.69
5	19.77	19.64	19.64	18.87
6	9.59	9.49	9.49	8.88
Σ	90.07	89.12	89.12	83.46

Table 2: Values of concentrated load masses

3.1 Numerical model

Nonlinear analysis of the ISPRA numerical model in Figure 2 has been conducted by SeismoStruct (2016) [21] in which the behavior of concrete elements was simulated with force-based plastic hinge (FBPH) elements with plastic hinges at the ends of the elements using Mander's model of confined concrete proposed by Mander et al. [22] and the Menegotto-Pinto model [23] for reinforcing steel.

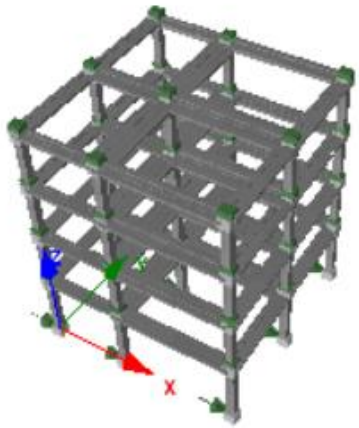

Figure 2: Numerical model in Seismostruct 2016 [21]

The accuracy of numerical model compared to the experimental one is firstly obtained by the comparison of natural periods for experimental and numerical model in Table 3.

Mode	Experiment	Numerical model	Error (%)
1	0,560	0,592	5,7
2	0,195	0,213	8,5
3	0,115	0,123	6,9

Table 3: Comparison of natural periods for experimental and numerical model

The other check of compatibility of numerical to experimental model are resulted relative errors and correlation of values obtained from numerical modelling and experimental test for displacement, and base shear. From the Table 4Table 4, it can be seen that the nonlinear numerical model also gave excellent results in terms of compatibility with hysteretic curves presented in Figure 3. The mean relative error of the observed variables (displacement, base shear) was 15.92%, while the correlation R was an excellent 0.95. That proves the compliance and applicability of the calibrated numerical nonlinear model for the parametric analysis of a model building with infilled frames according to expected behaviour.

Four-storey building ISPRA		Mean relative error [%]/correlation R
Displacement	1st floor	14.94/0.94
	2nd floor	11.11/0.95
	3rd floor	15.21/0.95
	4th floor	16.11/0.95
Base shear		17.24/0.95
Mean values		14.92/0.95

Table 4: Mean relative error [%] and correlation R

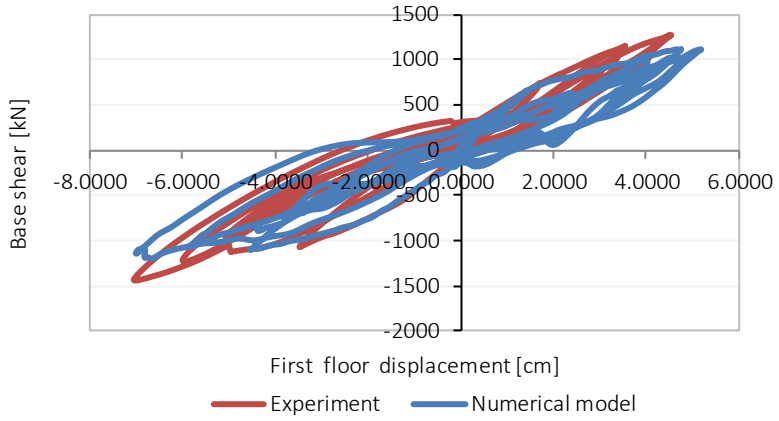

Figure 3: Comparison of Experimental and Numerical hysteretic curves for ISPRA model

4 SELECTION OF DIFFERENT EARTHQUAKE SCENARIO

Spectral matching is the most commonly proposed earthquake record selection method by seismic codes and, as such, can be utilized in the framework of both force-based and performance based design [12]. In the past 15 years, the use of spectrum matched records has become increasingly widespread for the estimation of nonlinear structural response. Spectrum matched records are artificially generated time histories of ground motion acceleration, or other relevant parameter, whose response spectral shapes are matched to a predetermined target spectrum and used as input to dynamic analysis [13].

While selecting the ground motion records, main aim is to select representative records of the ground motion at the site of interest and at the consistent source-to site distance. Also there

will generally be a requirement to ensure that the records of ground motion conform to some specified level of agreement with the ordinates of the design response spectrum, whether records are selected by performing searches in terms of response spectral ordinates or in terms of seismological and geophysical parameters [8]. If structural response is to be estimated by selecting ground motions to match a target response spectrum, typical response spectrum associated with the specified large amplitude Sa value at a single period must be found [14]. For graphical explanation of earthquake scenario selection method, flow chart in Figure 4 is presented.

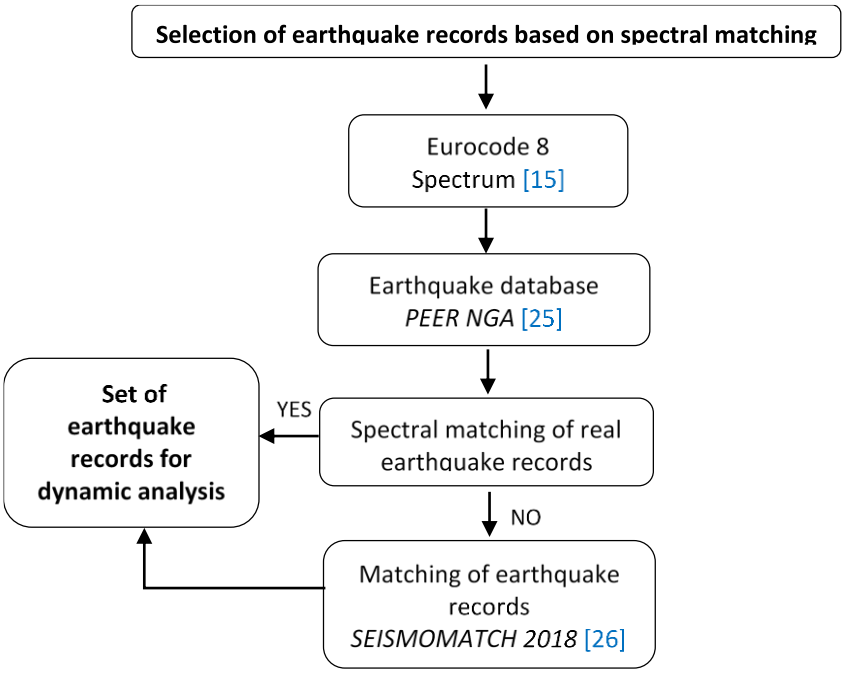

Figure 4: Flow chart of earthquake selection method

4.1 General data of used spectrums

Based on the experimental model, earthquake record from the location Friulli with longitude: 13-103365 and latitude: 46.225918 shown in Figure 5 a) was chosen for obtaining general data of used spectrum. For definition of Eurocode 8 [15] spectrum, elastic spectrum type 2 was used with expected PGA as shown in Figure 5 b) according to Hazard map for Italy.

a) b)

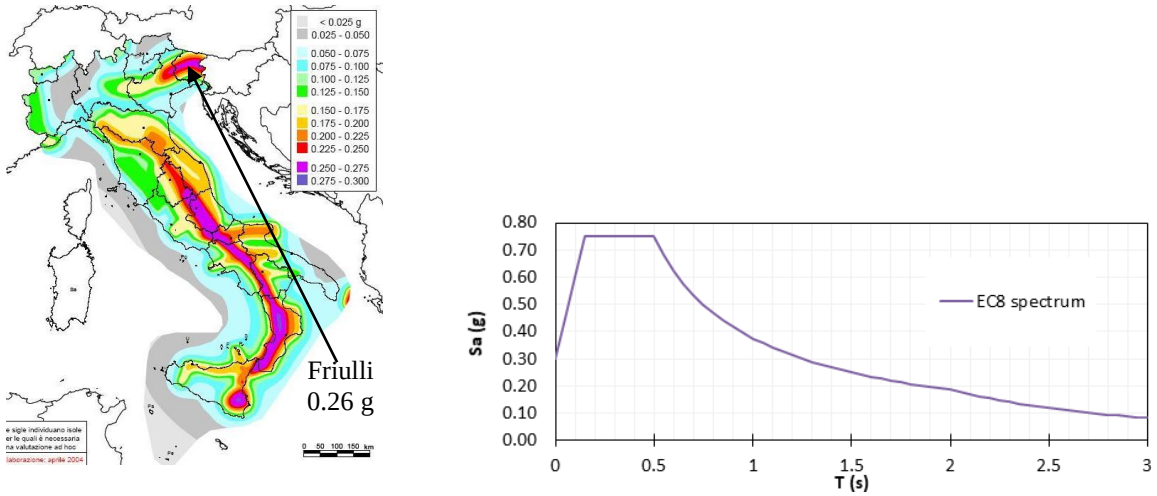

Figure 5: Seismic hazard map for Italy [35]; b) EC8 spectrum selected as target spectrums

4.2 Earthquake records set selection

Set of ground motion records was selected from PEER Ground Motions Database (The new NGA West 2 database) [25]. On Figure 6 is presented comparison of EC8 target spectrum with model spectrum obtained from PEER database.

Subfigures on left hand side are showing unscaled model spectrum, while on the right hand side are scaled model spectrum. In Table 5 are evaluated some of performance measures as Mean Absolute Error (MAE), Root Mean Squared Error (RMSE), and Mean Absolute Percentage Error (MAPE) from which can be seen that scaling model spectrums to target spectrums shows better results of performance measures.

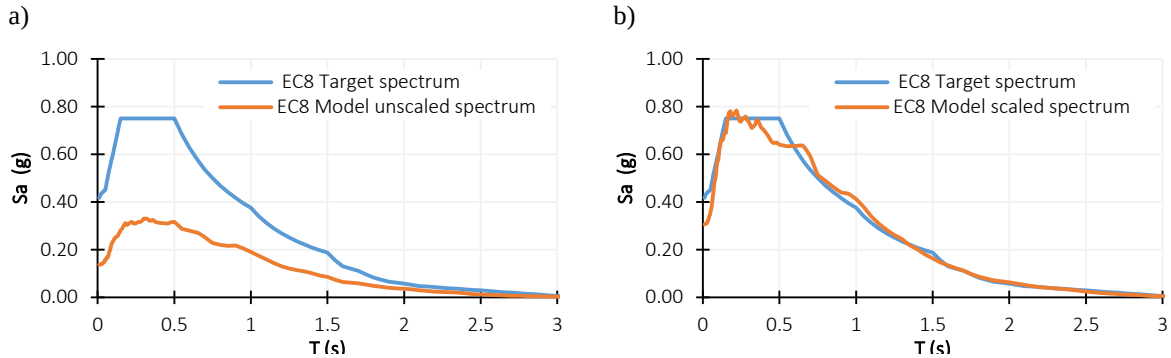

Figure 6: Comparison between spectrum obtained by PEER NGA database [25] for real (unscaled) spectrum and scaled or matched EC8 spectrum

However, comparing original spectrum obtained from the real accelerogram and target spectrum obtained from PEER NGA database [25] as shown on subfigures on the left hand side in Figure 7, great differences were observed and spectrums based on real unscaled earthquake records could not be used. Thus, real unscaled individual accelerograms were matched to target spectrum in SeismoMatch 2018 [26] to obtain mean target spectrum. Total of 30 earthquake records have been chosen (30 spectrums for 30 records). Subfigure on Figure 7 from the right hand side are presenting original and matched accelerogram.

Spectrum	Type of records	Mean absolute error (MAE)	Root mean squared error (RMSE)	Mean absolute percentage error (MAPE)
EC8	unscaled	0,24	0,49	55,31
	scaled	0,04	0,16	11,38
UHS	unscaled	0,09	0,27	44,67
	scaled	0,03	0,19	25,99
CMS	unscaled	0,03	0,15	70,84
	scaled	0,02	0,13	17,39

Table 5: Evaluation of selection of records based on real and scaled records according to performance measures

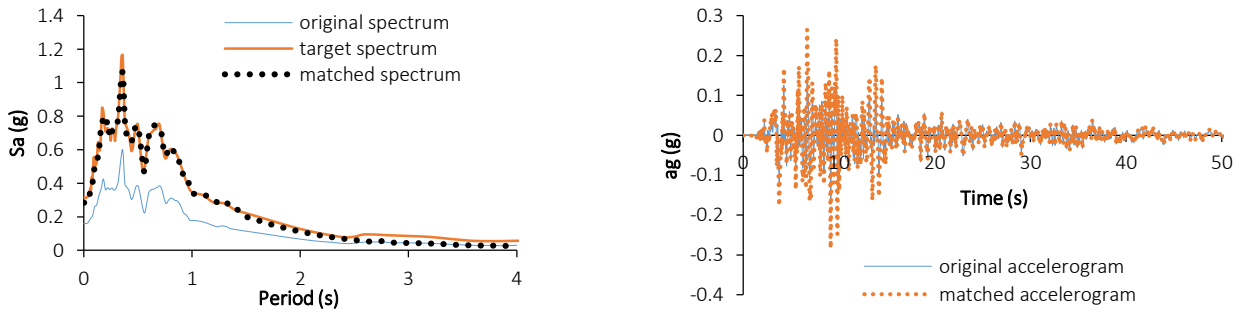

Figure 7: Example of spectral matching of earthquake records with aEC8 spectrum

Difference between the target and matched spectrum consequently have caused the change in values of performance measures Mean Absolute Error (MAE), Root Mean Squared Error (RMSE), and Mean Absolute Percentage Error (MAPE), and final shapes of evaluated spectrums on Figure 8.New, finally obtained values of performance measures are presented in Table 6.

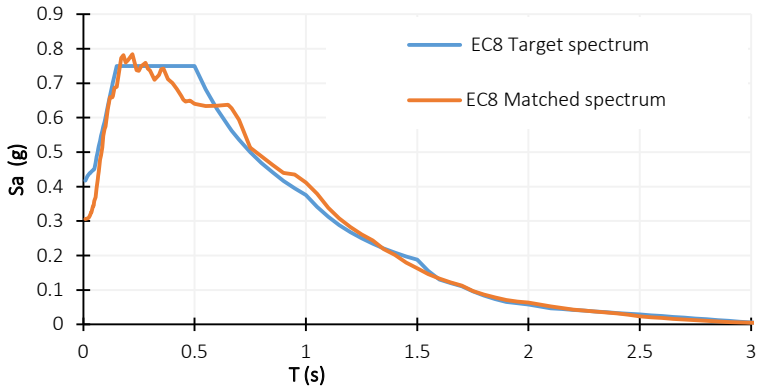

Figure 8: Example of spectral matching of earthquake records

Spectrum	Type of records	Mean absolute error (MAE)	Root mean squared error (RMSE)	Mean absolute percentage error (MAPE)
EC8	matched	0,03	0,11	9,21

Table 6: Evaluation of performance measures for matched spectrums in respect to target spectrums

5 RESULTS AND DISCUSSION

From seismic analysis are obtained results regarding Inter-storey Drift Ratio (IDR) of four-storey ISPRA building for all earthquake records and each target spectrum. These results are presented on Figure 9 and it can be seen that for target spectrum and belonging 30 matched earthquake records, average IDR is obtained.

Performance levels of structures under the earthquake loads describes the damage condition that must be satisfactory for a given building and a given ground motion. They are presenting the physical damage of buildings that may occur during the earthquake event. Damage for every structural performance level is defined by value of Inter-storey Drift Ratio (IDR) by Ghobarah [27] and description of damage condition needed to understand the physical state of the building for the end user.

a)

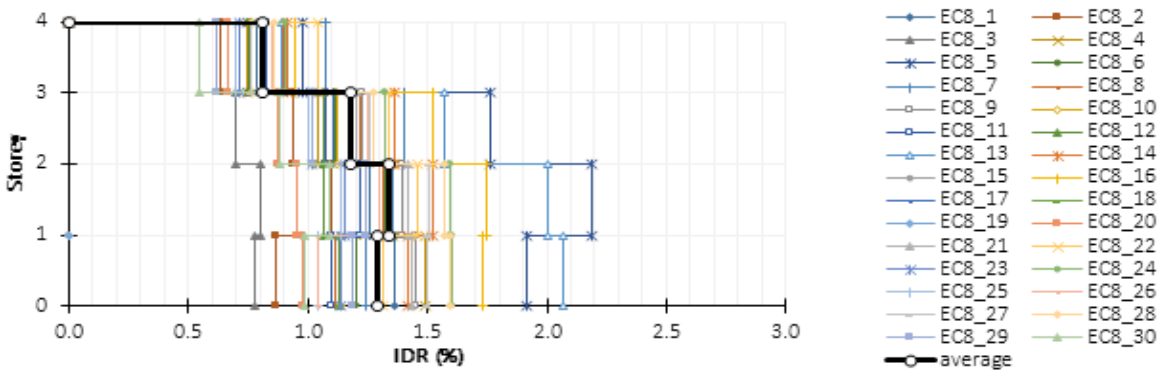

Figure 9: IDR profiles for EC8 target spectrum

Possible performance levels as shown in Table 7 are: slight damage=immediate occupancy; moderate damage=damage control; extensive damage=life safety; near collapse=collapse prevention according to HAZUS [28].

	Structural performance level	RC frames IDR(%)
	Slight damage	<0.20
	Moderate damage	<1.0
	Extensive damage	>1.0
	Near collapse	>3

Table 7: Comparison of IDR (%) according to structural performance levels and structure type [29]

In order to make an evaluation of obtained results in regard to defined performance levels and possible damage, mean IDR profiles from Figure 9 are summarized in Figure 10 with damage level limits.

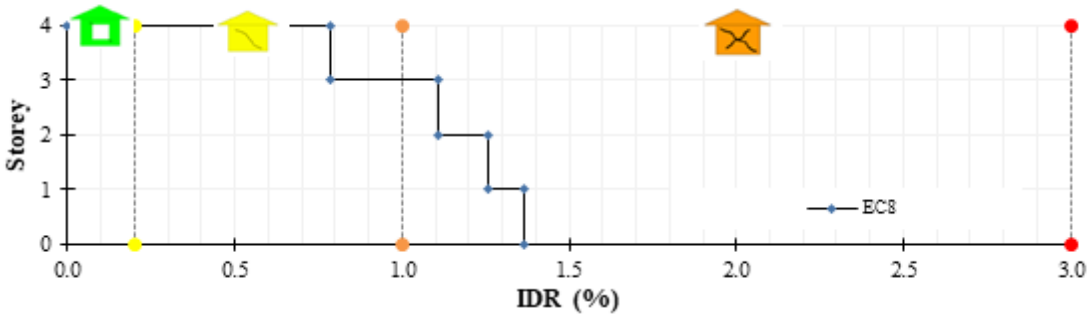

Figure 10: Mean IDR profiles for three spectrum in accordance with performance levels

Experimental results of low level (0.15 g) and high level (0.57 g) test conducted on ISPRA building [28] considering IDR are shown in Figure 10. In order to be able to compare results from the experiment and the ones obtained from seimic analysis, IDR is obtained by interpolation for PGA of 0.26 g, which is the PGA of observed location Friulli and result is shown in Figure 11. This IDR is further compared on Figure 12 with the ones obtained earlier from seismic analysis for EC8 target spectrum.

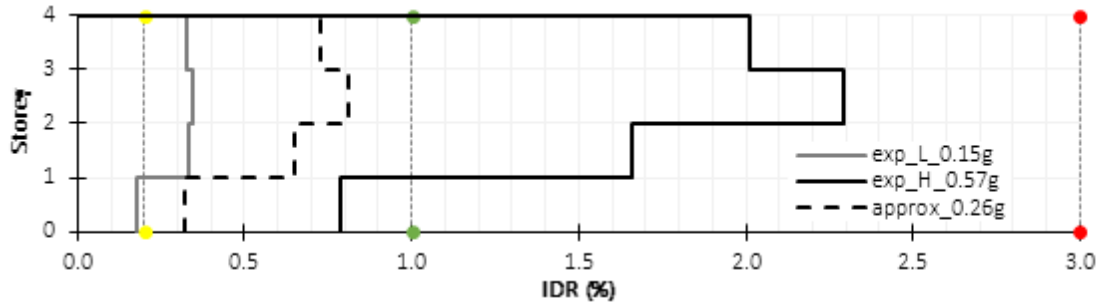

Figure 11: Mean IDR profiles for experimental results of low and high test and approximation of possible damage for 0.26g

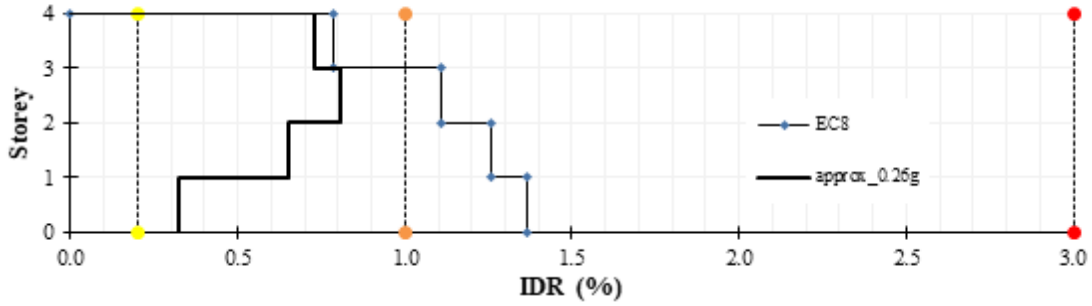

Figure 12: Comparison between approximated results for 0.26g and observed results from EC8 spectrum

6 CONCLUSION

The selection of appropriate seismic records is the one of the most critical steps while performing the nonlinear dynamic time history analysis in order to estimate the seismic performance in the basis of the hazard at the site where the structure is located. There are different ways of selecting ground motions, however in this paper 30 ground motion records are selected based on spectral matching according to EC8 spectrum.

Seismic analysis was performed on numerical model based on the experimentally tested ISPRA building. Accuracy of numerical model is obtained and approved by performance measures and comparison of displacements, base shear and hysteretic curve. Time history analysis for 30 earthquake records were obtained. As a result, Inter-story Drift Ratios (IDR) as a main damage measure were presented in order to make comparison with defined performance levels of reinforced concrete bare frames. There damage levels are defined with four limiting values of IDR. According to EC8 this IDR is within the limits that describe extensive damage.

Comparing these results with the ones from interpolation based on low and high test of ISPRA experimental model, it was concluded that IDR obtained from experimental model is lower compared to the IDR obtained for EC8 target spectrum. It can be concluded that EC8 is over conservative that can be good for design reserve, but in that case it is not efficient. However, for better results and comparison it is recommended to do larger number of numerical analysis including also conditional mean target spectrum and uniform hazard target spectrum.

REFERENCES

[1] S. K. Deb and G. S. Kumar, Seismic Damage Assessment of Reinforced Concrete Buildings Using Fuzzy Logic. 13th *World Conference on Earthquake Engineering*, p. 8., 2004

[2] M. Nooraie and F. Behnamfar, A New Procedure for Selection and Modification of ground motion for nonlinear dynamic Dynamic analysis. *15th World Conference on Earthquake Engineering*, p. 10., 2012.

[3] M. Araújo, L. Macedo, M. Marques, and J. M. Castro, Code-based record selection methods for seismic performance assessment of buildings. *Earthq. Eng. Struct. Dyn.*, vol. 45, no. 1, pp. 129–148, 2016.

[4] J. W. Baker, An introduction to Probabilistic Seismic Hazard Analysis (PSHA). *White Pap*, 2008.

[5] J. W. Baker, T. Lin, S. K. Shahu, and N. Jayaram, New Ground Motion Selection Procedures and Selected Motions for the PEER Transportation Research Program. 2011.

[6] J. W. Baker and C. A. Cornell, Spectral shape, epsilon and record selection. *Earthq. Eng. Struct. Dyn.*, 2006.

[7] J. Baker, Ground motion selection for performance-based engineering, and the Conditional Mean Spectrum as a selection tool. *10th Pacific Conference on Earthquake Engineering*, p. 8., 2015.

[8] J. J. Bommer and A. B. Acevedo, The use of real earthquake accelerograms as input to dynamic analysis. *J. Earthq. Eng.*, Vol. 8, No. Sup001, Pp. 43–91, Jan. 2004.

[9] C. C. Lin, C. E. Wang, H. W. Wu, and J. F. Wang, On-line building damage assessment based on earthquake records. *Smart Mater. Struct.*, vol. 14, no. 3, pp. S137–S153, Jun. 2005.

[10] C. A. Cornell, Engineering Seismic Risk Analysis. *Bull. theSeismologycal Soc. Am.*, vol. 58, no. 5, pp. 1583–1606, 1968.

[11] E. H. Field, Probabilistic Seismic Hazard Analysis (PSHA) A Primer.

[12] E. I. Katsanos, A. G. Sextos, and G. D. Manolis, Selection of earthquake ground motion records: A state-of-the-art review from a structural engineering perspective. *Soil Dynamics and Earthquake Engineering*, 2010.

[13] J. E. Carballo and C. A. Cornell, Probabilistic seismic demand analysis: Spectrum matching and design. *Report No. RMS-41*, 2000.

[14] A. Whittaker et al., Selecting and Scaling Earthquake Ground Motions for Performing Response-History Analyses | NIST. *Grant/Contract Reports*, - 11-917-15, Nov. 2011.

[15] European Standard EN 1998-1:2004, Eurocode 8: Design of Structures for earthquake resistance - Part 1: General Rules, Seismic Actions and Rules for Buildings, 2005.

[16] I. Iervolino and G. Manfredi, A review of ground motion record selection strategies for dynamic structural analysis. *CISM International Centre for Mechanical Sciences, Courses and Lectures*, 2008.

[17] P. Bazzurro and C. A. Cornell, Disaggregation of Seismic Hazard. *Bull. Seismol. Soc. Am.*, vol. 89, no. 2, pp. 501–520, 1999.

[18] J. W. Baker, Conditional Mean Spectrum: Tool for Ground-Motion Selection. *Journal of Structural Engineering*, vol. 137, no. 3, pp. 322–331, Mar. 2011.

[19] European Standard EN 1992-1-1:2004, Eurocode 2: Design of concrete structures - Part 1-1: General rules and rules for buildings, 2004.

[20] M. Dolšek, OS Modeler - Examples of Application. *Report*, Faculty of Civil and Geodetic Engineering, University of Ljubljana, 2008.

[21] SeismoStruct 2016. [Online]. Available: https://www.seismosoft.com/seismostruct. [Accessed: 12-Feb-2019].

[22] J. B. Mander, M. J. N. Priestley, and R. Park, Theoretical Stress‐Strain Model for Confined Concrete. *Journal of Structural Engineering*, vol. 114, no. 8, pp. 1804‐1826, Sep. 1988.

[23] Menegotto M. and Pinto P.E., Method of analysis for cyclically loaded reinforced concrete plane frames including changes in geometry and non-elastic behavior of elements under combined normal force and bending. *IABSE Symposium on Resistance and Ultimate Deformability of Structures Acted on by Well Defined Repeated Loads*, pp. 15–22., 1973.

[24] T. H. Jordan, W. Marzocchi, A. J. Michael, and M. C. Gerstenberger, Operational Earthquake Forecasting Can Enhance Earthquake Preparedness. *Seismol. Res. Lett.*, vol. 85, no. 5, pp. 955–959, Sep. 2014.

[25] PEER Ground Motion Database - PEER Center. [Online]. Available: https://ngawest2.berkeley.edu/site. [Accessed: 12-Feb-2019].

[26] SeismoMatch | Seismosoft. [Online]. Available: https://www.seismosoft.com/seismomatch. [Accessed: 12-Feb-2019].

[27] A. Ghobarah, On drift limits associated with different damage levels. Hamilton, 2004.

[28] HAZUS-MH 2.1, Advanced Engineering Building Module. Washington D.C.

COMPDYN 2019
7th ECCOMAS Thematic Conference on
Computational Methods in Structural Dynamics and Earthquake Engineering
M. Papadrakakis, M. Fragiadakis (eds.)
Crete, Greece, 24–26 June 2019

SHAKE TABLE TESTING FOR SEISMIC PERFORMANCE EVALUATION OF NON-STRUCTURAL ELEMENTS

D.Perrone[1], E. Brunesi[2], and S. Peloso[2]

[1] University School for Advanced Studies IUSS Pavia
Piazza della Vittoria 16, 27100, Pavia, Italy
e-mail: daniele.perrone@iusspavia.it

[2] European Centre for Training and Research in Earthquake Engineering
Via Ferrata 1, 27100, Pavia, Italy
{emauele.brunesi,simone.peloso}@eucentre.it

Abstract

In the last years an increasing interest has been addressed to the assessment of the expected mean annual losses of single buildings as well as of building portfolio(s). Field observation of damage/failure in the aftermath of past earthquakes demonstrates that the losses related to the non-structural elements could significantly exceed the structural losses. At the same time, it is worth noting that the damage related to the non-structural elements could affect the functionality of the buildings and critical facilities. Based on these considerations, a detailed assessment of the expected annual losses requires data both on the structural and non-structural elements. In comparison to structural elements and systems, however, there is much less information and experimental data to undertake the assessment and design of non-structural elements for multiple-performance levels. Shake table testing could thus be very useful to assess the seismic performance of non-structural elements and to achieve the required information for loss estimation studies. In this paper, the results of shake table testing of acceleration-sensitive non-structural elements are presented. Equivalent single degree of freedom numerical models of the analyzed acceleration-sensitive non-structural element was developed using the results of the tests and a performance evaluation was carried out.

Keywords: Non-structural elements, shake table testing, loss estimation, fragility analysis, experimental testing.

1 INTRODUCTION

In the last years many efforts have been spent to develop advanced or simplified methodologies in order to evaluate the earthquake related losses and to ensure a desired building performance for a given intensity of seismic excitation [1-2]. Figure 1 illustrates the four steps required to perform the probabilistic seismic assessment according to the Performance-Based Earthquake Engineering (PBEE) framework [3].

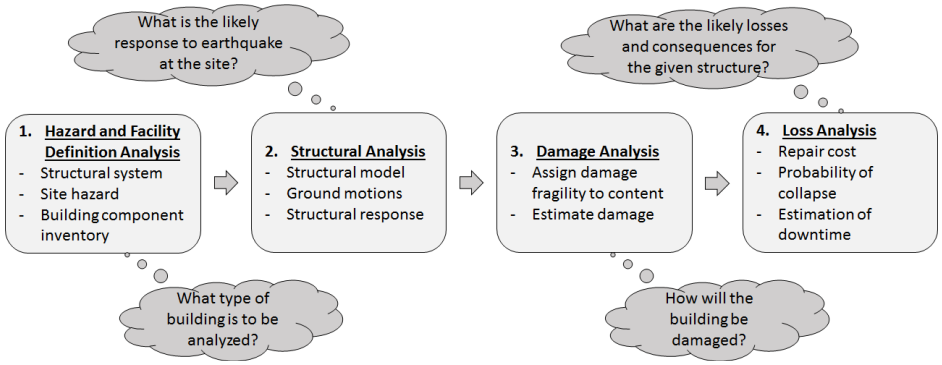

Figure 1: Overview of the four stages of PEER PBEE framework, after [3].

Within the PBEE framework the non-structural elements (NSEs) are of paramount importance, in particular in the damage (step 3) and loss analyses (step 4). During the damage analysis, the probability that a certain element (structural or non-structural) in the building will exceed a certain damage state for a given intensity level is established. At this stage, the availability of fragility functions for both structural and non-structural elements is necessary. In the literature, few experimental investigations are available for non-structural elements [4-7]. For this reason, many fragility functions are based on expert judgments. In loss estimation frameworks, the influence of non-structural elements is of paramount importance because they represent most of the total investments in typical buildings as well as because the non-structural elements show damage for low seismic intensities with respect to the structural ones [8-9]. The influence of non-structural elements has been demonstrated both looking at the damage reported during past earthquakes [10-11] as well as from loss estimation studies on buildings both at single and regional scale [12-14].

The lower seismic performance of non-structural elements is often related to the fact that, in comparison to structural elements, there is much less information and specific guidance available on the seismic design of NSEs for multiple-performance levels. The seismic qualification of NSEs by means of shake table tests could thus be a very useful tool to characterize the seismic response of the NSEs and to evaluate the performance parameters required for their seismic design. In this context, the ASCE 7-16 [15] standard in the US requires that certain critical non-structural elements must be seismically qualified to demonstrate their functionality after being subjected to design earthquake motions. The implementation of such seismic qualification procedure in the US resulted in significant benefits in terms of seismic performance of NSEs (i.e. definition of damage state, improved safety, reduced losses, etc.). According to ASCE 7-16 [15], the seismic qualification testing can be accomplished by either shake table testing, analysis or experience data.

This paper focuses on the definition of a simple procedure to evaluate the seismic performance of non-structural elements through the results of shake table tests. Shake tables tests were used both to qualify the case study non-structural element and to develop a simplified numerical model for the non-structural element of interest such that the outcomes of the testing could be reproduced and complemented with numerical simulations that in turn propagate the

effects of uncertainties/variability in the seismic input (and eventually in the non-structural element and the building). For this specific application, the developed numerical model allowed the authors to verify the performance of the tested non-structural element, when installed in a case study building. The simplified modeling approach, based on the results of shake table tests, could significantly help in the assessment of the seismic performance of non-structural elements and could be applicable to both fragility analysis as well as loss estimation frameworks.

2 CASE STUDY NON-STRUCTURAL ELEMENT

The seismic performance of a coaling machine was investigated in this study (see Figure 2). Shake table seismic qualification tests according to AC156 [16] and ISO13033 [17] were performed at the EUCENTRE laboratories using a multi-axial shaking table developed to test non-structural elements. The cooling machine is characterized by the following geometrical properties: length = 1000 mm, width = 890 mm, height = 1980 mm, operating weight = 4.51 kN. The specimen was connected to the shake table using custom interface plates designed by the staff of EUCENTRE. Every plate was connected to the shake table using four M30 bolts; threaded holes were manufactured at the Laboratory to fit the standard base connecting bolts of the tested unit (4 M10 bolts).

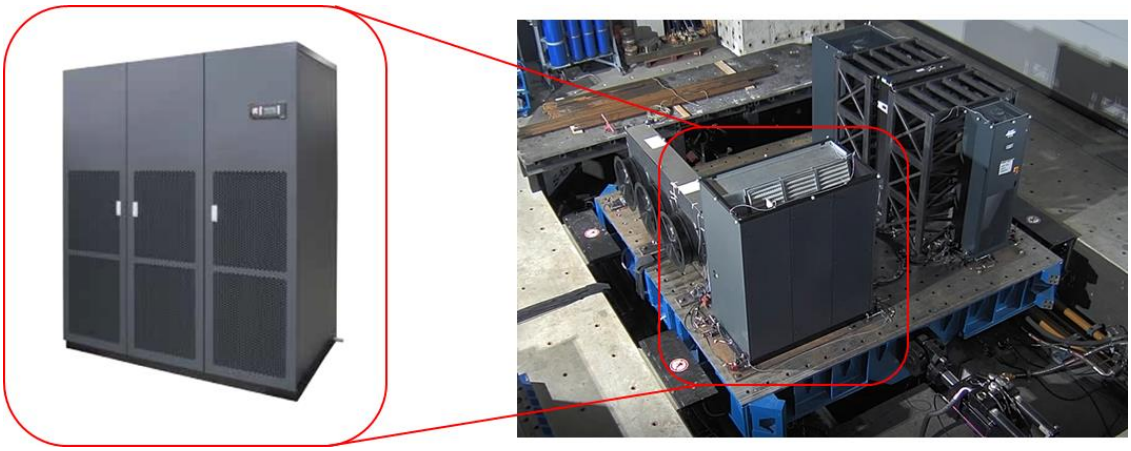

Figure 2: Tested Unit.

3 SEISMIC QUALIFICATION BY SHAKE TABLE TESTING

In this section, the main results of the experimental tests are reported. Only the results related to the shake table test performed according to ISO13033 [17] are reported. The ISO13033 document is the first document in Europe to provide recommendations about the procedures to be adopted for the verification of NSEs capacity and to ensure that those capacities exceed the seismic demands. In this study the original ISO13033 was modified and contextualized to the force-based formulation included in Eurocode 8 [18] to verify/design the non-structural elements.

3.1 Modal identification

Besides the seismic qualification tests, resonance search tests were also carried out, as specified by both AC156 [16] and ISO 13033 [17] test protocols. The resonance search was performed using white noise as input signal. The white noise consisted of a low-level acceleration (1.0 m/s^2 peak nominal) flat spectrum with frequency content from 0.25 Hz to 50 Hz, with approximately 60 seconds duration. Each axis (longitudinal and vertical) was tested separately. The white noise signal was generated using the MTS Systems Corporation Seismic Testing

Execution (STEX) software. Figure 3 shows an example of the acceleration time-histories used for the resonant frequencies search along the longitudinal direction.

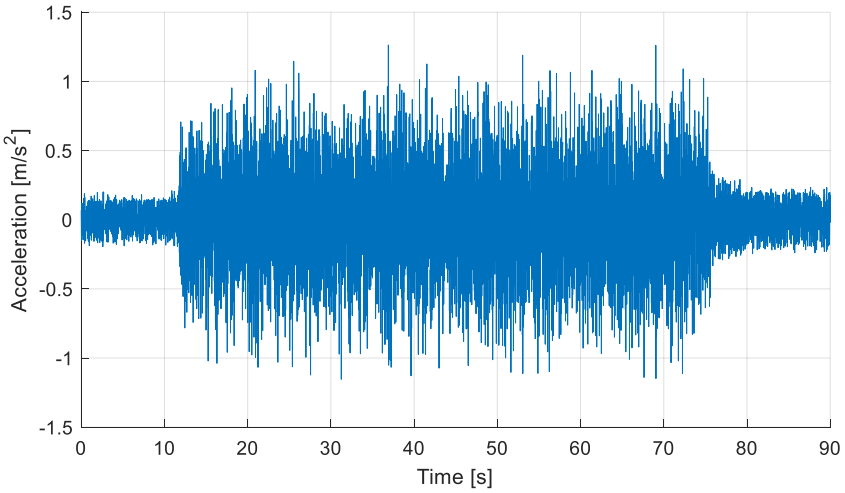

Figure 3: Time history of the white noise input for the longitudinal dof.

Data was analyzed using a transfer function algorithm with a frequency resolution of 0.0625 Hz. Based on the obtained results, the identified fundamental frequencies in the two main directions are 10.2 Hz (X direction) and 10.7 Hz (Y direction), respectively. The damping ratios were also estimated; they resulted equal to 7.1% and 6.3% respectively in the X and Y direction.

3.2 Shake table testing

The seismic qualification tests were performed according to a modified ISO13033 protocol [17] evaluating the Required Response Spectrum (RRS) for different seismic zones in Italy. Tests were conducted simultaneously in the longitudinal and vertical directions, with each direction excited by an independently (uncorrelated) generated table acceleration profile. The bi-directional testing protocol was conducted twice, in two horizontal testing directions rotated 90° from one another.

According to ISO 13033, the RRS can be evaluated for generic or specific buildings. The generic RRS can be evaluated according to the following equations:

$$A_{fleible} = k_{I(u\ or\ s)} \cdot k_{H,i} \cdot k_{R,p,flexible} \tag{1}$$

$$A_{rigid} = k_{I(u\ or\ s)} \cdot k_{H,i} \cdot k_{R,p,rigid} \tag{2}$$

where:

- $A_{flexible}$ is the design horizontal acceleration at the center of mass of flexible NSEs;
- A_{rigid} represents the design horizontal acceleration at the center of mass of rigid NSEs;
- $k_{I(u\ or\ s)}$ is the ground motion intensity factor to be provided by regional and national standards. The subscript u and s are referred to the PGA, modified to account for the soil conditions, at ultimate and serviceability limit state, respectively;
- $k_{H,i}$ is the floor response amplification factor. It is equal to:

$$k_{H,i} = \left[1 + \alpha \left(\frac{z_i}{H}\right)\right] \tag{3}$$

in which α is a parameter function of the type of seismic force-resisting system ($\alpha \leq 2.5$), z_i is the elevation of level i relative to the grade elevation, H is the average roof elevation of the structure relative to the grade elevation;

- $k_{R,p,flexible}$ is the NSEs amplification factor for flexible systems. This parameter is related to the NSEs element period, damping ratio, geometry, method of attachment, and inelastic behaviour. According to ISO 13033, $k_{R,p,flexible}$ can vary between 1 and 2.5 (or more). See ANNEX D of ISO 13033 for more information about the allowed values;

- $k_{R,p,rigid}$ is the NSEs amplification factor for rigid systems. It is assumed equal to 1.0.

The approach proposed by ISO13033 to define the RRS has been modified in order to make it compatible with the design horizontal equivalent static force evaluated according to Eurocode 8 [18]. In Eurocode 8, the spectral acceleration, S_a, used to calculate the horizontal equivalent static force to be applied to the NSE is given by:

$$S_a = \alpha \cdot S \cdot \left[3 \cdot \frac{\left(1+\frac{z_i}{H}\right)}{\left(1+\left(1-\frac{T_a}{T_1}\right)^2\right)} - 0.5 \right] \tag{4}$$

The parameter α in Eq. 4 represents the ratio of the design ground acceleration on soil type A to the acceleration of gravity g, while S is the soil amplification factor. The term in square brackets in Eq. 4 is used to replace the product $k_{H,i} \cdot k_{R,p}$ in Equations 1 and 2. This term accounts for the amplification of the peak floor acceleration due to the location of the NSEs in the building and for the spectral amplification as a function of the ratio of the fundamental period of the NSEs (T_a) to the fundamental period of the building (T_1). In order to define the spectral acceleration for flexible and rigid NSEs in the RRS, the ratio T_a/T_1 is assumed equal to 1 for flexible NSEs and equal to 0 for rigid NSEs. Based on this assumption, it is possible to reproduce the RRS by replacing Equations 1 and 2 with the following two equations:

$$A_{flexible} = k_{i(u\ or\ s)} \cdot \left[3 \cdot \left(1 + \frac{z_i}{H}\right) - 0.5 \right] \tag{5}$$

$$A_{rigid} = k_{i(u\ or\ s)} \cdot \left[3 \cdot \frac{\left(1+\frac{z_i}{H}\right)}{2} - 0.5 \right] \tag{6}$$

The vertical RRS is assumed to be 2/3 of the horizontal RRS with $z_i/H=0$, as suggested by AC156 [16]. The corner frequencies are also defined according to AC156: f_0=1.3 Hz, f_1=8.3 Hz and f_3=33.3 Hz.

Four seismic intensity levels were considered for the seismic qualification tests. The selected seismic intensities are representative of the Italian context. The probabilistic seismic hazard assessment proposed by Stucchi et al. [19], that provides the horizontal peak ground acceleration (PGA) with a 10% probability of exceedance in 50 years, was used to select the seismic intensities. In particular, seismic sites characterized by the following PGA on firm soil were taken into account: 0.05g (low intensity), 0.14g (medium intensity), 0.21g (medium-high intensity) and 0.27g (high intensity).

Figure 4 shows the comparison between the RRS and TRS for the vertical and horizontal testing directions. A good match between the RRS and TRS spectra is observed both for the horizontal and the vertical directions.

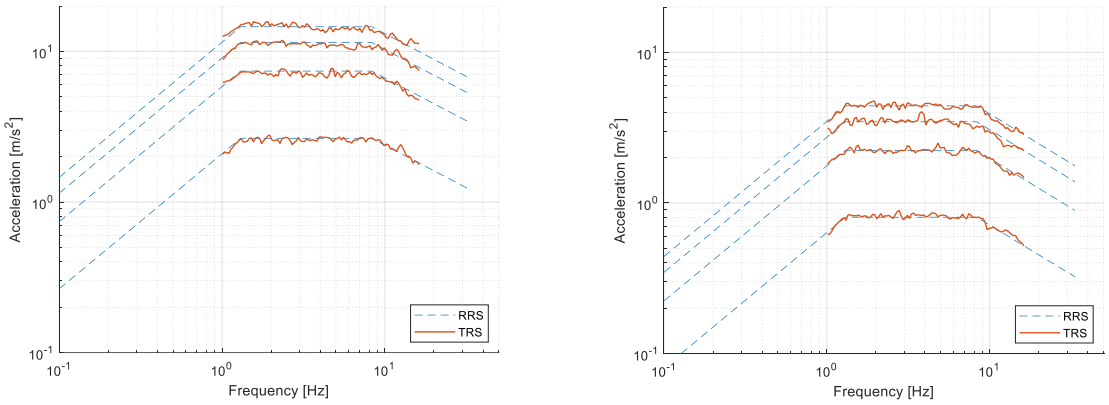

a) Horizontal component b) Vertical component

Figure 4: Comparison between RRS according to modified ISO13033 and TRS.

After each test, a visual inspection was undertaken to verify the structural integrity of the cooling machine as well as the presence of damage in the anchoring system. No evident sign of damage was observed after the tests for all considered intensities. Figure 5 shows photographs of the cooling machine after the test in the Y direction for the highest seismic intensity. Only a small distortion of the covering panels was observed, but the structural integrity was not compromised. A functionality test was also performed after the seismic qualification and the machine functioned perfectly.

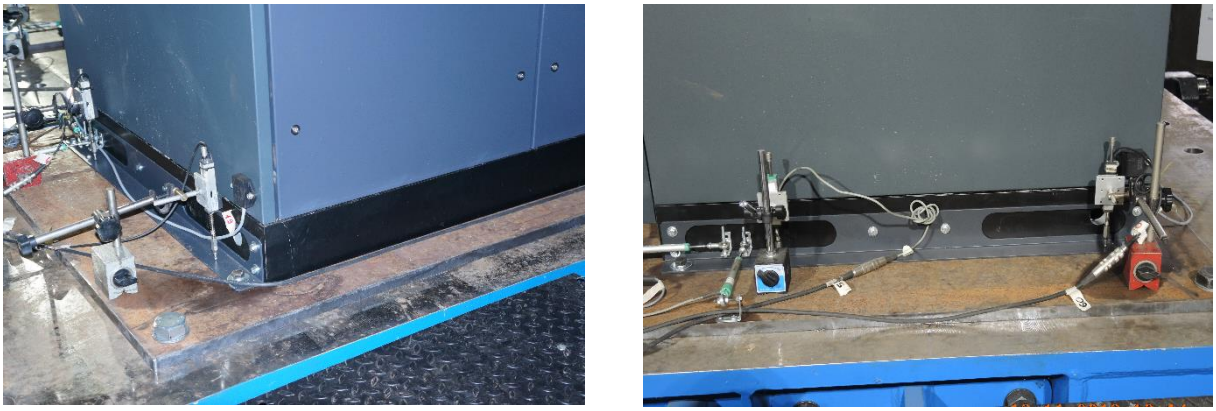

a) Deformation panels **b) Deformation panels**

Figure 5: Visual inspection after the seismic qualification tests.

4 SEISMIC PERFORMANCE EVALUATION OF THE CASE STUDY NON-STRUCTURAL ELEMENT

The results of the shake table seismic qualification tests were used to derive an easy-to-use modeling idealization for the investigated cooling machine and to carry out seismic performance evaluation of it, when integrated in a case study structure. In what follows, account is given of the main characteristics of the studied building archetype along with a description of the ground motion sets and seismic intensity levels assumed for the assessment. Capacity modeling was then treated, leading to seismic performance evaluation of the selected non-structural element.

4.1 Case study structure

A four-story RC moment-resisting frame was designed according to Eurocode 8 [18] assuming a ductility class B (q = 3.75) and a firm soil condition. The frame was supposed to be located in construction site near Cassino, Italy characterized by a design peak ground acceleration of 0.21g (return period of 475 years). The seismic weight of each floor was defined assuming a tributary width of 5 m. The strength of the concrete (f'c) was taken equal to 32 MPa, while the yield strength of the steel was taken equal to 375 MPa. The dimensions of the frame are shown in Figure 6.

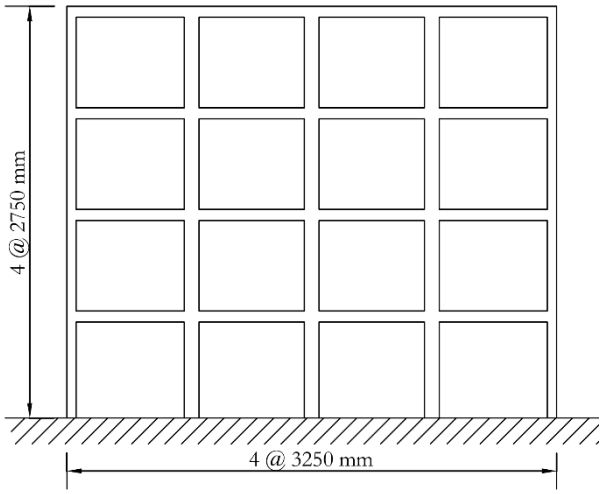

Figure 6: Case study RC frame

The model of the frame was developed using the Opensees software [20]. The numerical models were developed assuming the fiber force-based approach [21]. Inelastic beam-column fiber elements were used to model the frame members, explicitly including geometric and material nonlinearities. A distributed plasticity approach was thus adopted to simulate the spreading of inelasticity over the member length and cross section. The uniaxial confinement model proposed by Chang and Mander [22] was considered to simulate the cyclic behavior of concrete, the hysteretic rules of which were established based on statistical regression analysis on the experimental data from cyclic compression tests conducted by a number of researchers. A simple bilinear constitutive model with isotropic strain hardening was assigned to the steel rebars.

4.2 Ground motion selection

A set of 20 horizontal accelerograms at the site of the case-study buildings were selected from the PEER NGA-West database [23]. Based on a preliminary estimation of the Italian and European seismicity, the selection of the site was carried out in order to represent a medium-to-high seismicity in Italy. The selected intensity corresponds with the medium-high intensity used in the seismic qualification tests.

Hazard-consistent record selection was based on spectral compatibility (matching of the geometric mean) with a conditional mean spectrum according to the methodology proposed by Jayaram et al. [24]. This approach considers the conditional variance given a return period of spectral acceleration at the selected period. The conditional period, T*, to be used for the nonlinear time history analyses (NLTHAs) of RC frame was selected based on the results of eigenvalue analyses, and it is equal to 0.5 sec. Five return period of the seismic intensity were selected to perform the NLTHAs (50, 200, 475, 975 and 2475 years). Figure 7 shows the mean response

spectrum and all individual record response spectra for the 20 considered ground motions for a return period equal to 475 years.

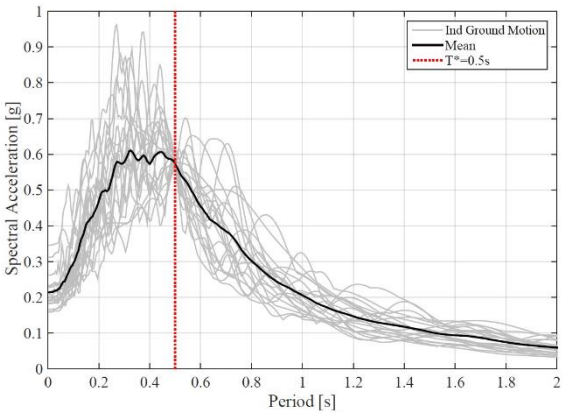

Figure 7: Mean response spectrum and acceleration response spectra of all considered ground motions for a conditional period, T*, equals to 0.5 sec

In order to perform the time history analyses tangent stiffness proportional Rayleigh damping was introduced to the 1st and 3rd modes of the structure. The inherent damping ratio was assumed to be 5.0% of the critical.

4.3 Numerical modeling of the case study cooling machine

For the purposes of this study, the non-structural element of interest was modeled as a simple bilinear idealization, with the initial elastic stiffness being computed according to test data from modal identification. More in detail, the initial stiffness of the bilinear single degree of freedom (SDoF) system was calculated as reported by Equation 7:

$$k = m \cdot (2\pi \cdot f)^2 \tag{7}$$

where m is the mass of the cooling machine and f is its fundamental frequency in the most critical of the two main directions. By taking Y-direction as reference, f equals 10.7 Hz and, hence, k equals 2078 kN/m.

Furthermore, the peak capacity of the bilinear model was assumed to correspond to the shear resistance of the 4 M10 bolts used to anchor the cooling machine to the shake table for the tests. Equation 8 reports how the total shear yield/ultimate capacity of the bolts ($V_{y/u}$) was computed:

$$V_{y/u} = 0.6 \cdot A_s \cdot n \cdot f_{y/u} = 0.6 \cdot A_s \cdot 4 \cdot f_{y/u} \tag{8}$$

where A_s is the cross-section area of the bolt, n is the number of bolts, and $f_{y/u}$ is the yield/ultimate stress of steel. The class of the bolts is 4.6, meaning that f_y is equal to 240 MPa. The bilinear model is presented in the S_a-S_d format in order to easily undertake performance evaluation and compare the results with the absolute acceleration – relative displacement floor response spectra obtained by the NLTHAs. In order to convert $V_{y/u}$ in the acceleration format, the maximum shear capacity is simply divided by the seismic mass of the cooling machine.

A simple parametric study was also performed to evaluate the bilinear model varying the bolts' diameter. To this end, three diameters were considered: 6, 8 and 10 mm. Figure 8 shows the S_a-S_d relationship of the calculated bilinear models.

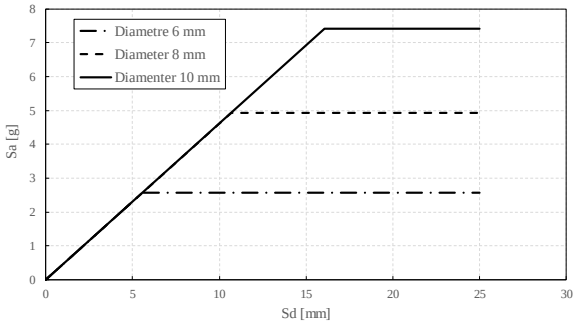

Figure 8: Bilinear model tested cooling machine

4.4 Seismic demand and assessment of the non-structural element

In order to carry out the performance evaluation, the absolute acceleration – relative displacement floor response spectra for the analyzed case study building were first calculated, for different return periods of the seismic intensities. Note that the cooling machine is supposed to be installed at the third floor of the building, and hence Figure 9a reports the median S_a-S_d response spectra corresponding to this floor. As reported in Figure 9b, all considered bolt's diameters satisfy the performance evaluation, for all considered return periods. It is worth to be noted that high return periods, such as 975 and 2475 years, are generally not considered for non-structural elements performance evaluation but are reported here as illustrative example.

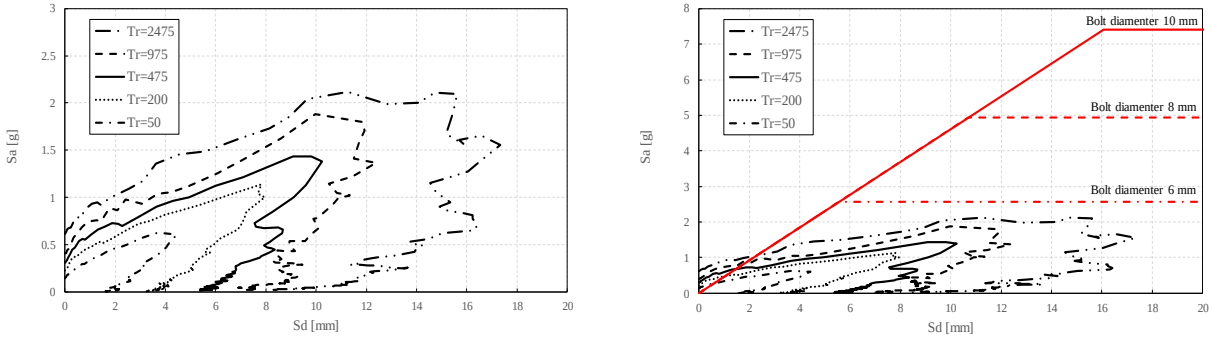

a) Floor response spectra b) Performance evaluation

Figure 9: Floor response spectra and performance evaluation

As a closing remark, it is worthy of mention that the adopted assessment methodology could be also used and extended to perform fragility analysis and develop fragility functions in which probabilities of exceeding given damage state conditions are expressed in terms of spectral accelerations at the fundamental period of the non-structural elements $S_a(T_1)$. The assumption of $S_a(T_1)$ as engineering demand parameter could significantly improve the loss estimation evaluation for acceleration-sensitive non-structural elements, with respect to the peak floor accelerations, because it takes into account the dynamic amplification due to the non-structural element stiffness.

5 CONCLUSIONS

The damage observed during past earthquakes demonstrated the importance of the non-structural elements in the performance-based seismic design of buildings. However, few experimental data are available to characterize the performance on non-structural elements and to

carry out seismic performance assessment. Within this context, this paper describes the results of shake table seismic qualification tests on a cooling machine. The shake table tests were first presented and then used to define a simple SDoF bilinear model of the investigated cooling machine. The proposed mechanics-based idealization was used to undertake the performance evaluation of the case study cooling machine, when installed in a typical four-storey RC frame. The results of the assessment demonstrated the effectiveness of the proposed approach, which could be extended and applicable to fragility analysis assuming a new, and more consistent, engineering demand parameter.

6 ACKNOWLEDGMENTS

The work presented in this paper has been developed within the framework of the project "Dipartimenti di Eccellenza", funded by the Italian Ministry of Education, University and Research at IUSS Pavia. Part of the current work was carried out under the financial support of the Italian Civil Protection, within the framework of the triennial agreement 2019-2021 (WP11 – Seismic characterization of non-structural elements).

REFERENCES

[1] D.P. Welch, T.J. Sullivan, G.M. Calvi, Developing direct displacement-based procedures for simplified loss assessment in performance-based earthquake engineering. *Journal of Earthquake Engineering*, **18**, 290-322, 2014.

[2] FEMA, FEMA P-58 Seismic Performance Assessment of Buildings, *Federal Emergency Management Agency*, Washington, DC, 2012.

[3] G.M. Calvi, T.J. Sullivan, D.P. Welch, A seismic performance classification framework to provide increased seismic resilience, *Perspectives on European Earthquake Engineering and Seismology*, **34**, 361-400, 2014.

[4] G. Gabbianelli, A. Kanyilmaz, C. Bernuzzi, C.A. Castiglioni, A combined experimental-numerical study on unbraced pallet rack under pushover loads, *Ingegneria Sismica*, **34**, 18-38, 2017.

[5] Y. Tian, A. Filiatrault, G. Mosqueda, Experimental Seismic Fragility of Pressurized Fire Suppression Sprinkler Piping Joints, *Earthquake Spectra*, **30**, 1733-1748, 2014.

[6] A. Silva, Y. Jiang, L. Macedo, J.M. Castro, R. Monteiro, N. Silvestre, Seismic performance of composite moment-resisting frames achieved with sustainable CFST members, *Frontiers of structural and civil engineering*, **10**, 312-332, 2016.

[7] C. Petrone, G. Magliulo, G. Manfredi, Shake table tests on standard and innovative temporary partition walls, *Earthquake engineering and structural dynamics*, **46**, 1599-1624, 2017.

[8] A. Filiatrault T.J. Sullivan, Performance-based seismic design of nonstructural building components: The next frontier of earthquake engineering, *Earthquake Engineering and Earthquake Vibration*, **13,**17-46, 2014.

[9] A. Filiatrault, D. Perrone, R. Merino, G.M. Calvi, Performance-Based Seismic Design of Non-Structural Building Elements, *Journal of Earthquake Engineering*, 2018. https://doi.org/10.1080/13632469.2018.1512910

[10] D. Perrone, P.M. Calvi, R. Nascimbene, E.C. Fischer, G. Magliulo, Seismic performance of non-structural elements during the 2016 Central Italy Earthquake, *Bulletin of Earthquake Engineering*, 2018. https://doi.org/10.1007/s10518-018-0361-5

[11] E. Miranda, G. Mosqueda, R. Retamales, G. Pekcan, Performance of nonstructural components during the 27 February 2010 Chile Earthquake, *Earthquake Spectra*, **28(S1)**, S453-S471, 2012.

[12] G. J. O'Reilly, D. Perrone, M. Fox, R. Monteiro, A. Filiatrault, Seismic assessment and loss estimation of existing school buildings in Italy, *Engineering Structures*, **168**, 142-162, 2018.

[13] A. Vecere, R. Monteiro, W.J. Ammann, S. Giovinazzi, R.H. Melo Santos, Predictive models for post disaster shelter needs assessment, *International Journal of Disaster Risk Reduction*, **21**, 44-62, 2017.

[14] D. Rogrigues, H. Crowley, V. Silva, Earthquake loss assessment of precast RC industrial structures in Tuscany (Italy), *Bulletin of Earthquake Engineering*, **16**, 203-228, 2018.

[15] ASCE, ASCE 7-16 Minimum design loads for buildings and other structures, *American Society of civil engineers*, Reston, Virginia, 2016.

[16] ICC-ES, AC156 Acceptance criteria for seismic qualification by shake table testing of nonstructural components and systems, *International Code Council Evaluation Service*, Whittier, CA, 2012.

[17] ISO, ISO13033 Bases for design of structures – loads, forces and other actions -Seismic actions on nonstructural components for building applications, *International Organization for Standardization*, Geneva, Switzerland, 2013.

[18] CEN, Eurocode 8 – Design provisions for earthquake resistant structures, EN-1998-1:2004, *Comite Europeen de Normalization*, Brussels, Belgium, 2004.

[19] M. Stucchi, C. Meletti, V. Montaldo, H. Crowley, G.M. Calvi, E. Boschi, Seismic hazard assessment (2003-2009) for the Italian Building Code, *Bulletin of the seismological society of America*, **11**, 1885-1911, 2011.

[20] S. Mazzoni, F. McKenna, M.H. Scott, G.L. Fenves, OpenSees Command language manual, *Pacific Earthquake Engineering Research*, 2006.

[21] E. Spacone, F.C. Filippou, F.F. Taucer, Fibre beam-column model for non-linear analysis of RC frames: Part 1. Formulation, *Earthquake Engineering and Structural Dynamics*, **25**, 711-725, 1996

[22] G.A. Chang, J.B. Mander, Seismic Energy Based Fatigue Damage Analysis of Bridge Columns: Part 1 – Evaluation of Seismic Capacity, *NCEER Technical Report No. NCEER-94-0006 State University of New York*, Buffalo, N.Y, 1994.

[23] PEER NGA-West database, available on-line: http://peer.berkeley.edu/ngawest

[24] N. Jayaram, T. Lin, J.W. Baker, A computationally efficient ground-motion selection algorithm for matching a target response spectrum mean and variance, *Earthquake Spectra*, 27, 797-815, 2011.

COMPDYN 2019
7th ECCOMAS Thematic Conference on
Computational Methods in Structural Dynamics and Earthquake Engineering
M. Papadrakakis, M. Fragiadakis (eds.)
Crete, Greece, 24-–26 June 2019

DAMAGE INVESTIGATION OF ADOBE WALLS USING NUMERICAL SIMULATIONS

Hala Damerji[1], Santosh Yadav[1], Yannick Sieffert[1], Florent Vieux-Champagne[1], Yann Malecot[1]

[1]Univ. Grenoble Alpes, CNRS, Grenoble INP*, 3SR, 38000 Grenoble, France
address
e-mail:
{hala.damerji,santosh.yadav,yannick.sieffert,yann.malecot,florent.vieux-champagne}@3sr-grenoble.fr

Keywords: adobe walls, traditional construction, vulnerability, abaqus,simplified micro-modelling approach, concrete damage plasticity.

Abstract. *Nowadays, traditional construction methods still widespread in developing countries despite the dominance of reinforced concrete structures in urban area. These traditional methods are generally based on the use of available local materials and old techniques characteristic of each region. Since, this kind of structure is poorly studied in the literature there is a strong need to better understand their mechanical behaviour in order to optimize their design.In this paper, the shear behaviour of an adobe wall, made of natural earth materials, is modeled using a simplified micro-modelling approach in order to investigate its behaviour under cyclic loading. The concrete damage plasticity model is used for the adobe modelling while interfaces between adobes are defined using cohesive and frictional elements. Then 2D numerical simulations are performed using Abaqus/Standard. The numerical model is first used to reproduce the experimental shear cyclic behaviour of a wall.The results show the different damage patterns while all numerical data were compared with the results of the experimental test.*

1 INTRODUCTION

Adobe structure is known as one of the oldest structures in the world. This type of construction is still widely used in several countries, especially in the developing ones because of its economical advantages characterized by the low cost of the materials and it's local availability since it's mainly composed of earth and water. In addition, there is no need to high engineering skills where non experienced labour are capable to construct adobe buildings relying on the traditional construction techniques [1]. Moreover, earth construction has revived in several developed countries due to the energy and environmental issues that create an urgent need to re-adopt sustainable construction techniques [2].
However, the adobe buildings are known as fragile structures that cannot withstand earthquakes. In fact, there is only few studies on the behaviour of these structures whereas nowadays most of research are concentrating on the developing and the enhancement of the reinforced concrete constructions. Therefore, there is a strong need to improve the earth construction by analysing their vulnerability using experimental and numerical techniques.
The paper presents a numerical simulation of adobe wall under cyclic loading that will be compared to a real experimental test in order to validate its efficiency. This model will be used in the future to simulate masonry walls under dynamic loading.

2 NUMERICAL MODELLING APPROACH

A finite element model was generated in Abaqus/Standard [3] to simulate the wall behaviour where 2D was chosen over 3D modelling in order to compromise between time consuming and real wall configuration. Where another decision that must be taken regarding the representation of masonry walls.
Based on the literature [4], there is different modelling strategies that can be divided into three types depending on the desired level of accuracy, see figure 1, two of them take into account the heterogeneous nature of the masonry walls, figure 1 (b) and (c), while (d) neglects the interface and takes the wall as a one homogeneous material. Among these techniques the simplified micro modelling was adopted where adobe units are expanded to the half of the mortar thickness in each direction in order to conserve the original wall dimension. They are represented by continuum elements while the interface is represented using discontinuous elements.

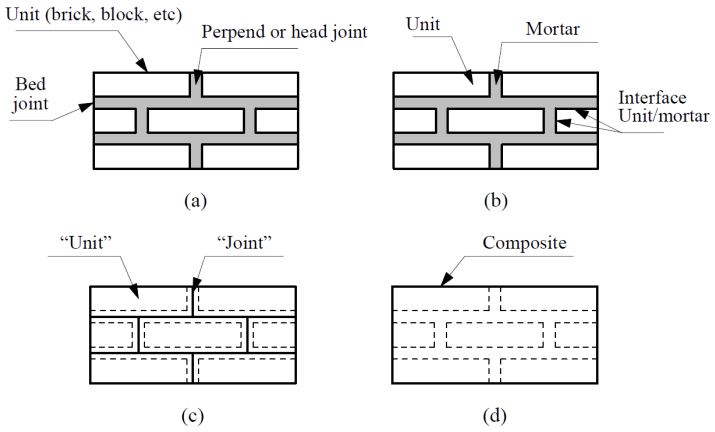

Figure 1: Modeling strategies for masonry structures: (a) masonry sample; (b) detailed micro-modeling; (c) simplified micro-modeling; (d) macro modeling.[4]

This technique was used by several studies on the masonry modelling [6, 7, 8] and it has several advantages: it gives accurate results despite of the simplified representation of the joints, since right before failure the non linear deformation occurs mostly in the joints [5]. It also allows to study the crack patterns and the shear behaviour. It should be mentioned that the CPS4R elements were using for adobe modelling in Abaqus.

2.1 Constitutive model of masonry units

The concrete damage plasticity model (CDP) was used to simulate the non-linearity of the adobes, it's based on the work of Lubliner [10], Lee and Fenves [11]. It's a continuum damage model for concrete or other quasi-brittle material which are subjected to monotonic, cyclic and /or dynamic loading [9]. It assumes that the uniaxial tension and compression response of the material is characterized by the damage plasticity where this damage is governed by the degradation of the stiffness, it's defined under unixial loading as:

$$\sigma = (1 - d)E_0(\epsilon - \epsilon^{pl}) \tag{1}$$

where $\sigma, \epsilon, \epsilon^{pl}, E_0$ are respectively, stress, strain, plastic strain, the (undamaged) modulus and d is the damage variable that can take from zero, for the undamaged material, to one when it's fully damaged. The model allows also the stiffness recovery, it's more evident when the load changes from tension to compression where the tensile cracks closure occurs resulting the recovery of the compressive stiffness, figure 2.

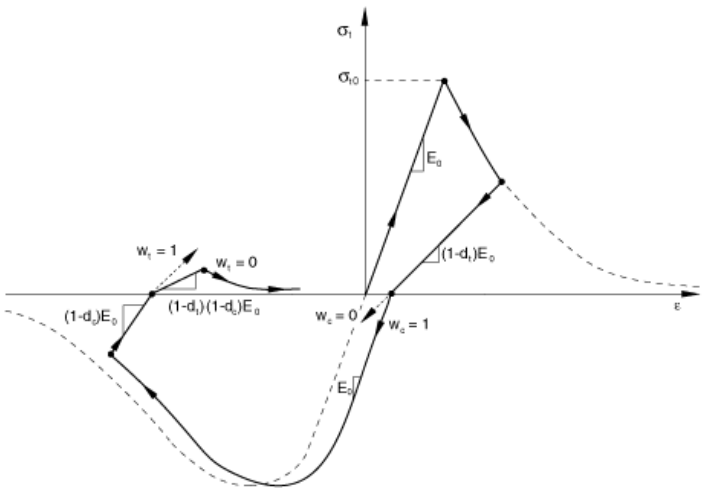

Figure 2: Response of the CDP material under uniaxial load cycle(tension and compression)[9]

In this work, most of the material properties of the adobe units were calibrated based on the experimental compression and tension tests [12]. The elastic properties are shown in the table 1 while the table 2 shows the CDP parameters that were calibrated by Agüera & al [13].Moreover, the compression-tension behaviour was introduced as a stress-strain values where compressive and tensile strengths are respectively equal to 6.4 and 0.48 MPa. Hence, the damage factor is identified using the following formula[10]:

$$d = 1 - \frac{\sigma}{f} \tag{2}$$

f is either the compressive or the tensile strength of the material.

Mass density (Kg/m^3)	E modulus (GPa)	Poisson coefficient
200	4	0.2

Table 1: Elastic characteristics of adobe.

Dilation angle	Eccentricity	fb0/fc0	k	Viscosity parameter
7	0.1	1.16	0.66	0.0005

Table 2: CDP characteristics of abode units

2.2 Surface-based cohesive model for joints

The surface based cohesive model was chosen to create the link between the units in order simulate the interface response. The interaction is defined based on a traction separation law [9] that allows to simulate the joint failure caused by normal tensile cracking, in plane and out of plane shear sliding. This law assumes initially linear traction-separation behaviour which is defined in terms of an elastic matrix K that relates the nominal shear stresses t and the separation vectors δ:

$$t = \left\{ \begin{array}{c} t_n \\ t_s \\ t_t \end{array} \right\} = \begin{bmatrix} K_{nn} & 0 & 0 \\ 0 & K_{ss} & 0 \\ 0 & 0 & K_{tt} \end{bmatrix} \left\{ \begin{array}{c} \delta_n \\ \delta_s \\ \delta_t \end{array} \right\} = K\delta \tag{3}$$

This linear law is followed by a failure mechanism which consists of a damage initiation criterion that refers to the beginning of the cohesive degradation at the interface contact and a damage evolution that ended with total joints failure. In this study the maximum stress was adopted to initiate the degradation of the cohesive bond, it's when the maximum contact stress ratio reached the value of one, see equation 4. The cracks propagation in the joints impose a stiffness degradation that affect the contact stress according to equation 5 where D is the damage coefficient that starts from 0 and it reaches 1 when the joints failure occurs. D is calculated in Abaqus based on a linear softening evolution, equation 6, by specifying the maximum value of the effective separation δ_m^{max} which is attended during loading history.

$$max \left\{ \begin{array}{c} \langle \frac{t_n}{t_n^0} \rangle ; \frac{t_s}{t_s^0} ; \frac{t_t}{t_t^0} \end{array} \right\} = 1 \tag{4}$$

$$t = (1 - D)K\delta \tag{5}$$

$$D = \frac{\delta_m^f (\delta_m^{max} - \delta_m^0)}{\delta_m^{max} (\delta_m^f - \delta_m^0)} \tag{6}$$

Moreover, the friction between adobes is defined by Coulomb friction model. The sliding begins after the failure of the cohesive bond and when the shear stress attends the critical sliding stress which is defined by the coefficient of friction μ and the normal compressive stress. The following table shows the different linear and non linear properties for joint interfaces, the rigidities are calculated based on the equations 7 [4] and the other parameters are deduced experimentally based on Casagrande tests:

μ	$K_{nn}(N/m^3)$	$K_{ss}(N/m^3)$	$K_{tt}(N/m^3)$	t_n^{max}(kPa)	C (kPa)	δ^{max} (mm)
0.9	102E9	43E9	43E9	200	13.9	1.56

Table 3: Properties for the joint interfaces.

$$K_{nn} = \frac{E_u E_m}{h_m(E_u - E_m)} \tag{7}$$

$$K_{ss} = K_{tt} = \frac{G_u G_m}{h_m(G_u - G_m)} \tag{8}$$

E_u and E_m are the Young's modulus, G_u and G_m are the shear modulus, respectively, for adobe and mortar and hm is the thickness of the joint.

3 MODEL OUTPUT AND DISCUSSION

The configuration of the FE model in Abaqus/Standard is showed in the figure 3. The model includes the wall which is composed of the adobe units and the contact is applied at their edges. The other two parts(base and top) are the metallic supports where they used to impose the boundary conditions like in real experimental test.

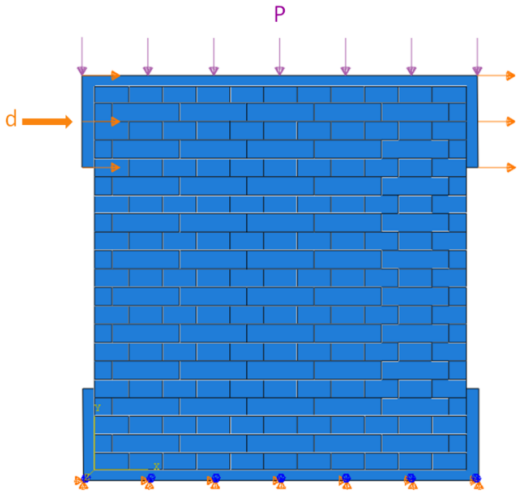

Figure 3: Numerical model of the adobe wall

The base support was fixed and on the surface of the top one a normal pressure loading P of 88 kN per surface was applied. Finally a cyclic loading (horizontal displacement d) was

imposed at the edges of the upper support. The wall has been meshed using the CPS4R elements where the number of elements in each unit vary between 4, 6 or 14 depending of their dimension, where 1506 is the total number of elements.

The figure 4 shows the damage pattern of the real experiment [12] and the numerical simulation at the end of the loading. In both cases, the cracks begin from the top and go down to the bottom of the wall in the two directions which is due to the high shear stress triggering the failure of the joints contact and creating an X shape pattern.

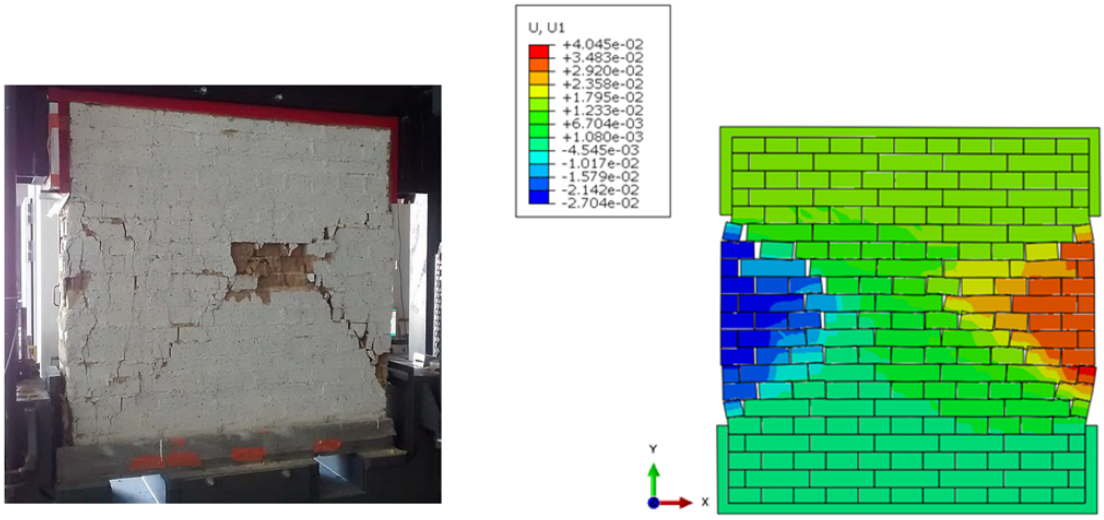

Figure 4: Crack patterns of the experimental and the numerical simulation(lateral displacement in m) of the wall

In addition, a comparison between numerical and experimental hysteresis loops is represented in the figure 5 where it shows the horizontal force (kN) in function of the displacement (mm). An asymmetrical loop is obtained from the experimental test where the positives peak forces attend 45.9 kN while the negative ones are limited at 23 kN. It can be assumed that this asymmetry is due to the cracks generation and the failure of several joints right from the beginning of the test, it makes the wall less resistant in a direction than the other one where the wall preserve it's resistance for several cyclic loading. As it's shown in the same figure the numerical simulation represents fairly enough the positive side of the experimental results than the negative one. Moreover, the experimental forces attend high values right from the beginning of the test which is not the case for the numerical forces. Therefore, the numerical wall withstand the first cycles where a symmetrical hysteresis loop is obtained.

The maximum numerical force is equal to 48.34 kN which is relatively close to the experimental value mentioned above. The effective stiffness K_{eff}, eq. 9, is calculated in function of: F_{eff} which is the maximum obtained force and d_{cr} its corresponding displacement. K_{eff} corresponds to the stiffness at the moment of the first cracks creation. The experimental stiffness is equal to 58.14 kN/mm while the numerical one is 10.35 kN/mm, and it also shows that the cracks start at an early stage experimentally while it's not the case for the numerical model.

$$K_{eff} = \frac{F_{cr}}{d_{cr}} \tag{9}$$

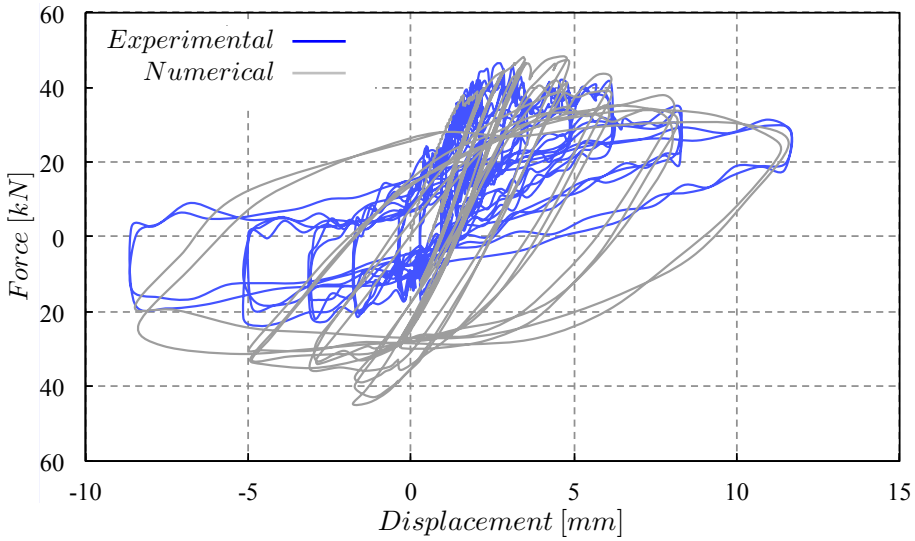

Figure 5: Hysteresis loop of experimental and numerical results, the horizontal force is presented in function of the horizontal displacement

The final graph, figure 6, represents the dissipated energy, in Joules, of each cycle. For the experimental results, the energy starts to dissipate from the first cycles and increases progressively with the increasing of the applied displacement. However, the numerical dissipated energy is negligible at the beginning, it starts to increase after the ninth cycle.

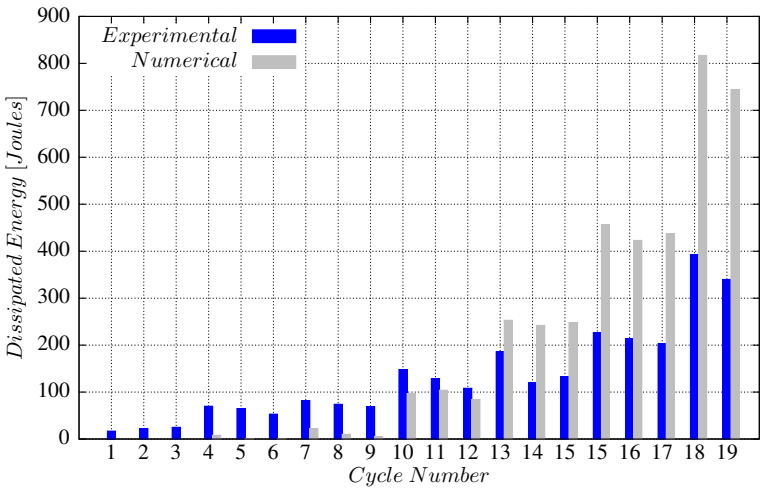

Figure 6: Comparison between the experimental and the numerical dissipated energy of each cycle.

All the results above indicate that the damage of the wall occurs at an early stage in the experimental test compared to the numerical one.

4 Conclusion

The numerical model is able to describe the adobe walls behaviour under cyclic loading. The simplified micro modelling is accurate enough to describe and predict the damage pattern

while the comparison of force-displacement curves was done only on the positive part of the values because of the asymmetrical shape of the experimental hysteresis loop. The forces and the dissipated energies show that the damage starts earlier in the experimental test than in the numerical model.
Therefore, additional analysis must be done on the experimental test and their results in order to specify and implement the exact boundary conditions in the numerical model. Moreover, 3D modelling will be performed to represent the real configuration of the wall and thus to improve the numerical results. In future, the model will be used to perform dynamic simulations that will allow to study more precisely the masonry walls behaviour.

REFERENCES

[1] A. G. Costa , J. Guedes, H. Varum, Structural Rehabilitation of Old Buildings *Building Pathology and Rehabilitation (Vol. 2)*,2014.

[2] M. I. Gomes, M. Lopes, J. De Brito, Seismic resistance of earth construction in Portugal *Engineering Structures*, **33(3)**, 932–941 ,2011.

[3] Abaqus/Standard *Dassault Systems Simulia Corporation*, Johnston, RI, USA, 2016.

[4] P. B. Lourenço, Computational strategies for masonry structures, *PhD Thesis* , 1996.

[5] A. W. Page, Finite element model for masonry, *New Analysis Techniques for Structural Masonry*, 1985.

[6] G. Milani , 3D upper bound limit analysis of multi-leaf masonry walls *International Journal of Mechanical Sciences*, **50(4)**, 817–836,2008.

[7] M. Bolhassani ,A. A. Hamid ,A. C. W. Lau , F. Moon , Simplified micro modeling of partially grouted masonry assemblages, *Construction and Building Materials*,**83** , 159–173,2015.

[8] A. Stavridis , P. B. Shing, Finite-Element Modeling of Nonlinear Behavior of Masonry-Infilled RC Frames, *Journal of Structural Engineering*, **136(3)**, 285–296,2010.

[9] Dassault Systems, *Abaqus analysis user's manual 6.13-3*, RI2013; Dassault Systems Providence: Waltham, MA,USA, 2013

[10] J. Lubliner , J. Oliver , S. Oller , and E. O˜nate, A plastic-damage model for concrete *Int. J. Solid. Struct.*, **25(3)** , 299–326.

[11] J. Lee , G. L. Fenves, Plastic-Damage Model for Cyclic Loading of Concrete Structures *Journal of Engineering Mechanics,vol. 124, no.8, pp. 892–900*, 1998.

[12] J. D. Aranguren Rodriguez, Analyse du comportement parasismique des murs en maçonnerie de terre crue renforcés et non-renforcés *Rapport de stage, INSA Toulouse*, France,2017

[13] N. D. Agüera, M. E. Tornello, C. D. Frau, Structural Response of Unreinforced Masonry Walls *Journal of Civil Engineering and Architecture* ,**10(2)**,2016

COMPDYN 2019
7th ECCOMAS Thematic Conference on
Computational Methods in Structural Dynamics and Earthquake Engineering
M. Papadrakakis, M. Fragiadakis (eds.)
Crete, Greece, 24–26 June 2019

THE INFLUENCE OF THE STEEL GRADE ON THE PROBABILISTIC THEORY OF PLASTIC MECHANISM CONTROL FOR STEEL MOMENT RESISTING FRAMES

Alessandro Pisapia[1*], Vincenzo Piluso[1]
[1] University of Salerno
Via Giovanni Paolo II, 132, 84084 Fisciano SA
e-mail: alpisapia@unisa.it, v.piluso@unisa.it

Abstract

This work aims at the extension of the Probabilistic Theory of Plastic Mechanism Control (P-TPMC) for Steel Moment Resisting Frames (MRFs) to other steel grades. P-TPMC is based on the application of First Order Reliability Method and Ditlevsen Bounds, which represents the reliability method for series systems, considering as random variable the yield strength of steel members. As in previous work, only the S275 steel grade has been investigated in this paper the analyses are extended to a different grade of steel, in particular, S235 and S355, to evaluate its influence on the failure probability of TPMC. Finally, a simple relationship to computing the value of the overstrength factor needed to include the importance of random material variability in the application of TPMC is proposed.

Keywords: Theory of Plastic Mechanism Control, collapse mechanisms, moment resisting frames, stochastic frames, probability of failure, series systems.

1 INTRODUCTION

In the seismic design of structures, modern seismic codes [Eurocode 8, AISC] [1],[2] provide simplified design rules to prevent unsatisfactory collapse mechanisms. In particular, in case of Moment Resisting Frames (MRFs), the use of the so-called beam-column hierarchy criterion is suggested, but it is widely demonstrated it is only able to prevent soft storey mechanism not assuring the development of a collapse mechanism of global type. The Theory of Plastic Mechanism Control (TPMC) [3]-[5] has been developed to design structures able to show a collapse mechanism of global type after aseismic events. This design procedure is based on the extension of the kinematic theorem of plastic collapse to the concept of mechanism equilibrium curve. Besides, the design conditions to be satisfied to prevent all the undesired collapse mechanisms, up to an ultimate displacement compatible with the local ductility supply of structural members, are derived. Up to now, TPMC has been successfully applied to deterministic structures having different seismic resistant schemes both for steel structures [5]-[15] and reinforced concrete structures [16]. However, even in the case of structures designed by TPMC, undesired collapse mechanisms could occur when the effects of random material variability are taken into account. The Theory of Plastic Mechanism Control has been extended to the case of stochastic MRFs to account for the influence of random material variability on the collapse mechanism of steel structures subjected to horizontal seismic forces. The method proposed evaluates the probability of failure in the attainment of a collapse mechanism of global type. It constitutes the probabilistic version of the Theory of Plastic Mechanism Control (TPMC) [17]-[19]. It is important to underline that, within structural reliability analysis and within the contest of failure mode control, the term “failure” denotes the attainment of a collapse mechanism different from the global one. In fact, many experimental investigations made by shaking table test [20]-[22] or Incremental Dynamic Analyses (IDA) [24]-[29] have shown that different failure mode can occur in structures under destructive earthquakes, and the reliability of having a collapse mechanism of global type sometimes is very low. Through the probabilistic procedure, it was possible to define an overstrength factor to apply to the deterministic version of TPMC with a given success probability, taking account the effects of random material variability.

In this work, a parametric analysis has been carried out to develop a mathematical relationship for computing the overstrength factor as a function of the main features of the analysed MRFs and with a fixed reliability value in the application of the deterministic version of Theory of Plastic Mechanism Control.

2 THEORY OF PLASTIC MECHANISM CONTROL

It is well known that under earthquake excitation, it is necessary to assure adequate global ductility and high energy dissipation. In the design of MRFs, it is important to guarantee the development of a global mechanism, where the dissipative zones are concentrated at beam ends and at the base of the columns of the first storey, avoiding the development of partial failure mechanisms, as depicted in Figure 1. For this reason, in the nineties, a theory on the plastic mechanism control has been proposed by Mazzolani et al. [3]. In particular, this theory is based on the extension of the kinematic theorem of plastic collapse to the concept of mechanism equilibrium curve. Therefore, for each collapse mechanism, it is possible to define the equilibrium curve as follows:

$$\alpha = \alpha_0 - \gamma\delta_u \tag{1}$$

where α is a collapse multiplier of structures, α_0 represents the first order multiplier, γ is the slope of curve depending on the second-order effects, and finally, δ_u is the ultimate displacement of the structure. Eq. (1) is provided by the equality between the internal work of

the plastic hinges and the external work of the horizontal forces. Remembering that, in the rigid-plastic analysis, the collapse multiplier is the smallest of the kinematically admissible multipliers, to assure the collapse mechanism of global type, it is necessary to satisfy the following design condition:

$$\alpha^{(g)} \leq \alpha^{(t)} => \alpha_0^{(g)} - \gamma^{(g)}\delta_u \leq \alpha_{0.i_m}^{(t)} - \gamma_{i_m}^{(t)}\delta_u \;\; for\; t = 1,2,3\; and\; i_m = 1,2,\ldots n_s \qquad (2)$$

where "g" indicates the global mechanism while "t" represents a generic collapse mechanism different by the global type and i_m is the generic storey of the structure. Eq.(2) assures that the curve of the global mechanism type is located below those corresponding to all the other undesired mechanisms until the ultimate displacement δ_u, compatible with the ductility supply of the dissipative zones, as depicted in Figure 2.

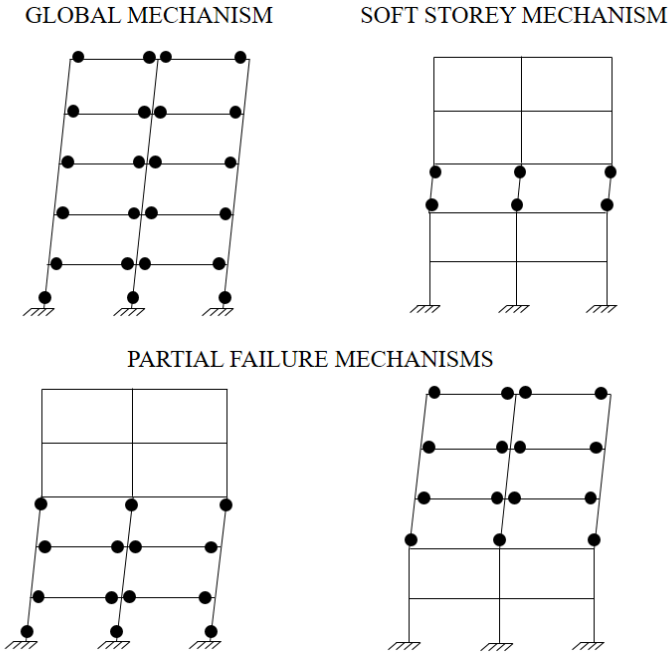

Figure 1: Collapse mechanism typologies.

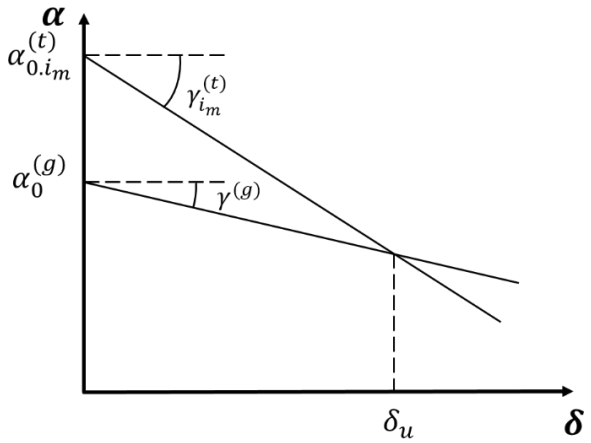

Figure 2: Design Condition of Theory of Plastic Mechanism Control (TPMC).

3 PROBABILISTIC VERSION OF TPMC

An advanced method for designing MRFs showing at collapse an assured probability of developing a collapse mechanism of global type is herein proposed. It means that the failure in the attainment of the design goal means the development of an undesired mechanism different

from the global one. Therefore, as reported in Figure 2, the failure is achieved when the mechanism equilibrium curve corresponding to any unwanted mechanism is located above the one corresponding to the global mechanism.

3.1 Definition of the failure events according to TPMC

Seeing the problem from the failure point of view, we can rearrange the design condition needed to prevent undesired collapse mechanism reported in Eq. (2) representing the occurrence of any failure event. The failure events, thus identified, are random events constituting a series system of binary components. Each failure event can be expressed by means of the following safety margin parameter $E_{i_m}^{(t)}$:

$$E_{i_m}^{(t)} = \left(\alpha_{0.i_m}^{(t)} - \gamma_{i_m}^{(t)}\delta_u\right) - (\alpha_0^{(g)} - \gamma^{(g)}\delta_u) < 0 \quad (3)$$

The safety margin is negative when "failure" occurs, i.e. an undesired mechanism develops. The number of the considered inequalities is equal to the whole number of collapse mechanisms different from the global one. Starting from the above consideration, in order to apply the reliability series method, some preliminarily assumptions are made:

1. Plastic moments of members are jointly Gaussian random variables because of random variability of steel yield strength;
2. Second order rigid-plastic analysis is carried out to include the influence of second order effects;
3. Horizontal seismic forces are deterministically distributed according to the first vibration mode of the structures evaluated following code provisions;
4. Vertical loads are assumed as deterministic quantities;
5. Plastic moments of columns are independent of the axial load.

3.2. FORM Method and Ditlevsen Bounds

As mentioned in a previous section, the failure events are events located in series, for this reason, it is possible to study the problem from the point of view of series system reliability [31],[32]. First Order Reliability Method (FORM) [32] and Ditlevsen Bounds [30] are applied to estimate the probability of failure. In particular, through FORM method it is possible to define the probability of failure of the single event, while Ditlevsen Bounds represent the Lower and Upper bounds of the failure probability of the TPMC, taking into account the correlation of random variables.

Following, the probabilistic procedure is reported. In particular, the random variables are collected into a vector **x** whose expectation and covariance matrix are respectively given by:

$$\boldsymbol{\mu}_{\mathbf{x}} = E[\mathbf{x}] \quad (4)$$

$$\boldsymbol{C}_{\mathbf{x}} = E[(\mathbf{x} - \boldsymbol{\mu}_{\mathbf{x}})(\mathbf{x} - \boldsymbol{\mu}_{\mathbf{x}})^T] \quad (5)$$

When the limit state condition defines a manifold surface $\mathrm{G}(\mathbf{x}) = 0$ constituted by n hyperplanes (being *n* the number of failure events), it means that any failure event is defined by a limit state function linear in **x**. The linearity of the expectation operator *E*, allows an easy determination of the first two moments of **G** as a function of the random vector **x**:

$$\mathbf{G}(\mathbf{x}) = \mathbf{a_0} + \mathbf{B}^{\boldsymbol{T}}\mathbf{x} \quad (6)$$

where $\mathbf{a}_0$ is a vector representing known quantities and **B** is a matrix of deterministic coefficients. Starting form Eq. (4) it is possible to obtain:

$$\boldsymbol{\mu}_{\mathbf{G}} = \boldsymbol{E}[\mathbf{G}] = \mathbf{a_0} + \mathbf{B}^{\boldsymbol{T}}\boldsymbol{E}[\mathbf{x}] = \mathbf{a_0} + \mathbf{B}^{\boldsymbol{T}}\boldsymbol{\mu}_{\mathbf{x}} \quad (7)$$

where $\boldsymbol{\mu}_G$ is a vector of mean values and $\boldsymbol{\mu}_{\mathbf{x}}$ is a vector containing the expected values of random variables of vector x. From Eq. (5), is possible to obtain the matrix of covariance $\boldsymbol{\sigma}_{\mathrm{G}}^2$ as:

$$\boldsymbol{\sigma_G^2 = E[(G - \mu_G)^2] = B^T E[(x - \mu_x)(x - \mu_x)^T]B = B^T C_x B} \quad (8)$$

where $\mathbf{C_x}$ is the matrix of second-order moments of random variables. Given the above, the Cornell reliability indexes corresponding to the different failure events are collected in the vector $\boldsymbol{\beta}_C$ [33], which is computed as the ratio between the mean value and the standard deviation of G.

$$\boldsymbol{\beta_C = \frac{\mu_G}{\sigma_G} = \frac{a_0 + B^T \mu_x}{\sqrt{B^T C_x B}}} \quad (9)$$

The theoretical justification of the above-reported index lies in the fact that when the distribution of **x** is jointly Gaussian than G is also Gaussian, being a linear combination of Gaussian variables. In this case, the distribution of G is completely defined by $\boldsymbol{\mu}_G$ and $\boldsymbol{\sigma}_G$. For this reason, the vector collecting the probability of the failure events given by Eq. (3) of the event $\boldsymbol{p}_f$ is expressed in this way:

$$\boldsymbol{p_f = \Phi\left(-\frac{\mu_G}{\sigma_G}\right) = \Phi(-\beta_C)} \quad (10)$$

which establishes a bi-univocal relationship between the Cornell indexes and the failure probability of the events constituting the series system.

However, because the events, i.e. each row of the **B** matrix, are correlated, it is needed to account for the correlation between each couple of events. To this scope the correlation coefficients ρ_{ij} have to be computed:

$$\boldsymbol{\rho_{ij} = \frac{b_i^T C_x b_j}{\sqrt{(b_i^T C_x b_i)(b_j^T C_x b_j)}}} \quad (11)$$

where $\mathbf{b}_i$ and $\mathbf{b}_j$ are the i-th and j-th row of **B** matrix. The values of ρ_{ij} ranges between -1 and 1. Concerning the whole series system identified by the failure events given by Eq.(3), the failure probability P_f can be approximated by the individual components failure probabilities P_{fi} which are the elements of the vector provided in Eq. (10) and of their intersection up to the second order using upper and lower bounds, so-called Ditlevsen bounds, which are generally close enough to provide an acceptable estimate [30],[32].

The failure probability has the following lower bound:

$$P_f \geq p_{f1} + \sum_{i=2}^{n} max\left\{p_{fi} - \sum_{j=1}^{i-1} p_{f.ij}, 0\right\} \quad (12)$$

and upper bound:

$$P_f \leq \sum_{i=1}^{n} p_{f.i} - \sum_{i=2}^{n} \max_{j<1}\{p_{f.ij}\} \quad (13)$$

where $p_{f.i}$ is the i-th component of the vector $\boldsymbol{p}_f$. However, the bounds require the calculation of joint probabilities of every pair of elements *i* and *j* by means of the following equation by exploiting the Cornell index and the correlation factors:

$$\boldsymbol{P_{f.ij} = \Phi_2(-\beta_i; -\beta_j; \rho_{ij})} \quad (14)$$

The joint probabilities can be computed according to the following equation:

$$p_{f.ij}(y_1;\, y_2; \rho_{ij}) = \Phi(y_1)\Phi(y_2) + \int_0^{\rho_{ij}} \frac{exp\left[-\frac{y_1^2 + y_2^2 - 2y_1 y_2 \rho^2}{2(1-\rho_{ij}^2)}\right]}{2\pi\sqrt{1-\rho^2}} d\rho \quad (15)$$

where a change of base is needed according to Cholesky decomposition of covariance matrix leading to:

$$\begin{bmatrix} y_1 \\ y_2 \end{bmatrix} = \begin{bmatrix} 1 & 0 \\ \rho & \sqrt{1-\rho^2} \end{bmatrix} \begin{bmatrix} -\beta_1 \\ -\beta_2 \end{bmatrix} \tag{16}$$

The mathematic procedure to define the Lower and Upper bounds for the failure events given by in Eq. (3), is provided by Piluso et al. [17].

4 CALIBRATION OF OVERSTRENGTH FACTOR

In a previous section, the procedure to compute the probability of failure of Theory of Plastic Mechanism Control is provided. Now, a procedure to define the overstrength factor γ_{ov} to apply to the deterministic version of TPMC is presented, considering the random material variability.

So, the following design procedure can be suggested, starting from the assumption that the maximum bending moment which the beams can transmit to the columns is given by $\gamma_{ov} M_b$ where M_b is the nominal plastic moment, while γ_{ov} is the overstrength factor to be calibrated according to the step reported in the flowchart (Figure 3).

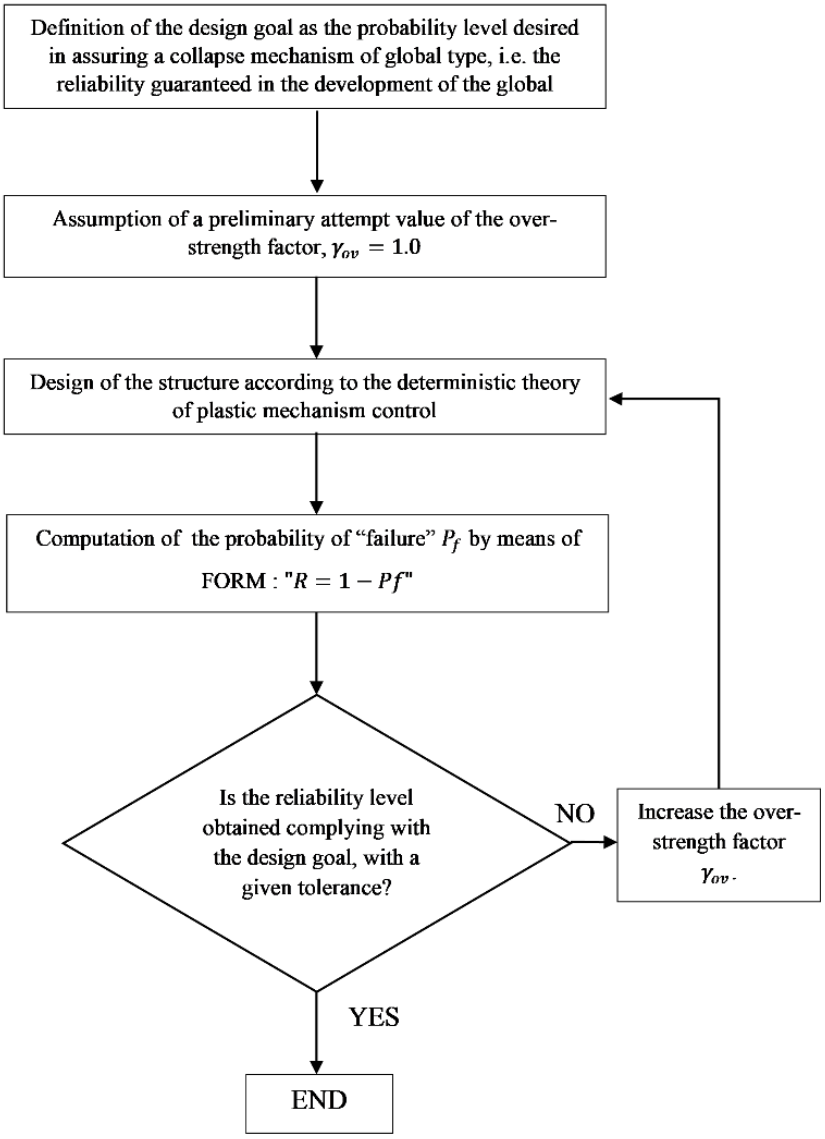

Figure 3: Design procedure flowchart.

5 PARAMETRIC ANALYSES

The parametric analyses have been performed to achieve a predefined level of reliability in the attainment of the design goal, i.e. the development of a collapse mechanism of global type. To this scope, 27-moment resisting steel frames have been considered by varying the number of storeys n_s, of bays n_b and the steel grade. The plastic moments of beams and columns are considered Gaussian random variables depending on the randomness of material properties. Moreover, three values of the coefficient of variation equal to 0.05, 0.10 and 0.15 have been accounted for. The parametric analysis has been repeated for increasing values of γ_{ov} aiming to its calibration. The analyzed moment resisting frames has a bay span equal to 6.00 m and an interstorey height equal to 3.50 m. The beams are the same for each frame, and they are designed to withstand distributed gravity loads whose values are $G_k = 15.00\ kN/m$ and $Q_k = 6.00\ kN/m$ for permanent and live load, respectively. Concerning the non-seismic load combination, the maximum gravity load acting on the beams is equal to $q_v = 1.3G_k + 1.5Q_k = 28.5\ kN/m$. The selected beam section is IPE 330. As the results of deterministic TPMC are not influenced by the magnitude of the seismic forces but are only sensitive to their distribution, a triangular distribution of the horizontal seismic forces has been assumed. Successively, for each frame, the plastic moments of the columns are defined according to the deterministic TPMC which is applied for increasing values of the overstrength factor assigned to the beam plastic moments. The resulting frames are analyzed using the stochastic approach herein presented, i.e. the corresponding lower and upper bounds of the probability of failure are computed. The results gained by means of such parametric analyses provide the variation of the probability of failure as a function of the overstrength factor adopted for the beams in the deterministic design and of the coefficient of variation, as depicted in Figure 4 to Figure 6.

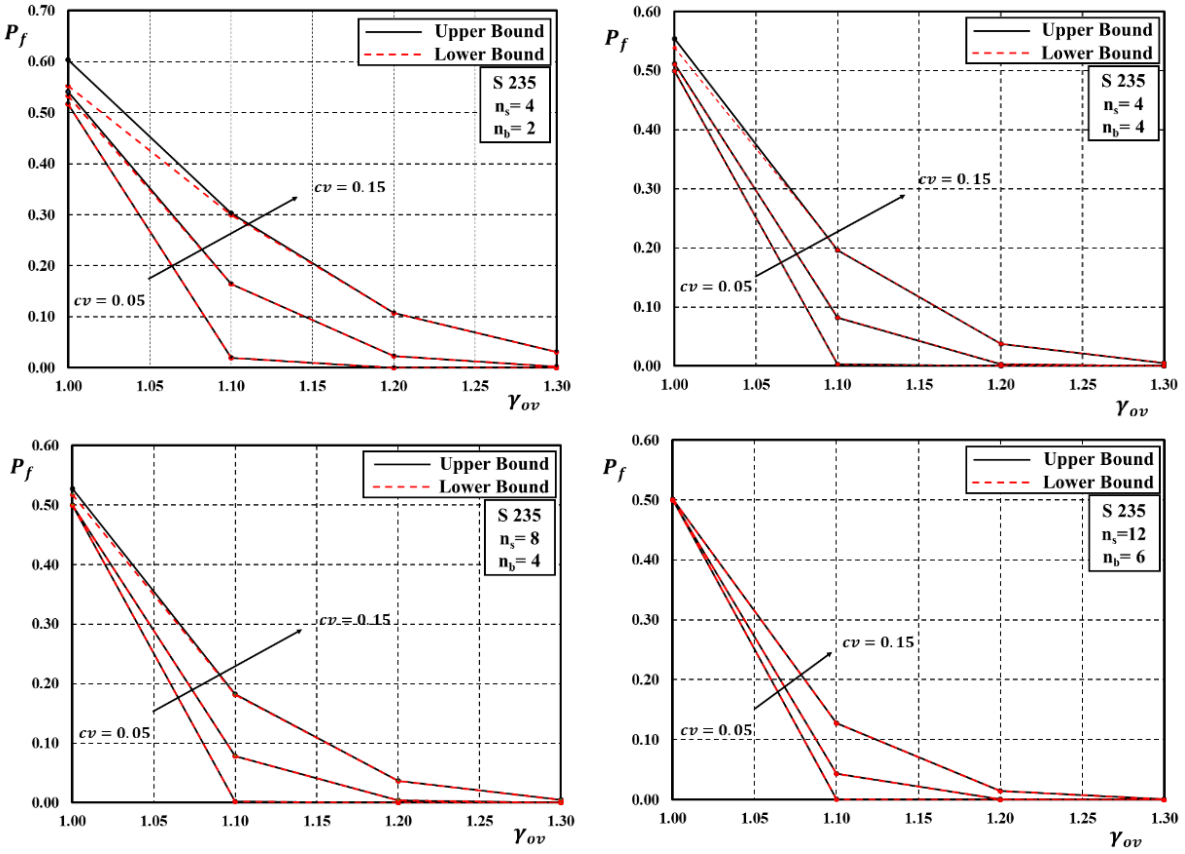

Figure 4: Upper and Lower bound of the failure probability for steel grade S235.

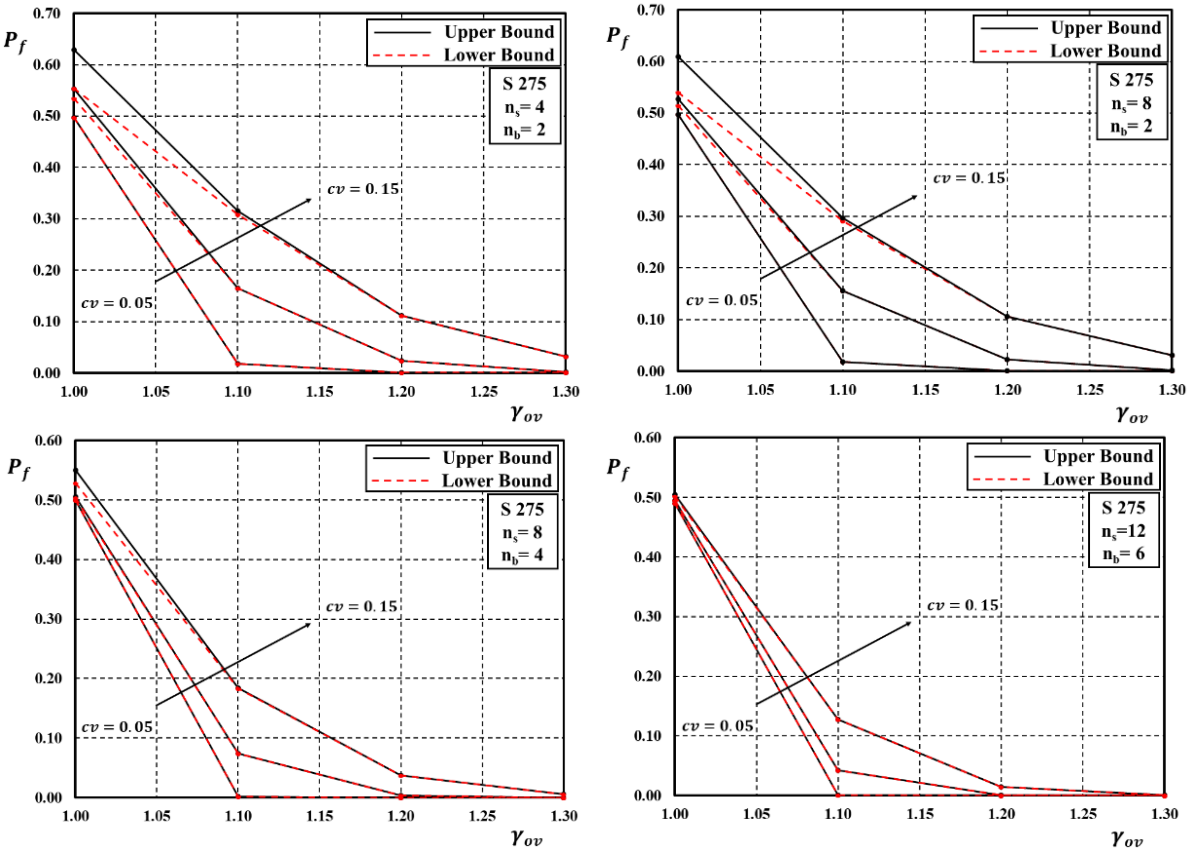

Figure 5: Upper and Lower bound of the failure probability for steel grade S275.

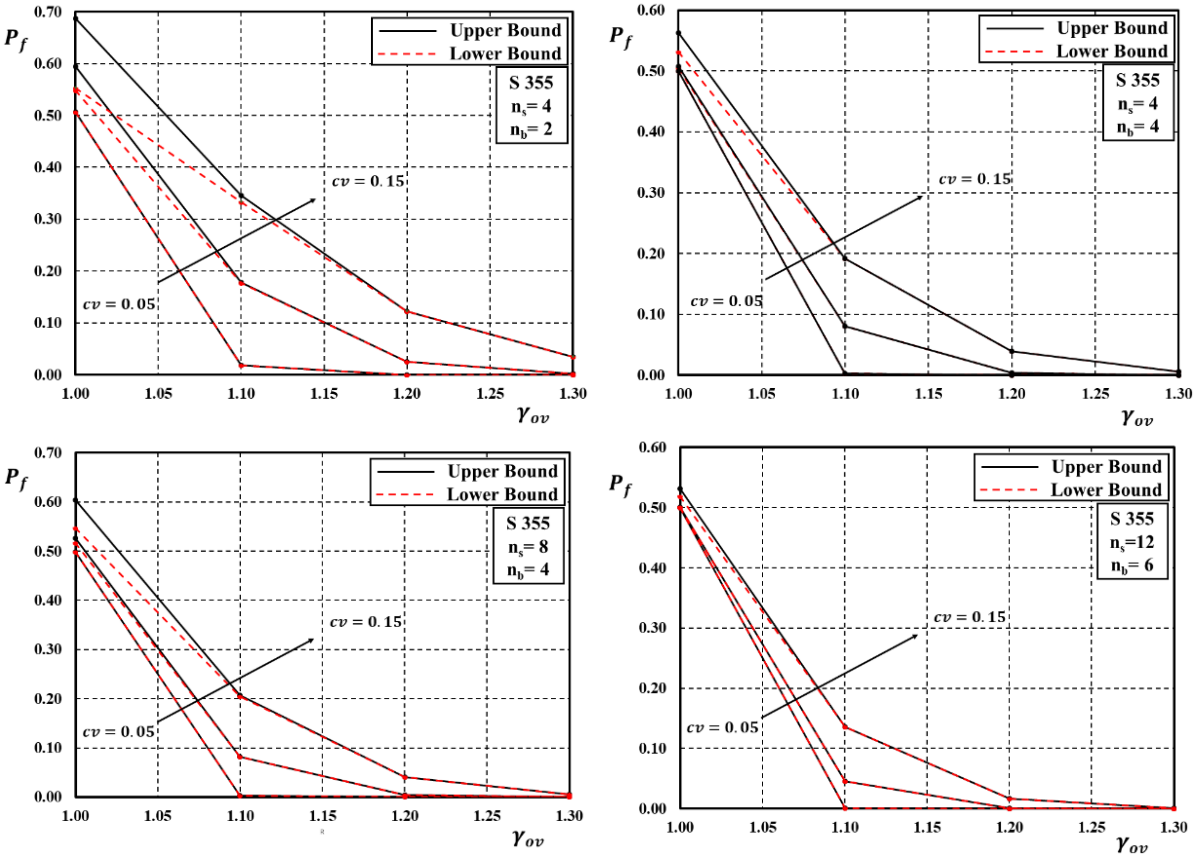

Figure 6: Upper and Lower bound of the failure probability for steel grade S355.

6 DEFINITION OF MATHEMATIC RELATIONSHIP

A mathematical relation can be suggested to compute the overstrength factor to apply the deterministic version of TPMC for fixed reliability level. Starting from the parametric analysis, previously described, it was easy to observe:

1. both the upper and lower bounds of the failure probability increase as the coefficient of variation of the yield strength cov increase, independently of the overstrength factor adopted in the design.
2. Independently of the coefficient of variation, both the upper bound and the lower bound of the probability of failure decrease as the overstrength factor adopted in the design is increased.
3. The value of the overstrength factor γ_{ov} decreases when the number of bays n_b increases, for fixed values of the number of storeys n_s and the failure probability.
4. Finally, for fixed values of the failure probability, the coefficient of variation cov and the number of bays n_b, the overstrength factor γ_{ov} results is not very influenced by varying the steel grade and the number of storeys n_s.

For these reasons, a mathematical formula has been developed with reference only Upper Bound of failure probability and with fixed reliability level R ($R = 1 - P_f$). In Table 1, the overstrength values are reported for a different number of bays n_b and coefficient of variation cov for a fixed value of R equal to 95%:

	Number of bays " n_b"		
cov	2	4	6
0.05	1.1148	1.1104	1.1096
0.10	1.3334	1.3201	1.3152
0.15	1.3846	1.3432	1.3200

Table 1: Values of the overstrength factor for reliability level of 0.95.

In Eq. (17) the mathematical relationship is provided, while the coefficients C_i are reported in:

$$\gamma_{ov} = [C_1(n_b)^{C_2}](cov)^2 + [C_3(n_b)^{C_4}](cov) + (c_5 n_b + c_6) \quad (17)$$

C_1	C_2	C_3	C_4	C_5	C_6
-34.2282	0.0502	9.8668	-0.012	0.0024	0.7075

Table 2: Coefficients of Eq.(17).

The comparison between the overstrength factor resulted by Eq. (17) and the values of γ_{ov} obtained by parametric analysis is provided in Figure 7. It is immediate observing that the accuracy of the mathematical formula proposed by the authors, is very high. The linear correlation coefficient R^2 is equal to 0.9977, while the standard deviation and the relative maximum error are equal respectively 0.0016. In the end, the corrective factor of regression has been computed at the 95% fractile, that is 1.0027.

7 CONCLUSIONS

- This work aims at the extension of the Probabilistic Theory of Plastic Mechanism Control (P-TPMC) for Steel Moment Resisting Frames (MRFs) to other steel grades
- Parametric analyses have been carried out starting from the Probabilistic version of Theory of Plastic Mechanism Control.

- The analyses were performed by varying the steel grade, the number of bays, number of storeys and the coefficient of variation of the stochastic variable.
- For a specific value of the reliability equal to 95%, a simple mathematical formula is defined to estimate the overstrength coefficient to apply to the deterministic version of TPMC, considering the material randomness.

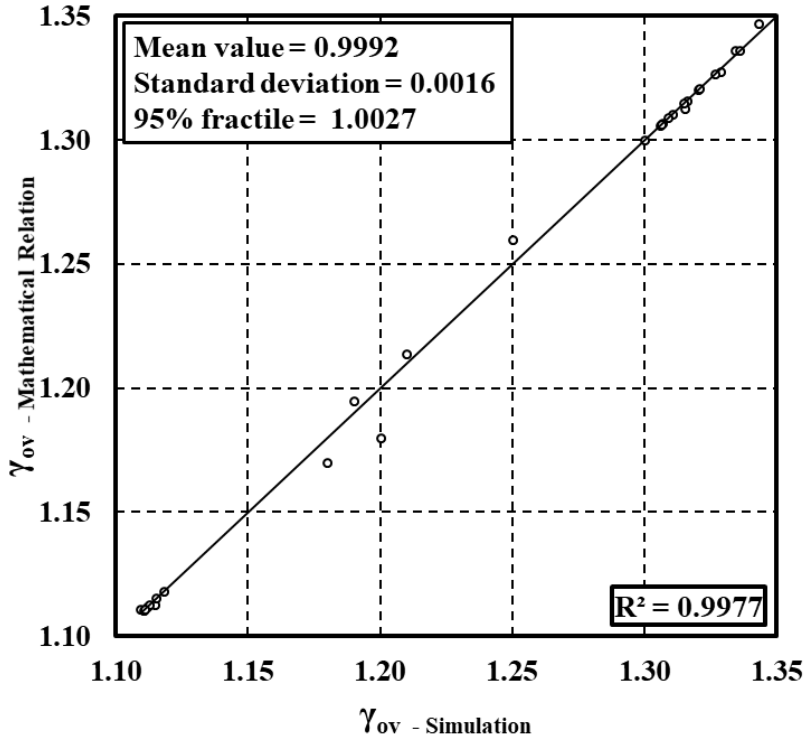

Figure 7: Accuracy of the relationship proposed for evaluating the overstrength factor.

REFERENCES

[1] CEN (2005) EN 1998-1-1: Eurocode 8 - Design of Structures for Earthquake Resistance. Part 1: General Rules, Seismic Actions and Rules for Buildings, Comite Europeen de Normalisation, CEN/TC 250.

[2] ANSI/AISC 341-10, "Seismic Provisions for Structural Steel Buildings", American Institute of Steel Construction, Chicago, IL, 2010.

[3] F.M. Mazzolani, V. Piluso, Plastic design of seismic resistant steel frames, *Earthquake Engineering and Structural Dynamics*, **26**, pp. 167-191, (1997).

[4] A. Longo, E. Nastri, V. Piluso, Theory of plastic mechanism control: State-of-the-art, *Open Construction and Building Technology Journal*, **8**, Pages 262-278, (2014).

[5] V. Piluso, E. Nastri, R. Montuori, "Advances in Theory of Plastic Mechanism Control: Closed Form Solution for MR-Frames", *Earthquake Engineering and Structural Dynamics*, **44**, Issue 7, Pages 1035-1054, (2015).

[6] R. Montuori, E. Nastri, V. Piluso, "Theory of Plastic Mechanism Control for MRF-EBF dual systems: Closed form solution", Volume **118**, *Engineering Structures*, Pages 287-306, (2016).

[7] V. Piluso, R. Montuori, E. Nastri, A. Paciello, "Seismic response of MRF-CBF dual systems equipped with low damage friction connections" *Journal of Constructional Steel Research*, **154**, pp. 263-277, (2019).

[8] Nastri, E., D'Aniello, M., Zimbru, M., Streppone, S., Landolfo, R., Montuori, R., Piluso, V. "Seismic response of steel Moment Resisting Frames equipped with friction beam-to-column joints" *Soil Dynamics and Earthquake Engineering*, **119**, pp. 144-157, (2019).

[9] G. Dell'Aglio, R. Montuori, E. Nastri, V. Piluso, "A critical review of plastic design approaches for failure mode control of steel moment resisting frames" *Ingegneria Sismica*, **34** (4), pp. 82-102, (2017).

[10] R. Montuori, E. Nastri, V. Piluso, "Influence of the bracing scheme on seismic performances of MRF-EBF dual systems" *Journal of Constructional Steel Research*, **132**, pp. 179-190, (2017).

[11] R. Montuori, E. Nastri, V. Piluso, M. Troisi, "Influence of connection typology on seismic response of MR-Frames with and without 'set-backs'" *Earthquake Engineering and Structural Dynamics*, **46** (1), pp. 5-25, (2017).

[12] Montuori, R., Sagarese, V. "The use of steel rbs to increase ductility of wooden beams" *Engineering Structures*, **169**, pp. 154-161, (2018).

[13] R. Montuori, E. Nastri, V. Piluso, "Theory of Plastic Mechanism Control for MRF-EBF dual systems: Closed form solution" *Engineering Structures*, **118**, pp. 287-306, (2016).

[14] E. Nastri, "Eccentrically braced frames designed for the energy dissipation optimization" *ECCOMAS Congress 2016 - Proceedings of the 7th European Congress on Computational Methods in Applied Sciences and Engineering*, **4**, pp. 8476-8491, (2016).

[15] A. Longo, R. Montuori, E. Nastri, V. Piluso, "On the use of HSS in seismic-resistant structures" *Journal of Constructional Steel Research*, **103**, pp. 1-12, (2014).

[16] R. Montuori, R. Muscati, "A general design procedure for failure mechanism control of reinforced concrete frames", *Engineering Structures*, **118**, pp. 137-155, (2016).

[17] V. Piluso, A. Pisapia, P. Castaldo, E. Nastri, "Probabilistic Theory of Plastic Mechanism Control for Steel Moment Resisting Frames" *Structural Safety*, **76**, pp. 95-107(2019).

[18] P. Castaldo, E. Nastri, V. Piluso, A. Pisapia, "Stochastic Approach for Theory of Plastic Mechanism Control", *XXIII Conference AIMETA 2017*, September 4–7, 2017, Salerno, Italy.

[19] P. Castaldo, E. Nastri, V. Piluso, A. Pisapia, Stochastic Theory of Plastic Mechanism Control: Parametric analysis, *XXIII Conference AIMETA 2017*, September 4–7, 2017, Salerno, Italy.

[20] L. Fiorino, V. Macillo, R. Landolfo, "Shake table tests of a full-scale two-story sheathing-braced cold-formed steel building" *Engineering Structures*, Elsevier Science. ISSN 0141-0296, **151**, pp. 633–647, (2017).

[21] L. Fiorino, M.T. Terracciano, R. Landolfo, "Experimental investigation of seismic behaviour of low dissipative CFS strap-braced stud walls". *Journal of Constructional Steel Research*, Vol. **127**, pp. 92-107, (2016).

[22] V. Macillo, L. Fiorino, R. Landolfo, "Seismic response of CFS shear walls sheathed with nailed gypsum panels: Experimental tests" *Thin-Walled Structures*. Vol. **120**, pp. 161-171, (2017).

[23] V. Macillo, O. Iuorio, M.T. Terracciano, L. Fiorino, R. Landolfo, "Seismic response of Cfs strap-braced stud walls: Theoretical study" *Thin-Walled Structures*, Vol. **85**, pp. 301-312, (2014).

[24] Y. Wang, E. Nastri, L. Tirca, R. Montuori, V. Piluso, "Comparative response of earthquake resistant CBF buildings designed according to Canadian and European code provisions" *Key Engineering Materials*, **763**, pp. 1155-1163, (2018).

[25] C.Bernuzzi, C. Chesi, D. Rodigari, R. De Col, "Remarks on the approaches for seismic design of moment-resisting steel frames" *Ingegneria Sismica*, **35** (2), pp. 37-47, (2018).

[26] M.A. Aiello, P.L. Ciampoli, A. Fiore, D. Perrone, G. Uva, "Influence of infilled frames on seismic vulnerability assessment of recurrent building typologies" *Ingegneria Sismica*, **34** (4), pp. 58-80, (2017).

[27] R. Montuori, E. Nastri, V. Piluso, "Preliminary analysis on the influence of the link configuration on seismic performances of MRF-EBF dual systems designed by TPMC" *Ingegneria Sismica*, **33** (3), pp. 52-64, (2016).

[28] R. Montuori, E. Nastri, V. Piluso, M. Troisi, "Influence of the cyclic behaviour of beam-to-column connection on the seismic response of regular steel frames" *Ingegneria Sismica*, **33** (1-2), pp. 91-105, (2016).

[29] L. Mastrandrea, E. Nastri, V. Piluso, "Validation of a design procedure for failure mode control of EB-Frames: Push-over and IDA analyses" *Open Construction and Building Technology Journal*, **7**, pp. 193-207, (2013).

[30] O.V. Ditlevsen, Narrow reliability bounds for structural systems", *Journal of Structural Mechanics*, **7**, No. **4** (1979), pp. 453-472, (1979).

[31] S. Krishnan, M. Muto, Mechanism of collapse of Tall Steel Moment-Frame Buildings under Earthquake Excitation, *Journal of Structural Engineering*, ASCE, **138**,1361-1387, (2012).

[32] P.E. Pinto, R. Giannini, P. Franchin, "Seismic Reliability Analysis of Structures", IUSS Press, (2004).

[33] C.A. Cornell, "A Probability-Based Structural Code", *ACI-Journal*, **66**, 1969, pp. 974-985, (1969).

COMPDYN 2019
7th ECCOMAS Thematic Conference on
Computational Methods in Structural Dynamics and Earthquake Engineering
M. Papadrakakis, M. Fragiadakis (eds.)
Crete, Greece, 24–26 June 2019

A SLAMA-BASED ANALYTICAL PROCEDURE FOR THE COST/PERFORMANCE-BASED EVALUATION OF BUILDINGS

Simona Bianchi[1], **Jonathan Ciurlanti**[1], **and Stefano Pampanin**[1]

[1] Sapienza University of Rome
Department of Structural and Geotechnical Engineering, Via Eudossiana 18, 00184, Rome, Italy
simona.bianchi@uniroma1.it,
jonathan.ciurlanti@uniroma1.it, stefano.pampanin@uniroma1.it

Abstract

The decision-making process for seismic risk is affected by the assessment/design procedure adopted and rigorous methodologies have been developed to estimate performance metrics relevant to stakeholders to take informed decisions. Input data for loss estimations of buildings are typically floor accelerations and inter-storey drift ratios, generally obtained from: 1) simplified evaluations, based on linear models and static analysis, 2) more accurate non-linear static analyses, or 3) more complex and time-consuming non-linear history analyses.
Considering that non-linear static analyses are arguably the best compromise between accuracy and simplicity, this paper proposes the application of an analytical non-linear static procedure, based on the Simplified Lateral Mechanism Analysis (SLaMA) of the NZSEE 2017 Guidelines, for the cost/performance-based evaluation of Reinforced Concrete structures. In order to validate the accuracy of the method, multi-storey case-study buildings are analyzed using different structural analysis methods (the proposed SLaMA-based approach vs. numerical Pushover vs. Time-History) and through sophisticated or simplified loss assessment methodologies (FEMA P-58, 2012; D.M. n.65, 2017).
The results in terms of Expected Annual Losses from the SLaMA-based approach are quite satisfactory - increase of 7-18% or 3-7% compared to numerical Pushover results from probabilistic or simplified loss estimations, increase of 20-40% compared to numerical Time-History results - and, in general, more accurate than static analyses results, even though no numerical modelling is needed. Therefore, the SLaMA-based method can be a promising tool for a daily use of practicing engineers for a rapid evaluation of economic losses for both the seismic assessment of existing buildings and the initial feasibility studies of new structures.

Keywords: Cost/performance-based, SLaMA procedure, Pushover analysis, Time-history analysis, Expected Annual Losses.

1 INTRODUCTION

Seismic design philosophy is based on controlling the building response under low-to-high intensity earthquakes, including either structural and non-structural components. Traditionally the design aimed to prevent the damage of these elements under low-intensity earthquakes, to reach repairable conditions in medium-intensity shakings and to avoid building collapse under high-intensity earthquakes. However, past earthquakes (e.g. Northridge 1994 and Kobe 1995, confirmed by more recent events such as Christchurch earthquake 2010-2011) highlighted very high economic losses in terms of repair costs and business interruption even for code-compliant buildings, leading in the mid-1990s to the development of the performance-based earthquake engineering (PBEE) concept [1, 2].

Vision 2000 [3] is one of the first documents where there is evidence of this new philosophy. Different structural and non-structural performance levels at various intensity demands (frequent, occasional, rare, and very rare) are described and classified as fully operational, operational, life safety, and near collapse, thus design objectives for building typologies are identified through the combination of performance levels and seismic hazard. Following this original concept, a series of additional documents were published considering the same design philosophy and representing the first generation of PBEE [4, 5, 6]

Nevertheless, the initial PBEE procedures were deterministic-based and affected by many shortcomings, such as the relations between engineering demand and component performance based on relations measured from laboratory tests or assumed considering engineering judgement [7]. Therefore, a more rigorous and probabilistic methodology was developed by the Pacific Earthquake Engineering Research (PEER) Center and its framework is summarized in Figure 1.

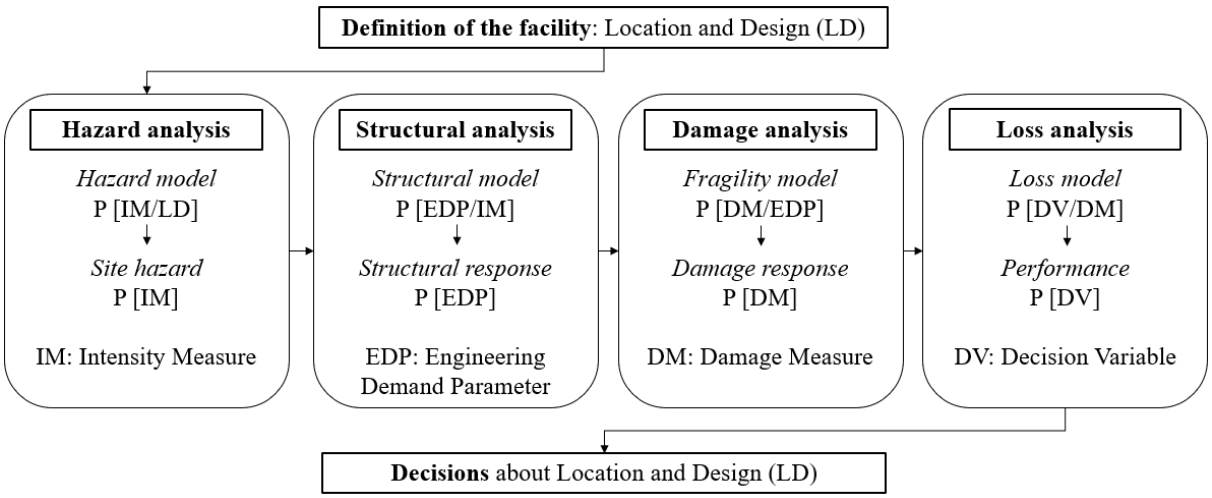

Figure 1: Performance-Based Earthquake Engineering (PBEE) methodology (modified after [8]).

The PEER methodology allows the direct evaluation (estimation) of performance measures such as economic losses, downtime and casualties that are relevant to stakeholders to manage decisions about seismic risk mitigation. The comprehensive framework includes the description, definition and qualification of different variables considering all the inherent uncertainties in the earthquake performance assessment. The process starts with the definition of the ground motion hazard (*Intensity Measure*) which affects the structural response, then the building structural response can be evaluated in terms of accelerations, deformations or other quantities (*Engineering Demand Parameter*). Finally, the system response is related to the

damage of each building component (*Damage Measure*) and the damage is transformed into quantities useful for decision-making processes (*Decision Variable*).

For the practical implementation of the probabilistic procedure, the US Federal Emergency Management Agency (FEMA) commissioned to the Applied Technology Council (ATC) the development of an electronic tool to apply this methodology, referred to as Performance Assessment Calculation Tool (PACT) and provided with the publication of the FEMA P-58 Document [9].

The application of the PBEE procedure is primary for the seismic loss evaluation of new buildings as well as for taking decisions on intervention/retrofit strategies of existing structures, particularly in the initial feasibility studies of the building/intervention. However, the fully probabilistic procedure can be time-consuming in its implementation, because it also requires the definition of numerical models to evaluate the building response through non-linear static and dynamic analyses. For this reason, this paper presents the application of an analytical procedure for non-linear static analysis, based on the Simplified Lateral Mechanism Analysis (SLaMA) of the NZSEE 2017 Guidelines, that can be rapidly implemented providing acceptable results for the loss estimation and can thus be a promising tool for a daily use of engineers for a rapid yet quite reliable initial evaluation of the post-earthquake losses.

2 EVALUATION OF BUILDING RESPONSE

Structural analysis is conducted to determine the building response to earthquake shaking, obtaining values for those key parameters that are predictive of structural and non-structural damage, such as floor accelerations, floor velocities, story drift ratios and residual drift ratios.

Alternative procedures can be used to estimate the peak values of these parameters: 1) *simplified procedures*, which consider linear models and static analyses to estimate the lateral yield strength and generate median demand values, thus determining the building response at each floor through simplified and numerically calibrated formulas; 2) *non-linear static analyses*, which allow the definition of the building capacity curve from numerical modelling as well as the performance points for the various seismic intensity (i.e. Capacity Spectrum Method), giving more accurate predictions than the previous ones; 3) non-linear response (time) history analysis, that is the most sophisticated method, where the structure is numerically modelled in its full non-linear cyclic and dynamic behavior, sets of demand parameters are generated from sets of earthquake input motions and are used to develop statistics (median values and dispersions) for each parameter of interest. Among all the aforementioned analysis methods, the non-linear static procedures (pushover) are the best compromise between accuracy and simplicity.

In the recently developed New Zealand Seismic Assessment Guidelines [10] an analytical non-linear static analysis procedure has been proposed for the seismic assessment of reinforced concrete existing buildings, the Simplified Lateral Mechanism Analysis (SLaMA), that is shown schematically in Figure 2. This assessment method, mandatory for every assessment prior to carry out any numerical modeling, is able to predict the building capacity curve (pushover) through an analytical study that, starting from the local section and member analysis and through the hierarchy of strengths evaluation of subassemblies, evaluate the local and global building mechanisms.

Notwithstanding the SLaMA procedure has been primarily implemented for the assessment existing structures, in this paper the method is applied, for the sake of simplicity, to rapidly estimate the seismic response of new reinforced concrete buildings, because it can be very useful for initial feasibility studies. The proposed simplified loss-assessment method based on a SLaMA approach, can be however used and properly exploited for either assessing existing structures and comparing alternative retrofit strategies.

In the case of a new building, the procedure can be modified and simplified as follows: 1) in terms of input data, the building characteristics are not already available but obtained from a preliminary building design that aims to already respect the hierarchy of strengths determining a final beam-sidesway mechanism, as required by the seismic codes; 2) the capacity curve of such type of building mechanism is analytically determined considering the results from the section analysis evaluation; 3) finally, introducing the capacity curve into the Acceleration-Displacement Response Spectra and combining it with the demand spectra, the expected maximum accelerations and displacements at different seismic intensities can be determined.

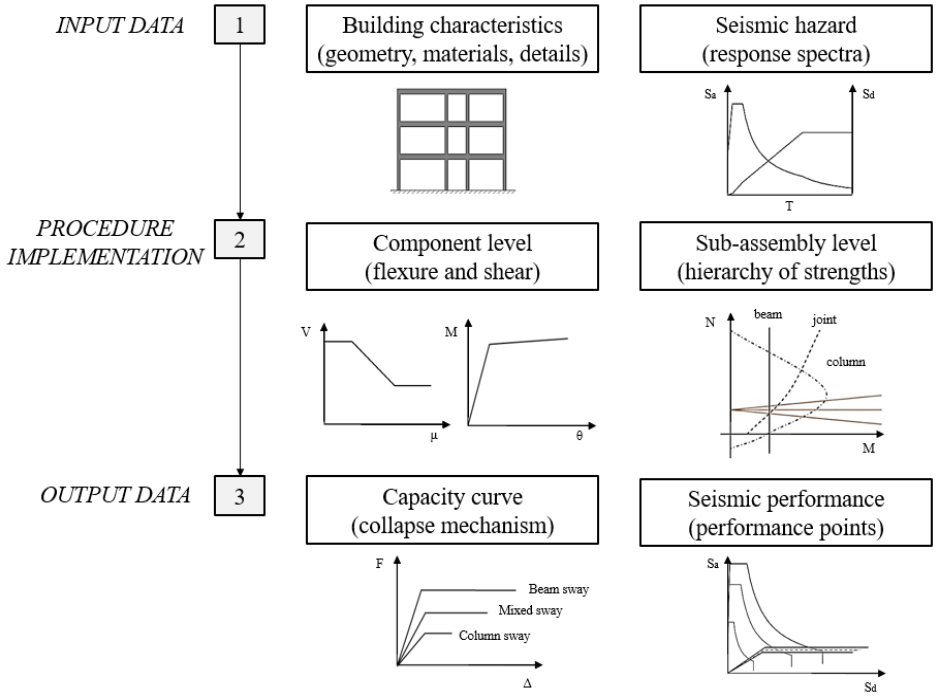

Figure 2: Framework of the SLaMA assessment procedure for reinforced concrete buildings.

3 RESEARCH MOTIVATION

In the current international seismic codes, the building design aims to guarantee the Life-Safety performance objective. However, as the reliability of design and construction practice in meeting this goal has improved, there has been an increasing demand for engineers to provide building design capable of reducing both damage and business interruption [11] and new tools able to determine these parameters in the philosophy of the performance-based earthquake engineering have been developed.

Apart from the seismic assessment process of existing buildings, the need for loss estimation in the common design process is starting to spread, therefore practical and efficient tools must be developed to be used by engineers. As alternative to more sophisticated procedures based on non-linear dynamic analyses, as previously described, more rapid estimations of post-earthquake losses can be determined through non-linear static (pushover) evaluations, especially as part of an initial feasibility study of the building design features.

This paper proposes the application of an analytical non-linear static analysis procedure, based on the Simplified Lateral Mechanism Analysis (SLaMA), for a rapid evaluation of post-earthquake losses of buildings without the need of more complicated numerical models.

A set of multi-storey case-study buildings is considered to apply and validate the proposed procedure, as described below.

4 VALIDATION OF THE SLAMA-BASED ANALYTICAL PROCEDURE

Cost/performance evaluations are implemented for a set of multi-storey buildings considering different approaches: the proposed SLaMA-based analytical procedure and numerical analyses through both non-linear Push-Over and Time-History analyses.

The numerical investigations are implemented with the aim of validating the analytical approach and confirming whether acceptable results in terms of economic losses can be expected from the SLaMA evaluation when compared to more sophisticated numerical results.

4.1 Description of the case-study buildings

The procedure is implemented considering four 5-storeys monolithic reinforced concrete buildings located in a high seismic zone in Italy (Soil type C, PGA of 0.35 g at the Life-Safety Limit State). The benchmark case-study structure has a plan configuration of 32m x 18 m, inter-storey height of 3.8 m; the building has commercial use for the first two floors, residential use for the other two floors, while the top floor is a roof. Lateral resistance against seismic action is provided by two seismic resistant four-bay frames in the longitudinal direction and two shear walls in the transverse direction. The other buildings are derived from the initial case-study structure (*Case1*) by varying: the beam span length in both seismic directions (*Case2*); the inter-storey height to 4.5 m (*Case3*); both the beam span length and the inter-storey height (*Case4*). Figure 3 presents the plan view of the benchmark building (Plan1) and its variation (Plan2), while all the case-study structures are summarized in Figure 4.

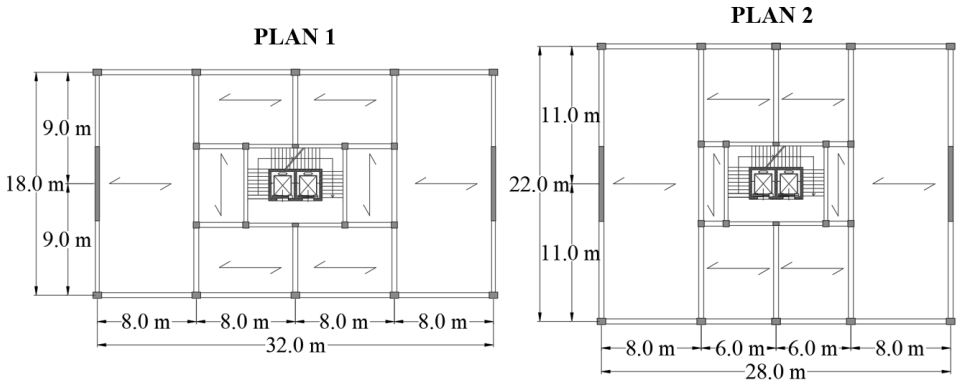

Figure 3: Plan view and dimensions of the benchmark building (left) and modified plan (right).

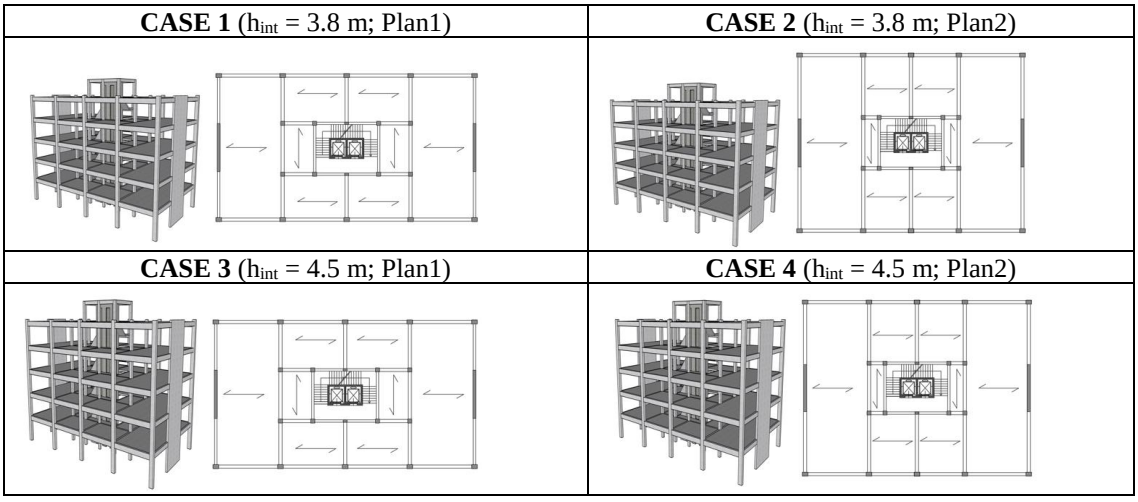

Figure 4: Case-study buildings.

In terms of dimensions of the structural members: the seismic beams and columns have same dimensions for both building plan (400 x 700 mm and 500 x 700 mm, respectively); while the wall is 6 m long, but its thickness varies depending on the plan configuration (350 mm for Plan1 and 400 mm for Plan2). Finally, the gravity beams connecting the wall are 300 x 600 mm and 400 x 700 mm, respectively for Plan 1 and Plan 2.

4.2 Building design

Referring to this structural scheme, geometry and related gravity loads, all the buildings are designed following the Direct Displacement Based Design (DDBD) procedure by [12, 13]. The DDBD procedure has been performed at the ULS limit state (Life-Safety) considering an appropriate value for the inter-storey drift limit, i.e. 2% for the frame direction and 1.2% for the wall direction for all case-study structures.

Table 1 shows the DDBD results for all the buildings in terms of yielding displacement (Δ_y), design displacement (Δ_d), effective mass (m_e), effective height (H_e), equivalent viscous damping (ξ_{eq}), effective period (T_e), effective elastic stiffness (K_e), and base shear (V_b).

Parameter	Case 1		Case 2		Case 3		Case 4	
	Frame	Wall	Frame	Wall	Frame	Wall	Frame	Wall
Δ_y [mm]	62.17	50.29	62.15	50.26	73.38	70.14	73.36	70.10
Δ_d [mm]	223.80	163.19	223.74	163.13	264.36	192.63	264.28	192.56
m_e [t]	2760.15	2627.80	2914.20	2774.46	2834.12	2698.27	2991.83	2848.42
H_e [m]	13.24	13.60	13.24	13.60	15.63	16.05	15.62	16.05
ξ_{eq} [%]	19.19	18.35	19.19	18.35	19.19	16.90	19.19	16.90
T_e [s]	2.65	1.91	2.65	1.91	3.13	2.22	3.13	2.21
K_e [kN/m]	15533.5	28383.0	16409.6	29987.5	11429.8	21705.3	12072.43	22928.2
V_b [kN]	3476.42	4631.94	3671.44	4891.99	3021.56	4181.03	3190.55	4415.01

Table 1: Parameters from the DDBD procedure for all the case-study buildings.

Distributing the base shear obtained by the DDBD throughout each structure, the internal actions in the structural members are determined, and the required steel reinforcement of each component can be designed.

4.3 Building seismic response

The building response is initially estimated through the SLaMA procedure described in the NZSEE 2017 Seismic Assessment Guidelines [10]. The seismic design considers capacity design principles, therefore it is sufficient to evaluate the capacity curves related to the beam-sway mechanism. In Figure 5 the so-obtained analytical capacity curves are presented for each building and structural direction. The ultimate limit state represents the achievement of the displacement corresponding to the first element reaching the ultimate rotational capacity.

Converting the base shear/displacement relationships into acceleration/displacement responses and considering the demand spectra from the Italian Code [14] of either elastic or ultimate limit states, the building performance points at each intensity level can be identified in the Acceleration Demand Response Spectrum (ADRS) domain. The demand spectra of the ultimate limit states (life-safety SLV and near collapse SLC) have been reduced considering the area-based equivalent viscous damping evaluated through the formulation proposed by Priestley in 2007 [12].

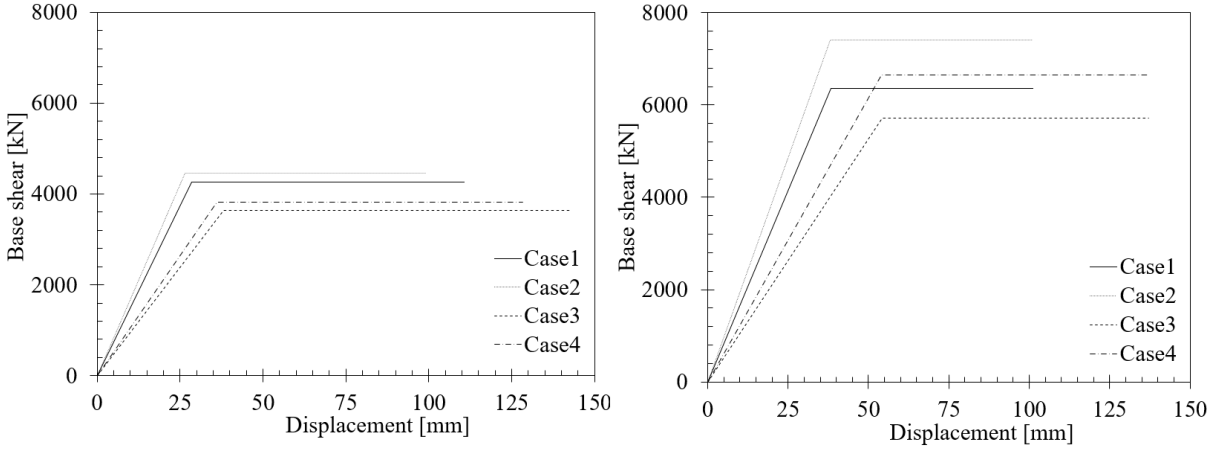

Figure 5: SLaMa-based non-linear (analytical) pushover capacity curves for the case-study buildings. Left: frame direction; Right: wall direction

The SLaMA capacity curves are compared to those obtained from numerical non-linear static analyses. The numerical models of each building are implemented using Ruaumoko 2D analysis program [15] through a lamped-plasticity approach. Therefore, the structural members are represented by elastic components where the non-linearity is concentrated within plastic hinge regions at the end sections (Giberson elements). The plastic hinges are described using proper moment-curvature relationships and a Takeda stiffness-degrading hysteresis rule.

Applying the Capacity Spectrum Method [16], where the area-based equivalent viscous structural damping is directly evaluated from push-pull analyses, the performance points can be also evaluated for this analysis approach.

As example, in Figure 6 can be found a comparison between the push-over curves and performance points obtained from both the analytical and numerical methods.

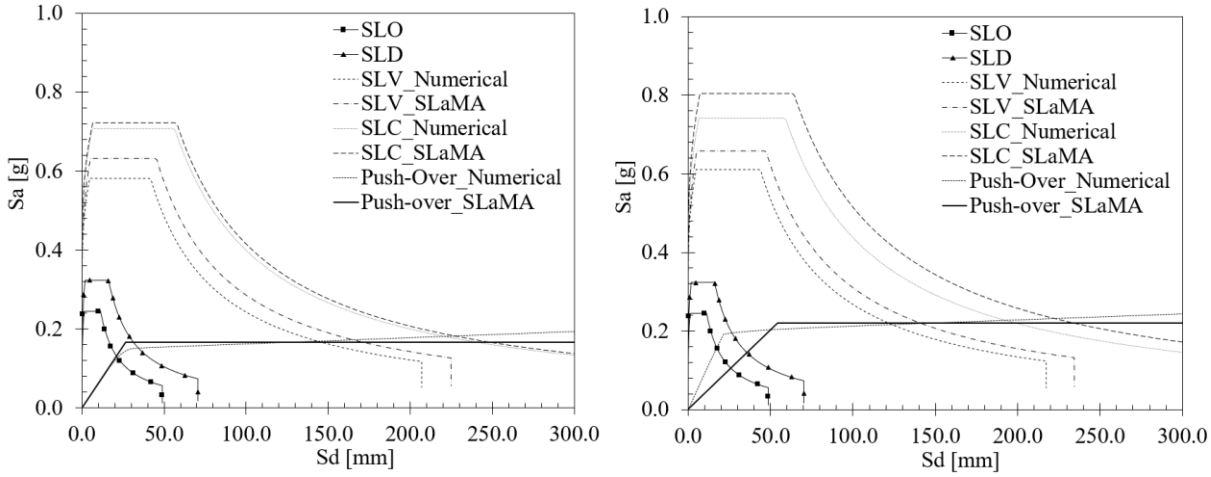

Figure 6: Analytical and numerical capacity curves in the ADRS domain for the *Case2* considering both frame (left) and wall (right) directions.

It can be observed from the previous graphs that the analytical curves well predict the building seismic behavior. The two analyses methods produce very similar performance points for all the case study-buildings in the frame directions, apart from the collapse limit state because of the increasing slope of the numerical curve and the inherent limit of the analytical curve itself which is not modeling the collapse point. Regarding the wall directions, the main differences in the performance points are obtained for the lower limit states (fully opera-

tional and operational) because of the modeling of the wall as equivalent frame which produces a very high initial stiffness when compared to the one from the analytical procedure.

In order to further validate the accuracy of the SLaMA method as a loss-modeling simplified procedure, non-linear time history analyses are also performed using sets of 7 accelerograms obtained from REXEL [17] for each seismic intensity. The accelerograms, extrapolated from the European Strong Motion database, are, thereby, properly scaled to guarantee the spectro-compatibility to each demand spectrum. For the Life-Safety intensity level, Figure 7 presents the response spectra related to the 7 accelerograms, the average and target spectra, the lower and upper tolerances, as well as the range of periods (0.15 s ÷ 2 s) selected for the spectro-compatibility to be satisfied.

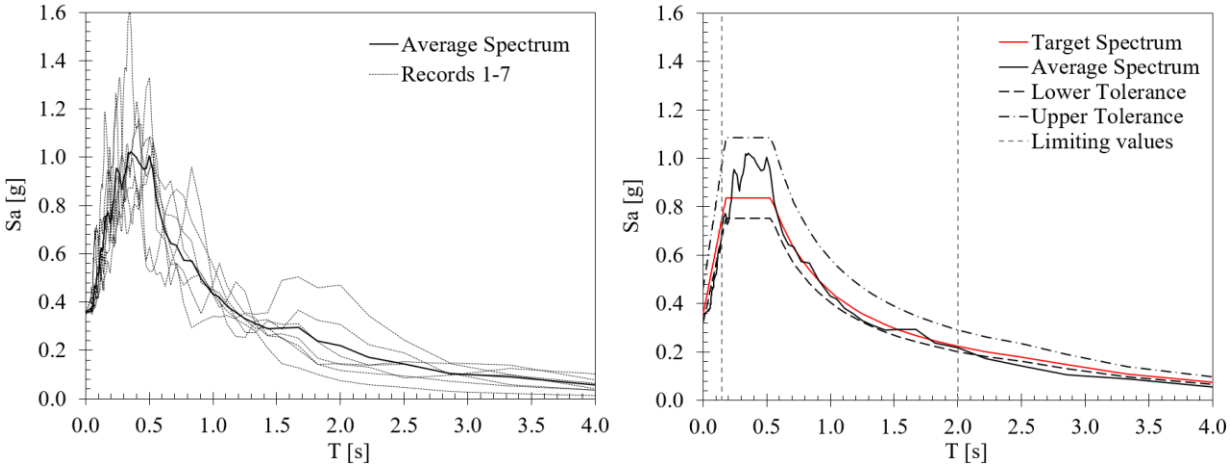

Figure 7: Spectro-compatibility at Life-Safety intensity level.

From time-history analyses a direct estimation of the floor accelerations and inter-storey drift ratios can be determined. As example, the results are presented for one case-study structure and one seismic intensity level in Figure 8. These key engineering demand parameters (EDPs) can be used as direct input data for the loss assessment investigations, while for the analytical and numerical non-linear static assessments they are estimated from the performance points, representing the behavior of the equivalent SDOF system, at each seismic intensity. In fact, considering the effective building height the EDPs at each floor can be estimated assuming proper displacement and acceleration profiles for the SLaMA procedure or the exact profiles determined from the numerical Push-Over results.

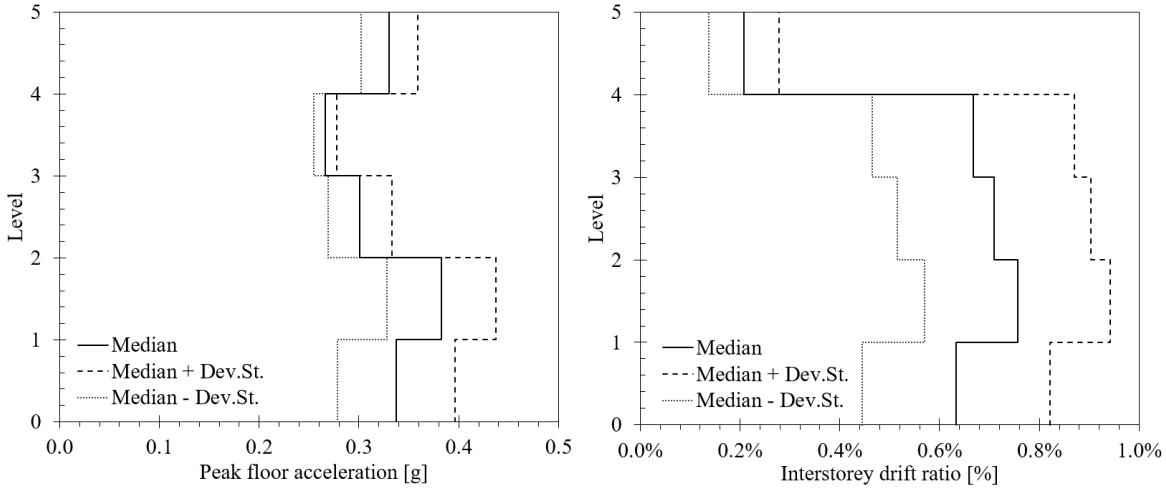

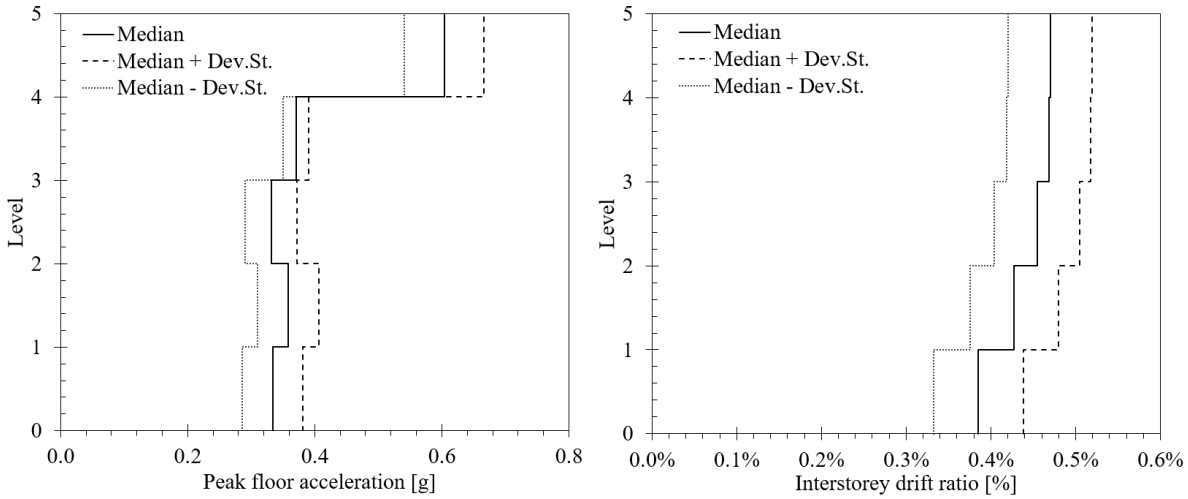

Figure 8: Time-history results for the Life-Safety demand level of *Case2*: peak floor acceleration and inter-storey drift ratio profiles for both building directions.

4.4 Loss assessment investigations: SLaMA vs numerical Pushover

Loss assessment estimations are performed using the PACT software [9] where all the case-study buildings are implemented. The input data for the analysis are: 1) the total replacement cost and time, calculated referring to 338 euro/m^3 and estimating the proper number of man-days; 2) the population model of the building, provided by the software depending on the building use; 3) the component fragilities, considering all the structural members, non-structural components, building services and contents present into the building; 4) the seismic building response, estimated using the different structural analyses methods; 5) finally, the seismic hazard, whose function is built referring to the demand intensity levels reported in the Italian Code [14] (T_R=30 years, fully operational; T_R=50 years, operational; T_R=475 years, life-safety; T_R=975 years, near collapse). Regarding the non-structural systems, it is assumed that all the structural skeletons are covered by external curtain walls, while interior components include lightweight partitions, suspended ceilings, electrical and mechanical services and contents. All the structural and non-structural components are defined using the fragility curves and consequence functions already available in the fragility database.

The results obtained for all the case-study buildings are reported in Figure 9 and Table 2.

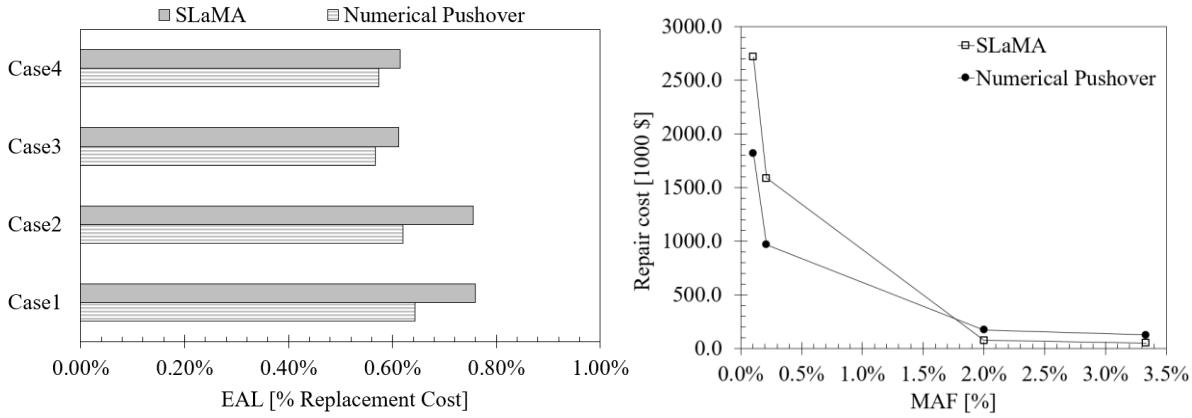

Figure 9: EAL values for all the four case-study buildings considering different structural analysis results (left) and Repair cost/Median Annual Frequency functions (right) for one case-study structure (*Case 2*).

	Case 1	Case 2	Case 3	Case 4
EAL $_{SLaMA}$ [%RC]	0.759	0.755	0.612	0.614
EAL $_{PO}$ [%RC]	0.644	0.621	0.567	0.573
ΔEAL $_{SLaMA/\ PO}$	15.16	17.79	7.31	6.70

Table 2: EAL values from non-linear static analyses results: SLaMA versus numerical Pushover (PO).

The loss estimations are carried out considering the floor accelerations and inter-storey drift ratios from: 1) for the SLaMA approach, these parameters are evaluated assuming a proper displacement profile for the building beam-sway mechanism, as suggested in NZSEE Guidelines [10], and considering the floor acceleration profile proposed by FEMA P-58 [9] for simplified procedures, 2) for the numerical analysis, the floor accelerations and inter-storey drift ratios are determined from the performance points considering both the displacement and acceleration profiles resulting from the numerical investigation. All the loss estimations have been performed, in this initial validation of the SLaMA procedure, without including the effects of the building collapse fragility or the residual drift into the results.

It can be observed that the application of SLaMA gives quite satisfactory results in terms of Expected Annual Losses (EAL) when compared to the results obtained from the numerical investigations, i.e. approximately 7-18% higher (conservative side).

Estimations of direct economic losses are also developed through the simplified procedure presented in the 2017 Italian Guidelines for Seismic Risk Classification [18]. This document describes a simple methodology to determine the expected annual losses, that is generally applied for the seismic assessment of existing buildings to investigate the benefits of retrofit strategies and regulate financial incentives provided to private owners to improve the risk/losses of their building. In this research the same approach is applied to new buildings. The building analytical and numerical capacity curves are the starting points of this procedure, which requires the determination of the median annual frequencies, MAF, associated to the achievement of specific limit states in the structure. Particularly, in this study, two limit states (Damage Control and Life-Safety) are identified taking into account just the structural behaviour (achievement of yielding and ultimate rotations of structural members) and used to estimate other limit states related to the structural and non-structural system, as explained in the Guidelines [18].

The results from this simplified methodology are presented in Figure 10 and Table 3.

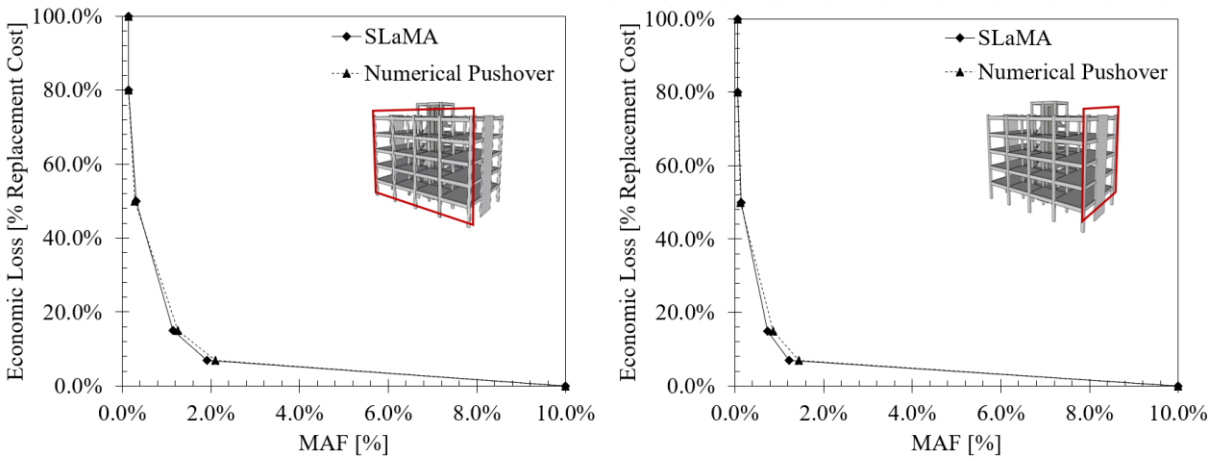

Figure 10: Economic loss/Median Annual Frequency functions estimated following the Italian Guidelines for Seismic Risk Classification [18] for *Case 2* and both building directions referring to the capacity curves obtained from SLaMA or numerical studies.

	Case 1		Case 2		Case 3		Case 4	
	X Dir.	Y Dir.	X Dir.	Y Dir.	X Dir.	Y Dir.	X Dir.	Y Dir.
EAL_{SLaMA} [%RC]	0.810	0.717	0.892	0.669	0.789	0.631	0.865	0.595
EAL_{PO} [%RC]	0.872	0.749	0.920	0.704	0.849	0.648	0.891	0.623
$\Delta EAL_{PO/SLaMA}$	7.17	4.22	2.99	4.94	7.27	2.68	2.91	4.49

Table 3: EAL (as a percentage of the Replacement Cost, RC) values from the simplified procedure [18] using the building capacity curves from analytical (SLaMA) and numerical (PO) Pushover analyses.

As it can be observed from the previous table, the differences between the EAL values from the SLaMA-based approach and numerical analysis are minor, in the range of 3-7% for both building directions. It is also noticed that the EALs associated to the numerical Pushover curves are now higher than those derived from the simplified SLaMA procedure, thus it seems that the estimation is not on the conservative side. This can be justified considering that the elastic and ultimate limit state points are identified on the numerical capacity curves respectively for lower and greater accelerations compared to the same points on the simplified elasto-plastic capacity curves. In any case, the differences are relatively low and well acceptable, thus the SLaMA method can be considered a valuable alterative tool to numerical methods for an initial cost-based building evaluation.

4.5 Loss assessment investigations: SLaMA vs Pushover vs Time-history

Loss assessment investigations are finally performed using the results from the time-history non-linear analyses, therefore the peak floor accelerations and inter-storey drift ratios from all the 7 records of each seismic intensity are directly introduced in the PACT software.

Figure 11 and Table 4 summarize the EAL values obtained from all the structural analysis procedures (analytical push-over, numerical push-over, time-history).

The percentage difference between the EAL values from SLaMA approach and Time-History analysis is in the range of 20-40%, while between numerical Pushover and Time-History results a difference of 15-30% is estimated. Notwithstanding the differences between the EAL values from the simplified SLaMA procedure and the sophisticated Time-History investigation are in this case not negligible, the SLaMA method still produces acceptable results and, in any case, more accurate than those obtained when application of linear static analysis suggested within the FEMA P-58 methodology as an alternative simplified investigation compared to the non-linear response history analysis. This statement is based on parallel work being carried out and to be presented in a future companion research publication.

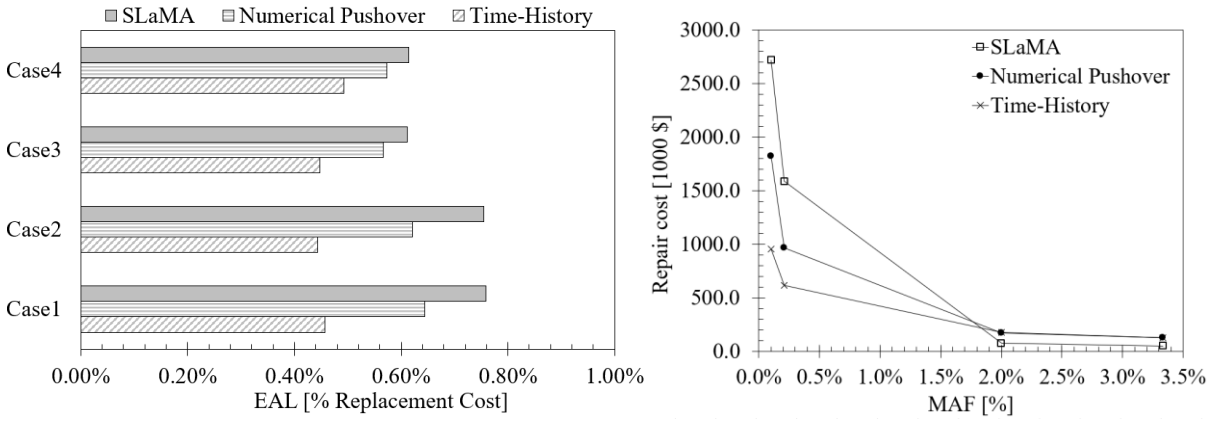

Figure 11: EAL values for all the four case-study buildings considering different structural analysis results (left) and Repair cost/Median Annual Frequency functions (right) for one case-study structure (*Case 2*).

	Case 1	Case 2	Case 3	Case 4
EAL_{SLaMA} [%RC]	0.759	0.755	0.612	0.614
EAL_{PO} [%RC]	0.644	0.621	0.567	0.573
EAL_{TH} [%RC]	0.457	0.444	0.447	0.493
$\Delta EAL_{SLaMA / PO}$	15.16	17.79	7.31	6.70
$\Delta EAL_{SLaMA / TH}$	39.76	41.18	26.84	19.75
$\Delta EAL_{PO / TH}$	28.98	28.44	21.07	14.02

Table 4: EAL values from different non-linear analyses results: SLaMA versus numerical Pushover (PO) versus Time-History (TH).

5 CONCLUSIONS

In the engineering community the estimation of performance metrics, such as repair costs or downtime, relevant to management decisions for seismic risk mitigation is becoming more consolidated not only for the assessment of existing buildings and thus for the evaluation of optimal retrofit strategy, but also in the seismic design of new buildings.

Probabilistic methodologies have been proposed to implement socio-economic loss estimations, which requires as input data engineering demand parameters, EDPs, such as floor accelerations and inter-storey drift ratios. The latter are usually obtained from simplified linear or non-linear analyses, requiring the implementation of simple or more-sophisticated numerical building models. The more complex the model the more accurate are typically expected to be the results in terms of seismic response, although very time-consuming modeling and analyses are required (i.e. Non-linear Time-History analyses).

With the aim of avoiding the implementation of un-necessary complex numerical models and knowing that non-linear static procedures are a very valuable compromise between accuracy and simplicity, the paper proposes the application of an analytical non-linear static analysis procedure, based on the Simplified Lateral Mechanism Analysis (SLaMA), for the cost/performance-based evaluation of buildings.

The Expected Annual Losses of four case-study reinforced concrete buildings are estimated referring to different structural analyses (SLaMA, numerical Pushover, Time-Histories) and loss assessment methodologies [9, 18]. The results highlighted that the SLaMA-based approach can provide satisfactory and acceptable results when compared to more complex numerical procedures. The method can be a promising tool for the daily use of practicing engineers for a rapid evaluation of the post-earthquake losses and it can be suggested both for the seismic assessment of existing buildings and retrofit interventions as well as part of the design feasibility study of new reinforced concrete structures.

Notwithstanding the good results obtained from this initial study, more investigations are needed to incorporate, for example, the building collapse limit states and the effects of residual drifts, which have been neglected in the loss estimations of this initial work.

6 REFERENCES

[1] C.A. Cornell, F. Jalayer, R.O. Hamburger, D.A. Foutch, Probabilistic basis for 2000 SAC Federal Emergency Management Agency steel moment frame guidelines. *ASCE Journal of Structural Engineering*, **128**, 4, 526-533, 2002.

[2] H. Krawinkler, E. Miranda, *Performance-based earthquake engineering. Earthquake Engineering: from engineering seismology to performance-based engineering*. Bertero VV (eds), CRC Press: Boca Raton, 2004.

[3] Structural Engineers Associate of California, *Performance-based seismic engineering*. SEAOC Vision 2000, Sacramento, California, USA, 1995.

[4] Applied Technology Council, *Seismic evaluation and retrofit of concrete buildings, Volume 1*. Technical Report ATC 40, Redwood City, California, USA, 1996.

[5] Federal Emergency Management Agency, *NEHRP Guidelines for Seismic Rehabilitation of Buildings*. FEMA-273, Building Seismic Safety Council, Washington, D.C, 1997.

[6] American Society of Civil Engineers, *FEMA 356 Prestandard and Commentary for the Seismic Rehabilitation of Buildings*. ASCE for the Federal Emergency Management Agency, Washington, D.C., 2000.

[7] J. Moehle and G. Deierlein, A framework methodology for performance-based earthquake engineering. *13th World Conference on Earthquake Engineering (13WCEE)*, Vancouver, B.C., Canada, August 1-6, 2003.

[8] K.A. Porter, An Overview of PEER's Performance-Based Earthquake Engineering Methodology. *9th International Conference on Applications of Statistics and Probability in Civil Engineering (ICASP9)*, San Francisco, California, USA, July 6-9, 2003.

[9] Federal Emergency Management Agency, *Seismic Performance Assessment of Buildings, Volume 1 – Methodology*. Technical Report FEMA-P-58-1, Washington, D.C., USA, 2012.

[10] New Zealand Society for Earthquake Engineering, *The Seismic Assessment of Existing Building – Technical Guidelines for Engineering Assessments*. NZSEE 2017, New Zealand, 2017.

[11] R.O. Hamburger, Implementing performance based seismic design in structural engineering practice. *11th World Conference on Earthquake Engineering (11WCEE)*, Acapulco, Mexico, June 23-28, 1996.

[12] M.J.N. Priestley, G.M. Calvi, M.J. Kowalsky, *Direct Displacement-Based Seismic Design of Structures*. 1st edition, IUSS Press, Pavia, Italy, 2007.

[13] S. Pampanin, D. Marriott, A. Palermo, and New Zealand Concrete Society, *PRESSS Design Handbook*, Auckland, New Zealand, 2010.

[14] Ministero delle Infrastrutture, *Aggiornamento delle Norme Tecniche per le Costruzioni*, Suppl. ordinario n°8 alle G.U. n° 42 del 20/02/2018, serie generale, Rome, Italy, 2018.

[15] A.J. Carr, *Ruaumoko Program for Inelastic Dynamic Analysis – User Manual*, University of Canterbury, Christchurch, New Zealand, 2003.

[16] S.A. Freeman, J.P. Nicoletti, J.V. Tyrell, Evaluations of Existing Buildings for Seismic Risk – A Case Study of Puget Sound Naval Shipyard, Bremerton, Washington. *U.S. National Conference on Earthquake Engineering*, Ann Arbor, Michigan,18-20 June, 1975.

[17] I. Iervolino, C. Galasso, E. Cosenza, REXEL: computer aided record selection for code-based seismic structural analysis. *Bulletin of Earthquake Engineering*, **8**, 339-362, 2009.

[18] Ministero delle Infrastrutture, *Linee guida per la classificazione del rischio sismico delle costruzioni*, Decreto Ministeriale 58 del 28/02/2017, Rome, Italy, 2017.

COMPDYN 2019
7th ECCOMAS Thematic Conference on
Computational Methods in Structural Dynamics and Earthquake Engineering
M. Papadrakakis, M. Fragiadakis (eds.)
Crete, Greece, 24–26 June 2019

A METHOD FOR PERFORMANCE-BASED SEISMIC DESIGN OF REINFORCED CONCRETE FRAME BUILDINGS

Soha H. ElKassas, Mohamed N. AbdelMooty, Ezzat H. Fahmy and Ezzeldin Y. Ahmed[1]

[1] Department of Construction Engineering,

The American University in Cairo (AUC)

New Cairo, 11835, Egypt

{shkassas, mamooty, ezzat, eyahmed}@aucegypt.edu

Keywords: Performance-based seismic design, Reinforced concrete structures, Moment-resisting frames, Maximum displacement estimates, Drift**.**

Abstract *A method for preliminary design of reinforced-concrete frames to satisfy predefined performance objectives is developed. It is directly based on performance targets and therefore fits in the context of emerging next-generation performance-based engineering. The key objective of the proposed method is achieving designs that are more reliable in meeting the targeted performance so that subsequent performance assessment iterations are minimized, while at the same time maintaining traditional design formats. The procedure is an adaptation of the force-based design where a force-reduction factor is still used; however, its value is calculated based on displacement parameters that are estimated at the initial design stage. Extensive parametric studies encompassing the inelastic response of regular moment-resisting frames to several ground motion records are performed, employing hundreds of nonlinear time-history analyses where the seismic records are scaled to different intensities to drive the structures to different levels of inelastic excursion. By conducting statistical analysis of the created response databank, a mathematical expression that relates the maximum displacement to some geometrical factors as well as a performance and damage metrics can be developed, while being independent of the frame section dimensions, such that it can be used at the initial stage of design. Using this estimate of maximum displacement, designers can calculate approximate values of force-reduction factors that are well correlated to performance, and then design can proceed in the conventional way.*

1 INTRODUCTION

Seismic design procedures have been in a continuing process of evolution, much more than design for any other load cases because it is difficult to replicate the complex geological nature of an earthquake in an experiment, and therefore major code changes remains an interminable requisite in response to actual performance of buildings during damaging earthquakes. Although earthquakes impose deformations on structures rather than forces, almost all current codes and standards, like Eurocode 8 (EC8) [1], still adopt the force-based design (FBD) approach for seismic design, which uses seismic forces as the primary design parameter. The main advantages of FBD are that it allows simple combination of all possible load cases being an extension of the traditional design format and that it involves linear analysis in conjunction with the familiar acceleration response spectrum. Inelastic behavior is allowed and is implicitly accounted for by dividing the ordinates of the elastic spectrum by a factor, referred to as response reduction factor (R) in American codes and behavior factor (q) in Eurocode, where its values are empirically stipulated to reflect the ductility and over-strength of the structural system [1, 2].

In the past 20 years, there has been an increasing shift in seismic design concept towards satisfying various levels of structural and nonstructural performance. Based on the increased demands from stakeholders for better accountability of new and existing designs in order to be able to make reliable economic and life-safety decisions, performance-based seismic design (PBSD) – a design whose objectives are in terms of multiple performance levels – has emerged as the future trend of seismic design. The latest approach for PBSD was first liberally described in the FEMA-445 document published by the Federal Emergency Management Agency of the United States [3], which explains how probabilities of exceeding certain values of some performance metrics can be converted to real-world losses such as casualties, time lost without operation, repair and replacement costs. The presented approach consists of three main steps: (1) defining the performance objectives, (2) performing preliminary building design, and (3) assessing the performance of the designed building; where steps (2) and (3) are iteratively repeated until the objectives in step (1) are achieved. The performance assessment stage, step (3), has been extensively studied and its methodology presented in the P-58 report [4] as a relatively long process that involves advanced structural analysis techniques and complex probabilistic approaches, however there is still limited research on efficient preliminary building designs, step (2). The FEMA-445 report acknowledges the challenge of developing such efficient design methods that can meet the desired objectives without extensive iterations and defines this challenge as the major decisive factor of the success of the whole framework of performance-based design, because otherwise the implementation process will be inefficient and uneconomical due to the length assessment process. The key requirement is that this design needs to address the system geometrical attributes as well as proportioning it in a manner consistent with the defined performance objectives [3].

The current state of knowledge renders two options for preliminary design in the context of the emerging performance-based methodology: either the aforementioned building code provisions for force-based design (FBD) or alternatively displacement-based design (DBD) that have been developed along with the growing interest in PBSD, and which use displacement parameters as the starting point of design; therefore, effectively control damage. Among the most common DBD procedures are the displacement coefficient method and the equivalent-linearization method [5]. These methods represent real seismic behavior more rationally by imposing displacement restrictions; however, they lack practicality and acceptance in the design community when compared to conventional FBD methods due to the use of the nonfamiliar displacement response spectrum, as evidenced by results of a recent survey of

practicing engineers in North America about their current seismic design practice [6]. Moreover, these procedures have other limitations, where they involve many approximations especially in adopting an equivalent single-degree-of-freedom (SDOF) representation of the structure, which does not recognize the basic differences in response due to different lateral load resisting systems. More importantly, they require a predesigned structure to get a starting estimate for the displacement demand, which renders these DBD methods more applicable to performance evaluation of existing structures for rehabilitation, rather than new designs [7]. On the other hand, concerning the applicability of the FBD method for performance-based design, it is recognized that most seismic codes (e.g. EC8 [1]) embody two performance levels in FBD: the first is the "life safety" performance level under the design basis earthquake at which strength requirements are obtained, and the second is the "serviceability or damage limitation" performance level under the frequently occurring earthquake at which deformation checks are performed. However, the latter performance level is only a final design check rather than a design criterion, which usually results in an iterative process and additionally include several approximations that can lead to inaccurate estimates of displacement [8]. Therefore, because FBD is likely to remain the mainstream of seismic design practice for some time, there is a need to adjust FBD to fit into the multi-level performance-based framework, by minimizing iterations required to achieve various performance objectives, and bringing damage and displacement control upfront at the beginning of the design process.

This paper proposes an efficient seismic design approach for reinforced concrete (RC) moment-resisting frames (MRF) based on the simple FBD scheme that can serve to meet the rising call for performance-based engineering without sacrificing practicality of application. A modification to the FBD procedure is envisaged, whereby, based on the structures' structural system and geometrical configuration, maximum roof displacement can be estimated according to preselected performance levels, and then the behavior factor (q) can be rationally calculated, so that damage and performance can be incorporated in the initial design stage. The study focuses on low-to-moderate height concrete frames with limited ductility, which is a common construction practice in some moderately seismic zones, for example, Egypt and Turkey, where the level of seismicity does not necessitate more complicated preliminary designs. The scope of this paper is presenting the computational methodology for obtaining the roof displacement estimates as associated with specific performance levels and other structural geometrical characteristics. More than 1750 nonlinear time history analyses are performed, employing rigorous models of RC members that captures both material and geometrical inelasticity which are particularly critical in case of RC structures. The results are postprocessed in order to understand the dependency of the story displacement values on the different variables chosen to be included in the displacement prediction equation for later use in the modified FBD method.

2 MODIFIED FORCE-BASED DESIGN METHOD

The basis of the designated method has been first proposed for steel moment resisting frame structures by Bazeos and Beskos [9], later developed and validated in detail specifically for PBD [10-18] and is still under refinement till present. This group of researchers have termed it the hybrid force/displacement (HFD) method. The main principle of this methodology is that it converts target limiting values of damage metrics associated with predefined performance levels to a target roof displacement that can be used to calculate a more meaningful behavior factor "q" such that ductility demands are bounded by the estimated target roof displacement ductility, and thus the design can control both strength and drift performance for several levels of seismic action. In addition to the benefit of using displacement parameters as input variables for the design process, the HFD method retains the use of conventional elastic

response spectrum analysis and design in line with current seismic codes. An initiative to apply the same procedure for composite steel/concrete structures was recently proved successful [19]. The method was also just newly extended to RC structures [20] where Piana and his co-researchers have developed a HFD method for RC structures based on numerical analyses of structures of varying height only and employing phenomenological models (lumped plasticity) to represent nonlinear behavior. The present work is an additional effort along the same frontier of applying the HFD design method to RC structures for preliminary PBD but through employing distributed plasticity fiber-element modeling to represent inelasticity along members cross sections and lengths, which, despite being much more computationally demanding, is deemed more accurate in accounting for the complex hysteretic behavior of RC structures. The steps of the envisaged modified force-based method can be summarized as follows:

(1) Selection of performance levels

According to the PBD philosophy, a performance level is defined by a pair of a post-earthquake damage and functional state objective and a level of seismic action. For example, a common multiple performance objective is: Immediate Occupancy (IO) under the frequently occurring earthquake (FOE), Life Safety (LS) under the design basis earthquake (DBE), and Collapse Prevention (CP) under the maximum considered earthquake (MCE). The DBE is given in seismic codes, while the FOE and MCE can be estimated from the DBE based on hazard studies. Limiting values of a response parameter associated with the damage level are identified based on performance-based codes for example FEMA-356 [21]. Inter-story Drift Ratio (IDR) is the chosen response parameter because there is consensus in the literature that it best correlates to damage at the global level [22-24]. IDR is defined as the relative lateral displacement between two successive floors normalized by the height between the floors

(2) Definition of building attributes

Some building characteristics such as the number of storeys, n_F, and the number of bays, n_B, are identified. The criteria for application of the FBD method as stated in the code are checked, for example, regularity in plan and elevation.

(3) Estimation of the maximum roof displacement

The maximum roof displacement, $\mu_{r,max}$, is estimated using a relationship that will be developed as a second stage of this research, given as $\mu_{r,max}= f(IDR_{max,}\ n_F,\ n_B,\ H)$, where H is the total height of the building.

(4) Elastic design under the FOE

Perform an elastic design of the frame with a behavior factor q= 1 only for strength requirement under the FOE. The resulting roof displacement serves as an estimate of the global yield displacement $\mu_{r,y}$

(5) Calculation of the behavior (strength reduction) factor, q

Based on the equal displacement rule [25], the behavior factor q is calculated based on the global displacement parameters by dividing the estimated maximum roof displacement ($\mu_{r,max}$) at the desired seismic event by the global yield displacement $\mu_{r,y}$

(6) Design of the structure

The ordinates of the elastic acceleration response spectrum are divided by the q-factor corresponding to the target deformation, and design proceeds in the conventional way.

3 DESCRIPTION OF PROTOTYPE BUILDINGS

In order to develop the expression that estimate the maximum roof displacement at the beginning of design, the performance of nine prototype RC structures varying in height (4, 7 and 10 floors) and number of bays (3, 5 and 7 bays) is studied. The structures are assumed to have the same symmetrical and square plan, as representatives of typical medium-rise RC office buildings. The floor height and bay width are fixed at 3.0m and 6.0m, respectively. The buildings are assumed to be constructed in a moderate seismic zone (featuring a design peak ground acceleration (PGA) of 0.3g).

3.1 Design and structural properties

The buildings were designed and detailed to resist combination of gravity and seismic loads, according to the Egyptian design codes ECP-203 [26], and ECP-201 [27] which are fundamentally in line with the regulations of EC8 [1]; a typical modern seismic code applicable to many countries. For gravity loading, the dead loads assumed comprise the self-weights of the concrete structural elements, typical floor finishing of 1.5 kN/m^2, and weight of masonry infill panels of 12 and 25cm thickness on interior and exterior beams respectively with a density of 18 kN/m^3. A live load of 3.0 kN/m^2 is also included. For seismic design, the lateral load resisting system is chosen as a space frame, and acceleration elastic response spectrum for shallow crustal earthquakes in non-Mediterranean areas is adopted known as Type 1 in ECP-201 [27], and as Type 2 in EC8 [1], for a "Soil Class C", which is soft soil, or dense or medium-dense sand, gravel or stiff clay as given in ECP-201[27] and EC8 [1]. Based on the norm and knowledge of reinforcement detailing in Egypt and many other countries with similar low-to-moderate seismicity, limited ductility (ordinary) frames are chosen and thus a FRF with a value of five is used in the design. Characteristic material properties are utilized, and they are presented in Table 1 using units consistent with those that will be subsequently used in the program for nonlinear time-history analysis. Gravity and seismic loading are combined using the appropriate coefficients from ECP-203 [26]. The only capacity design rule applied is that resulting from the prescribed reduction in the effective flexural stiffness of members where the reduction for beams (50%) is higher than that for columns (30%). All floors are assumed to have a solid rigid slab with a constant thickness of 150mm, and columns are selected to have a square cross-section and to be symmetrically reinforced on the four sides, in order to have equal resistance to the changing direction of earthquake loading. The reinforcement is selected minimally according to the structural analysis and code requirements, to avoid overstrength and unnecessary margins reflecting personal designers' choices. Figure 1 summarizes the notations used for the study cases together with their corresponding geometrical characteristics, and member cross-section sizes and reinforcements.

	Material parameter	Values used
Concrete	Compressive cube strength, f_{cu}	25 N/mm^2
	Modulus of elasticity, E_c	22 kN/mm^2
	Poisson's ratio	0.2
Steel (36/52)	Yield strength, F_y	360 N/mm^2
	Ultimate strength, F_u	520 N/mm^2
	Modulus of elasticity, E_s	205.9 kN/mm^2

Table 1: Material properties employed in design and time-history analysis

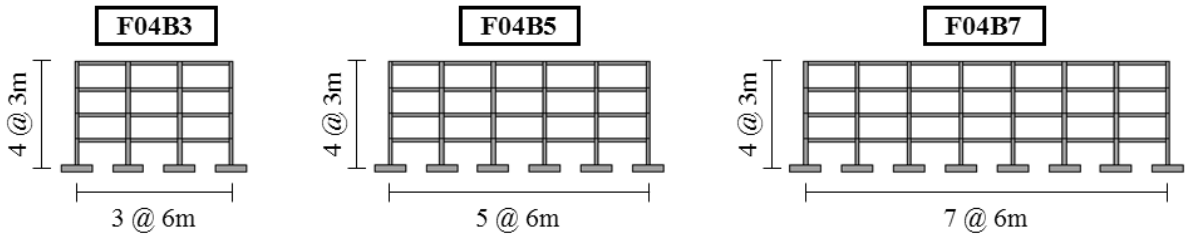

	Column (dimension (mm)/RNF)	**Beam** (depth (mm)/RNF)
Floors 1-4	450/8φ22 (outer) and 600/16φ20 (inner)	750 / 8φ18

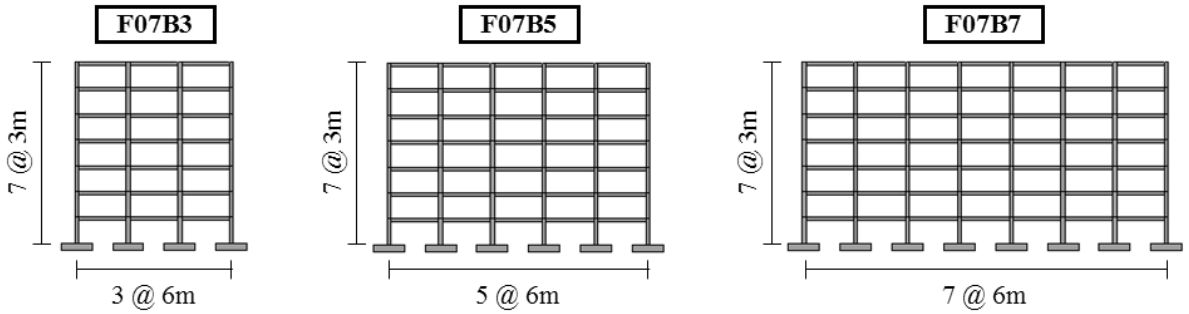

	Column (dimension (mm)/RNF)	**Beam** (depth (mm)/RNF)
Floors 5-7	450/8φ22 (outer) and 450/8φ22 (inner)	650 / 7φ18
Floors 1-4	550/12φ20 (outer) and 650/16φ22 (inner)	750 / 7φ20

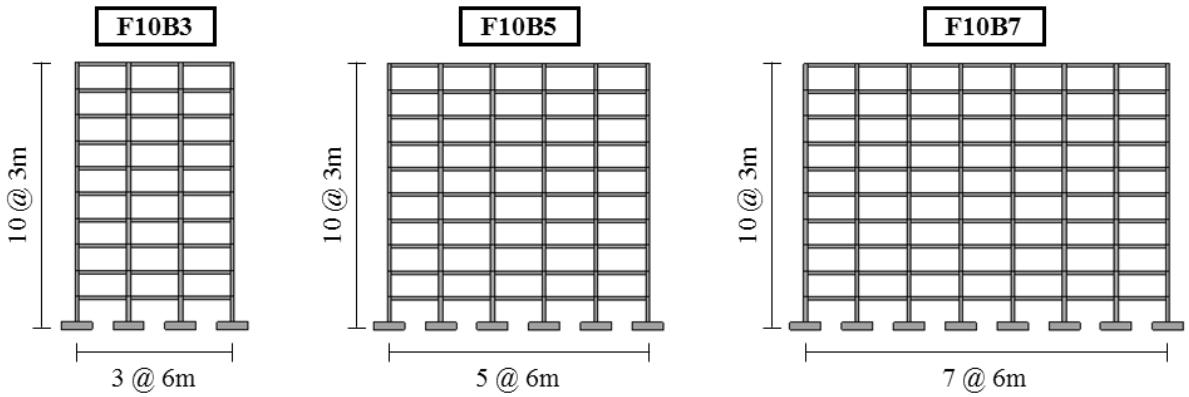

	Column (dimension (mm)/RNF)	**Beam** (depth (mm)/RNF)
Floors 8-10	450/8φ22 (outer) and 400/8φ20 (inner)	600 / 7φ16
Floors 5-7	550/12φ22 (outer) and 650/16φ22 (inner)	650 / 6φ20
Floors 1-4	650/20φ22 (outer) and 750/20φ22 (inner)	750 / 7φ20

Figure 1: Prototype buildings' configurations, members' cross-sections and reinforcement

3.2 Nonlinear analytical model

Taking advantage of the symmetry of the buildings with the insignificance of torsional effects, a two-dimensional nonlinear model of the structures was developed in order to simplify the post-processing of results. The simulation platform of the Mid-America Earthquake Center (MAE), called "ZEUS-NL", is selected for nonlinear Time History Analysis (THA). This

software was developed at the University of Illinois at Urbana- Champaign [28] specifically for earthquake engineering applications, based on the older analysis packages ADAPTIC [29] and INDYAS [30]. The stability and robustness of ZEUS-NL in its present or previous forms have been extensively tested and validated by many researchers [31-32]. ZEUS-NL uses the fiber analysis approach in modeling nonlinear behavior. This type of models, usually referred to as the distributed plasticity models, is considered a middle ground between the computationally efficient lumped plasticity models which represent inelasticity as a zero-length hinge with hysteretic properties, only at defined locations at ends of elements (for example SAP2000 and ETABS) and continuum analysis which monitors stress-strain behavior through every single point of the entire structure (for example ABACUS and ANSYS). The latter is unquestionably the most accurate and powerful modeling method, however because of its excessive computational demand, the fiber modeling approach is often the method of choice for research about large displacement analysis of frame structures in the inelastic range.

In distributed plasticity models, cross-sections at specific integration points along the element length are divided into fibers where each fiber is associated with a uniaxial stress-strain relationship (constitutive model) for one material. The number of section fibers needs to be defined by the user and they usually range between 100 and 200. During the entire multi-step analysis, making use of the Euler-Bernoulli assumption that plane sections remain plane after bending, fiber stresses are calculated from the fiber strains considering the migration of the position of the section neutral axis during the loading history. Then sectional stress-strain state in the form of moment-curvature relationship is obtained through the integration of the nonlinear response of the individual material fibers over the cross-sectional area, thus fully accounting for the spread of inelasticity across the whole section depth. This is followed by integrating the moment-curvature relationship of the sections along the length to obtain the moment-rotation response, and thus simulating the distributed inelasticity along the member length. This discretization process is illustrated for reinforced concrete frames in Figure 2.

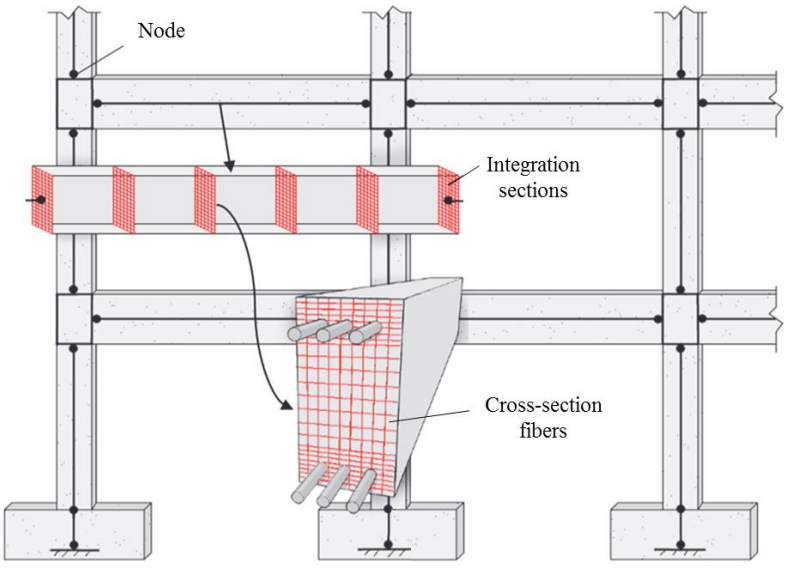

Figure 2: Fiber-element modeling of a reinforced concrete frame (after ATC, 2016 [33])

Some of the advantages of the fiber element method are that: it directly simulates interaction between axial force and bending moment; it does not need any prior moment-curvature analysis of members; and it automatically accounts for concrete cracking and growth in crack length, as well as gradual progression of steel yielding through the member cross sections and

lengths. Also, local buckling of steel reinforcing bars or steel webs and flanges can be reasonably modeled by incorporating it in a steel constitutive model that degrades the structural properties of the steel elements when they reach a certain critical buckling stress. The model can also impose equilibrium in the deformed state of the structure and thus represent geometrical nonlinearity and P-delta effects.

3.3 Material models

Concrete is represented using the uniaxial nonlinear concrete model that has a balance of simplicity and accuracy. This model adopts the constitutive relationship formulated by Mander et al. [34] integrated with the improved cyclic rules proposed by Martinez-Rueda and Elnashai [35] which can predict the continuing cyclic degradation of strength and stiffness and helps to achieve better numerical stability in case of large displacements analysis. Two separate concrete material models are used for the core concrete (confined) and cover concrete (unconfined) to reflect the different confinement factors included. The model assumes constant active confinement pressure throughout the entire stress-strain range, which is considered as the maximum confining pressure that occurs at yielding of transverse reinforcement.

The steel reinforcing bars (longitudinal bars) are modeled using a bilinear (elasto-plastic) model with a kinematic strain-hardening rule for the yield surface assumed as 0.5% of the elastic initial stiffness [36].

3.3.1. Cross-sections

The cross-sections of each element are defined based on their design details and the material models chosen. In order to account for the slab contribution to beam stiffness and strength, all beam sections are modeled as T-section with effective flange width equals to threefold the slab thickness on each side, corresponding to the specifications of ECP-203 [27] in case of seismic loading and amounting to 1.15m. Columns are modeled using square sections. ZEUS-NL built-in section models for RC T-section and RC Rectangular section are used to model beams and columns respectively as shown in Figure 3. Each structural member is modeled using several elements having different cross sections to reflect the change in reinforcement detailing along the member length. The cross-section definition covers the actual arrangement of longitudinal reinforcement while the arrangement of transverse reinforcement is approximated through the confinement factor in the constitutive material model discussed in section 3.2.1. Figure 3 also illustrates the discretization of the cross-section into fibers at the material level. The accuracy of the model increases as the number of fibers discretization increases; thus, it was chosen to use 200 monitoring points per section to monitor nonlinear behavior.

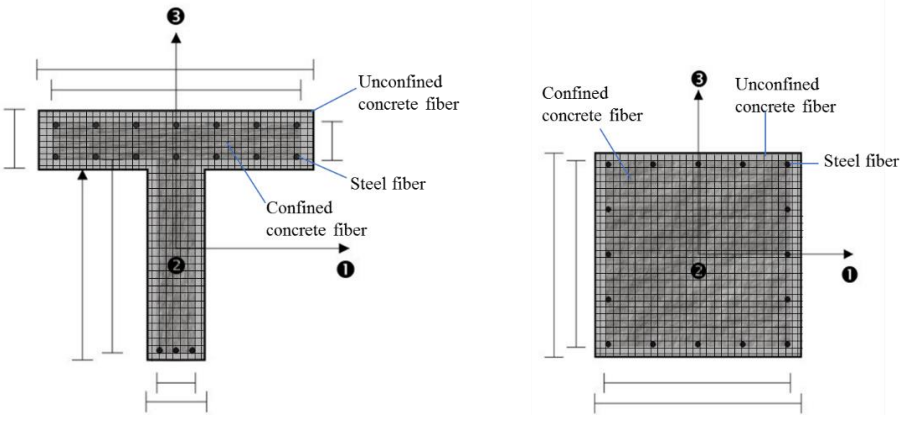

Figure 3: Cross sections used in modeling beams and columns

3.3.2. Elements

A 3-D cubic elasto-plastic element formulation was applied to model the spatial behavior of both column and beam elements accounting for inelasticity across element depth and length [37]. As the name implies, this elasto-plastic element utilizes a cubic shape function to provide the transverse displacement. For evaluation of the element forces and displacement, numerical integration of the cubic formulation equation is performed at two Gauss integration points whose location is depicted in Figure 4. The cross-section at each Gauss point is divided into a number of monitoring areas as discussed earlier, where the appropriate material constitutive model is applied, and strains and stresses are monitored and then integrated to model the response of the whole element cross-section and length employing the fiber approach. Geometrical nonlinearity due to second order effects is also accounted for. Since each element has a displacement-based formulation and just two integration points, several short length elements were used in order to ensure reasonable accuracy in inelastic modeling.

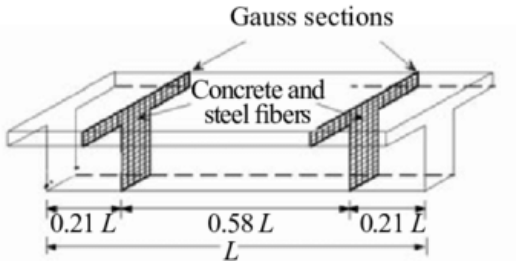

Figure 4: Location of the two Gaussian sections

Rayleigh damping elements were selected to model equivalent viscous damping in the structure, which can result from friction in concrete opened micro-cracks and interaction of nonstructural elements. Although, this damping part is very small compared to the more important hysteretic damping due to inelastic behavior and yielding (which is already implicitly accounted for within the nonlinear material models that allows energy dissipation though cyclic loading), it was chosen to still employ some viscous damping in order to provide numerical stability, where the damping matrix results in stabilizing the system of equations of motion. For this end, stiffness-proportional Rayleigh damping coefficient is calculated based on the periods of the structure in the first two modes of significant mass participation [38]. Although the Egyptian code ECP-201 [26] provides the design spectrum based on 5% first mode critical damping, this percentage also indirectly comprises the effect of inelastic behavior which is covered in the material models in nonlinear analysis. Therefore, 2% critical damping in the first mode was considered following the code provisions for wind load analysis in which structures are assumed to behave completely elastically. Also 5% of critical damping was assumed in the second mode.

Masses were represented by lumped 2D mass elements at beam-column intersections in dynamic analysis, in order to reduce computational demand, since the current work is focused on estimating structural global responses (like roof drift) rather than local stress state of members. Modeling infill walls was not included in the nonlinear dynamic analysis, except for their masses considered, because infill walls usually get damaged at low drift values and thus their contribution to stiffness stops at relatively low seismic action [39] and since the effect of infill walls is not as critical on the displacement behavior, which is the core of this study, as it is on the stress behavior.

4 IMPLEMENTATION OF NONLINEAR MODEL IN SEISMIC ANALYSIS

4.1 Seismic Input and Scaling

In this study, it was selected to use an ensemble of artificial accelerograms (acceleration time history ground motion records) for earthquake representation, with a single criterion which is compatibility of their 5% damped elastic spectra with the code spectrum used in the seismic design of the buildings over the period range of significance. Using artificial records provided the advantage of best fit to target spectrum as well as limiting the variability in results. It was opted to use a suite of seven ground motion records, and then to average the results pertinent to the provisions of ECP-201 [26] for THA. Accordingly, seven 20-seconds artificial accelerograms were generated using the program SIMQKE [40] such that their average matches the ECP-201 [26] "Type 1" elastic response spectrum for soft soil class "Type C" at PGA= 0.3g. The records were selected to have reasonable variability of frequency and energy content to reduce the bias in response. The software SEISMOSIGNAL [41] was used to evaluate some of the characteristics of the generated records, where maximum acceleration to maximum velocity (A/V) ratio serves as an energy content indicator, and the earthquake predominant period, T_p, as a frequency content indicator. Characteristics of the records that have been used with their reference notation are given in Table 2.

Earthquake reference	Predominant period (T_p)	A_{max}/V_{max}
EQ1	0.26	11.2
EQ2	0.12	8.6
EQ3	0.2	13.9
EQ4	0.28	9.4
EQ5	0.18	11.8
EQ6	0.16	14.1
EQ7	0.22	10.5

Table 2: Characteristics of selected artificial ground motion records

For the purpose of scaling the ground motion records, it was chosen to use the peak ground acceleration (PGA) as the intensity measure (IM) for scaling accelerograms later in the dynamic analysis rather than the most widely used IM, which is the 5%-damped spectral acceleration at the first-mode period of the structure. The latter has a major deficiency when used in analysis involving high excursion into the inelastic response range, where it does not consider the elongation of the first modal period of vibration as a result of nonlinear behavior. Additionally, PGA is considered the most important IM from a structural point of view because the resulting inertia forces in a structure are directly proportional to the acceleration, according to Newton's Second Law. And till present PGA is the key aspect of definition of seismic hazard in most seismic design standards including the ECP-201 [26], where it represents the first point on the elastic design response spectrum. Also, because relative spectral matching at all periods is closely achieved during the generation of the spectrum-compatible records, there is no need to provide separate scaling factors for each different height building depending on its fundamental period. PGA is measured as the maximum absolute amplitude on a recorded or synthetic accelerogram. In order to be used for scaling, at each incremental step a of analysis, each record is simply multiplied by a scale factor $Si_{ft} = a_i / a_1$, where a_i is the PGA

of ground motion record used in the analysis, and a_1 is the PGA of the original unscaled earthquake record (i.e. PGA =0.3g).

4.2 Performance Criteria

In order to identify the factors that affect the maximum displacement at various levels of seismic action, certain levels of performance were preselected and defined for studying their associated response. Three discrete structural performance levels corresponding to three major damage and functional states were investigated in the present work, following the definition of the guidelines of FEMA-356 [21]:

- Immediate Occupancy (IO) level, at which the structure is safe to be occupied immediately after the associated seismic event and repairs are minor, i.e. negligible damage.
- Life Safety (LS) level, at which the structure remains stable and has significant reserve capacity at the associated seismic event, and hazardous nonstructural damage is also controlled to ensure life safety.
- Collapse-Prevention (CP) level, at which the structure is barely standing after the associated seismic event, i.e. most severe damage before collapse.

Limiting values for the chosen response parameter, which is IDR, were assumed, following the acceptance criteria specified in the FEMA-356 document [21], and presented in Table 3. Therefore, the upper limits of IDR used to define the IO and LS performance levels were selected as 1% and 2%, respectively, while the limiting IDR for the CP level was chosen as 3% (less than the 4% specified by FEMA 356) for added conservatism in the global failure criteria as proved by several previous studies [42-42].

Structural Performance Levels and Damage – Vertical Elements				
		Structural Performance Levels		
Elements	**Type**	**Collapse Prevention**	**Life Safety**	**Immediate Occupancy**
Concrete Frames	Primary	Extensive cracking and hinge formation in ductile elements. Limited cracking and/or splice failure in some nonductile columns. Severe damage in short columns.	Extensive damage to beams. Spalling of cover and shear cracking (<1/8" width) for ductile columns. Minor spalling in nonductile columns. Joint cracks <1/8" wide.	Minor hairline cracking. Limited yielding possible at a few locations. No crushing (strains below 0.003).
	Secondary	Extensive spalling in columns (limited shortening) and beams. Severe joint damage. Some reinforcing buckled.	Extensive cracking and hinge formation in ductile elements. Limited cracking and/or splice failure in some nonductile columns. Severe damage in short columns.	Minor spalling in a few places in ductile columns and beams. Flexural cracking in beams and columns. Shear cracking in joints <1/16" width.
	Drift	4% transient or permanent	2% transient; 1% permanent	1% transient; Negligible permanent

Table 3: Definition of structural performance levels for RC frames (after FEMA 356 [21])

4.3 Incremental Dynamic Analysis

In order to derive maximum displacement expressions for RC frames corresponding to different levels of performance, it is required to study each prototype structure under various levels of seismic actions to investigate the factors that influence its maximum displacement pattern. This type of parametric analysis involving the extension of a single nonlinear THA into an incremental one by progressively scaling the seismic load is generally referred to as "Incremental Dynamic Analysis" (IDA). The scaling interval and limit is selected to adequately push the structure through the entire range of behavior under study, from elastic to inelastic and finally to collapse (or close to collapse). Appropriate postprocessing can present the structural response results as IDA curves, for each ground motion record, of the structural response parametrized by a seismic intensity level. For the purpose of IDAs performed herein, the following procedure is undertaken in order to develop IDA curves and create a response databank with the post-processed results at the study performance levels:

1. Multiply the accelerogram with the initial SF_1, which is taken as the reciprocal of the FRF used in design (FRF =5); therefore SF_1= 0.2.
2. Run nonlinear dynamic analysis with the ground motion record acceleration set as a_i = $SF_i \times PGA_{design}$ (0.3g), where i is the run number.
3. Extract all nodal displacements and calculate:
   - $(IDR_{max})_i$ = the maximum instantaneous inter-storey drift ratio at run i (the maximum difference between the lateral displacements of any two consecutive floors at any instance)
   - $(\mu r_{max})_i$ = maximum roof displacement at run i (the maximum difference between the lateral displacement of the roof and the base at any instance)
4. A reasonably small increment of 0.2 is chosen for progressively increasing the scale factors. Therefore, the new scale factor is computed as: SF_{i+1}= SF_i + 0.2. This is equivalent to having a PGA increment of 0.06g (0.2x 0.3g).
5. Repeat steps 2 to 3 until the (IDR_{max}) is greater than or equal 3%.
6. Plot the SF_i versus $(IDR_{max})_i$ and by linear interpolation, determine the scale factors SF_{IO}, SF_{LS}, SF_{CP} corresponding to the three following predefined performance levels (respectively):
   - IO when IDR_{max} equals to 1%
   - LS when IDR_{max} equals to 2%
   - CP when IDR_{max} equals to3%
7. Re-run the model using SF_{IO}, SF_{LS} and SF_{CP} and check that the IDR_{max} properly corresponds to the selected performance levels. If the target IDR_{max} is not achieved, interpolation is repeated, and scale factors are corrected until reaching the specified limits of IDR_{max} for the three study performance levels. In other words, for each pair of structure and accelerogram, three scale factors are identified for running the models.
8. For the same prototype structure, repeat steps 1 to 7, for the rest of the 7 artificially generated ground motion records.
9. Repeat steps 1 to 8 for the rest of the 9 prototype structures.

5 RESULTS AND DISCUSSION

This section discusses some of the results of IDA that are used to identify the factors and the form of the expression to be used for estimation of maximum roof displacement. The whole computational volume required to identify the selected performance levels was in the order of 1750 nonlinear THA runs, however for the presentation of the displacement profiles,

only the results at the study performance levels are included, after averaging the response of the seven ground motions for each prototype building.

5.1 Height-wise displacement profiles

The maximum displacement profiles for the study cases are presented based on the mean values of story displacement (average of the response for the seven ground motion records) that occurs at the seismic intensity identified for each performance level. Based on the results presented in Figures 5-7, it can be observed that the number of stories (n_F) is the main geometrical characteristics that affects the values of storey displacement and the shape of the displacement profile. Taller frames display higher displacement response, and their displacement profile shapes reflect higher modes of vibration than the fundamental translational mode. Shorter frames exhibit an almost linear displacement profile. Also, it can be inferred that an increase in the number of bays (n_B) produces a reduction in the maximum floor displacement due to the increased stiffness. This influence is more prominent in the nonlinear range for the LS and CP performance levels, with the reduction in displacement as related to the increased number of bays being more observed in the higher floors, especially for the roof displacement.

.

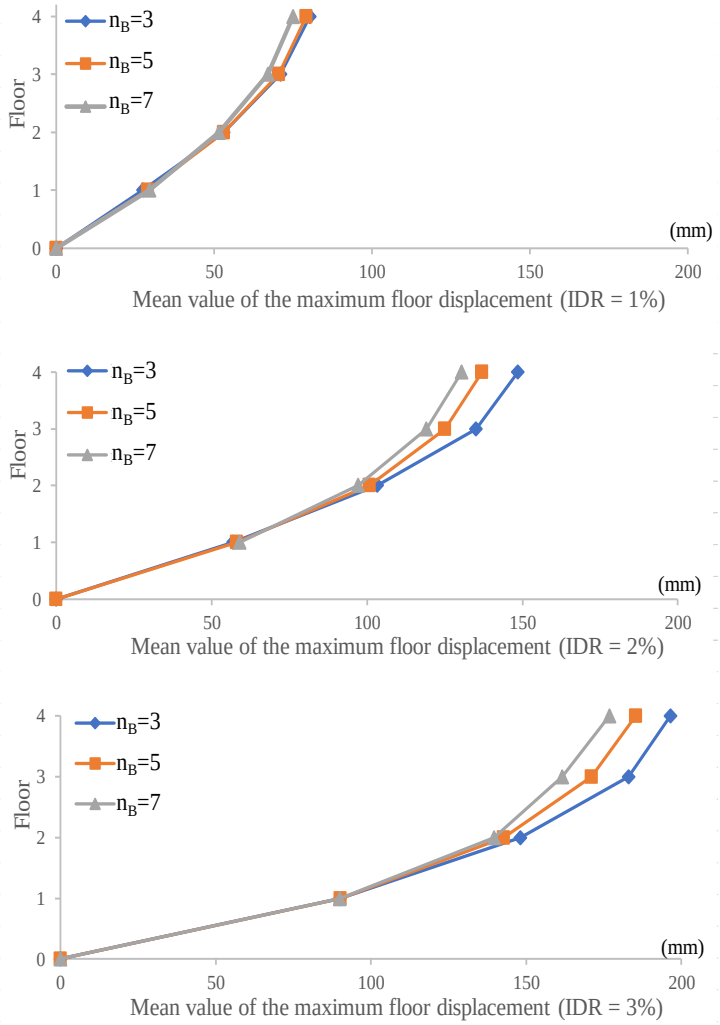

Figure 5: Mean values of the maximum floor displacements that represent the drift profile of the 4-story frames associated with the IO level (IDR =1%), LS level (IDR =2%), and CP level (IDR =3%).

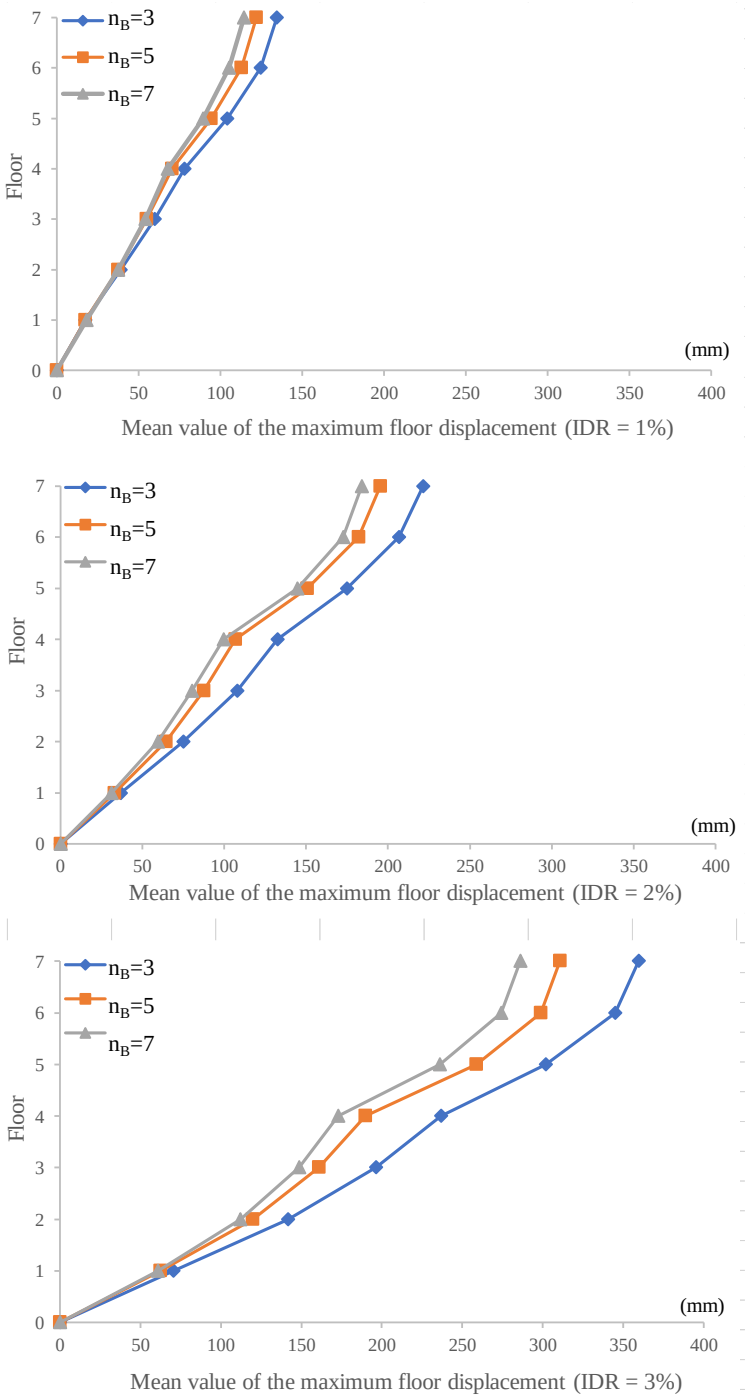

Figure 6: Mean values of the maximum floor displacements that represent the drift profile of the 7-storey frames associated with the IO level (IDR =1%), LS level (IDR =2%), and CP level (IDR =3%).

5.2 Parametric study

Three parameters are studied to understand their effects on the value of the maximum roof displacement, namely the number of floors (n_F), the number of bays (n_B) and the $IDR_{r,max}$ damage metric. Two of the parameters are alternatively fixed in order to be able to visualize the effects of the third parameter. The results of the parametric including all the results of the nonlinear THA are shown in Figures 8 and 9. By comparing the roof displacement versus IDR

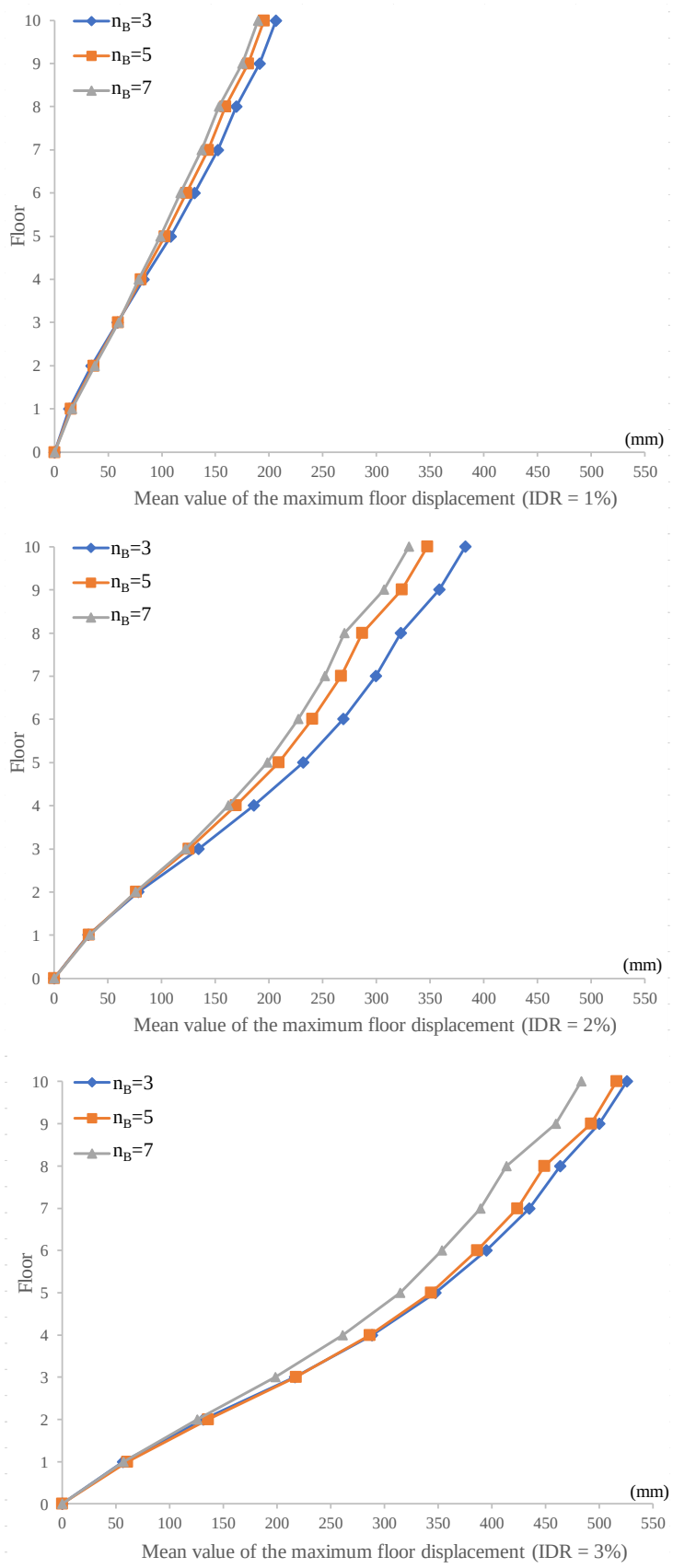

Figure 7: Mean values of the maximum floor displacements that represent the drift profile of the 10-storey frames associated with the IO level (IDR =1%), LS level (IDR =2%), and CP level (IDR =3%)

for the different height and width frames, a general increasing trend is observed with increasing building n_F and decreasing n_B. The effect of the number of stories is much more substantial, as clear in the plots. Also, there is higher sensitivity to the ground motion characteristics with increasing number of floors as proven by the higher dispersion of results in Figure 8, especially with higher excursion into inelastic action (higher IDR values). It can be observed that there is a change in slope with increasing IDR for the different height frames, which proves the interaction of these two factors in contributing to the estimate of maximum roof displacement. Figure 9 reiterates the same relationships and displays the range of sensitivity of the maximum roof displacement to the change in number of bays. The increase in roof displacement with decreasing number of bays is quite negligible for the 4 stories buildings, and the effect of number of bays becomes more prominent with increasing number of floors and especially at higher IDR values associated with more damage.

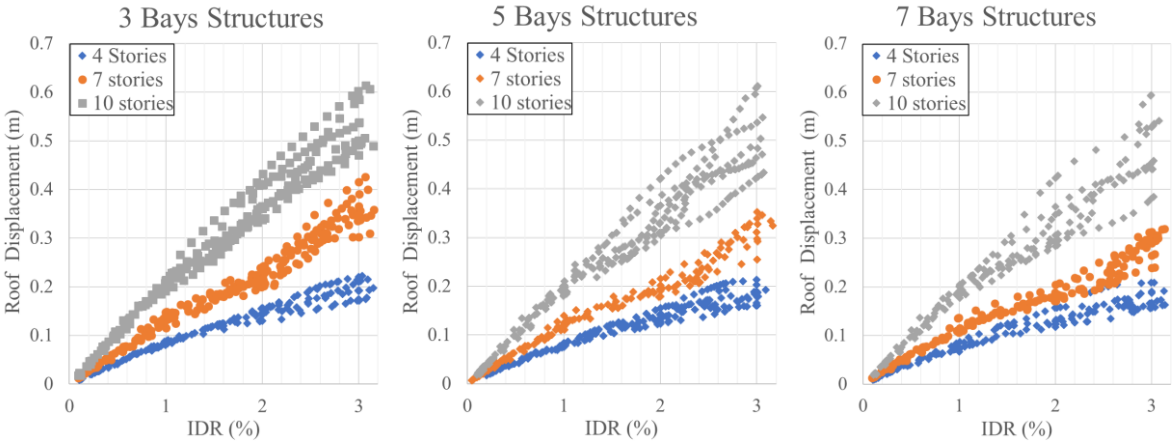

Figure 8: Dependency of the maximum roof displacement on IDR and n_F (for a given number of bays)

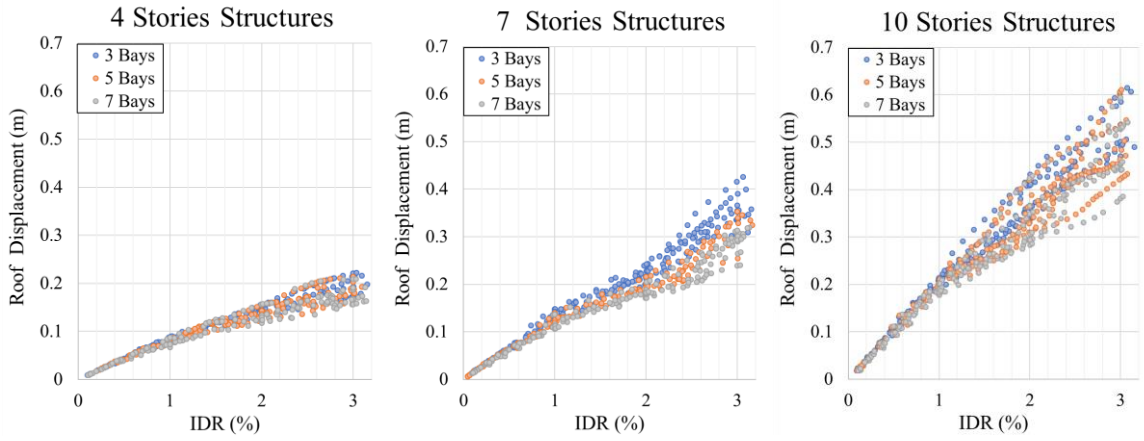

Figure 9: Dependency of the maximum roof displacement on IDR and n_B (for a given number of stories)

6 CONCLUSIONS

In order to incorporate damage in the initial stages of seismic design, a method is proposed for design of RC frame structures that involves modification of the familiar FBD method, where the design starts with a displacement variable that is converted into a force parameter,

and then design can proceed in the conventional way. The use of the proposed modification can yield designs with higher accuracy and more reliability in achieving the preselected performance targets, where the damage is controlled at every performance level. Additionally, due to minimizing the amount of iterations, this method can be considered a valid contribution to the stage of "Preliminary Building Design" of the framework of "next-generation performance-based seismic design" nominated by FEMA-445 [3].

This paper presents the modification envisaged which requires development of a mathematical that can estimate maximum roof displacement based on required performance objectives, and independent of the members cross sections, such that it can be used at the start of design. The computational methodology for development of such expressions are presented which requires developing rigorous nonlinear models of the RC structures and performing extensive parametric studies using nonlinear time-history analysis in order to identify the parameters that will be included in the displacement prediction relation. The effect of changing the number of floors and number of bays together with changing the performance level, on the displacement behavior is observed, so that they can be later incorporated by the authors in nonlinear regression to develop the required expressions. It should be noted that the conclusions herein are only valid for the range of structures under study and for areas with similar seismicity. In the long run, the recommended design scheme can present a promising design tool that can be implemented in design codes and textbooks, pending verification and validation on a wider range of structural systems and materials.

ACKNOWLEDGEMENTS

The MAE Center and the National Science Foundation (Award Number EEC-9701785) are acknowledged for the use of the finite-element analysis platform ZeusNL.

REFERENCES

[1] EC8. EuroCode 8, Design of Structures for Earthquake Resistance. Part 1: General rules, seismic actions and rules for buildings (EN 1998-1:2004). CEN, Brussels, 1998.

[2] FEMA-450, The 2003 NEHRP recommended provisions for new buildings and other structures. Part 1: provisions. Washington D.C: Federal Emergency Management Agency, 2003.

[3] FEMA-445, Next-Generation Performance-Based Seismic Design Guidelines: Program Plan for New and Existing Buildings. Federal Emergency Management Agency, report FEMA-445, Washington, D. C., August 2006.

[4] FEMA, P-58, Next-generation Seismic Performance Assessment for Buildings, Volume 1 – Methodology. Report prepared by the Applied Technology Council (ATC) for the Federal Emergency Management Agency, Washington, D.C., 2012.

[5] FEMA-440, Improvement of nonlinear static seismic analysis procedures. Federal Emergency Management Agency, report FEMA-440. Washington, D.C.,2004.

[6] S.L. Kramer, Performance-based design in geotechnical earthquake engineering practice. *Proceedings of the 5th international conference on earthquake geotechnical engineering*, Santiago, Chile, 2011.

[7] T. J. Sullivan, G. M. Calvi, M. N. Priestley, and M. J. Kowalsky, The Limitations and Performances of different Displacement Based Design Methods. *Journal of Earthquake Engineering*, **vol. 7(1)**, 2003, pp 201-241.

[8] S. Sattar, Evaluating the consistency between prescriptive and performance-based seismic design approaches for reinforced concrete moment frame buildings. *Engineering Structures*, **174**, 919–931, 2018.

[9] N. Bazeos and D. E. Beskos, New seismic design method for building framed structures, In: S. N. Atluri, D. E. Beskos, D. Polyzos, (Eds.) *Proceedings of International Conference on Computational and Experimental Engineering and Sciences.* Corfu, Greece: Tech Science Press; 2003.

[10] T. L. Karavasilis, N. Bazeos and D. E Beskos, A hybrid Force/Displacement Seismic Design Method for Plane Steel Frames. In *Proceedings of 1st European conference on earthquake engineering and seismology (1st ECEES)*, Geneva, Switzerland, Paper No 1013, –8 September 2006.

[11] T. L. Karavasilis, N. Bazeos and D. E Beskos, Estimation of Seismic Drift and Ductility Demands in Planar Regular X-Braced Steel Frames. *Journal of Earthquake Engineering and Structural Dynamics*, **36**, 2273–2289, 2007.

[12] T. L. Karavasilis, N. Bazeos and D. E Beskos, Behavior Factor for Performance-Based Seismic Design of Plane Steel Moment Resisting Frames. *Jr. of Earthquake Engineering*, **1(4)**, 531-559, 2007.

[13] T. L. Karavasilis, N. Bazeos and D. E Beskos. A hybrid Force/Displacement Seismic Design Method for Steel Building Frames. *The 14th world conference on Earthquake Engineering*, Beijing, China, October 12-17, 2008.

[14] T. L. Karavasilis, N. Bazeos and D. E Beskos. Seismic Response of Plane Steel MRF with Setbacks: Estimation of Inelastic Deformation Demands. *Journal of Constructional Steel Research*, **64(6)**, 644–654, 2008.

[15] N. Bazeos, Comparison of three seismic design methods for plane steel frames. *Journal of Soil Dynamics and Earthquake Engineering*, **29**, 553– 562, 2009.

[16] T. L. Karavasilis, N. Bazeos and D. E Beskos, A new Seismic Design Method for Steel Structures. Chapter 15. In: Fardis, M.N. (Ed). *Advances in Performance-Based Earthquake Engineering*. **13**: Springer e-books. 2010.

[17] A. S. Tzimas, T. L. Karavasilis, N. Bazeos and D. E Beskos, A Hybrid force/displacement seismic design method for steel building frames. *Engineering Structures*, **56**, 1452-1463, 2013.

[18] A. S. Tzimas, T. L. Karavasilis, N. Bazeos and D. E Beskos, Extension of the hybrid force/displacement (HFD) seismic design method to 3D steel moment-resisting frame buildings. *Engineering Structures*, **147**, 486-504, 2017.

[19] K. A. Skalomenos, G.D. Hatzigeorgiou, D.E Beskos, Application of the hybrid force/displacement (HFD) seismic design method to composite steel/concrete plane frames. *Journal of Constructional Steel Research*, **115**, 179-190, 2015.

[20] C. Piana, J. Qiana, E. V. Muhoa,, D. E. Beskos, A hybrid force/displacement seismic design method for reinforced concrete moment resisting frames. *Soil Dynamics and*

Earthquake Engineering, in press, available online Sept. 2018, https://doi.org/10.1016/j.soildyn.2018.09.002

[21] FEMA-356, Pre-standard and Commentary for the Seismic Rehabilitation of Buildings," Federal Emergency Management Agency. Report FEMA-356, Washington, D. C., 2000.

[22] B. B. Algan, Drift and Damage Considerations in Earthquake Resistant Design of Reinforced Concrete Buildings. Ph. D. thesis, University of Illinois, Urbana Champaign, III, 1982.

[23] J. P. Moehle, Strong Monitor Drift Estimates for R/C Structures. *Jr. of Structural Engineering*, **110(9)**, 1988-2001, 1984

[24] P. Gulkan and M. A. Sozen, Procedure for determining seismic vulnerability of building structures. *ACI structural Jr.*, **96(3)**, 336-342, 1999

[25] N. M. Newmark. and W. J. Hall, Earthquake spectra and design. Earthquake Engineering Research Institute, Berkeley, California, 1982.

[26] ECP– 201-2008, "The Egyptian Code of Practice no-201 for Design Loads for Construction Works," Research Center for Housing and Construction, Cairo, Egypt, 2012.

[27] ECP–203-2007, "The Egyptian Code of Practice no-203 for Design and Construction of Concrete Structures," Research Center for Housing and Construction, Cairo, Egypt, 2007.

[28] A. S. ElNashai, V. Papanikolau, and D. H. Lee, Zeus Non-linear: A system for inelastic analysis of structures. User Manual, version 1.8.7. Urbana-Champaign, IL, 2003.

[29] B. A. Izzudin, and A. S. ElNashai, ADAPTIC, a Program for Adaptive Large Displacement Elastoplastic Dynamic Analysis. Research Report ESEE, Report No. 89/7, Imperial College. London, 1989.

[30] A. S. ElNashai, R. Pinho, and S. Antoniou, INDYAS – A Program for INelastic DYnamic Analysis of Structures. *Engineering Seismology and Earthquake Engineering*, Report No. ESEE 00-2, 2000.

[31] R. Pinho,"Selective Repair &Strengthening of RC Buildings. *PhD. Thesis, Imperial College*, London, 2000.

[32] S. Jeong, and A. S. ElNashai, Analytical Assessment of an Irregular RC Frame for Full-Scale 3D Pseudo- Part I: Analytical Model. *Journal of Earthquake Engineering*, vol. 9(1), 2005, pp. 95-128.

[33] ATC, 2016, Guidelines for Nonlinear Structural Analysis for Design of Buildings: Part IIb – Reinforced Concrete Moment Frames. Draft report for the Applied Technology Council Project, 114, 2016.

[34] J. B. Mander, M. J. N. Priestley, and R. Park, Theoretical stress-strain model for confined concrete. *Jr. of Structural Engineering*, ASCE, **114(8)**, 1804-1826, 1988.

[35] J. E. Martinez-Rueda, and A. S. ElNashai, Confined concrete model under cyclic load. *Materials and Structures*, **30(197)**, 139-147, 1997.

[36] A. S. ElNashai, and B. A. Izzuddin, Modeling of material non-linearities in steel structures subjected to transient dynamic loading. *Earthquake Engineering & Structural Dynamics*, **22**, 509-532, 1993.

[37] B.A. Izzuddin, and A.S. Elnashai, 1993, Eulerian Formulation for large displacement analysis of space frames. *Journal of Engineering Mech*anics, **119(3**), 549-569, 1993.

[38] A. K. Chopra, Dynamics of Structures: Theory and Applications to Earthquake Engineering. Second Edition, Prentice-Hall of India, 2005.

[39] V. Bertero, M. Bendimerad, and C. Shah, C. Fundamental Period of Reinforced Concrete Moment Resisting Frame Structures. Report no. 87, Stanford University, 1988.

[40] D. A. Gasparini and H. E. Vanmarcke , SIMQKE a Program for Artificial Motion Generation: User's Manual and Documentation, MIT, USA 1976.

[41] Seismosoft, Seismosignal v 3.2.0, www.seismosoft.com, 2008.

[42] B. M. Broderick, and A. S. Elnashai, "Proposal for behaviour factors for composite frames in Eurocode 8", European Seismic Design Practice: Research and Application, *Proceedings, 5th SECED Conference,* Balkema, Rotterdam, 1995, pp. 333-340.

[43] A. J. Kappos, "A comparative assessment of RJC structures designed to the 1995 Eurocode 8 and the 1985 CEB seismic code", *The Structural Design of Tall Buildings*, Vol. 6 (1), 1997, pp. 59-83.

COMPDYN 2019
7th ECCOMAS Thematic Conference on
Computational Methods in Structural Dynamics and Earthquake Engineering
M. Papadrakakis, M. Fragiadakis (eds.)
Crete, Greece, 24–26 June 2019

RINTC-E PROJECT: TOWARDS THE ASSESSMENT OF THE SEISMIC RISK OF EXISTING BUILDINGS IN ITALY

Iunio Iervolino,[1] Andrea Spillatura,[2] Paolo Bazzurro[3]

[1] Dipartimento di Strutture per l'Ingegneria e l'Architettura
Università degli Studi di Napoli Federico II Naples, Italy
e-mail: iunio.iervolino@unina.it

[2] European Centre for Training and Research in
Earthquake Engineering (EUCENTRE) Pavia, Italy
andrea.spillatura@gmail.com

[3] University School for Advanced Studies of Pavia
(IUSS Pavia) Pavia, Italy
paolo.bazzurro@iusspavia.it

Abstract

The 2019-2021 RINTC project is the extension of the 2015-2017 RINTC project that assessed, explicitly, the seismic risk of code-conforming Italian structures (i.e., designed according to the seismic code currently enforced). The aim of the new RINTC project is to extend the methodological framework developed in RINTC to the existing structures (designed and built before 2008), which constitute the vast majority of Italian building stock. In 2018 some analyses, preliminary with respect to the 2019-2021 project, were carried out; i.e., the 2018 RINCT-e project. In particular, five structural typologies were considered: masonry, reinforced concrete, pre-cast reinforced concrete, steel, and seismically isolated buildings. In the framework of the 2018 project, several archetype structures for each typology have been designed and/or retrofitted according to standard practices consistent with outdated codes, enforced since the eighties, for five sites across Italy spanning a wide range of seismic hazard levels (evaluated according to current standards). The seismic vulnerability of the designed structures was assessed by subjecting three-dimensional nonlinear computer models to multi-stripe non-linear dynamic analysis. Integration of the probabilistic hazard and probabilistic vulnerability (i.e., fragility) yields the annual failure rate for each of the designed and modeled structure. In the paper, the 2019-2021 RINTC project is introduced and the preliminary failure rates of the existing structures are presented.

Keywords: Reliability, Structures, Earthquake Engineering, Failure, Damage.

1 INTRODUCTION

The 2015-2017 RINTC (*Rischio Implicito delle strutture progettate secondo le NTC*) project was a large research effort aimed at assessing the seismic structural reliability, expressed in terms of annual failure rate, of code-conforming structures in Italy [1][3]. For the purposes of the project three sites exposed to comparatively low- mid- and high-seismic hazard were considered; i.e., Milan (MI), Naples (NA) and L'Aquila (AQ). At these sites, residential/industrial buildings belonging to five structural typologies were designed according to the recent Italian seismic code; i.e., un-reinforced masonry (URM), reinforced concrete (RC), pre-cast reinforced concrete (PRC), steel (S), and base-isolated (BI) structures. All typologies were designed at all sites with reference to two limit states considered by the code; *damage control* and *life-safety*. Three-dimensional non-linear models were developed for the buildings, with the aim of running dynamic analysis for performance assessment with respect to two ad-hoc defined failure conditions*: usability-preventing damage* (UPD) and *global collapse* (GC). Earthquake records for the non-linear dynamic analysis were selected according to the *conditional-spectrum* (CS) [4] approach. The results mainly indicate that the seismic structural reliability changes by orders of magnitude as the seismic hazard changes from site-to-site, despite homogeneity of the exceedance return period of the design ground motion and of the other design and modelling choices. The contribution of uncertainty in modelling assumptions and soil-structure interaction was also quantified and found of relatively minor importance.

Herein the 2019-2021 RINTC project is introduced. It targets the seismic structural reliability of *low-* and *pre-code* structures in Italy. This is because these structures constitute the vast majority of the Italian building stock. To compare the reliability results to those already obtained for the code-conforming structures, the modelling and analysis framework is retained from the previous project. Three code levels, previous to the contemporary era, are broadly identified for the existing structures in Italy: (1) the 80-90s; (2) the 70s; (3) the pre-70s era. While (1) and (2) represent ages of evolution of the codes toward modern earthquake-resistant design, (3) is when most of the buildings in Italy were designed basically for gravity loads.

In this short paper, the workplan, in terms of analyzed structures, is presented together with the preliminary results from the preparatory activity developed in 2018. In particular the 2018 RINTC-e project is discussed. To this aim, the following is organized such that the case studies of the 2019-2021 RINTC project are illustrated. Subsequently, the structures analyzed in 2018, mostly referring to design or seismic upgrade of structures according to the codes enforced in the 80-90s (some also from the 70s) in Italy, are described along with the representation of the ground motion for reliability assessment via non-linear dynamic analysis. Then, the failure criteria considered, analogous to the 2015-2017 RINTC project are recalled. Finally, the, very preliminary, results in terms of failure rates are discussed. Final remarks close the paper.

2 RINTC-E SITES, STRUCTURES AND BUILDING CODES

The RINTC 2019-2021 project deals with existing buildings built, essentially, in the XX century, in which the design in Italy evolved from only gravity-load-design all-over the country to earthquake-resistant design in most of the country [5]. All the considered codes precede the contemporary era in which seismic actions are based on probabilistic seismic hazard analysis and the principle of seismic design (e.g., *capacity design*) are fully acknowledged by the code.

Table 1 provides a matrix where the buildings considered in the 2019-2021 project are associated to the design/construction age and the sites where they are supposed[1] to be located. It is to note that two sites, Rome (RM) and Catania (CT), have been specifically-considered for the purposes of the RINTC-e project. In particular, Catania has been considered as a site with relatively high seismic hazard according to the current code, yet characterized by gravity-load design only since a few decades ago. The addition of Rome downtown allowed to consider large URM buildings typical of historical downtowns in Italy, similar to Naples, yet exposed to different seismic hazard. Figure 1 (left), shows the considered sites overlaid on the map of the *peak ground acceleration* (PGA) with 475 years exceedance return period on rock, which is adopted by the current code as a basis to determine the current design actions [6],[7]. Figure 1 (right) shows the PGA on rock hazard curves for the five sites, ad-hoc computed, yet consistent with the probabilistic seismic hazard study at the basis of the current code [8]. The relative seismic design hazard levels can be observed from the figure. MI is the less hazardous and AQ is the most hazardous.

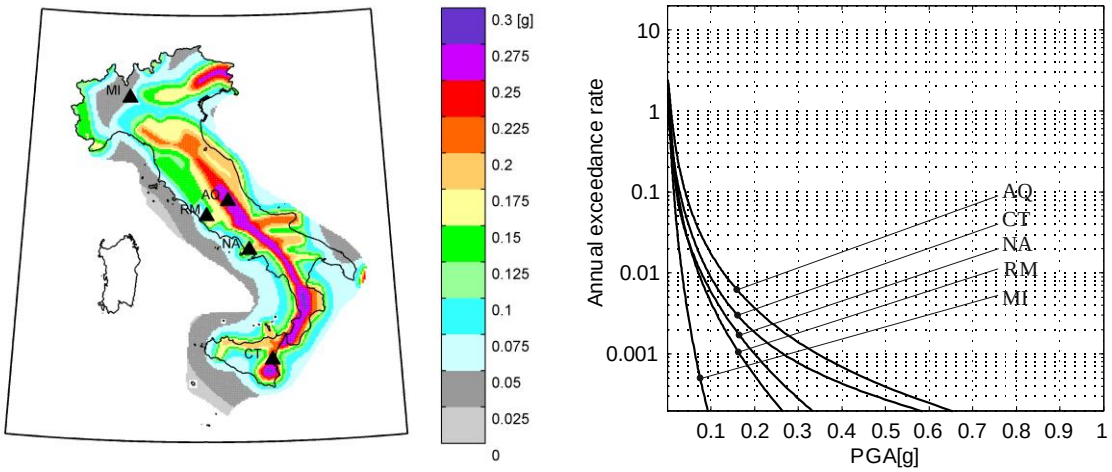

Figure 1: Left – considered sites on the map of peak ground acceleration (PGA) with 475 years exceedance return period on rock, adopted by the current code; right – PGA hazard curves on rock for the five sites.

Table 1: Building/sites matrix for the existing buildings to be studied in the 2019-2021 RINTC project and those analyzed in the 2018 RINTC-e project (in bold).[2]

	Milan (MI)	*Rome (RM)*	*Naples (NA)*	*Catania (CT)*	*L'Aquila (AQ)*
RC	G(50s-60s), **G(70s)**, G(80s-90s),		G(50s-60s), **G(70s)**, G(80s-90s),	G(50s-60s), **G(70s)**, G(80s-90s)	S(50s-60s), S(70s), **S(80s-90s)**
URM	G(<20s), G(20s-40s)	G(90s), SU(80s-90s), SU(08-18), **SU(NTC)rs1**, **SU(NTC)rs2**	G(<20s), **SU(NTC)str1**, **SU(NTC)str2**, **SU(POR)str1**, **SU(POR)str2**	G(<20s), G(50s-60s)	G(<20s), SU(80s-90s), SU(2008-2018)

[1] URM buildings in Rome are actual buildings located in the city's downtown.

[2] G = gravity-load-design; S = earthquake-resistant design; SU = seismically upgraded (see [9] for RC and [10] for PRC); NTC = current Italian code [6], POR = analysis method (see [11]), str-1,2= structure type, rs-1,2 = rehabilitation strategy (see [11]); HP = portal with Hinges, FP= fully constrained portal, SP = sandwich panels, TS = trapezoidal sheeting (see [12]); BI-G,S= RC structures isolated with high-damping rubber bearing and/or sliders (HDRB) or double-curvature friction pendulums (DCFP) (see [13]). Numbers in the parentheses represent reference years for code provisions used for design.

PRC	**G(70s),** G(60s-80s), G(80s-90s)		**G(70s),** G(60s-80s), S(80s-90s)	**G(70s)**	S(60s-80s), S(80s-90s), **S(80s-90s)**
S	FP-SP(80s-90s), HP-TS(80s-90s), HP-SP(80s-90s)		FP-SP(80s-90s), HP-TS(80s-90s), HP-SP(80s-90s)		FP-SP(80s-90s), **HP-BF(80s-90s), HP-TS(80s-90s)**, **HP-SP(80s-90s)**
BI			BI-G(50s-60s), **BI-G(70s),** G(80s-90s)		BI-S(50s-60s), BI-S(70s), **BI-S(80s-90s)**

The failure rates of buildings in bold in Table 1 are preliminarily addressed in this paper. The considered codes, although modern, are not at the contemporary level of seismic design, at least in terms of definition of design action and resistant mechanism rules such as capacity design. In most of cases, buildings were designed according to these codes; however, in the case of unreinforced masonry, older buildings were upgraded according to the considered code or, in some cases according to the current code, indicated as NTC [6]. In the following, few details for each typology are given; however, the interested reader should refer to the specific papers cited for a more comprehensive discussion about design, modelling and analysis.

2.1 URM buildings

For what concerns URM buildings, the 2018 RINTC-e plan was to retrofit older buildings. Retrofit interventions on URM buildings were designed according to the code, issued 1981, for repair and strengthening of buildings damaged by earthquakes [14], and the associated guidelines [15]. These documents incorporate the so-called POR method, originally proposed by Tomazevic [16], for the seismic analysis of retrofitted URM buildings. The relevance of this code is that it was published after the magnitude (M) 6.5 1976 (Friuli, northern Italy), M5.8 1979 (Norcia, southern Italy) and M6.9 1980 (Irpinia, southern Italy) earthquakes, and then extensively used in the reconstruction phases. Interventions were also alternatively designed according to the current code (NTC). Eventually, retrofit interventions were assessed according to the code update published in 2018 [7]. As an example, Figure 2 reports the upgraded buildings in Naples, about which further details can be found in [11].

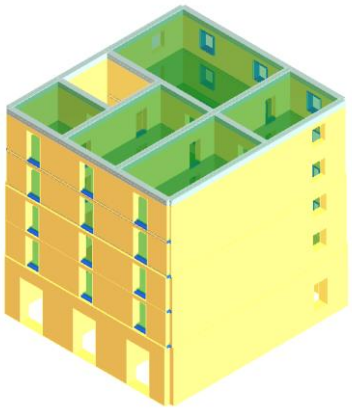

Figure 2: the URM building analyzed in Naples.

2.2 RC buildings

In 2018, case-study structures representative of the existing residential RC building stock in Italy were defined through a simulated design process. These structures were three-storey

buildings, designed for gravity loads only during the 70s (gravity-load-design, G) or for seismic loads during 80s-90s (seismic-load-design, S). G-buildings were designed according to [17]. S-buildings were designed according to [18], as technical code, and to [19], for seismic load provisions. S-buildings were assumed to be located in L'Aquila (*second seismic category* at the time of design; i.e., mid seismic loads in a set of three), and thereby they were designed with a base shear equal to 0.07 times the building weight, adopting a linear static analysis method. Both for G- and S-buildings, the allowable stress design method was used. In all cases modelling considered infilled structures. Details are given in [9], while Figure 3 provides an example of a three-storey RC building.

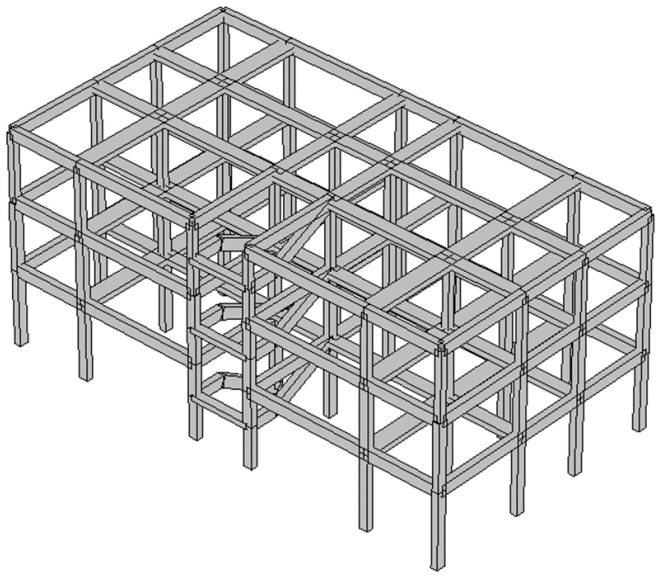

Figure 3: Three-dimensional view of a three-storey S building.

2.3 PRC buildings

Six different single-story PRC buildings were designed according to [17] and [20], enforced in Italy in the 70s, for three different sites (MI, NA, CT) and for two different heights of the columns (6 and 9 m).. The considered codes do not take into account seismic loads and the design follows a deterministic approach according to the allowable stress design. Roof elements and beams are designed only for vertical loads (dead and live loads), whereas the design of columns takes into account the wind load and temperature variations, which are the only horizontal forces acting on the buildings in the design phase. In fact, single-story PRC buildings are also designed according to the seismic codes enforced in Italy in 80s and 90s. Details are given in [10], while Figure 4 provides the front and plan views of the typical PRC buildings designed and modelled in the project.

2.4 S buildings

The building structures were obtained by simulating a design carried out according to the code and standards for steel buildings enforced in the years 1980s-1990s [19],[21][22]. In more detail, [21] contained information regarding variable load values (i.e., wind and snow loads and variable gravity loads). Instead, [19] contained information about the site seismic

classification and the consequent calculation of the equivalent static forces, for both horizontal and vertical components. In addition, [22] was a well know guideline for specific design of steel structures, in terms of resistance, stability and deformability checks. Steel structures design contemplated only hinged-portal (HP) in 2018, while corresponding fully-constrained portals (FP) will be examined in 2019-2021. Concerning the cladding, both sandwich panels (SP) and trapezoidal sheeting (TS), were considered. Details are given in [12], while Figure 3 provides a three-dimensional view of the typical steel building designed and modelled in the project.

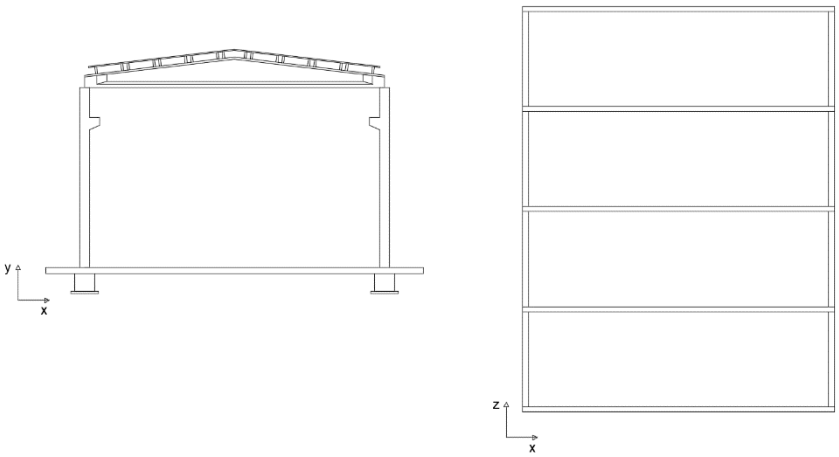

Figure 4: Front (left) and plan (right) views of the typical PRC buildings designed and modelled in the project.

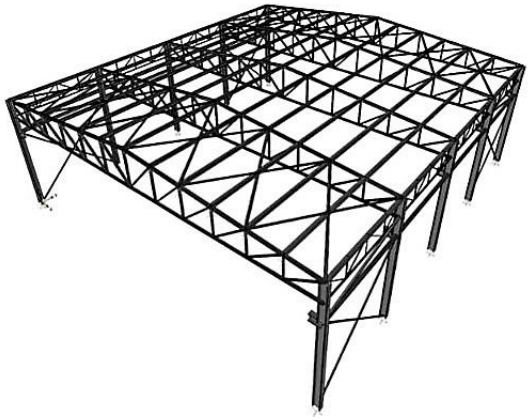

Figure 5: Three-dimensional view of the topical steel building designed herein.

2.5 BI buildings

For the case of BI, the objective was not to design the isolation system according to old codes, yet to protect the existing buildings according to the current code [6],[7]. In particular, for the existing fixed-base RC building (see Table 2), the base shear associated with the onset of plastic deformations was first identified by pushover analysis, assuming a uniform distribution of lateral forces. After that, the lowest value of the fundamental period of the base isolated building was derived entering the design spectrum with the spectral acceleration associated to the occurrence of the first plastic hinge. Next, the maximum displacement of the isolation system was evaluated using the displacement (code) spectrum at the *collapse* limit-state.

Based on the target period and required displacement capacity, suitable devices were selected from the manufacturers' catalogues. The verification of the base-isolated building was carried out through response spectrum analysis of a three-dimensional model of the structure, considering the performance requirements and compliance criteria specified in the current code. See [13] for details.

3 FAILURE CRITERIA

The failure rates were computed with respect to two performance levels, global collapse and usability-preventing damage. In general, the GC criterion is based on the deformation capacity corresponding to a certain level of strength deterioration, measured on the nonlinear static capacity curves of the structural models (Figure 6, left).[3] For all the structural models in any dynamic analysis, the occurrence of GC was checked using the maximum demand-over-capacity ratio in the two directions.

The criteria for UPD are based on a multi-criteria approach (Figure 6, right) that considers the onset of any of the following three conditions: (a) light damage in 50% of the main non-structural elements (e.g., infills); (b) at least one of the non-structural elements reached a severe damage level leading to significant interruption of use; (c) attainment of 95% of the maximum base-shear of the structure. Although these are the general criteria, several existing buildings belonging to the case studies analyzed required ad-hoc adjustments and further considerations about failure. The details on these issues are given in the companion articles for these specific typologies.

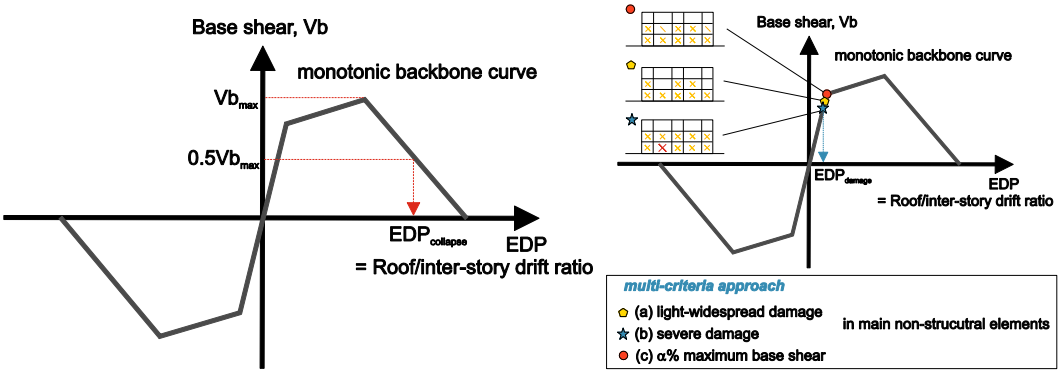

Figure 6: left – general definition for the GC e failure criterion; right – general definition of the UPD failure criterion. (Figure adapted from [3])

4 SEISMIC HAZARD AND RECORDS FOR DYNAMIC ANALYSIS

To compute the failure rates, hazard curves are required (see section 8). The ground motion intensity measures (IMs) considered are pseudo-spectral acceleration Sa at periods (T) close to the first-mode periods of the developed structural models. Table 2 reports the ground motion intensity measures the pseudo-spectral accelerations considered at the sites. The table acknowledges that the soil class for the analysis (and for the design, where applicable), was C according to the site classification of Eurocode 8 [23].

The hazard curves, expressed in terms of annual exceedance rate, $\lambda_{Sa(T)}(x)$, versus ground motion intensity, needed for the calculations, were computed as described in [3], that

[3] The GC condition for BI buildings was assumed to occur either if the superstructure fails or if the base isolation system fails.

is using the seismic zone source model of [8], with the magnitude distribution and rates described in [24], and the ground motion prediction equation of [25] (or that of [26] for the longer spectral periods not covered by [25]). Hazard calculations have been carried out via the OPENQUAKE platform [27].

Table 2: periods at which pseudo-spectral acceleration hazard has been computed at each site for record selection and failure rate computation.

Site	Soil C
MI	$T=\{0.5s,1.0s,2.0s\}$
NA	$T=\{0.25s,0.5s,1.0s,2.0s,3.0s\}$
RM	$T=\{0.15s,\ 0.5s\}$
CT	$T=\{0.5s,1.0s,2.0s\}$
AQ	$T=\{0.5s,1.0s,\ 2.0s,3.0s\}$

Hazard curves were discretized in ten IM values corresponding to the following return periods (T_R) in years: $T_R=\{10,50,100,250,500,1000,2500,5000,10000,100000\}$. No IM-values with exceedance return period longer than $T_R=100000\,yr$ were calculated, to avoid large extrapolations.

To select the ground motion records to be used as input for dynamic analysis, the CS approach has been considered, in analogy to what done in [3]. It accounts for seismic hazard disaggregation, to fit the scopes of non-linear dynamic multi-stripe analysis (MSA), which was used to assess seismic structural vulnerability.

The record selection procedure was that available at http://web.stanford.edu/~bakerjw/research/conditional_spectrum.html. The selected records were extracted mainly from the Italian accelerometric archive (http://itaca.mi.ingv.it/; [28]) and only if no records with similar spectra were available there, suitable records in the NGAwest2 (http://peer.berkeley.edu/ngawest2/) database [29] were selected instead.

The record selection delivered two-hundreds pairs of records for each IM; twenty records for each one of the ten stripes. Hence, two-hundred records have been employed in the analysis of each individual structural model. To reduce the computational demand from non-linear dynamic analysis, the selected records have been post processed to remove the parts of the signal outside $\{t_{0.05\%},t_{99.95\%}\}$ range, where $D_{99.90\%}=t_{99.95\%}-t_{0.05\%}$ is the 99.90% significant duration of the record [30], yet keeping synchronization of horizontal components.

5 STRUCTURAL ANALYSIS AND FAILURE RATES

The failure rates (λ_f) shown in the following, were evaluated via equation (1):

$$\lambda_f=\int_0^{x_{10^{-5}}} P\left[\,failure\middle|Sa(T)=x\right]\cdot\left|d\lambda_{Sa(T)}(x)\right|+10^{-5}. \qquad (1)$$

In the equation, $d\lambda_{Sa(T)}(x)$ is the derivative of the hazard curve of interests, and $P\left[\, failure \middle| Sa(T)=x \right]$ is the failure probability of the structure for which the failure rate is being evaluated; i.e., the structural fragility. The integral stops at the last IM value $\left(x_{10^{-5}}\right)$ for which hazard is computed; i.e., that with 10^{-5} annual exceedance rate. Thus, to account for this truncation 10^{-5} is added to the integral. This is an approximation that assumes structural failure, with certainty, for IMs larger than $x_{10^{-5}}$.

It has been briefly recounted in the previous section how $\lambda_{Sa(T)}$ (i.e., the seismic hazard) has been computed. For what concerns $P\left[\, failure \middle| Sa(T)=x \right]$, it has been evaluated for each structure via MSA (see [3]). In particular, each (three-dimensional) structural model has been subjected to 20 records (two horizontal pairs), ad-hoc selected (see section 4) for each of ten IM values corresponding to the return periods at which probabilistic seismic hazard was computed. The sample of 20 response values collected in this way forms a so-called *stripe*, because, in a hypothetical plot of response vs IM, they are all aligned. For each stripe, the fragility was computed via equation (2):

$$P\left[\, failure \middle| Sa(T)=x_i \right] = \left\{ 1-\Phi\left[\frac{log\left(edp_f\right)-\mu_{log(EDP)|Sa(T)=x_i}}{\sigma_{log(EDP)|Sa(T)=x_i}} \right] \right\} \left(1-\frac{N_{col,Sa(T)=x_i}}{N_{tot,Sa(T)=x_i}} \right) + \frac{N_{col,Sa(T)=x_i}}{N_{tot,Sa(T)=x_i}} \quad (2)$$

where EDP is the *engineering demand parameter*), representing a structural response measure (e.g., maximum inter-storey drift ratio) and edp_f is the structural capacity for the performance of interest. The quantities $\left\{ \mu_{log(EDP)|Sa(T)=x_i}, \sigma_{log(EDP)|Sa(T)=x_i} \right\}$ are the mean and standard deviation of the logarithms of EDP when $Sa(T)=x_i$, $i=\{1,\ldots,10\}$, while $\Phi(\bullet)$ is the cumulative Gaussian distribution function and $N_{col,Sa(T)=x_i}$ is the number of collapse cases (i.e., those reaching global instability according to the terminology in [31]). Finally, $N_{tot,Sa(T)=x_i}$ is the number of ground-motion records, here 20, with $Sa(T)=x_i$, $i=\{1,\ldots,10\}$.

Although equation (2) is the general framework, in selected cases $P\left[\, failure \middle| Sa(T)=x \right]$ has been empirically evaluated by counting the number of records for which failure has been observed, $N_{f,Sa(T)=x_i}$, as shown in equation (3).

$$P\left[\, failure \middle| Sa(T)=x_i \right] = \frac{N_{f,Sa(T)=x_i}}{N_{tot,Sa(T)=x_i}} \quad (3)$$

5.1 Preliminary results

Figure 7 provides the preliminary failure rates for the buildings analyzed in 2018. The figure contemplates both the UPD as well as the GC rates for soil C. Data are arranged per increasing design hazard of the sites according to the current code. It can be seen that the trend observed in [1][3] for current-code-conforming structures, which implied decreasing reliability for increasing design hazard, is less clear for existing buildings, likely due to the large heterogeneity of the buildings analyzed. Moreover, as expected these rates are generally larger than those of new constructions. Nevertheless, these are very preliminary and are far to be

considered consolidated yet. For example, rates for UPD and GC for BI structures, needs further deepening.[4]

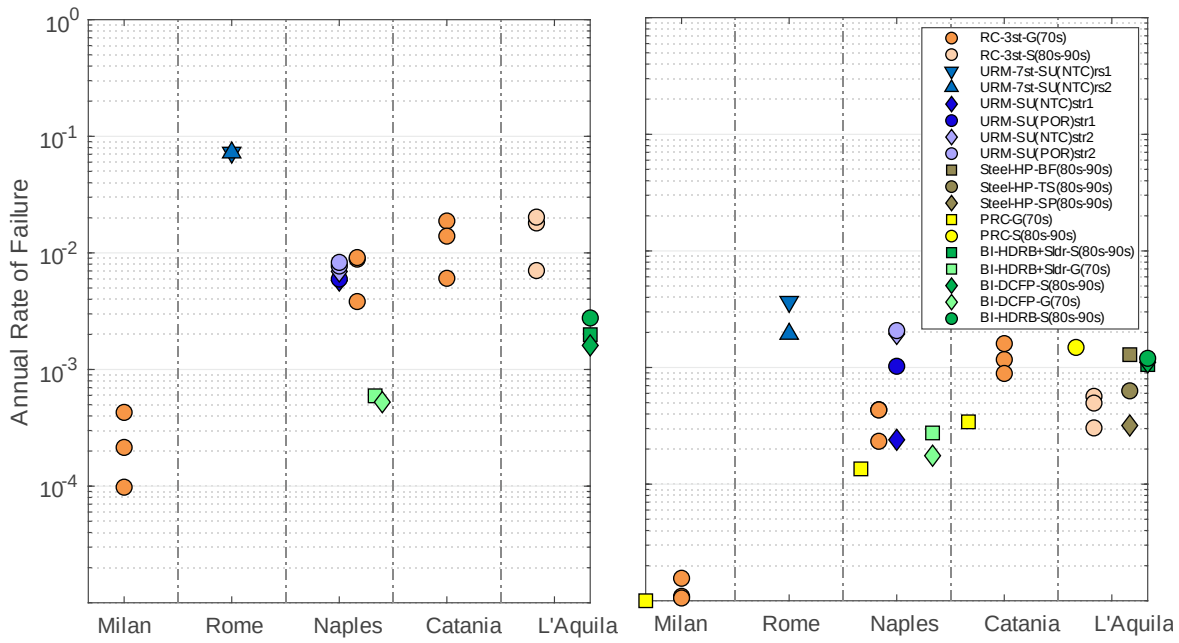

Figure 7: preliminary failure rates from the 2018 RINTC-e project for soil C; left is UPD, right is GC.

6 FINAL REMARKS

In this paper the 2019-2021 RINTC project was introduced. The project deals with the seismic reliability assessment of the existing building designed for earthquake resistance via obsolete codes or for gravity loads only. The project has the ambition to consider a wide range of Italian codes, following the evolution of construction practice in the XX century. As a preliminary work, some cases were investigated in 2018, in the framework of the RINTC-e project propaedeutic to the 2019-2021. These are mostly buildings designed according to 70s or 80s-90s codes as well as older buildings seismically upgraded according to codes from 80s-90s. Finally, base-isolated buildings are existing buildings of the mentioned type seismically upgraded according to the current code. Failure rates computed for these cases show a less clear trend with respect to what observed for current-code-conforming structures and generally higher values, as expected. Nevertheless, these results are not yet consolidated and will be likely revisited during the course of the 2019-2021 RINTC project.

7 ACKNOWLEDGEMENTS

The study was developed between 2017 and 2018 in the framework the ReLUIS-DPC and EUCENTRE-DPC projects, funded by the *Presidenza del Consiglio dei Ministri, Dipartimento della Protezione Civile* (DPC).

8 REFERENCES

[1] RINTC Workgroup, *Results of the 2015-2016 RINTC project*. ReLUIS report, ReLUIS, Naples, Italy, 2017. Available at https://goo.gl/j8H7MV

[4] With regard to BI, also note that the UPD rates presented herein also include the failure of the isolation system, differently from what discussed in [13], where damage conditions were only referred to the super-structure.

[2] I. Iervolino, A. Spillatura, and P. Bazzurro, Assessing the (Implicit) Seismic Risk of Code-Conforming Structures in Italy, in *COMPDYN 2017 - 6th ECCOMAS Thematic Conference on Computational Methods in Structural Dynamics and Earthquake Engineering*, Rhodes Island, Greece, 2017.

[3] I. Iervolino, A. Spillatura, P. Bazzurro, Seismic reliability of code-conforming Italian buildings. *J. Earthq. Eng.*, **22**(S2), 5-27, 2018.

[4] T. Lin, C.B. Haselton, J.W. Baker, Conditional spectrum-based ground motion selection. Part I: Hazard consistency for risk-based assessments. *Earthq. Eng. Struct. D.*, **42**, 1847-1865, 2013.

[5] I. Iervolino, F. Petruzzelli, NODE v.1.0 beta: attempting to prioritize large-scale seismic risk of engineering structures on the basis of nominal deficit, in XIV *Convegno Nazionale L'Ingegneria Sismica in Italia*, Bari, 2011.

[6] CS.LL.PP., Norme tecniche per le costruzioni. *Gazzetta Ufficiale della Repubblica Italiana*, **29**, 2008. (In Italian.)

[7] CS.LL.PP., Aggiornamento delle norme tecniche per le costruzioni. *Gazzetta Ufficiale della Repubblica Italiana*, **42**, 2018. (In Italian.)

[8] M. Stucchi, C. Meletti, V. Montaldo, H. Crowley, G.M. Calvi, E. Boschi, Seismic hazard assessment (2003–2009) for the Italian building code. *B. Seismol. Soc. Am.*, **101**, 1885-1911, 2011.

[9] P. Ricci, V. Manfredi, F. Noto, M. Terrenzi, M.T. De Risi, M. Di Domenico, G. Camata, P. Franchin, A. Masi, F. Mollaioli, E. Spacone, G.M. Verderame, RINTC-e: Towards seismic risk assessment of existing residential reinforced concrete buildings in Italy, in *COMPDYN 2019 - 7th ECCOMAS Thematic Conference on Computational Methods in Structural Dynamics and Earthquake Engineering*, Crete, Greece, 2019.

[10] G. Magliulo, D. Bellotti, C. Di Salvatore, F. Cavalieri, RINTC-e project: towards the seismic risk of low and pre-code single-story r/c precast buildings in Italy, in *COMPDYN 2019 - 7th ECCOMAS Thematic Conference on Computational Methods in Structural Dynamics and Earthquake Engineering*, Crete, Greece, 2019.

[11] S. Bracchi, S. Cattari, S. Degli Abbati, S. Lagomarsino, G. Magenes, M. Mandirola, S. Marino, A. Penna, M. Rota, RINTC-e project: towards the seismic risk of retrofitted existing Italian URM buildings, in *COMPDYN 2019 - 7th ECCOMAS Thematic Conference on Computational Methods in Structural Dynamics and Earthquake Engineering*, Crete, Greece, 2019.

[12] G. Cantisani, G. Della Corte, RINTC-e: Seismic risk of pre-code single-story non-residential steel buildings in Italy, in *COMPDYN 2019 - 7th ECCOMAS Thematic Conference on Computational Methods in Structural Dynamics and Earthquake Engineering*, Crete, Greece, 2019.

[13] L. Ragni, D. Cardone, N. Conte, A. Dall'Asta, A. Di Cesare, A. Flora, N. Lamarucciola, F. Micozzi, F. Ponzo, RINTC-e project: the seismic risk of existing Italian RC buildings retrofitted with seismic isolation, in *COMPDYN 2019 - 7th ECCOMAS Thematic Conference on Computational Methods in Structural Dynamics and Earthquake Engineering*, Crete, Greece, 2019.

[14] MIN.LL.PP., Decreto ministeriale 2 luglio 2981. *Gazzetta Ufficiale della Repubblica Italiana*, **198**, 1981. (In Italian.)

[15] MIN.LL.PP., Circolare 30 luglio 1981, Istruzioni relative alla normativa tecnica per la riparazione ed il rafforzamento degli edifici in muratura danneggiati dal sisma, Rome, Italy. (In Italian.)

[16] M. Tomaževič, *The computer program POR*, Report ZRMK, Institute for Testing and Research in Materials and Structures, Ljubljiana, Slovenia, 1978. (In Slovenian.)

[17] CS.LL.PP., Norme tecniche per la esecuzione delle opere in cemento armato normale e precompresso e per le strutture metalliche. *Gazzetta Ufficiale della Repubblica Italiana,* **198**, 1974. (In Italian.)

[18] CS.LL.PP., Norme tecniche per le opere in c.a. normale e precompresso e per le strutture metalliche. *Gazzetta Ufficiale della Repubblica Italiana,* **65**, 1992. (In Italian.)

[19] CS.LL.PP., Norme tecniche relative alle costruzioni antisismiche. *Gazzetta Ufficiale della Repubblica Italiana,* **108**, 1986. (In Italian.)

[20] C.N.R., *UNI 10012-67 – Ipotesi di carico sulle costruzioni.* UNI, Milan, Italy, 1967. (in Italian.)

[21] CS.LL.PP., Istruzioni relative ai carichi, ai sovraccarichi ed ai criteri generali per la verifica di sicurezza delle costruzioni. *Gazzetta Ufficiale della Repubblica Italiana*, **140**, 1982.

[22] C.N.R., *UNI 10011-88* – Costruzioni di acciaio: istruzioni per il calcolo, l'esecuzione, il collaudo e la manutenzione. UNI, Milan, Italy, 1988. (in Italian.)

[23] C.E.N., Eurocode 8: *Design of Structures for Earthquake Resistance: Part 1: General Rules, Seismic Actions and Rules for Buildings*, European Committee for Standardization, Bruxelles, Belgium, 2004.

[24] S. Barani, D. Spallarossa, P. Bazzurro, Disaggregation of probabilistic ground-motion hazard in Italy. *B. Seismol. Soc. Am.*, **99**, 2638-2661, 2009.

[25] N.N. Ambraseys, K.U. Simpson, J.J. Bommer, Prediction of horizontal response spectra in Europe. *Earthq. Eng. Struct. D.*, 25, 371-400, 1996.

[26] S. Akkar, J.J. Bommer, Empirical Equations for the Prediction of PGA, PGV, and Spectral Accelerations in Europe, the Mediterranean Region, and the Middle East. *Seismol. Res. Lett.*, 81, 195-206, 2010.

[27] D. Monelli, M. Pagani, G. Weatherill, V. Silva, H. Crowley, The hazard component of OpenQuake: The calculation engine of the Global Earthquake Model, in *15WCEE - 15th world conference on earthquake engineering*, Lisbon, Portugal, 2012.

[28] L. Luzi, S. Hailemikael, D. Bindi, F. Pacor, F. Mele, F. Sabetta, ITACA (ITalian ACcelerometric Archive): a web portal for the dissemination of Italian strong-motion data, *Seismol. Res. Lett.*, 79, 716-722, 2008.

[29] T.D. Ancheta, R.B. Darragh, J.P. Stewart, et al., NGA-West2 database. *Earthq. Spectra,* 30, 989-1005, 2014.

[30] R. Dobry, I.M. Idriss, E. Ng, Duration characteristics of horizontal components of strongmotion earthquake records. *B. Seismol. Soc. Am.*, 68, 1487-1520, 1978.

[31] N. Shome, C.A. Cornell, Structural seismic demand analysis: Consideration of "Collapse", in *PMC2000 - 8th ASCE Specialty Conference on Probabilistic Mechanics and Structural Reliability*. University of Notre Dame, South Bend, Indiana, 2000.

COMPDYN 2019
7th ECCOMAS Thematic Conference on
Computational Methods in Structural Dynamics and Earthquake Engineering
M. Papadrakakis, M. Fragiadakis (eds.)
Crete, Greece, 24–26 June 2019

ASSESSMENT OF THE RESISTANCE MODEL UNCERTAINTIES IN PLANE STRESS NLFEA OF CYCLICALLY LOADED REINFORCED CONCRETE SYSTEMS

D. Gino[1], P. Castaldo[2], A. Dorato[3] and G. Mancini[4]

[2] Department of Structural, Geotechnical and Building Engineering (DISEG), Politecnico di Torino, Turin, Italy
corso Duca degli Abuzzi 24, 10129 Torino, ITALY
e-mail: diego.gino@polito.it

[2] Department of Structural, Geotechnical and Building Engineering (DISEG), Politecnico di Torino, Turin, Italy
corso Duca degli Abuzzi 24, 10129 Torino, ITALY
e-mail: paolo.castaldo@polito.it

[2] Department of Structural, Geotechnical and Building Engineering (DISEG), Politecnico di Torino, Turin, Italy
corso Duca degli Abuzzi 24, 10129 Torino, ITALY
e-mail: alessandro.dorato@polito.it

[2] Department of Structural, Geotechnical and Building Engineering (DISEG), Politecnico di Torino, Turin, Italy
corso Duca degli Abuzzi 24, 10129 Torino, ITALY
e-mail: giuseppe.mancini@polito.it

Abstract

The present work is devoted to estimate the resistance model uncertainty within plane stress non-linear finite element analyses (NLFEAs) of reinforced concrete structures subjected to cyclic loads. Specifically, various shear walls experimentally tested are considered for the investigation. The comparison between the plane stress NLFE structural model results and the experimental outcomes is carried out considering the possible modelling hypotheses available to describe the mechanical behaviour of reinforced concrete members subjected to cyclic loads. Several NLFE structural models are defined for each experimental test in order to investigate the resistance model uncertainty.

Keywords: model uncertainties, NLFEAs, reinforced concrete structures, modeling hypotheses, cyclic loads.

1 INTRODUCTION

In the last decades, non-linear finite element analyses (NLFEAs) have increasingly become the most common and practical instruments able to model the actual mechanical behaviour of structural systems, such as reinforced concrete elements, in any loading condition (i.e., service limit state (SLS) and ultimate limit state (ULS)). In this context, although several guidelines for NLFEAs have been recommended by [1]-[4] in order to assure an accurate calibration and definition of the structural FE model, the results from such complex modelling need to be properly processed in order to satisfy safety and reliability requirements for engineering purposes [5]-[6]. To this aim, Bayesian finite elements have been proposed by [7] to take into account the model uncertainties for structural analysis. Contextually, different safety formats for NLFEAs have been proposed and commented in literature by several authors [8]-[13] and international codes [14]-[15] as well as their applications have been discussed by [16]-[18]. In these safety formats, uncertainties regarding the material (i.e., aleatory uncertainties) and the definition of the structural model (i.e., epistemic uncertainties) should be properly addressed in order to derive reliability-consistent design values of the global structural resistances. With regard to the material uncertainty, the corresponding randomness is usually well known and assessed, whereas the model uncertainty (i.e., uncertainty mainly related to the definition of the resistance model) associated with NLFEAs is not typically simple to be evaluated due to the different modelling hypotheses for the definition of a non-linear FE structural model. In fact, the prediction of the actual structural response through NLFEAs is characterized by a certain level of uncertainty because any numerical model aims to describe the essential characteristics of the overall behaviour neglecting other aspects.

All the research studies evidence the need to assess the model uncertainties by means of a comparison between simulations and experimental outcomes with the consequence that an in-depth characterization of the model uncertainties for NLFEAs of reinforced concrete structures is necessary to incorporate their effects on the global structural resistance assessment within the safety formats for cyclic loads. However, the assessment of the model uncertainties for calibration of a partial safety factor should also considers the different modelling hypotheses to run NLFEAs due to the different assumptions regarding the parameters that govern the equilibrium, kinematic compatibility and constitutive equations in dynamic conditions. In fact, different choices related to the described above parameters may lead to discordant results (i.e., epistemic uncertainty [19]).

With this aim, this work compares different experimental tests known from the literature [20]-[22], concerning different walls having different behaviours and failure modes in terms of global structural resistance with the numerical outcomes achieved by means of appropriate two-dimensional non-linear FE structural models (i.e., plane stress configuration). Several non-linear FE structural models are defined for each experimental test in order to investigate the influence of the model uncertainties on 2D NLFEAs of reinforced concrete members. Precisely, the assessment of the resistance modelling uncertainties in 2D NLFEAs, that belong to the group of the epistemic uncertainties, is herein based on the definition of eighteen (18) plausible structural models using different types of software and different mechanical behaviours for the reinforced concrete elements (i.e., modelling hypotheses [19]) in dynamic conditions.

2 RESISTANCE MODEL UNCERTAINTIES FOR NLFEAS

In general, the uncertainties in structural engineering can be classified in two families: aleatory and epistemic [19]. The aleatory uncertainties concern the intrinsic randomness of the variables that governs a specific structural problem, whereas the epistemic uncertainties are

mainly related to the lack of knowledge in the definition of the structural model [19],[23]-[25] and sometimes represented also by auxiliary non-physical variables/choices [19]. The safety assessment of a structural system by means of NLFEAs should account for explicitly both these sources of uncertainty.

Within the semi-probabilistic limit state method [26]-[28], the safety assessment of a structural system requires a reliable definition and characterization of the structural resistances, which increasingly often derive from NLFEAs. For this purpose, different safety formats have been proposed in the literature [8]-[15]. In particular, EN 1992 [14] defines a safety format based on the definition of the partial safety factors descending from representative values and design values of the material strengths (i.e., concrete compressive strength and reinforcement steel yielding strength). While, *fib* Model Code 2010 [15] provides three different methodologies for the assessment of the structural reliability: the probabilistic method, the global resistance method and the partial factor method. These different safety formats (with the exception for the partial factor method) allow the estimation of the design structural resistance R_d, that represents the global structural resistance of a structure with its behaviour and failure mode, as expressed by Eq.(1):

$$R_d = \frac{R_{rep}}{\gamma_R \gamma_{Rd}} \tag{1}$$

where R_{rep} denotes the value representative of the global structural resistance estimated by means of NLFEAs and in compliance with the selected safety format, γ_R is the partial safety factor accounting for the randomness of material properties (i.e., aleatory uncertainties) and γ_{Rd} represents the partial safety factor related to the modelling uncertainties (i.e., epistemic uncertainties). Therefore, the aleatory uncertainties are separated from the epistemic uncertainties within *fib* Model Code 2010 safety formats for NLFEAs [8],[15]. The procedure for the estimation of the partial factor γ_R is suggested by the corresponding safety format. Conversely, the value of the partial safety factor for the resistance model uncertainties γ_{Rd} remains an object of investigation. More recently, *fib* Model Code 2010 [15] has suggested to assume different values of γ_{Rd} depending on the level of validation of the structural model. The γ_{Rd} factor equal to 1 may be adopted for models with no epistemic uncertainties (i.e., presence of evidences of model validation in the actual design conditions [15]).

However, when NLFEAs have to be performed for dynamic simulations on structures having more complex geometry (that may differ from the simple case of the beam in the failure mode), the epistemic uncertainties related to the definition of the resistance model may be larger than expected. Therefore, an in-depth characterization of the partial safety factor γ_{Rd} needs to be addressed.

3 EVALUATION OF THE RESISTANCE MODEL UNCERTAINTIES

This section describes the methodology adopted in the present work for the assessment of the partial safety factor related to the resistance model uncertainties in the definition of 2D NLFEAs under cyclic loads. As discussed by [10],[29]-[30], the following aspects have to be considered in order to identify the resistance model uncertainties for NLFEAs:

- the database of the experimental data should contain, if possible, all the parameters necessary for the reproduction of the tests and for the definition of non-linear FE structural models; note that some information, related to the material properties, is so often missing and, in the practice, usually is derived from the available data under appropriate assumptions according to the scientific literature with an increase of the model uncertainty;

- the experimental results should be related to different typologies of structures with different failure modes;
- a probabilistic analysis of the observed model uncertainties needs to be carried out in order to define the most likely probabilistic distribution with the corresponding parameters.

In compliance with [8],[15], the resistance model uncertainty, separated from the aleatory one (Eq. (1)) and denoted as ϑ_i, can be expressed by a multiplicative law. This latter relates the i-th actual global resistance (response) estimated from an experimental test $R_i(X,Y)$ to the i-th global resistance (or response) estimated by a NLFEA $R_{NLFEA,i}(X)$ and, may be expressed as follows:

$$R_i(X,Y) \approx \vartheta_i R_{\mathrm{NLFEA},i}(X) \tag{2}$$

where X is a vector of basic variables included into the resistance model, Y is a vector of variables that may affect the resisting mechanism but are neglected in the model. Note that the unknown effects of Y variables, if present, are indirectly incorporated and covered by ϑ_i. As widely explained in the next section, different modelling hypotheses are possible to model a specific reinforced concrete structure by means of NLFEAs. A comprehensive calibration of the resistance model uncertainties for 2D NLFEAs requires to account for the different modelling hypotheses which may be selected by engineers for seismic analyses.

4 NON-LINEAR SIMULATIONS: PARAMETRIC ANALYSIS RESULTS

In this section, different experimental tests corresponding to different structural systems are considered and reproduced by means of NLFEAs. These simulations are performed considering a set of modelling hypotheses in order to estimate the resistance model uncertainties with the aim to calibrate the corresponding values of the partial safety factor within the safety formats proposed by [15]. Note that all the numerical simulations have been performed by the authors after a sensitivity/calibration analysis and this is an important requirement for the proposal of this study because leads to a reduction of the epistemic uncertainties, in other words, the designers, involved in NLFEAs for the structural verification process, should be confident with this approach. As known, the structural analysis is based on the fundamental principles of mechanics such as equilibrium, of displacement compatibility and of constitutive laws [31]. In the field of NLFEAs, these principles are attended by iterative calculation procedures which inevitably lead to a certain degree of error in the final solution. Moreover, the definition of a specific structural model [31] requires different assumptions about the parameters describing the equilibrium, kinematic compatibility, constitutive equations leading to different numerical outcomes, which may be more or less realistic. Therefore, the multiplicity of choices (i.e., epistemic uncertainties) which can be assumed during the definition of a non-linear FE model leads to have a certain degree of uncertainty in the final solution. It follows that, consistently with the framework of the safety formats for NLFEAs [14]-[15], the estimation of the partial safety factor γ_{Rd} for the resistance modelling uncertainties is necessary. Considering different experimental tests known from the literature [20]-[22], Subsection 4.1 describes the different modelling hypotheses that any engineer may assume during the computational phase. The numerical results in terms of global structural resistance from the NLFEAs are described in Subsection 4.2 and also compared to the experimental outcomes.

4.1 Different modelling hypotheses within NLFEAs

A multitude of modelling hypotheses is available to carry out 2D (plane stress) NLFEAs of reinforced concrete structures. In this work, two software [32]-[33], identified anonymously by Software A, and Software B in order to avoid advertising for the different codes, are adopted in order to reproduce the outcomes of a set of experimental tests. For each software, several choices about the hypotheses and mechanical parameters related to equilibrium, compatibility and constitutive laws can be performed. Specifically, in each software four-node quadrilateral iso-parametric plane stress finite elements, based on linear polynomial interpolation and 2x2 Gauss point's integration scheme, are used for the numerical simulations as well as the FE meshes are properly defined after a calibration procedure. The non-linear system of equations is solved by means of the standard Newton-Raphson iterative procedure based on the hypothesis of linear approximation [1]. Moreover, for each software the following main characteristics for the FE models are also assumed:

- non-linear behaviour of concrete in compression including softening with a reduction of the compression strength and shear stiffness (shear retention factor variable from a minimum value of 0.1 to a maximum value of 0.3) after cracking [34]. In detail, the mono-axial constitutive model for concrete proposed by EN 1992-1-1 [14], the constitutive model described by Model Code 1990 [15] and the constitutive model described by Thorenfeldt et al. [35] have been selected in order to fit as much as possible the experimental results with each software [32]-[33];
- smeared cracking with fixed crack direction model [36]-[38];
- tri-linear σ–ε curve for the reinforcement steel [34];
- discrete and smeared models of the reinforcement, assuming a perfect bond between the reinforcement and the surrounding concrete [34];
- Young's modulus and tensile concrete strength, as also explained previously, are the material properties derived as a function of the experimental compressive strength, according to [27].

The summary of the main hypotheses assumed in the definition of the simulations for 2D NLFEAs, adopting Software A and B [32]-[33], is listed in Table 1.

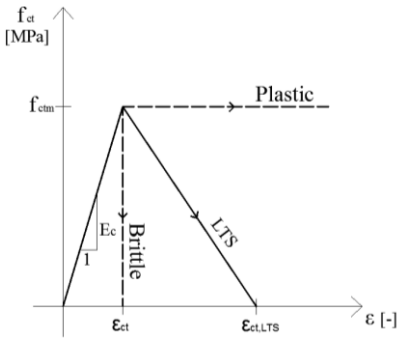

Figure 1: Different constitutive laws for concrete tensile behaviour.

In addition to the described above differences inherent to the use of two software, another important differentiation in the definition of non-linear FE models has been considered with respect to the concrete tensile mechanical behavior and the shear stiffness in cracked concrete. As known, concrete is considered as quasi-brittle material in compression and purely brittle in tension. However, the local interaction between reinforcing bars and concrete between cracks gives rise to the "tension stiffening effect" [38]. In numerical simulations, this effect may be taken into account through a modification of the constitutive tensile behavior of the concrete matrix. In general, this modification refers to the definition of a tension softening law in the

post peak concrete tensile behavior. In the present paper, three different constitutive laws for concrete in tension are considered in order to cover different hypotheses accounting for the tension stiffening effect [34]: elastic-brittle, elastic-plastic and a linear tension softening as shown in Figure 1. The first two constitutive laws are conceived as upper and lower limit (non-physical) approaches. While, the constitutive law having a linear tension softening for the concrete tensile behavior represents the physical modelling hypothesis and has been calibrated by means of an iterative specific process in each software with the aim to best fit each experimental result. In this iterative process, the ultimate deformation in tensile of concrete (i.e., $\varepsilon_{ct,LTS}$ in Figure 1) is assumed as a function of the corresponding elastic one (i.e., ε_{ct} in Figure 1) varying in a range from $2\varepsilon_{ct}$ to $10\varepsilon_{ct}$ without highlighting any dependence on the software and on the compressive strength.

	Software A	Software B
Equilibrium	*- Standard Newton-Raphson based on the hypothesis of linear approximation [1]* *- Convergence criteria based on strain energy* *- Load step sizes defined in compliance with the experimental procedure*	
Compatibility	*Finite Elements* - Isoparametric plane stress 4 nodes (2x2 Gauss points integration scheme with linear interpolation) - Discrete reinforcements - Element size defined by means of an iterative process of numerical accuracy	*Finite Elements* - Isoparametric plane stress 4 nodes (2x2 Gauss points integration scheme with linear interpolation) - Smeared reinforcements/discrete reinforcements - Element size defined following an iterative process of numerical accuracy
Constitutive laws	*CONCRETE* - Fixed crack model, smeared cracking, constant shear retention factor equal to: 1) 0.1 2) Variable 3) 0.3 - Mono-dimensional model extended to biaxial stress state - Compression: Non-linear with post peak linear softening branch - Tension (differentiating between 3 modelling hypotheses): 1) Elastic - Brittle (BRITTLE) 2) Elastic with post peak linear tension softening (LTS) 3) Elastic - perfectly plastic (PLASTIC) *REINFORCEMENTS STEEL* - Tri-linear elastic – plastic	

Table 1: Summary of the basic hypotheses assumed in the definition of non-linear FE numerical models.

Once the tensile behavior has been established, for each of the three tensile behaviours the same investigation procedure was used to calibrate the shear retention factor (β) with a value between 0.1 and 0.3. Specifically, for each software and experimental test, three different models for the different tensile behaviour are defined and for each one 0.1 and 0.3 are imposed as limits for β, and, in addition, an iterative process is used to define the most appropriate value of β to best fit the experimental tests.

Altogether, 18 different structural models (i.e., modelling hypotheses which belong to the group of the epistemic uncertainties because a specific choice can lead to a reduction of the

uncertainty [19]) can be defined combining the three different concrete tensile behaviours with the three different values of shear retention factor and the two software codes. A scheme of the modelling hypotheses adopted in this study is summarized in Figure 2. By this way, the resistance model uncertainties can be identified and computed for the different experimental tests of the 9 specimens as described in the following subsection, leading to a total number of NLFEAs equal to 162, as shown in Fig. 2.

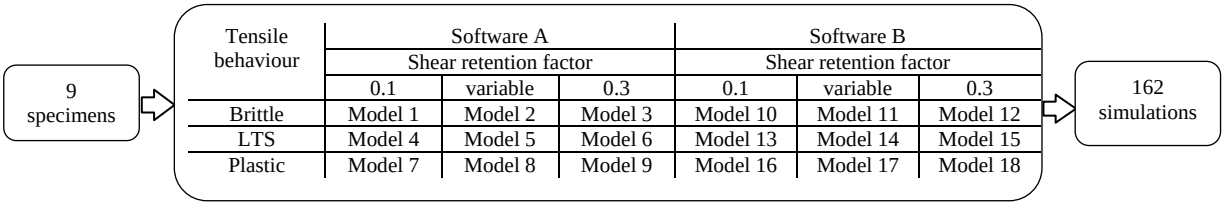

Figure 2: Distinction between the 9 structural models (Mo.1-9 for each software) for the resistance model uncertainty investigation and summary of the benchmark NLFEAs.

4.2 NLFEAs of different experimental tests: results and comparison

In this section, the experimental results presented in the scientific literature [20]-[22] and related to 9 different r.c. walls are considered and assumed as benchmark test set. All these experimental tests, have been performed through a cyclic loading process up to failure as discussed by [20]-[22]. The specimens have been realized in laboratory and supported by statically determined configurations. The experimental results, in terms of load vs displacement, are compared to the outcomes from the different 162 2D NLFEAs carried out taking into account the resistance model uncertainties as previously discussed. It is worthy to specify that some experimental systematic errors (e.g., modifications in the geometry or in the constraints) can affect the experimental results and represent another source of uncertainties, as commented below for the comparison with some experimental results [29],[39].

In the following, the experimental and numerical tests are described in details and illustrated in Figures 3-11.

The experimental tests described by Pilakoutas and Elnashai [20], analyzed six reinforced concrete walls designed in pairs so as to have the same percentage of bending reinforcement and differing in the percentage of shear reinforcement. For this work, only 3 of the all walls have been taken into consideration denoted respectively as SW4, SW6, SW8, with the following geometrical properties: 1.20 m high, 0.6 m wide, 0.06 m thick and stiffened by a 0.2 m thick and 0.25 m high lower beam, and by a 0.2 m thick and 0.15 m high upper beam where the load is applied. All walls are subjected to the same load history. The test was carried out in displacement control from 2 mm up to failure, performing two complete cycles with a 2 mm increment. The concrete compressive strength ranges from 36.9 to 45.8 MPa in the different tests, while the flexural reinforcement remains constant in the web and the shear reinforcement and the vertical reinforcement vary in the boundary elements. The numerical results in terms of global structural resistance of the simulations are listed in Table 2 and 3. The results from NLFEAs, in Figures 3-5 (a)-(f), are plotted for the same shear hypothesis, for the different tensile behaviors and for the two software codes. The lowest results in terms of maximum load are achieved when the brittle constitutive law is adopted for concrete tensile behavior, while the plastic constitutive law always leads to an overestimation of the maximum load and of stiffness. It can also be noted that the best results are obtained for a shear retention factor of 0.1 or in any case close to this value. In general, all the simulations overestimate the maximum load and then the structural resistance, but underestimate the ductility because a lot of simulations failure before then experimental tests. Figure 3-5 (a-c) and (d-f) show the in-

trinsic dependence of the results on the software choice (software A and B, respectively), in which the simulations (a-c) fail the simulation before the end of the load history, while the simulations (d-f) reach the end of the analysis but they overestimate the resistance, especially in the case of the models 12, 15, 18. The failure mode occurs with the progressive yielding of the tensile reinforcements and concrete crushing in the boundary element compressed on the opposite side. This failure is in compliance with the experimental results. When the ultimate deformation for the concrete in compression is reached, all the simulations have been stopped due to the convergence loss of the numerical procedure.

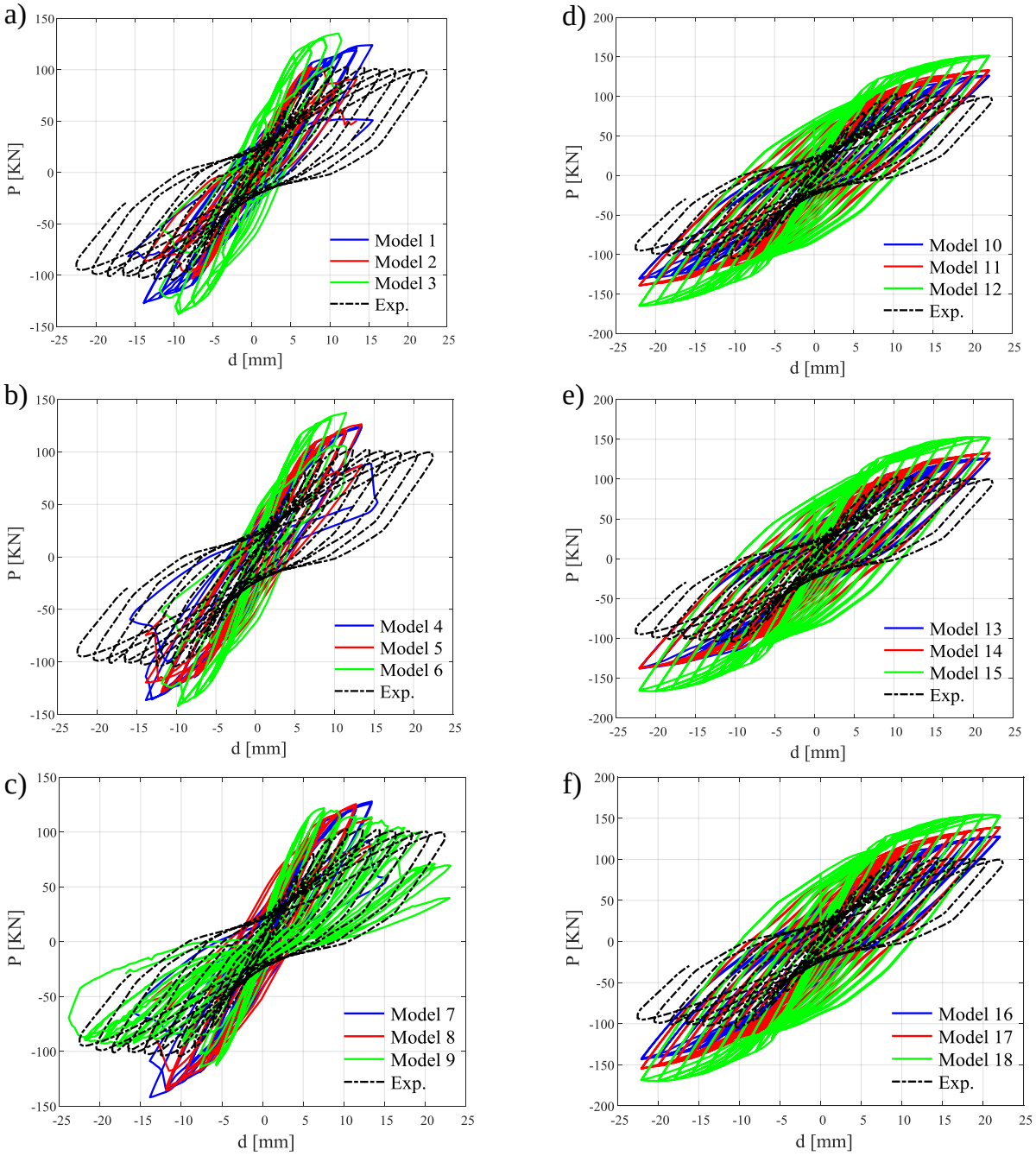

Figure 3: Load vs displacement diagrams from experimental tests SW4 of Pilakoutas [20] and NLFEA results; (a-c) Software A, (d-f) Software B.

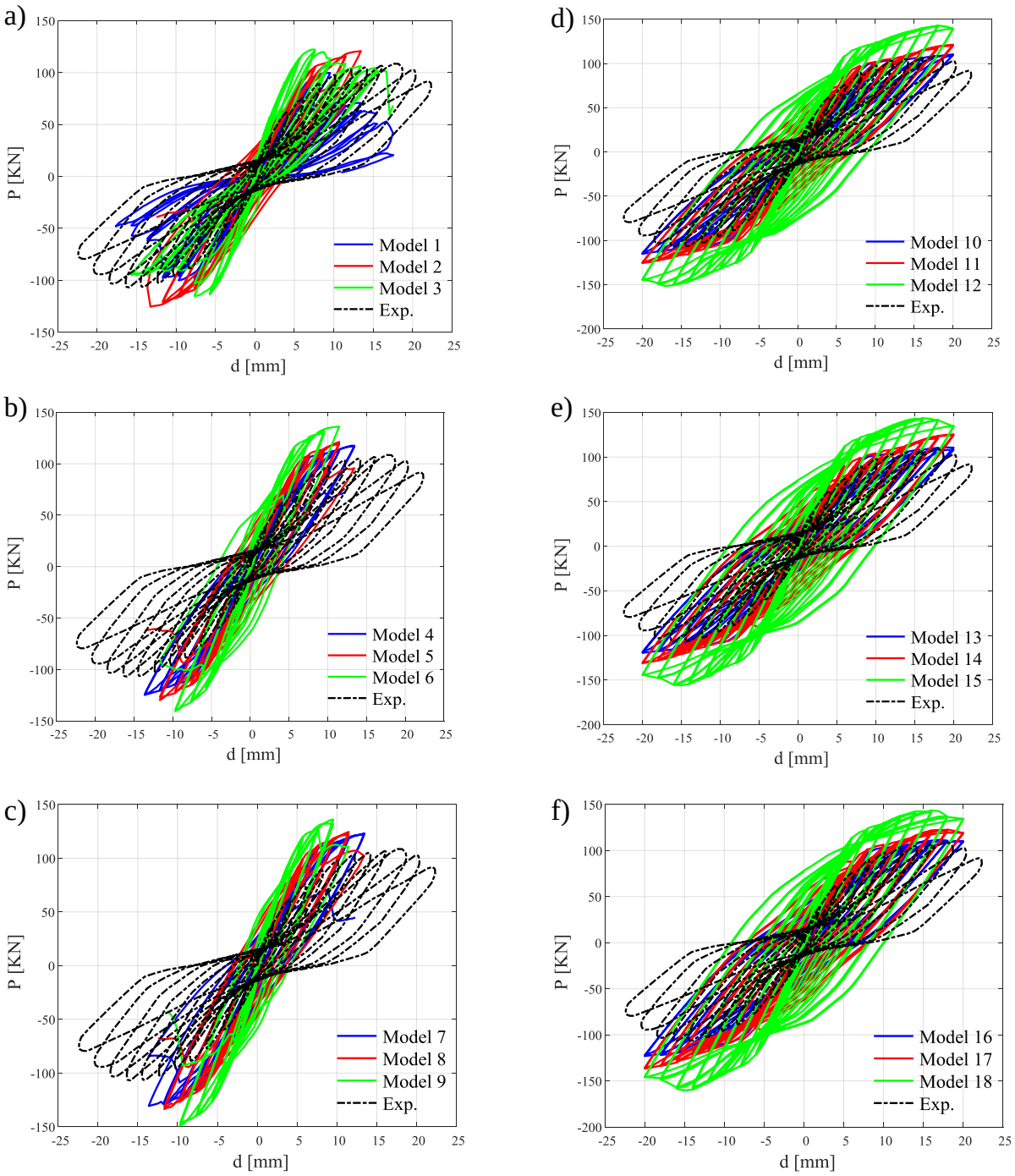

Figure 4: Load vs displacement diagrams from experimental tests SW6 of Pilakoutas [20] and NLFEA results; (a-c) Software A, (d-f) Software B.

Ref. [*]	**Exp. test**	$R_{EXP,i}$ **[kN]**	$R_{NLFEA,i}$ **[kN]**								
			Mo. 1	*Mo. 2*	*Mo. 3*	*Mo. 4*	*Mo. 5*	*Mo. 6*	*Mo. 7*	*Mo. 8*	*Mo. 9*
[20]	SW4	103.0	124.0	103.4	135.4	124.9	126.4	137.4	127.8	125.5	121.8
	SW6	108.6	100.1	120.8	122.2	117.6	121.3	134.3	123.0	124.5	136.0
	SW8	95.1	128.5	127.3	142.2	133.0	130.9	149.1	137.7	135.2	152.8

Table 2: Results in terms of resistance from the experimental tests $R_{EXP,i}$ [20] and NLFEAs $R_{NLFEA,i}$ for the different structural models, Software A.

Ref. [*]	Exp. test	$R_{EXP,i}$ [kN]	$R_{NLFEA,i}$ [kN]								
			Mo. 10	*Mo. 11*	*Mo. 12*	*Mo. 13*	*Mo. 14*	*Mo. 15*	*Mo. 16*	*Mo. 17*	*Mo. 18*
[20]	SW4	103.0	126.3	133.5	151.6	125.8	133.1	152.8	127.8	139.1	154.3
	SW6	108.6	110.3	121.3	142.9	110.8	125.4	142.7	111.6	122.7	143.7
	SW8	95.1	128.0	139.4	159.2	127.8	137.7	160.4	131.9	140.8	160.5

Table 3. Results in terms of resistance from the experimental tests $R_{EXP,i}$ [20] and NLFEAs $R_{NLFEA,i}$ for the different structural models, Software B.

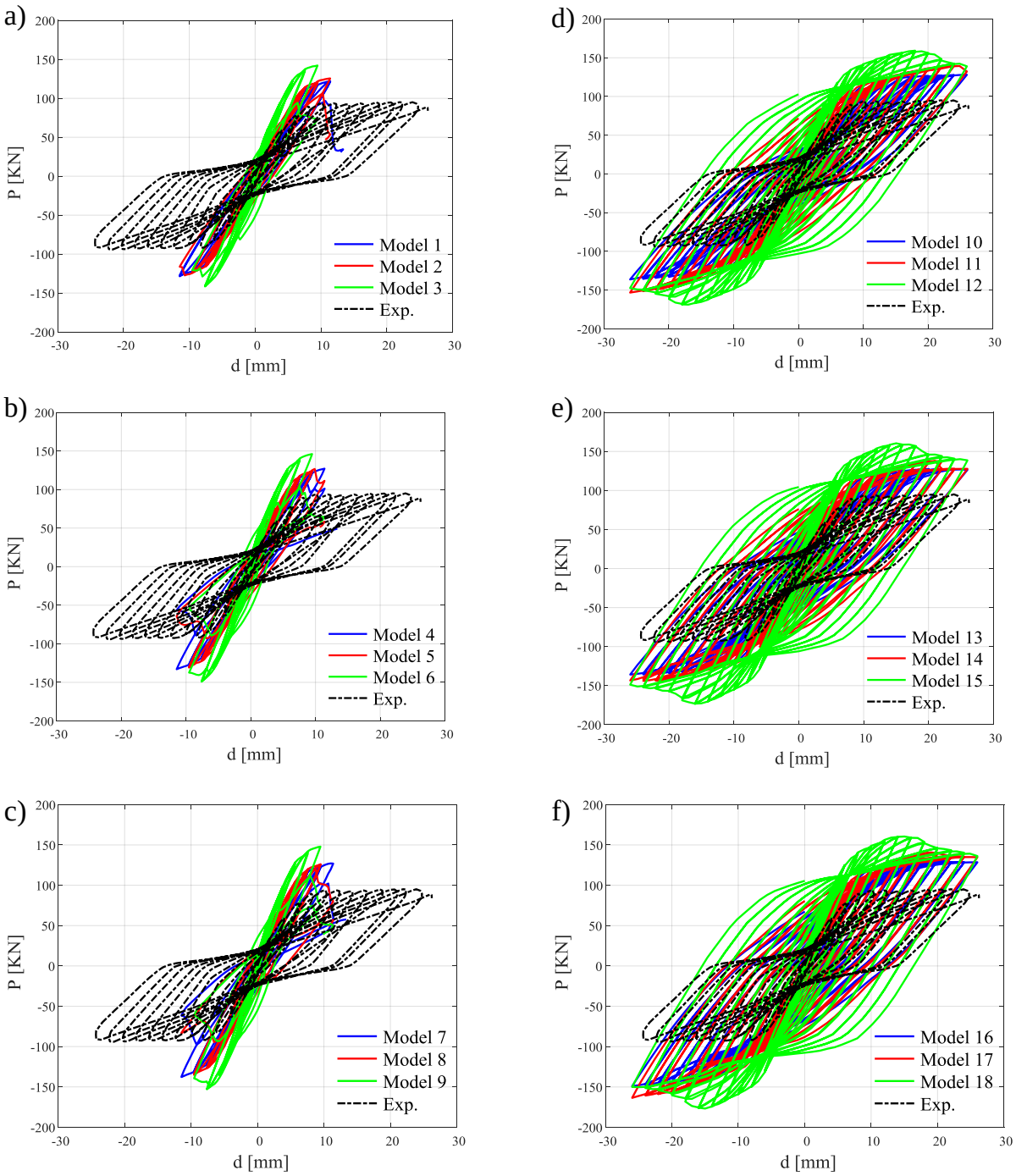

Figure 5: Load vs displacement diagrams from experimental tests SW8 of Pilakoutas [20] and NLFEA results; (a-c) Software A, (d-f) Software B.

The experimental results of Lefas and Kotsovos [21] are related to four identical walls of dimensions 1300x650x65mm, that are constrained inferiorly by a beam of section 200x300mm which simulates a rigid foundation. At the top there is a rigid beam to uniformly transmit the imposed displacement on the top of the wall. The flexural reinforcement is made up of ϕ8/100mm in the web, while the distance is reduced to 70mm in the boundary elements. Similarly, the shear reinforcement is composed of ϕ6.25/260mm over the entire width of the wall and additional stirrups in the boundary elements with ϕ4/130mm. The imposed displacement tests present a load history composed of four or five cycles with displacements of a few millimeters and then an increase of monotonic displacement up to failure. The concrete compressive strength varies in the range 35-53 MPa in the different tests. The numerical results in terms of global structural resistance of the simulations are listed in Tables 4-5. Figures 6-8 (a)-(f) show that models (3, 6, 9, 12, 15, 18) related to elastic-plastic constitutive law for the concrete tensile behavior, always lead to an overestimation of the resistance and stiffness, while models elastic-brittle and with a linear tension softening in tension have more or less the same behavior, with a stiffness similar to the real one in the cyclic phase, but, in general, an underestimation of the resistance. It can be also noted that as the shear retention factor increases, the dissipated energy also increases. The failure mode occurs with the progressive yielding of the tensile flexural reinforcements on the side where the displacement is imposed and concrete crushing at the bottom of the boundary element in the other side. Some simulations don't reach the ultimate experimental displacement but fail upon reaching the maximum load or for a slightly greater displacement than that achieved in the cyclic phase.

Ref. [*]	**Exp. test**	$R_{EXP,i}$ **[kN]**	$R_{NLFEA,i}$ **[kN]**								
			Mo. 1	*Mo. 2*	*Mo. 3*	*Mo. 4*	*Mo. 5*	*Mo. 6*	*Mo. 7*	*Mo. 8*	*Mo. 9*
[21]	SW31	115.9	111.9	120.8	160.2	121.3	133.3	168.9	127.7	139.3	174.4
	SW32	111.0	110.3	114.8	142.8	114.9	118.3	142.7	119.1	131.1	144.3
	SW33	111.5	107.2	111.5	129.8	110.4	114.0	139.4	113.8	117.6	143.8

Table 4. Results in terms of resistance from the experimental tests $R_{EXP,i}$ [21] and NLFEAs $R_{NLFEA,i}$ for the different structural models, Software A.

Ref. [*]	**Exp. test**	$R_{EXP,i}$ **[kN]**	$R_{NLFEA,i}$ **[kN]**								
			Mo. 10	*Mo. 11*	*Mo. 12*	*Mo. 13*	*Mo. 14*	*Mo. 15*	*Mo. 16*	*Mo. 17*	*Mo. 18*
[21]	SW31	115.9	87.8	117.5	139.8	98.0	127.2	147.6	98.9	131.8	151.2
	SW32	111.0	93.7	101.6	129.4	93.9	101.9	129.5	99.4	102.2	129.7
	SW33	111.5	94.6	96.0	118.7	95.2	101.1	122.8	95.7	98.8	126.9

Table 5: Results in terms of resistance from the experimental tests $R_{EXP,i}$ [21] and NLFEAs $R_{NLFEA,i}$ for the different structural models, Software B.

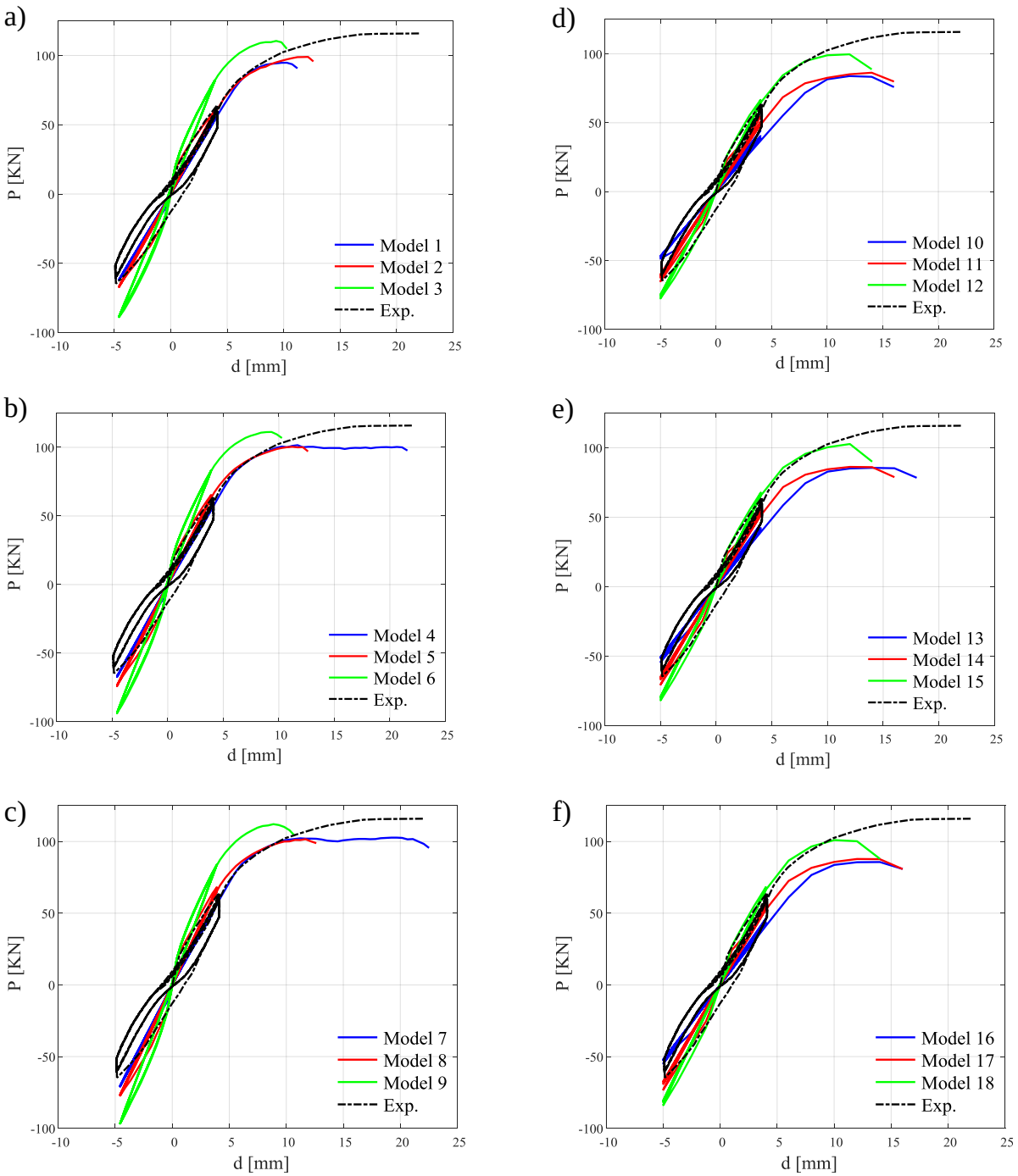

Figure 6: Load vs displacement diagrams from experimental tests SW31 of Lefas and Kotsovos [21] and NLFEA results; (a-c) Software A, (d-f) Software B.

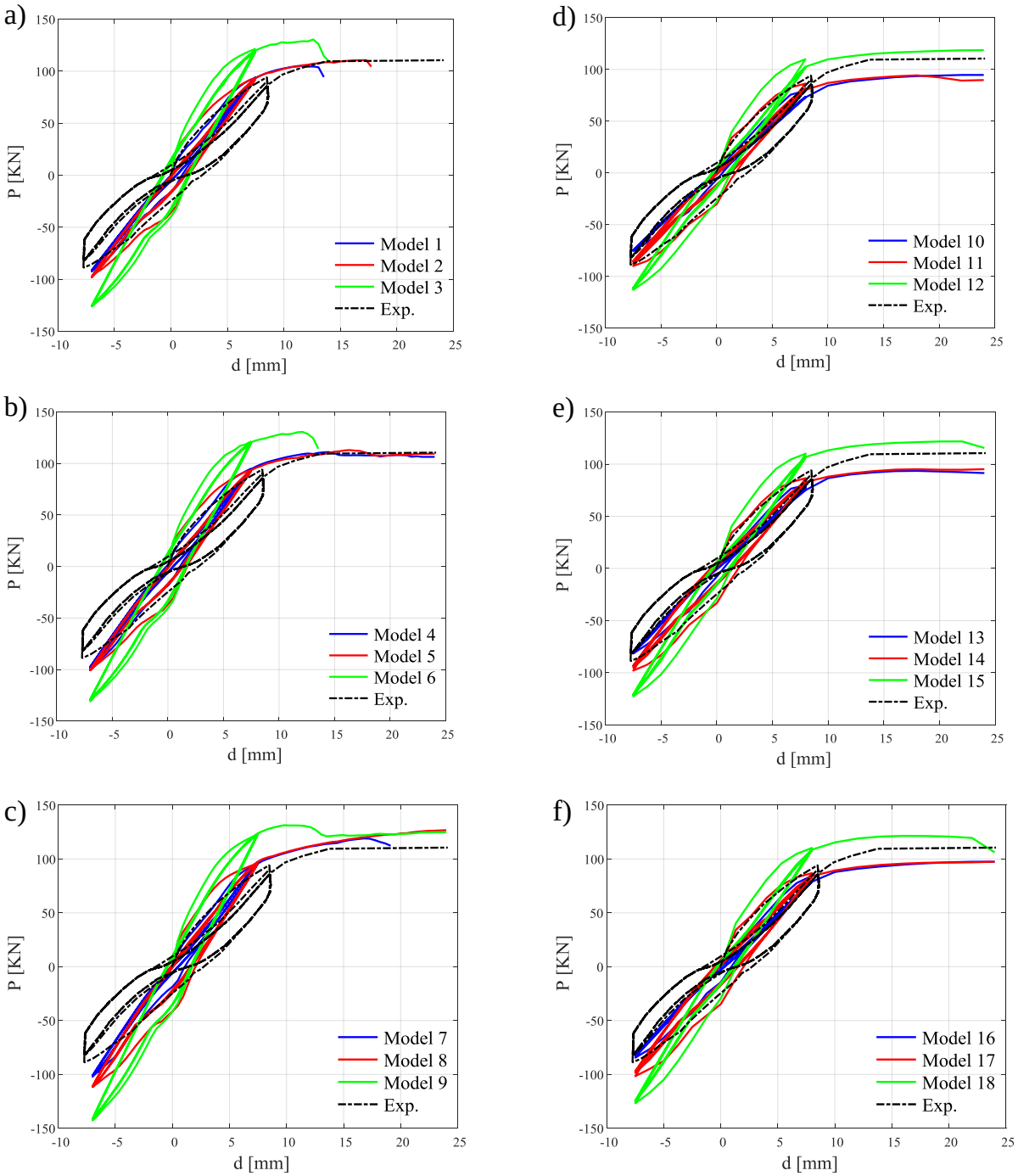

Figure 7: Load vs displacement diagrams from experimental tests SW32 of Lefas and Kotsovos [21] and NLFEA results; (a-c) Software A, (d-f) Software B.

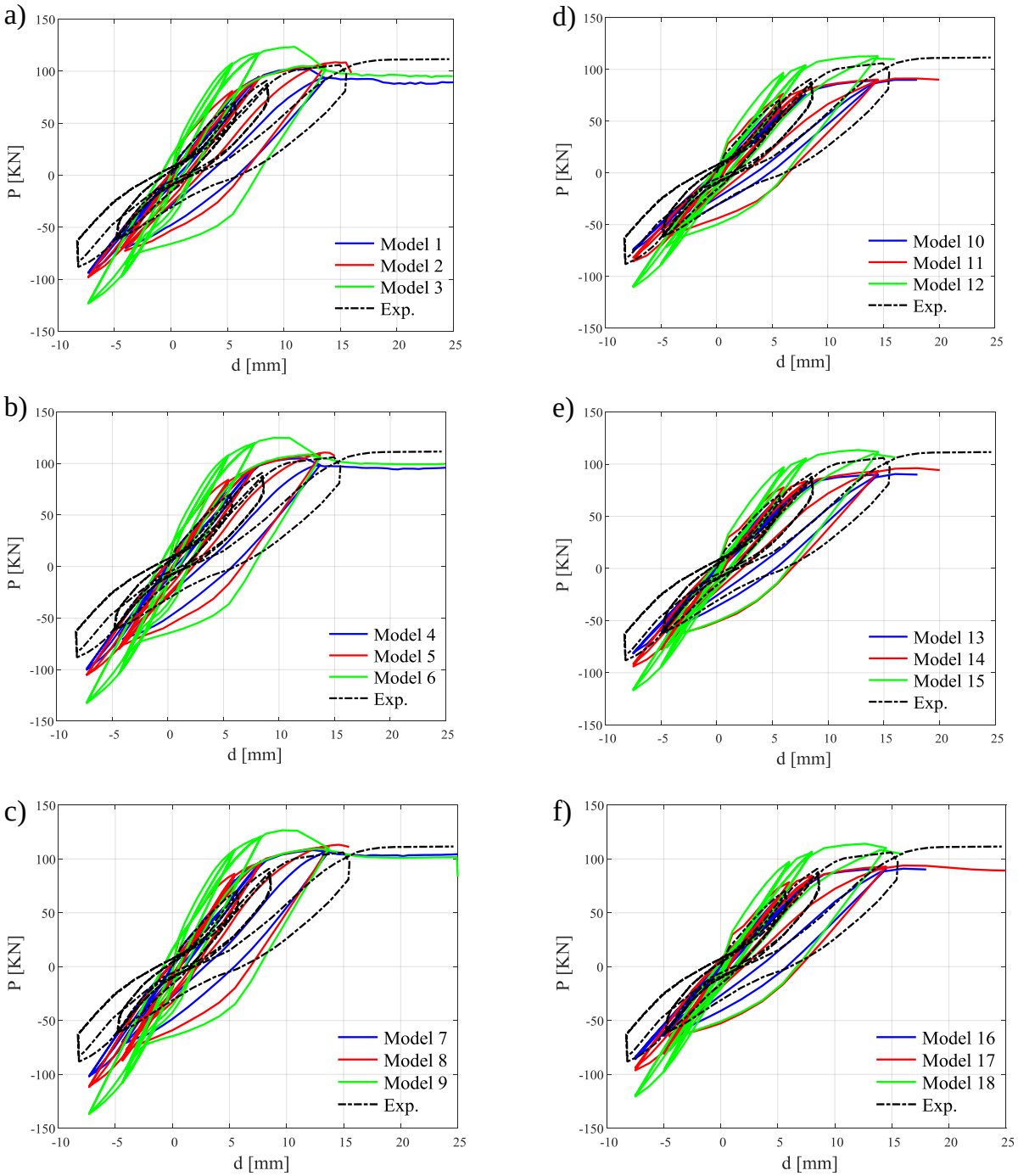

Figure 8: Load vs displacement diagrams from experimental tests SW33 of Lefas and Kotsovos [21] and NLFEA results; (a-c) Software A, (d-f) Software B.

The experimental results discussed by Zhang and Wang [22], focused on four reinforced concrete walls, denoted as SW7, SW8 and SW9 being 1.75 m high, 0.7 m wide, 0.1 m thick. The structural member is fully restrained at the base with a 0.5 m high and 0.4 m wide beam and loaded by an axial force at the top, that is considered evenly distributed at 25 cm from the top surface of the wall, while the horizontal imposed displacement is applied at 1.5 m from the base of the wall. Hence, the effective height of the wall is 1.5 m. The walls SW7 and SW8 have the same reinforcement that consist of ϕ8/150mm as flexural reinforcement in the web,

while for shear ϕ8/100mm over the total width of the wall and hoops ϕ6/50mm in the boundary elements. The difference is in flexural reinforcement in the boundary elements of the wall which consists respectively of 4ϕ14 and 4ϕ12 on each side of the wall. The SW9 is more reinforced, and presents 4ϕ20 on each boundary element, and a greater amount of shear reinforcement than the previous ones with ϕ8/75mm+ ϕ6/150mm over the total width of the wall and hoops ϕ6/75mm in the boundary elements. The walls also differ in the axial load: SW7 and SW9 have an axial-load ratio of 0.24 while SW8 has a greater axial-load ratio equal to 0.35. The loading histories are quite similar and follow the same procedure: at the first time the axial load is applied in small incremental steps, after that the wall is subjected to the cyclic phase with horizontal load divided in two parts. The first consists in 10 cycles until the yielding of flexural reinforcement; in the second phase at each cycle it is proceeded with a displacement increase equal to half that recorded for yielding. The numerical results in terms of global structural resistance of the simulations are listed in Table 6-7. The NLFEA results, plotted in Figure 9-11 (a)-(f), show that models related to elastic-plastic constitutive law for the concrete tensile behavior, always lead to an overestimation of the stiffness. Models elastic-brittle in tension do not always represent the lower bound. Figure 9-11 (a-c) and (d-f) show the dependence of the results on the software choice (software A and B, respectively), in which (a-c) reflect the real behavior for small displacement and reach the experimental maximum load, while for bigger displacement there is a progressive reduction of stiffness and resistance and in many cases the simulation fails (especially for models with elastic-plastic tensile behavior). For Software B instead, in general, all the models overestimate the structural resistance, but reach the end of the loading history by following the real behavior quite well.

Ref. [*]	**Exp. test**	$R_{EXP,i}$ **[kN]**	$R_{NLFEA,i}$ **[kN]**								
			Mo. 1	*Mo. 2*	*Mo. 3*	*Mo. 4*	*Mo. 5*	*Mo. 6*	*Mo. 7*	*Mo. 8*	*Mo. 9*
[22]	SW7	201.2	189.7	195.7	206.4	203.3	202.5	209.9	212.1	206.3	224.9
	SW8	224.0	223.6	220.1	236.7	227.0	223.7	239.9	239.8	234.6	254.4
	SW9	303.5	323.6	325.0	345.0	345.7	338.1	360.4	360.4	345.3	367.4

Table 6. Results in terms of resistance from the experimental tests $R_{EXP,i}$ [22] and NLFEAs $R_{NLFEA,i}$ for the different structural models, Software A.

Ref. [*]	**Exp. test**	$R_{EXP,i}$ **[kN]**	$R_{NLFEA,i}$ **[kN]**								
			Mo. 10	*Mo. 11*	*Mo. 12*	*Mo. 13*	*Mo. 14*	*Mo. 15*	*Mo. 16*	*Mo. 17*	*Mo. 18*
[22]	SW7	201.2	226.0	223.2	241.5	240.3	236.9	255.1	252.4	249.3	264.2
	SW8	224.0	232.3	226.9	243.8	244.6	239.8	250.4	255.9	247.8	252.2
	SW9	303.5	322.7	318.1	344.4	335.1	329.2	352.3	345.1	337.4	357.4

Table 7. Results in terms of resistance from the experimental tests $R_{EXP,i}$ [22] and NLFEAs $R_{NLFEA,i}$ for the different structural models, Software B.

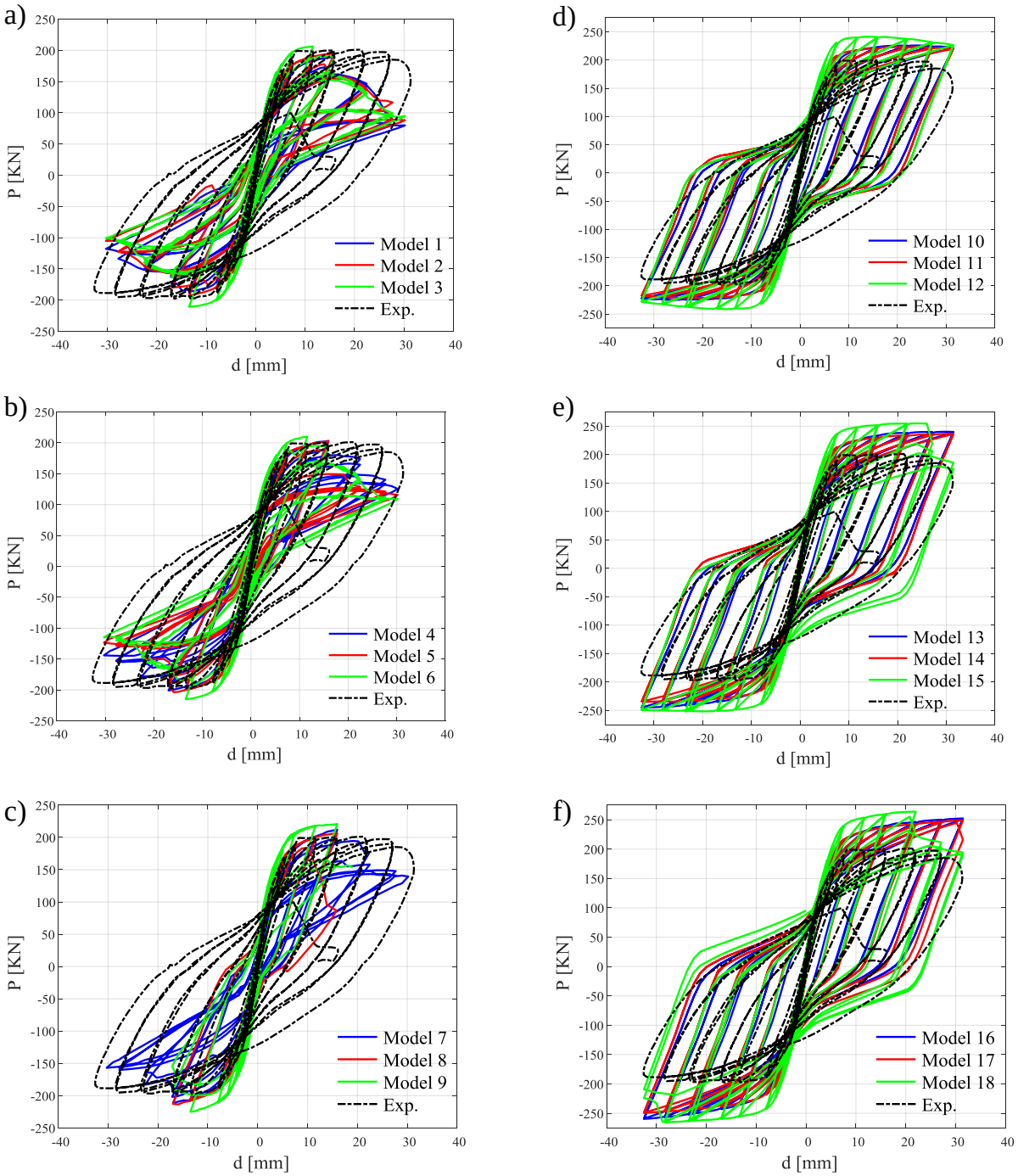

Figure 9: Load vs displacement diagrams from experimental tests SW7 of Zhang and Wang [22] and NLFEA results; (a-c) Software A, (d-f) Software B.

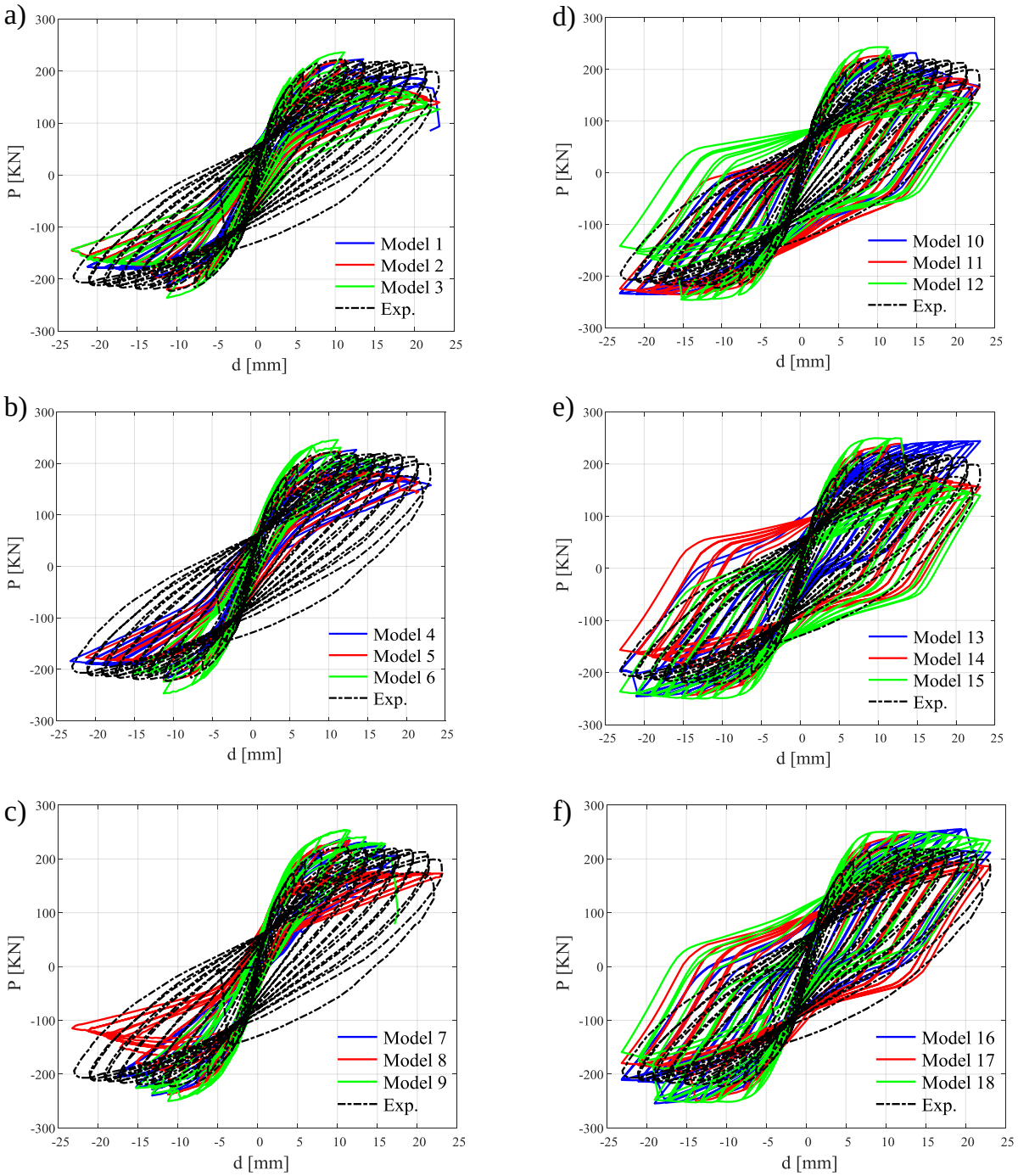

Figure 10: Load vs displacement diagrams from experimental tests SW8 of Zhang and Wang [22] and NLFEA results; (a-c) Software A, (d-f) Software B.

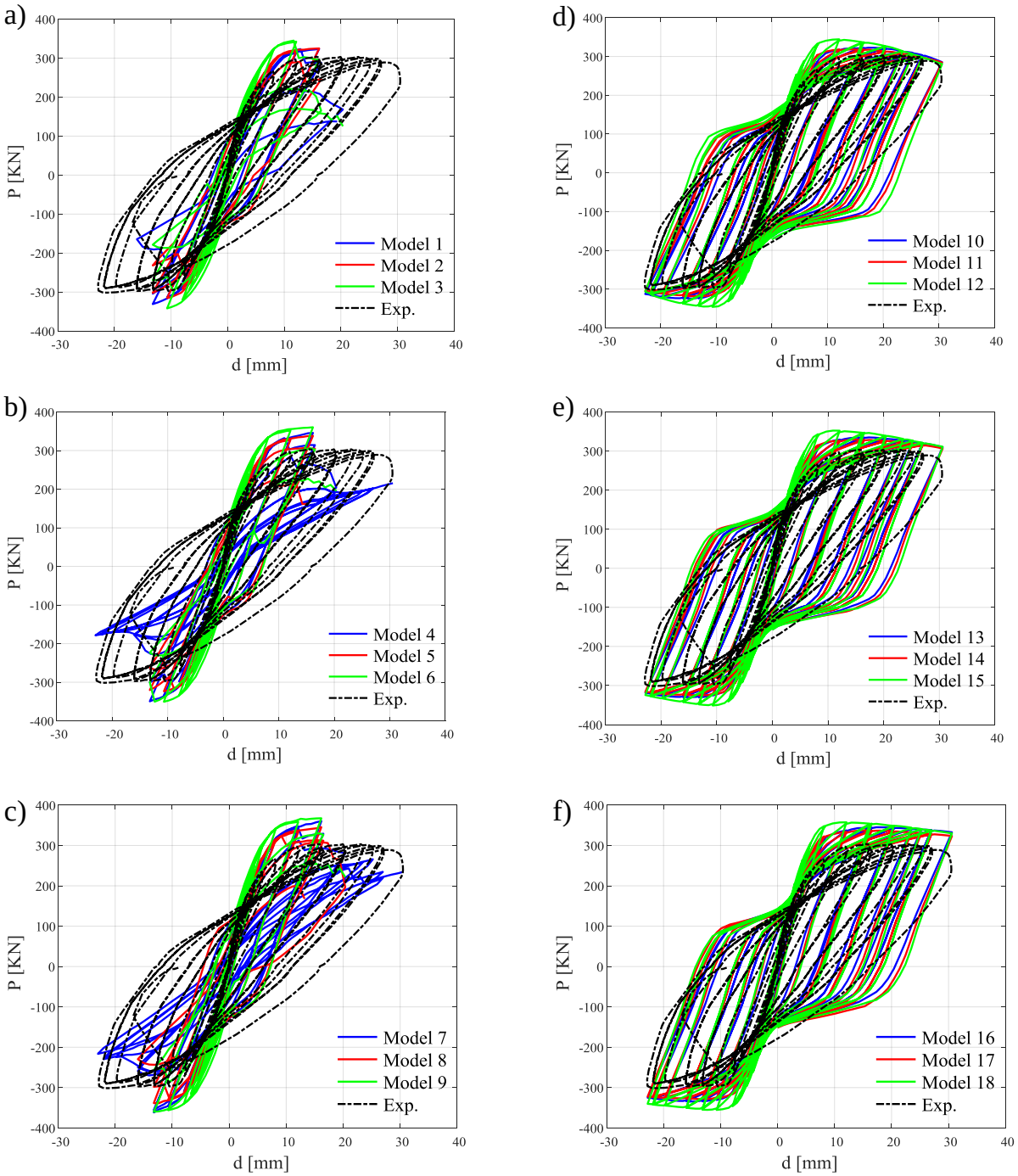

Figure 11: Load vs displacement diagrams from experimental tests SW9 of Zhang and Wang [22] and NLFEA results; (a-c) Software A, (d-f) Software B.

The results deriving from the abovementioned 162 non-linear FE simulations are useful to assess the resistance model uncertainties in 2D NLFEAs of reinforced concrete structures characterised by different failure modes under cyclic loads. These results have also demonstrated the several difficulties, which commonly occur considering different types of software and constitutive laws, in reproducing the actual failure behaviour of structural members.

5 CONCLUSIONS

This work evaluates the values of the model uncertainties (i.e., epistemic uncertainties) regarding the global structural resistance for 2D non-linear finite element method analyses of reinforced concrete systems under cyclic loads. Various experimental tests concerning different walls subject of cyclic shear action, have been numerically simulated by means of appropriate 162 NLFEAs considering two different software codes, three different constitutive laws for the behaviour of concrete in tension and three different shear behaviour after cracking. From the comparison with the experimental outcomes, the FE results have demonstrated the several difficulties, which commonly occur employing different types of software and constitutive laws, in reproducing the actual failure behaviour and the actual failure load of the all structural members considered. In general, it can be observed that a tensile behavior of the concrete perfectly plastic always gives a greater overestimation of the structural resistance, and that the variation of the shear retention factor varies the amplitude of the cycle, and therefore the dissipated energy. However, in terms of resistance, a shear retention factor close to 0.1 is the one that best fits the experimental test.

ACNOWLEDGEMENTS

This work is part of the collaborative activity developed by the authors within the framework of the Committee 3 – Task Group 3.1: *"Reliability and safety evaluation: full-probabilistic and semi-probabilistic methods for existing structures"* of the International Federation for Structural Concrete (*fib*).

REFERENCES

[1] *fib* Bulletin N°45. Practitioner's guide to finite element modelling of reinforced concrete structures – State of the art report. Lausanne; 2008.

[2] Belletti B, Damoni C, Hendriks MAN. Development of guidelines for nonlinear finite element analyses of existing reinforced and prestressed beams. European Journal of Environmental and Civil Engineering 2011;15(9): 1361-1384.

[3] DNV-RP-C208. Determination of structural capacity by non-linear FE analysis methods, Recommended Practice, DET NORSKE VERITAS AS 2013, http://www.dnv.com.

[4] Most T. Assessment of structural simulation models by estimating uncertainties due to model selection and model simplification. Computers and Structures 2011; 89(17-18): 1664-1672.

[5] Piluso V., Pisapia A., Castaldo P., Nastri E., (2019) "Probabilistic Theory of Plastic Mechanism Control for Steel Moment Resisting Frames", Structural Safety, (2019), 76:95-107, https://doi.org/10.1016/j.strusafe.2018.08.003.

[6] Basone, F., Castaldo, P., Cavaleri, L., Di Trapani, F. (2019) Response spectrum analysis of frame structures: reliability-based comparison between complete quadratic combination and damping-adjusted combination, Bulletin of Earthquake Engineering.

[7] Haukaas T, Gardoni P. Model Uncertainty in Finite-Element Analysis: Bayesian Finite Elements. Journal of Engineering Mechanics 2011; 137(8): 519-526.

[8] Allaix DL, Carbone VI, Mancini G. Global safety format for non-linear analysis of reinforced concrete structures. Structural Concrete 2013; 14(1): 29-42.

[9] Castaldo P., Gino D., Carbone V.I., Mancini G. (2018) Framework for definition of design formulations from empirical and semi-empirical resistance models, Structural Concrete, 19(4): 980-987.

[10] Castaldo P, Gino D, Bertagnoli G, Mancini G. Partial safety factor for resistance model uncertainties in 2D non-linear finite element analysis of reinforced concrete structures, Engineering Structures, 176(2018), 746-762.

[11] Shlune H, Gylltoft K, Plos M. Safety format for non-linear analysis of concrete structures. Magazine of Concrete Research 2012; 64(7): 563-574.

[12] König G, Nguyen T, Ahner C. Consistent safety format. In: CEB, editor. CEB bulletin 239 – non-linear analysis: discussion papers from the working party in commission 1. CEB 1997. Lausanne.

[13] Ftima MB, Massicotte B. Development of a reliability framework for the use of advanced nonlinear finite elements in the design of concrete structures. Journal of Structural Engineering 2012; 138:1054–64.

[14] CEN EN 1992-2 Eurocode 2 – Design of concrete structures, Part 2: concrete bridges. CEN 2005. Brussels.

[15] fib Model Code for Concrete Structures 2010. fib 2013. Lausanne.

[16] Blomfors M, Engen M, Plos M. Evaluation of safety formats for non-linear finite element analyses of statically indeterminate concrete structures subjected to different load paths. Structural Concrete 2016; 17(1): 44-51.

[17] Val D, Bljuger F, Yankelevsky D. Reliability evaluation in nonlinear analysis of reinforced concrete structures. Structural Safety 1997; 19(2): 203-217.

[18] Cervenka V. Reliability-based non-linear analysis according to fib Model Code 2010. Structural Concrete 2013; 14(1): 19-28.

[19] Kiureghian AD, Ditlevsen O. Aleatory or epistemic? Does it matter?. Structural Safety 2009; 31: 105-112.

[20] Kypros Pilakoutas and Amr Einashai. Cyclic Behaviour of Reinforced Concrete Cantilever Walls, Part I : Experimental Results. ACI structural journal no.92-S25, 1995.

[21] Ioannis D. Lefas and Micheal D. Kotsovos. Strength and deformation characteristics of reinforced concrete walls under load reversals. ACI structural journal no.87-S74, 1990.

[22] Yunfeng Zhang and Zhihao Wang. Seismic behaviour of reinforced concrete shear walls subjected to high axial loading. ACI structural journal no.97-S75, 2000.

[23] Patè-Cornell ME. Uncertainties in risk analysis: six levels of treatment, Reliability Engineering and System Safety 1996; 54: 95-111.

[24] Ditlevsen O. Model uncertainty in structural reliability. Structural Safety 1982; 1: 73-86.

[25] Bulleit WM. Uncertainty in structural engineering. Practice Periodical on Structural Design and Construction ASCE 2008; 13: 24-30.

[26] CEN. EN 1990: Eurocode – Basis of structural design. CEN 2013. Brussels.

[27] CEN. EN 1992-1-1: Eurocode 2 – Design of concrete structures. Part 1-1: general rules and rules for buildings. CEN 2014. Brussels.

[28] Allen TM , Nowak AS, Bathurst RJ. Calibration to determine load and resistance factor for geotechnical a structural design. Transport research board circular N° EC-079 2005. Washington.

[29] Holický M, Retief JV, Sikora M. Assessment of model uncertainties for structural resistance. Probabilistic Engineering Mechanics 2016; 45: 188-197.

[30] Sikora M, Holicky M, Prieto M, Tanner P. Uncertainties in resistance models for sound and corrosion-damaged RC structures according to EN 1992-1-1. Materials and structures 2014; 48: 3415-3430.

[31] Engen M, Hendriks MAN, Øverli JA, Åldtstedt E. Solution strategy for non-linear finite element analyses of large reinforced concrete structures. Str. Concrete 2015; 3: 389-397.

[32] ATENA 2D v5. Cervenka Consulting s.r.o. . Prague. Czech Republic. 2014.

[33] DIANA FEA BV. Delftechpark 19a 2628 XJ Delft. The Netherlands. 2017.

[34] Bertagnoli G, La Mazza D, Mancini G. Effect of concrete tensile strength in non –linear analysis of 2D structures: a comparison between three commercial finite element softwares. 3rd International Conference on Advances in Civil, Structural and Construction Engineering – CSCE 2015. Rome. 104-111. 10-11 December 2015.

[35] Thorenfeldt E, Tomaszewicz A and Jesen J, 1987 "Mechanical properties of high-strength concrete and applications in design", Proc. Symp. Utiliz. of High-Strength Concrete,149-159.

[36] De Borst R, Nauta P. Non-orthogonal cracks in a smeared finite element model. Engineering Computations 1985; 2: 35-46.

[37] Riggs HR, Powell GH. Rough crack model for analysis of concrete. J. Eng. Mech. Div. ASCE 1986; 112(5): 448-464.

[38] Massicotte B, Elwi AE, MacGregor JG. Tension-stiffening models for planar reinforced concrete members. Journal of Structural Engineering 199; 116(11): 3039-3058.

[39] Sykora M., Krejsa J., Mlcoch J., Prieto M., Tanner P. Uncertainty in shear resistance models of reinforced concrete beams according to *fib* MC2010, Struc. Concrete. 2018, 19(1):284-295.

COMPDYN 2019
7th ECCOMAS Thematic Conference on
Computational Methods in Structural Dynamics and Earthquake Engineering
M. Papadrakakis, M. Fragiadakis (eds.)
Crete, Greece, 24–26 June 2019

EXPERIMENTAL AND NUMERICAL EVALUATION OF CORING EFFECTS IN REINFORCED CONCRETE COLUMNS

Giuseppe Santarsiero[1], Angelo Masi[1], Andrea Digrisolo[1], Vincenzo Manfredi[1], Giuseppe Ventura[1], Domenico Nigro[1], Biagio Difina[1]

School of Engineering, University of Basilicata, viale dell'Ateneo Lucano, 10, Potenza, Italy

{giuseppe.santarsiero, angelo.masi, andrea.digrisolo, enzo.manfredi, giuseppe.ventura}@unibas.it;

Abstract

The knowledge of in-situ material properties is the first step in the assessment process of existing structures and, where needed, in the design of the consequent strengthening interventions. In order to achieve this goal, destructive (DT; e.g., cores) and non-destructive (NDT; e.g., ultrasonic, rebound) test methods are generally adopted, either alone or combined. Although many literature papers and guidelines propose to minimize the number of cores in the estimation of the concrete strength in reinforced concrete structures, the European and Italian codes prescribe that the estimation of in-situ strength has to be mainly based on cores drilled from the structure (DT). In this framework, the paper reports results of an experimental program aimed at evaluating the effects of core tests on RC columns, as well as the effectiveness of the structural restoration of drilling holes. Specifically, three sets of column specimens have been considered: (i) drilled columns, (ii) drilled and subsequently restored columns, and (iii) reference not drilled (as-built) columns. Compression tests have been carried out on each column and the results have been compared with the prediction based on codes or other literature approaches. This helped to recognize the main phenomena affecting the column members behavior under axial loads.
At the same time, the authors calibrated detailed finite element models based on the experimental results of the tests carried out on column specimens. An advanced Fem tool was used to set-up 3D models. Numerical simulations aimed at better understanding the failure mechanism, especially in the presence of the hole related to the core extraction. The role of longitudinal and transverse reinforcement has been evaluated, highlighting that concrete crushing in the areas around the hole causes the early buckling of rebars, leading to premature failure of drilled column specimens.

Keywords: Destructive tests, concrete strength, core drilling, finite element model, nonlinear numerical simulation.

1 INTRODUCTION

The investigation of structural characteristics (geometry, structural details, materials quality, etc.) is a crucial step in the assessment of existing reinforced concrete (RC) structures [1, 2] and, where needed, in the design of consequent strengthening interventions [3]. Specifically, the knowledge of in-situ material properties is the first step in the assessment process of existing structures. In order to achieve this goal, destructive (DT; e.g., cores) and non-destructive (NDT; e.g., ultrasonic, rebound) test methods are generally adopted, either alone or combined. Although many literature papers and guidelines propose to minimize the number of cores in the estimation of the concrete strength in reinforced concrete structures, the European and Italian codes prescribe that the estimation of in-situ strength has to be mainly based on cores drilled from the structure (destructive test, DT). Non-destructive tests (NDTs) can only supplement coring, thus permitting a more economical and representative determination of concrete properties throughout the whole structure under examination. In this framework, the paper reports results of an experimental program aimed at evaluating the effects of core tests on RC columns, as well as the effectiveness of the structural restoration of drilling holes. Twenty RC column specimens (dimension 30cm x 30cm x 80cm) have been purposely built and tested by both non-destructive and destructive tests. Specifically, after the preliminary campaign of ultrasonic tests performed on all structural members, three sets of column specimens have been considered: (i) drilled columns (3 specimens), (ii) drilled and subsequently restored columns (4 specimens), and (iii) reference not drilled (as-built) columns (3 specimens). Compression tests have been carried out on extracted cores and, finally, on each column.

After the experimental campaign was concluded, the authors calibrated detailed finite element models based on the experimental results of the tests carried out on specimens. A software package able to fully account for the main nonlinear properties of concrete like, for instance, cracking and crushing, as well as the reduction of shear and compressive strength after cracking, has been used in setting up the finite element models made up of 3D tetrahedral elements [4]. The numerical models have been used to carefully evaluate the failure mode, especially for drilled specimens. This latter, indeed, are characterized by failure mechanisms different from as-built and restored specimens that causes their premature failure.

2 EXPERIMENTAL PROGRAM

In the framework of the experimental program carried out at the Laboratory of Structures of the University of Basilicata, totally 10 columns (out of 20 specimens available) have been subjected to compression test until failure. The program was intended to explore the effects of core drilling in RC members and the effectiveness of the holes' restoration. This latter, in comparison to the capacity of as-built specimens, not subjected to drilling nor restoration. For this reason, the specimens' range comprised as-built, drilled and drilled-restored columns, according to table 1. Restoration grout is an anti-shrinkage thixotropic mortar having compressive strength after one day equal to 30 MPa, and 50 MPa after 28 days.

Columns are 80 cm high with a cross-section of 30x30 cm with different longitudinal reinforcement. They were extracted from other specimens, namely full-scale beam-column joints tested in the same laboratory [7] during a previous experimental campaign. As can be seen in table 1, specimens are named "NS" or "S", depending on the beam-column joint they are extracted from, where S specimens are extracted from seismically designed joints and are provided of 8 mm diameter hoops (spaced 20 cm) and six 14mm diameter longitudinal bars. The only difference for NS specimens is that the number of longitudinal rebars is four instead of six.

This has no influence when computing confining effect according to confining models reported in the following, since the additional bars of S specimens are not restrained. Specimens show typical defects of real constructions, such as the variability of concrete cover thickness due to movements of the reinforcement during the casting operations.

Type	Column ID	f_c	Mean concrete cover
		MPa	mm
As-built	NS4	-	35.7
	NS7	-	37.5
	S4	-	45.0
Drilled	NS1	39.56	36.6
	S2	34.60	35.0
	S9	39.80	40.3
Drilled-restored	NS6	39.06	39.1
	S6	34.64	40.3
	S11	38.85	40.0
	S12	37.92	44.4

Table 1: List of 10 columns under investigation with concrete strength of extracted cores f_c, and detected concrete cover thickness.

In fact, table 1 reports also the concrete cover measured by means of the pacometer survey before testing. Only for drilled and drilled-restored columns, a concrete cylinder strength is shown. These values derive from the compression tests carried out on the extracted cores corrected through the method reported in [8]. This method allows taking into account drilling damage, shape factor of the core and possible presence of reinforcement inside the core specimen. Mean value of concrete strength reported in table 1 is f_{med}=37.88 MPa while the standard deviation is σ=2.09 MPa. Being the low value of the coefficient of variation CV=0.055, the mean value can be properly assumed as the concrete strength of as-built specimens.

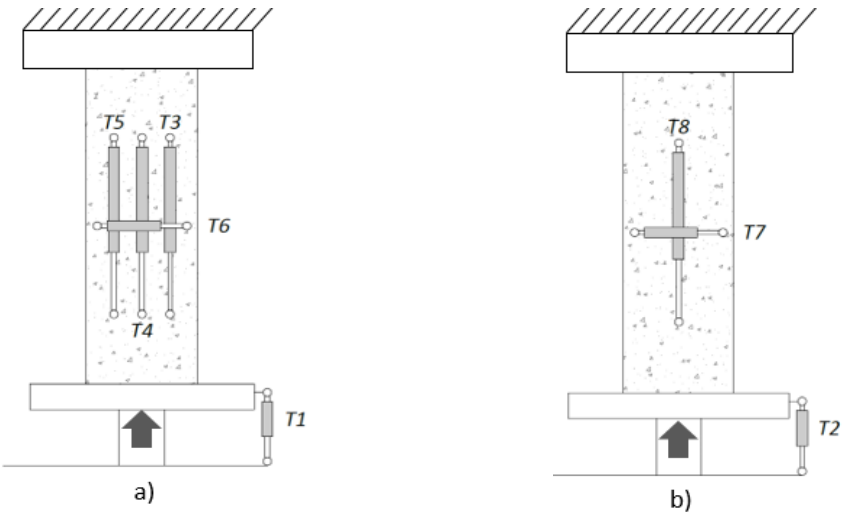

Figure 1: Loading schema and main instrumentation: a) on the front face and b) on the rear face.

The compression test machine applies the load moving his bottom plate and contrasting the top face of the specimen. The machine capacity is 3000 kN and the testing procedure is load controlled by applying increments of 30 kN/s until the peak load is found. When the load decreasing (after the peak is achieved) reaches 20% of the peak load, the machine unloads the specimen to start a new loading cycle. Figure 1 describes the loading scheme along with the instrumentation which consists of four Linear Variable Displacement Transducers (LVDT) placed on the front face of the specimens, one LVDT to measure the displacement of the bottom plate of the testing machine and additional 3 LVDT on the rear face. Out of these, two are placed on the concrete surface and one to measure the plate displacement on its opposite corner. Sometimes, an additional horizontal LVDT has been placed on the front face of the specimen like for example in fig. 2a). As examples, figure 2 shows the three types of tested columns placed on the Universal testing machine used throughout the experimental campaign. The front face is that where the core, if any, is drilled and possibly restored.

a) b) c)

Figure 2: a) as-built b) drilled and c) drilled-restored specimens before testing.

3 TEST RESULTS AND DISCUSSION

Different collapse mechanisms have been observed during the compression tests carried out on the three typologies of columns. Similar mechanisms have been found in as-built and drilled-restored in which a progressive deterioration of concrete cover is observed generally before reaching the peak load. The ultimate condition is, however, represented by the rebars' buckling which is poorly restrained due to the low amount of hoops. The drilled columns, as could be expected, are characterized by quite different behaviour especially in the first phases of compression tests. The first damage appears on the side of the hole in the front face, usually where the rebar is nearest to the hole. Figure 3 shows two stages of the compression test on S2 specimen. The first vertical crack appears on the left side of the hole (figure 3a) when the load is approaching the peak. In the following load cycles damage further concentrates in that region causing the buckling of the left bar (figure 3b). Uneven damage distribution causes eccentricity between load and resisting cross-section, which is an additional source of damage.

Results in terms of ultimate load measured on tested specimens are displayed in figure 4. The experimental ultimate load is averagely equal to 2293 kN for as-built specimens, 2260 kN for restored specimens and 1981 kN for drilled ones, respectively. So, drilled columns show a mean capacity reduction compared to as-built columns equal to about 14%. Restored columns show a reduction of only 1.4%, meaning that current procedures for restoring interventions

are effective. This conclusion has been drawn neglecting differences in terms of longitudinal reinforcement which can be considered small.

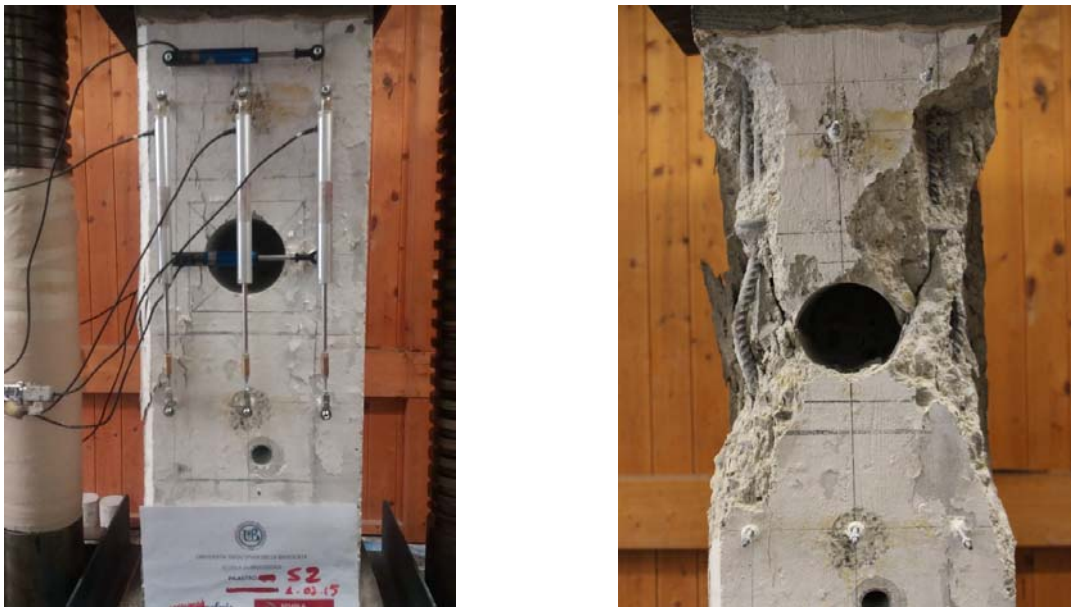

a) b)

Figure 3: S2 column: a) before peak load and b) at the end of the test.

Along with experimental results, also the analytical predictions of ultimate load for each column is reported. It is related to the gross concrete area times the compressive strength of each specimen added to the reinforcement contribution, as in expression (1):

$$F_{ug} = A_c \cdot f_c + A_s \cdot f_{ys} \tag{1}$$

where: A_c is the gross concrete area, A_s is the total steel area, f_{ys} is the steel yielding strength. For drilled specimens, A_c is obtained subtracting the horizontal projection of the hole which has 104 mm diameter and 220 mm depth.

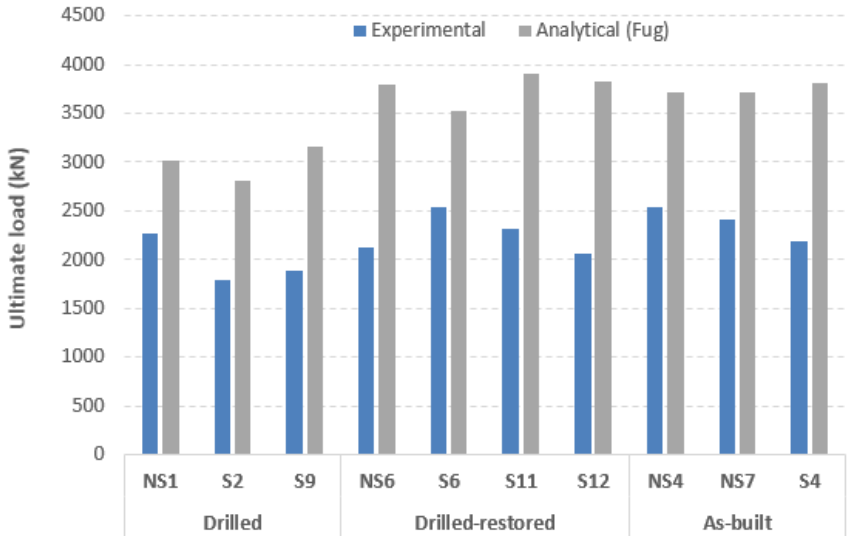

Figure 4: Comparison between experimental and analytical ultimate load values (gross section).

As can be seen, the analytical prediction of the ultimate load F_{ug} provides far higher values than the experimental ones. The observed scatter between experimental and analytical values is 52%, 67% and 58% for drilled, drilled-restored and as-built specimens, respectively. This difference strongly suggests that a much smaller value of the effective resisting cross section needs to be considered. This is also suggested by observing that in all tests concrete cover was spalled before reaching the peak load.

As a result, the effective section is assumed equal to the area confined by the steel cage, i.e. the gross section minus the concrete cover area (dashed area in figure 5). Moreover, in order to comply with international standards and codes for the design of concrete structures, the role of confining effect on concrete strength has been considered.

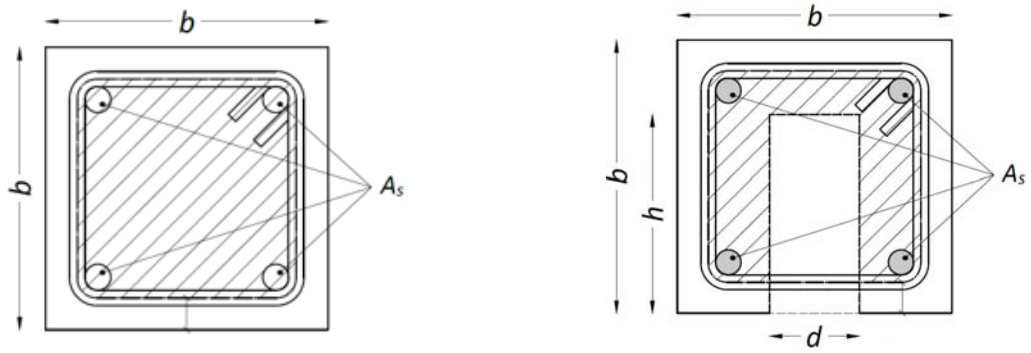

Figure 5: Effective cross section of a) as-built and drilled-restored and b) drilled specimens.

Some confinement models available in the literature [9,10] as well as the model reported in the Italian seismic code [1] have been considered. In the following, reference only to the model reported in [9] is made, because it provided the best matching with experimental results, while, for the sake of brevity, results obtained with the application of the other models are not discussed in the paper. By applying the confinement model in [9], a 5% increment of concrete strength is averagely obtained. Taking into account this concrete strength increase and the modified effective section displayed in figure 5, updated analytical values are computed and the comparison with the related experimental values is reported in figure 6.

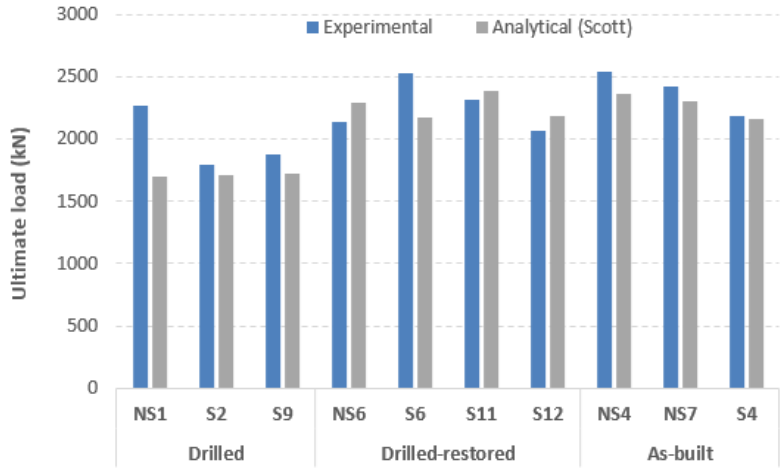

Figure 6: Comparison between experimental and analytical ultimate load values (confining model [9]).

As can be seen, the difference exp-num values remarkably decreases being averagely equal to 13%, 11% and 4% for drilled, drilled-restored and as-built specimens, respectively. Larger difference for drilled and drilled-restored specimens is somehow expected, due to the additional influence of the presence of the hole or the restoration unit on the collapse mechanism. Further, it is worth noting that, analytical results are always on the safe side for both as-built and drilled specimens, while, for drilled-restored specimens, they are generally higher thus unconservative.

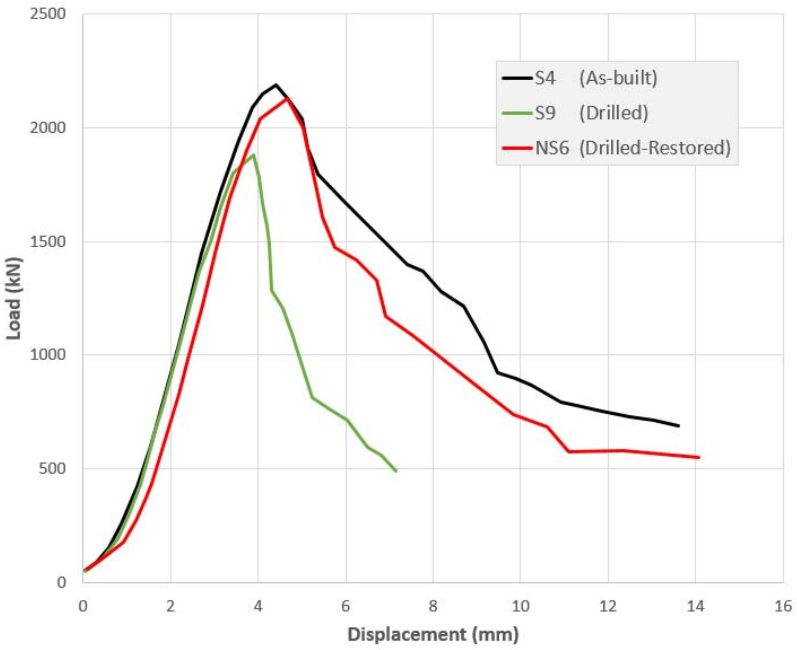

Figure 7: Envelope of skeleton curves of NS6, S4 and S9 specimens.

Although it seems inappropriate speaking of ductility for specimens whose failure is characterized by fragile mechanisms (concrete crushing and rebars' buckling), some differences have been found among the columns' typologies. In order to highlight this issue, the skeleton curves of the load-displacement envelopes have been plotted in figure 7 for three specimens: S4 (as-built), S9 (drilled) and NS6 (drilled-restored).

Beyond the expected lower failure load of the drilled column, degrading phenomena affecting as-built and drilled restored elements are more gradual. In fact, a 50% load reduction is found at displacements of 8 and 9 mm for drilled-restored and as-built specimens, respectively, while the drilled one shows the same reduction at around 5 mm. It is important to underline that restoration is able to provide the columns with almost the same ductile capacity compared with the as-built ones. Instead, more brittle failure is expected in drilled columns.

In addition to the previous discussion, it is worth remembering that specimens subject of this study belonged to seismically tested beam-column joints, whose concrete cover was mostly cracked at the moment of compression tests. Therefore, the reported results are particularly meaningful for seismically damaged structures for which residual capacity to carry vertical loads must be carefully evaluated, neglecting the contribution of the concrete cover.

4 FINITE ELEMENT ANALYSES

Nonlinear finite element models using ATENA 3D software package [4] were developed in order to more deeply investigate the failure mode found in drilled columns. The software is

based on the nonlinear fracture mechanics [11] and is capable to take into account compression softening as well as crushing and cracking of concrete.

For concrete, the robust smeared crack model "CC3DNonLinCementitious2" was used. The modelled column is NS1, that is a drilled one. The main properties of concrete are derived from the results of the compression test on the core extracted from the same column, that is f_c = 39.5MPa, f_t = 2.89 MPa, ν = 0.2, and E_c = 32.5 GPa, being respectively the compressive strength, tensile strength, Poisson ratio, and elastic modulus. Actually, with the exception of the compressive strength f_c, all other mechanical properties are derived from literature expressions based on f_c. As previously discussed, in accordance with the confinement model in [9], the concrete strength has been increased by 5%, assuming f_c=41.5 MPa in the numerical simulations.

A fictitious uniaxial stress-strain law (figure 8-a) with displacement based softening has been adopted [12].

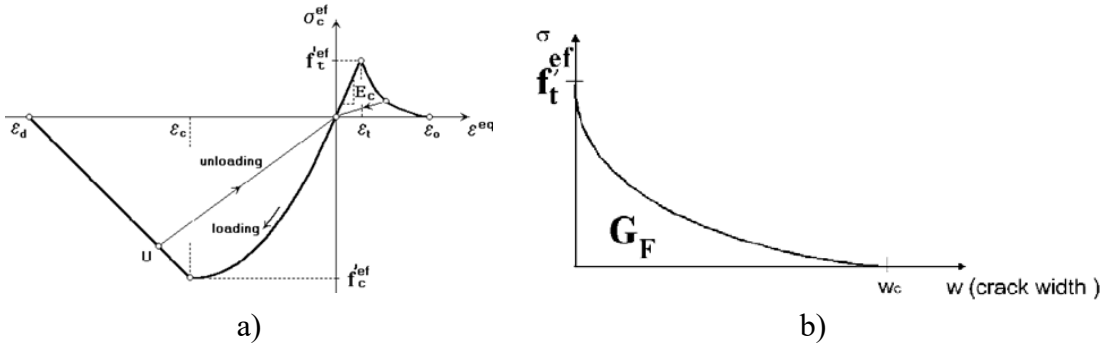

Figure 8: a) Uniaxial compressive stress-strain law and b) crack opening law for tensile stresses for concrete.

Under tensile stress, concrete behavior is governed by a crack opening law, as in figure 8-b defining the fracture energy (G_F). The tensile strength presents an exponential degrading law. The fracture energy was computed by means of Remmel's law [13].

An elastoplastic law with hardening was chosen for the reinforcing steel stress-strain relationship, with yielding strength f_y=480 MPa and failure strength f_t=590 MPa. These values were based on experimental tests carried out on rebars belonging to the same steel supply used for the specimens' construction. No bond slip between concrete and steel has been considered since the column is provided of ribbed bars and slip phenomena are not significant to global behavior under compression loads.

The global finite element model is referred to column NS1 without the concrete cover, based on the previous considerations, after having verified that the concrete cover is ineffective to increase the maximum load carrying capacity of the members under study. This means that only the concrete core inside the steel cage has been modeled giving a cross section 260mm x 260 mm.

Due to the presence of the core's hole, having diameter 104 mm and depth 220 mm, the mesh could not be structured (i.e. made of an ordinate repetition of elements having the same size). The mesh, in fact, is made of tetrahedral elements whose mean size near the hole is 10 mm while far from it, is set equal to 25 mm. The final mesh size has been determined by a sensitivity analysis gradually decreasing the element size. Despite only a short column is under study a huge model has been generated (figure 9-a). As a whole, the model is made up of 264 straight truss elements (i.e. carrying only axial loads) to simulate the steel reinforcement

(figure 9-b), 40347 tetrahedral elements to simulate concrete and the upper steel plate, and 9009 nodes. Analyzing such a model under cyclic loads is time expensive even using a powerful workstation, thus only monotonic analyses have been made to save time. Loading history was displacement controlled, applying to the top plate 5 mm displacement subdivided into 100 steps which the program can divide into further sub-steps based on numerical solution needs.

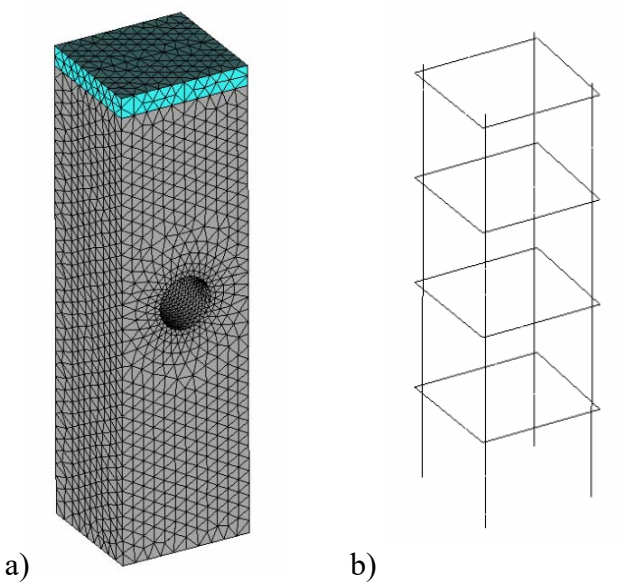

Figure 9: a) Mesh of NS1 FE model, b) steel reinforcement.

Firstly, to evaluate the effectiveness of the FEM model, experimental and numerical load-displacement curves are compared. As can be seen from figure 10, the peak load is well predicted by the numerical simulation, while differencence are found in the ascending branch, mainly ascribable due to the presence of a neoprene layer placed between the top face of column and the machine plate, having the role of uniformly applying the compression load during the test. Descending branches are not coincident due to the fact that numerical analysis is not cyclic and, then, generates less damage accompanied by a lower strength degradation.

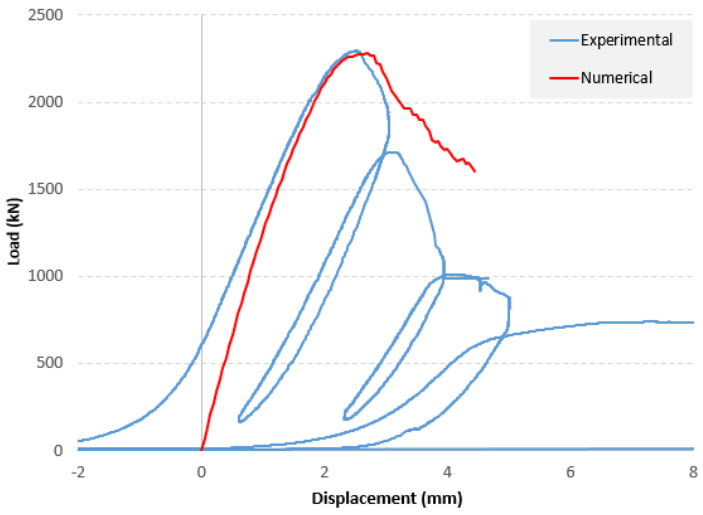

Figure 10: Experimental and numerical load-displacement curves for NS1 specimen.

4.1 Analysis of the failure mechanism

By studying the model of the drilled column NS1, the failure mode of the specimen due to presence of the extraction hole can be better understood. Specifically, figure 11a shows the deformed shape of the specimen by means of an isometric view and a side view. The presence of the hole determines an eccentricity between the applied load, directed along the column axis, and the center of the resisting section, not coincident with the column axis. This eccentricity introduces a bending moment around the X-axis with consequent displacements in the Y direction, especially for the column region around the hole.

Figure 11 shows the deformed shape at the peak load. Although horizontal displacements in the Y direction are low (below 1.0 mm), this involves an asymmetry of vertical (Z) displacements too.

This latter can be seen in figure 12a, where the relation between vertical displacements measured during the experimental tests by LVDT no. 4 (on the front face) and no. 8 (on the rear face) is displayed. As can be seen, there is a remarkable difference, matching the deformed shape obtained by the FEM model (figure 11).

Figures 12b and c display the colormap of Z displacements on the same faces of the specimen. From this colormap, similar differential displacements can be found between the points where the aforementioned LVDT are anchored.

This latter demonstrates the good calibration of the FEM model and its ability to predict the column's behavior.

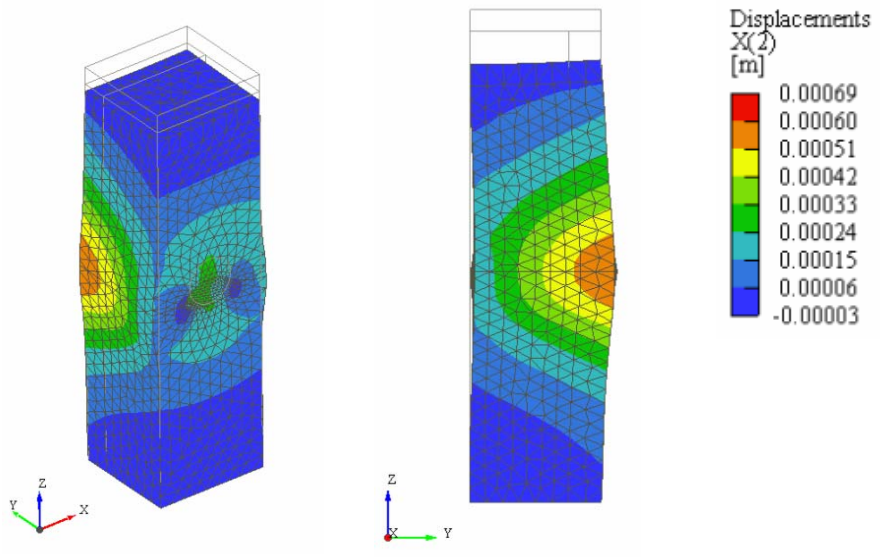

a) b)

Figure 11: Colormap of Y displacements as a) isometric view and b) side view.

In order to complete the description of the collapse mechanism, figure 13 shows the rebars' stresses at peak load. Longitudinal reinforcement (figure 13a) overcomes the yielding stress in compression (f_y=480 MPa), being the minimum value equal to 484 MPa. They are yielded for most of their length as can be seen by the evolution plotted along the bars' development. Going beyond the peak load of the specimen, the stress increases to about a maximum value of 500 MPa. This means that the bars do not fail being their tensile strength equal to 590 MPa.

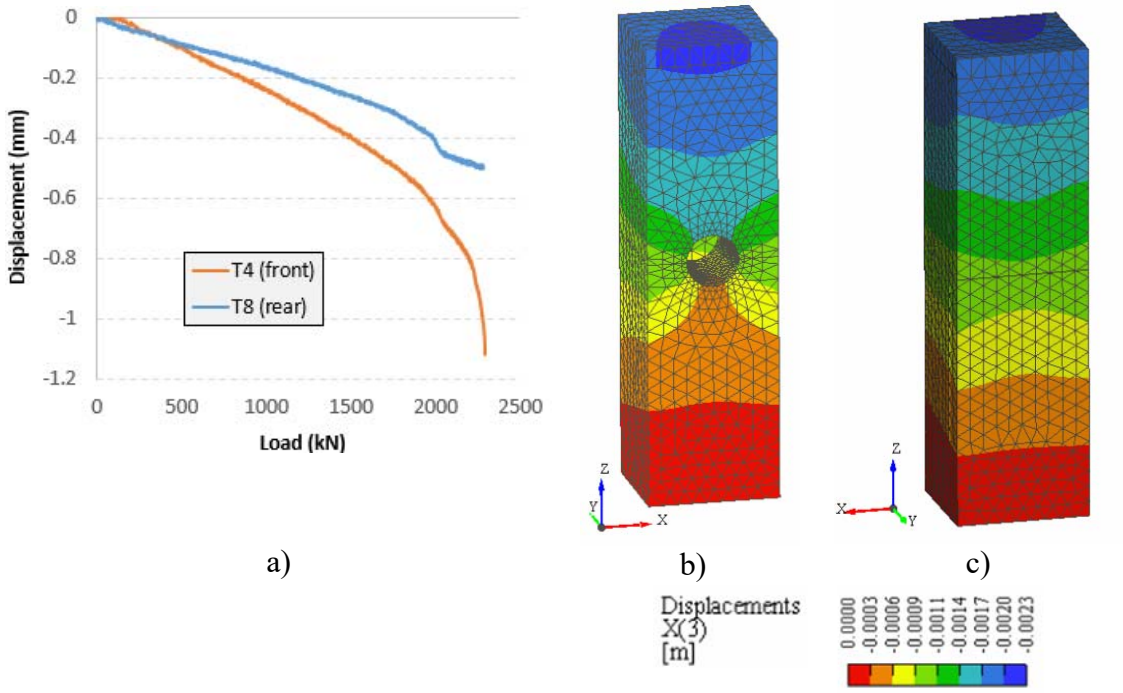

Figure 12: a) Experimental displacements and numerically evaluated on the front face (b) and on the rear face (c)

Hoops' stress is equal to 480 MPa corresponding to the yielding strength of steel. After the peak load, the hoops reach tensile stress values lower than 485 MPa. The most stressed branches of hoops are those normal to the core axis according to the deformed shape shown in figure 11a.

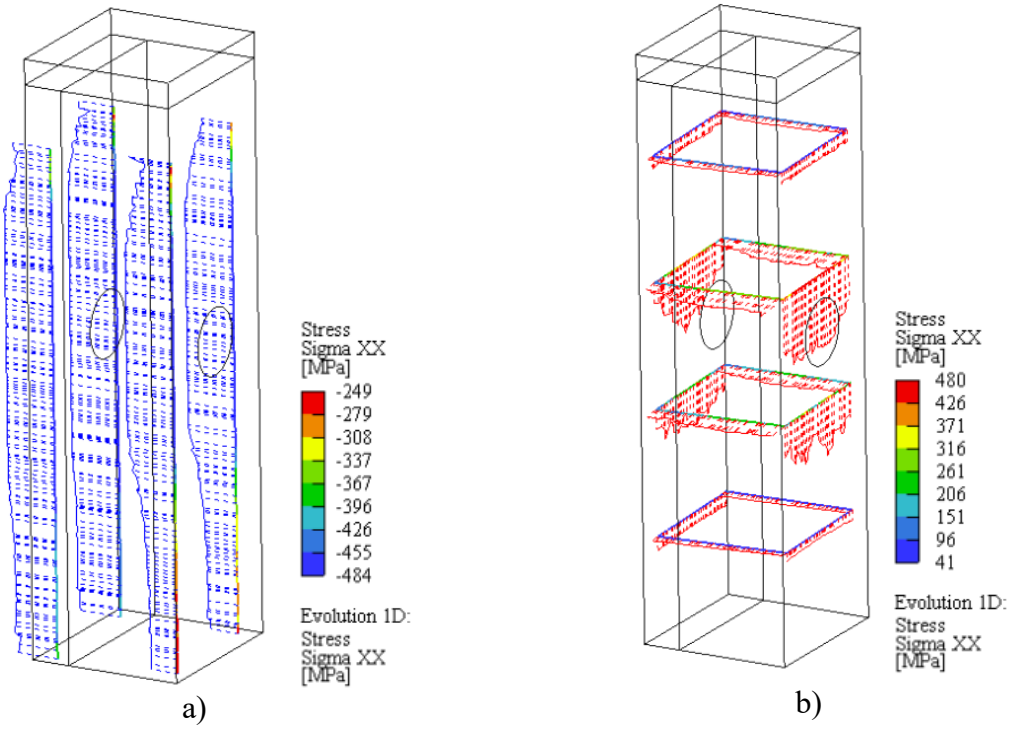

Figure 13: a) Longitudinal reinforcement and b) transverse reinforcement stresses distributions.

Summarizing, steel strength and ductility is not fully exploited as shown by the stress values achieved by longitudinal and transverse reinforcement. This happens because crushing of concrete on the core sides leads to the early buckling of reinforcement and consequent failure.

5 CONCLUSIONS

This paper reports a study on the behavior of reinforced concrete columns under axial compression load previously subjected to a seismic loading history as part of beam-column joints. By means of compression tests, the behavior of as-built, drilled and drilled-restored columns is investigated in order to evaluate the effect of core drilling and the effectiveness of the holes' restoration according to a standard procedure in the in-situ destructive testing campaign on RC buildings. Further, nonlinear finite element models were developed in order to better investigate the failure mode found in drilled columns.

The main findings from the experimental and numerical study are:

- Experimental results show that the failure of columns is characterized by early concrete cover spalling and consequent bar buckling. In particular, concrete cover spalling happens before reaching the peak load. Analytical ultimate load evaluated accounting for the gross concrete section is far higher than the correspondent experimental value.
- Based on the previous result, analytical prediction of the columns' strength can be done by considering only the confined concrete section, accounting also the confining effect. The most accurate capacity prediction is related to the confinement model reported in [9].
- Drilled specimens show a mean compression load capacity reduction equal to about 14% compared to as-built specimens. Restored specimens, instead, exhibit a negligible reduction (about 1.4%).
- Also, drilled specimens show a significant ductility reduction which has not been observed in restored specimens. This means that restoration is able to provide the columns with almost the same capacity of the as-built condition.
- The nonlinear FEM model of a drilled specimen showed a satisfying predictive capacity proved by the good agreement between experimental and numerical load-displacement curves.
- The failure behavior of columns is characterized by the eccentricity between the axial load and the resisting cross-section at the hole's location. This is clearly shown by the deformed shape of the numerical model that matches the experimental measurements of the LVDT placed on the front and rear face of the column.
- Finally, the failure of the studied column is characterized by the concrete crushing of regions around the hole. This causes the early spalling of concrete cover and consequent buckling of longitudinal bars that reach the compression yielding stress but are unable to exploit their full strength.

The experimental and numerical investigation on column specimens here reported suggests that the compression load carrying capacity of previously seismically loaded column members is far lower than that obtained from code-based analytical predictions accounting for the full cross-section. This is particularly true for weakly reinforced concrete columns as those of the present study, for which bar buckling can be not effectively restrained by hoops and ties.

ACKNOWLEDGEMENTS

The work reported in this paper was carried out within the framework of the DPC-ReLUIS 2018 Project, Research Line "Reinforced Concrete Structures", WP3-"Upgrading and Retrofitting of RC Existing Structures".

REFERENCES

[1] Aggiornamento delle *"Norme tecniche per le costruzioni"*, Ministry of Infrastructure DM 17 gennaio 2018, Suppl. ord. alla "Gazzetta Ufficiale n. 42 del 20 febbraio 2018 - Serie generale (in Italian), 2018.

[2] Masi A., Chiauzzi L. and Manfredi V., Criteria for identifying concrete homogeneous areas for the estimation of in-situ strength in RC buildings, *Construction and Building Materials*, **121**, 576-587, September 2016.

[3] Masi, A., Digrisolo, A., Santarsiero, G., Concrete strength variability in Italian RC buildings: Analysis of a large database of core tests. *Applied Mechanics and Materials,* ***5*97**, 283-290, 2014.

[4] Červenka V., Jendele L., Červenka J., *ATENA Program Documentation, Part 1, ATENA Theory Manual*. Cervenka Consulting, Praha, 2018.

[5] Z. P. Bažant, Q. Yu, Universal Size Effect Law and Effect of Crack Depth on Quasi-Brittle Structure Strength, *Journal of Engineering Mechanics,* **135**, 78-84, 2009.

[6] M. Brocca, Bažant Z.P., Size Effect in Concrete Columns: Finite-Element Analysis with Microplane Model, *Journal of Structural Engineering,* **127**(12), 1382-1390, 2001.

[7] Masi, A., Santarsiero, G., Nigro, D., Cyclic tests on external rc beam-column joints: Role of seismic design level and axial load value on the ultimate capacity. *Journal of Earthquake Engineering,* **1**7(1), 110-136, 2013.

[8] A. Masi, A. Digrisolo, and G. Santarsiero, Experimental Evaluation of Drilling Damage on the Strength of Cores Extracted from RC Buildings. *International Journal of Structural and Construction Engineering*, **7**, 2013.

[9] Scott, B.D., Park, R., and Priestley, M.J.N., *Stress-strain behavior of concrete confined by overlapping hoops at low and high strain rates*. J. American Concrete Institute, **79**, 13-27, 1982.

[10] J.B. Mander, M.J.N. Priestley, R. Park, Theoretical stress–strain model for confined concrete, *Journal of Structural Engineering*, ASCE **114** (8), 1804–1826, 1988.

[11] Z P. Bazant, *Fracture Mechanics Of Concrete Structures*, Elsevier Applied Science, London, 1992.

[12] Chen, W.F, Saleeb, A.F., *Constitutive Equations For Engineering Materials*, John Willey \& Sons, ISBN 0-471-09149-9, 1982.

[13] Remmel G., *Zum Zug-und Schubtragverhalten von Bauteilen aus Hochfestem Beton*. DAfStb, Heft 444, Beuth Verlag: Berlin, Germany, 1994.

COMPDYN 2019
7th ECCOMAS Thematic Conference on
Computational Methods in Structural Dynamics and Earthquake Engineering
M. Papadrakakis, M. Fragiadakis (eds.)
Crete, Greece, 24–26 June 2019

DISPLACEMENT-BASED DESIGN OF DAMPED BRACES FOR EXISTING R.C. BUILDINGS WITH DEGRADING SEISMIC RESPONSE

Fabio Mazza[1]

[1] Dipartimento di Ingegneria Civile
Università della Calabria
87036, Rende (Cosenza), Italy
e-mail: fabio.mazza@unical.it

Abstract

The widespread use of damped braces is closely related to the availability of simplified yet reliable design procedures along with the new generation of seismic codes based on the performance-based design. On the other hand, the seismic retrofitting of a reinforced concrete (r.c.) framed building goes through a proper evaluation of the structural behaviour before failure and sensitivity to damage. In fact, lack of knowledge on strength and stiffness degradation may not be compensated for in the following calculation of a passive control system. A Displacement-Based Design (DBD) procedure to proportion hysteretic damped braces (HYDBs) is proposed in order to take into account the effects of the seismic degradation of a structure that needs to be retrofitted. To this end, a hysteretic model based on plastic and damage mechanisms is adopted to describe the inelastic response of r.c. frame members. Then, nonlinear seismic analysis of a single-degree-of-freedom system, equivalent to a multi-degree-of-freedom model of the structure, is used to generate the capacity boundary curve by means of the hysteretic model defined starting from the initial backbone curve. Two-, four- and eight-storey r.c. framed structures, representative of low-, mid- and high-rise r.c. framed buildings, are designed for a medium-risk seismic zone of a former Italian code. These structures are then to be retrofitted by inserting HYDBs to attain performance levels imposed by current Italian code in a high-risk seismic zone. Different retrofitting solutions are compared, considering for each retrofitted structure: i) variable damper ductility coupled with constant frame ductility; ii) variable frame ductility coupled with constant damper ductility. The effects of different damage levels and different damage evolution laws are also investigated.

Keywords: R.C. Framed Structures, Strength Degradation, Stiffness Degradation, Hysteretic Damped Braces, Displacement-Based Design Procedure, Seismic Retrofitting.

1 INTRODUCTION

Thanks to the displacement and velocity dependent mechanisms (e.g. hysteretic and viscous) with in-built amplification (e.g. toggle and scissor jack brace configurations), the effectiveness of supplementary energy dissipation devices inserted on steel braces (i.e. damped braces) has been widely recognised as reducing the level of seismic energy to building structures [1, 2]. The widespread use of this technology is closely related to the availability of simplified yet reliable design procedures along with the new generation of seismic codes based on the performance-based design that combines seismic limit levels with hazard levels [3]. The most promising ideas are those in which the estimation of seismic demand and capacity of the structure is based on Displacement-Based-Design (DBD) and Energy-Based-Design (EBD) procedures. In particular, in the DBD approaches the design starts from a target deformation, combining the nonlinear static analysis of the multi-degree-of-freedom (MDOF) model of the actual structure with the response spectrum analysis of an equivalent single-degree-of-freedom (SDOF) system [4-6]. The EBD approaches, on the other hand, explicitly address cumulative and localized structural damage, assessing the energy absorption and the dissipation mechanisms that can be made to balance the total seismic energy input, through use of nonlinear dynamic analysis or optimization procedures [7-9].

Structural behaviour in past earthquakes confirms that reinforced concrete (r.c.) framed buildings, poorly reinforced with regard to the requirements of the seismic damage control, may suffer permanent damage from a combination of highly inelastic excursions and severe cyclic loading [10]. This observation opens up the search for a more realistic estimation of the deformation capacity through a displacement based approach in which strength and stiffness degradation of the MDOF system are evaluated starting from the initial backbone curve of the corresponding SDOF system [11]. Various types of hysteretic models can be used to study the effects of the deterioration modes of structural components on their hysteretic behaviour under sizeable inelastic deformations [12]. In the present work, to account for the cyclic behaviour, the initial backbone curve is replaced by a sequence of N linear segments defined by a combination of as many elastic-perfectly plastic (EPP) mechanisms as necessary. Then, cyclic deterioration is reproduced by introducing N elastic-softening damage (ESD) mechanisms acting in-parallel with the EPP ones, controlled by a damage variable (ψ) and corresponding damage index (Ψ).

To evaluate the effectiveness of the proposed Displacement-Based Design (DBD) procedure of hysteretic damped braces (HYDBs), accounting for the cyclic behaviour of r.c. frame members, two-, four- and eight-storey r.c. framed structures are adopted as test structures. These are first designed in line with a former Italian code for a medium-risk seismic zone [13] and then retrofitted to attain performance levels imposed by the current Italian code in a high-risk seismic zone [14]. Six solutions are compared, considering for each retrofitted structure: three design values of the damper ductility (i.e. μ_D=10, 15 and 20), coupled with a constant design value of the frame ductility (i.e. μ_F=1.5); three design values of the frame ductility (i.e. μ_F=1.2, 1.5 and μ_{Fu}), coupled with a constant design value of the damper ductility (i.e. μ_D=15). Moreover, six hysteretic laws, corresponding to different levels of degradation, are assessed: i.e. low (i.e. Ψ=0.33), medium (i.e. Ψ=0.5) and high (i.e. Ψ=0.83) constant values of the damage index (Ψ); continuous damage evolution with linear (i.e. ε=1.0) and nonlinear (i.e. ε=0.5 and 0.2) laws related to the parameter (ε) governing the rate of degradation. Finally, pushover curves of the original (unbraced) and retrofitted (damped braced) structures are evaluated, with and without considering degradation of the hysteretic response of r.c. frame members on the DBD procedure of the HYDBs.

2 DISPLACEMENT-BASED DESIGN PROCEDURE OF DAMPED BRACES

A multistep iterative DBD procedure, for proportioning HYDBs in order to get a designated performance level of an existing r.c. regular framed structure for a specific level of seismic intensity [5], is proposed to take account of the main modes of cyclic deterioration of r.c. frame members during seismic loads. The main steps of the new procedure are briefly summarized below, with the main focus on the strength and stiffness degradation of the SDOF system equivalent to the original MDOF system.

2.1 Nonlinear static analysis of the original multi-degree-of-freedom system

Nonlinear static analysis of the original unbraced frame, under constant gravity loads and monotonically increasing horizontal loads (Figure 1a), is carried out to obtain the base shear versus (e.g. roof) displacement ($V^{(F)}$-d) curve (Figures 1b,c) of the MDOF system, where the modal participation factor (Γ) controls the transformation to the equivalent SDOF system (Figure 1d). The lowest capacity curve is selected from those corresponding to constant lateral-load patterns based on "modal" and "uniform" displacement shapes, in line with provisions of the European seismic code [15] for regular structures: i.e. a "first-mode" pattern, obtained by multiplying the first-mode components (ϕ_1, ϕ_2, ..., ϕ_n) by the corresponding floor masses (m_1, m_2, ..., m_n); a "uniform" pattern, only proportional to the floor masses.

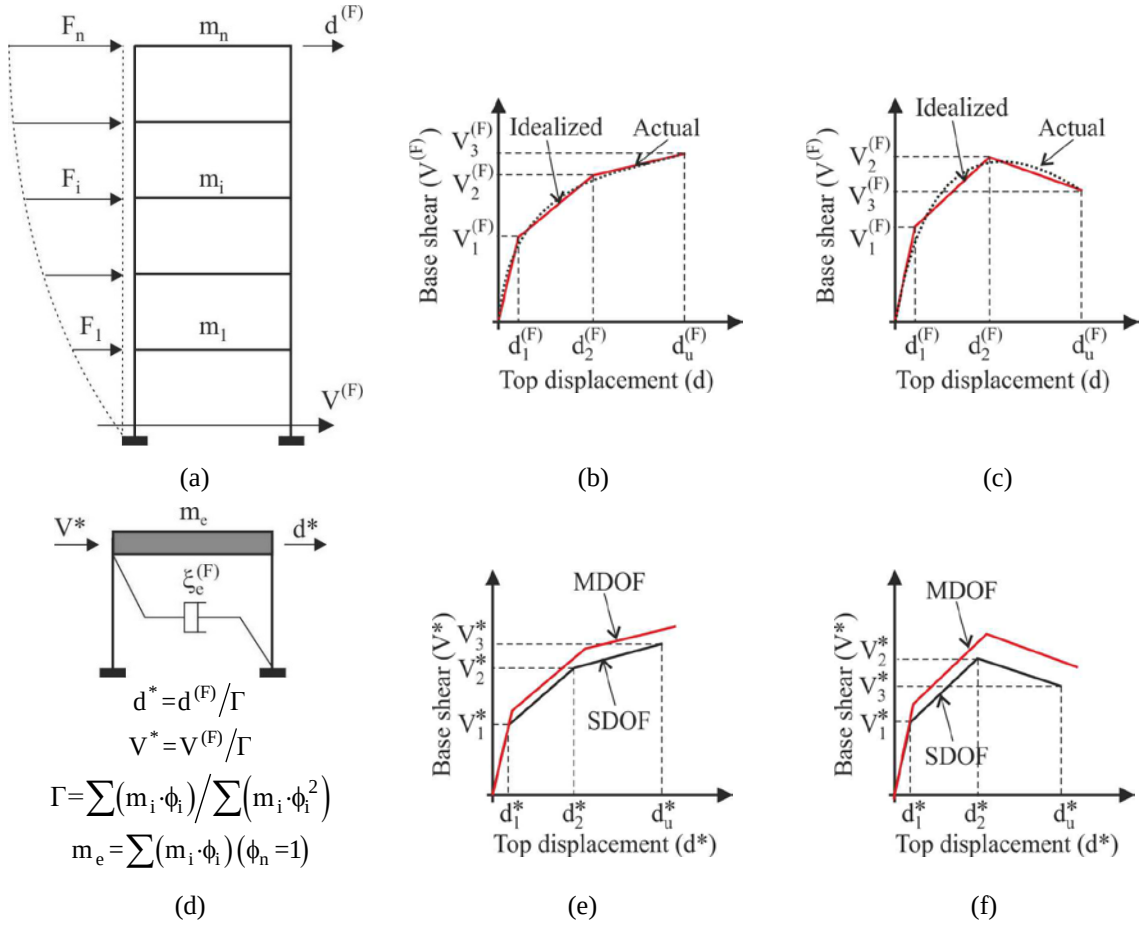

Figure 1: Pushover curves of the original (MDOF) and equivalent (SDOF) systems.

Then, the initial backbone curve of the SDOF system, incorporating yielding and positive (e.g. hardening in Figures 1b and 1e) and negative (e.g. hardening and softening in Figures 1c

and 1f) stiffness, is fitted by means of a piecewise linear function. By using this piecewise linear fit and leaving aside damage (i.e. a damage index Ψ=0), it is possible to account for the cyclic behaviour considering the hysteretic model obtained as a combination of N elastic-perfectly plastic (EPP) mechanisms corresponding to a sequence of N linear segments. Moreover, the i-th linear segment is coupled with the corresponding i-th plastic mechanism described by an EPP law expressed as (Figure 2):

$$V_{P,i}^{*\pm}=K_{P,i}^{\pm}\cdot\left(d^{*\pm}-d_{y,i-1}^{*\pm}\right),\ \left|d_{y,i-1}^{*\pm}\right|<\left|d^{*\pm}\right|\leq\left|d_{y,i}^{*\pm}\right| \tag{1}$$

$$V_{P,i}^{*\pm}=V_{yP,i}^{*\pm}=K_{P,i}^{\pm}\cdot\left(d_{y,i}^{*\pm}-d_{y,i-1}^{*\pm}\right),\ \left|d^{*\pm}\right|>\left|d_{y,i}^{*\pm}\right| \tag{2}$$

$V^*_{yP,i}$ and $d^*_{y,i}$ being the force and displacement at the i-th yielding point and $K_{P,i}$ the elastic stiffness. It should be noted that the initial backbone curve can exhibit multi-linear elastic hardening with a final positive (Figure 2a) or negative (Figure 2b) stiffness segment. In this case, the last (i.e. N-th) plastic mechanism of the hysteretic model will be represented by an elastic-linear law. Moreover, the unloading stiffness of the i-th plastic mechanism is assumed to be the same as the elastic one.

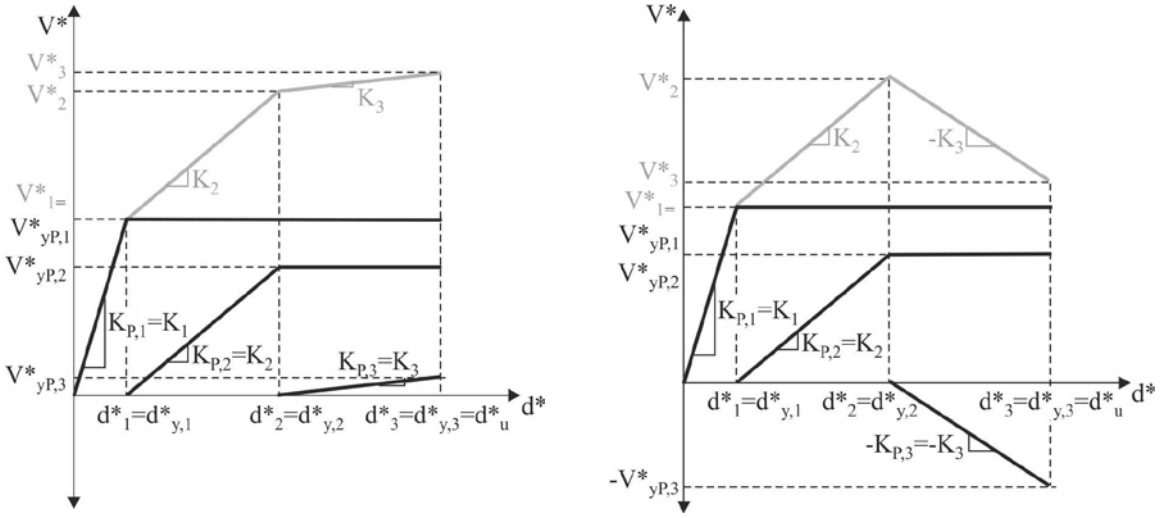

Figure 2: Illustration of the plastic mechanisms (Ψ=0).

2.2 Nonlinear dynamic analysis of the equivalent single-degree-of-freedom system

Nonlinear dynamic analysis of the equivalent SDOF system includes the cyclic deterioration by modifying the initial backbone curve, representative of the response for monotonically increasing loading, as function of the seismic loading history. One way of achieving this is to overlap N damage mechanisms onto the previously defined N plastic mechanism. In particular, the i-th damage mechanism presents an elastic-softening law characterized by a first linear upward branch until the attainment of yield displacement of the corresponding i-th plastic mechanism (Figure 3)

$$V_{D,i}^{*\pm}=K_{D,i}^{\pm}\cdot\left(d^{*\pm}-d_{y,i-1}^{*\pm}\right),\ \left|d_{y,i-1}^{*\pm}\right|<\left|d^{*\pm}\right|\leq\left|d_{y,i}^{*\pm}\right| \tag{3}$$

with an elastic stiffness of

$$K_{D,i}^{\pm}=\Psi^{\pm}\cdot K_i^{\pm} \tag{4}$$

Ψ being a damage index. Since the stiffness of the i-th segment of the backbone curve results from an in parallel combination of plastic (Figure 2) and damage (Figure 3) mechanisms

$$K_i^{\pm}=K_{P,i}^{\pm}+K_{D,i}^{\pm} \tag{5}$$

the initial plastic stiffnesses can be written as

$$K_{P,i}^{\pm}=\left(1-\Psi^{\pm}\right)\cdot K_i^{\pm} \tag{6}$$

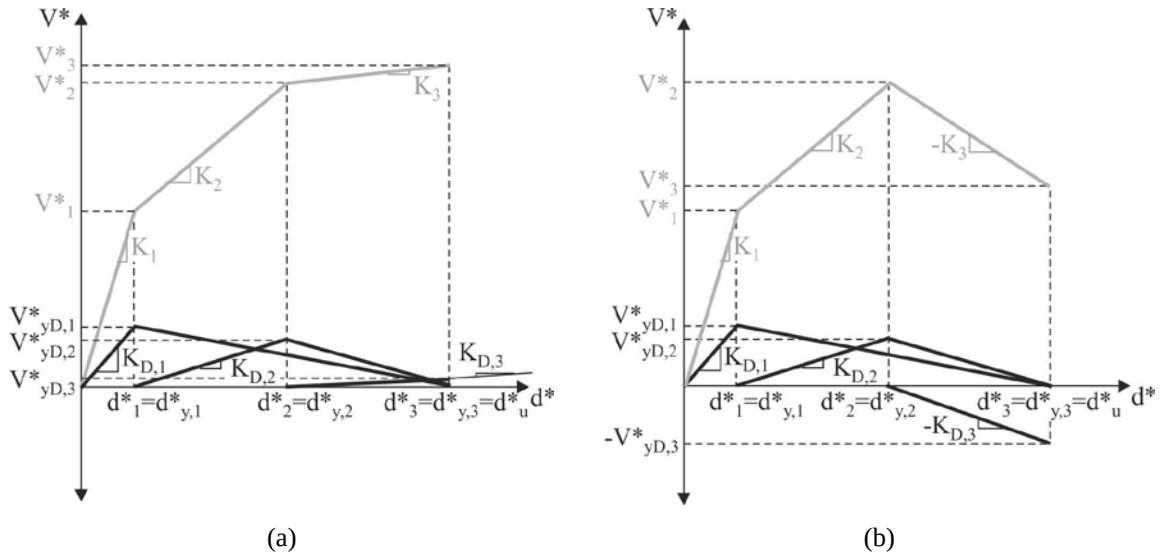

(a) (b)

Figure 3: Illustration of the damage mechanisms (0<Ψ<1).

With regard to the second linear downward branch of the i-th monotonic elastic-softening damage (ESD) mechanism the following expression can be used (Figure 3)

$$V_{D,i}^{*\pm}=V_{yD,i}^{*\pm}-K_{sD,i}^{\pm}\cdot\left(d^{*\pm}-d_{y,i}^{*\pm}\right),\ \left|d_{y,i}^{*\pm}\right|<\left|d^{*\pm}\right|\leq\left|d_u^{*\pm}\right| \tag{7}$$

where the stiffness of the softening branch is equal to

$$K_{sD,i}^{\pm}=\alpha_i^{\pm}\cdot K_{D,i}^{\pm}=\alpha_i^{\pm}\cdot\Psi^{\pm}\cdot K_i^{\pm} \tag{8}$$

by placing

$$\alpha_i^{\pm}=\frac{d_{y,i}^{*\pm}-d_{y,i-1}^{*\pm}}{d_u^{*\pm}-d_{y,i}^{*\pm}} \tag{9}$$

The unloading stiffness of the i-th cyclic elastic-softening damage (ESD) mechanism is assumed equal to:

$$K_{uD,i}^{\pm}=\beta_i^{\pm}\cdot K_{D,i}=\beta_i^{\pm}\cdot\Psi^{\pm}\cdot K_i^{\pm} \tag{10}$$

given

$$\beta_i^{\pm}=\alpha_i^{\pm}\frac{d_u^{*\pm}-d_i'^{*\pm}}{d_i'^{*\pm}} \tag{11}$$

where d' is the displacement of the softening branch corresponding to the initial point of the

unloading phase. In so doing, the unloading branch of the i-th ESD mechanism is oriented towards the origin.

The cyclic deterioration of the plastic and damage mechanisms described above is controlled by damage index Ψ, which involves one or more damage variables ψ (e.g. inelastic deformation and hysteretic energy) and represents a dimensionless parameter varying between Ψ=0, when there is no damage, and Ψ=1, when failure occurs [16]. Furthermore, a lower bound threshold of the damage variable ψ (i.e. ψ_e) corresponds to a substantially linear elastic response, while $\psi=\psi_u$ is the upper bound threshold corresponding to part or all of the ultimate capacity of the system under a monotonically increasing load (i.e. ψ_{mon}). An additional degradation parameter ε needs to be introduced in order to characterize the shape of the ever-increasing Ψ-ψ law:

$$\Psi^{\pm}=0, \text{ for } \psi^{\pm}\leq\psi_e^{\pm} \tag{12}$$

$$\Psi^{\pm}=\left(\frac{\psi^{\pm}-\psi_e^{\pm}}{\psi_u^{\pm}-\psi_e^{\pm}}\right)^{\varepsilon} \quad \text{for } \psi^{\pm}>\psi_e^{\pm},\ \varepsilon\geq 0 \tag{13}$$

ψ being the current value of the damage variable from nonlinear seismic analysis [17-21]. Moreover, the displacement of the SDOF system is considered as damage variable (ψ=d*) where ψ_e=d*$_{y1}$ and ψ_u=d*$_u$ are assumed as elastic and ultimate thresholds, respectively.

Finally, the force deformation curve that envelopes the hysteretic behaviour of the equivalent SDOF system subjected to seismic loads (i.e. the cyclic envelope V*-d*) can be evaluated (Figure 4a) and idealized as bilinear (Figure 4b), where $d_y^{(F)}$ and $V_y^{(F)}$ represent yielding values of displacement and base shear, respectively. Once the displacement corresponding to a selected performance level (d_p) is fixed, base shear at the performance displacement ($V_p^{(F)}$), stiffness hardening ratio (r_F) and ductility μ_F(=$d_p/d_y^{(F)}$) can be also evaluated for the frame.

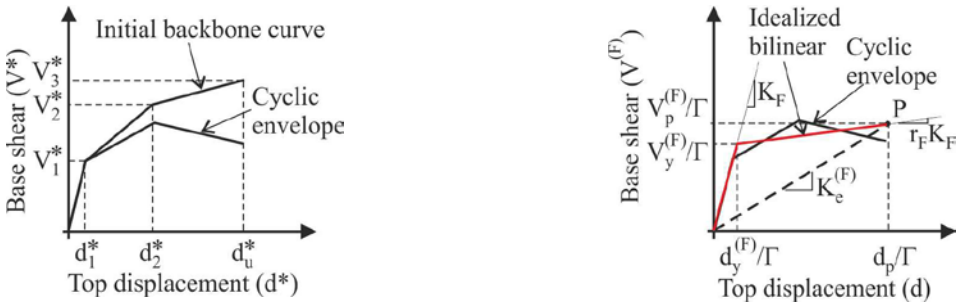

Figure 4: Idealization of the cyclic envelope for the equivalent SDOF system.

2.3 Equivalent viscous damping of the frame with damped braces

The equivalent viscous damping of the in-parallel system of framed structure (F) and damped brace (DB) can be evaluated iteratively by using the following expression, where a suitable value of the elastic viscous damping for the framed structure is assumed (e.g. ξ_V= 5%)

$$\xi_e(\%)=\xi_V+\frac{\xi_F^{(h)}\cdot V_p^{(F)}+\xi_{DB}\cdot V_p^{(DB)}}{V_p^{(F)}+V_p^{(DB)}} \tag{14}$$

being

$$\xi_F^{(h)}(\%)=\frac{1}{3}\left(63.7\frac{\left(\mu_F-1\right)\cdot\left(1-r_F\right)}{\mu_F\cdot\left[1+r_F\cdot\left(\mu_F-1\right)\right]}\right) \tag{15}$$

and

$$\xi_{DB}(\%)=63.7\frac{\left(\mu_{DB}-1\right)\cdot\left(1-r_{DB}\right)}{\mu_{DB}\left[1+r_{DB}\cdot\left(\mu_{DB}-1\right)\right]} \tag{16}$$

A bilinear base shear-displacement curve represents the response of the equivalent hysteretic damped braces (HYDBs) of the actual structure ($V^{(DB)}$-d), where $\mu_{DB}(=d_p/d_y^{(DB)}$, with $d_y^{(DB)}$ displacement corresponding to yielding of the HYDBs) and r_{DB} are ductility demand and stiffness hardening ratio, respectively.

2.4 Design of the equivalent damped brace

Once the effective period (T_e) of the damped braced frame (DBF) is evaluated as the vibration period of the design spectrum corresponding to the equivalent viscous damping (ξ_e) and performance displacement (d_p), it is possible to calculate the effective stiffness of the equivalent damped brace

$$K_e^{(DB)}=K_e-K_e^{(F)}=\frac{4\cdot\pi^2\cdot m_e}{T_e^2}-K_e^{(F)} \tag{17}$$

and shear contributions at the performance and yielding points ($V_p^{(DB)}$ and $V_y^{(DB)}$, respectively)

$$V_p^{(DB)}=K_e^{(DB)}\cdot d_p,\ V_y^{(DB)}=\frac{V_p^{(DB)}}{1+r_{DB}\cdot\left(\mu_{DB}-1\right)} \tag{18a,b}$$

2.5 Design of the hysteretic damped braces for the framed structure

If the structure is assumed to be regular, a proportional stiffness criterion can be used to assess the vertical distribution of the HYDBs, although more refined criteria are available in the literature [22]. In particular, the same value of stiffness ratio $K^*_{DB}(=K_{DB}/K_F$, K_{DB} being the elastic lateral stiffness of the damped braces and K_F that of the unbraced frame) is assumed at each storey. At a given storey, for a diagonal brace with hysteretic damper inclined at angle α with respect to the horizontal direction, the elastic stiffness of the damped brace ($K_i^{(DB)}$) and the yield-load (N_{yi}) can be expressed as

$$K_i^{(DB)}=\frac{V_{yi}^{(DB)}}{\left(\phi_i-\phi_{i-1}\right)\cdot d_y^{(DB)}}\frac{1}{cos^2\alpha_i},\ N_{yi}=\frac{V_{yi}^{(DB)}}{cos\alpha_i} \tag{19a,b}$$

as function of the shear at that storey

$$V_{yi}^{(DB)}=\sum_{j=i}^{n}F_{yj}^{(DB)}=\sum_{j=i}^{n}\frac{m_i\cdot\phi_i}{\sum_{j=1}^{n}m_j\cdot\phi_j}V_y^{(DB)} \tag{20}$$

3 ORIGINAL AND RETROFITTED TEST STRUCTURES

Two- (F2), four- (F4) and eight-storey (F8) r.c. framed structures, with a symmetric plan with 5m long bays (Figure 5a) and a constant interstorey height of 3 m (Figures 5b,c), are

considered as test structures. Note that cross sections of the r.c. frame members at the upper two and four levels of the F8 structure correspond to those of the F2 and F4 structures, respectively. A simulated design of the original (unbraced) buildings is carried out in accordance with a former Italian code [13], for a medium-risk seismic region (seismic coefficient: C=0.07) and a medium subsoil class (subsoil parameter: ε =1). The gravity loads are represented by a dead load of 5.0 kN/m^2 on all the floors, and a live load of 1.5 kN/m^2 on the top floor and 2.0 kN/m^2 on the other floors. A dead load of 1.9 kN/m^2 is also considered for the masonry infill walls. The cross sections of columns (i.e. corner, perimeter and central) and beams (i.e. deep and flat) are reported in Figures 5b,c, where for clarity the dimensions of the r.c. frame members are indicated with reference to Y direction, which will be considered to be the same as the one for the nonlinear static and dynamic analyses. Concrete cylindrical compressive strength of 25 MPa and steel yield strength of 375 MPa are assumed. Finally, the fundamental vibration period (T_{1Y}) and effective mass ($m_{e,1Y}$) of the test structures along Y, expressed as percentage of the total mass (m_{tot}), are reported in Figure 5a. Further details regarding the design can be found in previous work [23].

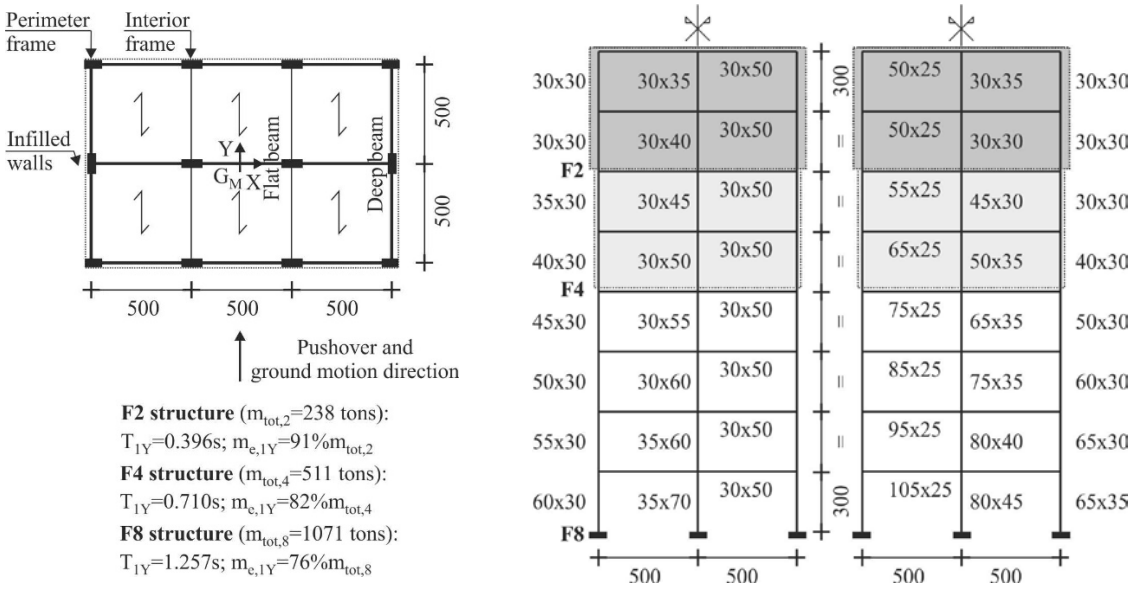

(a) Plan. (b) Perimeter frame. (c) Interior frame.

Figure 5: Original r.c. test structures (units in cm).

First, the nonlinear static analysis of the framed structures along the Y direction is carried out, considering horizontal loads applied at the centre of mass (G_M) of each storey [23]. A lumped plasticity model constituted of two parallel elements, one linearly elastic and the other elastic-perfectly plastic, describes the inelastic behaviour of a r.c. frame member [24]. For a more accurate estimation of the seismic capacity that takes into account the degradation of the Fi under cyclic loading, a piecewise linear fit of the initial backbone curve is used when applying the hysteretic model described in Section 2.1 to the equivalent SDOF system. Then, the nonlinear dynamic analysis of the SDOF systems, equivalent to the corresponding MDOF ones, is carried out along the Y direction, coupling the elastic perfectly-plastic (EPP) and elastic-softening damage (ESD) mechanisms. To this end, seven recorded accelerograms, reflecting the provisions of the current Italian seismic code [14] for the geographical coordinates (longitude 16.17° and latitude 39.31°) at the site in question (i.e. subsoil class C), are selected from the European Strong Motion database [25] and scaled to match, on average, the design spectrum [26]. Cyclic curves resulting from the proposed hysteretic model are evaluated, with

reference to constant and variable values of the damage index (Ψ), in terms of base shear (V_{base}) versus top (roof) displacement (d_{top}). Moreover, monotonic curves that envelope the hysteretic response of the equivalent SDOF systems (i.e. the capacity boundary curves) are plotted in Figure 6, together with the monotonic backbone curve resulting from the nonlinear static analysis (i.e. Ψ=0). In detail, the capacity boundary curves correspond to constant (i.e. Ψ=0.33, 0.5 and 0.83) and variable (i.e. assuming rate degradation of damage governed by ε=1.0, 0.5 and 0.2) values of Ψ.

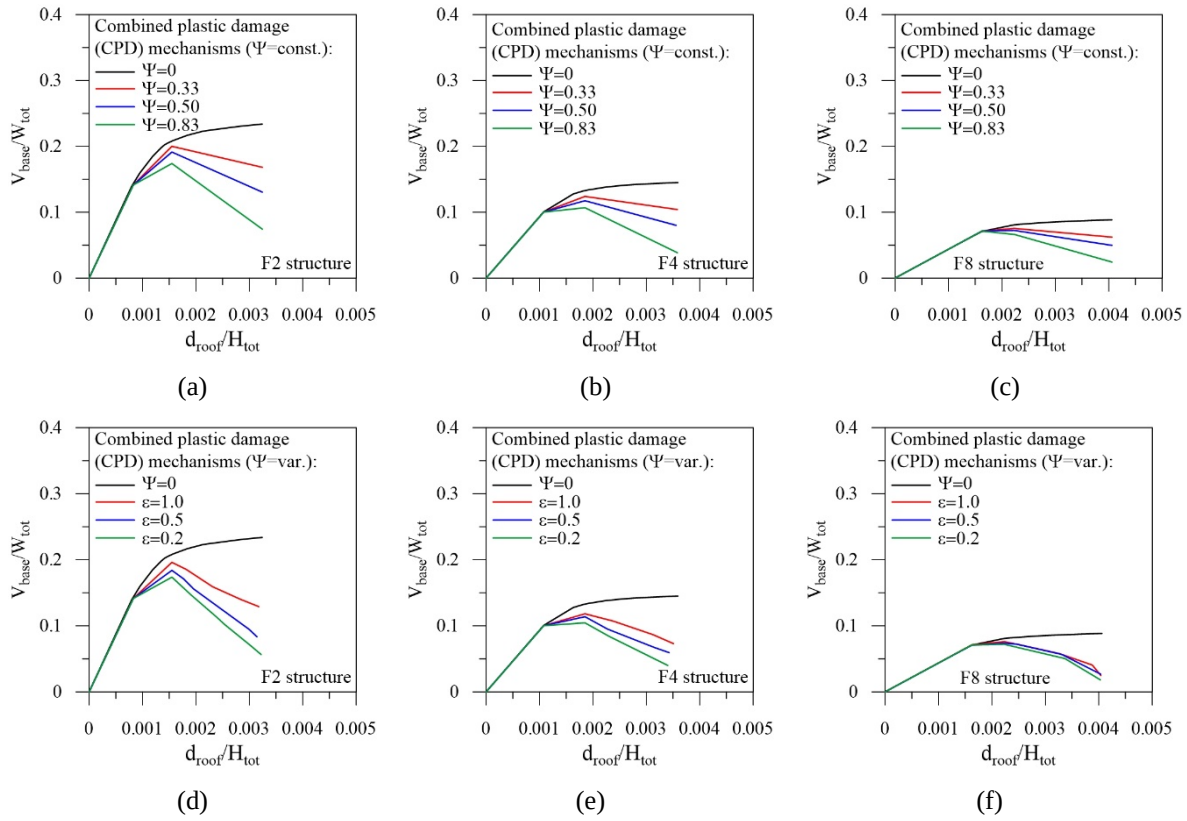

Figure 6: Monotonic and cyclic envelopes for the equivalent SDOF system: constant (a, b, c) and variable (d, e, f) values of damage index Ψ.

For the purpose of retrofitting the original r.c. framed structures (i.e. Fi, i=2, 4 and 8) to the performance levels imposed by NTC18 provisions, in a high-risk seismic zone (peak ground acceleration on rock, a_g=0.26g at the life-safety limit state) and medium subsoil class (type B, site amplification factor S=1.14), diagonal steel braces equipped with hysteretic dampers (HYDs) are inserted in the perimeter frames. Specifically, the damped braced (retrofitted) structures (i.e. DBFi, i=2, 4 and 8) are characterized by HYDBs placed in the central bay, in the X direction, and in both bays, in the Y direction, of the perimeter frames (Figure 7). The Displacement-Based design (DBD) procedure of HYDBs presented in Section 2 is used to proportion the HYDBs. In detail, six retrofitting solutions are considered for each structure, assuming: three design values of the damper ductility (i.e. μ_D=10, 15 and 20) with a constant design value of the frame ductility (i.e. μ_F=1.5); three design values of the frame ductility (i.e. μ_F=1.2, 1.5 and μ_{Fu}) with a constant design value of the damper ductility (i.e. μ_D=15). Moreover, six design solutions are evaluated for each selection of the design parameters, considering the capacity boundary curves corresponding to constant (i.e. Ψ=0.33, 0.5 and 0.83) and variable (i.e. ε=1.0, 0.5 and 0.2) values of the damage index. Finally, the monotonic backbone

curve (i.e. Ψ=0) corresponding to a simplified Displacement-Based Design (DBD) procedure is also examined to provide a comparison. The design results, omitted for the sake of brevity, highlight that the effective stiffness $K_e^{(DB)}$ is underestimated in all examined cases when the force-displacement curve that envelopes the hysteretic behaviour is not considered. As expected, increasing values of effective stiffness of the equivalent HYDB are obtained when stiffness and strength degradation rules depend on increasing (constant) values of the damage index. Assuming different rates of degradation, a similar trend is observed when the variability of Ψ with the current value of inelastic deformation is also taken into account. On the other hand, note that the yield-load is less sensitive than effective stiffness to degrading assumptions. Negligible effects of the μ_D variability are observed throughout, while significant variations of $V_y^{(DB)}$ are highlighted when μ_{Fu} is assumed as the design value of frame ductility.

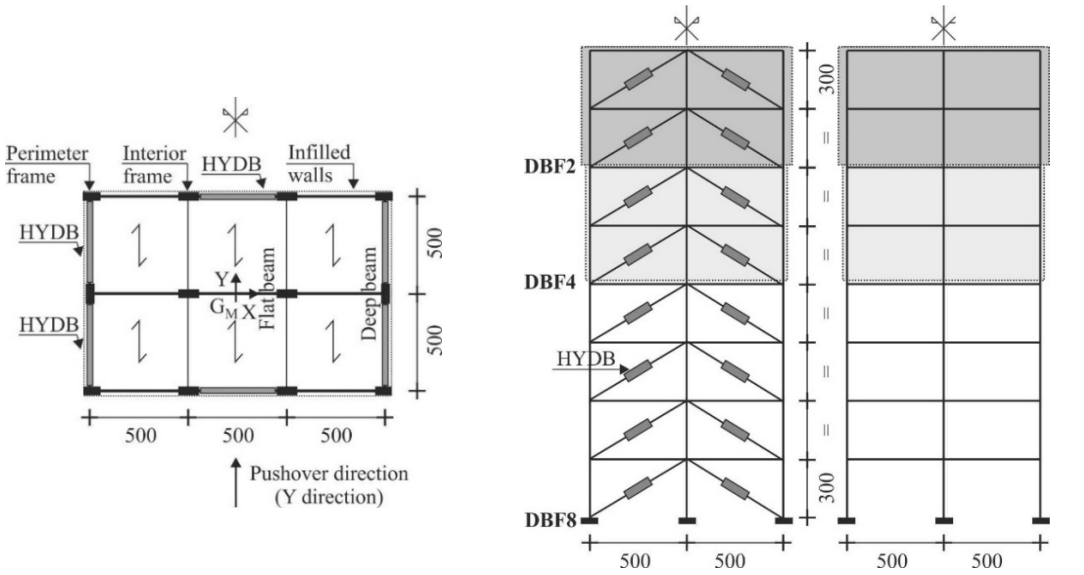

(a) Plan. (b) Perimeter frame. (c) Interior frame.

Figure 7: Retrofitted r.c. test structures (units in cm).

4 NUMERICAL RESULTS

To evaluate how different nonlinear modelling assumptions of the degrading hysteretic behaviour affect the seismic retrofitting with hysteretic damped braces (HYDBs), a new displacement-based-design (DBD) procedure is developed. Different damage levels on the DBD procedure of HYDBs are investigated based on a damage index (Ψ) on which the capacity boundary curve depends. Specifically, constant values of Ψ, from no damage up to light and moderate repairable damage ($0 \leq \Psi \leq 0.5$) and irreparable damage up to partial or total collapse ($0.5 < \Psi < 1$), are compared with different evolution laws of Ψ, referring to linear ($\varepsilon = 1$) and nonlinear ($\varepsilon < 1$) degradation rules. Stiffness and strength properties of the HYDBs are evaluated on the assumption that the deformability of the steel brace is negligible given its rigidity (i.e. $K_{DB} \cong K_D$, where K_{DB} and K_D are the lateral stiffnesses of the damped brace and hysteretic damper, respectively). An analogous assumption is made for the stiffness hardening ratio of the HYDBs (i.e. $r_{DB} \cong r_D$).

To evaluate the effectiveness of the proposed DBD procedure of HYDBs for the seismic retrofitting of the original two- (F2), four- (F4) and eight-storey (F8) r.c. framed structures, capacity curves of the DBFi structures are plotted in Figure 8, where dashed lines represent

results obtained for the corresponding Fi ones. In view of the low impact of the damper ductility on design properties of the HYDBs, only the value μ_D=15 is assumed in combination with the hardening ratio r_D=3%. Moreover, a frame ductility μ_F=1.5, limiting the inelastic demand to the original structures, is selected together with hardening ratio r_F=1%. The nonlinear static analysis of the DBFi is terminated once the ultimate value of damper ductility is attained (i.e. μ_{Du}=30). An ultimate ductility check has also been carried out for the r.c. frame members for both Fi and DBFi. In detail, HYDBs are designed with reference to constant (Figures 8a,c,e) and variable (Figures 8b,d,f) values of the damage index Ψ.

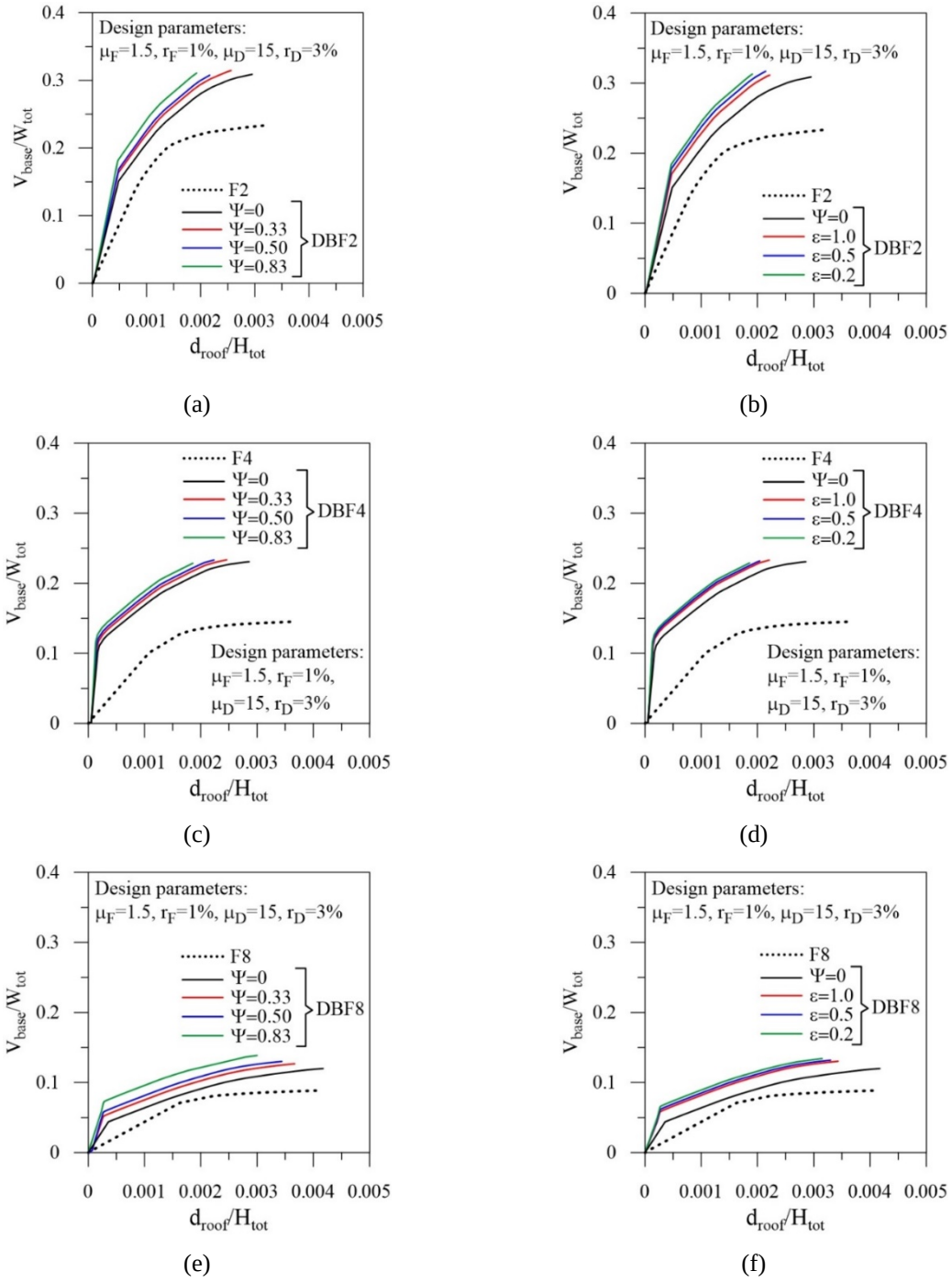

Figure 8: Pushover curves of retrofitted structures designed with and without considering degrading response of original r.c. framed structures, assuming constant (a, c, e) and variable (b, d, f) values of Ψ.

The DBD procedure is shown to be more effective for the low- (i.e. F2) and medium-rise (i.e. F4) structures than for the high-rise (i.e. F8) ones, where the lowest level of seismic protection is obtained. Capacity curves where the HYDBs are designed with the simplified DBD procedure, without considering the degrading response (Ψ=0), are also plotted. Significant variation in the results occurs when constant or variable values of the damage index Ψ are assumed. Moreover, the shear strength capacity of the DBFi structures increases for increasing values of damage index Ψ (Figures 8a,c,e) and decreasing values of rate parameter ε (Figures 8b,d,f). The opposite is observed for the lateral displacement capacity, for which there is a significant overestimation when the simplified DBD procedure is applied (i.e. Ψ=0). This behaviour highlights the need for special attention to the degrading cyclic response of r.c. frame members to ensure a successful retrofit.

Next, local structural damage along the building height of the Fi and DBFi structures is shown in Figures 9 and 10, in terms of maximum curvature ductility demand at the end sections of beams and columns.

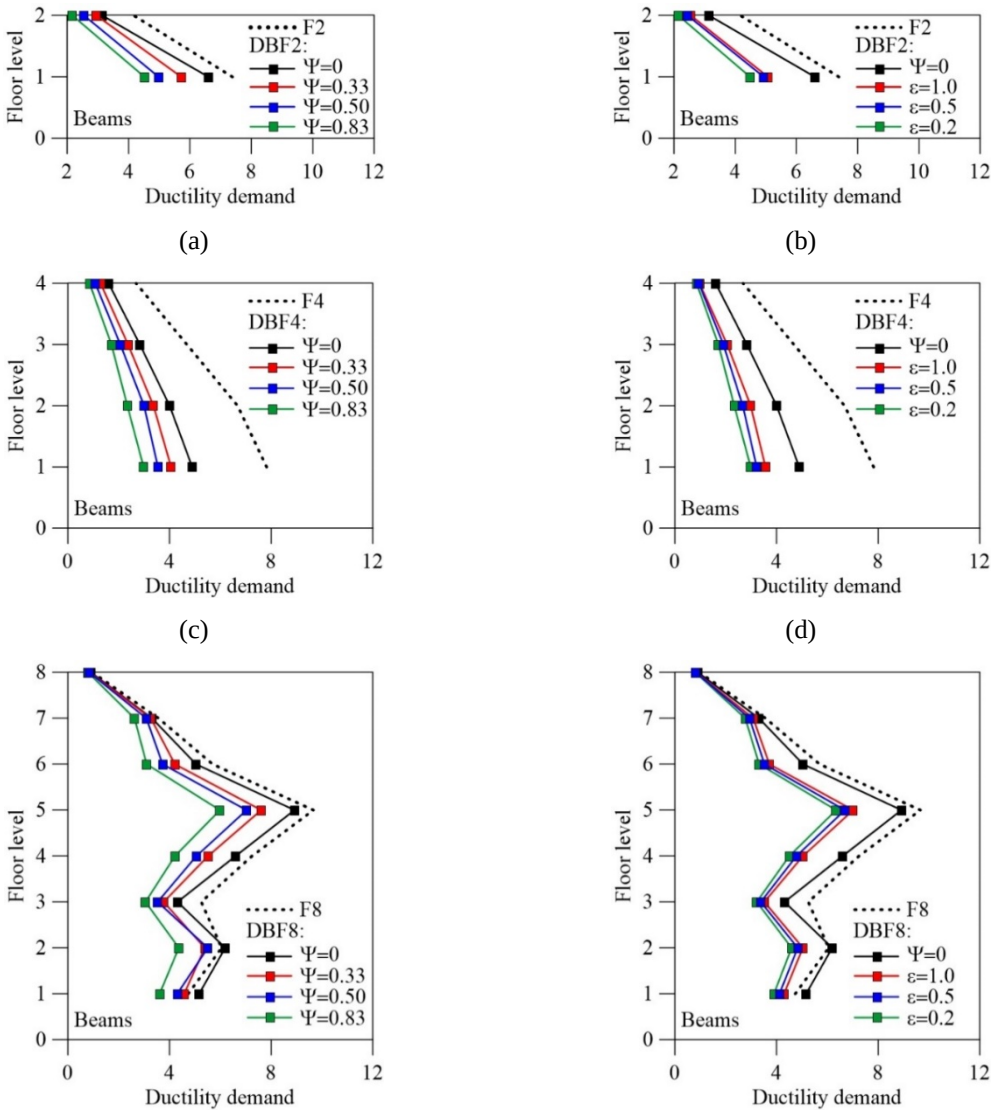

Figure 9: Local response of beams of retrofitted structures designed with and without degrading seismic response of original r.c. framed structures.

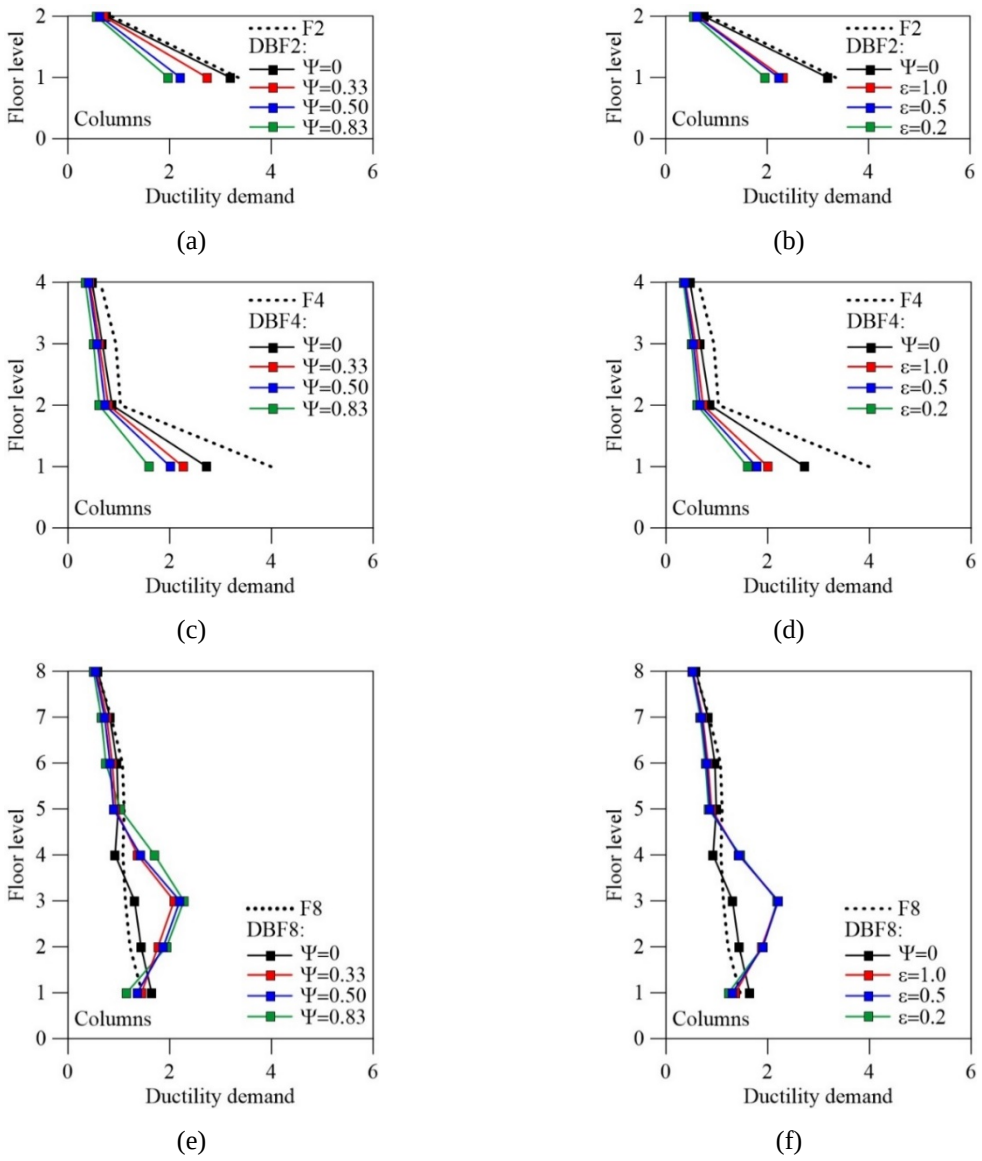

Figure 10: Local response of columns of the retrofitted structures designed with and without considering a degrading seismic response of original r.c. framed structures.

In particular, perimeter and interior frames in the Y direction are examined, assuming μ_F=1.5 combined with μ_D=15. The DBFi suffer collapse due to the attainment of the ultimate value on the ductility demand of HYDBs, before reaching inelastic capacity of r.c. frame members, while the Fi are characterized by a "strong-column weak-beam mechanism". The DBD procedure ensures notable reductions in the ductility demand of beams, for both increasing values of Ψ (Figures 9a,c,e) and decreasing values of ε (Figures 9b,d,f). Moreover, brittle failure phenomena do not occur, with maximum ductility demand of columns (Figure 10) which is always lower than that of the beams (Figure 9). A slight increase in ductility demand is observed for increasing values of Ψ, only for columns at lower storeys of the DBF8 (Figures 10e,f). This effect can be explained by observing that the DBFi are characterized by higher values of the axial load in the columns than the Fi, but the balanced compressive load is exceeded only at the lower storeys where ductility demand is increased. Finally, all design parameters being equal, the simplified DBD procedure (Ψ=0) leads to an overestimation of the ductility demand of r.c. frame members compared to the new DBD (Ψ>0) procedure.

5 CONCLUSIONS

A Displacement-Based Design (DBD) procedure is developed for retrofitting with hysteretic damped braces (HYDBs) a given framed structure, also considering the effects of degrading cyclic response of the r.c. frame members. Specifically, a piecewise linear approximation of the capacity boundary curve instead of initial backbone is adopted to obtain seismic capacity of the entire structure with reference to an equivalent nonlinear SDOF system. A combined plastic-damage (CPD) hysteretic model, resulting from an in-parallel combination of elastic-perfectly plastic (EPP) and elastic-softening damage (ESD) mechanisms, is adopted to describe the degrading hysteretic response represented by the capacity boundary curve. To verify the reliability of the DBD procedure, two-, four- and eight-storey r.c. framed buildings are retrofitted by sizing HYDBs in a high-risk seismic zone of the current Italian code. Six structural solutions are compared for each structure, considering: i) variable damper ductility combined with constant frame ductility; ii) variable frame ductility combined with constant damper ductility. Moreover, six design solutions are compared for each assortment of the design parameters, considering the cyclic envelopes corresponding to constant (i.e. Ψ=0.33, 0.5 and 0.83) and variable (i.e. ε=1.0, 0.5 and 0.2) values of the damage index. As a comparison, the results for the monotonic backbone curve (i.e. Ψ=0) are also examined. The seismic response from the nonlinear static analysis of the retrofitted structures confirms the effectiveness of the DBD procedure, especially for the low- and medium-rise framed buildings. Specifically, the shear strength capacity of the DBFi structures increases for increasing values of damage index Ψ and decreasing values of parameter ε. The opposite is observed for the lateral displacement capacity, where a significant overestimation is obtained assuming Ψ=0. Moreover, the DBD procedure makes it possible to obtain notable reductions of local ductility demand, for both increasing values of Ψ and decreasing values of ε, unlike the simplified DBD procedure corresponding to Ψ=0, leading to an overestimation of the ductility demand of r.c. frame members. As a final remark, special attention to the degrading cyclic response of r.c. frame members is advisable for a successful retrofit with HYDBs.

ACKNOWLEDGEMENTS

The present work was financed by Re.L.U.I.S. (Italian network of university laboratories of earthquake engineering), in accordance with the “Convenzione D.P.C.-Re.L.U.I.S. 2019-2021, WP15, Code Revisions for Isolation and Dissipation”.

REFERENCES

[1] M.D. Symans, F.A. Charney, A.S. Whittaker, M.C. Constantinou, C.A. Kircher, M.W. Johnson, R.J. McNamara, Energy dissipation systems for seismic applications: current practice and recent developments. *Journal of Structural Engineering*, **134**, 3-21, 2008.

[2] J.M. Londoño, D.J. Wagg, S.A. Neild, Supporting brace sizing in structures with added linear viscous fluid dampers: A filter design solution. *Earthquake Engineering and Structural Dynamics*, **43**, 1999-2013, 2014.

[3] M.N. Fardis, From force- to displacement-based seismic design of concrete structures and beyond. *Recent Advances in Earthquake Engineering in Europe. Geotechnical, Geological and Earthquake Engineering, K. Pitilakis eds. Procs. of the 6th European Conference on Earthquake Engineering*, Thessaloniki, Greece, June 17-21, 2018.

[4] J. Kim, H. Choi, Displacement-based design of supplemental dampers for seismic retrofit of a framed structure. *Journal of Structural Engineering*, **132**, 873-883, 2006.

[5] F. Mazza, A. Vulcano, Displacement-based design procedure of damped braces for the seismic retrofitting of r.c. framed buildings. *Bulletin of Earthquake Engineering*, **13**, 2121-2143, 2015.

[6] A. Segovia, S.E. Ruiz, Direct displacement-based design for buildings with hysteretic dampers, using best combinations of stiffness and strength. *Journal of Earthquake Engineering*, **21**, 752-775, 2017.

[7] H. Choi, J. Kim, Energy-based seismic design of buckling-restrained braced frames using hysteretic energy spectrum. *Engineering Structures*, **28**, 304-311, 2006.

[8] N. Pollini, O. Lavan, O. Amir, Minimum-cost optimization of nonlinear fluid viscous dampers and their supporting members for seismic retrofitting. *Earthquake Engineering and Structural Dynamics*, **46**, 1941-1961, 2017.

[9] G. Terenzi, Energy-based design criterion of dissipative bracing systems for the seismic retrofit of frame structures. *Applied Sciences*, **8**, 1-22, 2018.

[10] Applied Technology Council, Effects of strength and stiffness degradation on seismic response. *Technical Report ATC 62/FEMA P440A, Washington, D.C., Federal Emergency Management Agency*, 2009.

[11] D. Vamvatsikos, C.A. Cornell, Direct estimation of seismic demand and capacity of multidegree-of-freedom systems through incremental dynamic analysis of single degree of freedom approximation. *Journal of Structural Engineering*, **131**, 589-599, 2005.

[12] Federal Emergency Management Agency (FEMA), Prestandard and commentary for the seismic rehabilitation of buildings. *Report No. FEMA-356*, Washington, DC, 2000.

[13] DM96, Norme tecniche per le costruzioni in zone sismiche e relative istruzioni. *Italian Ministry of Public Works*, D.M. 16-01-1996 and C.M. 10-04-1997.

[14] NTC18, Technical Regulations for the Constructions. *Italian Ministry of the Infrastructures and Transports*, D.M. 17-01-2018.

[15] EC8, Eurocode 8. Design of structures for earthquake resistance - part 3: assessment and retrofitting of buildings. *C.E.N., European Committee for Standardization*, 2004.

[16] A.J. Kappos, Seismic damage indices for RC buildings: evaluation of concepts and procedures. *Progress in Structural Engineering and Materials*, **I**, 78-87, 1997.

[17] T.N. Do, F.C. Filippou, A damage model for structures with degrading response. *Earthquake Engineering and Structural Dynamics*, **47**, 311-332, 2018.

[18] Y.J. Park, A.M. Reinhorn, S.K. Kunnath, IDARC: Inelastic damage analysis of reinforced concrete frame-shear-wall structures. *Buffalo, NY, State University of New York at Buffalo 1987; Technical Report*, NCEER-87-0008.

[19] W. Krätzig, I. Meyer, K. Meskouris, Damage evolution in reinforced concrete members under cyclic loading. *In: Structural Safety and Reliability American Society of Civil Engineers*, San Francisco, California, USA, 795-804, 1989.

[20] M. Rahnama, H. Krawinkler, Effects of soft soil and hysteresis model on seismic demands. *Technical Report, John A. Blume Earthquake Engineering Center Report No. 108*, Department of CEE, Stanford University: Palo Alto, California, USA, 1993.

[21] Y. Bozorgnia, V.V. Bertero, Damage spectra: characteristics and applications to seismic risk reduction. *Journal of Structural Engineering*, **129**, 1330-1340, 2003.

[22] F. Mazza, Nonlinear seismic analysis of r.c. framed buildings with setbacks retrofitted by damped braces. *Engineering Structures*, **126**, 559-570, 2016.

[23] F. Mazza, Shear modelling of the beam-column joint in the nonlinear static analysis of r.c. framed structures retrofitted with damped braces. *Bulletin of Earthquake Engineering*, **108**, 111-129, 2018.

[24] F. Mazza, M. Mazza Nonlinear analysis of spatial framed structures by a lumped plasticity model based on the Haar-Kàrmàn principle. *Computational Mechanics*, **45**, 647-664, 2010.

[25] ESD, European Strong Motion database. http://esm.mi.ingv.it/.

[26] I. Iervolino, C. Galasso, E. Cosenza, REXEL: computer aided record selection for code-based seismic structural analysis. *Bulletin of Earthquake Engineering*, **8**, 339-362, 2009.

COMPDYN 2019
7th ECCOMAS Thematic Conference on
Computational Methods in Structural Dynamics and Earthquake Engineering
M. Papadrakakis, M. Fragiadakis (eds.)
Crete, Greece, 24–26 June 2019

COMPARISON OF BOND BEHAVIOR MODELS FOR LAP-SPLICES CONFINED BY TRANSVERSE REINFORCEMENT

Petros M. Chronopoulos[1], and Miltiadis P. Chronopoulos[2]

[1] Structural Expert, DB Engineering & Consulting GmbH
231, Suhaim Bin Hamad Street, Doha, Qatar
petros.chronopoulos@gmail.com

[2] Research Fellow, Lab. of RC, Nat. T. U. of Athens/GR
9, Iroon Polytechniou, Zografos Campus, Athens, Greece
chronmil@central.ntua.gr

Abstract

Bond related failures still pose a significant threat to the structural integrity of an increasing number of aging reinforced concrete structures. An accurate theory-based method for determining detailing parameters of a lap splice is not yet available. For this reason, modern codes are still relying on semi-empirical formulas for describing the bond behavior of bars in anchorages or splices. The most recent design recommendations are that of Model Code 2010 (MC 2010), which have already been used as the basis for the draft revision of EN 1992 to be published in 2023. Experience has shown that the application of MC 2010 provisions can lead to even longer laps compared to those required by EN 1992 (2004). In this paper, a comparison of the key available design models for determining the tension lap strength will be presented, focusing mainly on the influence of the internal transverse reinforcement (stirrups) present within the lap length. Conclusions regarding the shortcomings of the available design models will also be made.

Keywords: Reinforced Concrete, Bond Strength, Lap splices, Design Codes & Models, Transverse Reinforcement.

1 INTRODUCTION

Bond is one of the key interaction mechanisms between concrete and reinforcing bars that ensures proper structural performance of reinforced concrete structures. This has been widely known since the early stages of reinforced concrete design, as demonstrated by a very rich scientific research and some relevant design provisions included in the earliest available Design Standards (as early as 1966 by ACI and 1978 by CEB-FIP). The most recent codified design recommendations can be found in Model Code 2010, while the latest background data and design methods' development are presented and discussed in ACI 408R-03 and fib Bulletins N^o 10 (more detailed) and N^o 72 (more recent).

Two critical steps in the research history of bond were: a) the development of "local" bond stress–slip (τ-s) relationships (calibrated using experimental data), and b) the recognition and differentiation of the two possible failure modes, that of splitting (SP) and pull-out (PO), depending on whether or not the concrete cover splits. Bars in unconfined (or passively confined, by concrete cover and stirrups) concrete usually fail by splitting of the surrounding concrete, while bars in actively confined concrete fail by being pulled-out of the concrete (concrete is sheared on the surface defined by the ribbed profile of the bars). Passively confined bars may also fail with a pull-out failure mode depending on available cover and bar spacing. These two main assumptions, along with the following generic descriptive equation for bond strength, have been the subject of the most important scientific research in this field: $f_b=(\Delta\sigma_s A_b)/(\pi d_b l_b)$, where f_b: average bond stress over l_b, $\Delta\sigma_s$: change of bonded bar stress over l_b, A_b: cross section area of bonded bar, d_b: bar diameter, and l_b (or l_d later): bond (development) length.

Structural characteristics
Concrete cover & bar spacing
Development & splice length
Transverse reinforcement
Bar casting position
Percentage of bars lapped in one section
Non-contact lap-splices
Bar properties
Bar size
Bar geometry
Steel stress & yield strength
Bar surface condition (cleanliness, epoxy coated bars, etc.)
Concrete properties
Compressive strength
Aggregate type & quantity
Tensile strength & fracture energy
Ligthweight concrete
Concrete slump & workability admixtures
Mineral admixtures
Fiber reinforcement
Consolidation (vibration, construction related vibrations, revibration, etc.)

Table 1: Parameters affecting bond.

However, this last expression is a major simplification of the complex engineering problem of evaluating bond resistance. In reality, and contrary to earlier beliefs, bond strength is affected by many parameters and is not just a concrete material property (as it might be implied by the previous expression). ACI 408R-03 includes a detailed discussion on the major factors affecting bond and separates them in three main categories: structural characteristics, bar properties and concrete properties (see also Table 1). Although there is a general consensus regarding which parameters affect bond resistance, there have been significantly different scientific approaches and conclusions regarding the quantification of each parameter's influence.

Over the years, there have been many attempts to capture and explain all key aspects of the problem, with researchers relying on different type of models. Earliest attempts used simplified force equilibrium models on a plane perpendicular to the axes of the bonded reinforcement. In this way, bond-slip relations could not be applied. Alternatives have been also proposed based on kinematic relations between longitudinal bar displacements (slip) and radial displacement (dilatancy) of surrounding concrete. Both types of models were semi-empirical. Some purely analytical attempts have been made, but their accuracy and applicability is questionable since they are usually based on pull-out failure modes and tend to estimate bond behaviour only along the axis of the longitudinal reinforcement. More recently, numerical models offering full three-dimensional assessment of the bond mechanism have been developed. However, their calibration has been proved to be too complex and unreliable for routine design, limiting their applicability.

In most practical applications of lap-splices in columns or beams, splitting is the governing failure mode. The presence of transverse reinforcement within the lap-splice length can potentially increase the RC member's bearing capacity by increasing the bond strength and limiting the splitting crack width. Previous works by the authors (see Chronopoulos et al. 2012, Chronopoulos & Tassios 2013, Chronopoulos et al. 2016) have shown differences in that relevant design code provisions. In this paper, some key design models will be shortly presented and compared in terms of their estimation of the transverse reinforcement influence on bond strength and lap-splice performance in general.

2 INFLUENCE OF TRANSVERSE REINFORCEMENT

Tepfers (1973) and Orangun et al. (1977) has already established that legs of transverse reinforcement crossing the splitting crack can enhance bond behaviour by delaying crack progression and increasing the bar stress required to cause failure. In this sense, transverse reinforcement acts in a similar way with confining pressure (due to a different source), which if sufficiently high may lead to a pull-out type of failure (instead of a splitting one). It is rather obvious, that once pull-out failure is ensured, the effectiveness of additional transverse reinforcement is significantly reduced (or even becomes negligible).

Most of the available design models agree that the additional contribution of confining reinforcement to bond shall be represented in the relevant expressions as summative (except Esfahani & Kianoush 2005, who represent it as multiplicative). Considering this, a simplified expression of the total bond force can be written as: $T_b=T_c+T_s$, where T_c: bond force due to concrete (without transverse reinforcement) and T_s: bond force due to transverse reinforcement. It is important here to highlight that according to Zuo & Darwin (1998, 2000) T_c is affected by the presence of transverse reinforcement. This study has shown that in order to achieve better correlation with test data, an effective value of bar clear spacing c_{si} (actually internal "side cover", greater that the actual value, see Figure 1) shall be used in the relevant expression and taken equal to: $c_{si,eff}=1.6c_{si}$. However, for bars with transverse reinforcement, better match is achieved by using a reduced value for the effective bar spacing equal to: $c_{si,eff}=$

c_{si}+0.25in (c_{si}+6.4mm), still greater that the clear distance between bars (c_{si}). As a general conclusion, the influence on T_c is small, but measurable.

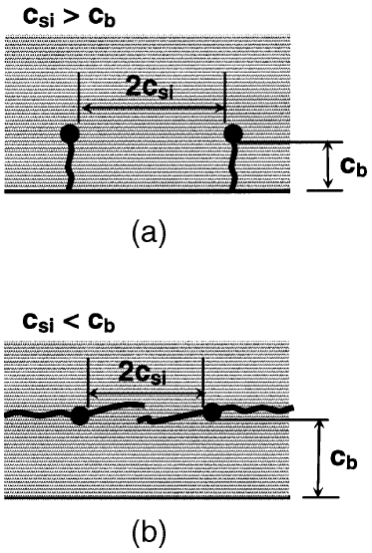

Figure 1: Bond cracks according to ACI408R-03: (a) $c_{si} > c_b$; and (b) $c_{si} < c_b$.

The two most important parameters that determine the transverse steel contribution to the total bond force T_s are the area of reinforcement crossing the potential crack planes A_{st} and the effective transverse reinforcement stress. Values of A_{st} can differ even for the same transverse reinforcement arrangement (same number of legs) depending on concrete cover and bar spacing (which affect splitting crack patterns, see also Chronopoulos et al. 2012). Different researchers have proposed various expressions that also consider other factors, which amongst others include concrete strength, bonded bar size and deformation properties (relative rib area), and yield strength of reinforcement (see also next paragraph). An increase in either bar size or relative rib area (rib size and spacing) leads to an increase in the wedging action exerted by the slipping bonded bars to the transverse reinforcement. This effect produces transverse dilatancy and mobilises tension stresses into the confining reinforcements, that causes an increase to the clamping force acting on the bonded bars.

It is worth noting that contrary to earlier beliefs, it has been observed during a lot of experimental studies that in such cases transverse reinforcements rarely yields. This observation is clearly stated in ACI408R-03 and is based on the studies of Maeda et al. (1991), Sakurada et al. (1993), and Azizinamini et al. (1995). The authors are also in support of and have already offered further justification for this opinion, even in zones with high shear forces. The relevant test results presented in Chronopoulos & Tassios (2013) and Chronopoulos et al. (2016), including monitoring of internal stirrups and external jacket strains, have shown maximum values of hoop strains of approx. 1‰ for stirrups. This observation raises some serious concerns about earlier works of e.g. Orangun et al. (1977) and Giuriani et al. (1991, see also Figure 2), which rely on transverse steel yield strength and both have influenced past design code provisions.

Fib Bulletin No 72 (2013) also highlights one other issue regarding the calibration of some key available semi-empirical models for estimating bond strength: “all have been calibrated based on test results of a data base where the majority of the tests were on specimens with no confining reinforcement (crossing potential splitting planes). The additional contribution from confining reinforcement was then estimated from the difference between strengths obtained

from otherwise identical specimens with confining reinforcement". This observation proves that at least a verification (if not a new calibration) of these expressions is required based on tests specifically designed for this purpose.

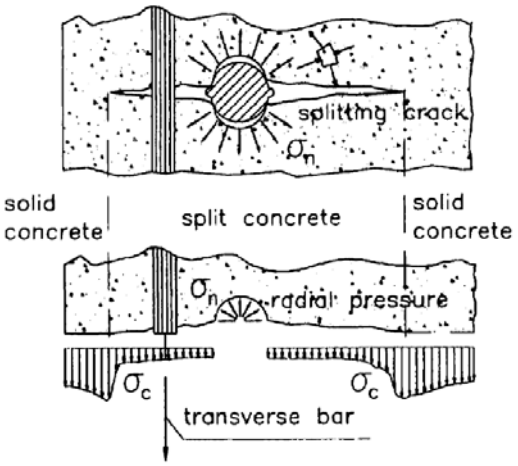

Figure 2: Splitting crack and confining actions around a ribbed bar according to ACI408R-03.

3 BOND MODELS CONSIDERING TRANSVERSE REINFORCEMENT

As already discussed in previous paragraphs, an accurate theory-based expression for calculating the additional bond resistance offered by the presence of transverse reinforcement is not yet available. In the following, a comparison of the key available semi-empirical design models is made, along with a short commentary of the major affecting parameters. This paragraph concludes with a short parametric study of the transverse reinforcement's influence to bond strength .

3.1 Orangun et al. (1977)

Orangun et al. developed their model for estimating the total bond force $T_b=T_c+T_s$ (expressed in relation to $\sqrt{f_c}$, see next sub-paragraph) using statistical analyses on a data base consisting of 62 specimens. Their model assumes that splitting failure governs (see Eq. 2) and that transverse reinforcement yield strength is mobilised (see relevant discussion in §2).

$$T_s/\sqrt{f_c} = [(\pi l_d A_{tr})/(41.5sn)]f_{yt} \quad (1)$$

$$1/d_b[c_{min}+0.4d_b+(l_d A_{tr})/(10.34sn)]f_{yt} \leq 2.5 \quad (2)$$

where: c_{min}: minimum concrete cover, A_{tr}: area of transverse reinforcement normal to the plane of splitting, f_{yt}: yield strength of transverse reinforcement, s: spacing of transverse reinforcement, and n: number of bars developed or spliced at the same location. The development length expression first incorporated in ACI318-95 was based on this study.

3.2 Darwin et al. (1992)

Darwin et al. (1992) reanalysed the data used by Orangun et al. (1997) and incorporated the effect of the relative maximum and minimum concrete cover (c_{max}/c_{min}), which however didn't affect the transverse reinforcement's influence. Eventually they also expanded the relevant database to include 133 specimens without and 166 with confining reinforcement. These additional data showed that a better for could be achieved by expressing T_b in relation to $f_c^{1/4}$,

compared to $\sqrt{f_c}$ used by Orangun et al. (1977). One new addition was the factors accounting for the influence of relative rib area and bar size, which can be seen in Eq. 4 and 5, here below:

$$T_s/f_c^{1/4} = 53.3t_rt_d(NA_{tr})/n+1019 \quad (3)$$

$$t_r = 9.6R_r+0.28 \quad (4)$$

$$t_d = 0.028d_b+0.28 \quad (5)$$

$$1/d_b[(c_{min}+0.5d_b)(0.1c_{max}/c_{min}+0.9)+(35.3t_rt_dA_{tr})/(sn)] \leq 4.0 \quad (6)$$

where: N: number of transverse stirrups (or ties) within the bond length, t_r, t_d: relative rib area and bar size (respectively) influence factors, and R_r: relative rib area, equal to: R_r = (projected rib area normal to bar axis) / (nominal bar perimeter x center-to-center rib spacing).

3.3 Zuo and Darwin (2000)

Zuo and Darwin (2000) further increased the data base, adding mainly specimens with high-strength concrete (f_c > 55 MPa). Their data base comprised of 171 specimens without and 196 with transverse reinforcement. They concluded that $f_c^{1/4}$ indeed offered a better representation of the effect of concrete compressive strength to the bond resistance of bars not confined by transverse reinforcement, as observed by Darwin et al. (1992). However, their calibration also proved that the use of $f_c^{3/4}$ in estimating T_s offered a much better fit for bars with confining reinforcement, based on below expressions:

$$T_s/f_c^{1/4} = [9t_rt_d(NA_{tr})/n+744]\ f_c^{1/2} \quad (7)$$

$$t_r = 9.6R_r+0.28 \quad (8)$$

$$t_d = 0.03d_b+0.22 \quad (9)$$

$$1/d_b[(c_{min}+0.5d_b)(0.1c_{max}/c_{min}+0.9)+(6.26t_rt_dA_{tr})/(sn)f_c^{1/2}] \leq 4.0 \quad (10)$$

3.4 Eligehausen & Lettow (2006)

Eligehausen and Lettow (2006) proposed an expression to calculate the average bonded bar stress f_{stm} (Eq. 11). A slightly modified version of this expression was finally included in Model Code 2010 (Eq. 12), which also followed the format proposed by Canbay & Frosch (2005). This expression was based on a data base of approx. 850 tests, which was created by supplementing the database of ACI Committee 408 (used in the previous studies) with additional data from mainly European and a few Asian scientific programs. It is a rather extensive database, including both anchorages and lap splices, with or without transverse reinforcement. The first part of this expression (Eq.12) represents the bond strength for some base reference conditions of confinement: minimum cover equal d_b, bonded bar spacing equal to $2d_b$, and no confining reinforcement. The second part of their expression (the one enclosed in the square brackets) modifies the reference bond strength to account for its enhancement due to concrete cover and transverse reinforcement.

$$f_{stm} = 24.2(f_c)^{0.25}(20/d_b)^{0.20}(l_d/d_b)^{0.55}(c_{min}/d_b)^{0.33}(c_{max}/c_{min})^{0.10}[1+10K_{tr}] \quad (11)$$

$$f_{stm} = 54(f_c/25)^{0.25}(20/d_b)^{0.20}(l_d/d_b)^{0.55}[(c_{min}/d_b)^{0.25}(c_{max}/c_{min})^{0.10}+k_mK_{tr}] \quad (12)$$

$$T_s = [54(f_c/25)^{0.25}(20/d_b)^{0.20}(l_d/d_b)^{0.55}k_mK_{tr}]\pi d_b^2/4 \quad (13)$$

where: c_{min}=min{(clear bar spacing)/2, top/bottom or side cover} and c_{max}=max{(clear bar spacing)/2, side cover}. The effectiveness factor k_m can be equal to 12 or 6 for confinement by legs of links perpendicular to the splitting plane or by straight bars inside the cover, respec-

tively, or 0 for other circumstances. $K_{tr}=n_t A_{st}/(n_b d_b s_t) \leqslant 0.05$, where n_t: number of transverse reinforcement legs intersecting the potential failure plane, A_{st}: one transverse reinforcement leg cross section area, s_t: longitudinal spacing of transverse reinforcement, and n_b: number of pairs of spliced bars in the failure plane. The relevant expression is valid for: $f_{stm} \leqslant f_y$ and $f_{stm} \leqslant$(2.5 or 1.25)$\sqrt{f_c}4(l_b/d_b)$ for good or bad bond conditions, respectively, 15 MPa$<f_{cm}<$110 MPa, 0.5$<c_{min}/d_b<$3.5 and 1.0$<c_{max}/c_{min}<$5.0.

3.5 Mancini et al (2018) and Vollum & Goodchild (2019)

Mancini et al. (2018) performed a consistent calibration based on a Monte Carlo method for the reliability assessment of the semi-empirical model of Eligehausen & Lettow (2006), in the form that is included in Model Code 2010. The purpose of their study was to formulate design lap-splice and anchorage length expressions according to a specific level of reliability (compliant with EN 1990). Their work proved that at Ultimate Limit State (ULS), EN 1992 tends to be unsafe for high values of longitudinal reinforcement stress f_{stm}, while Model Code 2010 is too conservative when low levels of f_{stm} should be transferred (see also Figure 3 here below).

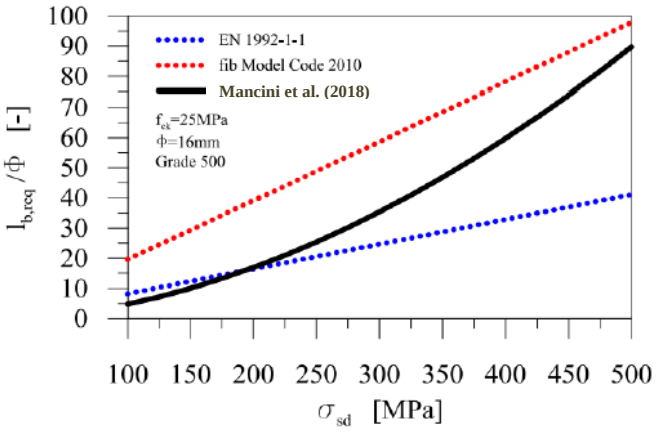

Figure 3: Comparison of Mancini et al (2018) to EN 1992 and Model Code 2010 provisions, according to Gino et al. (2018); Note: $\sigma_{sd} \approx 0.67\ \sigma_{sm}$ (or f_{stm} in this paper).

Vollum et al. (2019) expanded on this previous work, statistically investigating further the relevant Model Code 2010 expression and separating the database into four stress bands based on the measured bonded bar stress $f_{st,test}$: $f_{st,test} <$ 300 MPa, 300 $< f_{st,test} <$ 400 MPa, 400 MPa $< f_{st,test} <$ 500 MPa, 500 MPa $< f_{st,test}$. Each stress range was analysed separately based on the same procedure followed by Mancini et al. (2018). Based on this effort, Vollum & Goodchild were able at the end to calibrate a design expression focused on test results with $f_{st,test}$ values close to 435 MPa (design yield strength of modern steel reinforcements). This expression could be used to support a design method less conservative than the one included in Model Code 2010, but with a suitable reliability level that could be considered for the revision of EN 1992 to be published in 2023 (see also Vollum & Goodchild 2018 for more details on the development of their proposed design method). Based on this separation, they proposed a modified version of Eq. 12 with different probabilistic coefficient ζ_j for each stress range, which if expressed in terms of average bond strength f_{bj} (where j=m: mean, j=k: characteristic, or j=d: design) can be written as:

$$f_{bj} = 2.44\ \zeta_j^{1.82}\ (f_c/25)^{0.45}(20/d_b)^{0.36}[(c_{min}/d_b)^{0.25}(c_{max}/c_{min})^{0.10}+k_m K_{tr}] \quad (14)$$

$$f_{bm} = 2.8\,(f_c/25)^{0.45}(20/d_b)^{0.36}[(c_{min}/d_b)^{0.25}(c_{max}/c_{min})^{0.10}+k_m K_{tr}] \quad (15)$$

$$T_s = [2.8(f_c/25)^{0.45}(20/d_b)^{0.36}k_m K_{tr}]\pi d_b l_d \quad (16)$$

where for $\sigma_{sd} > 435$ MPa, the bond strength should be multiplied by $(435/\sigma_{sd})^{0.82}$, and or $\sigma_{sd} \leq 435$ MPa, bond strength is independent of reinforcement stress, which is unlike the expression used by Mancini et al. (2018) and Eligehausen & Lettow (2006).

4 COMPARISON OF DESIGN MODELS

In Table 2 here below, the parameters affecting the transverse steel contribution to the transverse steel attributed bond force T_s according to each key design model are summarised. A first generic comment on the relevant expressions is that over time researchers have tried to produce more detailed expressions, with individual coefficients and exponents applied to each parameter (e.g. Eligehausen & Lettow 2006), compared with earlier approaches, where a simple theory-based expression was used along with just a few generic experimental correction coefficients (e.g. Orangun et al. 1977). There is also a general agreement on the way that the influence of the transverse reinforcement is estimated, based on the reinforcement area that crosses the potential splitting crack planes. However, there are two main differentiations: a) In earlier models (Orangun et al 1977 to Zuo & Darwin 2000), the total reinforcement area within the bond length is considered by using the ratio of l_d/s or N (see §§3.1 to 3.3), compared to Eligehausen & Lettow (2006), where K_{tr} is calculated based on the number of stirrup legs within the stirrups' spacing (s). This may lead to further differentiations between estimations when the stirrups' spacing is not constant all along the bond length e.g. lap splices longer that the critical regions of columns. b) Eligehausen & Lettow (2006) introduced an effectiveness coefficient k_m, which quantified the widely-accepted common knowledge that poorly detailed and arranged transverse reinforcement may offer no enhancement at all (k_m can take values as low as zero, see §3.4).

	Orangun et al. (1977)	Darwin et al. (1992)	Zuo and Darwin (2000)	Eligehausen & Lettow (2006)	Mancini et al (2018)	Vollum & Goodchild (2019)
l_d	✓	×	×	✓	✓	✓
A_{tr}	✓	✓	✓	✓	✓	✓
f_{yt}	✓	×	×	×	×	×
s	✓	×	×	✓	✓	✓
n	✓	✓	✓	✓	✓	✓
t_r	×	✓	✓	×	×	×
t_d	×	✓	✓	×	×	×
N	×	✓	✓	✓	✓	✓
f_c	×	×	✓	✓	✓	✓
d_b	×	×	×	✓	✓	✓

Table 2: Parameters affecting transverse reinforcement influence to bond strength considered by each design model; Note: see §3 for parameters' description.

In Figures 4 and 5 here below, the results of a short parametric investigation on the influence of the area of transverse reinforcement is presented. These diagrams were produced using the equations presented in §3, which were solved for T_s (in kN) under the following conditions: R_r=0.056 (typical for B500C rebars with d_b>12mm), d_b=20mm, f_c=25MPa, f_{yt}= 500MPa, and l_d=20d_b or 30d_b. For this comparison, the Eligehausen & Lettow (2006) design

model is used in the form included in Model Code 2010. Eq. 1, 3 and 7 where transformed so that an equivalent parameter to K_{tr} of Eq. 16 could be incorporated in order to make all these equations easily comparable. For this transformation it was assumed that $[K_{tr}]_{Eq.16} = [A_{tr}/(snd_b)]_{Eq.1,3,7}$ and $N = l_d/s$. This analysis show that over time the latest scientific evidence follow a trend in reducing the contribution of passive confinement by transverse reinforcement to bond strength (see e.g. differences between Orangun et al. 1977 and Zuo & Darwin 2000). Contrary to that trend, Eligehausen & Lettow (2006) proposed a model with relatively increased values of additional bond strength due to stirrups, but later studies by Mancini et al. (2018) and Vollum et al. (2019) has proven that a more comprehensive reliability analysis of the same expression, along with a separation of the available database into a stress range closer to modern reinforcement yield strengths (400 to 500 MPa), can lead to less conservative but adequately safe and reliable design provisions.

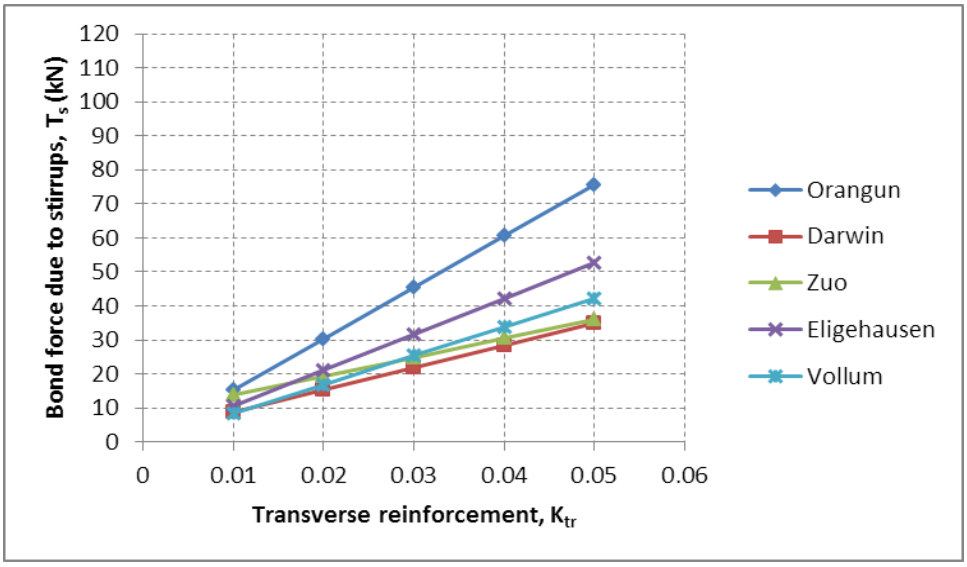

Figure 4: Comparison of the influence of K_{tr} to bond force due to transverse reinforcement for an available bond length of $20d_b$.

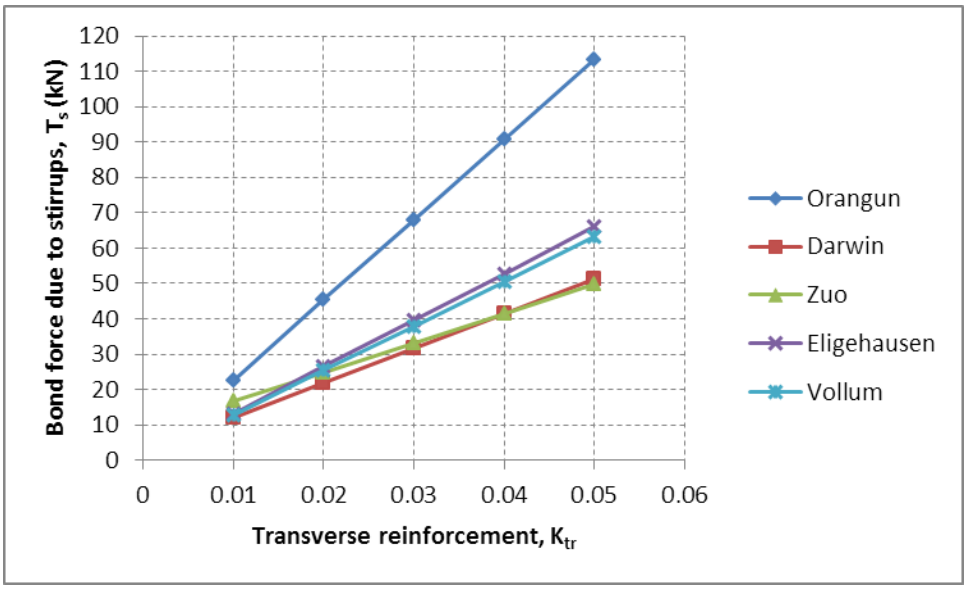

Figure 5: Comparison of the influence of K_{tr} to bond force due to transverse reinforcement for an available bond length of $30d_b$.

5 CONCLUSIONS

Contrary to past scientific knowledge and design codes, nowadays it is widely accepted that the strength of anchorages and lap-splices can be described by the same expressions. For example, today we know that lap-splices do not generate twice the splitting (bursting) force compared to that of an "equivalent" single bar anchorage, as it was predicted by the earlier "hydraulic pressure" physical models. In the last 30 or 40 years, a lot of relevant research was performed, with a lap considered as an almost "double" (in the past, see Model Code 1990) to an almost "single" anchorage (recently, see Model Code 2010), depending on a number of parameters. This shift of the Codes to a more uniform approach regarding both anchorages and lap-splices has been discussed, amongst others, by the authors in Chronopoulos et al. (2012), including a more detailed presentation of design code provisions. One of the conclusions of that study was that almost every 10 years lap-splice related factor values (e.g. the one for percentage of reinforcement lapped in one section) have been gradually reduced to approx. 1,1 (coming closer to the bond resistance of a single bar anchorage). In the present paper, a more detailed comparison of the progression of bond strength estimation models over the past 40 years was presented, focused mainly on the influence of the internal transverse reinforcement. Based on the previous discussion and observations, the following conclusions can be made:

- There is a general consensus that splitting is the governing failure mode in virtually all practical applications of anchorages or lap-splices without active (external) confinement.
- Most recent approaches suggest that the influence of passive confinement, by concrete cover and transverse reinforcement (stirrups, ties, secondary reinforcement, etc.), can be estimated as an enhancement to a basic bond strength corresponding to some minimum confinement conditions.
- Although theoretically reasonable, influence of rib area is excluded by most recent design models (Model Code 2010), mainly due to the relative scarcity of comprehensive test data and reliable calibrations. The opinion of Task Group 4.5 that produced Model Code 2010 argues that rib area has only a modest impact in the presence of some minimum confinement.
- On the other hand, since the early '90s it has been established that both bar size effects and relative maximum and minimum concrete cover affect passive confinement.
- There is an obvious effort to supplement the available bond strength databases with tests on specimens with transverse reinforcement crossing the splitting crack plane, as opposed to earlier design code expressions (e.g. Model Code 1990) which were based on databases that predominantly contained bond strength tests on unconfined bars with short bond lengths.
- As a general conclusion, the most recent scientific investigations of bond strength have shown that there is still room for considerable improvement of the available design code provisions.

REFERENCES

[1] A. Azizinamini, M. Chisala, S.K. Ghosh, Tension Development Length of Reinforcing Bars Embedded in High-Strength Concrete, *Engineering Structures*, **17(7)**, 512-522, 1995.

[2] ACI 408R-03. Bond and development of straight reinforcing bars in tension. *Report by American Concrete institute Committee 408*; 2003.

[3] C.O. Orangun, J.O. Jirsa, J.E. Breen, A reevaluation of test data on development length and splices, *ACI Structural Journal*, **74(3)**, 114-122, 1977.

[4] D. Darwin, S.L. McCabe, E.K. Idun, S.P. Schoenekase, Development Length Criteria: Bars Not Confined by Transverse Reinforcement, *ACI Structural Journal*, **89(6)**, 709-720, 1992.

[5] D. Gino, G. Bertagnoli, P. Castaldo, G. Mancini, Probabilistic assessment of laps and anchorages strength in reinforced concrete structure, *WMCAUS 2018 Conference Proceedings*, Prague, Czech Republic, 2018.

[6] E. Canbay, R.J. Frosch, Bond Strength of Lap Spliced Bars, ACI Structural Journal, **102(4)**, 2005.

[7] E. Giuriani, G.A. Pizzari, C. Schumm, Role of stirrups and residual tensile strength of cracked concrete on bond, *ASCE Journal of Structural Engineering*, **117(1)**, 1-18, 1991.

[8] EN 1992-1-1:2004/A1:2015, Eurocode 2: Design of concrete structures, P.1-1: General rules and rules for buildings, Amendment.

[9] *fib* Bulletin N^{o} 10: Bond of reinforcement in concrete, *Report by former Task Group 2.5, federation international du beton*, Lausanne, 2000.

[10] *fib* Bulletin N^{o} 72, Bond and anchorages of embedded reinforcements – Background to the *fib* Model Code for Concrete Structures, *federation international du beton*, Lausanne, 2000.

[11] *fib* Model Code for Concrete Structures 2010, *federation international du beton*, Lausanne, 2013.

[12] G. Mancini, V.I. Carbone, G. Bertagnoli, D. Gino, Reliability-based evaluation of bond strength for tensed lapped joints and anchorages in new and existing reinforced concrete structures, *Structural Concrete*, **19(3)**, 904–17, 2018.

[13] J. Zuo, D. Darwin, Bond Strength of High Relative Rib Area Reinforcing Bars, *SM Report No. 46, University of Kansas Center for Research, Lawrence, Kans.*, 350 pp, 1998.

[14] J. Zuo, D. Darwin, Splice Strength of Conventional and High Relative Rib Area Bars in Normal and High-Strength Concrete, *ACI Structural Journal*, **97(4)**, 630-641, 2000.

[15] M. Esfahani, M.R. Kianoush, Development/Splice Length of Reinforcing Bars, *ACI Structural Journal*, **102(1)**, 2005.

[16] M. Maeda, S. Otani, H. Aoyama, Bond Splitting Strength in Reinforced Concrete Members, *Transactions of the Japan Concrete Institute*, **13**, 581-588, 1991.

[17] P. Chronopoulos, C. Trezos, M. Chronopoulos, Behaviour of RC elements with inadequate lap splices, before and after upgrading by welding of reinforcement, *4th International Symposium "Bond in Concrete" Proceedings*, Brescia, Italy, 2012.

[18] P. Chronopoulos, E. Astreinidis, S. Giokaris, Experimental behaviour of externally confined concrete columns with inadequate lap spliced rebars under fully reversed cyclic loading, *19th IABSE Conference on "Challenges in Design and Construction of an Innovative and Sustainable Built Environment" Proceedings*, Stockholm, Sweden, 2016.

[19] P. Chronopoulos, T. Tassios, Retrofitting of RC columns with inadequate lap splices by means of external confinement, *2nd Conference on "Smart Monitoring, Assessment and Rehabilitation of Civil Structures" Proceedings*, Istanbul, Turkey, 2013.

[20] R. Eligehausen, S. Lettow, Formulation of application rules for lap splices in the new fib Model Code, *Task Group 4.5 "Bond Models" of the fib (federation international du beton)*, Stuttgart; 2006.

[21] R. Tepfers, A theory of bond applied to overlapped tensile reinforcement splices for deformed bars, *Publication 73:2, Chalmers University of Technology*, Goteborg, Sweden, 1973.

[22] R. Tepfers, Lapped tensile reinforcement splices, *ASCE Structural Division Journal*, **108**, 283-200, 1982.

[23] R. Vollum, C. Goodchild, Proposed EN 1992 tension lap strength equation for good bond, *Structures*, **19**, 5-18, 2019.

[24] S.P. Tastani, E. Brokalaki, S.J. Pantazopoulou, State of Bond along Lap Splices, *Journal of Structural Engineering*, **141(10)**, 2015.

[25] S.P. Tastani, S.J. Pantazopoulou, Direct Tension Pullout Bond Test: Experimental results, *Journal of Structural Engineering*, **136(6)**, 731-743, 2010.

[26] T. Sakurada, N. Morohashi, R. Tanaka, Effect of Transverse Reinforcement on Bond Splitting Strength of Lap Splices, *Transactions of the Japan Concrete Institute*, **15**, 573-580, 1995.

COMPDYN 2019
7th ECCOMAS Thematic Conference on
Computational Methods in Structural Dynamics and Earthquake Engineering
M. Papadrakakis, M. Fragiadakis (eds.)
Crete, Greece, 24–26 June 2019

COMPUTATIONAL VALIDATION OF DISSIPATIVE DEVICE FOR THE SEISMIC UPGRADE OF HISTORIC BUILDINGS

Victor Melatti[1], Dina D'Ayala[1], Erica Modolo[2]

[1] University College London Gower St, Bloomsbury, London WC1E 6BT

victor.melatti.16@ucl.ac.uk, d.dayala@ucl.ac.uk

[2] University of Padua Via 8 Febbraio 1848, 2, 35122 Padova PD, Italy

erica.modolo@studenti.unipd.it

Abstract

The lack of effective connections between sets of perpendicular walls often determines the local or global failure of heritage structures in case of seismic event. In order to address this problem, the paper focuses on retrofitting systems for masonry structures undergoing seismic load. Particularly, it concerns the behavior of two different types of anchoring stabilization systems that avoid the out-of-plane collapse mechanism of a masonry wall and restore the box-like behavior. The response of the corner connection between two walls was investigated by numerical simulations. Initially, the model was tested in its original configuration to determine the type and the extent of the failure mode when a base acceleration is imposed. Afterwards, a traditional steel anchoring system was implemented in the corner connection to prevent the relative detachment of the walls for the same seismic input. Finally, a friction-based dissipative device was added to the steel ties to provide ductility to the system by allowing for a controlled relative displacement of the walls and reducing the concentration of stresses. The computational analysis showed that implementation of a dissipative device integrated with traditional steel anchors is effective in delaying the complete failure of the anchoring system. Moreover, it provides energy dissipation capacity through controlled displacement, reducing the stress in the surrounding material and allowing the model to withstand a larger intensity input.

Keywords: Dissipative devices, Friction, Masonry, Energy Dissipation

1 INTRODUCTION

In the last decades, a variety of systems able to dissipate seismic input energy has been designed, enhancing the global response of structures in earthquake prone areas [1] [2]. Historic buildings represent a singular case: the implementation of systems based on the modern concept of ductility and energy dissipation is often in contrast with the limitations promulgated to protect the aesthetic and structural integrity of architectural assets. Therefore, the common retrofitting practice still relies on traditional techniques of intervention and historic centres are still considerably affected by earthquakes [3] [4].

It is recognised that poor-quality connections between orthogonal structural elements greatly affect the dynamic performance of heritage masonry structures causing the relative detachment of masonry panels and ultimately the out-of-plane failure of the structure [5]. A way of tackling this issue is to insert steel cross-ties at the corner of two perpendicular walls in order to restore the box-like behaviour and distribute the seismic forces through all the resisting elements. This practice is not exempt from drawbacks, as the increased local stiffness at the corners might lead to high-stress concentration in case of seismic events and consequently to severe damage to the valuable parent material in which the cross-ties are embedded [6].

Therefore, in the last decades alternative systems have been developed to provide energy dissipation capacity to heritage structures, in line with the modern principle of performance-based design. This approach optimizes the structure for different seismic action level, encouraging the use of devices able to provide ductility by shifting the response of the structure from the elastic-only range to an elasto-plastic one [7].

These innovative systems are tailored for historic masonry structures as they reflect the conservation principles enshrined in international and national guidelines such as the ICOMOS/ISCARSAH principles [8] and the Italian DPCM 2011 [9]. According to these documents, the benefits of possible upgrade interventions in terms of seismic performance must be weighed against the impact on the original aesthetic and structural authenticity of the building. A variety of systems are available [10],[11], [12], but technical codes are vague on design procedures and their implementation hardly follows.

The present work proposes an innovative dissipative anchoring system to improve the global response of historic structures to seismic events. The proposed friction-based anchoring system offers an innovative alternative to traditional systems for the repair and strengthening of heritage structures, using performance-based design principles, i.e. control of displacements and reduction of accelerations and concentration of stress. The innovative system comprises a friction device, shown in Figure 1a, connected to longitudinal stainless steel bars grouted within the thickness of the walls. The assembly is designed to be inserted at the connection between perpendicular walls (Figure 1b): the stainless steel profiles improve the box-like behaviour of the building, while the device allows for a relative displacements between orthogonal sets of walls and the dissipation of the seismic energy input to the structure. The system aims at preventing typical failure mechanism of reinforced and unreinforced masonry buildings under seismic loading, such as punching failure and excessive crack opening.

a) b)

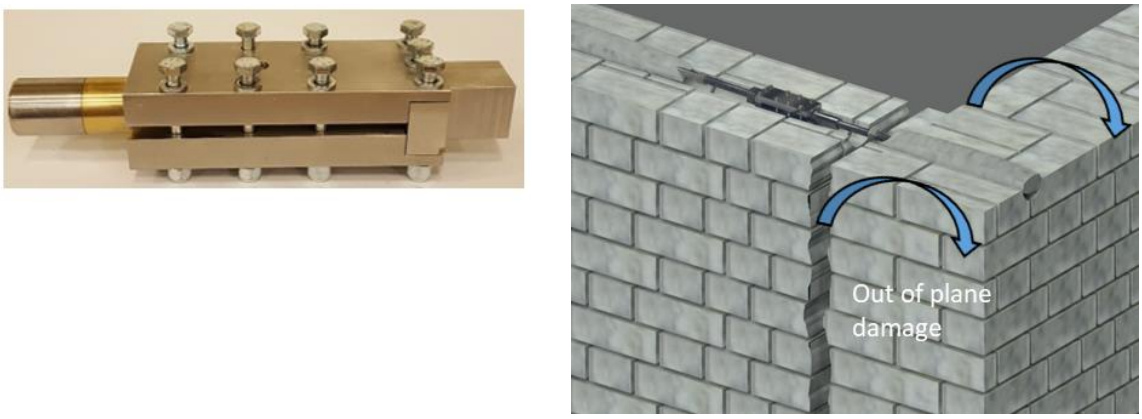

Figure 1: a) Patented design of the dissipative device, b) Insertion of the device at the connection between perpendicular walls (Paganoni 2015)

In the first part of this work, the experimental and numerical activities that led to the development and refinement of the dissipative device are presented. The experimental tests carried out on the device in its isolated configuration allowed for the identification of the meaningful parameters governing the functioning of the device. The dissipative anchoring system was then connected to a brickwork masonry specimen and tested under pseudo-static monotonic loading (pull- out test). The experimental activity demonstrate the beneficial effects of the dissipative anchoring system with respect to his strength-only counterpart.

Drawing on the experimental results, FE models were implemented using the commercial software Abaqus. The numerical simulations led to the refinement of the device's design to obtain a stable and repeatable behaviour. Moreover, the model allows simulating the response of the innovative system to a range of simulated inputs and provides information about the distribution of stresses both in the device and in the masonry wall.

A number of parameters have been analysed to determine which give the best results in terms of computational expediency and accuracy in respect to the behaviour of the laboratory samples.

In the second part of this work, the identified parameters feed in the model of a structure that is used to study the effect of standard and dissipative anchors ties on a larger scale. The building geometry provides a suitable case study as the analyses showed that it could be affected by local/global overturning damage of the walls in case of a seismic event. The model is used to predict the structural response in different scenarios, to guide future experimental activities and to fulfil the computational validation of the dissipative devices with respect to future applications to real case buildings.

2 THE FRICTION-BASED DISSIPATIVE ANCHORING SYSTEM

2.1 Optimization of the friction-based dissipative device

The design of the friction device draws on the Coulomb equation of friction:

$$F_{//} = n\,\mu\,F_{\perp} \tag{1}$$

Where $F_{\perp}$, the perpendicular force, represents the force transferred from the external plates to the internal slider by tightening two lines of bolts that pass through the assembly as shown in Figure 2. The friction force resisting the sliding motion is the combination of the perpendicular force, the friction coefficient, μ, and the number of surfaces in contact, n . The relative motion between the slider and the plates is initiated when the force acting in their own plane, $F_{//}$, exceeds the static friction force. Finally, a steel pin inserted in the device limits the sliding run of the internal part. Figure 2 shows in detail the elements composing the final design and the way the bolt load is transferred.

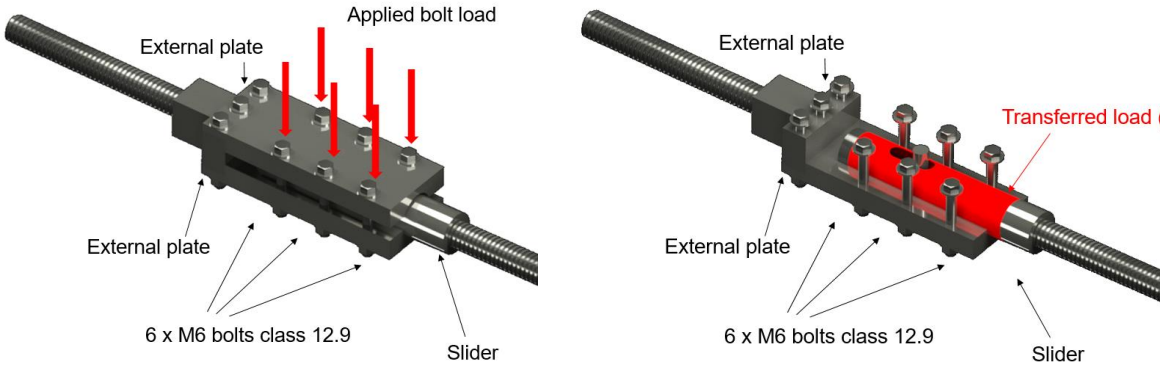

Figure 2: In friction-based device the force is transferred to the internal slider by tightening two lines of bolts

The validation process of the dissipative anchoring system is carried out through experimental and computational activities. Starting from the friction-based device developed by D'Ayala and Paganoni within the partnership between Cintec International and the University of Bath [13], the design was refined on the basis of experimental results conducted at University College London under a new collaboration agreement [14]. The fatigue tests conducted on the initial prototype had shown that the ratio between slip load and applied perpendicular force (Φ) significantly increases with the number of cycles. This variation is mainly caused by the wearing of the contact surfaces, which led to cold welding and interlocking phenomenon. Therefore, a detailed 3D FE model was developed in Abaqus FEA 6 .14 to achieve a more stable and reliable behaviour under cyclic loading. From the analysis of the stress distribution, it was concluded that a cylindrical shape for the sliding leads to a more homogeneous distribution of the shear stresses in the contact area. Figure 3 reports this evidence showing the larger contact area achieved by a cylindrical slider with respect to a squared one [14].

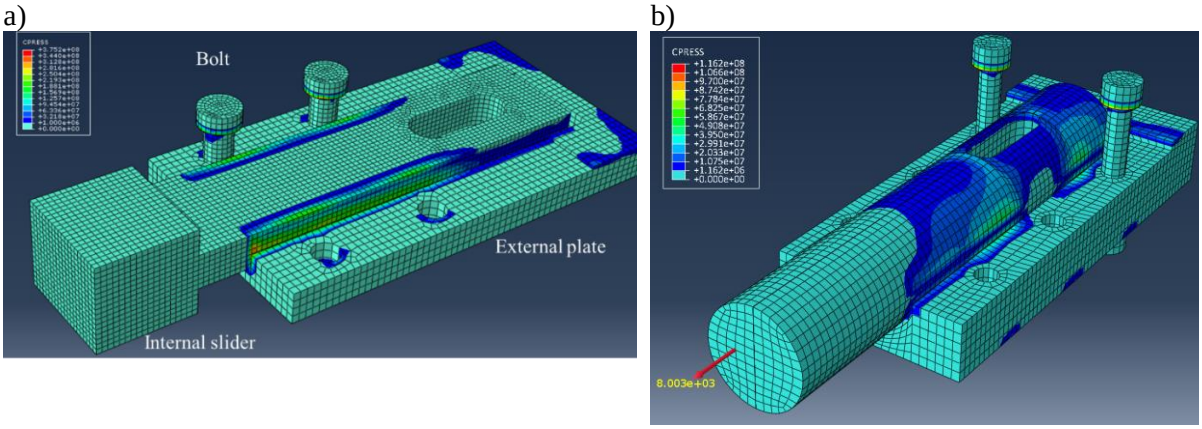

Figure 3: Numerical model: contact area a) of the initial prototype featuring a squared slider and b) of revised prototype featuring a cylindrical slider

2.2 Monotonic pull-out tests – Experimental and numerical analysis

A second experimental campaign aims at evaluating the behaviour of the dissipative device connected in series to a stainless steel bar grouted into a masonry panel. To this purpose a set of pull-out tests were performed to analyse the behaviour of a connection between two vertical elements, i.e. walls, strengthened by the dissipative anchoring system. The focus is on the performance of the anchor, and the damage caused to the wall perpendicular to the anchoring direction by the monotonic action of pull-out. The test set-up consists of the portion of stainless steel anchor embedded in a masonry panel perpendicular to the main seismic action, while the pulling action of the testing apparatus simulates the reaction of the anchor lying within the wall parallel to the main shock direction. Finally, the device is installed as add-on element between the grouted anchor and the pull-out jack as shown in Figure 4.

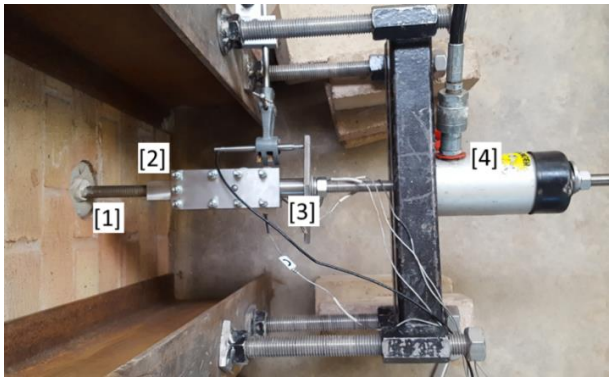

Figure 4: Description of elements composing the testing set up.

After visual inspection of the masonry panel, it was concluded that the devices can address some of the drawbacks that are identified for standard anchors, such as the presence of damage in the substratum, even for small relative displacement between the grouted anchor and the masonry. Conversely, the friction device improves the response of anchors, considerably reducing, or eliminating damage to the parent material. The activation load that initiates its sliding motion can be tuned to the point that almost no relative displacement is detected in the other elements of the anchor assembly.

A Finite Element model is implemented in Abaqus FEA 6.14 to understand the interaction between parent material and anchoring system. This is a central task of the validation process as the bond between the masonry and the grout determines the load at which the failure mode occurs. A numerical model of the dissipative device connected to a steel bar embedded in a masonry wall was generated, as shown in Figure 5.

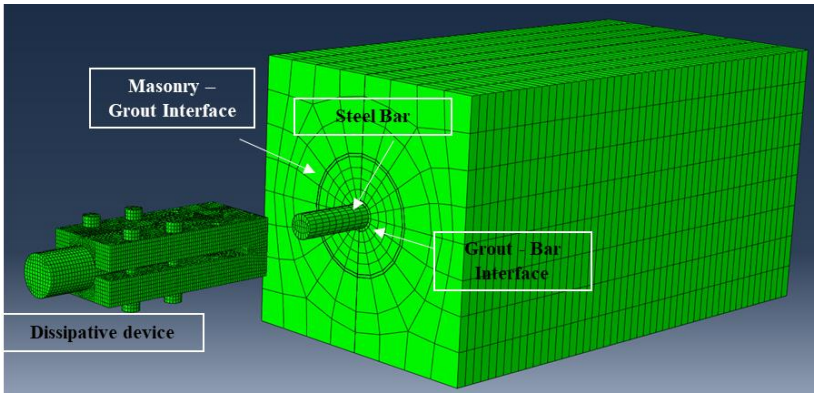

Figure 5: Numerical model – Undeformed shape and components of the model.

Three-dimensional volume elements were used for the mesh since an accurate stress distribution is relevant for a clear understanding of the stress field and of the structural behaviour. The motion of the steel bar is rigidly coupled to the device's end plate. The mesh discretization was defined to achieve a compromise between accuracy and efficiency. Brick elements (C3D8R, eight-node linear brick with hourglass control) are used for the mesh of all the parts, except for the simulation of the bond between different materials, where tri-dimensional cohesive elements (COH3D8, eight nodes in each surface) were used. The generated mesh includes 41309 nodes and 31111 elements.

According to the failure mechanism observed in the experimental activity, interface elements around the steel bar (inner interface) and between the grout and the masonry (outer interface) were included. The interfaces aim to simulate the bonding properties among the single components, i.e. the steel bar, the grout and the masonry. Abaqus FEA allows for the selection of cohesive elements to which a linear elastic traction-separation law before damage has been assigned. When the maximum traction resistance is reached, the interface elements display a progressive degradation, which is driven by a damage process. The numerical parameters defining the mechanical properties of these cohesive elements were calibrated to replicate the experimental behaviour of the sample under out-of-plane loading and reproduce the different failure mechanism.

The shear stiffness of the external interface is defined according to the pull-out tests performed on the specimens of anchors embedded in the masonry wall.. In order to define the traction-separation law that describes the behaviour of the cohesive interface, the values of maximum traction resistance τ_{max} and ultimate dispacement δ_{ult} need to be provided. On the basis of the experimental data, a mean value of F_{max}= 24 KN was considered to compute the maximum shear resistance τ_{max} :

$$\tau_{max} = \frac{F_{max}}{A_{interf}} = 0.29\ MPa \tag{2}$$

The change in stiffness exhibited by the anchors at a recorded displacement of 0.5mm determines the end-point of the linear correlation between the shear stress and the shear deformation. The Shear modulus (G) is therefore equal to:

$$G = \frac{\tau_{max}}{\gamma} = \frac{0.29}{0.25} = 1.16 \text{ MPa} \tag{3}$$

The pull-out tests performed on the anchor embedded in the masonry wall highlighted that the most likely failure was slippage of the bar-socket assembly, caused by the loss of adherence between the grouted socket and the surrounding material. Therefore, the ultimate displacement refers to the relative displacement of the grout with respect to the masonry at which the anchoring system is no longer able to provide any resistance to the pull-out force. According to the experimental data and crack propagation this value was assumed equal to δ_{ult} = 5 mm. The analytical curve implemented in the numerical model shown in Figure 6.

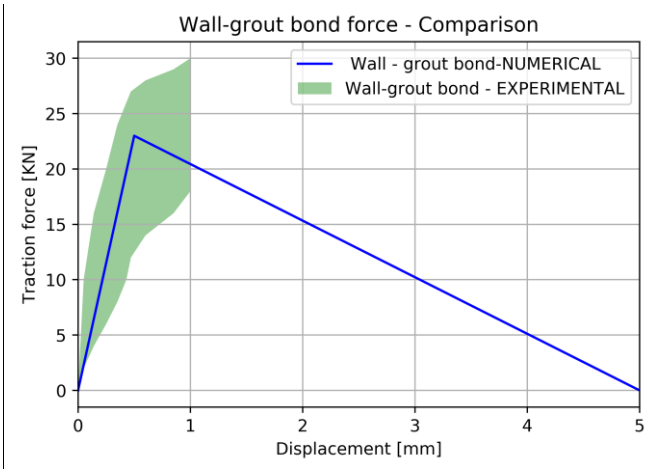

Figure 6: Comparison between the experimental envelope and the numerical analysis

Regarding the physical and mechanical properties of the grout and the steel, information from the technical sheet were used. Table 1 provides the mechanical properties adopted for the materials, as well as the parameters needed to define the traction-separation law for the interfaces.

Part	E	G1	τmax	displacement at τmax	Ultimate damage
	[Pa]	[Pa]	[Pa]	[m]	[m]
Wall	1.50E+09				
OUT Interface	-	1.16E+06	2.90E+05	5.00E-04	5.00E-03
INT Interface	-	2.00E+08	5.00E+07	5.00E-04	5.00E-03
Grout	3.00E+10				
Steel bar	2.10E+11				

Table 1: mechanical properties of model materials

The stress field attained in various parts of the model can be visualised through an analysis run setting a maximum displacement of 40 mm to the internal slider of the device. Figure 7 shows the failure of the outer interface caused by the imposed displacement.

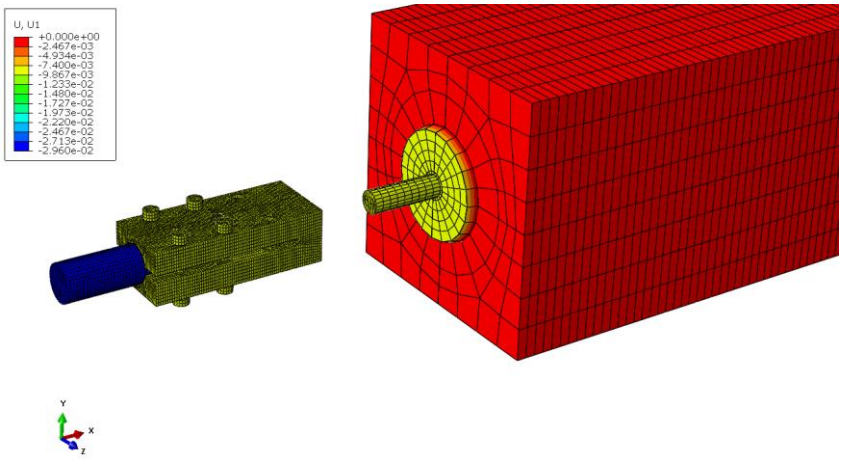

Figure 7: Numerical model – Deformed shape, failure at wall-grout interface.

In conclusion, the FE model of the pull-out test succeeds in replicating the bond failure between the parent material and the grouted element of the standard anchor, this being the failure mode that controls the performance of the whole assembly. The definition of a fictitious

part located between the grouted socket and the parent material and defined by traction-separation low is suitable for this purpose. The material properties of the fictitious part are defined on the basis of experimental results, creating an equivalent stress-strain curve compatible with the chosen failure criterion. Therefore, the numerical model tuned on the obtained experimental results can be considered good approximation of the physical test and can be used as a valid tool for the optimization of an upgrade intervention. Drawing on these conclusions, a second numerical model was developed to investigate the structural behaviour of a portion of an idealized masonry building under seismic loading.

3 FE MODELS OF AN IDEALIZED CASE-STUDY STRUCTURE

The positive outcome of the model of the pull-outs means that the modelling technique of fictitious parts and equivalent material curves can be applied to numerically describe the bonding capacity of a grouted anchor. The parameters identified for the pull-out model are applied for the model of a structure that is used to study the effect of standard and dissipative anchoring system on a larger scale. The analysed structure is composed of a front wall connected to two sidewalls representing an idealized portion of a masonry building with poor quality connection between adjacent walls. The geometry and dimensions of the subassembly are shown in Figure 8.

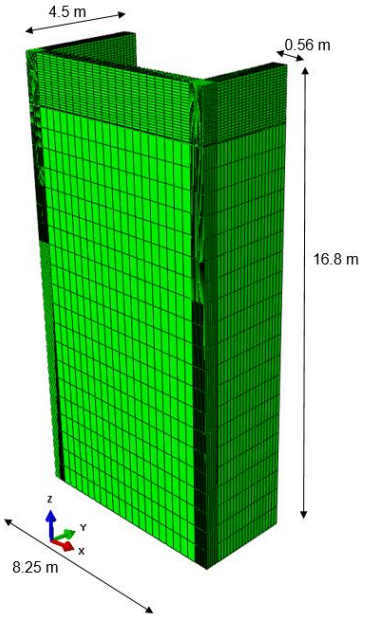

Figure 8: a) Dimensions of the analyzed corner connection

Modelling a smaller portion of the building allows for a more detailed analysis of the behaviour of the connection both in the unstrengthened and strengthened configuration. Three FE models are implemented: a first model represents the original structure, where the connection between the adjacent walls relies on their shear capacity only. A second model represents the structure when traditional grouted ties are inserted at the corner connection. In a last model, a friction-based dissipative device is implemented in series with the strength-only anchors to provide the connection with energy dissipation capacity. The response of the structure is evaluated imposing a seismic base acceleration in the out of plane direction of the front wall. The ground acceleration of the 2009 L'Aquila earthquake (Mw 6.3 main shock), as recorded at the station of L'Aquila – Valle Aterno (station code AQV) is used as input for the analysis. The walls are defined assuming that the mortar joints and brick units are smeared into

one isotropic material, with average mechanical properties according to the principle of macro-modelling [15].

3.1 The original structure

In the first model, the connection between cross walls relies on the equivalent traction resistance of a set of interfaces. An equivalent traction capacity is assigned to these interfaces in the direction of their thickness (T= 0.002m). This allows for the modelling of the shear resistance that opposes the out-of-plane loading that causes the wall's separation. If the external load exceeds the shear force the detachment of the adjacent walls is no longer prevented and the front wall experiences outward tilting. A traction-separation law is assigned to describe the mechanical constitutive behaviour of the interface. According to the Mohr-Coulomb criterion, the linear relationship between the shear strength τ and the normal compressive stress σ is given by the formula:

$$\tau = c + \sigma \tan(\varphi) \tag{4}$$

Where c denotes the cohesion and φ the angle of internal friction. For this study, the average cohesion and friction angle in the bed joints are respectively 0.35 MPa and 0.5 rad. The equivalent traction force ($F_{traction}$) is therefore the integral of the shear stress over the interface's area:

$$F_{\text{traction}} = \int \tau \, dA = \tau \cdot A_{interface} \tag{5}$$

$$\sigma_{\text{traction}} = \frac{F_{\text{traction}}}{A_{interface}} = \tau \tag{6}$$

Therefore for the purpose of this model the traction tress (σ) is equivalent to the the shear stress (τ). The shear stress linearly increases with the compressive stress, which means that the interfaces have higher equivalent traction resistance moving from the top to the bottom of the wall. The graph Figure 9b shows the values of equivalent traction resistance according to the location of the interfaces as measured from a control point (CP), referenced in Figure 9. To consider the damage evolution a post-damage effective separation at failure is defined and a coefficient of friction (μ) is specified to prevent components' penetration. Figure 9a shows the location of the upper cohesive interface with respect to the side and front walls.

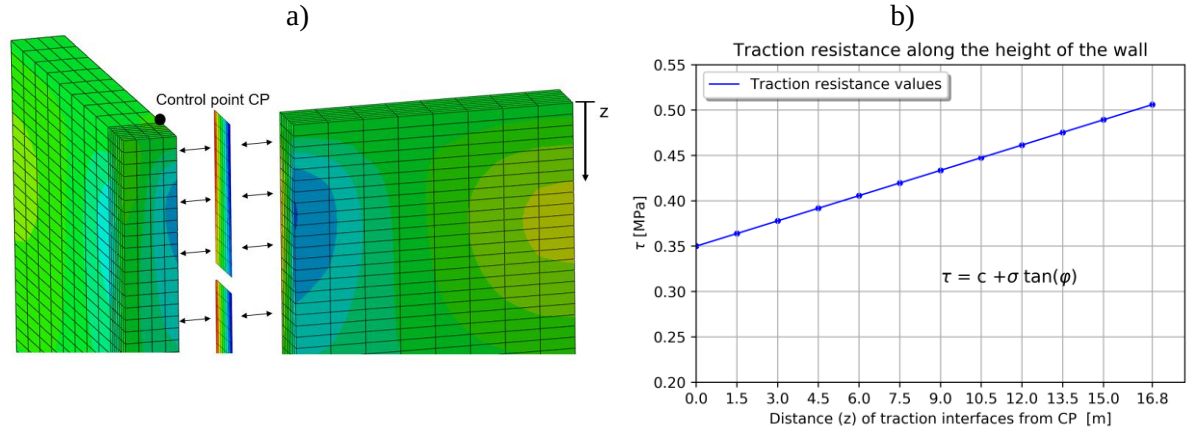

Figure 9: Model of unstrengthened walls: a) location of interface part with respect to walls b) Traction resistance of the cohesive interfaces along with the height of the wall.

As a result of the applied base acceleration shown in Figure 11a, the orthogonal walls separate when the strain in the direction of the interfaces' thickness (T) exceed the maximum strains defined by the traction-separation low. The strain limits depend on the maximum traction stress σ_{max} assigned to the interface according to Equation 4. The computation carried out to determine the ultimate shear resistance for the upper interface are:

$$F = K\,\Delta u = \frac{EA}{T}\,\Delta u \tag{7}$$

$$\sigma_{\text{traction}} = \frac{E}{T}\,\Delta u = \frac{E}{0.002}\,\Delta u = E\,\varepsilon \tag{8}$$

$$\varepsilon_{elastic} = \frac{\sigma_{\text{traction}}}{E} = \frac{3.5\ 10^{6}}{3.0\ 10^{6}} = 0.116 = 11\% \tag{9}$$

$$\varepsilon_{ultimate} = \frac{\Delta u_{max}}{T} = \frac{0.005}{0.002} = 2.5 = 250\,\% \tag{10}$$

Where E and A are the Young modulus and area of the interface, respectively and the maximum elastic strain ($\varepsilon_{elastic}$) and ultimate strain ($\varepsilon_{ultimate}$) are expressed as a percentage of the initial thickness of the interface (T=2 mm). The resulting constitutive laws assigned to the cohesive interface at z = 0 m (upper interface) and the cohesive interface at z = 15 m (lower interface) are shown in Figure 10a.

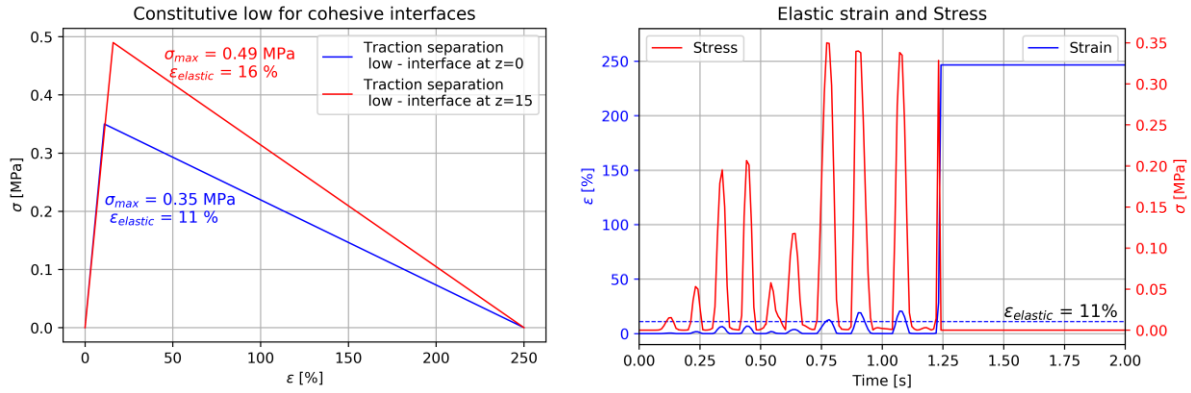

Figure 10: a) Cconstitutive law for the cohesive interface, b) strain and stress field for the upper cohesive interface

The graph reported in Figure 10b shows that the seismic acceleration applied to the base of the model produces in the upper interface a strain field equal to 11% and 250% after 0.76 s and 1.25 s respectively. For these values of strain, the interface elements experience the maximum values of traction stress(0.35 MPa)and the failure. Once the damage is initiated, it propagates down the height of the wall and the orthogonal walls start oscillating independently. The CP experiences a maximum relative displacement from the sidewall of 0.35 m at time step 1.25 s and the height of the separation is 6.8 meters as shown in Figure 11.

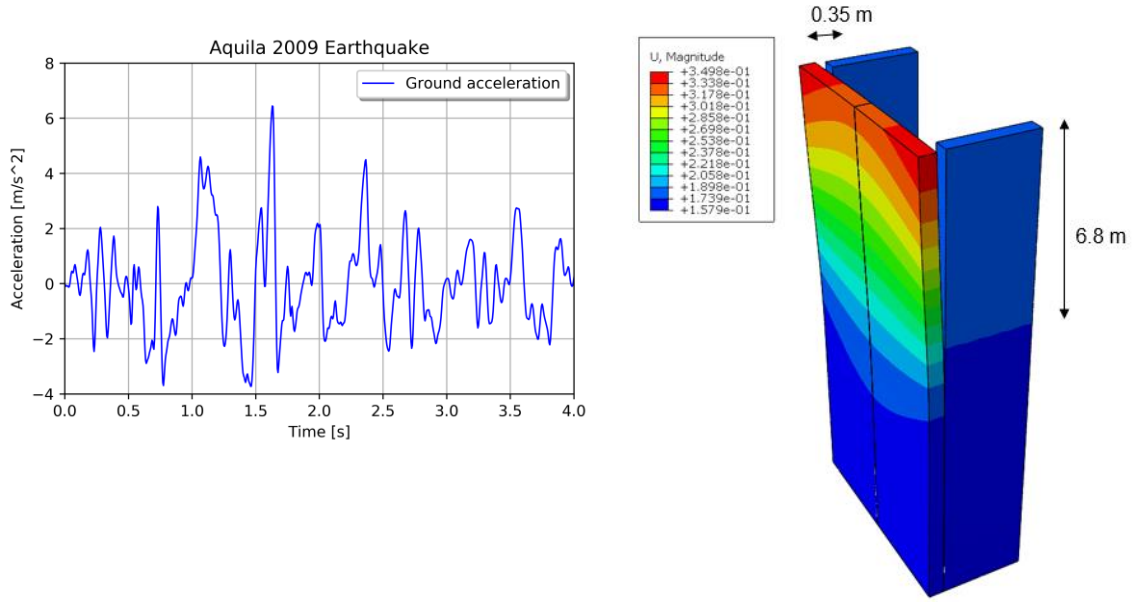

Figure 11: a) Applied base acceleration, b) deformed shape of FE model at time step 1.25 seconds.

These results show that the FE model is able to reproduce the typical failure mechanism detected on site in the aftermath of a seismic event, when major cracks at the interface between cross walls are often observed. The analysis shows that the connection capacity simulated by the interfaces is not sufficient to restrain the walls. The lack of effective lateral constrains determines the façade detachment form the side walls and it deforms similarly to a cantilever beam undergoing bending, as shown in Figure 11b. The model is deemed suitable for predicting the response of the structure in other case scenarios, for instance by inserting the anchors and dissipative devices characterised in section 2.2.

3.2 The strengthened structure

A second model is implemented to investigate the benefit of introducing a reinforcement scheme able to improve the connection between the cross walls that experienced mutual separation. Damage experienced by the structure is accounted for by removing the interfaces for the extent they failed in the previous analysis.

Material properties are the same as for the undamaged model, as cracking is localised and does not affect other parts of the structure; thus, it is not necessary to reduce the stiffness of the parent material. Table 2 provides the mechanical properties adopted for the materials.

Part	E	G1	G2	Density	Maxs Damage	First Damage	Ultimate damage
	[Pa]	[Pa]	[Pa]		normal[Pa]	[m]	[m]
Wall	1.50E+09			2.14E+03			
Interface	3.00E+06	3.00E+06	3.00E+06	1.75E+03	3.50E+05	2.33E-04	5.00E-03
Steel bar	2.10E+11			8.00E+03			

Table 2: mechanical properties of model's materials

A first FE analysis is performed on a model including standard stainless steel ties. A common retrofit practice is to grout the ties within the masonry inside a drilled hole to restore the box-like behaviour of masonry structures. Therefore, in the numerical model the metallic elements run along the whole length of the side walls, reconnecting the sets of perpendicular walls.

Paganoni and D'Ayala [16] used mono-dimensional truss elements to model the ties and a bonded contact was implemented at the interface between truss and elements representing the masonry. In the present work the anchors are modelled by means of three-dimensional elements and an interface part is defined to govern the mutual behaviour between the anchor and the parent material. The insertion of the grouted steel anchors is modelled through cohesive interfaces which reproduce the bonding between the ties and the masonry. A traction-separation law with sub-options governing the post damage behaviour is assigned to the cohesive elements. The parts representing the front and side walls are rigidly connected for 10 meters from the base by numerically defining tie constrains which prevent the relative motion of nodes belonging to the side and front wall. The two parts are disconnected for the remaining 6.8 meters and a frictionless contact coefficient (μ) is specified to prevent components' penetration. This means that, for this portion of the wall, the only link preventing the relative motion of the orthogonal walls is provided by the anchors running through the two parts representing the walls.

Compared to the model without any strengthening solution, the insertion of metallic ties does not improve the overall behaviour of the structure. The interface controlling the bonding capacity between the anchor and the surrounding part reaches the maximum traction capacity after 0.18 seconds and the anchor is pulled out of the front wall after 0.51 seconds when the interface experiences the maximum allowable displacement, namely 5 mm. The pull-out failure does not extend to the whole length of the anchor, but affects instead the portion adjacent to the disconnection, i.e. the portion bridging the vertical crack between front and side wall. Before failure, the maximum stress concentrations are registered in the proximity of the anchorage point on the façade face, as shown in Figure 13. The model shows a punching/pull-out failure at the head of the anchorage, which is a recurring failure mode for this type of retrofitting system in case of weak substratum, as shown in Figure 12.

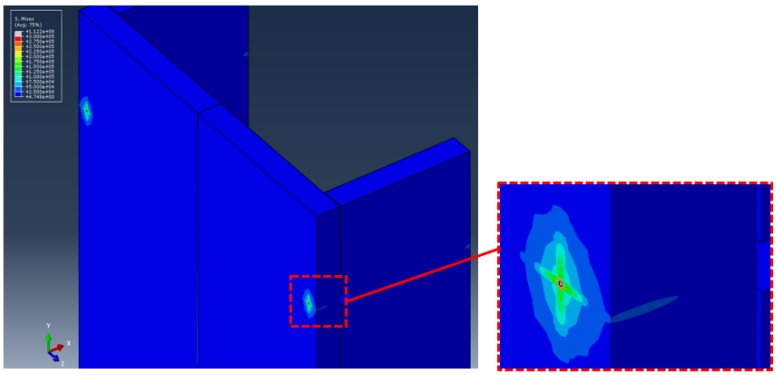

Figure 12: Punching failure of standard metallic ties - FEM

To observe in detail the stress field in the material surrounding the anchorage, the parts composing the model are sectioned along the x-z plane where the longitudinal axis of the anchor lies. Figure 13 shows the stress distribution along the length of the interface. As the front wall tilts outwards, the part representing the grouted bars are bent along their longitudinal axis. This mechanism determines that the maximum tensions are equal in value but opposite in sign as shown in Figure 13.Two critical points in the time history are identified, namely the time steps when the maximum traction and the maximum displacement are reached.

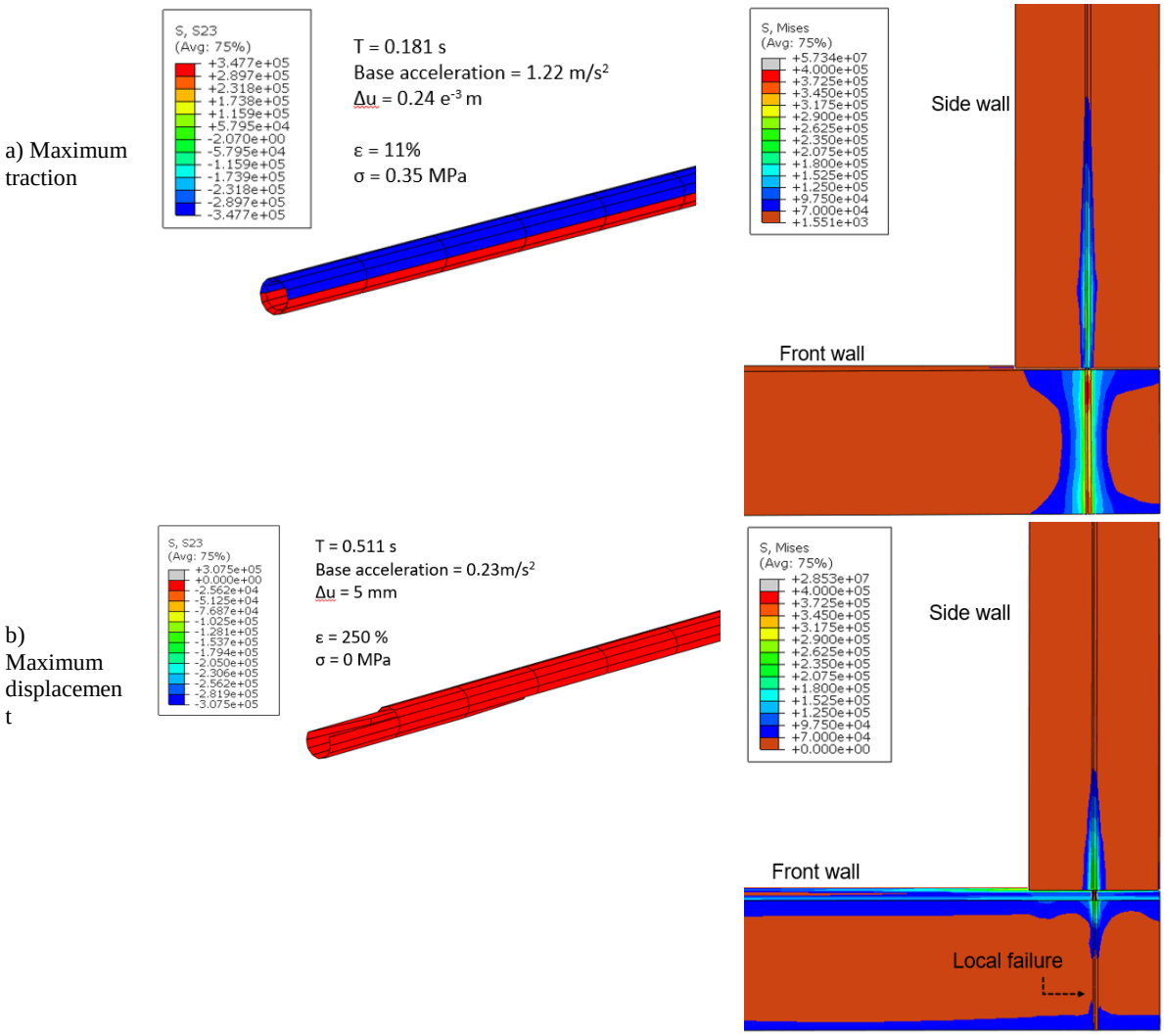

Figure 13: Distribution of Shear stresses along the cohesive interface and V. Mises stresses as transferred from the anchors to the masonry walls

A second model including a friction-based device inserted at the joint between front and side walls undergoes the same input as the model with standard steel ties. The dissipative device is modelled with solid elements reproducing all the parts composing the final assembly and is connected rigidly to the steel bars. The friction force resisting the slider's motion is induced by defining a "bolt load" in the element reproducing the bolts of the real devices. Each bolt-part is loaded with a transversal force equal to 2700 N and the resulting friction force is computed according to Equation 1:

$$F_{//} = n\,\mu\,F_{\perp} = 4 \cdot 0.2 \cdot (4 \cdot 2700) = 8.6\,KN \quad (11)$$

As for the previous model, one cohesive interface connecting the bars to the surrounding elements complete the assembly. Figure 14a shows the sliding motion of the device's slider along with the acceleration experienced at the anchor's location, namely at 14 meters from the base. From the graph, it is clear that the device activates twice depending on the experienced acceleration: the first time at T = 0.26, when it oscillates between its initial position and 2.5 mm and the second time at T = 1.16s when it fully exploits the allowable run of 20 mm. Since the device is tuned to start sliding for a resulting force (8.6 KN) lower than the one that would

cause the pull-out failure of the assembly (11 KN) the stress distribution in the wall's part are lower than the maximum traction capacity.

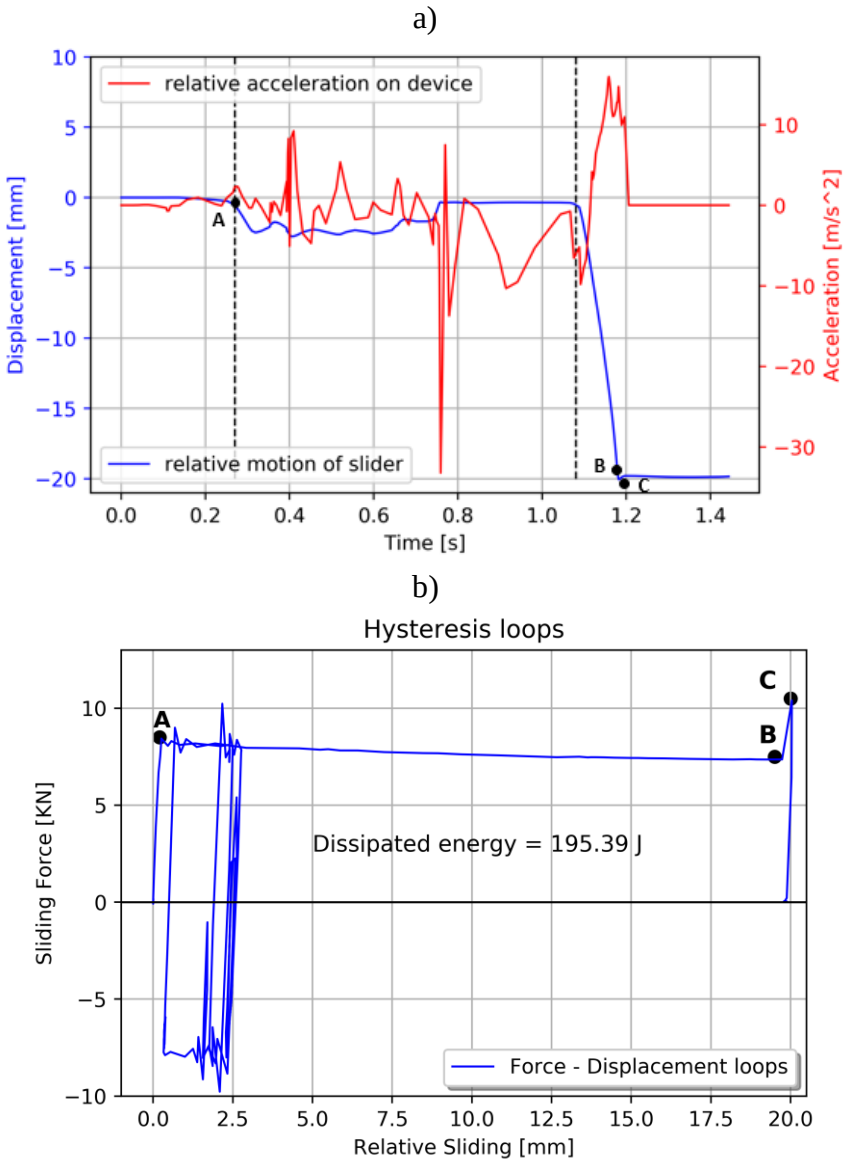

Figure 14: Sliding motion of the internal part and relative acceleration at anchor's location, b) Hysteresis loops of friction-based dissipative device

Figure 14b shows the load-displacement curve experienced by the device. When the sliding force exceeds the friction resistance force (Point A), the sliding central part starts moving according to the direction of the applied base acceleration. In particular, the slider completes a hysteresis loop oscillating between its initial position and 2.5 mm. At T= 1.16s, it slides out for 20 mm, thus reaching the maximum controlled displacement of the device (Point B). Point C in Figure 14 represents the ultimate traction resistance that the interface around the steel bar part can provide, after which the interface displays a gradual degradation. The areas between the force-displacement curve and the x-axis represents the total energy that the system can provide to resist the applied motion.

Figure 15 shows the stress distribution at the time step corresponding to the maximum traction and maximum displacement in the interface part. At time T=1.18 s the frictional sliding occurring in the device is equal to 20 mm and the internal part hits the central pin that controls

the allowed motion of the slider. At time T= 1.20 s the system, now working as a traditional strength-only anchor, fails as the interface between the bar and the masonry has reached the maximum displacement, namely 5 mm. By comparing the stress distribution in the parts surrounding the anchors, it can be noted that the insertion of the dissipative device reduces the shear stresses transferred from the anchor to the walls.

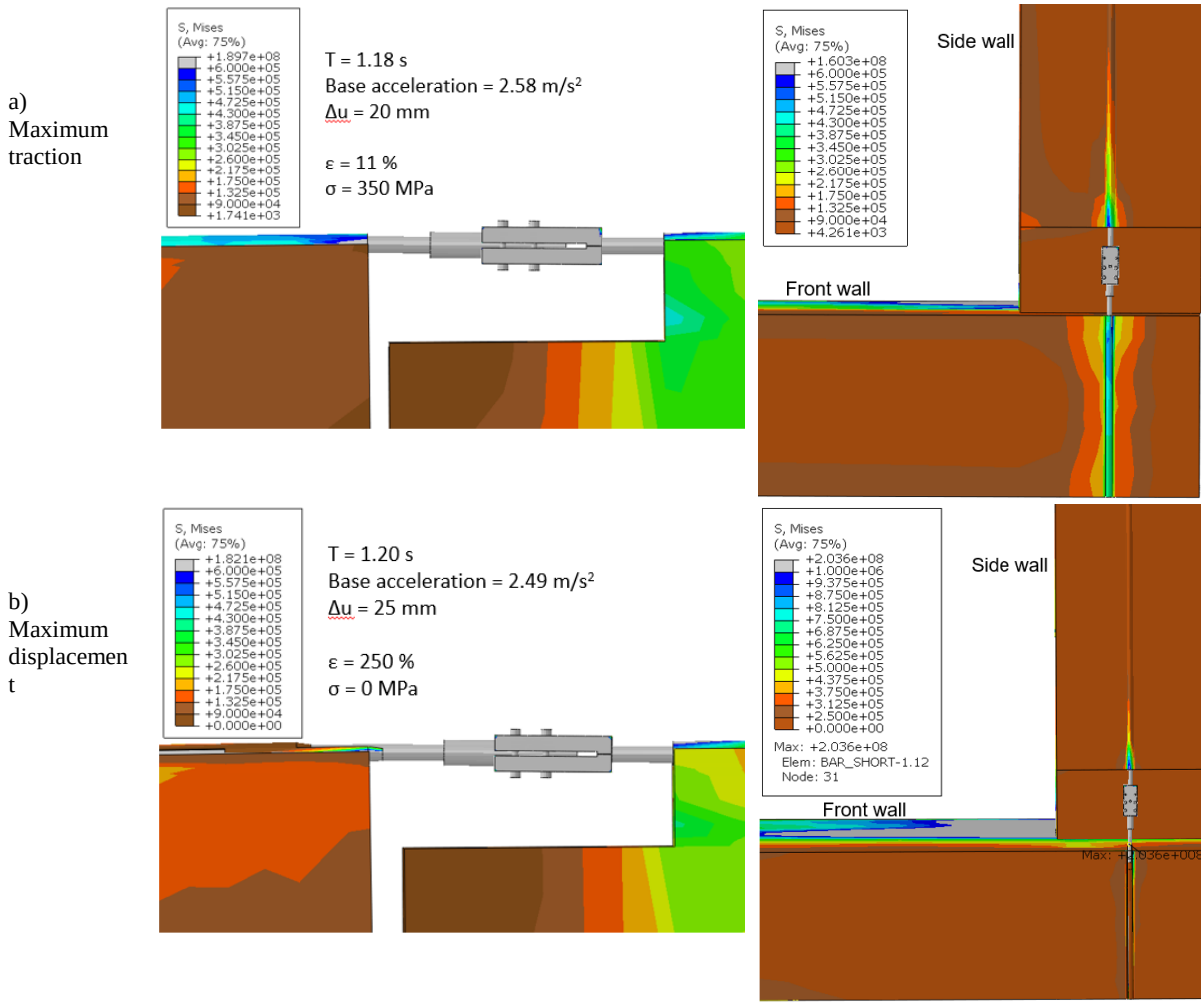

Figure 15: FE model of a corner connection strengthened by means of dissipative anchoring system. Deformed shape and stress distribution at maximum traction and maximum displacement

Figure 16a shows the relative acceleration experienced by the orthogonal walls at 14 m from the base, namely where the strengthening systems are inserted. From the graph, it is clear that the corner connection strengthened by means of the dissipative device withstands the applied base acceleration for a longer period. The ultimate failure is reached at T = 1.2 s, whilst it was reached at T= 0.5 s for the traditional anchor.

a)

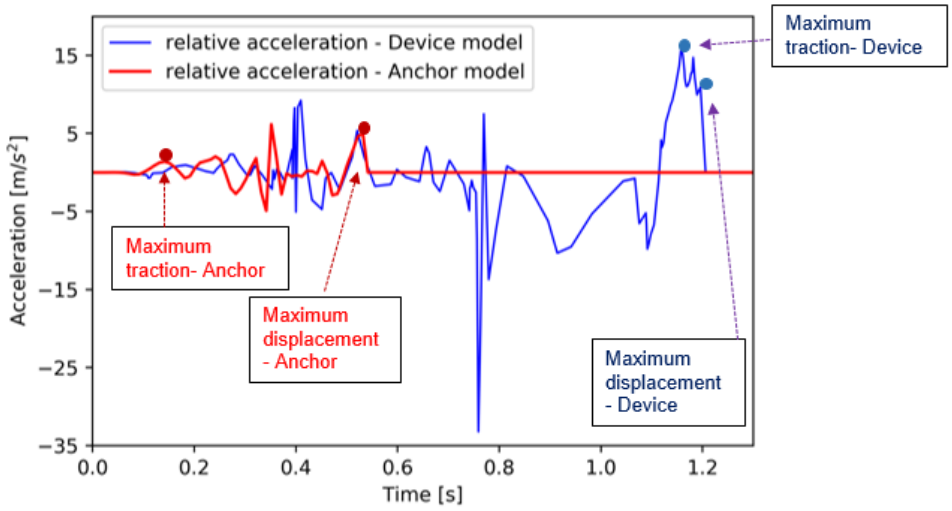

b)

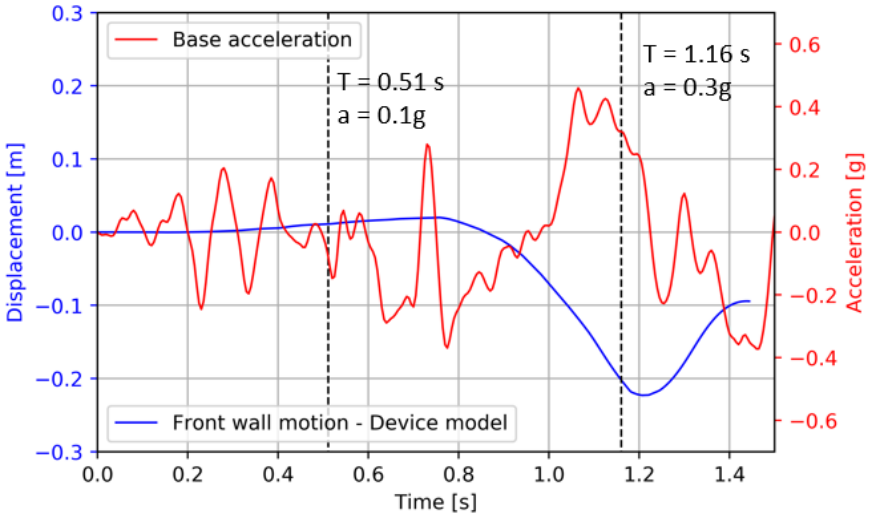

Figure 16: a) Relative acceleration experienced by the strengthening systems, b) base acceleration and displacement time history of front wall

By comparing the time steps at which the ultimate failure takes place, Figure 16b shows that the dissipative anchoring system experiences a pull-out failure for a base acceleration equal to 0.3g while the model representing the traditional strengthening system fails for a base acceleration equal to 0.1g.

4 CONCLUSIONS

The lack of effective connections between perpendicular walls often determines the failure of a historic masonry structure under seismic loading. To restore the box-like behaviour and provide these particular buildings with sufficient ductility to withstand shaking, the authors developed a friction-based dissipative anchoring system.

Such system comprises a device installed in series with standard metallic anchors grouted at the joint between perpendicular sets of walls of historic structures. The purpose of the strengthening system is to reconnect structural elements that might have become detached as

result of seismic events, but also to control relative displacements and reduce accelerations in case of further earthquakes, so that damage to the precious wall finishes can be reduced.

The device provides ductility to the connection, mitigating the width of the cracks in the parent material and preventing fragile failures, such as pull-outs. This, of course, entails allowing a controlled out-of-plane deformation, rather than completely relying on the in-plane stiffness of side walls.

The paper presents the experimental and computational work carried out to assess the performance of the dissipative anchoring system and its applicability to an idealized case study.

A series of FE models were implemented using the commercial software Abaqus to refine the device's shape and optimize its design in terms of stress distribution, stability and reliability

The pull-out tests performed on the device connected to steel bars and embedded in a masonry panel confirmed that the innovative system is effective in reducing the damage propagation to the subtratum in respect to its strength-only counterpart. The experimental results feed in the calibration of a computational model, which reproduces the experimental set up in order to understand better the rules that governs the behaviour of the dissipative anchoring system. A model of a wall panel strengthened by the anchoring devices was created and run and the FE model succeeds in replicating the bond failure between the parent material and the grouted element of the standard anchor, this being the failure mode that controls the performance of the whole assembly. Therefore, the numerical model tuned on the obtained experimental results was used as a starting point to develop a numerical model of an idealized case-study building in need of seismic upgrade. The numerical model reproduces the behaviour of a three-panel corner connection when a seismic base acceleration is applied. The front panel disconnects from the sidewalls for a hight of 6.8 meters and undergo out-of-plane motion. The outward tilting of walls is a recurring mode of failure for historic masonry structures, and the proposed system aims at controlling the opening of cracks and taking advantage of. The model of the corner connection is therefore "strengthened" by implementing an anchoring system with and without the addition of the dissipative device. Fictitious interfaces were used to define the bonding capacity between the parts representing the steel bars and the masonry. This method allows for the definition of an equivalent stress-strain curve compatible with the available experimental results. The dissipative anchoring system experiences a pull-out failure for a base acceleration equal to 0.3g while the model representing the traditional strengthening system fails for a base acceleration equal to 0.1g.

It should be noted that the applied base acceleration caused the pull-out failure of both strengthening systems meaning that the full scale signal was too demanding for traction capacity of the interfaces. Therefore, a future set of analysis will include a parametric study investigating the strengthening systems for smaller range of accelerations. Moreover, in the proposed work only one system was inserted in each corner connection, whilst in a real-case application several devices should be included. Therefore, the reported results will feed into a more complex model where a number of dissipative anchoring system will restrain simultaneously the out-of-plane motion of the front wall.

REFERENCES

[1] S. Zhu and Y. Zhang. 2014. "Seismic Behaviour of Self-Centring Braced Frame Buildings with Reusable Hysteretic Damping Brace." *(February):1329–46.*

[2] Christopoulos, C., R. Tremblay, H. Kim, and M. Lacerte. 2008. "Self-Centering Energy Dissipative Bracing System for the Seismic Resistance of Structures : Development and Validation." *134(January):96–107.*

[3] Lagomarsino, Sergio. 2012. "Damage Assessment of Churches after L ' Aquila Earthquake (2009)." 73–92.

[4] Wilkinson, Sean et al. 2013. "Observations and Implications of Damage from the Magnitude Mw 6.3 Christchurch, New Zealand Earthquake of 22 February 2011." *Bulletin of Earthquake Engineering* 11(1):107–40.

[5] Paganoni, Sara and Dina D'Ayala. 2014. "Testing and Design Procedure for Corner Connections of Masonry Heritage Buildings Strengthened by Metallic Grouted Anchors." *Engineering Structures* 70:278–93.

[6] D'Ayala, Dina F. and Sara Paganoni. 2011. "Assessment and Analysis of Damage in L'Aquila Historic City Centre after 6th April 2009." *Bulletin of Earthquake Engineering* 9(1):81–104.

[7] 1998:2005, EN. 2011a. "Eurocode 8: Design of Structures for Earthquake Resistance. Part 1 : General Rules, Seismic Actions and Rules for Buildings." 1(2004).

[8] ICOMOS. 2003. "Principles for the Analysis, Conservation and Structural Restoration of Architectural Heritage (2003)." *Architectural Heritage* 3–6.

[9] D.P.G.M. 2011. "Linee Guida per La Valutazione e La Riduzione Del Rischio Sismico Del Patrimonio Culturale Con Riferimento Alle Norme Tecniche per Le Costruzioni Di Cui Al Decreto Del Ministero Delle Infrastrutture e Dei Trasporti Del 14 Gennaio 2008 (09/02/2011)." 1(c):1–83.

[10] Indirli, Maurizio and Maria Gabriella Castellano. 2008. "Shape Memory Alloy Devices for the Structural Improvement of Masonry Heritage Structures." *International Journal of Architectural Heritage* 2(2):93–119.

[11] D'Ayala, D. F. and S. Paganoni. 2014. "Testing and Design Protocol of Dissipative Devices for Out-of-Plane Damage." *Proceedings of the Institution of Civil Engineers: Structures and Buildings* 167(1).

[12] Casciati, Fabio and Lucia Faravelli. 2009. "A Passive Control Device with SMA Components : From the Prototype to the Model." (June 2008):751–65.

[13] Paganoni, Sara. 2015. "Dissipative Anchor Devices for the Seismic Retrofit of Heritage Buildings." *Ph.D. Thesis, University of Bath, Department of Architecture and Civil Engineering* 1.

[14] Melatti, Victor and Dina D'Ayala. 2018. "Dissipative Device for the Seismic Protection of Masonry Structures." *16th European Conference on Earthquake Engineering* 1–12.

[15] Lourenco, Paulo B., Gabriele Milani, Antonio Tralli, and Alberto Zucchini. 2007. "Analysis of Masonry Structures : Review of and Recent Trends in Homogenization Techniques 1." 1457:1443–57.

[16] Paganoni, S. and D. F. D'Ayala. 2012. "Numerical Simulation of Dissipative Anchor Devices in Historic Masonry." *Proceedings of the Fifthteenth world Conference on earthqueake Engineering, Listbon, 2012*

COMPDYN 2019
7th ECCOMAS Thematic Conference on
Computational Methods in Structural Dynamics and Earthquake Engineering
M. Papadrakakis, M. Fragiadakis (eds.)
Crete, Greece, 24–26 June 2019

STATISTICAL ANALYSIS ON MECHANICAL PROPERTIES OF FRP MATERIALS FOR STRUCTURAL STRENGTHENING

P. Salzano[1], A. Bonati[2], F. Ceroni[3], G. Crisci[4], A. Franco[5], A. Occhiuzzi[6]

[1]Ph.D student, Engineering Department, University of Naples 'Parthenope',
Centro Direzionale is. C4, 80143, Napoli,
piera.salzano@uniparthenope.it

[2]Researcher, Construction Technologies Institute, Italian National Research Council ITC-CNR,
antonio.bonati@itc.cnr.it

[3]Associate professor, Engineering Department, University of Naples 'Parthenope',
Centro Direzionale is. C4, 80143, Napoli,
francesca.ceroni@uniparthenope.it

[4]Ph.D student, Engineering Department, University of Naples 'Parthenope',
Centro Direzionale is. C4, 80143, Napoli,
giovanni.crisci@uniparthenope.it

[5]Researcher, Construction Technologies Institute, Italian National Research Council ITC-CNR,
franco@itc.cnr.it

[6]Full Professor, Engineering Department, University of Naples 'Parthenope',
Centro Direzionale is. C4, 80143, Napoli,
antonio.occhiuzzi@uniparthenope.it

Abstract

In the last decades Fiber Reinforced Plastic (FRP) have been widely adopted for strengthening and repair of damaged structures. Design indications about the use of FRP materials as external strengthening techniques for structures are available in Italy since 2004, while only in 2015 the Italian Ministry of Infrastructure and Transportation published Guidelines for the qualification of FRP products. This paper summarizes the results of several experimental activities for the qualification of preformed FRP products. Statistical analyses were carried out in order to provide indications on variability of FRP's mechanical properties and assess the reliability of the classes individuated by the Italian guidelines.

Keywords: Preformed FRP products, tensile strength, Young's modulus, probabilistic models, design value.

1 INTRODUCTION

The demand for structural safety in civil construction in Italy is increasingly more widespread, especially after recent seismic events. In the last years, huge progress has been made in understanding the structural behaviour of concrete and masonry structures strengthened by means of innovative materials and techniques. In particular, ever-increasing resources have been used for both the retrofit and the strengthening of existing concrete and masonry structures with externally bonded composite materials, i.e. Fiber Reinforced Plastic (FRP) materials. Such a strengthening technique has been emerging for just over two decades becoming a system widely adopted by professionals and construction companies. Consequently, the Italian Ministry of Infrastructure and Transportation published Guidelines on the qualification of such products in 2015 [3], which were enforced by the end of 2016. These Guidelines add up to previous guidelines specific for the design of structural reinforcement through FRP materials (CNR DT 200/R1, 2013, [2]), with reference to both pre-formed and cured-in-situ (or wet-lay-up) systems.

Currently, any FRP manufacturer interested in the Italian market had to apply to the Ministry for the corresponding qualification, demonstrating the outcomes of the needed testing activity. According to the recent Italian Guidelines [3], the results of the qualification tests in terms of mean value of the Young's modulus E and of characteristic value (5th percentile) of the tensile strength f_{tk} place a given product in a certain class. The nominal classes provided in [3] are listed in *Table 1*.

Class	**Type of fibres**	**E** [GPa]	**f_{tk}** [MPa]
E17	Glass/Basalt	17	170
E23	Glass/Basalt	23	240
G38/600	Glass/Basalt	38	600
G38/800	Glass/Basalt	38	800
G45	Glass/Basalt	45	1000
C120	Carbon	120	1800
C150/1800	Carbon	150	1800
C150/2300	Carbon	150	2300
C190/1800	Carbon	190	1800
C200/1800	Carbon	200	1800
A55	Aramid	55	1200

Table 1: *Classes for pre-formed FRP systems given by Italian Guidelines [3].*

Moreover, the FRP systems' environmental durability should also be checked. In particular, strength to freeze/thaw cycles, humidity, salt water and alkaline environment needs to be investigated with further tensile tests.

In this paper, the results of tensile tests on several pre-formed FRP materials are analysed according to a statistical approach. The main aims of the analysis are: a) check the reliability of the classes suggested by the Italian Guidelines [3], b) assess the best fitting probabilistic model

able to describe the experimental distributions, c) estimate the average and characteristic values, and d) evaluate the safety factors according to Eurocode 0 [9].

The experimental data come from several laboratories, many of which are located in Italian universities, and were collected by the Construction Technologies Institute (ITC) of the Italian National Research Council (CNR).

2 TESTING ACTIVITY

Pre-formed FRP materials are made of fibres pre-impregnated with resins in the form of a sheet, characterized by initial axial rigidity and a mono-directional behaviour. They can be produced by pultrusion or lamination processes according to different shapes and thicknesses and are generally glued to the structural elements through an epoxy adhesive.

The number of pre-formed FRP products collected are listed in *Table* 2. They are all made of carbon fibres. According to the Italian Guidelines [3], the number of single tensile tests required for the qualification of each product is 15, thus obtaining the total number of individual tests shown in *Table* 2. The specimens have width variable in the range 25-70 mm and length from 250 to 350 mm. The recommended range of speed for tensile tests is 0.5-2.0 mm/min. Since the classes C150/1800, C190/1800, and C200/1800 are little populated (1, 2 or 3 products, respectively), the only experimental data belonging to the more populated class, i.e. the class C150/2300 having 5 pre-formed products, have been analysed in detail in this paper.

FRP Mechanical characterization		
Class	N° products	N° of single tests
C150/1800	1	15
C150/2300	5	75
C190/1800	2	30
C200/1800	3	45
Total	11	165

Table 2: *Pre-formed FRP products and number of single tests.*

2.1 Analysis of experimental data of class C150/2300

According to [3], the qualification tests have to be carried out on 15 specimens in order to evaluate the mean value of the Young's modulus, E, and the characteristic value of the tensile strength, f_{tk}. Thus, there are a total of 75 experimental pairs of values of E and f_t for the 5 types of products belonging to class C150/2300.

The experimental data were used to construct normalized recurrence histograms, in which the bins have width of 5 GPa for E and 100 MPa for f_t (see Figures 1a and 2a, respectively). Therefore, the Empirical Cumulative Density Function (ECDF) was calculated and plotted for both E and f_t in Figures 1b and 2b, respectively.

The empirical histograms show that the experimental data are more concentrated around values greater than the threshold values provided by [3] for the reference class, i.e. 150 GPa for E and 2300 MPa for f_t, and certainly produce some non-symmetric distributions of experimental data. This would mean that the definition of the threshold values of the classes for FRP pre-formed systems should be reviewed, since all the products exceed them, especially in terms of tensile strength.

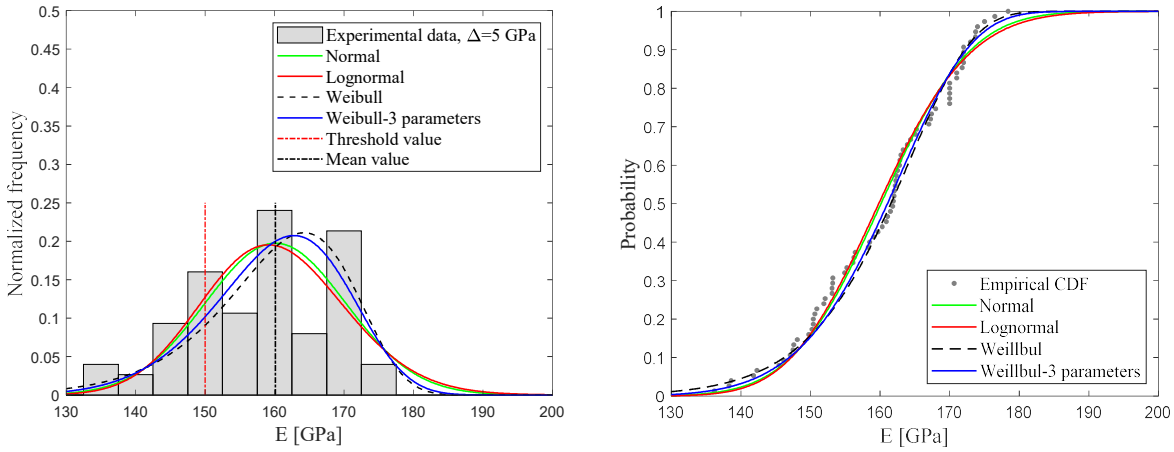

(a) (b)

Figure 1 – *Distribution of E for pre-formed FRP systems (class C150/2300) - Comparison between: a) empirical histograms and theoretical PDF; b) empirical and theoretical CDF.*

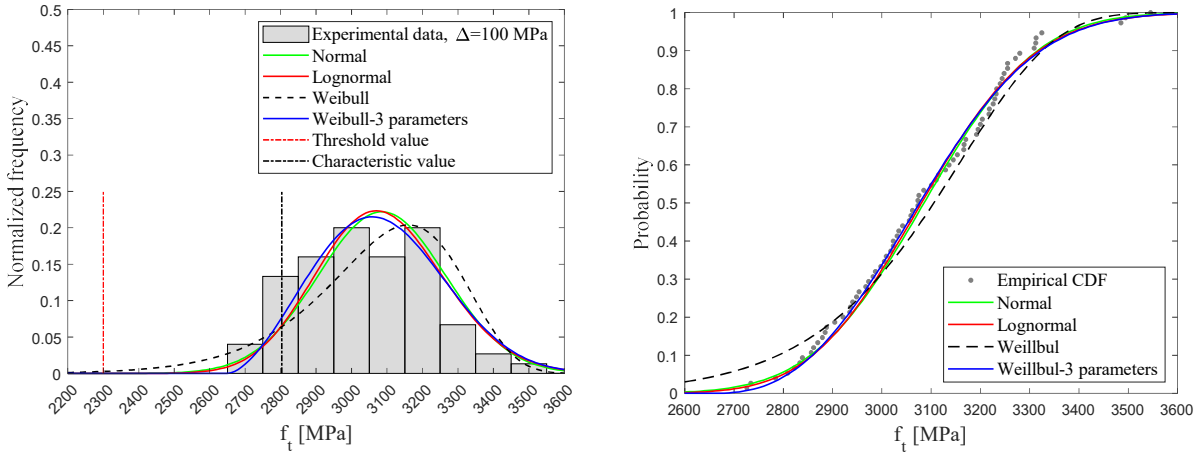

(a) (b)

Figure 2 – *Distribution of f_t for pre-formed FRP systems (class C150/2300) - Comparison between: a) empirical histograms and theoretical PDF; b) empirical and theoretical CDF.*

Therefore, the experimental data were compared with four theoretical probabilistic distributions: normal, lognormal, 2-parameters Weibull [4, 5] and 3-parameters Weibull [4, 5]. In Table 3, the Probability Density Functions (PDF) and the identifying parameters associated to these distributions are listed. In particular, the normal and lognormal distribution require the calculation of the parameters μ (average value) and σ (standard deviation). Whereas, the Weibull distribution is described by the shape (κ) and scale (λ) parameters, with the addition of a third parameter 'ϑ' for the 3-p Weibull distribution.

The software "SPC for Excel" [6] was used to calculate the parameters associated with the probability law from the experimental data. This software estimates the optimal parameters using the Maximum Likelyhood Estimate (MLE) method. In *Table* 4, the final values of the parameters adopted for data adaptation are listed.

Probability distributions	PDF	Parameters
Normal	$y = f(x \mid \mu, \sigma) = \frac{1}{x \cdot \sigma\sqrt{2\pi}} e^{-\frac{(x-\mu)^2}{2\cdot\sigma^2}}$	μ, σ
Lognormal	$y = f(x \mid \mu, \sigma) = \frac{1}{x \cdot \sigma\sqrt{2\pi}} e^{-\frac{(\ln x-\mu)^2}{2\cdot\sigma^2}}$	μ, σ
Weibull	$y = f(x \mid \lambda, \kappa) = \begin{cases} \frac{\kappa}{\lambda}\left(\frac{x}{\lambda}\right)^{\kappa-1} e^{-\left(\frac{x}{\lambda}\right)^{\kappa}} & x \geq 0 \\ 0 & x < 0 \end{cases}$	k, λ
3-p Weibull	$y = f(x \mid \lambda, \kappa, \vartheta) = \begin{cases} \frac{\kappa}{\lambda}\left(\frac{x-\vartheta}{\lambda}\right)^{\kappa-1} e^{-\left(\frac{x-\vartheta}{\lambda}\right)^{\kappa}} & x \geq 0 \\ 0 & x < 0 \end{cases}$	k, λ, ϑ

Table 3: *Probability models - systems falling in class C150/2300.*

Probability distributions	Variable	Values of fitting parameters		
Normal	*E*	μ = 160.1	σ = 10.1	
	ft	μ = 3085.5	σ = 179.7	
Lognormal	*E*	μ = 5.07	σ = 0.06	
	f_t	μ = 8.03	σ = 0.06	
Weibull	*E*	λ = 164.7	*k* = 18.9	
	f_t	λ = 3171.0	*k* = 17.6	
3-p Weibull	*E*	λ = 60.1	*k* = 6.7	ϑ = 104.2
	f_t	λ = 488.9	*k* = 2.6	ϑ = 2651.2

Table 4: *Parameters of probability models – pre-formed FRP systems (class C150/2300)*

The PDFs and the associated CDFs are plotted in Figure 1a-2a and 1b-2b, respectively, for comparison with experimental data. In order to have a quantitative estimate of the fitting goodness, the Kolmogorov-Smirnov (KS) test was used for comparing the different distributions and choose the most suitable model fitting the experimental data. The test is based on the comparison between the maximum absolute difference between the experimental CDF and the CDF associated with each theoretical probability distribution. Such a difference is calculated as follows:

$$D_{MAX} = \max\{|F(x) - \varphi(x)|\} \quad (1)$$

where F(x) is the ECDF and φ(x) is the CDF of each theoretical probability distribution.

The hypothesis regarding the distributional form is rejected if D_{MAX} is greater than a certain critical value, which depends on the specimen size, N, and the level of significance, α, of the test. There are several values available in the literature for the level of significance; some of them (Massey, 1951; Lilliefors, 1967) [7, 8] are reported in *Table* 5. Typically, the Kolmogorov-Smirnov test has a level of significance of 0.05, which means that in 5% of cases the null hypothesis (the estimation of the difference between the empirical and the theoretical CDF is based solely on chance) is rejected.

The Kolmogorov-Smirnov test was, thus, conducted for both the distribution of tensile strength (see *Table* 6) and Young's modulus (see *Table* 7) by comparing the maximum differences with the critical values suggested by (Massey, 1951; Lilliefors, 1967) [7, 8]. The results reported in *Table* 6 and *Table* 7 show that for both E and f_t the values of D_{MAX} allow do not reject the null hypothesis for the four selected probability distributions and for all significant levels and critical values provided by (Massey, 1951, [7]) and (Lilliefors, 1967, [8]). Note that in (Lilliefors, 1967, [8]) lower critical values are provided. The Normal distribution appears to be the best fitting distribution of the experimental data, since it has the lowest value of D_{MAX} in all cases. However, any of the considered distributions appears to be fairly adequate to describe the experimental data.

Sample size (N)		**Level of significance (α)**				
Massey, 1951 [7]	Over 35	0.20	0.15	0.10	0.05	0.01
		$\frac{1.07}{\sqrt{N}}$	$\frac{1.14}{\sqrt{N}}$	$\frac{1.22}{\sqrt{N}}$	$\frac{1.36}{\sqrt{N}}$	$\frac{1.63}{\sqrt{N}}$
Lilliefors, 1967 [8]	Over 30	0.20	0.15	0.10	0.05	0.01
		$\frac{0.736}{\sqrt{N}}$	$\frac{0.768}{\sqrt{N}}$	$\frac{0.805}{\sqrt{N}}$	$\frac{0.886}{\sqrt{N}}$	$\frac{1.031}{\sqrt{N}}$

Table 5: *Critical values for K-S test.*

Distribution	D_{MAX}	Critical values Massey, 1951			Critical values Lilliefors, 1967		
		α = 0.10	α=0.05	α=0.01	α = 0.10	α=0.05	α=0.01
Normal	0.076	**0.141**	**0.157**	**0.188**	**0.093**	**0.102**	**0.119**
Lognormal	0.088	**0.141**	**0.157**	**0.188**	**0.093**	**0.102**	**0.119**
Weibull	0.082	**0.141**	**0.157**	**0.188**	**0.093**	**0.102**	**0.119**
3-p Weibull	0.08	**0.141**	**0.157**	**0.188**	**0.093**	**0.102**	**0.119**

Table 6: *K-S test for elastic modulus E of pre-formed FRP product (class C150/2300).*

Distribution	D_{MAX}	Critical values Massey, 1951			Critical values Lilliefors, 1967		
		α = 0.10	α=0.05	α=0.01	α = 0.10	α=0.05	α=0.01
Normal	0.043	**0.141**	**0.157**	**0.188**	**0.093**	**0.102**	**0.119**
Lognormal	0.050	**0.141**	**0.157**	**0.188**	**0.093**	**0.102**	**0.119**
Weibull	0.078	**0.141**	**0.157**	**0.188**	**0.093**	**0.102**	**0.119**
3-p Weibull	0.049	**0.141**	**0.157**	**0.188**	**0.093**	**0.102**	**0.119**

Table 7: *K-S test for tensile strength f_t of pre-formed FRP product (class C150/2300).*

3 EFFECT OF ARTIFICIAL AGEING

According to Italian Guidelines [3], the FRP systems' environmental durability should also be checked. In particular, strength to freeze/thaw cycles, humidity, saltwater and alkaline

environment needs to be investigated with further tensile tests.

In order to verify the strength to freeze/thaw cycles, the conditioning procedure requires specimens to be placed in environments characterized by Relative Humidity (RH) ≥ 90% and Temperature T = 38 ± 2°C for 7 days, then 20 freeze/thaw cycles are performed. Each cycle consists of 4 hours at a -18 ± 1°C, followed by 12 hours at RH ≥ 90% and T = 38 ± 2°C.

For the other artificial ageing, the conditioning procedures are the following ones:

a) Strength to wet environment: curing at RH ≥ 90% and T = 38 ± 2°C for 1000 or 3000 hours (ASTM D 2247-11 [10] and ASTM E 104-02 [11]);
b) Strength to saltwater environment: immersion in saltwater at 23 ± 2 °C for 1000 or 3000 hours (ASTM D 1141-98 [12] and ASTM C 581-03 [13]);
c) Strength to alkaline environment: immersion in aqueous solution with pH = 12 and T= 23 ± 2 °C for 1000 or 3000 hours (ASTM D7705/D7705M [14]).

After each conditioning process, samples are visually examined in order to describe eventual surface changes and, then, the tensile tests are carried out. If the average values of E and f_t obtained by the tensile tests on the conditioned samples are not lower than 85% of the average values of the not conditioned samples in case of 1000 hours of exposure (80% in case of 3000 hours), the check is considered positive.

Table 8 reports a summary of the results of the unconditioned and conditioned specimens and shows that all the examined products passed the check on the environmental durability. It is worth to note that for each conditioning procedure, 4 conditioned and 4 unconditioned specimens are involved; the unconditioned specimens are extracted from the same batch, but do not correspond to the ones used for the mechanical characterization previously carried out under standard environmental conditions. However, it was verified that the results of such a second series of unconditioned specimens do not significantly differ from the ones of the first series used for the mechanical characterization (see Fig. 1a and 2a).

Artificial ageing effects are summarized in the following sections. In all cases, bins with width of 5 GPa E and 100 MPa for f_t have been adopted. The only Normal, Lognormal and Weibull probabilistic laws were considered, since the 3-p Weibull distribution was not always applicable.

Conditioning	***Elastic Modulus E[GPa]***			***Tensile Strength f_t [MPa]***		
Type	*Mean value unconditioned*	*85% mean value unconditioned*	*Mean value conditioned*	*Mean value unconditioned*	*85% mean value Unconditioned*	*Mean value conditioned*
Freeze/Thaw	160.0	136.0	**161.0**	3120	2652	**3087**
Humidity	160.4	136.3	**161.5**	3098	2634	**3099**
Saltwater	157.7	134.0	**162.0**	3121	2652	**3084**
Alkaline	162.4	138.0	**162.4**	3106	2640	**3115**

Table 8: *Parameters of probability models – C150/2300 class - exposure to freeze/thaw cycles.*

3.1 Exposure to freeze/thaw

Figure 3 and Figure 4 show the experimental data and the analytical interpretation for the specimens exposed to freeze/thaw cycles. *Table* 9 shows the parameters adopted for the data fitting of the conditioned sets of specimens, while *Table 10* shows the results of the corresponding K-S tests.

Probability distributions	Variable	Values of fitting parameters	
Experimental/ Normal	E	$\mu = 161.0$	$\sigma = 7.1$
	f_t	$\mu = 3087.3$	$\sigma = 207.9$
Lognormal	E	$\mu = 5.1$	$\sigma = 0.04$
	f_t	$\mu = 8.0$	$\sigma = 0.07$
Weibull	E	$\lambda = 164.2$	$k = 25.2$
	f_t	$\lambda = 3172.7$	$k = 22.6$

Table 9: *Parameters of probability models – C150/2300 class - exposure to freeze/thaw cycles.*

Variable	Distribution	D_{MAX}	Critical values Massey, 1951			Critical values Lilliefors, 1967		
			$\alpha = 0.10$	$\alpha=0.05$	$\alpha=0.01$	$\alpha = 0.10$	$\alpha=0.05$	$\alpha=0.01$
Elastic modulus E	**Normal**	0.088	**0.273**	**0.304**	**0.364**	**0.180**	**0.198**	**0.231**
	Lognormal	0.086	**0.273**	**0.304**	**0.364**	**0.180**	**0.198**	**0.231**
	Weibull	0.119	**0.273**	**0.304**	**0.364**	**0.180**	**0.198**	**0.231**
Tensile strength f_t	**Normal**	0.208	**0.273**	**0.304**	**0.364**	0.180	0.198	**0.231**
	Lognormal	0.213	**0.273**	**0.304**	**0.364**	0.180	0.198	**0.231**
	Weibull	0.180	**0.273**	**0.304**	**0.364**	**0.180**	**0.198**	**0.231**

Table 10: *K-S test for elastic modulus E and tensile strength f_t - exposure to freeze/thaw cycles*

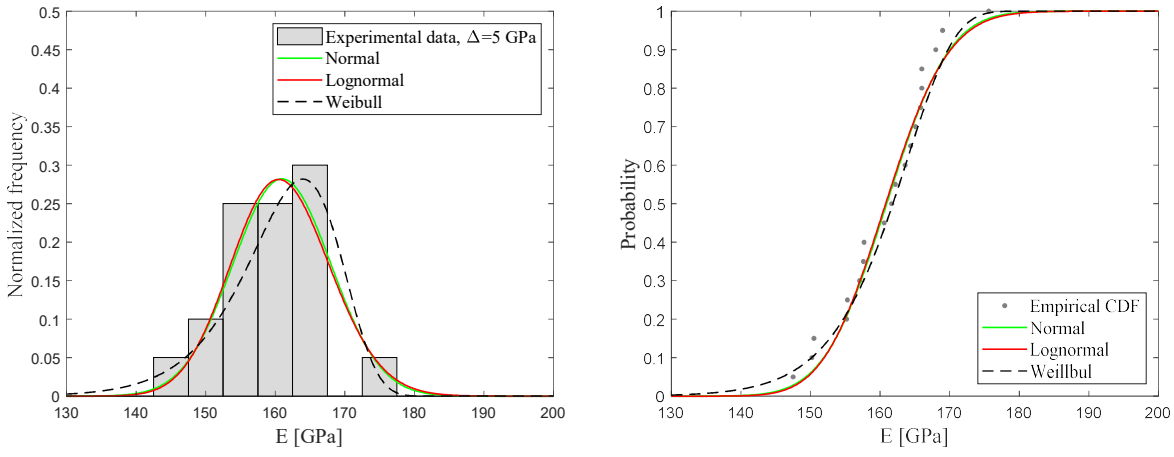

(a) (b)

Figure 3 – *Distribution fitting for E in pre-formed FRP systems (class C150/2300) exposed to freeze/thaw cycles: comparison between: a) empirical histograms and PDF, and b) empirical and theoretical CDF.*

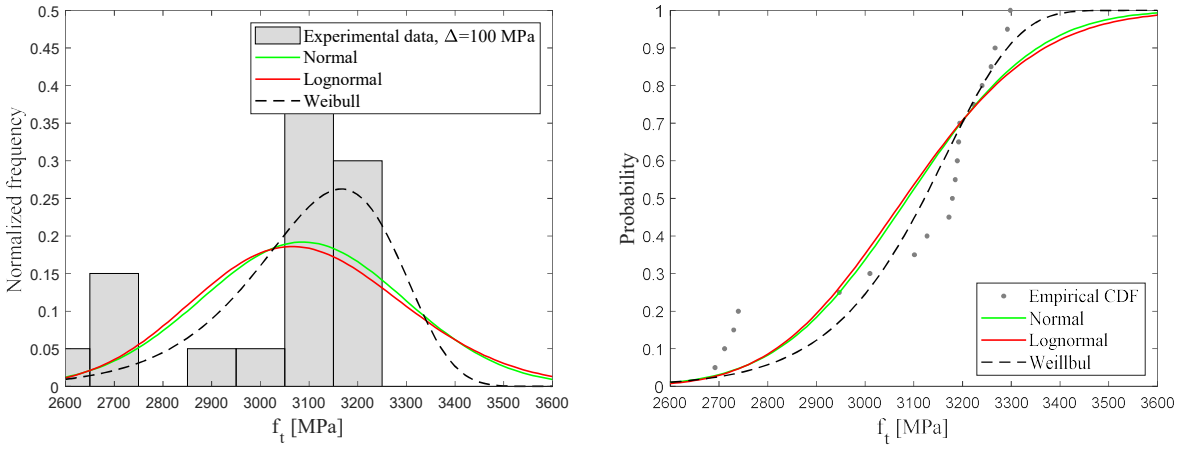

(a) (b)

Figure 4 – *Distribution fitting for f_t in pre-formed FRP systems (class C150/2300) exposed to freeze/thaw cycles: comparison between: a) empirical histograms and PDF, and b) empirical and theoretical CDF.*

3.2 Exposure to humidity

Figure 5 and Figure 6 show the experimental data and the analytical interpretation for the 20 specimens exposed to humidity for 1000 hours. *Table* 11 shows the parameters adopted for the data fitting of the conditioned sets of specimens, while *Table* 12 shows the corresponding K-S tests.

Probability distributions	**Variable**	**Values of fitting parameters**	
Experimental/ Normal	E	$\mu = 161.5$	$\sigma = 7.2$
	f_t	$\mu = 3098.6$	$\sigma = 233.9$
Lognormal	E	$\mu = 5.1$	$\sigma = 0.04$
	f_t	$\mu = 8.0$	$\sigma = 0.08$
Weibull	E	$\lambda = 164.9$	$k = 26.1$
	f_t	$\lambda = 3205.7$	$k = 14.5$

Table 11: *Parameters of probability models – C150/2300 class – exposure to humidity.*

Variable	**Distribution**	D_{MAX}	Critical values Massey, 1951			Critical values Lilliefors, 1967		
			$\alpha = 0.10$	α=0.05	α=0.01	$\alpha = 0.10$	α=0.05	α=0.01
Elastic modulus E	**Normal**	0.088	**0.273**	**0.304**	**0.364**	**0.180**	**0.198**	**0.231**
	Lognormal	0.086	**0.273**	**0.304**	**0.364**	**0.180**	**0.198**	**0.231**
	Weibull	0.142	**0.273**	**0.304**	**0.364**	**0.180**	**0.198**	**0.231**
Tensile strength f_t	**Normal**	0.090	**0.273**	**0.304**	**0.364**	**0.180**	**0.198**	**0.231**
	Lognormal	0.090	**0.273**	**0.304**	**0.364**	**0.180**	**0.198**	**0.231**
	Weibull	0.097	**0.273**	**0.304**	**0.364**	**0.180**	**0.198**	**0.231**

Table 12: *K-S test for elastic modulus E and tensile strength f_t - exposure to humidity.*

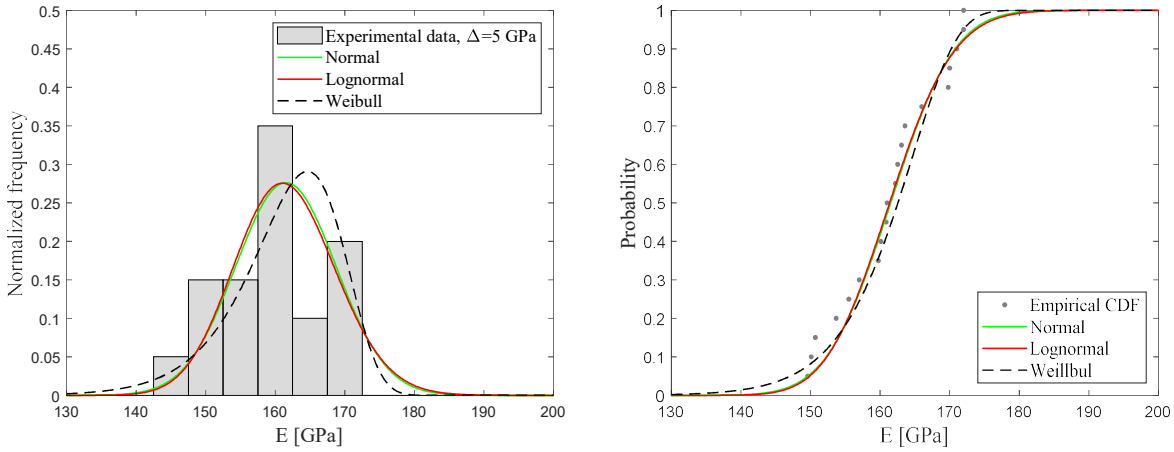

(a) (b)

Figure 5 – *Distribution fitting for E in pre-formed FRP systems (class C150/2300) exposed to humidity: comparison between: a) empirical histograms and PDF, and b) empirical and theoretical CDF.*

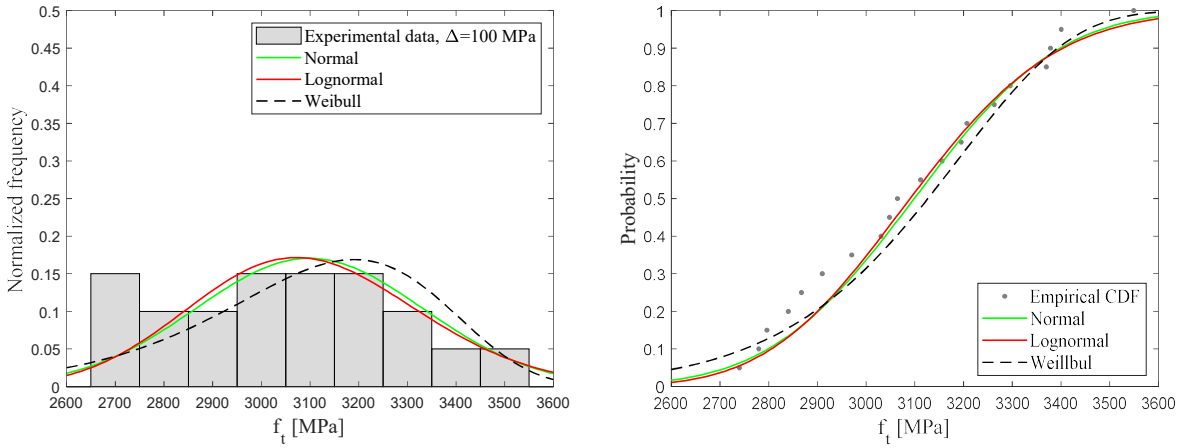

(a) (b)

Figure 6 – *Distribution fitting for f_t in pre-formed FRP systems (class C150/2300) exposed to humidity: comparison between: a) empirical histograms and PDF, and b) empirical and theoretical CDF.*

3.3 Exposure to saltwater

Figure 7 and Figure 8 show the experimental data and the analytical interpretation of the specimens exposed to saltwater for 1000 hours. *Table* 13 shows parameters adopted for the data fitting of the conditioned sets of specimens and *Table* 14 shows the corresponding K-S tests.

Probability distributions	Variable	Values of fitting parameters	
Experimental/ Normal	E	$\mu = 162.0$	$\sigma = 8.4$
	f_t	$\mu = 3083.7$	$\sigma = 191.8$
Lognormal	E	$\mu = 5.1$	$\sigma = 0.05$
	f_t	$\mu = 8.0$	$\sigma = 0.06$
Weibull	E	$\lambda = 165.8$	$k = 23.5$
	f_t	$\lambda = 3176.6$	$k = 14.7$

Table 13: *Parameters of probability models – C150/2300 class – exposure to saltwater.*

Variable	Distribution	D_{MAX}	Critical values Massey, 1951			Critical values Lilliefors, 1967		
			α = 0.10	α=0.05	α=0.01	α = 0.10	α=0.05	α=0.01
Elastic modulus E	**Normal**	0.155	**0.273**	**0.304**	**0.364**	**0.180**	**0.198**	**0.231**
	Lognormal	0.145	**0.273**	**0.304**	**0.364**	**0.180**	**0.198**	**0.231**
	Weibull	0.207	**0.273**	**0.304**	**0.364**	0.180	0.198	**0.231**
Tensile strength f_t	**Normal**	0.167	**0.273**	**0.304**	**0.364**	**0.180**	**0.198**	**0.231**
	Lognormal	0.156	**0.273**	**0.304**	**0.364**	**0.180**	**0.198**	**0.231**
	Weibull	0.221	**0.273**	**0.304**	**0.364**	0.180	0.198	**0.231**

Table 14: *K-S test for elastic modulus E and tensile strength f_t - exposure to humidity.*

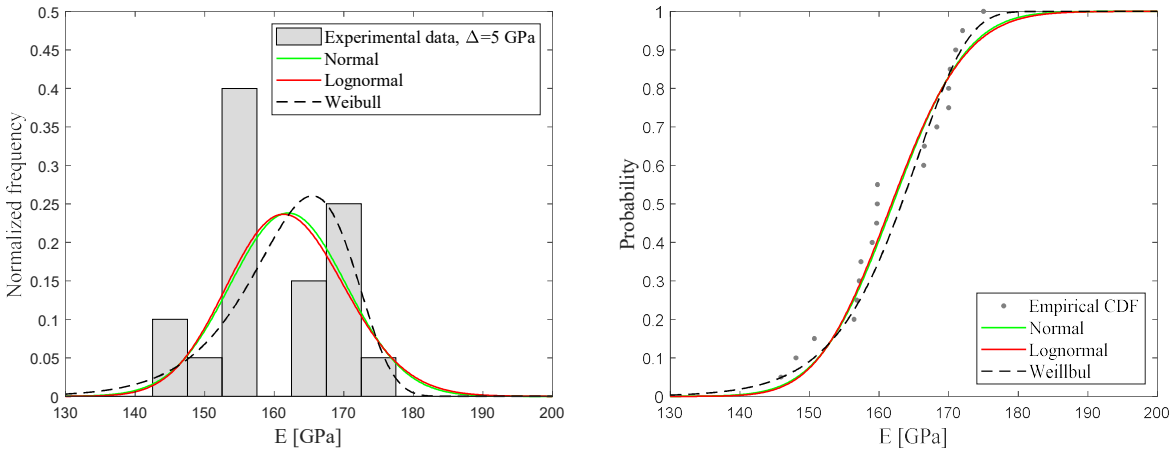

(a) (b)

Figure 7 – *Distribution fitting for E in pre-formed FRP systems (class C150/2300) exposed to saltwater: comparison between: a) empirical histograms and PDF, and b) empirical and theoretical CDF.*

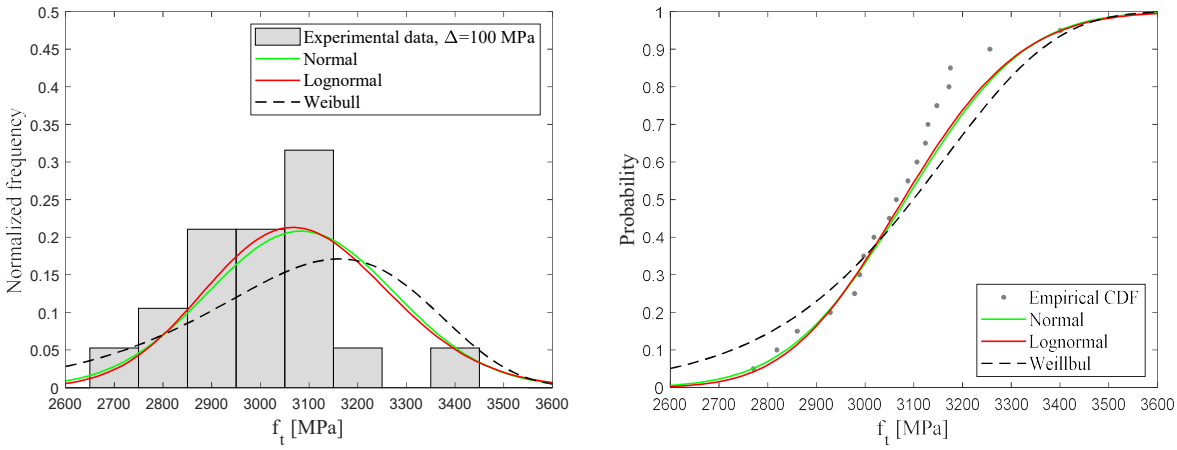

(a) (b)

Figure 8 – *Distribution fitting for f_t in pre-formed FRP systems (class C150/2300) exposed to saltwater: comparison between: a) empirical histograms and PDF, and b) empirical and theoretical CDF.*

3.4 Exposure to alkaline environment

Figure 9 and Figure 10 show the experimental data and the analytical interpretation of the specimens exposed to alkaline environment for 1000 hours. *Table* 15 shows the parameters adopted

for the data fitting of the conditioned sets of specimens, while *Table* 16 shows the corresponding K-S tests.

Probability distributions	Variable	Values of fitting parameters	
Experimental/ Normal	E	$\mu = 162.4$	$\sigma = 8.1$
	f_t	$\mu = 3115.2$	$\sigma = 170.3$
Lognormal	E	$\mu = 5.1$	$\sigma = 0.05$
	f_t	$\mu = 8.0$	$\sigma = 0.06$
Weibull	E	$\lambda = 166.3$	$k = 19.2$
	f_t	$\lambda = 3191.0$	$k = 23.3$

Table 15: *Parameters of probability models – C150/2300 class – exposure to alkaline environment.*

Variable	Distribution	D_{MAX}	Critical values Massey, 1951			Critical values Lilliefors, 1967		
			$\alpha = 0.10$	α=0.05	α=0.01	$\alpha = 0.10$	α=0.05	α=0.01
Elastic modulus E	**Normal**	0.128	**0.273**	**0.304**	**0.364**	**0.18**	**0.198**	**0.231**
	Lognormal	0.122	**0.273**	**0.304**	**0.364**	**0.18**	**0.198**	**0.231**
	Weibull	0.156	**0.273**	**0.304**	**0.364**	**0.18**	**0.198**	**0.231**
Tensile strength f_t	**Normal**	0.121	**0.273**	**0.304**	**0.364**	**0.18**	**0.198**	**0.231**
	Lognormal	0.127	**0.273**	**0.304**	**0.364**	**0.18**	**0.198**	**0.231**
	Weibull	0.155	**0.273**	**0.304**	**0.364**	**0.18**	**0.198**	**0.231**

Table 16: *K-S test for elastic modulus E and tensile strength ft - exposure to alkaline environment.*

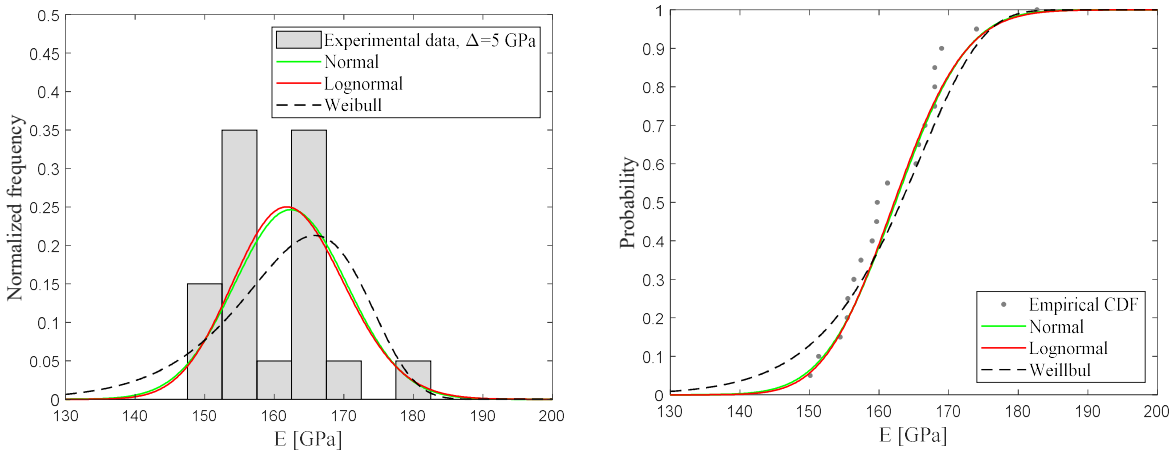

(a) (b)

Figure 9 – *Distribution fitting for E in pre-formed FRP systems (class C150/2300) exposed to alkaline environment: comparison between: a) empirical histograms and PDF, and b) empirical and theoretical CDF.*

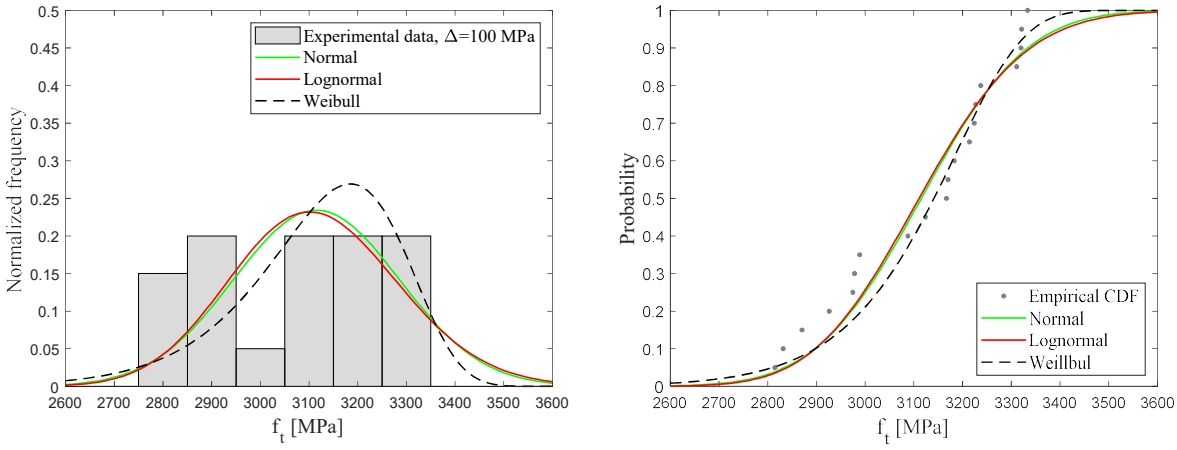

(a) (b)

Figure 10 – *Distribution fitting for f_t in pre-formed FRP systems (class C150/2300) exposed to alkaline environment: comparison between: a) empirical histograms and PDF, and b) empirical and theoretical CDF.*

3.5 Discussion on artificial ageing effects

Table 17 and *Table 18* summarize the values of D_{MAX} for the theoretical distributions related to the different effects of artificial aging. It is worth to note that for the Young's modulus, E, the minimum values of D_{MAX} occurs for the lognormal distribution for whatever aging procedure. Conversely, for the tensile strength f_t, the minimum values of D_{MAX} occurs again for the lognormal distribution for exposure to humidity and saltwater, while for exposure to freeze/thaw cycles and to alkaline environment the best fitting distributions are the Weibull and the Normal ones, respectively.

Distribution	*Freeze/thaw*	*Humidity*	*Saltwater*	*Alkaline enviroment*
Normal	0.088	0.088	0.155	0.128
Lognormal	**0.086**	**0.086**	**0.145**	**0.122**
Weibull	0.119	0.142	0.207	0.156

Table 17: *Minimum values of D_{MAX} for the best fitting distributions of E.*

Distribution	*Freeze/thaw*	*Humidity*	*Saltwater*	*Alkaline enviroment*
Normal	0.208	0.090	0.167	**0.121**
Lognormal	0.213	**0.090**	**0.156**	0.127
Weibull	**0.180**	0.097	0.221	0.155

Table 18: *Minimum values of D_{MAX} for the best fitting distributions of f_t.*

Consequently, the 5th percentile, f_{t5}, of the tensile strength was calculated with reference to the best distribution for each condition of artificial aging, in particular by adopting the Weibull probability model for *Freeze/Thaw* effect, the Lognormal probability model for *Humidity* and *Saltwater* effects, the Normal probability model for *Alkaline environment* effect. In *Table 19*

the experimental and theoretical mean value of the Young's modulus E and the 5th percentile, f_{t5}, and the mean value, $f_{tm,}$ of the tensile strength are listed for the reference unconditioned samples and the variously conditioned ones. The experimental and analytical percentual differences between unconditioned and conditioned samples are listed in brackets too.

		Unconditioned	*Freeze/Thaw*	*Humidity*	*Saltwater*	*Alkaline*
E [GPa]	empirical	160	161 (+0.5%)	162 (+0.9%)	162 (+1.2%)	162 (+1.4%)
	analytical	160 *Normal*	161 (+0.4%) *Lognormal*	162 (+0.9%) *Lognormal*	162 (+1.2%) *Lognormal*	162 (+1.4%) *Lognormal*
f_{tm} [MPa]	empirical	3086	3087 (+0.1%)	3099 (+0.4%)	3084 (-0.1%)	3115 (+1.0%)
	analytical	3086 *Normal*	3098 (+0.4%) *Weibull*	3099 (+0.4%) *Lognormal*	3084 (-0.1%) *Lognormal*	3115 (+1.0%) *Normal*
f_{t5} [MPa]	empirical	2803	2692 (-4.0%)	2740 (-2.3%)	2771 (-1.2%)	2815 (+0.4%)
	analytical	2790 *Normal*	2782 (-0.3%) *Weibull*	2730 (-2.2%) *Lognormal*	2785 (-0.2%) *Lognormal*	2835 (+1.6%) *Normal*

Table 19: *Mechanical parameters of C150/2300 products – unconditioned and variously conditioned.*

Table 19 shows no substantial variation of the mean value of Young's modulus after all the considered artificial ageing procedures. For both empirical and analytical data, the values vary, indeed, from 0.4% (*Freeze/Thaw*) to 1.4% (*Alkaline environment*).

Analogously, no variations were observed for the mean tensile strength (0.1-1%), while a light reduction of the 5th percentile of the tensile strength, i.e. ranging from -4.0% to -1.2%, was attained for all aging procedures, with exception of exposure to alkaline environment which induced a negligible increase (+0.4%).

In conclusion, ageing effects on the mean value of the Young's modulus and tensile strength of the tested products are negligible, whereas a slight reduction (maximum 4%) of the 5th percentile of the tensile strength is attained, especially in case of freeze/thaw cycles and exposure to humidity.

The Italian Guidelines [1] prescribes environmental conversion factors equal to 0.95, 0.85 and 0.85 for, respectively, indoor, outdoor and aggressive environments in the case of carbon fibres. The obtained experimental results show that for the most aggressive ageing effect (freeze/thaw cycles), the 5th percentile values of tensile strength reduces of only 4%. Such a reduction is slightly lower than the one induced when the highest value of the conversion factor (0.95) is assumed, confirming, thus, that the conversional factors suggested by [1] are safe for preformed carbon FRP products.

4 ASSESSEMENT OF DESIGN VALUE

According to the Eurocode 0 [9], the design value of a product property can be expressed as:

$$X_d = \eta \frac{X_k}{\gamma_m} \tag{2}$$

where X_d is the design value, X_k is the characteristic value (herein the 5th percentile of the probability distribution), η is a conversion factor associated to environmental conditions, and γ_m is the material partial factor. By neglecting in a first stage the conversion factor (i.e., assuming η=1), the material partial factor can be calculated as:

$$\gamma_m = X_k / X_d \tag{3}$$

For the Normal probability law, the characteristic value of the tensile strength of the tested products is f_{t5}=2790 MPa and the mean value is f_{tm}=3086 MPa (see *Table 19*). Since the Normal law is the best fitting distribution for the experimental results, the theoretical 5^{th} percentile value is calculated as follows:

$$f_{t5} = f_{tm} - 1.647 \cdot \sigma = 3086 - 1.647 \cdot 180 = 2790 \text{ MPa} \quad (4)$$

being f_{tm} and σ the mean value and the standard deviation of the distribution of the tensile strength. The experimental value of the 5th percentile of the tensile strength is 2803 MPa, which is practically equal to the theoretical value. The acceptance criteria described in the Italian Guidelines [3] assume the characteristic tensile strength equal to the mean value minus 2 times the standard deviation, as suggested by Eurocode 0 [9]. This procedure leads to f_{t5}=2726 MPa, which, thus, lightly underestimates (-3%) the real 5th percentile of the tensile strength.

Since under ordinary environmental conditions, the Normal probability model resulted the most suitable distribution law for the tensile strength, the corresponding design value, f_{td}, can be expressed as follows:

$$f_{td} = f_{tm} - \alpha_R \cdot \beta \cdot \sigma \quad (5)$$

being α_R the FORM (First Order Reliability Method) sensitivity factor and β the target reliability index. By assuming α_R = 0.8 and β = 3.8 (Consequences Class CC2, Reliability Class RC2, 50 years return period according to EN 1990 [9]), the design value results f_{td}=2450 MPa and, thus, the material partial factor of the tested population can be calculated as:

$$\gamma_m = f_{t5} / f_{td} = 2790/2450 = 1.10 \quad (6)$$

The partial factor suggested by the Italian Guidelines [1] for the strength of reinforcing material is 1.10 for composite kits fully certified, as the preformed ones are, whereas 1.25 is suggested for composites where only materials, not the installation, is certified. The lowest value, 1.10, exactly coincides with the strength partial factor related to the experimental data presented before, while the highest one, 1.25, leads to a more conservative design in order to take into account uncertainties related to operations on the construction site.

5 CONCLUSIONS

The analysis of experimental data related to the qualification of several preformed FRP products allowed to define a global perspective of the main mechanical parameters, i.e. tensile strength and Young's modulus.

Qualification procedures, as well as the values of design parameters, are prescribed in recent Italian guidelines [3]. The analysis of a discrete database, which could certainly be further expanded, allowed to carry out several statistical inquires. The analyses proved that the Normal probabilistic law is able to adequately describe the distribution of tensile strength and Young's modulus, mainly under standard environmental conditions.

Under the artificial ageing procedures prescribed by the Italian Guidelines [3] (exposure to freeze/thaw cycles, humidity, salt water, and alkali environment), the study fails to determine a single distribution law able to interpolate to the best the analysed specimens. This is mainly due to the low number of samples tested and to the higher scattering that affects the conditioned specimens in comparison with the unconditioned ones.

However, the experimental results showed that the ageing procedures did not affect sensibly

both the average and the 5th percentile values of the mechanical properties of the examined FRP products, confirming the reliability of the environmental factors suggested in the Italian guidelines for the design of strengthening interventions with FRP materials [1, 2].

Finally, it was also verified that the safety factors suggested by the Italian Guidelines [1, 2] in case of tensile failure of the FRP materials are safe.

The reliability of the results presented in this paper can be further checked, if more numerous experimental data will be available.

6 REFERENCES

[1] Linee guida per la Progettazione, l'Esecuzione ed il Collaudo di Interventi di Rinforzo di strutture di c.a., c.a.p. e murarie mediante FRP, in Italian, Ministry of Infrastructure and Transportation, 2009 (*in Italian*).

[2] CNR DT 200/R1 (2013). Guide for the Design and Construction of Externally Bonded FRP Systems for Strengthening Existing Structures, Advisory Committee on Technical Recommendation for Construction of National Research council, Rome, Italy.

[3] Linee Guida per la identificazione, la qualificazione ed il controllo di accettazione di compositi fibrorinforzati a matrice polimerica (FRP) da utilizzarsi per il consolidamento strutturale di costruzioni esistenti, in Italian, Ministry of Infrastructure and Transportation, 2015 (*in Italian*).

[4] Weibull W. (1951) A statistical distribution function of wide applicability, J. Appl. Mech., 13: 293–297.

[5] Alqam M., Bennett R.M., ZureickA.-H. (2002). Three-parameter vs. Two-parameter Weibull distribution for pultruded composite material properties, Compos. Struct., 58: 497–503.

[6] https://www.spcforexcel.com/.

[7] Massey F. J. (1951). The Kolmogorov-Smirnov test for goodness of fit. Journal of the American Statistical Association, 46 (2539): 68-78.

[8] Lilliefors H.W. (1967). On the Kolmogorov-Smirnov Test for Normality with Mean and Variance Unknown, Journ. of the American Statistical Association, 62 (318): 399-402.

[9] EN 1990:2002, Eurocode – Basis of structural design, CEN, 2002.

[10] ASTM D2247-11 (2011), Standard Practice for Testing Water Resistance of Coatings in 100% Relative Humidity, ASTM International, West Conshohocken, PA.

[11] ASTM E104-02 (2012), Standard Practice for Maintaining Constant Relative Humidity by Means of Aqueous Solutions, ASTM International, West Conshohocken, PA.

[12] ASTM D1141-98 (2013), Standard Practice for the Preparation of Substitute Ocean Water, ASTM International, West Conshohocken, PA.

[13] ASTM D7705 / D7705M-12 (2019), Standard Test Method for Alkali Resistance of Fiber Reinforced Polymer (FRP) Matrix Composite Bars used in Concrete Construction, ASTM International, West Conshohocken, PA.

[14] ASTM C581-03 (2008), Standard Practice for Determining Chemical Resistance of Thermosetting Resins Used in Glass-Fiber-Reinforced Structures Intended for Liquid Service, ASTM International, West Conshohocken, PA.

COMPDYN 2019
7th ECCOMAS Thematic Conference on
Computational Methods in Structural Dynamics and Earthquake Engineering
M. Papadrakakis, M. Fragiadakis (eds.)
Crete, Greece, 24–26 June 2019

DESIGN PROVISIONS FOR END-ANCHORING DEVICES IN CONCRETE AND MASONRY ELEMENTS EXTERNALLY BONDED WITH FRP MATERIALS

F. Ceroni

Associate professor, Engineering Department, University of Naples 'Parthenope', Centro Direzionale is. C4, 80143, Napoli,
e-mail: francesca.ceroni@uniparthenope.it

Abstract

Anchoring devices for external strengthening systems made of Fiber Reinforced Plastic (FRP) materials represent a solution to avoid or delay debonding phenomena in concrete and masonry strengthened elements. Several types of anchoring devices were tested by researchers and used in real applications in the last years, but clear design indication for estimating the effectiveness of each anchoring type are still not available.
Basing on the examination of the available experimental results of bond tests in concrete and masonry specimens externally bonded with FRP materials, this paper is aimed to furnish design indications for calculating the effectiveness of two types of common end anchoring systems in term of theoretical debonding load increase: 1) transversal FRP strips and 2) FRP spike anchors.

Keywords: FRP materials, externally bonded reinforcement, concrete, masonry, debonding load, anchoring devices.

1 INTRODUCTION

Anchoring devices for external strengthening systems made of Fiber Reinforced Plastic (FRP) materials represent a solution to avoid or delay debonding phenomena in concrete and masonry strengthened elements. The increase of failure loads may be, thus, attained by placing anchoring devices at the end of flexural or shear externally bonded FRP reinforcements. Moreover, anchoring devices may be useful also for increasing the ductility of the strengthened elements, since debonding is usually a very brittle failure mode, which often does not allow exploiting the full tensile strength of fibres (CNR DT 200/R1, 2013, [12]; *fib* bulletin 90, 2019, [15]).

Several types of anchoring devices were tested by researchers and used in real applications, but clear design indication for estimating the effectiveness of each anchoring type are still not available. Effectiveness of anchoring into increase strength and ductility of the strengthened elements depends on strengthening configuration (flexural, shear, confinement), type and geometry of the anchoring devices, mechanical properties of the substrate.

Design indications for predicting end debonding load in concrete and masonry elements externally bonded with FRP materials are now well consolidated, since the amount of available experimental tests are very relevant and allowed reliable statistical analysis and 'design by testing' calibrations used in code indications (CNR DT200/R1, 2013, [12]; fib bulletin 90, 2019, [15]).

Basing on the examination of the available experimental results of bond tests in concrete and masonry specimens externally bonded with FRP materials, this paper is aimed to furnish design indications for calculating the effectiveness of two types of common end anchoring systems in term of theoretical debonding load increase: transversal FRP strips and FRP spike anchors. Predictions are separately furnished for concrete and masonry elements.

2 LITERATURE REVIEW ON EFFICIENCY OF ANCHORING SYSTEMS

For flexural and shear strengthening configurations the most common anchorage system is given by a FRP sheet or a FRP or steel laminate glued transversally to the strengthening direction (Fig.1). This may be a reliable solution when the FRP-to-concrete width ratio, b_f/b, is lower than 1, because the transversal strip allows extending the width of concrete covered by the FRP strengthening (Ceroni and Pecce, 2010, [9], Ceroni et al., 2008, [10]; Al-Mahaidi and Kalfat, 2011, [2]). Conversely, when the ratio b_f/b increases, the effectiveness of the transversal strip reduces and becomes unhelpful when it approaches to 1. In these cases, U-shaped fiber sheets might be successfully used (Ceroni 2010, [6]; Khan and Fareed, 2014, [18]; Al-Amery and Al-Mahaidi, 2006, [1]; Buyle-Bodin and David, 2004, [4]; Orton et al., 2008, [25]; Spadea et al., 1998, [30]). For such an application, sharp edges of the section are recommended to be mechanically rounded with a minimum radius of 30 mm.

An alternative solution is represented by fiber spike systems, which are becoming a very diffuse anchoring system for wet-lay-up FRP reinforcements bonded to concrete and masonry elements (Ceroni and Pecce, 2010, [9]; Niemitz et al., 2010, [24]; Eshwar et al., 2008, [13]; Zhang and Smith, 2012, [31]; Zhang et al., 2012, [32]; Caggegi et al., 2014, [5]; Fagone et al., 2014, [14]; Ceroni, 2017, [7]) for several strengthening configurations, i.e. flexural reinforcement (Orton et al., 2008, [25]; Smith et al., 2011, [28]; Smith et al., 2013, [29]), confinement (Karantzikis et al., 2005, [17]), and shear reinforcement (Kim et al., 2011, [19]; Koutas and Triantafillou, 2013, [22]; Jinno et al. 2001, [16]; Kobayshi et al., 2001, [21]).

Fiber spike systems are usually made of a dry fiber cord or by a rolled dry fiber sheet (Fig.2a); carbon or glass fibers are usually adopted, even if some applications with steel cords

are also available (Prota et al., 2005, [27]). One end of the spike is impregnated by epoxy resin in order to form a dowel. A hole is drilled in the substrate on the same plane of the strengthening and the dowel is forced through the FRP reinforcement into the predrilled hole (Fig.2b). The fibers of the not impregnated end are splayed outwards over the reinforcement in order to form a fan with variable angle of splaying (α in Fig. 2b) and, then, fixed with epoxy resin. Fibers of the fan may be splayed parallel to the loading direction, in the opposite direction or along both of them (bow-tie configurations, Zhang and Smith, 2012, [31]). Other geometrical parameters of the spike anchor influencing its effectiveness are: the diameter, ϕ, of the cord, the embedded length of the dowel, l_{emb}, and the splaying radius, r, of the fibers.

The great advantage of such a system is the possibility to be applied also when b_f/b=1 or tends to 1, since it is a punctual anchoring system applied orthogonally to the reinforced surface. The effectiveness of the spike anchors may be influenced by details and accuracy of application procedures too.

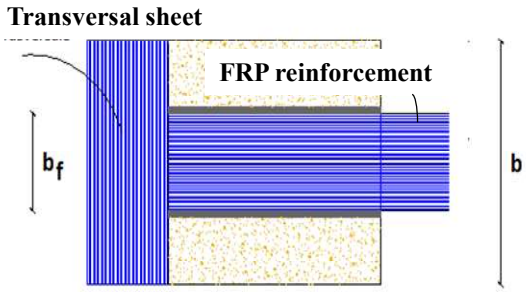

Figure 1: Transversal strip as anchoring device.

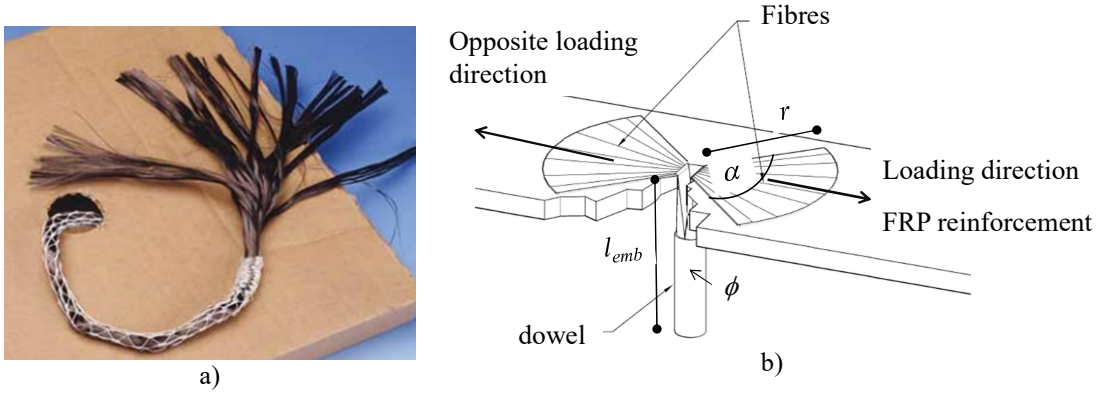

Figure 2: a) example of carbon fibers cord for spike anchors; b) geometry of spike anchor.

2.1 Effectiveness of end anchoring in concrete elements

2.1.1. Transversal and U-shape strips

The good performance of transversal strips as end anchoring system was proved by bond tests on concrete elements externally bonded with CFRP sheets (Ceroni and Pecce, 2010, [9], Ceroni et al., 2008, [10]; Al-Mahaidi and Kalfat, 2011, [2]). In all these tests, the bonded length was comparable with the effective one as defined in (Chen and Teng, [11]; CNR DT 200/R1, 2013, [12]) or higher.

In particular, in the bond tests carried out by (Ceroni and Pecce, 2010, [9]) for specimens with b_f/b = 0.67, the increase of maximum load of the anchored specimens ranged in 10-20%, while for b_f/b = 0.33, the strength increase was even higher (+52-57%). Analogously, in (Ce-

roni et al., 2008) for specimens with b_f/b = 0.33, a load increase of 55% was observed for the anchored specimens in comparison with the not anchored ones.

Also in the bond tests of (Al-Mahaidi and Kalfat, 2011, [2]), for specimens with b_f/b=0.4, a relevant load increase was attained in presence of transversal strips (+39-43%).

As the experimental results evidenced, when the FRP-to-concrete width ratio increases, the effectiveness of the transversal strip reduced and becomes unhelpful when it approaches to 1; in these cases U-shaped fiber sheets might be used. In (Ceroni, 2010, [6]) the use of U-shaped strip at the end of RC beams strengthened in bending with carbon FRP sheets led to an increase of the ultimate load of 5-10% depending on the steel reinforcement percentage (1% or 1.5%). In case of U-shaped strips distributed along the beam, a higher increase of ultimate load was attained, i.e. 10-20% for the same values of steel percentage. Nevertheless such a limited load increase, the use of end and especially of distributed U-shaped strips allowed increase ductility even greater than 50% at failure compared with the not anchored strengthened beam.

Also, in (Khan and Fareed, 2014, [18]) the effect of U-shaped fiber sheets to strengthen RC beams in bending was studied. The beams were characterized by different value of the span-to-depth ratio (a/d) and the end anchorages was wrapped all along the cross-section of the beam. It was observed a load increase of 6% and 15% for the anchored beams compared with the reference ones for the ratio a/d=3.4 and 2.5, respectively.

Further research conducted by (Al-Amery and Al-Mahaidi, 2006, [1]) evidenced that the use of the CFRP U-jackets, 200 mm spaced along the length of the beam, reduced the interfacial slip between the CFRP reinforcement and the concrete by up to only 1/10 of the values attained without anchoring devices. Moreover, the U-jackets allowed the full utilization of the CFRP flexural tensile capacity with an increase of the flexural strength up to 95% compared with the unstrengthened beam and up to 15% compared with the strengthened beam without the U-jackets.

In (Spadea et al., 1998, [30]), flexural tests on CFRP-strengthened RC beams with U-shaped steel anchors were carried out. The anchoring devices were installed both at the plate ends and distributed throughout the span, aimed to improve especially the ductility. In presence of anchoring devices, the experimental strains in the fibers at failure reached the 80% of their maximum strain with an enhancement of 67% compared with the not-anchored beam. Moreover, in the strengthened beams without anchorage the ductility reduced by 70–80% in comparison with the unstrengthened beams, whereas, in presence of anchoring devices, the loss of ductility ranged in 45–70%.

In (Mofidi et al., 2012, [23]), externally bonded CFRP strip and mechanically fixed double-aluminum-plates were used as end anchoring systems for concrete beams strengthened in shear by means of externally bonded CFRP sheets. The load increase attained in the anchored beams respect to the not anchored strengthened beam was 18% and 14%, respectively, for the two systems.

2.1.2. Spike anchors

Several pull-out tests aimed to check the effectiveness of spike anchors in concrete elements were carried out by (Özdemir, 2005, [26]). Basing on the experimental results, the following suggestions were provided: 1) anchors have to be inserted at least 50 mm into the core of the concrete (depth of 130–150 mm); 2) the cross-sectional area of anchor has to be at least two times greater than the cross-sectional area of the longitudinal sheet; 3) splitting the anchor into as many smaller anchors at about a 40 mm spacing as possible.

In (Ceroni and Pecce, 2010, [9]), bond tests on concrete specimens bonded with CFRP sheets with b_f = 100 mm (b_f/b = 0.67), provided that 1 spike anchor made of carbon fibesr

(ϕ=10mm, r=50 mm, α=90°, l_{emb}=50 mm) allowed a debonding load increase of 28% in comparison with equal not anchored specimens.

The bond tests of (Eshwar et al., 2008, [13]) evidenced similar bond strength increase; in particular, the increase was 25% in case of 1 spike anchor made of glass fibers (ϕ=10 mm, r=50 mm, α=360°) with l_{emb}=50 mm or 75 mm. A more significant load improvement (+230%) was attained in case of two adjacent glass anchors with the same geometry and l_{emb}=75 mm.

In the bond tests of (Niemitz et al., 2010, [24]), several configurations for two spike anchors made of carbon fibers were tested. When the two anchors (ϕ=13 mm, r=25mm, α=360°, l_{emb}=150 mm) were positioned side by side along the reinforcement width (Fig. 3a), the load increase was about +70%, while, when they were placed along a row (Fig. 3b), the efficiency was lower (+47%). The efficiency of the row configuration resulted improved (load increase +61%), if the diameter of the cord and the splaying radius were both increased (i.e., ϕ=19 mm, r=30mm).

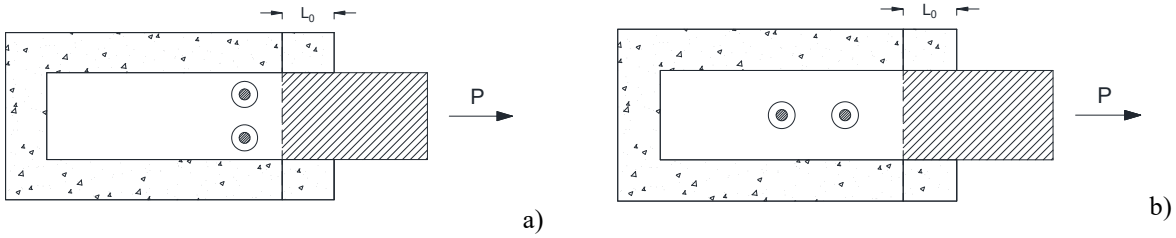

Figure 3: Spike anchor configurations in the test of (Niemitz et al., 2010 [24]): a) side by side configurations; b) row configuration (L_o is an unbonded length).

In the bond tests of (Zhang and Smith, 2012, [31]; Zhang et al., 2012, [32]) on concrete specimens bonded with CFRP sheets with b_f = 50 mm, a load increase ranging in 73-100% was attained when a single spike anchor made of carbon fibers (ϕ=12 mm, r=50 mm, α=60°, l_{emb}=40 mm), with the fibers splayed in the direction of load, was applied. Conversely, for the same anchor geometry, when the fibers were splayed in the reverse direction of the load, the increase was only 60%. Moreover, when a bow-tie configuration for the same anchor geometry was used, the load increase was again 100%, but, clearly, the fiber content was twice in this case. In case of single spike anchor made of glass fibers (ϕ=12 mm, r= 50 mm, a=60°, l_{emb}=40 mm) splayed in the direction of load, the load increase was 53%.

In the tests carried out by (Zhang and Smith, 2012 [31]), the influence of the dowel angle respect to the load direction was also investigated by ranging it in 45° - 157°. As the angle of the anchor dowel was increased, the failure load increased more relevantly. In particular, the highest effectiveness (+160% of load increase in comparison with the not anchored specimen) was attained for an angle of 157° (Figure 4a) and the lowest (+24%) for an angle of 45° (Figure 4b). However, it was observed that the ductility of the joint decreased when the dowel angle increased, as observed from the brittle anchor failure and the lack of a post-peak behavior. When the anchor dowel angle exceeded 90°, indeed, the anchor tended to rupture simultaneously with complete debonding of the reinforcement, the strength of the joint was increased, but at the expense of ductility loss. Conversely, for dowel angles less than 90°, the anchor remained intact and was able to accommodate large slippage with a lower strength increase.

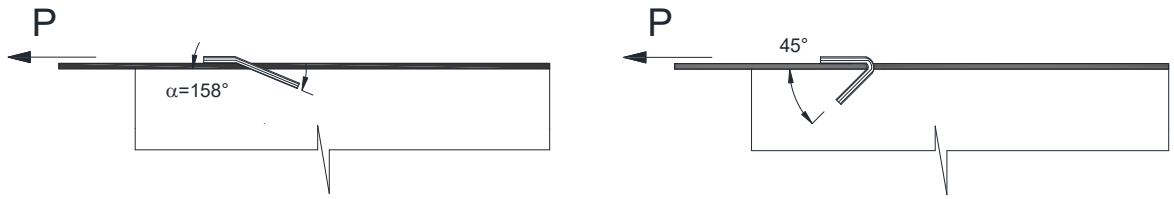

a) b)

Figure 4: Inclination of spike dowel in the tests of (Zhang and Smith, 2012, [31]): a) α=157°; b) α =45°.

In (Orton et al., 2008, [25]), attention was focused on the constructive detailing for warrant the best efficiency of spike anchor systems. In particular, bending tests on concrete beams strengthened with CFRP were conducted to evaluate the size, number, and spacing of spike anchors and to compare the performance of not anchored beams with beams provided of spike anchors or U-wraps. The experimental results showed that, without additional anchorage, the CFRP sheets debonded at about 37% of the tensile strength of fibers. Two single layer U-wraps placed at both ends of the strengthened beam allowed to increase the tension in the CFRP sheet up to 70% of its capacity, induced debonding of the flexural reinforcement and shear failure of the U-wraps, and led to a load increase of 75% in comparison with the not anchored beam. Two double layer U-wraps allowed a load increase of 150%, while two rows of three spike anchors (10 mm diameter) allowed developing the CFRP sheet's full tensile capacity with a final load increase of 170%. In addition, it was found that a greater number of smaller anchors and reduced spacing were more effective than larger spacing, which did not anchor the entire width of the FRPs and did not allow avoiding a partial debonding.

The bending tests conducted by (Smith et al., 2011, [28]) investigated the strategic use of different types and positions of spike anchors made of carbon fibers with bow-tie configuration to increase both strength and deflection capacity of strengthened slabs. A load increase variable between 24-30% in comparison with the reference not-anchored strengthened specimen was attained by using several spike anchors (r= 50 or 100 mm, α=60°, l_{emb}=50 mm) distributed along the span length with different spacing. The anchors allowed a relevant increase of ductility, which increased until 110 % in comparison with that of the unanchored strengthened slab.

Smith et al., 2013, [29] carried out further bending tests on concrete slabs in order to check the efficiency of single and bow-tie spike anchors located at the end or distributed along the reinforcement into increase strength and ductility. As in (Smith et al., 2011, [28]), the spike were made of carbon fibers with r = 50 mm, α= 60°, l_{emb}=50 mm and a suitable configuration of the anchors allowed to attained a load increase of 44%.

Spike anchors were used also in shear strengthening according to several configurations by (Jinno et al., 2001, [16]; Kobayshi et al., 2001, [21]) to solve the problem of passing fibers of reinforcement through the web of a 'T-section' and anchor the fibers of the shear reinforcement in the compressive zone of the section.

Analogously, in (Kim et al., 2011, [20]) 'T-section' beams were reinforced in shear by applying 'U-shaped' CFRP strips anchored using spike anchors made of carbon fibers just below the flange. A 40-45% increase in shear strength was observed.

In (Koutas and Triantafillou, 2013, [22]), a wide experimental investigation was carried out in order to check the effectiveness of various types of spike anchors into increase the capacity of concrete beams strengthened in shear by 'U-shaped' FRP sheets. Orientation of the cord, number and spacing of anchors, type of fibers constituent the anchors (carbon or glass) were the investigated parameters. With refer to the beam strengthened in shear without any anchors, the use of different lay-out of spike anchors led to the following load increase: +8%

for three horizontal anchors, +46% and +53% for three or five inclined anchors (angle of inclination approximately 25° with respect to the vertical). In case of five anchors, the increase in effectiveness of the jacket was only 53% because the anchors placed not above the shear cracks were not activated.

For confinement of columns where walls physically obstacle the complete wrapping of the elements, application of spike anchors (Jinno et al.2001, [16]; Kobayshi et al. 2001, [21]) can be used for giving continuity to the reinforcement.

Spike anchors provide a low cost solution also to anchor the confinement jacket to the existing structure, especially for the attachment of FRP jackets at the reentrant corners of L-shaped cross section columns, as tested in (Karantzikis et al., 2005, [17]). Experimental tests evidenced, indeed, that in FRP jacked specimens without anchors the strength increase respect to the reference specimen ranged in 32%-48% when the jacket was made of lightweight or heavyweight FRP sheets. In case of partial depth spike anchors, the strength increase respect to the not-anchored specimens ranged in 59-72%, and, in case of full depth anchors, the strength increased by 97% in both case of lightweight or heavyweight jacketing sheets.

2.2 Effectiveness of end anchoring in masonry elements

For masonry elements externally bonded with FRP materials, the efficiency of end-anchoring systems into improving the failure load may depend on the substrate typology.

Several bond tests were carried out by (Caggegi et al., 2014, [5]) and (Fagone et al., 2014, [14]) in order to analyze the performance of spike anchors applied to a brick substrate reinforced with CFRP sheets, as well as the influence of different test apparatus implementing the same test set-up. Different configuration for the spike anchors, made of carbon fibers, were considered varying the splaying angle of the fan (α=75° or 360°), the number of fan (1, 2 or 3), the diameter of fan radius splayed over the reinforcement (r = 25 or 40 mm). In all cases, the embedded length was l_{emb}=50 mm.

In the tests of (Caggegi et al. 2014, [5]), the load increase ranged between 26-87% respect to the not anchored specimen, with the higher increase (+87%) attained for the specimens with three anchors with r=25 mm and α=75°; such a configuration allows covering the whole width of the FRP reinforcement. A lower efficiency (+66%) was attained when two anchors with r=40 mm and α=75° were applied, even if also this configuration allowed entirely covering the FRP reinforcement. Conversely, similar load increases (26-31%) were attained when a single anchor was applied either with r=25 mm or 40 mm and α=75° and with r=40 mm and α=360°. In case of r=40 mm and α=75°, the use of two anchors allowed doubling the efficiency compared to the case of only one (+66% vs. +31%).

In (Fagone et al., 2014, [14]) the same specimens and testing configuration used by (Caggegi et al., 2014, [5]) were adopted. The same operators prepared the specimens. Nevertheless, the maximum loads attained in the tests of (Fagone et al., 2014, [14]) resulted higher than those obtained in the tests of (Caggegi et al., 2014, [5]) with differences ranging from 10% to 30%. Such differences were due the different deformability of the test set-up used by (Caggegi et al., 2014, [5]). In particular, for the same anchor configurations previously described, the load increases ranged in 34-116% instead of 26-87%, in the case of three anchors, while were variable in 34-48% instead of 26-31% in case of single spike anchor.

In (Ceroni, 2017, [7]), the effectiveness of spike anchors made of carbon fibers (ϕ=10 mm) was tested by means of bond tests on both single tuff stones and clay brick prisms. Tuff is a volcanic stone very used for buildings in the Southern Italy. For specimens made of single tuff stone, a similar effectiveness in terms of failure load increase (about +18%) was registered when a single anchor with α=360° and r=50 mm or two anchors with α=75° and r=40

mm, both having an embedded length of l_{emb}=80 mm, were applied. Conversely, in case of longer embedded length of the cord (i.e., 180 mm), the effectiveness of two anchors with α=75° was higher compared with a single fan with α=180° (i.e., +25% vs. 17%). It is worth to note that the effectiveness of the spike anchors in tuff stones was, however, limited by the very low tensile strength of the tuff, which make it sensible to shear/tensile failures in the blocks (Figure 5).

Figure 5: Failure surface at the end of anchored specimens made of tuff stone (Ceroni, 2017, [7]).

In (Ceroni, 2017, [7]), the efficiency of spike anchors was tested also on prisms made by clay bricks externally strengthened with carbon fibers. For these specimens, a similar effectiveness was experimentally observed when two spike anchors made of carbon fibers with ϕ=10 mm, α=75° and r=40 mm or when a single anchor with ϕ=10 mm, α= 360° and r=50 mm, both with l_{emb}=80 mm, were used (the load increase ranged, indeed, in 37-40%).

The experimental load increase observed for such specimens (+40%) was higher than the one observed in the specimens made of tuff stones (+25%) for similar anchoring configurations, showing again the sensibility of the failure load to the mechanical properties of the masonry support also when the anchoring devices are present. For both types of specimens, a squared quadriaxial sheet made of carbon fibers (side 100 mm) was applied over the anchors in order to improve their correct placement during the curing of the epoxy adhesive.

3 DESIGN INDICATIONS

Basing on the literature review previously discussed, some proposals of design indications are furnished for two types of anchoring systems for wet-lay-up FRP externally reinforcements, i.e. transversal strips and spike anchors, which are two of the most common used in practical applications.

For strengthening of concrete elements, both use of transversal strips and spike anchors are suggested, while for masonry elements, only design indications for spike anchors are proposed due the higher experimental data available for such an anchoring system. Since the effectiveness of spikes in terms of failure load increase depends strongly both on the anchor geometry and on the mechanical properties of the substrate, different strengthening configurations and design indications are suggested for concrete and masonry substrates.

For each selected anchoring configuration, with refer to common existing bond strength models (i.e., CNR DT200/R1, 2013, [12] or fib bulletin 90, 2019, [15]), an increasing of the theoretical debonding load is suggested basing on the experimental outcomes previously discussed.

A typical strength model for calculating the maximum stress in the FRP reinforcement in case of end debonding is the well-know one adopted by several authors and codes (Chen and Teng, 2001, [11]; CNR DT200/R1, 2013, [12]; fib bulletin 90, 2019, [15]):

$$f_{fb} = \beta_l \sqrt{\frac{2E_f \cdot G_f}{t_f}} \tag{1}$$

where β_l is a factor that depends on the bond length l_b, (i.e., it is lower than 1, if l_b is lower than the effective length), E_f and t_f are Young's modulus and thickness of the external reinforcement, G_f is the fracture energy associated to the reinforcement/substrate interface failure.

Starting from the general approach given by Eq. (1), most design formulations provide numerical coefficients derived from statistical regression analysis of experimental results of bond tests. In the new version of *fib* bulletin for external strengthening of concrete elements with FRP materials (*fib* bulletin 90, 2019, [15]), the following expression is suggested for calculating the mean debonding strength, $f_{deb,m}$, in the FRP reinforcement in case of debonding at the end anchorage zone:

$$f_{deb,m} = k_m \cdot k_b \cdot \beta_l \sqrt{\frac{2E_f}{t_f} \cdot f_{cm}^{2/3}} \qquad \text{[N, mm]} \qquad k_b = \sqrt{\frac{2 - b_f / b}{1 + b_f / b}} \tag{2}$$

where f_{cm} is mean compressive strength of concrete. The coefficient k_m= 0.25 was calibrated by (Bilotta et al., 2011, [3]) according to a statistical procedure as the least-square coefficient minimizing the difference between theoretical values and experimental results.

A similar approach is adopted also by (CNR DT200/R1, 2013) for predicting the end-debonding stress for strengthening of both concrete and masonry elements according to the following expression:

$$f_{deb,m} = \sqrt{\frac{2 \cdot E_f}{t_f} \cdot t_f \cdot k_b \cdot k_{G,m} \cdot \sqrt{f_{cm} \cdot f_{tm}}} \qquad k_b = \sqrt{\frac{3 - b_f / b}{1 + b_f / b}} \tag{3}$$

where the coefficient $k_{G,m}$ was differently calibrated according to the substrate (concrete or different types of masonry, i.e. tuff stones, limestone, calcarenite, clay bricks). An upgraded calibration of such a coefficient is provided in (Ceroni et al., 2017 [33]) for different masonry substrates, taking into account also the effects of the mortar joints on the bond strength.

The increased bond strength provided by each anchoring system can be used for calculating the global capacity of concrete or masonry strengthened elements in case of reinforcement configurations based on bond behavior and, thus, affected by end-debonding failure (i.e., mainly flexural and shear reinforcement). For both shear and flexural strengthening, the load increase provided by the anchoring system depends, indeed, not only on its type and geometry, but also on the original capacity of the not-strengthened element and the amount of external reinforcement. Thus, it is not simple to generalize the efficiency of an anchoring system, since it depends on the strengthening configuration. Conversely, with refer to the only bond behavior and, thus, to the end-debonding load, it is simpler to provide a generalized methodology for calculating the efficiency of the anchoring system into increase the bond strength for end debonding.

3.1 Design indications for concrete elements

3.1.1 Transversal strips

For transversal strips having the same width of the element, b, or U-shaped strips, the following increase of the theoretical end debonding load can be considered:
- +40% for strengthening configuration with $b_f/b = 0.33$;
- +20% for strengthening configuration with $b_f/b = 0.67$;
- linearly interpolated values between 20% and 40% for $0.33 < b_f/b < 0.67$.

For strengthening configurations with $b_f/b > 0.67$, the use of a transversal strip is not suggested as end anchoring system, but other configurations should be used.

3.1.2 Spike anchors

Basing on the experimental outcomes previously described, the following anchoring configurations can be considered:

1) for strengthening made of FRP sheets with b_f=100mm:

1a) single spike anchor made of carbon fibers with ϕ=10mm, r=50mm, α=360° and l_{emb}=100mm (Fig. 3a). For this configuration, an increase of the theoretical failure load of 25% can be assumed, safely based on the results of (Ceroni and Pecce, 2010, [9]; Eshwar et al., 2008, [13]);

1b) two adjacent spike anchors made of carbon fibers with ϕ=12mm, r=25mm, α=360° and l_{emb}=100mm (Fig. 3b). The two anchors have to be spaced of 50 mm in order to cover all the reinforcement width, b_f. For such a configuration, an increase of the theoretical failure load of 50% can be assumed, safely based on the results of (Niemitz et al., 2010, [24]);

2) for strengthening made of FRP sheets with b_f=50mm:

- 1 spike anchor made of carbon fibers with ϕ=12mm, r=50mm, α=60° and l_{emb}=100mm (Fig. 3c). For such a configuration, an increase of the theoretical failure load of 50% can be assumed, safely based on the results of (Zhang et al., 2012, [32]; Zhang and Smith, 2012, [31]).

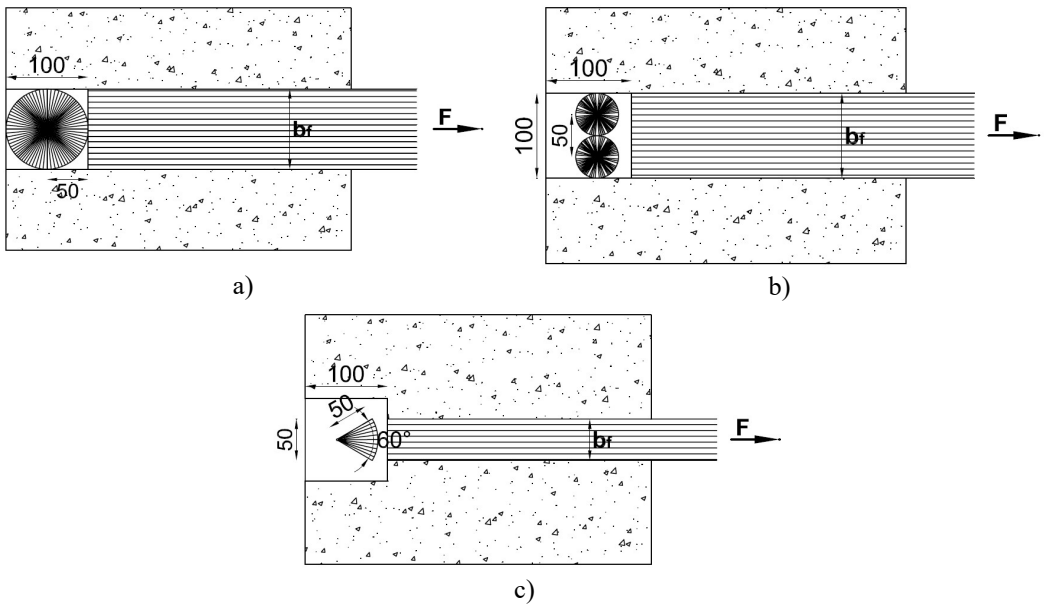

Figure 6: Recommended geometrical configurations for spike anchors in concrete elements: for b_f=100 mm a) 1 spike anchor with l_{emb} =100 mm, α = 360°, r = 50mm, and b) 2 spike anchors with l_{emb} =100 mm, α = 360°, r = 25 mm; for b_f=50mm c) 1 spike anchor with l_{emb} =100 mm, α = 60° e r =50 mm (dimensions in mm).

As further detail, for whatever spike anchor configuration, it is suggested to:

- apply a square quadriaxial FRP sheet (side 100 mm) over the splayed fibers in order to improve their correct placement during the curing of the epoxy adhesive;
- smooth the hole contour in order to avoid local failure of the splayed fibers.

3.2 Design indications for masonry elements

Bond behaviour of FRP strengthening systems applied on masonry substrates depends on masonry typology (Ceroni et al., 2014, [8]) with refer to both their mechanical and physical properties. Due to the variability of these properties, univocal design indications for whatever masonry substrate cannot be provided. Moreover, due to the wide variability of masonry substrates, especially in case of natural stones, which can be very variable depending on the geographical area, a consistent number of experimental results is not always available for each masonry substrate. Thus, basing on the most numerous experimental results now available, attention will be focussed on only two masonry substrates: clay bricks and tuff stone.

Clay bricks represent a very common building material all over the world, while tuff is a volcanic stone typical of the Southern Italy and very used in that area for realizing buildings, mainly because of its lightness and workability. These two materials are rather different both for the physical (unit weight, porosity) and mechanical properties (Young's modulus, compressive and tensile strength). Different indications will be provided for these two types of substrates basing on the outcomes of the experimental results described in section 2.2.

For masonry elements made of tuff stones and strengthened with FRP sheet having width b_f=100 mm, the following anchor configuration is suggested (see Figure 7a):

- 2 spike anchors made of carbon fibers with diameter of cord ϕ= 10 mm, embedded length l_{emb} = 150 mm, angle of splaying α=75°, and radius r = 40 mm.

The two spikes have to be applied at a distance of 50 mm in order to do not overlay each other and cover the reinforcement width as larger as possible. For such configuration, an increase of the theoretical debonding load of 25% can be considered, basing on the results of (Ceroni, 2017).

For masonry elements made of clay bricks and strengthened with FRP sheet having width b_f=100 mm, the following anchor configurations are suggested:

- 1 spike anchor made of carbon fibers with diameter of cord ϕ= 10 mm, embedded length l_{emb} = 80 mm, angle of splaying α=75°, and radius r = 40 mm (Figure 7b);
- 2 spike anchors made of carbon fibers with diameter of cord ϕ= 10 mm, embedded length l_{emb} = 80 mm, angle of splaying α=75°, and radius r = 40 mm. The two anchors have to be applied with a spacing of 50 mm in order to not overlap each other and to cover most part of the reinforcement width (Figure 7c).

For these two configurations, the increase of the theoretical failure load may be safely estimated in 30% and 50%, respectively, basing on the results of (Ceroni, 2017, [7]; Fagone et al., 2014, [14]; Caggegi et al., 2104, [5]).

As previously indicated for concrete elements, for both types of masonry substrates and for whatever spike anchor configuration, it is suggested to apply a squared quadriaxial FRP sheet (side 100 mm) over the splayed fibers and smooth the hole contour.

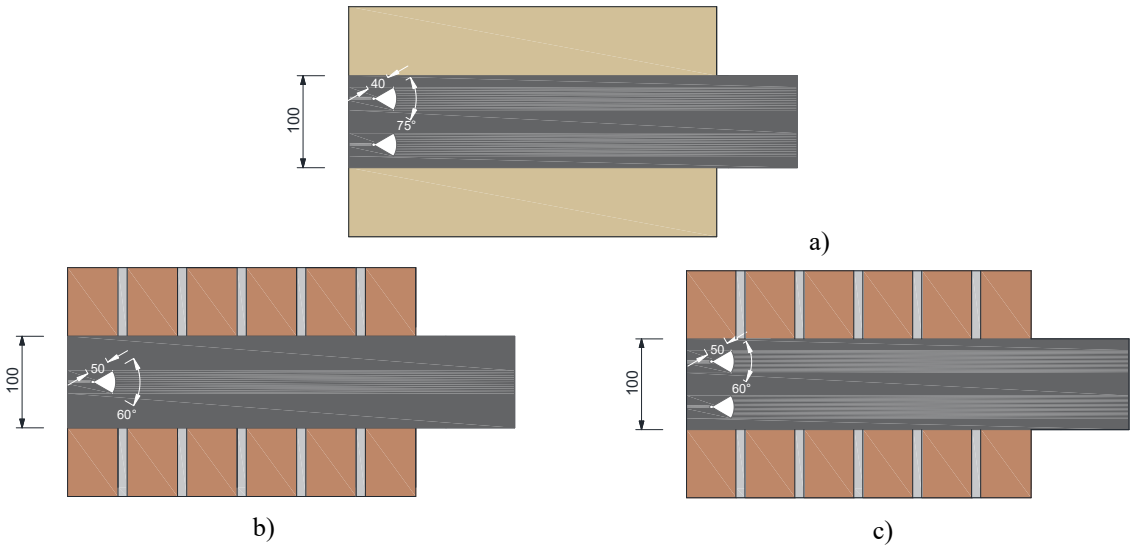

Figure 7: Recommended geometrical configurations for spike anchors in masonry elements for b_f=100 mm: a) 2 spike anchors for tuff stones with l_{emb} = 150 mm, α = 75°, r = 40 mm; b) 1 spike anchor for clay bricks with l_{emb} =80 mm, α = 60° e r =50 mm; c) 2 spike anchors for clay bricks with l_{emb} =80 mm, α = 60° e r =50 mm (dimensions in mm).

4 CONCLUSIONS

The paper presents a detailed state-of-art of the knowledge about the effectiveness of different types of anchoring systems for externally bonded FRP materials applied to concrete and masonry substrates.

The analysis of technical literature evidenced that the efficiency of anchoring systems varies sensibly according to both the strengthening configuration (flexural, shear, confinement) and type and geometry of the anchoring systems. Also detailing can influence the efficiency of each anchoring system.

The design indications proposed in this paper represent suggestions for calculating an increase of the theoretical end-debonding load provided by two common anchoring systems, i.e. transversal strips and spike anchors, since for these two devices more homogeneous and numerous experimental data are now available. The theoretical end-debonding load can be calculated with refer to existing well-established bond strength models for end-debonding failure.

The increased bond strength in presence of anchoring devices can be, indeed, used for calculating the global capacity of concrete or masonry elements strengthened with FRP materials in shear or bending, i.e. for strengthening configurations governed by the bond behavior at the FRP-substrate interface and eventually affected by end-debonding failure.

Extension of similar design indications to other types of anchoring devices request, clearly, availability of homogeneous experimental results.

REFERENCES

[1] Al-Amery, R., and Al-Mahaidi, R. (2006). Coupled flexural-shear retrofitting of RC beams using CFRP straps. Compos. Struct., 75(1–4), 457–464.

[2] Al-Mahaidi R., Kalfat R. (2011). Investigation into CFRP plate end anchorage utilizing unidirectional fabric wrap, Composite Structures, 93(2), 821–830.

[3] Bilotta, A., Ceroni, F., Nigro, E. And Pecce, M. (2011), Design by testing procedure of debonding load for RC elements strengthened with EBR FRP materials, in Proceedings of 10th FRPRCS International Symposium, ACI SP-275 Fiber-Reinforced Polymer Reinforcement for Concrete Structures, R. Sen, R. Seracino, C. Shield and W. Gold (eds), Tampa, Florida, CD-rom.

[4] Buyle-Bodin, F., and David, E. (2004). Use of carbon fibre textile to control premature failure of reinforced concrete beams strengthened with bonded CFRP plates. J. Ind. Text., 33(3), 145–157.

[5] Caggegi C., Pensée V., Fagone M., Cuomo M., Chevalier L. (2014). Experimental global analysis of the efficiency of carbon fiber anchors applied over CFRP strengthened bricks, Construction and Building Materials, Elsevier, 53: 203–212.

[6] Ceroni, F. (2010). Experimental performances of RC beams strengthened with FRP materials. Construction and Building Material, 24, 1547–1559.

[7] Ceroni F. (2017). Bond tests to evaluate the effectiveness of anchoring devices for CFRP sheets epoxy bonded over masonry elements, Composites Part B, 113: 317-330.

[8] Ceroni F., Ferracuti B., Savoia M., Pecce M., (2014). Assessment of a bond strength model for FRP reinforcement externally bonded over masonry blocks, Composite part B, Elsevier, 61: 147-161.

[9] Ceroni F., Pecce M., (2010). Evaluation of bond strength in concrete elements strengthened with CFRP sheets and anchorage devices, Journal of Composites in Construction, 14(5): 521-530.

[10] Ceroni F., Pecce M., Matthys S., Taerwe L. (2008). Debonding strength and anchorage devices for reinforced concrete elements strengthened with FRP sheets, Composites: Part B, 39: 429–441.

[11] Chen, J. F. and Teng, J. G. (2001), Anchorage strength models for FRP and steel plates bonded to concrete, ASCE Journal of Structural Engineering, 127(7), 784-791.

[12] CNR DT 200/R1 (2013). Guide for the Design and Construction of Externally Bonded FRP Systems for Strengthening Existing Structures, Advisory Committee on Technical Recommendation for Construction of National Research council, Rome, Italy

[13] Eshwar N., Nanni A., Ibell T.J. (2008). Performance of two anchor systems of externally bonded fiber-reinforced polymer laminates, ACI Materials Journal, 105: 72-80.

[14] Fagone, M., Ranocchiai, G., Caggegi, C., Briccoli, Bati, S., Cuomo, M. (2014). The efficiency of mechanical anchors in CFRP strengthening of masonry: An experimental analysis, Composites Part B, 64: 1–15.

[15] *fib* Bulletin 90 (2019), Externally applied FRP reinforcement for concrete structures, International Federation for Structural Concrete, Lausanne.

[16] Jinno, Y., Tsukagoshi, H., & Yabe, Y. (2001). RC beams with slabs strengthened by CF sheets and bundles of CF strands. In T. Telford (Ed.), Proceedings of FRPRCS-5 International symposium, July 2001, Cambridge, UK, pp. 981–987.

[17] Karantzikis, M., Papanicolaou, C.G., Antonopoulos, C.P., Triantafillou, T.C. (2005). Experimental investigation of nonconventional confinement for concrete using FRP, ASCE, Journal of Composite for Construction, Vol. 9, No. 6, pp. 480-487.

[18] Khan, A., R. and Fareed, S. (2014). Behaviour of Reinforced Concrete Beams Strengthened by CFRP Wraps with and without End Anchorages. Procedia Engineering 77, 123–130.

[19] Kim, I.S., Jirsa, J.O. and Bayrak, O. (2011). Use of Carbon Fiber-Reinforced Polymer Anchors to Repair and Strengthen Lap Splices of Reinforced Concrete Columns. ACI Structural Journal, 108(5), 630-640.

[20] Kim, Y., Quinn, K., T., Satrom, C., N., Ghannoum, W., M. and Jirsa, J., O. (2011). Shear Strengthening RC T-beams Using CFRP Laminates and Anchors. Special Publication, 275, 1-18.

[21] Kobayshi, K., Fujii, S., Yabe, Y., Tukagoshi, H., & Sugiyama, T. (2001). Advanced wrapping system with CF-anchor: stress transfer mechanism of CF-anchor. In T. Telford (Ed.), Proceedings of FRPRCS5 International symposium, July 2001, Cambridge, UK.

[22] Koutas, L. and Triantafillou, T., C. (2013). Use of Anchors in Shear Strengthening of Reinforced

[23] Mofidi, A., Chaallal, O., Benmokrane, B. and Kenneth, N. (2012). Performance of End-Anchorage Systems for RC Beams Strengthened in Shear with Epoxy-Bonded FRP. Journal of composites for construction, 16.

[24] Niemitz, C. W., James, R., & Breña, S. F. (2010). Experimental behavior of carbon fiber-reinforced polymer CFRP sheets attached to concrete surfaces using CFRP anchors. Journal of Composites for Construction, 14(2), 185–194.

[25] Orton, S. L., Jirsa, J. O., & Bayrak, O. (2008). Design considerations of carbon fiber anchors. ASCE Journal of Composites for Construction, 12(6), 608–616.

[26] Özdemir, G. (2005). Mechanical Properties of CFRP Anchorages, Master of Science Thesis, Middle East Technical University, Istanbul Turkey.

[27] Prota, A., Manfredi, G., Balsamo, A., Nanni, A., & Cosenza, E. (2005). Innovative technique for seismic upgrade of RC square columns. Proceedings of FRPRCS7.

[28] Smith, S., Hu, S., Kim, S., J. and Seracino, R. (2011). Strength and Deflection Enhancement of RC Slabs with Anchored FRP Strengthening. Special Publication, 275, 1–14.

[29] Smith, S., Zhang, H., & Wang, Z. (2013). Influence of FRP anchors on the strength and ductility of FRP-strengthened RC slabs. Construction and Building Materials, 49, 998–1012.

[30] Spadea, G., Bencardino, F., and Swamy, R. N. (1998). Structural behavior of composite RC beams with externally bonded CFRP. J. Compos. Constr., 2(3), 132–137.

[31] Zhang H., Smith S. (2012). Influence of FRP anchor fan configuration and dowel angle on anchoring FRP plates, Composites Part B Engineering, 43(8): 3516–3527.

[32] Zhang H.W., Smith S.T., Kim S.J. (2012). Optimisation of carbon and glass FRP anchor design, Construction and Building Materials, 32: 1–12.

[33] Ceroni F., Leone M., Rizzo V., Bellini A., Mazzotti C. (2017). Experimental bond behaviour of FRP materials bonded over different masonry substrates: effect of mortar joints, Engineering Structures, 153: 550–568.

COMPDYN 2019
7th ECCOMAS Thematic Conference on
Computational Methods in Structural Dynamics and Earthquake Engineering
M. Papadrakakis, M. Fragiadakis (eds.)
Crete, Greece, 24–26 June 2019

RINTC-E PROJECT: TOWARDS THE SEISMIC RISK OF RETROFITTED EXISTING ITALIAN URM BUILDINGS

Stefano Bracchi[1,2], Serena Cattari[3], Stefania Degli Abbati[3], Sergio Lagomarsino[3], Guido Magenes[1], Martina Mandirola[1], Salvatore Marino[3], Andrea Penna[1,2], Maria Rota[1]

[1] EUCENTRE Foundation, Dept. Buildings and Infrastructures
Via Ferrata 1, 27100 Pavia, Italy
martina.mandirola@eucentre.it, maria.rota@eucentre.it

[2] University of Pavia, Dept. of Civil Engineering and Architecture
Via Ferrata 3, 27100 Pavia, Italy
stefano.bracchi@unipv.it, guido.magenes@unipv.it, andrea.penna@unipv.it

[3] University of Genoa, Dept. of Civil, Chemical and Environmental Engineering
Via Montallegro 1, Genoa, Italy
{serena.cattari, stefania.degliabbati, sergio.lagomarsino}@unige.it, salvatore.marino@edu.unige.it

Abstract

This paper presents the results of the work carried out in an ongoing Research Project, funded by the Italian Civil Protection Department, aimed at computing the risk of collapse of existing masonry buildings. Other papers submitted to this conference describe the overall Research Project [1], its different areas of application ([2][3][4][5][6]), the overall seismic risk calculation procedure, the seismic hazard assessment and the ground motion selection process followed to identify the recorded ground motions used for nonlinear dynamic analyses. Several unreinforced masonry buildings were considered, characterized by stone and clay masonry, regular and irregular geometries and number of storeys varying from two to seven. These buildings were retrofitted according to the prescriptions of different Italian seismic codes, applying commonly adopted retrofit techniques (e.g. floor stiffening, injection of masonry, addition of tie beams, etc). The paper presents the results for a single case study building. Equivalent frame models are used to simulate the in-plane response, whereas out-of-plane failure modes are prevented by the selected strengthening interventions. Pushover analyses are performed to estimate the capacity in terms of a properly selected engineering demand parameter, whereas the demand is obtained by multi-stripe nonlinear dynamic analyses for ten different earthquake's return periods. The results allow to understand the different level of risk implicit in buildings retrofitted according to various codes and strategies.

Keywords: Unreinforced masonry, Nonlinear static and dynamic analysis, Equivalent frame models, Multi-stripe analysis, Seismic retrofit.

1 INTRODUCTION

RINTC-e is an ongoing research project, funded by the Italian Civil Protection Department, aimed at computing the risk of collapse of existing buildings. As a continuation of the previous work, which concerned new buildings [7], [8], [9], this paper focuses on understanding the different level of risk implicit in existing unreinforced masonry (URM) buildings retrofitted according to the prescriptions of different Italian seismic codes.

Several building configurations, realised with stone and clay masonry, with regular and irregular geometries, a number of storeys ranging from two to seven, and located in three different towns (L'Aquila, Naples and Rome) were analysed within the project. These buildings were retrofitted adopting common retrofit techniques aiming at improving wall-to-wall and wall-to-diaphragm connections, at increasing the in-plane stiffness of diaphragms and, in some cases, enhancing the strength of masonry by grout injections or other techniques.

The risk assessment in terms of global failure was performed by multi-stripe nonlinear dynamic analyses for ten different earthquake's return periods. The equivalent frame model implemented in the Tremuri program [10] was adopted, using the available macroelement models ([11], [12]). Pushover analyses were performed to estimate the capacity in terms of maximum wall inter-storey drift. Out-of-plane failure modes were not considered, as strengthening interventions are supposed to be appropriately designed to prevent their activation.

The results shown in this paper refer to one of the case study structures analysed, located in Naples and representative of a typical typology of the late nineteenth century.

2 IDENTIFICATION OF THE SELECTED CASE STUDY

The case study discussed in this paper consists of a 5-storey unreinforced yellow tuff masonry structure, with flexible wooden floors and different wall thicknesses and inter-storey heights (Table 1).

Figure 1 (a) shows two photos of the existing building and the corresponding plans of the ground and upper floors (Figure 1b), whereas Figure 2 shows the elevations views, obtained from a slight simplification of the real situation.

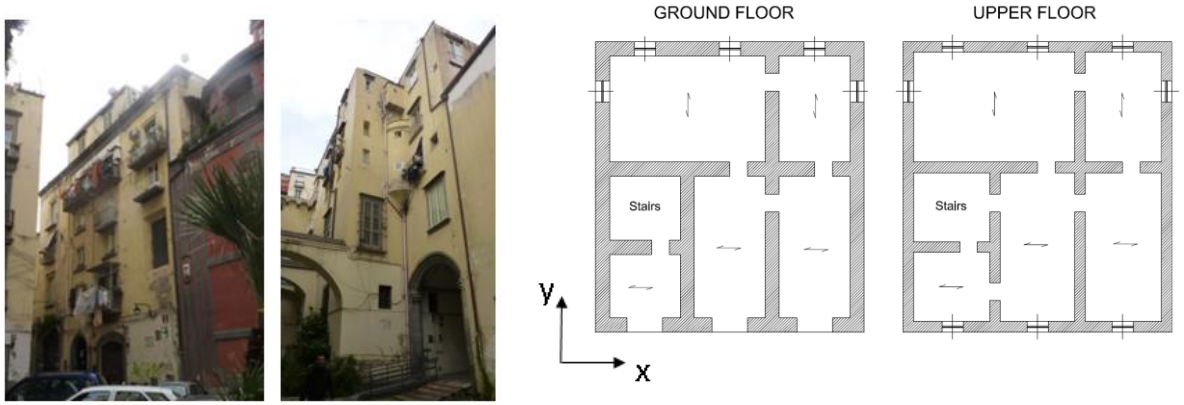

(a) (b)

Figure 1: Photos of the considered existing building prototype (a) and corresponding plans (b), obtained from a simplification of the real building. X and Y indicate the directions of analysis.

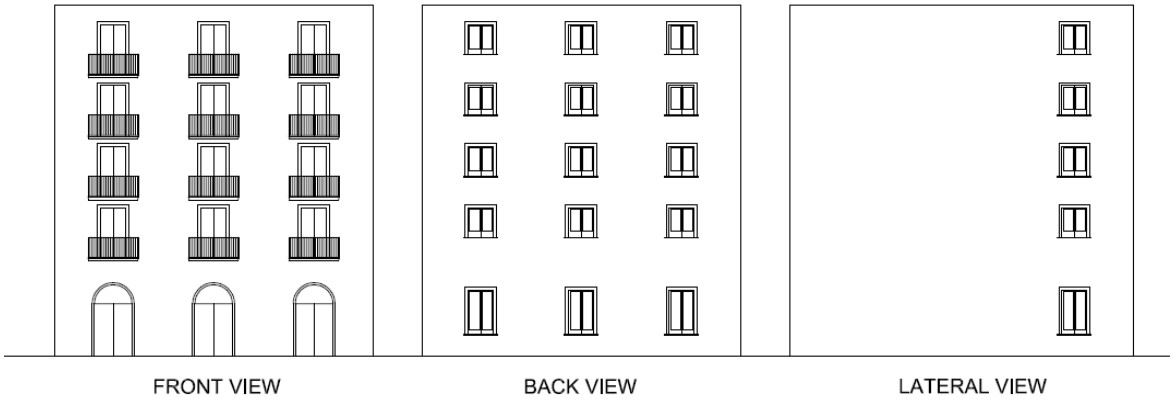

Figure 2: Elevations of the considered building, obtained from a simplification of the real building.

	Ground Floor	1st - 2nd Floor	3rd Floor	4th Floor
Wall thickness [m]	0.8	0.6	0.4	0.4
Inter-storey height [m]	4.5	2.7	2.7	3
Total Length [m]	15.2			
Total Height [m]	15.6			
Total Width [m]	16.4			

Table 1: Main geometrical properties of the different floors of the considered case study building

3 DESIGN OF RETROFIT SOLUTIONS USING DIFFERENT CODES

The retrofit interventions on the considered URM buildings were designed according to the "Code for repair and strengthening of buildings damaged by earthquakes," issued by the Ministry of Public Works in 1981 (D.M. 1981, [13]), and the associated guidelines [14], incorporating the POR method, originally proposed by Tomaževic [15] for the seismic analysis of retrofitted URM buildings. Such documents were published after the 1976 (Friuli), 1979 (Norcia) and 1980 (Irpinia) earthquakes and extensively used in the reconstruction phase. The procedures presented in this code were then included, with minor modifications, in the national seismic codes and largely implemented in the retrofit interventions designed in the last two decades of the 20th century.

Interventions were also alternatively designed according to the Italian building code issued in 2008 (NTC08, [17]) and its guidelines [18], which came into force after the 2009 L'Aquila earthquake. Eventually, retrofit interventions were assessed according to the code update published in 2018 (NTC18, [19]) and its guidelines [20].

3.1 D.M. 1981 (POR method)

The POR approach is an equivalent static, simplified nonlinear assessment method, proposed and developed by Tomaževič [15]. The method, which has undergone several refinements in the subsequent years, is based on the so-called "storey-mechanism" approach, which assumes that failure occurs only in the piers (shear failure), without any damage in the spandrels. Each masonry pier is modelled by a linear elastic-perfectly plastic shear spring, with limited ductility and effective height equal to the net height of the openings, as indicated in [14]. Alternative definitions of the effective height aiming at accounting for the orientation of

cracks at the pier edges and for the deformability of spandrels were proposed for example by Dolce [16].

Applying the POR method, according to the guidelines in force at the time of construction of the building [14], the effects of the following seismic retrofit strategies were investigated and verified:

- realisation of a reinforced concrete ring beam at the storey levels;
- stiffening of the floors by casting collaborating reinforced concrete rigid slabs.

Figure 3 shows the definition of the equivalent frame mesh of two significant walls of the numerical model adopted for the analyses according to the POR method.

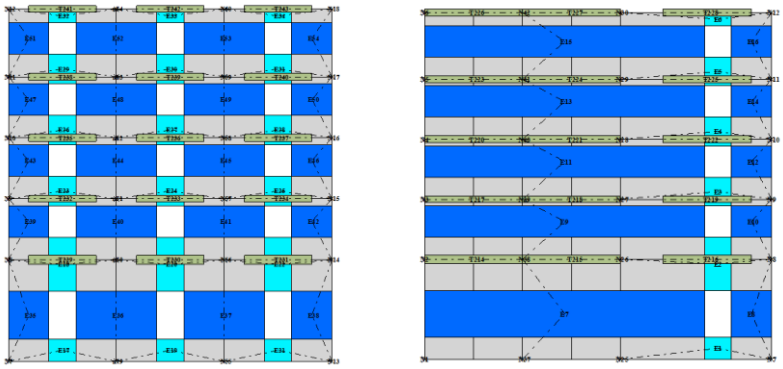

Figure 3: Equivalent frame mesh for two significant walls of the numerical model adopted in the analyses according to the POR method for the selected building.

The mechanical properties of masonry were assumed based on the values proposed in the guidelines [14] for tuff masonry. The adopted values are summarized in Table 2, in which f_m is the mean compressive strength of masonry, τ_0 is the mean shear strength of masonry, E and G the mean values of the elastic and shear moduli of elasticity and w is the masonry specific weight.

f_m [MPa]	τ_0 [MPa]	E [MPa]	G [MPa]	w [kN/m^3]
2.5	0.1	660	110	16

Table 2: Adopted mechanical properties of tuff masonry, assumed according to [14].

To be consistent with the assumptions of the POR method, the maximum shear strength of the structure was calculated under the hypothesis of fixed floor rotations, performing nonlinear static analysis (pushover), with a force distribution proportional to the first vibration mode. The seismic demand was computed as a percentage of the building weight, depending on the degree of seismicity of the considered area (Table 3).

Seismic Zone	Building weight, W_{tot} [kN]	Seismic Force, F_t [kN]	F_t / W_{tot} [-]
3	11489	1838	0.16

Table 3: Seismic forces computed according to [14].

Figure 4 shows the results of the analyses, in terms of shear strength normalized with respect to the weight of the structure (V/W_{tot}) versus top displacement. Since the strength in both

the directions of analysis clearly exceeds the seismic demand (dashed red line), the adopted retrofit strategies satisfy the code requirements of the period.

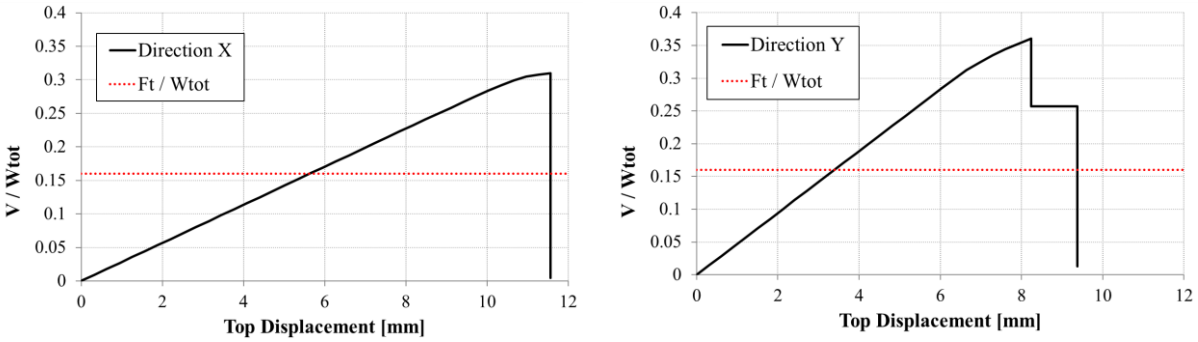

Figure 4: Results of the POR method, in terms of shear strength normalized to the weight of the structure versus top displacement: comparison between the strength of the structure in both the directions of analysis (longitudinal (left) and transversal (right)) and the seismic demand (dashed red line).

3.2 NTC08

For the same building prototype, different retrofit solutions were designed and analysed to fulfil the prescriptions of NTC08.

In particular, the effects of the following seismic retrofit strategies were investigated:

- stiffening of the floor diaphragm by adding a reinforced concrete collaborating slab, with lightweight concrete;
- improvement of the masonry quality by grout injections;
- enhancement of the wall-to-diaphragm connections by means of L-shaped steel ring beams at each floor level, except for reinforced concrete ring beams at the roof level;
- steel framing of all the openings of the longitudinal wall at the back (Figure 1b) by S275 HEB100 profiles.

These retrofit strategies were verified by applying the adopted equivalent-frame modelling strategy implemented in the 3Muri program and based on an elastic-perfectly plastic constitutive law of the structural element [10]. Figure 5 shows the 3D views of the numerical model of the retrofitted building.

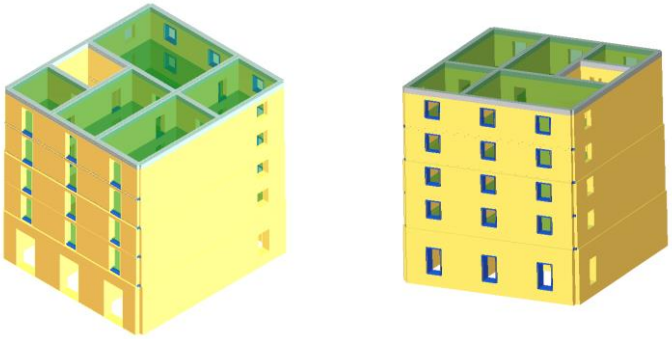

Figure 5: 3D views of the numerical models of the structures retrofitted according to NTC08.

The mechanical properties of masonry were defined based on the values proposed by the guidelines for NTC08 [18] for tuff masonry, assuming a confidence factor of 1.2 (knowledge level 2). The selected building was analysed in Naples, soil type A and C (topographic category T1). Figure 6 reports the pushover curve and damage pattern of one significant wall, ob-

tained in one of the critical analyses (minimum capacity over demand ratio) carried out according to NTC08 (soil type C). A damage concentration at the ground storey can be observed, with shear failure and flexural damage of the masonry piers of the longitudinal wall at the back (the one with steel profiles around all the openings).

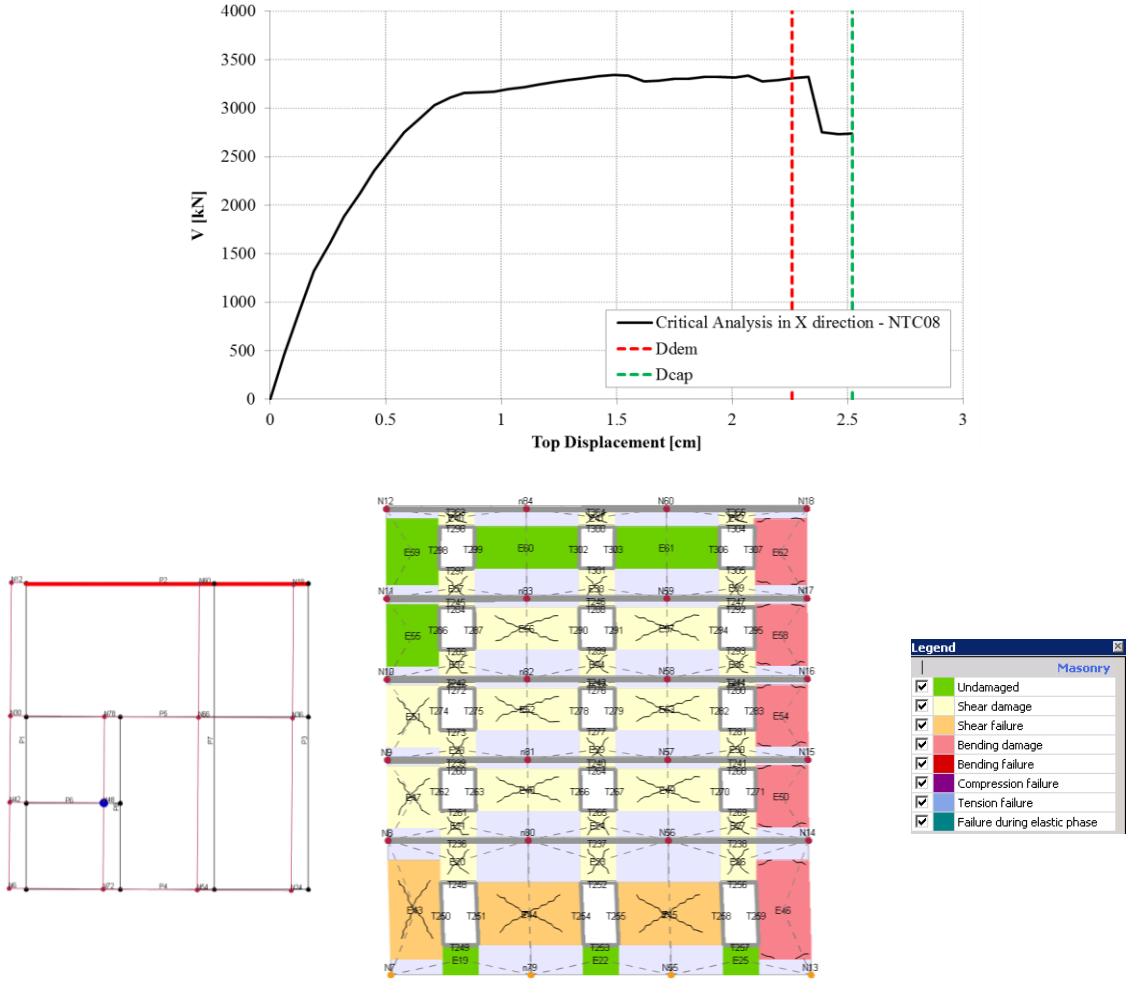

Figure 6: Results obtained for the critical analysis in the X direction (Figure 1), soil type C, for the building retrofitted according to NTC08: damage pattern of one significant wall (bottom) and pushover curve with indication of the demand (D_{dem}) and capacity (D_{cap}) displacement thresholds (top).

The retrofitted model was checked to fulfil also the prescriptions of NTC18 for both soil type A and C, for the two ultimate limit states of life safety and collapse. In particular, for the analyses carried out for soil type C, the maximum ratio between the maximum seismic capacity of the structure and the maximum seismic demand used for the design of new buildings (ζ_E) resulted equal to 90%, satisfying the requirements of the code ($\zeta_E \geq 80\%$).

4 SEISMIC PERFORMANCE OF RETROFITTED BUILDINGS

4.1 D.M. 1981

The seismic vulnerability of the retrofitted building was assessed by means of nonlinear static (pushover) and dynamic analyses, using the equivalent frame macroelement approach

implemented in the computer program Tremuri [10] and adopting for the piers an improved version [21] of the macroelement proposed by Penna *et al.* [11].

The mechanical properties of the macroelement model were calibrated starting from experimental tests on masonry of similar characteristics [22], consisting of in-plane cyclic shear-compression tests carried out on specimens made of cement mortar and tuff units obtained from demolished buildings erected in Naples in the last two centuries.

Figure 7 reports the comparison between the experimental results (black curve) and the numerical simulation (red curve), obtained for two of the unreinforced masonry piers tested.

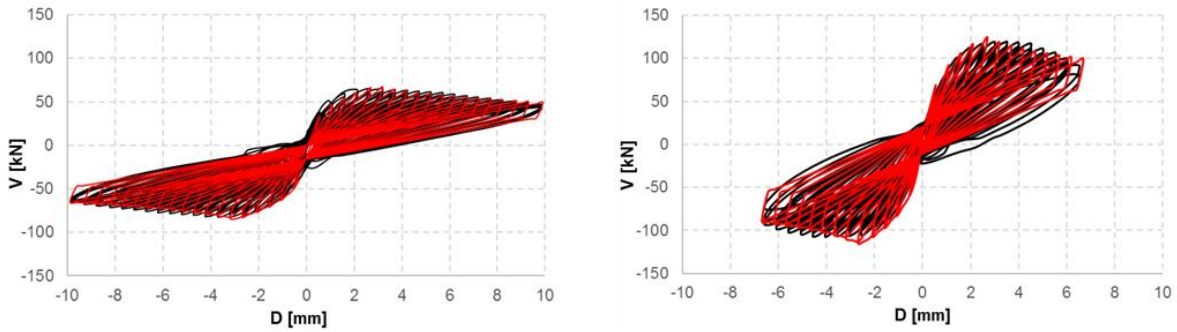

Figure 7: Comparison between the experimental results (black curve) and the numerical simulation (red curve), obtained for two of the unreinforced masonry piers tested by [22]: specimen T1-1 (left) and T1-3 (right).

Based on the comparison with experimental results, it was possible to calibrate only the parameters related to shear failure modes, since all experimental specimens failed in shear. The missing flexural parameters were derived from indications reported in the literature [24].

The seismic vulnerability was assessed in terms of frequency of exceedance of given thresholds of a selected Engineering Demand Parameter (EDP). As in [9], the maximum inter-storey drift (among all walls and all stories), accounting for the average rotations of the nodes of the storey, was selected as EDP. The EDP thresholds were computed by pushover analyses with an inverse triangular load pattern, considering the different behaviour of the building in the two directions of analysis, X and Y (positive and negative). The maximum inter-storey drift was evaluated separately for each direction and the EDP was calculated as the minimum value between the positive and negative direction for X and Y separately.

Two different limit states were considered: usability-preventing damage, UPD, evaluated according to the multi-criteria approach discussed in [1], and global collapse, GC, corresponding to a total base shear loss equal to 50% of the maximum base shear.

Figure 8 shows the pushover curves in the two directions of analysis, with the identification of the thresholds for the considered limit states (Table 4).

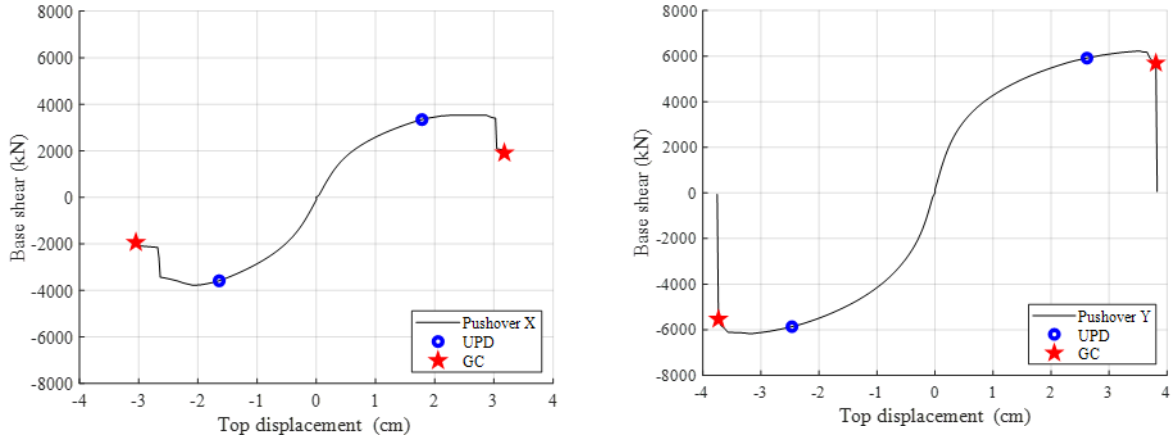

Figure 8: Pushover curves in the two directions of analysis for the building retrofitted according to D.M. 1981, with the identification of the thresholds for the considered limit states.

UPD threshold [%]		GC threshold [%]	
X direction	**Y direction**	**X direction**	**Y direction**
0.125	0.193	0.525	0.516

Table 4: Values of EDP thresholds corresponding to usability-preventing damage (UPD) and global collapse (GC) limit states, for the building retrofitted according to D.M. 1981.

The criterion governing the UPD limit state was the one associated with the attainment of 95% of the building lateral strength, corresponding to a condition in which the structure is still fully capable of withstanding horizontal forces. Figure 9 shows the damage in the structural elements at the end of analyses (GC limit state).

By means of nonlinear dynamic analyses, it was possible to calculate the percentage of exceedance of the two considered limit states, for increasing values of the return period. The time history analyses were carried out with a set of accelerograms (representative of the seismicity of Naples) selected for buildings with a fundamental period close to 0.25s, since the building fundamental vibration periods in undamaged conditions is about 0.28s in one direction and 0.2s in the other. A set of 20 ground motions was selected for each of the 10 return periods considered. The results in terms of frequency of exceedance of the two limit states are reported in Figure 10.

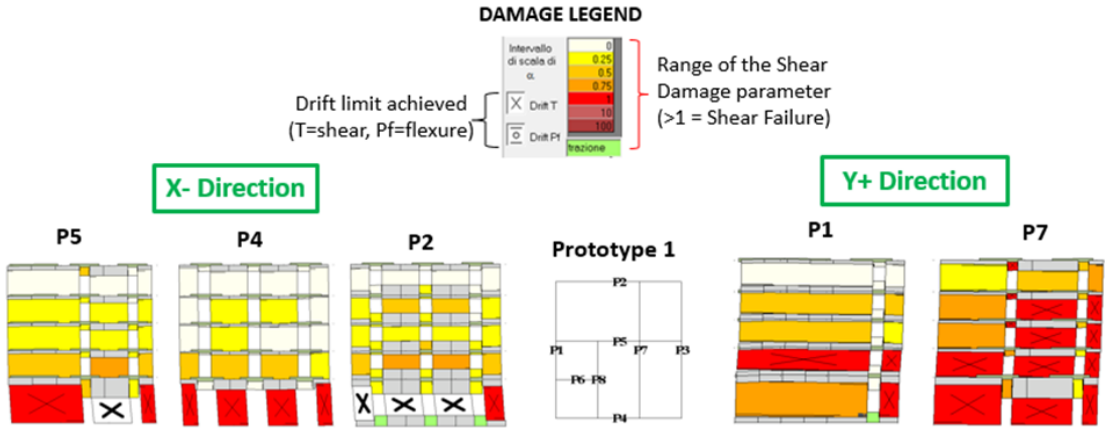

Figure 9: Damage in meaningful structural walls of the building retrofitted according to D.M. 1981 at the end of the pushover analyses carried out in the two directions of loading.

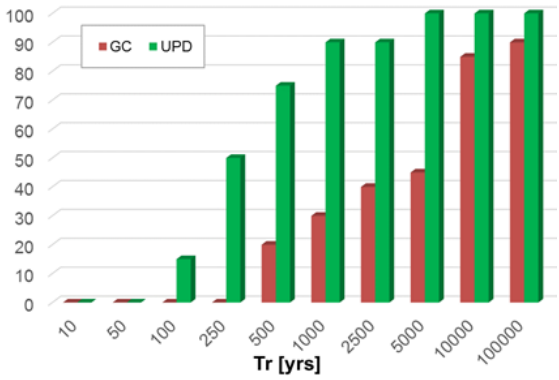

Figure 10: Frequency of occurrence (%) of UPD and GC limit states, as a function of the return period, for the building retrofitted according to D.M. 1981 (soil type C).

4.2 NTC08

The same approach described before was followed to assess the seismic performance of the building retrofitted according to NTC08. The mechanical properties of the macroelement were calibrated starting from the experimental campaign already considered for D.M. 1981, considering only the specimens strengthened by grout injections [22].

Figure 11 reports the comparison between the experimental results (black curve) and the numerical simulation (red curve), obtained for two of the considered walls.

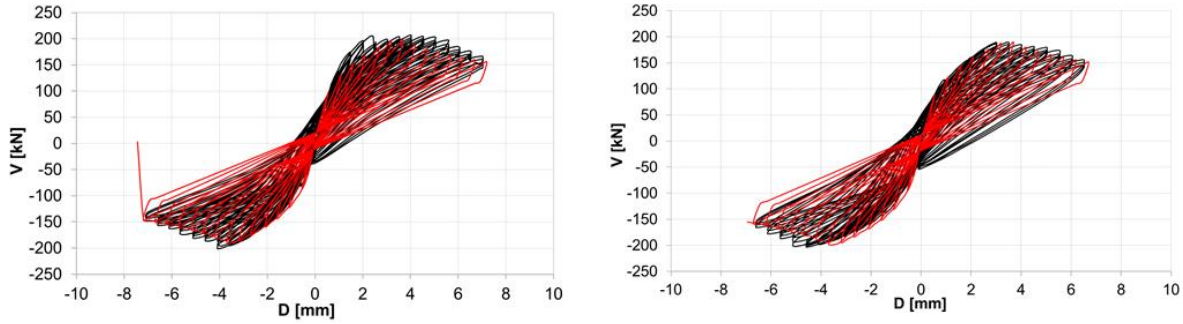

Figure 11: Comparison between the experimental results (black curve) and the numerical simulation (red curve), obtained for two of the retrofitted masonry piers tested by [22]: specimen T3-7 (left) and T3-9 (right).

The in-plane and out-of-plane stiffness of the floors was modelled assuming equivalent mechanical properties, calibrated on experimental shaking table tests on full scale stone masonry buildings with floor diaphragms and ring beams of similar characteristics [25].

Figure 12 shows the pushover curves obtained in the two directions of analysis, with the identification of the thresholds for the considered limit states (Table 5). The higher displacement capacity exhibited, with respect to the building retrofitted according to D.M. 1981 (Figure 8), is mostly due to the development of a global behaviour and failure mechanism different from what observed with the retrofit strategies designed in that case.

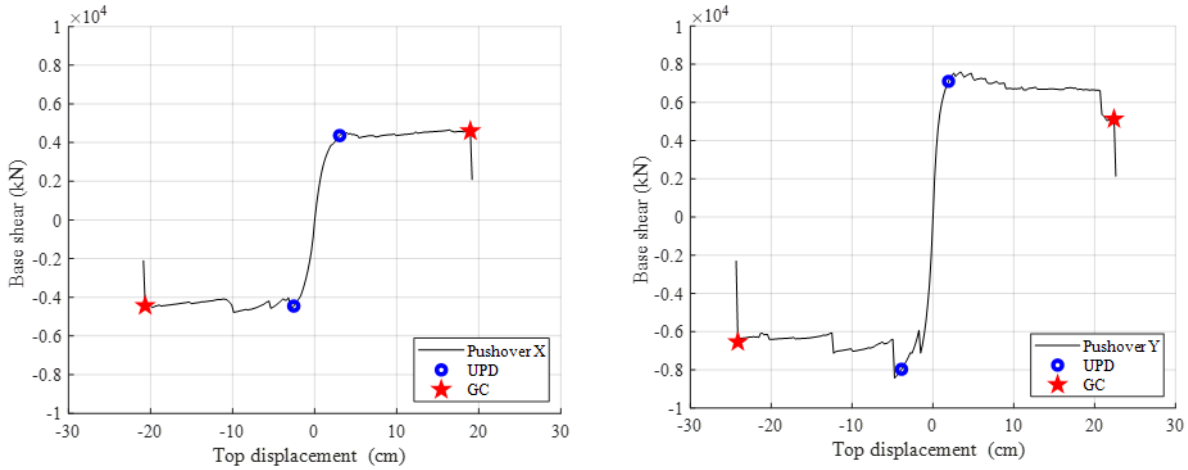

Figure 12: Pushover curves in the two directions of analysis, for the building retrofitted according to NTC08, with the identification of the thresholds of the considered limit states.

UPD threshold [%]		GC threshold [%]	
X direction	**Y direction**	**X direction**	**Y direction**
0.153	0.135	1.125	0.943

Table 5: Values of EDP threshold corresponding to the considered limit states for the building retrofitted according to NTC08

Also in this case, the dominant criterion identifying the attainment of UPD was associated with the attainment of 95% of the peak shear strength. The damage occurred in the structural elements at the end of the analyses (GC limit state) is reported in Figure 13.

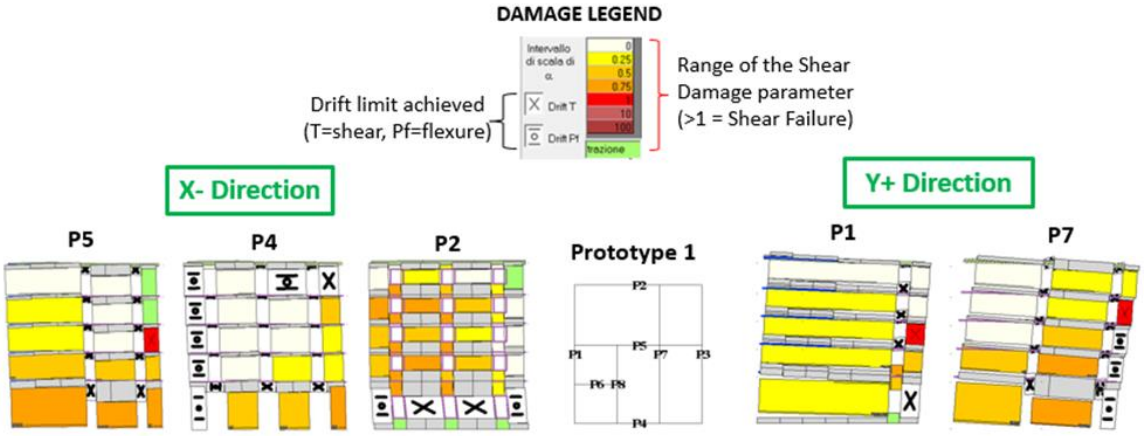

Figure 13: Damage observed in significant structural walls of the building retrofitted according to NTC08 at the end of the pushover analyses carried out in the two directions of loading.

Nonlinear time history analyses were then performed using the same two sets of ground motions of D.M. 1981, to obtain the percentage of exceedance of the two considered limit states (UPD and GC), for increasing values of the return period. Figure 14 shows the results for a reference period of 0.25 s and soil type C.

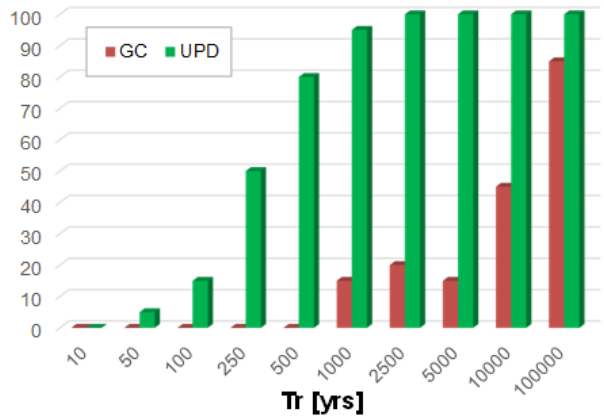

Figure 14: Frequency of occurrence (%) of UPD and GC limit states, as a function of the return period, for the building retrofitted according to NTC08.

5 DISCUSSION AND CONCLUSIONS

The assessment of the seismic performance of the building retrofitted according to the prescriptions of the two considered codes and associated hazard, allows to conclude that, for the considered case study, the vulnerability at the global collapse (GC) limit state is lower in the case of retrofit strategies designed according to NTC08, with respect to D.M. 1981. On the contrary, similar performances were obtained at the usability-preventing damage (UPD) limit state. This difference could be in part explained by the different global behaviour and failure mechanisms exhibited by the structure: a global rocking behaviour with failure of most of the spandrels occurred in case of NTC08, whereas the activation of an evident soft-storey mechanism, with shear failure of the piers, was observed in case of D.M. 1981. Observation of the global displacement capacity of the pushover curves confirms these results, showing in the two cases similar EDP thresholds for the usability preventing damage limit state and different thresholds for the global collapse limit state.

ACKNOWLEDGEMENTS

The study was developed between 2017 and 2018 in the framework of the ReLUIS-DPC and EUCENTRE-DPC projects, funded by the Italian Civil Protection Department (DPC).

REFERENCES

[1] I. Iervolino, A. Spillatura, P. Bazzurro RINTC-E project: towards the assessment of the seismic risk of existing buildings in Italy, RINTC-e: Towards seismic risk assessment of existing residential reinforced concrete buildings in Italy. *Proc. COMPDYN 2019 - 7th ECCOMAS Thematic Conference on Computational Methods in Structural Dynamics and Earthquake Engineering*, Crete, Greece, 2019.

[2] P. Ricci, V. Manfredi, F. Noto, M. Terrenzi, M.T. De Risi, M. Di Domenico, G. Camata, P. Franchin, A. Masi, F. Mollaioli, E. Spacone, G.M. Verderame, RINTC-e project: Towards seismic risk assessment of existing residential reinforced concrete buildings in Italy. *Proc. COMPDYN 2019 - 7th ECCOMAS Thematic Conference on Computational Methods in Structural Dynamics and Earthquake Engineering*, Crete, Greece, 2019.

[3] G. Magliulo, D. Bellotti, C. Di Salvatore, F. Cavalieri, RINTC-e project: towards the seismic risk of low and pre-code single-story r/c precast buildings in Italy. *Proc. COMPDYN 2019 - 7th ECCOMAS Thematic Conference on Computational Methods in Structural Dynamics and Earthquake Engineering*, Crete, Greece, 2019.

[4] M.E. Bressanelli, A. Belleri, P. Riva, G. Magliulo, D. Bellotti, B. Dal Lago, Effects of modeling assumptions on the evaluation of the local seismic response for RC precast industrial buildings. *Proc. COMPDYN 2019 - 7th ECCOMAS Thematic Conference on Computational Methods in Structural Dynamics and Earthquake Engineering*, Crete, Greece, 2019.

[5] G. Cantisani, G. Della Corte, RINTC-e project: Seismic risk of pre-code single-story non-residential steel buildings in Italy. *Proc. COMPDYN 2019 - 7th ECCOMAS Thematic Conference on Computational Methods in Structural Dynamics and Earthquake Engineering*, Crete, Greece, 2019.

[6] L. Ragni, D. Cardone, N. Conte, A. Dall'Asta, A. Di Cesare, A. Flora, N. Lamarucciola, F. Micozzi, F. Ponzo, RINTC-e project: the seismic risk of existing Italian RC buildings retrofitted with seismic isolation. *Proc. COMPDYN 2019 - 7th ECCOMAS Thematic Conference on Computational Methods in Structural Dynamics and Earthquake Engineering*, Crete, Greece, 2019.

[7] I. Iervolino, A. Spillatura, P. Bazzurro, Seismic reliability of code-conforming Italian buildings. *Journal of Earthquake Engineering*, **22** - Issue sup2, 5-27, 2018.

[8] C.F. Manzini, G. Magenes, S., A. Penna, F. da Porto, D. Camilletti, S. Cattari, S. Lagomarsino, Masonry Italian code-conforming buildings. Part 1: case studies and design methods. *Journal of Earthquake Engineering*. **22** - Issue sup2, 54-73, 2018.

[9] S. Cattari, D. Camilletti, S. Lagomarsino, S. Bracchi, M. Rota, A. Penna, Masonry Italian code-conforming buildings. Part 2: nonlinear modelling and time-history analysis. *Journal of Earthquake Engineering*. **22** - Issue sup2, 2010-2040, 2018.

[10] S. Lagomarsino, A. Penna, A. Galasco, S. Cattari, TREMURI program: an equivalent frame model for the nonlinear seismic analysis of masonry buildings. *Engineering Structures*, **56**, 1787-1799, 2013.

[11] A. Penna, S. Lagomarsino, A. Galasco, A nonlinear macroelement model for the seismic analysis of masonry buildings. *Earthquake Engineering and Structural Dynamics*, **43**(2), 159-179, 2014.

[12] S. Lagomarsino, S. Cattari, Seismic Performance of Historical Masonry Structures Through Pushover and Nonlinear Dynamic Analyses. *In: Ansal A. (eds) Perspectives on European Earthquake Engineering and Seismology. Geotechnical, Geological and Earthquake Engineering*, Springer, **39**, 265–292, 2015

[13] MPW Ministry of Public Works, D.M. 2 luglio 1981 "Normativa per le riparazioni ed il rafforzamento degli edifici danneggiati dal sisma nelle regioni Basilicata, Campania e Puglia", 1981.

[14] MPW Ministry of Public Works, Circolare 30 luglio 1981 N. 21745 (1981) "Istruzioni relative alla normativa tecnica per la riparazione ed il rafforzamento degli edifici in muratura danneggiati dal sisma", 1981.

[15] M. Tomaževič, The computer program POR, Report ZRMK, Ljubljana, Slovenia, 1978 (in Slovenian).

[16] M. Dolce, Schematizzazione e modellazione degli edifici in muratura soggetti ad azioni sismiche, *L'Industria delle Costruzioni*, **25**(242), 44-57, 1991 (in Italian).

[17] MIT Ministry of Infrastructures and Transport, D.M. 14 Gennaio 2008 - "Nuove Norme Tecniche per le Costruzioni", S.O. n.30 alla G.U. del 4.2.2008, No. 29, 2008.

[18] MIT Ministry of Infrastructures and Transport, Circolare (2009) - Circolare 617 del 02/02/2009, "Istruzioni per l'applicazione delle Nuove norme tecniche per le costruzioni di cui al DM 14 gennaio 2008", 2009.

[19] MIT Ministry of Infrastructures and Transport, D.M. 17 Gennaio 2018 - "Aggiornamento delle Norme tecniche per le costruzioni", S.O. n.42 alla G.U. del 20.2.2018, No. 8, 2018.

[20] MIT Ministry of Infrastructures and Transport, Circolare (2019) - Circolare 7 del 21/01/2019, "Istruzioni per l'applicazione dell'Aggiornamento delle Norme tecniche per le costruzioni di cui al decreto ministeriale 17 gennaio 2018.", 2019.

[21] S. Bracchi, A. Galasco, A. Penna, G. Magenes, An improved macroelement model for the nonlinear analysis of masonry buildings. *10th Australasian Masonry Conference*, Sydney, Australia, February 11–14, 2018.

[22] G. Faella, G. Manfredi, R. Realfonzo, Comportamento sperimentale di pannelli in muratura di tufo sottoposti ad azioni orizzontali di tipo ciclico. *5th Italian Conference on Earthquake Engineering*, Palermo, Italy, 1991.

[23] G. Magenes, G.M. Calvi, In-plane seismic response of brick masonry walls. *Earthquake Engineering and Structural Dynamics*. **26**, 1091-1112, 1997.

[24] F. Vanin, D. Zaganelli, A. Penna, K. Beyer, Estimates for the stiffness, strength and drift capacity of stone masonry walls based on 123 quasi-static cyclic tests reported in the literature. *Bulletin of Earthquake Engineering*, **15**(12), 5435-5479, 2017.

[25] A. Penna, I. Senaldi, A. Galasco, G. Magenes G., Numerical Simulation of Shaking Table Tests on Full-Scale Stone Masonry Buildings. *International Journal of Architectural Heritage*, **10**(2-3), 146-163, 2016.

COMPDYN 2019
7th ECCOMAS Thematic Conference on
Computational Methods in Structural Dynamics and Earthquake Engineering
M. Papadrakakis, M. Fragiadakis (eds.)
Crete, Greece, 24–26 June 2019

LONG-TERM SEISMIC RESPONSE OF BUILDINGS WITH ISOLATION DEVICES AFFECTED BY DETERIORATION EFFECTS

Fabio Mazza[1]

[1] Dipartimento di Ingegneria Civile,
Università della Calabria
87036, Rende (Cosenza), Italy
e-mail: fabio.mazza@unical.it

Abstract

Base-isolation technique has long been used worldwide but seismic codes generally do not take into account ageing and environmental effects on the evolution and extent of the deterioration of elastomeric (e.g. high-damping-rubber bearings, HDRBs) and friction (e.g. flat sliding bearings, FSBs) isolators during their lifetime and on their impact on the nonlinear seismic behaviour of the superstructure. The aim of the present work is to investigate the effects of variability of the mechanical properties of elastomeric and sliding bearings on the nonlinear dynamic response of base-isolated reinforced concrete (r.c.) framed structures, focusing the attention on ageing and air temperature effects. First, six-storey base-isolated r.c. framed structures are designed in accordance with the current Italian code in a high-risk seismic zone, considering nominal values of mechanical properties of the isolation system. Specifically, nine structural configurations are examined, considering two alternative arrangements: i) elastomeric base-isolation (EBI) systems, with three different elastomer compounds for the HDRBs (i.e. soft, normal and hard); ii) hybrid elastomeric-sliding base-isolation (ESBI) systems, with the aforementioned elastomer compounds of the HDRBs and two friction coefficients (i.e. low and medium) of the FSBs. Then, based on experimental results from accelerated ageing tests at high temperature, mathematical models are implemented to account for oxidation of elastomers and friction changes. The variability of mechanical properties at different mean temperatures, due to seasonal thermal variations, are also considered. The results of nonlinear time-history analysis are used to build fragility curves based on simple regression in the logarithmic space of structural response versus seismic intensity.

Keywords: Ageing Effects, Air Temperature Effects, Elastomeric Bearings, Sliding Bearings, Nonlinear Seismic Analysis, Fragility Curves.

1 INTRODUCTION

During the lifetime of the elastomeric (e.g. high-damping-rubber bearings, HDRBs) and sliding (e.g. flat sliding bearings, FSBs) bearings, representing some of the most widely used types of isolation systems, ageing and air temperature are important factors that affect the degradation of rubber and friction coefficient of the sliding surface, respectively. The introduction of the property modification factor approach to bound the likely seismic response of isolators has first been applied in the American code for new buildings [1], while a similar approach is implemented in the European code for bridges [2]. In detail, maximum or minimum factors for each type of event (e.g. ageing, air temperature and variations observed during testing) and an adjustment factor, taking into account the reduced probability of cumulative effects during an earthquake, are multiplied in order to define upper- and lower-bound force-displacement laws. However, other codes (e.g. the Italian code, [3]) are limited to establish the maximum variation of the mechanical properties of the isolators, vis-à-vis the corresponding nominal values, only for the purpose of qualification tests.

The mechanical properties of the HDRBs change uniformly along the radial direction of the isolator in a relatively short time, until a stable equilibrium state is reached in the inner region bounded by an external critical depth [4], the latter being an exponential function of the temperature [5]. The outer region is also affected by an oxidation process, related to time and depending on the amount of oxygen, which produces a degradation of properties whose effects diminish moving towards the critical depth. Moreover, the HDRBs considerably increase their horizontal and vertical stiffnesses for decreasing values of the air temperature through rubber crystallization due to prolonged exposure to cold weather, while their cyclic behaviour does not change significantly at high air temperatures [6]. Finally, it should be noted that ageing [7, 8] and air temperature [9] do not affect the equivalent viscous damping ratio of the HDRBs significantly. On the other hand, the friction coefficient of the FSBs presents an age-related increase that can be considered because of changes in the adhesive properties depending on creep of materials and subsequent increase in the contact area between the sliding pad and sliding plate [10]. In particular, creep affects the static friction coefficient during lifetime of the isolator while at the onset the dynamic friction coefficient remains almost unchanged. The significant frictional heating during seismic loading moderates the effects of low temperatures at the sliding interface that combined with isolators placed in normal environment obviates the air temperature effects on the friction coefficient [11].

While the analytical and experimental studies above-mentioned have provided considerable insight into how to predict the long-term behaviour of elastomeric and sliding bearings when subjected to aging and air temperature effects, more investigation is required to evaluate the effects of these phenomena on the nonlinear seismic analysis of base-isolated buildings. This study is also devoted to investigate the level of reliability of the property modification factor approach adopted in ASCE 7-2016 [1] predicting, conservatively, the nonlinear seismic response of base-isolation system and superstructure. First, six-storey r.c. framed structures, base-isolated with HDRBs acting alone or in combination with FSBs, are designed in accordance with the current Italian code [2] in a high-risk seismic zone, considering nominal values of mechanical properties of the isolation system. Specifically, nine structural configurations are examined, combining three elastomer compounds of HDRBs (i.e. soft, normal and hard) and two sliding friction coefficients of FSBs (i.e. low and medium). The results of nonlinear time-history analysis are used to build fragility curves based on simple regression in the logarithmic space of structural response versus seismic intensity [12], considering ground motions selected from the Pacific Earthquake Engineering Research center database [13] and scaled in line with the design hypotheses adopted.

2 AGEING EFFECTS ON THE ISOLATION SYSTEM

Mechanical properties of the HDRBs inevitably change over time and tend to cause an increase of the horizontal and vertical stiffnesses, with a reduction of the fundamental vibration periods that may affect the seismic response of a base-isolated structure. Ageing is dependent on the rubber compound and improper vulcanization and substantially increases for either very high damping or very low shear modulus [14]. Assuming linear material behaviour, the nominal horizontal (K_{H0}) and vertical (K_{V0}) stiffnesses of an HDRB can be evaluated as function of the initial (unaged) shear (G_0) and axial (E_0) moduli

$$K_{H0} = \frac{G_0 \cdot A}{t_r} = \frac{G_0 \cdot \pi \cdot D^2}{4 \cdot t_r}; K_{V0} = \frac{E_0 \cdot A}{t_r} = \frac{E_0 \cdot \pi \cdot D^2}{4 \cdot t_r} \tag{1a,b}$$

A and D being the cross-sectional area and the diameter of a circular bearing, respectively, and t_r the total thickness of the rubber. The ageing depends on chemical reactions and diffusion rate of oxygen and is characterized by a fast stage during which the mechanical properties change almost uniformly over the whole area and a slow stage governed by oxidation of the external part until a critical depth [4]

$$d^* = \alpha \cdot e^{\beta/T} \tag{2}$$

increasing for lower values of air temperature [15], where coefficients α(=1.2x10^{-4} mm) and β(=3.82x10^3 K^{-1}) can be evaluated with thermal oxidation tests [7]. That is why the aged shear modulus (G(t)) depends on the position inside the bearing and the horizontal stiffness can be expressed as

$$K_H(t) = \frac{Q_H(t)}{t_r} \tag{3}$$

having

$$Q_H(t) = \int G_{aged} \cdot dA = G_0 \cdot \int_0^{2\pi D/2} \int_0 f(r,\theta) \cdot dr \cdot d\theta \tag{4}$$

where $f(r,\theta)$ is a function describing the spatial variability of the shear modulus because of ageing. More specifically, Equation (4) can be divided in internal

$$Q_{Hi}(t) = 2 \cdot \pi \cdot G_0 \cdot \int_0^{R-d^*} (1 + \Delta f_{fast}) \cdot r \cdot dr \tag{5a}$$

and external

$$Q_{He}(t) = 2 \cdot \pi \cdot G_0 \cdot \int_{R-d^*}^{R} [1 + \Delta f_{fast} + w(r) \cdot \Delta f_{slow}] \cdot r \cdot dr \tag{5b}$$

contributions calculated on the corresponding reduced circular areas. In detail, fast and slow increases of the initial shear modulus are governed by the following expressions [7]

$$\Delta f_{fast} = 88.4 \cdot e^{-1887.2/T}, \ \Delta f_{slow} = 9.3 \times 10^{-4} \cdot t_{ref} \tag{6a,b}$$

where t_{ref} is the equivalent ageing time (expressed in days) at the reference temperature T_{ref} (expressed in degree Kelvin) of accelerated ageing tests while T represent the temperature under the service condition. It should be noted that constant parameters of Equations 6a and 6b

are assumed equal to the values proposed by [7] on the basis of investigation on different rubber compounds. Moreover, a parabolic law describes the spatial variation of Δf_{slow} in the external part of a circular bearing with radius R. Finally, an equivalent aged shear modulus can be evaluated for each elastomer compound as

$$G(t) = \frac{K_H(t)}{K_{H0}} \cdot G_0 \tag{7}$$

by which an equivalent aged axial modulus can be assessed

$$E(t) = \left(\frac{1}{6 \cdot G(t) \cdot S_1^2} + \frac{4}{3 \cdot E_b} \right)^{-1} \tag{8}$$

where E_b represents the volumetric compression modulus of the rubber (e.g. E_b=2000 MPa), whose variation over time is neglected, and S_1=D/(4t) is the primary shape factor, t being the thickness of the single layer of elastomer. Finally, the corresponding vertical stiffness is

$$K_V(t) = E(t) \cdot A / t_r \tag{9}$$

On the other hand, time variation of the static friction coefficient during the stick-slip phases has been experimentally studied through durability tests [10], highlighting an increase attributed primarily to creep of the materials and a corresponding increase in the contact area between sliding pad and sliding plate; moreover, negligible changes of the dynamic friction coefficient have been observed. Specifically, the following expression has been proposed to represent variability of the static friction coefficient over time:

$$\mu_s(t) = \mu_{s0} + 0.016 \cdot t^{0.1} \tag{10}$$

μ_{s0} being the initial (unaged) value of the static friction while t is the age, measured in years.

In line with International codes (e.g. [16]), the accelerated ageing process of elastomeric and sliding bearings are based on exposure of specimens to high temperatures T_{ref} (typically in the range 60°-80°) in a vacuum for known (generally relatively short) periods of time t_{ref}. However, the age of the treated specimens represented in these laboratory tests is not specified, confirming that this approach can be useful in the comparison of various rubber compounds but is unsuitable for the prediction of life expectancy of the elastomeric bearings [17]. For just that purpose, in the present work the Arrhenius methodology is adopted to correlate the accelerated ageing results with the ageing under service conditions [18, 19]:

$$\ln\left(t_{ref} / t\right) = E_a / R_g \cdot \left(T_{ref}^{-1} - T^{-1}\right) \tag{11}$$

t being the real time; E_a(=9.04x10^4 J/mol) the activation energy of the rubber; R_g(=8.31 J/mol/K) the gaseous constant.

Curves representing variability of the mechanical properties with time of accelerated ageing (t_{ref}), at the controlled temperature T_{ref}=80°C and service mean temperature T=20°C, are plotted in Figure 1. Specifically, shear modulus of the HDRBs (i.e. G(t) in Figure 1a), for three elastomer compounds (i.e. soft, S, normal, N, and hard, H) and static friction coefficient of the FSBs (i.e. μ_s(t) in Figure 1b), for low- (L) and medium (M) friction, are represented starting from the nominal (unaged) value. As a comparison, an additional axis of abscissa is reported in order to represent the equivalent time of ageing obtained with the Arrhenius method. It is worth noting that heat ageing tests after an expected time of 17, 33, 50 and 67 days correspond to 25, 50, 75 and 100 years when T_{ref}=80°C is considered, but an unrealistically high value of the reference time should be considered for the prediction of the life expectancy

when T_{ref}=60°C or T_{ref}=70°C are assumed. As expected, an increase of stiffness (Figure 1a) and friction threshold (Figure 1b) is observed for increasing values of t_{ref}.

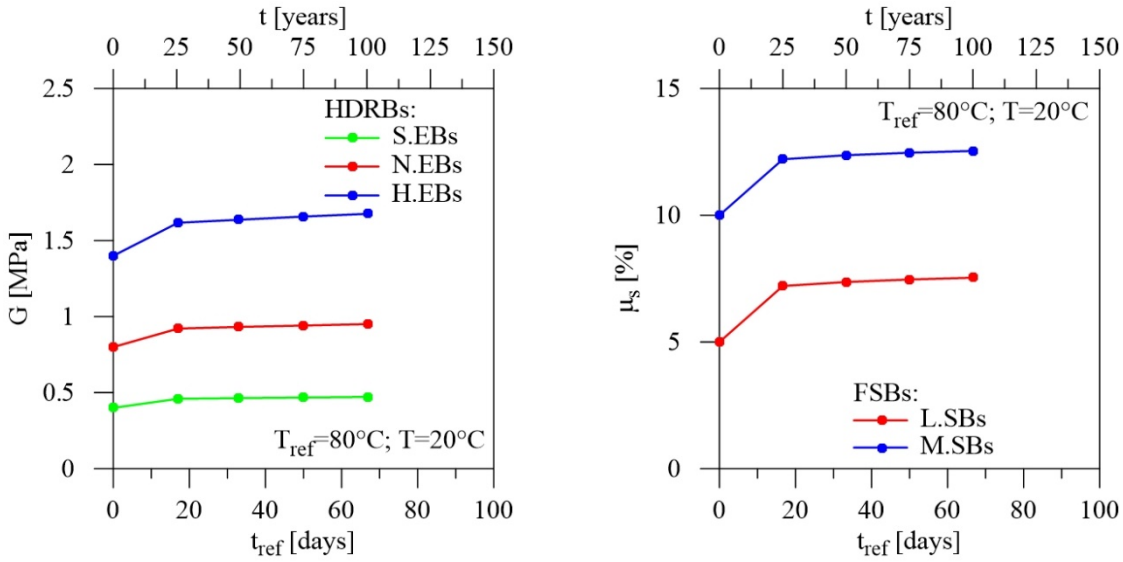

(a) HDRBs. (b) FSBs.

Figure 1: Effects of ageing on mechanical properties of the isolation system.

3 AIR TEMPERATURE EFFECTS ON THE ISOLATION SYSTEM

Mechanical properties of the HDRBs can also change significantly due to weather conditions: i.e. variations in the environmental temperature over long periods of time, such as wide variations in air temperature between winter (e.g. with a mean value of 10°C) and summer (e.g. with a mean value of 25°C). Specifically, experimental tests carried out on the HDRBs show that both the stress level and the area encompassed by the hysteresis loop increase more than linearly while air temperature is decreasing, especially when the temperature drops below zero [6]. Moreover, at a given temperature, these effects increase from soft-to-normal and from normal-to-hard elastomer compounds [9]. Furthermore, undetectable sensitivity of the cyclic behaviour to the thermal history of the specimen is observed, while the equivalent viscous damping remains practically unchanged over the whole range of air temperature. The results also indicate that the lateral stiffness increases more than linear when the air temperature falls significantly compared to the mean working condition (i.e. T=20°C); at the same time, rising temperatures do not lead to abrupt variations in lateral stiffness. Based on the experimental curves at 100% of shear strain [9], the secant shear modulus variability with air temperature (T) can be expressed by the following polynomial laws, distinguishing soft (SC)

$$G_{SC}=0.508-9.779\cdot10^{-3}\cdot T+3.603\cdot10^{-4}\cdot T^2-8.843\cdot10^{-6}\cdot T^3+8.967\cdot10^{-8}\cdot T^4 \ [MPa] \quad (12)$$

normal (NC)

$$G_{NC}=1.039-1.468\cdot10^{-2}\cdot T+4.204\cdot10^{-4}\cdot T^2-2.275\cdot10^{-5}\cdot T^3+4.29\cdot10^{-7}\cdot T^4 \ [MPa] \quad (13)$$

and hard (HC)

$$G_{HC}=1.752-2.493\cdot10^{-2}\cdot T+4.704\cdot10^{-4}\cdot T^2-7.452\cdot10^{-6}\cdot T^3+1.147\cdot10^{-7}\cdot T^4 \ [MPa] \quad (14)$$

elastomer compounds. It should be noted that the selected compounds (i.e. SC, NC and HC) present the nominal values of the shear modulus (i.e. 0.4 MPa, 0.8 MPa and 1.4 MPa) provided by FIP [20] when the selected temperature corresponds to the mean working temperature

(i.e. T=20°C). The corresponding axial moduli are evaluated through an expression similar to Equation 8

$$E_{..}(T) = \left(\frac{1}{6 \cdot G_{..}(T) \cdot S_1^2} + \frac{4}{3 \cdot E_b} \right)^{-1} \tag{15}$$

Curves representing variability of mechanical properties of HDRBs with air temperature are plotted in Figure 2. Specifically, shear (Figure 2a) and axial (Figure 2b) moduli of the HDRBs for SC, NC and HC elastomer compounds are represented in the range of temperatures from -20°C to 40°C. Vertical lines corresponding to winter and summer mean seasonal temperatures are also reported as threshold values considered in the numerical study. As can observed, the rate of reduction of the axial modulus with temperature (Figure 2b) is less evident than that observed for the shear modulus (Figure 2a) as a result of Equation 10 where $G_{..}(T)$ only concerns the first part of $E_{..}(T)$.

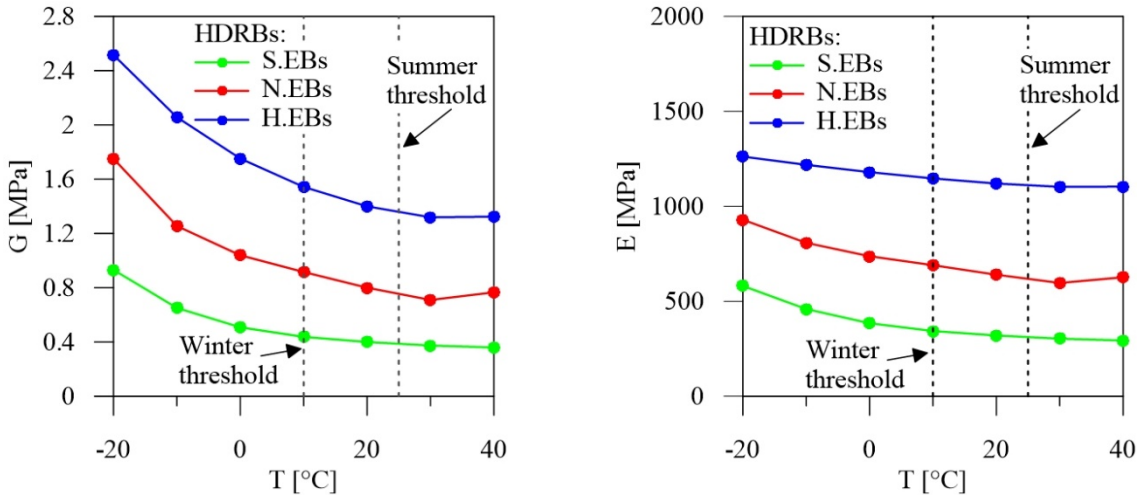

(a) Shear modulus. (b) Axial modulus.

Figure 2: Effects of air temperature on the mechanical properties of the HDRBs.

Finally, experimental results corresponding to different pressure-velocity couples of values highlight the fact that the dynamic friction coefficient decreases for increasing values of the air temperature [21]. Specifically, the rate of reduction is greater at low-to-medium (i.e. -10°C to 20°C) than from medium-to-high (i.e. 20°C to 50°C) temperatures, highlighting a decrease of about 2.5 times in the rate when the dynamic fast (μ_{fast}) instead of dynamic low (μ_{low}) friction coefficient is considered. Moreover, the dynamic friction coefficient is practically independent of the contact pressure. However, variation of the dynamic friction coefficient with temperature is significantly reduced in the range from 10°C to 25°C and therefore will not be considered in the present study.

4 TEST STRUCTURES

Six-storey residential buildings with a reinforced concrete (r.c.) framed structure isolated at the base by twenty identical HDRBs (i.e. elastomeric isolation system) or fourteen HDRBs combined with six FSBs (i.e. hybrid isolation system) are considered for the numerical investigation (Figure 3). In view of the symmetric plan of the building, only the plane frames orientated along the horizontal ground motion direction (Y), perpendicular to the floor slab direction (X), are considered as reference.

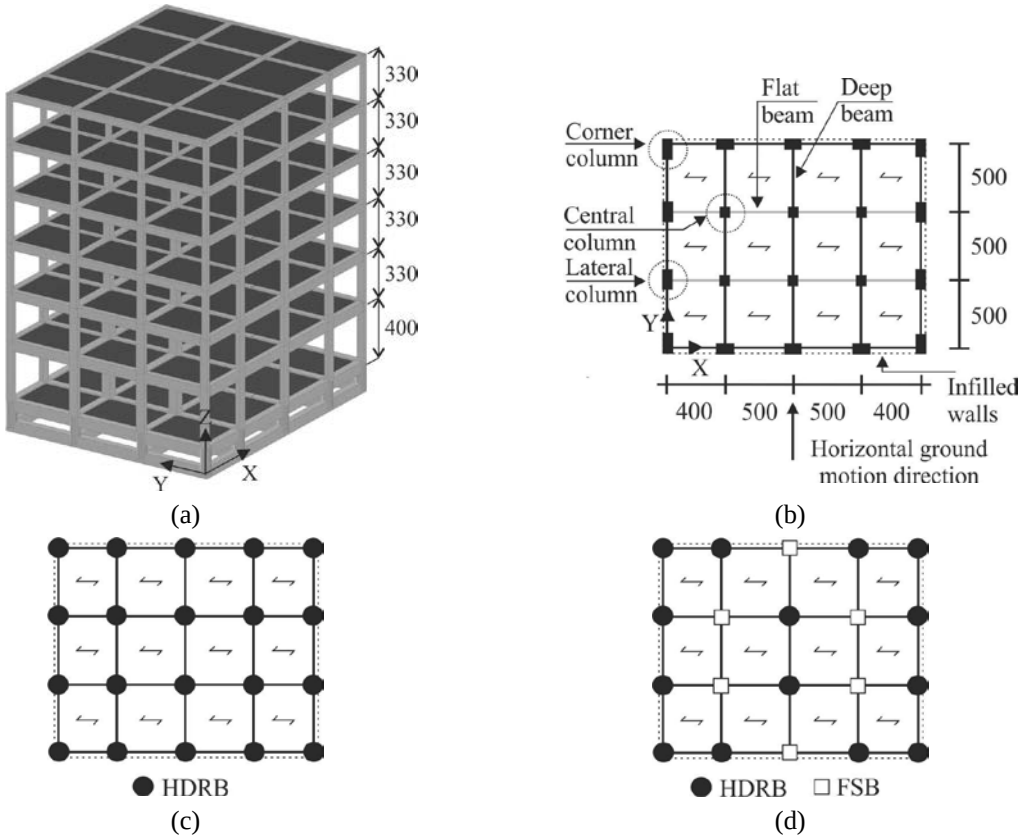

Figure 3: 3D view and plans and of the base-isolated structures (units in cm).

The design vertical loads are divided in structural dead loads and non-structural live loads equal, respectively, to 3.5 kN/m^2 and 2 kN/m^2 at all floors. Non-structural dead-loads are also applied, assuming: 1.67 kN/m^2, for the sixth floor; 3.47 kN/m^2, for the zero floor, and 3.07 kN/m^2, for the other floors. Non-structural masonry infills are taken into account through an additional dead load of 2.70 kN/m^2 along the perimeter. A cylindrical compressive strength of 25 N/mm^2 for the concrete and a yield strength of 450 N/mm^2 for the steel are assumed for the r.c. frame members. Horizontal and vertical seismic loads are evaluated in line with the current Italian code [3], assuming: high risk seismic zone; elastic response of the superstructure (i.e. behaviour factors for the horizontal and vertical seismic loads, q_H=q_V=1.0); medium subsoil type (i.e. subsoil class B); flat terrain (i.e. topographic class T1). The fundamental vibration period of the base-isolated structures is assumed equal to 2.1 s in the horizontal direction. The dimensions of the cross sections assumed for the beams and columns are reported in Table 1 where masses at the floor levels (i.e. m_i) are also presented. The design of the superstructure is carried out at the LS limit state so as to satisfy minimum conditions for the r.c. frame members in line with the provisions imposed by NTC18 [3].

Storey	Corner column	Lateral column	Central column	Deep beam	Flat beam	m_i
6	30x30	30x30	30x30	30x45	40x25	2.600
5	30x35	30x40	40x40	30x45	40x25	2.846
4	30x40	30x50	50x50	30x50	50x25	2.989
3	30x40	30x50	50x50	30x55	50x25	3.123
2	30x50	30x60	60x60	40x60	60x25	3.458
1	30x50	30x60	60x60	40x70	60x25	3.671
0	-	-	-	50x100	50x100	4.418

Table 1: Geometrical properties of the superstructure (units in cm and ton).

The elastomeric base-isolation (EBI) systems consist of three elastomer compounds for the twenty identical HDRBs and comply with the CP limit state, assuming a seismic design displacement equal to 28.9 cm and a nominal stiffness ratio α_{K0}(=K_{V0}/K_{H0}) equal to 800. Specifically, soft (S.EBs, Figure 4a), normal (N.EBs, Figure 4b) and hard (H.EBs, Figure 4c) compounds are characterized by an unaged shear modulus (G_0) equal to 0.4 MPa, 0.8 MPa and 1.4 MPa, respectively, and a volumetric compression modulus of the rubber (E_b) equal to 2000 MPa. All three compounds ensure the same values of the equivalent viscous damping ratio for the EBI systems: i.e. ξ_H=10%, in the horizontal direction; ξ_V=5%, in the vertical direction. The following geometrical properties of the HDRBs are reported in Table 2: diameter of the steel layer (D_s) and that of the elastomer (D_e); total thickness (t_e) and thickness of the single layer (t_i) of elastomer; number (n_{si}) and thickness (t_{si}) of the interior steel shims; thickness of the exterior steel plates (t_{se}); total height of the bearing (h).

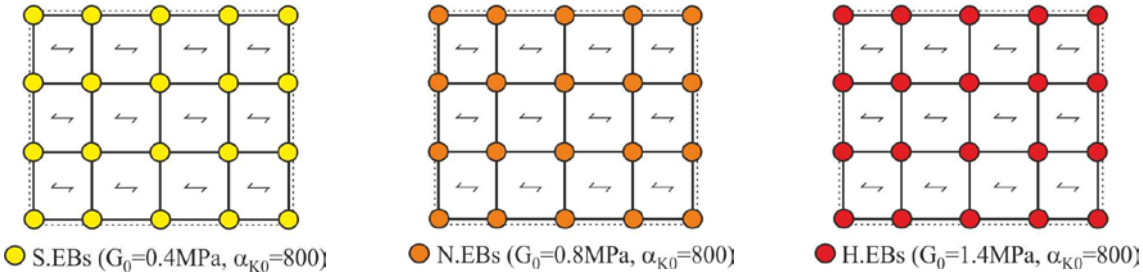

(a) (b) (c)

Figure 4: Elastomeric isolation systems with different elastomer compounds for the HDRBs.

Compound	D_s	D_e	t_e	t_i	n_{si}	t_{si}	t_{se}	h
Soft (S)	68	68	14.1	1.3	11	0.21	3	22.1
Normal (N)	50	50	18.3	0.9	19	0.28	3	29.7
Hard (H)	46	46	22.4	0.5	45	0.40	3	45.9

Table 2: Geometrical properties of the HDRBs for the elastomeric isolation systems (units in cm).

Six hybrid elastomeric-sliding base-isolation (ESBI) systems are designed at the CP limit state, given fourteen identical HDRBs, with three elastomer compounds (i.e. S.EBs, N.EBs and H.EBs), acting in parallel with six FSBs (four internally placed and two along the perimeter) and characterized by low- (i.e. L.SBs in Figures 5a-5c) and medium-type (i.e. M.SBs in Figures 5d-5f) friction properties. This arrangement corresponds to a value 0.37 for the nominal sliding ratio α_{S0}(=$F_{S0}/F_{S0,max}$) of the FSBs under gravity loads, defined as the sliding force (F_{S0}) of the entire sliding system divided by the maximum sliding force ($F_{S0,max}$) corresponding to a sliding bearing below each column of the test structure. The nominal stiffness ratio adopted for the ESBI systems is the same as the EBI ones (i.e. α_{K0}=800). The set of static (μ_s) and dynamic (μ_{slow} and μ_{fast}) friction parameters of the FSBs assumed in the analyses are reported in Table 3, where axial loads in the quasi-permanent combination (P_{sd}) are also shown. It should be noted that for FSBs with medium-type friction the coefficients are twice those for low-type friction. Damping properties of the ESBI systems are shown in Table 4, where: $W_{s,HDRBs}$ and $W_{s,FSBs}$ represent the strain energies at the secant stiffness corresponding to the design displacement; $W_{h,HDRBs}$ and $W_{h,SBs}$ represent the hysteretic energies in a cycle of motion at the same displacement. Finally, Table 5 summarises the geometrical properties for HDRBs of the ESBI systems with reference to low- and medium-type friction of the FSBs. Further details about the design of the test structures can be found in a previous work by the author [22].

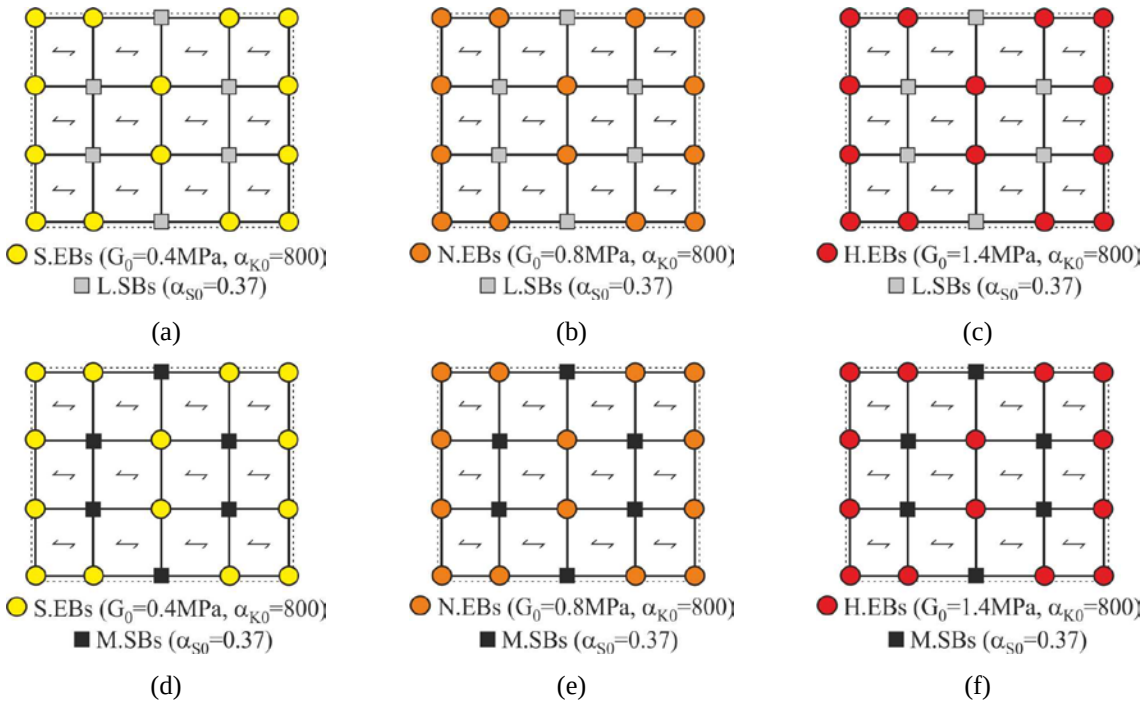

Figure 5: Hybrid elastomeric-sliding isolation systems with different elastomer compounds for the HDRBs and friction threshold for the FSBs.

Friction type	μ_{st}	μ_{slow}	μ_{fast}	P_{Sd} (lateral)	P_{Sd} (central)
Low (L)	5%	1%	2.5%	905	1243
Medium (M)	10%	2.5%	5%	905	1243

Table 3: Mechanical properties of the FSBs (units in kN).

Friction type	$W_{h,HDRBs}$	$W_{s,HDRBs}$	$W_{h,FSBs}$	$W_{s,FSBs}$	$\xi_{H,HDRBs}$	$\xi_{H,FSBs}$	$\xi_{V,HDRBs}$	$\xi_{V,FSBs}$
Low (L)	88992	83960	19593	2449	8	2	5	-
Medium (M)	69399	81511	39186	4898	7	3	5	-

Table 4: Damping properties of the hybrid isolation systems (units in kN and cm).

Friction type	Compound	D_s	D_e	t_e	t_i	n_s	t_{si}	t_{se}	h
Low (L)	Soft (S)	81	81	14.5	1.6	9	0.21	3	22.2
	Normal (N)	61	61	16.3	1.0	16	0.28	3	26.5
	Hard (H)	46	46	16.1	0.5	32	0.4	3	34.6
Medium (M)	Soft (S)	80	80	14.5	1.5	9	0.21	3	22.2
	Normal (N)	61	61	16.8	1.0	17	0.28	3	27.2
	Hard (H)	46	46	16.6	0.5	33	0.4	3	35.5

Table 5: Geometrical properties of the HDRBs for the hybrid isolation systems (units in cm).

4. NUMERICAL RESULTS

A numerical study is carried out to investigate the effects produced by the variability of the mechanical properties of elastomeric (EBI systems) and hybrid elastomeric-sliding (ESBI systems) bearings due to ageing and air temperature. In order to reflect the increase of both stiffness of the HDRBs and static friction coefficient of the FSBs over their lifetime, different ageing times (i.e. t_{ref}=17, 33, 50 and 67 days) are taken into account in the accelerated thermal oxidation test at reference temperature of T_{ref}=80°C. Moreover, the sensitivity of the HDRBs to air temperature variations is evaluated by referring to mean seasonal (i.e. T=10°C in the

winter and T=25°C in the summer) and annual (i.e. T=20°C) values. For comparison, system properties modification factors proposed by the American code for new buildings [1] are also considered. Specifically, all the maximum or minimum λ factors for each event are multiplied together [11]

$$\lambda_{\min} = \left[1 - f_a\left(\lambda_{ae,\min} - 1\right)\right] \cdot \lambda_{test,\min} \cdot \lambda_{spec,\min} \tag{16a}$$

$$\lambda_{\max} = \left[1 - f_a\left(\lambda_{ae,\max} - 1\right)\right] \cdot \lambda_{test,\max} \cdot \lambda_{spec,\max} \tag{16b}$$

where factors λ_{ae}, λ_{test} and λ_{spec} encompass, respectively, ageing and environmental effects, variation observed during tests and specification tolerances, while adjustment factor f_a provides for the reduced probability that several additive effects occur simultaneously. In the present work, different modification factors are applied to the HDRBs (i.e. $\lambda_{min,HDRBs}$=1 and $\lambda_{max,HDRBs}$=1.225) and FSBs (i.e. $\lambda_{min,FSBs}$=1 and $\lambda_{max,FSBs}$=1.42), on the assumption that λ_{test}=λ_{spec}=1.0 and with reference to ordinary buildings (i.e. f_a=0.75).

A lumped plasticity model based on the Haar-Kàrmàn principle is used to describe the inelastic behaviour of r.c. frame members of the superstructure [23], assuming a bilinear moment-curvature law with hardening ratio equal to 3%. Plastic conditions are checked at the potential critical sections of beams (i.e. end, quarter-span and mid-span sections of the sub-elements in which a beam is discretized) and columns (i.e. end sections). With a view to studying the effects of advanced nonlinear modelling of the EBI and ESBI isolation systems, the formulations of the HDRBs and FSBs described in a previous paper [22] are implemented through a computer code already proposed [23]. In the Rayleigh hypothesis, the damping matrix of the superstructure is assumed as a linear combination of the mass and stiffness matrices, assuming horizontal and vertical viscous damping ratios (i.e. $\xi_{H,S}$ and $\xi_{V,S}$) equal to 2% with reference to the corresponding fundamental vibration periods (i.e. T_{1H} and T_{1V}). Nonlinear dynamic analyses of the EBI and ESBI structural systems, subjected to the horizontal and vertical components of near-fault earthquakes, are terminated once the ultimate state of the superstructure (in terms of curvature ductility of beams and columns) and ultimate shear deformations (i.e. $\gamma_{tot,u}$=1.5x5=7.5 and $\gamma_{s,u}$=1.5x2=3) and ultimate axial loads (i.e. P_{cr} and P_{tu}) of the HDRBs are attained.

The twenty near-fault ground motion records selected for this numerical investigation are selected from the Pacific Earthquake Engineering Research center database [13] and are classified as pulse-type in accordance with a pulse indicator [24]. Specifically, the two-sided (i.e. forward-directivity) long-period horizontal velocity pulses are characterized by shear-wave velocity of the subsoil in the top 30 m, generally within the range corresponding to the subsoil type at the site in question (i.e. subsoil class B, 360m/s ≤ $V_{s,30}$ ≤ 800m/s). The Modified Acceleration Spectrum Intensity (MASI) measure is evaluated for both the horizontal components, integrating spectral values of acceleration in the range of vibration periods between a lower limit (i.e. 0.5·T_{BI}=1.05s), accounting for the contribution of higher modes to structural response, and an upper limit (i.e. 1.25·T_{BI}=2.63s), including the lengthening of vibration period due to the nonlinear structural behaviour [25]. This structure-specific integral seimic intensity measure can be considered efficient for predicting engineering demand parameters [26]. Note that only the horizontal component with the highest value of MASI is considered in the nonlinear dynamic analyses. In Table 6 the main data of the selected near-fault motions are shown: i.e. earthquake location, date, recording station, magnitude (M_w), closest distance to the fault (Δ), peak ground acceleration (PGA_H) and $MASI_H$ of the selected horizontal component.

Earthquake	Date	Station	M_w	Δ [km]	$V_{S,30}$ [m/s]	PGA_H [g]	$MASI_H$ [m/s]
Coyote Lake	06/08/1974	Gilroy Array #6	5.7	3.11	663.3	0.422	3.16
Tabas	16/09/1978	Tabas	7.4	2.05	766.8	0.854	8.29
Mammoth Lak06	27/05/1980	Long Valley Dam	5.9	16.03	537.2	0.414	2.80
Superstition Hills	24/11/1987	Parachute Test Site	6.5	0.95	348.7	0.432	12.89
Loma Prieta	18/10/1989	Gilroy - Gavilan Coll.	6.9	9.96	729.7	0.359	6.71
Erzincan	13/03/1992	Erzincan	6.7	4.38	352.1	0.496	5.70
Cape Mendocino	25/04/1992	Petrolia	7.0	8.18	422.2	0.591	5.19
Landers	28/06/1992	Barstow	7.3	34.86	370.1	0.135	3.04
Northridge	17/01/1994	Rinaldi Receiving Station	6.7	6.50	282.3	0.874	12.01
Kobe	16/01/1995	Takatori	6.9	1.47	256.0	0.618	18.27
Kocaeli	17/08/1999	Arcelik	7.5	13.49	523.0	0.134	5.53
Chi-Chi	20/09/1999	TCU068	7.6	0.32	487.3	0.512	10.68
Chi-Chi	20/09/1999	TCU076	7.6	2.70	615.0	0.428	1.42
Chi-Chi	20/09/1999	TCU079	7.6	10.70	364.0	0.592	5.76
Chi-Chi	20/09/1999	TCU102	7.6	1.49	714.3	0.304	8.27
Parkfield	28/09/2004	Cholame 2E	6.0	4.08	522.7	0.477	1.15
Parkfield	28/09/2004	Cholame 3E	6.0	5.55	397.4	0.800	0.83
Parkfield	28/09/2004	Cholame 4W	6.0	4.23	410.4	0.575	1.39
Chuetsu-oki	16/07/2007	Oguni Nagaoka	6.8	20.0	561.6	0.625	2.64
L'Aquila	06/04/2009	V. Aterno - Centro Valle	6.3	6.27	475.0	0.664	4.24

Table 6: Main data of the selected ground motions.

First, the nonlinear dynamic analysis of the EBI and ESBI structural systems subjected to the set of twenty unscaled ground motion histories is performed. For each record, the final instant of simulation is assumed as that corresponding to the attainment of an ultimate condition of r.c. frame members of the superstructure and/or HDRBs of the base-isolation system in the conventional design configuration (i.e. t=0 days and T=20°C). Afterwards, in order to make the results comparable, the analyses are repeated assuming this value as the final instant of simulation for each ground motion and base-isolated system. The cloud method is adopted for the fragility analysis [12], based on fitting a linear regression model in the logarithmic scale to the pairs of an engineering demand parameter (EDP), representative of the structural response, versus an intensity measure (IM) for a suite of unscaled ground motions. In Figures 6 and 7 are reported cloud data of the EBI and ESBI structures, respectively, obtained by combining a scalar demand to capacity ratio of the EDP, that is equal to unity at the onset of the ultimate limit state, with an IM [27]. In particular, maximum values of ductility demand at the end sections of the beams (Figures 6a,b,c and 7a,b,c) and total shear strain of the HDRBs (Figures 6d,e,f and 7d,e,f) are plotted against the MASI values corresponding to the elastic response spectra of acceleration of the interrupted records. Plots refer to three elastomer compounds of the HDRBs (i.e. the EBI.S, EBI.N and EBI.H structures) which may be combined with low friction of the FSBs (i.e. the ESBI.SL, ESBI.NL and ESBI.HL structures). The dependence of mechanical properties of the HDRBs on air temperature variations is taken into account by considering winter (T=10°C) and summer (T=25°C) mean values of temperature, in the aged state corresponding to t_{ref}=33days and T_{ref}=80°C. Results for the lower (λ_{min}) and upper (λ_{max}) bound limit values of the ASCE modification factor are also presented for comparison.

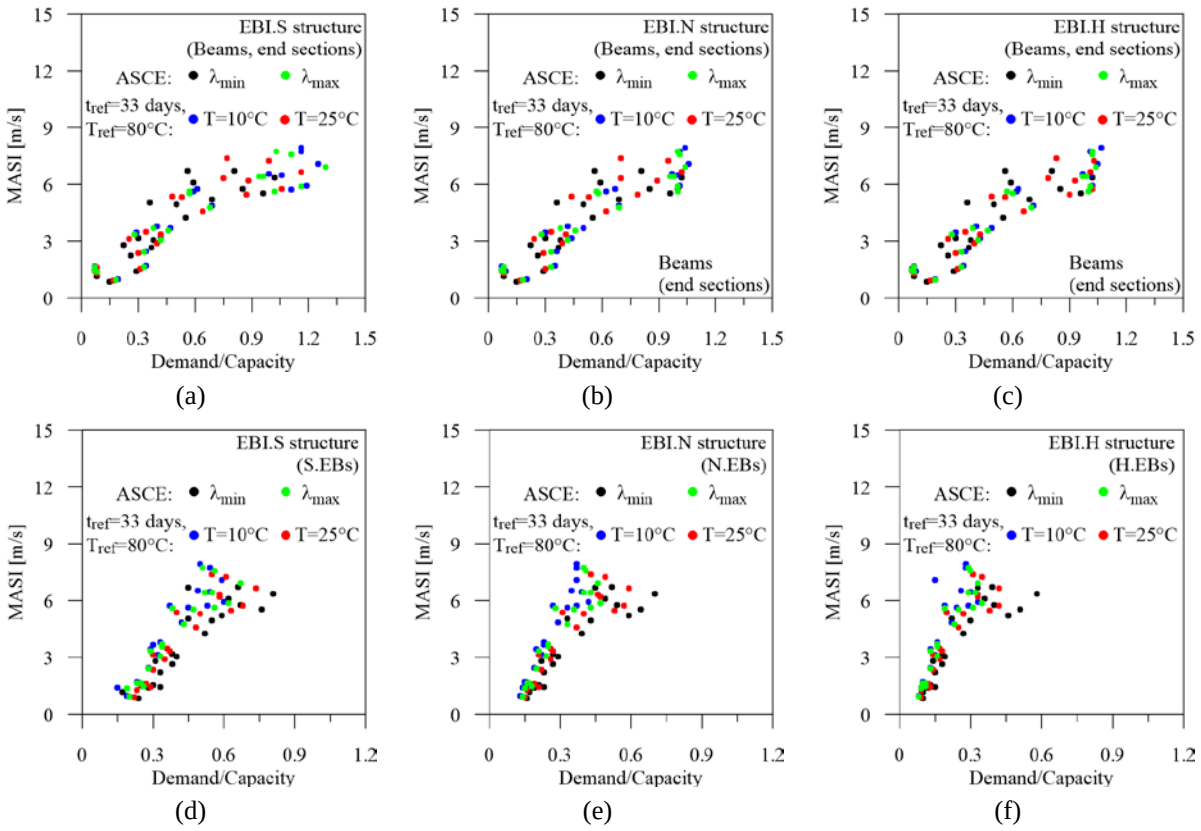

Figure 6: Cloud data of the structural systems with elastomeric base-isolation system: (a, b, c) ductility demand of beams; (d, e, f) total shear strain of HDRBs.

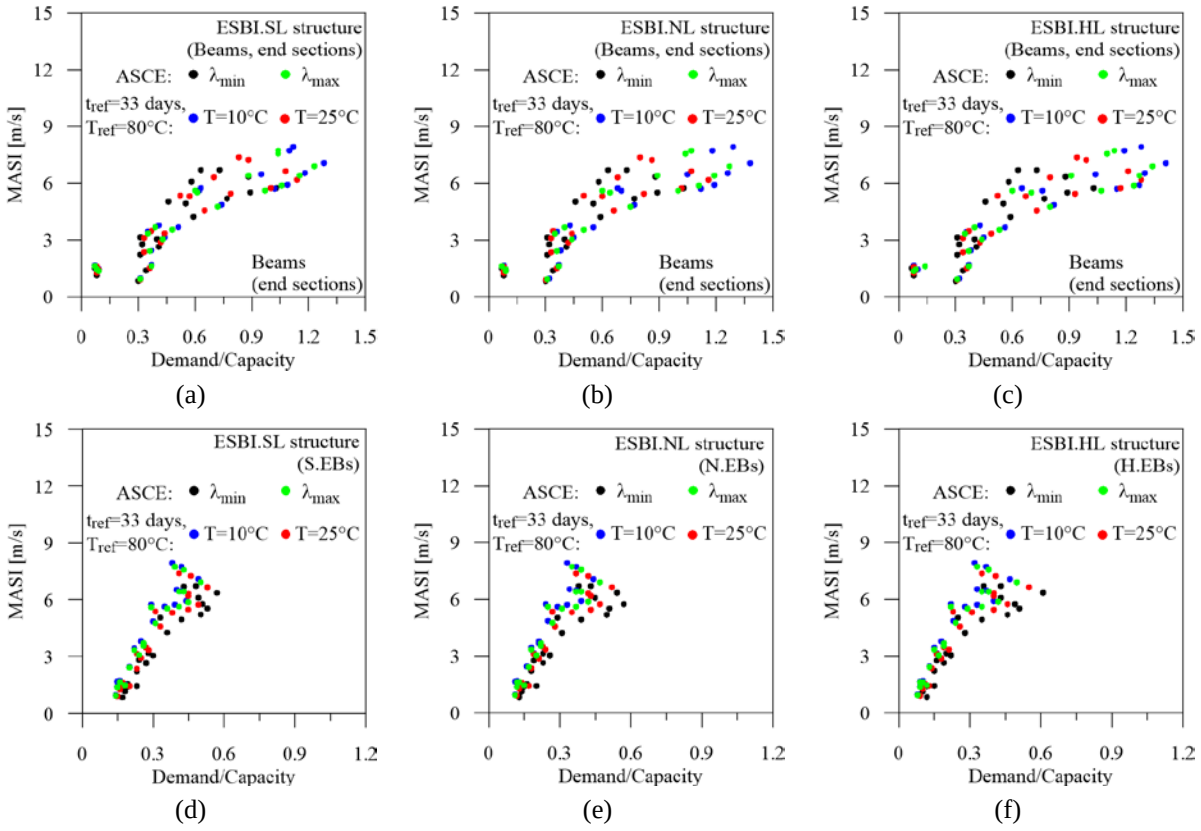

Figure 7: Cloud data of the structural systems with hybrid elastomeric-friction base-isolation system: (a, b, c) ductility demand of beams; (d, e, f) total shear strain of HDRBs.

As can be observed, the significant dispersion in the MASI values of the selected ground motions and the occurrence of a number of demand to capacity EDP ratios greater than unity leads to reasonable fragility estimates. Specifically, the maximum ductility demand of beams at the lower storeys of the test structures is always responsible for the conventional structural failure at t=0 days and T=20°C, (i.e. λ_{min}). The decrease in temperature leads to an increase of the ductility demand (see blue points in Figures 6a,b,c and 7a,b,c), while the opposite happens for the total shear strain when air temperature rises (see red points in Figures 6d,e,f and 7d,e,f).

In order to estimate the probability that a given level of damage will occur in the EBI and ESBI structures, undergoing a given ageing time at different air temperatures, fragility analysis needs to be developed. To this end, a robust fragility software based on the cloud data above described, is adopted for an efficient fragility assessment [27]. Fragility curves of the EBI and ESBI structures are reported in Figures 8 and 9, respectively, with reference to the superstructure and base-isolation system. Namely, the fragility curves plotted in Figures 8a,b,c and 9a,b,c provide information about the probability of exceeding a particular state of damage of the superstructure conditioned on ductility demand, while total shear strain-based fragility functions return a similar result for the base-isolation system (Figures 8d,e,f and 9d,e,f). It is noted that fragility curves referring to the minimum (λ_{min}) and maximum (λ_{max}) values of ASCE modification factors almost always envelope curves which are the effects of the long-term behaviour of the superstructure (i.e. blue and red lines in Figures 8a,b,c and 9a,b,c), unlike base isolation systems of the EBI (Figures 8d,e,f) and ESBI (Figures 9d,e,f) structures whose fragility curves for T=10°C exceed those related to λ_{min}. Furthermore, the selection of different elastomer compounds produces a significant variability of fragility curves of the HDRBs while less pronounced effects are observed for the superstructure.

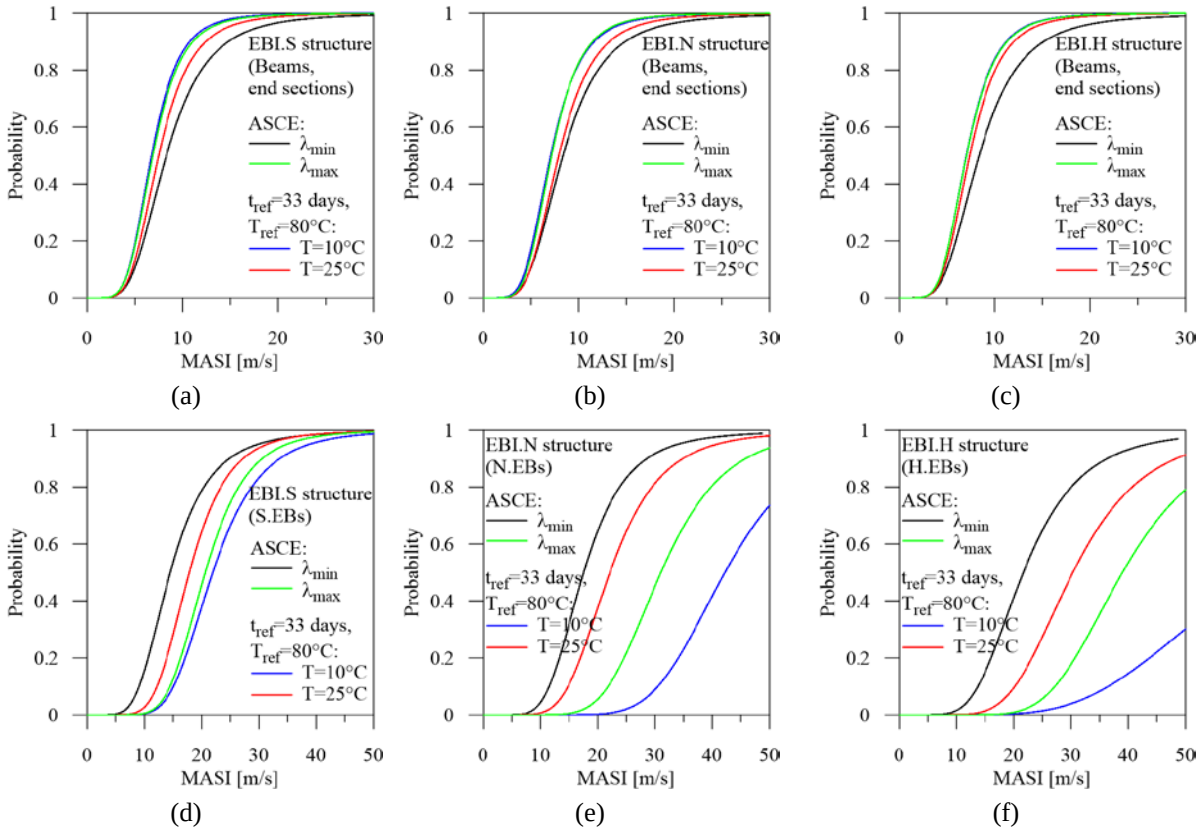

Figure 8: Fragility curves of the structural systems with elastomeric base-isolation system: (a, b, c) ductility demand of beams; (d, e, f) total shear strain of HDRBs.

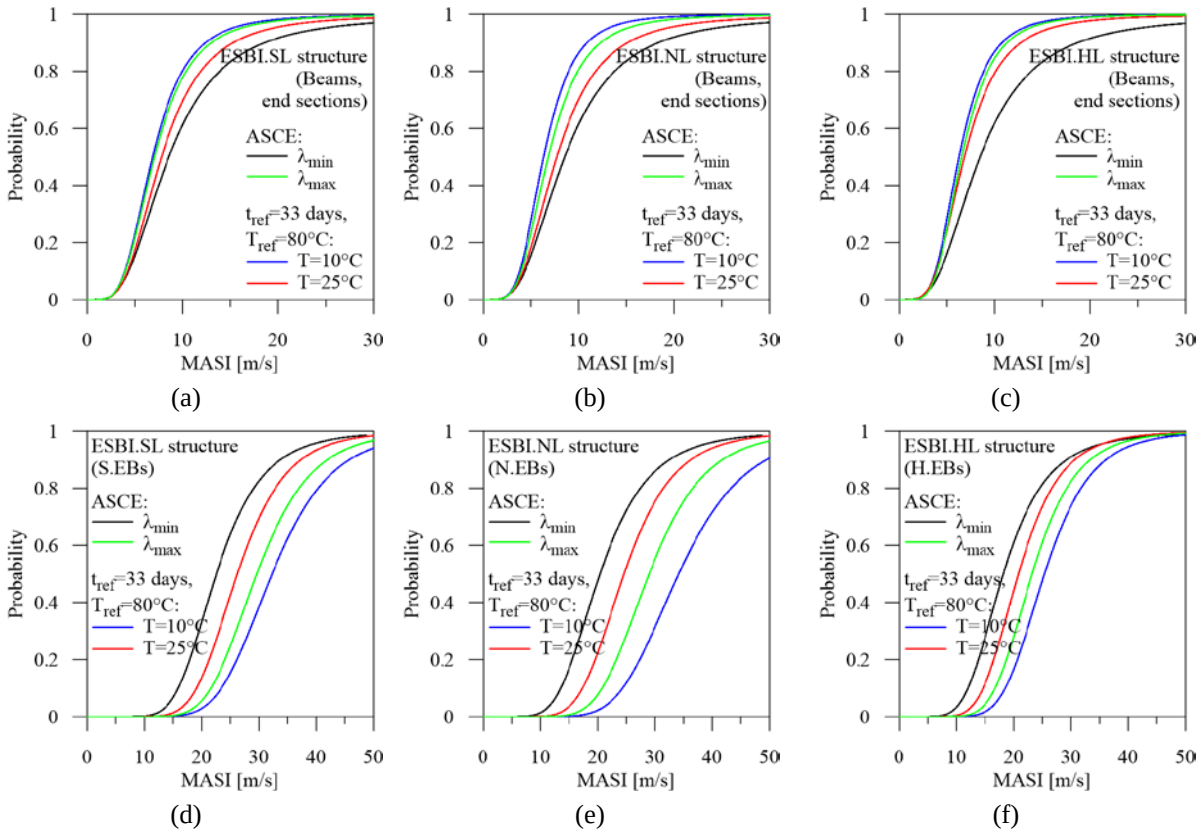

Figure 9: Fragility curves of the structural systems with hybrid elastomeric-friction base-isolation system: (a, b, c) ductility demand of beams; (d, e, f) total shear strain of HDRBs.

5 CONCLUSIONS

With the aim of quantifying the effects of mechanical property variability in elastomeric and sliding bearings on the nonlinear seismic response of base-isolated r.c. framed structures, a numerical model is proposed based on experimental results available in literature. Specifically, the influence of ageing and air temperature on the horizontal and vertical stiffnesses of the HDRBs and friction coefficient of the FSBs are investigated, while the equivalent viscous damping ratio of the HDRBs was found non-sensitive to these effects. First, nine structural solutions for the base-isolation system of six-storey r.c. framed structures are designed assuming nominal values of mechanical properties and considering two alternative arrangements: i) elastomeric base-isolation (EBI) systems, with three different elastomer compounds for the HDRBs (soft, normal and hard); ii) hybrid elastomeric-sliding base-isolation (ESBI) systems, with the aforementioned elastomer compounds of the HDRBs and two friction coefficients (low and medium) of the FSBs. Finally, fragility analysis of the test structures subjected to the horizontal components of unscaled earthquakes is carried out together with nonlinear dynamic analysis under the horizontal and vertical components of earthquakes scaled at the ultimate limit state. The results for the lower and upper bound property modification factors proposed by ASCE provide a comparison. The following conclusions can be drawn from the results presented in this study. Curves representing effects of accelerated ageing confirm that an increase of the horizontal stiffness of the HDRBs, and to a lesser extent vertical stiffness, and static friction coefficient of the FSBs is obtained for increasing values of the reference time. The equivalent time of ageing obtained with the Arrhenius method highlights that 25, 50, 75 and 100 years correspond to 17, 33, 50 and 67 days, respectively, when accelerated heat ageing tests at T_{ref}=80°C are considered, but an unrealistically high value of t_{ref} should be as-

sumed for the prediction of life expectancy when T_{ref}=60°C or T_{ref}=70°C is assumed. Variability of shear and axial moduli of the HDRBs is observed for mean seasonal and annual temperatures, with an increase moving from summer to winter values. However, variation of the dynamic friction coefficient of the FSBs with temperature can be neglected. Fragility curves referring to the minimum (λ_{min}) and maximum (λ_{max}) ASCE values almost always envelope curves representing effects of the long-term behaviour of the superstructure, unlike for the base isolation systems of the EBI and ESBI structures whose fragility curves for T=10°C exceed those related to λ_{min}. The selection of different elastomer compounds produces a significant variability of fragility curves of the HDRBs while less pronounced effects are observed for the superstructure.

ACKNOWLEDGEMENTS

The present work was financed by Re.L.U.I.S. (Italian network of university laboratories of earthquake engineering), in accordance with the "Convenzione D.P.C.-Re.L.U.I.S. 2019-2021, WP15, Code Revisions for Isolation and Dissipation".

REFERENCES

[1] American Society of Civil Engineers, Minimum Design Loads for Buildings and Other Structures, ASCE/SEI 7-16, 2017.

[2] Eurocode 8, Design of Structures for Earthquake Resistance. Part 2: Bridges. *European Committee for Standardization*, EN1998-2, 2005.

[3] N.T.C., Technical Regulations for the Constructions. Italian Ministry of the Infrastructures, D.M. 17-01-2018.

[4] Y. Itoh, H.S. Gu, Prediction of aging characteristics in natural rubber bearings used in bridges. *Journal of Bridge Engineering*, **14**, 122-128, 2009.

[5] Y. Itoh, H.S. Gu, K. Satoh, Y. Yamamoto, Long-term deterioration of high damping rubber bridge bearing. *Journal of Structural Mechanics and Earthquake Engineering*, **62**, 595-607, 2006.

[6] K.N.G. Fuller, J. Gough, A.G. Thomas, The effect of low temperature crystallization on the mechanical behaviour of rubber. *Journal of Polimer Science, Part B*, **42**, 2181-2190, 2004.

[7] Y. Paramashanti, Y. Itoh, Y. Kitane, H.S. Gu, Long-term performance evaluation of high damping rubber bearings by accelerated thermal oxidation test. *2nd International Conference on Advances in Experimental Structural Engineering*, Tongji University, Shanghai, China, December 4-6, 2007.

[8] Y. Paramashanti, Y. Kitane, Y. Itoh, S. Kito, K. Muratani, Experimental investigation of aging effect on damping ratio of high damping rubber bearing. *Journal of Structural Engineering*, **57A**, 769-779, 2011.

[9] D. Cardone, G. Gesualdi, D. Nigro, Effects of air temperature on the cyclic behavior of elastomeric seismic isolators. *Bulletin of Earthquake Engineering*, **9**, 1227-1255, 2011.

[10] M. Higashino, H. Hamaguchi, S. Minewaki, S. Aizawa, Basic characteristics and durability of low-friction sliding bearings for base isolation. *Earthquake Engineering and Engineering Seismology*, **4**, 95-105, 2003.

[11] W.J. McVitty, M.C. Constantinou, Property modification factors for seismic isolators:

design guidance for buildings. *MCEER-15-0005,* MCEER, Buffalo, NY, 2015.

[12] F. Jalayer, R. De Risi, G. Manfredi, Bayesian cloud analysis: efficient structural fragility assessment using linear regression. *Bulletin of Earthquake Engineering*, **13**, 1183-1203, 2015.

[13] PEER, Pacific Earthquake Engineering Research Center database. http://ngawest2.berkeley.edu, 2014.

[14] I.G. Buckle, M. Constantinou, M. Dicleli, H. Ghasemi, Seismic isolation of highway bridges. *Special report, MCEER-06-SP07, Multidisciplinary Center for Earthquake Engineering Research*, Buffalo, New York, 2006.

[15] Y. Muramatsu, I. Nishikawa, A study for the prediction of the long-term durability of seismic isolators. *Showa Electr. Wire Rev.*, **45**, 44-49, 1995.

[16] ASTM, Standard Test Methods for Vulcanized Rubber and Thermoplastic Rubbers and Thermoplastic Elastomers. *American Society for Testing and Materials*, D412, 1988.

[17] M. Constantinou, A.S. Whittaker, Y. Kalpakidis, D.M. Fenz, G.P. Warn, Performance of seismic isolation hardware under service and seismic loadings. *Technical report MCEER-07-0012*, August 24, 2007.

[18] W. Nelson, Accelerated testing. J. Wiley & Sons, New York, 1990.

[19] M. Le Huy, G. Evrard. Methodologies for lifetime predictions of rubber using Arrhenius and WLF models. Die Angewandte Makromolekulare Chemie, **261-262**, 135-142, 1998.

[20] FIP Industriale S.p.A. Catalogue S04: Curved Surface Sliders. Padova, http://www.fipindustriale.it, 2013.

[21] M. Dolce, D. Cardone, F. Croatto, Frictional behavior of steel-PTFE interfaces for seismic isolation. *Bulletin of Earthquake Engineering*, **3**, 75-99, 2005.

[22] F. Mazza, Effects of the long-term behaviour of isolation devices on the seismic response of base-isolated buildings. *Structural Control and Health Monitoring*, 10.1002/stc.2331, 2019.

[23] F. Mazza, A. Vulcano, Effects of the near-fault ground motions on the nonlinear dynamic response of base-isolated r.c. framed buildings. *Earthquake Engineering and Structural Dynamics*, **41**, 211-232, 2012.

[24] S.K. Shahi, J.W. Baker, An efficient algorithm to identify strong-velocity pulses in multicomponent ground motions. *Bulletin of the Seismological Society of America*, **104**, 2456-2466, 2014.

[25] F. Mollaioli, A. Lucchini, Y. Cheng, G. Monti, Intensity measures for the seismic response prediction of base-isolated buildings. *Bulletin of Earthquake Engineering*, **11**, 1841-1866, 2013.

[26] F. Mazza, R. Labernarda, Structural and non-structural intensity measures for the assessment of base-isolated structures subjected to pulse-like near-fault earthquakes. *Soil Dynamics and Earthquake Engineering*, **96**, 115-127, 2017.

[27] F. Jalayer, H. Ebrahimian, A. Milano, G. Manfredi, H. Sezen, Analytical fragility assessment using unscaled ground motion records. *Earthquake Enginering & Structural Dynamics*, **46**, 2639-2663, 2017.

COMPDYN 2019
7th ECCOMAS Thematic Conference on
Computational Methods in Structural Dynamics and Earthquake Engineering
M. Papadrakakis, M. Fragiadakis (eds.)
Crete, Greece, 24–26 June 2019

TUNED VIBRATION ABSORBERS FOR CONTROL OF TALL BUILDINGS UNDER WIND AND EARTHQUAKE LOADS

S. Elias[1], R. Rupakhety[2], and S. Olafsson[2]

[1] Post PhD Scholar
Earthquake Engineering Research Centre (EERC), University of Iceland
e-mail: said@hi.is

[2] Professor
Earthquake Engineering Research Centre (EERC), University of Iceland
{rajesh,simon}@hi.is

Abstract

This study presents an application of tuned vibration absorbers (TVAs) to reduce dynamic response of tall buildings under multiple excitations such as wind and earthquake ground motion. A finite element model of a typical tall building is prepared with rotational degrees of freedom reduced by static condensation. Mechanical models of TVAs are incorporated in the model. The coupled equations of motion are formulated and solved using numerical methods. The uncontrolled building (NC) and the controlled building are subjected to a number of near fault earthquake ground motions and wind forces (mass excitations). The effectiveness of using multiple TVAs as opposed to a single TVA (STVA) is investigated. The design parameters affecting the effectiveness of the TVA arrangements are chosen to investigate optimal setups. It is observed that STVA are more effective for wind response mitigation than seismic response mitigation of tall buildings. Multiple TVAs are, however, found to be effective for controlling both wind and earthquake induced vibrations. It is concluded that optimally designed TVAs are effective in controlling vibration of buildings subjected to action of wind and earthquake loads.

Keywords: Buildings, Earthquake, Multi-Hazard, Tuned Vibration Absorbers (TVAs), Wind Loads.

1 INTRODUCTION

Wind response control of structures using passive tuned vibration absorbers (TVAs) were extensively investigated in last few decades. Commonly, it was reported by the researchers that the optimum devices achieved significant improvement in the performance to increase the response reduction as compared to the conventional design of the devices. Recently, a detailed review is presented by Elias and Matsagar [1] for development of the passive vibration control of structures. Lu et al. [2] reported that the particle TVAs are more effective than the optimal TVAs. The researchers presented the multi-mode response control of tall structure by different TVA schemes [3-10]. They concluded that the distribution of the multiple TVAs (d-MTVAs) as per modal properties of the structures caused maximum responses reduction. However, in all the studies the devices were designed for consideration of single hazard either wind or earthquake excitations. Only few studies are exist that the researchers checked the performance of the controllers for wind and earthquake excitations [11, 12]. Based on detailed literature survey conducted no such study is seen that the effect of multi-hazard on the performance of the tall building without control (NC) and controlled by different passive TVAs were taken into account. Therefore, it is deemed important to investigate the performance tall buildings equipped by TVAs subjected to wind and earthquake. In this study the proper TVA scheme is designed to be effective while subjected to wind and earthquakes. The device which designed for wind vibration control of tall building may not be as effective for seismic vibration mitigation. Therefore, a robust multi-mode response control of tall buildings is presented using multiple TVAs. Initially, based on modal properties of the NC building, the TVAs' optimal locations are anticipated. Then, the effects of the addition of masses are taken into consideration for selection of the optimal placement for multi-hazard assessment of tall buildings. The basic assumption is to design a device for one hazard to be effective for both hazards or at least not to amplify the responses of the building while subject to the second hazard.

2 GENERAL THEORY

In this study the benchmark building is considered which was reported by many researchers to be wind sensitive. However, Aly and Abburu, [11] concluded that the tall building subjected to earthquake excitation could exhibit large floor acceleration due to higher modal contribution and higher drift ratio while subjected to wind forces. They recommended proper device controller needs to be installed to control the responses of the building under both wind and earthquake excitations. Therefore, it is important to investigate the effectiveness of adding TVA schemes for mitigation of the responses of the benchmark building subjected to wind and or earthquake excitations. The benchmark building equipped with the single TVA (STVA) shown in Figure 1(a), with multiple TVAs all installed at top floor (MTVAs-all.top) is shown in Figure 1(b). MATLAB code is prepared to conduct the numerical simulation of the uncontrolled and controlled buildings subjected to wind or earthquake excitations. The complete information of the building can be seen in the study presented by Elias et al. [10]. The three TVA schemes designed for the wind sensitive building and then subjected to the earthquake excitations. Then, the schemes designed to control the seismic response of the building and then subjected to the wind forces. In this procedure the optimal scheme is identified to be robust under both wind and earthquake excitations. To be noted that the cross wind forces are applied on the N degrees of freedom (DOFs) of the structure with zero forces on n DOFs of the TVAs ($\{F_t\} = \begin{Bmatrix} \{F_t\}_{N\times 1} \\ \{0\}_{n\times 1} \end{Bmatrix}$). For the system under consideration, the governing equations of motion for the benchmark building installed with the TVA schemes are obtained by

considering the equilibrium of forces at the location of each degree of freedom during the wind or earthquake excitation as

$$[M_s]_{(N+n)\times(N+n)}\{\ddot{X}_s\}_{(N+1)\times1}+[C_s]_{(N+n)\times(N+n)}\{\dot{X}_s\}_{(N+1)\times1}+[K_s]_{(N+n)\times(N+n)}\{X_s\}_{(N+1)\times1}=\{F_t\}_{(N+n)\times1} \quad (1)$$

where $[M_s]$, $[C_s]$, and $[K_s]$ are the mass, damping, and stiffness matrices of the building, respectively; $\{X_s\}$, $\{\dot{X}_s\}$, and $\{\ddot{X}_s\}$ are the unknown relative floor displacement, velocity, and acceleration vectors, respectively; and $\{F_t\}$ is the load vector. In case of earthquake excitations, $\{F_t\}=-[M_s]\{I\}\ddot{x}_g$ where $\{I\}$ is the influence vector and $\ddot{x}_g$ is the earthquake ground acceleration.

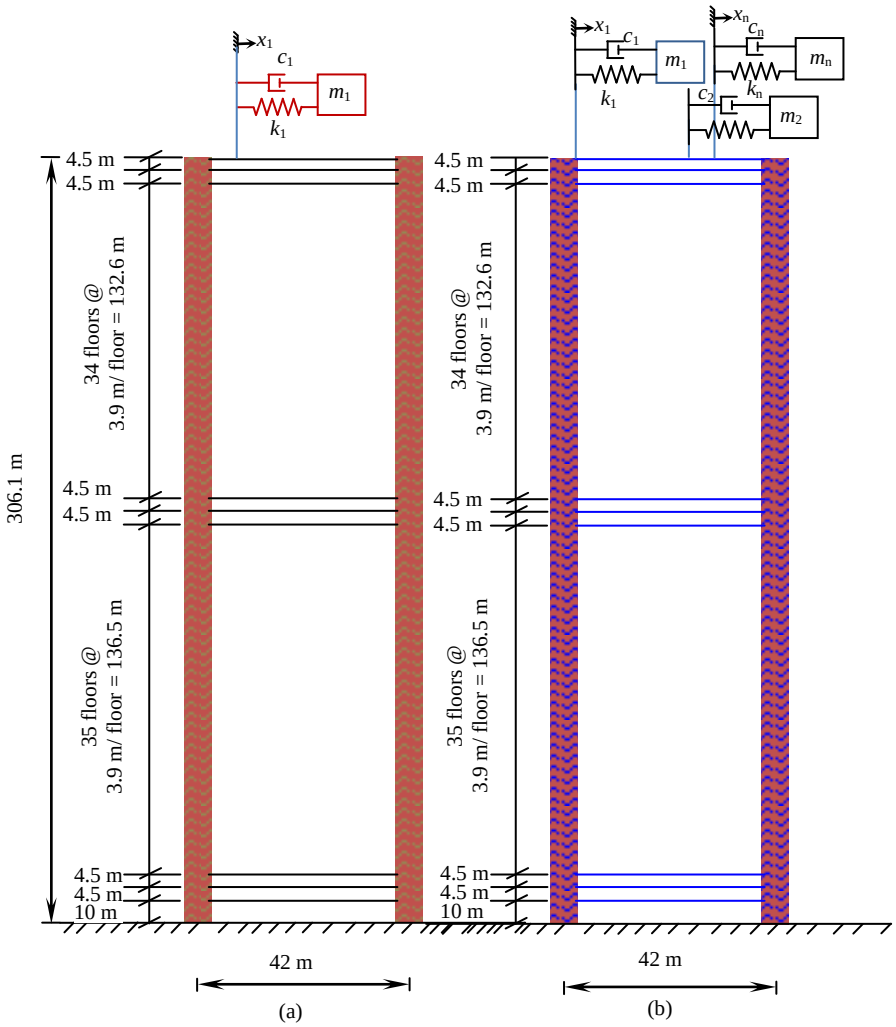

Figure 1: Model of benchmark building (a) installed with STMD, and (b) installed with MTVAs-all.top

3 NUMERICAL STUDY

The benchmark building is having height of more than 300 m and it is classified as a wind sensitive structure. However, if such structure is located at earthquake prone area, the question arises if the safety of the structure is underestimated. Similarly, different methodologies were proposed by the researchers to mitigate the wind response of the same building. Again it is not clear if those devices will be effective during the earthquakes. In this study the comparative analysis are conducted to find out a proper answer to the un-cleared questions. In Fig-

ures 2 and 3 show respectively the time variation of top floor displacement and acceleration for 76-storey benchmark building installed with the STVA, MTVAs-all.top under wind forces or Kobe, 1995 earthquake excitation. The figure shows that both the displacement and acceleration of the building are quite high while subjected to the earthquake ground excitation. Therefore, it is underestimated to design high-rise buildings only for a single hazard especially if the structure is located in seismic prone area. For such situation a multi-hazard scheme is required to design a robust structure to be safe under multiple hazards. The optimal STVA designed as per the parameters suggested by Patil and Jangid [13]. The optimal parameters of the STVA are 0.94, 0.06 respectively for frequency tuning ratio and damping ratio for total mass of 1250 ton.

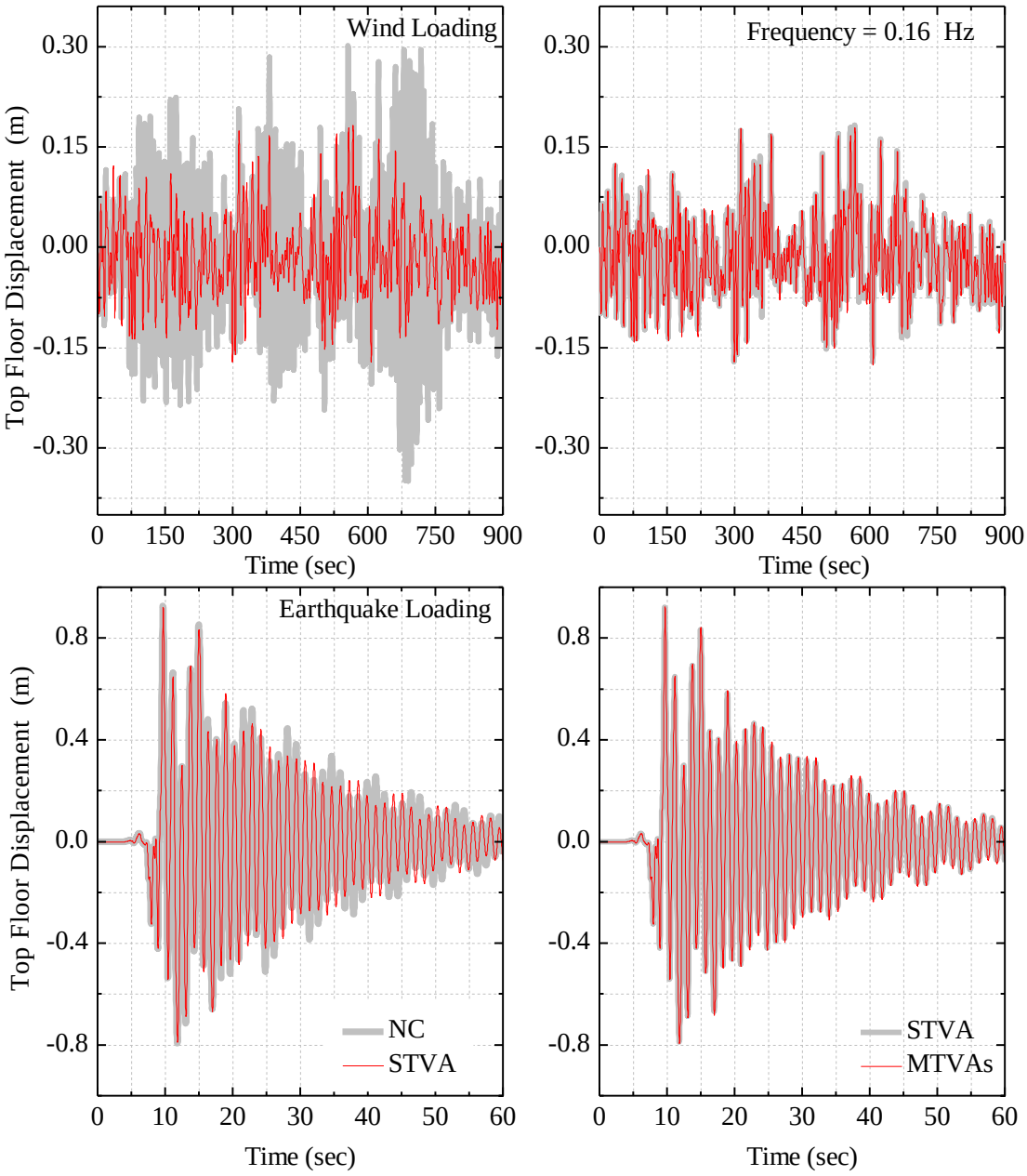

Figure 2: Time variation of top floor displacement for 76-storey benchmark building installed with the STVA, MTVAs-all.top under wind forces or Kobe, 1995 earthquake excitation.

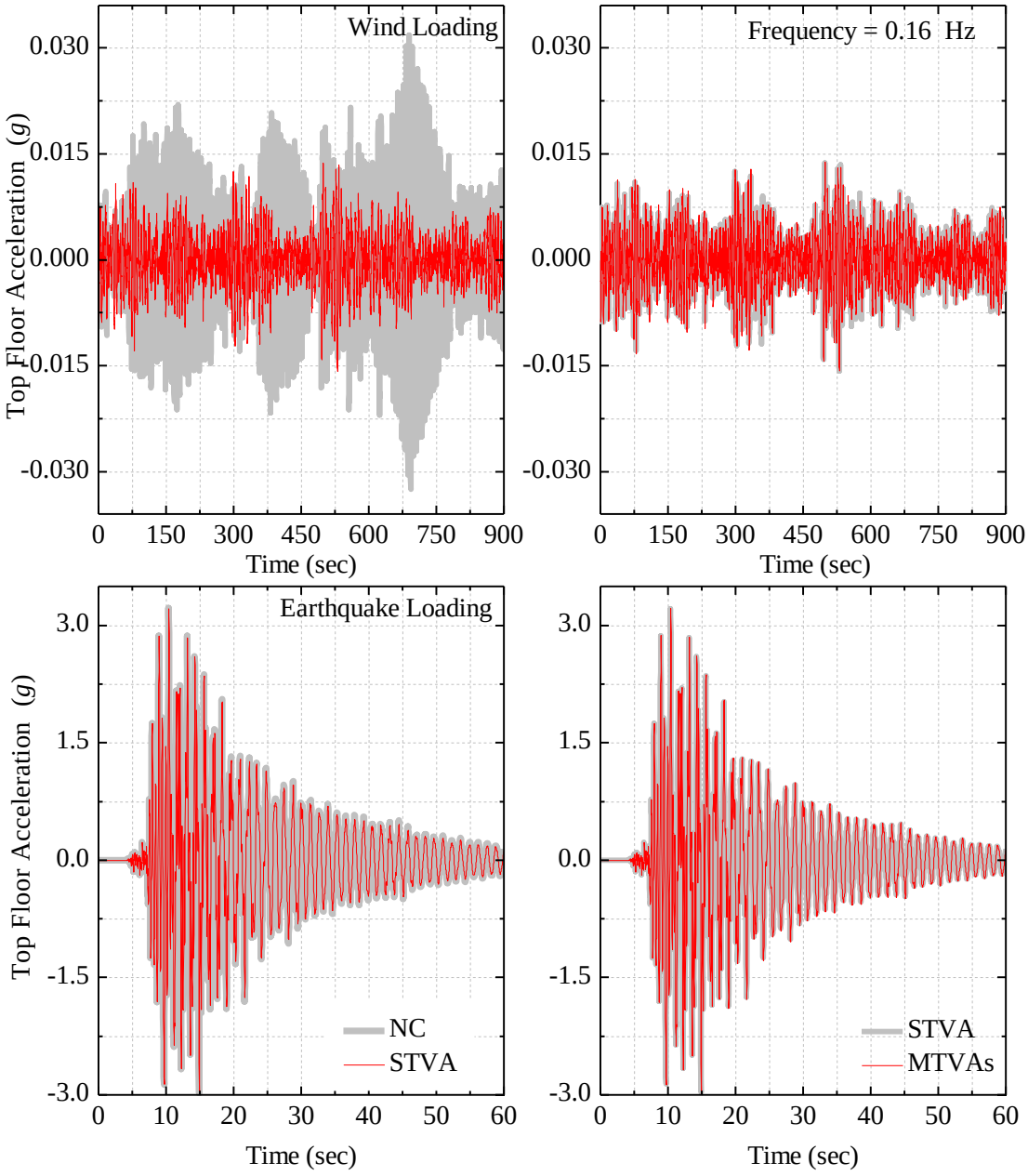

Figure 3: Time variation of top floor acceleration for 76-storey benchmark building installed with the STVA, MTVAs-all.top under wind forces or Kobe, 1995 earthquake excitation.

The STVA is designed for control of the building subjected to the wind forces. In the figure it is clearly shown that the STVA is quite effective for response reduction of the building while subjected to wind forces. However, it is noticed that the STVA designed for the reduction of wind response of the structure may not be as effective for earthquake response reduction. Even the scheme is not effective to reduce the peak displacement response of the benchmark building under Kobe earthquake. Having same mass (1250 ton) into consideration, the MTVAs are designed as per the optimal parameters suggested by Patil and Jangid [13]. The optimal parameters for MTVAs having five TVAs are 0.1, 0.94, and 0.05 for the frequency bandwidth, frequency tuning ratio, and damping ratio respectively. The MTVAs shows similar response reduction, which quite effective under wind forces but not much effective under earthquake ground excitation.

The STVA and MTVAs designed as per the closed formulation proposed by Sadeck et al. [14] for seismic response reduction of the buildings are presented in Figures 4 and 5. The system designed for earthquake response mitigation is subjected to wind forces. From the figures it is observed that the overall root mean square (RMS) of the responses are reduced significantly but not the peak responses while subjected to Kobe earthquake excitation.

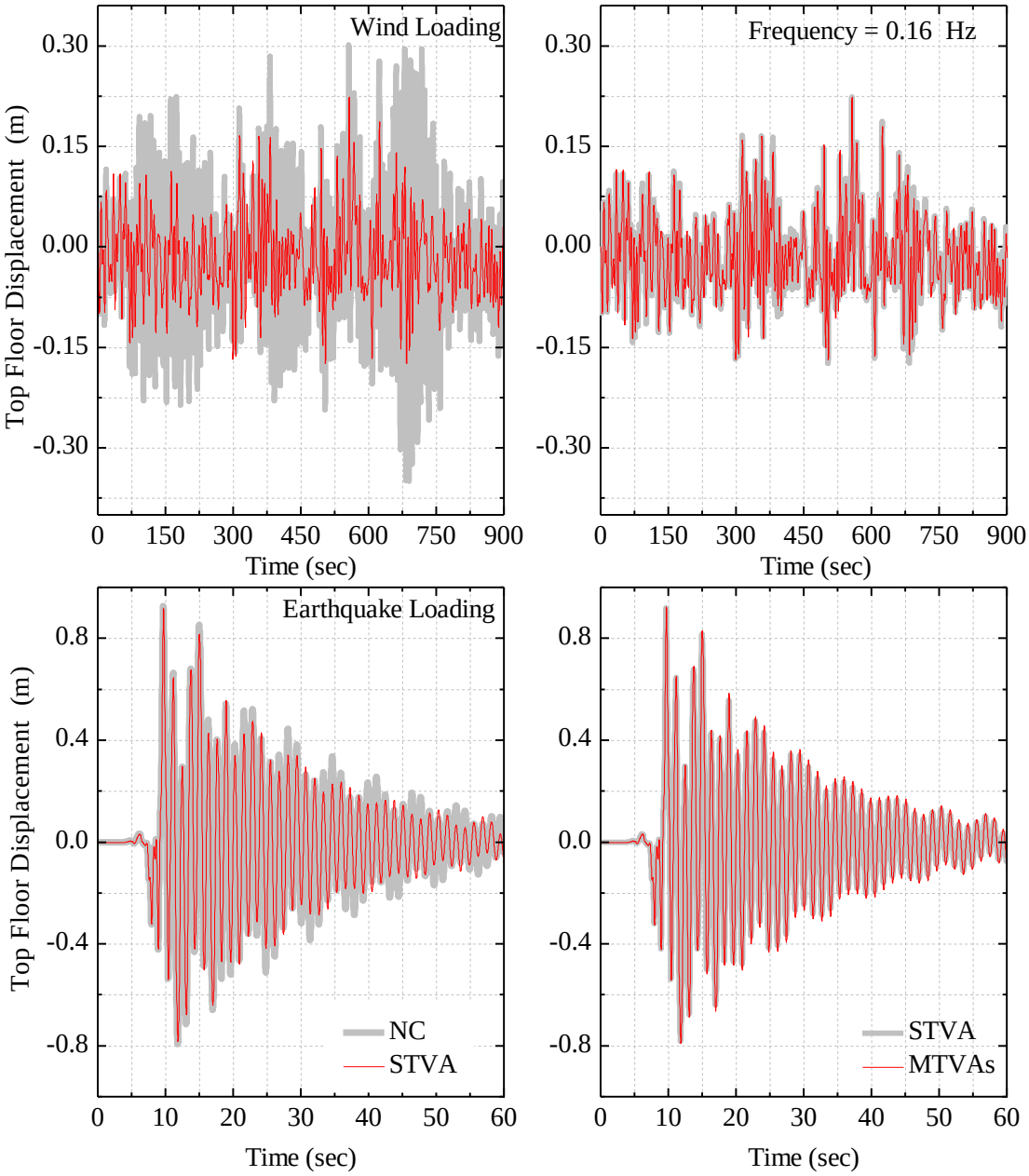

Figure 4: Time variation of top floor displacement for 76-storey benchmark building installed with the STVA, MTVAs-all.top under wind forces or Kobe, 1995 earthquake excitation.

The STVA and MTVAs perform good while the system subjected to wind forces. Although, the performances were not the same as the optimal devices designed for wind excitation. But the devices are not amplifying the responses of the benchmark building. Therefore, it is concluded that the optimal designed TVA schemes designed for wind sensitive situation would be vulnerable while subjected to the earthquakes, but the TVA schemes designed for

earthquake sensitive situation can still be effective for response reduction of structure subjected to wind forces.

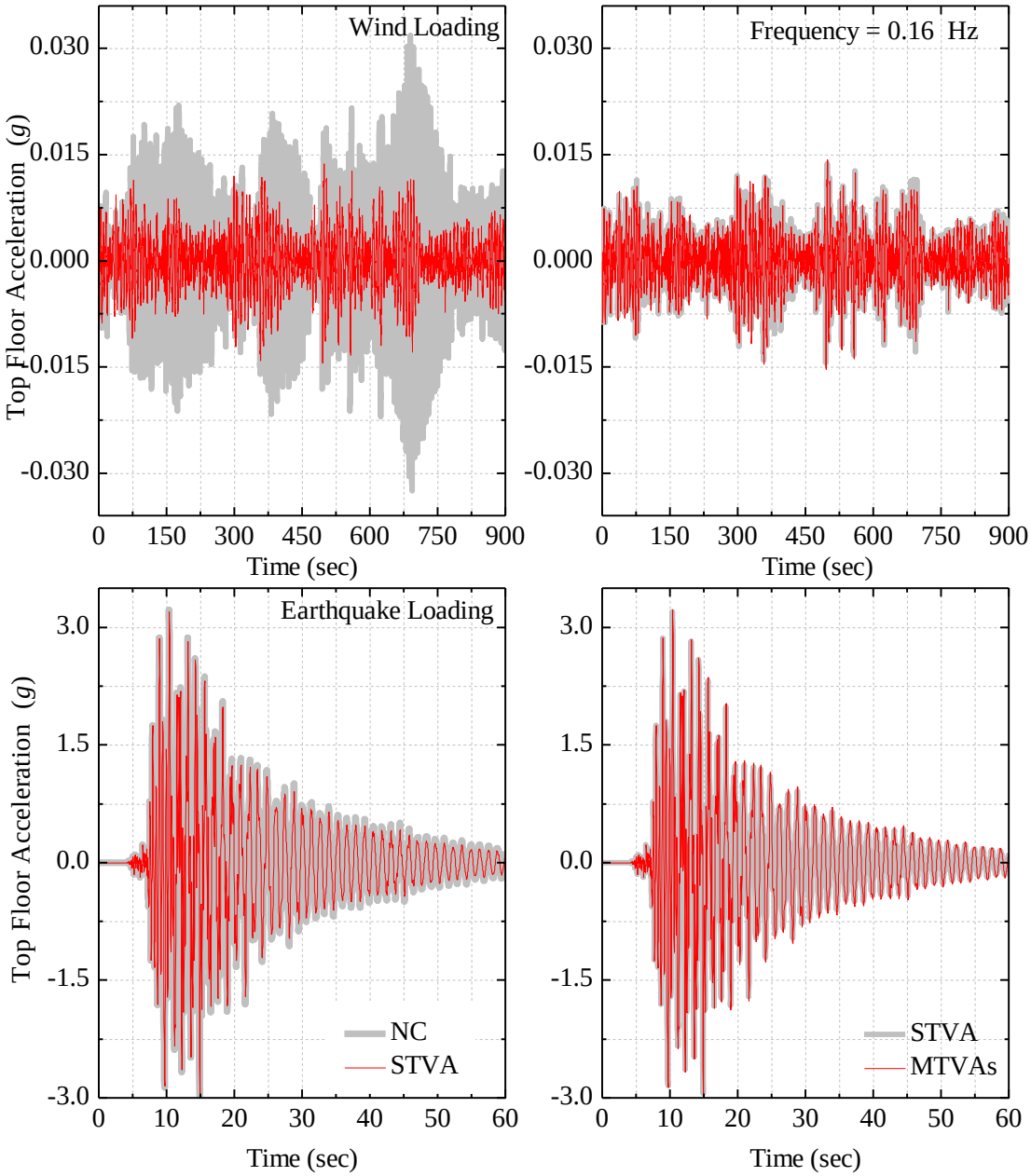

Figure 5: Time variation of top floor acceleration for 76-storey benchmark building installed with the STVA, MTVAs-all.top under wind forces or Kobe, 1995 earthquake excitation.

Multi-mode control is reported to be effective procedure for both wind and earthquake vibration mitigations. Elias et al. [7, 8] presented the detailed procedure for seismic response control of buildings considering multi-mode control. Very recently Elias et al. [9, 10] showed the effectiveness of the multi-mode control of the structures subjected to wind forces. In both methods the designed parameters showed to be quite different for earthquake vibration control the devices were designed having equal masses but for wind vibration control the devices designed considering equal stiffness. In this study for response mitigation of the benchmark building subjected to wind and earthquake excitations, both the designs applied to compare

the performance of the devices under multi-hazards. The MTVAs designed as per the procedure defined by Elias et al. [7, 8] named as e-MTVAs and the MTVAs designed as per the procedure defined by Elias et al. [9, 10] named as w-MTVAs. In Figures 6 and 7 the comparisons of the performances of the w-MTVAs and e-MTVAs for vibration control of benchmark structure are presented.

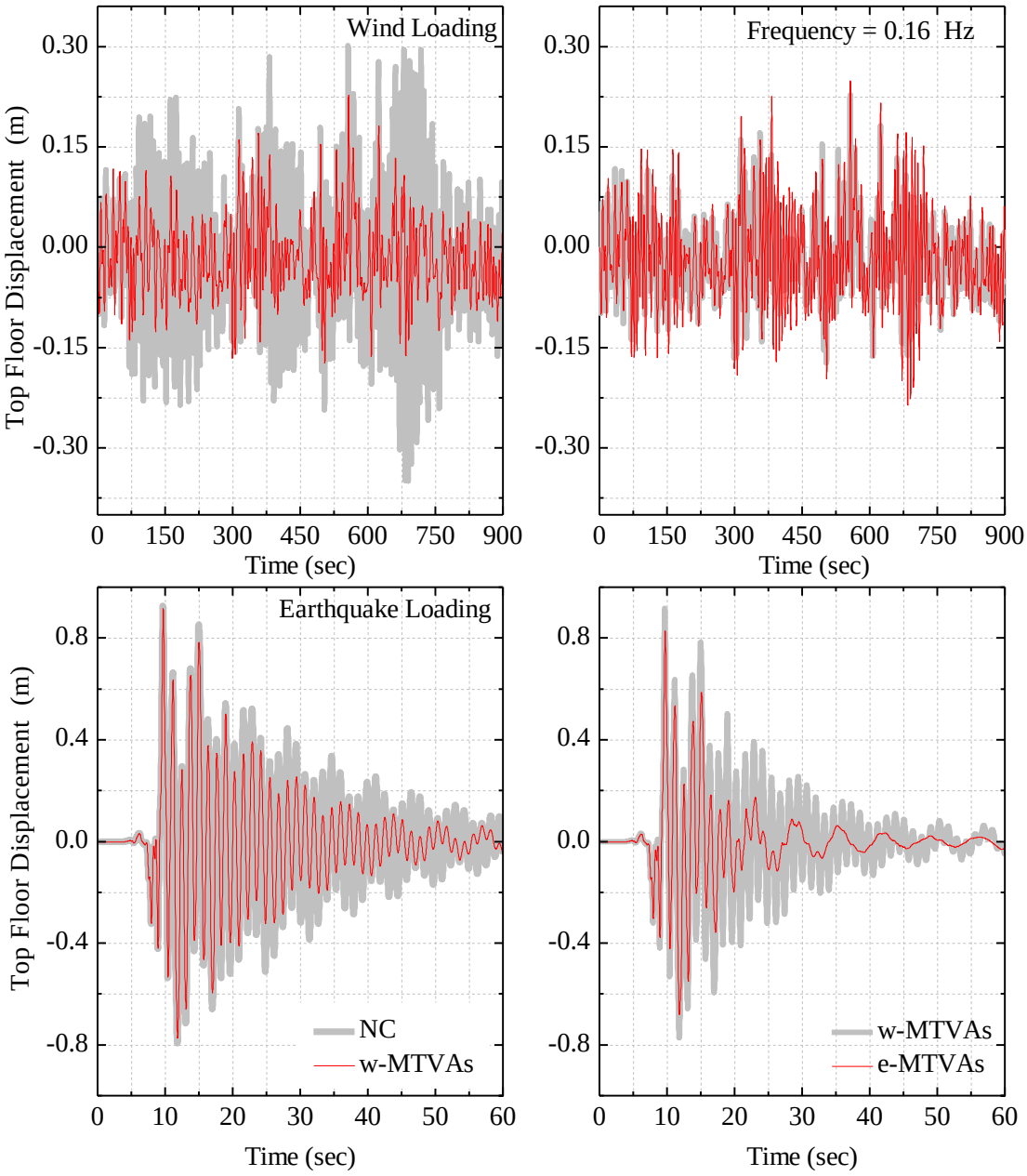

Figure 6: Time variation of top floor displacement for 76-storey benchmark building installed with the w-MTVAs, e-MTVAs under wind forces or Kobe, 1995 earthquake excitation.

It is observed that multi-mode control is quite effective procedure under both wind and earthquake excitations. The peak and RMS responses of the building are controlled significantly each subjected to earthquake or wind forces. It is to be noted that still the multi-mode control scheme designed for earth response mitigation is more effective as compared to the system designed for wind response mitigation (while subjected to Kobe earthquake). For wind

response mitigation still both the schemes are effective. It is found that the recent advancement proposed by Elias et al. [7-10] were the most effective solution for the benchmark building under multiple loading condition.

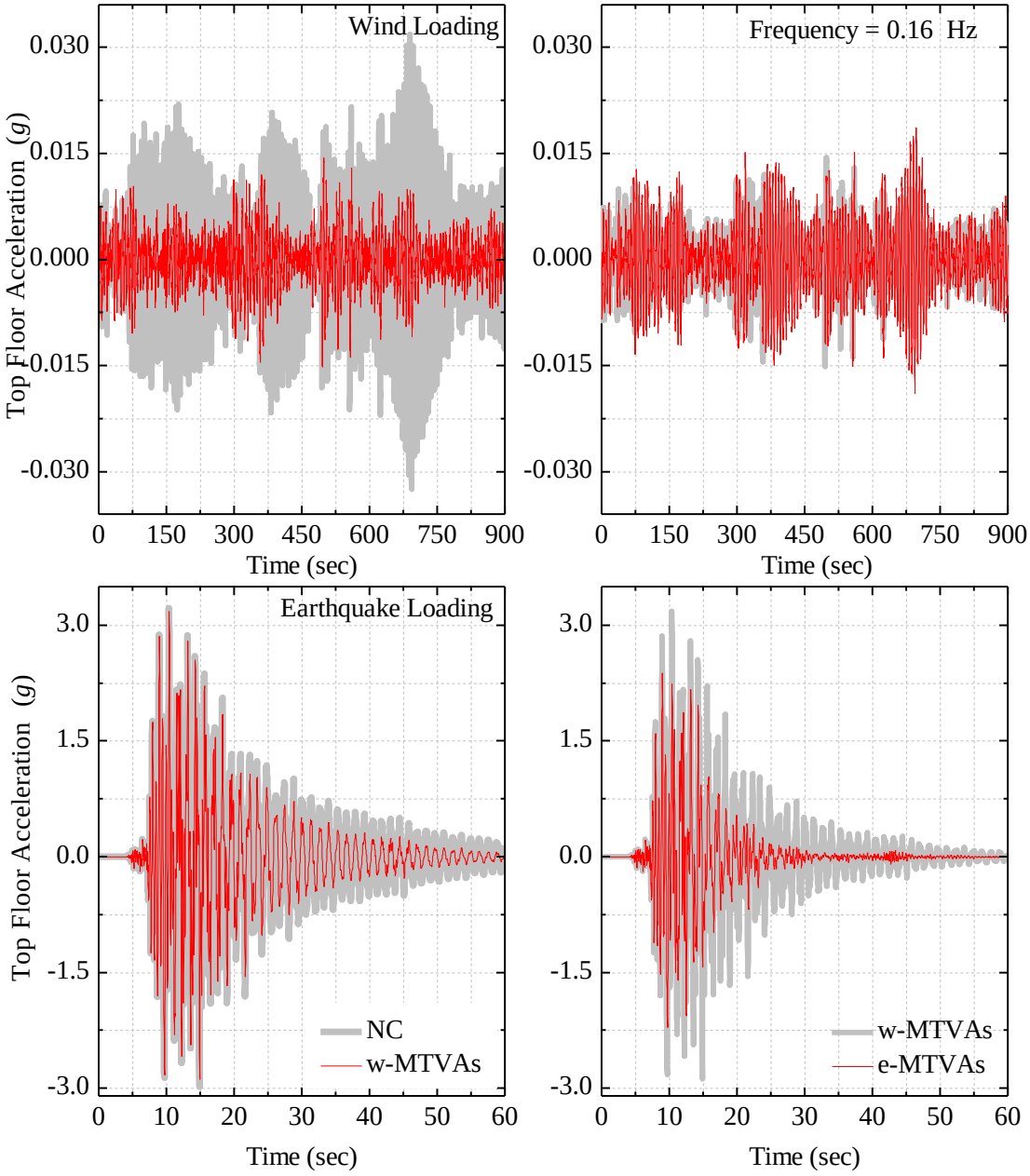

Figure 7: Time variation of top floor acceleration for 76-storey benchmark building installed with the w-MTVAs, e-MTVAs under wind forces or Kobe, 1995 earthquake excitation.

The effect of the mean wind speed at top of the building is also studied by having the speed of 40 m/sec, 50 m/sec, and 60 m/sec (see Table 1). It was found that by increasing the mean wind speed at the top of the building the responses increased by about 50%. But the increase the speed did not reduce the performance of the TVA schemes and same response reduction is achieved. The w-MTVAs reduced the top floor displacement by about 35% and e-MTVAs reduced about 30%. The top floor acceleration of the building is reduced by about 54% and 42% for w-MTVAs and e-MTVAS respectively while subjected to wind forces. While the

schemes subjected to different earthquake ground motion, still both performed. Generally for acceleration response reduction the e-MTVAs performed significantly better than the w-MTVAs while subjected to earthquakes. By accepting 12% less acceleration response reduction of the building while subjected to wind forces, therefore the e-MTVAs is the best solution among the schemes investigated in this study. However, for displacement response reduction there is not much difference in both devices while subjected to wind forces.

Scheme	Response	Wind Forces with Different Velocities at Top of the Building (m/sec)			Earthquakes		
		40	50	60	Imperial Valley 1940	Mexico City, 1995	Duzce, 1999
NC	Top Floor Displacement (m)	0.2507	0.3917	0.5640	0.9089	0.8784	0.2084
	Top Floor Acceleration (g)	0.0233	0.0364	0.0524	1.6523	0.6529	4.5354
w-MTVAs	Top Floor Displacement (m)	0.1629	0.2545	0.3664	0.4750	0.6421	0.2086
	Top Floor Acceleration (g)	0.0108	0.0169	0.0244	1.6504	0.6031	4.5164
e-MTVAs	Top Floor Displacement (m)	0.1782	0.2784	0.4010	0.6570	0.7423	0.1758
	Top Floor Acceleration (g)	0.0136	0.0212	0.0306	1.5292	0.5084	3.4534

Table 1: Peak responses of the schemes under different loading conditions.

4 CONCLUSIONS

Tuned vibration absorbers (TVAs) for control of tall buildings under wind and earthquake loads are investigated. The comparison of different TVA schemes such as single TVA (STVA), multiple TVAs (MTVAs) are presented. Based on the results presented the following conclusions can be drawn:

- The tall buildings designed for wind are not safe under strong earthquake loads. Nevertheless, it is important to mention that nonstructural systems may represent a high percentage of loss exposure of buildings to earthquakes due to high floor acceleration. Therefore, suitable vibration control techniques are recommended for response reduction of the buildings under wind and earthquake loads.
- The optimal devices designed only for wind sensitive structures may not be effective while subjected to earthquakes, but the device designed for earthquake sensitive structures may still be less effective under the wind forces.

- The multi-modal response control is a robust technique for vibration mitigation of the structures under multiple hazard situations.

REFERENCES

[1] S. Elias, V. Matsagar, Research developments in vibration control of structures using passive tuned mass dampers. *Annual Reviews in Control*, **44**, 129-156, 2017.

[2] Z. Lu, K. Li, Y. Zhou, Comparative studies on structures with a tuned mass damper and a particle damper. *Journal of Aerospace Engineering*, **31**(6), 04018090, 2018.

[3] S. Elias, Seismic energy assessment of buildings with tuned vibration absorbers, *Shock and Vibration*. 2018.

[4] S. Elias, Effect of SSI on vibration control of structures with tuned vibration absorbers, *Shock Vibration*, 2019.

[5] S. Elias and V. Matsagar, Wind response control of tall buildings with flexible foundation using tuned mass dampers, In Wind Engineering for Natural Hazards: Modeling, Simulation, and Mitigation of Windstorm Impact on Critical Infrastructure, 55-78, 2018.

[6] S. Elias and V. Matsagar, Seismic vulnerability of non-linear building with distributed multiple tuned vibration absorbers, *Structure and Infrastructure Engineering*, Accepted.

[7] S. Elias, V. Matsagar and T. K. Datta, Effectiveness of distributed tuned mass dampers for multi-mode control of chimney under earthquakes, *Engineering Structures.* **124** 1-16, 2016. https://doi.org/10.1016/j.engstruct.2016.06.006.

[8] S. Elias, V. Matsagar and T. K. Datta, Distributed tuned mass dampers for multi-mode control of benchmark building under seismic excitations, J. Earthquake Engineering, in press, http://dx.doi.org/10.1080/13632469.2017.1351407.

[9] S. Elias, V. Matsagar and T. K. Datta, Along-wind response control of chimneys with distributed multiple tuned mass dampers, *Structural Control and Health Monitoring*. **26**(1) e2275, 2019.

[10] S. Elias, V. Matsagar and T. K. Datta, Dynamic response control of a wind-excited tall building with distributed multiple tuned mass dampers, *International Journal of Structural Stability and Dynamics*, **26**(6), 2019.

[11] A.M. Aly, and S. Abburu, On the design of high-rise buildings for multi-hazard: fundamental differences between wind and earthquake demand. *Shock and Vibration*, 2015.

[12] T. Roy, and V. Matsagar, Effectiveness of passive response control devices in buildings under earthquake and wind during design life. *Structure and Infrastructure Engineering*, 1-17, 2019.

[13] V. B. Patil and R. S. Jangid, Optimum multiple tuned mass dampers for the wind excited benchmark building, *Journal of Civil Engineering and Management*. **17**(4), 540-557, 2011.

[14] F. Sadek, B. Mohraz, A.W. Taylor, and R.M. Chung, A method of estimating the parameters of tuned mass dampers for seismic applications. *Earthquake Engineering and Structural Dynamics*, **26**(6), 617-635, 1997.

COMPDYN 2019
7th ECCOMAS Thematic Conference on
Computational Methods in Structural Dynamics and Earthquake Engineering
M. Papadrakakis, M. Fragiadakis (eds.)
Crete, Greece, 24–26 June 2019

CONTROL OF MULTI STOREY BUILDING STRUCTURES WITH A NEW PASSIVE VIBRATION CONTROL SYSTEM COMBINING BASE ISOLATION WITH KDAMPER

K. A. Kapasakalis[1*], I. A. Antoniadis[2], E. J. Sapountzakis[1]

[1] Institute of Structural Analysis and Antiseismic Reasearch
School of Civil Engineering, National Technical University of Athens
Zografou Campus, GR-157 80 Athens, Greece
kostiskapasakalis@hotmail.com, cvsapoun@central.ntua.gr

[2] Mechanical Design and Control Systems Section
Mechanical Engineering Department, National Technical University of Athens
Zografou Campus, GR-157 80 Athens, Greece
antogian@central.ntua.gr

Abstract

Contemporary seismic isolation systems for building structures provide drastic reduction to the structure's interstorey drifts and absolute accelerations. However, their major drawback is the large increase of the base displacement. Due to the high equivalent damping ratio, the novel KDamper passive vibration isolation and damping concept can provide an alternative approach for seismic protection. The KDamper is based on the optimal combination of appropriate stiffness elements, which include a negative stiffness element. The main advantage of the KDamper over other similar concepts including negative stiffness elements, is that no reduction in the overall stiffness of the system is required.

This paper considers the application of a KDamper system to 3 storey concrete building structure. A dynamic system consisting from a simplified flexible structure model and KDamper devices is considered and is subjected to artificial accelerograms designed to match the EC response spectra. The KDamper is designed to higher frequencies compared to the isolated system with seismic isolation bearings, exploiting the extraordinary damping properties it offers.

A comparison with a base isolated structure using Lead Rubber Bearings designed to greatly increase the fundamental period of the system (2.0-2.5 sec), confirms that KDamper base seismic absorption designs can provide great reduction to the interstorey drifts and absolute accelerations reducing at the same time the base displacement.

Keywords: Seismic isolation, negative stiffness, KDamper, damping.

1 INTRODUCTION

Throughout the last decades, the need for updated seismic design codes, incorporating advanced techniques and technologies, has been intensified, due to the damages of major earthquake events occurring in densely populated areas. Especially, considering structures whose functionality needs to be preserved even after a seismic event, such as hospitals, bridges etc., numerous novel methods have been developed, promising to improve each structure's dynamic behavior. Focusing on bridge structures, numerous devices have already been implemented, under the scope of seismic isolation, whose main principle is reducing the earthquake forces induced on a structure instead of increasing the structure's capacity. Devices of this kind enable the decoupling of the superstructure – in this case the bridge's deck – from the substructure – in this case the bridge's piers and abutments. As a result, the system gains in flexibility and lower forces are imposed to the superstructure (the isolated system's fundamental period leads to a design acceleration value that is obtained from the descending branch of the response spectrum).

Recently, scientific interest focuses on the use of innovative devices and configurations based on the introduction of an additional mass to the structure, namely the Tuned Mass Dampers (TMDs). Since their first application by Frahm [5], TMDs have been frequently used to absorb vibrations of skyscrapers under earthquake and/or wind loading (Luft [10]), (McNamara [11]), (Qin et al. [15]), with the Taipei 101 Tower (101 stories, 54 m) in Taiwan (Haskett et al. [6]) being one of the most characteristic examples. The implementation of TMDs on bridge structures, in order to mitigate the effects of seismic or other types of vibrations, has been, lately, included in many research studies (Debnath et al. [3]). The optimal design theory proposed by Den Hartog [4] is usually employed when designing a system with TMDs. Their salient performance feature is the tuning of the TMD's natural frequency in resonance with the fundamental frequency of the primary structure. This way, a large amount of the structural vibrating energy is transferred for the superstructure to the TMD and then dissipated through damping. Besides their effectiveness, TMDs demonstrate two basic drawbacks: a) their performance is vulnerable to even slight changes of external and environmental factors that cause detuning phenomena (Weber & Feltrin [20]) and b) a large oscillating mass is required in order for the device to be effective and the resulting isolated system to exhibit an improved dynamic behavior.

Furthermore, the use of negative stiffness elements as parts of vibration absorption configurations becomes more and more popular. True negative stiffness is defined as a force that assists motion instead of opposing it. The use of negative stiffness elements was first introduced in the pioneer publication of Molyneaux [12], as well as in the milestone developments of Platus [14]. Specifically, many researchers have demonstrated the effectiveness of "Quasi Zero Stiffness" (QZS) oscillators, aiming to reduce the system's stiffness and, by extent, its natural frequency to almost zero levels (Carella et al. [2]), regarding the seismic protection of structures through the alleviation of dynamic forces (Ibrahim [7]), (Nagarajaiah et al. [13]). Negative stiffness behavior is achieved by special mechanical designs involving conventional positive stiffness pre-stressed elastic mechanical elements (e.g. post-buckled beams, plates, shells and pre-compressed springs), arranged in appropriate geometric configurations (Winterflood et al. [21]), (Virgin et al. [19]). Interesting applications of QZS oscillators in seismic isolation are described in Iemura and Pradono [8] and Sarlis et al. [17]. However, the drastic reduction of the total structural stiffness to almost negligible levels, namely, the main feature of QZS oscillators, is, also, its fundamental drawback, as it is accompanied by a decrease of the structure's static load capacity.

Inspired by the two aforementioned technologies (TMDs and QZS oscillators), a novel passive vibration absorption and damping concept is proposed, the KDamper concept. A detailed presentation of this concept can be found in Antoniadis et al. [1]. The KDamper devices comprise of both negative and positive stiffness elements, as well as an additional mass and an artificial damper, properly arranged, in order to exhibit an extraordinary damping behavior. Even though negative stiffness elements usually demonstrate an unstable behavior, the KDamper is designed to be both statically and dynamically stable, presenting the same overall (static) stiffness as a traditional reference oscillator. Thus, the proposed concept overcomes the previously mentioned disadvantages of TMDs and QZS oscillators. The salient feature of the KDamper concept is the transfer of the vibrating structural energy from the primary structure to the additional mass, which is then dissipated through damping. The resulting isolated system exhibits an improved dynamic behavior. A first approach to the implementation of the KDamper concept for base isolation of structures can be found in Kapasakalis et al [9].

In this paper, the implementation of the KDamper concept to a 3 storey concrete building structure for base isolation, is considered. The Structure is subjected to 10 Artificial Accelerograms designed to match the EC8 response spectra. A comparison with a highly damped conventional seismic isolation system (Lead Rubber Bearings), designed to greatly increase the fundamental period of the structure (2.0 sec), confirms that KDamper base seismic absorption designs can provide great reduction to the interstorey drifts and absolute accelerations, reducing at the same time the base displacement, offering high damping properties.

2 OVERVIEW OF BASE ISOLATION AND THE KDAMPER CONCEPT

The principle on which seismic isolation is based on, is that increasing the structure's fundamental period leads to the transition branch of the response accelerations spectrum, as presented in Figure 1a. However, it should be mentioned here, that excessively high values of the fundamental period could result in an undesirable increase of the structure's displacements as it can be observed in Figure 1b. It is also observed, that further increase of the base's damping ratio ζ (*20%*) does not improve the dynamic behavior of the system.

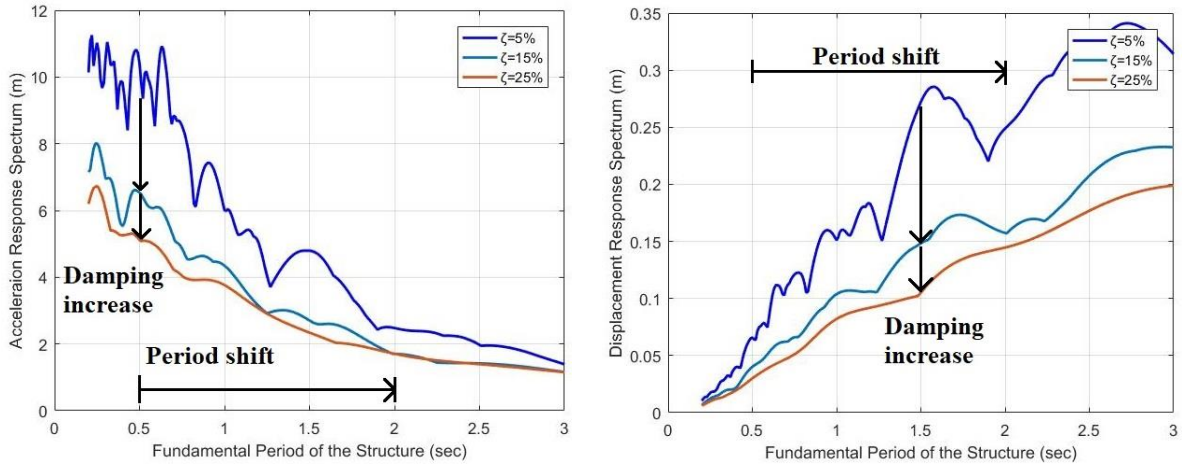

Figure 1. Indicative examples of response spectra of (a) accelerations and (b) displacements and their variation over damping.

Even though the implication of dampers seems a rather effective choice to overcome this problem, it is not always a feasible solution, because relatively high values of damping are usually required. An optimum compromise between accelerations and displacements, within

an acceptable range of structural fundamental periods, results in a region of feasible solutions. This region is referred to as design window and its lower and upper bounds are shown in Figure 2.

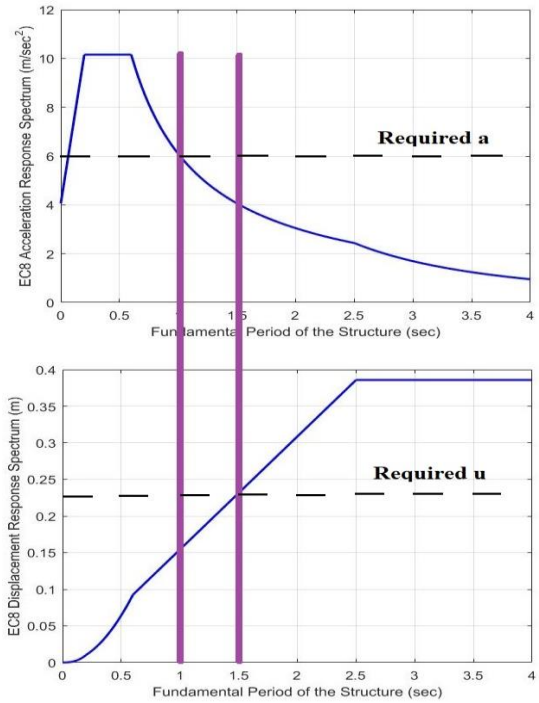

Figure 2. Conceptual illustration of the design window for isolation systems.

More specifically, the left boundary of the design window is imposed by the necessity to reduce accelerations. Its value generally depends on the soil of the structure's foundation (soil properties define the margin between the branch of constant accelerations and the descending one) and it is roughly estimated to be equal to 2 seconds. On the contrary, the right boundary cannot be defined as easily as the left one, as it is relevant to the displacement performance requirements of each structure. Consequently, the upper limit of the design window depends on each structure's functionality, security and implementation demands. In light of the above, the need to employ an optimization procedure, in order to efficiently design a seismic isolation system, is inherently apparent.

Figure 3 presents the basic layout of the proposed vibration isolation and damping concept, the KDamper concept, where k_N denotes the algebraic value of the negative stiffness element. An initial SDoF system is considered (Figure 3.a), consisting of a mass m_S and static stiffness *ko*, which may be undamped or have a low damping ratio. As it can be observed from Figure 3.b, the additional mass, m_D inside the device creates a second degree of freedom. Thus, the resulting isolated system is a 2-DoF system.

The device's performance is controlled by three parameters, μ, κ and ζ_D designated by the following equations:

$$\mu = \frac{m_D}{m_s},\ \kappa = -\frac{k_N}{k_e + k_N},\ \zeta_D = \frac{c_D}{2\sqrt{(k_e + k_N)m_D}} \tag{1}$$

Where ζ_D represents the equivalent damping ratio of the additional artificial damper with constant c_D.

Further information including a detailed description of the proposed device's optimized performance, the equations of motion of the isolated system, the realization and treatment of

the negative stiffness element and a possible implementation of such a device can be found in Antoniadis et al. [1].

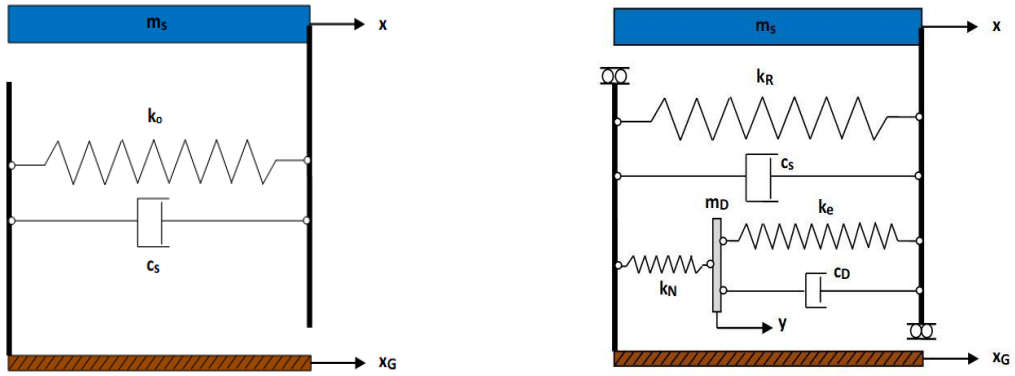

(a) (b)

Figure 3. (a) Undamped SDoF system and (b) schematic representation of the considered vibration absorption and damping concept, the KDamper.

The effect of the mass ratio on the Transfer Function of the system is presented in Figure 4 and the variation of the KDamper basic parameters are presented in Figure 5.

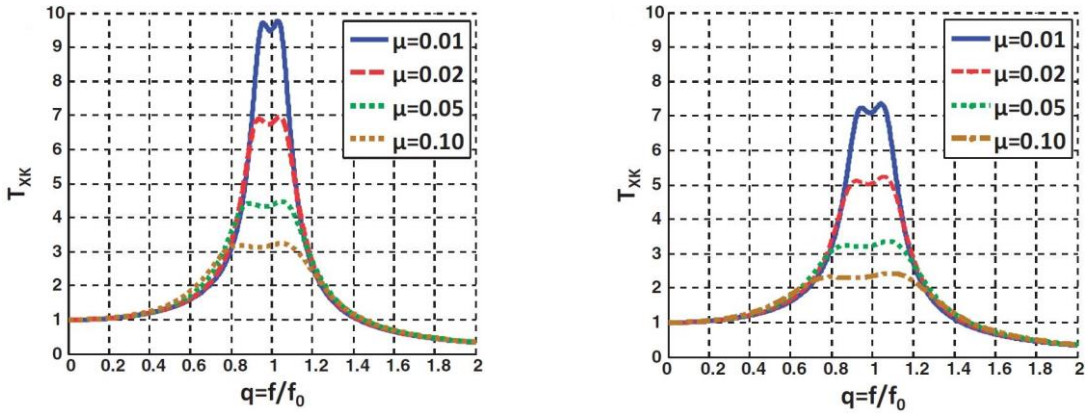

(a) (b)

Figure 4. Effect of the mass ratio μ on the Transfer Function T_{XK} of the KDamper for (a) $\kappa=0.5$ and (b) $\kappa=1.0$.

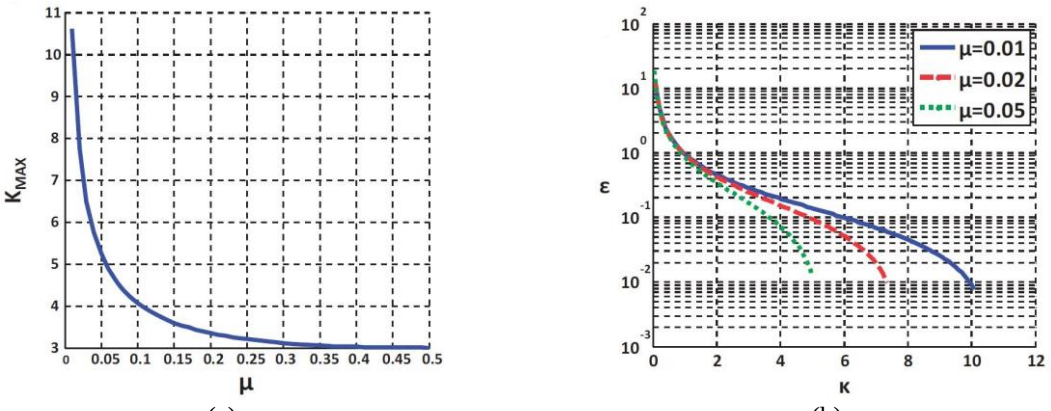

(a) (b)

Figure 5. Variation of KDamper parameters. (a) Effect of the mass ratio μ on the maximum value κ_{MAX} of κ and (b) effect of κ and μ over the static stability margin ε.

Based on these three parameters (Eq.1), all the other constants (regarding either stiffness or damping) of the KDamper elements are defined. Certain limitations are imposed to the values of the three parameters in order for the device to be economical and easy to place, regarding each structure's safety and functionality requirements and demands. Restrictions concerning the maximum allowable displacement (stroke) of both DoFs (internal and external) have to be also taken into consideration. More specifically, the maximum allowable value of the internal DoF depends on the mechanical equipment used to realize the negative stiffness element at each specific case/structure. For all these reasons, proposing an accurate optimization procedure is of paramount importance to facilitate the selection of the device's basic parameters and, by extent, the implementation of the KDamper concept.

3 IMPLEMENTATION ON 3-STOREY CONCRETE BUILDING STRUCTURE

A 3-storey concrete building structure as shown in Figure 6 (*C20/25, H_{floor}=3.1 m, g_{tot}=3.5 kN/m^2, q=2.5 kN/m^2*), is examined. The structure is idealized as a three storey shear type building as shown in Figure 6.b. The building is modeled as a 3-DoF system for fixed base, as a 4-DoF system for base isolated condition, using Lead Rubber Bearings, and as a 5-DoF system for base isolation using KDamper devices. The structure is modeled using one lateral degree of freedom at each floor. The damping of the superstructure is assumed as Rayleigh's mass and stiffness proportional damping, for that critical damping is considered as ξ=5% in all modes.

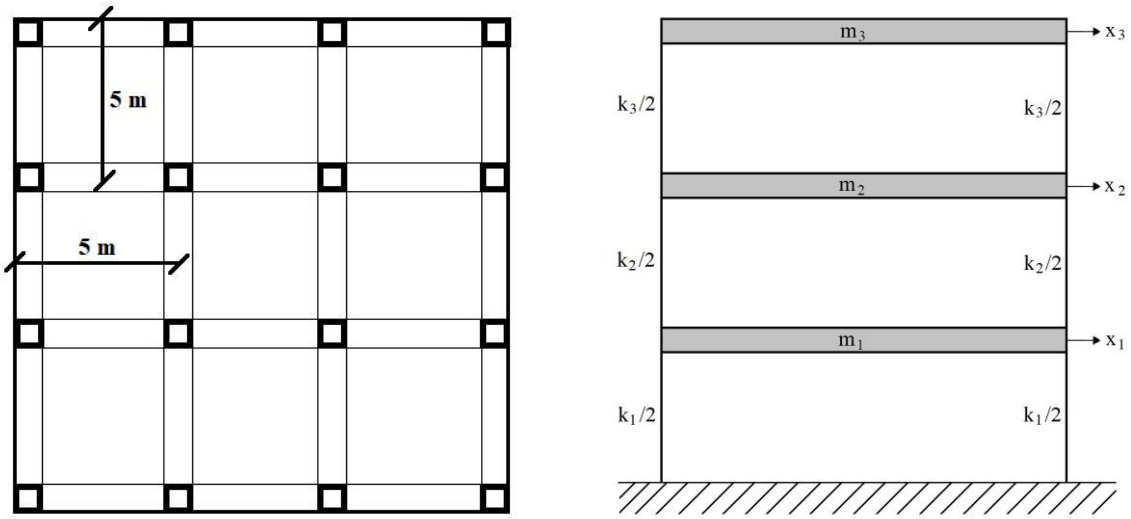

(a) (b)

Figure 6. (a) Ground floor plan of a typical floor of the structure and (b) schematic presentation of a 3-Dof system mounted on a fixed base.

The various assumptions made for the modeling of the structure are:

a) The system is subjected to a single horizontal component of the earthquake ground motion.
b) The total mass of the structure is concentrated at the levels of the floors.
c) The slabs ad grinders on the floors are rigid as compared to the columns.
d) The columns are inextensible and weightless providing the lateral stiffness.
e) The effect of soil-structure-interaction is not taken into consideration.

In addition to this for base isolated buildings we assume that the superstructure is considered to remain within the elastic limit during the seismic excitation. This is a reasonable assumption as the isolation attempts to reduce the earthquake response in such a way that the structure remains within the elastic range.

The system is subjected to Artificial Accelerograms designed to match the EC8 response spectra, as in Figure 7. The Artificial Accelerograms are generated using the SeismoArtif Software [18], for spectral acceleration *0.36 g*, ground type C, spectrum type I, importance class II, calculation method Artificial Accelerogram Generation and Adjustment using an envelope shape by Saragoni & Hart [16]. In Figure 7b, it is observed that the acceleration response spectrum of an Artificial Acclerogram, calculated as described above, is matched very accurately with the EC8 response spectrum, with characteristics: spectral acceleration *0.36 g*, ground type C, spectrum type I, importance class II.

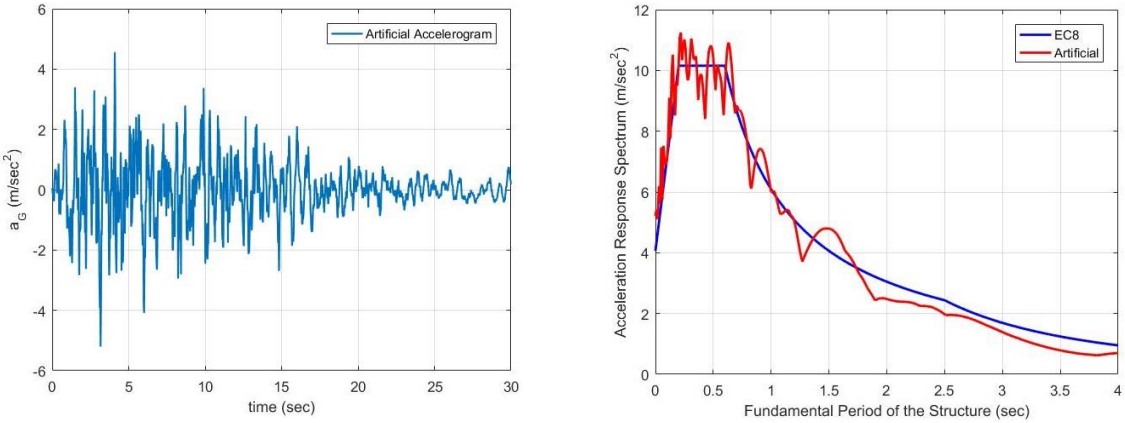

(a) (b)

Figure 7. (a) Artificial ground excitation and (b) Artificial Acceleration response spectra vs EC8 response spectra.

Figure 8 presents the seismic isolation concepts considered in this paper. The SDoF system with mass m_S, stiffness k_S and damping coefficient c_S represents the superstructure, which in this case is the 3 storey building structure. It must be noted here that the presentation of the structure as a superstructure, in Figure 8, is made only for comprehensibility reasons.

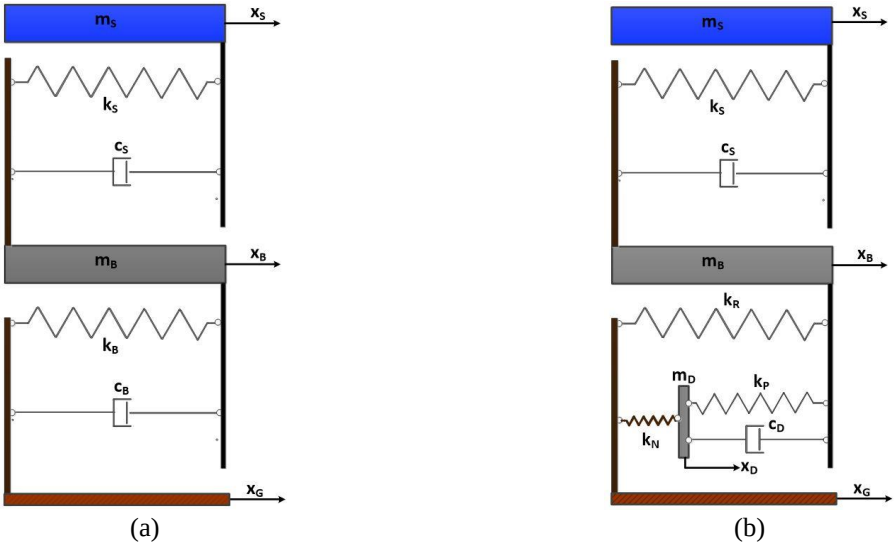

(a) (b)

Figure 8. (a) Flexible structure on a conventional seismic isolation base and (b) possible implementation of the KDamper concept on a seismic isolation base.

The base isolated system with Lead Rubber Bearings (Figure 8.a) is designed to provide an increased fundamental period of the structure of *T=2.0 sec* and an equivalent base's damping

ratio *20%* of critical. The hysteresis loop is modelled as bilinear, as presented in Figure 9. The parameters d_1, F_1, d_2 and F_2 define the bilinear curve and are given for a standard LRB.

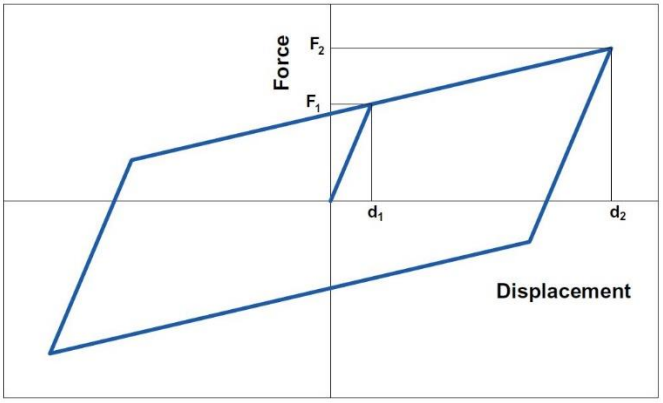

Figure 9. Bilinear hysteresis loop of an LRB.

The hysteretic behavior of an LRB can also be modelled as linear, by means of the effective stiffness K_e and the equivalent viscous damping coefficient ξ_e, which depend on the maximum displacement d_2, and on the corresponding force F_2 to which they refer:

$$K_e = F_2 / d_2 \,,\ \xi_e = \frac{2}{\pi}\left[\frac{F_1}{F_2} - \frac{d_1}{d_2}\right] \tag{2}$$

The system controlled with KDamper devices (Figure 8.b) is designed to increase the fundamental period of the structure to *1 sec*. The additional mass ratio μ_D is *5%* of the total superstructures mass. The stiffness elements are obtained through an optimization procedure with an objective function the base's displacement and proper constraints concerning the floor's accelerations and displacements. The KDamper elements are presented in Table1.

m_D (*tn*)	k_N (*kN/m*)	k_P (*kN/m*)	k_R (*kN/m*)	c_D (*kNs/m*)
17	-14389	18858	74146	405.7

Table 1. Dimensional KDamper parameters.

4 RESULTS

Fig.10 presents the Transfer Functions of the main system responses. As it can be observed, the effect of the conventional seismic isolation system is to shift the natural period of the structure from *0.45 sec* to *2.0 sec*, well below the main frequency content of the earthquakes.

The effect of the KDamper, implemented to the base isolation system, leads to a significant reduction of the initial Transfer Function H_{US} of the Structure's displacement. However, the Transfer Function H_{AS} of the Structure's acceleration retains a significant frequency content.

The Transfer Function of the base's displacement is dramatically improved with the KDamper compared with the conventional seismic isolation base, in all the frequency range, except very high frequencies (5-6 *Hz or 0.15-0.2 sec*).

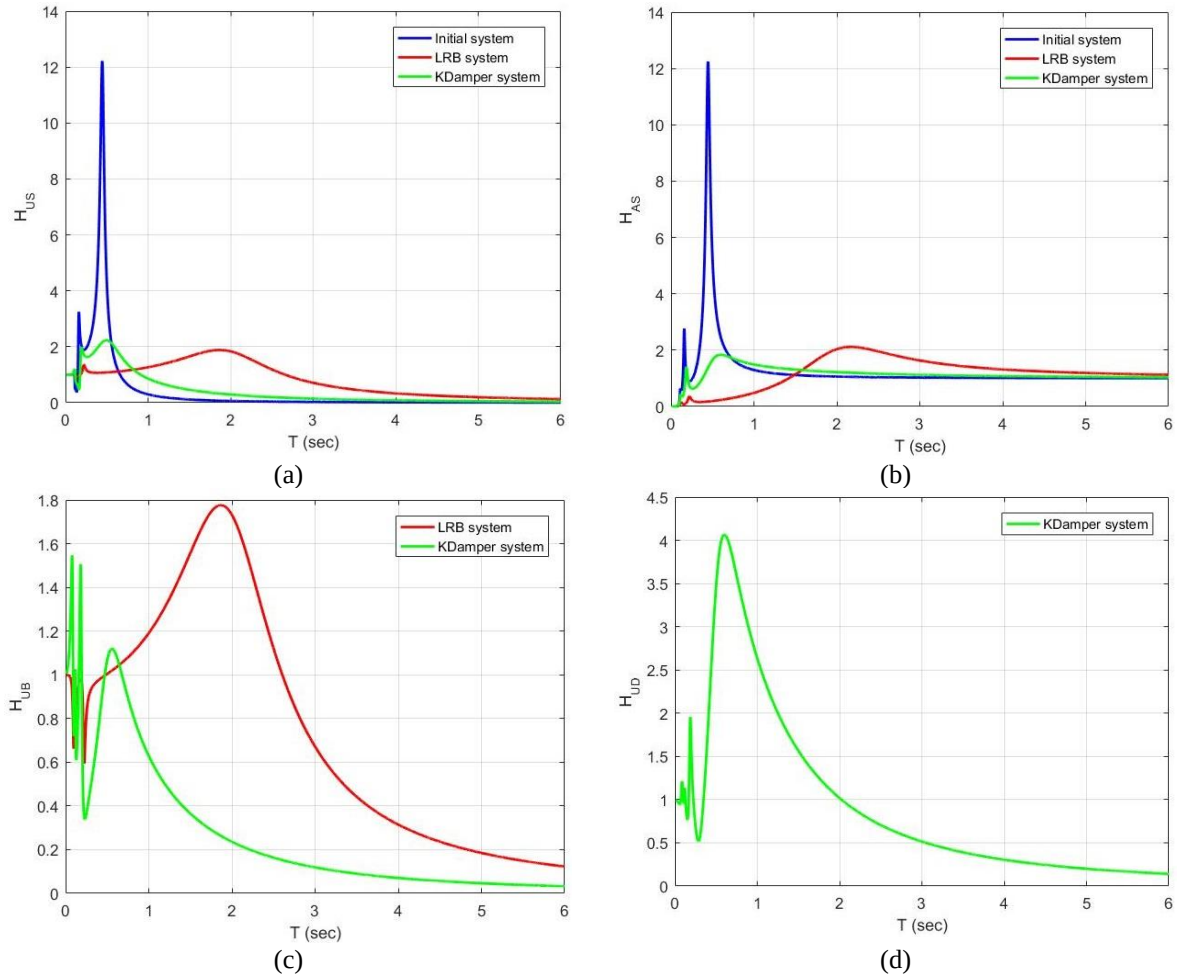

Figure 10. Transfer Functions of the initial system and the isolated system with a conventional seismic isolation base and with a KDamper (a) structure's relative displacement, (b) structure's absolute acceleration, (c) base's displacement and (d) KDamper's displacement.

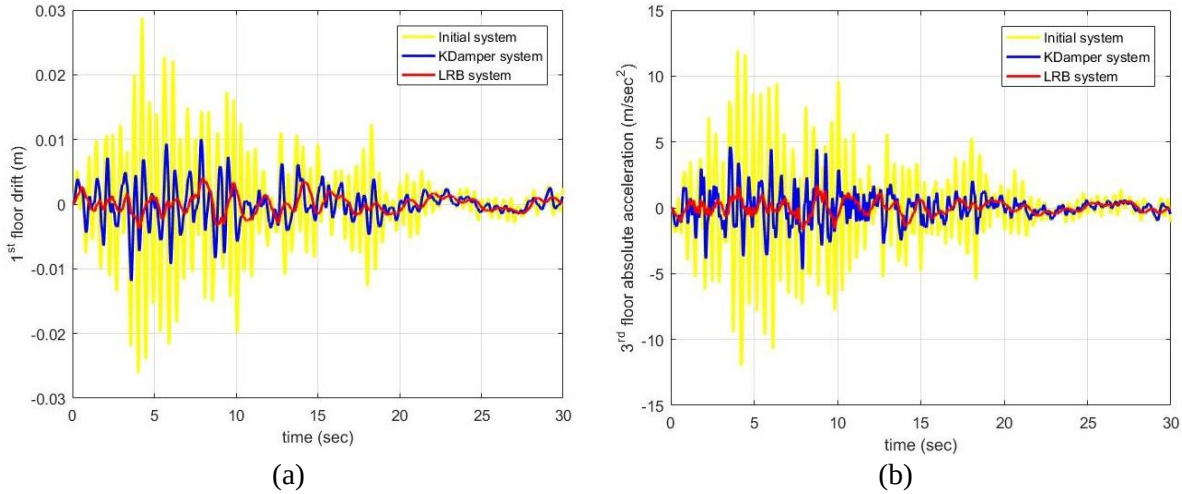

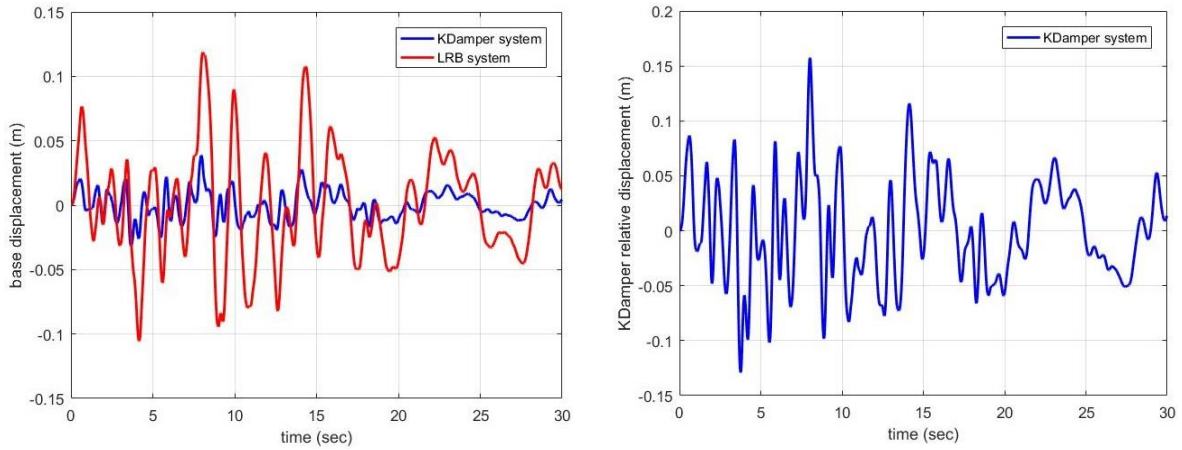

(c) (d)

Figure 11. Dynamic response of the structure under the base isolation concepts considered (a) Structure relative displacements, (b) Structure absolute accelerations, (c) Base relative displacements and (d) KDamper relative displacement

The system is solved using the Newmark-β method with linear acceleration. The responses of the structure to an Artificial Acceleration (Art. Acc. No1), are presented in Figure 11. Figure 11a and 11b confirms that the proposed implementation of the KDamper to the base isolation system, results to a drastic reduction of the structure's dynamic response in both terms of relative displacement and absolute acceleration, at acceptable levels compared to the highly damped conventional base isolation system (LRB). The base's displacement is dramatically improved with the KDamper system than the LRB system *(~70%* reduction), as presented in Figure 11.c.

The responses of the structure are presented in Table2 and 3, for 10 Artificial Accelerograms for the initial system as well as the base isolated system using conventional seismic isolation bearings (LRB) and KDamper.

	LRB - System			Initial - System	
	1st floors drift (m)	3rd floors as (m/sec2)	Base's displacement (m)	1st floors drift (m)	3rd floors as (m/sec)
Artificial_1	0,0040	1,7132	0,1188	0,0288	12,0015
Artificial_2	0,0046	2,0803	0,1358	0,0242	11,0234
Artificial_3	0,0042	1,7209	0,1297	0,0262	13,6332
Artificial_4	0,0045	1,8279	0,1318	0,0301	13,7464
Artificial_5	0,0037	1,6126	0,1091	0,0257	12,7395
Artificial_6	0,0047	2,1782	0,1372	0,0258	11,3612
Artificial_7	0,0058	2,3536	0,1694	0,0303	13,6703
Artificial_8	0,0047	1,8687	0,1359	0,0276	11,8371
Artificial_9	0,0044	1,8221	0,1268	0,0313	13,3713
Artificial_10	0,0058	2,3536	0,1694	0,0303	13,6703
Average	**0,0046**	**1,9531**	**0,1364**	**0,0280**	**12,7054**
STDEV	0,0007	0,2698	0,0194	0,0025	1,0613

Table 2. Dynamic responses of the initial structure and the base isolated structure using conventional seismic isolation bearings (LRB), for 10 Artificial Accelerograms.

	KDamper - System			
	1st floors drift (m)	3rd floors as (m/sec2)	Base's displacement (m)	KDamper's displacement (m)
Artificial_1	0,0119	4,6647	0,0387	0,1575
Artificial_2	0,0110	4,9931	0,0396	0,1603
Artificial_3	0,0112	4,9598	0,0286	0,1178
Artificial_4	0,0108	4,8125	0,0348	0,1414
Artificial_5	0,0115	5,8799	0,0364	0,1413
Artificial_6	0,0104	4,7467	0,0365	0,1452
Artificial_7	0,0121	4,6694	0,0504	0,2047
Artificial_8	0,0118	5,4170	0,0417	0,1612
Artificial_9	0,0107	4,7444	0,0442	0,1797
Artificial_10	0,0121	4,6694	0,0504	0,2047
Average	**0,0113**	**4,9557**	**0,0401**	**0,1614**
STDEV	0,0006	0,3980	0,0068	0,0280

Table 3. Dynamic responses of the base isolated structure using KDamper, for 10 Artificial Accelerograms.

5 CONCLUSIONS

The implementation of the KDamper concept for base isolation of a 3 storey concrete building structure subjected to Artificial Accelerogramms designed to match the EC8 response spectra for ground type C, reveals that the KDamper concept can provide a realistic alternative approach to the existing base isolation schemes.

The application of the KDamper leads to reductions of more than *50%* for the structure's maximum relative displacements and absolute accelerations, while retaining the base's relative displacement to acceptable levels more that *70%* lower than that of the high damped conventional seismic isolation systems (LRB), designed to shift the natural period of the structure to *2.0 sec*.

Provided that efficient technological realizations of the negative stiffness element can result, the KDamper can offer further advantages in terms of complexity and reliability, compared to a conventional highly damped base isolation system. Moreover, the inherit non-linear nature of the negative stiffness force can be exploited to offer further advantages of the KDamper concept, such as robustness, broadband response and energy sinks.

6 ACKNOWLEDGMENTS

This research has been co-financed by the European Union and Greek national funds through the Operational Program Competitiveness, Entrepreneurship and Innovation, under the call RESEARCH – CREATE – INNOVATE (project code:T1EDK-02827).

REFERENCES

[1] I. Antoniadis, S. Kanarachos, K. Gryllias, I. Sapountzakis, KDamping: A stiffness based vibration absorption concept. *Journal of Vibration and Control*, DOI: 10.1177/1077546316646514, 2016, 2016.

[2] A. Carella, M. Brennan, T. Waters, Static analysis of a passive vibration isolator with quasi-zero-stiffness characteristic. *Journal Sound and Vibration* **301**, 678-689, 2007.

[3] N. Debnath, S. K. Deb, A. Dutta, Multi-modal vibration control of truss bridges with tuned mass dampers under general loading. *Journal of Vibration and Control*, DOI: 10.1177/1077546315571172, 2015.

[4] J.P. Den Hartog, *Mechanical Vibrations*, 4th Edition. McGraw Hill, 1956.

[5] H. Frahm, Device for Damping Vibrations of Bodies. US patent #989958, 1909.

[6] T. Haskett, B. Breukelman, J. Robinson, J. Kottelenberg, *Tuned mass dampers under excessive structural excitation*. Report of the Motioneering Inc. Guelph, Ontario, Canada NIK 1B8, 2003.

[7] R. Ibrahim, Recent advances in nonlinear passive vibration isolators. *Journal of Sound and Vibration* **314**, 371–452, 2008.

[8] H. Iemura, M.H. Pradono, Advances in the development of pseudo-negative stiffness dampers for seismic response control. *Structural Control and Health Monitoring*, **16**, 784-799, 2009.

[9] K.A. Kapasakalis, E.J. Sapountzakis, I.A. Antoniadis, Kdamper concept in seismic isolation of building structures with soil structure interaction, *The 13th International Conference on Computational Structures Technology (CST2018)*, Sitges, Barcelona, Spain, 4-6 September, 2018.

[10] R.W. Luft, Optimal tuned mass dampers for buildings. *Journal of the Structural Division ASCE*, **103**, 1985-1998, 1977.

[11] R.J. McNamara, Tuned mass dampers for buildings. *Journal of the Structural Division ASCE*, **105**, 2766-2772, 1979.

[12] W. Molyneaux, *Supports for vibration isolation.* ARC/CR-322, Aer Res Council, G. Britain, 1957.

[13] S. Nagarajaiah, A.M. Reinhorn, M.C. Constantinou, D. Taylor, D.T.R. Pasala, A.A. Sarlis, Adaptive negative Stiffness: A New Structural Modification Approach for Seismic Protection. *5th World Conference on Structural Control and Monitoring (WCSCM 2010)*, p. no. 103, 2010.

[14] D. L. Platus, Negative-stiffness-mechanism vibration isolation systems. *SPIE's International Symposium on Optical Science, Engineering, and Instrumentation*, 98–105, 1999.

[15] L. Qin, W. Yan, Y. Li, Design of frictional pendulum TMD and its wind control effectiveness. *Journal of Earthquake Engineering and Engineering Vibration*, **29**, 153-157, 2009.

[16] G.R. Saragoni, G.C. Hart, Simulation of artificial earthquakes. E*arthquake Engineering-and Structural Dynamics*, **2**, 219-267, 1974.

[17] A.A. Sarlis, D.T.R. Pasala, A.M. Reinhorn, M.C. Constantinou, S. Nagarajaiah, D. Taylor, Negative stiffness device for seismic protection of structures. *Journal of Structural Engineering,* **139**, 1124-1133, 2012.

[18] Seismosoft [2018], SeismoArtif - A computer program for generating artificial earthquake accelerograms matched to a specific target response spectrum. *http://www.seismosoft.com*, 2018.

[19] L. Virgin, S. Santillan, R. Plaut, Vibration isolation using extreme geometric nonlinearity. *Journal of Sound and Vibration,* **315**, 721-731, 2008.

[20] B. Weber, G. Feltrin, Assessment of long-term behaviour of tuned mass dampers by system identification. *Engineering Structures,* **32**, 3670-3682, 2010.

[21] J. Winterflood, D. Blair, B. Slagmolen, High performance vibration isolation using springs in Euler column buckling mode. *Physics Letters A,* **300**, 122-130, 2002.

COMPDYN 2019
7th ECCOMAS Thematic Conference on
Computational Methods in Structural Dynamics and Earthquake Engineering
M. Papadrakakis, M. Fragiadakis (eds.)
Crete, Greece, 24-26 June 2019

A PSEUDOELASTIC FLOOR ISOLATION SYSTEM FOR HOSPITAL SEISMIC RETROFITTING

Lorenzo Casagrande[1,2,*], **Antonio Bonati**[2], **Antonio Occhiuzzi**[2,3], **Ferdinando Auricchio**[1]

[1]University of Pavia, Civil Engineering and Architecture Department (DICAr)
Via Ferrata 3, 27100 Pavia (Italy)
e-mail: lorenzo.casagrande01@universitadipavia.it, ferdinando.auricchio@unipv.it

[2] National Research Council (CNR), Institute for Construction Technologies (ITC),
Viale Lombardia 49, 20098 San Giuliano Milanese (Italy)
e-mail: {casagrande, bonati, occhiuzzi}@itc.cnr.it

[3] University Parthenope, Department of Engineering,
Centro Direzionale Isola C4, 80143 Naples (Italy)
e-mail: antonio.occhiuzzi@uniparthenope.it

Keywords: Multistory buildings, Floor isolation system, Passive damper, Shape-memory alloy, Non-structural elements, Hospitals.

Abstract. *Healthcare facilities symbolize the principal lifeline activity whose operability should be assured after a natural calamity. However, hospital post-disaster functionality is closely related to both structural and nonstructural response, highlighting how facilities can lose their operability just for medium intensity earthquakes. Accordingly, this work aims to focus on a novel pseudoelastic isolation prototype when adopted to damp floor systems, therefore potentially relevant to isolate and retrofit, respectively, new and existing hospitals.*

Initially, based on tests accomplished at the Italian National Research Council (CNR), dedicated numerical simulations are performed to interpret the tensile response of the proposed shape-memory alloy (SMA) passive damper. In this regard, static and dynamic, as well as hint of coupled thermo-mechanic analyses are performed to clarify and predict the physical phenomena underpinning the complex SMA-based damper response.

Finally, focusing on the concept of hospital resilience, the paper demonstrates and updates reasons behind floor isolation systems, underlining structural and non-structural enhanced capabilities when applied to multistory moment resisting frame (MRF) healthcare facilities.

1 INTRODUCTION

In seismic areas a higher level of structural performance is desired for hospital systems than for residential buildings: on one hand, working continuity of such systems depend on the proper functioning of technical installations; on the other hand, medical facilities need to sustain life-line activities in post-emergency healthcare [1].

Although it is generally possible to make medical structures able to remain in function, even after severe seismic events, conspicuous financial losses are related to poorly planned hospital evacuation procedures and lack in operability [2]. Moreover, California is the only country having a specific code for hospital seismic retrofitting [3]. However, according to [4], meet these code requirements approximately consists in retrofit an equivalent 50% of medical facilities (or close them over the next 28 years), and therefore renovate 75% of non-structural components over the same period, for a total cost of $41.7 billion. Numerous guidelines on the hospital seismic assessment have been developed by the World Health Organization (WHO) within the 'Safe Hospitals' campaign, better known as the Hyogo Framework [5]; nonetheless, it is recognized that these guidelines are more practical policies than ad-hoc technical standards.

Resilience is described as the capacity of the system to reduce chances, to absorb and recover after a shock [6]. Especially, hospital resilience intimately depends both on structural and non-structural components, as well as on strategical vulnerabilities (such as emergency planning) toward a performance key indicator that describes the serviceability state of the system [7, 8, 9]. For instance, to prevent and minimize medical record losses, modern complementary techniques implement strategies that protect data in a double perspective, i.e., safeguarding non-structural hardware contents and formulating both Business Continuity (BCP) and Disaster Recovery plans (DRP) [10, 11].

As a result, our study pursues three main goals: (i) numerically model innovative dampers to be adopted as floor isolation systems (indicated as 'FIS', according to [12]) in a novel retrofitting perspective; (ii) highlight local and global isolation performance when dampers are equipped in multistory hospitals; (iii) face main non-structural vulnerabilities, protecting delicate human processes as ones conducted in laboratories, computer and operating rooms.

Therefore, the work is organized as follows: in Section 2 we discuss the novel passive damper developed by Nespoli et al. [13], composed by a parallel system of shape-memory alloy wires (indicated as 'SMA device'). Initially, we focus on the device dynamics, both empirically (through experimental tests performed by Nespoli et al. [14]) and numerically (by means of 3D finite element models developed using the software Abaqus [15], in Section 2.1). Afterwards, we display the effectiveness of the SMA device both in modifying the hospital structural dynamics and in reducing the non-structural vulnerability, when floor passive dampers are considered as a retrofitting procedure (Section 3). In detail, most relevant structural modeling stages (Section 3.1) and the device equivalent 1D model reduction (Section 3.2) are presented. Subsequently, local and global effects of FIS in structural response are discussed, highlighting attenuation in non-structural response and safeguarding human sensitive healthcare procedures (Section 4). Concluding remarks are presented in Section 5.

2 MATERIAL AND METHODS

The main stages fulfilled in this section can be outlined as follows:

- to summarize experimental tests previously performed by Nespoli et al. [14];
- to numerically reproduce the experimental tests;

- to establish the physical and mechanical effects on the response of the SMA damper;
- to re-design the device for floor isolation system applications;

To describe these stages, the consistency of modeling assumptions is discussed.

2.1 Shape-memory alloy (SMA) device

The scope is to study the mechanical response of the damper described in [14], investigating on shape-memory alloy physical peculiarities such as high strain recovery (known as shape memory effect) and recentering capabilities (due to pseudoelasticity) [16, 17]. In detail, pseudoelasticity is a recoverable deformative process induced by a thermo-elastic transformation between two different solid phases, martensite and austenite. This process is the base mechanism for the damper behavior, of which we concisely recapitulate the functioning in the following.

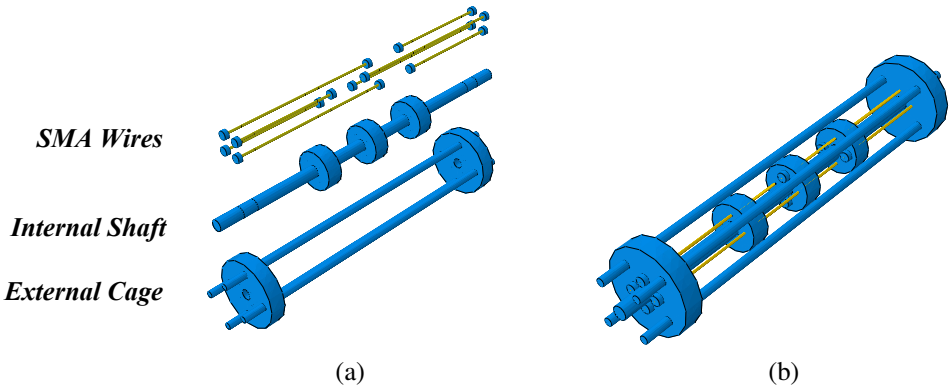

Figure 1: Shape-memory alloy device, components (a) & assembly (b).

The device is constituted by two groups of SMA wires with the same diameter (1.2 mm) and different length (210 and 132 mm), organized in a specular parallel disposition (Figs. 1(a), yellow). According to Indirli et al [18] and Ren et al [19], this wire disposition tunes the stress-strain response of different length wire groups, composing multi-plateau force levels and improving the overall damping capacity. Externally, a steel cage protects the wires and support an internal steel sliding shaft: the shaft puts in tension the SMA wires through three fixed disks (Fig. 1(a), blue), providing bi-directionality to the damper.

Quasi-static and dynamic cyclic tests have been performed by Nespoli et al. [13, 14] to assess the mechanical behavior, initially on single SMA wires, subsequently on pseudoelastic systems (composed by groups of two wires), and finally on the global device (Fig. 1(b)). Tests have been fulfilled by means of a servo-hydraulic thermo-mechanical MTS equipment and temperatures have been measured by thin thermocouples. Quasi-static tests have been executed at controlled deformation rate (1% min^{-1}), while dynamic tests have been performed at 0.5-1 Hz for 1000 working cycles, stretching wires up to 6.4% strain.

Therefore, we develop 3D finite element (FE) models by means of the software ABAQUS [15], employing 8-node brick-based models in an isoparametric framework, in accordance with [20]. Geometrical and material non-linearities are considered. In order to reduce numerical analyses, we model the external cage rigidly, while we assume the rate-independent Von Mises yielding principle to reproduce the metal plasticity of shaft components [21]. The shape-memory alloy constitutive model is derived by Auricchio et al. [16].

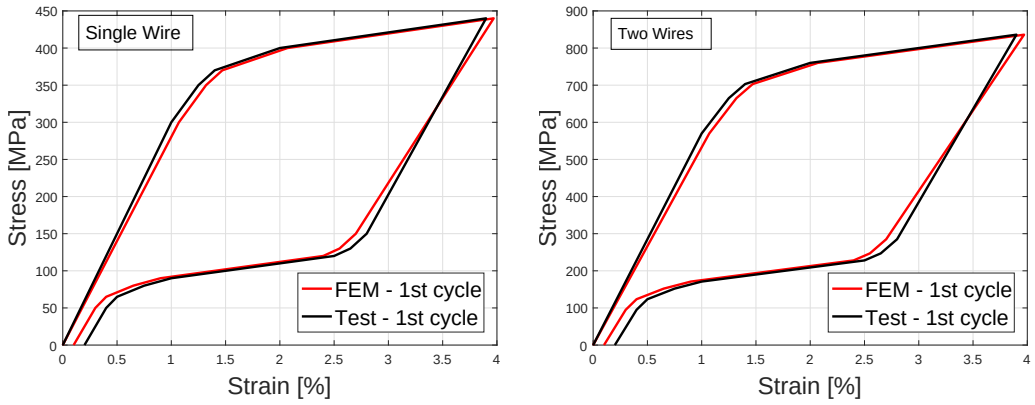

(a) (b)

Figure 2: Model calibration, tests on one- (a) & two-wire (b) pseudoelastic system.

At first, based on quasi-static experimental tests, we calibrate a single wire model capable to reproduce the one- and the two-wire experimental system, stretching such system up to 4% strain. Fig. 2 display the correlation between experimental and numerical results.

Afterwards, to numerically interpret the dynamic behavior of the whole damper, and therefore to characterize material property variations due to the exothermic transition from austenite to stress-induced martensite, single wire dynamic stress-strain response is expressed by functions of temperature in a coupled thermo-mechanical problem. Even if the simulated problem has an uniaxial nature, the response is explored in a three-dimensional domain. Specifically, dynamic analyses are performed in ABAQUS [15] by means of full-scale coupled temperature-displacement models, accounting for transient heat transfer: the external stagnant air is simulated applying a convective film coefficient to each free surface, while conduction is considered negligible. According to [22], although it is known that the expansion coefficient and the thermal conductivity may depend on the solid phase of SMA (whether alloy is austenite or martensite), these coefficients are considered to be independent from strain or temperature, as well as the specific heat and the film coefficient [15].

As a result, numerical tests are performed in a tensile/compressive fashion loading the wires for 1000 working cycles toward a 6.4% strain for the short wire (132 mm) and 4% strain for the long one (210 mm). Fig. 3 displays the heat radiation, moving from the center to the external surface in short- and long-wire sections.

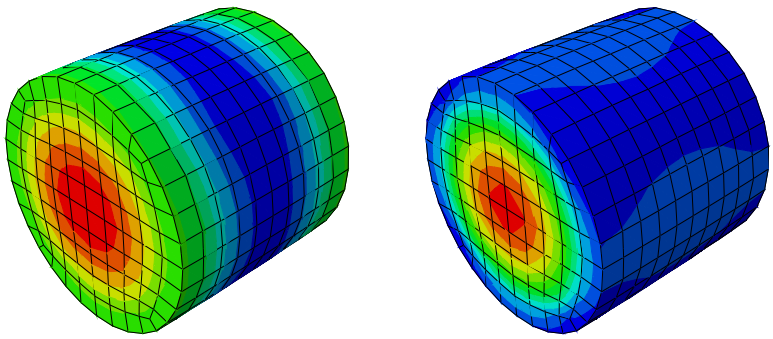

(a) (b)

Figure 3: Model calibration, thermo-mechanical tests on short- (a) & long-wire (b) sections.

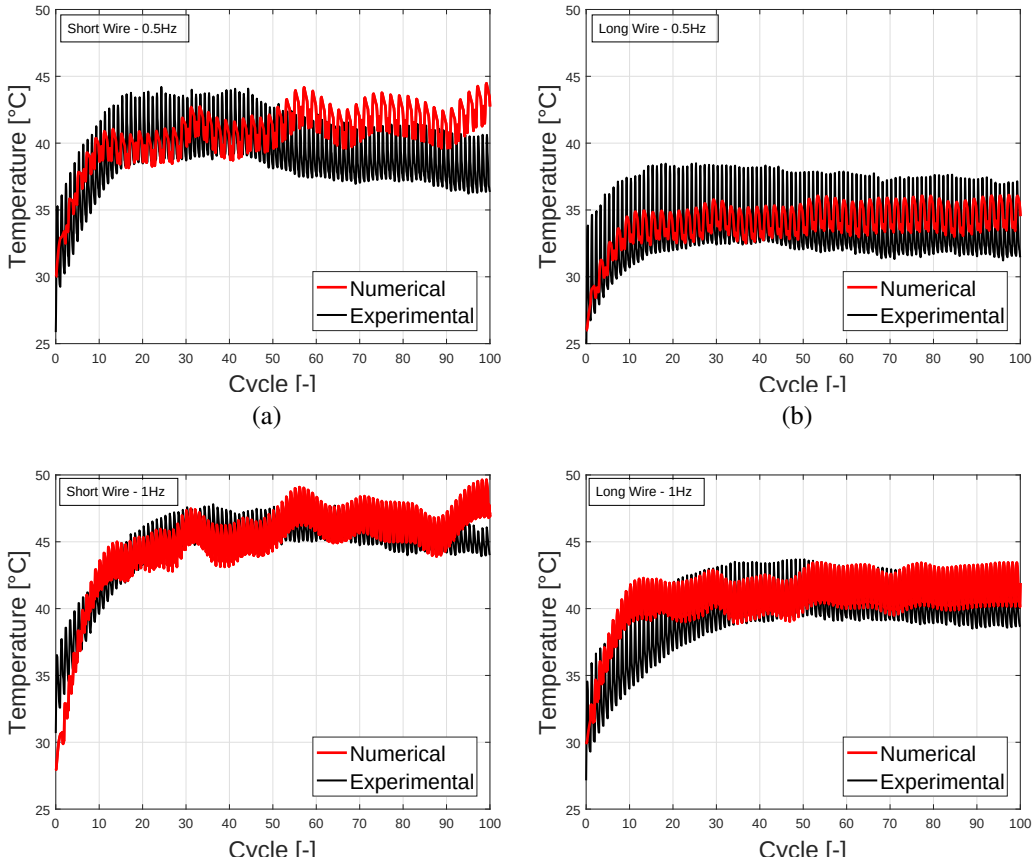

Figure 4: Coupled thermo-mechanical simulation, 0.5Hz - short wire (a) & 0.5Hz - long wire (b) & 1Hz - short wire (c) & 1Hz - long wire (d), numerical and experimental results.

Fig. 4 compares the experimental [14] and numerical temperature variation for the short and the long wire during the first 100 working cycles. The sinusoidal trend is due to the exothermic phase transition. Finally, we assemble the damper global model with tested wires: Fig. 5 depicts force-displacement diagrams during the first working cycle, registered at 0.5 and 1Hz.

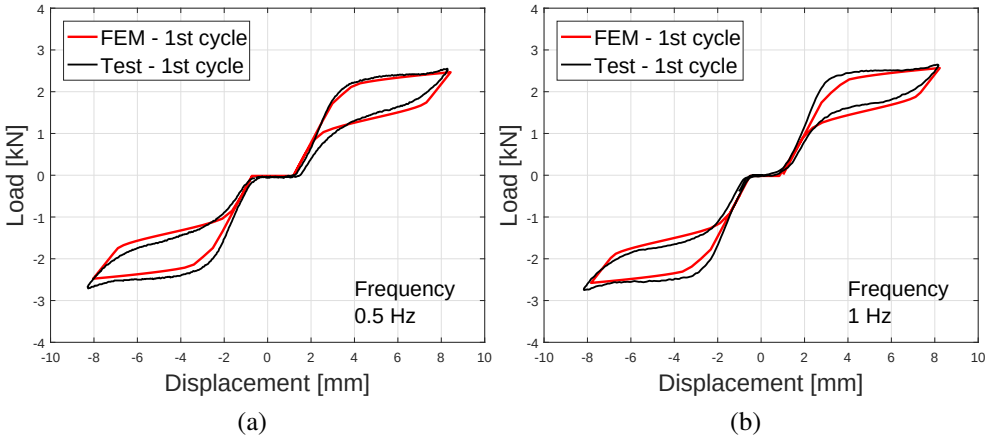

Figure 5: Numerical and experimental tests on the global device: 0.5Hz (a) & 1 Hz (b).

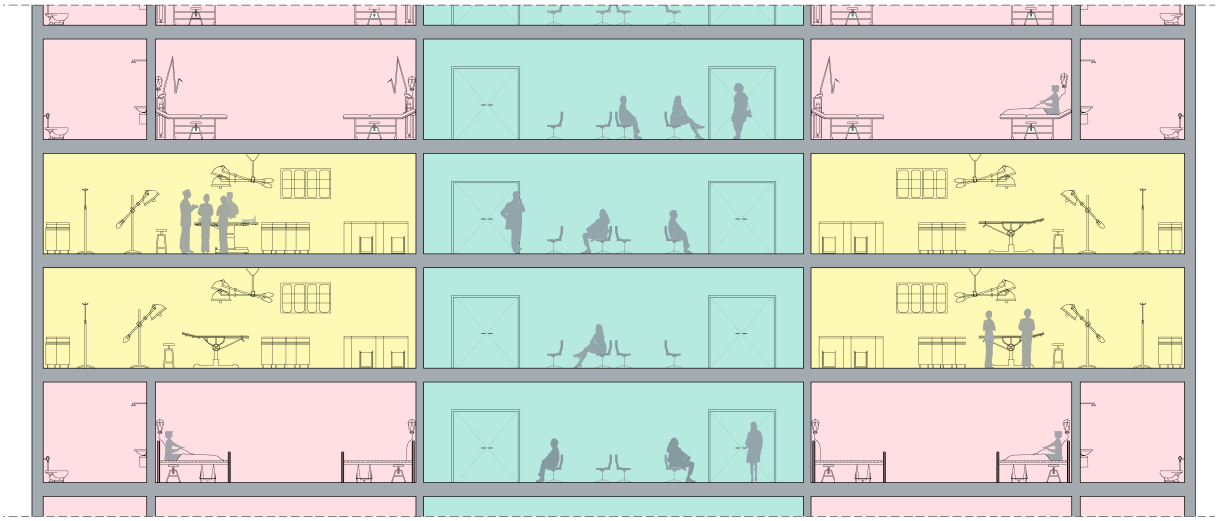

Figure 6: Model of hospital facility, the hazard color code.

2.2 SMA devices for hospital floor isolation systems

As illustrated in Fig. 6, several key activities are daily performed in hospitals: these activities can be conceptually gather according to an hazard color code. As a sample, in yellow we highlight delicate procedures, such as procedures executed in laboratories or operating rooms; in pink we depict recovery rooms and in green the waiting rooms. Interruption of yellow activities may affect life-saving operations or result in safety and economic losses. As a result, we decide to adopt floor isolation techniques to seismically protect non-structural elements, equipment and fragile building contents of yellow areas. Particularly, the isolation is achieved by decoupling secondary floor systems form the motion of structural frame by means of horizontally flexible links called isolators (Fig. 7(a)). However, despite preserving the content of critical facilities might produce the greatest cost-benefit ratio, floor isolation systems have not been codified yet; additionally, distinctions from conventional base isolation systems arise on the supported weight and on the seismic input, generally making floor isolation technique laborious. By contrast, thanks to SMA devices we propose an intuitive floor isolation scheme (Fig. 7(b)).

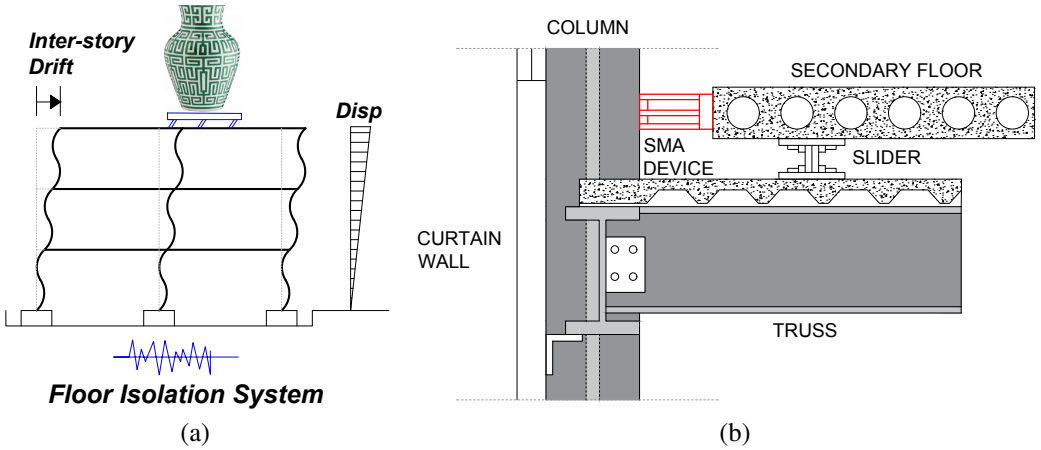

Figure 7: Floor isolation system, conceptual model (a) & application scheme (b).

In this scheme, the secondary floor system is supported by a low friction slider, while laterally the motion is damped by SMA devices. Successively, we perform a parametric numerical campaign, iterating numerical simulations presented in Section 2.1 in order to re-design a SMA-based damper, capable to support a 50mm inter-story drift in displacement and a 6kN lateral load in force. In Fig. 8 we depict the new damper geometries (8(a)) and the force-displacement dynamic response (8(b)).

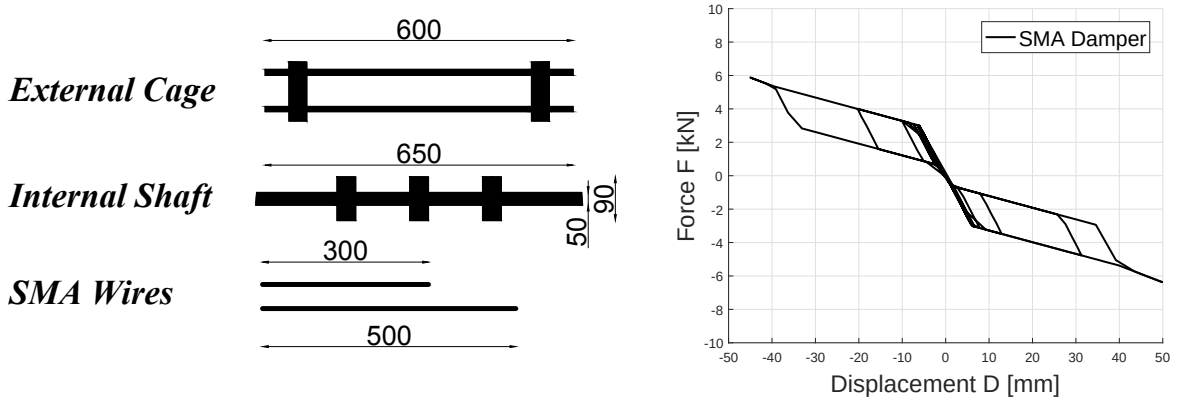

(a) (b)

Figure 8: Shape-memory alloy device, geometries (a) & dynamic response (b).

3 NONLINEAR TIME HISTORY ANALYSES

The main objective of this work is to highlight the potentiality of SMA devices as a retrofitting tool, in order to isolate hospital floors safeguarding lifeline activities during extreme events, throughout these main stages:

- to reproduce, by means of fiber-based models, the seismic response of four multistory hospital facilities introduced in Section 3.1;
- to reduce 3D device numerical simulations (introduced in Section 2.1) in equivalent 1D fiber-based link elements;
- to assess the potential impact obtained by implementing SMA-based floor isolation techniques, correlating structural and non-structural seismic response attenuation demonstrated by means of nonlinear time history analyses.

In this regard, the main conceptual simplifications will be discussed.

3.1 Description of the case-study buildings

We design four hospital prototypes (Fig. 9) according to Eurocode 8 [23], consisting in 6 x 6-bay buildings extrapolated from reference 5-,10-,15- and 30-storey three-dimensional structures. We consider high seismicity areas (i.e. PGA = 0.40 g) with soil class C (180 m/s $\leq$ Vs $\leq$ 360 m/s) and a medium ductility class (DCM). Fig. 9 displays the lateral force resisting system (LFRS): internally, a braced core redistributes vertical loads and guarantee stability against horizontal forces; externally, outriggers arranged every 15 floors impede lateral displacements

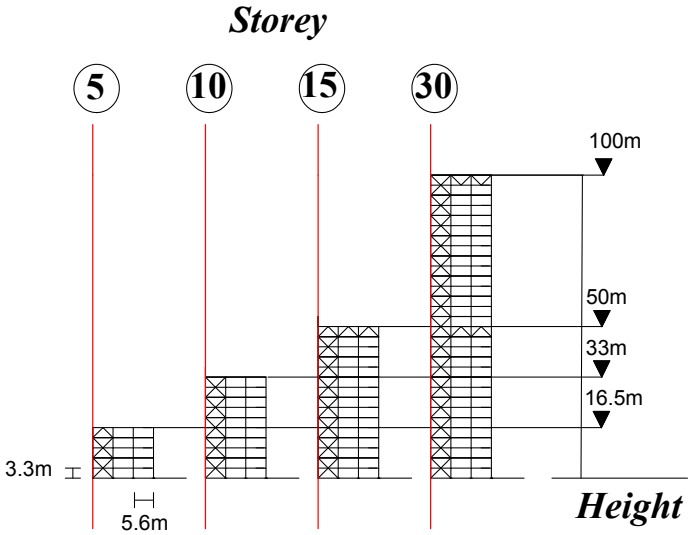

Figure 9: Reference hospital structures.

and inter-story drifts. As specified in 6.3 of EC8, we conservatively assume the behaviour factor (q) equal to 2, considering V bracing systems. Moreover, we hypothesize 2 and 4 kN/m^2, respectively, for dead and live loads; additional 3.5 kN/m^2 are assumed to consider medical equipment and permanent non-structural weights in laboratories and operating rooms (yellow areas according to the hazard color code introduced in Fig.6), 2 kN/m^2 otherwise. Furthermore, in areas susceptible to overcrowding (green code according to Fig.6) we combine vertical permanents with 60% of live loads. In order to explore the dynamic response of reference hospital prototypes, we perform nonlinear time history analyses (NLTHAs), symbolizing an efficient technique to evaluate global and local seismic performances. In detail, we develop inelastic force-based fiber element models through the open source platform OpenSees [24], efficient in predict distributed plasticity and geometric nonlinearities in a classical corotational transformation framework: the plastic propagation in key structural elements is simulated through the bilinear stress-strain relationship by Menegotto-Pinto [25]. Gusset plate connection is specified in Fig. 10, along with the main modeling assumptions. Structures are subjected to a set of 10 natural records [26], scaled in displacement to match the design response spectrum defined by EC8. For additional information on the fiber-based modeling the reader may refer to [27].

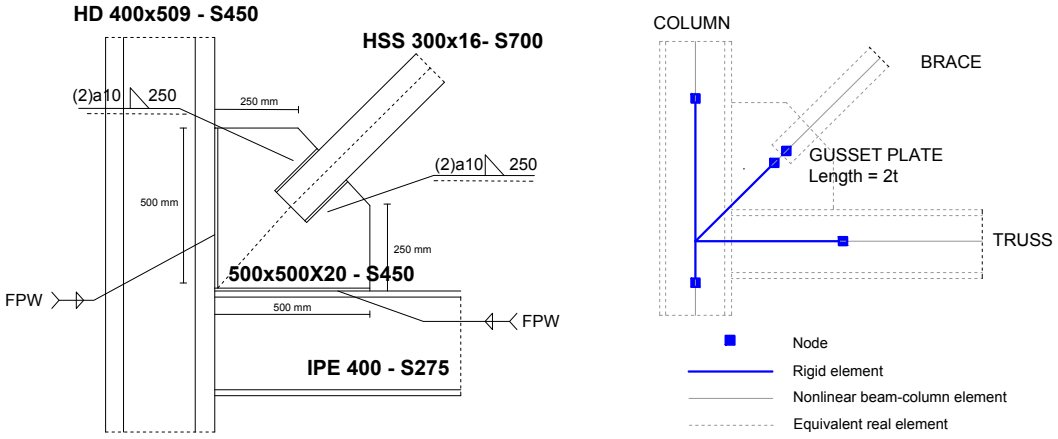

Figure 10: Designed gusset-plate connection with modeling assumptions.

3.2 SMA device equivalent 1D model reduction

Finite element approaches acquire efficiency when the computational cost decreases; however, model veracity tends to be deeply sensitive to the numerical simplifications [28]. By contrast, particularized three-dimensional simulations may become excessively onerous in terms of computational time [29]. According to [30], we calibrate equivalent mono-dimensional links capable to extensively describe the dynamic response of the SMA damper, legitimized by the need in developing predictive models that reduce the demand of expensive experimental tests. Fig. 11 depicts the 3D global model and the schematic of the mono-dimensional spring model, achieved by calibrating and combining non-linear links that individually represent one out of six lumped plasticity constitutive curve.

The proposed scheme is flexible and adaptable to secondary floor system geometry changes and mass variability. As a result, input parameters are deduced by means of iterative numerical calibration of Section 2.2.

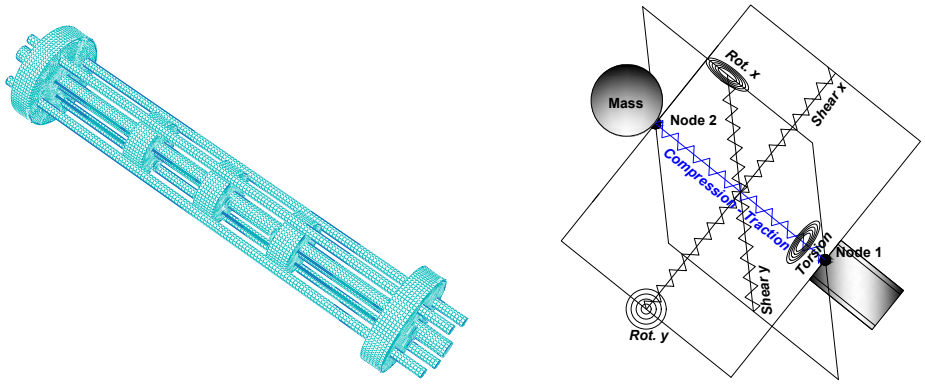

(a) (b)

Figure 11: Shape-memory alloy device, 3D (a) & equivalent 1D model (b).

4 RESULTS AND COMPARISONS

This work explores the employment of shape-memory alloy dampers in original floor isolation applications: specifically, we wish to study modifications in hospital structural dynamics associated to reductions in non-structural vulnerability. Therefore, in this section we highlight main results, provided in terms of global and local performance of four reference medical structures. Accordingly, each diagram display the comparison between NLTHA average response achieved by the retrofitted structure (SMA) and the correspondent bare moment resisting frame (MRF), along with individual earthquake (MRF EQs) acceleration result.

4.1 Global performance

We equip floor isolation systems in hospital frames in order to limit absolute displacement and acceleration demands on sensitive medical equipment. Thereafter, we wish to highlight the dual effect of FIS in limiting the maximum instantaneous seismic demand on such equipment: on one hand, reducing the structural response; on the other hand, decoupling non-structural elements.

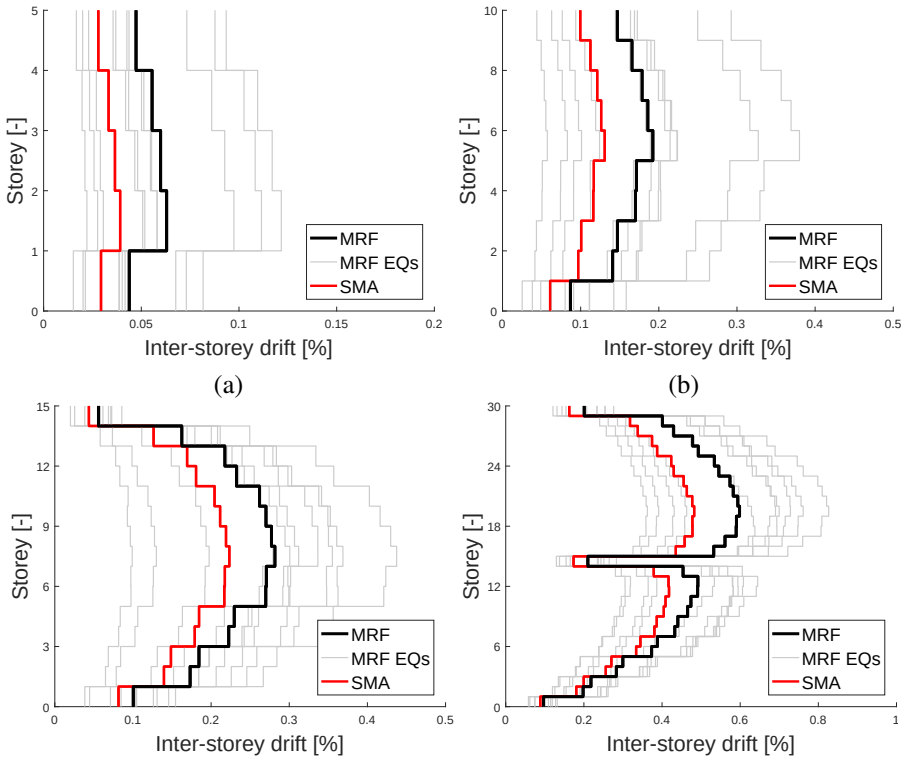

Figure 12: NLTHA Avg peak values for SMA & MRF, inter-storey drift.

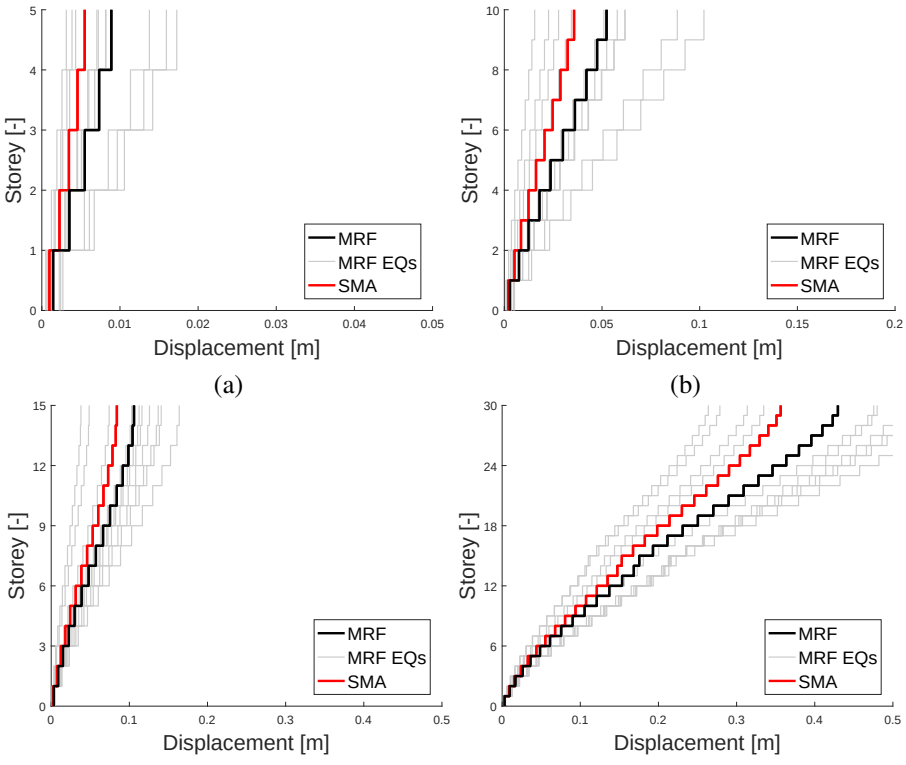

Figure 13: NLTHA Avg peak values for SMA & MRF, displacement.

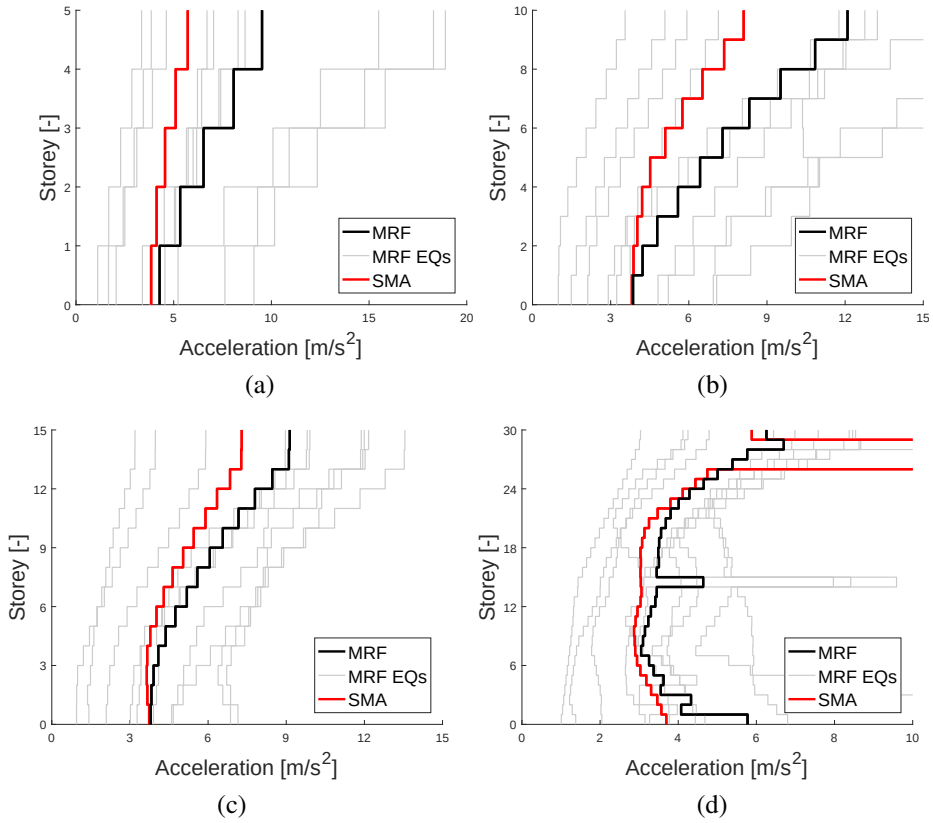

Figure 14: NLTHA Avg peak values for SMA & MRF, acceleration.

Accordingly, a series of nonlinear time history analyses are performed to validate the damper design: we analyze the global performance of four hospital frames (introduced in Section 3.1) in terms of maximum inter-storey drift, peak displacement and acceleration peak profiles, together with their average values. Specifically, Fig. 12 compares inter-storey drifts in bare moment resisting frames and in SMA-based isolated structures. SMA-based results deviate from MRF average at approximately mid-height: the drift appears clearly reduced when the floor isolation system is considered, up to an attenuation of 37.77%, 31.84%, 20.70%, 18.23%, showing a inversely proportional trend along the height. These values remain under the threshold of 0.5% for deformation sensitive equipment [31, 32].

In Fig. 13 we summarize peak displacements: the response assumes a rough cantilevered shape with maximum values on top. The percentage attenuation is respectively 38.28%, 31.79%,

Performance	**5 Storey**		**10 Storey**		**15 Storey**		**30 Storey**	
	SMA	**MRF**	**SMA**	**MRF**	**SMA**	**MRF**	**SMA**	**MRF**
Inter-storey Drift [%]	0.039	0.054	0.13	0.17	0.22	0.27	0.42	0.50
Displacement [mm]	5.5	7.6	35.7	47.1	84.2	101.6	356.4	417.1
Acceleration [m/s^2]	5.72	8.00	8.10	11.77	7.29	8.76	5.54	5.88
Drift Attenuation [%]	**37.77**	-	31.84	-	20.70	-	18.23	-
Disp. Attenuation [%]	**38.28**	-	31.79	-	20.69	-	17.04	-
Accel. Attenuation [%]	**39.94**	-	32.98	-	20.20	-	6.09	-

Table 1: NLTHA Avg peak values for SMA & MRF, global performance.

20.69% and 17.04%, once again displaying more pronounced percentage attenuation in low-rise respect to medium-rise structures. Significant top accelerations are experienced in dynamic simulations, i.e. 0.82g, 1.10g, 0.89g and 0.60g, underlining the stiffest behavior of lower structures. Moreover, the performance survey suggest that floor isolation efficiently reduces absolute structural acceleration demands recorded at the base of acceleration sensitive equipment: results are illustrated in Fig. 14, where peak percentage attenuation of 39.94%, 32.98%, 20.20% and 6.09% are reached.

We wish to recall that global performance values (inter-storey drift, displacement and acceleration summarized in Tab. 1) are recorded at structural level. Therefore, these results suggest that the use of FIS is an efficient technique for protecting sensitive equipment, reducing the overall structural response. However, in a control strategy perspective, either passive or semi-active, non-structural demand can be limited even modulating the decoupling effects provided by FIS. In detail, equipment displacements and accelerations might be effectively damped by the isolation system, establishing a response modification factor that scales the structural global performance, obtaining the corresponding non-structural local demand [33, 34]. Qualitatively, in Fig. 15 we represent the isolation scheme with the correlated stress-strain response: accordingly, from such response it is possible to specify the stiffness and damping properties of the floor isolation system, evaluating the transmissible primary floor level demand.

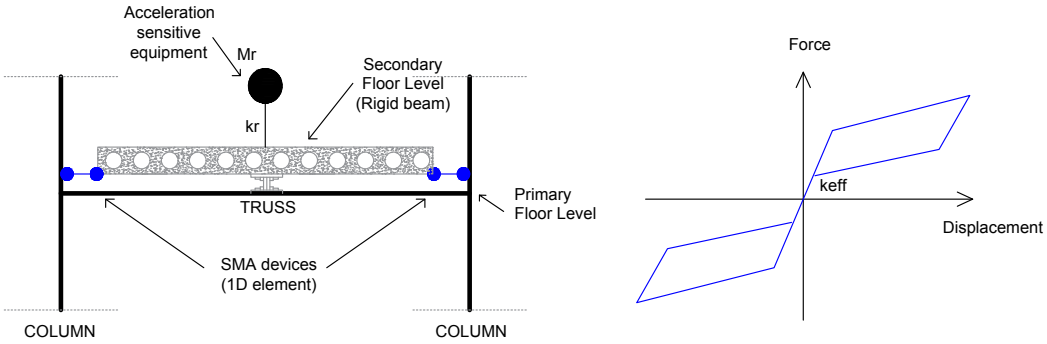

Figure 15: Secondary floor isolation scheme.

4.2 Local performance

According to Casagrande et al. [27], key components that support the seismic action in MRFs are internal core columns: the reader may refer to Fig. 16 where we display the extent of seismic overburden in such columns. Thereafter, the response in terms of axial load, bending and shear peak profiles in critical members is displayed. In addition, the percentage attenuation between MRF and SMA-based isolated structure results is illustrated.

Specifically, in Fig. 17 compressive peak forces of most critical columns are depicted, along with their average. The obtained peaks reach a maximum in 30-storey frame with 19823kN, reduced up to 9.33% with the SMA-based isolation. A proportional demand is obtained in 5, 10 and 15 storey buildings, as a consequence of the structural weight increment, where is demonstrated that modeling the structure without FIS conduce to overestimate NLTHAs results up to 32.22%. In Figs. 18-19 we summarize the seismic peak bending moments and shear forces in columns: diagrams depict a comparison between forces observed considering the moment resisting frame with the external floor isolation and the supporting structure alone: values are almost stable along the height, reaching a maximum at the base.

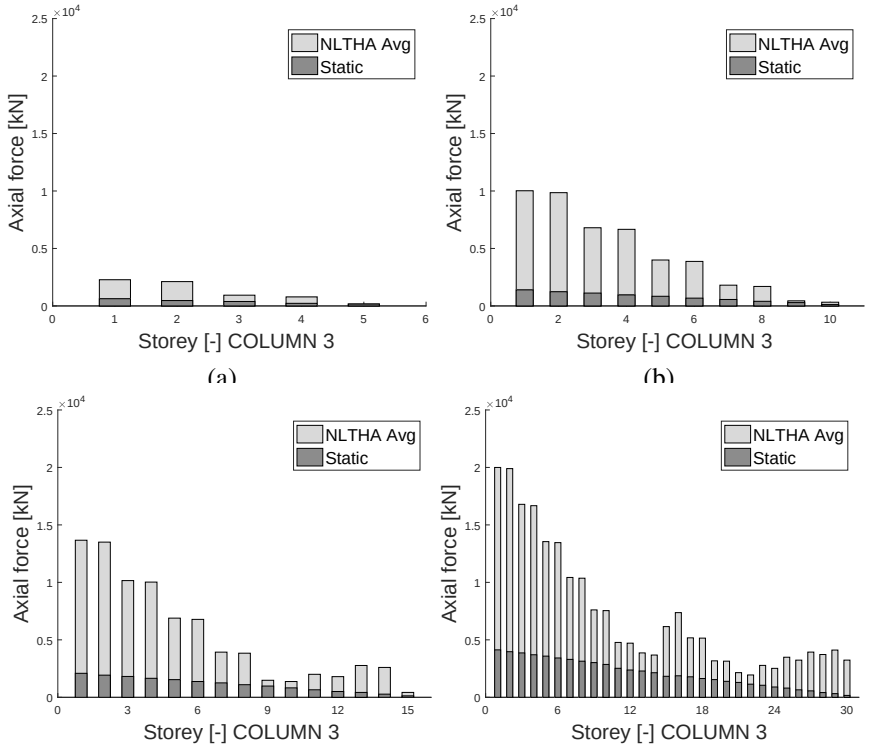

Figure 16: NLTHA Avg peak values and static loads, axial forces.

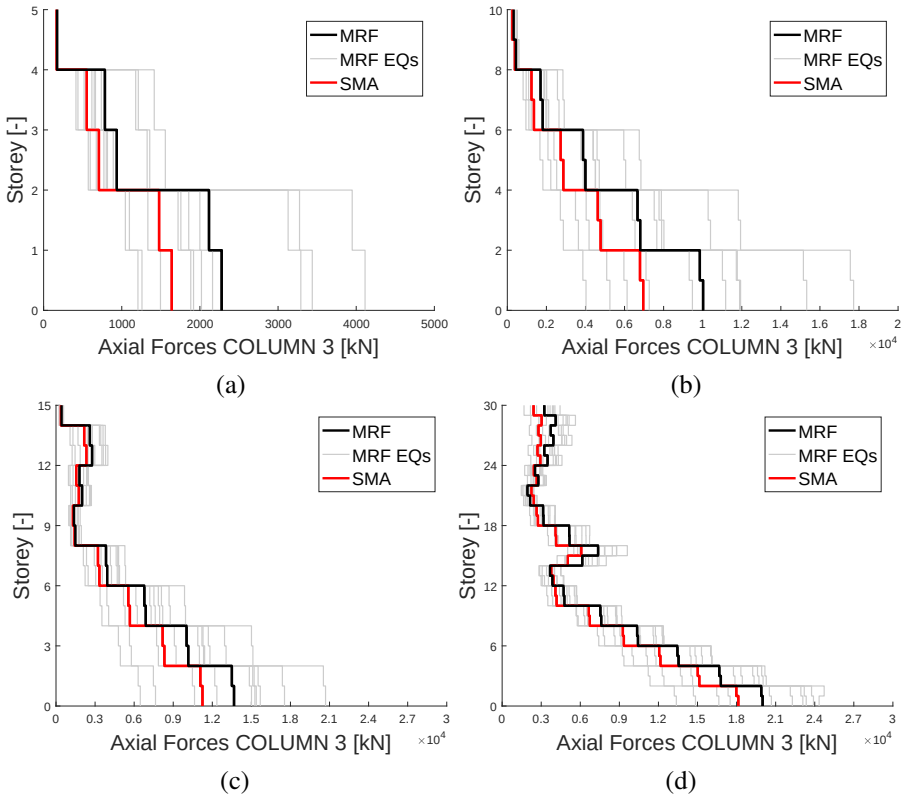

Figure 17: NLTHA Avg peak values for SMA & MRF, axial forces in columns.

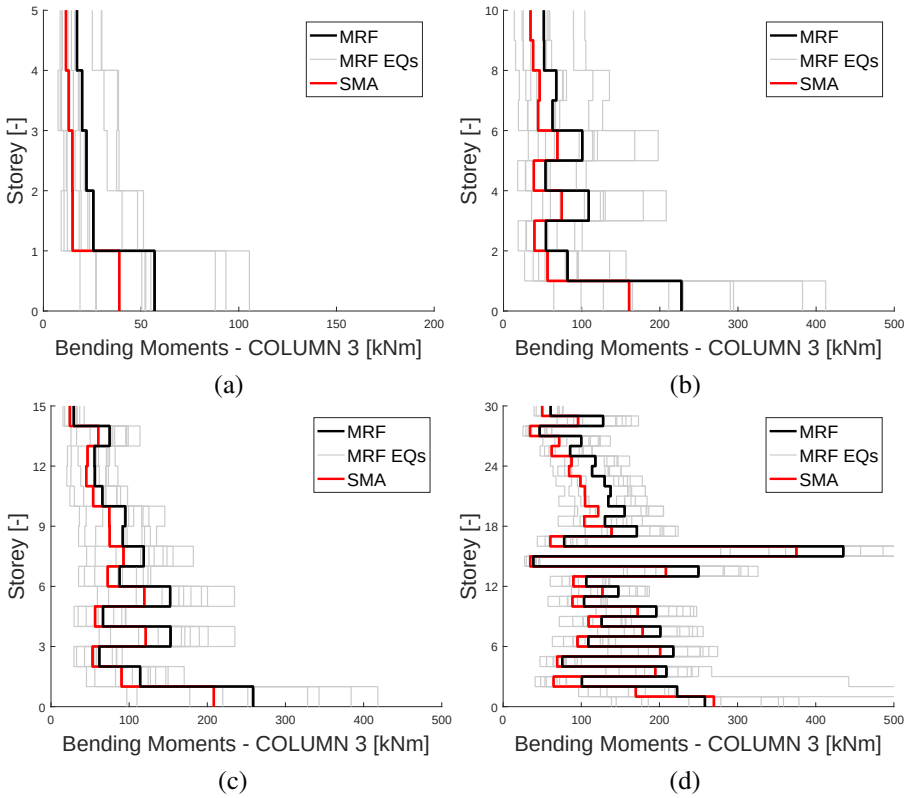

Figure 18: NLTHA Avg peak values for SMA & MRF, bending moments in columns.

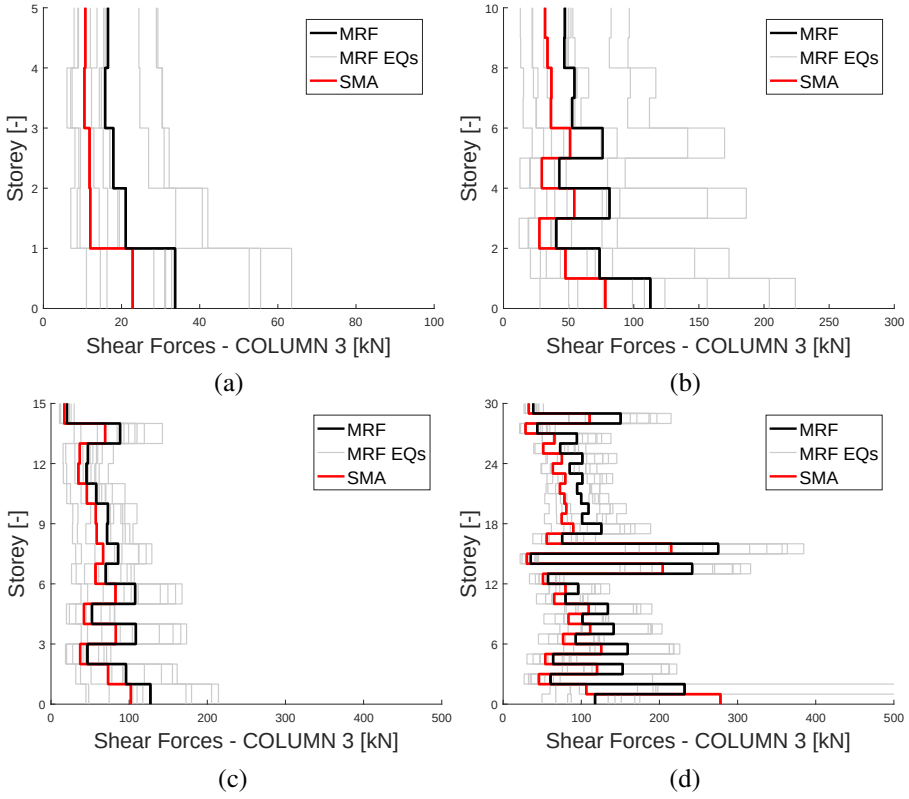

Figure 19: NLTHA Avg peak values for SMA & MRF, shear forces in columns.

Performance	5 Storey		10 Storey		15 Storey		30 Storey	
	SMA	**MRF**	**SMA**	**MRF**	**SMA**	**MRF**	**SMA**	**MRF**
Col. Axial Force [kN]	1640	2168	6955	9082	11245	13237	18132	19823
Col. Bending [kNm]	38.78	51.13	160.66	207.97	208.38	248.87	375.21	426.91
Col. Shear [kN]	22.83	30.19	78.13	102.10	102.21	122.28	214.98	262.00
Col. Axial Attenuation [%]	**32.22**	-	30.59	-	17.72	-	9.33	-
Col. Bend. Attenuation [%]	**31.85**	-	29.45	-	19.43	-	13.78	-
Col. Shear Attenuation [%]	**32.23**	-	30.68	-	19.64	-	21.87	-

Table 2: NLTHA Avg peak values for SMA & MRF, local performance.

Even if similar percentage attenuation are achieved between bending moments and shear forces, a larger mismatch is determined for the 5-storey structure, up to approximately 32%. This discrepancy reflects that particular care has to be paid in evaluating the earthquake-induced demand, expressly during the design phase of low rise structures with FIS. Results are summarized in Tab.2, where peak responses are collected together with their percentage attenuation.

5 CONCLUSIONS

The work presented investigates on some critical challenges of interest for the seismic isolation of hospitals. Initially, shape-memory alloy devices have been explored, experimentally and numerically, to be adopted as a novel isolation device. Afterwards, we have focused on the advantageous features related to floor isolation systems (FISs) when equipped in multistory medical structures exposed to nonlinear time history analyses. Finally, analogies and contrasts between SMA-based floor isolated structures and traditional moment resisting frames have been discussed. The main conclusions may be summarized as follows.

Shape-memory alloy floor isolation systems:

- suggest attenuation in inter-storey drifts, displacements and accelerations, up to 40%, 38% and 37%, respectively. As a result, SMA-based dampers globally decrease seismic demand on non-structural contents;
- reveal a beneficial increment in energy dissipation capacity, resulting in local force attenuation (up to 32% in columns, the most seismically overloaded element);
- may be designed to remain elastic, locally decoupling accelerations and displacements directed to non-structural elements;
- result to be more effective in low-rise frames (5-storey). Dampers also decrease the structural period when increasing the structural eight.
- reasonably boost the reliability of sensitive equipment located in secondary floor systems;
- may be adopted in existing buildings as a retrofitting technique.

Additional applications under assessment, compatible with this results, regard either extending the survey to other damper typologies or deeply investigating the thermo-mechanically coupled SMA device response.

REFERENCES

[1] Y. Kuwata, S. Takada, Seismic risk assessment and upgrade strategy of hospital-lifeline performance. *Advancing Mitigation Technologies and Disaster Response for Lifeline Systems*, 82-91, 2003.

[2] KM. Taaffe, E. Tayfur, Evaluating the robustness of hospital evacuation plans. *IIE Annual Conference. Proceedings. Institute of Industrial and Systems Engineers (IISE)*, 2006.

[3] Office of Statewide Health Planning and Development, Seismic evaluation procedures for hospital buildings, SB 1953. *California building standards administrative code*, 2007.

[4] C. Meade, J. Kulick, R. Hillestad, Estimating the Compliance Costs for California SB 1953. *Oakland: California HealthCare Foundation*, 2002.

[5] United Nations inter-agency secretariat of the international strategy for disaster reduction (UNISDR), Hyogo Framework for Action 2005-2015: Building the Resilience of Nations and Communities to Disasters. *World Conference on Disaster Reduction*, 2005.

[6] GP. Cimellaro, AM. Reinhorn, M. Bruneau, Seismic resilience of a hospital system. *Structure and Infrastructure Engineering*, **6.1-2**,127-144, 2010.

[7] R. Miniati, C. Iasio, Methodology for rapid seismic risk assessment of health structures: Case study of the hospital system in Florence, Italy. *International journal of disaster risk reduction*, **2**, 16-24, 2012.

[8] S. Zhong, M. Clark, XY. Hou, YL. Zang, G. Fitzgerald, Development of hospital disaster resilience: conceptual framework and potential measurement. *Emerg Med J*, **31.11**, 930-938, 2014.

[9] S. Zhong, M. Clark, XY. Hou, Y. Zang, G. FitzGerald, Development of key indicators of hospital resilience: a modified Delphi study. *Journal of health services research and policy*, **20.2**, 74-82, 2015.

[10] V. Lozupone, Disaster recovery plan for medical records company. *International Journal of Information Management*, **37.6**, 622-626, 2017.

[11] N. Sahebjamnia, SA. Torabi, SA. Mansouri, Integrated business continuity and disaster recovery planning: Towards organizational resilience. *European Journal of Operational Research*, **242.1**, 261-273, 2015.

[12] S. Liu, GP. Warn, Seismic performance and sensitivity of floor isolation systems in steel plate shear wall structures. *Engineering structures*, **42**, 115-126, 2012.

[13] A. Nespoli, D. Rigamonti, M. Riva, E. Villa, F. Passaretti, Study of pseudoelastic systems for the design of complex passive dampers: static analysis and modeling. *Smart Materials and Structures*, **25**, 105001, 2016.

[14] A. Nespoli, E. Bassani, D. Della Torre, R. Donnini, E. Villa, An experimental study on pseudoelasticity of a NiTi-based damper for civil applications. *Smart Materials and Structures*, **26**, 105041, 2017.

[15] M. Smith, ABAQUS/Standard User's Manual, Version 6.9. *Simulia*, 2009.

[16] F. Auricchio, RL. Taylor, Shape-memory alloys: modelling and numerical simulations of the finite-strain superelastic behavior. *Computer methods in applied mechanics and engineering*, **143.1-2**, 175-194, 1997.

[17] L. Casagrande, J. Sisinni, A. Bonati, A. Occhiuzzi, F. Auricchio, Integrated shape memory alloy devices toward a high-performance glazed curtain wall seismic retrofit. *Engineering Structures*, **179**, 540-555, 2019.

[18] M. Indirli, MG. Castellano, Shape memory alloy devices for the structural improvement of masonry heritage structures. *International Journal of Architectural Heritage*, **2.2**, 93-119, 2008.

[19] W. Ren, H. Li, G. Song, An innovative shape memory alloy damper for passive control of structures subjected to seismic excitations. *World Conference on Earthquake Engineering*, 2008.

[20] L. Casagrande, A. Bonati, F. Auricchio, A. Occhiuzzi, Dissipating effect of glazed curtain wall stick system installed on high-rise mega-braced frame-core buildings under nonlinear seismic excitation. *Eccomas Proceedia COMPDYN*, 3711-3727, 2017.

[21] R. Hill, A theory of the yielding and plastic flow of anisotropic metals. *Proc. R. Soc. Lond. A*, **193.1033**, 281-297, 1948.

[22] JA. Shaw, Simulations of localized thermo-mechanical behavior in a NiTi shape memory alloy. *International journal of plasticity*. **16.5**, 541-562, 2000.

[23] British Standard, Eurocode 8: Design of structures for earthquake resistance. Part 1. *European Committee for Standardization*, 1998-1, 2005.

[24] S. Mazzoni, F. McKenna, MH. Scott, GL. Fenves, OpenSees command language manual. *Pacific Earthquake Engineering Research (PEER) Center*, **264**, 2006.

[25] M. Menengotto, Method of Analysis for Cyclically Loaded Reinforced Concrete Plane Frames Including Changes in Geometry and Nonelastic Behavior of Elements under Combined Normal Force and Bending. *IABSE Symposium on Resistance and Ultimate Deformability of Structures Acted on by Well-Defined Repeated Loads, Final Report*, 1973.

[26] TJ. Maley, R. Roldan, A. Lago, TJ. Sullivan, Effects of response spectrum shape on the response of steel frame and frame-wall structures. *Pavia (Italy): IUSS Press*, 2012.

[27] E. Brunesi, R. Nascimbene, L. Casagrande, Seismic analysis of high-rise mega-braced frame-core buildings. *Engineering Structures*, **115**, 1-17, 2016.

[28] AMG. Coelho, Rotation capacity of partial strength steel joints with three-dimensional finite element approach. *Computers and Structures*, **116**, 88-97, 2013.

[29] AK. Chopra, RK. Goel, A modal pushover analysis procedure for estimating seismic demands for buildings. *Earthquake engineering and structural dynamics*, **31.3**, 561-582, 2002.

[30] L. Casagrande, A. Bonati, A. Occhiuzzi, N. Caterino, F. Auricchio, Numerical investigation on the seismic dissipation of glazed curtain wall equipped on high-rise buildings. *Engineering Structures*, **179**, 225-245, 2019.

[31] CG. Gordon, Generic criteria for vibration-sensitive equipment. *Vibration Control in Microelectronics, Optics, and Metrology.*, **1619**, 71-86, 1992.

[32] JS. Hwang, YN. Huang, YH. Hung, JC. Huang, Applicability of seismic protective systems to structures with vibration-sensitive equipment. *Journal of Structural Engineering*, **130.11**, 1676-1684, 2004.

[33] A. Filiatrault, TJ. Sullivan, Performance-based seismic design of nonstructural building components: The next frontier of earthquake engineering. *Earthquake Engineering and Engineering Vibration*, **13.1**, 17-46, 2014.

[34] TJ. Sullivan, PM. Calvi, R. Nascimbene, Towards improved floor spectra estimates for seismic design. *Earthquakes and Structures*, **4.1**,109-132, 2013.

COMPDYN 2019
7th ECCOMAS Thematic Conference on
Computational Methods in Structural Dynamics and Earthquake Engineering
M. Papadrakakis, M. Fragiadakis (eds.)
Crete, Greece, 24–26 June 2019

SEISMIC MONITORING OF BUILDINGS WITH BASE ISOLATION

A. Salvatori[1], **A. Di Cicco**[1] and **P. Clemente**[2]

[1] University of L'Aquila
DICEAA Via Giovanni Gronchi 18, L'Aquila
e-mail: antonello.salvatori@univaq.it

[2] ENEACasaccia Research Centre
Via Anguillarese 301, 00123 ROMA
e-mail: paolo.clemente@casaccia.enea.it

Abstract

The seismic monitoring of buildings is important for two fundamental reasons:
- evaluate the possible dynamic behavior of these structures during earthquakes;
- gain experience on the general seismic behavior of the structures so that the experience and the database can be used in the future for design and analysis.
The results of previous efforts in seismic monitoring of the structures have facilitated the development of a database, which in turn was used in the creation of new formulas and reference values for the estimation of the fundamental periods of the structures and the percentage of critical damping from use during dynamic analyzes. The database is very well supplied with data on traditional buildings, but there is still not enough data for buildings isolated at the base. Some different structures with seismic base isolation have been monitored during recent strong earthquakes in Italy, namely Amatrice earthquake (2016/08/24, M_w=6.0) and Norcia earthquake (2016/10/30, M_w=6.5).
For the structure under examination, amplification phenomena have been noticed, up to about twice the accelerations on the superstructure, for very low energy value inputs. In these cases, however, it is noted that the amplified accelerations are extremely small, and very far from being able to damage the structure. Records from the ENEA permanent accelerometric network, installed on the structure under examination, and the tests carried out on the same isolators used for the qualification tests of the devices mounted below the analyzed structure, permit to describe the behavior of the isolators in terms of force and displacement defining two non-linear laws, derived from experimental data.

Keywords: Seismic isolation, monitoring.

1 INTRODUCTION

It's well known that seismic isolation of a structure in order to uncouple the ground motion from the one of the super-structure represents the better solution to prevent seismic damage to buildings, by introducing a disconnection in the structure which is then divided into two parts: the substructure, rigidly connected to the ground, and the superstructure.

Seismic isolation, instead of increasing the capacity of the structure, use RID's strategy, drastically reducing the energy transmitted from the ground to the building. The substructure, generally very rigid, has roughly the same acceleration of the ground and must be designed in elastic field, while the superstructure benefits from the increased deformability resulting from the introduction of isolating devices.

Typically, response spectra in terms of accelerations of most earthquakes have a strong amplification in the range 0.1÷ 0.8 sec, where the main vibration period of many traditional buildings stands. Assuming, for simplicity's sake, that the isolators have an elastic or comparable behaviour, the increase of deformability consequent to their installation brings the own period of the structural system (Substructure-isolating system-superstructure) in a zone of spectral lower acceleration. As a result, the earthquake-generated accelerations on the isolated structure are drastically lower than those produced in the fixed-base configuration, to such an extent that the structure can be easily designed to withstand violent earthquakes without suffering damage both in structural and in non-structural components. Of course, increase in period also produces an increase in displacement, but they are concentrated in the devices, where most of the energy of the earthquake is low-pass filtered and also, in part, dissipated.

From analysis of experimental data on isolated structures, performed in the present study, however, it has been noticed that for low acceleration values the system has vibration periods not suited to those of an isolated structure but closer to the ones of a fixed base traditional structure, as can be observed from recordings of low energy seismic events carried out by the authors in the structure under examination.

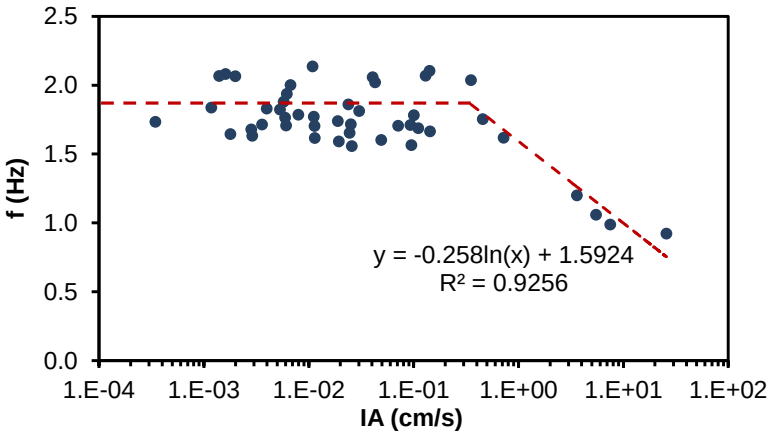

Figure 1 Base energy/frequencies

In figure 1 Arias intensity versus frequency of the system is shown. The Arias intensity (1) is an integral parameter, obtained as cumulative measure of seismic motion during its duration, and it represents the energy at the base of the structure.

$$\mathrm{IA} = \frac{\pi}{2g} \cdot \int_0^t a_x^2 + a_y^2 + a_z^2 \; dt \tag{1}$$

Corresponding to low input energies at the base of the structure the frequency of the structure itself leads to frequency values different from those for which it was designed (< 0.5 Hz). The reduction of the vibration period increases the acceleration more than the case of higher period.

These accelerations are higher than those evaluated in the design with consequent possible damage to the superstructure. In figure you can see the accelerations recorded on the structure at levels 0 (structure solidary to the ground), 1 (at the first level) and 2 (in correspondence of the cover).

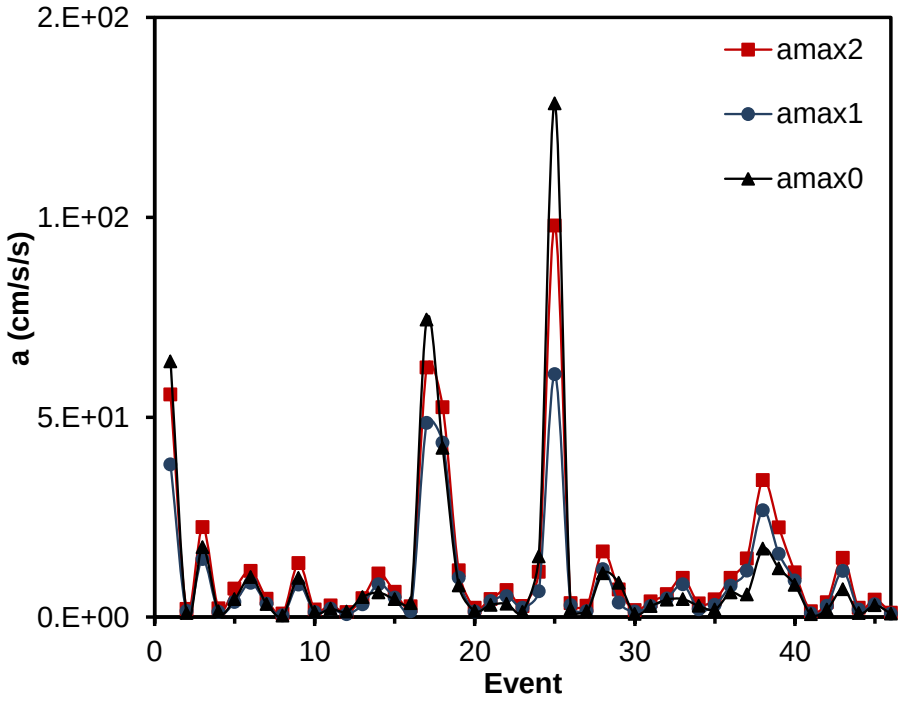

Figure 2 Base acceleration/number of events

For events characterized by small base acceleration there is an amplification of the acceleration from the bottom upwards. The two accelerations peaks are related respectively to the earthquake of Amatrice (2016/24/08, M_w 6.0) and Norcia (2016/30/10, M_w 6.5).

2 THE MONITORED STRUCTURE: REGIONAL CIVIL PROTECTION CENTER (UMBRIA REGION, ITALY)

The regional civil Protection center of the Umbria region (highlighted in red in the following figure), is located in Foligno. The Regional Center is composed by a building (operative room, analyzed in detail in the present work), a regional building (emergency and training) where the Special Office for Reconstruction (Umbria Region) is currently located and a third building (Amphitheatre – Plants building). The first two buildings are seismically isolated and the third is a traditional one.

The structure under consideration has three floors above ground and a basement for a total area of about 1532.25 m^2 above ground, and a volume equal to 8,630.00 m^3; it has built with reinforced concrete and it is seismically isolated by ten high damping elastomeric isolators, located externally on the ground floor. The isolated superstructure has a dome supported by ten half arches with cross section 40 x 120 cm, converging towards a single ring from which two concentric cylinders of 16 cm thickness are suspended, with a prestressed reinforced concrete. The size of the dome is 22 meters in height and 31 meters in diameter base.

Figure 3 Monitored isolated building location

Figure 4 Operation Room

The two concentric cylinders have inside a spiral staircase and an elevator placed inside the innermost cylinder. The outermost cylinder stops at the height of the first floor while the innermost cylinder continues to the basement, at a height of -4.00 m.

The foundation system consists of plinths based on four piles each, linked together by a reinforced concrete beam with cross section 80 x 80 cm, and by radial beams converging in a ring beam with cross section 50 x 140 cm and diameter, measured on the longitudinal axis, equal to 7.20 m inside which descends, until the basement, the elevator core. There is no

connection between the elevator core and the ring beam above.

Above the beams connecting the plinths there is a 20 cm thick slab which is also the base of the dome. The pedestrian access to the structure is possible by means of a slab (18 cm thick) that extends as a cantilever from the core elevator suspended on the base of the dome. There is no connection between the slab for pedestrian access and the base of the structure. Above the foundation plinths, there are 10 concrete supports on which the elastomeric isolation devices are fixed. The floors, with a radial dimension descending from the bottom towards the top of the structure, are supported by circular and radial beams that connect the half arches to the outer vertical cylinder.

Figure 5 base for pedestrian access

Figure 6 Support of an isolator during the construction and after its completion

In the innermost cylinder are also contained the plants of the various levels down to the basement level which remains separate, and therefore suspended, by the foundations.

The two upper floors are used as offices for the Civil protection operative room and more precisely:

- The first floor consists of 14 offices, in addition to the services and organized through furniture-equipped walls;

- The second floor is divided into a meeting room of about 145.50 m^2, a direction hall of about 60.00 m^2, a meeting hall of about 136.60 m^2 and services.
- The third floor contains other offices and a room for air conditioning systems.

3 SEISMIC ISOLATOR USED IN STRUCTURE

The isolators are elastomeric one with soft-type rubber, namely SI-S 1000/240. Their mechanical characteristics are shown in table 1.

.

Figure 7 SI-S 1000/240 elastomeric isolator installed

External diameter	D_g	1000	mm
Total high without anchorage plates	H	392	mm
Total high with anchorage plate	H	472	mm
Volume of the nucleus	Vol	307.88	dm^3
Total weight without anchorage	W	1834	kg
Maximum horizontal force with maximum seismic displacement	F_{xy}	497	kN
Maximum seismic uniform pression = V / A'	$\sigma_{v\,s,max}$	**3.98**	Mpa
Mimimun sesismic uniform pressure = V_{min} / A'	$\sigma_{v\,s,min}$	**0.00**	Mpa
Vertical stiffness = $E_c \cdot A' / t_e$	K_v	**2310**	kN/mm
Horizontal equivalent stiffness = $G_{din} \cdot A \cdot t_e$	K_e	**1.31**	kN/mm
Stiffness ratio	K_v/K_e	**1764**	

Table 1 – Mechanical properties of seismic isolators

Type test were performed for the determination and control of the isolator characteristics. In this case was evidenced an increasing cyclical stress at constant frequency and the corresponding strength of resistance of the isolator.
Being the test carried out on isolators of dimensions equal to half of the installed ones, their mechanical properties are then related to the real dimension of installed isolators.
The results reported the following values for the shear resistance module and damping:
the devices have an increase in the damping and in the shear stiffness modulus with the decrease in the deformation.
In particular, for a deformation values from 30% to 5%, there is a sharp increase in stiffness and damping values.

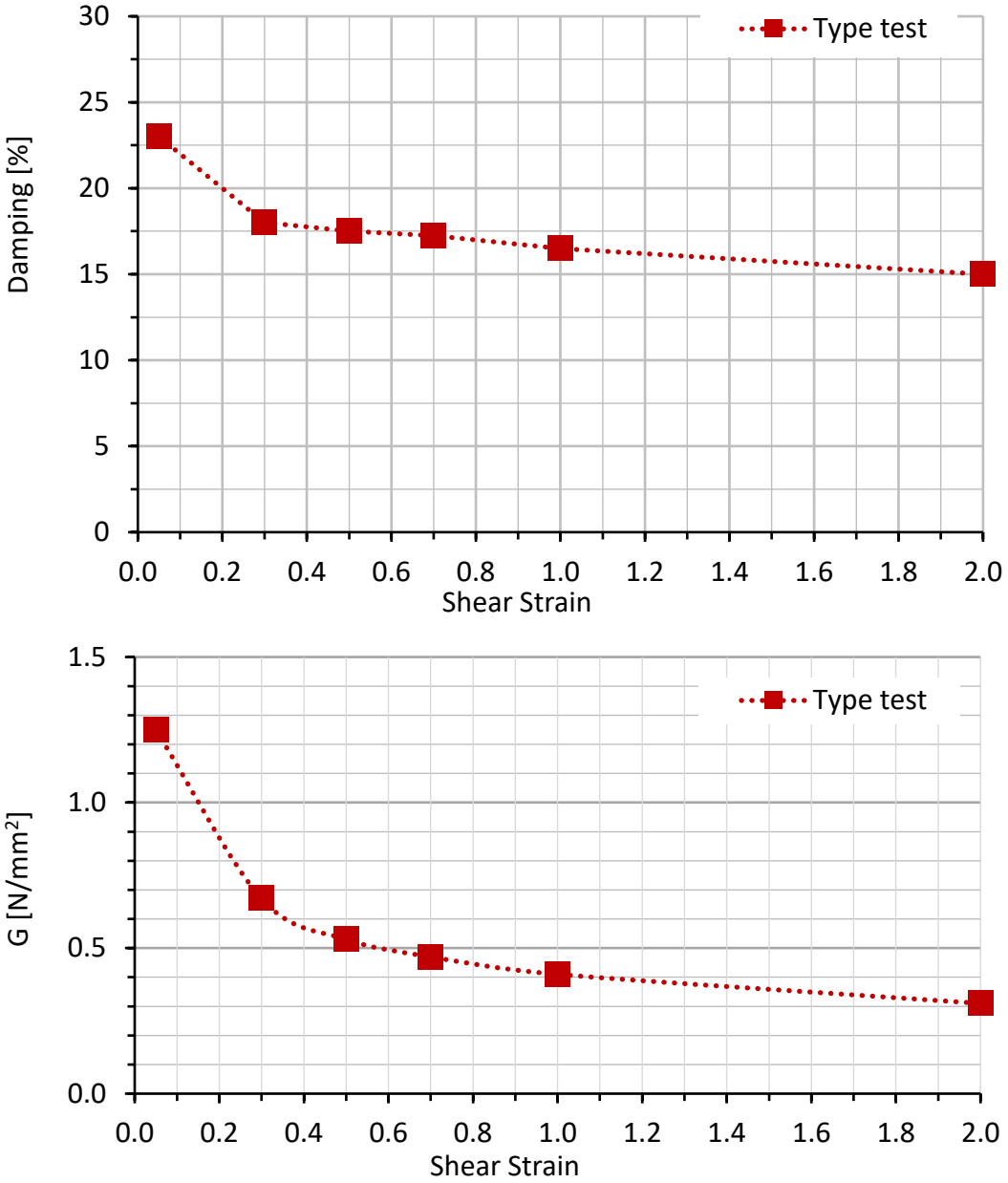

Figure 8 Increase in damping and shear modulus as strain varies.

4 MONITORING SYSTEM INSTALLED ON THE STRUCTURE

In order to monitor the structure a control equipment was installed in August 2014, with:
- Acquirer Kinemetrics K2, absolute timing using GPS, equipped with 24-bit A/D converter (digital analogue), 12 acquisition channels, 3 of which are connected to the sensor triad inside the acquirer and 9 connected to the external sensors;
- 12 Sensors Kinemetrics Type Force Balance with dynamic > 120 DB and full scale 2 G, three of which, orthogonal each other, are contained in the acquirer; the remaining 9 are arranged at the level of the first deck, below the floating floor (also used for cable passage).

The instrumentation is arranged on the structure according to the diagram shown in the following figure, where the arrows indicate direction and positive sensors and the point corresponds to the arrowhead, so the sensors for the channels A02, A04, A05 and A06 are vertical.

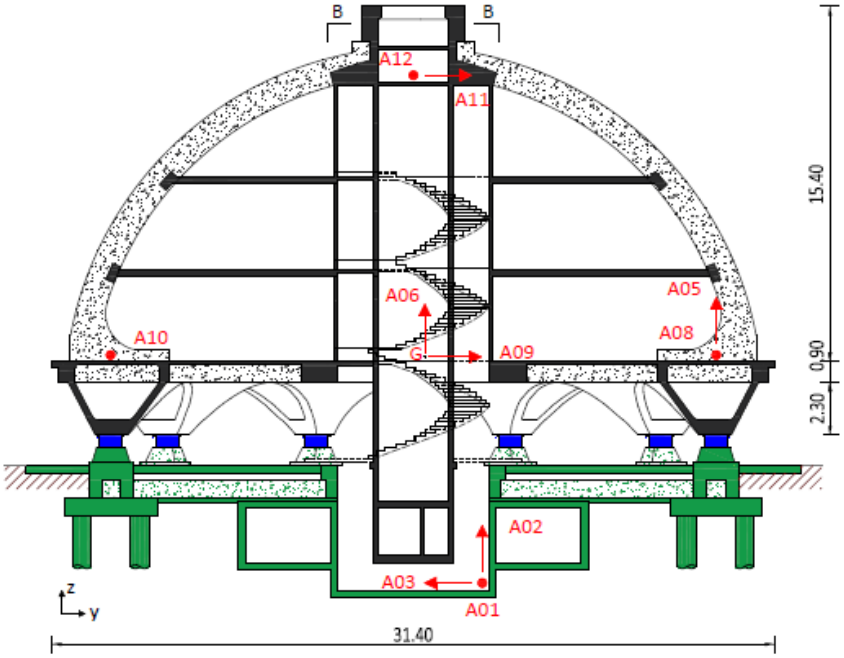

Figure 9 Provision in section of the instrument and fixes installed

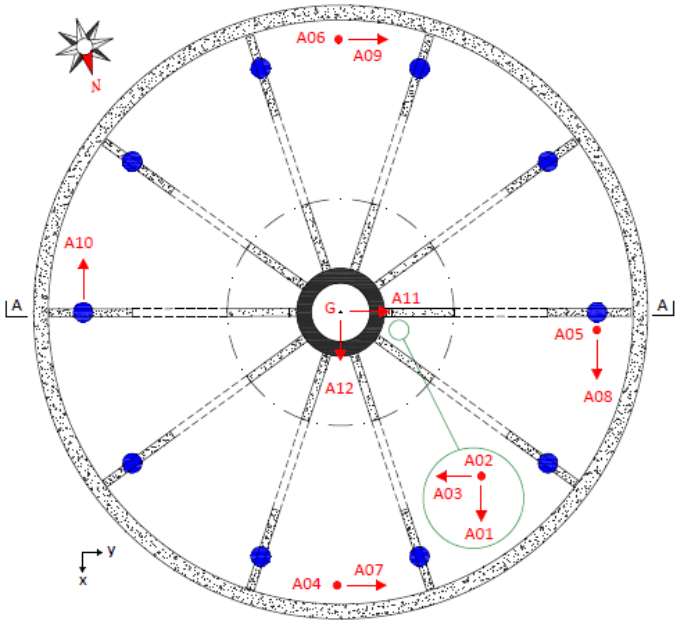

Figure 10 Plant arrangement of installed equipment

The sensor group inside the acquirer, A01, A02 and A03, is positioned below the isolating plane, in the lowest attainable position, near the terminal part of the Elevator Core. The positioning of sensors on the structure, the accelerometers relative to the channels from A04 to A10 are located to the share of the first deck, immediately above the isolating plane, while the sensors related to channels A11 and A12 are positioned at the top of the inner core.

The recognition of seismic events is carried out in STA/LTA logic (Short Term Average/Long Term average), i.e. by comparing the mean signal measured by each sensor, filtered pass 0.1-10 Hz band, in a short time interval, in this case 0.6 s, (STA) and the mean signal rate

detected by the same sensor, band pass filtered 0.1-10 Hz, in a long time interval, in this case 60 s, (LTA).

If the STA/LTA value exceeds a preset value, in this case equal to 4, the signal from the channel generates a trigger command.

Figure 11 GPS antenna and accelerometers (A04 and A07) below the floating floor.

Figure 12 Accelerometers A11 and A12 (internal core top)

To reduce the amount of recorded spurian signals, the trigger condition for a single channel is not sufficient to initiate the recording. To start the recording a determined number of sensors must exceed simultaneously trigger conditions. In this case were delegated to this task the sensors at the base and the two sensors at the top, clearly less affected by local disturbances. If 2 Sensors exceeds at the same time the trigger condition starts recording on a card of memory PCMCIA internal to the acquirer.

To record the entire signal the acquirer adds to the head of the recording the portion of the signal prior to the trigger for a preset duration, in this case 30 s. The detected event is considered terminated when the selected sensors check the condition of detrigger, i.e. the signal amplitudes fall below a preset value, in this case the 40% of the trigger conditions. Starting from the time of detrigger, the acquirer still continues the recording for a preset time, post event, in this case 30 s

5 EVENTS RECORDED BY THE ACCELEROMETRIC NETWORK

In table 2 are reported all the seismic event recordings with M_W or $M_L \geq 4.0$ relative to the seismic sequence started on August 24, 2016 (with an event of magnitude M_W= 6.0) until 31 December 2017. The table lists the events defined from time source, localization (latitude, longitude, depth), the source of the data (Seismic Bulletin INGV), the name of the registration (ENEA internal code for the archiving of events), the epicentral distance and eventual notes.

SOURCE Time [Utc]	Latit.	Longit.	Depth [km]	Magnitude	Source	Name Record.	D_{Epi} [Miles]
24/08/2016 01:36:32	42,698	13,234	8.1	6.0-Mw	BULLETIN	**TN015**	53
24/08/2016 01:56:01	42,601	13,276	7.7	4.3-Mw	BULLETIN	**TN018**	62
24/08/2016 02:33:29	42,792	13,151	8.0	5.4-Mw	BULLETIN	**TN032**	41
24/08/2016 03:40:11	42,614	13,244	10.7	4.1-Mw	BULLETIN	**TN045**	59
24/08/2016 04:06:51	42,771	13,124	6.2	4.4-Mw	BULLETIN	**TN047**	41
24/08/2016 11:50:31	42.82	13.16	9.8	4.5-Mw	BULLETIN	**TN066**	41
24/08/2016 17:46:09	42,659	13,215	10.3	4.2-Mw	BULLETIN	**TN074**	54
24/08/2016 23:22:06	42,654	13.21	11.8	4.0-Mw	BULLETIN	**TN078**	54
25/08/2016 03:17:17	42,745	13,193	9.0	4.3-Mw	BULLETIN	**TN080**	47
25/08/2016 12:36:05	42.6	13,282	7.5	4.4-Mw	BULLETIN	**TN083**	63
26/08/2016 04:28:26	42,605	13,292	8.7	4.8-Mw	BULLETIN	**TN086**	63
27/08/2016 02:50:59	42,843	13,238	7.8	4.0-Mw	BULLETIN	**TN093**	46
28/08/2016 15:55:35	42,823	13,232	8.7	4.2-Mw	BULLETIN	**TN102**	46
03/09/2016 01:34:12	42.77	13,132	8.9	4.2-Mw	BULLETIN	**TO015**	41
03/09/2016 10:18:51	42,861	13,217	8.3	4.3-Mw	BULLETIN	**TO017**	43
16/10/2016 09:32:35	42,748	13,176	9.2	4.0-Mw	BULLETIN	**TP016**	47
26/10/2016 17:10:36	42.88	13,128	8.7	5.4-Mw	BULLETIN	**TP021**	36
26/10/2016 19:18:06	42,909	13,129	7.5	5.9-Mw	BULLETIN	**TP026**	35
26/10/2016 21:42:02	42,863	13,121	9.9	4.5-Mw	BULLETIN	**TP053**	36
27/10/2016 03:19:27	42,843	13,143	9.2	4.0-Mw	BULLETIN	**TP071**	38
27/10/2016 03:50:24	42,984	13.12	8.7	4.1-Mw	BULLETIN	**TP073**	34
27/10/2016 08:21:46	42,873	13,097	9.4	4.3-Mw	BULLETIN	**TP086**	34
27/10/2016 17:22:23	42,839	13,099	9.0	4.2-Mw	BULLETIN	**TP103**	35
29/10/2016 16:24:33	42,811	13,095	10.9	4.1-Mw	BULLETIN	**TP144**	36
30/10/2016 06:40:17	42,832	13,111	9.2	6.5-Mw	BULLETIN	**TP151**	36
30/10/2016 07:34:48	42,922	13,129	9.9	4.0--ML	Survey	**TP170**	35
30/10/2016 11:58:17	42.84	13,056	10.2	4.0-Mw	Survey	**TP235**	32
30/10/2016 12:07:00	42,845	13,078	9.7	4.5-Mw	Survey	**TP237**	33
30/10/2016 13:34:54	42,803	13,165	9.2	4.1-Mw	Survey	**TP251**	42
30/10/2016 18:21:09	42.79	13,152	9.6	4.0-Mw	Survey	**TP275**	42
31/10/2016 03:27:40	42,766	13,085	10.6	4.0-Mw	Survey	**TP310**	38
31/10/2016 07:05:45	42,841	13,129	10.0	4.0-Mw	Survey	**TP322**	37
01/11/2016 07:56:40	43	13,158	9.9	4.8-Mw	Survey	**TP354**	37
03/11/2016 00:35:01	43,029	13,049	8.4	4.7-Mw	Survey	**N.R.**	29
12/11/2016 14:43:34	42,723	13,209	10.1	4.1-Mw	Survey	**TQ077**	49
14/11/2016 01:33:44	42.86	13,158	11.0	4.0--ML	Survey	**TQ092**	39
29/11/2016 16:14:03	42,529	13.28	11.1	4.4-Mw	BULLETIN	**TQ171**	68
11/12/2016 12:54:53	42.9	13,113	8.3	4.3--ML	Survey	**TR018**	34

Table 2 – Recorded events

The process of processing the recorded data requires that the following processing be carried out for each registration:

- Transformation of data from acquirer units, Volt, into CM/s/s units.
- Calculation and graphical representation of Fourier transforms to select the filtering frequencies.
- Instrumental correction for the characteristics of each sensor, natural frequency and damping, with a change of direction for sensors related to ch03 and ch10, frequency filtering and dual integration to obtain the temporal histories corrected in terms of acceleration, speed and displacement.
- For magnitude ≥ 5.0, the calculation of the Accelerometric Group response spectra at the base was also carried out.
- For all recordings, the maximum, in acceleration and displacement, for each channel was

calculated, the maximum for each recording and the channel on which that value was obtained. The following table shows the maximum acceleration values expressed in cm/s^2.

Rec	CH01	CH02	CH03	CH04	CH05	CH06	CH07	CH08	CH09	CH10	CH11	CH12	Max	Ch
TN015	59.9	27.2	43.4	42.3	37.7	40.1	40.4	36.1	33.5	35.9	51.0	46.5	59.9	CH01
TN018	0.9	0.5	0.7	0.9	0.7	0.7	1.6	1.0	1.4	1.2	2.0	1.3	2.0	CH11
TN032	16.9	9.0	14.9	16.2	12.8	13.7	10.9	14.1	12.3	14.5	22.2	18.5	22.2	CH11
TN045	1.1	0.7	1.3	1.2	1.2	1.0	1.2	1.3	1.3	1.2	2.1	1.4	2.1	CH11
TN047	3.3	2.1	4.4	4.9	3.9	4.4	3.9	3.0	3.7	3.5	7.1	4.0	7.1	CH11
TN066	7.3	5.2	8.7	6.6	7.4	7.0	7.5	9.8	8.0	7.7	10.5	11.2	11.2	CH12
TN074	2.5	1.8	2.4	2.1	2.0	1.7	3.4	2.5	3.3	2.1	4.6	2.8	4.6	CH11
TN078	0.3	0.2	0.3	0.4	0.4	0.4	0.5	0.2	0.5	0.3	0.8	0.3	0.8	CH11
TN080	6.6	2.7	9.3	5.2	6.7	4.9	7.9	4.8	8.9	5.8	13.3	8.5	13.3	CH11
TN083	0.9	0.5	1.3	0.9	0.8	0.8	1.3	1.1	1.2	1.0	1.6	1.5	1.6	CH11
TN086	2.0	1.1	1.9	2.0	1.4	1.6	2.2	1.5	1.7	1.6	2.9	2.0	2.9	CH11
TN093	1.3	0.5	0.8	0.7	0.7	0.7	0.6	0.8	0.7	0.6	1.1	1.0	1.3	CH01
TN102	4.5	2.1	4.2	3.7	2.8	2.9	3.0	2.6	3.4	2.4	4.6	3.3	4.6	CH11
TO015	5.1	3.4	5.8	3.3	2.9	4.8	9.1	4.8	7.7	5.3	10.8	6.0	10.8	CH11
TO017	4.5	1.5	2.1	2.2	2.3	2.0	2.7	5.3	2.7	4.7	3.7	6.3	6.3	CH12
TP016	2.6	1.3	2.8	2.3	2.0	2.0	1.4	1.2	1.6	1.5	2.4	1.9	2.8	CH03
TP021	67.6	26.2	51.4	27.3	24.6	21.7	44.3	22.7	48.2	23.6	62.1	37.9	67.6	CH01
TP026	36.3	21.5	37.3	35.4	28.2	30.4	44.8	36.1	42.4	32.1	51.1	36.3	51.1	CH11
TP053	7.7	2.7	7.2	4.9	4.4	4.3	8.1	6.0	9.3	6.1	10.7	7.6	10.7	CH11
TP071	1.5	1.0	0.9	1.6	1.3	1.9	1.3	1.1	1.7	1.1	2.3	1.3	2.3	CH11
TP073	1.8	1.7	3.0	2.4	2.2	2.3	3.3	3.9	3.5	3.1	4.3	4.3	4.3	CH11
TP086	3.2	1.7	3.3	3.3	2.4	2.3	5.2	5.0	4.6	4.8	5.9	5.8	5.9	CH11
TP103	1.0	1.0	1.2	1.5	1.2	1.4	2.4	1.8	2.1	1.4	2.7	2.0	2.7	CH11
TP144	12.4	6.8	8.9	8.3	8.2	7.1	4.1	7.6	3.4	7.0	7.3	9.3	12.4	CH01
TP151	74.8	61.6	118.4	67.0	70.7	67.6	60.0	42.4	60.4	46.6	96.0	61.6	118.4	CH03
TP170	1.4	1.3	2.0	2.0	1.1	1.2	3.0	1.5	3.0	1.5	3.5	1.9	3.5	CH11
TP235	1.4	1.2	1.2	2.1	1.8	1.8	1.7	1.0	1.3	0.8	2.8	1.4	2.8	CH11
TP237	6.3	6.4	10.9	8.2	8.6	7.1	11.3	5.5	11.6	5.6	16.4	7.6	16.4	CH11
TP251	7.4	4.4	4.4	4.2	3.4	3.5	3.3	2.9	3.6	3.1	5.6	5.8	7.4	CH01
TP275	0.5	0.4	0.7	0.6	0.5	0.4	1.2	0.8	1.3	0.7	1.7	0.8	1.7	CH11
TP310	2.6	1.5	2.7	2.2	1.8	2.1	2.1	2.8	2.2	2.7	3.3	3.6	3.6	CH12
TP322	3.3	3.4	3.9	4.3	4.0	3.8	4.5	1.8	4.8	1.9	5.7	3.0	5.7	CH11
TP354	4.1	2.9	4.1	5.9	4.7	5.5	6.2	8.5	6.2	8.1	8.6	9.4	9.4	CH12
TQ077	1.7	0.8	2.7	1.3	1.3	1.3	1.7	1.9	1.9	2.1	3.1	2.4	3.1	CH11
TQ092	1.7	1.0	1.4	1.5	1.6	1.5	2.2	2.9	2.6	2.9	3.7	3.5	3.7	CH11
TQ171	6.2	2.0	5.5	3.2	3.6	3.4	4.2	8.0	3.2	7.6	6.1	9.8	9.8	CH12
TR018	3.6	2.2	5.6	2.6	2.6	2.4	11.6	4.7	11.6	4.5	14.2	5.4	14.2	CH11

Table 3 – Maximum acceleration values of recorded events

In the table below, the maximum in terms of displacement expressed in cm is shown.

Rec	CH01	CH02	CH03	CH04	CH05	CH06	CH07	CH08	CH09	CH10	CH11	CH12	Max	Ch
TN015	1.48	0.92	0.70	0.91	0.91	0.92	1.05	1.75	1.02	1.70	1.08	1.77	1.77	CH12
TN018	0.01	0.01	0.01	0.01	0.01	0.01	0.01	0.02	0.01	0.02	0.01	0.02	0.02	CH08
TN032	0.11	0.07	0.10	0.07	0.07	0.07	0.16	0.19	0.15	0.18	0.15	0.20	0.20	CH12
TN045	0.00	0.00	0.00	0.00	0.00	0.00	0.01	0.01	0.01	0.01	0.01	0.01	0.01	CH12
TN047	0.02	0.01	0.01	0.01	0.01	0.01	0.02	0.03	0.02	0.03	0.02	0.03	0.03	CH08
TN066	0.03	0.02	0.04	0.02	0.02	0.02	0.07	0.09	0.07	0.09	0.07	0.09	0.09	CH12
TN074	0.01	0.00	0.01	0.00	0.00	0.00	0.02	0.02	0.02	0.02	0.02	0.02	0.02	CH11
TN078	0.00	0.00	0.00	0.00	0.00	0.00	0.00	0.00	0.00	0.00	0.00	0.00	0.00	CH11
TN080	0.02	0.01	0.02	0.01	0.01	0.01	0.06	0.04	0.06	0.04	0.07	0.04	0.07	CH11
TN083	0.01	0.01	0.01	0.01	0.01	0.01	0.01	0.01	0.01	0.01	0.01	0.01	0.01	CH08
TN086	0.02	0.01	0.02	0.01	0.01	0.01	0.02	0.03	0.02	0.03	0.02	0.03	0.03	CH12
TN093	0.01	0.00	0.00	0.00	0.00	0.00	0.01	0.01	0.01	0.01	0.01	0.01	0.01	CH11
TN102	0.01	0.01	0.02	0.01	0.01	0.01	0.03	0.03	0.03	0.03	0.03	0.03	0.03	CH11
TO015	0.03	0.02	0.02	0.02	0.02	0.02	0.08	0.06	0.08	0.06	0.09	0.07	0.09	CH11
TO017	0.03	0.01	0.01	0.01	0.01	0.01	0.02	0.05	0.02	0.05	0.03	0.05	0.05	CH12
TP016	0.01	0.00	0.01	0.00	0.00	0.00	0.01	0.01	0.01	0.01	0.01	0.01	0.01	CH12
TP021	0.30	0.22	0.29	0.21	0.22	0.22	0.70	0.44	0.68	0.44	0.72	0.47	0.72	CH11
TP026	0.86	0.69	0.95	0.68	0.70	0.69	1.41	1.38	1.39	1.32	1.45	1.28	1.45	CH11
TP053	0.03	0.02	0.04	0.02	0.02	0.02	0.08	0.05	0.08	0.05	0.09	0.06	0.09	CH11
TP071	0.00	0.00	0.01	0.00	0.00	0.00	0.01	0.01	0.01	0.01	0.01	0.01	0.01	CH11
TP073	0.02	0.02	0.03	0.02	0.02	0.02	0.04	0.04	0.04	0.04	0.04	0.04	0.04	CH07
TP086	0.02	0.02	0.03	0.02	0.02	0.02	0.05	0.05	0.05	0.05	0.05	0.05	0.05	CH11
TP103	0.01	0.01	0.01	0.01	0.01	0.01	0.03	0.02	0.02	0.02	0.03	0.02	0.03	CH11
TP144	0.02	0.01	0.01	0.01	0.01	0.01	0.02	0.05	0.01	0.05	0.01	0.05	0.05	CH12
TP151	2.59	1.74	1.79	1.72	1.72	1.72	2.60	2.89	2.35	2.92	2.20	3.13	3.13	CH12
TP170	0.00	0.00	0.01	0.00	0.00	0.00	0.02	0.01	0.02	0.01	0.03	0.01	0.03	CH11
TP235	0.00	0.00	0.00	0.00	0.00	0.00	0.01	0.01	0.01	0.01	0.01	0.01	0.01	CH11
TP237	0.02	0.01	0.02	0.01	0.02	0.02	0.07	0.06	0.07	0.05	0.08	0.06	0.08	CH11
TP251	0.01	0.00	0.01	0.01	0.01	0.01	0.01	0.03	0.01	0.02	0.01	0.03	0.03	CH12
TP275	0.02	0.01	0.01	0.01	0.01	0.01	0.01	0.02	0.01	0.02	0.01	0.02	0.02	CH12

TP310	0.01	0.00	0.01	0.01	0.00	0.01	0.02	0.02	0.02	0.02	0.02	0.03	0.03	CH12
TP322	0.01	0.01	0.01	0.01	0.01	0.01	0.04	0.02	0.04	0.02	0.04	0.02	0.04	CH11
TP354	0.04	0.02	0.03	0.02	0.02	0.02	0.07	0.09	0.07	0.08	0.08	0.09	0.09	CH12
TQ077	0.00	0.00	0.00	0.00	0.00	0.00	0.01	0.01	0.01	0.01	0.01	0.01	0.01	CH08
TQ092	0.01	0.00	0.00	0.00	0.00	0.00	0.01	0.02	0.01	0.02	0.01	0.02	0.02	CH12
TQ171	0.01	0.00	0.01	0.00	0.00	0.00	0.02	0.04	0.01	0.04	0.02	0.05	0.05	CH12
TR018	0.02	0.02	0.04	0.02	0.02	0.02	0.09	0.04	0.09	0.04	0.10	0.05	0.10	CH11

Table 4 – Maximum displacement values of recorded events

The event which gave the major values had magnitude $M_w = 6.5$, registered under the name TP151 (Norcia earthquake PG of 30/10/2016). This event is discussed in more detail.
To test the finite element model implemented and the isolator characteristics, the event recordings were also used with the name TN015, relative to the effects of the event of 24/08/2016 with magnitude $M_w = 6.0$ with epicentral zone near Amatrice (RI).

5.1 RECORDING ANALYSIS TP151

The comparison between the temporal histories of the accelerations at the three monitored levels and for the two directions, shown below, shows that seismic actions are different in both directions.
Moving from the ground motion to the motion above the isolator plane, there is a decrease in the amplitude of the accelerations and a noticeable lowering of the frequency content.
Moving from the level above the isolator plane there is an increase in accelerations, which are still lower than those of the ground.
The dominant frequency appears to be still the same but it is evident, more in the direction of CH11, the presence of higher frequencies.

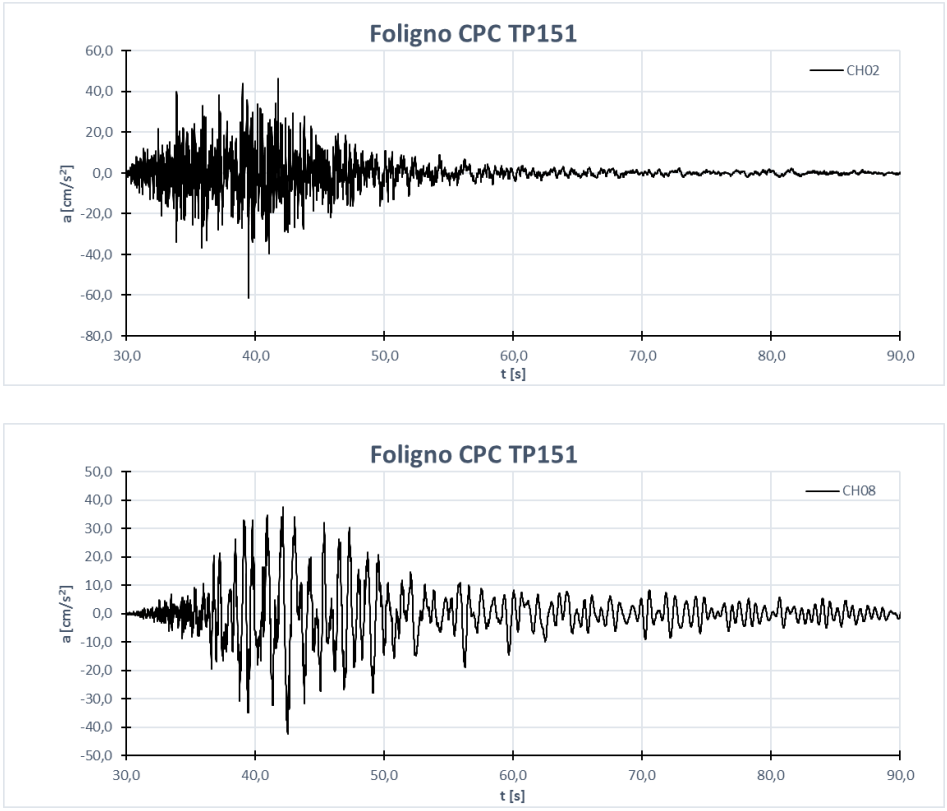

Figure 13 TP151 comparison of the time history signals

The analogous comparison between the Fourier spectra, shown below, shows that the frequency content in the two measuring points above the isolator plane, CH08 and CH12 in one Direction and CH07 and CH11 in the other direction, is substantially identical, for each direction, below 2 Hz. In the direction of Ch07 and Ch11 A significant frequency content is manifested between 7 and 9 Hz, even dominant for Ch11. Such frequency content is not justified in a structure with seismic isolation at the base.

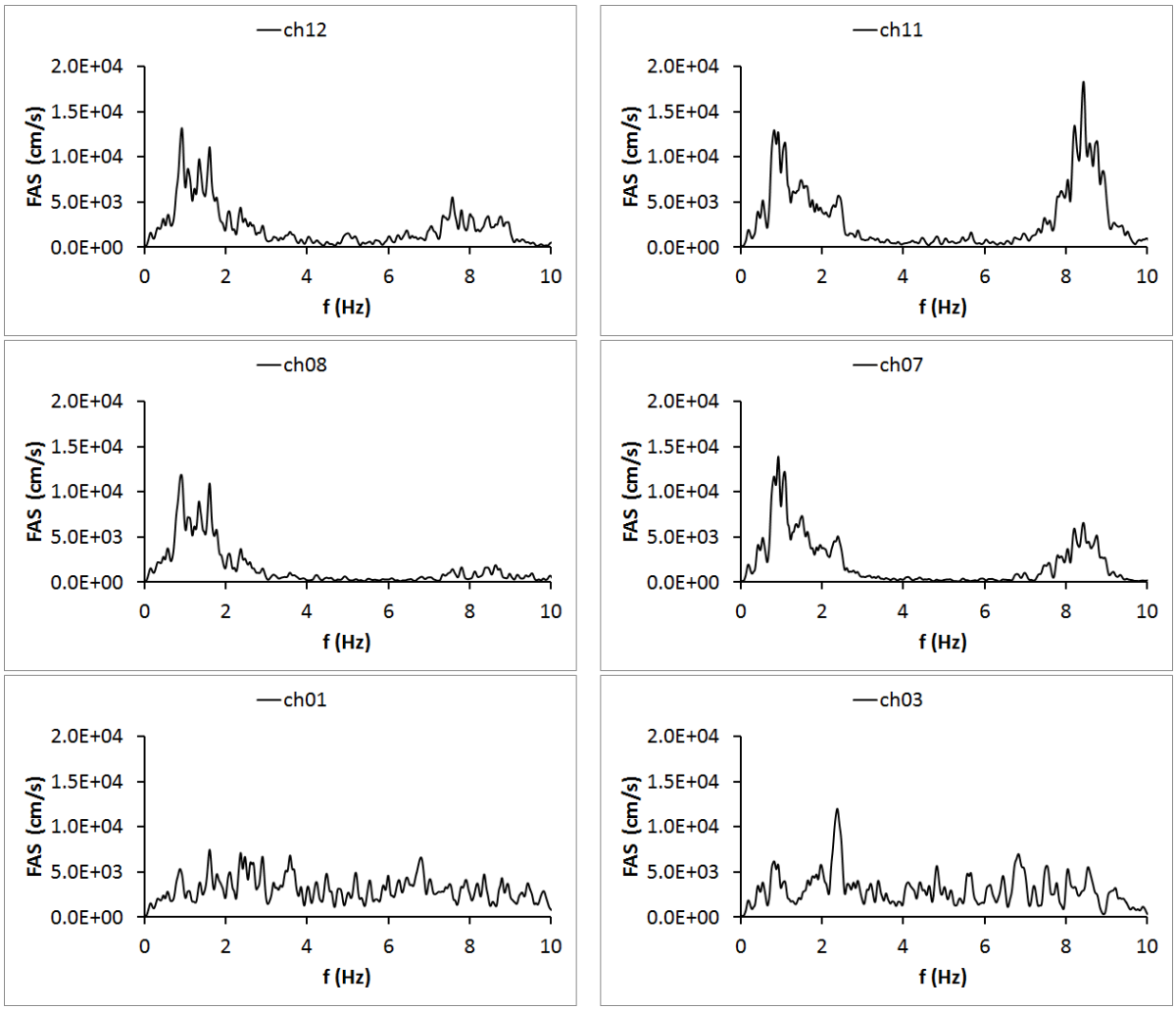

Figure 14 TP151 comparison of the Fourier spectra of accelerations

Cross-spectral analysis, Ch08 Ch12 and Ch07 Ch11, stresses that the motion of the structure above the isolator plane increases very little by proceeding upwards in the range in frequency less than 2 Hz, and it is also consistent and in phase.
This frequency range can be considered representative of the motion of the isolated structure.
The frequency content between 7 and 9 Hz has much greater amplitudes on the top of the structure and in the direction of Ch11, which decrease by going downwards; Consistency is high and the motion of the two points of measurement is in opposition to phase. It can be stressed that the motion at these frequencies is originated within the isolated superstructure.
To explain the presence of several frequency peaks in the recordings examined, a time-frequency analysis was carried out for the CH11 and CH12 channels. From these it is evident that the dominant frequency varies during the seismic action as it is expected for a structure with seismic isolation at the base [Bongiovanni et al, 2017].

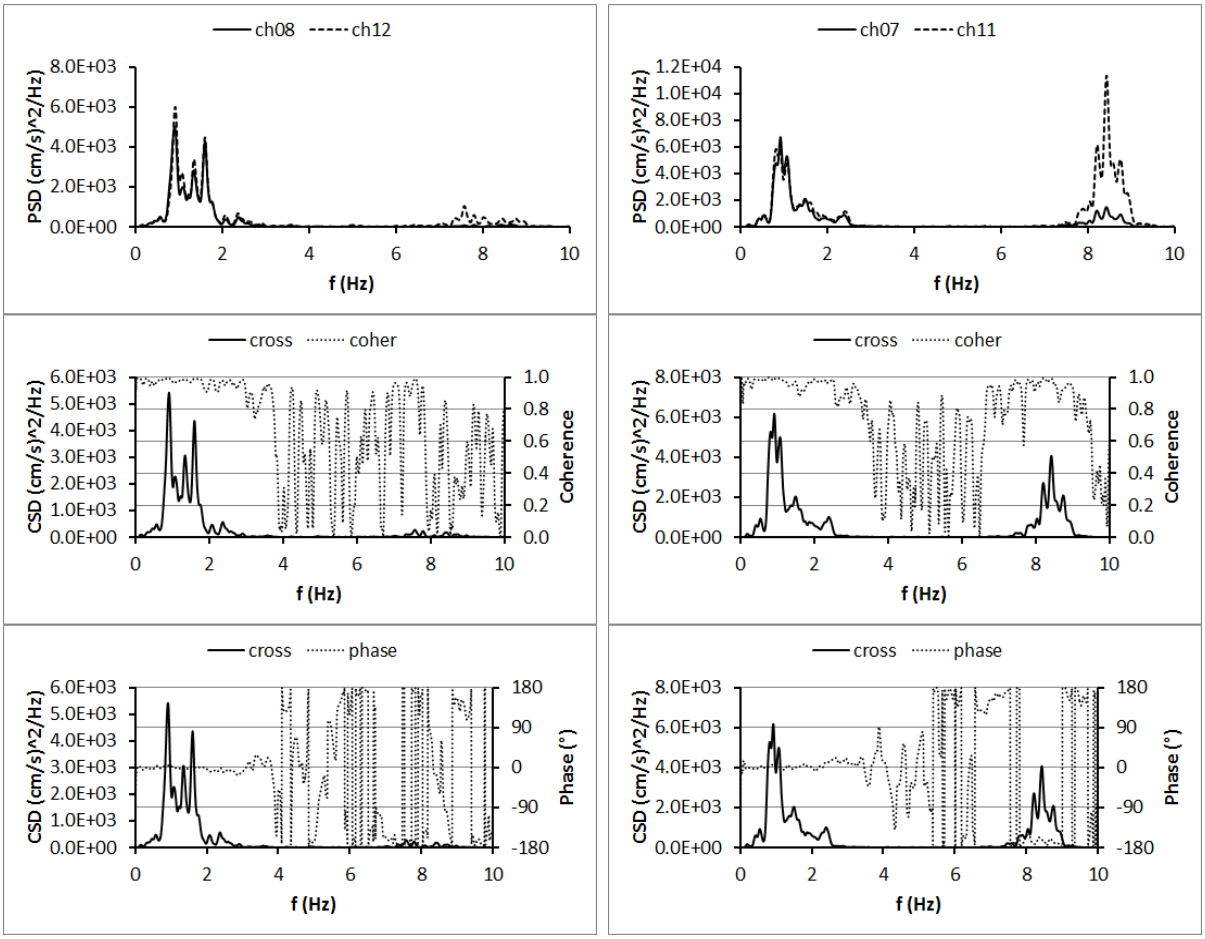

Figure 15 Cross-Spectral analysis

6 EXPERIMENTAL TEST ON SEISMIC ISOLATOR

In order to know the actual characteristics of the isolator for deformations less than 5% was performed a test on the same isolators used for the Type Test of the isolators mounted on the structure under examination using as input data the relative displacements between the isolated structure and the ground, deriving from the double integration of the accelerations recorded by the "CH03" accelerometer located at the base of structure under examination and integral to the ground and the barycentric displacement of the structure, calculated by mediating the movements deriving from the recordings of the accelerometers "CH07" and "CH09" placed in correspondence of the first scaffold, in diametrically position Opposite, just above the elastomeric isolators.

The registrations for the TP151 event were used for the test. The event TP151 is the recording, of the accelerometers installed on the structure, of the event of the day 30/10/2016 06:40:17 of magnitude Moment (M_w) of 6.5, with an epicenter at a distance of about 36 Km, near Norcia (PG).

The deformation of the test is below 5% deformation of the isolator, the height of the isolator is equal to 240 mm. The results obtained from the test are shown in the following shift-force graph: in blue are shown the curves related to the test with the time history obtained from the data of the event TP151 while the curves in red are those related to a test of type Type-Test for a 5% deformation performed at constant frequency.

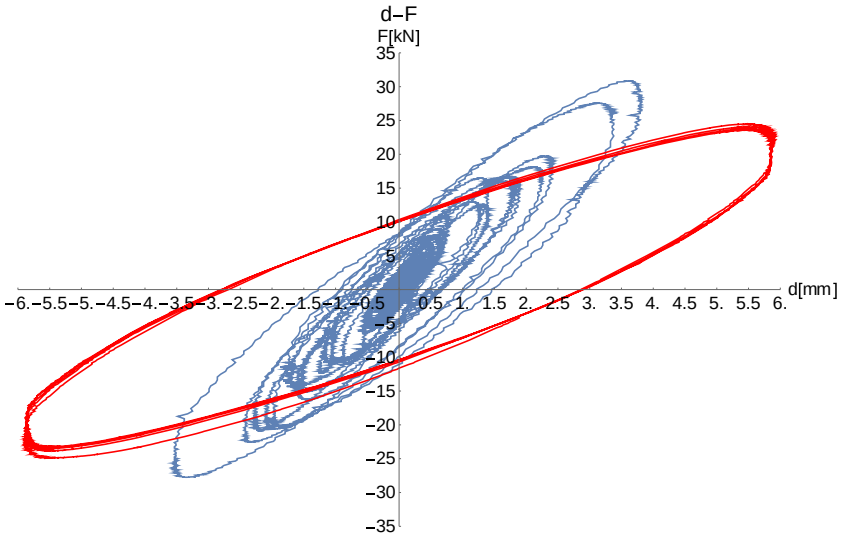

Figure 16 curves related to the test with the time history obtained from the data of the event TP151

7 NON LINEAR ANALYSIS WITH TIME HISTORIES AND NON LINEAR ISOLATOR'S LAW

To verify the validity of the law and analyze the structure's behaviour, a finite element model of the structure was analyzed. The definition of a model that is correct and adherent to that which is the real situation is a very delicate operation, also through the model you have to recreate, in the most likely way possible, the condition of load present on the structure at the time when you are verified recorded events.

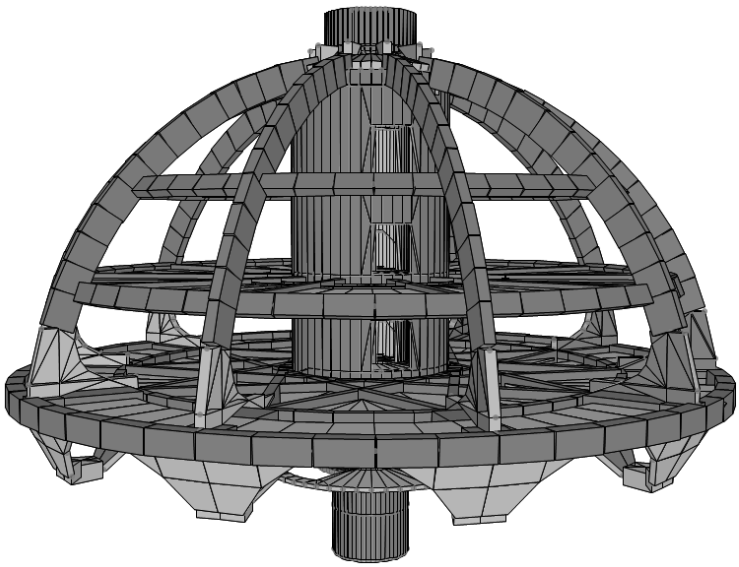

Figure 17 Set view of the Realized calculation model

On the model a nonlinear dynamic modal analysis was conducted, (considering the first 50 modes of vibration of the structure), using as input the time histories in terms of acceleration recorded directly on the structure, optimizing the model by inserting the nonlinear behavior of the elastomeric isolator by using the laws obtained from the results of the test, performed on the isolator based on the displacement recordings of the TP151 event.

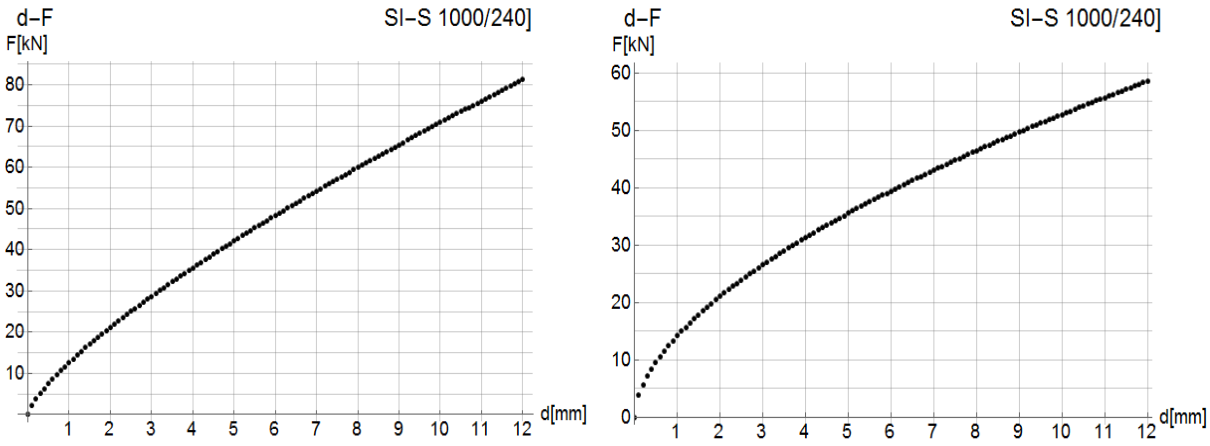

Figure 18 Local and global isolator non linear curves

The laws have been appropriately discretized in a number of points with step 1 mm and have been inserted inside the model. The results were then extrapolated in terms of displacement and acceleration of the same points where the accelerometers used in the monitoring are compared with the actual recordings of accelerations and displacement recorded during the analyzed events.

It is known that the orientation of the accelerometers with respect to the structure is the same even within the model and in particular:

- The CH03 is oriented in the model according to the X-axis
- The CH01 is oriented in the model according to the Y-axis
- The CH02 is oriented in the model according to the Z-axis

The results of the various analyses carried out below are shown below. It was inserted into the finite element model, as input data, the time history of the recording at the base, in terms of acceleration, of the event named TP151.

The input accelerations are as follows:

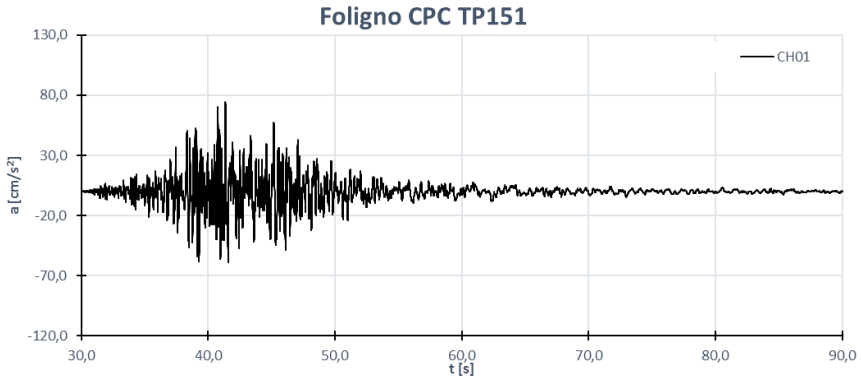

Figure 19 Nonlinear input acceleration TP151 CH01

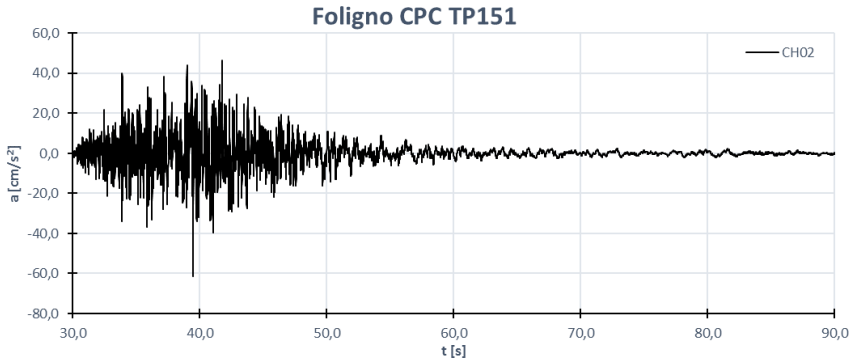

Figure 20 Nonlinear input acceleration TP151 CH02

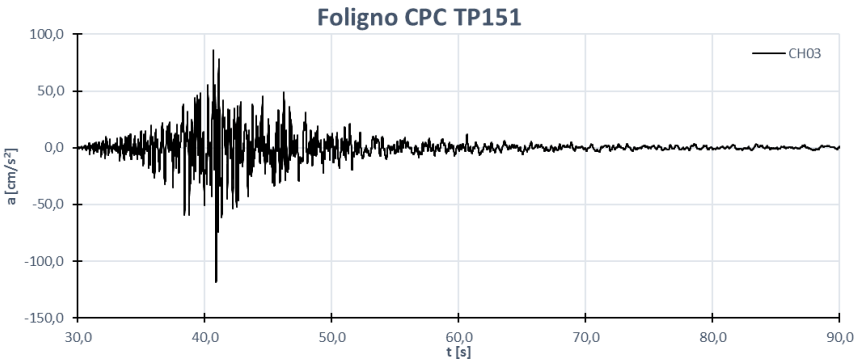

Figure 21 Nonlinear input acceleration TP151 CH03

Some of the results obtained for displacement, compared with the recordings made on the structure, are shown below:

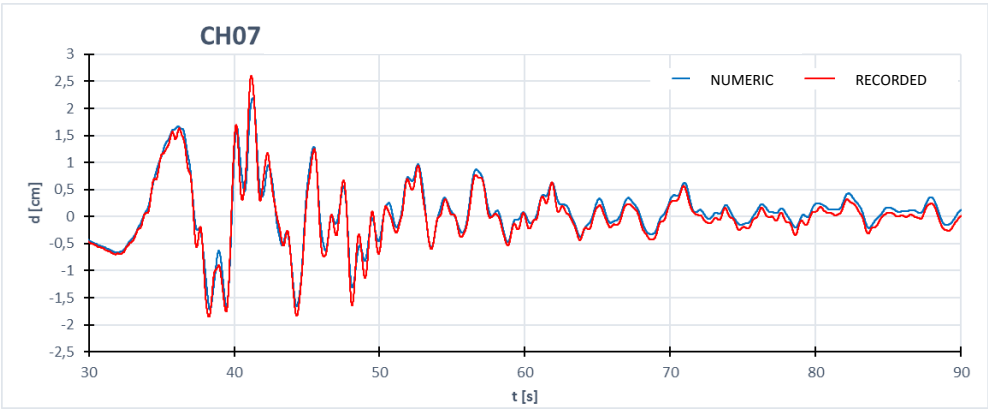

Figure 22 Comparison of recorded displacement with numeric ones

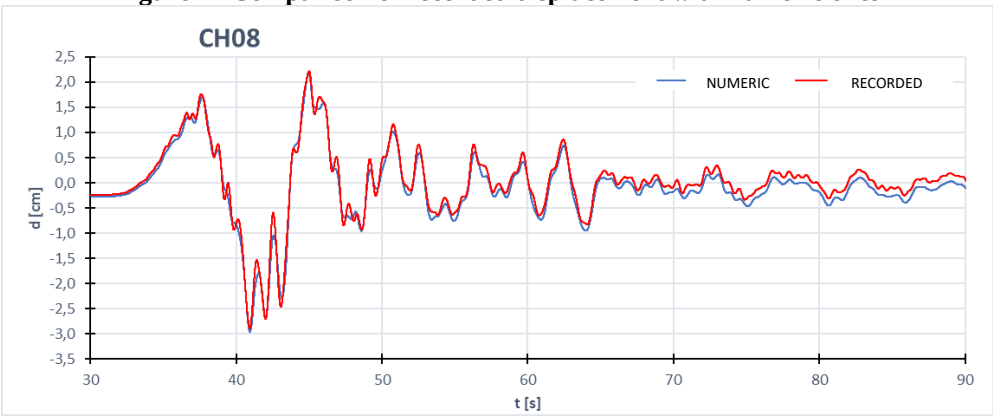

Figure 23 Comparison of recorded displacement with numeric ones

Below are the results in terms of acceleration compared, as in the previous case, with the recordings made on the structure:

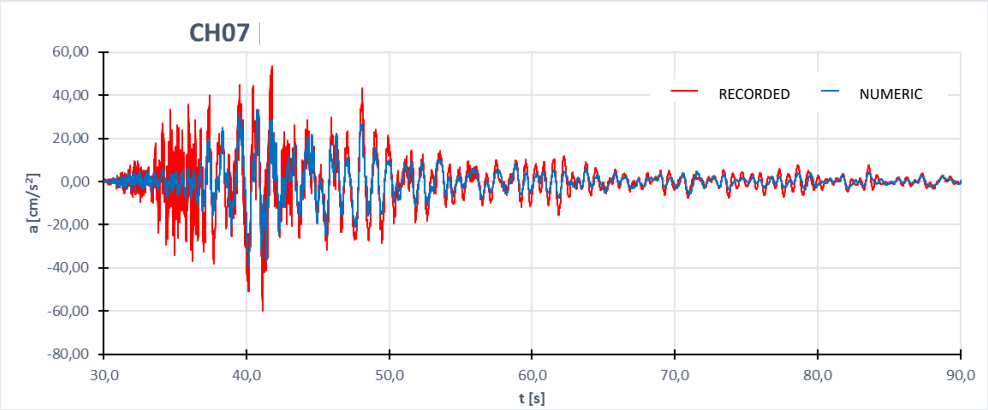

Figure 24 Comparison of recorded acceleration with numeric ones

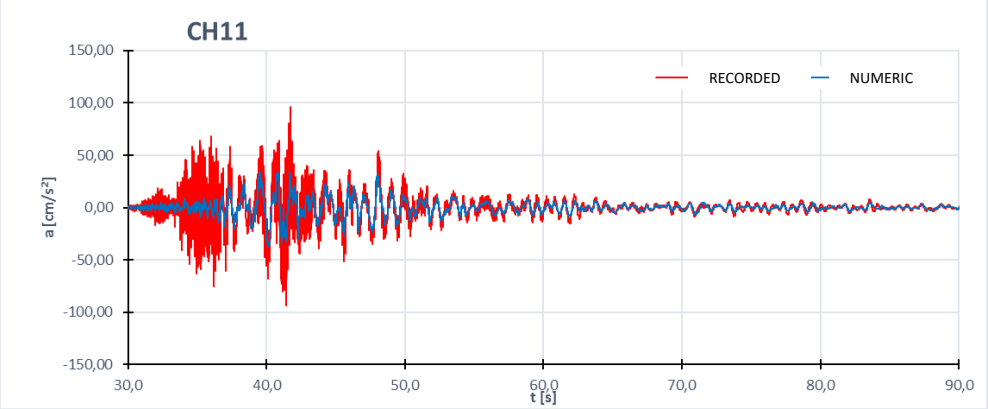

Figure 25 Comparison of recorded acceleration with numeric ones

It can be seen that the model, equipped with the non-linear law of the isolator, has an excellent correspondence with the recorded data. Note above all how, in acceleration terms, present a frequency, in most cases, almost equal to the one recorded, but with slightly lower values. As in the previous case, even the model implemented with the global law turns out to have a good correspondence with the recordings.

It is worthwhile to point out the effectiveness of the model and the implementation of the latter with the non-linear characteristics of the isolator, to conduct a linear analysis using the equivalent horizontal stiffness of isolators K_e = 1.31 KN/mm, by using acceleration recordings of the TP151 event in the three main directions as input data.

The results on two channels at the level of the first deck, one in the X-direction (CH09) and another in the Y-direction (CH08) are shown below, both as displacement and as acceleration.

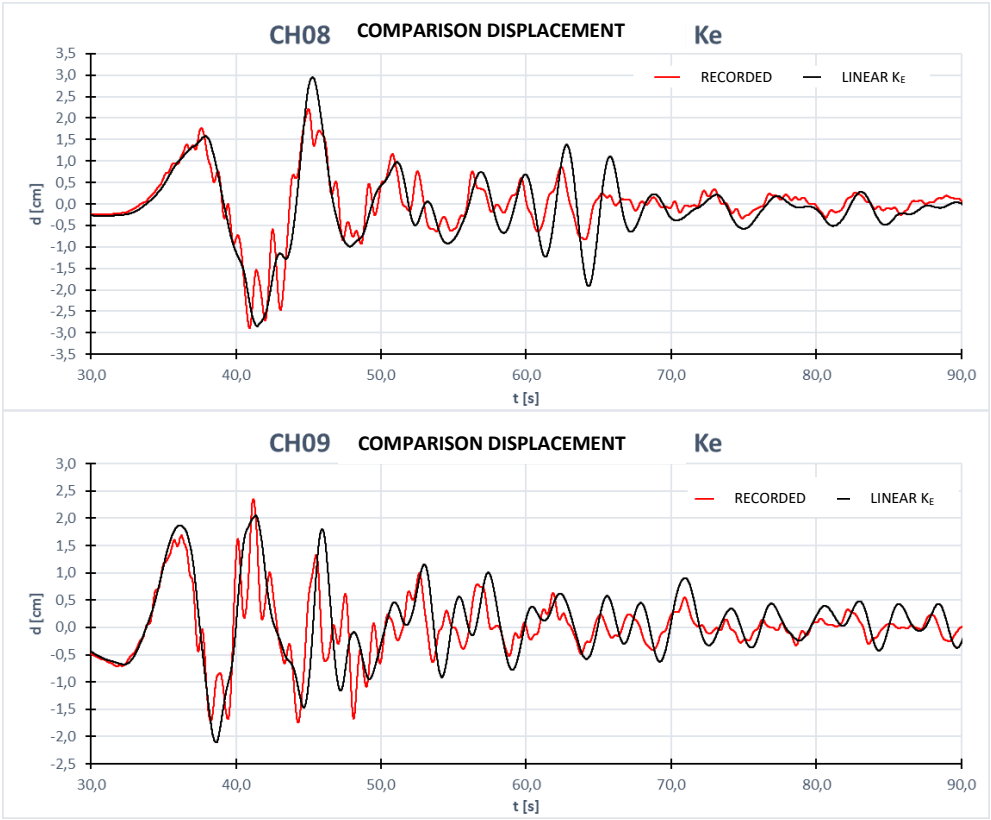

Figure 26 Comparison of displacement between linear analysis and recorded data

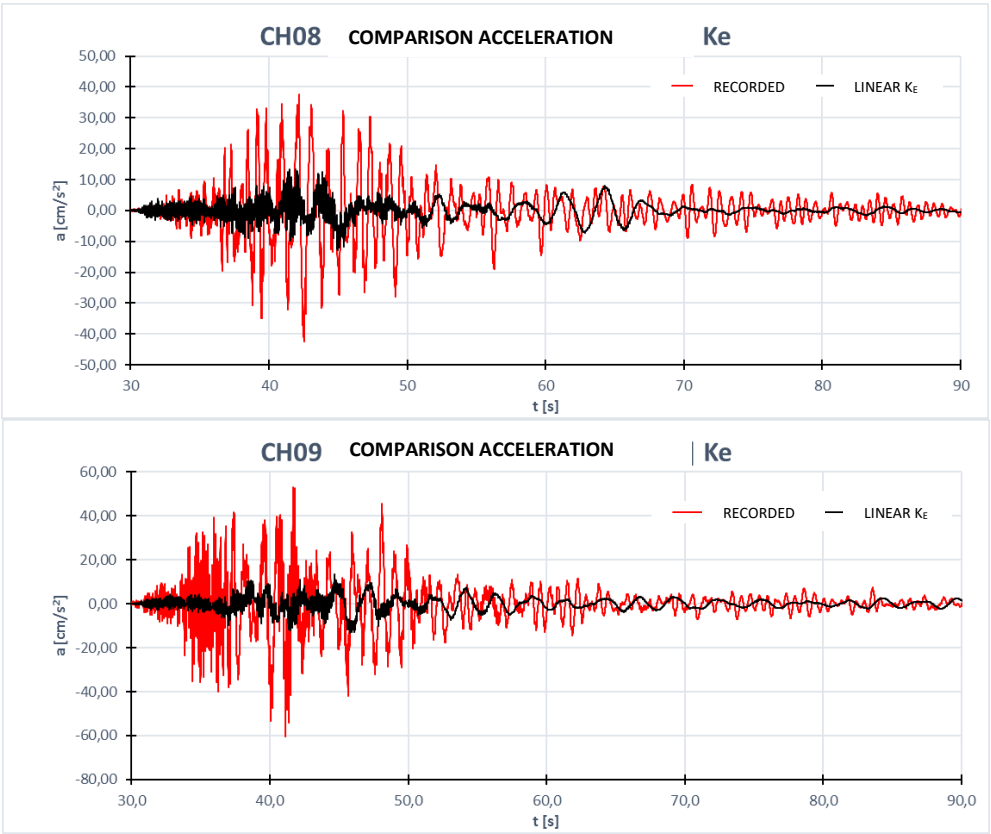

Figure 27 Comparison of acceleration between linear analysis and recorded data

The differences between linear analysis with K_e and the analysis with the non-linear characteristics of the isolator are very pronounced. As for displacement, the highest recorded peak is more or less reached, but the trend does not align with the movements recorded. As for acceleration, however, it is noticed that the numerical solution obtained by conducting the linear analysis heavily underestimates the acceleration of the structure, and the time sequence of the accelerations does not respect the recorded law.
There is also a preponderant frequency within the accelerations of the model, certainly different from that recorded on the actual structure.

8 CONCLUSIONS

For the structure under examination, amplification phenomena have been noticed, up to about twice the acceleration on the superstructure, for very low input energy values. In these cases, however, it is noticed that the amplified accelerations are extremely small entities, and very far from damaging the structure. This is because, as seen, isolation systems with high-damping elastomeric isolators have a stiffness that increases as the deformation decreases (as required to avoid disturbing vibrations even under weak horizontal loads such as wind, etc.), with nonlinear performance; in the case of low-energy seismic input, the insulation system is more rigid even than the equivalent horizontal stiffness K_e.
However, the isolation devices have been shown to function also in low stress conditions, with frequencies higher than those for which they were designed, but still carrying out a filter function, in fact, less than extremely low acceleration, there is no upward acceleration amplification.
It can be observed, from the recordings, the presence of a content in frequency different from that of the fixed-base structure. At the same time, it was also verified that the stresses on the structure were less than those of design.
Thanks to the recordings of ENEA permanent accelerometric network, installed on the test structure, and to the tests carried out on the same isolators used for the qualification, it was possible to describe the behavior of isolators in terms of force and displacement by defining two non-linear laws, derived from experimental data. Obviously, while the first local law seems more suitable to describe the behavior of the isolator for deformations below 5%, the global law is also suitable for uses that for which the isolator is deformed even beyond that value.
The developed finite element model is very faithful to what is the actual behavior of the structure and, accompanied by the non-linear laws of the isolator, has a very good feedback with the experimental measurements of seismic events. Consider however that we cannot expect that the results of the numerical model match exactly to the recording ones, because, of course, there are many other variables to consider in a calculation model.
By performing linear analyses using the equivalent horizontal stiffness modulus and comparing the results with the recordings of low energy seismic events, there are major differences, especially in terms of accelerations that are considerably undervalued (75% less than about).
The differences between the two analyses decrease in the case of higher-entity input accelerations, as could be seen by repeating the linear analysis in the case of the Norcia earthquake, considering the structure in the epicentral zone. The structure also lends itself very well to this type of analysis, both for a geometric factor being essentially a half sphere, and because it appears to have an extremely rigid superstructure.

9 REFERENCES

[1] Clemente P. (2002). L'analisi dinamica sperimentale nella salvaguardia dei beni culturali. ENEA, Roma, marzo, ISBN 88-8286-012-4.

[2] Çelebi M., Bazzurro P., Chiaraluce L., Clemente P., Decanini L., De Sortis A., Ellsworth W., Gorini A., Kalkan E., Marcucci S., Milana G., Mollaioli F., Olivieri M., Paolucci R., Rinaldis D., Rovelli A., Sabetta F. and Stephens C. (2010). "Recorded Motions of the Mw6.3 Apr. 6, 2009 L'Aquila (Italy) Earth. and Implications for Building Structural Damage: A Review". Earth. Spectra, Vol. 26, No. 3, 651-684, Aug. 2010, EERI.

[3] Rinaldis D., Clemente P., Buffarini G. (2010). "Dynamic Behavior of a Historical Building". In Advanced Materials Research Vols. 133-134 (2010), Proc. 7th International Conference on Structural Analysis of Historic Constructions, pp 659-664, © (2010) Trans Tech Publications, Switzerland, doi:10.4028/www.scientific.net/AMR.133-134.659.

[4] Clemente P., Buffarini G., Rinaldis D. (2010). "Application of limit analysis to stone arch bridges". In Baochun Chen and Jiangang Wei (Eds) ARCH'10, Proc. 6th Int. Conf. on Arch Bridges , pp 465-472, SECON-HDGK, New Art Color-Plate & Printing Co., LTD, Fujian, China. ISBN: 978-953-7621-10-0.

[5] Clemente P. and Buffarini G. (2010). "Base isolation: design and optimization criteria". J. of Seismic Isolation and Protection Systems, 1-1(2010), 17-40, Mathematical Science Publisher, DOI 10.2140.siaps.2010.1.17.

[6] Martelli A., Clemente P., Saitta F. and Forni M. (2012). "Recent worldwide application of seismic isolation and energy dissipation to steel and other materials structures and conditions for their correct use". In Mazzolani F.M. & Herrera R. (eds) STESSA 2012 (Proc., Seventh Int. Conf. Structures in Seismic Areas, Santiago del Chile, 9-11 Jan), Keynote Lecture, Taylor & Francis Group, London, ISBN 978-0-415-62105-2.

[7] Rinaldis D., Clemente P. (2013). "Seismic input characterization for some Italian sites". In Brebbia C.A & Hernández S. (eds), Earth. Resistant Eng. Structures IX (Proc. ERES 2013, A Coruña, Jul 8-10), Vol. 79, 13-21, WIT Press, Southampton, UK, ISSN 1743-3509 (on-line), DOI: 10.2495.ERES130021.

[8] Clemente P., Bongiovanni G., Buffarini G. & Saitta F. (2015). "Seismic input in the structural design: considerations and application to the Italian territory". Int. J. of Safety and Security Eng., WIT Pres, Vol. 5, No. 2 (2015) 101-112, ISSN 2041-9031 (paper format), ISSN 2041-904X (on-line), DOI: 10.2495/SAFE-V5-N2-101-112.

[9] Martelli A., Clemente P. (2015). "Need for an Adequate Seismic Monitoring of Seismically Isolated Buildings to Ensure Safety During Their Life". In De Stefano A. (ed), Proc. 7th Int. Conf. on Structural Health Monitoring of Intelligent Infrastructure (SHMII-7, 1-3 July 2015, Turin), RS2, ISHMII & Politecnico di Torino.

[10] Martelli A., Clemente P., Forni M. (2015). "Worldwide state-of-the-art of development and application of anti-seismic systems based on the information provided at the ASSISi Sendai Conference in 2013 and later and conditions for their correct use". Proc. 14th World Conf. on Seismic Isolation, Energy Dissipation and Active Vibration Control of Structures (San Diego, Sep 9-11 2015), Keynote lecture, Univ. of California San Diego, CA USA.

[11] Bongiovanni G., Buffarini G., Clemente P., Saitta F., De Sortis A., Nicoletti M., Rossi G. (2015). "Behaviour of the base isolated Jovine School in San Giuliano di Puglia, Italy, under the December 20th 2013 earthquake". Proc. 14th World Conf. on Seismic Isolation, Energy Dissipation and Active Vibration Control of Structures (San Diego, Sep 9-11 2015), Univ. of California San Diego, CA USA.

[12] Clemente P. (ed) (2015). "Avezzano 1915 – 2015: Cento anni di ingegneria sismica".

Energia, Ambiente e Innovazione, No. 5, ENEA, Roma.
[13] De Stefano A., Matta E., Clemente P. (2016). "Structural health monitoring of historical heritage in Italy: some relevant experiences". J. of Civil Structural Health Monitoring, Vol. 6, No. 1, 83-106, Springer, DOI 10.1007/s13349-016-0154-y (published on line 23 Feb 2016).
[14] Bongiovanni G., Buffarini G., Clemente P., Saitta F., Serafini S., Felici P. (2016). "Ambient vibration analysis of a strategic base isolated building". Proc. 6th Int. Civil Struct. Health Monitoring Workshop (CSHM-6, Belfast, 26-27 May, 2016), Queen's University Belfast.
[15] Clemente P., Bontempi F., Boccamazzo A. (2016). "Seismic Isolation in masonry buildings: Technological and economic issues". In Modena C., da Porto F. & Valluzzi M.R. (eds), Brick and Block Masonry: Trends, Innovation and Challenges (Proc. 6th Int. Conf. IB^{2}MAC, 26-30 Jun 2016, Padua), 2207-2215, Taylor & Francis Group, London, UK, ISBN 978-1-138-02999-6.
[16] Clemente P., Bongiovanni G., Buffarini G. and Saitta F. (2016). "Experimental analysis of base isolated buildings under low magnitude vibrations". Int. J. of Earthquake and Impact Engineering, Vol. 1, No. 1-2, 199-223, Inderscience Publishers, DOI: 10.1504/IJEIE.2016.10000961.
[17] Clemente P., Martelli A. (2017). "Anti-seismic systems: Worldwide application and conditions for their correct use ". Proc. 16th World Conf. on Earth. Eng., (16WCEE, Santiago, Chile, Jan 9-13), Keynote lecture, IAEE & ACHISINA.
[18] Martelli A., Clemente P., Benzoni G. (2017). "State-of-the-art of development and application of anti-seismic systems in Italy". Proc. New Zealand Society for Earthquake Annual Conf. and 15th World Conf. on Seismic Isolation, Energy Dissipation and Active Vibration Control of Structures (NZSEE2017 and 15WCSI, Wellington, Apr 27-29).
[19] Clemente P., Bongiovanni G., Benzoni G. (2017). "Monitoring of seismic isolated buildings: state of the art and results under high and low energy inputs". Proc. New Zealand Society for Earthquake Annual Conf. and 15th World Conf. on Seismic Isolation, Energy Dissipation and Active Vibration Control of Structures (NZSEE2017 and 15WCSI, Wellington, Apr 27-29).
[20] Clemente P. (2017). "Seismic isolation: past, present and the importance of SHM for the future". J. of Civil Structural Health Monitoring, Vol. 7, No. 2, 217-231, Springer, DOI 10.1007/s13349-017-0219-6 (on line 18 March 2017).
[21] Clemente P., Martelli A. (2018). "Seismically isolated buildings in Italy: state-of-the-art and applications".
[22] M. Dolce, D.Cardone, F. C. Ponzo, A. Di Cesare, "Progetto di edifice con isolamento sismico", IUSS Press.
[23] Trevor E Kelly, S.E., Base isolation of structures - Design Guidelines, Holmes Consulting Group Ltd
[24] Farzard Naeim, James M. Kelly, Design of Seismic Isolated Structures, John Wiley & sons inc.
[25] Anil K. Chopra, Dynamics of structures, Prentice hall
[26] Bendat J.S., Piersol A.G., *Engineering application of correlation and spectral analysis*, J. Wiley & Sons, New York, 1982.

COMPDYN 2019
7th ECCOMAS Thematic Conference on
Computational Methods in Structural Dynamics and Earthquake Engineering
M. Papadrakakis, M. Fragiadakis (eds.)
Crete, Greece, 24–26 June 2019

EXPERIMENTAL INVESTIGATION OF THE BEHAVIOR OF VARIABLE FRICTION BASE ISOLATION SYSTEMS

Tianye Yang[1], Ugurcan Ozcamur[2], Paolo M. Calvi[1], Richard Wiebe[1], Eleonora Bruschi[3], Virginio Quaglini[3], Haluk Sucuoglu[4], Igor Lanese[5], Alberto Pavese[5]

[1] University of Washington
More Hall, Department of Civil and Environmental Engineering, Seattle, WA 98195, USA
tianyy3@uw.edu, pmc85@uw.edu, rwiebe@uw.edu

[2] TIS Technological Isolation Systems
Emirgazi Mahallesi No 35, M Kahramankazan, Ankara, Turkiye
ugurcan.ozamur@tis.com.tr

[3] Politecnico di Milano
Piazza Leonardo da Vinci, 32, 20133 Milano MI, Italy
eleonora.buschi@polimi.it, virginio.quaglini@polimi.it

[4] Middle East Technical University
Universiteler Mh., Dumlupinar Blv. No:1, 06800 Cankaya/Ankara, Turkey
sucuoglu@metu.edu.tr

[5] EUCENTRE
Via Adolfo Ferrata, 1, 27100 Pavia PV, Italy
igor.lanese@eucentre.it, a.pavese@eucentre.it

Abstract

This paper describes a preliminary experimental study aimed at investigating the force-displacement behavior of Variable Friction base isolation Systems (VFSs). Full-scale VFS prototypes were tested under cyclic loading conditions. A series of dynamic hybrid tests simulating the response of a full-scale single-story structure isolated with VFS devices and subjected to ground motions with different intensities, was also performed.
The results of the experiments are presented and used to provide some preliminary validation of a previously developed numerical model. Overall, the results of the experiments were in good agreement with the predictions provided by the numerical analyses.

Keywords: Friction Pendulum bearing, variable friction, bearing testing, dynamic hybrid testing.

1 INTRODUCTION

In the context of developing innovative, high-performance seismic isolation devices, Variable Friction base isolation Systems (VFSs) were recently proposed [1, 2]. Preliminary numerical studies have indicated that VFSs may represent promising solutions because of their capability of providing adaptive response for increasing displacement demands [3].

This paper summarizes some recent experimental results achieved as part of an ongoing international research project focused on the development of VFSs. Two full-scale Variable Friction prototypes were tested under cyclic loading conditions, considering realistic values of vertical load and peak horizontal velocities. Numerical simulations were run alongside the experiments to verify the reliability of a recently proposed numerical model [4] implemented in *OpenSees* [5].

A series of dynamic hybrid tests of a full-scale single-story structure isolated with a VFS prototype was also performed. A natural ground motion time history was used as the acceleration input and different acceleration scale factors were implemented throughout the tests. Horizontal displacement, forces, velocities, and accelerations of the base isolation system and of the numerical superstructure were evaluated throughout the tests.

The results of the bearing tests were generally in good agreement with the numerical predictions. However, during the experiments some technological limitations emerged pertaining to the properties of the low friction materials employed to fabricate the Variable Friction prototypes that were addressed over the course of the project. The first refurbished VFS prototype (tested in the context of the dynamic hybrid simulations) showed improved force-displacement behavior, and its response matched well with the numerical predictions.

2 EXPERIMENTAL SETUP AND OVERVIEW

Full-scale experiments were conducted on a total of three VFS prototypes at the experimental facilities of EUCENTRE (European Centre for Training and Research in Earthquake Engineering) in Pavia (Italy) using the Bearing Tester System (BTS) shown in Figure 1. The Bearing Tester System, consists of a prestressed reinforced concrete frame equipped with a series of servohydraulic actuators providing five degrees of freedom to the testing device: vertical load, horizontal load and rotation about three axes (roll, pitch and jaw). Both horizontal and vertical actuators can be used to apply static and dynamic loads, with a peak velocity of 2,200 mm/s in the horizontal direction and 250mm/s in the vertical direction. The Vertical load capacity of the Bearing Testing System is 50,000 kN (40,000 kN static and ± 10,000 kN dynamic) with displacement capacity of ±60 mm, and the Horizontal load capacity is 2,100 kN, with ±580 mm of displacement. The BTS controller is a real-time, digital controller that provides PID closed loop control with a delta-p feedback signal, which enables the BTS to perform real-time dynamic hybrid testing. More details can be found in [6].

2.1 Test specimens

Each prototype bearing consisted of a conventional single friction pendulum system with rigid slider, but the concave stainless steel sliding surface was treated using different polishing techniques to achieve spatially varying frictional properties. Namely, two areas with different surface roughness were obtained: an inner circular area of radius r_1 with smooth surface finish ("low friction area"), and an outer ring area of external radius r_2 with rough finish ("high friction area"). A schematic drawing and a plan view of the full-scale prototype VFS bearing are shown in Figure 2.

(a) (b)

Figure 1. (a) The EUCENTRE BTS; (b) Elevation view of the bearing test setup.

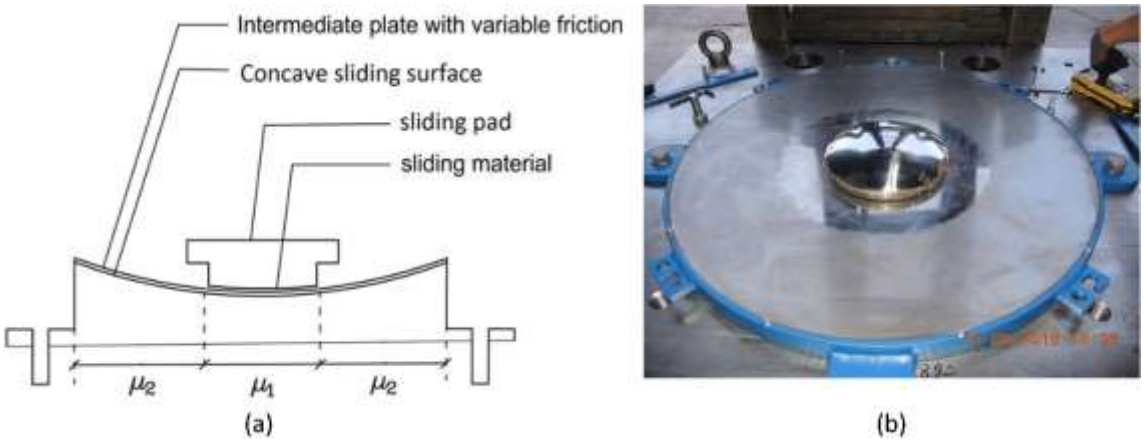

Figure 2. (a) Schematic drawing of a two-ring VFS bearing; (b) Plan view of the concave sliding surface and the slider of the prototype VFS bearing.

The main properties of the tested VFS prototypes are summarized in Table 1. The parameters reported in the table represent the radius of the sliding pad (r_0), the radius of the low friction area (r_1), the external radius of the high friction area (r_2), the coefficient of friction between the sliding pad and the low friction area (μ_1), the coefficient of friction between the sliding pad and the high friction area (μ_2), and the radius of curvature of the sliding surface (R).

Group #	Prototype #	r_0 (m)	r_1 (m)	r_2 (m)	μ_1 (%)	μ_2 (%)	R
1	1	0.125	0.150	0.450	7.0	9.2	4.5
	2	0.125	0.225	0.450	7.0	9.2	4.5
2	1	0.100	0.150	0.450	7.0	9.2	4.5

Table 1. Properties of the tested VFS prototypes

The dynamic coefficients of friction between the sliding pad and the sliding surface were equal to 7.0% and 9.2% for the smooth and the rough areas, respectively. These values were

provided by the bearing manufacturer and were confirmed through friction characterization tests performed in the laboratory.

2.2 Testing program

Following the friction characterization tests, the Group 1 VFS prototypes were subjected to the testing program recommended by the European standard EN 15129 [7]. The program comprised a series of unidirectional harmonic displacement histories, with different displacement amplitudes and frequencies. A list of the tests conducted is summarized in Table 2. For brevity, only the results pertaining to one test for each prototype are presented in this paper. For the presented tests, the displacement amplitude of the harmonic motion was 0.3 m, and the peak velocities were 500 mm/sec and 200 mm/sec, for prototype 1 and prototype 2, respectively.

Test name	Ampl. [m]	Max.vel. [m/s]	load shape	Vert.load [kN]	cycles
Frictional resistance	±0.006	0.0001	triangle	2000	1
Service	±0.060	0.005	sine	2000	20
Benchmark	±0.300	0.050	sine	2000	3
Dynamic 1	±0.075	0.500	sine	2000	3
Dynamic 2	±0.150	0.500	sine	2000	3
Dynamic 3	±0.300	0.500	sine	2000	3
Seismic	±0.300	0.500	sine	1000	3
Seismic	±0.300	0.500	sine	2500	3
Bidirectional	±0.300	0.500	sine	2000	3
Property verification	±0.300	0.500	sine	2000	3

Table 2. Testing program on Group 1 VFS prototypes

The Group 2 prototype was subjected to hybrid tests, simulating the response of a single-story structure isolated with VFS devices. The stiffness of the superstructure (treated as a linear-elastic single-degree of freedom system) was selected to achieve a natural period of vibration of 0.4 seconds, considering a seismic weight of 785 kN. A 785 kN vertical load was also adopted in the hybrid simulations, which resulted in an average pressure on the sliding pad of 25 MPa. The tests were performed under the application of recorded ground motions with different intensities. The peak velocity recorded during these tests reported was approximately 950 mm/sec.

3 PRELIMINARY RESULTS AND NUMERICAL COMPARISON

3.1 Bearing testing

The horizontal force-displacement response characterizing the Group 1 VFS prototypes [8] is reported in Figure 3. The black lines represent the first-cycle response, while the grey lines refer to the second and third loading cycles. It can be seen that the first-cycle response differs quite significantly from that of the subsequent cycles [9]. In particular, the effects of the variable friction are clearly visible in the first cycle, but they tend to disappear in later loops. This undesirable discrepancy was ascribed to the creation of a transfer film of the sliding material on the mating surface, which smoothed the surface and made the sliding behavior more uniform over the two areas with different roughness [10]. At the current stage, this still represents a major challenge and one of the main constraints limiting the possible frictional properties that

can be selected for a VFS. Additionally, μ_1 and μ_2 are only marginally different in their initial values, thus the variability of the friction coefficient is low.

However, Figure 3 shows that the numerical predictions based on the VFS model developed by [4] and briefly described in Section 3.3, successfully predicts the first-cycle experimental response of the systems tested.

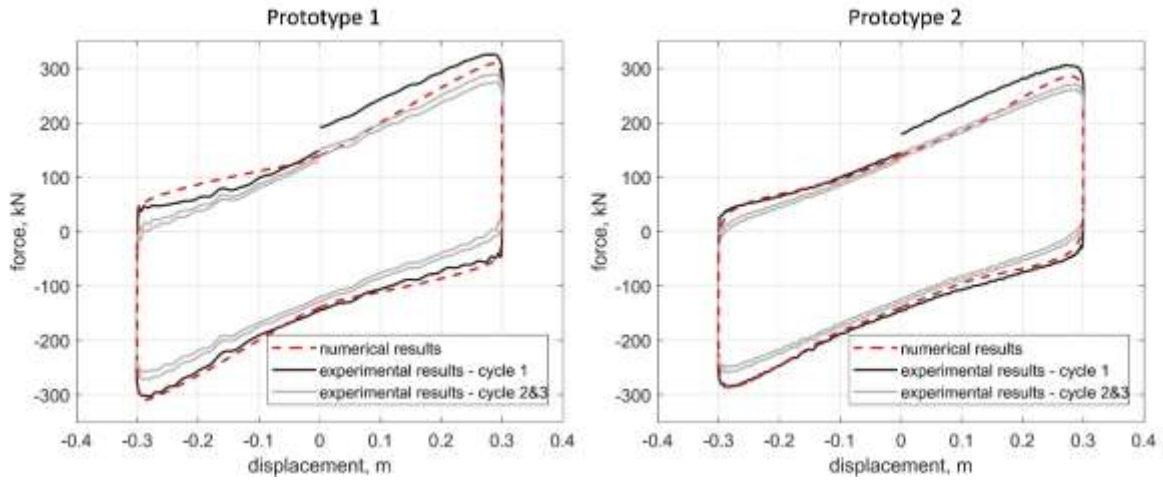

Figure 3. Comparison between the hysteretic curves from numerical model and experimental data for Group 1 VFS prototypes

3.2 Dynamic hybrid testing

The horizontal force-displacement responses characterizing the Group 2 VFS prototype undergoing a realistic ground motion in the context of hybrid testing is shown in Figure 4. The black dashed lines represent the experimental results, while the grey solid lines represent the numerical predictions. The numerical predictions are in good agreement with the experimental results. These preliminary results are very promising and suggest that the numerical element developed by the Authors [4] can adequately capture the mechanics of the VFSs tested, in the context of time history analyses. However, more experimental evidence is needed (including 3-D testing) before definitive conclusions can be drawn.

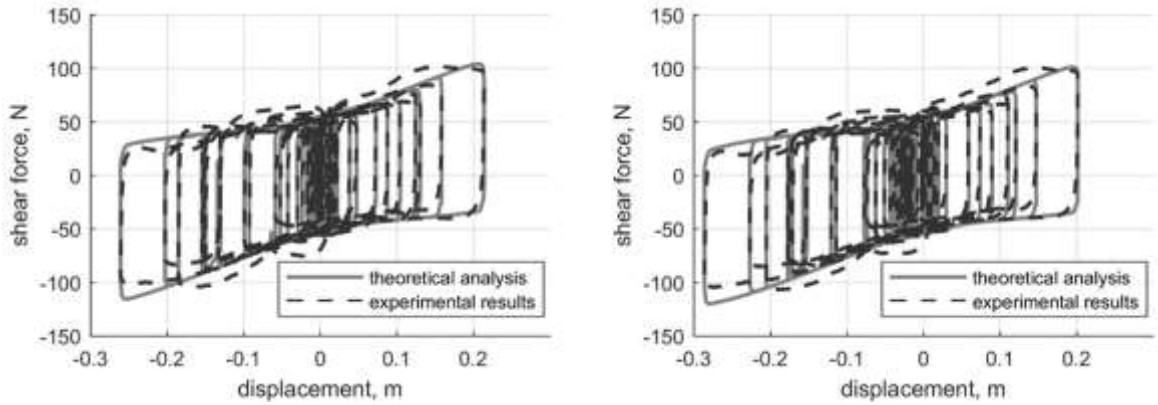

Figure 4. Comparison between the hysteretic curves from numerical model and experimental data for Group 2 VFS prototype.

3.3 Numerical modeling

The response predictions outlined in Figure 3 and Figure 4 were obtained using a newly developed numerical model that was recently implemented in *OpenSees* [4]. The numerical model was developed based on the bi-directional plasticity model proposed by [11]. The model accounts for complex aspects of the bearing response, such as simultaneous influence of velocity and axial force on the coefficient of friction, and vertical-horizontal coupling effect due to the geometric radius of curvature.

For this project, a velocity-dependent friction model was used while pressure-dependency was neglected because the axial force remained approximately constant throughout the tests. The relationship between the sliding velocity and the coefficient of friction can be described by the exponential function proposed in [12], shown in Equation 1:

$$\mu(v) = \mu_{max} \times (1 - (1 - \tilde{\mu}_v)e^{-av}) \quad (1)$$

where μ(v) represents the coefficient of friction as a function of sliding velocity, μ_{max} is the coefficient of friction at high sliding velocity, $\tilde{\mu}_v$ is the ratio between the coefficient of friction at slow sliding velocity and μ_{max}, and a is a constant describing the transition rate from low to high sliding velocity regimes. Past studies suggest that the value of the coefficient a can range from 20 sec/m to over 100 sec/m depending on the sliding material utilized [13]. In the present work, it was found that setting a equal to 20 sec/m provided the best match between the experimental results and the numerical predictions. The parameter $\tilde{\mu}_v$ was set equal to 0.5, which is consistent with past studies [14].

4 CONCLUSIONS AND FUTURE WORK

Preliminary experimental evaluation of three VFS prototypes are presented in this paper. The experimental results from both the bearing testing and the dynamic hybrid testing were in good agreement with the analytical results obtained using the numerical model presented in [4].

The results of the dynamic hybrid testing collected with respect to the behavior of the superstructure will be analyzed and discussed as part of future work. Further 2-D and 3-D bearing tests will also be performed in the future to further validate and improve the numerical model.

In addition, the development of more suitable sliding materials to be used in the context of implementing high-performance VFSs, persists as one of the key objectives of the ongoing research investigation.

REFERENCES

[1] P.M. Calvi, D.M. Ruggiero, Numerical modelling of variable friction sliding base isolators. *Bulletin of Earthquake Engineering*, **14**, 549-568, 2016.

[2] P.M. Calvi, M. Moratti, G.M. Calvi, Seismic isolation devices based on sliding between surfaces with variable friction coefficient. *Earthquake Spectra*, **32**, 2291-2315, 2016.

[3] S. Timsina, P.M. Calvi, Variable friction base isolation systems: seismic performance and preliminary design. *Journal of Earthquake Engineering*, DOI: 10.1080/13632469.2018.1504837

[4] T. Yang, P.M. Calvi, R. Wiebe, Numerical implementation of variable friction sliding base isolators and preliminary experimental results. *Earthquake Spectra*, under review, 2019.

[5] *Open System for Earthquake Engineering Simulations (OpenSees)*, 2006. Pacific Earthquake Engineering Research Center. http://OpenSees.berkeley.edu.

[6] S. Peloso, A. Pavese, C. Casarotti, Eucentre trees lab: laboratory for training and research in earthquake engineering and seismology. *Geotechnical and Geology Earthquake Engineering*, **20**, 65-81, 2012.

[7] *EN 15129. Antiseismic devices*, Comité Européen de Normalisation (CEN), 2009.

[8] EUCENTRE, *Dynamic Testing of Variable Friction Seismic Isolation Devices and Isolated Systems, Tech. Rep. EUC179/2017E_TR_1*, EUCENTRE Laboratory, Pavia, Italy, 2018.

[9] V. Quaglini, M. Bocciarelli, E. Gandelli, P. Dubini, Numerical assessment of frictional heating in sliding bearings for seismic isolation. *Journal of Earthquake Engineering*, **18**, 1198–1216, 2014.

[10] V. Quaglini, P. Dubini, D. Ferroni, C. Poggi, Influence of counterface roughness on friction properties of engineering plastics for bearing application. *Materials and Design*, **30**, 1650-1658, 2009.

[11] G. Mosqueda, A.S. Whittaker, G.L. Fenves, Characterization and modeling of friction pendulum bearings subjected to multiple component of excitation. *Journal of Structural Engineering*, **231**, 433-442, 2004.

[12] A. Mokha, M.C. Constantinou, A.M. Reinhorn, *Teflon bearing in aseismic base isolation: experimental studies and mathematical modeling. Report No. 88-0038*, National Center for Earthquake Engineering Research, 1988.

[13] M.C. Constantinou, P. Tsopelas, A. Kasalanati, E. Wolff, *Property modification factors for seismic isolation bearings. Report No. 99-0012*, Multidisciplinary Center for Earthquake Engineering Research, 1999.

[14] D.M. Fenz, M.C. Constantinou, *Development, implementation, and verification of dynamic analysis models for multi-spherical sliding bearings. Report No. 08-0018*, Multidisciplinary Center for Earthquake Engineering Research, 2008.

COMPDYN 2019
7th ECCOMAS Thematic Conference on
Computational Methods in Structural Dynamics and Earthquake Engineering
M. Papadrakakis, M. Fragiadakis (eds.)
Crete, Greece, 24–26 June 2019

SEISMIC PROTECTION OF HIGH-VOLTAGE EQUIPMENT BY FRICTION DAMPERS: NUMERICAL MODELLING CORRELATED WITH FULL-SCALE COMPONENT TESTS

Shakhzod Takhirov[1], Leon Kempner[2], Michael Riley[3], Eric Fujisaki[4] and Brian Low[5]

[1] Civil and Environmental Engineering Department, University of California at Berkeley; 337 Davis Hall, UC Berkeley, Berkeley, California, 94720, USA; e-mail: takhirov@berkeley.edu

[2] Bonneville Power Administration, Vancouver, WA 98666, USA; e-mail: lkempnerjr@bpa.gov

[3] Bonneville Power Administration, Vancouver, WA 98666, USA; e-mail: mjriley@bpa.gov

[4] InfraTerra, Inc., 5 Third Street, San Francisco, CA 94103, USA; e-mail: e.fujisaki.01@gmail.com

[5] Pacific Gas and Electric, San Ramon, CA 94583, USA; e-mail: brian.low@pge.com

Abstract

The usage of seismic protective devices in the electric power industry for improving seismic resiliency of high-voltage substation equipment is increasing worldwide. Friction or viscous dampers represent the most common devices used by the industry to reduce the seismic demand by incorporating supplemental damping and thus increasing the equivalent viscous damping of the system. Although viscous dampers are quite common in the building industry, an application of friction dampers is gaining traction as an efficient alternative for seismic protection of high-voltage equipment. To study the performance, friction dampers of a typical design were selected and studied. This paper summarizes the results of a research program that includes full-scale component testing and numerical modelling. A special test setup was created for component testing of the damper. A numerical model of a substation high-voltage equipment protected by friction dampers was developed. A numerical model of the damper was calibrated based on the results of component tests. A newly developed time history matched to the IEEE693 spectrum for use in seismic qualification of substation equipment by analysis/testing were used as excitation input motion. In the research program, the performance of the well-calibrated numerical model of the seismically protected high-voltage equipment was analyzed. The conclusions of the study demonstrate the benefits of using dampers for improving seismic resiliency of the electric power grid.

Keywords: Seismic Qualification Testing, IEEE693, Nonlinear System, Shaking Table Tests, Friction Dampers, Seismic Protection, Component Testing.

1 INTRODUCTION

The usage of seismic protective devices in the electric power industry for improving seismic resiliency of high-voltage substation equipment is increasing worldwide. Friction or viscous dampers represent the most common devices used by the industry to reduce the seismic demand by incorporating supplemental damping and thus increasing the equivalent viscous damping of the system. Although viscous dampers are quite common in the building industry, an application of friction dampers is gaining traction as an efficient alternative for seismic protection of high-voltage equipment. To study the performance, friction dampers of a typical design were selected and studied. This paper summarizes the results of a research program that includes full-scale component testing and numerical modelling.

2 COMPONENT TESTING OF FRICTION DAMPERS

A special test setup was created for component testing of the dampers. It is presented in Figure 1 and it simulates loading of the friction damper in a typical installation when the damper is installed as a stiffness and damping component of the anchoring system. Friction dampers from Ringfeder [1] were used in this study. Since the friction dampers work in compression only, there are several ways of using friction dampers as seismic protection devices. For example, if only one friction damper is used in the so-called single-acting configuration, the force will be developed in compression only as presented in the left side image of Figure 2. In this case, another spring or friction damper needs to be used on the tension side that corresponds to positive force and displacement to resist tension forces. When there is one damper on each side of the loading point, they create the so-called double-acting configuration. The force versus displacement curve is more symmetric in this case as presented in the right image of Figure 2.

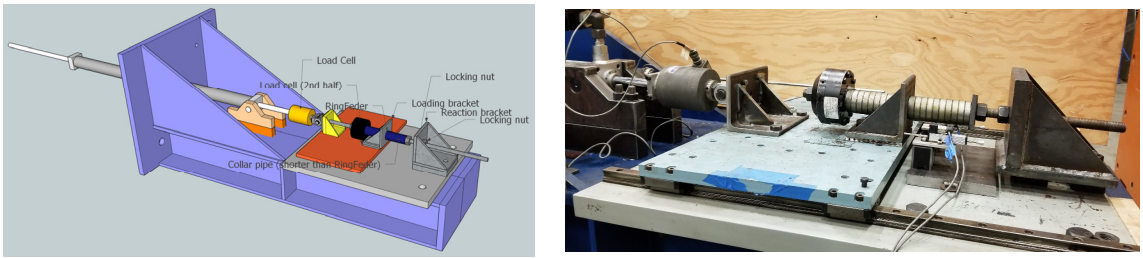

Figure 1: Component testing setup for Ringfeder friction dampers: sketch (left) and photo (right).

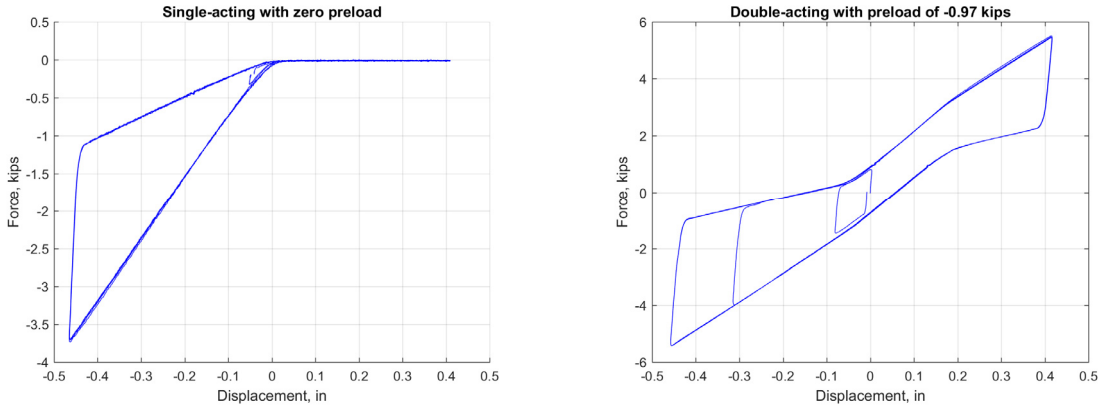

Figure 2: Force vs. displacement from component testing in single-acting with no preload (left) and double-acting with preload (right) configurations.

In addition to that, one of the dampers can be preloaded in compression, which is very common when the dampers are installed in a vertical configuration and the bottom damper is compressed under the dead weight of the equipment. The case with a preload of -0.97 kips is presented in the right image of Figure 2.

The dampers used in this study were installed in a double-acting configuration, when there is a dumper on each side of the loading point. The latter results in symmetric behavior in tension and compression. A testing protocol followed recommendations of the upcoming version of the IEEE693 document [3], which is presented in Figure 3 on the left. The displacement D_{PL} corresponds to the maximum displacement of the device to be achieved at High Performance Level [4]. A typical result for cyclic tests with increasing amplitude is presented in the right image of Figure 3.

It is worth noting, that for structural applications, the friction dampers are studied in many publications (see [2] as an example).

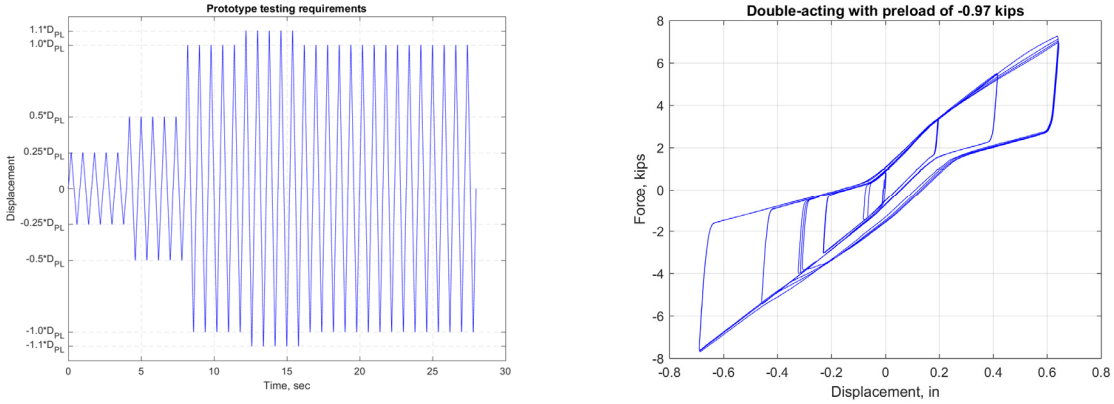

Figure 3: Component testing: protocol (left) and sample test results (right).

As presented in the left image of Figure 4, the equivalent viscous damping of the damper is estimated from a single cycle based on the well-known expression (see, for example, [5] – the graphical representation of which is shown in the right image of Figure 4):

$$\zeta_{eq} = E_D/E_{S0}/(4\pi), \tag{1}$$

where E_D is the energy dissipated over the cycle, E_{S0} is the strain energy, which is calculated from equivalent stiffness, k, and the cycle's amplitude, u_o:

$$E_{S0} = k u_o^2/2. \tag{2}$$

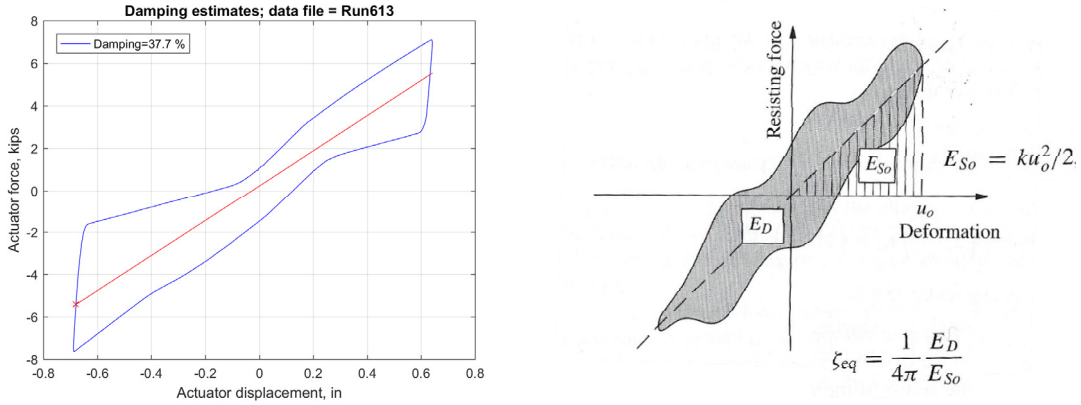

Figure 4: Estimation of equivalent viscous damping (left) based on [5] - right.

The equivalent viscous damping of the double-acting friction damper with a preload of -0.97-kips was estimated at 37.7% as presented in the left image of Figure 4.

3 HIGH-VOLTAGE EQUIPMENT AND FE MODEL

In this study, a typical model of high voltage equipment consisting of a 230-kV porcelain insulator with a terminal pad assembled on top of a steel support structure was studied. It is presented in Figure 5. A similar model was studied earlier [6] when it was isolated by Wire Ropes. The fixed based configuration was also previously tested on the shaking table [7]. In both cases studied earlier, the support structure was supported by eight anchors. In this study, only four anchors were considered at the bottom of the support structure as shown in Figure 5c. The modelling is conducted in SAP2000 [8]. The results of numerical simulations are reduced in the Matlab environment [9].

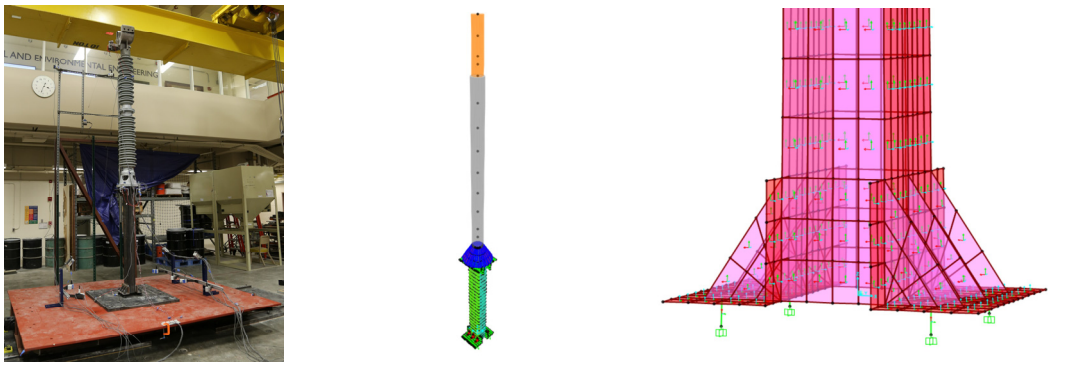

a) Fixed base configuration on shaking table

b) FE model

c) Number of anchors is limited to four

Figure 5: High-voltage equipment on a support structure.

Several finite element (FE) models were created. The first model (Model A) was simulating a fixed base configuration. The second model (Model B) was isolated by utilizing a model of the friction damper [8] without a preload. There were several models simulating HV equipment isolated by friction dampers with different values of preload as presented in Table 1. The resonant frequency of the fixed based model was close to that measured by a snap-back test of a real specimen [7] as shown in Table 1. The latter means that the dynamic properties of the equipment's model were closely correlated to that of real equipment.

To ensure that the resonant frequency for each model is captured correctly in nonlinear numerical analysis, all models were subjected to a sine sweep excitation in the X axis. The level of excitation was the same and high enough to cause about the same axial force in the friction damper. In other words, the demand of sine sweep excitation on the models was about the same at the resonant frequency of the system.

The normalized transfer functions of top accelerations from numerical simulations with the sine sweep excitation are presented in Figure 6. The transfer function plot of models with a preload steadily widens while the preload is increasing. It means that the damping of the model is increasing. The damping based on the half-power bandwidth method (see [5], for example) is estimated in the same figure. Since the half-power bandwidth method works for relatively low values of critical damping, only few damping estimations for some models are presented in this plot. Two major conclusions can be made from these results. First, the force versus displacement curve of the friction dampers with a preload is much wider than that

without a preload. Second, the resonant frequency of the isolated equipment steadily increases while the preload increases.

In the next step, all models were subjected to a seismic excitation by using a strong motion time history matched to the IEEE693 spectrum at 5% damping, TestQke4IEEE5-4 [10]. The excitation was only applied in the X direction.

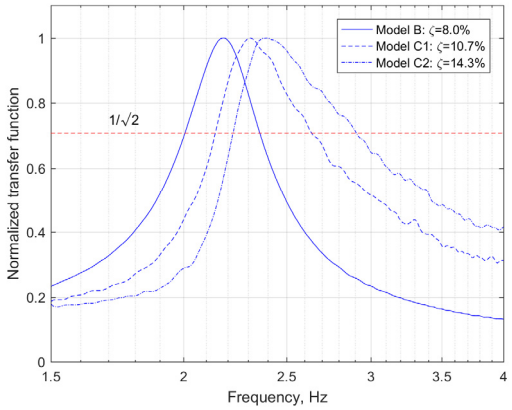

Figure 6: Normalized transfer functions from sine sweep runs were used in the damping estimates based on half-power bandwidth method [5].

Configuration	Resonant frequency (X), Hz	Damping, %	Preload, in
Snap-back test of actual specimen	4.9	NA[!]	NA
Model A: fixed base	5.0	5.0	NA
Model B: friction damper	2.2	8.0	0.0
Model C1: friction damper	2.3	10.7	-0.05
Model C2: friction damper	2.4	14.3	-0.07
Model C3: friction damper	2.9	NA[&]	-0.10
Model C4: friction damper	3.5	NA[&]	-0.15

[!] – damping was not estimated in the test; [&] - damping is too high to be estimated by means of half-power band-width method

Table 1: Resonant frequencies and damping values of actual specimen and FE models.

The friction damper model [8] was based on the stiffnesses of the Ringfeder damper experimentally measured in the component testing. The resultant hysteresis loops of the friction dampers for Model B and Model C4 are presented in Figure 7.

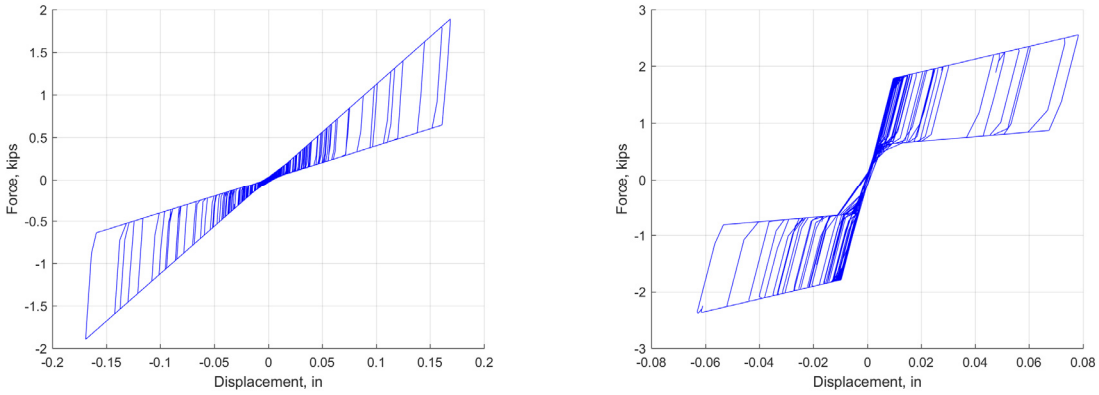

Figure 7: Force vs. displacement without (left) and with (right) preload: Model B vs. Model C4.

For all models, the peak maximum acceleration and displacement on top and moment at the bottom of the insulator is investigated. All these results are normalized to corresponding peak values for Model A. The normalized values are summarized in Table 2.

Normalized peak value	Model A	Model B	Model C1	Model C2	Model C3	Model C4
Acceleration on top	100%	90%	86%	78%	70%	55%
Moment at bottom of insulator	100%	96%	88%	85%	79%	61%
Displacement on top	100%	448%	381%	352%	302%	186%

Table 2: Normalized peak values of seismic performance.

As shown in Table 2, the peak acceleration on top and moment at the bottom of the insulator is less than that of the non-isolated model (Model A). Preloading improves the performance of the isolated equipment and the highest reduction of peak acceleration and moment resulted in Model C4. In the case of the latter model, the peak acceleration was reduced by about 45% and the moment at the bottom by about 39%. Since excessive moments can lead to failure of the porcelain insulators, this parameter is very important for acceptable seismic performance of the HV equipment.

This reduction of moments is closely correlated to the reduction in peak accelerations as presented in Figure 8. This serves as evidence that the first mode vibrations are dominating and that they control the seismic performance of the HV equipment.

The IEEE693 spectrum decreases when the damping is increasing as presented in Figure 8. The latter figure presents all other spectral plots normalized to the plateau of the IEEE693 spectrum with damping of 5%. As it can be seen from Figure 8, the reduction factors are somewhat consistent with the reduction estimated by the IEEE693 spectral plots [4]. In the figure, all lines correspond to the IEEE693 spectra for different damping values, the points correspond to the normalized peak values at the system frequency.

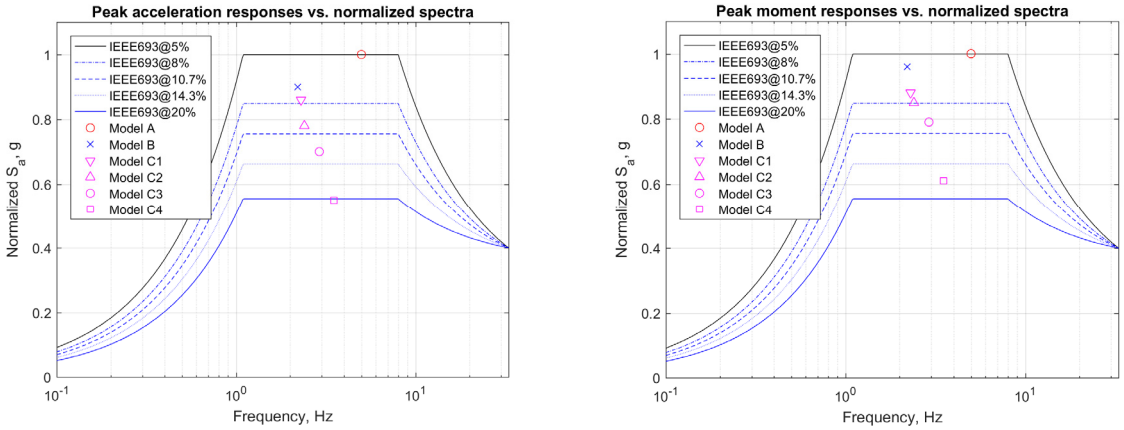

a) Peak acceleration responses b) Peak moment responses

Figure 8: Normalized peak responses vs. normalized spectra.

The peak relative displacement on top of the isolated equipment with no preload (Model B) increased about 4.5 times in respect to the fixed base model (Model A) as presented in Table 2. This increase is expected due to increased flexibility of the base support dampers. Preloading increases the effective damping of the system and as such the peak displacement decreases and for Model C4 is it just 1.86 time greater than the fixed based model. The relative

displacements at the insulator's terminal location are very important for estimating the cable length when the HV equipment is connected to other substation equipment by flexible bus power cables.

The results of this study demonstrate that even simple models of the friction damper shows its efficiency. In the next phase of the study, the friction dampers will be installed at the bottom of the HV equipment and the system will be tested on a long stroke 1D shaking table and 6D shaking table. A more accurate model of the friction damper will be utilized and a nonlinear time history will be conducted on a FE model isolated by friction dampers. The results of the shaking table tests will be compared to the numerical predictions of this simplified model and to that with more sophisticated model of friction damper. This phase of the project is ongoing.

4 CONCLUSIONS

- This paper highlights results of component tests conducted on friction dampers. The test results show that the effective viscous damping of the friction dampers can be as high as 37.7%.
- Based on a simplified model of the friction damper [8], the efficiency of the seismic isolation is demonstrated. It was shown that the peak moments and accelerations can be reduced by about 39% and 45%, respectively. The peak displacements on top of the equipment will increase in respect to the fixed base model, that can be reduced by increasing preload.
- There is a need for a study with a more sophisticated model of friction dampers to be investigated in a nonlinear time history numerical simulation. The sophisticated model of the HV equipment needs to be calibrated based on the system level tests on a shaking table. A study on these issues is ongoing.

ACKNOWLEDGEMENTS

The project is sponsored by the Electric Power Research Institute (EPRI) whose support is greatly appreciated. The research team thanks Mr. Robert Cochran of Seattle City Light for donating Ringfeder friction dampers. Special thanks are due to the staff of the Structure Laboratory at the University of California, Berkeley. Special thanks are due to Mr. Llyr Griffith, Mr. Phillip Wong, and Mr. Matthew Cataleta. The successful completion of the testing phase of the project would not be possible without their technical support. Technical help by Ms. Sage Shamsai (CEE, UC Berkeley) on preparing 3D drawings and testing is greatly appreciated.

REFERENCES

[1] Ringfeder Power Transmission, 2016. Ringfeder Damping Technology. http://www.Ringfeder.com/Documents/Products/Ringfeder/Damping_US.pdf.

[2] Bishay-Girges, N.W. & Carr, Athol. (2014). Ring spring dampers: Passive control system for seismic protection of structures. 47. 173-180. BULLETIN OF THE NEW ZEALAND SOCIETY FOR EARTHQUAKE ENGINEERING, Vol. 47, No. 3, September 2014.

[3] P693/D18, July 2018. Draft 18 of Recommended Practice for Seismic Design of Substations.

[4] IEEE, 2005. IEEE STANDARD 693-2005 - IEEE Recommended Practice for Seismic Design of Substations.

[5] Chopra, Anil (2007). Dynamics of structures. Pearson Education, Inc.

[6] Shakhzod Takhirov, Eric Fujisaki, Brian Low, Leon Kempner, Michael Riley (2018). Seismic Performance of Nonlinear System Subjected to Multiple Time Histories Matched to the Same Spectrum: Evaluation of Mean and Maximum Response Approaches. The 16th European Conference on Earthquake Engineering (16ECEE), Thessaloniki, Greece, June 18-21, 2018.

[7] Shakhzod Takhirov, Eric Fujisaki, Leon Kempner, Michael Riley and Brian Low. 'Nonlinear Systems Subjected to Multiple Seismic Excitations Matched to the Same Spectrum: Numerical Predictions versus Shaking Table Tests'. COMPDYN2017, 6th International Conference on Computational Methods in Structural Dynamics and Earthquake Engineering, 15-17 June 2017, Rhodes Island, Greece.

[8] Computers and Structures, Inc. (CSI), 2014. SAP2000 Ultimate Version 16.1.1. Structural Analysis Program.

[9] The MathWorks, Inc. (2016): Matlab Version R2016b.

[10] Shakhzod Takhirov, Eric Fujisaki, Leon Kempner, Michael Riley and Brian Low (2017). 'Development of Time Histories for IEEE693 Testing and Analysis (Including Seismically Isolated Equipment)'. PEER Report No. 2017/10, Pacific Earthquake Engineering Research Center, Berkeley, December 2017.

COMPDYN 2019
7th ECCOMAS Thematic Conference on
Computational Methods in Structural Dynamics and Earthquake Engineering
M. Papadrakakis, M. Fragiadakis (eds.)
Crete, Greece, 24-26 June 2019

ACCURATE AND EFFICIENT MODELING OF THE HYSTERETIC BEHAVIOR OF SLIDING BEARINGS

N. Vaiana, S. Sessa, M. Paradiso and L. Rosati

Department of Structures for Engineering and Architecture, University of Naples Federico II
Via Claudio, 21, 80124 Naples, Italy
e-mail: nicolovaiana@outlook.it

Keywords: Sliding Bearing, Hysteretic Behavior, Phenomenological Model.

Abstract. *This paper presents a uniaxial phenomenological model for the simulation of the hysteretic behavior typically exhibited by sliding bearings deforming along one of their transverse directions under the effect of an axial compressive load. The proposed hysteretic model is able to take into account the dependency of the device restoring force on the velocity of sliding, on the bearing pressure, and on the condition of the sliding interface. Furthermore, it allows for a considerable reduction of the computational effort of nonlinear dynamic analyses since the model hysteretic variable is evaluated by solving an algebraic equation. The numerical accuracy and computational efficiency of the proposed model are assessed by means of numerical simulations.*

1 INTRODUCTION

Base isolation represents one of the most effective techniques for the seismic protection of buildings and bridges [1, 2, 3]. Such a technique requires the use of special devices, called seismic isolation bearings, having flexibility and energy dissipation capacity along their transverse directions and a large axial stiffness [4, 5].

Seismic isolation bearings can be divided into two main categories, that is, elastomeric and sliding bearings. The latter, of particular interest in this work, are devices made up of rigid plates that can slide with respect to each other. Looking at the type of sliding surface, it is possible to distinguish between flat surface sliding bearings and curved surface sliding bearings [6].

Sliding bearings deforming along one of their transverse directions under the effect of an axial compressive load display a hysteretic behavior due to the friction occurring at the sliding interface. Experimental tests results available in the literature show that the device restoring force depends not only on the device transverse displacement but also on the device transverse velocity. In particular, the dependency of the device restoring force on the velocity of sliding is due to the variation of the kinetic friction coefficient with the sliding velocity [7, 8].

Several hysteretic models have been proposed in the literature for simulating the complex behavior occurring in sliding bearings [9]. Among existing models, the one proposed by Mokha et al. [10] seems to be the most suitable one since it allows for an accurate prediction of the hysteretic response of both flat and curved surface sliding bearings by using a relatively small number of parameters. In particular, such a model is able to take into account the dependency of the restoring force on the velocity of sliding, on the bearing pressure, and on the condition of the sliding interface. Unfortunately, this model is not computationally efficient since it requires the numerical solution of a first-order nonlinear ordinary differential equation for the evaluation of the hysteretic variable at each time step of a nonlinear dynamic analysis.

This paper presents a uniaxial phenomenological model able to predict the hysteretic behavior generally displayed by sliding bearings. Compared to the model formulated by Mokha et al. [10], the proposed one not only offers the important advantage of accurately simulating the response of such devices, but it also allows for a considerable reduction of the computational effort required by nonlinear dynamic analyses since the model hysteretic variable is evaluated by solving an algebraic equation. Furthermore, it is based on a smaller set of parameters and can be easily implemented in a computer program.

2 SLIDING BEARINGS

Sliding bearings are seismic isolation devices consisting of a slider that moves on a sliding surface. Such devices, having an axial stiffness that is very much greater than the transverse one, display an energy dissipation capacity due to the friction damping occurring at the sliding interface [4].

According to the type of sliding surface, sliding bearings can be classified into two main categories, namely, Flat Surface Sliding Bearings (FSSBs) and Curved Surface Sliding Bearings (CSSBs) [6].

In this section, the main characteristics of the two above-mentioned types of sliding bearings are illustrated with particular emphasis on the brief description of the hysteretic behavior displayed along their transverse directions under the effect of an axial compressive load.

2.1 Flat Surface Sliding Bearings

Figure 1a shows the sectional view of a typical FSSB in deformed configuration. Such a device has a slider generally made up of an upper sliding plate and a lower polished stainless steel plate. The flat sliding surface is typically overlain by unfilled or filled Polytetrafluoroethylene, referred to as PTFE or Teflon.

FSSBs deforming along one of their transverse directions under the effect an axial compressive load display both rate-dependent and rate-independent hysteretic behaviors. Indeed, experimental test results available in the literature [7, 8] show that the device restoring force f depends not only on the device transverse displacement u but also on the device transverse velocity $\dot{u}$. Figure 1b shows the typical hysteresis loop shape displayed by FSSBs.

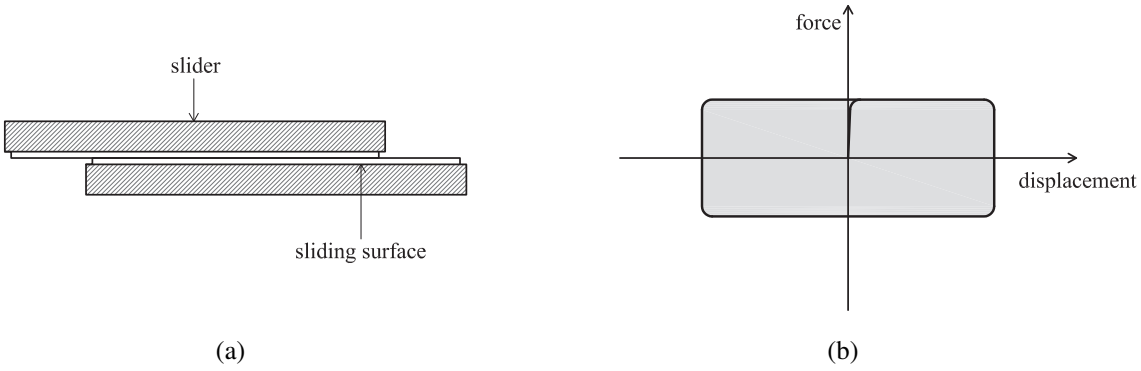

Figure 1: Typical FSSB: sectional view in deformed configuration (a) and hysteresis loop shape (b).

2.2 Curved Surface Sliding Bearings

Figure 2a shows the sectional view of a typical CSSB in deformed configuration. Such a device, denominated Friction Pendulum Bearing (FPB), has an articulated slider generally coated with a low-friction and high-pressure capacity composite material, typically PTFE. The curved sliding surface, having radius of curvature R, is generally overlain by polished stainless steel.

FPBs deforming along one of their transverse directions under the effect an axial compressive load display both rate-dependent and rate-independent hysteretic behaviors. Figure 2b shows the typical hysteresis loop shape displayed by FPBs.

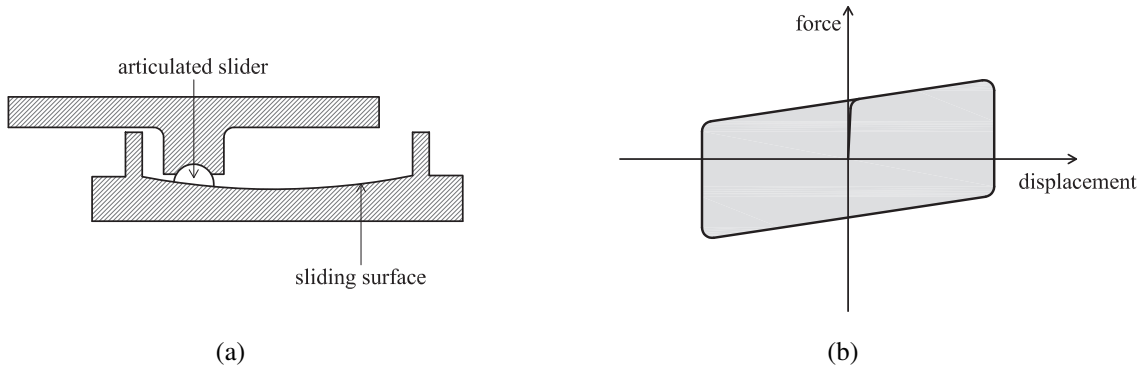

Figure 2: Typical FPB: sectional view in deformed configuration (a) and hysteresis loop shape (b).

3 PROPOSED HYSTERETIC MODEL

In this section, we first present the proposed hysteretic model formulation; subsequently, we illustrate a schematic flowchart of the model to allow for an easy computer implementation.

3.1 Model Formulation

The restoring force of a sliding bearing may be evaluated as [10]:

$$f\left(u,\dot{u}\right)=\frac{N}{R}u+\mu\left(\dot{u}\right)Nz\left(u\right), \tag{1}$$

where N is the axial compressive force acting on the bearing, R is the radius of curvature of the sliding surface, $\mu\left(\dot{u}\right)$ is the kinetic coefficient of friction, $z(u)$ is a dimensionless hysteretic variable, whereas u and $\dot{u}$ are the bearing transverse displacement and velocity, respectively.

The kinetic friction coefficient $\mu\left(\dot{u}\right)$ may be computed as [8]:

$$\mu\left(\dot{u}\right)=\mu_{max}-\left(\mu_{max}-\mu_{min}\right)e^{-a|\dot{u}|}, \tag{2}$$

where μ_{max} (μ_{min}) is the value of the kinetic friction coefficient at large (low) bearing transverse velocity, and a is a parameter, having units of time per unit length, that rules the velocity of transition of $\mu\left(\dot{u}\right)$ from μ_{min} to μ_{max}. Note that the values of μ_{max}, μ_{min}, and a depend on the bearing pressure, temperature, as well as condition of the sliding surface.

The dimensionless hysteretic variable $z(u)$ is a function of u and has a unit maximum absolute value, that is, $max\left\{|z(u)|\right\}=1$; in particular, if u cycles between two values, $z(u)$ traces a hysteresis loop bounded by two parallel horizontal straight lines.

In the model proposed by Mokha et al. [10], such a variable is evaluated by solving the following differential equation, typical of the celebrated Bouc-Wen model [11, 12]:

$$Y\dot{z}+\gamma\left|\dot{u}\right|z\left|z\right|^{n-1}+\beta\dot{u}\left|z\right|^{n}-A\dot{u}=0, \tag{3}$$

where $Y>0$ is a parameter having dimension of displacement, whereas A, β, γ, and n are dimensionless parameters. Unfortunately, the numerical solution of Equation (3) for each time step of a nonlinear dynamic analysis may significantly increase the overall computational effort.

To decrease the computational burden of the analyses without decreasing the accuracy of the numerical results, we propose to evaluate $z(u)$ by employing a specific instance of the general class of uniaxial phenomenological models formulated by Vaiana et al. [13, 14].

According to such a general formulation, a generic hysteresis loop, in the z-u plane, can be described by means of four types of curves, that is, the upper c_u and the lower c_l limiting curves and the generic loading c^+ and unloading c^- curves.

As shown in Figure 3, the upper (lower) limiting curve c_u (c_l) intercepts the vertical axis at $z=\bar{f}$ ($z=-\bar{f}$). Furthermore, the generic loading (unloading) curve has a starting point, lying on the lower (upper) limiting curve, having abscissa u_i^+ (u_i^-) and an ending point, lying on the upper (lower) limiting curve, having abscissa u_j^+ (u_j^-), with $u_i^+=u_j^+-2u_0$ ($u_i^-=u_j^-+2u_0$).

In the generic loading case, $z=c^+$ when $u_i^+\leq u<u_j^+$, and $z=c_u$ when $u>u_j^+$, whereas, in the generic unloading case, $z=c^-$ when $u_j^-<u\leq u_i^-$, and $z=c_l$ when $u<u_j^-$.

Specifically, in this work, the expressions of the upper c_u and lower c_l limiting curves are:

$$c_u=\bar{f}, \tag{4}$$

$$c_l=-\bar{f}, \tag{5}$$

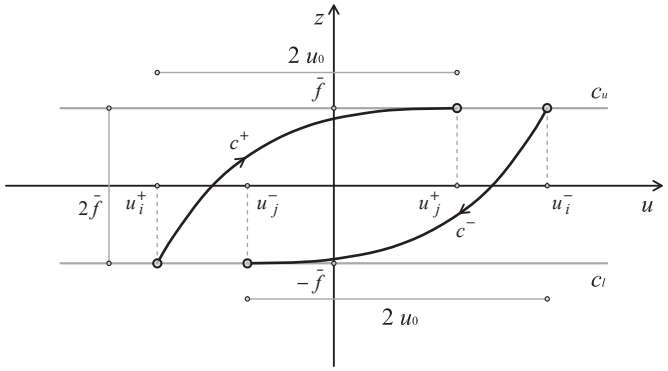

Figure 3: Curves c_u, c_l, c^+, and c^- defining the dimensionless hysteretic variable $z(u)$.

whereas, the ones of the generic loading c^+ and unloading c^- curves are:

$$c^+\left(u, u_j^+\right) = k_a \left[\frac{\left(1 + u - u_j^+ + 2u_0\right)^{(1-\alpha)}}{1-\alpha} - \frac{(1+2u_0)^{(1-\alpha)}}{1-\alpha} \right] + \bar{f}, \tag{6}$$

$$c^-\left(u, u_j^-\right) = k_a \left[\frac{\left(1 - u + u_j^- + 2u_0\right)^{(1-\alpha)}}{\alpha-1} - \frac{(1+2u_0)^{(1-\alpha)}}{\alpha-1} \right] - \bar{f}, \tag{7}$$

where k_a and α are model parameters to be calibrated from experimental tests, whereas u_0 and $\bar{f}$ are two internal model parameters that can be expressed as a function of k_a and α. In particular, $k_a > 0$, $\alpha > 0$, $\alpha \neq 1$, $u_0 > 0$, and $\bar{f} > 0$.

The internal model parameters u_0 and $\bar{f}$ can be evaluated as follows:

$$u_0 = \frac{1}{2}\left[\left(\frac{k_a}{\delta_k} \right)^{\frac{1}{\alpha}} - 1 \right], \tag{8}$$

$$\bar{f} = \frac{k_a}{2}\left[\frac{(1+2u_0)^{(1-\alpha)} - 1}{1-\alpha} \right], \tag{9}$$

where δ_k may be set equal to 10^{-20}, as explained in [13, 14].

Finally, for the generic loading case, the expression of the history variable is:

$$u_j^+ = 1 + u_P + 2u_0 - \left\{ \frac{1-\alpha}{k_a} \left[f_P - \bar{f} + k_a \frac{(1+2u_0)^{(1-\alpha)}}{1-\alpha} \right] \right\}^{\left(\frac{1}{1-\alpha}\right)}, \tag{10}$$

whereas, for the generic unloading case, it becomes:

$$u_j^- = -1 + u_P - 2u_0 + \left\{ \frac{\alpha-1}{k_a} \left[f_P + \bar{f} + k_a \frac{(1+2u_0)^{(1-\alpha)}}{\alpha-1} \right] \right\}^{\left(\frac{1}{1-\alpha}\right)}, \tag{11}$$

where (u_P,f_P) are the coordinates of the initial point P of the generic loading or unloading curve.

Note that, in order to have $max\left\{|z(u)|\right\} = 1$, the parameters k_a and α need to be selected so that Equation (9) gives a unit value of $\bar{f}$.

1. Initial settings.
1.1 Set the model parameters: N, R, μ_{max}, μ_{min}, a, k_a, and α.
1.2 Compute the internal model parameters: $u_0 = \frac{1}{2}\left[\left(\frac{k_a}{\delta_k}\right)^{\frac{1}{\alpha}} - 1\right]$ and $\bar{f} = \frac{k_a}{2}\left[\frac{(1+2u_0)^{(1-\alpha)}-1}{1-\alpha}\right]$, with $\delta_k = 10^{-20}$.
2. Calculations at each time step.
2.1 If $s_t s_{t-\Delta t} < 0$, update the history variable: $u_j = u_{t-\Delta t} + s_t\,(1+2u_0) - s_t\left\{\frac{s_t(1-\alpha)}{k_a}\left[z_{t-\Delta t} - s_t\bar{f} + k_a\frac{(1+2u_0)^{(1-\alpha)}}{s_t(1-\alpha)}\right]\right\}^{\left(\frac{1}{1-\alpha}\right)}$.
2.2 Evaluate the dimensionless hysteretic variable at time t: if $u_j s_t - 2u_0 \leq u_t s_t < u_j s_t$: $z_t = k_a\left[\frac{(1+s_t u_t - s_t u_j + 2u_0)^{(1-\alpha)}}{s_t(1-\alpha)} - \frac{(1+2u_0)^{(1-\alpha)}}{s_t(1-\alpha)}\right] + s_t\bar{f}$, otherwise: $z_t = s_t\bar{f}$.
2.3 Compute the kinetic friction coefficient at time t: $\mu_t = \mu_{max} - (\mu_{max} - \mu_{min})\,e^{-a\lvert\dot{u}_t\rvert}$.
2.4 Evaluate the restoring force of the sliding bearing at time t: $f_t = \frac{N}{R}u_t + \mu_t N z_t$.

Table 1: Proposed hysteretic model algorithm.

3.2 Computer Implementation

To allow for an easy computer implementation, Table 1 presents a schematic flowchart of the proposed hysteretic model. To this end, we suppose that a sliding bearing is subjected to a given transverse displacement history and that a displacement-driven solution scheme has been adopted. Because of these assumptions, the displacements $u_{t-\Delta t}$ and u_t, the velocities $\dot{u}_{t-\Delta t}$ and $\dot{u}_t$, as well as the restoring force $f_{t-\Delta t}$ are known over a time step Δt, and the restoring force f_t has to be evaluated.

The implementation scheme of the proposed hysteretic model, summarized in Table 1, is composed of two parts. In the first one, called *Initial settings*, the model parameters, that is, N, R, μ_{max}, μ_{min}, a, k_a, and α are assigned and the internal ones, namely, u_0 and $\bar{f}$, are evaluated. In the second one, called *Calculations at each time step*, the history variable u_j is updated if the sign of the transverse velocity at time t, that is, $s_t = sgn(\dot{u}_t)$, changes with respect to the one at time $t - \Delta t$, that is, $s_{t-\Delta t} = sgn(\dot{u}_{t-\Delta t})$; then, the dimensionless hysteretic variable z_t is computed by using the expression of the generic loading/unloading curve if $u_j s_t - 2u_0 \leq u_t s_t < u_j s_t$; otherwise, it is computed by adopting the expression of the upper/lower limiting curve. Finally, after updating the value of the kinetic friction coefficient μ_t, the restoring force of the sliding bearing f_t is evaluated.

4 VERIFICATION OF THE PROPOSED MODEL

This section presents the validation of the Proposed Hysteretic Model (PHM), described in Section 3. Specifically, numerical accuracy and computational efficiency of the proposed model are assessed by performing Nonlinear Time History Analyses (NLTHAs) on a base-isolated rigid block and comparing the results obtained by modeling the restoring force of each sliding bearing on the basis of the PHM with those obtained by using the model developed by Mokha et al. [10], given by Equations (1)-(3) and referred to as the Mokha Hysteretic Model (MHM) for simplicity.

4.1 Analyzed Mechanical System

Figure 4 illustrates the analyzed mechanical system that consists of a rigid block isolated by two FPBs placed between a shaking table and the rigid block.

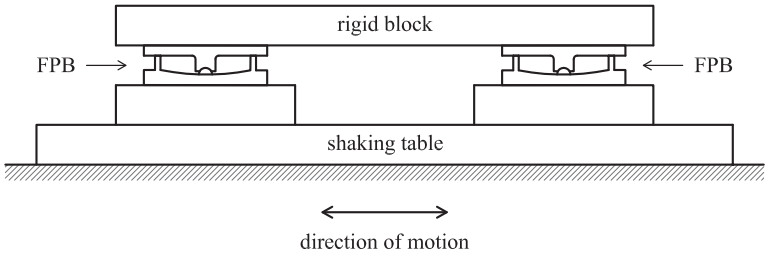

Figure 4: Mechanical system adopted for the numerical verification.

The motion of such a system is described by the following equation:

$$m\ddot{u} + 2c\dot{u} + 2f(u, \dot{u}) = p(t), \tag{12}$$

where m denotes the rigid block mass, c the viscous damping coefficient of each bearing, u, $\dot{u}$, and $\ddot{u}$ the mechanical system displacement, velocity, and acceleration relative to the ground, respectively, f the restoring force of each FPB, and p the external force depending upon time t.

If the mechanical system is subjected to an earthquake excitation, p represents the effective earthquake force, that is, a force acting opposite to the acceleration and equal to mass m times the ground acceleration $\ddot{u}_g$. Thus, Equation (12) is replaced by:

$$m\ddot{u} + 2c\dot{u} + 2f(u, \dot{u}) = -m\ddot{u}_g(t). \tag{13}$$

The rigid block has a mass of 11685.94 $\mathrm{Ns^2m^{-1}}$, whereas the two FPBs, characterized by negligible mass and viscous damping coefficient, have the same properties as the one tested by Mokha et al. [10]. Their nonlinear behavior is simulated by using the hysteretic models parameters listed in Table 2.

4.2 Applied External Forces

The nonlinear dynamic response of the mechanical system is evaluated for two different external forces, namely, a harmonic force and an earthquake force.

The harmonic force, shown in Figure 5a, is a sinusoidal force characterized by an amplitude p_0 that increases linearly with time from 0 to 10^4 N, a forcing frequency $\omega_p = 2\pi$ rad/s, and a time duration $t_d = 10$ s.

MHM	N [N]	R [m]	μ_{max}	μ_{min}	a [s/m]	Y [m]	A	β	γ	n
	57300	0.247	0.075	0.040	43.30	0.0001	1	0.1	0.9	1.1
PHM	N [N]	R [m]	μ_{max}	μ_{min}	a [s/m]	k_a [m^{-1}]	α			
	57300	0.247	0.075	0.040	43.30	15500	7750			

Table 2: Hysteretic models parameters.

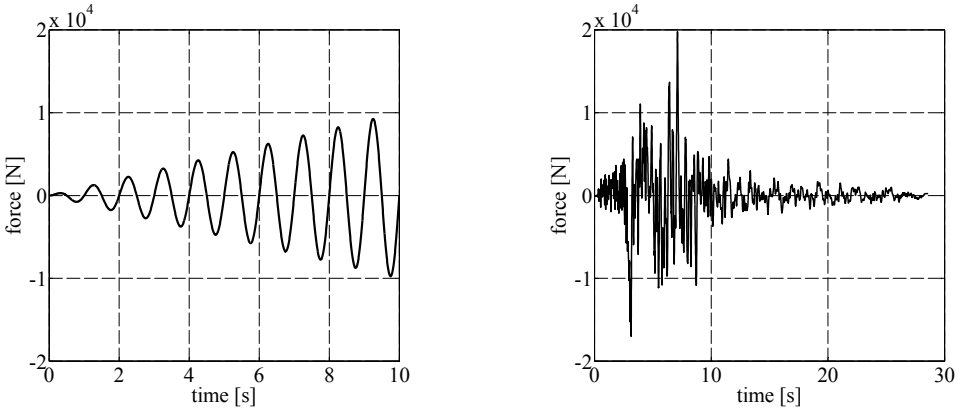

(a) (b)

Figure 5: Applied external forces: harmonic (a) and earthquake force (b).

The earthquake force, shown in Figure 5b, is evaluated by adopting the SN component of horizontal ground acceleration recorded at the Jensen Filter Plant station during the Northridge earthquake of January 17, 1994. The original ground acceleration record, having time step equal to 0.005 s, has been scaled by a factor of 1/3 in order to reach a peak mechanical system displacement, relative to the ground, that is close to the maximum displacement attained by the FPB during the experimental tests conducted by Mokha et al. [10].

4.3 Results of the Nonlinear Time History Analyses

In this subsection, the results of some numerical simulations are presented to assess the numerical accuracy and the computational efficiency of the PHM.

The equation of motion, given by Equation (12) or (13), according to the type of applied external force, has been numerically solved by employing a widely used explicit time integration method, that is, the central difference method [15, 16], and adopting a time step of 0.005 s. In addition, the first-order nonlinear ordinary differential equation characterizing the MHM has been numerically solved by adopting the unconditionally stable semi-implicit Runge-Kutta method [17] and using 50 steps. The numerical time integration algorithm as well as the hysteretic models have been implemented in MATLAB and run on a computer having an Intel®Core™i7-4700MQ processor and a CPU at 2.40 GHz with 16 GB of RAM.

Tables 3 and 4 present the NLTHAs results obtained for the harmonic and earthquake forces, respectively.

The numerical results confirm the accuracy of the PHM since the maximum and minimum

			$u\,[\mathrm{m}]$		$\dot{u}\,[\mathrm{ms}^{-1}]$		$\ddot{u}\,[\mathrm{ms}^{-2}]$	
	$tct\,[\mathrm{s}]$	$tctp$	max	min	max	min	max	min
MHM	9.55	-	0.0350	-0.0321	0.2078	-0.2255	1.4296	-1.5581
PHM	0.07	0.73%	0.0350	-0.0320	0.2077	-0.2253	1.4286	-1.5573

Table 3: NLTHAs results obtained by applying the harmonic force.

			$u\,[\mathrm{m}]$		$\dot{u}\,[\mathrm{ms}^{-1}]$		$\ddot{u}\,[\mathrm{ms}^{-2}]$	
	$tct\,[\mathrm{s}]$	$tctp$	max	min	max	min	max	min
MHM	27.00	-	0.0218	-0.0345	0.1392	-0.1406	1.6221	-1.1974
PHM	0.22	0.81%	0.0218	-0.0346	0.1391	-0.1408	1.6227	-1.1896

Table 4: NLTHAs results obtained by applying the earthquake force.

values of the relative displacement, velocity, and acceleration of the mechanical system, evaluated by employing the proposed model, are quite close to those predicted by the MHM.

Furthermore, the numerical results also show that the computational burden of the PHM, expressed by the total computational time tct, is significantly smaller than the one characterizing the MHM. Since the parameter tct depends upon the amount of the back-ground process running on the computer, the relevant memory, as well as the CPU speed, a fully objective measure of the computational benefits, associated with the use of the PHM with respect to the MHM, is obtained by normalizing such a parameter as follows:

$$\mathrm{PHM}\ tctp\ [\%] = \frac{\mathrm{PHM}\ tct}{\mathrm{MHM}\ tct} \cdot 100\ . \tag{14}$$

Figures 6, 7, and 8 illustrate, respectively, the time histories of the relative displacement, velocity, and acceleration of the mechanical system, whereas Figure 9 shows the restoring force-displacement hysteresis loops displayed by each FPB. Generally speaking, the comparison between the responses simulated with the PHM and the MHM shows a very good agreement.

5 CONCLUSIONS

We have presented a uniaxial phenomenological model able to simulate the complex hysteretic behavior typically displayed by sliding bearings deforming along one of their transverse directions under the effect of an axial compressive load.

The proposed model allows for the evaluation of the device restoring force taking into account its dependency on the sliding velocity, bearing pressure, and sliding surface conditions. Furthermore, such a model requires the solution of an algebraic equation for the evaluation of the hysteretic variable and can be easily implemented in a computer program.

The numerical accuracy and the computational efficiency of the proposed model have been assessed by performing nonlinear time history analyses on a single degree of freedom mechanical system, for two different external forces, that is, a harmonic force and an earthquake force, and comparing the results of the PHM with those associated with the MHM. Specifically, the following conclusions can be drawn:

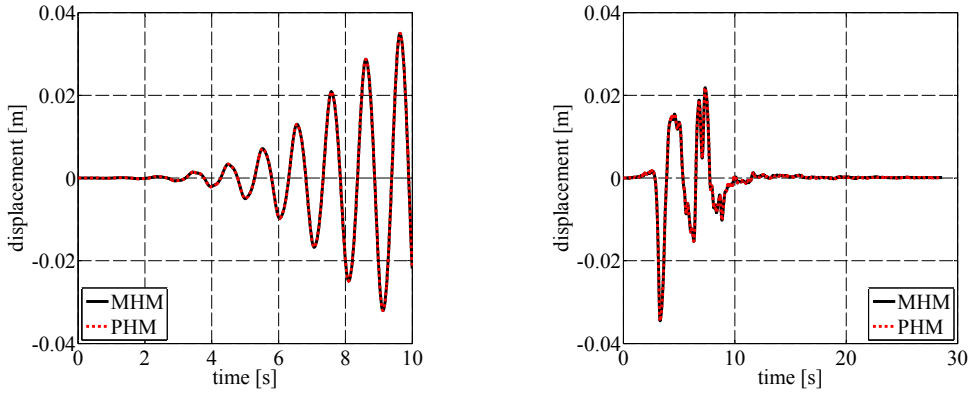

(a) (b)

Figure 6: Relative displacement time history obtained by applying the harmonic (a) and the earthquake force (b).

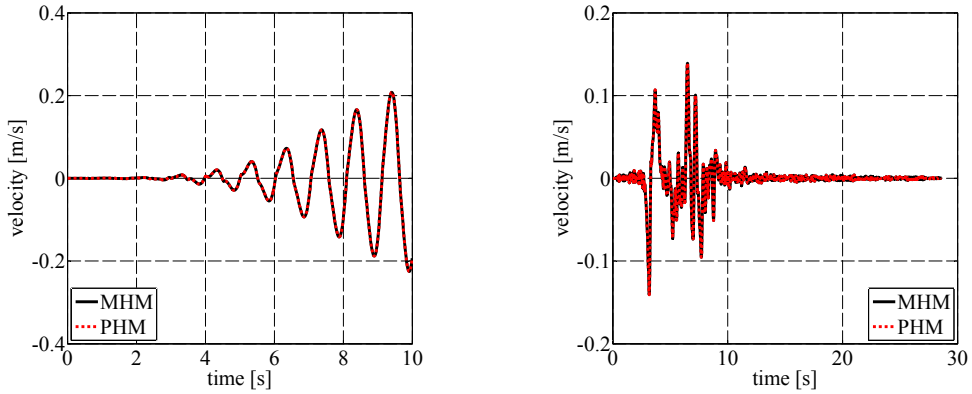

(a) (b)

Figure 7: Relative velocity time history obtained by applying the harmonic (a) and the earthquake force (b).

- the numerical results of the PHM closely match those predicted by the MHM, for both types of external force;
- the total computational time required by the PHM is equal to 0.73% (0.81%), for the harmonic (earthquake) force case, of the one associated with the MHM.

Current research is focusing on the extension of the proposed model to the two-dimensional case through the definition of an interaction domain involving restoring forces. Furthermore, in forthcoming papers, the presented model will be combined with recent strategies to address the nonlinear behavior of framed [18] or shear wall structures [19] in order to analyze base-isolated buildings by exploiting the concept of seismic response envelopes [20].

ACKNOWLEDGMENTS

The present research was supported by the Italian Government, ReLuis 2017 project [AQ DPC/ReLUIS 2014-2018, PR2, Task 2.3] and PRIN 2015 grants [2015JW9NJT-PE8, WP2, Task 2.1], which is gratefully acknowledged by the authors.

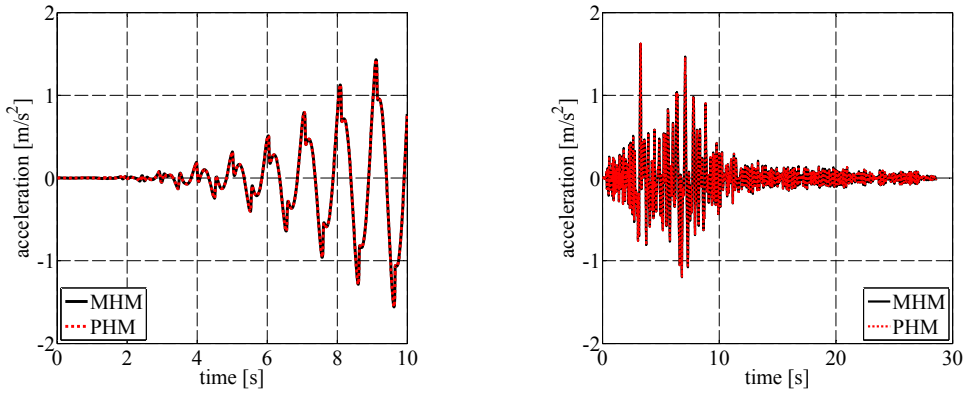

Figure 8: Relative acceleration time history obtained by applying the harmonic (a) and the earthquake force (b).

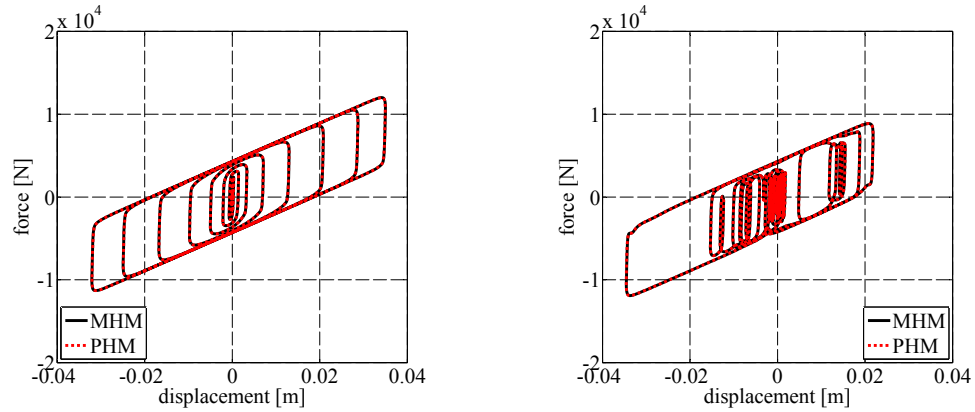

Figure 9: Hysteresis loops obtained by applying the harmonic (a) and the earthquake force (b).

REFERENCES

[1] D. Losanno, M. Spizzuoco, G. Serino, Optimal design of the seismic protection system for isolated bridges. *Earthquakes and Structures*, **7**(6), 969–999, 2014.

[2] H.A. Hadad, A. Calabrese, S. Strano, G. Serino, A base isolation system for developing countries using discarded tyres filled with elastomeric recycled materials. *Journal of Earthquake Engineering*, **21**(2), 246–266, 2017.

[3] I.E. Madera Sierra, D. Losanno, S. Strano, J. Marulanda, P. Thomson, Development and experimental behavior of HDR seismic isolators for low-rise residential buildings. *Engineering Structures*, **183**(1), 894–906, 2019.

[4] F. Naeim, J.M. Kelly, *Design of seismic isolated structures: from theory to practice*. John Wiley and Sons Inc, 1999.

[5] N. Vaiana, M. Spizzuoco, G. Serino, Wire rope isolators for seismically base-isolated lightweight structures: experimental characterization and mathematical modeling. *Engineering Structures*, **140**(1), 498–514, 2017.

[6] M.C. Constantinou, A.S. Whittaker, Y. Kalpakidis, D.M. Fenz, G.P. Warn, *Performance of seismic isolation hardware under service and seismic loading*. Report No. MCEER-07-0012, State University of New York, Buffalo, NY, USA, 2007.

[7] A. Mokha, M.C. Constantinou, A.M. Reinhorn, Teflon bearings in base isolation. I: Testing. *Journal of Structural Engineering*, **116**(2), 438–454, 1990.

[8] M.C. Constantinou, A. Mokha, A.M. Reinhorn, Teflon bearings in base isolation. II: Modeling. *Journal of Structural Engineering*, **116**(2), 455–474, 1990.

[9] P.C. Tsopelas, P.C. Roussis, M.C. Constantinou, R. Buchanan, A.M. Reinhorn, *3D-BASIS-ME-MB: Computer program for nonlinear dynamic analysis of seismically isolated structures*. Report No. MCEER-05-0009, State University of New York, Buffalo, NY, USA, 2005.

[10] A. Mokha, M.C. Constantinou, A.M. Reinhorn, V.A. Zayas, Experimental study of friction-pendulum isolation system. *Journal of Structural Engineering*, **117**(4), 1201–1217, 1991.

[11] R. Bouc, Modele mathematique d'hysteresis. *Acustica*, **24**(1), 16–25, 1971.

[12] Y.K. Wen, Method for random vibration of hysteretic systems. *Journal of the Engineering Mechanics Division*, **102**(2), 249–263, 1976.

[13] N. Vaiana, S. Sessa, F. Marmo, L. Rosati, A class of uniaxial phenomenological models for simulating hysteretic phenomena in rate-independent mechanical systems and materials. *Nonlinear Dynamics*, **93**(3), 1647–1669, 2018.

[14] N. Vaiana, S. Sessa, F. Marmo, L. Rosati, An accurate and computationally efficient uniaxial phenomenological model for steel and fiber reinforced elastomeric bearings. *Composite Structures*, **211**(1), 196–212, 2019.

[15] K-J. Bathe, *Finite element procedures*. Prentice Hall, 1996.

[16] F. Greco, R. Luciano, G. Serino, N. Vaiana, A mixed explicit-implicit time integration approach for nonlinear analysis of base-isolated structures. *Annals of Solid and Structural Mechanics*, **10**(1), 17–29, 2018.

[17] H.H. Rosenbrock, Some general implicit processes for the numerical solution of differential equations. *The Computer Journal*, **5**(4), 329–330, 1963.

[18] F. Marmo, L. Rosati, The fiber-free approach in the evaluation of the tangent stiffness matrix for elastoplastic uniaxial constitutive laws. *International Journal for Numerical Methods in Engineering*, **94**(9), 868–894, 2013.

[19] N. Valoroso, F. Marmo, S. Sessa, A novel shell element for nonlinear pushover analysis of reinforced concrete shear walls. *Bulletin of Earthquake Engineering*, **13**(8), 2367–2388, 2015.

[20] S. Sessa, F. Marmo, N. Vaiana, L. Rosati, A computational strategy for Eurocode 8 - compliant analyses of reinforced concrete structures by seismic envelopes. *Journal of Earthquake Engineering*, 1–34, 2018. https://doi.org/10.1080/13632469.2018.1551161

COMPDYN 2019
7th ECCOMAS Thematic Conference on
Computational Methods in Structural Dynamics and Earthquake Engineering
M. Papadrakakis, M. Fragiadakis (eds.)
Crete, Greece, 24–26 June 2019

ANALYTICAL VS NUMERICAL DETERMINATION OF THE AXIAL AND LATERAL STIFFNESS OF FIBER REINFORCED ISOLATORS

Daniele Losanno[1], Ingrid E. Madera Sierra[2,3], Andrea Calabrese[4], Johannio Marulanda[3] and Peter Thomson[3]

[1] Construction Technologies Institute, National Research Council of Italy, San Giuliano Milanese, Milano, Italy
e-mail: losanno@itc.cnr.it

[2] Departamento de Ingeniería Civil e Industrial, Pontificia Universidad Javeriana Cali
Calle 18 #118-200, Santiago de Cali, Colombia
e-mail: ingridm@javerianacali.edu.co

[3] Escuela de Ingeniería Civil y Geomática, Universidad del Valle
Calle 13 #100-00, Santiago de Cali, Colombia
e-mail: {johannio.marulanda, peter.thomson}@correounivalle.edu.co

[4] Department of Civil Engineering & Construction Engineering Management
California State University Long Beach, Long Beach, CA, USA
e-mail: andrea.calabrese@csulb.edu

Abstract

This paper presents the results of a numerical and experimental study aiming to define the vertical and horizontal stiffness of Fiber-Reinforced Elastomeric Isolators (FREIs). In FREIs, the conventional steel shims of laminated rubber bearings are replaced by flexible fiber reinforcements. The axial and lateral response of these bearings is influenced by the flexibility of these layers. This study describes results of an analytical model capable of providing an accurate estimation of the vertical and horizontal stiffness of the bearings under static and dynamic loads. Results of this analytical model are compared to output of finite element analysis (FEM) available in literature. The influence of the geometry of the isolator (i.e., strip and circular shape), its shape factor and type of reinforcement on the vertical and horizontal stiffness are discussed. Considerations are also given on the effects of the compressibility of the rubber on the axial and lateral response of the devices.

Keywords: FREI, Unbounded Isolators, Analytical Modeling, FEM modeling, Low cost Isolators.

1 INTRODUCTION

The fiber-reinforced elastomeric isolators (FREIs) have been developed in the last years as alternative to the conventional steel reinforced elastomeric isolators (SREIs) [1] in the attempt of reducing the weight, manufacturing time and cost of rubber based devices [2]–[4], and with this to permit their application to all type of structures, including low-cost residential buildings.The main characteristics of the FREIs are: traditional steel plates are replaced with fabric reinforcement layers of different kind [5]–[9]; and the bearings are not bonded to the structure. This latter feature together with the lack of flexural rigidity of the fiber-reinforcements allow the bearings to roll-of the supports when deformed in shear, eliminating the high tensile stresses developed in a bonded isolator when it is displaced horizontally [10], [11].
Studies have been conducted to determine the vertical and horizontal behaviour, under cyclic and monotonic loads, of FREIs based on the behaviour of the SREIs, leading to a better understanding of their performance. These investigations have considered the influence of the variation of the reinforcement and matrix materials as well as the influence of the vertical pressure by comparing experimental investigations and finite element analyses [6], [12]–[17]. However, the lack of a complete analytical solution that combines the lateral and vertical response of FREIs has limited the possibility ofpredicting their response under large levels of deformation (i.e., strain up to 100%) [16].
The aim of this paper is to compare the vertical and horizontal behavior of FREIs with different reinforcement, shape and geometry under cyclic and monotonic loads. This comparison will be based on the results of analytical model proposed by the authors in a previous investigation [18] and results of finite element analysis (FEM) available in literature [15].

2 ANALYTICAL MODEL

Based on experimental outcomes, the authors confirmed that the vertical stiffness obtained by Eq. 1 proposed by Konstantinidis and Kelly [19] can satisfactorily estimate the vertical stiffness, K_{Vd}, of FREIs :

$$K_{Vd} = \frac{E_c^f A}{H_r} \tag{1}$$

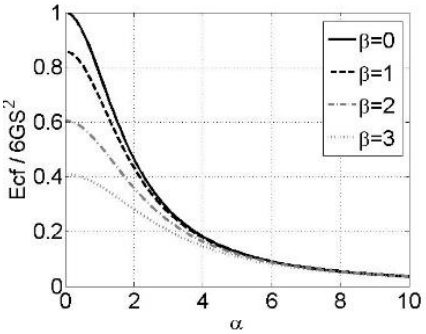

Figure 1: Dimensionless ratio of fiber-reinforced and steel-reinforced compression moduli as a function of parameter α [20].

where E_c^f is the compression modulus of the confined elastomeric compound, when fiber reinforcements are used [20]. For circular bearings, this equivalent compression modulus can be determined from Figure 1, where $\alpha^2 = 12(1-\upsilon^2)G_{20}R^2/(E_f t_f\ t_r)$ and $\beta^2 = 12G_{20}R^2/Kt_r^2$, with υ as the Poisson's ratio of the fiber, G_{20} is the shear modulus at a strain level of

20%, R is the radius of the isolator, E_f is elastic modulus of the fiber, t_f is the thickness of the fiber reinforcement and K is the bulk modulus of the rubber [18]. E_c^s is the compression modulus for steel reinforced isolators defined as $E_c^S = 6G_{20}S^2$, where the shape factor is $S = D/(4t_r)$, with D as the diameter of the device and t_r the thickness of each rubber layer.
In a previous work [18], the authors developed an accurate analytical model capable of predicting both the horizontal and the vertical stiffness of U-FREIs. The main steps required to estimate the horizontal stiffness of FRBs are summarized below. The method adopts an formulation in which the horizontal stiffness $K_H = G_{eff}\, A_{eff}/t_r$ is function of both the effective shear modulus of the rubber and the contact area of the bearings. This procedure also takes into account the axial load on the bearings. The method can be divided into four steps:

Step 1: In the first step, the effective shear modulus (G_{eff}) is obtained from the rubber characterization curve for the expected deformation levels. This curve is usually supplied by the rubber manufacturer.

Step 2: In the second step, the height of the compressed isolator (h), defined as $h = H - u_P$, is estimated analytically once a compression test on a prototype isolator has been performed. The authors derived an expression that considers the vertical displacement under the design load (u_P) as the summation of the displacement of the unconfined (u_r) and confined rubber (u_{rf}) (Eq. 2):

$$u_P = u_r + u_{rf} \tag{2}$$

The first part, u_r, is calculated as the product of the initial height H and the deformation ε at the stiffness change limit point ($u_r = H\varepsilon$). This deformation ε is obtained from the compression test results carried out on the pure rubber once the stiffness change limit point is known from the isolator under study. The second part, u_{rf}, is calculated using the expression $u_{rf} = \Delta P/K_{Vd}$, where ΔP is the maximum applied load (P) minus the load in the stiffness change limit (P_{sc}). The theoretical vertical stiffness K_{Vd} is obtained from Eq. 1. Further investigations will be devoted to studying the stiffness change point depending on the reinforcement type.

Step 3: The effective area is calculated according to the strain level. For this purpose, the Russo et al. [6] method was applied. As a result, the isolator's portion in contact with the support and subjected to pure shear (A_{eff}) will be equal to the total area (A) minus the area of the detached semicircle (A_d) (Figure 2a). In the case of circular isolator, the detached area is calculated as $A_d = R^2/2 * (\theta - sin\theta)$, with $\theta = 2\arcsin(c/2R)$ and the length $c = \sqrt{((R - s/2) * 8s)}$. The detachment point ($d_0$) and the detached portion length (s) are calculated as $d_0 = \sqrt{H^2 - h^2}$ and $s = d - d_0$, respectively. A_{eff} is calculated as in Eq. 3 based on d_0 and the displacement level (d):

$$\begin{cases} A_{eff} = A & for\ d \le d_0, \\ A_{eff} = A - A_d & for\ d > d_0 \end{cases} \tag{3}$$

In the case of rectangular or strip isolator, the effective area is equal to the product of the isolator side length in the direction perpendicular to the applied load, L, and the side length, B, minus the detached portion, s, in the direction parallel to the applied load [6] (Eq. 4, Figure 2b).

$$A_{eff} = L * (B - s) \tag{4}$$

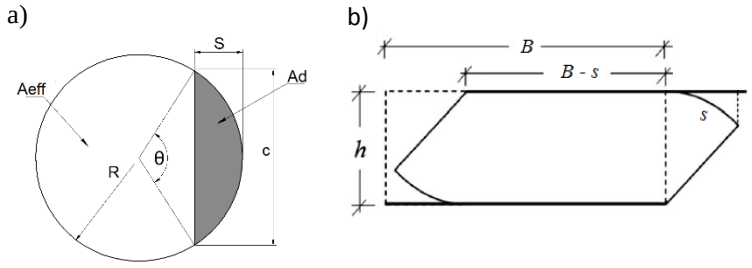

Figure 2. Effective area for isolators (A_{eff}): a) circular [18], and b) strip [12].

Step 4: In the final step, K_H is calculated at different levels with the obtained values of G_{eff} and A_{eff}. Two important aspects of this method should be highlighted. First, it is possible to assume that all the lateral surface will be in contact with the top support when $s = s_{max} = \pi H/2$. This means that the total rollover displacement is $d_{max} = d_o + s_{max}$. The method could be applied until that point with good accuracy, i.e. until the rollover is completed. Based on the proposed equations, it can be stated that isolators experiencing higher vertical displacement under the design load *P* are expected to be stiffer in the horizontal direction, because the detachment process will take longer to start, thus ensuring a full contact area.

The above mentioned formulation has been applied for a comparison to a numerical model available in literature [15].

3 NUMERICAL FINITE ELEMENT ANALYSIS

In a previous study, Kelly and Calabrese [15] studied the mechanics of FREIs comparing linear elastic theory and the outputs of finite element (FEM) analyses. The former had been previously developed by Kelly and Takirov [20] by pressure solution.

The authors of [15] developed an accurate FEM model accounting for rubber incompressibility and flexibility of the fiber layers.

The rubber is modeled by a single Mooney-Rivlin material (i.e., Neo-Hookean) with strain energy function that is the constant shear modulus $G = 0.7MPa$ and a bulk modulus $k = 2000MPa$. The reinforcement is modeled as a rebar element, i.e. a tension element of a linear elastic isotropic material with Young's modulus $E = 14.000\ Pa$ and thickness $t_f = 0{,}07mm$ (SET1) or $t_f = 0{,}25mm$ (SET2).

Two analysis cases are considered in the following for the sake of comparison:

Infinitely long strip isolator under lateral loading: different shape factors are obtained by increasing the values of the base of the device (B=250; 300; 350; 400; 450; 500 mm), to which the following shape factors correspond ($S = B/(2t_r)$; S = 19,6; 23,5; 27,5; 31,4; 35,3; 39,2 for SET1; and S = 20,3; 24,3; 28,4; 32,4; 36,5; 40,5 for SET2 by a $t_r = 6.37mm$ and $t_r = 6.17mm$ for SET1 and SET2, respectively. Each device is made of 29 fiber layers with 28 interleaf rubber sheets (

1. Figure 3). The total height of isolators is 180.4mm for SET1 and 180.0mm for SET2.

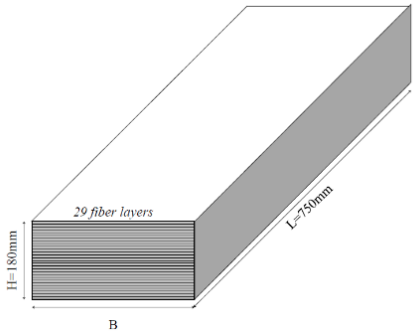

Figure 3: Strip type bearing showing reinforcements and dimensions [15].

2. Circular bearings under vertical loading: different shape factors ($S = \varphi/(4t_r)$; S = 10,1; 12,2; 14,2; 16,2; 18,2; 20,3) are obtained by increasing the values of the diameter of the device (φ =250; 300; 350; 400; 450; 500 mm). Each device is made of 29 fiber layers with 28 interleaf rubber sheets. Each rubber layer is $t_r = 5.75mm$ (Figure 4).

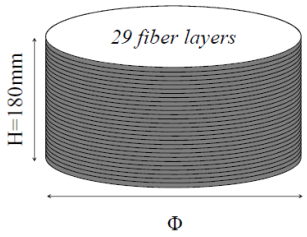

Figure 4: Circular type bearing showing reinforcements and dimensions [15].

4 COMPARISON BETWEEN MODELS

4.1 Vertical behavior

In Figure 5, the graphic comparison between the different formulations is given:

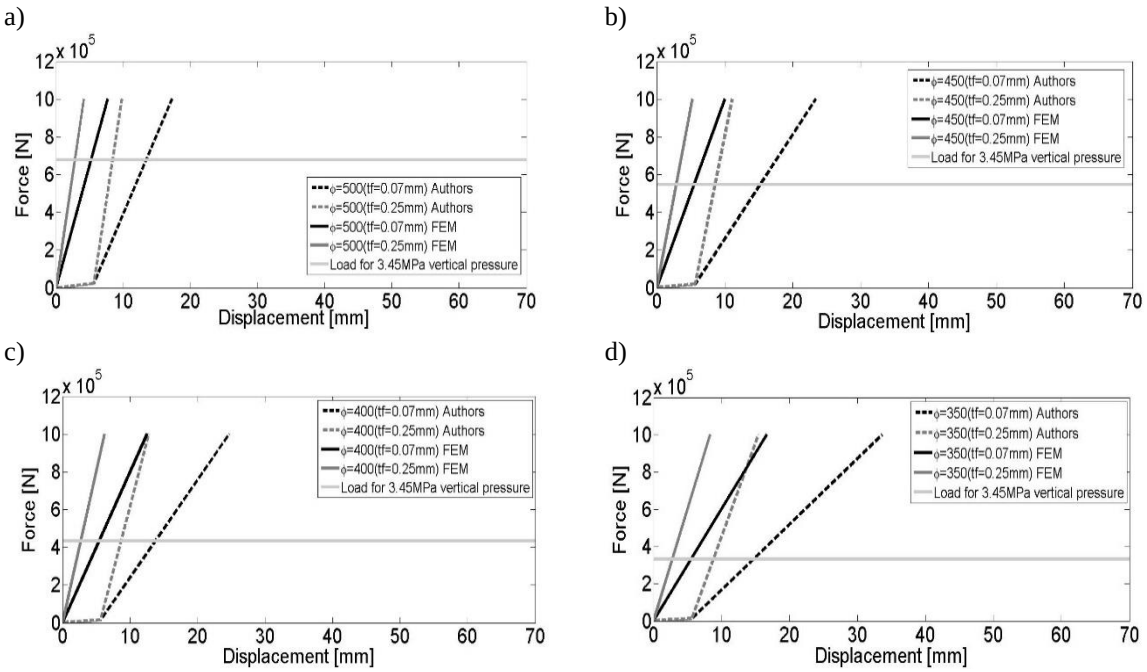

e) f)

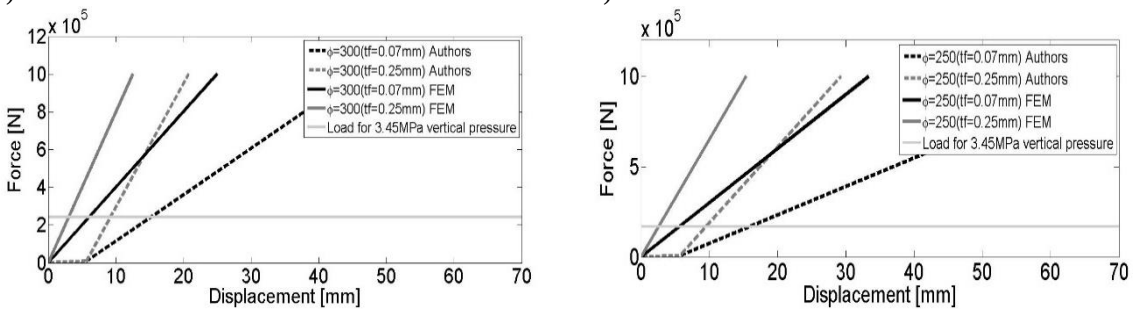

Figure 5: Vertical test results (authors vs. authors solution) for isolator with diameter of: a) 500mm, b) 450mm, c) 400mm, d) 350mm, e) 300mm, and f) 250mm.

The main difference between the models lies in the different assumption at the initial load phase. In particular, the analytical model provided a bilinear behavior in order to take into account the initial unconfined behavior with the pure rubber carrying the load (u_r). This phenomenon has been mentioned for other authors, also [6]. Once the internal fibers have been preloaded, the tangent stiffness is practically the same according to pressure solution and FEM estimate. The stiffness change limit point is calculated assuming a rubber deformation of 3,5 % according to experimental results from a previous investigation [18]. With the bilinear model, the vertical displacement under design load is approximately two times higher than with linear model. This difference also affected the estimation of the horizontal stiffness and as a result the selected design period of the structure [18]. The secant vertical stiffness at the design load of 3,45MPa has been calculated and is plotted in the following Figure 6:

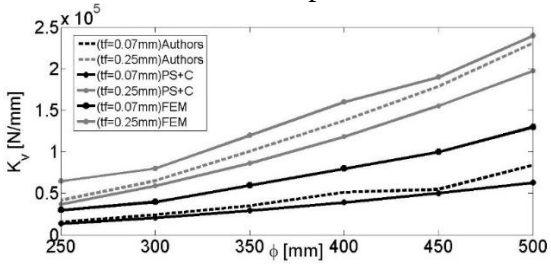

Figure 6: Secant vertical stiffness results

It can be noted that authors' formulation falls between FEM and elastic theory provision, the latter obtained according to the pressure solution also assuming compressibility of rubber (PS+C).

4.2 Horizontal behavior

In Figure 7, the graphic comparison between the authors' and FEM results is given for the strip isolators of

Figure 3:

a) b)

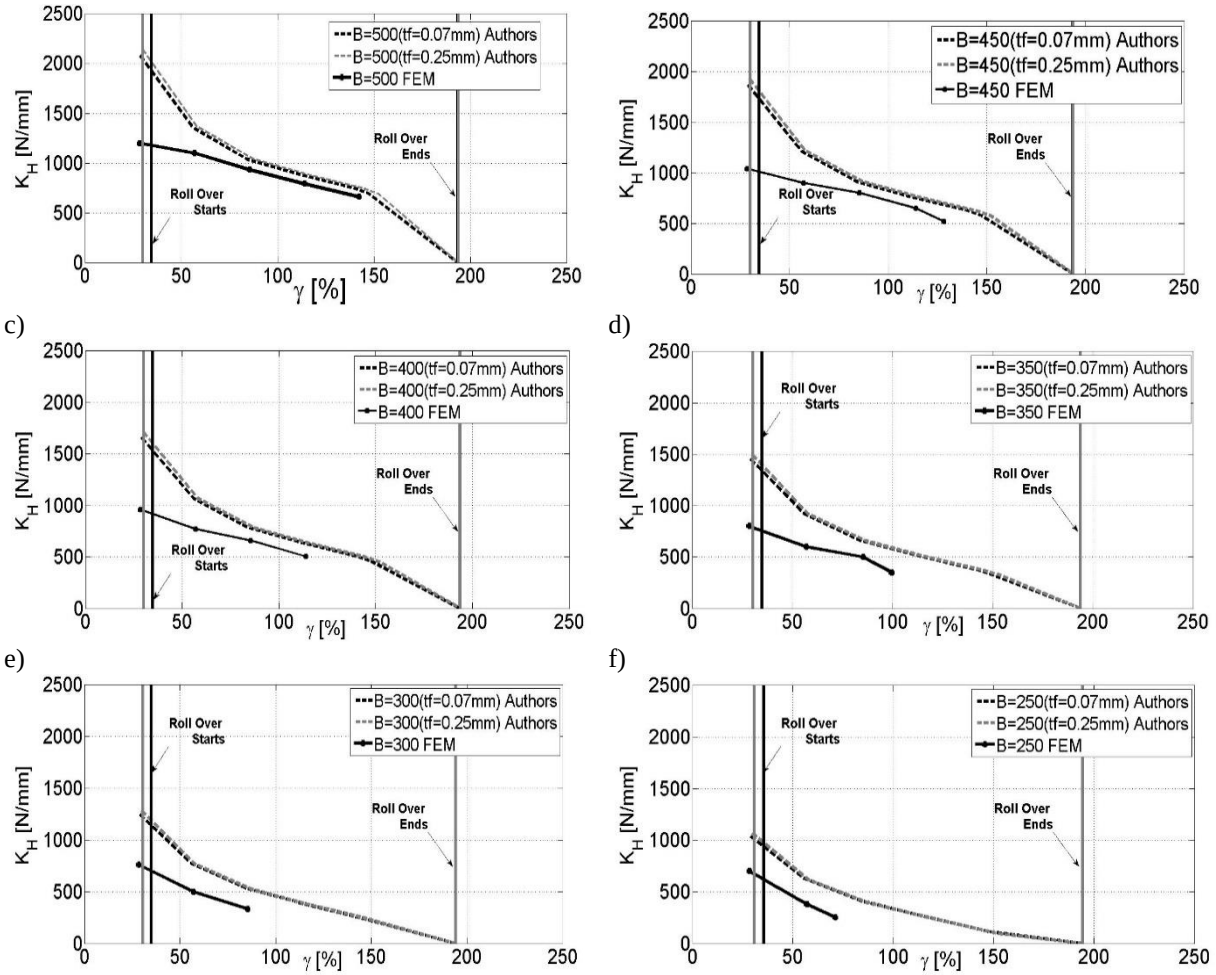

Figure 7: Horizontal stiffness vs deformation (authors vs. authors solution) for isolator with base of: a) 500mm, b) 450mm, c) 400mm, d) 350mm, e) 300mm, and f) 250mm.

It can be noted that analytical formulation provides a higher value of lateral stiffness, due to initial contribution of rubber compressibility to vertical displacement under design load. This was also confirmed by experimental observations [18], [21]. It can be noted that displacements where roll-over begins and is complete change for all geometries. This is due to the following: in order to determine the total vertical displacement (u_P), while u_r remains constant (H_r is almost constant for all prototypes), u_{rf} changes according to the characteristics of the fiber and the geometrical dimensions of the isolator. Numerical provision is only given up to a limited value of the shear strain $\gamma = B/(2H_r)$, according to stability limit found by the authors as corresponding to horizontal tangent stiffness of the force-displacement curve. As far as the influence of the fiber reinforcement is concerned, it can be said that according to analytical model, for a constant value of the total rubber height, SET1 was expected to be stiffer in the horizontal direction due to higher settlement under design load. In reality, SET 1 was lightly more flexible in horizontal direction due to lower total rubber height than SET2 thus determining a lower contribution of u_r. No difference arises in terms of FEM provision.
For the analytical model, a different value of G was assumed for each strain level, according to experimental results from a previous investigation, where a value of 0.6 MPa for large strain levels (up100%) was obtained, which is similar to the value used in the FEM analysis (0.7 MPa) [21].

5 CONCLUSIONS

The paper presented an interesting comparison between analytical formulations and numerical FEM results available from literature. The following conclusions can be drawn:

- The analytical model provided a bilinear constitutive behavior for the vertical stiffness of FREIs, considering a first part where the pure rubber is carrying the load and a second part with the fiber becoming effective in confining the rubber.
- The horizontal stiffness assessment by analytical formulation permits to account for both contact area and modulus reduction whereas FEM analysis are usually stable under particular model assumptions;
- The horizontal behavior can be investigated by analytical formulations even at larger displacements up to a complete rollover of the bearing;
- The analytical model can be applied with excellent accuracy for different geometries (square, strip or circular), materials, and dimensions of the isolators by implementing the suggested formula and steps in a simple spreadsheet.

ACKNOWLEDGEMENTS

The research of the corresponding author was funded by STAR 2017 project LO-CO-ISO from University of Naples Federico II and Foundation "Compagnia di San Paolo". This research was also financially supported by grant P44842-020-2017 from the Administrative Department of Science and Technology of Colombia COLCIENCIAS and the Universidad del Valle through Convocatoria 745-2016. The authors would like to acknowledge the scholarship for Colombian Doctoral Formation No. 617 / 2013, which was provided by COLCIENCIAS.

REFERENCES

[1] I. G. Buckle, Passive control of structures for seismic loads. *Bull. New Zeal. Soc. Earthq. Eng.*, vol. 33, no. 3, pp. 209–221, 2000.

[2] B. Y. Moon, G. J. Kang, B. S. Kang, and J. M. Kelly, Design and manufacturing of fiber reinforced elastomeric isolator for seismic isolation. *J. Mater. Process. Technol.*, vol. 130–131, pp. 145–150, 2002.

[3] J. M. Kelly and D. Konstantinidis, *Mechanics of rubber bearings for seismic and vibration isolation*. John Wiley & Sons, 2011.

[4] I. E. Madera, J. Marulanda, and P. Thomson, Matrix and reinforcement materials for low-cost building isolators: an overview of results from experimental tests and numerical simulations. *Appl. Res. Technol. J.*, vol. 16, pp. 99–111, 2018.

[5] G. J. Kang and B. S. Kang, Dynamic analysis of fiber-reinforced elastomeric isolation structures. *J. Mech. Sci. Technol.*, vol. 23, no. 4, pp. 1132–1141, 2009.

[6] G. Russo, M. Pauletta, and A. Cortesia, A study on experimental shear behavior of fiber-reinforced elastomeric isolators with various fiber layouts, elastomers and aging conditions. *Eng. Struct.*, vol. 52, pp. 422–433, 2013.

[7] A. Strauss, E. Apostolidi, T. Zimmermann, U. Gerhaher, and S. Dritsos, Experimental investigations of fiber and steel reinforced elastomeric bearings: Shear modulus and damping coefficient. *Eng. Struct.*, vol. 75, pp. 402–413, 2014.

[8] F. Hedayati Dezfuli and M. S. Alam, Performance of carbon fiber-reinforced

elastomeric isolators manufactured in a simplified process: experimental investigations. *Struct. Control Heal. Monit.*, vol. 21, no. 11, pp. 1347–1359, 2014.

[9] A. Mordini and A. Strauss, An innovative earthquake isolation system using fibre reinforced rubber bearings. *Eng. Struct.*, vol. 30, no. 10, pp. 2739–2751, 2008.

[10] H. Toopchi-Nezhad, M. J. Tait, and R. G. Drysdale, Bonded versus unbonded strip fiber reinforced elastomeric isolators: Finite element analysis. *Compos. Struct.*, vol. 93, no. 2, pp. 850–859, 2011.

[11] N. C. Van Engelen, P. M. Osgooei, M. J. Tait, and D. Konstantinidis, Partially bonded fiber-reinforced elastomeric isolators (PB-FREIs). *Struct. Control Heal. Monit.*, vol. 22, no. 3, pp. 417–432, 2015.

[12] T. Van Ngo, A. Dutta, S.K. Deb, Evaluation of horizontal stiffness of fibre-reinforced elastomeric isolators. *Earthq. Eng. Struct. Dyn.*, vol. 46, pp. 1747–1767, 2017.

[13] H. Toopchi-Nezhad, Horizontal stiffness solutions for unbonded fiber reinforced elastomeric bearings. *Struct. Eng. Mech.*, vol. 49, no. 3, pp. 395–410, 2014.

[14] U. Gerhaher, Faserverstärkte Elastomerlager – Konzeption und Bemessung. BOKU University, 2010.

[15] J. M. Kelly and A. Calabrese, PACIFIC EARTHQUAKE ENGINEERING Mechanics of Fiber Reinforced Bearings, no. February, 2012.

[16] N. Vaiana, S. Sessa, F. Marmo, L. Rosati, An accurate and computationally efficient uniaxial phenomenological model for steel and fiber reinforced elastomeric bearings. *Compos. Struct.*, vol. 211, no. 1, pp. 196–212, 2019.

[17] N. Vaiana, S. Sessa, F. Marmo, L. Rosati, A class of uniaxial phenomenological models for simulating hysteretic phenomena in rate-independent mechanical systems and materials. *Nonlinear Dynamics*, vol. 93, no. 3, pp. 1647–1669, 2018.

[18] D. Losanno, I.E. Madera Sierra, M. Spizzuoco, J. Marulanda, P. Thomson, Experimental assessment and analytical modeling of novel fiber-reinforced isolators in unbounded configuration, *Compos. Struct.*, vol. 212, pp. 66-82, 2019.

[19] D. Konstantinidis and J. M. Kelly, Advances in Low-Cost Seismic Isolation With Rubber. *Tenth U.S. Natl. Conf. Earthq. Eng. Front. Earthq. Eng.*, 2014.

[20] J. Kelly and S. Takhirov, Analytical and experimental study of fiber-reinforced bearings. *Pacific Earthq. Eng. Res. Center, Univ. California, Berkeley, CA*, vol. Rept. No., 2002.

[21] I. E. Madera Sierra, D. Losanno, S. Strano, J. Marulanda, P. Thomson, Development and experimental behavior of HDR seismic isolators for low-rise residential buildings. *Eng. Struct.*, vol. 183, pp. 894–906, 2019.

COMPDYN 2019
7th ECCOMAS Thematic Conference on
Computational Methods in Structural Dynamics and Earthquake Engineering
M. Papadrakakis, M. Fragiadakis (eds.)
Crete, Greece, 24–26 June 2019

EXPERIMENTAL BEHAVIOR OF FULL-SCALE UNBOUNDED POLYESTER-FIBER REINFORCED RUBBER ISOLATORS FOR RESIDENTIAL BUILDINGS

Ingrid E. Madera Sierra[1,2], Daniele Losanno[3], Johannio Marulanda[2] and Peter Thomson[2]

[1] Departamento de Ingeniería Civil e Industrial, Pontificia Universidad Javeriana Cali
Calle 18 #118-200, Santiago de Cali, Colombia
e-mail: ingridm@javerianacali.edu.co

[2] Escuela de Ingeniería Civil y Geomática, Universidad del Valle
Calle 13 #100-00, Santiago de Cali, Colombia
e-mail: {johannio.marulanda, peter.thomson}@correounivalle.edu.co

[3] Department of Structures for Engineering and Architecture, University of Naples Federico II
Via Claudio 21, 80125, Naples, Italy
e-mail: daniele.losanno@unina.it

Abstract

This paper presents the results of an investigation on full-scale innovative low-cost unbounded polyester-fiber reinforced high-damping elastomeric isolators (UPFREIs) to be used for seismic protection of residential buildings in Colombia, South America. In order to characterize the mechanical behavior of the UPFREIs, two full-scale prototypes were manufactured and tested at the Structures Laboratory of the Universidad del Valle. The experimental results were compared with results from the same test performed with two traditional connected steel reinforced isolators (SREIs). Both isolation systems were designed for a residential 5-story building with a target period of 2,5s located in a medium-high seismicity region. A dedicated set-up was designed and built specifically for the experimental tests. Results from shear tests up to 100% shear strain with sustained axial load exhibited very satisfactory behavior of the UPFREIs versus the SREIs with no residual deformation after unloading. An enhanced damping mechanism with damping ratio between 10 and 15 % was provided by the frictional fiber interface. Lower horizontal stiffness of the UPFREIs was obtained at higher deformation levels due to the typical rollover deformation. Despite the higher axial flexibility with respect to SREIs, UPFREIs also provided an adequate vertical to horizontal stiffness ratio. The results show that the developed UPFREIs have great potential to be implemented as a low-cost seismic isolation system of residential buildings.

Keywords: *UPFREIs, SREIs,* High Damping Rubber, Unbounded Isolators, Polyester Fiber Reinforcement, Seismic Isolation.

1 INTRODUCTION

Base isolation is a technique through which the structure is uncoupled from the ground by installing flexible bearings at the foundation's level. This reduces the potentially damaging motion that earthquakes transmit to the structure and decreases the economic and human life losses after the event [1]. The isolation system has been widely studied [2]–[5] and implemented in developed countries with more than 12000 projects [6], and its effectivity has been proved during different seismic events worldwide [7], [8]. An important number of developing countries are considered as high seismic activity regions, with the most devastating earthquake records in the last decades; however, the isolation system is rarely implemented in their infrastructure. Colombia is a distinct example of this, with seismic events like Armenia (January 1992, magnitude 6.6) earthquakes, which caused more than 2500 human losses, 6000 wounded, 43000 houses damaged and 50000 destroyed, in total. However, until 2016, only three buildings were isolated for a special use (education and health). The limited implementation is related to two main aspects. First, the most common type of isolation device is the steel-reinforced multilayer elastomeric isolator (SREI) [9], which is generally large, heavy and expensive due to the highly labor-intensive manufacturing process [10]. Second, the absence of manufacturing companies in Colombia requires the devices be imported which considerably increases the final cost of the isolator. For these reasons, their application has been only justified for large and expensive buildings, and they have not been accepted for typical residential buildings [11]. The production of low-cost seismic isolation systems, using a relatively simple manufacturing process, could encourage the applications of this type of earthquake-resistant strategy to ordinary housing and commercial low-rise buildings (three to five stories), which represent more than 80% of the constructions projects in the urban areas of the country.

Reducing an isolators' cost and weight can be achieved by replacing the traditional steel plates with fabric reinforcement [12]. This type of device is known as fiber-reinforced elastomeric isolator (FREI), which can be manufactured using conventional fiber, such as carbon (bi-directional or quadri-directional fabrics), glass or nylon [13]–[17]; and non-conventional fibers, such as carbon-fiber-reinforced plastic meshes, polyamide and engineering plastic sheets [18]–[21]. The type of connection used between the FREIs and the structure is another aspect that can be modified [22] by selecting between fully anchored (bonded condition) or unanchored (unbonded condition). In the first case, the isolator is bonded to two steel end plates that are mechanically fastened to the supports; in the second case, these plates are eliminated and the isolator is placed between the upper and lower supports with no mechanical restraints [23]. This option results in less weight, lower cost and easier installation of the isolator. Regarding the behavior, during horizontal displacements the corners of unbonded FREIs roll off the supports due to the unbonded condition and the lack of flexural rigidity of the fiber reinforcement. This eliminates the high tensile stress regions developed in a bonded isolator when it is displaced horizontally [24], [25].

The aim of this paper is to evaluate a novel unbounded polyester-fiber reinforced high-damping elastomeric isolators UP-FREIs, proposed for low-rise residential buildings, which are the most common type of projects in the principal cities of Colombia. The full-scale devices were manufactured with materials and technology commercially available in Colombia, in an unbonded condition, without lead core and with a high damping rubber (HDR) matrix. As a reinforcement material, a polyester fiber mesh was proposed and compared with the tra-

ditional SREIs. The specimens were tested under shear and compression loads applied simultaneously, to determine mechanical properties, such as stiffness and damping.

2 DESIGN AND MANUFACTURING OF THE PROTOTYPES

The prototypes were designed for a five-story structure whose dimensions are shown in Fig. *1*, and represents a typical building in the city of Santiago de Cali, Colombia. The structure has a total self-weigh of 21310kN with a natural period of 0.5s in the fixed base configuration and 2.5s in the base isolated one. The assumed location of the structure was the seismic Zone 2 of the city, which has a design acceleration of SM1=0.50g corresponding to a 950-year return period event. The prototypes were design according to FEMA450 requirements [26], adopting the formulations developed by Naeim and Kelly [27], the characteristics of the ground motion at the site and the properties of the materials used for manufacturing. The maximum design displacement (D_M = 320mm) was calculated according to the maximum acceleration at the site, assuming an equivalent damping ratio of 6%. The building is considered to be supported by 20 isolators, each one designed for an ultimate vertical load of 2000kN and a target stiffness of 681N/mm. Assuming a design shear strain of 114% and a vertical pressure of 6.8 MPa, an isolator with 277.4 mm total rubber height and 620 mm diameter is defined. According to these characteristics, the building was modelled in SAP2000 for an assessment of the expected behavior. In particular, the maximum base shear, story drift and accelerations reduce by 60 to 70% in the isolated configuration with respect to the fixed base one, thus confirming the capacity of the isolation system to reduce most relevant response parameters.

With the aim of selecting an efficient reinforcement and connection system for the isolators, from both economical and functional point of view, a different configuration was investigated using a high damping rubber compound developed by the authors [22]. Instead of the classical steel reinforcement, polyester fibers were considered. SREIs were only tested in bolted configuration in order to define a benchmark for FREIs. SREIs were not considered in unbolted configuration since this alternative is not deemed satisfactory in terms of both mechanical behaviour, due to flexural rigidity of internal steel shims, and higher cost and weight with respect to FREIs. Konstantinidis and Kelly [23] demonstrated that the usual thick and inflexible steel plates can be replaced by thin and flexible reinforcements to produce low-cost rubber isolators one order of magnitude cheaper. Considering the influence of the internal reinforcement cost (fiber layers versus steel plates) and different manufacturing process, the cost of UP-FREIs is estimated in the order of 30% less than the SREIs. Additionally, UP-FREIs have lower weight and provide additional benefits in terms of handling and installation process.

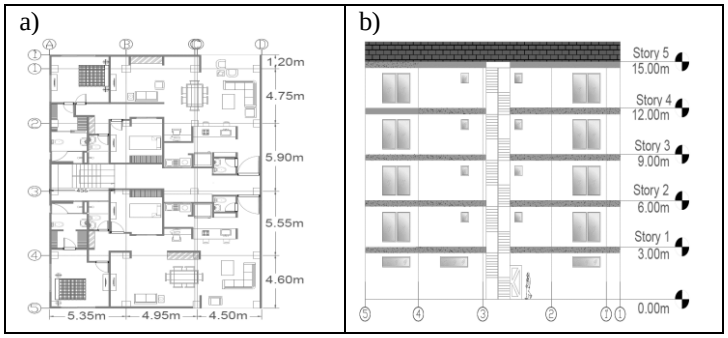

Fig. 1. Dimensions of the design structure a) plan view and b) front view.

Two different sets of isolators were manufactured with a different reinforcement and the same number of layers ($n_f = 37$): i) (SREI) type 1 (T1), 1.9mm A-36 steel plates with yield stress of 254MPa and ultimate stress of 408MPa (*Fig. 2*a); and ii) (UP-FREI) type 2 (T2), 1.1mm bidirectional polyester fiber fabric with an elastic modulus of 1.176MPa (*Fig. 2*b). For all prototypes, the same diameter (exterior $\phi_e = 620$mm and interior $\phi_i = 610$mm), rubber thickness ($t_r = 7.3$mm) and number of layers ($n_r = 38$) were assumed, with a secondary shape factor (external diameter/total rubber height) of 2.2. Steel top and bottom plates ($t_{T,B} = 25$mm) with six fixed bolts of 22mm diameter were provided for the connection system of the SREIs. In total, four specimens were tested, two for each type (Table 1).

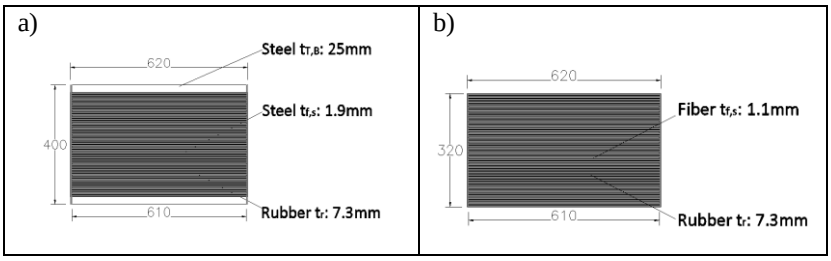

Fig. 2. Cross section of the prototypes: a) type T1, and b) type T2.

Type	Sample	Reinforcement	Connection
1	a b	Steel plates	Bolted
2	a b	Polyester fiber	Unbolted

Table 1. Types of isolators for experimental campaign.

3 SHEAR TEST SETUP AND PROTOCOL

The prototypes were tested under simultaneous shear and compression loads. In the vertical direction, a 2000kN load was used and the corresponding vertical displacement was measured. A displacement protocol, considering the testing program in FEMA450 [26], was applied horizontally, which should be carried out on the isolators prior to installation by using the design displacement as the maximum deformation (114%). The protocol was composed by three parts: part 1, consisted of three fully reversed cycles of loading at each increment of displacement ($0.25D_M$, $0.50D_M$, $0.67D_M$, $1.00D_M$); in part 2 three fully reversed cycles of loading at the maximum displacement ($1.00D_M$) were applied; in part 3 ten continuous fully reversed cycles of loading at 0.75 times the total maximum displacement ($0.75D_M$) were used (*Fig. 3*a) [26]. Due to the characteristics of the setup and the rollover process of the T2 prototypes, the third part of the protocol was applied up to $0.90D_M$ (102% strain) (*Fig. 3*b); and for both cases, according to the control system of the setup a period of $T = 100s$ was possible used. The correspondence between the percentage of D_M and γ_s is presented in Table 2.

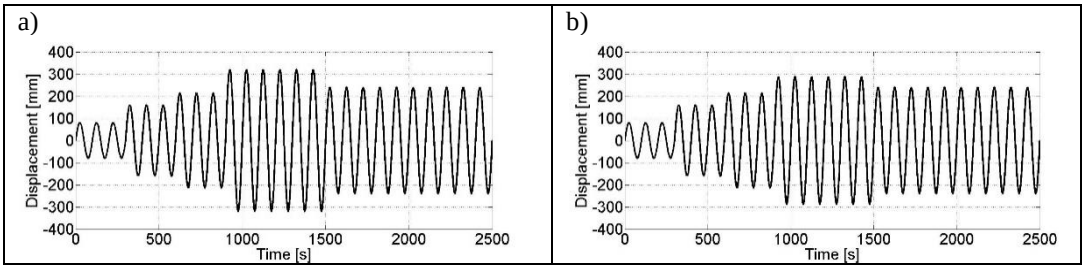

Fig. 3. Displacement protocols for the shear tests for: a) T1, and b) T2.

$\%D_M$	γ_s [%]	Displacement [mm]
0.25	29	80
0.50	57	160
0.67	77	214
0.75	86	240
0.90	105	290
1.00	114	320

Table 2. Equivalence between percentage of D_M and γ_s.

For the shear test program an experimental platform was designed and built at the Laboratorio de Pruebas para Homologaciones (MaP-H) of the Universidad del Valle. The setup was made by steel frames with a dedicated reaction framework. The setup allows to apply a total cyclic horizontal load up to 1000kN to two isolators in double shear configuration under a constant vertical load of 2000kN. The vertical load was applied through two hydraulic actuators with a capacity of 1000kN each and 100 mm stroke. For the horizontal load a hydraulic actuator with a stroke of ±500mm and a force capacity of 1000kN was used. Finally, instruments to measure the sliding guides position, the vertical load and the lateral load time-histories were employed (*Fig. 4*).

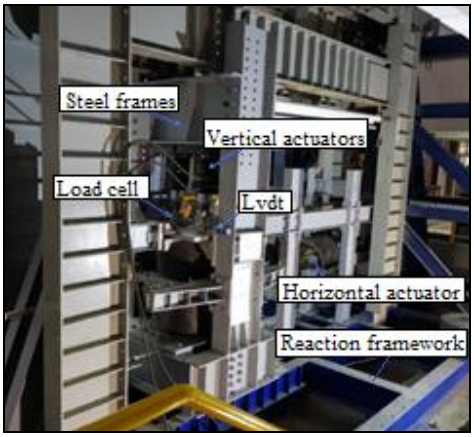

Fig. 4. Shear test setup.

4 SHEAR TESTS RESULTS

Through the shear tests, the hysteresis loops shown in *Fig. 5* were obtained. In all cases, a stiffness reduction with respect to the first cycles was observed for each deformation levels, due to the rupture of the bonds among the polymer chains and the reinforcement particles (Mullins effect) [28]. Secant stiffness and equivalent damping ratios parameters [29] were calculated for each step of the applied protocol (*Fig. 6* and *Fig. 7*). The T2 prototypes showed lower stiffness than T1 (50% less for the design level) due to the reduction of the contact area, when top and bottom faces roll off the contact supports, as a result of their unbonded conditions (rollover deformation) [14]. However, these prototypes showed a stable rollover and returned to their initial position after each test without residual deformation. Regarding the target horizontal stiffness (680N/mm), with T1 a lower period in the building will be obtained (2.3s); however, due to the minimum difference (8%), an acceptable behavior in the isolated building could be expected. Meanwhile, with T2 a period higher than the design one will be achieved (3.2s) because, for compari-

son purpose, the same dimensions of T1 was used without taking account the detachment of the area during the roll over process.

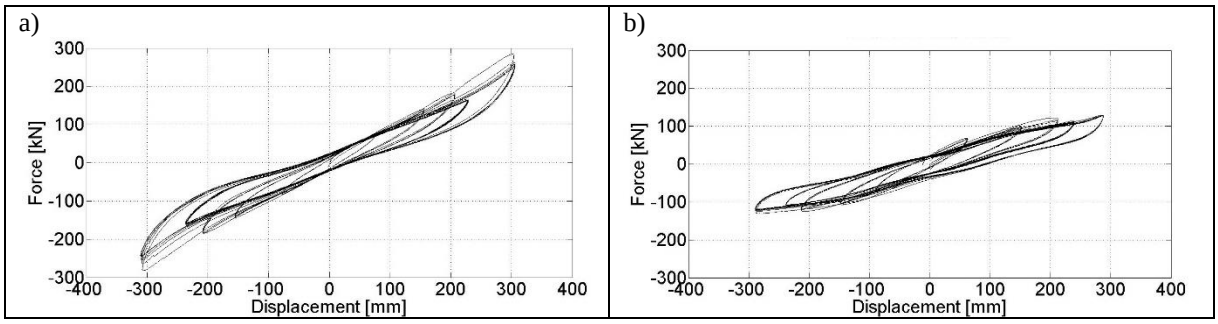

Fig. 5. Hysteresis loops isolators: a) T1, and b) T2.

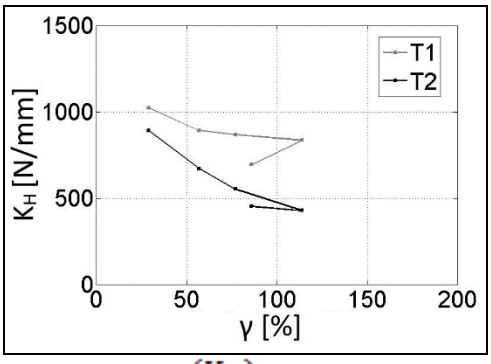

Fig. 6. Horizontal stiffness (K_H) versus shear deformation (γ_s).

As expected, in all cases the damping ratio was higher than the one obtained for the pure rubber (*Fig. 7*) [15], due to interaction with the reinforcement, being this effect more significant in prototypes T2. However, for both cases the damping ratio was higher than the required value for the design process (6%). It can be noticed that, for all deformation levels, the damping ratios of the unbonded isolators tends to be larger than those of the corresponding bolted one. Specifically, for T2 damping ratios higher than 10% were always attained, which are expected values for FREIs with high damping rubber [14]–[16], [30], [31]. Even though the secant stiffness of UP-FREIs was lower than steel reinforced one (T1) (*Fig. 6*), higher values of damping ratios can ensure a superior hysterical behavior of UP-FREIs with respect to SREIs (*Fig. 7*). With respect to the design target stiffness, UP-FREIs exhibited a 37% lower value despite to SREIs having 22% higher stiffness.

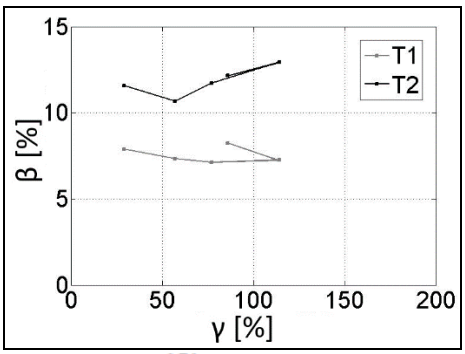

Fig. 7. Damping ratio (β) versus shear deformation (γ_s).

In T2, the flexibility of the reinforcement allowed the unbonded surfaces to roll off the loading surfaces and relieving the tensile stresses [12], achieving the design deformation without damage (*Fig. 8*b). In one of prototypes T1, the failure occurred due to the delamination of some layers. This detachment may be produced by a deficient impregnation process when the adherence material was applied to the steel plates and by the high tensile stress regions developed in this bonded device (*Fig. 8*a). In Table 3, the results for the tested deformation levels are summarized.

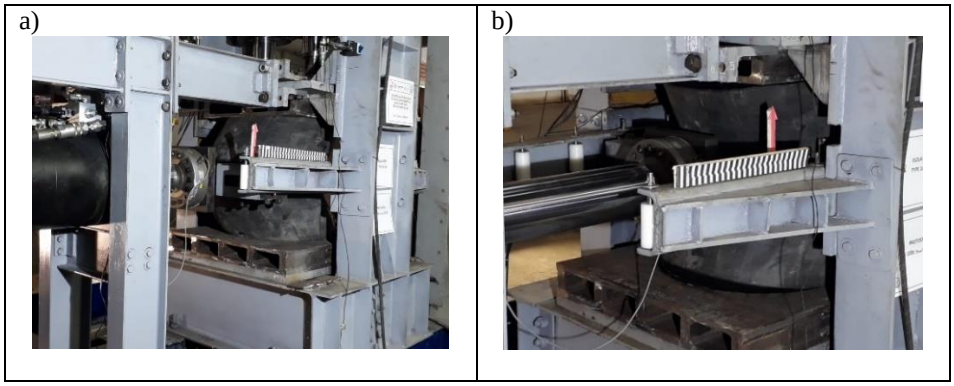

Fig. 8. Deformation of the isolators during the shear test: a) T1, and b) T2.

	γ_s=29%		γ_s=57%		γ_s=77%		γ_s=105%		γ_s=114%	
Type	K_{Hex} [N/mm]	β [%]	K_{Hex} [N/mm]	β [%]	K_{Hex} [N/mm]	β [%]	K_{Hex} [N/mm]	β [%]	K_{Hex} [N/mm]	β [%]
T1	1023	8	891	7	867	7	-	-	835	7
T2	893	12	671	11	552	12	429	13	-	-

Table 3. Isolator's properties for $\gamma_s = 29\%, 57\%, 77\%, 105\%$ and 114%.

Regarding the vertical behavior, displacements during initial axial loading were measured in order to estimate a secant vertical stiffness (K_{Vs}) of the devices (Table 4) to be compared with the horizontal one at the design displacement level. The lower vertical stiffness of FREIs compared with classical SREIs has been commonly acknowledged [23]. This aspect can be seen in Table 4, where, as expected, UP-FREIs are more flexible than SREIs in the vertical direction due to lower stiffness of fiber layers [13]. Since the horizontal to vertical stiffness ratio is one order of magnitude lower in the case of UP-FREIs, at the current state of development these isolators could be mainly devoted to low rise buildings that would produce lower settlements under self-weight. (Table 4). Results on UP-FREIs confirmed that analytical models for stiffness evaluation have to take into account both contact area and shear modulus reduction [32]. A deeper investigation is ongoing on stability issues and vertical stiffness of FREIs, as well as different fiber reinforcing layers.

Type	K_{vs} [kN/mm]	K_H [kN/mm]	K_{vs}/K_H
T1	2500	0.84	2976
T2	100	0.43	233

Table 4. Isolator's vertical stiffness and vertical and horizontal stiffness ratio.

5 CONCLUSIONS

- This paper presents a preliminary investigation of novel FREIs reinforced with polyester fiber, whose mechanical properties were obtained through a full-scale experimental program, according to the requirements of FEMA450.

- Compared to SREIs, the UP-FREIs showed a satisfactory behavior with a lower horizontal stiffness due to the rollover deformation and higher damping ratio. In order to obtain a target horizontal stiffness in unbounded applications, the variation of the contact area and the shear modulus should be considered simultaneously.

- A satisfactory behavior of UP-FREIs was obtained in the horizontal direction, thanks to lower stress at the interface between different layers, achieving the design strain without failure. They showed a positive tangent stiffness and stable roll over. Also, the UP-FREIs provided an adequate vertical to horizontal stiffness ratio, which could ensure a stable behavior of the isolators under vertical and horizontal loads.

- The results highlight an interesting comparison between UP-FREIs and SFREIs, with both satisfying required design values. Nevertheless, taking into account the fact that the price of polyester fiber is less than steel plates and that manufacturing process of the UP-FREIs is cheaper, this seems to be a very promising option, with greater potential to be implemented as a lighter and lower-cost seismic isolation system for developing countries.

ACKNOWLEDGEMENTS

This research was supported financially by grant P44842-020-2017 from the Administrative Department of Science and Technology of Colombia COLCIENCIAS and the Universidad del Valle through Convocatoria 745-2016. The authors would like to acknowledge the scholarship for Colombian Doctoral Formation No. 617 / 2013, which was provided by COLCIENCIAS.

REFERENCES

[1] B. S. Kang, G. J. Kang, and B. Y. Moon, “Hole and lead plug effect on fiber reinforced elastomeric isolator for seismic isolation,” *J. Mater. Process. Technol.*, vol. 140, no. 1–3 SPEC., pp. 592–597, 2003.

[2] D. Losanno, H. A. Hadad, and G. Serino, “Design charts for eurocode-based design of elastomeric seismic isolation systems,” *Soil Dyn. Earthq. Eng.*, no. January, pp. 1–11, 2018.

[3] D. Losanno, H. A. Hadad, and G. Serino, “Seismic behavior of isolated bridges with additional damping under far-field and near fault ground motion,” *Earthq. Struct.*, vol. 13, no. 2, pp. 119–130, 2017.

[4] D. Losanno, Daniele;Spizzuoco, Mariacristina;Serino, “Optimal design of the seismic protection system for isolated bridges,” *Earthquakes Struct.*, vol. 7, no. 6, pp. 969–999, 2014.

[5] F. Greco, R. Luciano, G. Serino, and N. Vaiana, “A mixed explicit–implicit time integration approach for nonlinear analysis of base-isolated structures,” *Ann. Solid Struct. Mech.*, 2017.

[6] W. Mason, "Seismic Isolation--The Gold Standard of Seismic Protection," *Struct. Mag*, 2015.
[7] D. Gomez, J. Marulanda, and P. Thomson, "Control systems for dynamic loading protection of civil structures," *Dyna-Colombia*, vol. 75, no. 155, pp. 77–89, 2008.
[8] M. Melkumyan, "Seismic Isolation Retrofitting Experience in Armenia and New Structural Concept for an Existing 8-Story Reinforced Concrete Hospital Building to be Retrofitted by Base Isolation," vol. 3, 2014.
[9] I. G. Buckle, "Passive control of structures for seismic loads," *Bull. New Zeal. Soc. Earthq. Eng.*, vol. 33, no. 3, pp. 209–221, 2000.
[10] B. Y. Moon, G. J. Kang, B. S. Kang, and J. M. Kelly, "Design and manufacturing of fiber reinforced elastomeric isolator for seismic isolation," *J. Mater. Process. Technol.*, vol. 130–131, pp. 145–150, 2002.
[11] B. Y. Moon, G. J. Kang, B. S. Kang, G. S. Kim, and J. M. Kelly, "Mechanical properties of seismic isolation system with fiber-reinforced bearing of strip type," *Int. Appl. Mech.*, vol. 39, no. 10, pp. 1231–1239, 2003.
[12] J. M. Kelly and D. Konstantinidis, *Mechanics of rubber bearings for seismic and vibration isolation*. John Wiley & Sons, 2011.
[13] G. J. Kang and B. S. Kang, "Dynamic analysis of fiber-reinforced elastomeric isolation structures," *J. Mech. Sci. Technol.*, vol. 23, no. 4, pp. 1132–1141, 2009.
[14] G. Russo, M. Pauletta, and A. Cortesia, "A study on experimental shear behavior of fiber-reinforced elastomeric isolators with various fiber layouts, elastomers and aging conditions," *Eng. Struct.*, vol. 52, pp. 422–433, 2013.
[15] A. Strauss, E. Apostolidi, T. Zimmermann, U. Gerhaher, and S. Dritsos, "Experimental investigations of fiber and steel reinforced elastomeric bearings: Shear modulus and damping coefficient," *Eng. Struct.*, vol. 75, pp. 402–413, 2014.
[16] F. Hedayati Dezfuli and M. S. Alam, "Performance of carbon fiber-reinforced elastomeric isolators manufactured in a simplified process: experimental investigations," *Struct. Control Heal. Monit.*, vol. 21, no. 11, pp. 1347–1359, 2014.
[17] A. Mordini and A. Strauss, "An innovative earthquake isolation system using fibre reinforced rubber bearings," *Eng. Struct.*, vol. 30, no. 10, pp. 2739–2751, 2008.
[18] A. Karimzadeh Naghshineh, U. Akyüz, and A. Caner, "Comparison of fundamental properties of new types of fiber-mesh-reinforced seismic isolators with conventional isolators," *Earthq. Eng. Struct. Dyn.*, vol. 43, no. 2, pp. 301–316, 2014.
[19] A. Bakhshi, M. H. Jafari, and V. Valadoost Tabrizi, "Study on dynamic and mechanical characteristics of carbon fiber- and polyamide fiber-reinforced seismic isolators," *Mater. Struct.*, vol. 47, no. 3, pp. 447–457, 2013.
[20] P. Tan, K. Xu, B. Wang, C. M. Chang, H. Liu, and F. L. Zhou, "Development and performance evaluation of an innovative low-cost seismic isolator," *Sci. China Technol. Sci.*, vol. 57, no. 10, pp. 2050–2061, 2014.
[21] I. E. Madera Sierra; J. Marulanda; P. Thomson, "Matrix and reinforcement materials for low-cost building isolators: an overview of results from experimental tests and numerical simulations," *Appl. Res. Technol. J.*, vol. 16, pp. 99–111, 2018.
[22] I. E. Madera Sierra; D. Losanno; M. Spizzuoco; J. Marulanda; P. Thomson, "Development and experimental behavior of HDR seismic isolators for low-rise residential buildings," *Eng. Struct. J.* vol. 183, pp. 894-906, 2018.
[23] D. Konstantinidis1 and J. M. Kelly, "Advances in Low-Cost Seismic Isolation With Rubber," *Tenth U.S. Natl. Conf. Earthq. Eng. Front. Earthq. Eng.*, 2014.
[24] H. Toopchi-Nezhad, M. J. Tait, and R. G. Drysdale, "Bonded versus unbonded strip fiber reinforced elastomeric isolators: Finite element analysis," *Compos. Struct.*, vol.

93, no. 2, pp. 850–859, 2011.
[25] N. C. Van Engelen, P. M. Osgooei, M. J. Tait, and D. Konstantinidis, "Partially bonded fiber-reinforced elastomeric isolators (PB-FREIs)," *Struct. Control Heal. Monit.*, vol. 22, no. 3, pp. 417–432, 2015.
[26] Building Seismic Safety Council (BSSC) of the National Institute of Building Sciences, "FEMA 450 Edition Recommended Provisions For Seismic Regulations For New Buildings And Other Structures P2," no. Fema 450, 2003.
[27] F. Naeim and J. M. Kelly, *Design of seismic isolated structures: from theory to practice*. John Wiley & Sons, 1999.
[28] L. Mullins, "Softening of Rubber by Deformation.," *Rubber Chem. Technol.*, vol. 42, pp. 339–362, 1969.
[29] A. K. Chopra and A. K. Chopra, *Dynamics of structures: theory and applications to earthquake engineering*, vol. 3. Pearson/Prentice Hall Upper Saddle River, NJ, 2007.
[30] R. G. Toopchi-Nezhad, H.; Tait, M.J.; Drysdale, "Shake table study on an ordinary low-rise building seismically isolated with SU-FREIs (stable unbonded-fiber reinforced elastomeric isolators)," *Earthq. Eng. Struct. Dyn.*, vol. 38, pp. 1335–1357, 2009.
[31] FIP Industriale, "FIP Industriale," 2018. [Online]. Available: https://www.fipindustriale.it/.
[32] D. Losanno; I. E. Madera Sierra; M. Spizzuoco; J. Marulanda; P. Thomson, "Experimental assessment and analytical modeling of novel fiber-reinforced isolators in unbounded configuration," *Compos. Struct.*, vol. 212, pp. 66-82, 2018.

COMPDYN 2019
7th ECCOMAS Thematic Conference on
Computational Methods in Structural Dynamics and Earthquake Engineering
M. Papadrakakis, M. Fragiadakis (eds.)
Crete, Greece, 24-–26 June 2019

ON THE USE OF META-FOUNDATIONS FOR SEISMIC ISOLATION: A PRACTICAL APPLICATION FOR CONVENTIONAL BUILDINGS

P. Martakis[1], **V. Dertimanis**[1], **E. Chatzi**[1]

[1]ETH Zurich
Stefano-Franscini-Platz 5, 8093, Zurich, Switzerland
e-mail: {martakis,v.derti,chatzi}@ibk.baug.ethz.ch

Keywords: Seismic isolation, Metamaterials, Periodic structures, local resonant foundation

Abstract. *This paper presents an attempt to evaluate the feasibility and the effectiveness of an innovative foundation, which relies on the concept of local resonance, from a practical point of view. The proposed composite foundation integrates the well-established isolation system of lead rubber bearings in a layered structure form with reinforced concrete slabs, in order to tackle the inherent drawbacks of the bearing isolation. The novel foundation concept is implemented in a realistic structural geometry, designed according to the current standards, and the seismic performance is evaluated and compared against the corresponding typical base isolated and conventional stiff designed buildings. The results show that the proposed foundation concept achieves superior seismic performance in comparison to standard base isolation, providing an applicable and cost efficient solution in the framework of metafoundations.*

1 Introduction

The often catastrophic consequences of earthquakes have stimulated research in the field of seismic isolation (SI) since more than 100 years. Many works summarize the state of the art in SI ([1], [2]). As stated by [1] "achieving the level of performance provided by seismic isolation is virtually impossible through conventional construction". From the designer's point of view, SI systems are displacement- rather than force-sensitive and better comply to displacement-based design methods as these are more physically consistent [3]. Furthermore, the nonlinear response of SI systems is concentrated in the isolator and damping devices with known force-displacement relations, thereby facilitating the realistic modelling of the behavior of the system in the nonlinear range. The idea to decouple the structure from the ground motion, though conceptually simple, fails to prevail conventional fixed-based designs in the majority of the implementations. The failure of SI to establish itself as a broadly applicable design solution stems from the inherent weaknesses of the existing seismic isolation solutions, namely the large deformations at the isolation level during ground motions and the resulting displacements. These problems are usually tackled with additional costly damping devices that, however, rarely reach an equivalent global viscous damping above 20%, setting questions on the efficiency of the displacement reduction through energy dissipation [3], [4]. Therefore, it becomes essential to further optimize the base isolation concepts, in order to extend their applicability to conventional structures.

The aforementioned limitations of typical base isolation systems led numerous researchers to the possibility of employing new anisotropic materials to develop innovative earthquake protection systems. Several studies present applications of such materials on foundations, introducing the term periodic foundations or metafoundations [5, 6]. The potential advantage of metafoundations against conventional base isolation is in reducing the large displacement demand by reflecting the incoming energy on the interfaces and/or by dissipating energy through local resonance. Since the pioneering works on phononic crystals and metamaterials [7, 8, 9], a lot of recent interesting studies in the framework of metafoundations have been published [5, 6, 10, 11, 12, 13, 14, 15, 16]. The crucial challenge is the realisation of a sufficient band gap, targeting the main frequency content of the earthquake excitation and the characteristic frequencies of the isolated structure (normally between 0.5-10 Hz), while maintaining the dimensions of the foundation in a realistic range. Dertimanis et al. [17], [18] analytically investigated the feasibility of reaching a frequency band gap focusing in the range of [0.5, 5] Hz by implementing locally resonant structures. Recently, Casablanca et al. [19] designed a composite foundation comprising four reinforced concrete slabs, each vertically disconnected from the others through a combination of steel and Teflon layers. The foundation was tested experimentally under harmonic excitation, without considering the coupling between foundation and superstructure, the effect of realistic vertical loads and the lateral stiffness against minor horizontal loads. Although recent works provide optimistic results, the proposed concepts are far from applicable to engineering practice. The disproportional large dimensions of the proposed unit cells cannot be justified even for special structures, while there are still plenty of unresolved issues, for instance the reach of an effective band gap, the transmission of the vertical loads to the ground and the reach of sufficient lateral stiffness against minor horizontal loads. To this end, a novel local resonant foundation, tailored to an example realistic structure, is designed to fulfil the codal requirements and its performance is numerically tested and compared against the current state of the art.

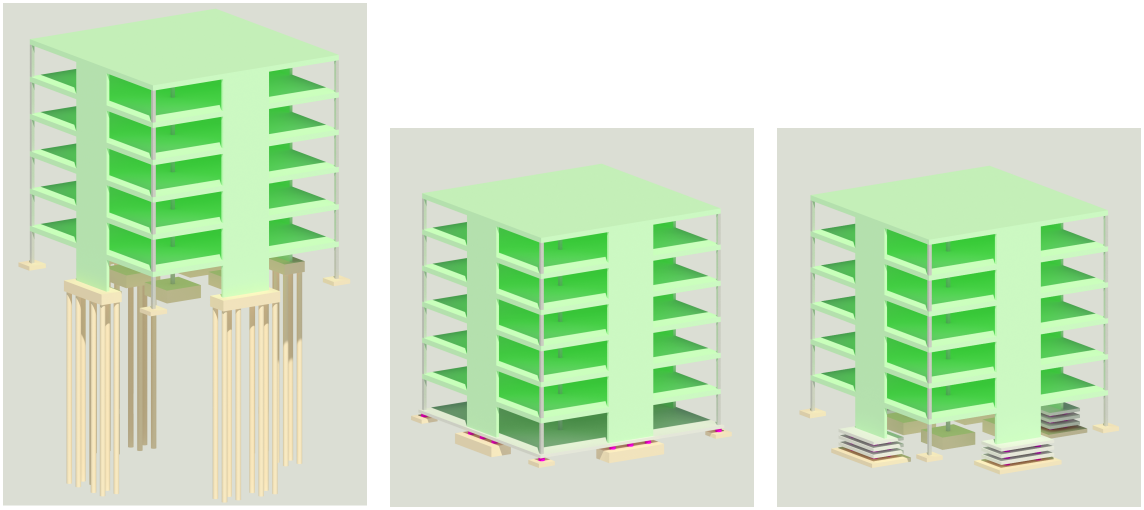

(a) Fixed base (FX) (b) Base isolation (BI) (c) Local resonance (LR)

Figure 1: Overview of the foundation concepts

2 Conceptual design of the novel foundation

In this study, we present an innovative foundation concept, namely local resonant foundation (LR), based on the combination of alternating lead rubber bearings (LRB) and reinforced concrete slabs (Figure 1c). The substantial vertical stiffness and bearing capacity pertaining to the LRBs guarantee the safe transfer of the vertical loads to the ground, while the lead core and the high damping coefficient provide increased initial stiffness and suppress the oscillations due to wind and ambient excitations. The concrete slabs provide masses that introduce additional degrees of freedom to the system in the horizontal direction. The additional modes act as a filter on the induced seismic motion through local resonance of the concrete slabs. With proper tuning, the filter range can target the frequency of the oscillating superstructure and essentially reduce the induced seismic response. In order to further optimize the foundation geometry, the metafoundation blocks are placed directly below the stiffening elements of the structure. The novel foundation concept is implemented in a realistic structural geometry and the seismic performance is evaluated and compared with the corresponding typical base isolated and conventional stiff-designed buildings (Figure 1). The performance of a proper designed local resonant foundation, tailored to the specific structure, proves to be remarkably superior and more robust in comparison to the equivalent base isolated structure, while keeping the costs in approximately the same range.

3 Application on the seismic design of a conventional building

In order to evaluate the performance of the novel foundation in a realistic framework, a simplified, though realistic, structural geometry was selected. A six-storey, shear wall building was designed according to the current standards for three different foundation cases: conventional fixed base structure (FX), base isolated structure (BI) and local resonant isolated structure (LR). An overview of the building geometry and the different foundation concepts is given in Figure 1. In order to focus on the effect of the foundation, the structural geometry is selected to be symmetric and to conform with the simplicity criteria prescribed in Eurocode 8 (EC8). The seismic design was conducted according to EC8 for a region of high seismicity (PGA = $0.36g$). The target spectrum, illustrated in Figure 2, corresponds to soil conditions C and equivalent

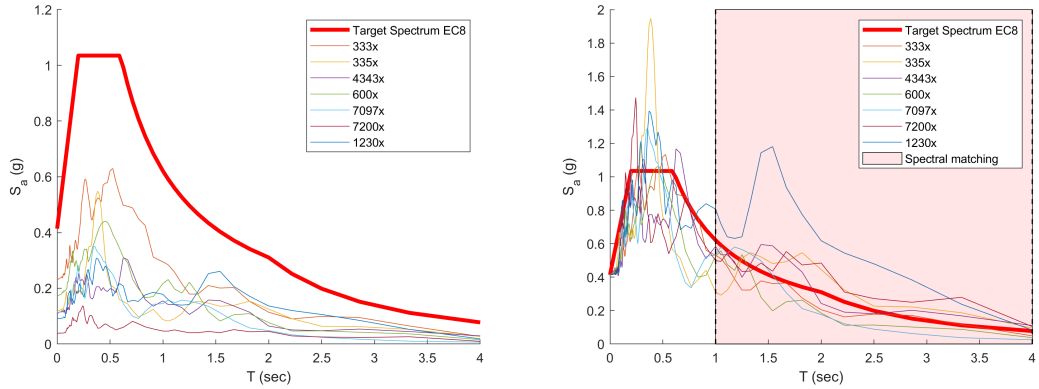

(a) Non scaled motions

(b) Scaled motions

Figure 2: Target spectrum and ground motions

Magnitude [R]	Epicentric distance [km]	Soil class (EC8)
$6-9$	$20-100$	C

Table 1: Preliminary criteria for the selection of ground motions

viscous damping $\zeta = 5\%$. The vertical loads were considered based on realistic assumptions from the practice: dead load $4\ \frac{kN}{m^2}$ and live load $3\ \frac{kN}{m^2}$.

Waveform ID	Station ID	Earthquake name	Date	Scale factor (x/y)
4343	ST2574	Izmit	1999	3.77/3.63
0600	ST223	Umbria Marche	1997	2.41/3.90
7200	ST184	Avej	2002	10.71/5.59
0333	ST121	Alkion	1981	1.80/1.34
7097	ST856	Ishakli	2002	3.67/4.45
0335	ST121	Alkion	1981	3.55/3.45
1230	ST576	Izmit	1999	4.52/3.21

Table 2: Selected ground motions

For the comparison of the different foundation configurations nonlinear time-history analyses were conducted. A group of seven ground motion records, combatable with preliminary criteria summarized in Table 1, was selected from the European Strong-motion Database (ESD). Both horizontal components of each record were simultaneously applied on the 3D numerical models, according to EC8. The selected ground motions were properly scaled to match the target spectrum. The selection and scaling of the ground motions was conducted with the software packet REXEL [21]. Information regarding the selected ground motions are summarized in Table 2, while the corresponding frequency spectra are depicted in Figure 2.

The conventional fixed-base design yields tension forces on the foundation level due to the high bending moment. A pile foundation is designed in order to transfer these forces to the ground. It is well understood that in order to eliminate or reduce the tension forces, it could be possible to optimize the dimensions of the shear walls. For comparison reasons, however,

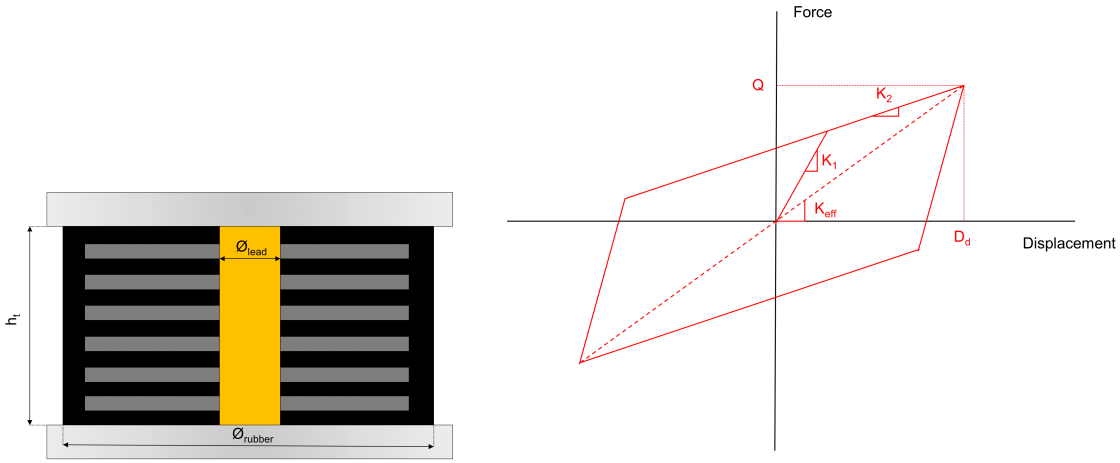

(a) schematic cross-section (b) bilinear modelling of LRBs

Figure 3: Lead rubber bearings

the structural system is considered identical for all different foundation cases. The BI case was designed based on the current standards. The nonlinear modelling of the isolators is based on the bilinear approximation, as suggested by [20] (Figure 3). The properties of the isolators are summarized in the Tables 3 and 4. A total of 28 isolators was implemented for the design of the base isolated building (Figure 1b).

$\varnothing_{rubber}$ [mm]	$\varnothing_{lead}$ [mm]	h_{total} [mm]	h_{rubber} [mm]
600	150	350	176

Table 3: Geometry of the lead rubber bearings

G [kPa]	D_d [mm]	K_{eff} [kN/m]	K_2 [kN/m]	K_1/K_2 [-]	Q [kN]
600	206	964	729	10	48

Table 4: Material and structural properties of the lead rubber bearings

The LR foundation is designed to support the vertical loads according to the current standards. The performance against horizontal excitation is studied through nonlinear time-history analysis. To further optimize the material and the geometry, the novel foundation is designed for placement directly beneath the stiff elements of the structure. In the present case, the shear walls form the horizontal resisting system that transfers the seismic energy to the upper floors. The columns are supported directly to the ground with pinned joints, in order to allow for minor displacements and rotations due to horizontal loads. For a direct comparison, the same isolator configurations, as for the BI case, were used for the design of the LR foundation. For the proposed configuration a total amount of 48 isolators was implemented. The novel foundation concept is presented in Figure 1c.

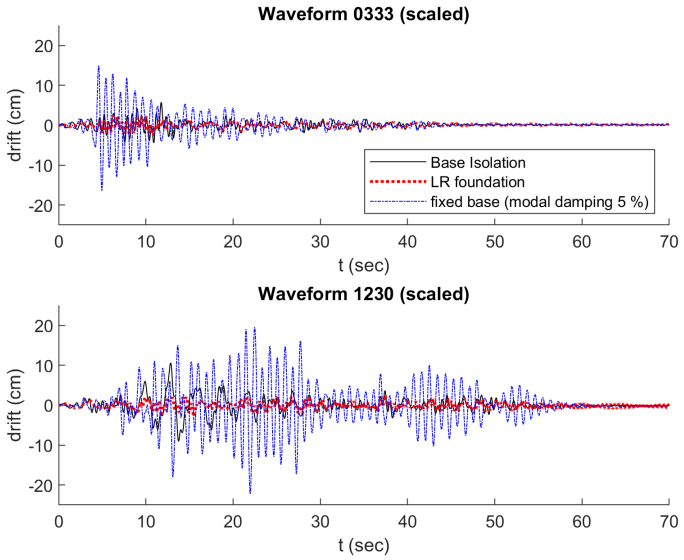

Figure 4: Top - bottom drift

Waveform ID	FX	BI	LR
0333	16.4	5.8	2.6
1230	22.2	10.6	2.8

Table 5: Maximum top-bottom drift [cm]

4 RESULTS

4.1 Modal characteristics

This section overviews the dominant modal shapes that primarily contribute to the response of each system. The fundamental period of the fixed-base structure (FX) is 0.88 sec and corresponds to the bending mode of the building. The BI structure initially responds as a rigid body, with a fundamental period of 2.67 sec. The second characteristic period is equal to 0.56 sec and refers to the bending mode of the building. The LR foundation system also mainly responds as a rigid body with a period of 5.65 sec. The second modal shape describes the rotation around the central vertical axis of the building (1.18 sec). In the third mode (0.53 sec) the bending response of the building is activated. Finally, the fourth mode describes the local resonance of the foundation layers (0.4 sec). It is important to mention that the local-resonance mode is tuned to result close to the characteristic mode that expresses the bending response of the building. As a result, the seismic energy in this frequency range is significantly dissipated already at the level of the foundation, before reaching the structure, leading to a remarkable reduction of the internal demand (Figure 4).

4.2 Displacement response

This section discusses the response of the systems, in terms of displacements. For reasons of clarity, only the results of two representative time history analyses are examined. The Waveform 0333 is requires the lowest scale factor to match the target spectrum, providing more realistic results, while the Waveform 1230 comprises a broad frequency content in the vicinity of the

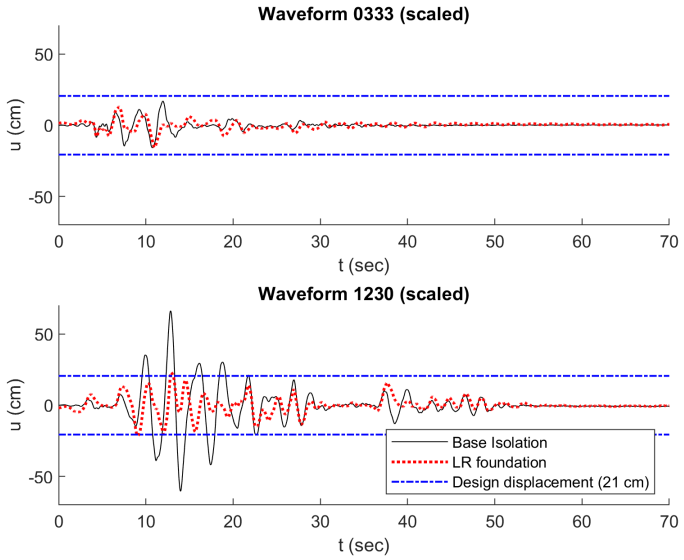

Figure 5: Bottom displacements

Waveform ID	BI	LR
0333	17	16.6
1230	66.2	24.2

Table 6: Maximum bottom displacements [cm]

structural bending mode (Figure 2b). Considering that the structural stiffness is uniformly distributed both in plane and in height, the top-bottom drift comprises a reliable indicator of the structural demand. Figure 4 contrasts the top-bottom drift response of the three different systems. The absolute maximum drift-displacements are summarized in Table 5. As it would be expected, the BI structure yields $50-65\%$ reduced drift-displacements in comparison to the fixed-base structure. The LR foundation provides a further reduction of 74% in comparison to the drift of the BI structure. In other words, the LR foundation reduces the elastic structural demand up to 85% compared to the FX structure.

In order to obtain an overview of the global response of the novel foundation, it is of interest to examine the base displacements of the two isolated systems. Figure 5 illustrates the base displacements due to the examined ground motions. The absolute maximum base displacements are summarized in Table 6. For the waveform 0333 both systems yield displacements of approximately similar amplitude, lower than the design displacement of the LRBs (20.6 cm). For Waveform 1230, however, the BI structure yields displacements up to 66 cm corresponding to more than three times the design displacement of the isolators. For a regular BI design this would require the application of external dampers to the system, in order to reduce the displacements to the acceptable range. For the same excitation, the LR foundation experiences displacements in the range of the design displacement, 63% lower than the BI system. Overall, the performance of the LR foundation proves to be superior to the performance of regular base isolation. By filtering out the frequency content in the vicinity of the structural bending mode, the LR foundation manages to reduce the structural demand without compromising the stability of the structure.

4.3 Cost considerations

Taking into account the applicability and the cost efficiency of an engineering solution is crucial even at the very beginning of the conceptual design. For this reason, the proposed novel foundation concept is designed according to the current standards, while the structural details are formed as simple as possible. Since the LR foundation is actually a composite structure, consisting of precast concrete slabs and LRBs, the application should not remarkably affect the overall costs. Considering that the LR foundations are placed locally beneath the structural walls, the extent of the application is limited, compared to base isolation, which extends to the whole ground floor area. According to the actual market prices, the designed isolators would cost ca. $5'000$ Euro/piece. The BI was designed with a total amount of 28 LRBs, while for the LR foundation the amount of the isolators increases to 48. This translates to an additional investment of approximate $100'000$ Euro for this specific example. According to the analyses, the BI system requires additional damping units to provide acceptable performance, the application and the material costs of which are expected to exceed this amount. Finally, regarding the FX structure, the installation and application costs for a pile foundation is certainly the most expensive solution. One should also consider the additional time for the necessary installations and the execution of the pile driving. Once again it is mentioned that in such a case it would be more reasonable to adjust the structural system in order to reduce or even eliminate the need for a pile foundation. For comparison reasons, however, the structural system is here considered the same for all foundation concepts.

5 CONCLUSIONS

The application of metamaterials for the development of a new generation of seismic isolation is currently a very attractive field for interdisciplinary research. Scientists combine knowledge from different domains in order to build a new line of defence against the destructive force of earthquakes. So far, however, no practical configurations, of reasonable dimensions, that could provide desirable performance against vertical and horizontal loads exist. In the present study, a novel foundation concept, consisting of LRBs and precast concrete slabs is designed to fulfill the normative requirements for the support of vertical and minor horizontal loads. The seismic performance proves to be remarkably superior to the equivalent base-isolated and fixed-base structures, for an example realistic geometry of a conventional building. The promising results of this preliminary study set the basis for the further investigation on the use of composite local resonant foundations to filter out the seismic energy content in the frequencies of interest.

REFERENCES

[1] Farzad Naeim. *Seismic Design Handbook*. 1989.

[2] JM Kelly and D Konstantinidis. *Mechanics of rubber bearings for seismic and vibration isolation*. 2011.

[3] M. J.Nigel Priestley, Gian Michele Calvi, and Mervyn J. Kowalsky. *Displacement Based Seismic Design of Structures*. 2007.

[4] Costas Providakis. Effect of supplemental damping on LRB and FPS seismic isolators under near-fault ground motions. *Soil Dynamics and Earthquake Engineering - SOIL DYNAM EARTHQUAKE ENG*, 29:80–90, jan 2009.

[5] Antonio Palermo, Sebastian Krödel, Kathryn H. Matlack, Rachele Zaccherini, Vasilis K. Dertimanis, Eleni N. Chatzi, Alessandro Marzani, and Chiara Daraio. Hybridization of Guided Surface Acoustic Modes in Unconsolidated Granular Media by a Resonant Metasurface. *Physical Review Applied*, 9(5):54026, 2018.

[6] R. Zaccherini, V.K. Dertimanis, A. Palermo, S. Krödel, A. Marzani, C. Daraio, and Eleni N. Chatzi. Resonant Metabarriers as Seismic Attenuators in Granular Media. In *ISMA2018 conference on Noise and Vibration Engineering*, Leuven, 2018.

[7] Michael Sigalas and Eleftherios Economou. Band structure of elastic waves in two dimensional systems. *Solid State Communications*, 86(3):141–143, 1993.

[8] M. S. Kushwaha, P. Halevi, G. Martínez, L. Dobrzynski, and B. Djafari-Rouhani. Theory of acoustic band structure of periodic elastic composites. *Physical Review B*, 49(4):2313–2322, jan 1994.

[9] Liu, Zhang, Mao, Zhu, Yang, Chan, and Sheng. Locally resonant sonic materials. *Science (New York, N.Y.)*, 289(5485):1734–6, sep 2000.

[10] H. J. Xiang, Z. F. Shi, S. J. Wang, and Y. L. Mo. Periodic materials-based vibration attenuation in layered foundations: Experimental validation. *Smart Materials and Structures*, 21(11), 2012.

[11] Zhifei Shi, Zhibao Cheng, and Hongjun Xiang. Seismic isolation foundations with effective attenuation zones. *Soil Dynamics and Earthquake Engineering*, 57(5-12):143–151, feb 2014.

[12] Vincenzo La Salandra, Moritz Wenzel, Oreste S. Bursi, Giorgio Carta, and Alexander B. Movchan. Conception of a 3D Metamaterial-Based Foundation for Static and Seismic Protection of Fuel Storage Tanks. *Frontiers in Materials*, 4(October):1–13, 2017.

[13] Francesco Basone, Moritz Wenzel, Oreste S. Bursi, and Marinella Fossetti. Finite locally resonant Metafoundations for the seismic protection of fuel storage tanks. *Earthquake Engineering and Structural Dynamics*, (October):1–21, 2018.

[14] Z. B. Cheng and Z. F. Shi. Composite periodic foundation and its application for seismic isolation. *Earthquake Engineering and Structural Dynamics*, 47(4):925–944, 2018.

[15] Elena Gabbianelli. *Layered Periodic Metafoundations for Seismic Isolation*. PhD thesis, Università di Bologna, 2017.

[16] Giulia Agguzi. *Investigation of layered metafoundations for seismic waves attenuation*. PhD thesis, Università di Bologna, 2017.

[17] Vasilis K Dertimanis and Ioannis A Antoniadis. Feasibility Analysis on the Attenuation of Strong Ground Motions Using Finite Periodic Lattices of Mass – in – Mass Barriers. *Journal of Engineering Mechanics*, 142(9):1–10, 2015.

[18] Paul Remo Wagner, Vasilis K. Dertimanis, Ioannis A. Antoniadis, and Eleni Chatzi. On the feasibility of structural metamaterials for seismic-induced vibration mitigation. *International Journal of Earthquake and Impact Engineering*, 1(1/2):20–56, 2016.

[19] O. Casablanca, G. Ventura, F. Garescì, B. Azzerboni, B. Chiaia, M. Chiappini, and G. Finocchio. Seismic isolation of buildings using composite foundations based on metamaterials. *Journal of Applied Physics*, 123(17), 2018.

[20] Farzad Naeim and James M. Kelly. *Design of Seismic Isolated Structures*. 1999.

[21] Iunio Iervolino, Carmine Galasso, and Edoardo Cosenza. REXEL: Computer aided record selection for code-based seismic structural analysis. *Bulletin of Earthquake Engineering*, 8(2):339–362, 2010.

COMPDYN 2019
7th ECCOMAS Thematic Conference on
Computational Methods in Structural Dynamics and Earthquake Engineering
M. Papadrakakis, M. Fragiadakis (eds.)
Crete, Greece, 24–26 June 2019

NUMERICAL OPTIMIZATION OF SEISMIC PERFORMANCE OF TALL AND SLENDER SYSTEM PROTECTED BY SEISMIC PROTECTION DEVICE

Shakhzod Takhirov[1], Hiroko Kuse[2], Keiko Yoshida[3], Seiichi Murase[4] and Eric Fujisaki[5]

[1] Civil and Environmental Engineering Department, University of California at Berkeley; 337 Davis Hall, UC Berkeley, Berkeley, California, 94720, USA; e-mail: takhirov@berkeley.edu

[2] Transmission & Distribution Systems Center, Mitsubishi Electric Corporation, Japan; email: Kuse.Hiroko@dp.MitsubishiElectric.co.jp

[3] Transmission & Distribution Systems Center, Mitsubishi Electric Corporation, Japan; email: Yoshida.Keiko@dw.MitsubishiElectric.co.jp

[4] Transmission & Distribution Systems Center, Mitsubishi Electric Corporation, Japan; e-mail: smurasehome@ybb.ne.jp

[5] InfraTerra, Inc., 5 Third Street, San Francisco, CA 94103, USA; e-mail: e.fujisaki.01@gmail.com

Abstract

High-voltage equipment representing a tall and slender system is quite common. Capacitor racks and valve towers are common examples of such equipment. A representative example of such equipment is analyzed in this paper. Due to electrical isolation purposes, this type of equipment is usually comprised of brittle porcelain insulators or polymer insulators with low damping. The insulators are used as columns, main load carrying elements. The system is relatively tall and slender. Because of the large masses installed at various elevations of the system and the narrow footprint in one of the horizontal directions, the system has a relatively low resonant frequency. Seismic protection of such systems with a potentially large overturning moment and low resonant frequency is quite challenging. For example, a regular seismic isolation has limited use. To improve the seismic performance of the system, friction dampers are introduced into the system. The friction dampers are studied extensively in full-scale component tests, as it is required by the current draft of the IEEE693 document. The results of component tests are used in the development of a numerical finite element model, which is subjected to an IEEE693-spectrum compatible strong motion to evaluate the seismic performance of the seismically protected system.

Keywords: Seismic Qualification Testing, IEEE693, Nonlinear Time History Analysis, SAP2000, Nastran, Friction Damper, Seismic Protection, Component Testing.

1 INTRODUCTION

High-voltage equipment representing a tall and slender system is quite common. Capacitor racks and valve towers are common examples of such equipment. A representative example of such equipment is analyzed in this paper. Due to electrical isolation purposes, this type of equipment is usually comprised of brittle porcelain insulators or polymer insulators with low damping. The insulators are used as columns, main load carrying elements. The fully assembled system is relatively tall and slender. Because of the large masses installed at various elevations of the system and the narrow footprint in one of the horizontal directions, the system has a relatively low resonant frequency. Seismic protection of such systems with a potentially large overturning moment and low resonant frequency is quite challenging. For example, a regular seismic isolation has limited use. To improve the seismic performance of the system, friction dampers are introduced into the system at its base. Performances of fixed base and isolated base equipment are discussed in this paper.

2 ELASTIC FINITE ELEMENT MODEL OF UNPROTECTED EQUIPMENT

A detailed finite element model of the equipment was generated in Nastran [1] as presented in the left image of Figure 1. It represented a five-story structure without any bracing system. The footprint of the system is very narrow in the Y direction of the global coordinate system. The shelving system is loaded with concentrated masses as presented in the left image of Figure 1. To increase the capacity in the Y direction, five insulators are installed in each row along the Y direction at the first two levels.

The first mode of vibration is presented in the right image of Figure 1. The second and the third modes of vibration are presented in Figure 2.

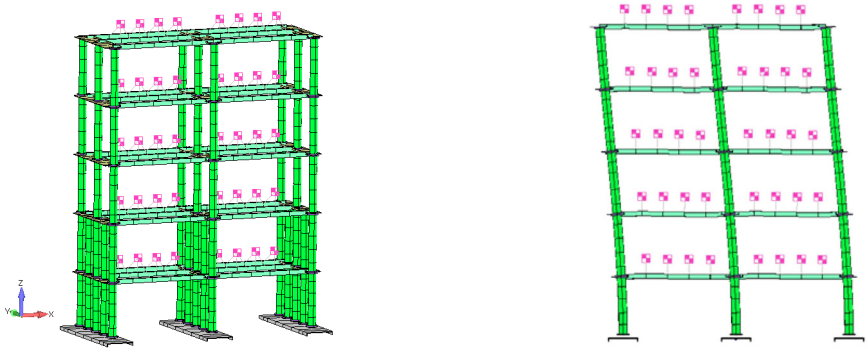

Figure 1: FE model (left) and first mode of vibration (right).

Figure 2: Second (left) and third (right) modes of vibration.

The first mode is a bending vibration mode in the X direction, the second mode is a bending vibration mode in the Y direction, and the third mode is related to the torsional vibrations of the model.

The Nastran model was used to perform an elastic spectral analysis. The IEEE693 spectra at 3% damping anchored at 0.5g was used in this analysis [2], which is presented in Figure 3. As required by the IEEE693 document [2], the same scaling factor of unity was used for spectral demands in the X and Y axes, whereas the spectral demand in the Z direction was at 80% of the one presented in Figure 3.

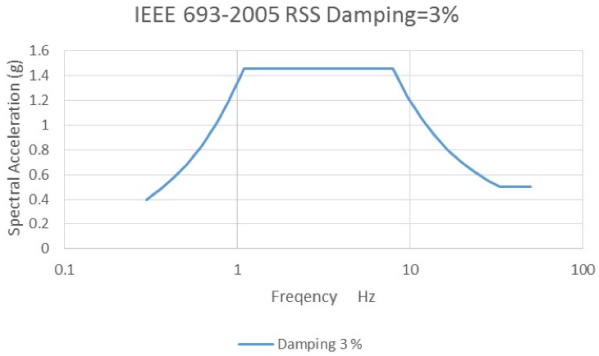

Figure 3: IEEE693 high required response spectrum (RRS) at 3% damping [2].

The spectral analysis revealed that the peak displacement on the top of the shelving system is 315.8 mm. Due to clearance issues, it is anticipated that the peak displacement on the top of the shelving system will remain under 200 mm. More importantly, the stresses in the insulator's polymer tubing were exceeding allowable stresses. The allowable stresses were estimated for a polymer tubing with cantilever load on the top at the half of Specified Mechanical Load (SML) value [2]. The capacity of polymer insulator controls acceptancy of the system's seismic performance, whereas the clearance limitations can be addressed by creating more separation from the neighboring equipment. A summary of the spectral analysis results is presented in Table 1.

Peak value	Results of spectral analysis	Clearance requirements or capacity	Demand to capacity ratio
Displacement at the top	315.8 mm	200 mm	158%[&]
Stress at the bottom of polymer tubing	147 MPa	95 MPa[§]	155%

Note: [§]-corresponds to 50% of SML stress in cantilever loading; [&]-not critical and can be addressed by increasing clearance

Table 1: Results of spectral analysis compared to clearance requirements or capacity.

Since the equipment could not meet both the clearance requirements and the tensile stress capacity of the polymer insulator, there was a need to use a protection device to improve its seismic performance. Based on previous successful applications (see [3], as an example), it was decided to introduce friction dampers [4] at the bottom of the shelving system and study the feasibility of using friction dampers in improving seismic performance of the system.

To follow the requirements of the upcoming version of the IEEE693 document [5], the friction dampers were tested in a component test setup to quantify their properties and performance.

3 COMPONENT TESTING OF FRICTION DAMPERS

The friction dampers were tested in a special test setup that was created for component testing of the dampers. As presented in Figure 4, the test setup simulates loading of the friction damper in a typical installation when the damper is installed as a stiffness and damping component of the anchoring system. Since the friction dampers work in compression only, there are several ways of using friction dampers as seismic protection devices. For example, if only one friction damper is used in the so-called single-acting configuration, the force will be developed in compression only as presented in the left side image of Figure 5. In this case, another spring or friction damper needs to be used on the tension side that corresponds to positive force and displacement to resist tension forces. When there is a damper on each side of the loading point, they create the so-called double-acting configuration. The force versus displacement curve is more symmetric in this case as presented in the right image of Figure 5.

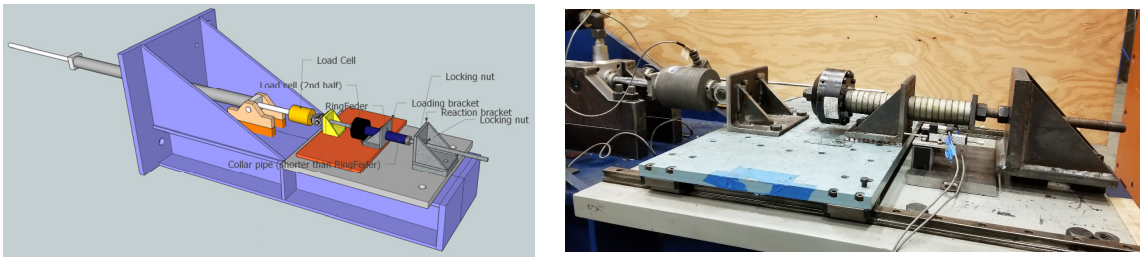

Figure 4: Component testing setup for Ringfeder friction dampers: sketch (left) and photo (right).

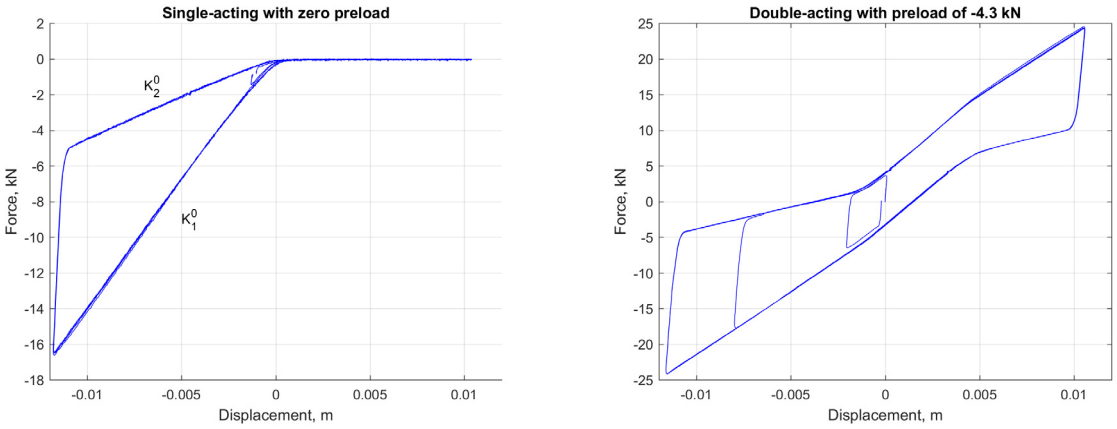

Figure 5: Force vs. displacement from component testing in single-acting with no preload (left) and double-acting with preload (right) configurations.

In addition to that, one of the dampers can be preloaded in compression, which is very common when the dampers are installed in a vertical configuration and the bottom damper is compressed under the dead weight of the equipment. The case with a preload of -4.3 kN is presented in the right image of Figure 5.

The dampers used in this study were installed in a double-acting configuration, where there is a damper on each side of the loading point. The latter results in symmetric behavior in tension and compression. A testing protocol followed recommendations of the upcoming version of the IEEE693 document [5], which is presented in Figure 6 on the left. The displacement D_{PL} corresponds to the maximum displacement of the device to be achieved at High Perfor-

mance Level [2]. A typical result for cyclic tests with increasing amplitude is presented in the right image of Figure 6.

More details on the numerical analysis of a high-voltage system with a double-acting friction damper can be found in [6].

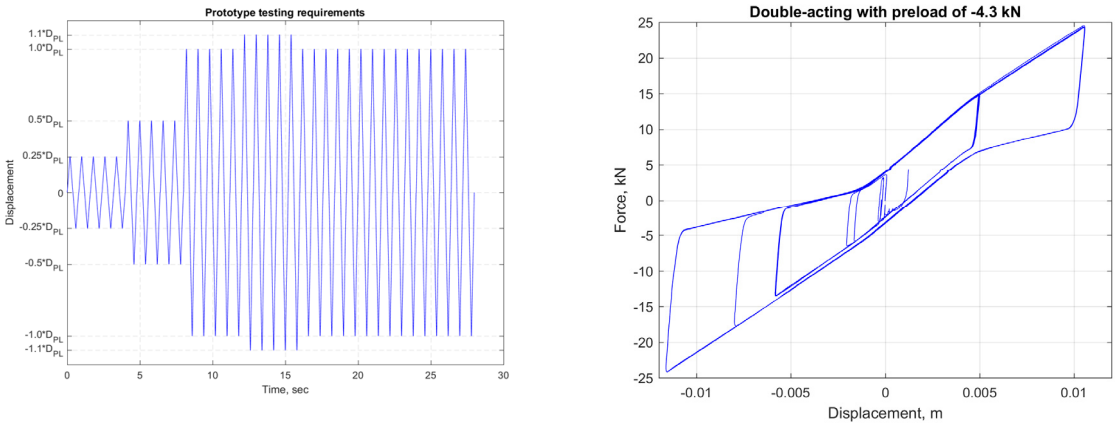

Figure 6: Component testing: protocol (left) and sample test results (right).

4 NONLINEAR FINITE ELEMENT MODEL OF PROTECTED EQUIPMENT

Another model of the equipment was generated in SAP2000 to utilize the friction damper model of this finite element software package [7].

The resonant frequencies are summarized in Table 2. The first three modes of vibration are the same as for the Nastran model as shown in Figure 7. The frequencies of the model generated in SAP2000 are slightly lower than that of the Nastran model as presented in Table 2, which is considered acceptable.

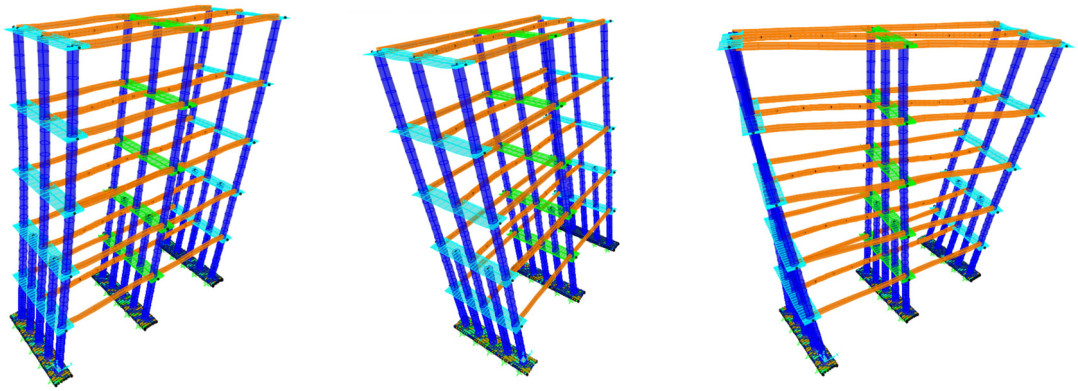

a) First mode b) Second mode c) Third mode

Figure 7: Elastic modes of SAP2000 model.

Model	Frequency of mode 1, Hz	Frequency of mode 2, Hz	Frequency of mode 3, Hz
Nastran	1.35	1.88	2.46
SAP2000	1.28	1.87	2.41

Table 2: Resonant frequencies of two elastic models.

In the next step of the study, the model generated in SAP2000 was subjected to tri-axial seismic excitation by utilizing TestQke4IEEE2, the IEEE693-spectrum compatible time histo-

ry [8]. This three-component time history was matched in a time domain to the IEEE693 spectra at 2% damping. Since the latter damping was closer to the critical damping of 3% estimated for this equipment shelving system, the newly generated IEEE693-spectrum compatible time histories matched to 5% spectra were not used [9]. The response spectra of each component of the input time history are presented in Figure 8. All results of experiments and numerical simulations presented herein are reduced in the Matlab environment [10].

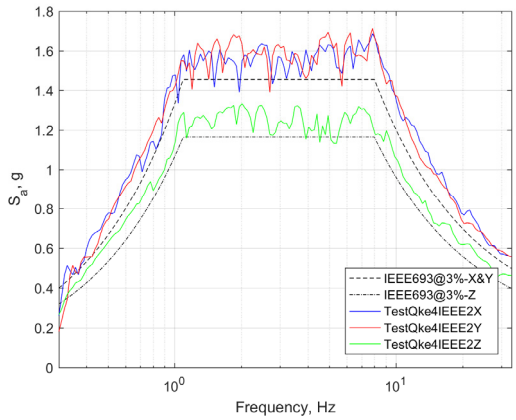

Figure 8: Response spectra of TestQke4IEEE2 [8] versus IEEE693 spectra.

Several finite element (FE) models were created. The first model, Case A, was simulating a fixed base configuration. All other FE models were generated by introducing friction dampers at the anchor locations attaching the bottom channels to the foundation as presented in Figure 9.

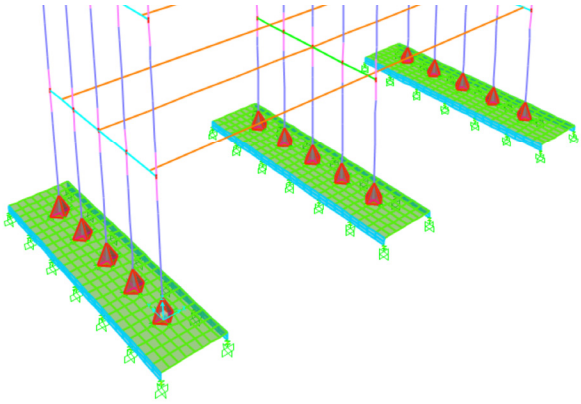

Figure 9: Friction dampers were introduced at anchor locations attaching bottom channels to foundation.

Depending on the presence of a preload, a finite element model of the friction damper [7] yields two typical force versus displacement diagrams as presented in Figure 10. It is worth noting that a simplified model of a friction damper [8] was utilized in this study. It was considered acceptable to investigate the feasibility of the system's performance improvement, if any.

The next model, Case B, was isolated by utilizing a model of the friction damper without a preload. There were several models simulating HV equipment isolated by friction dampers with different stiffness variations while keeping the preload the same as presented in Table 2.

All other models (Cases C1 through C4) were utilizing a model of a friction damper with the same preload. The stiffnesses K_1 and K_2 (shown in Figure 10a) varied from model to model as presented in Table 3. The stiffnesses were scaled up from the corresponding values measured in the test, which are shown in the left image of Figure 5.

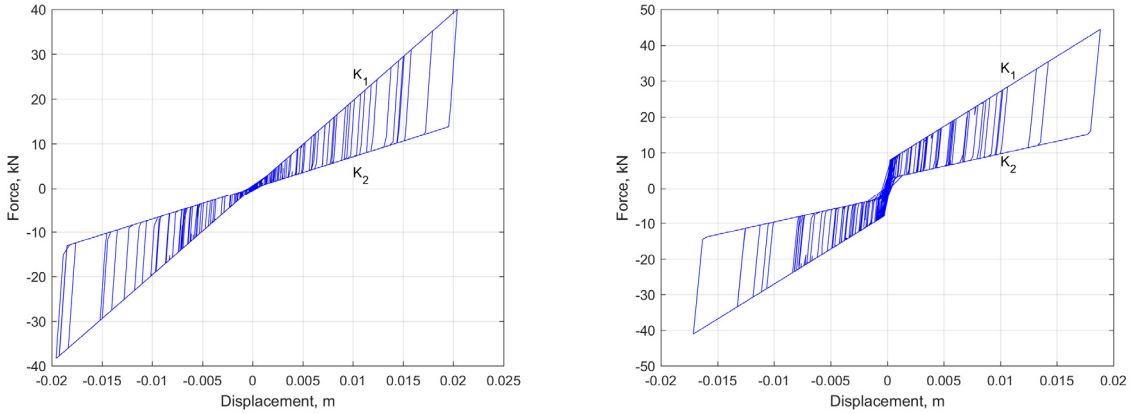

Figure 10: Typical force vs. displacement for double-acting configurations without (left) and with (right) preload: Case B vs. Case C1.

FE model	K_1/K_1^0	K_2/K_2^0	Preload, mm	1st frequency, Hz
Case A: fixed base	1.0	1.0	NA	1.28
Case B: friction damper	1.0	1.0	0.0	0.90
Case C1: friction damper	1.0	1.0	-3.81	0.90
Case C2: friction damper	2.0	2.0	-3.81	0.95
Case C3: friction damper	5.0	5.0	-3.81	1.01
Case C4: friction damper	10.0	10.0	-3.81	1.04

Table 3: SAP2000 FE models studied.

As it shown in Table 3, the low stiffness of the friction damper results in low frequency of the system, which is expected. The system with the lowest resonant frequency corresponds to the friction dampers tested in the component testing with no preload (Case B). The bending stress in the insulator is the smallest in this case as presented in Figure 11. However, the maximum displacement on the top of the system is very large (0.480 m in X direction and 0.243 m in Y direction). This is related to the fact that this system is much more flexible than the original system with a fixed base. The situation can be improved by pre-loading the friction dampers. In this case (Case C1), the maximum bending stress is still much lower than that of the fixed base system and peak displacements are reduced to 0.468 m. The bending stress is a little better for Case C1, but the system is still too flexible. Further optimization of the system performance leads to the Case C2 system, where maximum bending stress of which is slightly lower than the capacity of the polymer insulator. The maximum displacements go down to 0.424 m, which still requires a relatively large clearance around the system. All other FE models resulted in the bending stress that does not provide enough reduction in respect to the original system with a fixed base. A summary of the results is presented in Table 3. It worth noting that all systems with friction dampers have resonant frequencies below 1.1 Hz which is a corner frequency of the IEEE693 spectral plateau [2]. In other words, the demand on the systems is also reduced because the frequencies are located on the descending side of the

spectrum. Hence, the reduction of bending stress can be explained by both reduction of spectral demand and increase in overall damping of the system.

The following conclusion was made from the analysis of numerical models. The most optimal seismic performance is achieved for the Case C2 model. The results of nonlinear time history numerical simulations of the latter model show that the bending stress is right under the capacity of the polymer insulator. The peak displacement is still relatively high at 0.424 m, which is difficult to avoid due to increased flexibility of the system. The stiffnesses of the corresponding friction damper model are two times greater than those of the friction dampers tested in the component testing. The damper is used in the double-acting configuration with a preload.

More numerical simulations are planned for the future. A more sophisticated model closely replicating the actual performance of the friction damper depicted in the right image of Figure 5 will be utilized in the future study. Based on the results of this and future studies, the manufacturer of the friction damper will be approached with a request to provide this type of friction damper.

	Case A	Case B	Case C1	Case C2	Case C3	Case C4
Bending stress at bottom of polymer insulator to capacity, %	155.0%	77.2%	82.9%	99.8%	124.7%	133.7%
Displacement in X direction, mm	334	480	468	424	427	457
Displacement in Y direction, mm	154	243	233	217	194	169

Table 3: Summary of bending stress at the bottom of insulator divided by capacity at 50% of SML and peak displacements.

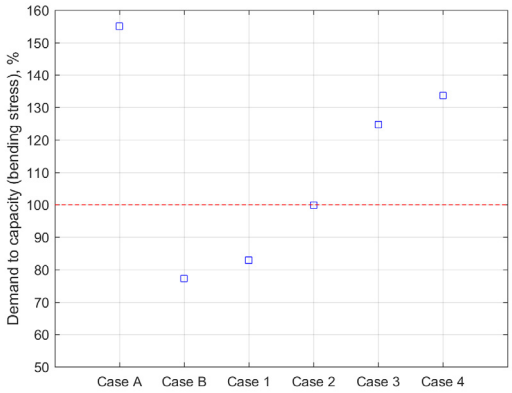

Figure 11: Variation of bending stress of the polymer insulator in respect to its capacity

5 CONCLUSIONS

- Based on a simplified model of the friction damper [7], the efficiency of the seismic isolation is demonstrated. It was shown that the peak moments can be reduced to remain under or meet the capacity. The peak displacements on top of the equipment will increase in respect to the fixed base mode. The peak displacement can be reduced by increasing the preload, but this reduction is limited.
- The most optimal seismic performance is achieved for the Case C2 model. The results of nonlinear numerical simulations show that the bending moment is right under the capaci-

ty of the polymer insulator. The stiffnesses of the corresponding friction damper model are two times greater than those of the friction dampers tested in the component testing.

- There is a need for a study with a more sophisticated model of friction dampers to be investigated in a nonlinear time history numerical simulation. A study on these issues is ongoing.

ACKNOWLEDGEMENTS

The project is sponsored by the Mitsubishi Electric Corporation whose support is greatly appreciated. The research team thanks Mr. Robert Cochran of Seattle City Light for donating Ringfeder friction dampers. Special thanks are due to the staff of the Structure Laboratory at the University of California, Berkeley. Special thanks are due to Mr. Llyr Griffith, Mr. Phillip Wong, and Mr. Matthew Cataleta. The successful completion of the testing phase of the project would not be possible without their technical support. Technical help by Ms. Sage Shamsai (CEE, UC Berkeley) on preparing 3D drawings and testing is greatly appreciated.

REFERENCES

[1] Nastran reference comes here…MSC Software, 2014. MSC NASTRAN 2014.1. https://www.mscsoftware.com/product/msc-nastran.

[2] IEEE, 2005. IEEE STANDARD 693-2005 - IEEE Recommended Practice for Seismic Design of Substations.

[3] Bishay-Girges, N.W. & Carr, Athol. (2014). Ring spring dampers: Passive control system for seismic protection of structures. 47. 173-180. BULLETIN OF THE NEW ZEALAND SOCIETY FOR EARTHQUAKE ENGINEERING, Vol. 47, No. 3, September 2014.

[4] Ringfeder Power Transmission, 2016. Ringfeder Damping Technology. http://www.Ringfeder.com/Documents/Products/Ringfeder/Damping_US.pdf.

[5] P693/D18, July 2018. Draft 18 of Recommended Practice for Seismic Design of Substations.

[6] Shakhzod Takhirov, Leon Kempner, Michael Riley, Eric Fujisaki and Brian Low (2019). Seismic Protection of High-voltage Equipment by Friction Dampers: Numerical Modelling Correlated with Full-scale Component Tests. COMPDYN 2019. 7th ECCOMAS Thematic Conference on Computational Methods in Structural Dynamics and Earthquake Engineering. M. Papadrakakis, M. Fragiadakis (eds.), Crete, Greece, 24–26 June 2019.

[7] Computers and Structures, Inc. (CSI), 2014. SAP2000 Ultimate Version 16.1.1. Structural Analysis Program.

[8] Takhirov S., Fenves G., Fujisaki E., and Clyde D. 2005. Ground Motions for Earthquake Simulator Qualification of Electrical Equipment. Pacific Earthquake Engineering Research Center, University of California at Berkeley, PEER report PEER 2004/07, January 2005.

[9] Shakhzod Takhirov, Eric Fujisaki, Leon Kempner, Michael Riley and Brian Low (2017). 'Development of Time Histories for IEEE693 Testing and Analysis (Including Seismically Isolated Equipment)'. PEER Report No. 2017/10, Pacific Earthquake Engineering Research Center, Berkeley, December 2017.

[10] The MathWorks, Inc. (2016): Matlab Version R2016b.

COMPDYN 2019
7th ECCOMAS Thematic Conference on
Computational Methods in Structural Dynamics and Earthquake Engineering
M. Papadrakakis, M. Fragiadakis (eds.)
Crete, Greece, 24–26 June 2019

SEISMIC RISK ASSESSMENT OF MULTI-SPAN BRIDGES USING NONLINEAR STATIC PROCEDURES

Camilo Perdomo[1], Ricardo Monteiro[1], and Haluk Sucuoğlu [2]

[1] IUSS – University Institute for Advances Studies, Pavia, Italy
address
e-mail: {camilo.perdomo, ricardo.monteiro}@iusspavia.it

[2] Department of Civil Engineering, Middle East Technical University, Ankara, Turkey
address
sucuoglu@metu.edu.tr

Abstract

Over the past decades the shift towards performance-based design and assessment of structures has led to the consideration of additional measures of structural performance other than just the structural response. Among these measures of performance, the expected economic losses after an earthquake event have attracted the attention of the research community because of their direct link with seismic risk and utility for post-earthquake emergency planning. The main objective of this study is to assess the accuracy and suitability of Nonlinear Static Procedures (NSP) for the computation of seismic fragility curves, which are then employed in the quantification of seismic risk, through annual rates of collapse exceedance and expected annual losses (EAL), for reinforced concrete (RC) bridges. The relative accuracy of different NSPs, when applied to a bridge population, is compared with estimations obtained implementing Nonlinear Time History Analysis (NTHA), considered as the benchmark prediction. Seven NSP approaches, from single-mode conventional pushover-based methods to multi-mode conventional or adaptive pushover-based procedures are implemented. Results indicate that when bridges can be classified as higher-mode sensitive, the performance of multi-mode procedures is marginally superior, whereas for first mode dominated bridges, although the latter still present advantages, the relative performance of single-mode procedures justifies its implementation.

Keywords: Bridges, multi-mode pushover, non-classical first mode, fragility assessment, loss assessment.

1 INTRODUCTION

Over the past decades, bridges have been identified as one of the most seismically vulnerable components within transportation networks [1, 2]**.** It is therefore necessary, for proper risk assessment and development of earthquake loss models in a certain region of interest, to reliably characterise of the seismic response of such structures. Several steps are key for the development of earthquake loss models at the regional (or individual) level and, in general, they encompass: the characterization of the seismic hazard, the assessment of the structural response and the development of measures of seismic vulnerability, and the implementation of tools for the calculation of economic losses (direct and indirect) based on the assessed seismic hazard and seismic vulnerability. Such framework has been implemented in the past in tools such as HAZUS [3, 4]. HAZUS manages the vulnerability assessment of a bridge stock with the use of fragility curves, which relate the expected intensity level of an earthquake event with the expected level of damage in the structure(s). Furthermore, HAZUS proposes fragility curves for typical bridge configurations, although it is allowed (and expected) that the user will input case-specific fragility curves for any type of configuration [4].

Seismic vulnerability assessment methods have been extensively studied during past decades [5, 6], from these, analytical fragility curves emerge a suitable and reliable tool to this end. Analytical fragility curves are constructed from results of structural analysis, which can be implemented with Linear Elastic, Nonlinear Static, or Nonlinear Dynamic approaches. Analytical fragility curves are often preferred over other approaches because they overcome the perceived subjectivity and/or scarce post-earthquake damage information that other methodologies require. Regarding RC bridges specifically, past studies have implemented analytical fragility curves for the seismic vulnerability assessment of individual bridges, bridge classes and bridge populations, Linear Elastic (e.g. [7]), Nonlinear Static (e.g. [8-10]) and Nonlinear Dynamic (e.g. [12-14]) analyses have been implemented for the structural response estimation.

Studies that have implemented Nonlinear Dynamic analyses for the estimation of the structural response have the advantage of working with "exact" predictions for the construction of fragility curves; however, when developing them for large portfolios of structures, this analysis approach becomes seldom practical, in terms of computational effort and time demand. Furthermore, past research for the development of fragility curves using alternative structural analysis procedures (i.e. Linear Elastic and Nonlinear Static analyses) have been limited in a number of ways, e.g., considering a unique or few similar structural configurations, evaluating the performance of a single or few Nonlinear Static Procedures (NSP), or comparing the response in terms of engineering demand parameters only, without extending it to the computation of expected economic losses. It is thus clear that additional research for identifying a more efficient, yet accurate alternative, for the computation of seismic risk in bridge populations is necessary.

The main goal of this study, in view of the above discussion, is to assess the suitability of NSPs for the computation of seismic risk of multi-span reinforced concrete (RC) bridges. For this purpose, a portfolio of 50 bridges is constructed using data from existing bridges. Structural response estimations are computed and fragility curves are developed using results from Nonlinear Time History Analysis (NTHA), was well as seven NSPs, namely, the N2 Method (N2), Capacity Spectrum Method (CSM), Extended N2 Method (Ext-N2), Modal Pushover Analysis (MPA), Generalized Pushover Analysis (GPA), Improved Modal Pushover Analysis (IMPA), and Adaptive Capacity Spectrum Method (ACSM). These fragility curves are then used to develop loss curves and then perform the computation of Expected Annual Losses (EAL) implementing the HAZUS approach, considering only direct losses due to physical damage, which serves as a measure of seismic risk. The assessment of the accuracy of the different NSPs is made by direct comparison of EAL results with those coming from NTHA.

2 CASE-STUDY PORTFOLIO

The case-study portfolio is composed of 50 RC bridges taken from a previous study [1]. These bridges are part of the Italian bridge stock, all belonging to the same typology, namely, multi-span with continuous, non-monotonically connected deck with circular section piers. The case-study portfolio features bridges with the number of spans ranging from 3 to 56 and with total length from approximately 95m to 2000m. The span length is rather uniform within the portfolio with a mean value of approximately 31m. The piers cross section diameter varies from 1m to 4.8m. With respect to piers reinforcement layouts and materials, the longitudinal reinforcement ratio varies from 0.5% to 1% with mean yield strength of 440MPa. Furthermore, the cover concrete compressive strength accumulates around 40 MPa, whereas the core concrete compressive strength varies between 42MPa and 52MPa. Pier heights are highly variable among bridges and sometimes within the same bridge, which indicates that the case-study portfolio contains both regular and irregular layouts.

2.1 Preliminary classification

For the expedite assessment of irregular behaviour in bridges, previous research has proposed several indexes that relate the stiffness of the structure and/or its geometrical configuration. Among these, the Relative Stiffness Index [15] and the Irregularity Index [16] were implemented in this study. However, no clear trends could be identified in using these indexes, particularly because the bridge configurations used in this study seem to be outside the scope for which they were originally tested. Since this study makes use of NSPs, single-mode and multi-mode based, it is rather significant to determine the sensitivity to higher modes in the bridges of the case-study portfolio. Such preliminary classification allows for the division of the case-study based on the expected behaviour, i.e., first-mode dominated or higher mode sensitive, and also defines the expectations for the performance of NSP approaches, i.e., single-mode based procedures are expected to perform similarly to multi-mode based approaches in first dominated bridges, whereas the use of multi-mode based procedures should be encouraging in higher-mode sensitive structures.

A critical evaluation of modal analysis results allows for identification of bridges where a classical dominant first mode (defined as the fundamental mode where all piers displace in the same direction) develops and bridges where a classical first mode does not develop or does not strictly exists. A sample of these results is shown in Figure 1. Building on these observations, respectively, 23 bridges were classified as “Classical” whereas 27 bridges were classified as “Non-Classical”. Generally, “Classical” type bridges have a number of spans less than or equal to six and modal mass participating the first mode of no less than 65%, pointing out that this type of bridge can be seen as first mode dominated. “Non-Classical” type bridges are always higher mode sensitive with a modal mass participating in the first mode less than 70%. Observations of this nature seem to indicate that inspection of modal shapes is more efficient than previously proposed indexes for identifying sensitivity to higher modes in bridge structures.

2.2 Structural Modelling Approach

All the bridges were modelled considering the following general characteristics: the deck was modelled as a linear elastic element, the piers were modelled with force-based fibre elements, the Kent-Park model was implemented for concrete whereas a bilinear hysteresis with a post-yield hardening ratio of 0.002 was employed for the reinforcement fibres. The mechanical behaviour of the abutments was considered via a simplified bilinear model, with an initial stiffness of 1400kN/mm, yield force of 4800kN and post-yield hardening ratio of 0.005. Shear keys were employed in the deck-to-pier connection to transfer horizontal forces but not moments.

With this modelling strategy, support devices were not modelled and shear keys are considered (implicitly) with a shear strength always larger than de shear developed in the piers. The foundation was considered as fully fixed, as has been suggested by other studies for bridges belonging to the Italian stock [14]. The structural mass is computed as that contributing from the deck and 1/3 of the piers [17]. Nonlinear geometry was considered via incorporation of P-Delta effects. All structural models were developed in the software OpenSees [18], which allows for the integration of the structural analysis results (either static or dynamic) with the construction of fragility curves and the assessment of economic losses. Furthermore, since not all sources of energy dissipation were considered in the modelling, an inherent tangent stiffness proportional viscous damping ratio [19] of 2% at the predominant period was adopted for NTHA.

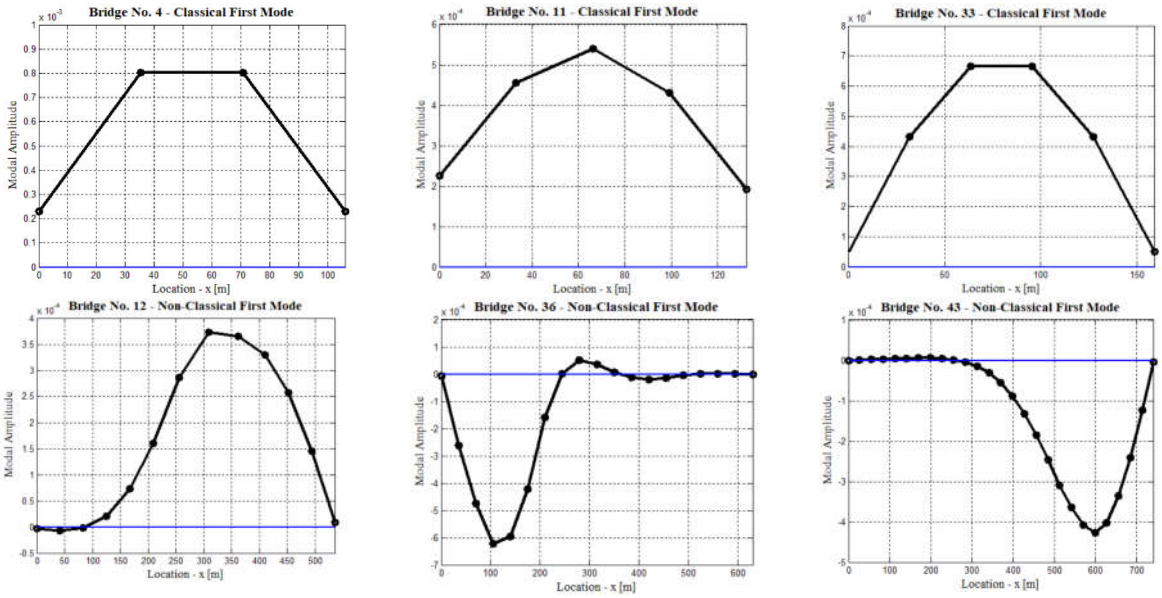

Figure 1: First Mode Shapes, 'Classical' and 'Non-Classical'.

2.3 Nonlinear Static Procedures

Seven NSPs were implemented to assess their capability of computation of EAL in the case-study portfolio. While the reader is referred to specific literature for a complete presentation of the methods, a brief description of their main features as implemented in this study is presented.

- **N2 Method (N2) [20]:** Capacity curves are constructed with a first-mode proportional lateral load vector; performance points are computed using an inelastic spectrum formulation. If the modal mass participating in the first mode is less than 55% of the total seismic mass, a mass proportional lateral load vector is implemented.
- **Capacity Spectrum Method (CSM) [21]:** It is implemented in the same fashion as the N2, however, performance points are computed implemented an overdamped spectrum formulation as presented in FEMA-440 [20].
- **Extended N2 Method (Ext-N2) [22]:** Results from a first mode proportional N2 assessment are updated via correction factors computed using Response Spectrum Analysis (RSA).
- **Modal Pushover Analysis (MPA) [23]:** Capacity curves are computed for each i^{th} mode proportional lateral load vector and corresponding performance points are computed via NTHA on the i^{th} equivalent Single-Degree-of-Freedom-System (SDOF). 'Modal' responses are combined using the Squared-Root-of-the-Sum-of-the-Squares (SRSS) rule.

- **Generalized Pushover Analysis (GPA) [24]:** Generalized Force Vectors and target displacement demand are computed according to Perdomo et al. [25]. The envelope of the response for each Generalized Force Vector is taken as the total seismic demand.
- **Improved Modal Pushover Analysis (IMPA) [26]:** A GPA analysis is first carried out to determine updated 'modal shapes', these updated 'modal shapes' are used to determine the updated displaced state of the structure per each mode. 'Updated modal' responses are combined using the SRSS rule.
- **Adaptive Capacity Spectrum Method (ACSM) [27]:** An adaptive equivalent SDOF is constructed with results from a Force-Based Adaptive Pushover Analysis (FAP) and the tools from Direct Displacement-Based Assessment (DBA). Performance points are computed using an overdamped spectrum formulation following the recommendation from Casarotti et al. [28].

3 GROUND MOTION SELECTION AND SCENARIO EARTHQUAKES

The ground motion record selection method implemented in study is the Conditional Spectrum (CS) Method [29]. For its implementation the method requires input from Probabilistic Seismic Hazard Analysis (PSHA), disaggregation of the PSHA and Ground Motion Models (GMM) information. At each bridge location, the PSHA and its disaggregation was carried out with the software OpenQuake [30] along with a simplified version of the 2013 Harmonized European Seismic Hazard Model (SHARE) [31], for which only the GMM from Akkar and Bommer [32] is required. The Intensity Measure (*IM*) chosen to characterize the expected ground motion input at the site was the spectral acceleration at the first mode period ($S_a(T_1)$), according the results of a recent study [33] that shows that, despite not being always optimal (in terms of efficiency and sufficiency) in general it presents better performance that the commonly used Peak Ground Acceleration (PGA). The first mode period (T_1) was estimated for each bridge through a bilinear fitting to a first-mode proportional capacity curve. Twelve return periods were considered for the characterization of the structural response, construction of loss curves and computation of EAL: 19975, 9975, 4975, 975, 475, 225, 141, 98, 73, 55, 32 and 22 years (probabilities of exceedance of 0.0025, 0.005, 0.01, 0.05, 0.1, 0.2, 0.3, 0.4, 0.5, 0.6, 0.8 and 0.9 in 50 years, respectively).

Once the PSHA and its disaggregation were carried out, the CS was computed for each determined *IM* level at each particular site and 25 records were selected per *IM* level in order to match the CS mean and variance. Real earthquake records were scaled and selected from a databank of approximately 11500 waveforms (one direction) obtained from the European Strong Motion Database, K-Net Japanese database and the PEER NGA West2 database. Sample results for two bridges, three *IM* levels each, are presented in Figure 2, which includes the CS (target mean and standard deviation), the selected records spectra with their corresponding mean and standard deviation and the conditioning period and the limits for matching (from $0.2T_1$ to $2.5T_1$ in all cases), shown with vertical lines. It can be seen in Figure 2 that within the limits for matching the agreement between the target mean and standard deviation and the records' mean and standard deviation is very good, this observation can be extended to all target CS computed and records selected.

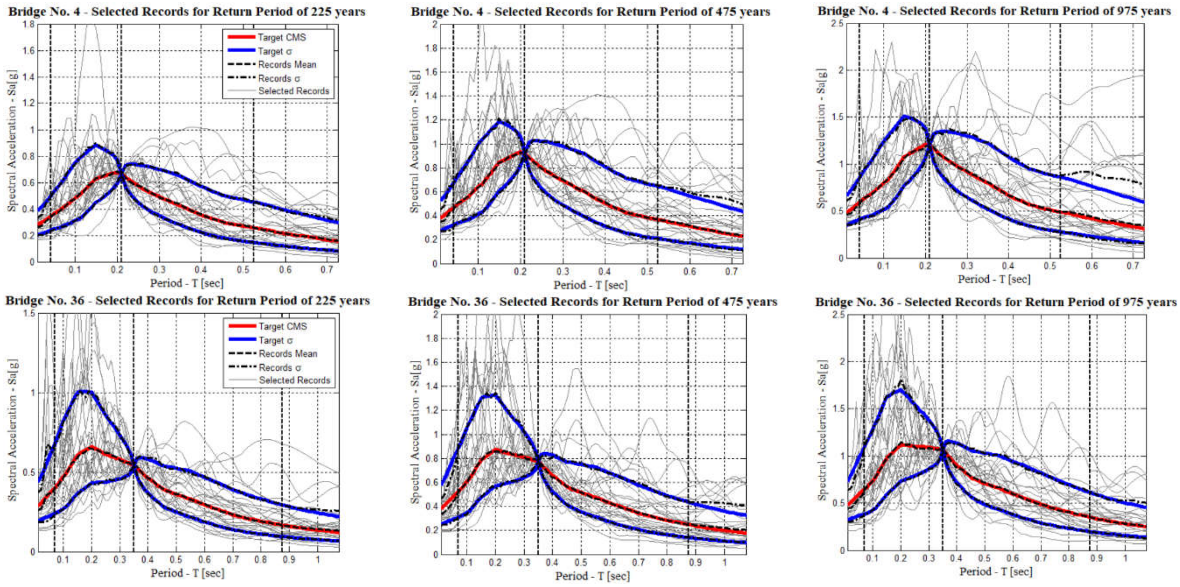

Figure 2: Sample results for CS and selected records.

4 DAMAGE LIMIT STATES AND FRAGILITY CURVES

A structure level criterion, in which an element damage evaluation serves for the quantification of the damage state for the whole structure, was adopted in this study. Keeping in mind the characteristics of the case-study portfolio and based on the work presented on HAZUS [3] and Nielson [34], further developed in Monteiro et al. [35], pier displacement ductility (μ_Δ) was adopted as Engineering Demand Parameter (EDP) and the maximum ductility among the different piers was used for the characterization of the damage state of the entire bridge. Accordingly, four discrete Damage Limit States (DLS) were identified: Slight, Moderate, Extensive and Collapse. The thresholds for the identification of the damage state of any particular pier in terms of displacement ductility are presented in Table 1. The EDP associated with the DLS requires the computation of the piers' top displacement and their yield displacement; the former was obtained directly from the structural analysis results.

DLS	μ_Δ
Slight	1.00
Moderate	1.20
Extensive	1.76
Collapse	3.00

Table 1: DLS in terms of displacement ductility.

Extensive experimental and analytical evidence, summarized in Priestley et al. [36], indicates that the yield displacement of columns is essentially independent from the amount of longitudinal reinforcement, transverse reinforcement and external axial load. Following their recommendations, the yield displacement of a cantilever column (behaviour presented in all piers of the case-study portfolio) can be computed adequately using Equation 1, wherein Δ_y is the yield displacement, H_p is the pier height, ϕ_y is the yield curvature, given in Equation 2, and L_{sp} is the strain penetration length, given in Equation 3.

$$\Delta_y = \phi_y \left(H_p + L_{sp}\right)^2 / 3 \tag{1}$$

In Equation 2, ε_y is the longitudinal reinforcement yield strain whilst D is the pier diameter. Additionally, in Equation 3, f_y is the longitudinal reinforcement yield strength and d_{bl} is the longitudinal reinforcement bar diameter.

$$\phi_y = 2.25\varepsilon_y/D \tag{2}$$

$$L_{sp} = 0.022 f_y d_{bl} \tag{3}$$

Consequently, the displacement ductility at any given pier can be computed according to Equation 4, in which $\Delta_{analysis}$ is the maximum displacement in absolute value found in the structural analysis and μ_Δ is the corresponding displacement ductility.

$$\mu_\Delta = \Delta_{analysis}/\Delta_y \tag{4}$$

The largest value of μ_Δ among the different piers of the bridge was taken as representative of the system and used for the evaluation of the exceedance of the predefined DLS.

Demand estimations from NTHA and all the tested NSP, *IM* levels, and bridges within the case-study portfolio were then obtained and fragility curves for each individual bridge and structural analysis approach were generated. Multiple Stripes Analysis (MSA) [37] was selected for the development of the fragility curves for two reasons: it allows the use of different records in different *IM* levels, and it is not necessary for all records to reach the *IM* level that leads to reaching the DLS under consideration, which is its main advantage. With respect to the fitting, Maximum Likelihood Method (MLE) was preferred for their computation, as it has proven successful in previous research [37]. Moreover, following current practice, a log-normal Cumulative Distribution Function (CDF) was chosen for the description of vulnerability for each structural analysis approach, DLS and individual bridge within the case-study portfolio.

5 EXPECTED ANNUAL LOSSES COMPUTATION

In this study, the simplified HAZUS [3] approach was used for the computation of scenario earthquake losses, loss curves, and finally, Expected Annual Losses (EAL), considering only direct losses due to physical damage. Several past studies [38-41] have used the same approach for the computation of direct losses for bridges at the regional level. Scenario losses were computed based on the compound damage ratio (μ_D), as shown in Equation 5, where DR_j is the damage ratio for DLS j and $P[DLS_j]$ is the probability of being in DLS j.

$$\mu_D = \sum_{j=1}^{4} DR_j P\left[DLS_j\right] \tag{5}$$

Damage ratios, DR_j, for each DLS were taken the same as in previous studies [40, 41], which match the recommendations contained in HAZUS [3], as shown in Table 2. Furthermore, for a scenario earthquake with a given *IM* level, the probabilities of being at each DLS are given by Equation 6.

$$\begin{gathered} P\left[DLS_j\right] = P\left(DLS_j \middle| IM = Sa(T_1)\right) - P\left(DLS_{j+1} \middle| IM = Sa(T_1)\right) \; for \; j = 1, 2, 3 \\ P\left[DLS_j\right] = P\left(DLS_j \middle| IM = Sa(T_1)\right) for \; j = 4 \end{gathered} \tag{6}$$

In Equation 6, $P\left(DLS_j \middle| IM = Sa(T_1)\right)$ is the probability of exceedance for DLS j read from the fragility function for a scenario with $IM = Sa(T_1)$ as determined in the PSHA. Direct mean economic losses for the scenario earthquake were computed according to Equation 7, where C_{REP} is the bridge's replacement cost, computed with Equation 8. In Equation 8, the unit re-

placement cost (UC_{REP}) was taken constant with a value of 2306 €/m^2 according to the recommendations of Dong & Frangopol [38]. The deck width (W) was also taken constant with a value of 10m whereas the length (L) was retrieved for each bridge.

DLS	j	DR_j
Slight	1	0.03
Moderate	2	0.08
Extensive	3	0.25
Collapse	4	1.00

Table 2: Damage ratios per DLS.

$$\mu_L = C_{REP}\,\mu_D \;\leq\; C_{REP} \tag{7}$$

$$C_{REP} = UC_{REP}\,W\,L \tag{8}$$

Mean direct losses were computed for each of the twelve earthquake scenarios determined in the PSHA, using fragility curves corresponding to each individual bridge developed with NTHA and each tested NSP. Loss curves were produced by plotting together the mean rate of exceedance of each earthquake scenario (as indicated in Section 3) with their corresponding mean direct losses, therefore, for each individual bridge and structural analysis approach. Finally, the area under each generated loss curve was assessed and EAL (as percentage of the replacement cost) were computed with results from NTHA and each tested NSP.

6 EXPECTED ANNUAL LOSS RESULTS

Fragility curves, loss curves and ELA were computed using structural response estimations from NTHA and each of the NSP presented in Section 2, for the scenario earthquakes and selected records presented in Section 3, following the guidelines presented in Sections 4 to 6. Sample results for a "Classical" type configuration and a "Non-Classical" type configuration are presented in Figures 3 and 4, respectively.

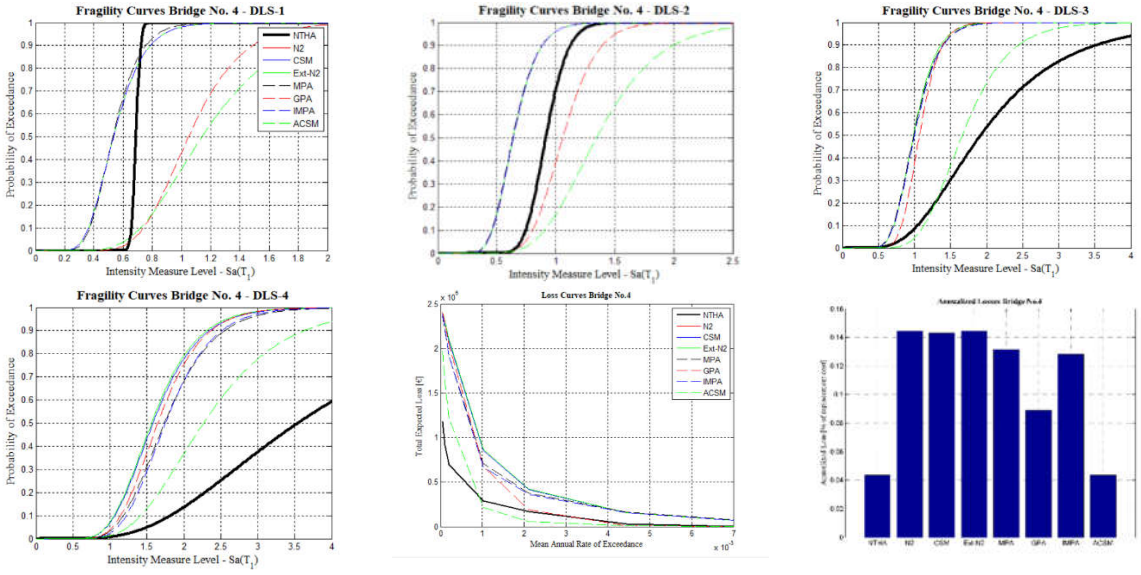

Figure 3: Sample results for fragility curves, loss curves and MLA. "Classical" type configuration.

Figure 3 shows that for this specific "Classical" Type configuration fragility curves computed with NSPs do not present a good agreement with NTHA estimations, except for ACSM

in DLS-3 and DLS-4 where it is the closest. It is also seen that in this case most NSPs yielded similar results in terms of fragility for DLS-3 and DLS-4. This observation clearly translates to the computed loss curves where all NSP tend to cluster in the same shape, except for GPA, that gets closer to NTHA for higher probability of exceedance events, and ACSM which is the closest across all evaluated scenarios. EAL results follow quite clearly this behaviour with N2, CSM, Ext-N2, MPA, and IMPA presenting a similar performance in prediction and ACSM being the closest to NTHA followed only by GPA.

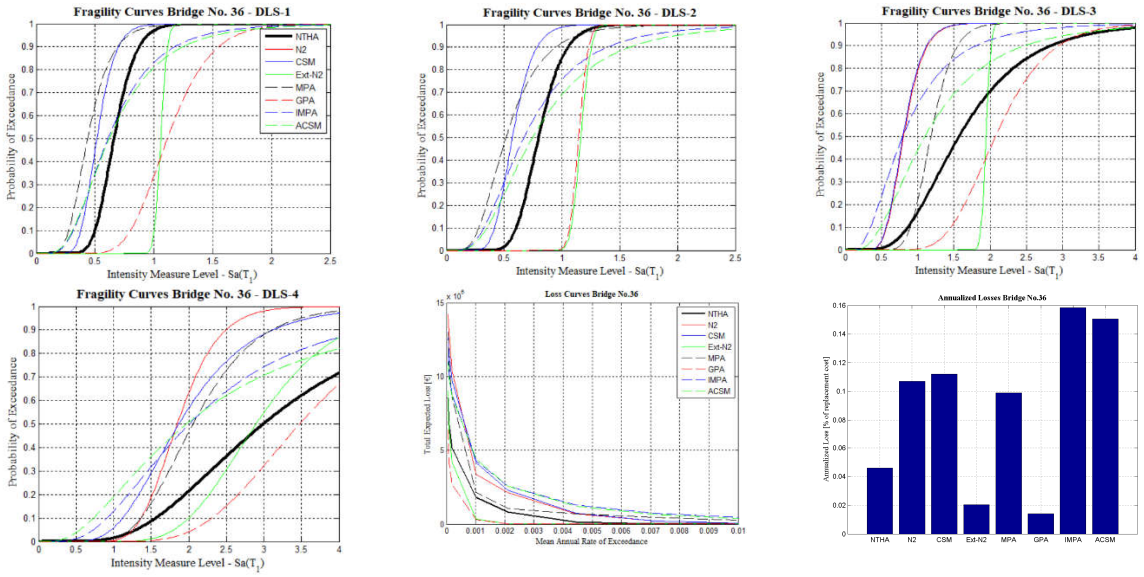

Figure 4: Sample results for fragility curves, loss curves and MLA. “Non-Classical” type configuration.

Figure 4, in turn, shows that for the specific “Non-Classical” type configuration the fragility curves computed with NSPs diverge greatly among them, for all considered DLSs, with different levels of agreement with NTHA. Remarkably, in this case, Ext-N2 and GPA computed slightly less vulnerable behaviour for all DLSs whereas the rest of NSP present opposite results, predicting a more vulnerable system with respect to NTHA. These observations are again clearly sustained by the loss curves and EAL values, where Ext-N2 and GPA curves are below the NTHA curve for low probability of exceedance events, the MPA curve is close to NTHA for some of the low probability of exceedance events, but it is always higher for more frequent events. It is also seen that despite computing different fragility functions, loss curves for other NSPs tend to cluster with a similar shape, higher than NTHA results. EAL values, again, capture this behaviour perfectly, with N2, CSM, MPA, IMPA and ACSM leading to higher losses and Ext-N2 and GPA to lower losses with respect to NTHA. Comparatively, the latter two present the best match to the benchmark results, although their predictions would be non-conservative.

The results presented in Figures 3 and 4 are not fully representative of the behaviour of the case-study portfolio hence the results for EAL values are further scrutinized and analysed statistically. In order to compare NSP results with respect to NTHA predictions, the error in the EAL estimation is computed for each bridge according to Equation 9. In Equation 9, EAL_{NTHA} is the EAL estimated with NTHA, EAL_{NSP} is the EAL estimated with a given NSP (e.g. N2) and EAL_{ε} is the associated error in the prediction.

$$EAL_{\varepsilon} = (EAL_{NSP} - EAL_{NTHA})/EAL_{NTHA} \tag{9}$$

Moreover, EAL_ε values are grouped according to the behaviour typology (i.e., "Classical" and "Non-Classical") and their results are treated separately. EAL_ε results are presented in boxplots in Figure 5. These boxplots present the 25th and 75th percentiles enclosed by the blue box whereas the horizontal red line marks the median of the results and two horizontal green lines are also presented in the plots which mark 30% difference with respect to NTHA predictions.

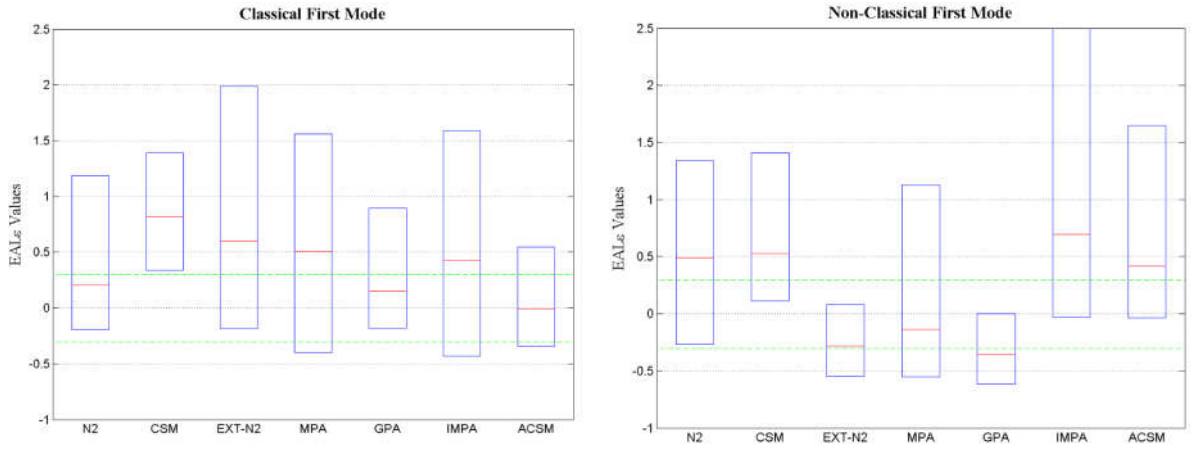

Figure 5: MALε values. "Classical" and "Non-Classical" type configuration.

Figure 5 shows, in terms of median EAL_ε values for "Classical" type configurations, that CSM performs the worst among the tested NSP alternatives, whereas N2 performs better, being within the 30% accuracy with respect to NTHA. Ext-N2, MPA and IMPA perform similarly, however their median EAL_ε values are slightly less accurate than that obtained with the N2. GPA presents itself as the second best alternative with a median EAL_ε value slightly more accurate than N2, whilst ACSM is the best performing method, with a median EAL_ε value essentially matching NTHA predictions. When the dispersion in EAL_ε values is taken into account, ACSM and GPA are still the first and second best performing methods, Ext-N2, MPA and IMPA present similar values of dispersion, larger than other approaches. N2 presents a larger dispersion than CSM nevertheless it is overall more accurate than the latter. In view of the simplicity in implementation of the N2 method, it is seen a viable alternative for the assessment of "Classical" type configurations within the case-study population.

For what concerns the "Non-Classical" type configurations, the median EAL_ε values for N2 and CSM are similar and both outside the 30% accuracy threshold, with respect to NTHA, overpredicting EAL and generally losing accuracy with respect to the "Classical" configurations, especially N2. IMPA and ACSM also lose performance with respect to the "Classical" configurations, with the ACSM median EAL_ε value being just slightly more accurate than N2. Ext-N2 ad GPA have very similar median EAL_ε values, being just on the boundary with the 30% accuracy with respect to NTHA. MPA presents the closest match with respect to NTHA in terms of median EAL_ε value. When considering the dispersion, MPA loses performance with respect to GPA and Ext-N2, with the former having a dispersion quite larger than the latter two, which have similar levels. ACSM would present almost identical performance to N2 and CSM, however it seems just slightly superior. IMPA presented the largest level of dispersion on EAL_ε values among the tested NSP for "Non-Classical" configurations. It is seen that for "Non-Classical" type configurations the use of multi-mode based NSP is encouraging in terms of improved accuracy. Results for the tested case-study portfolio tend to favour Ext-N2 and GPA, with the downside of underpredicting median ELAs. MPA and ACSM present overall a marginally better performance than N2 and CSM.

7 SUMMARY AND CONCLUSIONS

This work studied the accuracy of Nonlinear Static Procedures (NSP) in the prediction of seismic risk levels of reinforced concrete (RC) bridges, using Expected Annual Losses (EAL) as metric. For this purpose, a case-study portfolio of 50 multi-span bridges with continuous but non-monotonically connected deck has been selected from the Italian bridge stock. The bridges were divided in two typologies, "Classical", where a classical first mode shape develops, and "Non-Classical" where a classical first mode shape does not develop or does not exist. Twelve earthquake scenarios have been defined using Probabilistic Seismic Hazard Analysis (PSHA) for chosen mean return periods. The measure of earthquake intensity for each scenario was characterized via the spectral acceleration at the first mode period, allowing for the computation and selection of records using the Conditional Spectrum (CS) method. Furthermore, for the characterization of the structural response at each intensity measure level, 25 real earthquake recordings were scaled and matched in order to fit the CS mean and variance. Structural response estimations were obtained for each record and intensity measure level using Nonlinear Time History Analysis, considered the benchmark results, and seven NSPs, namely, N2 Method (N2), Capacity Spectrum Method (CSM), Extended N2 Method (Ext-N2), Modal Pushover Analysis (MPA), Generalized Pushover Analysis (GPA), Improved Modal Pushover Analysis (IMPA) and Adaptive Capacity Spectrum Method (ACSM). Four discrete damage limit states were defined and fragility curves were developed for each bridge within the case-study portfolio, for each DLS using structural response estimations from NTHA and each of the tested NSPs. The developed fragility curves were then used to compute Expected Annual Losses (EAL) for each of the earthquake scenarios defined previously, implementing the HAZUS approach. The accuracy of each tested NSP for EAL computation was assessed with direct comparison with NTHA predictions using an error measure. For the case-study portfolio investigated in this study, the findings suggest that the following conclusions can be drawn.

When the bridges can be classified as "Classical", the results favour ACSM as the best performing alternative, followed by GPA. At the same time, N2 presents a good performance and in view of its simplicity could be considered as viable alternative for the risk assessment of the "Classical" type configurations of the case-study portfolio. When bridges can be classified as "Non-Classical", results tend to favour multi-mode based NSP, in particular Ext-N2 and GPA, with the downside of yielding slightly non-conservative predictions. MPA and ACSM present only a marginally superior performance than N2 or CSM. Single-mode based NSPs, especially N2, lose performance when compared to the "Classical" type configurations.

Considering the results obtained for the overall portfolio, multi-mode NSPs that consider higher mode effects offer an improvement in the prediction of EAL. With generally similar median prediction estimates and dispersion levels for different types of structures, the choice would likely be made between GPA and ACSM. On the other hand, other aspects, such as computational demand or ease of implementation, should be considered. In such a case, N2 would be confirmed as a viable alternative for what concerns first mode dominated structures or structures where a classical first mode develops.

Overall, these results support the idea that NSPs can be used for large scale seismic assessment of bridge portfolios, while keeping in mind some limitations and improvements for future research. In particular, more research for higher mode sensitive bridges is required to improve the accuracy of alternative structural analysis approaches. It is also emphasized that the simplified approach implemented in this study for the calculation of EAL, i.e. structure level fragility curves along with compounded damage ratios, could conceal further deficiencies (or capabilities) of NSP approaches. As such, studies at the element level, as those currently implemented

for earthquake loss assessment in buildings, are necessary for the loss estimation in bridge structures. Efforts in these directions are expected in the near future.

8 ACKNOWLEDGEMENTS

The first and second authors greatly acknowledge the support provided by the research project INFRA-NAT (783298-UCPM-2017-PP-AG), co-funded by the European Commission ECHO – Humanitarian Aid and Civil Protection, and the project "Dipartimenti di Eccellenza," funded by the Italian Ministry of Education, University and Research at IUSS Pavia.

REFERENCES

[1] C. Zelaschi, R. Monteiro, R. Pinho, Parametric characterization of RC bridges for seismic assessment purposes. *Structures*, **7**, 14-24, 2016.

[2] J. Simon, L.G. Vigh, Seismic reliability assessment of typical road bridges in Hungary. *Journal of Earthquake Engineering*, published online DOI:10.1080/13632469.2017.1297270, 2017.

[3] Federal Emergency Management Agency (FEMA), *Multi-Hazard Loss Estimation Methodology Earthquake Model, HAZUS,* Washington D.C., 2003.

[4] C.A. Kircher, R.V. Withman, W.T. Holmes, HAZUS Earthquake loss estimation methods. *Natural Hazards Review*, **7**(2), 45-59, 2006.

[5] G.M. Calvi, R. Pinho, G. Magenes, J.J. Bommer, L.F. Restrepo-Vélez, H. Crowley, Development of seismic vulnerability assessment methodologies over the past 30 years. *ISET-Journal of Earthquake Technology*, Paper No. 472 **43**(3), 75-104, 2006.

[6] D. Perrone, P.M. Calvi, R. Nascimbene, E.C. Fischer, G. Magliulo, Seismic performance of non-structural elements during the 2016 Central Italy Earthquake, Bulletin of Earthquake Engineering, 2018. https://doi.org/10.1007/s10518-018-0361-5

[7] J.B. Jernigan, H. Hwang, Development of bridge fragility curves, *7th US Conference in Earthquake Engineering*.

[8] S. Banerjee, M. Shinozuka, Nonlinear static procedures for seismic vulnerability assessment of bridges, *Computer-Aided Civil and Infrastructure Engineering*, **22**, 293-305, 2007.

[9] I.F. Moschonas, A.J. Kappos, P. Panetsos, V. Papadopoulos, T. Makarios, P. Thanopoulos, Seismic fragility curves for Greek bridges: Methodology and case studies, *Bulletin of Earthquake Engineering*, **7**, 439-468, 2009.

[10] D. Perrone, M. Leone, M.A. Aiello, Non-linear behavior of masonry infilled RC frames: Influence of masonry mechanical properties, Engineering Structures, 150, 875-891, 2018.

[11] C. Perdomo, R. Monteiro, H. Sucuoğlu, Development of Fragility Curves for Multi-Span Bridges using Nonlinear Static Procedures, *Earthquake Spectra*, Under review, 2019.

[12] E. Choi, R. DesRoches, B. Nielson, Seismic fragility of typical bridges in moderate seismic zones, *Engineering Structures*, **26**, 187-199, 2004.

[13] B. Nielson, R. DesRoches, Analytical fragility curves for typical bridges in the central and southeastern United States, *Earthquake Spectra*, **23**(3), 615-633, 2007.

[14] B. Borzi, P. Ceresa, P. Franchin, F. Noto, G.M. Calvi, P.E. Pinto, Seismic vulnerability of the Italian roadway bridge stock, *Earthquake Spectra*, **31**, 2137-2161, 2015.

[15] H. Dwairi, M. Kowalsky, Implementation of inelastic displacement patterns in direct displacement-based design of continuous bridge structures, *Earthquake Spectra*, **22**(3), 631-662, 2006.

[16] C. Zelaschi, Seismic assessment of spatially distributed RC bridge portfolios, *PhD. Thesis*, Scuola Universitaria Superiore IUSS, Pavia, Italy, 2017.

[17] M.J.N. Priestley, F. Seible, G.M. Calvi, *Seismic design and retrofit of bridges*, John Wiley & Sons, 1996.

[18] Pacific Earthquake Engineering Research Institute (PEER), *OpenSees (Open System for Earthquake Engineering Simulation)*, available at http://opensees.berkeley.edu

[19] M.J.N. Priestley, D.N. Grant, Viscous damping in seismic design and analysis, *Journal of Earthquake Engineering*, **9**(2), 229-255, 2005.

[20] P. Fajfar, A nonlinear analysis method for performance based design, *Earthquake Spectra*, **16**(3), 573-592, 2000.

[21] Applied Technology Council (ATC), Seismic evaluation and retrofit of concrete buildings, *ATC-40*, Redwood City, 1996.

[22] P. Fajfar, M. Kreslin, The extended N2 method taking into account higher mode effects in elevation, *Earthquake Engineering and Structural Dynamics*, **40**, 1571-1589, 2011.

[23] A.K. Chopra, R.K. Goel, A modal pushover analysis procedure for estimating seismic demands on buildings, *Earthquake Engineering and Structural Dynamics*, **40**, 561-582, 2002.

[24] H. Sucuoğlu, M.S. Günay, Generalized force vectors for multi-mode pushover analysis, *Earthquake Engineering and Structural Dynamics*, **40**, 55-74, 2010.

[25] C. Perdomo, R. Monteiro, H. Sucuoğlu, Generalized force vectors for multi-mode pushover analysis of bridges, *Bulletin of Earthquake Engineering*, **15**, 5427-5280, 2017.

[26] T.S. Paraskeva, A.J. Kappos, Further development of a multimodal pushover analysis procedure for seismic assessment of bridges, *Earthquake Engineering and Structural Dynamics*, **39**(2), 211-222, 2010.

[27] C. Casarotti, R. Pinho, An adaptive capacity spectrum method for assessment of bridges subjected to earthquake action, *Bulletin of Earthquake Engineering*, **5**(3), 377-390, 2009.

[28] C. Casarotti, R. Monteiro, R. Pinho, Verification of spectral reduction factors for the seismic assessment of bridges, *Bulletin of the New Zealand Society for Earthquake Engineering*, **42**(2), 111-122, 2009.

[29] N. Jayaram, T. Lin, J.W. Baker, A computationally efficient ground motion selection algorithm for matching target response spectrum mean and variance, *Earthquake Spectra*, **27**(3), 797-815, 2011.

[30] M. Pagani, D. Monelli, G. Weatherill, L. Danciu, H. Crowley, V. Silva, P. Henshaw, L. Butler, M. Nastasi, L. Panzeri, M. Simionato, D. Vigano, OpenQuake engine: an open hazard (and risk) software for the global earthquake model, *Seismological Research Letters*, **85**(3), 692-702, 2014.

[31] J, Woesner, D. Laurentiu, D. Giardani, H. Crowley, F. Cotton, G. Grünthal, G. Valensise, R. Arvidsson, R. Basili, M.B. Demirciouglu, S. Hiemer, C. Meleti, R.W. Musson, A.N. Rovida, K. Sesetyan, M. Stucchi, The Consortium, The 2013 European seismic hazard model: key components and results, *Bulleting of Earthquake Engineering*, **13**, 3553-3596, 2015.

[32] S. Akkar, J.J. Bommer, Empirical Equations for the prediction of PGA, PGV and spectral acceleration in Europe, the Mediterranean and Middle East, *Seismological Research Letters*, **81**(2), 195-206, 2010.

[33] C. Zelaschi, R. Monteiro, R. Pinho, Critical assessment of intensity measures for seismic response of Italian RC bridge portfolios, *Journal of Earthquake Engineering*, published online DOI: 10.1080/13632469.2017.1342293, 2017.

[34] B.G. Nielson, Analytical fragility curves for highway bridges in moderate seismic zones, *PhD Thesis*, Georgia Institute of Technology, US.

[35] R. Monteiro, C. Zelaschi, R. Pinho, A. Silva, Derivation of fragility functions for seismic assessment of RC bridge portfolios using different intensity measures, *Journal of Earthquake Engineering*, published online DOI: 10.1080/13632469.2016.1264334, 2017.

[36] M.J.N Priestley, G.M. Calvi, M.J. Kowalsky, *Direct Displacement-Based Design of Structures*, IUSS Press, 2007.

[37] J.W. Baker, Efficient analytical fragility function fitting using dynamic structural analysis, *Earthquake Spectra*, **31**(1), 579-599, 2015.

[38] Y. Dong, D.M. Frangopol, Risk and resilience assessment of bridges under mainshock and aftershocks incorporating uncertainties, *Engineering Structures*, **83**, 198-208, 2015.

[39] A. Milano, F. Jalayer, R. De Risi, A. Prota, G. Manfredi, Model updating and seismic loss assesssment for a portfolio of bridges, *Bulletin of Earthquake Engineering*, **14**, 699-719, 2016.

[40] M.N. Furtado, A.A. Alipour, Cost assessment of highway bridge network subjected to extreme seismic events, *Transportation Research Record: Journal of the Transportation Research Board*, **2459**, 29-36, 2014.

[41] J.E. Padgett, R. DesRoches, E. Nilsson, Regional seismic risk assessment of bridge network in Charlestone, South Carolina, *Journal of Earthquake Engineering*, **14**, 918-933, 2010.

COMPDYN 2019
7th ECCOMAS Thematic Conference on
Computational Methods in Structural Dynamics and Earthquake Engineering
M. Papadrakakis, M. Fragiadakis (eds.)
Crete, Greece, 24–26 June 2019

SEISMIC FRAGILITY ASSESSMENT OF LNG PIPE RACK ACCOUNTING FOR SOIL-STRUCTURE INTERACTION

Luigi Di Sarno[1,2,*], **George Karagiannakis**[1]

[1] University of Sannio
Piazza Roma, 21, 82100 Benevento, Italy
ldisarno@unisannio.it
karagiannakis@unisannio.it

[2] University of Liverpool, Liverpool L69 3BX, UK
Luigi.Di-Sarno@liverpool.ac.uk

Abstract

The increasing momentum for Natural Gas exploitation in Europe and worldwide constitutes Liquified Gas terminals indispensable links of energy supply network. Infrastructures of this kind should be resilient against the earthquake hazard and thus designed accounting for as much as possible sources of uncertainty such as modelling issues, analysis methods, seismic input selection, soil effects and others. To date, research efforts have not assessed the response of pipe racks sufficiently, let alone the interaction between the rack and piping system and analysis methods of the past have proved to be neither adequate nor efficient towards evaluating the earthquake hazard potentiality. Further, soil-structure-interaction has not been incorporated into a fragility analysis framework; albeit it is considered as a critical parameter since midstream and downstream facilities are usually rested on alluvial deposits.
In the present work, a supporting RC rack is analysed through a 3D finite element model in the nonlinear regime both as coupled and decoupled vis-à-vis a piping system. The fragility functions are evaluated for structural components and limit states in the global and meso-scale, through the Incremental Dynamic Analysis (IDA) considering far-field conditions. In the end, the SSI is encountered accounting for linear and nonlinear soil, and soil effects are demonstrated by the fragility curves. It is inferred that the fragility of the rack soars considerably by the piping system boundary conditions in the coupled case and the SSI has detrimental impact, and thus should be accounted, particularly, for industrial structures that are located at coastal sites.

Keywords: RC pipe rack, pipelines, dynamic interaction, fragility assessment, far-field, soil-structure-interaction.

1 INTRODUCTION

The strategic role of Liquified Natural Gas (LNG) terminals all over the world and particularly in Europe due to the high energy demands, which have been increasing recently, makes these infrastructures focal points of energy world network. Climate changes due to global warming was, is and will be high on the agenda of societies, and thus the consumption of more environmental friendly fuels e.g. LNG will be prioritized in the future. There are currently 28 LNG terminals (24 ground and 4 floating) along European coastline some of which are planned or being expanded and the number is going to increase considerably in the Mediterranean Sea by the first half of the next decade since the LNG imports are expected to soar by almost 20% by 2040 compared to 2016 levels [1]. Furthermore, ongoing European projects, e.g. EastMed or future exploitation of natural resources in the East Mediterranean regions, will probably support exports to global markets and Europe via LNG or pipelines increasing even more the need for constructing LNG terminals in the region. The terminals play an essential part since their purpose is to store, process and distribute natural gas mainly by freight and pipelines at regional or supra-regional level. There are two types of terminals, namely liquefaction and regasification (or off-loading facility); in the first type, the gas is liquified by compression and cooling to low temperature, whereas in the second case, the LNG is converted to its gaseous form for further distribution to the market (Figure 1a). The natural gas is liquified because it takes up approximately 1/600 less volume compared to gaseous form. In this view, LNG terminals are made of a port, storage tanks and the main process area (Figure 1b) that includes pipe racks, knock-out drum (or vapor-liquid separator) and other process equipment.

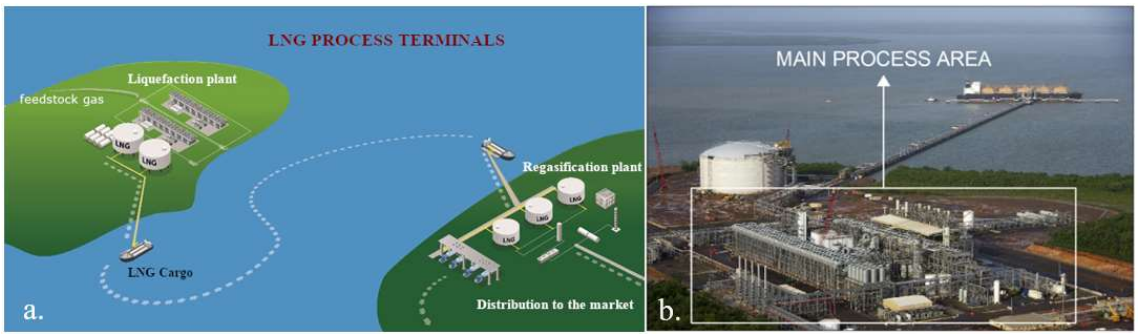

Figure 1: a. LNG process pathway and b. an LNG liquefaction plant ([2])

Many of LNG terminals could impose high risk to human and countries financial state considering that they might be vulnerable against natural hazards such as inundations, fire, earthquake and others. The earthquake hazard potentiality, which the present study intends to examine, is high in Central and East Mediterranean basin in which countries e.g. Italy, Greece and Turkey have experienced severe seismic events during the last decades. The seismic hazard is a key one to be addressed in the analysis of major accident hazards within a well-completed risk assessment of industrial facilities as clearly proved in [3]. A literature review that was conducted at the time showed that 14 seismic events caused damages to 182 equipment items and the 70% of that damage led to Loss of Containment (LOC) events. The number of non-building structures e.g. pipe rack and nonstructural components e.g. pipelines that an LNG or oil refinery encompasses are numerous. To adjudicate what the most vulnerable structures in a process plant are in order to account for their fragility during a quantitative risk assessment process (this kind of risk assessment is out of the scope of the present work), we should examine the seismic behaviour during past seismic events. In particular for oil refinery pipe racks, it has been found that are not the most vulnerable structures themselves against seismic hazard,

however, they could be due to the differential displacement of pipe supports that are not compatible with the pipelines ([4]). Supporting structures or pipe racks carry complex systems of nonbuilding structures and nonstructural components that transfer hazardous substances from one unit to another and thus their seismic integrity is critical.

To-date, the seismic research has focused on the decoupled case by investigating the seismic response of critical components such as elbows, t-joints or bolted flange joints without analyzing the rack and piping system in unison (coupled case) ([5], [6]). This engineering practice of decoupling the response of structural and nonstructural components has been adopted not only for research purposes but also in industrial sector in virtue of simplifying the design process due to the lack of code provisions or due to possible limitation of structural analysis software in the market that causes engineers to overlook important design aspects and overestimate or underestimate the seismic response. These limitations along with the ones that refer to modelling of pipes, the soil deformability or the selection of seismic input increase considerably the number of uncertainties (epistemic and aleatory since they are based both on the lack of knowledge e.g. modelling as well as inherent/unavoidable randomness e.g. soil properties or seismic excitation characteristics) that comes in stark contrast with the magnitude of process plants cruciality. Additionally, the Limit States (LSs) of common building structures are not applicable e.g. for pipe racks considering the exceptional high human, environmental or financial risk that a failure of structural or nonstructural component may induce [7]. That being said, it is essential to assess in a detailed fashion the dynamic interaction of pipe racks vis-à-vis pipelines or other supported components considering also that testing campaigns on this research topic cannot be found in the literature.

Another important aspect that may increase the seismic vulnerability particularly of mid- and down-stream facilities is the soil deformability. The soil beneath LNG terminals and oil refineries that are located at the seaside is rather weak, and thus strengthening measures are undertaken e.g. pile foundation so as to decrease possible settlement by dead loads or enhance the lateral capacity against earthquake loading. As it has been investigated up to a point for common buildings, the soil deformability affects mainly squat and heavy structures by increasing the lateral deformation and lessening the force demand ([8]). Steel and concrete pipe racks come in many sizes and layouts and it is definitely impossible for someone to deduce whether the soil should be considered or not in the final design. This is the reason that seismic code provisions encourage the incorporation of Soil-Structure Interaction (SSI) in the design, however, European ones in particular fail to form a practical way so as the SSI to be considered in the modelling of common buildings let alone for pipe racks that differentiate in many ways e.g. irregularity along the height and in plan. Furthermore, the decision could be even more complex by considering that pipelines are supported flexibly on racks and may be affected by the soil-induced higher displacements. To the best of our knowledge, there is no a probabilistic approach that undertake the seismic vulnerability of mid- or down-stream pipe racks – pipelines systems accounting for SSI, even though the demand for acquiring a better insight of the seismic vulnerability of existing or under design process plants is rather essential.

The present paper is organized as follows: first, the peculiarities of analysis methodologies of nonbuilding structures and nonstructural components as can be found in the current literature and codes of practice are presented in Section 2. Furthermore, it follows a brief review of soil-structure interaction effects and two models for linear and nonlinear soil that are adopted for the case-study (Section 3). In the last section, an LNG RC pipe rack is considered as a representative case study and the vulnerability at global- and meso-scale accounting for the coupled case is evaluated. The objective of the work herein is twofold: i) evaluation of the importance of dynamic interaction between an LNG RC rack and steel pipelines and ii) investigation of soil-deformability effects on structural components by means of Fragility Functions (FFs).

2 ANALYSIS METHODOLOGIES FOR PIPE RACKS

Petrochemical plant pipe racks are usually made by steel to avoid corrosion due to harsh environmental conditions that process plants are exposed to, however, concrete modular frames could be found as more preferable option due to the lower cost of the material, the high uncertainty in the welding process and time constraints relating to the long installation period of steel frames. They are complex systems since numerous nonbuilding structures and nonstructural components are supported on them (Figure 2). The detailed analysis methods of supported components specifically are excluded in this section; however, some references will be made to the point that are related to the connection with the supporting structure.

2.1 Code provisions

The main European (EN) contribution for seismic-resistant design of structures [9] do not make reference to oil refinery pipe racks yet to irregular building structures that, of course, differentiate in many ways e.g. different types of loading due to the supported nonbuilding and nonstructural components or importance class definition compared to nonbuilding structures. Even though EN regulations deal with other type of structures included in process plants such as tanks, silos, towers and pipelines ([10], [11]), the important design aspects of pipe racks along with the pipelines that are outfitted by are not mentioned. On the other hand, the American (AM) code [12] or the petrochemical plant structures guideline [13] encompass a few regulations for the design and analysis of pipe racks. Oil refinery pipe racks are called nonbuilding structures similar to buildings in the codes since they are designed and constructed in a manner similar to buildings, respond to strong ground motion in a fashion similar to buildings and constitute moment, braced or dual systems. Building-like structures share many design parameters and expected behaviour with regard to common building structures but there are also considerable differences.

Figure 2: An oil refinery complex with pipe racks and supported components (source: www.rainbow941.fm)

According to the AM code [12], several parameters should be considered for determining the analysis methodology of nonbuilding structures similar to buildings, viz the vertical and horizontal irregularities, the configuration of nonbuilding structures e.g. heat exchanger or tower vessels mass, the relative rigidity of beams that should not be confused with the rigid or flexible way of supporting e.g. a piping system on a nonbuilding structure, the Seismic Design Category (the SDS in the AM code is defined as a function of importance class, seismicity and site class) and the fundamental period, T. In contrast with the EN codes that are not dealt with

pipe racks, AM ones specify several analysis methodologies and give high latitude to the engineer in selecting the most suitable. Petrochemical pipe racks are usually subjected to vertical irregularities in comparison with horizontal ones (the last are defined in the code based upon the differential drift between perimetrical points when there is diaphragmatic behaviour but pipe racks most commonly have no diaphragms). The vertical irregularity could be due to the inequality of stiffness, strength, geometry and/or weight of adjacent storeys. For instance, it is rather common when a unique floor supports significant mass, whereas other adjacent carry inconsiderable nonstructural components, the equivalent lateral force analysis method may be applied since the response is dominated by the first mode; however, it is also common dissimilarities in stiffnesses and strength to exist due to the distinct vibration of concentrated masses on upper floors as well as geometry e.g. side overhang cantilevers that are necessary to support nonstructural components that run out of the main frame. The fact that pipe racks or other building-like structures present similar skeleton to buildings does not mean necessarily that behave like them. The resulting pendulum modes that come from the support of suspended vessels and other equipment may have strong impact on pipe rack response depending on the clearance and make the use of dynamic analysis inevitable. Another reason that necessitates the use of response spectrum or time history analysis is the higher local modes that come from the weakness of beams compared to columns or braces and may contribute substantially to the total response. This is a common behaviour of nonbuilding structures with absence of floor slab.

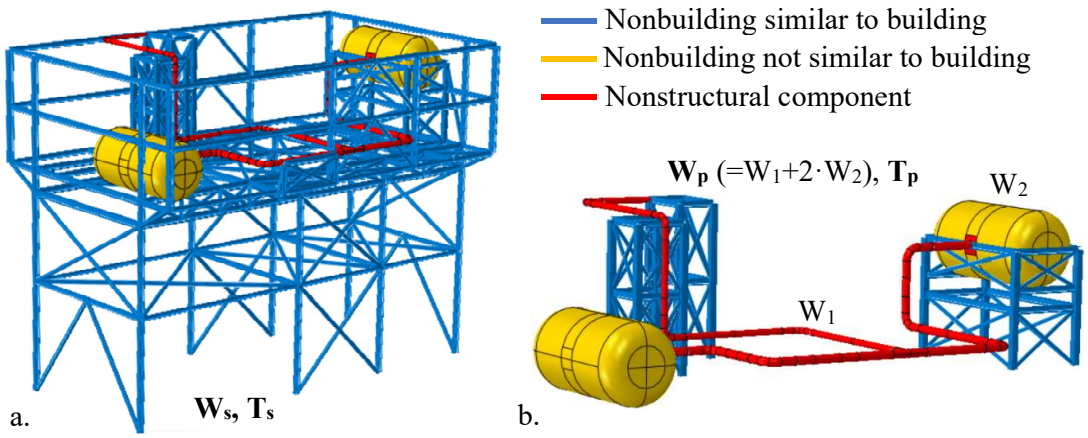

Figure 3: a. A steel nonbuilding structure, b. the piping system considering the towers that is support

To assess further what the AM code proposes regarding the interaction between supported nonbuilding structures and/or nonstructural components and supporting structure, a nonbuilding steel rack is demonstrated in Figure 3a consisting of a unique pipeline that runs across the third floor and connects two horizontal pressure vessels. When the weight of nonbuilding structure similar to building W_s (Figure 3a) and nonbuilding structures not similar to buildings as well as nonstructural components W_p (Figure 3b) is less than the 25% of the W_t (W_s+W_p), the decoupled case (no interaction) between them should be considered according to the code requirements. This is a very rough rule that relies on the low influence the supported components will have on the system response and intents some nonlinearity to be appeared on the nonbuilding structure to avoid resonance response and lessen the interaction. Also, the supporting structure and nonstructural components design parameters e.g. behaviour factor or component amplification factor a_p (this factor multiplies the design force and takes value between 1 and 2.5 for rigid and flexible supported components) are defined separately. Should this not be the

case, the dynamic interactıon is accounted for; however, if nonbuilding structures and/or non-structural components (the AM code states only the nonbuilding structure but implies the non-structural components e.g. pipes) are rigidly attached to the supporting structure (T_p<0.06s, the value is estimated by considering the flexibility of beams that the components is attached to e.g. the towers in Figure 3b), they should be analysed as rigid elements considering only the behaviour factor of the rack, otherwise both the supporting and nonbuilding structure should be modelled together in a combined model (Figure 3a) adopting the lesser behaviour factor between them. Finally, the two predominant dynamic analyses proposed by the code is the response spectrum and dynamic linear analysis probably due to safety reasons since nonlinearity increases the number of uncertainties in modelling and interpretation of results, however, the code implicitly recommends the use of nonlinear time-history to be used with caution.

2.2 Previous studies

According to [14], the most commonly causes of industrial accidents are the human factor (commission or omission errors), the organization/management errors e.g. design deficiencies or lack of maintenance and equipment/mechanical failure e.g. material failure or malfunctioning of equipment. The investigation of 284 case studies that referred solely to chemical process plants accidents by [15] was in unison with the previous statement, but it yielded additionally that the majority of accidents (25%) was related to piping system. That conclusion indicates that the piping network is one of the most prone parts within a process plant and due consideration should be given to technical human errors e.g. defective design by positioning unjustifiably the pipes on the rack or incorrect pipe bents configuration for increasing the flexibility of the system due to thermal pressure.

To-date, it still remains to be examined the dynamic interaction between a supporting structure and a piping system towards highlighting the most critical design challenges and preventing accidents in the future that put human lives and environment at risk. To the best of our knowledge, the research is rather limited on this topic; the majority of research has focused on the analysis of piping system or critical components individually ([5] &[16] among others), whereas the analysis of the combined models (supporting structure and piping) is rather obscure. An interesting research upon the effects of dynamic interaction on pipe-way and piping system response by considering different weight ratio, diameters and end-condition of pipes as well as thickness of U-ring elements (they are used to capture the pipes along the perimeter restraining only the movement in vertical and transverse direction) was conducted in [17]. The governing result of the case-study referred to the significant role the end-conditions and the stiffness of U-bolt rings played in the seismic response; the last two parameters may sensationally affect the whole system more than the weight ratio. The outcomes of the research showed that in case of multi-secondary structures e.g. pipelines that are multiply supported on a supporting structure, the relative stiffness of connection and the end-conditions except for the weight ratio should be examined; however, these parameters are missing from the codes which deal with singe secondary systems that are rigidly or flexibly supported on a nonbuilding structure.

3 SOIL-STRUCTURE INTERACTION

This section is devoted in the review of SSI models and effects on buildings and similar to building structures. More attention will be given to former structural type due to the higher research interest depicted in the literature. The limited research on soil deformability influence on the latter structural type demands a better insight to be acquired that can assist during the design process both of structural and nonstructural components. The fact that oil refineries are

located close to seaside where the soil is rather weak makes the examination of SSI phenomenon a sine qua non for the seismic integrity.

3.1 State-of-the-art

Except for the well-known effects of SSI on system response, namely period elongation and damping increase, the SSI has been found to affect mostly heavy and stiff structures. The longer period as well as the added damping in the system reduce the seismic demand forces (lower response spectrum) and thus SSI could be beneficial from this point of view. On the other hand, the higher displacement demand due to the soil deformation could be strictly necessary within the displacement-based design particularly for pipe racks that are outfitted by sensitive to high-deformation pipelines. According to [8], the ratio of $h/(V_s \cdot T)$ (h is the effective height, V_s is the shear velocity and T is the natural period) could be a reliable indicator of the degree of period elongation and damping increase.

Depending on the structural type under investigation, different parameters are of interest to evaluate the effects of SSI. For instance, foundation settlement or sliding and change in dynamic properties could be of interest for common building structures. However, when it comes to nonbuilding structures such as bridges, pipe racks or nuclear power plant reactors, the seismic demand on piles as well as the peak floor acceleration for checking the response of nonstructural components are of importance. Usually, pile foundations are adopted for pipe racks due to the liquefiable alluvial deposits existing at coastal sites and the high area that oil refineries cover making the replacement of soil practically or financially infeasible.

Except for the identification of changes in the response of structures, which is still a challenging task particularly when soil nonlinearity is accounted for, the researchers have been trying during the last decade to evaluate the effects of SSI in a probabilistic manner by estimating fragility functions that constitute an essential tool for assessing the response of existing or under design structures for further loss estimation and risk management. Even though this attempt has been partially completed for common building structures and bridges ([18]–[20]), the research lacks clearly of a probabilistic methodology that investigates the damage of pipe racks in a probabilistic manner accounting for dynamic and soil-structure interaction. The influence of SSI has been examined mostly for storage tanks and nuclear containment structures ([21], [22]), although process plant pipe racks could be stiff due to the vertical and horizontal bracing that intend to keep low the ductility as well as heavy since other nonbuilding structures and components are usually supported on them [7].

3.2 SSI models

This section is the forerunner for the case-study that follows, thus SSI models will be examined in connection with the ones that have been adopted afterwards. The literature abounds with models that are used to describe the soil-foundation-structure interaction. These models can be categorized into three main categories, namely ‘domain type models’ that refer to local scale since the soil is examined by constitutive laws, macroelements (intermediate-scale) where the soil-foundation-structure interface is described by a link element and finally soil springs which is the simpler type of model that is mostly used by practitioners and is based on impedance functions by considering mostly only for the fundamental frequency of the superstructure (global scale). The last type of model could be computationally efficient accounting for soil nonlinearity response and is suggested by code-of-practice provisions as a practically acceptable method [8]. Having said that, this latter type of model will be described hereafter and used for the fragility analysis in the following case study.

Lumped springs that represent the soil compliance are used mainly for shallow foundations making the assumption that the superstructure is underneath by a homogeneous, elastic and semi-infinite medium [23]. The assumption of linear behaviour in the vicinity of foundation could be an acceptable approximation when the foundation is rigid and the seismic excitation is not enough to develop soil inelasticity. The energy dissipation of soil due to radiation and hysteretic damping is represented by dampers. Although the stiffness and damping of soil is frequency-dependent, usually, they are modelled as frequency independent at the fundamental frequency of the structure since the analysis is conducted in time domain.

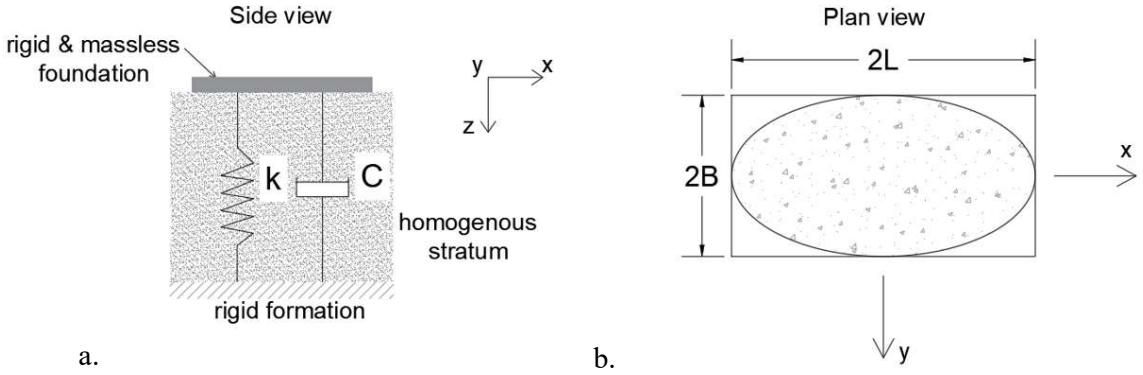

Figure 4: a. Idealisation of soil and foundation as a spring, dashpot and mass system, b. general shaped foundation (L>B) for the calculation of impedance functions

	K_i	C
u_z	$\frac{2GL}{1-\nu}(0.73+1.54\chi^{0.75})$	$\rho V_{La} B^2 \bar{c}_z$
u_y	$\frac{2GL}{2-\nu}(2+2.5\chi^{0.85})$	$\rho V_s A_b \bar{c}_z$
u_x	$K_y - \frac{0.2}{0.75-\nu} GL\left(1-\frac{B}{L}\right)$	$\rho V_s A_b$
r_z	$\frac{G}{1-\nu} J_t^{0.75}\left(4+11\left(1-\frac{B}{L}\right)^{10}\right)$	$\rho V_s J_t$
r_y	$\frac{G}{1-\nu} I_{by}^{0.75} 3\left(\frac{L}{B}\right)^{0.15}$	$\rho V_{La} I_{by} \bar{c}_{ry}$
r_x	$\frac{G}{1-\nu} I_t^{0.75}\left(\frac{L}{B}\right)^{0.25}\left(2.4+\frac{0.5B}{L}\right)$	$\rho V_{La} I_{bx} \bar{c}_{rx}$

I & J_t area and polar moment of inertia of the soil-foundation surface around the pertinent axis, $\bar{c}$ a damping factor with $\bar{c}=\bar{c}(L/B, a_o)$, $\chi = A_b/(4L^2)$, G the soil shear modulus, A_b foundation area

Table 1: Static stiffness K and radiation damping coefficient C for arbitrary shaped foundations ([24])

The dynamic impedance function of the system shown in Figure 4a is given by:

$$K(\omega) = \bar{K} + i \cdot \omega \cdot C \tag{1}$$

where both $\bar{K}$ and C are functions of frequency ω. In particular, $\bar{K}$ is called dynamic stiffness and represents the soil stiffness and inertia being frequency independent up to a good approximation for soil properties. The dynamic stiffness is given by:

$$\bar{K} = K_i \cdot k(\omega) \tag{2}$$

The static soil stiffness K_i in the three modes of vibration for a general shaped foundation (Figure 4b) rested on homogenous half-space is given in Table 1. The dynamic stiffness coefficient (k) is a function of L/B, the soil Poisson ratio ν and the dimensionless parameter a_o ($=\omega \cdot B/V_s$, ω is the fundamental angular frequency of the superstructure and V_s is the average soil shear wave velocity commonly estimated at the upper 30 m of a soil deposit). The coefficient k can be found by plots existing in the literature as a function of the aforementioned parameters. Furthermore, the total damping is represented by the product $\omega \cdot C$ where C is the radiation damping (hysteretic damping is zero for linear soil) coefficient that for a general shaper foundation are given also Table 1, where ρ is the soil density, V_{La} is the Lysmer's analog wave velocity ($=3.4V_s/(\pi \cdot (1-\nu))$) and c_i is a factor that is given by plots being a function of the dimensionless ratio α_o and the ratio L/B. The interested reader may find more information about the methodology for the soil springs configuration and the forms of rotational modes of vibration in [24].

The soil behaves in the nonlinear regime under strong-ground motion and in the vicinity of foundation interface (near-field) even at low strain levels. The hysteretic behaviour is described by the inclination (that refers to soil stiffness) and the size of the loop (the larger the loop the higher the energy dissipation, Figure 5a). Usually, the secant stiffness ($G_{sec}=\tau_c/\gamma_c$) is used to describe the average stiffness of soil along an entire loop instead of the tangent G_{tan} and the damping ξ for the dissipation of energy due to the material nonlinearity. The G_{sec} and ξ constitute the equivalent linear soil properties; the increase of shear strain amplitude decreases the secant modulus and increases the energy dissipation due to the hysteresis phenomenon. The change in shear modulus and damping are usually depicted through the G-γ-D curve ([25]) (Figure 5b).

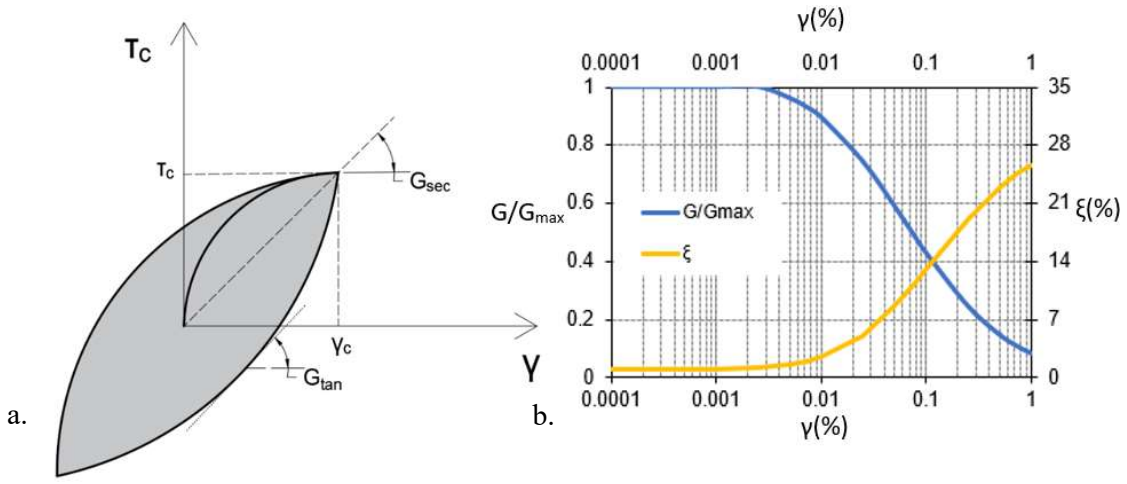

Figure 5: a. hysteresis loop of soil element subjected to symmetric cyclic loafing ([25]), and b. typical G-γ-D curves of a soil deposit

The simplest way to estimate the soil nonlinearity is the equivalent linear method that accounts for the modification of secant and damping during an iterative analysis procedure by considering a percentage (roughly 65%) of the peak strain from the previous step. More information about this method can be found in [26]. The equivalent nonlinear method is a straightforward and simple to be implemented procedure, however, it still remains an approximation of the actual soil behaviour. Thus, plentiful nonlinear constitutive models of different rigorousness and complexity exists in the literature. Soil models with hysteretic behaviour can be rather difficult to be calibrated since they require a lot of parameters. In this regard, a simplified model will be used in the sequel to account for the nonlinear behaviour of soil underneath an LNG RC

rack. That model relies on the Ramberg-Osgood (RO) curve [27], which is described by the following equation:

$$\frac{\gamma}{\gamma_y} = \frac{\tau}{\tau_y}\left(1 + a\left|\frac{\tau}{\tau_y}\right|^{r-1}\right) \tag{3}$$

where γ_y and τ_y are the yield strain and stress ($G_{max}=t_y/\gamma_y$) and the parameters α and r are positive constants ($r\geq1$ and $a\geq0$). When the strain is very small ($\gamma\rightarrow0$ and $\tau\rightarrow0$ given that $r>1$), the eq. 7 can be rewritten according to Masing's rule as follows:

$$\frac{\gamma}{\gamma_y} = \frac{\tau}{G_{max}\cdot\gamma_y}\left(1 + a\cdot\left|\frac{\tau}{G_{max}\cdot\gamma_y}\right|^{r-1}\right) \tag{4}$$

Also, the hysteretic damping according to RO model is defined as:

$$\frac{G}{G_{max}} = 1 - \frac{D\cdot\pi\cdot(r+1)}{2(r-1)} \tag{5}$$

The parameters a, r and γ_y are to be determined by using a code that tries repetitively to estimate the best fit given a soil type with G_{max}. This code has been developed in MATLAB and the results are presented in the following section. Once the parameters are known, D-γ curve can be determined as well.

To represent the soil properties of the following case study by using the G-γ-D curves shown in Figure 5b and calibrate the pertinent curves of RO model, afterwards, the empirical formulae by [28] have used that refer to alluvium deposit of sandy clay to clayey sand with plasticity I_p. The quotation of those formulae is omitted herein for brevity.

4 FRAGILITY ANALYSIS OF A RC PIPE RACK

The seismic fragility of a RC pipe rack is examined herein considering a 3D model in dynamic nonlinear analysis of framed structures software Seismostruct ([27]). Towards achieving robustness in the assessment methodology, a particular number of steps were followed for that purpose: i) material and frame element modelling, ii) modal analysis for identifying the fundamental modes in horizontal and vertical direction, iii) pushover analysis of the rack for determining the weakest direction, iv) selection of 7 spectrum compatible seismic records considering the predefined fundamental period, v) definition of the acceptance criteria for the assessment of structural components and, vi) time-history analyses and results compilation and representation via probabilistic functions. All the following steps are explained in more details in the sequel.

4.1 Model Description

The pipe rack that is examined comes from an existing LNG terminal plant (Figure 6a) and is shown in Figure 6b. Although the LNG terminal is originally placed and designed in a low-seismicity region, the pipe rack is replaced to Priolo Gargalo, a high seismicity area in southeast Sicily, in order to acquire a better insight of the seismic performance. The pipe rack under assessment consists of 2 sub-racks; a 6x9x8.3 m short rack that supports the pipelines that come immediately from the LNG storage tank and a 102x6x7.3 long rack that transfer LNG to nearby units (Figure 6c). All the intermediate spans by the beams are 3 m long. The structural components are made by concrete class C40/50, whereas the 7 pipelines that run along the rack by steel grade ASTM A312/TP304L with yield and ultimate strength 370 MPa and 461 MPa, respectively. More information about the mechanical properties of the rack and pipelines can be

found in [29] and [30]. The concrete material is described by the Mander model, which accounts for transverse reinforcement, and the Menegotto-Pitto one is used for the ribbed reinforcement. The inelasticity of beams and columns is described by force-based frame elements that rely on nonlinear fibre section method [27]. A five-element non-uniform subdivision is adopted for the members.

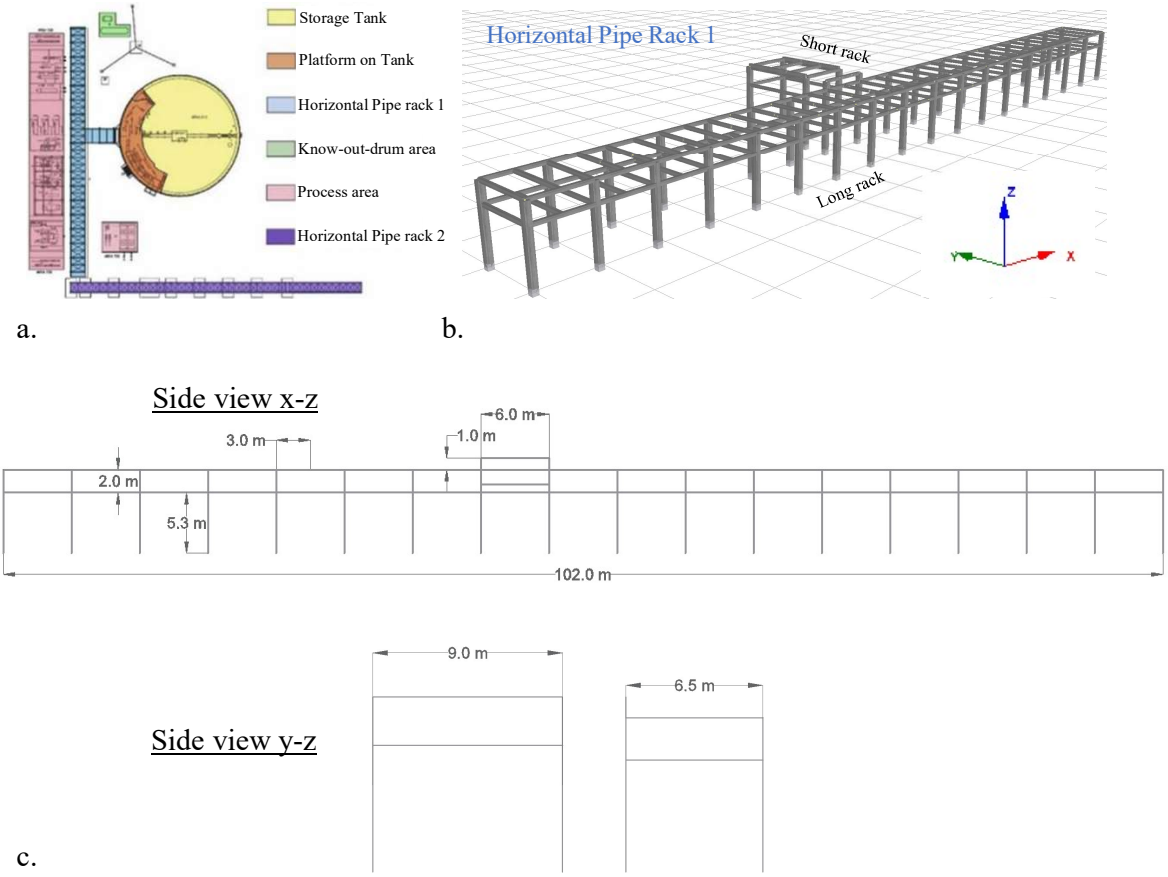

Figure 6: a. LGN terminal layout ([30]), b. RC pipe rack under assessment and c. dimension of the rack

Since the modelling of the entire terminal is not practically feasible due to the excessive computational cost, the assumption of pinned connections at the edges of the pipes that run beyond the pipe rack main frame is made. This decision is an approximation and states on the safe side since pipes that present relative flexibility -mostly bend downwards or upwards after the main frame of the rack- are considered more rigidly restrained. Furthermore, another type of modelling constraint refers to pipe modelling. Although EN and AM codes of pipelines design do not make reference of shell elements yet only to beam ones, the last type of element may be incapable of capturing the exact strain-stress response [7]. In view of the large model under investigation and the availabilities of the analysis software [27] for pipe modelling, stick models both for straight and curved pipe have been used and calibrated according to [32]. It is worth mentioning that the internal operating pipe pressure is low (P_{max}=1.63 MPa) as quoted in [30] and thus neglected in order to remain on the safe side since the pressure increases at low operating levels the bending stiffness of pipe bends ([32]). The pipelines are supported mainly in a flexible way on the rack by keeping free the displacement in the axial direction of the pipe as well as all the degrees of freedom.

Finally, to account for the SSI effects, an elastic footing and strip beams foundation system is designed according to [33] for the new site. A coastal sandy clay to clayey sand soil profile with V_s=210 m/s and G_{max}=105 GPa (STC according to [9]) has been adopted and the linear soil springs for the 6 modes of vibration are estimated according to [24] and placed both under the footings and strip beams as shown in Figure 7.

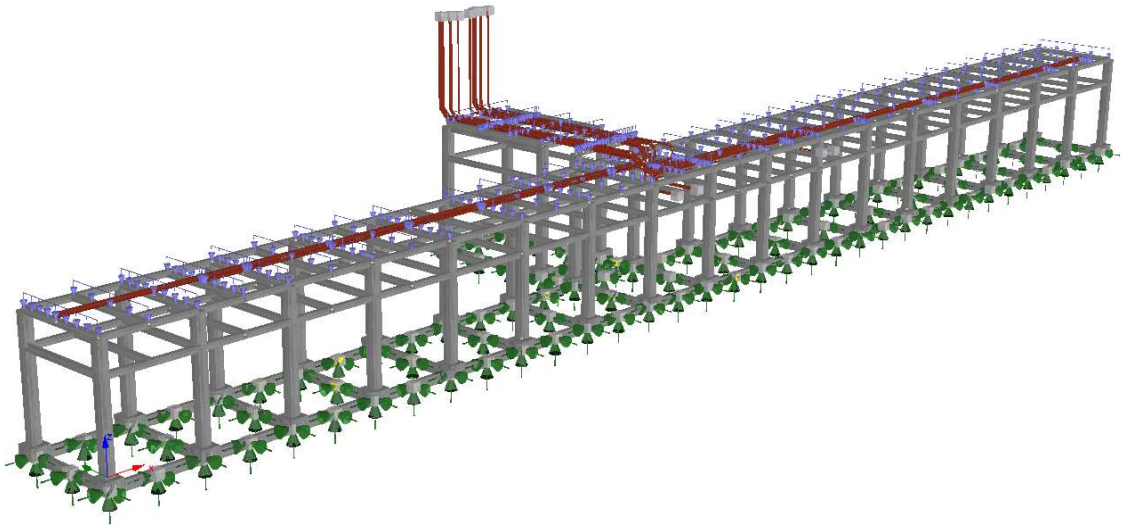

Figure 7: The soil-foundation, pipe rack and pipelines in the same model on Seismostruct ([27])

The original G-γ-D curves of the soil type, which rely on the formulae of [28] are shown in Figure 5. As mentioned in the section 3, the soil nonlinearity is described by calibrating the RO model included in the toolset of [27] for the STC. For that purpose, the unknown parameters of the model are estimated by building up a code in MATLAB ([34]) and the yielded G-γ-D curves are shown in Figure 8a&b for two fitting methods, namely the Root Mean Square Error (RMSE) and the coefficient of determination (R^2). The former was found to calibrate better the G-γ curve and thus the parameters of that fitting are adopted.

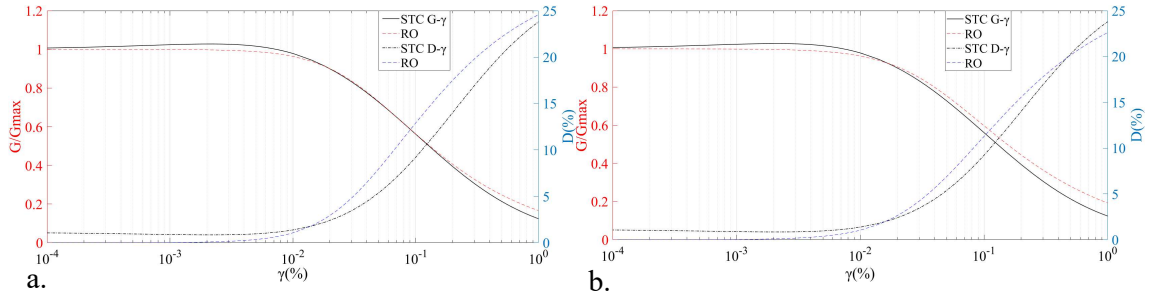

Figure 8: Calibration of RO model for the STC using a. the RMSE and b. R^2 fitting methods

4.2 Seismic assessment

Initially, a modal analysis is conducted for the pipe rack shown in Figure 7 with (W/) and without (W/O) SSI to identify the fundamental modes, which are quoted in Table 2. The maximum increase of the period fluctuated between 17 and 20% for the two modes. To select the seismic records for the fragility assessment of the rack, it is necessary to identify the fundamental period along the weakest direction. This is achieved by means of pushover analysis both for uniform and 1st mode load distribution as well as for the two modes shown in Table 2. The

capacity curves are illustrated in Figure 9 where it is obvious that the principal mode in the Y direction (T_3=0.276 sec) is the weakest one.

	$T_{W/O}$ (sec)	$T_{W/}$ (sec)	ΔT (%)	$M_{W/O}$ (%)	$M_{W/}$ (%)
Mode 3(Y)	0.269	0.315	17	43	34
Mode 5 (X)	0.230	0.276	20	87	55

Table 2: The two fundamental modes of the pipe rack

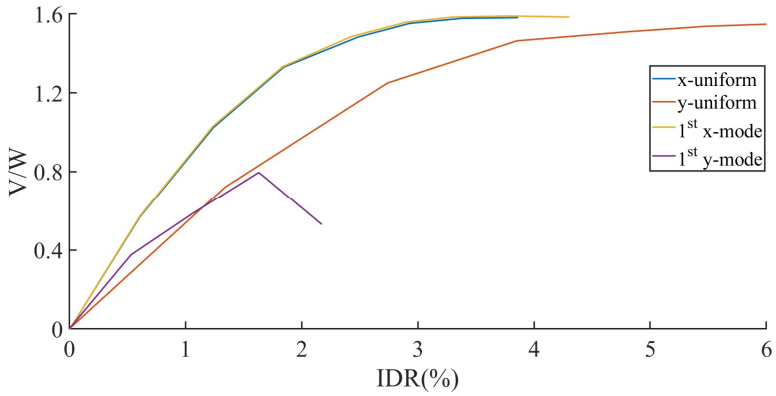

Figure 9: The capacity curves of the first mode and uniform load pattern distribution

Furthermore, 7 compatible records are selected through REXEL software ([35]) in the [0.2 T_3, 2T_3] period range. The spectrum that the compatibility is achieved for refers to SLV limit state, STC and Usage Class III ([36]), although three LSs, namely Serviceability (SLS), Safe Life Limit State (SLLS) and Collapse (CLS) are accounted for the assessment in the following. This topic is under investigation by the Authors since the best option could be records compatibility for each LS. It is also noteworthy that the compatibility of records is difficult to be attained both for the two horizontal and one vertical component, thus, the records shown in Figure 8 have compatibility for the two horizontal ones at least (the vertical component is used in all cases). The epicentral distance of the seismic records is greater than 15 kms (far-field, [37]) and the duration of the records selected for the analysis is bracketed with a_g>0.05 g.

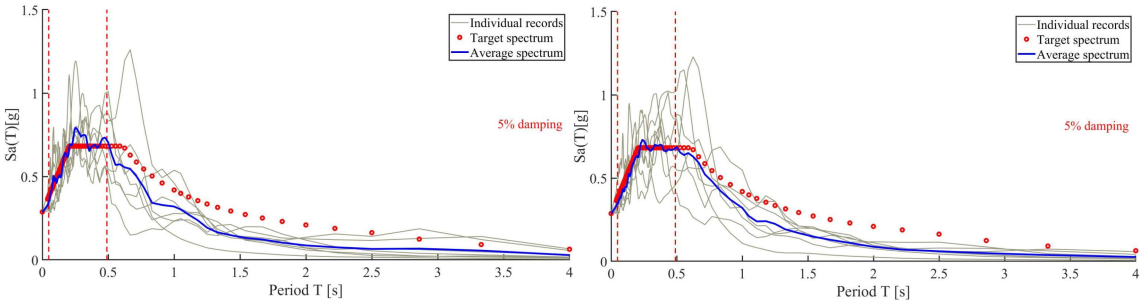

Figure 10: The spectrum-compatible seismic records in far-field conditions for the a. X and b. Y component

4.3 Derivation of fragility functions

Numerous methodologies exist in the literature for the evaluation of fragility functions. A common methodology that proposes the successive scaling of records till structural collapse onset, viz Incremental Dynamic Analysis (IDA, [38]), is adopted in the framework of this study.

The method has the competitive edge against other methodologies such as Multi-Stripes Analysis (MSA) or Cloud Analysis that it can be used even if a limited number of spectrum compatible records can be found for a particular site accounting also for the constraint in the epicentral distance, whereas other methodologies need a considerably greater number ([39]). The constraint of limited number of records is also in connection with the model scale. Before assessing the structural damage, the LSs should be determined. Only the structural members are assessed herein, whereas the nonstructural components will be presented in future publications.

Accounting for the fact that an LNG pipe rack is a critical structure that carries nonstructural components, a multi-scale approach should be considered by discriminating the collapse in local scale e.g. pipelines, meso-scale (structural members) and global scale in order to be utilized in the future within a quantitative risk framework. In particular, the Engineering Demand Parameter (EDP) that is adopted for the meso-scale is the shear force V_E, since it is related to the response of individual macroelement whilst the chord rotation θ_E or IDR can describe the global collapse (joint of more than one element, Table 3). More information about the EDPs of structural components can be found in [40].

Mechanism	Serviceability LS (SLS)	Safe Life LS (SLLS)	Collapse LS (CLS)
Flexure (rad)	$\theta_E \leq \theta_y$	$\theta_E \leq \theta_y$	$\theta_E \leq \theta_{u,\,m\text{-}\sigma}$
Shear (kN)	$V_E \leq V_{Rd.EC2}$	$V_E \leq 0.75 \cdot V_{Rd.EC8}$	$V_E \leq V_{Rd.EC8}$

Table 3: Limit states of concrete members in meso- and global-scale ([40])

The fragility functions of columns and beams are shown in Figures 11&12 only for the meso-scale investigation since the failure under bending was not found to be predominant. The SSI affects detrimentally the response of structural components both in linear and nonlinear case. An interesting result pertains to the dispersion of damage when the two cases are compared. The soil nonlinearity yields much lower dispersion (Table 4) and that might be due to the independence of structural damage vis-à-vis the modelling parameters caused by the energy dissipation of soil. We mention that the probability of exceedance of columns CLS for PGA=0.6g in the decoupled case W/ and W/O SSI soars by 43% and 81% for the linear and nonlinear soil, respectively. The pertinent values for the beams are equal to 55% and 270%.

When it comes to decoupled and coupled case, it is shown that the vulnerability of the pipe rack goes up further, however, the tendency is much higher for the beams since they become considerably fragile. The comparison of beams and columns response W/O SSI deduces that the beams fail earlier for SLS, however, the columns get more fragile for the two consecutive LSs. However, this is not the case for the coupled case for which the beams fail in advance of columns for all LSs. The fragility of beams for the CLS W/O SSI and PGA=0.6g increases by 455% from the decoupled to coupled case. The pertinent raise for the columns is only 40%. This response is justified due to the immediate dynamic interaction of beams with the pipelines. Also, noteworthy is that the pipe rack was initially designed for a low-seismicity area and that make the support of pipes totally inappropriate for the seismicity of the new placement. Also, this proves our statement in the introduction that the type of BCs is considerable in the design of the racks and should be taken into account by the codes in a clear manner considering that only the weight and the rigidity of supported equipment is presently prescribed to be accounted for the analysis.

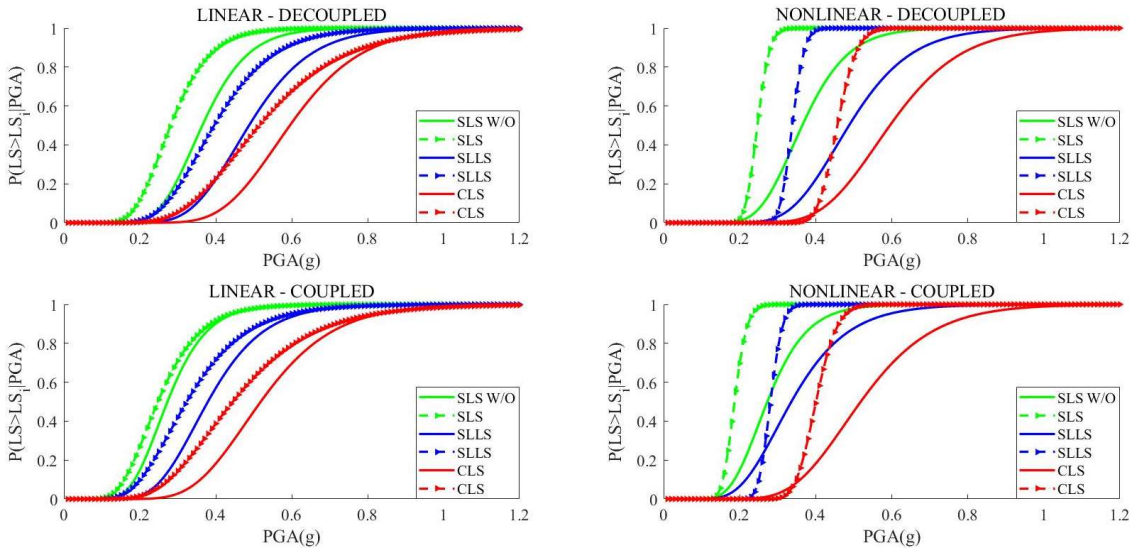

Figure 11: Fragility function for columns

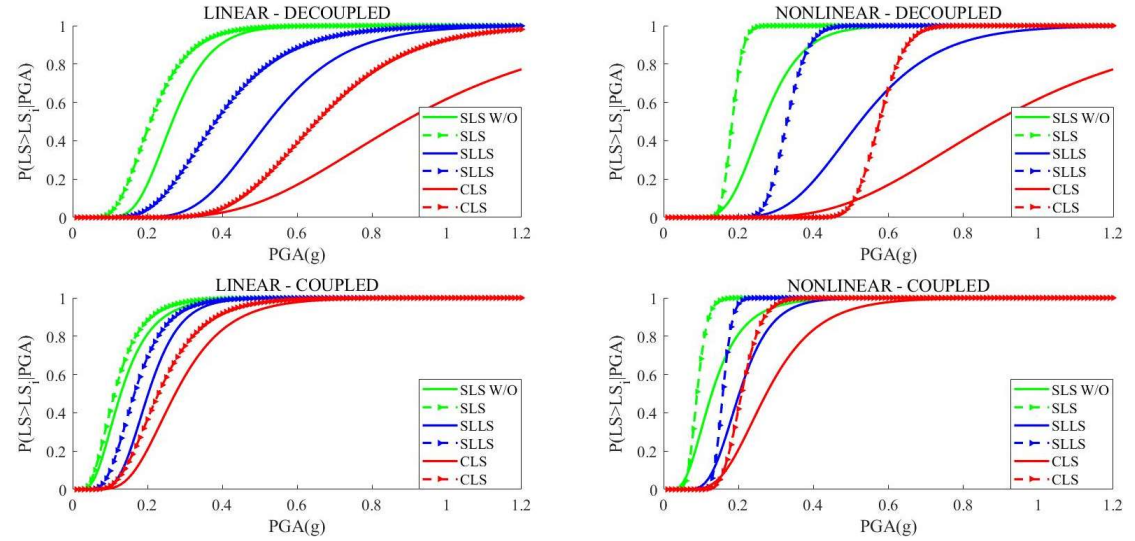

Figure 12: Fragility function for beams

Decoupled	W/O SSI			W/ SSI - Linear			W/ SSI - Nonlinear		
	SLS	SLLS	CLS	SLS	SLLS	CLS	SLS	SLLS	CLS
Columns	0.26	0.26	0.24	0.29	0.30	0.34	0.10	0.07	0.09
Beams	0.31	0.31	0.41	0.37	0.38	0.32	0.12	0.13	0.09

Table 4: Dispersion of damages for columns in decoupled case

5 CONCLUSIONS

In the present analytical paper, a two-fold purpose was addressed; first the investigation of dynamic interaction between a number of pipelines with the supporting structure, and secondly,

the effects of soil-structure interaction on structural components response. The initial review of codes and technical literature showed that there is a gap of information of code provisions upon the parameters to be considered for the analysis methodology selection. The lack of code prescriptions was confirmed by the case-study, since it was shown by means of fragility curves the tremendous impact the pipeline might have on structural components and beams specifically. The rise on beams fragility was greater than 400% for the ultimate limit state without considering the effects of soil-structure interaction. When the last interaction is considered as well, the fragility of pipe rack increases further over than 50% and 250% for linear and nonlinear soil, respectively. It was also demonstrated that the soil nonlinearity or the higher energy dissipation might constitute the response of the rack independent of modelling and therefore reduce the dispersion of damage. Finally, both beams and columns failure was observed due to shear (meso-scale).

The investigation of pipes fragility and correlation of stress-strain values with LSs of the structural components is considered essential in order to confirm that common LSs cannot apply for nonbuilding structures like the present LNG rack. Also, another important parameter in the design process will be the evaluation of peak floor acceleration that is usually proposed by the codes when nonstructural components exist. Finally, records in near-field conditions as well as compatibility for the vertical component should be considered as well to examine possible variations of the pipe rack-pipes damage. The research on the aforementioned topics is still under investigation by the Authors.

ACKNOWLEDGEMENTS

The work presented herein has received funding from the European Union's Horizon 2020 research and innovation programme under the Marie Sklodowska-Curie grant agreement No 721816. This support is gratefully acknowledged.

REFERENCES

[1] European commission, press release database: EU-U.S. Joint Statement of 25 July: European Union imports of U.S. Liquefied Natural Gas (LNG) are on the rise (http://europa.eu/rapid/press-release_IP-18-4920_en.htm#_ftn1), Brussels, 9 August 2018.

[2] "Center for liquified natural gas information upon the market and regulatory process in the United States", (https://lngfacts.org/about-lng/lng-process/).

[3] G. Antonioni, G. Spadoni, and V. Cozzani, "A methodology for the quantitative risk assessment of major accidents triggered by seismic events", *J. Hazard. Mater.*, 2007.

[4] F. Paolacci, R. Giannini, and M. De Angelis, "Analysis of the Seismic Risk of Major-Hazard Industrial Plants and Applicability of Innovative Seismic Protection Systems," in *Petrochemicals*, InTech, 2012.

[5] E. Salimi Firoozabad, B. G. Jeon, H. S. Choi, and N. S. Kim, "Seismic fragility analysis of seismically isolated nuclear power plants piping system," *Nucl. Eng. Des.*, 2015.

[6] G. DeGrassi, J. Nie, and C. Hofmayer, *Seismic Analysis of Large-scale Piping Systems for the JNES-NUPEC Ultimate Strength Piping Test Program*, 2008.

[7] L. Di Sarno and G. Karagiannakis, "Petrochemical steel pipe rack: Critical assessment of existing design code provisions and a case-study (under revision)," *Int. J. Steel Struct.*,

2019.

[8] A. S. Elnashai and L. Di Sarno, Fundamentals of Earthquake Engineering: From Source to Fragility, Second. Wiley, 2015.

[9] EN 1998-1, *Eurocode 8: Design of structures for earthquake resistance - Part 1 : General rules, seismic actions and rules for buildings*, vol. 1, no. English. 2004.

[10] E. 1998-4, Design of structures for earthquake resistance – Part 4: Silos, tanks and pipelines [Authority: The European Union Per Regulation 305/2011, Directive 98/34/EC, Directive 2004/18/EC], 2006.

[11] EN13480-3, "BSI Standards Publication Metal industrial piping Part 3 : Design and calculation," 2012.

[12] ASCE/SEI 7-16, Minimum Design Loads and Associated Criteria for Buildings and Other Structures. 2017.

[13] ASCE (2011), Guidelines for Seismic Evaluation and Design of Petrochemical Facilities. (2011). Reston, VA: American Society of Civil Engineers, 2nd Edition.

[14] M. Konstandinidou, Z. Nivolianitou, N. Markatos, and C. Kiranoudis, "Statistical analysis of incidents reported in the Greek Petrochemical Industry for the period 1997-2003," *J. Hazard. Mater.*, 2006.

[15] K. Kidam and M. Hurme, "Analysis of equipment failures as contributors to chemical process accidents," *Process Saf. Environ. Prot.*, vol. 91, no. 1–2, pp. 61–78, Jan. 2013.

[16] H. B. Surh *et al.*, "Seismic response analysis of a piping system subjected to multiple support excitations in a base isolated NPP building," *Nucl. Eng. Des.*, 2015.

[17] O. Azizpour and M. Hosseini, "A Verification Study of ASCE Recommended Guidelines for Seismic Evaluation and Design of Combination Structures in Petrochemical Facilities," *J. Appl. Sci.*, vol. 9, no. 20, pp. 3609–3628, 2009.

[18] C. Mitropoulou, C. Kostopanagiotis, M. Kopanos, D. Ioakim, and N. D. Lagaros, "Influence of soil-structure interaction on fragility assessment of building structures," *Structures*, 2016.

[19] S. T. Karapetrou, S. D. Fotopoulou, and K. D. Pitilakis, "Seismic vulnerability assessment of high-rise non-ductile RC buildings considering soil-structure interaction effects," *Soil Dyn. Earthq. Eng.*, 2015.

[20] O. Kwon and A. S. Elnashai, "Fragility Analysis of a Bridge with Consideration of Soil-Structure-Interaction Using Multi-Platform Analysis," 2007.

[21] D. Peña Ruiz and S. Guzmán Gutiérrez, "Finite element methodology for the evaluation of soil damping in LNG tanks supported on homogeneous elastic halfspace," *Bull. Earthq. Eng.*, 2015.

[22] X. Wang, Q. Zhou, K. Zhu, L. Shi, X. Li, and H. Wang, "Analysis of Seismic Soil-Structure Interaction for a Nuclear Power Plant (HTR-10)," *Sci. Technol. Nucl. Install.*, vol. 2017, pp. 1–13, 2017.

[23] G. Gazetas, "Foundation Vibrations," in *Foundation Engineering Handbook*, 1991, pp. 553–593.

[24] G. Mylonakis, S. Nikolaou, and G. Gazetas, "Footings under seismic loading: Analysis

and design issues with emphasis on bridge foundations," *Soil Dyn. Earthq. Eng.*, vol. 26, no. 9, pp. 824–853, Sep. 2006.

[25] G. Tsinidis, "On the seismic design and behaviour of tunnels", Doctoral Thesis, Aristotle University of Thessaloniki, 2015.

[26] S. L. Kramer, "Geotechnical Earthquake Engineering," in *Prentice-Hall, Inc.*, vol. 6, 1996, p. 230.

[27] SeismoSoft, "A computer program for static and dynamic nonlinear analysis of framed structures," *Available from URL: www. seismosoft. com*. 2018.

[28] I. Ishibashi and X. Zhang, "Unified dynamic shear moduli and damping patios of sand and clay.," *SOILS Found.*, 1993.

[29] "Bursi, et al., 2016a. Report on Mechanical Characterization of Selected Steel for Cyclic Loading and Temperature Sensitivity. Deliverable 4.1, INDUSE-2-SAFETY, Grant No. RFSR-CT-2014–20100025."

[30] O. S. Bursi, R. di Filippo, V. La Salandra, M. Pedot, and M. S. Reza, "Probabilistic seismic analysis of an LNG subplant," *J. Loss Prev. Process Ind.*, 2018.

[31] A. Klar and A. M. Marshall, "Shell versus beam representation of pipes in the evaluation of tunneling effects on pipelines," *Tunn. Undergr. Sp. Technol.*, 2008.

[32] O. S. Bursi, F. Paolacci, and S. Reza, "Performance-Based Analysis Of Coupled Support Structures And Piping Systems Subject To Seismic Loading," *ASME 2015 Press. Vessel. Pip. Conf.*, vol. 00032, no. July 2015, pp. 1–8.

[33] M. N. Fardis, *Seismic Design, Assessment and Retrofitting of Concrete Buildings*, vol. 8. Dordrecht: Springer Netherlands, 2009.

[34] "MATLAB and Statistics Toolbox Release 2018a, The MathWorks, Inc., Natick, Massachusetts, United States." .

[35] I. Iervolino, C. Galasso, and E. Cosenza, "REXEL: Computer aided record selection for code-based seismic structural analysis," *Bull. Earthq. Eng.*, vol. 8, no. 2, pp. 339–362, 2010.

[36] NTC, 2018*,* "Norme Tecniche per le costruzioni"*, DM Infrastructure, 14 January*. (in Italian).

[37] M. Heydari and M. Mousavi, "The Comparison of Seismic Effects of Near-field and Far-field Earthquakes on Relative Displacement of Seven-storey Concrete Building with Shear Wall," *Curr. World Environ.*, 2015.

[38] D. Vamvatsikos and C. Allin Cornell, "Incremental dynamic analysis," *Earthq. Eng. Struct. Dyn.*, vol. 31, no. 3, pp. 491–514, 2002.

[39] J. W. Baker, "Efficient analytical fragility function fitting using dynamic structural analysis," *Earthq. Spectra*, 2015.

[40] "Fardis M.N. (2014) From Performance- and Displacement-Based Assessment of Existing Buildings per EN1998-3 to Design of New Concrete Structures in fib MC2010. In: Ansal A. (eds) Perspectives on European Earthquake Engineering and Seismology. Geotechnical, Geological and Earthquake Engineering, vol 34. Springer, Cham".

COMPDYN 2019
7th ECCOMAS Thematic Conference on
Computational Methods in Structural Dynamics and Earthquake Engineering
M. Papadrakakis, M. Fragiadakis (eds.)
Crete, Greece, 24–26 June 2019

SEISMIC VULNERABILITY ASSESSMENT OF NON-ENGINEERED MASONRY BUILDINGS IN MALAWI

Viviana Novelli[1], Ignasio Ngoma[2], Panos Kloukinas[3], Innocent Kafodya[4], Raffaele De Risi[5], John Macdonald[6] and Katsuichiro Goda[7]

[1, 5, 6] Department of Civil Engineering, University of Bristol, Bristol, BS8 1TR, UK
e-mail: {viviana.novelli, raffaele.derisi, john.macdonald}@bristol.ac.uk

[3] Faculty of Engineering & Science, University of Greenwich, Chatham, ME4 4TB, UK
e-mail: {p.kloukinas}@greenwich.ac.uk

[2, 4] University of Malawi - The Polytechnic, Malawi
e-mail: {ingoma, ikafodya}@poly.ac.mw

[7] Department of Earth Sciences, Western University, London, N6A 5B7, Canada
e-mail: {kgoda2@uwo.ca}

Abstract

Malawi is located within the southern branch of the active East African Rift System, where earthquakes of Mw 7.0 (or greater) can occur along major faults. In Malawi, the majority of dwellings in both formal and informal settlements are non-engineered unreinforced masonry constructions, built by local artisans with little input from engineers. These constructions are highly vulnerable to seismic events due to poor materials and lack of construction detailing. This study develops analytical vulnerability functions that enable the assessment of seismic capacity of typical buildings in Malawi. Since the seismic vulnerability greatly depends on building characteristics, geometrical and structural data are collected by conducting semi-rapid surveys of 300 houses located in urban and rural areas of Central and Southern regions of Malawi. Mechanical properties of the local materials are also obtained from an experimental campaign. In this work, a mechanical method FaMIVE (Failure Mechanism Identification and Vulnerability Evaluation) is adopted and the effects of both in-plane and out-of-plane behaviour of the masonry structures are taken into consideration to derive capacity curves for seismic vulnerability assessment. Special attention is given to 1) the Malawian building typologies as described in the Word Housing Encyclopedia and 2) failure mode classes for the Malawian constructions as calculated by FaMIVE. Hence, the derived vulnerability functions can serve as a benchmark for typical buildings in Malawi. The results and conclusions are also relevant for other East African countries, where similar construction techniques are adopted.

Keywords: non-engineered masonry constructions, mechanical approach, seismic vulnerability, capacity curves, East African Rift System

1. INTRODUCTION

Malawi is located in Sub-Saharan Africa and shares borders with Mozambique, Zambia, and Tanzania. The country is ranked as the third poorest country in the world [1, 2]; where the main economic sector is agriculture, which is often negatively affected by adverse environmental disturbances and hazards (e.g. drought, poor health, heavy rains, windstorms, and floods).

Malawi is also a seismic-prone country within the southern branch of the active East African Rift System, where M_w 7.0 (or greater) earthquakes can occur near major geological faults [3, 4]. In recent years, the most significant earthquake in the country occurred in 1989 with Mw 5.7 in Central Malawi, making 50,000 people homeless [5].

In Malawi, residential buildings are made of unreinforced masonry and are regarded as non-engineered constructions, since they are built by local artisans with little input from qualified engineers. These dwellings are built informally, using poor-quality materials and inadequate structural detailing. Issues related to seismic vulnerability of non-engineered masonry structures need to be investigated through methods for building performance assessment by taking into account geometry and strengths/weakness of local structures. In fact, such an undesirable situation is prevalent across many countries in East Africa and most developing countries around the world.

During the first preliminary investigation carried out in Malawi by the authors to identify the prevalent building features and understand local construction practice, information was gathered from the Malawi Housing and Population Census [6] and World Housing Encyclopedia [7], and the Malawian Safer Housing Construction Guidelines [8]. As discussed in [9], collected data underlined high inconsistencies between datasets, highlighted by different criteria adopted to identify building typologies and distributions and non-compliance with design standards and guidelines.

To overcome discrepancies identified in the available data, in this work on-site investigations on local constructions are carried out with the aim at investigating the real distribution of the local buildings and identify parameters affecting the seismic vulnerability of the selected regions. Based on the collected data, seismic performance of the inspected houses is estimated by using a viable mechanical approach FaMIVE (Failure Mechanism Identification and Vulnerability Evaluation; [10, 11]), which evaluates failure modes and capacity curves by taking into account geometrical/structural features observed on site and mechanical parameters derived experimentally. Results will provide useful data for the development of structural vulnerability evaluation tools for masonry structures in Malawi, and for the implementation of risk assessment frameworks for East African countries [12].

2. METHODOLOGY

In order to enhance the data on building features of the Malawian buildings available from local/global datasets and guidelines [6, 7, 8], on-site structural surveys were carried out on 300 buildings. Data collected during the on-site inspections characterize urban and rural settlements of the Central-Southern Malawi, selected as a representative country in the East African Rift region, where rapid expansion of informal settlements is occurring. Recorded information includes geometry in plan and elevation, structural condition related to connections between walls, roof structures, masonry type and fabric quality, as discussed in Section 3. With reference to the collected data, in Section 4 inspected buildings are classified in building typologies. The adopted classification for the Malawian constructions was proposed by the authors in a World Housing Encyclopedia report [13], where three typologies were identified to classify buildings according to their expected seismic vulnerability.

Seismic performance and actual vulnerability of the three identified building typologies are evaluated in Section 5 using the mechanical approach FaMIVE [10, 11]. The proposed approach was adopted to capture failure modes and derive capacity curves as a function of the geometrical/structural data collected on site. Furthermore, since the major factors influencing the building performance are correlated the strength properties of masonry materials commonly used for housing construction in Malawi, these are also defined following an experimental campaign, carried out on local materials [14]. Results obtained from the laboratory testing and their correlation with different types of materials observed on site are discussed in Section 5.1.

The building performances derived from the urban settlements of Balaka and in the rural settlements in Lifidzi are focused upon. The seismic vulnerability of these buildings is discussed in Section 5.2 where failure mode distributions are illustrated and in Section 5.3, where capacity curves are presented. The results for the two different sites highlight how buildings with the same material types and roof structures, within the same (broad) building class, behave differently and have, consequently, dissimilar vulnerability. This is due to a high variety of construction details (e.g. different fabric quality and connection levels between walls observed for each identified typology) between rural and urban settlements which is extremely dependent on material and resource availability of a specific area.

3. ON-SITE STRUCTURAL SURVEYS

On-site structural surveys were carried out on 300 non-engineered buildings located in formal and informal settlements in the urban areas of Salima and Balaka and in the informal settlements of the rural villages Lifidzi and Golomoti (see Figure 1(a) and 1(b)). For each building, data were collected only for two orthogonal façades, since parallel walls of the inspected buildings had similar opening layouts. Data collection consisted of taking a few geometrical measurements as the ones illustrated in Figure 1 (c) (i.e. plan geometry, building/gable height, and opening dimensions and layout). Information related to structural features, such as masonry and mortar types, roof structure, connection levels between walls, and between walls and roof, were also collected.

Furthermore, since the inspected houses were constructed using locally-sourced materials with poor quality control, and construction materials differ considerably in shape, homogeneity, consistency, density, and brittleness, the fabric quality of the observed construction materials was recorded and defined as:

(1) good fabric quality: bricks have regular shapes and regular mortar layers. The clay has a homogeneous texture. Overlapping of bricks is regular. The bricks might have hairline cracks or cracks are apparently absent.
(2) medium fabric quality: bricks have uneven shapes and partially regular mortar layers. The clay has a medium porosity. Overlapping of bricks is partially regular. The bricks might have light cracks or small holes.
(3) poor fabric quality: bricks have irregular shapes and mortar layers. The clay has high porosity. Overlapping of bricks is irregular. The bricks have deep cracks or are partially lost.

Deficiencies derived from poor structural detailing, presence of damage, material loss and lack of maintenance were also investigated during the structural survey to take into account how existing structural weakness impacts on the performance of the investigated buildings.

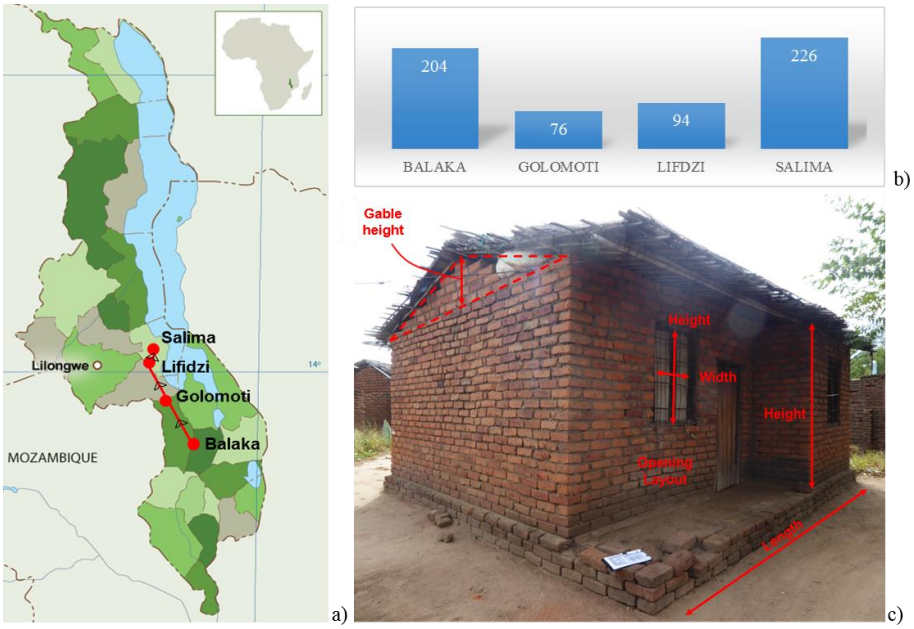

Figure 1: a) Building survey locations, Balaka, Golomoti, Lifidzi, and Salima; b) number of façades collected for each site c) geometrical measurments collected for each inspected façade

4. BUILDIGN CLASSIFICATION

Data collected on site were used to classify the inspected buildings in typologies, which are adopted in Section 5 to derive the vulnerability of the Malawian constructions. In Table 1, the inspected buildings are classified according to material type (a: unfired bricks, b: unfired bricks), fabric quality (1: good, 2: medium; 3: poor), and roof type (thatched/metallic sheet roof). Main features of the inspected constructions are reported in Figure 2.

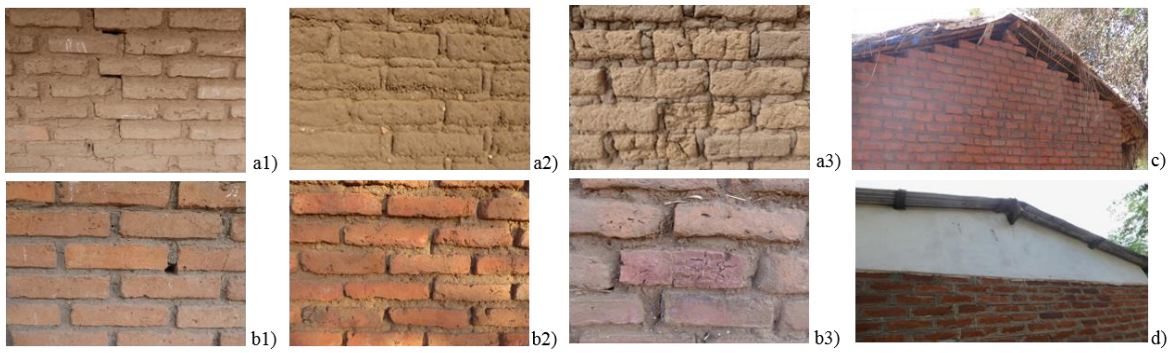

Figure 2: a1) and b1) good; a2) and b2) medium and a3) and b3) poor fabric quality of unfired and fired bricks, respectively c) thrached roof and d) metallic sheet roof

Most of the observed buildings (82%) were made of fired bricks, since these are affordable materials to be sourced on-site, and they do not require high construction skills. Mud mortar was identified for 76% of the inspected buildings, while cement mortar, observed for the remaining inspected houses, is gradually being adopted. Fabric quality varies considerably from poor to good and underlines the need of assessing the building performance by defining mechanical properties which reflect the actual masonry strength according to the different fabric quality identified on site (see Section 5.1).

The majority of the inspected houses (55%) were built with single-skin walls with thickness varying from 100 mm to 160 mm. For these constructions, the connections between adjacent walls were assumed poor, while for the remaining inspected houses with double-skin walls and thickness varying from 210 mm to 260 mm, the connections between walls were assumed stronger only if cement mortar was employed. Regarding building roofs, these were made of timber rafters supporting thatch for 21% of the inspected buildings or light metallic corrugated sheets for the remaining ones. Both roof types were inspected on site and classified as light systems, as they are not rigid along the entire plane do not act as rigid diaphragm.

According to the collected data described above, inspected buildings, as illustrated in Table 1, are classified in three typologies: A, B, and C (shown in Figure 3) introduced in the World Housing Encyclopedia by the authors [9, 13] Typology A is representative for 20% of the inspected buildings, characterized by low seismic vulnerability (Figure 3 (a)). These buildings were made of mud mortar combined with fired bricks of poor fabric quality (see Figure 2(b3)) and unfired bricks from poor to high fabric quality (see Figure 2(a1), (a2), and (a3)). Generally, these houses have smaller building footprints than the typical floor plan of 8 m × 6 m. Most of these houses (17%) have thatch supported by light timber elements, while the remaining are made with metallic sheet roof. Roof structures are characterized by a poor structural detailing (e.g. lack of connection between walls and between the walls and roof).

	Thatched roof				
	Unfired bricks + mud mortar			Fired bricks +mud mortar	
	a1	a2	a3	b2	b3
	1.2%	11.3%	1.8%	4.6%	2.5%
typology	A			B	A

	Metallic sheet roof							
	Unfired bricks + cement mortar			Fired bricks +mud mortar			Fired bricks + cement mortar	
	a1	a2	a3	b1	b2	b3	b1	b2
	0.3%	2.5%	0.6%	3.7%	41.4%	6.4%	11.7%	12.0%
typology	A			B			C	

Table 1: Building distribution with reference to material type (a: unfired brick, b: fired brick), fabric quality (1: good; 2: medium and 3: poor), and roof type (thatched or metallic sheet roof).

The most common typology observed in Malawi, B, representing 52 % of the buildings, is rated as medium seismic vulnerability (see Figure 3(b)). These buildings were made of fired bricks characterized from poor to a good quality fabric (Figure 2(b1), (b2), and (b3)). Due to the presence of mud mortar in these houses, the bonding between bricks is considered poor, therefore connections between walls were assumed weak. The construction details varied significantly, as well as maintenance levels.


a) b) c)

Figure 3: Typical one-story masonry building in Malawi. a) typology A; b) typology B; c) typology C

Typology C covers 28% of the inspected houses (see Figure 3(c)). These were made of fired bricks from poor to good quality fabric (Figure 2(b1), (b2), and (b3)) and cement mortar. Generally, these houses had a larger floor plan than the typical plan. Due to the extended plan

size, irregularities were likely to occur (e.g. portico and re-entrant corner). Most of these houses had corrugated metallic sheets supported by timber elements or truss, and good structural detailing (e.g. adjacent walls and walls/roof are connected). The good structural quality of these houses can be also attributed to the presence of strengthening elements (e.g. ring beams).

5. DERIVATION OF SEISMIC PERFORMANCE FOR BUILDING TYPOLOGIES

In this work, results are shown for two locations: Lifidzi and Balaka, classified as a rural and an urban area, respectively. These sites are adopted in this study with the scope of illustrating that buildings with the same construction material types and roof structures, classified in the same typologies (i.e. A, B and C), they may have a different seismic response. This is stated because, during the on-site survey, it was observed that buildings of the same typology are often characterized by a different geometry (i.e. plan size, height, and opening layouts) or a different fabric quality (dimensions of the bricks, bonding between brick-mortar in terms of friction and cohesion) or a different level of structural conditions (connections between orthogonal walls, and between the walls and roof). Therefore, there is a high possibility that the different observed parameters could impact on the behaviour of the individual building and consequently, on the vulnerability of the specific typology.

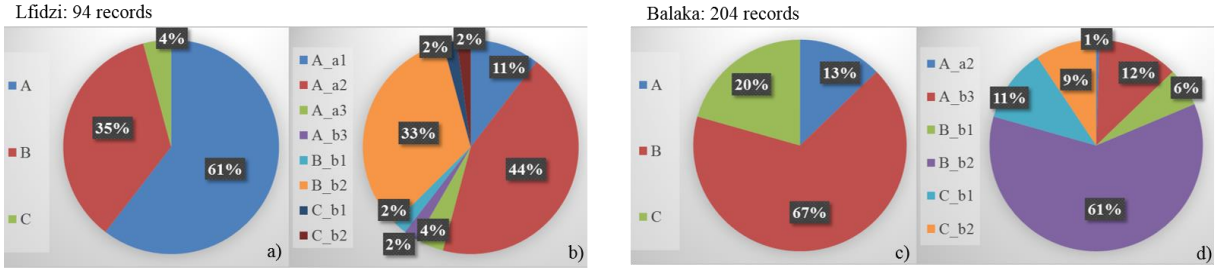

Figure 4: a) and c) Building typology distribution (A, B and C) identified in Lifidzi and Balaka; b) and c) each identified building typology is associated to inspected material type and fabric quality, where a1 and b1 is good; a2 and b2 is medium and a3 and b3 poor fabric quality for unfired and fired bricks.

Before discussing the results obtained for the two different sites, Figure 4(a) and 4(c) are presented to illustrate the building distributions identified for building typologies A, B and C for Lifidzi and Balaka, respectively. As expected, the weakest typologies A, built with unfired bricks and low low-quality of fired bricks, has a higher concentration in Lifidzi, where houses are constructed in rural communities by local builders/artisans in absence of technical guidance. Building typologies B and C are more concentrated in Balaka, where houses are built using materials with better mechanical properties than the ones in rural areas. Figure 4(b) and 4(d) present the fabric quality observed in the three typologies, underlining, as expected, that materials adopted in Balaka have better fabric quality than the ones observed in Lifidzi. This can be underlined by typology A, where 79% of the houses belonging to this class for Lifidzi are made of unfired bricks of medium/poor fabric quality against the 4% in Balaka, where houses are mainly made of fired bricks of poor fabric quality. For typology B, 16% of the houses in Balaka are made with bricks of high fabric quality compared to 6% identified in Lifidzi, while the remaining houses for both sites are made of bricks with medium fabric quality. For typology C, houses belonging to this class, cover only 4% of the inspected houses in Lifidzi, whereas 20% observed in Balaka. Mechanical properties defined for the different material types are indicated in Section 5.1. As discussed in Section 4, roofs are made in thatch or metallic corrugated sheets supported by timber elements, therefore in both cases it is assumed

that the roof structures behave as flexible horizontal systems. Furthermore, for the classes A and B, it is assumed that the roof structure is completely detached from the walls, in order to be consistent with the observations on site. As for the connections between walls, they are assumed absent for houses constructed with single-skin walls, features belonging to 63% of the inspected houses in Lifidzi and Balaka.

5.1 Strength of local masonry in Malawi

Strength properties of masonry materials commonly used for housing construction in formal and informal settlements in Malawi, were investigated by means of laboratory testing, conducted on masonry prisms and panels [14]. The tests were conducted with the scope at reproducing actual field conditions and construction practices in the country. Based on the observations from the on-site structural surveys, specimens were prepared by local artisans using local commercial production of brick batch and mortar types in mud and cement, which were cured in uncontrolled conditions. The results revealed that the behaviour of the masonry in compression is governed by the low compressive strength of the brick units. It was also found that the quality of the brick-mortar bonding governs the in-plane shear and out-of-plane flexural behaviour, which are the critical parameters of the resistance to horizontal loading, such as earthquake action. These are directly related to the quality of the brick-mortar interface bonding and the thickness of the walls. Values for interface cohesion, measured by means of standard triplet shear testing, vary between 0.01-0.02 MPa for mud mortar and between 0.2-0.25 MPa for cement mortar configurations. Friction angles were measured at around 32 degrees.

With reference to these measured values, they are used to define the mechanical properties of the observed fired bricks with mud and cement mortar with a good fabric quality. In evaluating seismic vulnerability of the houses based on FaMIVE, typologies with poor/medium structural features are penalized by considering that their fabric quality and brick-mortar bonding are inferior compared to the ones derived from the tested materials [11].

5.2 Estimation of load factor multipliers and failure mode distribution

The seismic performance of the buildings inspected in Lifidzi and Balaka is assessed using FaMIVE [10, 11, 15, 16]. The approach is based on a mechanical procedure, relying on the assumption that buildings behave as an assemblage of macro elements, held together by compressive forces. Analyses are performed using equilibrium equations, where earthquake actions are simulated as a horizontal static force, proportional to the mass of the single inspected façade. The analysis is static equivalent and aims to predict the horizontal static actions, quantified by means of collapse load factor multipliers (λ), corresponding to a percentage of gravity acceleration, g [10, 11]. The factor λ is calculated for each of the failure modes, which are defined as all possible collapse mechanisms that can occur for a masonry building subjected to earthquake shaking. The estimated values of λ indicate the lower bounds of the level of shaking which trigger the identified failure modes. Among the computed collapse load factor multipliers, the failure mode with the smallest multiplier is considered to occur on a façade (as the weak link). In implementing the FaMIVE method, geometrical/structural features described in Sections 3 and 4 for the inspected houses in Malawi are used as input of the proposed approach. Furthermore, since masonry type, fabric quality, and connection level between walls have a considerable impact on the building responses, both angle of friction and cohesion taken from Section 5.1, and relative dimensions of bricks and walls taken from the survey carried on site were adopted to assess the capacity of the inspected buildings.

The occurrence of λ, evaluated for the selected building stocks in Lifidzi and Balaka are illustrated in Figure 5(a). The median of λ, being 0.24g and 0.38g for Lifidzi and Balaka re-

spectively, underlines that the buildings inspected in Lifidzi are weaker than the ones inspected in Balaka, as they fail for lower values of λ. This is also highlighted by the slope of the cumulative curve: the one derived for Lifidzi has a higher slope than the one derived for Balaka (i.e. for λ = 0.35g, 72% and 35% of the inspected buildings fail in Lifidzi and Balaka, respectively).

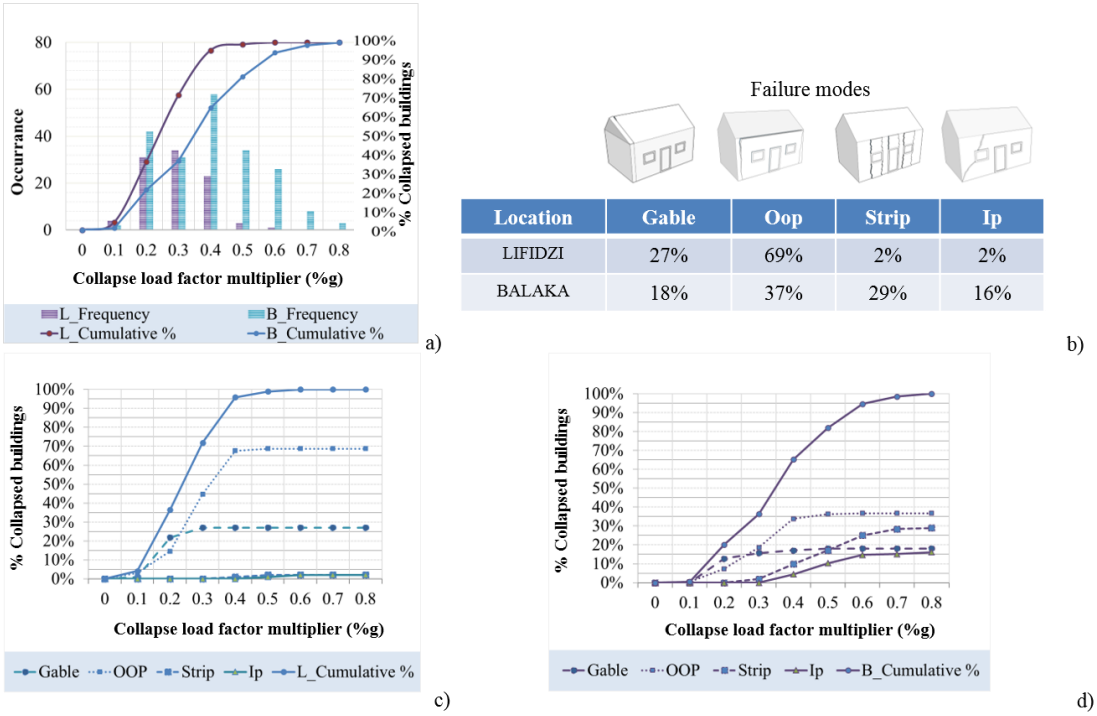

Location	Gable	Oop	Strip	Ip
LIFIDZI	27%	69%	2%	2%
BALAKA	18%	37%	29%	16%

Figure 5: a) Collapse load factor multiplier distribution in the selected building stocks in Lifidzi (L) and Balaka (B); b) failure modes distribution; c) collapse load factor multiplier distribution for the failure modes identified in Lifidzi (L) and d) collapse load factor multiplier distribution for failure modes identified in Balaka (B)

The failure modes associated with the identified collapse load factor multipliers are illustrated in Figure 5(b). These are classified into four categories: 1) *Gable*: predominantly occurs on walls with gables which are not connected to roofs, and therefore fail in overturning; 2) *Oop*: Out of plane, predominantly occurs on single-skin walls with a low-quality material and poor connection with orthogonal walls and roof, causing overturning of a single façade; 3) *Strip*: predominantly occurs on single-/double-skin walls with a medium-quality material and a good connection with orthogonal walls and roof; causing overturning of a strip of piers and spandrels; and 4) *Ip*: In-plane, predominantly occurs on single/double-skin walls with a medium-quality material and a good-quality connection with orthogonal walls and roof; causing shear failure of a single façade.

As expected from the on-site surveys, since a lack of connections between the walls and roof and low-quality construction materials were frequently observed in the inspected buildings in Lifidzi, *Oop* is the most likely failure mode with a percentage of 69%. By contrast in Balaka, there is a smaller percentage of buildings failing in *Oop* (37%), and a higher percentage of buildings failing for *Strip* (29%), where the latest occurs on buildings with stronger connections, belonging to typologies B or C. Only a small percentage of the inspected buildings fail for *Ip* (16%), emphasizing that even buildings of typology C, built with double-skin walls, fired bricks of better quality and cement mortar, mostly fail due to overturning of ga-

bles, walls, and spandrels and piers, due to use of poor construction materials and construction practice details.

Figure 5(c) and 5(d) show the distribution of collapse load factor multipliers for the failure modes identified in Lifidzi and Balaka, respectively. *Gable* failure modes occur for the lowest values of λ (smaller than 0.3g) for inspected buildings with tall gables, resulting in separation of their roofs. Buildings in classes B and C, classified in a medium high-quality class, mostly fail for *Strip* and *Ip* failure modes with the highest values λ, (greater than 0.3g). Regarding *Oop*, λ varies from a minimum value of 0.1, values identified for buildings belonging to typology A, to 0.4, values identified for buildings belonging to typologies B and C.

5.3 Derivation of capacity curves

In this section, capacity curves are derived for the building typologies identified in Lifidzi and Balaka with reference to [10, 11, 16, 17, 18]. Derived capacities strictly correspond to the parameters defining the geometry, structural conditions, connection level between walls, material types and fabric quality of the inspected buildings in the case study. Multiple capacity curves, one for each analysed façade, are derived for a single building. This is because capacity curves are directly developed from the load factor multipliers, which are also calculated for each inspected façade, as illustrated in Section 5.2.

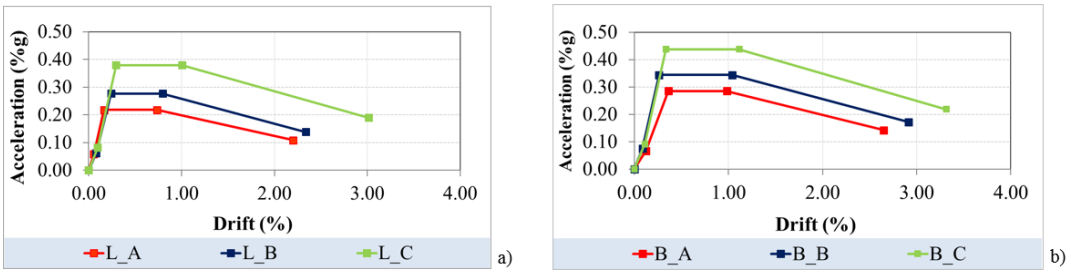

Figure 6: Median capacity curves for a) the building typologies: A, B and C for Lifidzi and Balaka, respectively

The maximum strength or maximum acceleration (g) in a capacity curve is taken equal to the minimum collapse load factor estimated by FaMIVE for each inspected façade. The elastic limit displacement of each façade is calculated as a function of the elastic stiffness and the mass of the façade, involved in the identified failure mode. The ultimate displacement is defined as the displacement identifying the geometrical instability of the façade and hence its collapse. Computed these displacements, these are divided by the height of the single inspected façade to derive the drift.

Figure 6 shows the different capacity curves derived for the building typologies A, B, and C identified in Lifidzi and Balaka, respectively. As expected from the definition of the three typologies, it is noticeable that the building typology A (class of buildings characterized by low-quality materials and construction details) has the lowest values of acceleration and drift compared to B and C. Clearly, the derived capacity curves are capable of capturing the different performances for the single typology. Furthermore, they underline that classifying buildings according to structural conditions and differentiating mechanical properties with respect to the fabric quality improve the reliability of the vulnerability obtained for the single typology. This can be observed particularly for the different values of acceleration obtained for typologies B (maximum acceleration is 0.29g, and 0.35g for Lifidzi and Balaka, respectively), and C (maximum acceleration is 0.38g, and 0.43g for Lifidzi and Balaka, respectively) which point out that buildings of the same typology (same construction materials and roof

types) located at different sites and subjected to different levels of quality control are likely to behave differently under seismic events. Conversely for the typology A, the values of maximum acceleration are the same (0.21g), underlining that the two classes in the two sites have same vulnerability, as they are constructed using poor materials with same mechanical properties.

6. CONCLUSIONS

This paper has shown the results derived from a seismic vulnerability study carried out for representative non-engineered masonry buildings in Central-Southern Malawi. The presented work integrates an effective methodology for collecting data, classifying non-engineered masonry buildings in main typologies, correlating observed masonry types to their strength measured experimentally, and assessing vulnerability. The data collected during the structural investigations and presented in this paper have enhanced the available information related to building distribution and typologies compared with local/global datasets that were previously available for the Malawian constructions (Ngoma & Sassu, 2002; National Statistical Office of Malawi, 2008; Bureau TNM, 2016). Furthermore, this work illustrates the importance of gathering detailed structural information, including masonry type, fabric quality, bonding between masonry and mortar, and connection levels between walls. Moreover, the vulnerability calculated for this work can offer notable advantages to identify failure modes and derive capacity curves for non-engineered masonry buildings which could be further implemented in a risk assessment tool together with enhanced local data.

DATA ACCESS STATEMENT

The underlying data can be obtained by contacting the first author.
DOI: 10.5523/bris.2dqckine9t2rk2k1t0ifxt1ac5

ACKNOWLEDGEMENT

This work is supported by the Engineering and Physical Science Research Council through the PREPARE project (EP/P028233/1) and by the EEFIT research grant.

REFERENCES

[1] Food and Agriculture Organization of the united Nations (FAO), International fund for Agricultural Development (IFAD), &World Food Programme (WFP), Achieving Zero Hunger The critical role of investments in social protection and agriculture. *Rome, FAO,* 2015.

[2] World Bank. World Bank Annual Report 2017 (English). *Washington, D.C. World Bank Group. http://documents.worldbank.org/curated/en/143021506909711004/World-Bank-Annual-Report-2017,* 2017

[3] M. Hodge, J. Biggs, K. Goda, W. Aspinall, Assessing infrequent large earthquakes using geomorphology and geodesy: the Malawi Rift. *Natural Hazards, 76(3), 1781-1806,* 2015.

[4] V. Poggi, R. Durrheim, G. M. Tuluka, G. Weatherill, R. Gee, M. Pagani, A. Nyblade, & D. Delvaux, Assessing seismic hazard of the East African Rift: a pilot study from GEM and AfricaArray. *Bulletin of Earthquake Engineering, 15(11), 4499-4529,* 2017.

[5] V. Midzi, B. Manzunzu, Large recorded earthquakes in sub-Saharan Africa. Extreme Natural Hazards. *Disaster Risks and Societal Implications, 1, 214,* 2014.

[6] National Statistical Office of Malawi, Population and Housing Census 2008. *National Statistical Office, Zomba, Malawi*, 2008.

[7] I. Ngoma, M. Sassu, Rural mud wall building (Report 43). *World Housing Encyclopedia, Earthquake Engineering Research Institute, California, USA*, 2002.

[8] Bureau TNM, Safer House Construction Guidelines. *Available at https://issuu.com/saferconstructionguidelines/docs/no-crocini*, 2016.

[9] V. Novelli, P. Kloukinas, R. De Risi, I. Kafodya, I. Ngoma, J. Macdonald, K. Goda, Seismic Mitigation Framework for Non-engineered Masonry Buildings in Developing Countries: Application to Malawi in the East African Rift. *Book Title: Resilient Structures and Infrastructure, Chapter 8. DOI 10.1007/978-981-13-7446-3_8. Publisher: Springer Singapore*, 2019.

[10] D. D'Ayala, E. Speranza, Definition of collapse mechanisms and seismic vulnerability of historic masonry buildings. *Earthquake Spectra, 19(3), 479-509*, 2003.

[11] D. D'Ayala, Force and displacement-based vulnerability assessment for traditional buildings. *Bulletin of Earthquake Engineering, 3(3), 235-265*, 2005.

[12] K. Goda, P. Kloukinas, R. De Risi, M. Hodge, I. Kafodya, I. Ngoma, J. Biggs, A. Crewe, A. Fagereng, J. Macdonald, Scenario-based seismic risk assessment for Malawi using improved information on earthquake sources and local building characteristics. *16th European Conference on Earthquake Engineering (16ECEE): 18-21 June 2018*: *Thessaloniki, Greece*, 2018.

[13] V. Novelli, P. Kloukinas, I. Ngoma, I. Kafodya, J. Macdonald, K. Goda, Unreinforced masonry houses made of fired clay bricks (Report 205). *World Housing Encyclopedia, Earthquake Engineering Research Institute, California, USA*, 2018.

[14] P. Kloukinas, I. Kafodya, I. Ngoma, V. Novelli, J. Macdonald, K. Goda, Strength of materials and masonry structures in Malawi. SEMC 2019: *The Seventh International Conference on Structural Engineering, Mechanics and Computation: 2-4 September 2019: Cape Town, South Africa*, 2019.

[15] C. Casapulla, D. D'Ayala, In-plane collapse behaviour of masonry walls with frictional resistances and openings. *5th International Seminar on Structural Analysis of Historical Constructions: 6-8 November 2006, New Delhi, India*, 2006.

[16] V. I Novelli, D. D'Ayala, N. Makhloufi, D. Benouar, A. Zekagh, A procedure for the identification of the seismic vulnerability at territorial scale. Application to the Casbah of Algiers. *Bulletin of Earthquake Engineering, 13(1), 177-202*, 2015.

[17] D. D'Ayala, V. Novelli, Seismic Vulnerability Assessment: Masonry Structures. *In: Beer M., Kougioumtzoglou I., Patelli E., Au IK. (eds) Encyclopedia of Earthquake Engineering. Springer, Berlin, Heidelberg*, 2014.

[18] V. Novelli, D. D'Ayala, Assessment of the most damaged historic centres of the Region Emilia Romagna due to the earthquake of the 20th and 29th of May 2012. *Ingegneria Sismica, 29(2-3), 59-71*, 2012.

COMPDYN 2019
7th ECCOMAS Thematic Conference on
Computational Methods in Structural Dynamics and Earthquake Engineering
M. Papadrakakis, M. Fragiadakis (eds.)
Crete, Greece, 24–26 June 2019

IDENTIFYING UNCERTAINTY CONTRIBUTIONS TO THE SEISMIC FRAGILITY ASSESSMENT OF A NUCLEAR REACTOR STEAM LINE

Pierre Gehl[1], Marine Marcilhac-Fradin[2], Jeremy Rohmer[1], Yves Guigeno[2], Nadia Rahni[2], Julien Clément[2]

[1] BRGM
Orléans, France
p.gehl@brgm.fr, j.rohmer@brgm.fr

[2] IRSN
Fontenay-aux-Roses, France
marine.marcilhacfradin@irsn.fr, yves.guigueno@irsn.fr, nadia.rahni@irsn.fr, julien.clement@irsn.fr

Abstract

In nuclear applications, fragility curves are an essential element of the seismic probabilistic safety assessment that is performed at the level of the power plant. They are required to account for the aleatory randomness and the epistemic uncertainty generated by various sources of variability, such as the representation of the seismic input by intensity measures, the assumptions in the structural model (e.g., mechanical or geometrical parameters) and the confidence in the statistical estimation of the fragility parameters (i.e., related to number of data points used). Therefore, this study investigates the relative contributions of such variables to the dispersion of the resulting fragility functions, while ensuring the separation between aleatory and epistemic uncertainty sources, as advocated by the standards in effect in the nuclear industry. To this end, vector-valued fragility functions, based on two intensity measures, are also investigated: it appears that they allow for a partial transfer from the record-to-record variability to an epistemic uncertainty component that is related to the description of the seismic loading given the hazard at the studied site.
The proposed uncertainty decomposition is applied to the fragility assessment of the main steam line of a nuclear reactor: the total dispersion of the resulting fragility models is then decomposed into different aleatory and epistemic components. Although it is found that vector-valued intensity measures contribute to a significant part of the total dispersion, the uncertainty due to the variability of mechanical and geometrical parameters appears to be even larger.

Keywords: Fragility curves, intensity measures, dynamic analysis, epistemic uncertainty.

1 INTRODUCTION

The quantification of the vulnerability of structures and equipment constitute a crucial step of the seismic Probability Safety Assessment (PSA) of a Nuclear Power Plant (NPP). To this end, fragility curves are common tools developed in the nuclear industry. The vulnerability of a component may then be represented by the so-called High Confidence Probability of Failure (HCLPF) capacity, which corresponds to the value of the intensity measure (IM) leading to a failure probability of 5% on the 95% confidence interval of the fragility curve (EPRI, 2003). Therefore a rigorous distinction between aleatory and epistemic uncertainty sources is required, following for instance the decomposition proposed by Kennedy et al. (1980): the total dispersion β of the fragility curve is decomposed into a term β_R representing aleatory randomness (i.e., the "slope" of the curve) and a term β_U representing epistemic uncertainty (i.e., the width of the confidence interval).

$$P_f(im) = \Phi\left(\frac{\ln im - \ln \alpha + \beta_U \Phi^{-1}(Q)}{\beta_R}\right) \quad (1)$$

where P_f is the conditional probability of reaching or exceeding a given damage state, Φ is the normal cumulative distribution function, α is the median of the fragility function, and Q is the confidence level

Due to the complexity of a ground-motion time history, the description of the seismic loading through a single IM is acknowledged as a significant source of uncertainty, usually referred to as the record-to-record variability. Several studies have addressed this issue, either by searching for adequate IMs (Luco & Cornell, 2007; Padgett et al., 2008) or by deriving vector-IM fragility functions or surfaces (Baker & Cornell, 2005; Seyedi et al., 2010; Modica & Stafford, 2014). Generally, a decrease in the dispersion of the fragility functions is observed, however its interpretation in terms of uncertainty transfer remains to be clarified. Therefore, the aim of this study is to quantify the various uncertainty sources that may contribute the total dispersion of the derived fragility models. In particular, the comparison between single-IM fragility curves and vector-IM fragility functions should offer insight on the treatment of record-to-record variability and on its impact on the aleatory uncertainty component.

The proposed analysis will be demonstrated on the fragility assessment of the main steam line of a pressurizer water reactor (Rahni et al., 2017), using a set of nonlinear time-history analyses (Section 2). Then, several criteria for the selection of IMs will be investigated (Section 3), before deriving vector-IM fragility functions with multivariate regression models (Section 4). Finally, in Section 5, three main types of uncertainty will be compared thanks to different fragility formulations: *(i)* the aleatory uncertainty due to the record-to-record variability, *(ii)* the epistemic uncertainty due to the number of simulations (data points) used, and *(iii)* the epistemic uncertainty due to the variability of mechanical and geometrical parameters. As a result, this work will allow to decompose the total dispersion into several components, thus identifying the terms that deserve the most attention when computing the HCPLF.

2 NUMERICAL MODEL AND ANALYSES

This section details the modelling assumptions for the main steam line of the reactor, as well as the design of experiment for the dynamic analyses.

2.1 Modelling assumptions

The coupled model of a supporting structure and a secondary system is considered here, corresponding to the main steam line of a pressurised water reactor. The model, built and

computed with the CAST3M finite-element software (Combescure et al., 1982), is taken from Rahni et al. (2017). Structural elements, representing the containment building, are modelled with multi-degree-of-freedom stick formulations. The containment building has a double-wall structure, with an inner reinforced prestressed concrete wall and an outer reinforced concrete wall (see Figure 1). The steel steam line is modelled by means of beam elements, representing pipe segments and elbows, as well as several valves, supporting devices and stops at different elevations of the supporting structure. The stick models, which have the benefit of enabling fast computations, have been calibrated from detailed finite-element 3D models of the containment building (Rahni et al., 2017).

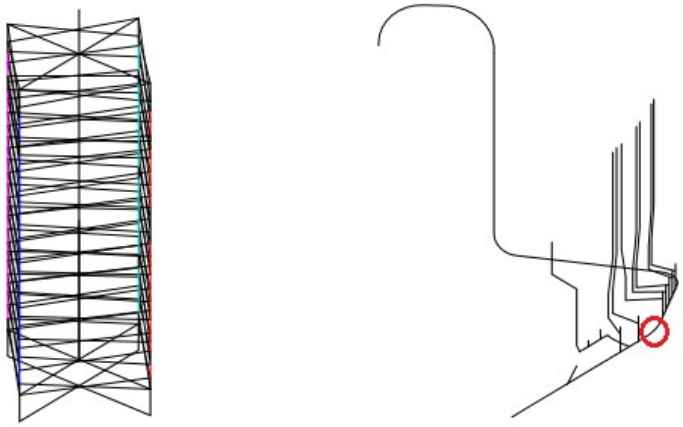

Figure 1:Left: stick model of the containment building (inner wall, outer wall and internal structures); Right: steam line beam model, where the red circle points to the location of the vertical stop.

Dynamic analyses are performed in two successive steps: first, the seismic loading is applied at the base of the building; and the resulting time history of structural displacements is then applied to the steam line model in order to estimate the induced strains and stresses on the beam elements. Rahni et al. (2017) have proposed several mechanical failure criteria for the verification of the steam pipe line integrity, such as the equivalent stress at any point of the pipe line (conservative assumption), the total plastic deformation at the pipe location corresponding to the containment penetration (i.e., accounting for the non-linear behaviour of the steel material), and the effort calculated at the beam model's node corresponding to a vertical stop (see Figure 1). For simplicity purposes, the latter failure criterion is considered here for the fragility analysis. The threshold for the occurrence of the damage state considered (i.e., failure at the vertical stop) is arbitrarily set at EDP_{th} = 400 kN for the maximum transient effort: this choice is made in order to obtain a relatively good balance between data points corresponding to intact or damaged states, for demonstration purposes.

As a preliminary to the non-linear time-history analyses, a modal analysis of the supporting structure is carried out, in order to identify the main vibration modes (see Table 1).

Mode #	Period [s]	3D mass participation factor [%]
1	0.38	61
2	0.38	65
3	0.15	35
4	0.14	97

5	0.14	31

Table 1: Modal analysis of the model of the containment building.

Modes #1 and #2 correspond to the excitation of the structure in the *Y*- and *X*-direction, respectively: due the almost symmetrical properties of the building, they are almost identical. Therefore, the fundamental period of the structure is taken as $T_1 = 0.38$s, while the second one is taken as $T_2 = 0.15$s (i.e., cluster of modes #3, #4 and #5).

In order to integrate the epistemic uncertainties due to the identification of some mechanical and geometrical parameters, ten variables are sampled within a Latin Hypercube Sampling design (see Table 2), following the values provided by Rahni et al. (2017).

Variable	Description	Uniform distribution interval
E_{IC}	Young's Modulus – Inner containment	[27700 – 45556] MPa
ξ_{RPC}	Damping ratio – reinforced prestressed concrete	[4 – 6] %
ξ_{RC}	Damping ratio – reinforced concrete	[6 – 8] %
e_1	Pipe thickness – Segment #1	[29.8 – 38.3] mm
e_2	Pipe thickness – Segment #2	[33.3 – 42.8] mm
e_3	Pipe thickness – Segment #3	[34.1 – 43.9] mm
e_4	Pipe thickness – Segment #4	[33.3 – 42.8] mm
e_5	Pipe thickness – Segment #5	[53.4 – 68.6] mm
e_6	Pipe thickness – Segment #6	[34.1 – 43.9] mm
ξ_{SL}	Damping ratio – steam line	[1 – 4] %

Table 2: Range of variation of the ten uncertain parameters considered, based on Rahni et al. (2017). A uniform distribution is assumed.

2.2 Selection of input ground-motion records

The conditional spectrum method (Lin et al., 2013) is used here for the selection of the input ground motions, for subsequent dynamic analyses. This approach has the benefit of enabling a light scaling of a set of natural records, while saving the consistency of the associated response spectra. Therefore, it is especially suited for the use of spectral values, such as *SA* (spectral acceleration) at various periods. The main steps of this procedure are the following:

- *Probabilistic hazard assessment of the studied site*: here, an arbitrary location in Southern Europe is selected. Hazard curves are generated with the OpenQuake platform (www.globalquakemodel.org), accounting for 13 seismogenic areas which have been characterized in the SHARE project (Woessner et al., 2013).

- *Selection of a period of interest and of scaling levels*: here, the response spectrum is chosen to be conditioned on $SA(T_1=0.38\text{s})$, with 6 scaling levels ranging from 0.185g to 3.882g, corresponding to return periods from 20 years to 20 000 years.

- *Identification of reference earthquakes*: for the studied site, the OpenQuake software performs a hazard disaggregation for each scaling level in order to identify a reference earthquake scenario.

• *Generation of the target response spectrum* and *selection of spectrum-compatible ground-motion records* (Jayaram et al., 2011). The final selection from the PEER database (PEER, 2013) consists of 30 records for each of the 6 scaling levels (i.e., 180 ground-motion records in total), as shown in Figure 2.

The ground-motion selection using conditional spectrum implies the evaluation of the seismic hazard at a given site, along with the identification of reference earthquakes at various return periods: as a result, this approach leads to site-specific fragility functions, which are well suited to the context of NPPs.

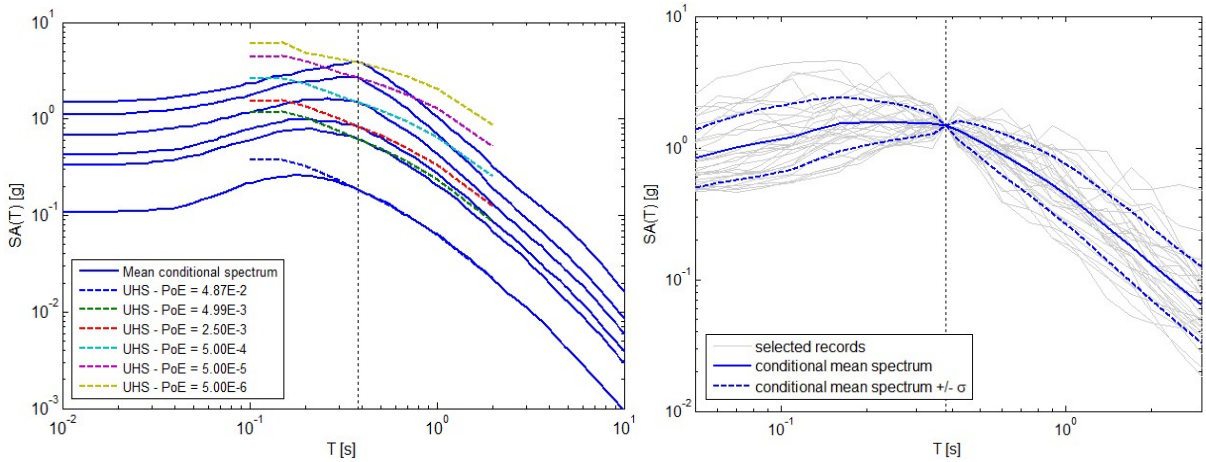

Figure 2: Left: conditional mean spectra and uniform hazard spectra for the 6 scaling levels; Right: conditional spectrum for scaling level #4 and corresponding set of 30 selected ground-motion records.

2.3 Non-linear time-history analyses

The 180 ground-motion records are applied to the base of the 3D model of the containment building, in the form of a 3-component loading. In total, 360 models of the PWR structure are built in the CAST3M environment, so that each ground-motion record may be applied to two different models, with the objective of generating enough data points. As an example, some simulation outcomes are presented in Figure 3, with PGA and SA(0.5s).

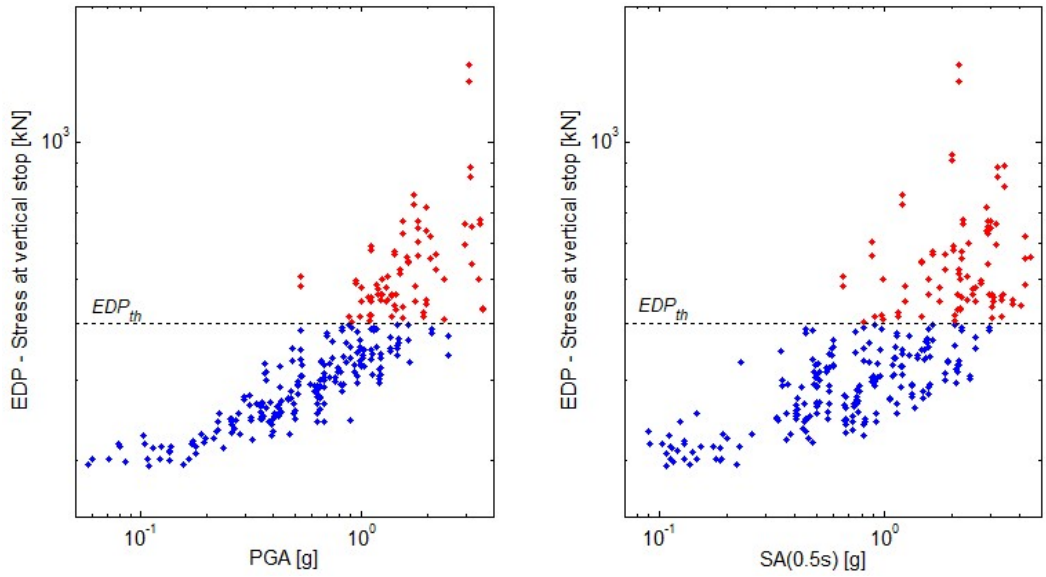

Figure 3: IM-EDP data points, with respect to PGA (left) and SA(0.5s) (right).

3 SELECTION OF SCALAR IMS

From Figure 3, it may be observed that a linear fit between the logarithms of IM and EDP is not justified for this specific case study: it is proposed here to apply the maximum estimation approach (MLE – cf. Shinozuka et al., 2000) approach, which only requires a separation between the intact and damaged states (i.e., respectively blue and red points in Figure 3). To this end, a large number of ground-motion parameters is evaluated as potential IMs:

- Spectral acceleration at various periods: *SA*(*T*)
- Peak parameters (acceleration, velocity and displacement): *PGA*, *PGV*, *PGD*
- Arias Intensity parameters: *AI* (Arias Intensity), *A95*[1], *SL75-95*[2]
- Spectral intensities: *SI* (Housner Intensity), *ASI* (Acceleration Spectral Intensity)
- Duration parameters: *RSD75-95*[3]
- Cyclic parameters: *NCy* (number of effective cycles), *DCy* (cyclic damage parameter)
- Energy-related parameters: *NED* (Normalised Energy Density)
- Parameters related to time-integrated acceleration: *CAV* (Cumulative Absolute Velocity), *ARMS* (Root-Mean-Square Acceleration)

The adequacy of IMs for the derivation of fragility curves has been addressed by many studies, using efficiency and sufficiency indicators (Luco & Cornell, 2007), statistical classifiers (Lancieri et al., 2015) or the concept of hazard compatibility (Hariri-Ardebili & Saouma, 2016). Based on these previous works, it is proposed to use three performance metrics in order to estimate the adequacy of the considered IMs:

1. **Standard-deviation β of the fragility curve:** although the MLE approach is used here, the estimated dispersion parameter β may be interpreted as the quantity described by Padgett et al. (2008) as the *proficiency* measure (i.e. combination of efficiency and practicability measures).
2. **Akaike Information Criterion (AIC):** this criterion quantitatively assesses the goodness-of-fit of a given model. The AIC accounts for the number of parameters used in a model through the variable k, in order to penalize the over-parametrization of some models. In the case of scalar-IM fragility curves, $k = 2$ (i.e., parameters α and β). The AIC is then expressed as follows:

$$AIC = 2k - 2\ln L \tag{2}$$

   where L is the likelihood function of the fragility model, which is computed as a product of the 360 conditional probabilities corresponding to the 360 simulation outputs. Therefore, a small AIC value implies a great statistical fit given the data.
3. **Area under the ROC curve (AUC):** the ROC curve is a possible representation of a ROC analysis, where the ability of a given model to be both specific and sensitive is evaluated by plotting the true positive rate versus the false positive rate. This approach has been applied by Gehl et al. (2013) to the evaluation of fragility curves (i.e. ability of the model to accurately predict the damage state or not, given an IM taken as a predictor). Therefore, the AUC provides a quantification of how well the fragility model

[1] Level of acceleration that contains 95% of the Arias Intensity

[2] Slope of the Husid plot (cumulative *AI* over time) between 5% and 75% (or 95%) of the total *AI*

[3] Relative Significant Duration: length of time interval between when *AI* first exceeds 5% of total value and when *AI* first exceeds 75% (or 95%) of total value

works as a classifier: a large AUC value (i.e., area close to 1) implies a model that works significantly better than a random classifier (i.e., the 1:1 diagonal).

These three criteria are first estimated for *SA* at various periods, ranging from 0.05s to 2s (see Figure 4). The curves reveal an optimum at T = 0.29s, whatever the metric considered. Local optima are also found at periods equal to 0.14s and 0.50s. The three identified periods are close to the periods that corresponding to the first two vibration modes (i.e., T_1 = 0.38s and T_2 = 0.15s). However, they are not exactly identical, and these differences may be explained by two factors, i.e. *(i)* the combination of superior modes that may be excited by some ground motions and *(ii)* the lengthening of the fundamental period due to the loss of elasticity of the structural components.

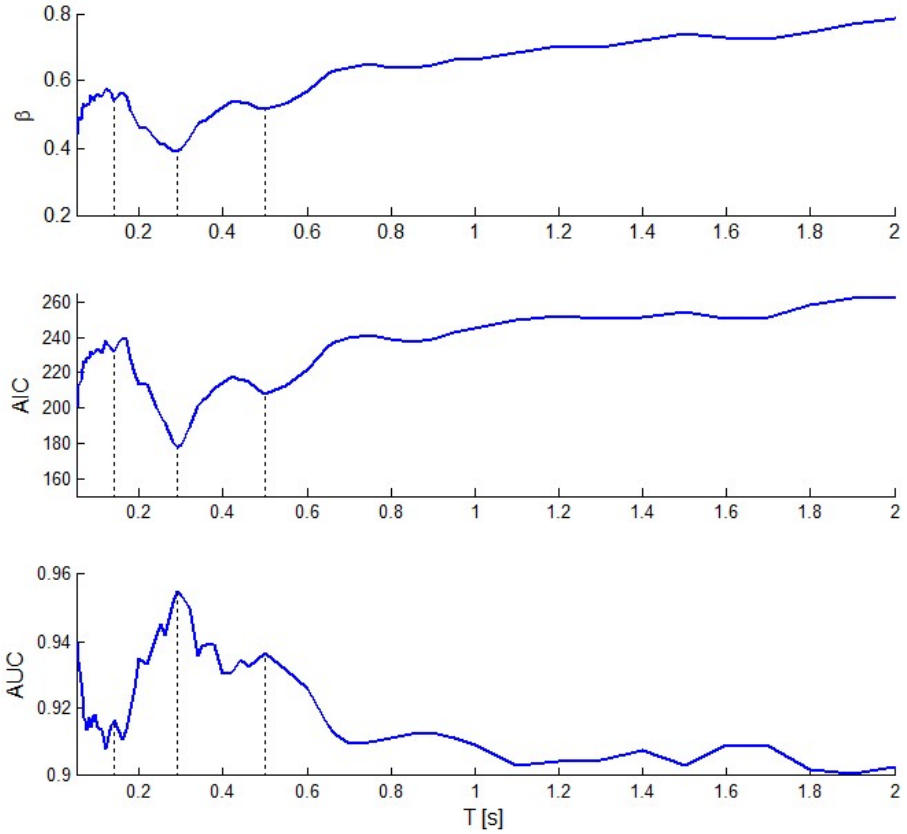

Figure 4: Evolution of the three performance metrics considered, with SA at different periods.

As a result, *SA* at the three identified periods (0.14s, 0.29s and 0.50s) are considered as potential IMs; and their performance is compared to other ground-motion parameters (see Table 3).

IM	β	AIC	AUC
SA(0.14s)	0.5415	229.91	0.9166
SA(0.29s)	0.3898	175.82	0.9547
SA(0.50s)	0.5144	206.12	0.9363
PGA	0.4403	198.45	0.9399
PGV	0.4928	205.73	0.9381
PGD	1.2622	308.93	0.8469

AI	0.7674	182.13	0.9485
A95	0.4041	192.88	0.9389
SL75	0.9471	206.91	0.9325
SL95	0.7681	176.59	0.9508
SI	0.5293	213.94	0.9347
ASI	0.3775	176.23	0.9519
RSD75	-	-	-
RSD95	-	-	-
NCy	-	-	-
DCy	0.8123	191.58	0.9412
NED	1.4284	259.27	0.8968
CAV	0.6012	247.15	0.8951
ARMS	0.5728	240.45	0.9073

Table 3: Estimated values of the three performance metrics, for different potential IMs. The gray cells indicate the five best performing IMs, for each metric.

It is found that the parameters *SA*(0.29s) and *ASI* are the most consistent, since they show a satisfying performance across the three metrics. Other well performing parameters are *PGA*, *PGV*, *AI*, *A95*, *SL95* and *DCy*. However, it should be noted that *DCy*, *SL95* and *A95* may not be easily computed from current GMPEs (see **Erreur ! Source du renvoi introuvable.**). The metrics cannot be evaluated for some parameters (*RSD75*, *RSD95*, *NCy*) because the fragility estimation has not converged due the poor IM-EDP correlation: these parameters may still be used as secondary IMs when deriving fragility surfaces, if the right IM combination is found.

4 DERIVATION OF VECTOR-IM FRAGILITY FUNCTIONS

In order to improve the predictive power of the fragility curves and to reduce the dispersion due to the record-to-record variability, it is proposed to combine two IMs and to use this vector-valued predictor for the derivation of the fragility functions. To this end, the following functional form for the damage probability is assumed:

$$\begin{aligned} P_f(im_1, im_2) &= P(ds \geq DS | IM_1 = im_1, IM_2 = im_2) \\ &= \frac{1}{2}[1 + erf(c_1 + c_2 \ln im_1 + c_3 \ln im_2)] \end{aligned} \quad (3)$$

where *erf* is the error function and c_1, c_2 and c_3 are the coefficients to be estimated (i.e., fragility parameters).

A composite variable im_V may then be introduced as follows:

$$\mathrm{im_V} = \mathrm{im_1}^{\frac{c_2}{c_2+c_3}} \cdot \mathrm{im_2}^{\frac{c_3}{c_2+c_3}} \quad (4)$$

Using im_V as the IM, the functional form in Eq. 3 is expressed as:

$$
\begin{aligned}
P_f(im_V) &= P(ds \geq DS|IM_V = im_V) = P(ds \geq DS|IM_1 = im_1, IM_2 = im_2) \\
&= \frac{1}{2}[1 + \mathrm{erf}(c_1 + c_2 \ln im_1 + c_3 \ln im_2)] \\
&= \frac{1}{2}\left[1 + \mathrm{erf}\left(\frac{\frac{c_1}{c_2+c_3} + \ln im_1^{\frac{c_2}{c_2+c_3}} + \ln im_2^{\frac{c_3}{c_2+c_3}}}{\frac{1}{c_2+c_3}}\right)\right] \\
&= \frac{1}{2}\left[1 + \mathrm{erf}\left(\frac{\ln im_V + \frac{c_1}{c_2+c_3}}{\frac{1}{c_2+c_3}}\right)\right] \\
&= \frac{1}{2}\left[1 + \mathrm{erf}\left(\frac{\ln im_V - \ln a_V}{\beta_V\sqrt{2}}\right)\right]
\end{aligned}
\tag{5}
$$

where α_V and β_V are the "fragility parameters" of the composite IM im_V, which are finally identified as follows:

$$
\begin{cases}
\alpha_V = exp\left(-\frac{c_1}{c_2+c_3}\right) \\
\beta_V = \frac{1}{(c_2+c_3)\sqrt{2}}
\end{cases}
\tag{6}
$$

The coefficients c_1, c_2 and c_3 are estimated with a MLE approach, using the same likelihood function as for scalar-IM fragility curves (expect that there are now three parameters to find, instead of two).

Thanks to the identification of the "composite" dispersion parameter β_V, it is possible to compute the same three of types of performance metrics, as for the case of scalar-IM fragility curves. More than sixty combinations of vector-valued IMs are tested, and the results for the most promising couples of IMs are detailed in Table 4.

IM_1	IM_2	β_V	AIC	AUC
SA(0.14s)	*SA*(0.29s)	0.3724	173.71	0.9568
SA(0.14s)	*SI*	0.3464	167.19	0.9508
SA(0.29s)	*SA*(0.50s)	0.3834	173.74	0.9571
SA(0.29s)	*PGA*	0.3370	161.33	0.9424
SA(0.29s)	*PGV*	0.3718	171.22	0.9591
SA(0.29s)	*AI*	0.4687	171.69	0.9530
SA(0.29s)	*SI*	0.3659	167.43	0.9610
SA(0.29s)	*RSD95*	0.4371	174.11	0.9559
SA(0.50s)	*PGA*	0.3348	158.25	0.9439
PGA	*PGV*	0.3389	166.18	0.9532
PGA	*AI*	0.5027	170.79	0.9468
PGA	*SI*	0.3225	155.43	0.9339
PGA	*ASI*	0.3447	169.06	0.9416
PGV	*ASI*	0.3668	173.61	0.9526

Table 4: Estimation values of the three performance metrics, for different vector-valued IMs. The gray cells indicate the three best performing couples of IMs, for each metric.

It is found that the vector-valued IMs tend to perform slightly better than the scalar IMs, judging from the values of the three metrics. Some scalar IMs that were not identified as ade-

quate (e.g., *RSD95*) become much more efficient when combined together. Some examples of vector-valued fragility functions are displayed in Figure 5, for selected combinations of IMs.

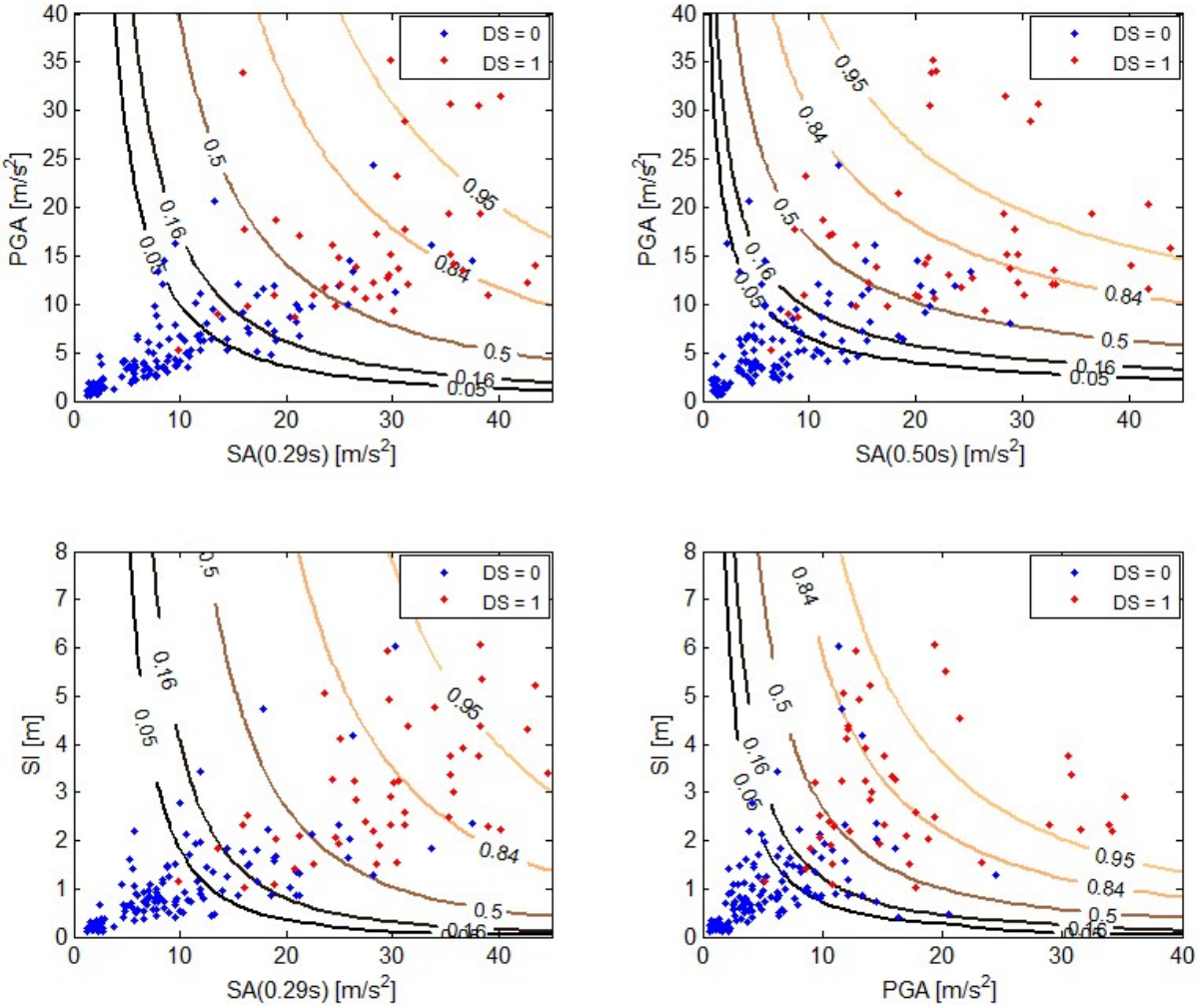

Figure 5: Iso-probability lines corresponding to some examples of vector-valued fragility function (i.e., probabilities of 0.05, 0.16, 0.5 0.84 and 0.95). The dots represent the outcomes of the NLTHAs in the vector-IM space.

5 COMPARATIVE ANALYSIS OF UNCERTAINTY SOURCES

This section discusses a set of procedures for the quantitative estimation of some uncertain components, namely the record-to-record variability, the uncertainty due to the number of data points, and the in-situ variability due to the variability of mechanical and geometrical parameters

5.1 Decomposition of the record-to-record variability

The contribution of the record-to-record variability to the global uncertainty structure may be estimated thanks to the comparison between scalar-IM fragility curves and vector-IM fragility surfaces. To this end, as an example, it is proposed to reduce the fragility surface w.r.t. [*PGA* ; *SA*(0.29s)] (see top left plot in Figure 5) into a fragility curve w.r.t. *SA*(0.29s) only. This operation should consider the correlation between the two IMs, in order to preserve the hazard consistency of the applied loading. Therefore, a first step consists in estimating the distribution of the secondary IM (i.e, *PGA*) w.r.t. *SA*(0.29s), using the dataset of the input ground-motion records: a median line and its 16%-84% confidence intervals are then plotted

(see Figure 6, left). The space delimited by this interval provides also practical guidance on the validity domain of the fragility surface, in the sense that it identifies the IM combinations that are very unlikely.

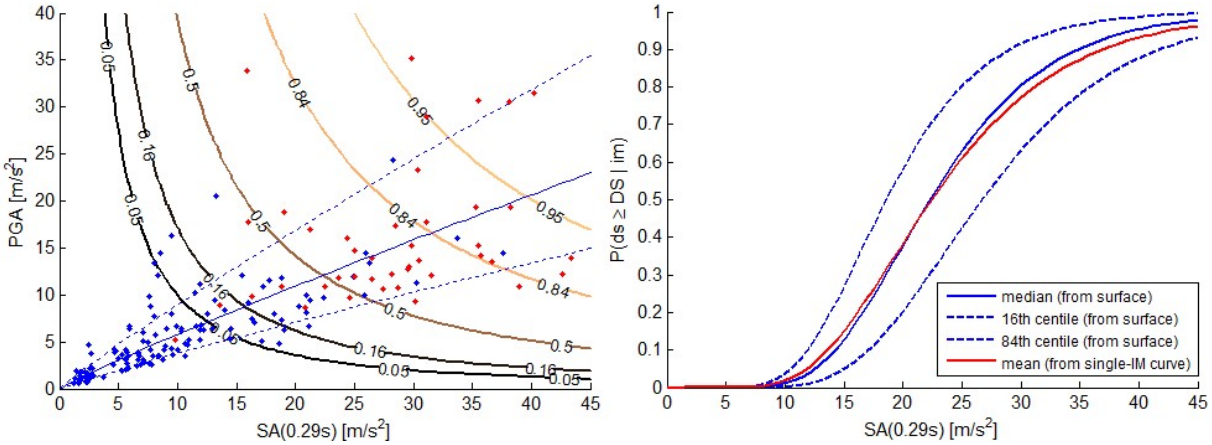

Figure 6: Left: fragility surface w.r.t. PGA and SA(0.29s), the solid blue line represents the median of the PGA-SA(0.29s) distribution and the dashed blue lines the 16%-84% confidence intervals; Right: equivalent fragility curves w.r.t. SA(0.29s).

It is then proposed to generate "slices" of the fragility surfaces by following the distribution of *PGA* as a function of *SA*(0.29s) (i.e., solid and dashed lines in Figure 6, left). As a result, the "slices", now represented as a function of the single IM *SA*(0.29s), may be compared to the original scalar-IM fragility curve. The fragility curves in Figure 6, right, are identified as follows:

- *Solid red line*: "mean" fragility curve corresponding to the scalar-IM fragility curve, derived w.r.t. *SA*(0.29s) only;
- *Solid blue line*: median fragility curve corresponding to the "median" slice of the fragility surface;
- *Dashed blue lines*: 16%-84% confidence intervals around the median fragility, corresponding to the lower and upper bounds of the slices of the fragility surfaces.

Finally, this family of fragility functions corresponds to the probabilistic framework by Kennedy et al. (1980), where the identification of aleatory and epistemic uncertainties (β_R and β_U, respectively), as introduced in Eq. 1. The mean fragility curve, w.r.t. to *SA*(0.29s), has a total standard deviation $\beta_{tot} = (\beta_R^2 + \beta_U^2)^{1/2} = 0.390$. Meanwhile, the median fragility curve, obtained from the fragility surface w.r.t. *PGA* and *SA*(0.29s), has a standard deviation of 0.349, which actually corresponds to the aleatory randomness term only (i.e., β_R). The confidence intervals obtained from the graphical construction in Figure 6 are then used to estimate the epistemic uncertainty term, i.e. $\beta_U \approx 0.174$.

It may be concluded that the vector-IM fragility functions lead to the transfer of a part of the record-to-record variability into a form of epistemic uncertainty, which is related to the description of the seismic loading given the hazard at the specific site.

5.2 Uncertainty due to the number of data points

The epistemic uncertainty due to the number of data points in the simulations, i.e. related to the quality of the statistical estimation of the fragility parameters, may also be evaluated in the case of vector-IM fragility functions. To this end, a bootstrap sampling approach is ap-

plied to the fragility surface w.r.t. of *PGA* and *SA*(0.29s). The outcomes of the bootstrap sampling are displayed in Figure 7, in the case of 16%-84% confidence intervals.

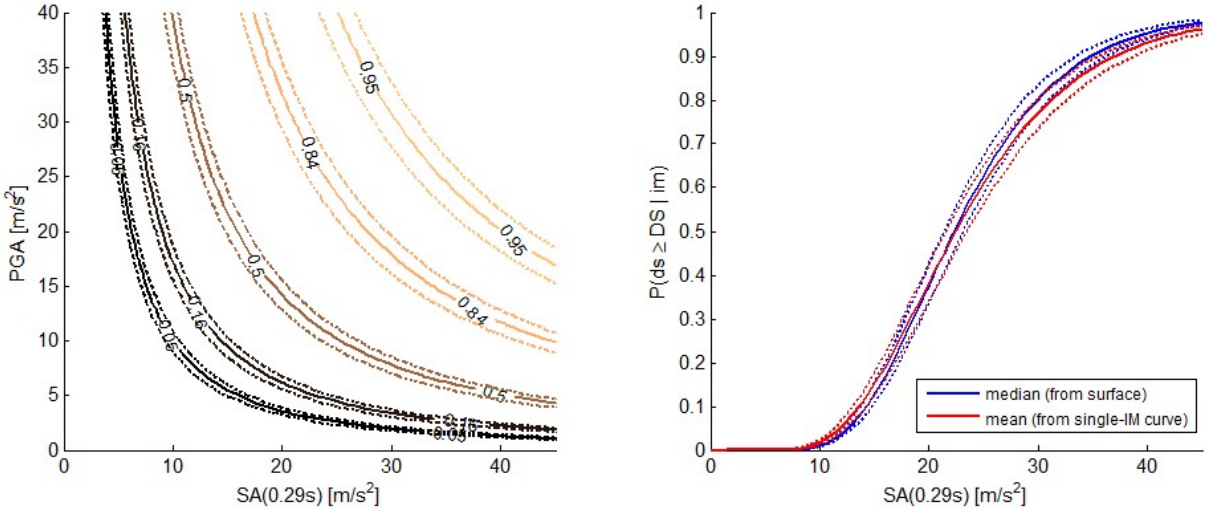

Figure 7: Left: fragility surface w.r.t. PGA and SA(0.29s), with the 16%-84% confidence intervals (dashed lines) due to the statistical estimation; Right: equivalent fragility curves w.r.t. SA(0.29s) and related 16%-84% confidence intervals due to the statistical estimation.

In order to compare these confidence intervals with the ones estimated for the corresponding scalar-IM fragility curves, the fragility surface is reduced to a scalar case w.r.t. *SA*(0.29s) only, following the same approach as before (i.e., use of a "median" slice of the fragility surface). The curves in Figure 7, right, reveal a similar order of magnitude for the confidence intervals due to the amount of data points, both for the single-IM fragility curve ($\beta_U = 0.043$) and for the vector-IM fragility function ($\beta_U = 0.048$).

5.3 Uncertainty due to the variability of mechanical and geometrical parameters

Based on the 360 randomly generated structures, a new vector-IM fragility curve is derived by incorporating the effect of the epistemic uncertainties related to the $p = 10$ mechanical and geometrical parameters (described in Table 2). This is done by adding linear terms in Eq. 3 as:

$$\frac{1}{2}\left[1 + \mathrm{erf}(c_1 + c_2 ln\, im_1 + c_3 ln\, im_2 + \sum_{i=1}^{p} c_{x_i} x_i)\right] \tag{7}$$

where x_i is the i^{th} uncertain parameter and c_{x_i} the corresponding regression coefficient.

When the ten parameters are considered at the same time, it is found that the MLE-based regression cannot converge, due to the limited number of data points. Therefore, partial combinations of parameters are tested until the most influent parameters are identified. As a result, the MLE regression on Eq. 7 has been carried out with three geometrical parameters, namely the thicknesses e_2, e_4 and e_6 (see Table 5). The analysis by the *p*-value of the Wald test has been used to decide whether the corresponding parameter is significant or not, using a significance threshold at 5%. Interestingly, the mechanical parameters barely affect the mean of the vector-IM fragility function (at 5% significance).

Parameter	Regression coefficient	Std. Error	*p*-value (Wald statistic)
c_1 - Intercept	-22.008	4.030	4.73e-8
c_2 - *SA*(0.29s)	1.991	0.359	2.98e-8

c_3 - *PGA*	1.284	0.342	1.75e-4
c_4 - Thickness e_2	95.504	46.303	0.0392
c_5 - Thickness e_4	135.553	46.184	0.0033
c_6 - Thickness e_6	98.819	44.217	0.0254

Table 5: Regression coefficients, standard error and *p*-value of the Wald statistic of the vector-IM fragility function.

On this basis, a new vector-IM fragility function is plotted in Figure 8, left, by incorporating only the significant geometrical parameters. The median surface is obtained by setting the thickness parameters at the median of their uniform distribution interval (cf. Table 2), while its 16%-84% confidence bounds account for the corresponding variations of these parameters. The same approach is applied to the construction of the single-IM fragility curve, enabling the comparison between the two approaches (see Figure 8, right).

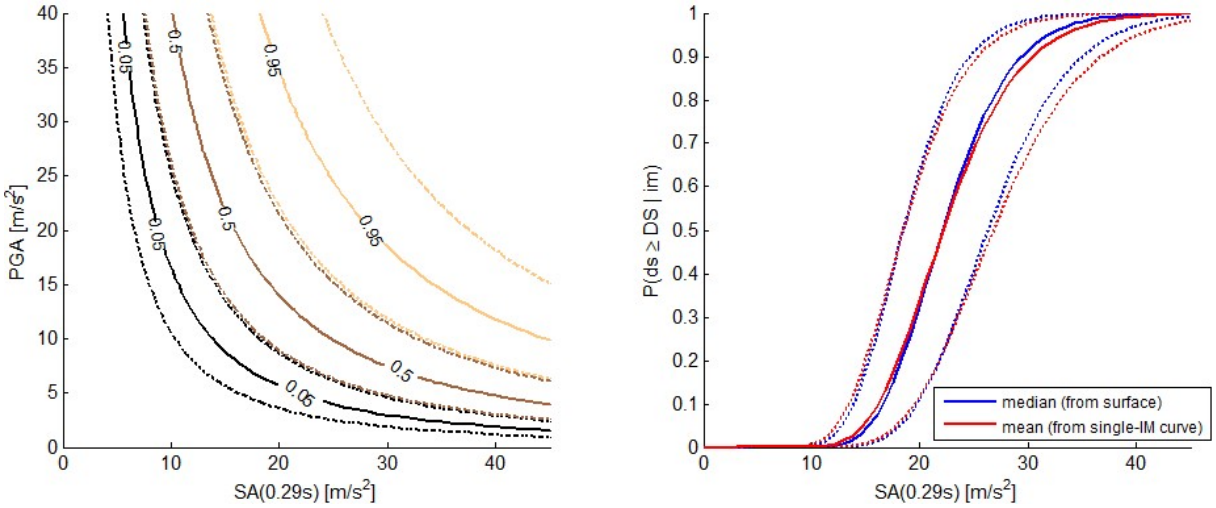

Figure 8: Left: fragility surface w.r.t. PGA and SA(0.29s) with the 16%-84% confidence intervals (dashed lines) due to variability in the parameters; Right: equivalent fragility curves w.r.t. SA(0.29s) and related 16%-84% confidence intervals due to variability in the parameters.

These fragility models, based on the disaggregation of the variability of some mechanical or geometrical, show a significantly reduced dispersion, when compared to the ones that do not use these parameters as input variables (i.e., models in Figures 6 and 7). However, it should be noted that some regression coefficients have been estimated with a significant standard error (see Table 5), which implies that much more data points from simulations should be necessary in order to get stable estimates.

5.4 Discussion on the respective contribution of uncertainty sources

The previous statistical analyses have helped identifying the uncertainty sources at play in different fragility modelling strategies (see Figure 9):

- *Single-IM fragility curve*: the aleatory dispersion β_R includes most of the variability, with a very small contribution of the epistemic uncertainty due to the number of data points.

- *Vector-IM fragility function*: a part of the record-to-record variability may be interpreted as an epistemic uncertainty term. The uncertainty term due to the number of data points is slightly larger, without becoming significant.
- *Vector-IM fragility function accounting for mechanical and geometrical parameters*: a multivariate MLE-based regression has allowed to explicitly account for the most influent mechanical and geometrical, further reducing the aleatory dispersion.

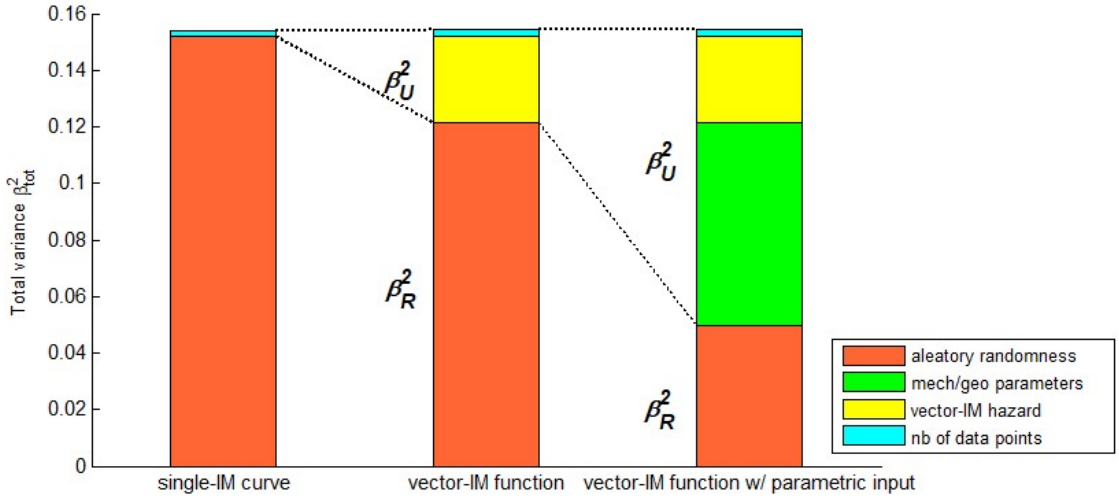

Figure 9: Decomposition of the uncertainty sources in terms β_R (aleatory) and β_U (epistemic), depending on the modelling strategy used.

It may be noted that, for the considered application, the use of vector-IMs contributes to a significant part of the total dispersion, although the uncertainty due to the variability of mechanical and geometrical parameters appears to be much larger. When computing the HCLPF, the uncertainty decomposition from Figure 9 is preserved, according to the following equation derived from Eq. 1:

$$SA(0.29s)_{HCLPF} = \alpha_{SA} \cdot exp[-(\beta_R + \beta_U) \cdot \Phi^{-1}(0.95)] \quad (8)$$

Therefore, when assessing a given element from an NPP, its HPCLPF may be gradually reduced if the following measures are taken to lower the epistemic uncertainty term:

- Reduction of β_U due to the number of data points, by performing more simulations (i.e., increased confidence in the statistical estimation);
- Reduction of β_U due to the description of the seismic loading, by performing a vector probabilistic hazard assessment of the considered site (i.e., more accurate knowledge of the excepted vector-IM distribution);
- Reduction of β_U due to the variability of mechanical and geometrical parameters, by testing or qualifying the materials used (i.e., increase of knowledge).

6 CONCLUSIONS

This study has confronted the concept of vector-IM fragility functions to the probabilistic framework commonly employed in nuclear applications. This exercise has then allowed for a systematic analysis of various sources of aleatory or epistemic uncertainty.

Regarding the selection of IMs, carefully selected vector-IMs make excellent candidates in terms of IM sufficiency and efficiency, when compared to scalar IMs. As a result, vector-IM

fragility functions tend to generate less dispersion (i.e., aleatory uncertainty due to record-to-record variability) than single-IM fragility curves: this difference may be interpreted as a partial transfer from the record-to-record variability to an epistemic uncertainty component that is related to the description of the seismic loading given the hazard at the studied site. However, in the present example, it appears that the epistemic uncertainty due to the variability of mechanical and geometrical parameters is still much larger.

Although a wide range of statistical tools are available for the quantification and propagation of sources of uncertainties, it appears that all the epistemic uncertainties usually cannot be adequately covered and accounted for (e.g., much more simulations would be required in order to accurately model the variability of the mechanical and geometrical parameters). In most cases, expert judgment would be necessary in order to constrain the assumptions and to interpret the simulation results.

Finally, the present study has followed the lognormal assumption for the functional form of the fragility functions. This constraint, while convenient for the combination of nested uncertainty terms, is bound to introduce significant biases in the statistical estimates (i.e., the outcomes of the MLE-based regression). A similar analysis based on undefined functional forms would also be able to deliver valuable lessons.

7 ACKNOWLEDGEMENT

This study has been carried out within the NARSIS project, which has received funding from the European Union's H2020-Euratom Program under grant agreement N° 755439. The Pacific Earthquake Engineering Research Center is gratefully acknowledged for providing access to their database of ground-motion records.

REFERENCES

[1] EPRI, *Seismic Probabilistic Risk Assessment Implementation Guide*. EPRI Report TR-1002989, Palo Alto, CA, 2003.

[2] R.P. Kennedy, C.A. Cornell, R.D. Campbell, S. Kaplan, H.F. Perla, Probabilistic seismic safety study of an existing nuclear power plant. *Nuclear Engineering and Design*, **59**(2), 305-338, 1980.

[3] N. Luco, C.A. Cornell, Structure-specific scalar intensity measures for near-source and ordinary earthquake ground motions. *Earthquake Spectra*, **23**(2), 357-392, 2007.

[4] J.E. Padgett, B.G. Nielson, R. DesRoches, Selection of optimal intensity measures in probabilistic seismic demand models of highway bridge portfolios. *Earthquake Engineering & Structural Dynamics*, **37**(5), 711-725, 2008.

[5] J.W. Baker, C.A. Cornell, A vector-valued ground motion intensity measure consisting of spectral acceleration and epsilon. *Earthquake Engineering & Structural Dynamics,* **34**, 1193-1217, 2005.

[6] D.M. Seyedi, P. Gehl, J. Douglas, L. Davenne, N. Mezher, S. Ghavamian, Development of seismic fragility surfaces for reinforced concrete buildings by means of nonlinear time-history analysis. *Earthquake Engineering & Structural Dynamics*, **39**(1), 91-108, 2010.

[7] A. Modica, P.J. Stafford, Vector fragility surfaces for reinforced concrete frames in Europe. *Bulletin of Earthquake Engineering,* **12**, 1725-1753, 2014.

[8] N. Rahni., M. Lancieri, C. Clement, G. Nahas, J. Clement, L. Vivan, Y. Guigueno, E. Raimond, An original approach to derived seismic fragility curves – Application to a PWR main steam line. *Proceedings of the International Topical Meeting on Probabilistic Safety Assessment and Analysis (PSA2017)*, Pittsburgh, PA, 2017.

[9] A. Combescure, A. Hoffmann, P. Pasquet, The CASTEM finite element system. Brebbia C.A. eds. *Finite Element Systems*, Springer, Berlin, Heidelberg, 1982.

[10] T. Lin, C.B. Haselton, J.W. Baker, Conditional spectrum-based ground motion selection. Part I: hazard consistency for risk-based assessments. *Earthquake Engineering & Structural Dynamics*, **42**(12), 1847-1865, 2013.

[11] J. Woessner, L. Danciu, P. Kaestli, D. Monelli, *Database of seismogenic zones, Mmax, earthquake activity rates, ground motion attenuation relations and associated logic trees*. FP7 SHARE Deliverable Report D6.6, 2013.

[12] N. Jayaram, T. Lin, J.W. Baker, A computationally efficient ground-motion selection algorithm for matching a target response spectrum mean and variance. *Earthquake Spectra*, **27**(3), 797-815, 2011.

[13] PEER, *PEER NGA-West2 Database*. Pacific Earthquake Engineering Research Center, https://ngawest2.berkeley.edu, 2013.

[14] M. Shinozuka, M. Feng, J. Lee, T. Naganuma, Statistical analysis of fragility curves. *Journal of Engineering Mechanics*, **126**(12), 1224-1231, 2000.

[15] M. Lancieri, M. Renault, C. Berge-Thierry, P. Gueguen, D. Baumont, M. Perrault, Strategy for the selection of input ground motion for inelastic structural response analysis based on naïve Bayesian classifier. *Bulletin of Earthquake Engineering*, **13**(9), 2517-2546, 2015.

[16] M.A. Hariri-Ardebili, V.E. Saouma, Probabilistic seismic demand model and optimal intensity measure for concrete dams. *Structural Safety*, **59**, 67-85, 2016.

[17] P. Gehl, D.M. Seyedi, J. Douglas, Vector-valued fragility functions for seismic risk evaluation. *Bulletin of Earthquake Engineering*, **11**(2), 365-384, 2013.

COMPDYN 2019
7th ECCOMAS Thematic Conference on
Computational Methods in Structural Dynamics and Earthquake Engineering
M. Papadrakakis, M. Fragiadakis (eds.)
Crete, Greece, 24–26 June 2019

SEISMIC VULNERABILITY OF THE RESIDENTIAL BUILDINGS OF FLORENCE

V. Cardinali[1], S. Viti[2], and M. Tanganelli[2]

[1] Department of Architecture (DiDA), University of Florence,
Via della Mattonaia 14, 50121 Firenze, Italy
e-mail: vieri.cardinali@unifi.it

[2] Department of Architecture (DiDA), University of Florence, Sezione Materiali e Strutture
Piazza Brunelleschi 6, 50121 Firenze, Italy
e-mail: stefania.viti@unifi.it
e-mail: marco.tanganelli@unifi.it

Abstract

The city of Florence, famous all over the world for its historical and artistic heritage, experienced public housing interventions since the XIX century. They consist both in RC and masonry constructions developed during several interventions in the external areas around the historical centre. Florence has been classified "seismic zone" just in 1982 so, most part of the considered population of buildings have been built without seismic criteria. Masonry buildings represent the most significant part of public housing population, characterized by the oldest constructions. This work deals with the vulnerability assessment of masonry public housing interventions at urban scale in Florence. A meaningful database with a large number of selected buildings has been made. Every construction has been investigated adopting an empirical approach based on geometrical and mechanical parameters; houses have been divided into typological classes in function of geometrical and architectonical features. This information has been collected on a GIS platform into a geo-referred system. This allowed a ranking of the public housing population that defines a vulnerability index for different classes of buildings. Further studies will be developed to mix vulnerability features with seismic microzonations of soils and to combine the proposed empirical approach to numerical one in order to investigate representative case-studies adopting mechanical models.

Keywords: Urban Scale, Public Housing Intervention, Pre-normative Buildings, Masonry Buildings, Seismic Assessment.

1 INTRODUCTION

The seismic assessment of existing buildings plays a crucial role in the evaluation - and mitigation - of the seismic risk. Italy joints a high seismic hazard to rich and complex monumental goods and constructive tradition. A huge number of historical buildings, in Italy, needs to be preserved, retrofitted and improved in order to assure the required safety standards, and to preserve the National and local history and traditions.

The earthquakes occurred during the last century (L'Aquila, Emilia Romagna, Central Italy) remarked the vulnerability of stocks where people live [1-3]; the majority of existing buildings has been realized before the introduction of seismic codes and without anti-seismic criteria. This vulnerability affects all types of buildings; masonry buildings, however, for their number and age, deserve a special attention. Nowadays, indeed, masonry structures still represent a large percentage of urban fabric.

The most studied masonry structures consist of monumental historical buildings; indeed, they have a special value for their cultural and architectural importance and collected the most part of the research efforts and contributions. However, most part of masonry buildings is represented by residential ones; the assessment of these buildings is usually left to the will of the single owners, since they are too many to be faced by the Government. For this reason, the researchers are facing their assessment at the urban scale, in order to provide some general and useful benchmark for the assessment of single cases [4-6].

Since the last century, many different studies (empirical, analytical and hybrid methods) have been carried on for a vulnerability assessment of urban stocks at urban scale [7-10]. Empirical methods are the most basic ones; they reduce computational costs analyzing the vulnerability based on statistic damage examinations of past earthquakes, achieving a consequent typological classification. They use macroseismic scales (MSK and MCS scales are the most used); even if these methodologies cannot be considered as advanced approaches they are important to connect vulnerability assessment with historic seismology of places since historical documentaries are based on damage testimonies [11]. Analytical methods assess the damage with numerical analysis performing mechanical computational models; they demand an adequate knowledge of the structure and usually they refer to individual structural units or specific building classes. They are based on simplified tuning of the Capacity Spectrum Method [12-13] and they lead to acceleration-displacement response spectra evaluated in terms of damage limit states [14]. Finally, hybrid methods start from the definition of buildings-types which are representative of different constructions, combining empirical and analytical techniques for an implementation of the empirical typological classifications with specific mechanical analysis. Computational costs of the assessment at urban scale are then limited to the evaluation of selected case-studies [15].

The research project deals with the vulnerability assessment of the residential buildings of Florence. In this work the empirical approach is applied to a relevant database, consisting of almost 300 buildings. In this area of interest, different studies have been carried out during the last years [16-17] combining typological features of buildings with the soil specification investigated such as amplification factors or period ground motions. In this paper, seismic assessment of part of the Florentine residential stock has been evaluated in a systematic way. Public Housing Interventions have been selected as a scattered homogeneous database, more trackable. For a relevant database of buildings referred into a GIS system the GNDT second level approach has been used. Buildings have been divided according to their architectonical and typological features into nine classes. Vulnerability indices have been then expressed in terms of macroseismic intensities and related to the historical seismology of the city. Finally, the expected damage of the nine classes of buildings have been defined.

2 FLORENCE: RESIDENTIAL VULNERABILITY AND SEISMIC RISK

2.1 The residential stock of Florence

The city of Florence is characterized by important architectures and monuments famous all over the world. Since December 1982 the centre is considered UNESCO World Heritage Centre and it concerns both the copious number of Medieval and Renaissance buildings, and the historic urban pattern of the districts. However, external areas of the city centre have grown just in a recent period. Starting with the demolition of the city walls in the XIX century and the support at the urbanization of a multitude of different new districts and areas, the contemporary face of the city has been defined. Perimetral zones of Florence are mainly composed by residential buildings which have been designed according to the zoning theories of the last centuries; they were settled far from the other functions and supported by urbanistic regulations [18]. The most significant part of this residential stock (and the most ancient) has been realized through masonry buildings.

Nowadays, in the city of Florence, 24308 residential buildings of the total residential stock (31070 buildings) are composed by masonry structures (78,2%), while just 4840 are composed by RC (15,5%) and 1110 with different technologies (6,3%). From a legislative point of view, the city is classified as "seismic zone" just since 1982 so, most part of the residential heritage has been made without anti-seismic criteria. Furthermore, the last important Florentine earthquake is dated 1895, before the main development of satellite stocks; seismic performance of most part of pre-modern buildings has never been checked by relevant ground motions, and their vulnerability never been assessed.

Together with the grow of the city, many Public Housing Interventions have been promoted. Starting from the XIX century different institutions built several buildings. These houses are characterized both for masonry and RC structures. During more than a century, according to Pierini [19], more than 20000 apartments have been realized. In this paper, Public Interventions have been selected to assess the seismic vulnerability of a relevant percentage of the residential buildings of Florence. Social houses interventions have been made by few institutions, which provide private archives with technical information and, if still of public domain, they are accessible to in-depth studies and more specific analysis.

2.2 History of Public Housing Intervention in Florence

Public housing interventions in Florence started in 1848 with the institution of SAE (Società Anonima Edificatrice). The society dealt with the construction of houses for the working class in the external areas of the historical centre. In the years between 1885 and 1911, the *"Comitato per le Case ad uso degli indigenti"*, built 342 houses for needy people divided into 14 different interventions. Since 1912, Railway Society built other new residential buildings for their workers. The "*Istituto Autonomo per le Case Popolari*" (*IACP*) was established in 1909. It represented the main promoter of the last century. Starting from the oldest interventions, IACP adopted different architectonical typologies, realizing both "ring" large buildings with internal courtyards and line-type having different spatial configurations. Many different interventions were constructed from 20's by *IACP* and *ENCEP* ("*Ente Nazionale Combattenti Edilizia Popolare*") during the fascist period. It concerned small urban villages like the stock in *via Carlo del Prete*, modern architectures like the residential buildings of *via Erbosa* or public housing interventions for middle classes like the district of *Romito*. Constructions arrested during the Second World War; as a consequence of its destructions, many reconstruction projects were planned in Florence and in the entire peninsula. The "*INA-Casa*" plan, financed by state fundings, represents the most meaningful project. In the 50s it supported dif-

ferent large interventions of which the *Isolotto* district, projected by important architects or Italian modernism (such as Michelucci, Tiezzi, Pastorini, Pellegrini, Fagnoni, Gamberini) is the most important one. In 1956 a further important public housing intervention, *Sorgane*, had been built in reinforce concrete buildings. After *INA-Casa* and its continuation with "*Gescal*" (*Gestione Case per Lavoratori*), in the 60s the residential building constructions got slower, while, from 70s they had been mostly characterized by RC structures. During the last decays most part of these public housing interventions has been privatized with hire-purchase procedures, so nowadays social houses heritage follows private regulations and is not fully available to the will of institutions.

This research, besides regarding a large number of residential buildings in Florence, could present an higher effectiveness, since many further interventions have been made even in other cities according to the *INA-Casa* standards.

2.3 Technological information of the investigated stock

A meaningful archive research has been made. It concerned different catalogues in Florence (*Archivio Ater/Casa SPA*, *Archivio Storico del Comune di Firenze*, *Archivio delle Ferrovie dello Stato*) and has found a relevant number of projects of residential buildings. For each project has been founded the final design and the related technical specifications and quantity surveying of materials. The detail level of the achieved information is not always the same, depending on the catalogue, the contractor society, the years of constructions, the researched intervention. *Ferrovie dello Stato* records represent the most precious source of information for the quantity and the quality of specifications and details.

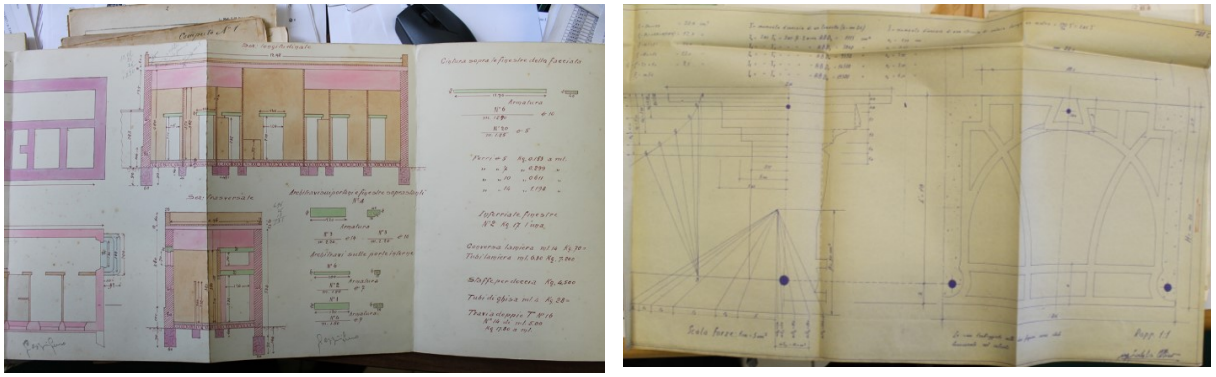

Fig. 1. From left to right: Details of masonry structures; particular of slabs in hollow bricks and RC joists.

The collected database allowed a technical characterisation of residential modern buildings in Florence. They are composed by bearing walls in coursed rubble stone masonry and plain bricks. The coursed rubble masonry is generally made of irregular stones of various dimensions subdivided by horizontal courses, 1 meter spaced, made of clay bricks. It is usually adopted in the largest walls of the perimeter at the lower floors. The plain brick masonries, instead, are made with lime mortar.

The floors are made of RC joists alternated to hollow bricks, topped by a 4-cm concrete slab, and they have a thickness of 20 cm. The hollow bricks can have different shapes that can lead at different distances between the joists. The top storey floors, used for crawl spaces where there are not live loads, in some cases have the same technology but lower (12/16 cm) depths, while in other examples are composed by steel beams alternated to

hollow tiles generally without concrete slab. Roofs are generally made with wooden beams covered by wooden planks and roof tiles; otherwise, they are composed by prefabricated RC joists, hollow tiles and finally hollow roof tiles. Generally, the crawl space has the concrete kerb over the perimeter of the building and it is joined with the level floor, while the roof structure is not linked with the concrete ring.

2.4 Seismic history of Florence

During the last years many studies on the soil stratigraphy and the consequent classification have been conducted. Florentine area has a sedimentary base originated by the Late Pliocene activities [20]. According to the geological history, deposits can be divided into three typologies: the Synthem of the Basin, the Ancient Arno River Deposits and Recent Arno River Deposits [21].

The area is characterized by a moderate telluric activity; historical earthquakes has been estimated at 5 ML and their epicenter were located around Florence (Mugello 1542 and 1919, Impruneta 1456 and 1895, Valdarno 1770). Historical seismology is the main source of information to define the hazard of a place. Historical records show that the most severe earthquakes were occurred in 09/28/1453 and 05/18/1895, both estimated at VII-VIII MCS level.

During the last years more than 2000 drillings of the soil have been made, implemented by 52 downhole tests. These works have permitted the definition of a mapped grid with the main subsoil information such as Fundamental Period of the soil, Amplification Factor, bedrock depth and its stratigraphy.

3 VULNERABILITY ASSESSMENT OF THE RESIDENTIAL STOCK

3.1 GIS Database

A GIS database of public housing interventions in Florence has been made. It concerns a large number of selected buildings. Preliminarily they have been distinguished in three categories, depending on their structure: masonry buildings, RC buildings and mixed typologies. Masonry interventions have been amply recorded. Each single project has been identified with an *ID* number and geo-referred; using the archive drawings, they have been re-drawn in CAD and related to the GIS identification number. Actually, the main part of the masonry database consists of 286 buildings.

3.2 The GNDT 2nd level approach

The collected interventions have been classified according to the GNDT second level vulnerability assessment method, and a vulnerability index, *Iv*, for every building has been found. The assessment is composed of 11 parameters, which are listed in Table 1. They concern many different types of information, and they are "weighted" through proper coefficients, ranging from 0.25 to 1.5, on the basis of their importance and influence. The Vulnerability Index, *Iv*, can be found on the basis of the assumed classification, through the following expression:

$$I_v = \sum P_i \, x \, w_i \tag{1}$$

Finally, the vulnerability index is normalized between 0 and 100.

Parameter	P_i				w_i
	A	B	C	D	
P1 Type of resisting system	0	5	20	45	1,5
P2 Quality of resisting system	0	5	25	45	0,25
P3 Conventional strength	0	5	25	45	1,5
P4 Location and soil condition	0	5	25	45	0,75
P5 Horizontal diaphragms	0	5	15	45	variable
P6 Planimetric configuration	0	5	25	45	0,5
P7 Regularity in height	0	5	25	45	variable
P8 Maximum distance between masonries	0	5	25	45	0,25
P9 Roofing system	0	15	25	45	variable
P10 Non-structural elements	0	0	25	45	0,25
P11 conservation state	0	5	25	45	1

Table 1: GNDT Vulnerability Index.

3.3 The data-base classification

Each building of the database has been classified according to the GNDT criteria, and a Vulnerability Index ranging between 13% and 39% has been found, with a *mean* value equal to 29%. Figure 2 and Table 2 show the database classification. As can be noted, some parameters do not seem to be sensitive to the database features, since almost all buildings present the same classification. In particular, the parameters most sensitive to the database features are parameters #3, #6, #7, #8 and #9.

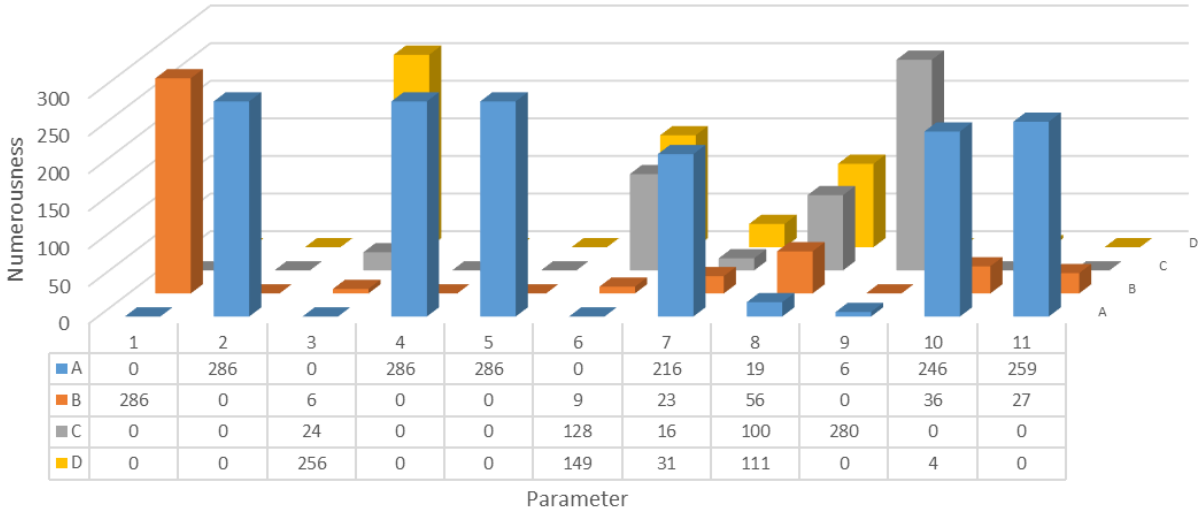

	1	2	3	4	5	6	7	8	9	10	11
A	0	286	0	286	286	0	216	19	6	246	259
B	286	0	6	0	0	9	23	56	0	36	27
C	0	0	24	0	0	128	16	100	280	0	0
D	0	0	256	0	0	149	31	111	0	4	0

Fig. 2. Distribution of GNDT parameters applied to the database.

Parameter P3 is based on geometrical and mechanical data like: the resistant area along x and y directions, the total area, the number of storeys and some non-investigated mechanical features, like density of materials ρ and tangential resistance τ_k as well live loads. Because of the lack of detailed studies for this type of buildings, mechanical characteristics have been chosen following normative guidelines considering their values constant, so, variability of parameter P3 is given mainly by geometrical features such as height, number of storeys, plan area and resistant areas. Resistant area varies in a range from 8 to 22 % of the total area of

buildings. It is usually not equi-distributed between *x* and *y* directions depending on typological and architectonical features.

	A	B	C	D
P1	0%	100%	0%	0%
P2	100%	0%	0%	0%
P3	0%	2%	8%	90%
P4	0%	3%	45%	52%
P7	76%	8%	6%	11%
P8	7%	20%	35%	39%
P9	2%	0%	98%	0%
P10	86%	13%	0%	1%
P11	91%	9%	0%	0%

Table 2: GNDT Vulnerability Index.

P7 is one of the most sensible parameters to the quality of considered drawings projects. It is referred to "elevated configuration of buildings" and concerns the percentage decrease of resistant area along the height of the fabric. Masonries setback are typical of historic masonry buildings in which flexible wooden slabs are wedge into bearing walls; anyway, modern pre-normative buildings are characterized by clear-cut interruptions of masonry due to the presence of the perimetral RC kerb. In the database of buildings, there is some variability of results; it is mainly given by the change of material in the making of the walls. If the lowest levels of the buildings are composed by rubble stone masonries with larger depths, while upper level are generally made with hollow bricks and lower thicknesses. In some case the top floors are composed by perforated bricks with the drillings along the horizontal set.

P8 parameter provides better scores to buildings with bearing walls disposed along two directions, while it penalizes houses with walls along one direction. Each building of the database can be considered to have a box-behavior with concrete rings and rigid slabs. However, when the distance between two consecutive bearing walls is excessive, undesirable torsional effects can occur.

Finally, parameter P9 concerns the roof type of buildings through a quality assessment; most part of the considered buildings resulted to have the same classification.

3.4 Macroseismic methodology assessment

In order to find the damage level which the building could experience at the occurring of a ground motion, the GNDT vulnerability index I_v presented in § 3.3 has been transformed in a macroseismic vulnerability index, V, assuming different levels of seismic intensity according with the EMS-98 [22].

Macroseismic methodology allows to determine the expected damage μ_D for different levels of intensity, I. For each building, vulnerability curves have been found with the following expression:

$$\mu_D = 2.5\left[1+\tanh\left(\frac{I+6.25V-13.1}{Q}\right)\right] \quad ; \quad 0 \le \mu_D \le 5 \tag{2}$$

where Q is the ductility factor. Recent studies have provided different values for Q; in this work Q has been assumed equal to 3, according to the Sandi and Floricel [23] suggestion. The

macroseismic vulnerability index V has been determined through the relationship proposed by Vicente et al. [7]:

$$V = 0.58 + 0.0064\, I_v \tag{3}$$

Seismic intensity can be related to the historical seismology of Florence. The definition of EMS-98 intensity applied in a specific area is related to the vulnerability of buildings that suffered earthquakes in past centuries; so, the comparison of this parameter with "more recent" buildings that never experienced seismic shocks can be not so proper. Seismic intensity of Florence can be estimated between grade VI and grade VIII MCS scale; for each expected measure it is possible to define the respective damage level. The definition of damage according the EMS-98 defines five levels of increasing damage, from D_0 (No damage) to D_5 (Collapse). The damage distribution has been evaluated according to the macroseismic approach through a binomial function based on the damage collection of Italian earthquakes [24]. The probability to have a certain level of damage corresponding to a specific intensity has been assessed according to the probability mass function of the binomial distribution:

$$PMF: \; p_k = \frac{n!}{k!(n-k)!} \times d^k \times (1-d)^{n-k} \quad n \geq 0; \tag{4}$$

where p_k ranges between 0 and 1 and it expresses, in terms of percentage, the continuous damage level for each value of μ_D. Finally, expected damage of the database for different levels of macroseismic intensity can be defined.

In the technical literature there are many formulas to convert the macroseismic intensity measure in PGA. In this work the correlation defined by Giovinazzi and Lagomarsino [24] has been used:

$$a_g = c_1 c_2^{(I-5)} \tag{5}$$

where C_1 is the value of the vulnerability curve for macroseismic intensity I, and C_2 represents the slope of the correlation curve. In this work correlation factors C_1 and C_2 have been estimated respectively equal to 0.03 and 2.05 according to Margottini et al. [25] and traced back on MCS macroseismic scale by Bernardini et al. [26]. PGA of Florence is equal to 0.131 g [27]. Considering the latest soil information about the area of Florence, the amplification factor induced by the soil stratigraphy can vary between 0.7 and 1.7. In this paper only amplification factors greater than 1 have been considered, generating a range of g between 0.131 g and 0.223 g. Fig. 3 shows the *minimum*, *mean* and *maximum* values presented in the database and correlated to the seismic action expressed in terms of macroseismic intensity and PGA.

3.5 Building classification

Building database has been classified in order to determine more specific analyses on buildings. In this work buildings have been divided from a typological point of view into nine building-types, depending on the global shape of their plans. Buildings with a rectangular plan are named "stairs-building-type", and they are further distinguished on the basis of the number of stairs (i.e. their slenderness in plan) in: one-stairs-building-type (1SBT), two-stairs-building-type (2SBT), three-stairs-building-type (3SBT), four/five-stairs-building-type (4SBT). Moreover, there are buildings with a different plan shape: L-buildings (LBT), C-buildings (CBT), T-buildings (TBT), and two further classes: terraced-houses (TH) and irregular buildings (XBT). SBT-types are characterized by central stairwells that serve two apartments for each story. Terraced houses are low buildings aggregated one after the other in a

continuous structural unit. Their vulnerability is most estimable from the length of the construction and the number of unities repetitions than for other parameters. Finally, XBT includes all the interventions not clearly identifiable in the previous classification.

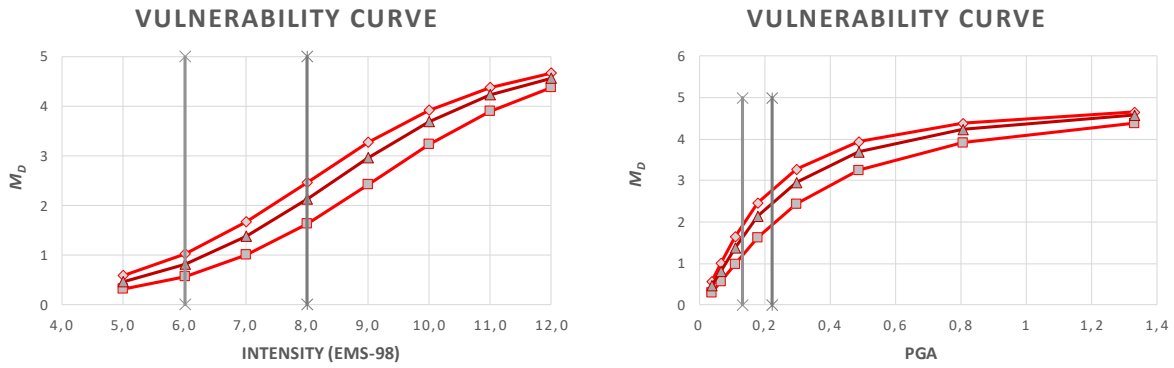

Fig. 3. Vulnerability curves of the database expressed in terms of macroseismic scale (EMS-98) and in PGA (*g*).

The proposed classification (presented in Table 4) can be finally assessed for the expected level of damage for the assumed seismic intensities. According with (4) for each building-type the probability to achieve a certain level of damage for intensities VI, VII and VIII has been assessed. Fig. 4 shows, for each building typology, some examples of real buildings belonging to the database.

Damage distributions of building-types according to the probability mass function of the binomial distribution are finally presented in Fig. 5. Results are very similar from each other because of the lack of variability in terms of Vulnerability Index and, consequently, of macroseismic intensity *I*.

Type	n.	%	I_v range	I_v mean	dev. St.
1SBT	131	43%	21-38	29,72	0,0430
2SBT	58	19%	12-37	28,23	0,0634
3SBT	22	7%	20-32	28,07	0,0344
4SBT	8	3%	29-32	28,13	0,0432
TH	30	10%	22-33	29,14	0,0451
LBT	28	9%	22-32	29,83	0,0209
TBT	12	4%	22-33	29,14	0,0300
XBT	15	5%	20-34	30,03	0,0347
CBT	3	1%	28	28,99	0

Table 4: The proposed classification of buildings.

For seismic intensity equal to VI the probability to have a damage between D_0 and D_1 holds the 80% of the full sample, almost equally distributed. Percentages descend significantly for the other damage levels. Intensity VII leads more scattered results, with the peak of probability (*mean* value 37%) for D_1. D_2 value settles at 29%, while D_0 obtains 20% of the total. Finally, for the most severe intensity expected in the area, VIII, D_2 is the most possible damage configuration of the database (34%), with D_3 at 26% and D_1 at 2 % of probability.

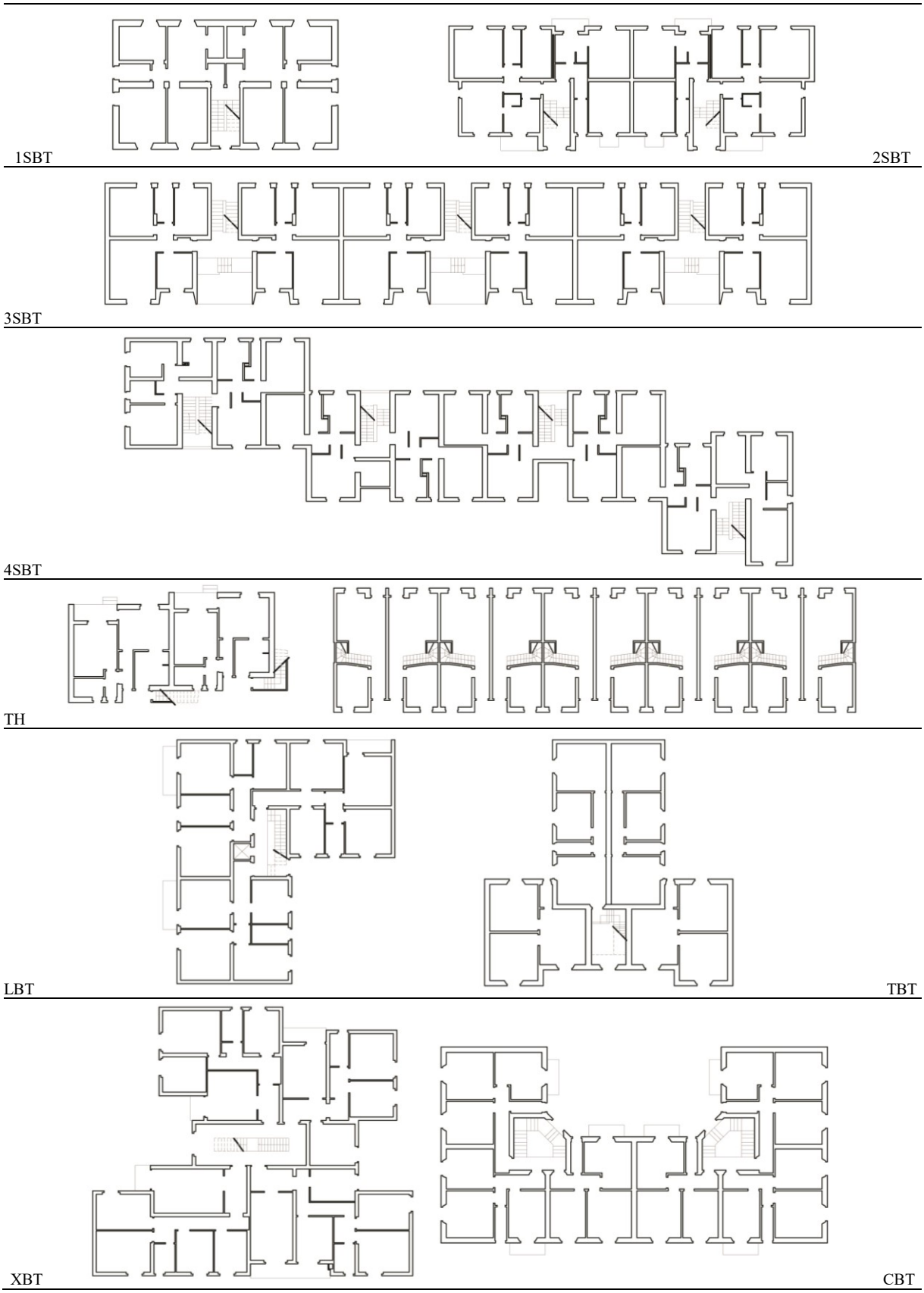

Fig. 4: Examples of buildings selected by the database and classified according the proposed specifications.

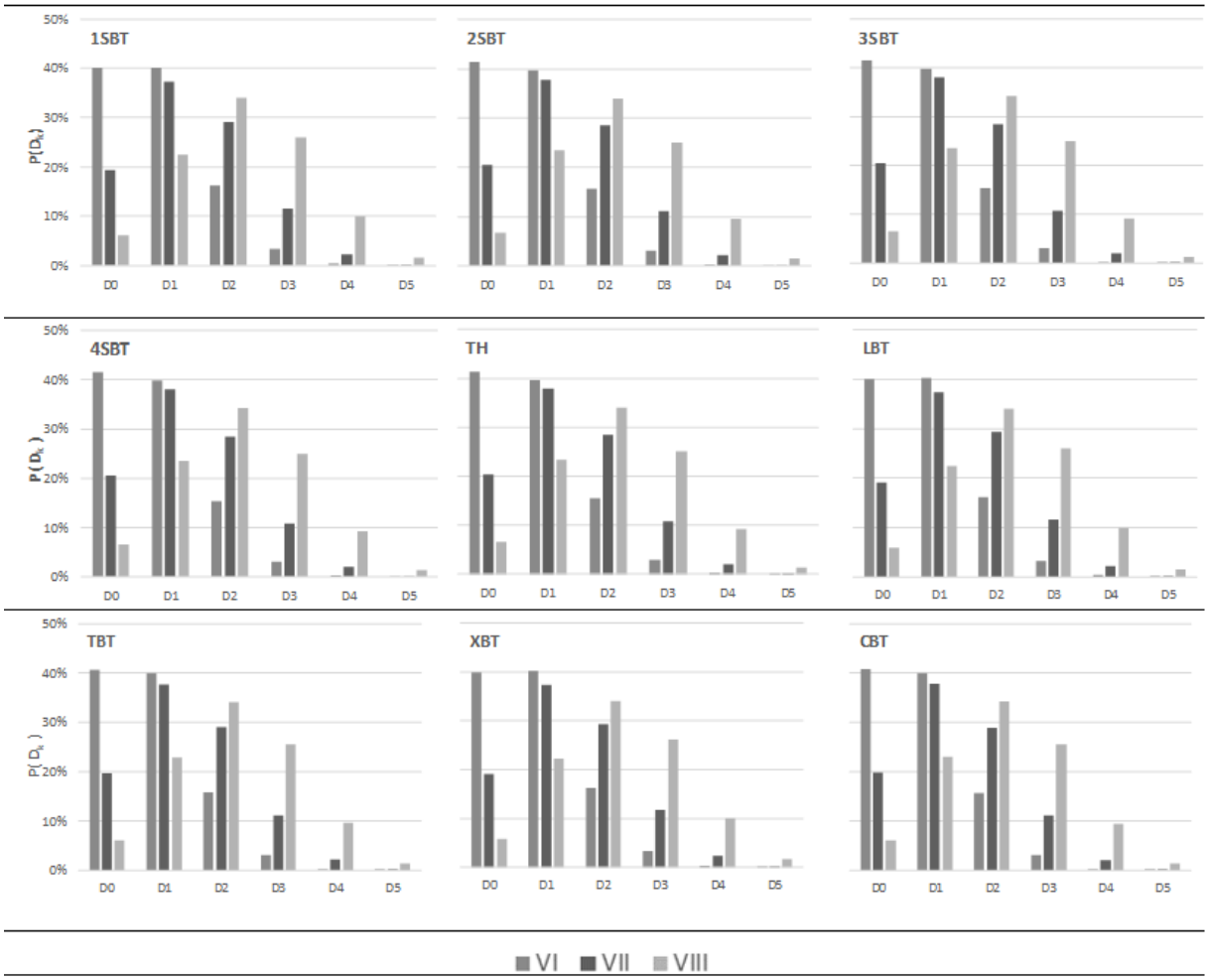

Fig. 5: Probability damage distributions for the three levels of seismic intensity expected in the considered area.

4 CONCLUSIONS

In this paper a systematic assessment of the residential buildings of Florence has been made. Public Housing Interventions have been chosen like representative of the residential stock because of their numerosity and scattered localization. Information about buildings have been collected through an extensive archive research. Finally, each building has been gathered into a geo-referred system. The GNDT second level method has been applied and a vulnerability index I_v for each building has been found. Through expressions presented in literature and based on statistical seismic damage observations, the seismic vulnerability has then been converted in terms of vulnerability curves. The database has been then expressed in terms of macroseismic intensity and peak ground accelerations. The building database has been divided into nine classes, as a function of typological parameters. Finally, the probability of damage for different levels of seismic intensity has been defined for each different class. Seismic scenarios for the residential stock are not dramatic; for Intensity VIII the most expected damage levels is D_2 with the 34% of probability of occurrence and D_3 with the 26% of probability of occurrence.

The results are sensitive to the quality of the vulnerability assessment. Since the database is related to modern homogeneous buildings, the GNDT second level approach, is probably too much broad to catch the database variability. Previous works [28] have shown through analytical analyses the sensitivity of the seismic performance of one-stairwell-building-type to dif-

ferent parameters. A calibration of the presented empirical methodology is expected, to quantify the effects related to single parameters through hybrid approaches, such as analytical models based on performance-based assessments and mechanical characteristics by *in-situ* tests and dynamic identifications.

REFERENCES

[1] Augenti N., Parisi F. (2010). Learning from construction failures due to the 2009 L'Aquila, Italy, earthquake, Journal of Performance of Constructed Facilities, 24(6), 536-555, 2010.

[2] Parisi F., De Luca F., Petruzzelli F., De Risi R., Chioccarelli E., Iervolino I. (2012). Field inspection after the May 20thand 29th2012 Emilia-Romagna earthquakes, available on http://www.reluis.it.

[3] GL-INGV [Gruppo di Lavoro INGV sul terremoto di Amatrice] 2016. Secondo rapporto di sintesi sul Terremoto di Amatrice Ml 6.0 del 24 Agosto 2016 (Italia Centrale), doi:10.5281/zenodo.154400.

[4] Gruppo Nazionale per la Difesa dai Terremoti - GNDT-SSN, (1994). Scheda di esposizione e vulnerabilità e di rilevamento danni di primo e secondo livello (muratura e c. a.). Gruppo Nazionale per la Difesa dai Terremoti, Rome (in Italian).

[5] Zuccaro G., De Gregorio D., Dolce, M., Speranza E., Moroni C., (2014). Manuale per la compilazione della scheda Cartis 2014, Dipartimento Protezione Civile, Rete dei Laboratorio Universitari di Ingegneria Sismica (in Italian).

[6] RINTC Workgroup (2018). Results of the 2015-2017 Implicit seismic risk of codeconforming structures in Italy (RINTC) project. ReLUIS report, Rete dei Laboratori Universitari di Ingegneria Sismica (ReLUIS), Naples, Italy, available at http://www.reluis.it/

[7] Vicente R., Parodi S., Lagomarsino S., Varum H., Mendes Silva J. A. R., (2011). Seismic vulnerability and risk assessment: case study of the historic city centre of Coimbra, Portugal, Bull Earthquake Eng (2011) 9:1067–1096 DOI 10.1007/s10518-010-9233-3.

[8] Silva V., Crowley H., Pinho R., Varum H., Sousa R. (2014). Evaluation of analytical methodologies to derive vulnerability functions". Earthquake Engineering and Structural Dynamics, 43(2):181-204.

[9] Preciado A., Ramirez-Gaytan A., Salido-Ruiz R.A., Caro- Becerra J.L., Lujan-Godinez R., (2015). Earthquake risk assessment methods of unreinforced masonry structures: Hazard and vulnerability. // Earthquakes and Structures, 9, 4(2015), pp. 719-733.

[10] Cavaleri L., Di Trapani F., and Ferrotto M.F., (2017). A new hybrid procedure for the definition of seismic vulnerability in Mediterranean cross-border urban areas, Nat. Hazards, vol. 86, pp. 517-541, 2017. [http://dx.doi.org/10.1007/s11069-016-2646-9]

[11] Giovinazzi S., Lagomarsino S., (2004). A macroseismic model for the vulnerability assessment of buildings. In: Proceedings of 13th world conference on earthquake engineering. Vancouver, Canada.

[12] HAZUS 1999. Earthquake Loss Estimation Methodology. Federal Emergency Management Agency, Washington, D.C.

[13] Risk-UE Project. An advanced approach to earthquake risk scenarios with applications to different European towns. http://www.risk-ue.net

[14] Cattari S., Curti E., Giovinazzi S., Lagomarsino S., Parodi S., Penna A. (2004). A mechanical model for the vulnerability assessment and damage scenario of masonry buildings at urban scale. In: Proc. 11th Italian conference on earthquake engineering. Genoa, Italy.

[15] Lamego P., Lourenço P.B., Sousa M.L., Marques R., (2017). Seismic vulnerability and risk analysis of the old buildingstock at urban scale: Application to a neighbourhood in Lisbon. Bull. Earthq. Eng.2017,15, 2901–2937.

[16] M. Ripepe, G. Lacanna, P. Deguy, M. De Stefano, V. Mariani and M. Tanganelli (2015). Large-scale seismic vulnerability assessment method for urban centres. An application to the city of Florence. Key Engineering Materials Vol 628 (2015) pp 49-54.

[17] Ripepe M., Lacanna G., Deguy P., Cristofaro M. T., De Stefano M., Tanganelli M., Barbara Paoletti B., Vieri Cardinali C., Viti S., Bertaccini B., Rocco E., Giommi A. (2018). Rischio sismico di aree urbane complesse: progetto Sismed. In: ReUSO 2018: VI Convegno Internazionale sulla documentazione, conservazione e recupero del patrimonio architettonico e sulla tutela paesaggistica, Messina, 11-13 ottobre 2018, Gangemi Editore spa, pp. 903-910, ISBN:9788849236590 (in Italian).

[18] Fantozzi Micali O., Lolli E. Novoli: alla periferia delle grandi trasformazioni: edilizia economica e popolare del secondo dopoguerra, Firenze, Alinea, 2007, ISBN: 978-88-6055- 197-9 (in Italian).

[19] Pierini R. La citta distante: piani e progetti di edilizia residenziale pubblica. Pisa, ETS, 2001. ISBN: 88-467-0497-5 (in Italian).

[20] Coli M., Guerri L. & Rubellini P., (2015). Geotechnical characterization of the Florence (Italy) soils. Proc. 5th Asian Regional Conference on Soil Mechanics and Geotechnical Engineering, Fukuoka November 9-13, Japan.

[21] Coli M. & Rubellini P. (2013). Geological anamnesis of the Florence area, Italy. Z. Dt. Ges. Geowiss. (German J. Geosci.), 164 (4), p. 581–589.

[22] Grunthal G (1998). European Macroseismic Scale. Chaiers du Centre Européen de Géodynamique et de Séismologie, vol. 15 Luxembourg.

[23] Sandi H, Floricel I (1995). Analysis of seismic risk affecting the existing IX building stock. In: Proceedings of the 10th European conference on earthquake engineering, vol 3, pp 1105–1110.

[24] Lagomarsino S, Giovinazzi S (2006). Macroseismic and mechanical models for the vulnerability assessment of current buildings. Bull Earthquake Eng. doi:10.1007/s10518-006-9024-z.

[25] Margottini C, Molin D, Narcisi B, Serva L (1992). Intensity versus ground motion: a new approach using Italian data. Eng Geol 33(1):45–58, ISSN 0013-7952. doi:10.1016/0013-7952(92)90034-V.

[26] Bernardini A., Giovinazzi S., Lagomarsino S., Parodi S., (2007). Matrici di probabilità di danno implicite nella scala EMS-98. XIII Congresso Nazionale "L'ingegneria Sismica in Italia", Pisa (in Italian).

[27] NTC (2008). Norme tecniche per le costruzioni. D.M. Ministero Infrastrutture e Trasporti 14 gennaio 2008, G.U.R.I. 4 Febbraio 2008, Roma (in Italian).

[28] Tanganelli M., Rotunno T., Cardinali V., Stefania Viti S., (2018). Public Housing in Florence: Seismic Assessment of Masonry Buildings. PROCEDIA STRUCTURAL INTEGRITY, pp. 266-273, ISSN:2452-3216.

COMPDYN 2019
7th ECCOMAS Thematic Conference on
Computational Methods in Structural Dynamics and Earthquake Engineering
M. Papadrakakis, M. Fragiadakis (eds.)
Crete, Greece, 24–26 June 2019

AN ASSESSMENT OF THE STRUCTURAL BEHAVIOUR OF THE GARISENDA TOWER IN BOLOGNA THROUGH FINITE ELEMENT MODELLING AND STRUCTURAL HEALTH MONITORING

Simonetta Baraccani[1], Alessandro Piccolo[1], Giada Gasparini[1], Michele Palermo[1]Tomaso Trombetti[1]

[1] University of Bologna
Viale del Risorgimento 2, Bologna, Italy
e-mail: simonetta.baraccani2@unibo.it

alessandro.piccolo2@studio.unibo.it

giada.gasparini4@unibo.it

michele.palermo7@unibo.it

tomaso.trombetti@unibo.it

Abstract

The Garisenda Tower, built in the XI century in Bologna (Italy) is a tilted Tower of 48 m high, with a square cross section, that represent the cultural symbol of the city. From the date of its construction, the tower was subjected to various accidents (such as fires, lightings and earthquakes) and interventions of consolidation. Nevertheless its structural configuration and the natural decay of the materials during the years, makes the tower inherently vulnerable to static and seismic actions, thus requiring a constant evolution of its structural health. The purpose of the study is to evaluate the current structural health of the Garisenda tower, through the development of a number of Finite Element models, in order to account for the influence of the geometrical configuration (actual inclination, cross section variability), peculiar construction techniques ("a sacco" masonry) and potential material degradation. To this aim, it has been of fundamental importance to integrate information related to both the actual geometrical configuration from data provided through static and dynamic monitoring and masonry texture, quality and material mechanical properties. In particular, to evaluate the effects caused by an eventual reduction in the material properties at the base, composed by selenitic stones, on the structural behavior, Three Dimensional Finite Element models with brick elements have been developed. The results of the FE analyses indicate that a material degradation at the base of the Tower could lead to local increase of stress levels close to material strength. Moreover, the analyses results also allow to better interpret some trends of behavior as resulted from the monitoring data.

Keywords: Masonry tower, Structural Health Monitoring, Three Dimensional Finite Element Methods

1 INTRODUCTION

The correct management of the historical buildings is a matter of crucial importance that passes through a deep knowledge of their present state and its eventual evolutions during the centuries. The availability of only partial information regarding the original project and the construction techniques, together with strong limitations in the number and extent of in-situ tests for materials characterizations (related to preservation issues), make the assessment of the actual safety level of a monumental building of extreme difficulty [1]. For this reason, data acquired from a structural health monitoring system become of fundamental importance since their proper interpretation may help in increasing the knowledge and better understanding the structural behavior of the monument. The aim of the present study is the analysis of the current structural health of the Garisenda tower. The Garisenda tower is a masonry tilt tower built in the XI century in Bologna (Italy). Although several studies and strengthening interventions have been carried out in the last decades, a continuous attention should be payed on the evaluation of the structural health and on the consequences of the natural decay of material properties in terms of safety and stability [2]. In the present work, the assessment of the current structural behavior of the Garisenda tower is conducted through different Finite Element (FE) models able to take into account the actual geometrical state and variation of inclination as detected from the monitoring system as well potential material degradation at the base. First, the available knowledges related to the tower geometrical configuration and material properties are illustrated and correlated/integrated with the information obtained from the static and dynamic monitoring. Then, the results of structural analysis carried out by mean of FE models with different levels of complexity and accuracy are presented. In particular, to evaluate the effects caused by a material degradation at the base on the structural behavior, Three Dimensional Elements models were performed.

2 GARISENDA TOWER

The Garisenda tower, built in the heart of the city of Bologna in the 11th century, together with its nearby Asinelli tower, is known as one of the “The Two Towers”, that are the main cultural symbol of the city (Fig.1a)[3]. It has a height of 48 m and with an overhang of 3.4 m towards South-East. It is one of the most leaning Tower in Italy.

a) b)

Figure 1-a) The Two Towers of Bologna (Asinelli and Garisenda towers). b) The Garisenda tower

2.1 Geometrical configuration and material proprieties

The cross section of the tower, approximately square, is composed by two external skins and an internal infill. Its thickness decreases with the height as shown in Figure 2a. Starting from the foundation, the first few meters of the tower are composed by an external and internal perimeter of selenitic stones (thickness of around 50-60 cm). In 1889, another external selenitic layer was added to cover the heterogeneous and unsightly portion of the wall in the first 3.5 m (Figure 2b) [4].The properties of the material, summarized in Table 1, have been characterized through in situ tests (both destructive and non-destructive) [5].

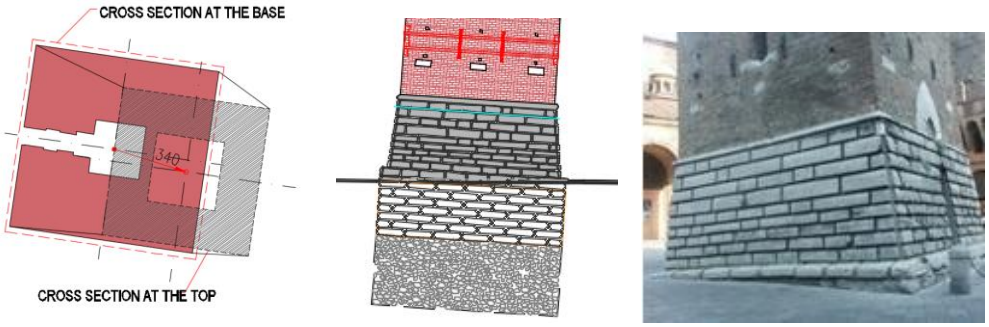

(a) (b) (c)

Figure 2-a) Tower cross section at two different heights (b) Foundation (c) External selenitic stones

Material	Specific Weight γ	υ	Elastic Modulus E_m	Compressive strength f_m	Shear strength $f_{v,m}$
	[KN/m^3]		[MPa]	[MPa]	[MPa]
Masonry bricks	18	0.2	3000	4	0.5
Selenitic stone	24	0.2	5000	7	0.7
infill	17	0.2	2500	4	0.5

Table 1: Material properties

2.2 The Static Structural Health Monitoring (SHM) results

A static SHM system was installed on the Garisenda tower at the beginning of 2011. This system allows monitoring: movements of the main cracks, deformations of critical portions of masonry, inclination, strains along the steel ties (installed on the height of the tower to provide a lateral confinement to the masonry) and environmental parameter (such as temperature, wind speed). Additional details on the monitoring system are available in previous work developed by some of the authors [6], [7]. The results obtained from the analyses of the data recorded by the SHM system highlighted a slight evolutionary trend especially in relation to the inclination. Six inclinometers are installed in the East and South fronts at different levels (13.20 m, 30.65m and 43.3m). The data recorded show an increase in the Tower inclination toward East of around 1.3 mm/year and also a slight inclination northwards.

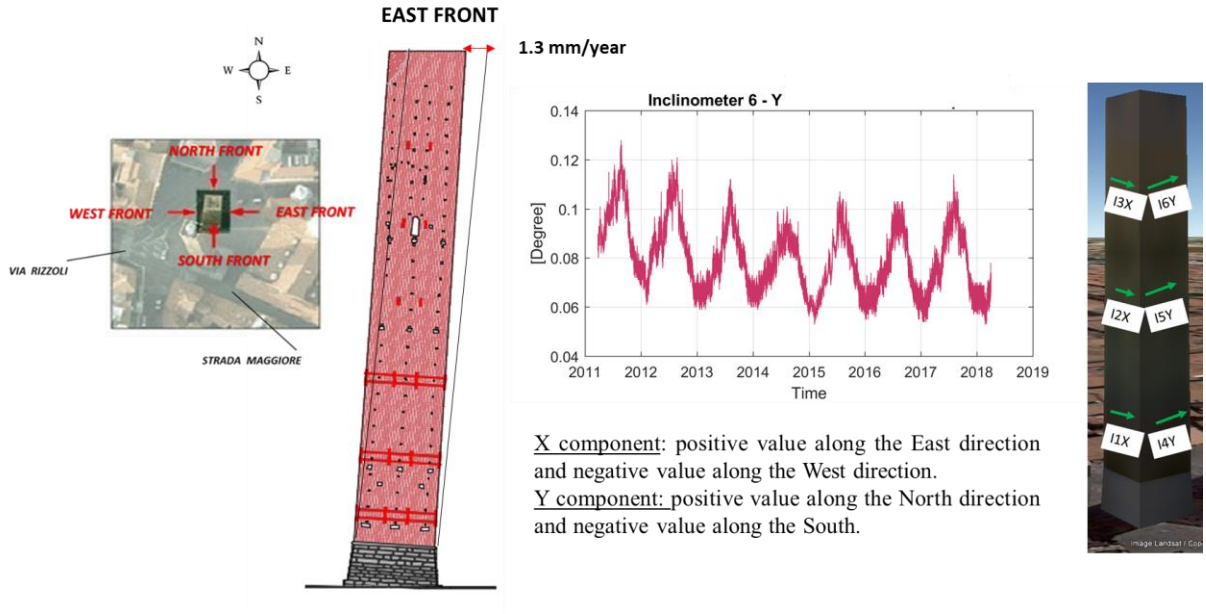

Figure 3-(a) Inclination detected toward East from the X-component of the inclinometers. (b)Inclination detected towards North Y-component of the inclinometers

2.3 Actual state of degradation

Over the last year, some surveys and visual inspections revealed that small portions of the selenitic layer are degrading and becoming chalk, with a significant reduction of the mechanical characteristics of the original stone. This phenomenon is observed at the base in the corner under slope, both on the outside and in the inner side (Figure 4a). Externally the selenitic blocks, that cover the first meters of the tower, have suffered relative displacements mainly concentrated on the East front (Figure 4b). The internal selenitic stones, on the other hand, show the presence of a deterioration process underway due to chemical processes linked to humidity. This phenomenon is particularly pronounced in the South-East corner (Figure 4c).

Figure 4-(a) Corner mainly affected by the degradation phenomenon. (b) Displacements of the selenitic blocks of the East front (c) Degradation of the internal selenite basement

3 NUMERICAL ANALYSES

Structural analyses have been carried out on 3D FE models of the tower in order to assess (i) the effect of static loads and wind accounting for the tower inclination and thermal variations, (ii) the dynamic properties through comparisons with data from SHM, (iii) behavior under earthquake loadings, (iv) the influence of the material degradation at the basement on the structural behavior, (v) possible cause of specific trend detected through the SHM [2]. In

this section, for sake of conciseness, the attention is focused only on the study of the variation of the stress levels due to the material degradation at the base of the tower by means of a Three-Dimensional Finite Element Model (Figure 5a). In detail, the following models/limit cases have been considered:

1) UNDmodel: model with materials having full strengths and elastic moduli according to values provided in Table1,
2) DEGmodel_1: model with a portion of the external and internal selenitic stones having reduced values of elastic moduli (Figure 6a);
3) DEGmodel_2: model with a portion of the entire wall (including the internal infill) with reduced elastic moduli,
4) DEGmodel_3: model with the entire East side with the external selenitic stones having reduced values of elastic moduli.

First, the stress levels as obtained from UNDmodel are reported in figure 5b. It can be noted that the maximum compressive stresses accumulates on the external selenitic blocks concentrated on the South-East corner (around 2 MPa), while the internal infill achieves compressive stresses of the order of 1 MPa.

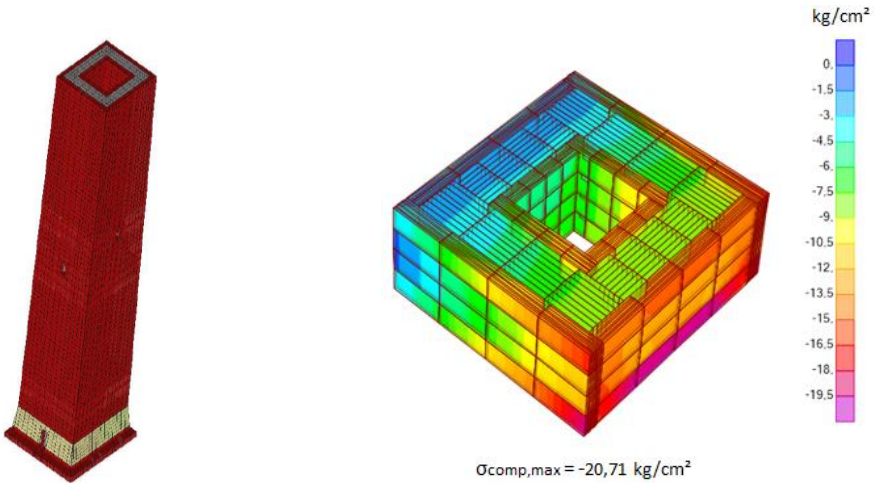

(a) (b)

Figure 5-(a) Three-Dimensional Finite Element Model of the Garisenda Tower. (b)Stress levels at the base of the tower considering the material not degraded.

In model DEGmodel_1, the degradation detected in the external and internal perimeter constituted by blocks of selenite has been simulated progressively decreasing the elastic modulus of the material in the South-East corner, evidenced in green in Figure 6a (in particular several analyses have been carried out reducing the elastic moduli from 2500 to 250 MPa). The analyses have been conducted considering only the self-weight. The results obtained in terms of contour maps, considering an elastic modulus of the corner equal to 250 MPa, are presented in figure 6b. It can be noticed that the maximum value of the compressive stress in selenitic blocks remains of the same order of magnitude whilst increase in the infill (reaching values of the order of 2.6 MPa).

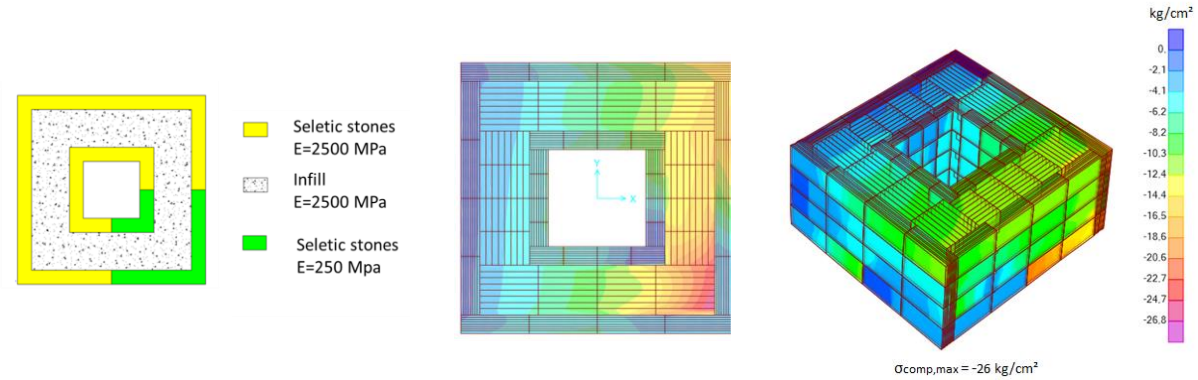

(a) (b)

Figure 6-(a) Identification of the areas interested by the reduction of the Elastic modulus. (b) Contour maps, considering an elastic modulus of the corner equal to 250 MPa

DEGmodel_2 includes the effect of a possible deterioration in the infill material through 2 reductions in the elastic moduli: (i) from 3000 MPa (initial value) to 1500 MPa, (ii) from 3000 MPa (initial value) to 300 MPa. Figure 7 displays the contour maps of the stresses levels in the selenitic stones and infill for the two cases. It can be noticed that the degradation of the infill causes a redistribution of the tension moving the maximum stresses in the selenitic stones close to the deteriorate corner (peaks of the order of 3.2 MPa and 5.7 MPa).

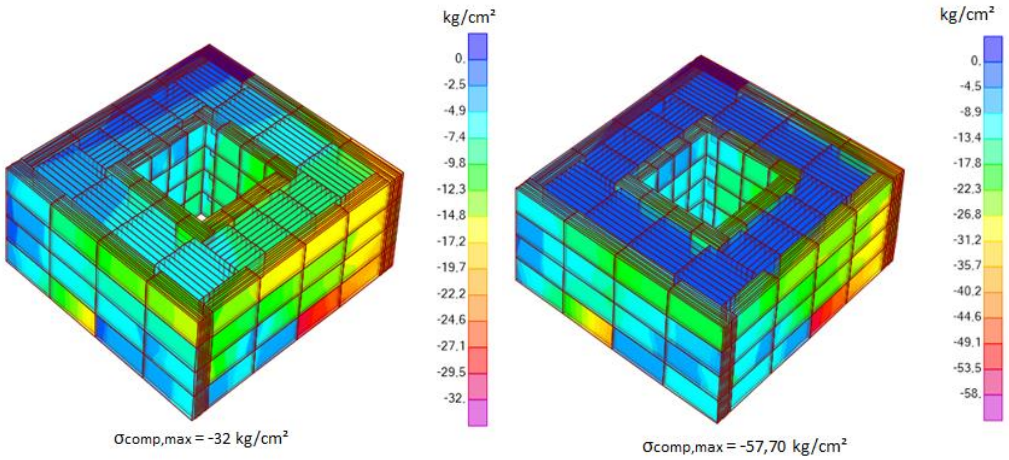

(a) (b)

Figure 7-(a) Contour maps of the stress level at the base section obtained reducing the infill Elastic modulus by: (a) 50% and (b) 90%

DEGmodel_3 investigates the possible cause of the inclination detected by the inclinometers in the North direction of the tower. In this model, the properties of the selenic stone for all the external portion of the East side were reduced to 250 MPa. This phenomenon could be related to the results obtained by recent investigations that detect a small cavity on the Eastern front towards the edge opposite to the one actually under slope, causing a weakening of the section. From this latter case, it can be inferred that if all the side under slope as well as the internal infill would become completely deteriorated, there would be peaks of tension in the infill of the order of 3.5 MPa and close to material strength. Analysing the displacements in the Y-direction of this model (corresponding to North direction of the tower), it has been possible noticed that the presence of a degradation in all the side under slope actually provokes a displacement, although of the order of tenths of millimetres, in North direction.

4 CONCLUSIONS

The main conclusion of the present work can be summarized as follows:

- The structural health of the Garisenda tower has been investigated with a particular attention to the effects of the potential material degradation detected at the base of the tower. First, the present state of the tower has been studied through survey and non-destructive tests correlated to the data obtained by a static and dynamic monitoring system.
- The effects caused by a reduction in the material properties at the base, composed by selenitic stones, on the structural behavior, has been investigated by means of Three Dimensional Finite Element models with brick elements.
- Considering the degradation only in the selenitic stone and with a concentration in the South-East front, the results obtained reveal that the maximum compression value in the selenite blocks remains substantially unchanged but creates a sort of arc effect that leads to the loading of the first blocks alongside the deteriorated ones.
- A deterioration of the infill material would cause tensions that could reach the limit of the material strength with a considerable reduction of the safety levels of the building.
- In addition, it has been confirmed that the tower is undergoing a slight displacement northwards due to a deterioration of the coating portion on the North-East front.

ACKNOWLEDGEMENT

The authors gratefully acknowledge Dott. Ing. Gilberto Dallavalle who provided valuable information related to geometrical and material properties.

REFERENCES

[1] ISCARSAH (International Scientific Committee for Analysis and Restoration of Structures of Architectural Heritage), “Recommendations for the analysis, conservation and structural restoration of Architectural Heritage,” *Icomos*, no. June, pp. 3–6, 2003.

[2] S. Baraccani, G. Gasparini, M. Palermo, S. Silvestri, and T. Trombetti, “The structural strengthening of the Garisenda Tower in Bologna, Italy Simonetta,” 2017.

[3] T. Costa, *Il grande libro delle Torri Bolognesi*. 1984.

[4] G. Francisco, *La Torre Garisenda*. 2000.

[5] C. Ceccoli, P. Diotallevi, P. Pozzati, L. Sanpaolesi, and G. Dallavalle, “Indagini inerenti le strutture murarie e fondali e consolidamento delle parti in elevazione della Torre Garisenda".” 2001.

[6] S. Baraccani, M. Palermo, R. M. Azzara, G. Gasparini, S. Silvestri, and T. Trombetti, *Structural interpretation of data from static and dynamic structural health monitoring of monumental buildings*, vol. 747 KEM. 2017.

[7] S. Baraccani, G. Gasparini, M. Palermo, S. Silvestri, and T. Trombetti, “A possible interpretation of data acquired from monitoring systems,” *Civil-Comp Proc.*, vol. 106, 2014.

COMPDYN 2019
7th ECCOMAS Thematic Conference on
Computational Methods in Structural Dynamics and Earthquake Engineering
M. Papadrakakis, M. Fragiadakis (eds.)
Crete, Greece, 24–26 June 2019

UNCERTAINTY OF PROPERTIES AND FAILURE LOAD IN COMPOSITE MATERIALS

Piotr Kędziora

Cracow University of Technology
31-155 Kraków, ul. Warszawska 24, Poland
e-mail: piotr.kedziora@mech.pk.edu.pl

Abstract

The impreciseness (uncertainty) of the experimentally obtained data can be described using fuzzy sets theory. It is proposed the fuzzy set method for the correct and concise evaluation of various geometrical and mechanical properties or final failure load. The variability (understood as the fuzziness) of the fiber and matrix properties is described by a membership function. Based on experimental results it is possible to determine the effect of the fuzziness of the mechanical properties. The fuzzy sets theory allows to build the lower and upper bounds of the failure envelopes for the Tsai-Wu criterion. The linear qualifier function is applied to analyze the composite structure subjected to the load.

Keywords: Composite Materials, Fuzzy Set, Fuzzy Logic, Material Uncertainty.

1 INTRODUCTION

The use of fiber-reinforced composite materials in modern engineering structural design has become a common practice. However, since more design variables typically exist when composite materials are employed and the manufacturing processes for producing composites are more complex, more variability can exist in a design procedures with composites compared to conventional (isotropic) materials [1]. Thus, the variability of properties that occurs in composite structures leads directly to a random field of variables describing constructions. A scatter of properties has a different origin including geometrical and mechanical properties, environmental effects and the influence of the applied technology or existence of the internal defects of flaws, see e.g. papers [2-5]. Therefore, there is a fundamental question: how many and which of the above factors can (or should) be incorporated in the design process and how can we manage to take into account the existing variability of parameters. A broader discussion of those problems can be found in reference [6].

The majority of available references in literature discussing design problems of composite structures is devoted to the analysis conducted in a pure deterministic way. However, the random field of parameters describing composites may be taken into account by the standard use of different variants of the statistical analysis or by the application of non-stochastic methods – a fuzzy set approach.

Referring to composite materials the origin and the source of imprecision (or uncertainty) lies mainly in the lack of information dealing with their microstructure, mechanical properties, behavior and the number of factors responsible for gradual degradation of their properties and final failure. Commonly, the theoretical (deterministic) analysis of composites is based on the homogenization theories that may include an increasing number of different parameters [7, 8]. However, it is unknown in advance what number of parameters is sufficient to describe satisfactorily the problem considered. On the other hand, the material parameters are evaluated in the experimental way being the source of randomness in the traditional (deterministic) analysis or impreciseness or vagueness in the fuzzy set approach. The imprecise, vague, qualitative, linguistic or incomplete information may be present in geometry, material properties, degradation of properties, applied loads or boundary conditions.

Different kinds of methods are investigated for different types of uncertainties. Oskay and Fish [9] calibrated material properties in a deterministic fashion with the aid of genetic algorithms and gradient-based techniques. Jiang et al. [10] proposed the deterministic model to identify the uncertain elastic modulus of braided composites using modal data. Mustafa et al. [11] presented a probabilistic model for estimating the fatigue life of composite laminates using a high fidelity, multi-scale approach called M-LaF (Micromechanics based approach for Fatigue Life Failure). They developed a unified framework for the representation and quantification of uncertainty present in the fiber and matrix properties with the use of the Bayesian inference approach in order to calculate probabilistic composite fatigue failure. Chandrashekhar and Ganguli [12] performed probabilistic analysis using the Monte Carlo Simulation on a refined composite plate finite element model to calculate the statistical properties of the variation in modal parameters of a cantilever composite plate due to structural damage and material uncertainty.

If the system parameters are described in imprecise or linguistic terms the fuzzy theory can be implemented to predict the structural response in the sense of evaluation of its upper and lower bounds, respectively. Various problems connected with fundamentals and concepts used in the fuzzy set theory are presented in a few representative monographs: McNeill and Thro [13], Cox [14], Tsoukalas and Uhrig [15], Dubois and Prade [16], Zadeh et al. [17], Kosko [18].

Fuzzy concepts are used in various areas of mechanics. Moens and Hanss [19] presented an overview of the research activities on non-probabilistic finite element analysis and its application in the representation of parametric uncertainty in applied mechanics. Sodoke et al. [20] used a fuzzy logic model to obtain a simplified view of linguistic variables representing the modulus of elasticity and to reconcile different modules by including the uncertainty inherent to the different measuring techniques. Altmann et al. [21] introduced a fuzzy-probabilistic approach to assess the durability of strain-hardening cement-based composites. Karbhari and Stein [22] described the application of a fuzzy probabilistic approach to reflect the impact of the inherent uncertainty in determining the reinforcing fibers of polymer jackets for the seismic retrofit of columns. Bohlooli et al. [23] presented a suitable model based on fuzzy logic to predict the compressive strength of inorganic polymers with seeded fly ash and rice husk bark ash. Syamsiah et al. [24] proposed the role of input selection using a neuro-fuzzy approach to predict the physical properties of degradable composites, namely the melt flow index and density. Rassbach and Lehnert [25] developed a model based on the mathematical methods of fuzzy-logic which can describe the plasto-mechanical behavior of functionally gradient materials during the deformation process. Muc and Kędziora [26] employed a fuzzy-set based approach in conjunction with a finite element analysis and fracture mechanics. In the numerical analysis four parameters were considered to be fuzzy, namely, three mechanical parameters (Young's moduli, Kirchhoff's modulus) and one geometrical parameter describing the position of the crack center. Kędziora and Muc [27-29] proposed the fuzzy set analysis in order to estimate the uncertainty in the evaluation of critical number of cycles corresponding to the final fatigue damage. Experimental data obtained during fatigue tests conducted for tension and compression were represented by the lower and upper bounds of the stiffness degradation, i.e., as stiffness versus the number of cycles relationships [28, 29].

Therefore, in this way the impreciseness (uncertainty) of the experimentally obtained data can be described using fuzzy sets theory. In this paper, it is proposed the fuzzy set method for the correct and concise evaluation of various mechanical properties or final failure load. The variability (understood as the fuzziness) of the fiber and matrix properties is described by a membership function. Based on experimental results it is possible to determine the effect of the fuzziness of the mechanical properties. The fuzzy sets theory allows to build the lower and upper bounds of the failure envelopes for the Tsai-Wu criterion. The linear qualifier function is applied to analyze the composite structure subjected to the load.

2 FUNDAMENTAL DEFINITIONS

2.1 Representations of Fuzzy Sets

The data "integer less than 10" is the definition of characteristic function Π_A and is represented in the following way:

$$\Pi_A : IN \rightarrow \{0,1\}$$
$$\Pi_A(\eta) = \begin{cases} 1, & \text{if less than } 10 \\ 0, & \text{otherwise} \end{cases} \tag{1}$$

that yields a value 1 for each element of space IN that belongs to set A and a value 0 for each element that does not. The above representation is commonly called a crisp set. However, this concept cannot be used directly as we intend to characterize the typical property for composite materials, e.g. the failure of carbon fiber reinforced polymer under tension occurring as tensile strain ε_x is equal to the ultimate value of 0.015. The characteristic function of this set is depicted in Figure 1a. For the three-dimensional analysis, all the components of the strain ten-

sor can be evaluated in a similar manner. A problem arises if the linguistic term “failure under tension” has to be described. The value of a failure strain in composites depends on various parameters such as the fiber and matrix materials, loading conditions, porosity, environmental effects, etc. It is well-known that from the micromechanical point of view that failure starts from microcracks in the matrix for strain values much lower than the value 0.015. In addition, the value 0.015 is usually an average value characterizing rather a scatter of a random values of macrocracks appearing at the strain level 0.015. Therefore, for some specimens one can observe the final (macroscale) failure as ε_x is equal to 0.0159 or to 0.0141. A possible solution to this problem is to generalize the definition of the characteristic function in a way that it yields values from interval [0, 1] and not just the two values of the {0, 1}. This leads to the notion of a fuzzy set.

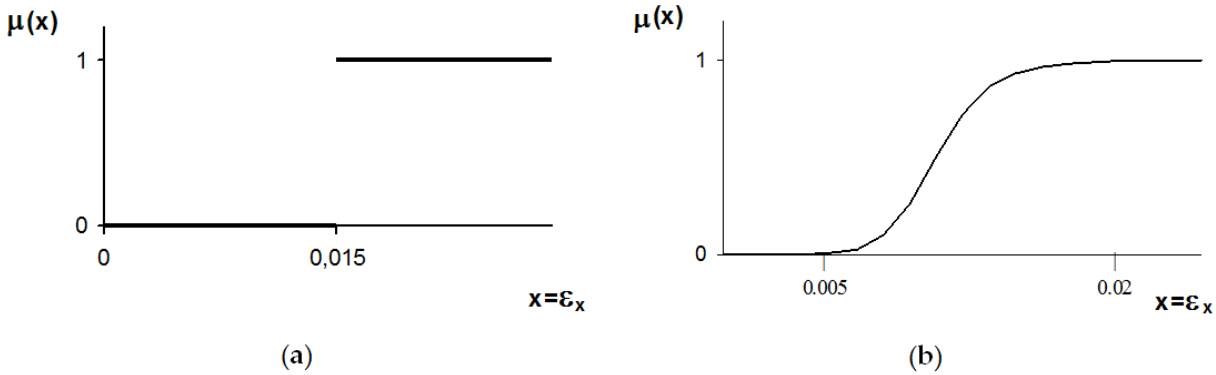

Figure 1: Representation of term “failure under tension”: (a) crisp set; (b) fuzzy set.

Fuzzy set μ of X is a function that maps space X into the unit interval, i.e.:

$$\mu : X \rightarrow [0,1] \tag{2}$$

Value μ(x) denotes the membership function of x to fuzzy set μ. Figure 1b shows (subjectively defined) a membership function of fuzzy set μ describing the linguistic meaning of the term “failure under tension”. The use of fuzzy sets to formally represent vague data is often done in an intuitive way because in many applications there is no model that provides a clear interpretation of the membership degrees, though we want or we try to base it on various experimental data.

The application of fuzzy methodologies requires the knowledge of the membership functions of fuzzy quantities. In general, fuzzy numbers are sets that represent numeric quantity. It can be done in a variety of ways. Of course, there are different possibilities to determine and represent membership functions characterizing a fuzzy set. If subspace S contains only a finite number of elements, a fuzzy set μ of X will be defined by specifying for each element $x \in X$ its membership degree μ(x). If the number of elements is very large or a continuum is chosen for X, then μ(x) can be better defined by a function that can use parameters which are adapted to the actual modeling problem. For instance, if we want to represent the term “Young’s modulus is equal to 200 GPa” in the sense of a fuzzy set having a finite amount of experimental data, we can select one of the different representations given in Figure 2.

The determination of the membership functions is difficult. There are different forms of them and in the description of the fuzzy numbers the triangular, trapezoidal, Π, B, Gaussian or Weibull curves are commonly used, whereas in the case of fuzzy qualifiers – the sigmodal or linear curves – see reference [3]. However, the first attempt or trial in building the membership functions can be based on the statistical data – see e.g. the description of failure.

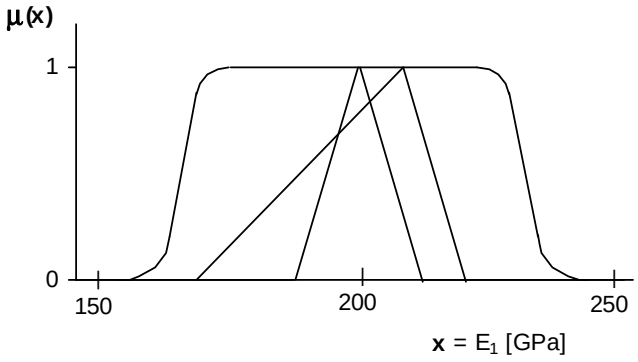

Figure 2: The used descriptions of uncertainty.

One of the possible fuzzy set representations was presented there. Another approach is the so-called horizontal representation of fuzzy sets. This is introduced by using their α-cuts instead of membership functions μ(x) which are called vertical representations.

Let $\mu \in F(x)$ and $\alpha \in [0, 1]$. The set is called the α-cuts of μ:

$$[\mu]_\alpha = \{x \in X | \mu(x) \geq \alpha\} \tag{3}$$

Let μ be the triangular function on IR given in Figure 3. The α-cuts of μ are in this case defined as follows:

$$[\mu]_\alpha = \begin{cases} [a + \alpha \cdot (m-a), b - a \cdot (b-m)] & \text{if } 0 < \alpha \leq 1 \\ IR & \text{if } \alpha = 0 \end{cases} \tag{4}$$

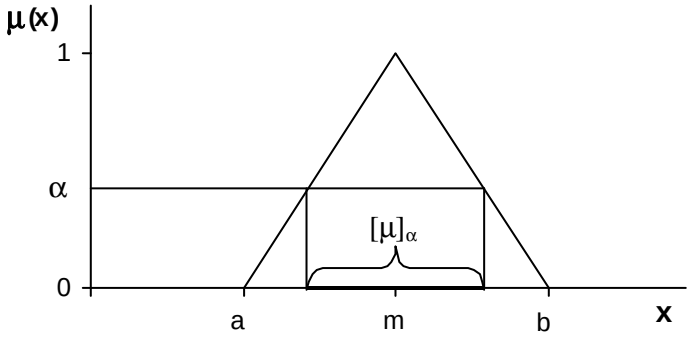

Figure 3: Definition of α-cuts.

There are, generally, two kinds of fuzzy sets:

- numbers that represent an approximate numeric quantity; those values can represent uncertainty (impreciseness, fuzziness) of Young's (see Figure 2) or Kirchhoff's moduli, geometric properties of structures (dimensions, fiber orientations) or allowable strengths/strains in appropriate directions;
- qualifiers that characterize open-ended concepts; these sets provide the framework for describing unbounded concepts (or concepts that are theoretically unbounded), e.g. qualifiers of failure or constraints in various optimization problems – see e.g. Rao [30].

2.2 Vertex Method

Let us introduce N fuzzy parameters describing the material or geometric parameters of the considered composite structure. The membership functions are discretized using several α-cuts – Equation (4). Considering the left and right end points of the α-cut s intervals $[\mu]_\alpha$ (see Figure 3) for all the fuzzy parameters, one can find the total number of combinations $N_{c/\alpha}$ per α-cut in the following form:

$$N_{c/\alpha} = \begin{cases} 2^N & for\ 0 \le \alpha < 1 \\ 1 & \text{for } \alpha = 1 \end{cases} \tag{5}$$

An output response denoted by p is an unknown function of input fuzzy parameters x_i (i=1, 2, …, N), so that:

$$p = f(x_1,...,x_N) \tag{6}$$

Using the α-cut concept combined with binary representation (5) of fuzzy parameters x_i (i=1,2,…,N) relation (6) can be rewritten in the abbreviated form:

$$p = f(C_{\lambda,j}); \quad j = 1, 2, ..., N_{c/\alpha} \tag{7}$$

Since output response p as a function of fuzzy parameters is a fuzzy set, the corresponding interval in p is obtained from relation (6):

$$[p_\alpha^L, p_\alpha^R] = [\min_{\lambda,j} f(C_{\lambda,j}), \max_{\lambda,j} f(C_{\lambda,j}); \ \lambda \ge \alpha, \ j = 1, 2, ..., N_{c/\alpha} \tag{8}$$

As may be seen, relation (8) allows one to obtain a scatter of the output parameters and then to build the appropriate probability distributions and reliability functions by a sweep of α-cut at different possibility levels.

In order to conduct the computations and to evaluate the upper and lower boundaries of output response (8), it is necessary to outline the deterministic method of the definition of function f given in Equation (6). It can be defined in a purely analytical way or alternatively in a purely numerical way. As may be noticed, the vertex method resembles here the Monte Carlo simulation method where the output response also has a deterministic, and therefore unique form.

Function f existing in Equation (6) may describe an arbitrary failure criterion for composites, e.g. buckling, delamination, first-ply-failure (FPF) etc., whereas symbol p denotes the corresponding value of the failure load.

3 FUZZY SET ANALYSIS

The origin and source of imprecision (or uncertainty) can result from the lack of information dealing with their microstructure, mechanical properties, behavior and the number of factors responsible for gradual degradation of their properties and final failure of composite materials.

3.1 Mechanical Properties

Commonly, the theoretical (deterministic) analysis of composites is based on homogenization theories. In the micromechanics analysis the development of the model of repeating unit cells is based on the assumption that the unidirectional composite is represented by fibers which are aligned in the x_1–direction and distributed regularly in the matrix and finally the components form a doubly periodic array in the x_2 and x_3 directions – see Figure 4. In Figure

4 the fibers have a circular cross-section and the same diameter d and are arranged at distances h, l apart. The unit cell is showed in Figure 4b.

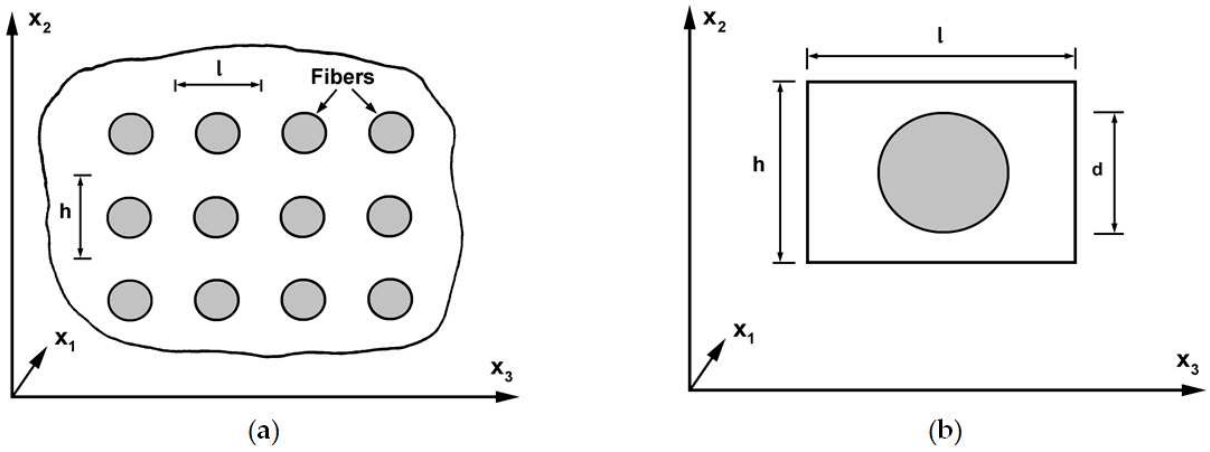

Figure 4: Micromechanics unit cell geometry: (a) periodic array of circular fibers extending in the x_1 direction; (b) representative cell.

At the micromechanics level, the transversely isotropic material is expressed in terms of the five engineering constants. They are functions of the material variables, i.e. of the fiber and the matrix properties E_{f1}, E_{f2}, G_{f12}, ν_{f12}, ν_{f13}, E_m, ν_m, V_f, where f denotes fiber property, m – a matrix property, E – the Young's modulus, G – the Kirchhoff's modulus, ν – Poisson's ratio and V_f is the fiber volume fraction (assuming $V_f + V_m = 1$, where V_m is the matrix volume fraction).

The impreciseness in the modeling is obvious: the ideal forms of the constituents and of representative cells, an influence of the interface is completely eliminated – there are two components in the model fibers and matrices, the matrix and fibers have constant values (there is no defects inside them) etc.

Now, let us assume that the variables characterizing the fiber and matrix properties are fuzzy variables and their fuzziness is described by a triangular membership function – see Figure 3. It is assumed that the variability (understood as the fuzziness) of material parameters is taken to be equal to ±10 %. The nominal (average) values correspond to α=1 (see Figure 3) whereas the parameters of the triangular membership function given by Equation (4) are following :

$$m = \frac{a+b}{2}, \quad a = 0.9 \cdot m \quad b = 1.1 \cdot m \tag{9}$$

Having the Halpin–Tsai model equations of the relation (6) and using the procedure proposed in the Section 2 for a given α-cut one can evaluate the upper (the right end point of the interval (8)) and lower bounds (the left end point of the interval (8)) of the effective longitudinal and transverse Young moduli. The results are evaluated for the unidirectional long glass fibers/epoxy resin, i.e. the nominal properties (denoted by m in relation (10) and Figure 3) E_{f1}=73GPa, E_m=3.5GPa from [31]. The results of computations are plotted in Figure 5. As it may be seen, the nominal curve denoted by the value α=1 (the solid red line in Figure 5) is obtained for nominal values of E_{f1} and E_m. The lower and upper bounds of the curves denoted by the value α=0 plotted in Figure 5 (denoted by the superscripts L and R), are evaluated with the use of Equation (8). As it may be observed the biggest effect of fuzziness is for the maximal values of the fiber volume fraction.

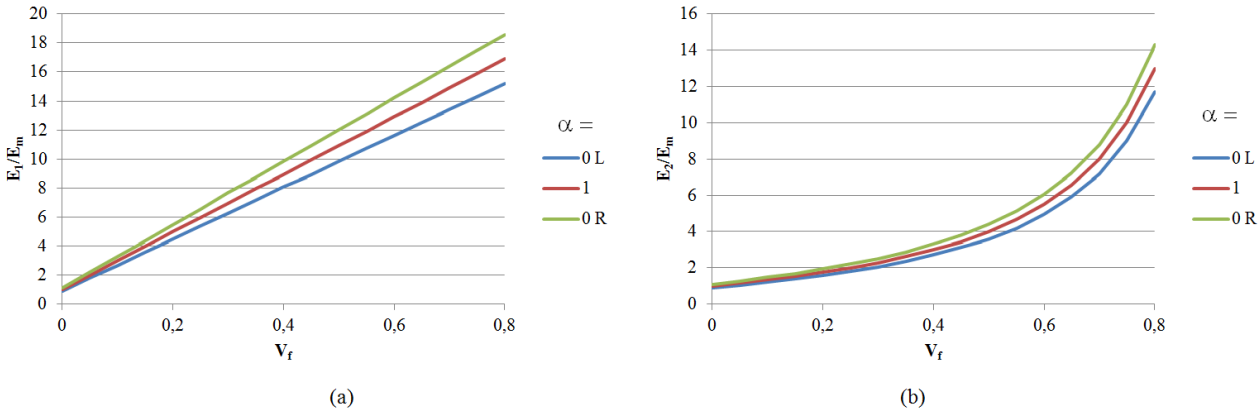

Figure 5: Distributions of the effective longitudinal E_1 (a) and transverse E_2 (b) Young moduli at α= 0 and 1 (L – lower bound, R – upper bound).

3.2 First-ply-failure

One of failure criterion in order to consider these uncertain material properties is applied to the calculation. For example, uncertainties in elastic moduli of laminates are due to several factors, such as e.g. the misalignment of fibers or imperfect bonding between fibers and matrix.

The classical first-ply-failure (FPF) envelopes (e.g. the Tsai-Wu criterion) are described with the aid of variety of material constants characterizing different modes of failures (tension, compression etc.). Those values may be treated as fuzzy ones and in this way the fuzzy set theory allows us to build the lower and upper bounds of the failure envelopes for each fiber orientations of plies in the laminate. Assuming that five strength constants are fuzzy parameters such envelopes have been built and the plot is presented in Figure 6. For compressive deformations the uncertainty of failure locations (at plies having fibers oriented at 0° or 45°) is the characteristic feature of the resulting curves.

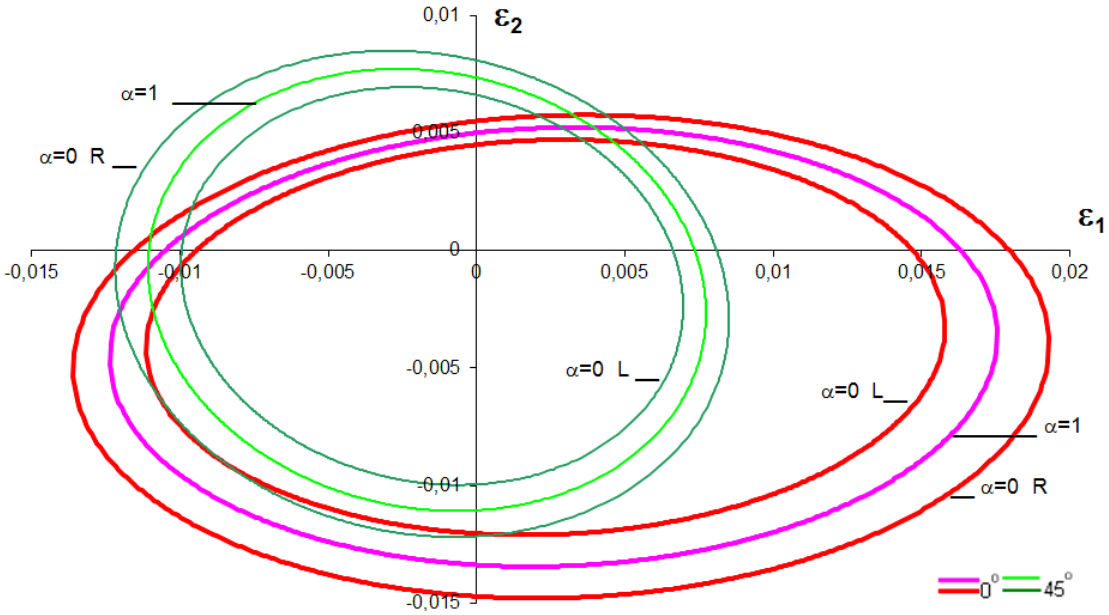

Figure 6: Upper and lower bounds of FPF envelopes – the Tsai-Wu criterion (plies having fibers oriented at 0° or 45°; L – lower bound, R – upper bound).

The results demonstrate evidently that the classical deterministic approach to the FPF analysis can lead to the inconsistency and incorrectness with experimental data. For compression in both directions it is possible to obtain experimentally the FPF initiation at plies oriented both at 0° and 45°. They show simply the limitations of the classical global elastic approach since the matrix cracking associated with the FPF is connected with inelastic deformations (in the global sense), especially for fibers oriented at 45° or with the appearance of intralaminar cracks (a micromechanical approach).

3.3 Fuzzy Constrains

The deformation of composite structure subjected to in-plane and/or bending loads can be considered using fuzzy maximum strain criteria. Fuzzy constrains are defined by maximum strain criteria in the following way:

$$\begin{aligned} \varepsilon_{1c}^{ult} - \Delta\varepsilon_{1c} \le \varepsilon_1^{\pm}(\theta_k) \le \varepsilon_{1t}^{ult} + \Delta\varepsilon_{1t} \\ \varepsilon_{2c}^{ult} - \Delta\varepsilon_{2c} \le \varepsilon_2^{\pm}(\theta_k) \le \varepsilon_{2t}^{ult} + \Delta\varepsilon_{2t} \\ \left|\varepsilon_6^{\pm}(\theta_k)\right| \le \varepsilon_{6t}^{ult} + \Delta\varepsilon_{6t} \end{aligned} \tag{10}$$

where ± denotes upper and lower surface of k-th layer, respectively. t designates tension and c – compression. θ denotes fiber orientation. Ultimate strain strengths (maximum) ε^{ult} are dealt with as fuzzy numbers by using $\Delta\varepsilon$ and β in the following manner:

$$\Delta\varepsilon_{ij} = \beta \cdot \varepsilon_{ij}^{ult} \quad i = 1,2,6 \quad j = t, c \tag{11}$$

The value of the parameter β denotes the level of fuzziness in the problem. When β is equal to 0% it denotes a crisp optimization problem. The degree of satisfaction of constraint is determined using the membership functions $\mu_\varepsilon(\varepsilon(\theta))$ (see reference [3]) which are represented by linear qualifier function in the form of asymmetrically trapezium. For the positive value of strain $\varepsilon(\theta)$, the membership functions $\mu_\varepsilon(\varepsilon(\theta))$ is given by

$$\mu_{\varepsilon_t}(\varepsilon(\theta_k)) = \begin{cases} 1 & \varepsilon(\theta_k) < \varepsilon_t^{ult} - \Delta\varepsilon_t \\ \alpha_t & \varepsilon_t^{ult} - \Delta\varepsilon_t \le \varepsilon(\theta_k) \le \varepsilon_t^{ult} + \Delta\varepsilon_t \\ 0 & \varepsilon(\theta_k) > \varepsilon_t^{ult} + \Delta\varepsilon_t \end{cases} \tag{12}$$

where

$$\alpha_t = 1 - \frac{\varepsilon(\theta_k) - \left(\varepsilon_t^{ult} - \Delta\varepsilon_t\right)}{\varepsilon_t^{ult} + \Delta\varepsilon_t - \left(\varepsilon_t^{ult} - \Delta\varepsilon_t\right)} \in [0,1] \tag{13}$$

and presented in Figure 7a. For the negative value of strain $\varepsilon(\theta)$, the membership functions $\mu_\varepsilon(\varepsilon(\theta))$ is showed in Figure 7b.

The maximum stress criterion has a similar form. Then, in Equations (10)-(13), the notation σ is used in place of ε.

CONCLUSIONS

The present study is a practical tool for engineering activities dealing with evaluating the degradation of real material structure. As it remains an open problem, it is connected with the total number of uncertain parameters that should be considered in order to describe the real

behavior of engineering structures with an acceptable accuracy. However, it can be solved for each individual problem only.

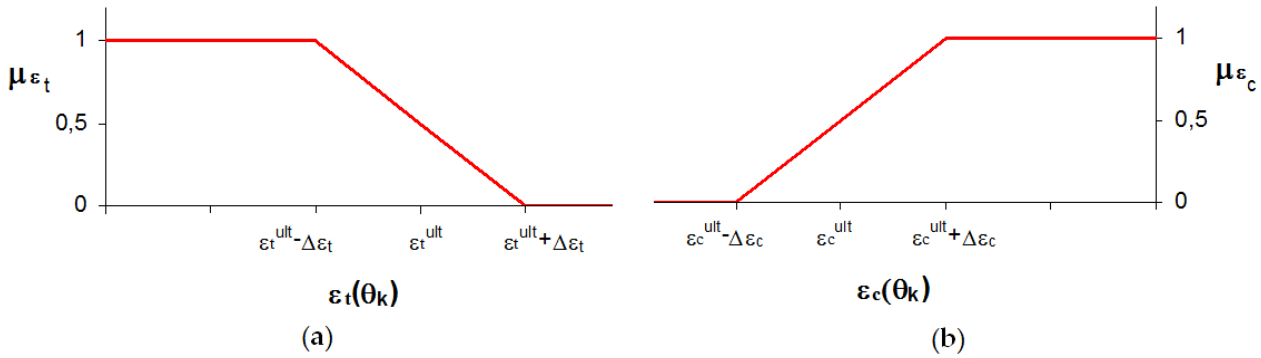

Figure 7: The membership functions for: (a) the positive value of strain; (b) the negative value of strain.

The presented method allows one to build the appropriate membership functions for the evaluated values of the Young moduli.

The fuzzy set theory allows us to build the lower and upper bounds of the failure envelopes for FPF and the linear qualifier function (in the form of asymmetrically trapezium for maximum strains criteria). Fuzziness of failure strain has a great influence on a surface of limit load values. The above conclusions depend on structural geometry and load parameters.

REFERENCES

[1] A. Muc, M. Chwał, *Analytical discrete stacking sequence optimization of rectangular composite plates subjected to buckling and FPF constraints*, Journal of Theoretical and Applied Mechanics, **54**, 423-436, 2016.

[2] J. Lee, B. Harris, D.P. Almond, F. Hammett, *Fibre composite fatigue-life determination*, Composites Part A, **28**, 5-15, 1997.

[3] A. Muc, P. Kędziora, P. Krawczyk, M. Sikoń, *Failure analysis of FRP panels with a cut-out under static and cyclic load*, In: Proceedings of Third International Conference on Thin-Walled Structures (3-ICTWS), Elsevier: London, UK, 313-320, 2001.

[4] A. Muc, A. Stawiarski, P. Romanowicz, *Experimental investigations of compressed sandwich composite/honeycomb cylindrical shells*, Applied Composite Materials, **25**, 177-189, 2018.

[5] A. Muc, A. Stawiarski, *Location of delaminations in curved laminated panels, Composite Structures*, **133**, 652-658, 2015.

[6] A. Muc, P. Kędziora, *Application of the fuzzy set theory in mechanics of composite materials*, In: Soft Computing in Textile Sciences; Sztandera, L., Pastore, C., Eds.; Springer-Verlag: Heidelberg, Germany, 16-50, 2003.

[7] A. Muc, M. Jamróz, *Homogenization models for carbon nanotubes, Mechanics of Composite Materials*, **40**, 101-106, 2004.

[8] M. Chwał, A. Muc, *Transversely isotropic properties of carbon nanotube/polymer composites*, Composites B, **88**, 295-300, 2016.

[9] C. Oskay, J. Fish, *On calibration and validation of eigendeformation-based multiscale models for failure analysis of heterogeneous systems*, Computational Mechanics, **42**, 181-195, 2008.

[10] D. Jiang, Y. Li, Q. Fei, S. Wu, *Prediction of uncertain elastic parameters of a braided composite*, Composite Structures, **126**, 123-131, 2015.

[11] G. Mustafa, C. Crawford, A. Suleman, *Fatigue life prediction of laminated composites using a multi-scale M-LaF and Bayesian inference*, Composite Structures, **151**, 149-161, 2016.

[12] M. Chandrashekhar, R. Ganguli, *Damage assessment of composite plate structures with material and measurement uncertainty*, Mechanical Systems and Signal Processing, **75**, 75-93, 2016.

[13] F.M. McNeill, E. Thro, *Fuzzy Logic: a Practical Approach*. Academic Press: Boston, USA, 1996.

[14] E. Cox, *The Fuzzy Systems Handbook*. Academic Press: Boston, USA, 1996.

[15] L.H. Tsoukalas, R.E. Uhrig, *Fuzzy and Neural Approaches in Engineering*. John Wiley and Sons: New York, USA, 1997.

[16] D. Dubois, H. Prade, *Fuzzy Sets and System: Theory and Applications*. Academic Press: Boston, USA, 1996.

[17] L.A. Zadeh, K.-S. Fu, K. Tanaka, M. Shimura, *Fuzzy Sets and Their Application to Cognitive and Decision Process*. Academic Press: Boston, USA, 1996.

[18] B. Kosko, *Neural Networks and Fuzzy Systems*. Prentice Hall: Englewood Cliffs, USA, 1991.

[19] D. Moens, M. Hanss, *Non-probabilistic finite element analysis for parametric uncertainty treatment in applied mechanics: Recent advances*, Finite Elements in Analysis and Design, **47**, 4-16, 2011.

[20] K.F. Sodoke, L. Laperrière, L. Toubal, R.S. Khakestar, *Fuzzy logic response to Young's modulus characterization of a flax–epoxy natural fiber composite*, Materials and Design, **89**, 273-285, 2016.

[21] F. Altmann, J.U. Sickert, V. Mechtcherine, M. Kaliske, *A fuzzy-probabilistic durability concept for strain-hardening cement-based composites (SHCCs) exposed to chlorides: part1: concept development*, Cement and Concrete Composites, **34**, 754-762, 2012.

[22] V.M. Karbhari, M. Stein, *Fuzzy logic based approach to FRP retrofit of columns*, Composites Part B, **38**, 651-673, 2007.

[23] H. Bohlooli, A. Nazari, G. Khalaj, M.M. Kaykha, S. Riahi, *Experimental investigations and fuzzy logic modeling of compressive strength of geopolymers with seeded fly ash and rice husk bark ash*, Composites Part B, **43**, 1293-1301, 2012.

[24] A.B. Syamsiah, M.D. Rosma, B.A. Ajab, H.W.H. Wan, *Role of input selection prediction of physical properties of degradable composites using ANFIS*, International Journal of Materials, Mechanics and Manufacturing, **3**, 213-217, 2015.

[25] S. Rassbach, W. Lehnert, *Modelling of the deformation behaviour of FGM by fuzzy-logic*, Computational Materials Science, **16**, 167-175, 1999.

[26] A. Muc, P. Kędziora, *A fuzzy set analysis for a fracture and fatigue damage response of composite materials*, Composite Structures, **54**, 283-287, 2001.

[27] P. Kędziora, A. Muc, *Optimal design of composite structures subjected to fatigue loading in a fuzzy environment*. In: Engineering Optimization IV; Rodrigues et al., Eds.; Taylor & Francis Group: London, UK, 961-966, 2015.

[28] P. Kędziora, A. Muc, *Fuzzy Set Approach in the Fatigue Damage Analysis of Composite Structures*, Advanced Materials Research, **1025-1026**, 1041-1046, 2014.

[29] A. Muc, P. Kędziora, *The application of fuzzy logic in fatigue damage analysis*, Composites Theory and Practice, **14**, 60-63, 2014.

[30] S.S. Rao, *Multi-objective optimization of fuzzy structural systems*, International Journal for Numerical Methods in Engineering, **24**, 1157-1171, 1987.

[31] H. Ahn, W.-R. Yu, *Mechanical analysis of 3D braided and woven composites using fiber-based continuum analysis*, Composite Structures, **160**, 1105-1118, 2017.

COMPDYN 2019
7th ECCOMAS Thematic Conference on
Computational Methods in Structural Dynamics and Earthquake Engineering
M. Papadrakakis, M. Fragiadakis (eds.)
Crete, Greece, 24–26 June 2019

USE OF ARTIFICIAL NEURAL NETWORKS IN THE R/C BUILDINGS' SEISMIC VULNERABILTY ASSESSMENT: THE PRACTICAL POINT OF VIEW

Konstantinos E. Morfidis[1] **and Konstantinos G. Kostinakis**[2]

[1] Assistant Researcher, Earthquake Planning and Protection Organization (EPPO-ITSAK)
Terma Dasylliou, 55535, Thessaloniki, Greece
e-mail: konmorf@gmail.com

[2] Assistant Professor, Department of Civil Engineering, Aristotle University of Thessaloniki
Aristotle University campus, 54124, Thessaloniki, Greece
e-mail: kkostina@civil.auth.gr

Keywords: Artificial Intelligence, Artificial Neural Networks, Seismic Vulnerability, Seismic damage assessment, R/C buildings.

Abstract. *The implementation of methods which belong to the field of Artificial Intelligence such as the Artificial Neural Networks (ANN) based methods is continuously increased in many scientific and technological applications. As regards the civil engineering applications, the investigation for the utilization of these methods has led to very promising results. More specifically, the experimental application of ANN-based methods for the seismic vulnerability assessment of structures has proved that they can be utilized as alternative methods in parallel of the well-documented existing methods. However, despite their promising results there is no wide acceptance of ANNs as computational tools for the prediction of the seismic damage level of structures. This can possibly be attributed mainly to the fact that the vast majority of civil engineers who investigate methods for structures' seismic vulnerability assessment has no the minimum required background about the abilities and the utilization of the ANN-based methods. The current paper attempts to present a different point of view of the ANN-based methods and to prove that the research for their further implementation can be approachable by civil engineers provided that the corresponding formulation is defined in certain stages. In the framework of the current paper it is also proved that by the utilization of ANNs the definition of relatively simple equations for the preliminary estimation of the seismic damage level of R/C buildings in near-real time is possible.*

---

1 INTRODUCTION

The utilization of the Artificial Neural Networks (ANNs) for the solution of civil engineering problems was examined for the first time at the end of eighties [1, 2]. Their alternative approach to these problems' solution as well as their very promising results led to a further study of them. More specifically, in the field of earthquake engineering the corresponding studies are enough but less than the studies which are focused on other scientific fields of civil engineering (see e.g. [3-9]). Thus, for the seismic vulnerability assessment of existing buildings at urban scale or at regional state, methods such as the seismic vulnerability curves were developed and widely used (e.g. [10, 11]). It must be noticed that, besides the fact that significant efforts have been done globally for the utilization of ANNs in the seismic vulnerability assessment of existing buildings, the correspondence of the civil engineering research community and the amount of the corresponding research was not sufficient. Among the possible reasons which led to this situation, perhaps the most significant according to the authors' opinion concerns the fact that the utilization of ANNs requires not only specialized software for their configuration (e.g. [12, 13]), training and evaluation, but also the corresponding knowledge. This knowledge is not given in the framework of the civil engineers' mandatory education. Thus, either the cooperation with scientists specialized on the ANNs or the post graduate education of civil engineers on the basic principles of ANNs is required. In order to fulfill this demand, the ANN based methods must be performed through specific stages:

(a) The stage of the problems' definition and the generation of the ANNs' training data-set. At this stage the civil engineer describes the computational problem to the ANN expert and collects the required data for its solution. Thus, significant problems such as the number and the types of ANNs' input and output parameters as well as the quality of the training data-set are initially detected and partly solved at this preliminary stage. The final solution of these issues is achieved in the following stage (b).

(b) The stage of the selection of problem's formulation in terms of ANNs' structure as well as the type, the configuration, the training and the optimization of ANNs' parameters. The available options for these selections are suggested by the ANN expert. In stage (b) final decisions about the selection of the input and output parameters of ANNs are made, perhaps through sensitivity analyses. This stage also includes the evaluation of the trained ANNs using data which were not used for their training (generalization tests).

(c) The final stage in which the most efficient trained networks must be encoded by the ANN expert in order to be produced a computer code ready for use by the civil engineer. It must be noted that it is possible to extract closed-form expressions which can be directly used for the problem's solution if specific conditions (e.g. small number of input parameters and small number of neurons) are valid.

The current paper attempts to prove that the ANN-based methods can have practical applications in a way which is more approachable to civil engineers, if the results which are extracted by them are appropriately processed. Thus, the present paper focuses on the detailed description of the stages of the r/c buildings' seismic vulnerability assessment using ANN-based procedures, and mainly on the final stage. It must me stressed that only Multilayer Feedforward Perceptron Networks (MFPN) are utilized. The problem is separated in the configuration and the training stage for which only a general description is presented, and the stage after the training for which a detailed formulation is given. Finally, closed-form equations which relate the seismic damage index MIDR (Maximum Interstorey Drift Ratio) with various seismic parameters (e.g. PGA, Arias Intensity, etc.) are developed. Thus, it is proved that the utilization of ANNs for the r/c buildings' seismic vulnerability assessment can lead to expressions which can be easily used by engineers.

2 THE STAGES FOR THE FORMULATION AND SOLUTION OF R/C BUILDINGS' SEISMIC VULNERABILITY ASSESSEMENT PROBLEM USING ANNS

The formulation and solution of the problem of R/C buildings' seismic vulnerability assessment using ANNs consists of three distinct stages. These stages are briefly presented in Figure 1. More detailed description of them will be given in the following subsections.

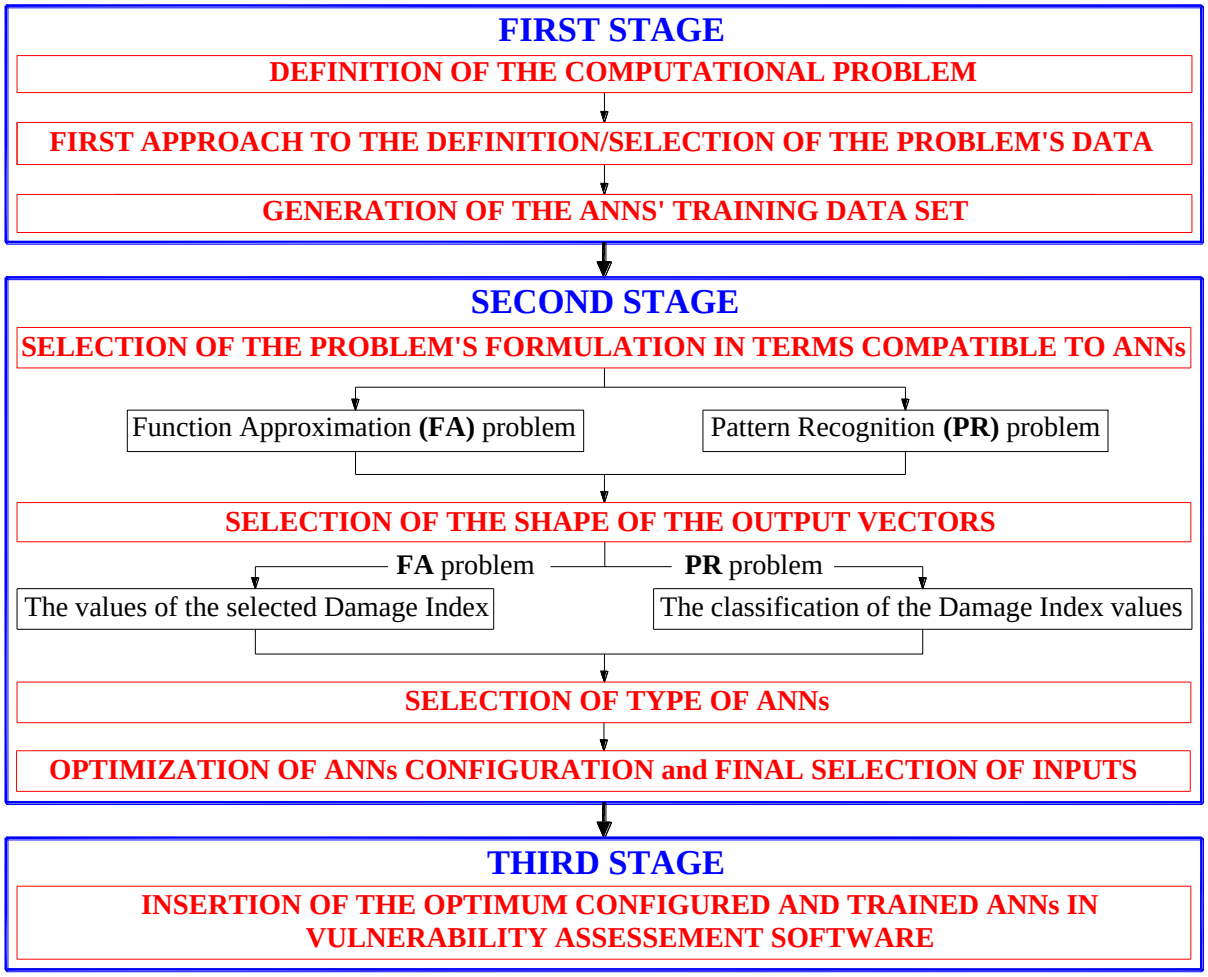

Figure 1: The three stages of problem's formulation and solution using ANNs

2.1 The first stage of problem's formulation

The first stage requires the cooperation between the civil engineer and the ANN expert. This stage consists of three individual steps as shown in Figure 1. These steps are explicitly described in Figure 2. In the first step the civil engineer describes the mathematical formulation of the problem to the ANN expert. This description contains the detailed presentation of the models and the methods which are used for the simulation of R/C buildings, earthquakes as well as their interaction. Thus, in this step the ANN expert receives the required knowledge about the problem's parameters in order to give instructions for the next step (Figure 2). In the framework of the next step (step two) the parameters which are considered as more suitable to be used as input and output parameters of ANNs are suggested. This suggestion is the result of the combination of the expertise of civil engineer and of the ANN expert. In particular, the civil engineer indicates the input parameters (structural, seismic and soil parameters) which widely used for the modeling of the seismic response of R/C buildings. It must be stressed

that this indication must be accompanied by the information about the type of input parameters (i.e. integers or real numbers) as well as the range in which they fluctuate. This information can be deployed by the ANN expert in order to give certain instructions about the effective composition of the input vectors at this (first) stage. Thus, combinations of input parameters which will cause problems to the efficient training of ANNs can be excluded at this early stage of the overall procedure.

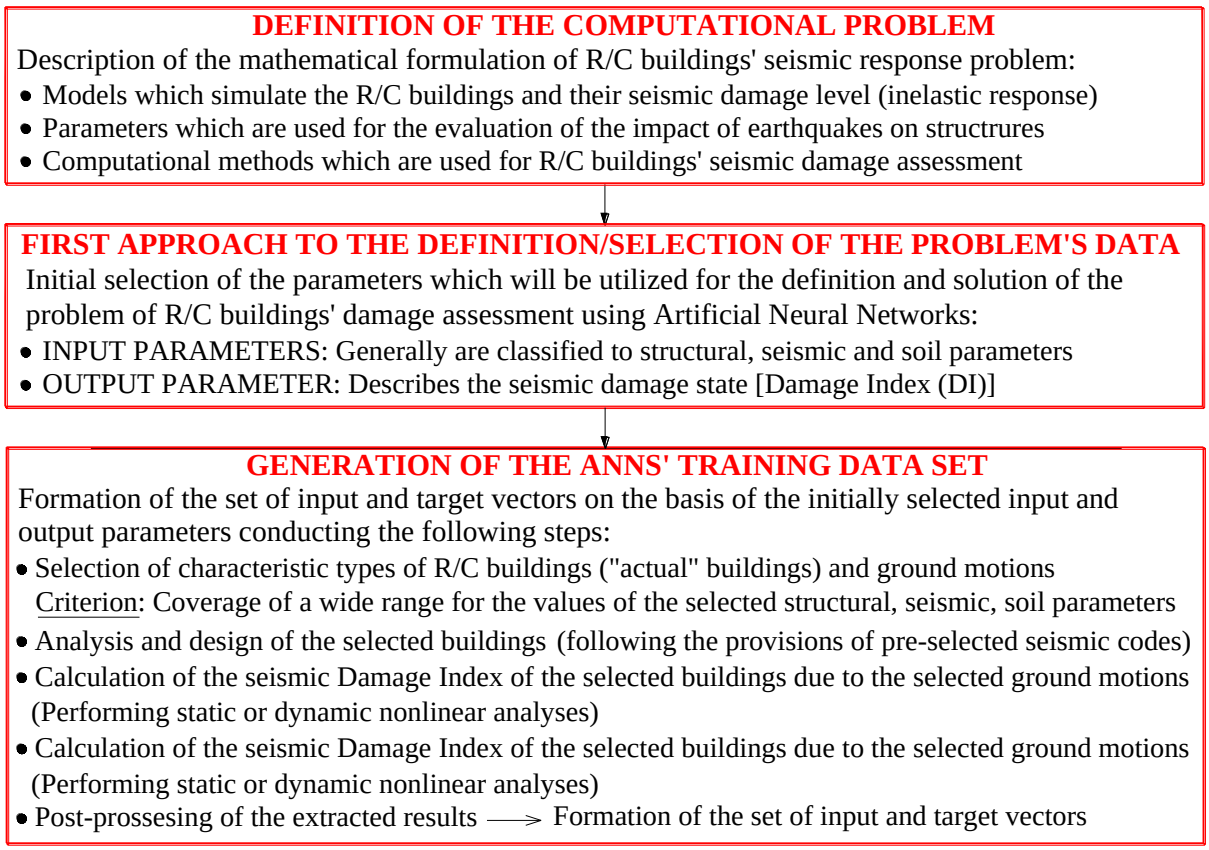

Figure 2: Detailed description of the steps of the first stage of problem's formulation

The third step of the first stage concerns the generation of the data-set (i.e. a set of samples) which is required for the training of ANNs (see e.g. [14]). The procedure of this generation for the problem of R/C buildings' vulnerability assessment is explicitly presented in [9, 15]. Having already available the information about the permissible choices for the input and the output parameters, the selection of the R/C buildings and the ground motions must correspond to a wide range of values of these parameters [for example in case of generation of training data-set which correspond to R/C buildings in Greece the height of the selected buildings must fluctuates between 3 meters (one storey buildings) and 30 meters (ten storey buildings)].

Finally, as regards the software packages which must be utilized for the accomplishment of the first stage it must be noted that only computer programs for the linear and the non-linear analysis and design of R/C buildings are required. The application of these software packages appertains to the scientific field of civil engineers. Thus, the role of the ANN expert in the first stage is limited to the instructions about the initial selection of the input and output parameters i.e. the parameters which will not cause significant malfunction to ANNs.

2.2 The second stage of problem's formulation

The second stage is mainly performed by the ANN expert. This stage consists of four individual steps as shown in Figure 1. First of all, a decision about the formulation of the problem in terms compatible to the ANNs function must be made. This decision is mainly based on the required application of the trained ANNs.

The formulation as a Function Approximation (FA) problem is intended if the prediction of the numerical value of the selected R/C buildings' Damage Index (DI) is required [9]. In the framework of this formulation, the DI is considered a (initially unknown) function of the selected structural, seismic and soil parameters:

$$DI = F\left(strP_1,...,strP_i,....,strP_n,seP_1,...,seP_j,...,seP_m,soP_1,...,soP_k,...,soP_l\right) \quad (1)$$

Where: $strP_i$ are the n selected structural parameters, seP_j are the m selected seismic parameters and soP_k are the l selected soil parameters. The Eq. (1) can be expressed in matrix form especially when a large number of input parameters is considered:

$$DI = F\left([StrP],[SeP],[SoP]\right) \quad (2)$$

Where: [StrP], [SeP] and [SoP] are the vectors which include the selected structural, seismic and soil parameters respectively.

The solution of the FA problem using ANNs leads to an approximation of the unknown function F by means of a combination of elementary linear or non-linear functions [14]. More specifically the approximate function F is also depended on a number of real numbers which are called synaptic weights and biases [14]. The calculation of these numbers is the object of the ANNs' training. The procedure for the development of function F by using the Eqs. (1), (2) as well as basic principles of the function of the trained Multilayer Feedforward Perceptron Networks (MFPN) will be explicitly presented in Section 3.

The formulation as a Pattern Recognition (PR) problem is intended if the prediction of the classification of R/C buildings to pre-defined seismic damage categories on the basis of the value of the selected DI is required (see e.g. [9, 16]). In this case, first of all the decision about the number of these categories is necessary. This is a decision which must be taken by the civil engineer. However, independently of this decision a significant difference between the FA and PR problems is the number of ANNs' outputs. In the solution of the FA problem the required output is a real number, i.e. the value of the selected DI. On the contrary, in the solution of the PR problem a mapping between the DI values and the pre-defined seismic damage classes is needed. Thus, in case of the formulation of the PR problem the required output is a vector. The dimension of this vector is (nx1), where n is the number of the pre-defined seismic damage classes. The description of the required mapping between the DI values and the seismic damage classes is presented in Figure 3.

DAMAGE CLASS	DI values	Output vector **o**
1	$0<DI\le DI_1$	$\longrightarrow o_1$
2	$DI_1<DI\le DI_2$	$\longrightarrow o_2$
⋮	⋮	⋮
i	$DI_i<DI\le DI_{i+1}$	$\longrightarrow o_i$
⋮	⋮	⋮
n	$DI_{n-1}<DI\le DI_n$	$\longrightarrow o_n$

$$\Rightarrow \text{ if } DI_i<DI\le DI_{i+1} \xrightarrow[\text{definition}]{\text{By}} \mathbf{o}=\begin{bmatrix}o_1\\o_2\\\vdots\\o_i\\\vdots\\o_n\end{bmatrix}=\begin{bmatrix}0\\0\\\vdots\\1\\\vdots\\0\end{bmatrix}$$

Figure 3: The mapping between the DI values and the pre-defined damage classes in case of PR formulation

The next step of the second stage is the selection of the type of ANNs' (Figure 1). This selection is based on the experience of the ANN expert. However, although several types of ANNs have been proposed (see e.g. [14, 17, 18]) the problem of R/C buildings' seismic vulnerability assessment is mainly approached using MFPN. This conclusion is based on the investigation of the relevant literature (see e.g. [3-9, 15]). More specifically, the choice of MFPN in the framework of the FA problem's formulation and solution is based on the fact that this type of networks can approach continuous functions with any desirable level of accuracy (e.g. [19, 20]). As regards the solution of the PR problem the MFPN are also a reliable option as it was presented in many references (see e.g. [8, 9, 21, 22, 23]).

The final (fourth) step of the second stage concerns the optimization of the networks' performance. This optimization consists of a parametric investigation with two components, namely the parametric investigation for the optimum configuration of networks as well as the parametric investigation for the optimum combination of their input parameters which were initially selected in the framework of the first stage (Figure 2). The target of the two aforementioned parametric investigations is the maximization of generalization ability of them. The generalization ability of the trained ANNs concerns their ability to extract reliable solutions for problems with data which are unknown to them. It must be stressed that in this step the contribution of the ANN expert is very critical because, as it was proved, a great danger during the ANNs' training is the so-called "overfitting" (see e.g. [24, 25]). The "overfitting" concerns the phenomenon of high performance of ANNs in problems with data which were used for their training and in parallel their poor performance in cases in which the data are unknown to them. Several techniques for the avoidance of the overfitting are available (for example the early stopping of the training procedure, the utilization of a part of the training data set for the generalization testing, the multiple trainings using different parts of the available training data set see etc., e.g. [12, 25]). In any case, the ANN expert is the most efficient to suggest the most proper technique to overcome this weakness.

The procedure for the above described parametric investigations is schematically presented in Figure 4. However, it must be stressed that this procedure is based on specific assumptions. The main assumption is the utilization of the Forward Stepwise Method (see e.g. [8, 15, 26]) for the parametric investigation for the optimum combination of input parameters. Thus, the procedure of Figure 4 is not a unique option for the accomplishment of the optimum performance of the utilized networks.

In the procedure which is described in Figure 4, the two components of the parametric investigation are not independent. The investigation for the optimum configuration of utilized MFPNs is included in the procedure for the investigation of the optimum combination of input parameters. Thus, in every step of the investigation of the optimum combination of input parameters a complete investigation procedure for the optimum configuration of the utilized networks is included. An additional comment which arises from the study of Figure 4 is the extremely big number of the required trainings in particular in cases of big number of initially selected input parameters and networks with more than one hidden layer. To overcome this problem – which can lead to time consuming procedures – the expertise of the civil engineer as well as of the ANN expert must be deployed. More specifically, the civil engineer can give advices about the input parameters which have significant influence on the seismic response of R/C buildings thus reducing the number of the initially selected input parameters and, as a result, the number of their different combinations. On the other hand, the ANN expert can give specific advices as regards the choices for parameters which must be defined for the MFPNs' configuration, thus reducing the number of the different configurations which must be evaluated (i.e. the restriction of the number of hidden layers, the exclusion of specific types of the activation functions, the optimum choice of training algorithms etc.).

STEP 1: Configuration of ***n*** MFPN [Each MFPN has as input one of the ***n*** examined parameters]

INDIVIDUAL STEPS: (For each one of the ***n*** MFPN)

(a) Parametric investigation for the optimum configured MFPN *

*(a1) Configuration of **m** MFPN with different configuration parameters***

*(a2) Multiple trainings of the **m** MFPN* (using the selected training algorithms)***

*(a3) Detection of the optimum configured MFPN (between the **m** configured networks) i.e. the network which exports the optimum results (i.e. the results with the smallest error)*****

(b) Ranking of the n MFPN on the basis of the error of their results

(This ranking leads to the network which exports results with the smallest error. This network indicates the most significant input parameter i.e. the input parameter which leads to the optimum performance between the examined input parameters)

STEP 2: Configuration of ***n-1*** MFPN

[Each MFPN has as input 2 of the ***n*** examined input parameters: The most significant parameter of the former step and one of the remaining ***n-1*** examined parameters]

INDIVIDUAL STEPS: (For each one of the ***n-1*** MFPN)

(a) Parametric investigation for the optimum configured MFPN * [Sub-steps (a1)-(a3)]

(b) Ranking of the n-1 MFPN on the basis of the error of their results

(This ranking leads to the network which exports results with the smallest error. This network indicates the combination of 2 input parameters which leads to the optimum performance between the examined input combinations of 2 parameters)

.....

STEP j: Configuration of ***n-(j-1)*** MFPN

[Each MFPN has as input j of the ***n*** examined input parameters: The most significant combination of the (j-1) parameters of the former step and one of the remaining ***n-(j-1)*** examined parameters]

INDIVIDUAL STEPS: (For each one of the ***n-(j-1)*** MFPN)

(a) Parametric investigation for the optimum configured MFPN * [Sub-steps (a1)-(a3)]

(b) Ranking of the n-(j-1) MFPN on the basis of the error of their results

(This ranking leads to the network which exports results with the smallest error. This network indicates the combination of j input parameters which leads to the optimum performance between the examined input combinations of j parameters)

.....

STEP n: Configuration of ***1*** MFPN

[This MFPN has as input all the ***n*** examined input parameters]

INDIVIDUAL STEPS:

(a) Parametric investigation for the optimum configured MFPN * [Sub-steps (a1)-(a3)]

STEP n+1: Comparison of values of the performance parameter of the ***n*** optimum MFPN which are exported from the ***n*** steps. The minimum of these values indicates the most significant (or optimum) combination of the examined parameters and the corresponding network

Notes

* After the completion of the individual step (a) networks with the same number of input parameters but with different combination of them are exported.

**These networks have the same number and the same combination of input parameters but different: number of hidden layers, number of neurons in hidden layers, types of activation functions partitioning ratios of the total training data set to training, validation and testing subsets.

*** Each one of the configured MFPN is trained several times using different part of the total training data set. The training which leads to the optimum results is selected.

**** The error is measured using ANNs' performance parameters such as the Mean Square Error (MSE)

Figure 4: Procedure for the detection of the optimum configured MFPN and the corresponding optimum combination of the input parameters by means of Forward Stepwise Method in case of a problem with n initially selected input parameters

Closing the description of the second stage, a special mention about the meaning of the term "training of MFPNs" must be given, because this is essential for the better understanding of the potential of separation of the second and third stage. In order to specify the MFPNs' training procedure using a simple and widely known terminology, we can describe it as an iterative procedure for the optimum definition of the values of the synaptic weights and biases of the neurons which are the structural units of MFPNs (Figure 5). The synaptic weights and the biases can be characterized as generalized "degrees of freedom" of networks in the sense that they give to networks the ability for the adaptation of their function to the problem's requirements. This optimum definition of the values of the synaptic weights and biases is the subject of the training algorithms which are complicated mathematical procedures (e.g. [14, 17, 24]). The criterion which is utilized for the optimum definition of the values of the synaptic weights and biases is the minimization of the error between the networks' outputs and the expected (known) outputs for a set of samples (i.e. a set of input vectors and output-target vectors) which comprise the training data set. Thus, after the completion of the training procedure the set of the values of the synaptic weights and biases which optimizes the generalization ability of the network on the basis of the available training data set is available. In other words, the training procedure leads to the calibration of the values of the synaptic weights and biases using the available input data having as target the optimum performance of the networks. Thus, the difference between a trained network and an untrained network with the same configuration parameters is only the set of the values of their synaptic weights and biases. Therefore, after the completion of the second stage is available (in matrix form) the optimum set of values of the synaptic weights and biases and the next challenge (in the framework of the third stage) is the simulation of the trained NFPN as it will be described in the next subsection. Furthermore (as it also can be extracted from the study of Figure 5) the process of the NFPNs leads to the expression of the Damage Index not only as a function of the input parameters (see Eq. 2) but also as a function of the matrices of values of the synaptic weights [W] and biases [B]. Thus the Eq. 2 can be rewritten as follows:

$$DI = \{ \underbrace{[StrP],[SeP],[SoP]}_{Input\ Parameters}, \underbrace{[W],[B]}_{Weights\ and\ Biases} \} \tag{3}$$

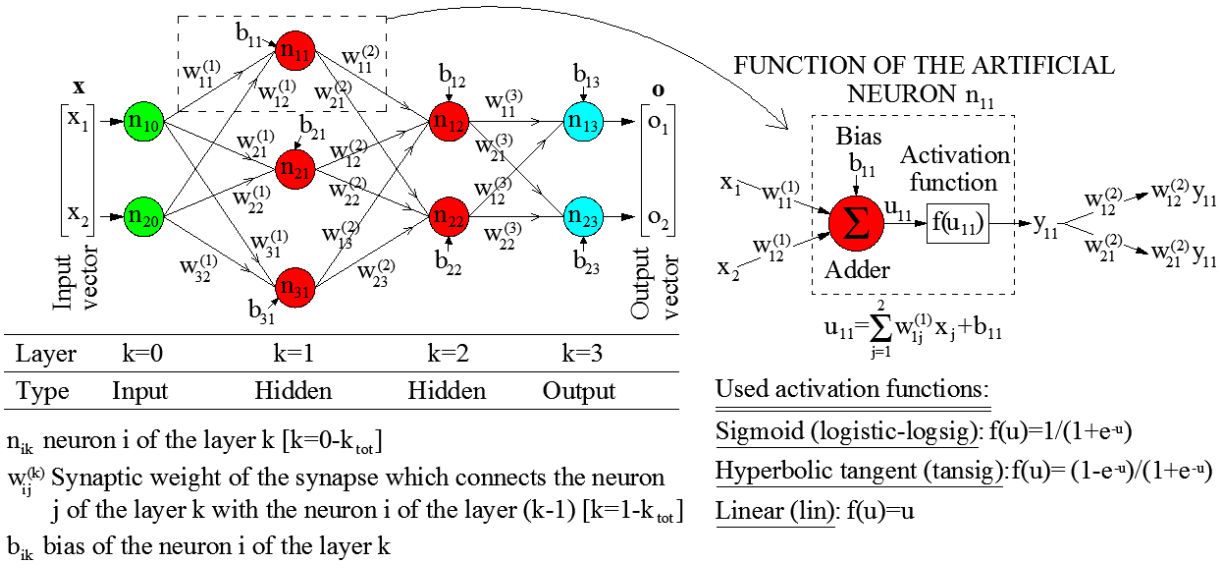

Figure 5: Description of the function of a MFPN and of the function of an artificial neuron as a unit

2.3 The third stage of problem's formulation

The third stage concerns the implementation of optimum configured and trained MFPN. In other words, in this stage the optimum configuration of the selected MFPN (i.e. number of hidden layers, number of neurons in the hidden layers, activation functions of neurons, number and combination of the input parameters), as well as the matrices with the values of synaptic weights and biases (Figure 5) which are best adapted to the utilized training data set (after the training procedure) are available. Thus, in this stage the unique target is the utilization of the optimum configured and trained MFPN in practical applications. This means that the MFPN will be implemented for the prediction of the seismic vulnerability of (known or unknown) R/C buildings which are subjected to (known or unknown) earthquakes. It must be stressed that the terms "known" and "unknown" in present case mean that the R/C buildings (or/and the earthquakes) have parameters which belong or not to the training data set's samples respectively. For example, the trained MFPN can be used for the prediction of the seismic damage state of a "known" R/C building (i.e. a building whose structural parameters have values which have been utilized as parts of at least one training vector) which is subjected to an "unknown" earthquake (i.e. an earthquake whose seismic parameters have values which have not been utilized as parts of at least one training vector).

The implementation of trained MFPNs for the solution of problems with unknown some or all of their data is called "network's simulation". The "network's simulation" requires the fully understanding of the MFPNs' function. This function can be formulated in matrix form. More specifically, it can be shown that the function of MFPNs is based on a matrix transformation of the input vector to the output vector with the aim of a sequence of matrices' operations. This sequence can be presented using a MFPN with n input parameters, p=1 output parameter and 1 hidden layer with m neurons (Figure 6).

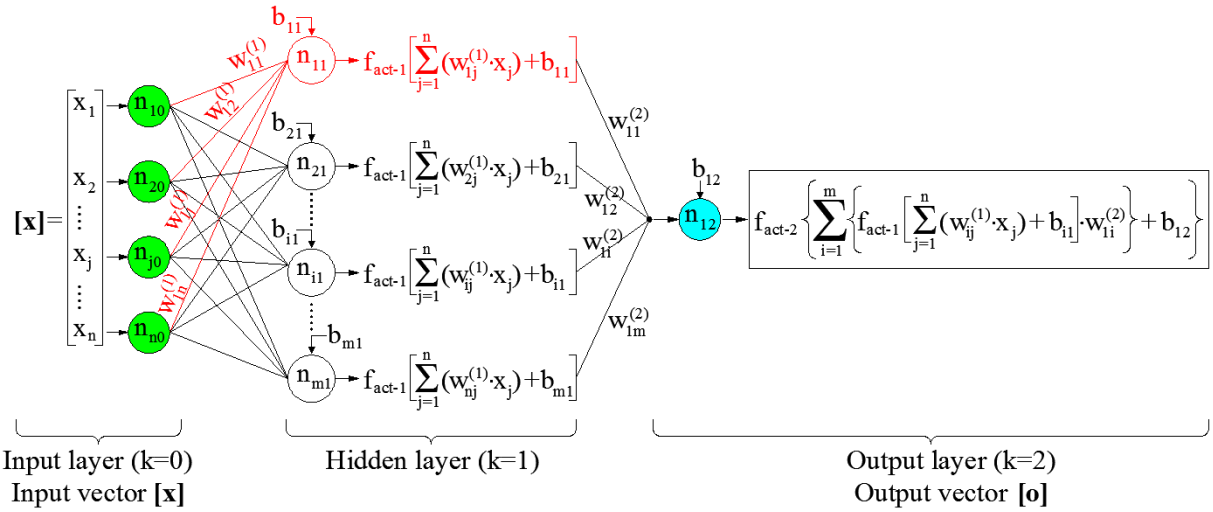

Figure 6: Indicative presentation of the MFPNs' function for the solution of the FA problem

On the basis of the configuration of the MFPN which is presented in Figure 6, the matrix operations for the transformation of the input vector **[x]** to the output vector **[o]** (which is in the present case a scalar parameter and not a vector) can be separated in 3 steps. In the first step the matrix $\mathbf{[A_1]}$ which contains the arguments of the activation functions $f_{act\text{-}1}$ of hidden layer's neurons is calculated. This matrix arises from the multiplication of the input vector **[x]** by the matrix $\mathbf{[W_1]}$ which contains the synaptic weights of synapses that connect the neurons of input layer with neurons of the hidden layer, and the addition of the corresponding product to the vector which contains the biases of hidden layer's neurons:

$$\begin{bmatrix} A_{11} \\ A_{21} \\ ..... \\ A_{i1} \\ ..... \\ A_{m1} \end{bmatrix} = \begin{bmatrix} w_{11}^{(1)} & w_{12}^{(1)} & w_{13}^{(1)} & ... & w_{1j}^{(1)} & ... & w_{1n}^{(1)} \\ w_{21}^{(1)} & w_{22}^{(1)} & w_{23}^{(1)} & ... & w_{2j}^{(1)} & ... & w_{2n}^{(1)} \\ ..... & .... & .... & ... & .... & ... & ..... \\ w_{i1}^{(1)} & w_{i2}^{(1)} & w_{i3}^{(1)} & ... & w_{ij}^{(1)} & ... & w_{in}^{(1)} \\ ..... & .... & ..... & ... & .... & ... & ..... \\ w_{m1}^{(1)} & w_{m2}^{(1)} & w_{m3}^{(1)} & ... & w_{mj}^{(1)} & ... & w_{mn}^{(1)} \end{bmatrix} \cdot \begin{bmatrix} x_1 \\ x_2 \\ .... \\ x_j \\ .... \\ x_n \end{bmatrix} + \begin{bmatrix} b_{11} \\ b_{21} \\ .... \\ b_{i1} \\ .... \\ b_{m1} \end{bmatrix} \tag{4}$$

The Eq. 4 can be written in a symbolic form as follows:

$$\mathbf{[A_1]} = \left[\mathbf{W_1}\right] \cdot \left[\mathbf{x}\right] + \left[\mathbf{B_1}\right] \tag{5}$$

In the framework of the second step the selected activation function of the hidden layer's neurons is applied to all elements of the matrix **[A1]**. Thus, the matrix **[A2]** arises:

$$\begin{bmatrix} A_{12} \\ A_{22} \\ ..... \\ A_{i2} \\ ..... \\ A_{m2} \end{bmatrix} = \begin{bmatrix} f\left(A_{11}\right) \\ f\left(A_{21}\right) \\ ..... \\ f\left(A_{i1}\right) \\ ..... \\ f\left(A_{m1}\right) \end{bmatrix} \tag{6}$$

The Eq. 6 can be written in a symbolic form as follows:

$$\mathbf{[A_2]} = f_{act-1}\mathbf{[A_1]} \tag{7}$$

The third step concerns the manipulation of the matrix **[A2]** by the vector **[W2]** (which contains the synaptic weights of synapses that connect the neurons of the hidden layer with neuron of the output layer), and the addition of the corresponding product to the bias of output layer's neuron. The result of these operations A_3 is the argument of the activation function f_{act-2} of the output layer's neuron:

$$A_3 = \left[w_{11}^{(2)} \;\; w_{12}^{(2)} \;\; .... \;\; w_{1i}^{(2)} \;\; .... \;\; w_{1m}^{(2)} \right] \cdot \begin{bmatrix} A_{12} \\ A_{22} \\ ..... \\ A_{i2} \\ ..... \\ A_{m2} \end{bmatrix} + b_{12} \tag{8}$$

The Eq. 8 can be written in a symbolic form as follows:

$$A_3 = \mathbf{[W_2]} \cdot \mathbf{[A_2]} + b_{12} \tag{9}$$

Thus, the output o of the MFPN is:

$$o = f_{act-2}\left(A_3\right) = f_{act-2}\left(\mathbf{[W_2]} \cdot \mathbf{[A_2]} + b_{12}\right) \tag{10}$$

The combination of Eqs. (5), (7) and (10) leads to an equation which relates the input vector **[x]** with the output o:

$$o = f_{act-2}\left\{[\mathbf{W_2}]\cdot\left[\, f_{act-1}\left\{[\mathbf{W_1}]\cdot[\mathbf{x}]+[\mathbf{B_1}]\right\}\right]+b_{12}\right\} \tag{11}$$

The combined study of Eq. 3 and Eq. 11, leads to the conclusion that the Eq. 11 is a specific expression of the Eq. 3. Thus, we can write the following MFPN-based expression for the seismic Damage Index:

$$DI = f_{act-2}\left\{[\mathbf{W_2}]\cdot\left[\, f_{act-1}\left\{[\mathbf{W_1}]\cdot[StrP\ SeP\ SoP]^T+[\mathbf{B_1}]\right\}\right]+b_{12}\right\} \tag{12}$$

The above described procedure concerns the calculation of MFPNs' output in case of solution of the FA problem in which the outputs are scalar parameters (i.e. the real value of the DI). However, in case of the problem's formulation as a PR problem the MFPNs' outputs are vectors which include the information about the classification of DI to the pre-defined seismic damage classes (Figure 3). In Figure 7 a MFPN with one hidden layer which is used for the solution of the PR problem with three pre-defined seismic damage classes is presented.

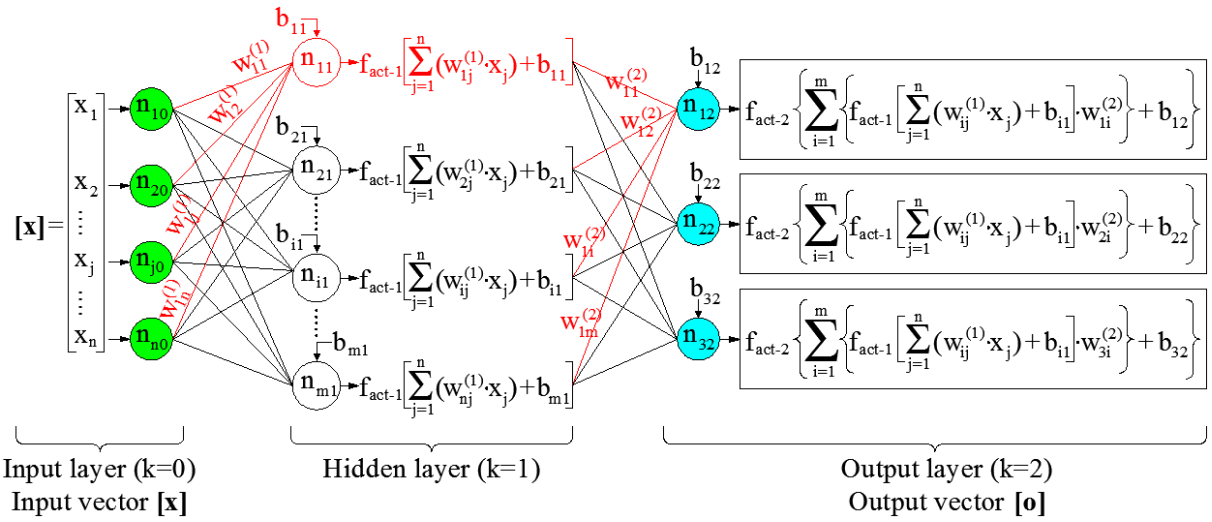

Figure 7: Indicative presentation of the MFPNs' function for the solution of the PR problem (3 damage classes)

Following the procedure which is based on Eqs. (4)-(11) it can be proved that in case of solution of the PR problem using a MFPN with one hidden layer with *m* neurons, *n* input parameters and *p* output parameters (i.e. *p* seismic damage classes), the (*p*x1) output vector (in form which is presented in Figure 3) is:

$$[\mathbf{o}] = \left[f_{act-2}\left\{[\mathbf{W_2}]\cdot\left[\, f_{act-1}\left\{[\mathbf{W_1}]\cdot[StrP\ SeP\ SoP]^T+[\mathbf{B_1}]\right\}\right]+[\mathbf{B_2}]\right\}\right] \tag{13}$$

Where:

$$[\mathbf{B_2}]^T = \left[b_{12}\ \ b_{22}\ \ldots\ b_{t2}\ \ldots\ b_{p2}\right]$$

is the vector of the biases of the output layer's neurons.

Equations similar to Eqs. 12 and 13 arise in case of MFPNs with more than one hidden layer. Certainly, the complexity of these equations is increased as long as the number of hidden layers is also increased. However, even in cases of equations with high complexity the corresponding coding is straightforward provided that the matrices of values of synaptic

weights and biases are available (after the completion of the second stage of the problem's formulation). Thus, no specialized software is required for the performance of the third stage. For this reason, the insertion of a trained MFPN in a system (e.g. [27]) which collects data from earthquakes in near-real time after the event is an easy procedure provided that the stages 1 and 2 have successfully completed at a pro- or a post-seismic period.

Finally, it must be stressed that the dependence of the value of the seismic DI on the values of the synaptic weights and biases of a trained MFPN has as a consequence the dependence of the corresponding equation on the composition of the training data set. For this reason, the form of the MFPN-based equations of DI can be altered if new data for the training of the MFPN are available. This is the case of re-training which gives to MFPN-based equations of DI the versality to improve their prediction ability if new data about the structures' seismic damage are collected.

3 PRACTICAL APPLICATIONS: CLOSED-FORM EQUATIONS FOR THE PREDICTION OF THE SEISMIC DAMAGE OF R/C BUILDINGS

In the current section the procedure that was presented in the section 2.3 for the formulation of closed-form equations which can be used in practice for the seismic vulnerability assessment of R/C buildings is applied. This formulation is based on optimum configured and trained MFPNs which are presented in research works of Morfidis and Kostinakis [8, 15]. More specifically, closed-form expressions which correspond to the solution of the FA and the PR problem will be developed.

3.1 Formulation of closed-form equations for the solution of the FA problem

In case of solution of the FA problem the MFPNs' output is the value of the DI. Thus, the Eq. 12 is valid if MFPNs' with one hidden layer are used. In the reference [15] this type of networks was used for the prediction of R/C buildings' DI, and the parametric investigation which is described in Figure 4 was applied. As DI the Maximum Interstorey Drift Ratio (MIDR) was selected. The utilized input vector [**x**] was comprised of 4 structural parameters [the total height of building H_{tot}, the structural eccentricity e_o, and the ratio of the base shear that is received by r/c walls (if they exist) along two perpendicular directions (axes x and y): n_{vx} and n_{vy}], whereas the number of seismic parameters was mutable. More specifically, the number of the utilized seismic parameters was fluctuated between 1 and 14 in order to detect the optimum configuration of the seismic parameters which led to the most reliable prediction of DI's (MIDR) value. Soil parameters were neglected. A training data-set which was comprised of 1950 samples (extracted by nonlinear time history dynamic analyses of 30 R/C buildings subjected to 65 seismic excitations) was created for the MFPNs' training.

The performance of the parametric investigation (Figure 4) led to the conclusion that the most reliable predictions about the MIDR values for a set of 293 samples (unknown to the trained MFPNs) arise from networks which have as input parameters at least 6 seismic parameters. Furthermore, from the parametric investigation the conclusion that the activation functions logsig and tansig (Figure 5) for the neurons of the hidden layer lead to similar results (i.e. predictions of similar reliability as regards the MIDR values) was extracted. Regarding the activation function of the neuron of the output layer it must be stressed that a linear (lin) function (Figure 5) was used, because this function exports real and not restricted values just as the MIDR values. Thus, the network with the configuration and the input parameters which is presented in Figure 8a is the most efficient between the networks with 6 seismic input parameters (these parameters are: the Housner Intensity (HI), the Peak Ground Acceleration (PGA), the ratio of Peak Ground Velocity to Peak Ground Acceleration (PGV/PGA), the Acceleration Spectrum Intensity (ASI), the Significant Duration (SD) of earthquake and the

Bracketed Duration (BD) of earthquake). This network was selected in the present paper for the presentation of a more specific shape of Eq. 12. Furthermore, for the same reason the network which is presented in Figure 8b with one seismic input parameter (the parameter HI) was selected. This network led to the most reliable predictions of the MIDR value between the networks with one seismic input parameter [15].

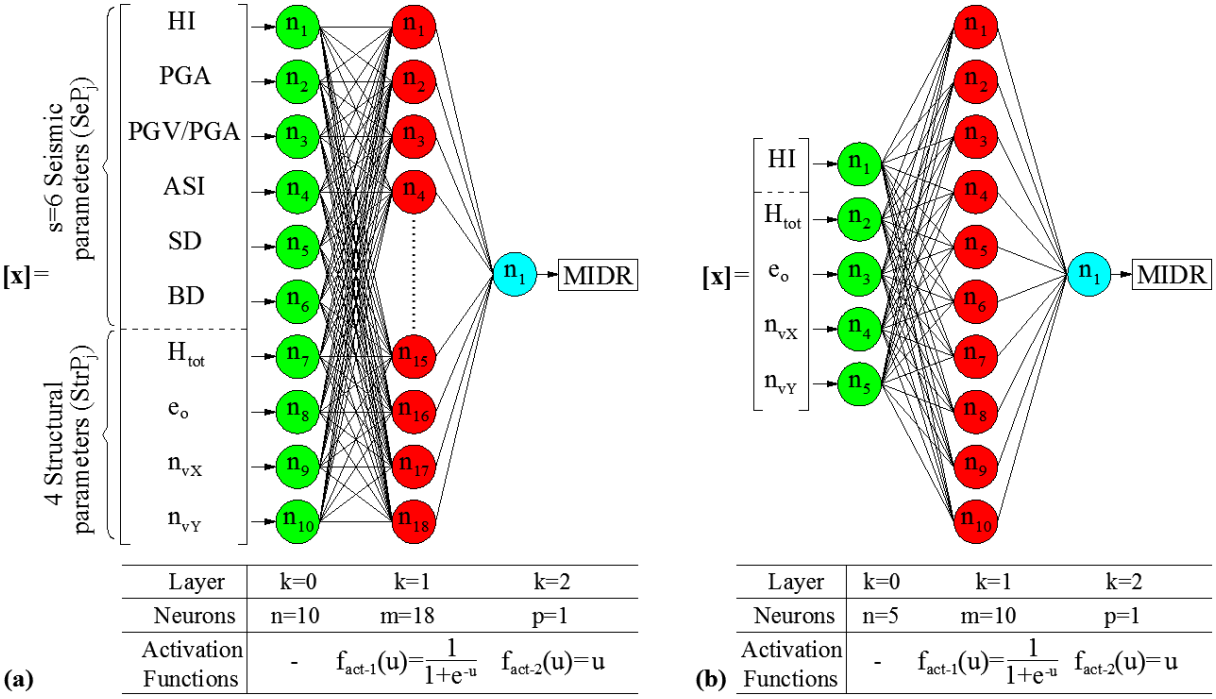

(a)

Layer	k=0	k=1	k=2
Neurons	n=10	m=18	p=1
Activation Functions	-	$f_{act\text{-}1}(u)=\frac{1}{1+e^{-u}}$	$f_{act\text{-}2}(u)=u$

(b)

Layer	k=0	k=1	k=2
Neurons	n=5	m=10	p=1
Activation Functions	-	$f_{act\text{-}1}(u)=\frac{1}{1+e^{-u}}$	$f_{act\text{-}2}(u)=u$

Figure 8: Parameters of optimum configured MFPNs which are utilized for the prediction of MIDR values

Introducing the data of networks of Figures 8a and 8b to Eq. 12 the following expressions for the calculation of MIDR values arise respectively:

$$MIDR=\sum_{i=1}^{18}\left(\frac{w_{1i}^{(2)}}{1+e^{-\left[\sum_{j=1}^{6}\left(w_{ij}^{(1)}\cdot SeP_j\right)+\sum_{j=7}^{10}\left(w_{ij}^{(1)}\cdot StrP_j\right)+b_{i1}\right]}}\right)+b_{12} \tag{14a}$$

$$MIDR=\sum_{i=1}^{10}\left(\frac{w_{1i}^{(2)}}{1+e^{-\left[w_{i1}^{(1)}\cdot SeP_1+\sum_{j=2}^{5}\left(w_{ij}^{(1)}\cdot StrP_j\right)+b_{i1}\right]}}\right)+b_{12} \tag{14b}$$

For the application of the two above equations, the matrices of the synaptic weights and biases of the neurons of the hidden and the output layer are required. These matrices are extracted from the networks' training procedure. Thus, while the shape of Eqs. 14a and 14b is independent of the utilized training data set, the values of the constants which are introduced to them (i.e. the values of the elements of the matrices of the synaptic weights and biases of the neurons of the hidden and the output layer) are depended on the training data set. In the Appendix A the values of these constants (i.e. the matrices of the synaptic weights and biases of the neurons of the hidden and the output layer) that arise from the parametric investigation which was conducted in the framework of the reference [15] are presented.

3.2 Formulation of closed-form equations for the solution of the PR problem

In case of solution of the PR problem the MFPNs' output is the classification of R/C buildings to pre-defined seismic damage classes on the basis of the selected expression of DI. Thus, in this case the Eq. 13 leads to the problem's solution if MFPNs' with one hidden layer are used. Following the procedure of the parametric investigation which is presented in Figure 4 the optimum configuration of MFPNs with one hidden layer as well as the optimum combination of their seismic input parameters (using also the 4 structural parameters which are referred in subsection 3.1) was extracted by Morfidis and Kostinakis in [8]. In this research work the DI was expressed by means of the MIDR, and five seismic damage classes were predefined. The configuration parameters as well as the optimum combination of the seismic input parameters of the most efficient MFPN are presented in Figure 9a. This network led to the most reliable predictions about the correct classification of 293 samples (unknown to the trained MFPNs) to the five pre-defined seismic damage classes. The network of Figure 9a was selected in the current paper for the presentation of a more specific shape of Eq. 13. Additionally, for the same reason the network which is presented in Figure 9b with one seismic input parameter (the parameter HI) was selected. This network led to the most reliable predictions for the classification of the 293 samples to the correct damage classes, between the networks with one seismic input parameter [8].

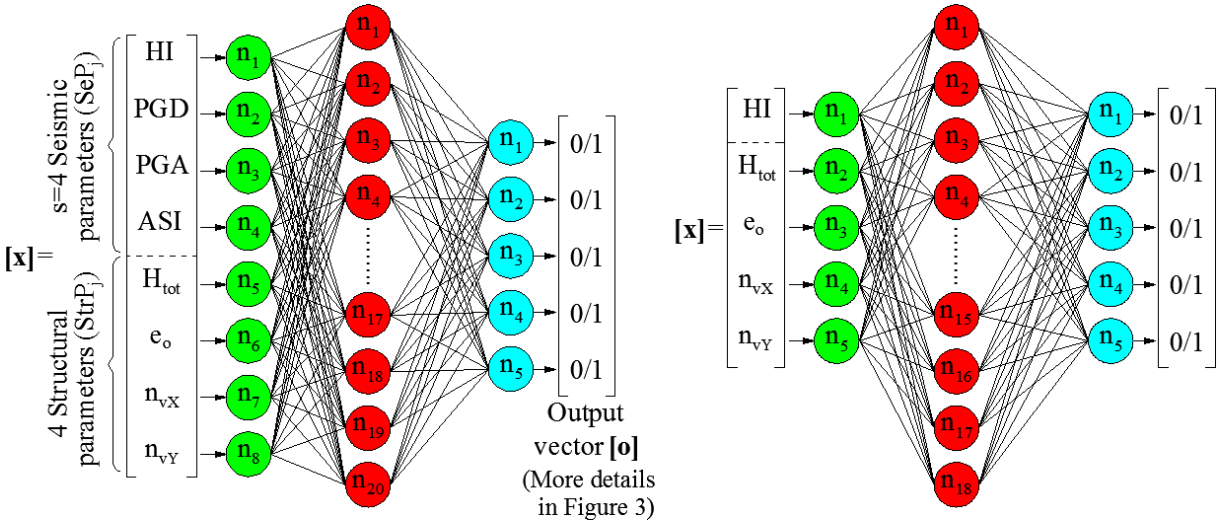

(a)

Layer	k=0	k=1	k=2
Neurons	n=8	m=20	p=5
Activation Functions	-	$f_{act\text{-}1}(u)=\frac{1-e^{2u}}{1+e^{2u}}$	$f_{act\text{-}2}(u)=f_{act\text{-}1}(u)$

(b)

Layer	k=0	k=1	k=2
Neurons	n=5	m=18	p=5
Activation Functions	-	$f_{act\text{-}1}(u)=\frac{1-e^{2u}}{1+e^{2u}}$	$f_{act\text{-}2}(u)=f_{act\text{-}1}(u)$

Figure 9: Parameters of optimum configured MFPNs which are used for prediction of the seismic damage class

Introducing the data of MFPNs of Figures 9a, 9b to Eq. 13 the following vectors which give the classification of R/C buildings to 5 damage classes (Figure 3) arise respectively:

$$[\mathbf{o}]^T=\left[o_1 \quad o_2 \quad o_3 \quad o_4 \quad o_5\right]=\left[\frac{e^{2u_1}-1}{e^{2u_1}+1} \quad \cdots\cdots \quad \frac{e^{2u_t}-1}{e^{2u_t}+1} \quad \cdots\cdots \quad \frac{e^{2u_5}-1}{e^{2u_5}+1}\right]$$

$$u_t=b_{t2}+\sum_{i=1}^{20}\left\{\frac{e^{2\cdot\left[b_{i1}+\sum_{j=1}^{4}\left(SeP_j\cdot w_{ij}^{(1)}\right)+\sum_{j=5}^{8}\left(StrP_j\cdot w_{ij}^{(1)}\right)\right]}-1}{e^{2\cdot\left[b_{i1}+\sum_{j=1}^{4}\left(SeP_j\cdot w_{ij}^{(1)}\right)+\sum_{j=5}^{8}\left(StrP_j\cdot w_{ij}^{(1)}\right)\right]}+1}\cdot w_{ti}^{(2)}\right\} \tag{15a}$$

$$[\mathbf{o}]^T = \begin{bmatrix} o_1 & o_2 & o_3 & o_4 & o_5 \end{bmatrix} = \begin{bmatrix} \dfrac{e^{2u_1}-1}{e^{2u_1}+1} & \cdots\cdots & \dfrac{e^{2u_t}-1}{e^{2u_t}+1} & \cdots\cdots & \dfrac{e^{2u_5}-1}{e^{2u_5}+1} \end{bmatrix}$$

$$u_t = b_{t2} + \sum_{i=1}^{18} \left\{ \frac{e^{2\cdot\left[b_{i1}+\left(SeP_1\cdot w_{i1}^{(1)}\right)+\sum_{j=2}^{5}\left(StrP_j\cdot w_{ij}^{(1)}\right)\right]}-1}{e^{2\cdot\left[b_{i1}+\left(SeP_1\cdot w_{i1}^{(1)}\right)+\sum_{j=2}^{5}\left(StrP_j\cdot w_{ij}^{(1)}\right)\right]}+1} \cdot w_{ti}^{(2)} \right\} \tag{15b}$$

For the application of the two above equations, the matrices of the synaptic weights and biases of the neurons of the hidden and the output layer are required. These matrices are extracted from the networks' training procedure. Thus, while the shape of Eqs. 15a and 15b is independent of the utilized training data set, the values of the constants which are introduced to them (i.e. the values of the elements of the matrices of the synaptic weights and biases of the neurons of the hidden and the output layer) are depended on the training data set. In the Appendix B the values of these constants (i.e. the matrices of the synaptic weights and biases of the neurons of the hidden and the output layer) that arise from the parametric investigation which was conducted in the framework of the reference [8] are presented.

4 CONCLUSIONS

In the current paper the procedure of implementation of Artificial Neural Networks (ANN) for the solution of the problem of R/C buildings' seismic vulnerability assessment is presented. For the scope of this presentation Multilayer Feedforward Perceptron Networks (MFPN) were utilized because their ability in the successful approach to solution of the studied problem has been proven in many relevant research studies. More specifically, the present paper is focused on the presentation of the practical point of view of MFPNs' implementation i.e. on the presentation of the procedure for the generation of the required data which are used for their training (pre-training stage) and their function after the training (simulation of MFPNs).

The procedure for R/C buildings' seismic vulnerability assessment using ANNs is comprised of three stages. At the first stage a preliminary selection of the parameters which describe the mathematical formulation of the problem is made. These parameters are the input parameters (i.e. the parameters that affect the R/C buildings' seismic response) and the output parameters (i.e. the parameters which quantitative the R/C buildings' seismic damage). This preliminary selection of the input and output parameters must be made taking into consideration the ANNs' features. Thus, at the first stage the collaboration between a civil engineer (which is expert in earthquake engineering) and an ANN expert can lead to parameters' selection which will ensure against possible malfunctions of ANNs. In the framework of the first stage the data-set for the ANNs' training is also generated. This generation must be compatible to the preliminary selection of the problems' parameters. At the second stage decisions must be made as regards the type of the ANNs and the formulation of the problem in terms compatible to the ANNs' function. The most common selection for the solution of the problem of R/C buildings' seismic vulnerability assessment is the MFPNs, whereas as regards the formulation of the problem the two possible options are the formulation as Function Approximation (FA) problem and the formulation as Pattern Recognition (PR) problem. Finally, at the second stage the training procedure and the parametric investigations for the optimum configuration of the selected ANNs, as well as for the optimum combination of their input parameters, must be performed. The target of these investigations is the optimization of the ANNs' generalization ability (i.e. the ability of ANNs to extract reliable results in case in which the values of the input parameters were no utilized for their training). At the second

stage the ANN expert possesses central role because the deep knowledge of the networks' function aids to the avoidance of problems which are related to low generalization ability (overfitting). The third stage concerns the implementation of the optimum configured and trained networks for the prediction of the seismic damage of R/C buildings in near-real time after a seismic event. This implementation is based on a mathematical procedure which is familiar to the civil engineers since it consists of matrix operations.

In the framework of the current paper the mathematical formulation of the third stage (i.e. the function of the trained MFPNs) is presented in details. This presentation leads to the conclusion that the utilization of the trained networks is based on a procedure which can be separated from their training procedure. Thus, the implementation of MFPNs in the research for the improvement of the R/C buildings' seismic vulnerability assessment methods is a very promising option provided that the civil engineers will gain knowledge about the basic principles of ANNs' function. This knowledge is a kind of a "common language" which can be used by civil engineers in order to efficiently collaborate with ANN experts for the implementation of neural networks in the earthquake engineering research field. In this sense, the present paper attempts to give a description not only of the overall procedure for the solution of the problem of R/C buildings' seismic vulnerability assessment, but also to describe the mathematical framework of the trained MFPNs' function.

Finally, in the present paper was proven that in case of implementation of MFPNs with one hidden layer it is possible to develop closed-form expressions which lead to the problem's solution either it is formulated as FA problem or it is formulated as PR problem. This ability results from the matrix formulation of the trained MFPNs' function. Furthermore, this ability is a proof of the fact that the algorithm which simulates the function of trained MFPNs can be inserted (independently of the procedure which was performed for their training and the computational tools which were used for this procedure) to systems which are dedicated to the recording and processing of data that arise from strong seismic motions in near-real time after the seismic events. Thus, the expansion of the services of these systems in the extraction of data for the seismic damage of a large amount of R/C buildings is possible. The aforementioned conclusion illustrates once again the great importance of understanding of the need for separation of procedure for the solution of the problem of R/C buildings' seismic vulnerability assessment in three stages, since the first two must be integrated in pre- or post-seismic periods (because they are time consuming) while the third can be performed instantly after the seismic event. Another one (but not insignificant) contribution of the present paper is the notation that the simulation of the trained MFPN (and consequently the matrix equations which are used for this purpose) is depended on the utilized training data set. This means that the ability of ANNs to predict reliably the damage state of R/C buildings can be improved if new data are available for their re-training.

REFERENCES

[1] H. Adeli, C. Yeh, Perceptron learning in engineering design, *Microcomputers in Civil Engineering*, **4(4)**, 247–256, 1989.

[2] H. Adeli, Neural Networks in Civil Engineering: 1989-2001, *Computer-Aided Civil and Infrastructure Engineering*, **16**, 126-142, 2001.

[3] G. Molas, F. Yamazaki, Neural Networks for quick Earthquake Damage Estimation, *Earthquake Engineering and Structural Dynamics*, **24**, 505-516, 1995.

[4] O.R. Lautour, P. Omenzetter, Prediction of seismic-induced structural damage using artificial neural networks, *Engineering Structures*, **31**, 600-606, 2009.

[5] M.H. Arslan, An evaluation of effective design parameters on earthquake performance of RC buildings using neural networks, *Engineering Structures*, **32(7)**, 1888-1898, 2010.

[6] F.R. Rofooei, A. Kaveh, F.M. Farahani, Estimating the vulnerability of the concrete moment resisting frame structures using artificial neural networks. *Int J Optim Civ Eng*, **3**, 433–48, 2011.

[7] M. Vafaei, A.B. Adnan, A.B.A. Rahman, Real-time seismic damage detection of concrete shear walls using artificial neural networks. *J Earthquake Eng*, **17**, 137–54, 2013.

[8] K.E. Morfidis, K.G. Kostinakis, Approach to prediction of R/C buildings' seismic damage as pattern recognition problem using Artificial Neural Networks, In: Proceedings of *4th Conference in Computational Methods in Structural Dynamics and Earthquake Engineering* (COMPDYN2017), Rhodes island, Greece, June 15-17, 2017.

[9] K. Morfidis, K. Kostinakis, Approaches to the rapid seismic damage prediction of r/c buildings using artificial neural networks. *Eng Struct*, **165**, 120-141, 2018.

[10] ATC, Earthquake Damage Evaluation Data for California, ATC-13 Report. Redwood City, CA: Applied Technology Council, 1985.

[11] A.J. Kappos, G. Panagopoulos, Ch. Panagiotopoulos, Gr. Penelis, A Hybrid Method for the vulnerability assessment of R/C and URM buildings. *Bulletin of Earthquake Engineering*, **4(4)**, 391-413, 2006.

[12] Matlab, Neural networks toolbox user's guide, 2015.

[13] Wolfram Research, Inc., Mathematica, Version 11.2.0.0, Champaign, IL, 2017.

[14] S. Haykin, *Neural Networks and Learning Machines, 3rd Edition*, Prentice Hall, 2009.

[15] K. Morfidis, K. Kostinakis, Seismic parameters' combinations for the optimum prediction of the damage state of R/C buildings using neural networks. *Advances in Engineering Software*, **106**, 1-16, 2017.

[16] S. Theodoridis, K. Koutroumbas, *Pattern Recognition, 4th Edition*. Elsevier, 2008.

[17] L. Fausett, *Fundamentals of Neural Networks: Architectures, Algorithms and Applications*. Pearson, 1994.

[18] B. Muller, J. Reinhardt, M.T. Strickland, *Neural Networks: An Introduction*. Springer, 1995.

[19] K. Hornik, M. Stinchcombe, H. White, Multilayer Feedforward Networks are Universal Approximators, *Neural Networks*, **2(5)**, 359-366, 1989.

[20] K-I Funahashi, On the Approximate Realization of Continuous Mappings by Neural Networks. *Neural Networks*, **Vol. 2**, 183-192, 1989.

[21] B.D. Ripley, *Pattern Recognition and Neural Networks*. Cambridge University Press, 1996.

[22] C.M. Bishop, *Neural Networks for Pattern Recognition*. Oxford University Press, 1995.

[23] K. Tai-Hoon, Pattern Recognition Using Artificial Network: A Review. *4th International Conference (ISA 2010)*, Miyazaki, Japan, June 23-25, 138-148, 2010.

[24] M.T. Hagan, H.B. Demuth, M.H. Beale, *Neural Network Design*. MA: PWS Publishing, Boston, 1996.

[25] R. Caruana, S. Lawrence, L. Giles, Overfitting in neural nets: backpropagation, conjugate gradient, and early stopping. *In: Proceedings of neural information processing systems*, Denver, Colorado, USA, 402–8, 2000.

[26] M. Gevrey, I. Dimopoulos, S. Lek S, Review and comparison of methods to study the contribution of variables in artificial neural network models. *Ecological Modelling*, **160**, 249-264, 2003.

[27] D.J. Wald, V. Quitoriano, T. H. Heaton, H. Kanamori, C. W. Scrivner, and C. B. Worden, TriNet "ShakeMaps": Rapid generation of peak ground motion and intensity maps for earthquakes in southern California. *Earthq. Spectra*, **15**, 537–555, 1999.

APPENDIX A: Matrices with values of the synaptic weights and the biases of MFPNs in case of problem's solution by means of the FA problem

A.1 Matrices of the network of Figure 8a

$[W_1]=$

0.800	1.175	2.939	0.114	1.959	0.350	0.649	0.121	-1.059	1.112
0.239	-2.045	1.708	-0.014	0.584	1.479	2.046	0.224	-0.767	-0.988
-2.755	-0.262	1.108	1.864	-0.077	-0.384	1.207	0.382	1.581	-0.083
0.337	-1.711	-0.365	1.897	0.051	0.657	2.240	-0.637	-2.313	1.027
1.150	0.865	-2.014	-1.217	-0.745	0.108	0.510	-0.307	0.214	0.791
2.526	1.613	1.491	1.303	1.204	-0.652	0.068	0.054	-0.370	0.081
0.218	-0.465	-0.555	0.917	-1.449	2.342	0.626	0.102	-0.345	-0.247
-2.259	-0.319	-1.812	1.896	0.642	0.903	1.336	-0.043	-0.790	-0.137
-0.109	2.536	-1.184	-0.467	-0.436	-0.459	0.635	-0.275	-0.137	1.194
-2.158	1.631	1.771	1.990	0.568	-0.034	-0.901	-0.239	0.240	-0.320
-2.526	2.774	-1.885	-0.305	0.716	0.746	0.986	-0.144	-0.670	-0.078
1.197	1.042	-0.279	-1.951	-0.424	0.523	1.196	-1.161	-1.923	1.110
-1.716	2.416	0.245	-0.163	1.604	-2.115	1.053	-0.364	-2.167	0.102
1.264	-0.005	-1.296	-2.627	0.738	-0.463	0.337	-1.730	0.944	-0.457
-2.048	1.832	-1.037	-3.341	-0.313	0.572	0.681	0.666	-0.286	0.085
-1.449	-1.431	1.601	-0.855	1.127	0.021	0.822	0.249	1.472	-1.863
-0.440	0.076	-0.184	-0.640	0.997	-0.094	1.004	-0.495	-2.999	-0.901
0.447	-1.076	-1.711	1.600	-0.970	1.066	-0.345	-1.158	1.365	0.889

Table A.1: Matrix of the synaptic weights of the synapses between the input and the hidden layer's neurons

$[B_1]^T=$ [-4.19 -4.35 4.62 -2.42 -1.58 -1.16 0.90 0.27 -0.94 1.90 0.52 0.86 -3.10 0.62 -3.05 -2.68 -3.64 4.05]

Table A.2: Matrix of the biases of hidden layer's neurons

$[W_2]^T=$ [0.39 0.21 -0.99 -0.23 -1.06 0.48 0.47 -0.88 0.68 -0.97 0.81 -0.16 0.27 -0.03 -0.66 -0.05 -0.23 -0.2]

Table A.3: Matrix of the synaptic weights of the synapses between the hidden and the output layer's neurons

Bias of the output layer's neuron: b_{12}=1.1265

A.2 Matrices of the network of Figure 8b

$$[W_1]=\begin{bmatrix} -18.811 & 1.426 & -0.569 & -0.807 & 0.502 \\ -0.316 & -2.592 & 1.066 & -3.779 & -5.590 \\ -12.095 & 1.232 & -0.354 & -0.492 & 0.366 \\ 1.686 & -1.073 & -5.817 & -3.798 & -1.615 \\ 3.029 & 1.922 & 0.371 & -0.029 & 0.405 \\ -6.922 & 2.634 & -1.670 & 2.486 & -3.515 \\ -1.418 & -5.935 & 3.106 & 0.402 & 3.301 \\ 1.342 & -0.096 & -0.673 & 0.468 & 0.322 \\ -0.333 & -0.314 & -6.342 & 0.994 & 1.404 \\ 1.873 & -3.287 & -5.756 & -1.474 & -3.511 \end{bmatrix}$$

Table A.4: Matrix of the synaptic weights of the synapses between the input and the hidden layer's neurons

$$[B_1]^T=\begin{bmatrix} 12.62 & 6.99 & 7.92 & -3.53 & -0.43 & -0.15 & -2.14 & 1.69 & -3.41 & -17.42 \end{bmatrix}$$

Table A.5: Matrix of the biases of hidden layer's neurons

$$[W_2]^T=\begin{bmatrix} 2.16 & 0.02 & -2.37 & 0.14 & 0.16 & -0.10 & -0.06 & 1.02 & -0.30 & 5.96 \end{bmatrix}$$

Table A.6: Matrix of the synaptic weights of the synapses between the hidden and the output layer's neurons

Bias of the output layer's neuron: b_{12}=-1.2272

APPENDIX B: Matrices with values of synaptic weights and biases of MFPNs in case of problem's solution by means of the PR problem

B.1 Matrices of the network of Figure 9a

$$[W_1]=\begin{bmatrix} 0.406 & -0.728 & -0.315 & 0.520 & -0.548 & -0.511 & -1.233 & 0.629 \\ 4.159 & 0.508 & -3.191 & 4.894 & 0.682 & 2.150 & -0.959 & -0.246 \\ 0.629 & -0.699 & -1.161 & -0.602 & -0.212 & -0.146 & -0.163 & 0.307 \\ 2.544 & 0.230 & -0.249 & 3.381 & -1.142 & 0.523 & -1.506 & -0.459 \\ 0.755 & -1.532 & -0.246 & 0.964 & -0.133 & -0.735 & 0.045 & 0.425 \\ -11.401 & 1.742 & -0.232 & -4.292 & 0.182 & -0.886 & 0.929 & 0.012 \\ -0.780 & -0.599 & 0.363 & 1.443 & -0.183 & 0.386 & -0.170 & -0.320 \\ 0.414 & -0.175 & -0.887 & -1.064 & -0.094 & 0.645 & 0.117 & -0.564 \\ -0.462 & -0.650 & 0.360 & 0.816 & 0.329 & -0.240 & -0.071 & -0.677 \\ -0.395 & -1.000 & 1.328 & 2.526 & 0.098 & 0.380 & -0.100 & -0.218 \\ 0.427 & 1.487 & 1.459 & 0.507 & 0.138 & -1.162 & 0.314 & 0.057 \\ -1.099 & -0.971 & -0.918 & 0.457 & -0.095 & 0.295 & -0.309 & 0.730 \\ 0.168 & -0.494 & 1.318 & 3.008 & 0.035 & 0.540 & -0.259 & -0.222 \\ 0.885 & -0.630 & -0.167 & 0.097 & 0.659 & 0.635 & -0.095 & 0.745 \\ -0.583 & -0.271 & 3.279 & -2.731 & 0.120 & 0.813 & 0.122 & -0.215 \\ -0.477 & 0.118 & -0.263 & 8.522 & 1.581 & 0.964 & -0.509 & -0.312 \\ 0.147 & 0.250 & -0.943 & 0.471 & -0.077 & -0.796 & 0.314 & 0.569 \\ -1.080 & 0.053 & -1.650 & -4.243 & 2.373 & 0.272 & 0.126 & 1.556 \\ 1.618 & -0.303 & 1.282 & 0.053 & -0.693 & 0.206 & -0.287 & -0.120 \\ 1.127 & 0.187 & -0.180 & 1.351 & -0.142 & -0.143 & 0.678 & 1.232 \end{bmatrix}$$

Table B.1: Matrix of the synaptic weights of the synapses between the input and the hidden layer's neurons

$$[B_1]^T=\begin{bmatrix}-2.06 & 0.59 & -1.66 & -2.08 & 1.62 & -1.30 & 0.70 & -0.94 & 2.45 & 1.82\\ 0.19 & -0.70 & 1.90 & 0.71 & 1.27 & 1.20 & 1.58 & 2.43 & 1.73 & 1.93\end{bmatrix}$$

Table B.2: Matrix of the biases of hidden layer's neurons

$$[W_2]^T=\begin{bmatrix}-0.022 & 0.419 & 0.443 & -0.145 & 0.618\\ 0.478 & 0.290 & -0.304 & -0.814 & 0.775\\ 2.330 & -0.845 & 0.085 & -0.172 & -0.396\\ 0.061 & 0.262 & 0.247 & -0.417 & 0.550\\ -0.383 & -0.237 & -1.029 & -0.624 & -0.235\\ -0.005 & 0.325 & 0.906 & 0.056 & -0.870\\ -3.992 & -0.707 & -0.297 & 0.313 & 0.426\\ 3.188 & 0.208 & -0.029 & 0.172 & -0.478\\ -0.615 & -0.760 & -0.414 & -0.493 & -0.519\\ -1.984 & 1.177 & 1.508 & 0.258 & 0.289\\ -0.082 & -0.348 & 0.830 & 0.100 & -1.090\\ 1.133 & 0.156 & -0.162 & 0.264 & -0.204\\ -0.165 & -2.547 & -0.471 & 1.144 & 0.133\\ -0.929 & 0.276 & 0.040 & 0.185 & -0.208\\ -0.750 & -0.750 & 0.317 & -0.173 & -0.988\\ -0.195 & -0.204 & -0.792 & 0.168 & 0.344\\ 0.026 & -0.488 & -0.324 & -0.200 & -0.060\\ -0.725 & -0.681 & 0.309 & -0.045 & -0.174\\ -0.586 & 0.624 & 0.100 & -0.162 & -0.599\\ -0.690 & -0.071 & 0.024 & -0.151 & 0.562\end{bmatrix}$$

Table B.3: Matrix of the synaptic weights of the synapses between the hidden and the output layer's neurons

$$[B_2]^T=\begin{bmatrix}1.227 & 0.525 & -0.294 & -0.840 & 1.241\end{bmatrix}$$

Table B.4: Matrix of the biases of output layer's neurons

B.2 Matrices of the network of Figure 9b

$$[W_1]=\begin{bmatrix}-2.401 & -0.666 & 0.929 & -0.827 & -1.517\\ 3.734 & 1.627 & -1.330 & -0.898 & -0.102\\ 0.042 & 0.530 & -0.247 & 1.132 & -1.229\\ 4.021 & 0.006 & 0.045 & -0.505 & -0.022\\ 3.699 & 0.127 & 0.180 & -0.705 & 0.095\\ 0.134 & -1.811 & 1.337 & -0.678 & 0.058\\ 1.560 & -0.670 & 0.180 & -0.532 & -1.716\\ 1.565 & 1.482 & 0.099 & 0.134 & -0.157\\ 0.393 & 0.513 & 1.509 & -0.185 & -1.350\\ 0.209 & -0.370 & 0.764 & -0.267 & 0.911\\ 2.098 & 0.437 & -0.620 & 0.515 & -0.123\\ 6.303 & 0.370 & 1.631 & -0.896 & -0.403\\ 4.579 & 1.202 & 2.087 & -1.395 & 0.597\\ -4.873 & -0.448 & -0.786 & 0.456 & 0.185\\ 3.367 & 0.070 & 0.235 & -0.139 & -0.139\\ -2.076 & -0.058 & -0.664 & 0.182 & 0.234\\ 0.274 & 3.540 & 3.114 & 2.543 & 0.688\\ -1.034 & -0.961 & -2.340 & 0.456 & 0.077\end{bmatrix}$$

Table B.5: Matrix of the synaptic weights of the synapses between the input and the hidden layer's neurons

$$[\mathbf{B_1}]^{\mathbf{T}}=\begin{bmatrix}3.126 & -2.327 & 3.321 & -1.581 & -1.681 & -0.827 & -0.770 & -0.484 & 0.362 \\ -1.845 & 0.923 & 0.820 & -1.399 & -1.618 & 2.445 & -2.055 & 2.048 & -1.183\end{bmatrix}$$

Table B.6: Matrix of the biases of hidden layer's neurons

$$[\mathbf{W_2}]^{\mathbf{T}}=\begin{bmatrix}0.584 & 3.1E\text{-}04 & -0.315 & -0.443 & 0.496 \\ -0.169 & 0.078 & -0.306 & 0.221 & -0.657 \\ 0.195 & -0.387 & -0.250 & -0.599 & -0.657 \\ 0.128 & -0.329 & 0.012 & -0.389 & 1.209 \\ 0.513 & 0.532 & 0.475 & -0.612 & 0.463 \\ 0.077 & -0.113 & -0.086 & 0.388 & 0.393 \\ -0.149 & 0.172 & 0.300 & 0.009 & 0.151 \\ -0.087 & 0.113 & 0.216 & 0.456 & 0.478 \\ 0.948 & -0.030 & -0.202 & 0.010 & -0.254 \\ -0.152 & 0.317 & 0.839 & -0.072 & -0.028 \\ -1.378 & 0.157 & 0.336 & -0.182 & 0.115 \\ -0.227 & 0.018 & -0.765 & -0.816 & 0.428 \\ 0.073 & -0.287 & -0.085 & -0.247 & 0.603 \\ -0.040 & 1.365 & 1.212 & -0.947 & -0.522 \\ -1.299 & -0.163 & 1.189 & 0.424 & 0.174 \\ 3.695 & 0.011 & -0.255 & -0.087 & -0.334 \\ 0.134 & 0.061 & 0.050 & -0.352 & 0.250 \\ -0.213 & -0.158 & -0.332 & -0.254 & 0.248\end{bmatrix}$$

Table B.7: Matrix of the synaptic weights of the synapses between the hidden and the output layer's neurons

$$[\mathbf{B_2}]^{\mathbf{T}}=\begin{bmatrix}-1.69 & -0.831 & -0.485 & -0.854 & 0.992\end{bmatrix}$$

Table B.8: Matrix of the biases of output layer's neurons

COMPDYN 2019
7th ECCOMAS Thematic Conference on
Computational Methods in Structural Dynamics and Earthquake Engineering
M. Papadrakakis, M. Fragiadakis (eds.)
Crete, Greece, 24–26 June 2019

A MODEL OF GOOD PRACTICE FOR URBAN REGENERATION AS A BALANCE BETWEEN DIFFERENT REQUESTS

B. Manganelli[1], **and P. Pontrandolfi**[2]

[1] School of Engineering, University of Basilicata,
Viale dell'Ateneo Lucano, 85100 Potenza, Italy
benedetto.manganelli@unibas.it

[2] Department of European and Mediterranean Cultures, University of Basilicata
Via San Rocco, 3, 75100, Matera, Italy
piegiuseppe.pontrandolfi@unibas.it

Abstract

The success of the urban regeneration of an entire district, where the total or partial replacement of the building is planned because it is obsolete in terms of energy, seismic and social aspects, involves the balance between different requests. The process involves the demolition of old buildings still occupied and their replacement with a new sustainable building in turn supported by the construction of new equipped public spaces. The cost of these interventions should be covered by private capital. It is therefore essential the initiative of entrepreneurs who find economic convenience in the operation. Revenues are those expected from the sale of tradable surfaces (residences or other uses) obtained as volume premiums compared to the existing or as residual with respect to the amount returned to the old residents. In fact, the latter will have to accept a new equivalent residential surface lower than the existing property. The relationship between these two surfaces for each resident owner, the new one and the old one, should at least reflect the ratio of the corresponding market values. Another actor who can play a fundamental role in the success of the regeneration intervention is the public administration. The latter in view of the collective benefits deriving from urban regeneration on the entire district and on those adjacent to it (in which no intervention is planned), should implement a series of actions aimed at favoring the process. These include the aforementioned volumetric premiums, incentives for investors and residents in terms of tax exemption. This work aims, also through an application example, to implement a model able to define the balance between the different instances in order to manage the fundamental parameters that characterize the regeneration intervention and guarantee its success.

Keywords: Urban Regeneration, Sustainability, Housing Market, Cost Effectiveness, Social Benefit.

1 INTRODUCTION

In Italy, the construction industry market has long been in a heavy crisis partly produced by external contingencies and partly also generated by the inefficiency of the administration. In particular, the absence or lack of urban planning requirements suitable for rational development has played an important role in limiting investments. This theme is combined with that of the poor condition of the building heritage of many cities, built in the post-war period and often today characterized by a high socioeconomic degradation. In turn, this condition of degradation discourages investments, thus making the spontaneous renewal of these areas much more difficult and thus contributing to strengthening social exclusion [1].

It is known, both in Italy and in Europe, the existence of a considerable percentage of residential buildings that has now exceeded the performance efficiency limit, both due to the widespread obsolescence and the lack of maintenance interventions. It is therefore necessary to identify new intervention strategies that give concrete possibilities for re-launching the sector. Sustainable urban regeneration, due to the depletion of energy resources and the poor condition of the building stock, is the priority issue in the development policies of the coming years.

The new approaches to sustainable development should favor actions aimed at limiting urban sprawl, reducing environmental impacts, curbing the consumption of new territory, by concentrating volumes in some areas against clearing out of other urbanized areas, to be transformed into services and places of aggregation, thus also relaunching a socio-economic redevelopment [2].

On the one hand, the demand from users who are now aware of the environmental problems linked to energy waste, oriented towards buildings characterized by higher quality and new technological energy standards, located in areas with adequate services, shops, meeting places, green areas and parking lots ; on the other hand, the need to limit the consumption of soil leads to thinking of regenerating already urbanized but degraded areas.

The redevelopment of real estate assets is a forced choice to guarantee citizens the quality and safety of living and to improve the social and environmental quality of degraded suburbs. It is also a great opportunity to promote local entrepreneurship employment. We therefore need policies that involve the legislative, institutional and financial framework capable of activating private capital more than the volumetric incentives done so far [3].

We need to put in place solutions capable of identifying, supporting and developing sustainability policies that balance social, environmental and economic interests.

Social sustainability, on the other hand, can be fostered through social inclusion, the coexistence of social classes with different economic capacities, through a mix of housing that has been ceded in ownership and leased with economic contributions to families.

Environmental sustainability must be pursued by means of strategies capable of acting on the transformation of urban spaces, reducing the consumption of new soil, increasing the resilience of the existing area or reducing their vulnerability to possible natural events or environmental changes.

Finally, economic sustainability can be achieved through the planning and execution of urban regeneration based on concerted and partnership forms [4]. The dissemination of negotiation practices involving private investors in the construction of social housing and in the renewal / redevelopment of the existing real estate and the use of specific financial and fiscal instruments can guarantee the success of urban regeneration processes.

This work focuses on the development of a model capable of defining a fair compromise between the different needs of the actors of an urban redevelopment program. It therefore constitutes a useful tool for defining urban planning and economic parameters capable of guaranteeing the success of the operation within a given regulatory and territorial constraints.

2 LITERATURE REVIEW AND MODEL BASES

Urban regeneration policies must address the issue taking care of the multiple dimensions involved. The definition of urban regeneration provided by Roberts and Sykes [5] emphasizes this interaction of the physical, economic and social dimensions of urban problems: "*Comprehensive and integrated vision and action which leads to the resolution of urban problems and which seeks to bring about a lasting improvement in the economic, physical , social and environmental condition of an area that has been subject to change*."

Urban regeneration interventions must go beyond physical regeneration and, although the latter is an important component, the main objectives are economic growth, the reduction of social inequalities and the increase in community cohesion [6,7,8] and environmental sustainability, through infrastructure provision and building specifications, and indirectly through making possible and incentivizing more sustainable lifestyles [9].

A process of urban regeneration also involves many subjects, existing residents and those arriving, investors and the public administration. The most important challenge in the practice of urban regeneration is to avoid imbalances in the distribution of benefits, i.e. to avoid that at the end of it there are winners and losers, to avoid that the benefits are captured by the strongest groups (external investors) and that the disadvantages instead fall on existing residents [10,11].

A response to this issue can be given by public-private partnership (PPP) and other participation mechanisms, and by the definition of long-term monitoring policies [12]. PPP attempt to build mutually beneficial cooperation between public and private partners. They facilitate the urban regeneration process because they lighten the public financial burden determined by infrastructure costs, thus transferring risks from the public to the private sector. The intervention of the latter is fundamental because it makes the process more efficient, in turn the risk that the private investor assumes is compensated by an expectation of economic return. Negotiating and organizing how risks and benefits are distributed is crucial to the success of the process.

Urban regeneration involves financial and market risks for external investors who spend time and resources on the expectation of a profit. Dedicated financing mechanisms, direct public investments, fiscal mechanisms are the possible actions of the public administration which, for this reason, assumes financial and political risks with the aim of maximizing collective well-being (social integration, economic development, environmental sustainability). Finally there are the residents who have to face difficult and risky choices.

In fact, many of them are not aware of living in buildings that are vulnerable to the earthquake [13]. It will therefore be necessary first of all to make them aware of the benefit resulting from the replacement of their old home with a new one. Although in the trade-off they will lose in quantitative terms they will gain in terms of quality, sustainability and security, while indirectly they will get the benefit of a changed and better social condition.

The challenge of this work is to try to combine the interests of public and private partners in a fair compromise.

3 THE MODEL

The hypothesis underlying the model is that the three actors, the public, the private investor and the residents are involved in a process of urban regeneration of an entire dormitory area (lack of services) in a seismic risk area. A neighborhood characterized by poor quality construction, inadequate both with regard to earthquake regulations, and those on containing energy

consumption [14,15], as well as by a consequent condition of social degradation also due to the lack of suitable infrastructures both in terms of quantity and quality.

Each of them has different needs and interests. Regeneration involves the demolition of existing residential volumes and their replacement with new buildings that are environmentally sustainable and seismically safe. The transformation process requires the private sector to take on the burden of upgrading the infrastructures and services in the neighborhood and to integrate the existing ones with new facilities and services (parking, green areas, etc.). The process involves an increase in the existing volumes as a reward to be attributed to the private investor and tax incentives for reaching the condition of convenience.

The parameters and variables involved are:

- Current Value (*start*) of the residential units (*Vs*);
- Future Value (*arrival*) that is predictable at the end of the regeneration. It corresponds to the difference in terms of cost between the two buildings (the old and the new) plus a differential to be commensurate with the increase in urban income resulting from the regeneration process (*Va*);
- Current surfaces (*start*) (*Ss*);
- Final surfaces (*arrival*) (*Sa*);

The difference *Sa*-*Ss* constitutes the premium (Δ) guaranteed by the public administration. 30% is the upper limit of Δ, considering the national and local regulations;

- New surfaces replacing the old ones assigned to residents (trade-off) (Sra);
- Demolition costs for old buildings (*Cd*);
- Total Cost of building transformation (new residences, infrastructures and services) (*Ct*);
- Tax incentives commensurate with a percentage of the cost (*Ti*).

The model involves the construction of utility functions to be maximized for each actor involved. The independent variables are subject to constraints. The aggregation of the individual functions takes place through the assignment of weights that express the contractual capacity of the different subjects in participatory programming.

All utility functions are assumed to be linear and are normalized in the range 0-1.

$$\frac{Vs}{Va} = i \quad \text{with } i < 1 \tag{1}$$

$$\text{constrain} \quad Ss \cdot i \leq Sra \leq Ss \tag{2}$$

$$Sa = Ss + \Delta \cdot Ss \tag{3}$$

$$\text{constrain} \quad 0 \leq \Delta \leq 0.30 \tag{4}$$

Amount of real estate (surface) sold by the private investor:

$$Sa - Sra = Si \tag{5}$$

Possible income of the private investor:

$$Si \cdot Va \tag{6}$$

Additional revenues (or tax deductions):

$$Ti \cdot (Cd + Ct) \ \ constrain \ 0 \leq Ti \leq Timax \tag{7}$$

3.1 Utility function of the residents (*Ur*)

Figure 1 shows the utility function of the residents, then formalized in equation (8).

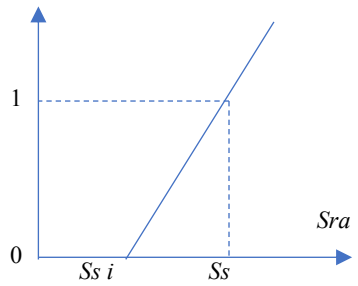

Figure 1: Utility function of the residents.

$$Ur = \frac{Sra - Ss \cdot i}{Ss \cdot (1 - i)} \tag{8}$$

The redevelopment of public spaces, affecting the quality of life of the inhabitants and their sense of belonging to places can, in fact, be a decisive factor in reducing disparities between rich and poor neighborhoods, helping to promote greater social cohesion.

However, the quantification in the utility functions of improving social welfare is excluded from this outline. The benefit is partly directed to residents and partly to the entire community (public sector).

3.2 Utility function of the public sector (*Upb*)

This utility function is associated only with the reduction of land consumption. Figure 2 shows the utility function of the public sector, then formalized in equation (9).

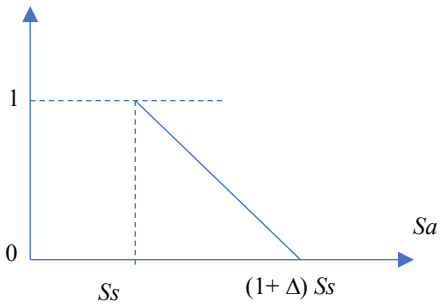

Figure 2: Utility function of the public sector.

$$Upb = \frac{Ss - Sa}{\Delta \cdot Ss} + 1 \tag{9}$$

3.3 Utility function of the private investor (*Upv*)

The investor has the goal of obtaining the maximum profit. In this scheme we assume to neglect the time dimension. Therefore, the calculation of the net present value (NPV) of urban regeneration operated only with private capital can be simplified with the expression (10), with *r* equal to the minimum expected rate of return, and *n* the time required for regeneration

$$\text{NPV}= \left[\frac{Si \cdot Va-(Cd+Ct)\cdot(1-Ti)}{(1+r)^n}\right] \tag{10}$$

The utility function, which must be normalized in the range 0-1, is constructed by calculating the maximum value of the NPV (*NPVmax*). The latter is obtained by setting the Delta and Ti equal to the maximum values (see the constraints) and the surface assigned to the residents (*Sra*) in the trade off equal to the minimum threshold (*Ss i*).

Calculating in this way the *NPVmax*, the utility function, as shown in Figure 3 and Equation (11), depends on the variables already described.

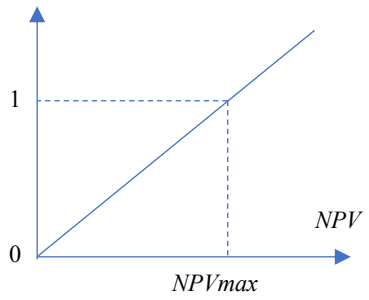

Figure 3: Utility function of the private investor.

$$Upv = \frac{NPV}{NPVmax} \tag{11}$$

3.4 Function aggregation and solution

At this point it is necessary to attribute the weights to the utility functions (ρ). Since the objective function and the constraints of the optimization problem are linear functions, then the mathematical programming problem is a linear programming problem.

$$Max\ f(Sra, \Delta, Ti) = \sum_i U_i.\rho_i \tag{11}$$

4 CONCLUSIONS

The "urban regeneration" project already contains within itself the economic resources that, with adequate financial instruments and public incentives, volumetric bonuses and European funds, can generate income and make this challenge realizable.

Through a new urban conception and, therefore, through an adequate tool, it is possible to trigger a virtuous economic flow able to recover those parts of the city, where the lack of services and the deterioration of public spaces have produced forms of tension and exclusion social. We need to implement programs that, in addition to urban and building redevelopment with the use of sustainable materials and the use of alternative energies, also favor the elimination of social problems. Because the first recipient of Sustainable Urban Regeneration must be the citizen. Also, for this reason his contribution is fundamental. It is necessary for him to become aware of the state of security of living and the patrimonial conditions of his property so that he

accepts the choice of replacing his old real estate unit in a tradeoff that would see him lose in quantitative terms but gain in qualitative terms.

To achieve this, however, the contribution of private capital is fundamental, i.e. the intervention of investors who see in these initiatives the possibility of a profit. The model presented in this research represents a tool capable of facilitating negotiation among the stakeholders, trying to outline a condition of sustainable balance between the different interests and expectations.

REFERENCES

[1] P. Cheshire, Resurgent Cities, Urban Myths and Policy Hubris: What We Need to Know. *Urban Studies*, **43** (8), 1231–1246, 2006.

[2] P. Pontrandolfi, B. Manganelli, Urban regeneration for a sustainable and resilient city: An experimentation in Matera. O. Gervasi et al. eds. *18th International Conference on Computational Science and Its Applications, ICCSA 2018*. Melbourne, Australia, July 2-5, 2018.Vol.10964 LNCS, 31-43, 2018.

[3] L. Della Spina, F. Calabrò F. Decision Support Model for Conservation, Reuse and Valorization of the Historic Cultural Heritage. O. Gervasi et al. eds. *18th International Conference on Computational Science and Its Applications – ICCSA 2018*. Melbourne; Australia; July 2-5 2018. Vol 10962 LNCS, 3-17, 2018.

[4] L. Noring, Public asset corporation: A new vehicle for urban regeneration and infrastructure finance. *Cities*, **88**, 125-135, 2019.

[5] P. Roberts, H. Sykes (eds.), *Urban Regeneration: a Handbook*. London: Sage, 2000

[6] P. Jones, J. Evans, *Urban Regeneration in the UK*. London: Sage, 2013.

[7] J. McCarthy, *Partnership, Collaborative Planning and Urban Regeneration*. Aldershot: Ashgate, 2007.

[8] R. Imrie, L. Lees, M. Raco (eds.), *Regenerating London: Governance, Sustainability and Community in a Global City*. Abingdon: Routledge, 2009.

[9] J. Flint, M. Raco (eds.), T*he Future of Sustainable Cities: Critical Reflections*. Bristol: Policy Press, 2012.

[10] R. Imrie, H. Thomas, The limits of property-led regeneration, Environment and Planning. *C: Government and Policy*, **11**, 87-102, 1993

[11] E. Swyngedow, F. Moulaert, A. Rodriguez, Neoliberal urbanisation in Europe: Large-scale urban development projects and the New Urban Policy. Antipode, **34** (3), 542-577, 2002.

[12] M. Ball, P. Maginn, Urban Change and Conflict: Evaluating the Role of Partnerships in Urban Regeneration in the UK. *Housing Studies*, **20** (1), 9-28, 2005.

[13] B. Manganelli, M. Vona, P. De Paola, Evaluating the cost and benefits of earthquake protection of buildings. *Journal of European Real Estate Research*, **11** (2), 263-278, 2018.

[14] M. Vona, M. Mastroberti, B. Manganelli, Novel models and tools to evaluate the economic feasibility of retrofitting intervention, *6th International Conference on*

Computational Methods in Structural Dynamics and Earthquake Engineering, COMPDYN 2017, Rhodes Island, Greece, June 15-17 2017. Code 133542 Vol. 2, , 3213-3224, 2017.

[15] B. Manganelli, M. Mastroberti, M. Vona, Evaluation of benefits for integrated seismic and energy retrofitting for the existing buildings. *3rd International New Metropolitan Perspectives. Local Knowledge and Innovation dynamics towards territory attractiveness through the implementation of Horizon/Europe2020/Agenda2030, 2018*, Reggio Calabria, Italy, May 22-25, 2018, Code 213639 Smart Innovation, Systems and Technologies, Vol. 101, 654-662, 2019.

COMPDYN 2019
7th ECCOMAS Thematic Conference on
Computational Methods in Structural Dynamics and Earthquake Engineering
M. Papadrakakis, M. Fragiadakis (eds.)
Crete, Greece, 24–26 June 2019

SEISMIC RISK MAP FOR THE ITALIAN RESIDENTIAL BUILDING STOCK

M. A. Zanini[1*], L. Hofer[1], F. Faleschini[1], K. Toska[1] and C. Pellegrino[1]

[1] University of Padova
Via Marzolo 9, 35131 Padova
e-mail: marianoangelo.zanini@dicea.unipd.it

Abstract

The paper illustrates the seismic risk maps derived for the residential building stock of Italy by using a general framework specifically set up by the authors for mapping seismic risk for a generic asset of interest. Seismic risk maps are computed taking into account a seismogenic model of the analyzed area, and properly characterizing vulnerability and exposure of an asset of interest. A risk-targeted indicator named Municipal Expected Annual Loss (MEAL) is introduced and used as suitable metric for the development of the maps, and for the subsequent seismic risk rating.

Keywords: Seismic risk map, Italy, Expected Annual Loss, Risk Reduction, Structural retrofit

1 INTRODUCTION

In the last decade, the number of significant losses following natural disasters worldwide, has been rapidly growing [1]. This is mainly due to the growing of urbanization, world population and Gross Domestic Product (GDP). This main three factors, imply a concentration of people, thus increasing the exposure of our society to natural hazards more than in the past [2]. In addition, the vulnerability of many structures and infrastructures is still high, since retrofitting and re-building are time and money consuming processes. Furthermore, in many cases the vulnerability of old structure is increased by degradation phenomena [3]. Earthquake represent one of the most destructive natural events that can significantly affect the economy of a region and lead to long-term restoration processes [4]. In particular, in Italy, several significant losses occurred in the last decades: in 2009 a moment magnitude M_w = 6.1 stroke the Abruzzo Region, in 2012 a M_w = 6.0 and M_w = 6.1 earthquake occurred in Emilia Romagna, while within the summer of 2016 and the winter of 2017 several significant seismic events with M_w = 6.0-6.5 occurred in the Central Italy area [5-6]. The rapid succession of these seismic events unavoidably ended up to weight on public financial funds. For this reason, the Italian government has recently approved specific incentives for householders interested in seismically retrofitting their properties [7]. In this way, a private citizen can take advantage of a tax relief when reducing the seismic vulnerability of his private home with structural retrofit and improvement. The reduction of structural vulnerability is the most immediate way for addressing the problem of the seismic risk mitigation. Nowadays seismic risk evaluation is a well-known and established procedure, mostly applied for the risk assessment of punctual structures or spatially distributed portfolio of structures [8-9]. The use of this procedures is then commonly extended for a quantitative assessment of seismic risk at regional level. In this case, a multidisciplinary approach is needed for fully describing the seismic activity of the region of interest, its vulnerability distributions, and the associated exposure. In particular, the development of seismic risk maps is the key point when dealing with the seismic risk assessment at territorial level, since they provide a quantitative representation of the current risk and are a fundamental tool for computing the benefit associated to the structural retrofit. Their use is thus needed when dealing with the design of possible sustainable risk reduction programs at regional and national scale. In scientific literature, several authors investigated issues related to the computation of seismic risk maps. In 2000, Musson [10] proposed a framework the seismic risk assessment at regional level adopting as reference measure the EMS-98 scale [11], and highlighting the significant difference between hazard and risk curves. In Germany, Tyagunov et al. [12] developed a risk map based on the EMS-98 macroseismic intensity, in which they computed the mean damage ratio and losses for the German residential building stock. Worldwide, Zhongchun et al. [13] computed the seismic risk mortality map for the Chinese state, Huttenlau and Stotter analyzed the seismic risk of the Austrian Province of Tyrol [14], and Frolova et al. showed different approaches for the seismic risk computation in Russia, basing on the different extension of the considered area [15]. Regarding Italy, some first works adopting the MCS intensity scale for representing the seismic hazard and damage probability matrices can be found in [16-17-18]. Recently, researcher focused their attention on the development of more detailed fragility functions [19] and seismic risk maps, adopting quantitative intensity measures for the ground shaking, as the Peak Ground Acceleration (PGA). In 2011, Rota et al. [20] developed typological seismic risk maps for Italy, by simply convolving hazard, in terms of PGA, and vulnerability expressed by empirical typological fragility curves derived from data collected during post-earthquake survey after the main Italian events of the past 30 years. In [20], authors did not included exposure, due mainly to the lack of data. The

contribute of exposure has been considered by Asprone et al. 2013 [21], who computed a possible seismic insurance premium for five different types of building categories within all the Italian territory, starting from the Italian seismic hazard map. In the last few years, the OpenQuake engine [22] has been adopted for developing maps of losses conditioned on ground motion with a specific return period, for Portugal [23], Nepal [24] and Turkey [25]. In these latter cases, the OpenQuake engine has been used with the s-called PSHA-approach, consisting in the calculation of the loss exceedance curve starting from the output of the hazard analysis, coupled with vulnerability and exposure. Literature review, showed as the computation of seismic risk maps is mainly subdivide into two main steps, the hazard computation, and then the risk estimation starting from hazard outputs. For this reason, this work proposes a novel-approach for computing the Italian seismic risk map for the residential building stock, directly starting from simulation of earthquake scenario consistent with the national seismogenic source model. This paper adopts as seismic synthetic risk indicator the Expected Annual Loss (EAL) that represents the potential economic loss to be yearly sustained to repair the seismic damage to the residential building asset of each Italian municipality. EAL is computed at three different levels of granularity, i.e. the most detailed municipal level (Municipal Expected Annual Loss, MEAL), the intermediate provincial level (Provincial Expected Annual Loss, PEAL), and the less refined regional level (Regional Expected Annual Loss, REAL), accordingly with the cogent administrative subdivision of Italy.

2 SEISMIC RISK COMPUTATION FRAMEWORK

The computation of the seismic risk in each municipality, and concretely the EAL estimation, requires a set of suitable models able to represent the spatial distribution of the hazard and the exposure, and the all the possible structural classes of the considered buildings assets.

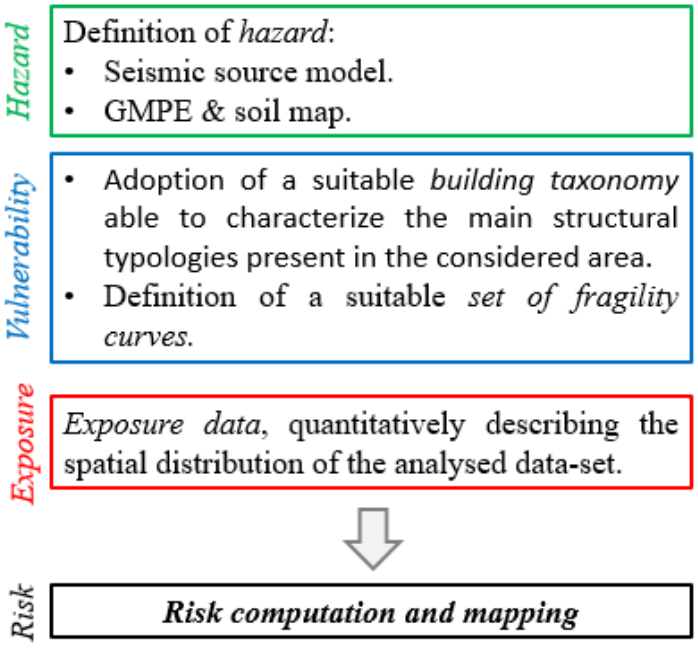

Figure 1: Main steps of the proposed framework

Figure 1 shows the main steps for the *MEAL* computation, whose input data are:

- Seismic source model represented by a set of *s* seismogenic zones (ZSs). Each ZS is characterized by a specific spatial shape, and by a Gutenberg–Richter law representing the seismogenic potential of the considered ZS. Furthermore, a suitable Ground

Motion Prediction Equation (GMPE) has to be adopted for the computation of the shaking field, jointly with a soil map representing the shear wave velocity in the first 30 m soil-depth ($v_{s,30}$);

- A building taxonomy able to represent all the structural typologies that are present in the considered area. Each of the *p* taxonomy classes (TCs) is characterized by common seismic vulnerability features. Formally, each TC is characterized by a set of fragility curves able to express the exceedance probabilities of a set of *q* mutually-exclusive and collectively-exhaustive damage states (DSs). Commonly, fragilities are derived analytically via the use of structural models [26], or empirically, starting from evidences of structural damage due to occurred earthquakes [27].
- Exposure data: they have to provide the spatial distribution of the analysed asset. In particular, exposure data provides the built area of each *p* taxonomy class, for every municipality.

The first passage consists in the creation of a grid of *e* epicenter, and in the definition of a set of *m* magnitude values between $M_{w,min}$ and $M_{w,max}$ for each i^{th} SZ, with $t=1\ldots s$. Earthquakes scenario analysis have thus to be run in every x^{th} municipality centroid ($x = 1 \ldots n$), for every j^{th} epicenter ($j = 1\ldots e$) and for every k^{th} ($k = 1 \ldots m$) magnitude, belonging to each i^{th} SZ ($i = 1 \ldots s$). By using the GMPE it is possible to compute the correspondent value of the adopted intensity measure *IM*, in each x^{th} municipality, namely $IM_{x,k,j,i}$, and consequently the associated total losses $L_{x,k,j,i}$ as sum of direct losses over the *p* TCs

$$L_{x,k,j,i} = \sum_{y=1}^{p} L_{x,k,j,i,y} \tag{1}$$

where $L_{x,k,j,i,y}$ can be computed as

$$L_{x,k,j,i,y} = RCR_{Tot,y,x,k,j,i} \cdot A_{y,x} \cdot URC_y \tag{2}$$

In Equation (2), $A_{y,x}$ represents the built area of the y^{th} TC in the x^{th} municipality, URC_y is the unit repair cost for the y^{th} TC (in €/m^2), and $RCR_{Tot,y,x,k,j,i}$ is the total repair cost ratio of the y^{th} TC, that can be computed as

$$RCR_{Tot,y,x,k,j,i} = \sum_{z=0}^{q} P\left[DS_{z,y} \mid IM_{x,k,j,i}\right] \cdot RCR_{z,y} \tag{3}$$

where $RCR_{z,y}$ are a set of repair cost ratios (i.e., ratio between unit cost to repair a building in a specific damage state and the unit replacement cost), assumed deterministic and homogeneous for each y^{th} TC. In Equation (3), $P\left[DS_{z,y} \mid IM_{x,k,j,i}\right]$ is computed as

$$P\left[DS_{z,y} \mid IM_{x,k,j,i}\right] = P\left[DS_{z,y} \mid \geq ds_{z,y} \mid IM_{x,k,j,i}\right] - P\left[DS_{z+1,y} \mid \geq ds_{z+1,y} \mid IM_{x,k,j,i}\right] \tag{4}$$

and assuming $P[DS_{0,y} \geq ds_{0,y} \mid IM_{x,k,j,i}] = 1$ and $P[DS_{5,y} \geq ds_{5,y} \mid IM_{x,k,j,i}] = 0$.

The damage state exceedance probability of the z^{th} DS for the y^{th} TC, in each x^{th} municipality centroid, in computed via fragility curves as

$$P\left[DS_{z,y} \geq ds_{z,y} \mid IM_{x,k,j,i}\right] = \Phi\left[\frac{1}{\sigma_{DS_{z,y}}} \ln\left(\frac{IM_{x,k,j,i}}{\mu_{DS_{z,y}}}\right)\right] \quad (5)$$

At this stage, for each x^{th} municipality a set of e losses caused by each k^{th} magnitude, generated by the i^{th} SZ is available. This vector of data represents the probability density function (*pdf*) of direct losses conditioned on the specific magnitude value k^{th}. From this samples, is thus straightforward to compute *ad hoc* statistics, as the sample mean, representing the distribution expected value, and other percentile of interest (25th, 50th, 75th ecc). In the following the paper assumes the mean value as relevant statistic, namely $L_{x,k,mean,i}$. The final step of the proposed procedure consists in the computation of the $MEAL_{x,mean,i}$ in each x^{th} municipality due to losses cause by the i^{th} SZ. This calculation can be performed according to Figure 2 by associating to each $L_{x,k,mean,i}$ the corresponding mean annual rate $\nu_{k,i}$ of exceeding a certain moment magnitude $M_{k,i}$ in the i^{th} SZ, and applying the total probability theorem. $\nu_{k,i}$ can be easily computed from the Gutenberg-Richter (GR) recurrence law, given by the following expression

$$\log\left(\nu_{k,i}\right) = a_i - b_i \cdot M_{k,i} \quad (6)$$

where a_i is the total seismicity rate and b_i is the negative slope of the GR law for the i^{th} SZ. The expected annual loss, in the x^{th} municipality, due to seismicity arising from the i^{th} SZ is thus given by

$$MEAL_{x,mean,i} = \int_0^{\nu_{M_{\min,i}}} L_{x,mean,i}\left(M\right)\left|d\nu_{M,i}\right| \quad (7)$$

As Figure 2 shows, two additional points are introduced for the computation of Eq. (7), consistently with the following assumption:

- A minimum magnitude value $M_{min,i}$ is assumed for each zone, aiming to remove small events characterized by negligible impacts in terms of structural damage and thus losses. For this reason, earthquakes with magnitudes lower than $M_{min,i}$ are associated to zero loss;
- Since every zone, basing on its seismological characteristics, is characterized by a maximum magnitude $M_{max,i}$, the loss exceedance curve is truncated in correspondence of $M_{max,i}$, excluding in this way from the computation higher impossible losses.

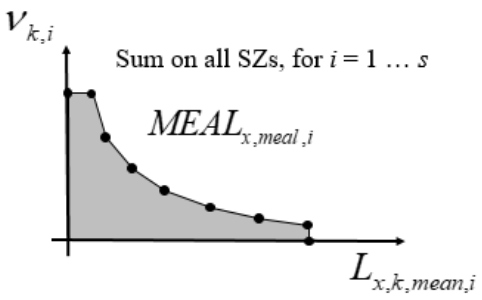

Figure 2: MEAL computation.

The MEAL considering the contribution of every SZ determining the seismicity of the considered x^{th} municipality, can be computed by simply adding each contribution as:

$$MEAL_{x,mean} = \sum_{i=1}^{s} MEAL_{x,mean,i} \tag{8}$$

Once the $MEAL_{x,mean}$ is computed for each n municipalities, results can be mapped thus obtaining the seismic risk map. Since $MEAL_{x,mean}$ is strongly influenced by the exposure, it is possible to refer the $MEAL_{x,mean}$ to the build surface in each municipality, i.e. the $MEAL_{x,mean}$ for 1 m^2 of built area in each x^{th} municipality, obtaining in this way the $UMEAL_{x,mean}$ as:

$$UMEAL_{x,mean} = \frac{MEAL_{x,mean}}{\sum_{y=1}^{p} A_{y,x}} \tag{9}$$

Finally, a dimensionless indicator is introduced to easily rank seismic risk throughout a country, i.e. the Municipality Seismic Risk Class (*MSRC*, in % of replacement cost), estimated as:

$$MSRC_{x,mean} = \frac{UMEAL_{x,mean}}{URC_y} \tag{10}$$

The same three risk indicators can be easily computed also for different granularity levels, as the provincial and regional level. The development of a seismic risk map is therefore a key-starting point for the definition of a rational seismic mitigation program for a country, since it allows government to understand needs and priorities, and compare resulting benefits with costs associated to the implementation of specific seismic retrofitting schemes [28].

3 APPLICATION TO ITALY

The proposed framework is applied to compute the seismic risk map for the residential building stock of Italy, considering as target losses the reconstruction cost of damaged structural elements (i.e. the so-called *direct losses*). However, the framework is general and flexible and can be applied to different target losses, as losses due to business interruption [29], losses due to failure of spatially distributed networks [30-31], or losses arising from different natural hazards [32], for which the same conceptual scheme can be applied.

3.1 Hazard model

The ZS9 model [33] has been adopted for describing the Italian seismicity; parameters of the GR law for each i^{th} SZ are taken from [34] and the values showed in Figure 3. In particular, a 5-km mesh grid of epicenters is adopted, for a total of 7237 points. Sardinia has not been considered in the computation, since the ZS9 model does not provide SZs for this region.

Regarding the GMPE model, the formulation proposed by Bindi et al. [35] is adopted, jointly with the $v_{s,30}$ soil map provided by the United States Geological Survey (USGS) [36]. Finally, for each i^{th} SZ a total of m = 6 magnitudes between $M_{min,i}$ and $M_{max,i}$ have been adopted.

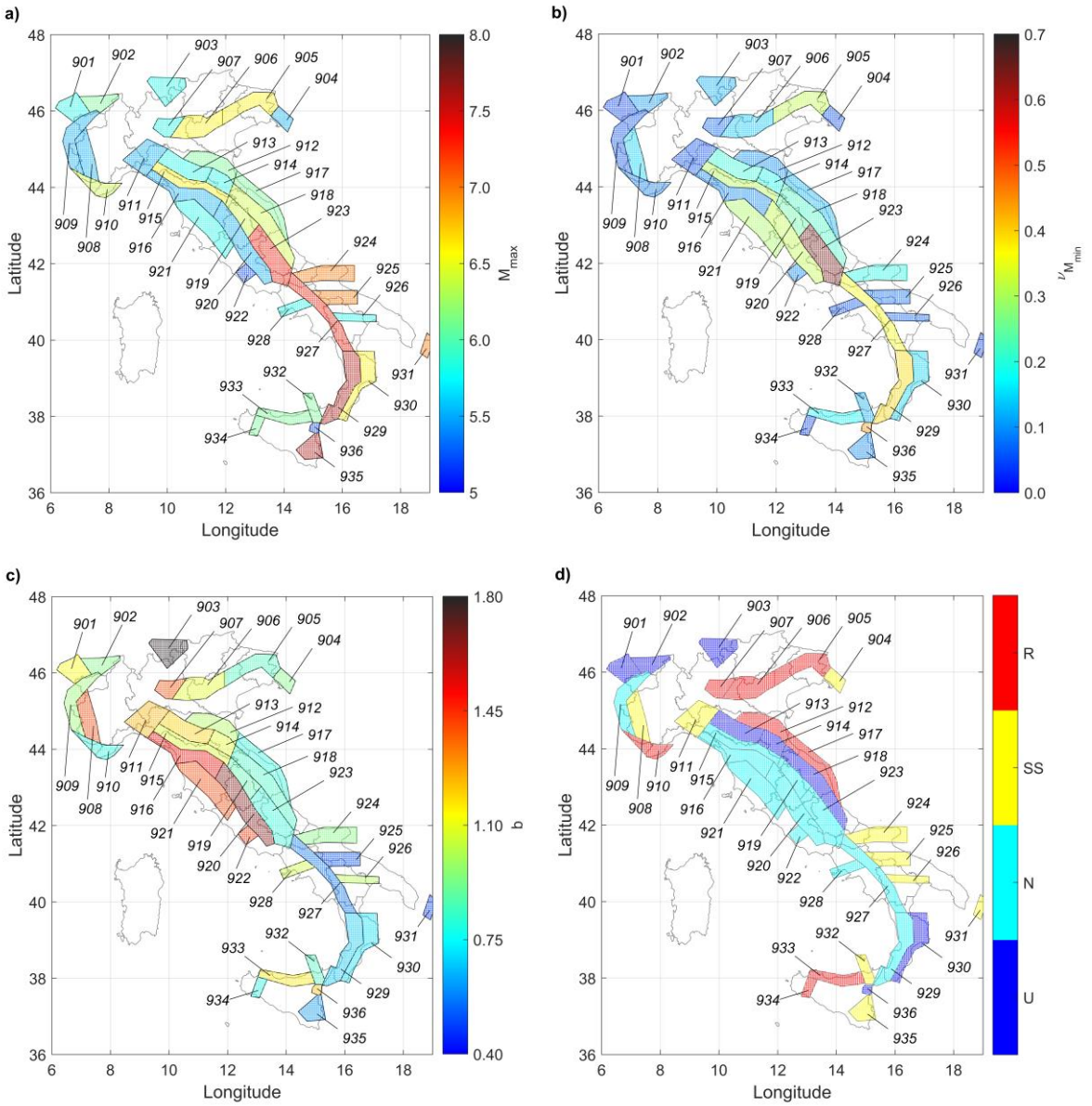

Figure 3: Seismogenic source model: M_{max} (a) and $\nu_{M_{min}}$ (b) values, G-R *b* coefficients, and d) prevailing mechanism of faulting for each SZ (U = undetermined, N = normal, SS = strike-slip, R = reverse).

3.2 Vulnerability Model

For characterizing the seismic vulnerability of the analyzed building stock, a suitable building taxonomy has been adopted. In particular, 8 TC classes have been adopted for representing the residential building stock of Italy, each one characterized by a set of fragility curves related to four mutually exclusive and collectively exhaustive damage states (i.e. DS_1, DS_2, DS_3, DS_4 respectively related to slight, moderate, extensive and complete damage), according to [37]. Two masonry classes have been adopted for characterize masonry buildings, according to Kostov et al. [38]: masonry building built before 1919, and after 1919. As regards reinforced concrete (RC) structures, the first important distinction is between gravity load designed and seismic load designed. The subdivision for each municipality between the two classes, have been performed by using the ECS-IT software which provide the temporal

evolution of the Italian seismic code in each municipality [39]. Moreover, since the census data is classified per decade (i.e. in 1971, 1981, and 2001), a linear variation with time was assumed in order to bridge the gap between the milestone years marking the code evolution and the census ten-year classification. A further subdivision has also been performed both for RC-gravity and RC-seismic buildings, considering the number of stories and thus defining two additional subclasses (1-2 story, 3 or more stories). Fragility parameters for the four reinforced concrete TCs have been taken from Ahmad et al. [40]. Finally, two TCs have been considered representative of "other" mixed structural types, particularly combined RC-masonry, again subdivided in gravity-load and seismic-load designed, with the same approach adopted for RC classes [35]. All main parameters of the adopted fragilities are listed in Table 1.

Taxonomy Class	Damage State	$\mu_{DS_{z,y}}$ [g]	$\sigma_{DS_{z,y}}$
Masonry – pre 1919	DS_1	0.10	0.79
	DS_2	0.14	0.80
	DS_3	0.17	0.81
	DS_4	0.24	0.80
Masonry – post 1919	DS_1	0.12	0.79
	DS_2	0.17	0.81
	DS_3	0.19	0.79
	DS_4	0.33	0.79
RC - Gravity | 1-2	DS_1	0.09	0.33
	DS_2	0.12	0.44
	DS_3	0.25	0.37
	DS_4	0.33	0.36
RC - Gravity | 3+	DS_1	0.08	0.32
	DS_2	0.11	0.43
	DS_3	0.17	0.40
	DS_4	0.22	0.38
RC - Seismic | 1-2	DS_1	0.09	0.33
	DS_2	0.12	0.44
	DS_3	0.24	0.37
	DS_4	0.48	0.36
RC - Seismic | 3+	DS_1	0.08	0.32
	DS_2	0.11	0.41
	DS_3	0.17	0.39
	DS_4	0.31	0.36
Other - Gravity	DS_1	0.11	0.79
	DS_2	0.16	0.78
	DS_3	0.27	0.78
	DS_4	0.35	0.79
Other - Seismic	DS_1	0.12	0.79
	DS_2	0.19	0.79
	DS_3	0.30	0.79
	DS_4	0.41	0.79

Table 1: Main parameters of fragility curves for each TC and DS.

3.3 Exposure Model

The exposure of the national residential building is based on the 15th census database of the National Institute of Statistics [41], from which the built area of each TC has been computed, as in [34]. The unit repair cost has been assumed constant among the eight TCs and equal to 1200 €/m^2. Figure 3a shows the total build area in each municipality, while Figure 3b shows the exposed value. Regarding, the percentage disaggregation of the TCs, Figure 3c shows that masonry structures are the most diffused structural typology within all the Italian municipalities. Regarding the $RCR_{z,y}$, they have been assumed constant among the TCs and equal to [0.15, 0.40, 0.65, 1], respectively for DS_1, DS_2, DS_3 and DS_4, resulting from statistical post-processing of rough data [42].

3.4 Seismic Risk computation

For the *MEAL* computation the expected value of the loss distribution *f(L|M)* has been assumed as reference statistic. *EAL* is computed first at municipality level (*MEAL*), and then aggregated for obtaining the *EAL* at provincial level (*PEAL*), and the EAL at regional level (*REAL*), according to the administrative subdivision of Italy.

Figure 4 shows results for the three adopted granularity levels. In particular, it is worth to note as in this case the risk maps in terms of absolute EAL are highly influenced by the spatial distribution of the exposure. The contribution of each SZ to the *EAL* of each municipality can be found in Zanini et al. [43].

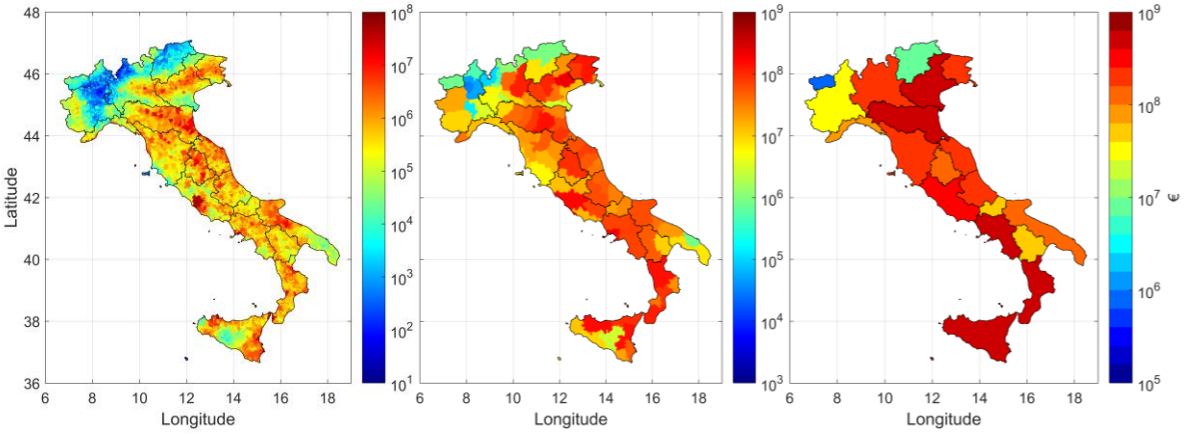

Figure 4: The seismic risk map of Italy in terms of MEAL (left), PEAL (center), REAL (right).

The same maps can therefore be expressed in relative terms using the following unitary metric, the *UMEAL* (i.e. the *MEAL* for 1 m^2 built area in each municipality, in €/m^2), the *UPEAL* (i.e. the *PEAL* for 1 m^2 built area in each province, in €/m^2), and the *UREAL* (i.e. the *REAL* for 1 m^2 built area in each region, in €/m^2). *UMEAL*, *UPEAL* and *UREAL* map, showed in Figure 5, allows to better detail the effective spatial distribution of seismic risk, since they represent risk in relative terms, and can be used as a basic metric when dealing with defining insurance coverage schemes.

In particular, Figure 5 shows the beneficial effect of computing seismic risk at higher granularity levels than respect to the more refined municipal level. Indeed, the maximum amount of *UMEAL* of 17-18 €/m^2 drops to 5-6 17-18 €/m^2 for *UPEAL* and *UREAL*. Previous risk maps reported in Figure 4 and Figure 5, detail seismic risk of Italy quantifying in economic terms its impact: such risk maps are therefore relevant for stakeholders (e.g. government, research institutes, insurance, industry, banks).

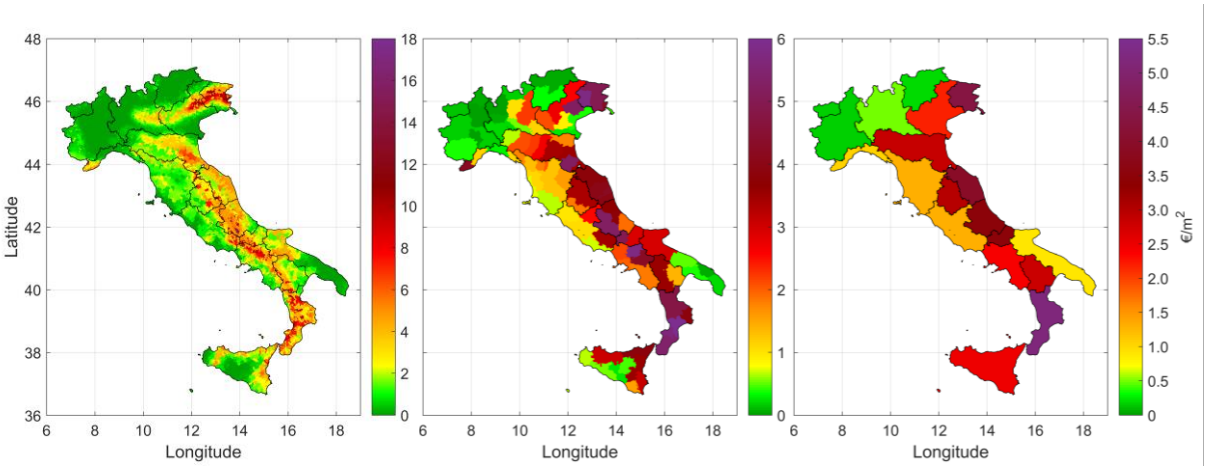

Figure 5: The seismic risk map of Italy in terms of *UMEAL* (left), *UPEAL* (center), *UREAL* (right).

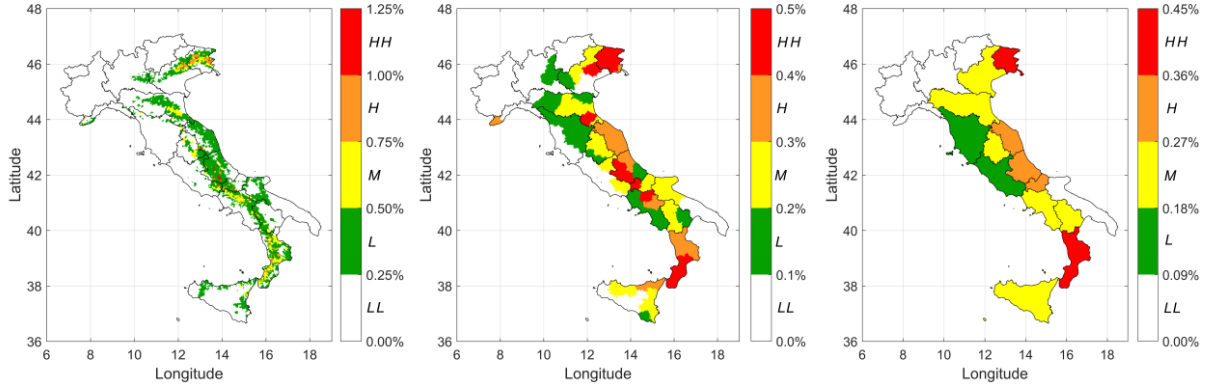

Figure 6: The seismic risk map of Italy in terms of *MSRC* (left), *PSRC* (center), *RSRC* (right).

A qualitative and dimensionless seismic risk indicator can be obtained from the ratio between *UMEAL* and the *URC* value, namely the Municipality Seismic Risk Class (*MSRC*). The same calculation can be performed also at provincial level, obtaining the Provincial Seismic Risk Class (*PSRC*), and at regional level (*RSRC*, Regional Seismic Risk Class).

For all three different granularity levels the range between 0 and the correspondent maximum value, has been subdivided in 5 classes, finding five different risk levels: Very Low Seismic Risk (*LL*), Low Seismic Risk (*L*), Medium Seismic Risk (*M*), High Seismic Risk (*H*), and Very High Seismic Risk (*HH*). Table 2 shows the range on each class for the three granularity levels, while Figure 5 show the *MSRC*, *PSRC* and *RSRC* map.

	LL	*L*	*M*	*HH*	*HH*
MSRC [%]	0.00 - 0.25	0.25 - 0.50	0.50 - 0.75	0.75 - 1.00	1.00 - 1.25
PSRC [%]	0.00 - 0.10	0.10 - 0.20	0.20 - 0.30	0.30 - 0.40	0.40 - 0.50
RSRC [%]	0.00 - 0.09	0.09 - 0.18	0.18 - 0.27	0.27 - 0.36	0.36 - 0.45

Table 2: *MSRC*, *PSRC* and *RSRC* range values for the adopted seismic risk ratings.

4 CONCLUSION

Seismic risk maps are a key tool for public authorities of countries prone to significant losses due to earthquakes, for developing suitable seismic risk transferring solutions. The described formulation deals with this specific topic, proposing an overall framework for computing the seismic risk and introducing some useful risk indicators. In particular, an application to the Italian residential building stock is reported and seismic risk maps for Italy are computed. For this scope, a detailed hazard, vulnerability and exposure models are assumed. Seismogenic zones are used for representing the seismicity of Italy, while eight taxonomy classes are assumed for describing the different vulnerability of the residential Italian buildings. The Expected Annual Loss is used as suitable risk indicator, representing the yearly amount that has to be save for facing possible significant future losses. In the application, *EAL* computation is performed at three granularity levels, municipal (*MEAL*), provincial (*PEAL*), and regional level (*REAL*). Results showed as this first risk indicator, in the Italian case, is strictly related to the exposure. Seismic risk maps have been computed also in terms of *UMEAL*, *UPEAL* and *UREAR*, that represent each municipal, provincial and regional *EAL* referred to the corresponding built area of each municipality, province and region. Results show as considering less refined granularity has an averaging effect on the risk computation. Finally, adimensional seismic risk maps have been computed and used for providing qualitative and immediate risk maps of Italy. Resulting maps depict national seismic risk spatial distribution, thus providing reliable information to government agencies, which can promote specific mitigation intervention at the territorial scale to reduce the impact of future earthquakes in the areas mostly. Risk maps are a fundamental tool for knowing the current exposure to seismic risk of a wide territory, and provide a quantitative tool for evaluating the benefit associated to a possible national retrofit scheme, and for designing possible sustainable financial risk reduction programs.

REFERENCES

[1] Munich RE, 2017, Natural catastrophes 2016 - Analyses, assessments, positions, 2017 Issue.

[2] J.E. Daniell, B. Khazai, F. Wenzel, A. Vervaeck, *The CATDAT damaging earthquakes database*, Nat. Hazards Earth Syst. Sci., **11**, 2235–2251, 2011.

[3] F. Faleschini, M.A. Zanini, L. Hofer, Reliability-based analysis of recycled aggregate concrete under carbonation, *Advances in Civil Engineering*, ID 4742372, 2018.

[4] H. Cutler, M. Shields, D. Tavani, and S. Zahran, Integrating engineering outputs from natural disaster models into a dynamic spatial computable general equilibrium model of Centerville, *Sustainable and Resilient Infrastructure*, **1(3-4)**, 169-187, 2016.

[5] L. Luzi, S. Hailemikael, D. Bindi, D. F. Pacor, F. Mele, F. Sabetta, ITACA (ITalian ACcelerometric Archive): A Web Portal for the Dissemination of Italian Strong-motion Data, *Seismological Research Letters*, **79(5)**, 716–722, 2008.

[6] F. Pacor, R. Paolucci, L. Luzi, F. Sabetta, A. Spinelli, A. Gorini, M. Nicoletti, S. Marcucci, L. Filippi, M. Dolce, Overview of the Italian strong motion database ITACA 1.0, *Bulletin of Earthquake Engineering*, **9(6)**, 1723–1739, 2011.

[7] DM 65, Sisma Bonus – Linee guida per la classificazione del rischio sismico delle costruzioni e relativi allegati. Modifiche all'articolo 3 del Decreto Ministeriale n° 58 del 28/02/2017. Ministero delle Infrastrutture e dei Trasporti, Roma (in Italian), 2017.

[8] K.A. Porter, An Overview of PEER's Performance-based Earthquake Engineering Methodology, *Proceedings of Ninth International Conference on Applications of Probability and Statistics in Engineering*, San Francisco, CA, 2003.

[9] K.A., Porter, J.L. Beck, R. Shaikhutdinov, Simplified Estimation of Economic Seismic Risk for Buildings, *Earthquake Spectra*, **20(4)**, 1239−1263, 2004.

[10] R. M. W. Musson, Intensity-based seismic risk assessment, *Soil Dynamic and Earthquake Engineering*, **20**, 353–360, 2000.

[11] G. Grünthal, European Macroseismic Scale 1998. European Seismological Commission, Subcommission on Engineering Seismology, Working Group Macroseismic Scales, *Cahiers du Centre Européen de Géodynamique et de Séismologie*, Luxemburg, 1998.

[12] S. Tyagunov, G. Grunthal, R. Wahlstrom, L. Stempniewski, J. Zschau, Seismic risk mapping for Germany, N*at. Hazards Earth Syst. Sci.*, **6(4)**,573–586, 2006.

[13] X. Zhongchun, W. Shaohong, D. Erfu, L. Kaizhong, Quantitative assessment of seismic mortality risks in China, *J. Resour. Ecol.*, **2(1)**, 83–90, 2011.

[14] M. Huttenlau, J. Stotter, Risk-based damage potential and loss estimation of earthquake scenarios in the moderate endangered Austrian Federal Province of Tyrol, *Georisk: Assess. Manag. Risk Eng. Syst. Geohazards*, **6(2)**, 105–127, 2012.

[15] N.I. Frolova, V.I. Larionov, J. Bonnin, S.P. Sushchev, A.N. Ugarov, M.A. Kozlov, Seismic risk assessment and mapping at different levels, *Natural Hazards*, **88**, S43–S62, 2017.

[16] A. Lucantoni, V. Bosi, F. Bramerini, R. De Marco, T. Lo Presti, G. Naso, F. Sabetta, Seismic risk in Italy, *Ingegneria Sismica*, **17(1)**, 5-36, 2001 (in Italian).

[17] G. Zuccaro, Inventory and vulnerability of the residential building stock at a national level, seismic risk and socio/economic loss maps. CD-ROM, Naples, Italy, 2004 (in Italian).

[18] F. Bramerini, G. Di Pasquale Updated seismic risk maps for Italy. *Ingegneria Sismica*, **15(2)**, 5-23, 2009 (in Italian).

[19] H. Crowley, M. Colombi, B. Borzi, M. Faravelli, M. Onida, M. Lopez, D. Polli, F. Meroni, R. Pinho, A comparison of seismic risk maps for Italy, *Bullettin of Earthquake Engineering*, **7(1)**, 149–180, 2009.

[20] M. Rota, A. Penna, C. Strobbia, G. Magenes, Typological seismic risk maps for Italy, *Earthquake Spectra*, **27(3)**, 907–926, 2011.

[21] D. Asprone, F. Jalayer, S. Simonelli, A. Acconcia, A. Prota, G. Manfredi, Seismic insurance model for the Italian residential building stock, *Structural Safety*, **44**, 70–79, 2013.

[22] V. Silva, H. Crowley, M. Pagani, D. Monelli, R. Pinho, Development of the OpenQuake engine, the Global Earthquake Model's open-source software for seismic risk assessment, *Natural Hazards*, **72**, 1409–1427, 2012.

[23] V. Silva, H. Crowley, H. Varum, R. Pinho, Seismic risk assessment for mainland Portugal, *Bulletin of Earthquake Engineering*, **13**, 429–457, 2015.

[24] H. Chaulagain, H. Rodrigues, V. Silva, E. Spacone, H. Varum, Seismic risk assessment and hazard mapping in Nepal, *Natural Hazards*, **78**, 583–602, 2012.

[25] V. Silva, H. Crowley, M. Pagani, R. Pinho, D. Monelli, Development and Application of OpenQuake, an Open Source Software for Seismic Risk Assessment, *Proceedings of 15th World Conference on Earthquake Engineering - WCEE*, Lisbon, Portugal, September 24-28 2012.

[26] M.A. Zanini, L. Hofer, F. Faleschini, C. Pellegrino, The influence of record selection in assessing uncertainty of failure rates, *Ingegneria Sismica*, **34 (4)**, pp. 30-40, 2017.

[27] L. Hofer, P. Zampieri, M.A. Zanini, F. Faleschini, C. Pellegrino, Seismic damage survey and empirical fragility curves for churches after the August 24, 2016 Central Italy earthquake, *Soil Dynamics and Earthquake Engineering*, **111**, 98-109, 2018

[28] F. Faleschini, J. Gonzalez-Libreros, M.A. Zanini, L. Hofer, L. Sneed, C. Pellegrino, Repair of severely-damaged RC exterior beam-column joints with FRP and FRCM composites, *Composite Structures*, **207**, pp. 352-363, 2019.

[29] L. Hofer, M.A. Zanini, F. Faleschini, C. Pellegrino, Profitability Analysis for Assessing the Optimal Seismic Retrofit Strategy of Industrial Productive Processes with Business-Interruption Consequences, *Journal of Structural Engineering (United States)*, **144(2)**, 4017205, 2018.

[30] M.A. Zanini, C. Vianello, F. Faleschini, L. Hofer, G. Maschio, A framework for probabilistic seismic risk assessment of NG distribution networks, *Chemical Engineering Transactions*, **53**, pp. 163-168, 2016

[31] M.A. Zanini, L. Hofer, F. Faleschini, P. Franchetti, C. Pellegrino, Maintenance and seismic retrofit cost assessment of existing bridges, Maintenance, *Monitoring, Safety, Risk and Resilience of Bridges and Bridge Networks - Proceedings of the 8th Interna-*

tional Conference on Bridge Maintenance, Safety and Management, IABMAS 2016, pp. 1106-1112, 2016.

[32] M.A. Zanini, L. Hofer, F. Faleschini, C. Pellegrino, Building damage assessment after the Riviera del Brenta tornado, northeast Italy, *Natural Hazards*, **86(3)**, pp. 1247-1273, 2017

[33] C. Meletti, F. Galadini, G. Valensise, M. Stucchi, R. Basili, S. Barba, G. Vannucci, E. Boschi, A seismic source zone model for the seismic hazard assessment of the Italian territory, *Tectonophysics*, **450**, 85–108, 2008

[34] S. Barani, D. Spallarossa, P. Bazzurro, Disaggregation of probabilistic ground-motion hazard in Italy, *Bull. Seismol. Soc. Am.*, **99 (5)**, 2638–2661, 2009.

[35] D. Bindi, F. Pacor, L. Luzi, R. Puglia, M. Massa, G. Ameri, R. Paolucci, Ground motion prediction equations derived from the Italian strong motion database, *Bulletin of Earthquake Engineering*, **9(6)**, 1899–1920, 2011.

[36] T.I. Allen, D.J. Wald, Topographic slope as a proxy for global seismic site conditions (v_{s30}) and amplification around the globe: U.S. Geological Survey Open-File Report2007-1357, 69 pp.

[37] M.A. Zanini, l. Hofer, C. Pellegrino, A framework for assessing the seismic risk map of Italy and developing a sustainable risk reduction program, *International Journal of Disaster Risk Reduction*, **33**, 74–93, 2019.

[38] M. Kostov, E. Vaseva, A. Kaneva, N. Koleva, G. Verbanov, D. Stefanov, E. Darvarova, D. Salakov, S. Simeonova, L. Cristoskov, Application to Sofia. RISK-UE, WP13, 2004.

[39] ECS-IT; 2015: Evoluzione della Classificazione Sismica in Italia. Retreived online at www.reluis.it/index.php?option=com_content&view=article&id=399&Itemid=185&lang=it

[40] N. Ahmad, H. Crowley, R. Pinho, Analytical fragility functions for reinforced concrete and masonry buildings aggregates of Euro-Mediterranean regions – UPAV methodology. Internal report, Syner-G Project, 2009/2012, 2011.

[41] Istituto Nazionale di Statistica, 15-esimo Censimento Generale della popolazione e delle abitazioni, 2011. Postel Editore, Roma (in Italian), 2011.

[42] M. Dolce, G. Manfredi, Libro bianco sulla ricostruzione privata fuori dai centri storici nei comuni colpiti dal sisma dell'Abruzzo del 6 aprile 2009. Doppiavoce Edizioni, pp.224 (in Italian), 2015.

[43] M.A. Zanini, L. Hofer, F. Faleschini, K. Toska, C. Pellegrino, Municipal expected annual loss as an indicator to develop seismic risk maps in Italy, *Bollettino di Geofisica Teorica ed Applicata*, DOI 10.4430/bgta0262, Accepted.

COMPDYN 2019
7th ECCOMAS Thematic Conference on
Computational Methods in Structural Dynamics and Earthquake Engineering
M. Papadrakakis, M. Fragiadakis (eds.)
Crete, Greece, 24–26 June 2019

EXPERIMENTAL AND NUMERICAL ANALYSIS OF THE SEISMIC RESISTANCE OF TECHNOLOGY

Juraj Králik[1]

[1] Faculty of Civil Engineering, STU Bratislava, Radlinského 11; 810 05, Bratislava; SK

juraj.kralik@stuba.sk

Abstract

This paper gives the methodology to get the floor response spectra of the buildings on the base of the results of the probabilistic assessment. On the base of the geophysical and seismo-logical monitoring of locality the peak ground acceleration and the uniform hazard spectrum of the acceleration was defined for the return period 10 000 years. The algorithms to generate a synthetic ground motion accelerogram compatible with a response spectrum are described. The methodology of the seismic resistance of the cable support structures are presented. The experimental and numerical analysis of the seismic resistance of the technology structures are discussed.

Keywords: Structural Dynamics, Earthquake Engineering, Safety, Technology, NPP, ANSYS.

1 INTRODUCTION

The earthquake resistance analysis of NPP (Nuclear Power Plant) buildings in Mochovce were based on the recommends of IAEA (International Agency of Energy Atomic) in Vienna to get international safety level of nuclear power plants [1]. Three logical possibilities of the source zones were defined for Mochovce site – contact of Eastern Alps and Western Carpathians, Dobra Voda and alternative fault. The seismic load was defined by PGA (Peak Ground Acceleration) and local seismic spectrum in dependence on magnitude and distance from source zone of earthquake [2, 3]. Two principal methods are appropriate for assessing the seismic safety of facilities, the SMA (Seismic Margin Assessment) method and the SPSA (Seismic Probabilistic Safety Assessment) method [3, 4]. The RLE (Review Level Earthquake) is very effective method to reevaluation of NPP safety then the new seismic hazard is defined. The SMA methodology is based on the RLE determination. The first seismic reevaluation of the seismic hazard of the Mochovce site was established on the deterministic method and seismic-tectonical consideration of the Mochovce site was analyzed on the base of probabilistic method. The design response spectra were prepared based on results of the PSHA (Probabilistic Seismic Hazard Analysis) study for the NPP Mochovce site developed by GFÚ SAV [4].

Basic parameters of the design GRS (Ground Response Spectrum) are as follows [2]:

- Spectral shape MDE (SL-2) (Maximum Design Earthquake) corresponds to 84% NEP (Non Exceedence Probability) (i.e. median + 1 sigma);
- Seismic event with annual recurrent frequency 10^{-4};
- PGA for horizontal direction $PGA_H = 0.150$ g;
- PGA for vertical direction $PGA_V = 0{,}100$ g;
- Vertical response spectra

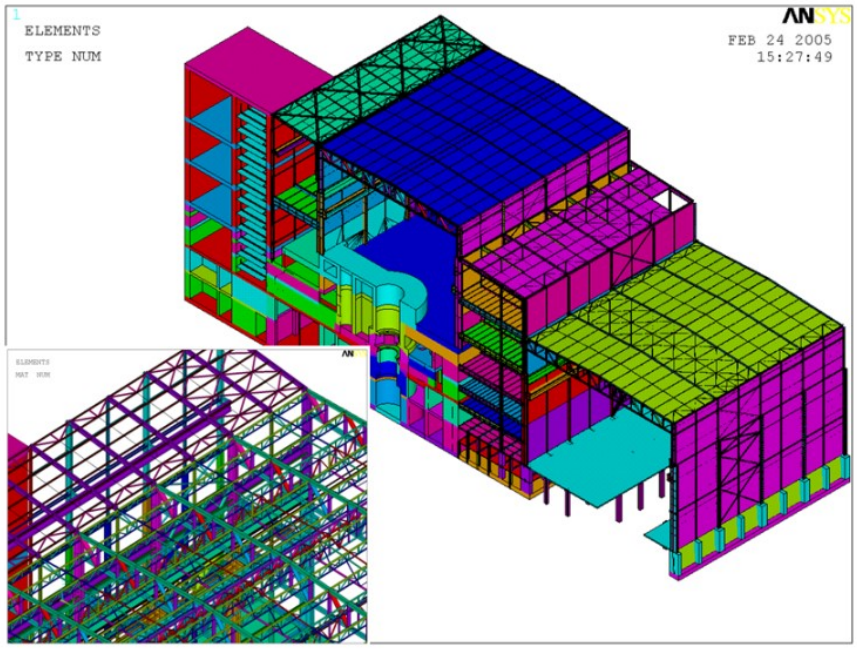

Figure 1: Calculation model of NPP V2.

Firstly the value of PGA was defined at 1994 (PGA_{RLE}=0,1g) follow in accordance of the results of seismological monitoring this locality at 2003 (PGA_{UHS}=0.142g and

PGA_{HS}=0.143g). The last PGA for horizontal direction was defined as PGA_{HS} = 0.150 g on base of the seismic-tectonic investigation of Mochovce NPP site.

The Mochovce NPP structures are typically the same as the NPP structures for reactor VVER 440. Around of the reinforced concrete structures of the box SG and bubbler tower are the steel structures of the reactor hall, longitudal and transversal electrical buildings are built. The calculation model of NPP structures (Fig.1) created by VUT Brno [5] and modified by STU Bratislava has 161 856 elements and 135 629 nodes [2]. The foundation of the reactor building is embedded into the rock subsoil.

2 SEISMIC EVALUATION METHODOLOGY

To provide input excitations to structural models for sites with no strong ground motion data, it is necessary to generate synthetic accelerogram. It has long been established that due to parameters such as geological conditions of the site, distance from the source, fault mechanism, etc. different earthquake records show different characteristics [6 - 9].

The program COMPACEL was created by J. Králik [2] to generate synthetic accelerograms. The methodology of structure resistance verification is elaborately described in [1 - 4]. There are illustrated the procedures, requirements and criterion of calculation models and methods for design of structure reliability. There are two principal methodology available for seismic design of NPP structures - deterministic (SMA- seismic margin assessment) and probabilistic (SPRA – seismic probabilistic risk assessments). The CDFM method is very similar to the design procedure followed in the industry, except that the parameter values have been liberalized. The objective of seismic margin assessment (SMA) is to determine for a nuclear power plant the high-confidence-of-a-low-probability-of-failure (HCLPF) capacity for a pre-selected seismic margin earthquake (SME), which is always chosen higher than the design basis input. In probabilistic terms, the HCLPF is expressed as approximately a 95% confidence of about a 5% or less probability of failure.

Based on Kanai's investigation regarding the frequency content of different earthquake records [7], Tajimi proposed the following relation for the spectral density function of the strong ground motion with a distinct dominant frequency

$$S(\omega) = \frac{\left[1 + 4\xi_g^2 \left(\omega/\omega_g\right)^2\right]}{\left[1 - \left(\omega/\omega_g\right)^2\right] + 4\xi_g^2 \left(\omega/\omega_g\right)^2} S_0 \tag{1}$$

Here ξ_g and ω_g are the site dominant damping coefficient and frequency, and S_0 is the constant power spectral intensity of the bedrock excitation. The Kanai-Tajimi power spectral density function may be interpreted as corresponding to an "ideal white noise" excitation at the bedrock level filtered through the over-laying soil deposit at site [7].

3 ACCEPTABLE EVALUATION METHODS

For seismic analyses of structures and technological equipment, following methods are acceptable [2, 7 - 9]:

- Response Spectrum Modal Analysis Method – RSMAM,
- Methods of direct time integration of the motion equations system (Linear Time History Method – LTH and Non-linear Time History Method – NTH are discerned),
- Equivalent Static Method – ESM (or also “approximate equivalent static seismic loads method”).

The equivalent static seismic loading method is used in cases when a structure or an equipment component is, in the viewpoint of the mechanics, a simple single-degree of free-

dom (SDOF) or 2-degree-of-freedom (2-DOF) system and when the intention of the analysis is to determine only the seismic forces and moments in the point of anchorage to the civil structure or to perform the stress analysis in some critical cross-section (when such a simple substitution is obviously sufficient).

The spectral analysis is based on linear behavior of the structures, while damping takes into account the plastic deformations and the over thrust of friction-type connections. The response spectrum will be obtained by a combination of a response magnitudes for the individual shapes by the CQC method (considering the proximity) as follows [7]:

$$R_{CQC} = \left\{ \left| \sum_{i=1}^{N} \sum_{j=1}^{N} k.\varepsilon_{ij}.R_i.R_j \right| \right\}^2, \qquad k = \begin{cases} 1 \; ak \; i = j \\ 2 \; ak \; i \neq j \end{cases}, \qquad r = \omega_j/\omega_i, \tag{2}$$

where $\varepsilon_{ij} = \dfrac{8\left(\xi_i \, \xi_j\right)^{1/2}\left(\xi_i + r\xi_j\right).r^{3/2}}{\left[1-r^2\right]^2 + 4\xi_i \, \xi_j \, r\left(1+r^2\right) + 4\left(\xi_i^2 + r\xi_j^2\right).r^2}$ and ξ_i is the modal damping.

Overall response R_k in the cross-section k has been obtained by the envelope of combinations of responses alongside the individual excitation directions in the direction of the axes X, Y and Z.

$$R_k = \max\{R_{xk} + 0{,}4R_{yk} + 0{,}4R_{zk}\,;\; R_{xk} + 0{,}4R_{yk} + 0{,}4R_{zk}\,;\; R_{xk} + 0{,}4R_{yk} + 0{,}4R_{zk}\} \tag{3}$$

where R_{xk}, R_{yk} and R_{zk} are the responses in the cross-section k from excitation by the acceleration spectra in the direction X, Y and Z.

Test segment	Static resistance [N]	Dynamic resistance experimentally determined				
		Horizontal force [N]		Vertical force [N]		Ratio [%]
		Min	Max	Min	Max	
1A	3 000	0	1040	450	810	35
2A	12 000	0	6370	2700	4864	53
3A	11 000	0	12530	5400	9730	88

Table 1. Recapitulation of the experimental tests of OBO Bettermann segments

All tested segments were satisfied for the static and dynamic loads defined in Tab.1. In the case of the tested connection OBO2A the plastic deformation of 9mm occurred, but this connection was not damaged. This connection was not used in the final cable trays structures in NPP finally.

4 NUMERICAL ANALYSIS OF THE SEISMIC RESISTANCE

The seismic resistance of the various typical cable support structures based on OBO Bettermann segments were numerically analysed in software ANSYS (Fig.3) [1].

The principal structures was made from the columns 5xI8/3680, beams 6xUS7/1500, consoles 60xAS30/41/410 and the cable segments. These structures were used with the cable trays 48xWKSG140/1500 (OBO1Z) and the cable ladders 44xLG640N/1500 (OBO1R) (Fig.4). The seismic response was solved by the method of the seismic response spectra from the floor spectra envelope in the horizontal direction as well as vertical direction at the level of the ceiling +5,4 m; upon considering 7% damping [1] (Fig.3).

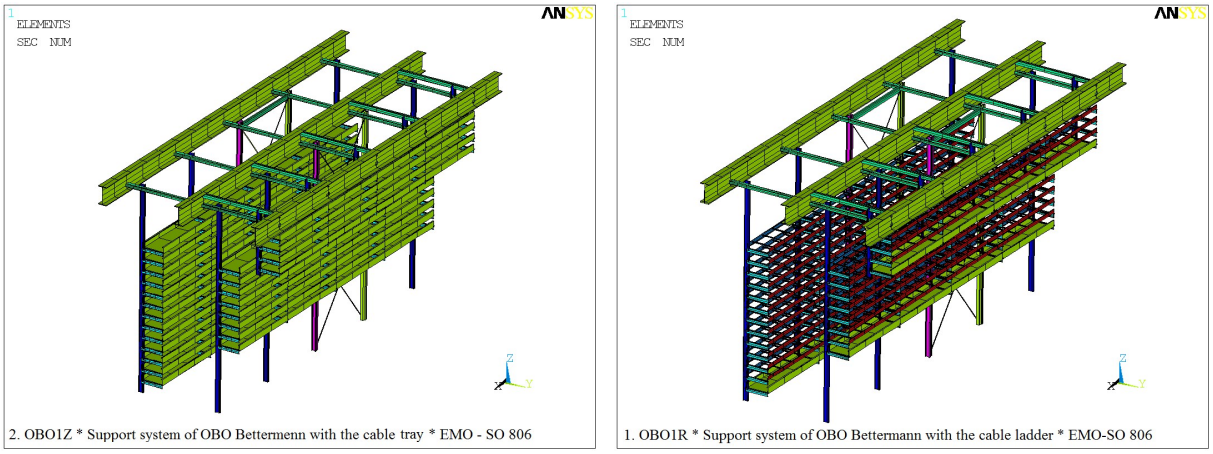

Fiure.2. Calculation models of the support structures with the cable tray EKS640 (OBO1Z) and the cable ladder LG640 (OBO1R)

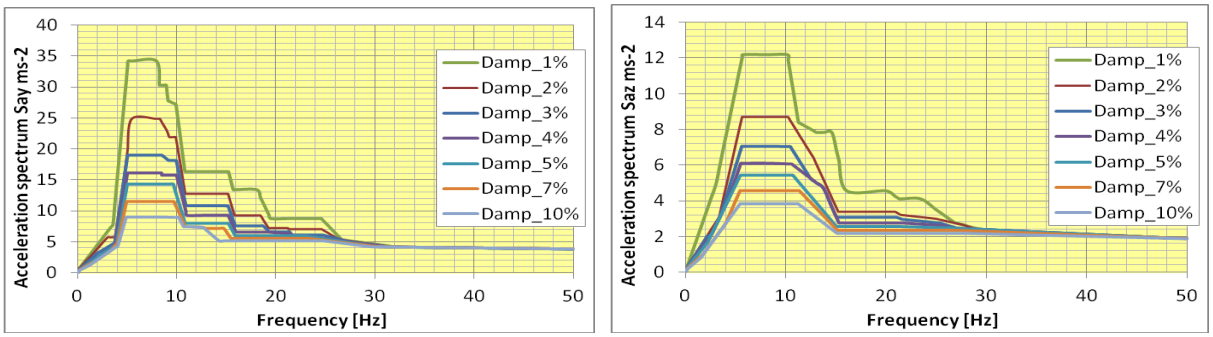

Figure 3. FRS for horizontal and vertical direction at the level of +5,4m of SO805/806

The value of the HCLPF parameter depends on the equipment structure or component resistance (R) and the corresponding effect of action (E) using elastic or inelastic behavior. Generally, it follows

$$\text{HCLPF (CDFM)} = (\text{FS})_{ep} \cdot \text{PGA}_{RLE} = \text{SL-2} \tag{4}$$

Model	f_o[Hz] in direct. X	Part. factor [%]	f_o[Hz] in direct. Y	Part. factor [%]	f_o[Hz] in direct. Z	Part. factor [%]
OBO1Z	10.27	84.8	3.88	84.3	9.64	47.3
OBO1R	0.85	58.5	2.98	76.5	8.99	67.4

Table 2. Principal eigenvalues of the OBO Bettermann structures

Model	Cable masses [kg/bm]	Column [g]	Beam [g]	Console [g]	Bracing [g]
OBO1Z	390	0.33	0.31	5.79	6.85
OBO1R	390	0.18	0.29	0.19	3.70

Table 3. Parameter HCLPF for the segments of OBO Bettermann structures

The optimal configuration of the support systems of the cable trays was determined by the acceleration peaks of FRS, which are in intervals 5-10Hz [1]. The seismic effective structures are with the principal modes out from this interval. There are presented two different conceptions of the structures. The principal frequencies of model OBO1Z and OBO1R are out of this

critical interval in direction *X* and *Y* (Tab.2). The total masses of the structure OBO1Z is equal to 19 719ton and OBO1R is equal to 22 176ton .

The seismic resistance of these support structures is determined by the lowest resistance of the structure segments (Tab.3). The minimal HCLPF parameter of the structure OBO1Z is 0.31g and the structure OBO1R is 0.18g.

5 CONCLUSIONS

This paper presented the methodology of the seismic reevaluation of NPP in Mochovce due to new results from the geological and seismic-tectonic monitoring of this site. The deterministic methodology of seismic design based on CFDM methodology was presented. The synthetic spectrum compatible accelerograms generated in program COMPACEL (created by Králik) were presented in comparison with requirements ASCE4/98 standard. The methodology of the seismic resistance of the cable support structures were described. This methodology was used for the optimal design of the cable support systems from the structural elements of OBO Bettermann experimentally tested.

Acknowledgements

The project was performed with the financial support of the Grant Agency of the Slovak Republic (VEGA 1/1039/12).

REFERENCES

[1] IAEA, *Safety Guide No. 28, Seismic Evaluation of Existing Nuclear Power Plants*, IAEA, Vienna, 2003.

[2] J. Králik, *Safety and Reliability of Nuclear Power Buildings in Slovakia. Earthquake-Impact-Explosion*. Ed. STU Bratislava, 307pp. 2009.

[3] J. Králik, Risk Assessment of Safety Analysis of NPP Structures Due to Earthquake Events, *Applied Mechanics and Materials,* Vol 769, pp 235-240, © Trans Tech Publications, Switzerland, doi:10.4028/www.scientific.net/AMM.769.235, 2015.

[4] J. Králik, Comparison of Probabilistic and Deterministic Assessments for Evaluation of Seismic Safety of Nuclear Power Plants in Slovakia. In: *First European Conference on Earthquake Engineering and Seismology*. 3-8 September, Geneve, p. 422, 2006.

[5] J. Novotný, V. Kanický, V. Salajka, P. Štepánek, Seismic Analysis of selected structures of the NPP Dukovany. Influence of Modeling on the Corectness of Results. In proc. *1.th international conference. DYNA 2006*, VUT Brno, UAM Brno, ČSM VEDA Brno. Pp. 229-237, ISBN 80/214/3164-4.

[6] J. Králik, M. Šimonovič, Earthquake response analysis of nuclear power plant buildings with soil structural interaction. *Mathematics and Computers in Simulation 50. IMACS*/Elsevier Science B.V., Pp. 227-236, 1999.

[7] R. W. Clough, J. Penzien, *Dynamics of Structures*, Mc Graw-Hill, Inc. 1998.

[8] Z. X. Li, Z. C. Li, W. X. Shen, Sensitivity analysis for floor response spectra of nuclear reactor buildings, *Hedongli Gongcheng / Nuclear Power Engineering*, 26 (1), pp. 44-50. ISSN: 02580926, 2005.

[9] W. T. Lin, M. H. Hsieh, Y. C. Wu, C. C. Huang, Seismic Analysis of the Condensate Storage Tank in a Nuclear Power Plant. Journal of Vibroengineering, 14 (3), pp. 1021-1030. ISSN: 1392-871, 2012.

COMPDYN 2019
7th ECCOMAS Thematic Conference on
Computational Methods in Structural Dynamics and Earthquake Engineering
M. Papadrakakis, M. Fragiadakis (eds.)
Crete, Greece, 24–26 June 2019

ASSESSMENT OF PROBABILITY VARIABLES OF RELIABILITY ANALYSIS FOR SEISMIC DESIGN OF UNDERGROUND STRUCTURES

Young-bin Park[1], Do Kim[1], Seung-beom Ock[1], Yo-Seph Byun[2], Seong-Won Lee[2]

[1] Woosung D&C
CO 06562, Seoul, Korea
civilkkaby@empas.com

[2] Korea Institute of Civil Engineering and Building Technology
CO 10223, Seoul, Korea
byunyoseph@kict.re.kr

Abstract

In order to estimate failure probabilities of underground structure under seismic load, probability variables should be considered in reliability analysis. Normally underground structures are applied from both vertical and horizontal loads at the same time, and have nonlinear boundary conditions, so the behavior of structure not correspond to the superposition principle. In first, in order to obtain load(L) in the limit state function(Q=R-L), member forces of underground structure applied combined loads in seismic condition are analyzed from 2D frame model, and then combined probability variables such as means and variances are determined from a new approach developed in this study. Probabilities of failure are calculated on load combinations by using MCS(Monte-Carlo Simulation) technique. As a result, from the estimation of reliability indices on load combinations, target reliability index in seismic condition are determined in order to develop a specification for limit state design of underground structures.

Keywords: Failure Probability, Underground Structures, Seismic Condition, Limit State Function, Reliability Analysis, MCS, Target Reliability Index.

1 INTRODUCTION

Recently AASHTO presented "LRFD 2017 Road tunnel design and construction guide specifications" [1], and BSI suggested "PAS 8810 - Design of concrete segmental tunnel linings - code of practice" [2]. Korea also has been developing the LSD specification for underground structures and has been researching probabilities of variables and establishing of target reliability indices.

In this study, structural analysis is performed to 2D frame model applied all of loads entirely with nonlinear boundary conditions, because analysis of underground structure not correspond to the superposition principle. In order to obtain probability variables of resistance(R) and load (L) for reliability analysis in seismic condition, existing research materials and pre-researched data are considered.

It is calculated to probabilities of failure in the limit state function through MCS (Monte-Carlo Simulation), then, probabilities of failure convert to reliability indices by function described by Nowak and Collins (2013) [3]. The analysis result in strength limit state are made out in order to compare with assessment of underground structure in the general condition, then target reliability index is suggested in final.

2 REVIEW MODEL

2.1 Modeling and Boundary Condition

In this study, the analysis model of underground structure is as shown in Fig. 1, and the model is consist of 2D frame members and nonlinear boundary conditions.

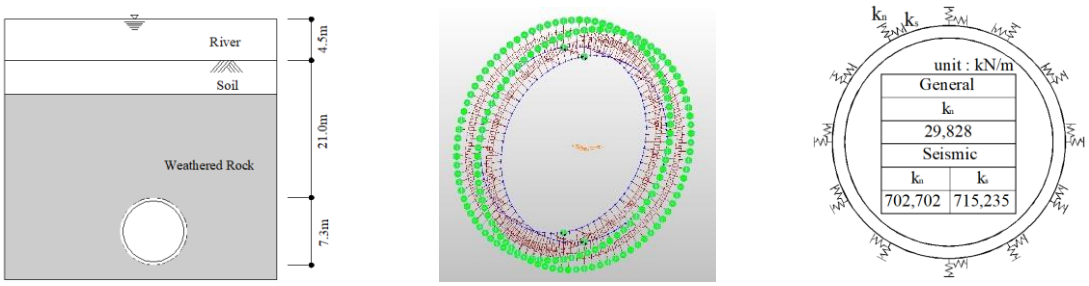

Figure 1: Analysis model of underground structure

2.2 Applied Loads

The loads applied on underground structure are considered to self-weight, horizontal & vertical earth pressure, water pressure, and earthquake load as shown in Fig. 2.

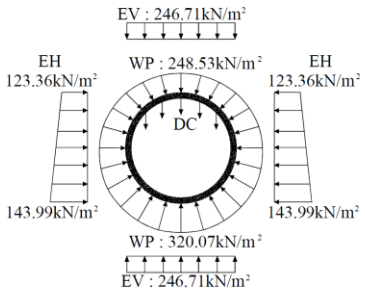

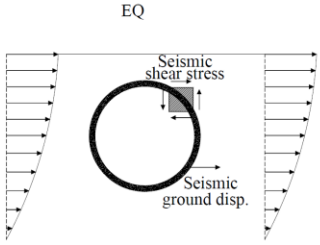

Type Name		Load Cases
L1	DC	Self-weight (Dead Load)
L2	EH	Horizontal Earth Pressure
L3	EV	Vertical Earth Pressure
L4	WP	Water Pressure
L5	EQ	Earthquak Load

Figure 2: Loads applied on underground structure

3 STRUCTURAL ANALYSIS

3.1 Analysis in the General Condition

The enveloped result of load combinations in the general condition is shown as follows, the results are performed through preliminary study [4].

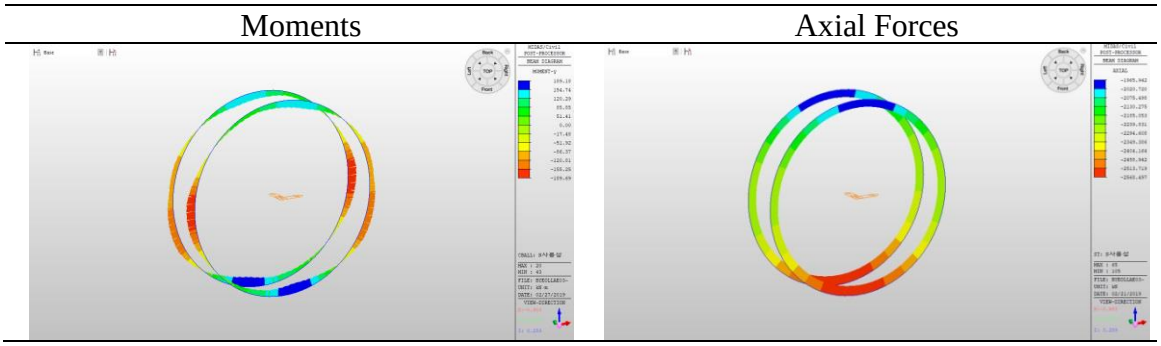

Figure 3: Member forces in the general condition

3.2 Analysis in the Seismic Condition

Underground structures in the seismic condition are loaded from inertia force and ground displacement as well as seismic shear stress. Thus, member forces generated by inertia force and ground displacement load are shown in Fig. a, member forces generated by seismic shear stress are shown in Fig. b.

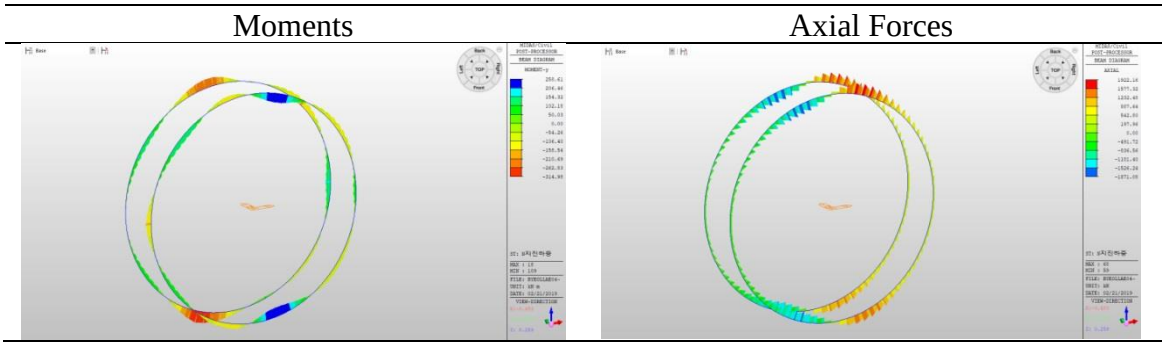

a. Member forces generated by inertia force and ground displacement

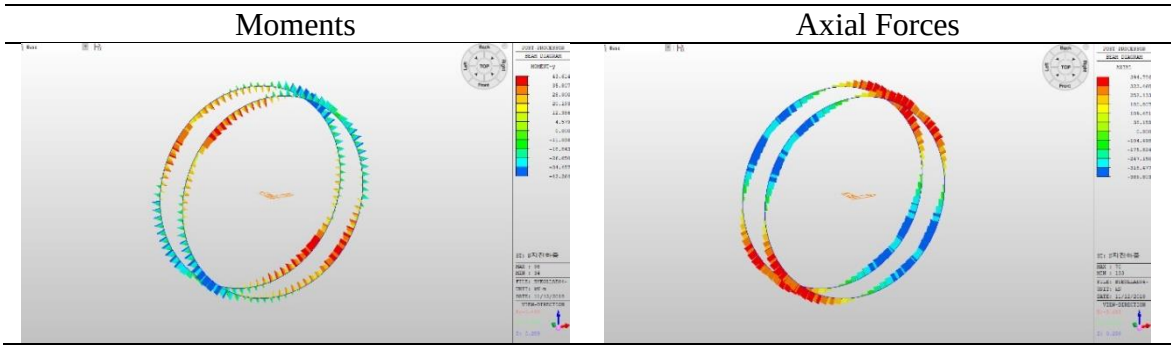

b. Member forces generated by seismic shear stress

Figure 4: Member forces in the seismic condition

4 RELIABLITY ANALYSIS

4.1 Probability variables of loads

It is considered to probability variable which is presented by Nowak as shown Table 1 [5]. As mentioned in the introduction, however, variations separately are not applicable to analysis reliability for underground structures because of not corresponding to the superposition principle. Thus, the variance of combined COV of all loads which are proposed through the research process with KICT is calculated and applied for this study.

	Loads	Bias factors	Variations (COV)
L1	Dead load	1.05	0.10
L2	Horizontal earth pressure	0.95	0.15
L3	Vertical earth pressure	1.00	0.14
L4	Water pressure	0.90	0.15
L5	Seismic load	0.95	0.15
L_{comb}	Combined load (Seismic)	0.95	0.15
L_{comb}	Combined load (General)	1.00	0.37

Table 1: Probability variables of loads

4.2 Probability variable of resistance

The probability variable of resistance, COV(coefficient of variation), is used 0.08 which is presented by Nowak and Rakoczy [6].

4.3 MCS (Monte Carlo Simulation)

In this study, MCS program was developed to calculate probabilities of failure, results are obtained as shown in Fig. 5.

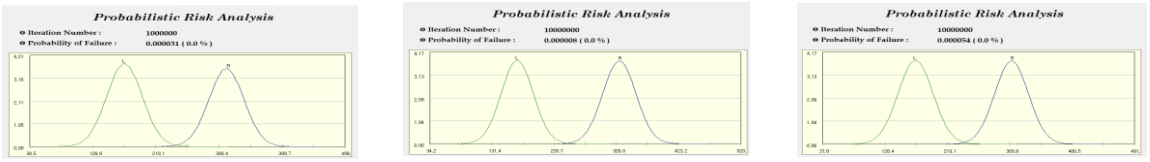

Figure 5: Applied loads on underground structure

4.4 Probability of failure and reliability index

The probability of failure and reliability index for the existing design cases (5sections) in Korea are calculated as following Table 2.

Models	Prob. of failure (P_f)	Reliability Index(β)
M-1	3.10e-5	4.01
M-2	8.00e-6	4.31
M-3-a	5.40e-5	3.87
M-3-b	1.23e-7	5.16
M-3-c	1.00e-11	6.71

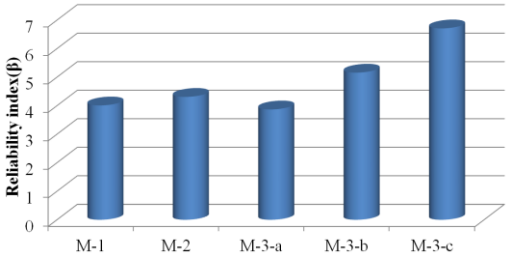

Table 2: Probability of failure and reliability index for the existing design cases.

5 REVIEW OF RELIABILITY INDEX

The load combinations for reviewing the target reliability index are based on the AASHTO LRFD TUNNEL SPECIFICATION (2017) [1], and the load factors that affect the section force are analyzed by calculating the member forces according to the change of load factors in units of 0.05. Also, the sensitivity of the load is identified by analyzing of the reliability index depend on the change of load factors.

5.1 Sensitivity of load factors

The load combinations in this study are considered as follows.

LC 1 : 1.25DC + 1.35EV + 1.35EH + 1.00WA + 1.00EQ

LC 2 : 1.25DC + 1.35EV + 0.75EH + 1.00WA + 1.00EQ

The results according to load combination are as following Fig. 6, from the results, it is confirmed that horizontal earth pressure (EH) and seismic load (EQ) are more sensitive than others in the variation of member forces according to the change of load factors.

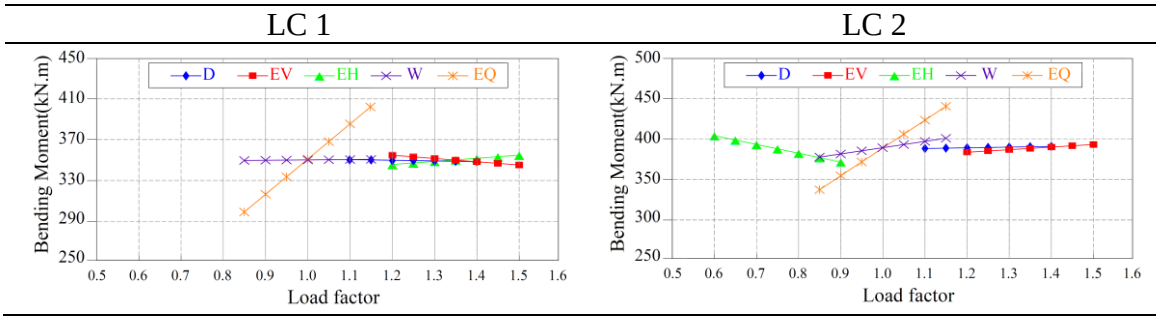

Figure 6: Variations of member forces depend on load combinations

5.2 Review on reliability index according to variation of load factors

The reliability indices according to variation of load factors are calculated as follows, earthquake load (EQ) mainly effects to the variation of reliability index as shown Table 3.

	Adjustment of Factors						
	-0.15	-0.10	-0.05	0.0	+0.05	+0.10	+0.15
EH	2.46	2.37	2.29	2.20	2.11	2.03	1.94
EQ	1.38	1.65	1.93	2.22	2.47	2.74	3.02

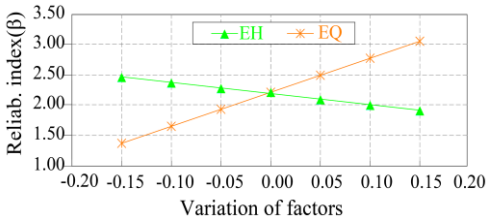

Table 3: Reliability Indices according to variations of load factor.

Earthquake load is not only an extreme load, but also a main load to effect to the variation of reliability index. Thus, it is reasonable to apply the load factor of earthquake load is 1.00, it may be applicable to consider the code calibration of horizontal earth pressure depending on the regional characteristics.

5.3 Target reliability index

For bridge structures, a sufficient number of bridges have studied to establish the target reliability. Nowak presented a normal target reliability index of 3.5 in the NCHRP Report 368

[7], and Ghosn et al. proposed a seismic target reliability index of 2.4 ~ 2.9 in the NCHRP Report 489 [8].

On the other hand, though enough research has not been done yet for underground structures, it may propose that the target reliability in seismic is 2.3 considering the existing research on the bridge and results of this study. And, the target reliability index was proposed through limited number of design sample, so it should be to advance based on sufficient number of samples and data in the future.

6 CONCLUSIONS

- It is conformed that horizontal earth pressure (EH) and earthquake load (EQ) are more sensitive than others in the seismic condition.
- It is presented that the earthquake load factor is 1.00 in this study, and that the code calibration of horizontal earth pressure may be needed depending on the regional characteristics.
- In the study, considering the existing research on the bridge and results of this study, it is supposed that target reliability is 2.3 under seismic condition.

ACKNOWLEDGMENT

This research was supported by a grant (19SCIP-B105148-05) from the Construction Technology Research Program, funded by the Ministry of Land, Infrastructure, and Transport (MOLIT) of the Korean government.

REFERENCES

[1] AASHTO. (2017), *AASHTO LRFD - Road Tunnel Design and Construction Guide Specifications*, AASHTO, Washington DC., USA

[2] British Standards Institution. (2015), *PAS 8810 - Design of concrete segmental tunnel linings - Code of practice*, PSI, London, U.K

[3] Nowak, A. S., Collins K. R., "Reliability of structures", CRC Press, New York, 2013.

[4] Y.S. Byun, S.W. Lee, etc., "A Study of Reliability Analysis for the Tunnels", International Conference on Environmental and Civil Engineering Innovation, 2018.

[5] Nowak, S. A., Park, C-H, and Ojala, P, "Calibration of design code for buried structures", *Canadian Journal of Civil Engineering*, V. 28, No. 4, 2001, pp.574-582.

[6] Nowak Andrzej S. and Rakoczy, Anna M. "Statistical Resistance Models for R/C Structural Components", ACI SP-284-6, Vol. 248, pp. 1-16, 2012

[7] Nowak, A. S. (1999) Calibration of LRFD Bridge Design Code, NCHRP Report 368, National Academy Press, Washington, DC.

[8] Ghosn, M. Moses, F. and Wang J. (2003) Design of Highway Bridges for Extreme Events, NCHRP Report 489, National Academy Press, Washington, DC.

COMPDYN 2019
7th ECCOMAS Thematic Conference on
Computational Methods in Structural Dynamics and Earthquake Engineering
M. Papadrakakis, M. Fragiadakis (eds.)
Crete, Greece, 24–26 June 2019

ON THE EQUAL DISPLACEMENT APROXIMATION FOR MID-RISE REINFORCED CONCRETE BUILDINGS

Yeudy F. Vargas[1], Luís G. Pujades[1], José R. González-Drigo[1], Rodrigo E. Alva[1] and Luis A. Pinzón[1]

[1]Universitat Politècnica de Catalunya, Dep. of Civil and Environmental Engineering
C. Jordi Girona 1-3, Campus Nord UPC, Barcelona, Spain
{yeudy.felipe.vargas, lluis.pujades, jose.ramon.gonzalez, rodrigo.esteban.alva, luis.pinzon}@upc.edu

Abstract

The equal displacement approximation is a well-known procedure for estimating the non-linear behavior of structures subjected to earthquake ground motions. This procedure plays a significant role in current seismic design, since it constitutes the basic assumption for defining strength reduction factors. In this paper, calculation of the performance point based on this rule is used to estimate engineering demand parameters such as those obtained by advanced probabilistic non-linear dynamic analysis, NLDA. We present a modification to the classic approach, to improve the predictability of the equal displacement rule. Uncertainties in seismic action and structural properties are considered. Mid-rise reinforced concrete buildings will be used as a testbed. To obtain a representative sample of buildings for statistical analysis, we describe the development through implementation of a numerical tool for calculating probabilistic NLDA. This tool, which is expected to evolve into interoperable software for assessing the seismic risk of structures, is developed within the framework of the KaIROS project. The results presented in this paper could be used to estimate the seismic risk of structures in a very simplified manner.

Keywords: equal displacement approximation, probabilistic non-linear dynamic analysis, mid-rise reinforced concrete buildings, KaIROS project

1 INTRODUCTION

Disaster risk reduction is a major concern of world communities. The 2030 Agenda for Sustainable Development includes 17 goals to end poverty, fight inequality and injustice and tackle climate change. The eleventh goal is *sustainable cities and communities*, as half of humanity now lives in urban areas and almost 60 per cent will live in cities by 2030. Thus, an important target for 2030 is to ensure universal access to basic services and to adequate, safe, affordable housing. Achievement of this target is at risk if the negative impact of catastrophes is not reduced. The importance of resilient communities has been shown in past and recent earthquakes. However, the negative impact of these catastrophic events on mankind is increasing due to

globalization. Sustainability, resilience and well-being are affected negatively at global level. Accordingly, a continuous effort to reduce seismic risk is fundamental to develop a stronger society.

Seismic loss mainly depends on the capacity of civil structures to withstand strong ground motions. Thus, the development of advanced numerical tools for assessing the seismic response of civil structures will contribute positively to the planning of optimal strategies for reducing seismic risk. Currently, several research projects are focused on reducing seismic risk. One is the Kairos project [1], which is aimed at maintaining and increasing the resilience and sustainability of communities against earthquakes. One research area in the Kairos project is the development of numerical tools to estimate the seismic risk of structures. In this paper, we present the development of one of the tools. To correctly estimate seismic risk scenarios, uncertainties in seismic hazard action and in the main features of the structures should be considered. The numerical tool presented herein takes into account uncertainties relating to the geometry of the structure, the mechanical properties of the materials and the seismic action, amongst many others. Moreover, the tool can be used to estimate several engineering demand parameters (EDP), which can be related to seismic damage of structures. The tool is developed through implementation of a hypothetical case study. To achieve this, the probabilistic seismic response of mid-rise reinforced concrete buildings is calculated via NLDA. A thousand numerical models were created and subjected to a set of earthquake records with different properties. The numerical tool, combined with information on variables characterizing the exposure of an urban environment, will help to estimate the seismic risk of the area precisely. However, the main target of the paper was to develop a procedure based on the equal approximation rule for estimating EDPs in a very simple way. Due to the amount of numerical data available, this simplified procedure could be developed easily based on a maximum correlation criterion.

2 PROBABILISTIC CONSIDERATIONS

The main factors affecting earthquake risk are hazard, exposure and vulnerability. Hazard refers to seismic actions and their occurrence probabilities. Probabilistic seismic hazard analysis [2] is estimated based on past seismicity, statistical models, ground motion prediction equations and site effects. Exposure concerns structures, facilities and properties in the stricken area. The quantification of exposure requires a considerable amount of data on facilities, population and built environment, including special and essential buildings and lifelines. Vulnerability is related to susceptibility to damage of exposed goods. It connects hazard and exposure to obtain risk, that is, expected damage and cost. Regarding exposure, it has been a common practice to classify structures with similar features within a structural class. For instance, buildings are often classified as low-rise (1-3 stories), mid-rise (4-7 stories) and high-rise (>7 stories). Of course, many other features are used to identify a structural class. Generally, the seismic behavior of buildings in the same structural class is represented using probabilistic functions. This classification within structural classes simplifies the characterization of exposure when the seismic risk is estimated at urban level. The finer the characterization of the exposure, the more precise is the quantification of the seismic risk. Thus, inventory is a critical issue in risk assessments, and geographical information systems (GIS) can be used to enhance characterization at urban scale. Thus, if precise inventory information is available, it should be included when exposure is modelled.

2.1 Characterizing exposure

It is important to distinguish between two types of random variables when exposure is characterized: those that refer to the population of buildings, for example, in a neighborhood, district or city, and those that refer to intrinsic properties of a building, which can be considered epistemic uncertainty. Consideration of these types of random variables depends on whether the intended application is the classes of structures considered in urban risk assessment or individual buildings. Modeling the random variation in building-to-building structural characteristics within a structural class is standard practice. This modelling must reflect the epistemic uncertainty and how many structural types are grouped together into a single class.

2.2 Building-to-building variation

The main variables that characterize buildings in a structural class are random. In this section, we explain how building-to-building random variation will be considered within a structural class. Buildings belonging to the structural class 'reinforced concrete mid-rise buildings' are used as a testbed. Through implementation of this simulation, a numerical tool will be created that allows consideration of specific distributions within a structural class. Several variables that characterize a building are considered as input random variables. These variables will be the input of the software to be developed, once the simulation is achieved. In real cases, characterization of these random variables strongly depends on the information stored by local institutions. This information can be enhanced using GIS tools. For the purpose of the present study, the distribution of these variables will be assumed, and it will be mainly uniform or Gaussian. Thus, the number of stories, N_{st}, the number of spans, N_{sp}, the story height, H_{st} and the span length, S_l, are considered as the input random variables. N_{st} follows a uniform, discrete distribution in the interval (4, 7); N_v also follows a uniform, discrete distribution in the interval (2, 8). H_{st} is distributed uniformly in the interval (2.8, 3.2) m. S_l is distributed uniformly in the interval (4, 6) m. Functions based on the design of various hypothetical structures belonging to the structural class are used to assign the cross area to the structural elements. These models were designed by supposing that they are located in a moderate seismic area. Based on the results, several functions are developed. Thus, the width, W_c, and depth, D_c, of the columns of the first story will depend on the number of stories of the building and will be calculated using the following equation:

$$W_c \; or \; D_c = c_1 * \ln(N_{st} - c_2) + c_3 * \Phi_{1,0} + c_4 \tag{1}$$

where c_n are coefficients that could be adjusted depending on the data distribution of the analyzed area. For the study, $c_1 = 0.15$, $c_2 = 3$, $c_3 = 0.02$ and $c_4 = 0.35$. $\Phi_{1,0}$ is the standard normal distribution. Note that the columns are not necessarily square, that is, one random sample is generated for the width and one for the depth of the columns according to Equation 1. Moreover, the values generated are rounded to the nearest multiple of 5 cm. Figure 1a shows the size of the columns in the first story and Figure 1b shows the cross-sectional area. For the upper stories, the size of the columns will decrease systematically by 5 cm every two stories. To assign the steel percentage of the columns, ρ_c, a continuous Gaussian distribution is assumed. The mean value is 1.5% and the standard deviation is 0.15%. The width of the beams will also depend on the number of stories of the building model and will be calculated using the following equation:

$$W_b = b_1 * N_{st} + b_2 \tag{2}$$

where b_n are again coefficients that depend on the data distribution of the urban area. For the hypothetical case of study, $b_1 = 0.0053$ and $b_2 = 0.2947$. The depth of the beams will not only depend on the number of stories but also on the span length. The following equation has been used to calculate the depth of the beams:

$$D_b = g_1 * N_{st} + g_2 * S_l + g_3 \quad (3)$$

where g_1 = 0.0157, g_2 = 0.075 and g_3 = -0.0157. A random term was not considered for the beams. Either the coefficients, or the type of equation considered, can be modified so that they better represent the urban environment under consideration. Figure 2a shows the width of the beams as a function of the number of stories and Figure 2b depicts the depth of the beams as a function of the number of stories and the span length. To assign the steel percentage of the beams, ρ_b, a continuous Gaussian distribution is assumed whose mean value is 1% and standard deviation is 0.1%.

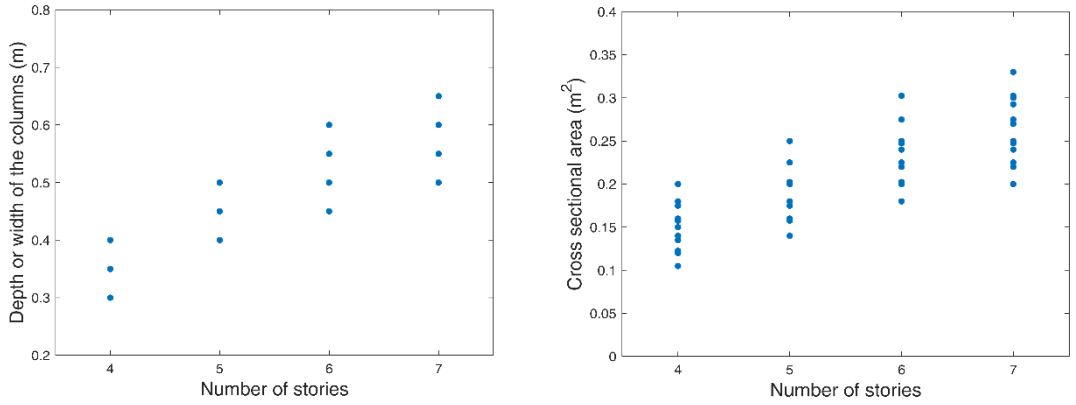

Figure 1 a) Depth and width of the columns of the first story and b) Cross-sectional area

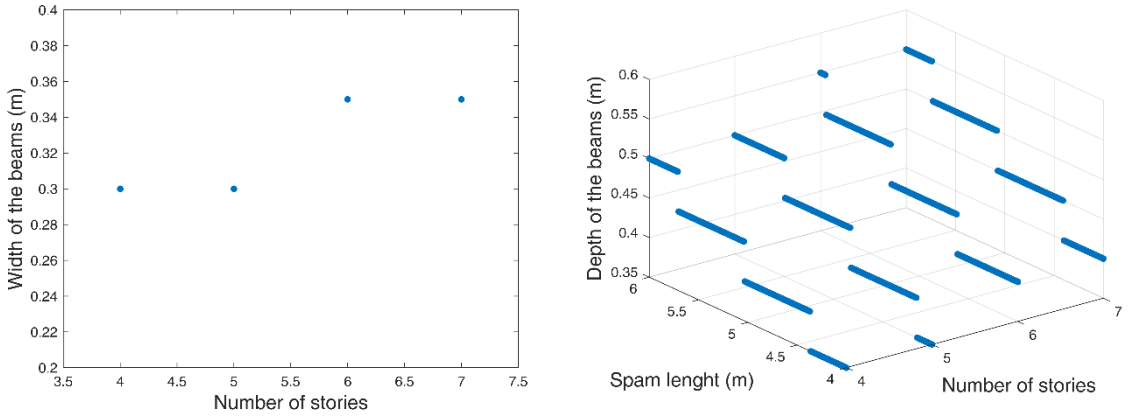

Figure 2 a) Width of the beams as a function of the number of stories and b) Depth of the beams as a function of the number of stories and the span length

2.3 Epistemic uncertainty

Several random variables should be considered when the behavior of a single building is modelled. Amongst many other variables, the mechanical properties of the materials, the loads acting on the structure and the participation of non-structural elements introduce epistemic uncertainty to the system. In this paper, the live loads, *LL*, the superimposed loads, *SL*, the compressive strength of the concrete, *fc*, the tensile strength of the steel, *fy*, the elastic modulus of

the concrete, *Ec*, and the elastic modulus of the steel, *Es*, are considered random variables. A continuous Gaussian distribution is assumed for these variables. The mean values, μ, and standard deviations, σ, are summarized in Table 1.

Variable	μ	σ
LL (kPa)	1	0.15
SL (kPa)	2	0.3
fc (kPa)	2.1e4	2.1e3
fy (kPa)	4.2e6	4.2e5
Ec (kPa)	2e7	2e6
Es (kPa)	2e8	2e7

Table 1 Mean and standard deviation of the random variables

2.4 Monte Carlo simulation

The Monte Carlo method is a relatively modern technique that allows modelling of complex systems with a large number of random parameters. This method has been used to generate 1000 random samples of buildings, according to the established distributions described above. An algorithm was implemented with MATLAB to this end. This algorithm will be part of the source code of the software under development. Figure 3 shows ten building samples generated with this algorithm. In this figure, we can see how the geometrical properties of the models vary within the intervals considered.

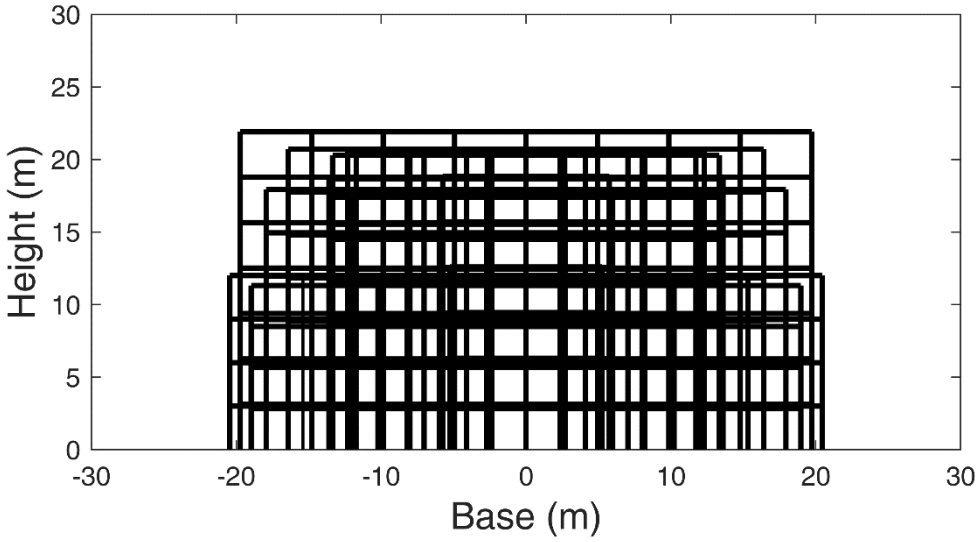

Figure 3 Building samples generated by the code

One question at this point relates to the validity of the models that are generated: do they properly describe the behavior of real structures? This question can be answered by comparing some properties of the models with a physical property of the real structures. For instance, Figure 4a shows a comparison between the fundamental period of the simulated models and those measured in real reinforced concrete buildings [3]. The fundamental periods of the buildings that are generated agree with those measured on real structures. Moreover, if the fundamental periods are tabulated into a histogram (Figure 4b) one can observe that the values are in agreement with those expected, according to the number of stories.

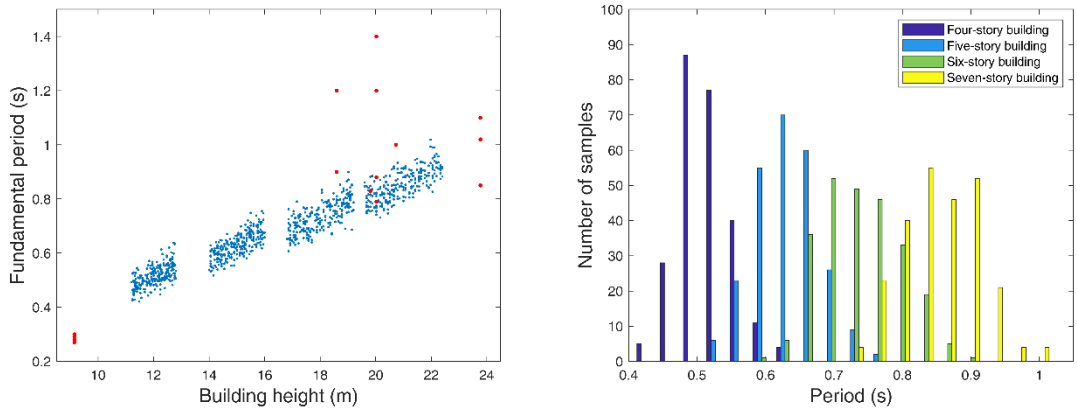

Figure 4 a) Variation in the fundamental period as a function of the building height and b) Histogram of the fundamental periods of the structural models that are generated

3 SEISMIC HAZARD

One of the main important sources of uncertainty in estimations of the seismic risk of structures is the random variability of the ground motion. There are several methodologies to properly select ground motion records that are consistent with the site-dependent spectral shape. However, the main objective of this paper is not to assess the seismic risk of an area, but to develop a simplified procedure for estimating EDPs, like those obtained with NLDAs. With this objective in mind, the most important requirement is to have earthquakes that demand the structural models at different intensity levels. To achieve this, based on the fundamental period range of the generated models (see Figure 4b), groups of earthquakes are selected whose mean spectral acceleration in the interval (0.4-1) s is between a stripe limited by two intensity levels. The intensity levels defining the upper and lower limits of each stripe range from 0 to 1.5 g at intervals of 0.15 g. The objective is to obtain 1000 records (as many as structural models generated) whereby 100 earthquake records per interval should be found. The database of Ambraseys et al. [4] is considered for the earthquake selection. Figure 5 shows 100 earthquake records (approximately 10 per interval) selected according to the procedure described.

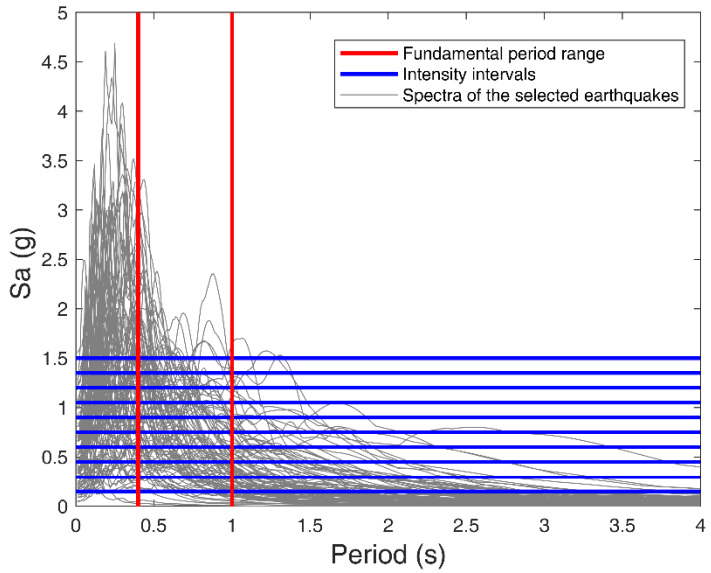

Figure 5 Response spectra of the selected earthquakes

However, because of the high number of earthquakes requested, several will be scaled versions of the ones that naturally fulfil the interval condition. Thus, if an interval does not contain 100 earthquakes records, because there are not enough records within the database, the number of missing records will be selected from the previous interval. This criterion avoids excessive scaling of the earthquake records.

4 NON-LINEAR DYNAMIC ANALYSIS

An NLDA allows simulation of the time history response of a structure, which enters or does not enter the nonlinear range when it is subjected to an earthquake. This analysis allows calculating EDPs such as the maximum displacement at the roof, δ_{roof}, the maximum interstory drift ratio (MIDR) and damage indices, among others. A key issue when an NLDA is performed is the hysteresis law assigned to the structural elements. The modified Takeda hysteresis law [5] has been used to perform the simulations. In-cycle strength degradation has also been considered. The yielding surfaces are defined by the bending moment-axial load interaction diagram for columns and bending moment-curvature for beams. Based on these modeling assumptions, the 1000 NLDA are performed. Ruaumoko software has been used to calculate the structural analyses [6]. Figures 6a and 6b show the histograms of δ_{roof} and MIDR, respectively. These EDP are commonly used in several methodologies to assess the seismic risk of structures. The maximum global drift ratio (MGDR), obtained as the ratio between the δ_{roof} and the height of the building, is also considered as EDP. Note that the MIDR is the envelope of the MGDR, as can be seen in Figure 7. Another important aspect of the relationship between these two EDP is their high correlation, which indicates that if one of them is known an accepted estimation of the other can be made. Pearson's linear correlation coefficient is also presented in Figure 7. This coefficient will always be used in this paper to measure the correlation between two variables. Although NLDA requires a high computational effort, it should be the reference procedure to correctly estimate the seismic risk of structures. Nevertheless, it would be of practical interest to have a simpler methodology to obtain similar results to those based on NLDA.

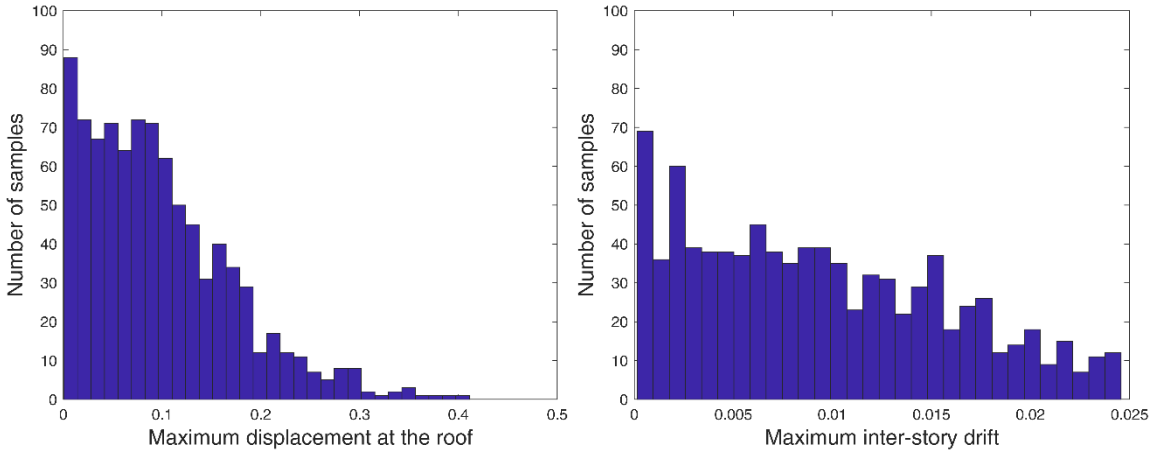

Figure 6 a) Histogram of $\boldsymbol{\delta_{roof}}$ and b) histogram of the MIDR (NLDA)

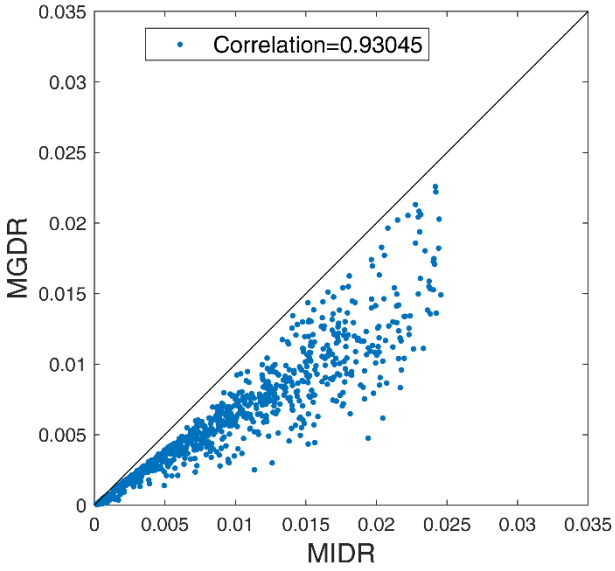

Figure 7 MGDR vs. MIDR

5 EDP ESTIMATION BASED ON THE EQUAL DISPLACEMENT APPROXIMATION

The most simplified assumption, and one of the most commonly used in practice, is to estimate the expected seismic response of the structure based on the equal displacement approximation, EDA. EDA is a well-known empirical rule for the assessment of non-linear behavior of structures subjected to earthquake ground motions. This procedure states that the predicted inelastic displacement response of oscillators is often very similar to the predicted displacement response of elastic oscillators with the same period. Noticeably, oscillators with short periods of less than approximately 0.5 seconds are often significantly larger than the predicted response of elastic structures of the same period. Accordingly, most of the structures analyzed in this paper meet the requirements for a good prediction based on this simplified rule. The displacement calculated using EDA, commonly known as a performance point, corresponds to a single-degree-of-freedom (SDOF) approximation of the structure; if the δ_{roof} of the represented multi-degree-of-freedom system (MDOF) is the target, the spectral displacement should be multiplied by the participation load factor [7], *PF1*, as shown in Equation 4:

$$\delta_{roof,EDA} = PF1 * Sd(T_f) \tag{4}$$

where T_f is the fundamental period of the structure. In this way, after applying the EDA rule to the structural models described above, and factoring the results by *PF1*, the δ_{roof} based on EDA is obtained. Figure 8a shows the comparison between the δ_{roof} obtained using NLDA and EDA methodologies. The dispersion increases as the displacement rises. The EDA rule allows the δ_{roof} of a building to be estimated, but the MIDR cannot be directly estimated based on this approximation. However, an MGDR based on EDA can be calculated by dividing the δ_{roof} by the height of the building, *H*. According to Figure 7, there is a high correlation between MIDR and MGDR. Consequently, it is expected that this correlation also exists between these variables when EDA is applied. Thus, the following equation can be used to estimate the MIDR from the $\delta_{roof,EDA}$:

$$MIDR_{EDA} = \alpha * \frac{\delta_{roof,EDA}}{H} \quad (5)$$

where α is a coefficient intended to minimize the mean square error between the MIDR drift based on NLDA and the MIDR based on EDA. It was found that α=1.3675. Figure **8**b shows this comparison. Noticeably, the correlation between these variables is similar to that observed when δ_{roof} (Figure 8a) is analyzed. Nevertheless, the EDA rule does not consider, explicitly, either the higher mode response or the structural period elongation because of the accumulation of damage.

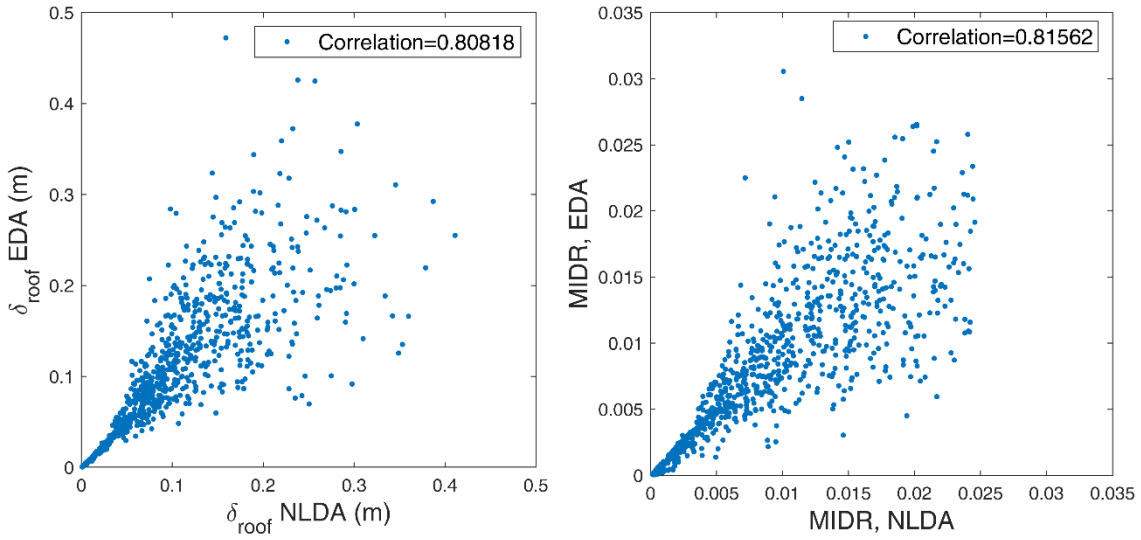

Figure 8 a) Comparison between the $\boldsymbol{\delta_{roof}}$ via NLDA and EDA and b) MIDR comparison obtained via NLDA and EDA

5.1 Modification to the EDA rule

When a structure undergoes inelastic deformation due to a dynamic action, a change of in its vibrational elastic properties is expected, whereby the participation of periods that are longer than the elastic ones becomes important. Moreover, depending on the mass participation factor of higher modes of the structure and the frequency content of the dynamic action, the contribution of these modes can become significantly high, even in low-rise buildings. Neither of these effects are considered explicitly by the EDA rule. More advanced methodologies, also based on the principles of the capacity spectrum method, e.g. FEMA 440 [8], allow such effects to be considered. Nevertheless, these methodologies are intended for spectral shapes that are smooth, and they can provide multiple solutions when real earthquakes are considered. If earthquakes are selected to fit a smooth spectral shape, such as a design or a uniform hazard spectrum, these methodologies provide very good results [9]. The most important aspect of the EDA, at least in our opinion, is its ease of use. Thus, a modification of the EDA rule, aimed at maintaining its simplicity, is presented. The new performance point will be calculated not as the response of the oscillator related to the fundamental period but as the average spectral displacement of several SDOF systems. Therefore, the term *Sd* from Equation 4 becomes the average spectral displacement of several oscillators as follows:

$$\delta_{roof,MEDA} = PF1 * \frac{\sum_{i=1}^{n} Sd(T_i)}{n} \quad (6)$$

Of course, the periods of these oscillators should consider softening of the structure due to the accumulation of damage and the participation of higher modes. These periods will be equally spaced, with an interval of 0.01 s, in the $\beta_{inf} \cdot T_f$ to $\beta_{sup} \cdot T_f$ range. T_f represents the fundamental period of the structure. Moreover, it is expected that β_{inf} <=1 and β_{sup}>=1. We designed an algorithm based on Monte Carlo to find the coefficients β_{inf} and β_{sup} that minimize the mean square error between the δ_{roof} obtained via NLDA and the modified EDA. It has been found that β_{inf} = 0.1 and β_{sup}= 1.8 are the coefficients that fulfil the minimization condition. Figure 9a shows the comparison between the δ_{roof} obtained using NLDA and the modified EDA. A significant increase in the correlation can be seen after the applied modification. Then, to calculate the MIDR based on the modified EDA, the MGDR based on EDA are recalculated and a new α coefficient is obtained. In this case, it has been found that α=1.6976. Figure 9b shows the comparison between the MIDR using NLDA and the modified EDA. Again, the correlation between these variables is similar to that obtained for the δ_{roof} comparison (Figure 9a).

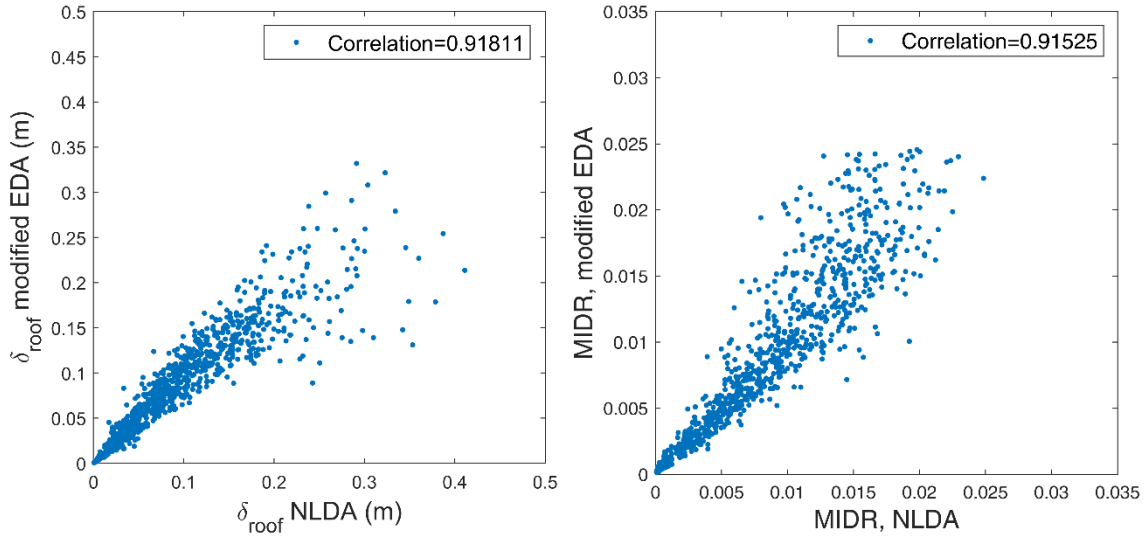

Figure 9 a) Comparison between the maxima $\boldsymbol{\delta_{roof}}$ via NLDA and modified EDA and b) MIDR comparison obtained via NLDA and modified EDA

6 DISCUSSION AND CONCLUSIONS

In this paper two main issues were considered. The first is related to the development of a numerical tool that can be used to estimate the seismic risk of structures through the implementation of a hypothetical case study. This tool considers several sources of uncertainties such as those related to geometry, the mechanical properties of the materials and the seismic hazard. Currently, the source code used to obtain the results presented herein is being reviewed and enhanced. It is expected that an interoperable version for potential users will be created by the end of the KaIROS project [1]. This tool could be used to develop detailed vulnerability models as the one presented in [10]. The second is a statistical analysis of the results aimed at developing a simplified procedure for estimating commonly used EDPs. The EDA rule principle was employed as the basis of a modified version that can be used to calculate similar results to those obtained via NLDA. This simplified procedure can be used to estimate, for instance, fragility curves via cloud analysis [11] without the need to perform NLDAs. Thus, the fragility curves for several damage state thresholds, related to MIDR 0.005, 0.01, 0.015 and 0.02, for the reinforced concrete six-story building shown in Figure 10a will be obtained based on the NLDA

and the modified EDA. The fundamental period of this structure is 0.84 s. Table 2 summarizes the details of the building. The epistemic uncertainties are considered according to the values presented in Table 1.

Story	W_c (m)	B_c (m)	W_b (m)	D_b (m)	ρ_c (%)	ρ_b (%)
1	0.7	0.7	0.35	0.4	1.2	0.8
2	0.7	0.7	0.35	0.4	1.2	0.8
3	0.65	0.65	0.3	0.35	1.1	0.8
4	0.65	0.65	0.3	0.35	1.1	0.8
5	0.6	0.6	0.3	0.3	1	0.8
6	0.6	0.6	0.3	0.3	1	0.8

Table 2 Characteristic of the building analyzed (Figure 10a)

Fifty earthquake records are selected in similar way to the procedure presented in Section 3, but in this case the spectral acceleration is related to the fundamental period of the structure. The values defining the upper and lower limit of each stripe range from 0 to 1 g, at intervals of 0.1 g (Figure 10b).

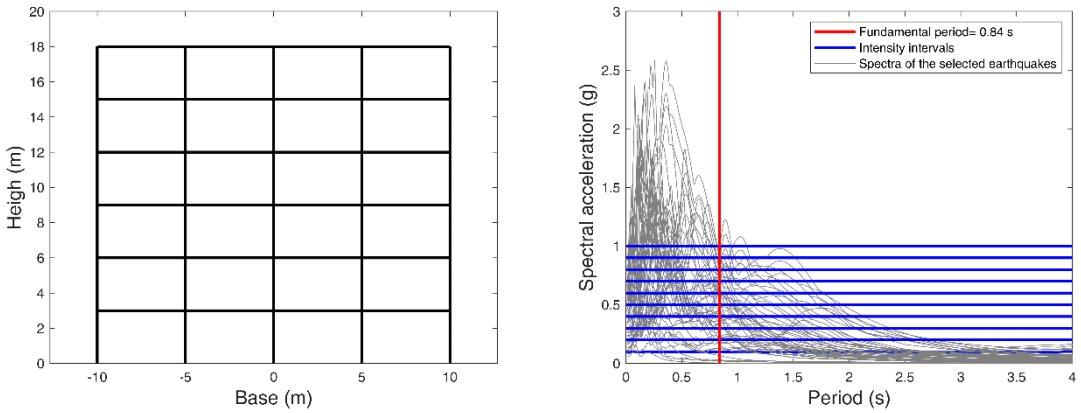

Figure 10 a) Six-story building and b) Spectra of the selected earthquakes

The fragility curves are then obtained using the cloud analysis via NLDA and the modified EDA. Figure 11a shows the comparison between the fragility curves obtained with both approaches. Significant differences can be seen between both curves. Nevertheless, these curves have been calculated for α=1.6976, which is a value that minimizes the error of all the structural models analyzed in the paper. If one analyzes the evolution of α depending on the number of stories, we will find that α increases with the number of stories. This makes sense, because the higher the building the higher the participation of superior modes of vibration. Figure 12 shows the evolution of α as a function of the number of stories. Then, after performing the calculations using α=1.85, obtained from the regression analysis presented in Figure 12, the fragility curves shown in Figure 11b are obtained. Noticeably, a better fit is achieved. This example proves the ability of the proposed procedure to estimate EDP in a very simplified way. Of course, the building that is analyzed should be in the domain of the simulation performed in this paper.

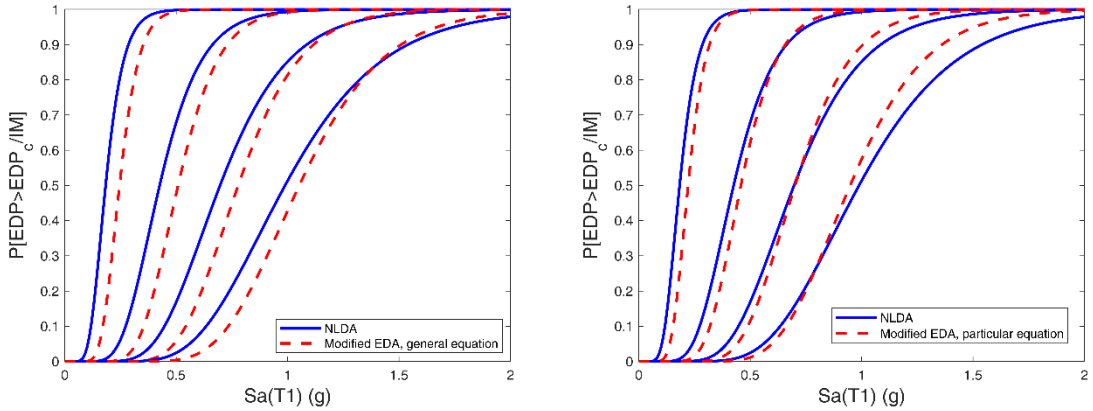

Figure 11 a) Fragility curves via cloud analysis with α=1.6976 and b) α=1.85

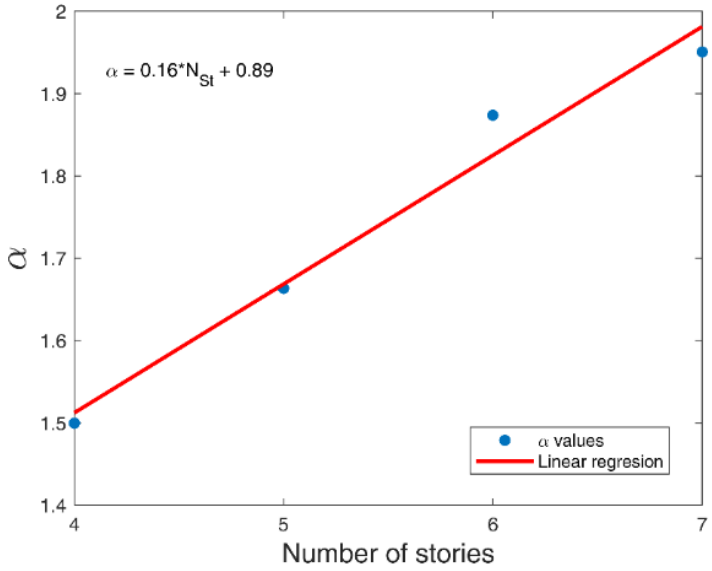

Figure 12 Evolution of α as a function of the number of stories

Finally, the key to reducing seismic risk is to decrease the vulnerability of existing structures and provide new insights to improve the design of new structures and protect them against seismic events. The current capacity of computers, combined with the versatility offered by probabilistic numerical methods, helps face this fundamental challenge in current society.

Acknowledgments

We thank Lucille Banham for her assistance in the preparation of the English manuscript. Yeudy F. Vargas-Alzate has been granted an Individual Fellowship (IF) in the research grant program of the Marie Sklodowska-Curie Actions (MSCA), European Union/European (H2020-MSCA-IF-2017) No 799553. Rodrigo E. Alva holds a PhD fellowship from the Centro Nacional de Ciencia y Tecnología (CONACyT) in Mexico. The authors acknowledge the support of these institutions. This research was partially funded by the Spanish Government's Ministry of Economy and Competitiveness (MINECO) and by the European Regional Development Fund (ERDF) of the European Union (EU) through projects with references CGL2015-65913 -P (MINECO/ERDF, EU) and EFA158/16/POCRISC (INTERREG/POCTEFA. EU).

REFERENCES

[1] KaIROS Project. Keeping and Increasing Resilience Opportunities and Sustainability of communities against earthquakes. https://cordis.europa.eu/project/rcn/215743/fact-sheet/en

[2] Baker J.W., An Introduction to Probabilistic Seismic Hazard Analysis (PSHA). White Paper, Version 1.3, 72 pp. Available at: http://web.stanford.edu/~bakerjw/publications.html.

[3] Goel R., Chopra A., Period Formulas for Moment-Resisting Frame Buildings. *Journal of Structural Engineering*, **123**, 1454-1461, 1997.

[4] Ambraseys N., Smit, p., Sigbjornsson r., Suhadolc P., Margaris b., Internet-Site for European Strong-Motion Data, European Commission, Research-Directorate General, Environment and Climate Programme. http://www.isesd.hi.is/ESD_Local/frameset.htm (Last visited on March 12, 2019)

[5] Otani S. Inelastic analysis of RC frame structures, *Journal of Structural Division, ASCE*. **100**, 1974.

[6] Carr, A.J. *Ruaumoko-Inelastic Dynamic Analysis Program*. Department of Civil Engineering, University of Canterbury, Christchurch, New Zealand 2000.

[7] ATC-40. *Seismic evaluation and retrofit of concrete buildings. ATC*-40, Redwood City, California, 1996.

[8] FEMA-440, Improvement of Nonlinear Static Seismic Procedures, ATC-55, Redwood City, 2005.

[9] Vargas-Alzate Y.F., Pujades L.G., Barbat A.H., Hurtado J.E, An efficient methodology to estimate probabilistic seismic damage curves. *Journal of Structural Engineering, ASCE*. **145**, 2019.

[10] Silva V., Crowley H., Varum H., Pinho R., Sousa L., Investigation of the characteristics of Portuguese regular moment-frame RC buildings and development of a vulnerability model. *Bulletin of earthquake engineering*, **13**, 1455-1490, 2015.

[11] Bakalis K., Vamvatsikos D., Seismic fragility functions via nonlinear dynamic methods. ASCE *Journal of Structural Engineering, ASCE*, **144**, 2018.

COMPDYN 2019
7th ECCOMAS Thematic Conference on
Computational Methods in Structural Dynamics and Earthquake Engineering
M. Papadrakakis, M. Fragiadakis (eds.)
Crete, Greece, 24–26 June 2019

THE USE OF SEISMIC RISK MAPS IN THE DEVELOPMENT OF SEISMIC RISK REDUCTION PROGRAMS

M.A. Zanini[1*], L. Hofer[1], C. Pellegrino[1]

[1] University of Padova, Dept. of Civil, Environmental and Architectural Engineering
Via Marzolo 9
e-mail: marianoangelo.zanini@dicea.unipd.it

Abstract

Mapping seismic risk at the territorial scale is a key process in earthquake-prone countries since it allows to understand the spatial distribution of risk and its quantification in economic terms. Seismic risk maps can be used by governments to outline short-, mid- or long-terms risk mitigation and/or transfer actions. The present contribution aims to show how the seismic risk mapping framework detailed by the authors in a companion paper can be used to investigate the financial sustainability of national seismic risk reduction programs, focusing the attention on the specific case of the national residential building stock of Italy.

Keywords: Seismic risk map, Italy, Seismic risk reduction programs, risk mitigation, cost-benefit analysis

1 INTRODUCTION

For practitioners and authorities, seismic risk computation and mapping are fundamental knowledge tools for understanding and managing the risk at which communities are exposed. For these reasons, reliable seismic risk indicators are needed for quantitatively approach the problem of reducing and/or transferring the risk at with an extended territory is exposed. The Expected Annual Loss (EAL) is a widely adopted synthetic risk indicator, considering and weighing all possible loss scenario than can occur in a specific point. Furthermore, it allows quantifying benefits associated to a retrofit intervention and also provides a reasonable estimate the insurance premium that can be expected based on the design or strengthening decision taken [1].

In last years, many applications adopted the EAL for the evaluation of the best seismic strategy to be adopted, but mostly related to specific structures and addressing specific problems, most of time at punctual level and not at regional level. In [2], Beigi et al. performed a cost-benefit analysis for buildings retrofitted using a gapped-inclined brace system (GIB), while [3] discussed the possible criteria for the mitigation of seismic risk and for the structural strengthening in case of reinforced concrete structures [3]. In 2018, Hofer et al. [4] proposed a methodology for determining the most profitable seismic retrofit strategy to be adopted in an industrial productive plant. In this context, seismic risk evaluations have been extended to spatially distributed assets, for assessing seismic risk at regional level. Map of losses, conditioned on a specific return period, have thus been developed with the OpenQuake engine [5] for Portugal [6], Nepal [7], and Turkey [8]. In 2013, Asprone et al. [9] computed a possible seismic insurance premium for five different types of building categories within all the Italian territory, while in 2018 Zanini et al. developed the first seismic risk map in terms of EAL, for the Italian territory [10]. In particular, he performed the calculation for three different level of granularity according to the Italian administrative subdivision, obtaining in this way the Municipal Expected Annual Loss map (*MEAL*), the Provincial Expected Annual Loss map (*PEAL*), and the Regional Expected Annual Loss map (*REAL*). In addition, [10] showed the effect of different granularity levels on the EAL referred to 1 m^2 of build area (€/m^2), highlighting the averaging effect of assuming a less refined granularity.

This work wants to propose a possible seismic retrofit scenario for the entire Italian residential building stock, and accordingly compute the seismic risk maps for the retrofitted assets. From the difference between the two maps, it is thus possible to quantify the benefit associated to the retrofit interventions. Furthermore, this paper provides an insight on the problem of evaluating the profitability of retrofit interventions at national scale when a significant number of vulnerable structures is involved, and thus scale-effects may happen on the cost-benefit analysis. The paper thus proposes a possible sustainable risk reduction program for the Italian residential building stock and shows some possible applications of it. More details, and the complete procedure description can be found in [10, 11].

2 A RETROFIT SCENARIO FOR REDUCING THE CURRENT SEISMIC RISK

2.1 The current seismic risk map of Italy

Zanini et al. [12], showed the construction of the seismic risk map for Italy, computing the Expected Annual Loss for every Italian municipality, province and region. For the hazard representation, [10] adopted the seismogenic model of [13], jointly with the Gutenberg-Parameter of [14], the Ground Motions Prediction Equations of [15], and the soil map of [16].

A suitable building taxonomy have been adopted for representing the seismic vulnerability of the Italian residential building stock, which has been subdivided in eight Taxonomy Classes TCs. Masonry buildings have been subdivided in two TCs, masonry buildings built before and after 1919, respectively TC1 and TC2. Reinforced concrete structures have been subdivided in two main classes, depending if gravity-load design, or seismic-load design. Each one of these two classes have been furtherly subdivided in two classes, on the base of the number of storeys (1-2, or 3+), respectively TC3 and TC4 for the gravity-load design, and Tc5 and TC6 for the seismic-load design. Finally, two more TCs (again Other – gravity design TC7, and Other – seismic design TC8) have been adopted for describing structures other than masonry and RC, mainly combined RC-masonry structures. All parameters of the adopted fragilities can be found in [10].

About exposure data, they have been retrieved from the 15th census database of the National Institute of Statistics [17]. Figure 1 shows the seismic risk maps in terms of *MEAL*, *PEAL* and *REAL*, that are representations of the seismic risk in the so-called *as-built* condition.

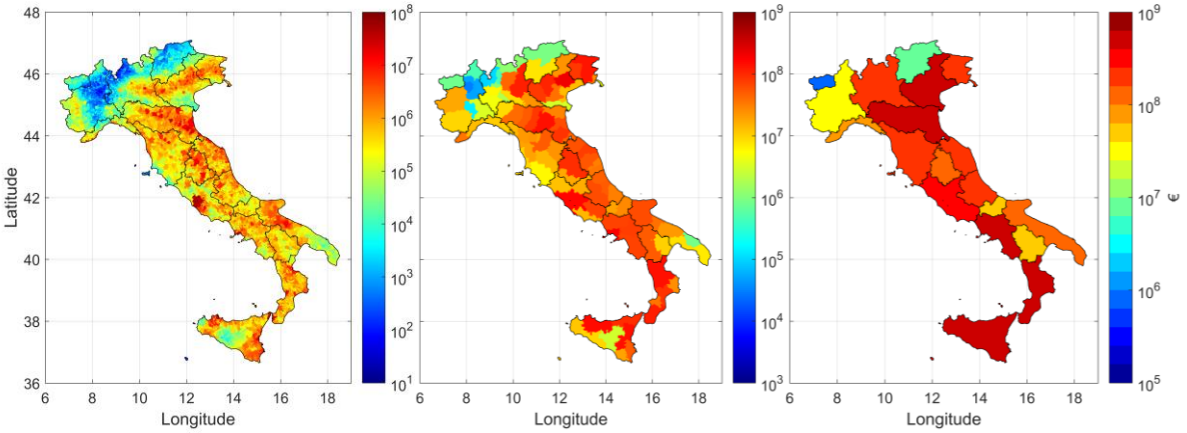

Figure 1: The seismic risk map of Italy in terms of MEAL (left), PEAL (center), REAL (right).

2.2 The seismic risk map of Italy after the retrofit of the building stock

This work investigates benefits of implementing a full seismic retrofit of the Italian residential building stock. For this scope, a seismic retrofit scenario for the entire building asset at national scale, has to be determined, and improved suitable fragilities have to be assumed.

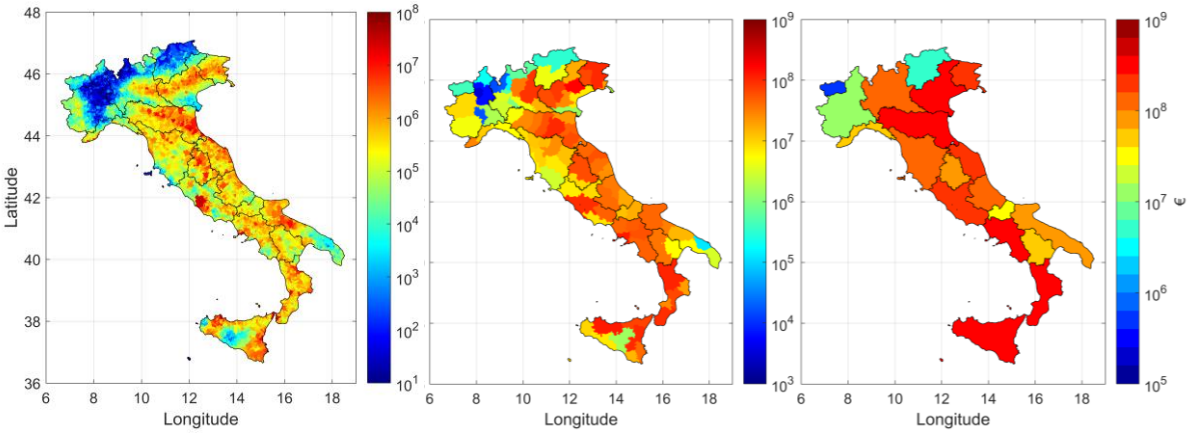

Figure 2: The seismic risk map in terms of MEAL (left), PEAL (center), REAL (right), for the retrofitted asset.

In particular, this paper assumes to improve the structural behavior or masonry buildings (TC1 and TC2), RC gravity load-designed structures (TC3 and TC4), and "Other" gravity load-designed structures (TC7). Retrofitting implies a change of the fragilities for the above-mentioned TCs: in particular it has been assumed that in the retrofitted configuration they behave like the respective seismic-designed classes, i.e. TC1, TC2, TC3 change in TC5, TC4 is modified as TC6, and TC7 is characterized as TC8.Under these assumptions, seismic risk maps have been recomputed for the three level of granularity. Figure 2 shows results in terms of *MEAL*, *PEAL* and *REAL*.

2.3 Assessing the retrofit convenience

For assessing the financial sustainability of the proposed seismic retrofit program, a cost-benefit analysis (CBA) is needed [18]. The main aim of CBA is to assess the profitability of a retrofit intervention, usually performed by computing the break-even time t_{BE}, i.e. the temporal point at which total cost and total revenue are equal. The $t_{BE,x}$ for each x^{th} municipality can thus be computed as:

$$t_{BE,x} = \frac{C_x}{B_x} \tag{1}$$

where C_x represents the cost to be sustained by the x^{th} municipality for retrofitting TC1, TC2, TC3, TC4 and TC7, and B_x is the benefits in terms of EAL provided by the all the retrofit interventions in the x^{th} municipality. B_x can be computed as the different between the *MEAL* in the as-built condition, and the *MEAL* after the structural improvement interventions as

$$B_x = MEAL_{x,as-built} - MEAL_{x,retrofit} \tag{2}$$

Similarly, the benefit due to seismic retrofit can be computed at provincial and regional level. Figure 3 shows the three benefit maps, highlighting how higher benefits are expected in the area of higher Annual Expected Losses.

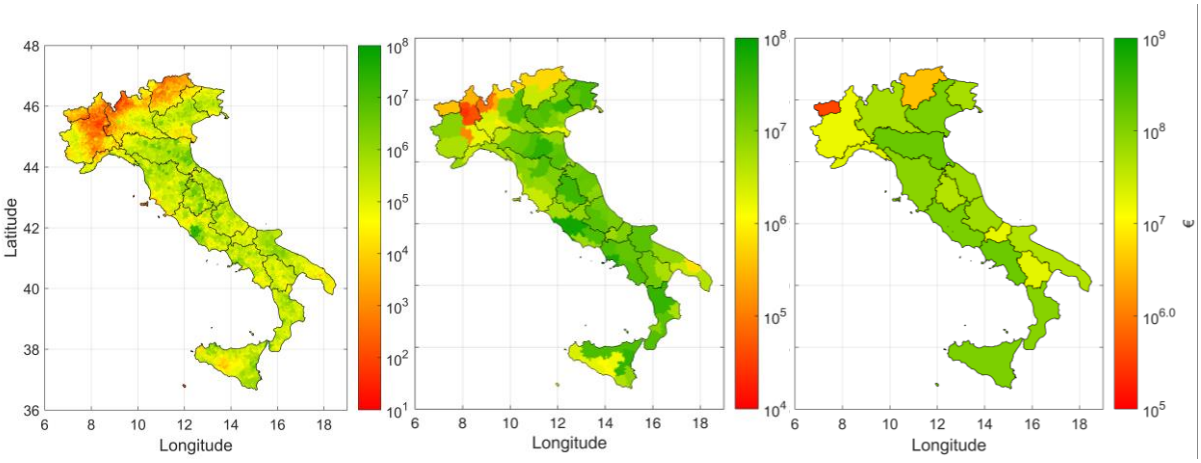

Figure 3: Benefit map at municipal (left), provincial (center), and regional (right) level.

Cost at municipal level C_x in Eq. (1) strictly depends on the planned seismic retrofit interventions for p = 5 TCs that need a structural improvement, and can be computed as

$$C_x = \sum_{y=1}^{p} A_{y,x} \cdot SRC_y \tag{3}$$

where $A_{y,x}$ is the built area of the y^{th} TC that needs seismic retrofit, and SRC_y is the unitary seismic retrofit cost for the y^{th} TC. The SRC_y values have been assumed equal to 68 €/m^2 for TC1, TC2, TC7 structures (i.e. retrofit schemes consisting in the insertion of tie-roads [19] and reinforced plaster) and 34 €/m^2 to for TC3, TC4 buildings (i.e. interventions based in FRP wrapping [20] or reinforced concrete jacketing of RC frame elements) in accordance to Prota [21]. Figure 4 shows the break-even time map, computed at municipal, provincial and regional level. Basing on this indicator, the Italian territory is mainly divided into two parts: in the first zone, coinciding with the Appennini area and northeastern Italy, seismic retrofit is recommended and t_{BE} ranges between few decades till about one hundred years. In the second case, for northwestern Italy, Puglia and the Tyrrhenian coast, retrofit interventions seem not to be convenient, since the break-even time is hundreds of years. Even in this case, the calculation at provincial and regional level, has an averaging effect, increasing the lower t_{BE} values at municipal level, and reducing the higher t_{BE} values.

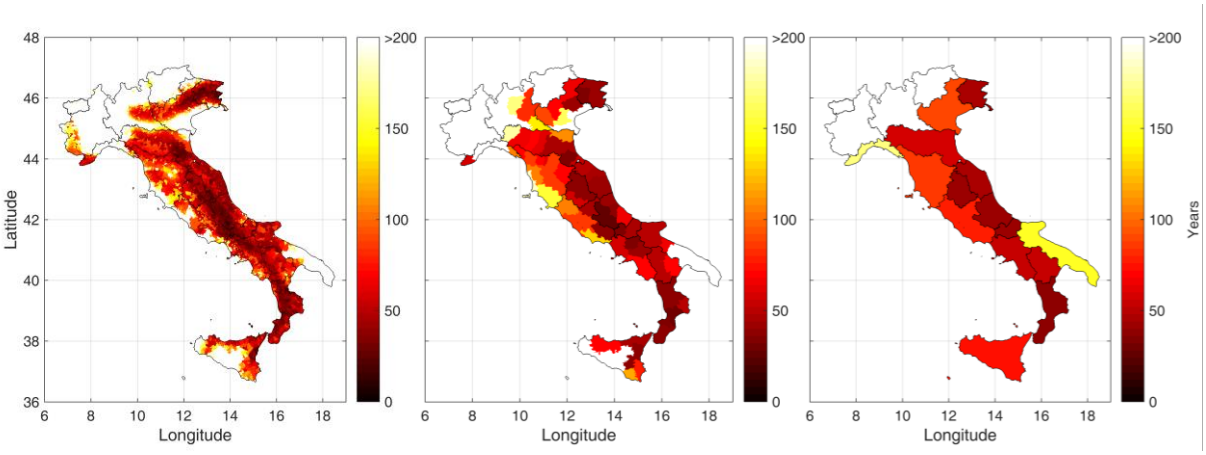

Figure 4: Break-even time map at municipal (left), provincial (center), and regional (right) level.

In general, for the entire national territory, structural retrofit implies gains in a medium-long term, and, except for some municipalities and provinces where it is highly recommended, seems not to be a convenient strategy for reducing seismic risk. However, the safety of citizens and the national risk reduction, cannot be neglected basing on cost-effectiveness analysis. For this reason, a financially sustainable seismic risk reduction program is proposed in the next section.

3 DEVELOPMENT OF SUSTAINABLE RISK REDUCTION PROGRAMS

The financial sustainability of implementing a nationwide retrofit program, has to be investigated in order to guarantee reasonable break-even times. The idea is that the implementation of the national seismic risk reduction program, should be managed by the Italian Government, or, better, by an *ad hoc* national public agency, which have to support the seismic retrofit at municipal level (or provincial and regional). The cost-effectives of the initial investment, and thus a reasonable financial return time, should be guaranteed by increasing benefits due to the seismic retrofit. This can be obtained by introducing for each x^{th} municipality (or Province and Region) a property tax PT_x, that can be seen as an additional income to be summed to the benefit B_x, thus reducing the break-even time:

$$t_{BE,x} = \frac{C_x}{B_x + PT_x} \tag{4}$$

In each x^{th} municipality, PT_x can be computed as a fraction PTR_x (property tax rate) of the total municipal cadastral income

$$PT_x = PTR_x \cdot CI_x \cdot A_x \tag{5}$$

where A_x is the total built area in the x^{th} municipality, and CI_x is the municipal cadastral income in €/m^2: in this application CI has been assumed constant and equal to 484 €/m^2 [22]. From Eq. (4) and Eq. (5) it is thus possible to compute the PTR_x, given a specific t_{BE}, and, on the contrary, compute the break-even time corresponding to a specific PTR_x. Figure 5 shows the map of the break-even time for PTR_x = 1 ‰ while Figure 6 shows the map for PTR_x = 2 ‰. Further examples for PTR_x = 0.5 ‰ and PTR_x = 3 ‰, and the calculation of PTR_x for a specific payback period can be found in [10].

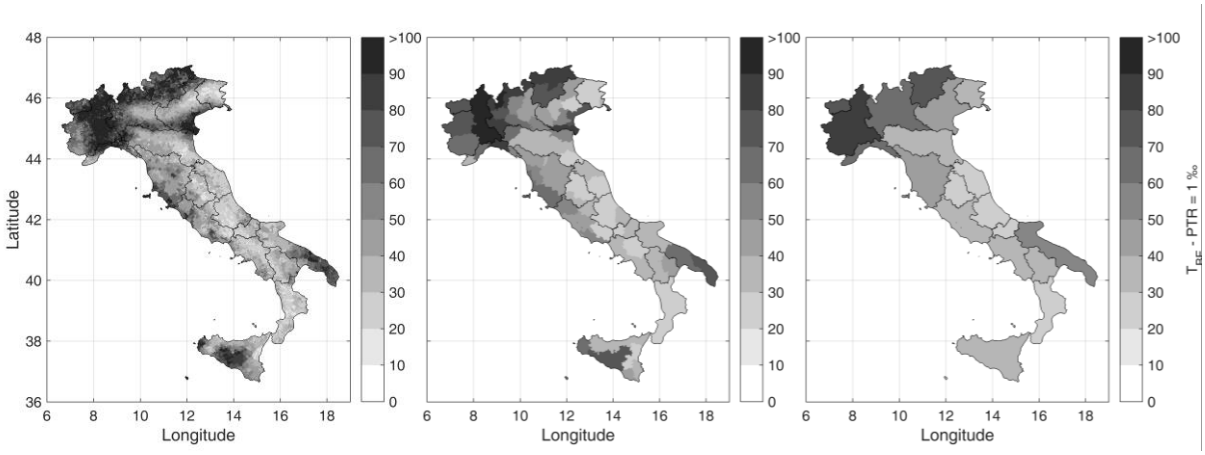

Figure 5: Break-even time map with PTR = 1 ‰ at municipal (left), provincial (center), and regional (right) level.

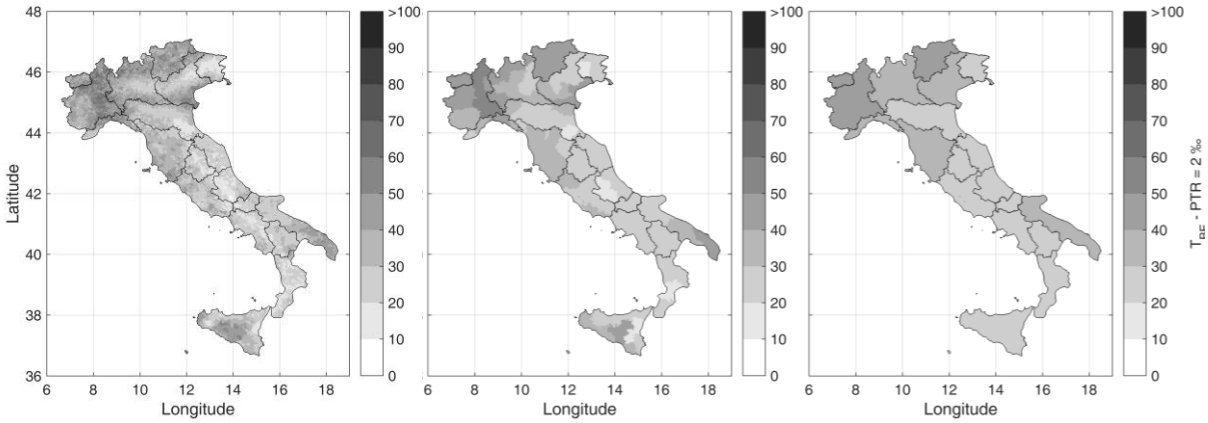

Figure 6: Break-even time map with PTR = 2 ‰ at municipal (left), provincial (center), and regional (right) level.

Figure 5 and Figure 6 clearly show the benefit of introducing this contribution. In particular, with PTR_x = 2 ‰ almost the entire national territory has a payback period lower than 30 years. Even in this case, considering less refined granularity has an averaging effect on t_{BE}, increasing the lower values, and reducing the higher ones.

4 CONCLUSIONS

In earthquake-prone countries, the development of financially sustainable risk reduction programs, is a key issue that has to be addressed starting from a deep knowledge of the risk at which the national territory is exposed. For this scope, suitable hazard, vulnerability and exposure models have to be defined, and then combined for computing the seismic risk map of the area of interest. The seismic risk map is the representation of the current *as-built* condition, from which the benefit due to seismic retrofit has to be computed. It is thus possible to compute the seismic risk map for the *retrofitted* configuration, and by subtraction the map of the expected benefit. The cost-benefits analysis performed for the Italian territory, showed a wide range of variability for the payback period, highlighting Italian regions in which seismic retrofit is highly recommended, and others in which it has a lower impact with high break-even times. For this reason, this work proposed a financially sustainable risk reduction strategy, based on the introduction of a property tax to be paid by citizen for achieving in a shorter time the financial break-even. The Italian Government, or, better, an *ad hoc* national public agency, has thus to support the seismic retrofit, whose cost-effectives is guaranteed by the introduction of this additional contribution. The flexibility of the proposed strategy allows computing the expected payback period corresponding to a given level of property tax rate, or vice versa, the property tax rate to be applied for re-entering the investment in a specific number of years. Results shows as a property tax rate of 2 ‰ assures for almost the entire national territory a payback period lower than 30 years. In this paper, all calculations are performed at three granularity levels, i.e. municipal, provincial and regional level, according to the Italian administrative subdivision. In particular, a less refined granularity has an averaging effect on the final break-even time, increasing the lower values, and reducing the higher ones. The use of different granularity levels is highly informative and, together with the developed maps, allows national authorities to take rational decisions for reducing the impact of future earthquakes that can occur in the Italian peninsula.

5 REFERENCES

[1] Applied Technology Council (ATC), Guidelines for Seismic Performance Assessment of Buildings, ATC-58, Redwood City, California, 2011.

[2] H.A. Beigi, C. Christopoulos, Sullivan T.J., G.M. Calvi, Cost-Benefit Analysis of Buildings Retrofitted Using GIB Systems, *Earthquake Spectra*, **32(2)**, 861-879, 2016.

[3] G.M. Calvi, Choices and Criteria for Seismic Strengthening, *Journal of Earthquake Engineering*, **17**:769–802, 2013.

[4] L. Hofer, M.A. Zanini, F. Faleschini, C. Pellegrino, Profitability Analysis for Assessing the Optimal Seismic Retrofit Strategy of Industrial Productive Processes with Business-Interruption Consequences, *Journal of Structural Engineering (United States)*, **144(2)**, 4017205, 2018.

[5] V. Silva, H. Crowley, M. Pagani, D. Monelli, R. Pinho, Development of the OpenQuake engine, the Global Earthquake Model's open-source software for seismic risk assessment, *Natural Hazards*, **72**, 1409–1427, 2012.

[6] V. Silva, H. Crowley, H. Varum, R. Pinho, Seismic risk assessment for mainland Portugal, *Bulletin of Earthquake Engineering*, **13**, 429–457, 2015.

[7] H. Chaulagain, H. Rodrigues, V. Silva, E. Spacone, H. Varum, Seismic risk assessment and hazard mapping in Nepal, *Natural Hazards*, **78**, 583–602, 2012.

[8] V. Silva, H. Crowley, M. Pagani, R. Pinho, D. Monelli, Development and Application of OpenQuake, an Open Source Software for Seismic Risk Assessment, *Proceedings of 15th World Conference on Earthquake Engineering - WCEE*, Lisbon, Portugal, September 24-28 2012.

[9] D. Asprone, F. Jalayer, S. Simonelli, A. Acconcia, A. Prota, G. Manfredi, Seismic insurance model for the Italian residential building stock, *Structural Safety*, **44**, 70–79, 2013.

[10] M.A. Zanini, l. Hofer, C. Pellegrino, A framework for assessing the seismic risk map of Italy and developing a sustainable risk reduction program, *International Journal of Disaster Risk Reduction*, **33**, 74–93, 2019.

[11] M.A. Zanini, L. Hofer, F. Faleschini, K. Toska, C. Pellegrino, Municipal expected annual loss as an indicator to develop seismic risk maps in Italy, *Bollettino di Geofisica Teorica ed Applicata*, DOI 10.4430/bgta0262, Accepted.

[12] M.A. Zanini, l. Hofer, F. Faleschini, C. Pellegrino, Seismic risk map for the Italian residential building stock, *Proceedings of the 7th ECCOMAS Thematic Conference on Computational Methods in Structural Dynamics and Earthquake Engineering – COMPDYN 2019*, Crete, Greece, 24–26 June 2019.

[13] C. Meletti, F. Galadini, G. Valensise, M. Stucchi, R. Basili, S. Barba, G. Vannucci, E. Boschi, A seismic source zone model for the seismic hazard assessment of the Italian territory, *Tectonophysics*, **450**, 85–108, 2008

[14] S. Barani, D. Spallarossa, P. Bazzurro, Disaggregation of probabilistic ground-motion hazard in Italy, *Bull. Seismol. Soc. Am.*, **99 (5)**, 2638–2661, 2009.

[15] D. Bindi, F. Pacor, L. Luzi, R. Puglia, M. Massa, G. Ameri, R. Paolucci, Ground motion prediction equations derived from the Italian strong motion database, *Bulletin of Earthquake Engineering*, **9(6)**, 1899–1920, 2011.

[16] T.I. Allen, D.J. Wald, Topographic slope as a proxy for global seismic site conditions (v_{s30}) and amplification around the globe: U.S. Geological Survey Open-File Report2007-1357, 69 pp.

[17] Istituto Nazionale di Statistica, 15-esimo Censimento Generale della popolazione e delle abitazioni, 2011. Postel Editore, Roma (in Italian), 2011.

[18] P. Gardoni, F. Guevara-Lopez, A. Contento, The Life Profitability Method (LPM): a financial approach to engineering decisions, *Structural Safety*, **63**, 11–20, 2016.

[19] L. Hofer, P. Zampieri, M.A. Zanini, F. Faleschini, C. Pellegrino, Seismic damage survey and empirical fragility curves for churches after the August 24, 2016 Central Italy earthquake, *Soil Dynamics and Earthquake Engineering*, **111**, 98-109, 2018

[20] F. Faleschini, J. Gonzalez-Libreros, M.A. Zanini, L. Hofer, L. Sneed, C. Pellegrino, Repair of severely-damaged RC exterior beam-column joints with FRP and FRCM composites, *Composite Structures*, **207**, pp. 352-363, 2019.

[21] A. Prota, Seismic retrofit solutions for existing structures: the Abruzzo 2009 earthquake experience on private buildings, in: Proceedings of Workshop on the Seismic Risk Prevention between Sustainability and Resilience, ENEA – Italian National Agency for New Technologies, Energy and Sustainable Economic Development, 20th October 2016, Rome (in Italian).

[22] OMI – Osservatorio del Mercato Immobiliare, Cadastral statistics 2017: urban land registry. National Tax Office of Italy – Office for Statistics and Research on the real estate market, Rome. (in Italian), 2017.

COMPDYN 2019
7th ECCOMAS Thematic Conference on
Computational Methods in Structural Dynamics and Earthquake Engineering
M. Papadrakakis, M. Fragiadakis (eds.)
Crete, Greece, 24–26 June 2019

RINTC-E: SEISMIC RISK OF PRE-CODE SINGLE-STORY NON-RESIDENTIAL STEEL BUILDINGS IN ITALY

Gaetano Cantisani[1], **Gaetano Della Corte**[1]

[1] Department of Structures for Engineering and Architecture, University of Naples Federico II
Naples, Italy
e-mail: {gaetano.cantisani, gaetano.dellacorte}@unina.it

Abstract

The paper summarizes results from numerical investigations on seismic response of single-story non-residential steel buildings designed and built in Italy during the 1980s-1990s, i.e. prior to code enforcement of modern capacity design and ductility detailing rules. A typical geometry and structural layout were selected to generate an archetype building, considering trussed portal frames in the building transverse direction and concentric braces in the building longitudinal direction. Following the simulated design, the case study building was modelled and analysed using OpenSEES. First, the paper describes the mathematical modelling of the mechanical response of critical building components as well as the global building model. The model represented explicitly the shear force-displacement response of bolted connections for truss members, as well as the axial-shear force-displacement response for column base connections. Low-cycle fatigue of buckling braces was considered following literature models to represent triggering of brace fracture. Two different envelope types were analysed and explicitly modelled. Following description of the finite element model, results from non-linear static analysis are summarized and critical building components are identified. Subsequently, results from response history analysis with multiple sets of ground motions selected for increasing seismic intensity levels are also provided and commented on. Finally, conclusions from the presented numerical results are traced and future developments of the work are discussed.

Keywords: Building, collapse, risk, steel

1 INTRODUCTION

Single story steel buildings are frequently used in Italy for non-residential buildings. Often, in old buildings, trussed beams were employed to carry the gravity loads distributed on large spans, while braced frames were used to obtain out-of-plane member stability and stiffness in the orthogonal direction. Because of the relatively small values of structural and non-structural masses, design of this buildings is dictated by gravity and wind actions, as well as slenderness and other geometric limitations. Besides, due to the absence of capacity design and ductility detailing rules in the old structural codes, post-buckling member behaviour, connection failures and other relatively brittle failure modes are phenomena that could govern response under increasing horizontal actions. Eventually, an adequate model of the building envelope could be necessary, if a realistic estimate of the seismic performance would be required. The case study presented in this paper refers to typical similar structures designed and built in Italy during the years 1980s-1990s. First, the paper provides a description of the case studies and the relevant design assumptions, as well as the main design output. Second, a description of the structural model, including the building envelope, is presented. Finally, results are presented in terms of non-linear static and dynamic analyses on a 3D finite element (FE) model. The paper discusses the results, with a focus on evaluating the building ultimate failure, and the effect on response of the building envelope, in comparison to the bare frame response. The presented work is framed within the activity of a broader research project, the ReLUIS-DPC project named RINTC, aimed at evaluating the seismic reliability of structures in Italy with emphasis on ultimate failure [1, 2]. In specific, the behaviour of existing steel structures is under investigation, following a similar work already carried out for new structures [3].

2 CASE STUDY STRUCTURE

2.1 General design assumption

The building depicted in Figure 1 represents the case study of this work. A simulated design was carried out, according to codes and standards of practice adopted in Italy in the years 1980s-1990s [4,5,6]. The archetype building was made of five portal frames with a main trussed beam in the transverse direction (X), while concentric braced frames were adopted in the longitudinal direction (Y). In addition, Figure 1 highlights the presence of the envelope and their openings in the two main building directions.

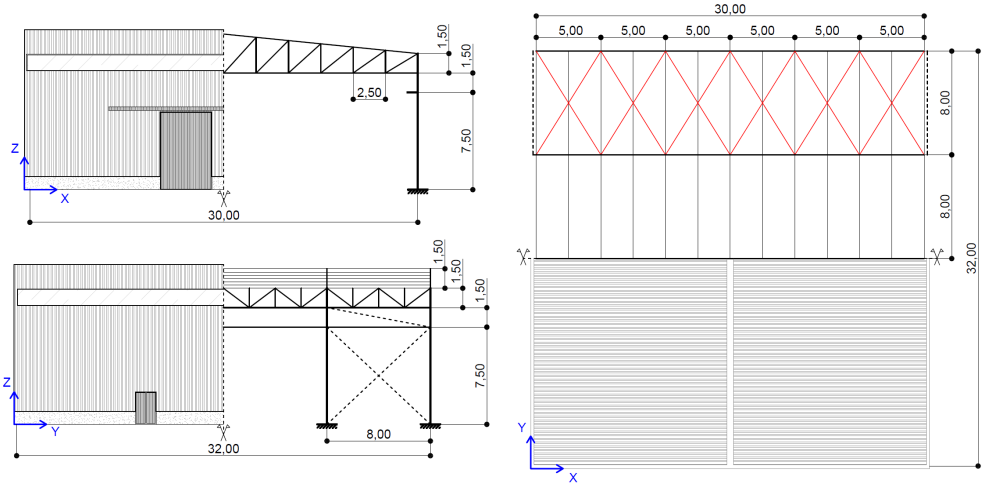

Figure 1: Global geometry of the case study building.

The building was located at L'Aquila (Italy), a small city in central Italy where seismic hazard is significant. The design assumed two main load combinations: (i) a gravity load combination; (ii) a horizontal load combination. The effects of seismic actions were included in the combinations (for both horizontal and vertical actions), but neither capacity design rules nor detailing requirements for ductility were implemented. The simulated design was carried out according to the allowable stress method, considering an old "Fe 430" steel with an allowable stress of σ_a=190 MPa.

2.2 Design results

Figure 2 shows the member cross sections for the main structural members. The choice of the trussed beam element cross sections was governed by the gravity loads, while the column cross section was governed by the horizontal loads. The brace cross sections were selected based on a codified slenderness limitation ($\lambda \leq 200$ for main members and $\lambda \leq 250$ for secondary members).

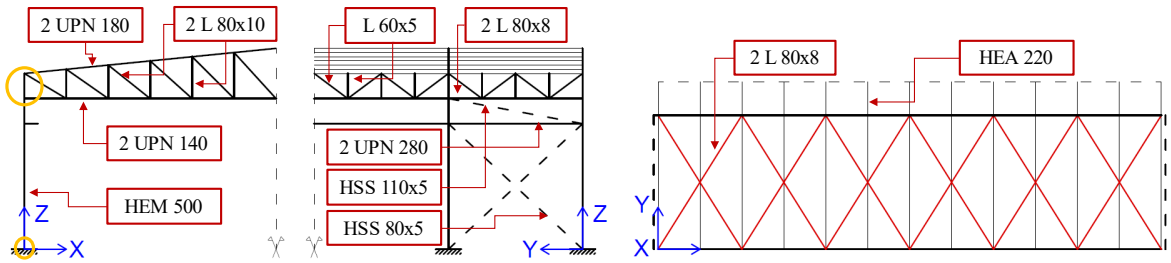

Figure 2: Cross sections of main structural members.

Bolted connections were used for truss members. The gravity load combination led to connections for members at midspan stronger than the connections for members at the column face (Figure 3(a)). Simple column base connections were assumed for the design. Column base anchor cross sections were selected to resist only shear forces, because no tension developed under the design loads. The anchor length was conservatively selected equal to the minimum suggested by the code for tension bars. In addition, to provide stability during column erection, four anchors were used (Figure 3(b)).

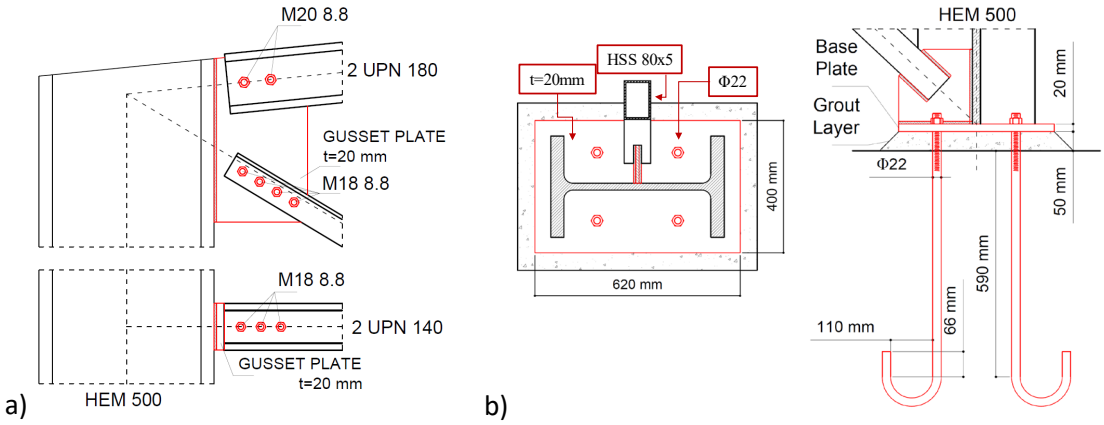

Figure 3: Connection design: (a) Truss-to-Column connection; (b) Column base connection.

Two alternative types of lateral cladding were considered: (i) sandwich panels (Figure 4(a)), and (ii) trapezoidal sheeting (Figure 4(b)). The roofing panels were always made of sin-

gle trapezoidal sheeting, eventually completed on-site with thermal insulation and weather shield. Bolted connections between secondary steelwork and panels were assumed in the case of sandwich panels, because of the experimental results used for modelling the panels [7]. Instead, screw connections were assumed in the case of trapezoidal sheeting, according to the experimental results used for modelling the panels [8].

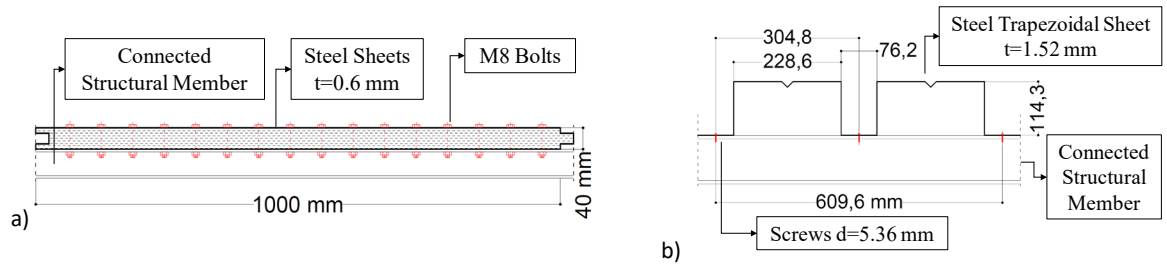

Figure 4: Cladding and roofing elements: (a) sandwich panel detail; (b) trapezoidal sheeting detail.

3 NON-LINEAR MODELLING FOR SEISMIC ASSESSMENT

3.1 General modelling issues

The open source finite element software "OpenSEES" [9] was adopted to analyse the seismic performance of the case study building. The stress-strain relationship was defined by Young modulus E_s = 210 GPa, yielding strength f_y = 316.25 MPa, post-elastic kinematic hardening ratio $E_p = 0.01E_s$, and Poisson ratio ν=0.30.

A classical Rayleigh damping model was adopted, with damping ratio set equal 5% for two main vibration modes in the two main building directions. Generally, members of both transverse and longitudinal trusses were modelled as "truss" elements. An exception is represented by the bottom chords of the main trusses, where "beam" elements were used to provide more realistic out-of-plane stiffness of the truss. Columns were modelled as elastic "beam-column" elements, because preliminary analysis indicated that connection and brace failures anticipated column yielding.

3.2 Structural modelling issues

Figure 5 shows two views of the structure finite element model, highlighting: (i) the main structure elements; (ii) the secondary steelwork elements; (iii) the cladding/roofing panel-equivalent brace elements. Openings (dashed lines) were considered by applying a 50% reduction to both the initial stiffness and resistance [10].

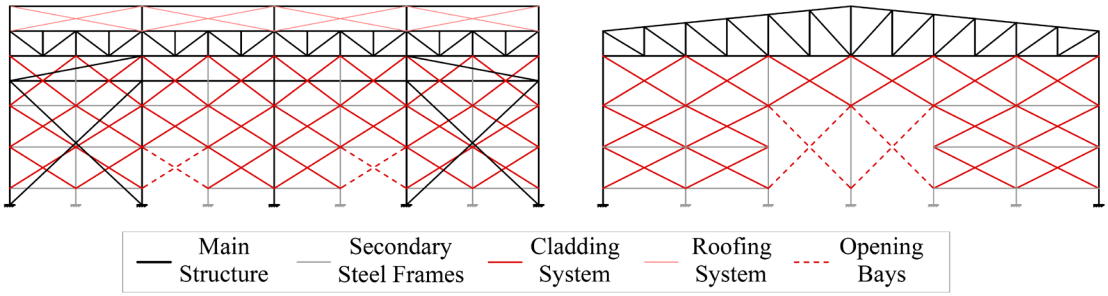

Figure 5: Structure finite element model

Both roof and vertical braces were modelled as non-linear fiber beam-column elements, with equivalent member imperfections calibrated to obtain buckling loads according to the

Eurocode general method [11]. The Giuffré-Menegotto-Pinto uniaxial material model was selected, considering the steel mechanical parameters described previously. The Bauschinger effect was considered assuming values of relevant parameters suggested in the OpenSEES user manual. Figure 6 shows one example of vertical brace modelling: brace discretization and member equivalent imperfection (Figure 6(a)), out-of-plane rotational behaviour of the gusset plate connection (Figure 6(b) and Figure 6(c)) according to Hsiao *et al.* [12]. Figure 6(d) shows an example of component response.

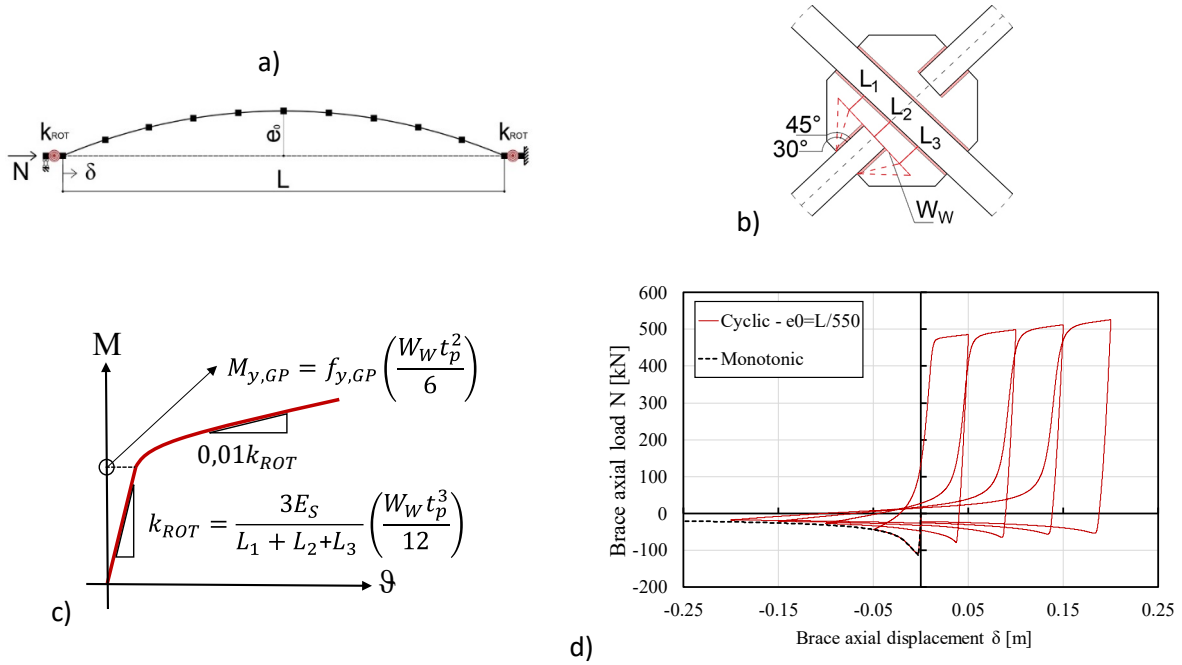

Figure 6: Brace modelling: (a) element modelling; (b) connection detail and (c) model; (d) element response.

Figure 7(a) shows the mechanical model used for the generic element of the main truss, where the flexibility and resistance of end connections was considered [13]. For the bolted connection between the columns and the truss ends, analysis indicated shear failure of bolts and the relevant non-linear behaviour ($\delta_{U,conn}$, $F_{U,conn}$) was modelled using results provided by Henriques *et al.* [14].

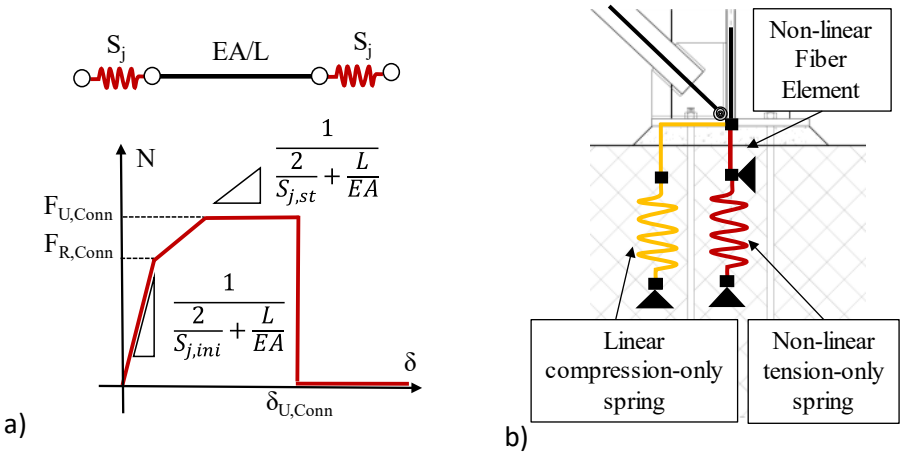

Figure 7: Connection modelling: (a) truss connection model; (b) column base connection model.

Figure 7(b) shows the model for column base connections in the longitudinal braced frame direction. An equivalent circular non-linear fiber element was used to simulate the anchor length outside the foundation block, thus considering the shear-axial force interaction. In addition, a unilateral tension spring was used to simulate the anchor length embedded into the concrete foundation including the hook [15]. The compression behaviour of the connection was considered by means of an elastic unilateral compression spring. Additional information about modelling can be found in Cantisani *et al*. [16].

Figure 8(a) shows the mechanical response of sandwich panels with bolted connections (SPs). The model comprises both the mechanical response of the panel and the non-linear response of the connection between panels and secondary steelwork. According to the experimental results [7], failure of the specimen occurred by bolt bearing against the sheet holes. Figure 8(b) shows the mechanical response of the trapezoidal sheeting (TS), considering the non-linear response of the screw connections. The response for TS comprises also the side-by-side connections between adjacent sheets [8].

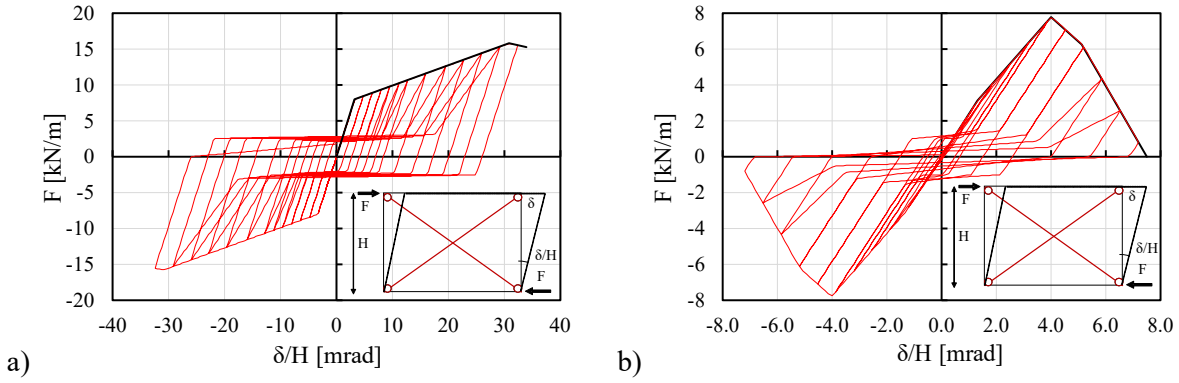

Figure 8: Envelope component modelling: (a) SPs response; (b) TSs response.

In addition to panel and panel-to-frame connection response, the model comprises also the non-linear response of connections between siderails and columns (Figure 9(a)). The shear connection model was implemented following the same rules already used in modelling truss-to-column connections (Figure 9(b)), considering a horizontal zero-length element in each siderail-to-column intersection in both the main direction of the building.

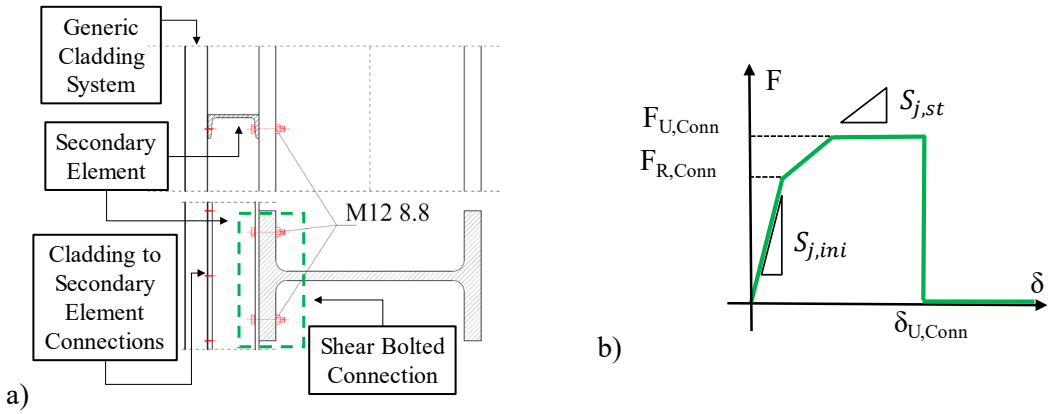

Figure 9: Cladding connection modelling: (a) connection geometry; (b) connection model; (c) connection arrangement.

4 ANALYSIS RESULTS

4.1 Modal analysis results

Table 1 provides information about periods of vibration (T) corresponding to modes having the largest modal participating mass (indicated as m^* in the table, and given as percentage of the total building mass) in the main building directions. Results are shown for different 3D models: (i) a bare frame model (BF), (ii) a model with sandwich panels (SP), and (iii) a model with trapezoidal sheeting. The values of T for the transverse X-direction (i.e., the direction of the main trusses) demonstrate significant increase of stiffness when changing from a bare frame model to a model incorporating envelope panels. Such increase in global stiffness was due to both the diaphragm effect of the roofing panels and the lateral stiffness contribution from the panels located at the two front and back portal frames. The diaphragm effect provided by the roofing panels is demonstrated by the different modes of vibration illustrated in Figure 10 for the bare frame model (Figure 10(a)) and the models with the envelope panels (Figure 10(b)). There was no significant difference between the SP and TS models, because the two models showed almost the same elastic stiffness in the transverse direction. Considering that SP and TS exhibited appreciable difference in their initial stiffness, one can conclude that the increase in the lateral stiffness compared with the bare frame model was mainly due to the diaphragm effect of the roofing panels. Instead, the longitudinal Y-direction (i.e., the direction of the concentrically braced frames) was neither qualitatively nor quantitatively affected to any significant extent by the presence of the envelope panels.

Model	X-direction		Y-direction	
Bare frame (BF) model	T = 1.06 s	m*=59.5%	T = 0.25 *s*	m*=71.2%
Model with sandwich panels (SP)	T = 0.54 s	m*=95.2%	T = 0.22 s	m*=81.6%
Model with trapezoidal sheeting (TS)	T = 0.54 s	m*=95.2%	T = 0.22 s	m*=81.6%

Table 1: Modal analysis results for the 3 cases study

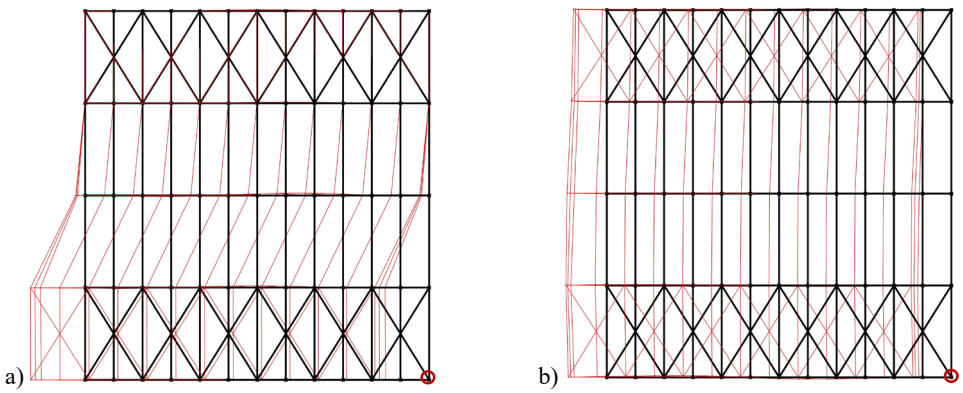

Figure 10: Transverse vibration mode in plain view: (a) BF model; (b) SP/TS model. Note: A circle highlights the control node for the pushover analysis discussed in section 4.2.

4.2 Pushover analysis results

Figure 11 summarizes the results of non-linear static (i.e., pushover) analysis. The figure shows the relationship between the base shear force ($V_{B,X}$ and $V_{B,Y}$) and the column drift ratio (d_X/H and d_Y/H, with H=10.50 m) (the control node is shown in Figure 10). Two types of lateral force patterns were used: (i) a modal force (MF)pattern, in which forces are proportional

to the product of node mass and displacement component of the relevant vibration mode in the direction considered; (ii) a uniform force (UF)pattern, in which forces have the same intensity at all the nodes of the model. The pseudo-static analysis method suggested by Hall [17] was adopted in cases in which convergence problems occurred.

Pushover results show that the structural response is significantly different between the two main directions. Failure of truss-to-column connections leads to collapse of the building in the transverse direction, in all the examined models. The presence of the cladding did not change the collapse mechanism of the building. During the whole loading process until collapse, rather complex interaction developed between claddings and the main structure. A detailed explanation of the interaction phenomena, as well as the evolution of the claddings damage, is provided by Cantisani and Della Corte [18].

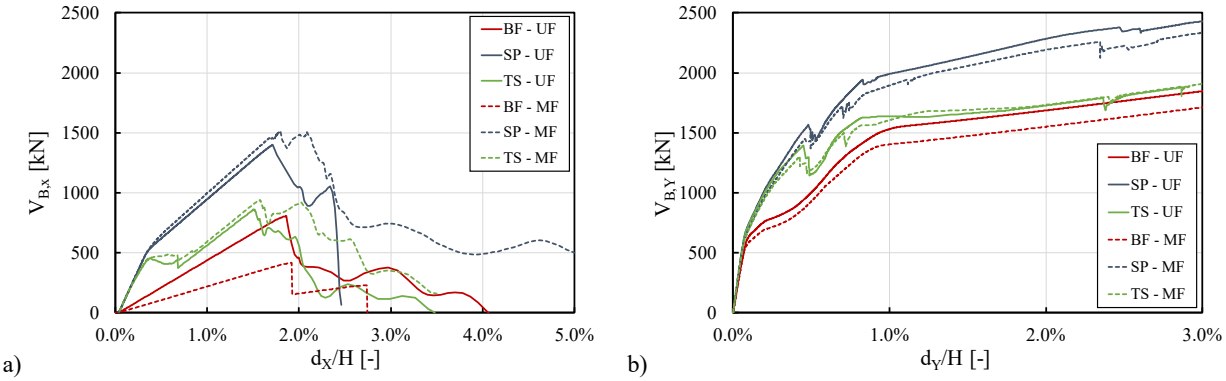

Figure 11: Non-linear static analysis results: (a) transverse direction; (b) longitudinal direction.

4.3 Ultimate failure criteria

Pushover analysis was used to identify the building ultimate failure [1]. Global failure of the building during a generic non-linear dynamic analysis was assumed to occur when the drift ratio at the pushover control node exceeded a limit value. The limit value to the drift ratio was assumed as that corresponding to a 50% loss in the global base shear force resistance obtained from the pushover curve. The drift limits were identified for the transverse response, because of the descending branch of the pushover curves. Ultimate failure for the longitudinal response was monitored by post-processing results in terms of brace and column base anchor strains. In fact, brace fracture was assumed to occur when the maximum brace strain range ($\Delta\varepsilon_{peak}$) reached the limit value by Hsiao *et al.* [12]. Similarly, column base anchor fracture was assumed to occur when the peak strain in the anchors (ε_{peak}) exceeded the expected steel ultimate strain (ε_{u}=34%, [19]).

4.4 Non-linear dynamic analysis results

4.4.1. Seismic hazard and record selection

Non-linear time history analyses were performed using bidirectional ground motions which were selected by the coordinators of the RINTC project [1]. The spectral (pseudo-) acceleration at the system fundamental period of vibration ($S_a(T_1)$) was used as intensity measure (IM). Ten different IM values corresponding to return periods (T_R) varying from 10 years to 100000 years were considered. At each IM value, 20 pairs of ground motions (GMs) were provided. Consequently, a total of 200 non-linear dynamic analyses were carried out. For instance, Figure 12(a) shows the two selected site hazard curves in terms of mean annual frequency of exceedance (λ_{Sa}). Figure 12(b) shows the mean (pseudo-)acceleration elastic response spectra of

ground motions selected with a conditioning period $T = 0.5\ s$ and for each return period, T_R, considered in the analysis.

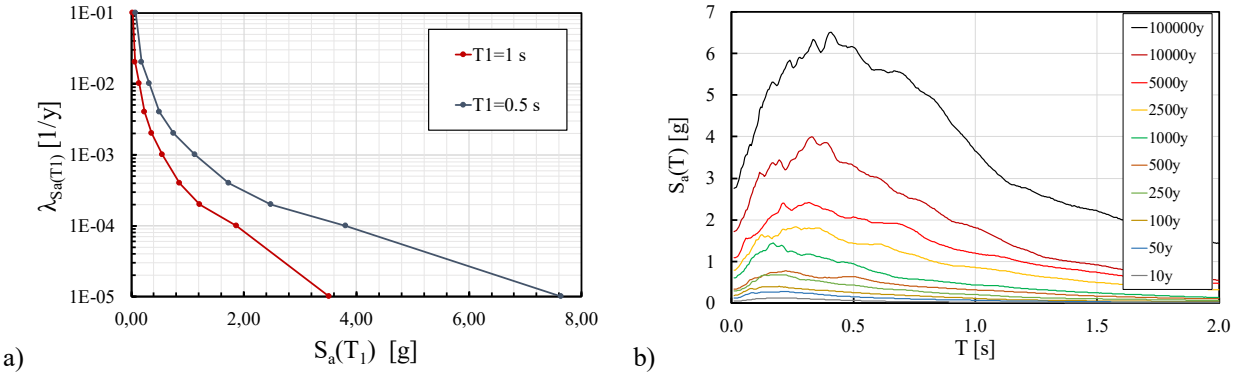

Figure 12: Seismic hazard: (a) Hazard curves for L'Aquila (Italy); (b) mean elastic acceleration response spectra for GMs selected with conditioning period T=0.5 s.

4.4.2. Multi-stripe analysis results

Using the selected ground motions, a multi-stripe dynamic analysis (MSA) was carried out [20]. Figure 13 summarizes the results in terms of relationship between IM and an engineering demand parameter (EDP), which was chosen to represent the global building response. For the transverse direction (X), the peak drift ratio ($d_{X,peak}/H$) among the five portals was selected as EDP. For the longitudinal direction (Y), the brace strain range ($\Delta\varepsilon_{peak}$) among the vertical braces and the anchors peak strain (ε_{peak}) were selected as EDPs, in order to check possibility to trigger steel fracture in braces or anchors. The results are shown for the BF model (Figure 13 (a), (b)), the SP model (Figure 13 (c), (d)), and the TS model (Figure 13 (e), (f)). The figures also report the various ultimate failure limits of the EDPs, as introduced previously.

The MSA of the bare frame model was already described by Cantisani *et al.* [14]. Results are reported here for comparison purposes. The figure shows the number of failure cases (if larger than 0) in a box for each value of IM. As shown in Figure 13, failure in the transverse direction starts to occur at IM = 6 (i.e., $T_R = 1000\ yrs$). Only one failure case was observed in the longitudinal direction due to brace fracture. No anchor fractured in the bare frame model.

Concerning the SP (Figure 13 (c), (d)) and TS models (Figure 13 (e), (f)), results essentially confirmed the pushover results, with ultimate failure cases predominantly occurring in the transverse direction, starting at IM = 6 (i.e., $T_R = 1000\ yrs$) and IM = 7 (i.e., $T_R = 10000\ yrs$) for the TS and SP models respectively. The SP model shows much less failure cases at IM = 7 and IM = 8, while there is practically no difference at IM = 9 and IM = 10. A small number ($\leq$3 for both models) of failures in the longitudinal direction were observed, but they only occurred at IM = 10, when also failure in the transverse direction takes place for any ground motions.

MSA results are reported in terms of peak strains in the column base anchors in Figure 14(a) and (b), for the SP and TS models respectively. Though there were no fractures predicted to occur in column base anchors, large ductility demand could occur, with values as high as 28% for one ground motion at IM=10.

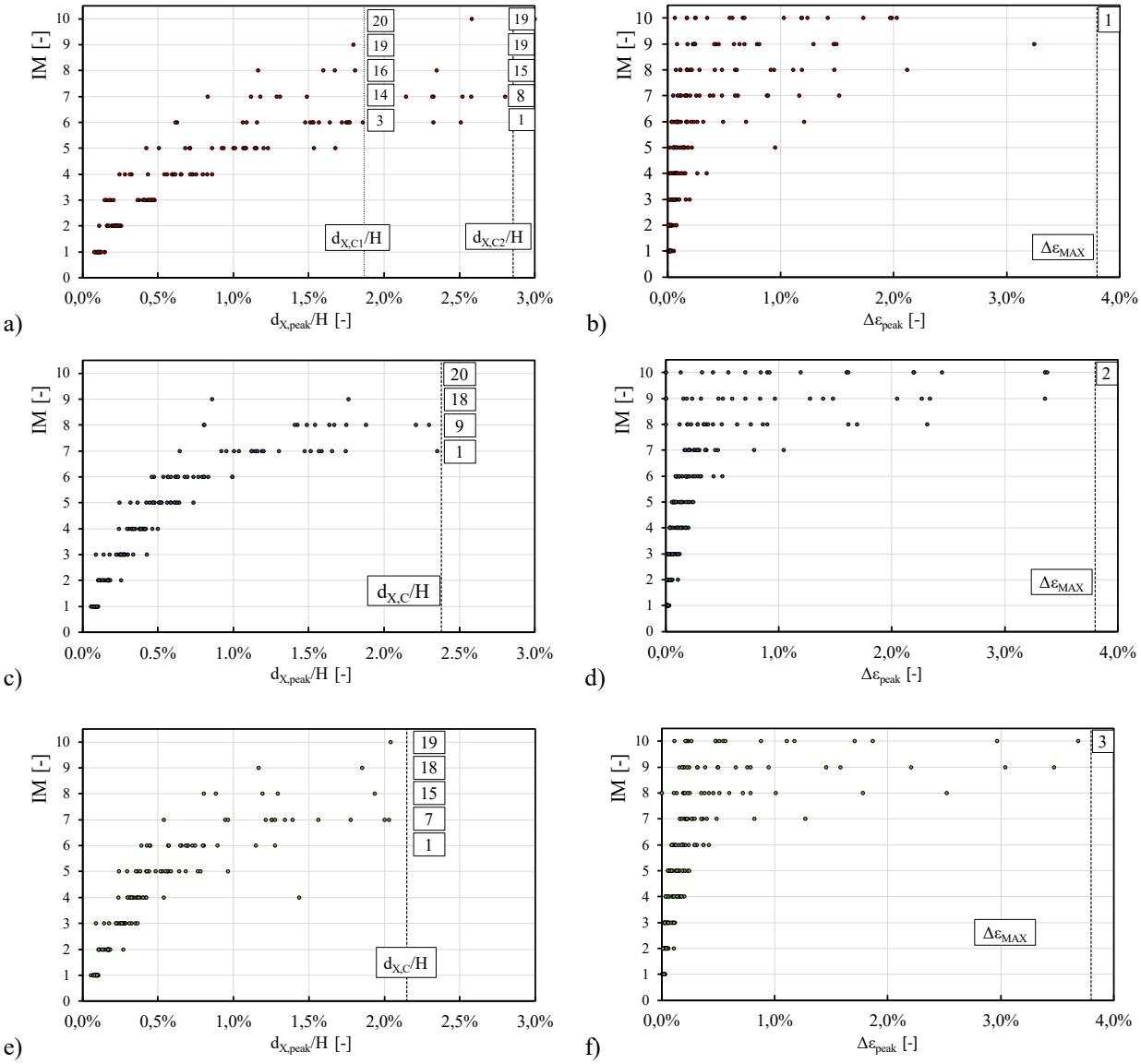

Figure 13: MSA results for the three models: (a) X-BF; (b) Y-BF; (c) X-SP; (d) Y-SP; (e) X-TS; (f) Y-TS.

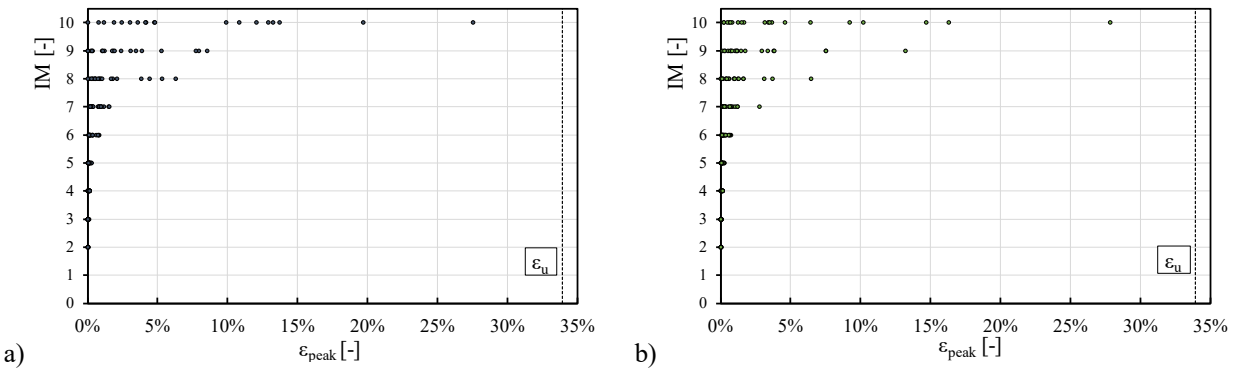

Figure 14: MSA results in terms of column base anchor peak strain: (a) SP model; (b) TS model.

Because of the bi-directional ground motion input, columns were subjected to axial forces and bi-directional bending moments, differently from the pushover analyses. For this reason, and for also investigating any potential difference in the dynamic response compared with the predictions from the static non-linear analysis, column buckling was checked step-by-step during post-processing of the numerical results. Figure 15 shows the peak demand over capacity ratio (*D/C*) for the columns in the SP model (Figure 15(a)) and TS model (Figure 15(b)). The Figure shows the results considering all the GMs at the last two stripes of the analysis (i.e., IM = {9,10}). Since columns were elastic elements in the model, three checks were necessary: (i) resistance check (labelled as *R*); (ii) in-plane buckling check (labelled as *IP*); out-of-plane buckling check (labelled as *OOP*). The member capacities for the *R*, *IP* and *OOP* failure modes were evaluated according to Eurocode 3 [9]. Looking at Figure 15, one can observe that there were no column failures in the SP model, while there was one failure case in the TS model (IM=10, GM=19). However, for this specific GM brace fracture anticipated column buckling. For both models, the ratio *D/C* varies in the range (0.4, 0.8), approximatively.

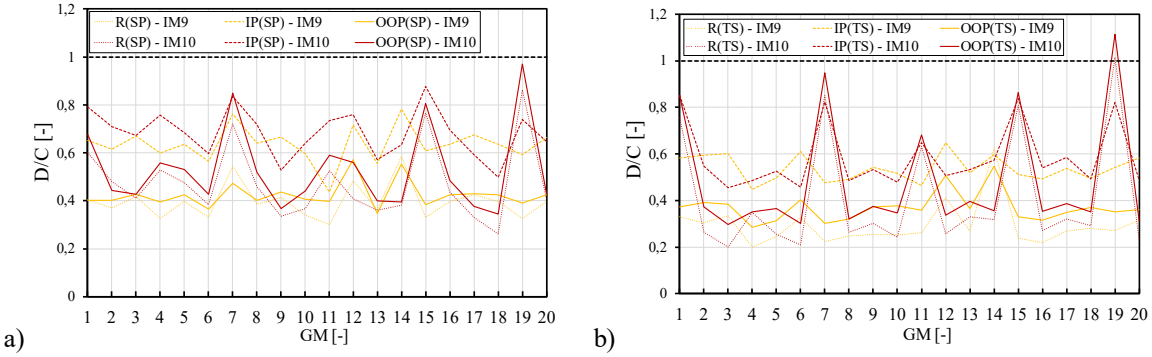

Figure 15: Demand-capacity ratio for columns: (a) SP model; (b) TS model

4.4.3. Model-to-model comparison

Figure 16 provides further comparison between the three analysed models. Figure 16(a) shows statistical comparison among the median values of the peak drift ratio demand ($(d_{X,peak}/H)_m$) in the transverse direction at each IM. IM levels at which global failures occurred (i.e., IM > 6) were discarded in this statistical analysis. The comparison in Figure 16(a) is in agreement with the comparison made by the pushover analysis: the two types of envelope panels shows reductions of displacements compared with the bare frame model in all the analysed intensity. Comparing the models with envelope, although median drift values were similar until IM=6, dispersion between SP and TS became different from IM>4. This assertion is discussed showing the coefficient of variation (*COV*) for the same data as a function of the IM parameter in Figure 16(b). Comparing the results from the two models with envelope panels (i.e., SP and TS plots in the figure), one can observe similar values of *COV* up to IM = 4, whilst the dispersion became larger for the TS model when yielding of TS started (i.e., IM > 5). It is worth noting that one GM at IM=4 for the TS model was excluded from the statistical analysis, because of the anomalously larger value of the peak drift demand in that case. Figure 16(c) summarizes the number of global failures observed for the three examined models as a function of the IM value. The better performance of the building with SPs compared with the BF model response is apparent. On the contrary, the building with TS had a response comparable to the BF model, except at very large IM values for which almost all the GMs produced global failure anyway. The relatively smaller increase in the lateral force resistance

provided by the selected trapezoidal sheeting, and the fact that the panel resistance was completely lost during severe earthquakes, could explain the observed response. Figure 16(d) shows the fraction of global failures (i.e., the ratio between the number of GMs producing global failure at a given IM and the total number of GMs considered) as a function of the $S_a(T_1)$ value. The median value of $S_a(T_1)$ to global failure is also highlighted in the figure. Although number of global failures is similar between the BF and TS models, differences in the hazard curves leads to significant differences in the median value of the first-mode spectral acceleration leading to failure.

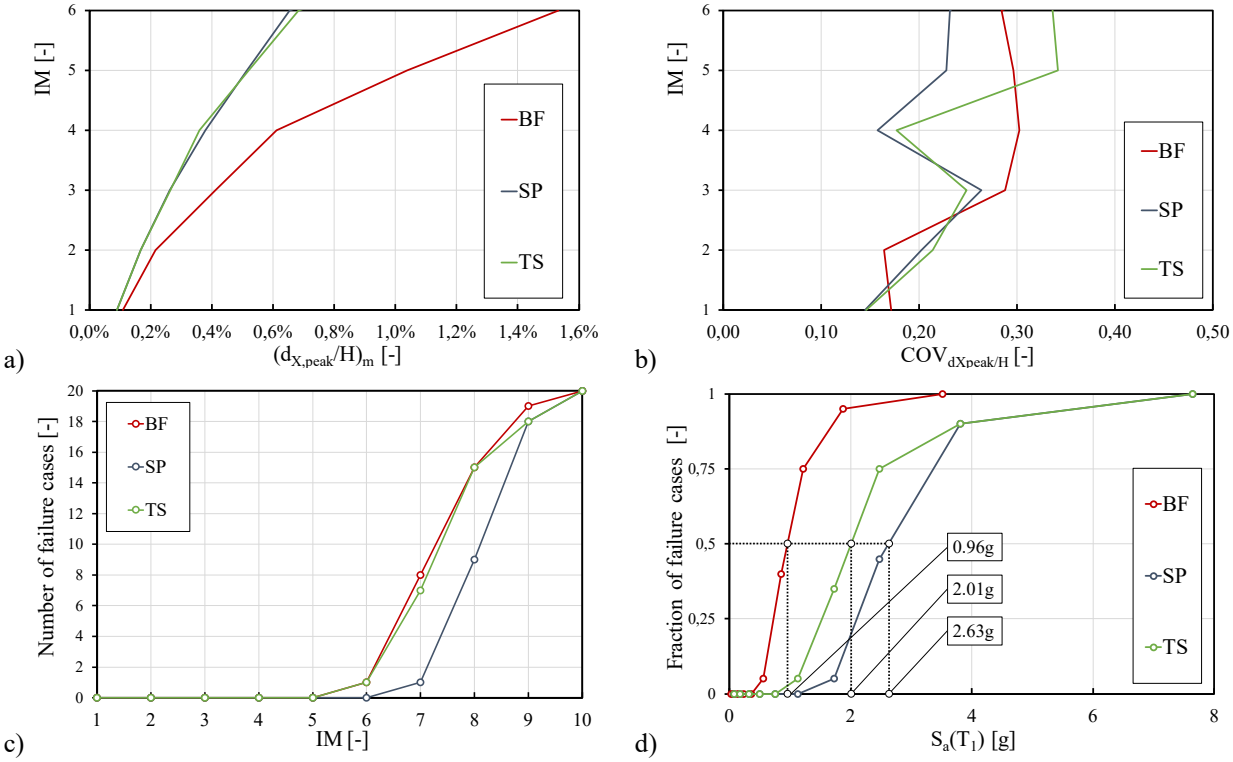

Figure 16: Model-to-model comparison in terms of (a) median peak drift and (b) COV, (c) failure cases and (d) median spectral acceleration that led to building failure.

4.4.4. Components response

This section highlights some aspects of local responses observed in the building components. To this end, Figure 17 shows a sketch of (i) the structural plan layout with a portion of a transverse elevation, (ii) one column where vertical braces are connected in the longitudinal direction, and (iii) a clos-up view of the corresponding column base joints. The sketch of structural layout highlights (i) the location of the transverse trusses (labelled as TR_i), (ii) the location of two critical truss-to-column connections (labelled as TCC_{iL} and TCC_{iR} in the figure), and (iii) the portal frame transverse displacements ($d_X(t)$). To describe the local response at the brace-column-foundation connections, the views on the braced column highlight (i) the column top displacement ($d_{Y,CTD}$) and the displacement of the node at the brace-to-column connection ($d_{Y,CD}$). Knowing these displacements, it is possible to identify the column relative displacement ($d_{Y,CRD}$). Finally, the close-up view of the column base highlights the force and displacement parameters used to describe the column base connection response.

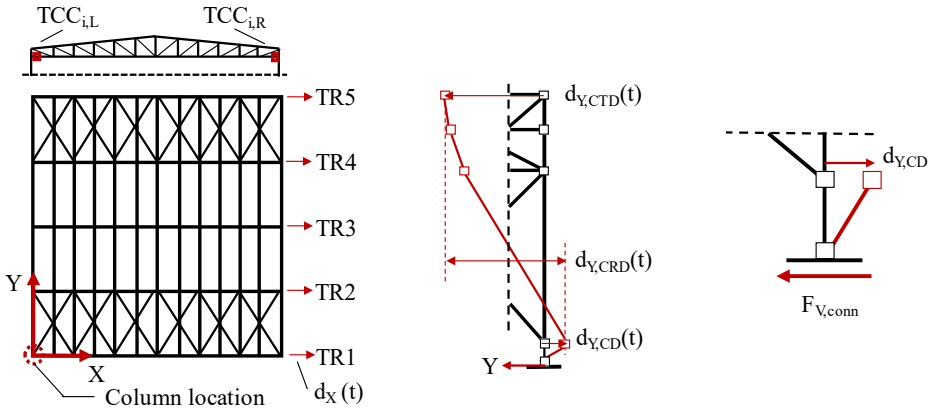

Figure 17: Sketch of trusses and column locations with identification of displacement components.

Figure 18(a) shows response histories of portal frame displacements. In the figure, TR_i identifies the i-th truss (Figure 17). The drift plotted in the figure is the mean value between the two columns for each portal frame. The assumed limit value of the drift for the ultimate failure is also indicated by a dashed line. As shown in the plot, similar drift values were observed among the five portals, especially when the limit value was reached. Figure 18(a) emphasizes the relatively brittle overall system response, with the five portal frames reaching almost simultaneously the limit corresponding to global failure. Divergence of the lateral displacement response at a time during the shaking is also apparent from the plot. This behaviour is further highlighted by the results plotted in Figure 18(b), showing the relationship between the drift of each portal frame and the corresponding shear force in the truss-to-column connections (forces labelled as F_{iL}, F_{iR} corresponding to TCC_{iL} and TCC_{iR} as shown in Figure 17). The figure clearly shows that all the connections reached their deformation capacity.

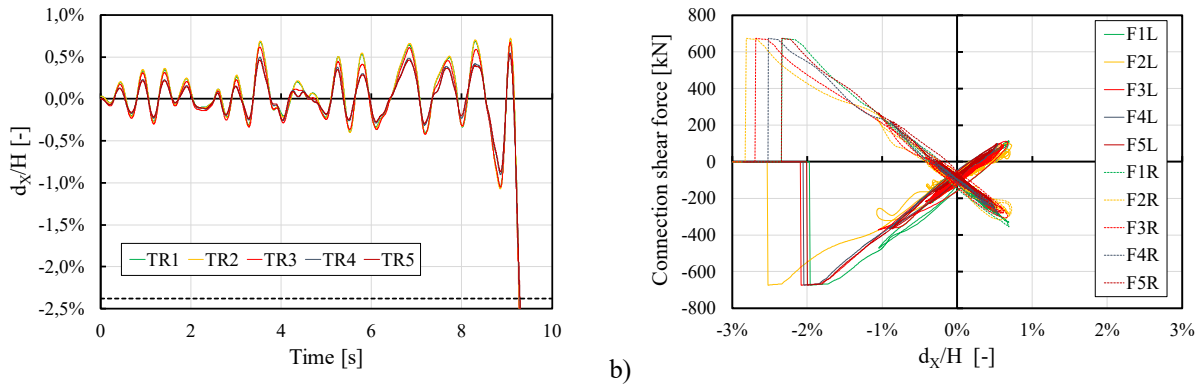

Figure 18: Sample time history response at IM10: (a) transverse drift; (b) forces on truss-to-column connections.

Figure 19(a) shows one sample response history for the column longitudinal displacements. The connection contribution to the column total displacement $d_{Y,CTD}$ was negligible in the first part of the response history, i.e. when the column base connection remained in the elastic range of response. When yielding of the column base connection started, a difference also started to develop between $d_{Y,CTD}$ and $d_{Y,CRD}$, i.e. a difference between total displacement at the column top cross section and column displacement relative to the base. The plot shows that $d_{Y,CRD}$ could either be smaller or larger than $d_{Y,CTD}$ depending on the response time. This behaviour can be explained because of the connection residual deformation that accumulated during the response history, as shown in Figure 19(b).

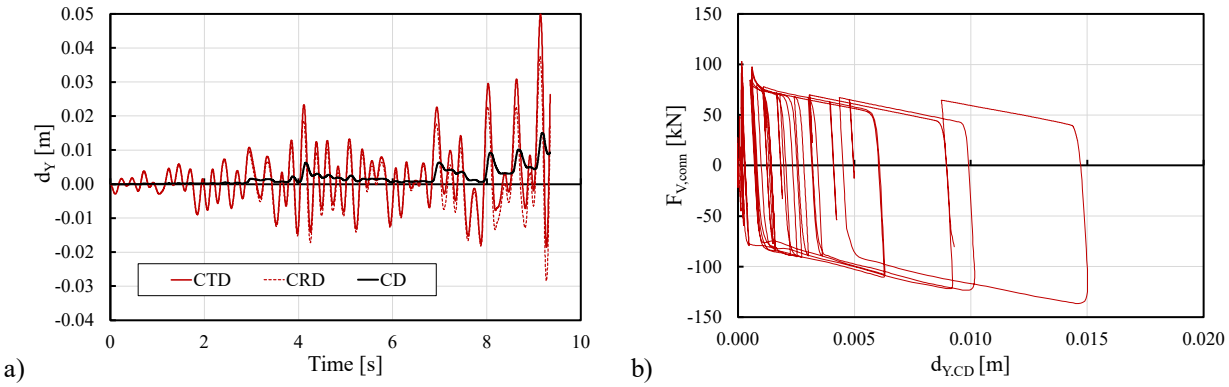

Figure 19: Sample time history at IM10: (a) effect of the column base connection displacements to the column displacement; (b) column base connection response.

5 CONCLUSIONS

This paper presented the results of an ongoing research project on seismic performance evaluation of existing non-residential single-story steel buildings in Italy. Non-linear static and dynamic analyses were carried out on a 3D finite element model of an archetype building. The following main conclusions could be drawn:

- Because of quasi-brittle shear failure of truss-to-column connections, the building response in the transverse direction was much less ductile than in the longitudinal direction. Consequently, global failure of the building was always governed by failures occurring in the trussed beams.
- The envelope panels provided significant benefits to the seismic structural performance. The two types of examined panels, i.e. sandwich panels and trapezoidal sheeting, provided significant increase of the initial lateral stiffness and resistance in the direction of the main portal frames. On the contrary, the effect was much smaller in the longitudinal braced frame direction.

REFERENCES

[1] Iervolino, I., Spillatura, A., Bazzurro, P., Seismic reliability of code-conforming Italian buildings. *Journal of Earthquake Engineering*, **22(S2)**, 5-27, 2018.

[2] Iervolino, I., Spillatura, A., Bazzurro, P., RINTC-E project: towards the assessment of the seismic risk of existing structures in Italy. *Proceedings of the 7th ECCOMAS Thematic Conference on Computational Methods in Structural Dynamics and Earthquake Engineering*, Crete, Greece, 2018.

[3] Scozzese, F., Terracciano, G., Zona, A., Della Corte, G., Dall'Asta, A., Landolfo, R., Modelling and seismic response analysis of Italian code-conforming single-storey steel buildings. *Journal of Earthquake Engineering*, **22:sup2**, 2104-2133, 2018.

[4] CS.LL.PP. C 24 Maggio, Istruzioni relative ai carichi, ai sovraccarichi ed ai criteri generali per la verifica di sicurezza delle costruzioni. *Gazzetta Ufficiale della Repubblica Italiana*, **140**, 1982.

[5] CS.LL.PP. DM 24 Gennaio, Norme tecniche per le costruzioni in zone sismiche. *Gazzetta Ufficiale della Repubblica Italiana*, **108**, 1986.

[6] CNR – Consiglio Nazionale delle Ricerche, Costruzioni di acciaio: Istruzioni per il calcolo, l'esecuzione, il collaudo e la manutenzione. *CNR-UNI 10011*, 1988.

[7] De Matteis G., Landolfo R., Structural behaviour of sandwich panel shear walls: An experimental analysis. *Material and Structures*, **32**, 331-341, 1999.

[8] O'Brien P., Eatherton M.R., Easterling W.S., Characterizing the load-deformation behavior of steel deck diaphragms using past test data. *Cold-Formed Steel Research Consortium Report Series*, CFSRC R-2017-02, 2017.

[9] Mazzoni S., McKenna F., Scott M.H., Fenves G.L., OpenSEES Command Language Manual. *PEER Website*, 2007.

[10] ECCS – European Convention for Constructional Steelwork, European Recommendations for the Application of Metal Sheeting acting as a Diaphragm – Stressed Skin Design. *ECCS – Technical Committee 7 "Thin-walled, cold-formed sheet steel in Building", Technical Working Group 7.5 – "Practical Improvement of Design Procedures"*, **88**, 1995.

[11] CEN – European Committee for Standardization, Eurocode 3: Design of steel structures – part 1-1: General rules and rules for buildings. *EN 1993-1-1, Eurocode 3*, Brussells, 2005.

[12] Hsiao P.C., Lehman D.E., Roeder W., A model to simulate special concentrically braced frames beyond brace fracture. *Earthquake Engineering & Structural Dynamics*, **42**: 183-200, 2012.

[13] CEN – European Committee for Standardization, Eurocode 3: Design of steel structures – part 1-8: Design of joints. *EN 1993-1-8, Eurocode 3*, Brussells, 2005.

[14] Henriques J, Jaspart J.P, Da Silva L.S., Ductility requirements for the design of bolted lap shear connections in bearing. *Advanced Steel Constructions*, **10**(1): 33-52, 2014.

[15] Fabbrocino G, Verderame G.M, Manfredi G, Cosenza E., Structural models of critical regions in old-type r.c. frames with smooth rebars. *Engineering Structures*, **26**: 2137-2148, 2004.

[16] Cantisani G, Della Corte G., Landolfo R., Modelling and analysis of an archetype non-residential old steel building for collapse risk evaluation. *16th European Conference on Earthquake Engineering*, Thessaloniki, Greece, 2018.

[17] Hall J.F., On the descending branch of the pushover curve for multistory buildings. *Earthquake Engineering and Structural Dynamics*, **47**, 772-783, 2018.

[18] Cantisani G., Della Corte G., Seismic response of non-conforming single-storey non-residential buildings considering envelope panels. *Proceedings of the Ninth International Conference on Advances in Steel Structures*, Hong Kong, China, 2018.

[19] Badalassi, M., Braconi, A., Cajot, L.-G., Caprili S., et al., Influence of variability of material mechanical properties on seismic performance of steel and steel-concrete composite structures, *Bulletin of Earthquake Engineering*, **15**, 1559-1607, 2017.

[20] Jalayer, F. and Cornell, C. A., Alternative non-linear demand estimation methods for probability-based seismic assessments. *Earthquake Engineering & Structural Dynamics* **38**(8), 951–972, 2009.

COMPDYN 2019
7th ECCOMAS Thematic Conference on
Computational Methods in Structural Dynamics and Earthquake Engineering
M. Papadrakakis, M. Fragiadakis (eds.)
Crete, Greece, 24–26 June 2019

THE ROLE OF UNCERTAINTY OF MODEL PARAMETERS IN PSHA

L. Hofer[1] **and M.A. Zanini**[1]

[1] University of Padova, Department of Civil, Environmental and Architectural Engineering
Via Marzolo 9
e-mail: lorenzo.hofer@dicea.unipd.it
e-mail: marianoangelo.zanini@dicea.unipd.it

Abstract

Current approaches for the seismic hazard assessment, are mainly based on the classical formulation of the probabilistic seismic hazard analysis, widely known with the acronym PSHA. This procedure is able to compute the annual rate of exceedance of a set of ground motion intensity measures at a site of interest. During years, several efforts were performed for understanding and including the influence of uncertainties underlying the PSHA calculation. PSHA integral is a correct application of the total probability theorem, but it does not account for the uncertainties in model parameters which can be significant, since most of times they are derived from historical data and/or statistical catalogues. For this reason, this work aims to develop a robust semi-analytical formulation, able to assess how uncertainties in model parameters influence the seismic hazard curve's reliability. The proposed mathematical procedure uses the reliability index and its standard deviation for computing a design hazard curve, whose points are characterized by a fixed accepted level of risk. Results show how uncertainties in model parameters affect the hazard curve's dispersion, and how a better parameters' knowledge allows defining lower design values, with the same assumed risk.

Keywords: Instructions, ECCOMAS Thematic Conference, Structural Dynamics, Earthquake Engineering, Proceedings.

1 INTRODUCTION

Current approaches for the seismic hazard assessment, are mainly based on the classical formulation of the probabilistic seismic hazard analysis, widely known with the acronym PSHA**.** For its nature, PSHA deals with several sources of uncertainties and aims describing effects of stochastic and unpredictable events. For this reason, since its early beginning, several efforts have been made for guaranteeing that all uncertainty sources were correctly accounted for [1]. Usually, scientific literature subdivides uncertainties into two main types: aleatory uncertainty and epistemic uncertainty. The former is the variability naturally inherent to a physical phenomenon, while the latter is due to the limited knowledge about the true model describing the aleatory variability ([2], [3]). Currently, on of the most widely adopted strategy for addressing seismic hazard epistemic uncertainty is the so-called logic-tree approach [4]. In the logic-tree, every node represents a potential source of epistemic uncertainty, and the corresponding outcoming branches represent the possible alternatives. This approach is general and considers both the inter-model uncertainty, due to uncertainty in model parameters, and the inter-model uncertainty, due to the uncertainty among models. Despite its wide adoption in PSHA [5], the use of logic trees is often debated, and there are many potential pitfalls that should be considered [6], mainly due to the fact that two potential interpretation of the logic-tree are possible ([7], [8], [9], [10]). For an extended discussion on the subject the reader is referred to [11] and [12]. In any case, logic tree results strictly depend on how logic tree branches are populated and on the weight assigned on each branch. In this context, the present work wants to contribute to the discussion on the reliability of seismic hazard estimate. In particular, this contribution aims to develop a standardized robust semi-analytical formulation, able to assess the influence of all possible source on variability involved in the seismic hazard computation, by treating them as random variables. The proposed method needs a carefully election of the best functional forms to be adopted in the calculation but does not need the definitions of any branches or weights. The formulation herein presented allows thus computing a given quantile of the seismic hazard demand by treating model parameters as random variables. The required computational time is limited, since no sampling or distribution fitting is required.

2 PROPOSED FORMULATION

The proposed formulation introduces a further development to the classical PSHA formulation, that is able to consider the variability of the hazard curve arising from uncertainties in model parameters ([13], [14]). For this reason, only a brief presentation of the consolidated PSHA procedure will be provided in the following, leaving space to a complete and extensive explanation of the proposed method. Classical PSHA integral aims computing the annual rate of exceedance $\lambda_{\mathrm{IM}\geq\mathrm{im}}$ of a set of ground motion intensity measures IM at a site of interest with the following formula:

$$\lambda_{IM\geq im}=\sum_{i=1}^{n_{sources}} \nu_{m_{min,i}} \int_{m_{min,i}}^{m_{max,i}} \int_{0}^{r_{max,i}} P\left[IM\geq im|m,r\right] f_{M,i}\left(m\right) f_{R,i}\left(r\right) dr dm \tag{1}$$

where $\nu_{m_{min,i}}$ is rate of occurrence of earthquakes greater than a suitable minimum magnitude $m_{min,i}$ of the i^{th} seismogenic sources (SZ), $f_{M,i}\left(m\right)$ is the magnitude distribution for the i^{th} ZS and $f_{R,i}\left(r\right)$ is the distribution of the source i^{th} -to-site distance. The exceedance probability of a threshold *im*, given a magnitude *m* and a distance *r* is provided by $P\left[IM\geq im|m,r\right]$. Once

calculating $\lambda_{IM \geq im}$, using the Poissonian distribution it is possible to compute the probability of exceeding each ground motion level *im* in the next *T* years as

$$P\left[IM \geq im,T\right]=1-e^{-T\cdot\lambda_{IM\geq im}} \tag{2}$$

The exceedance annual rate computed in Eq. (1) depends on $v_{m_{min,i}}$ and on parameters which define $f_{M,i}(m)$, $f_{R,i}(r)$ and $f_{IM}(im)$ distributions; in the following, these model parameters are summarized in vector $\boldsymbol{\Theta}$. As a consequence, probability computed in Eq. (2), called in the following P_f (probability of failure), is function of *im*, *T*, and parameters $\boldsymbol{\Theta}$:

$$P\left[IM \geq im,T\right]=P_f\left(im,T,\boldsymbol{\Theta}\right)=1-e^{-T\cdot\lambda_{IM\geq im}(\boldsymbol{\Theta})} \tag{3}$$

Following Gardoni et al. [15] the solid line of Fig. 1 is a point estimate $\hat{P}_f(im,T)$ of P_f calculated by computing $P_f\left(im,T,\boldsymbol{\Theta}\right)$ at a point estimate of $\boldsymbol{\Theta}$ (i.e., $\boldsymbol{\Theta}=\hat{\boldsymbol{\Theta}}$, where $\hat{\boldsymbol{\Theta}}$ could be the mean or median of $\boldsymbol{\Theta}$), or the predictive estimate $\tilde{P}_f(im,T)$ of $P_f\left(im,T,\boldsymbol{\Theta}\right)$ computed as the expected value of over $\boldsymbol{\Theta}$ ($\tilde{P}_f(im,T)=\int P_f\left(im,T,\boldsymbol{\Theta}\right)f(\boldsymbol{\Theta})d\boldsymbol{\Theta}$). The risk-based hazard curve $P_{f,d}(im,T)$ (where *d* stands for design) is characterized by fixed accepted level of risk (Fig. 1); in other words, we want to define a quantile *q* such that the probability of having P_f bigger than $P_{f,d}$ due to uncertainties in model parameters it is equal to *q*; more formally

$$P\left[P_f\left(im,T,\boldsymbol{\Theta}\right)\geq P_{f,d}\left(im,T\right)\right]=q \tag{4}$$

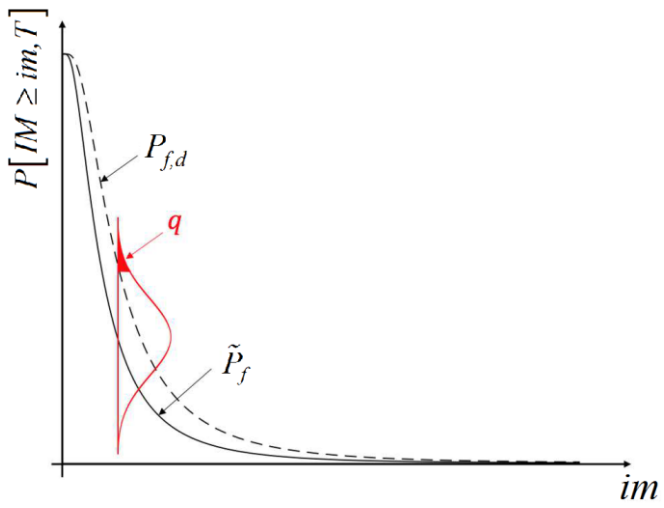

Figure 1: Definition of the $P_f\left(im,T,\boldsymbol{\Theta}\right)$ distribution, $\tilde{P}_f$, $P_{f,d}$ and *q*.

Since the exact evaluation of the $P_f\left(im,T,\boldsymbol{\Theta}\right)$ distribution requires nested calculation ([16]), this formulation adopts approximated quantile obtained by a first order analysis ([15]). The design failure probability $P_{f,d}$ can thus be obtained as

$$P_{f,d}\left(im,T\right)=\Phi\left[-\tilde{\beta}\left(im,T\right)+k\cdot\sigma_{\beta}\left(im,T\right)\right] \tag{5}$$

where $\Phi(\cdot)$ is standard normal cumulative function, $\tilde{\beta}(im,T)$ is the reliability index computed according to the definition of reliability index as $\tilde{\beta}(im,T)=\Phi^{-1}\left[1-\tilde{P}_f(im,T)\right]$ and $k\cdot\sigma_\beta(im,T)$ is the quantile of the distribution reflecting the assumed level of risk. Assuming β normally distributed, *k* is shown to be equal to:

$$k=\Phi^{-1}[1-q] \tag{6}$$

According to [16] the standard deviation of the reliability index σ_β can be computed by using a first order Taylor series expansion around the mean vector of the model parameters $\mathbf{M}_{\boldsymbol{\Theta}}$ as

$$\sigma_\beta{}^2(im,T)\approx\nabla_{\boldsymbol{\Theta}}\beta(im,T)^T\,\boldsymbol{\Sigma}_{\boldsymbol{\Theta}\boldsymbol{\Theta}}\nabla_{\boldsymbol{\Theta}}\beta(im,T) \tag{7}$$

where $\boldsymbol{\Sigma}_{\boldsymbol{\Theta}\boldsymbol{\Theta}}$ is the covariance matrix and contains the variances of the model parameters and their possible correlation. The gradient of β $\nabla_{\boldsymbol{\Theta}}\beta(im,T)$, is computed by applying the chain rule to the definition of reliability index as

$$\nabla_{\boldsymbol{\Theta}}\beta(im,T)=-\frac{1}{\varphi\left[\tilde{\beta}(im,T)\right]}\nabla_{\boldsymbol{\Theta}}P_f(im,T) \tag{8}$$

where $\varphi(\cdot)$ is the standard normal probability density function and $\nabla_{\boldsymbol{\Theta}}P_f(im,T)$ is the gradient column vector of $P_f(im,T,\boldsymbol{\Theta})$ evaluated in $\mathbf{M}_{\boldsymbol{\Theta}}$, that can be numerically computed with the definition of derivative as

$$\nabla_{\boldsymbol{\Theta}}P_f(im,T)=\left[\frac{P_f(im,T,\Theta+\delta\Theta)-P_f(im,T,\Theta)}{\delta\Theta}\right]_{\mathbf{M}_{\boldsymbol{\Theta}}} \tag{9}$$

3 CASE STUDY

The proposed formulation is applied to a case study, represented by a residential building structure (T = 50 years) located in Gemona (13.145, 46.288) and built on a soil-type C [17]. Two seismogenic zones SZs of the Italian source model are considered, SZ 904 and SZ 905 [18]. Main model parameters for each zone are derived from Barani et al. [19] and are reported in Tab. 1

	$m_{max,i}$	$m_{min,i}$	b_i	$v_{m_{min,i}}$
i = 1 – SZ 904	5.5	4.3	0.939	0.05
i = 2 – SZ 905	6.6	4.3	0.853	0.316

Table 1: Main parameters of each SZ.

Fig. 2 shows a map representing the site of interest and the considered seismogenic zones. Calculations are performed referring to two *IMs*, i.e. Sa (T = 0 sec.), the so-called Peak Ground Acceleration (PGA), and for Sa (T = 0.1 sec.). In this work, the ground motion prediction equation GMPE proposed by Bindi et al. [20] has been adopted.

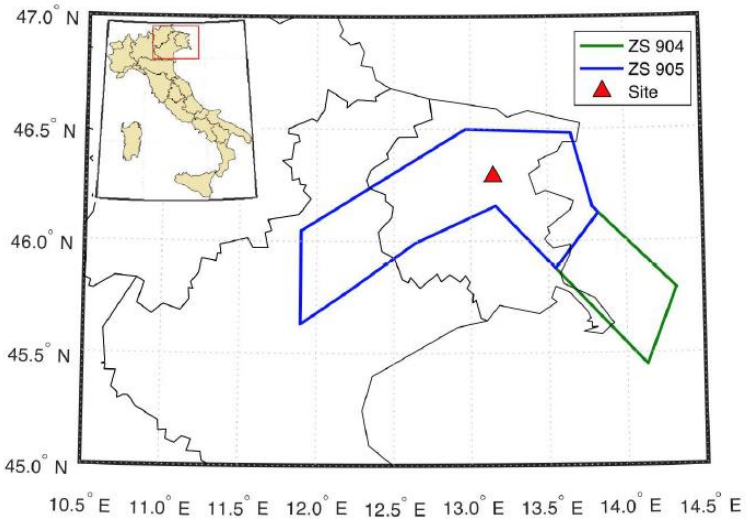

Figure 2: Site of interest and adopted SZs

The parameters that have been assumed as random are the G-R law parameters ($m_{max,i}$, $m_{min,i}$, b_i and $v_{m_{min,i}}$), and the main parameters contained in the adopted GMPE, i.e. e_1 that is the constant term of the regression, F_S and F_{sof} representing respectively the site amplification and the faulting mechanism, and σ_{tot} that is the standard deviation of the predicted *IM* logarithm. The final vector of model parameters $\boldsymbol{\Theta}$, is thus composed by the following 12 elements

$$\boldsymbol{\Theta}=\left[m_{max,1},m_{max,2},m_{min};b_1;b_2;v_{m_{min,i}};v_{m_{min,i}};e_1,F_S;F_{sof,1};F_{sof,2};\sigma_{tot} \right] \tag{9}$$

In this way, all the main possible sources of uncertainty, associated to model's parameters involved in the PSHA calculation, are considered. Table 2 lists the mean value and the standard deviation of each parameter, where the mean values are the elements of the vector $\mathbf{M}_{\boldsymbol{\Theta}}$, while the variances represent the diagonal term of the covariance matrix $\boldsymbol{\Sigma}_{\boldsymbol{\Theta\Theta}}$. For $m_{max,i}$, m_{min}, b_i, $v_{m_{min,i}}$ and σ_{tot}, a coefficient of variation $\delta=\sigma/\mu$ has been assumed, since no information on the parameters' standard deviation was available.

	$m_{max,1}$	$m_{max,2}$	b_i	b_i	$v_{m_{min,i}}$	$v_{m_{min,i}}$	m_{min}	σ_{tot}
μ	5.5	6.6	0.939	0.853	0.05	0.316	4.3	0.337
σ	0.55	0.66	0.0939	0.0853	0.005	0.0316	0.43	0.0337
δ = σ/μ	0.1	0.1	0.1	0.1	0.1	0.1	0.1	0.1
	e_1	F_S	$F_{sof,1}$	$F_{sof,2}$	e_1	F_S	$F_{sof,1}$	$F_{sof,2}$
	Sa (T = 0 sec.)				Sa (T = 0.1 sec.)			
μ	3.672	0.24	-0.0544	0.105	3.796	0.247	-0.0451	0.111
σ	0.316	0.0322	0.0355	0.0296	0.365	0.0357	0.0367	0.0351
δ = σ/μ	0.086	0.134	0.652	0.282	0.096	0.145	0.814	0.316

Table 2: Mean value and standard deviation of the adopted parameters.

Finally, two percentile values have been assumed $q=\{0.05,0.15,0.25\}$ corresponding to $k=\{1.64,1.04,0.67\}$; when q = 0.5, P_f is computed (Eq. (2)), without any further information related to parameter uncertainties (k = 0). When $k \approx \pm 1$ the approximate 15% and 85% per-

centile bounds of P_f are calculated. Fig. 3 shows results of the proposed formulation which allows characterizing P_f uncertainty and its distribution; each design hazard curve is characterized by a constant level of assumed risk q (for completeness also curves corresponding to (1- q) have been plotted). The two different spectral accelerations show a similar behavior; in particular, quantiles of Sa (T = 0.1 sec.) are less close, in absolute terms, to the hazard curve computed without considering parameters uncertainties.

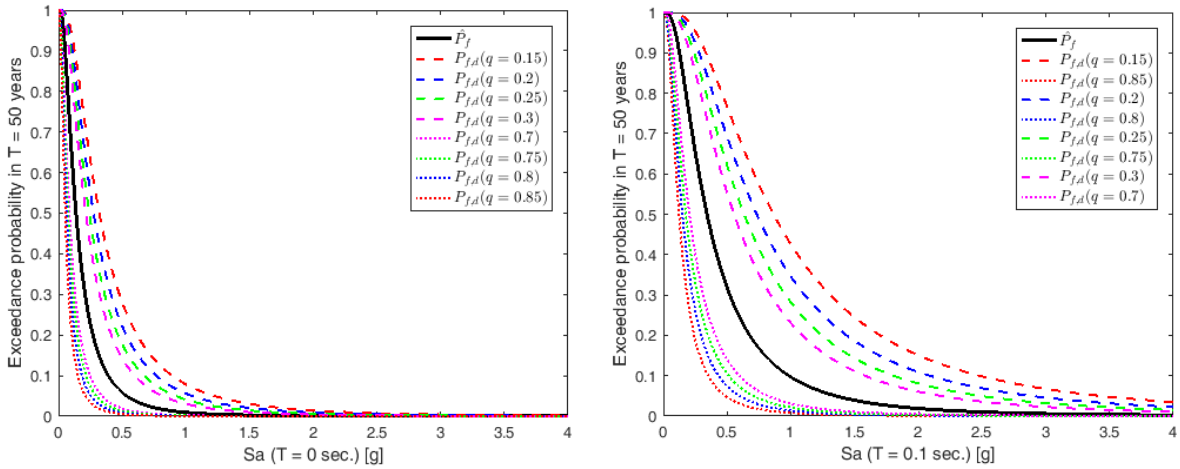

Figure 3: Hazard curve for different values of *q:* a) Sa (T = 0 sec.), b) Sa (T = 0.1 sec.).

For sake of completeness and for showing the influence of the covariance matrix, a smaller fictitious covariance matrix $\boldsymbol{\Sigma}_{\boldsymbol{\Theta\Theta}}^{\text{small}}$ is assumed with the coefficient of variation of all parameters equal to $\delta^{\text{small}} = \delta / 2$ representing a hypothetical case in which a more accurate knowledge of the distribution parameters is available. Table 3 lists the mean value and the standard deviation of each parameter adopted in this second case.

	$m_{max,1}$	$m_{max,2}$	b_i	b_i	$v_{m_{min,i}}$	$v_{m_{min,i}}$	m_{min}	σ_{tot}
μ	5.5	6.6	0.939	0.853	0.05	0.316	4.3	0.337
σ	0.275	0.330	0.047	0.043	0.003	0.016	0.215	0.017
δ = σ/μ	0.050	0.050	0.050	0.050	0.050	0.050	0.050	0.050
	e_1	F_S	$F_{sof,1}$	$F_{sof,2}$	e_1	F_S	$F_{sof,1}$	$F_{sof,2}$
	Sa (T = 0 sec.)				Sa (T = 0.1 sec.)			
μ	3.672	0.24	-0.0544	0.105	3.796	0.247	-0.0451	0.111
σ	0.158	0.016	0.018	0.015	0.182	0.018	0.018	0.018
δ = σ/μ	0.043	0.067	0.326	0.141	0.048	0.072	0.407	0.158

Table 3: Mean value and standard deviation of the adopted parameters.

Fig. 3 shows as that $P_{f,d}$ curves are closer to the one computed without considering parameters' variability. This behavior is clearly due to the lower uncertainty associate to the input parameters. In other words, a better initial knowledge allows considering a lower seismic hazard curve with the same assumed level of risk q.

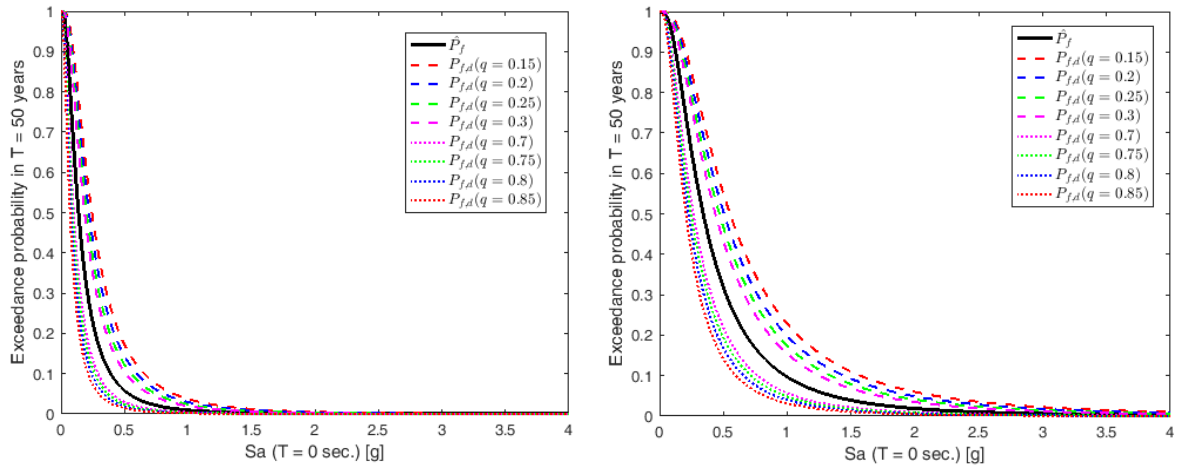

Figure 3: Hazard curve for different values of q computed with a reduced covariance matrix $\boldsymbol{\Sigma}_{\boldsymbol{\Theta\Theta}}^{\text{small}}$: a) Sa (T = 0 sec.), b) Sa (T = 0.1 sec.)

4 CONCLUSIONS

This work presented a mathematical formulation able to consider the effect of parameters' uncertainty, on the seismic hazard curve. In particular, a procedure for the seismic hazard computation based on a fixed level of risk was proposed. The proposed framework allows computing a specific target quantile of the hazard curve, by mean of an immediate semi-analytical procedure that does not need any sampling or distribution fitting. The formulation is general and flexible and can be easily extended to hazard curve obtained by considering the entire seismic sequence, with foreshocks and aftershocks. Furthermore, the proposed methodology is also an important knowledge tool, since it allows finding the most impacting parameter on final results without running extensive analysis.

REFERENCES

[1] R. K. McGuire, Effects of uncertainties in seismicity on estimates of seismic hazard for the east coast of the United States. *Bulletin of the Seismological Society of America*, **67**: 827-848, 1977.

[2] R.K. McGuire, K.M. Shedlock, Statistical uncertainties in seismic hazard evaluations in the United States, *Bulletin of the Seismological Society of America*, **71**: 1287-1308, 1981.

[3] Senior Seismic Hazard Analysis Committee (SSHAC), Recommendations for Probabilistic Seismic Hazard Analysis: Guidance on Uncertainty and Use of Experts, U.S. Nuclear Regulatory Commission, U.S. Dept. of Energy, Electric Power Research Institute, NUREG/CR- 6372, UCRL-ID-122160, 1997.

[4] R.B. Kulkarni, R.R. Youngs, K.J. Coppersmith, Assessment of confidence intervals for results of seismic hazard analysis. *Proceedings of the Eighth World Conference on Earthquake Engineering*, San Francisco, **1**, 263–270, 1994.

[5] E. H. Field, R.J. Arrowsmith, G.P. Biasi, P. Bird, T.E. Dawson, K.R. Felzer, D.D. Jackson, K.M. Johnson, T.H. Jordan, C. Madden, A.J. Michael, K.R. Milner, M.T. Page, T.

Parsons, P.M. Powers, B.E. Shaw, W.R. Thatcher, R.J. Weldon II, Y. Zeng, Uniform California Earthquake Rupture Forecast, Version 3 (UCERF3)-The Time-Independent Model, *Bulletin of the Seismological Society of America*, **104 (3)**: 1122–1180, 2014.

[6] J.J. Bommer, F. Scherbaum, The use and misuse of logic-trees in probabilistic seismic hazard analysis, *Earthquake Spectra*, **24**, 997–1009, 2008.

[7] R.K. McGuire, C.A. Cornell, G.R. Toro, The case for using mean seismic hazard, *Earthquake Spectra*, **21**: 879-886, 2005.

[8] R. Musson, Against fractiles, *Earthquake Spectra*, **21**: 887-891, 2005.

[9] N.A. Abrahamson, J.J. Bommer, Probability and uncertainty in seismic hazard analysis, *Earthquake Spectra*, **21**, 603–607, 2005.

[10] M. Stucchi, C. Meletti, V. Montaldo, H. Crowley, G. M. Calvi, E. Boschi, Seismic hazard assessment (2003–2009) for the Italian Building Code, *Bulletin of the Seismological Society of America*, **101**, 1885–1911, 2011

[11] W. Marzocchi, M. Taroni, J. Selva, Accounting for Epistemic Uncertainty in PSHA, logic Tree and Ensamble Modeling, *Bulletin of the Seismological Society of America*, **105**, 4, 2015.

[12] W. Marzocchi, T.H. Jordan, A unified probabilistic framework for seismic hazard analysis. *Bulletin of the Seismological Society of America*, **107(6)**, 2738-2744, 2017.

[13] C. Cornell, Engineering seismic risk analysis, *Bulletin of Seismological Society of America*, **58(5)**: 1583-1606, 1968.

[14] J.W. Baker, Introduction to Probabilistic Seismic Hazard Analysis. White Paper Version 2.1, 77 pp, 2015.

[15] P. Gardoni, A. Der Kiureghian, K.M. Mosalam, Probabilistic Capacity Models and Fragility Estimates for Reinforced Concrete Columns based on Experimental Observations, *Journal of Engineering Mechanics*, **128(10)**: 1024-1038, 2002.

[16] A. Der Kiureghian, Measures of structural safety under imperfect states of knowledge, *Journal of Structural Engineering*, **115(5)**, 1119–1140, 1989.

[17] Italian Ministry of Infrastructures (2008) Technical Standards for Constructions, NTC-2008-1-14 (in Italian).

[18] C. Meletti, F. Galadini, G. Valensise, M. Stucchi, R. Basili, S. Barba, G. Vannucci, E. Boschi, A seismic source zone model for the seismic hazard assessment of the Italian territory, *Tectonophysics*, **450**, 85–108, 2008

[19] S. Barani, D. Spallarossa, P. Bazzurro, Disaggregation of probabilistic ground-motion hazard in Italy, *Bulletin of Seismological Society of America*, **99 (5)**, 2638–2661, 2009.

[20] D. Bindi, F. Pacor, L. Luzi, R. Puglia, M. Massa, G. Ameri, R. Paolucci, Ground motion prediction equations derived from the Italian strong motion database, *Bulletin of Earthquake Engineering*, **9(6)**, 1899–1920, 2011.

COMPDYN 2019
7th ECCOMAS Thematic Conference on
Computational Methods in Structural Dynamics and Earthquake Engineering
M. Papadrakakis, M. Fragiadakis (eds.)
Crete, Greece, 24–26 June 2019

SOIL NON-LINEARITY ON HIGH SPEED RAILWAY LINES

K. Dong[1], P. Alves Costa[2], O. Laghrouche[1], P.K. Woodward[3], D. P. Connolly[3]

[1] Heriot Watt University
Edinburgh, Scotland, UK
e-mail: kd11@hw.ac.uk, O.Laghrouche@hw.ac.uk

[2] University of Porto
Porto, Portugal
pacosta@fe.up.pt

[2] University of Leeds
Institute of High Speed Rail and System Integration
Leeds, UK
d.connolly@leeds.ac.uk, p.k.woodward@leeds.ac.uk

Abstract

Increases in operational train speed have resulted in an elevated probability that dynamic effects will occur inside the railway track and subgrade structure. This is problematic because it causes soil non-linearity, thus resulting in reduced soil stiffness. Therefore, this paper outlines a numerical semi-analytical frequency domain model to compute and analyse non-linear stiffness degradation below railway lines. An equivalent linear approach is used to incorporate non-linear stiffness and damping changes into a thin-layer element frequency-wavenumber domain formulation. The model is validated using published data and then used to analyse non-linearity. It is shown that non-linearity plays an important role in track-ground response, with track displacements increasing significantly in magnitude. It is also shown that the critical velocity can be reduced significantly, which is important because many high speed lines set their dynamic threshold at 70% of the linearly calculated value. Similar findings are made for track velocities and soil strain levels, thus indicating it is vital to consider soil non-linearity when modelling high speed rail track behaviour.

Keywords: Railway track dynamics, non-linear soil, thin-layer element method

1 INTRODUCTION

Operational railway speeds have increased over the past 40 years since the inception of high speed rail. This means it is increasingly likely that trains will induce high levels of dynamics within the track-soil structure. This occurs when the trains peed approaches the natural wave speeds of the track-ground system. The speed at which maximum dynamic amplification occurs is the 'critical velocity' ([1], [2]). This is undesirable because it is a safety risk, increases track degradation and can induce ground-borne vibration ([3],[4], [5]).

To analyze critical velocity, early approaches modelled the problem analytically [6]. Then, with the aim of simulating more complex ground conditions (e.g. layered soil), integral transform methods [7] were proposed. To allow for the track to also be modelled in a more detailed manner, 'two-and-a-half' dimensional models (2.5D) were also developed ([8], [9], [10]). These assumed the track was invariant in the direction of vehicle travel, thus allowing the problem to be discretized in 2D. This provided greater model flexibility, while maintaining a relatively low number of degrees of freedom.

The majority of railway vibration models are formulated in the frequency-wavenumber domain, meaning they are typically limited to considering linearly elastic material behavior. This assumption is suitable for many situations, however limits the analysis of non-linearity's such as wheel-rail contact ([11]) and soil stiffness degradation. Soil stiffness degradation is particularly important on heavy haul and high speed rail lines were the elevated loads and high speeds can cause high strain levels. These strains can then reduce the soil stiffness by a significant percentage, thus causing higher track deflections.

To include non-linear material effects, [1] manually adjusted the soil shear wave velocity at different speeds to account for the reduced stiffness effect. A challenge with this approach is that manually choosing stiffness' values is open to error and difficult to apply over multiple soil regions. Therefore [12], [13] proposed 3D time-domain constitutive non-linear time domain formulations and validated results against field data recorded in Sweden. A challenge with this approach is that such models are computationally intensive and often require a large number of material input properties that are challenge to quantify.

As an alternative, [14] proposed the use of a frequency-wavenumber domain 2.5D finite/infinite element model which although was linear, used an iterative procedure implement non-linearity. Again the model was compared to the data recorded in Sweden and strong agreement was found but with reduced run times compared to the 3D constitutive approach.

This paper builds upon this iterative linear equivalent approach. Instead of a 2.5D model though, a semi-analytical approach is preferred because it further reduces run times thus allowing for larger sensitivity studied to be performed. The track is modelled analytical while the soil is modelling using the thin-layer element method. It is validated and then used to make findings into the effect of non-linearity of dynamic amplification curves.

2 NUMERICAL MODEL

The model uses a semi-analytical method to compute vertical track deflections. It consists of an analytical track model, and a semi-analytical thin-layer element model for the soil. These sub-models are formulated in the frequency-wavenumber domain, and then coupled assuming a relaxed boundary condition at their interface. To do so, although the 2 models have different numbers of degrees of freedom, they are only coupled in the vertical direction. As will be shown, this approach produce accurate results, yet allows for the simulation of deep-wave propagation in an efficient manner [15].

2.1 Track model

The track is modelled upon a generic slab track, using springs for the railpads and beam elements for the rail and slab (Figure 1). The equations of motion are formulated in the wave-number-frequency domain and shown in Equation 1. Further details of the track formulation are found in [15].

$$\begin{bmatrix} EI_r k_x^4 + k_p^* - {}^2 m_r & -k_p^* \\ -k_p^* & EI_s k_x^4 + k_p^* - \omega^2 m_s + k_{eq} \end{bmatrix} \begin{Bmatrix} \tilde{u}_r(k_x,\omega) \\ \tilde{u}_s(k_x,\omega) \end{Bmatrix} = \begin{Bmatrix} \tilde{P}(k_x,\omega) \\ 0 \end{Bmatrix} \quad (1)$$

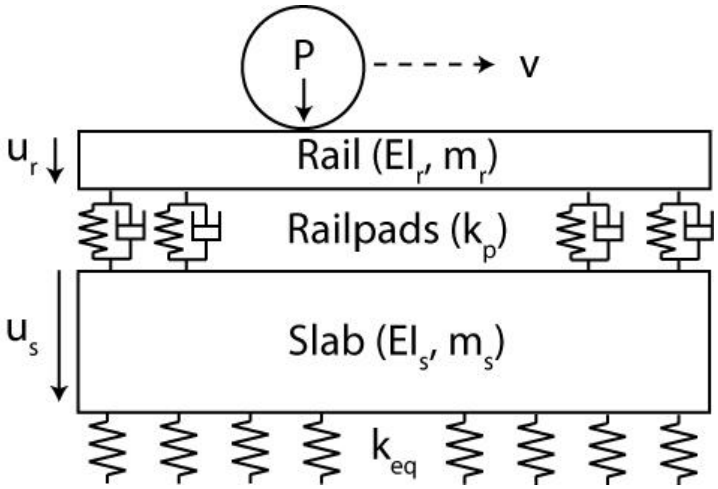

Figure 1: Track model

2.2 Ground model

The ground behavior is simulated using the thin-layer element method. First the soil stratum is discretized into a series of thin and horizontal elements, each with 3 nodes (Figure 2). This ensures that the stresses and strains are accurately reproduced, which is important for the linear equivalent updating procedure. Again, the equations of motion are formulated in the frequency-wavenumber domain as shown in Equation 2, where **K** and **M** are the global stiffness and mass matrices respectively, **U** is displacement, ω is frequency and **P** is the load.

$$([\mathbf{K}] - \omega^2[\mathbf{M}])\mathbf{U} = \mathbf{P} \quad (2)$$

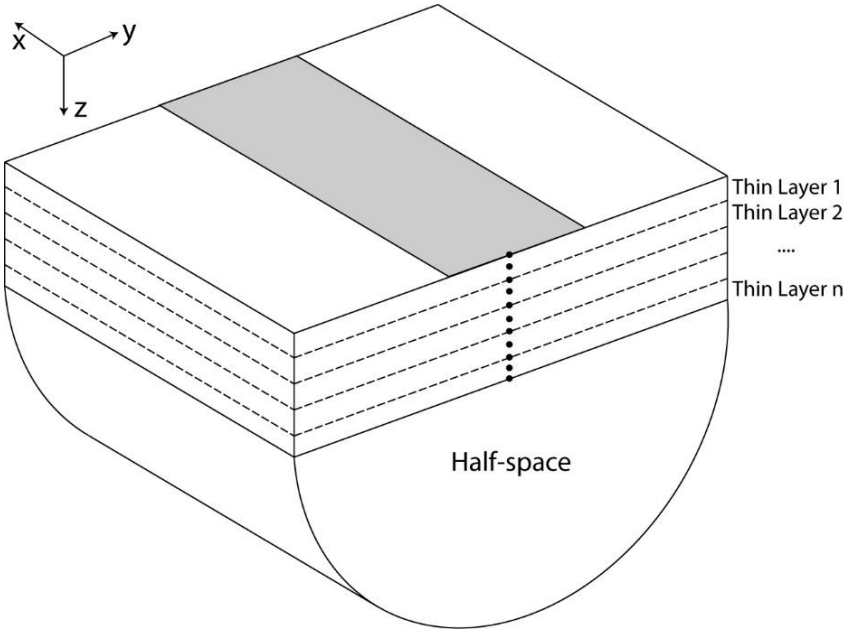

Figure 2: Soil model

2.3 Track-soil coupling

The track model and soil model are coupled using a frequency-wavenumber dependent stiffness. This is computed using the thin-layer method and assumes that there is an equilibrium of loads and a compatibility of displacements at the track-ground interface. It is important that the interaction across this boundary is accurately resolved because when the train speed nears the critical velocity there is very significant wave propagation within the soil stratum.

2.4 Linear equivalent implementation

At high train speeds, large strains can be induced in the underlying soil, causing a reduction in its stiffness, as illustrated in Figure 3. To capture this non-linear behaviour, a 'linear equivalent' approach is implemented.

This is useful because it can be implemented with frequency domain models, to approximate non-linear soil behavior in a much faster timeframe in comparison to time-domain constitutive models. By definition, it means that while the analysis remains linear, the soil properties are updated as function of the strain level, thus simulating non-linear type effects. It is implemented within the thin-layer formulation using the following steps:

- Low strain properties assumed for all thin-layer soil elements
- Strain time histories computed for all elements and determine effective octahedral shear strain values
- Use the maximum strain value to update the element stiffness, based upon stiffness-strain reduction curves (e.g. [14])
- Use the maximum strain value to update the element damping, based upon damping-strain reduction curves
- Repeat the above steps until convergence between consecutive iterations is below 3%

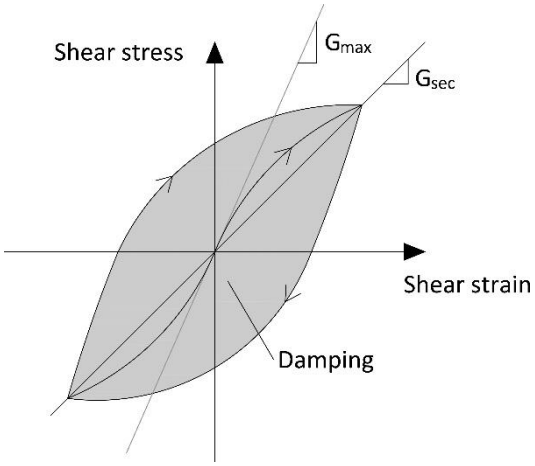

Figure 3: Stress-strain path

3 VALIDATION

The model was validated using field data recorded at Ledsgard, Sweden. This site was subject to large rail deflections and suspected high soil non-linearity during the passage of X2000 trains shortly after opening. This occurred because the track was constructed over soft ground, with a sandwiched layer of uncharacteristically soft organic clay. The detailed track and ground properties, including soil degradation curves, are given in [14], [16] and [17].

Figure 4 shows the time history response of the field the TLM signals at a train speed of 70 km/h. It is seen that the numerical model replicates the field result accurately in terms of magnitude and shape. The same is true for the faster speed of 180km/h, which is shown in Figure 5. Additional speeds were also computed with similar findings. Therefore is was concluded that the model was able to accurately predict track response in the presence of non-linear soil behavior.

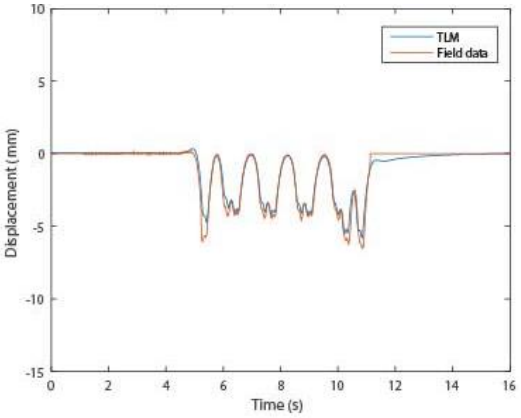

Figure 4: Displacement time history at 70km/h

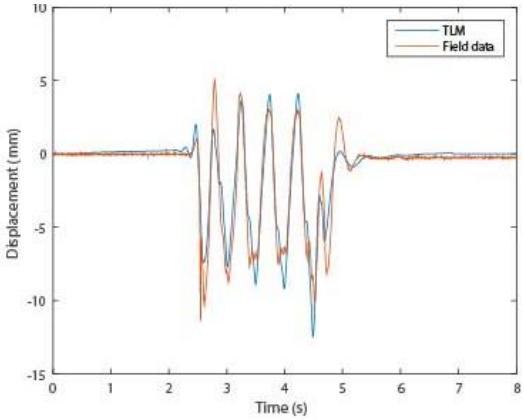

Figure 5: Displacement time history at 180km/h

4 NUMERICAL ANALYSIS

To investigate the role of soil non-linearity on high speed lines in more depth, an infinitely deep, homogenous soft soil was analysed. It had a small-strain stiffness of 45MPa, a Poisson's ratio of 0.35, a density of 1800kg/m^3 and damping of 0.03. The stiffness and damping degradation curves were identical to those used for the validation case. The vehicle was a single 18 tonne axle load moving at speeds ranging between 10-140m/s.

Figure 6 shows the rail dynamic amplification curve across the full speed range. It is seen that the linear and linear-equivalent curves have similar shape. The linear response yields lower displacements at the majority of speeds, except around its critical velocity peak at 90m/s. Further, the linear equivalent case has 29% higher maximum rail deflections compared to the linear case. Also, the critical velocity for the non-linear case reduces by 21% compared to the linear case. Both the change in deflection magnitude and critical speed are due to the drop in soil stiffness below the moving load, thus allowing the track to deflect more. However, it should be noted that the result is for a single wheel and that non-linearity is highly sensitive to multiple-wheel spacing and loading magnitude.

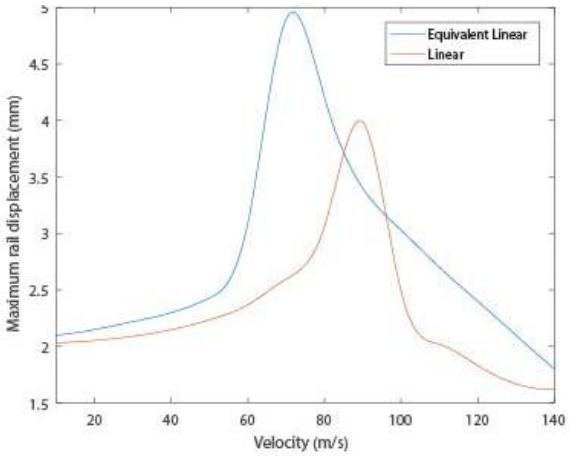

Figure 6 – DAF curves for linear and non-linear behavior

Finally, Figure 7 shows the effect of vehicle speed on strain levels with depth. Two speeds are shown: 10m/s (well below the critical speed) and 70m/s (at the linear equivalent critical speed). It is seen that the maximum strains occur for both speeds close to 1m below

the soil surface. However, at all depths, the maximum octahedral strains are significantly lower for the linear case. This is the primary cause of the reduction of soil stiffness and the ultimate increase in rail deflections.

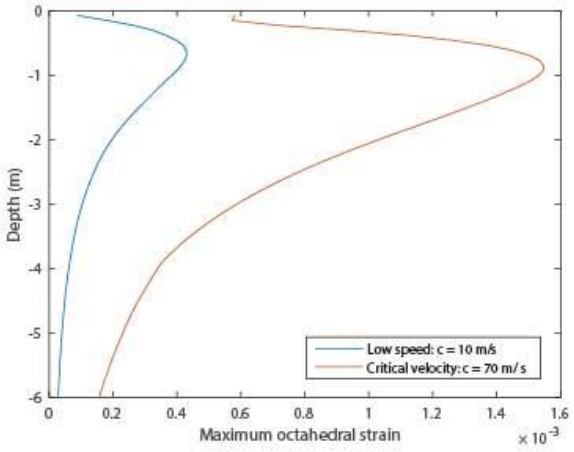

Figure 7 – Strain versus depth for linear and non-linear behavior

5 CONCLUSIONS

This paper presented a wavenumber-frequency domain model to predict railway track displacements in the presence of non-linear soil stiffness degradation. Analytical expressions were used for the track and the soil was simulated using the thin-layer method. Linear equivalent soil behavior was implemented using an iterative procedure where the soil strains were calculated during train passage and then used to update the stiffness and damping material properties. The model was validated using field data collected on a railway line with high non-linearity in Sweden. Finally, the model was used to investigate the effect of non-linearity on a homogenous half-space. It was found that the linear equivalent approach showed yielded significantly higher deflections compared to the linear case and that the critical speed was also lower.

REFERENCES

[1] C. Madshus and A. M. Kaynia, “High-Speed Railway Lines on Soft Ground: Dynamic Behaviour At Critical Train Speed,” *J. Sound Vib.*, vol. 231, no. 3, pp. 689–701, Mar. 2000.

[2] V. Krylov, “Generation of ground vibrations by superfast trains,” *Appl. Acoust.*, vol. 44, no. 2, pp. 149–164, 1995.

[3] G. Kouroussis, D. P. Connolly, K. Vogiatzis, and O. Verlinden, “Modelling the environmental effects of railway vibrations from different types of rolling stock - A numerical study,” *Shock Vib.*, 2015.

[4] D. López-Mendoza, A. Romero, D. P. Connolly, and P. Galvín, “Scoping assessment of building vibration induced by railway traffic,” *Soil Dyn. Earthq. Eng.*, vol. 93, no. June, pp. 147–161, 2017.

[5] B. Olivier, D. P. Connolly, P. Alves Costa, and G. Kouroussis, “The effect of embankment on high speed rail ground vibrations,” *Int. J. Rail Transp.*, vol. 4, pp. 229–246, 2016.

[6] L. Fryba, *Vibration of Solids and Structures Under Moving Loads*. Groningen, The Netherlands: Noordhoff International Publishing, 1972.

[7] X. Sheng, C. J. C. Jones, and D. J. Thompson, “A theoretical model for ground vibration from trains generated by vertical track irregularities,” *J. Sound Vib.*, vol. 272, no. 3–5, pp. 937–965, May 2004.

[8] S. François, P. Galvín, M. Schevenels, G. Lombaert, and G. Degrande, “A 2.5D coupled FE-BE methodology for the prediction of railway induced vibrations,” *Notes Numer. Fluid Mech. Multidiscip. Des.*, vol. 118, pp. 367–374, 2012.

[9] P. Galvín, D. L. Mendoza, D. P. Connolly, G. Degrande, G. Lombaert, and A. Romero, “Scoping assessment of free-field vibrations due to railway traffic,” *Soil Dyn. Earthq. Eng.*, vol. 114, no. May, pp. 598–614, 2018.

[10] A. Colaço, P. Alves Costa, and D. P. Connolly, “The influence of train properties on railway ground vibrations,” *Struct. Infrastruct. Eng.*, no. April 2015, pp. 1–18, Apr. 2015.

[11] G. Kouroussis, K. Vogiatzis, and D. P. Connolly, “A combined numerical/experimental prediction method for urban railway vibration,” *Soil Dyn. Earthq. Eng.*, vol. 97, pp. 377–386, 2017.

[12] J. Y. Shih, D. J. Thompson, and A. Zervos, “The influence of soil nonlinear properties on the track/ground vibration induced by trains running on soft ground,” *Transp. Geotech.*, vol. 11, pp. 1–16, 2017.

[13] P. K. Woodward, O. Laghrouche, S. B. Mezher, and D. P. Connolly, “Application of coupled train-track modelling of critical speeds for high-speed trains using three-dimensional non-linear finite elements,” *Int. J. Railw. Technol.*, vol. 4, no. 3, pp. 1–35, 2015.

[14] P. Alves Costa, R. Calcada, A. S. Cardoso, and A. Bodare, “Influence of soil non-linearity on the dynamic response of high-speed railway tracks,” *Soil Dyn. Earthq. Eng.*, vol. 30, pp. 221–235, 2010.

[15] S. B. Mezher, D. P. Connolly, P. K. Woodward, O. Laghrouche, J. Pombo, and P. A. Costa, “Railway critical velocity - Analytical prediction and analysis,” *Transp. Geotech.*, 2015.

[16] K. Dong, D. P. Connolly, O. Laghrouche, P. K. Woodward, and P. A. Costa, “The stiffening of soft soils on railway lines,” *Transp. Geotech.*, 2018.

[17] I. Ishibashi and X. Zhang, “Unified dynamic shear moduli and damping ratio of sand and clay,” *Soils Found*, vol. 33, no. 1, pp. 182–191, 1993.

COMPDYN 2019
7th ECCOMAS Thematic Conference on
Computational Methods in Structural Dynamics and Earthquake Engineering
M. Papadrakakis, M. Fragiadakis (eds.)
Crete, Greece, 24-–26 June 2019

HYBRID FREQUENCY-TIME DOMAIN METHOD FOR THREE-DIMENSIONAL SEISMIC ANALYSES OF NONLINEAR SOILS

Francesca Taddei[1], **Thi Hoa Nguyen**[1], **and Gerhard Müller**[1]

[1]Chair of Structural Mechanics,Technical University of Munich
Arcisstr. 21, 80333 Munich
e-mail: {francesca.taddei, hoa.nguyen, gerhard.mueller}@tum.de

Keywords: Soil-Structure Interaction (SSI), Wave Propagation Theory, Hybrid frequency–time domain (HFTD), Nonlinear Soil, 3D Effects, Integral Transform Method (ITM)

Abstract. *The simulation of the behavior of soil-structure interaction (SSI) systems subjected to seismic waves can be conveniently carried out in the frequency domain, to account for the frequency-dependent properties of the infinite soil. However, the soil exhibits nonlinear behavior even at small values of the strain level, so that its shear modulus and damping ratio vary as a functions of the strain. It is important to consider the strain- and frequency-dependent properties of the soil in a seismic SSI simulation. Since frequency domain (FD) analyses are not suitable for nonlinear systems, time domain (TD) integration algorithms are commonly adopted. An accurate way of including the frequency-dependent soil into a transient analysis is to use convolution integrals, which requires linearity of the system and leads to a high computational cost. Hybrid frequency–time domain (HFTD) methods represent an efficient alternative. Most of the existing HFTD methods idealize the soil behavior according to the one-dimensional (1D) wave propagation theory, which is a major simplification of the complex three dimensional (3D) theory.*

In this contributions we present a HFTD method, where the soil is described as a 3D continuum governed by Lamé's equation of elastodynamics and the problem is solved with the integral transform method (ITM). The shear modulus and the damping of the soil are nonlinear functions of the strain level. The seismic waves (the loading) can be represented by spatial waves with an arbitrary distribution in time and space. The response of the soil to the seismic waves is first solved in the FD assuming a linearized elastic soil subjected to input waves, the response is transformed into the TD and the maximum strain is evaluated at different depths. According to the maximum strain, the shear modulus and the damping at different depths is updated and the process is iterated until convergence. The proposed method is compared to the reference 1D nonlinear method and it is applied for a multi-dimensional analysis of a nonlinear soil. The limitations of the method are also described.

1 INTRODUCTION

Structures and the underlying soil can exhibit nonlinear behavior during strong earthquakes. Nonlinearities can arise in the structure, in the soil, or/and at the interface between structure and soil (i.e. base isolation, uplift). In order to simulate the nonlinear interaction between the soil and the structure during a seismic event, transient analyses in the time domain are necessary. It is common to use discretized numerical models for simulating structural problems in civil engineering; in particular, the finite element method (FEM) is the most established approach, thanks to its suitability for nonlinear and anisotropic materials.

However, the FEM fails to represent the real endless dimension of the soil because the energy cannot be transported to infinity. A possible solution is to enlarge the soil domain and move its boundary away from the structure at a sufficient distance. This leads to a model with a large number of elements, for which the run time becomes prohibitive.

Another complex aspect of nonlinear seismic analysis is the correct estimation of the seismic loads, which do not act directly on the structures but result from the spatial and temporal variation of the seismic displacement field. The latter, in turn, can be influenced by the foundation and the structure. This aspect must be taken into account when selecting the analysis method.

In the past decades, much effort has been made in order to find valid alternatives to the classical FEM representation for nonlinear soil-structure interaction (SSI) problems. The different methods can be classified into two main groups: direct methods and substructure methods. In both cases the aim is to overcome the difficulty of modeling the unbounded domain of the soil, accounting for the radiation conditions at infinity and the nonlinearities of the system due to seismic events.

In the direct methods, the structure and part of the soil near the foundation (near field) are modeled using the same technique, usually the FEM. In order to satisfy the radiation condition, mathematical artifacts at the boundary of the soil's near field must be added. These are called transmitting boundaries (TB) and are local approximations of boundary conditions (local in time and space) and their coefficients are frequency-independent. Direct methods can account for nonlinearities in the structure as well as in the soil's near field and can be solved using direct time integration methods such as central difference method or Newark method. The soil's far field is assumed to remain linear. Applications of direct methods can be found in [8]. The direct method for nonlinear SSI system is computationally demanding.

The substructure methods involve the application of different techniques for different parts of the systems and their coupling at the interaction surfaces. Usually the FEM is used for the structure and a different numerical method is used for the soil. If nonlinearities occur, the soil model must be defined in the TD and this would involve convolution integrals. In this case, the SSI boundary conditions are global in time and space, as they require the information of all the time steps from the beginning and all the degrees of freedom (DoF) at the substructure interface. Substructure methods can account for nonlinearities in the structure as well as at the soil-structure interface, whereas the soil is assumed to remain linear. A classical reference for the theory of substructure methods is Wolf [23]. An example of application can be found in [18].

Alternatives to transient analysis are the hybrid time-frequency domain (HTFD) approaches, where the system of equations is solved iteratively transforming back and forth from the TD to the FD and vice versa. The existing HFTD methods assume the soil approximated as a one-dimensional system (either as a compressional bar for P-waves or as a shear beam for S-waves).

In this contribution we present an extension of the HTFD, where the three-dimensionality

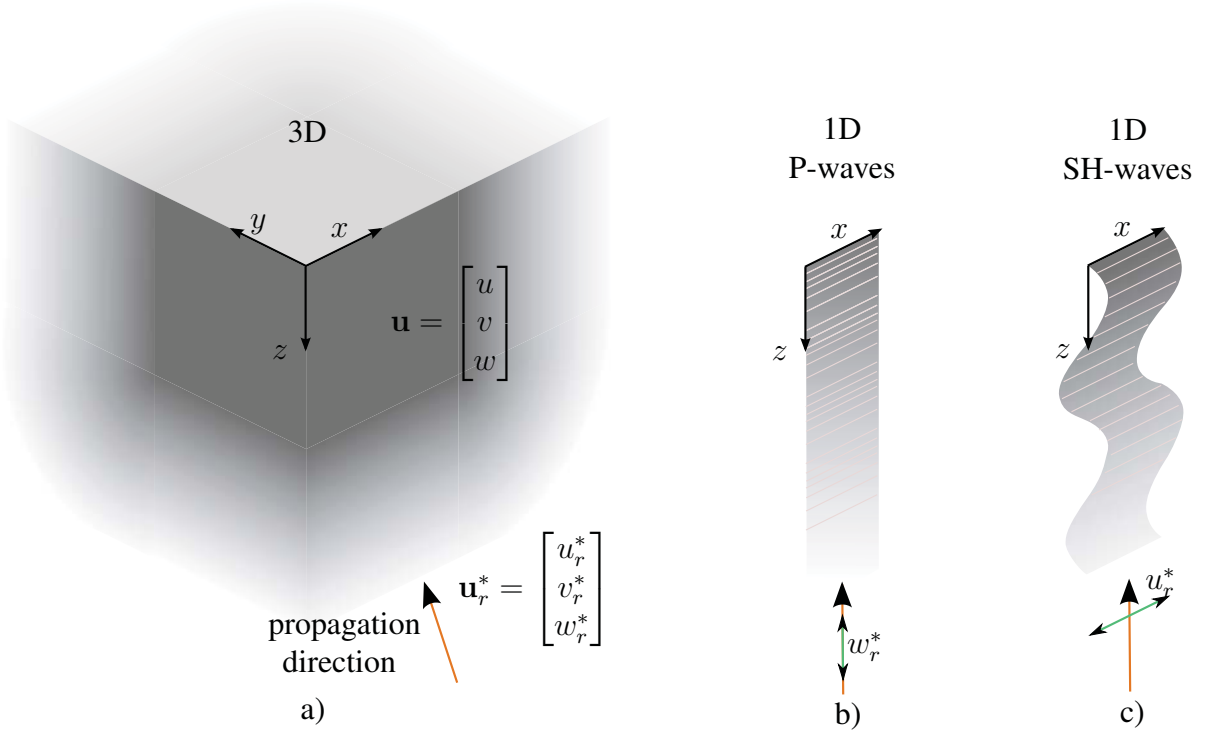

Figure 1: a) 3D free field, b) 1D representation of the free field subjected to P-waves, c) 1D representation of the free field subjected to S-waves.

of the problem can be account for and the solution is found iteratively using both time- and frequency-domain results. The focus in on the nonlinear response of the free field and the equations are derived only for the nonlinear soil. However, a coupling to a nonlinear structure using transfer functions is straightforward.

2 THREE-DIMENSIONAL PROPAGATION OF SEISMIC WAVES

Let us first analyze a linear isotropic soil. The propagation of seismic waves through the soil can be described using the theory of elasticity applied to a three dimensional homogenous half space. Different forms of waves (shear, compressional and *Rayleigh* waves) can propagate simultaneously, generating a complex three dimensional displacement field $\mathbf{u}$. In seismic analysis it is of interest 1) how the soil amplifies or de-amplifies the signal as the waves propagate through the medium towards the structure, and 2) how its flexibility influences the overall dynamic response of the structure. For both aspects, the extent of the effects depends on the properties of the soil and on the frequency content and spatial distribution of the seismic excitation. The propagation of seismic waves through a non-homogenous half space is even more complicated, because of additional *Stoneley* waves, *Lov*e waves and evanescent modes.

The problem is shown in Fig. 1a and can be described with the *Lamé* equation in index notation:

$$G u^i|_j^j + (\lambda + G) u^j|_j^i - \rho \ddot{u}^i = 0 \quad \text{with} \quad i, j = x, y, z \tag{1}$$

where $u^x = u$,$u^y = v$ and $u^z = w$ are the componenet of the displacement vector $\mathbf{u}$, ρ is the soil mass density, λ and G are the *Lamé*-constant and can be estimated from the *Youngs*'s modulus

E and *Poisson*'s ratio ν:

$$G = \frac{E}{2(1+\nu)} \quad \text{and} \quad \lambda = \frac{\nu E}{(1+\nu)(1-2\nu)} \quad . \tag{2}$$

The *Lamé* equation, Eq. (1), is defined in the original space (x, y, z, t) and is valid for a linear elastic isotropic and homogeneous continuum. Using the *Helmholtz* decomposition and a threefold *Fourier* transformation one obtains a system of four decoupled ordinary differential equations which can be solved with an exponential approach in the image space (k_x, k_y, z, ω) [4]. This approach is referred to as integral transform method (ITM). The solution expressed in terms of potentials $\bar{\phi}$ and $\bar{\psi}_i$ reads:

$$\begin{aligned} \bar{\phi}(k_x, k_y, z, \omega) &= A_1 e^{\lambda_1 z} + A_2 e^{-\lambda_1 z} \\ \bar{\psi}_i(k_x, k_y, z, \omega) &= B_{i1} e^{\lambda_2 z} + B_{i2} e^{-\lambda_2 z} \quad \text{with} \quad i = x, y, z \end{aligned} \tag{3}$$

$$\text{with} \quad \lambda_1 = -i\sqrt{\frac{\omega^2}{c_p^2} - k_x^2 - k_y^2} \quad ,$$

$$\lambda_2 = -i\sqrt{\frac{\omega^2}{c_s^2} - k_x^2 - k_y^2} \quad , \tag{4}$$

$$k_p = \frac{\omega}{c_p} \quad \text{and} \quad k_s = \frac{\omega}{c_s}$$

where c_p and c_s are the compressional and shear wave velocity respectively and k_x and k_y are the horizontal wave numbers. One can demonstrate that the potential $\bar{\psi}_z$ can be set to zero, still maintaining the complete correct 3D solution [6]. The displacements in the image space can be obtained as:

$$\bar{\mathbf{u}} = \begin{pmatrix} \bar{u} \\ \bar{v} \\ \bar{w} \end{pmatrix} = \underbrace{\begin{bmatrix} ik_x & ik_x & 0 & 0 & -\lambda_2 & \lambda_2 \\ ik_y & ik_y & \lambda_2 & -\lambda_2 & 0 & 0 \\ \lambda_1 & -\lambda_1 & -ik_y & -ik_y & ik_x & ik_x \end{bmatrix}}_{\boldsymbol{K}_{\bar{\mathbf{u}}}} \underbrace{\begin{pmatrix} A_1 e^{\lambda_1 z} \\ A_2 e^{-\lambda_1 z} \\ B_{x1} e^{\lambda_2 z} \\ B_{x2} e^{-\lambda_2 z} \\ B_{y1} e^{\lambda_2 z} \\ B_{y2} e^{-\lambda_2 z} \end{pmatrix}}_{\boldsymbol{c}} \tag{5}$$

where the vector $\boldsymbol{c}$ contains the 6 unknown coefficients of the solution. The stresses can be estimated and expressed as:

$$\begin{pmatrix} \bar{\sigma}_x \\ \bar{\sigma}_y \\ \bar{\sigma}_z \\ \bar{\sigma}_{xy} \\ \bar{\sigma}_{yz} \\ \bar{\sigma}_{zx} \end{pmatrix} = G \underbrace{\begin{bmatrix} -(2k_x^2 + \frac{\lambda}{G}k_p^2) & -(2k_x^2 + \frac{\lambda}{G}k_p^2) & 0 & 0 & -2ik_x\lambda_2 & 2ik_x\lambda_2 \\ -(2k_y^2 + \frac{\lambda}{G}k_p^2) & -(2k_y^2 + \frac{\lambda}{G}k_p^2) & 2ik_y\lambda_2 & -2ik_y\lambda_2 & 0 & 0 \\ 2k_r^2 - k_s^2 & 2k_r^2 - k_s^2 & -2ik_y\lambda_2 & 2ik_y\lambda_2 & 2ik_x\lambda_2 & -2ik_x\lambda_2 \\ -2k_xk_y & -2k_xk_y & ik_x\lambda_2 & -ik_x\lambda_2 & -ik_y\lambda_2 & ik_y\lambda_2 \\ 2ik_y\lambda_1 & -2ik_y\lambda_1 & \lambda_2^2 + k_y^2 & \lambda_2^2 + k_y^2 & -k_xk_y & -k_xk_y \\ 2ik_x\lambda_1 & -2ik_x\lambda_1 & k_xk_y & k_xk_y & -(\lambda_2^2 + k_x^2) & -(\lambda_2^2 + k_x^2) \end{bmatrix}}_{\boldsymbol{K}_{\bar{\boldsymbol{\sigma}}}} \boldsymbol{c} \tag{6}$$

with

$$k_r^2 = k_x^2 + k_y^2 \tag{7}$$

In short notation, we can write:

$$\begin{aligned} \bar{\mathbf{u}} &= \boldsymbol{K}_{\bar{\mathbf{u}}}\boldsymbol{c} \quad , \\ \bar{\boldsymbol{\sigma}} &= \boldsymbol{K}_{\bar{\sigma}}\boldsymbol{c} \quad . \end{aligned} \tag{8}$$

The two matrices $\boldsymbol{K}_{\bar{\mathbf{u}}}$ and $\boldsymbol{K}_{\bar{\sigma}}$ depend on the excitation circular frequency ω, the soil material and the horizontal wave numbers k_x and k_y. Based on given boundary conditions at certain z-coordinates the unknown coefficients vector $\boldsymbol{c}$ can be found.

The application of the the material law delivers the strain components in the original space :

$$\begin{aligned} \sigma_x &= \lambda\widehat{\varepsilon} + 2G\varepsilon_x & \tau_{xy} &= \tau_{yx} = G\gamma_{xy} \\ \sigma_y &= \lambda\widehat{\varepsilon} + 2G\varepsilon_y & \tau_{yz} &= \tau_{zy} = G\gamma_{yz} \\ \sigma_z &= \lambda\widehat{\varepsilon} + 2G\varepsilon_z & \tau_{zx} &= \tau_{xz} = G\gamma_{zx} \end{aligned} \tag{9}$$

with

$$\widehat{\varepsilon} = \varepsilon_x + \varepsilon_y + \varepsilon_z \quad . \tag{10}$$

Adding σ_x, σ_y and σ_z, $\widehat{\varepsilon}$ is estimated as:

$$\widehat{\varepsilon} = \frac{\sigma_x + \sigma_y + \sigma_z}{3\lambda + 2G} \quad . \tag{11}$$

The strain components ε_x, ε_y and ε_z result from inserting Eq. (11) into Eq. (9). The three shear strain components γ_{xy}, γ_{yz} and γ_{zx} can be estimated directly from the respective shear stress through division by the shear modulus G. Thus, a matrix formulation of the stress-strain relationship reads:

$$\underbrace{\begin{pmatrix} \varepsilon_x \\ \varepsilon_y \\ \varepsilon_z \\ \gamma_{xy} \\ \gamma_{yz} \\ \gamma_{zx} \end{pmatrix}}_{\boldsymbol{\varepsilon}} = \underbrace{\begin{bmatrix} \frac{1}{2G}(1 - \frac{\lambda}{3\lambda+2G}) & -\frac{1}{2G}\frac{\lambda}{3\lambda+2G} & -\frac{1}{2G}\frac{\lambda}{3\lambda+2G} & 0 & 0 & 0 \\ -\frac{1}{2G}\frac{\lambda}{3\lambda+2G} & \frac{1}{2G}(1 - \frac{\lambda}{3\lambda+2G}) & -\frac{1}{2G}\frac{\lambda}{3\lambda+2G} & 0 & 0 & 0 \\ -\frac{1}{2G}\frac{\lambda}{3\lambda+2G} & -\frac{1}{2G}\frac{\lambda}{3\lambda+2G} & \frac{1}{2G}(1 - \frac{\lambda}{3\lambda+2G}) & 0 & 0 & 0 \\ 0 & 0 & 0 & \frac{1}{G} & 0 & 0 \\ 0 & 0 & 0 & 0 & \frac{1}{G} & 0 \\ 0 & 0 & 0 & 0 & 0 & \frac{1}{G} \end{bmatrix}}_{\boldsymbol{K}_{\varepsilon\sigma} = \boldsymbol{K}_{\bar{\varepsilon}\bar{\sigma}}} \underbrace{\begin{pmatrix} \sigma_x \\ \sigma_y \\ \sigma_z \\ \sigma_{xy} \\ \sigma_{yz} \\ \sigma_{zx} \end{pmatrix}}_{\boldsymbol{\sigma}} \tag{12}$$

The assumption of linearized elastic material allows the application of the material law also in the image space. Thus,

$$\begin{aligned} \boldsymbol{K}_{\varepsilon\sigma} &= \boldsymbol{K}_{\bar{\varepsilon}\bar{\sigma}} \quad \text{and} \\ \bar{\boldsymbol{\varepsilon}} &= \boldsymbol{K}_{\bar{\boldsymbol{\varepsilon}}\bar{\boldsymbol{\sigma}}}\bar{\boldsymbol{\sigma}} \quad . \end{aligned} \tag{13}$$

Combining Eq. 8 and Eq. 13, the relationship between the strains $\bar{\boldsymbol{\varepsilon}}$ and the vector of the unknowns coefficients $\boldsymbol{c}$ is established:

$$\bar{\boldsymbol{\varepsilon}} = \underbrace{\boldsymbol{K}_{\bar{\boldsymbol{\varepsilon}}\bar{\boldsymbol{\sigma}}}\boldsymbol{K}_{\bar{\boldsymbol{\sigma}}}}_{\boldsymbol{K}_{\bar{\boldsymbol{\varepsilon}}}}\boldsymbol{c} \quad . \tag{14}$$

For a layered half space with N isotropic layers, the system of equations is obtained by overlapping the matrices of the adjacent layers and by enforcing continuity and equilibrium

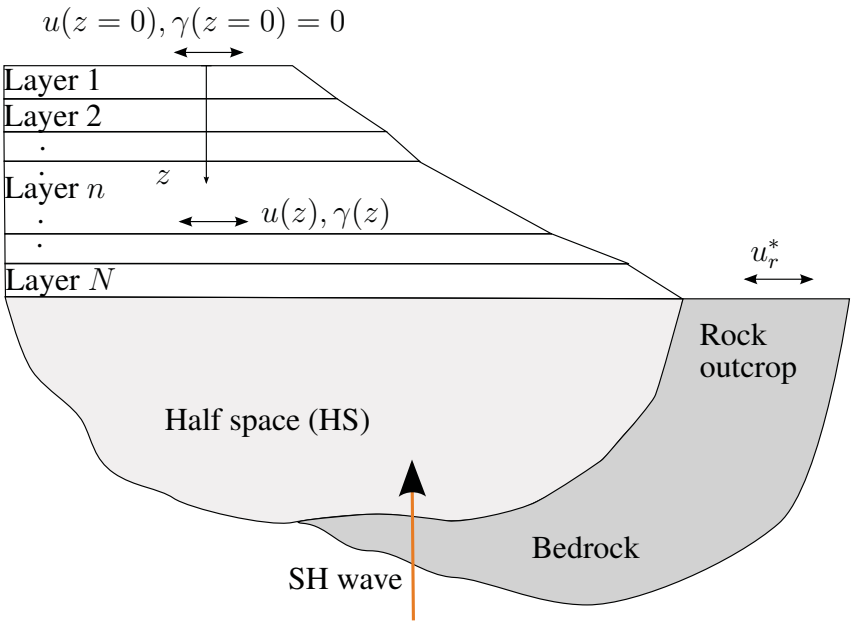

Figure 2: One-dimensional representation of the load application for a seismic analysis of the free field.

at their interfaces. If at the base of the layers there is a bedrock, a fixed boundary condition is enforced at the base and the system has $6N$ unknowns. If the layers are underlain by an homogenous half space, the radiation condition must be satisfied and the system has 6(N-1)+3 unknowns.

The unknowns are found with the additional boundary conditions concerning the load. For a free field (soil without a coupled structure) subjected to a seismic excitation, one of the boundary conditions is the zero-stress condition at the surface. A further boundary condition is the equilibrium of stresses at the location where the seismic excitation is applied, which leads to a condition between stresses and displacements at that location and therefore to the remaining unknowns of the problem.

The definition of the seismic input and its location depends on the available information about the seismic event and on the aim of the analysis. In this contribution, according to Kausel [11][1], we assume that the seismic input is known in form of a motion $\mathbf{u}_r^*$ at the rock outcrop, which is the surface of the rock without taking into consideration the layers (see Fig. 2).

If at the base of the layers there is a bedrock, $\mathbf{u}_r^*$ can be directly used as a root-point-excitation condition, after transformation into the image space. If the layers are underlain by an homogenous half space, equivalent seismic stresses are computed according to Kausel [11] and applied at the interface between half space and layers.

Once the problem is solved in the image space, the solution is transformed back into the original space for further calculations (see Fig. 3). In the following paragraphs, $\bar{...}$ indicates the quantity in the image space.

2.1 Three-Dimensional Transfer Functions for the Free Field

Using the ITM, it is possible to express the relationship between various response parameters of the soil, such as displacements, velocities, accelerations, stresses and strains, and an input motion parameter such as the bedrock displacement vector $\mathbf{u}_r^*$. This relationship is referred

[1]Pages 356-357

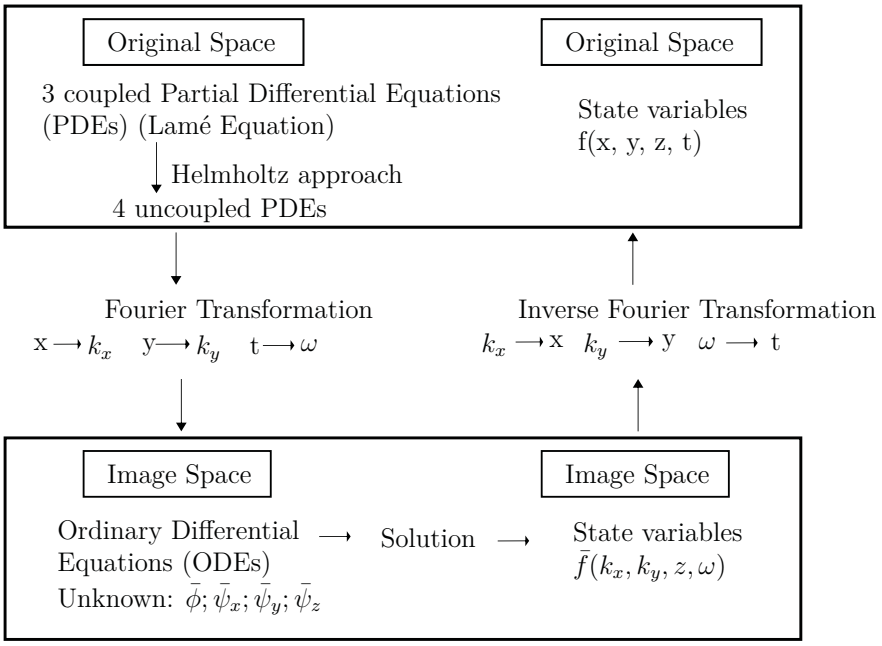

Figure 3: Integral transform method for the solution of the *Lamé* equations.

to as transfer function. This paragraph explains how to obtain the three-dimensional transfer functions for the displacements and the formulation is shown for a single stratum with thickness h subjected to input motions, to maintain clarity. The same procedure can be applied to any arbitrary horizontally layered soil over a bedrock or an elastic half space.

For a stratum subjected to input motions at the bedrock level, the boundary conditions are:

- BC 1: zero stresses at the soil surface
  $\rightarrow [\bar{\sigma}_z(k_x, k_y, z = 0, \omega), \bar{\sigma}_{yz}(k_x, k_y, z = 0, \omega), \bar{\sigma}_{zx}(k_x, k_y, z = 0, \omega)]^T = [0, 0, 0]^T$,
- BC 2: the displacements at the interface bewteen bedrock and stratum are given
  $\rightarrow [\bar{u}(k_x, k_y, z = h, \omega), \bar{v}(k_x, k_y, z = h, \omega), \bar{w}(k_x, k_y, z = h, \omega)]^T = [\bar{u}_r^*, \bar{v}_r^*, \bar{w}_r^*]^T$,

which lead to the following expression:

$$\begin{pmatrix} A_1 \\ A_2 \\ B_{x1} \\ B_{x2} \\ B_{y1} \\ B_{y2} \end{pmatrix} = \left[\underbrace{G \begin{bmatrix} 2k_r^2 - k_s^2 & 2k_r^2 - k_s^2 & -2ik_y\lambda_2 & 2ik_y\lambda_2 & 2ik_x\lambda_2 & -2ik_x\lambda_2 \\ 2ik_y\lambda_1 & -2ik_y\lambda_1 & \lambda_2^2 + k_y^2 & \lambda_2^2 + k_y^2 & -k_xk_y & -k_xk_y \\ 2ik_x\lambda_1 & -2ik_x\lambda_1 & k_xk_y & k_xk_y & -(\lambda_2^2 + k_x^2) & -(\lambda_2^2 + k_x^2) \\ ik_xe^{\lambda_1 h} & ik_xe^{-\lambda_1 h} & 0 & 0 & -\lambda_2 e^{\lambda_2 h} & \lambda_2 e^{-\lambda_2 h} \\ ik_ye^{\lambda_1 h} & ik_ye^{-\lambda_1 h} & \lambda_2 e^{\lambda_2 h} & -\lambda_2 e^{-\lambda_2 h} & 0 & 0 \\ \lambda_1 e^{\lambda_1 z} & -\lambda_1 e^{-\lambda_1 h} & -ik_ye^{\lambda_2 h} & -ik_ye^{-\lambda_2 h} & ik_xe^{\lambda_2 h} & ik_xe^{-\lambda_2 h} \end{bmatrix}}_{\boldsymbol{K}_{BC}} \right]^{-1} \begin{pmatrix} 0 \\ 0 \\ 0 \\ \bar{u}_r^* \\ \bar{v}_r^* \\ \bar{w}_r^* \end{pmatrix} \tag{15}$$

The coefficients A_1, A_2, B_{x1}, B_{x2}, B_{y1}, B_{y2} are then introduced in Eq. 8 to find the displacements and stresses in the image space. Finally, the inverse *Fourier* transformation leads to the spatial and temporal distribution of the ground motions due to the input motions $\mathbf{u}_r^*$. Because both input $\mathbf{u}_r^*$ and output $\mathbf{u}$ have three components and each component depends on the position in space and time, it is not possible to establish a simple definition for the three-dimensional transfer functions, which usually relate scalar values.

However, for the method proposed in this contribution, it is necessary to choose a representative value of the strain vector for each horizontal plane in the middle of each layer, which will be used in the nonlinear material model. This can be done either observing a specific point of horizontal coordinate $\widehat{x}$ and $\widehat{y}$ or using a spatial averaging method to estimate a representative value.

In order to overcome this difficulty, in most studies on free field response analysis, a major assumption is commonly adopted: the seismic input was generated far enough from the area of interest, so that the wavefront can be considered plane and all the point in the horizontal plane moves in phase and experience the same motion. In the image space, this condition is represented by a function which is equal to zero everywhere except for k_x=k_y=0. In this special case, Eq. 5 and Eq. 15 shows that $\bar{u}$ only depends on A_1 and A_2 (related to $\bar{\Phi}$, P-waves), which in turn only depend on u_r^*, so that a straightforward definition for the transfer function u/u_r^* is possible. Analogously, this apply for v/v_r^* and w/w_r^*. This means that for k_x=k_y=0, the three dimensional problem can be treated as a one dimensional problem, where each component of the displacement vector can be treated independently.

2.2 One-Dimensional Transfer Functions for the Free Field

Under the assumption of a plane horizontal wavefront (k_x=k_y=0), the problem in x-direction is uncoupled from the problem in y- direction and the axial and shear motions do not affect each other. Fig. 1b and Fig. 1c shows that, in 1D, P-waves and SH-waves can be treated separately and the vertical and horizontal transfer functions for a layered soil, $w(z)/w_r^*$ and $u(z)/u_r^*$ respectively, can be computed independently at different soil depths. The transfer functions are defined in frequency domain and take into account the frequency-dependent steady-state response of the 1D free field.

We consider a soil made up of N layers with thickness h_n, shear wave velocity $c_{s,n}$, shear modulus G_n and density ρ_n underlain by a homogenous half space, subjected to a SH-wave. The transfer functions $\boldsymbol{F}_1$ for the displacements, evaluated at the top of each layer, are obtained using the stiffness matrix of the soil $\boldsymbol{K}$:

$$\boldsymbol{F}_1(\omega) = \begin{pmatrix} u_1/u_r^* \\ u_2/u_r^* \\ u_3/u_r^* \\ \dots \\ u_n/u_r^* \\ u_r/u_r^* \end{pmatrix} = \boldsymbol{u}_{1D}/u_r^* = \boldsymbol{K}^{-1} \begin{pmatrix} 0 \\ 0 \\ 0 \\ \dots \\ 0 \\ K_{HS} \end{pmatrix} \tag{16}$$

where $\boldsymbol{K}$ is the stiffness matrix of the layered soil and K_{HS}=$i\omega\rho_{HS}c_{s,HS}$ is the stiffness of the underlying half space. The dependency on the circular frequency ω is omitted for clarity.

This transfer matrix can be applied also to estimate the velocity at different z-coordinates:

$$\frac{\dot{\boldsymbol{u}}_{1D}}{\dot{u}_r^*} = \frac{i\omega\boldsymbol{u}_{1D}}{i\omega u_r^*} = \frac{\boldsymbol{u}_{1D}}{u_r^*} = \boldsymbol{F}_1 \tag{17}$$

For the purposes of this contribution, it is necessary to define a second transfer function type, $\boldsymbol{F}_2$, which estimates the shear strain transfer functions w.r.t the velocity of the seismic excitation $\dot{u}_r^*$. This transfer function $\boldsymbol{F}_2$ is obtained from the relationship between shear strains and displacements:

$$\boldsymbol{\gamma}_{1D} = \boldsymbol{F}_{\boldsymbol{\gamma}\mathbf{u}}^{1D}\boldsymbol{u}_{1D} \tag{18}$$

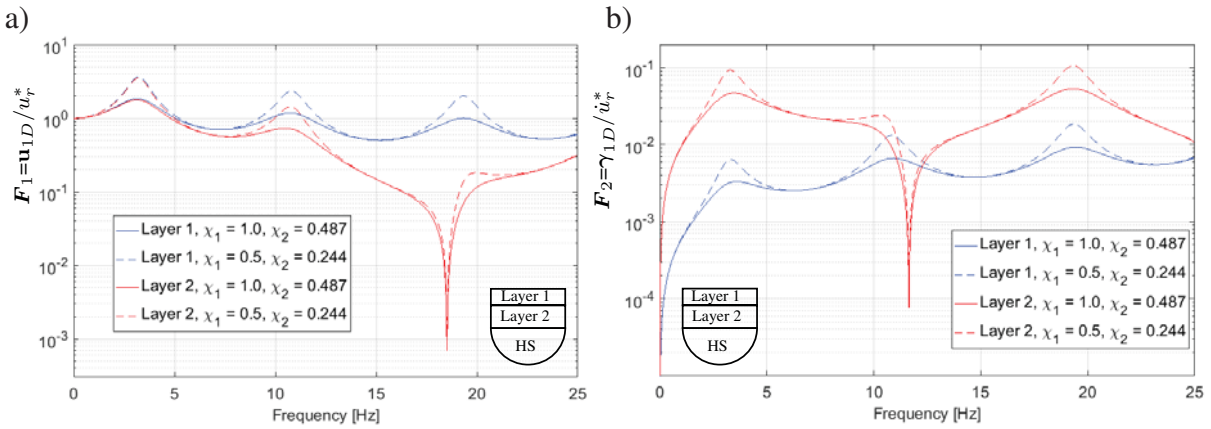

Figure 4: a) Displacement transfer function $\boldsymbol{F}_1$ and b) strain transfer functions $\boldsymbol{F}_2$, for the soils investigated in paragraph 2.3.

where the matrix $\boldsymbol{F}^{1D}_{\boldsymbol{\gamma}\mathbf{u}}$ of the N-layered soil system reads:

$$\boldsymbol{F}^{1D}_{\boldsymbol{\gamma}\mathbf{u}} = \begin{bmatrix} -F_1 & F_{12} & 0 & ... & 0 & 0 \\ -0.5F_{12} & 0.5(F_1-F_2) & 0.5F_{23} & 0 & ... & 0 \\ 0 & -0.5F_{23} & 0.5(F_2-F_3) & 0.5F_{34} & ... & 0 \\ ... & ... & ... & ... & ... & ... \\ 0 & ... & ... & -0.5F_{N-1,N} & 0.5(F_{N-1}-F_N) & 0.5F_{N,N+1} \\ 0 & ... & ... & 0 & -0.5F_{N,N+1} & 0.5(F_N+F_{HS}) \end{bmatrix} \tag{19}$$

with

$$\begin{aligned} n_n &= \omega/c_{s,n} \\ F_n &= n_n cot(n_n h_n) \quad \text{and} \quad F_{n,n+1} = n_n sin^{-1}(n_n h_n) \\ F_{HS} &= \frac{K_{HS}}{G_{HS}} = \frac{i\omega\rho_{HS}c_{s,HS}}{G_{HS}} \end{aligned} \tag{20}$$

Inserting Eq. (17) in Eq. (18), the functions $\boldsymbol{F}_2$ can be obtained from the functions $\boldsymbol{F}_1$:

$$\begin{aligned} &\boldsymbol{\gamma}_{1D} = \boldsymbol{F}^{1D}_{\boldsymbol{\gamma}\mathbf{u}}\mathbf{u}_{1D} = \boldsymbol{F}^{1D}_{\boldsymbol{\gamma}\mathbf{u}}\frac{1}{i\omega}\dot{\boldsymbol{u}}_{1D} = \boldsymbol{F}^{1D}_{\boldsymbol{\gamma}\mathbf{u}}\frac{1}{i\omega}\boldsymbol{F}_1\dot{u}_r^* = \boldsymbol{F}_2\dot{u}_r^* \\ \rightarrow &\boldsymbol{F}_2 = \boldsymbol{\gamma}/\dot{u}_r^* = \boldsymbol{F}^{1D}_{\boldsymbol{\gamma}\mathbf{u}}\frac{1}{i\omega}\boldsymbol{F}_1 \end{aligned} \tag{21}$$

The 1D transfer functions are a special case of the 3D relationships between input and output. It can be demonstrated that the 1D transfer functions $\boldsymbol{F}_1$ and $\boldsymbol{F}_2$ can be obtained from the 3D procedure described in paragraph 2.1 by setting k_x=k_y=0.

2.3 Example: 1D Linear Transfer Function of a Layered Soil

This example shows the transfer functions for a layered soil both in terms of $\boldsymbol{F}_1$ and $\boldsymbol{F}_2$. The investigation is carried out for two different soils, both made up of two undamped layers underlain by an elastic half space. The displacements transfer functions $\boldsymbol{F}_1$ are evaluated at the top surface of each layer, while the strain transfer functions $\boldsymbol{F}_2$ are evaluated at the center of each layer.

For both soils, the two layers have different thicknesses and shear velocities but same mass density:

- Thickness h_1 = 2.1336 m and h_2 = 3.9624 m
- Mass density $\rho_1 = \rho_2$ = 1922 kg/m^3
- Shear wave velocity $c_{s,1}$ = 158 m/s and $c_{s,2}$ = 0.488 $c_{s,1}$ = 77 m/s

The ratios χ_i, which relate the impedance of the layers with the impedance of the half space, vary according to Tab. 1. Fig. 4 shows the linear transfer functions and the influence of the ratios χ_i on the amplification effect of the soil layering on the seismic input.

	$\chi_1 = \frac{\rho_1 c_{s,1}}{\rho_{HS} c_{HS}}$	$\chi_2 = \frac{\rho_2 c_{s,2}}{\rho_{HS} c_{HS}}$
Soil 1 (continuous lines in Fig. 4)	1.0	0.488
Soil 2 (dashed lines in Fig. 4)	0.5	0.244

Table 1: Impedance ratios for the soils investigated in paragraph 2.3.

3 NONLINEAR SOIL BEHAVIOUR

Experiments and past seismic events have shown that the soil material behaves non linearly when the strain exceeds 10^{-5}, which is often the case during strong earthquakes [20, 3]. Adequate three-dimensional models for the description of the inelastic soil behavior are still under investigation today (for example in [15]). The salient characteristics of the behavior of the material is the degradation of the stiffness and the increasing dissipation with increasing strain. Fig. 5 shows typical degradation curves for the shear modulus G normalized to the maximum shear modulus G_0 and for the hysteretic damping ξ as a function of the cyclic strain γ for sand material. The gray areas are the envelopes of experimental data according to [14], which show the influence of the confining pressure p and of the void ratio e on the degradation curves.

The most common models are based on the one-dimensional wave propagation theory and consider only one stress and one strain component at a time. Most of these models assume the behavior to be rate independent and fully characterized by the initial loading curve, or backbone. The most widely used stress-strain constitutive law is the Masing's rule [17]. This model assumes that unloading and reloading paths are scaled and/or inverted replicas of the initial stress–strain path for monotonic loading. In this model, when unloading or re-loading, the history of some or all of the reversal points must be tracked, so that when an unloading or re-loading episode intersects a previously taken path, that previous path is reestablished. Hence, this nonlinear model has memory of the previous strain history, but the path does not depend on the deformation speed. One can simulate any rate-independent, inelastic material obeying Masing's rule by means of a set of elasto-plastic springs in parallel [10]. The implementation of this model is much easier than the one for a non-linear backbone where many reversal points need to be tracked [7]. Other 1D models are the hyperbolic model [21] and the Ramberg-Osgood [19, 16] model and more recent extensions of them, e.g. [5]. These assume that the stress-strain curve is independent of the cycle number, the void ratio, the confining pressure and the sand type.

In this contribution, we focus on the Assimaki et al. model [2], called MITS1, which is defined by 4 parameters and gives the strain-dependent values for the shear modulus and the hysteretic damping (or material damping) and takes into account the confining pressure.

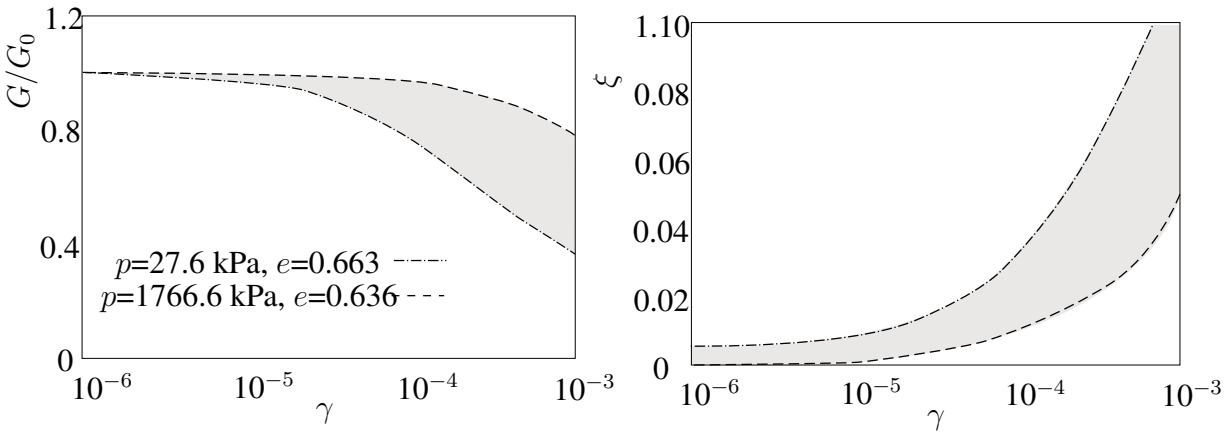

Figure 5: Experimental evidences of the dependency of the shear modulus G and of the material damping ξ on the strain γ, the confining pressure p and on the void ratio e (adapted from [2]).

Furthermore, to obtain a scalar measure of the shear deformation on a given point from the 3D strain vector, we use the octahedral shear strain [9]:

$$\gamma_{\text{oct}} = \frac{2}{3}\sqrt{(\varepsilon_x - \varepsilon_y)^2 + \varepsilon_y - \varepsilon_z)^2 + (\varepsilon_z - \varepsilon_x)^2 + 6\gamma_{xy}^2 + 6\gamma_{yz}^2 + 6\gamma_{zx}^2} \tag{22}$$

where ε_i are the normal strains and γ_i are the shear strains. This value is used as a reference for the degradation curves of the material model. It is important to notice that, if only shear strains in one direction would occur (ε_x=ε_y=ε_z=γ_{xy}=γ_{yz}=0, $\gamma_{zx} \neq$0), the octahedral shear strain γ_{oct} does not coincide with the 1D shear strain γ_{zx} (γ_{oct}=1.63γ_{zx}).

4 1D HFTD Method

When a nonlinear constitutive material for the soil is assigned to the model, a time-integration algorithm is necessary, because the properties of the soil depends on the strain and the model must be updated at each time step. This task is computationally demanding and produces a large database of transient signal, which are difficult to interpret. An alternative to time integration schemes are the hybrid frequency-time domain (HFTD) methods, which assume a linearized material and solve the problem iteratively.

In the one dimensional case, the HFTD method involves the following steps:

1. discretize the soil in N thin numerical layers;
2. assume initial linearized soil parameters;
3. evaluate the strain spectrum $\bar{\gamma}_n(\omega)$ at the center of each n-th numerical layer using the transfer functions $\boldsymbol{F}_2$, described earlier;
4. transform the response back into the time domain $\gamma_n(t)$ and evaluate the maximum of the signals;
5. for each layer, use this maximum to scale the strain spectrum, obtaining an effective strain spectrum $\bar{\gamma}_{n,\text{eff}}(\omega)$;
6. for each frequency ω of the spectrum, read the effective spectral strain value $\bar{\gamma}_{n,\text{eff}}(\omega)$ and use the constitutive laws (for example the hyperbolic model or the MITS1 model) to update the shear modulus $G_n(\bar{\gamma}_{n,\text{eff}}(\omega))$ and the material damping $\xi_n(\bar{\gamma}_{n,\text{eff}}(\omega))$;

7. repeat the analysis until the maximum of the strain of two subsequent analysis converge.

With these procedure the frequency- and amplitude-dependent nature of the strains is approximated, which in turn requires the model's material to be frequency-dependent.

The effective strain spectra obtained in step 5 can be smoothed before using the strain value in the constitutive laws, in order to obtain a more stable iterative algorithm. The HFTD procedure presented by Kausel et al. [12] is summarized in Fig. 6.

4.1 Example: 1D HFTD Analysis of a Nonlinear Stratum

As an example, a layer underlain by a bedrock (a stratum) is computed considering a linear and a nonlinear material. The soil properties are taken from [12]-Example 1. The total depth h of the stratum is 25 m, the density ρ is 2000 kg/m^3, the shear velocity c_s 200 is m/s and the material damping ξ_s is 5%. The nonlinear behavior follows the material model MITS1 [2]. The stratum is subjected to a transient signal of the Kobe Earthquake scaled to a maximum acceleration of 0.5g. The physical layer is discretized into 10 numerical layers and the exponential smoothing technique described in Fig. 6 is used.

Fig. 7a shows the influence of the nonlinearity on the displacement transfer function $\boldsymbol{F}_1(\omega)$ evaluated at the surface. In the nonlinear case, the amplitudes of the peaks are decreased and the peaks for the first three resonances occur at lower frequencies then in the linear case. Fig. 7b,c and d show the spectrum of the strains at the center of the top layer, the transient accelerations and the transient displacements at the surface respectively, for the linear and non linear case.

Several alternative smoothing functions can be used to improve the method. Kwack et al. [13] compared different smoothing techniques found in literature. Wang and Zhao [22] proposed a smoothing method based on a moving average method and a different scaling technique for the computation of the effective strain. Fig. 8 shows the influence of the different smoothing techniques for the effective strain (Fig. 8d) on the converged results, e.g. on the accelerations of the free field at the surface (Fig. 8a) and on the displacement transfer functions (Fig. 8b). The moving average method (MAM) gives the most stable and realistic results.

Fig. 8c shows the frequency-dependent behavior of the material parameters for the MITS1 model using different smoothing techniques, evaluated at the center of the physical layer. It can be observed that the shear modulus is strongly degraded at low frequencies. The opposite applies to the hysteric damping, which decreases strongly at high frequencies. This is also confirmed in Fig. 9, where the distribution of the material properties with depth is shown for different frequencies, for the converged solution.

Fig 10 shows a validation of the 1D HFTD method against a fully transient nonlinear analysis carried out with the aid of a series of elasto-plastic springs, according to the *Ivan*'s Model [11][2]. The comparison shows the great agreement between the two approaches, confirming the suitability of the hybrid method.

5 3D HFTD Method

All the existing studies on HFTD methods for the SSI simulations neglect the effects of the three dimensions of the system and focus only on one strain component at time. Therefore, we propose to extend the HFTD methods by computing the three dimensional strains for the free field and iteratively solve the problem analogously to the 1D procedure. Fig. 11 shows the proposed algorithm for the 3D HFTD methods. The main difference between the 1D and the

[2]Pages 555

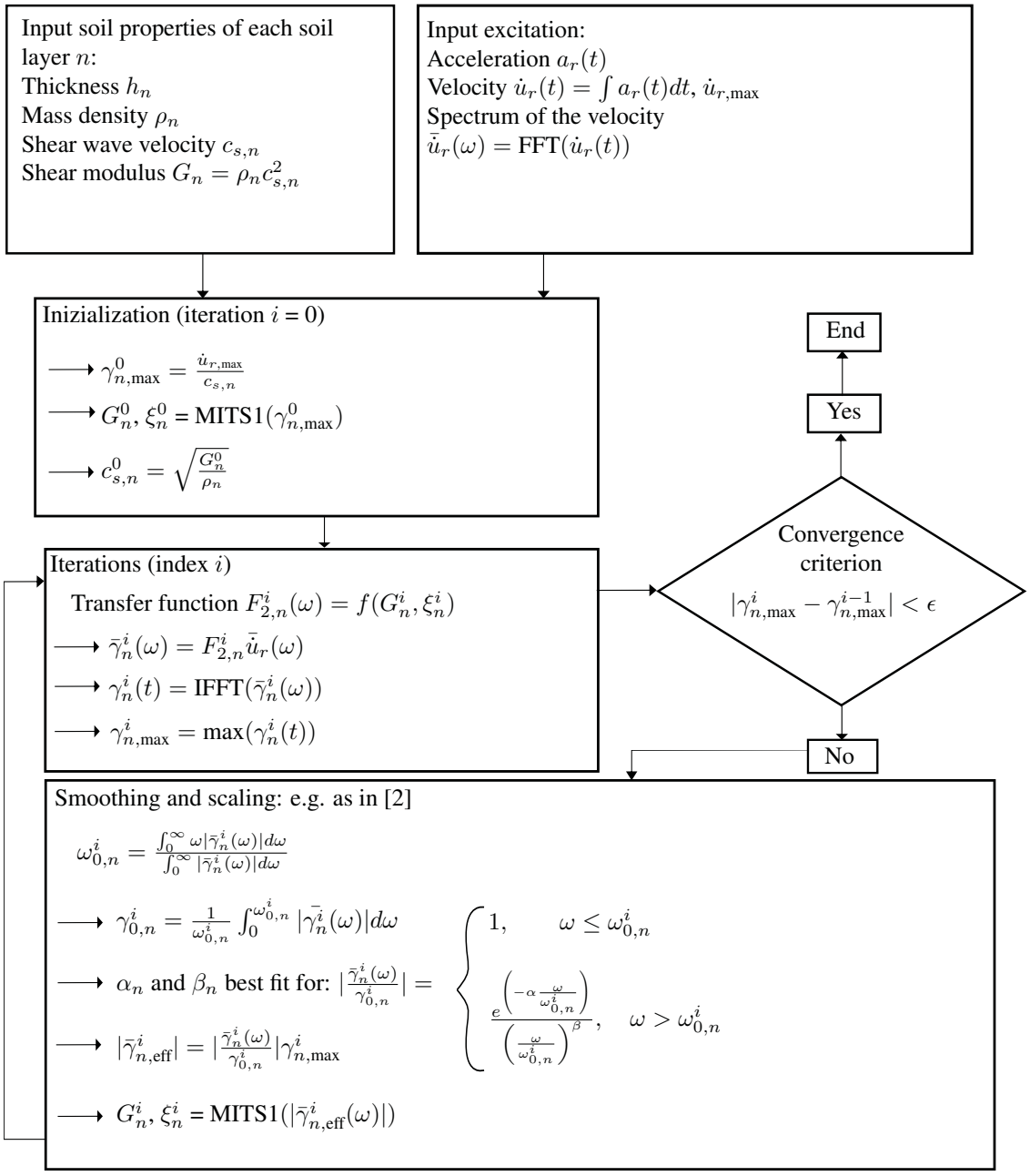

Figure 6: 1D iterative process according to [2] for non-linear soil properties based on the MITS1 constitutive laws.

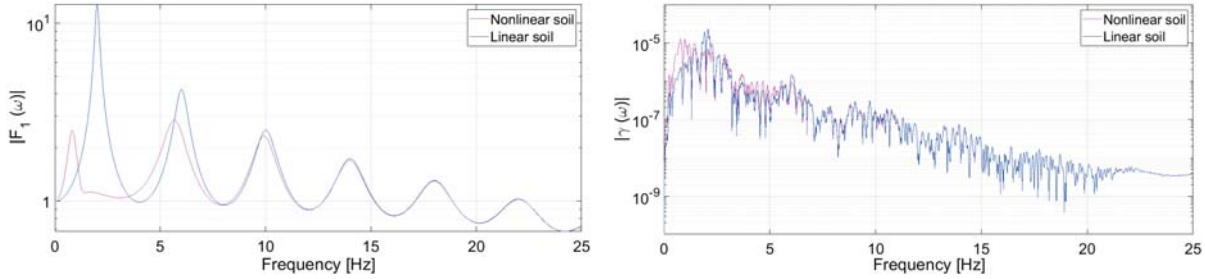

(a) Transfer function F_1 at the surface

(b) Strain spectrum at center of the numerical layer on top

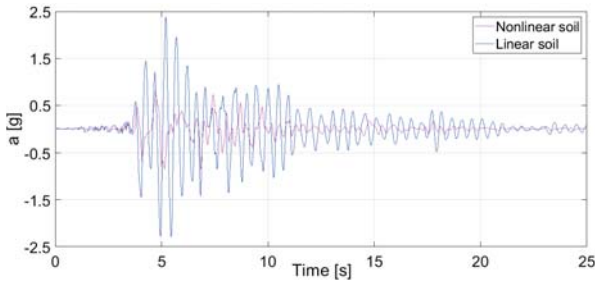

(c) Acceleration response at the surface

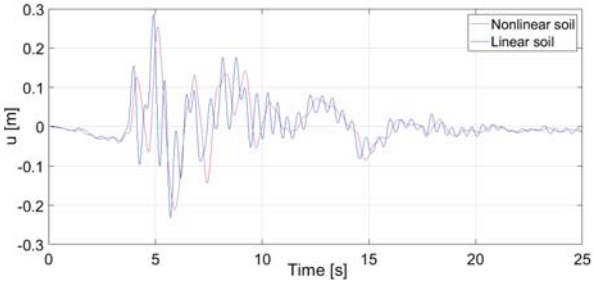

(d) Displacement response at the surface

Figure 7: Comparison between the nonlinear soil response resulting from the 1D HFTD method and the linear soil response.

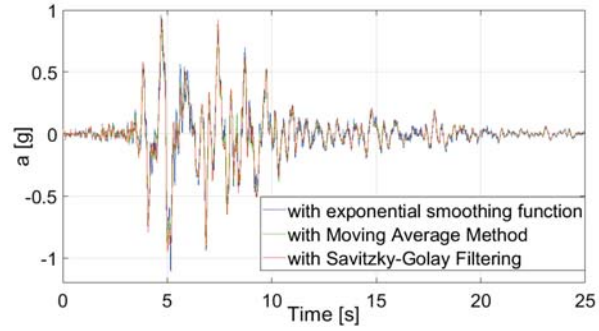

(a) Acceleration at surface

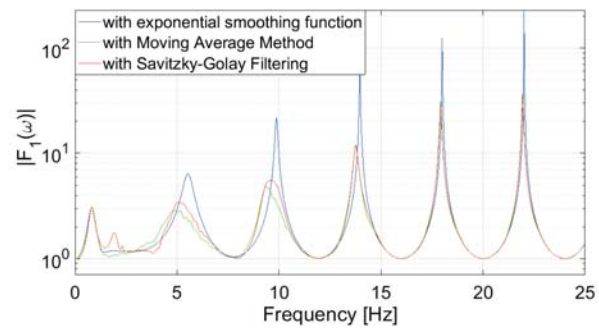

(b) Transfer function F_1

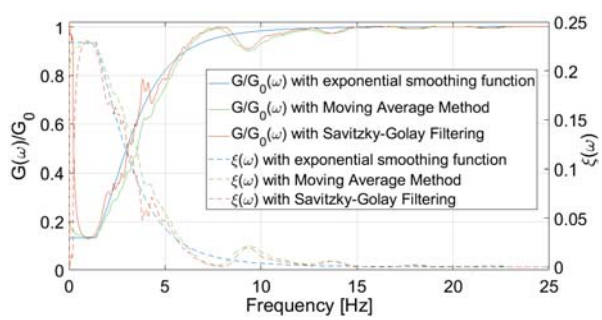

(c) Degradation curves at center of the physical layer

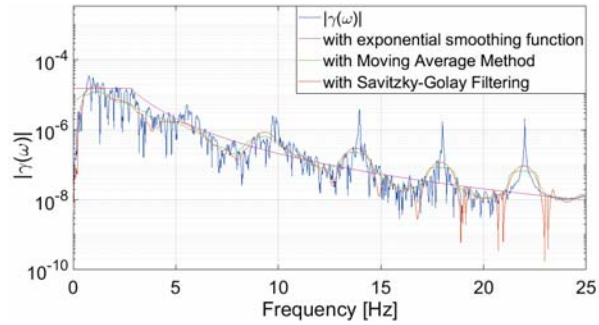

(d) Strain spectrum at center of the upper numerical layer

Figure 8: Nonlinear soil response with different smoothing techniques for the 1D case.

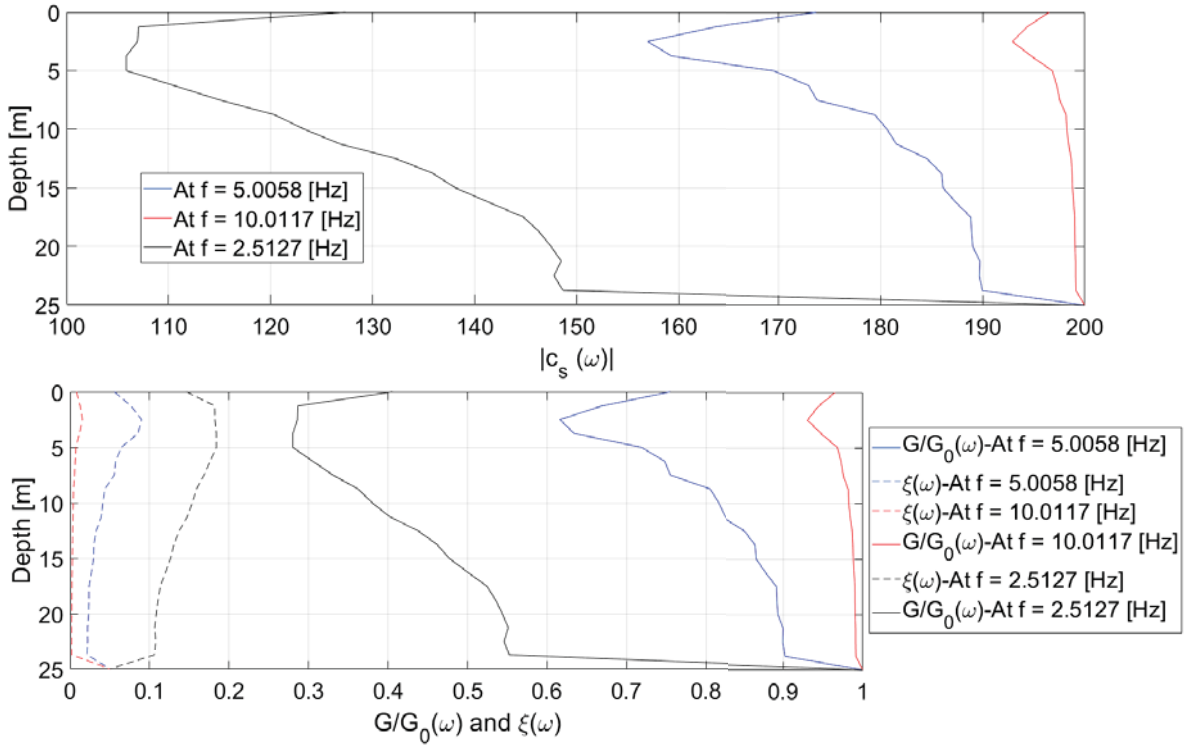

Figure 9: Nonlinear soil properties over depth at frequency of 2.5 Hz, 5 Hz and 10 Hz.

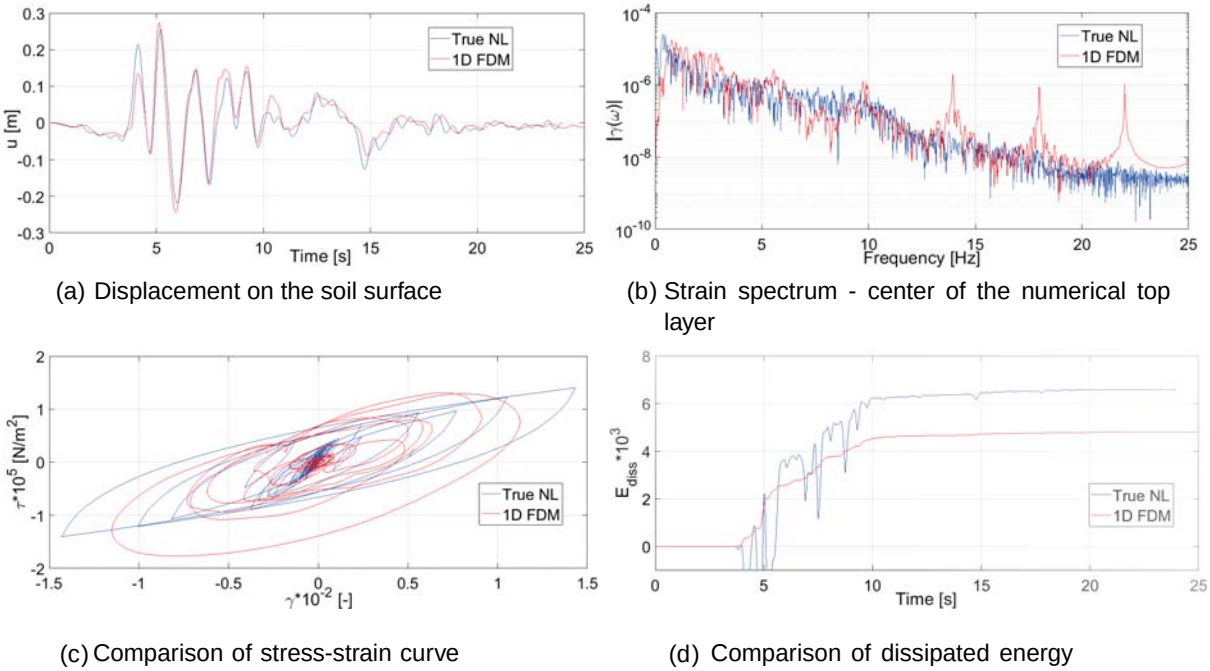

(a) Displacement on the soil surface

(b) Strain spectrum - center of the numerical top layer

(c) Comparison of stress-strain curve

(d) Comparison of dissipated energy

Figure 10: Comparison between the results according to the 1D HFTD method and a true nonlinear simulation using elasto-plastic springs after *Ivan* [11].

3D lies on the computation of the strains: in the 1D case, the strains at different depths in the free field are obtained through the 1D transfer functions $\boldsymbol{F}_2$ according to Eq. (21); in the 3D case, the strains are obtained with the ITM according to Eq. (13).

In the 3D HFTD method, it is possible to consider a complex spatial distribution of the input at the rock outcrop or at any point of the soil. Consequently, also the displacements and strains become a function of the coordinates x, y and z. These can be used to update the soil properties locally, thus obtaining a non-homogenous anisotropic soil. However, one of the assumption of the ITM method is that the soil has the same properties in x-direction and y-direction and that the properties in z-direction are homogenous within each horizontal layer. Therefore, for the iterative part of the method, we approximate the 3D strain distribution through a distribution which is constant for each horizontal layer and the reference strain vector $\boldsymbol{\varepsilon}_n$ for each layer n corresponds to the octahedral shear strain evaluated at the coordinate z_n (depth of the center of each layer), $\widehat{x}$ and $\widehat{y}$ (horizontal coordinate of the evaluation points, e.g. directly underneath the potential structure coupled to the free field). With the components of the reference strain vector, the octahedral shear strain according to Eq.(22) is computed and used to update the material properties of each layer with the chosen nonlinear material law. The more horizontal numerical layers are considered, the more accurate is the approximation. Alternatively one can used directly the 6 components of the the reference strain vector $\boldsymbol{\varepsilon}_n$ and a 3D nonlinear material model to update the soil model.

5.1 Comparison Between the 1D and 3D HFTD Method

In order to compare the 1D and 3D results, a free field subjected to a plane S-wave is considered. The wave propagates vertically while the particles move horizontally in x-direction (v_r^*=w_r^*=0, $u_r^* \neq$0) according to the Kobe earthquake signal[12]. In each plane x-y, all the particles experience the same horizontal motion, therefore the three dimensional case coincide with a one-dimensional problem. The soil is made up of a physical layer underlain by an elastic half space and the properties are specified in Tab. 2. The physical layer is divided into 10 numerical layers. The evaluation points for the ITM quantities are at the coordinate x_n=y_n=0 and at the z_n corresponding to the depths of the center of the N numerical layers.

For the solution of the ITM, the following boundary conditions are applied:

- BC 1: zero stresses at the soil surface;
- BC 2: the product of the dynamic stiffness of the half space with the relative displacements at the lowest interface of the layer is equal to the stresses at this interface,

$$\begin{aligned}&[\bar{\sigma}_{zx}(z=h), \bar{\sigma}_{yz}(z=h), \bar{\sigma}_z(z_1=h)]^T = \\ &\mathbf{K}_{HS}\left[(\bar{u}(z=h)-\bar{u}_r^*), (\bar{v}(z=h)-\bar{v}_r^*), (\bar{w}(z=h)-\bar{w}_r^*)\right]^T;\end{aligned}$$

- BC 3: continuity at interfaces between layers.

Where h is the thickness of the physical soil layer. By applying these boundary conditions, the coefficient vector $\boldsymbol{c}$ can be found and consequently the free field soil response in the image space (k_x, k_y, z, ω) is obtained. The solution in the original space (x, y, z, t) is computed through the inverse *Fourier* transformation.

The strain at the layer center and the acceleration at the surface resulting from 1D (blue curves) and 3D-model (red curves) are plotted in Fig. 12a and c. It can be seen that strains and accelerations resulting from both models is nearly identical. The 3D model achieved the convergence after eight iterations while the 1D model required six iteration steps. Also the

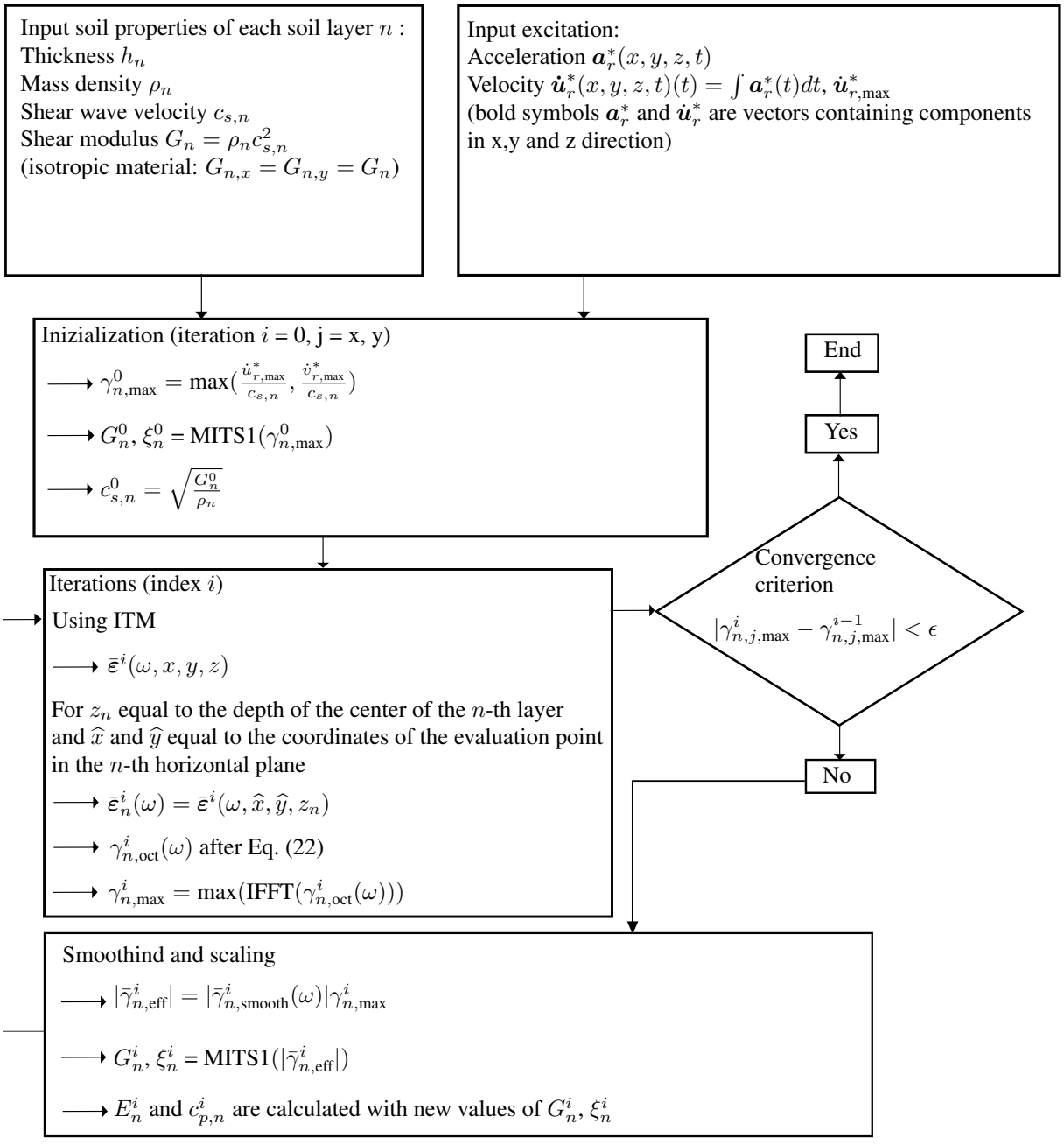

Figure 11: Proposed 3D iterative process for non-linear soil properties based on the MITS1 constitutive laws.

	h [m]	ρ [kg/m^3]	c_s [m/s]	ξ [-]	ν [-]
Layer	6.096	2002	244	0.05	0.3
Half space (HS)	-	2102	265	0.05	0.3

Table 2: Soil properties - Example with ITM

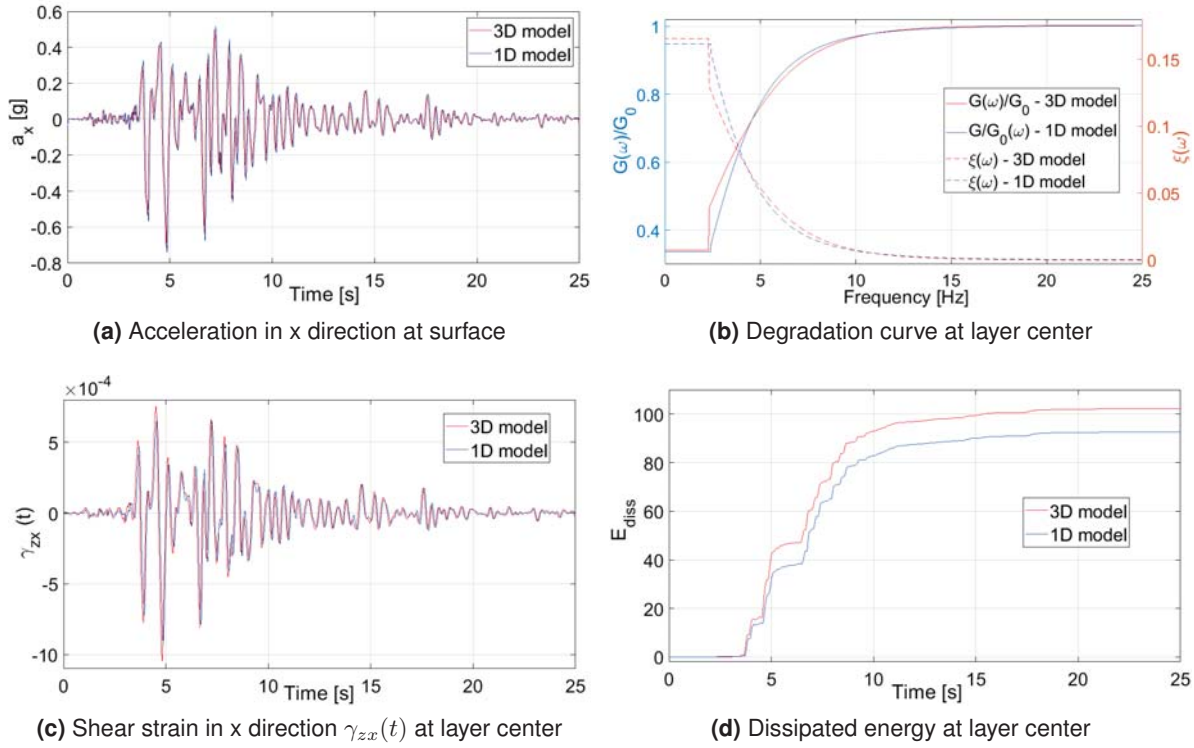

(a) Acceleration in x direction at surface

(b) Degradation curve at layer center

(c) Shear strain in x direction $\gamma_{zx}(t)$ at layer center

(d) Dissipated energy at layer center

Figure 12: Nonlinear response of one heterogeneous layer on elastic half space, subjected to a plane wave: 3D-HFTD method with ITM versus 1D-HFTD method.

degradation curves and the dissipated energy shows agrrement between the 1D and the 3D method.

5.2 3D HFTD Method Considering a Spatially Varying Seismic Excitation

In this example a layered soil is subjected to a seismic excitation with a non-constant horizontal distribution, applied at the interface between layer and half space, as shown in Fig 13. The material properties are shown in Tab. 3. Fig. 14 shows the transient signals and the spectra of the input u_r^* in x-direction and of v_r^* in y-direction, applied to all the particles of the area highlighted in Fig 14. The loaded area is 0.625 m $\times$ 0.625 m, symmetric with respect to the point (x, y) = (0, 0). Because of the small size of the loaded area, the excitation which would results from this excitation would be very small. Therefore, the equivalent seismic loads $[\bar{\sigma}_{zx}(z=h), \bar{\sigma}_{yz}(z=h), \bar{\sigma}_z(z_1=h)]^T$ are scaled with a factor of 1200 in order to introduced enough energy into the system. This scenario does not represents a real seismic loading condition but serves the purpose of showing the effect of a localized excitation. The soil is discretized into 10 numerical layers and the MITS1 material model is assumed. The reference strains for the iterative process are evaluated at the center of each layer and the the points (x, y) = (0,0). The results of this scenario are compared to the results of the same scenario considering a linear material behavior.

Fig. 15 shows the time history of the displacement response of the soil surface at (x,y,z) = (0,0,0), and the strain response at a depth of 5m (center of the physical layer), for the nonlinear and linear case. Fig. 16 shows the contour of the displacement response in x- and y-direction over the considered area on the soil surface at a chosen time t = 5.5s. Finally, Fig. 17 shows the transfer functions $F_{1,x} = u/u_r^*$ and $F_{1,y} = v/v_r^*$ (defined as in the 1D case) as well as the spectrum of the total displacements $u_{tot}(\omega, x = y = z = 0) = \sqrt{u^2 + v^2 + w^2}$ at the soil

	h [m]	ρ[kg/m^3]	c_s [m/s]	ξ[-]	ν[-]
Layer	10.0	2002	100	0.05	0.3
Half space	-	2102	265	0.05	0.3

Table 3: Soil properties for the 3D investigation in paragraph 5.2.

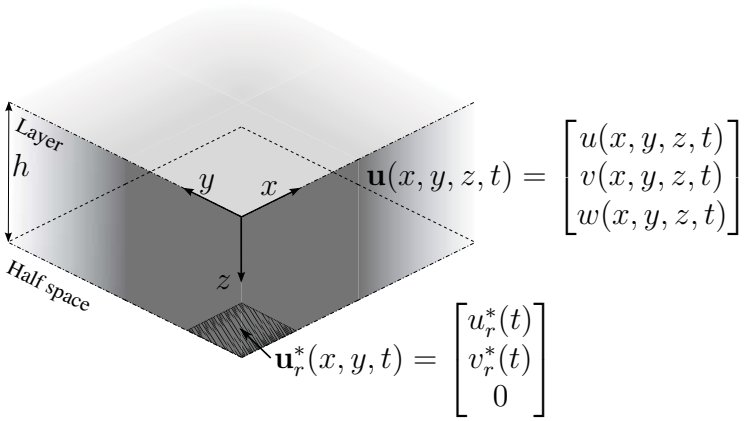

Figure 13: Non-constant spatial distribution of the seismic excitation at the layer-HS interface for the example in paragraph 5.2.

surface for the linear and the nonlinear case. The results show the influence of the nonlinear behavior on the frequency response and on the transient response.

5.3 Limitations of the 3D HFTD Method

The proposed method owns several advantages with respect to fully transient nonlinear analysis such as efficiency, simplicity of application and recued amount of output data. However, several limitations are also present and discussed in the following:

- Linearization: as in the 1D HFTD method, we assume that the transient nonlinear behavior of the 3D ground can be approximated by a superposition of steady-state linearized frequency-dependent responses. The convergence criteria focuses on the strain and affect the accuracy of the iterative process. This assumption needs to be investigated in more details, with a comparison against a fully transient nonlinear analysis.

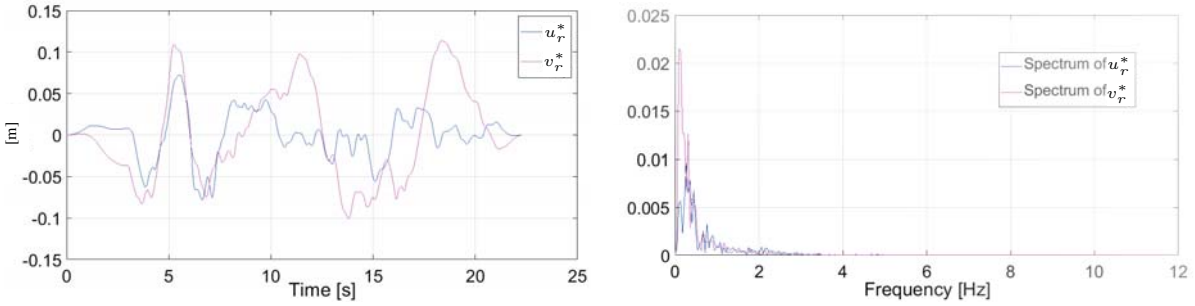

(a) Transient signals of the input motion (b) Spectra of the input motion

Figure 14: Displacement input in x and y direction applied at a portion of the layer-HS interface - 1987 earthquake in Superstition Hills, California, USA (downloaded from the PEER Strong Motion Database Record [1]).

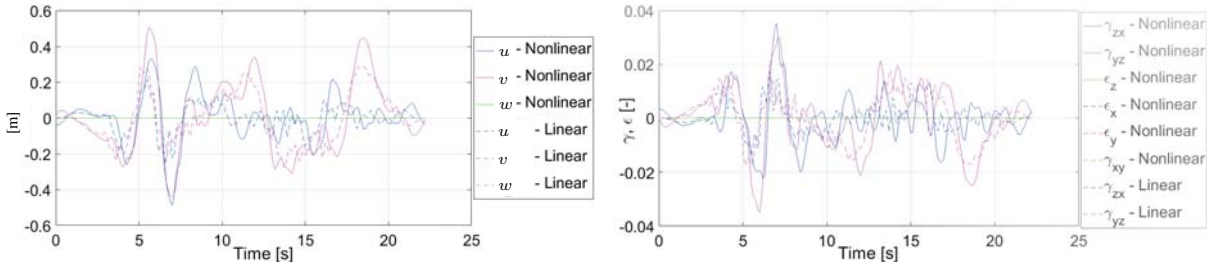

(a) Displacements at the soil surface (b) Strains at $z = 5\ m$

Figure 15: Comparison of the displacement and strain response at (x, y) = (0,0) for the linear and the nonlinear 3D HFTD method.

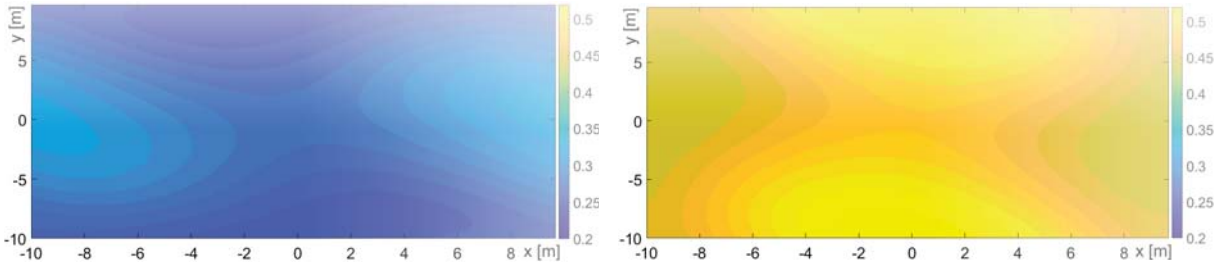

(a) Contour plot of the displacement $u(x, y, z = 0, t = 5.5\ s)$

(b) Contour plot of the displacement $v(x, y, z = 0, t = 5.5\ s)$

Figure 16: Contour of the displacement response of the soil surface at t = 5.5s for the nonlinear case.

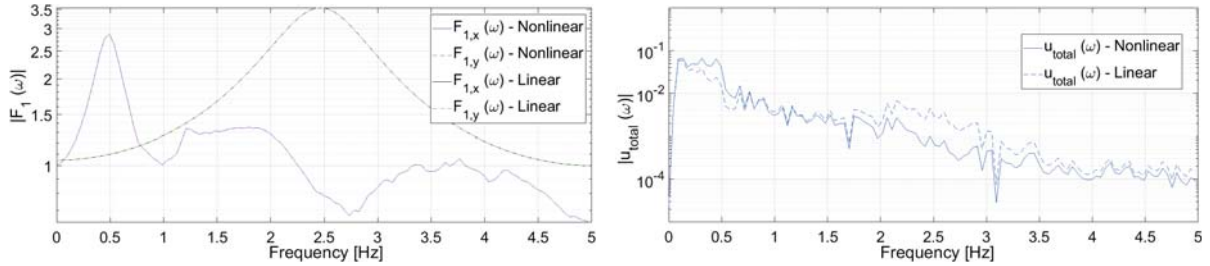

(a) Transfer functions of the displacement response on the soil surface

(b) Spectrum of the total displacement response on the soil surface

Figure 17: Comparison of the transfer functions and total displacement spectrum at the soil surface at (x, y) = (0, 0) - Linear versus nonlinear soil system.

- Material model: most of the nonlinear material model for soils are one-dimansional and the material parameters are defines as a function of the shear deformation. In the 3D HFTD method, one obtains a more detailed picture of strain deformation with 6 components, which could be the input of a realistic three-dimensional model for the description of the inelastic soil behavior. However, 3D material models are still under investigation. Therefore, we opted for established 1D material models, such as the MITS1, which depend only on one component of the strain. Here, we take the octahedral shear strain as a scalar measure of the shear deformation on a given point. This aspect can be improved integrating more complex 3D material models.

- Spatial averaging: in the 1D HFTD method, the system is approximated by a one dimensional model and all the particles in the x-y-planes, perpendicular to the depth-direction (z-axis), moves in phase and with the same amplitude. In the 3D HFTD method, the distribution of the motions and strains in the x-y-planes is not constant, being the input arbitrarily spatially distributed. One could use this information to update the soil model locally. However, in the current formulation of the ITM, we assume that each horizontal layer is isotropic. Therefore, the material properties, such as G and ξ, are constant for the whole x-z-plane and over the whole depth of the layer. For this reason, we have to summarize the spatial distribution into one reference value, for example observing one specific horizontal point $(\widehat{x},\widehat{y})$ to obtain the reference strain for the material model. In future developments, we plan to reformulate the method including spatial averaging based on energy consideration and to extend the ITM solution for anisotropic and locally inhomogeneous soils.

6 CONCLUSIONS

In this contribution we gave an overview of the one-dimensional (1D) hybrid frequency-time domain (HFTD) method for the simulation of the seismic response of nonlinear soils. The 1D HFTD method does not takes into account the three dimensional (3D) effects that characterize the wave propagation in the soil. To fill this gap, we presented a 3D HFTD method, where the seismic input motions can be applied at any point of the soil and can be spatially variable. The effective strains in the soil are computed based on the 3D theory of elasticity through the integral transform method (ITM). The 3D strain vector is used to find the linearized properties of the nonlinear soil and the problem is solved iteratively transforming from the image space into the original space and viceversa and updating the soil properties until convergence. Several examples show the comparison between the 1D and the 3D formulations and between linear and nonlinear simulations.

In the proposed method the main assumptions are that the soil is isotropic in the horizontal plane and that the properties of the material are homogenous within each horizontal layer. Moreover, the nonlinear material model used to update the materiel properties is one-dimensional. In future works, the 3D HFTD method will be extended for anisotropic soils and for three dimensional non linear material models.

REFERENCES

[1] Peer strong motion database record. `https://ngawest2.berkeley.edu/`. Accessed: 2019-01-15.

[2] Dominic Assimaki, Eduardo Kausel, and Andrew Whittle. Model for dynamic shear modulus and damping for granular soils. *J Geotech Geoenviron*, 126(10):859–869, 2000.

[3] Igor A Beresnev and Kuo-Liang Wen. Nonlinear soil response—a reality? *Bulletin of the Seismological Society of America*, 86(6):1964–1978, 1996.

[4] Julian Freisinger and Gerhard Müller. Modellierung eines halbraums mit sphärischem oder zylinderförmigem hohlraum für dreidimensionale boden-bauwerk-interaktion. *Forschung im Ingenieurwesen*, pages 1–12, 2018.

[5] David R Groholski, Youssef MA Hashash, Byungmin Kim, Michael Musgrove, Joseph Harmon, and Jonathan P Stewart. Simplified model for small-strain nonlinearity and strength in 1d seismic site response analysis. *Journal of Geotechnical and Geoenvironmental Engineering*, 142(9):04016042, 2016.

[6] Manuela Hackenberg and Gerhard Müller. Modeling a halfspace with tunnel using a coupled integral transform method–finite element method approach. *PAMM*, 15(1):389–390, 2015.

[7] Youssef MA Hashash and Duhee Park. Non-linear one-dimensional seismic ground motion propagation in the mississippi embayment. *Eng Geol*, 62(1):185–206, 2001.

[8] George D Hatzigeorgiou and Dimitri E Beskos. Soil–structure interaction effects on seismic inelastic analysis of 3-d tunnels. *Soil Dynamics and Earthquake Engineering*, 30(9):851–861, 2010.

[9] Chitas P.; Santos J.A.; Lopes I.F. A three-dimensional extension of the ramberg-osgood model. comparison with other formulations. In *Proceedings of the 15WCEE*, 2012.

[10] Wilfred D Iwan. On a class of models for the yielding behavior of continuous and composite systems. *J Appl Mech*, 1967.

[11] Eduardo Kausel. *Advanced structural dynamics*. Cambridge University Press, 2017.

[12] Eduardo Kausel and Dominic Assimaki. Seismic simulation of inelastic soils via frequency-dependent moduli and damping. *Journal of Engineering Mechanics*, 128(1):34–47, 2002.

[13] Dong-Yeop Kwak, Chang-Gyun Jeong, Duhee Park, and Sisam Park. Comparison of frequency dependent equivalent linear analysis methods. In *The 14th World Conference on Earthquake Engineering*, page 8, 2008.

[14] JP Laird and KH Stokoe. Dynamic properties of remolded and undisturbed soil samples tested at high confining pressures. *Geotechnical Engineering Report GR93*, 6, 1993.

[15] Chao Ma, Dechun Lu, Xiuli Du, and Annan Zhou. Developing a 3d elastoplastic constitutive model for soils: A new approach based on characteristic stress. *Computers and Geotechnics*, 86:129–140, 2017.

[16] Luan Maotian. Ramberg-osgood constitutive model with variable parameters for dynamic nonlinear analysis of soils. *Earthq Eng Eng Vib*, 2:007, 1992.

[17] Georg MASING. Eigenspannungen und verfestigung beim messing. In *Proceedings, second international congress of applied mechanics*, pages 332–335, 1926.

[18] Hossein Rahnema, Sassan Mohasseb, and Behtash JavidSharifi. 2-d soil-structure interaction in time domain by the sbfem and two non-linear soil models. *Soil Dynamics and Earthquake Engineering*, 88:152–175, 2016.

[19] Walter Ramberg and William R Osgood. *Description of stress-strain curves by three parameters*. National advisory committee for aeronautics, 1943.

[20] Julie Régnier, Héloïse Cadet, and Pierre-Yves Bard. Empirical quantification of the impact of nonlinear soil behavior on site response. *Bulletin of the Seismological Society of America*, 106(4):1710–1719, 2016.

[21] H Bolton Seed, Robert T Wong, IM Idriss, and Kohji Tokimatsu. Moduli and damping factors for dynamic analyses of cohesionless soils. *J Geotech Eng*, 112(11):1016–1032, 1986.

[22] Duguo Wang and Chenggang Zhao. Strain-threshold-and frequency-dependent seismic simulation of nonlinear soils. *Earthquake Science*, 27(6):615–626, 2014.

[23] J Wolf and William Hall. *Soil-structure-interaction analysis in time domain*. Number LCH-BOOK-2008-037. A Division of Simon & Schuster, 1988.

COMPDYN 2019
7th ECCOMAS Thematic Conference on
Computational Methods in Structural Dynamics and Earthquake Engineering
M. Papadrakakis, M. Fragiadakis (eds.)
Crete, Greece, 24–26 June 2019

BASIN EDGE EFFECT AT TURKISH BASINS: THE CASE STUDY OF DINAR AND DUZCE BASINS

H. Khanbabazadeh[1], R. Iyisan[2], M.E. Hasal[3] and C. Zulfikar[4]

[1, 4] Assistant Professor, Gebze Technical University
Civil Eng. Department, 41400 Gebze, Kocaeli, Turkey
e-mail: hadikhanbabazadeh@gmail.com

[2] Professor, Istanbul Technical University
Civil Engineering Faculty, 34469 Maslak, Istanbul, Turkey
iyisan@itu.edu.tr

[3] Project Director, Bursa Metropolitan Municipality
Department of Construction, Bursa, Turkey
hasal@hotmail.com

[4] Assistant Professor, Gebze Technical University
Civil Eng. Department, 41400 Gebze, Kocaeli, Turkey
aczulfikar@gtu.edu.tr

Abstract

Several studies have revealed that the inclined bedrock at the sides of the basins bring about the concentration of damages, which well known as basin edge effect. As a seismically active area much of the Turkey lies on the Anatolian Plate. This small plate bounded by two major strike-slip fault zones, the North Anatolian Fault and East Anatolian Fault. During the history, Turkey has been the site of devastating earthquakes.

Severe structural damage at basin sides during recent major earthquakes around the world strongly pointed out the importance of basin edge effect. Some of its notable examples can be tracked in Turkey. With respect to the fact that Turkey is among the top 20 percent of all countries exposed to earthquake hazard with regard to mortality and economic losses, the necessity of the investigation and consideration of the basin edge effect in earthquake design codes is revealed. In this study, the dynamic behavior at the edge of two real basins is investigated. In this study, at the first, the basin edge model of the basins are extracted from the data obtained from extensive microtremor surveys and geotechnical investigations as well as in-situ studies including SPT, CPT, PS logging tests. Then, the idealized geometry of the Dinar and Duzce basins edge models are proposed.

Afterwards, the basins are subjected to the collection of strong ground motions using a fully nonlinear method which works based on explicit finite difference scheme FLAC3D code. The

idealized 2D model of the Dinar and Duzce basins are subjected to the collection of sixteen strong ground motions with different peak ground accelerations (PGA) level of 0.1, 0.2, 0.3 and 0.4 g, four motions for each PGA level. For missing the effect of soil layers on selected real accelerograms they have been chosen from among those recorded on stiff layers during real earthquakes, or deconvoluted to the corresponding bedrock motion.

After the application of the strong ground motions from the bottom of the models in time domain, the acceleration of the surface points were recorded. For each surface point, the maximum spectral amplification factor under each earthquake is calculated then the average of resulted spectral amplification for four earthquakes of the same PGA level was estimated and reported.

The results of the dynamic analysis of Duzce basin showed the dominant effect of the inclined bedrock at the basin edge. Also, variation of its effect under excitations with different PGA levels is evident. At this basin the highest amplification factor occurs under the motions with PGA of 0.2g. Also, unlike the rest of the curves, a de-amplification of 0.85 along about 200 meters from the basin edge occurred at Duzce basin edge which shows that the basin edge can sometimes have decreasing effect on amplification. Regarding the influenced distance by the basin edge, while this distance is bout 800m and 1000m for the motions with the PGA of 0.1g and 0.2g, it increases to 1250m and 1500m for the motions with the PGA of 0.3g and 0.4g, respectively.

For asymmetric Dinar basin, two different amplification behaviors were seen at the eastern and western edges of the basin in terms of amplification amount and influenced distance by the basin edge. The higher basin edge effect at the eastern part with lower bedrock inclination with respect to western part was seen. This shows the higher effect of bedrock with lower angles. While the highest amplification factor at the western side occurs under the motions with PGA of 0.3g, it happens under the motions with PGA of 0.1g at the eastern side. Also, it was seen that at the eastern part of the basin has affected the distance about 1500 m from the outcrop while this distance for the steeper bedrock angle at the western side is about 700 m from outcrop. Between these distances 1D behavior is dominant.

The results show that the dynamic behavior of the both Dinar and Duzce basins at their sides is under the effect of basin edge in terms of amplification amount and influenced distance by the basin edge. At the basin edges, comparable amplification amounts with respect to the inner parts of the basins were seen.

Keywords: Site effect, Dynamic behavior, Numerical modeling, Microtremor, Basin edge effect, Dinar Basin, Duzce Basin.

1 INTRODUCTION

Several studies have revealed that the inclined bedrock at the sides of the basins bring about the concentration of damages, which well known as basin edge effect [1-3]. Ashigara Valley [4] and Ohba Valley [5] in Japan, Parkway Valley in New Zealand [6], Coachella Valley in southern California [7], Volvi Basin in Greece [8], Heathcote Valley in the Christchurch City of New Zealand [9] are among the sites with extensive seismic array observation instruments that have been used for validation of the theoretical studies regarding basin effects. In the meantime, investigations carried out at basins like Miyagi and Fukushima (Japan) [10], Fraser Delta [11] and Euroseistest site [12], among others, provided more accurate data about the basin edge effect.

As a seismically active area much of the Turkey lies on the Anatolian Plate. This small plate bounded by two major strike-slip fault zones, the North Anatolian Fault and East Anatolian Fault. During the history, Turkey has been the site of devastating earthquakes. A devastating earthquake hit the city of Duzce on November 12, 1999 with a moment magnitude (Mw) of 7.2 causing heavy damage and fatalities in Duzce province. The seen damage pattern during 1st October 1995 earthquake at Dinar town, Turkey, where located at the edge of an alluvial basin is another example of such effect. With respect to the statistical investigations, the resulting losses place Turkey in the top 20 percent of all countries exposed to earthquake hazard with regard to mortality and economic losses [13]. Severe structural damage at basin sides during recent major earthquakes around the world strongly pointed out the importance of basin edge effect and land-use planning [14-15]. Some of its notable examples can be tracked in Turkey. The recorded damage patterns during 1996 Dinar earthquake [16] as well as November 12, 1999 Duzce earthquake [17] revealed the necessity of the consideration of the basin edge effect in earthquake design codes. In this study, the different dynamic behavior at the edge of two basins with respect to the basin center is investigated. The results of such investigations can be used as the critical data in land-use planning projects as instrument of earthquake hazard mitigation.

In this study, at the first, the edge models of are extracted from the data obtained from performed microtremor surveys as well as geotechnical investigation. In this way, the basin stratification and shear wave velocity profile as well as geotechnical properties of the layers are obtained. Based on these data, the idealized geometry of Dinar and Duzce basins are proposed. Then, in order to estimate the dynamic behavior of the basins, a fully nonlinear method based on explicit finite difference scheme which solve the full equations of motion using FLAC3D code [18] is performed.

2 BASIN EDGE EFFECTS AT DINAR AND DUZCE BASINS

The existence of the inclined bedrock underlying the Duzce Basin has aroused the ideas of the effect of the basin edge on the dynamic behavior of basin. Also, the concentration of the damages at the edges of the non-symmetric alluvial Dinar basin indicates the involvement of the inclined bedrock in the different dynamic behavior of the basin at its sides [19-20].

2.1 Geology and seismo-tectonics of the basins

Dinar town is located at the edge of an alluvial basin in the southwest Anatolia, Turkey. To reveal its geology and geotechnical conditions, extensive in-situ studies including SPT, CPT, PS logging tests as well as microtremor measurements were carried out throughout the town [21].

There are two main fault systems around Dinar Town. One of them is Dinar-Civril fault which lays in the NW-SE direction and the other is Akdag fault with N-S direction. The Di-

nar-Civril fault has got a 75 km long normal fault with a slight oblique left lateral component [22]. These two fault systems had caused to form a seismotectonic structure consisting of two grabens and a horst.

In order to estimate the shear wave velocity profile of soil layers, at two of the pre-drilled boreholes suspension PS-logging tests until the approximate depths of 40 m were done. In Fig. 1 a characteristic geological section of Dinar laying in the E-W direction which reveals the horst-graben structure as well as an example of the results of the SPT and PS-logging test that were carried out at Dinar meteorological station site are presented.

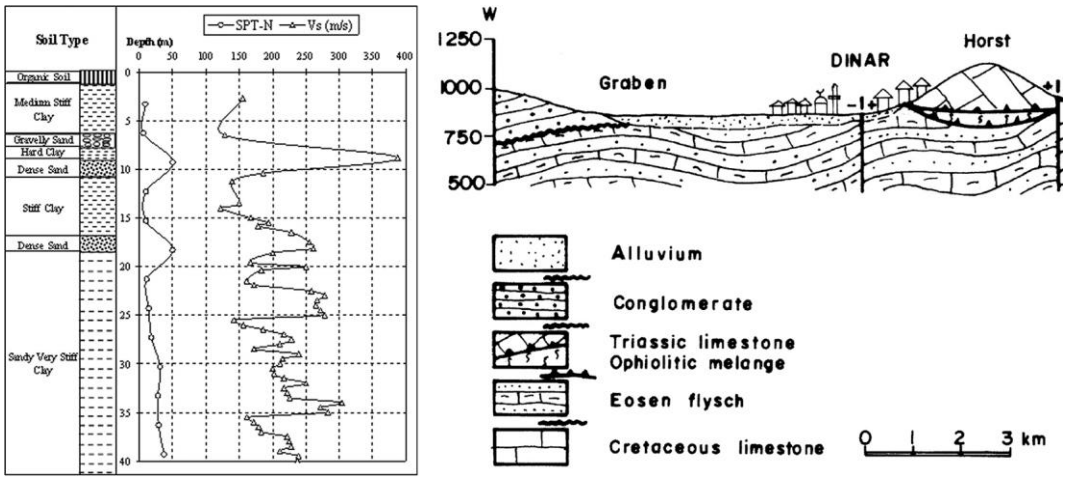

Figure 1: East-West geological section of Dinar basin and an example of the SPT and PS-logging test results.

Duzce basin is a graben-like basin which was formed by the activities of the North Anatolian Fault. From geological point of view there is a low inclined topography toward the southwest (toward Lake Eftani). In order to constitute the basin model and extract shear wave velocity profile of the Duzce basin a microtremor survey was performed. Also, Single point microtremor measurements were carried out at 25 different points in the basin along an S-N line. The thickness value for each top layer was estimated by providing the best fit between the H/V curve and theoretical Rayleigh wave ellipticity [23]. Based on microtremor measurements, the basin is composed of seven separate layers with different shear wave velocities. The layer with a shear wave velocity greater than 800 m/s was considered as seismic bedrock. The depth of seismic bedrock was estimated by the method conducted by Kudo et. al.(2002) [24]. In Fig. 2 the proposed Duzce basin stratification and the shear wave velocity profile of the basin edge is presented.

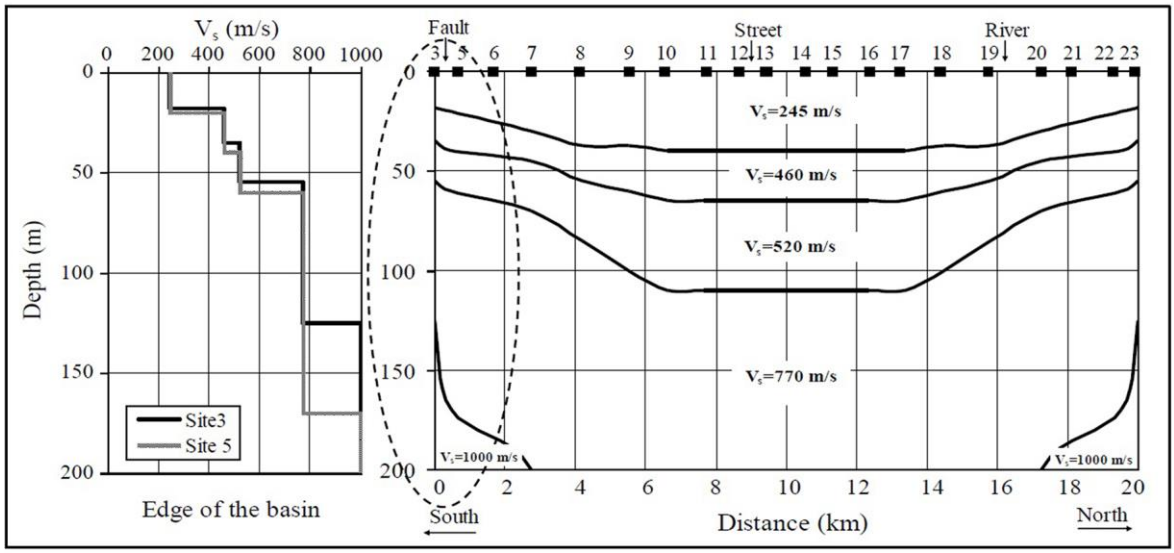

Figure 2: The proposed Duzce basin stratification and the shear wave velocity profile of the basin edge.

2.2 Idealized basin geometry and geotechnical properties

Based on the results of the microtremor measurements, underground explorations and laboratory tests, and with respect to the extracted geologic cross sections of the areas given at Fig. 1 and Fig.2 the idealized geometry of the Dinar and Duzce basins are proposed at Fig. 3.

As can be seen, for Dinar basin which is located between two horsts, the bedrock has got 6° inclination at the east edge until the180m depths. Then, until the depth of 220 m the bedrock angle decreases to 2°. At the west part steeper bedrock with 20° angle continues until the depth of 220 m. At the other parts, horizontal bedrock with the depth of 220 m is modeled. The width of the 2D basin model has been taken 6km.Corresponding soil specifications are presented at Table 1.

For Duzce basin, the findings of the 2D shear wave velocity profile indicate the seismic bedrock inclination of 6° at the basin edge which continues until 2km inside the basin. The soil layers were assumed to extend horizontally within 2.2 km from the basin edge. Also, in order to effectively catch the 2D behavior of the basin, the selected modeling length should exceed the region that is affected by inclined bedrock. Such point is considered as the beginning of the 1D behavior of the basin; the region that the effect of the inclined bedrock is missed. So, the left 2.2km of the basin has been modeled.

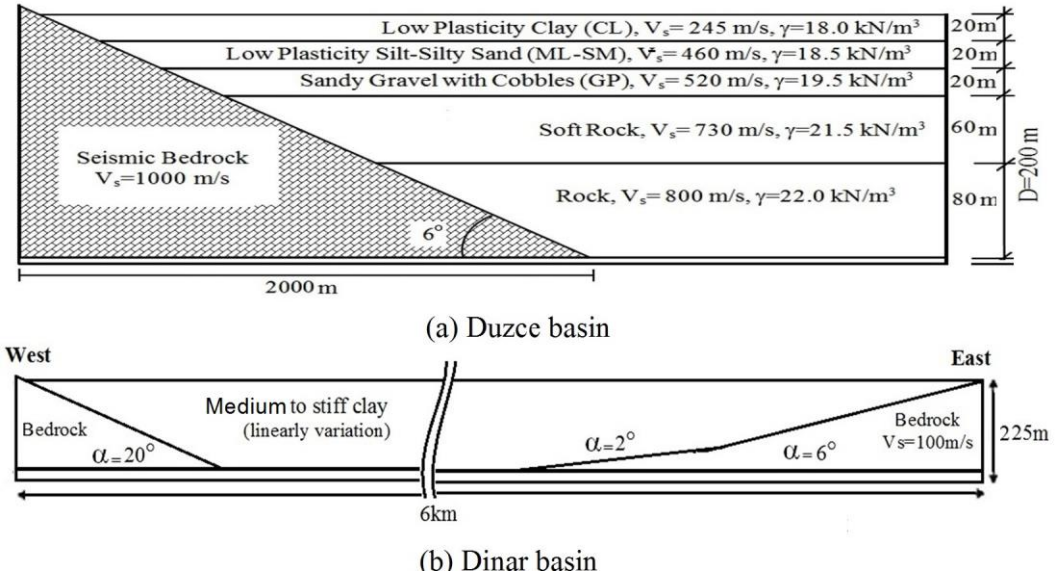

Figure 3: The idealized geometry of the (a) Duzce and (b) Dinar basins.

Regarding geotechnical properties of the basins, the 220 m basin depth of the Dinar basin is divided to two 200 m and 20 m layers on the bedrock in order to model the 20 m transient layer between bedrock and basin (underlying a 5m bedrock layer). A linear variation of the properties over basin depth has been provided for Dinar basin. Duzce basin and its surrounding area consists of alluvium deposits and lake sediments, which are composed of fine grained gravel, sand and silt mixture with clay layers. The geotechnical properties of the idealized Dinar and Duzce basins soils are presented at Table 1.

Soil Type	c' (kPa)	ϕ' (°)	Vs (m/s)	G (MPa)	K (MPa)	g(kN/m$^{3)}$
Dinar Basin						
Basin	50-140	10	175-600	55.1-828	143.7-2159	18-21.6
Transient part	140-150	10	600-700	828-1127	2159-2939	216-22
Bedrock	-	-	1000	2200	3600	22
Duzce Basin						
Stiff Low Plasticity Clay with Sand (CL)	10	26	245	108	282	18
Medium Dense-Dense Silty Sand (SM)	3	33	460	391.5	1020	18.5
Dense-Very Dense Sandy Gravel with Cobbles (GP)	-	38	520	527.3	1375	19.5
Medium Weathered Soft Rock	350	35	730	1120	2918	21
Slightly Weathered Soft Rock	450	37	800	1410	3672	22
Elastic Bedrock	-	-	1000	2500	4160	25

Table 1: The geotechnical properties of the idealized Dinar and Duzce basins

The idealized 2D model of the Dinar and Duzce basins are subjected to the collection of sixteen strong ground motions with different peak ground accelerations (PGA) level of 0.1, 0.2, 0.3 and 0.4 g, four motions for each PGA level. These records are of different peak ground accelerations, frequency contents and durations. They are baseline corrected and filtered by a 25 Hz low-pass filter. The excitations are applied as SV waves to the model bot-

toms. For missing the effect of soil layers on selected real accelerograms they have been chosen from among those recorded on stiff layers during real earthquakes, or deconvoluted to the corresponding bedrock motion. At Table 2 the specification of the applied earthquakes are presented.

Earthquakes	Station	Amax (g)	Magnitude	Significant Duration (s)	Arias Intensity (m/s)
Anza (25.02.1980)	PinyonFlat	0.1	Mw=4.9	1.945	0.0218
Mammoth lakes (25.05.1980)	LongValleyDam	0.1	Mw=6.0	7.46	0.0666
Chalfant (21.07.1986)	LongValleyDam	0.1	Mw=6.2	10.24	0.0638
Palm springs1986	Silent Valley	0.1	ML=5.9	6.14	0.0658
Livermore (27.01.1980)	Morgan Terr Park	0.2	Mw=5.4	3.42	0.1877
Düzce (12.11.1999)	Lamont-531	0.2	Mw=7.1	10.57	0.5283
Dinar 1995	Dinar station	0.2	ML=5	14.95	0.8096
Sakarya (11.11.1999)	Develop. burea	0.2	Md=5.7	3.11	0.1397
Firuzabad 20.06.1994	Firuzabad-ZRT	0.3	Mw=5.9	7.14	0.687
Parkfield (28.06.1966)	Temblor pre	0.3	Mw=6.1	4.29	0.3615
Coyotelake (06.08.1979)	Coyote Lake Dam	0.3	Mw=5.7	3.68	0.4003
Mendocino 1992	EEL River valley	0.3	ML=6.5	4.82	0.8079
South Iceland (17.06.2000)	Thjorsarbru	0.4	Mw=6.5	4.29	1.6125
UmbriaMarche (10.16.1997)	Colfiorito	0.4	Mw=4.3	4.57	0.6902
Parkfield (28.06.1996)	Temblorpre	0.4	Mw=6.1	3.19	0.5537
Kocaeli1(7.08.1999)	Develop. burea	0.4	Md=7.4	9.74	1.5843

Table 2: The specification of the applied strong ground motion collection.

3 ANALYSIS METHOD

To estimate the dynamic behavior of the Dinar and Duzce basins a fully nonlinear analysis using FLAC3D code (Fast Lagrangian Analysis of Continua) based on explicit finite difference scheme which solves the full equations of motion is applied. In this method, both shear and compressional waves are propagated together in a single simulation, and the material responds to the combined effect of both components. This aspect gets more important in the 2D modeling of the basin edge where the waves are trapped at low angle bedrock inclinations. Also, the method follows any prescribed nonlinear constitutive relation and since the strain increments (not tensors) relate to the stress tensors, therefore plastic yielding is modeled appropriately [18]. With respect to the selected soil properties, the corresponding G/Gmax curves have been estimated based on relation proposed by Ishibashi and Zhang (1993) [25] and is presented at Fig. 5.

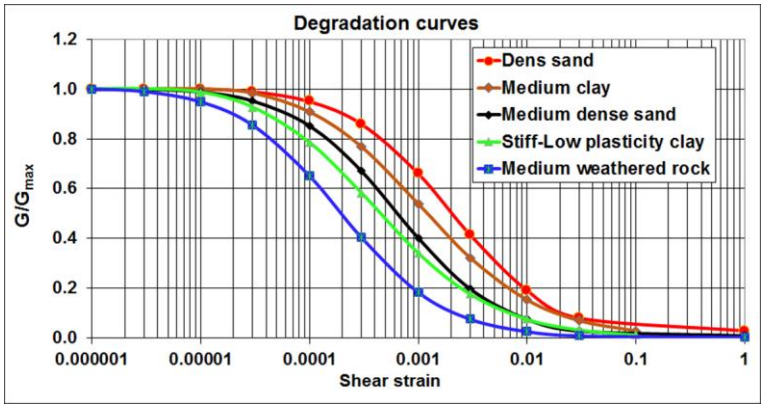

Figure 4: The corresponding G/Gmax degradation curves of the basins' soils.

At the bottom boundary of the model the quiet boundary scheme, which involves dashpots, are attached independently in the normal and shear directions to prevent the reflection of outward propagating waves back into the model as well as allow the necessary energy radiation. For vertical boundaries, the approach used in the continuum finite difference code NESSI [26] are developed via Free-Field boundary condition which involving the execution of free-field calculations in parallel with the main-grid analysis. Also, to provide the accurate transmission of the wave through modeled mesh, based on Kuhlemeyer and Lysmer (1973) [27], with respect to the frequency content of the input waves and the wave speed characteristics of the system, the spatial mesh size was selected smaller than one tenth to one eighth of the wavelength associated with the highest frequency component of the wave.

The verification of this analysis has been done by comparing to the solution of Kawase and Aki (1989) [28], and presented at Iyisan and Khanbabazadeh (2013) [29] and Khanbabazadeh and Iyisan (2014 a,b) [30-31]. The solution of the trapezoidal valley by Kawase and Aki (1989) [28] has been tested by Zahradnik (1995) [32] and Gil-Zepeda et al. (2003) [33], among the others.

4 RESULTS AND DISCUSSION

After the application of the strong ground motions presented at Table 2 from the bottom of the models in time domain, the acceleration of the surface points were recorded. For each surface point, the maximum spectral amplification factor under each earthquake is calculated then the average of resulted spectral amplification for four earthquakes of the same PGA level was estimated and reported. At Fig. 6 and Fig. 7, the maximum spectral amplification variation at the surface of the Dinar and Duzce basins under excitations with four different PGA levels are presented.

4.1 Dinar basin

As seen at the idealized geometry of the Dinar basin, this basin has got an asymmetric geometry with different bedrock angles at its sides. The effect of such geometry can also be seen in the dynamic behavior of Dinar basin at Fig. 6. Two different amplification behaviors are seen at the eastern and western edges of the Dinar basin in terms of amplification amount and influenced distance by the basin edge. Also, the effect of the motion strength on the dynamic behavior of the basin is evident.

The results show that while the highest amplification factor at the western side occurs under the motions with PGA of 0.3g (with the maximum amplification factor of 3.75), it hap-

pens under the motions with PGA of 0.1g at the eastern side (with the maximum amplification factor of 3.82).

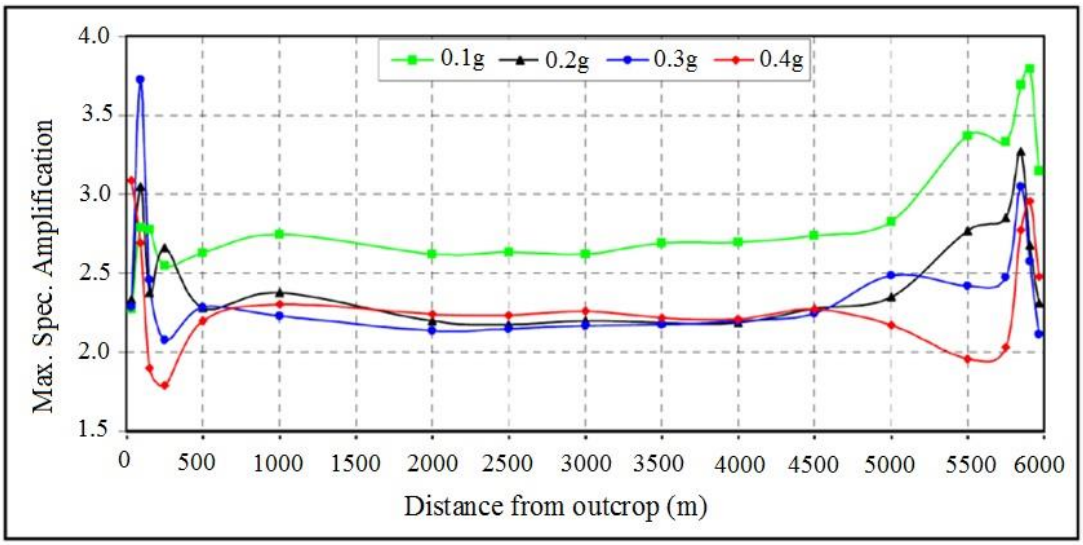

Figure 5: The maximum spectral amplification variation at Dinar basin surface.

There are two different amplification trends at two sides. Because of the enough distance between two edges, no interference of the edges effect is seen. In fact, Dinar basin is divided to three areas, two areas with independent 2D behavior at edges and a middle area with 1D behavior. The point that the amplification curve turns to a flat curve, which continues towards the inner parts of the basin, is usually considered as the beginning of the 1D behavior of the basin; the region that the effect of the inclined bedrock is missed.

It is seen that the milder bedrock inclination at the eastern part of the basin has affected the distance about 1500 m from the outcrop while this distance for the steeper bedrock angle at the western side is about 700 m from outcrop. Between these distances, the effects of the basin edges are cancelled. In this region the basin turns to behave one dimensionally. The highest 1D amplification factor belongs to the motions with PGA of 0.1g. For other PGA levels, relatively close 1D amplification factor is seen. While the sustained spectral amplification of the basin center under the motions of 0.1g PGA is about 2.7, it decreases to about 2.25 for stronger motions with higher PGAs.

4.2 Duzce basin

The amplification curves of the Duzce basin clearly show the influence of the basin edge on the dynamic behavior of Duzce basin. Also, the variation of its effect under excitations with different PGA levels is evident. As can be seen, while the highest amplification factor occurs under the motions with PGA of 0.2g, the lowest amplification factor belongs to the motions with PGA of 0.1g.

Despite the increasing trend of the amplification under the motions with the PGA of 0.1g and 0.2g, it begins to decrease under the motions with higher PGAs. The seen amplification factors under the motions with the PGA of 0.3g and 0.4g reach to 3.4 and 3, respectively.

Also, the maximum amplification curve of the basin surface under the motions with the PGA of 0.3g shows a de-amplification of 0.85 along about 200 meters from the basin edge, unlike the rest of the curves. This shows that the basin edge can sometimes have decreasing effect on amplification. This phenomenon can be the result of the trapping of the waves at the half space between inclined bedrock and surface at the edges.

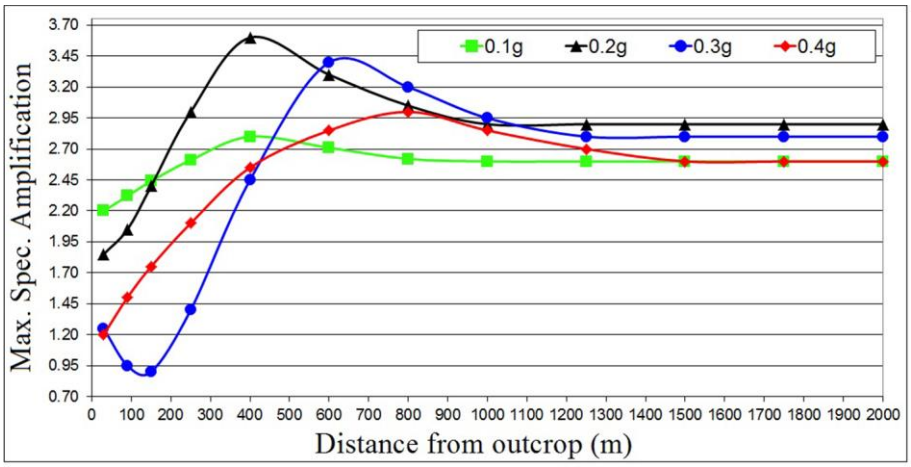

Figure 6: The maximum spectral amplification variation at Duzce basin surface.

As mentioned earlier, from the point that the effect of the inclined bedrock is missed the 1D behavior of the basin begins. For Duzce basin the beginning of 1D behavior under the motions with different strengths is different. While this behavior for motion with the PGA of 0.1g begins at 800m from the outcrop (with the maximum amplification factor of 2.6), it reaches to about 1000m under the motions with the PGA of 0.2g (with the maximum amplification factor of 2.9). Despite the decrease in the maximum amplification factor under the motions with the PGA of 0.3g and 0.4g (with respect to the motions with the PGA of 0.2g), the beginning point of the 1D behavior stretches more. It begins from 1250m and 1500 for the motions with the PGA of 0.3g and 0.4g, respectively. In shorts, inside these areas the effect of the basin edge is dominant.

5 CONCLUSIONS

- In this study, in order to investigate the basin edge effect, at the first, the basin edge model is extracted from the data obtained from extensive microtremor surveys and geotechnical investigations as well as in-situ studies including SPT, CPT, PS logging tests. Using these findings the basin stratification and shear wave velocity profile as well as geotechnical properties of the layers of the basins were obtained. Then, the idealized geometry of the Dinar and Duzce basins edge models were proposed. Afterwards, the basins were subjected to the collection of sixteen strong ground motions with different peak ground accelerations (PGA) levels using a fully nonlinear method which works based on explicit finite difference scheme and solve the full equations of motion using FLAC3D code. Using the recorded acceleration at 12 surface points along the basin edge the variation of the maximum spectral amplification factor was reported.

- The results show that the dynamic behavior of the both Dinar and Duzce basins at their sides is under the effect of basin edge. Comparable amplification amounts with respect to the inner parts of the basins were seen. For asymmetric Dinar basin, two different amplification behaviors were seen at the eastern and western edges of the basin in terms of amplification amount and influenced distance by the basin edge. The higher basin edge effect at the eastern part with lower bedrock inclination with respect to western part was seen. This shows the higher effect of bedrock with lower angles. While the highest amplification factor at the western side occurs under the motions with PGA of 0.3g, it happens under the motions with PGA of 0.1g at the eastern side. Also, it was seen

that at the eastern part of the basin has affected the distance about 1500 m from the outcrop while this distance for the steeper bedrock angle at the western side is about 700 m from outcrop. Between these distances 1D behavior is dominant.

- The results of the dynamic analysis of Duzce basin showed the dominant effect of the inclined bedrock at the basin edge. Also, variation of its effect under excitations with different PGA levels is evident. At this basin the highest amplification factor occurs under the motions with PGA of 0.2g. Also, unlike the rest of the curves, a de-amplification of 0.85 along about 200 meters from the basin edge occurred at Duzce basin edge which shows that the basin edge can sometimes have decreasing effect on amplification. Regarding the influenced distance by the basin edge, while this distance is bout 800m and 1000m for the motions with the PGA of 0.1g and 0.2g, it increases to 1250m and 1500m for the motions with the PGA of 0.3g and 0.4g, respectively.

- By consideration of the all aspects of this study, the results of such investigations can be used as the critical data in land-use planning projects as instrument of earthquake hazard mitigation.

REFERENCES

[1] H. Khanbabazadeh, A. Janalizadeh, Investigation of the site effect on seismic ground motions using elasto-plastic constitutive model. *Elec. J. Geotech. Eng.,* 11(Bundle A), 2006.

[2] D. Assimaki, S. Jeong, Coupled topography-stratigraphy effects during the m 7.0 Haiti earthquake: the case of hotel Montana. *4th IASPEI/IAEE international symposium,* Santa Barbara: University of California, USA, 2011.

[3] M. E.Hasal, R. Iyisan, H. Khanbabazadeh, A. Bayin, G. Cevikbilen, O. Kepceoglu. A, Preliminary Seismic Microzonation Study Based on Microtremor Measurements. *International Conference on Earthquake Engineering*, Skopje, Macedonia, 2013.

[4] A. Ohtsuki, H. Yamahara, T. Tazoh, Effect of lateral inhomogeneity on seismic waves, II: Observation and analysis. *Earthq Eng Struct Dyn.,* **12**:795-816, 1984.

[5] G. Gazetas, K. Fan, T. Tazoh, K. Shimizu. Seismic response of the pile foundation of Ohba Ohashi Bridge. *Proceedings of the 3rd International Conference on Case History in Geotechnical Engineering*, 1803-1809, 1993.

[6] F.J. Chavez-Garcia, M. Rodriguez, W.R. Stephenson. 1D vs. 2D site effects: the case of Parkway Basin, New Zealand. *11th European Conference on Earthquake Engineering*, Balkema, Rotterdam, 1998.

[7] E.H. Field, Spectral amplification in a sediment-filled valley exhibiting clear basin edge induced waves. *Bull Seismol Soc Am,* **86**, 991-1005, 1996.

[8] K. Pitilakis, Site effects. Recent Advances in Earthquake Geotechnical Engineering and Microzonation. *Kluwer Academic Publishers*, Netherlands, 1:139-193, 2004.

[9] F. Gelagoti, R. Kourkoulis, D. Tsirantonaki, G. Gazetas, 2-dimensional non-linear valley effects at Heathcote Valley during the 2011 Canterbury earthquake: A case study. *2nd European Conference on Earthquake Engineering and Seismology*, Istanbul, 2014.

[10] M. Kamiyama, T. Satoh, Seismic response analysis of laterally inhomogeneous ground with emphasis on strains. *Soil Dyn Earthq Eng*, **22**, 877–84, 2002.

[11] W.D. Finn, E. Zhai, T. Thavaraj, X.S. Hao, C.E. Ventura, 1D and 2D analyses of weak motion data in Fraser Delta from 1966 Duvall earthquake. *Soil Dyn Earthq Eng*, **23**, 323–9, 2003.

[12] K. Makra, F.J. Chavez-Garcıa, D. Raptakis, K. Pitilakis, Parametric analysis of the seismic response of a 2D sedimentary valley: implications for code implementations of complex site effects. *Soil Dyn Earthq Eng*, 25, 303–15, 2005.

[13] M. Erdik, Earthquake Risk in Turkey. *Am Assoc Advanc Sci*, **341(6147)**,724-725, 2013. DOI: 10.1126/science.1238945.

[14] K. Beyen, M. Erdik, Two-dimensional nonlinear site response analysis of Adapazarı plain and predictions inferred from aftershocks of the Kocaeli earthquake of 17 August 1999. *Soil Dyn Earthq Eng*, **24**, 261-279, 2004. DOI:10.1016/j.soildyn.2003.10.009.

[15] H. Khanbabazadeh, R. Iyisan, A. Ansal, C. Zulfikar, Nonlinear dynamic behavior of the basins with 2D bedrock. *Soil Dyn Earthq Eng*, **107**,108-115, 2018;. DOI: 10.1016/j.soildyn.2018.01.011.

[16] KOERI. Dinar earthquake of 1.10. Reconnaissance Report, October 9, 1995. Bogazici University, Kandilli Observatory and Earthquake research Institute (KOERI); 1995.

[17] M.E. Hasal, R. Iyisan, H. Yamanaka, Basin Edge Effect on Seismic Ground Response: A Parametric Study for Duzce Basin Case, Turkey. *Arab J Sci Eng*, **43(4)**, 2069–2081, 2018.

[18] P.A. Cundall. FLAC3D Manual: A Computer Program for Fast Lagrangian Analysis of Continua (Version 4.0), Minneapolis, Minnesota, USA; 2008.

[19] B.S. Bakir, M.Y. Ozkan, S. Ciliz, Effects of basin edge on the distribution of damage in 1995 Dinar, Turkey earthquake. *Soil Dyn Earthq Eng*, **22**, 335–45, 2002.

[20] H. Khanbabazadeh, R. Iyisan. A. Ansal, M.E. Hasal, 2D non-linear seismic response of the Dinar basin,TURKEY. *Soil Dyn Earthq Eng*, **89:5**–11, 2016.

[21] M.A. Ansal, R. Iyisan, H. Güllü, Microtremor measurements for the microzonation of Dinar. Pure Appl Geophys, **158**, 2525–41, 2001.

[22] A. Ozturk, Tectonics of Dinar Sandıklı-Isıklı region, Communications of Faculty of Science. Ankara, Turkey: University of Ankara; .pp 1–58, 1982.

[23] H. Yamanaka, M. Kato, M. Hashimoto, U. Gulerce, R. Iyisan, A. Ansal, Microtremor and earthquake observations in Adapazari and Duzce, Turkey, for estimations of site amplifications. *Proceedings of the Assessment of Seismic Local Site Effects at Plural Test Sites, Ministry of Education, Science, Sports and Culture, Research Grant No: 11694134*, Japan, 129-136, 2002.

[24] K. Kudo, T. Kanno, H. Okada, O. Ozel, M. Erdik, T. Sasatani, S. Higashi, M. Takahashi, K. Yoshida, Site-specific issues for strong ground motions during the Kocaeli, Turkey, earthquake of 17 August 1999, as inferred from array observations of microtremors and aftershocks. *Bulletin of Seismological Society of America,* **92 (1),** 448-465, 2002.

[25] I. Ishibashi, X. Zhang, Unified dynamic shear moduli and damping ratios of sand and clay. *Soils Found Jpn Soc Soil Mech Found Eng*, **33(1),** 182–91, 1993;.

[26] P.A. Cundall. et al., NESSI–Soil Structure Interaction Program for Dynamic and Static Problems, *Norwegian Geotech. Institute; Report*, **51**,508-509, 1980.

[27] R.L. Kuhlemeyer, J. Lysmer, Finite element method accuracy for wave propagation problems. *J Soil Mech Found Div ASCE*, **99(SM5)**, 421–7, 1973.

[28] H. Kawase, K. Aki, A study on the response of a soft basin for incident. S, P and Rayleigh waves with special reference to the long duration observed in Mexico City. *Bull Seismol Soc Am*, **79**, 1361–82, 1989.

[29] R. Iyisan, H. Khanbabazadeh, A numerical study on the basin edge effect on soil amplification. *Bull Earthq Eng*, **11**, 1305–23, 2013.

[30] H. Khanbabazadeh, R. Iyisan, A numerical study on the 2D behavior of the single and layered clayey basins. *Bull Earthq Eng*, **12(4)**, 1515–36, 2014.

[31] H. Khanbabazadeh, R. Iyisan, A numerical study on the 2D behavior of the clayey basins. *Soil Dyn Earthq Eng*, **66**, 31-41, 2014. DOI:10.1016/j.soildyn.2014.06.029

[32] J. Zahradnik, Simple elastic finite-difference scheme. *Bull Seismol Soc Am*, **85**, 1879–87, 1995.

[33] S.A. Gil-Zepeda, J.C. Montalvo-Arrieta, R. Vai, F.J. Sanchez-Sesma, A hybrid indirect boundary element-discrete wave number method applied to simulate the seismic response of stratified alluvial valleys. *Soil Dyn Earthq Eng* , **23**, 77–862003.

COMPDYN 2019
7th ECCOMAS Thematic Conference on
Computational Methods in Structural Dynamics and Earthquake Engineering
M. Papadrakakis, M. Fragiadakis (eds.)
Crete, Greece, 24-–26 June 2019

TRANSIENT RESPONSE OF A TUNNEL EMBEDDED IN A HETEROGENOUS ELASTIC FULL SPACE

H.Bouare[1], A. Mesgouez[1] and G. Lefeuve-Mesgouez[1]

[1] Avignon Université, UMR EMMAH
Campus Jean-Henri Fabre, Agroparc, 301 rue Baruch de Spinoza, BP 21239, 84916 Avignon cedex 9 - France
e-mail: {hamed.bouare, arnaud.mesgouez, gaelle.mesgouez}@univ-avignon.fr

Keywords: Dynamic response, Transient regime, Imperfect interface, Semi-analytical approach, Heterogeneous elastic medium

Abstract. *The two dimensional transient response of a tunnel subjected to an uniform load is described in this paper. The concrete tunnel is embedded in a limestone massif with a heterogeneous chalk layer. The theoretical approach presented here is based on a semi-analytical approach in which the Helmholtz decomposition is used for the separation of wave motion and the solutions of wave equations are written using the Bessel-Fourier serie expansion method in the Laplace domain. The inversion of the Laplace transforms are performed numerically by using the Durbin algorithm. An imperfect contact is used to take into account the discontinuities at the interfaces between the different media. The results of hoop stress and radial displacement on the outer boundary of the tunnel are presented.*

1 INTRODUCTION

Seismic methods have been used for several decades increasingly to asssist in rock mass characterization in many geotechnical engineering applications. The present work concerns the study of mechanical wave propagation in a specific underground environment constituted by a system of cylindrical galleries, some of them presenting a concrete layer, embedded in an elastic full space. The site under study is located at the LSBB (Low Noise Inter-Disciplinary Underground Science and Technology, Rustrel, France). A bibliographical survey has been carried out with a special attention to select articles focusing on configurations close to the LSBB-kind geometry. Fang et al. [1] studied the dynamic response of a non-circular tunnel subjected to longitudinal and transversal waves (P, SV). They used a visco-elastic interface to model the contact between the rock mass and the tunnel. They concluded that the viscosity has a small influence on the dynamic stress in high frequency areas compared to low frequency areas. Fang et al. [2] analyzed the dynamic stress distribution around a circular tunnel subjected to SH waves. Using an elastic slip interface to represent the contact between the alluvial valley and the lined tunnel, they found that the dynamic stress increases when the elastic modulus of the tunnel lining increases, and that the interface effect decreases for larger dimension tunnels. The work described here extends the approach originally proposed by Yi et al. [3] who studied the harmonic response of a cylindrical elastic tunnel, impacted by a plane compressional wave and embedded in an infinite elastic ground. The interface between the rock mass and the linen is considered as an imperfect contact and is modeled with two spring parameters (Achenbach et al. [4]). The extension concerns the heterogeneous aspect around the tunnel called the damaged zone. The heterogeneous description of this area consists in a finite number of isotropic and elastic layers with imperfect contacts at each interface. We propose a cylindrical chalk layer to take into account the heterogeneous area around the tunnel. The main steps of the theoretical approach are: i) applying the Helmholtz decomposition, ii) solving the wave equation based on the separation method and iii) use the Laplace transform and the expansion in Bessel function series in the Laplace domain. We consider a step load that acts on the inner surface of the tunnel, the solutions for each layer are derived and expressed in terms of Bessel-Fourier series. Using the boundary conditions associated with the orthogonality conditions, a global stiffness matrix is constructed and assembled. The Durbin algorithm [5] is used for the inverse transformation in the time domain. The results obtained have been validated by comparison with Zakout et al. [6] and a first set of new results with the configuration under study is proposed.

2 STATEMENT OF PROBLEM

An infinitely long cylindrical tunnel in an infinite limestone massif is subjected to a load acting on the inner surface of the cavity (Figure 1).

The limestone massif is considered to be elastic, homogeneous and we propose a cylindrical layer ($k = 2$) approach to model the heterogeneous area surrounding the concrete tunnel ($k = 3$). We also consider the tunnel and the heterogeneous layer to be elastic and isotropic. Taking into account these hypotheses, the displacement equations of motion in each medium can be written as follows

$$\mu_k \nabla^2 \mathbf{u}_k + (\lambda_k + \mu_k) \nabla \nabla \cdot \mathbf{u}_k = \rho_k \ddot{\mathbf{u}}_k \ , \quad k = \{1, 2, 3\} \tag{1}$$

where the displacement vector $\mathbf{u}$ with subscript k represents motion in a given layer, $\{\lambda_k, \mu_k\}$ are the Lamé constants, ρ_k is the density and the superposed dot denotes time derivative ($\ddot{\mathbf{u}}$ is the second derivative with respect to time).

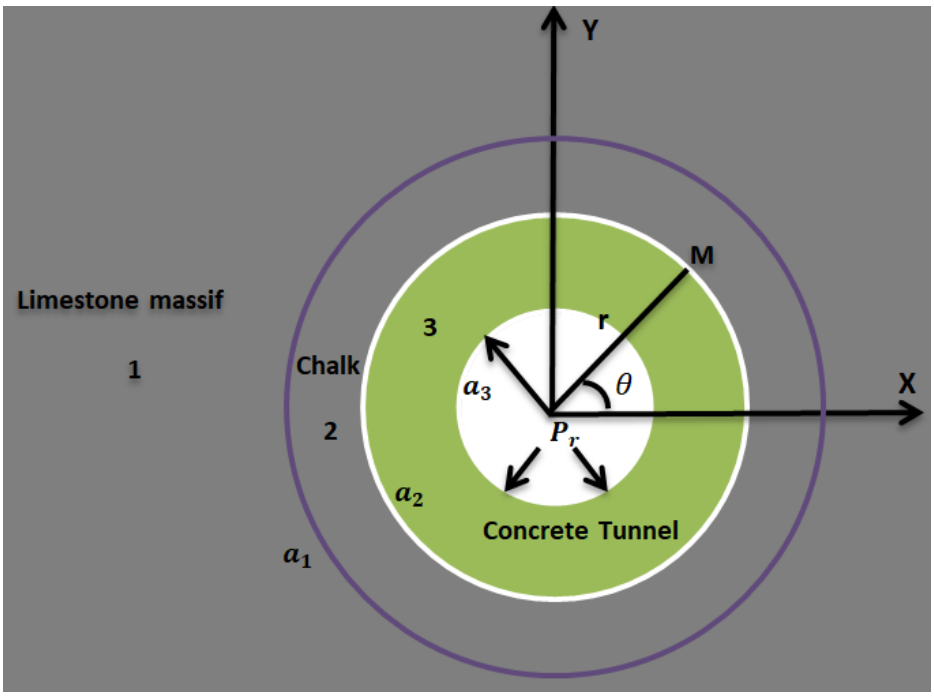

Figure 1: Problem geometry

The displacement field may be separated into scalar ϕ and vector Ψ potentials with the usual Helmholtz decomposition. The problem does not depend on the z-coordinate due to the two dimensional configuration, Ψ has only one single component ψ_z and for the sake of clarity it will be written as ψ. It comes thus

$$\mathbf{u}_k = \nabla\phi_k + \nabla \times \psi_k \tag{2}$$

Substituting equation (2) into (1), two wave equations are obtained

$$\nabla^2\phi_k - \frac{1}{c_{pk}^2}\ddot{\phi}_k = 0 \tag{3}$$

$$\nabla^2\psi_k - \frac{1}{c_{sk}^2}\ddot{\psi}_k = 0 \tag{4}$$

Equations (3) and (4) are relative to P and SV waves, respectively. $c_{pk} = \sqrt{\frac{\lambda_k+2\mu_k}{\rho_k}}$ and $c_{sk} = \sqrt{\frac{\mu_k}{\rho_k}}$ are the P and SV wave velocities in the elastic medium under consideration, ∇^2 is the the Laplace operator in polar coordinates.

The Laplace transforms is defined as

$$\overline{F}(r,\theta,s) = \int_0^\infty F(r,\theta,t)e^{-st}\,\mathrm{d}t \tag{5}$$

Applying the Laplace transform with respect to time to Eqs (3) and (4), we obtain

$$\nabla^2\overline{\phi_k} + \overline{\alpha_k}^2\overline{\phi_k} = 0 \tag{6}$$

$$\nabla^2\overline{\psi_k} + \overline{\beta_k}^2\overline{\psi_k} = 0 \tag{7}$$

where over-bar hereafter denotes the Laplace transform, $\{\overline{\alpha_k} = \dfrac{is}{c_{pk}},\ \overline{\beta_k} = \dfrac{is}{c_{sk}}\}$ are the P and SV wave numbers in the Laplace domain for a given layer and $i^2 = -1$ is the imaginary complex number.

When the step load acts on the inner surface of the tunnel, two incoming cylindrical waves (P, SV) and two outgoing cylindrical ones propagate in the tunnel medium. The same phenomenon is observed in the heterogeneous area, i.e two incoming and two outgoing cylindrical waves (P, SV). The two incoming (P, SV) waves are expressed with Hankel functions of the second kind. The two outgoing (P, SV) are written with Hankel functions of the first kind. The total displacement potentials in the Laplace domain for the heterogeneous area ($k = 2$) and the tunnel ($k = 3$) are

$$\overline{\phi_{kt}} = \sum_{n=0}^{\infty}[L_{nk}H_n^{(2)}(\overline{\alpha_k}r) + P_{nk}H_n^{(1)}(\overline{\alpha_k}r)]cos(n\theta) \tag{8}$$

$$\overline{\psi_{kt}} = \sum_{n=0}^{\infty}[Q_{nk}H_n^{(2)}(\overline{\beta_k}r) + Z_{nk}H_n^{(1)}(\overline{\beta_k}r)]sin(n\theta) \tag{9}$$

where L_{nk}, P_{nk}, Q_{nk}, Z_{nk} are respectively the expansion coefficients per mode of the (P, SV) waves in the tunnel and the heterogenoues area. $\{H_n^{(1)},\ H_n^{(2)}\}$ are the Hankel function of the first and second kind of an integer order n.

Two transmitted waves (P, SV) propage in the limestone massif from the interface $r = a_1$. They are expressed by Hankel functions of the first kind that represent outgoing cylindrical waves.

$$\overline{\phi_{1t}} = \sum_{n=0}^{\infty} E_n H_n^{(1)}(\overline{\alpha_1}r)\cos(n\theta) \tag{10}$$

$$\overline{\psi_{1t}} = \sum_{n=0}^{\infty} F_n H_n^{(1)}(\overline{\beta_1}r)\sin(n\theta) \tag{11}$$

where E_n and F_n are respectively the expansion coefficients per mode of the two transmitted waves (P, SV).

Based on the Helmholtz potential-displacement (11), displacement-strain relations (12) and stress-strain relations generalized by Hooke's law for a linear isotropic material (13), stress and displacement components for the different media $\{k = 1, 2, 3\}$ in the Laplace domain in polar coordinates can be expressed as

$$\overline{u_{r,k}} = \frac{\partial\overline{\phi_{kt}}}{\partial r} + \frac{1}{r}\frac{\partial\overline{\psi_{kt}}}{\partial\theta} \qquad \overline{u_{\theta,k}} = \frac{1}{r}\frac{\partial\overline{\phi_{kt}}}{\partial\theta} - \frac{\partial\overline{\psi_{kt}}}{\partial r} \tag{12}$$

$$\overline{\varepsilon_{rr,k}} = \frac{\partial\overline{u_{r,k}}}{\partial r} \qquad \overline{\varepsilon_{\theta\theta,k}} = \frac{1}{r}\frac{\partial\overline{u_{\theta,k}}}{\partial\theta} + \frac{\overline{u_{r,k}}}{r} \qquad \overline{\varepsilon_{r\theta,k}} = \frac{1}{2}(\frac{\partial\overline{u_{\theta,k}}}{\partial r} - \frac{\overline{u_{\theta,k}}}{r} + \frac{1}{r}\frac{\partial\overline{u_{r,k}}}{\partial\theta}) \tag{13}$$

$$\overline{\sigma_{rr,k}} = \lambda_k(\overline{\varepsilon_{rr,k}}+\overline{\varepsilon_{\theta\theta,k}})+2\mu_k\overline{\varepsilon_{rr,k}} \quad \overline{\sigma_{\theta\theta,k}} = \lambda_k(\overline{\varepsilon_{rr,k}}+\overline{\varepsilon_{\theta\theta,k}})+2\mu_k\overline{\varepsilon_{\theta\theta,k}} \quad \overline{\sigma_{r\theta,k}} = 2\mu_k\overline{\varepsilon_{r\theta,k}} \tag{14}$$

3 BOUNDARY CONDITIONS

The heterogeneous area chalk surrounding the tunnel contains fractures which can modify the mechanical parameters of the materials. We propose an interface model developed by Achenbach et al. [4] to take into account the discontinuities at the interfaces located at $r = a_1$ and $r = a_2$. The basis of the model is that a fracture represents a displacement discontinuity whereas the stresses are continuous. It is applicable to cases for which the fractures are large in extent but small in thickness compared to the wavelength of the mechanical waves. We consider that a fracture of circular shape separates two successive layers. Two stiffness ($k_{r,k}$, $k_{\theta,k}$) constants are useful for modeling the fracture in the radial and angular directions at the interface between two successive layers. The constant $k_{r,k}$ models the fracture in the radial direction and the constant $k_{\theta,k}$ in the circumferential direction. Physically, the contact is assumed to be perfect between two successive layers for largest values of $k_{r,k}$ and $k_{\theta,k}$. For very low values of $k_{r,k}$, $k_{\theta,k}$ two successive layers are detached but present identical traction conditions. The interface conditions at $r = \{a_1,\ a_2\}$ are thus written as

$$\begin{cases} \overline{\sigma_{rr,1}} = \overline{\sigma_{rr,2}} \\ \overline{\sigma_{r\theta,1}} = \overline{\sigma_{r\theta,2}} \\ \overline{u_{r,1}} - \dfrac{1}{k_{r,1}}\overline{\sigma_{rr,1}} = \overline{u_{r,2}} \\ \overline{u_{\theta,1}} - \dfrac{1}{k_{\theta,1}}\overline{\sigma_{r\theta,1}} = \overline{u_{\theta,2}} \\ \overline{\sigma_{rr,2}} = \overline{\sigma_{rr,3}} \\ \overline{\sigma_{r\theta,2}} = \overline{\sigma_{r\theta,3}} \\ \overline{u_{r,2}} - \dfrac{1}{k_{r,2}}\overline{\sigma_{rr,2}} = \overline{u_{r,3}} \\ \overline{u_{\theta,2}} - \dfrac{1}{k_{\theta,2}}\overline{\sigma_{r\theta,2}} = \overline{u_{\theta,3}} \end{cases} \tag{15}$$

We consider a step load which acts on the inner boundary of the tunnel at ($r = a_3$). The relative equations are

$$\begin{cases} \overline{\sigma_{rr,3}} = \dfrac{P_r}{s} \\ \overline{\sigma_{r\theta,3}} = 0 \end{cases} \tag{16}$$

We choose to expand term $\dfrac{P_r}{s}$ of Eq (15) into Fourier cosine series so that the Fourier series appears on each side

$$\frac{P_r}{s} = \sum_{n=0}^{\infty} \kappa_n cos(n\theta) \tag{17}$$

where $\kappa_n = \dfrac{P_r}{s}$ for $n = 0$ and $\kappa_n = 0$ for $n \geq 1$.

Substituting Eqs (11-13) into Eqs (14-15), and applying the orthogonality conditions, n sets of linear algebraic equations are obtained in the Laplace domain

$$[X]_{n,\{10,10\}}\{C\}_{n,10} = \{Y\}_{n,10} \tag{18}$$

$$X = \begin{pmatrix} \times & \times & \times & \times & \times & \times & 0 & 0 & 0 & 0 \\ \times & \times & \times & \times & \times & \times & 0 & 0 & 0 & 0 \\ \times & \times & \times & \times & \times & \times & 0 & 0 & 0 & 0 \\ \times & \times & \times & \times & \times & \times & 0 & 0 & 0 & 0 \\ 0 & 0 & \times & \times & \times & \times & \times & \times & \times & \times \\ 0 & 0 & \times & \times & \times & \times & \times & \times & \times & \times \\ 0 & 0 & \times & \times & \times & \times & \times & \times & \times & \times \\ 0 & 0 & \times & \times & \times & \times & \times & \times & \times & \times \\ 0 & 0 & 0 & 0 & 0 & 0 & \times & \times & \times & \times \\ 0 & 0 & 0 & 0 & 0 & 0 & \times & \times & \times & \times \end{pmatrix}$$

$$\{C\} = \begin{pmatrix} E_n & F_n & L_{n2} & P_{n2} & Q_{n2} & Z_{n2} & L_{n3} & P_{n3} & Q_{n3} & Z_{n3} \end{pmatrix}^T$$

$$\{Y\} = \begin{pmatrix} 0 & 0 & .. & .. & .. & .. & .. & .. & \frac{P_r}{s} & 0 \end{pmatrix}^T$$

The symbol $\times$ denotes non-zero terms.

The inversion of the Laplace transforms are performed numerically by using the following Durbin's formula [5] on the interval $[0, T_0]$

$$F(t) = \frac{e^{at}}{T_0}\{\frac{1}{2}Re[\overline{F}(a)] + \sum_{\varsigma=0}^{M}[Re[\overline{F}(a + \frac{i\pi\varsigma}{T_0})]\cos(\frac{\pi\varsigma t}{T_0}) - Im[\overline{F}(a + \frac{i\pi\varsigma}{T_0})\sin(\frac{\pi\varsigma t}{T_0})]] \quad (19)$$

where M is the truncation parameter, a is an arbitrary real number and $\overline{F}(a)$ can be any of $\overline{u_{r_k}}$, $\overline{u_{\theta_k}}$, $\overline{\sigma_{rr_k}}$.....

4 NUMERICAL RESULTS

The phenomenon of dynamic stress concentration, namely the sharp increase in the stress over some normal value in a localized region of a structural body due to geometric discontinuities such as cavities, corners or notches, is related to the propagation of elastic waves. Structures embedded in a medium act as discontinuities resulting in an amplification of the dynamic signal. Baron et al. [7, 8] have analysed the dynamic stress and displacement fields produced around a circular cylindrical cavity in an infinitely extending elastic medium due to the passage of harmonic or transient waves.

For numerical inversion with the Durbin method [5], the numerical parameters are as follows:

$$aT_0 = 5, \;\; T_0 = 200, \;\; M = 2000$$

At first, we are interested in the validation of our numerical code. Zakout et al. [6] study the transient response of a circular cavity with and without a bonded shell in an infinite elastic medium. We consider the same configuration for the case of the circular cavity unlined by assuming that media 2 and 3 are identical to medium 1. We also consider perfect contacts at interfaces $r = a_1$ and $r = a_2$. Using the same mechanical parameters as Zakout et al. [6], in Figure 2 we compare the nondimensional radial displacement and a good agreement is obtained.

Parameters	Limestone massif	Chalk	Concrete tunnel
$\rho\ (kg/m^3)$	2700	3100	2500
$c_p\ (m/s)$	6000	2600	4216
$c_s\ (m/s)$	3300	1300	2582

Table 1: Mechanical parameters of the media

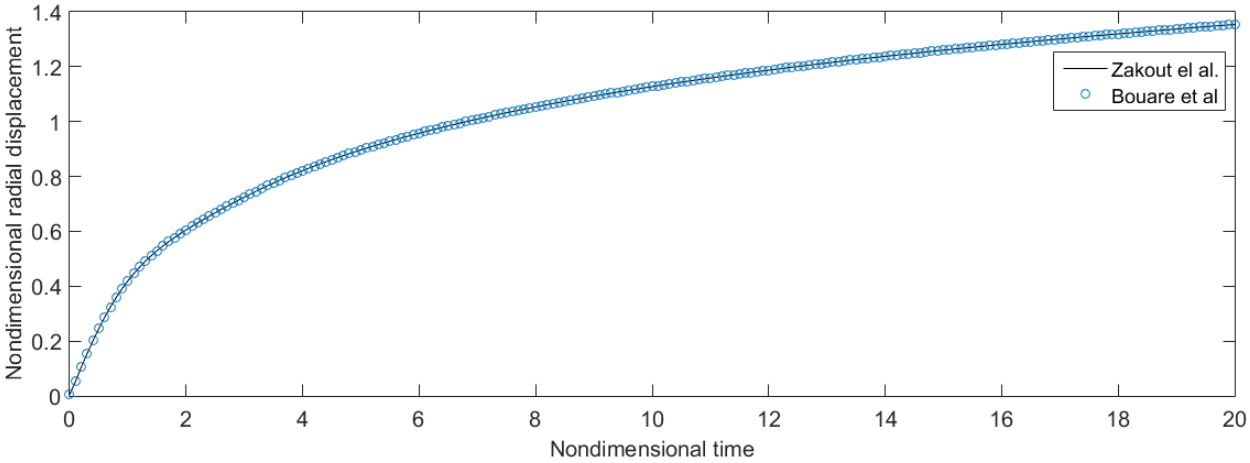

Figure 2: Nondimensional radial displacement for mode ($n = 1$) at the inner surface of the tunnel $r = a_3$ and $\theta = 0$, comparision with Zakout et al. [6].

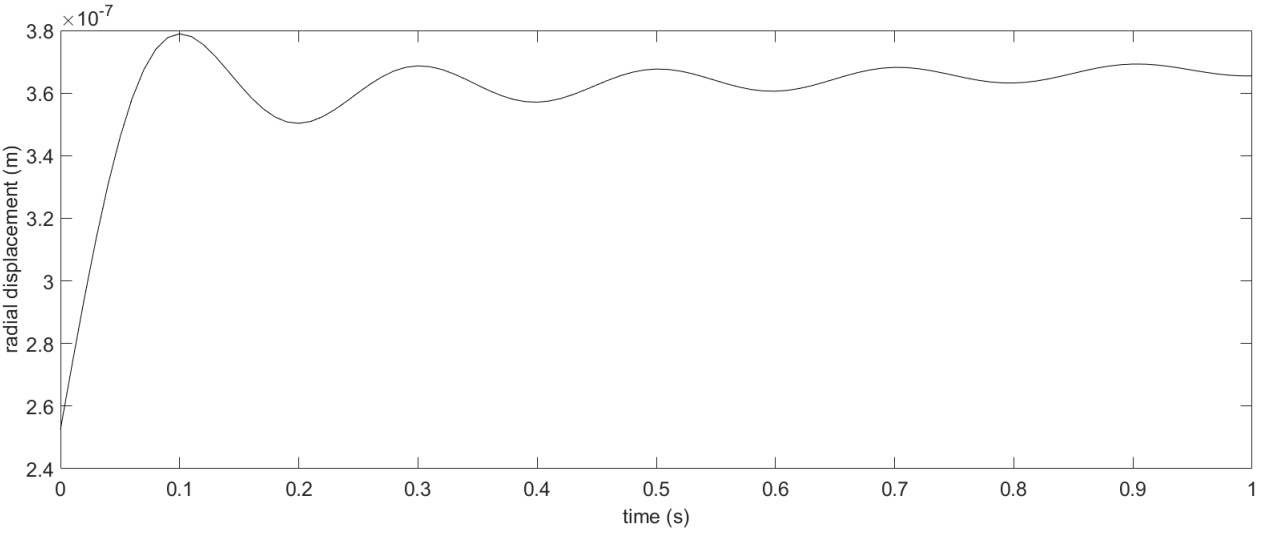

Figure 3: Radial displacement for mode ($n = 0$) at the outer surface of the tunnel $r = a_2$ and $\theta = 0$

The numerical parameters for the geometric points in Figure 1 are $a_1 = 2.2\ m,\ a_2 = 1.2\ m,\ a_3 = 1\ m$.

We consider imperfect contacts, the stiffness constants have the values $k_{r1} = k_{r2} = k_{\theta 1} = k_{\theta 2} = 86.42\ \ Pa/m$ and the charge Pr is equal to $\pi\ Pa$. The mechanical parameters of the media are shown in table 1. The results presented are obtained only for the first mode (n = 0) and at the angle $\theta = 0$. Figures 3 and 4 show the radial displacement and the hoop stress on the outer surface of the tunnel at $r = a_2$. We observed a fast increase in the amplitudes of the

radial displacement and the hoop stress followed by a progressive attenuation over the time. The attenuation is certainly impacted by the quality of the contact at the interfaces which has a considerable effect on the seismic wave signals. Figures 3 and 4 are the first sets of results, other complementary results will be investigated in the near future.

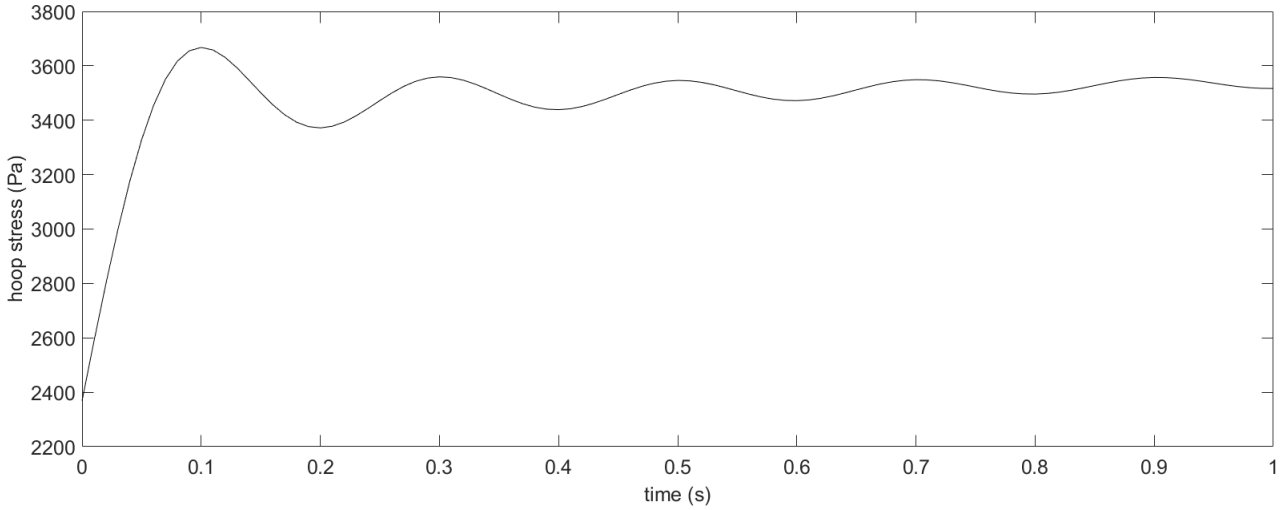

Figure 4: Hoop stress for mode ($n = 0$) at the outer surface of the tunnel $r = a_2$ and $\theta = 0$

5 CONCLUSIONS

We have proposed a transient analysis of an elastic model describing the dynamic response of a circular tunnel lined embedded in a limestone massif with a heterogeneous chalk layer. An imperfect contact model is used to take into account the heterogeneous chalk area surrounding the concrete tunnel. The numerical results are validated with those of Zakout et al. [6] and a first set of results relating to the hoop stress and the radial displacement on the outer surface of the tunnel is presented. Other results will be examined in the near future and we also hope an experimental validation of the numerical results in some distant future.

ACKNOWLEDGEMENT

This work has been carried out under a PhD grant from Conseil Général Provence-Alpes-Côte d'Azur, France. This support is gratefully acknowledged.

REFERENCES

[1] X.Q. Fang, H.X. Jin. Visco-elastic imperfect bonding effect on dynamic response of a non circular lined tunnel subjected to P and SV waves. Soil Dynamics and Earthquake Engineering **88** 1-7 2016.

[2] X.Q. Fang, T.F. Zhang, H.Y. Li. Elastic-slip interface effect on dynamic response of a lined tunnel in a semi infinite alluvial valley under SH waves. Tunnelling and Underground Space Technology **74** 96-106 2018.

[3] C.P. Yi, W.b. Lu, P. Zhang, D. Johansson, U. Nyberg. Effect of imperfect interface on the dynamic response of a circular lined tunnel impacted by plane P-waves. Tunnelling and Underground Space Technology **21** 68-74 2016.

[4] J.D. Achenbach, H. Zhu. Effect of interfacial zone on mechanical behavior and failure of fiber reinforced composites. Journal of the Mechanics and Physics of Solids **37** 381–393 1989.

[5] F. Durbin. Numerical inversion of Laplace transforms : an efficient improvement to Dubner and Abate's method. Journal of computer **17** 371-376 1974.

[6] U. Zakout, N. Akkas. Transient response of a cylindrical cavity with and without a bonded shell in an inifinite elastic medium. International Journal Engineering Science **35** 1203-1220 1997.

[7] [20] M.L. Baron, A. T. Matthews. Diffraction of a pressure wave by a cylindrical cavity in an elastic medium. Applied Mechanics **28** 347-354 1961.

[8] M.L. Baron, R. Parnes. Displacements and Velocities produced by the diffraction of a pressure wave by a cylindrical cavity in an elastic medium. Applied Mechanics **29** 385-395 1962.

COMPDYN 2019
7th ECCOMAS Thematic Conference on
Computational Methods in Structural Dynamics and Earthquake Engineering
M. Papadrakakis, M. Fragiadakis (eds.)
Crete, Greece, 24–26 June 2019

CONSEQUENCE OF SPATIALLY VARYING GROUND MOTIONS FOR THE RESPONSE OF A BRIDGE STRUCTURE

Z. Yang, C. Kun, and N. Chouw

Department of Civil and Environmental Engineering, the University of Auckland, Auckland 1142, New Zealand

zyan511@aucklanduni.ac.nz, ckun005@aucklanduni.ac.nz, n.chouw@auckland.ac.nz

Abstract

In earthquakes propagating seismic waves will arrive at adjacent bridge piers at different instants. Consequently, the ground motion will not excite all bridge piers at the same time, but with a time delay. Since the soil development along the bridge is never uniform, the spreading waves will be altered by the unequal soil properties along the wave path. The bridge will therefore experience spatially non-uniform ground excitation. The research focuses on the consequence of this non-uniform ground excitation for the response of a bridge structure. The left-hand abutment, bridge pier and right-hand abutment were excited by three separate large-scale shake tables, respectively. The influence of the spatial variation of ground motions on the seismic response is discussed.

Keywords: Spatial variation; Seismic response; Bridge; Shake tables; Earthquake; Pounding

1 INTRODUCTION

Major earthquakes, e.g. the 1995 Kobe earthquake [1], the 1999 Chi-Chi earthquake [2], the 2008 Wenchuan earthquake [3], the 2010 Chile earthquake [4] and the 2011 Canterbury earthquake [5] have shown the seismic vulnerability of bridges. Previous research found that for long bridges, the non-uniform ground motions at adjacent bridge supports is one of the main reasons of the relative movements between bridge structures. This is because the ground motions at adjacent bridges will never be the same due to the finite speed of propagating waves and heterogeneous properties of soil medium along the bridge. Many studies have been conducted to investigate the influence of spatially varying ground motions. Some earlier research [6-8] revealed that a time delay of ground motions has a considerable influence on the response of bridges. After the installation of the Strong Motion Array (SMART-1 array) in Taiwan [9], Chouw and Hao [10] found that for adjacent bridge segments with similar natural frequencies, the ground motion variation is one of the dominant factors for causing the out-of-phase movements between the bridge structures. The work showed the significant influence of wave passage, incoherence and site-response effects on the bridge response during earthquakes.

During strong earthquakes the collisions between adjacent bridge structures are normally impossible to avoid because of a relatively small expansion gap. Research has shown that poundings could reduce bending moments of the piers due to the dissipation of the energy as well as the restriction of the girder movements. However, poundings might also cause the damage at the contact location and increase the unseating probability of the bridge girder own to the transfer of the momentum [11]. Pounding response of bridges subjected to spatially varying excitations has been studied by many researchers. Hao et al. [12], for instance, revealed that the spatially varying ground motions could increase the accelerations and impact forces of adjacent bridge segments, which in turn resulted in an increasing number of collisions. Sextos et al. [13] found in their numerical study that when considering pounding, ignoring ground motion variation could on average result in a 25% underestimation on the ductility demand of bridge piers. Bi et al. [14] showed that the spatially varying ground motions with weak correlation could increase the pounding responses of bridges in both transverse and vertical directions.

Experimental research on the topic is limited. Crewe and Norman [15] were among the few that using the experimental method to investigate the spatial variation effects of ground motions. In their study, a 1:50 scale bridge model was fabricated to evaluate the pounding response of short-span bridges under non-uniform ground motions. The result showed that even for the same input ground motions with only a small time delay the girder displacements was significantly increased. Li and Chouw [16] constructed a two-span bridge model to study the influence of the plastic deformation of the bridge piers when subjected to non-uniform excitations. In a later study [17], a three-span bridge model was chosen to investigate the influence of the size of gap at the expansion joints with considering two-side poundings. The result of their studies indicated that neglecting the spatial variation of ground motions can underestimate the seismic responses of bridges, e.g. the pounding forces and the relative displacements between the neighbouring bridge girders. Shrestha et al. [18] carried out a shake table testing for a large-scale reinforced concrete bridge model subjected to non-uniform ground motions. The authors reported that spatially varying ground motions would increase the longitudinal peak accelerations of the girder.

The moveable abutment is, however, not considered in the studies mentioned above. Because of the significantly dissimilar structural characteristic, the abutments will inevitable influence the seismic responses of the bridge girder, which has been confirmed by many former

researcher [19-22].

To the authors' knowledge the experimental study on the pounding behaviour of bridge structures subjected to the spatially varying ground motions is scarce. To narrow the knowledge gap, in this research a series of shake table tests have been performed on a bridge-abutment model. The effects of spatially varying ground motions and pounding was physically investigated by fixing the left-hand abutment, bridge pier and right-hand abutment on three separate large-scale shake tables, respectively. The ground motions were stochastically simulated based on the target design spectrum specified in the New Zealand standard [23] for soft soil (Class D) condition with low correlation.

2 METHODOLOGY

2.1 Prototype structure and scaled model

The prototype structure is a segment of the Newmarket Viaduct Bridge located in Auckland, New Zealand. The bridge segment is 100 m long and 15.5 m high. The pier-to-pier distance is 50 m. The longitudinal fundamental frequency of the prototype is 0.98 Hz.

The experimental model has been constructed using steel with a dimensional scale of 1:20. The similitude approach followed in this study has been proposed by Chen et al. [24] and Qin et al. [25]. Details of the model are summarised in Table 1. Two abutments were simulated using steel frames, which are significantly stiffer compared to the bridge model in terms of having a much higher fundamental frequency of 330 Hz. The abutment, bridge and adjacent abutment were fixed on a shake table array located in the National Engineering Laboratory for Construction Technology of High-Speed Railway at Central South University, China. The shake table array consists of three 4 m × 4 m independent shake tables with an edge-to-edge distance of 2 m. The bridge-abutment system with shake tables is shown in Figure 1.

Parameter	Model dimension
Bridge span	5000 mm
Pier height	775 mm
Pier-to-pier distance	2500 mm
Pier width	100 mm
Pier thickness	6 mm
Second moment of area of the pier	1.8×10^{3} mm^4
Bending stiffness	1.86×10^{4} N/m
Effective mass	488 kg
Longitudinal frequency	0.98 Hz

Table 1 Parameters of model

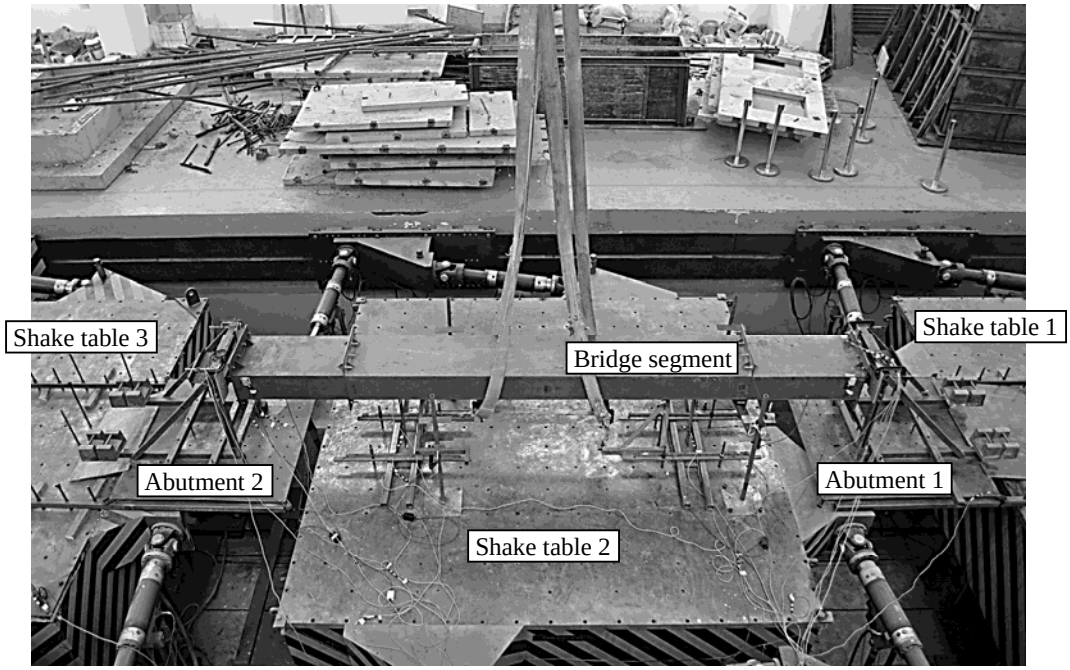

Figure 1 Bridge-abutment model on shake tables

2.2 Experimental set-up

The pounding response of bridges was investigated using pounding heads attached at each girder end. The pounding head has a contact block with a dimension of 310 mm × 56 mm. Since pounding occurs via a contact area, the actual state of impact behaviour of bridges, i.e. surface-to-surface contact, can be simulated effectively. For the case of pounding, the bridge span and adjacent abutments were fixed 5 mm apart from each other. When pounding was not considered, they were sufficiently far apart.

The MEAS 4000A accelerometers with a capacity of ± 2g were used to capture the girder accelerations. Laser displacement transducers were fixed at girder ends to measure the opening and closing displacements of the girder relative to the abutments. The pounding forces developed at the bridge-abutment interface were calculated using the force sensors. The strain gauges were placed near the top and support of each pier for measuring the strains for calculating the bending moments.

2.3 Ground motions

Spatially non-uniform ground motions were simulated stochastically based on the target design spectrum specified in the New Zealand seismic codes [22] for soft soil conditions. Details of the simulation can be found in Chouw and Hao [26]. Two sets of ground motions are considered for each of uniform and non-uniform ground motions, hereafter referred to as Set 1 and Set 2, respectively. The ground displacements at different supports of are presented in Figure 2.

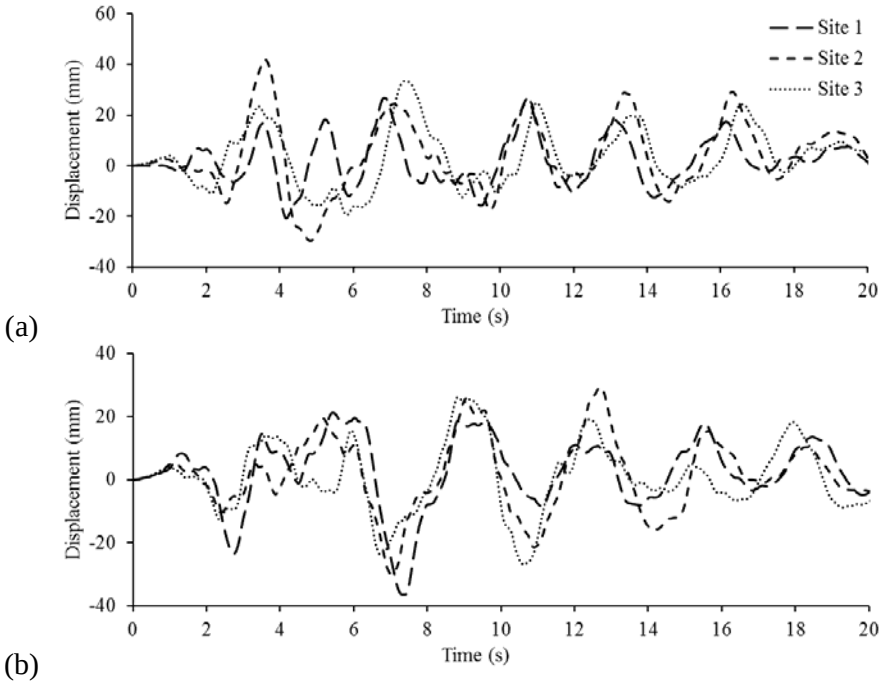

Figure 2 Ground displacements of (a) Set 1 and (b) Set 2

3 RESULTS AND DISCUSSION

To investigate the influence of spatially non-uniform ground excitations, the relative displacements obtained in the case of spatially varying ground excitations (SVGM) are compared to those obtained from an assumption of uniform excitations (UGM). The maximum displacements in both no pounding and pounding cases are present in Figure 3. Fig. 3(a) shows the effect of spatially non-uniform ground motions. It increases the maximum opening displacements of the girder in all considered cases. Fig. 3(b) shows that in the case without considering pounding, non-uniform ground motions increase the maximum displacements by 20%, whereas in the pounding case a significant larger amplification factor of 64% can be observed compared to that of the no pounding case. This result shows that an assumption of uniform ground motions could underestimate the relative movements of the girder whether or not pounding was considering. In the case of considering the spatially varying ground motion the amplitude of the relative displacement increases significantly due to poundings.

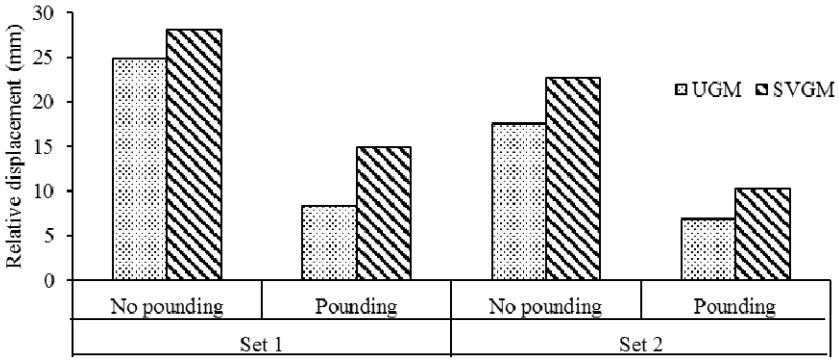

(b)

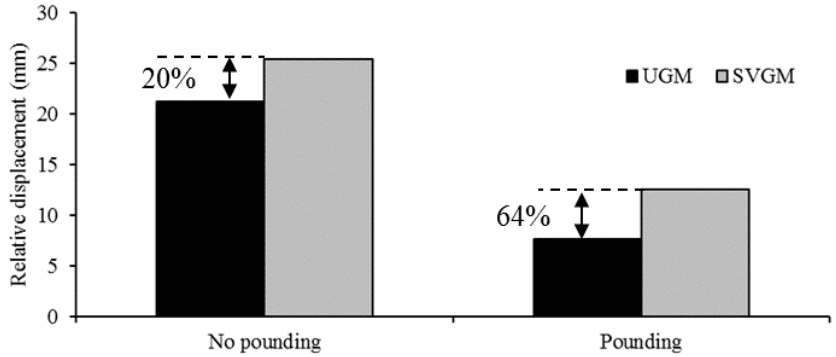

Figure 3: Effects of spatially varying ground motions and pounding on the (a) maximum and (b) average maximum longitudinal relative displacements of the bridge girders due to ground motions Sets 1 and 2.

Figure 4 shows the influence of the spatially varying ground motions on the bending moment developed at the base of piers when pounding was considered. The spatially varying ground motions increase the maximum bending moment by 18% and 27% due to the ground motions Sets 1 and 2, respectively. The results show that with considering pounding the non-uniform ground motions increases the maximum bending moments of piers. However, the influence of the effect on the bending moments is smaller than that of on the relative displacements of the girder (see Fig. (3).

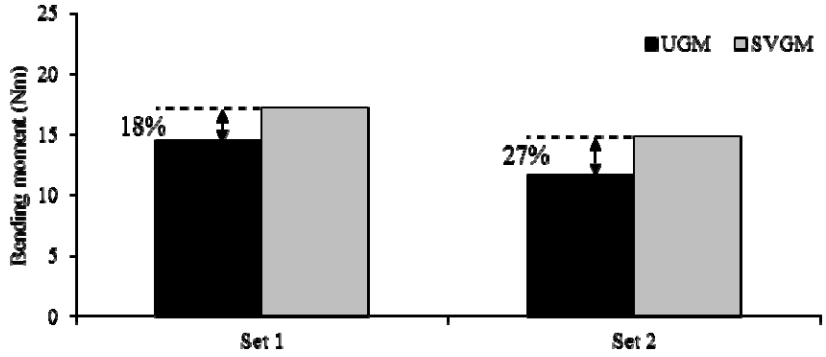

Figure 4: Simultaneous effects of spatially varying ground motions and pounding on the maximum bending moments of the bridge girders due to ground motions Sets 1 and 2.

To investigate the influence of ground motion variations on the pounding response, the pounding forces developed at girder-abutment interface due to ground motions Sets 1 and 2 are plotted in Figure 5. The result shows that the effect of spatially non-uniform ground motions increases the maximum pounding force from 194.43 N to 275.27 N due to ground motions Set 1, whereas the maximum pounding force is increased from 108 N to 240 N due to ground motions Set 2.

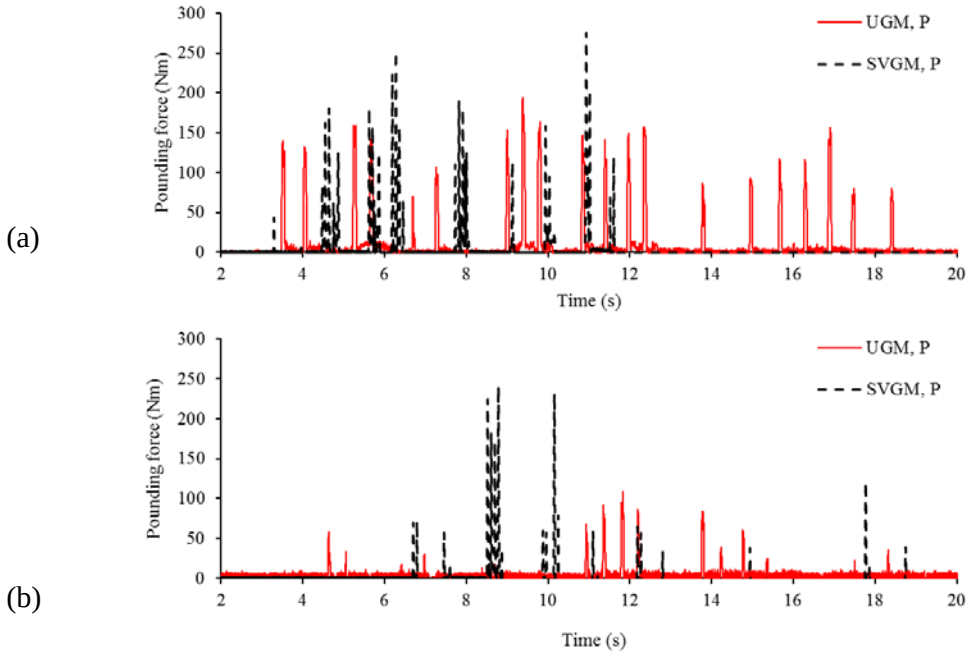

Figure 5: Effects of spatially varying ground motions on the pounding force due to (a) Set 1 and (b) Set 2 ground motions

4 CONCLUSIONS

This paper discussed the simultaneous influence of spatially varying ground motions and pounding on the seismic response of bridges. The following conclusions are drawn:

- The effect of spatially varying ground motions could aggravate the seismic response of bridges whether or not pounding was considered.
- In the case with considering pounding the effect of spatially varying ground motions causes a larger amplification on the relative displacements than the no pounding case.
- Poundings and the spatially varying ground motions have more influence on the relative displacements of the girder than on the bending moments at the bridge pier supports.

ACKNOWLEDGMENTS

The authors would like to thank the Ministry of Business, Innovation, and Employment for the support of this research through the Natural Hazards Research Platform under the Award 3708936. The authors would like to extend their gratitude to China Scholarship Council (CSC) for supporting the Ph.D. research of the first author at the University of Auckland.

REFERENCES

[1] N. Chouw, Effect of the earthquake on 17th of January 1995 on Kobe, *Proceedings of the D-A-CH meeting of the German, Austrian and Swiss Society for Earthquake Engineering and Structural Dynamics*, University of Graz, Austria, 135-169, 1995.

[2] Y.T. Hsu, C.C. Fu, Seismic effect on highway bridges in Chi-Chi earthquake, *Journal*

of Performance of Constructed Facilities, **18**(1), 47-53, 2004.

[3] C.J. Lin, H. Hung, , Y. Liu, J. Chai, Reconnaissance report of 0512 China Wenchuan earthquake on bridges, *Proceedings of the 14th World Conference on Earthquake Engineering*, Beijing: 13, 2008.

[4] K. Kawashima, S. Unjoh, J.I. Hoshikuma, K. Kosa, Damage of bridges due to the 2010 Maule, Chile, earthquake. *Journal of Earthquake Engineering*, **15**(7), 1036-1068, 2011.

[5] N. Chouw, H. Hao, Pounding damage to buildings and bridges in the 22 February 2011 Christchurch earthquake. *International Journal of Protective Structures*. **3**(2), 123-140, 2012.

[6] J.L. Bogdanoff, J.E. Goldberg, A.J. Schiff, The effect of ground transmission time on the response of long structures, *Bulletin of the Seismological Society of America*, **55**(3), 627-640, 1965.

[7] N.E. Johnson, R. Galletly, The comparison of the response of a highway bridge to uniform ground shock and moving ground excitation, *The Shock and Vibration Bulletin*, **42**, 75-85, 1972.

[8] S.D. Werner, L.C. Lee, H.L. Wong, M.D. Trifunac, An evaluation of the effects of traveling seismic waves on the three-dimensional response of structures, *Agbabian Associates*, National Science Foundation. AA-R-7720-4514, 1977.

[9] B.A. Bolt, C.H. Loh, J. Penzien, Y.B. Tsai, Y.T. Yeh, Preliminary report on the SMART-1 strong motion array in Taiwan. *Earthquake Engineering Research Center*, University of California Berkeley. CA, 1982.

[10] N. Chouw, H. Hao, Seismic design of bridge structures with allowance for large relative girder movements to avoid pounding, *Bulletin of the New Zealand Society for Earthquake Engineering*, **42**(2), 75-84, 2009.

[11] A. Ruangrassamee, K. Kawashima, Relative displacement response spectra with pounding effect. *Earthquake Engineering and Structural Dynamics*, **30**(10), 1511-1538, 2001.

[12] H. Hao, , X.Y. Liu, J. Shen, Pounding response of adjacent buildings subjected to spatial earthquake ground excitations, *Advances in Structural Engineering*, **3**(2), 145-162, 2000.

[13] A.G. Sextos, A.J. Kappos, K.D. Pitilakis, Inelastic dynamic analysis of RC bridges accounting for spatial variability of ground motion, site effects and soil–structure interaction phenomena. Part 2: Parametric study, *Earthquake Engineering and Structural Dynamics*, **32**(4), 629-652, 2003.

[14] K.M. Bi, H. Hao, N. Chouw, 3D FEM analysis of pounding response of bridge structures at a canyon site to spatially varying ground motions. *Advances in Structural Engineering*, **16**(4), 619-640, 2013.

[15] A.J. Crewe, J. Norman, Experimental modelling of multiple support excitation of long span bridges, *Proceedings of the 4th International Conference on Earthquake Engineering*, Taipei, Taiwan, 2006.

[16] B. Li, N. Chouw, Experimental investigation of inelastic bridge response under spatially varying excitations with pounding, *Engineering Structures*, **79**, 106-116, 2014.

[17] B. Li, N. Chouw, Field tests on total gap of modular expansion joints to avoid bridge pounding, *Frontiers in Built Environment*, 2:7. DOI: 10.3389/fbuil.2016.00007, 2016.

[18] B. Shrestha, L.X. He, H. Hao, K.M. Bi, W.X. Ren, Experimental study on relative displacement responses of bridge frames subjected to spatially varying ground motion and its mitigation using superelastic SMA restrainers. *Soil Dynamics and Earthquake Engineering*, **109**, 76-88, 2018.

[19] C. Kun, Z. Yang, N. Chouw, Seismic response of skewed bridges including pounding effects, Earthquakes and Structures, **14**, 467-476, 2018.

[20] C. Kun, L.Z. Jiang, N. Chouw, Influence of pounding and skew angle on seismic response of bridges, *Engineering Structures*, **148**, 890-906, 2017.

[21] C. Kun, N. Chouw. Estimation of response of skewed bridges considering pounding and supporting soil, *Engineering Structures*, **184**, 469-479, 2019.

[22] C. Kun, N. Chouw. Influence of ground motion characteristics on seismic response of skewed bridges, Structure and Infrastructure Engineering, 2019.

[23] Standards New Zealand, *Structural design actions Part 5: Earthquake actions – (NZS 1170.5)*. Wellington, New Zealand, 2005.

[24] Y. Chen, T. Larkin, N. Chouw, Experimental assessment of contact forces on a rigid base following footing uplift. Earthquake Engineering and Structural Dynamics, **46**(11): 1835-1854, 2017.

[25] X. Qin, , Y. Chen, , N. Chouw, Effect of uplift and soil nonlinearity on plastic hinge development and induced vibrations in structures, *Advances in Structural Engineering*, **16**(1), 135-147, 2013.

[26] N. Chouw, H. Hao, Study of SSI and non-uniform ground motion effect on pounding between bridge girders, *Soil Dynamics and Earthquake Engineering*, **25**, 717-728, 2005.

COMPDYN 2019
7th ECCOMAS Thematic Conference on
Computational Methods in Structural Dynamics and Earthquake Engineering
M. Papadrakakis, M. Fragiadakis (eds.)
Crete, Greece, 24–26 June 2019

NUMERICAL ANALYSIS OF STRUCTURE-SOIL-STRUCTURE INTERACTION FOR TWO DIFFERENT BUILDINGS DURING EARTHQUAKES

Felipe Vicencio[1], **Nicholas A. Alexander**[2]

[1] Researcher, Department of Civil Engineering, University or Bristol
Queens School of Engineering, Room 2.11, University Walk, Bristol, UK
e-mail: fv16607@bristol.ac.uk

[2] Reader in Structural Dynamics, Department of Civil Engineering, University of Bristol
Queens School of Engineering, Room 0.37b, University Walk, Bristol, UK
nick.alexander@bristol.ac.uk

Abstract

A simple reduced-order discrete model is used to investigate the problem of dynamic through soil structure to structure interaction via an analytical 2-D formulation that is solved in the time domain. This new model includes sufficient degrees of freedom (DOF) for each of the buildings to analyses the structure-soil-structure interaction between tall and short buildings. This extends the parametric scope of previous studies. Additionally, we employ real ground motion, that are classified into three groups: Near-Field Pulse-Like (NFPL), Near-Field Without Pulse (NFWP) and Far-Field (FF). These records have differences in amplitude, duration, envelope shape, and power spectral content. Over 3 million different structural cases are analysed in Matlab for this extensive parametric study. Interaction between mode one of the short building and mode 2 of the tall building is considered. These mode 1-to-2 interactions along with the mode 1-to-1 interaction suggests that adverse/beneficial structure-soil-structure behaviour occurs for may more buildings than previous studies suggest.

Keywords: Structure-Soil-Structure Interaction (SSSI), Time History, Seismic Analysis, Dynamics.

1 INTRODUCTION

Conventionally, buildings in urban areas are designed by considering the response of structures in isolation, i.e. without any neighbouring structures. However, the high density of buildings in cities inevitably results in the possibility of seismic interaction of adjacent buildings through the underlying or surrounding soil. This phenomenon is widely known as structure-soil-structure interaction (SSSI) and has been reported in the pioneering works of Luco and Contesse [1], Kobori et al. [2], Lee and Wesley [3], Murukami and Luco [4] and Wong and Trifunac [5].

The complexity of the multi-structural interaction problem has also been emphasized in more recent investigations based on numerical two or three-dimensional Finite Element Method (FEM), Boundary Elements Method (BEM) or a combination of these two FEM/BEM procedures. For example the works of Qian and Beskos [6], Karabalis and Mohammadi [7], Lehmann and Antes [8], Qian et al. [9], Yahyai et al. [10], Padron et al. [11], among others. These studies have identified important factors that control the seismic interaction behaviour such as: (i) the separation building distance, (ii) the direction of the orientation between foundations, (iii) the height ratio and dynamic characteristics of adjacent buildings, (iv) the aspect ratio (the building height to width ratio), and (v) the soil type beneath the buildings. One advantage of using such methods is the possibility of modelling complex geometries and considering nonlinearities in the elements. However, those models have a large number of degrees of freedom involved, producing computationally costly and time-consuming analyses.

Another approach is physical modelling, which has been implemented in the last years for the SSSI phenomenon. Trombetta et al. [12] and Mason et al. [13], model the nonlinear behaviour of soil and structure. Knapett et al. [14] analysed similar and highly dissimilar building on shallow foundations using centrifuge modelling. Aldaikh [15] has indicated that the presence of neighbouring buildings could produce favourable/detrimental changes in seismic response. These represent important validation points for numerical models and provide preliminary estimates of the effects of complex interaction problems. However, these experiments are technically challenging because of the problem of scaling and represent a statistically small sample. Thus, a large-scale parametric exploration of this problem requires a different method.

The alternative is to use system models, with a relatively limited number of degrees of freedom, for a parametric study. These low-order models (i) capture the most important dynamic behaviour, (ii) have a relatively small amount of system parameters and (iii) are computationally simple for exploring a vast number of generic cases. These parametric studies should be viewed as a preliminary investigation of the problem. They are not meant to substitute advanced computational models and experimental work of specific cases. Mulliken and Karabalis [16] calculated the interaction between adjacent two and three identical rigid surface foundations supported by a homogeneous half-space soil, and subjected to impulsive, moment, sinusoidal and random loads. Most recently, Alexander et al. [17] proposed a set of frequency-independent rotational coupling spring coefficient that is used to modelling the interaction between adjacent closely spaced buildings. Additionally, Aldaikh et al. [18] proposed an alternative closed-form analytical expression for these interaction springs based on a Boussinesq formulation of the surficial displacement and rotation fields. On the other hand, Vicencio and Alexander [19] extended these previous analyses further by allowing nonlinear hysteretic behaviour in the soil. Results indicate that SSSI effects can increase with soil nonlinearity. Vicencio and Alexander [20] suggest that there are significant interactions between different structures, employed a large database of real records.

Based on the previous discussion, this paper aims to introduce a mathematical formulation of the problem of SSSI, where the model enables an extra mode for each structure, and it is

included the case of a low-rise structure next to a neighbouring much taller structure. We explore over 3 million different systems/ground motion cases. This computationally challenging study required the High-Performance Computing (HPC) machine, BlueCrystal, at the University of Bristol. The objective of this research is to answer the following two questions: (i) does the taller buildings can affect the size of adverse/beneficial SSSI behaviour? and (ii) Is there evidence to suggest that different types of earthquakes can affect the SSSI behaviour?

2 THEORY

Considering the following system shown in Figure 1. It is a pair of building described in terms of six DOFs and coupled by a rotational ground spring κ. The soil/foundation system of each building has one rotational DOF at the foundation level θ_j. The building super-structures have two translational DOFs relative to the ground (x_{2j-1} and x_{2j}). Thus, the three DOFs of each building can be viewed as a projection, onto a three modes vector basis, of a generalised multi-storey building. In the same way, this extended simplified low-order model allows SSSI between the 'second sway mode' of a tall building, and the 'first sway mode' of a shorter building. A known ground displacement field is applied at both foundations, i.e. wave passage effects and spatially heterogeneous ground displacement are neglected in the present work. The kinetic energy and potential energy for this system are given by the equations (1) and (2) respectively.

$$T_E = \frac{1}{2}\sum_{j=1}^{2}\left(\frac{1}{2}m_{bj}\left(\dot{x}_{2j-1} + \dot{x}_g - \frac{1}{2}h_j\dot{\theta}_j\right)^2 + \frac{1}{2}m_{bj}\left(\dot{x}_{2j} + \dot{x}_g - h_j\dot{\theta}_j\right)^2 + m_{sj}r_j^2\theta_j^2\right) \quad \textbf{(1)}$$

$$U_E = \frac{1}{2}\sum_{j=1}^{2}\left(k_{bj}x_{2j-1}^2 + k_{bj}\left(x_{2j} - x_{2j-1}\right)^2 + k_{sj}\theta_j^2\right) + \frac{1}{2}\kappa(\theta_2 - \theta_1)^2 \quad \textbf{(2)}$$

where h_j is the total height of the structures and m_{bj} is the total mass of the buildings. m_{sj} are the foundation/soil masses underneath building 1 and 2, r_j are the soil/foundation masses radius of gyration, $m_{sj}r_j^2$ are the foundation/soil mass polar second moments of area (moments of inertia). k_{bj} are the building lateral stiffnesses, κ is the stiffness of the inter-building soil rotational spring and b_j are the width of the buildings' foundation. The equation of motion of the complete dynamic system can be derived using the Euler-Lagrange as follows.

$$\mathbf{M\ddot{u}} + \mathbf{C\dot{u}} + \mathbf{Ku} = \mathbf{p}\ddot{u}_g \quad \textbf{(3)}$$

The system's linear viscous damping matrix $\mathbf{C}$ defined in equation (3) assumes that each natural mode $n \in [1,6]$ is damped at $\xi_n = 0.05$ of critical damping. $\boldsymbol{\phi}_n$ is the eigenvector for mode n, ω_n are the natural frequencies of the systems. Thus, the Caughey orthogonal damping matrix $\mathbf{C}$ can be calculated as [21]:

$$\mathbf{C} = \mathbf{M}\left(\sum_{n=1}^{6}\frac{2\xi_n\omega_n}{\boldsymbol{\phi}_n^T\mathbf{M}\boldsymbol{\phi}_n}\boldsymbol{\phi}_n\boldsymbol{\phi}_n^T\right)\mathbf{M} \quad \textbf{(4)}$$

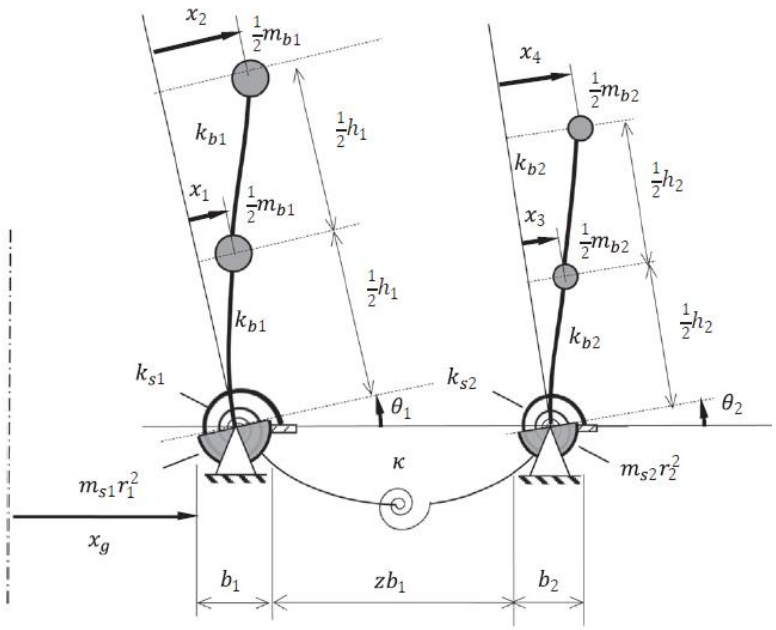

Figure 1: Two buildings discrete model.

The scope of this analysis is restricted to a special case, by assuming the following.

- The same soil profile (loose sand with an average soil density of $\rho_s = 1300kg/m^3$) exists under both buildings.
- Both buildings have a similar square plan area of $b = b_1 = b_2$.
- The buildings can be of different heights h_j, where the first building frequency is estimated using the approximation of the SEAOC Blue Book [22] for the natural period of a structure on a rigid foundation equal to $T = h_1/32$.
- The buildings are spaced at some arbitrary distance from each other zb.
- Building pounding is not permitted as inter-building spacing is assumed large enough to avoid pounding.

Newmark and Rosenblueth [23] proposed that the dynamic mass of soil beneath buildings is equal to $m_s = 0.35b^3\rho_s$. The mass of the buildings can be calculated as $m_{bj} = \rho_b h_j b^2$, where ρ_s and ρ_b are the densities of soil and building respectively. Based on typical spans and floor loading, the average building density is 400-800 kg/m^3. In this research, we used $\rho_b = 600kg/m^3$. Hence, the proportionality constant is equal to $c_1 = 0.76$. The radius of gyration of the soil-cylinder (directly under the rigid foundation) is evaluated using the Newmark's empirical expression $r \approx 0.33b$. We defined the following geometric parameters *Height ratio* ε and *Aspect ratio* s.

$$\varepsilon = \frac{h_2}{h_1}, \quad s = \frac{h_1}{b}, \quad c_1 = 0.35\frac{\rho_s}{\rho_b} \tag{5}$$

Empirical forms for the rotational and inter-building interaction spring defined in Alexander et al. [17] are considered. These springs were validated by (i) finite element models [14], (ii) physical experimental models in shaking table and centrifuge [14, 15] and (iii) closed-form analytical Boussinesq models [18]. Therefore, the values of foundation rotational spring $k_{s1} = k_{s2}$, and the interaction spring stiffness κ are written as an inverse cube power function of non-

dimensional inter-building separation distance z. The rotational stiffness spring coefficient k_s is obtained by using the empirical formulae deducted by Pais and Kausel [24] in the absence of building interaction.

$$k_{s1} = k_{s2} = k_s q_2, \;\; \kappa = k_{s1} q_k, \;\; q_k = -\frac{0.25}{(1+z)^3}, \;\; q_2 = 1 + \frac{0.5}{(1+z)^3}, \;\; k_s = \frac{1}{2}\frac{G_s b^3}{1-\mu} \tag{6}$$

Thus, the Euler-Lagrange equation of motion expressed in matrix form is as follows,

$$\mathbf{M} = \frac{1}{2}\begin{bmatrix} 1 & 0 & -\frac{3}{2}s & 0 & 0 & 0 \\ 0 & 1 & -3s & 0 & 0 & 0 \\ -\frac{3}{2}s & -3s & \frac{45}{4}s^2 + 2c_1 s^{-1} & 0 & 0 & 0 \\ 0 & 0 & 0 & \varepsilon & 0 & -\frac{3}{2}\varepsilon^2 s \\ 0 & 0 & 0 & 0 & \varepsilon & -3\varepsilon^2 s \\ 0 & 0 & 0 & -\frac{3}{2}\varepsilon^2 s & -3\varepsilon^2 s & \frac{45}{4}\varepsilon^3 s^2 + 2c_1 s^{-1} \end{bmatrix} \tag{7}$$

$$\mathbf{K} = \begin{bmatrix} 2 & -1 & 0 & 0 & 0 & 0 \\ -1 & 1 & 0 & 0 & 0 & 0 \\ 0 & 0 & c_1 c_2 q_2 s \bar{V}_s^2 (1+q_k) & 0 & 0 & -c_1 c_2 q_2 q_k s \bar{V}_s^2 \\ 0 & 0 & 0 & 2\varepsilon^{-1} & -\varepsilon^{-1} & 0 \\ 0 & 0 & 0 & -\varepsilon^{-1} & \varepsilon^{-1} & 0 \\ 0 & 0 & -c_1 c_2 q_2 q_k s \bar{V}_s^2 & 0 & 0 & c_1 c_2 q_2 s \bar{V}_s^2 (1+q_k) \end{bmatrix}, \mathbf{p} = \frac{1}{2}\begin{bmatrix} -1 \\ -1 \\ \frac{9}{2}s \\ -\varepsilon \\ -\varepsilon \\ \frac{9}{2}\varepsilon^2 s \end{bmatrix} \tag{8}$$

Therefore, in this analysis, we need only 3 geometric non-dimensional parameters, (i) Aspect ratio $s = h_1/b$ (for building 1), (ii) The height ratio $\varepsilon = h_2/h_1$ (building 2 to 1) and (iii) the normalised inter-building distance ratio z (ratio of the distance between buildings to building width). The soil parameters are reduced to c_1, c_2, $\bar{V}_s$, ρ_s and μ.

In this paper, we will employ two system performance measures (the following displacement and total acceleration) to calculate the difference between the response of the coupled (SSSI) and uncoupled (SSI) systems.

$$U_{2j} = u_{2j} - 3\frac{h_j}{b}\theta_j, \;\; A_{2j} = \ddot{u}_{2j} + \ddot{u}_g - 3\frac{h_j}{b}\ddot{\theta}_j \tag{9}$$

where A_{2j} are respectively the total (sway + ground + rotational) accelerations for the top of buildings "j" in non-dimensional form. Therefore, we can state the percentage change in power caused by SSSI as follows,

$$\ddot{\chi}_{ii} = 100\frac{[E_s(A_i)]_{SSSI} - [E_s(A_i)]_{SSI}}{[E_s(A_i)]_{SSI}} \tag{10}$$

where subscript i is from 1 to 4 and $E_s(A_i)$ is the total power spectral density (which is based on all data points of response timeseries A_i), which is defined using the Parseval's theorem according to equation (11).

$$E_s(U_i) = \int_{-\infty}^{\infty} |A_i(\tau)|^2 d\tau = \frac{1}{2\pi}\int_{-\infty}^{\infty} |A_i(\omega)|^2 d\omega \tag{11}$$

where $A_i(\omega)$ is the continuous Fourier transform of $A_i(\tau)$. This difference term $\ddot{\chi}_{ii}$ is zero if there is no change between SSSI and SSI analyses or no interaction between the different structures. Using the total power as a comparative variable, produces a statistical estimate of magnitude that is more robust than employing a single peak of the function (displacement and acceleration). To obtain the uncoupled system response (SSI) case, it is possible to calculate the following system (i) increase inter-building distance z to a very large value or (ii) set $q_\kappa = 0$ and $q_2 = 1$.

3 RESULTS AND DISCUSION

3.1 Ground Motion Selection

To calculate the effect of SSSI on the system we consider three types of ground acceleration motion. This includes Far-Field (FF), Near-Field Without Pulse (NFWP) and Near-Field Pulse-Like (NFPL) record sets [25]. The ground motions database is obtained from FEMA P695 [26]. The recorded acceleration series of these ground motions are selected from the Pacific Earthquake Engineering Research (PEER-NGA) West database. The FEMA P695 recommends a set of 22 FF records that are taken from 14 events that occurred between 1971 and 1999. Eight of them occurred in California, and six of them are taken from different places around the world. Each record has two horizontal components. Event magnitudes range from $M_w = 6.5$ to $M_w = 7.6$ with an average magnitude of $M_w = 7.0$. Values of their peak ground accelerations (PGAs) vary from 0.21g to 0.82g with a mean value of 0.43g. The next figure shows the elastic response spectra from all records set used in this research.

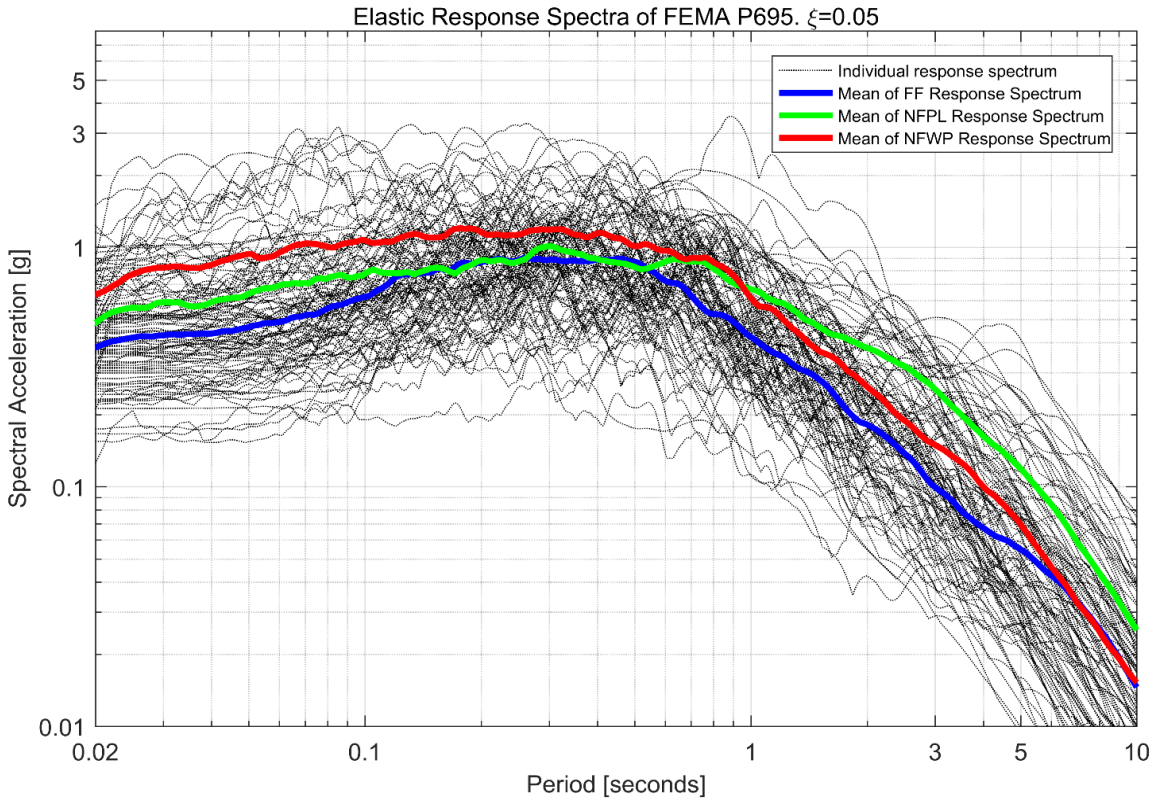

Figure 2: Elastic response spectra of FEMA P695 ground motions.

3.2 Response of the system for a set of parameters

In this section, initial results for the Near-Field Pulse-Like Imperial Valley earthquake is presented. For this, we examine the case when the two buildings are placed in very close proximity to each other, at $z = 0.1$, i.e. at a spacing distance equal to $0.1b$.

Figure 3 displays the response for a system that the second building is 2.6 times the first building, and building one has a height to width ratio equal to 2.6 (aspect ratio $s = h_1/b = 2.6$ and height ratio $\varepsilon = h_2/h_1 = 2.5$). Figure 3(a) shows the uncoupled SSI (blue line) and coupled SSSI (red line) responses for the upper DOFs of building 1, that is the displacement U_2 and the total acceleration A_2. Comparing the uncoupled SSI and coupled SSSI responses, we

observe that the maximum displacement and acceleration of buildings increases for the SSSI case.

Figure 3(b) shows the power spectral density for the displacements and total accelerations of the building 1 (SSI and SSSI cases). We perceive that building 1's total response power increase about $\chi_{22} = 63.7\%$ and $\ddot{\chi}_{22} = 51.3\%$ in the displacement and acceleration respectively. In general, for height ratios greater than 2.0, higher amplifications are observed for displacement than for acceleration.

There is a significant amplification in the displacement power spectral density for a Fourier frequency equal to 0.61Hz. This is mainly due to building 2's first uncoupled natural frequency. An important characteristic of the SSSI system is that the eigenfrequencies for the coupled and uncoupled system are very similar (there is a maximum of 9% variation in natural frequencies). However, the eigenmodes are different for the coupled system as they span the two buildings rather than a single building in the uncoupled system. The resonance at 0.61Hz is not significant for acceleration, mainly because the acceleration response is not as susceptible to low-frequency content by definition. This is a result of the Eulerian relationship $\ddot{\mathbf{v}}(\omega) = (i\omega)^2\mathbf{v}(\omega)$. The second resonance in the displacement and acceleration occurs at a Fourier frequency equal to 2.1Hz (which corresponds to building 1's first uncoupled natural frequency), while the third resonance is due to building's 2 second uncoupled natural frequency.

Figure 3(c) and Figure 3(d) displays the norm of the transfer function for the displacement and acceleration for building 1 and 2 respectively. There is a transfer of earthquake energy between building 2 to building 1, producing a reduction in building 2's responses of $\chi_{44} = -12.3\%$ and $\ddot{\chi}_{44} = -4.1\%$ in the displacement and acceleration respectively. For this parameter setting, the 'first modal frequency' of building 1 (represented by the second peak with a Fourier frequency of 2.1Hz) is close to the natural frequency of the second mode in building 2 (represented by the third peak in Figure 3(d) with a Fourier frequency of 3.4Hz). This produces an additional amplification in the response of building 1. Thus, adding an extra degree of freedom to building 1 and 2 may increase the interaction between the buildings. Nevertheless, incorporating further additional DOF into the buildings (i.e. greater than 3 degree of freedom per buildings) does not significantly influence the SSSI system response. This is because the modal participation factors of additional higher system modes are very small.

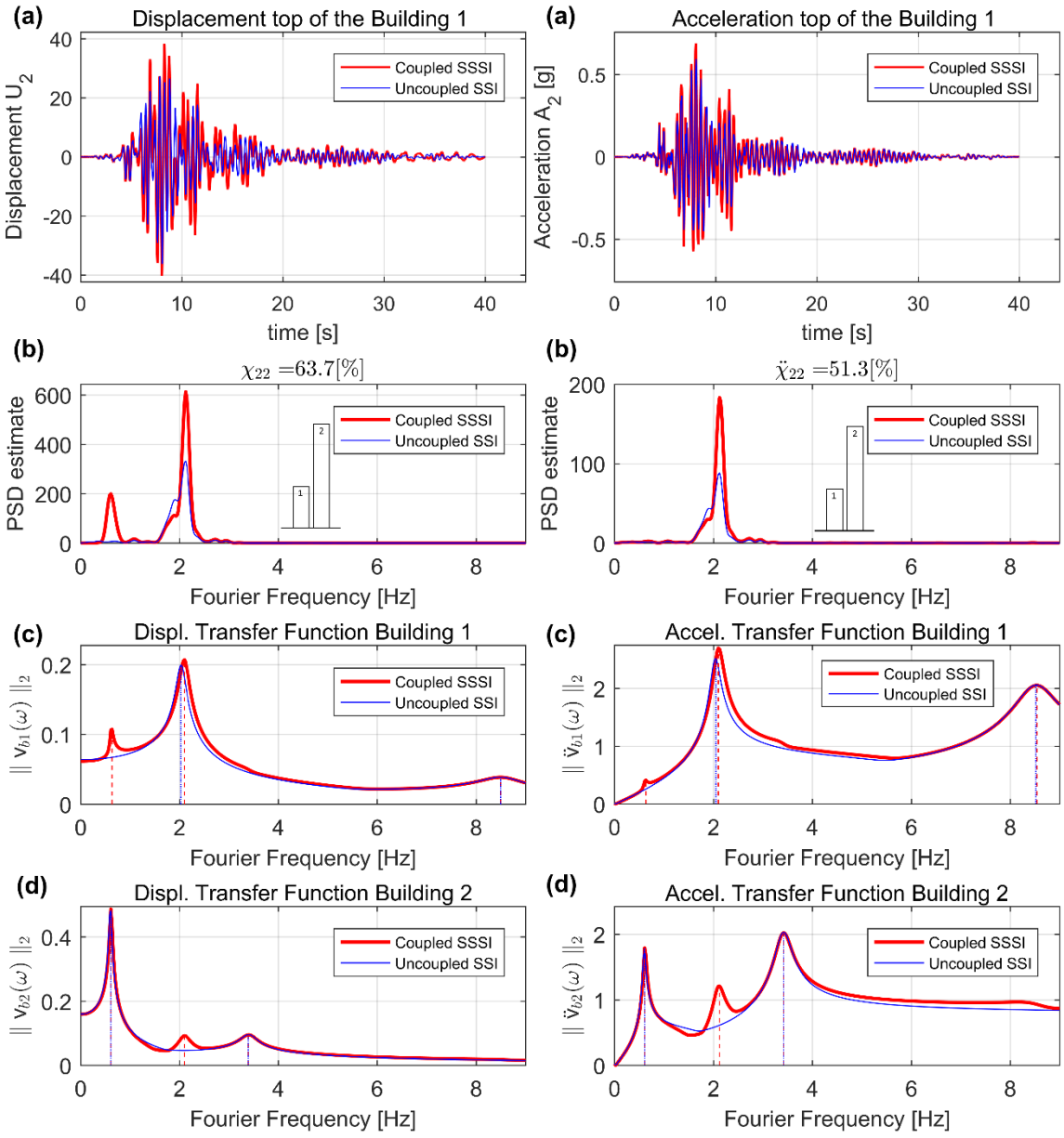

Figure 3: (a) Displacement and acceleration responses of building 1, (b) Power spectral density of displacement and acceleration responses of building 1, (c) Transfer function of displacement and acceleration for building 1 and (d) Transfer function f displacement and acceleration for building 2.

3.3 Change in power with variation in aspect ratio and height ratio

We now take a look at the total change in power of building 1, defined in equation (10) for the acceleration $\ddot{\chi}_{22}(s,\varepsilon)$. This difference term would be zero if there is no difference between the coupled (SSSI) and uncoupled (SSI) analyses.

The variation of error in power, with height $\varepsilon = h_2/h_1$ and aspect ratio $s = h_1/b$ for loose soil and inter-building spacing of $z = 0.1$, is plotted. The system is subjected to all earthquake events, classified by Far-Field (FF), Near-Field Without Pulse (NFWP) and Near-Field Pulse-Like (NFPL) record sets. For each of these record sets, the maximum of maxima error (for this record set), the mean error (for this record set) and the standard deviation of error (for this record set) are presented.

Figure 4 displays the contour plots of variation of error $\ddot{\chi}_{22}(s,\varepsilon)$ for the displacement and acceleration A_2 on top of building 1, for the Far-Field records. Figure 4 contains the results of nearly half million different time-histories analyses. We employed University of Bristol's supercomputer, BlueCrystal, for these simulations. The critical zones in the figure are red, i.e. where the total response power of building 1 is amplified by the presence of building 2. Blue indicates when the response power is reduced.

For the displacement, the worst possible building parametric configuration lies around $\chi_{22}(2.6,1.1) = 110\%$, and when the height ratio is greater than 2. In the case of acceleration, for height ratios greater than 1, i.e. when adjacent buildings are taller, the response of building 1 is amplified. The maximum increase in total acceleration power response occurred when the building parametric configuration lies around $\ddot{\chi}_{22}(2.5,1.1) = 110\%$ and its average is approximately $\ddot{\chi}_{22}(\mathrm{s},1.1) = 40\%$. The dispersion of the values is small, with a maximum of 40%, for the whole range of analysed parameters.

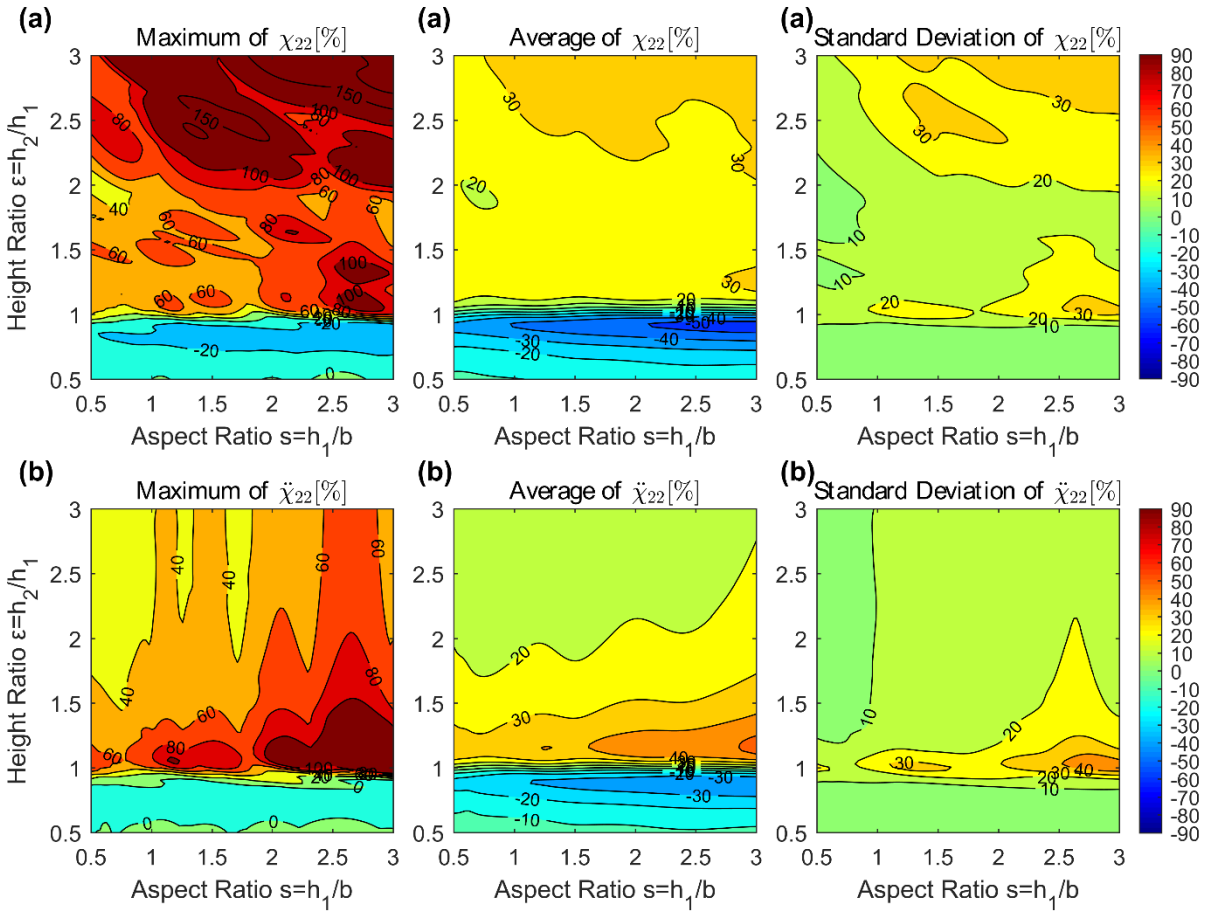

Figure 4: Response for Far-Field records. Maximum value, average and standard deviation for change in (a) displacement and (b) acceleration power.

Figure 5 displays the contour plots of variation of error in power $\ddot{\chi}_{22}(s,\varepsilon)$ for the displacement and acceleration A_2 considering the Near-Field Pulse-Like records. Again, in Figure 5 and Figure 6 over half a million different time-histories analyses are developed. As with the FF records, the maximum increase in total acceleration power response occurred when the structure configuration lies around $\ddot{\chi}_{22}(2.6,1.1) = 110\%$ and reaching values above 400% for the displacement (height ratio greater than 2). The dispersion of the values is small, with a maximum of 32%, for the whole range of analysed parameters.

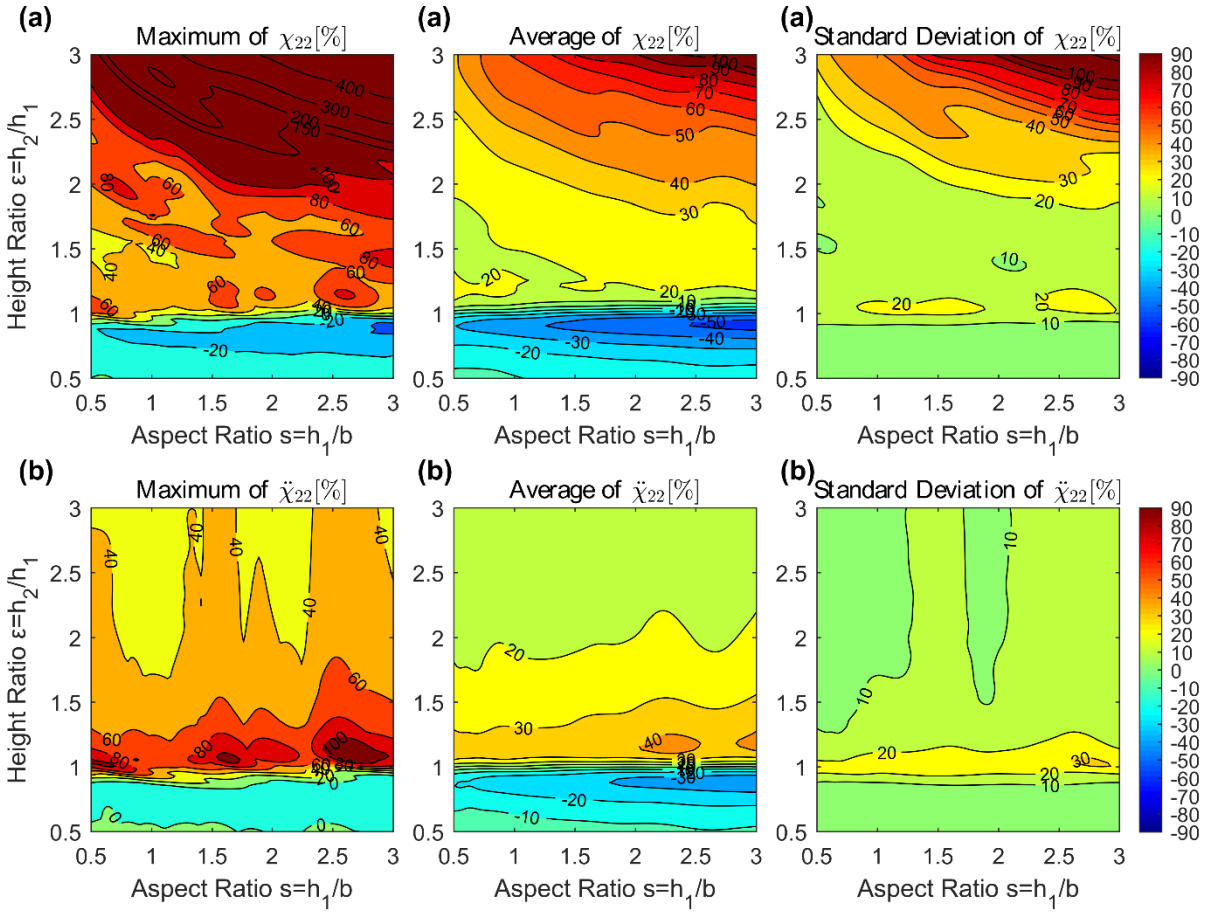

Figure 5: Response for Near-Field Pulse-Like records. Maximum value, average and standard deviation for change in (a) displacement and (b) acceleration power.

Figure 6 shows the variation of change in power for the displacement and acceleration A_2 considering Near-Field Without Pulse records. In general, the behaviour of NFPL and NFWP earthquakes follows a similar pattern for maximum values, averages and standard deviation. Comparing the FF and NF earthquakes, the contour plots suggest that the low-frequency content of the earthquake (especially for Near-Field records) can affect the size of adverse SSSI effects, especially for response displacements when the height ratio is greater than 2.0.

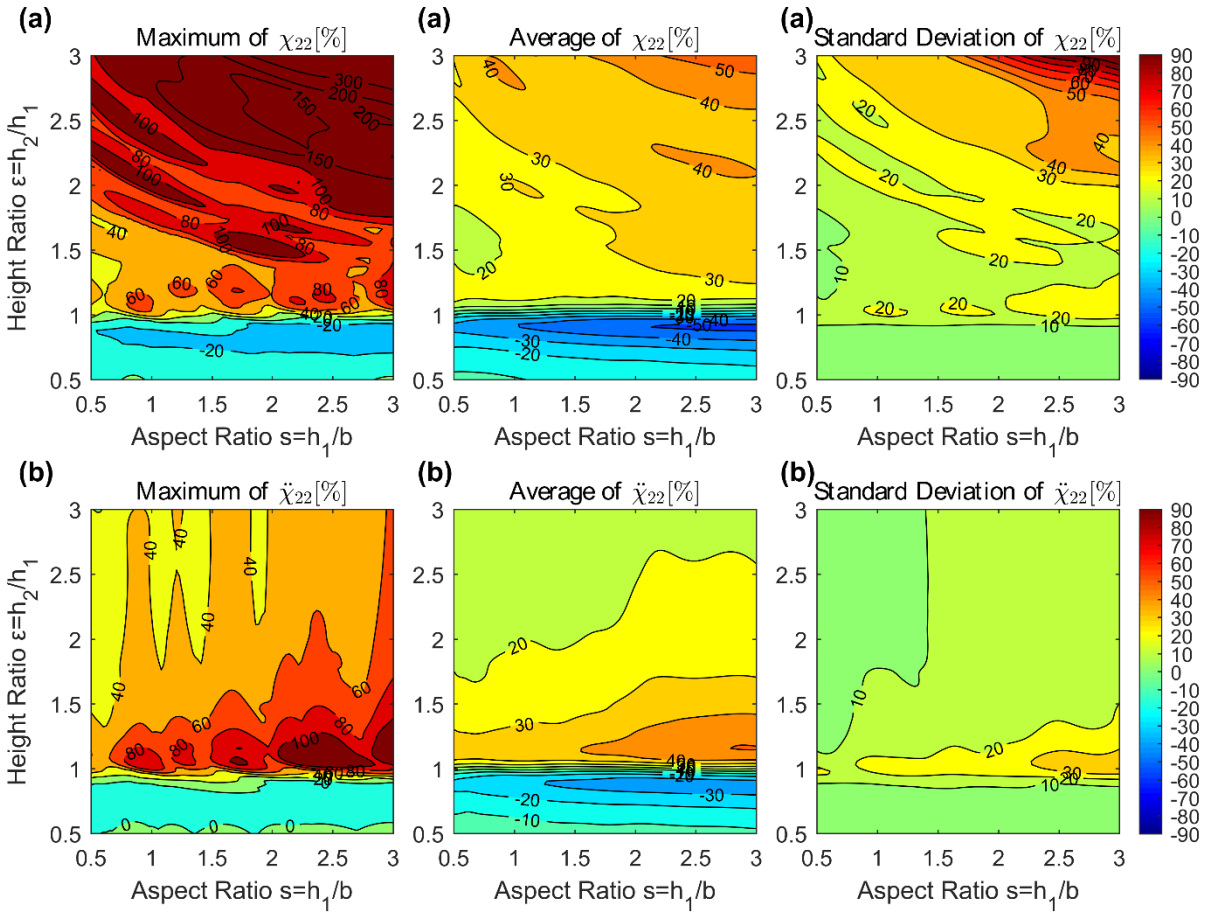

Figure 6: Response for Near-Field Without-Pulse records. Maximum value, average and standard deviation for change in (a) displacement and (b) acceleration power.

4 CONCLUSION

In this paper, we present a theoretical formulation for SSSI between two buildings. These structures are coupled through the underlying soil. Three types of ground motion were considered (Far-Field, Near-Field Without Pulse and Near-Field Pulse-Like records sets), selected from FEMA P695. The analyses have been undertaken for loose soil.

The computational analysis for loose soils showed that there are unfavourable and beneficial configurations for the dynamic characteristics of buildings. Regardless of the seismic event, it is found that the effect of interaction is adverse for building 1 when building 2 is taller: i.e. the power of the earthquake passed from the taller building to the smaller building. For the displacement responses, there is an increase in the response of up to 400%, when there is a large difference of height (height ratio $\varepsilon = h_2/h_1 > 2.0$) between the buildings. This result was not observed in previous studies [15,17]. The taller building imposes a low-frequency 'rigid body rocking mode' on the smaller building. If this behaviour is combined with ground motions that have a larger low-frequency content (i.e. the near field records), then there is significant error in using SSI analyses rather than SSSI analyses for these cases. This behaviour is observed in displacement responses alone because acceleration responses are, by definition, much less susceptible to low-frequency excitation. For the acceleration responses, the greatest amplifications, of up to 120%, are observed for buildings of 10% difference in height. This finding confirms the results of previous studies [17].

This research also indicated that there is a favourable geometric configuration ($\varepsilon = h_2/h_1 < 1.0$) where the seismic risk is reduced in building 1 by the presence of a smaller structure. The most beneficial configuration produces a reduction of the change in power in -45% for displacement and acceleration.

Results obtained from this 6dof model suggest that the introduction of two additional degree of freedoms can affect the size of interaction between the structures. Therefore, the 6dof model allows the interaction of the second sway mode of a much taller structure with the first sway mode of a shorter structure of less than half its height. This suggests that modal coupling between the buildings is possible between more than just the primary modes of each structure and therefore indicates a significant interaction between a taller building 1 and much shorter building 2.

REFERENCES

[1] Luco JE, Contesse L. Dynamic structure–soil–structure interaction. *Bull Seismol Soc Am* 1973; 63:1289–303.

[2] Kobori T, Minai R, Kusakab K. Dynamical characteristics of soil–structure cross-interaction system. *Bull Disaster Prevent Res Inst* 1973; 22. Kyoto University.

[3] Lee TH, Wesley DA. Soil–structure interaction of nuclear reactor structures considering through-soil coupling between adjacent structures. *Nucl Eng Des* 1973; 24:374–87.

[4] Murakami H, Luco JE. Seismic response of a periodic array of structures. *Journal of Engineering Mechanics*, ASCE 1977; 103(5):965-77.

[5] Wong HL, Trifunac MD. Two-dimensional, antiplane, building–soil–building interaction for two or more buildings and for incident planet SH waves. *Bull Seismol Soc Am* 1975; 65:1863–85.

[6] Qian J, Beskos DE. Dynamic interaction between 3-D rigid surface foundations and comparison with the ATC-3 provisions. *Earthq Eng Struct Dyn* 1995; 24:419–37.

[7] Karabalis DL, Mohammadi M. 3-D dynamic foundation-soil-foundation interaction on layered soil. *Soil Dyn Earthq Eng* 1998; 17:139-152.

[8] Lehmann L, Antes H. Dynamic structure–soil–structure interaction applying the Symmetric Galerkin Boundary Element Method (SGBEM). *Mech Res Commun* 2001; 28:297–304.

[9] Qian J, Tham LG, Cheung YK. Dynamic cross-interaction between flexible surface footings by combined BEM & FEM. *Earthq Eng Struct Dyn* 1996; 25:509–26.

[10] Yahyai M, Mirtaheri M, Mahoutian M, Daryan AS. Soil structure interaction between two adjacent buildings under earthquake load. *Am J Eng Appl Sci* 2008; 1:121–5.

[11] Padron LA, Aznarez JJ, Maeso O. Dynamic structure–soil–structure interaction between nearby piled buildings under seismic excitation by BEM–FEM model. *Soil Dyn Earthq Eng* 2009;29:1084–96.

[12] Trombetta NW, Mason HB, Chen Z, Hutchinson TC, Bray JD, Kutter BL. Nonlinear dynamic foundation and frame structure response observed in geotechnical centrifuge experiments. *Soil Dyn Earthq Eng* 2013; 50:117–33.

[13] Mason HB, Trombett NW, Chen Z, Bray JD, Hutchinson TC, Kutter BL. Seismic soil–foundation–structure interaction observed in geotechnical centrifuge experiments. *Soil Dyn Earthq Eng* 2013; 48:162-174.

[14] Knappett J, Massen P, Caucis K. Seismic structure-soil-structure interaction between pairs of adjacent building structures. *Geotechnique* 2015; 65(5):429-41.

[15] Aldaikh H, Alexander N, Ibraim E, Knappett J. Shake table testing of the dynamic interaction between two and three adjacent buildings (SSSI). *Soil Dyn Earthq Eng* 2016; 89:219-232.

[16] Mulliken JS, Karabalis DL. Discrete model for dynamic through-the-soil coupling of 3D foundations and structures. *Soil Dyn Earthq Eng* 1998; 27:678-710.

[17] Alexander NA, Ibraim E, Aldaikh H. A simple discrete model for interaction of adjacent buildings during earthquakes. *Comput Struct* 2013; 124:1–10.

[18] Aldaikh H, Alexander NA, Ibraim E, Knappett J. Evaluation of rocking and coupling rotational stiffness coefficient of adjacent foundations. *Int J Geomech*, ASCE 2018; 18(1):04017131.

[19] Vicencio F, Alexander NA. Dynamic interaction between adjacent buildings through nonlinear soil during earthquakes. *Soil Dyn Earthq Eng* 2018; 108: 130–41.

[20] Vicencio F, Alexander NA. Higher mode seismic structure-soil-structure interaction between adjacent building during earthquakes. *Eng Struct* 2018; 174:322–37.

[21] Chopra AK. Dynamics of structures: Theory and applications to earthquake engineering. 2nd ed. Prentice-Hall; 2000.

[22] SEAOC Bluebook: The Recommended Lateral Force Requirements of the Structural: SEAOC, 1959.

[23] Newmark NM, Rosenblueth E. Fundamentals of earthquake engineering. Prentice-Hall; 1971.

[24] Pais A, Kausel E. Approximate formulas for dynamic stiffnesses of rigid foundations. *Soil Dyn Earthq Eng* 1988;7(4):213–27.

[25] PEER Strong Motion Database <http://ngawest2.berkeley.edu/ >.

[26] FEMA P695, Federal Emergency Management Agency. Quantification of Building Seismic Performance Factors, June 2009.

COMPDYN 2019
7th ECCOMAS Thematic Conference on
Computational Methods in Structural Dynamics and Earthquake Engineering
M. Papadrakakis, M. Fragiadakis (eds.)
Crete, Greece, 24-26 June 2019

HOW BUILDING ADJACENCY AFFECTS OCCUPANT-PERCEIVABLE VIBRATIONS DUE TO URBAN SOURCES: A PARAMETRIC STUDY

Peter Persson[1], **Loukas F. Kallivokas**[2], **Lars V. Andersen**[3], **Andrew T. Peplow**[4]

[1]Department of Construction Sciences, Lund University
P.O. Box 118, SE-221 00 Lund, Sweden
e-mail: peter.persson@construction.lth.se

[2] Department of Civil, Architectural and Environmental Engineering, The University of Texas at Austin
Austin, TX 78712-1068, USA
e-mail: loukas@mail.utexas.edu

[3] Department of Engineering, Aarhus University
8000 Aarhus C, Denmark
e-mail: lva@eng.au.dk

[4] Department of Natural Sciences and Public Health, Zayed University
P.O. Box 144534, Abu Dhabi, United Arab Emirates
e-mail: andrew.peplow@zu.ac.ae

Keywords: Building Vibrations, Building Adjacency Effects, Ground Vibrations, Coupled FEM, Frequency Domain, Parametric Study

Abstract. *Urban densification, despite the economic and social opportunities it offers, brings with it challenges to the well-being of citizens. A direct effect of densification is the rise in noise- and vibration-producing sources, which can lead to both health and comfort issues. In determining the risk associated with excessive vibration levels, the distance between the source and the receiver or target building, the ground properties, and the building type, are all important factors. In this paper, we are concerned with the effect that adjacent buildings have on the prediction of the vibration levels in a residential building, caused by external ground surface loads. The parametric studies were conducted using a coupled finite element model of the ground and the buildings. The analyses were conducted in the frequency domain, and vibrational velocity levels were computed at the receiver building in order to assess how building adjacency affects the receiving building's vibrational response.*

1 INTRODUCTION

The densification of urban areas, driven mostly by economic forces, continues unabated. Urban densification, despite the economic and social opportunities it offers, brings with it challenges to the well-being of citizens. A direct effect of densification is the rise in noise- and vibration-producing sources, which can lead to vibrations that exceed human-tolerable levels. Current construction trends, which tend to favor the use of lighter materials (e.g., timber), promote higher levels of human-perceivable vibrations. In addition, in dense urban settings, the proliferation of vibration-producing sources has an effect on vibration-sensitive equipment, whether in hospitals, research laboratories, or industrial facilities, that cannot be ignored.

Of the many different vibration sources, of interest herein is the analysis of traffic-induced building vibrations, since it remains one of the dominant sources of vibrations in urban environments, further aggravated by densification. The traffic-induced vibration analysis is demanding, since the problem involves a large number of difficult-to-estimate parameters. In broad strokes, the problem can be divided into the three different parts illustrated in Fig. 1: the external source; the medium; and the receiver. The parameters and the properties of each part affect the vibration levels in the receiver building. In devising numerical models to estimate the vibration levels, adjacent buildings are usually not taken into account—it is common practice to only include the receiving building within the model. The effect of adjacent buildings in the response of a receiver building has been primarily studied in the context of earthquake engineering, the so-called structure–soil–structure interaction and/or "site–city effects", where the presence of adjacent buildings can significantly alter the response dynamics (see, for example, [1, 2]). However, the influence of these interaction effects is not a well-studied area for traffic-induced building vibrations. Exceptions include the study of the effect of structural modifications to the receiving building and its surroundings in order to mitigate the vibrational response induced by ground sources [3, 4, 5, 6, 7, 8].

In the present study, we investigate the effect of structural modifications to an adjacent building on the receiving building's vibrational response due to ground surface loading. An example of a suitable and commonly-arising application is the study of traffic-induced building vibrations were residents may be complaining due to increased vibrational levels. In Section 2 we describe modeling of externally induced building vibrations, and in Section 3 we discuss the developed computational model. Section 4 presents the conducted parametric study and the numerical results. In Section 5 we discuss pertinent conclusions of the study.

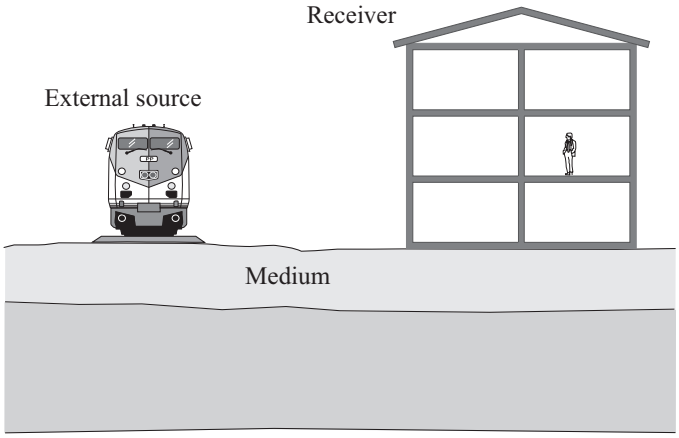

Figure 1: Illustration of typical components of a building vibration problem in the built environment.

2 MODELING OF EXTERNALLY INDUCED BUILDING VIBRATIONS

The modeling procedure used in the present study is based on the assumption of linear elastic behavior, since we consider only low-amplitude vibrations induced by, for example, train and/or road traffic. The analyses of the dynamic loading is performed in the frequency domain and the finite element (FE) method is used to compute velocity levels. Since the spatial variability of the soil and of the building properties occur at scales much smaller than the wavelengths that correspond to the frequency range of interest, in additional to linearity, we assumed homogeneous and isotropic material behavior throughout.

After spatial discretization, the FE model of a linear dynamic system provides a semi-discrete equation of motion in the form of the following system of ordinary differential equations:

$$\mathbf{M}\ddot{\mathbf{u}} + \mathbf{C}\dot{\mathbf{u}} + \mathbf{K}\mathbf{u} = \mathbf{f}, \tag{1}$$

where $\mathbf{M}$, $\mathbf{C}$, and $\mathbf{K}$ denote the mass, damping, and stiffness matrices, respectively, whereas $\mathbf{u}$ denotes the displacements and $\mathbf{f}$ the loads. Dots indicate derivatives with respect to time. In case of steady state displacement response to harmonic excitation, $\mathbf{u}$ and $\mathbf{f}$ can be expressed as complex harmonic functions:

$$\mathbf{f} = \hat{\mathbf{f}}\mathrm{e}^{\mathrm{i}\omega t}, \quad \mathbf{u} = \hat{\mathbf{u}}\mathrm{e}^{\mathrm{i}\omega t}, \tag{2}$$

where $\hat{\mathbf{f}}$ and $\hat{\mathbf{u}}$ denote the complex load amplitude and the displacement amplitude, respectively, i denotes the imaginary unit, ω denotes the angular frequency, and t denotes time. Introducing Eq. (2) in the equation of motion (Eq. 1) yields the equation of motion in the frequency domain:

$$\mathbf{D}(\omega)\hat{\mathbf{u}} = \hat{\mathbf{f}}, \tag{3}$$

where the dynamic stiffness matrix $\mathbf{D}(\omega)$ can be expressed as:

$$\mathbf{D}(\omega) = -\omega^2\mathbf{M} + \mathrm{i}\omega\mathbf{C} + \mathbf{K}. \tag{4}$$

We used a rate-independent (hysteretic) damping model, and thus, the damping can be described by a loss factor [9], as in:

$$\mathbf{K}\eta = \omega\mathbf{C}. \tag{5}$$

Inserting Eq. (5) into Eq. (4), we arrive at:

$$\mathbf{D}(\omega) = -\omega^2\mathbf{M} + (1 + \mathrm{i}\eta)\mathbf{K}. \tag{6}$$

The imaginary part of the stiffness matrix is often referred to as the structural damping matrix. Equation (6) was used to model both the structures and the soil. We note that for the soil, the linear elastic model accounts for the bulk compressional and shear waves, as well as for any interface waves (Rayleigh on the free surface, and Stoneley along any interfaces between soil layers). As is often the case, the FE model occupies a finite computational domain, which is truncated via the introduction of suitable absorbing boundaries. Here, to reduce the computational effort, we used dashpots [10], which are effective when waves impinge at normal incidence.

3 COMPUTATIONAL MODEL

The coupled FE model comprises both the soil and the building structures, which are fully coupled. See Fig. 2 for a schematic of the model. Plane strain conditions were applied, thus a line load as well as an elongated building exposed to planar waves were assumed.

The soil in the example case consists of a stiff 10 m deep soil layer resting on top of bedrock—conditions common in the south of Sweden; see Fig. 3 for the Youngs modulus E, Poissons ratio ν, mass density ρ, and the loss factor η for the soil materials. Treating the bedrock as a linear elastic material rather than a rigid foundation is an important parameter in this study. The dimensions of the building are shown in Fig. 2. The building structure consists of 200 mm thick concrete walls and 300 mm thick concrete slabs. The reinforcing bars are assumed to not influence the response; the isotropic material properties used for the concrete are given in Table 1. The model is excited by a vertical harmonic unit load applied on the ground surface 50 m from the receiver building; the load frequency was varied between 1 and 80 Hz in steps of 0.5 Hz. The frequency range was set to relate to human response, on the basis of the ISO standard [12].

Abaqus 6.13 [11] was used to compute the coupled response. To ensure that the FE analyses provide results of adequate accuracy, the influence of various parameters such as the aspect ratio of the finite elements, the size of the computational domain, and the reflection of waves at artificial boundaries have been studied, while the mesh density was adjusted to account for typical minimum number of nodes per wavelength criteria. The soil, as well as the buildings, were modeled with eight-node (serendipity) plane strain elements. Given the materials and fre-

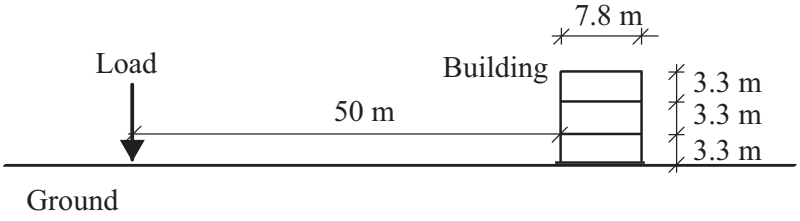

Figure 2: Schematic of the model. Center-to-center dimensions are also shown.

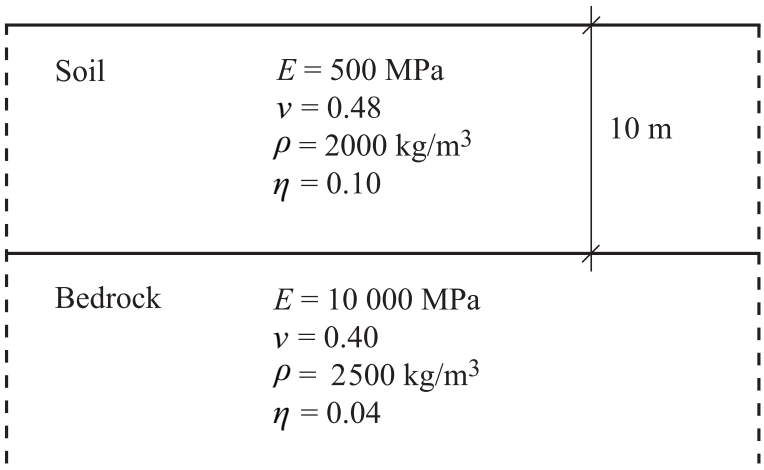

Figure 3: Schematic of the ground profile; inserts describe the ground material properties.

Property	Value
Young's modulus	32 GPa
Poisson ratio	0.2
Mass density	2500 kg/m^3
Loss factor	0.04

Table 1: Material properties used for concrete.

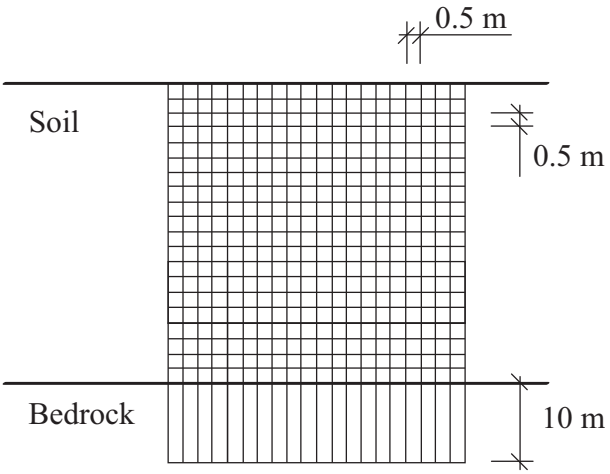

Figure 4: Schematic of the soil element mesh.

quency range of interest, the mesh convergence study resulted in an element size of 0.5×0.5 m^2 for the soil layer and 0.5×10 m^2 for the bedrock. Generally, an element size of 0.3×0.3 m^2 was used for the slabs, and 0.2×0.3 m^2 for the walls. The FE mesh of the soil is shown in Fig. 4.

4 PARAMETRIC STUDY

In order to investigate the effects that various parameters of the adjacent building have on the receiving building's vibration response, a single parameter at a time was varied while the others were kept constant. In total, five different parameters related to the adjacent building were varied, and the results are presented in the following five subsections 4.1–4.5. Specifically, we report on the effect of:

1. Distance between the buildings
2. Size of adjacent building footprint
3. Adjacent building cellar depth
4. Adjacent building mass
5. Adjacent building damping

In computing one value representing the vibration response we want to use a metric that is sensitive to the peaks in the response spectra. We are therefore using a Root Mean Quad value (RMQ), calculated as follows:

$$\text{RMQ} = \frac{1}{n}\left(\sum |V|_j^4\right)^{1/4}, \tag{7}$$

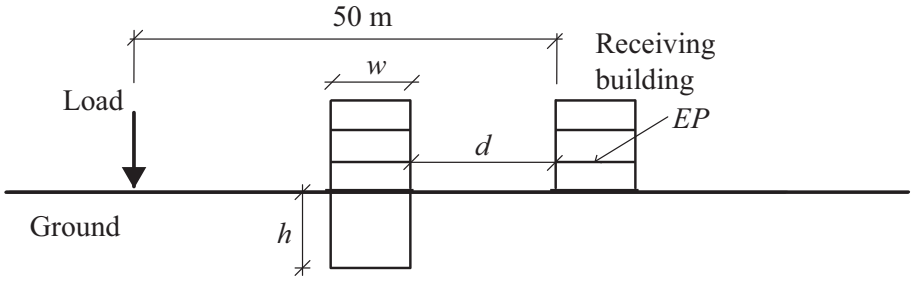

Figure 5: Setup with adjacent building in front of receiving building.

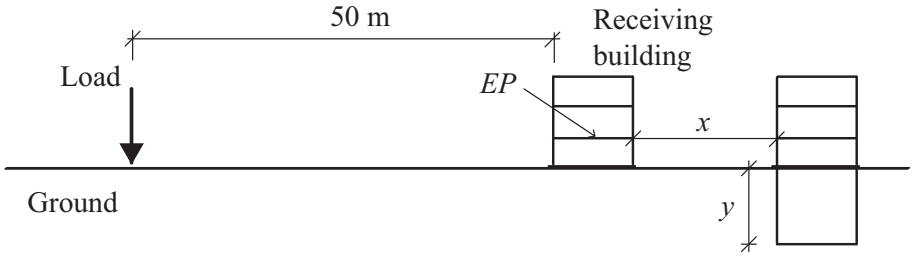

Figure 6: Setup with adjacent building behind receiving building.

where j denotes each discrete frequency, and n is the total number of frequencies. The vertical velocities, $|V|$, were evaluated as complex magnitudes at the mid-point of the first floor level; the specific locations are indicated in Figs. 5 and 6 as *EP* (Evaluation Point).

4.1 Distance between the buildings

In this subsection we evaluate to what extent the distance between the buildings affects the vibrations in the receiving building.

First we consider the case when the adjacent building ($h = 0$, $w = 8$ m) is located in front of the receiving building as seen in Fig. 5. Figure 7 shows that having an adjacent building between the vibration source and the receiving building affects the response significantly. It also shows that the gap-distance d has a minor effect on the response, and that no clear trend can be seen.

Secondly, we consider the case of having an adjacent building without a cellar ($h = 0$) located behind the receiving building. The calculations showed that the response was not affected to any appreciable extent, independently of the distance x between the buildings (cf. Fig. 6). Therefore, we do not show the corresponding frequency response. However, if an 8 m-deep cellar is considered, i.e. $y = 8$ m, the response in the receiving building is affected. The effect of various distances, x, between the buildings for this case is presented in Fig. 8. As seen in the figure, there is an effect on the response depending on the distance to the adjacent building. The effect on the spectrum is rather small but since it affects the large frequency peaks, it still results in a considerable change in the evaluated metric of the response. However, no apparent general trends can be seen other than that the distance between the buildings is of importance.

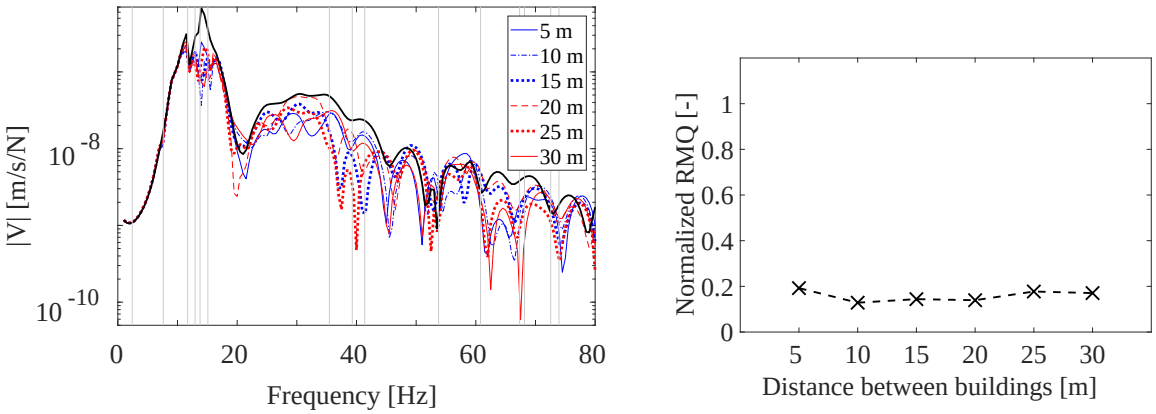

(a) Frequency spectrum for tested values of d. (b) RMQ value normalized to the reference case.

Figure 7: Vibration levels computed with the adjacent building in front of the receiving building. The distance d is being varied. A setup with no adjacent building represents the reference case. In the left subfigure, the solid black line represents the reference case and the gray vertical lines show the receiving building's eigenfrequencies.

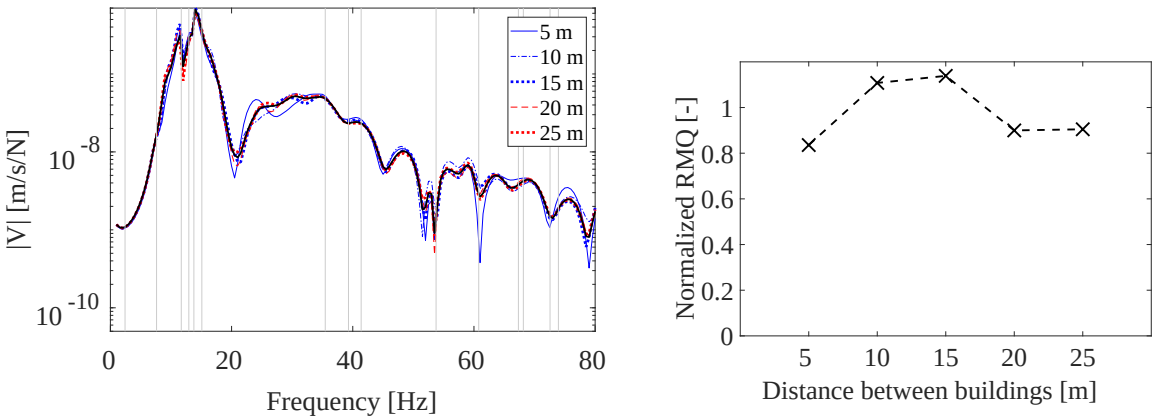

(a) Frequency spectrum for the tested values of x. (b) RMQ value normalized to the reference case.

Figure 8: Vibration levels computed with the adjacent building having 8 m cellar behind the receiving building. The gap-distance x being varied. A setup with no adjacent building represents the reference case. In the left subfigure, the solid black line represents the reference case and the gray vertical lines show the receiving building's eigenfrequencies.

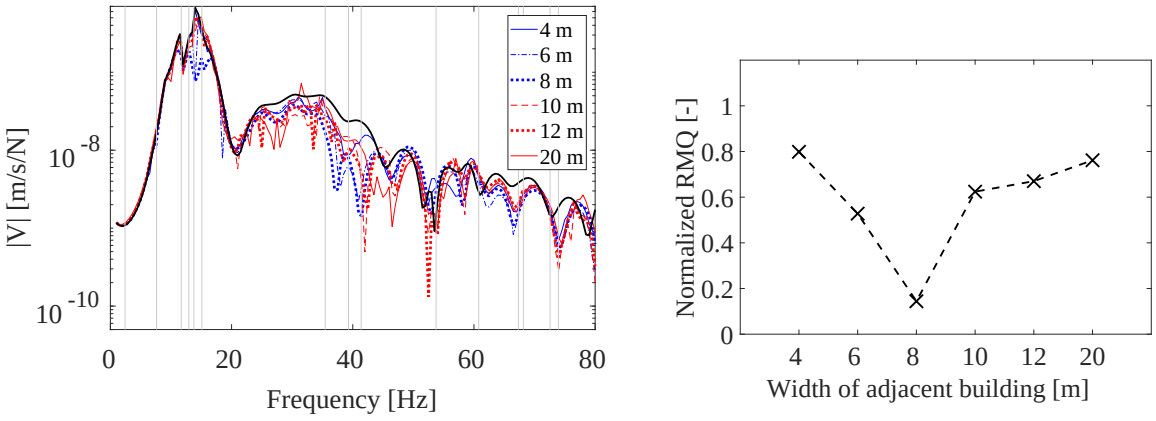

(a) Frequency spectrum for the tested values of w.

(b) RMQ value normalized to the reference case. Note the inconsistent scale on the horizontal axis.

Figure 9: Vibration levels computed with the adjacent building in front of the receiving building. The width of the adjacent building w being varied. A setup with no adjacent building represents the reference case. In the left subfigure, the solid black line represents the reference case and the gray vertical lines show the receiving building's eigenfrequencies.

4.2 Size of building footprint

In this subsection we investigate the effects of the footprint size of the adjacent building, when located in front of the receiving building, on the receiving building's response. The model can be seen in Fig. 5, where the footprint size is varied by changing of the width w of the adjacent building. As seen in Fig. 9, the footprint size can have a marked influence on the response. The most significant effect is seen when the adjacent building has the same footprint as the receiving building ($w = 8$ m), where a large reduction in the vibration response is evident. In this setup, the adjacent and receiving buildings have the same modal properties.

4.3 Cellar depth

The influence of the cellar depth for two different locations of the adjacent building is investigated in this subsection. In the first case, the adjacent building is located in front of the receiving building as seen in Fig. 5. The distance d is fixed at 15 m, and the width of the adjacent building is 8 m; we vary the cellar depth h. As seen in Fig. 10, there is a large effect of the cellar depth on the vibration response. The largest influence occurs when the cellar goes all the way down to the bedrock, i.e. $h = 10$ m. The reflection of waves from the concrete cellar walls is then significant.

As was noted in Section 4.1, having the adjacent building without cellar located behind the receiving building did not, to any appreciable extent, affect the vibrational response for any of the tested distances between the buildings. However, the distance has an influence when the adjacent building has a cellar. Now we vary the cellar depth y of the adjacent building located behind the receiving building. The distance x is fixed at 15 m and the width of the adjacent building is 8 m; see Fig. 6 for the model. As seen in Fig. 11, there is only a small effect of varying the cellar depth, but a clear trend is shown; with deeper cellar the reflected waves amplify (normalized RMQ value greater than 1) the response in the receiving building.

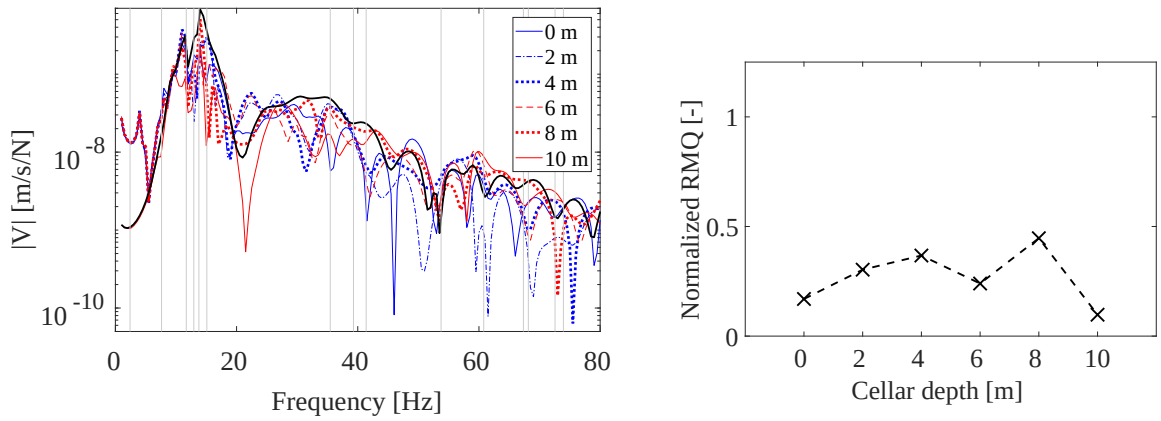

(a) Frequency spectrum for the tested values of h. (b) RMQ value normalized to the reference case.

Figure 10: Vibration levels computed employing the adjacent building with cellar in front of the receiving building. The cellar depth h being varied. A setup with no adjacent building represents the reference case. In the left subfigure, the solid black line represents the reference case and the gray vertical lines show the receiving building's eigenfrequencies.

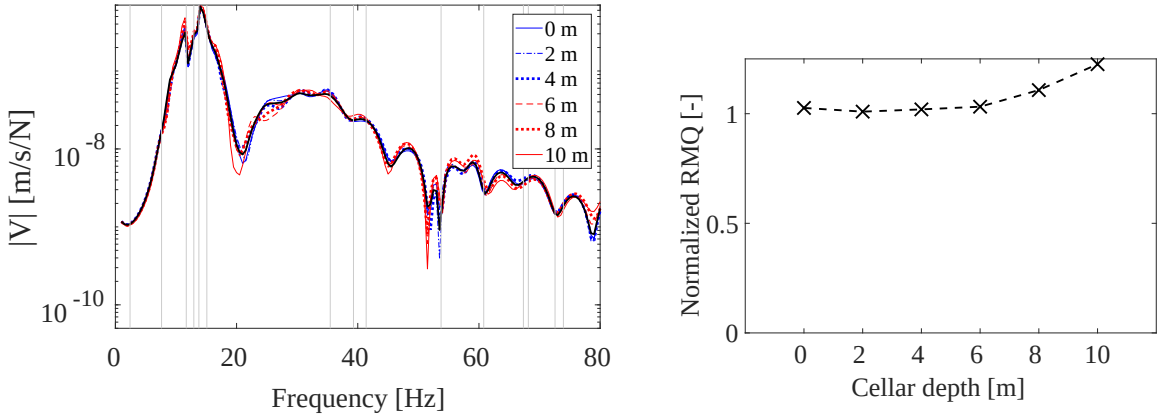

(a) Frequency spectrum for the tested cellar depths of the adjacent building. (b) RMQ value normalized to the reference case.

Figure 11: Vibration levels computed with the adjacent building with cellar behind the receiving building. The cellar depth y being varied. A setup with no adjacent building represents the reference case. In the left subfigure, the solid black line represents the reference case and the gray vertical lines show the receiving building's eigenfrequencies.

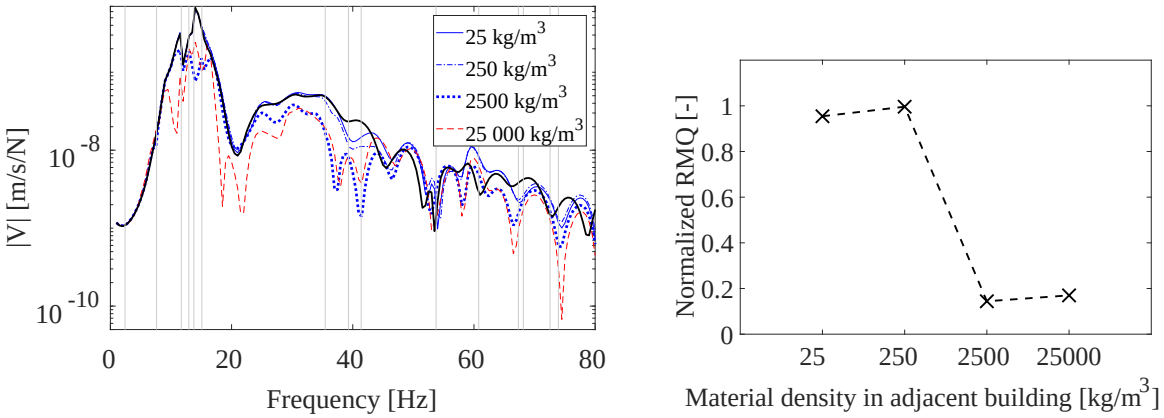

(a) Frequency spectrum for the tested density values of the adjacent building.

(b) RMQ value normalized to the reference case. Note the scale on the horizontal axis.

Figure 12: Vibration levels computed with the adjacent building in front of the receiving building. The mass density of the adjacent building being varied. A setup with no adjacent building represents the reference case. In the left subfigure, the solid black line represents the reference case and the gray vertical lines show the receiving building's eigenfrequencies.

4.4 Building mass

In this subsection we vary the mass of the adjacent building by changing the material density of the concrete. The adjacent building is located in front of the receiving building; see Fig. 5 for the model. The distance d is fixed at 15 m, the width of the adjacent building is 8 m, and the building does not have a cellar, i.e. cellar depth $h = 0$.

As seen in Fig. 12 the mass of the adjacent building has a significant effect on the response. A heavier adjacent building in front of the receiving building mitigates the vibrations to a larger extent than a lighter building. Note that the lowest as well as the highest tested mass densities are not realistic—however, they indicate that the largest influence occurs for mass densities between 250 and 2500 kg/m^3.

4.5 Building damping

The amount of damping in the adjacent building, which is located in front of the receiving building according to Fig. 5, is varied. The distance d is fixed at 15 m, and the width of the adjacent building is 8 m and it does not have a cellar, i.e. cellar depth $h = 0$. The loss factor was varied between 0.02 and 0.2. It was seen that varying the damping in the adjacent building had a minor effect on the evaluated vibration levels in the receiving building; see Fig. 13 for the response.

5 CONCLUSIONS

The paper presents a conceptual study of the effects of structural parameters of an adjacent building on the vibration response in a receiving building. The FE method was used to create a coupled soil and structure model that was excited by a ground surface load. The analysis was conducted in the frequency domain with plane strain conditions, and the velocity levels were computed in the frequency range of 1–80 Hz and evaluated at the midpoint of the first floor.

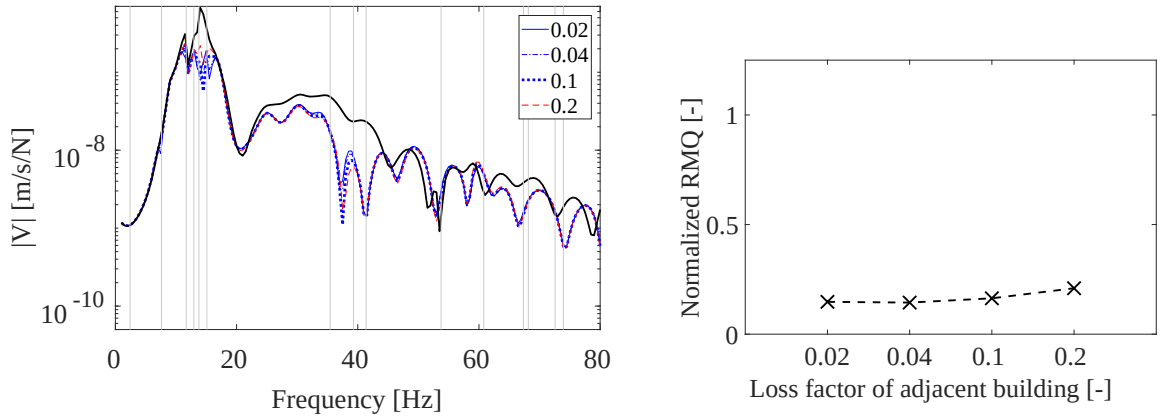

(a) Frequency spectrum for the tested damping values of the adjacent building.

(b) RMQ value normalized to the reference case. Note the scale on the horizontal axis.

Figure 13: Vibration levels computed with the adjacent building in front of the receiving building. The amount of damping in the adjacent building being varied by use of the loss factor η. A setup with no adjacent building represents the reference case. In the left subfigure, the solid black line represents the reference case and the gray vertical lines show the receiving building's eigenfrequencies.

Two main general tendencies were observed: (i) to place a building between the vibration source and the receiving building may work as a wave obstacle, thus mitigating the incoming ground vibrations—the benefit is greater when the intervening building is heavier; (ii) having building(s) with a cellar behind the receiving building may amplify the response and should therefore be considered in a vibration analysis.

This conceptual study clearly points that there are so-called "site–city effects" in the problem of ground-surface induced building vibrations, and that adjacent buildings must be considered in an analysis aiming at determining vibrations levels in a building.

6 ACKNOWLEDGMENTS

The research presented in this paper was partly funded by several agencies. They being: Swedish Governmental Agency for Innovation Systems, grant ref.no. 2018-04159; The city of Helsingborg through Plattformen; and The Swedish Foundation for International Cooperation in Research and Higher Education (STINT). The financial supports are gratefully acknowledged. The former Master's student Johansson [13] is gratefully acknowledged for his contribution to the research presented in the paper.

REFERENCES

[1] A. Kham, J.F. Semblat, P.Y. Bard, P. Dangla, Seismic site–city interaction: Main governing phenomena through simplified numerical models. *Bulletin of the Seismological Society of America*, **96**(5), 1934–1951, 2006.

[2] J. Liang, B. Han, M.I. Todovorska, D.M. Trifunac, 2D dynamic structure-soil-structure interaction for twin buildings in layered half-space I: Incident SH-waves. *Soil Dynamics and Earthquake Engineering*, **102**, 172–194, 2017.

[3] M. Villot, P. Ropars, P. Jean, E. Bongini, F. Poisson, Modeling the influence of structural modifications on the response of a building to railway vibration. *Noise Control Engineering Journal*, **59**(6): 641651, 2011.

[4] L.V. Andersen, Influence of dynamic soil-structure interaction on building response to ground vibration. M.A. Hicks, R.B.J. Brinkgreve, A. Rohe eds. *Numerical Methods in Geotechnical Engineering VIII*, 2, pp. 1087–1092, 2014.

[5] P. Persson, K. Persson, G. Sandberg, Numerical study on reducing building vibrations by foundation improvement. *Engineering Structures*, **124**, 361–375, 2014.

[6] P. Persson, L.V. Andersen, K. Persson, P. Bucinskas, Effect of structural design on traffic-induced building vibrations. *Procedia Engineering*, **199**, 2711–2716, 2017.

[7] A. Clot, R. Arcos, J. Romeu, Efficient three-dimensional building-soil model for the prediction of ground-borne vibrations in buildings. *Journal of Structural Engineering*, **143**(9), ASCE, 2017.

[8] P. Persson, L.V. Andersen, Efficient finite-element analysis of the influence of structural modifications on traffic-induced building vibrations. A.S. Cardoso, J.L. Borges, P.A. Costa, A.T. Gomes, J.C. Marques, C.S. Vieira eds. *Numerical methods in geotechnical engineering IX*, 2, pp. 1557–1564, 2018.

[9] R.R. Craig Jr, A.J. Kurdila, *Fundamentals of structural dynamics*. John Wiley & Sons, New Jersey, 2006.

[10] J. Lysmer, R.L. Kuhlemeyer, Finite dynamic model for infinite media. *Journal of Engineering Mechanics Division*, **95**(4), 859–877, ASCE, 1969.

[11] Dassault Systémes SIMULIA. Abaqus 6.13.

[12] International Organization for Standardization, *Mechanical vibration and shock – Evaluation of human exposure to whole-body vibration – Part 1: General requirements*. ISO 2631-1:1997.

[13] A. Johansson, *Structural effects on externally induced building vibrations*. Report TVSM-5230 (Master's dissertation), Department of Construction Sciences, Lund University, 2018.

COMPDYN 2019
7th ECCOMAS Thematic Conference on
Computational Methods in Structural Dynamics and Earthquake Engineering
M. Papadrakakis, M. Fragiadakis (eds.)
Crete, Greece, 24–26 June 2019

IMPEDANCE FUNCTIONS OF ADJACENT STRIP FOUNDATIONS WITH DIFFERENT DEPTHS OF EMBEDMENT

Vasiliki G. Terzi[1]

[1] Laboratory Teaching Staff
Laboratory of Statics and Dynamics of Structures,
Civil Engineering Department, 54124, Thessaloniki, Greece
e-mail: terziv@civil.auth.gr

Abstract

The present study refers to the interaction between two adjacent strip foundations that have different depths of embedment. In particular, one foundation is characterized as deep and is embedded in an elastic isotropic soil layer which is resting on a rigid substratum, while the other foundation is characterized as surface and is resting on the soil layer's surface. The two foundations have an equal value of half-width, B and the embedment depth, D of the deep foundation is equal to B. The distance ratio S/L, where S is the distance between the foundations and L is the width of each foundation receives the values of 0.5,3,5 and 10. In order to investigate the effect of the soil layer's depth H, the distance ratio is kept constant and equal to 0.5 while the H/B ratio receives the values of 2, 4, 8 and 32.

The main target is the calculation of the impedance matrix of the two interacting foundations and is achieved by the use of the finite element method. The accuracy of the finite element model is verified by comparison studies with the rigorous results from the boundary element method, concerning a single strip foundation, embedded or surface.

Each strip foundation has three degrees of freedom; the vertical translation, the horizontal translation and the rotational one. Therefore, harmonic type of loading is applied at each foundation for each degree of freedom and the flexibility matrix is calculated for a normalized frequency range of $0.1<\alpha o<2$, where $\alpha o=\omega B/Vs$; ω is the loading frequency and Vs is the shear wave velocity. The final flexibility matrix is a 6x6 symmetric matrix, which consists of terms referring to the deep or surface foundation response and the coupled response between them. The flexibility functions are presented for typical values of S/L and H.

The main conclusions are focused on the comparison between the response of each foundation which belongs to the system of the two and the response of a single foundation, deep or surface. Additional comments refer to the effect of the soil layer's depth on the coupling terms of the flexibility matrix of the two adjacent foundations.

Keywords:
Structure-soil-structure interaction, Strip footings, Finite Element Method.

1 INTRODUCTION

The assumption of fixed base boundary conditions for a structure can be considered appropriate only in very limited cases of a hard substratum time. Consequently, the soil-structure interaction (SSI) phenomenon must be taken into account, especially during dynamic structural design analysis. Furthermore, in dense populated areas, of closely spaced structures or structures on relatively close supports, the cross interaction through the soil between adjacent foundations might also be important [1]. Therefore, in order to evaluate the dynamic characteristics or the response of adjacent structures, it is necessary not only to investigate the classical interaction between the foundation and the soil medium, but also the interaction between the adjacent foundations through the soil [2]. Each foundation which diffracts the incident wave field can be regarded as a disturbance producing a secondary wave field affecting its neighboring [3]. This phenomenon is known as dynamic cross interaction (DCI) problem [2], structure-soil-structure interaction (SSSI, 3SI) problem [4] or foundation-soil-foundation interaction (FSFI) problem [5].

The interaction of soil medium and a surface strip foundation was investigated by many researchers. Some researches refer to the coupling between horizontal and rocking response. Luco and Westmann (1972) studied the coupling under the assumption of welded soil contact. Horizontal-rocking coupling arises during the application of lateral forces (e.g. wind), earthquake loading or machine vibrations [7]. The coupled and uncoupled horizontal-rocking response of a surface foundation under the assumption of relaxed and welded as well boundary conditions was studies by Karasudhi et al. (1968). The dynamic response of a surface strip foundation without accounting for horizontal-rocking coupling was investigated by Hryniewicz (1981). Furthermore, some additional researches focus on the properties of the soil medium. Wickham's study (1977) referred to a rigid strip foundation in smooth contact with a semi-infinite elastic solid. A semi-analytical technique was applied by Gazetas and Roesset (1976) in order to estimate the dynamic compliances of a rigid strip foundation resting on an elastic, linearly hysteretic, layered half-space. Von Estorff and Schmid (1984) analyzed the dynamic behavior of a strip foundation resting on a soil layer using the BEM. A frequency domain BEM formulation has been used by Dominguez and Abascal (1989) in a 2-D analysis of a strip footing on zoned viscoelastic soils. Jendoubi et al. (2008) studied the response of a strip footing resting on a half-space with constant or variable shear wave velocity.

The first studies concerning the through-the-soil coupling of adjacent surface foundations referred to the two-dimensional space. Cruze and Rizzo (1968) applied a frequency domain BEM formulation in order to study two and three dimensional elastodynamic problems, between two rigid surface foundations. The dynamic cross interaction of adjacent infinitely long shear walls, supported on semi-cylindrical foundations under the prism of two-dimensional anti-plane shear problem, was studied by Luco and Contesse (1973) for the case of two structures, by Wong (1975) and Wong and Trifunac (1975) for the case of several structures and by Murakami and Luco (1977) for the case of an infinite number of equally space structures. The finite element method was applied for the study of two-dimensional plane-strain models by Lysmer et al. (1974, 1975), Liang (1974) and Aydinoglu and Cakiroglu (1977), whereas the boundary integral equation approach was applied by Nakai and Fukuwa (1982), Antes and v. Estorff (1986) and Kokkinos and Spyrakos (1991) for the same problem.

The soil-structure interaction of an embedded foundation was studied by many researchers as well. Karabalis and Beskos (1986) applied the full-space Green's functions in order to investigate the dynamic response of an arbitrarily shaped embedded rigid foundation. The dynamic response under vertical and horizontal loadings of arbitrarily shaped embedded foundation was calculated by Gazetas et al. 1985 and Gazetas et al. 1987. Rajapakse and Shah

(1988) studied also the dynamic response of rigid strip foundations of arbitrary geometry embedded in a homogeneous elastic half-space. Hatzikonstantinou et al. 1989 estimated the static and dynamic stiffness coefficients while Fotopoulou et al. 1989 estimated the radiation damping coefficients of arbitrarily shaped rigid foundations embedded in an elastic homogeneous half-space. The dynamic response of an arbitrary shaped rigid strip foundation embedded in an orthotropic elastic soil under time-harmonic vertical, horizontal and moment loading was studied by Wang and Rajapakse (1991). The impedance functions of rigid massless soil-structure interfaces, embedded in arbitrarily heterogeneous half-spaces were calculated by Esmaeilzadeh Seylabi et al. (2016).

The dynamic performance of an embedded strip foundation was investigated by many researchers. In particular, Kobori et al. (1982) and Nakai et al. (1984) applied the boundary integral equation scheme. Israil and Ahmad (1989) investigated the dynamic response of surface and embedded rigid strip foundation in viscoelastic soils under vertical excitation. The research was continued by Ahmad and Bharadwaj (1991) who investigated in detail the influence on key mechanical and geometrical parameters on the dynamic horizontal stiffness of rigid strip foundations embedded in layered soil, while the research of Bharadwaj and Ahmad (1992) referred to the rocking degree of freedom.

Although, many studies refer to the dynamic behavior of a single, massless, rigid embedded foundation, very few deal with the dynamic cross-interaction problem of two adjacent embedded foundations. It is worth mentioning that Rajapakse and Shah (1988) investigated the effect on impedances due to the presence of an adjacent embedment for various distances between foundations and embedment ratios. Furthermore, Betti (1997) studied the dynamic cross-interaction between two identical rigid square foundations embedded in a homogeneous viscoelastic half-space by the application of the boundary element method.

The present study refers to the dynamic cross interaction between two adjacent strip foundations that have different depths of embedment and is a step further to previous investigations concerning two adjacent surface or embedded foundations [39, 40]. Difference in depth of embedment may appear in cases where there is a basement in one of the adjacent structures. The complete 6x6 impedance matrix of the coupled system is calculated for various values of the distance ratio S/L, while the height of the soil stratum is kept constant. The study is completed by the investigation of the effect of the height of the soil stratum on the foundations coupling for the minimum value of S/L.

2 PROBLEM AND MODEL DESCRIPTION

The problem under study is depicted in Fig.1. The main target of the study is the degree of interaction between two rigid, massless, strip foundations that have different depths of embedment. Therefore, the left foundation is embedded to a depth D, in a soil layer which is resting on a rigid substratum while the right foundation is resting on the free soil surface. The welded contact condition [9] issues at each foundation-soil interface. Consequently, complete continuity of displacements is assumed for the area of contact (perfect bond). The adjacent foundations have the same length, L or half-width, B and their separation distance is denoted as S. Each foundation has three degrees of freedom: horizontal translation, u_i; vertical translation, w_i; and rotation, φ_i. the corresponding loadings that activate the three degrees of freedom are denoted as: H_i, horizontal force; V_i, vertical force; and M_i, moment. In the following figure the positive direction of the external loads and the corresponding displacements are depicted. Subscript 1 refers to the deep foundation while subscript 2 refers to the surface foundation. The soil comprises of a layer of thickness, H which is assumed as elastic, homogeneous and isotropic.

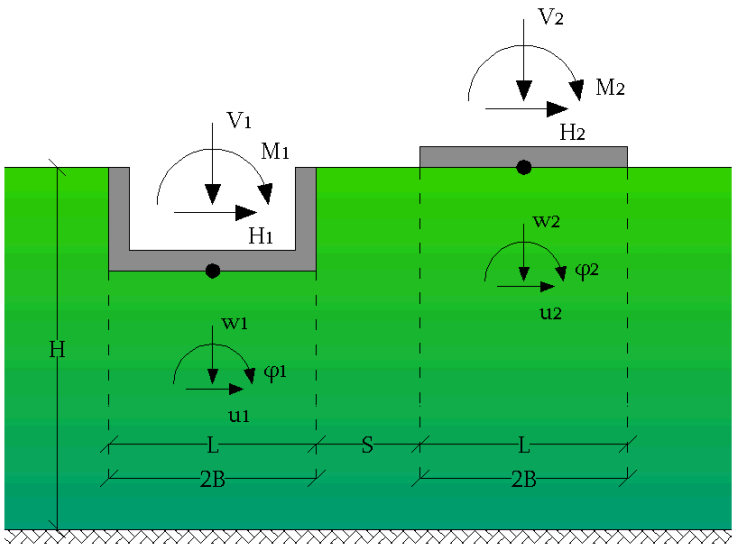

Figure 1: Adjacent strip foundation with different depths of embedment.

The system of the adjacent foundations has six degrees of freedom in total. The loading and displacement vector are related by the impedance matrix, K which takes the following form.

$$\begin{Bmatrix} V_1 \\ H_1 \\ M_1 \\ V_2 \\ H_2 \\ M_2 \end{Bmatrix} = \begin{bmatrix} K_{11} & K_{12} & K_{13} & K_{14} & K_{15} & K_{16} \\ & K_{22} & K_{23} & K_{24} & K_{25} & K_{26} \\ & & K_{33} & K_{34} & K_{35} & K_{36} \\ & & & K_{44} & K_{45} & K_{46} \\ & \text{symm.} & & & K_{55} & K_{56} \\ & & & & & K_{66} \end{bmatrix} \cdot \begin{Bmatrix} w_1 \\ u_1 \\ \varphi_1 \\ w_2 \\ u_2 \\ \varphi_2 \end{Bmatrix} \tag{1}$$

The 6x6 matrix is symmetrical. Each term is a frequency dependent complex number. The real part (in-phase component) represents the true stiffness, the restraining action of the soil and can be taken into account in the form of springs in a discrete model. Moreover, the imaginary part (out-of-phase component) represents the energy dissipation due to radiation and in a discrete model corresponds to dashpots [4, 5].

Therefore, the complete displacement field of the two foundations is needed in case where the external loading is applied at the deep foundation while the displacement field only of the surface foundation itself is needed in case where the external loading is applied at the surface foundation. The reverse issues if the surface foundation is denoted with subscript 1 and the deep with subscript 2.

The main tool used for the estimation of the response of the complex system under different excitation frequencies is the finite element method. In the case of a strip foundation, related to a track, dam or building foundation with a high ratio of length to width, the assumption of plane strain conditions can be considered to be reasonable [2]. Therefore, the finite element model is created in 2D space with the aid of 9-node quadrilateral 2-D solid elements.

The foundation-soil-foundation problem is typically a wave propagation problem. Thus, the minimum finite element size for each excitation frequency is equal to $\lambda_R/10$, where λ_R is the wavelength of minimum wave propagation velocity in the model, which usually corresponds to Rayleigh waves. Furthermore, the wave propagation problem in a model constructed by the used of the finite element method, cannot be simulated perfectly due to the restriction imposed by the model length and the finite element size [41]. In particular, the model must be large enough in order to reduce any reflected waves at its boundaries [42] and

the finite elements' size must be as small as possible in order to accurately describe a wavelength. Therefore, in order to avoid any wave reflections, quiet boundaries suggested by Lysmer and Kuhlemeyer (1969) were used.

The soil characteristics are the following: shear modulus, G equals to 132MPa, Poisson's ratio, v equals to 0.4 and density, ρ equals to 1.75t/m^3. The ratio between the foundation's depth and its half-width, D/B is kept constant and equal to unity. The problem is first studied for H/B equal to 2 and for various values of S/L ratio (0.5, 3, 5, 10). Furthermore, in order to maximize the foundation-soil-foundation interaction effects, the distance ratio, S/L is also kept constant and equals to 0.5. The interaction is studied for various typical values of the soil layer's depth ratio, H/B (2, 4, 8 and 32).

3 FINITE ELEMENT RESULTS

3.1 Validation studies

In order to validate the finite element model two validation studies were performed. The first one refers to the calculation of flexibility matrix of a deep foundation while the second one of a surface foundation.

Huh (1986) calculated the flexibility matrix of a rigid, massless, strip foundation embedded to a depth, D of a soil layer resting on rigid substratum by the use of the boundary element method. Figure 2 depicts the comparison between the researcher's results and the results of the present study by the use of the finite element method. The horizontal axis of the charts represents the normalized frequency α_o, $\alpha_o = (\omega \cdot B)/V_s$, where V_s is the shear wave velocity and the vertical axis is normalized by the parameters π, G and B.

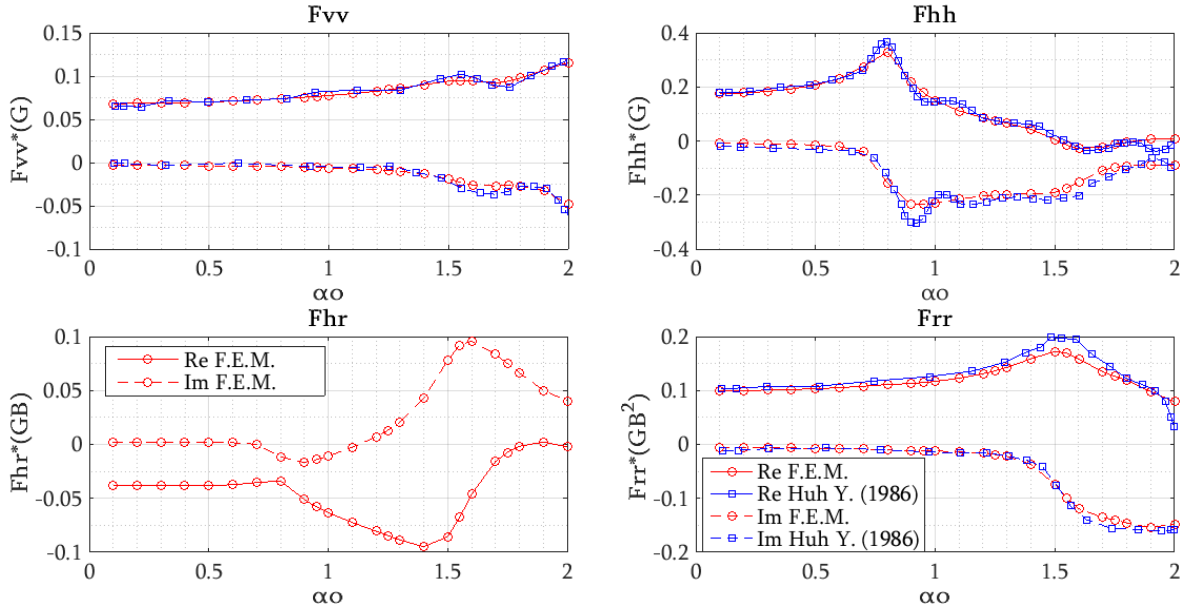

Figure 1: Validation study results for the case of an isolated, rigid, massless strip foundation embedded to a soil layer resting on a rigid substratum.

The vertical loading of an isolated deep foundation does not produce any horizontal or rocking displacement. Therefore, no coupling terms exist for the vertical degree of freedom. On the other hand, the horizontal/moment loading produces rotations/horizontal translations, respectively. Therefore, the coupling terms of motion are presented in Fig.2.c. Unfortunately

no information is given by Huh (1986) regarding the coupled horizontal-rocking degree of freedom. The results of the finite element method are in very good agreement with the result of the boundary element method. Consequently, the validation study referring to the deep foundation can be considered successful.

Luco and Westmann (1972), Hryniewicz (1981) and Wang et al. (2015) calculated the flexibility matrix of a rigid, massless, strip foundation bonded to the free surface of an elastic half-space. Figure 2 depicts the comparison between the researchers' results and the results of the present study by the use of the finite element method.

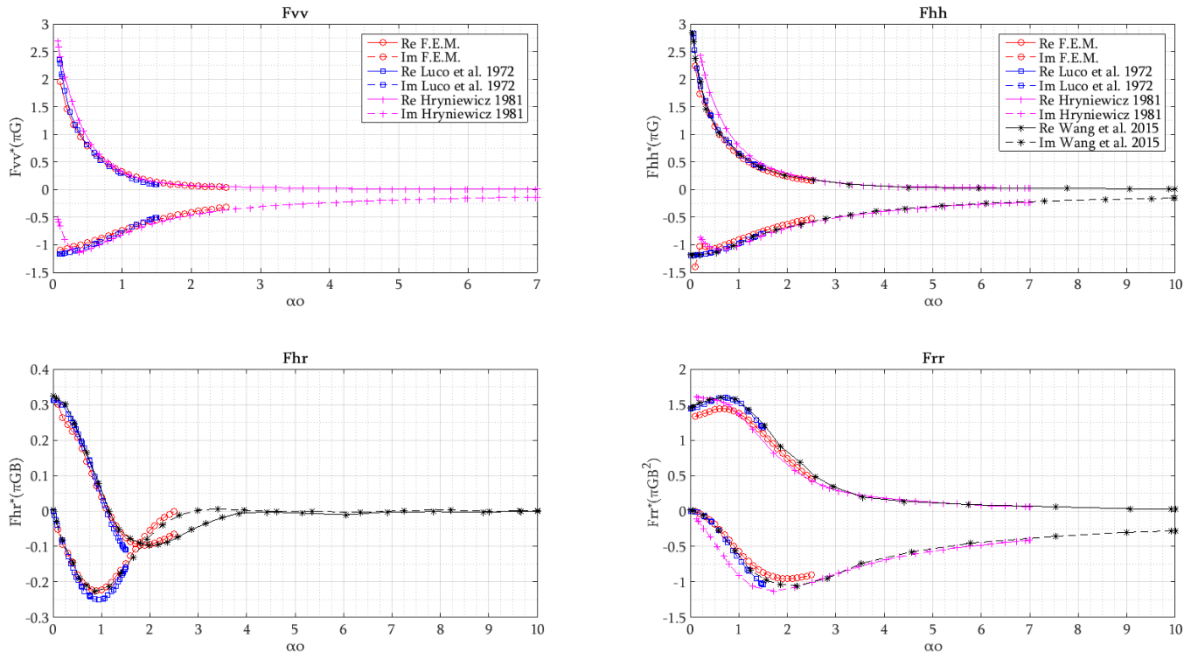

Figure 3. Validation study results for the case of an isolated, rigid, massless strip foundation bonded to an elastic half-space.

Once again, the vertical loading of an isolated surface foundation does not produce any coupling terms with the other degrees of freedom. Taking into account that the researchers' results are produced by the boundary element method, which treats accurately the wave propagation problem in half-space, it can be concluded that the finite element results are in good agreement. Therefore, the second validation study referring to a single surface foundation can also be considered successful.

3.2 Study of coupling between two foundations with different embedment depths

The main core of the present study refers to the estimation of the dynamic cross interaction between two rigid, massless, strip foundations that have different depths of embedment. Therefore, the question that must be answered is the following: How much an external loading imposed on a foundation affects the dynamic behavior of its adjacent one? In order to answer the above question two features must be examined. The first feature refers to the deviation of the behavior of each coupled foundation from the behavior of an isolated one, while the second feature refers to the coupling terms of the 6x6 flexibility matrix. Therefore, additional analyses were performed in order to calculate the flexibility matrices of an isolated deep and an isolated surface foundation as well. The distance ratio, S/L receives the following values: 0.5, 3, 5 and 10 while the soil layer's depth, H/B is constant to 2.

Based on the analyses results, it was found that the displacement field of each foundation is attributed not only on its external loading but on the adjacent foundation's loading as well. The smaller the ratio S/L is the bigger the effects of the foundation-soil-foundation interaction phenomenon are. Therefore, not only there are coupling terms between the horizontal and rocking movement of the foundation itself but coupling terms also appear between the two foundations even for the vertical excitation. In particular, Fig. 4 depicts the foundations movement at a random time frame for the case of S/L=0.5. It can be observed that even the vertical excitation causes a rocking movement not only on the foundation itself but on the adjacent foundation as well. The blue color depicts the initial position of the foundations while the cyan the deformed one.

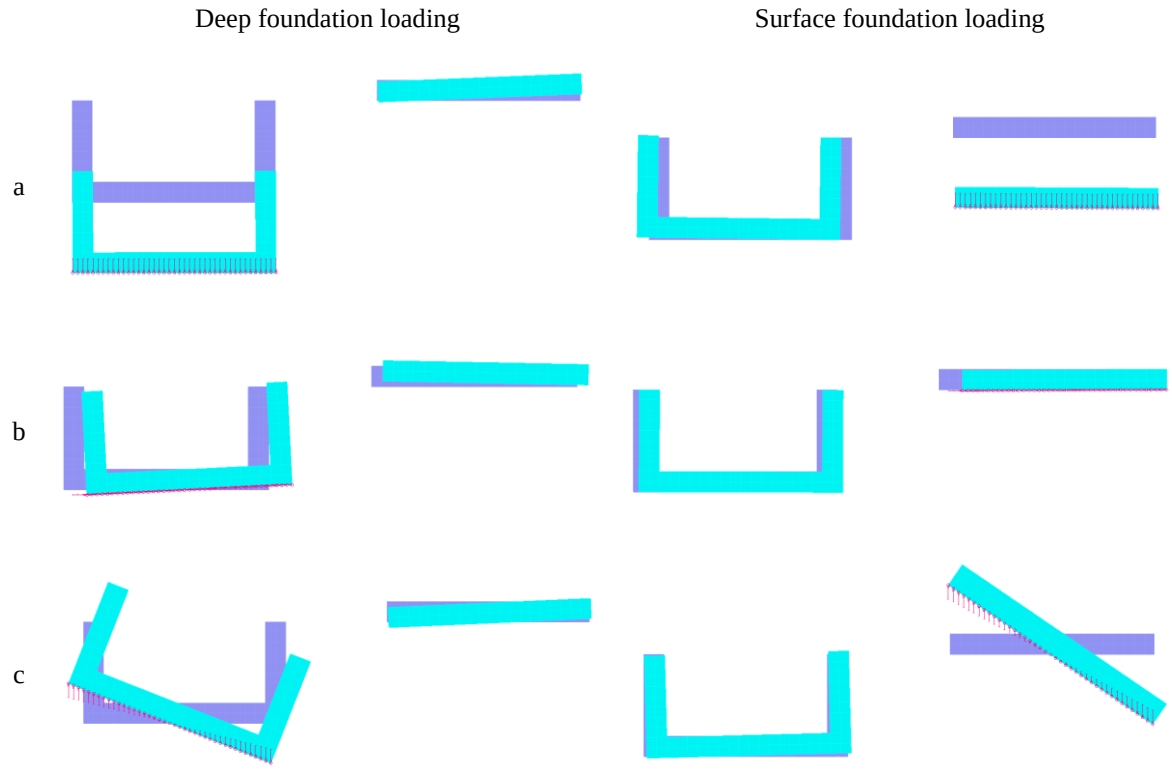

Figure 3. Foundations response at a random time frame for the case of S/L=0.5: a) vertical loading, b) horizontal loading, c) moment loading.

The foundation-soil-foundation interaction is expressed by the flexibility matrix, which is the inverse of the impedance matrix. The necessary terms, real and imaginary parts, for the definition of the impedance matrix, according to equation (1) that are related to the behavior of the deep foundation are depicted in Fig. 4 and Fig.5. The horizontal axis of the charts represents the normalized frequency αo and the vertical axis is normalized by the parameters π, G and B. The deviation from the behavior of an isolated deep foundation is observed at the coupling terms between vertical loading and translational and rocking degrees of freedom. Therefore, in the case of adjacent foundations, the vertical loading produces a complete displacement field on the foundation itself. This phenomenon is intense for small values of distance ratios, such as S/L=0.5 or 3. However, taking into account the small values of the aforementioned coupling terms in comparison to the other terms of the matrix, it can be concluded that they can be ignored, especially in the low frequency range.

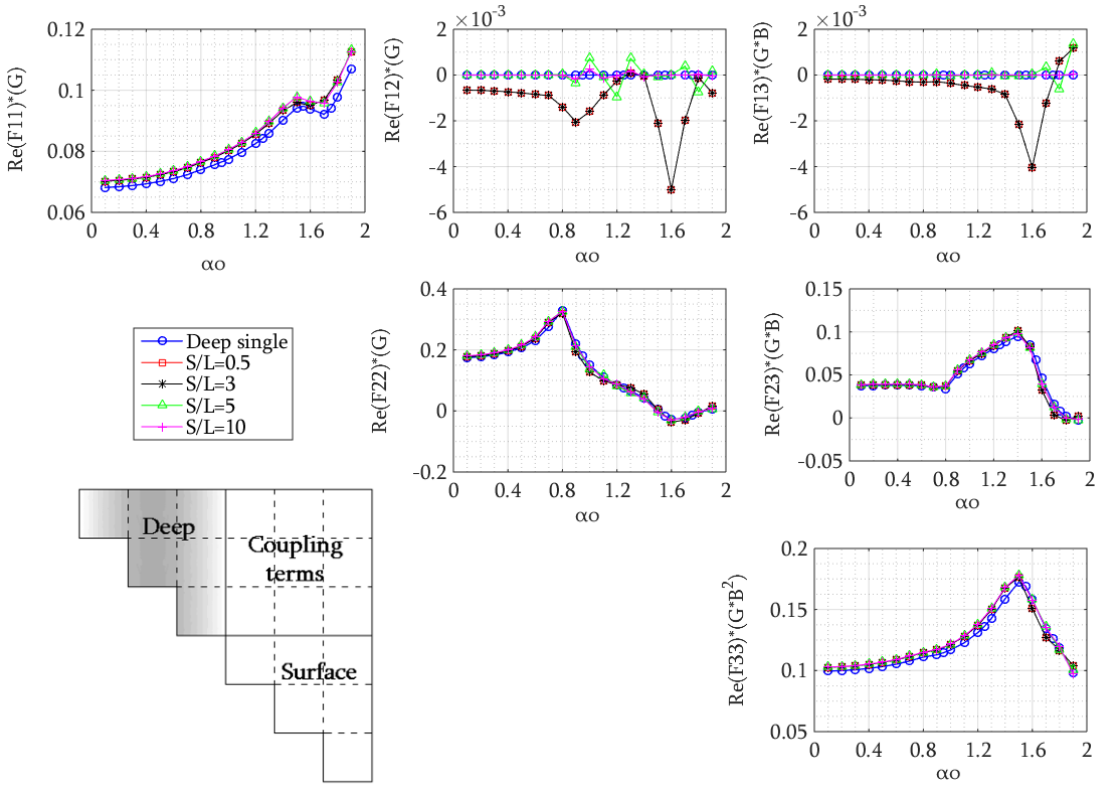

Figure 4. Real parts of the necessary terms for the definition of the flexibility matrix referring to the response of the deep foundation for various values of S/L (H/B=2).

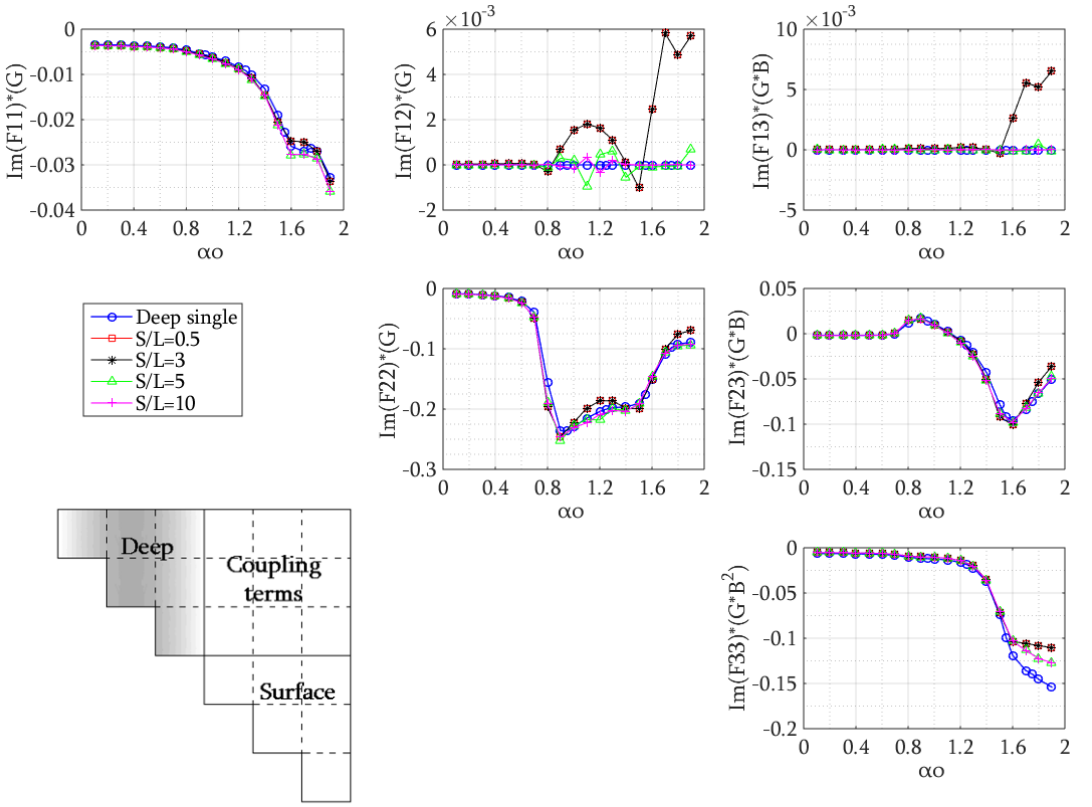

Figure 5. Imaginary parts of the necessary terms for the definition of the flexibility matrix referring to the response of the deep foundation for various values of S/L (H/B=2).

In Fig.6 and Fig.7 the real and imaginary parts of the flexibility matrix that are related to the behavior of the surface foundation are depicted. The deviation from the behavior of an isolated surface foundation is intense, especially in the high frequency range. Furthermore, the coupling terms that relate the vertical loading to the horizontal and rocking degree of freedom receive higher values than in the case of the deep foundation. Therefore, it can be concluded that the surface foundation is affected in a higher level than the deep foundation from the through-the soil- coupling.

In Fig.8 and Fig.9 the real and imaginary parts of the flexibility matrix that are related to the pure coupling between the two foundations are depicted. Their values are a significant portion of the values of the corresponding degrees of freedom of the two foundations. The coupling is intense for small values of distance ratios, S/L=0.5 and 3. Furthermore, the interaction is stronger for horizontal and moment loading than for vertical loading, especially in the high frequency range.

Consequently, for the case of a constant value of H/B=2, the through-the-soil coupling of two rigid, massless, strip foundations with different depths of embedment cannot be ignored for small values of distance ratios and in the high frequency range. Even though, the behavior of each foundation does not decline from the behavior of an isolated one, the coupling terms control the final behavior of the complex system.

Taking into account that the through-the-soil coupling of the adjacent foundations is strongest for the smallest distance ratio, another question that arises is related to the effect of the soil layer's depth ratio, H/B. Therefore, the 6x6 flexibility matrix is calculated for typical values of H/B: 2, 4, 8 and 32.

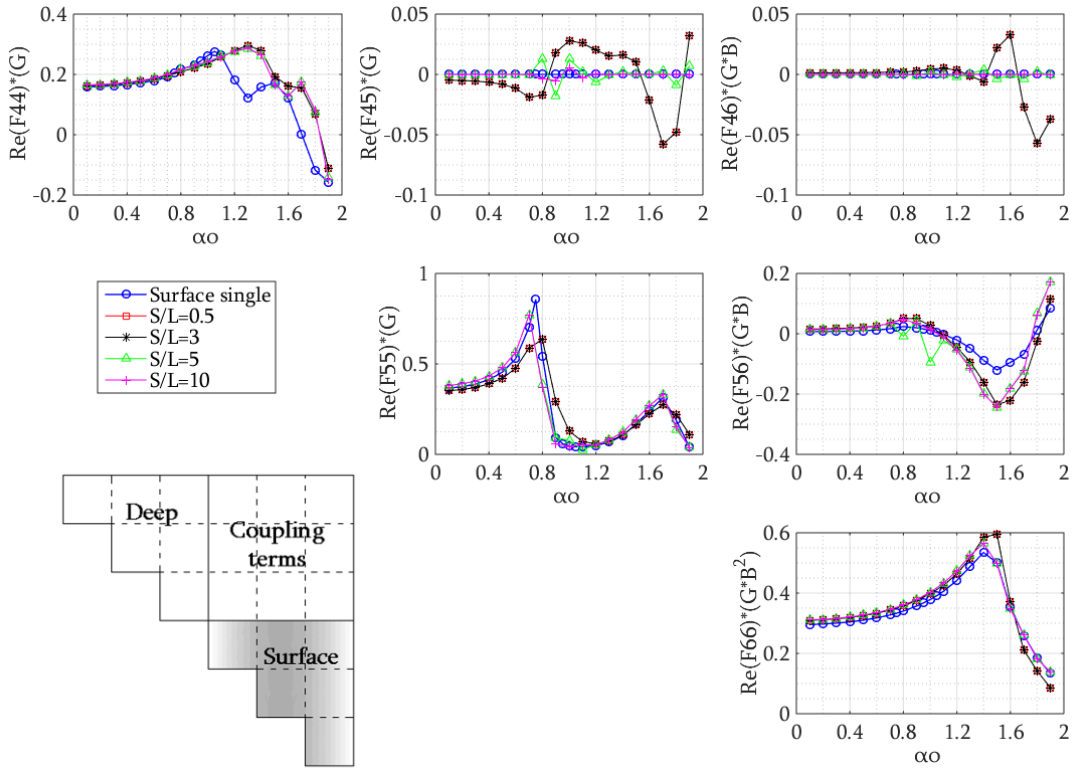

Figure 6. Real parts of the necessary terms for the definition of the flexibility matrix referring to the response of the surface foundation for various values of S/L (H/B=2).

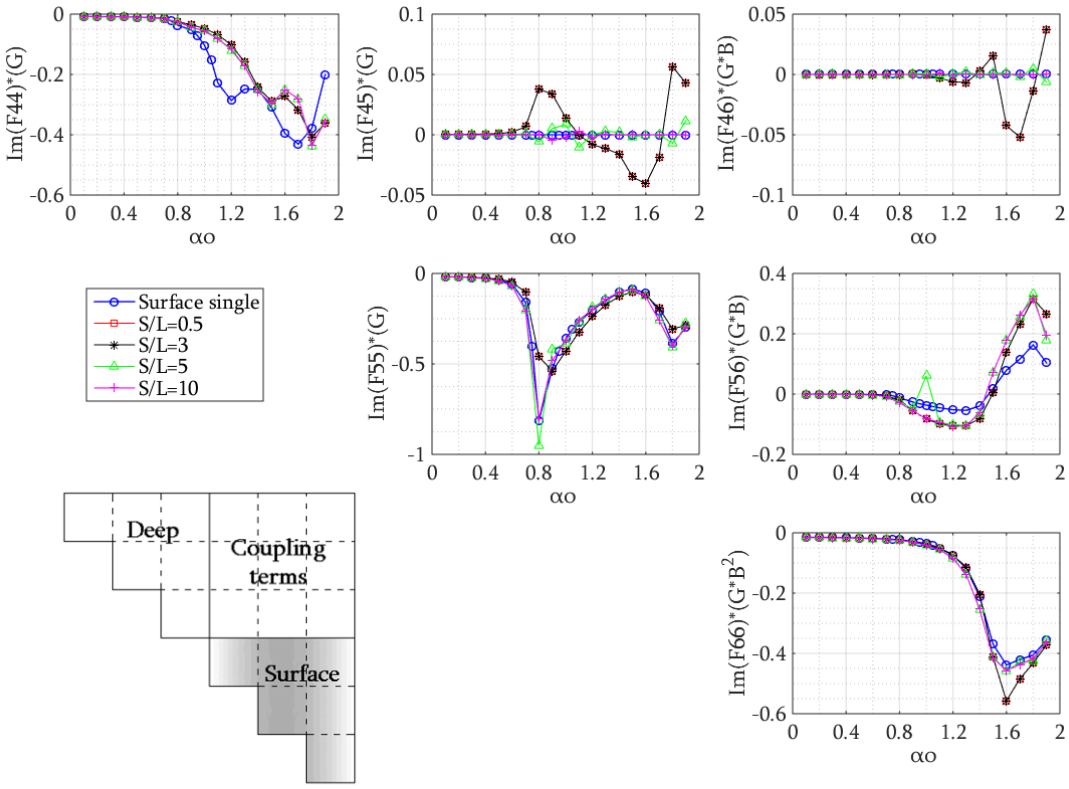

Figure 7. Imaginary parts of the necessary terms for the definition of the flexibility matrix referring to the response of the surface foundation for various values of S/L (H/B=2).

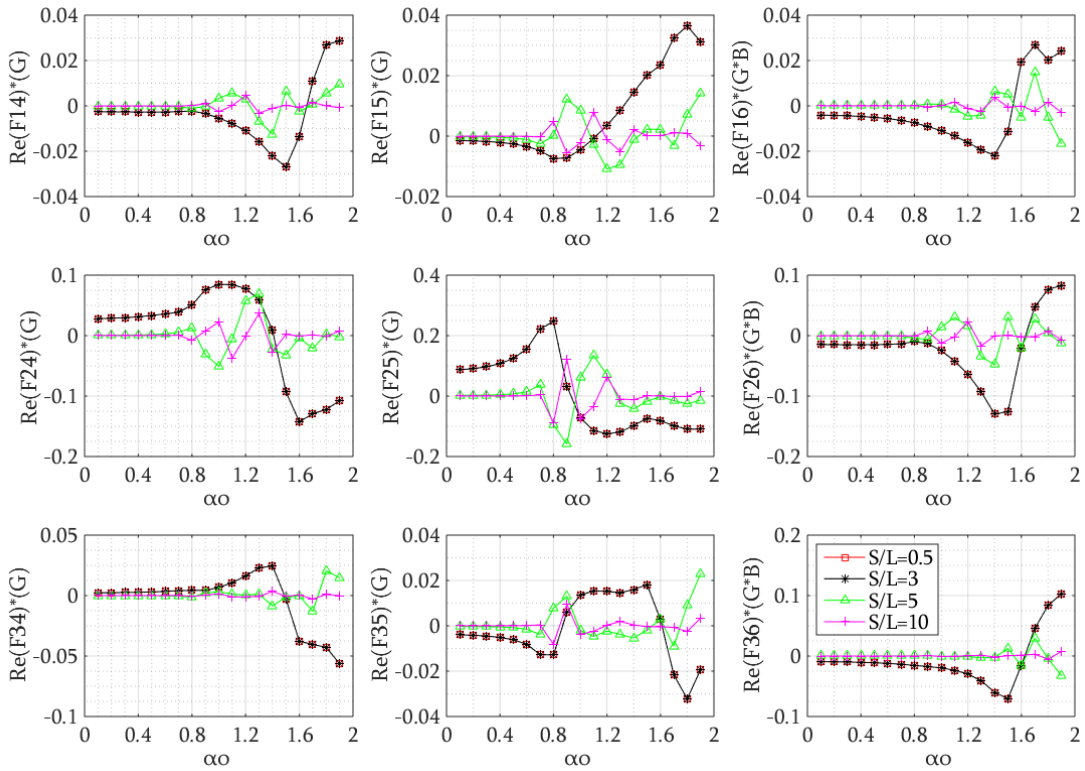

Figure 8. Real parts of the necessary terms for the definition of the flexibility matrix referring to the coupling terms between the deep and the surface foundation for various values of S/L (H/B=2).

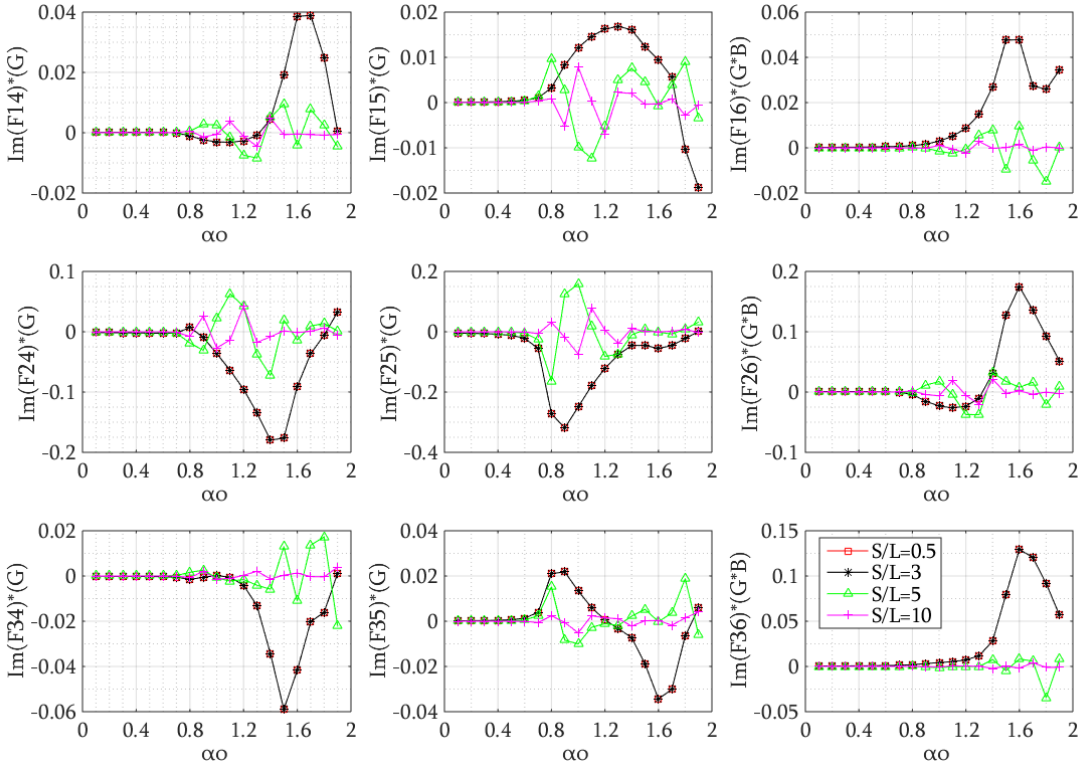

Figure 9. Imaginary parts of the necessary terms for the definition of the flexibility matrix referring to the coupling terms between the deep and the surface foundation for various values of S/L (H/B=2).

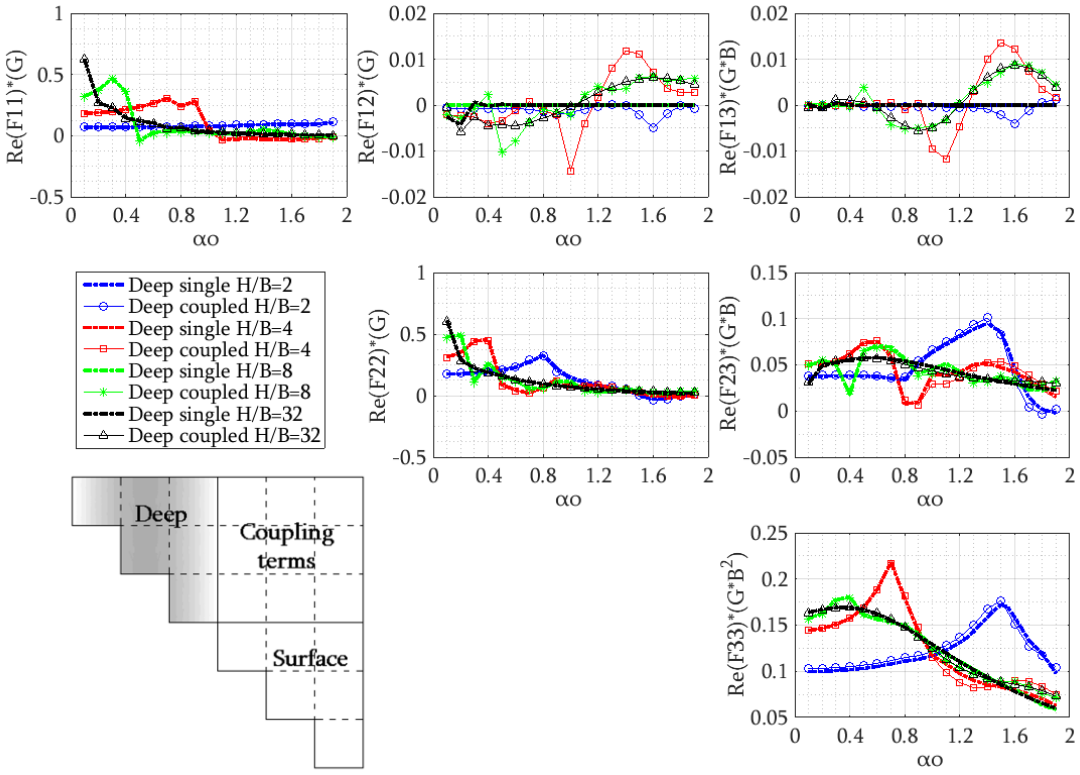

Figure 10. Real parts of the necessary terms for the definition of the flexibility matrix referring to the response of the deep foundation for various values of H/B (S/L=0.5).

In Fig.10 and Fig.11 the real and imaginary parts of the flexibility matrix related to the response of the deep foundation are depicted. The thick lines represent the behavior of an isolated deep foundation at various values of H/B. The behavior of the coupled foundations does not deviate substantially from the behavior of the isolated one, except for the coupling terms between the vertical loading and the horizontal/rotational degrees of freedom. The coupled effect cannot be ignored especially in the high frequency range for the real parts and for total frequency range for the imaginary parts. Moreover, the coupling effect does not weaken with the increase of H/B ratio.

In Fig.12 and Fig.13 the real and imaginary parts of the flexibility matrix related to the response of the deep foundation are depicted. The response of the coupled surface foundation deviates substantially from the response of the isolated foundation according to the degree of freedom excited and to the H/B ratio. In particular, the largest degree of deviation is presented for the rocking motion, while the smallest one for the vertical motion. Furthermore, the deviation is strongest for H/B=2, while it still remains significant for larger values of H/B. The coupling terms between the vertical excitation and the horizontal/rocking degree of freedom receive the highest values for small values of H/B and only in the high frequency range. The aforementioned behavior is expected for a surface foundation.

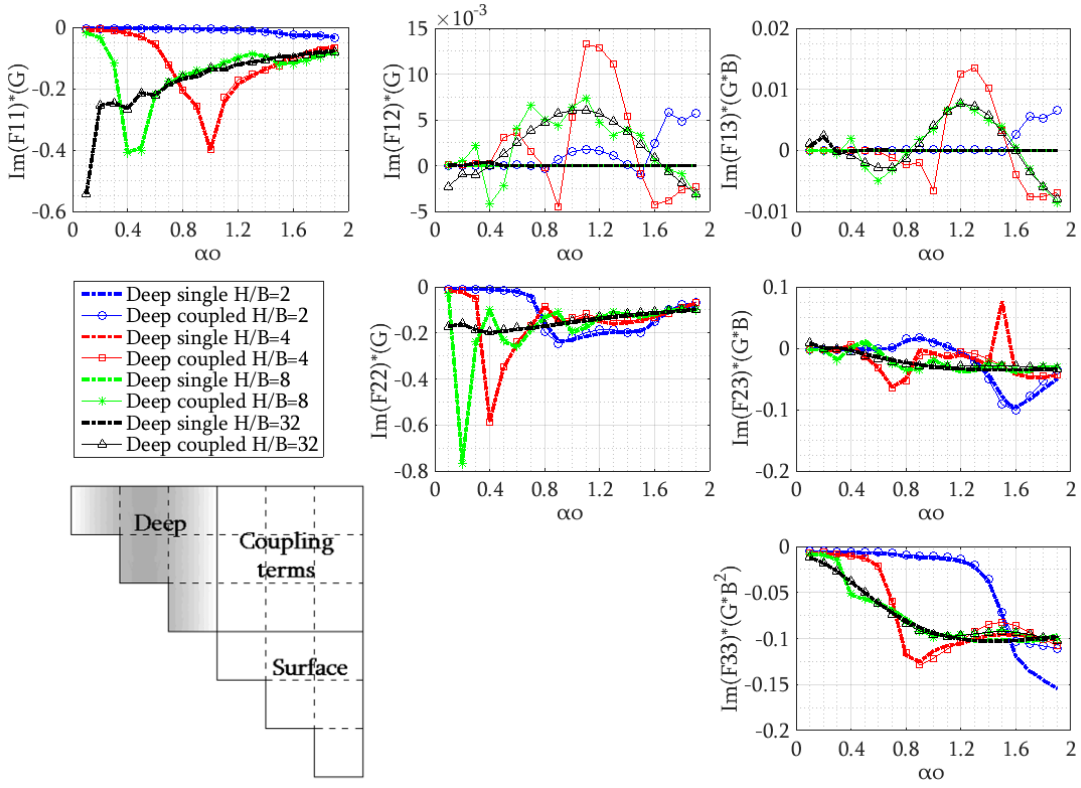

Figure 11. Imaginary parts of the necessary terms for the definition of the flexibility matrix referring to the response of the deep foundation for various values of H/B (S/L=0.5).

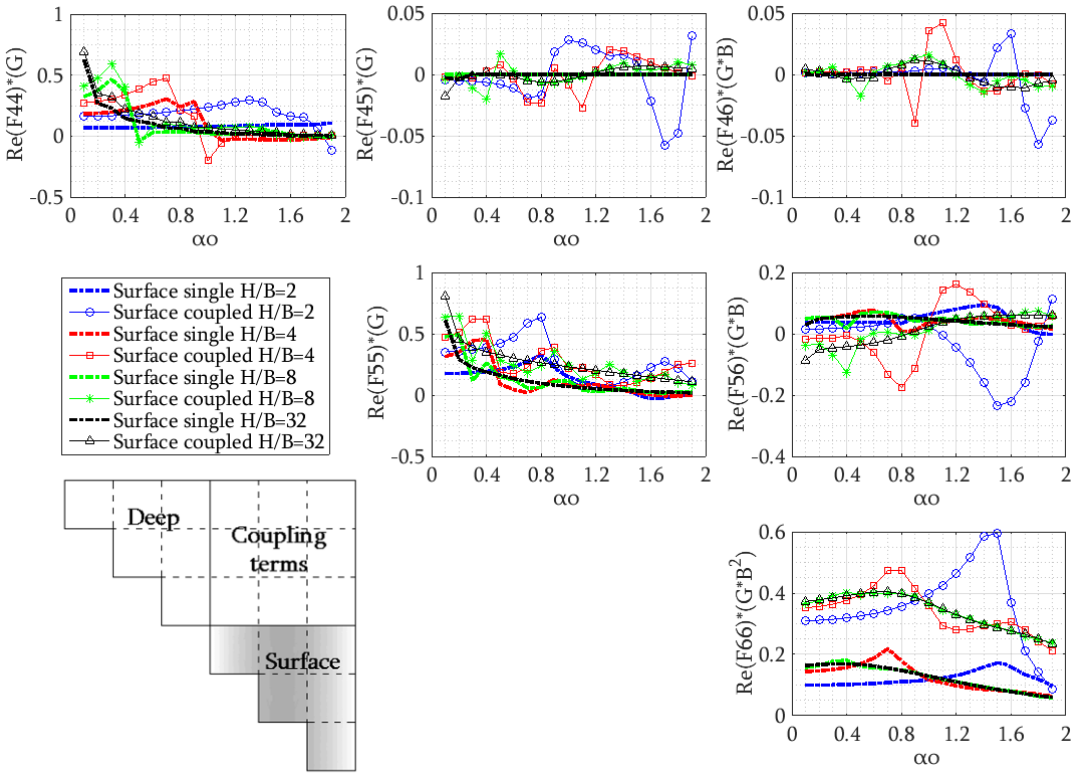

Figure 12. Real parts of the necessary terms for the definition of the flexibility matrix referring to the response of the surface foundation for various values of H/B (S/L=0.5).

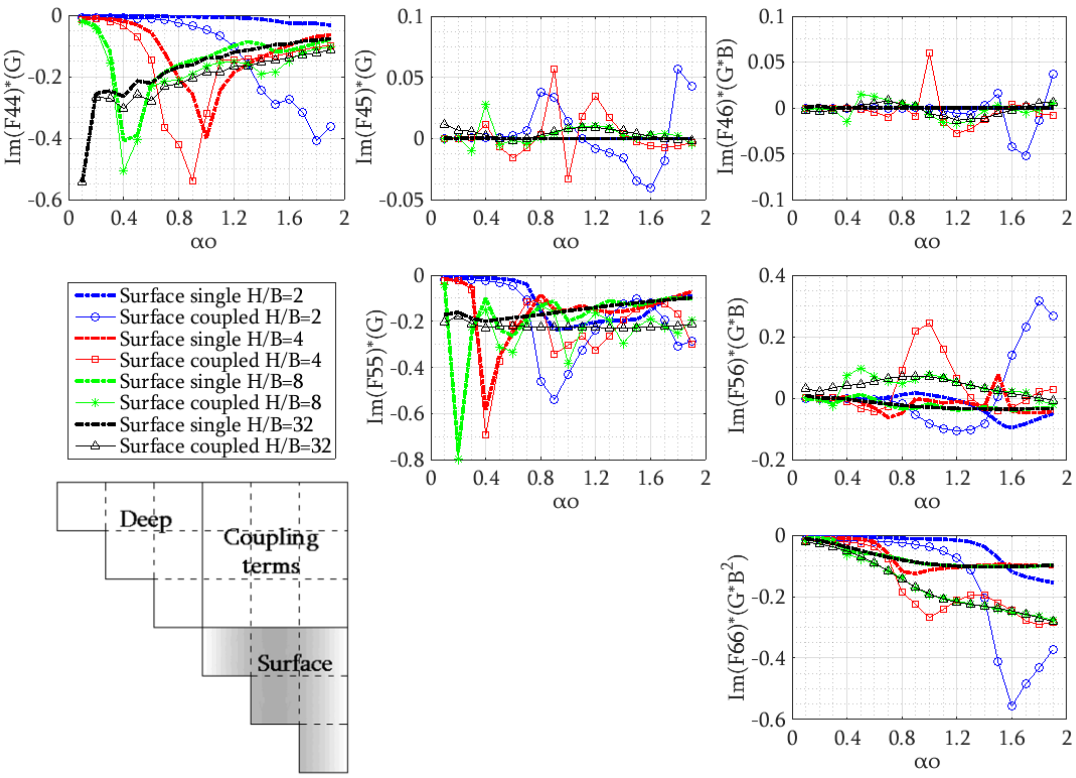

Figure 13. Imaginary parts of the necessary terms for the definition of the flexibility matrix referring to the response of the surface foundation for various values of H/B (S/L=0.5).

In Fig.14 and Fig.15 the real and imaginary parts of the flexibility matrix related to the coupling terms between the two foundations are depicted. Comparing the maximum normalized values of the coupling terms with the values of the corresponding degrees of freedom of the two foundations, it is obvious that the through-the soil coupling cannot be ignored. For the vertical loading, the coupling terms receive their smallest values for H/B=2. As the ratio H/B increases, the coupling due to vertical excitation covers the total frequency range with larger values. For horizontal loading, the coupling terms receive higher values for small ratios of H/B. Furthermore, for moment loading the interaction of the two foundations for small values of H/B dominates in the high frequency range but as H/B increases the phenomenon covers the total frequency range.

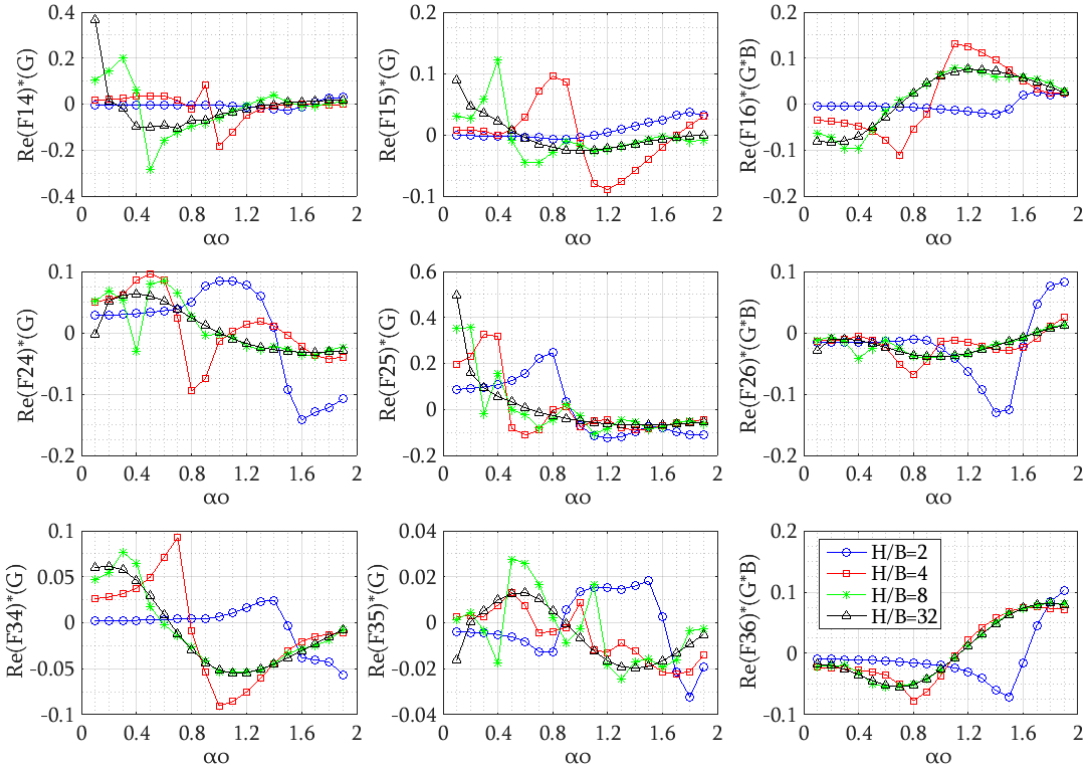

Figure 14. Real parts of the necessary terms for the definition of the flexibility matrix referring to the coupling terms between the deep and the surface foundation for various values of H/B (S/L=0.5).

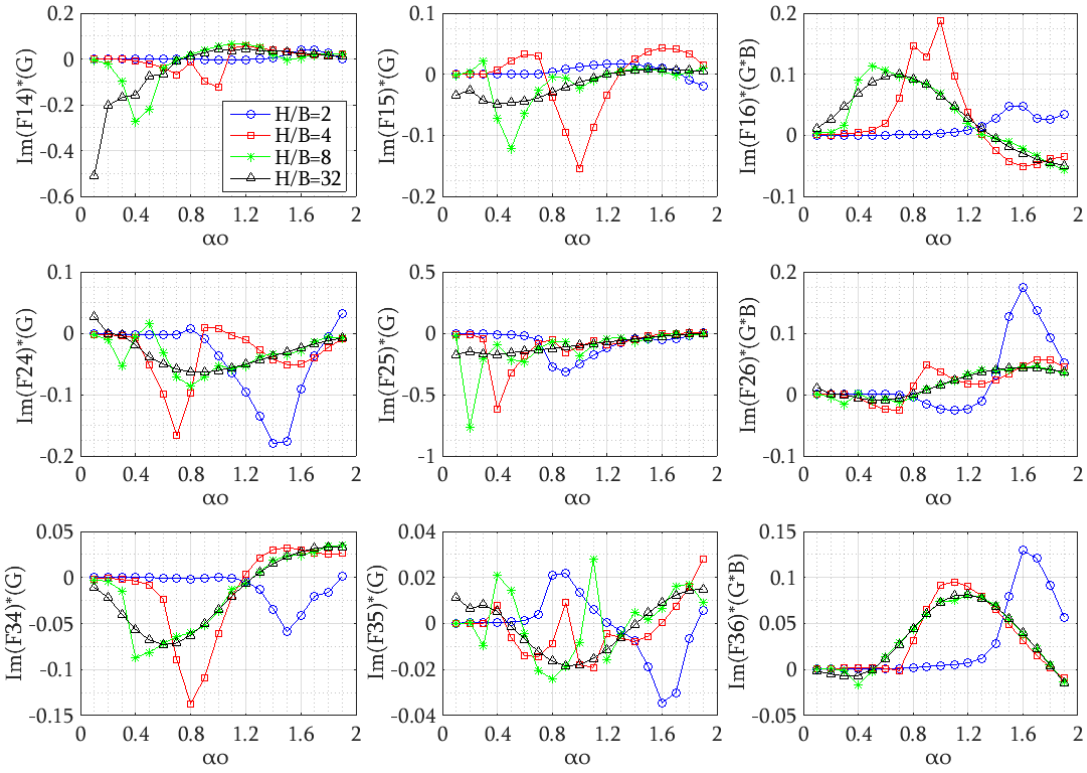

Figure 15. Imaginary parts of the necessary terms for the definition of the flexibility matrix referring to the coupling terms between the deep and the surface foundation for various values of H/B (S/L=0.5).

4 CONLCUSIONS

The through the soil coupling of two rigid, massless strip foundations with different depths of embedment has been studied by the use of the finite element method. The accuracy of the finite element model was verified by the comparison studies referring to an isolated surface and an isolated deep strip foundation. The foundation-soil-foundation is expressed by the impedance or flexibility matrix of the coupled system.

In the case of H/B=2, the response of the deep foundation deviates from the behavior of an isolated one only at the coupling terms of horizontal and rocking motion, caused by a vertical loading, especially for small values of S/L (0.5 and 3) and in the high frequency range. On the other hand, the surface foundation is more susceptible to the dynamic cross interaction. In particular, not only the aforementioned coupling terms are affected but also the terms due to horizontal and moment loading. Finally, the coupling terms between the two foundations receive important values at small distances and in the high frequency range, especially for horizontal and moment loading. Therefore, the through-the-soil coupling between the two foundations cannot be ignored for small values of distances at shallow bedrocks.

In the case of S/L=0.5, the response of the deep foundation deviates from the behavior of an isolated one only at the coupling terms of horizontal and rocking motion, caused by a vertical loading. The aforementioned deviation is obvious for all values of H/B. On the contrary, the response of the surface foundation deviates substantially for all degrees of freedom and for all values of H/B. Finally, the coupling terms between the two foundations receive high values only in the high frequency range for small values of H/B. On the contrary, as the H/B ratio increases, the coupling becomes stronger in the whole frequency range. Therefore, the

through-the-soil coupling between two closely spaced foundations cannot be ignored even for high values of H/B.

The charts of real and imaginary parts of the impedances can be used in a simplified model of springs and dashpots of the two foundations.

REFERENCES

[1] R. Betti, Effects on the dynamic cross-interaction in the seismic analysis of multiple embedded foundations. *Earthquake Engineering and Structural Dynamics*, 26, 1005-1019, 1997.

[2] J. Wang, D. Zhou and W. Liu, Simplified model for coupled vibration of adjacent strip footings. M. Papadrakakis, V. Papadopoulos, V. Plevris eds. *5th ECCOMAS Thematic Conference on Computational Methods in Structural Dynamic and Earthquake Engineering (COMPDYN 2015)*, Crete Island, Greece, May 25-27, 2015.

[3] L.G. Tham, J. Qian and Y.K. Cheung, Dynamic response of a group of flexible foundations to incident seismic waves. *Soil Dynamic and Earthquake Engineering*, 17, 127-137, 1998.

[4] A. Bharadwaj and S. Ahmad, Rocking impedance of embedded strip foundations in layered soil. *Journal of Geotechnical Engineering*, 118(5), 796-813, 1992.

[5] D.L. Karabalis and M. Mohammadi, 3-D dynamic foundation-soil-foundation interaction on layered soil. *Soil Dynamics and Earthquake Engineering*, 17, 139-152, 1998.

[6] J.E. Luco and R.A. Westmann, Dynamic response of a rigid footing bonded to an elastic half-space. *Journal of Engineering Mechanics Division ASME*, 39(2), 527-534, 1972.

[7] B. Suhol and L.C. Hong, Coupled horizontal-rocking impedance functions for embedded square foundations at high frequency factors. *Journal of Earthquake Engineering*, 3(4), 561-587, 1999.

[8] P. Karasudhi, L.M. Keer and S.L. Lee, Vibratory motion of a body on an elastic half plane, *Journal of Applied Mechanics ASME*, 35(4), 697-705, 1968.

[9] Z. Hryniewicz, Dynamic response of a rigid strip on an elastic half-space. *Computer methods in applied and mechanical engineering*, 25, 355-364, 1981.

[10] G.M. Wickham, The forced two dimensional oscillations of a rigid strip in smooth contact with a semi-infinite elastic solid. Mathematical Proceedings of Cambridge Philosophical Society, 81 (2), 291-311, 1977.

[11] G. Gazetas and J.M. Roesset, Forced vibrations of strip footing on layered soils. *Proceedings of Methods in Structural Analysis ASCE*, 1, 115-131, 1976.

[12] O. Von Estorff and G. Schmid, Application of the boundary element method to the analysis of the vibration behavior of strip foundations on a soil layer. *Proceedings of the International Symposium on Dynamic Soil-structure interaction*, A.A. Balkema, Minneapolis, Minn., 11-17, 1984.

[13] J. Dominguez and R. Abascal, Seismic response of strip footings on zoned viscoelastic soils. *Journal of Engineering Mechanics*, 115, 913-934, 1989.

[14] A. Jendoubi, F. Legeron and M. Karray, Numerical simulation of displacement functions of strip footings. *Geotechnical Earthquake Engineering and Soil Dynamics IV Congress*, 1-10, 2008.

[15] T.A. Cruze and F.J. Rizzo, A direct formulation and numerical solution of the general transient elastodynamic problem. *International Journal of Mathematical Analysis and Applications*, 22, 244-259, 1968.

[16] J.E. Luco and L. Contesse, Dynamic structure-soil-structure interaction. *Bulletin of the Seismological Society of America*, 63(4), 1289-1303, 1973.

[17] H.L. Wong, Dynamic soil-structure interaction. *Report EERL-75-01*, Earthquake Engineering Research Lab., California Institute of Technology, Pasadena, California, 1975.

[18] H.L. Wong and M.D. Trifunac, Two dimensional, antiplane, building-soil-building interaction for two or more buildings and for incident plane SH-waves. *Bulleting of the Seismological Society of America*, 65(6), 1863-1885, 1975.

[19] M. Murakami and J.E. Luco, Seismic response of a periodic array of structures, *Journal of the Engineering Mechanics Division ASCE*, 103 (EM5), 967-977, 1977.

[20] J.T. Lysmer, T. Udaka, H.B. Seed and R. Hwang, A computer program for complex response analysis of soil-structure interaction. *Report EERC 74-4*, Earthquake Engineering Research Center, University of California, Berkeley, CA, 1975.

[21] V.C. Liang, Dynamic response of structures in layered soils. *Report 1274-10*, Department of Civil Engineering, Massachusetts Institute of Technology, Cambridge, 1974.

[22] M.N. Aydinoglu and A. Cakiroglu, Dynamic interaction between soil and a group of buildings. *Proceeding of the 6th World Conference on Earthquake Engineering*, New Delhi, India, 2, 1596-1601, 1977.

[23] S. Nakai and N. Fukuwa, Boundary element analysis of approximate three-dimensional soil-structure interaction. *Proceedings of the 6th Japan Earthquake Engineering Symposium*, Tokyo, Japan, 1633-1640, 1982.

[24] H. Antes and V. O. Estorff, Dynamic soil-structure interaction by BEM in the time and frequency domain. *8th European Conference on Earthquake Engineering*, Lisbon, Portugal, 1986.

[25] F.T. Kokkinos and C.C. Spyrakos, Dynamic analysis of flexible strip-foundations in the frequency domain. *Computers and Structures*, 39 (5), 473-482, 1991.

[26] D.L. Karabalis and D.E. Beskos, Dynamic response of 3-D embedded foundations by the boundary elements method. *Journal of Computer Methods in Applied Mechanics and Engineering*, 56, 91-119, 1986.

[27] G. Gazetas, R. Dobry and L.J. Tassoulas, Vertical response of arbitrarily shaped embedded foundations. *Journal of Geotechnical Engineering*, ASCE, 111(6), 750-777, 1985.

[28] G. Gazetas and L.J. Tassoulas, Horizontal stiffness of arbitrarily shaped embedded foundations. *Journal of Geotechnical Engineering*, ASCE, 113(5), 440-457, 1987.

[29] G. Gazetas and L.J. Tassoulas, Horizontal damping of arbitrarily shaped embedded foundations. *Journal of Geotechnical Engineering*, ASCE, 113(5), 458-475, 1987.

[30] R.K.N.D Rajapakse and A.H. Shah, Impedances of embedded rigid strip foundations. *Earthquake Engineering and Structural Dynamics*, 16, 255-273, 1988.

[31] E. Hatzikonstantinou, L.J. Tassoulas, G. Gazetas, P. Kotsanopoulos and M. Fotopoulou, Rocking stiffness of arbitrarily shaped embedded foundations. *Journal of Geotechnical Engineering*, 115(4), 457-472, 1989.

[32] M. Fotopoulou, P. Kotsanopoulo, G. Gazetas and L.J. Tassoulas, Rocking damping of arbitrarily shaped embedded foundations. *Journal of Geotechnical Engineering*, 115(4), 473-490, 1989.

[33] Y. Wang and R.K. Rajapakse, Dynamics of rigid strip foundations embedded in orthotropic elastic soils. *Earthquake Engineering and Structural Dynamics*, 20, 927-947, 1991.

[34] E. Esmaeilzadeh Seylabi, C. Jeong and E. Taciroglu, On numerical computation of impedance functions for rigid soil-structure interfaces embedded in heterogeneous half-spaces. *Computers and Geotechnics*, 72, 15-27, 2016.

[35] T. Kobori, Y. Shinozaki and A. Mita, Soil-structure interaction analysis by boundary integral equation method. *Proceedings of the 6th Japan Earthquake Engineering Symposium*, Tokyo, Japan, 1982

[36] S. Nakai, N. Fukawa and M. Hasegawa, Approximate three-dimensional analysis of embedded structures. *Proceedings of the 8th World Conference on Earthquake Engineering*, San Francisco, California, 1984.

[37] A.S.M. Israil and S. Ahmad, Dynamic vertical compliance of strip foundations in layered soils. *Earthquake Engineering and Structural Dynamics*, 18, 933-950, 1989.

[38] S. Ahmad and A. Bharadwaj, Horizontal impedance of embedded strip foundations in layered soil. *Journal of Geotechnical Engineering*, 117(7), 1021-1041, 1991.

[39] V.G. Terzi, Impedance functions of adjacent strip foundations. *Proceedings of the 6th ECCOMAS Thematic Conference on Computational Methods in Structural Dynamic and Earthquake Engineering (COMPDYN2017),* Rhodes Island, Greece, 15-17 June, 2017.

[40] V.G. Terzi, Impedance functions of adjacent embedded strip foundations. *Proceedings of the 16th European Conference on Earthquake Engineering*, Thessaloniki, Greece, 18-21 June, 2018.

[41] Smith W (1974). A non-reflecting plane boundary for wave propagation problem, *Journal of Computer Physics*, 15: 492-503.

[42] Roesset J.M, Ettouney M.M (1977). Transmitting boundaries: comparison, *Journal of numerical and analytical methods in geomechanics*, 1(2): 151-176.

[43] J. Lysmer and R.L. Kuhlemeyr, Finite dynamic model for infinite media. *Journal of the Engineering Mechanics Division ASCE*, 95, 859-878, 1969.

[44] Huh Y (1986). Die Anwendung der Randelementmethode zur Untersuchung der dynamischen Wechselwirkung zwischen Bauwerl und geschichtetem Baugrund, *RUB, SFB 1551- Mitteilung*, 86 (13).

[45] J.E. Luco and R.A. Westmann, Dynamic response of a rigid footing bonded to an elastic half-space. Journal of Engineering Mechanics Division ASME, 39(2), 527-534, 1972.

COMPDYN 2019
7th ECCOMAS Thematic Conference on
Computational Methods in Structural Dynamics and Earthquake Engineering
M. Papadrakakis, M. Fragiadakis (eds.)
Crete, Greece, 24–26 June 2019

IMPACT OF SEISMIC UPLIFT AND SOIL SUPPORT ON THE ACCELERATION OF A LIQUID STORAGE TANK

Diego Hernandez-Hernandez[1], **Tam Larkin and Nawawi Chouw**
University of Auckland
Department of CEE
20 Symonds Street Auckland
[1]dher840@aucklanduni.ac.nz
{t.larkin, n.chouw}@auckland.ac.nz

Abstract

A rigid base is assumed in most seismic studies of liquid storage tanks. Additionally, recent studies have shown that permitting uplift can significantly reduce the damage to tanks. Uplift is the transient partial separation of the tank base from the supporting foundation. However, uplift of storage tanks is still not well studied and a rigid base is assumed in numerical studies. In this work, the simultaneous effect of uplift and a soil foundation are utilised to evaluate experimentally the effect of these two factors on the acceleration in the tank wall. A low-density polyethylene tank and a shake table were employed. Stochastically generated seismic excitation is employed based on the New Zealand design standard, NZS 1170.5, for medium soil, classification B. Three base conditions were considered: 1) fixed-base tank on a rigid support, 2) free-base tank on a rigid support and 3) free-base tank on a flexible support.

To simulate the rigid support condition, the tank is resting on a steel plate rigidly attached to the shake table. A laminar box infilled with sand is utilised to represent a flexible soil condition. Results revealed that the highest acceleration at the tank top occurred when the tank is resting freely on a rigid supporting base. Furthermore, for this case the maximum uplift occurred at the same time as the maximum acceleration. However, for the case of a flexible support, the maximum acceleration occurred at the tank base and did not coincide with the time of maximum uplift. The maximum uplift occurred for a flexible supporting base and is not related to the maximum acceleration at the tank top. Thus, the distribution of the maximum acceleration, and hence uplift, depends significantly on the support condition.

Keywords: Liquid storage tank, Uplift, Soil-Structure Interaction, Earthquake Engineering

1 INTRODUCTION

Liquid storage tanks are required to supply and regulate water, petrol or other chemicals following damaging seismic events. Hence, their integrity after emergencies is essential, especially for the fast recovery of the affected area. Experiences with strong earthquakes have repeatedly shown the vulnerability of tanks under dynamic loads. The vulnerability lies from the complex uncertainties originating from the interaction between the liquid, the tank wall and the supporting soil. However, these complications are usually incorporated by simplifications in the design analysis and may not represent adequately the real behaviour of the tank under seismic loads.

Damage to a tank wall is generally associated with high concentration of both hoop and axial stress. Hoop stress is related to the hydrodynamic pressure due to the liquid. Axial stress is associated with uplift, which is the transient separation of a part of the tank base from the supporting foundation. Uplift in liquid storage tanks depends on several parameters that include the dimensions of the tank, the ratio of the tank radius to the liquid height (aspect ratio *h/r*), the stiffness of the base plate and supporting foundation. Another factor that may amplify the risk of failure is soil-structure interaction (SSI).

SSI involves factors that are not generally addressed in a holistic design. The majority of studies in this topic have been numerical, but opinions differ on some of the key parameters of SSI. On the one hand, a flexible support condition is beneficial to the tank response, i.e. the magnitude of acceleration and stresses are reduced [1–3]. According to Larkin [4], on the other hand, the tank response depends on the soil and tank properties. Additionally, the changes in the fixed base natural frequencies that may occur produce significant changes in the system response. If the natural frequency of the tank is close enough to the predominant frequency of the soil site, amplification in the response may occur [5–7]. Hence, during the design phase, assuming a rigid support condition does not always guarantee conservative results [8].

Limited experimental studies have been conducted considering SSI [9-14]. Ormeño et al. [10] utilised an aluminium tank on a shake table, focusing on the development of the acceleration of the tank and associated uplift. To simulate a flexible base support, a rigid box with sand was utilised. It was concluded that the maximum acceleration for aspect ratios $h/r = 1$ and 2.5, when SSI is considered, presented similar magnitude. However, the maximum acceleration is less than that of the case when the tank is resting on a rigid base.

The present paper evaluates, through an experimental study using a laminar box, the combined effects of uplift and a flexible support foundation (sand) on the earthquake-induced acceleration of a storage tank.

2 EXPERIMENTAL SET-UP

2.1 Tank model

A low-density polyethene (LDPE) tank, 750 mm in height and 450 mm in diameter, is used to model a prototype steel tank. Neglecting the influence of oscillations at the fluid free surface, i.e. the convective mode of response, the model can be analysed as a Single-Degree-of-Freedom (SDOF) system based only on the impulsive inertia forces on the tank wall [3]. Thus, the similitude conditions may be defined using the Buckingham π theorem, along with the Cauchy number for a SDOF system [15]. The model and prototype properties are shown in Table 1, and the scale factors are shown in Table 2. The fundamental periods were estimated according to the work reported in NZSEE [16], for an anchored-roofless tank on a rigid support condition.

	Model	Prototype
Material	LDPE	Steel
Elastic Modulus E (GPa)	1.12	210
Radius r (m)	0.225	4.5
Liquid Height H (m)	0.675	13.5
Maximum liquid Mass (kg)	107	858 833
Fundamental period (s)	0.034	0.14

Table 1. Properties of the model and prototype

Dimension	Scale factor
Length	20
Mass	8000
Time	4.2
Acceleration	1.16

Table 2. Scale factors

Two support conditions for the tank were utilised, i.e. 1) a rigid steel plate fixed to the shake table, representing a rigid support condition, i.e. rock, Figure 1(a); 2) sand contained in a laminar box (described in Section 2.3) i.e. a flexible support condition representing a soil site, **Error! Reference source not found.**(b). All tests were performed with a liquid height of 675 mm, which corresponds to an aspect ratio of three. Three tank base conditions are utilised: 1) The tank is fixed to the rigid steel plate, 2) the tank is unanchored and is placed directly on the rigid steel plate, and 3) the tank is resting freely on sand in the laminar box.

Two columns of three accelerometers, i.e. at 0° and 180°, see Figure 1(c), at heights of 30 mm, 375 mm and 700 mm, were attached to the external face of the LDPE tank, see Figure 1(c). All the accelerometers were oriented at the same direction, i.e. positive in the direction from 180° to 0 °. In both support cases (rigid and flexible), an accelerometer was attached to the shake table.

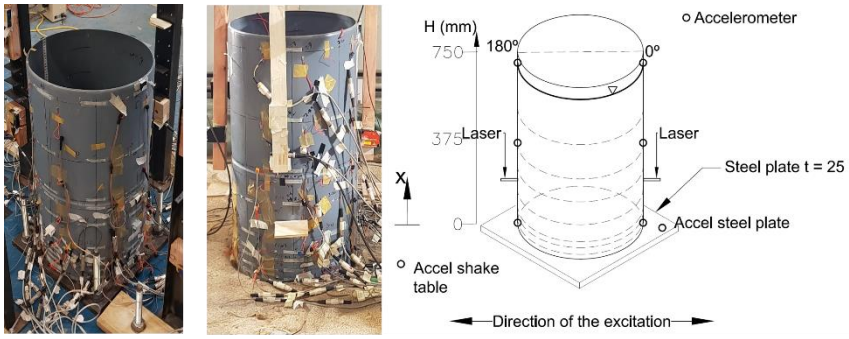

Figure 1. LDPE tank (a) fixed and free-rigid base, (b) free-flexible base, and (c) measurements locations.

2.2 Anchorage

The LDPE tank was fixed to a rigid steel plate of $t = 25\ mm$ thickness through eight M8 bolts. A round steel plate of 3 mm thickness was placed inside the tank to avoid stress concentration on the base plate due to the pressure from the bolts, as shown in Figure 2. Hence, modifications to the tank wall stiffness were avoided. An extra accelerometer was placed on the steel plate to record the acceleration of the tank base (see Figure 1(c)).

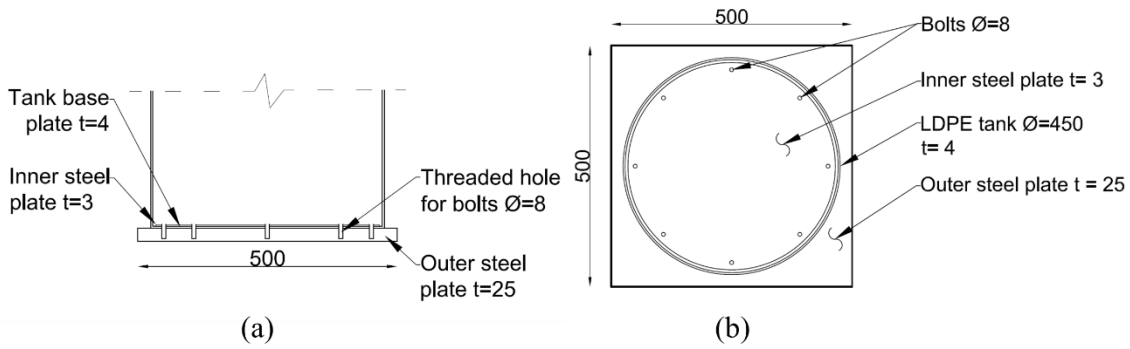

Figure 2. Fixing of LDPE tank base (a) Front view, and (b) top view (units in mm).

2.3 Laminar box

A 2 m cubic laminar box is used to simulate the earthquake-induced shear deformation of the sand that results from seismic motion (Fig. 3). The maximum permitted displacement of each layer of the laminar box is 175 mm in the direction of the shake table motion. More information regarding the characteristics of the box can be found in [17]. The box is filled to a height of 1.43 m with sand with an average density of 1.58 $\mathrm{t/m^3}$. One accelerometer was placed on the sand surface, next to the tank base.

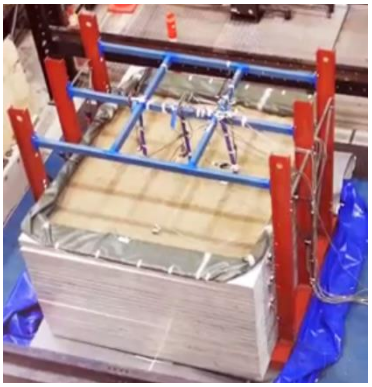

Figure 3. Cubic laminar box filled with sand.

The shear wave velocity was measured at the beginning of the experiment by creating an impulse, to ascertain the shear stiffness of the sand. The experimental set-up and the recorded accelerations are shown in Figure 4. A circular steel plate was placed on the sand surface. A horizontal impact from a hammer on the steel plate produces a downward travelling shear wave that was recorded by two accelerometers a distance of $700\ mm$ apart. The average shear wave velocity v_{s_m} may be estimated by dividing the travel distance ΔL by the travel time Δt. From Figure 4, the travel time is $\Delta t = 1.1554 - 1.1514 = 0.004\ s$. The estimated mean velocity is $v_{s_m} = 175\ m/s$. An empirical method to estimate the shear wave velocity is by Equation (1) [18]:

$$v_s = \sqrt{\frac{D_r + 25}{100}} \sqrt{\frac{0.422 \times 10^6\ (\sigma'_m)^{\frac{1}{2}}}{\rho}} \tag{1}$$

where v_s is the shear wave velocity in m/s, D_r is the sand relative density, $\mathrm{D_r} = 56\%$; ρ is the sand mass density, 1580 $\mathrm{kg/m^3}$; σ'_m is the mean effective stress at the respective depth, estimated as $\sigma'_\mathrm{m} = (\sigma'_\mathrm{v} + 2\sigma'_\mathrm{h})/3$; σ'_v is the effective vertical stress and σ'_h is the horizontal effective stress.

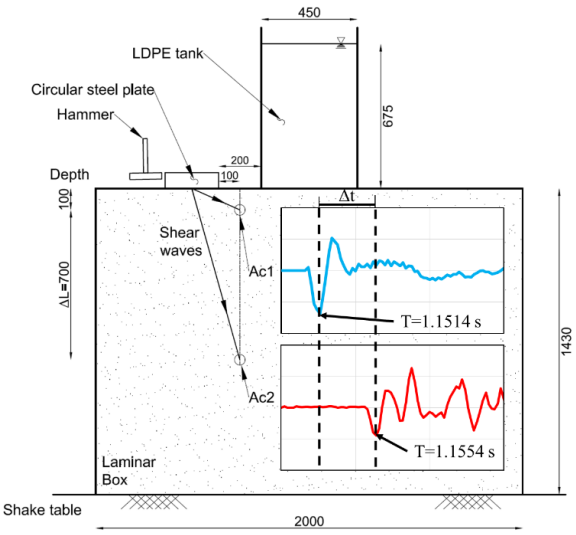

Figure 4. Configuration of impulse test and shear waves recorded by both accelerometers (units in mm).

The stresses may be estimated by elastic solutions for a uniform surface stress over a circular area, in this case, $675\ kPa$. The mean stress is $\sigma'_{m_{100}} = 405\ Pa$ and $\sigma'_{m_{800}} = 135\ Pa$. Hence, the shear wave velocity is $v_{s_{100}} = 222\ m/s$, $v_{s_{800}} = 169\ m/s$, and $v_{s_m} = 196\ m/s$. The subscript indicates the depth from the ground surface and the "m" indicates the mean value. The estimated mean shear wave velocity is similar to the result obtained experimentally.

2.4 Excitation applied

The shake table excitation was stochastically simulated based on the target spectrum for a medium fine grained soil, i.e. classification C of the design standard NZS 1170.5, Figure 5(a). The target spectrum was calculated utilising the NZSEE recommendations for time domain analysis of liquid storage tanks [16], [19]. However, the NZ 1170.5 code specifies the lower limit of the frequency range of interest $T_{min} > 0.4\ s$, and Ormeño, et al. [20] found application of this lower limit of period underestimates the response of some tanks. The $0.4\ s$ limit was established for structures, not specifically tanks, because periods below this figure are difficult to determine and hence have relatively high uncertainty, especially when structures present complex geometries and diverse materials. For tanks, which usually have a regular geometry and are made of a single material, this restriction may lead to an underestimate of the response. Thus, the lower limit of frequency given by NZS 1170.5 was not applied in this work. The lower limit applied was $0.4T_{pro} = 0.057\ s$ and the upper limit was $1.3T_{pro} = 0.186\ s$, as specified in the recommendations of NZSEE [14]. The response spectrum of the simulated excitation and the target spectrum are shown in Figure 5(b). The range of frequencies of interest for matching the response and the natural period of vibration of the tank with an assumed fixed base are shown.

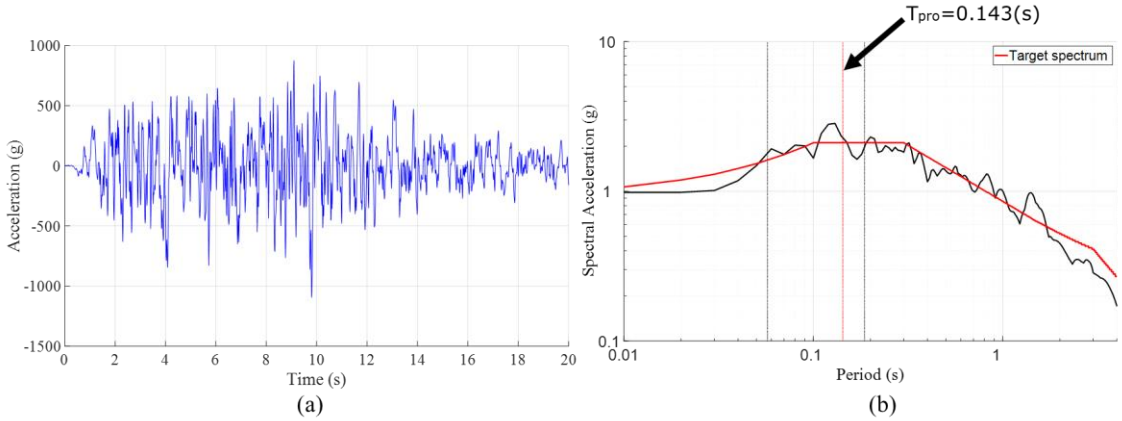

Figure 5. Base excitation. (a) Simulated motion for a medium soil condition defined by NZS 1170.5 and (b) response spectrum of the simulated ground motion and target spectrum of the NZS 1170.5.

3 RESULTS

Table 3 shows the maximum acceleration recorded at the tank base. For the rigid base conditions, the maximum acceleration is given by the accelerometer on the steel plate; for the flexible base condition, by the accelerometer on the sand surface. The results hereafter have been normalised by the maximum base acceleration to remove minor fluctuations in the applied motion.

	Base case		
	Fixed rigid	Free rigid	Flexible
Maximum acceleration (g)	0.14	0.13	0.17

Table 3. Maximum acceleration at the base of the tank

Table 4 shows the normalised absolute maximum accelerations for the bottom, middle and top of the tank, for the three base conditions. For the fixed base condition, the amplification of acceleration at the tank top is 25% referred to the acceleration at the tank base. For the free-base case, on a rigid foundation, the tank top experienced the highest amplification of 260% with respect to the acceleration at the tank base. Thus, if the tank is resting on a rigid foundation, fixed or free to uplift, the design of the tank wall should recognise the acceleration is not constant over the height of the tank.

The normalised acceleration of the tank resting on sand has two main differences compared with the results of the tank on a rigid foundation. Firstly, the highest acceleration of the tank on sand occurred at the bottom of the tank, i.e. 30 mm from the supporting base, that is 81% higher than the acceleration of the sand surface, adjacent to the tank base. This result is perhaps counter intuitive, i.e. the maximum acceleration may be expected to occur at the top of the tank. Based on the experiment results, the interaction of the supporting soil and the tank base resulted in differences in the development of the acceleration along the tank height.

Secondly, the maximum amplification of the base acceleration on a rigid base (3.6) is almost three times the maximum acceleration experienced when the tank is supported by a flexible foundation (1.3). These results suggest that the maximum acceleration that should be considered for design of the tank wall is given by the case when the tank is resting freely on a rigid foundation (may be interpreted as a rock site), and occurs at the top of the tank.

Hence, the design of an anchored tank on a hard rock site would results in high tie-down forces and lower wall stresses than the same tank free to uplift.

	Base case		
	Fixed rigid	Free rigid	Flexible
Top	1.25	3.60	0.91
Middle	1.08	1.64	0.90
Bottom	0.98	0.93	1.34

Table 4. Variation of maximum normalised acceleration in the tank wall

Figure 6 shows the time-histories of the angle of rotation α for the time $t = [8,12]\ s$, being the time interval containing the time of the maximum of acceleration. The rotation angle α is the angle formed between the supporting soil and the tank base when uplift occurs at one side of the tank (see Figure 7). It is assumed that the base plate is rigid, hence it did not experienced any deformation. The angle α is calculated using the time-history of uplift. It is worth noting that in the cases of the rigid and flexible base the maximum uplift for each side of the tank occurred at the same instant of time. Those results suggest that in the considered case the occurrence of uplift depends more on the characteristics of the earthquake rather than the supporting soil condition.

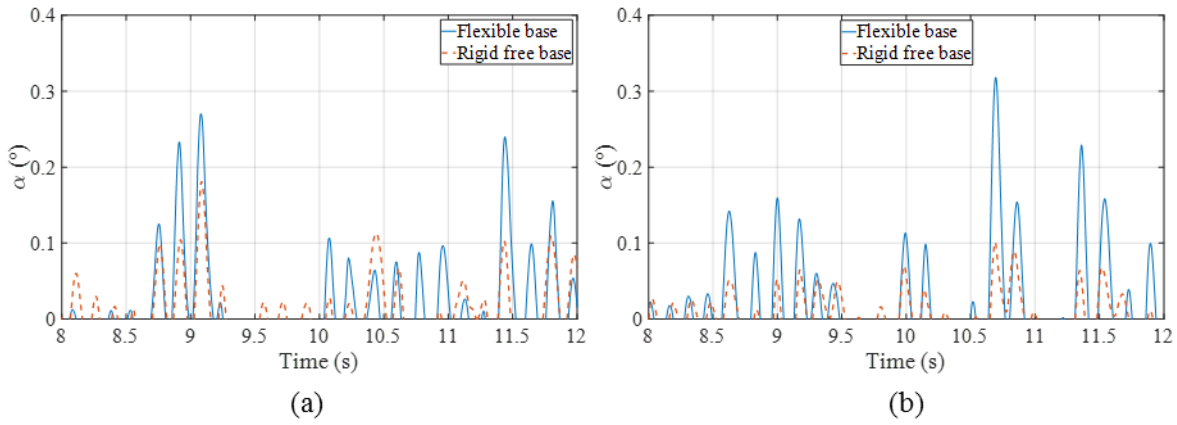

Figure 6. Comparison of angle of rotation α for free rigid and flexible base at (a) 180° and (b) 0°

Table 5 shows the times when the maximum acceleration of the shake table, acceleration of the tank wall and uplift occurred, for both rigid and flexible base cases. These values were extracted from time-history records as shown in Figure 6. Figure 7 shows sketches of the tank configuration when the maximum uplift occurred and the normalised acceleration profiles along the dimensionless height x/H for each supporting case. It is assumed that the acceleration profiles follow a linear distribution along the tank wall. The three accelerometers are indicated by circles.

From Table 5, for the case of a rigid base, at the same side of the tank (180°), the maximum acceleration in the tank wall occurred 10 ms before the maximum uplift. Figure 7(a) shows the acceleration profile at the time at the maximum uplift. The tank top has the maximum acceleration of the profile. Considering the profile at 180°, for a flexible supporting soil the maximum acceleration occurs 10 ms after the maximum uplift, while simultaneously the maximum uplift takes place at the side of 0° (see Figure 7(b)). The lowest accelerometer of the tank recorded the maximum acceleration of the profile of 0°. Even though the tank on a flexible base soil experienced around 30% uplift more than that of the rigid base case, the development of acceleration was almost three times higher when the tank was on a rigid base.

From the observation of the water in the tank, it was generally observed that the water was vibrating out-of-phase with respect to the tank wall, and from time to time changed to being in-phase. This suggests that for both rigid and flexible base cases, the time when the maximum acceleration of the shake table occurred does not coincide with the time of the maximum acceleration of the tank wall and maximum uplift.

	Maximum acceleration shake table		Maximum acceleration tank wall		Maximum Uplift			
					Rigid base		Flexible base	
	Rigid	Flexible	Rigid	Flexible	0°	180°	0°	180°
Time (s)	11.305	11.305	9.075	10.705	10.69	9.085	10.695	9.08

Table 5. Comparison of the time of maximum acceleration of the shake table, tank wall and uplift

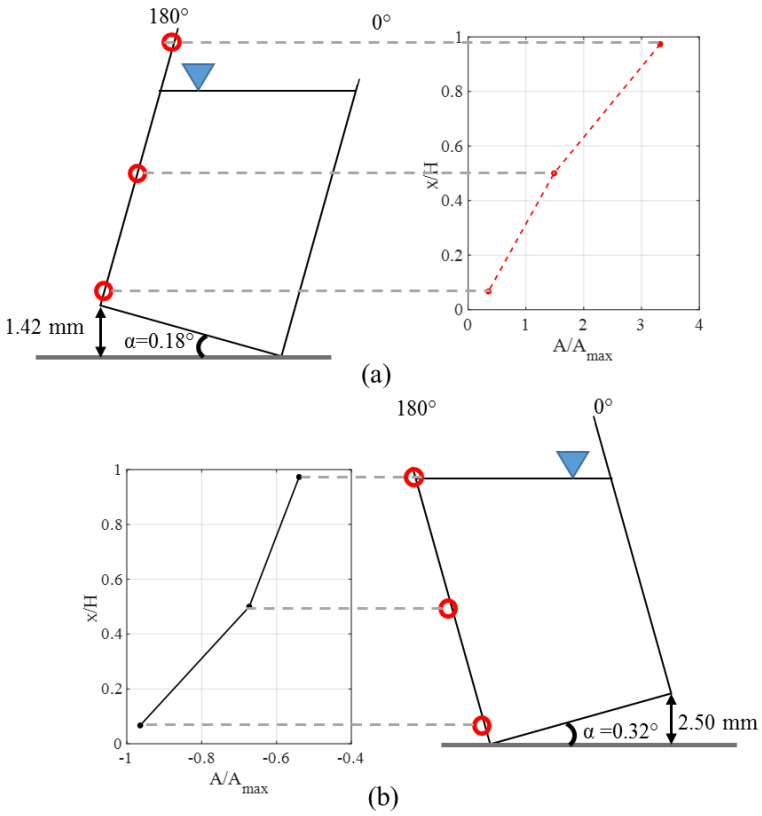

Figure 7. Acceleration profiles in the tank wall when maximum uplift occurred. (a) Rigid supporting case $t = 9.085\ s$ and (b) flexible base case $t = 10.695\ s$

4 CONCLUSIONS

A low-density polyethylene tank was used as a model for a steel tank and tested on a shake table. One stochastically simulated base motion based on the design spectrum of NZS1170.5 for a class C site was used. Two support conditions were utilised, i.e. 1) on a rigid base (steel plate); 2) on a flexible base (sand). Results from three base conditions were compared: i) fixed on a rigid base, ii) free on a rigid base and iii) free on sand. The experiments were performed with an aspect ratio of three. The main aim was to investigate the combined effects of a flexible foundation on uplift and tank acceleration. The results of the experiments reveal:

1) The highest acceleration occurred for a free-rigid base condition, at the top of the tank. It was thrice the maximum acceleration of the case with a fixed-base condition and twice

of the case for the tank on sand. In the cases considered, soil-structure interaction reduces the development of acceleration in the tank wall.

2) The maximum acceleration did not always occur at the top of the tank. For a flexible base, the maximum acceleration occurred at the bottom of the tank. This location of the maximum acceleration may be due to the interaction between the soil and the structure as well as the interaction between the fluid and the tank wall (out-of-phase vibrations).
3) In all cases considered the maximum uplift of occurred for the case of supporting sand, even though the maximum acceleration occurred when the tank was on a rigid base. However, the occurrence of the maximum uplift in both cases of a rigid and flexible base coincided.

ACKNOWLEDGEMENT

The authors wish to thank the Mexican Government for awarding the first author the doctoral scholarship "CONACyT-SENER Hidrocarburos" for his PhD research at the University of Auckland.

5 REFERENCES

[1] K. H. Cho, M. K. Kim, Y. M. Lim, and S. Y. Cho, "Seismic response of base-isolated liquid storage tanks considering fluid-structure-soil interaction in time domain," *Soil Dyn. Earthq. Eng.*, vol. 24, no. 11, pp. 839–852, 2004.

[2] M. A. Haroun and W. Abou-Izzeddine, "Parametric study of seismic soil-tank interaction. I: Horizontal excitation," *J. Struct. Eng.*, vol. 118, no. 3, pp. 783–797, 1992.

[3] A. S. Veletsos and Y. Tang, "Soil-Structure Interaction effects for laterally excited liquid storage tanks," *Earthq. Eng. Struct. Dyn.*, vol. 19, pp. 473–496, 1990.

[4] T. Larkin, "Seismic response of liquid storage tanks incorporating soil structure interaction," *J. Geotech. Geoenvironmental Eng.*, vol. 134, no. 12, pp. 1804–1814, 2008.

[5] H. Daysal and W. A. Nash, "Soil structure interaction effects on the seismic behavior of cylindrical liquid storage tanks," in *Eighth World Conference on Earthquake Engineering*, 21-28 July, 1984.

[6] A. Durmus and R. Livaoglu, "A simplified 3 DOF model of a FEM model for seismic analysis of a silo containing elastic material accounting for soil-structure interaction," *Soil Dyn. Earthq. Eng.*, vol. 77, pp. 1–14, 2015.

[7] L. Ma and C. S. Chang, "Pressures exerted on soil due to rocking of liquid storage tanks," *J. Geotech. Eng.*, vol. 119, no. 11, pp. 1679–1695, Nov. 1993.

[8] R. Seeber, F. D. Fischer, and F. G. Rammerstorfer, "Analysis of a three-dimensional tank-liquid-soil interaction problem," *Trans. ASME*, vol. 112, pp. 28–33, 1990.

[9] N. Hori, "Effects of soil on the dynamic response of liquid-tank systems.," *Am. Soc. Mech. Eng. Press. Vessel. Pip. Div. PVP*, vol. 127, no. May 1990, pp. 339–347, 1987.

[10] M. Ormeño, T. Larkin, and N. Chouw, "Influence of uplift and SSI on liquid storage tanks during earthquakes," in *15th World Conference on Earthquake Engineering*, 24-28 September, 2012.

[11] M. Ormeño, T. Larkin, and N. Chouw, "Effect of foundation conditions on the seismically induced stresses of liquid storage tanks," in *2013 NZSEE Conference*, 26-28 April, 2013.

[12] M. Ormeño, T. Larkin, and N. Chouw, "Effects of subsoil on seismic wall stresses in liquid storage tanks: Experimental findings," in *New Zealand-Japan Workshop on Soil Liquefaction during Recent Large-Scale Earthquakes*, 2013, pp. 233–240.

[13] D. Hernandez-Hernandez, T. Larkin, and N. Chouw, "Seismic wall stresses of liquid storage tanks

considering soil-structure interaction," in *16th European Conference on Earthquake Engineering*, 18-21 June, 2018.

[14] D. Hernandez-Hernandez, T. Larkin, N. Chouw, and D. Engelvin, "Seismic response of a storage tank with fluid-structure- soil interaction," *NZSEE 2018 Conf.*, 12-15 April, 2018.

[15] X. Qin, Y. Chen, and N. Chouw, "Effect of uplift and soil nonlinearity on plastic hinge development and induced vibrations in structures," *Adv. Struct. Eng.*, vol. 16, no. 1, pp. 135–147, Jan. 2013.

[16] NZSEE, *Seismic design of storage tanks, 2009: Recommendations of a study group of the New Zealand Society for Earthquake Engineering*. Wellington: New Zealand Society for Earthquake Engineering, 2009.

[17] X. Qin and N. Chouw, "Shake table study on the effect of mainshock-aftershock sequences on structures with SFSI," *Shock Vib.*, vol. 2017, no. 9850912, pp. 1–12, 2017.

[18] T. Larkin, "Report N° 51508/6," Norwegian Geotechnical Institute, Oslo, Norway, 1978.

[19] NZS 1170.5, *Structural design actions, Part 5: earthquake actions—New Zealand. Code and supplement. Standards New Zealand*, vol. 5. 2004.

[20] M. Ormeño, T. Larkin, and N. Chouw, "Evaluation of seismic ground motion scaling procedures for linear time-history analysis of liquid storage tanks," *Eng. Struct.*, vol. 102, pp. 266–277, 2015.

COMPDYN 2019
7th ECCOMAS Thematic Conference on
Computational Methods in Structural Dynamics and Earthquake Engineering
M. Papadrakakis, M. Fragiadakis (eds.)
Crete, Greece, 24-–26 June 2019

RESPONSE OF PERIODIC ELEVATED STRUCTURES ACCOUNTING FOR SOIL-STRUCTURE INTERACTION

Pieter Reumers, Kirsty Kuo*, Geert Lombaert, and Geert Degrande

KU Leuven, Department of Civil Engineering, Structural Mechanics Section
Kasteelpark Arenberg 40, Box 2448, 3001 Leuven, Belgium
e-mail: pieter.reumers@kuleuven.be

Keywords: periodic elevated structures, dynamic soil-structure interaction, wave finite element method

Abstract. *This paper presents a methodology to study wave propagation in periodic elevated structures consisting of a series of identical cells. The wave finite element method is used to determine the dynamic response of the structure while only a single reference cell is modeled. A substructuring approach is used to efficiently compute the condensed dynamic stiffness matrix of the reference cell. To demonstrate the methodology, the receptance of a slab track is computed. The results are validated with the Floquet transform method and the classical wave finite element method.*

*Presently at Wood, Australia

1 INTRODUCTION

Predicting the dynamic response of large-scale structures is computationally expensive, especially when dynamic soil-structure interaction (SSI) is taken into account. For periodic structures, the SSI problem can be solved for a single reference cell using periodic structure theory [1, 2]. A periodic finite element-boundary element (FE-BE) formulation using Green-Floquet functions has been proposed to solve periodic SSI problems [3, 4]. The Floquet transformation is used to transform the equilibrium equations to the wavenumber domain. The wave finite element method (WFEM) avoids this transformation by employing the free wave characteristics of the reference cell [5, 6]. In this paper, a methodology based on the WFEM is presented to study wave propagation in periodic elevated structures. The periodic reference cell is divided in four parts to efficiently compute its condensed dynamic stiffness matrix. Section 2 introduces the WFEM and elaborates the methodology for elevated structures. In Section 3, the methodology is demonstrated by computing the receptance of a floating slab track. The results are validated using the classical WFEM and the Floquet transform method. Section 4 concludes the paper.

2 METHODOLOGY

In this section, the classical WFEM to compute the forced vibration response of one-dimensional waveguides is briefly recapitulated [5]. Next, the method is adapted to efficiently study wave propagation in periodic elevated structures.

2.1 The wave finite element method (WFEM)

Figure 1 shows an infinitely long periodic structure which is divided in periodic cells with length L. The dynamic stiffness matrix $\mathbf{D} = \mathbf{K} + \mathrm{i}\omega\mathbf{C} - \omega^2\mathbf{M}$ of a reference cell k relates the forces $\mathbf{f}_k$ to the displacements $\mathbf{u}_k$:

$$\begin{Bmatrix} \mathbf{f}_{\mathrm{L}k} \\ \mathbf{f}_{\mathrm{I}k} \\ \mathbf{f}_{\mathrm{R}k} \end{Bmatrix} = \begin{bmatrix} \mathbf{D}_{\mathrm{LL}} & \mathbf{D}_{\mathrm{LI}} & \mathbf{D}_{\mathrm{LR}} \\ \mathbf{D}_{\mathrm{IL}} & \mathbf{D}_{\mathrm{II}} & \mathbf{D}_{\mathrm{IR}} \\ \mathbf{D}_{\mathrm{RL}} & \mathbf{D}_{\mathrm{RI}} & \mathbf{D}_{\mathrm{RR}} \end{bmatrix} \begin{Bmatrix} \mathbf{u}_{\mathrm{L}k} \\ \mathbf{u}_{\mathrm{I}k} \\ \mathbf{u}_{\mathrm{R}k} \end{Bmatrix}. \tag{1}$$

The subscripts L, I, and R denote the degrees of freedom (DOFs) on the left interface, the interior DOFs, and the DOFs on the right interface of the reference cell, respectively. If no external forces are applied to cell k ($\mathbf{f}_{\mathrm{I}k} = \mathbf{0}$), the condensed dynamic stiffness matrix $\tilde{\mathbf{D}}$ is

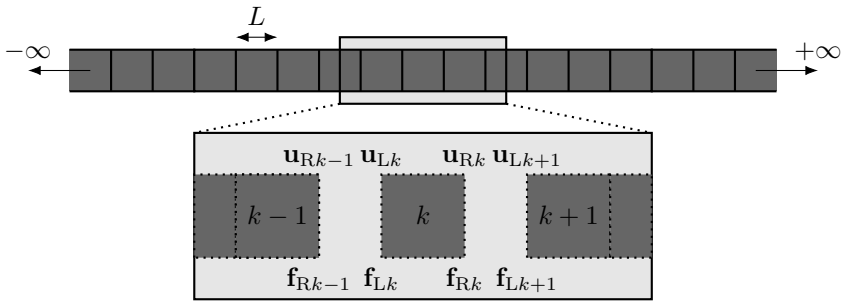

Figure 1: Periodic structure consisting of an infinitely long array of identical cells.

obtained after elimination of the interior DOFs:

$$\begin{Bmatrix} \mathbf{f}_{\mathrm{L}k} \\ \mathbf{f}_{\mathrm{R}k} \end{Bmatrix} = \begin{bmatrix} \tilde{\mathbf{D}}_{\mathrm{LL}} & \tilde{\mathbf{D}}_{\mathrm{LR}} \\ \tilde{\mathbf{D}}_{\mathrm{RL}} & \tilde{\mathbf{D}}_{\mathrm{RR}} \end{bmatrix} \begin{Bmatrix} \mathbf{u}_{\mathrm{L}k} \\ \mathbf{u}_{\mathrm{R}k} \end{Bmatrix} \tag{2}$$

where

$$\begin{bmatrix} \tilde{\mathbf{D}}_{\mathrm{LL}} & \tilde{\mathbf{D}}_{\mathrm{LR}} \\ \tilde{\mathbf{D}}_{\mathrm{RL}} & \tilde{\mathbf{D}}_{\mathrm{RR}} \end{bmatrix} = \begin{bmatrix} \mathbf{D}_{\mathrm{LL}} & \mathbf{D}_{\mathrm{LR}} \\ \mathbf{D}_{\mathrm{RL}} & \mathbf{D}_{\mathrm{RR}} \end{bmatrix} - \begin{bmatrix} \mathbf{D}_{\mathrm{LI}} \\ \mathbf{D}_{\mathrm{RI}} \end{bmatrix} \mathbf{D}_{\mathrm{II}}^{-1} \begin{bmatrix} \mathbf{D}_{\mathrm{IL}} & \mathbf{D}_{\mathrm{IR}} \end{bmatrix}. \tag{3}$$

If the number of interior DOFs is large, this condensation is computationally expensive.

Free wave propagation in periodic media is described by Floquet theory which states that waves propagate from cell to cell with only a change in amplitude and phase [1]. This is represented by the propagation constant μ that relates the displacements and forces at the interfaces of neighboring cells k and $k+1$:

$$\mathbf{u}_{\mathrm{L}k+1} = e^{-\mu}\mathbf{u}_{\mathrm{L}k}, \tag{4}$$

$$\mathbf{f}_{\mathrm{L}k+1} = e^{-\mu}\mathbf{f}_{\mathrm{L}k}. \tag{5}$$

Furthermore, continuity of displacements and equilibrium of forces is imposed at the cell interfaces:

$$\mathbf{u}_{\mathrm{L}k+1} = \mathbf{u}_{\mathrm{R}k}, \tag{6}$$

$$\mathbf{f}_{\mathrm{L}k+1} + \mathbf{f}_{\mathrm{R}k} = \mathbf{0}. \tag{7}$$

The following relation is obtained from equations (4) and (6):

$$\mathbf{u}_{\mathrm{R}k} = e^{-\mu}\mathbf{u}_{\mathrm{L}k}, \tag{8}$$

while combining equations (5) and (7) results in:

$$\mathbf{f}_{\mathrm{R}k} = -e^{-\mu}\mathbf{f}_{\mathrm{L}k}. \tag{9}$$

Equation (9) is further elaborated using equation (2):

$$\tilde{\mathbf{D}}_{\mathrm{RL}}\mathbf{u}_{\mathrm{L}k} + (\tilde{\mathbf{D}}_{\mathrm{LL}} + \tilde{\mathbf{D}}_{\mathrm{RR}})\mathbf{u}_{\mathrm{R}k} = -\tilde{\mathbf{D}}_{\mathrm{LR}}e^{-\mu}\mathbf{u}_{\mathrm{R}k}. \tag{10}$$

Equations (8) and (10) are combined into the following eigenvalue problem from which the free wave characteristics (propagation constants and free wave modes) of the reference cell are obtained [5]:

$$\begin{bmatrix} \mathbf{0} & \mathbf{I} \\ -\tilde{\mathbf{D}}_{\mathrm{LR}}^{-1}\tilde{\mathbf{D}}_{\mathrm{RL}} & -\tilde{\mathbf{D}}_{\mathrm{LR}}^{-1}(\tilde{\mathbf{D}}_{\mathrm{LL}} + \tilde{\mathbf{D}}_{\mathrm{RR}}) \end{bmatrix} \begin{Bmatrix} \mathbf{u}_{\mathrm{L}k} \\ \mathbf{u}_{\mathrm{R}k} \end{Bmatrix} = e^{-\mu} \begin{Bmatrix} \mathbf{u}_{\mathrm{L}k} \\ \mathbf{u}_{\mathrm{R}k} \end{Bmatrix}. \tag{11}$$

Note that this eigenvalue problem can be reformulated to improve the numerical conditioning [7, 8]. It can be shown that the propagation constants μ appear in pairs (μ,$-\mu$) [8]. The real part $\mathrm{Re}(\mu)$ of the propagation constant μ determines the wave attenuation, while the imaginary part $\mathrm{Im}(\mu)$ determines the phase change over the cell length L. A wave is called positive-going if its amplitude decreases towards the right ($\mathrm{Re}(\mu) > 0$) or, if power is flowing towards the right ($\mathrm{Im}(\mu) > 0$), when its amplitude is constant ($\mathrm{Re}(\mu) = 0$). A wave is called negative-going if its amplitude decreases towards the left ($\mathrm{Re}(\mu) < 0$) or, if power is flowing towards the left ($\mathrm{Im}(\mu) < 0$), when its amplitude is constant ($\mathrm{Re}(\mu) = 0$). The number of positive- and

negative-going waves is equal to the number of DOFs n at the interface between two cells. Furthermore, three wave types are observed: (1) non-decaying waves ($\mathrm{Re}(\mu) = 0$), (2) evanescent waves ($\mathrm{Im}(\mu) = 0$), and (3) decaying waves (all other cases).

The propagation constants of positive- and negative-going waves are denoted by μ_p and μ_n, respectively. The corresponding free wave modes $\boldsymbol{\psi}_\mathrm{p}$ and $\boldsymbol{\psi}_\mathrm{n}$ are the eigenvectors in equation (11). Each mode $\boldsymbol{\psi}_\mathrm{p}$ or $\boldsymbol{\psi}_\mathrm{n}$ is associated with a force vector $\boldsymbol{\rho}_\mathrm{p}$ or $\boldsymbol{\rho}_\mathrm{n}$, which is computed as:

$$\boldsymbol{\rho}_\mathrm{p} = \left(\tilde{\mathbf{D}}_\mathrm{LL} + e^{-\mu_\mathrm{p}}\tilde{\mathbf{D}}_\mathrm{LR}\right)\boldsymbol{\psi}_\mathrm{p} \tag{12}$$

for the positive-going waves, and as:

$$\boldsymbol{\rho}_\mathrm{n} = \left(\tilde{\mathbf{D}}_\mathrm{RR} + e^{+\mu_\mathrm{n}}\tilde{\mathbf{D}}_\mathrm{RL}\right)\boldsymbol{\psi}_\mathrm{n} \tag{13}$$

for the negative-going waves. The modes $\boldsymbol{\psi}_\mathrm{p}$ and $\boldsymbol{\psi}_\mathrm{n}$ are collected in the matrices $\boldsymbol{\Psi}_\mathrm{p}$ and $\boldsymbol{\Psi}_\mathrm{n}$, while the force vectors $\boldsymbol{\rho}_\mathrm{p}$ and $\boldsymbol{\rho}_\mathrm{n}$ are collected in the matrices $\mathbf{R}_\mathrm{p}$ and $\mathbf{R}_\mathrm{n}$.

Subsequently, the free wave characteristics are used to construct the condensed dynamic stiffness matrix of a semi-infinite part of the structure. First, consider the semi-infinite part to the left of cell k where only negative-going waves are propagating (figure 1). Hence, the displacements $\mathbf{u}_{\mathrm{R}k-1}$ at the right side of cell $k-1$ are written as a linear combination of the wave modes $\boldsymbol{\Psi}_\mathrm{n}$:

$$\mathbf{u}_{\mathrm{R}k-1} = \boldsymbol{\Psi}_\mathrm{n}\boldsymbol{\alpha}_\mathrm{n} \tag{14}$$

with $\boldsymbol{\alpha}_\mathrm{n}$ the modal coordinates of the negative-going waves. Similarly, the forces $\mathbf{f}_{\mathrm{R}k-1}$ are written as a linear combination of the force vectors $\mathbf{R}_\mathrm{n}$:

$$\mathbf{f}_{\mathrm{R}k-1} = \mathbf{R}_\mathrm{n}\boldsymbol{\alpha}_\mathrm{n}. \tag{15}$$

Eliminating the modal coordinates $\boldsymbol{\alpha}_\mathrm{n}$ results in an expression for the dynamic stiffness matrix $\mathbf{S}_\mathrm{n}$ of the semi-infinite part to the left of cell k:

$$\mathbf{S}_\mathrm{n} = \mathbf{R}_\mathrm{n}\boldsymbol{\Psi}_\mathrm{n}^{-1}. \tag{16}$$

A similar approach is followed to construct the dynamic stiffness matrix $\mathbf{S}_\mathrm{p}$ of the semi-infinite part to the right of cell k where only positive-going waves are propagating, relating the forces $\mathbf{f}_{\mathrm{L}k+1}$ to the displacements $\mathbf{u}_{\mathrm{L}k+1}$:

$$\mathbf{S}_\mathrm{p} = \mathbf{R}_\mathrm{p}\boldsymbol{\Psi}_\mathrm{p}^{-1}. \tag{17}$$

Finally, the condensed dynamic stiffness matrix of a finite part of the structure consisting of N cells is constructed, accounting for both positive- and negative-going waves. The displacements $\mathbf{u}_{\mathrm{L}1}$ at the left side of the first cell and $\mathbf{u}_{\mathrm{R}N}$ at the right side of the Nth cell are written as a linear combination of the wave modes $\boldsymbol{\Psi}_\mathrm{p}$ and $\boldsymbol{\Psi}_\mathrm{n}$:

$$\begin{Bmatrix}\mathbf{u}_{\mathrm{L}1}\\ \mathbf{u}_{\mathrm{R}N}\end{Bmatrix} = \begin{bmatrix}\boldsymbol{\Psi}_\mathrm{n}e^{+N\mu_\mathrm{n}} & \boldsymbol{\Psi}_\mathrm{p}\\ \boldsymbol{\Psi}_\mathrm{n} & \boldsymbol{\Psi}_\mathrm{p}e^{-N\mu_\mathrm{p}}\end{bmatrix}\begin{Bmatrix}\boldsymbol{\alpha}_\mathrm{n}\\ \boldsymbol{\alpha}_\mathrm{p}\end{Bmatrix}. \tag{18}$$

A similar expression is used for the forces $\mathbf{F}_{\mathrm{L}1}$ and $\mathbf{F}_{\mathrm{R}N}$ as a linear combination of the force vectors $\mathbf{R}_\mathrm{p}$ and $\mathbf{R}_\mathrm{n}$, respectively:

$$\begin{Bmatrix}\mathbf{F}_{\mathrm{L}1}\\ \mathbf{F}_{\mathrm{R}N}\end{Bmatrix} = \begin{bmatrix}-\mathbf{R}_\mathrm{n}e^{+N\mu_\mathrm{n}} & \mathbf{R}_\mathrm{p}\\ \mathbf{R}_\mathrm{n} & -\mathbf{R}_\mathrm{p}e^{-N\mu_\mathrm{p}}\end{bmatrix}\begin{Bmatrix}\boldsymbol{\alpha}_\mathrm{n}\\ \boldsymbol{\alpha}_\mathrm{p}\end{Bmatrix}. \tag{19}$$

The modal coordinates $\boldsymbol{\alpha}_{\mathrm{n}}$ and $\boldsymbol{\alpha}_{\mathrm{p}}$ are eliminated from equations (18) and (19), as follows:

$$\begin{Bmatrix} \mathbf{F}_{\mathrm{L}1} \\ \mathbf{F}_{\mathrm{R}N} \end{Bmatrix} = \begin{bmatrix} -\mathbf{R}_{\mathrm{n}} e^{+N\mu_{\mathrm{n}}} & \mathbf{R}_{\mathrm{p}} \\ \mathbf{R}_{\mathrm{n}} & -\mathbf{R}_{\mathrm{p}} e^{-N\mu_{\mathrm{p}}} \end{bmatrix} \begin{bmatrix} \boldsymbol{\Psi}_{\mathrm{n}} e^{+N\mu_{\mathrm{n}}} & \boldsymbol{\Psi}_{\mathrm{p}} \\ \boldsymbol{\Psi}_{\mathrm{n}} & \boldsymbol{\Psi}_{\mathrm{p}} e^{-N\mu_{\mathrm{p}}} \end{bmatrix}^{-1} \begin{Bmatrix} \mathbf{u}_{\mathrm{L}1} \\ \mathbf{u}_{\mathrm{R}N} \end{Bmatrix}$$
$$= \begin{bmatrix} \tilde{\mathbf{S}}_{\mathrm{LL}} & \tilde{\mathbf{S}}_{\mathrm{LR}} \\ \tilde{\mathbf{S}}_{\mathrm{RL}} & \tilde{\mathbf{S}}_{\mathrm{RR}} \end{bmatrix} \begin{Bmatrix} \mathbf{u}_{\mathrm{L}1} \\ \mathbf{u}_{\mathrm{R}N} \end{Bmatrix}. \tag{20}$$

The properties of a block matrix are used to compute the matrix inverse. The condensed dynamic stiffness matrix $\tilde{\mathbf{S}}$ relates the forces to the displacements at both ends of the finite part. Note that the dynamic stiffness matrix is denoted by $\mathbf{S}$ for parts consisting of multiple cells, while $\mathbf{D}$ is used for a single cell. A tilde is used to denote a dynamic stiffness matrix after condensation.

2.2 Periodic elevated structures

In this section, the WFEM is used to compute the forced vibration response of periodic elevated structures such as the bridge shown in figure 2. Waves propagate through both the bridge deck and the soil (one-dimensional waveguides), and interact through the bridge piers. The dynamic response of this structure is computed efficiently by substructuring the reference cell into four parts (figure 2): the bridge pier (part a), the foundation (part b), the bridge deck between two piers (part c), and the soil between two foundations (part d). Instead of constructing an FE model of the entire reference cell, each part is modeled separately. This reduces the computational effort, particularly when the number of interior DOFs in the reference cell is large.

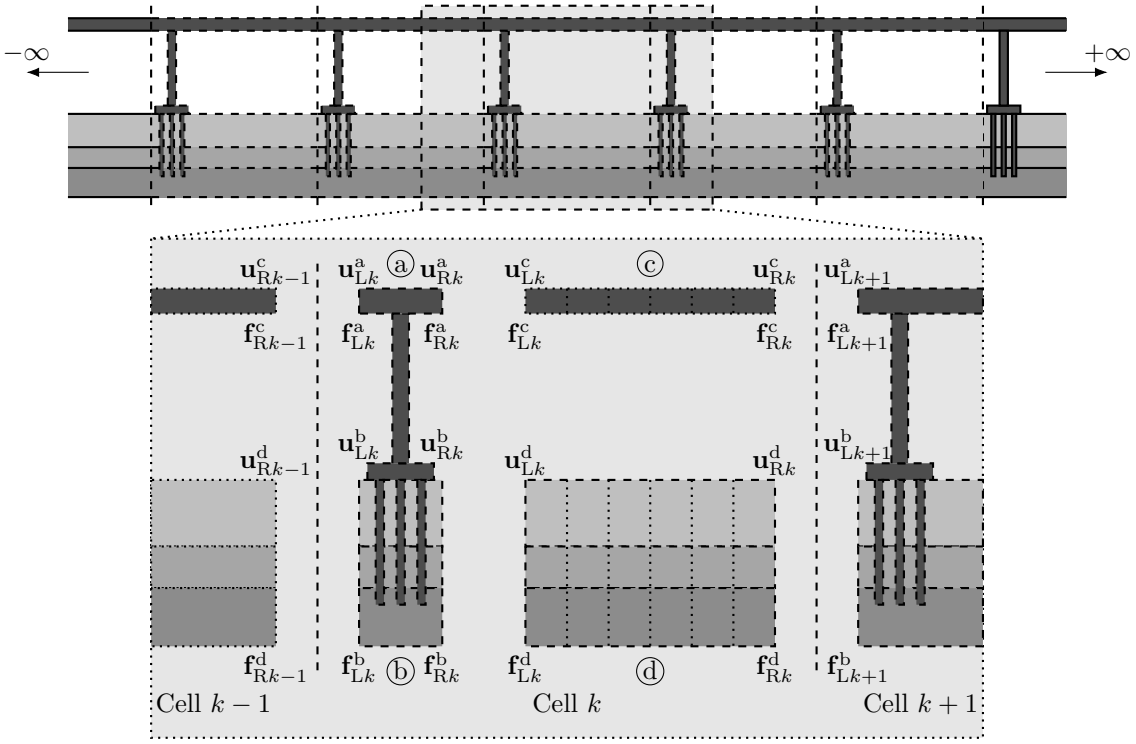

Figure 2: Periodic elevated structure consisting of an infinitely long array of identical cells. The reference cell is divided into four parts a, b, c, and d.

2.2.1 Substructuring of the reference cell

The dynamic stiffness matrix of the coupled parts a and b is denoted by $\mathbf{D}_{\mathrm{ab}}$, where the subscript ab denotes the union of parts a and b:

$$\begin{Bmatrix} \mathbf{f}^{\mathrm{a}}_{\mathrm{L}k} \\ \mathbf{f}^{\mathrm{b}}_{\mathrm{L}k} \\ \mathbf{f}^{\mathrm{a}}_{\mathrm{I}k} \\ \mathbf{f}^{\mathrm{b}}_{\mathrm{I}k} \\ \mathbf{f}^{\mathrm{a}}_{\mathrm{R}k} \\ \mathbf{f}^{\mathrm{b}}_{\mathrm{R}k} \end{Bmatrix} = \begin{bmatrix} \mathbf{D}^{\mathrm{aa}}_{\mathrm{LL}} & \mathbf{D}^{\mathrm{ab}}_{\mathrm{LL}} & \mathbf{D}^{\mathrm{aa}}_{\mathrm{LI}} & \mathbf{D}^{\mathrm{ab}}_{\mathrm{LI}} & \mathbf{D}^{\mathrm{aa}}_{\mathrm{LR}} & \mathbf{D}^{\mathrm{ab}}_{\mathrm{LR}} \\ \mathbf{D}^{\mathrm{ba}}_{\mathrm{LL}} & \mathbf{D}^{\mathrm{bb}}_{\mathrm{LL}} & \mathbf{D}^{\mathrm{ba}}_{\mathrm{LI}} & \mathbf{D}^{\mathrm{bb}}_{\mathrm{LI}} & \mathbf{D}^{\mathrm{ba}}_{\mathrm{LR}} & \mathbf{D}^{\mathrm{bb}}_{\mathrm{LR}} \\ \mathbf{D}^{\mathrm{aa}}_{\mathrm{IL}} & \mathbf{D}^{\mathrm{ab}}_{\mathrm{IL}} & \mathbf{D}^{\mathrm{aa}}_{\mathrm{II}} & \mathbf{D}^{\mathrm{ab}}_{\mathrm{II}} & \mathbf{D}^{\mathrm{aa}}_{\mathrm{IR}} & \mathbf{D}^{\mathrm{ab}}_{\mathrm{IR}} \\ \mathbf{D}^{\mathrm{ba}}_{\mathrm{IL}} & \mathbf{D}^{\mathrm{bb}}_{\mathrm{IL}} & \mathbf{D}^{\mathrm{ba}}_{\mathrm{II}} & \mathbf{D}^{\mathrm{bb}}_{\mathrm{II}} & \mathbf{D}^{\mathrm{ba}}_{\mathrm{IR}} & \mathbf{D}^{\mathrm{bb}}_{\mathrm{IR}} \\ \mathbf{D}^{\mathrm{aa}}_{\mathrm{RL}} & \mathbf{D}^{\mathrm{ab}}_{\mathrm{RL}} & \mathbf{D}^{\mathrm{aa}}_{\mathrm{RI}} & \mathbf{D}^{\mathrm{ab}}_{\mathrm{RI}} & \mathbf{D}^{\mathrm{aa}}_{\mathrm{RR}} & \mathbf{D}^{\mathrm{ab}}_{\mathrm{RR}} \\ \mathbf{D}^{\mathrm{ba}}_{\mathrm{RL}} & \mathbf{D}^{\mathrm{bb}}_{\mathrm{RL}} & \mathbf{D}^{\mathrm{ba}}_{\mathrm{RI}} & \mathbf{D}^{\mathrm{bb}}_{\mathrm{RI}} & \mathbf{D}^{\mathrm{ba}}_{\mathrm{RR}} & \mathbf{D}^{\mathrm{bb}}_{\mathrm{RR}} \end{bmatrix} \begin{Bmatrix} \mathbf{u}^{\mathrm{a}}_{\mathrm{L}k} \\ \mathbf{u}^{\mathrm{b}}_{\mathrm{L}k} \\ \mathbf{u}^{\mathrm{a}}_{\mathrm{I}k} \\ \mathbf{u}^{\mathrm{b}}_{\mathrm{I}k} \\ \mathbf{u}^{\mathrm{a}}_{\mathrm{R}k} \\ \mathbf{u}^{\mathrm{b}}_{\mathrm{R}k} \end{Bmatrix}. \tag{21}$$

The superscript a denotes the DOFs of part a, while the superscript b denotes the DOFs of part b. The subscripts L, I, and R are used to distinguish between the DOFs on the left interface, the interior, and the right interface, respectively. In those cases where the left and right interface are not directly coupled, the coupling terms with subscripts LR and RL are zero. Assuming $\mathbf{f}^{\mathrm{a}}_{\mathrm{I}k} = \mathbf{0}$ and $\mathbf{f}^{\mathrm{b}}_{\mathrm{I}k} = \mathbf{0}$, the condensed dynamic stiffness matrix $\tilde{\mathbf{D}}_{\mathrm{ab}}$ is obtained by eliminating the interior DOFs (equation (3)):

$$\begin{Bmatrix} \mathbf{f}^{\mathrm{a}}_{\mathrm{L}k} \\ \mathbf{f}^{\mathrm{b}}_{\mathrm{L}k} \\ \mathbf{f}^{\mathrm{a}}_{\mathrm{R}k} \\ \mathbf{f}^{\mathrm{b}}_{\mathrm{R}k} \end{Bmatrix} = \begin{bmatrix} \tilde{\mathbf{D}}^{\mathrm{aa}}_{\mathrm{LL}} & \tilde{\mathbf{D}}^{\mathrm{ab}}_{\mathrm{LL}} & \tilde{\mathbf{D}}^{\mathrm{aa}}_{\mathrm{LR}} & \tilde{\mathbf{D}}^{\mathrm{ab}}_{\mathrm{LR}} \\ \tilde{\mathbf{D}}^{\mathrm{ba}}_{\mathrm{LL}} & \tilde{\mathbf{D}}^{\mathrm{bb}}_{\mathrm{LL}} & \tilde{\mathbf{D}}^{\mathrm{ba}}_{\mathrm{LR}} & \tilde{\mathbf{D}}^{\mathrm{bb}}_{\mathrm{LR}} \\ \tilde{\mathbf{D}}^{\mathrm{aa}}_{\mathrm{RL}} & \tilde{\mathbf{D}}^{\mathrm{ab}}_{\mathrm{RL}} & \tilde{\mathbf{D}}^{\mathrm{aa}}_{\mathrm{RR}} & \tilde{\mathbf{D}}^{\mathrm{ab}}_{\mathrm{RR}} \\ \tilde{\mathbf{D}}^{\mathrm{ba}}_{\mathrm{RL}} & \tilde{\mathbf{D}}^{\mathrm{bb}}_{\mathrm{RL}} & \tilde{\mathbf{D}}^{\mathrm{ba}}_{\mathrm{RR}} & \tilde{\mathbf{D}}^{\mathrm{bb}}_{\mathrm{RR}} \end{bmatrix} \begin{Bmatrix} \mathbf{u}^{\mathrm{a}}_{\mathrm{L}k} \\ \mathbf{u}^{\mathrm{b}}_{\mathrm{L}k} \\ \mathbf{u}^{\mathrm{a}}_{\mathrm{R}k} \\ \mathbf{u}^{\mathrm{b}}_{\mathrm{R}k} \end{Bmatrix}. \tag{22}$$

Parts c and d are uncoupled and assumed to be periodic. Equation (20) is used to construct the condensed dynamic stiffness matrix $\tilde{\mathbf{S}}_{\mathrm{cc}}$ of part c, consisting of N_{c} cells, from the free wave characteristics of a reference cell. A similar approach is followed to construct the condensed dynamic stiffness matrix $\tilde{\mathbf{S}}_{\mathrm{dd}}$ of part d consisting of N_{d} cells. The condensed dynamic stiffness matrix $\tilde{\mathbf{S}}_{\mathrm{cd}}$ of the union of parts c and d then becomes:

$$\begin{Bmatrix} \mathbf{f}^{\mathrm{c}}_{\mathrm{L}k} \\ \mathbf{f}^{\mathrm{d}}_{\mathrm{L}k} \\ \mathbf{f}^{\mathrm{c}}_{\mathrm{R}k} \\ \mathbf{f}^{\mathrm{d}}_{\mathrm{R}k} \end{Bmatrix} = \begin{bmatrix} \tilde{\mathbf{S}}^{\mathrm{cc}}_{\mathrm{LL}} & \mathbf{0} & \tilde{\mathbf{S}}^{\mathrm{cc}}_{\mathrm{LR}} & \mathbf{0} \\ \mathbf{0} & \tilde{\mathbf{S}}^{\mathrm{dd}}_{\mathrm{LL}} & \mathbf{0} & \tilde{\mathbf{S}}^{\mathrm{dd}}_{\mathrm{LR}} \\ \tilde{\mathbf{S}}^{\mathrm{cc}}_{\mathrm{RL}} & \mathbf{0} & \tilde{\mathbf{S}}^{\mathrm{cc}}_{\mathrm{RR}} & \mathbf{0} \\ \mathbf{0} & \tilde{\mathbf{S}}^{\mathrm{dd}}_{\mathrm{RL}} & \mathbf{0} & \tilde{\mathbf{S}}^{\mathrm{dd}}_{\mathrm{RR}} \end{bmatrix} \begin{Bmatrix} \mathbf{u}^{\mathrm{c}}_{\mathrm{L}k} \\ \mathbf{u}^{\mathrm{d}}_{\mathrm{L}k} \\ \mathbf{u}^{\mathrm{c}}_{\mathrm{R}k} \\ \mathbf{u}^{\mathrm{d}}_{\mathrm{R}k} \end{Bmatrix}. \tag{23}$$

Continuity of displacements and equilibrium of forces is imposed at the interface between parts a and c:

$$\mathbf{u}^{\mathrm{a}}_{\mathrm{R}k} = \mathbf{u}^{\mathrm{c}}_{\mathrm{L}k}, \tag{24}$$

$$\mathbf{f}^{\mathrm{a}}_{\mathrm{R}k} + \mathbf{f}^{\mathrm{c}}_{\mathrm{L}k} = \mathbf{0}. \tag{25}$$

Similarly, the following relations hold at the interface between parts b and d:

$$\mathbf{u}^{\mathrm{b}}_{\mathrm{R}k} = \mathbf{u}^{\mathrm{d}}_{\mathrm{L}k}, \tag{26}$$

$$\mathbf{f}^{\mathrm{b}}_{\mathrm{R}k} + \mathbf{f}^{\mathrm{d}}_{\mathrm{L}k} = \mathbf{0}. \tag{27}$$

Relations (24) to (27) are used to combine equations (22) and (23) into the following system of

equations:

$$\begin{Bmatrix} \mathbf{f}^{\mathrm{a}}_{\mathrm{L}k} \\ \mathbf{f}^{\mathrm{b}}_{\mathrm{L}k} \\ \mathbf{f}^{\mathrm{c}}_{\mathrm{R}k} \\ \mathbf{f}^{\mathrm{d}}_{\mathrm{R}k} \\ \mathbf{0} \\ \mathbf{0} \end{Bmatrix} = \begin{bmatrix} \tilde{\mathbf{D}}^{\mathrm{aa}}_{\mathrm{LL}} & \tilde{\mathbf{D}}^{\mathrm{ab}}_{\mathrm{LL}} & \mathbf{0} & \mathbf{0} & \tilde{\mathbf{D}}^{\mathrm{aa}}_{\mathrm{LR}} & \tilde{\mathbf{D}}^{\mathrm{ab}}_{\mathrm{LR}} \\ \tilde{\mathbf{D}}^{\mathrm{ba}}_{\mathrm{LL}} & \tilde{\mathbf{D}}^{\mathrm{bb}}_{\mathrm{LL}} & \mathbf{0} & \mathbf{0} & \tilde{\mathbf{D}}^{\mathrm{ba}}_{\mathrm{LR}} & \tilde{\mathbf{D}}^{\mathrm{bb}}_{\mathrm{LR}} \\ \mathbf{0} & \mathbf{0} & \tilde{\mathbf{S}}^{\mathrm{cc}}_{\mathrm{RR}} & \mathbf{0} & \tilde{\mathbf{S}}^{\mathrm{cc}}_{\mathrm{RL}} & \mathbf{0} \\ \mathbf{0} & \mathbf{0} & \mathbf{0} & \tilde{\mathbf{S}}^{\mathrm{dd}}_{\mathrm{RR}} & \mathbf{0} & \tilde{\mathbf{S}}^{\mathrm{dd}}_{\mathrm{RL}} \\ \tilde{\mathbf{D}}^{\mathrm{aa}}_{\mathrm{RL}} & \tilde{\mathbf{D}}^{\mathrm{ab}}_{\mathrm{RL}} & \tilde{\mathbf{S}}^{\mathrm{cc}}_{\mathrm{LR}} & \mathbf{0} & \tilde{\mathbf{S}}^{\mathrm{cc}}_{\mathrm{LL}} + \tilde{\mathbf{D}}^{\mathrm{aa}}_{\mathrm{RR}} & \tilde{\mathbf{D}}^{\mathrm{ab}}_{\mathrm{RR}} \\ \tilde{\mathbf{D}}^{\mathrm{ba}}_{\mathrm{RL}} & \tilde{\mathbf{D}}^{\mathrm{bb}}_{\mathrm{RL}} & \mathbf{0} & \tilde{\mathbf{S}}^{\mathrm{dd}}_{\mathrm{LR}} & \tilde{\mathbf{D}}^{\mathrm{ba}}_{\mathrm{RR}} & \tilde{\mathbf{S}}^{\mathrm{dd}}_{\mathrm{LL}} + \tilde{\mathbf{D}}^{\mathrm{bb}}_{\mathrm{RR}} \end{bmatrix} \begin{Bmatrix} \mathbf{u}^{\mathrm{a}}_{\mathrm{L}k} \\ \mathbf{u}^{\mathrm{b}}_{\mathrm{L}k} \\ \mathbf{u}^{\mathrm{c}}_{\mathrm{R}k} \\ \mathbf{u}^{\mathrm{d}}_{\mathrm{R}k} \\ \mathbf{u}^{\mathrm{a}}_{\mathrm{R}k} \\ \mathbf{u}^{\mathrm{b}}_{\mathrm{R}k} \end{Bmatrix}. \tag{28}$$

The displacements $\mathbf{u}^{\mathrm{a}}_{\mathrm{R}k}$ and $\mathbf{u}^{\mathrm{b}}_{\mathrm{R}k}$ are subsequently eliminated by taking the Schur complement of the coefficient matrix in equation (28). This results in the condensed dynamic stiffness matrix of the reference cell, which relates forces to displacements at the cell interfaces. This condensed dynamic stiffness matrix is used to compute the free wave characteristics of the reference cell by solving the eigenvalue problem (11). The dynamic stiffness matrices $\mathbf{S}_{\mathrm{n}}$ and $\mathbf{S}_{\mathrm{p}}$ of the semi-infinite parts to the left and the right of the reference cell are computed using equations (16) and (17).

2.2.2 Forced vibration response

In order to study the forced vibration response due to a moving load, the transfer functions between the force and receiver locations are required in the frequency domain. Since the force moves along the bridge deck, two cases are distinguished: (1) a force $\mathbf{p}$ applied to the interior DOFs of part a (figure 3a), and (2) a force $\mathbf{p}$ applied to the interior DOFs of part c (figure 3b).

In the first case (figure 3a), the force $\mathbf{p}$ is applied to the interior DOFs of part a. Hence, the dynamic stiffness matrix $\mathbf{D}_{\mathrm{ab}}$ of the union of parts a and b is used in the following. At the interface between parts a and b, and the semi-infinite part on the left, continuity of displacements ($\mathbf{u}^{\mathrm{c}}_{\mathrm{R}k-1} = \mathbf{u}^{\mathrm{a}}_{\mathrm{L}k}$ and $\mathbf{u}^{\mathrm{d}}_{\mathrm{R}k-1} = \mathbf{u}^{\mathrm{b}}_{\mathrm{L}k}$) and equilibrium of forces ($\mathbf{f}^{\mathrm{c}}_{\mathrm{R}k-1} + \mathbf{f}^{\mathrm{a}}_{\mathrm{L}k} = \mathbf{0}$ and $\mathbf{f}^{\mathrm{d}}_{\mathrm{R}k-1} + \mathbf{f}^{\mathrm{b}}_{\mathrm{L}k} = \mathbf{0}$) is imposed. Furthermore, at the interface between parts c and d, and the semi-infinite part on the right, continuity of displacements ($\mathbf{u}^{\mathrm{c}}_{\mathrm{R}k} = \mathbf{u}^{\mathrm{a}}_{\mathrm{L}k+1}$ and $\mathbf{u}^{\mathrm{d}}_{\mathrm{R}k} = \mathbf{u}^{\mathrm{b}}_{\mathrm{L}k+1}$) and equilibrium of forces ($\mathbf{f}^{\mathrm{c}}_{\mathrm{R}k} + \mathbf{f}^{\mathrm{a}}_{\mathrm{L}k+1} = \mathbf{0}$ and $\mathbf{f}^{\mathrm{d}}_{\mathrm{R}k} + \mathbf{f}^{\mathrm{b}}_{\mathrm{L}k+1} = \mathbf{0}$) is imposed. The continuity of displacements and equilibrium of forces between the substructures in the reference cell are expressed in equations (24) to (27). The force-displacement relations are given by the dynamic stiffness matrices defined in equations (16), (17), (21) and (23). Subsequently, the force equilibrium equations are combined in the following system of equations:

$$\begin{Bmatrix} \mathbf{0} \\ \mathbf{0} \\ \mathbf{p} \\ \mathbf{0} \\ \mathbf{0} \\ \mathbf{0} \\ \mathbf{0} \\ \mathbf{0} \end{Bmatrix} = \begin{bmatrix} \mathbf{S}^{\mathrm{cc}}_{\mathrm{n}} + \mathbf{D}^{\mathrm{aa}}_{\mathrm{LL}} & \mathbf{S}^{\mathrm{cd}}_{\mathrm{n}} + \mathbf{D}^{\mathrm{ab}}_{\mathrm{LL}} & \mathbf{D}^{\mathrm{aa}}_{\mathrm{LI}} & \mathbf{D}^{\mathrm{ab}}_{\mathrm{LI}} & \mathbf{D}^{\mathrm{aa}}_{\mathrm{LR}} & \mathbf{D}^{\mathrm{ab}}_{\mathrm{LR}} & \mathbf{0} & \mathbf{0} \\ \mathbf{S}^{\mathrm{dc}}_{\mathrm{n}} + \mathbf{D}^{\mathrm{ba}}_{\mathrm{LL}} & \mathbf{S}^{\mathrm{dd}}_{\mathrm{n}} + \mathbf{D}^{\mathrm{bb}}_{\mathrm{LL}} & \mathbf{D}^{\mathrm{ba}}_{\mathrm{LI}} & \mathbf{D}^{\mathrm{bb}}_{\mathrm{LI}} & \mathbf{D}^{\mathrm{ba}}_{\mathrm{LR}} & \mathbf{D}^{\mathrm{bb}}_{\mathrm{LR}} & \mathbf{0} & \mathbf{0} \\ \mathbf{D}^{\mathrm{aa}}_{\mathrm{IL}} & \mathbf{D}^{\mathrm{ab}}_{\mathrm{IL}} & \mathbf{D}^{\mathrm{aa}}_{\mathrm{II}} & \mathbf{D}^{\mathrm{ab}}_{\mathrm{II}} & \mathbf{D}^{\mathrm{aa}}_{\mathrm{IR}} & \mathbf{D}^{\mathrm{ab}}_{\mathrm{IR}} & \mathbf{0} & \mathbf{0} \\ \mathbf{D}^{\mathrm{ba}}_{\mathrm{IL}} & \mathbf{D}^{\mathrm{bb}}_{\mathrm{IL}} & \mathbf{D}^{\mathrm{ba}}_{\mathrm{II}} & \mathbf{D}^{\mathrm{bb}}_{\mathrm{II}} & \mathbf{D}^{\mathrm{ba}}_{\mathrm{IR}} & \mathbf{D}^{\mathrm{bb}}_{\mathrm{IR}} & \mathbf{0} & \mathbf{0} \\ \mathbf{D}^{\mathrm{aa}}_{\mathrm{RL}} & \mathbf{D}^{\mathrm{ab}}_{\mathrm{RL}} & \mathbf{D}^{\mathrm{aa}}_{\mathrm{RI}} & \mathbf{D}^{\mathrm{ab}}_{\mathrm{RI}} & \mathbf{D}^{\mathrm{aa}}_{\mathrm{RR}} + \tilde{\mathbf{S}}^{\mathrm{cc}}_{\mathrm{LL}} & \mathbf{D}^{\mathrm{ab}}_{\mathrm{RR}} & \tilde{\mathbf{S}}^{\mathrm{cc}}_{\mathrm{LR}} & \mathbf{0} \\ \mathbf{D}^{\mathrm{ba}}_{\mathrm{RL}} & \mathbf{D}^{\mathrm{bb}}_{\mathrm{RL}} & \mathbf{D}^{\mathrm{ba}}_{\mathrm{RI}} & \mathbf{D}^{\mathrm{bb}}_{\mathrm{RI}} & \mathbf{D}^{\mathrm{ba}}_{\mathrm{RR}} & \mathbf{D}^{\mathrm{bb}}_{\mathrm{RR}} + \tilde{\mathbf{S}}^{\mathrm{dd}}_{\mathrm{LL}} & \mathbf{0} & \tilde{\mathbf{S}}^{\mathrm{dd}}_{\mathrm{LR}} \\ \mathbf{0} & \mathbf{0} & \mathbf{0} & \mathbf{0} & \tilde{\mathbf{S}}^{\mathrm{cc}}_{\mathrm{RL}} & \mathbf{0} & \tilde{\mathbf{S}}^{\mathrm{cc}}_{\mathrm{RR}} + \mathbf{S}^{\mathrm{aa}}_{\mathrm{p}} & \mathbf{S}^{\mathrm{ab}}_{\mathrm{p}} \\ \mathbf{0} & \mathbf{0} & \mathbf{0} & \mathbf{0} & \mathbf{0} & \tilde{\mathbf{S}}^{\mathrm{dd}}_{\mathrm{RL}} & \mathbf{S}^{\mathrm{ba}}_{\mathrm{p}} & \tilde{\mathbf{S}}^{\mathrm{dd}}_{\mathrm{RR}} + \mathbf{S}^{\mathrm{bb}}_{\mathrm{p}} \end{bmatrix} \begin{Bmatrix} \mathbf{u}^{\mathrm{a}}_{\mathrm{L}k} \\ \mathbf{u}^{\mathrm{b}}_{\mathrm{L}k} \\ \mathbf{u}^{\mathrm{a}}_{\mathrm{I}k} \\ \mathbf{u}^{\mathrm{b}}_{\mathrm{I}k} \\ \mathbf{u}^{\mathrm{a}}_{\mathrm{R}k} \\ \mathbf{u}^{\mathrm{b}}_{\mathrm{R}k} \\ \mathbf{u}^{\mathrm{c}}_{\mathrm{R}k} \\ \mathbf{u}^{\mathrm{d}}_{\mathrm{R}k} \end{Bmatrix}. \tag{29}$$

The system of equations (29) can be further condensed, for instance by eliminating the displacements $\mathbf{u}^{\mathrm{c}}_{\mathrm{R}k}$ and $\mathbf{u}^{\mathrm{d}}_{\mathrm{R}k}$.

In the second case, the force $\mathbf{p}$ is applied to the interior DOFs of part c (figure 3b). Part c is divided in the loaded cell c_2 and two unloaded parts c_1 and c_3 consisting of N_{c_1} and N_{c_3} cells, respectively. The dynamic stiffness matrix of the loaded cell is denoted by $\mathbf{D}_{\mathrm{c}_2}$. The

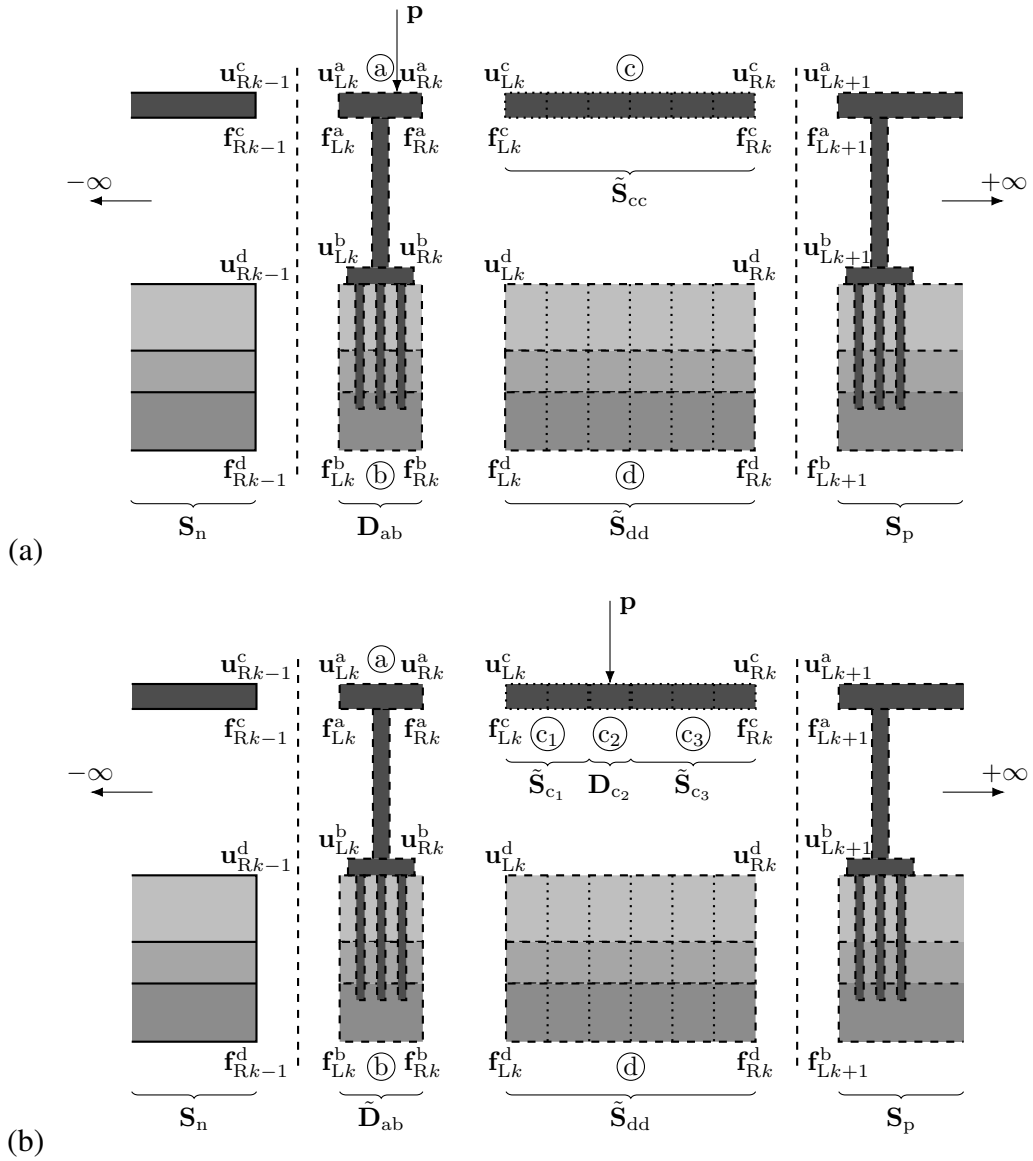

Figure 3: Force $\mathbf{p}$ applied to the interior DOFs of (a) part a, and (b) part c of the reference cell.

condensed dynamic stiffness matrices $\tilde{\mathbf{S}}_{\mathrm{c1}}$ and $\tilde{\mathbf{S}}_{\mathrm{c3}}$ of parts c_1 and c_3 are obtained from equation (20). The dynamic stiffness matrices of the substructures are now assembled into one global dynamic stiffness matrix by expressing continuity of displacements and equilibrium of forces on the interfaces between the substructures (as in the first case). Additionally, continuity of displacements is imposed between parts c_1 and c_2, and c_2 and c_3, respectively:

$$\mathbf{u}^{\mathrm{c}_1}_{\mathrm{R}k} = \mathbf{u}^{\mathrm{c}_2}_{\mathrm{L}k}, \tag{30}$$

$$\mathbf{u}^{\mathrm{c}_2}_{\mathrm{R}k} = \mathbf{u}^{\mathrm{c}_3}_{\mathrm{L}k}, \tag{31}$$

as well as equilibrium of forces:

$$\mathbf{f}^{\mathrm{c}_1}_{\mathrm{R}k} + \mathbf{f}^{\mathrm{c}_2}_{\mathrm{L}k} = \mathbf{0}, \tag{32}$$

$$\mathbf{f}^{\mathrm{c}_2}_{\mathrm{R}k} + \mathbf{f}^{\mathrm{c}_3}_{\mathrm{L}k} = \mathbf{0}. \tag{33}$$

The force-displacement relations are given by the dynamic stiffness matrices defined in equations (16), (17), (22) and (23), and the dynamic stiffness matrix $\mathbf{D}_{\mathrm{c}_2}$ of the loaded cell. Sub-

sequently, the force equilibrium equations are combined in the following system of equations:

$$\begin{Bmatrix} \mathbf{0} \\ \mathbf{0} \\ \mathbf{0} \\ \mathbf{0} \\ \mathbf{0} \\ \mathbf{p} \\ \mathbf{0} \\ \mathbf{0} \\ \mathbf{0} \end{Bmatrix} = \begin{bmatrix} \mathbf{S}_{\mathrm{n}}^{\mathrm{cc}} + \tilde{\mathbf{D}}_{\mathrm{LL}}^{\mathrm{aa}} & \mathbf{S}_{\mathrm{n}}^{\mathrm{cd}} + \tilde{\mathbf{D}}_{\mathrm{LL}}^{\mathrm{ab}} & \tilde{\mathbf{D}}_{\mathrm{LR}}^{\mathrm{aa}} & \tilde{\mathbf{D}}_{\mathrm{LR}}^{\mathrm{ab}} & \mathbf{0} & \mathbf{0} & \mathbf{0} & \mathbf{0} & \mathbf{0} \\ \mathbf{S}_{\mathrm{n}}^{\mathrm{dc}} + \tilde{\mathbf{D}}_{\mathrm{LL}}^{\mathrm{ba}} & \mathbf{S}_{\mathrm{n}}^{\mathrm{dd}} + \tilde{\mathbf{D}}_{\mathrm{LL}}^{\mathrm{bb}} & \tilde{\mathbf{D}}_{\mathrm{LR}}^{\mathrm{ba}} & \tilde{\mathbf{D}}_{\mathrm{LR}}^{\mathrm{bb}} & \mathbf{0} & \mathbf{0} & \mathbf{0} & \mathbf{0} & \mathbf{0} \\ \tilde{\mathbf{D}}_{\mathrm{RL}}^{\mathrm{aa}} & \tilde{\mathbf{D}}_{\mathrm{RL}}^{\mathrm{ab}} & \tilde{\mathbf{D}}_{\mathrm{RR}}^{\mathrm{aa}} + \tilde{\mathbf{S}}_{\mathrm{LL}}^{\mathrm{c_1}} & \tilde{\mathbf{D}}_{\mathrm{RR}}^{\mathrm{ab}} & \tilde{\mathbf{S}}_{\mathrm{LR}}^{\mathrm{c_1}} & \mathbf{0} & \mathbf{0} & \mathbf{0} & \mathbf{0} \\ \tilde{\mathbf{D}}_{\mathrm{RL}}^{\mathrm{ba}} & \tilde{\mathbf{D}}_{\mathrm{RL}}^{\mathrm{bb}} & \tilde{\mathbf{D}}_{\mathrm{RR}}^{\mathrm{ba}} & \tilde{\mathbf{D}}_{\mathrm{RR}}^{\mathrm{bb}} + \tilde{\mathbf{S}}_{\mathrm{LL}}^{\mathrm{dd}} & \mathbf{0} & \mathbf{0} & \mathbf{0} & \mathbf{0} & \tilde{\mathbf{S}}_{\mathrm{LR}}^{\mathrm{dd}} \\ \mathbf{0} & \mathbf{0} & \tilde{\mathbf{S}}_{\mathrm{RL}}^{\mathrm{c_1}} & \mathbf{0} & \tilde{\mathbf{S}}_{\mathrm{RR}}^{\mathrm{c_1}} + \mathbf{D}_{\mathrm{LL}}^{\mathrm{c_2}} & \mathbf{D}_{\mathrm{LI}}^{\mathrm{c_2}} & \mathbf{D}_{\mathrm{LR}}^{\mathrm{c_2}} & \mathbf{0} & \mathbf{0} \\ \mathbf{0} & \mathbf{0} & \mathbf{0} & \mathbf{0} & \mathbf{D}_{\mathrm{IL}}^{\mathrm{c_2}} & \mathbf{D}_{\mathrm{II}}^{\mathrm{c_2}} & \mathbf{D}_{\mathrm{IR}}^{\mathrm{c_2}} & \mathbf{0} & \mathbf{0} \\ \mathbf{0} & \mathbf{0} & \mathbf{0} & \mathbf{0} & \mathbf{D}_{\mathrm{RL}}^{\mathrm{c_2}} & \mathbf{D}_{\mathrm{RI}}^{\mathrm{c_2}} & \mathbf{D}_{\mathrm{RR}}^{\mathrm{c_2}} + \tilde{\mathbf{S}}_{\mathrm{LL}}^{\mathrm{c_3}} & \tilde{\mathbf{S}}_{\mathrm{LR}}^{\mathrm{c_3}} & \mathbf{0} \\ \mathbf{0} & \mathbf{0} & \mathbf{0} & \mathbf{0} & \mathbf{0} & \mathbf{0} & \tilde{\mathbf{S}}_{\mathrm{RL}}^{\mathrm{c_3}} & \tilde{\mathbf{S}}_{\mathrm{RR}}^{\mathrm{c_3}} + \mathbf{S}_{\mathrm{p}}^{\mathrm{aa}} & \mathbf{S}_{\mathrm{p}}^{\mathrm{ab}} \\ \mathbf{0} & \mathbf{0} & \mathbf{0} & \tilde{\mathbf{S}}_{\mathrm{RL}}^{\mathrm{dd}} & \mathbf{0} & \mathbf{0} & \mathbf{0} & \mathbf{S}_{\mathrm{p}}^{\mathrm{ba}} & \mathbf{S}_{\mathrm{p}}^{\mathrm{ab}} + \tilde{\mathbf{S}}_{\mathrm{RR}}^{\mathrm{dd}} \end{bmatrix} \begin{Bmatrix} \mathbf{u}_{\mathrm{L}k}^{\mathrm{a}} \\ \mathbf{u}_{\mathrm{L}k}^{\mathrm{b}} \\ \mathbf{u}_{\mathrm{L}k}^{\mathrm{c}} \\ \mathbf{u}_{\mathrm{L}k}^{\mathrm{d}} \\ \mathbf{u}_{\mathrm{L}k}^{\mathrm{c_2}} \\ \mathbf{u}_{\mathrm{I}k}^{\mathrm{c_2}} \\ \mathbf{u}_{\mathrm{R}k}^{\mathrm{c_2}} \\ \mathbf{u}_{\mathrm{R}k}^{\mathrm{c}} \\ \mathbf{u}_{\mathrm{R}k}^{\mathrm{d}} \end{Bmatrix}. \tag{34}$$

This system of equations can further be condensed, for instance by eliminating the displacements $\mathbf{u}_{\mathrm{L}k}^{\mathrm{a}}$ and $\mathbf{u}_{\mathrm{L}k}^{\mathrm{b}}$.

3 CASE STUDY

In this section, the proposed methodology is demonstrated by computing the receptance of a floating slab track. The track properties are taken from Lombaert et al. [9].

Figure 4 shows the model of an infinitely long floating slab track. The track is symmetric in its cross-sectional plane. Hence, only one rail and half of the slab are modeled. The track consists of a UIC60 rail which is periodically supported by rail pads, which are modeled as spring-damper connections with stiffness $k_{\mathrm{r}} = 213.2 \times 10^6$ N/m and viscous damping constant $c_{\mathrm{r}} = 14.8 \times 10^3$ Ns/m. The slab with height $H = 0.55$ m and width $2B = 2.5$ m is made of concrete with a Young's modulus of 30 GPa, a Poisson's ratio of 0.25, a density of 2500 kg/m^3, and a hysteretic material damping ratio of 2%. The slab rests on a slab mat which is modeled as a continuous spring-damper connection with stiffness $K_{\mathrm{s}} = 15 \times 10^6$ N/m^3 and viscous damping constant $C_{\mathrm{s}} = 30 \times 10^3$ Ns/m^3. Multiplying K_{s} and C_{s} with B results in the stiffness $\bar{k}_{\mathrm{s}}$ and damping constant $\bar{c}_{\mathrm{s}}$ per unit length of the slab. The rail and the slab are modeled as Euler-Bernoulli beams consisting of n elements per periodic length $L = 0.6$ m. The external force $\mathbf{p}$ is a vertical unit harmonic point force applied to the rail at $y = 0$ m.

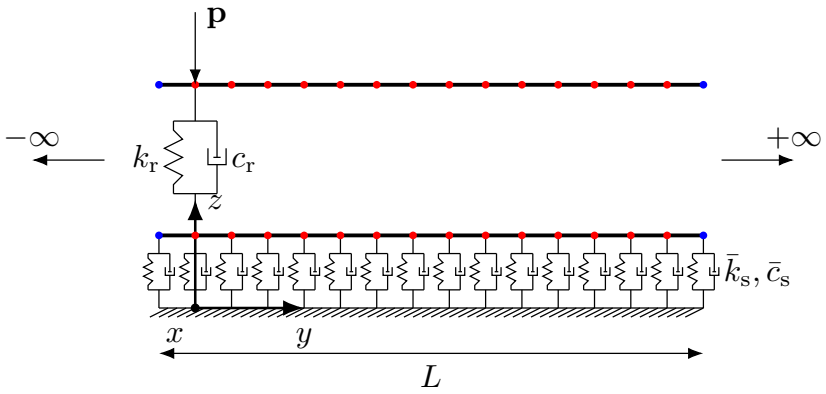

Figure 4: Model of one reference cell of the periodic slab track. The interface nodes are indicated in blue, while the interior nodes are indicated in red. The number of beam elements in the rail and slab is equal to n per length L. The external force $\mathbf{p}$ is applied to the rail at $y = 0$ m in the vertical direction.

Figure 5 shows the modulus and the phase of the vertical rail displacement at $y = 0$ m as a function of the excitation frequency. Figure 6 shows the modulus and the phase of the vertical

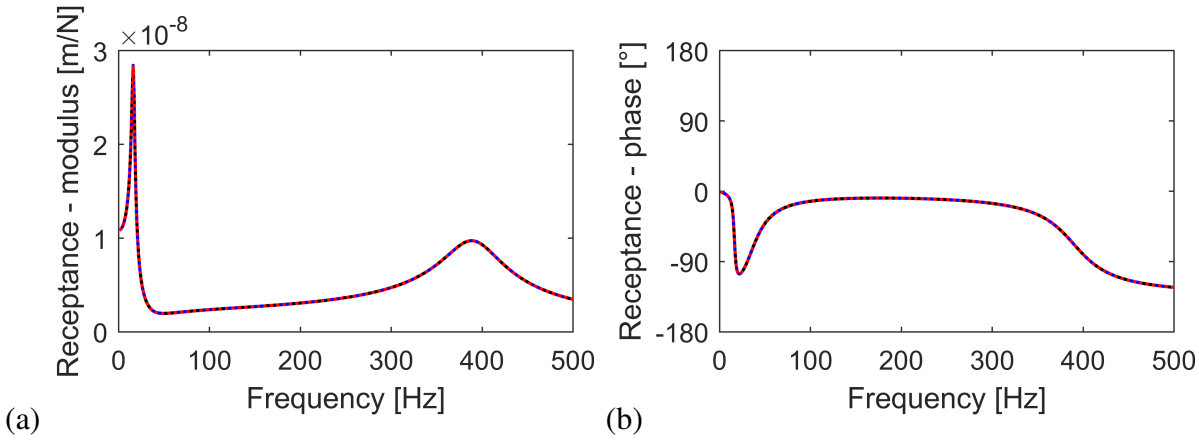

Figure 5: (a) Modulus and (b) phase of the vertical rail displacement at $y = 0$ m as a function of the excitation frequency computed with the Floquet transform method (black solid line), the classical WFEM (blue dashed line), and the adapted WFEM (red dotted line). The number of rail and slab elements in the FE model is $n = 10$.

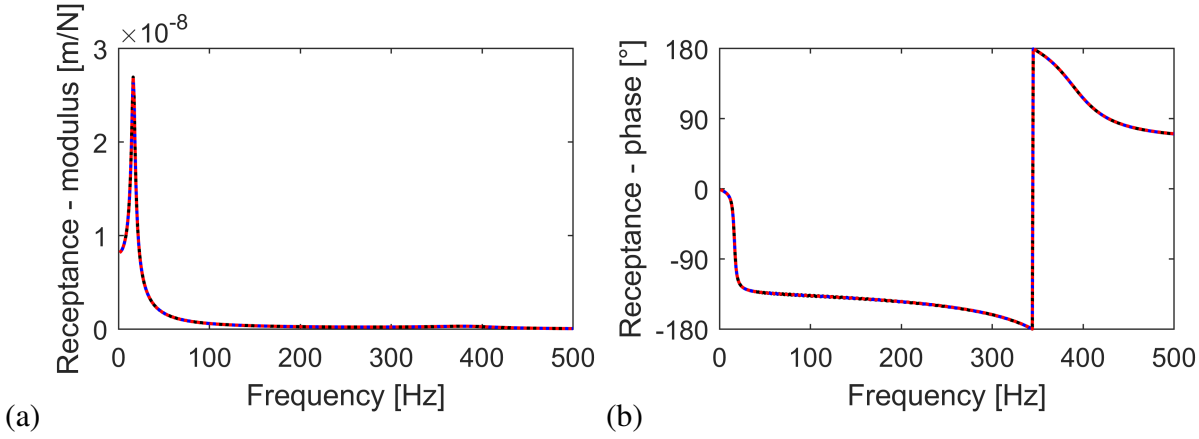

Figure 6: (a) Modulus and (b) phase of the vertical slab displacement at $y = 0$ m as a function of the excitation frequency computed with the Floquet transform method (black solid line), the classical WFEM (blue dashed line), and the adapted WFEM (red dotted line). The number of rail and slab elements in the FE model is $n = 10$.

slab displacement at $y = 0$ m as a function of the excitation frequency. Reference solutions are computed with (1) the classical WFEM and (2) the Floquet transform method. The frequency is sampled between 1 and 500 Hz with a frequency bin of 1 Hz, while the wavenumber κ_y in the Floquet transform method is sampled between $-\pi/L$ and π/L with a wavenumber bin of $\pi/(200L)$. The correspondence between the three methods is excellent over the entire frequency range. The resonance peaks correspond to the natural frequencies of a simplified 2DOF system of the periodic reference cell. The resonance of the rail and slab on the slab mat occurs at 16.3 Hz, while the resonance of the rail on the rail pads occurs at 393.1 Hz. In the low frequency range, the rail and slab move in phase and their amplitude is similar. In the high frequency range, the displacement of the slab reduces significantly and the system behaves as a rail on rail pads.

Table 1 gives an overview of the total computation time for each method with increasing number of elements n. It is observed that for the Floquet transform method and the classical WFEM the total computation time increases by increasing n. However, for the adapted WFEM the total computation time is unaffected, since the number of DOFs in parts a and b does not

increase by increasing n. For $n = 1000$, the computation time increases significantly for the classical WFEM. A breakdown of the computation time results in the following: 47% is required for the condensation of the dynamic stiffness matrix (equation (2)), while 44% is needed to solve the system of equations. For $n = 10$ on the other hand, the largest part of the total computation time is in the construction of the FE model and the computation of the free wave characteristics using equation (11). The computations for $n = 1000$ are not performed with the Floquet transform method.

	$n = 10$	$n = 100$	$n = 1000$
Classical WFEM	0.002	0.024	7.186
Adapted WFEM	0.003	0.003	0.003
Floquet transform method	0.091	14.842	-

Table 1: Comparison of the total computation time (in s) per frequency as a function of the number of elements n per length L. The results are not computed with the Floquet transform method for $n = 1000$.

Finally, it should be pointed out that the construction of a full FE model of the periodic reference cell is avoided in the adapted WFEM. This reduces memory requirements, which is a very important advantage when solving large-scale SSI problems.

4 CONCLUSIONS

An adapted wave finite element method is presented for structures consisting of two one-dimensional wavequides which are periodically coupled. The method exploits the periodicity of the waveguides between the coupling points to efficiently assemble the dynamic stiffness matrix of the entire periodic reference cell. In this way, the construction of a full FE model of the reference cell is avoided. The methodology is demonstrated by computing the response of a floating slab track. It is shown that the computational effort is significantly reduced. This is very promising for the solution of large-scale periodic soil-structure interaction problems such as railway bridges on piled foundations.

REFERENCES

[1] D. Mead. Free wave propagation in periodically supported, infinite beams. *Journal of Sound and Vibration*, 11(2):181–197, 1970.

[2] D. Mead. The forced vibration of one-dimensional multi-coupled periodic structures: an application to finite element analysis. *Journal of Sound and Vibration*, 319(1–2):282–304, 2009.

[3] D. Clouteau, M. Arnst, T.M. Al-Hussaini, and Degrande G. Freefield vibrations due to dynamic loading on a tunnel embedded in a stratified medium. *Journal of Sound and Vibration*, 283(1–2):173–199, 2005.

[4] H. Chebli, R. Othman, and D. Clouteau. Response of periodic structures due to moving loads. *Comptes Rendus Mécanique*, 334(6):347–352, 2006.

[5] D. Duhamel, B. Mace, and M. Brennan. Finite element analysis of the vibrations of waveguides and periodic structures. *Journal of Sound and Vibration*, 294(1–2):205–220, 2006.

[6] J.-M. Mencik and D. Duhamel. A wave-based model reduction technique for the description of the dynamic behavior of periodic structures involving arbitrary-shaped substructures and large-sized finite element models. *Finite Elements in Analysis and Design*, 101:1–14, 2015.

[7] Y. Waki, B. Mace, and M. Brennan. Numerical issues concerning the wave and finite element method for free and forced vibrations of waveguides. *Journal of Sound and Vibration*, 327(1–2):92–108, 2009.

[8] W.X. Zhong and F. Williams. On the direct solution of wave propagation for repetitive structures. *Journal of Sound and Vibration*, 181(3):485–501, 1995.

[9] G. Lombaert, G. Degrande, B. Vanhauwere, B. Vandeborght, and S. François. The control of ground borne vibrations from railway traffic by means of continuous floating slabs. *Journal of Sound and Vibration*, 297(3-5):946–961, 2006.

COMPDYN 2019
7th ECCOMAS Thematic Conference on
Computational Methods in Structural Dynamics and Earthquake Engineering
M. Papadrakakis, M. Fragiadakis (eds.)
Crete, Greece, 24–26 June 2019

SOIL-STRUCTURE INTERACTION MODELING FOR THE DYNAMIC ANALYSIS OF CONCRETE GRAVITY DAMS

A. De Falco[1], M. Mori[2], and G. Sevieri[2]

[1] Dept. of Energy, Systems, Territory and Constructions Engineering, Pisa University, Largo Lucio Lazzarino, 1 – 56122 Pisa (Italy)
a.defalco@ing.unipi.it

[2] Dept. of Energy, Systems, Territory and Constructions Engineering, Pisa University, Largo Lucio Lazzarino, 1 – 56122 Pisa (Italy)
morimatteo123@gmail.com

[2] Dept. of Civil and Industrial Engineering, Pisa University, Largo Lucio Lazzarino, 1 – 56122 Pisa (Italy)
giacomo.sevieri@unifi.it

Abstract

During earthquake shaking, the dam-reservoir-foundation system has to be considered a coupled system. In this paper Soil-Structure Interaction (SSI) effect is investigated on a 2D plane model of a concrete gravity dam under earthquake excitation. Firstly, different approaches to simulate the unboundedness of soil domain are explored: the Perfectly Matched Layer (PML) technique, the Low Reflecting Boundary (LRB) condition and the Infinite Elements (IEs). Different options are compared in the time domain in the case of linear elastic material. The importance of taking into account the SSI in the seismic assessment of concrete dams is also highlighted by the energy balance during time. Successively, the effects of SSI are analysed on a full interacting nonlinear plane model. The results which are obtained in terms of material damage and dissipated energy through a parametric SSI simulation in the time domain show the importance of the choice of the damage constitutive law of the material.

Keywords: Gravity dams, Soil Structure Interaction, Perfectly Matched Layer, Low Reflecting Boundary, Infinite Elements, Time history analysis.

1 INTRODUCTION

The soil effects on the seismic behavior of buildings are seldom explicitly taken into account in finite element models. More often, in order to overcome the difficulties involved in modeling soil-structure interaction, code-provided response spectra depending on suitable soil categories are used. The particular characteristics of the retaining structures do not allow us to use the simplified methods which are commonly applied to ordinary buildings, so dam earthquake safety assessment requires the direct modeling of soil structure interaction.

Soil Structure Interaction is described to have two main components: kinematic and inertial interaction [1]. In the literature two contributions are relevant in approaching the problem of soil-structure interaction, those by Wilson [2] and Wolf [1]. Wilson describes the "massless foundation" method, basing on the consideration that the recorded ground motions are acquired at the terrain surface where the response has already experienced the effects of the soil. This model is governed by soil flexibility. The massless foundation model proposed by Clough in 1980 [3] has been extensively used in seismic analysis of dam-foundation problems. In this context, recorded displacements are imposed at the boundaries of the domain and the input motion reaches instantaneously the base of the dam disregarding the inertial interaction. In the massless model, the wave velocity in foundation becomes infinite, so the input motion reaches instantaneously the base of the dam and the structure takes all kinetic energy. These assumptions seem in general unrealistic [4].

Inertial interaction is generated by elastic waves that develop under dynamic loads, promoting the energy transport through the soil volume. Such a phenomenon that carries energy away from the structure is often referred as "radiation damping". So, while in static SSI analysis the simple truncation of the far field with setting of appropriate boundary conditions gives very often good results, in dynamic cases it makes results to be erroneous because of reflection waves.

The present paper addresses Soil-Structure Interaction (SSI) for existing concrete gravity dams, investigating its effects numerically on a 2D plane system under earthquake excitation. In order to simulate the unboundedness of soil domain, different modelling approaches are explored: the Perfectly Matched Layer (PML) technique [5], the Low Reflecting Boundary (LRB) condition [6] and the Infinite Elements (IEs) [7]. Moreover, the analysis in the time domain is performed in order to compare the response of the model in terms of base shear, using different modelling options. The energy balance during time shows the importance of modeling the SSI in the seismic assessment of concrete dams. The results in terms of base shear values for several modeling approaches are compared in order to highlight the differences among different modelling strategies.

Finally the effects of SSI are analysed on a full interacting nonlinear plane model with nonlinear material constitutive behaviour. The results in terms of material damage are obtained from a parametric SSI simulation in the time domain, in order to take into account the presence of soil beneath the dam.

The main contribution of this work is to compare different modeling strategies and to highlight the importance of SSI modelling for the evaluation of the seismic behaviour of concrete gravity dams.

2 MODELLING UNBOUNDED SOIL

Dam models seldom take into account full interaction effects, because of the lack of adequate numerical implementations or computational resources required by three dimensional detailed models. Recently, SSI for concrete retaining structures is addressed by many authors searching for a reliable simulation of wave propagation in a semi-infinite medium, modeling

the far field part of the foundation. The unboundedness of the terrain was first considered by Lamb [8] in its classical problem of a point load on a half space, for which he provided an analytical solution. Wolf [4], on the other hand, developed a formulation for appropriate spring-dashpot coefficients and boundary conditions. Some worth noting methods are Lysmer boundary conditions [6], hyperelements [9], infinite elements [10], [11], rational boundary conditions [12], boundary element method [13], scaled boundary element method [14] and high order non-reflecting boundary conditions [15].

In order to simulate the unboundedness of both solid and fluid domains, three different modeling options are explored in this work, the Perfectly Matched Layer (PML) technique, the Low Reflecting Boundary (LRB) condition and the Infinite Elements (IEs). PML have been widely used for simulating wave propagation in unbounded media to effectively avoid spurious wave reflections from the computational domain boundaries. This technique is able to absorb incident waves under any angle and frequency, preventing them from returning back to the medium after incidence to the model boundaries [16]. The procedure, which was first introduced by Berenger in 1994 [5], may be applied to different physical problems. It comes to a complex coordinate stretching of the domain to introduce a decay of the oscillation avoiding any reflection in the source domain, thus simulating a perfectly absorbing material. The rational scaling of PML is expressed by the following function of the dimensionless coordinate ξ [16]

$$f(\xi) = s \cdot \xi \left(\frac{1}{3p(1-\xi)+4} - \frac{i}{3p(1-\xi)} \right) \tag{1}$$

where p is the curvature parameter and s the scaling parameter.

Implementation of PML into most commercial FE software packages is performed only in the frequency domain, because the majority of the formulations in the time domain highly affect the computational time and resources.

IEs, which are used to incorporate unbounded domains into the finite element method, have a formulation similar to those of FEM, except for the infinite extent of the element region and shape function in one direction. IEs is based on a function which maps the global to the local coordinate system

$$f(\xi) = \frac{\xi}{\gamma - \xi} \Delta p \tag{2}$$

where Δp is the pole distance,

$$\gamma = \frac{\Delta s + \Delta p}{\Delta s} \tag{3}$$

and Δs is the scaled thickness [7].

Finally, the LRB condition is obtained by imposing a mechanical impedance on the foundation boundary of the model, following the equation

$$[T] \cdot n = -[D] \frac{du}{dt} \tag{4}$$

where u is the displacement vector, $[T]$ the stress tensor, n the unit vector of the boundary tangent plane, $[D]$ is the impedance matrix [17]

$$[D]=\frac{c_p+c_s}{2}[\mathbf{I}], \quad c_s=\sqrt{\frac{G}{\rho}}, \; c_p=\sqrt{\frac{K+4/3\,G}{\rho}} \tag{5}$$

where K is the bulk modulus of the soil, G the shear modulus, ρ the material's density and [I] the identity matrix.

3 A COMPARISON AMONG SSI MODELING STRATEGIES

Different modeling strategies are analyzed and compared in terms of resultant base shear force of a 2D plane strain system under earthquake excitation. The analyses are carried out in the time domain using COMSOL Multiphysics [18].
The dam and soil domains are modeled by applying the standard Solid Mechanics equations. Three different techniques which have been discussed above are used to simulate the unboundedness of the soil: the Perfectly Matched Layer (PML) technique, the Low Reflecting Boundary (LRB) condition and the Infinite Elements (IEs). The study in the time domain is performed on an Italian concrete gravity dam 65 meters tall, with a base of about 45 m, using four plane strain models, as shown in figure 1.
The reference model 1 simulates the dam on a rigid terrain. The solid mesh is composed by 453 default second-order serendipity elements and the displacements of the base nodes are restrained along both directions.
In this case, the basin was simulated by the added mass model [19].

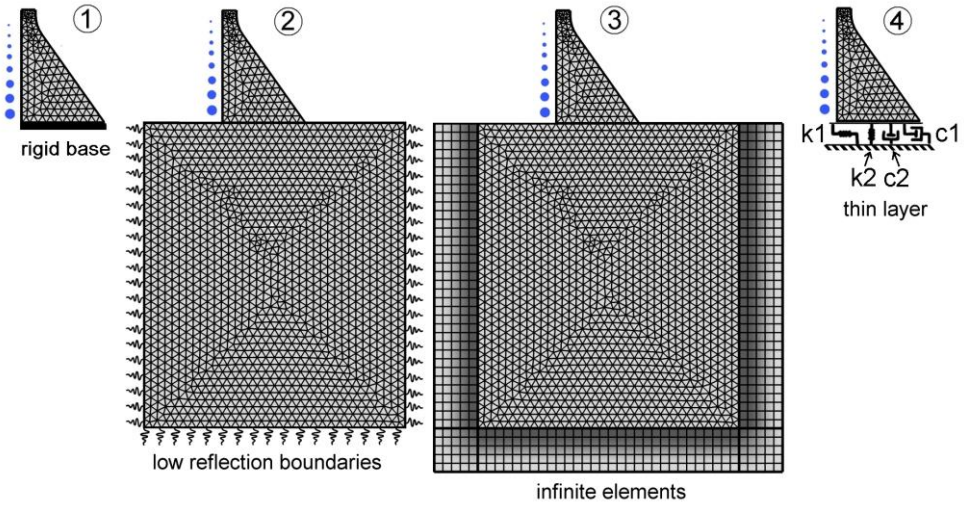

Figure 1. Different SSI modeling strategies for a plane strain model of an Italian dam.

The other three models account for massed foundation as an unbounded half-space.

The second model simulates the dam with the soil equipped by low reflection boundaries. The solid mesh is composed by 3146 default second-order serendipity elements for both the soil and the dam. The low reflecting boundary condition is defined on the boundary of the soil domain. Its impedance parameter values derive from the elastic properties of the soil domain. The third model is similar to the second one, but in addition there are 550 infinite elements surrounding the physical soil region. The solid mesh is thus composed by 3696 default second-order serendipity elements. Infinite element pole distance is 400 m and the scaled thickness is $10^3 \cdot 400$ m.

The fourth model of fig. 1 simulates the unboundedness of the soil through the PMLs applied at the bottom and on the sides. Unfortunately, PML technique is not always available in

each program code or, if present, may not be compatible with time domain analyses. For this reason, a suitable 2D simplified model with horizontal and vertical springs and dashpots at the base was created in [20] to take into account the SSI by using tools and standard boundary conditions. Two viscous damping coefficients and two spring stiffness coefficients were calibrated in [20], starting from a model which is similar to that of case 2 of figure 1, but is equipped by PML boundary elements around the soil domain, instead of low reflecting boundaries. Calibration has been performed to provide the same resultant shear force at the base of the dam in the frequency domain for both models: a simplified model and the interacting 2D model with PML boundary condition. The result is that there is a set of coefficients which are capable to simulate SSI in terms of resultant shear force at the base of the dam. Their values are independent from the frequency in the range between 0 Hz and 25 Hz with good approximation and they are reported in table 1.

Table 1: Resulting parameters of the simplified model approximating the PML boundary technique.

parameter	[N/sqm]	[N·s/sqm]
k_1	8,6e+9 ± 1,1e+9	
k_2	9,7e+8 ± 9,3e+7	
c_1		3,6e+7 ± 2,3e+6
c_2		1.5e+7 ± 6,8e+6

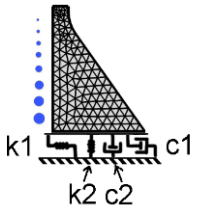

The four models share the same plane-strain setting and material properties, whose values are reported in Table 2.

Table 2. Material properties which are assumed for the comparison among SSI modelling strategies.

Material property value	*Concrete*	*Foundation rock*
Density **ρ** *(kg/m^3)*	2450	2300
Young modulus **E** *(MPa)*	20500	22000
Poisson modulus **ν**	0.2	0.2
Damping coefficient ξ	0.05	0.05

In order to perform the analysis in the time domain for the fourth model of fig. 1, the Thin Elastic Layer boundary condition of COMSOL is applied at the base of the dam. It has both elastic and damping properties and can model a thin elastic layer with specified stiffness and damping properties.

The dynamic excitation which was used in the model belongs to one of the Italian strongest events occurred in the last 30 years, the earthquake of Central Italy of October 30th 2016 (06:40:17 UTC, 6.5 MW). It is the E-W component with about 7.8 m/sqs PGA, which was recorded by Savelli (PG) station [21] (Fig. 2). The duration of transient load is 30 s and the sampling is 5/1000 s.

The analysis has been carried out by assigning the seismic shaking in form of volume loads to the dam domain, in addition to the self-weight and the hydrostatic load. The results in form of base shear are reported in Fig. 3, where the graphs are overlapped. The similarity between the results obtained with the different modelling strategies for the semi-finite soil is remarkable, while a certain difference between these and the rigid case is noteworthy, although the heights of some main peaks remain quite unchanged.

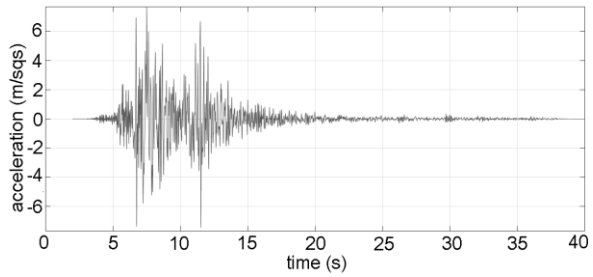

Figure 2. The acceleration time history recorded on October 30th 2016 by Savelli station (record 1).

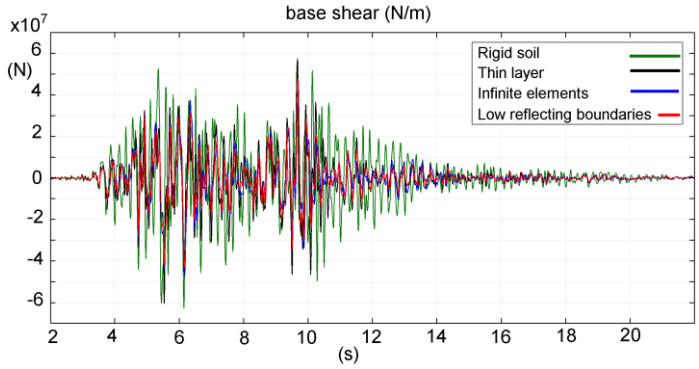

Figure 3. Base shear resultant force obtained from the transient analysis for the four different modeling options.

The FFT of the signal of Fig. 3 is reported in figure 4. The FFT graphs for the different modeling approaches substantially coincide except for the amplitude of some peaks, while, as expected, the graph of the rigid case shows higher peak frequencies and relative peak values.

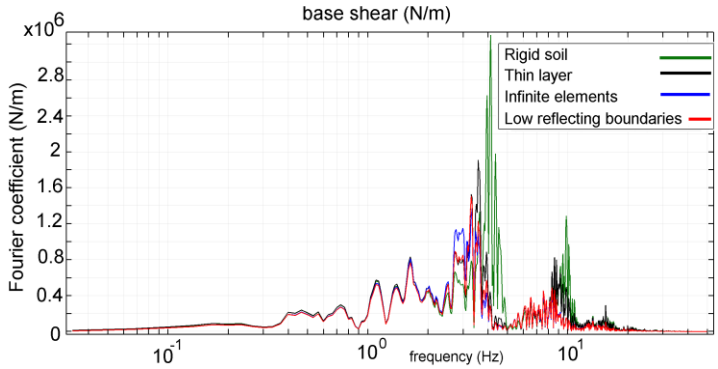

Figure 4. FFT of the base shear history for the different SSI modeling approaches.

Finally, in Fig. 5 the Root Mean Square value of the resultant base shear for different modeling options is displayed. Also this time, it may be observed that RMS values for the cases of thin layer, low reflection boundary and infinite elements are very similar to each other, while they substantially differ from the rigid base case. In addition, the models with IEs and LRB almost coincide.

The graph of the energy balance during the time history analysis on the model with LRB is displayed in Fig. 6. One can note that the most part of dissipated energy is radiated and the energy dissipated within both dam and soil material is about 45% of the radiated one. In its turn, the energy dissipated within the dam material only is about 70% of the energy dissipated within the solid domain. The contribution of radiation damping is therefore a no-negligible part of the total dissipated energy.

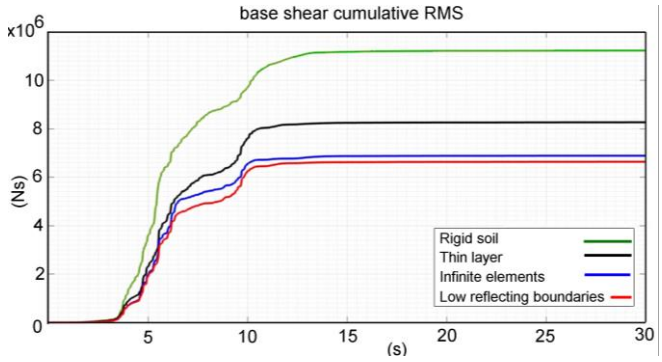

Figure 5. Base shear Root Mean Square value for different modeling options.

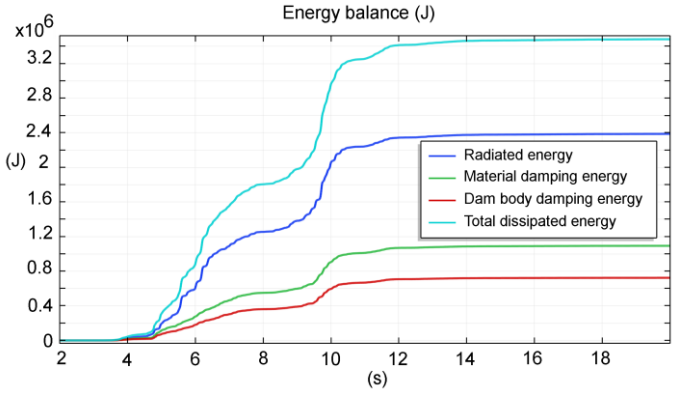

Figure 6. Energy balance (J) during the time history analysis for the LRB model.

4 SSI IN NONLINEAR 2D MODELS

In order to evaluate the effects of taking into account SSI in a more detailed nonlinear model, a 2D full interacting model was created in Abaqus r.6.14 [22]. It simulates a dam 55 m tall, with a base length of 40 m, in plane stress state. The soil domain dimensions are 260 m x 110 m and the reservoir level is 53 m high. The thickness of the plane model is 1 m.

The standard Solid Mechanics equations are applied to the dam and soil domains. The solid mesh is composed by 774 linear quadrilateral elements CPS4R for the soil domain and by 1149 linear triangular elements CPS3 for the dam domain. 79 infinite elements CINPS4 surrounding the soil domain allow one to simulate the soil unboundedness.

The fluid subsystem is simulated by the Helmoltz equation derived from the full Navier-Stokes equation, assuming small vibrations and neglecting viscosity. The mesh of the fluid domain is composed by 2912 linear triangular elements AC2D3.

As for the boundary condition for the fluid domain, a zero pressure condition is imposed at the free surface of the water and a rigid wall condition at the bottom of the reservoir. The fluid-structural interaction condition at the interface between the two domains is the following

$$\begin{cases} -\boldsymbol{n}\left(\frac{1}{\rho}\nabla\sigma\right) = -\boldsymbol{n}\cdot\boldsymbol{u}_{tt} \\ F_A = \sigma\cdot\boldsymbol{n} \end{cases} \tag{6}$$

where σ is the fluid pressure, $\boldsymbol{n}$ is the normal direction to the interface, F_A is the acoustic force on the structure and $\boldsymbol{u_{tt}}$ is the solid acceleration. The first equation transfers the structural acceleration to the fluid, while the second applies the fluid pressure load on the structure. Such a

system of equations expresses a *fully coupled* problem, where the solid and the acoustic parts have to be solved simultaneously.

In order to simulate the unboundedness of the fluid domain, an acoustic impedence in form of Improved Planar nonreflecting boundary condition was introduced at the upstream side of the fluid domain. The total number of elements within the model is 4914, whereas the total number of nodes is 3170.

The constitutive model selected for the dam is the Concrete Plastic Damage Model (CPDM) following the formulation proposed by Lee and Fenves [23], which uses the concepts of fracture-energy-based damage and stiffness degradation in continuum damage mechanics. In order to avoid mesh-dependency problem when simulating damage, a constitutive law formulation in terms of displacements was selected. The values of material properties are reported in table 2 and the parameters of the CPDM implementation in Abaqus [22] are reported in table 3 [24].

The seismic shaking of figure 1 was applied in form of displacement to 12 nodes of the base contour of the solid domain, once it was reduced with a scale factor of 0.6.

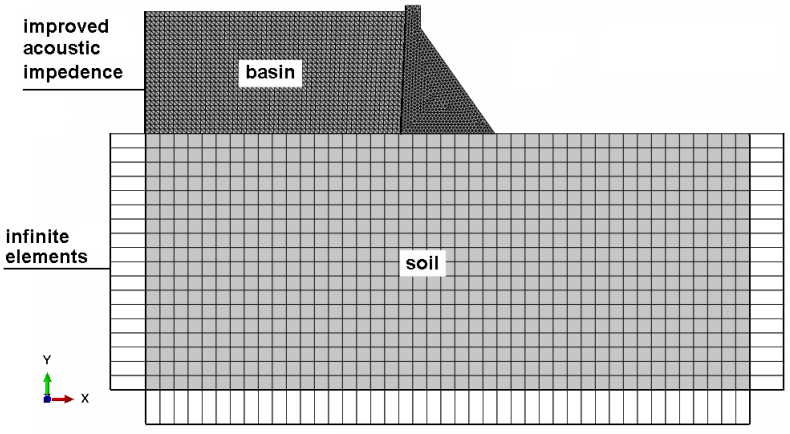

Figure 7. The model for nonlinear time history analysis.

Table 3. Parameters of the CPDM [22].

parameters for the concrete	
Dilation angle *(°)*	32
Flow potential eccentricity ε	0.1
σ_{b0}/σ_{c0} ratio of initial equibiaxial compressive yield stress to initial uniaxial compressive yield stress	1.16
Shape factor Kc	0.66
Compressive strength *(MPa)*	17
Tensile strength *(MPa)*	1
Fracture energy *(Nm)*	150

In order to apply the recorded seismic shaking to the base of the soil model, the deconvolution of the signal was performed through the algorithm of Sooch and Bagchi [24].

As a first evaluation on the SSI effects, one can wonder whether the interaction forces are able to change the basement motion as compared to the free-field ground motion (i.e. motion recorded on the free surface of the soil without structure). To this aim, in Fig. 8 the acceleration of a point on the soil surface near to the dam base (red dashed line) has been compared with the acceleration of the same point in a model that does not include the dam (black continuous line). In Fig. 9 the FFT of both signals is reported. One can note that the peak acceleration is higher in the free-field model. The FFT shows that the greatest amplifications of the

free-field model in respect to the model with dam take place in the interval between 5 Hz and 10 Hz, although the peak frequencies remain almost unchanged. It can be concluded that the interaction forces are able to considerably change the soil motion in this case.

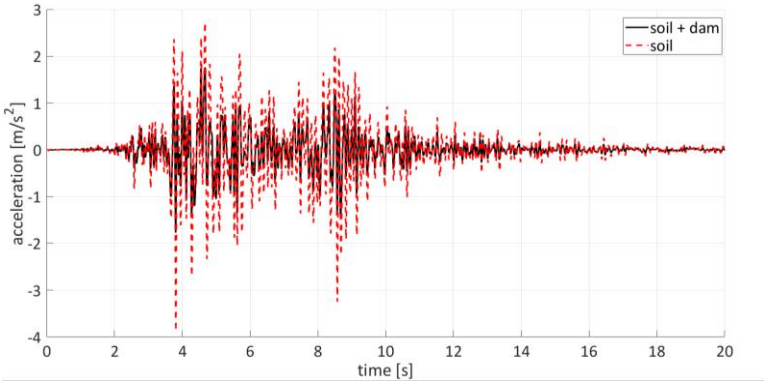

Figure 8. Acceleration history on a point of the soil surface for the model including the dam (red dashed line) and for the free-field model (black continuous line).

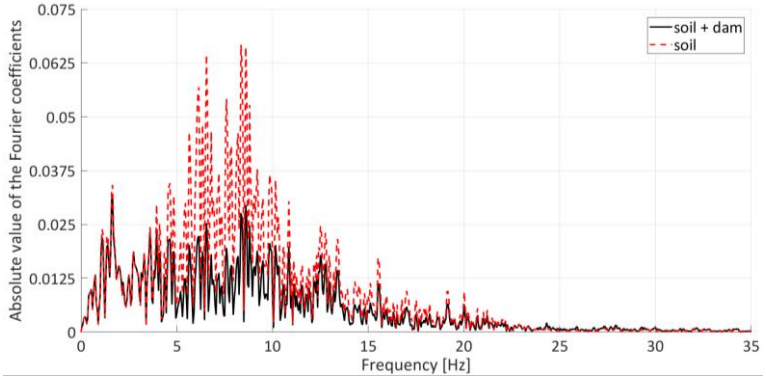

Figure 9. FFT of the signals of Fig. 8.

Another issue concerns the damaging mode of the dam after shaking when CPDM is used to simulate the material behaviour. In this regard, the influence of both soil density and damping ratio variation was investigated and the effects of different acceleration records applied to the model were explored.

As soil density seems to be a key parameter for SSI effects [20], it was varied in order to evaluate the damaged state of the dam after shaking. In Figure 10 the damage level after the seismic sequence is presented. The legend reports the values of the complement to unity of the ratio between damaged deformability modulus and undamaged one. Cracks begin on the upstream side and at the interface between dam and soil and develop downstream across the dam body. Two different soil density values are considered: the first is greater than the actual density of an order of magnitude and the second is near to zero. Figure 10 reports the damaged areas in the two extreme cases in comparison with the case with actual density. Despite the considerable variation in the soil density value, the influence in terms of material damage is not significant. One can conclude that there are no effects on the type and extent of damage as a result of the different or incorrect appreciation of the soil density value.

The influence of viscous damping can be evaluated for the full interacting nonlinear system in term of dissipated energy. Two different values for damping ratio were considered: $\xi = 1\%$ and $\xi = 5\%$. The energy balance was calculated in both cases. In figure 11 the dam body damping dissipated energy versus time is represented by a red line, the plasticity dissipated energy is indicated by a yellow line and the damage dissipated energy by a blue line.

One can note that in both cases the dissipated energy due to plasticity is of the same order of magnitude as the dam body damping energy, while material damage dissipates a very low energy amount in respect to the other two quantities.

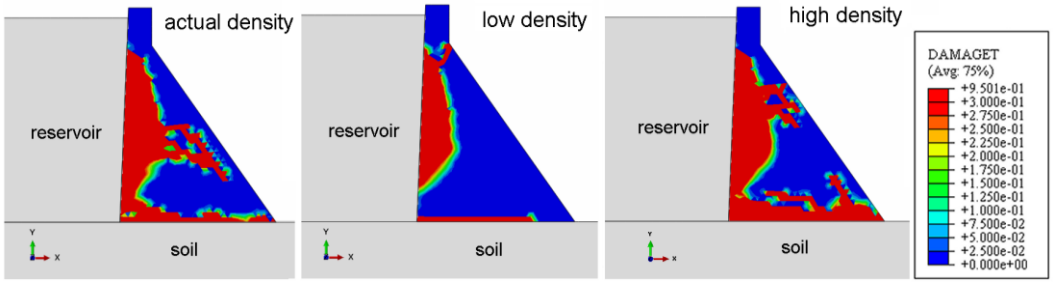

Figure 10. Damage on the dam, varying density.

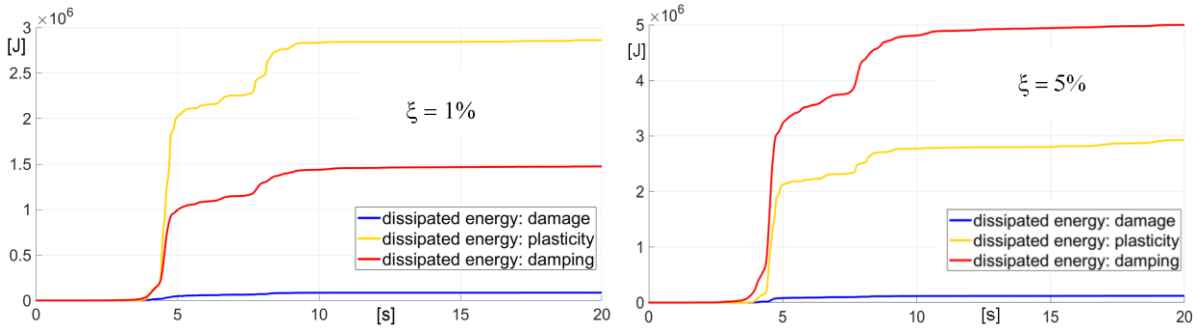

Figure 11: Dissipated energy for damage, plasticity and dam body damping for different values of ξ.

The effect of the type of seismic shaking was evaluated, in its turn, by comparing the damaged state after the shaking of October 30th 2016 (record 1) with that after the shaking of August 24th 2016 (record 2) in Central Italy (Fig. 12).

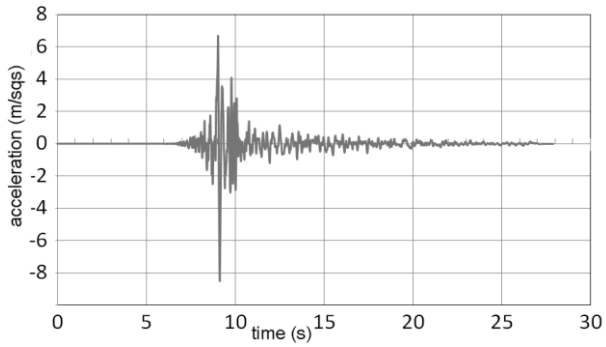

Figure 12. The acceleration time history recorded on August 24th 2016 by Amatrice station (record 2).

This latter, belonging to the seismic sequence of August 24th 2016 (03:36:32 UTC, 6 MW), is the E-W component recorded by Amatrice (RI) station [21] with about 8.5 m/sqs PGA. As in the previous case, it was reduced by 0.6 before being applied.

Resulting damage of the dam is displayed in figure 13 for both dynamic excitations applied at the base of the soil domain. For each record, the initial and final damage state are reported. The damaged state is different in the two cases both in the initial and in the final phase. In the case of record 1 and tensile strength of 1 MPa, cracks initiate from the upstream side of the dam, whereas in the second case, they initiate from the downstream side. Damage evolves in a very different way, as can be seen from the figures of final damage.

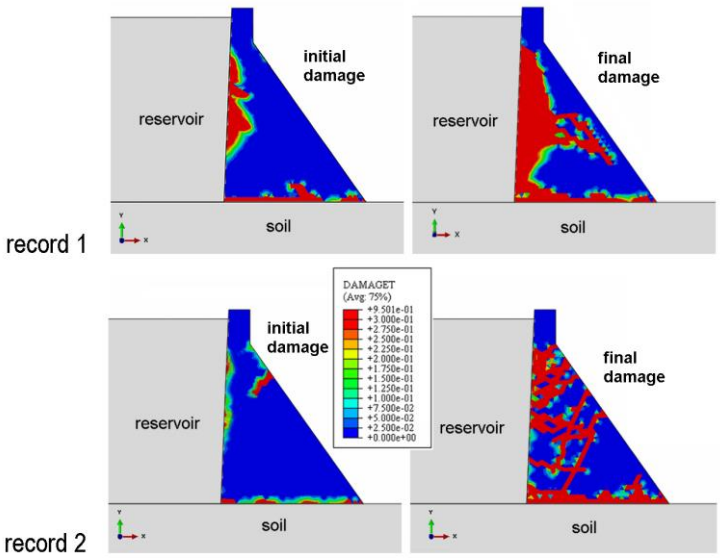

Figure 13: Damage of the dam during the shaking of October 30th 2016 (record 1) and August 24th 2016 (record 2).

5 CONCLUSIONS

We can conclude that different modelling strategies for simulating the soil unboundedness provide very similar results in terms of base shear force and dissipated energy. Moreover, the most part of dissipated energy is the radiated one, thus, the simulation of the unbounded soil appears very important.

When the material is nonlinear, the amount of dissipated energy due to plastic deformation has the same order of magnitude of the dissipated energy due to material damping. On the contrary, the energy that is dissipated by the material damage is particularly low. Hence, the assumption of plastic behaviour of the material could provide large consequences in terms of dissipated energy. Finally, the damaged state of the dam is not affected by the variation of soil density, nor by that of the material damping, but it is largely influenced by the frequency content of the shaking. In conclusions, in order to obtain reliable results, SSI modeling and the material damage law selection must be carefully considered.

REFERENCES

[1] J.P. Wolf, *Dynamic Soil Structure Interaction*. Englewood Cliffs, New Jersey, Prentice-Hall, 1985.

[2] E.L. Wilson, *Three-Dimensional Static and Dynamic Analysis of Structures, A Physical Approach With Emphasis on Earthquake Engineering*. Computers and Structures, Inc., Berkeley, California, 2002.

[3] R.W. Clough, Non-linear mechanisms in the seismic response of arch dams. *International Conference on Earthquake Engineering*. Skopje, Yugoslavia, 1980.

[4] H. Tan, A.K. Chopra, Earthquake analysis of arch dams including dam-water foundation rock interaction. *Earth. Eng. and Struct. Dyn.*, **24**, 1453-1474, 1995.

[5] J.P. Berenger, A perfectly matched layer for the absorption of electromagnetic waves, *J. Comput. Phys.*, **114**, 185-200, 1994.

[6] J. Lysmer, R.L. Kuhlemeyer, Finite dynamic model for infinite media. *J. Eng. Mech., ASCE* **95**, 859-878, 1969.

[7] O.C. Zienkiewicz, C. Emson, P. Bettess, A novel boundary infinite element. *Int. J. for Numerical Methods in Engineeering*. **19**, 1983.

[8] H. Lamb, On the Propagation of Tremors over the Surface of an Elastic Solid, *Philosophical Transactions of the Royal Society of London*. Series A, **203**, 1–42, 1903.

[9] V. Lofti, J.L. Tassoulas, J.M. Roesset, A technique for the analysis of dams to earthquakes, Earthquake. *Engineering & Structural Dynamics*. **15**, 463–490, 1987.

[10] D.K. Kim, C.B. Yun, Time domain soil-structure interaction analysis in two dimensional medium based on analytical frequency-dependent infinite elements. *Int. J. Numer. Meth. Eng.,* **47**, 1241-1261, 2000.

[11] C.B. Yun, D.K. Kim, J.M. Kim, Analytical frequency-dependent infinite elements for soil-structure interaction analysis in two-dimensional medium. *Engineering Structures*, **22**, 258-271, 2000.

[12] G. Feltrin, *Absorbing boundaries for the time-domain analysis of dam-reservoir-foundation systems*. Report Swiss Federal Institute of Technology Zurich, 1997.

[13] M. Yazdchi, N. Khalili, S. Valliappan, Nonlinear seismic behaviour of concrete gravity dams using coupled finite element-boundary element technique. *International Journal for Numerical Methods in Engineering*, **44**, 101-130, 1999.

[14] C. Song, J.P. Wolf, The scaled boundary finite-element method, a primer: solution procedures. *Comput. Struct.*, **78**, 211–225, 2000.

[15] D. Givoli, High-order local non-reflecting boundary conditions: a review. *Wave. Mot.*, **39**, 319–326, 2004.

[16] S. Johnson, *Notes on perfectly matched layers (PMLs).* Massachusetts Institute of Technology, Tech. Rep., 2007.

[17] G.A. Holzapfel *Nonlinear Solid Mechanics: A Continuum Approach for Engineering*. John Wiley & Sons, 2000.

[18] COMSOL® Multiphysics, *User's Guide, Version 5.3*, COMSOL, 2017.

[19] A. De Falco, M. Mori, G. Sevieri, Simplified Soil-Structure interaction models for concrete gravity dams. R. Owen, R. de Borst, J. Reese and C. Pearce Eds. *6th European Conference on Computational Mechanics (ECCM 6) 11-15 June 2018,* Glasgow, UK.

[20] H. M. Westergaard, Water pressures on dams during earthquakes. *Trans. ASCE,* **98**, 418-433, 1933.

[21] L. Luzi, R. Puglia, E. Russo & ORFEUS WG5, Engineering Strong Motion Database, Istituto Nazionale di Geofisica e Vulcanologia, Observatories & Research Facilities for European Seismology, doi: 10,13127/ESM, 2016.

[22] Abaqus r.6.14 *Reference Guide*.

[23] J. Lee, G.L Fenves, Plastic-damage concrete model for earthquake analysis of dams. *Earthquake Engineering and Structural Dynamics*, **27**, 937-956, 1998.

[24] J. Lubliner, S. Oliver, S. Oller, E. Oñate, A plastic-damage model for concrete, *International Journal of Solids and Structures*, **25**, 299-326, 1989.

[25] G.S. Sooch, A. Bagchi, A new Iterative procedure for deconvolution of seismic ground motion in dam-reservoir-foundation systems. *Journal of Appl. Math.*, **2014**, 2014.

COMPDYN 2019
7th ECCOMAS Thematic Conference on
Computational Methods in Structural Dynamics and Earthquake Engineering
M. Papadrakakis, M. Fragiadakis (eds.)
Crete, Greece, 24–26 June 2019

ANALYSIS OF THE EFFECT OF LAYERED SUBSOIL ON THE SEISMIC EXCITATION OF NUCLEAR FUEL STORAGE STRUCTURES

Juraj Králik[1], **Juraj Králik, jr.**[2]

[1] Faculty of Civil Engineering, STU Bratislava, Radlinského 11, 810 05 Bratislava, SK

juraj.kralik@stuba.sk

[2] Academy of Fine Arts and Design in Bratislava, Hviezdoslavovo nám. 18, 814 37 Bratislava, SK

ing.kralikj@hotmail.com

Abstract

During the last couple of decades, it was recognized that the soil on which a structure is constructed might interact dynamically with the structure during earthquakes, especially when the soil is relatively soft and the structure is stiff. This kind of dynamic soil-structure interaction can sometimes modify significantly the stresses and deflections of the full structural system from the values that can be developed if the structure were designed on a rigid foundation. Two important characteristics that distinguish the dynamic soil-structure interaction system from other general dynamic structural systems are the unbounded nature and the nonlinearity of the soil medium. Generally, when establishing numerical dynamic soil-structure interaction models, the following problems should be taken into account.

Keywords: Seismic, Safety, Reliability, SSI, Nuclear Power Plants, ANSYS.

1 INTRODUCTION

After the accident of nuclear power plant (NPP) in Fukushima the IAEA in Vienna adopted a large-scale project "Stress Tests of NPP", which defines new requirements for the verification of the safety and reliability of NPP. Based on the recommendations of the ASCE standard and IAEA in Vienna [1- 3], the effective seismic resistance of objects is assessed in PGA sites up to 0.3g according to the "Seismic Margin Assessment" methodology (SMA) [1].

The required methodology was based on a reference earthquake (RLE) or a "Seismic Margin Earthquake" (SME) earthquake, which is an earthquake with seismological parameters of a given site and response spectrum at the free terrain level corresponding to 84.1% probability of non-elevation (median overs), including Peak Ground Acceleration (PGA) for a given acceptable annual occurrence probability (typically 10^{-4}/year). The dynamic soil-structure interaction can sometimes modify significantly the stresses and deflections of the structural system.

The building of the nuclear fuel storage VJP in the J. Bohunice is located near the NPP areal [4]. This building consists of a reinforced concrete and steel hall. The nuclear fuel storage capacities are located in seven modules by 7 meters (Fig.1). The dimensions of the object in the plan view are 58.8m.x.36m. The elevation of the building is designed asymmetrically from 14m to 30m. The building is based on a massive reinforced concrete slab with a thickness of 1.5m. The base joint is located at a depth of -6.5 m.

The design response spectra were prepared based on results of the PSHA (Probabilistic Seismic Hazard Analysis) study for the NPP J. Bohunice site developed by GFÚ SAV [4]. The value of the PGA for horizontal and vertical excitation for the annual occurrence probability (typically 10^{-4}/year) is following

- horizontal acceleration peak $PGA_{H.iRLE} = 0.250g$, $PGA_{H.RLE} = 0.367g$
- vertical acceleration peak $PGA_{V.iRLE} = 0.130g$, $PGA_{V.RLE} = 0.229g$

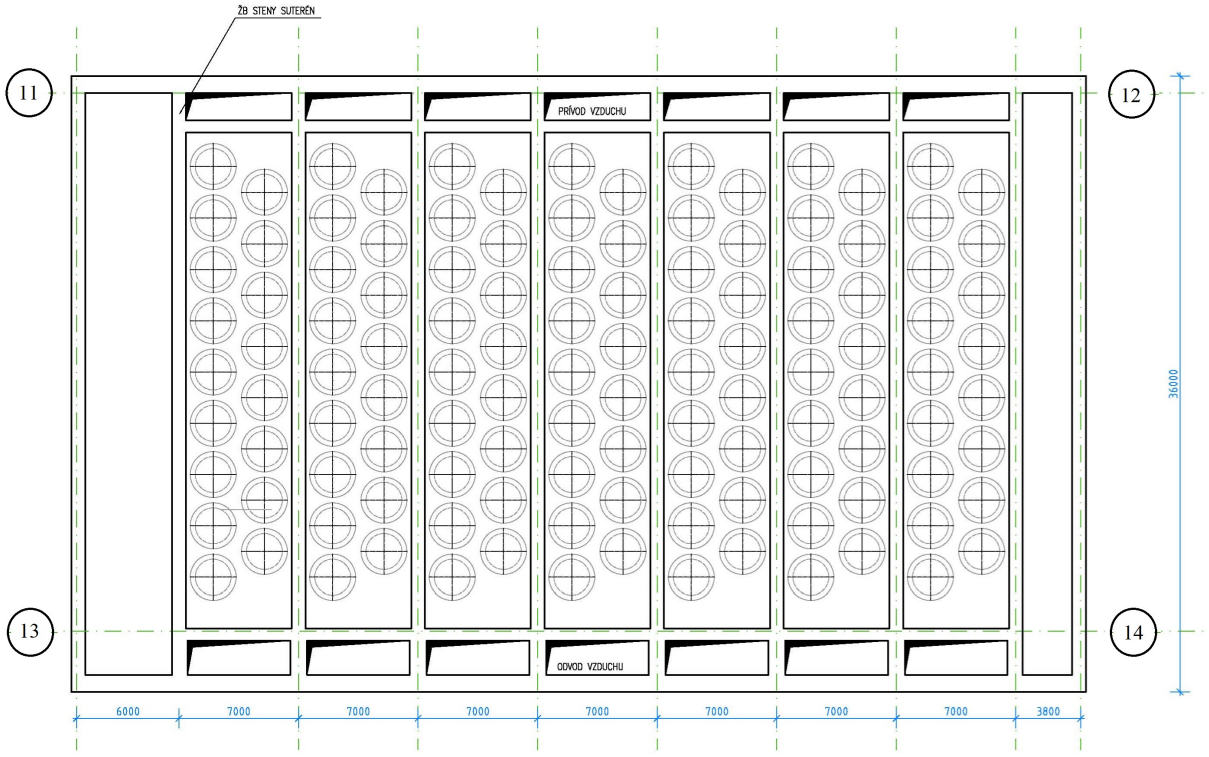

Figure 1: Ground floor basement of the nuclear fuel storage VJP SO841M_B-VT

The values of seismic motion (see Fig.2) for the nuclear fuel storage VJP are taken from the report of the Geophysical institute [4]. The horizontal and vertical response spectrum RLE are shown in the graphs. These spectra were used as inputs for generating a synthetic three-component accelerograms.

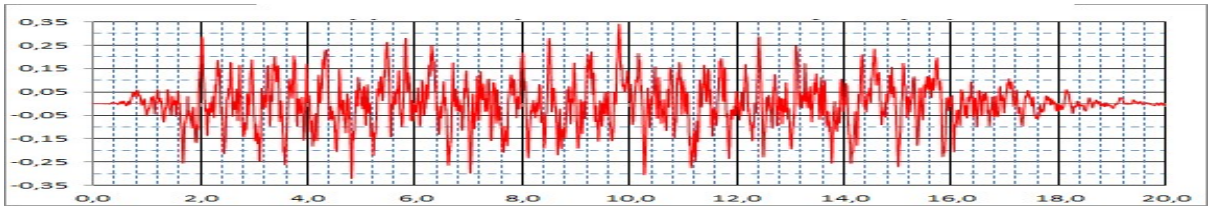

Figure 2: The spectrum compatible synthetic accelerogram.

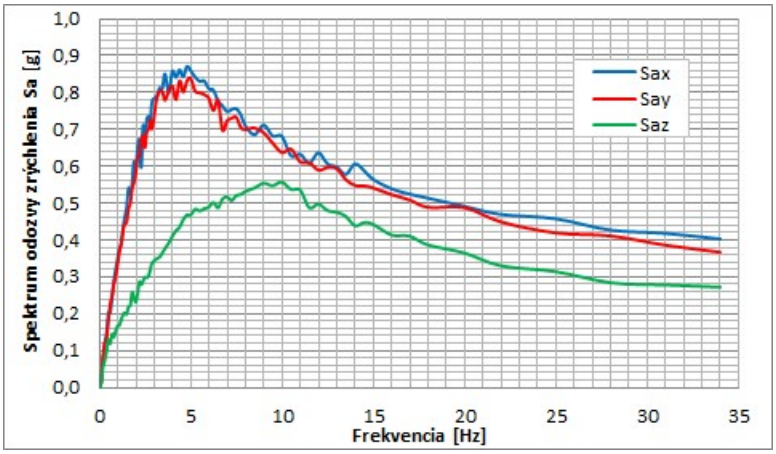

Figure 3: The response spectrum from the synthetic accelerograms in direction *X*, *Y* and *Z* for 5% damping

2 GEOPHYSICAL SUBSOIL PROPERTIES OF THE LOCALITY

For seismic analyzes, it was recommended to use the seismic assignment for the nuclear fuel storage VJP at J. Bohunice site according to data in the feasibility study.

BV11			BV12			BV13			BV14			BVX		
Depth	v_s	ρ	Depth	v_s	ρ	Depth	v_s	ρ	Depth	v_s	ρ	Depth	v_s	ρ
[m]	[m/s]	[t/m3]	[m]	[m/s]	[t/m3]	[m]	[m/s]	[t/m3]	[m]	[m/s]	[t/m3]	[m]	[m/s]	[t/m3]
0.0	100	2.0	0.0	100	2.0	0.0	100	2.02	0.0	100	2.0	0.0	100	2.0
10.2	230	2.0	8.3	210	2.0	4.8	190	1.98	5.5	200	2.0	6.9	210	2.0
10.2	260	2.0	8.3	250	2.0	4.8	230	2.03	5.5	250	2.0	6.9	250	2.0
18.0	410	2.1	17.4	380	2.1	16.6	370	2.11	17.1	370	2.1	18.5	420	2.1
18.0	440	2.2	17.4	410	2.2	16.6	400	2.15	17.1	400	2.2	18.5	460	2.2
25.2	460	2.2	25.3	470	2.2	24.0	470	2.20	24.5	470	2.2	24.9	480	2.2
25.2	460	2.0	25.3	470	2.0	24.0	470	1.95	24.5	470	2.0	24.9	480	2.0
28.8	500	2.1	28.5	500	2.1	30.1	510	2.05	29.4	510	2.1	28.7	500	2.1
28.8	500	2.2	28.5	500	2.2	30.1	510	2.20	29.4	510	2.2	28.7	500	2.2
40.7	650	2.3	40.8	650	2.3	39.6	650	2.25	39.9	650	2.3	41.8	650	2.3
40.7	650	2.1	40.8	650	2.1	39.6	650	2.05	39.9	650	2.1	41.8	650	2.1
100.0	860	2.2	100.0	860	2.2	100.0	860	2.20	100.0	860	2.2	100.0	860	2.2

Table 1: Geological profile under the building of the nuclear fuel storage VJP SO841M_B-VT

This seismic assignment corresponds to the results of the original seismological surveys (see Tab.1) based on the recommendations of the standards IAEA 50-SG-S1 and NS-G-3.3.

Dynamic soil characteristics were obtained with sufficient accuracy from the refractive and reflexive survey of a given site [3, 5, 6]. Depending on the propagation rates of the longitudinal and transverse waves in the soil, we can determine its physical characteristics.

The basic rigid parameter characterizing the earth body for dynamic calculations is the dynamic G_{dyn} (or Young's elastic modulus modulus)

$$G_{dyn} = v_s^2 \rho, \quad E_{dyn} = v_s^2 \rho 2\left(1+\nu_{dyn}\right), \quad \nu_{dyn} = \left(v_p^2 - 2v_s^2\right) / \left[2\left(v_p^2 - v_s^2\right)\right] \tag{1}$$

where ρ is the soil density, v_s - the velocity of the shear waves propagation in the respective earth (layer), v_p is the velocity of the longitudinal waves.

3 STIFFNESS AND DAMPING SOIL PARAMETERS IN THE SUBSOIL

Dynamic soil characteristics were obtained with sufficient accuracy from the refractive and reflexive survey of a given site [4]. Depending on the propagation rates of the longitudinal and transverse waves in the soil, we can determine its physical characteristics [3].

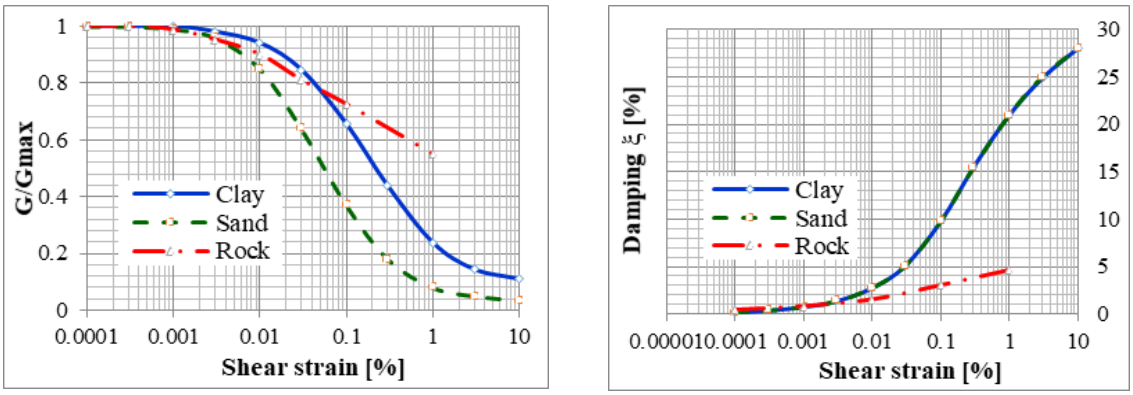

Figure 4: Shear modulus dependence on the shear strain and proportional damping.

In the case of earthquakes, there is a large movement of the soil, and because of plastic deformation, the value of the dynamic soil module also drops. According to the recommendations of international standards, this reduction will maximally reach 65% of the dynamic module measured for small seismic events. The process of the shear modulus and the damping can be seen in Fig. 4 depending on the shear strain [3].

4 SEISMIC HAZARD CONSIDERING SITE EFFECTS

The methodology for analyzing the influence of the layered subsoil of type 3 (for $v_s < 300$ m/s) according to the requirements of the IAEA NS-G-3.6 was used to define the seismic load for the nuclear fuel storage. The seismic load RLE was defined assuming that seismic waves are transformed from the source to the site in a rock bed (for $v_s > 1100$m/s).

Local design acceleration spectra were calculated considering the SSI effects used the SHAKESI program in accordance with the recommendations of the standards IAEA [2] and U.S. NRC.

Therefore, the methodology for calculating local design spectra is based on the following assumptions:

- PGA values for RLE seismicity were determined for the free field assuming the rigidity of the bed of the corresponding to the rock subsoil (for $v_s > 1100$m/s)

- The response spectrum acceleration for SL-2 [3] were defined based on a probabilistic analysis of the site effects,
- Synthetic 3D accelerograms compatible with response spectra were generated in accordance with the requirements [3].

Based on these input data, the calculation of local design spectra, taking into account the real geological composition at the location of the VJP object, is carried out in the following steps:

- Calculation of the synthetic accelerograms on the base at level -100m from the free level in accordance with IAEA [2] standards,
- Calculation of the local synthetic accelerograms and the design response spectra at level of foundation (-6.5m) and at level of the pile foundations (-18.5m) from the excitation synthetic accelerations using the program SHAKESI for original and modified geological conditions,
- Calculation of the smoothed design spectra at foundation level (-6.5m) and pile level (-18.5m) than the median values and the statistical envelope for 84.5% probability of failure is based on previous analyzes for characteristic excitation frequencies.

For these analyses, the modified SHAKESI [3] program was used to determine a best estimate of the transformation from free field to base level for the 1D model of the subsoil.

The amplification factors of the program SHAKESI are presented in the fig.5.

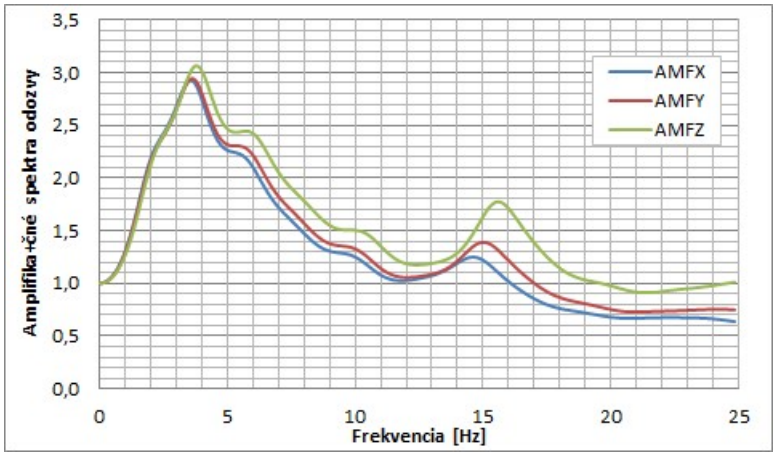

Figure 5: The amplification factors between the base and free field - SHAKESI

Acceleration response spectrum [m/s^2]								
Frequency [Hz]	Level "Base"				Level "Free Field"			
	RLE		Local (SSI)		RLE		Local (SSI)	
	Sah	Sav	Sah	Sav	Sah	Sav	Sah	Sav
0.5	0.050	0.015	0.059	0.067	0.050	0.030	0.084	0.050
2	0.364	0.085	0.159	0.382	0.364	0.172	1.891	0.708
5	0.837	0.199	0.293	0.264	0.837	0.422	1.402	0.863
10	0.780	0.215	0.240	0.269	0.780	0.524	0.836	0.759
33	0.367	0.103	0.136	0.167	0.367	0.229	0.581	0.394

Table 2: Comparison of the global and local acceleration response spectrum

The smoothing response spectra were calculated in program SHAKESI at defined frequencies recommended by IAEA standards (Fig.6).

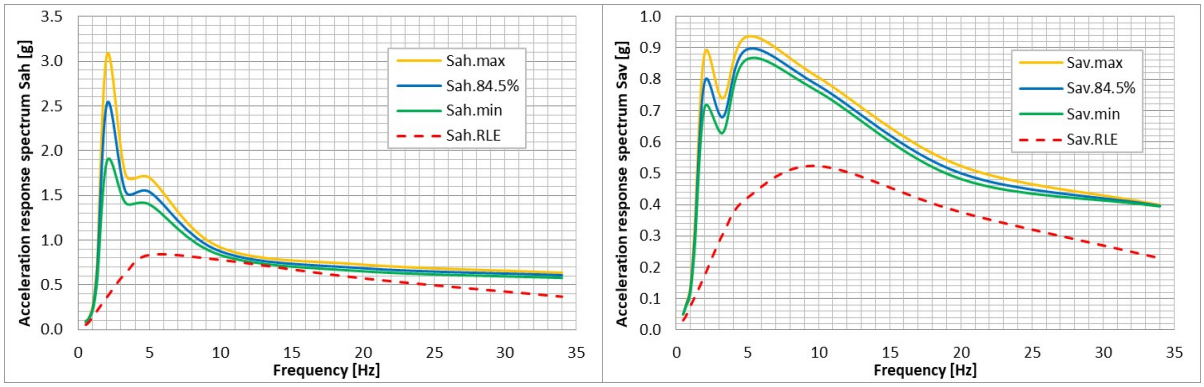

Figure 6: The smoothing horizontal and vertical response spectra at level -6.5m

5 CONCLUSIONS

This paper describes the soil-structure interaction effects in the case of the nuclear fuel storage VJP during earthquake excitation. The methodology of the calculation of the soil-structure interaction effects was presented. The local design acceleration spectra were calculated considering the SSI effects used the SHAKESI program in accordance with the recommendations of the standards IAEA. The considering the local effects in accordance with the subsoil properties is very significant.

Acknowledgement

This project was performed with the financial support of the Grant Agency SR (VEGA 1/0265/16 and 1/0412/18).

REFERENCES

[1] EPRI, *A Methodology for Assessment of Nuclear Power Plant Seismic Margin*, Rep. EPRI NP-6041-SL, Rev. 1, EPRI, Palo Alto, CA, (1991).

[2] IAEA, *Specific Safety Guide No. SSG-9, Seismic Hazards in Site Evaluation for Nuclear Installations. International Atomic Energy Agency*, Vienna, 2010.

[3] J. Králik, *Safety and Reliability of Nuclear Power Buildings in Slovakia. Earthquake-Impact-Explosion*. Ed. STU Bratislava, 2009, 307pp.

[4] J. Králik, *Dynamic analysis of the soil-structure interaction to the sesmic loads of the nuclear fuel storage building in J. Bohunice*, Rep. 0086-A*3*1-VUJE-R2-2/18.

[5] S. M. Hsiung, H. Asadul, A.H. Chowdhury, *Seismic Effects on Soil-Structure Interactions*, NRC–02–07–006, NRA, San Antonio, Texas, 2011.

[6] T. Zouaghi, *Earthquakes Tectonics, Hazard and Risk Mitigation*, Monography, In Tech Open, February 1st 2017, DOI: 10.5772/63173, ISBN: 978-953-51-2886-1.

[7] J. Králik, M. Šimonovič, Earthquake response analysis of nuclear power plant buildings with soil-structural interaction. *Mathematics and Computers in Simulation 50. IMACS*/Elsevier Science B.V. 1999, Pp. 227-236.

[8] J. Králik, Risk-Based Safety Analysis of the Seismic Resistance of the NPP Structures, In Proc. of the *8th International Conference on Structural Dynamics, EURODYN 2011*, Leuven, Belgium, 4-6 July 2011, Vol.2, p. 292-299.

COMPDYN 2019
7th ECCOMAS Thematic Conference on
Computational Methods in Structural Dynamics and Earthquake Engineering
M. Papadrakakis, M. Fragiadakis (eds.)
Crete, Greece, 24–26 June 2019

ANALYSIS OF RECTANGULAR CONCRETE-FILLED DOUBLE SKIN TUBULAR SHORT COLUMNS WITH EXTERNAL STAINLESS STEEL TUBES

Omnia Kharoob[1], **Nashwa Yossef**[2]

[1] Department of Structural Engineering, Faculty of Engineering, Tanta University
Tanta, Egypt
omnia_m102020@yahoo.com

[2] Department of Structural Engineering, Faculty of Engineering, Tanta University
Tanta, Egypt
nashwa.yossef@gmail.com

Abstract

Concrete-filled double skin steel tubular (CFDST) columns could be utilized in structures such as bridges, high-rise buildings, viaducts and electricity transmission towers due to its great structural performance. Alternatively, lean duplex stainless steel has recently gained significant interest for its high structural performance, similar corrosion resistance and lower cost compared to the austenitic steel grade. Hence, this paper presents nonlinear numerical simulations of rectangular outer lean duplex stainless steel (EN 1.4162) CFDST short columns under compression, based on the finite element (FE) method, The FE model and its validation were initially presented. Then, the effect of the key parameters that influence the behavior of these types of columns was introduced. Based on that model, the behavior and design of rectangular outer lean duplex stainless steel (EN 1.4162) CFDST short columns under compression were discussed. All classes of the outer rectangular hollow section according to the depth-to-thickness (D/t) ratios were considered. The results showed that the axial ultimate strength of rectangular CFDST short columns increased linearly by increasing the concrete compressive strength, while it does not influence when changing the hollow ratios. Finally, the axial capacities were compared with the available design methods, and recommendations were conducted for the design strength of this type of column. The presented design model, for calculation of the ultimate axial strength of rectangular CFDST short columns with external lean duplex stainless steel outer tubes, gave suitable conservative results if compared with the other literature model.

Keywords: Concrete-filled double skin columns, Finite element analysis, Ultimate axial strength, Short columns, Lean duplex stainless steel, Compressive strength.

1 INTRODUCTION

Steel-concrete composite columns represent a very attractive structural form that is now benefiting from extensive success. The composite construction ideally combines the advantages of both steel and concrete elements, where's the high strength and the light weight of steel combine the inherent mass, stiffness, damping, and economy of concrete [1, 2]. To reduce the weight of the structure while still maintaining a large energy absorption capacity against different loading cases, concrete-filled double skin steel tubular (CFDST) columns were suggested. With composite construction advantages, CFDST columns were recognized to have a series of beneficial properties, such as a good fire and seismic performance [3-6]. CFDST columns consist of concentric inner and outer steel tubes with infill concrete between them. The steel tubes are hollow structural sections, it may be supplied with carbon steel material, these sections can be circular (CHS) [3-9], square (SHS) [10] and rectangle (RHS) [11, 12].

On the other hand, Stainless steel materials have many advantages like the aesthetic appearance, high corrosion resistance, smooth and uniform surface, high fire resistance, high ductility and impact resistance, reuse and recycling capability. Due to these advantages many researchers [13-18] encouraged to investigate the behaviour of this material on the concrete-filled tubular columns with different cross-section, and motivated the authors to perform this study on the short concrete-filled double skin steel tubular (CFDST) stub columns with external stainless steel material as an introduction study of the long CFDST.

The austenitic stainless steels have been used for many years in structural applications as minor elements; see [19-21]. Due to the lower cost of lean duplexes compared with austenitic stainless steel, its applications are spread recently. However, most design codes [22-24] consider duplexes as the same design as austenitic stainless steels because the majority of the presented numerical and experimental results were for austenitic or duplex alloys as discussed by Gardner [19]. Many studies show that, the structural behaviour of stainless steel and carbon steel are differ, the main difference is that stainless steel has no definite yield strength, it has a round stress-strain curve, and shows an early departure from linear elastic behaviour with strong strain hardening [19-21]. The carbon steel has high proportional limit stress (at least 70% of the yield point) compared to stainless steel (from 36%- 60% of the yield stress) [25].

The rectangular sections are preferred when large major-axis bending moments occur in beam or beam–column. Based on the above background, the behaviour of rectangular CFDST short columns with external lean duplex tubes of Grade EN 1.4162 has never been studied. Hence, the present paper focuses on the behaviour and strength of short rectangular CFDST columns with external lean duplex tubes. The nonlinear analysis, behaviour and design of rectangular lean duplex stainless steel-concrete-carbon steel double skin tubular short (CFDST) columns were presented. The finite element (FE) model for CFDST short columns, were developed by using the general purpose finite element package ABAQUS [26]. Different classification of cross-sections of outer tubes; fully effective (F), slender (S) and very slender (VS) cross-sections were considered. The high and ultra-high strength concrete (HSC and UHSC) were also investigated for current rectangular CFDST short columns. The results were discussed and compared with the available design strength found in the literature.

2 NUMERICAL MODELLING

Nonlinear numerical simulations, based on the FE method and utilizing the software package ABAQUS/Standard [26], were made in this section to widen the available results on short rectangular CFDST columns which are not found in the literature. The FE model and its vali-

dation were initially presented. Finally, the effect of key parameters that influence the behaviour of these types of columns was discussed.

2.1 General description of FE model

A detail of the current FE model was previously presented in several papers published by the first author, such as [15-17]. The FE model can be summarized as following:

- Both inner and outer steel tubes were modelled using element S3 ABAQUS [26], S3 is a three-node triangular general-purpose shell element with finite membrane strains element.
- The sandwiched concrete and the two end plates were modelled by C3D4 ABAQUS [26], where C3D4 is a three dimensional four-node linear tetrahedron solid element.
- The initial imperfections were neglected in the FE modelling as previously discussed by Tao et al. [27]. Because of the reduction in strength of the thin-walled hollow tubes is not significant (about 1% in average) owing to the delaying effect of the concrete core on the tube buckling.
- The mesh size was chosen as approximately 25 mm for modelling the tubes and the sandwiched concrete.
- Interface between tubes and the sandwiched concrete was modelled by surface-based interaction with a contact pressure-overclosure model in the normal direction and a Coulomb friction model in the longitudinal direction; more details of interaction between surfaces were discussed by Hassanein et al. [15, 16].
- Only a quarter of the short rectangular CFDST columns were modelled, where's the geometry and the loads were symmetric, as shown in Figure 1 (a), in which the upper end plates at the loaded end were removed to illustrate the cross-section.

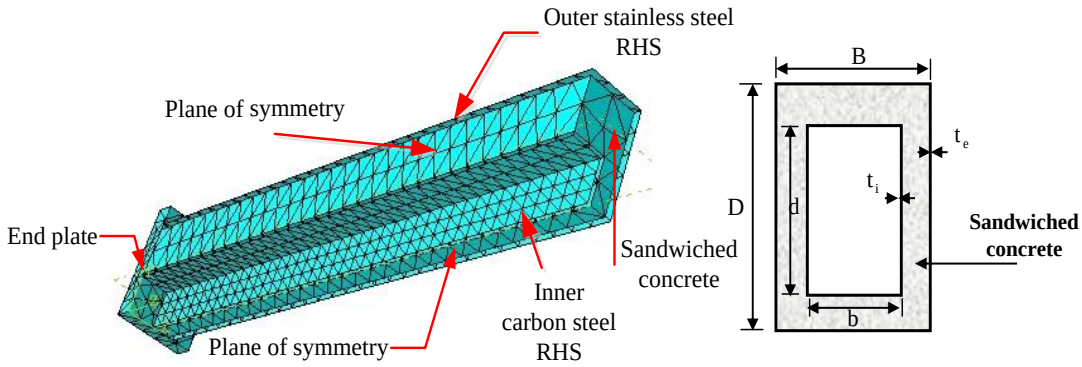

Figure 1(a). FE mesh of short rectangular CFDST column

Figure 1(b): Cross-section CFDST column

Figure 1: FE mesh and Cross-section of short rectangular CFDST column

2.2 Stainless steels material model

Lean duplex stainless steel Grade EN 1.4162 was used in this study with proof stress ($\sigma_{0.2}$) and ultimate strength (σ_u) of 530 MPa and 700 MPa, respectively according to EN 10088-4 [24]. The material behaviour can be modelled using a multi-linear stress-strain curve in ABAQUS [26], as shown in Figure 2; see Ref. [15, 18].

2.3 Carbon steels material model

The carbon steel tube with steel grade S235 material was used. According to EN 1993-1-1 [28], S235 has a minimum yield (f_{sy}) of 235 MPa, an ultimate strength (f_{su}) of 360 MPa and the Young's modulus of E_0 = 210 GPa. A von Mises material with isotropic hardening was used for modelling the steel material. The bilinear elastic-plastic stress-strain curve with linear strain hardening was used to model the steel material.

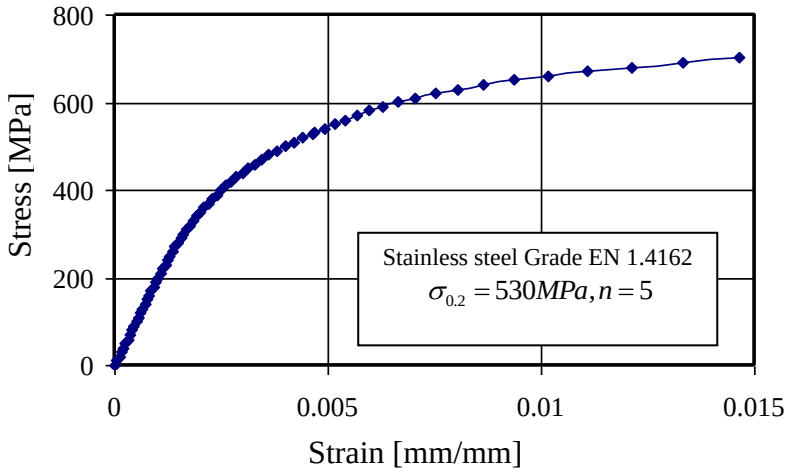

Figure 2. Stress-strain curve of the lean duplex stainless steel material Grade EN 1.4162

2.4 Sandwich concrete material model

The confinement of concrete by steel tube occurred at the four corners of the rectangular CFST column. This confinement does not have a considerable effect on the compressive strength of the concrete core so that it can be ignored in the analysis and design of rectangular CFST columns, as studied by Patel et al. [29]. In spite of that, the ductility of the concrete core in rectangular CFST columns was improved and was included in the presented concrete model, as discussed by Liang [30] and Patel et al. [29].

2.5 Validation of the FE model

2.5.1 CFDST short columns with both carbon steel tubes

To assess the accuracy of the generated FE models, the validity of the current FE model is made in this section. First, the model was verified by the behaviour of carbon rectangular CFDST short axial columns tested by Tao et al. [12]. A short specimen of a rectangular cross-section of CFDST short axial column was given in Figure 1 (b). Two replicate tests for this specimen were tested. The details of the specimens' simulation are given in Table 1, where D, B and t_e are the depth, width and thickness of the outer square tube, and d, b and t_i are the depth, width and thickness of the inner square tube respectively. Second, additional simulation to validate the FE model was developed, the model was used to predict the behaviour of square tubes CFDST short axial columns with inner circular tubes tested by Han et al. [31]. The comparison between the current FE ultimate strengths ($P_{ul,FE}$) and the experimental results ($P_{ul,Exp}$) is listed in Table 1. The mean value of $\frac{P_{ul,FE}}{P_{ul,Exp}}$ is 0.96 with a coefficient of variations of 0.043.

Figure 3 (a) shows a comparison between the experimental and FE load-axial strain curve for the rectangular CFDST column tested by Tao et al. [12]. Also, Figure 3 (b) shows a com-

parison between the experimental specimens tested by Han et al. [31] and FE load-axial strain curves of sample results of square CFDST columns with circular inner tubes presented by the first author with the same model [10]. It can be observed that the FE model gives good predictions for the ultimate load and axial load-strain curves for the short CFDST columns with both square and rectangular cross-sections.

Details of the tested short rectangular CFDST columns [12]									$P_{ul,FE}$ [kN]	$P_{ul,Exp}$ [kN]	$\frac{P_{ul,FE}}{P_{ul,Exp}}$
Column	$D*B*t_e$ [mm]	$d*b*t_i$ [mm]	L [mm]	f_{ye} [MPa]	f_{ue} [MPa]	f_{yi} [MPa]	f_{ui} [MPa]	f'_c [MPa]			
DST-SC1	150*100*3.2	75*45*3.2	450	380	476	429	473	42.88	1315	1320	0.996
DST-SC2	150*100*3.2	75*45*3.2	450	380	476	429	473	42.88	1315	1300	1.012
Details of the tested short square CFDST columns [31]											
Column	$D \times t_e$ [mm]	$d \times t_i$ [mm]	L [mm]	f_{ye} [MPa]		f_{yi} [MPa]		f'_c [MPa]			
scc3-1	120*3	58*3	360	275.9		374.5		37.44	946	990	0.96
scc3-2	120*3	58*3	360	275.9		374.5		37.44	946	1000	0.95
scc7-1	300*3	165*3	900	275.9		320.5		37.44	3050	3240	0.94
scc7-2	300*3	165*3	900	275.9		320.5		37.44	3050	3430	0.89
Mean											**0.96**
Standard deviation											**0.043**

The subscript ($_e$) and ($_i$) for external and internal properties respectively, f'_c is the compressive cylinder strength of the concrete.

Table 1: Details of the tested short CFDST columns and the comparison of the experimental and predicted strength.

2.5.2 Short columns with external stainless steel tubes

In this subsection, the verification of the FE model to simulate the behaviour of stainless-steel tubes was assessed. The developed FE model was used to predict the behaviour of square and rectangular hollow section (SHS and RHS) short columns with the lean duplex stainless steel tubes, tested by Theofanous et al. [32]. Table 2 presents the dimensions and material properties of these columns. The ultimate axial loads and end shortening at the ultimate load of SHS and RHS columns obtained from the finite element analyses were compared with the test data in Table 3. The FE model yields good predictions of both ultimate loads (P_{ul}) and end shortening at the ultimate load (δ_u) of SHS and RHS columns. The mean values of $\frac{P_{ul,FE}}{P_{ul,Exp}}$ and $\frac{\delta_{u,FE}}{\delta_{u,Exp}}$ are 0.98 and 0.95 with a coefficient of variations of 0.019 and 0.042, respectively. Figure 3 (c) shows the comparison of predicted FE and experimental results with respect to the load-axial strain relationships for SHS and RHS columns with a lean duplex stainless steel tubes. It can be concluded that the FE model gives good predictions for the behaviour of axial load-strain relationships compared with the tested specimens.

On the other hand, other verifications were made by the first author on circular CFDST short columns tested by Han et al. [14] with external stainless steel tubes and inner carbon tubes [17].

Column	$D*B*t$ [mm]	L [mm]	E [MPa]	$\sigma_{0.2}$ [MPa]	σ_u [MPa]	n
80*80*4-SC2	80*80*3.81	332.2	199900	679	773	6.5
80*40*4-SC2	79.5*39.6*3.81	237.8	199500	734	817	10.1

Table 2: Details of the tested lean duplex stainless steel short columns tested by Theofanous et al. [32]

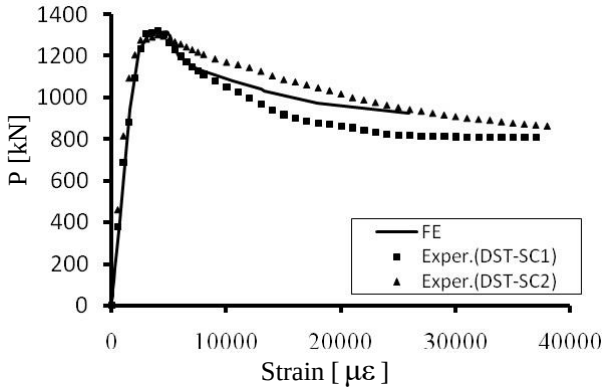

Figure 3(a): Comparisons of experimental and FE axial load-strain curves for short rectangular CFDST column tested by Tao *et al*. [12]

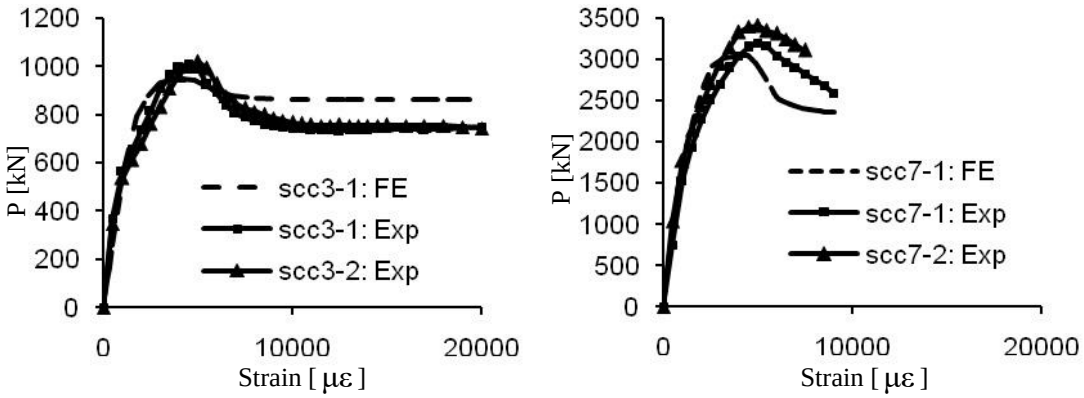

Figure 3(b): Comparisons of experimental and FE axial load-strain curves for short square CFDST columns with inner CHSs presented by Hassanein *et al*. [10]

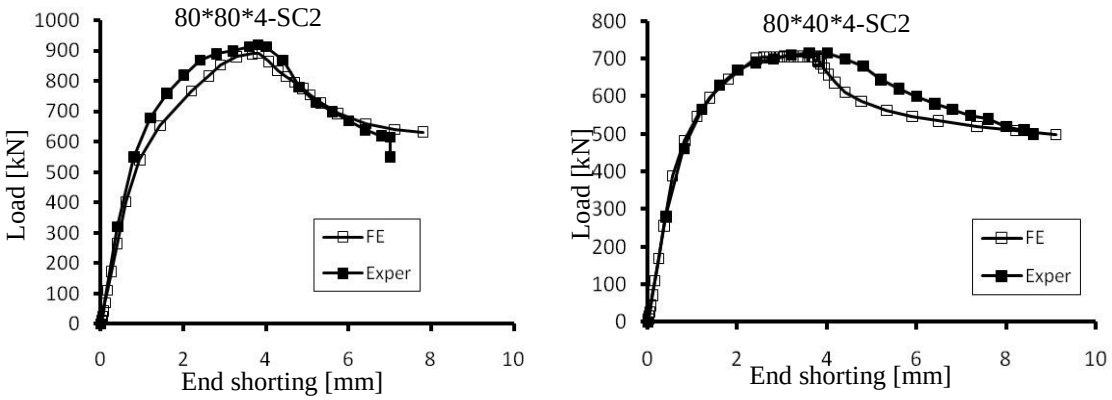

Figure 3(c): Verification of load-end shortening relationships of Lean duplex stainless steel columns Theofanous *et al*. [32]

Figure 3: Verification of the current FE model

Column	Ultimate load (P_{ul}) [kN]			End shortening at ultimate load δ_u [mm]		
	$P_{ul,FE}$	$P_{ul,Exp}$	$\frac{P_{ul,FE}}{P_{ul,Exp}}$	$\delta_{u,FE}$	$\delta_{u,Exp}$	$\frac{\delta_{u,FE}}{\delta_{u,Exp}}$
80*80*4-SC2	890	915	0.97	3.82	3.88	0.98
80*40*4-SC2	708	710	0.997	3.8	4.12	0.92
Mean			**0.98**			**0.95**
Standard deviation			**0.019**			**0.042**

Table 3: Comparison between FE and Experimental results of short lean duplex stainless steel columns

3 PARAMETRIC STUDY

The verified FE model was used to generate parametric results for short rectangular CFDST columns. The length of the column (L) was taken as three times the external depth (D) of the outer rectangular hollow section (RHS) to avoid global buckling effects. Table 4 shows the dimensions of the current cross-sections considered in this study. The material properties were considered as discussed in sections 2.3 to 2.5. The outer RHSs were classified into three groups (G1, G2 and G3) based on the maximum depth-to-thickness ratios for the compression parts of the cross-sections $(D-2t_e)/t_e$ according to EC3 Part 1.4 [24]. The first group (G1) was fully-effective (F: $(D-2t_e)/t_e \leq 30.7$), and the second group (G2) was considered as slender sections (S: $(D-2t_e)/t_e > 30.7$); $\varepsilon = \sqrt{235/f_{ye}}$. Finally, the value of $(D-2t_e)/t_e$ exceeded the maximum value of 52ε for group 3 (G3) as specified in EC4 [33], hence these cross-sections were considered to be very slender (VS). It worth pointing out that, in the current paper, the inner tubes were selected to have full-effective cross-sections.

The cylinder strength (f'_c) of the concrete and the hollow section ratio ($\chi = \sqrt{\frac{b*d}{(B-2t_e)*(D-2t_e)}}$) were considered as the key parameters in the analyses. The values of f'_c ranging from 25 MPa to 120 MPa, covering the normal strength (NSC), high strength (HSC) and ultra-high strength concrete (UHSC) according to the EC4 [33] in each group. The values of the hollow section ratio (χ) are 0.34, 0.54 and 0.66 in each group. The ultimate axial loads of the current model were given in Table 4.

The failure mode of short rectangular CFDST column presented in Figure 4. The failure local buckling mode was observed clearly in the outer tube than the inner one. An outward local buckling failure mechanism of the outer tube was observed, this behaviour is similar to that observed by Tao et al. [11, 12] in CFDST specimens. A separation of the tube from the concrete core was noticed.

Group	Column	Outer tube				Inner tube				f'_c [MPa]	χ	$\frac{t_i}{t_e}$	$P_{u,FE}$ [kN]
		D [mm]	B [mm]	t_e [mm]	$\frac{D}{t_e}$	d [mm]	b [mm]	t_i [mm]	$\frac{d}{t_i}$				
G1	C1	200	120	10	20	60	35	5	12	25	0.34	0.50	5036
	C2	200	120	10	20	60	35	5	12	40	0.34	0.50	5298
	C3	200	120	10	20	60	35	5	12	60	0.34	0.50	5611
	C4	200	120	10	20	60	35	5	12	80	0.34	0.50	5836
	C5	200	120	10	20	60	35	5	12	100	0.34	0.50	6240

	C6	200	120	10	20	60	35	5	12	120	0.34	0.50	6428
	C7	200	120	10	20	80	65	5	12	25	0.54	0.50	5003
	C8	200	120	10	20	80	65	5	12	40	0.54	0.50	5253
	C9	200	120	10	20	80	65	5	12	60	0.54	0.50	5470
	C10	200	120	10	20	80	65	5	12	80	0.54	0.50	5780
	C11	200	120	10	20	80	65	5	12	100	0.54	0.50	5951
	C12	200	120	10	20	80	65	5	12	120	0.54	0.50	6282
	C13	200	120	10	20	120	65	5	12	25	0.66	0.50	5047
	C14	200	120	10	20	120	65	5	12	40	0.66	0.50	5216
	C15	200	120	10	20	120	65	5	12	60	0.66	0.50	5462
	C16	200	120	10	20	120	65	5	12	80	0.66	0.50	5704
	C17	200	120	10	20	120	65	5	12	100	0.66	0.50	5894
	C18	200	120	10	20	120	65	5	12	120	0.66	0.50	6080
G2	C19	320	140	10	32	85	50	10	8.5	25	0.34	1.00	6883
	C20	320	140	10	32	85	50	10	8.5	40	0.34	1.00	7468
	C21	320	140	10	32	85	50	10	8.5	60	0.34	1.00	7920
	C22	320	140	10	32	85	50	10	8.5	80	0.34	1.00	8435
	C23	320	140	10	32	85	50	10	8.5	100	0.34	1.00	8954
	C24	320	140	10	32	85	50	10	8.5	120	0.34	1.00	9354
	C25	320	140	10	32	140	75	10	14	25	0.54	1.00	7167
	C26	320	140	10	32	140	75	10	14	40	0.54	1.00	7438
	C27	320	140	10	32	140	75	10	14	60	0.54	1.00	7890
	C28	320	140	10	32	140	75	10	14	80	0.54	1.00	8222
	C29	320	140	10	32	140	75	10	14	100	0.54	1.00	8657
	C30	320	140	10	32	140	75	10	14	120	0.54	1.00	9024
	C31	320	140	10	32	185	85	10	18.5	25	0.66	1.00	7375
	C32	320	140	10	32	185	85	10	18.5	40	0.66	1.00	7430
	C33	320	140	10	32	185	85	10	18.5	60	0.66	1.00	7865
	C34	320	140	10	32	185	85	10	18.5	80	0.66	1.00	8221
	C35	320	140	10	32	185	85	10	18.5	100	0.66	1.00	8543
	C36	320	140	10	32	185	85	10	18.5	120	0.66	1.00	8867
G3	C37	400	150	10	40	115	50	8	14.4	25	0.34	0.80	7521
	C38	400	150	10	40	115	50	8	14.4	40	0.34	0.80	7786
	C39	400	150	10	40	115	50	8	14.4	60	0.34	0.80	8309
	C40	400	150	10	40	115	50	8	14.4	80	0.34	0.80	9411
	C41	400	150	10	40	115	50	8	14.4	100	0.34	0.80	9977
	C42	400	150	10	40	115	50	8	14.4	120	0.34	0.80	10783
	C43	400	150	10	40	160	90	8	20	25	0.54	0.80	7501
	C44	400	150	10	40	160	90	8	20	40	0.54	0.80	7931
	C45	400	150	10	40	160	90	8	20	60	0.54	0.80	8258
	C46	400	150	10	40	160	90	8	20	80	0.54	0.80	9008
	C47	400	150	10	40	160	90	8	20	100	0.54	0.80	9613
	C48	400	150	10	40	160	90	8	20	120	0.54	0.80	10228
	C49	400	150	10	40	255	85	8	31.9	25	0.66	0.80	7544
	C50	400	150	10	40	255	85	8	31.9	40	0.66	0.80	7683
	C51	400	150	10	40	255	85	8	31.9	60	0.66	0.80	8094
	C52	400	150	10	40	255	85	8	31.9	80	0.66	0.80	9076
	C53	400	150	10	40	255	85	8	31.9	100	0.66	0.80	9458
	C54	400	150	10	40	255	85	8	31.9	120	0.66	0.80	9750

Table 4: Details of FE models of short rectangular CFDST columns

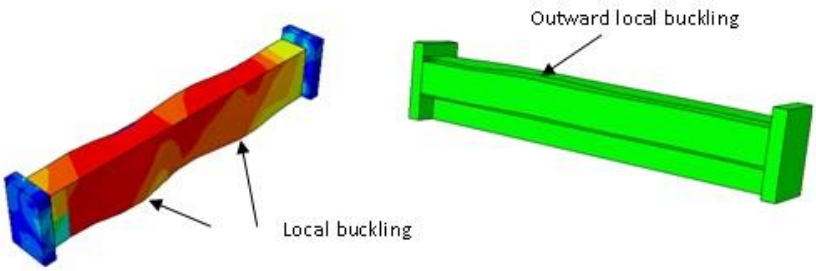

Figure 4: Failure mode of rectangular CFDST short columns with outer stainless steel

4 EFFECTS OF THE KEY PARAMETERS (f'_c & χ)

In this section, the effect of the cylinder strength (f'_c) of the concrete was discussed, as well as the hollow section ratio (χ) on the behaviour of the rectangular CFDST short columns. The effects of the key parameters on the axial load-strain relationships and the ultimate axial strength ($P_{u,FE}$) were provided.

4.1 Effects of concrete compressive strengths

To study the influence of the concrete compressive strengths (f'_c) on the behaviour of axial rectangular CFDST short columns, the compressive concrete strengths varied between 25 and 120 MPa, so that the current investigation includes normal strength concrete (NSCs) (25 and 40 MPa), high strength concrete (HSCs) (60 and 80 MPa) and ultra-high strength concrete UHSCs of 100 and 120 MPa EC2 [29]. Table 4 shows that increasing in the f'_c values of the sandwiched concrete increases the compressive strength of the rectangular CFDST short columns with full-effective, slender and very slender sections of outer stainless steel tubes for the same hollow ratio.

The relationship between the load and axial strain for sample results was provided in Figure 5. It can be concluded that, the increase in the concrete compressive strength (f'_c) caused increment in the ultimate axial strength of rectangular CFDST short columns in an almost linear manner as shown in Figure 6. Also, it was found that by increasing the concrete compressive strength the initial stiffness is nearly the same. Moreover, the CFDST short columns have favorable ductile behaviour.

4.2 Effects of hollow ratio

The effect of the hollow ratio (χ) on the ultimate axial strength ($P_{u,FE}$) of rectangular CFDST short columns under axial compression was studied for fully effective, slender and very slender sections, as shown in Figure 7. For the same concrete compressive strength (f'_c), it can be observed that, changing of the values of the hollow ratio has minimum effects on the ultimate compressive strength ($P_{u,FE}$). This can be explained, as the hollow ratio increases the area of sandwich concrete decreases, and the strength remains nearly the same due to the increase in the area of the inner tube, which raises the strength and covers the decrease caused by the concrete.

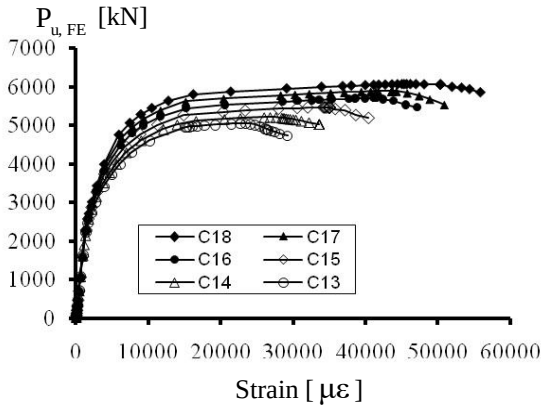

(a) Full-effective sections

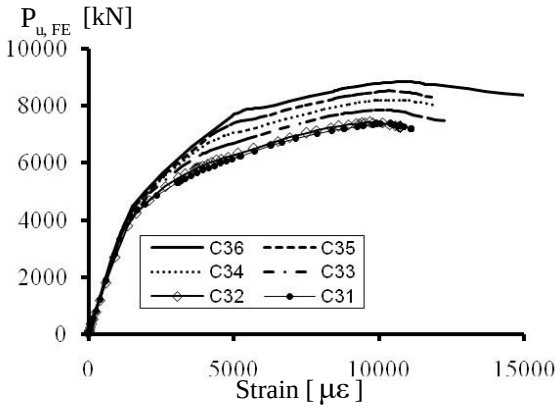

(b) Slender sections

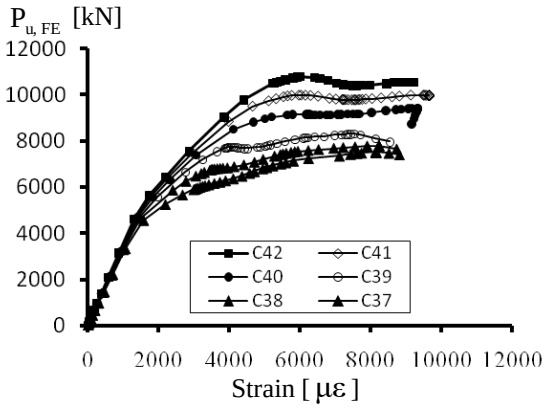

(c) Very slender sections

Figure 5: Axial load-strain curves for rectangular CFDST short columns for different concrete compressive strengths

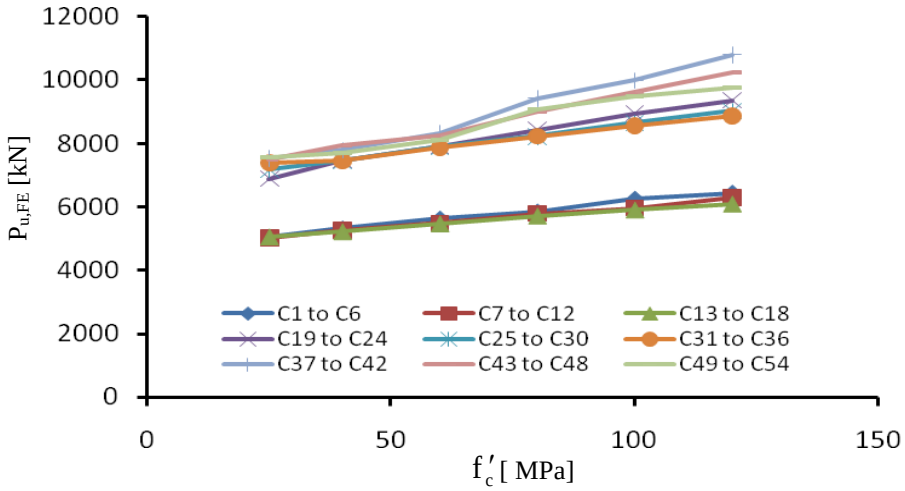

Figure 6: Effect of increasing the concrete compressive strengths on the compressive strength of the rectangular CFDST short column

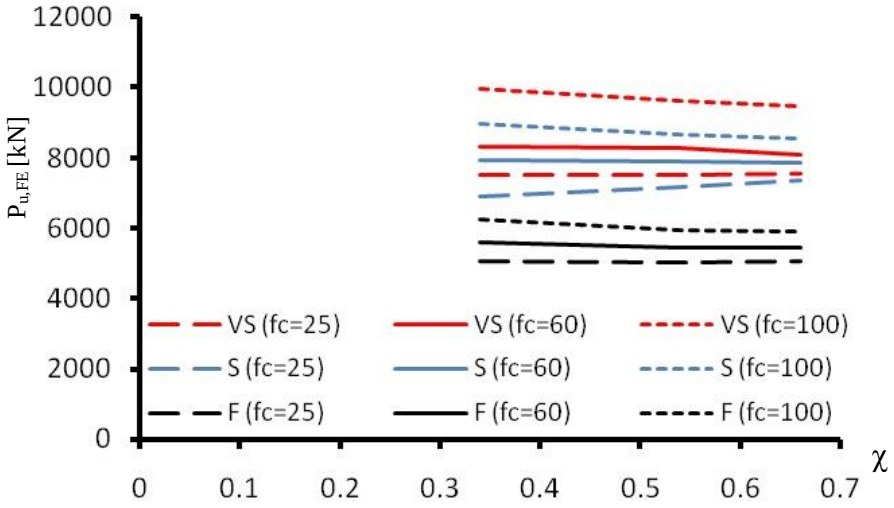

Figure 7: Effects of hollow ratio

5 DESIGN STRENGTH

A comparison of the FE strengths ($P_{u,FE}$) generated in the parametric study, the ultimate axial strength predicted according EC4 (P_{EC4}) [33] and AISC specification (P_{AISC}) [34] proposed for short stainless steel CFDST columns are discussed here.

Based on the design model proposed by Hassanein et al. [17] and developed by the same authors [15, 16], For determining the ultimate axial strength of short stainless steel CFDST columns, a new modified model was suggested for the rectangular (CFDST) specimens based on the current parametric study, whereas the proposed ultimate axial strength ($P_{ul,Prop}$) can be calculated as the summation of the component strength, as follow:

$$P_{ul,Prop} = \gamma_{ss}\sigma_{0.2}A_{se} + f_c'A_{sc} + \gamma_s f_{yi}A_{si} \quad (1)$$

where A_{sc}, A_{se} and A_{si} are the cross-sectional area of the sandwiched concrete, gross sectional area of the external and internal steel tube respectively, f_{yi} is the yield stress of the inner steel tube. γ_{ss} and γ_s are factors to consider the effects of strain hardening as given by Liang [30] and Hassanein et al [15-17], which can be calculated as follow:

$$\gamma_{ss} = 1.62\left(\frac{D}{t_e}\right)^{-0.1} \quad (\gamma_{ss} \le 1.2) \quad (2)$$

$$\gamma_s = 1.458\left(\frac{d}{t_i}\right)^{-0.1} \quad (0.9 \le \gamma_s \le 1.1) \quad (3)$$

Note that, for slender and very slender section, the gross sectional area of the external tube (A_{se}) is calculated as the effective cross-sectional area ($A_{se,eff}$). The effective cross-sectional areas ($A_{se,eff}$) of the external steel tubes were calculated by using EN 1993-1-5 [35] while the reduction factor ρ should be taken according to Eurocode 3 Part 1.4 [24].

$$\rho = \frac{0.772}{\overline{\lambda}_p} - \frac{0.125}{\overline{\lambda}_p^2} \text{ but } \le 1 \quad (4)$$

where; $\overline{\lambda_p}$ is the element slenderness defined as: $\overline{\lambda_p} = \frac{\bar{b}/t}{28.4\varepsilon\sqrt{k_\sigma}}$.

t is the relevant thickness, $k_\sigma$is the buckling factor corresponding to the stress ratio ψ and boundary conditions from Table 4.1 or Table 4.2 in EN 1993-1-5 [35].

A comparison of the FE strengths generated in the parametric study and predicted strengths were listed in Table 5. From Table 5, it can be observed that the average values of $\frac{P_{EC4}}{P_{ul,FE}}$ $\frac{P_{AISC}}{P_{ul,FE}}$, and $\frac{P_{ul,Prop}}{P_{u,FE}}$ are 0.82, 0.87 and 0.90 with standard deviations of 0.046, 0.095 and 0.031, respectively. Hence, the strength predictions using $P_{ul,Prop}$ are therefore recommended for short rectangular CFDST columns with an external lean duplex stainless steel outer tubes.

Group	Column	$P_{u,FE}$ [kN]	P_{EC4} [kN]	$\frac{P_{EC4}}{P_{ul,FE}}$	P_{AISC} [kN]	$\frac{P_{AISC}}{P_{ul,FE}}$	$P_{ul,Prop}$ [kN]	$\frac{P_{ul,Prop}}{P_{u,FE}}$
G1	C1	5036	3777	0.75	3690	0.73	4433	0.88
	C2	5298	4016	0.76	3890	0.73	4672	0.88
	C3	5611	4334	0.77	4158	0.74	4990	0.89
	C4	5836	4652	0.80	4425	0.76	5308	0.91
	C5	6240	4970	0.80	4692	0.75	5626	0.90
	C6	6428	5288	0.82	4959	0.77	5944	0.92
	C7	5003	3817	0.76	3741	0.75	4485	0.90
	C8	5253	4009	0.76	3903	0.74	4677	0.89
	C9	5470	4265	0.78	4118	0.75	4933	0.90
	C10	5780	4521	0.78	4334	0.75	5189	0.90
	C11	5951	4777	0.80	4549	0.76	5445	0.91
	C12	6282	5033	0.80	4764	0.76	5701	0.91
	C13	5047	3846	0.76	3780	0.75	4507	0.89
	C14	5216	3999	0.77	3909	0.75	4660	0.89
	C15	5462	4203	0.77	4081	0.75	4864	0.89
	C16	5704	4407	0.77	4253	0.75	5068	0.89
	C17	5894	4611	0.78	4424	0.75	5272	0.89
	C18	6080	4815	0.79	4596	0.76	5476	0.90
G2	C19	6883	5222	0.76	5833	0.85	5841	0.85
	C20	7468	5698	0.76	6234	0.83	6318	0.85
	C21	7920	6333	0.80	6769	0.85	6953	0.88
	C22	8435	6968	0.83	7302	0.87	7588	0.90
	C23	8954	7603	0.85	7835	0.88	8223	0.92
	C24	9354	8238	0.88	8368	0.89	8858	0.95
	C25	7167	5442	0.76	6075	0.85	6099	0.85
	C26	7438	5824	0.78	6397	0.86	6481	0.87
	C27	7890	6334	0.80	6827	0.87	6991	0.89
	C28	8222	6844	0.83	7256	0.88	7501	0.91
	C29	8657	7354	0.85	7684	0.89	8011	0.93
	C30	9024	7864	0.87	8113	0.90	8521	0.94
	C31	7375	5569	0.76	6222	0.84	6240	0.85
	C32	7430	5874	0.79	6479	0.87	6544	0.88
	C33	7865	6279	0.80	6821	0.87	6949	0.88

	C34	8221	6685	0.81	7162	0.87	7355	0.89
	C35	8543	7090	0.83	7503	0.88	7760	0.91
	C36	8867	7496	0.85	7844	0.88	8166	0.92
G3	C37	7521	5784	0.77	7051	0.94	6336	0.84
	C38	7786	6438	0.83	7603	0.98	6991	0.90
	C39	8309	7311	0.88	8337	1.00	7864	0.95
	C40	9411	8184	0.87	9071	0.96	8737	0.93
	C41	9977	9057	0.91	9804	0.98	9610	0.96
	C42	10783	9930	0.92	10536	0.98	10483	0.97
	C43	7501	5887	0.78	7186	0.96	6455	0.86
	C44	7931	6412	0.81	7629	0.96	6980	0.88
	C45	8258	7112	0.86	8218	1.00	7680	0.93
	C46	9008	7812	0.87	8807	0.98	8380	0.93
	C47	9613	8512	0.89	9396	0.98	9080	0.94
	C48	10228	9212	0.90	9984	0.98	9780	0.96
	C49	7544	6044	0.80	7370	0.98	6579	0.87
	C50	7683	6459	0.84	7721	1.00	6994	0.91
	C51	8094	7014	0.87	8189	1.01	7549	0.93
	C52	9076	7568	0.83	8655	0.95	8103	0.89
	C53	9458	8123	0.86	9122	0.96	8658	0.92
	C54	9750	8677	0.89	9588	0.98	9212	0.94
Mean				**0.82**		**0.87**		**0.90**
Standard deviation				**0.046**		**0.095**		**0.031**

Table 5: FE strengths compared to different design models

6 SUMMARY AND CONCLUSIONS

The main objective of this paper was to examine the behaviour of short rectangular concrete-filled double-skin tubular (CFDST) columns with external lean duplex stainless steel tubes. External rectangular hollow sections (RHSs) with different local slenderness (i.e. fully-effective, slender and very slender cross-sections) were considered. From this paper, the following conclusions can be drawn:

- Increasing in the cylinder strength values of the sandwiched concrete increases linearly the compressive strength of the rectangular CFDST short columns with full-effective, slender and very slender sections of outer stainless steel tubes for the same hollow ratio.
- Changing the values of the hollow ratio has minimum effects on the compressive strength of the rectangular CFDST.
- It was observed that the design strength of EC4 is high conservative compared with both the AISC and the proposed design method based on design method found in literature.
- The design strength of AISC and the proposed method gave suitable conservative results but the AISC has the highest standard deviation.
- Hence, the proposed design model was recommended to use for the prediction of the ultimate axial strength of rectangular CFDST short columns with external lean duplex stainless steel outer tubes which is suitable for all classifications of cross-sections under axial loading.

REFERENCES

[1] B. Uy, H.D. Wright, M.A. Bradford, Combined axial and flexural strength of profiled composite walls, Structures & Buildings, Proceedings of the Institution of Civil Engineers, 2001, pp. 129-139.

[2] A.H. Varma, J.M. Ricles, R. Sause, L.-W. Lu, Experimental Behavior of High Strength Square Concrete-Filled Steel Tube Beam-Columns, J. Struct. Eng. 128(3) (2002) 309-318.

[3] K. Uenaka, H. Kitoh, K. Sonoda, Concrete filled double skin circular stub columns under compression, Thin-Walled Struct. 48(1) (2010) 19-24.

[4] L.-H. Han, Y.-J. Li, F.-Y. Liao, Concrete-filled double skin steel tubular (CFDST) columns subjected to long-term sustained loading, Thin-Walled Struct. 49(12) (2011) 1534-1543.

[5] M.F. Hassanein, O.F. Kharoob, Compressive strength of circular concrete-filled double skin tubular short columns, Thin-Walled Struct. 77 (2014) 165-173.

[6] Y. Yao, H. Li, K. Tan, Theoretical and numerical analysis to concrete filled double skin steel tubular columns under fire conditions, Thin-Walled Structures 98 (2016) 547-557.

[7] H. Huang, L.-H. Han, Z. Tao, X.-L. Zhao, Analytical behaviour of concrete-filled double skin steel tubular (CFDST) stub columns, J. Constr. Steel Res. 66(4) (2010) 542-55.

[8] H. Lu, X.-L. Zhao, L.-H. Han, Testing of self-consolidating concrete-filled double skin tubular stub columns exposed to fire, J. Constr. Steel Res. 66(8-9) (2010) 1069-1080.

[9] Q.Q. Liang, Nonlinear analysis of circular double-skin concrete-filled steel tubular columns under axial compression, Eng. Struct. 131 (2017) 639–650.

[10] M.F. Hassanein, O.F. Kharoob, L. Gardner, Behaviour and design of square concrete-filled double skin tubular columns with inner circular tubes, Eng. Struct. 100 (2015) 410-424.

[11] Z. Tao, L.-H. Han, X. Zhao, Tests on stub columns of concrete filled double skin rectangular hollow sections, in: J. Loughlan (Ed.) International Conference on Thin Walled Structures, Institute of Physics Publishing, Bristol UK, 2004, pp. 885-892.

[12] Z. Tao, L.-H. Han, Behaviour of concrete-filled double skin rectangular steel tubular beam–columns, J. Constr. Steel Res. 62(7) (2006) 631-646.

[13] M.F. Hassanein, Numerical modeling of concrete-filled lean duplex slender stainless steel tubular stub columns, J. Constr. Steel Res. 66 (2010) 1057-1068.

[14] L.-H. Han, Q.-X. Ren, L. Wei, Tests on stub stainless steel-concrete-carbon steel double-skin tubular (DST) columns, J. Constr. Steel Res. 67 (2011) 437-452.

[15] M.F. Hassanein, O.F. Kharoob, Q.Q. Liang, Behaviour of circular concrete-filled lean duplex stainless steel tubular short columns, Thin-Walled Structures 68 (2013) 113-123.

[16] M.F. Hassanein, O.F. Kharoob, Q.Q. Liang, Behaviour of circular concrete-filled lean duplex stainless steel–carbon steel tubular short columns, Eng. Struct. 56 (2013) 83-94.

[17] M.F. Hassanein, O.F. Kharoob, Q.Q. Liang, Circular concrete-filled double skin tubular short columns with external stainless steel tubes under axial compression, Thin-Walled Struct. 73 (2013) 252-263.

[18] M.F. Hassanein, K.O. F., Analysis of circular concrete-filled double skin tubular slender columns with external stainless steel tubes, Thin-Walled Struct. 79 (2014) 23-37.

[19] L. Gardner, The use of stainless steel in structures, Prog. Struct. Eng. Mater. 7(2) (2005) 45-55.

[20] E. Ellobody, B. Young, Design and behaviour of concrete-filled cold-formed stainless steel tube columns, Eng. Struct. 28(5) (2006) 716-728.

[21] G. Gedge, Structural uses of stainless steel — buildings and civil engineering, J. Constr. Steel Res. 64(11) (2008) 1194-1198.

[22] EN 10088-1. Stainless steels, Part 1, List of stainless steels. CEN. , 1995.

[23] Design manual for structural stainless steel Third edition, Euro Inox and The Steel Construction Institute, 2006.

[24] CEN, Eurocode 3: Design of steel structures, Part 1-4: General rules–Supplementary rules for stainless steel. , EN 1993-1-4. , 2006.

[25] B. Young, Experimental and numerical investigation of high strength stainless steel structures, J. Constr. Steel Res. 64(11) (2008) 1225-1230.

[26] ABAQUS Standard User's Manual, The Abaqus Software is a product of Dassault Systèmes Simulia Corp, DassaultSystèmes, Providence, RI, USA, 2008.

[27] Z. Tao, B. Uy, L.-H. Han, Z.-B. Wang, Analysis and design of concrete-filled stiffened thin-walled steel tubular columns under axial compression, Thin-Walled Struct. 47 (2009) 1544-1556.

[28] EC3, Eurocode 3, Design of steel structures-, Part 1-1: General rules and rules for buildings, British Standards Institution, BS EN 1993-1-1, London, UK, 2005.

[29] V.I. Patel, Q.Q. Liang, M.N.S. Hadi, High strength thin-walled rectangular concrete-filled steel tubular slender beam-columns, Part I: Modeling, J. Constr. Steel Res. 70 (2012) 377–384.

[30] Q.Q. Liang, Performance-based analysis of concrete-filled steel tubular beam–columns, Part I: Theory and algorithms, J. Constr. Steel Res. 65(2) (2009) 363-372.

[31] L.-H. Han, Z. Tao, H. Huang, X.-L. Zhao, Concrete-filled double skin (SHS outer and CHS inner) steel tubular beam-columns, Thin-Walled Struct. 42(9) (2004) 1329-1355.

[32] M. Theofanous, L. Gardner, Testing and numerical modelling of lean duplex stainless steel hollow section columns, Eng. Struct. 31 (2009) 3047-3058.

[33] CEN, Eurocode 4: Design of composite steel and concrete structures Part 1-1: General rules and rules for buildings, European Committee for Standardization, ENV 1994-1-1, Brussels, 2004.

[34] AISC 360. Load and resistance factor design specification, for structural steel buildings, American Institute of Steel Construction, Chicago, 2010.

[35] CEN, EN 1993-1-5, Eurocode 3. Design of steel structures - Part 1-5, Plated structural elements., 2007.

COMPDYN 2019
7th ECCOMAS Thematic Conference on
Computational Methods in Structural Dynamics and Earthquake Engineering
M. Papadrakakis, M. Fragiadakis (eds.)
Crete, Greece, 24–26 June 2019

SEISMIC ANALYSES OF SINGLE-STOREY STEEL BUILDINGS FOR EVALUATING CLADDING DAMAGE

Fabrizio Scozzese[1], Alessandro Zona[1], and Gaetano Della Corte[2]

[1] University of Camerino, School of Architecture and Design
Viale della Rimembranza 9, 63100 Ascoli Piceno, Italy
e-mail: {fabrizio.scozzese, alessandro.zona}@unicam.it

[2] University of Napoli Federico II, Department of Structures for Engineering and Architecture
Via Claudio 21, 80125 Napoli, Italy
gaetano.dellacorte@unina.it

Abstract

The analysis of steel constructions for their seismic design is commonly based on structural models including just the main frame members and relevant connections, while cladding panels are considered only in evaluating the seismic mass. Exceptions to this common approach can be found in a few studies available in the literature. A recent contribution was presented on the cladding damage under seismic input, as well as on the role of cladding panels in the overall seismic response of single-storey steel buildings. The results pointed out that claddings might have an important role on seismic response and should not be neglected in a refined finite element model. Starting from the available previous studies, the current work contributes in terms of both methodology and results. Regarding the methodology, a multi-criteria approach adopted for evaluating damage to cladding panels is reviewed and its applicability is discussed based on the results of a probabilistic study performed via multiple-stripe analyses. Regarding the results, a case study designed according to the Eurocodes and the recent 2018 Italian National Building Code is analysed with the aim of investigating the influence of cladding panels with non-symmetric plan distributions, which introduce torsional effects even if the structural elements have a symmetric configuration.

Keywords: Cladding, Non-structural damage, Serviceability limit state, Steel structures.

1 INTRODUCTION

The analysis of steel constructions for their seismic design is commonly based on structural models where only beams, columns, and braces contribute to the seismic response, while cladding panels are considered in the overall seismic mass but are not included as components explicitly influencing the structural behaviour [1][2]. Few exceptions to this common approach can be found in the literature with studies involving the following aspects: (i) development of nonlinear cyclic models for cladding panels to be included in advanced models incorporating structural and non-structural elements; (ii) design of cladding panels as structural elements providing bracing functions; (iii) analysis of the influence of the cladding panels on the structural response under seismic conditions as compared to the results obtained when only beams, columns, and braces are considered in the model definition; (iv) analysis of the seismic damage that cladding panels undergo through explicit modelling of their response as component of the structural model. A review of the state of the art on such topics can be found in Scozzese et al. [3]. Attention is here focused on the latter two aspects, i.e. cladding panels are included in the structural model with two objectives: 1) evaluate their influence on the simulated seismic response, and 2) estimate their damage under seismic excitations.

Previous studies on single-storey steel buildings [3][4] pointed out that claddings have an important role on the seismic response and should not be neglected in a refined finite element model. Starting from the obtained outcomes [3], the current study contributes in terms of both methodology and results. Regarding the methodology, the multi-criteria approach proposed in [5] for reinforced concrete frames and used in [3] for the evaluation of the damage to the cladding panels is reviewed and its applicability is discussed. Regarding the obtained results in the description of the development and extent of non-structural damage, comparisons are made between two sets of a case study designed according to the Eurocodes [6][7] and the recent 2018 Italian National Building Code [8]. Specific attention is given to the investigation of the influence of cladding panels with non-symmetric distributions in plan, not previously evaluated in [3].

2 METHODOLOGY FOR ASSESSING NON-STRUCTURAL DAMAGE

2.1 Methodology review

According to the European [6][7] and Italian [8] seismic codes, the assessment of non-structural damage of buildings is conventionally pursued by monitoring global response quantities, such as the interstory drift. The main limit of this conventional approach is represented by the lack of an explicit relationship with the actual level of deformation of the non-structural elements, whose behaviour is not explicitly considered during seismic analyses, and the relevant lack of the description of the interactions between structural and non-structural elements. In this study, following former investigations [3][4], the damage evaluation of the non-structural elements is pursued through their inclusion in the structural model, thus, allowing an explicit estimation of their local seismic demand. A direct comparison with the outcomes achieved by means of a global drift-based approach applied to the conventional analysis of bare-frame models allows comparing the results of the proposed methodology to the results of the conventional code-based damage verifications.

Multi-criteria approach for the assessment of the Damage Limit State

In order to assess the onset of the Damage Limit State (DLS), a multi-criteria approach was adopted. Specifically, a three-level local damage criterion [3] was proposed to characterize

the attainment of the DLS of buildings: (1) low-damage level: a percentage of panels exceeds the elastic response limit (a 50% value is considered in this study); (2) medium-damage level: the totality of panels is beyond the elastic field; (3) strong-damage level: at least one panel exceeds its maximum shear resistance. A global condition is added besides the three-level local damage criterion, i.e. attainment of the 95% of the maximum base shear force resistance of the whole structural system, in order to consider cases where significant structural damage might occur before the development of damage in non-structural elements, as discussed in [3][4].

DLS fragility functions

A probabilistic unconditional approach [9], i.e., based on the Intensity Measure (IM), is used for the fragility functions estimation at the DLS. In particular, the widely used Multiple Stripe Analysis (MSA) method [10][11] is adopted to build the conditional demand model $P(D|IM) = P[D > d \mid IM = im]$, providing information about the probability that a given response quantity D exceeds a certain threshold value *d* characterising the attainment of given limit state (focus of this study is on DLS), conditional to different levels of seismic intensity, as described by specific values of IM. The seismic hazard curve is discretized in 10 intensity levels corresponding to the following return periods (expressed in years): 10, 50, 100, 250, 500, 1000, 2500, 5000, 10000, 100000. The spectral pseudo-acceleration $S_a(T_1)$ at the system period T_1 is assumed as IM. The seismic record-to-record variability is accounted by using a set of 20 pairs (two horizontal seismic components) of ground motion time-histories for each IM level. Further details about the adopted seismic records and related scale factors can be found in [12][13].

A simplified method based on pushover analyses is proposed for identifying the limit values (*d*) corresponding to the DLS attainment, in which the roof drift ratio is assumed as response quantity for the aim of the present work. The whole methodology used for estimating the fragility functions can be summarised through the following four steps: (1) Pushover analyses are performed separately along the two orthogonal directions (X, Y); (2) The control node displacements (nodes located at the roof level) corresponding to the attainment of all of three local damage conditions defined above (i.e., low, medium and strong damage) are evaluated and the corresponding drift ratios identified; (3) Nonlinear time-history analyses are performed within the probabilistic context of MSA; (4) A set of fragility functions is provided by comparing the roof drift ratios monitored during time-history analysis (for all of the ground motions and for different IM values) with the limit values identified via pushover analysis.

Non-structural element modelling approach

A class of lightweight sandwich panels widely used as enclosure elements in both industrial and civil constructions is considered in this study. In particular, the type A panels tested by De Matteis and Landolfo [14] were adopted. The panels consist of external embossed steel sheets (thickness of 0.6 mm) with slight stiffening ribs and insulating polyurethane core, for a total thickness of 40 mm. The connection of panels to the main structural frame is made through cladding rails (for vertical cladding panels) or purlins (for roof panels) by means of bolts (generally of 8 mm in diameter and 110-120 mm spacing) [14].

Each panel was modelled by means of a couple of diagonal truss elements with nonlinear axial behaviour following the Pinching4 model, able to catch the main features of the shear-

displacement experimental response of cladding panels typically used in steel constructions [14][15]. Further details about the Pinching4 implementation can be found in [3][4][16].

For the purposes of the present investigation, the Pinching4 model was calibrated based on the experimental results available from cyclic shear loading tests performed on individual units of panel type A, having size of 1000 mm × 2500 mm × 40 mm. The backbone curve for the panel at hand is schematically represented in Figure 1a, superimposed to the envelope of the experimental cyclic response. It consists of a trilinear model characterized by: a yielding point at 12 kN (d = 20 mm), a hardening behaviour until the maximum shear of 17 kN (d = 80 mm), and a gradual softening branch where the force drops to zero at d = 320 mm. The simulated quasi-static nonlinear response is shown in Figure 1b.

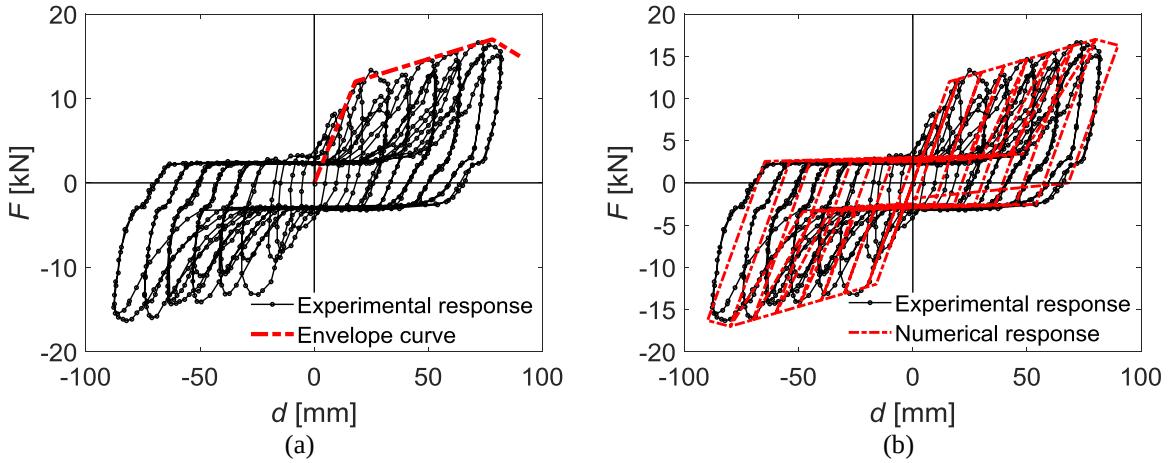

Figure 1: (a) Cyclic envelope curve of a panel unit and (b) experimental vs. numerical cyclic response.

It is worth noting that the panel type A presented above is not used as individual unit within the buildings, but panel assemblies are adopted, made of a number of single panels varying according to the specific geometric configuration of the structural system. To cope with that, the equivalent truss model calibrated for the single panel is extended to simulate the nonlinear contribution of whole panel assemblies, and this is done by making the following hypothesis: (i) the presence of several adjacent panels is accounted by increasing the strength and the stiffness of each pair of truss elements by a factor equal to the number of panels, i.e. the actual number of panels, which can also be a fractional number (this assumption is consistent with the condition of panels working in parallel); (ii) the presence of multiple rows of panels along the height is accounted by following the analogy of a system working in series, according to which the displacements of Ns rows of panels are Ns times larger than those of a single row, while the stiffness of the whole system is reduced by a factor equal to 1/Ns; (iii) the presence of concentrated openings is accounted by introducing a reduction factor equal to 0.5 for both stiffness and strength of the truss elements; (iv) the cladding panels are assumed not connected side by side. For sake of clarity, according to the assumption discussed above, a panel assembly located within a structural field with length 6 m and height 4.5 m will have strength and stiffness respectively 6 and 3.3 times higher than a single panel.

2.2 Applicability and open problems

The methodology as presented in the previous section was used in [3] to evaluate the intensity and extent of non-structural damage in steel buildings with cladding panels with symmetric distributions in plan in a high seismic hazard area in Italy (L'Aquila). On the other hand, in

the present work focus is made to the evaluation of the intensity and extent of non-structural damage in steel buildings with cladding panels with symmetric as well as non-symmetric distributions in plan in a medium seismic hazard area in Italy (Naples). Specifically, two different panel distributions are considered: perfectly symmetric along both X and Y directions; with asymmetric distribution along the X direction, as thoroughly discussed in the following section 3 of this article.

Moreover, the effect of the choice of the control node used to evaluate the drift ratio is analysed. This is an aspect of high relevance for the type of buildings herein investigated, characterized by the absence of a rigid diaphragm at the roof level. This implies that differential movements are not restraint among the frames, and, thus, the choice of the nodes with respect to which the drifts are computed might affect the outcomes. The relevance of this matter is further amplified by the consideration of panels with asymmetric distribution that introduce torsional effects even if the structural elements have a symmetric configuration.

3 CASE STUDY

3.1 Geometry and structural design

The considered case study is composed of five single span duo-pitch portal frames repeated in the longitudinal direction at a constant distance. The frames are connected in the longitudinal direction by hot-rolled beams at the apex, at the eaves and at the crane-supporting bracket level. A three-dimensional view of the structural system is presented in Figure 2. The transverse X-direction has its abscissa labelled with the letters A and B, the longitudinal Y-direction has its ordinates labelled with numbers. Horizontal forces are withstood by two different structure typologies: in the X-direction the resistance to lateral forces is due to moment resisting action of the portal frames, i.e. moment resisting frames (MRFs); in the Y-direction the resistance is provided by vertical concentric bracings, i.e. concentrically braced frames (CBFs), placed in the outer spans. The same geometry was considered in in the case studies analysed in [3][4][16] and a detailed description of its structural configuration, considered loading conditions, and general design approaches, can be found in [16].

The considered case study is located in Naples, soil type C, topography condition T1 [7][8]. The transverse bay width is L_x = 20.00 m, the longitudinal bay width is L_y = 6.00 m, the height at the eaves is H = 6.00 m, and the height of the crane-supporting bracket (measured at top surface of the bracket) is H_c = 4.50 m. The roof pitch is equal to 6°. Purlins are used to support the roof cladding and are positioned every 2.5 m. Roof bracings are arranged in the outer bays to transfer horizontal forces to the vertical bracings. Steel grade is S275.

The presence of a travelling overhead crane was considered as illustrated in details in [16]. Variable environmental loads (snow, wind, thermal actions) and seismic loads were determined accordingly to the Italian code prescription for the considered site [8]. Following the current European and Italian seismic code [7][8], the design model assumed that horizontal forces can be resisted by tension-only diagonal braces, i.e. the contribution of the compression diagonals to the lateral force resistance was neglected at the design stage. Equivalent geometric frame imperfections were included in the design according to the simplified approach suggested by the Italian code [8] and described in [16]. The roof purlins were modelled as simple spanned between two consecutive frames. All the columns were modelled as hinged at their base.

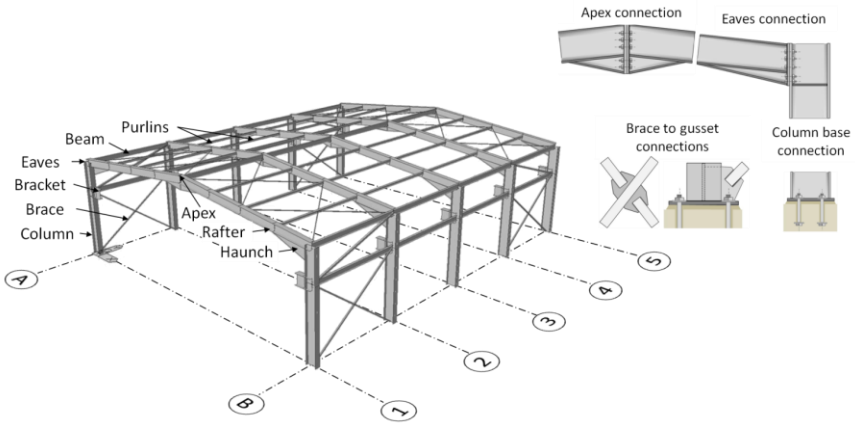

Figure 2: View of the steel structure of the considered case study.

Two different seismic designs were made by assuming a dissipative structural behaviour: 1) ductility class medium (DCM) of Eurocode 8 [7], providing a behaviour factor q = 4 for both the moment resisting frames and the frames with concentric braces; 2) ductility class high of the 2018 Italian Code [8] (indicated in the code as CD"A"), providing a behaviour factor q > 4 for the moment resisting frames and q = 4 for the frames with concentric braces. While it was assumed q = 4 for both designs and the same results were attained for the moment resisting frames (Table 1), a ductility requirement of the 2018 Italian Code [8] enforce a width-to-thickness ratio smaller than or equal to 18 for the box cross section of braces, leading to different brace designs. Efforts were made to select cross sections for the braces to reduce as much as possible the difference in resisting areas; inevitably the other inertial properties present large variations, as indicated in Table 2.

Element	Eurocode design	Italian code design
Column	HE 600 M	HE 600 M
Rafter	HE 450 A	HE 450 A
Vertical X braces	60x2	50x3
Vertical single brace	90x2.6	70x4
Longitudinal beam	IPE 270	IPE 270
Purlins	HE 160 A	HE 160 A
Roof bracings	L 20x3	L 20x3

Table 1: Designed cross section for the considered case study.

Property	60x2	50x3	90x2.6	70x4
Width b (mm)	60.00	50.00	90.00	70.00
Thickness t (mm)	2.00	3.00	2.60	4.00
Area A (mm^2)	450.30	554.00	885.70	1040.00
Inertia moment I (mm^4)	248300	202000	1112000	746000
Gyration radius i (mm)	23.48	19.10	35.43	26.78
b/t	30.00	16.67	34.62	17.50
Ductility class	1	1	2	1

Table 2: Comparisons of the properties of the designed brace sections.

Serviceability limit state verifications for the horizontal displacements of the portal frame for the characteristic combination of loads was limited to $\Delta_i/H=1/300$. For the damage limitation limit state (SLD), the horizontal drift was limited to 1/200. The difference of horizontal deflection between two consecutive portal frames, Δ_{ij}/L_y, was also checked to not exceed 1/200 [16].

3.2 Nonlinear finite element model and analysis

The nonlinear response of the case study was investigated using the finite element open source software OpenSees [17] including both geometric and material nonlinearities. All the structural elements were modelled using nonlinear fibre sections with nonlinear behaviour assigned to each section fibre using the Steel02 constitutive law (Giuffré-Menegotto-Pinto steel material object with isotropic strain hardening) available within the OpenSees libraries. Attention was given to the following aspects of the vertical brace modelling: description of the buckling phenomenon in compression; proper modelling of the gusset plate connections that in real structures are neither pinned nor fixed joints. The method followed for modelling the bracings is that proposed by Hsiao [18][19] and consisting in simulating the nonlinear out-of-plane rotational behaviour of the gusset plate connections by means of a rotational nonlinear spring located at the physical end of the brace. Details of the nonlinear finite element model of the structural elements can be found in [3][4]. Material parameters are considered as deterministic, being the evaluation of the influence of model uncertainties beyond the scope of this study. Studies involving response sensitivity analysis to material parameters, either using direct differentiation or finite difference strategies, e.g. [20][21], could be considered in possible future developments. Further information on model uncertainties can be found in [4] where the methodology illustrated in [22] was adopted.

Modelling of panels in OpenSees was made through couples of nonlinear truss elements adopted to reproduce the contribution of groups of assembled panels belonging to different structural fields. As already discussed, for each truss element, the Pinching4 uniaxial material available in the OpenSees library was adopted to simulate the nonlinear cyclic behaviour of the panel assembly, and the experimental results provided in [14][15] were used to calibrate the parameters required. The presence of concentrated openings was accounted by a reduction factor equal to 0.5 to both the stiffness and the strength of the truss elements. Details of the nonlinear finite element model of the non-structural elements can be found in [3][4].

MSA at 10 IM levels (with IM chosen to be the spectral pseudo-acceleration at the fundamental period of the system) were carried out, by using a set of 20 X-Y-pairs of ground motions for each IM level in order to simulate the seismic record-to-record variability, as already discussed. More details at this regard can be found in [3][4][13][16].

3.3 Numerical results

As previously introduced, the present work considers the influence of cladding panels with non-symmetric distributions in plan. Two different panel distributions are considered: 1) distribution with perfect symmetry along both X and Y directions (Figure 3a); 2) asymmetric distribution along the X direction, i.e., with cladding panels located within one extreme portal frame only (Figure 3b). Figures also show the opening locations, whose effects are numerically accounted by following the modelling strategy discussed in section 2.1.

Pushover analysis results

A preliminary study on the influence of the cladding panels was carried out by performing nonlinear static (pushover) analysis on the building designed in CD“A” according to the Italian seismic code [8]. It is worth noting that differential movements are possible among the portals (in X direction) and the braced frames (in Y direction), because of the lack of a rigid diaphragm at the roof level. Different control nodes were monitored in order to catch this phenomenon and consequently assess the impact on the results provided by both pushover analysis (as discussed in the current subsection) and MSA (discussed later). Despite the rela-

tive movements are mainly expected along the portal direction (X), because of both the presence of a middle portal not restrained by roof braces and the asymmetric panel distribution, a set of three control nodes was also utilized to monitor the longitudinal (Y) direction. The assumed control nodes are identified in Figure 3. The analyses were performed in control of displacement, by pushing the building in each direction by means of sets of uniform horizontal forces applied at the nodes of the roof level.

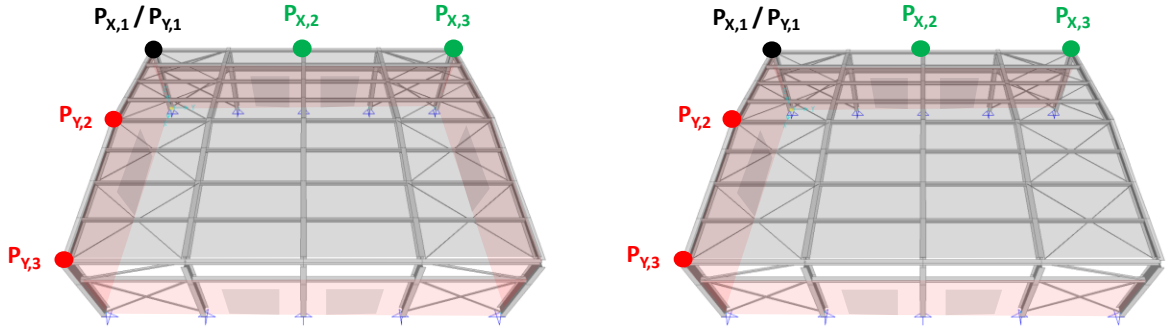

Figure 3: Scheme of panel distribution: (a) symmetric case; (b) asymmetric distribution along the X direction.

The capacity curves for the case with symmetric panels are reported in Figure 4, while those related to the asymmetric panel distribution are shown in Figure 5. Curves related to different control nodes are superimposed in the charts by using different colours. It is worth noting that the choice of the control node has no influence for the response along the longitudinal direction, because of the symmetry of both structural and non-structural components. On the contrary, a higher sensitivity is observed in the X direction, due to the following reasons: (1) the presence of a middle portal not restrained by roof braces, which experiences higher displacements with respect to the lateral ones even for a symmetric panel assemblies' configuration (see Figure 4a); (2) the asymmetric panel distribution, which amplifies the effect said above on the central portal frame and, moreover, leads the extreme portal frame without panels to experience higher deformability, as witnessed by the pushover curves comparison in Figure 5a. It is also worth noting the asymmetric distribution of panels along X modifies the lateral response of the system, as can be observed by the different trends of the capacity curves in X of Figure 4a (symmetric) and Figure 5a (asymmetric): hardening post-elastic behaviour with symmetric panels and softening branch with asymmetric ones.

For what concerns the local damage criterion, the four performance states introduced in section 2.1 are highlighted on the capacity curves of Figure 4 and Figure 5 by coloured markers: (GD) a green dot for the low-damage level; (RST) a red star for the medium-damage level; (BD) a blue diamond for the strong-damage level; (RSQ) a red square for the base-shear limit. According to these results, the following comments can be done: (1) low-damage and medium-damage levels are attained simultaneously, and this is due to the particular geometry of the building, with one storey only and panel assemblies of the same type and with the same heights along each direction; (2) the attainment of the limit on the base-shear (i.e., 95% $V_{b,max}$) is always posterior to the panel strong-damage state, except for the case with symmetric panels in X direction (Figure 5a), where a non-negligible structural damage occurs before the development of strong-damage level on panels; this testifies the worsening of the lateral structural response due to the presence of non-structural elements with asymmetric distribution in plan; (3) as expected, no differences are observed in the longitudinal direction (Y) in terms of both capacity curves and panel performance points.

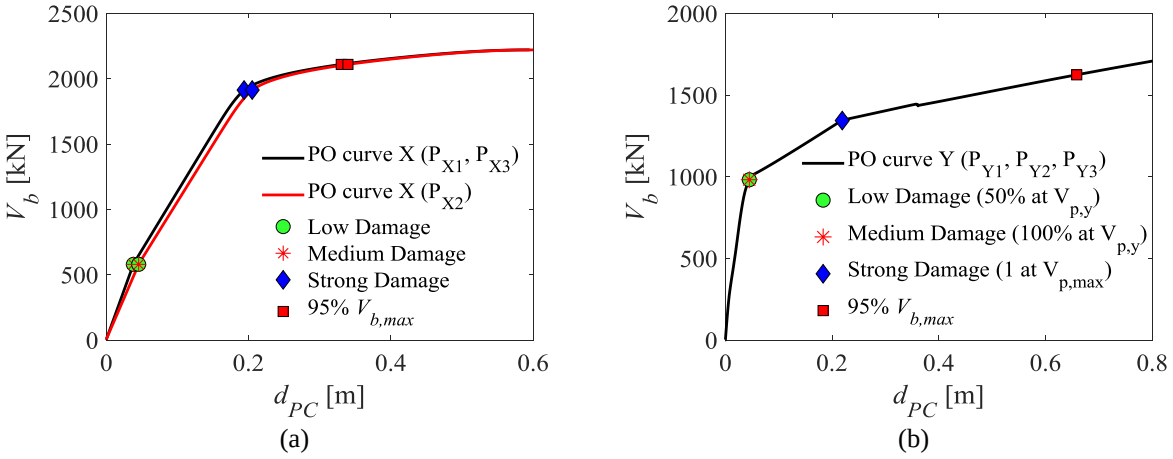

Figure 4: Pushover curves for symmetric panel distribution along X (MRF) (a) and Y (CBF) (b) direction.

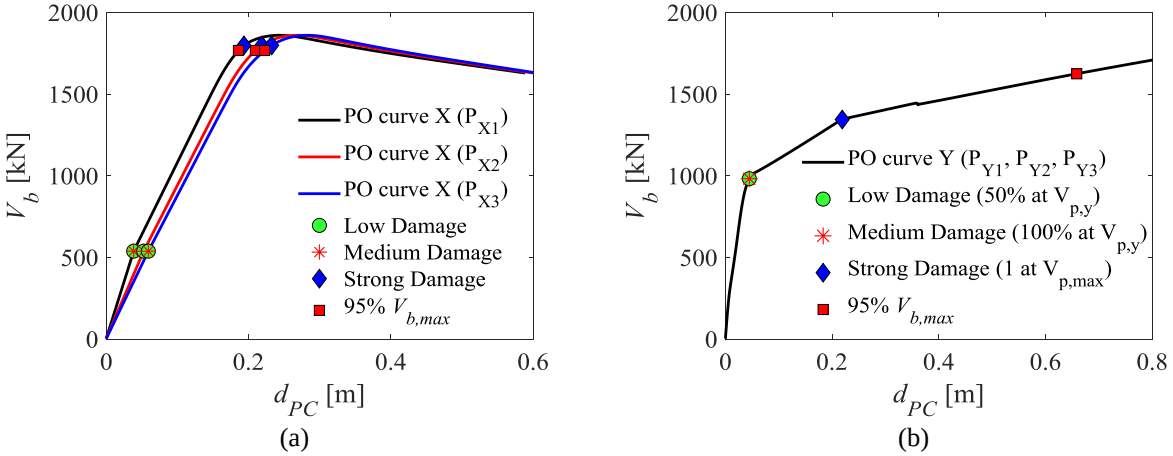

Figure 5: Pushover curves for asymmetric panel distribution: direction X (MRF) (a) and Y (CBF) (b).

	Control node	Low damage (50% at $V_{p,y}$)	Medium damage (100% at $V_{p,y}$)	Strong damage (1 at $V_{p,max}$)	95% $V_{b,max}$
Dir. X	P_{x1}	0.0060	0.0060	0.0307	0.0524
	P_{x2}	0.0072	0.0072	0.0325	0.0539
	P_{x3}	0.0060	0.0060	0.0307	0.0524
Dir. Y	P_{y1} / P_{y2} / P_{y3}	0.0071	0.0071	0.0348	0.1045

Table 3. DLS limit drift values for symmetric panel distribution.

	Control node	Low damage (50% at $V_{p,y}$)	Medium damage (100% at $V_{p,y}$)	Strong damage (1 at $V_{p,max}$)	95% $V_{b,max}$
Dir. X	P_{x1}	0.0061	0.0061	0.0307	0.0295
	P_{x2}	0.0083	0.0083	0.0347	0.0333
	P_{x3}	0.0094	0.0094	0.0369	0.0353
Dir. Y	P_{y1} / P_{y2} / P_{y3}	0.0070	0.0070	0.0348	0.0405

Table 4. DLS limit drift values for asymmetric panel distribution.

To conclude this section, the drift limit values, estimated by using the different control nodes of Figure 3, are summarised in Table 3 for the case with symmetric panels and in Table 4 for the case with asymmetric ones. These limits were used as threshold values to estimate and compare the conditional probability (fragility) functions at the DLS, as described in the next subsection.

Fragility functions estimated via MSA

The probability of exceeding the performance level corresponding to DLS at different intensity levels, is herein estimated for the building designed in CD"A" according to the Italian seismic code [8]. This task is achieved through the application of the local damage criteria introduced in section 2.1, i.e. the attainment of the DLS is defined by monitoring the onset of the damage levels of the cladding panels. MSA is used to estimate the fragility functions P(D|IM) = P[D > *d* | IM = im] at the DLS. Specifically, the drift ratios measured at the roof nodes (see Figure 3) of the models with infill panels are used as response parameter (D), while the limit threshold values *d* consist of the drift ratios computed via pushover analysis and summarised in Table 3 and in Table 4.

Fragility curves for the building with symmetric panels are shown in Figure 6 (X direction in Figure 6a and Y direction in Figure 6b). Given the panel symmetry, the probabilistic response does not change significantly by varying the control node, and, thus, only the results related to node $P_{X1/\ Y1}$ are shown in the chart. The fragility curves corresponding to the exceedance of the conventional code-based limit drift value of 0.5% are also provided in the same charts. It is worth noting that, in this case, the response parameter consists of the drift ratios monitored on the bare-frame model (with panel assemblies modelled as mass only), that is the most frequently adopted seismic analysis method for steel constructions.

Fragility curves for the building with asymmetric panels are shown in Figure 7 (X direction in Figure 7a,b,c and Y direction in Figure 7d). Given the panel asymmetry, the probabilistic response changes by varying the control node as can be observed comparing the results for the considered control nodes: P_{X1} (Figure 7a), P_{X2} (Figure 7b), P_{X3} (Figure 7c).

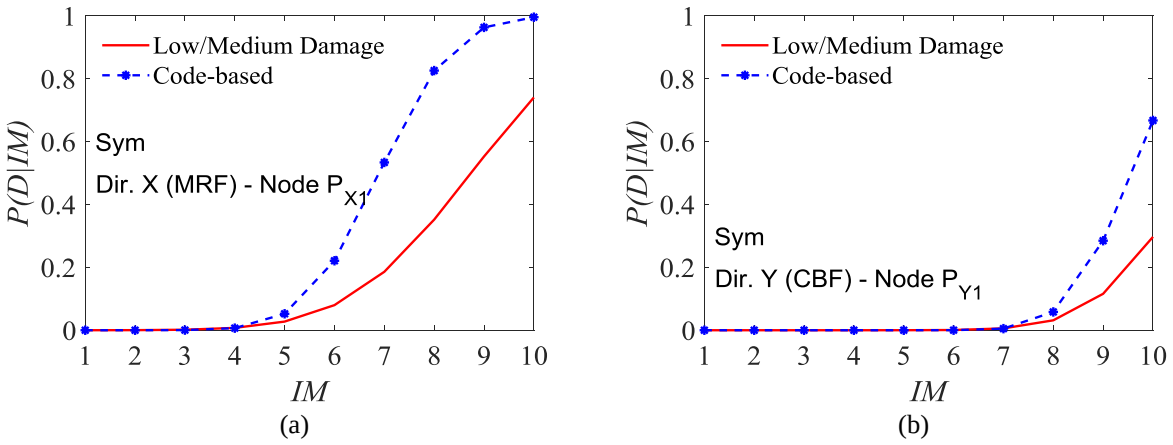

Figure 6: DLS fragility curves for symmetric panel distribution. Results along the X direction (MRF) refer to drift values computed on control node P_{X1} (a). Results along the Y direction (CBF) refer to node P_{Y1} (b).

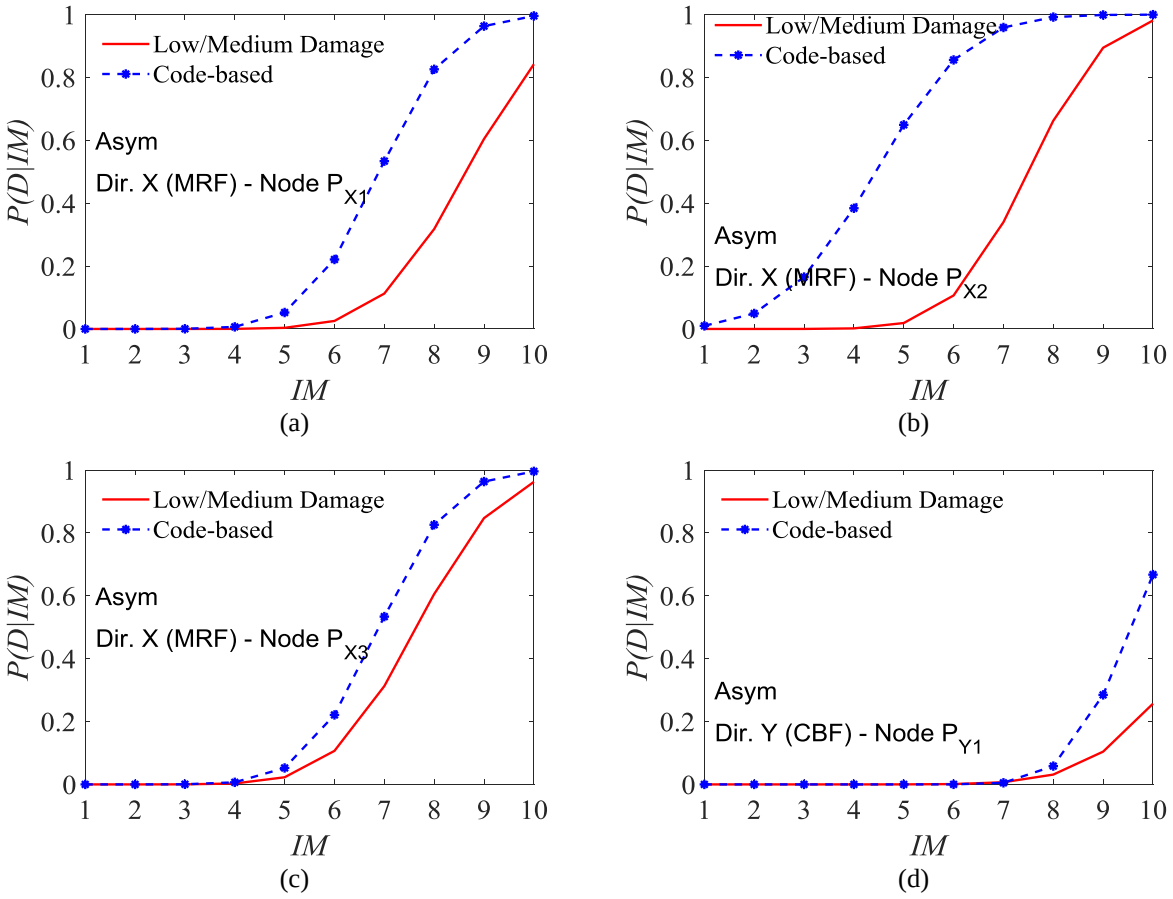

Figure 7: DLS fragility curves for asymmetric panel distribution. Results along the X direction (MRF) refer to drift values computed on different control nodes: P_{X1} (a), P_{X2} (b), P_{X3} (c). Results along the Y direction (CBF) refer to node P_{Y1} (d).

Influence of the design of braces

The probability of exceeding the performance level corresponding to DLS considering the differences in the design of the vertical braces as discussed in section 3.1 is herein presented. The methodology is the same illustrated in the previous section. The drift values are computed with respect to node P_1. Fragility curves for the building designed in DCM are shown in red (Figure 8), by using continuous lines for the curves exceeding the low-damage level (also equal to the medium-damage level) and dashed lines for the code-based curve with 0.5% conventional drift ratio). Fragility curves for the building designed in CD"A" are shown in black. Results for the two brace designs are generally comparable with the fragility of the building designed in medium ductility class (DCM) and slightly higher only at the very large IM = 10. Similar trends are observed in terms of code-based fragility curves.

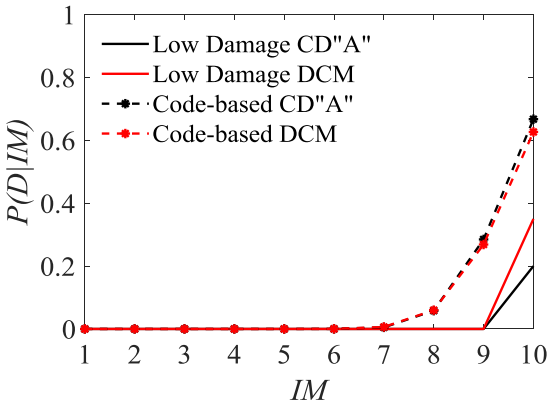

Figure 8: DLS fragility curves along the Y direction (CBF) for the buildings design in medium and high ductility. Results refer to drift values computed with respect to the node P_{X1}.

4 CONCLUSIONS

This paper focused on the influence of cladding panels on seismic response of non-residential single-storey steel buildings. Starting from a previous work carried out by the authors, where cladding panels were explicitly included in the structural seismic analysis, the current study aimed at investigating the influence of cladding panels with non-symmetric distributions in plan. In addition, as a supplementary work, two different seismic design philosophies were investigated: structural design in medium ductility class according to the Eurocodes and structural design in high ductility class according to the recent 2018 Italian National Building Code. Moreover, the effect of the choice of the control node used to evaluate the drift ratio was analysed. In order to assess the onset of the Damage Limit State (DLS), a multi-criteria approach was adopted. Multiple-stripe analysis was used to estimate the DLS fragility curves.

According to the outcomes provided in this work, the following main conclusions can be drawn:

- Because of the specific building geometry, characterized by the absence of a rigid diaphragm at the roof level, the choice of the nodes for which the drift ratio is evaluated might affect the fragility estimation, either underestimating or overestimating the conditional exceedance probabilities at the DLS. An asymmetric distribution of panels could exacerbate the changes of the fragility curves with respect to the control node.
- The ductility class selected for brace members was observed to have negligible effects on the DLS fragility functions.

For what concerns some possible future developments, these might be oriented to: (1) extend the current study to different typologies and different asymmetric configurations of cladding panels; (2) improve the local damage criterion and tailor it to better fit on single story buildings; (3) analyse the influence of structural and non-structural parameters on the obtained results through response sensitivity analysis; (4) evaluate the effect of model uncertainties both for structural and non-structural components. Regarding the second point, it is remarked that, due to the specific geometric features, all cladding panels experience almost simultaneously the same damage state, thus, reducing the usefulness of a criterion based on the attainment of a given damage condition by subsets of panel assemblies (such as, 50% of panels at a given damage condition).

REFERENCES

[1] G. Ballio, F.M. Mazzolani, *Theory and design of steel structures.* Chapman and Hall ltd, 1983.

[2] R. Landolfo, F.M. Mazzolani, D. Dubina, L.S. Da Silva, M. D'Aniello, *Design of steel structures for buildings in seismic areas (ECCS Eurocode Design Manuals*). Ernst & Sohn, 2015.

[3] F. Scozzese, G. Terracciano, A. Zona, G. Della Corte, A. Dall'Asta, R. Landolfo, Analysis of seismic non-structural damage in single-storey industrial steel buildings. *Soil Dynamics and Earthquake Engineering*, **114**, 505-519, 2018.

[4] F. Scozzese, G. Terracciano, A. Zona, G. Della Corte, A. Dall'Asta, R. Landolfo, Modelling and seismic response analysis of Italian code-conforming single-storey steel buildings. *Journal of Earthquake Engineering*, **22**(S2), 168-197, 2018.

[5] D. Cardone, G. Perrone. Developing fragility curves and loss functions for masonry infill walls. *Earthquakes and Structures*, **9**(1), 257-79, 2015.

[6] European Committee for Standardization. *Eurocode 3: Design of steel structures - Part 1-1: General rules and rules for buildings*. EN1993-1-1, August 2005.

[7] European Committee for Standardization, *Eurocode 8: Design of structures for earthquake resistance - Part 1: General rules, seismic actions and rules for buildings*. EN 1998-1, December 2004.

[8] Repubblica Italiana, Ministero delle Infrastrutture e dei Trasporti, *Nuove norme tecniche per le costruzioni*, D.M. 17 gennaio 2018 (Gazzetta Ufficiale n.42 del 20 febbraio 2018, supplemento ordinario n. 8) [In Italian].

[9] F. Jalayer, C.A. Cornell, Alternative non-linear demand estimation methods for probability-based seismic assessments. *Earthquake Engineering & Structural Dynamics*, **38**(8), 951-972, 2009.

[10] F. Scozzese, A. Dall'Asta, E. Tubaldi, Seismic risk sensitivity of structures equipped with anti-seismic devices with uncertain properties. *Structural Safety*, **77**, 30-47, 2019.

[11] B.A. Bradley, Practice-oriented estimation of the seismic demand hazard using ground motions at few intensity levels. *Earthquake Engineering & Structural Dynamics*, **42**(14), 2167-2185, 2013.

[12] I. Iervolino, A. Spillatura, P. Bazzurro, RINTC Project - Assessing the (implicit) seismic risk of code-conforming structures in Italy. M. Papadrakakis, M. Fragiadakis (eds.) *COMPDYN 2017 - 6th ECCOMAS Thematic Conference on Computational Methods in Structural Dynamics and Earthquake Engineering*, Rhodes Island, Greece, 15–17 June 2017.

[13] I. Iervolino, A. Spillatura, P. Bazzurro, Seismic reliability of code-conforming Italian buildings. *Journal of Earthquake Engineering*, **22**(S2), 5-27, 2018.

[14] G. De Matteis, R. Landolfo, Modelling of lightweight sandwich shear diaphragms for dynamic analyses. *Journal of Constructional Steel Research*, 53(1), 33-61, 2000.

[15] G. De Matteis, R. Landolfo, Structural behaviour of sandwich panel shear walls: An experimental analysis. *Materials and Structures*, **32**(5), 331-341, 1999.

[16] F. Scozzese, G. Terracciano, A. Zona, G. Della Corte, A. Dall'Asta, R. Landolfo, RINTC project: Nonlinear dynamic analyses of Italian code-conforming steel single-storey buildings for collapse risk assessment. M. Papadrakakis, M. Fragiadakis (eds.) *COMPDYN 2017 - 6th ECCOMAS Thematic Conference on Computational Methods in Structural Dynamics and Earthquake Engineering*, Rhodes Island, Greece, 15–17 June 2017.

[17] F. McKenna, OpenSees: a framework for earthquake engineering simulation. *Computing in Science & Engineering*, **13**(4), 58-66, 2011.

[18] P.C. Hsiao, D.E. Lehman, C.W. Roeder, Improved analytical model for special concentrically braced frames. *Journal of Constructional Steel Research*, **73**, 80-94, 2012.

[19] P.C. Hsiao, D.E. Lehman, C.W. Roeder, Evaluation of the response modification coefficient and collapse potential of special concentrically braced frames. *Earthquake Engineering & Structural Dynamics*, **42**(10), 1547-1564, 2013.

[20] A. Zona, M. Barbato, J.P. Conte, Finite element response sensitivity analysis of continuous steel-concrete composite girders. *Steel and Composite Structures*, 6(3), 183-202, 2006.

[21] Q. Gu, A. Zona, Y. Peng, A. Dall'Asta, Effect of buckling-restrained brace model parameters on seismic structural response. *Journal of Constructional Steel Research*, 98, 100-113, 2014.

[22] P. Franchin, L. Ragni, M. Rota, A. Zona, Modelling uncertainties of Italian code-conforming structures for the purpose of seismic response analysis. *Journal of Earthquake Engineering*, **22**(S2), 28-53, 2018.

COMPDYN 2019
7th ECCOMAS Thematic Conference on
Computational Methods in Structural Dynamics and Earthquake Engineering
M. Papadrakakis, M. Fragiadakis (eds.)
Crete, Greece, 24–26 June 2019

STRIP MODEL FOR STEEL PLATE SHEAR WALLS WITH BEAM-CONNECTED WEB PLATES

Yigit Ozcelik[1] **and Patricia Clayton**[2]

[1] Ozyegin University
Nisantepe M. Orman S., Cekmekoy, Istanbul, Turkey 34794
e-mail: yigit.ozcelik@ozyegin.edu.tr

[2] University of Texas at Austin
301 E. Dean Keeton St. Stop C1700, Austin, Texas, USA 78712
clayton@utexas.edu

Abstract

Steel plate shear walls (SPSWs) are a lateral force-resisting system in which thin infill plates (web plates) are connected to the boundary frame (i.e., beams and columns) along four edges. Despite shear buckling of thin plates upon lateral loading, web plates still provide lateral strength and stiffness in the post-buckling range owing to a mechanism called tension field action. The boundary frame (particularly columns) needs to satisfy stringent strength and stiffness requirements to anchor the inclined forces in web plates resulting from tension field action. An alternative system to conventional SPSWs, steel plate shear walls with beam-connected web plates (B-SPSWs), is proposed in the literature where web plates are connected to beams only. Therefore, high flexural and axial load demands in columns induced by tension field forces are eliminated. However, due to the difference in boundary conditions of web plates, the load path of steel plate shear walls with beam-connected web plates significantly differs from that of conventional SPSWs. In this study, a simplified strip model of beam-connected web plate is proposed to simulate the cyclic behavior of beam-connected web plates. As it is typical and conservative to ignore the compressive strength of strips, strip models underestimate the strain energy dissipated under cyclic loading. An equation for the compressive strength of strips is proposed to accurately capture the energy dissipation capacity of beam-connected web plates. A three-way comparison between the proposed strip model, a strip model from the literature, and a validated continuum model is provided. The results reveal that the proposed strip model is capable of successfully estimating the boundary frame demands, lateral load capacity, and energy dissipation of beam-connected web plates.

Keywords: Steel Plate Shear Walls, Beam-connected Web Plates, Strip Model, Partial Tension Field, Compressive Strength.

1 INTRODUCTION

Steel plate shear walls (SPSWs) are a reliable lateral force-resisting system with high ductility, high lateral stiffness, and stable hysteretic behavior [1–7]. SPSWs comprise thin infill plates (web plates) connected to beams and columns on all four edges. Under lateral loads, web plates experience shear buckling; however, they are still capable of resisting lateral loads and providing lateral stiffness in the post-buckling range due to diagonal tension stresses developing in web plates called tension field action (TFA) [8]. As the current design practices rely on TFA for the design of SPSWs, diagonal tension stresses in the web plates must be anchored to very stiff beams and columns to utilize TFA efficiently. This diagonal tension might cause significant force demands in beams and columns and require stringent stiffness requirements. It is worthwhile noting that the vertical component of TFA in the web plates of the adjacent stories acting on the intermediate-story beams are in the opposite direction. Consequently, except for the base and roof beams, the flexural demands in the beams of SPSWs might be minimal. However, as diagonal tension stresses in the web plates are exerted on the columns of SPSWs on one side only, the significant internal force demands develop in the columns, which is a design challenge. To mitigate high flexural and axial demands in the columns due to TFA and to facilitate field installation of web plates, an alternative SPSW configuration called SPSWs with beam-connected web plates (B-SPSW) is proposed, in which the web plates are connected to the beams of SPSWs only and the vertical edges of the web plates are free. Within the scope of this paper, the focus is on the modeling of beam-connected web plates. Details of B-SPSWs system design and seismic performance can be found in Ozcelik and Clayton [9–12].

The web plate behavior is typically simulated using two modeling techniques, namely, the continuum model and the strip model. In the former technique, the web plate is modeled using shell-based finite elements with specified initial out-of-straightness to explicitly simulate the shear buckling behavior and to capture the development of TFA under lateral loads. In the later approach, the strip model, the web plate is modeled using a series of inclined tension-only truss elements connected to beams and columns to represent the diagonal tension field of the web plate. The strip model has been utilized successfully by many researchers [2,8,13–17] to simulate the cyclic response of fully-connected web plates (i.e., web plates connected to beams and columns). However, there has been little work done on the development of a strip model for the simulation of cyclic behavior of beam-connected web plates in B-SPSWs.

In the strip model, it is essential to determine the extent and inclination angle of TFA and the hysteretic behavior of individual strips to simulate the cyclic behavior of web plates and to obtain member demands accurately. For fully-connected web plates, design codes [18,19] provide an equation for the inclination angle of tension field. In addition, recent research [20,21] proposed an inclination angle of 45 degrees for fully-connected web plates provided that beams and columns have sufficient stiffness to anchor the web plate to develop full TFA, i.e., diagonal tension stresses develop in the whole plate. As the beam-connected web plates are not restrained by columns along their vertical edges, the extent and inclination angle of the tension field differ from these of fully-connected web plates due to the formation of partial TFA (Figure 1) instead of full TFA. In addition, recent research [20,21] revealed that the tension-only strip behavior is not in alignment with experimental findings and the fully-connected web plates have non-negligible compressive resistance upon loading and unloading. As the compressive strength of the strips depends on the web plate connectivity and thickness, it should be investigated for beam-connected web plates.

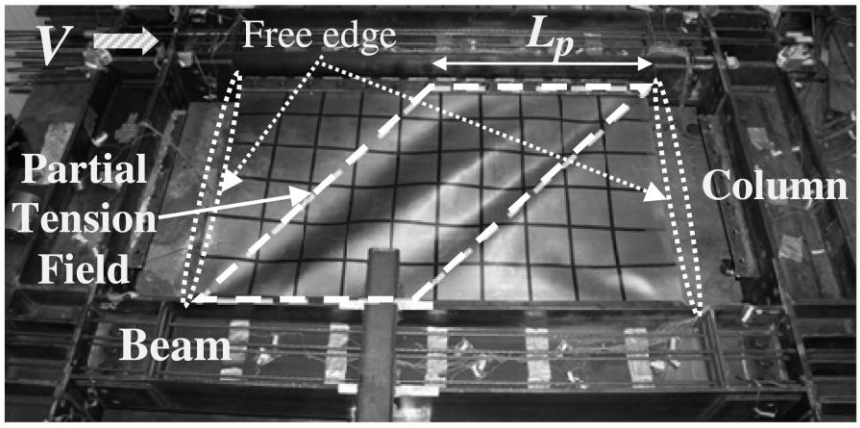

Figure 1: A test photo of partial tension field (adapted from Clayton et al. [16])

In this study, to simulate the beam-connected web plate behavior, a strip model is proposed, providing equations for the inclination angle of tension field and the compressive strength of strips. The details of the strip model are explained and a three-way comparison between the proposed strip, a strip model in the literature, and a continuum model is presented.

2 STRIP MODEL FOR BEAM-CONNECTED WEB PLATES

Thorburn et al. [8] was proposed a strip model for fully-connected web plates with infinitely flexible columns. In this model, Thorburn et al. [8] assumed that partial TFA would form in the web plate between the beams over the partial TFA length (L_p) as the columns could not anchor the diagonal tension stresses in the web plate. Assuming the PTF orients itself to resist the maximum shear force, Thorburn et al. [8] proposed an equation for the inclination angle of partial TFA (Equation 1), where γ is a non-dimensional inclination angle parameter given as 0.5.

$$\theta = \gamma \tan^{-1}(L/H) \tag{1}$$

Thorburn et al. [8] defined L_p based on web plate geometry and an assumed θ (Equation 2), where L and H are the web plate length and height, respectively:

$$L_p = L - H\tan\theta = L\left(1 - \frac{\tan\theta}{L/H}\right) \tag{2}$$

The strip model proposed by Thorburn et al. [8] can be extended to beam-connected web plates as partial TFA is observed in beam-connected web plates under lateral loads. Characterizing thin beam-connected web plate behavior adopting a mechanics-based analytical model and a validated detailed finite element of a beam-connected web plate, Equation 3 is proposed for γ. Details of Equation 3 can be found in Ozcelik and Clayton [22,23].

$$\gamma = 0.55 - 0.03\,(L/H) \geq 0.51 \tag{3}$$

As discussed herein, compressive strength of SPSW web plates is typically neglected since it is assumed that web plates have limited shear buckling strength. A parametric study was conducted by Ozcelik and Clayton [22] to quantify the compressive strength of strips representing beam-connected web plates. A parameter, β, is defined as the ratio of compressive strength of the strip to the yield strength, F_y, of the web plate material, given by Equation 4, where t_w is the web plate thickness:

$$\beta = -0.04 + 0.02\,(L/H) + \frac{2.75}{\sqrt{H/t_w}} \geq 0 \tag{4}$$

Adding an elasto-plastic material with a compressive strength determined by Equation 4 (Figure 2(b)) to the tension-only pinched material for which tensile stresses do not develop until reaching the maximum plastic strain from previous cycles (Figure 2(a)) in parallel, a parallel material (Figure 2(c)) can be used to simulate the strip behavior under cyclic loading. The normalized stress and strain diagrams of the materials are given in Figure 2, where σ is the stress in strips, ε is the normal strain of strips, and ε_y is the yield strain of the web plate material.

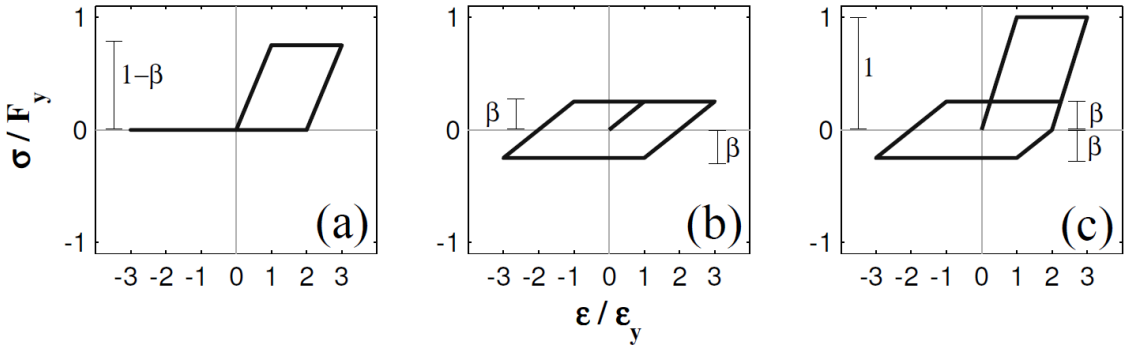

Figure 2: Material models for strips: (a) pinched tension-only material, (b) elasto-plastic tension-compression material, and (c) resulting strip response when (a) and (b) are used in parallel. (adapted from Ozcelik and Clayton [22])

The area of a strip, A_s, can be calculated using Equation 5, where n_s is the number of strips in each direction:

$$A_s = t_w\, L_p \cos\theta\, / n_s = t_w\, L \left(1 - \frac{\tan\theta}{L/H}\right) \cos\theta\, / n_s \tag{5}$$

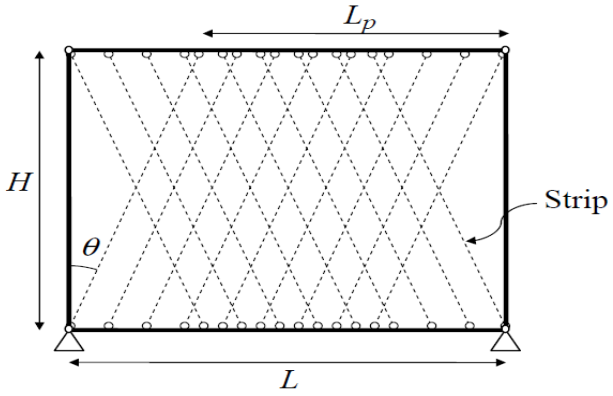

Figure 3: Strip model. (adapted from Ozcelik and Clayton [22])

The step-by-step modeling of the proposed strip model is described as follows:

- Determine γ and θ using Equations 3 and 1, respectively.
- Calculate L_p using Equation 2.
- Select the number of strips (at least 10 strips to improve accuracy) and calculate A_s from Equation 5.

- Estimate β from Equation 4.
- Define the strip material as a combination of materials in parallel given in Figure 2(a) and Figure 2(b).
- Create a series of evenly-spaced inclined strips using truss elements as shown in Figure 3.

3 COMPARISON OF B-SPSW MODELS

A three-way comparison between the proposed strip model, a strip model in the literature, and the continuum model is provided. B-SPSWs with various aspect ratios (L/H) between 0.8 and 2.5 keeping H constant (4 m) and height-to-thickness ratios between 160 and 3200 are analyzed under a cyclic drift history in ABAQUS [24] adopting the continuum model approach where the web plates are represented by shell elements (S4R) with an initial imperfection and beams and columns are modeled using very stiff line elements (B31). These models will be referred to as finite element models (FEM). The same B-SPSWs are modeled in OpenSEES adopting the strip model approach proposed herein. As the proposed strip model accounts for the compressive strength of the strips, it will be referred to as tension-compression strip model (TC). In addition to the proposed strip model, B-SPSWs are modeled in OpenSEES adopting the strip model proposed by Thorburn et al. [8], in which γ is 0.5 and β is 0 (i.e., tension-only strips). The strip model proposed by Thorburn et al. [8] will be referred to as tension-only strip model (TO). Similar to FEM, the beams and columns of the TC and TO models are modeled using very stiff line elements. Further details on the modeling of FEM, TC, and TO can be found in Ozcelik and Clayton [22].

The analysis results from the strip models (TC and TO) and FEMs are compared in terms of base shear capacity of beam-connected web plates, beam and column demands, and energy dissipation capacity of B-SPSWs. Figure 4 shows the comparison of the base shears, V, normalized with respect to the web plate lateral load capacities, V_y, of three models with an aspect ratio of 1.5 for various H/t_w ratios. V_y can be calculated from Equation 6:

$$V_y = 0.5\, F_y t_w L_p \sin 2\theta \tag{6}$$

As depicted in Figures 6(a) and 6(b), for thinner web plates (higher H/t_w), both TO and TC match the FEM results closely as the strips representing thinner web plates have limited compressive strength. The normalized base shear capacities and the normalized unloading base shears are closed to 1 and 0, respectively, for all models, as expected. For thicker plates (Figures 6(d) and 6(e)), TC still shows a very similar response to FEM while TO does not match FEM. As thicker plates are used, TC is able to predict peak capacities accurately; however, it does tend to underestimate the web plate strength during unloading and loading. The loading and unloading strengths might have a substantial impact on the energy dissipation capacity; however, they do not affect the peak beam and column demands as will be discussed.

By integrating the area under the base shear vs. displacement response for each model, energy dissipation (E) is determined. For a L/H of 1.5 and H/t_w of 213, Figure 5 shows E for each model normalized with respect to the total energy dissipated in FEM (E_{max}). As mentioned, the TC model underestimates the unloading and loading strengths; consequently, the TC model underpredicts E by approximately 25% for thicker plates with respect to the FEM results. On the other hand, the TO model underestimates E by approximately 75% for the same plate thickness with respect to the FEM results.

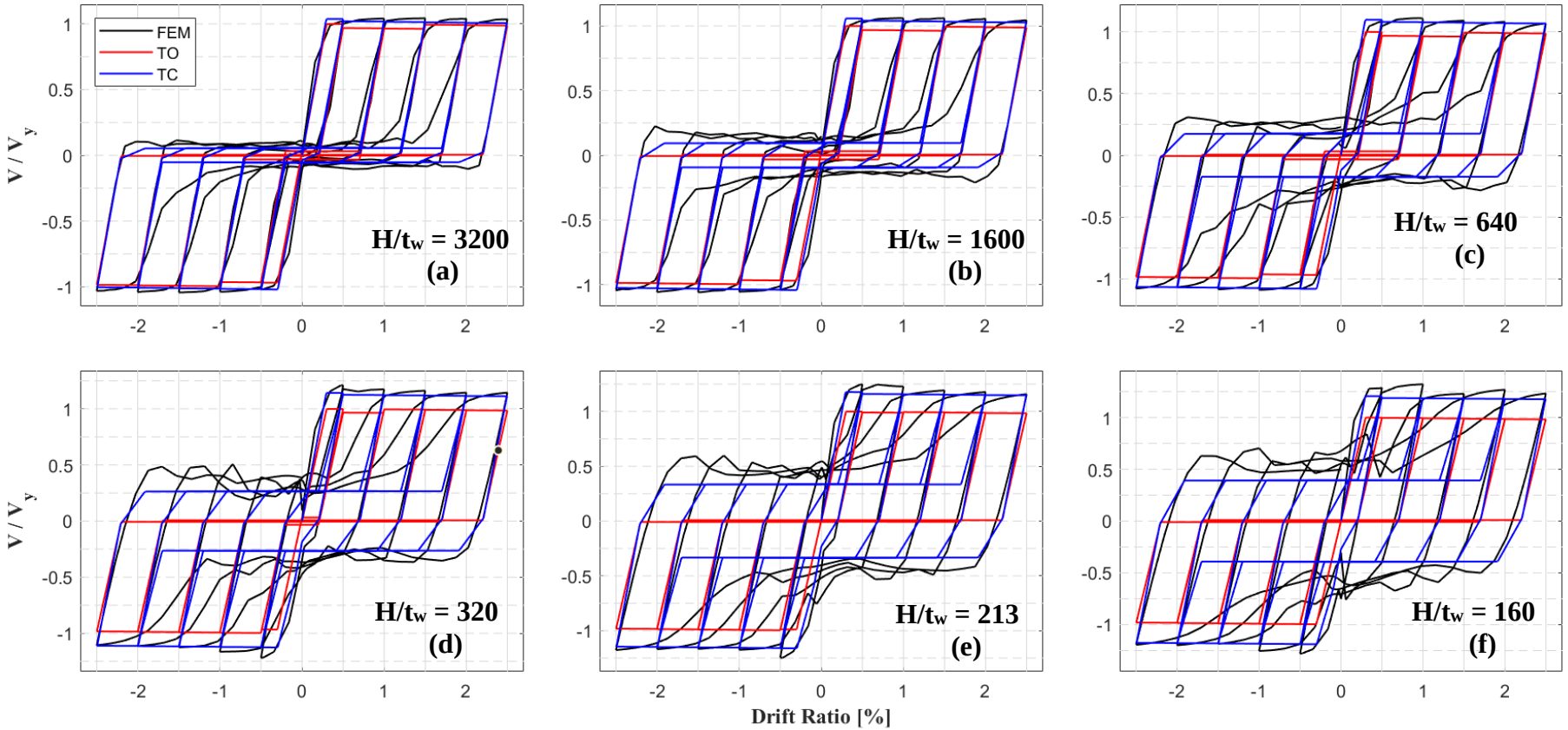

Figure 4: Comparison of normalized base shear vs. drift ratio for an aspect ratio of 1.5

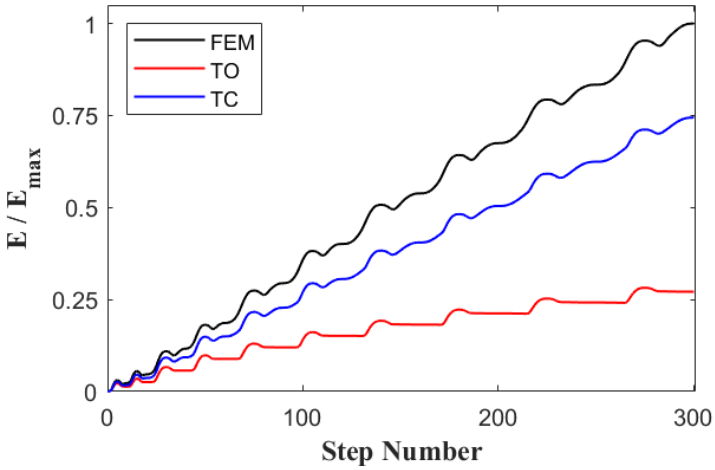

Figure 5: Normalized strain energy for a L/H of 1.5 and H/t_w of 213

For various L/H and H/t_w, the normalized strain energy (E/E_{max}) values are tabulated in Tables 1 and 2 for TC and TO models, respectively. For the thinnest and the thickest plates considered in this study ((H/t_w of 1600 and 160, respectively), TO can dissipate approximate 50% and 25% of E_{max} (on average), respectively. However, TC can dissipate as high as 84% of E_{max} on average. Despite underprediction of energy dissipation, TC shows a great improvement in simulating beam-connected web plate behavior compared to the existing TO in terms of energy dissipation capacity.

	M_{max}			P_{max}			V			E		
	H/t_w			H/t_w			H/t_w			H/t_w		
L/H	**160**	**320**	**1600**	**160**	**320**	**1600**	**160**	**320**	**1600**	**160**	**320**	**1600**
1.1	1.16	1.06	1.06	0.96	0.98	1.04	0.89	0.92	0.96	0.75	0.76	0.81
1.4	1.03	1.16	1.04	0.94	1.05	1.03	0.92	0.98	0.99	0.78	0.79	0.84
1.7	1.17	1.14	1.04	1.08	1.03	1.04	0.96	0.98	0.99	0.80	0.80	0.81
2.0	1.12	1.12	1.03	1.06	1.07	1.03	0.99	1.01	1.00	0.83	0.83	0.84
2.3	1.07	1.16	1.05	1.05	1.06	1.03	1.01	1.02	0.99	0.95	0.92	0.90
Average	1.09	1.09	1.04	1.01	1.03	1.04	0.94	0.98	0.98	0.82	0.84	0.85
Std. Dev.	0.07	0.06	0.02	0.06	0.04	0.01	0.07	0.04	0.02	0.08	0.06	0.04

Table 1: Beam Moment, Column Axial Load, Base Shear, and Energy Ratios (TC Model to ABAQUS Ratios)

	M_{max}			P_{max}			V			E		
	H/t_w			H/t_w			H/t_w			H/t_w		
L/H	**160**	**320**	**1600**	**160**	**320**	**1600**	**160**	**320**	**1600**	**160**	**320**	**1600**
1.1	1.45	1.24	1.15	1.09	1.08	1.10	0.64	0.80	0.94	0.24	0.30	0.54
1.4	1.31	1.37	1.13	1.07	1.15	1.09	0.76	0.82	0.94	0.23	0.30	0.51
1.7	1.48	1.37	1.14	1.23	1.15	1.10	0.77	0.87	0.95	0.27	0.33	0.51
2.0	1.44	1.35	1.14	1.21	1.19	1.09	0.79	0.88	0.95	0.27	0.33	0.50
2.3	1.36	1.36	1.12	1.21	1.17	1.09	0.82	0.88	0.96	0.28	0.35	0.53
Average	1.39	1.31	1.14	1.15	1.13	1.10	0.75	0.84	0.94	0.25	0.33	0.52
Std. Dev.	0.10	0.09	0.02	0.08	0.06	0.01	0.08	0.04	0.01	0.02	0.03	0.03

Table 2: Beam Moment, Column Axial Load, Base Shear, and Energy Ratios (TO Model to ABAQUS Ratios)

Tables 1 and 2 tabulate the ratios of maximum moment in beams (M_{max}), maximum axial compressive load in columns (P_{max}), and V of strip models to those of FEM. TO overestimates

M_{max} and P_{max} conservatively for all H/t_w values; however, TO becomes overly conservative as plate thickness increases. TO successfully predicts V for thinner plates while V of TO can be as low as 60% of V of FEM for thicker plates. These differences stem from the negligible compressive strength assumption for TO. TC predicts the M_{max} P_{max}, and V accurately regardless of the plate thickness as TC accounts for the compressive strength of strips. For the cases in which TC deviates from FEM, the member demands are typically conservatively overestimated and base shear tends to be conservatively underestimated for TC. In brief, TC can be used to model beam-connected web plates for a wide range of L/H and H/t_w values.

4 CONCLUSIONS

In this study, a simplified model called strip model is proposed to simulate the behavior of beam-connected web plates under cyclic loading. An equation is presented for the inclination of tension field action observed in beam-connected web plates and another equation is provided that estimates the compressive strength of strips. A three-way comparison between the proposed strip model, the strip model proposed by Thorburn et al. [8], and the shell-based finite element model is presented. The results of the comparative study appear to indicate that the proposed strip model matches the finite element results and shows a significant improvement in simulating beam-connected web plate behavior compared to the strip model proposed by Thorburn et al. [8].

REFERENCES

[1] Driver RG, Kulak GL, Kennedy DJL, Elwi AE. Seismic behavior of steel plate shear walls. Structural Engineering Report No. 298. University of Alberta. Edmonton, AB: 1997.

[2] Driver R, Kulak G, Elwi AE, Kennedy D. FE and simplified models of steel plate shear wall. J Struct Eng 1998;124:121–30. doi:10.1061/(ASCE)0733-9445(1998)124:2(121).

[3] Elgaaly M. Thin steel plate shear walls behavior and analysis. Thin-Walled Struct 1998;32:151–80. doi:10.1016/S0263-8231(98)00031-7.

[4] Kulak G, Kennedy D, Driver R. Discussion of "Experimental Study of Thin Steel Plate Shear Walls under Cyclic Load" by Vincent Caccese, Mohamed Elgaaly, and Ruobo Chen (February, 1993, Vol. 119, No. 2). J Struct Eng 1994;120:3072–3. doi:10.1061/(ASCE)0733-9445(1994)120:10(3072).

[5] Rezai M. Seismic behavior of steel plate shear walls by shaking table testing. University of British Columbia, 1999.

[6] Roberts TM, Sabouri-Ghomi S. Hysteretic characteristics of unstiffened perforated steel plate shear panels. Thin-Walled Struct 1992;14:139–51. doi:10.1016/0263-8231(92)90047-Z.

[7] Sabelli R, Bruneau M. Steel design guide: Steel plate shear walls. AISC; 2012.

[8] Thorburn L, Kulak G, Montgomery C. Analysis of steel plate shear walls. Structural Engineering Report No. 107. University of Alberta. Edmonton, AB: 1983.

[9] Ozcelik Y, Clayton P. Seismic design and performance of SPSWs with beam-connected web plates. J Constr Steel Res 2018;142:55–67.

[10] Ozcelik Y, Clayton PM. Behavior of columns of steel plate shear walls with beam-connected web plates. Eng Struct 2018;172:820–32.

doi:10.1016/j.engstruct.2018.06.087.

[11] Ozcelik Y, Clayton PM. Effect of flexural demands in the leaner columns on the column buckling strength. Proc. 11th Natl. Conf. Earthq. Eng., Los Angeles, CA: 2018.

[12] Ozcelik Y, Clayton PM. Seismis performance of SPSWs with beam-connected web plates designed for low-seismic regions. Proc. 16th Eur. Conf. Earthq. Eng., Thessaloniki, Greece: 2018.

[13] Clayton PM, Tsai C-Y, Berman JW, Lowes LN. Comparison of web plate numerical models for self-centering steel plate shear walls. Earthq Eng Struct Dyn 2015;44:2093–110. doi:10.1002/eqe.2578.

[14] Guo L, Li R, Zhang S, Yan G. Hysteretic analysis of steel plate shear walls (SPSWs) and a modified strip model for SPSWs. Adv Struct Eng 2012;15:1751–64. doi:10.1260/1369-4332.15.10.1751.

[15] Lubell AS, Prion HGL, Ventura CE, Rezai M. Unstiffened steel plate shear wall performance under cyclic loading. J Struct Eng 2000;126:453–60. doi:10.1061/(ASCE)0733-9445(2000)126:4(453).

[16] Clayton PM, Berman JW, Lowes LN. Seismic performance of self-centering steel plate shear walls with beam-only-connected web plates. J Constr Steel Res 2015;106:198–208. doi:10.1016/j.jcsr.2014.12.017.

[17] Shishkin J, Driver R, Grondin G. Analysis of steel plate shear walls using the modified strip model. J Struct Eng 2009;135:1357–66. doi:10.1061/(ASCE)ST.1943-541X.0000066.

[18] AISC. ANSI/AISC 341-16 Seismic provisions for structural steel buildings. Chicago, IL: American Institute for Steel Construction (AISC); 2016.

[19] CAN/CSA. CAN/CSA-S16-09 Design of steel structures. Mississauga, ON: Canadian Standards Association; 2009.

[20] Webster DJ, Berman JW, Lowes LN. The elastic and inelastic post-buckling behavior of steel plate shear wall web plates and their interaction with vertical boundary elements. Proc. Annu. Stab. Conf. Struct. Stab. Res. Counc., Grapine, TX: 2012.

[21] Webster DJ. The inelastic seismic response of steel plate shear wall web plates and their interaction with the vertical boundary members (Ph.D. Dissertation). University of Washington, 2013.

[22] Ozcelik Y, Clayton P. Strip model for steel plate shear walls with beam-connected web plates. Eng Struct 2017;136:369–79. doi:10.1016/j.engstruct.2017.01.051.

[23] Ozcelik Y, Clayton P. Tension field inclination angle in steel plate shear walls with beam- connected web plates. Second Int. Conf. Nat. Hazards Infrastruct., Chania, Greece: 2019.

[24] ABAQUS. ABAQUS version 6.10 documentation. Simulia; 2010.

COMPDYN 2019
7th ECCOMAS Thematic Conference on
Computational Methods in Structural Dynamics and Earthquake Engineering
M. Papadrakakis, M. Fragiadakis (eds.)
Crete, Greece, 24–26 June 2019

SEISMIC DESIGN CRITERIA TO IMPROVE THE PERFORMANCE OF X-CBFS

S. Costanzo[1], M. D'Aniello[1], G. Di Lorenzo[1], A. De Martino[1], and R. Landolfo[1]

[1] Department of Structures for Engineering and Architecture, University of Naples Federico II
e-mails: silvia.costanzo@unina.it, mdaniel@unina.it, gianmaria.dilorenzo@unina.it, atdemart@unina.it, landolfo@unina.it

Abstract

Cross concentrically braced frames are commonly used in seismic design of steel buildings at any seismicity, owing to their large lateral stiffness, simplicity of design and limited constructional cost. The seismic design criteria provided by current EC8 aim at assuring ductile global plastic mechanism occur, namely restraining the plastic deformation into the diagonals, while the remaining structural members and connections should elastically behave. However, several studies, show that the design process compliant to Eurocode 8 is affected by several criticisms, it entails several efforts and often leads to massive, uneconomical systems solution exhibiting poor seismic performance. EN1998-1 recommends estimating the lateral resistance of X-CBFs by performing structural analysis on a tension-only (T-O) diagonal scheme in which solely the tension braces resist the lateral loadings, while the contribution given by the compression diagonals is neglected. As highlighted by the comments given by European designers coming from the survey promoted by CEN TC 250/SC8 for the systematic review of EC8, this type of model can induce misleading interpretation of the structural behavior and relevant modelling of X-CBFs, leading to uneconomical and oversized systems characterized by heavy structural solutions and poor plastic engagement. The research presented in this paper is addressed to critically discuss and revise the detailing rules codified within the current EN 1998-1 for X-CBF, to simplify the design process and to improve the seismic behavior. Whit this aim, an extent set of nonlinear dynamic analyses has been performed on a set ow low, medium, and high-rise 2D frames extracted from residential steel buildings to assess the effectiveness of currently codified requirements and to validate the beneficial effects of the proposed revision.

Keywords: concentrically braced frames; seismic design; Eurocode 8; ductility demand; steel structures.

1 INTRODUCTION

Cross concentrically braced frames (X-CBFs) are widely used in multi-story steel buildings as seismic resisting systems at any seismicity, due to their simplicity of design and low constructional costs, although the limited available ductility and redundancy as respect to moment resisting frames (MRFs).

To ensure a global ductile behavior, seismic codes [1-3] provide capacity design criteria devoted restraining the plastic deformations into the diagonal members and preventing damage of beams, columns and connections.

Numerous researchers [4-22] critically discussed and revised the design rules codified within EN 1998-1 and even identified some issues needing upgrading and/or amendment.

EN1998-1 [1] recommends calculating the lateral resistance of cross bracings by performing structural analysis on a tension-only (T-O) diagonal scheme in which solely the tension braces withstand the lateral loadings, and the contribution given by the compression diagonals is neglected. As highlighted by the comments given by European designers coming from the survey promoted by CEN TC 250/SC8 for the systematic review of EC8, this type of model can induce misleading interpretation of the structural behavior and relevant modelling of X-CBFs. In detail, one of the most critical aspect deals with the evaluation of brace slenderness. Indeed, the use of T-O model instills in many designers that only the diagonal subjected to tensile forces is mechanically active and the mutual restraint between the braces could be disregarded, thus considering the entire length of the element as buckling length. Conversely, as highlighted by several Authors [12, 22-29], the presence of the complementary brace and the mutual connection degree at the diagonals mid length has considerably importance for the accurate prediction of both in-plane and out-of-plane buckling phenomena; theoretical and experimental results by [22-29] confirmed that the tension brace can effectively restrain both in-plane and out-of-plane displacements of the diagonal under compression at the brace-to-brace intersection. Therefore, to accurately evaluate the brace slenderness and the brace hysteretic response, half length of the brace can be conservatively assumed as buckling length.

According to current EC8 [1] the brace slenderness ratio should be in the range (1.3 – 2); the lower limit is introduced to avoid overloading of the columns due to the force demand transferred by the compression diagonals omitted in the models. However, the EC8 do not discriminate continuous and discontinuous diagonals, being likely unconservative: indeed, in absence of specific guidance, the designer can disregard the brace-to-brace mutual restraint, thus selecting diagonals that are stockier than expected.

Another critical aspect of EC8-compliant design is related to the requirement on the capacity-to-demand ratios $\Omega_i = N_{pl,br,Rd,i}/N_{Ed,br,i}$ (being $N_{pl,br,Rd,i}$ the brace yield strength and $N_{Ed,br,i}$ the design forces due to the seismic actions) which should vary in the range (Ω; 1.25Ω) to guarantee uniform distribution of plasticity along the building height and thus mitigating the tendency of CBFs to soft-story mechanisms. Several Authors [11-18] showed that this requirement is not adequate to guarantee an overall plastic engagement of the dissipative elements and it also leads to oversize the diagonals at lower and intermediate stories. Indeed, to contemporarily satisfy the requirements of slenderness limits and the overstrength variation often leads to impractical solutions with significant difficulties to select the proper member for braces, being both requirements closely interrelated and juxtaposed [4-9, 11-12, 14-15]. These considerations motivated the research presented in this paper, which is addressed to identify the main criticisms of the current EC8 [1] and to propose some amendments to design rules in order to obtain more cost-effective and structurally efficient X-CBFs.

With this aim, the paper is organized in three main parts: (i) Section 2 describes the design rules of the current Eurocode 8, providing a critical discussion; In Section 3, revised design

rules are proposed; the proposed design rules are validated by mean of a numerical parametric study described and discussed in Section 4

2 EC8 DESIGN PROCEDURE

For regular structures equipped with X-CBFs, EN 1998-1 recommends a behavior factor q equal to 4 to reduce the elastic spectrum for both medium and high ductility classes.

To calculate the internal forces, EC8 allows simplified design procedure, performing a linear-elastic analysis on a T-O model where the contribution of compression diagonals is neglected (Fig. 1a).

The slenderness ratio $\bar{\lambda}$ of diagonal members should be in the range [1.3, 2]. As mentioned in the previous Section, the lower bound limit ($\bar{\lambda} \geq 1.3$) is introduced to limit the forces transferred to the columns by compression braces, omitted in the T-O model, while upper bound limit ($\bar{\lambda} \leq 2$) is devoted to assure satisfactorily hysteretic behavior and undesired buckling under serviceability loads. The imposition of the lower bound limit ($\bar{\lambda} \geq 1.3$) is direct consequence of using T-O model and it entails significant difficulties in sizing of brace cross-section, and it often involves the need to increase the number of braced bays to select smaller diagonal members.

The upper bound limit for brace slenderness ($\bar{\lambda} \leq 2$) also influences the design process of bracing elements, especially due to its interrelation with the control of the variation of the brace overstrength ratios Ωi. To assure uniform distribution of plastic deformations along the building height, Eurocode 8 limits the variation of the brace overstrength ratios $\Omega_i = N_{pl,br,Rd,i}/N_{Ed,br,i}$ for braces at i-th story within the range [Ω - 1.25Ω], being Ω the minimum value.

The diagonal members at the roof story are indeed generally characterized by large overstrength ratio due to the need of selecting large cross section to satisfy the slender upper bound limit. As consequence, to meet the requirement on the Ω variation, the designer is forced to oversize the diagonals at all story. In such situation, typical values of Ω ratios for bracings in X configurations can largely overcome the unit, resulting in poor plastic engagement of dissipative zones and unsatisfactorily energy dissipation capacity [5,7,9].

The hierarchy of resistance is deemed to be satisfied by amplifying the seismic-induced effects evaluated by mean of the linear-elastic analysis by the overstrength factor Ω. In detail, the required strength of non-dissipative should meet the following:

$$N_{pl,Rd}(M_{Ed}) \geq N_{Ed,G} + 1.1 \cdot \gamma_{ov} \cdot \Omega \cdot N_{Ed,E} \tag{2}$$

where $N_{pl,Rd}(M_{Ed})$ is the design axial strength of the beam or column calculated in accordance with EN 1993:1-1 [31], taking into account the interaction with the design value of bending moment, M_{Ed}, in the seismic design situation; $N_{Ed,G}$ is the axial force in the beam or in the column due to the non-seismic actions included in the combination of actions for the seismic design situation; $N_{Ed,E}$ is the axial force in the beam or in the column due to the design seismic action; γ_{ov} is the factor accounting for random variability of the steel yield stress.

As previously mentioned, this design procedure often leads to uneconomical and oversized structures practically behave in elastic range [4-5, 8-9, 11-12, 34-39]. The reason for using T-O structural scheme is based on the assumption that compression diagonals have negligible contribution to resist lateral action due to buckling. However, this idealization is a reasonable approximation only for slender braces in post-buckling condition, while in the first stages of seismic response, as well as for stocky braces, both diagonals are active in tension and com-

pression and the axial force transferred to the columns and connections by the compression diagonals could be significant. In order to clarify this aspect, Figure 2 depicts the force transfer mechanisms obtained by considering T-O model (Fig. 1a) and by using a tension-compression (T-C) scheme in which both braces are explicitly accounted for (Fig. 1b). It is trivial to observe that T-O model underestimates the force acting in the columns, thus potentially resulting in unconservative design.

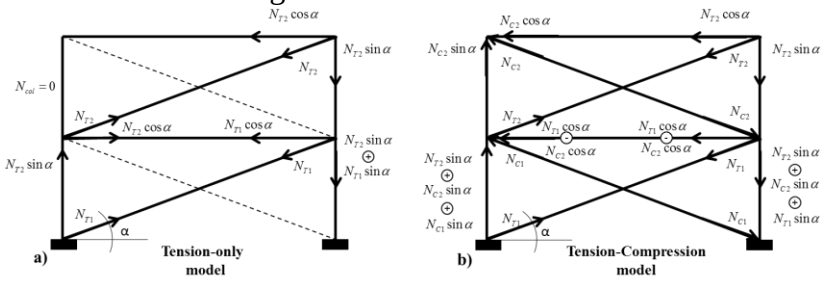

Figure 1: Tension-only (a) Tension-Compression (b) model.

Moreover, as previously mentioned, the use of T-O model can lead to misleading interpretation of structural behavior, inducing the designer to inaccurately calculate the buckling length of the diagonal disregarding the role of the complementary bracing and of the brace-to-brace mutual degree of connection.

3 SEISMIC DESIGN CRITERIA TO IMPROVE THE PERFORMANCE OF X-CBFS

The current section presents new design criteria to improve the ductility of X-CBFs and at the same time to simplify the design process. The suggested rules are consistent with those provided by Authors [11, 13] for chevron CBFs, to develop and validate a unified approach for seismic design of both cross and chevron bracings, thus avoiding the definition of two sub-categories based on the bracing configurations as it is in the current version of EC8.

The behavior factor currently recommended by EC8 for X-CBFs, i.e. q = 4, is retained.

The required strength of bracings is determined by performing global elastic analysis on the structural scheme with both braces active in tension and compression (T-C scheme). Thereby, the bracing members should be designed to meet the following condition:

$$N_{b,br,Rd,i} \geq N_{br,Ed,i} \tag{3}$$

Where $N_{\mathrm{b,br,Rd,i}}$ is the factored buckling capacity of the i-th bracing member evaluated according to EN 1993-1 [30]; $N_{\mathrm{br,Ed,i}}$ is the axial force acting in the bracing members evaluated according to the following equation:

(i) at the roof story:

$$N_{br,Ed,rf} = q \cdot N_{br,Ed,E,rf} + N_{br,Ed,G,rf} \tag{4}$$

where $N_{\mathrm{br,Ed,rf}}$ is the required strength in compression of bracings at the roof story; $N_{\mathrm{br,Ed,E,rf}}$ is the axial force contribution at the roof story due to the seismic action; $N_{\mathrm{br,Ed,G,rf}}$ is the axial force contribution at the roof story due to the non-seismic actions included in the combination of actions for the seismic design situation; q the behavior factor assumed at design stage.

(ii) at the i-th story:

$$N_{br,Ed,ri} = N_{br,Ed,E,i} + N_{br,Ed,G,i} \tag{5}$$

being $N_{\mathrm{br,Ed,i}}$ the required strength in compression of bracings at the i-th story; $N_{\mathrm{br,Ed,E,i}}$ the axial force at the i-th story due to the seismic action; $N_{\mathrm{br,Ed,G,i}}$ the axial force at the i-th story

due to the non-seismic actions included in the combination of actions for the seismic design situation.

The requirement expressed by Eq. 4 is devoted to favor uniform distribution of drift along the building height. Results of nonlinear dynamic analyses performed by [10, 12] showed that medium and high-rise multistory braced frames designed according to EN 1998 generally exhibit cantilever-like displacement profile with high damage concentration at the upper stories. Restraining the bracings at roof story in the elastic range allows to control the distribution of drift along the building height. Results from non-linear analyses performed within previous studies by the Authors [11-15] clearly validated the effectiveness of requirement expressed by Eqn. 4 in assuring shear-like behavior and more uniform distribution of drifts and plastic deformations along the building height. In low-rise buildings up to three story, such requirement can be neglected, being the behavior of low-rise buildings mostly shear-type.

Since, the brace under compression is explicitly accounted for in the global analysis, the lower bound limit currently provided for by EC8 is disregarded, while the maximum allowable slenderness is retained (i.e. $\overline{\lambda} \le 2$).

The brace slenderness is evaluated assuming that both in-plane and out-of-plane initial buckling is effectively restrained by the complementary brace, namely the buckling length is assumed equal to the half-length of the element.

The requirement on capacity-to-demand ratio variation is amended as follow:

$$[(\Omega_{b,i} - \Omega_b)/\Omega_b] \ge 0.25 \tag{6}$$

Where:

$$\Omega_b = \min(\Omega_{b,i}) = \mathrm{mi}\left(\frac{\chi \cdot N_{pl,br,Rd,i}}{N_{Ed,br,i}}\right);\ \ i \in [1,(n-1] \tag{7}$$

being n the number of stories.

The overstrength Ω_b at each story is defined considering the buckling strength of the brace $\chi N_{pl,br,Rd,i}$ rather than the tensile one, to better control the sequence of buckling and fostering uniform engagement of braces.

Differently from current EC8, the design forces acting in the non-dissipative members are evaluated by explicitly considering the force transfer mechanisms occurring in the post-buckling range; thereby the most severe condition among the following is considered:

1) pre-buckling stage: both braces are active, and their axial forces are equal to $\gamma_{ov}\chi_i N_{pl,br,Rd,i}$.

2) post-buckling stage: the design forces in the non-dissipative members are estimated by a free-body distribution of plastic forces corresponding to the braces fully yielded under tension and those under compression in the post-buckling range. In detail, the brace under tension is assumed transmitting its full plastic strength as follow:

$$N_T = 1.1 \cdot \gamma_{ov} \cdot N_{pl,br,Rd,i} \tag{8}$$

where, $N_{pl,br,Rd,i}$ is the design plastic strength of brace cross-section, γ_{ov} is the material randomness coefficient and 1.1 accounts for material strain-hardening.

The compression diagonal is assumed attaining its average post-buckling strength set equal to:

$$N_C = 0.3 \cdot \gamma_{ov} \cdot \chi \cdot N_{pl,br,Rd,i} \tag{9}$$

It should be noted that in current EN 1998, plastic mechanism analysis is recommended solely for calculating the unbalanced force occurring on the brace-intercepted beam in chevron concentrically braced frames. According to current EC8, the post-buckling strength of

brace under compression should be assumed equal to $\gamma_{pb}N_{pl,br,Rd,i}$, where the recommended value for γ_{pb} is 0.30. As observed in [9-12], $\gamma_{pb}N_{pl,br,Rd,i}$ leads to inconsistent distribution of forces when slender braces are used. Indeed, for very slender bracings close to the upper bound limit 2, the brace buckling strength tends to the 20% of the plastic resistance (the buckling reduction factor χ is about 0.2), thus resulting lower than the value suggested by the code to evaluate the brace post-buckling strength. Consistently to what recommended by AISC 341-16 [2] Eqn. 9 overcomes this criticism and it provides the post-buckling strength accounting for the brace slenderness by mean of the buckling coefficient χ.

In addition, consistently with CSA-S16 [3], the columns belonging to the braced bays are verified to withstand the combined action of the axial force evaluated for the condition (2) and bending moments with uniform distribution equal to the 20% of the plastic bending resistance of the column cross section.

Moreover, in order to enhance the redundancy of the system and to favor a uniform distribution of plasticity along the height the beam-to-column connections belonging to the braced bays are designed to be full strength and full-rigid (i.e. of moment resisting type).

4 NUMERICAL VALIDATION OF PROPOSED DESIGN CRITERIA

4.1 Parametric study

In order to validate the design criteria described in Section 3, a set of frames with three, six and twelve-story was alternatively designed according to the proposed design rules and the EC8-compliant criteria and analyzed by means of nonlinear dynamic analyses. In addition, in order to highlight the influence of brace-to-brace mutual restraint in the estimation of brace slenderness, the EC8 design criteria were applied twice, alternatively considering both design rules, namely:1) buckling length factor K = 1 (i.e. the effective length equal to the full length of the brace); 2) buckling length factor K = 0.5 (i.e. the effective length equal to the half-length of the brace).

The building archetypes is shown in Fig. 2. At each floor, the rigid diaphragm transmitting the horizontal actions is obtained by means of composite slabs with profiled steel sheetings supported by the hot-rolled steel beams (both primary and secondary), which are considered as restrained to avoid flexural-torsional buckling.

The structural design for gravity loads is carried out according to the non-seismic European codes [31-33] for all the examined frames, considering the Eurocode recommended parameters in place of those nationally determined. Permanent loads (G_k) and live loads (Q_k) are assumed equal to 5.20 kN/m^2 and 2.00 kN/m^2, at both intermediate and roof story. The inertial effects in the seismic design situation are evaluated in accordance with EN 1998-1 [1]. A reference peak ground acceleration equal to a_{gR} = 0.25g (being g the gravity acceleration), a type C soil, a type 1 spectral shape are assumed.

Cold formed circular hollow profiles are used for the diagonal members; IPE and HE profiles are used for beams; HE and HD for the columns. The cross sections of all steel members (i.e. beams, bracings and columns) are selected to satisfy the Class 1 requirements according to EN 1993:1-1 [31].

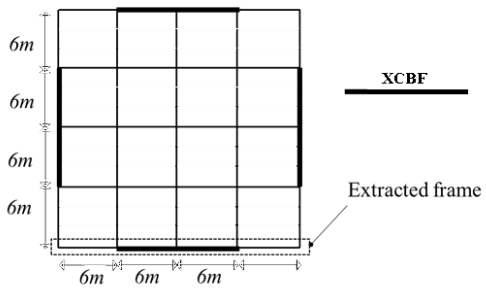

Figure 2: Reference building archetype

The geometrical properties of structural members for the three, six and twelve story buildings are reported in [12].

The non-linear behavior of the 2D examined frames is simulated by means of Seismostruct ; the modelling assumptions are described and validated against experimental results in [12]. A suite of 14 natural earthquake acceleration records has been considered to perform the non-linear dynamic analyses on the examined cases. More details on the selection of the signals and the relevant data can be found in [12].

4.2 Discussion of results

The plots in the current Section report the average values of performance parameters obtained for the 14 records. Figure 3 shows the average peak interstory drift ratios (IDR) for all examined cases. The frames designed according to the proposed design rules meet the requirement for non-structural damage at DL limit state, being the seismic demand smaller than 0.75% (i.e. EC8 limit for ductile non-structural elements). In addition, they exhibit more uniform distribution of displacements along the building height than EC8-compliant frames. These results confirm the effectiveness of proposed criteria to force a shear-type distribution od deformation and to avoid damage concentration at upper story. Figure 4 report the profiles of the maximum brace ductility demand $\mu = \left(\frac{d}{d_y} \right)$, where d is the axial elongation and dis the axial elongation and d_y is the value corresponding to the yielding. The frames designed according to proposed rules exhibit the lager plastic engagement of bracings, while limited ductility is recognized for EC8 frames with K = 0.5 and significant damage concentration is recognized solely at the upper story for EC8-compliant frames designed assuming K = 1.

5 CONCLUSIVE REMARKS

The paper discusses the main criticism of the design procedure for XCBFs currently codified in EN 1998-1 and seismic design criteria to improve the ductility of this type of systems are provided and numerically validated.

The interpretation of obtained results infers the following remarks:

T-C scheme (see Fig. 1b) with both braces active in tension and compression allows estimating the force-transfer mechanism induced by seismic action more effectively than T-O model (see Fig. 1a).

Using T-C model allows removing the lower bound limit on normalized brace slenderness making easier to select proper brace cross sections and allowing to obtain more ductile and effective systems.

The requirement of current EC8 on the capacity-to-demand variation of brace is not adequate to avoid soft-story mechanism and assuring uniform distribution of plasticity along the building height. In addition, it entails difficulties to design the brace cross sections and it leads to overdesigned and uneconomical structures, almost behaving elastically up to NC limit state. On the contrary, controlling the story-to-story variation of brace buckling overstrength is more effective to limit soft-story mechanisms and to assure uniform sequence of buckling along the building height.

The requirement devoted to keep the braces at the roof story in elastic range (Eqn. 4) is effective to obtain a shear-type overall structural response in six and twelve-story buildings with more uniform distribution of plastic deformations along the height.

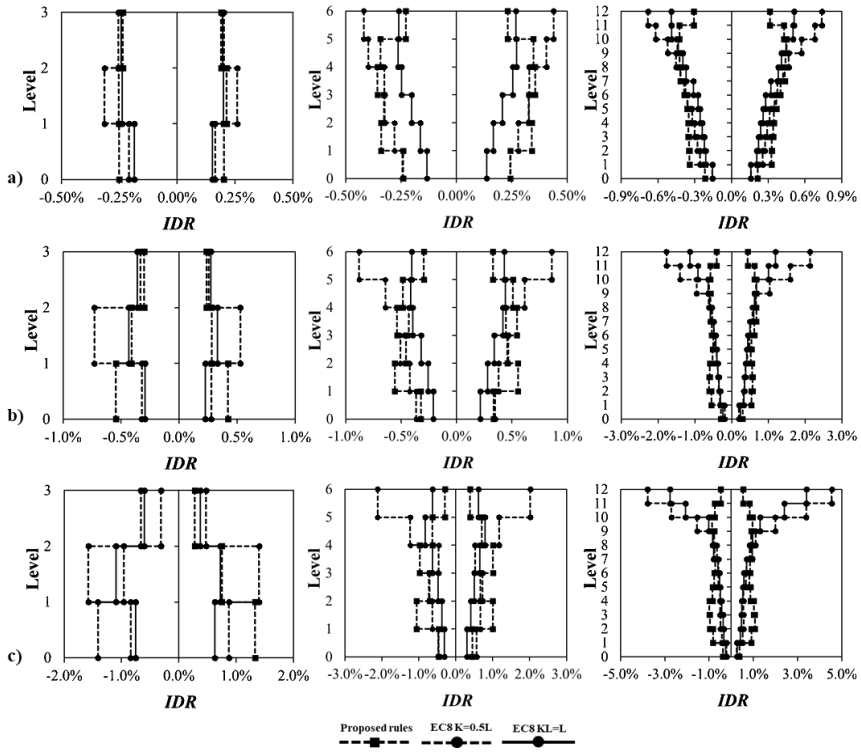

Figure 3. Comparison between proposed design criteria and EC8 compliant frames: Interstory drift ratios for three, six and twelve story buildings at DL (a), SD (b) and NC (c) limit state.

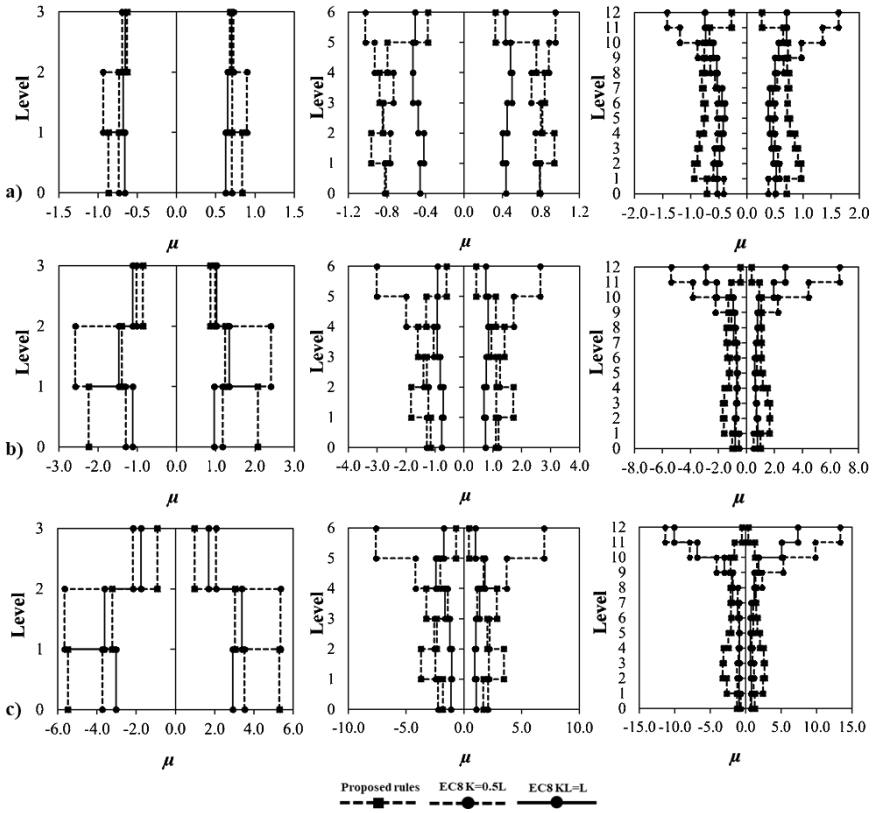

Figure 4. Comparison between proposed design criteria and EC8 compliant frames: Braces ductility demand for three, six and twelve story buildings at DL (a), SD (b) and NC (c) limit state

REFERENCES

[1] EN 1998-1-1. Eurocode 8: Design of structures for earthquake resistance – Part 1: General rules, seismic actions and rules for buildings. CEN; 2005.

[2] American Institute of Steel Construction, Inc. (AISC). (2016). Seismic Provisions for Structural Steel Buildings. ANSI/AISC Standard 341-16. AISC, Chicago, Illinois

[3] CSA. 2014. Design of Steel Structures, CSA-S16-14, Canadian Standards Association, Toronto, ON.

[4] A.Y. Elghazouli. Seismic design of steel structures to Eurocode 8. *Structural Engineer*, **85** (12), 26-31. 2017

[5] A.Y. Elghazouli. Assessment of European seismic design procedures for steel framed structures. *Bulletin of Earthquake Engineering*, **8**, 65-89. 2010

[6] B.M. Broderick, A.Y. Elghazouli, J.m. Goggins. Earthquake testing and response analysis of concentrically-braced-sub-frames. *Journal of Constructional Steel Reseach*, **64**:9, 997-1007. 2008

[7] G. Brandonisio, M. Toreno, E. Grande, E. Mele, A. De Luca. Seismic design of concentric braced frames. *Journal of Constructional Steel Research*, **78**, 22-37. 2012

[8] M. Bosco, G. Brandonisio, E.M. Marino, E. Mele, A. De Luca. Ω* method: An alternative to Eurocode 8 procedure for seismic design of X-CBFs. *Journal of Constructional Steel Research*, **134**, 135–147. 2017

[9] S. Costanzo, R. Landolfo. Concentrically braced frames: European vs North American seismic design provisions. *The Open Civil Engineering Journal*, **11**, (Suppl 1: M11) 453-463. DOI: 0.2174/1874149501711010453. 2017

[10] S. Costanzo, M. D'Aniello, R. Landolfo. Seismic design criteria for chevron CBFs: European vs North American codes (part-1), *Journal of Constructional Steel Research* **135**: 83–96; DOI: http://dx.doi.org/10.1016/j.jcsr.2017.04.018. 2017

[11] S. Costanzo, M. D'Aniello, R. Landolfo. Seismic design criteria for chevron CBFs: Proposals for the next EC8 (part-2), *Journal of Constructional Steel Research*, **138**: 17–37; DOI: http://dx.doi.org/10.1016/j.jcsr.2017.06.028. 2017

[12] S. Costanzo, M. D'Aniello, R. Landolfo. Proposal of design rules for ductile X-CBFS in the framework of EUROCODE 8, *Earthquake Engineering and Structural Dynamics*, **48**(1), 124-151. DOI: https://doi.org/10.1002/eqe.3128. 2019

[13] S. Costanzo, M. D'Aniello, R. Landolfo. The influence of moment resisting beam-to-column connections on seismic behavior of chevron concentrically braced frames. *Soil Dynamics and Earthquake Engineering*,**113**, 136-147. DOI: https://doi.org/10.1016/j.soildyn.2018.06.001. 2018

[14] S. Costanzo, M. D'Aniello, R. Landolfo. Critical review of seismic design criteria for chevron concentrically braced frames: the role of the brace-intercepted beam. *Ingegneria Sismica: International Journal of Earthquake Engineering*, **1-2**, 72-89. 2016

[15] S. Costanzo, M. D'Aniello, R. Landolfo, A. De Martino. Critical discussion on seismic design criteria for cross concentrically braced frames. *Ingegneria Sismica: International Journal of Earthquake Engineering*, **35**(2**)**, 23-36. 2018

[16] S. Costanzo, M. D'Aniello, R. Landolfo, A. De Martino. Remarks on seismic design rules of EC8 for inverted-V CBFs. *Key Engineering Materials*, **763**, 1147-1154. DOI: https://doi.org/10.4028/www.scientific.net/KEM.763.1147. 2018

[17] S. Costanzo, M. D'Aniello, R. Landolfo. The influence of beam stiffness on seismic response of chevron concentric bracings. Journal of Constructional Steel Research, 112, 305-324, DOI: https://doi.org/10.1016/j.jcsr.2015.05.021, 2015

[18] E.M. Marino. A unified approach for the design of high ductility steel frames with concentric braces in the framework of Eurocode 8. *Earthquake Engng Struct. Dyn*, **43**, 97–118. 2013

[19] L. Fiorino, M.T. Terracciano, R. Landolfo. Experimental investigation of seismic behaviour of low dissipative CFS strap-braced stud walls. *Journal of Con-structional Steel Research*, **127**, 92-107. doi:10.1016/j.jcsr.2016.07.027. 2016

[20] V. Macillo, L. Fiorino, R. Landolfo. Seismic response of CFS shear walls sheathed with nailed gypsum panels: Experimental tests. *Thin-Walled Structures*, **120**, 161-171. doi: 10.1016/j.tws.2017.08.022. 2017

[21] L. Fiorino, S. Shakeel, V. Macillo, R. Landolfo. Behaviour factor (q) evaluation the CFS braced structures according to FEMA P695. *Journal of Constructional Steel Research*, **138**, 324-339. doi:10.1016/j.jcsr.2017.07.014. 2017

[22] L. Fiorino, V. Macillo, R. Landolfo. Shake table tests of a full-scale two-story sheathing-braced cold-formed steel building. *Engineering Structures*, **151**, 633–647. doi: 10.1016/j.engstruct.2017.08.056. 2017

[23] G. Metelli. Theoretical and experimental study on the cyclic behaviour of X braced steel frames. *Engineering structures*, **46** 763-773. 2013

[24] A. Picard, D. Beaulieu. Design of cross-braced frames for predictable buckling behavior: Part 1 theoretical study. *Engineering Journal AISC*, third quarter. 1987

[25] A. Picard, D. Beaulieu. Design of cross-braced frames for predictable buckling behavior: Part 2 Experimental study. *Engineering Journal AISC*, third quarter. 1987

[26] A. Picard, D. Beaulieu.Theoretical study of the buckling strength of compression members connected to coplanar tension members. *Canadian Journal of Civil Engineering*, **16**(3), 239–248. 1989

[27] A. Picard, D. Beaulieu. Experimental study of the buckling strength of compression members connected to coplanar tension members. *Canadian Journal of Civil Engineering*, **16**(3), 249–257. 1989

[28] R. Sabelli, D. Hohbach. Design of cross braced frames for predictable buckling behaviou. *Journal of structural engineering ASCE*, **125**(2) 163-168. 1991

[29] R. Tremblay, M.H. Archambault, A. Filiarault. Seismic response of Concentrically Braced Steel Frames made with rectangular hollow bracing members. *Journal of Structural Engineering ASCE*, **129**(12) 1626-16-36. 2003

[30] K.D. Palmer, C.W. Roeder, D.E. Lehman, T. Okazaki, C. Shield. Experimental Performance of Steel Braced Frames Subjected to Bidirectional Loading. *Journal of Structural Engineering ASCE*, **139**(8): 1274-1284. 2013

[31] EN 1993:1-1, Eurocode 3: Design of steel structures – Part 1-1: General rules and rules for buildings. CEN; 2005.

[32] EN 1990 (2001) Eurocode 0: Basis of structural design;

[33] EN 1991-1-1 (2002) Eurocode 1: Actions on structures - Part 1-1: General actions - Densities, self-weight, imposed loads for buildings;

[34] M. Bosco, A. Ghersi, E.M. Marino, P.P. Rossi, A capacity design procedure for columns of steel structures with diagonals braces. *Open Construction and Building Technology Journal* **8**, 196-207, 2014.

[35] M. Bosco, E. Ferrara, A. Ghersi, E.M. Marino, P.P. Rossi, Improvement of the model proposed by Menegotto and Pinto for steel. *Engineering Structures*, **124**, 442-456, 2016

[36] M. Bosco, A. Ghersi, E.M. Marino, P.P. Rossi, Generalized corrective eccentricities for nonlinear static analysis of buildings with framed or braced structure. *Bulletin of Earthquake Engineering*, 2017

[37] M. Bosco, G.A.F. Ferrara, A. Ghersi, E.M. Marino, P.P. Rossi, Application of nonlinear static method with corrective eccentricities to steel multi-storey braced buildings. Geotechnical, *Geological and Earthquake Engineering*, **40**, 193-203, 2016

[38] V. Piluso, R. Montuori, E. Nastri, A. Paciello, Seismic response of MRF-CBF dual systems equipped with low damage friction connections. *Journal of Constructional Steel Research*, 154, 263-277, 2019.

[39] V. Piluso, A. Pisapia, P. Castaldo, E. Nastri, Probabilistic Theory of Plastic Mechanism Control for Steel Moment Resisting Frames. *Structural Safety* **76**, 95-107, 2019.

COMPDYN 2019
7th ECCOMAS Thematic Conference on Computational Methods in Structural Dynamics and Earthquake Engineering M. Papadrakakis, M. Fragiadakis (eds.)
Crete, Greece, 24–26 June 2019

COMPARISON OF DIFFERENT DESIGN REQUIREMENTS ON P-DELTA EFFECTS FOR STEEL MOMENT RESISTING FRAMES

R. Tartaglia[1], M. D'Aniello[1], G. Di Lorenzo[1], A. De Martino[1] and R. Landolfo[1]

[1] University of Naples Federico II
via Forno Vecchio 34, 80136 Naples (Italy)
e-mail: roberto.tartaglia@unina.it, m.daniel@ unina.it, gianmaria.dilorenzo@unina.it, attilio.demartino@unina.it, landolfo@unina.it

Abstract

Steel moment resisting frames (MRFs) compliant with EN1998-1 are largely overdesigned owing to the need to satisfy the severe requirements for lateral deformability and P-Delta effects. On the contrary, the North American codes (e.g. ASCE7) introduce different rules to consider the structural sensitivity to the P-Delta effects. In lines with the latter approach, the current draft version of the amended EN1998-1-1 introduces a different methodology to account for the structural lateral displacements. This work aims to investigate, using static non-linear analysis, the effectiveness of the new EC8 provisions with respect to the former version of EC8 and the current ASCE7. The analyses have been carried out by accounting for the real dimension of beam-to-column joints and their behavior, which was simulated by means of a non-linear spring, properly calibrated against experimental tests. The results show that the structures designed according to the latest draft version of the EN1998-1-1 and those compliant with the North American code have a similar behavior.

Keywords: Seismic design, moment resisting frame steel structures, non-linear analyses, P-Delta effect, extended stiffened joint.

1 INTRODUCTION

Moment resisting frames (MRFs) are largely used for steel multi-story low and medium rise buildings in seismic areas, since they can provide high ductile behavior thanks to the formations of plastic hinges at the ends of the beams and at the base of the column of the base level. [1-13].

However, owing to their large lateral deformability, MRFs are highly sensitive to second-order (P-Delta) effects as well as severely penalized by the verification checks of the drifts at damage limitation state [14]. The current version of EN1998-1-1 [15] recommends to verify the sensitivity of the structures to P-Delta effects by means of the Horne method, where the critical multiplier is estimated considering the secant stiffness of the structure assuming that the theoretical strength is set equal to the design base shear and the corresponding displacement is set equal to the seismic demand given by the equal displacement rule.

On the contrary, in the United States of America (USA), the rules given by the ASCE7 codes [16] account for the design overstrength, and the stiffness is evaluated at a displacement demand computed more efficiently and more accurately than the equal displacement rule adopted in EN1998-1-1. In addition, ASCE7 gives less stringent requirements for the limitations of lateral drifts for MRFs. In lines with this approach, the current draft version of the amended EN1998-1-1 evaluate the Horne secant stiffness accounting for the structural overstrength mainly due to (i) the selection of slightly larger members, (ii) the hardening related to the formation of plastic mechanism, and (iii) the expected strength of the materials, which are larger than the design values. All these aspects clarify the reasons why EC8-compliant MRFs are often overdesigned as shown by Tenchini et al. [17] and Cassiano et al. [18].

Therefore, the second order sensitivity coefficient (defined as θ) is evaluated considering two overstrength parameters. The aim of this work is to investigate, by means pf static non-linear analyses, the effectiveness of the new EC8 provisions with respect to the former version of EC8 and the current ASCE7. Therefore, for each of the investigated design approaches (current EC8, modified EC8 and ASCE7) a set of four MRFs was designed varying the spam length (6 or 8m). Moreover, since the MRF's response is strongly influenced by the beam-to-column joint typologies and behavior, the connections were modelled by a lumped non-linear spring.

The paper is organized into three main parts, namely (1) the introduction of the investigated parameters with the descriptions of the three design approaches; (2) the description of the geometrical features of the examined structures and the modelling assumptions; (3) the discussion of the results.

2 GENERAL SPECIFICATIONS

The current EN1998-1-1 (hereinafter also referred as "EC8-C") recommends to calculate the stability coefficient ($\theta_{EC8\text{-}C}$) for P-Delta effects as follows:

$$\theta_{EC8-C} = \frac{P_{tot} \cdot d_r}{V_{tot} \cdot h} \tag{1}$$

Where P_{tot} is the total vertical loads due to the gravity loads in the seismic loading combination, d_r is the design interstorey drift, V_{tot} is the total seismic shear and h is the interstorey height. If $\theta_{EC8\text{-}C}$ is smaller than 0.1, the second order effects can be neglected at design stage, while if $\theta_{EC8\text{-}C}$ is smaller than 0.2 the calculated internal effects should be magnified by the factor α equal to $1/(1-\theta_{EC8\text{-}C})$. If $\theta_{EC8\text{-}C}$ exceed 0.3 the structure should be re-designed.

The design interstorey drift (d_r) is evaluated as follows:

$$d_{r,i} = d_{s,i} - d_{s,i-1} \tag{2}$$

Where d_s is a structural displacements induced by the design seismic action and is evaluated on the basis of the equal displacement rule by the following equation:

$$d_s = q \cdot d_e \tag{3}$$

Where q is the adopted behavior factor and d_e is structural displacement evaluated by means a response spectrum linear analysis.

According to this method, the displacements are evaluated considering the secant stiffness of the structure by assuming that the ultimate resistance is equal to the design base shear, disregarding either any source of overstrength or the hardening effects associated with redundancy and plastic redistribution. From these considerations a proposal to amended EC8 rule (hereinafter referred as "EC8-M") may be to compute the stability coefficient by increasing the secant stiffness as follows:

$$\theta_{EC8-M} = \frac{P_{tot} \cdot d_r}{V_{tot} \cdot h \cdot \gamma_{ov} \cdot \Omega_d} \tag{4}$$

Where γ_{ov} accounts for the randomness of the yield stress of the steel and Ω_d is equal to $\min(R_{d,i}/E_{d,i})$ being $R_{d,i}$ the plastic resistance of the i-th dissipative component and $E_{d,i}$ is the corresponding design effect.

This criterion is very similar to the proposal by Vigh et al. [19], but it is more stringent because the overall hardening due to the redundancy of the structural system is not considered. The stability coefficient (θ_{ASCE}) recommended by ASCE7 is evaluated according to the following equation:

$$\theta_{ASCE} = \frac{P_x \cdot \Delta \cdot I_e}{V_x \cdot h_{sx} \cdot C_d} \tag{5}$$

Where P_x are the total vertical loads at level x (which perfectly corresponds to the P_{tot} in the European approach), I_e is the importance factor (which is assumed equal to 1 in this study), V_x is the seismic shear force acting between levels x and $x - 1$, h_{sx} is the storey height, C_d the deflection factor (that was assumed equal to 5.5) and Δ the design story drift occurring simultaneously with V_x. With this regard, the design interstorey drift Δ are computed as the largest difference of the displacement δ_x and δ_{x-1}, where δ_x is estimated as follows:

$$\delta_x = \frac{C_d \cdot \delta_{xe}}{I_e} \tag{6}$$

where δ_{xe} is the displacement determined by an elastic analysis.

If the stability coefficient is larger than 1, an amplification factor should be introduced to account for the P-Delta influence in the design analyses. However, θ_{ASCE} should not exceed the θ_{max} defined in Equation (7).

$$\theta = \frac{0.5}{\beta \cdot C_d} \tag{7}$$

Where β can be assumed equal to 1 in a conservatively way.

3 INVESTIGATED STRUCTURES

3.1 Geometrical features

The influence of the second order effects were investigated by the design and verification of six MRFs varying the span length (6-8m) and the method to account for the P-Delta effects. To highlight the influence of the secondary effects' limitation on the design phase, all the

structures were designed according to current Eurocodes (i.e. both the EN1993-1-1 [20] and EN1998-1-1 [15]), with the sole exception of the P-Delta effects. In line with this purpose, cold formed partition walls were assumed, thus being able to separate the structural response from the infill system [21-24].

The first set of structures were designed according to the current EN1998-1-1 (i.e. EC8-C), the second set of structures were designed considering a modification of the actual EN1998-1-1 (i.e. EC8-M) and finally, in the last set of MRFs the P-Delta effects were accounted for according the ASCE7 approach.

All structures have a height of 22m with 6 floors and a constant value of storey height of 3.5m, except for the first level that is equal to 4.5m.

The plane has a rectangular shape, with five MRF bays in the X direction and three bays in the Y direction, with a concentric braced frame (CBF) system in the central bay (see Figure 1). The span length is equal in both directions and was alternatively set equal to 6m and 8m. Both the structural design and verifications were done on a planar MRF system that was extracted from the 3D structure.

The vertical dead load was assumed equal to 4.5kN/m2 and the live loads were set equal to 2kN/m^2. The response spectrum was evaluated considering a peak ground acceleration (PGA) equal to 0.25*g*, soil type B and a damping ratio equal to 2%. In accordance with the EN1998-1-1 riles for seismic design, the torsional effects were taken into account by means of the amplification factor δ, assumed equal to 1.3.

As damage limitation requirement, the maximum interstorey drift (ISD) ratio was fixed equal to 1%, thus assuming non-structural elements fixed in a way so as not to interfere with structural deformations.

The design forces have been calculated by means of response spectrum analyses (RSA), according to EN1998-1-1, where all the vibration modes that contribute significantly to the global response were accounted for.

Full strength extended stiffened end-plate joints, designed according to the procedure described by D'Aniello et al. [25], were adopted for all the investigated structures.

The results in terms of cross section, amplification factor (α), interstorey drift and the design overstrength (Ω_d), are reported in Table 1 and Table 2 for the structures with 6 and 8m span respectively.

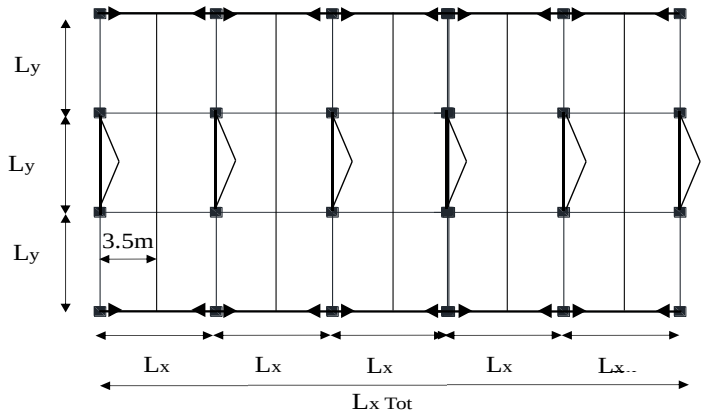

Figure 1: Structures geometrical features.

Floor	First bay		Second bay		Third bay		α	Drift	Ω_d
	Column	Beam	Column	Beam	Column	Beam			
I	HE450B	IPE500	HE500B	IPE500	HE500B	IPE500	1.21	0.60%	2.72
II	HE450B	IPE500	HE500B	IPE500	HE500B	IPE500	1.25	0.79%	
III	HE400B	IPE450	HE450B	IPE450	HE450B	IPE450	1.24	0.84%	
IV	HE400B	IPE450	HE450B	IPE450	HE450B	IPE450	1.19	0.80%	
V	HE360B	IPE360	HE400B	IPE360	HE400B	IPE360	1.15	0.78%	
VI	HE360B	IPE360	HE400B	IPE360	HE400B	IPE360	1.00	0.62%	
I	HE400B	IPE450	HE450B	IPE450	HE450B	IPE450	1.00	0.74%	2.2
II	HE400B	IPE450	HE450B	IPE450	HE450B	IPE450	1.13	0.98%	
III	HE360B	IPE400	HE400B	IPE400	HE400B	IPE400	1.13	1.07%	
IV	HE360B	IPE400	HE400B	IPE400	HE400B	IPE400	1.00	1.02%	
V	HE340B	IPE330	HE360B	IPE330	HE360B	IPE330	1.00	0.98%	
VI	HE340B	IPE330	HE360B	IPE330	HE360B	IPE330	1.00	0.78%	
I	HE400B	IPE400	HE450B	IPE400	HE450B	IPE400	0.04	0.63%	1.93
II	HE400B	IPE400	HE450B	IPE400	HE450B	IPE400	0.05	0.93%	
III	HE360B	IPE360	HE400B	IPE360	HE400B	IPE360	0.05	1.03%	
IV	HE360B	IPE360	HE400B	IPE360	HE400B	IPE360	0.05	1.00%	
V	HE340B	IPE300	HE360B	IPE300	HE360B	IPE300	0.04	0.95%	
VI	HE340B	IPE300	HE360B	IPE300	HE360B	IPE300	0.02	0.78%	

Table 1: Design results of the MRFs with span equal to 6m

Floor	First bay		Second bay		Third bay		α	Drift	Ω_d
	Column	Beam	Column	Beam	Column	Beam			
I	HE550M	IPE600	HE650M	IPE600	HE650M	IPE600	1.18	0.53%	2.28
II	HE550M	IPE600	HE650M	IPE600	HE650M	IPE600	1.25	0.79%	
III	HE500B	IPE600	HE550M	IPE600	HE550M	IPE600	1.25	0.84%	
IV	HE500B	IPE450	HE550M	IPE450	HE550M	IPE450	1.23	0.92%	
V	HE400B	IPE450	HE500B	IPE450	HE500B	IPE450	1.20	1.03%	
VI	HE400B	IPE450	HE500B	IPE450	HE500B	IPE450	1.00	0.77%	
I	HE550M	IPE550	HE650M	IPE550	HE650M	IPE550	1.00	0.55%	1.95
II	HE550M	IPE550	HE650M	IPE550	HE650M	IPE550	1.13	0.87%	
III	HE500B	IPE550	HE550M	IPE550	HE550M	IPE550	1.14	0.97%	
IV	HE500B	IPE400	HE550M	IPE400	HE550M	IPE400	1.13	1.08%	
V	HE400B	IPE400	HE500B	IPE400	HE500B	IPE400	1.12	1.21%	
VI	HE400B	IPE400	HE500B	IPE400	HE500B	IPE400	1.00	0.96%	
I	HE550B	IPE500	HE550M	IPE500	HE550M	IPE500	0.04	1.14%	1.77
II	HE550B	IPE500	HE550M	IPE500	HE550M	IPE500	0.05	1.83%	
III	HE450B	IPE450	HE550B	IPE450	HE550B	IPE450	0.06	2.11%	
IV	HE450B	IPE450	HE550B	IPE450	HE550B	IPE450	0.05	2.10%	
V	HE400B	IPE360	HE450B	IPE360	HE450B	IPE360	0.04	2.13%	
VI	HE400B	IPE360	HE450B	IPE360	HE450B	IPE360	0.02	1.83%	

Table 2: Design results of the MRFs with span equal to 8m

The influence of the adopted method to account for P-Delta effects can be directly recognised by comparing the design results. Indeed, the structures designed according to EC8-C are characterized by very large values of the magnification factor (α), which is equal to 1.25 in some cases. The EC8-M compliant structures have smaller values of the amplification factor (α), with a maximum value equal to the 1.14. On the contrary, in the cases designed according to the ASCE7 the P-Delta effects can be neglected.

The value of the amplification factor implies an important change in the dimensions of structural members and consequentially in the structural weight, as consistently showed in Figure 3.

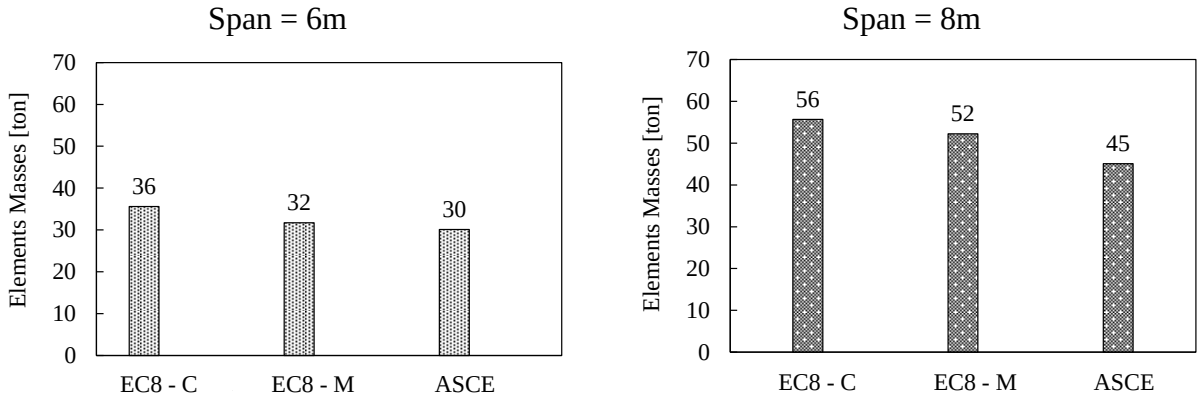

Figure 2 – *Structural weight (expressed in ton) for the frames with span equal to 6m and 8m*

3.2 FEM modelling

All the analyses were conducted on a 2D planar model build in Seismiostruct software [26]. As recommended by EN1998-1-1, the torsional effects were accounted for in the design phase by the introduction of δ (amplification factor), assumed equal to 1.3.

The slab's in-plane rigidity was simulated by the introduction of diaphragm constrains that connect all the MRF bays to the leaning column. The lumped masses at each floor and the concentrated forces, that model the gravity frame loads, are applied on the leaning column that has no lateral rigidity in order for it not to influence the structural lateral stiffness.

All the structural elements were modelled by a force-based (FB) distributed inelasticity elements. These elements account for distributed inelasticity through integration of material response over the cross section and integration of the section response along the length of the element. The cross-section behavior is reproduced by means of the fiber approach, assigning a uniaxial stress–strain relationship at each fiber. The Menegotto-Pinto [27] law was introduced to model the behavior of all steel elements, while the leaning column was modelled by an indefinitely elastic material.

Since their height seismic performance [28-31] extended stiffened joints were introduced in all the investigated structures; the real joint dimensions were modelled by the introduction of the rigid elements connected to the steel profiles by a lumped non-linear spring. that were properly calibrated against the experimental results obtained within the EQUALJOINTs research project (EQUALJOINTs [32], D'Aniello et al. [33]).

4 RESULTS

The pushover results are presented in terms of: elastic stiffness (K), the maximum resistance (V_{max}) and the overall overstrength factor (Ω), which are defined in Figure 3.

The V_{Ed} is the base shear at the design stage and V_y is the base shear at the formation of the first plastic hinge. For the sake of clarity, the overall overstrength factor (Ω) is given by the following ratio:

$$\Omega = \frac{V_{max}}{V_{Ed}} = \frac{V_y}{V_{Ed}} \cdot \frac{V_{max}}{V_y} \tag{8}$$

Where V_y/V_{Ed} is the ratio between force that corresponds to the formation of the first plastic hinge and the design force. The V_{max}/V_y ratio represents the overstrength due to the system redundancy (corresponding to α_u/α_1 the corresponding ratio in the EN1998-1-1).

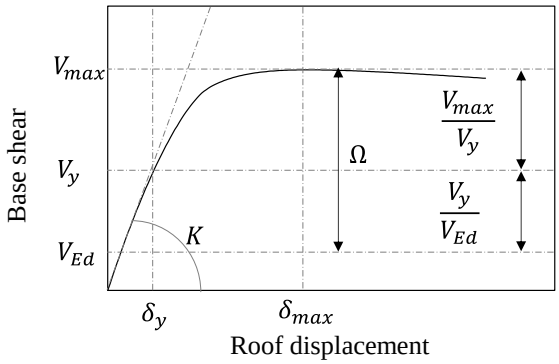

Figure 3: Monitored parameter in the pushover analysis

As a general consideration, it can be observed how, independently from the span length (6 or 8m) and the lateral force shape, the pushover results (see Figure 4) show that both the structural resistance and elastic stiffness are strongly influenced by the P-Delta effects limitation. The structures designed according to the current EN1998-1-1 are the stiffer and the more resistant, while, the MRF designed according to EC8-M have intermediate stiffness and resistance between the EC8-C and the ASCE compliant frames.

The shape of the response curves highlights that independently from the lateral force distribution the structures with 6m span exhibit the failure of the plastic hinges that corresponds to the drop in terms of strength and stiffness of the response curves. Contrariwise, most of the structures with span length equal to 8m show the formation of plastic hinges in the columns. In line with the design assumptions, the structures designed according to the current version of the EN1998-1-1 show the larger value of the V_y/V_{Ed} ratio. For instance, comparing the results of the structures with 6m of span subjected to a lateral force proportional to the masses, it can be recognized that the EC8-C structures have a V_y/V_{Ed} overstrength factor 1.22 and 1.58 times larger than the one of the EC8-M and ASCE structures, respectively. These differences are almost the same for all the investigated structures (see Figure 4). Contrariwise, independently from the design approach and the span length, the V_{max}/V_y overstregnth factors are comparable for all the investigated structures and vary in the range 2.10-2.80, values larger compared to the EN1998-1-1 recommendation of 1.3.

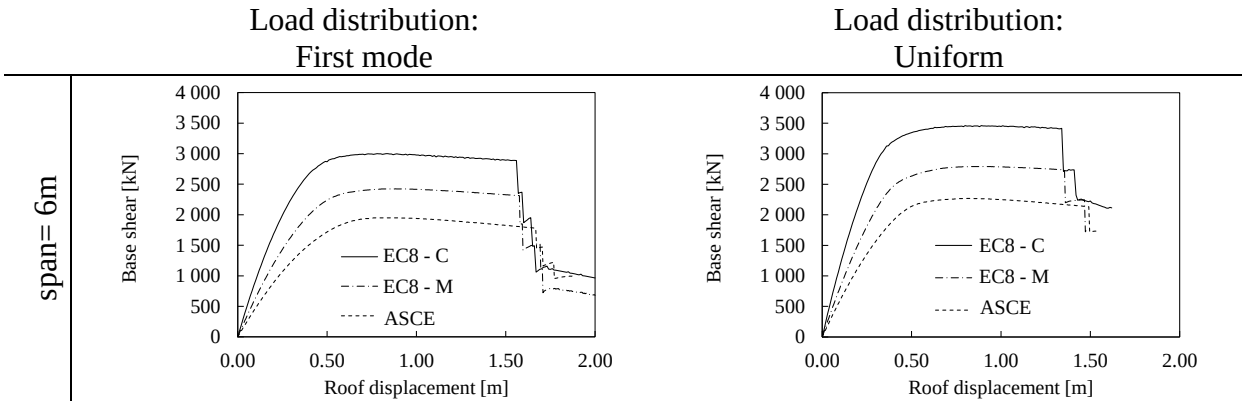

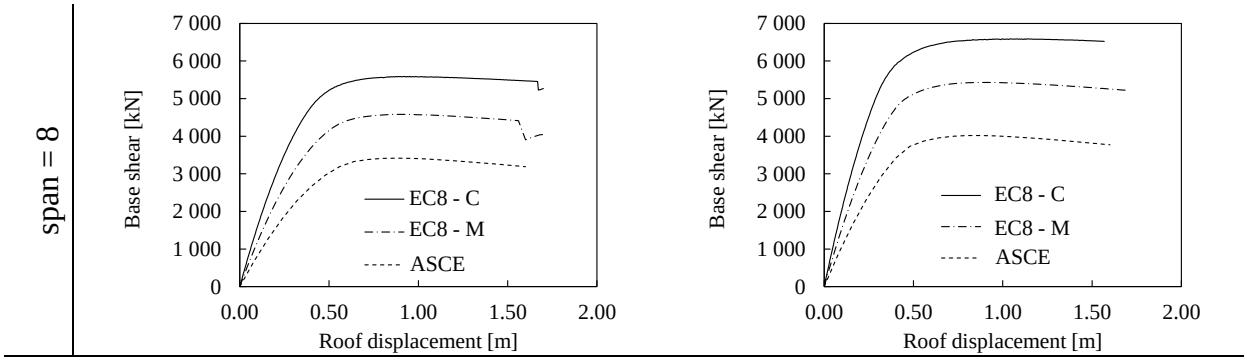

Figure 4: Push over results for both the 6 and 8m spam length structures

Moreover, the shape of the response curves highlights that independently from the lateral force distribution and the span length, the more deformable structures are more sensitive to the P-Delta effects, showing a more pronounced performance degradation.
Differently from the structures with a span length of 8m, where the plastic mechanism involves also the column of the first floor, all the structures with 6m span exhibit the failure of the plastic hinges that corresponds to the drop in terms of strength and stiffness of the response curves.
Regarding the overstrength factor, the structures designed according to the current version of the EN1998-1-1 show the larger values of the V_y/V_{Ed}. This result is consistent with the design assumptions.

5 CONCLUSIONS

- The design limitation on the P-Delta effects strongly influence the MRFs lateral stiffness; therefore, the structures designed according to the actual version of EN1998-1-1 are 1.13 and 1.2 times heavier than those designed according to the EC8-M and ASCE, respectively. This difference increases in the case of the frames with the longer spans (e.g. 8m).
- The pushover analysis confirms that, independently from the shape of the lateral loads and the span length, the structures compliant with EN1998-1-1 are the stiffer and the stronger among those examined. The EC8-C structures have overdesign factors ranging within 2.49-2.93 for 6m and 8m of span, respectively.
- Changing the evaluation method for the P-Delta effects leads to a strong variation of both the lateral stiffness and overstrength; therefore, the structures designed according to the EC8-M and ASCE have an overstrength factor varying in the ranges 1.88-2.40 and 1.58-1.85, respectively.

REFERENCES

[1] R. Montuori, E. Nastri, V. Piluso, Advances in theory of plastic mechanism control: Closed form solution for MR-Frames. *Earthquake Engineering and Structural Dynamics*, **44(7)**, 1035-1054, 2015.

[2] R. Montuori, E. Nastri, V. Piluso, M. Troisi, Influence of the cyclic behaviour of beam-to-column connection on the seismic response of regular steel frames. *Ingegneria Sismica - International Journal of Earthquake Engineering*, **33(1),** 91-105, 2016.

[3] R. Montuori, E. Nastri, V. Piluso, Influence of the bracing scheme on seismic performances of MRF-EBF dual systems. *Journal of Constructional Steel Research*, **132**, 179-190, 2017.

[4] R. Montuori, E. Nastri, V. Piluso, M. Troisi, Influence of connection typology on seismic response of MR-Frames with and without 'set-backs'. *Earthquake Engineering and Structural Dynamics*, **46(1),** 5-25, 2017.

[5] R. Montuori, E. Nastri, V. Piluso, S. Streppone, M. D'Aniello, M. Zimbru, R. Landolfo, Comparison between different design strategies for Freedam frames: Push-Overs and IDA Analyses. *The Open Construction and Building Technology Journal*, **12 (1)**, 140-153, 2018.

[6] E. Nastri, The influence of geometry, loads and steel grade for the development of a specific collapse type of MR-Frames. *COMPDYN 2017 – Proc. of the 6th International Conference on Computational Methods in Structural Dynamics and Earthquake Engineering*, **2**, 5014-5025, 2017.

[7] E. Nastri, Design and assessment of steel structures in seismic areas: Outcomes of the last italian conference of steel structures. *Ingegneria sismica - International Journal of Earthquake Engineering*, **35(2)**, 1-4, 2018.

[8] AY. Elghazouli, Assessment of European seismic design procedures for steel framed structures. *Bulletin of Earthquake Engineering*, **8(1),** 65–89, 2010.

[9] V. Giordano, C. Chisari, G. Rizzano, M. Latour, Prediction of seismic response of moment resistant steel frames using different hysteretic models for dissipative zones. *Ingegneria Sismica - International Journal of Earthquake Engineering*, **34(4)**, 42-56, 2017.

[10] E. Nastri, M. D'Aniello, M. Zimbru, S. Streppone, R. Landolfo, R. Montuori, V. Piluso, Seismic response of steel Moment Resisting Frames equipped with friction beam-to-column joints, *Soil Dynamics and earthquake Engineering*, **119** 144–157, 2019.

[11] M. Latour, M. D'Aniello, M. Zimbru, G. Rizzano, V. Piluso, R. Landolfo, Removable friction dampers for low-damage steel beam-to-column joints *Soil Dynamics and Earthquake Engineering*, **115**, 66–81, 2018.

[12] R. Tartaglia, M. D'Aniello, G.A. Rassati, J. Swanson, R. Landolfo, Influence of composite slab on the nonlinear response of extended end-plate beam-to-column joints. *Key Engineering Materials*, **763**, 818-825, 2018.

[13] AR. Medina, HJ. Krawinkler, Evaluation of drift demands for the seismic performance assessment of frames. *Structural Engineering*, **131(7)**, 1003–13, 2005.

[14] R. Tartaglia, M. D'Aniello, G. Di Lorenzo, A. De Martino, Influence of EC8 rules on P-Delta effects on the design and response of steel MRF, *Ingegneria Sismica - International Journal of Earthquake Engineering*, **35(3),** 104-120, 2018.

[15] EN 1998-1 (2005), Design of Structures for Earthquake Resistance - Part 1: General Rules, Seismic Actions and Rules for Buildings. CEN.

[16] ASCE/SEI. Minimum design loads for buildings and other structures, ASCE7-16. American Society of Civil Engineers/Structural Engineering Institute, Reston, VA; 2016.

[17] A. Tenchini, M. D'Aniello, C. Rebelo, R. Landolfo, R., L.S. da Silva, L. Lima, Seismic performance of dual-steel moment resisting frames. *Journal of Constructional of Steel Research*, **101**, 437-454, 2014.

[18] D. Cassiano, M. D'Aniello, C. Rebelo, R. Landolfo, L.S. da Silva, Influence of seismic design rules on the robustness of steel moment resisting frames. *Steel and Composite Structures*, **21(3)**, 479-500, 2016.

[19] L.G. Vigh, A. Zsarnóczay, J.M. Balogh, J.M. Castro, P-Delta effect and pushover analysis: Review of Eurocode 8-1. Report N.1 of WG2 CEN/TC 250/SC 8, 2016.

[20] EN 1993:1–1 (2005), Design of Steel Structures - Part 1–1: General rules and rules for buildings. CEN.

[21] L. Fiorino, V. Macillo, R. Landolfo, Shake table tests of a full-scale two-story sheathing-braced cold-formed steel building. *Engineering Structures*, **151**, 633–647, 2017.

[22] L. Fiorino, M.T. Terracciano, R. Landolfo, Experimental investigation of seismic behaviour of low dissipative CFS strap-braced stud walls. *Journal of Constructional Steel Research*, **127**, 92-107, 2016.

[23] L. Fiorino, S. Shakeel, V. Macillo, R. Landolfo, Behaviour factor (q) evaluation the CFS braced structures according to FEMA P695. *Journal of Constructional Steel Research*, **138**, 324-339, 2017.

[24] V. Macillo, L. Fiorino, R. Landolfo, Seismic response of CFS shear walls sheathed with nailed gypsum panels: Experimental tests. *Thin-Walled Structures*, **120**, 161-171, 2017.

[25] M. D'Aniello, R. Tartaglia, S. Costanzo, R. Landolfo, Seismic design of extended stiffened end-plate joints in the framework of Eurocodes. *Journal of Constructional Steel Research*, **128**, 512–527, 2017.

[26] SeismoStruct 2018 – A computer program for static and dynamic nonlinear analysis of framed structures," available from http://www.seismosoft.com.

[27] M. Menegotto, PE. Pinto, Method of analysis for cyclic ally loaded R.C. plane frames including changes in geometry and non-elastic behaviour of elements under combined normal force and bending. Proc. of Symposium on the Resistance and Ultimate Deformability of Structures Acted on by Well Defined Repeated Loads, 1973.

[28] R. Tartaglia, M. D'Aniello, G.A. Rassati, J. Swanson, R. Landolfo, Full strength extended stiffened end-plate joints: AISC vs recent European design criteria. *Engineering Structures*, **159**, 155–171, 2018.

[29] R. Tartaglia, M. D'Aniello, M. Zimbru, R. Landolfo, Finite element simulations on the ultimate response of extended stiffened end-plate joints. Steel and Composite Structures, **27(6)**, 727-745, 2018.

[30] R. Tartaglia, M. D'Aniello, R. Landolfo, The influence of rib stiffeners on the response of extended end-plate joints. Journal of Constructional Steel Research, **148**, 669–690, 2018.

[31] R. Tartaglia, M. D'Aniello, R. Landolfo, G.A. Rassati, J. Swanson, Finite element analyses on seismic response of partial strength extended stiffened joints. *COMPDYN 2017 – Proc. of the 6th International Conference on Computational Methods in Structural Dynamics and Earthquake Engineering* **2**, 4952–4964, 2017.

[32] EQUALJOINTS – European pre-QUALified steel JOINTS: RFSR-CT-2013-00021. Research Fund for Coal and Steel (RFCS) research programme.

[33] M. D'Aniello, R. Tartaglia, S. Costanzo, G. Campanella, R. Landolfo, A. De Martino, Experimental Tests on Extended Stiffened End-Plate Joints within Equal Joints Project. *Key Engineering Materials*, **763**, 406-413, 2018.

COMPDYN 2019
7th ECCOMAS Thematic Conference on
Computational Methods in Structural Dynamics and Earthquake Engineering
M. Papadrakakis, M. Fragiadakis (eds.)
Crete, Greece, 24–26 June 2019

WIND PERFORMANCE ASSESMENT OF TELECOMMUNICATION TOWERS: A CASE STUDY IN GREECE

Dimitrios V. Bilionis[1], **Dimitrios Vamvatsikos**[2]

[1] PhD Candidate
Institute of Steel Structures, School of Civil Engineering, National Technical University of Athens
Zografou Campus, Iroon Polytechneiou 9, 15780 Zografou, Athens, Greece
e-mail: dimbilionis@central.ntua.gr

[2]Assistant Professor
Institute of Steel Structures, School of Civil Engineering, National Technical University of Athens
Zografou Campus, Iroon Polytechneiou 9, 15780 Zografou, Athens, Greece
e-mail: divamva@mail.ntua.gr

Abstract

Steel lattice towers are widely used by telecommunication companies to install radiowave dish antennas for the expansion of their network. They are tall highly-optimized structures for which severe weather conditions including low temperatures, snow and high winds are the governing loading conditions. Specifically, high winds in combination with accumulated ice on the members of the structure and the dishes are the leading causes of collapse. The focus is on a standardized model of a telecommunication tower used by major telecommunication companies in Greece. The model is designed according to European Standards for areas located at distances lower than 10km from the coastline. The tower is 48 meters tall, having a square cross-section whose dimensions generally reduce with height and it employs channel and angle steel sections. Non-linear dynamic analyses were performed in order to estimate the fragility of the structure to wind and/or icing conditions. Wind loads were simulated via a 3D wind field fully capturing the spatial and temporal variation of wind speed over the entire profile of the tower for different reference values of wind speed. The impact of ice was assessed by considering a range of different uniformly thick layers of ice that increase the weight as well as the cross-section area of all members and dishes. The ultimate goal of this work is to provide the fragility functions for every potential combination of wind and icing conditions that could be observed during the service life of the structure. Thus, by incorporating the corresponding climactic hazard surfaces, the risk of tower collapse is estimated over its entire projected lifetime, offering a useful decision support tool to telecommunication companies regarding the need to replace or upgrade their existing tower network on a case-by-case basis.

Keywords: Telecommunication Tower, Steel Lattice Structure, Wind, Ice, Fragility

1 INTRODUCTION

Rapid advances in data transmission technology and telecommunications introduce new engineering challenges affecting not only the electromechanical components (e.g. microwave dishes) of a telecommunication network but also the supporting structures. Supporting structures are usually tall highly-optimized steel lattice towers. These structures are vulnerable to weather hazards with wind, low temperatures and corresponding ice accretion being the most critical loading conditions.

Relevant experience, especially from power transmission networks, has shown that storm events may lead to significant damage of steel lattice towers of a network resulting in total collapses with adverse impact for the whole operation of the network, in most of the times associated with considerable long downtime in service and significant economic loss. The above effect of strong winds is further enhanced when ice has accumulated on the exposed members of the structure due to low temperature and/or precipitation (e.g. snow) [1-3]. Under this perspective, the development of a framework for performance based assessment [4] for lattice steel structures used in telecommunication or power transmission networks is essential. The first step towards this effort is the estimation of the fragility of those structures under weather hazards and especially wind and icing conditions [5].

The most critical part for a performance based analysis of steel lattice structures requires detailed and precise calculations of the wind forces acting on the structure. Methodologies for estimation of wind force at lattice structures proposed by current standards (e.g. EN1991-1-4) are mainly based on the solidity ratio of the structure. In cases of a telecommunication tower carrying microwave dish antennas, the shielding effects of the antennas should be taken into account. However, due to the lack of sound guidelines in standards, the estimation of the shielding effects is usually based on wind tunnel tests [6-8].

Considering the above, the purpose of this paper is to present a case study of a telecommunication tower carrying four microwave dish antennas, and designed for coastal areas of Greece according to European standards [9]. The ultimate goal is the estimation of the structure's fragility under possible combinations of wind speed and icing conditions. For this reason, a 3D model was developed in open-source software and a 3D simulation of the wind field was conducted capturing the spatial and temporal variation of wind speed over the entire profile of the structure. Moreover, the impact of ice was assessed by considering a range of various uniformly thick layers of accumulated ice on the exposed tower members and dishes. The estimation of the fragility was based on the processing of the results of a large number of non-linear dynamic analyses via probabilistic methods.

The results could be elaborated for performance-based design and analysis of telecommunication towers. Furthermore, if the fragilities are used in combination with climatic data from the site of installation a risk assessment of this particular type of structure would be possible. This assessment could be valuable to telecommunication companies as a useful decision support tool regarding their needs to replace or upgrade their existing tower network.

2 TOWER MODEL

2.1 Geometry

The main body of the lattice tower of the study is 48 meters tall and has a square cross section [9]. At the top of the tower though, a pyramid that holds the lightning rod is formed and ends at a height of 51m. A complete view of the tower is presented in Figure 1a. The view of the tower can be divided into two main sections. The first section is an inclined one, whose

square cross section reduces with height and runs from 0 to 24m. The second section is a vertical one, which runs from 24 to 48m and has no inclination since it is designed to carry the antennas. The tower has horizontal diaphragms every 3 meters along its height (Figure 1b). It also includes five working platforms at heights of 12, 24, 42 and 45m (Figure 1c). Finally, a ladder and a waveguide rack for the cables of the antennas run connecting the centers of the horizontal diaphragms.

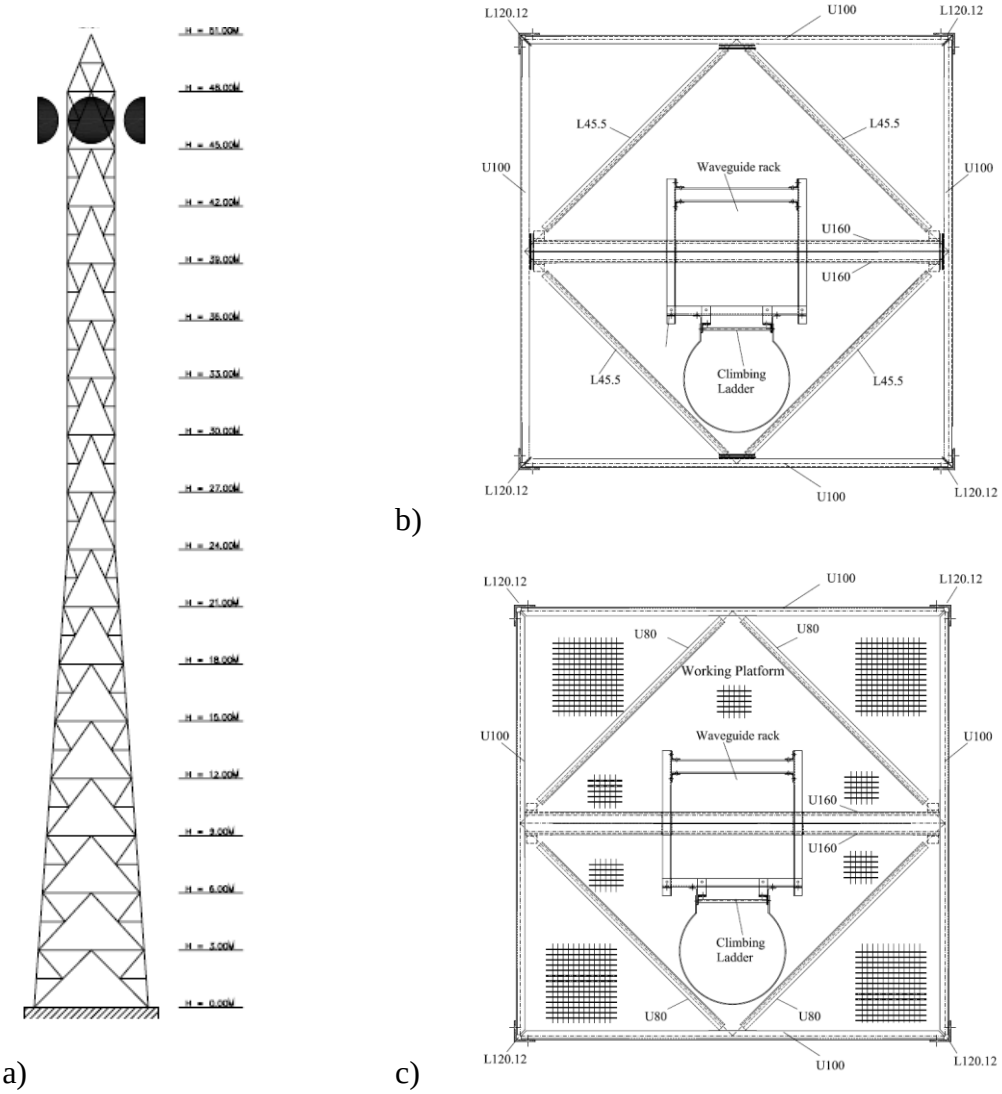

Figure 1: a) Complete view of the tower. b) Typical plan of a horizontal diaphragm. c) Typical plan of a working platform [9].

The structural members of the tower consist of channel and angle steel sections. The members could be characterized as (Figure 2): legs, (main) vertical diagonals/bracing members, secondary vertical bracing members, horizontals, horizontal diagonals and a central horizontal member at each diaphragm which carries the loads of the ladder, the waveguide rack and the cables.

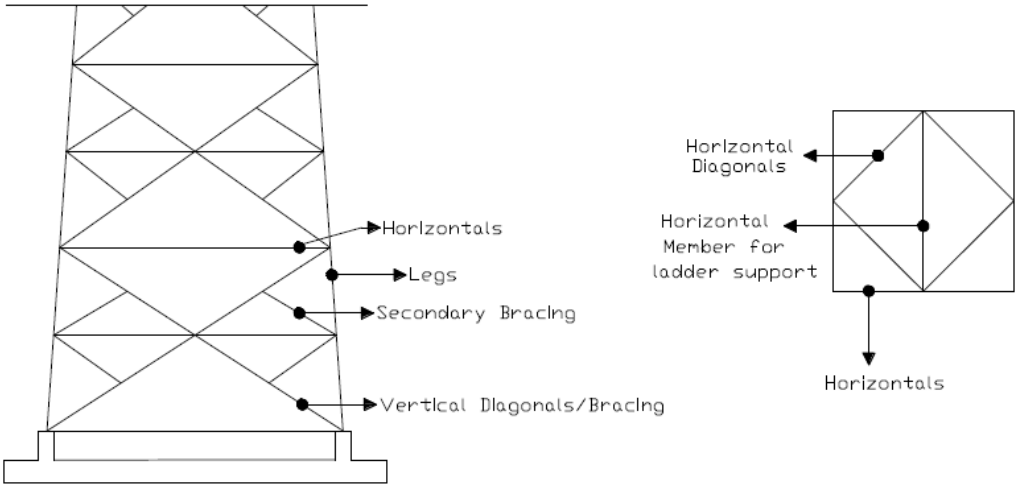

Figure 2: Designation of structural members [9].

As far as the legs are concerned, two types of angle sections were used. Specifically, the legs of the inclined section (height: 0-24m) were constructed from L160.15, while the legs of the vertical section (height: 24-48m) were constructed from L120.12. For the main vertical diagonals, an angle L70.7 section was used throughout the whole height of the structure, while for the secondary vertical diagonals a L45.5 section was used. The horizontal members of each diaphragm were constructed from a channel U100 section. For the horizontal diagonal members an angle L45.5 was used, except for the five levels of the working platforms where a channel U80 section was employed. On the other hand, the central horizontal member of each diaphragm was formed by 2 channel U160 sections welded on both edges. Finally, the members of the pyramid at the top of the tower (height: 48-51m) were made by L70.7.

2.2 Material

The structural steel grade was S355J2K2 for legs and S235J0JR for the rest of the members. At this point it should be noted that since the purpose of this work is not the design but a performance assessment for a lattice telecommunication tower, the real values of steel strength (as estimated by experimental work listed in the literature) were assumed in the analysis, instead of the nominal ones. Specifically, for steel grade S355J2K2, the (mean) yield strength f_y is equal to 454.90 MPa and the (mean) tensile strength f_u is equal to 546.84 MPa. On the other hand, for S235J0JR the corresponding values are 328.80 MPa and 435.41MPa, respectively [10]. The material stress-strain curve that was assumed in the analysis is presented in Figure 3. The value of E corresponds to steel Young's Modulus and is equal to 210 GPa, while the the buckling reduction factor χ was calculated for each structural member according to EN 1993-1-1 [11] to reduce its compression strength. Since the members of the tower have different properties according to their cross-section, the stress-strain curve is different for each member and thus Figure 3 presents only the general form of the stress-strain curve for all members.

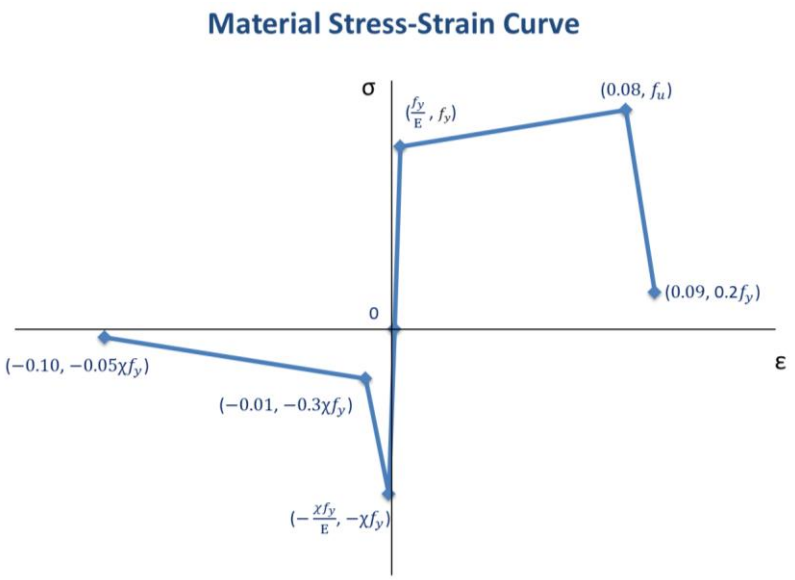

Figure 3: General form of a member stress-strain curve

2.3 Loads

2.3.1 Gravity loads

The unit weight of steel is equal to 78.50 kN/m^3. The weight of the climbing ladder is 15.30 kN and the weight of waveguide rack 14.60 kN. Four dish antennas are installed at the top (height 45-48m) of the tower. Each dish antenna has a weight of 2.30 kN. The weight of the cables is assumed to be 0.05 kN/m per dish. Finally, the weight of the five working platforms is 0.25 kN/m^2.The live load of the climbing ladder is 5.00 kN, while the live load at the working platforms is assumed to be 2.00 kN/m^2.

2.3.2 Wind loads

In the case of a telecommunication tower with dish antennas, the total wind force acting on the structure consists of two main components, namely the force acting on the tower (i.e. the structural members) and the force acting on the dish antennas [6,8,12]:

$$F_T = F_{tower} + F_{antennas} \quad (1)$$

Wind Force at the tower

The wind force acting on the tower is calculated by the Equation:

$$F_{tower} = qC_D A_{ref} \quad (2)$$

where: q is the dynamic pressure of the wind, C_D is the drag coefficient and A_{ref} is the area of the members projected normal to the level of the wind.

The dynamic pressure of the wind q depends on the air density ρ and the wind speed u and is estimated using the following Equation:

$$q = \frac{1}{2}\rho u^2 \quad (3)$$

Herein, ρ was assumed to be equal to 1.225 kg/m^3.

The drag coefficient C_D for lattice steel structures depends on the solidity ratio φ. According to EN1991-1-4 [13], the solidity ratio φ is the fraction of the sum of the projected area A

of the members of the structure's face normal to that face divided by the total enclosed area A_c by the face's boundaries projected normal to that face. Thus:

$$\varphi = \frac{A}{A_c} \tag{4}$$

In this work, the structure was divided into sixteen segments (every 3 m) along its height considering each horizontal diaphragm to be at the middle of the segment. For each segment the solidity ratio was calculated and the corresponding drag coefficient was estimated based on [13]. Finally, the forces of each segment were assigned to the level of the corresponding diaphragm.

Wind Force at the dish antennas

According to [12], the commonly used practice in the past for the estimation of the wind force on dish antennas was to calculate the drag coefficient of the isolated antenna, then the corresponding force, and finally adding the result to the force of the tower as calculated by Eq. (2). However, this practice would overestimate the total force since the antenna may shield part of the tower. This is also evident in case of multiple antennas installed on the tower. For this reason, except for the drag coefficient of the isolated antenna, an additional interference factor should be added in the estimation. Thus the wind force, in case of two identical in size antennas installed on the same height at the tower, is calculated as follows [6, 8]:

$$F_{antennas} = qA_a(C_{Da_1}f_{a_1} + C_{Da_2}f_{a_2}) \tag{5}$$

where: q is the dynamic pressure of the wind, A_α is the area of each antenna projected normal to the level of the wind, $C_{D\alpha 1}$ and $C_{D\alpha 2}$ are the drag coefficients for the two isolated antennas and $f_{\alpha 1}$ and $f_{\alpha 2}$ are the corresponding interference factors for each of the antennas.

The values of the drag coefficients and the interference factors of the antennas are mainly based on the wind angle and the solidity ratio. Those values are usually estimated experimentally [6-8]. Herein, in lack of experimental results for the tower and the antennas, proposed values by an experimental study of a similar case [8] for $C_{D\alpha 1}$, $C_{D\alpha 2}$, $f_{\alpha 1}$ and $f_{\alpha 2}$ were adopted.

2.3.3 Ice Loads

Apart from wind, another environmental hazard that should be taken into account is ice. In the case of a lattice telecommunication tower, ice accumulates on the surface of the structural members and the dish antennas. Ice accretion affects the loads of the structure in two major ways. First, the weight (i.e. dead load) of the members and the dish antennas increase and secondly, the projected area of the members and the antennas also increase. Following the previous section, where the estimation of the wind loads was discussed, it can be inferred that an increase in the projected area of the members affects the solidity ratio of the tower and the corresponding drag coefficients resulting in a larger wind force for the same wind speed value.

In this work, it was assumed that an ice layer of uniform thickness was formed on the surface of the exposed parts of the members and the dish antennas. In terms of the value of the ice thickness, three scenarios of different values were considered, namely 15mm, 30mm and 45mm. For each of those icing scenarios, the corresponding areas of the ice surface and the associated values of the affected parameters (e.g. weight, solidity ratio etc.) were estimated. Finally, it should be noted that the unit weight of ice was considered equal to 7.00 kN/m^3.

3 ANALYSIS

3.1 OpenSees model

For the analysis, the tower was modeled in OpenSees, an open-source software, provided by Pacific Earthquake Engineering (PEER) Center [14]. The final 3D model (Figure 3) was composed by 932 members, both trusses and beams. The members were also modeled as fiber sections sharing the same properties of the corresponding steel cross-sections used in the structure. In total, four different versions were analyzed, one for no icing conditions and one for each of the three different scenarios of ice thickness as presented in a previous section.

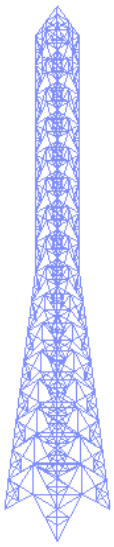

Figure 3: 3D model created in OpenSees.

The natural frequencies of the structure were determined by a modal analysis. The first two modes have the same period due to structure's and loads symmetry, although refer to different directions (X and Y). The third mode is torsional.

Modal analyses were also performed for each of the icing scenarios. Table 1 presents the periods of the first three modes for each scenario. The results show, as expected, that as the thickness of the ice layer increases, the corresponding periods increase. Certainly, this should be attributed to the increase of the tower (and dish antennas) mass.

Ice Thickness (mm)	T_1 (sec)	T_2 (sec)	T_3 (sec)
15	0.901	0.901	0.305
30	1.108	1.108	0.370
45	1.316	1.316	0.436

Table 1: Natural periods of the first three modes for the three icing scenarios considered.

3.2 Wind speed simulation

3.2.1 Wind speed profile

Wind speed increases with height following a specific pattern known as wind speed profile. Herein, a power law wind speed profile was considered. According to the power law profile, the value of wind speed at a height z is given by:

$$\frac{u}{u_{ref}} = \left(\frac{z}{z_{ref}}\right)^{a} \tag{6}$$

where: u is the wind speed at height z (in m/s), u_{ref} is the wind speed at a reference height z_{ref} (in m/s) and α is the power law exponent. In this work, a power law exponent α=0.20 was used, as proposed by IEC 61400-1 [15] for onshore structures. Eq. (6) gives the values of the wind speed along the height of the tower. Herein, the values of wind speed at the heights of the horizontal diaphragms and the center of the dish antennas were calculated. Based on these values, the wind force along the height of the tower is estimated by applying Eq. (1) and Eq. (2).

3.2.2 Wind field simulation

The simulation of the wind field where the tower is placed was performed in TurbSim software [16]. TurbSim has been developed by National Renewable Energy Laboratory of the USA and is mainly used in wind industry applications. The software simulates a 3D wind field. TurbSim can also generate timeseries of wind speed over a user-defined period (e.g. 10 min, 1 hour etc.) and for a specific wind speed value which is considered to be the mean wind speed (reference wind speed). The wind field is defined by a custom grid whose dimensions and resolution are specified by the user. The software finally outputs the corresponding timeseries of the values of the three wind speed components (for each of the three directions X, Y, Z) at the points of the grid of the wind field. For each of those components the corresponding wind force timeseries (mainly for the directions X and Y, since the component of direction Z is ignored in this study) were estimated by applying Eq. (2) for the wind force at the tower and Eq. (5) for the wind force at the antennas.

3.3 Pushover analysis

As a first step before the nonlinear dynamic analysis, a pushover (nonlinear static) analysis was performed in order to specify the failure mechanisms of the tower. The lateral load profile considered in the pushover was following the pattern of the wind force. Pushover analysis was conducted for no ice conditions and the three scenarios of icing. In all cases, the failure mechanism revealed a cascading effect shown in Figure 4. It is evident that the first member failure occurs at the point of the tower where the inclination of the legs changes to vertical, a change which also coincides with the change in the legs' cross-section from L160.15 to L120.12. The first element that fails could be either a leg or a main vertical bracing member (marked with a red circle in the figure). As lateral loads increase, the failure cascades to other elements resulting finally in a total collapse.

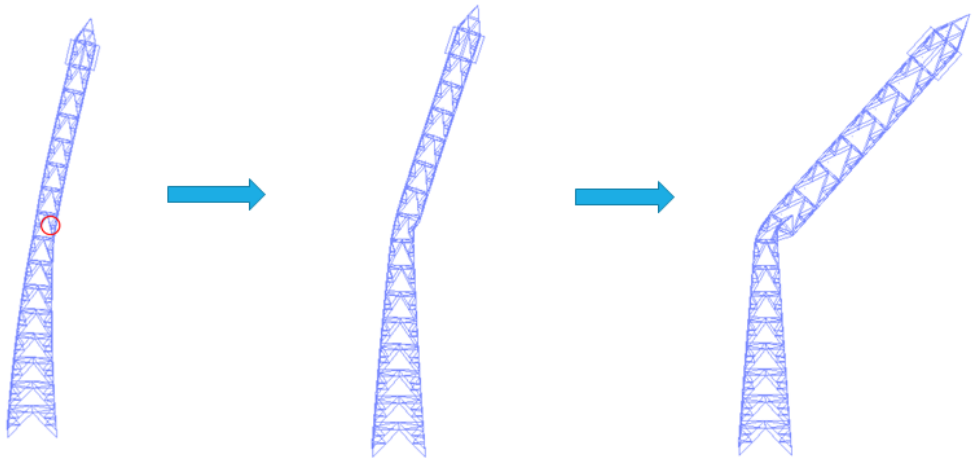

Figure 4: Failure mechanism as revealed by pushover analysis

Figure 5 presents the pushover curves for each of the four versions of tower (no ice and icing scenarios). The horizontal axis depicts the displacement of the top of the tower along the lateral loads direction, while the vertical axis depicts the shear force at the base of the tower. The curves show that the maximum shear force (i.e. the shear force when the first failure occurs) is approximately the same for the four versions and close to 470 kN. The corresponding displacement of the top (height 51m) at the time of the first failure is approximately 0.68 m in all versions.

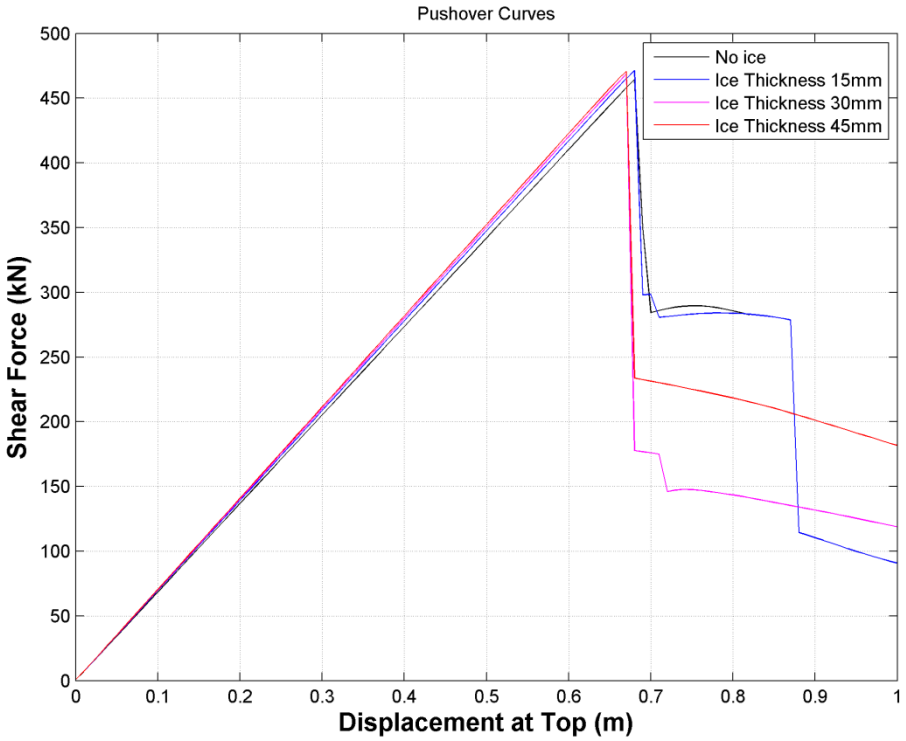

Figure 5: Pushover curves for each of the four versions of ice thickness considered.

3.4 Dynamic analysis

The main input for the nonlinear dynamic analysis was the timeseries of the wind speed created in TurbSim software as discussed above. Thus, the wind speed value (i.e. the wind speed profile) was estimated for specific points at the heights of the horizontal diaphragms of the tower. Figure 6 presents a typical form of the wind speed timeseries at the level of the top horizontal diaphragm (height 48m). The length of the timeseries was 1 hour (3600 seconds).

The next step of the analysis was to estimate the timeseries of wind force along the height of the tower (i.e. the wind force profile). The estimation was done by processing the results of the timeseries of wind speed and performing the necessary calculations by applying Eq. (1) along the two horizontal directions (X and Y). Thus, the wind force profile for the two horizontal directions was created. Those values constituted the inputs of the dynamic parameters for the OpenSees software where the dynamic analysis was performed.

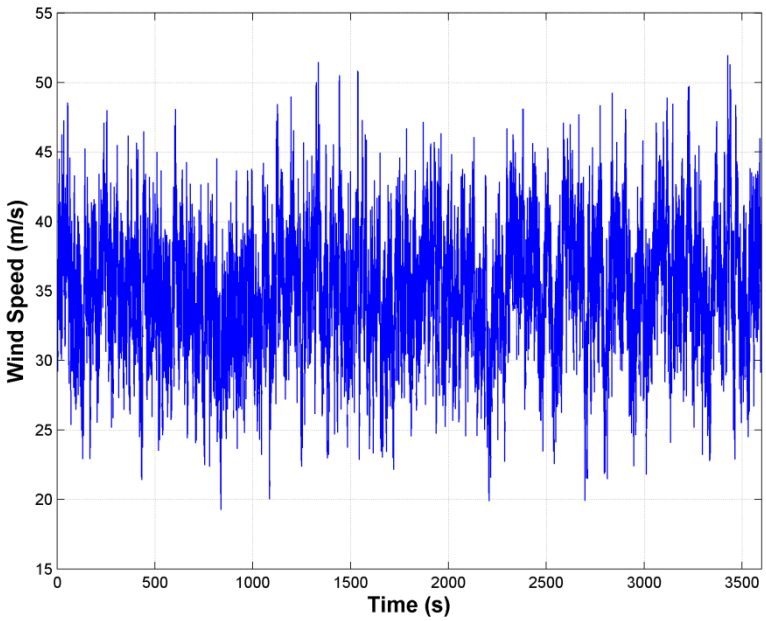

Figure 6: Typical form of 1hr wind speed timeseries (reference wind speed 35 m/s).

In an attempt to reduce computational effort and time, only five different values for wind speed with a horizontal angle of 0 degrees (i.e. parallel to X axis) were considered, namely 20, 25, 30, 35 and 40 m/s. Those values were actually the reference values of wind speed (constituting the inputs for TurbSim software) and their height was the height of the top horizontal diaphragm (height 48m). Moreover, for each of the above values, six timeseries were created resulting in a total of 5×6=30 different timeseries of wind speed. Consequently, 30 different wind dynamic analyses were performed in OpenSees software for each of the four tower versions (no ice conditions and the three icing scenarios) considered in this work. Finally, it should be noted that the same 30 timeseries of wind speed were used for the four versions in order the final results to be comparable. However, the resulting wind force timeseries were different since wind force is affected by ice thickness.

3.5 Fragility analysis

The ultimate goal of this work was to estimate the fragility of the tower to wind and/or icing conditions. Fragility could be defined as the probability of failure for a given intensity measure (*IM*), herein the value of wind speed. The results of such an analysis are reported in the form of fragility curves. The estimation of the fragility functions and corresponding curves is based on the probability of failure for the various values of the *IM*, i.e. the wind speed in this case. A common assumption is that the fragility curve is defined by a lognormal cumulative function (CDF) with the following mathematical expression [17]:

$$P(C|IM = x) = \Phi\left(\frac{ln(x/\theta)}{\beta}\right) \tag{7}$$

where: $P(C|IM=x)$ is the probability that a value of the *IM* (e.g. the wind speed) equal to x will cause a failure of the structure, $\Phi(\ )$ is the standard normal cumulative distribution function (CDF), θ is the median of the fragility function which corresponds to the value of *IM* with 50% probability of failure and β is the standard deviation of *lnIM*, sometimes referred to as dispersion of *IM*.

A simple method to estimate fragility is by performing stripe analysis. Stripe analysis is mainly applied when discrete values of *IM* are used, as in the case of this work. The first step of the process is to perform a number of dynamic analyses for each value of the *IM*, namely the wind speed, and then estimate the number of cases where a failure was occurred. Then for each wind speed the fraction of analyses causing failure could be estimated by simply dividing by the total number of analyses. This fraction is actually an estimator of the probability of failure for the corresponding value of the *IM*.

In this work, six dynamic analyses were performed for each of the five different reference values of wind speed based on the wind speed timeseries discussed in a previous section and for each of the four versions of tower considered. Finally, a failure was assumed that occurs in two ways. First, when the mean value of the inter-story drift during the first 10 minutes of the analysis is different from the corresponding mean value of the last 10 minutes of the analysis. Secondly, if the dynamic analysis was failed (i.e. it was incomplete) due to non-convergence of the algorithm used by the OpenSees software.

Figure 7 shows the stripe analysis results for no ice conditions. A blue circle denotes a non-failure result of the dynamic analysis. A red triangle denotes a failure result of a converged dynamic analysis, while a black asterisk denotes a non-converged dynamic analysis. Following the results of Figure 7, the estimation of the probability of failure for each combination of wind speed and ice thickness can be estimated by simply calculating the fraction of analyses causing failure, as presented in Table 2.

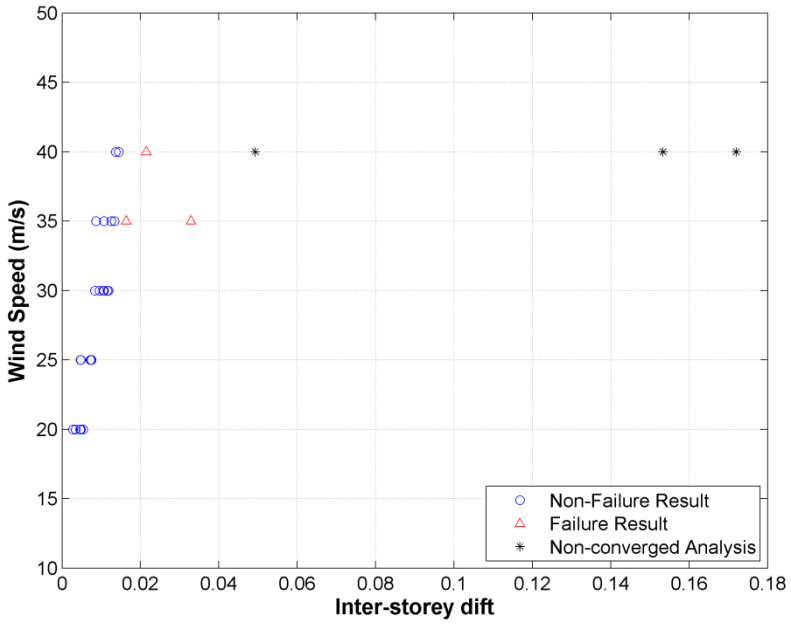

Figure 7: Stripe analysis for no ice conditions.

Wind Speed (m/s)	No Ice	Ice thickness 15 mm	Ice thickness 30 mm	Ice thickness 45 mm
20	0.00	0.00	0.00	0.00
25	0.00	0.00	0.00	0.17
30	0.00	0.33	0.50	0.33
35	0.33	0.67	0.67	1.00
40	0.67	1.00	1.00	1.00

Table 2: Fraction of analyses causing failure for combinations of wind speed and ice thickness

The next step is to fit a lognormal cumulative function (Eq. (7)) to the values listed in Table 2. The parameters θ and β can be easily estimated by maximum likelihood estimation method as in [17].

Results show that for no ice conditions, the median wind speed (θ) of the fragility function is 37.62 m/s. On the other hand, for ice thicknesses of 15mm, 30mm and 45mm, the corresponding values are 32.28 m/s, 31.48 m/s and 29.55 m/s, respectively. This means that as ice accumulates on the tower, the median wind speed of failure decreases. At the same time, the probability of failure increases, as the thickness of the ice layer increases. The last is also evident if the four fragility curves are plotted on the same graph as in Figure 8. It is obvious that the position of the fragility curve moves to the left as ice thickness increases. This finding should be attributed to the impact that ice has on the structure by increasing both the dead loads and the wind force for the same wind speed.

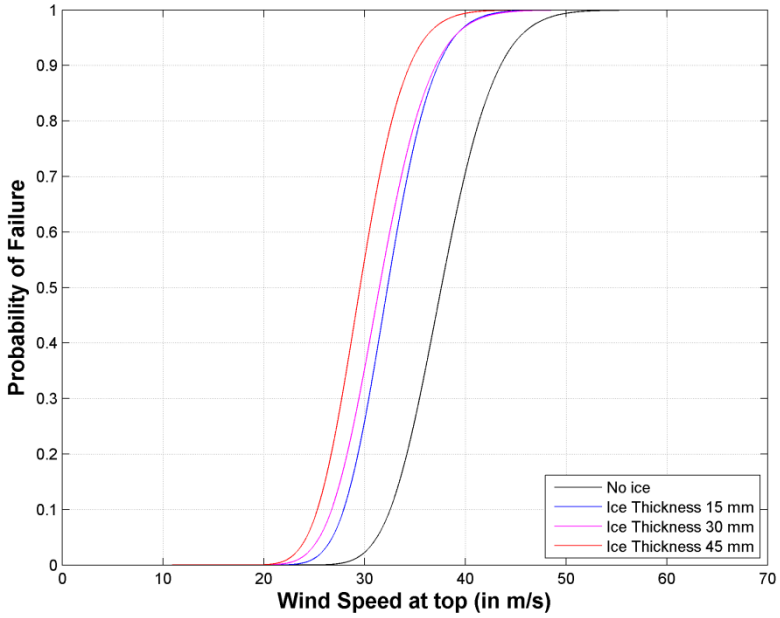

Figure 8: Fragility curves for wind speed and ice thickness combinations

4 CONCLUSIONS

Telecommunication towers are tall steel lattice structures vulnerable to weather hazards. In this paper, a case study of a telecommunication tower carrying four dish antennas and designed for coastal areas of Greece was presented. For the analysis of the tower a 3D model was developed in an open-source software.

A number of nonlinear dynamic analyses of the 3D model of the tower were performed in order to estimate the fragility of the tower to wind and icing conditions. For those analyses, timeseries of wind speed and corresponding force at the structure were created based on a detailed 3D simulation of the wind field along the entire profile of the tower. Furthermore, four different cases of icing conditions were examined by developing the corresponding models. Finally, the fragility of the structure for every combination of wind and icing conditions was estimated and the corresponding fragility curves were created following a probabilistic methodology.

The results confirm the significant effect of wind on steel lattice structures, especially when it is combined with ice accretion. Specifically, the probability of failure (and probably collapse) tends to increase as ice accumulates on the structure for the same wind speed value in comparison with no ice conditions. This finding is in accordance with related literature.

At the end, the elaboration of climatic data from the site of the structure could be proposed as an extension of this work. Based on climatic data, the probabilities of occurrence of all wind and icing combinations over a specified period (e.g. service life of structure) could be estimated. By incorporating these probabilities along with the fragility curves presented herein, one could estimate the risk of the structure over its projected lifetime. This risk estimation could be used as a useful decision tool by telecommunication companies in upgrading and/or expanding their network.

ACKNOWLEDGMENTS

This research has been financed by the European Commission (Research Program of the Research Fund for Coal and Steel) through the Program "ANGELHY - Innovative solutions for design and strengthening of telecommunications and transmission lattice towers using large angles from high strength steel and hybrid techniques of angles with FRP strips" with Grant Agreement Number: 753993.

REFERENCES

[1] C. Klinger, M. Mehianpour, D. Klingbeil, D. Bettge, R. Hacker, W. Baer, Failure analysis on collapsed towers of overhead electrical lines in the region Münsterland (Germany) 2005, *Engineering Failure Analysis*, **18**, 1873-1883, 2011.

[2] L. Makkonen, P. Lehtonen, M. Hirviniemi, Determining ice loads for tower structure design, *Engineering Structures*, **74**, 229-232, 2014.

[3] D.K. Davis, North American tower failures: causes and cures. *Consolidated Engineering Inc*, 2010.

[4] Y. Wang, D.V. Rosowsky, Characterization of joint wind-snow hazard for performance-based design, *Structural Safety*, **43**, 21-27, 2013.

[5] S.N. Rezaei, Fragility assessment and reliability analysis of transmission lines subjected to climatic hazards, *PhD Dissertation*, McGill University, Monteal, Quebec, Canada, 2016.

[6] J.D. Holmes, R.W. Banks, G. Roberts, Drag and aerodynamic interference on microwave dish antennas and their supporting towers, *Journal of Wind Engineering and Industrial Aerodynamics*, **50**, 263-270, 1993.

[7] C.F. Carril Jr, N. Isyumov, R.M.L.R.F. Brasil, Experimental study of the wind forces on rectangular latticed communication towers with antennas, *Journal of Wind Engineering and Industrial Aerodynamics*, **91**, 1007-1022, 2003.

[8] P. Martin, V.B. Elena, A.M. Loredo-Souza, E.B. Camano, Experimental study of the effects of dish antennas on the wind loading of telecommunication towers, *Journal of Wind Engineering and Industrial Aerodynamics*, **149**, 40-47, 2016.

[9] ANGELHY Deliverable 1.3, Report on analysis and design of 6 case studies, *Research Program of the Research Fund for Coal and Steel ANGELHY, Grant Agreement Number: 753993*, European Commission, Brussels, Belgium, 2019.

[10] A. Braconi et al. Optimising the seismic performance of steel and steel-concrete structures by standardising material quality control (OPUS), *Research Program of the Research Fund for Coal and Steel ANGELHY, Grant Agreement Number: RFSR-CT-2007-00039*, European Commission, Brussels, Belgium, 2013.

[11] EN 1993-1-1, Design of steel structures. Part 1-1: General rules and rules for buildings. Brussels. Comité Européen de Normalisation (CEN), 2005.

[12] J.D. Holmes, *Wind loading of structures, Third Edition*, CRC Press, Taylor & Francis Group, 2015.

[13] EN 1991-1-4, Design of steel structures. Part 1-4: General actions – Wind actions. Brussels. Comité Européen de Normalisation (CEN), 2005.

[14] S. Mazzoni, F. McKenna, M. Scott, G. Fenves, Open system for earthquake engineering simulation. User Command-Language Manual, Report NEES grid-TR 2004-21, Berkeley, CA: Pacific Earthquake Engineering Research, University of California, 2006. Retrieved http://opensees.berkeley.edu

[15] IEC 61400-1. "Wind Turbines-Part 1: Design Requirements," International Electrotechnical Commission, Geneva, Switzerland, 2005.

[16] B.J. Jonkman, L. Kilcher, TurbSim User's Guide. Technical Report NREL/TP-xxx-xxxx (Draft Version). NREL Technical Report, National Renewable Energy Laboratory, Golden, Colorado, 2012.
[17] J.W. Baker, Efficient analytical fragility function fitting using dynamic structural analysis, *Earthquake Spectra*, **31**, 579-599, 2015.

COMPDYN 2019
7th ECCOMAS Thematic Conference on
Computational Methods in Structural Dynamics and Earthquake Engineering
M. Papadrakakis, M. Fragiadakis (eds.)
Crete, Greece, 24–26 June 2019

SIMPLIFIED MODELS FOR THE NONLINEAR ANALYSIS OF ARSW STRUCTURES UNDER SEISMIC LOADING

D. Tsarpalis[1], D Vamvatsikos[2], and I. Vayas[2]

[1] National Technical University of Athens
Iroon Polytechniou Str 9, GR – 15780 Athens
e-mail: dimitrists93@central.ntua.gr

[2] National Technical University of Athens
Iroon Polytechniou Str 9, GR – 15780 Athens
{divamva, vastahl}@{mail.ntua.gr, central.ntua.gr}

Abstract

Automated Rack Supported Warehouses (ARSW) are the state of the art in storage technology, as they provide substantial savings in terms of cost, space and energy with respect to traditional solutions. Despite their lightness, ARSWs carry very high live loads, by far higher than their self-weight, in contrast to what happens in typical civil engineering structures. Thus, standard design approaches are not applicable, especially when one considers lateral loading, i.e. seismic and wind loading.
In the frame of the STEELWAR project, the behavior factor (q) as well as the seismic fragility shall be assessed for a number of archetype warehouses. FEM modelling for such structures is a tedious task; they consist of hundreds or thousands steel members and nodes connected to each other through simple and semirigid joints. Modern computers accompanied with efficient computational algorithms can handle linear systems with ease and thus, linear analysis can be performed by including all structural components in the analysis model. Problems arise when one considers nonlinear phenomena i.e. material and geometric nonlinearity. Simulations that take into account all ARSW members and their nonlinear response may lead to prohibitive computational costs, while introducing convergence and numerical stability problems. As a direct remedy, a reduced-order physical model is proposed that enables accurate assessment of nonlinear behavior without compromising convergence performance.

Keywords: Simplified models, steel racks, pallet racking systems, automated rack supported warehouses, nonlinear analysis.

1 INTRODUCTION

Pallet rack is a material handling storage aid system designed to store materials on pallets (or "skids"). Although there are many varieties of pallet racking, all types allow for the storage of palletized materials in horizontal rows with multiple levels. Forklift trucks are usually an integral part of any pallet rack system as they are usually required to place the loaded pallets onto the racks for storage.

1.1 Structural Components

The structural design of a warehouse (geometry, materials, cross-sections etc.) varies depending on the material handling system, the designer's preferences and the owner's requirements. However, the following structural components are commonly considered:

a) Upright frame

Also known as built-up column, this component is in-plane with the cross-aisle direction of the warehouse (Figure 1). It consists of two or three vertical elements known as uprights, which are usually made of cold-formed open cross-section. The uprights are connected with diagonal and horizontal bracings typically made of "C" cross-sections, which transfer shear forces by uniaxial compression-tension mechanism. Their assembly strategy defines different upright frame types (D, Z, K, X etc. [1]).

b) Beam

Similarly to steel frames, beams carry the pallet loads and transfer them to the upright frames (Figure 1). Usually, the have connecting claws that ensure a decent connection to the frames without the use of bolts or screws. They are made of hollowed cross-section of high bending resistance and thus, their weakest point is the beam-to-upright connection.

c) Down-aisle vertical bracing

In many cases the loose connection between uprights and beams is not capable to resist the lateral loads and a bracing system is assembled in down-aisle direction. Purpose of this system is to prevent soft-story collapse mechanism [2] and limit the displacements induced by earthquake excitations.

1.2 Automated Rack Supported Warehouses

At present, Automated Rack Supported Warehouses (ARSW) or clad rack warehouses are usually built by manufacturers specialized in structural systems for logistics with the same or similar cold formed profiles used for warehouse storage pallet racks although in the case of ARSW the rack forms the load bearing structure of the whole building by itself.

The research made up to now is mainly limited to steel storage racks which are a much smaller scale of automated warehouses ([3], [4]). Automated storage systems, which will probably be the future of the warehouse sector, have not been investigated to such an extent so far. Moreover, in Europe (and in the world) there is no official reference document specific for the design of Automated high-rise warehouses. Designers are obliged to work with a total lack of specific references and of commonly accepted design rules and procedures. As a result, these structures are vulnerable in extreme load scenarios, such as high wind speeds and seismic actions (Figure 2).

The aforementioned lack of knowledge and bibliography raises the demand for further research. Today, a variety of methods (Pushover, IDA etc.) exist to determine the nonlinear characteristics (overstrength, ductility, energy dissipation) of a structure, which require computationally expensive numerical analyses. By examining the FEA model of an ARSW, it is obvious that a nonlinear simulation of the whole structure is nearly impossible. Objective of

the present paper is to develop simplified models for the representation of complete warehouses in order to check their nonlinear response to seismic motion.

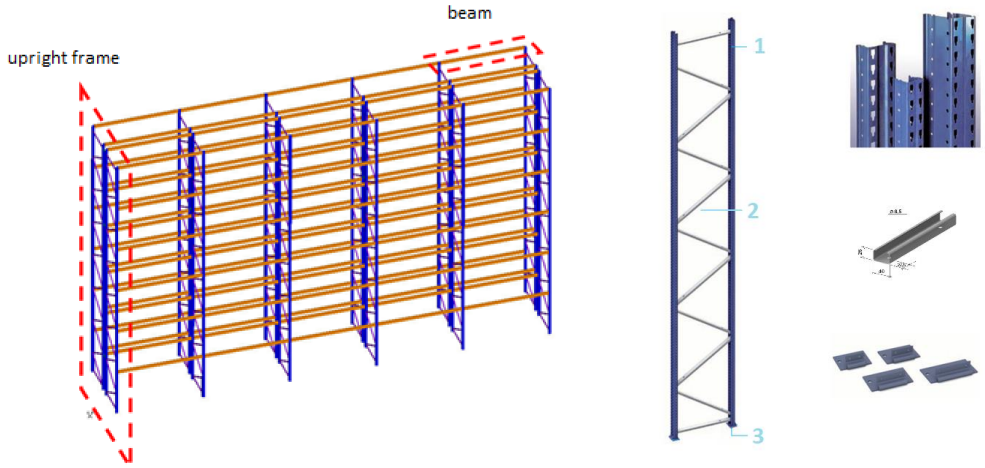

Figure 1: Configuration of a racking system: portal frame (left), upright frame's components (right)

Figure 2: Configuration of a racking system: portal frame (left), upright frame's components (right)

2 MODEL SIMPLIFICATION PROCEDURE

As mentioned before, the full simulation of an Automated Rack Supported Warehouse consists of hundreds of thousands of elements and nodes yielding to an extremely computationally cumbersome model, which is not only hard to be designed in a CAD program, but also nearly impossible to be solved nonlinearly. These problems motivate the search for an equivalent model which will be computationally efficient but also respect the behavior of the real structure. The solution suggested in the present papers is to substitute the built-up columns and the roof for simple beam elements whose degrees of freedom will be way lesser.

2.1 Elastic Properties of equivalent beam element in Cross-Aisle direction

The stiffness matrix of a prismatic homogeneous two-dimensional beam element with doubly symmetric cross-section depends on the material properties (i.e. E and G), length, cross-section area, moment of inertia and shear area. It is worth mentioning that shear deformation is usually neglected because in beams with typical lengths and cross sections this phenomenon is insignificant. However, in the case of upright frames, the "cross section" does not

remain perpendicular to the neutral axis [5] and so shear must be considered (Figure 3). If one neglects the effects of shear deformation, the equivalent element may be 10 to 30% more stiff, depending on the characteristics of the structure and the distribution of loads. Moreover, compatibility of deformations leads to fixed restraints on the equivalent beam.

Obviously, the equivalent element is made of the same material and has the same length, thus:

$$\begin{aligned} E_{eq} &= E \\ G_{eq} &= G \\ L_{eq} &= L \end{aligned} \tag{1}$$

Cross-section area of the simplified column is equal to the sum of upright's cross-section areas:

$$A_{eq} = \sum_{i=1}^{N} A_i \tag{2}$$

, where N is the total number of uprights and A_i is the cross-section area of i-upright.

In general, the equivalent moment of inertia of a built-up column consisted of N uprights is given by:

$$I_{eq} = \sum_{i=1}^{N} A_i \cdot h_i^2 \tag{3}$$

, where h_i is i-upright's distance from the center of gravity. For example, the upright frame shown in Figure 4 has moment of inertia equal to:

$$I_{eq} = A_c \left(-\frac{h_0}{2} \right)^2 + A_c \cdot 0 + A_c \left(\frac{h_0}{2} \right)^2 = A_c \frac{h_0^2}{2}$$

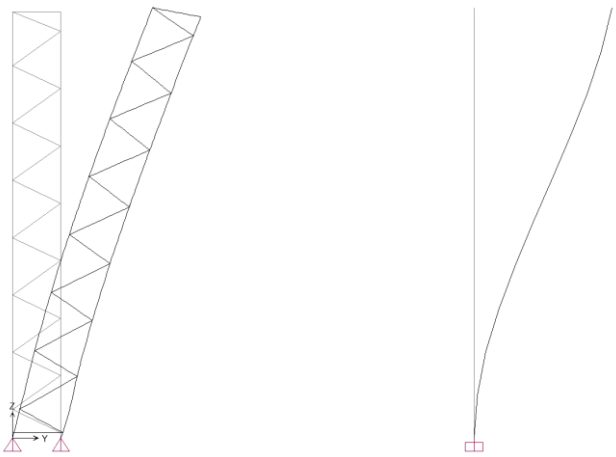

Figure 3: In built-up columns (left) "cross sections" do not remain perpendicular to the neutral axis. This effect must be considered when assigning equivalent element's properties (right)

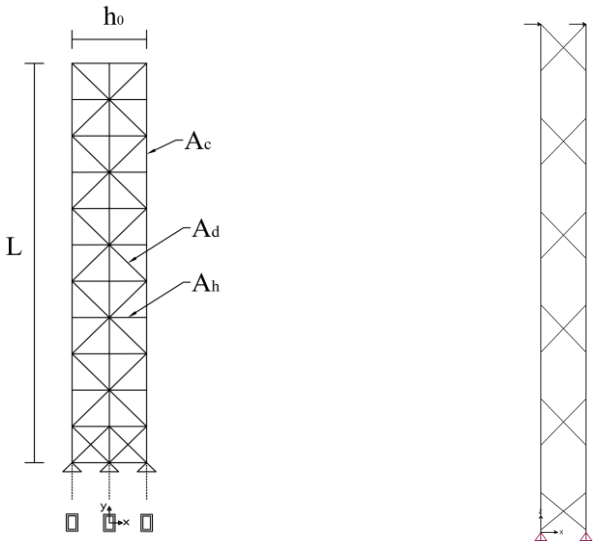

Figure 4: Example of a X-type column with 3 uprights (left) and an upright frame with arbitrary bracing (right)

Finally, shear area depends on the geometry and the type of the upright frame (X, D, Z and K systems. Closed form solutions can be easily derived for common systems, by considering a segment of the upright frame and enforce static equilibrium [6]. However, in the case of arbitrary bracing configuration like the one shown in Figure 4, no formula exists for the calculation of shear area. In order to overcome this difficulty, the following approximate procedure is introduced:

1. Isolate the column under consideration and pin the nodes at one end.
2. Apply a point load at the free end. If P is the applied load, then the corresponding displacement of the free end δ_{tot} is given by:

$$P=\frac{12}{4+\Phi}\frac{EI_{eq}}{L^3}\delta_{tot} \tag{4}$$

, where $\Phi=\frac{12EI_{eq}}{GA_{eff}L^2}$

3. Solve Eq. (4) for A_{eff} :

$$A_{eff}=\frac{P(3EI)L}{(3EI)\delta-PL^3}/G \tag{5}$$

2.2 Elastic Properties of equivalent beam element in Down-Aisle direction

In down-aisle direction the uprights of an upright frame are independent and thus they behave as springs in parallel. This assumption is valid as the bracings are commonly pinned to the uprights. As a result, we aggregate the moment of inertias of all uprights:

$$I_{eq,DA}=\sum_{i=1}^{N} I_{i,DA} \tag{6}$$

, where $I_{i,DA}$ is i-th's upright moment of inertia in down-aisle direction. Moreover, if the uprights are assumed partially fixed to the base plate by employing rotational springs, the sum of their stiffnesses has to be applied on equivalent beam's restrained end.

	Z-COLUMN SINGLE	**Z-COLUMN DOUBLE A**	**Z-COLUMN DOUBLE B**
	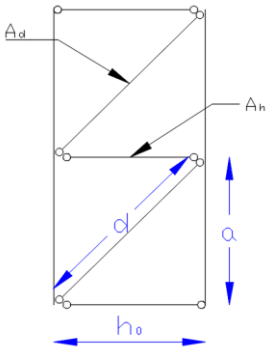	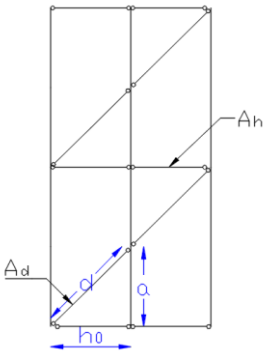	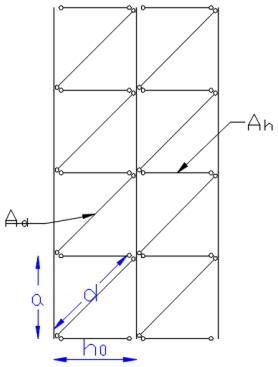
Nº uprights	2	3	3
A_{eq}	$2A_c$	$3A_c$	$3A_c$
I_{eq}	$A_c \frac{h_0^2}{2}$	$2A_c h_0^2$	$2A_c h_0^2$
A_{eff}	$\frac{\frac{EA_d}{G}\frac{h_0^2}{d^2}\frac{a}{d}}{1+\frac{h_0^3}{d^3}\frac{A_d}{A_h}}$	$\frac{\frac{EA_d}{G}\frac{h_0^2}{d^2}\frac{a}{d}}{1+\frac{h_0^3}{d^3}\frac{A_d}{A_h}}$	$2\cdot\frac{\frac{EA_d}{G}\frac{h_0^2}{d^2}\frac{a}{d}}{1+\frac{h_0^3}{d^3}\frac{A_d}{A_h}}$

Table 1: Equivalent properties of X-type columns

2.3 Nonlinear behavior of equivalent beam element

The nonlinear behavior of an upright frame can be distinguished in three main categories:

1. *Axial Failure*. This type of failure refers to flexural, local, distortional and lateral torsional buckling of the uprights [7]. It is common in rack-system technology to perform laboratory tests to evaluate uprights' compression resistance and thus, $N_{rd,upright}$ is usually a known value.
2. *Bending Failure*. Loads are not primarily carried by bending mechanisms, as bracings are considered to be pinned and uprights are usually simply supported to the foundation. However, when vertical bracing system is missing in down-aisle direction, horizontal loading may lead to development of bending moments in the uprights. However, their contribution is usually small with respect to the axial loads.
3. *Shear Failure*. Shear forces are transferred via axial tension-compression mechanism by bracings, which may fail due to buckling or tensile yielding.

The equivalent element must take into consideration all these failure mechanisms. For instance, open-source software OpenSees [8] provides the Two Node Link Elements (aka Link Elements, see Figure 5) with the capability to assign axial, rotational and shear springs.

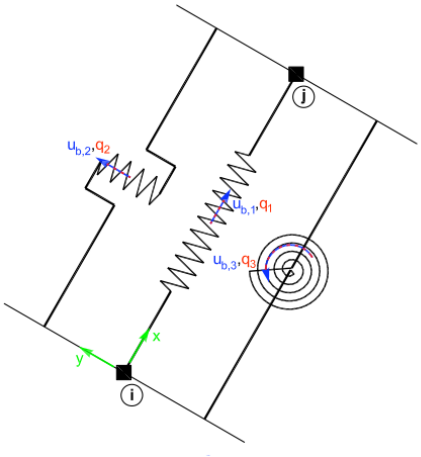

Figure 5: Concept of Two Node Link Element

One important characteristic of the equivalent element is the coupled behavior of the axial and rotational spring. Equivalent element's bending moment M_{eq} is linked to a set of axial forces N_b on the uprights, of opposite direction. As an example, for the Z-type upright frame shown in Figure 6 the following relation holds:

$$M_{eq} = N_b \cdot h_0 \tag{7}$$

On the other hand, equivalent axial force N_{eq} is related to a set of axial forces $N_{eq}/2$ on the uprights, of the same direction. Summing all together, if $N_{rd,upright}$ is upright's compression resistance and N, M the axial force and the bending moment acting on the equivalent element respectively, then the condition for axial failure is (same formulae can be derived for any number of uprights):

$$N_{rd,upright} = \frac{N_{eq}}{2} + \frac{M_{eq}}{h_0} \tag{8}$$

Eq. (8) indicates a linear interaction between moment and axial force of the equivalent element, which is conceptually illustrated in Figure 7.

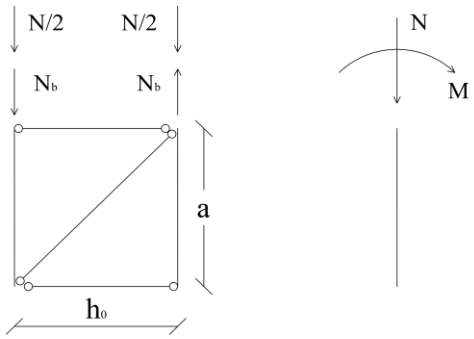

Figure 6: Relation between axial forces and bending moments of the two models

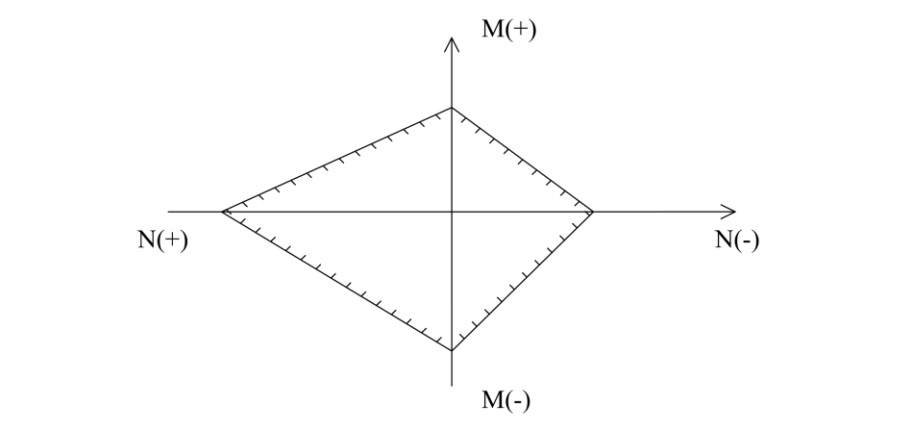

Figure 7: Interaction between the bending moment and axial force of the equivalent element

An important factor that dominates the nonlinear behavior of an upright frame in seismic loading is bracings' failure, as indicated in [9]. These structural components are responsible for the transfer of seismic shear forces to structure's foundation. If V_{eq} is equivalent element's shear force and $N_{rd,bracing}$ the axial resistance of the diagonal bracing shown in Figure 6, then failure occurs when:

$$N_{rd,upright} = \frac{V_{eq}}{\cos\varphi} \tag{9}$$

, where $\cos\varphi$ is the angle between upright and bracing. Eq. (9) holds for Z-type upright frames with two uprights, but it can be extended for any system.

Concluding, the substitution of an upright frame for simple beam elements does not reduce model's capabilities to simulate any type of structural failure. OpenSees' Link Elements comprise of two rigid linear segments and three or six springs in the center for 2D and 3D analysis respectively. These springs have to produce the same stiffness matrix as the classic finite beam elements. Table 2 shows the stiffness of each spring for the 2D case.

Type of beam	**EULER-BERNOULLI**	**TIMOSHENKO**
Axial Spring	$\frac{EA}{L}$	$\frac{EA}{L}$
Shear Spring	$\frac{12EI}{L^3}$	$\frac{1}{1+\Phi}\cdot\frac{12EI}{L^3}$
Bending Spring	$\frac{EI}{L}$	$\frac{EI}{L}$
P-delta input value (OpenSees users)	-0.1	$\frac{-0.1}{(1+\Phi)^2}$

Table 2: Springs' stiffnesses for 2D Two Node Link Element

3 ANALYSIS OF AN ARSW FRAME WITH SHEAR FAILURE

The nonlinear behavior of a single ARSW frame is examined in static and dynamic analysis. The uprights are class 1 steel sections and thus not expected to participate in structure's failure mechanism. This test case focuses solely to shear failure of the simplified model or equivalently to bracings' failure.

3.1 Configuration of test case and structural characteristics

The ARSW frame under consideration (geometry illustrated in Figure 8) consists of 2 external single X-type upright frames and 4 internal double X-type upright frames connected to a "truss" roof. The section and the material of the uprights and diagonal bracings vary in height while the horizontal bracing has constant properties (see Table 3 for more details). The roof is comprised of double angle sections 45x45x4 with steel grade S355.

Regarding the connections, it was assumed that the base plates do not offer additional stiffness and thus the uprights were simulated as pinned to the foundation and the roof. Horizontal and diagonal bracings were also assumed pinned as they are commonly connected to the uprights by 1 or 2 bolts. A common practice in the design of pallet racking systems is to reduce diagonal bracings' cross-section area to take into account the looseness of their connection. The magnitude of this reduction can be quite significant (e.g. 80%) and is verified by experimental shear tests. However, for this particular test case the existence of class 1 uprights and diagonals may lead to the safe assumption that this reduction is negligible and thus it was not considered.

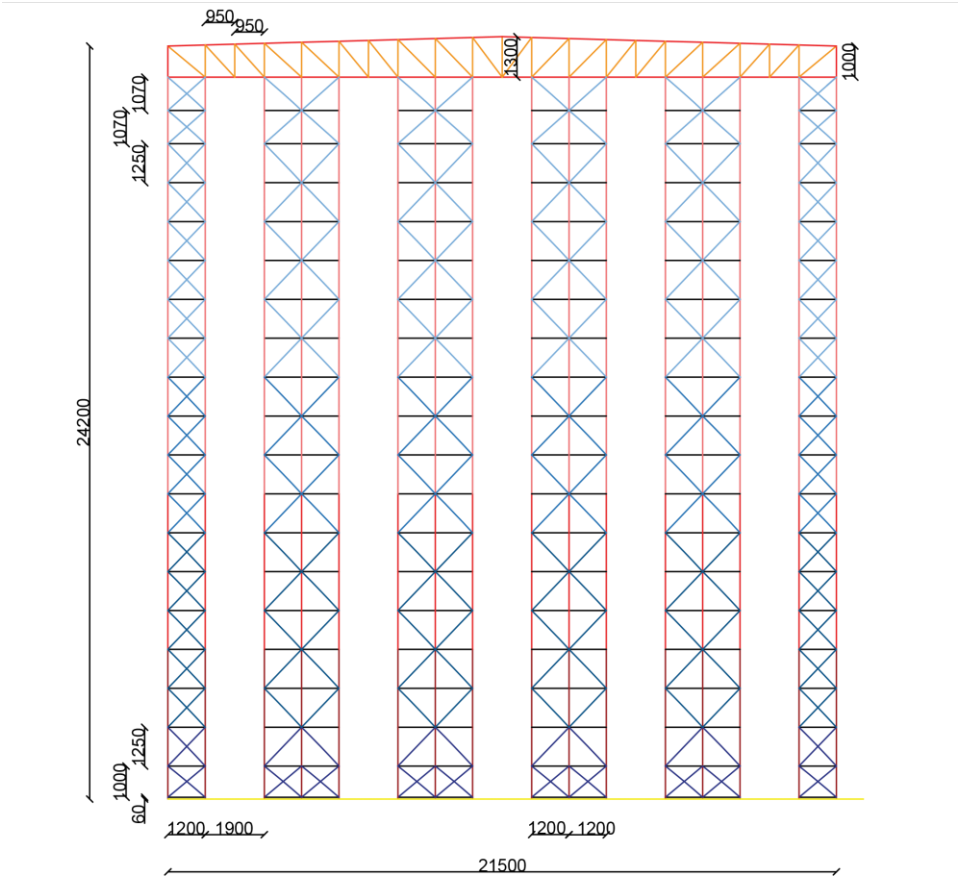

Figure 8: Configuration and geometric properties of ARSW frame test case (units in mm)

Height (m)	**Uprights (single)**	**Diagonal (single)**	**Diagonal (double)**	**Horizontal (both)**
0.00-2.31	RHS (S355) 120x80x10	L (S355) 40x40x5	L (S355) 40x40x5	DC (S355) 80x50x3
2.31-4.81	RHS (S355) 120x80x10	L (S275) 40x40x4	RHS (S355) 30x30x2.5	DC (S355) 80x50x3
4.81-9.75	RHS (S355) 120x80x6	L (S275) 40x40x4	RHS (S355) 30x30x2.5	DC (S355) 80x50x3
9.75-13.56	RHS (S355) 120x80x4	L (S275) 35x35x4	RHS (S275) 30x30x2.5	DC (S355) 80x50x3
13.56-23.2	RHS (S355) 120x80x4	L (S235) 30x30x4	RHS (S235) 30x30x2	DC (S355) 80x50x3

Table 3: Cross sections of upright frames. (RHS: Rectangular Hollowed Section, L: Angle, DC: Double Channel)

3.2 Reduced order models

Three models of decreasing accuracy will be examined:

1. *Fiber Model:* All structural members suspected to participate in structure's failure mechanism (i.e. uprights, diagonal and horizontal bracings) are simulated as force-based fiber elements [10] with 3 integration points. Especially for the diagonal bracings in compression, an imperfection L/200 is assumed, where L is the length of the element. For the rest elements classic Euler-Bernoulli beams where used.
2. *Truss Model:* In this case, uprights are assumed to behave linearly (class 1 sections), while the bracings are simulated by nonlinear truss elements. Their material law can be derived by EN1993 formulae or by isolating each bracing, simulate it by fiber elements, perform compression and tension arithmetic tests and use them to find an equivalent stress-strain diagram. For the rest elements classic Euler-Bernoulli beams where used.
3. *Link Model:* Here, an entire upright frame is substituted for a Two Node Link Element that includes shear failure. As mentioned before, Link Elements include axial, rotational and shear springs which may have nonlinear material laws. Here we will mainly focus on the characteristics of the shear spring.

To determine the elastic properties of the Link Elements first we have to substitute the upright frames for elastic Timoshenko Elements, using Eq (1) to Eq (6). Afterwards, spring's elastic stiffnesses can be readily evaluated using Table 2.

Next, the nonlinear behavior of the shear spring will be approximated. In initial configuration (Figure 9), shear forces are transferred through the diagonal bracings, while the horizontal bracing is unstressed due to symmetry. We define $N_{(+)}$, $N_{(-)}$ diagonal bracing's strength in tension and compression respectively and N_h buckling resistance of the horizontal bracing. The following relations hold:

- $N_{(+)} > N_{(-)}$, as in compression buckling phenomena are witnessed.

- $N_h > N_{(-)}$, as $h_0 < d$ and taking into account that horizontal bracing commonly is comprised of equal or even heavier section than the diagonal.

Thus, the first member exceeding its ultimate strength will be the diagonal bracing in compression, which corresponds to a *"yield shear strength"*:

$$V_y = 2N_{(-)} \frac{h_0}{d} \tag{10}$$

Figure 10 shows the failure mechanism of a X-type upright frame. One can claim that the system has transformed from X-type to Z-type and thus the shear area has changed. This will be referred as *"shear degradation"*. Link element's reduced shear stiffness after the degradation will be:

$$k_{y,shear} = \frac{12EI}{\left(1+\Phi_y\right)L^3} \tag{11}$$

, where Φ_y is calculated using the shear stiffness formula for the Z-type columns given in Table 1. Shear spring's *"yield deformation"* is derived by combining Eq (10), Eq (11) and:

$$\delta_y = \frac{V_y}{k_{y,shear}} \tag{12}$$

The upright frame has transformed from a X-type to a Z-type and thus, horizontal bracing is now compressed. The next structural member that will fail depends on their tensile and compressive strength. If $N_h < \cos\varphi N_{(+)} = \frac{h_0}{d} N_{(+)}$, the horizontal bracing in compression will fail first, otherwise the diagonal bracing in tension. Following a similar to Eq. (10), (11) and (12) procedure the complete force-displacement diagram can be calculated for each spring.

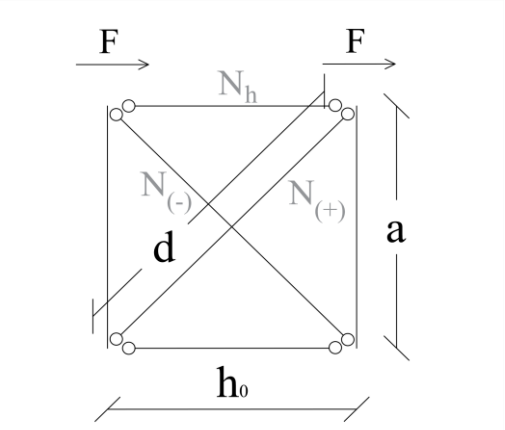

Figure 9: Shear transfer mechanism in initial configuration

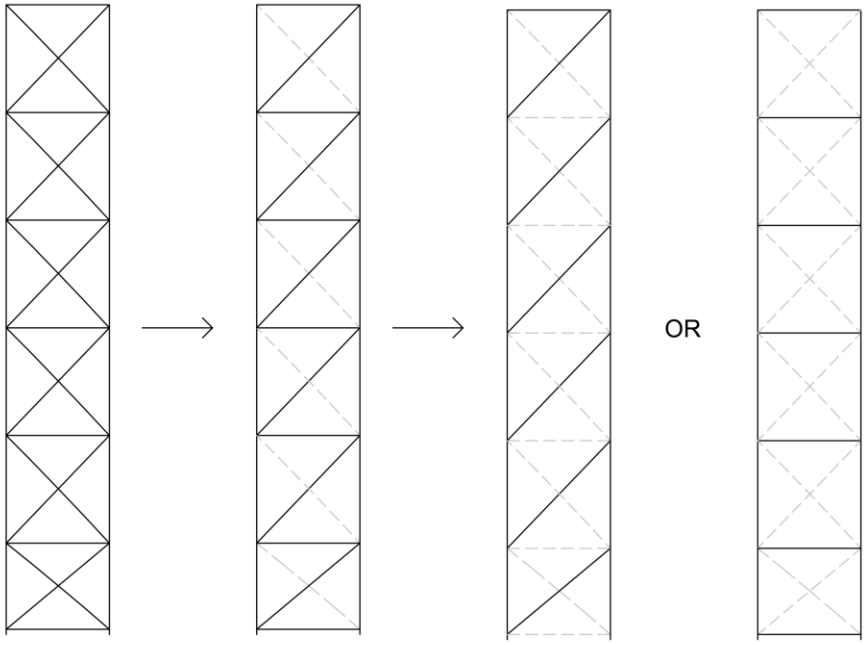

Figure 10: Failure sequence of X-type upright frame's bracing

3.3 Modal Analysis

First, Modal Analysis is performed to validate the Link Model in the elastic region. The masses are assumed to be lumped, of magnitude 10 kN at each level. The results for the five first eigenmodes are shown in Figure 11 and Figure 12. As it is observed, the Link Model predicts well even the higher modes of the system, and so, it is expected to give accurate results in linear dynamic analysis.

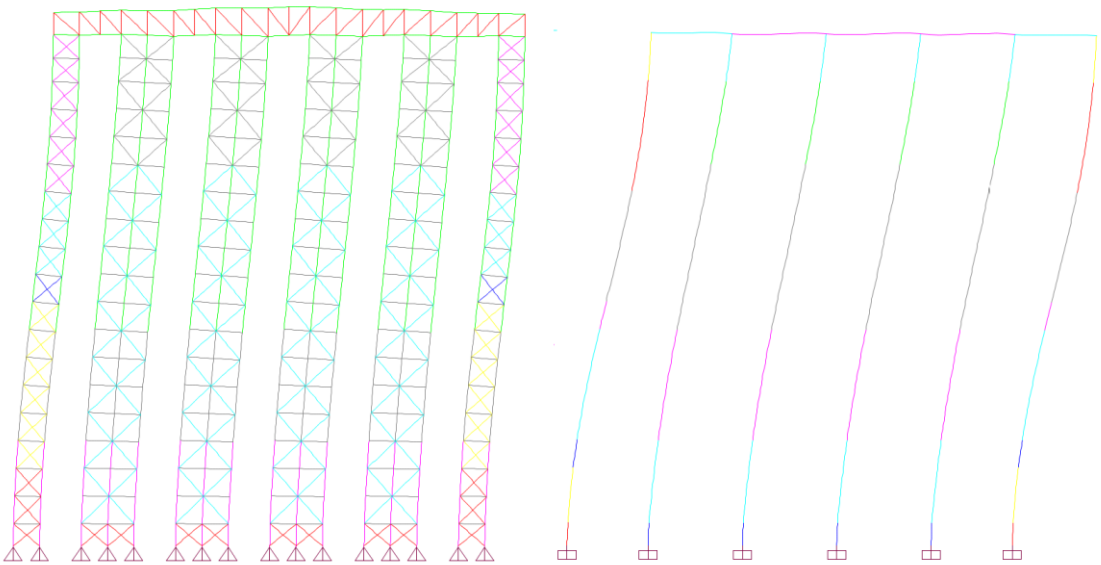

Figure 11: First Eigenmode of Full Model (T1,1=0.775 sec) and Link Model (T1,2=0.784 sec)

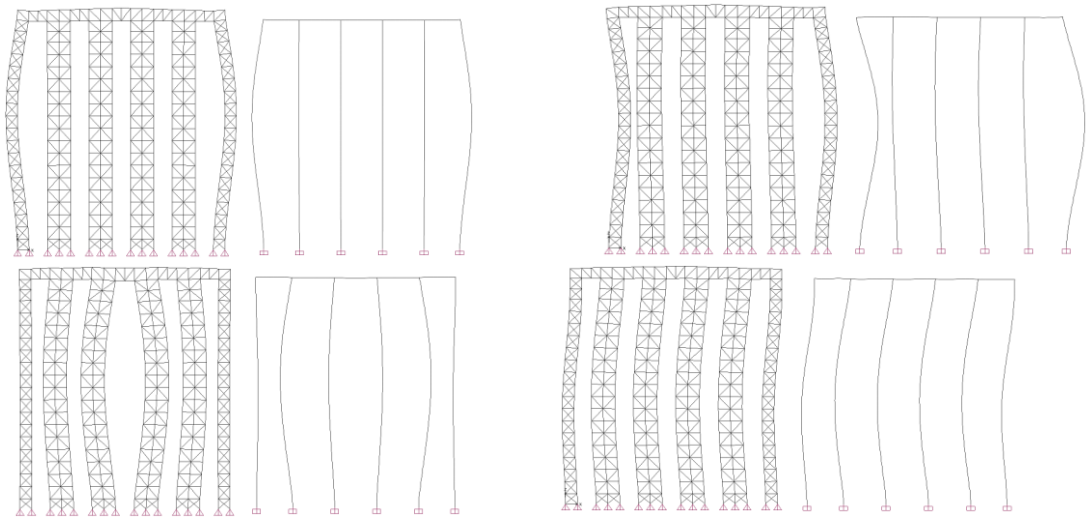

Figure 12: 2nd, 3rd, 4th and 5th mode shapes. 5% maximum relative error

3.4 Pushover Analysis

Next, Static Pushover Analyses were performed for the three models, assuming triangular distribution for the lateral loads. The analyses were executed until the system reached 10% roof drift or stability and non-convergence problems occurred. The Base-Shear vs Top Node Displacement diagrams are illustrated in Figure 13a and Figure 13b for 800 kg and 2000 kg pallet load respectively.

All models respond linearly and elastic until a roof displacement approximately equal to 150 mm is achieved. After this "limit state" is exceeded, the structure is highly nonlinear, and Pushover's slope decreases exponentially. This behavior was attributed to the successive failure of the diagonal bracings in tension. At about 500mm the slope has dropped to 7.2% of the elastic branch for the Link Model, 5.5% for the Truss Model and 7.7% for the Fiber Model. It is mentioned that steel's strain hardening was chosen equal to 5% which is roughly Pushover's residual slope.

Pallet load scenarios 800 and 2000 kg have a vast difference in post-capping behavior. In latter, P-delta phenomena are of major importance and the structure is not able to achieve high ductility and overstrength.

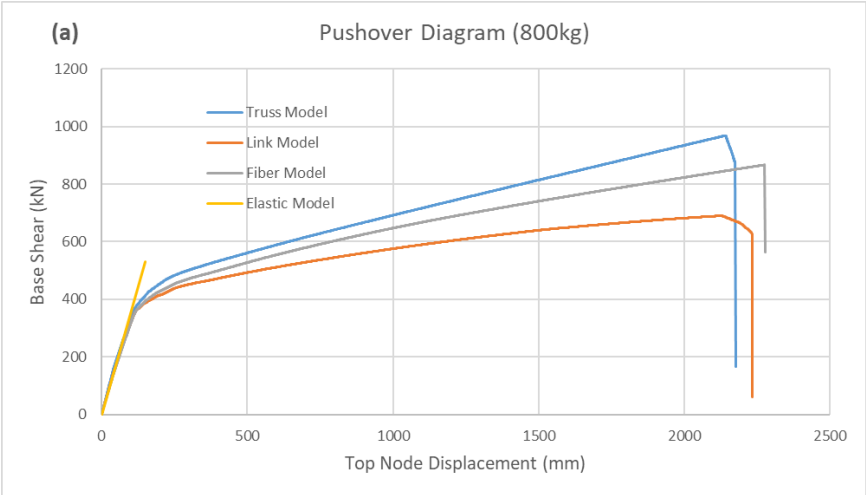

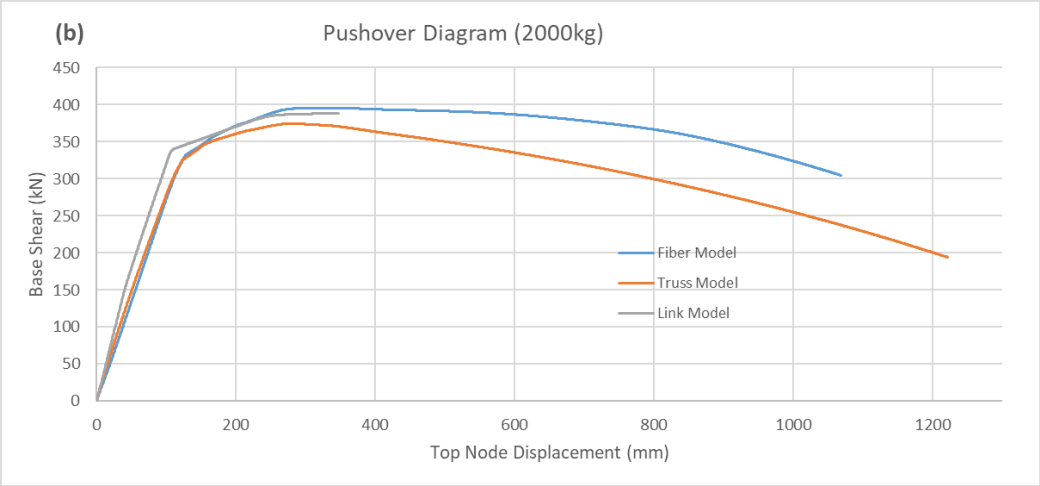

Figure 13: Base Shear vs Top Node Displacement of Pushover Analysis for the three models under examination; (a) 800 kg pallet load and (b) 2000 kg pallet load

3.5 Pushover Analysis

Nonlinear dynamic analyses were executed for the Truss and Link Model, and the time-history results are displayed in Figure 14a to 14d. Structural properties, geometry and distribution of masses were the same as in Pushover Analysis of 800 kg pallet load. In addition, both systems were assumed undamped, and thus residual oscillations are expected. It was observed that the Link Model was encouraging accurate, as it was able to predict adequately well the maximum displacement of the system.

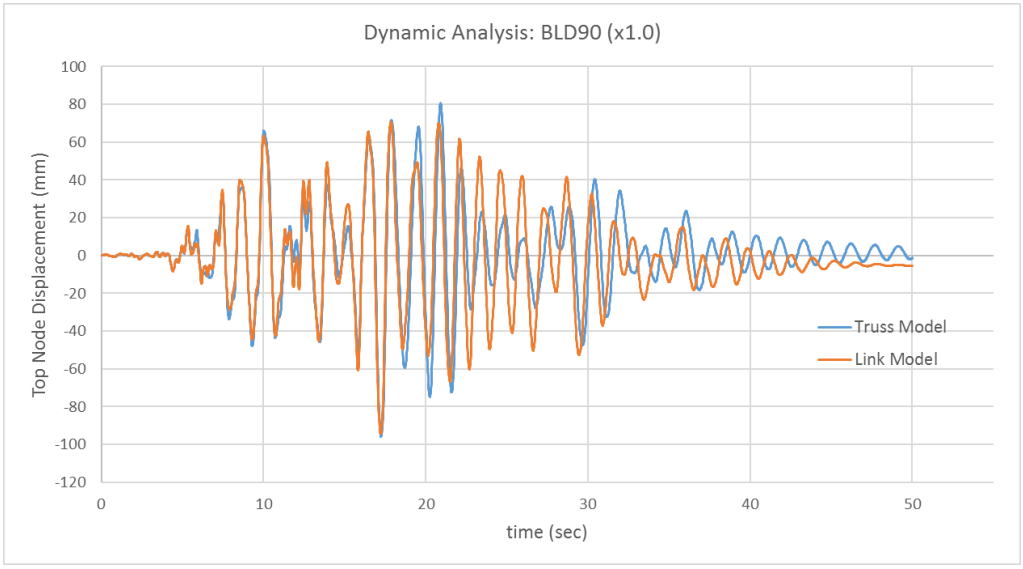

(a) Accelerogram BLD90 (x1.0)

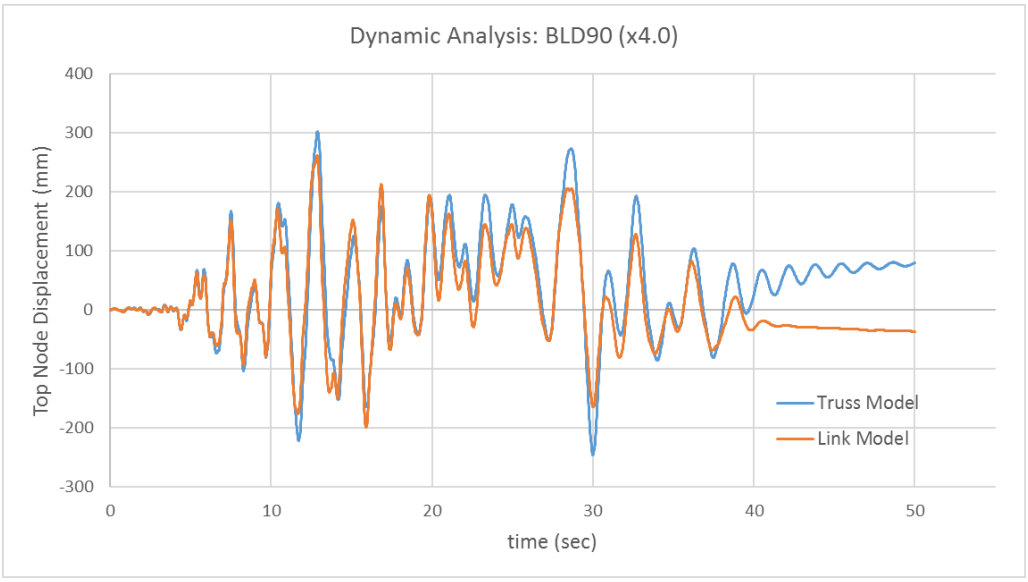

(b) Accelerogram BLD90 (x4.0)

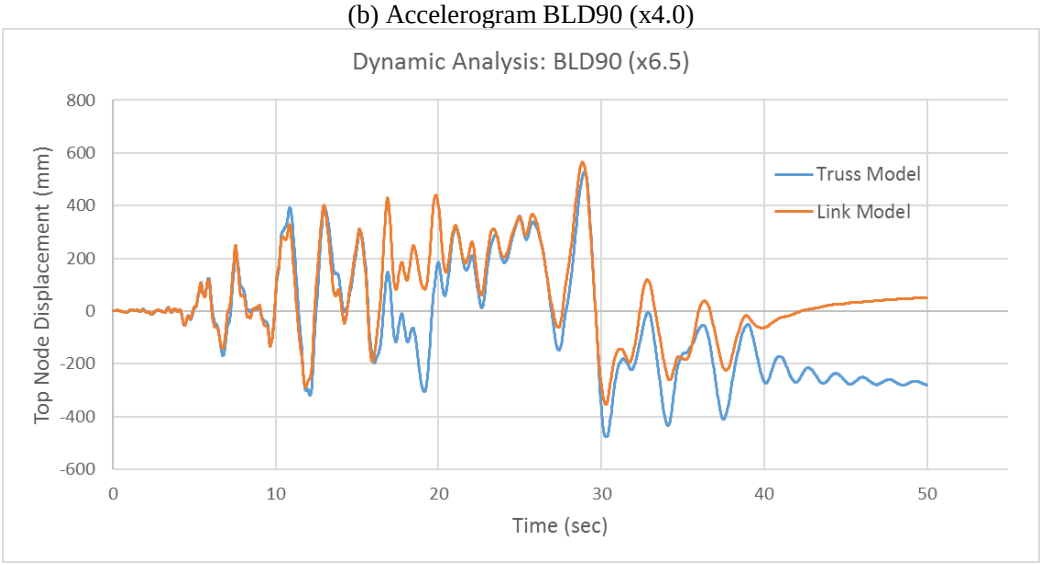

(c) Accelerogram, BLD90 (x6.5)

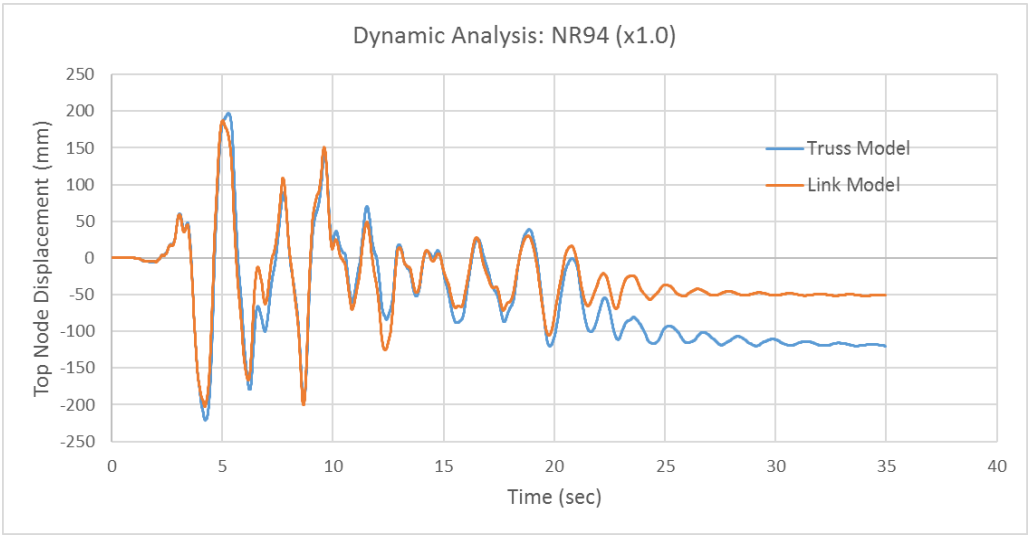

(d) Accelerogram NR94 (x1.0)

Figure 14: Results of time history analyses for the Truss and Link Model

4 CONCLUSIONS

The simplified method developed in present thesis was tested on a 2D Automated Rack Supported Warehouse frame for linear, nonlinear static and nonlinear dynamic analyses. In elastic region, the reduced-order model can predict extremely well even the higher eigenmodes of the real structure. A question remains about Linear Buckling Analysis, as upright's local buckling between bracings cannot be considered.

Concerning nonlinear analyses, the introduced model uses Two Node Link Elements to simulate the nonlinear response of upright frames and Timoshenko Beam Elements for the roof. In this specific test case, uprights were considerably stiff, so they did not participate in structure's plastic mechanism. Thus, we concentrated on bracings' compression and tension failure, which corresponds to shear degradation for the equivalent link element. As it was observed, X-column was "transformed" to Z-type after buckling of the diagonal bracing occurs and the system loses shear stiffness.

REFERENCES

[1] BS EN 15512-2009, *Terms and definitions,* Section 3

[2] EN 16681, *Low dissipative concept,* Section 8.3.2

[3] EU-RFCS Steel RTD Programme RFSR-CT-2004-00045 *SEISRACKS: Storage Racks in Seismic Areas,* 2004.12.01 - 2007.05.31

[4] EU-RFCS Steel RTD Programme RFSR-CT-2011-00031 *SEISRACKS2: Seismic Behavior of Steel Storage Pallet Racking Systems* 2011.07.01 - 2014.06.30.

[5] BS EN 15512-2009, *Simplified method for cross-aisle stability analysis in circumstances where there is uniform distribution of compartment loads over the height of the upright frame,* Annex G

[6] D.A. Tsarpalis, *Analysis of pallet racking systems with equivalent beam elements*, Master Thesis ISS MT 2018/10. Institute of steel structures, National Technical University of Athens, 2018

[7] BS EN 15512-2009, *Structural analysis,* Section 9

[8] http://opensees.berkeley.edu/

[9] EN 16681, *Structural types and behaviour factor*, Section 8.3

[10] Neuenhofer, A. and F. C. Filippou, *Evaluation of Nonlinear Frame Finite Element Models. Journal of Structural Engineering*, 123(7):958-966, 1997

COMPDYN 2019
7th ECCOMAS Thematic Conference on
Computational Methods in Structural Dynamics and Earthquake Engineering
M. Papadrakakis, M. Fragiadakis (eds.)
Crete, Greece, 24–26 June 2019

EXPERIMENTAL TESTS ON STEEL PLATES WITH CFRP STRENGTHENING

Konstantinos Vlachakis, Sofia Vlachaki-Karagiannopoulou and Ioannis Vayas

Institute of Steel Structures, National Technical University of Athens, Greece
e-mail: kostasvlachakis@yahoo.gr, sophia.vlachaki@gmail.com, vastahl@central.ntua.gr

Abstract

The application of Fiber Reinforced Polymer (FRP) strips is common for rehabilitation and strengthening of concrete structures. Still, the strengthening of steel profiles with FRPs has received little attention so far. In this direction, three tests were performed on steel plates strengthened with Carbon Fiber Reinforced Polymers (CFRP) at the Institute of Steel Structures, NTUA. They comprised one tensile and two four-point bending tests on composite specimens that consisted of one 3mm thick steel plate and one 1.2mm thick CFRP plate bonded together in order to make a preliminary estimation of the CFRP strengthening effect. The first four-point bending test was performed with the CFRP on the tension side, while the second test employed the CFRP on the compression side of the specimen. Analytical approaches as well as numerical nonlinear analyses using finite elements were employed to gain intuition and further substantiate the results. In conclusion, CFRP strengthening was found to be an effective strengthening method, which enhances ductility, tensile and bending capacity of the steel plate by almost five times, regardless of whether the CFRP is used under tension or compression. Notably, the CFRP plates, despite their slenderness were found to offer considerable resistance to compression stresses.

Keywords: Experimental tests, Carbon Fiber Reinforced Polymers (CFRP), Steel strengthening, numerical analyses, analytical procedure.

1 INTRODUCTION

The application of fiber-reinforced polymers (FRP) has been long established in teaching, research, design and regulation for strengthening and repair of concrete structures [1] – [4]. However, such an activity for steel structures is relatively new although strengthening of steel structures by means of FRPs has gained attention in recent times [5]. The main application fields refer to enhancing the moment capacity of steel or composite girders in building/bridge applications [6], [7], increasing the local buckling resistance of thin-walled compression elements [8], repair through crack-patching of fatigue prone details [9], or increase strength and ductility by means of confinement of steel or concrete filled steel tubes [10], [11]. It is therefore not surprising that, at least in Europe, there is a lack of regulations on the subject, except probably an Italian guideline [12], while the European seismic code for assessment and retrofitting of buildings [2] provides information for FRP-interventions in reinforced concrete structures only and not for steel or composite structures.

The potential for structural interventions in steel structures by means of FRPs is high, at least in some areas, despite the fact that conventional interventions with steel for steel structures are easier to implement than with concrete for concrete structures. Indeed, it is simpler to remove and repair damaged steel parts or entire structural members and easier to attach for strengthening purposes new to existing steel through welding or bolting, than remove, repair or strengthen through jacketing existing concrete members. An area where FRP composites might be applied with big advantages is for strengthening of masts and towers, like for telecommunication towers that are often in need of strengthening due to their occupation with more and larger antennas. Indeed, the classical method for strengthening tower legs where a second angle profile is added in a star battened configuration may be substituted by adhesive bonding of FRP plates to the existing angle profile. This leads to a smaller attack area of the strengthened member for the wind and a smaller periphery for the snow loading, leading to increased resistance and less loading, while the conventional method leads to increased resistance and higher loading. In addition, the operation could be handled easier due to less weight to be lifted, less space needed and, probably, lower susceptibility to environmental influences. Another area of potential beneficial application is for buildings in seismic areas where FRP plates could be attached to the beam flanges near the beam-to-column joints, in order to move the plastic hinges away from the joints, or added panel zones to increase their shear capacity. The interest for such research at European level appears to attract attention and is funded by the Research Fund for Coal and Steel (RFCS) in the ANGELHY project [13] and the German Academic Exchange Service (DAAD) in a project of hybrid strengthening methods [14].

Characteristic for these applications is that FRP composites are added in both tension and compression zones of elements, as well as in zones subjected to both compression and tension. Indeed, tower legs or bracing members may be subjected to compression or tension forces depending on the wind direction, flanges of beams in building frames in seismic areas are subjected alternatively to compression and tension, depending on the direction of the seismic excitation and the same happens to the applied shear forces of panel zones.

Design for FRP strengthening of steel elements is currently based on the nominal FRP material properties as supplied by the fabricators. These material properties, such as modulus of elasticity, tensile strength or elongation at fracture, refer exclusively to tension. Indeed, international test specifications for FRP material refer only to tensile testing, [15] to [18], obviously due to the fact that FRP material is predominantly used for tension and too thin to be directly tested for compression. The tension properties are also used, unchanged, in analytical formulae proposals for the prediction of the global or local buckling resistance of compression

members [8]. However, this approach may be questioned due to the fact that the compression resistance of FRPs is expected to be lower than the resistance to tension. It would be therefore beneficial to test the material under compression and check whether the compression properties are the same as for tension. Unfortunately, there is no international specification providing a test method, but for such a test the FRP material should be obviously attached to another element from the material that is intended to strengthen. Another issue, unspecified yet, is whether compression originates in the test from axial force or bending. For the current research it was accordingly considered necessary to investigate prior to the full-scale tests on angle leg columns, complete towers or beam-to-column joints, as planned in the relevant projects, the compression and tension behavior of FRP stripes bonded to steel plates. This would help the determination of the relevant properties and the correct design of the interventions.

This paper presents experimental, analytical and numerical investigations on the behavior of composite steel-CFRP specimens subjected to a tension and two four-point bending tests, one with the CFRP material on the tension side, the other on the compression side. The purpose was to determine the properties of FRP plates in tension separately from whether the tension arises from external axial forces or bending moments, and in compression arising from bending moments. Carbon fiber-reinforced polymer (CFRP) was used as composite material due to its high elastic modulus and tensile strength. The research was carried out in the frame of the MSc-Theses of the two first authors [19], [20].

2 GENERAL SPECIFICATIONS

The test specimens were constructed by the partner of the DAAD project [14] at the Brandenburg University of Technology (BTU) in Germany. They had the same dimensions and were made by the same materials. Each one was consisted by two parts, a 3mm thick steel plate with dimensions 80x250mm and a 1.2mm thick CFRP plate with the same dimensions (80x250mm). The two parts were bonded with a structural adhesive along their whole surface, with measured thicknesses of 1.3, 1.1 and 1.1 mm for the specimens 1, 2 and 3 respectively. Two aluminum tabs with dimensions 84x100x3mm were also used at the specimen's ends on the side of the CFRP plate, in order to protect the fibers and avoid a local failure or a fibers' break at the sections that are attached in the machine's grips in the tensile test or at the points of load application in bending tests. The side and plan view of the specimens are shown in Fig. 1, while Fig. 2 shows pictures of the specimens before testing.

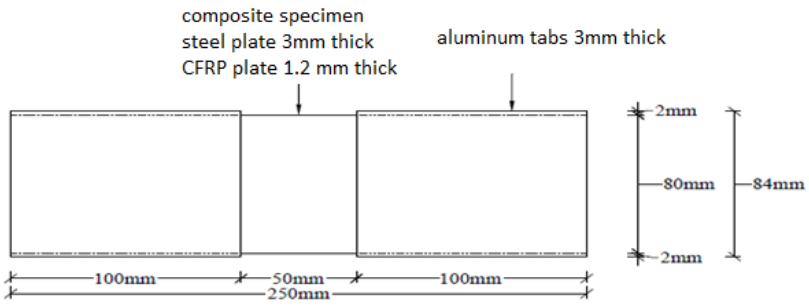

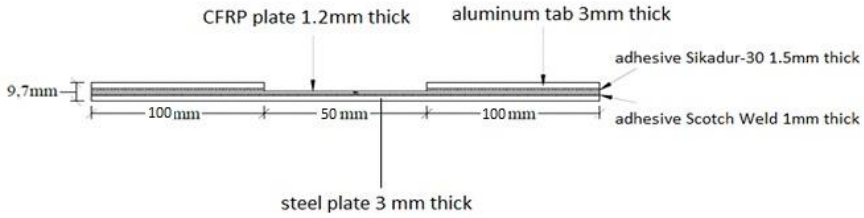

Figure 1: Plan and side view of the specimens

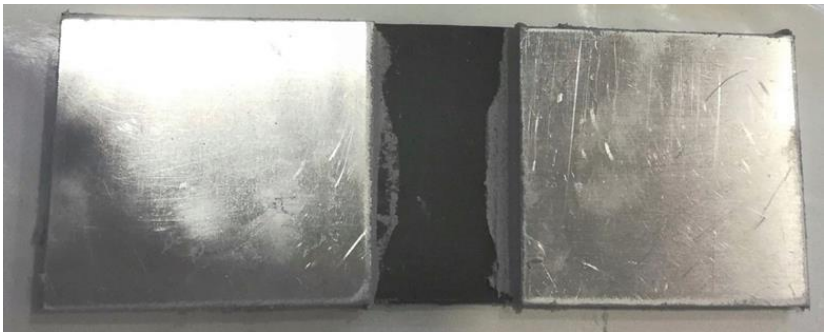

Figure 2: Picture of the specimen before testing

The mechanical properties of the constituent materials have been determined experimentally by tensile testing, carried out in an INSTRON 300XL universal machine with 300kN capacity. Steel has been tested by two tests in accordance with [21]. The resulting σ-ε-curve is shown in Fig. 3, the mechanical properties, as average from the two tests, in Table 1.

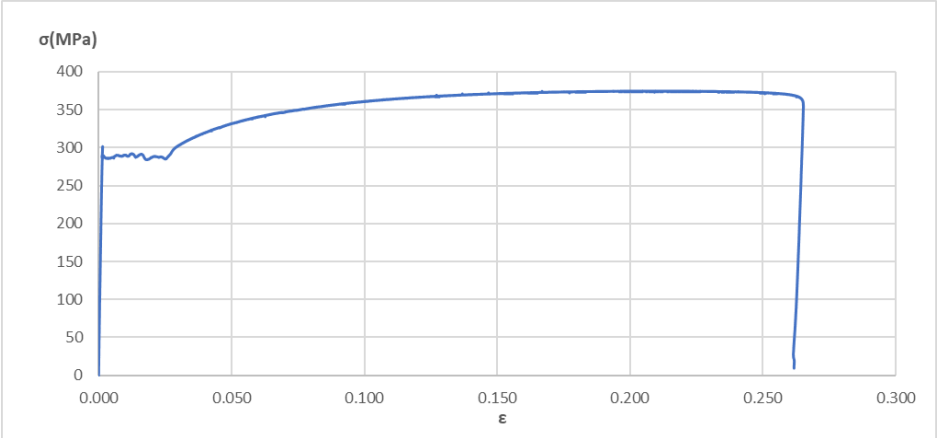

Figure 3: Experimental stress-strain curve for steel

E (MPa)	Yield stress σ_y (MPa)	Yield strain ε_y (%)	Hardening stress σ_R (MPa)	Hardening strain ε_R (%)	Ultimate stress σ_{max} (MPa)	Ultimate strain ε_{max} (%)
210000	287.5	0.1364	291	2.886	375	39.818

Table 1: Material properties of steel

The CFRP plates were made by MC Brauchemie and are considered as “low strength” plates. Their designation is 160/2400, i.e. the nominal modulus of elasticity is 160 GPa and the ultimate strength 2400 MPa. The plates were made using unidirectional fibers along the longitudinal axis of the plate. The actual mechanical properties have been determined by tensile tests on seven (7) specimens according to EN ISO 527-4 [16] and ASTM D638 -03 [17], D3039 [18]. The dimensions of the specimens were 300x25x1.5 mm, with their ends protected from the jaws of the machine by aluminum end tabs of dimensions 105x30x3 mm, as proposed by [16]. The loading speed was 1mm/min, lower than as specified in [16], in order to allow taking pictures by a thermic camera Flir B360 that was used to investigate if temperature changes take place in the material during the loading process. Strains were measured by both extensometer and strain gage. The material behaved linear elastic up to failure which was brittle and was due to the breakage of the carbon fibers, Fig. 4. Fig. 5 shows the resulting σ-ε-curves as derived from the extensometer and the strain gage measurements. The former indicates that slippage occurs between the extensometer and the specimen distorting the results. Accordingly, mechanical properties were determined on the basis of the strain gage measurements. The modulus of elasticity was determined by two methods: (a) as the slope of the curve between two predefined points with strains ε1 = 0,05% and ε2 = 0,25% proposed in [16] and (b) as the linear trendline of the σ-ε-curve from the origin up to failure. The average value from the tests was for method (a) ≈130 GPa, while for method (b) ≈141 GPa. Both methods delivered lower value than the nominal value provided by the producer, possibly due to the fact that only one strain gage was used on one side of the specimen so that effects of eccentricity were present. The average values for the ultimate stress was 2734 MPa, i.e. higher than the nominal value, as expected, and for the ultimate strain 1.91%.

Figure 4: CFRP specimens at failure

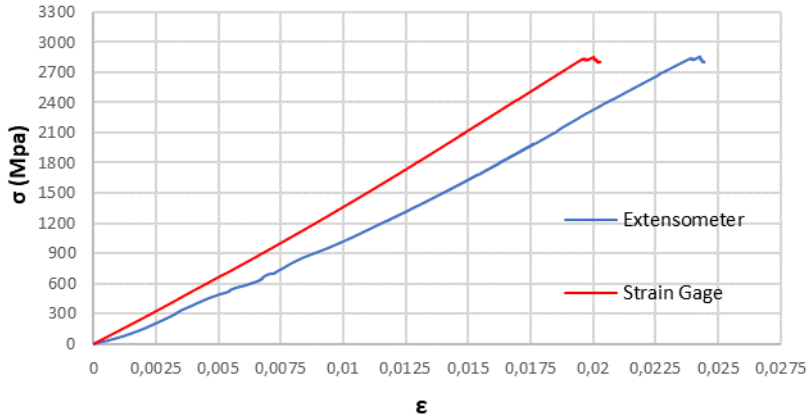

Figure 5: Experimental stress-strain curve for CFRP

The structural epoxy resin Scotch WeldTM DP 490 was used as adhesive to bond steel and CFRP plate, which is characterized by its simple and easy application and therefore recommended by its producer as appropriate for steel sections. Its ultimate shear stress τ_k and normal stress σ_k are estimated based on [5] and are shown in Table 2.

E_k (MPa)	Shear strength τ_k (MPa)	Shear modulus G_k (MPa)
3036	3.76	308.9

Table 2: Material properties of adhesive, average values

This adhesive was not strong enough to bond the aluminium tabs at the specimen's ends to the CFRP plates, so that Sikadur 30 from SIKA with nominal shear strength of 20 MPa was used instead.

As mentioned before, the specimens were fabricated at the Brandenburg University of Technology, Germany, following a specific procedure. Firstly, a special treatment using a hard brush was implemented to the steel surface, to increase the surface roughness in order to have better application of the adhesive. Then the surfaces of both steel and CFRP plates were cleaned with acetone. The adhesive was added using a special equipment, Fig. 6, to allow a uniform application of the adhesive with a thickness of approximately 0.2mm over the entire surface. For this purpose, small beads with diameter 0.105-0.20 mm made from glass were placed between the two surfaces as seen in Fig. 6. The two bonded plates remained under constant pressure for seven days until the adhesive reached its total strength. However, after this procedure the adhesive's thickness was measured, as well as possible, and was estimated to be 1.3, 1.1 and 1.1 mm for specimens 1,2, and 3 respectively.

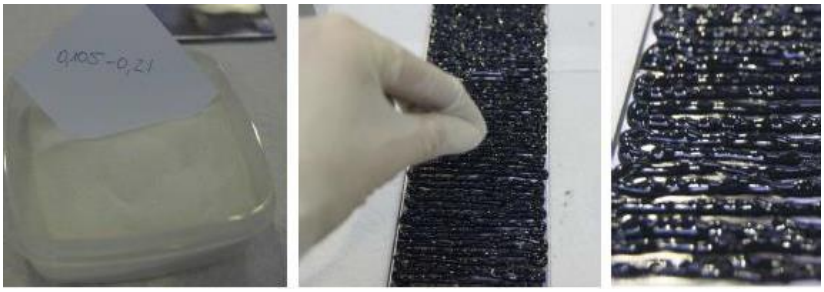

Figure 6: Application of the adhesive using special equipment

Subsequently, two aluminum tabs were also bonded on the CFRP side to protect it from the jaws of the machine. A different adhesive, Sikadur 30, was used to bond the aluminum plates to the CFRP plate**.** After that the three specimens remained seven more days under some heating lamps at a constant temperature of 33-36ºC, so that adhesive reaches its maximum strength.

3 TENSILE TEST

The tension test was carried out in the INSTRON 300XL machine. The specimen was loaded via displacement control at a testing speed of 0.2 mm/min, up to the maximum load capacity of the test machine, 300 kN, which is lower than its nominal failure load. Besides the load and the total elongation measured by the machine, strains on both the steel and the CFRP were measured by two strain gauges. The test set-up is shown in Fig. 7.

Figure 7: Test set-up for the tension test

The experimental force – displacement curve is shown in Fig. 8. The applied force is divided between the steel and the CFRP plates as in Fig. 9. It may be seen that steel behaves in the elastic-plastic, while CFRP purely in the elastic range. The force is distributed according to the stiffness of the constitutive parts as long as steel behaves elastic. When steel enters into the plastic region, it transfers only its yield force the other part transferred by the CFRP. This is because steel did not enter into the strain hardening region, as the strains measurements showed.

Assuming uniform strain distribution in the two materials, i.e. both materials are subjected to pure tension, the total force may be determined analytically and expressed by equations (1)

and (2). This assumption, which will be checked later, leads to acceptable results. This is shown in Fig. 8 where the simplified analytical curve is compared to the experimental curve.

$\varepsilon_s \leq \varepsilon_y$: $$P_{an} = E_s \cdot \varepsilon_s \cdot A_s + E_{cfrp} \cdot \varepsilon_{cfrp} \cdot A_{cfrp} \quad (1)$$

$\varepsilon_s > \varepsilon_y$: $$P_{an} = f_y + E_{cfrp} \cdot \varepsilon_{cfrp} \cdot A_{cfrp} \quad (2)$$

where:

E_s , E_{cfrp} are the modulus of elasticity of steel or correspondingly CFRP

ε_s, ε_{cfrp} are the, measured, strains of steel or correspondingly CFRP

A_s , A_{cfrp} are the cross-section areas of steel or correspondingly CFRP

ε_y, f_y are the actual yield strain and yield stress of steel

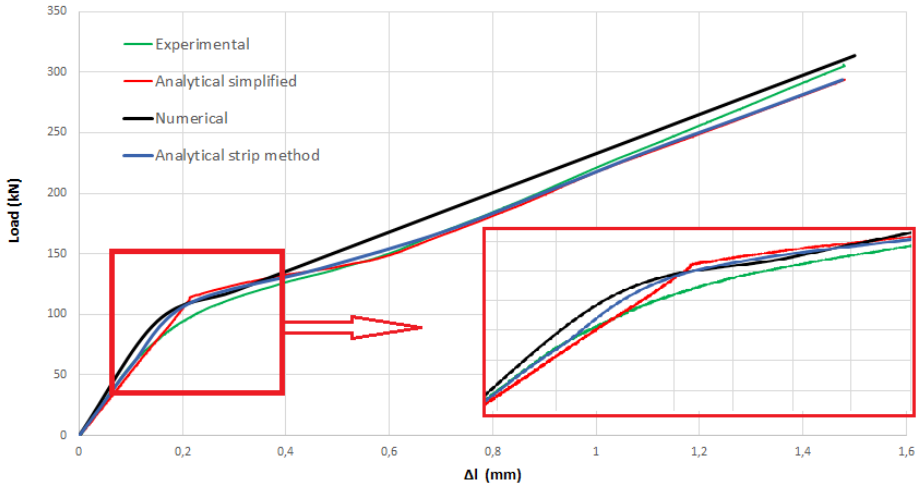

Figure 8: Experimental, analytical and numerical force – displacement curve

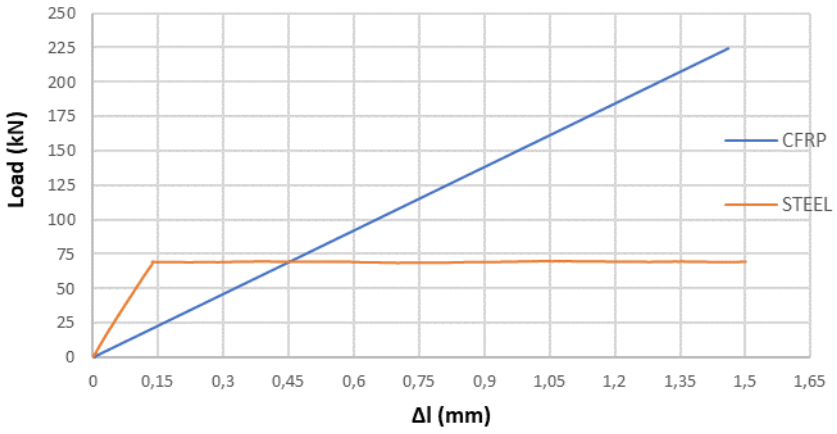

Figure 9: Partial forces transferred by the steel and CFRP plates

The specimen didn't reach failure at maximum load due to the limited capacity of the machine. However, the specimen exhibited a large permanent bow deformation after unloading as shown in Fig. 10, due to the fact that steel entered into the plastic range and exhibited a permanent tensile deformation. The corresponding plastic strain at unloading was measured by the strain gages as ε_{per} = 1,3%. This value is confirmed by appropriate geometrical measurements after the test and application of eq. (3).

$$\varepsilon_{perm} = \frac{1}{1-\frac{1}{\left(\frac{L/2}{f}\right)^2+1}} - 1 \quad (3)$$

where, Fig. 10:
f is the, measured, sagitta of the chord and
L is the, measured, chord length of the specimen.

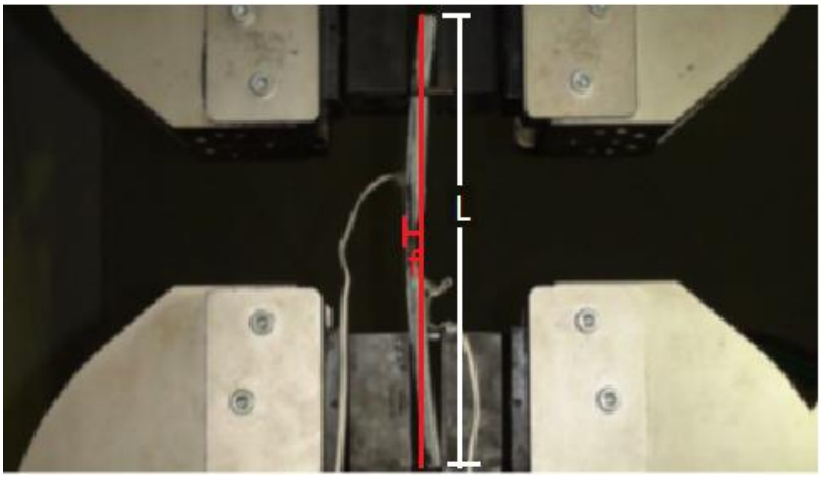

Figure 10: Permanent bow deformation after unloading. Steel on the tension (convex) side

The tension test was in addition investigated numerically using the ABAQUS Code [22]. Steel was modelled by application of solid elements of type C3D8R (Continuum solid element, 8-node linear brick, Reduced integration with hourglass control), while CFRP with shell elements of type S4R (Shell, 4-node double curved thick shell). The thickness of the shell was determined through the *Composite Layup*, by entering the number of carbon layers from which the CFRP is composed. Such a model is necessary when the orientation of the individual layers differs. In our case the same result could be achieved by a single layer with the total thickness. The end tabs and the epoxy resin were not included in the model. The interaction between steel and CFRP was introduced by connection of the two contact surfaces by means of tie constraints so that the two parts are rigidly connected with no slip between them.

The material properties of steel were introduced to follow the measured σ-ε-curve shown in Fig. 3. For the composite material the material properties were given separately for the fibers, type Graphite IM6 with modulus of elasticity E_f = 275.6 GPA, Poisson's ratio v = 0.2, ratio v_f = 51% and the matrix, type Epoxy 9310/9360 with E_m = 3.12 GPA, v_m = 0.38 and ratio v_m = 49%. The modulus of elasticity of the composite material in the longitudinal, 1, transverse, 2, and through thickness, 3, direction and the shear moduli are determined from eqs. (4) to (8) correspondingly [23]:

$$E_1 = E_f \cdot v_f + E_m \cdot v_m \quad (4)$$

$$E_2 = \frac{E_f \cdot E_m}{E_f \cdot v_f + E_m \cdot v_m} \quad (5)$$

$$E_3 = E_m \quad (6)$$

$$G_{12} = G_{13} = \frac{G_f \cdot G_m}{G_m \cdot v_f + G_f \cdot v_m} \quad (7)$$

$$G_{23} = G_m \quad (8)$$

where:

v_f, v_m are the fibers ratio and the matrix ration correspondingly and
$G = E / [2 \cdot (1+\nu)]$ for the fibers, f, and the matrix, m.
The Poisson's ratio of the composite material may be determined from:

$$\nu_{12} = \nu_{13} = \nu_f \cdot \nu_f + \nu_m \cdot \nu_m \quad (9)$$

$$\nu_{23} = \nu_m \quad (10)$$

The numerical model included the specimen over its entire length, but at the end regions where the jaws are acting the relevant displacements were restrained so that one end is fixed and the other can move freely in direction of the load application. The force – displacement curve of the numerical model is illustrated in Fig. 8, together with the experimental and analytical curves. The comparison shows a quite good agreement with the experimental and analytical results, indicating that the adopted input material parameters and the assumption of no slip between the two materials are acceptable.

However, the numerical model allows the determination of the strain and stress state separately in the two material as shown in Fig. 11 and 12. It may be seen that the stresses, and strains, at the external and internal surfaces of steel are not identical. Strains therefore vary through the specimen's thickness as shown in Fig. 13. The actual strains measured during the test were ε_{so} and ε_{cfrp} at the specimen's surface, which are similar but not identical to the strains at the centroids of the corresponding materials. The corresponding stress distribution gives rise to an internal moment that was calculated analytically by the strip method and numerically with ABAQUS and is shown in Fig. 14. This moment is in equilibrium with the external moment, calculated as the product between the applied force and the eccentricity between this force and the centroid of the composite section, calculated from eq. (11). The external moment is also illustrated in Fig. 14. There is a discrepancy between the curves of the external and internal moment that is due to the approximations made in the calculations of both. More specifically, the calculations for the internal moment assume pure axial tension with no moment in the initial loading steps, while moments arise later due to plasticity. On the other side, the external moment starts to develop from the beginning and is affine to the applied force since the eccentricity is considered unchanged during the test.

Besides the moment, the strip method was applied to calculate the axial force by integration of the axial forces in the individual strips. The relevant analytical curve is shown in Fig. 8. The comparison with the experimental curve indicates that the strip method is more accurate to the simplified one in the elastic region, while the two converge at larger strains in the plastic region of steel.

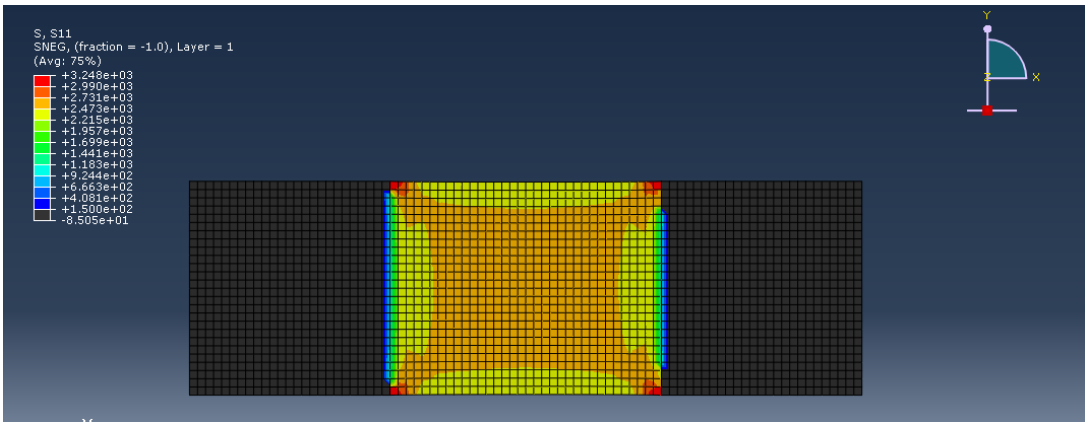

Figure 11: Stress distribution in the CFRP plate

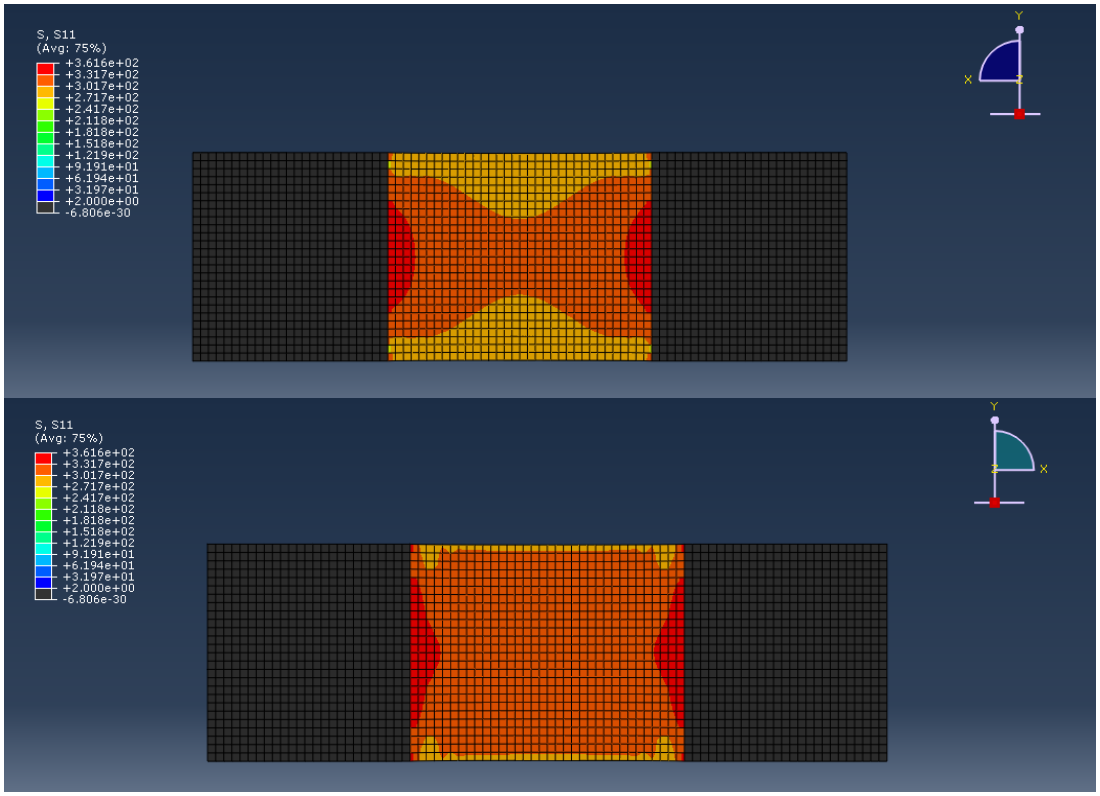

Figure 12: Stress distribution in the external and internal face of steel

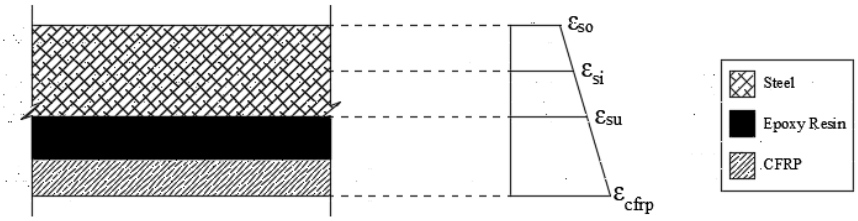

Figure 13: Actual strain distribution in the composite specimen

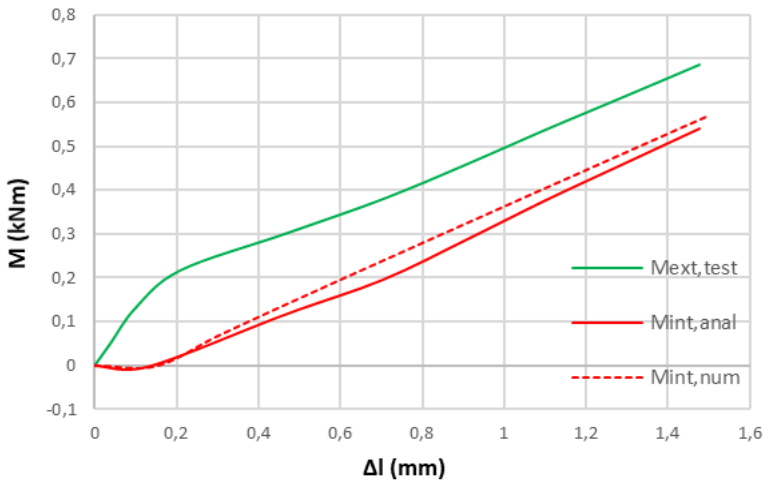

Figure 14: Moment – displacement curve of the specimen

4 FOUR-POINT BENDING TEST – FRP ON THE TENSION SIDE

The test set-up for the 4-point bending test, which was carried out in the INSTRON 300XL machine, is shown in Fig. 15. The specimen was loaded via displacement control at a testing speed of 0.42 mm/min. The recordings included the applied load, the deflection at mid-span, both measured from the machine recordings, and the strains of the steel and the FRP-plate at midspan, measured by two strain gauges. At late loading stages no steel's strain data were available because the strain gauge at the compression side was disconnected due to very high strains. Small slips also occurred at certain times during the test.

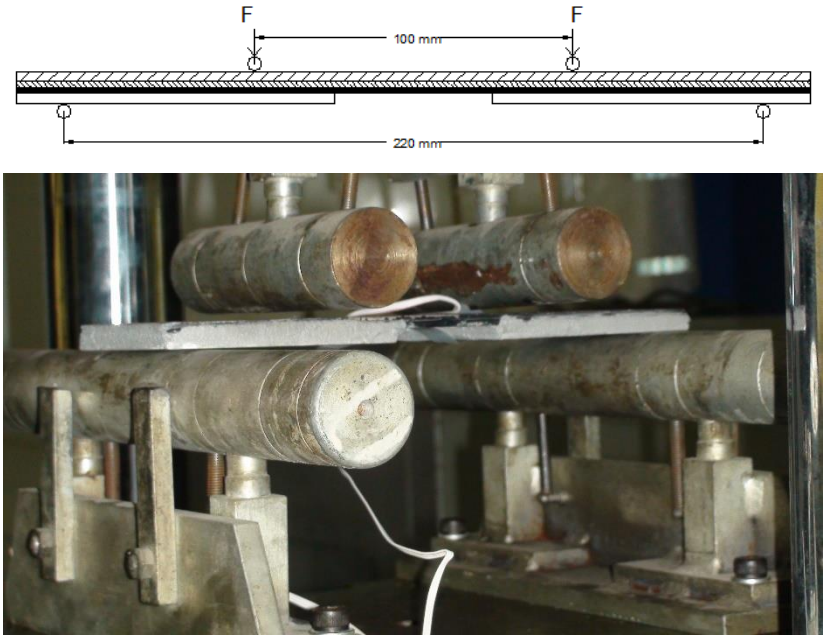

Figure 15: Test set-up for the 4-point bending test – CFRP in tension

The experimental force – deflection curve is shown in Fig. 16. At some points the load drops indicating small slips between the specimen and the supports. The experimental test was accompanied by analytical and numerical calculations. For the former two methods were adopted.

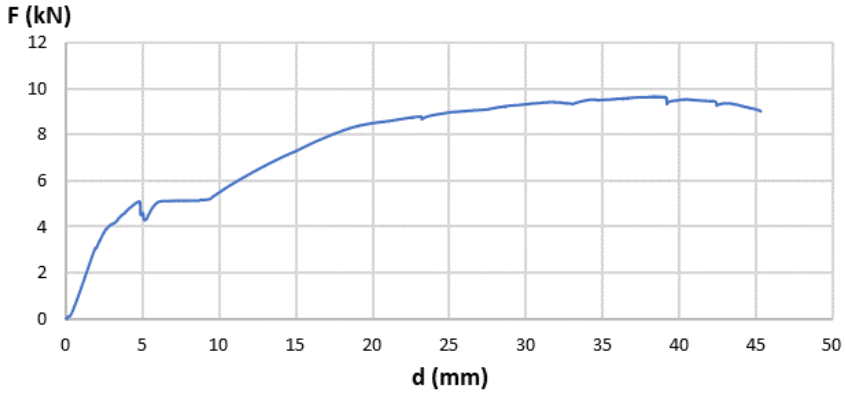

Figure 16: Experimental force – mid-span deflection curve

- Analytical Method 1

This is based on the Bernoulli-Euler beam theory for linear strain distribution over the cross section, Fig. 17. The centroid of the cross section, distance from the top side, is calculated from eq. (11):

$$zc = \frac{zs*As+(z_{res}*\frac{A_{res}}{n_{res}})+(z_{CFRP}*\frac{A_{CFRP}}{n_{CFRP}})}{As+\frac{A_{res}}{n_{res}}+\frac{A_{CFRP}}{n_{CFRP}}} \quad (11)$$

where:
z_s, z_{res}, z_{cfrp} are the centroids of steel, resin or CFRP correspondingly
A_s, A_{res}, A_{cfrp} are the cross-section areas of steel, resin or CFRP correspondingly
E_s, E_{res}, E_{cfrp} are the moduli of elasticity of steel, resin or CFRP correspondingly
$n_{res} = E_s/E_{res}$ is the modular ratio of the resin
$n_{cfrp} = E_s/E_{cfrp}$ is the modular ratio of the CFRP

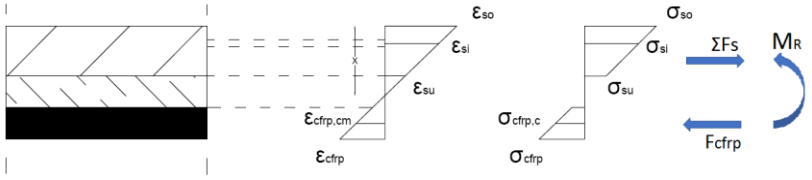

Figure 17: Calculation procedure for the internal moment – Analytical method 1

Starting from the strains as measured during the test, the internal moment is determined by the strip method as indicated in Fig. 17 neglecting the contribution of the resin. The analytical moment – deflection curve is illustrated in Fig. 18 and compared with the experimental one. The disadvantage of the analytical method 1 is that no experimental strain data are available at the late loading steps so that the moment can be calculated up to a certain point (up to a deflection 25 mm in Fig. 18).

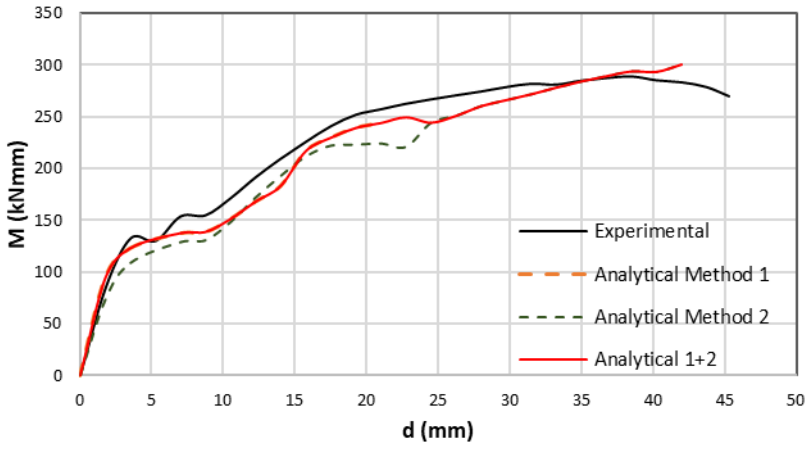

Figure 18: Experimental and analytical moment – deflection curves

- Analytical Method 2

In this method the computation process is reversed. The tension force in the CFRP, acting at its centroid, is determined from eq. (12):

$$F_{cfrp} = E_{cfrp} \cdot \varepsilon_{cfrp} \cdot A_{cfrp} \quad (12)$$

where:

ε_{cfrp} is the strain at the CFRP centroid of the CFRP. It is taken as ½ of the measured CFRP strain, since the plastic neutral axis of the composite section is considered to be within the adhesive.

The tension force in the CFRP is equal for equilibrium reasons to the compression force in steel, Fig. 19. The stress distribution in steel is assumed uniform across its thickness. The steel stress is determined from measurements as long as strain data for steel are available. After it, the steel stresses are estimated under consideration of strain hardening. The so calculated moments are shown in Fig. 18.

It may be seen that despite the missing strain measurements, method 2 is appropriate for the late loading steps at large strains where steel is yielding and strain hardening, while method 1 fits better for the early loading steps. Fig 18 shows that the combination of the two methods may provide a good estimate of the specimen's response.

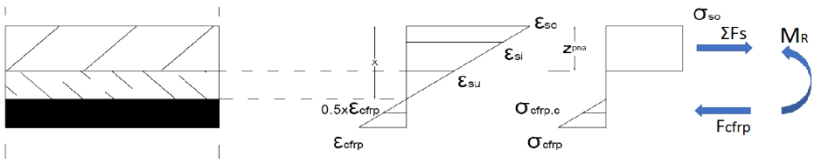

Figure 19: Calculation procedure for the internal moment – Analytical method 2

The bending test was also investigated numerically with the same modelling using the ABAQUS Code as previously described. Fig. 20 shows the test specimen in its deformed shape, together with the corresponding numerical model.

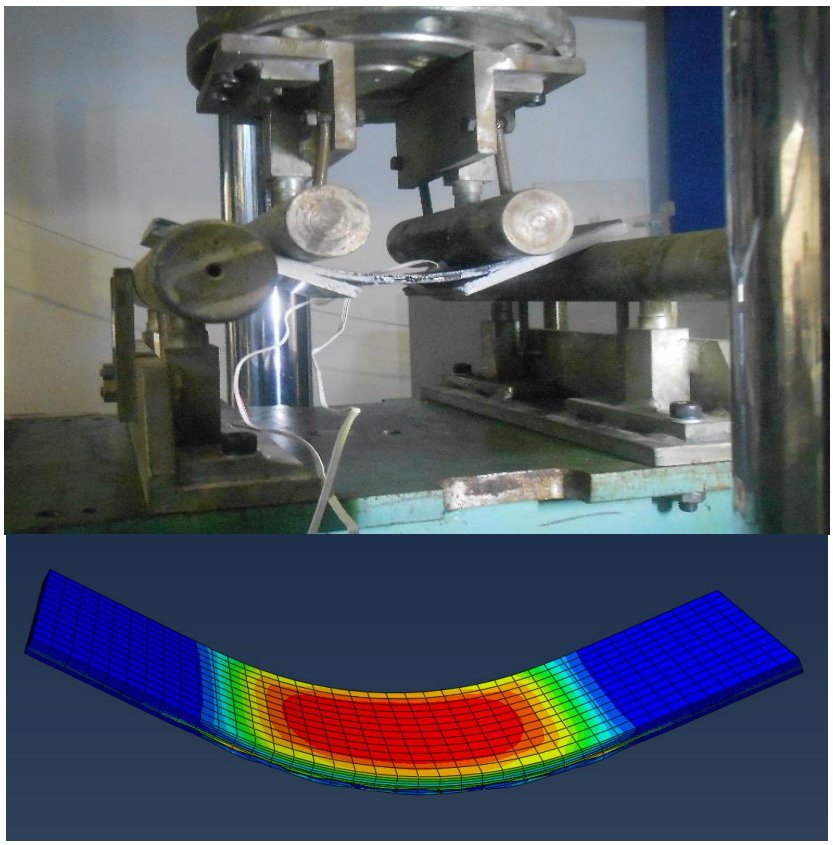

Figure 20: Experimental and numerical model at its deformed state

The calculations included MNA and GMNA analyses, where in the former only the material non-linearity and in the latter the geometric and material non-linearity were considered. Fig 21 shows the experimental and numerical results. It may be seen that the numerical results fit well with the experimental ones, especially when the effects of slip are removed from the experimental ones. The numerical models, especially the GMNA analysis, predict a smaller capacity due to the neglect of any contribution of the adhesive. However, the initial stiffness is very close to the experimental one.

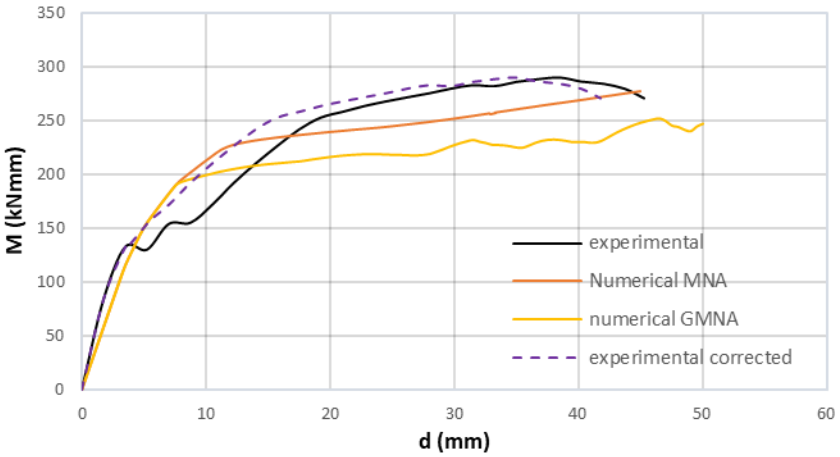

Figure 21: Experimental and numerical moment – deflection curves

5 FOUR-POINT BENDING TEST – FRP ON THE COMPRESSION SIDE

The test set-up, the measurements and all other data are the same as before, except that the specimen is put upside down, so that the CFRP is on the compression side, Fig. 22. For the same reasons as before, at late loading stages no CFRP strain data were available because the strain gauge was disconnected at the compression side due to very high strains.

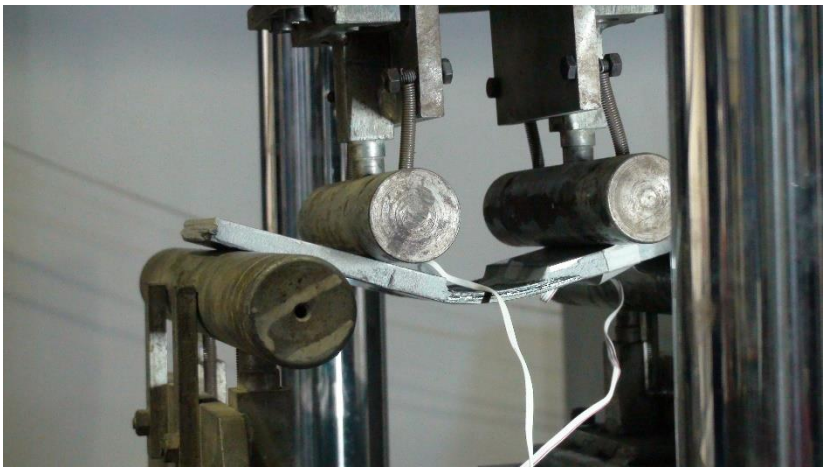

Figure 22: Test set-up for the 4-point bending test – CFRP in compression

Fig. 23 shows the experimental and analytical moment – deflection curves. The analytical curves were determined by the two methods described before. It may be seen that the combination of methods 1 and 2 provides acceptable results, even if the contribution of the resin

was neglected. Based on the analytical calculations, the compression strength of the CFRP is estimated to be 640 MPa.

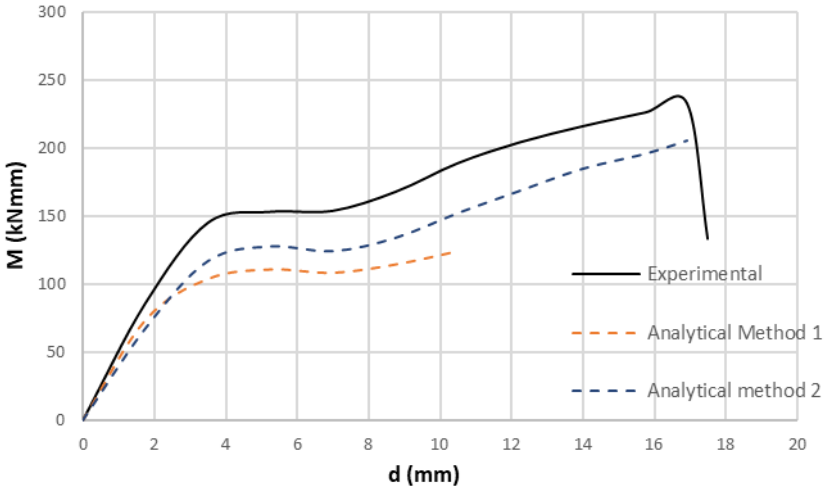

Figure 23: Experimental and analytical moment – deflection curves

This test was also studied numerically using the same model as in the other tests. Especially, the material properties of the CFRP were taken as those for tension. Both MNA and GMNA analyses were performed. The deformed shape of the model for the GMNA analysis is shown in Fig. 24 and may be compared to the deformed shape of the experimental model shown in Fig. 22.

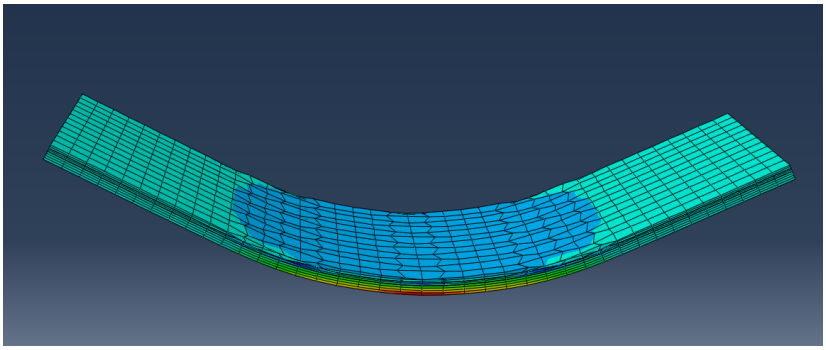

Figure 24: Deformed shape of the numerical model by GMNA analysis

Fig. 25 shows the experimental and numerical moment - deflection curves. It may be seen that for this test the GMNA analysis provides better results. However, the numerical analyses cannot predict the moment capacity due to the fact that for the CFRP material the linear elastic tension properties were introduced. Accordingly, the large deflections predicted numerically are not realistic if the tension properties of the material are adopted. Based on the stresses of the numerical model at the maximal deflections of the experiment, the compression strength of the CFRP is estimated as 700 MPa, which is similar to 640 MPa as determined with the analytical model. This is around 30% of the nominal tension strength. However, it should be noted that no local buckling occurred in this test.

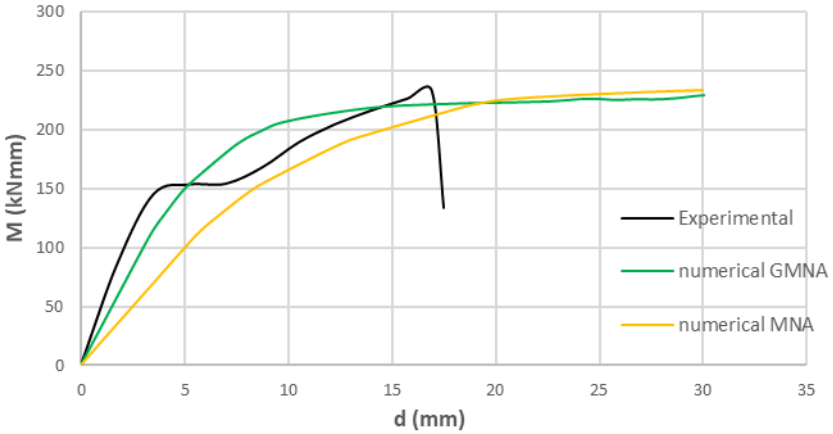

Figure 25: Experimental and analytical moment – deflection curves

The numerical model was further on used to calculate the 4-point bending response of the steel plate alone without any CFRP strengthening. Fig. 26 compares the derived curve in comparison with the experimental curves of the same steel plate strengthened with CFRP on the tension or the compression side. It may be seen that the bending capacity of the steel plate increased almost 6 times by strengthening it with CFRP in the tension side. When the CFRP was placed on the compression side this increase was less, around 4.6 times, confirming the lower strength of CFRP when it is used for compression. However, the stiffness of the strengthened specimens was equal indicating that the same modulus of elasticity may be used for the CFRP either in compression or tension. Important is that the ductility of the composite specimen is exhausted when the CFRP material is reaching its compression capacity.

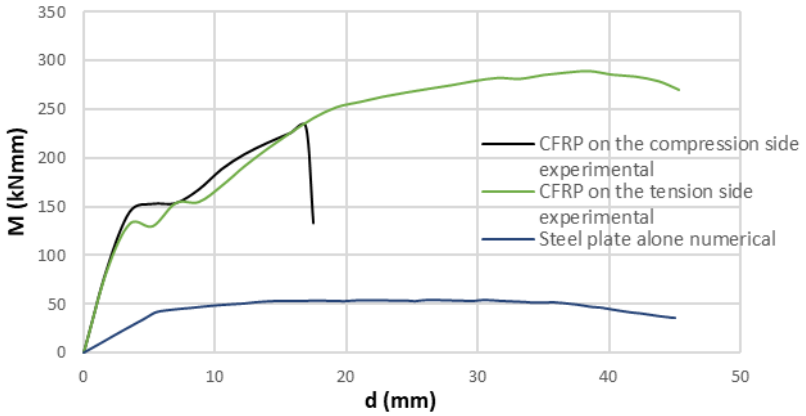

Figure 26: Moment – deflection curves for steel plates with and without CFRP reinforcement subjected to 4-point bending

6 CONCLUSIONS

The behavior of steel plates reinforced in one side with carbon fiber reinforced polymer (CFRP) has been studied experimentally, analytically and numerically. The properties of the source material have been determined experimentally. Subsequently, the composite material has been subjected to tension tests and four-point bending tests with the reinforcement on the tension and the compression side. The test material has been prepared in BTU Cottbus, Germany, while the tests have been executed in NTUA, Athens, Greece. Analytical relations have been derived on the basis of the Bernoulli assumption of linear strain distribution in the cross

section and numerical investigations with application of the FEM have been performed. From the studies carried out following conclusions may be drawn:

1. One-sided strengthened steel plates subjected to axial tension forces exhibit permanent bow deformations after unloading due to irreversible plastic deformations of steel.
2. Existing analytical relations for defining the properties of the CFRP plates in relation to the properties of the two constituent materials, the carbon fibers and the matrix, have been confirmed.
3. The modulus of elasticity of CFRP was equal, whether the CFRP was in the tension or in the compression side.
4. The strength of the CFRP was different for compression and tension, the former being a fraction of the latter.
5. The assumption of a composite section from two different materials, the Bernoulli assumption of linear strain distribution in the cross-section and the assumption of no slip between the two constituent materials are valid for this type of strengthening, provided that appropriate adhesives are used and their application follows the relevant specifications for their connection.
6. Design for CFRP strengthening of steel elements where the CFRP is in the tension side may be based on the nominal material properties of CFRP as determined by the specified tensile testing.
7. For CFRP strengthening of steel elements where the CFRP is in the compression side, only the modulus of elasticity of CFRP as determined by the tensile testing may be used, while its strength must be reduced
8. Four-point bending tests of the composite material with no local buckling as outlined here, where the CFRP is in the compression side are appropriate to define the properties of the CFRP material to compression.

ACKNOWLEDGEMENTS

The financial support of the Deutscher Akademischer Austauschdienst (DAAD) through the project “Verstärkungsmaßnahmen und innovative Messmethoden im Stahlbau“ and of the Research Fund of Coal and Steel (RFCS) through the project ANGELHY is gratefully acknowledged.

REFERENCES

[1] FRP EBR (2001), Design and use of externally bonded FRP reinforcement, FIP

[2] EN 1998-3 (2005). Eurocode 8. Earthquake resistant design of structures. Part 3 Assessment and retrofitting of buildings, European Committee for Standardization (CEN), Brussels, Belgium.

[3] ACI 440.2R-02 (2002), “Guide for the Design and Construction of Externally Bonded FRP Systems for Strengthening Concrete Structures”, American Concrete Institute

[4] National Cooperative Highway Research Program NCHRP Report 514 (2004), “Bonded Repair and Retrofit of Concrete Structures Using FRP Composites”

[5] Teng JG, Yu T, Fernando D (2012). Strengthening of steel structures with fiber-reinforced polymer composites, J. of Constructional Steel Research, Elsevier, 78, 131-143.

[6] Al-Saidy AH, Klaiber FW, Wipf TJ (2004), Repair of steel composite beams with carbon fiber-reinforced polymer plates, J. of Composites for Construction (ASCE), 8(2), 163-172

[7] Miller TC, Chajes MJ, Mertz DR, Hastings JN (2001), Strengthening of a steel bridge girder using CFRP plates, J. of Bridge Engineering (ASCE), 6(6), 514-522

[8] Silvestre N, Young B, Camotim D (2008) Non-linear behavior and load-carrying capacity of CFRP -strengthened lipped channel steel columns, Engineering Structures, 30, 2613-2630

[9] Bassetti A, Nussbauer A, Colombi P (2000), Repair of riveted members damaged by fatigue using CFRP materials, Advanced FRP Materials for Civil Structures, Bologna, Italy, 19th October, 33-42

[10] Haedir J, Zhao XL (2011), Design of short CFRP-reinforced steel tubular columns, J. of Constructional Steel Research, Elsevier, 67, 497-509

[11] Hu YM, Yu T, Teng JG (2011), FRP-confined circular concrete-filled thin steel tubes under axial compression, J. of Composite Construction (ASCE), 15(5), 850-860

[12] CNR-DT 202 (2005), "Guidelines for the Design and Construction of Externally Bonded FRP Systems for Strengthening Existing Structures – Metallic Structures", CNR, Rome, 2007

[13] EU DG Research and Innovation, Grant agreement 753993 – ANGELHY, 2017

[14] Deutscher Akademischer Austauschdienst (DAAD), Project 57339810, Verstärkungsmaßnahmen und innovative Messmethoden im Stahlbau, 2017

[15] ISO 527-1 (2012). Plastics: "General principles for determination of tensile properties"

[16] ISO 527-4 (1997). Plastics: "Test conditions for isotropic and orthotropic fiber-reinforced plastic composites"

[17] ASTM D638 – 03 (2003) "Standard Test Method for Tensile Properties of Plastics"

[18] ASTM D3039/D3039M – 17 (2017). "Standard Test Method for Tensile Properties of Polymer Matrix Composite Materials"

[19] Vlachaki-Karagiannopoulou S (2018) Behavior of fiber reinforced polymers with experimental and analytical methods, MSc-Thesis, NTUA

[20] Vlachakis K (2018) Analysis and design of a telecommunication steel tower strengthened with FRP plates, MSc-Thesis, NTUA

[21] EN ISO 6892-1 (2009), "Metallic materials - Tensile testing: Method of test at room temperature"

[22] ABAQUS (2008). *ABAQUS User's Manual*. Version 6.14, Dassault Systems Simulia Corp., Providence, RI, USA

[23] Pederson J (2008). Finite Element Analysis of Carbon Fiber Composite Ripping using Abaqus, All Theses, Paper 512, Clemson University, Clemson, SC

COMPDYN 2019
7th ECCOMAS Thematic Conference on
Computational Methods in Structural Dynamics and Earthquake Engineering
M. Papadrakakis, M. Fragiadakis (eds.)
Crete, Greece, 24–26 June 2019

EFFECT OF ARCHITECTURAL NON-STRUCTURAL COMPONENTS ON LATERAL BEHAVIOUR OF CFS STRUCTURES: SHAKE-TABLE TESTS AND NUMERICAL MODELLING

Alessia Campiche[1] and **Sarmad Shakeel**[1]

[1] Department of Structures for Engineering and Architecture

University of Naples "Federico II", Naples; Italy
e-mail: alessia.campiche@unina.it

sarmad.shakeel@unina.it

Abstract

This paper illustrates the effect of architectural non-structural components on the variation of dynamic properties and lateral seismic behaviour of Cold-Formed steel (CFS) buildings, using shake-table tests and numerical modelling. The seismic behaviour of a two-storey gypsum-sheathed building was investigated as a part of European project ELISSA. Shake-table tests were carried-out on this building under two different configurations: with and without architectural non-structural components. Dynamic properties, such as fundamental period and damping ratio, of both building configurations were evaluated and compared. Numerical models considering all the architectural non-structural components were developed in Opensees environment. Results highlight the importance of considering the contribution of architectural non-structural components, such as finishing materials of shear and gravity walls, partition walls and internal counter walls, in the process of structural analysis and modelling of CFS buildings.

Keywords: CFS structures, Shake-table test, Non-Structural Components, OpenSees modelling.

1 INTRODUCTION

Nowadays, Cold-Formed Steel (CFS) structures are often preferred to the traditional constructions as low-rise buildings in seismic areas due to their light weightiness and good seismic performance [1]. In fact, in the last decades numerous studies on elements [2–4], components [5–12] or whole buildings [13–15] have evaluated their seismic response. Although structural behaviour has been deeply investigated, only few experimental and numerical works have been carried out for the evaluation of the influence of architectural non-structural components on the global seismic response [16,17]. As demonstrated, the presence of non-structural architectural components offers a big contribution to the lateral resistance and stiffness of structure, but the current seismic design of CFS buildings does not take into account that contribution. To overcome this lack, as a part of European project ELISSA, the main task of University of Naples "Federico II" was the design and the execution of shake-table tests on full-scale two-storey CFS building in two different construction phases, which differ for the presence of architectural non-structural components. The influence of finishing material and other non-structural architectural components, i.e. partition walls and internal counter walls, on the dynamic properties of the structure (fundamental period of vibration and damping) has been evaluated, through the experimental results and numerical modelling. This paper summarises the experimental campaign and 3D building models developed in Opensees [18] software, focusing on the effect produced by non-structural architectural components on the seismic response.

2 EXPERIMENTAL CAMPAIGN

2.1 General

An experimental campaign aimed to deepen the knowledge of structural behaviour of CFS constructions, subjected to seismic excitations, was carried out at the Department of Structures for Engineering and Architecture of University of Naples "Federico II". In particular, the influence of architectural non-structural components on the seismic behaviour was investigated through cyclic tests and shake-table tests. The cyclic tests were carried out on two full-scale gypsum-sheathed shear wall configurations, which differ only for the presence of finishing and insulating materials, whereas shake-table tests were carried out on a full-scale 3D building mock-up with and without architectural non-structural components. In particular, the wall specimen without finishing and insulating materials is named as B wall Configuration, while the specimen wall with finishing and insulating materials is named as C wall Configuration. Equally, the building mock-up without architectural non-structural components is named as B mock-up Configuration, while the building mock-up in which the architectural non-structural components were added is named as C mock-up Configuration. The B and C wall Configurations were representative of the shear walls used in the B and C mock-up Configurations, respectively. More details about the research project are available in Landolfo et al. [19].

2.2 Shear wall testing

The effect of the presence of finishing materials was evaluated through cyclic tests. The wall specimens had a dimension of 2.4 × 2.3 m (length x height). The two wall configurations are shown in Fig.1. The steel frame of specimens was mainly composed of intermediate and chord studs and tracks. The studs had 147×50×10×1.5 mm (outside-to-outside web depth × flange size × lip size × thickness) lipped channel (C) sections mainly spaced at 625 mm on the centre. Tracks had 150×40×1.5 mm (outside-to-outside web depth × flange size × thickness)

unlipped channel (U) sections. All the steel members were made of S320GD+Z steel (characteristic yield strength: 320 MPa, characteristic ultimate tensile strength: 390 MPa). The steel frame was sheathed with 15.0 mm thick impact resistant gypsum board on both sides. In order to withstand the axial force due to overturning phenomena, back-to-back coupled studs and ad-hoc designed hold-down devices were placed at the wall ends. For the second test (C wall Configuration), the wall specimen was completed with insulation mineral wool, inserted among steel studs. The internal face was completed with an internal counter wall made of 20 mm thick vacuum insulated panel attached to the structural wall, 50×50×0.6 mm C vertical profiles spaced at about 600 mm, 50×40×0.6 mm U horizontal tracks, 50 mm thick insulation mineral wool. The steel frame of the internal counter wall was sheathed with double layer of 15 mm thick impact resistant gypsum board panels. The external face was completed with a ventilated façade made of a water proof membrane, 25×100 (outside-to-outside web depth × outside-to-outside flange size) slotted Ω horizontal profiles spaced at about 400 mm on the centre, sheathed with 12.5 mm thick cement-based outdoor board panels and finished with fibreglass mesh and cement plaster. Tests on wall specimens were conducted under displacement control in the reversed cyclic regime. The CUREE protocol, developed by Krawinkler et al. [20], was used.

Results are presented in the form of a comparison of cyclic behaviour obtained for the B and C Configurations walls (Fig. 2). Test results are shown in Table 1 in term of peak resistance per unit length (F_{max}/L), elastic resistance per unit length (F_e/L), which is the 40% of maximum resistance, drift corresponding to F_e (d_e/H), ultimate drift corresponding to a load equal to $0.80 \cdot F_{max}$ on the post-peak branch of the response curve (d_u/H) and conventional elastic stiffness per unit length (k_e/L) assumed equal to F_e / (L d_e). For both specimens the wall collapse was mainly governed by the tilting and pull-out of sheathing-to-frame connections. At global level, the steel frame deformed as a parallelogram with a consequent rigid rotation of the sheathing panels. In the case of C wall Configuration, the detachment of the sheathing panel, together with the wall lining of the internal face was also occurred for inter-storey drift ratios (IDR) higher than 4%. The presence of the finishing gave an increase in average of 48% for the wall strength and 39% for wall stiffness. Further details are available in Macillo et al. [21].

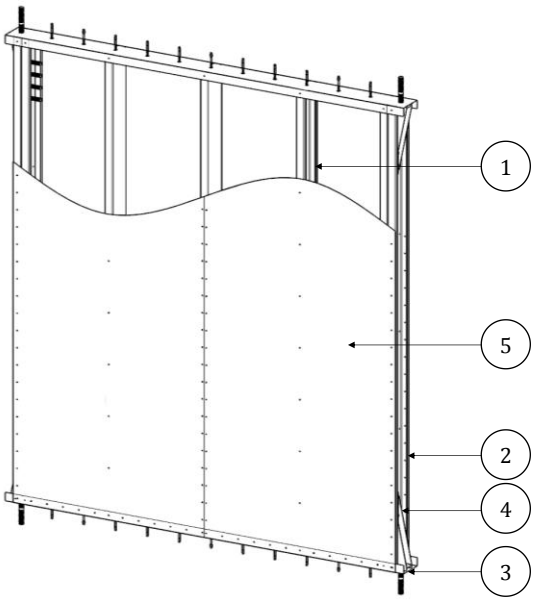

1. stud; 2. chord stud; 3. track; 4. hold-down; 5. gypsum board

a)

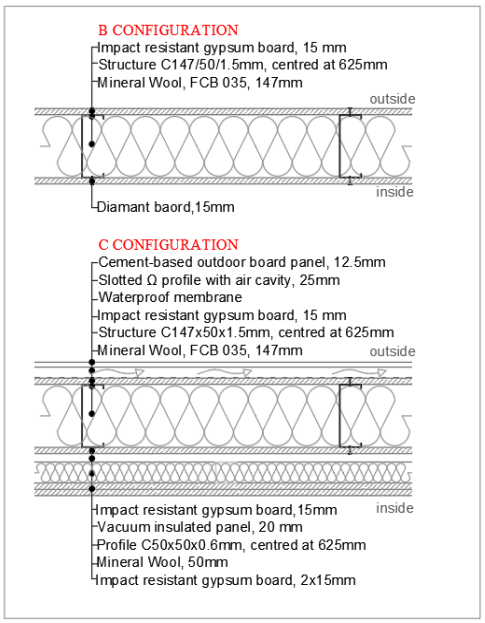

b)

Figure 1 a) View side of the B wall Configuration, b) Sections of B and C wall Configurations

Configuration		F_e/L [kN/m]	d_e/H [%]	k_e/L [kN/mm/m]	F_{max}/L [kN/m]	d_u/H [%]
B	Pos. Env.	5.60	0.19	1.28	14.00	1.97
	Neg. Env.	5.54	0.20	1.24	13.85	1.95
	Av.	5.57	0.19	1.26	13.92	1.96
C	Pos. Env.	8.47	0.23	1.63	21.17	2.71
	Neg. Env.	7.98	0.19	1.86	19.95	1.37
	Av.	8.22	0.21	1.75	20.56	2.04

Table 1 Cyclic test results of both B and C wall configurations

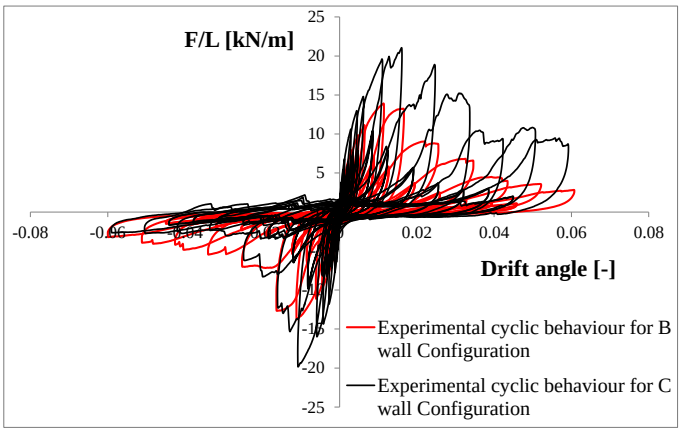

a) Experimental cyclic behaviours of B and C wall Configurations

b)Global deformation

c)Sheathing-to-frame connection collapse

d)Detachment of sheathing panel

Figure 2 Cyclic test results

2.3 Mock-up testing

A 3D building mock-up was tested on shaking table in two different construction phases: bare structure (B mock-up Configuration), consisting only of structural elements; and complete construction (C mock-up Configuration), in which architectural non-structural components were added. The mock-up was a 2.5×4.5×5.4 m (length x width x height) two storey building. The seismic resistant elements were made of CFS shear walls laterally braced by gypsum panels. A white noise signal was applied to the building (Random tests) in B and C Configurations in order to assess the main dynamic characteristics, i.e. first period of vibration and damping, while a natural ground motion record scaled by 5 to 150% (Earthquake tests) was applied only to C mock-up Configuration to evaluate its seismic response. Indeed, the experimental seismic response under an earthquake input is available only for the C mock-up Configuration.

The B mock-up Configuration consisted mainly of shear walls and gravity walls without finishing parts, internal partition walls, floors and roof. Shear walls had the same structure of the B wall Configuration tested under quasi-static cyclic regime (see Section 2.2). Gravity and partition walls had the same structural elements of shear walls. The main difference between shear and gravity walls was the presence of hold-down. In fact, in order to withstand the axial force due to overturning phenomena, ad hoc designed hold-down devices were placed only at the ends of shear walls. Internal partition walls, instead, were not designed to carry gravity loads. Floors and roof were made of back-to-back 197×50×10×2.0 mm C joists with a spacing of about 500 mm on the centre, connected at their end with 200×40×1.5 mm U floor tracks. The steel frame of the floors was sheathed on the top side with 28 mm thick high-density gyp-

sum fibre board panels. The bottom side of steel frame of second floor and roof was sheathed with 15 mm thick impact resistant gypsum board panels.

The C mock-up Configuration was completed with architectural non-structural components, which mainly consisted of internal counter walls and finishing parts of shear walls, gravity walls, and finishing parts of floors and roof. In particular, shear walls had the same structure of the C wall Configuration tested under quasi-static cyclic regime and gravity walls were completed in the same way of the shear walls (see Section 2.2), however certainly without the hold down devices. Top sides of first and second floors were sheathed with additional gypsum fibre board panels, while bottom sides of second floor and roof were completed with a ceiling. The seismic weight of the B mock-up Configuration was evaluated to be approximately 24 kN for the second floor and 14 kN for the roof, while for the C mock-up Configuration they were approximately 50 kN and 26 kN, respectively. More details about mock-up are available in Fiorino et al. [22].

Random test results are presented in term of fundamental period of vibration and damping ratio for B and C mock-up Configurations, while the Earthquake test results are presented in term of peak and residual inter-storey drifts for C mock-up Configuration. The fundamental period for the B mock-up Configuration was greater than that recorded for the C mock-up Configuration. In particular, the fundamental period of the B mock-up Configuration was about 0.13 s, while for C mock-up Configuration it was about 0.10 s. As far as the measurement of damping ratio is concerned, it resulted in the range from 1.4% to 3.1% for the B mock-up Configuration and from 1.2% to 2.0% for the C mock-up Configuration. As concerned the peaks of the inter-storey drift ratio (PIDR) measured during earthquake tests carried out on the C mock-up Configuration, the PIDRs were 0.80% for 1st storey and 0.52% for 2nd storey. All the PIDRs corresponded to the earthquake with maximum intensity (scale factor equal to 150%). In addition, the residual inter-storey drift ratios (RIDRs) were very small (under 0.05%) and the observed damage was limited to architectural non-structural components, i.e. presence of gypsum dust and small detachment of cover paper at some corner joints on the inner faces of internal counter walls.

2.4 Effect of architectural non-structural components based on experimental results

Non-structural components explicitly considered in this study included insulating and finishing materials of shear and gravity walls, partition walls and internal counter walls. On the bases of experimental results, the effect of architectural non-structural components can be evaluated both on subsystem (shear wall) and whole building (mock-up). The evaluation of this effect for the shear walls can be done in term of stiffness, strength and collapse mechanisms, i.e. the cyclic tests on the shear walls were carried out up to the collapse on both shear walls without (B wall Configuration) and with architectural non-structural components (C wall Configuration). In contrast to shear walls, for the mock-up the effect of architectural non-structural components can be evaluated only in term of first period of vibration and stiffness, because the experimental seismic response under earthquake inputs is only available for mock-up with architectural non-structural components (C mock-up Configuration). Moreover, the partition walls are present in both B and C mock-up Configurations, therefore a rigorous comparison between B and C mock-up Configurations focused to assess the effect of non-structural components is affected by this circumstance. A further evaluation of the effect of architectural non-structural components was carried out through numerical modelling (see Section 3.6).

As experimental results showed, the increasing in stiffness due to the effect of non-structural components on the single shear wall was estimated equal to about 1.4 times, while the increasing in resistance was estimated equal to about 1.5 times, by comparing the lateral

response of B and C wall Configurations. For the mock-up, the influence of non-structural components implied a global decreasing of the fundamental period of about 1.3 times from B to C mock-up configuration. Note that the variation of fundamental period of the mock-up was also affected by the variation of the mass, because the mass of the B mock-up Configuration was about one half than that of the C mock-up Configuration. Therefore, for the mock-up an increase of the estimated lateral stiffness equal to about 3 times can be associated to the decrease of the fundamental period. It is evident that the increase of lateral stiffness was greater for the mock-up than for the shear wall. This result confirms the important role of all architectural non-structural components, together with the box building behaviour, which increase significantly the lateral stiffness.

3 NUMERICAL MODELLING

3.1 General

Numerical models representative of B and C mock-up Configurations were developed in Opensees environment in order to capture their dynamic behaviour and seismic response. In particular, B Models are representative of the B mock-up Configuration and include shear walls (SW_B) and gravity walls (GW_B) without architectural non-structural components and partition walls, while C Models are representative of the C mock-up Configuration and include shear walls (SW_C) and gravity walls (GW_C) with non-structural finishing materials, partition walls (PW) and internal counter walls (ICW). Several modelling options were explored to deepen the knowledge of contribution offered by different structural and architectural non-structural components on the seismic response of the mock-up. They ranged from very simple models with only shear walls to more complex models, in which all the structural and architectural non-structural components were included. The effect of two different modelling choices for diaphragm was also evaluated. Diaphragm was either modelled as a rigid diaphragm constraint across all the nodes at floor or roof level, or as each joist (J) being modelled as a separate element without any constraint. Different modelling options are summarised in Table 2.

Mock-up Configuration	**Model**	**Structural***				**Non-structural***			
		SW_B	**IS**	**GW_B**	**J**	**PW**	**SW_C**	**GW_C**	**ICW**
B	**B1**	Yes	No	No	No	No	No	No	No
	B2	Yes	Yes	No	No	No	No	No	No
	B3	Yes	Yes	Yes	No	No	No	No	No
	B4	Yes	Yes	Yes	Yes	No	No	No	No
	B5	Yes	Yes	Yes	Yes	Yes	No	No	No
C	**C1**	Yes	Yes	Yes	Yes	Yes	Yes	No	No
	C2	Yes	Yes	Yes	Yes	Yes	Yes	Yes	No
	C3	Yes	Yes	Yes	Yes	Yes	Yes	Yes	Yes

*SW_B= shear wall without finishing materials, IS= intermediate studs, GW_B= gravity wall without finishing materials, J= floor joists, PW= partition walls, SW_C= shear wall with finishing materials, GW_C= gravity wall with finishing materials, ICW= internal counter wall

Table 2 Modelling options

3.2 Shear walls

The shear walls were modelled by a pair of diagonal trusses elements with a Pinching4 material, calibrated based on quasi static cyclic test response of the walls, as explained in the

Section 2.2. Pinching4 material is a material model, which represents a pinched load-deformation response and can exhibit degradation under cyclic loading, using the definition of the backbone envelope and the parameters governing the cyclic behaviour. In order to define the best-fit Pinching4 material for the shear walls, the force-displacement backbone curves assigned to diagonals were individuated first using the cyclic test results from the experiments, then the cyclic parameters were calibrated to best match the experimental response.

The shear wall models were subjected to the same loading protocol used in the cyclic tests. A parametrical analysis was performed to better match the cyclic behaviour of the walls through a quantitative comparison based on the energy dissipation per single cycle and cumulative cyclic energy. Figure 3 shows the comparison between experimental and numerical response in terms of load vs. displacement cyclic behaviour and cumulative dissipated energy. Hold-downs present at the ends of shear walls were modelled as ZeroLength elements with stiffness of 37kN/mm. The chord studs were modelled as truss elements with physical and mechanical properties representative of chord studs used in tested mock-up (147×50×1.5 mm C back-to-back sections), while the tracks were modelled as infinitely rigid truss elements. More details are available in Fiorino et al. [23]. Intermediate studs were neglected in the shear wall models as they are pin connected to their ends and do not contribute to the shear wall response.

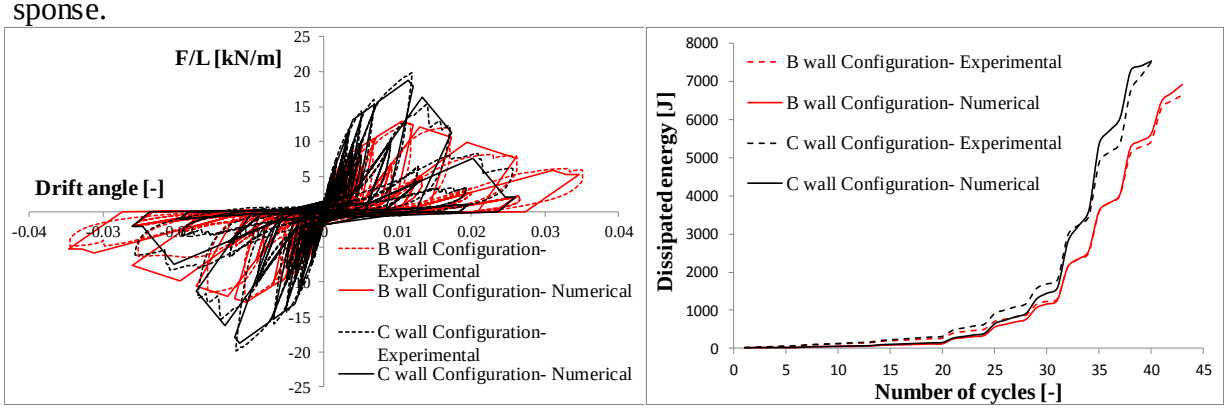

Figure 3: Experimental vs. numerical response in terms of load vs. displacement cyclic behaviour and cumulative dissipated energy

3.3 Other structural components

Apart from shear walls, other structural elements and components contribute to the seismic behaviour of the mock-up, i.e. intermediate studs, gravity walls, floors and roof. The intermediate studs were modelled as truss elements, with physical and mechanical properties representative of studs used in tested mock-up (147×50×1.5 mm C sections). The behaviour of gravity walls was also idealized as a pair of diagonal truss elements with Pinching4 material. The main difference between gravity and shear walls is the absence of hold-downs in gravity walls and the presence of hold down in shear walls. To reproduce the experimental rigid behaviour of the floors (ASCE 7-10), two different approaches were followed: rigid diaphragm or floor joists explicitly modelled. In the first approach the diaphragm was simulated by infinite rigid vertical and horizontal truss elements and in-plane X trusses applied at both floor intrados and extrados. In the second approach, joists were modelled as elastic beam column elements pin connected to the floor track elements, with the same properties of joists used in the mock-up (197×50×10×2.0 mm C back-to-back section. For further details see Campiche et al. [24].

3.4 Architectural non-structural components

Main architectural non-structural components present in the C mock-up Configuration were: finishing materials of shear walls and gravity walls, partition walls and internal counter walls. Finishing materials of shear and gravity walls were included directly in wall models, by using models representative of the walls with architectural non-structural components, i.e. model of shear wall with finishing materials (SW_C) and model of gravity wall with finishing materials (GW_C). The model of the partition walls was the same model used for the gravity walls. Since partition walls did not have present finishing materials, only test data of the B wall Configuration were used to calibrate the *Pinching4* material. The lateral force contribution provided by the double layer of impact resistant gypsum boards in counter walls was already lumped in the model of shear and gravity walls with finishing parts. Therefore, only the studs of internal counter walls were modelled as a truss element with their position in model and, the physical and mechanical properties being the representative of profiles used in tested mock-up (60×27×0.6 mm C sections). The end nodes of these studs were linked to the rigid truss elements of floors and they were constrained by the same rigid Diaphragm used to reproduce the rigid behaviour of the floor.

3.5 Numerical vs. Experimental response

In order to validate the numerical results, a comparison in term of dynamic properties (fundamental period of vibration) for B and C mock-up Configurations and seismic performance for C mock-up Configuration was performed. For each model, the fundamental period of vibration was evaluated via modal analysis (T_{NUM}) and was compared with the values evaluated on the bases of the experimental results (T_{EXP}), through the ratio $\Delta T = (T_{NUM} - T_{EXP})/T_{EXP}$ (Table 3) The models which gave the most accurate estimation of the fundamental period for the B and C mock-up Configurations were the B2 and C2 Models, respectively. They exhibited a fundamental period of vibration of about 0.12 s and 0.11 s, corresponding to a ΔT equal to about 3% and 7%, respectively.

For C Models, the peak inter-storey drifts were evaluated via non-linear time history analysis ($PIDR_{NUM}$) and were compared with the values obtained experimentally ($PIDR_{EXP}$), through the ratio $\Delta PIDR = (PIDR_{NUM} - PIDR_{EXP})/PIDR_{EXP}$. Moreover, experimental and numerical inter-storey drift time histories were compared. The model which gave the most accurate estimation of peak inter-storey drifts and better reproduced the experimental time history (Fig.4) was the C3 Model. It exhibited a PIDR equal to about 0.61% and 0.53% for the first and second storeys, corresponding to a $\Delta PIDR$ equal to about 24% and 2%, respectively.

Model	T_{NUM} [s]	T_{EXP} [s]	ΔT [%]
B1	0.143	0.130	13
B2	0.123		3
B3	0.118		7
B4	0.117		8
B5	0.100		21
C1	0.107	0.100	7
C2	0.095		5
C3	0.082		18

Table 3 Comparison between experimental and numerical fundamental period of vibration

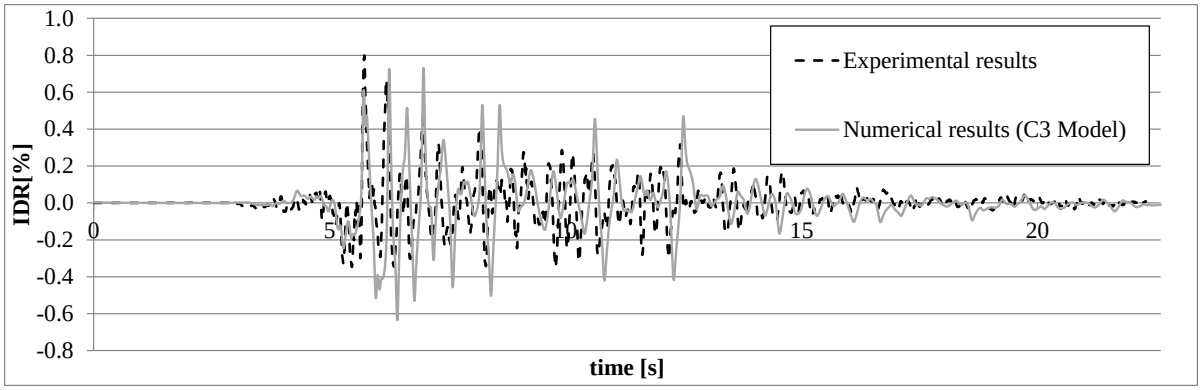

Figure 4: Comparison between experimental and numerical (C3 Model) IDR time history for the first storey

3.6 Effect of architectural non-structural components based on numerical results

Since the experimental data for the seismic response under earthquake input are not available for the B mock-up Configuration and partition walls were present in both B and C mock-up Configurations, the effect of architectural non-structural components on the seismic response of the mock-up was investigated numerically. The B4 Model, in which only all the structural components are modelled, and C3 Model, i.e. the model including all structural and non-structural components, were subjected to non-linear time history analysis and the results, in terms of IDR time history (Fig. 5), PIDR and residual inter-storey drift ratio (RIDR) were compared. PIDRs were 1.24% and 0.61%, while RIDRs were equal to 0.058% and 0.024% for B4 and C3 Models, respectively. The comparison of earthquake response of B4 and C3 Models shows the decreasing of the PIDR in C3 Model due to the effect of non-structural components on the whole building equal to about 2.0 times, while the decreasing of RIDR was estimated equal to about 2.4 times. Obviously, due to the non-linear response of the building under the earthquakes with higher intensity, the influence of the non-structural components in terms of PIDR reduction becomes lower in comparison with their effect on the increasing of initial lateral stiffness (see Section 2.4). However, also results in terms of earthquake response confirm the important role of all architectural non-structural components, which can significantly reduce peak and residual inter-storey drifts.

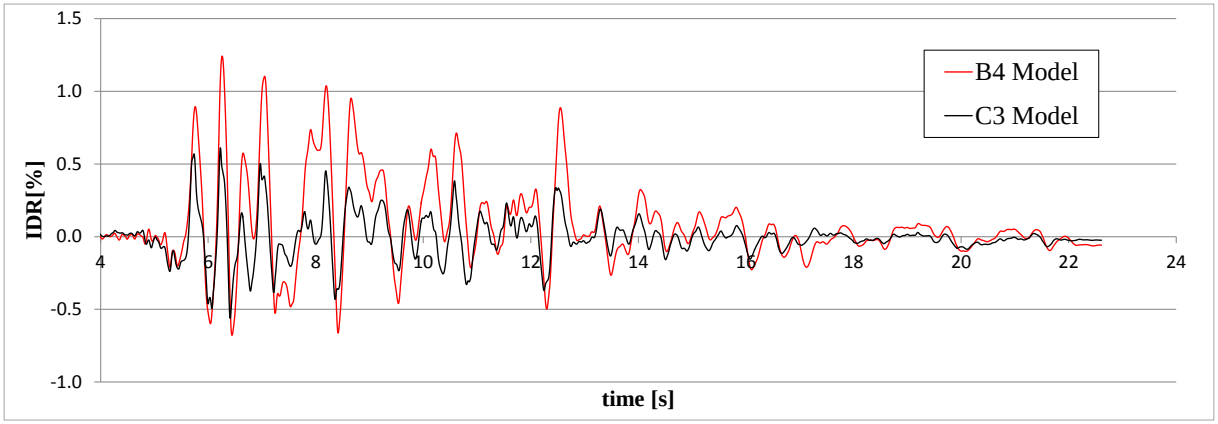

Figure 5: Inter-storey drift time history for B4 and C3 models

4 CONCLUSIONS

The present paper summarises the study on the effect of architectural non-structural components on the seismic behaviour of CFS structures, through the experimental test results and numerical modelling. Cyclic tests on full-scale gypsum sheathed shear walls with and without finishing materials and shake-table tests on full-scale two-storey CFS building with and without the architectural non-structural components and finishing materials were carried out. On the basis of the experimental results different numerical models of the building were developed in Opensees software, considering architectural non-structural components.

Based on the experimental results, the increasing in lateral stiffness and resistance due to the effect of non-structural components on the single shear wall was estimated equal to about 1.4 and 1.5 times, respectively; while for the building the effect of non-structural components, together with the box building behaviour, increased the lateral stiffness of about 3 times. Based on the numerical results, the decreasing of the inter-storey drift due to the effect of non-structural components was estimated equal to about 2.0 in terms of peak value and 2.4 times in terms of residual value.

Therefore, both experimental and numerical results confirm the important role of all architectural non-structural components, together with the box building behaviour, which significantly increase lateral stiffness and strength and reduce peak and residual inter-storey drifts.

REFERENCES

[1] R. Landolfo, Lightweight steel framed systems in seismic areas : Current achievements and future challenges, Thin-Walled Struct. 140 (2019) 114–131.

[2] L. Fiorino, V. Macillo, R. Landolfo, Experimental characterization of quick mechanical connecting systems for cold-formed steel structures, Adv. Struct. Eng. 20 (2017) 1098–1110. doi:10.1177/1369433216671318.

[3] L. Fiorino, T. Pali, B. Bucciero, V. Macillo, M. Teresa Terracciano, R. Landolfo, Experimental study on screwed connections for sheathed CFS structures with gypsum or cement based panels, Thin-Walled Struct. 116 (2017) 234–249. doi:10.1016/j.tws.2017.03.031.

[4] M.T. Terracciano, V. Macillo, T. Pali, B. Bucciero, L. Fiorino, R. Landolfo, Seismic design and performance of low energy dissipative CFS strap-braced stud walls, Bull. Earthq. Eng. 17 (2019) 1075–1098. doi:10.1007/s10518-018-0465-y.

[5] V. Macillo, O. Iuorio, M.T. Terracciano, L. Fiorino, R. Landolfo, Seismic response of Cfs strap-braced stud walls: Theoretical study, Thin-Walled Struct. 85 (2014) 301–312. doi:10.1016/j.tws.2014.09.006.

[6] L. Fiorino, O. Iuorio, V. Macillo, M.T. Terracciano, T. Pali, R. Landolfo, Seismic Design Method for CFS Diagonal Strap-Braced Stud Walls: Experimental Validation, J. Struct. Eng. 142 (2016) 04015154. doi:10.1061/(ASCE)ST.1943-541X.0001408.

[7] V. Macillo, S. Shakeel, L. Fiorino, R. Landolfo, Development and Calibration of a Hysteretic Model for CFS Strap braced stud walls, Adv. Steel Constr. 14 (2018) 337–360. doi: 10.18057/IJASC.2018.14.3.2

[8] L. Fiorino, M.T. Terracciano, R. Landolfo. Experimental investigation of seismic behaviour of low dissipative CFS strap-braced stud walls. J. Const. Steel Res. 127 (2016), pp. 92-107. doi:10.1016/j.jcsr.2016.07.027

[9] L. Fiorino, T. Pali, R. Landolfo, Out-of-plane seismic design by testing of non-structural lightweight steel drywall partition walls, Thin-Walled Struct. 130 (2018) 213–230. doi:10.1016/j.tws.2018.03.032.

[10] T. Pali, V. Macillo, M.T. Terracciano, B. Bucciero, L. Fiorino, R. Landolfo, In-plane quasi-static cyclic tests of nonstructural lightweight steel drywall partitions for seismic performance evaluation, Earthq. Eng. Struct. Dyn. 47 (2018) 1566–1588. doi:10.1002/eqe.3031.

[11] L. Fiorino, B. Bucciero, R. Landolfo, Evaluation of seismic dynamic behaviour of drywall partitions, façades and ceilings through shake table testing, Eng. Struct. 180 (2019) 103–123. doi:10.1016/j.engstruct.2018.11.028.
[12] R. Tartaglia, M. D'Aniello, G.A. Rassati, J.A. Swanson, R. Landolfo, Full strength extended stiffened end-plate joints: AISC vs recent European design criteria, Eng. Struct. 159 (2018) 155–171. doi:10.1016/j.engstruct.2017.12.053.
[13] L. Fiorino, O. Iuorio, R. Landolfo, Designing CFS structures: The new school bfs in naples, Thin-Walled Struct. 78 (2014) 37–47. doi:10.1016/j.tws.2013.12.008.
[14] L. Fiorino, S. Shakeel, V. Macillo, R. Landolfo, Behaviour factor (q) evaluation the CFS braced structures according to FEMA P695, J. Constr. Steel Res. 138 (2017) 324–339. doi:10.1016/j.jcsr.2017.07.014.
[15] R. Tartaglia, M. D'Aniello, A. De Martino, G. Di Lorenzo, Influence of EC8 rules on P-Delta effects on the design and response of steel MRF., Ing. Sismica Int. J. Earthq. Eng. 35 (2018) 104–1.
[16] V. Nikolaidou, C.A. Rogers, D.G. Lignos, Influence of Non-Structural Components on the Seismic Response of Cold - Formed Steel Structures, 3 (2017) 1–12.
[17] R. Montuori, E. Nastri, V. Piluso, Modelling of floor joists contribution to the lateral stiffness of RC buildings designed for gravity loads, Eng. Struct. 121 (2016) 85–96.
[18] S. Mazzoni, F. McKenna, M.H. Scott, G.L. Fenves, OpenSees, (2009).
[19] R. Landolfo, O. Iuorio, F. Luigi, Experimental seismic performance evaluation of modular lightweight steel buildings within the ELISSA project, Earthq. Eng. Struct. Dyn. (2018) 1–23. doi:10.1002/eqe.3114.
[20] H. Krawinkler, P. Francisco, L. Ibarra, A. Ayoub, R. Medina, CUREE publication No. W-02 Development of a Testing Protocol for Woodrame Structures, (2001).
[21] V. Macillo, L. Fiorino, R. Landolfo, Seismic response of CFS shear walls sheathed with nailed gypsum panels: Experimental tests, Thin-Walled Struct. 120 (2017) 161–171. doi:10.1016/j.tws.2017.08.022.
[22] L. Fiorino, V. Macillo, R. Landolfo, Shake table tests of a full-scale two-story sheathing-braced cold-formed steel building, Eng. Struct. 151 (2017) 633–647. doi:10.1016/j.engstruct.2017.08.056.
[23] L. Fiorino, S. Shakeel, V. Macillo, R. Landolfo, Seismic response of CFS shear walls sheathed with nailed gypsum panels: Numerical modelling, Thin-Walled Struct. 122 (2018) 359–370. doi:10.1016/j.tws.2017.10.028.
[24] A. Campiche, S. Shakeel, V. Macillo, M.T. Terracciano, B. Bucciero, T. Pali, L. Fiorino, R. Landolfo, Seismic Behaviour of Sheathed CFS Buildings: Shake Table Tests and Numerical Modelling, Ing. Sismica-International J. Earthq. Eng. 2 (2018) 106–123.

COMPDYN 2019
7th ECCOMAS Thematic Conference on
Computational Methods in Structural Dynamics and Earthquake Engineering
M. Papadrakakis, M. Fragiadakis (eds.)
Crete, Greece, 24–26 June 2019

EXPERIMENTAL AND NUMERICAL SIMULATIONS ON RBS CONNECTIONS INCORPORATING LARGE SECTIONS

T. Bogdan[1], D.V. Bompa[2], A.Y. Elghazouli[2], E. Nunez[3] M. Eatherthon[4], and R. Leon[4]

[1] ArcelorMittal Global Research and Development Esch, Esch sur Alzette, Luxembourg
e-mail: Teodora.bogdan@arcelormittal.com

[2] Department of Civil and Environmental Engineering, Imperial College London, UK
e-mails:d.bompa@imperial.ac.uk, a.elghazouli@imperial.ac.uk

[3] ArcelorMittal Global Research and Development Basque Country, Bilbao, Spain
e-mail: edurne.nunez@arcelormittal.com

[4] Via Department of Civil and Environmental Engineering, Virginia Tech, Blacksburg, USA
e-mail: meather@vt.edu; rleon@vt.edu

Abstract

Recent experimental tests have shown that RBS connections incorporating Jumbo specimens meet the current seismic design qualification protocols, allowing to further extend the current seismic provisions for prequalified steel connections with possible applications of heavy steel sections beyond their current use in ultra-tall buildings. The experimental results and observations described in this paper enabled a better understanding of the structural behaviour of RBS connections made of heavy structural sections for application in seismic regions. However, the results indicate that geometrical and material effects need to be carefully considered when designing welded RBS connections incorporating large steel profiles. To better interpret the experimental results, extensive detailed non-linear finite element simulations are conducted on the entire series of tests, comprising of three large-scale specimens with distinct sizes. The analyses intend to clarify the scale effects that influence the performance of these connections, both at material and geometric level, and particularly to understand the balance in deformation between the column panel zones and the reduced beam section and level of stress within the main connection components. It is shown that the numerical models for all three specimens reproduce accurately the overall load-deformation and moment-rotation time history.

Keywords: reduced beam sections; steel connections; welded connections; seismic design; non-linear modelling.

1 INTRODUCTION

Structural members with long uninterrupted spanning and large loading capacity are needed in the design of tall buildings, convention centres, sport arenas and airport concourses. The latest product developments made by ArcelorMittal permits the use of large jumbo steel profiles as W920x420x1377 (W36×925) with steel of 450 MPa in grades like S460 and HISTAR 460, available both on the US and European market. When such profiles are used in areas of high seismicity, the welded connection design requires a careful development from welding performance specifications (WPS) point to ensure that the required rotational capacities to reach interstudy drifts of 4% can be developed. One technique used to control the flexural demand from the beam is to utilize reduced beam sections (RBS), which effectively limit the demands at the beam-column interface (Figure 1).

The RBS concept was proposed initially by Plumier [1] in the late 1990s to alleviate problems encountered in the 1994 Northridge Earthquake with conventional welded connections. Following, different shapes of RBS have been studied along the time. For example, Iwankiw and Carter [2] studied the first polygonal cut and observed initial yielding in the column panel zone (PZ) followed by diagonal yield lines in the beam flanges. Englehart [3] observed that a higher performance goal might be achieved by changing the shape from constant to a radius cut dogbone. Moreover, Zekioglu et al [4] showed that the application of large plastic rotation capacities, without considering the strength degradation or rotation demand range, to justify a particular moment frame system, would not be a rational approach.

Popov et al. [5] showed in tests that the triaxial loading makes steel at a connection fail without exhibiting yielding ductile behaviour due to the state of stress and not because of material property. Later, Uang et al [6] used a database of 55 cyclically full-scale RBS moment connection tests to study the cyclic instability of such connections. They observed that the slenderness ratio for web local buckling affects the plastic rotation. Ultimately, Zhang and Ricles [7,8] investigated the RBS moment connections to a deep wide flange column and observed that thee composite floor can significantly reduce the lateral displacement of the beam bottom flange in the RBS and the amount of twist developed in the column.

The current AISC Provisions for Steel Buildings (AISC 360-16) [9], Seismic Provisions (AISC 341-16) [10] and the Provisions for Prequalified Connections for Special and Intermediate Steel Moment Frames (AISC 358-16) allow the use of these connections but only for sections up to 900 mm in depth and 450 kg/m in weight [11]. To extend the coverage of these specifications to much larger sections, a joint experimental and analytical program was undertaken by Virginia Tech and ArcelorMittal [12]. It is worth noting, that codified prequalification procedures for seismic steel connections are under development in Europe as a result of the recently completed Equaljoints research project [13].

In this paper, results and observations from an experimental program on three RBS connections provided with large section are reported. Complementary numerical studies are also undertaken using nonlinear finite element procedures which are validated against the experimental results from this study. Comparative assessments are also presented, including stiffness and strength as well as ductility and energy dissipation are examined.

2 EXPERIMENTAL AND NUMERICAL METHODOLOGY

2.1 Testing arrangement and specimen details

The experimental campaign is based on a trial design to determine the realistic member size in buildings with high seismicity area [12]. The study consisted of a square office building tower with fifteen stories and a large open atrium at the 1st floor. Special Moment Frames

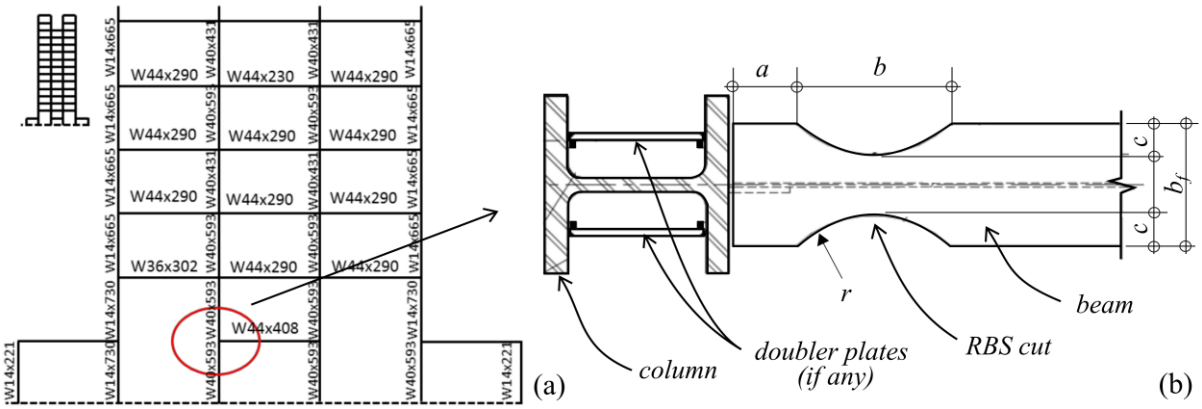

Figure 1: a) Sections at the lower storeys of the Case study building, b) Plan detail of the examined beam-column connections with doubler plates.

Spec.	Beam	Column	Doubler plate	RBS cut			Cont. plates
				A mm (in)	B mm (in)	C mm (in)	
SP2	W 44x408	W 14x873	None	200.5 (7.9)	708.5 (27.89)	68 (2.69)	None
SP3	W 36x925	W 14x873	5/8	236.5 (9.31)	710.5 (27.97)	99 (3.91)	None
SP4	W 44x408	W 40x503	None	305 (12.00)	950 (37.40)	85 (3.36)	None

Table 1: Specimen details

with RBS connections were considered exclusively for the seismic-load-resisting system. These frames are located at the perimeter and are typically three bays wide, except at the lower levels as shown in Figure 1a. From these typical frames, sample connections were extracted as possible test specimens. Table 1 presents the chosen configurations for the testing, whilst Figure 1b depicts the schematic of a specimen. Each specimen exceeds the size limitation outlined in the AISC 358-16 [11] in at least one regard.

The specimens were secured within a rigid frame that is affixed to the strong floor laboratory as illustrated in Figure 2 and the schematic representation in Figure 3a. The pieces in red indicates where the frame was being fixed to the strong floor. The frame connects to the strong floor in two different ways. The first set of connections to the strong floor is made up of eight stiffened W33×291 members. These eight members take load in the longitudinal direction (parallel to both the actuators and the W members embedded within the strong floor). Each of the members is secured to the W members embedded within the strong floor (depicted as grey strips in Figure 3a) with 42 × one-inch (25.4 mm) A490 bolts in slip-critical connection (achieved with pre-tensioning). The second set of connections to the strong floor involves two large steel wedge shape blocks, designed to take the load in the lateral direction.

As observed, the specimens were tested in the horizontal orientation in displacement control with the actuators reacting to the testing frame. The specimens were subjected to the loading protocol described in AISC 341-16 [10], as illustrated in Figure 3b. After two cycles at a story drift angle of 0.04 rad, the story drift increases by 0.01 rad increments every two cycles until failure. Due to stroke limitations in the actuators, the maximum achievable story drift during these tests was 0.06 rad, hence, the specimens were cycled at 0.06 rad until failure. Specimen instrumetation included a combination of linear and string potentiometers, strain gauges and rosettes, and an in-house imaging system (OJOS) in order to capture all pertinent measurements for analyzing the system as a whole. Results from these devices are later used for the numerical validation descriBed later.

Figure 2 Specimen in testing orientation with two actuators

Is is worth noting that besides the extension of prequalification limits in the AISC codes, another main objective of the experimental programme was to determine an acceptable balance between the deformation obtained from flexural yielding of the RBS and shear yielding of the column web PZ [12]

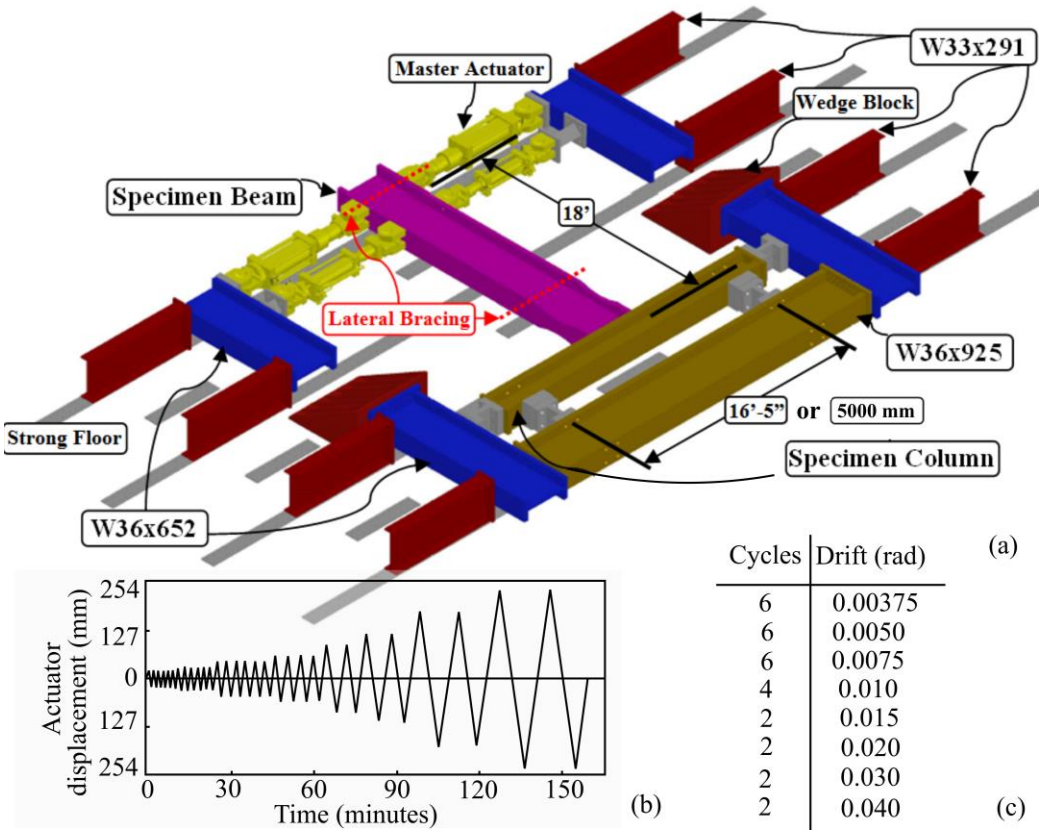

Figure 3 a) Test setup with four actuators, b) Loading protocol – AISC 2010..

2.2 Numerical procedures

The numerical simulations described in this paper were carried out using the non-linear finite element (FE) program ABAQUS [14]. Tri-dimensional (3D) models of RBS connections adopt eight node brick elements (C3D8R). Extruded solid elements from heavy W sections representing the column were connected to the beams using tie constraints. Special attention was given to the characteristics of the RBS region and the column PZ by considering the exact dimensions taken from the experimental specimens (Table 2). Initial studies indicated that the experimental stiffness of specimens with the largest cross-sections (SP3) differed from analytical assessments [12]. To address the potential influence from the test rig, two modelling approaches were considered. Firstly, the specimens, including the four stub elements made of W sections used as boundary conditions were modelled together. Multi-point constraints connected to reference points assigned with pinned boundary conditions to the exterior face of the W profile, whilst surface-to-surface interactions were assigned to the interface between the column element of the specimens and stub elements. Secondly, the specimens described in Section 2.1 were modelled along with the complete testing arrangement as illustrated in Figure 3a. Similarly, pinned boundary conditions were assigned to reference points that were connected through multi-points constraints to the rig elements. All contacts between specimens and rig elements were modelled using surface-to-surface interactions.

Cyclic displacements were applied to reference points that are connected to beam tips through constraints and transfer plates simulating firmly the experimental time history. Mesh sensitivity studies were undertaken assess the element size influence on the hysteretic response. These indicate that a relatively coarse mesh restricts a reliable inelastic strain propagation within the RBS and local buckling effects are not captured. On the other hand, a fine mesh within the RBS and column PZ ($l_m \approx$15-20 mm), combined with $l_m \approx$30-40 mm outside of the critical regions offer reliable deformations and strains, as described in the subsequent sections. A minimum of two mesh rows per flange thickness offer a good balance in terms of computational time and reliability of the results, whilst a much larger number of rows significantly increase the analysis time and reduce the ability of the model to capture local effects, primarily due to hourglass effects [15]. The Newton-Raphson approach was adopted for the numerical integration procedure. The steel material properties were modelled using a plastic multilinear kinematic hardening [14] constitutive representation in which the materials properties obtained from coupon testing, separately for webs and flanges, were accounted for. The yield strength varied between f_y=440-477 MPa and the ultimate strength varied between f_u=609-702 MPa.

3 TEST RESULTS AND NUMERICAL VALIDATION

A reliable failure mode of RBS connections is triggered by yielding at the RBS, followed by limited yielding of the PZ and ultimately local flange buckling at the RBS. The latter is an important mechanism as controls the connection behaviour acting as limit to hardening in flexurally governed yielding responses [12]. Close inspection on the slenderness parameters of the section showed that SP2 and SP4 were susceptible to such sequence of yielding and failure. As the slenderness of both web and flanges are relatively low for SP3, local buckling is unlikely to develop. As expected, SP2 and SP4, failed by flexural yielding and inelastic local buckling, and achieved the desired deformation capacity [12] as illustrated Figure 4a,c. The load-displacement curves for these specimens indicate typical, yielding post-buckling softening after maximum capacity was reached. In contrast, SP3, with significantly higher sections reached flexural yielding, failing relatively sudden without any evidence of softening (Figure 4b). This behaviour was attributed to the extreme demands on the very thick welds,

for which the conventional design procedures may substantially underestimate the local strain demands under cyclic displacements [12].

Non-linear numerical validation of the experimental results of Specimens SP2, SP3 and SP4 were undertaken by accounting for the procedures described in Section 2.2. Figures 4d-e present the relationship between load versus beam tip deflection of the above. The results indicate reliable prediction in terms of elastic stiffness, yielding characteristics, deformations and relatively good predictions of the hysteretic response for Specimen SP2. Remarkably, the model can closely capture the initiation of flange buckling and plastic development in the RBS region and PZ. It is worth noting that the numerical model of SP2 showed slightly larger deformations at RBS and slightly lower deformations at the PZ, recorded as displacement reaction from beam flanges in the column, in comparison to the test response.

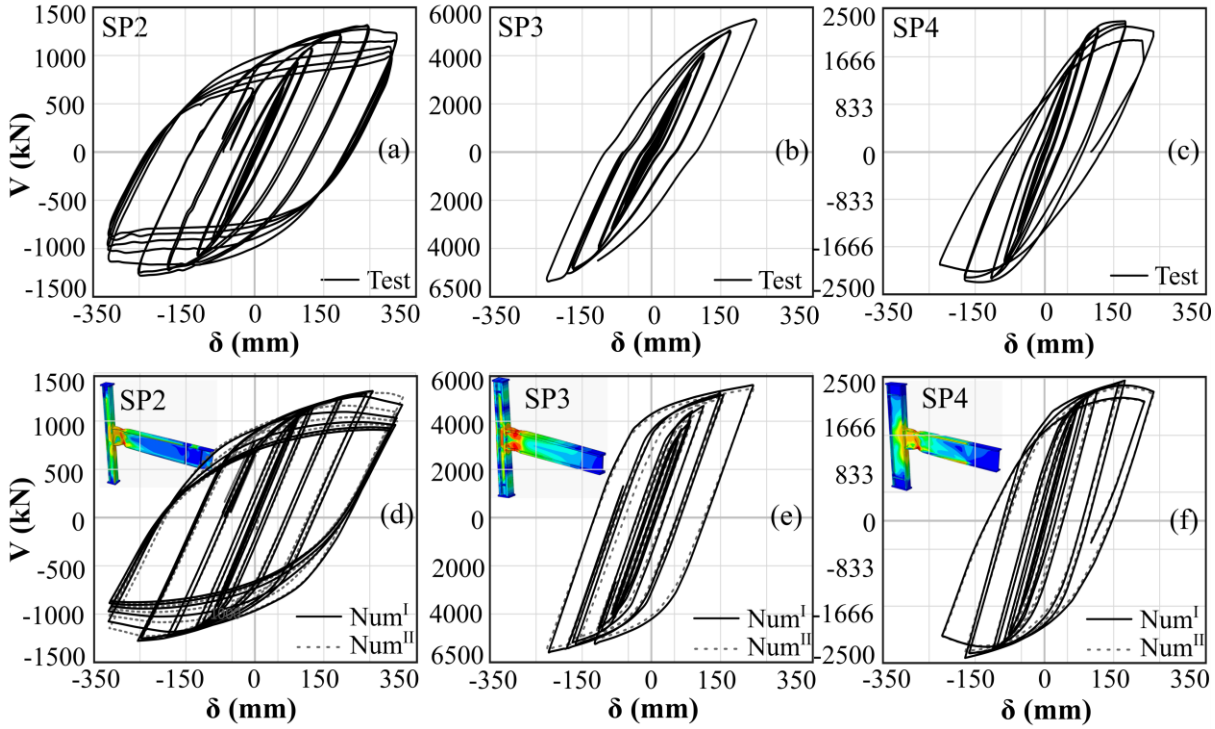

Figure 4: Test force – deflection (V-δ) a) SP2, b) SP3, c) SP4; Numerical validation d) SP2, e) SP3, f) SP4

On the other hand, the behaviour of SP3 was predicted well only in terms of capacity and corresponding displacement, with the numerical stiffness being more rigid in comparison to the experimental stiffness. The test load-displacement of SP3 shows some pinching and change in the unloading stiffness at load reversal, which is not captured with the adopted modelling approach, primarily since all connections between rig elements are modelled with tie constraints, whilst in tests these were rather discrete at the bolted connections. Simulation results of Specimen SP4 show good agreement in terms of stiffness, capacity and degradation, yet the energy dissipation, considered as the area enclosed under the hysteretic loops, is over-estimated. For this specimen the numerical displacements at RBS in tension is identical with the test response, whilst the compression is slightly over-estimated. This is however compensated by a decrease in the deformation at the PZ at which the numerical displacement is about 35% less than the test displacement (Figure 5).

The direct comparison between the models with and without testing rig allowed for an improved understanding of the rig compliance to the load-displacement response. Except the

post-buckling softening response, for SP2 and SP4, the test and numerical curves in Figures 4d,f are virtually identical in terms of key structural parameters and hysteretic response. For SP3, which had significantly larger section sizes in comparison to SP2 and SP4, there is some deviation in the elastic stiffness, primarily due to higher reactions at the boundary conditions of the specimen. Also, the numerical results indicated that the webs of the stub elements that connected the SP3 column to the reaction stubs developed inelastic strains. Additional modelling of the slip between elements fixed to the strong floor and connected rig elements, r by transducers, reduced the stiffness of SP3, being closer to the experimental stiffness, yet more rigid.

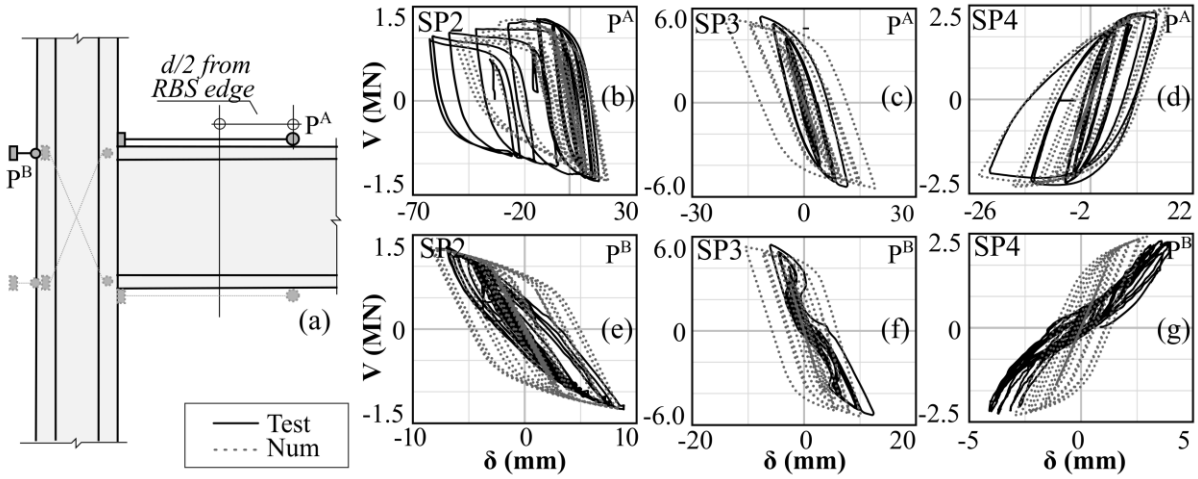

Figure 5 a) Instrumentation extract; Comparison of deformations at RBS b) SP2, c) SP3, d) SP4; at column flange due to force introduction from beam flanges e) SP2, f) SP3, g) SP4.

Observations from models indicate that although the welds were not explicitly modelled, the inelastic strain maps obtained from the SP3 model showed initiation of yielding in the beam at the column face and further in the web column panel, with lower stresses in the RBS flanges than in its web. Also, the direct comparison between the test hysteretic responses of SP2 and SP4 versus SP3 indicate a relatively distinct response. The latter depicts a less ductile behaviour with a lower amount of energy dissipated through the loops. These observations combined with test and numerical results from literature on RBS beam-to-column connections [5] with relatively large sections suggest a possible size effect in cyclic response of large size steel connections. As material models employed in numerical simulations are typically validated against tests on relatively small samples, at significant inelastic strains, these may not reliably represent the structural response when plastic strains develop on large areas.

4 COMPARATIVE ASSESSMENTS

This section describes a detailed analysis of the response of the connections investigated in terms of moment-rotation envelopes, ductility, energy dissipation and stiffness. Bending moments M were assessed at the face of the column from actuator loads in case of experiments and reaction forces at reference points for numerical models. For the global behaviour, chord rotations θ are assessed from beam tip displacements. Figure 6a depicts both test and numerical M-θ envelope curves determined from the V-δ from Figure 4. Besides M-θ curves, the yield moment M_y at the RBS, using assessed material strengths, for each specimen is presented. As observed, the yield moment, represented by a change in member stiffness for both test and numerical models intersects with the analytical assessments, marked with dashed lines.

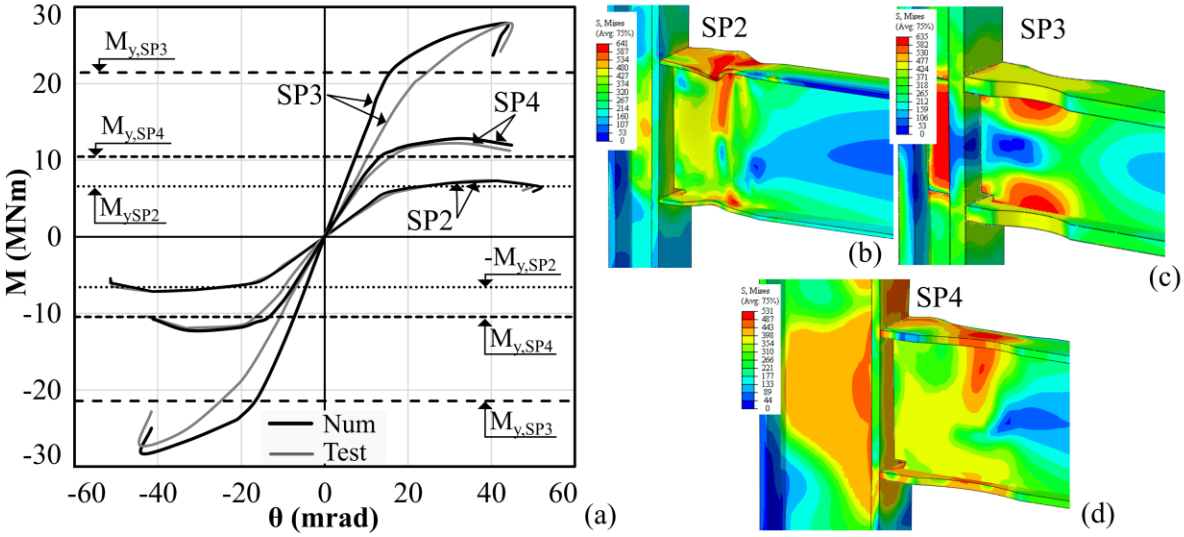

Figure 6 a) Moment – rotation envelopes; stress fields at peak displacement for b) SP2, c) SP3, d) SP4

All specimens exhibited acceptable levels of ductility at ultimate with values above 40 mrad. Specimens SP2 and SP4 had higher ductility and enhanced hysteretic response in comparison to SP3, as also described in previous sections. This is also highlighted by a direct comparison between the test and numerical M-θ curves. For SP2 and SP4 there is a very good agreement in terms of stiffness, yield moment M_y, hardening, ultimate moment M_u and softening. On the other hand, although the yield and capacity of SP3 are well captured by the numerical simulations, the test stiffness is lower than its numerical counterpart. It is worth noting that the size of SP3 was significantly higher than of the SP2 and SP4, hence the M_u at the column face for SP3 was in the range of 27.9 MNm, which is 2.3 × M_u of SP4 and 3.8 × M_u of SP2.

Figures 6b-d illustrate the Mises stress fields at the last cycle of the peak displacement applied. The stress distributions indicate (i) flange buckling at RBS for SP2 with a lower damage at the PZ (Figure 6b), (ii) concentration of stresses at PZ and beam web with lower stress levels at the RBS flanges at SP3 (Figure 6c), and (iii) non-symmetric stress distribution at RBS and PZ with out-of-plane column rotation for SP4 (Figure 6d). It is suggested that the cyclic degradation of SP2 resulted from buckling at the RBS, whilst at SP4 the initiation of buckling was combined with column twist and column web buckling. In contrast, as the RBS flanges of SP3 had lower stress levels than the remaining connection components, there was no degradation at RBS, yet significant column web panel distortion occurred.

The contributions of the RBS and column web PZ obtained from numerical simulations are depicted in Figures 7a-c. The rotation at RBS was assessed from the relative displacements of the top and bottom RBS cuts, and divided by the beam depths. The web column rotation was determined from the relative web displacements resulted from force induction by beam flanges and relative vertical panel displacements [16]. As indicated in the figure, SP2 an SP4, dissipated large energy proportions through the RBS, with the PZ contributing in the range of 15-25%; hence a stronger PZ. On the other hand, SP3 had a relatively even contribution of the two components indicating a relatively balanced behaviour. A close inspection on an identical model of SP3 without double plates showed a contribution of the web column panel of about 70% to the connection rotation, resulting in excessive distortional demands leading to unreliable performance of the components [17,18].

Figures 7d-e indicate the cumulative energy dissipation, integrated from the hysteretic loops converted in M-θ from Figure 4, and the decrease in secant stiffness in relation with θ. As described before, SP2 had stable hysteretic loops and a ductile response with θ_u=50.5 mrad. This is captured by the cumulative energy curve whose stiffness increases with rotation. Additionally, as the numerical response was in good agreement with the test curves, the test and numerical E_d curves of SP2 nearly overlap. On the other hand, SP3 and SP4 reached lower E_d indicating poorer hysteretic response in comparison to SP2 yet reaching reliable ductility levels (θ_u≈mrad). More importantly, considering that the yield rotation was around θ_y=15 mrad for all members, the plastic rotation θ_p=30-35 mrad indicating that these connections developed reliable response for connections in seismic resistant structures with θ_p being between the minimum requirements for ductility class medium ($\theta_{p,M}$=25 mrad) and for ductility class high ($\theta_{p,M}$=35 mrad) [19].

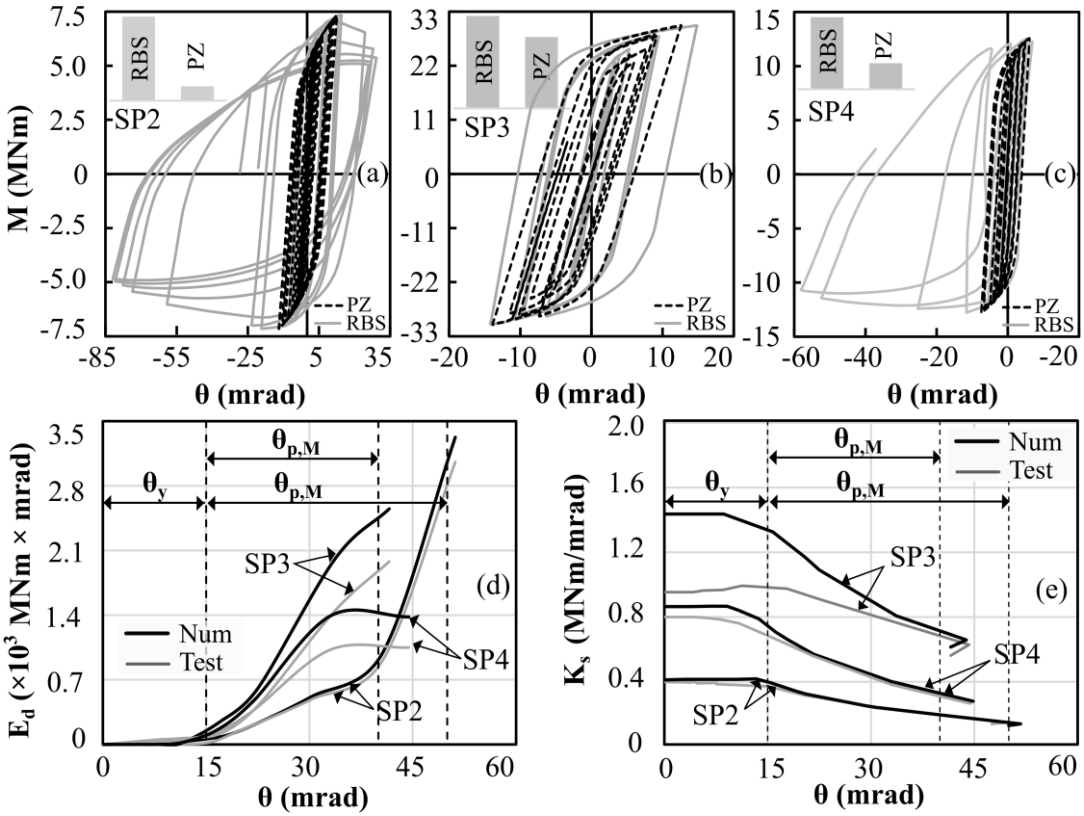

Figure 7 Contribution of connection components for Specimen a) SP2, b) SP3, c) SP4; d) Cumulative energy dissipation versus rotation; e) Stiffness versus rotation

5 CONCLUSIONS

The performance of reduced beam section (RBS) beam-to-column connections incorporating large jumbo steel profiles subjected to cyclic loading was investigated in this study. The experimental and numerical results showed that the strength, stiffness, ductility, hysteretic response and failure mode of such connections are largely dependent on the beam and column section sizes. The results indicated that RBS beam sections with relatively high depth-to-web thickness slenderness ratios develop reliable failure modes characterised by extensive yielding at the RBS, followed by yielding at the panel zone (PZ) and ultimately, flange buckling at RBS. Also, for relatively deep columns, force induction from beam flanges, combined with RBS flange buckling, could produce out-of-plane column rotation. These connections

developed responses characterised by stable hysteretic response, a relatively strong PZ and reliable ductility levels.

In contrast, compact sections with relatively low depth-to-web thickness ratios may develop unreliable response with yielding developing almost concomitantly and at RBS and PZ, having a relatively equal contribution to the total connection deformation. Numerical simulations showed that for connections with relatively compact sections, a higher concentration of stresses may occur at the PZ and at the beam, web with lower stress levels developing at the RBS flanges. These observations indicate the need for an alternative design procedure of RBS for connections incorporating large compact sections. More importantly, the connections investigated in this paper reached reliable rotational capacities, that correspond to inter-story drifts of 4% as a minimum required by North American prequalification standards. This corresponds to plastic rotations of above 25 mrad, indicating that these steel connections conform with the minimum European requirements for ductility class medium. Ultimately, the numerical models were able to capture the local effects, as well as the key structural response characteristics indicating that the modelling procedures can be employed for further extensive parametric investigations.

ACKNOWLEDGEMENTS

The financial support of the Research Fund for Coal and Steel of the European Community within the projects EQUALJOINTS Grant agreement no. RFSR-CT-2013-00021 and, EQUALJOINTS-PLUS Grant agreement no 754048 (2017) for the tests and numerical investigations in this paper are gratefully acknowledged.

REFERENCES

[1] Plumier A., New idea for safe structures in seismic zones, *IABSE Symposium: Mixed structures including new materials*, Brussels, 1990. p. 431-6. doi:10.5169/seals-46518

[2] N.R. Iwankiw C.J. Carter, Dogbone: a new idea to chew on, *Modern Steel Construction*, pp. 18-26, April 1996.

[3] M.D. Engelhart, T. Winneberger, A.J. Zekany, T.J. Potyraj, The dogbone connection: part 2 Selectively trimming a portion of a beam allows connection strength to exceed beam strength without the need to develop a stronger connection, *Modern Steel Construction*, 1996.

[4] A. Zekioglu, H. Mozaffarian, K. Le Chang, C.M. Uang, Designing after Northridge: a California engineering firm re redesigned a project's connections to ensure adequate seismic performance, *Modern Steel Construction*, March 1997.

[5] E. P. Popov, T.S. Yang, S.P. Chang, Design of steel MRF connections before and after 1994 Northridge earthquake, *Engineering Structures*, **20(12)**, 1030–1038, 1998 doi:10.1016/S0141-0296(97)00200-9

[6] C.M. Uang, C.C, Fan., Cyclic stability criteria for steel moment connections with reduced beam section, *Journal of Structural Engineering*, **127(9)**, 1021-1027, 2001. doi:10.1061/(ASCE)0733-9445(2001)127:9(1021)

[7] X. Zhang, J.M. Ricles, Seismic Behavior of Reduced Beam Section Moment Connections to Deep Columns, *Journal of Structural Engineering*, **132(3)**, 358-367, 2006. doi:10.1061/(ASCE)0733-9445(2006)132:3(358)

[8] X. Zhang, J.M. Ricles, Experimental Evaluation of Reduced Beam Section Connections to Deep Columns, *Journal of Structural Engineering*, **132(3)**,346-357, 2006. doi:10.1061/(ASCE)0733-9445(2006)132:3(346)

[9] ANSI 360-16, *AISC: Specification for Structural Steel Buildings*, 2016, Chicago, IL

[10] ANSI 341-16, *AISC. Seismic Provisions for Structural Steel Buildings*, 2016, Chicago, IL

[11] ANSI 358-14, *AISC: Prequalified Connections for Special and Intermediate Steel Moment Frames for Seismic Applications*, 2014, Chicago, IL

[12] L. Qi, J. Paquette, M. Eatherthon, R. Leon, T. Bogdan, N. Popa, E. Nunez Moreno, Analysis of Fracture Behaviour of Large Steel Beam Column Connections, *12th International Conference on Advances in Steel-Concrete Composite Structures (ASCCS)*, 2018 doi:10.4995/ASCCS2018.2018.7122

[13] R. Landolfo, M. D'Aniello, S. Costanzo, R. Tartaglia, A. Stratan, D. Dubina, C. Vulcu, C. Maris, C. Zub, L. Da Silva, C. Rebelo, H. Augusto, A. Shahbazian, F. Gentili, J.P. Jaspart, J.F. Demonceau, L.V. Hoang, A.Y. Elghazouli, A. Tsitos, O. Vassart, E. Moreno Nunez, V. Dehan, C. Hamreza, *European pre-QUALified steel JOINTS (EQUALJOINTS)*, Final Report, 2018-05-04, Directorate-General for Research and Innovation (European Commission). 2018 Available from: https://publications.europa.eu/s/j7q0 [Accessed 7th January 2019]

[14] DSS (Dassault Systèmes Simulia Corp). *ABAQUS Analysis user's manual 6.14-2*, DSS, Providence, RI, USA. 2014

[15] D.V. Bompa, A.Y. Elghazouli, Numerical modelling and parametric assessment of hybrid flat slabs with steel shear heads, *Engineering Structures*, **142**, 67-83, 2017. doi:10.1016/j.engstruct.2017.03.070

[16] H. Augusto, L. Simões da Silva, C. Rebelo, J.M. Castro, Cyclic behaviour characterization of web panel components in bolted end-plate steel joints. *Journal of Constructional Steel Research*, **133**, 310-333, 2017. doi:10.1016/j.jcsr.2017.01.021.

[17] J.M. Castro, F.J. Dávila-Arbona, A.Y. Elghazouli. Seismic design approaches for panel zones in steel moment frames. *Journal of Earthquake Engineering*, **12**, 34-51, 2008. doi:10.1080/13632460801922712.

[18] J.M. Castro, A.Y. Elghazouli, B.A. Izzuddin. Modelling of the panel zone in steel and composite moment frames. *Engineering Structures*, **27(1)**, 129-144, 2005. doi:10.1016/j.engstruct.2004.09.008.

[19] CEN (European Committee for Standardisation), *EN 1998-1, Eurocode 8: Design of structures for earthquake resistance - Part 1 : General rules, seismic actions and rules for buildings*, Brussels, 2004

COMPDYN 2019
7th ECCOMAS Thematic Conference on
Computational Methods in Structural Dynamics and Earthquake Engineering
M. Papadrakakis, M. Fragiadakis (eds.)
Crete, Greece, 24–26 June 2019

ASSESSMENT OF EXISTING STEEL FRAMES WITH INFILLS UNDER MULTIPLE EARTHQUAKES

Luigi Di Sarno[1], Jing-Ren Wu[1], Mario D'Aniello[2], Silvia Costanzo[2], Raffaele Landolfo[2], Oh-Sung Kwon[3], Fabio Freddi[4]

[1] Dept. of Civil Engineering and Industrial Design, University of Liverpool
The Quadrangle, Brownlow Hill, Liverpool, United Kingdom
{luigi.di-sarno, jingren.wu}@liverpool.ac.uk

[2] Dept. of Structures for Engineering and Architecture, University of Naples Federico II
Corso Umberto I 40, Naples, Italy
{mdaniel, silvia.costanzo, landolfo}@unina.it

[3] Dept. of Civil and Mineral Engineering, University of Toronto
35 St. George Street, Toronto, Canada
os.kwon@utoronto.ca

[4] Dept. of Civil, Environment and Geomatic Engineering, University College London
Gower Street, London, United Kingdom
f.freddi@ucl.ac.uk

Abstract

Many existing steel multi-storey frames in Europe were designed prior to the provisions of modern seismic design codes; therefore, they often exhibit low resistance to earthquakes due to their insufficient energy dissipation capacity. However, the current framework for assessing existing structures in EC8-3 is inadequate and should be reviewed. Particular attention should be paid to the contribution from masonry infill walls as they significantly affect the modal properties and the lateral stiffness of structures. To this end, two 3D models of a two-storey steel moment-resisting frame were developed to assess the applicability of the current framework in EC8-3 to the infilled structures under multiple earthquakes through nonlinear analyses. The modelling of masonry infill walls was achieved through a macro-model using equivalent diagonal struts. The ground motions utilised during the analyses took the records of the recent 2016 Central Italy earthquake sequence. As part of the project HITFRAMES, this paper serves as a preparation for the experiment to be conducted in Greece.

Keywords: Existing steel frames, Assessment, Pseudo-dynamic testing, Seismic response, Modal calibration.

1 INTRODUCTION

Nowadays, modern seismic design codes have recognised the importance of the inelastic behaviour of structures during earthquake and provided guidelines for designing ductile structures with sufficient capability of dissipating energy. However, numerous existing steel frames were designed prior to the provisions of model seismic design codes and were designed to gravity loading only. Those frames are often characterised by inadequate energy dissipation capacity due to their non-ductile connections and slender beams and columns [1], and therefore, high vulnerability to earthquakes. Global collapse and severe local damage have been observed in such frames in the aftermath of the 2016 Amatrice earthquake in Central Italy. Public attention has been attracted to the urgent need of a rigorous framework of assessing the seismic vulnerability of existing steel frames [1, 2].

Many code-based procedures for assessing and retrofitting existing steel frames has been developed so far, such as EC8-3 in Europe [3] and ASCE41-13 in the US [4]. Those codified assessment procedures generally adopt the concept of performance-based earthquake engineering and allow both linear and nonlinear analysis of frame models to be carried out, though with some restrictions on the linear methods. However, a recent review of the EC8-3 by Araújo and Castro [4] summarised some inconsistencies and limitations in the European code, for example, the different analysis methods provided in EC8-3 may cause significant inconsistencies in demand estimations and it seems that the predefined capacity criteria for different limit states in terms of member plastic rotations are a direct reproduction of the former version of American code ASCE41-06, which were based on tests of typical American cross section profiles rather than the European profiles [4]. Another important issue is that the current EC8-3 only defines the behaviour requirements of non-structural members in a qualitative manner, through the definition of each limit states. Besides, since the EC8-3 requires safety check of every individual member, the assessment process can be extremely time-consuming and the onset of failure of a limit state is simply decided by the first member that exceeds corresponding criteria, which tends to neglect the redundancy of a structure. Consequently, further revision of EC8-3 is necessary for the next generation of Eurocode 8 regarding both the analysis methods and compliance criteria.

As an important part of the assessment of existing steel frames, selection of the most appropriate numerical model is strongly dependent on the specific target that is set to achieve. A comprehensive model that contains more detailing than a bare frame may lead to higher reliability of structural performance estimation, but this is not always true because of the complex nature of the interactions among structural and non-structural components, such as the masonry infill walls, beam-to-column connections and composite slab. It is now widely accepted that the contribution of infill walls to the lateral stiffness and strength of steel frame is significant and should be taken into consideration in assessing existing steel frames [1, 5]. Several previous studies have tried to develop simple but reliable models of masonry infill walls and incorporated them into bare frame models. A macro-model of masonry infill wall was proposed which uses a single equivalent strut in each diagonal direction with appropriate strut mechanical properties to capture the strut action caused by infill walls to the confining frames [5, 6, 7, 8, 9]. This macro-model has an advantage in terms of its combined efficiency and accuracy in the assessment of global response, despite some compromise has to be made to the local behaviour of infill walls. A valid constitution law also plays an essential role in the equivalent strut model due to the non-homogenous nature of the material [5].

The main aim of this study is to present the assessment of a case steel moment resisting frame (MRF) based on the procedure in EC8-3. Nonlinear static and dynamic analysis was performed to estimate the demand and capacity for each limit states. The steel frame was designed to sustain gravity loading only following the design code EC3. A 3D model was established in the Open System for Earthquake Engineering Simulation (OpenSees) analysis

software [10]. Special attention was paid to the contribution of masonry infills to the overall performance of the frame. In addition, multiple earthquakes were applied to the frame model in the nonlinear dynamic analyses so that potential cumulative damage on the structure was investigated as well. Capacity was assessed based on the criteria proposed in EC8-3 in terms of member plastic rotation. Criteria based on inter-storey drift ratio (IDR), which accounts for the stability of structures, were also used to assess the reliability of plastic rotation criteria.

2 ASSESSMENT FRAMEWORK IN EC8-3

This paper is aimed to present the assessment procedure of a steel frame based on the non-linear analyses in EC8-3, therefore, a brief description of the framework is presented. The focus of this study is nonlinear analysis; hence the procedure of linear analysis is not included here.

Three limit states are defined in EC8-3, namely the Damage Limitation (DL) limit state, the Significant Damage (SD) limit state and the Near Collapse (NC) limit state, compared to two in EC8-1 for general rules [11], which are the DL and ultimate limit state. By definition, as concluded in Table 1, the return periods for the DL, SD and NC limit state are 225, 475 and 2475 years respectively, corresponding to probabilities of exceedance of 20%, 10% and 2% in 50 years. It is interesting to notice that the ultimate limit state in EC8-1 is equivalent to the SD limit state in EC8-3 in terms of their return periods, while NC limit state is actually closer to the real collapse of structures, hence associated with a much longer return period. The explanation given is that NC limit state makes full use of the deformation capacity of structural elements, while SD limit state (ultimate limit state) leaves some residual lateral drift and stiffness and loading carrying capacity of vertical elements [2]. It is also worth noting that the DL limit state in EC8-1 has a shorter return period than that in EC8-3, so the former is more conservative than the latter. The above comparisons indicate that the three limit states for existing buildings are defined to prevent collapse of buildings rather than upgrading them to satisfy the design requirements for new buildings [4].

	EC8-3			EC8-1	
	DL	SD	NC	DL	Ultimate
Hazard level	225 years	475 years	2475 years	95 years	475 years
	or				
	20% in 50 years	10% in 50 years	2% in 50 years	10% in 10 years	10% in 50 years

Table 1: Performance requirements for different limit states in EC8-1 and EC8-3.

The EC8-3 also provides some guidance on the data collecting of existing buildings, where information of geometry, detailing and materials should be gathered. Three knowledge levels are summarised to deal with the uncertainties during the process of surveying, from limited to full knowledge level. A confidence factor is assigned to each knowledge level, which is used in the assessment of capacity as a partial safety factor. For the purpose of this study, full knowledge is assumed, thus a confidence factor of 1.0 is taken and no reduction is required in the safety verification.

Safety check in terms of demand and capacity is the last stage in the assessment framework of EC8-3. In the context of nonlinear analysis, demand can be taken as the results of analysis directly, but capacity differs between ductile and brittle structural elements. For ductile elements, their deformation capacity will be compared with the deformation demand, while for brittle elements, internal force capacity shall be compared with the corresponding force demand. In the case of steel frames, which is the case of this study, EC8-3 requires safety check

to be done considering the plastic rotation of columns and beams, where the capacity for each limit state is dependent on the yield rotation of each element, as summarised in Table 2. The table applies to Class 1 and 2 cross-sections only and the dimensionless axial force ν should not exceed 0.3. EC8-3 does not give any limits on other cross-sections or with higher value of ν. Recall that the criteria in Table 2 is in fact the same as the one used to be adopted in the American code ASCE41 for dimensionless axial force ν less than 0.2. For the determination of demand, i.e. the target displacement, in nonlinear static analysis, N2 method [12] is recommended by EC8-3.

Class of cross-section	DL	SD	NC
1	$1.0\theta_y$	$6.0\theta_y$	$8.0\theta_y$
2	$0.25\theta_y$	$2.0\theta_y$	$3.0\theta_y$

Table 2: Plastic rotation capacity proposed in EC8-3 with dimensionless axial force $\nu \leq 0.3$.

For non-structural elements, requirements are described in the definition of three limit states qualitatively. For DL limit state, infill walls may experience some cracking, but damage shall be repaired at a low cost. For SD limit state, although infill walls are damaged, but out-of-plane failure shall not happen. Finally, the NC limit state allows infill walls to be significantly damaged or even collapse. Quantitative specifications are not included in the current version of EC8-3.

3 CASE STUDY AND NUMERICAL MODELLING

The building considered in this study is a two-storey steel MRF, which has a rectangular layout in plan. The frame is 13.5 metres long, consisting of three bays, 8.5 meters in width and 6.6 metres in height with a storey height of 3.3 metres. Figure 1 shows the plan and side view of the frame. Composite floor slab and masonry infill walls are omitted for clarity. The steel frame was designed to resist gravity load only and does not have sufficient lateral stiffness and strength to survive a strong earthquake. The steel grade for all beams and columns is S355. The primary and perimeter beams are designed to be IPE270, all other beams are IPE200 and columns are HE240A. Moreover, beam-to-column connections are full penetration weld connection and the infill walls consist of two layers of 80-mm thick perforated bricks with a compressive strength of 9.7 N/mm^2 bound together through M5 mortar. Regarding the loading conditions, the self-weight of slab was taken as 240 kg/m^2, the density of bricks is 855 kg/m^3 and a live load of 2 kN/m^2 is also accounted for in the design.

	Cracking	Ultimate	Residual
Axial force (kN)	183	239	24
Strain	0.00009	0.00034	0.01063

Table 3: Modelling parameters of the trilinear curve for masonry infill walls.

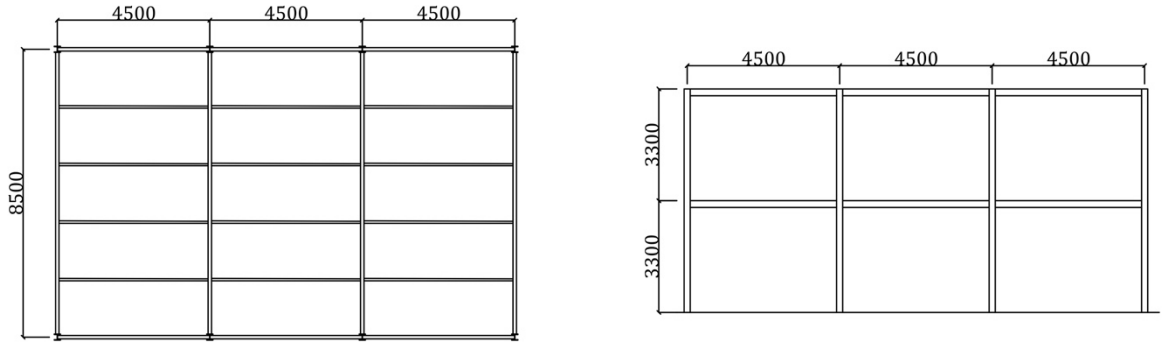

Figure 1: Plan layout and side view of the steel MRF.

Two 3D models of this steel MRF were established in OpenSees [10], namely a bare frame and an infilled frame. Columns were modelled using force-based beam-column elements with fibre section and 10 integration points along the length using Gauss-Lobatto integration method. Besides, the Steel01 material, which is a bilinear elastoplastic material model, was considered for structural steel with a hardening ratio of 0.02. Plastic hinges in beams were assumed to form at the ends of members, through lumped plasticity zero-length elements. The zero-length elements possess a trilinear moment-rotation relationship based on the Ibarra-Krawinkler-Deterioration (IKD) model [13, 14] to represent the rotational behaviour of beams. The parameters if the IKD model were calibrated based on finite element analyses carried out in ABAQUS 6.14. Rigid diaphragm action was achieved using rigid diagonal struts. Regarding the infills, the equivalent strut model [5] was chosen due to its simplicity and accuracy for evaluating global response. The constitution law was based on the Fardis-Panagiotakos model, which is a trilinear curve accounting for the cracking and ultimate strength of masonry infills, as well as degrading after the ultimate strength is reached [6]. The model applies to compression only and zero tension is considered. Since the modelling of infill walls is a key point in this study, the modelling parameters are summarised in Table 3. The analyses were performed in the longitudinal direction of the frame, as shown in Figure 1, where the weak axis of columns was involved and the contribution of infills were more significant.

4 ASSESSMENT RESULTS

4.1 Modal analysis

A modal analysis was performed at the beginning to capture the basic modal properties of the frame and the results are summarised in Table 4. The information obtained here will be helpful in the following assessment of the steel frame.

		1st mode	2nd mode
Period (sec)		0.74	0.25
Modal mass (%)		92%	8%
Mode shape	1st floor	0.42	1.00
	2nd floor	1.00	-0.54

Table 4: Modal property of the bare frame in the longitudinal direction.

It is anticipated from Table 4 that the seismic behaviour of the frame will be dominated by the fundamental mode, with a modal mass that accounts for 92% of the total mass. The modal

analysis was performed on the bare frame only. The presence of infills increases the initial lateral stiffness by a considerable amount, hence the initial fundamental period of the infilled frame is much lower than that of the bare frame, which is around 0.05 sec. However, since the masonry infills crack and fail quickly during the analysis, a quick drop was observed in the lateral stiffness of the infilled frame, hence the fundamental period was very unstable. It was also expected that the infilled frame would eventually have similar fundamental period to the bare frame after the loss of all infill walls.

4.2 Nonlinear static analysis

A total of four pushover analyses were carried out in this study. EC8-3 requires at least two lateral load patterns should be used in pushover analysis, namely a uniform pattern and a modal pattern. The uniform pattern (denoted as U) consists of lateral loads proportional to the lumped mass of each node, while the modal pattern (denoted as M) includes lateral loads proportional to both the mass and first mode shape of each node. Both of the two load patterns were applied to the bare and infilled frame. The performance points (demand) were determined based on the N2 method [12] suggested in EC8-1. The response spectrum adopts the Type 1 elastic response spectrum in EC8-1 for ground type B, and the reference peak ground acceleration was taken as 0.1975, 0.25 and 0.4275g for DL, SD and NC limit state, respectively. The choice of these parameters was based on the seismicity in Central Italy, where severe earthquake events have occurred in the past few years, causing collapse of numerous steel MRFs. Figure 2 shows the response spectrum in acceleration-displacement (AD) form for each limit state, as well as the capacity curves for the original frames and the equivalent SDOF systems. Since the uniform and modal lateral load patterns provided very similar capacity curves, only the seismic demands obtained from the modal pattern are presented in this paper. The global and inter-storey drift ratios at each performance point are also presented in Table 5.

It is clearly shown in Figure 2 that the presence of infill walls significantly increased the initial stiffness and maximum base shear of the frame. Besides, based on a damage assessment, it is found that columns in both models yield prior to the beams, which remain in elastic range up to NC limit state. This weak column-strong beam (WCSB) scenario is undesirable in modern seismic design code, which tends to concentrate plastic deformation within certain floors and increase seismic demands [15, 16]. It is also observed that for the bare frame, no plastic hinges were formed in columns at the DL and SD limit state. However, at NC limit state, plastic hinges were found in all ground floor columns of the bare frame, indicating that the frame was about to lose its load carrying capacity in the vertical direction. On the other hand, for the infilled frame, plastic hinges began to form at the point of maximum base shear, right after the exhaustion of ground floor infill walls. The turning point at 1.15% global drift marks the formation of plastic hinges in all ground floor columns. Apparently, the columns in the infilled frame failed quickly than those in the bare frame. This is possibly due to the strut action of the infill walls which caused higher local force on columns. In addition, as a result of the WCSB characteristic, all infills on the ground floor collapsed at the point of maximum base shear while those on the first floor barely cracked. Therefore, the presence of infills had great effects on the seismic behaviour of steel MRFs, emphasising the necessity of including infill walls in the seismic assessment.

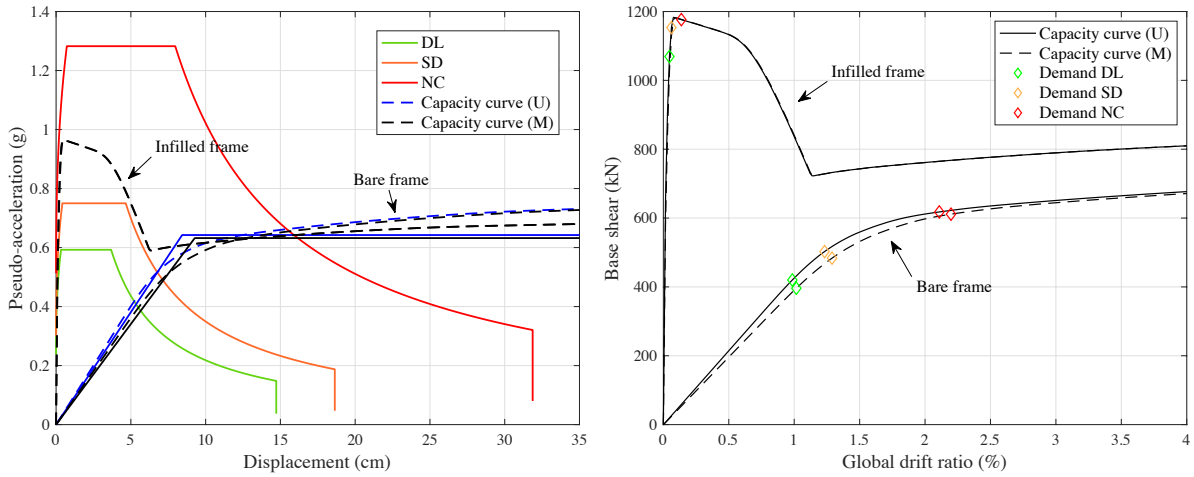

Figure 2: Response spectrum in AD form and capacity curves of the original frames (right) and the equivalent SDOF systems (left).

		Bare			Infilled		
		DL	SD	NC	DL	SD	NC
Global	Uniform	0.99	1.23	2.11	0.04	0.06	0.14
	Modal	1.02	1.29	2.20			
Ground floor	Uniform	1.13	1.45	2.88	0.08	0.09	0.26
	Modal	1.09	1.40	2.78			
1st floor	Uniform	0.81	0.98	1.27	0.02	0.02	0.01
	Modal	0.94	1.18	1.62			

Table 5: Global and inter-storey drift ratios (%) obtained from nonlinear static analyses.

An important step of the N2 method in EC8 is that an idealised bilinear curve should be derived to represent the behaviour of the equivalent SDOF system, as presented in Figure 2. However, a bilinear idealisation seems not appropriate in the case of infilled frames based on the shape of its capacity curve. As a result, the initial stiffness was adopted to continue the N2 method. Apparently, from Figure 2 and Table 5, the seismic demands on the infilled frame is much lower than those on the bare frame, because the presence of infill walls resulted in a sharp increase in the lateral stiffness and strength. However, the N2 may yield non-conservative estimation at the short-period range due to the high sensitivity of inelastic displacement to the change of structures [12]. In this study, the infill walls cracked and failed shortly after the start of pushover analysis, caused the global lateral stiffness to quickly decrease and eventually to be the same as that of the bare frame. Therefore, further research should be carried out to find out a more accurate rule for structures in the short-period range, where the effects due to changes of structural parameters are accounted for.

4.3 Nonlinear dynamic analysis

The time-history analysis utilised the records for the earthquake sequence initiated in Amatrice, a town in Central Italy, on 24th of August 2016. The Amatrice earthquake sequence includes one mainshock and four aftershocks whose peak ground accelerations are larger than 1.0g. The basic information of those strong ground motions is provided in Table 6, and the accelerogram and pseudo-acceleration spectrum for 5% damping are shown in Figure 3. EC8-3 requires at least 7 earthquake records to be involved in the time-history analysis, however,

the focus in this analysis is to investigate the potential effects of earthquake sequence and the presence of infill walls. Therefore, only one earthquake sequence is considered in this study.

As shown in the spectrum in Figure 3, the spectral acceleration of the unscaled record of mainshock at the fundamental period is 0.365g, which is less than the spectral acceleration at fundamental period corresponding to the DL limit state. This indicates that the frame may still be within the elastic range under the unscaled records. In order to observe some damage on the frame, the entire earthquake sequence was scaled by a factor of 1.37 and 2.36 such that the spectral acceleration of the new earthquake records at fundamental period equal to the one corresponding to the SD and NC limit state, thus the two scaled earthquakes are denoted as SD and NC, respectively. The spectral acceleration at fundamental period was used as the scaling parameter because as mentioned in the modal analysis, the seismic response of the steel frame in this study is dominated by the first mode, which takes up more than 90% of total mass. The mainshock record was applied to the frame alone at first and then with its aftershocks to represent single and multiple earthquakes.

Event	Date	M_w	M_L	R_{epi} (km)	PGA (g)	PGV (cm/s)	PGD (cm)
M/S	24-Aug-2016	6.0	6.0	8.5	0.87	43.5	8.5
A/S1	24-Aug-2016	4.3	4.5	3.6	0.19	6.8	0.5
A/S2	24-Aug-2016	5.3	5.4	20.9	0.11	5.1	0.9
A/S3	25-Aug-2016	4.4	4.3	3.6	0.23	9.6	0.6
A/S4	26-Aug-2016	4.8	4.7	3.1	0.34	11.0	0.6

Table 6: Summary of the Amatrice earthquake sequence.

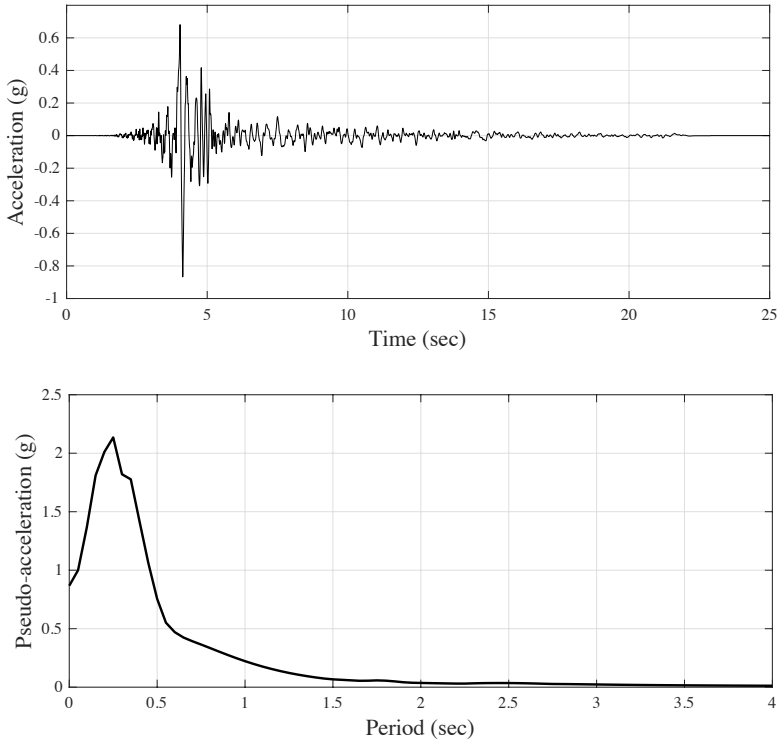

Figure 3: Accelerogram and pseudo-acceleration spectrum for 5% damping of the mainshock.

		Bare		Infilled	
		SD	NC	SD	NC
Global	single	1.26	2.18	0.26	1.34
	multiple	1.26	2.18	0.26	1.34
Ground floor	single	1.46	2.73	0.50	2.67
	multiple	1.46	2.73	0.50	2.67
1st floor	single	1.37	1.87	0.03	0.04
	multiple	1.37	1.87	0.03	0.04
Residual drift	single	0.05	0.44	0.02	0.60
	multiple	0.05	0.44	0.02	0.60

Table 7: Peak global and inter-storey drift ratio and residual drift ratio (%) obtained from nonlinear dynamic analyses.

The failure mechanisms in time-history analysis under single or multiple earthquakes are similar to those in the pushover analysis. The occurrence of column plastic hinges and infill failure is limited to the ground floor, while beams are too strong to enter plastic range. Besides, the presence of infill walls led to higher local force at beam-to-column connections and accelerated the yield of columns.

The peak global, inter-storey and residual drift ratios of the bare and infilled frame obtained under single and multiple earthquakes are presented in Table 7. It is observed that there is no difference between the peak and residual drift ratios under single and multiple earthquakes. This is primarily due to the WCSB characteristic of the frame which led to the failure of columns but kept beams safe. Also, as a matter of numerical modelling, deterioration in unloading and reloading was not considered in the columns, and the aftershocks were not strong enough to activate columns into plastic range again. This is a major limitation of this study and further study addressing this issue should be conducted in the future. It is also noticed in Table 7 that the ground floor drift ratio of the infilled frame was nearly twice the global drift ratio, indicating that the global drift was in fact equal to the ground floor drift. This behaviour is significantly different from that of the bare frame, possibly due to the quick failure of ground floor infill walls and columns, causing the lateral stiffness of ground floor to be much lower than the first floor. When comparing with the results from nonlinear static analyses, good consistency was found for the bare frame. However, for the infilled frame, nonlinear static analysis gives extremely underestimated prediction of seismic demands, although it captured the same behaviour of lateral drift as nonlinear dynamic analysis did.

4.4 Safety verifications

At the safety verification stage, the seismic demands obtained from the nonlinear analyses are compared with the capacity determined based on the compliance criteria in EC8-3, which are based on the rotation of beams and columns. EC8-3 also requires that no yielding or buckling shall occur in columns for DL and SD limit state. To calculate the yield rotation of columns, the following equation is adopted:

$$\theta_y = \frac{M_{pl,Rd} L_s}{3EI}\left(1 - \frac{N_{Ed}}{N_{pl,Rd}}\right) \quad (1)$$

This equation is not proposed in the EC8-3 and is slightly different from the one proposed in the American code which uses half the length of element in the equation rather than the actual shear span L_s. Apart from the criteria proposed in EC8-3, previous studies also suggested the

check of IDR to ensure the stability of structures [2, 17, 18]. The recommended criteria of IDR in [18] for SD and NC limit state is given in Table 9. The value for DL limit state was derived from the serviceability requirement in EC8-1. Recall that the DL limit state in EC8-1 is more conservative than the DL limit state defined in EC8-3, the value of 1% may also be slightly conservative.

The capacity curves from pushover analyses incorporated capacity points are presented in Figure 4. In Figure 4, R represents the capacity of element rotation while D represents the capacity of IDR. It is obvious that for both frames, the rotation criteria only give more conservative predictions at the DL limit state. This indicates that the performance level at SD and NC limit state are not guaranteed by only using the rotation criteria. Also, in the case of bare frame, the locations of capacity points well match the definition of each limit state in EC8-3. However, for the infilled frame, the capacity points tend to correspond to a worse situation than that defined in EC8-3. For the safety verification, the bare frame failed the DL limit state but fulfilled the requirement of SD and NC limit state.

	DL	SD	NC
IDR (%)	1.0	2.5	4.0

Table 8: Criteria in terms of IDR for each limit state.

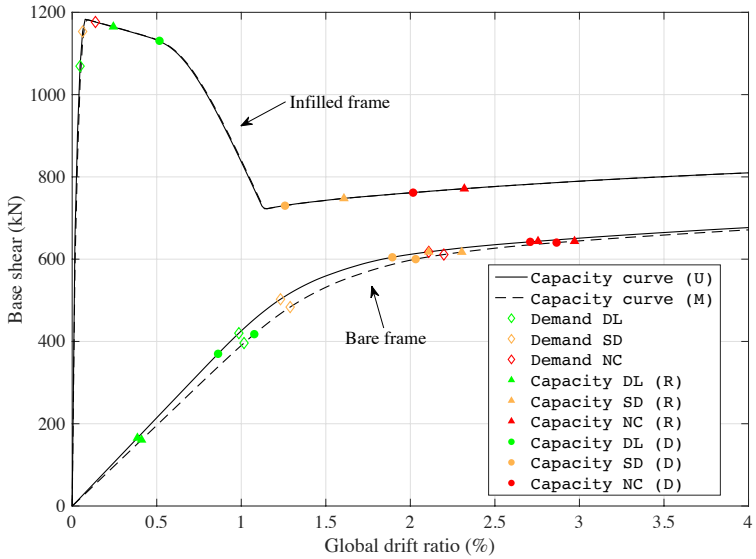

Figure 4: Capacity curves with demand and capacity points for safety verification.

The verification based on the results from nonlinear dynamic analyses was carried out by firstly checking each individual beam and column and then the IDR in Table 7. It is found that the bare and infilled frame survived the SD limit state under the SD earthquake, and survived the NC limit state only under the NC earthquake. Therefore, good consistency has been observed in the final verification results between the nonlinear static and dynamic analysis.

5 CONCLUSIONS

This paper presents a brief assessment of a steel MRF based on the framework in EC8-3 using nonlinear static and dynamic analysis. The potential effects of the presence of masonry infill walls and the use of multiple earthquakes instead of a single earthquake are investigated.

A modal analysis was performed at first, indicating that the seismic behaviour of the steel frame is dominated by its first mode, with a natural period of 0.74 sec. Nonlinear static and dynamic analyses were also performed and the following findings are concluded:

1. The presence of infill walls increases the initial lateral stiffness and strength significantly. An approximate 100% increase is found in the maximum base shear due to the incorporation of infill walls. The strut action induced by the infill walls causes the columns to fail earlier, which also affects the failure mechanism of the frame.
2. The sharp increase in the initial lateral stiffness puts the infilled frame in the short-period range, where the accuracy of N2 method is not guaranteed and non-conservative estimation may be provided. Big differences were found between the global and inter-storey drift ratios for the infilled frame from pushover and time-history analyses, while good consistency was observed in the performance points obtained for bare frame.
3. The use of multiple earthquakes does not influence the assessment results in this case study. This is because of the WCSB nature of the frame structure, whose failure mechanism is controlled by columns, as well as the modelling of structural steel for columns, which does not consider any deterioration in unloading and reloading stiffness.
4. The use of criteria based on beam and column rotation proposed by EC8-3 is not enough in this study, which does not address the issue due to stability. A criterion based on IDR gives more conservative capacity points than the rotation criteria for this case frame under SD and NC limit state.

Further research should be carried out to address the applicability of N2 method in the short-period range, which accounts for the presence of essential non-structural elements like the infill walls. This limitation of the N2 method also restrict the applicability of the bilinear idealisation proposed in EC8-1, which is no longer suitable for the case of an infilled frame. Further research using refined models which take degrading and deterioration of columns into consideration should also be conducted to assess the cumulative damage in columns under multiple earthquakes.

ACKNOWLEDGEMENT

The financial support from Seismic Engineering Research Infrastructure for HITFRAMES (SERA) Project, funded within the H2020-INFRAIA-2016-2017 Framework Programme of the European Commission under grant agreement No.730900 is greatly appreciated. Any opinions, findings and conclusions, or recommendations expressed in this paper are those of the authors and do not necessarily reflect those of SERA sponsors.

REFERENCES

[1] L. Di Sarno, F. Paolacci, A.G. Sextos, Seismic performance assessment of existing steel buildings: a case study, *InKey Engineering Materials,* 763, 1067-1076.

[2] M. Araújo, J.M. Castro, A critical review of European and American provisions for the seismic assessment of existing steel moment-resisting frame buildings. *Journal of Earthquake Engineering,* 22(8), 1336-1364, 2017.

[3] British Standards Institution, BS EN 1998-3:2005, Eurocode 8. *Design of structures for earthquake resistance – Part 3: Assessment and retrofitting of buildings,* London: BSI; 2005.

[4] American Society of Civil Engineers (ASCE), ASCE 41-13, *Seismic evaluation and retrofit of existing buildings,* Reston, Virginia: 2014.

[5] N.M. Noh, L. Liberatore, F. Mollaioli, S. Tesfamariam, Modelling of masonry infilled RC frames subjected to cyclic loads: State of the art review and modelling with OpenSees. *Engineering Structures,* 150, 599-621, 2018.

[6] M.N. Fardis, T.B. Panagiotakos, Seismic design and response of bare and masonry-infilled reinforced concrete buildings part II: infilled structures. *Journal of Earthquake Engineering,* 1(03), 475-503, 1997.

[7] P.G. Asteris, S.T. Antoniou, D.S. Sophianopoulos, C.Z. Chrysostomou, Mathematical macromodeling of infilled frames: state of the art. *J Struct Eng,* 137(12), 1508-1517, 2011.

[8] G. Al-Achaar, *Evaluating strength and stiffness of unreinforced masonry infill structures,* Construction Engineering Research Laboratories, Report No. ERDC/CERL TR-02-01, USA, 2002.

[9] A. S. Elnashai, L. Di Sarno, Fundamentals of Earthquake Engineering, Wiley and Sons, UK, 2008.

[10] S. Mazzoni, F. McKenna, M.H. Scott, G.L. Fenves, *OpenSees command language manual,* Pacific Earthquake Engineering Research (PEER) Centre, 264, 2006.

[11] British Standards Institution, BS EN 1998-1:2004, Eurocode 8. *Design of structures for earthquake resistance – Part 1: General rules, seismic actions and rules for buildings,* London: BSI; 2004.

[12] P. Fajfar, A nonlinear analysis method for performance-based seismic design. *Earthquake spectra,* 16(3), 573-92, 2000.

[13] L.F. Ibarra, R.A. Medina, H. Krawinkler, Hysteretic models that incorporate strength and stiffness deterioration, *Earthquake engineering & structural dynamics,* 34(12), 1489-511, 2005.

[14] D.G. Lignos, H. Krawinkler, Deterioration modeling of steel components in support of collapse prediction of steel moment frames under earthquake loading, *Journal of Structural Engineering,* 137(11), 1291-302, 2010.

[15] C.W. Roeder, S.P. Schneider, J.E. Carpenter, Seismic behavior of moment-resisting steel frames: analytical study, *Journal of Structural Engineering,* 119(6), 1866-84, 1993.

[16] S.P. Schneider, C.W. Roeder, J.E. Carpenter, Seismic behavior of moment-resisting steel frames: Experimental study, *Journal of Structural Engineering,* 119(6), 1885-902, 1993.

[17] T.L. Karavasilis, N. Bazeos, D.E. Beskos, Maximum displacement profiles for the performance based seismic design of plane steel moment resisting frames, *Engineering Structures,* 28(1), 9-22, 2006.

[18] SEAOC: Recommended lateral force requirements and commentary, 7th ed. 1999.

COMPDYN 2019
7th ECCOMAS Thematic Conference on
Computational Methods in Structural Dynamics and Earthquake Engineering
M. Papadrakakis, M. Fragiadakis (eds.)
Crete, Greece, 24–26 June 2019

NUMERICAL EVALUATION OF THE BEHAVIOUR FACTOR OF LIGHTWEIGHT STEEL LATERAL FORCE RESISTING SYSTEMS ACCORDING TO FEMA P695

Sarmad Shakeel, Luigi Fiorino, and Raffaele Landolfo

Department of Structures for Engineering and Architecture, University of Naples "Federico II", Italy
e-mail: sarmad.shakeel@unina.it

Abstract

Seismic design regulations rely on certain factors to reduce the earthquake actions due to inherent ductility and overstrength of the lateral force resisting systems. The behaviour factors given in Eurocodes are one such example, which when applied during the design process will ensure the life safety performance level of a building. Light-Weight Steel (LWS) structures fabricated with Cold Formed Steel (CFS) profiles are increasingly widespread in earthquake prone regions, however the current in practice edition of Eurocodes fails to acknowledge their seismic performance by not providing behaviour factors for them. The study presented herein addresses this issue by evaluating behaviour factor for the two commonly used LWS systems: CFS strap braced walls and CFS shear walls with gypsum board sheathing through FEMA P695 methodology. For each type of system, a set of archetypes, which represent a range of design parameters and building configurations are designed following the capacity design approach and their response is idealized by nonlinear numerical models. The performance of archetype models is evaluated systematically through the static pushover and the incremental dynamic analysis under a suite of forty-four normalized and scaled earthquake records, representing the probable seismic hazard to the buildings. Finally, by calculating the collapse probability while also considering the uncertainties from various sources, the suitability of a trial value of the behaviour factor used in the design phase of archetypes is evaluated. Based on the results, it is concluded that a behaviour factor of 2.5 and 2.0 for CFS strap braced walls and CFS shear walls with gypsum board sheathing is appropriate.

Keywords: Cold-formed steel, Shear walls, Gypsum board sheathing, Strap braced walls, Behaviour factor, FEMA P695

1 INTRODUCTION

Improved structural efficiency and superior environmental performance of Light-Weight Steel (LWS) constructions made with a Cold Formed Steel (CFS) frame and sheathing panels have made them stand out as a preferable alternative in contrast to traditional masonry or concrete constructions for low rise building applications. To resist the earthquake horizontal loads, two main energy dissipative solutions are used in LWS constructions: strap-braced and sheathed-braced. Lateral resistance can be provided by thin steel straps acting as braces in an X configuration or sheathing-braced solutions with steel sheets, wood or gypsum-based panels can provide the lateral bracing effect to withstand the horizontal loads.

Currently, only North American standard for seismic design of CFS structures AISI S400 [1] provides design guidelines for various typologies of Lateral Force Resisting Systems (LFRS) used in CFS constructions. In contrast with AISI S400, the main European earthquake standard EN 1998-1 [2] lacks guidelines for any type of LFRS used in LWS constructions. In order to bridge this gap, a series of numerical and experimental investigations were carried out at University of Naples Federico II, Italy, in recent years to better understand the seismic response of these constructions and to propose design guidelines within the European design framework. These studies are part of a wider effort [3–5] carried out at University of Naples Federico II to better understand the seismic performance of steel structures.

Behaviour factors are employed in EN 1998-1 for buildings equipped with LFRS to reduce the effect, of seismic actions due to building's inherent structural ductility and overstrength. The behaviour factor for any structural system can be evaluated preliminary through either a test-based or a numerical approach. In a test-based approach, usually monotonic and cyclic tests [6] of the prototypes representative of LFRS are used to evaluate the seismic response, while a numerical approach make uses of several building archetypes to evaluate the collapse probability of the LFRS system and to make a judgement on reasonable value of the behaviour factor. A more elaborate methodology is outlined by FEMA document P695 [7], which uses nonlinear numerical analysis techniques, and explicitly considers uncertainties in ground motions, modelling, design, and experimental data to achieve an acceptably low probability of collapse of the LFRS for a particular value of behaviour factor. The work presented in this paper uses this methodology to evaluate behaviour factor for CFS gypsum-sheathed shear walls and strap-braced walls (Fig. 1).

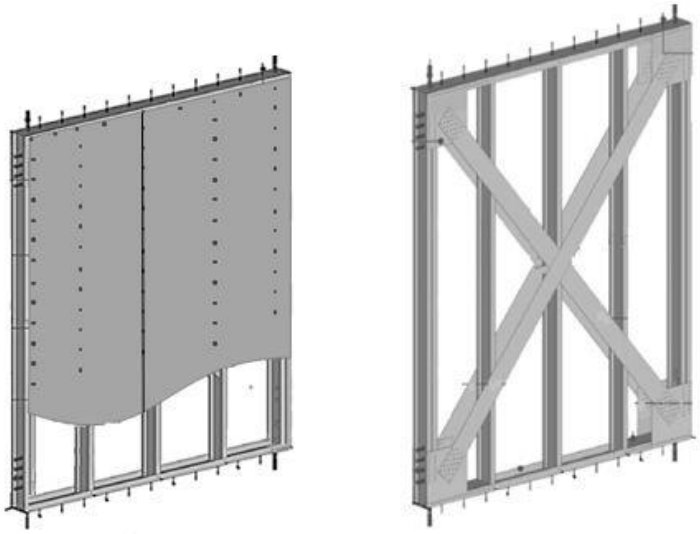

a) b)

Figure 1. a) CFS gypsum-sheathed shear wall b) CFS strap-braced wall.

The methodology outlined by FEMA P695 [7] considers an archetypes design space to characterize the system behaviour , which is designed using a trial value of behaviour factor and whose seismic response is idealized by nonlinear numerical models. A value of 2.5 and 2.0 is used as a trial value for CFS strap-braced walls and CFS gypsum-sheathed shear walls, respectively. The seismic performance of the archetypes is evaluated systematically through static pushover and incremental dynamic analysis techniques, by calculating the collapse probability, while also considering the uncertainties from various sources. On the basis of collapse probability, the suitability of trial value of behaviour factor used in the design phase of archetypes is evaluated. The organization of this paper also follows the arrangement of the different steps in defined by the FEMA methodology.

2 ARCHETYPE SELECTION AND DESIGN

A set of 14 archetypes (Table 1) are designed separately for each LFRS under investigation. The archetypes differed with each other in terms of occupancies, building heights (H) and seismic hazards. The complete design space is considered as one performance group due to the fact that the changes in structural configuration and gravity loads among different archetypes will not alter the behaviour of the LFRS significantly. Three anonymous geographical sites with low, medium and high seismic intensity levels representative of the type of seismic hazard exposed to European continent are assumed as location of the archetypes. The Low, Medium and High seismic hazard are assigned with reference peak ground acceleration ($a_{g,R)}$ values of 0.1g, 0.2g and 0.3g, respectively, in case of gypsum-sheathed shear walls and with the values of 0.15g, 0.25g and 0.35g, respectively in case of strap-braced walls. The reason for the choice of a comparatively lower hazard for gypsum-sheathed shear walls is due to their limited strength, with which it was not possible to design a reasonable number of archetypes at the same hazard level as that for strap-braced walls. All of the archetypes are assumed to be built on Soil class C and belong to an Importance class II according to EN 1998-1 [2].

CFS gypsum-sheathed shear walls			CFS strap-braced wall		
Archetype ID*	Design base shear [kN]	No of walls in each direction	Archetype ID*	Design base shear [kN]	No of walls in each direction
R1L	129	4	R2L	292	4
R2L	175	6	R3L	470	6
R3L	322	12	R4L	644	8
R4L	469	16	R2M	486	6
R1M	258	10	R3M	783	8
R2M	350	12	R4M	1073	10
R3M	528	18	R2H	681	8
R1H	387	14	R3H	1096	10
R2H	525	18	O1L	212	6
O1L	101	4	O2L	475	6
O2L	332	12	O1M	352	6
O1M	203	8	O2M	792	6
O2M	504	18	O1H	494	6
O1H	304	12	O2H	1108	10

*Archetype ID: First letter: (Type of Occupancy R-residential or O-office), Second number: umber of storeys, Third alphabet: Level of seismic hazard (L-low, M-medium or H-high)

Table 1. Archetype design space

Two type of occupancies are considered for the archetypes: residential and office. The major differences among the two occupancies is different intensity of the live loads they cause. In particular, EN 1990 [8] defines a live load of 2.0 kN/m^2 and 3.0 kN/m^2 for residential and office type of occupancies, respectively. The two occupancies also differ with each other in terms of accessibility to roof. In case of residential occupancy, the roof is considered accessible with an expected live load equal to the floors i.e. 2.0 kN/m^2, while the roof of the office archetype is considered inaccessible, except for normal maintenance and repair, which resulted in 0.4 kN/m^2 expected live load. Two different types of floor are used: a lightweight steel floor sheathed with panels (light solution) and a composite steel concrete deck (ordinary solution). The use of light floors is limited to archetypes with shear walls braced archetypes which resulted in an excessive design base shear, if an ordinary floor is used. In case of archetypes with strap-braced walls, only ordinary floors are used. The resulting dead loads on floors due to light or ordinary floor, ceilings and vertical partitions are 1.30 or 1.80, 0.10 and 0.80 kN/m^2, respectively, while the roof dead loads due to light or ordinary roof and ceilings are 1.40 or 2.30 and 0.10 kN/m^2, respectively. In addition to dead loads, a snow load of 1.00 kN/m^2 and a wind load of 0.35 kN/m^2 is assumed to be acting on the roof of archetypes. The height of the archetypes reflected the current trend of LWS construction application in seismic areas, which is only limited to low rise buildings. For residential building 3.0 to 12.0 m high archetypes are selected, while for office archetype maximum height of archetype is limited to 6.0 m. Total height of each storey for both type of occupancies is 3.0 m including a floor depth of 0.3 m.

The archetypes are structurally designed according to the relevant parts of Eurocodes. The design of archetypes against the gravity load is carried out using EN 1993-1-3 [9], which provides supplementary rules for CFS members and sheeting. The lateral loads acting on the archetypes included a wind load of 0.70 KN/m^2 and earthquake loads as explained earlier. Lateral force method in EN 1998-1 [2] is used to compute the design base shear, because all of the archetypes meet the criteria of regularity in structural plan and elevation. The seismic design base shear is distributed over height of structure corresponding to seismic mass of each floor or the first modal shape. Both types of lateral force distribution are used in pushover analysis of archetypes as explained in upcoming Sections in order to obtain the worst-case scenario response. A 2.40 m wide shear wall configuration, which is already tested by authors [6] and has shown acceptable performance under both cyclic [6] and shake table testing [10], is selected as the only configuration used here for archetypes with gypsum-sheathed shear walls as the LFRS. On the other hand, three wall configurations with Low, Medium and High shear force capacities were used for archetypes with strap-braced walls as LFRS. The low and medium capacity walls were tested experimentally in past [11], while high capacity wall was designed based on formulations given in [12].

3 NUMERICAL MODELLING

Numerical modelling of the archetypes is needed for their seismic performance evaluation. It is expected from the building using CFS gypsum-sheathed shear walls as LFRS, that it would mainly develop the nonlinear mechanism only at the sheathing connections, while rest of the element would remain elastic. For strap-braced wall, the main nonlinear mechanism only happens in steel straps due to their plastic yielding. Thus, the simulation of response of the walls is the single most important factor in the modelling of complete building response. OpenSees software [13] is used for developing the numerical models. A two-stage modelling approach is adopted. At first, numerical model for single wall is developed and calibrated based on the experimental results and then in the later stage, the model of the single wall is incorporated in

a complete building model representing the global response of the archetype. The choice of the type of model for single wall and different modelling options available in literature are explained in detail by authors in [14] for CFS gypsum-sheathed shear walls and in [12] for CFS strap-braced walls. A simplified model (Fig. 2), which relies on a pair of nonlinear diagonal truss elements is used to simulate the response of a wall. Pinching4 material available in OpenSees is used to represent the nonlinearity in truss elements, which have a unit area and are the representative of the behaviour of the walls as a whole. Rest of the wall elements, including chord studs and hold-down devices are also modelled as elastic elements, which are necessary for the transfer of forces to the rest of building.

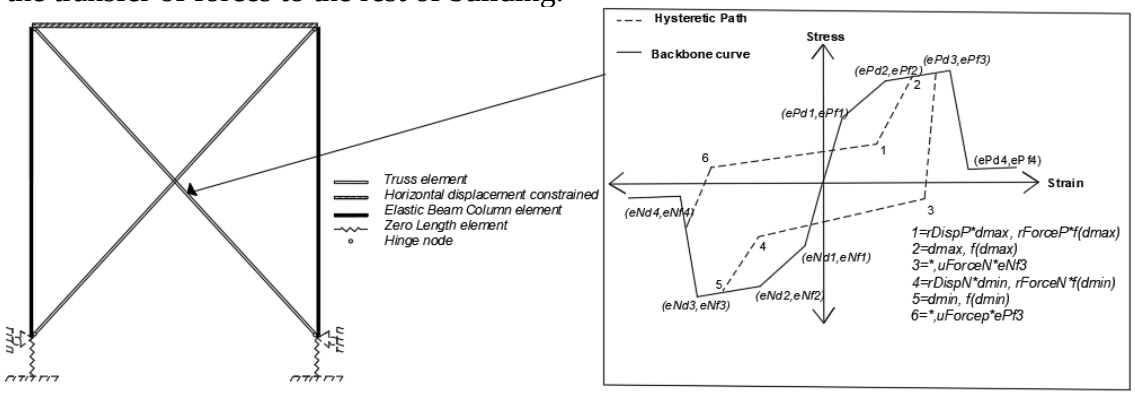

Figure 2. Simplified model for the walls

A three-dimensional model representing the most important structural elements that would have significant implications on the global seismic response of the building is created for each archetype. The skeleton of a typical CFS building is made by joining the wall elements, such as studs and wall tracks, to the floor elements, such as floor tracks and joists. The gravity studs are modelled using truss elements. Not all of the gravity load bearing studs are modelled, because the presence of gravity load bearing studs does not affect much the seismic performance of the archetypes since they cannot resist any bending moments. Moreover, adding all the studs in model would make the model unnecessarily complex. Floor elements (joist, tracks and composite floor) are modelled as the rigid elastic beam column elements. To capture the lateral displacement arising from P-delta effect, a rigid frame made of axially rigid elastic beam column elements having a co-rotational coordinate transformation is connected to the building in the direction of seismic action. Moment releases are created at the ends of columns of P-delta frame and are linked to the main building frame using the rigid truss elements. Moment releases at the ends of columns are intended to avoid any transfer of moments from P-delta fame to main frame and hence only transmitting the axial force, which induce an equivalent lateral displacement in the main frame. In the actual building, the studs are truss elements, and with the truss elements, it's not possible to simulate the p-delta effect. This is the main reason of using a separate frame. Gravity load is applied to the P-delta columns at floor levels. More information on modelling of CFS archetypes is give in [15]. For dynamic analysis, a 2% damping ratio is used based on the Rayleigh damping model. This 2% value reflected the measured damping values during the shaking table experiments [10] on a two storey CFS building.

4 SEISMIC ANALYSIS AND RESULTS

4.1 Non-linear static analysis

FEMA P695 [7] methodology uses non-linear static analysis to estimate archetype overstrength by calculating the ratio of maximum base shear resistance (V_{max}) of archetype obtained

through non-linear static analysis to the design base shear. After achieving the maximum base shear resistance, all archetype models have the concentration of damage at a ground storey in case of archetypes with shear walls, while in case of archetypes with strap-braced walls, the story with the damage concertation varied from case to case, depending on the distribution of shear resistance over the height of archetype. Moreover, this particular difference is due to the difference in design of both systems. In case of shear walls, all stories had a same design shear resistance, since there was only one configuration of gypsum-sheathed shear wall used in all archetypes on all floors. While in case of archetypes with strap-braced walls, the design shear resistance descended with ascending heights, since there were three different types of wall configurations used in archetypes design (see Section 2). The response in two planar directions do not differ much in terms of V_{max} in most cases, while the ultimate roof displacement (δ_u) presented slight differences. Ultimate roof displacement (δ_u) is taken as the roof displacement at the point of 20% strength loss ($0.8V_{max}$) in pushover analysis.

Additionally, the pushover analysis is also used to compute the period-based ductility according to formulations in FEMA, which is used to evaluate the effect of spectral shape of different earthquake records, used for dynamic analysis, on the archetype performance. Subsequently, the final value of over-strength and period-based ductility for each archetype is computed based on its average response in both planar directions and under both types of load distribution patterns based on FEMA P695 recommendations. These load patterns corresponded to the first modal shape, which has linearly increasing displacement over the height of an archetype or to the distribution of seismic mass of each floor over the height of an archetype.

4.2 Non-linear Incremental Dynamic Analysis (IDA)

The collapse performance of archetypes in terms of the Collapse Margin Ratio (CMR) can be assessed through Incremental Dynamic Analysis (IDA), which uses a set of ground motions scaled with increasing scaling factors to reach a magnitude that will cause the collapse. CMR is the ratio between median collapse intensity (S_{CT}) and maximum considered earthquake intensity (S_{MT}). The 4% inter storey drift ratio is used as a threshold value causing the collapse at global level for archetypes with CFS gypsum-sheathed shear walls. The 4% value is selected based on a similar study on shear walls sheathed with fibre cement board panels [16], which exhibit comparable behaviour as walls with gypsum board panels and are classified under the same category in AISI S400 [1]. Contrarily, a 5% inter storey drift value is chosen for archetypes with strap-braced archetypes as failure criterion. However, this value was chosen based on experiment results [11], in which strap-braced walls were able to sustain load carrying capacity until at least 5% drift in all specimens.

Far-field record set provided by FEMA P695 is used to conduct IDA in both planar directions with a 20% increment in intensity starting from a 20% (Scaling factor SF = 0.2) to 600% (SF = 6.0). Before applying the records to archetypes, they were normalized to remove the unwarranted variability between records due to inherent differences in event magnitude, distance to source, source type and site conditions, without eliminating overall record-to-record variability based on Peak Ground Velocity (PGV) and were matched to the archetype design response spectrum through the scaling of median response spectrum of all records within the range of fundamental vibration periods of archetypes. The SF=1.0 is representative of design level earthquake, while SF=1.5 corresponds to MCE (Maximum Considered Earthquake). Figure 3 shows the IDA curves for a three-storey residential (R3M) archetype for both types of LFRS under investigation.

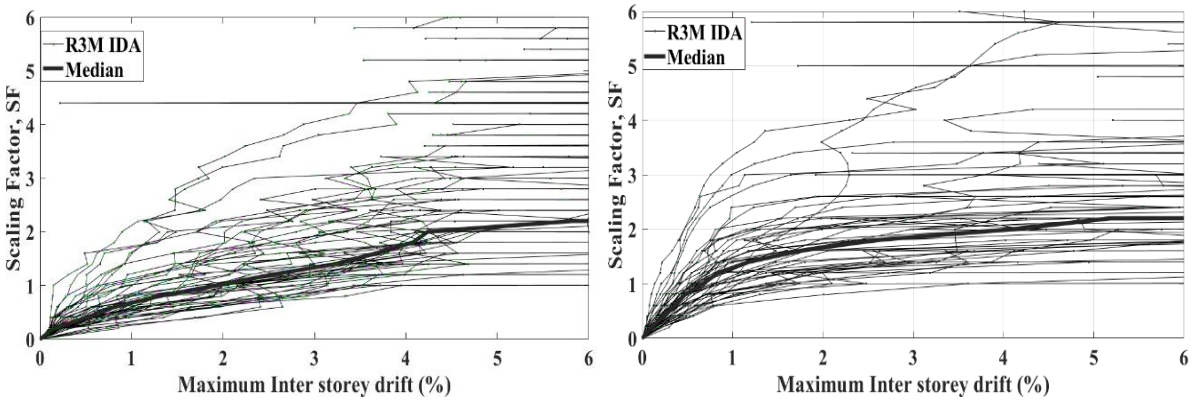

Figure 3. IDA curves: a) CFS Strap-braced walls, b) CFS gypsum-sheathed shear walls

5 SEISMIC PERFORMANCE EVALUATION

The acceptably low, yet reasonable, probability of collapse of structural systems is established by checking the suitability of the trial value of behaviour factor used in design as per performance evaluation criteria of FEMA P695. The CMR's obtained from the IDA analysis are adjusted to take into the spectral shapes of different records used for the analysis to obtain the adjusted CMR (ACMR), which is the product of CMR and a Spectral Shape Factor (SSF). Two performance criteria are defined by the methodology [7]: the average value of adjusted collapse margin ratio, $ACMR_{avg}$, for each performance group should be greater than $ACMR_{10\%}$, and the individual values of adjusted collapse margin ratio, $ACMR_i$, for each archetype within a performance group should be greater than $ACMR_{20\%}$. The values of $ACMR_{10\%}$ and $ACMR_{20\%}$ are the function of uncertainties, which are summed up as the total collapse uncertainty β_{TOT}, that takes into account the different sources of uncertainty which could contribute to the variability in collapse capacity. In particular, the main sources of uncertainty include: record to record uncertainty (β_{RTR}), design requirements uncertainty (β_{DR}), test data uncertainty (β_{TD}); and modelling uncertainty (β_{MDL}).

β_{RTR} represents the variability in response of the archetypes model under different ground motion records. FEMA P695 recommends to use β_{RTR} equal to 0.40 for archetypes having period-based ductility greater than 3, which is the case for all archetypes in this study. The other three uncertainty parameters β_{DR}, β_{TD} and β_{MDL}, are the qualitative measures. FEMA P695 provides the following qualitative scale to quantify them: (a) Superior: β=0.10, (b) Good: β=0.20, (c) Fair: β=0.35, and (d) Poor: β=0.50. A quality rating of 'Good' (β =0.20) is adopted for all of them in both cases except a 'superior' rating is given to test data available for gypsum-sheathed shear walls. In addition to quasi cyclic test data on the shear wall [6], there was also significant evidence on the seismic performance of gypsum-sheathed shear walls from shaking table tests [10]. Finally, the total collapse uncertainty β_{TOT} is computed to be 0.49 and 0.53 for gypsum-sheathed shear walls and strap-braced walls, respectively. Based on the value of β_{TOT}, $ACMR_{10\%}$ and $ACMR_{20\%}$ are obtained from Table 7-3 of FEMA P695. All of the archetypes in both cases passed the criterion, as it can be seen in Tables 2 and 3, and hence this concludes that the value of the behaviour factor equal to 2.5 and 2.0 used in design phase for strap-braced walls and gypsum-sheathed shear walls, respectively is appropriate.

Archetype ID	S_{CT}	S_{MT}	SSF	CMR	ACMR	$ACMR_{20\%}$	Pass/Fail	$ACMR_{avg}$	$ACMR_{10\%}$	Pass/Fail
R2L	3.40	1.50	1.14	2.27	2.58	1.57	Pass	2.05	1.97	Pass
R3L	3.67	1.50	1.14	2.45	2.79	1.57	Pass			
R4L	3.70	1.50	1.13	2.47	2.79	1.57	Pass			
O1L	2.87	1.50	1.14	1.91	2.18	1.57	Pass			
O2L	3.40	1.50	1.14	2.27	2.58	1.57	Pass			
R2M	2.27	1.50	1.14	1.51	1.73	1.57	Pass			
R3M	2.18	1.50	1.13	1.45	1.64	1.57	Pass			
R4M	2.53	1.50	1.12	1.69	1.89	1.57	Pass			
O1M	2.40	1.50	1.14	1.60	1.82	1.57	Pass			
O2M	2.50	1.50	1.14	1.67	1.90	1.57	Pass			
R2H	1.95	1.50	1.30	1.30	1.69	1.57	Pass			
R3H	1.94	1.50	1.31	1.29	1.69	1.57	Pass			
O1H	1.72	1.50	1.33	1.15	1.53	1.57	Near Pass			
O2H	2.16	1.50	1.30	1.44	1.87	1.57	Pass			

Table 2. Performance evaluation of archetypes with CFS strap-braced walls

Archetype ID	S_{CT}	S_{MT}	SSF	CMR	ACMR	$ACMR_{20\%}$	Pass/Fail	$ACMR_{avg}$	$ACMR_{10\%}$	Pass/Fail
R1L	2.70	1.50	1.12	1.80	2.02	1.51	Pass	1.91	1.88	Pass
R2L	2.80	1.50	1.11	1.87	2.07	1.51	Pass			
R3L	3.10	1.50	1.10	2.07	2.27	1.51	Pass			
R4L	3.33	1.50	1.08	2.22	2.39	1.51	Pass			
O1L	2.47	1.50	1.13	1.64	1.86	1.51	Pass			
O2L	2.90	1.50	1.09	1.93	2.11	1.51	Pass			
R1M	3.60	1.50	1.13	2.40	2.71	1.51	Pass			
R2M	2.25	1.50	1.09	1.50	1.64	1.51	Pass			
R3M	2.00	1.50	1.07	1.33	1.43	1.51	Near Pass			
O1M	2.09	1.50	1.10	1.39	1.53	1.51	Pass			
O2M	2.23	1.50	1.08	1.49	1.61	1.51	Pass			
R1H	2.57	1.50	1.25	1.71	2.13	1.51	Pass			
R2H	1.80	1.50	1.18	1.20	1.42	1.51	Near Pass			
O1H	1.83	1.50	1.23	1.22	1.50	1.51	Near Pass			

Table 3. Performance evaluation of archetypes with CFS gypsum-sheathed shear walls

6 CONCLUSIONS

Behaviour factor for CFS gypsum-sheathed shear walls and CFS strap-braced walls, which are not yet standardized as seismic force resisting system in EN 1998-1, is evaluated here through FEMA P695 [7] methodology. A total of fourteen residential and office archetypes representing heights up to 12 m are designed following capacity design approach to withstand the low, medium and high seismic load. Numerical models of archetypes with an ability to simulate nonlinear hysteretic response of walls are developed in OpenSees software and analysed under the action of 44 records in FEMA P695 far-field record set. The analysis of models followed an incremental dynamic analysis approach until the collapse happens. Finally, by gauging the collapse performance of models against the FEMA P695 acceptance criteria for adjusted collapse margin ratios, it is concluded that a behaviour factor value of 2.0 and 2.5 is

appropriate for buildings using CFS gypsum-sheathed shear walls and CFS strap-braced walls as main seismic force resisting system, respectively.

7 REFERENCES

[1] AISI, *S400-15 North American Standard for Seismic Design of Cold formed Steel Structural Systems*. *American Iron and Steel Institute (AISI)*, 2015.

[2] CEN, *EN 1998-1 Eurocode 8: Design of Structures for earthquake resistance-Part 1: General rules, seismic actions and rules for buildings*. *European Committee for Standardization*, Brussels, 2004.

[3] R. Tartaglia, M. D'Aniello, D.L. Gianmaria, and D.M. Attilio De Martino, Influence of EC8 rules on P-Delta effects on the design and response of steel MRF. *Ingegneria Sismica: International Journal of Earthquake Engineering*, vol. 13, no. 3, pp. 104–120, 2018.

[4] V. Piluso, A. Pisapia, P. Castaldo, and E. Nastri, Probabilistic Theory of Plastic Mechanism Control for Steel Moment Resisting Frames. *Structural Safety*, vol. 76, pp. 95–107, 2019.

[5] S. Costanzo, M. D'Aniello, and R. Landolfo, Proposal of design rules for ductile X-CBFS in the framework of EUROCODE 8. *Earthquake Engineering & Structural Dynamics*, vol. 48, no. 1, pp. 124–151, 2019.

[6] V. Macillo, L. Fiorino, and R. Landolfo, Seismic response of cold-formed steel shear walls sheathed with nailed gypsum panels: Experimental tests. *Thin-Walled Structures*, vol. 120, no. August, pp. 161–171, 2017.

[7] FEMA, *FEMA P695: Quantification of Building Seismic Performance Factors*. , Washigton, DC, USA, 2009.

[8] CEN, *EN 1990 Eurocode 0: Basis of structural design*. *European Committee for Standardization*, Brussels, 2002.

[9] CEN, *EN 1993-1-3 Eurocode 3: Design of steel structures-Part 1-3: General rules-Supplementary rules for cold-formed members and sheeting*. *European Committee for Standardization*, Brussels, 2006.

[10] L. Fiorino, V. Macillo, and R. Landolfo, Shake table tests of a full-scale two-story sheathing-braced cold-formed steel building. *Engineering Structures*, vol. 151, pp. 633–647, 2017.

[11] O. Iuorio, V. Macillo, M.T. Terracciano, T. Pali, L. Fiorino, and R. Landolfo, Seismic response of Cfs strap-braced stud walls: Experimental investigation. *Thin-Walled Structures*, vol. 85, pp. 466–480, 2014.

[12] V. Macillo, S. Shakeel, L. Fiorino, and R. Landolfo, Development and Calibration of a Hysteretic Model for CFS Strap braced stud walls. *Advanced Steel Construction*, vol. 14, no. 3, pp. 336–359, 2018.

[13] S. Mazzoni, F. McKenna, M.H. Scott, and G.L. Fenves, Open System for Earthquake Engineering (OpenSees), (2009).

[14] L. Fiorino, S. Shakeel, V. Macillo, and R. Landolfo, Seismic response of CFS shear walls sheathed with nailed gypsum panels: Numerical modelling. *Thin-Walled Structures*, vol. 122, pp. 359–370, 2018.

[15] L. Fiorino, S. Shakeel, V. Macillo, and R. Landolfo, Behaviour factor (q) evaluation the CFS braced structures according to FEMA P695. *Journal of Constructional Steel Research*, vol. 138, pp. 324–339, 2017.

[16] M. Zeynalian, A.Z. Shahrasbi, and H.T. Riahi, Seismic Response of Cold Formed Steel Frames Sheathed by Fiber Cement Boards. *International Journal of Civil Engineering*, vol. 16, no. 11, pp. 1643–1653, 2018.

COMPDYN 2019
7th ECCOMAS Thematic Conference on
Computational Methods in Structural Dynamics and Earthquake Engineering
M. Papadrakakis, M. Fragiadakis (eds.)
Crete, Greece, 24–26 June 2019

LATERAL STRUCTURAL BEHAVIOUR OF STEEL NETWORK ARCH BRIDGES

Cyrille Denis Tetougueni[1], **Paolo Zampieri**[1], **Carlo Pellegrino**[1]

[1]Dept. of Civil, Architectural and Environmental Engineering, Via Marzolo 9, 35121 Padua, Italy

e-mails: cyrille.tetougueni@dicea.unipd.it, paolo.zampieri@dicea.unipd.it, carlo.pellegrino@dicea.unipd.it

Keywords: Lateral deflection, traffic loads, critical loads, Finite element analysis

Abstract. *Network arch bridges are arch bridges where hangers intersect each other at least twice. The concept has been developed firstly by Prof. Per Tveit during his Ph.D. Several network arch bridges have been built around the world due to the advantage this type of bridge presents. However, Network arch bridges as to conventional arch bridges are sensitive to lateral displacement under vertical loads. In this study, lateral structural response of network arch bridges against traffic loads has been analyzed through extensive non-linear analyses. The structural response of the arch showed a relationship between the lateral displacement and applied stress. In addition, it is observed that lateral arch's bracing changes the development of plastic hinges in the arch.*

1 INTRODUCTION

In bridges' industry, tied-arch bridges represent types of bridges where hangers are used to transfer vertical loads from deck to arches. In this condition, the arches are substantially subjected to compression axial force instead of in the deck or tie beam there is a tensile axial force and reduced bending moment due to hangers. Network arch bridges are widely spread around the world due to several advantages from the aesthetical aspect to the cost-performance ratio. The bridge has been developed by Per Tveit with the aim to develop innovative tied-arch bridges [1]. According to Per Tveit [2], network arch bridges are defined as tied arch bridges where inclined hangers intersect each other at least twice. These bridges are often mistaken to Nielsen bridges, which provide also inclined hangers but only once [3]. Fig.1 provides the common cable distribution in arch bridges from the vertical arrangement to network arrangement.

Due to excessive axial force developed in the arches, they are sensitive to undergo instability phenomenon, either in plane or out-of-plane or both. For this reason, it is usually necessary to provide an optimum cable arrangement, which gives a minimum stress distribution into structural elements. Several authors [4 - 6] focused their researches to deliver an optimal cable distribution within the arch.

In regards to the arch's instability phenomenon, three different behaviors are often observed (fig.2). Amongst them, out-of-plane buckling has captured great attention recently. Sakimoto et al. [7] conducted experimental tests on arches with square hollow sections to study the out-of-plane buckling of the arch. New column curves for the out-of-plane verification have been derived as the outcome. La poutré et al. **Error! Reference source not found.** investigated the elasto-plastic out of plane buckling response of roller bent circular steel arches under a vertical force located at the crown. Several tests were performed and the presence of plastic zones in the arch rib featured the arches failure. Spoorenberg et al. **Error! Reference source not found.** performed sensitivity numerical analyses to evaluate the influence of initial imperfections on the out-of-plane buckling response of steel arches. The authors proposed a design rule to check the response of freestanding circular roller bent steel arches under symmetric loads. When dealing with the analysis of lateral displacement of the arch, it is important to consider the existing imperfections of the element developed during the manufacturing process of the structural steel. Lonetti et al. [10], through non-linear analyses, showed the influence of considering geometrical imperfections in the analysis while the influence of geometrical out-of-plane imperfections on the lateral buckling behavior using a highly detailed finite element model has been investigated by Backer et al. [11].

In this study, the global lateral behavior of network arch bridges under traffic loads has been studied throughout extensive nonlinear finite element analyses. Initial geometric imperfections equivalent to the first buckling mode of the free arch have been assigned in arch elements. Finally, the influence of the lateral bracing typologies and its position to the lateral displacement have been developed.

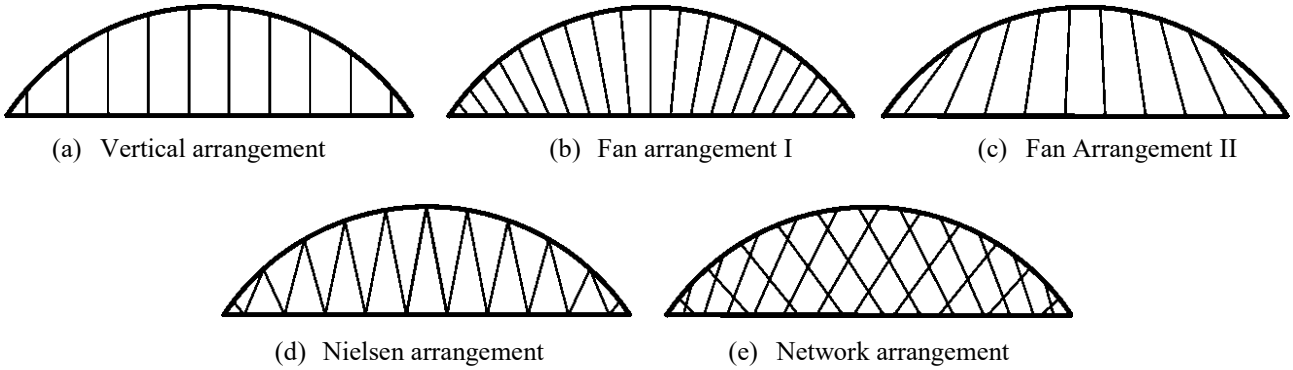

(a) Vertical arrangement (b) Fan arrangement I (c) Fan Arrangement II

(d) Nielsen arrangement (e) Network arrangement

Fig. 1. Hanger arrangement for existing tied-arch bridges

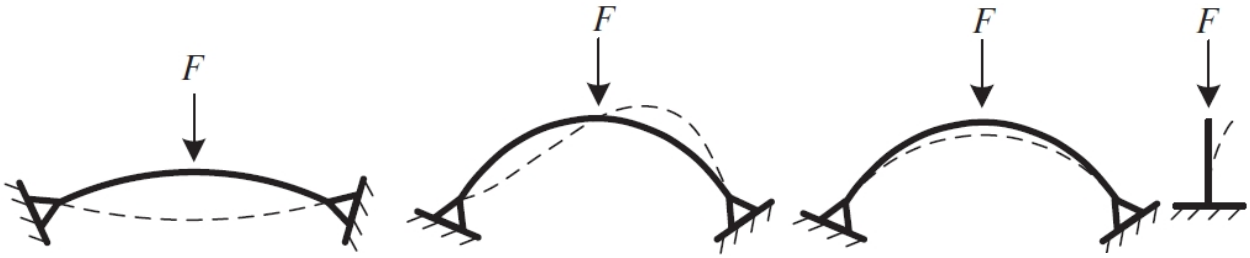

a) b) c)

Fig. 2. Global instability behaviour of free standing arch; a) Snap-through; b) In-plane buckling; c) Out-of-Plane buckling extracted from Spoorenberg et al. 2012 **Error! Reference source not found.**

2 DESCRIPTION OF THE BRIDGE

The bridge considered in this study is a 100 m span simply supported steel bridge. The height of the arch has been chosen to have a desired span/height ratio equal to 0.20. The bridge consists of two arch layouts with network arrangement of hanger. The two arches are welded directly to two lateral girder beams inter-connected throughout 10 m equally spaced transversal beams, which represents the width of the bridge. Each arch plane has 26 inclined cables to distribute the loads throughout structural elements. The structural response of an arch plane can be compared to an IPE section element where both arch and girder play the same role than the upper and lower flange and hangers are considered as the web. The deck will be composed of 8 m width traffic lane with two footways of 1 m width each. IPE lateral beams are used to connect altogether the two arches. To study the influence of lateral bracing, hollow circular elements have been used to connect the existing transversal arch beam. A global view of the arch bridge is presented in Fig.3 while the information regarding the dimension of the structural elements considered is presented in both Table 1.

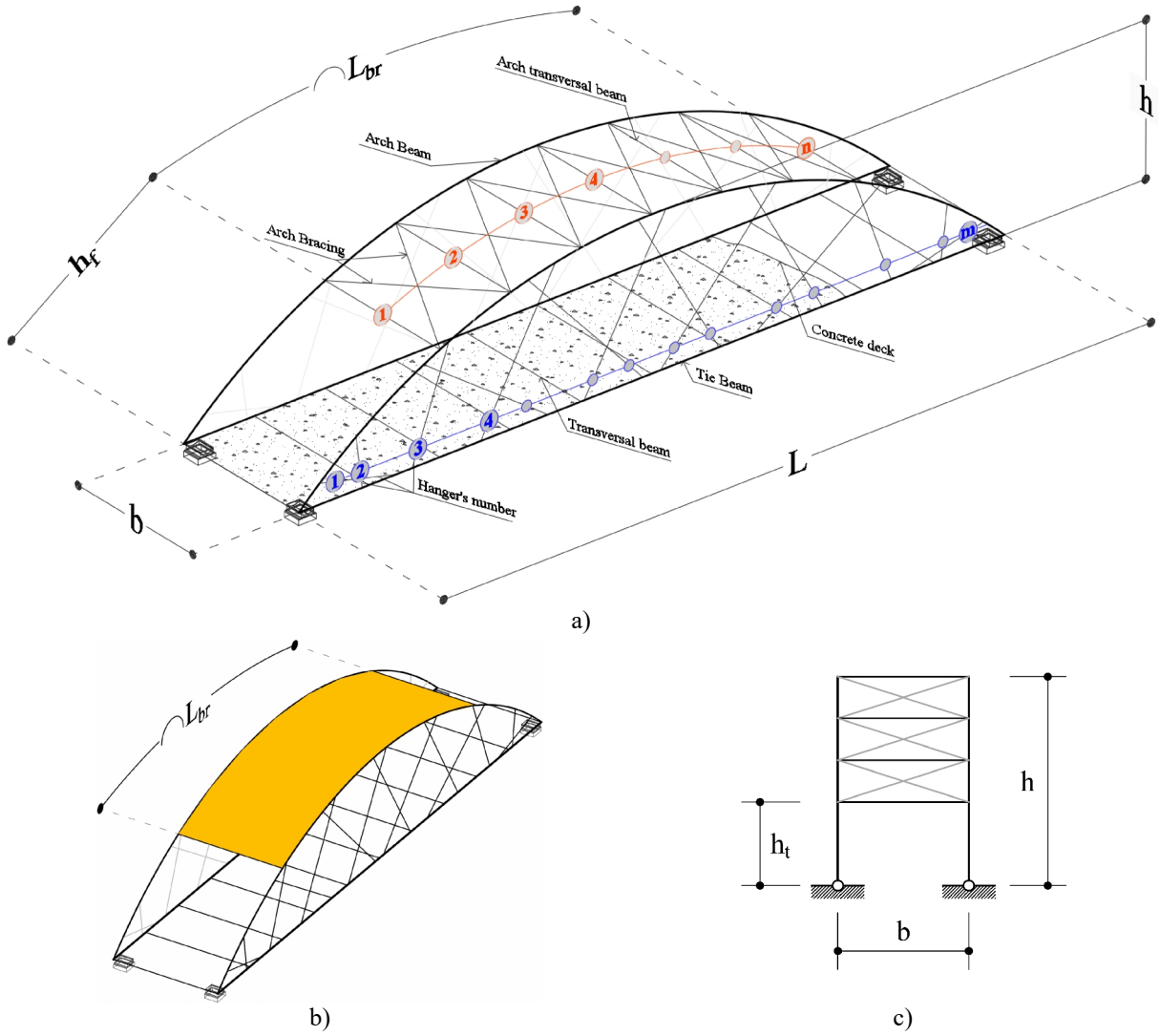

Fig. 3. Generic network arch bridge considered in the study

Structural elements	h [mm]	b [mm]	t_w [mm]	t_f [mm]	D [mm]	t [mm]
Tie Beam	1600	500	80	80		
Arch	474.6	424	47.6	77		
Secpondary beam	650	250	12	14		
Arch transversal beam	398	141.8	6.4	8.6		
Cable					12	
Lateral bracing					250	5

Table 1: Section dimensions of the structural elements considered in the analysis

3 DESCRIPTION OF THE FINITE ELEMENT MODEL

FEM analysis has been performed in this study considering 1D element for all structural elements unless cable and deck. The latter has been modelled as 2D shell elements with eight nodes quad8 and six degrees of freedom. Hanger's arrangement follows the radial distribution along the arches. Imperfections equal to first buckling mode of the arch has been applied to the arch before the buckling analysis of the whole model. To perform the GMNIA, a perfect

elasto-plastic steel material behavior has been considered. S420 and S355 steel classes were considered in the analysis while cables were modelled as tension only material to avoid any risk of buckling of slender cable section. An overview of the 3D FEM model is presented in Fig.4.

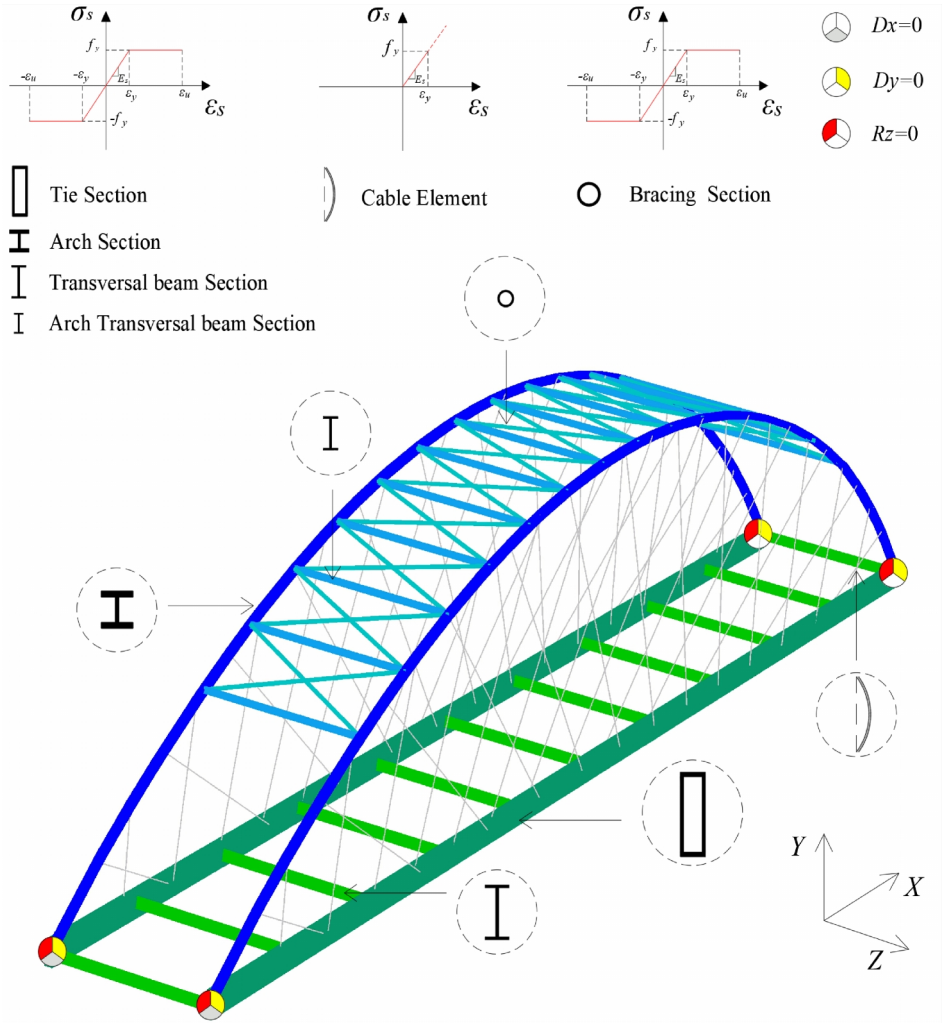

Fig. 4. 3D FEM model of a network arch bridge

4 LATERAL DISPLACEMENT OF NETWORK ARCH BRIDGES

In order to investigate the lateral sensitivity of the arches in network arch bridges, a geometrically and materially nonlinear analysis with imperfections (GMNIA) have been considered. Since the effect of traffic loads was primary investigated, analysis of the model with only permanent loads is run firstly. Then, progressively increasing the live loads to better figure out the influence of traffic loads in the out-of-plane structural response. The FEM analysis has been done following each step of the algorithm shown in Fig.5.

The results obtained from different braced length showed almost the same behaviour. The first hinge is formed when the vertical force in the arch is more or less 4000 kN for unbraced arches following successively the formation of second and third hinges. It is worth noting that the successive hinges in the arches are formed shortly after the first hinge. Fig. shows the stress level inducing the formation of the first three hinges. The benefit of wind bracing in the increase of lateral stiffness is evident as soon as both cases are drawn in the same graph. As

soon as the length of the braced zone of the arch increases, the critical load increases faster than the lateral displacement. For unbraced arches, the behaviour observed is the same for different cases studied while the situation is quite different for braced arches. In fact, for arches braced up to 80 and 90 %, softening behaviour is observed after the critical load is reached (Fig.). When the free end portal increase for arches with syst.1, a slight softening is observed after the critical buckling load of the arch.

Other results from FEM analysis showed that in general, the lateral sensitivity of both braced and unbraced arch bridges subjected to vertical loads is characterized by 3 states: one linear and two non-linear. From a stress point of view, the load increases linearly with the lateral displacement until the material reaches the yielding stress at point 2. Thus, the first hinge is formed with the partial plasticization of the section and will end the linear phase as shown in Fig. . The location of the first hinge may vary depending on the length of the arch where lateral bracing has been applied. It is worth noting that the first hinge is prone to be formed near the support due to the reaction of the abutment.

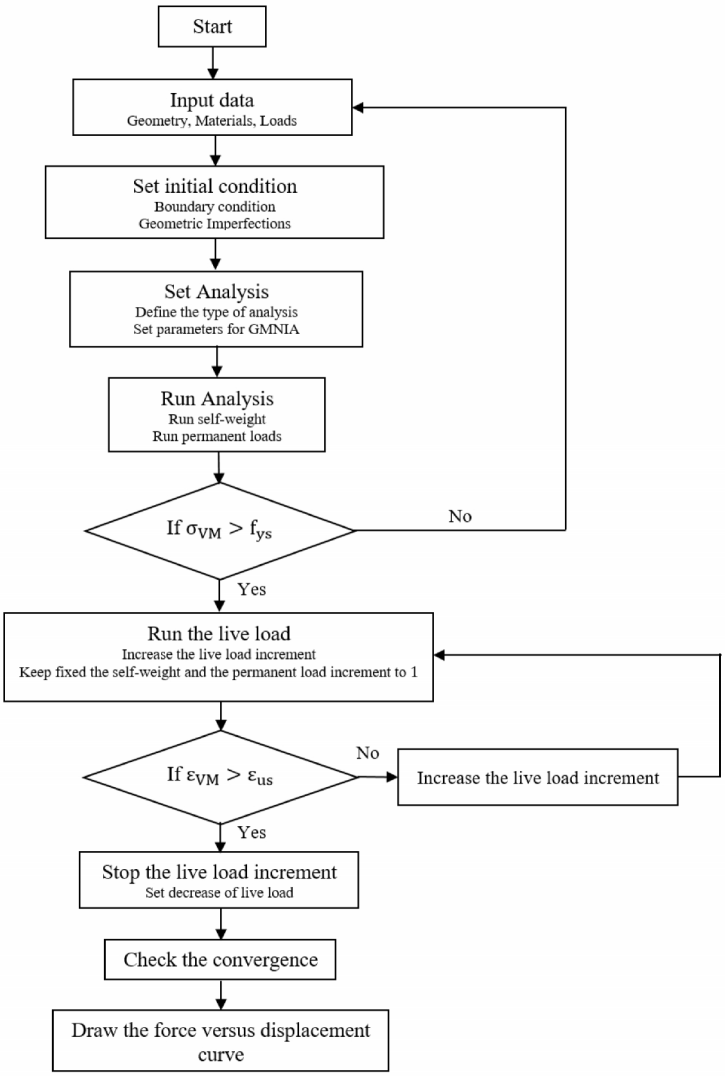

Fig. 5. Flowchart for the GMNIA procedure analysis in braced arches

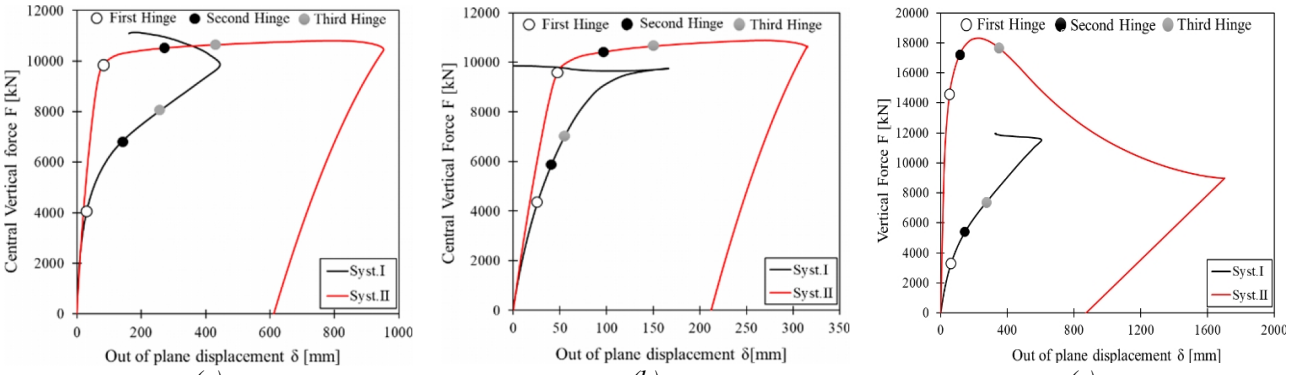

(a) *(b)* *(c)*

Fig. 6. Vertical live loads – lateral deflection curves for unbraced and braced arch bridge; (a) L^{Braced}=50 m; (b) L^{Braced}=70 m; (c) L^{Braced}=90 m;

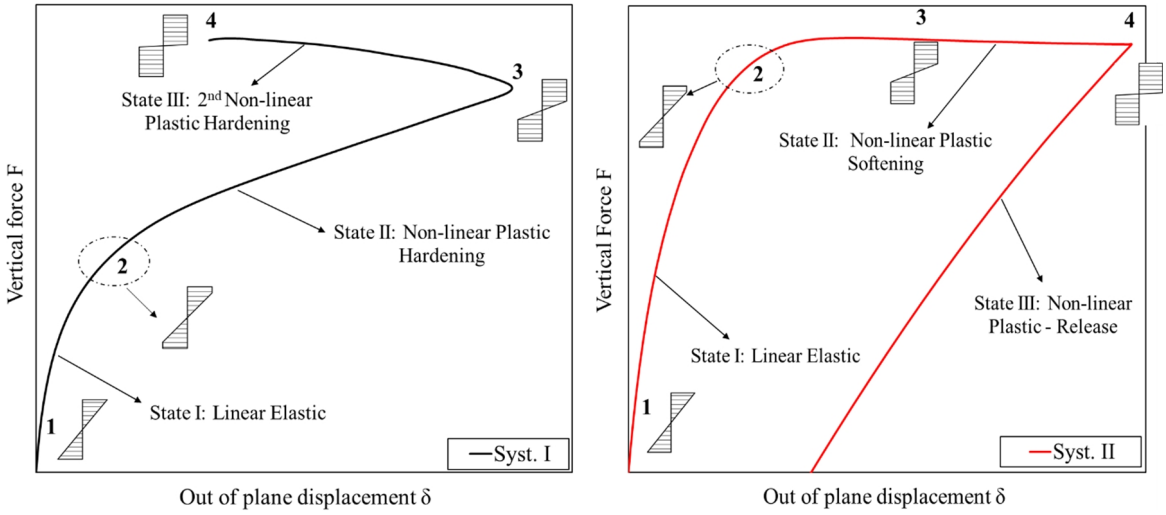

a) *b)*

Fig. 7. Global lateral behavior of the network arch bridge under vertical loads; a) Stress variation in the section of unbraced network arch bridge; b) Stress variation in the section of braced network arch bridge

5 CONCLUSION

The global out-of-plane behavior of network arch bridge has been studied in this paper through intensive nonlinear analysis. The results from finite element models show a gradual yielding of arch either from the support toward the arch midspan or from the arch midspan toward the support. The yielding process is fast for the early case and the hinges are formed rapidly until the braced region of the arch while in the latter case, the development of yielding is prevented by the bracing system. On the other hand, for arches without lateral bracing, multi-shape modes are observed. The arches move to the second buckling mode at the end of the first nonlinear phase. During this phase, an increase of vertical loads is still visible. On the other hand, another behavior is observed for braced arches, which display a slight softening at the end of the first nonlinear phase.

REFERENCES

[1] P. Tveit, The design of network arches, *The Structural Engineer*, **44** (7), 249-259, 1966.

[2] P. Tveit, "Bogebruer med skrå krysstilte hengestenger." ("Arch bridges with inclined intersecting hangers," in Norwegian.) *Ph.D. thesis presented at the Tech. Univ. of Norway*, 1959.

[3] A.W. Ostrycharczyk, Network arch timber bridges with light timber deck on transverse cross beams, *Ph.D. Dissertation Norwegian University of Science and Technology*, Norway, 2017.

[4] S. Teich, Fatigue Optimization in Network Arches, *4th International Conf. on Arch Bridges, ARCH'04*, Barcelona, Spain, 2004.

[5] A. De Zotti, C. Pellegrino, C. Modena, A parametric study of the hanger arrangement in arch bridges, *5th International Conf. on Arch Bridges, ARCH '07*, Madeira, Portugal, 2007.

[6] C. Pellegrino, G. Cupani, C. Modena, The effect of fatigue on the arrangement of hangers in tied arch bridges. *Engineering Structures*. **32** (4), 1140-1147, 2010.

[7] T. Sakimoto, T. Yamao, S. Komatsu, Experimental study on the ultimate strength of steel arches. *Proceedings in Japan Society of Civil Engineering*, **286,** 139-49, 1979.

[8] D. B. La Poutré, Inelastic spatial stability of circular wide flange steel arches. *Ph.D. Dissertation, Eindhoven University of Technology*. Eindhoven, 2004.

[9] R.C. Spoorenberg, H.H. Snijder, J.C.D. Hoenderkamp, D. Beg, Design rules for out-of-plane stability of roller bent steel arches with FEM. *Journal of Constructional Steel Research*, **79**, 9-21, 2012.

[10] P. Lonetti, A. Pascuzzo, S. Aiello, Instability design analysis in tied-arch bridges. *Mechanics of Advanced materials and Structures*, **0** (0) (2017) 1-11.

[11] H. De Backer, A. Outtier, P. Van Bogaert, Buckling design of steel tied-arch bridges, *Journal of Constructional Steel Research*, **103,** 159–167, 2014. https://doi.org/10.1016/j.jcsr.2014.09.004.

COMPDYN 2019
7th ECCOMAS Thematic Conference on
Computational Methods in Structural Dynamics and Earthquake Engineering
M. Papadrakakis, M. Fragiadakis (eds.)
Crete, Greece, 24-26 June 2019

DOMAIN DECOMPOSITION METHODS FOR CRACK GROWTH PROBLEMS USING XFEM

Serafeim Bakalakos, Manolis Georgioudakis and Manolis Papadrakakis

Institute of Structural Analysis & Antiseismic Research
School of Civil Engineering
National Technical University of Athens
GR 15780, Zografou Campus, Athens
e-mail: serafeim.bakalakos@outlook.com, geoem@mail.ntua.gr, mpapadra@centra.ntua.gr

Keywords: Crack Propagation, Domain Decomposition, FETI, XFEM.

Abstract. *The extended finite element method (XFEM) enriches the polynomial basis functions of standard finite elements with specialized non-smooth functions. The resulting approximation space can be used to solve problems with moving discontinuities, such as cracks, while avoiding the computational cost of remeshing. As the crack propagates, many artificial degrees of freedom are introduced near the crack tip, which can inflate the size of resulting linear system to be solved. In addition, the stiffness matrix of the cracked body may become ill-conditioned, causing slow convergence of iterative solvers. To overcome this, domain decomposition methods for solving the resulting linear systems of crack propagation problems is combined with XFEM to improve its performance. A suitable decomposition is proposed to avoid inter-subdomain boundaries near crack tip area. It is shown that choosing the proper FETI method, offers significant speedup compared to a direct solver that uses the common finite element solution techniques by means of Cholesky/LDL factorization, even if the execution is performed on a single-core systems.*

1 INTRODUCTION

The extended finite element method (XFEM) enriches the polynomial basis functions of standard finite elements with specialized non-smooth functions [1]. The resulting approximation space can be used to solve problems with moving discontinuities, such as cracks, while avoiding the computational cost of remeshing. Although the local enrichment strategy of XFEM is computationally efficient, it can rapidly increase the size of the resulting linear system in large scale problems. In addition, the stiffness matrix may become ill-conditioned, causing slow convergence of iterative solvers.

In this paper, the application of domain decomposition methods for solving the resulting linear systems is proposed. Among such methods we will focus to the family of finite element tearing and interconnecting (FETI) methods which were originally developed for the standard finite element method. In a FETI method, the finite element model is decomposed into several subdomains and the continuity at the boundary freedom degrees is enforced by applying Lagrange multipliers. These are the unknowns of an equivalent dual linear system, which can be solved by processing each subdomain independently. To speed up the solution process of each subdomain the standard preconditioners (e.g. preconditioned conjugate gradient method - PCG) are used. When FETI methods are combined with XFEM, the identification of rigid body motions of floating subdomains must be purely identified. Round-off errors in the computation of the rigid body motions can increase the PCG iterations that are required to solve the interface problem. Thus, a FETI method and can be combined with an effective mesh partitioning algorithm to ensure a decomposition into balanced subdomains that does not slow down the convergence.

A benchmark structure under fatigue crack growth is analyzed to demonstrate the capabilities of the proposed algorithm. A suitable decomposition is proposed to avoid inter-subdomain boundaries near crack tip area. It is shown that choosing the proper FETI method, offers significant speedup compared to a direct solver that uses the common finite element solution techniques by means of Cholesky/LDL factorization, even if the execution is performed on a single-core systems.

The paper is organized as follows: a brief description of modeling crack propagation with XFEM is given first, with special emphasis to fatigue crack growth. Subsequently, the FETI methods are discussed and their basic concepts are presented. Finally numerical tests are provided for illustrating the capabilities of the proposed methodology.

2 MODELING CRACK PROPAGATION USING XFEM

This paper focuses on the 2D mixed-mode linear elastic fracture mechanics (LEFM) formulation, where the size of cracked plastic zone is sufficiently small and it is embedded within an elastic zone around the crack tip. The inelastic behavior at the crack tip can cause a fatigue crack growth, meaning that the crack will grow under conditions of cyclic applied loading. The basic assumptions of LEFM in order to quantify crack growth around the crack tip in the presence of constant amplitude cyclic stress intensity, are given in the next sections.

2.1 XFEM basic ingredients

According to XFEM, special functions are added to the finite element approximation based on the partition of unity (PU) [2] and additional degrees of freedom are introduced to selected nodes of the finite element mesh near to discontinuities providing a higher level of accuracy. The quasi-static crack propagation simulations can be carried out without the need of remesh-

ing, modeling the domain with standard finite elements without explicitly meshing the crack surfaces.

Two basic types of enrichment functions are used: (i) the Heaviside function (step function) and (ii) the asymptotic crack-tip enrichment functions derived from LEFM [3]. The displacement field for a single "nominal" element can be expressed as a superposition of the standard $\vec{u}^{\text{std}}$, the crack-split $\vec{u}^{\text{H}}$ and the crack-tip $\vec{u}^{\text{tip}}$ fields as:

$$\vec{u}(\vec{x}) = \vec{u}^{\text{std}} + \vec{u}^{\text{enr}} = \vec{u}^{\text{std}} + \vec{u}^{\text{H}} + \vec{u}^{\text{tip}} \tag{1}$$

or more explicitly:

$$\vec{u}(\vec{x}) = \underbrace{\sum_{j=1}^{n} N_j(\vec{x})\vec{u}_j}_{\vec{u}^{\text{std}}} + \underbrace{\sum_{h=1}^{n_h} N_h(\vec{x})H(\vec{x})\vec{a}_h + \sum_{k=1}^{n_t} N_k(\vec{x})\Big(\sum_{l=1}^{n_f} F_l(\vec{x})\vec{b}_k^l\Big)}_{\vec{u}^{\text{enr}}} \tag{2}$$

The first contributing part ($\vec{u}^{\text{std}}$) on the right-hand side of Eq. (2) corresponds to the classical finite element approximation of the displacement field, while the second part ($\vec{u}^{\text{enr}}$) refers to the enrichment approximation which takes into account the existence of discontinuities. This second contributing part utilizes additional degrees of freedom to facilitate modeling of the discontinuous field, without modeling it explicitly. n is the number of nodes in each finite element model with standard degrees of freedom $\vec{u}_j$ and shape functions $N_j(\vec{x})$, n_h is the number of nodes in the elements containing the crack face (but not the crack tip), $\vec{a}_h$ is the vector of additional degrees of freedom for modeling crack faces defined by the Heaviside function $H(\vec{x})$, n_t is the number of nodes associated with the crack tip in its influence domain and $\vec{b}_k^l$ is the vector of additional degrees of freedom for modeling crack tips.

Furthermore, $F_l(\vec{x})$ are the crack-tip enrichment functions, given by:

$$\{F_l(r,\theta)\}_{l=1}^4 = \left\{\sqrt{r}\sin(\frac{\theta}{2}); \sqrt{r}\cos(\frac{\theta}{2}); \sqrt{r}\sin(\frac{\theta}{2})\sin(\theta); \sqrt{r}\cos(\frac{\theta}{2})\sin(\theta)\right\} \tag{3}$$

The elements which are cut entirely by the crack, are enriched with the Heaviside (step) function H. The Heaviside function is a discontinuous function across the crack surface and is constant on each side of the crack. Splitting the domain by the crack causes a displacement jump and the Heaviside function provides the desired behavior to approximate the real displacement field.

2.2 Crack representation by level sets

In association to XFEM, the level set method (LSM) [4] is adopted to describe the geometry of the crack. The LSM was originally proposed for tracking moving interfaces, and became a key ingredient of XFEM for describing complicated geometrical interfaces by computing their motion on a fixed finite element mesh. Thus, level set functions offer an elegant way of modeling cracks which take the form of signed distance functions. In order to fully characterize a crack discontinuity, two level set functions are defined as signed distance functions: (i) a normal level set function ϕ and (ii) a tangent level set function ψ. To define the signed distance functions, the interface Γ can be regarded as the zero level contour of the level set function $\phi(\vec{x})$. The distance d from a point $\vec{x}$ to the interface Γ is defined as:

$$d = \|\vec{x} - \vec{x}_\Gamma\| \tag{4}$$

where $\vec{x}_\Gamma$ is the normal projection of $\vec{x}$ on Γ. Mathematically, the signed distance function $\phi(\vec{x})$ can be defined as,

$$\phi(\vec{x}) = \min \|\vec{x} - \vec{x}_\Gamma\| \, \text{sign}(\vec{n_1} \cdot (\vec{x} - \vec{x}_\Gamma)) \tag{5}$$

where $\vec{n_1}$ is the unit normal vector to the crack at point $\vec{x_\Gamma}$ (see Fig. 1).

For the case of an edge crack, to construct the two level set functions, the approach proposed by Stolarska et al. [5] is adopted. The crack tip segment is extended to "meet" the boundary of the domain and the normal level set function ϕ is then defined using Eq. (5), from the original crack segment Γ (at crack tip j) and the virtual segments (extensions) ($\phi = 0$ and $\psi = 0$) (see Fig. 1). Similar, the tangent level set function ψ as the signed distance to the plane including

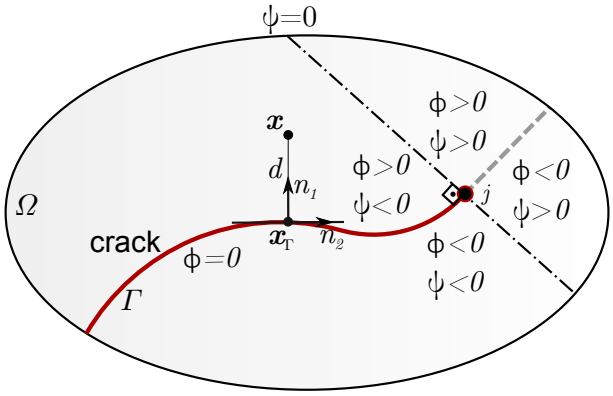

Figure 1: Signed distance definition, and corresponding level set functions ϕ and ψ in crack tip point $\vec{x}_\Gamma$.

the crack front and perpendicular to the crack surface, is defined as follows:

$$\psi(\vec{x}) = \min \|\vec{x} - \vec{x}_\Gamma\| \, \text{sign}(\vec{n_2} \cdot (\vec{x} - \vec{x}_\Gamma)) \tag{6}$$

where $\vec{n_2}$ is the unit vector tangent to the crack at its tip. The crack can now be represented by the two level set functions ϕ and ψ such that $\phi = 0$ for the crack surface Γ. Consequently, the crack tip j is identified on an intersection of normal and tangent zero level set functions, i.e. intersection of $\phi = 0$ and $\psi = 0$. In the remaining domain, ϕ has a positive value above the crack, while ψ has a positive value to the right of the unit normal vector $\vec{n_1}$ at the crack tip j. The crack tip level set ψ is generally assumed to be orthogonal to ϕ, i.e. $\phi\psi = 0$. It is also assumed that once a part of the crack has formed, that part will no longer change its shape or move.

2.3 Computation of the crack growth direction

The accuracy and reliability of the method primarily on the continuity and the determination of the crack path. Among the existing crack growth criteria, the maximum hoop stress criterion [7], is adopted. According to this criterion: (i) the crack initiation will occur when the maximum hoop stress reaches a critical value and (ii) the crack will grow along direction θ_{cr} in which circumferential stress $\sigma_{\theta\theta}$ is maximum.

The circumferential stress $\sigma_{\theta\theta}$ in a polar coordinate system (r, θ) (see Fig. 2) along the direction of the crack propagation is a principal stress. Hence, the critical crack propagation direction θ_{cr} is determined by setting the shear stress $\sigma_{r\theta}$ equal to zero, i.e.:

$$\sigma_{r\theta} = \frac{1}{2\sqrt{(2\pi r)}} cos\frac{\theta_{cr}}{2}\Big(K_I sin\theta_{cr} + K_{II}(3cos\theta_{cr} - 1)\Big) = 0 \tag{7}$$

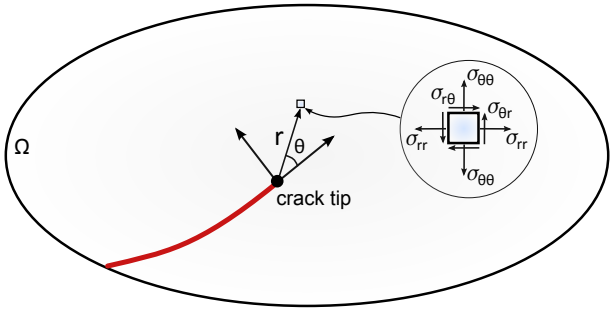

Figure 2: Polar coordinates in the crack tip coordinate system.

leading to the following expression of the crack growth direction θ_c, in terms of local crack tip coordinate system:

$$\theta_c = \theta_{cr} = 2arctan\frac{1}{4}\Big(\frac{K_I}{K_{II}} \pm \sqrt{\frac{K_I^2}{K_{II}} + 8}\Big) \tag{8}$$

2.4 Computation of fatigue cycles

Fatigue crack growth is quantified using Paris law [8], which is originally proposed for single mode deformation cases, and correlates crack propagation rate under fatigue loading with the stress intensity factors (SIFs). For the case of mixed-mode loading, a modified Paris law is defined using the effective stress intensity factor range $\Delta K_{\text{eff}} = K_{\max} - K_{\min}$. For a certain fatigue loading level, where the crack grows by length Δa in ΔN_c cycles, Paris law reads:

$$\frac{\Delta a}{\Delta N_c} \approx \frac{da}{dN_c} = C(\Delta K_{\text{eff}})^m \tag{9}$$

where C and m are empirical material constants. m is often called as the *Paris exponent* and is typically defined in the range of $3 \div 4$ for common steel and aluminium alloys. Eq. (9) represents a linear relationship between $log(\Delta K_{\text{eff}})$ and $log(\frac{da}{dN_c})$ which is used to describe fatigue crack propagation in Region II (Fig. 3). For calculating the effective mixed-mode stress

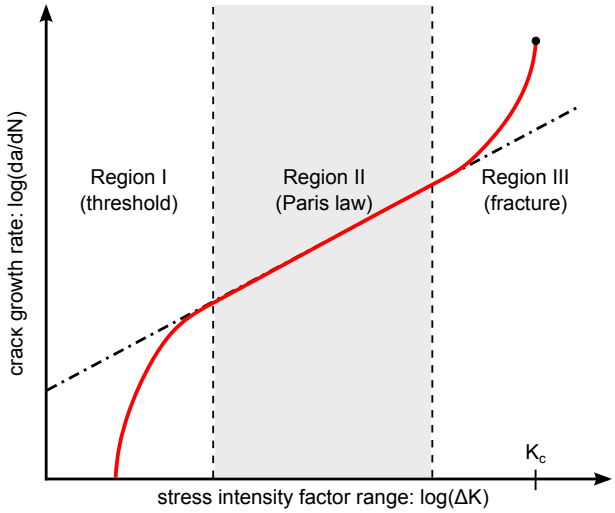

Figure 3: Logarithmic crack growth rate and effective region of Paris law.

intensity factor ΔK_{eff}, the energy release rate model is adopted, leading to:

$$\Delta K_{\text{eff}} = \sqrt{\Delta K_I^2 + \Delta K_{II}^2} \tag{10}$$

Subsequently, the number of the corresponding cycles for a crack growth Δa is computed according to [3]:

$$\Delta N_c = \frac{\Delta a}{C(\Delta K_{\text{eff}})^m} \tag{11}$$

Similar to strength of materials theory where the calculated stress is compared with an allowable stress defining the material strength, LEFM assumes that unstable fracture occurs when SIF K reaches a critical value K_c, called *fracture toughness*, which represents the capacity of a material to withstand a given stress field at the crack tip and to resist into the progressive tensile crack extension. In other words, K_c is a material constant and is used as a threshold value for SIFs.

3 FETI Methods

Domain decomposition methods (DDM) split the domain into smaller subdomains which can be processed independently. Among such methods, the finite element tearing and in interconnecting (FETI) DDMs exhibit the highest scalability, when executed in distributed computing environments. The first FETI method (FETI-1) was introduced by Farhat et al. [11], and is the first implementation of FETI methods which uses Lagrange multipliers to describe the forces between the subdomains. Later, dual-primal FETI (FETI-DP) was introduced by Farhat et al. [12], as a simpler and in many cases more efficient, alternative.

3.1 FETI-1

In FETI-1 method, the domain is divided into disconnected subdomains as in Fig. 4 and the continuity between them is retained by enforcing equal displacements for instances of the same boundary DOF (degree of freedom).

$$\left[\begin{array}{cc} 1 & -1 \end{array} \right] \left[\begin{array}{c} u_k^{(1)} \\ u_k^{(2)} \end{array} \right] = 0 \tag{12}$$

By gathering the 1, -1 and 0 coefficients in a signed boolean matrix $\boldsymbol{B}^s$ for all boundary DOFs of a subdomain:

$$\sum_{s=1}^{N_s} \boldsymbol{B}^s \boldsymbol{u}^s = \boldsymbol{0} \tag{13}$$

To solve the initial linear system in the presence of these constraints, we apply Lagrange multipliers at boundary DOFs. These are dual quantities and can be viewed as forces, while displacements are primal quantities. Using the superscript e to denote the aggregation of all subdomain matrices/vectors into an expanded matrix/vector, the resulting linear system is written as:

$$\left[\begin{array}{cc} \boldsymbol{K}^e & (\boldsymbol{B}^e)^T \\ \boldsymbol{B}^e & \boldsymbol{0} \end{array} \right] \left[\begin{array}{c} \boldsymbol{u}^e \\ \boldsymbol{\lambda} \end{array} \right] = \left[\begin{array}{c} \boldsymbol{f}^e \\ \boldsymbol{0} \end{array} \right] \tag{14}$$

A subdomain of FETI-1 can be floating, meaning there are not enough constrained DOFs and its stiffness matrix $\boldsymbol{K}^s$ is singular. To overcome this, we use a generalized inverse $(\boldsymbol{K}^s)^+$

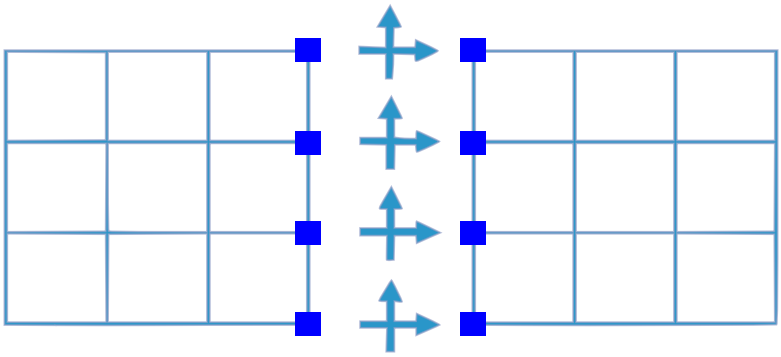

Figure 4: Langrange multipliers applied to boundary DOFs of subdomains.

and a normalized basis for its nullspace $\boldsymbol{R}^s$, which corresponds to the rigid body motions of the floating subdomain.

$$(\boldsymbol{K}^s)^+ = \begin{bmatrix} (\boldsymbol{K}^s_{11})^{-1} & \boldsymbol{0} \\ \boldsymbol{0} & \boldsymbol{0} \end{bmatrix} \tag{15}$$

$$\boldsymbol{R}^s = \begin{bmatrix} (\boldsymbol{K}^s_{11})^{-1}\boldsymbol{K}^s_{12} \\ \boldsymbol{I} \end{bmatrix} \tag{16}$$

where the subscripts 1/2 denote linearly independent/dependent rows and columns, respectively. If the subdomain has sufficient constraints then $\boldsymbol{R}^s = \emptyset$ and $(\boldsymbol{K}^s)^{-1}$. The interface problem of FETI-1 is as follows:

$$\begin{bmatrix} \boldsymbol{F}_I & -\boldsymbol{G}_I \\ -\boldsymbol{G}_I^T & 0 \end{bmatrix} \begin{bmatrix} \boldsymbol{\lambda} \\ \boldsymbol{a} \end{bmatrix} = \begin{bmatrix} \boldsymbol{d} \\ -\boldsymbol{e} \end{bmatrix} \tag{17}$$

where $\boldsymbol{a}$ expresses linear combinations of the normalized rigid body motions in $\boldsymbol{R}$, $\boldsymbol{F}_I$ is the flexibility matrix, $\boldsymbol{G}$ aggregates the rigid body motions, $\boldsymbol{d}$ are the displacements due to applied forces (boundary conditions and loading) and $\boldsymbol{e}$ is the work of rigid body motions due to these applied forces.

$$\boldsymbol{F}_I = \sum_{s=1}^{N_s} \boldsymbol{F}_I^s = \sum_{s=1}^{N_s} \boldsymbol{B}^s (\boldsymbol{K}^s)^+ (\boldsymbol{B}^s)^T \tag{18}$$

$$\boldsymbol{d} = \sum_{s=1}^{d_s} \boldsymbol{F}_I^s = \sum_{s=1}^{N_s} \boldsymbol{B}^s (\boldsymbol{K}^s)^+ \boldsymbol{f}^s \tag{19}$$

$$\boldsymbol{G}_I = \begin{bmatrix} \boldsymbol{B}^{(1)}\boldsymbol{R}^{(1)} & \boldsymbol{B}^{(2)}\boldsymbol{R}^{(2)} & \dots & \boldsymbol{B}^{(N_s)}\boldsymbol{R}^{(N_s)} \end{bmatrix} \tag{20}$$

The linear system of Eq. (17) is not symmetric positive definite. To solve it using the preconditioned conjugate gradient (PCG) method, we must project it into another space using a projection matrix $\boldsymbol{P}$ and then solve the following system:

$$\boldsymbol{P}^T \boldsymbol{F}_I \boldsymbol{P} \bar{\boldsymbol{\lambda}} = \boldsymbol{P}^T (\boldsymbol{d} - \boldsymbol{F}_I \boldsymbol{P} \boldsymbol{\lambda}_0) \tag{21}$$

where

$$\boldsymbol{P} = \boldsymbol{I} - \boldsymbol{G}_I (\boldsymbol{G}_I^T \boldsymbol{G}_I)^{-1} \boldsymbol{G}_I^T \tag{22}$$

$$\boldsymbol{\lambda}_0 = \boldsymbol{G}_I (\boldsymbol{G}_I^T \boldsymbol{G}_I)^{-1} \boldsymbol{e} \tag{23}$$

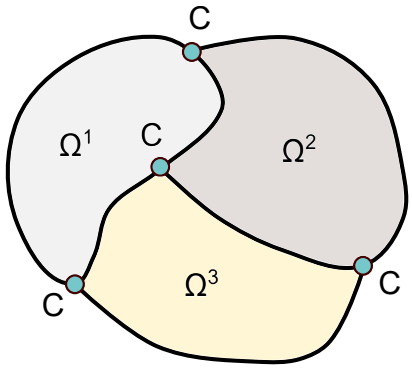

Figure 5: Definition of corner nodes (C).

$$\boldsymbol{\lambda} = \boldsymbol{\lambda}_0 + \boldsymbol{P}\bar{\boldsymbol{\lambda}} \tag{24}$$

$$\boldsymbol{a} = (\boldsymbol{G}_I^T \boldsymbol{G}_I)^{-1} \boldsymbol{G}_I^T (\boldsymbol{F}_I \boldsymbol{\lambda} - \boldsymbol{d}) \tag{25}$$

The coarse problem of FETI-1 is expressed in the linear system $\boldsymbol{G}_I^T \boldsymbol{G}_I x = y$ of Eq. (22) and it helps speed up convergence by globally distributing the error at each PCG iteration. Finally we calculate the displacements depending on if the subdomain is floating or not:

$$\boldsymbol{u}^s = (\boldsymbol{K}^s)^+ (\boldsymbol{f}^s - (\boldsymbol{B}^s)^T \boldsymbol{\lambda}) + \boldsymbol{R}^s \boldsymbol{a}^s \implies \boldsymbol{u}^s = (\boldsymbol{K}^s)^{-1} (\boldsymbol{f}^s - (\boldsymbol{B}^s)^T \boldsymbol{\lambda}) \tag{26}$$

3.2 FETI-DP

The FETI-DP method is based on a dual-primary formulation of the problem to be solved. The main difference between the FETI-DP method and the FETI-1 method is that in FETI-DP, in every iteration of the PCG method, the compatibility of displacements is imposed to a small subset of primal *corner* DOFs, while the compatibility of displacements to the remaining boundary DOFs is only achieved after convergence.

We define *corner* nodes and corner or primal DOFs (Fig. 5). All other DOFs are called *remainder* and are further separated into boundary-remainder and boundary-internal. We then perform static condensation of the remainder DOFs in each subdomain and assemble the resulting matrices/vectors into global ones:

$$\boldsymbol{K}_{cc}^* = \sum_{s=1}^{N_s} (\boldsymbol{L}_c^s)^T \left(\boldsymbol{K}_{cc}^s - (\boldsymbol{K}_{rc}^s)^T (\boldsymbol{K}_{rr}^s)^{-1} \boldsymbol{K}_{rc}^s \right) \boldsymbol{L}_c^s \tag{27}$$

$$\boldsymbol{f}_c^* = \sum_{s=1}^{N_s} (\boldsymbol{L}_c^s)^T \left(\boldsymbol{f}_c^s - (\boldsymbol{K}_{rc}^s)^T (\boldsymbol{K}_{rr}^s)^{-1} \boldsymbol{f}_r^s \right) \tag{28}$$

where the subscripts r and c denote the rows/columns corresponding to remainder and corner DOFs respectively. $\boldsymbol{L}_c$ are unsigned boolean matrices (entries are 0 or 1) mapping global corner displacements to subdomain corner displacements. With an appropriate selection of corner nodes, the matrices $\boldsymbol{K}_{rr}$ is invertible, thus there are no floating subdomains. For the signed boolean matrices $\boldsymbol{B}_r$, we will use the columns of $\boldsymbol{B}$ that correspond to remainder DOFs.

The interface problem of FETI-DP can be written as follows:

$$\left(\boldsymbol{F}_{Irr} + \boldsymbol{F}_{Irc}(\boldsymbol{K}_{cc})^{-1}(\boldsymbol{F}_{Irr})^{T}\right)\boldsymbol{\lambda} = \boldsymbol{d}_r - \boldsymbol{F}_{Irc}(\boldsymbol{K}_{cc})^{-1}\boldsymbol{f}_c^* \tag{29}$$

where $\boldsymbol{d}_r$ are the displacements due to boundary conditions and loading and $\boldsymbol{F}_{Irr}$ is the flexibility matrix. The linear system of Eq. (29) can be solved using the PCG method.

$$\boldsymbol{d}_r = \sum_{s=1}^{N_s} \boldsymbol{B}_r^s(\boldsymbol{K}_{rr}^s)^{-1}\boldsymbol{f}_r^s \tag{30}$$

$$\boldsymbol{F}_{Irr} = \sum_{s=1}^{N_s} \boldsymbol{B}_r^s(\boldsymbol{K}_{rr}^s)^{-1}(\boldsymbol{B}_r^s)^{T} \tag{31}$$

$$\boldsymbol{F}_{Irc} = \sum_{s=1}^{N_s} \boldsymbol{B}_r^s(\boldsymbol{K}_{rc}^s)^{-1}\boldsymbol{K}_{rc}^s\boldsymbol{L}_c^s \tag{32}$$

The coarse problem of FETI-DP is expressed in the linear system $\boldsymbol{K}_{cc} * x = y$ of Eq. (29) and it helps speed up convergence by globally distributing the error at each PCG iteration. After solving the interface problem the displacements can be calculated using:

$$\boldsymbol{u}_c = \left(\boldsymbol{K}_{cc}^*\right)^{-1}\left(\boldsymbol{f}_c^* + (\boldsymbol{F}_{Irc})^{T}\boldsymbol{\lambda}\right) \tag{33}$$

$$\boldsymbol{u}_r^s = (\boldsymbol{K}_{rr}^s)^{-1}\left(\boldsymbol{f}_r^s - \left(\boldsymbol{B}_r^s\right)^{T}\boldsymbol{\lambda} - \boldsymbol{K}_{rc}^s\boldsymbol{L}_c^s\boldsymbol{u}_c\right) \tag{34}$$

3.3 Preconditioning

Both FETI-1 and FETI-DP can use the same preconditioners to speed up the convergence of PCG when solving the interface problem. The idea is to approximate the inverse of the flexibility matrix, which is defined for the boundary DOFs. The most common preconditioners used are Dirichlet and lumped ones.

Dirichlet preconditioner

A Dirichlet preconditioner is defined as follows:

$$\boldsymbol{F}_I^{-1} = \sum_{s=1}^{N_s} \boldsymbol{B}_{pb}^s\boldsymbol{S}^s(\boldsymbol{B}_{pb}^s)^{T} \tag{35}$$

where $\boldsymbol{S}^s$ is the Schur complement of internal dofs (internal-remainder in FETI-DP)

$$\boldsymbol{S}^s = \boldsymbol{K}_{bb}^s - (\boldsymbol{K}_{ib}^s)^{T}(\boldsymbol{K}_{ii}^s)^{-1}\boldsymbol{K}_{ib}^s \tag{36}$$

$\boldsymbol{B}_{pb}$ are sparse matrices that perform mapping (like $\boldsymbol{B}$) and scaling, e.g. for a homogeneous stiffness distribution among subdomains:

$$\boldsymbol{B}_{pb}^s = \boldsymbol{B}_b^s(\boldsymbol{M}_b^s)^{-1} \tag{37}$$

where $\boldsymbol{B}_b$ are the columns of $\boldsymbol{B}$ corresponding to boundary DOFs (boundary remainder in FETI-DP) and $\boldsymbol{M}_b$ is a diagonal matrix whose diagonal entries are the multiplicity of the corresponding DOFs, i.e. how many subdomains have instances of the DOFs.

Lumped preconditioner

A lumped preconditioner is defined as follows:

$$\boldsymbol{F}_I^{-1} = \sum_{s=1}^{N_s} \boldsymbol{B}_{pb}^s \boldsymbol{K}_{bb}^s (\boldsymbol{B}_{pb}^s)^T \tag{38}$$

In general, a lumped preconditioner is faster to compute and implement, but does not speed up the convergence of PCG as much as Dirichlet.

Diagonal Dirichlet preconditioner

A Diagonal Dirichlet preconditioner is defined as follows:

$$\boldsymbol{F}_I^{-1} = \sum_{s=1}^{N_s} \boldsymbol{B}_{pb}^s \hat{\boldsymbol{S}}^s (\boldsymbol{B}_{pb}^s)^T \tag{39}$$

where $\hat{\boldsymbol{S}}^s$ is an approximation of the Schur complement of internal dofs (internal-remainder in FETI-DP).

$$\hat{\boldsymbol{S}}^s = \boldsymbol{K}_{bb}^s - (\boldsymbol{K}_{ib}^s)^T (\boldsymbol{D}_{ii}^s)^{-1} \boldsymbol{K}_{ib}^s \tag{40}$$

where $\boldsymbol{D}_{ii}^s$ is the diagonal of $\boldsymbol{K}_{ii}^s$. In general, the computational cost of computing and implementing a diagonal Dirichlet preconditioner, as well as the resulting reduction of PCG iterations falls between that of Dirichlet and lumped preconditioner.

4 Combining XFEM with FETI

Using FETI methods to solve the linear systems resulting from XFEM during crack propagation can speed up the process. FETI methods are inherently parallel and can be executed on distributed computing environments concurrently. Compared to other domain decomposition methods, FETI methods scale extremely well with the number of processors in a network environment.

Even on a single-core system, FETI methods can result in a speedup over direct solvers. Due to domain decomposition, the stiffness matrix of each subdomain will have lower bandwidth than the stiffness matrix of the global domain. Non zero entries of the stiffness matrix correspond to DOFs of the same element. These DOFs are numbered closer to each other in a subdomain that has fewer DOFs than the whole model. In contrast, direct solvers rely on factorizing the stiffness matrix and their main bottleneck is its bandwidth. The more subdomains a domain decomposition solvers uses, the smaller the bandwidth of the resulting stiffness matrices.

To use FETI-1 for XFEM one needs to correctly identify the rigid body motions of the floating subdomains defined in Eq. (16). Round-off errors in the computation of the rigid body motions can increase PCG iterations required to solve the interface problem. FETI-DP on the other hand requires an appropriate selection of corner nodes to avoid singular matrices. Both methods can use the standard preconditioners described in Section 3.3. They should also be combined with an effective mesh partitioning algorithm to ensure a decomposition into balanced subdomains that does not slow down convergence.

5 NUMERICAL EXAMPLE

The test case deals with a fatigue crack growth in a double cantilever beam (DCB) [10]. The geometry of the DCB are $h = 3.94$ in and $L = 3h = 11.82$ in, as shown in Fig. 6. The thickness of the beam is equal to 1 in. The first crack segment is horizontal at half the beam's height and has length $a = 3.95$ in. An extra crack segment is added with length $da = 0.5$ in with an inclination angle $d\theta = 5.71^o$, to avoid pure Mode I propagation. The right side of the DCB is fixed, while a cyclic load $P = 197$ lbs is applied on the top left and bottom left corners. The material properties are $E = 3 \cdot 10^7$ psi and $v = 0.3$, while plane stress conditions are considered.

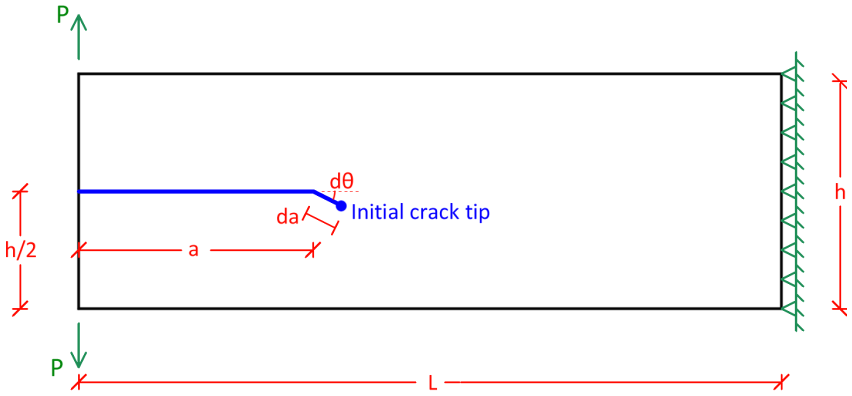

Figure 6: Geometry characteristics of the double cantilever beam.

The beam is discretized with standard QUAD4 finite elements, forming a uniform mesh. XFEM analysis is performed at 7 propagation steps, with topological tip enrichment. All analyses were conducted on a single-core system (Intel Core i7-6700 @3.40GHz CPU / 8 GB RAM) using three different types of solvers: i) a direct solver (with LDL factorization), ii) a FETI-1 solver and iii) a FETI-DP solver. In all analyses approximate minimum degree (AMD) reordering was used to reduce the bandwidth of the resulting stiffness matrices. Fig. 7 shows the crack path at the last step of the XFEM analysis.

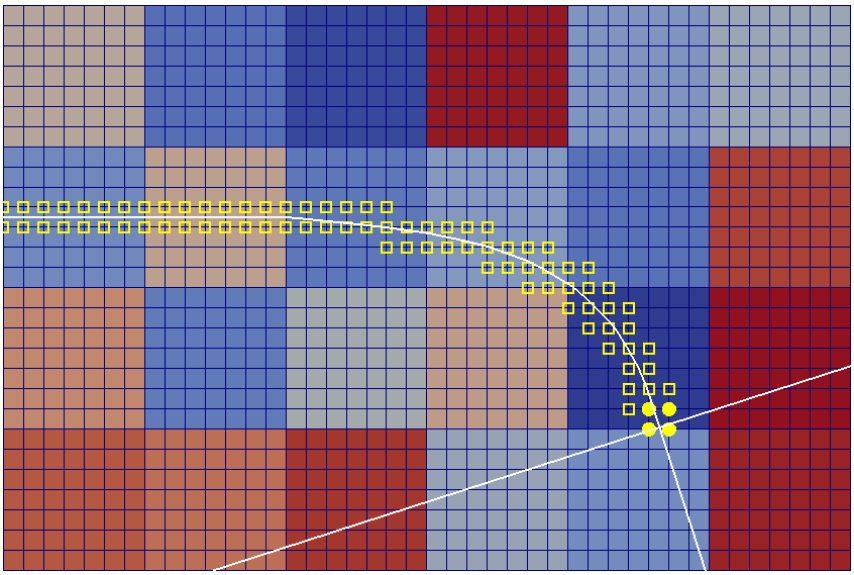

Figure 7: Crack propagation in a double cantilever beam.

The speedup of FETI-1 and FETI-DP solver over the direct solver is depicted in Fig. 8 versus the number of DOFs and the number of subdomains. It is shown that FETI-DP exhibits excellent performance compared to other two solvers. More specific, it offers significant speedup (up to 22X) compared to the direct solver for all meshes examined. Furthmore, the Dirichlet preconditioner outperforms lumped and diagonal Dirichlet (up to a factor of 10X). The average number of PCG iterations is depicted in Fig. 9 versus the number of DOFs and the number of subdomains. The number of required PCG iterations remained low throughout the crack propagation analysis and was not affected by the ill-conditioned due to the enriched DOFs, while the optimal number of subdomains depends on the mesh size. On the other hand, FETI-1 required more PCG iterations to converge, as more enriched DOFs are added to the system. Although FETI-1 is inferior to FETI-DP, it still results in a speedup of the solution phase compared to the direct solver (up to 12X). Again Dirichlet precondition outperforms the other two in terms of average number of iterations required for the convergence.

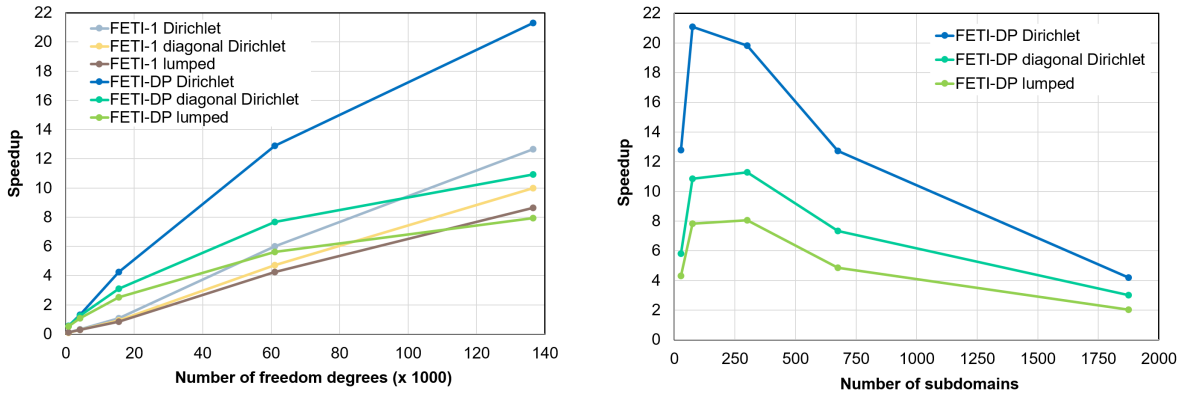

(a) (b)

Figure 8: Speedup over direct solver versus number of (a) dofs and (b) subdomains.

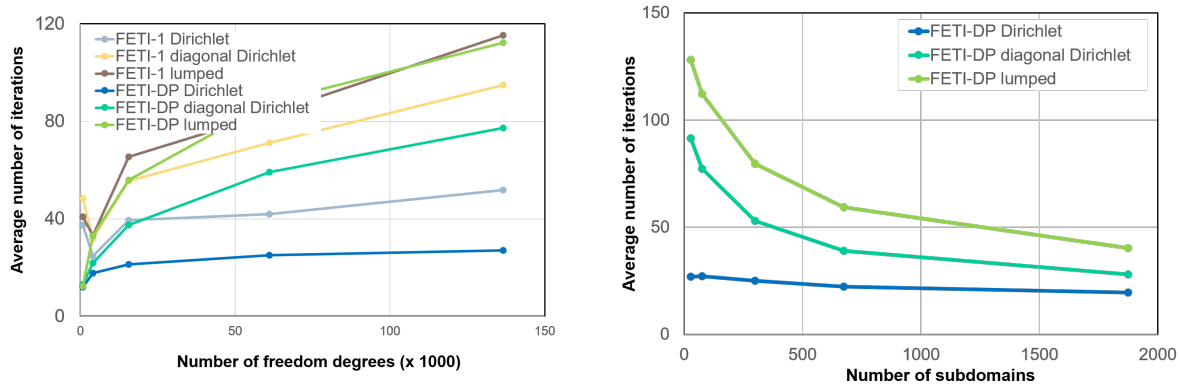

(a) (b)

Figure 9: Average number of PCG iterations vs number of (a) dofs and (b) subdomains.

6 CONCLUSIONS

- FETI-1 and FETI-DP can be used for the solution of the linear systems resulting from 2D crack propagation in the XFEM framework.
- They offer significant speedup compared to a direct solver that uses Cholesky/LDL factorization and reordering, even when run on a single-core system.
- Potentially they can be run on distributed computing environments to further reduce the computational time.
- FETI-DP is simpler to use than FETI-1 and more efficient, since the number of PCG iterations is marginally increased by the ill-conditioning caused by enriched dofs.
- For both methods, Dirichlet preconditioner performs the best, while lumped preconditioner performs the worst.

REFERENCES

[1] Moes, N., Dolbow, J. and Belytschko, T. A Finite Element Method for Crack Growth without Remeshing. *International Journal for Numerical Methods in Engineering*, **46**, 131–150, 1999.

[2] Babuška, I. and Melenk, J. M., The Partition of Unity Method. *International Journal for Numerical Methods in Engineering*, **40**, 727–758, 1997.

[3] Anderson, T. L., *Fracture Mechanics: Fundamentals and Applications*. 3rd Edition, CRC Press, 2004.

[4] Osher, S. and Sethian, J. A, The Partition of Unity Method. *Journal of Computational Physics*, **79**, 12–49, 1988.

[5] Stolarska, M. and Chopp, D. L. and Moës, N. and Belytschko, T., Modelling crack growth by level sets in the extended finite element method. *International Journal for Numerical Methods in Engineering*, **51**, 943–960, 2001.

[6] Rice, J. R., A path independent integral and the approximate analysis of strain concentrations by notches and cracks. *Journal of Applied Mechanics*, **35**, 379–386, 1968.

[7] Erdogan, F. and Sih, G. C., On the Crack Extension in Plates Under Plane Loading and Transverse Shear. *Journal of Fluids Engineering*, **51**, 519–525, 1963.

[8] Paris, P.C. and Gomez, M.P. and Anderson, W.E., On the Crack Extension in Plates Under Plane Loading and Transverse Shear. *The Trend in Engineering*, **13**, 9–14, 1961.

[9] Yau, J. F. and Wang, S. S. and Corten, H. T., A Mixed-Mode Crack Analysis of Isotropic Solids Using Conservation Laws of Elasticity. *Journal of Applied Mechanics*, **47**, 335–341, 1980.

[10] Belytschko, T. and Black, T., Elastic crack growth in finite elements with minimal remeshing. *International Journal for Numerical Methods in Engineering*, **45**, 601–620, 1999.

[11] Farhat, C. and Roux, F.-X., A method of finite element tearing and interconnecting and its parallel solution algorithm. *International Journal for Numerical Methods in Engineering*, **32**, 1205–1227, 1991.

[12] Farhat, C., Lesoinne, M. and Pierson, K., A scalable dualprimal domain decomposition method. *Numerical Linear Algebra with Applications*, **32**, 687-714, 2000.

COMPDYN 2019
7th ECCOMAS Thematic Conference on
Computational Methods in Structural Dynamics and Earthquake Engineering
M. Papadrakakis, M. Fragiadakis (eds.)
Crete, Greece, 24-26 June 2019

TRANSIENT RESPONSE MOMENT ANALYSIS OF A LINEAR SYSTEM SUBJECTED TO NON-GAUSSIAN RANDOM EXCITATION BY THE EQUIVALENT NON-GAUSSIAN EXCITATION METHOD

Takahiro Tsuchida and Kohei Kanno[1]

[1]Department of Systems and Control Engineering Tokyo Institute of Technology
2-12-1 Ookayama, Meguro-ku, Tokyo 152-8552, Japan
e-mail: ttsuchida@sc.e.titech.ac.jp, kanno.k@k.sc.e.titech.ac.jp

Keywords: Stochastic Dynamics, Non-Gaussian random excitation, Transient moment analysis, Moment Equation, Equivalent non-Gaussian excitation method, Kurtosis.

Abstract. *The transient response analysis of a linear system subjected to non-Gaussian random excitation is carried out by using the equivalent non-Gaussian excitation method. The non-Gaussian excitation is prescribed by both the probability density function and the power spectrum. Since the excitation is expressed by the Itô stochastic differential equation, moment equations for the response can be derived from the governing equations for the excitation and the system. However, the moment equations are generally not closed owing to the nonlinearity of the diffusion coefficient in the governing equation for the excitation. Thus, using the equivalent non-Gaussian excitation method, the diffusion coefficient is replaced approximately by the equivalent diffusion coefficient, which is expressed by a quadratic polynomial. After the replacement of the diffusion coefficient, we could derive a closed set of the moment equations and obtain the time evolution of the response moments by solving these equations. In numerical examples, the analytical method is applied to a linear system under non-Gaussian excitation with the widely different probability distributions and bandwidth. It is shown that the analytical results of the transient response kurtosis agree very well with the corresponding Monte Carlo simulation results in all cases considered in the examples.*

1 INTRODUCTION

Stochastic analysis of the response of machines and structures subjected to random excitation have been performed widely for many decades. In many cases, the random excitation has been assumed to be a Gaussian process. This assumption is due to the fact that many random processes in engineering problems have the probability density functions similar to the Gaussian distribution. However, some random excitations (e.g. road roughness[1], shallow water waves[2] and wind pressure acting on low-rise buildings[3]) possess highly non-Gaussianity. The response of systems under non-Gaussian excitation is generally also non-Gaussian even if the system is linear, and the response characteristics are quite different with those in the case of Gaussian excitation. Therefore, response analysis in consideration of the non-Gaussian nature of random excitation is important to evaluate system response and reliability correctly.

In recent years, the equivalent non-Gaussian excitation method was presented to obtain the statistical moments of the response of non-Gaussian randomly excited systems[4]. It was demonstrated that this method leads to the accurate results of the variance, skewness and kurtosis of the stationary response for the random excitation with a wide range of the non-Gaussian probability distributions and the bandwidth of the power spectrum. On the other hand, the effectiveness of the method in transient analysis has not been verified yet.

In this study, we carry out the transient response analysis of a linear system subjected to non-Gaussian random excitation by the equivalent non-Gaussian excitation method. The non-Gaussian excitation is prescribed by both the probability density function and the power spectrum. Since the excitation is expressed by the Ito stochastic differential equation, moment equations for the response can be derived from the governing equations for the excitation and the system. However, the moment equations are not closed in most cases due to the nonlinearity of the diffusion coefficient in the governing equation for the excitation. Accordingly, using the equivalent non-Gaussian excitation method, the diffusion coefficient is replaced by the equivalent diffusion coefficient approximately. The square of the equivalent diffusion coefficient is expressed by a quadratic polynomial. The coefficients of the polynomial are determined according to the criterion of the least mean square error between the original diffusion coefficient and the equivalent counterpart. After the replacement of the diffusion coefficient, we can derive a closed set of the moment equations and obtain the time evolution of the response moments by solving these equations.

In numerical examples, the above-mentioned method is applied to a linear system under non-Gaussian excitation with the widely different probability distributions and bandwidth. It is shown that the analytical results of the transient response moments up to the fourth order agree very well with the corresponding Monte Carlo simulation results in all cases considered in the examples.

2 DESCRIPTION OF SYSTEM AND NON-GAUSSIAN RANDOM EXCITATION

2.1 System

Consider a single-degree-of-freedom linear system described by

$$\ddot{X} + 2\zeta\dot{X} + X = U(t) \tag{1}$$

where ζ is the damping ratio, t is the non-dimensional time parameter and dot sign denotes the derivative with respect to time t. $U(t)$ is a zero-mean stationary non-Gaussian random excitation.

2.2 Non-Gaussian random excitation

The non-Gaussian random excitation $U(t)$ considered in this study is prescribed by both the marginal probability density function $p_U(u)$ and the power spectral density $S_U(\omega)$. As the excitation probability density $p_U(u)$, various shapes of non-Gaussian distributions are taken into account.

The power spectrum $S_U(\omega)$ is expressed by

$$S_U(\omega) = \frac{\alpha \mathrm{E}[U^2]}{\pi(\omega^2 + \alpha^2)} \tag{2}$$

where α is the bandwidth parameter and $\mathrm{E}[U^2]$ is the mean square value of the excitation. $S_U(\omega)$ is shown in Fig. 1. This spectral density has a peak at zero frequency. The excitation is wide-band when α is large, on the other hand, the low-frequency component of the excitation is dominant when α is small.

The excitation $U(t)$ with the specified probability density $p_U(u)$ and the power spectrum $S_U(\omega)$ given by Eq. (2) can be described by the following one-dimensional Itô stochastic differential equation[5]

$$dU = -\alpha U dt + D(U) dB(t) \tag{3}$$

where α is the bandwidth parameter in Eq. (2), $B(t)$ is a Wiener process and the diffusion coefficient $D(u)$ is expressed by

$$D^2(u) = -\frac{2\alpha}{p_U(u)} \int_{-\infty}^{u} s p_U(s) ds \tag{4}$$

It is found that the non-Gaussian distribution $p_U(u)$ is reflected in $D(u)$. On the other hand, the information on the power spectrum $S_U(\omega)$ is included in the drift coefficient in Eq. (3) (see Ref.[5]).

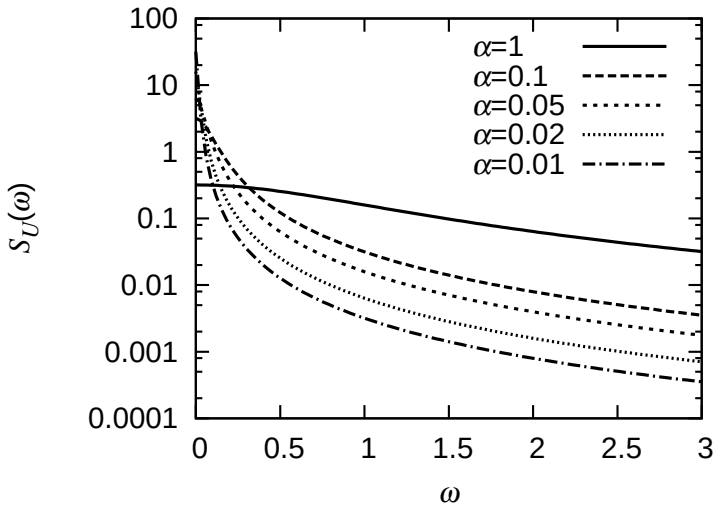

Figure 1: Power spectrum of excitation ($\mathrm{E}[U^2] = 1$).

3 EQUIVALENT NON-GAUSSIAN EXCITATION METHOD

3.1 Moment equations

The augmented system consisted of the equation of motion of the system (1) and the governing equation for the excitation (3) is described by a set of Itô stochastic differential equations as follows:

$$dX = \dot{X}dt \tag{5}$$

$$d\dot{X} = (-2\zeta\dot{X} - X + U)dt \tag{6}$$

$$dU = -\alpha U dt + D(U)dB(t) \tag{7}$$

Then, applying the Itô's formula[6] to Eqs. (5)-(7), the $(i+j+k)$th-order moment equations for the system response can be derived.

$$\begin{aligned}\frac{d}{dt}\mathrm{E}[X^i\dot{X}^jU^k] =& i\mathrm{E}[X^{i-1}\dot{X}^{j+1}U^k] - j\mathrm{E}[X^{i+1}\dot{X}^{j-1}U^k] - (2j\zeta + k\alpha)\,\mathrm{E}[X^i\dot{X}^jU^k] \\ &+ j\mathrm{E}[X^i\dot{X}^{j-1}U^{k+1}] + \frac{1}{2}k(k-1)\mathrm{E}[X^i\dot{X}^jU^{k-2}D^2(U)]\end{aligned} \tag{8}$$

However, $\mathrm{E}[X^i\dot{X}^jU^{k-2}D^2(U)]$ on the right-hand side of Eq. (8) is complicated form in most cases because of the nonlinearity of the diffusion coefficient $D^2(u)$ given by Eq.(4). Therefore, the moment equations (8) are generally not closed. In this paper, the equivalent non-Gaussian excitation method[4] is applied to obtain a closed set of the moment equations approximately.

3.2 Equivalent non-Gaussian excitation method

In the equivalent non-Gaussian excitation method, the diffusion coefficient $D(U)$ in Eq. (7) is replaced approximately with the equivalent diffusion coefficient $D_{eq}(U)$. The square of $D_{eq}(U)$ is expressed by a quadratic polynomial.

$$D_{eq}^2(U) = A_{eq}U^2 + B_{eq}U + C_{eq} \tag{9}$$

where the coefficients A_{eq}, B_{eq} and C_{eq} of the polynomial are adjusted according to the criterion of minimization of the mean square error $\mathrm{E}[e^2]$ between the square of the original diffusion coefficient $D^2(U)$ and the square of the equivalent one $D_{eq}^2(U)$.

$$\mathrm{E}[e^2] = \mathrm{E}[(D^2(U) - D_{eq}^2(U))^2] = \mathrm{E}[(D^2(U) - A_{eq}U^2 - B_{eq}U - C_{eq})^2] \tag{10}$$

Minimization of $\mathrm{E}[e^2]$ is realized when the following three conditions hold:

$$\frac{\partial \mathrm{E}[e^2]}{\partial A_{eq}} = 0, \quad \frac{\partial \mathrm{E}[e^2]}{\partial B_{eq}} = 0, \quad \frac{\partial \mathrm{E}[e^2]}{\partial C_{eq}} = 0 \tag{11}$$

Solving Eq. (11) with respect to A_{eq}, B_{eq} and C_{eq} leads to

$$\begin{aligned}A_{eq} =& \frac{(\mathrm{E}[U^2] - \mathrm{E}[U]^2)(\mathrm{E}[U^2D^2(U)] - \mathrm{E}[U^2]\mathrm{E}[D^2(U)])}{(\mathrm{E}[U^4] - \mathrm{E}[U^2]^2)(\mathrm{E}[U^2] - \mathrm{E}[U]^2) - (\mathrm{E}[U^3] - \mathrm{E}[U]\mathrm{E}[U^2])^2} \\ &- \frac{(\mathrm{E}[U^3] - \mathrm{E}[U]\mathrm{E}[U^2])(\mathrm{E}[U^2D^2(U)] - \mathrm{E}[U^2]\mathrm{E}[D^2(U)])}{(\mathrm{E}[U^4] - \mathrm{E}[U^2]^2)(\mathrm{E}[U^2] - \mathrm{E}[U]^2) - (\mathrm{E}[U^3] - \mathrm{E}[U]\mathrm{E}[U^2])^2}\end{aligned} \tag{12}$$

$$
\begin{aligned}
B_{eq} =& \frac{(\mathrm{E}[U^4] - \mathrm{E}[U^2]^2)(\mathrm{E}[UD^2(U)] - \mathrm{E}[U]\mathrm{E}[D^2(U)])}{(\mathrm{E}[U^4] - \mathrm{E}[U^2]^2)(\mathrm{E}[U^2] - \mathrm{E}[U]^2) - (\mathrm{E}[U^3] - \mathrm{E}[U]\mathrm{E}[U^2])^2} \\
&- \frac{(\mathrm{E}[U^3] - \mathrm{E}[U]\mathrm{E}[U^2])(\mathrm{E}[U^2D^2(U)] - \mathrm{E}[U^2]\mathrm{E}[D^2(U)])}{(\mathrm{E}[U^4] - \mathrm{E}[U^2]^2)(\mathrm{E}[U^2] - \mathrm{E}[U]^2) - (\mathrm{E}[U^3] - \mathrm{E}[U]\mathrm{E}[U^2])^2}
\end{aligned} \tag{13}
$$

$$
C_{eq} = \mathrm{E}[D^2(U)] - A_{eq}\mathrm{E}[U^2] - B_{eq}\mathrm{E}[U] \tag{14}
$$

Next, we derive the 2nd, 3rd and 4th order moment equations for the stationary excitation $U(t)$ by letting $(i, j, k) = (0, 0, 2), (0, 0, 3), (0, 0, 4)$ in Eq. (8) as follows:

$$
-2\alpha\mathrm{E}[U^2] + \mathrm{E}[D^2(U)] = 0 \tag{15}
$$

$$
-3\alpha\mathrm{E}[U^3] + 3\mathrm{E}[uD^2(U)] = 0 \tag{16}
$$

$$
-4\alpha\mathrm{E}[U^4] + 6\mathrm{E}[u^2D^2(U)] = 0 \tag{17}
$$

From Eqs. (12)-(17), it can be seen that the coefficients A_{eq}, B_{eq} and C_{eq} are evaluated by the moments up to the 4th order of $U(t)$. The moments $\mathrm{E}[U^n]$ $(n = 1, 2, 3, 4)$ can be calculated analytically or numerically from the non-Gaussian distribution $p_U(u)$, which is given beforehand to prescribe the excitation $U(t)$. Therefore, A_{eq}, B_{eq} and C_{eq} can be calculated, and the equivalent diffusion coefficient $D_{eq}(U)$ can be obtained by substituting the three coefficients into Eq. (9).

By replacing $D(U)$ in Eq.(7) with $D_{eq}(U)$ determined through the above procedure, the stochastic differential equation governing the equivalent non-Gaussian excitation can be obtained as

$$
dU = -\alpha U dt + \sqrt{A_{eq}U^2 + B_{eq}U + C_{eq}}dB(t) \tag{18}
$$

Finally, the $(i + j + k)$th-order moment equations are derived from Eqs. (5), (6) and (18).

$$
\begin{aligned}
\frac{d}{dt}\mathrm{E}[X^i\dot{X}^jU^k] =& i\mathrm{E}[X^{i-1}\dot{X}^{j+1}U^k] - j\mathrm{E}[X^{i+1}\dot{X}^{j-1}U^k] \\
&+ \left(-2j\zeta - k\alpha + \frac{1}{2}k(k-1)A_{eq}\right)\mathrm{E}[X^i\dot{X}^jU^k] \\
&+ j\mathrm{E}[X^i\dot{X}^{j-1}U^{k+1}] + \frac{1}{2}k(k-1)B_{eq}\mathrm{E}[X^i\dot{X}^jU^{k-1}] \\
&+ \frac{1}{2}k(k-1)C_{eq}\mathrm{E}[X^i\dot{X}^jU^{k-2}]
\end{aligned} \tag{19}
$$

In Eq.(19), the moments of order higher than $(i + j + k)$ do not appear. Therefore, Eq. (19) is closed form and can be solved analytically to obtain the time evolution of the response moments.

The solution of the 2nd-order response moment to Eq.(19) coincides perfectly with the exact solution. This is due to the following two facts:

- The power spectrum of the excitation given by Eq.(2) remains unchanged after replacing the diffusion coefficient $D(U)$ by $D_{eq}(U)$[4].
- The 2nd-order response moment of a linear system is determined from the excitation power spectrum $S_U(\omega)$ and the frequency response function $H(\omega)$ of the system as follows[7]:

$$\begin{aligned}\sigma_X^2(t) = \int_{-\infty}^{\infty} & S_U(\omega)|H(\omega)|^2 \\ & \times \{1 + \exp(-2\zeta t)\left[1 + \frac{2\zeta}{\sqrt{1-\zeta^2}}\sin\sqrt{1-\zeta^2}t\cos\sqrt{1-\zeta^2}t\right. \\ & - \exp(\zeta t)\left(2\cos\sqrt{1-\zeta^2}t + \frac{2\zeta}{\sqrt{1-\zeta^2}}\sin\sqrt{1-\zeta^2}t\right)\cos\omega t \\ & - \exp(\zeta t)\left(\frac{2}{\sqrt{1-\zeta^2}}\right)\sin\sqrt{1-\zeta^2}t\sin\omega t \\ & \left.\left. + \frac{2\zeta^2 - 1 + \omega^2}{1-\zeta^2}\sin^2\omega t\right]\right\} d\omega \end{aligned} \tag{20}$$

Furthermore, in the previous study[4], it was shown that since the coefficients A_{eq}, B_{eq} and C_{eq} are determined by the moments $\mathrm{E}[U^n]$ $(n = 1, 2, 3, 4)$, the equivalent non-Gaussian excitation governed by Eq. (18) retains the moments up to the 4th order which are the same as those of the original excitation, and this feature enables us to obtain the accurate results of the stationary response moments up to the 4th order.

In the next section, the validity of the equivalent non-Gaussian excitation method in transient response moment analysis will be examined.

4 NUMERICAL EXAMPLE

The equivalent non-Gaussian excitation method described in the previous section will now be applied to a linear system subjected to non-Gaussian excitation with the generalized Gaussian distribution.

4.1 Excitation probability distribution and diffusion coefficient

In this example, the generalized Gaussian distribution[8] is used for the non-Gaussian distribution of the excitation. The distribution with zero mean is defined as

$$p_U(u) = \frac{\kappa}{2a\Gamma(1/\kappa)}\exp\left(-\frac{|u|^\kappa}{a^\kappa}\right) \tag{21}$$

where $\Gamma(\cdot)$ is the gamma function and $\kappa(>0)$ represents the shape parameter. By varying κ, it is possible to characterize a large class of distributions with the widely different kurtosis. The Laplace, Gaussian and uniform distributions are special cases of the generalized Gaussian distribution with $\kappa = 1$, $\kappa = 2$ and $\kappa \to \infty$, respectively. a is the scale parameter. The variance σ^2 of the distribution is expressed by

$$\sigma^2 = a^2\Gamma\left(\frac{3}{\kappa}\right)\Gamma\left(\frac{1}{\kappa}\right)^{-1} \tag{22}$$

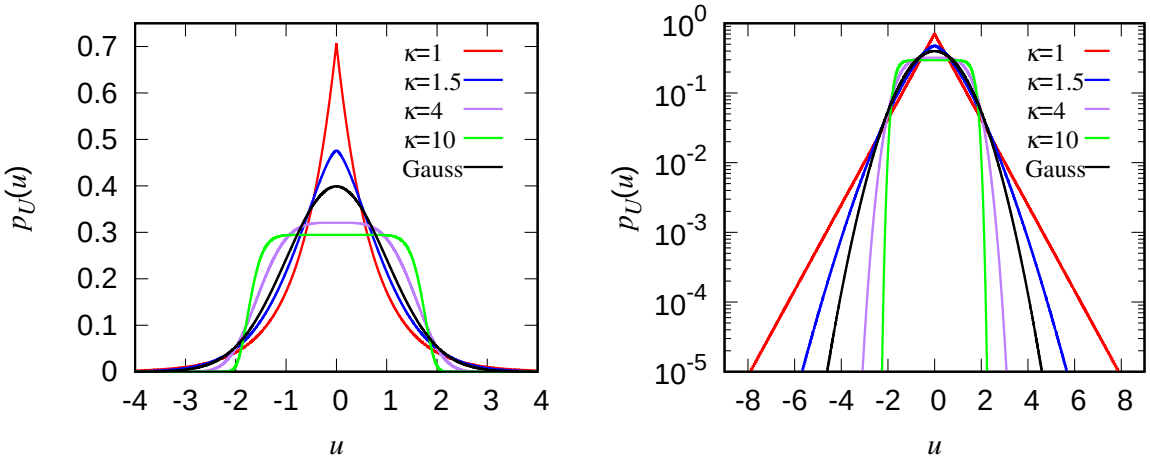

Figure 2: Generalized Gaussian distribution with zero mean and unit variance. Left : linear scale, Right : logarithmic scale.

In this study, a is adjusted so that σ^2 is equal to 1, irrespective of the shape parameter κ. The kurtosis γ_{4U} is given by

$$\gamma_{4U} = \Gamma\left(\frac{5}{\kappa}\right)\Gamma\left(\frac{1}{\kappa}\right)\Gamma\left(\frac{3}{\kappa}\right)^{-2} - 3 \tag{23}$$

In Fig. 2, the generalized Gaussian distributions for four types of κ are shown. In the case of $\kappa < 2$, the distribution has the heavier tail and larger kurtosis than those of a Gaussian distribution ($\kappa = 2$). On the other hand, the distribution for $\kappa > 2$ becomes the light-tailed distribution with smaller kurtosis compared to Gaussian distribution.

By Eq. (4), the diffusion coefficient $D(u)$ corresponding to the the generalized Gaussian distribution is derived as

$$D^2(u) = \frac{2\alpha a^2}{\kappa}\Gamma\left(\frac{2}{\kappa}, \frac{|u|^\kappa}{a^\kappa}\right)\exp\left(\frac{|u|^\kappa}{a^\kappa}\right) \tag{24}$$

where $\Gamma(\cdot,\cdot)$ is the upper incomplete gamma function.

4.2 Application of equivalent non-Gaussian excitation method

Since the diffusion coefficient $D(u)$ given by Eq. (24) is the complicated expression, the moment equations (8) are not closed. Therefore, the equivalent non-Gaussian excitation method is applied. $D(U)$ is replaced approximately with the equivalent diffusion coefficient $D_{eq}(U)$ expressed by Eq. (9). The moments up to the 4th order of the generalized Gaussian distribution are given as follows:

$$\begin{aligned} &\mathrm{E}[U^n] = a^n\Gamma\left(\frac{n+1}{\kappa}\right)\Gamma\left(\frac{1}{\kappa}\right)^{-1}, \quad n = 2, 4 \\ &\mathrm{E}[U] = \mathrm{E}[U^3] = 0 \end{aligned} \tag{25}$$

Using Eqs.(12)-(17) and (25), A_{eq}, B_{eq} and C_{eq} can be calculated. The coefficient B_{eq} is equal to 0 since the 1st and 3rd order moments of the excitation are zero. Then, substituting A_{eq}, B_{eq} and C_{eq} into Eq. (18) gives the stochastic differential equation for the equivalent non-Gaussian excitation. Finally, using this equation and Eqs. (5) and (6), the moment equations can be derived (Eq. (19)).

In this example, all the odd-order response moments are zero since the system is linear and the excitation distribution is symmetric. Thus, the second and fourth order moment equations are solved. These moment equations are written in appendix.

4.3 Parameters for numerical Example

- Damping ratio $\zeta = 0.05$
- Bandwidth parameter of excitation
  $\alpha = 0.01 \quad (\alpha/\zeta = 0.2)$
  $\alpha = 0.05 \quad (\alpha/\zeta = 1)$
  $\alpha = 1 \qquad (\alpha/\zeta = 20)$
- Shape parameter of generalized Gaussian distribution
  $\kappa = 1 \qquad$ (kurtosis $\gamma_{4U} = 3$)
  $\kappa = 1.5 \quad$ (kurtosis $\gamma_{4U} = 0.761954$)
  $\kappa = 4 \qquad$ (kurtosis $\gamma_{4U} = -0.811560$)
  $\kappa = 10 \quad$ (kurtosis $\gamma_{4U} = -1.11584$)

Three types of the excitation bandwidth parameter α are considered: $\alpha = 0.01$ (smaller than the damping ratio ζ which corresponds to the bandwidth of the frequency response function of a linear system), $\alpha = 0.05$ (the same as ζ) and $\alpha = 1$ (larger than ζ). The shape parameter κ of the generalized Gaussian distribution is also changed such that the shapes of the probability densities are quite different from each other. The distributions with $\kappa = 1$ and 1.5 have the larger kurtosis than that of a Gaussian distribution (kurtosis $= 0$), whereas the distributions with $\kappa = 4$ and 10 have the small kurtosis compared to a Gaussian distribution. The four types of the distributions are shown in Fig. 2.

Assume that the initial conditions of the system are $X(0) = 0$, $\dot{X}(0) = 0$ and the excitation is added to the system at $t = 0$.

4.4 Results

As mentioned above, all the odd-order response moments are zero since the system is linear and the excitation distribution is symmetric and zero-mean. Furthermore, when the equivalent non-Gaussian excitation method is used, the exact solution of the 2nd-order response moment can be obtained. Thus, the results of the response kurtosis, which is calculated from the 2nd and 4th order moments, is compared with the Monte Carlo simulation result.

The results of the transient displacement kurtosis are shown in Figs. 3-6. In these figures, the solid line and $\odot$ denote the analytical results and the corresponding Monte Carlo simulation results, respectively. The analytical results are in good agreement with the simulation results in all cases considered here. These results illustrate that the effectiveness of the equivalent non-Gaussian excitation method for transient response moment analysis of the system under non-Gaussian excitation with the widely different probability densities and a wide range of the bandwidth.

From Figs. 3-6, the following characteristics of the displacement response kurtosis could be found.

- Immediately after the excitation is applied to the system ($t \simeq 0$), the response kurtosis becomes almost the same as the excitation kurtosis, irrespective of the excitation bandwidth α.

- When the excitation bandwidth is narrower than the bandwidth of the system ($\alpha = 0.01$), the response kurtosis approaches zero (i.e., Gaussian) at period 2π and becomes a value close to the excitation kurtosis in steady state.
- In the case of the excitation bandwidth similar to the system bandwidth ($\alpha = 0.05$), the response kurtosis approaches zero at period 2π as in the case of $\alpha = 0.01$, on the other hand, the kurtosis of the stationary response is closer to 0 than that for $\alpha = 0.01$.
- When the excitation bandwidth is wider than that of the system ($\alpha = 1$), the response kurtosis changes almost monotonically and becomes a value close to zero in steady state.

These response characteristics will be investigated and discussed in detail in future work.

5 CONCLUSIONS

The transient response moment analysis has been performed for a linear system subjected to non-Gaussian random excitation using the equivalent non-Gaussian excitation method. The non-Gaussian random excitation is prescribed by both the probability density function and the power spectrum, and is described by an Itô stochastic differential equation. Since moment equations, which is derived from the governing equations for the excitation and the system, are generally not closed due to the nonlinearity of the diffusion coefficient in the stochastic differential equation for the excitation. Thus, by applying the equivalent non-Gaussian excitation method, the diffusion coefficient is replaced by the equivalent one approximately. The square of the equivalent diffusion coefficient is expressed by a quadratic polynomial. The coefficients of the polynomial are determined by minimizing the mean square error between the original diffusion coefficient and the equivalent counterpart. After the replacement of the diffusion coefficient, we can derive a closed set of the moment equations and obtain the transient response moments by solving these equations. The solution of the 2nd-order response moment coincides precisely with the exact solution because the replacement of the diffusion coefficient does not change the power spectrum of the excitation.

In numerical examples, the equivalent non-Gaussian excitation method has been applied to a linear system under non-Gaussian excitation with the generalized Gaussian distribution. It has been shown that the analytical results of the kurtosis of the transient response is in good agreement with the corresponding Monte Carlo simulation results in all cases considered in the examples. This is because the equivalent non-Gaussian excitation obtained by replacing the diffusion coefficient retains the moments up to the 4th order which are the same as those of the original excitation.

In this study, only the case of non-Gaussian excitation with a symmetric probability distribution has been considered. In our future work., application of the equivalent non-Gaussian excitation method to the case of random excitation with an asymmetric probability distribution will be performed to examine the validity of the method for various shapes of non-Gaussian distributions of the excitation.

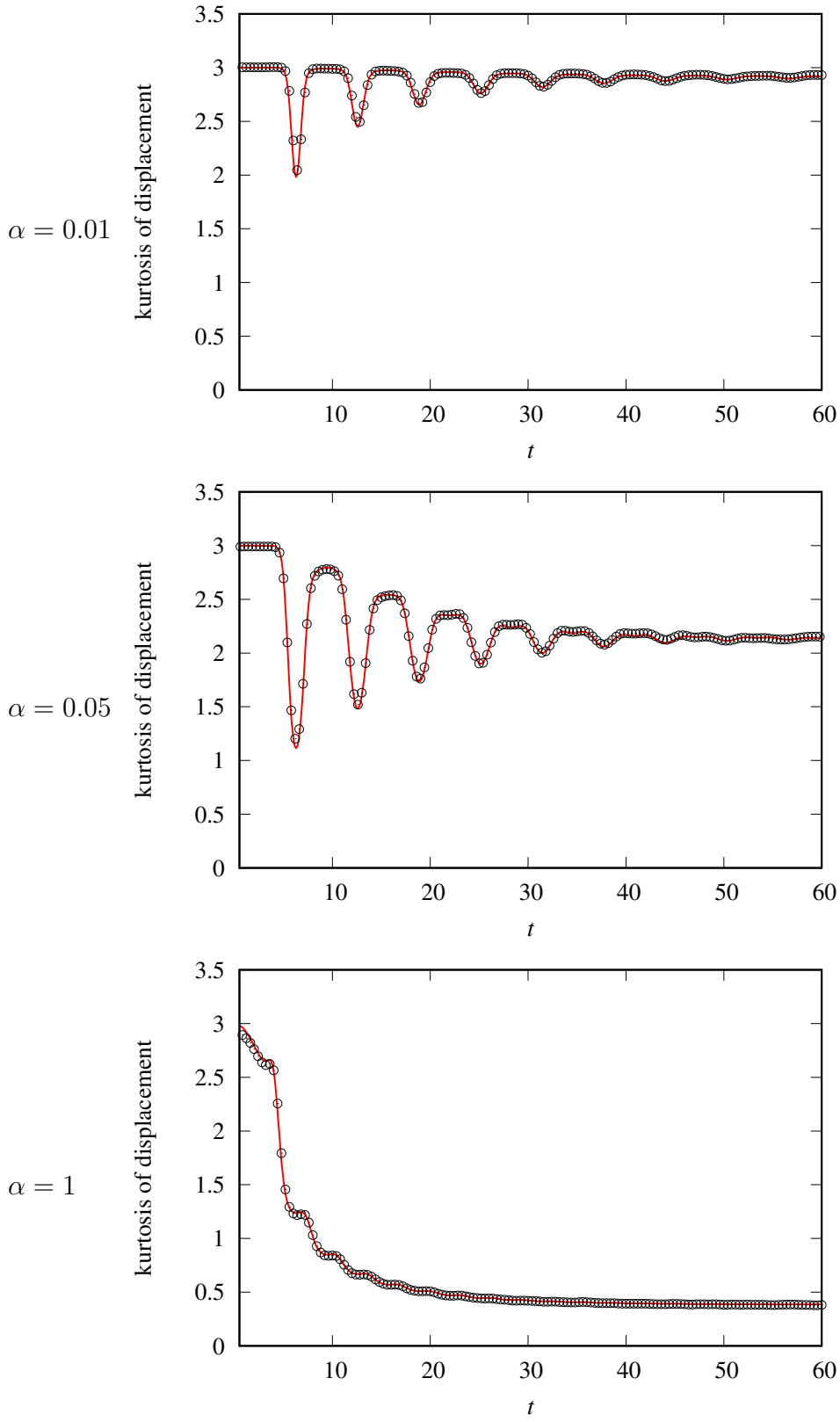

Figure 3: Kurtosis of displacement response, $\kappa = 1$, solid line : analysis, $\odot$: Monte Carlo simulation.

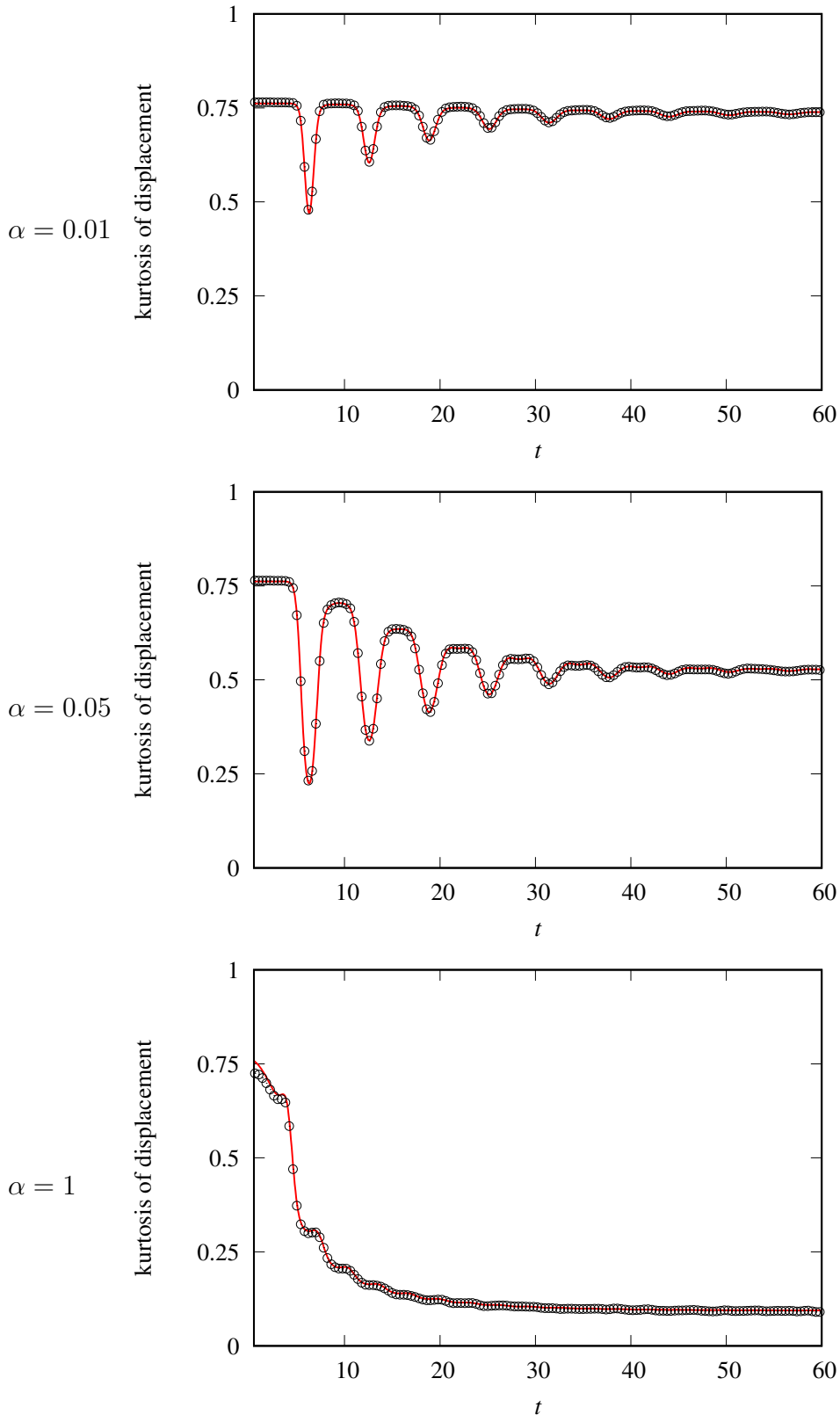

Figure 4: Kurtosis of displacement response, $\kappa = 1.5$, solid line : analysis, $\odot$: Monte Carlo simulation.

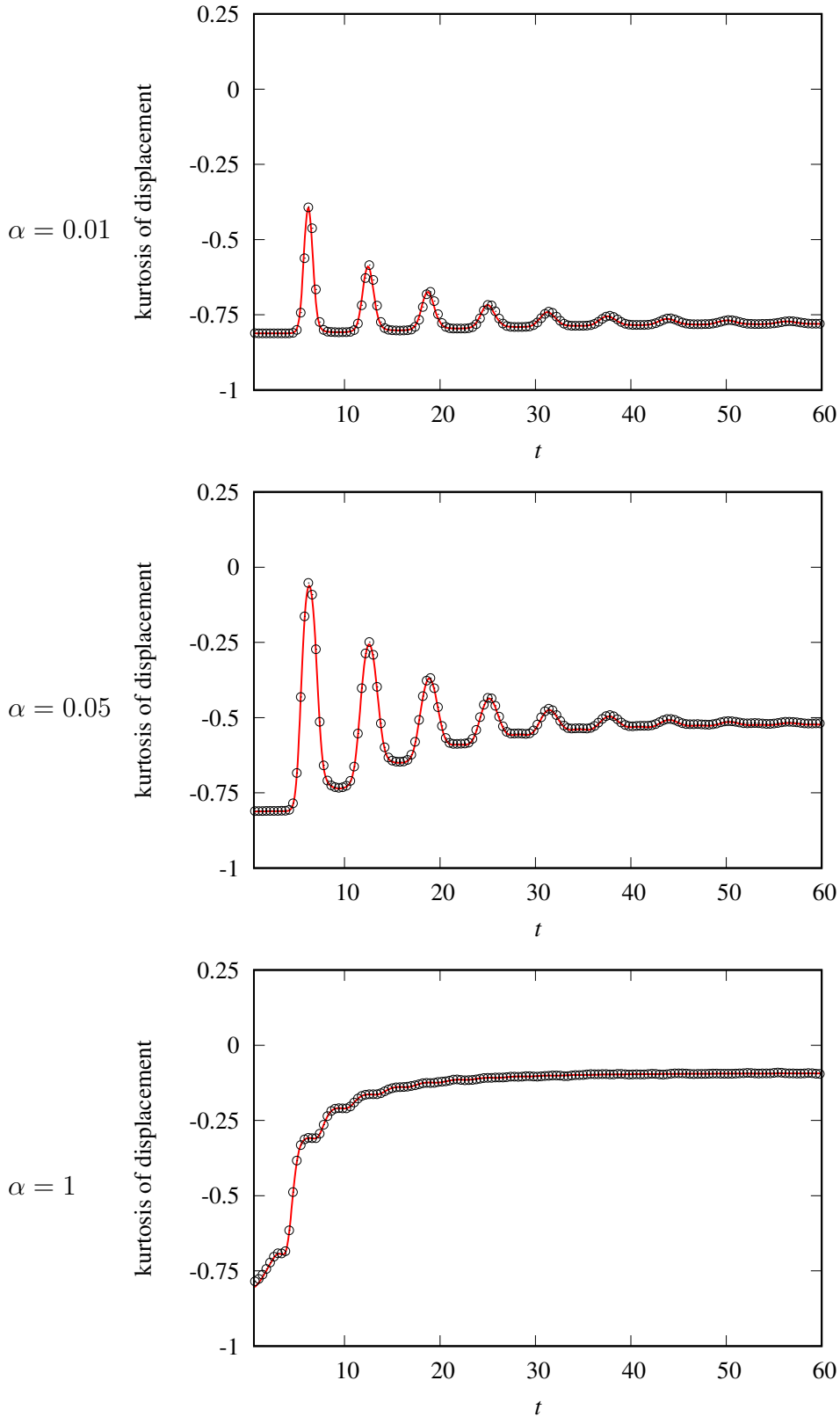

Figure 5: Kurtosis of displacement response, $\kappa = 4$, solid line : analysis, $\odot$: Monte Carlo simulation.

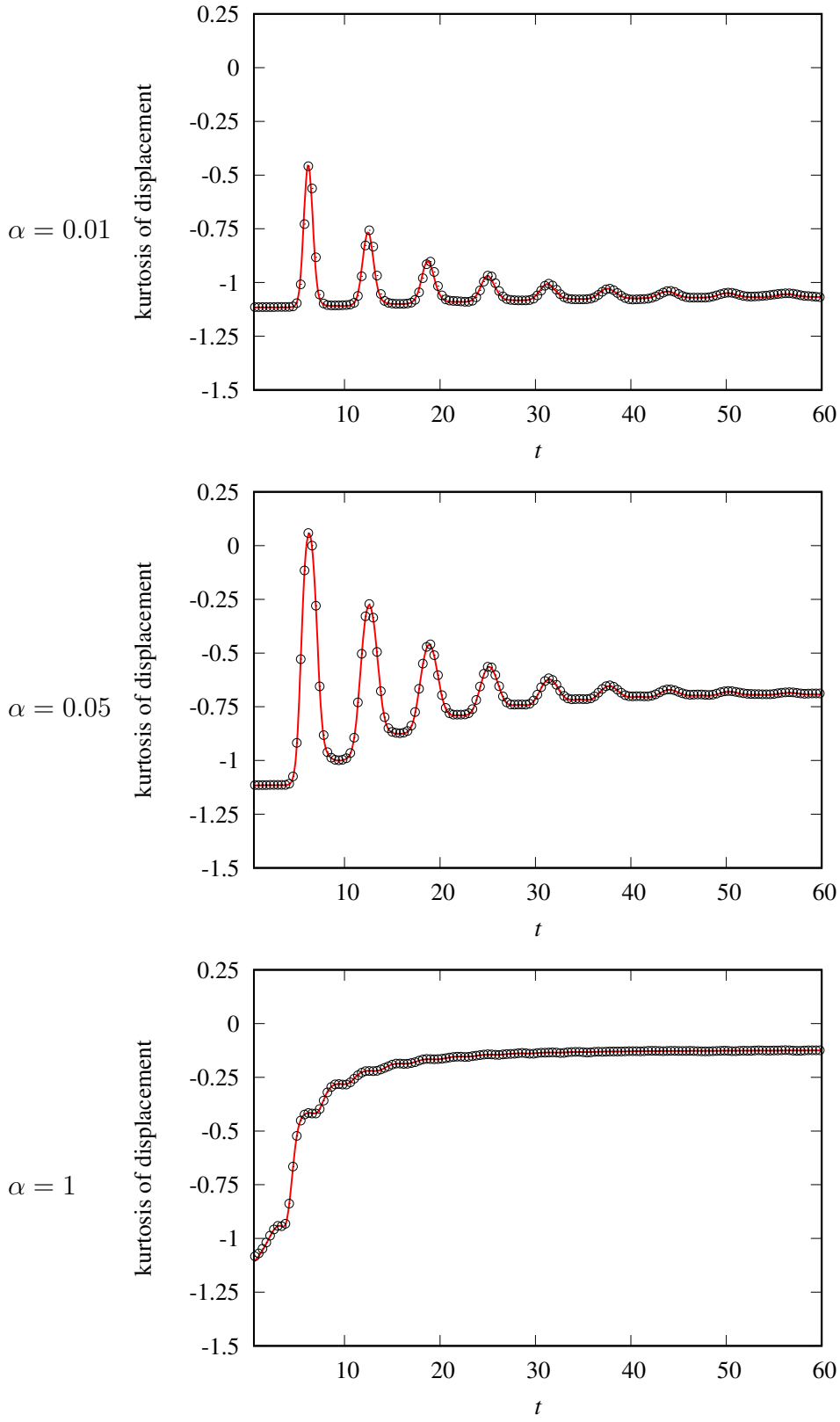

Figure 6: Kurtosis of displacement response, $\kappa = 10$, solid line : analysis, $\odot$: Monte Carlo simulation.

Appendix

The 2nd and 4th order moment equations to be solved are shown below. These equations can be derived from Eq. (19).

2nd-order moment equations

$$\frac{d\mathrm{E}[X^2]}{dt} = 2\mathrm{E}[X\dot{X}] \tag{26}$$

$$\frac{d\mathrm{E}[X\dot{X}]}{dt} = -\mathrm{E}[X^2] + \mathrm{E}[\dot{X}^2] - 2\zeta\mathrm{E}[X\dot{X}] + \mathrm{E}[XU] \tag{27}$$

$$\frac{d\mathrm{E}[XU]}{dt} = -\alpha\mathrm{E}[XU] + \mathrm{E}[\dot{X}U] \tag{28}$$

$$\frac{d\mathrm{E}[\dot{X}^2]}{dt} = -2\mathrm{E}[X\dot{X}] - 4\zeta\mathrm{E}[\dot{X}^2] + 2\mathrm{E}[\dot{X}U] \tag{29}$$

$$\frac{d\mathrm{E}[\dot{X}U]}{dt} - \mathrm{E}[XU] - (2\zeta + \alpha)\mathrm{E}[\dot{X}U] + 2\mathrm{E}[U^2] \tag{30}$$

$$\frac{d\mathrm{E}[U^2]}{dt} = (-2\alpha + A_{eq})\mathrm{E}[U^2] + C_{eq} \tag{31}$$

4th-order moment equations

$$\frac{d\mathrm{E}[X^4]}{dt} = 4\mathrm{E}[X^3\dot{X}] \tag{32}$$

$$\frac{d\mathrm{E}[X^3\dot{X}]}{dt} = -\mathrm{E}[X^4] - 2\zeta\mathrm{E}[X^3\dot{X}] + 3\mathrm{E}[X^2\dot{X}^2] + \mathrm{E}[X^3U] \tag{33}$$

$$\frac{d\mathrm{E}[X^2\dot{X}^2]}{dt} = -2\mathrm{E}[X^3\dot{X}] - 4\zeta\mathrm{E}[X^2\dot{X}^2] + 2\mathrm{E}[X\dot{X}^3] + \mathrm{E}[X^2\dot{X}U] \tag{34}$$

$$\frac{d\mathrm{E}[X\dot{X}^3]}{dt} = -3\mathrm{E}[X^2\dot{X}^2] - 6\zeta\mathrm{E}[X\dot{X}^3] + 3\mathrm{E}[X\dot{X}^2U] + \mathrm{E}[\dot{X}^4] \tag{35}$$

$$\frac{d\mathrm{E}[X^3U]}{dt} = -\alpha\mathrm{E}[X^3U] + 3\mathrm{E}[X^2\dot{X}U] \tag{36}$$

$$\frac{d\mathrm{E}[X^2U^2]}{dt} = (-2\alpha + A_{eq})\mathrm{E}[X^2U^2] + 2\mathrm{E}[X\dot{X}U^2] + C_{eq}\mathrm{E}[X^2] \tag{37}$$

$$\frac{d\mathrm{E}[XU^3]}{dt} = (-3\alpha + 3A_{eq})\mathrm{E}[XU^3] + \mathrm{E}[\dot{X}U^3] + 3C_{eq}\mathrm{E}[XU] \tag{38}$$

$$\frac{d\mathrm{E}[X^2\dot{X}U]}{dt} = -\mathrm{E}[X^3U] - (2\zeta + \alpha)\mathrm{E}[X^2\dot{X}U] + \mathrm{E}[X^2U^2] + 2\mathrm{E}[X\dot{X}^2U] \tag{39}$$

$$\frac{d\mathrm{E}[X\dot{X}^2U]}{dt} = -2\mathrm{E}[X^2\dot{X}U] - (4\zeta+\alpha)\mathrm{E}[X\dot{X}^2U] + 2\mathrm{E}[X\dot{X}U^2] + \mathrm{E}[\dot{X}^3U] \tag{40}$$

$$\begin{aligned}\frac{d\mathrm{E}[X\dot{X}U^2]}{dt} =& -\mathrm{E}[X^2U^2] - (2\zeta+2\alpha-A_{eq})\mathrm{E}[X\dot{X}U^2] + \mathrm{E}[XU^3] \\ &+ \mathrm{E}[\dot{X}^2U^2] + C_{eq}\mathrm{E}[X\dot{X}]\end{aligned} \tag{41}$$

$$\frac{d\mathrm{E}[\dot{X}]}{dt} = -4\mathrm{E}[X\dot{X}^3] - 8\zeta\mathrm{E}[\dot{X}^4] + 4\mathrm{E}[\dot{X}^3U] \tag{42}$$

$$\frac{d\mathrm{E}[\dot{X}^3U]}{dt} = -3\mathrm{E}[X\dot{X}^2U] - (6\zeta+\alpha)\mathrm{E}[\dot{X}^3U] + 3\mathrm{E}[\dot{X}^2U^2] \tag{43}$$

$$\frac{d\mathrm{E}[\dot{X}^2U^2]}{dt} = -2\mathrm{E}[X\dot{X}U^2] - (4\zeta+2\alpha-A_{eq})\mathrm{E}[\dot{X}^2U^2] + 2\mathrm{E}[\dot{X}U^3] + C_{eq}\mathrm{E}[\dot{X}^2] \tag{44}$$

$$\frac{d\mathrm{E}[\dot{X}U^3]}{dt} = -\mathrm{E}[XU^3] - (2\zeta+3\alpha-3A_{eq})\mathrm{E}[\dot{X}U^3] + \mathrm{E}[U^4] + 3C_{eq}\mathrm{E}[\dot{X}U] \tag{45}$$

$$\frac{d\mathrm{E}[U^4]}{dt} = (-4\alpha+6A_{eq})\mathrm{E}[U^4] + 6C_{eq}\mathrm{E}[U^2] \tag{46}$$

REFERENCES

[1] M. Grigoriu, *Applied Non-Gaussian Processes: Examples, Theory, Simulation, Linear Random Vibration, and MATLAB Solutions*, Prentice Hall, Englewood Cliffs, New Jersey, 1995.

[2] M.K. Ochi, Non-Gaussian random processes in ocean engineering, *Probabilistic Engineering Mechanics*, **1**, 1, 28–39, 1986.

[3] L. Yang, K.R. Gurley and D.O. Prevatt, Probabilistic modeling of wind pressure on low-rise buildings, *Journal of Wind Engineering and Industrial Aerodynamics*, **114**, 18–26, 2013.

[4] T. Tsuchida and K. Kimura, Response moments of dynamic systems under non-Gaussian random excitation by the equivalent non-Gaussian excitation method, *12th International Conference on Recent Advances in Structural Dynamics (RASD2016)*, Southampton, UK, 2168, 2016.

[5] G.Q. Cai and Y.K. Lin, Generation of non-Gaussian stationary stochastic processes, *Physical Review E*, **54**, 1, 299–303, 1996.

[6] C. Gardiner, *Stochastic Methods: A Handbook for the Natural and Social Sciences 4th ed.*, Springer-Verlag Berlin Heidelberg, 2009.

[7] Y.K. Lin, *Probabilistic Theory of Structural Dynamics*, McGraw-Hill, New York, 1967.

[8] K. Sharifi and A. Leon-Garcia, Estimation of shape parameter for generalized Gaussian distributions in subband decompositions of video, *IEEE Transactions on Circuits and Systems for Video Technology*, **5**, 1, 52–56, 1995.

COMPDYN 2019
7th ECCOMAS Thematic Conference on
Computational Methods in Structural Dynamics and Earthquake Engineering
M. Papadrakakis, M. Fragiadakis (eds.)
Crete, Greece, 24–26 June 2019

NUMERICAL STUDIES ON THE DYNAMIC BEHAVIOR OF A SUPER-LONG CURVED PONTOON BRIDGE UNDER WIND AND WAVE ACTIONS

Aksel Fenerci[1], **Yuwang Xu**[2] **and Ole Øiseth**[1]

[1] Norwegian University of Science and Technology, Department of Structural Engineering
Richard Birkelandsvei 1A 7034 Trondheim
e-mail: {aksel.fenerci,ole.oiseth}@ntnu.no

[2] School of Naval Architecture, Ocean & Civil Engineering, Shanghai Jiao Tong University
800 Dongchuan Road, Shanghai, China
xuyuwang@sjtu.edu.cn

Abstract

Floating bridges serve as attractive solutions where classical bridge concepts are not possible. However, compared to more commonly encountered bridge concepts such as cable-supported bridges, their dynamic behavior remains less investigated. Here, an end-supported pontoon bridge, currently under development by the Norwegian Public Roads Administration (NPRA) for the Bjørnafjord crossing in Norway, is considered as a case study to investigate its dynamic behavior under combined wind and wave loading. The stochastic dynamic behavior of the bridge are evaluated using state-of-the-art time domain analysis techniques. The frequency-dependent motion induced forces are modeled using state-space formulations, which are then embedded into the general-purpose finite element software ABAQUS, where the global dynamic analysis is carried out. Results of global response measures at the bridge girder are presented and the results are carefully discussed.

Keywords: floating bridge, buffeting, first-order waves, stochastic dynamics, radiation forces, self-excited forces, state-space model

1 INTRODUCTION

Although they are still relatively rare, floating bridges offer viable and economically efficient alternatives to the more classical long-span bridges. Span lengths so far has not been crossed with cable-supported bridges can possibly be crossed with floating bridges, without needing massive increase in the cost due to impractically large section dimensions. Such a solution for crossing the 5 km wide, Bjørnafjord in Norway is currently under evaluation of the Norwegian Public Roads Administration (Statens Vegvesen) as part of the Ferry Free E39 Coastal Highway Project [1]. In contrast to the cable-supported bridges, however, the dynamic behavior of such structures under environmental actions is far less investigated. The harsh nature of the Norwegian fjords together with its complex and mountainous topography in addition to the uniquely large scale of the structure makes such an evaluation increasingly challenging for the designing engineers. Significant efforts in understanding the underlying complex dynamics of the system are therefore necessary.

Dynamic analysis of floating bridges under random environmental loads require a stochastic dynamics approach, where the hydrodynamic effects at the pontoon locations and the aerodynamic interaction of the bridge girder with the wind should be modeled. Such an analysis can be carried out both in the frequency domain using spectral analysis [2,3] and in the time domain using Monte Carlo simulations [4,5]. Although significantly less time-efficient, time domain methods allow incorporation of the nonlinearities in the system. In a time domain approach, structural and geometric nonlinearities and nonlinear wind and wave forces can be included in the dynamic analysis, the effects of which might be important in case of such a slender structure. However, the frequency-dependent motion-induced forces, namely the aerodynamic self-excited forces and the hydrodynamic radiation forces that arise from the fluid-structure interaction, are more difficult to model in a time domain approach. For computational efficiency, radiation forces are conveniently modeled by state-space models [6,7] in analysis of large offshore structures and recently same approach was adopted for floating bridges [5]. Similar approaches can also be encountered in modeling of the self-excited forces in aerodynamic analysis of bridge decks [5,8,9].

Numerical simulations of the dynamic behavior of a super-long curved floating pontoon bridge under combined wind and wave actions are carried out in this study. The analysis is carried out in time domain, where the motion-induced forces are modeled using state-space models. The analysis results are presented in terms of standard deviations of the girder displacement and section forces.

Figure 1: Floating bridge crossing the Bjørnafjord

2 THE FLOATING BRIDGE CONCEPT

The floating bridge concept studied here is currently under concept development phase and considered a viable option for crossing the Bjørnafjord in Norway, which is a 5 km wide fjord in Hordaland, Norway. The fjord is exposed to strong winds and waves from the Norwegian Sea and the depth of the seabed does not allow for abutments, which would support a classical bridge. Therefore, a floating bridge with that is supported by pontoons is considered for the crossing (Figure 1). The proposed bridge consists of mainly three parts: a cable-stayed bridge that would allow the passage of ships underneath it, a high-bridge part that provides the transition between the cable-stayed bridge and the pontoon bridge, and the low bridge that sits on floating pontoons (Figure 2). On top of each pontoon, columns support the bridge girder, which has a streamlined girder of 31 meters wide and 3.5 meters deep. The bridge is also curved, providing an arching effect against the harsh environmental loading from the open-sea exposure.

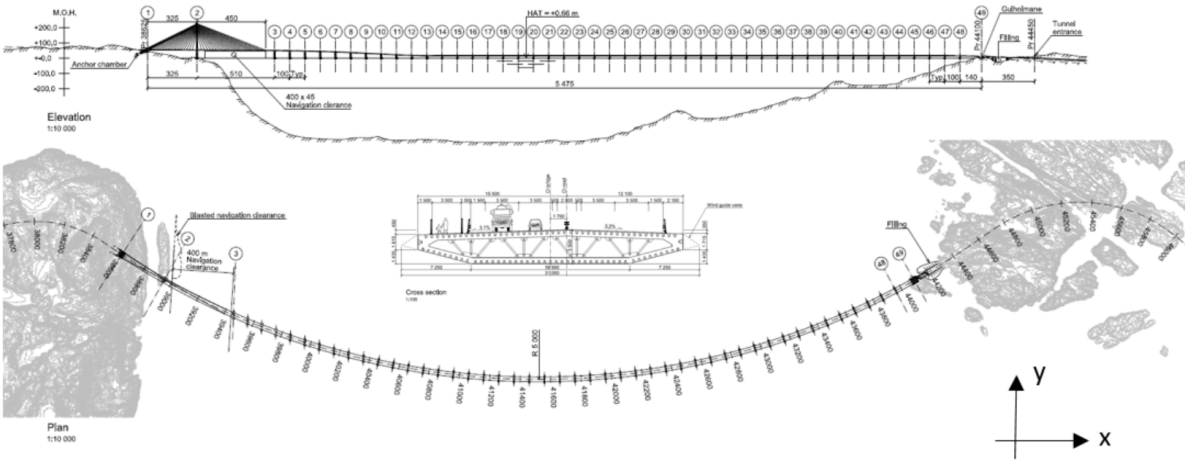

Figure 2: Technical Drawings (courtesy of Norwegian Public Roads Administration)

3 MODELING FRAMEWORK

In the framework of finite element discretization, the equation of motion of the structure under wind and wave loading, including the fluid-structure interaction terms, can be written as [5,7]

$$\mathbf{M}_s\ddot{\mathbf{u}}(t)+\mathbf{C}_s\dot{\mathbf{u}}(t)+(\mathbf{K}_s+\mathbf{K}_h)\mathbf{u}(t)=\mathbf{F}_{wind}+\mathbf{F}_{buff}(t)+\mathbf{F}_{se}(t)+\mathbf{F}_{wave}(t)-\mathbf{F}_{rad}(t) \quad (1)$$

where $\mathbf{M}_s$, $\mathbf{K}_s$, $\mathbf{C}_s$ are the structural mass, stiffness and damping matrices, $\mathbf{K}_h$ is the hydrostatic restoring stiffness matrix and $\mathbf{u}(t)$ is the vector of displacements. $\mathbf{F}_{wind}$ is the static wind load vector, $\mathbf{F}_{buff}(t)$ is the buffeting load vector and $\mathbf{F}_{wave}(t)$ is the first order wave load vector. $\mathbf{F}_{se}(t)$ and $\mathbf{F}_{rad}(t)$ denote the aerodynamic self-excited forces and the hydrodynamic radiation forces, respectively. The structural matrices are easily obtained using a finite element model of the structure (Figure 3), where the frequency-independent hydrostatic stiffness matrix can be obtained based on the buoyancy.

3.1 Motion-induced forces

The frequency-dependent motion-induced forces, $\mathbf{F}_{se}(t)$ and $\mathbf{F}_{rad}(t)$ will be modeled by state-space models for computational efficiency. The state-space model adopted for both terms can be written as

$$\begin{aligned}\dot{\mathbf{X}}(t) &= \mathbf{D}\mathbf{X}(t) + \mathbf{E}\mathbf{u}(t) \\ \mathbf{z}(t) &= \mathbf{Q}\mathbf{X}(t)\end{aligned} \tag{2}$$

where **X**(t) is the so-called state vector and **D, E, Q** are matrices of the model, $\mathbf{z}(t)$ denotes the frequency dependent part of the force vector. The system of equations given in the model gives a linear, continuous and time invariant system that describes the relationship between the motion of the structure and the motion-induced forces. The composition of the **D, E, Q** matrices depend on the functional form assumed to represent the forces. The detailed formulation of the models can be found in [5,10].

3.2 Buffeting and first-order wave forces

The buffeting forces due to wind turbulence and the wave forces are stochastic dynamic forces acting on the structure at pontoon locations and along the girder. They can be modeled as time-dependent nodal forces in the finite element framework described. However, the stochastic processes are generally defined in the form of spectral density matrices and Monte Carlo simulations are needed to obtain representative time-series of the processes.

Neglecting the aerodynamic admittance terms, the buffeting load vector for a girder node can be written assuming three degrees-of-freedom associated with the drag, lift and pitch motions of the girder as

$$F_{buff}(x,t) = \frac{\rho U B}{2}\begin{bmatrix} 2(D/B) & (D/B)C_D' - C_L' \\ 2C_L & C_L' + (D/B)C_D' \\ 2BC_M & BC_M' \end{bmatrix}\begin{bmatrix} u(x,t) \\ w(x,t) \end{bmatrix} \tag{3}$$

where ρ is the air density, U is the mean wind velocity and B is the width of the bridge deck. C_D, C_L and C_M are the aerodynamic static coefficients of the bridge deck. Lastly, $u(x,t)$ and $w(x,t)$ are the time-series of the along-wind and vertical turbulences.

Similarly, the first-order wave forces exerted upon pontoons by the incident waves, this time acting on a node with six degrees of freedom, can be written as

$$\begin{aligned} F_{wave}(x,y,t) &= \sum_n \sum_m \left|\mathbf{T}(\omega_n,\theta_m)\right|\eta_{nm}\cos\left(k_n(x\cos(\theta_m) + y\cos(\theta_m) - \omega_n t + \varepsilon_{mn} - \phi_{mn}\right),\ n,m = \{1,2,...6\} \\ \eta_{nm} &= \sqrt{2S_\eta(\omega_n,\theta_n)\Delta\omega\Delta\theta},\ \phi_{mn} = \tan^{-1}\left(\frac{\mathrm{Im}\left(\mathbf{T}(\omega_n,\theta_m)\right)}{\mathrm{Re}\left(\mathbf{T}(\omega_n,\theta_m)\right)}\right) \end{aligned} \tag{4}$$

where ω, θ, η and k denote the frequency, direction, wave amplitude and wave number, respectively and $\mathbf{T}$ is the transfer function, which can be obtained via potential theory.

4 NUMERICAL SIMULATIONS

A detailed finite element model of the bridge, which was created in the general-purpose commercial finite element software ABAQUS [11] was supplied by the Norwegian Public Roads administration. The model (Figure 3) consists of beam elements representing the bridge girder and the columns and nodes at the water level at the pontoon locations. At the pontoon nodes, structural springs are used to model the hydrostatic stiffness of the pontoons. Prior to modal and dynamic analyses, the static loading on the structure, namely the prestressing of the cables, self-weight of the structure and the static wind loads are applied to get the correct stiffness. Eigenvalue analysis is carried out after the application of static loads. The first four mode shapes, along with the corresponding natural frequencies are shown in Figure 4. The first natural period of the structure is found to be around 116 seconds.

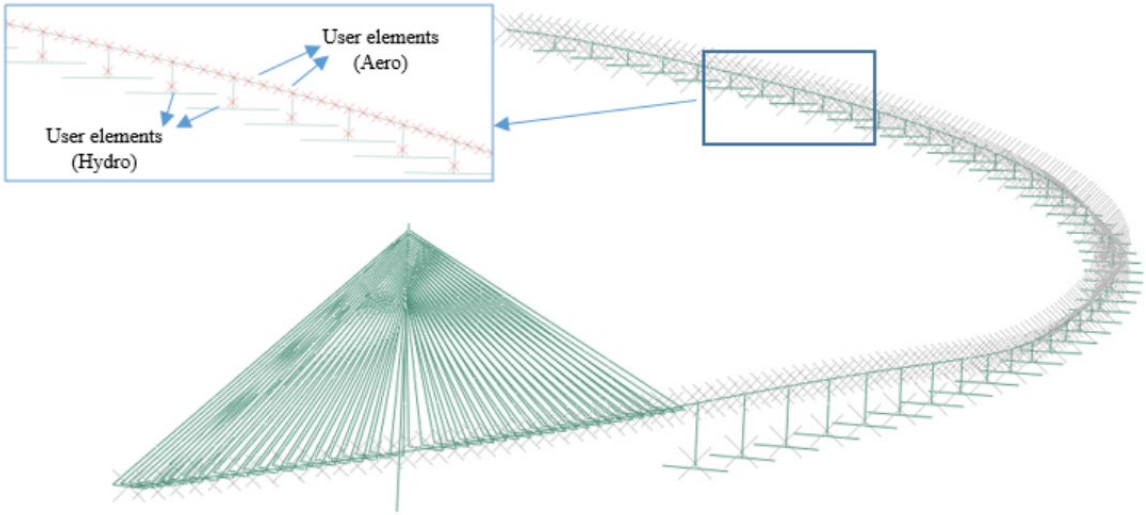

Figure 3: Finite element model of the bridge with aero and hydro user elements

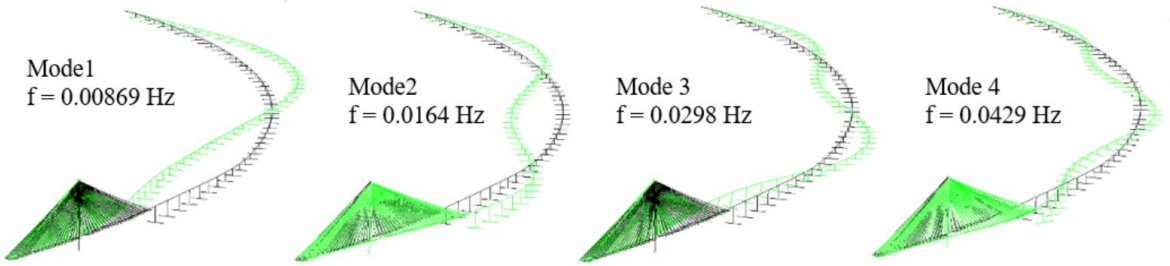

Figure 4: First four mode shapes and natural frequencies

4.1 Stochastic dynamic analysis

As discussed earlier, the definition of the stochastic environmental loads in the finite element model requires simulation of random time series from the processes defined by spectral characteristics. Time series of wind and wave forces are generated using an FFT-based simulation scheme [12]. The spectral densities of the processes are taken according to the design guidelines and the forms and parameters of the spectra are presented in Table 1. A Kaimal type of spectra along with Davenport coherence scheme is assumed for the wind turbulence,

where the Jonswap spectrum along with a cos-2s directional distribution is adopted for the wave spectrum.

Wind spectra	parameters					
$\frac{S_i f}{\sigma_i^2} = \frac{A_i f_z}{\left(1+1.5A_i f_z\right)^{5/3}},\ f_z = \frac{fz}{U},\ i = u, w$	U	30 m/s	C_{wy}	6.5	$C_D(C_D')$	0.53(0)
	A_u	6.8	C_{wz}	3	$C_L(C_L')$	0.133(4.87)
$\frac{S_{nm}(f)}{\sqrt{S_n(f)S_m(f)}} = C = \exp(-K\frac{f.\Delta x}{U}),\ m,n = \{u,w\}$	A_w	9.4	I_u	0.14	$C_M(C_M')$	0.042(0.056)
	C_{uy}	10	I_w	0.077		
	C_{uz}	10				
Wave spectra	**parameters**					
$S(\omega) = \frac{5H_s\omega_p{}^4\left(1-0.278\ln(\gamma)\right)}{16\omega_p}\exp\left(-1.25\frac{\omega_p{}^4}{\omega^4}\right)\gamma^{\exp\left(-\frac{(\omega-\omega_p)^2}{2\sigma^2\omega_p{}^2}\right)}$	s			3		
	Hs			2.4		
$\sigma = \begin{Bmatrix} 0.07 & for\ \omega \le \omega_p \\ 0.09 & for\ \omega > \omega_p \end{Bmatrix},\ \omega_p = 2\pi / T_p$	Tp			5.9		
$D(\theta) = \cos^{2s}\left(\frac{\theta}{2}\right)$						

Table 1: Analysis input

The self-excited forces are modeled using the state-space model described in Eqn (2). The self-excited forces obtained by the quasi-steady theory are curve fitted by rational functions and the obtained coefficients are used to deduce the aerodynamic state-space model. Similarly, the hydrodynamic added mass and damping obtained from potential flow analyses in WADAM software using a panel model of the pontoon. The coefficients, which are obtained only at discrete frequencies, are then curve fitted using the method developed in [13]. The results of the curve fitting are then used to deduce the hydrodynamic state-space model.

The state-space models cannot be directly incorporated into the commercial finite element software. To overcome this obstacle, additional node elements at the existing nodes of the finite element model, defined by a user subroutine are introduced into the model, following the work of [5], where details of the implementation can be found.

5 ANALYSIS RESULTS

Dynamic analysis of the bridge is carried in time domain using the ABAQUS model, including the aerodynamic and hydrodynamic effects. 5 simulations of 1-hour duration each have been performed. The global responses along the length of the bridge girder, namely the strong and weak axis bending moments, the axial force and the displacements in three degrees-of-freedom (drag, lift and pitch) are extracted by post-processing the analysis results. The standard deviations of the global responses are then calculated using the hour-long signals at each node or integration point along the girder. The resulting standard deviations of the responses are plotted in Figure 5 for each simulation, where the average of five simulations is also shown.

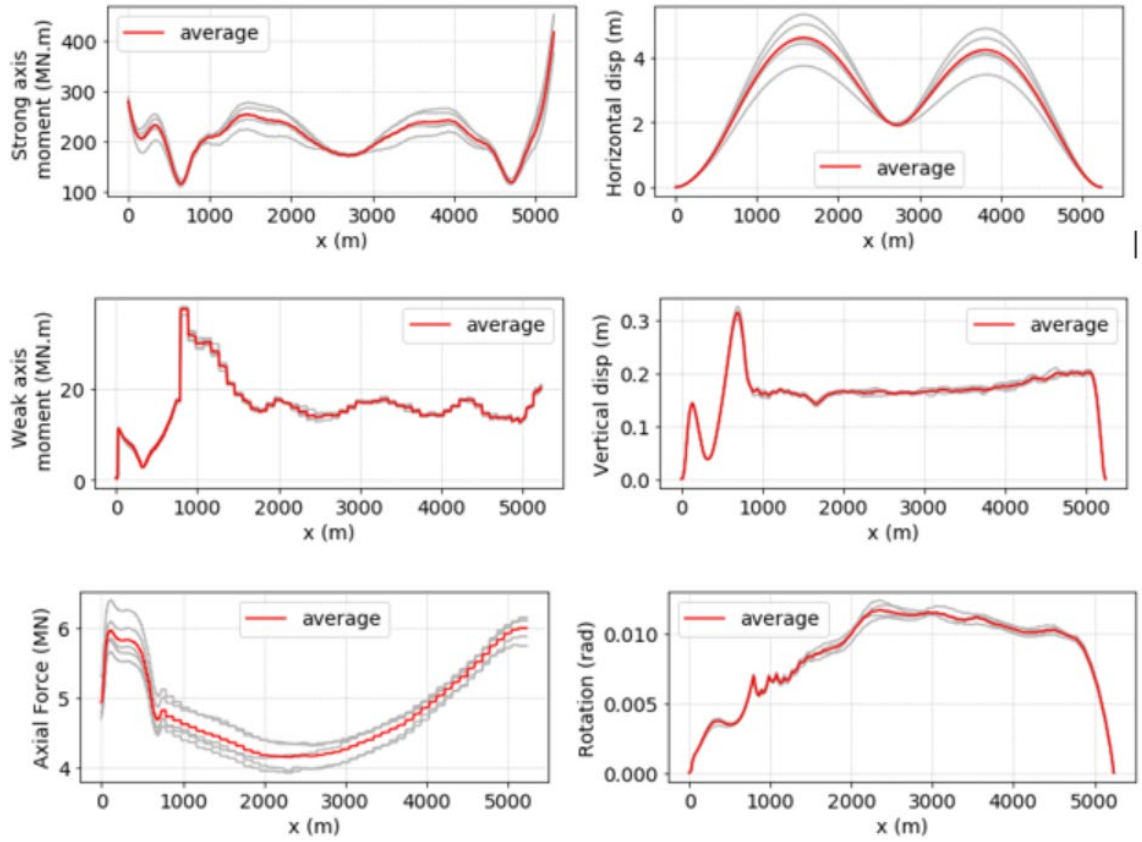

Figure 5: Standard deviations of the global responses of the bridge girder: the gray lines show different simulations, where the red lines are the averaged results

6 CONCLUSIONS

Dynamic behavior of a super-long curved pontoon bridge crossing the Bjørnafjord in Norway is investigated in this study under wind and wave loading. The analysis methodology is described and selected global responses under a certain environmental condition are presented.

Although the time-domain method discussed here has been used and verified against well-established frequency domain analyses before [5,10], comparisons are still necessary to ensure reliability of the approach. Such an analysis framework allows inclusion of also nonlinear phenomena with reasonable cost of computation, and opens possibilities for many investigations concerning the dynamic behavior of the structure. The contributions of wind and wave loadings and their interaction, different sources of damping, hydrodynamic interaction of the pontoons and global parametric stability of the entire bridge can be listed among others.

7 ACKNOWLEDGEMENTS

The research described here is financially supported by the Norwegian Public Roads Administration.

REFERENCES

[1] Dunham KK. Coastal Highway Route E39 - Extreme Crossings. Transp. Res. Procedia, vol. 14, 2016, p. 494–8. doi:10.1016/j.trpro.2016.05.102.

[2] Wirsching PH, Paez TL, Ortiz K. Random Vibrations: Theory and Practice. Dover Publications; 2006.

[3] Kvåle KA, Sigbjörnsson R, Øiseth O. Modelling the stochastic dynamic behaviour of a pontoon bridge: A case study. Comput Struct 2016;165:123–35. doi:10.1016/j.compstruc.2015.12.009.

[4] Shinozuka M. Monte Carlo solution of structural dynamics. Comput Struct 1972;2:855–74. doi:10.1016/0045-7949(72)90043-0.

[5] Xu Y, Øiseth O, Moan T. Time domain simulations of wind- and wave-induced load effects on a three-span suspension bridge with two floating pylons. Mar Struct 2018. doi:10.1016/j.marstruc.2017.11.012.

[6] Taghipour R, Perez T, Moan T. Hybrid frequency-time domain models for dynamic response analysis of marine structures. Ocean Eng 2008;35:685–705. doi:10.1016/j.oceaneng.2007.11.002.

[7] Naess A, Moan T. Stochastic Dynamics of Marine Structures. Cambridge: Cambridge University Press; 2012. doi:DOI: 10.1017/CBO9781139021364.

[8] Øiseth O, Rönnquist A, Sigbjörnsson R. Finite element formulation of the self-excited forces for time-domain assessment of wind-induced dynamic response and flutter stability limit of cable-supported bridges. Finite Elem Anal Des 2012;50:173–83. doi:10.1016/j.finel.2011.09.008.

[9] Xu Y, Øiseth O, Naess A, Moan T. Prediction of long-term extreme load effects due to wind for cable-supported bridges using time-domain simulations. Eng Struct 2017;148:239–53. doi:10.1016/j.engstruct.2017.06.051.

[10] Øiseth O, Rönnquist A, Sigbjörnsson R. Time domain modeling of self-excited aerodynamic forces for cable-supported bridges: A comparative study. Comput Struct 2011;89:1306–22. doi:10.1016/j.compstruc.2011.03.017.

[11] Dassault Systèmes Simulia, Fallis A., Techniques D. ABAQUS documentation. Abaqus 612 2013;53:1689–99. doi:10.1017/CBO9781107415324.004.

[12] Shinozuka M, Jan C-M. Digital simulation of random processes and its applications. J Sound Vib 1972;25:111–28. doi:10.1016/0022-460X(72)90600-1.

[13] Perez T, Fossen TI. A Matlab Toolbox for Parametric Identification of Radiation-Force Models of Ships and Offshore Structures. Model Identif Control A Nor Res Bull 2009;30:1–15. doi:10.4173/mic.2009.1.1.

COMPDYN 2019
7th ECCOMAS Thematic Conference on
Computational Methods in Structural Dynamics and Earthquake Engineering
M. Papadrakakis, M. Fragiadakis (eds.)
Crete, Greece, 24–26 June 2019

ESTIMATION OF EVOLUTIONARY POWER SPECTRA OF SEISMIC ACCELEROGRAMS

George Stefanou[1] **and Sokratis Tsiliopoulos**[1]

[1] Department of Civil Engineering, Aristotle University of Thessaloniki
54124 Thessaloniki, Greece
e-mail: gstefanou@civil.auth.gr, stsiliopoulos@gmail.com

Abstract

In this paper, the evolutionary (time varying) power spectra of seismic accelerograms are estimated using the recently proposed method of separation. The procedure is based on a number of sample functions of the non-stationary random process characterizing the seismic event. These sample functions are artificial accelerograms as well as natural ground motion records. The key advantage of the method of separation is the minimization of spectral dispersion due to optimum time-frequency localization. However, it requires at least approximate spectral separability of the input samples to achieve satisfactory accuracy. The estimated evolutionary spectra are found to be in good agreement with those of the input samples in an average sense and can be used to generate artificial accelerograms compatible with specific ground motion records.

Keywords: Accelerogram, Random Process, Evolutionary Spectrum, Spectral Representation.

1 INTRODUCTION

Acceleration time histories are usually used to represent the seismic ground motion as they contain information regarding both the nature of seismic wave propagation and the soil properties. Ground motion time histories are used as input in the nonlinear dynamic analysis of engineering structures. Since there are still not enough records of strong earthquakes at a specific site, the generation of artificial accelerograms becomes necessary. The lack of regulatory provisions regarding the algorithms for the generation of acceleration time histories and the underlying assumptions has led to the development of a wide variety of methods based on non-stationary random process theory. The basic distinction made between these methods is about whether the produced accelerograms are design spectrum compatible [2, 3, 5, 6] or their evolutionary (time varying) power spectra match recorded data [4, 7, 8, 12].

This paper assesses the performance of the method of separation proposed by Schillinger and Papadopoulos in [9] for the estimation of evolutionary power spectra using a number of sample functions of the random process characterizing the seismic event. These sample functions are artificial accelerograms generated by the algorithm of Sabetta and Pugliese [8] as well as natural ground motion records. The key advantage of the method of separation is the minimization of spectral dispersion due to optimum time-frequency localization. However, it requires at least approximate spectral separability of the input samples to achieve reasonable accuracy.

The paper is organized as follows: An introduction to evolutionary power spectra along with a detailed description of the method of separation are provided in Section 2. Section 3 is devoted to the estimation of evolutionary power spectra based on a set of artificial accelerograms whereas the case of natural ground motion records used as input is examined in Section 4. The paper closes with a discussion and related conclusions in Sections 5 and 6.

2 EVOLUTIONARY POWER SPECTRA - THE METHOD OF SEPARATION

One of the most widely used techniques for the simulation of earthquakes as random processes is the spectral representation method [10]. This method is based on the power spectrum, which is related to the average energy of the random process and is obtained in seismic applications from measured ground accelerations. Despite its importance in the dynamic analysis of structures, there is little experience so far in accurately determining the evolutionary (time-varying) power spectrum of seismic motion. This is mainly achieved with the adoption of time-frequency analysis techniques in the framework of digital time signal processing.

The evolutionary power spectrum $S(\omega,t)$ is dependent on both frequency ω and time t and can be defined as the distribution of the mean square of the stochastic process $f(t)$ over the time-frequency domain:

$$E\left[\left|f(t)\right|^2\right] = 2\int_0^\infty S(\omega,t)d\omega \tag{1}$$

The power spectrum $S(\omega,t)$ satisfies spectral separability if it can be decomposed into a homogeneous spectrum part $S_h(\omega)$ and a modulating time envelope $g_h(t)$ as follows:

$$S(\omega,t) = S_h(\omega)g_h(t) \tag{2}$$

The corresponding stochastic process is called separable. The homogeneous spectrum part of the above equation expresses the distribution of energy over the frequency space ω and can be determined from a series of samples $f^{(i)}(t)$ of the random process by the so-called periodogram:

$$\tilde{S}_h(\omega) = E\left[\frac{1}{2\pi L}\left|\int_0^L f^{(i)}(t) w\left(t-\frac{L}{2}\right) e^{-I\omega t} dt\right|^2\right] \tag{3}$$

where L is the total sample length and window w is centered at $t=L/2$. However, the distribution over time cannot be appropriately matched by Eq. (3), since it finds an average over the entire duration of the signal. This is achieved with the use of the evolutionary power spectrum. By combining Eqs. (1) and (2), we get:

$$E\left[\left|f(t)\right|^2\right] = 2\int_0^\infty S_h(\omega) g_h(t) d\omega = g_h(t) 2\int_0^\infty S_h(\omega) d\omega \tag{4}$$

from which it follows that:

$$\tilde{g}_h(t) = \frac{E\left[\left|f^{(i)}(t)\right|^2\right]}{2\int_0^\infty \tilde{S}_h(\omega) d\omega} \tag{5}$$

By combining Eqs. (2) and (5), the estimation of the evolutionary power spectrum by the method of separation is finally obtained as [9]:

$$S(\omega,t) = E\left[\left|f^{(i)}(t)\right|^2\right] \frac{\tilde{S}_h(\omega)}{2\int_0^\infty \tilde{S}_h(\omega) d\omega} \tag{6}$$

Factor 1/2 in the right-hand side fraction is necessary, because Eq. (6) takes into account only one side of the symmetric two-sided power spectrum. Eq. (6) can be interpreted as the distribution of the mean square of the samples $f^{(i)}(t)$ over the frequency domain at each time instant t.

3 EVOLUTIONARY SPECTRA ESTIMATION BASED ON ARTIFICIAL ACCELEROGRAMS

In this section, the method of separation will be used to compute the evolutionary power spectrum of a specific earthquake (Lazio-Abruzzo, May 1984) based on 50 artificial accelerograms with the characteristics of this earthquake, derived from the Sabetta and Pugliese algorithm [8]. The method of separation is implemented in MATLAB software.

The algorithm of Sabetta and Pugliese incorporates the dependence of the motion on the magnitude, the distance from the source and the geological conditions, in order to generate realistic accelerograms. Based on these parameters, the evolutionary power spectrum or physical spectrum of the motion $S(\omega,t)$ is computed using a lognormal function [8]. The accelerograms are generated by spectral representation where the transient nature of the seismic process is incorporated in the coefficients of the series $C_n(t)$, which are determined by the physical spectrum:

$$a(t) = 2\sum_{n=1}^{N} C_n(t) \cos(\omega_n t + \phi_n), \quad C_n(t) = \sqrt{S(\omega_n,t)\Delta\omega} \tag{7}$$

Parameters of the Lazio-Abruzzo earthquake (as recorded in Garigliano station) related to the geophysical characteristics of the site under consideration were first introduced in the Sabetta and Pugliese algorithm to produce 50 compatible artificial accelerograms. The generated

accelerograms have the same peak ground acceleration, time duration and small differences in their form. The parameters used as input are the following:

- Moment magnitude: $M_w = 5.8$
- Epicentral distance: R = 52.6 km
- Local soil conditions: deep alluvial soil

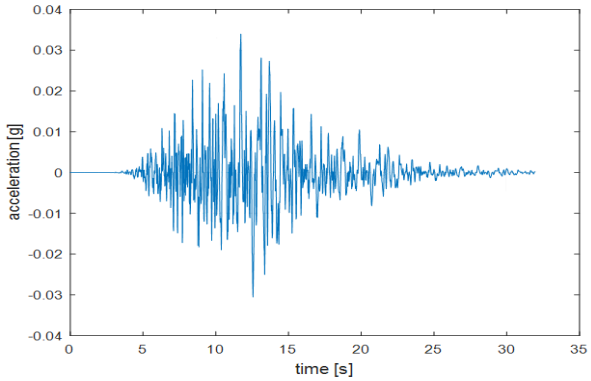

Figure 1: Typical accelerogram from Sabetta and Pugliese algorithm.

Fig. 1 shows a typical accelerogram out of the 50 produced for this paper. The estimation of the peak ground acceleration from the Sabetta and Pugliese algorithm for the parameters given above is 33.8 cm/s^2 and of the velocity is 2.5 cm/s. The duration of the time histories is approximately 32 s.

As demonstrated in [11], the algorithm achieves in most cases a very good match of the response spectrum of the input earthquake although it has not been developed with the aim of producing spectrum-compatible accelerograms. It is capable of delivering spectra that can satisfactorily be adapted to the Eurocode 8 design spectrum although the values of the maximum spectral accelerations of most spectra are smaller than the regulatory range for a particular combination of parameters. Finally, it has been shown that the computed spectra, although dispersed around the median, do not differ from this in their shape.

After generation of the artificial accelerograms with the Sabetta and Pugliese algorithm, their evolutionary power spectra have been computed using the method of separation discussed in the previous section. Figs. 2-4 show respectively the real spectrum of the Lazio-Abruzzo earthquake, the physical spectrum calculated by the Sabetta and Pugliese algorithm and the ensemble (mean) evolutionary power spectrum computed with the method of separation from 50 artificial accelerograms.

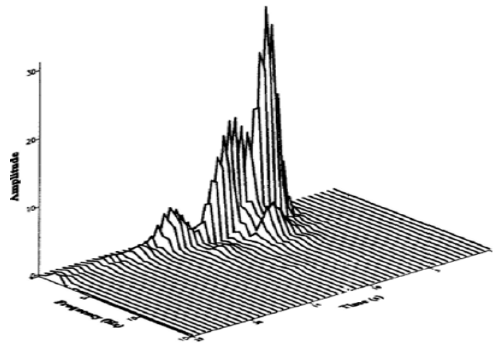

Figure 2: The real power spectrum of Lazio-Abruzzo earthquake [8].

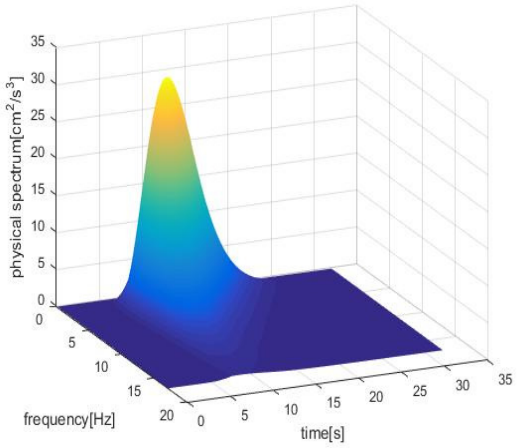

Figure 3: Lazio-Abruzzo earthquake: Physical spectrum calculated from Sabetta and Pugliese lognormal function.

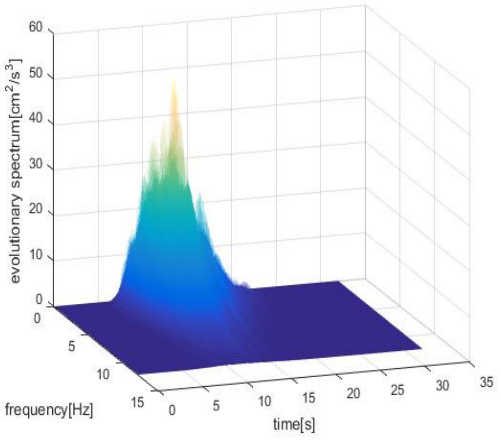

Figure 4: Evolutionary (mean) power spectrum computed using the method of separation from 50 artificial accelerograms.

50 accelerograms have been used because it was observed that the more samples were introduced in the separation algorithm, the more homogenized, smooth and close to the values of the real and the physical spectrum was the respective diagram. This is illustrated in Figs. 4-5 which show the evolutionary power spectra of 50, 1 and 10 artificial accelerograms with the parameters given above.

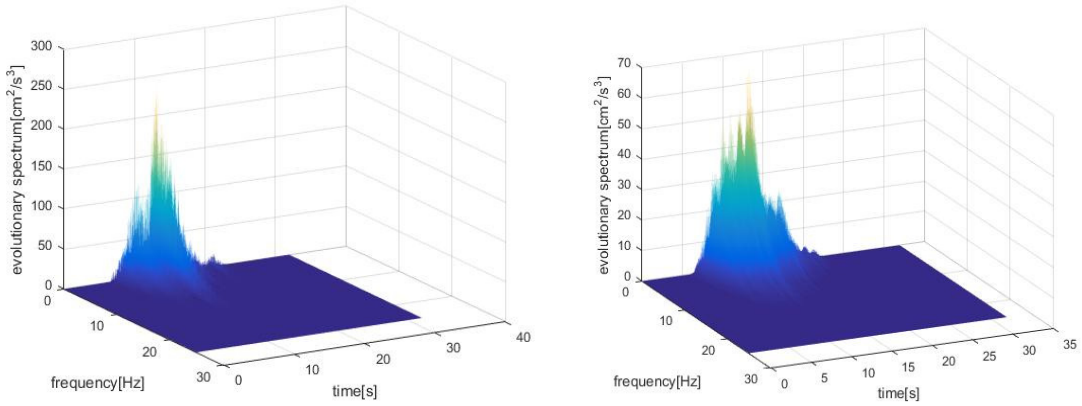

(a) (b)

Figure 5: Evolutionary power spectrum of (a) one and (b) ten artificial accelerograms computed using the method of separation.

4 EVOLUTIONARY SPECTRA ESTIMATION BASED ON REAL ACCELEROGRAMS

After producing the evolutionary spectra of artificial accelerograms derived from the Sabetta and Pugliese algorithm, some examples of evolutionary spectra of recorded accelerograms are also provided. The accelerograms were selected with peak ground accelerations in the range 0.9-2.3 m/s^2 from the European Strong-Motion Database (ESD) [1].

A. Earthquake: Montenegro (aftershock), Station: Bar-Skupstina Opstine

- Moment magnitude: $M_w = 6.2$
- Epicentral distance: R = 33 km
- Peak ground acceleration: PGA = 0.2g
- Date: 24/05/1979

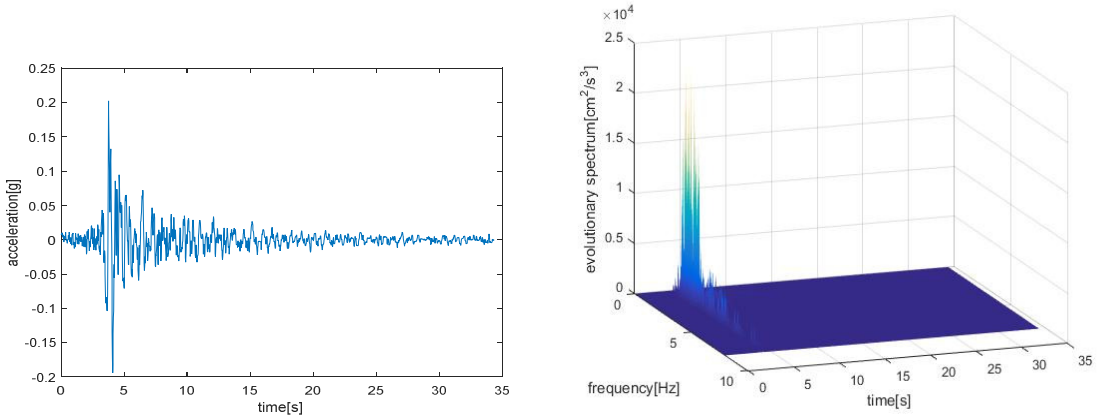

(a) (b)

Figure 6: (a) Accelerogram of earthquake A and (b) its evolutionary power spectrum computed using the method of separation.

B. Earthquake: Ano Liosia, Station: Athens 2 (Chalandri District)

- Moment magnitude: $M_w = 6$
- Epicentral distance: R = 20 km
- Peak ground acceleration: PGA = 0.09g
- Date: 07/09/1999

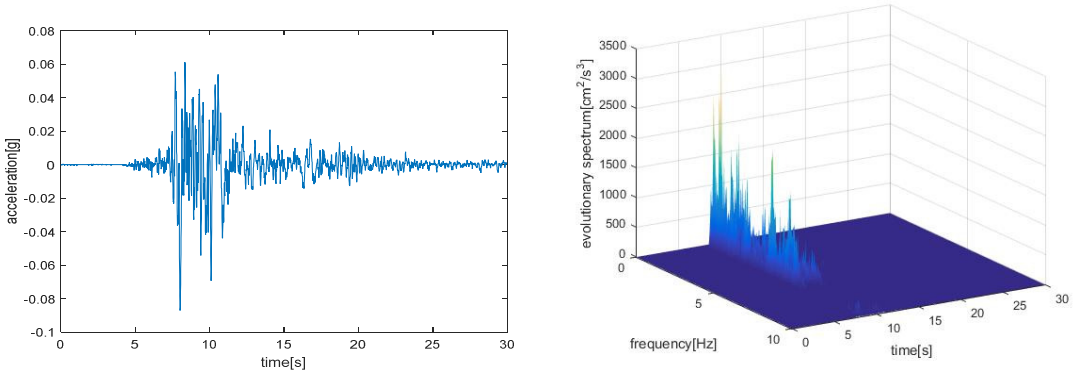

(a) (b)

Figure 7: (a) Accelerogram of earthquake B and (b) its evolutionary power spectrum computed using the method of separation.

C. Earthquake: Adana, Station: Ceyhan-Tarim Ilce Mudurlugu

- Moment magnitude: $M_w = 6.3$
- Epicentral distance: R = 30 km
- Peak ground acceleration: PGA = 0.23g
- Date: 27/06/1998

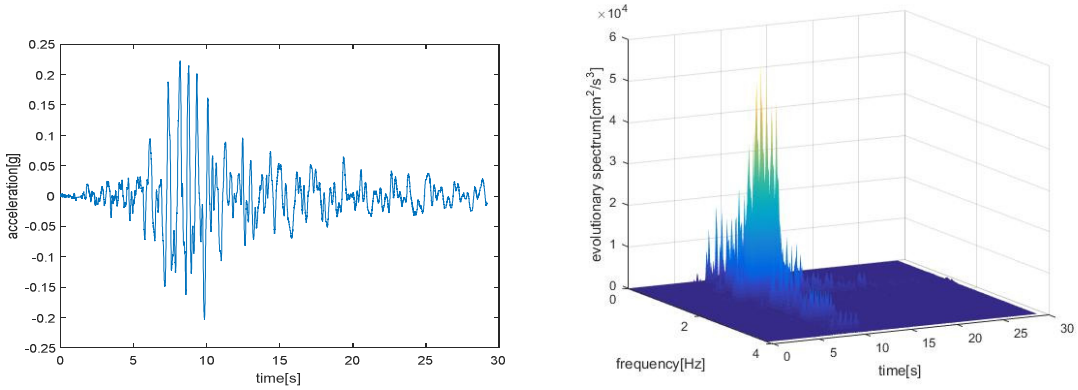

(a) (b)

Figure 8: (a) Accelerogram of earthquake C and (b) its evolutionary power spectrum computed using the method of separation.

5 DISCUSSION

Based on the above results, it can be noticed that the evolutionary power spectrum of the 50 artificial accelerograms (Fig. 4) approaches the physical spectrum of the Sabetta and Pug-

liese algorithm (Fig. 3) but is less smooth as it is not calculated by an analytical lognormal function. It is also similar to the real spectrum, which appears to exhibit a higher concentration of values at smaller frequencies (<5 Hz) than the other two. The evolutionary spectrum has larger values in this frequency range than the physical spectrum.

A general observation based on the power spectra of Figs. 4, 6b-8b is that the distribution of the seismic energy over time follows the corresponding accelerogram and is concentrated at time instants of high acceleration values. The evolutionary spectra present also a large fluctuation in the frequency domain.

6 SUMMARY AND CONCLUSIONS

- In this paper, the evolutionary power spectra of artificial and real accelerograms were computed using the method of separation. The Sabetta & Pugliese algorithm was used to produce artificial accelerograms. The analyses were performed in MATLAB using 50 artificial and three real accelerograms to implement the method of separation.
- The evolutionary power spectrum estimated using the method of separation was in general found to be similar to the physical spectrum of the Sabetta and Pugliese algorithm and to the real spectrum of the particular earthquake examined but it also presented some differences. This is mainly due to the small number of accelerograms that were used. As shown in [9], it took up to 10,000 samples of the stochastic process to obtain a smooth approximation of the spectrum.
- Another reason is that the physical spectrum used by the Sabetta and Pugliese algorithm to produce the accelerograms is not separable, which means that the method of separation requires at least approximate spectral separability of the input samples to achieve satisfactory accuracy.
- Further investigation is deemed necessary using a larger number of time histories as input and, perhaps, more reliable intensity measures, such as spectral acceleration, for the selection and/or generation of ground motions.
- The estimated evolutionary spectra can be used as input in the spectral representation method to produce artificial accelerograms compatible with given recordings.

REFERENCES

[1] N. Ambraseys, P. Smit, R. Sigbjornsson, P. Suhadolc, B. Margaris, Internet site for European strong-motion data. European Commission, Research-Directorate General, Environment and Climate Programme, 2002, http://www.isesd.hi.is.

[2] P. Cacciola, A stochastic approach for generating spectrum compatible fully nonstationary earthquakes. *Computers and Structures*, **88**, 889-901, 2010.

[3] D. Cecini, A. Palmeri, Spectrum-compatible accelerograms with harmonic wavelets. *Computers and Structures*, **147**, 26-35, 2015.

[4] J.P. Conte, B.F. Peng, Fully nonstationary analytical earthquake ground motion model. *Journal of Engineering Mechanics (ASCE)*, **123**(1), 15-24, 1997.

[5] D. Gasparini, E.H. Vanmarcke, SIMQKE: A program for artificial motion generation. Dept. of Civil and Environmental Engineering, Massachusetts Institute of Technology, Cambridge, MA, 1976.

[6] A. Giaralis, P.D. Spanos, Wavelet-based response spectrum compatible synthesis of accelerograms - Eurocode application (EC8). *Soil Dynamics and Earthquake Engineering*, **29**, 219-235, 2009.

[7] S. Rezaeian, A. Der Kiureghian, A stochastic ground motion model with separable temporal and spectral nonstationarity. *Earthquake Engineering and Structural Dynamics*, **37**, 1565-1584, 2008.

[8] F. Sabetta, A. Pugliese, Estimation of response spectra and simulation of non-stationary earthquake ground motions. *Bulletin of the Seismological Society of America*, **86**(2), 337-352, 1996.

[9] D. Schillinger, V. Papadopoulos, Accurate estimation of evolutionary power spectra for strongly narrow-band random fields. *Computer Methods in Applied Mechanics and Engineering*, **199**, 947-960, 2010.

[10] M. Shinozuka, G. Deodatis, Simulation of stochastic processes by spectral representation. *Applied Mechanics Reviews (ASME)*, **44**(4), 191-203, 1991.

[11] F. Vagionas, G. Stefanou, The effect of seismic loading simulation on the response variability of structures. M. Papadrakakis, M. Fragiadakis eds. *6th International Conference on Computational Methods in Structural Dynamics and Earthquake Engineering (COMPDYN 2017)*, Crete, Greece, June 15-17, 2017, pp. 4740-4751.

[12] C. Vlachos, K.G. Papakonstantinou, G. Deodatis, A multi-modal analytical non-stationary spectral model for characterization and stochastic simulation of earthquake ground motions. *Soil Dynamics and Earthquake Engineering*, **80**, 177-191, 2016.

COMPDYN 2019
7th ECCOMAS Thematic Conference on
Computational Methods in Structural Dynamics and Earthquake Engineering
M. Papadrakakis, M. Fragiadakis (eds.)
Crete, Greece, 24-26 June 2019

AN EFFICIENT TRANSMISSION OPERATOR FOR COMPUTING WAVE PROPAGATION BY DOMAIN DECOMPOSITION

Denis Duhamel[1]

[1]Ecole des Ponts ParisTech
Laboratoire Navier, Champs sur Marne, France
e-mail: denis.duhamel@enpc.fr

Keywords: Domain decomposition, wave, Helmholtz, finite element, transmission operator.

Abstract. *For large size problems, domain decompositions can be used to solve wave propagation problems such as the Helmholtz equation. Generally, this leads to an iterative process where data are exchanged at the boundary between subdomains. Depending on the quality of this exchange the number of iterations is more or less. Moreover, this number of iterations can depend on the frequency and on the number of domains. Here, we propose transmission operators approximating the Dirichlet to Neumann (DtN) operator which is known to be near optimal. We show this can be done using only the solution of problems involving sparse matrices and so keeping the computational time at an acceptable level. When this is combined with the double sweep preconditioner and that the computational domain is decomposed into a sequel of slices this results in an algorithm with a low number of iterations. Different examples are presented to support the precedent analysis.*

1 INTRODUCTION

Solving wave propagation problems described by the Helmholtz equation is important in many domains such as acoustics or elastic wave propagation. This can be difficult as the frequency increases because fine meshes have to be used in these cases. One possibility to increase the computing power is to use domain decompositions for which the domain is decomposed into subdomains on which the solutions can be computed more easily by solving small size problems. This generally involves an iterative scheme with a communication between the subdomains at each step, for instance by the transmission of data across the boundary of subdomains.

Many works have been done in the past on this subject where we find methods in which the subdomains overlap or not. In the field of non-overlapping methods we find the works on FETI methods as in [1] or for the application to the Helmholtz equation in [2] where interdomains fields continuity is obtained by Lagrange multipliers. These Lagrange multipliers are computed by solving a relatively small dual problem by a preconditioned conjugate gradient algorithm.

Another possibility is to use overlapping or non-overlapping Schwartz methods as in [3, 4, 5] where the solution is computed iteratively in each subdomain and transmission conditions are defined at the boundary of each domain from the solutions in the subdomains at the precedent step. The convergence rate mainly depends on this transmission operator at the boundary, the best one being the DtN map, see [6, 7], but it is too complicated to compute for being usable. Different methods have been proposed to approximate this complex non-local operator by a simpler one, often by local operators on the boundary, see for instance [8] and [9] for an uptodate view on the subject. A PML layer can also be used as in [10].

Here we propose a new transmission operator defined from the solution of a wave problem in domains around the computed subdomain as in the PML but with a simpler formulation which does not need modifications to the problem formulation or computations of new stiffness matrices. For being efficient, a preconditionner must be used with these methods such as the double sweep preconditionner found in [11, 12, 13].

In section 2, the method is described for the case of a problem posed on two half planes where analytical results can be found following the approach of [5] but with a new transmission operator, then this is applied to more general domains which can be decomposed into a sequel of slices. Finally, in section 3, numerical results are presented before a conclusion.

2 COMPUTATION BY DOMAIN DECOMPOSITION

The objective is to solve a wave propagation problem by domain decomposition. We consider here the case of the Helmholtz equation given by

$$\Delta p + k^2 p = 0 \tag{1}$$

with p the pressure, $k = \omega/c$ the wavenumber, c the sound velocity, $\omega = 2\pi f$ and f the frequency. This is defined on a domain Ω with a Neumann boundary condition as $\frac{\partial p}{\partial n} = q$ on the boundary Γ of Ω.

2.1 Case of two half-planes

Consider first the Helmholtz equation defined on a plane (x, y) which is divided into two half-plane subdomains by the line $x = 0$, see figure 1. Taking the Fourrier transform in the y variable with the wavenumber k_y, one obtains the following sequel of one-dimensional problems in the

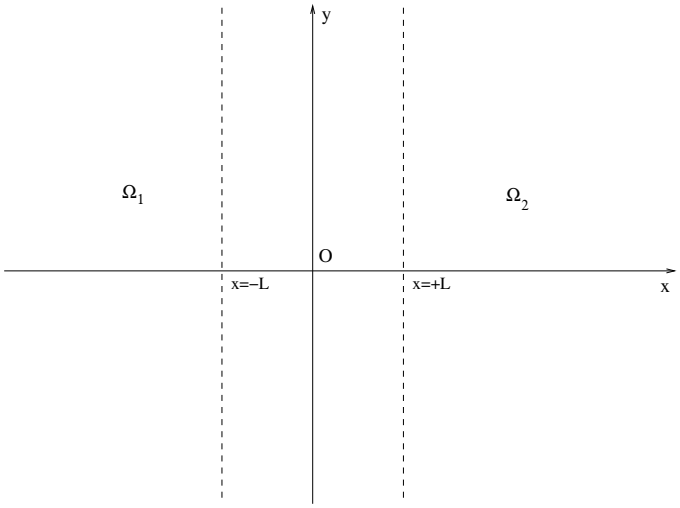

Figure 1: Two half-planes with additional slices of thickness L.

two sub-domains, which are respectively

$$\begin{aligned} \frac{\partial^2 p_1^{n+1}}{\partial x^2} + (k^2 - k_y^2) p_1^{(n+1)} &= 0 \quad for\ x < 0 \\ \frac{\partial p_1^{(n+1)}}{\partial x} + \sigma_1(k_y) p_1^{(n+1)} &= \frac{\partial p_2^{(n)}}{\partial x} + \sigma_1(k_y) p_2^{(n)} \quad at\ x = 0 \end{aligned} \tag{2}$$

$$\begin{aligned} \frac{\partial^2 p_2^{(n+1)}}{\partial x^2} + (k^2 - k_y^2) p_2^{(n+1)} &= 0 \quad for\ x > 0 \\ -\frac{\partial p_2^{(n+1)}}{\partial x} + \sigma_2(k_y) p_2^{(n+1)} &= -\frac{\partial p_1^{(n)}}{\partial x} + \sigma_2(k_y) p_1^{(n)} \quad at\ x = 0 \end{aligned} \tag{3}$$

with $\sigma_1(k_y)$ and $\sigma_2(k_y)$ two well chosen functions to assure the convergence of the iterative process. The solutions are respectively

$$\begin{aligned} p_1^{(n+1)}(x) &= e^{-\lambda(k_y)x} p_1^{(n+1)}(0) \quad for\ x < 0 \\ p_2^{(n+1)}(x) &= e^{\lambda(k_y)x} p_2^{(n+1)}(0) \quad for\ x > 0 \end{aligned} \tag{4}$$

with $\lambda(k_y) = i\sqrt{k^2 - k_y^2}$. From the transmission conditions (second lines of 2 and 3), one gets

$$\begin{aligned} p_1^{(n+1)}(0) &= \frac{\lambda(k_y) + \sigma_1(k_y)}{-\lambda(k_y) + \sigma_1(k_y)} p_2^{(n)}(0) \\ p_2^{(n+1)}(0) &= \frac{\lambda(k_y) + \sigma_2(k_y)}{-\lambda(k_y) + \sigma_2(k_y)} p_1^{(n)}(0) \end{aligned} \tag{5}$$

so that

$$p_1^{(2n)}(0) = \rho^n(k_y) p_1^{(0)}(0) \tag{6}$$

with

$$\rho(k_y) = \frac{\lambda(k_y) + \sigma_1(k_y)}{-\lambda(k_y) + \sigma_1(k_y)} . \frac{\lambda(k_y) + \sigma_2(k_y)}{-\lambda(k_y) + \sigma_2(k_y)} \tag{7}$$

Different possibilities for choosing the values of σ_1 and σ_2 are discussed in [5]. Here, we propose another way of building these functions. The value of $\sigma_1(k_y)$ is obtained from the solution of the problem in the slice $0 < x < L$ with absorbing boundary conditions at $x = L$, more precisely from the solution of the problem

$$\begin{aligned} \frac{\partial^2 p_1}{\partial x^2} + (k^2 - k_y^2) p_1 &= 0 \quad for\ 0 < x < L \\ p_1 &= p \quad for\ x = 0 \\ \frac{\partial p_1}{\partial x} - \gamma_1(k_y) p_1 &= 0 \quad for\ x = L \end{aligned} \tag{8}$$

and $\sigma_1(k_y)$ is defined such that $\frac{\partial p_1}{\partial x}(0) + \sigma_1(k_y) p = 0$. The solution of problem 8 is given by

$$p_1(x) = a e^{\lambda(k_y)x} + b e^{-\lambda(k_y)x} \tag{9}$$

with the coefficients a and b such that

$$\begin{aligned} a + b &= p \\ \lambda(k_y)(a e^{\lambda(k_y)L} - b e^{-\lambda(k_y)L}) - \gamma_1(k_y)(a e^{\lambda(k_y)L} + b e^{-\lambda(k_y)L}) &= 0 \end{aligned} \tag{10}$$

The second relation of 10 leads to $b = R_1 a$ with $R_1 = \frac{\lambda(k_y) - \gamma_1(k_y)}{\lambda(k_y) + \gamma_1(k_y)} e^{2\lambda(k_y)L}$, so that we get

$$\sigma_1(k_y) = -\lambda(k_y) \frac{1 - R_1}{1 + R_1} \tag{11}$$

Similarly one gets

$$\sigma_2(k_y) = -\lambda(k_y) \frac{1 - R_2}{1 + R_2} \tag{12}$$

In the case $k_y = 0$, taking $\gamma_1 = \gamma_2 = ik$, one gets $R_1 = R_2 = R$ and the classical values $\sigma_1 = \sigma_2 = -ik$. From (11) and (12) we obtain the value of $\rho(k_y)$ by relation 7 giving $\rho(k_y) = R^2$ in the case $\gamma_1 = \gamma_2 = ik$. The function $\rho(k_y)$ is plotted versus k_y/k for several values of kL in figure 2. For $kL = 0$, the evanescent waves are not attenuated and the process cannot converge. On the contrary, for $kL > 0$, the value of $\rho(k_y)$ is lower than one for the entire spectrum leading to the convergence of the iterative process and all the more so as the value of kL is high.

2.2 General method

We consider now a more general domain which is decomposed into vertical slices as shown in figure 3. In each vertical band i, one has to solve at step $n + 1$

$$\begin{aligned} \Delta p_i^{(n+1)} + k^2 p_i^{(n+1)} &= 0 \ in\ \Omega_i \\ \frac{\partial p_i^{(n+1)}}{\partial n_i} + S_{i,i-1} p_i^{(n+1)} &= g_{i,i-1}^{(n)} = -\frac{\partial p_{i-1}^{(n)}}{\partial n_{i-1}} + S_{i,i-1} p_{i-1}^{(n)} \ on\ \Gamma_{i-1,i} \\ \frac{\partial p_i^{(n+1)}}{\partial n_i} + S_{i,i+1} p_i^{(n+1)} &= g_{i,i+1}^{(n)} = -\frac{\partial p_{i+1}^{(n)}}{\partial n_{i+1}} + S_{i,i+1} p_{i+1}^{(n)} \ on\ \Gamma_{i,i+1} \end{aligned} \tag{13}$$

with the operators S as approximations of the DtN operators on the boundaries and the $g_{i,i+1}$ are updated by

$$\begin{aligned} g_{i,i+1}^{(n+1)} &= -\frac{\partial p_{i+1}^{(n+1)}}{\partial n_{i+1}} + S_{i,i+1} p_{i+1}^{(n+1)} \\ &= -g_{i+1,i}^{(n)} + (S_{i,i+1} + S_{i+1,i}) p_{i+1}^{(n+1)} \end{aligned} \tag{14}$$

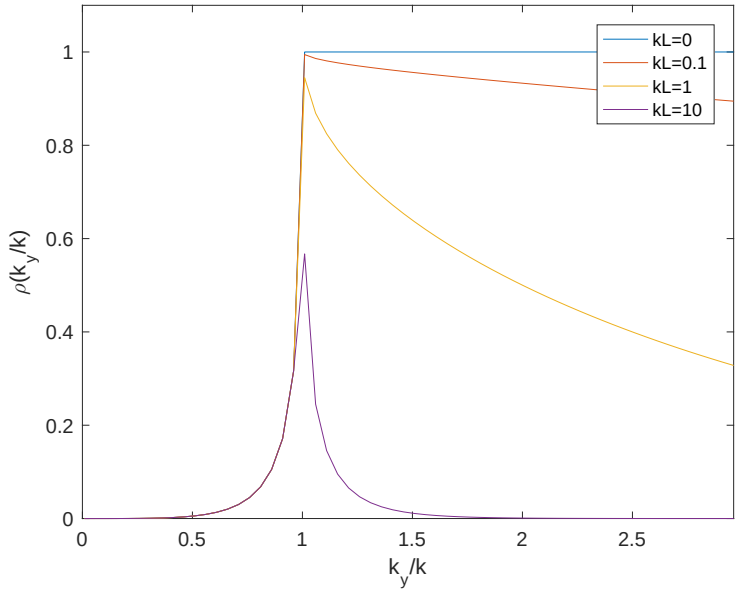

Figure 2: Values of ρ for different kL

with a similar formula for $g_{i,i-1}^{(n+1)}$.

The operator $S_{i,i+1}p_{i+1}^{(n+1)}$ is obtained by solving the Helmholtz equation in the domain Ω_{i+1} with an absorbing boundary condition on $\Gamma_{i+1,i+2}$, that is

$$\begin{aligned} \Delta u + k^2 u &= 0 \; in \; \Omega_{i+1} \\ \frac{\partial u}{\partial n_{i+1}} - iku + \frac{i}{4k}\frac{\partial^2 u}{\partial \tau^2} &= 0 \; on \; \Gamma_{i+1,i+2} \\ u &= p_{i+1}^{(n+1)} \; on \; \Gamma_{i,i+1} \end{aligned} \tag{15}$$

and $S_{i,i+1}p_{i+1}^{(n+1)} = \frac{\partial u}{\partial n_{i+1}}$ on $\Gamma_{i,i+1}$ giving an approximation of the DtN operator on that interface.

The operator $S_{i+1,i}p_{i+1}^{(n+1)}$ is obtained by solving the Helmholtz equation in the domain Ω_i with an absorbing boundary condition on $\Gamma_{i-1,i}$, that is

$$\begin{aligned} \Delta u + k^2 u &= 0 \; in \; \Omega_{i} \\ \frac{\partial u}{\partial n_{i}} - iku + \frac{i}{4k}\frac{\partial^2 u}{\partial \tau^2} &= 0 \; on \; \Gamma_{i-1,i} \\ u &= p_{i+1}^{(n+1)} \; on \; \Gamma_{i,i+1} \end{aligned} \tag{16}$$

with $\frac{\partial}{\partial \tau}$ the tangential derivative and $S_{i+1,i}p_{i+1}^{(n+1)} = \frac{\partial u}{\partial n_i}$ on $\Gamma_{i,i+1}$ giving an approximation of the DtN operator on that interface.

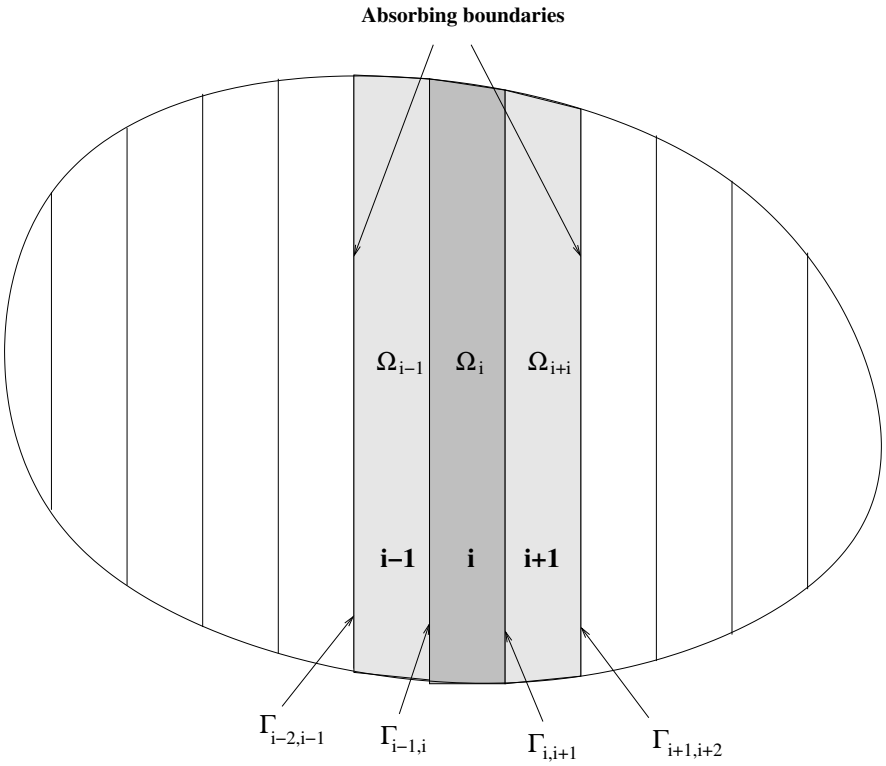

Figure 3: Domain and its decomposition into subdomains

Combining relations 13, 15 and 16, to update the solution in Ω_i, one has to solve

$$\begin{aligned}
\Delta p_i^{(n+1)} + k^2 p_i^{(n+1)} &= 0 \; in \; \Omega_i \\
\Delta u_{i-1}^{(n+1)} + k^2 u_{i-1}^{(n+1)} &= 0 \; in \; \Omega_{i-1} \\
\Delta u_{i+1}^{(n+1)} + k^2 u_{i+1}^{(n+1)} &= 0 \; in \; \Omega_{i+1} \\
\frac{\partial p_i^{(n+1)}}{\partial n_i} + \frac{\partial u_{i-1}^{(n+1)}}{\partial n_{i-1}} &= g_{i,i-1}^{(n)} \; on \; \Gamma_{i-1,i} \\
\frac{\partial p_i^{(n+1)}}{\partial n_i} + \frac{\partial u_{i+1}^{(n+1)}}{\partial n_{i+1}} &= g_{i,i+1}^{(n)} \; on \; \Gamma_{i,i+1} \\
\frac{\partial u_{i-1}^{(n+1)}}{\partial n_{i-1}} - iku_{i-1}^{(n+1)} + \frac{i}{4k}\frac{\partial^2 u_{i-1}^{(n+1)}}{\partial \tau^2} &= 0 \; on \; \Gamma_{i-2,i-1} \\
\frac{\partial u_{i+1}^{(n+1)}}{\partial n_{i+1}} - iku_{i+1}^{(n+1)} + \frac{i}{4k}\frac{\partial^2 u_{i+1}^{(n+1)}}{\partial \tau^2} &= 0 \; on \; \Gamma_{i+1,i+2}
\end{aligned} \tag{17}$$

The last equations of (15) and (16) provide the relations of continuity between the solutions in the adjacent domains. At the discrete level this problem is solved by assembling the dynamic stiffness matrices of the domains Ω_{i-1}, Ω_i and Ω_{i+1} and putting forces on the interfaces $\Gamma_{i-1,i}$ and $\Gamma_{i,i+1}$ defined respectively by the functions $g_{i,i-1}^{(n)}$ and $g_{i,i+1}^{(n)}$. For external boundaries, the boundary condition of the problem should be used, for instance $\frac{\partial p}{\partial n} = q_0$ for a Neumann boundary defined by a function q_0.

The problem is then solved by the GMRES algorithm associated to the double sweep preconditionner described in [11, 12, 13]. For the updating of $g_{i,i+1}$, one has to solve the problems

(15) and (16) and use their solutions in (14).

3 NUMERICAL EXAMPLES

3.1 Rectangle

We first consider the case of a rectangular domain of size $1m \times 1m$ with a boundary condition given by a plane wave e^{ikx} on the left and right boundaries as $\frac{\partial p}{\partial n} = ikn_x e^{ikx}$. The mesh is created with triangular elements of degree 2 (52633 nodes for 5 subdomains up to 80401 nodes for 100 subdomains). The mesh for 100 subdomains is shown on figure 4 where each domain is a fine vertical band. Computations are done for different frequencies and number of subdomains. Table 1 shows that in this case the number of iterations is very low and do not depend on the frequency or the number of subdomains. The solution for 100 subdomains and the frequency 2000Hz is shown on the right of figure 5.

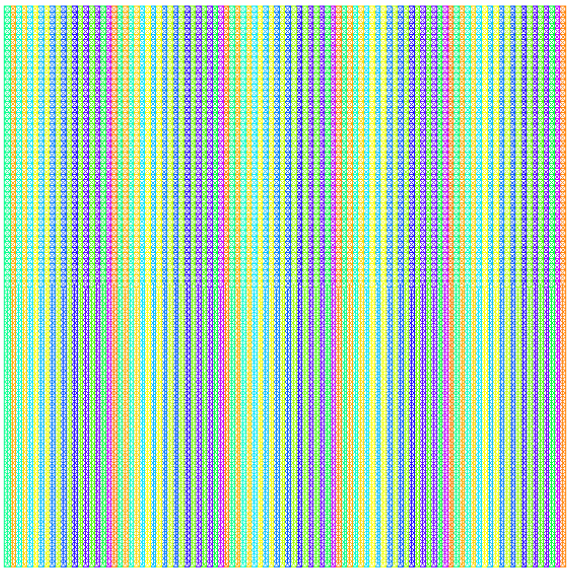

Figure 4: Rectangular domain with 100 subdomains

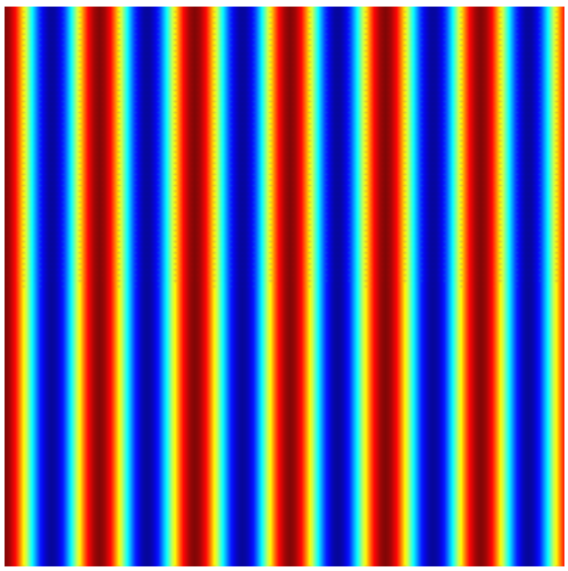

Figure 5: Solution at 2000Hz for 100 subdomains

Other computations are made with the boundary condition given by $cos(k_y y)e^{ik_x x}$ with $k_y = 4\pi/L_y$ and $k_x = \sqrt{k^2 - k_y^2}$. The number of iteration is given in table 2 while the solutions for 500 Hz and 2000 Hz are given in figures 6 and 7. In figure 6 the boundary condition leads to an evanescent wave while in figure 6 a propagating wave is clearly visible. This number of iterations is low except for 100 subdomains and low frequencies. This needs further studies to understand this phenomenon as usually the number of iteration is increasing with the frequency.

Frequency	Number of subdomains		
	5	25	100
500 Hz	4	4	4
1000 Hz	4	4	4
2000 Hz	4	4	4

Table 1: Number of iterations for different frequencies and number of subdomains.

Frequency	Number of subdomains		
	5	25	100
500 Hz	10	15	73
1000 Hz	13	15	41
2000 Hz	17	18	20

Table 2: Number of iterations for different frequencies and number of subdomains.

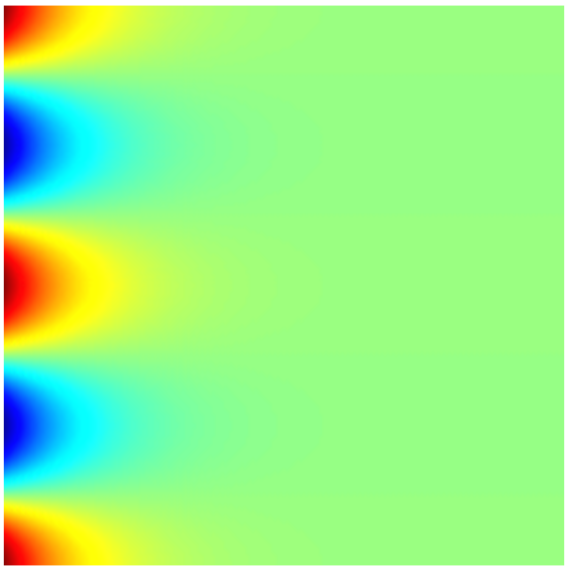

Figure 6: Solution at 500Hz for 100 subdomains

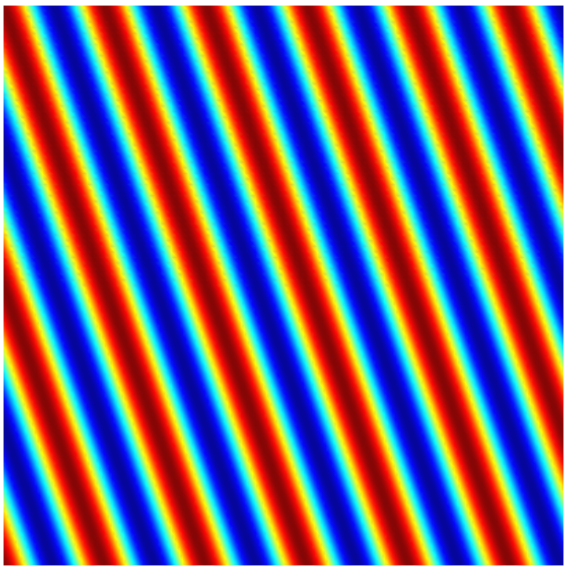

Figure 7: Solution at 2000Hz for 100 subdomains

3.2 Disk

The domain is now a disk of radius 1m whose mesh and decomposition into 100 subdomains is shown in figure 8. The solution for the plane wave excitation is shown in figure 9. In this case the number of iterations is shown in table 3. There is a slow increase in the number of iteration with the frequency and the number of subdomains.

Frequency	Number of subdomains		
	5	25	100
500 Hz	10	14	26
1000 Hz	15	17	23
2000 Hz	28	34	38

Table 3: Number of iterations for different frequencies and number of subdomains.

4 CONCLUSION

We have presented transmission conditions which are intermediate between the local conditions on the boundary and domain conditions as provided by a PML layer. So it gives an equilibrium between the ease of implementation and the efficiency. It involves only modified

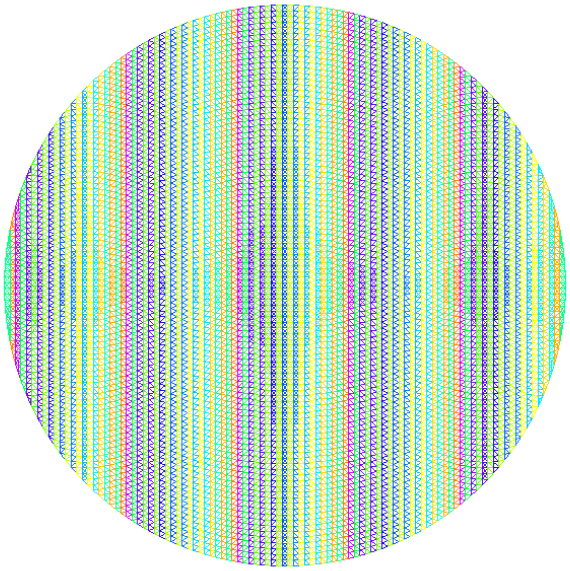

Figure 8: Disk domain with 100 subdomains

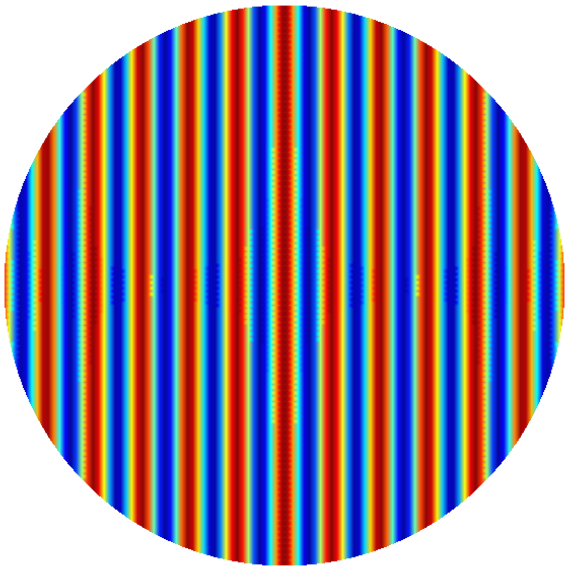

Figure 9: Solution at 2000Hz for 100 subdomains

matrices on the boundaries but no new matrix in the domains. Subsequent research should focus on the improvement of the boundary condition $\frac{\partial p}{\partial n} = ikp - \frac{i}{4k}\frac{\partial^2 p}{\partial \tau^2}$.

REFERENCES

[1] C. Farhat, F.X. Roux, An unconventional domain decomposition method for an efficient parallel solution of large-scale finite element systems, *SIAM J. Sci. Stat. Comput.*, **13**, 37996, 1992.

[2] C. Farhat, P. Avery, R. Tezaur, J. Li, FETI-DPH: A dual-primal domain decomposition method for acoustic scattering, *Journal of Computational Acoustics*, **13**, 499-524, 2005

[3] M.J. Gander, H. Zhang, Optimized Schwarz Methods with Overlap for the Helmholtz Equation, *SIAM Journal on Scientific Computing*, **38**, No. 5, A3195-A3219, 2016.

[4] M. Gander, Optimized Schwarz methods, *SIAM J. Numer. Anal.*, **44**, 699731, 2006.

[5] M. Gander, F. Magoules, F. Natar, Optimized Schwarz methods without overlap for the Helmholtz equation, *SIAM J. Sci. Comput.*, **24** 38-60, 2002.

[6] J.-C. Nédélec, Acoustic and electromagnetic equations, in: Applied Mathematical Sciences, vol. 144, Springer-Verlag, New York, 2001, Integral representations for harmonic problems.

[7] F. Nataf, Interface connections in domain decomposition methods, *In Modern methods in scientific computing and applications* (Montréal, QC, 2001), volume 75 of NATO Sci. Ser. II Math. Phys. Chem., pages 323364. KluwerAcad. Publ., Dordrecht, 2002.

[8] B. Thierry, A. Vion, S. Tournier, M. El Bouajaji, D. Colignon, N. Marsic, X. Antoine, C. Geuzaine, GetDDM: An open framework for testing optimized Schwarz methods for time-harmonic wave problems, *Computer Physics Communications*, **203**, 309-330, 2016

[9] Y. Boubendir, X. Antoine, C. Geuzaine, A quasi-optimal non-overlapping domain decomposition algorithm for the Helmholtz equation, *Journal of Computational Physics*, **231**, 262280, 2012.

[10] C.C. Stolk, A rapidly converging domain decomposition method for the Helmholtz equation, *Journal of Computational Physics*, **241**, 240-252, 2013.

[11] A. Vion, C. Geuzaine, Double sweep preconditioner for optimized Schwarz methods applied to the Helmholtz problem, *Journal of Computational Physics*, **266**, 171190, 2014.

[12] M. Eslaminia, M.N. Guddati, A double-sweeping preconditioner for the Helmholtz equation, *Journal of Computational Physics*, **314**, 800823, 2016.

[13] A. Vion, R. Bélanger-Rioux, L. Demanet, C. Geuzaine, A DDM double sweep preconditioner for the Helmholtz equation with matrix probing of the DtN map, *Proceedings of the 11th International Conference on Mathematical and Numerical Aspects of Waves (WAVES 2013)*, Tunis, Tunisia, June 3-7, 2013.

COMPDYN 2019
7th ECCOMAS Thematic Conference on
Computational Methods in Structural Dynamics and Earthquake Engineering
M. Papadrakakis, M. Fragiadakis (eds.)
Crete, Greece, 24-26 June 2019

MODELING TRAIN-INDUCED GROUND-BORNE VIBRATIONS USING FEM IN A MOVING FRAME OF REFERENCE

J. Malmborg[1], **K. Persson**[1] **and P. Persson**[1]

[1]Lund University, Department of Construction Sciences
P.O. Box 118 SE-221 00 Lund, Sweden
e-mail: {jens.malmborg,kent.persson,peter.persson}@construction.lth.se

Keywords: Train-induced ground-vibration, moving frame of reference, Kirchhoff plate slab track.

Abstract. *To predict ground-borne vibration levels caused by railway traffic, models for estimating the load from the vibration source, as well as the vibration transmission through the ground, are needed. In the present paper, a finite element formulation in a frame of reference following the moving load, is used for modeling a railway slab track. The response of the underlying soil is represented through a dynamic stiffness matrix, obtained via the Green's function for a horizontally layered visco-elastic half-space in a moving frame of reference in the frequency–wavenumber domain. The track can be modeled as continuously connected beams, but the use of plate elements allows for more general stress and displacement distributions in the transverse direction of the slab to be resolved. Here, the free-field response due to a harmonic load moving along a slab track, is evaluated and compared using different modeling strategies for the slab.*

1 INTRODUCTION

To predict the level of ground-borne vibration caused by railway traffic, models are needed to estimate the load from the vibration source as well as the vibration transmission through the ground. A number of techniques have been developed in the past decades to study ground vibrations caused by a passing train, ranging from empirical methods to analytical and numerical schemes.

Numerical schemes are often based on either the finite element (FE) or the boundary element (BE) method or a combination thereof. The strength of these methods lies in their ability to model arbitrary geometries and discontinuities. The downside is the high computational cost. The computational cost can be reduced if the soil and track system is assumed to be invariant in the track direction, leading to so called 2.5D models [1, 2, 3, 4]. Further, if the soil stratification is assumed to consist of horizontally layered visco-elastic layers, a fundamental solution (Green's function) for the soil response can be found efficiently in frequency–wavenumber domain. Sheng et al [5, 6] proposed a semi-analytical model, with the track represented by an infinite layered beam resting on a layered ground, where both the ground and the beam is described in the frequency–wavenumber domain. Kaynia et al [7] coupled a series of FE beams, representing the railway track, to a dynamic stiffness matrix of the ground calculated from the Green's function of a layered half-space.

Modeling the track as a beam on a layered half-space is a common approach in the field of ground-borne vibrations due to railway traffic. This approach, however, constricts the track–soil interface stress distribution. Steenbergen et al [8] studied the influence of different interface conditions between a beam on a half-space, subjected to a dynamic moving load, on the free-field response, using a semi-analytical model in the frequency–wavenumber domain. Galvin et al [4] compared the free-field response of a high-speed train passage on a ballasted track on an embankment, calculated using a 2.5D continuum model, to a model with a beam representation of the track, finding large differences attributed to the rigid cross-section of the embankment in the beam model.

In the present paper, a FE model is used for representing a railway slab track. The response of the underlying soil is represented by a dynamic stiffness matrix obtained via the Green's function for a horizontally layered visco-elastic half-space. The model is formulated in a frame of reference following the moving load. The slab and rails can either be modeled as continuously connected beams or by using Kirchhoff plate elements for representing the track slab. Plate elements allow for more general stress and displacement distributions in the track transveral direction to be resolved. Here, the free-field response due to a harmonic load moving along the track at constant velocity, is calculated and compared using different modeling strategies for the track.

In Section 2 an overview of the model is given and the studied case is presented in Section 3. Finally, conclusions are given in Section 4.

2 CALCULATION MODEL

2.1 Overview

The slab track is shown principally in Figure 1. It consists of a supporting layer, a concrete slab, rails and rail pads. Full interaction is assumed between the slab and the supporting layer, so that a homogeneous section with equivalent mass and bending stiffness may be utilized in the calculations. This homogeneous section is simply referred to as the slab in the following.

Three models, model a)–c), with different assumptions regarding the slab and the slab–soil

interface conditions, are established:

a) The slab is modeled with Bernoulli-Euler beam elements. Displacement continuity of the beam and the soil is enforced only along the beam center line. A uniform stress distribution between the beam and the soil is assumed in the transverse direction of the slab.

b) The slab is modeled with Bernoulli-Euler beam elements. The slab–soil interface is assumed rigid in the transverse direction. This is enforced by coupling the beam kinematically to a number of soil DoFs in the transverse direction over the width of the slab.

c) The slab is modeled with Kirchhoff plate elements, allowing for a more general slab–soil interface stress and displacement distribution in the transverse direction of the slab than by the two other models.

In all three models, the rails are modeled as Bernoulli-Euler beams, connected to the slab via a continuous visco-elastic interface layer representing the rail pads. The loading is assumed identical on both rails, hence in model a) and b) the two rails are modeled as one. In model c) symmetry around the track center line is utilized so that only half the track is modeled. The track is coupled to a ground model, represented by a dynamic stiffness matrix. The dynamic stiffness matrix of the ground is derived from the Green's function for a horizontally layered visco-elastic half-space. Both the ground model and the FE model are expressed in a moving frame of reference, following the vehicle at a given speed v. The models a)–c) are shown schematically in Figure 2.

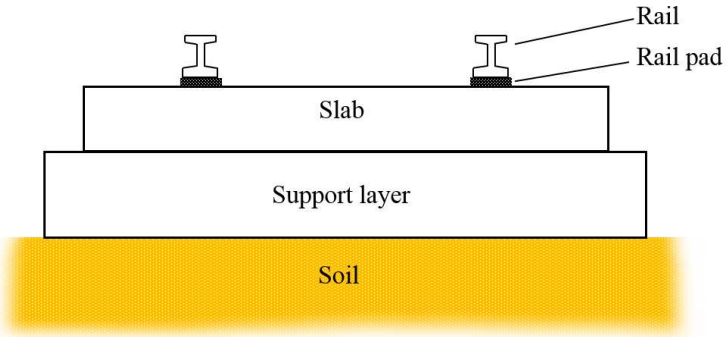

Figure 1: Section of slab track.

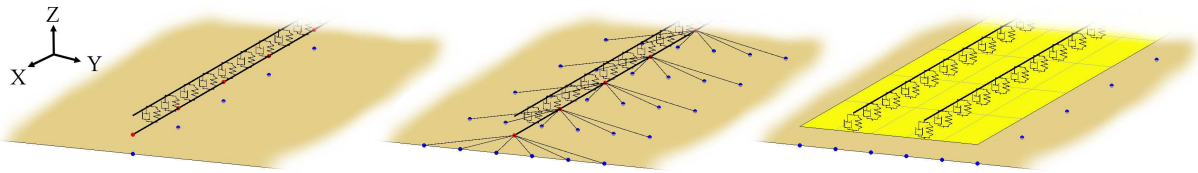

Figure 2: Finite element models of the slab track. From the left: Models a), b) and c). Blue points represent soil nodes at the slab–soil interface.

The soil model is described in Section 2.2. In Section 2.3 the governing equations for the beam, plate and interface finite elements are derived. The coupling between the finite elements and the soil is described in Section 2.4.

2.2 Soil model

The ground is assumed to be composed of horizontal visco-elastic layers. Neglecting body forces, the Navier equations for a single soil layer can be written as

$$(\lambda+\mu)\frac{\partial^2 u_j}{\partial x_i \partial x_j}+\mu\frac{\partial^2 u_i}{\partial x_j \partial x_j}=\rho\frac{\partial^2 u_i}{\partial t^2} \tag{1}$$

where $u_i = u_i(x_1, x_2, x_3, t)$ is the displacement in direction *i*. λ and μ are the Lame' parameters. Introducing a coordinate transformation as

$$(\tilde{x}_1, \tilde{x}_2, \tilde{x}_3) = (x_1 - vt, x_2, x_3), \tag{2}$$

where $\tilde{x}_1, \tilde{x}_2, \tilde{x}_3$ denotes the coordinates in the moving frame of reference, and v is the vehicle speed, transforms the Navier equations to

$$(\lambda+\mu)\frac{\partial^2 \tilde{u}_j}{\partial \tilde{x}_i \partial \tilde{x}_j}+\mu\frac{\partial^2 \tilde{u}_i}{\partial \tilde{x}_j \partial \tilde{x}_j}=\rho\Big(\frac{\partial^2 \tilde{u}_i}{\partial t^2}-2v\frac{\partial^2 \tilde{u}_i}{\partial t \partial \tilde{x}_1}+v^2\frac{\partial^2 \tilde{u}_i}{\partial^2 \tilde{x}_1}\Big), \tag{3}$$

where $\tilde{u}_i = \tilde{u}_i(\tilde{x}, \tilde{y}, \tilde{z}, t)$ is the displacement in the moving frame of reference [9].

Fourier transforming the Navier equations with respect to the horizontal coordinates and time, $(\tilde{x}_1, \tilde{x}_2, t)$, yields the Navier equations in frequency–wavenumber domain as

$$(\lambda+\mu)\tilde{\Delta} i\tilde{k}_1+\mu(\frac{d^2}{d\tilde{x}_3^2}-\tilde{k}_1^2-\tilde{k}_2^2)\tilde{U}_1=-\rho\tilde{\omega}^2\tilde{U}_1 \tag{4a}$$

$$(\lambda+\mu)\tilde{\Delta} i\tilde{k}_2+\mu(\frac{d^2}{d\tilde{x}_3^2}-\tilde{k}_1^2-\tilde{k}_2^2)\tilde{U}_2=-\rho\tilde{\omega}^2\tilde{U}_2 \tag{4b}$$

$$(\lambda+\mu)\frac{d\tilde{\Delta}}{d\tilde{x}_3}+\mu(\frac{d^2}{d\tilde{x}_3^2}-\tilde{k}_1^2-\tilde{k}_2^2)\tilde{U}_3=-\rho\tilde{\omega}^2\tilde{U}_3 \tag{4c}$$

where $\tilde{\Delta} = \tilde{\Delta}(\tilde{k}_1, \tilde{k}_2, \tilde{x}_3, \omega)$ is the Fourier transform, with respect to the horizontal coordinates and time, of the dilation $\Delta(\tilde{x}_1, \tilde{x}_2, \tilde{x}_3, t)$. The vibration frequency of a material point is $\tilde{\omega} = \omega - \tilde{k}_1 v$ and ω is the frequency of the moving load. The horizontal wavenumbers in the direction of $\tilde{x}_1$ and $\tilde{x}_2$ are $\tilde{k}_1$ and $\tilde{k}_2$, respecitvely.

As showed by Sheng [5, 6], the solution to Eq. 4 for an individual layer can be found analytically, and due to continuity of displacements and tractions over interfaces between layers, several layers can be assembled using the Thomson [10] and Haskell [11] layer transfer matrix approach, forming a relationship between the displacement and stresses at the top of the stratum and at the bottom of the stratum. With known boundary conditions at the lowest interface, a relationship between the traction and the displacement at the surface can be obtained as

$$\hat{\mathbf{u}} = \hat{\mathbf{G}}\,\hat{\mathbf{p}}, \tag{5}$$

where $\hat{\mathbf{u}} = \hat{\mathbf{u}}(\tilde{k}_1, \tilde{k}_2, \omega)$ and $\hat{\mathbf{p}} = \hat{\mathbf{p}}(\tilde{k}_1, \tilde{k}_2, \omega)$ are vectors containing the displacements and tractions respectively on the soil surface, $\hat{\mathbf{G}} = \hat{\mathbf{G}}(\tilde{k}_1, \tilde{k}_2, \omega)$ is the Green's function tensor, $\tilde{k}_1$ and $\tilde{k}_2$ are the horizontal wavenumbers. For certain frequencies and stratifications, the original Thomson and Haskell method suffers from loss-of-precision. To avoid these problems in the present work, the different soil layers are assembled in an orthonormalization procedure as proposed by Wang [12].

Equation 5 is evaluated for a set of discrete values of $\tilde{k}_1$ and $\tilde{k}_2$, and the displacement vector $\tilde{\mathbf{u}}(\tilde{x}_1, \tilde{x}_2, \omega)$ is obtained in Cartesian space through a double inverse Fourier transform of $\hat{\mathbf{u}}(\tilde{k}_1, \tilde{k}_2, \omega)$.

The procedure described above is used for calculating the response on the soil surface, due to a unit load with a rectangular spatial distribution, the size of which is determined by the element size in the connecting superstructure. From this single load case, a dynamic flexibility matrix $\mathbf{F}_g(\omega, v)$ is established for a set of DoFs where the superstructure interacts with the soil surface. These DoFs will be referred to as soil–structure interaction (SSI) DoFs. $\mathbf{F}_g$ is formed, column by column, by interpolating from $\tilde{\mathbf{u}}$. The flexibility matrix is then inverted to form the dynamic stiffness matrix of the soil, $\mathbf{D}_g(\omega, v) = \mathbf{F}_g^{-1}(\omega, v)$, which gives a relation between the steady-state displacements $\tilde{\mathbf{u}}_g$ and forces $\tilde{\mathbf{f}}_g$ for the SSI DoFs, at a certain load circular frequency ω and velocity v, as

$$\mathbf{D}_g\, \tilde{\mathbf{u}}_g = \tilde{\mathbf{f}}_g. \tag{6}$$

2.3 Finite element model of railway structure

The coordinate transformation used for expressing the governing FE equations in a moving frame of reference introduces convective terms in the damping and stiffness matrices. In Sections 2.3.1–2.3.3 below, the FE equations are derived for the beams, plates and visco-elastic interface elements, respectively.

2.3.1 Beam elements

The equilibrium equation for a Bernoulli-Euler beam reads

$$\frac{\partial^2 M}{\partial x^2} + q - m_b \frac{\partial^2 w}{\partial t^2} = 0, \tag{7}$$

where $M = M(x,t)$ is the bending moment. $q(x,t)$ is a loading force per unit length. m_b is the mass per unit length of the beam. $w = w(x,t)$ is the deflection. With the coordinate transformation described by Eq. 2, Eq. 7 can be written as

$$\frac{\partial^2 \tilde{M}}{\partial \tilde{x}^2} + \tilde{q} - m_b\left(\frac{\partial^2 \tilde{w}}{\partial t^2} - 2v\frac{\partial^2 \tilde{w}}{\partial \tilde{x}\partial t} + v^2\frac{\partial^2 \tilde{w}}{\partial \tilde{x}^2}\right) = 0, \tag{8}$$

where $\tilde{\cdot}$ denotes that a variable is expressed in the moving frame of reference. The weak form is obtained by multiplying Eq. 8 by an arbitrary weight function $g = g(\tilde{x})$ and integrating it over the region. It can be shown that the resulting weak form for the Bernoulli-Euler beam in a moving frame of reference is

$$\int_a^b \tfrac{\partial^2 g}{\partial \tilde{x}^2}\tilde{M}\,dx - [\tfrac{\partial g}{\partial \tilde{x}}\tilde{M}]_a^b + [g\tilde{V}]_a^b + \int_a^b g\tilde{q}\,dx - m_b\int_a^b g(\tfrac{\partial^2 \tilde{w}}{\partial t^2} - 2v\tfrac{\partial^2 \tilde{w}}{\partial \tilde{x}\partial t} + v^2\tfrac{\partial^2 \tilde{w}}{\partial \tilde{x}^2})\,dx = 0. \tag{9}$$

With the kinematic and constitutive assumptions for a Bernoulli-Euler beam, $\tilde{M}$ can be written as

$$\tilde{M} = -EI\frac{\partial^2 \tilde{w}}{\partial \tilde{x}^2}, \tag{10}$$

where EI is the bending stiffness. To obtain the FE formulation, the deflection $\tilde{w}(\tilde{x}, t)$ is approximated using the element nodal values $\mathbf{a}(t)$ and the shape functions $\mathbf{N}(\tilde{x})$, as $\tilde{w} = \mathbf{N}\mathbf{a}$.

Adopting the Galerking method, the mass, damping and stiffness matrices, as well as the load and boundary vectors, are identified as

$$\mathbf{K} = EI \int_a^b \Big(\frac{d^2\mathbf{N}(\tilde{x})}{d\tilde{x}^2}\Big)^T \frac{d^2\mathbf{N}(\tilde{x})}{d\tilde{x}^2}\, dx + m_b\, v^2 \int_a^b \mathbf{N}^T \frac{d^2\mathbf{N}}{d\tilde{x}^2}\, dx, \tag{11}$$

$$\mathbf{C} = -2m_b v \int_a^b \mathbf{N}^T \frac{d\mathbf{N}}{d\tilde{x}}\, dx, \tag{12}$$

$$\mathbf{M} = m_b \int_a^b \mathbf{N}^T\mathbf{N}\, dx, \tag{13}$$

$$\mathbf{f}_l = \int_a^b \mathbf{N}^T \tilde{q}\, dx, \tag{14}$$

$$\mathbf{f}_b = [\mathbf{N}^T\tilde{V}]_a^b - [\frac{\partial \mathbf{N}^T}{\partial \tilde{x}}\tilde{M}]_a^b. \tag{15}$$

A 2-node beam element with two DoFs per node (vertical displacement and one rotation), based on the above formulation, is implemented and used in the present work. Similar derivations for the convective Bernoulli-Euler beams can be found in e.g. [13, 14].

2.3.2 Plate elements

The equilibrium equation for a Kirchhoff plate reads, see e.g. [15],

$$\frac{\partial^2 M_{xx}}{\partial x^2} + 2\frac{\partial^2 M_{xy}}{\partial x \partial y} + \frac{\partial^2 M_{yy}}{\partial y^2} + q - \rho h \frac{\partial^2 w}{\partial t^2} = 0, \tag{16}$$

where $M_{xx} = M_{xx}(x, y, t)$, $M_{yy} = M_{yy}(x, y, t)$ and $M_{xy} = M_{xy}(x, y, t)$ are the bending moments in the x- and y-directions. $q(x, y, t)$ is a loading force per unit area. h and ρ is the plate thickness and the mass density respectively. $w = w(x, y, t)$ is the deflection of the mid-section. With the coordinate transformation described by Eq. 2, Eq. 16 can be written as

$$\frac{\partial^2 \tilde{M}_{xx}}{\partial \tilde{x}^2} + 2\frac{\partial^2 \tilde{M}_{xy}}{\partial \tilde{x} \partial \tilde{y}} + \frac{\partial^2 \tilde{M}_{yy}}{\partial \tilde{y}^2} + \tilde{q} - \rho h(\frac{\partial^2 \tilde{w}}{\partial t^2} - 2v\frac{\partial^2 \tilde{w}}{\partial \tilde{x}\partial t} + v^2\frac{\partial^2 \tilde{w}}{\partial \tilde{x}^2}) = 0. \tag{17}$$

The weak form is obtained by multiplying Eq. 17 by an arbitrary weight function $g = g(\tilde{x}, \tilde{y})$ and integrating it over the region. It can be shown that the resulting weak form for the Kirchhoff plate in a moving frame of reference is

$$\begin{aligned} &\textstyle\int_A (\tilde{\nabla} g)^T \tilde{\mathbf{M}}\, dA - \oint_{\mathscr{L}} \frac{dg}{dn}\tilde{M}_{nn}\, d\mathscr{L} + \oint_{\mathscr{L}} g(\tilde{V}_{nz} + \frac{d\tilde{M}_{nm}}{dm})\, d\mathscr{L} + \int_A g\tilde{q}\, dA \\ &\textstyle -\rho h \int_A (g\frac{\partial^2 \tilde{w}}{\partial t^2} - 2vg\frac{\partial^2 \tilde{w}}{\partial \tilde{x}\partial t} + v^2 g\frac{\partial^2 \tilde{w}}{\partial \tilde{x}^2})\, dA = 0, \end{aligned} \tag{18}$$

where the matrix differential operator $\tilde{\nabla}$ is defined as

$$\tilde{\nabla} = \begin{bmatrix} \frac{\partial^2}{d\tilde{x}^2} & \frac{\partial^2}{d\tilde{y}^2} & 2\frac{\partial^2}{d\tilde{x}d\tilde{y}} \end{bmatrix}^T, \tag{19}$$

and the moment vector $\tilde{\mathbf{M}}$ as

$$\tilde{\mathbf{M}} = \tilde{\mathbf{M}}(\tilde{x}, \tilde{y}, t) = \begin{bmatrix} \tilde{M}_{xx}(x, y, t) & \tilde{M}_{yy}(x, y, t) & \tilde{M}_{xy}(x, y, t) \end{bmatrix}^T. \tag{20}$$

The constitutive equation for the cross-section of a Kirchhoff plate can be written as $\tilde{\mathbf{M}} = -(h^3/12)\mathbf{D}\tilde{\nabla}\tilde{w}$ where $\mathbf{D}$ is the plane stress constitutive matrix for isotropic elasticity. To obtain the FE formulation, the deflection $\tilde{w}(\tilde{x},\tilde{y},t)$ is approximated using the element nodal values $\mathbf{a}(t)$ and the shape functions $\mathbf{N}(\tilde{x},\tilde{y})$, as $\tilde{w} = \mathbf{N}\mathbf{a}$.

Adopting the Galerking method, the mass, damping and stiffness matrices, as well as the load and boundary vectors, are identified as

$$\mathbf{K} = \frac{h^3}{12}\int_A (\tilde{\nabla}\mathbf{N})^T\mathbf{D}(\tilde{\nabla}\mathbf{N})\,dA \;+\rho h v^2\int_A \mathbf{N}^T\frac{\partial^2\mathbf{N}}{\partial\tilde{x}^2}\,dA\,, \tag{21}$$

$$\mathbf{C} = -2\rho h v\int_A \mathbf{N}^T\frac{\partial\mathbf{N}}{\partial\tilde{x}}\,dA, \tag{22}$$

$$\mathbf{M} = \rho h\int_A \mathbf{N}^T\mathbf{N}\,dA, \tag{23}$$

$$\mathbf{f}_l = \int_A \mathbf{N}^T\tilde{q}\,dA, \tag{24}$$

$$\mathbf{f}_b = \oint_{\mathscr{L}} \mathbf{N}^T(\tilde{V}_{nz} + \frac{d\tilde{M}_{nm}}{dm})\,d\mathscr{L} - \oint_{\mathscr{L}} (\nabla\mathbf{N})^T\mathbf{n}\tilde{M}_{nn}\,d\mathscr{L}. \tag{25}$$

A 4-node rectangular element with three DoFs per node (vertical displacement and two rotations), based on the above formulation, is implemented and used in the present work.

2.3.3 Visco-elastic interface elements

The rail pads are modeled by visco-elastic interface elements, representing continuous springs and dashpots. In the following derivation of the equations for the interface elements, an interface element is assumed to be located between two beam elements parallel with the x-axis. The loads on the upper and lower beams due to the visco-elastic interface are written

$$q_u(x,y,t) = -k(w_u - w_l) - c(\frac{\partial w_u}{\partial t} - \frac{\partial w_l}{\partial t}) = 0, \tag{26}$$

$$q_l(x,y,t) = -k(w_l - w_u) - c(\frac{\partial w_l}{\partial t} - \frac{\partial w_u}{\partial t}) = 0, \tag{27}$$

where $w_u = w_u(x,t)$ and $w_l = w_l(x,t)$ is the deflection in the upper and lower beam respectively, k is the spring stiffness and c is the damping coefficient. With the coordinate transformation described by Eq. 2,

$$\tilde{q}_u(\tilde{x},t) = -k(\tilde{w}_u - \tilde{w}_l) - c\Big\{(\frac{\partial\tilde{w}_u}{\partial t} - \frac{\partial\tilde{w}_l}{\partial t}) - v(\frac{\partial\tilde{w}_u}{\partial\tilde{x}} - \frac{\partial\tilde{w}_l}{\partial\tilde{x}})\Big\}, \tag{28}$$

$$\tilde{q}_l(\tilde{x},t) = -k(\tilde{w}_l - \tilde{w}_u) - c\Big\{(\frac{\partial\tilde{w}_l}{\partial t} - \frac{\partial\tilde{w}_u}{\partial t}) - v(\frac{\partial\tilde{w}_l}{\partial\tilde{x}} - \frac{\partial\tilde{w}_u}{\partial\tilde{x}})\Big\}. \tag{29}$$

The displacements of the upper and lower beam, w_u and w_l, are approximated using the shape functions $\mathbf{N}_u$ and $\mathbf{N}_l$ and element nodal displacements $\mathbf{a}_u(t)$ and $\mathbf{a}_l(t)$ for the upper and lower beams, respectively. With Eq. 14 the load vectors for the respective beams can be written

$$\begin{aligned}&\mathbf{f}_{l_u} = \textstyle\int_a^b \mathbf{N}_u^T\tilde{q}_u\,dx = -k\Big\{\int_a^b \mathbf{N}_u^T\mathbf{N}_u\,dx\,\mathbf{a}_u - \int_a^b \mathbf{N}_u^T\mathbf{N}_l\,dx\,\mathbf{a}_l\Big\} - \\ &c\Big\{\int_a^b \mathbf{N}_u^T\mathbf{N}_u\,dx\,\dot{\mathbf{a}}_u + \int_a^b \mathbf{N}_u^T\mathbf{N}_l\,dx\,\dot{\mathbf{a}}_l\Big\} + c\,v\,\Big\{\int_a^b \mathbf{N}_u^T\tfrac{\partial\mathbf{N}_u}{\partial\tilde{x}}\,dx\,\mathbf{a}_u - \int_a^b \mathbf{N}_u^T\tfrac{\partial\mathbf{N}_l}{\partial\tilde{x}}\,dx\,\mathbf{a}_l\Big\},\end{aligned} \tag{30}$$

$$\begin{aligned}&\mathbf{f}_{l_l} = \int_a^b \mathbf{N}_l^T \tilde{q}_l \, dx = -k\Big\{ \int_a^b \mathbf{N}_l^T \mathbf{N}_l \, dx \, \mathbf{a}_l - \int_a^b \mathbf{N}_l^T \mathbf{N}_u \, dx \, \mathbf{a}_u \Big\} - \\ &c\Big\{ \int_a^b \mathbf{N}_l^T \mathbf{N}_l \, dx \, \dot{\mathbf{a}}_l + \int_a^b \mathbf{N}_l^T \mathbf{N}_u \, dx \, \dot{\mathbf{a}}_u \Big\} + c\,v \Big\{ \int_a^b \mathbf{N}_l^T \tfrac{\partial \mathbf{N}_l}{\partial \tilde{x}} \, dx \, \mathbf{a}_l - \int_a^b \mathbf{N}_l^T \tfrac{\partial \mathbf{N}_u}{\partial \tilde{x}} \, dx \, \mathbf{a}_u \Big\}.\end{aligned} \tag{31}$$

With the shape function vectors $\tilde{\mathbf{N}}_u$ and $\tilde{\mathbf{N}}_l$ and the displacement vector $\mathbf{a}$ defined as

$$\begin{aligned}&\tilde{\mathbf{N}}_u(\tilde{x},\tilde{y}) = \begin{bmatrix}\mathbf{N}_u & 0\mathbf{N}_l\end{bmatrix}, \tilde{\mathbf{N}}_l(\tilde{x},\tilde{y}) = \begin{bmatrix}0\mathbf{N}_u & \mathbf{N}_l\end{bmatrix} \\ &\tilde{\mathbf{f}}_{l_u}(t) = \begin{bmatrix}\mathbf{f}_{l_u} & 0\mathbf{f}_{l_l}\end{bmatrix}, \tilde{\mathbf{f}}_{l_l}(t) = \begin{bmatrix}0\mathbf{f}_{l_u} & \mathbf{f}_{l_l}\end{bmatrix}, \mathbf{f}_L(t) = \begin{bmatrix}\mathbf{f}_{l_u} & \mathbf{f}_{l_l}\end{bmatrix}^T \\ &\tilde{\mathbf{a}}_u(t) = \begin{bmatrix}\mathbf{a}_u & 0\mathbf{a}_l\end{bmatrix}, \tilde{\mathbf{a}}_l(t) = \begin{bmatrix}0\mathbf{a}_u & \mathbf{a}_l\end{bmatrix}, \mathbf{a}(t) = \begin{bmatrix}\mathbf{a}_u & \mathbf{a}_l\end{bmatrix}^T\end{aligned} \tag{32}$$

it is possible to write the load vector as

$$\begin{aligned}&\mathbf{f}_L(t) = \tilde{\mathbf{f}}_{l_u}(t) + \tilde{\mathbf{f}}_{l_l}(t) = \\ &-k\Big\{ \int_a^b \tilde{\mathbf{N}}_u^T \tilde{\mathbf{N}}_u \, dx + \int_a^b \tilde{\mathbf{N}}_l^T \tilde{\mathbf{N}}_l \, dx - \int_a^b \tilde{\mathbf{N}}_u^T \tilde{\mathbf{N}}_l \, dx - \int_a^b \tilde{\mathbf{N}}_l^T \tilde{\mathbf{N}}_u \, dx \Big\} \mathbf{a} \\ &-c\Big\{ \int_a^b \tilde{\mathbf{N}}_u^T \tilde{\mathbf{N}}_u \, dx + \int_a^b \tilde{\mathbf{N}}_l^T \tilde{\mathbf{N}}_l \, dx + \int_a^b \tilde{\mathbf{N}}_u^T \tilde{\mathbf{N}}_l \, dx + \int_a^b \tilde{\mathbf{N}}_l^T \tilde{\mathbf{N}}_u \, dx \Big\} \dot{\mathbf{a}} \\ &+c\,v \Big\{ \int_a^b \tilde{\mathbf{N}}_u^T \tfrac{\partial \tilde{\mathbf{N}}_u}{\partial \tilde{x}} \, dx + \int_a^b \tilde{\mathbf{N}}_l^T \tfrac{\partial \tilde{\mathbf{N}}_l}{\partial \tilde{x}} \, dx - \int_a^b \tilde{\mathbf{N}}_u^T \tfrac{\partial \tilde{\mathbf{N}}_l}{\partial \tilde{x}} \, dx - \int_a^b \tilde{\mathbf{N}}_l^T \tfrac{\partial \tilde{\mathbf{N}}_u}{\partial \tilde{x}} \, dx \Big\} \mathbf{a}.\end{aligned} \tag{33}$$

The vector $\mathbf{f}_L(t)$ collects the forces on the upper and lower beam, caused by the interface element. The forces on the interface element are therefore $\mathbf{f}_i(t) = -\mathbf{f}_L(t)$, and the stiffness and damping matrices of the interface element can be identified from Eq. 33 as

$$\begin{aligned}\mathbf{K} = &k\Big\{ \int_a^b \tilde{\mathbf{N}}_u^T \tilde{\mathbf{N}}_u \, dx + \int_a^b \tilde{\mathbf{N}}_l^T \tilde{\mathbf{N}}_l \, dx - \int_a^b \tilde{\mathbf{N}}_u^T \tilde{\mathbf{N}}_l \, dx - \int_a^b \tilde{\mathbf{N}}_l^T \tilde{\mathbf{N}}_u \, dx \Big\} \\ &-cv\Big\{ \int_a^b \tilde{\mathbf{N}}_u^T \tfrac{\partial \tilde{\mathbf{N}}_u}{\partial \tilde{x}} \, dx + \int_a^b \tilde{\mathbf{N}}_l^T \tfrac{\partial \tilde{\mathbf{N}}_l}{\partial \tilde{x}} \, dx - \int_a^b \tilde{\mathbf{N}}_u^T \tfrac{\partial \tilde{\mathbf{N}}_l}{\partial \tilde{x}} \, dx - \int_a^b \tilde{\mathbf{N}}_l^T \tfrac{\partial \tilde{\mathbf{N}}_u}{\partial \tilde{x}} \, dx \Big\},\end{aligned} \tag{34}$$

$$\mathbf{C} = c\Big\{ \int_a^b \tilde{\mathbf{N}}_u^T \tilde{\mathbf{N}}_u \, dx + \int_a^b \tilde{\mathbf{N}}_l^T \tilde{\mathbf{N}}_l \, dx - \int_a^b \tilde{\mathbf{N}}_u^T \tilde{\mathbf{N}}_l \, dx - \int_a^b \tilde{\mathbf{N}}_l^T \tilde{\mathbf{N}}_u \, dx \Big\}. \tag{35}$$

The above expressions are also valid for an interface element between a beam element overlying a plate element in the xy-plane, such as in model c), with the shape functions for the plate evaluated at the y-coordinate of the beam.

2.4 Coupling to soil

Assuming steady-state conditions, the governing equation for the railway track structure can be written as

$$(-\omega^2 \mathbf{M}_r + i\omega \mathbf{C}_r + \mathbf{K}_r)\tilde{\mathbf{u}}_r = \tilde{\mathbf{f}}_r, \tag{36}$$

or

$$\mathbf{D}_r \tilde{\mathbf{u}}_r = \tilde{\mathbf{f}}_r, \tag{37}$$

where $\mathbf{M}_r$, $\mathbf{C}_r$ and $\mathbf{K}_r$ is the mass, damping and stiffness matrix respectively. $\mathbf{D}_r = (-\omega^2 \mathbf{M}_r + i\omega \mathbf{C}_r + \mathbf{K}_r)$ is the dynamic stiffness matrix, and $\tilde{\mathbf{u}}_r$ and $\tilde{\mathbf{f}}_r$ is the displacement and force vector for the track structure, respectively.

The track and soil is coupled in a standard FE manner. Only the vertical DoFs of the track structure and the soil are coupled. A global system of equations for the soil and the railway structure is formed by combining Eqs. 6 and 37, yielding

$$\mathbf{D}_t \tilde{\mathbf{u}}_r = \tilde{\mathbf{f}}_r, \tag{38}$$

where $\mathbf{D}_t$ represents the total dynamic stiffness matrix for the track structure and soil.

Once the track displacements $\tilde{\mathbf{u}}_r$, and thereby also the displacement in the soil DoFs $\tilde{\mathbf{u}}_g$, have been obtained by solving Eq. 38, the corresponding forces on the soil surface, $\tilde{\mathbf{f}}_g$ are calculated by Eq. 6. A second flexibility matrix $\mathbf{F}_{gf}(\omega, v)$ is established, in the same manner as $\mathbf{F}_g(\omega, v)$ as described in Section 2.2, expressing the displacements in free-field due to forces on the soil–structure interface. The free-field displacements, $\tilde{\mathbf{u}}_f$, are then calculated as

$$\tilde{\mathbf{u}}_f = \mathbf{F}_{gf}\tilde{\mathbf{f}}_g. \tag{39}$$

3 MODEL COMPARISON

To compare the effect of the three different modeling strategies for the track on the free-field response, each model is used for evaluating the response to a moving unit harmonic point load acting on the rail. The track properties are given in Table 1. The track rests on a 14 m deep layer of clay overlaying a half-space, with properties according to Table 2. An element length of 0.3 m is used, meaning that 12 elements are used in the transverse direction of the slab in model c). For model b) the slab is rigidly connected to 13 soil DoFs in the transverse direction. In all three models, the number of elements in the track direction is 500, yielding a total track length of 150 meters, which has been found to be sufficient to avoid problems with reflecting waves at the boundaries of the FE model in the studied case. The track gauge is 1.435 m.

Figure 3 shows the wavefield and the track deformation due to a harmonic point load with frequency $f = 50$ Hz traveling at $v = 60$ m/s, as obtained with the three different models. The difference in the slab deformation in the transverse direction due to the different modeling approaches is clearly visible. The displacements shown in Figure 3 are in the moving frame of reference, following the load at speed $v = 60$ m/s. In this frame of reference, the displacements are in steady state with the loading frequency $f = 50$ Hz. For a fixed point in the free-field, however, the response is transient and contains a broad band of frequencies due to the Doppler effect. A higher load speed results in a broader frequency content of the response in a fixed point. This can be seen in Figure 4 that shows the displacement spectrum for a fixed point 10 m and 25 m from the track, due to a harmonic 50 Hz load travelling at $v = 30$ m/s and $v = 60$ m/s. All three models yield similar results, however, the response obtained with model c) using plate elements is slightly higher than obtained with the other two models, for this particular load frequency.

To compare the three models for a range of excitation frequencies, a moving rms-value of the vibration velocity in a fixed point is calculated for each excitation frequency f, as

$$v_{rms}(t) = \sqrt{\frac{1}{T}\int_t^{t+T} \dot{u}(t)^2 dt}, \tag{40}$$

where $\dot{u}(t)$ is the velocity time history response for a fixed point. T is the window length and is here set to $T = 1$ s. In Figure 5 the maximum of $v_{rms}(t)$ is shown for each excitation frequency for the three models, for a fixed point located 10 and 25 m from the track respectively and the load speeds $v = 30$ and $v = 60$ m/s. For both load speeds, and both distances, the free-field response is very similar for all three models up to about $f = 50$ Hz. At higher frequencies, both models a) and b) underestimate the response. However, the underestimation with model b) is modest. For model a) the maximum underestimation is almost 10 dB at 70 Hz.

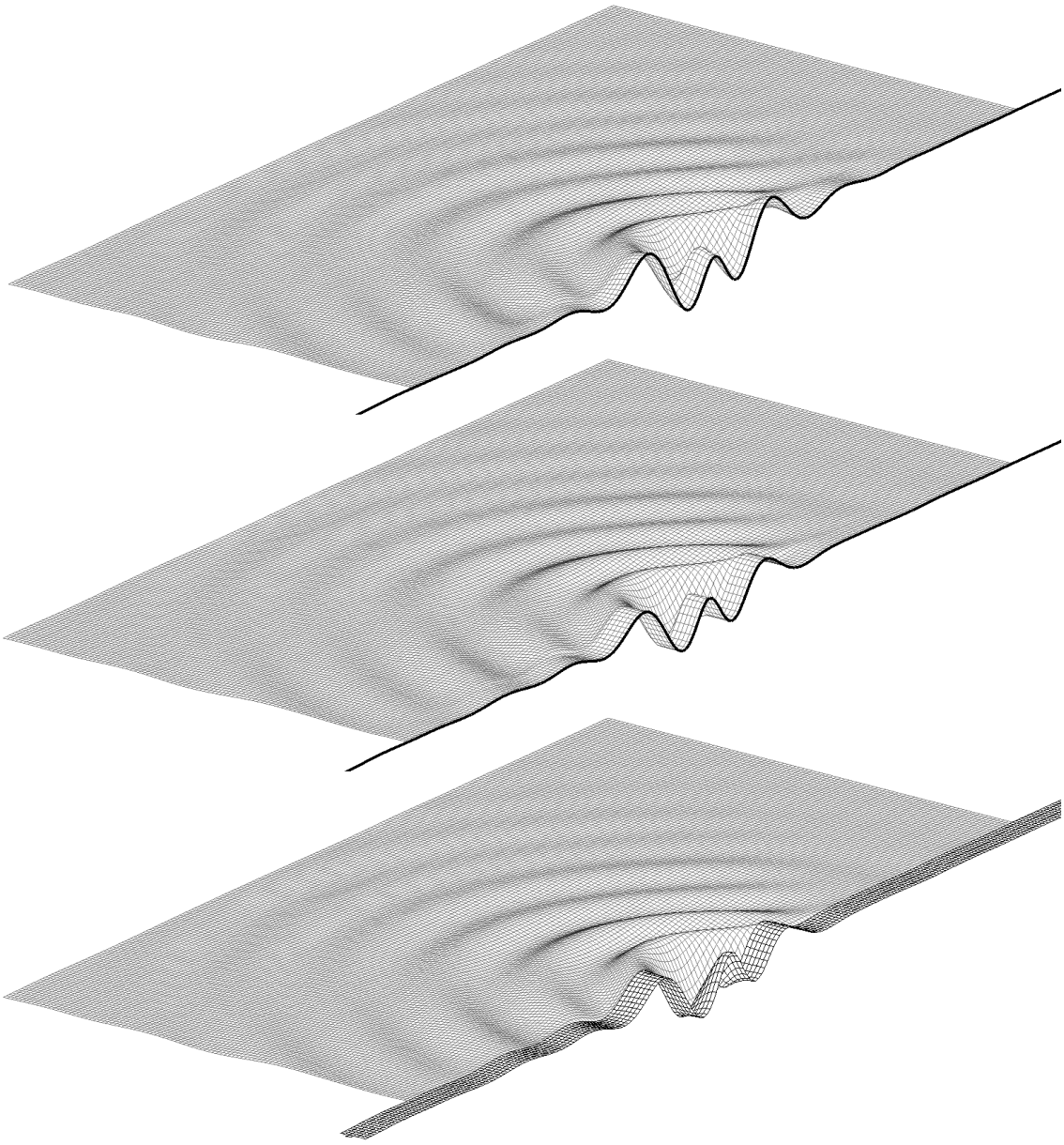

Figure 3: Soil and slab displacements in models a)–c), from top to bottom, when subjected to a harmonic load with frequency $f = 50$ Hz moving along the track at speed $v = 60$ m/s. The size of the displayed area is 60 m$\times$ 30 m.

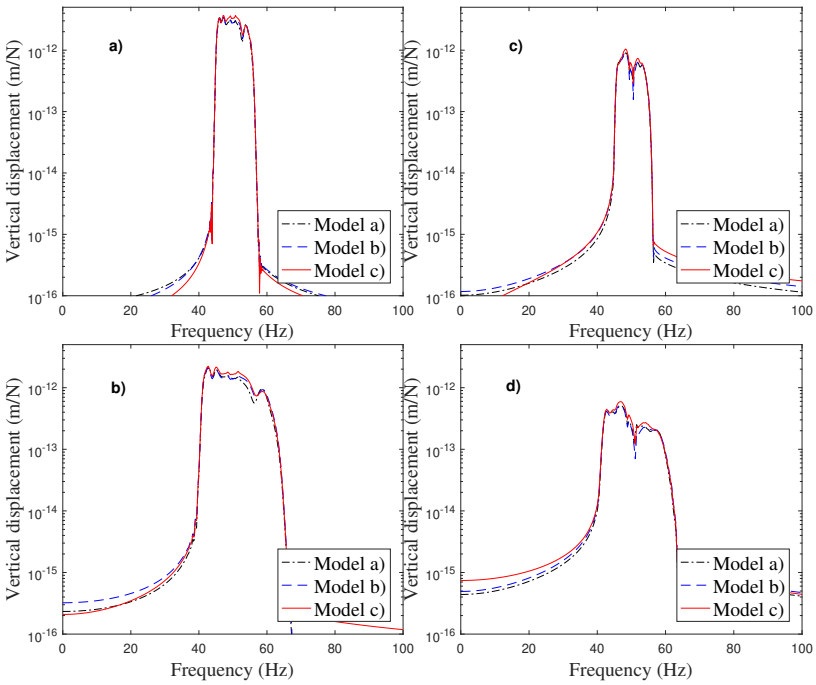

Figure 4: Response of a fixed point in the free-field due to a 50 Hz load traveling on the track. a) and b) show the results for a fixed point 10 meters from the track, with a load speed of $v = 30$ and $v = 60$ m/s, respectively. c) and d) are for a point 25 meters from the track.

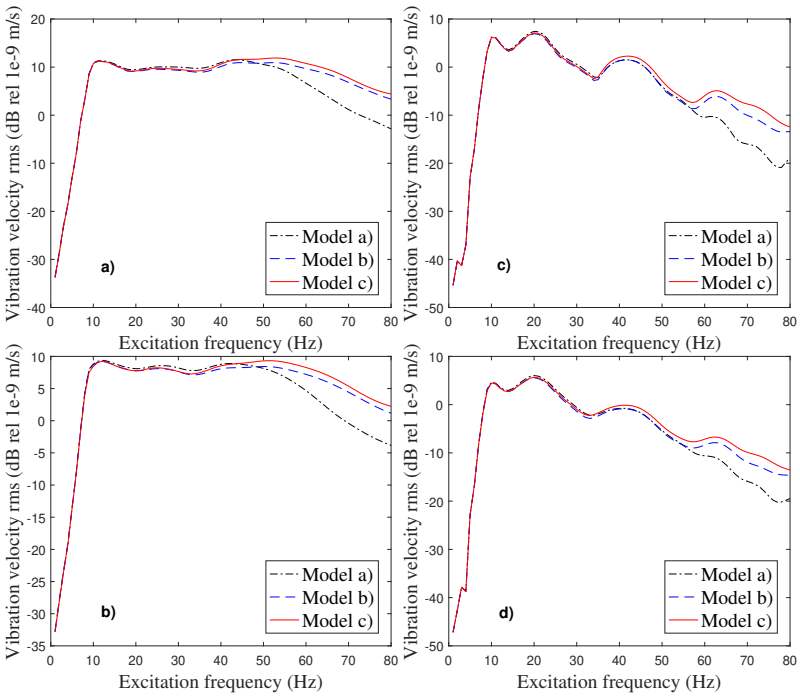

Figure 5: Velocity rms-value of a fixed point in the free-field due to a harmonic load traveling on the track. a) and b) show the results for a fixed point 10 meters from the track, with a load speed of $v = 30$ and $v = 60$ m/s, respectively. c) and d) are for a point 25 meters from the track.

	Parameter	Value
Rail	Mass (kg/m)	60
	Young's modulus (GPa)	210
	Second moment of inertia (m^4)	3.217×10^{-5}
	Loss factor (-)	0.01
Rail pads	Stiffness (MN/m^2)	92
	Damping (kNs/m^2)	73
Slab + support layer	Density (kg/m^3)	2310
	Young's modulus (GPa)	26.7
	Poisson's ratio	0.2
	Width (m)	3.6
	Thickness (m)	0.55
	Loss factor (-)	0.04

Table 1: Track properties.

4 CONCLUSIONS

In the paper a numerical prediction model for train-induced ground-vibration has been presented. The model is formulated in a frame of reference following the moving load, which offers some advantages over conventional FE models using a fixed frame of reference. Using a fixed frame of reference, the computational domain must be large for the moving load to stay within the model during the time of analysis. In the moving frame of reference following the load, on the other hand, the load stays at the same location in the model throughout the analysis, allowing a smaller model. Furthermore, frequency domain methods can be used for analyzing the moving load. A drawback of the model is that it is not suitable for analyzing load cases where the resulting wavelengths are very short, such as moving loads approaching the soil shear wave velocity. Short wavelengths, making the current approach inappropriate, may also result from non-moving loads, depending on the soil and track stiffness and the frequency of the load.

Three different models of a railway slab track have been established and compared. In the first two models, the railway track is modeled as a Bernoulli-Euler beam on a layered half-space, with different assumptions regarding the displacement and stress distribution at the track–soil interface. In the third model, the track slab is modeled using Kirchhoff plate elements, enabling a more general displacement and stress distribution in the track transverse direction to be resolved. It is shown that in the case studied here, the beam model where the track–soil interface is considered rigid over the width of the slab, only slightly underestimates the response, at higher frequencies. The beam model where a uniform traction is assumed at the track–soil interface, on the other hand, underestimates the response significantly at frequencies above 50 Hz.

5 Acknowledgments

Part of the project was funded by the City of Helsingborg through the call Plattformen. The authors of this work gratefully acknowledge the financial support.

Layer	Parameter	Value
Soil	Depth (m)	14.0
	Young's modulus (MPa)	475
	Poisson's ratio	0.48
	Density (kg/m^3)	2125
	Loss factor (-)	0.14
Bedrock	Depth (m)	∞
(half-space)	Young's modulus (MPa)	8800
	Poisson's ratio	0.40
	Density (kg/m^3)	2600
	Loss factor (-)	0.04

Table 2: Soil properties.

REFERENCES

[1] Y. Yang, H. Hung, A 2.5D finite-infinite element approach for modelling visco-elastic bodies subjected to moving loads. *International Journal for Numerical Methods in Engineering*, **51**. 1317–1336, 2008.

[2] X. Sheng, C.J.C. Jones, D.J. Thompson, Prediction of ground vibration from trains using the wavenumber finite and boundary element methods. *Journal of Sound and Vibration*, **293**. 575–586, 2006.

[3] G. Lombaert, G. Degrande, J. Kogut, S. Francois, The experimental validation of a numerical model for the prediction of railway induced vibrations. *Journal of Sound and Vibration*, **297**. 512–535, 2006.

[4] P. Galvin, S. Francois, M. Schevenels, E. Bongini, G. Degrande, G. Lombaert, A 2.5D coupled FE-BE model for the prediction of railway induced vibrations. *Soil Dynamics and Earthquake Engineering*, **30**. 1500–1512, 2010.

[5] X. Sheng, C.J.C. Jones, M. Petyt, Ground vibration generated by a harmonic load acting on a railway track. *Journal of Sound and Vibration* **225(1)**.3–28, 1999.

[6] X. Sheng, C.J.C. Jones, M. Petyt, Ground vibration generated by a load moving along a railway track. *Journal of Sound and Vibration*, **228(1)**. 129–156, 1999.

[7] A.M. Kaynia, C. Madshus, P. Zackrisson, Ground vibration from high-speed trains: prediction and countermeasure. *Journal of Geotechnical and Geoenvironmental Engineering*, **126(6)**. 531–537, 2000.

[8] M.J.M.M. Steenbergen, A.V. Metrikine, The effect of the interface conditions on the dynamic response of a beam on a half-space to a moving load. *European Journal of Mechanics A/Solids*, **26**. 33–54, 2007.

[9] L.V. Andersen, *Linear Elastodynamic Analysis*, Department of Civil Engineering, Aalborg University. DCE Lecture Notes, No. 3, 2006.

[10] W. Thomson, Transmission of elastic waves through a stratified solid medium. *Journal of Applied Physics*, **21**. 89–93, 1950.

[11] N. Haskell, The dispersion of surface waves on multilayered medium. *Bulletin of the Seismological Society of America*, **73**. 17–43, 1953.

[12] R. Wang, A simple orthonormalization method for stable and efficient computation of Green's functions. *Bulletin of the Seismological Society of America*, **89(3)**. 733–741, 1999.

[13] L. Andersen, S.R.K. Nielsen, P.H. Kirkegaard, Finite element modelling of infinite Euler beams on Kelvin foundations exposed to moving loads in convected co-ordinates. *Journal of Sound and Vibration*, **241(4)**. 587–604, 2001.

[14] X. Lei, J. Wang, Dynamic analysis of the train and slab track coupling system with finite elements in a moving frame of reference. *Journal of Vibration and Control*, **20(9)**. 1301–1317, 2014.

[15] N. Ottosen, H. Petersson, *Introduction to the finite element method*, Prentice Hall, 1992.

COMPDYN 2019
7th ECCOMAS Thematic Conference on
Computational Methods in Structural Dynamics and Earthquake Engineering
M. Papadrakakis, M. Fragiadakis (eds.)
Crete, Greece, 24-26 June 2019

ON THE EXPERIMENTAL VALIDATION OF THE NUMERICAL CALCULATION OF THE DISPERSION RELATIONS OF COMPLEX WOVEN COMPOSITES

V. Thierry[1], O. Mesnil[2], and D. Chronopoulos[1]

[1]Institute for Aerospace Technology and the Composites Research Group, University of Nottingham
Aerospace Technology Centre Innovation Park, Triumph Road Nottingham, NG7 2TU
e-mail: {victor.thierry, dimitrios.chronopoulos}@nottingham.ac.uk

[2]CEA List
Site DIGITEO Saclay, 91191 Gif-sur-Yvette
e-mail: olivier.mesnil@cea.fr

Keywords: Textile composite structures, Wave propagation, Periodic Structure Theory, Experimental validation, B-scan.

Abstract. *In this article, an attempt is made toward the experimental validation of a numerical method allowing vibroacoustic and ultrasonic wave propagation analysis of complex woven composites. For this validation, plates with a complex woven architecture were manufactured using Resin Transfer Molding (RTM) process. These composites can be considered as periodic structures composed of unit cells repeated in two directions. The unit cells of these three different woven patterns are modelled realistically at a mesoscopic scale, using information from micrographic cross-sections and the mechanical properties of the fibres and matrix materials provided by the various manufacturers. The numerical method combining the mode-based Component Mode Synthesis (CMS) and the Wave Finite Element (WFEM) methods allows for computing the dispersion relations of the modelled samples. Experimentally, a few dispersion relations are extracted from the samples by the mean of B-scan. These experimental results are compared with the numerical results. It is shown that this methodology has a good accuracy for determining the dispersion relations of complex woven composites. It is efficient time wise and provides more information on the dispersion relations than experimental testing.*

1 INTRODUCTION

Textile composites are increasingly used in modern industry due to their excellent mechanical properties [1] and especially for aerospace applications thanks to a low weight. These composite structures considered as an infinite assembly of identical elements called unit cells. The wide application of these periodic structures have attracted a lot of research for more than a decade [2, 3, 4, 5, 6]. 3D woven composites in particular are getting more and more interest over 2D laminates as they provide higher resistance in out-of-plane loading while 2D laminates are easily subjected to delamination. Textile composites are prone to many modes of failures such as fiber breakages, cracks and delamination. In the process of Structural Health Monitoring (SHM) - which consists of performing Non Destructive Evaluation (NDE) [7] - the earliest possible detection of damage is important. At present, approximately 27% of an average aircraft's life cycle cost is spent on maintenance [8]. To avoid that, a technique finding increasing popularity for 'on-line' inspection is ultrasound guided waves spectroscopy [9]. As guided wave propagation in thin plates is dispersive, the velocity of wave propagation depends on the frequency and the dispersion relations need to be known. These guided waves techniques are very efficient in traditional isotropic or even orthotropic materials as their wave propagation characteristics have been thoroughly investigated [10]. However in strongly anisotropic composites, such as woven composites for example, these properties are not straightforward to obtain. This paper proposes and experimentally validates a methodology for obtaining these dispersion relations for 3D woven composites.

2 SAMPLES MANUFACTURING

A 3D woven fabric of complex architecture was used [11] to manufacture plaque samples by resin transfer molding (RTM) (see Fig1). This process was chosen because it allows to have smooth surfaces which is extremely important for the experimental measurements using a laser Doppler vibrometer.

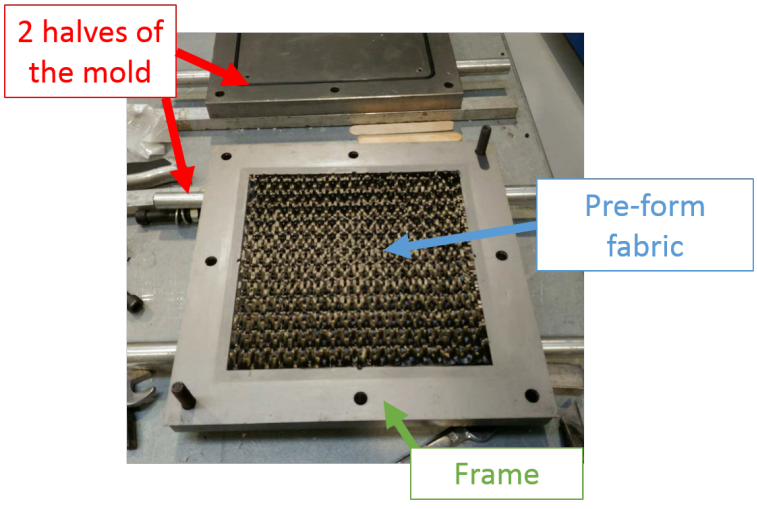

Figure 1: Photography showing the two halves of the mold, with the frame placed on on half and the pre-form fabric sheet fitted inside the frame

The plaques measure 250 x 250 x 2 mm. The fabric is an angle interlock weave. The fabric is made of carbon fibers while the matrix is made of epoxy resin. The dry preforms were given courtesy of Dr. Andreas Endruweit.

3 EXPERIMENTAL DETERMINATION OF THE DISPERSION RELATIONS

When performing a quantitative measurement of the dispersion relations in a thin structure , more than one mode can exist and propagate for any given frequency. That is why the two-dimensional fast Fourier transform (2D FFT) is used [12]. It allows for calculating the amplitude in the frequency-wavenumber domain from displacements or velocities amplitude in the space-temporal domain.

A broadband excitation signal (Fig.2 is transmitted to the studied structure by the mean of a glued piezoelectric transducer (PZT).

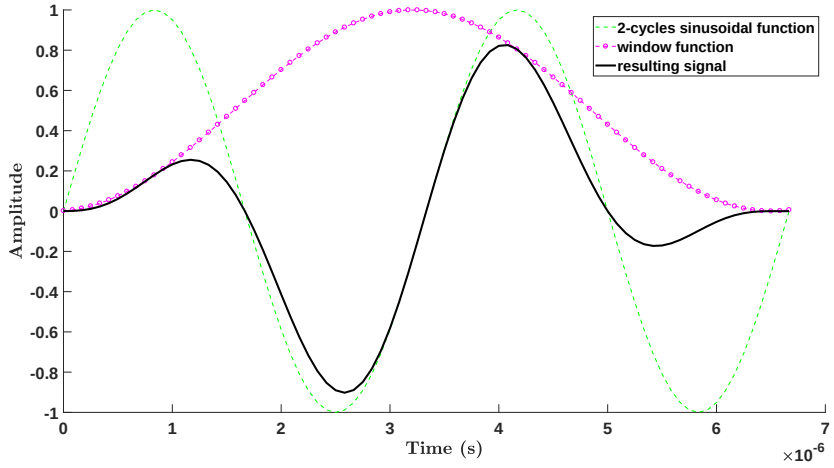

Figure 2: Broadband excitation signal, '- -' 2 cycles of a sinusoidal function mixed with a window function '-o-' gives the broadband signal '–'

Two cycles of a sinusoidal function are modulated by a window function.

The set-up (see Fig.3) is composed of a waveform generator that is used to generate the electrical waveform that will be transmitted to the piezoelectric transducer. The transducer is glued on the surface of the tested textile composite sample. Finally, the scanning laser Doppler vibrometer is programmed to measure the displacement at a set of discrete position on a straight line (B-scan). The B-scan is performed once in every direction of interest.

This output signal is transmitted to the oscilloscope for each discrete position along the defined line. A Fourier transform of the time history of the response at each discrete position is carried to compute the frequency spectrum for each position. A spacial Fourier transform is then applied to compute the amplitude-wavenumber-frequency information.

4 NUMERICAL METHOD

4.1 Microscale: Matrix and yarn mechanical properties

The mechanical properties of the fibers and matrix are provided by the supplier. A square arrangement of the fiber is assumed to calculate the mechanical properties of the yarn [13, 14, 15]. The homogenization from microscale (fibers & matrix) to mesoscale (yarn) gives us the following properties for the yarns (Tab.4.1)

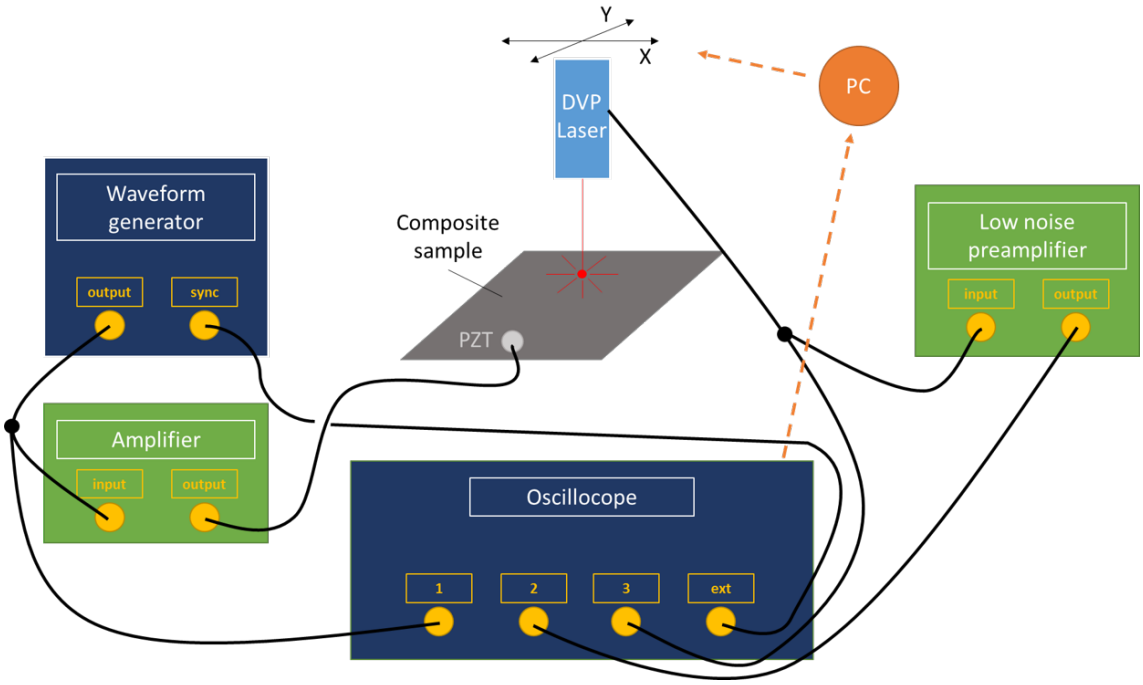

Figure 3: Experimental set-up for B-scan measurements

	Fibre	**Resin**	E_1	$E_{2,3}$	$G_{12,13}$	G_{23}	$\nu_{12,13}$	ν_{23}	**density**
Yarn - Mat1 V_f=0.41	TC33	IN2	116.3	7.40	2.87	2.31	0.27	0.37	1.450
	TC35	IN2	124.5	7.41	2.87	2.31	0.27	0.37	1.451

4.2 Mesoscale: Geometric modelling

The modelling of the textile is performed with TexGen which is a software developed by the Composites Research Group at the University of Nottingham [16, 17]. The geometric modeling is compared to micrographic cross sections of the actual composite (see Fig.2). This helps for an accurate modelling of the geometric shapes [18, 19].

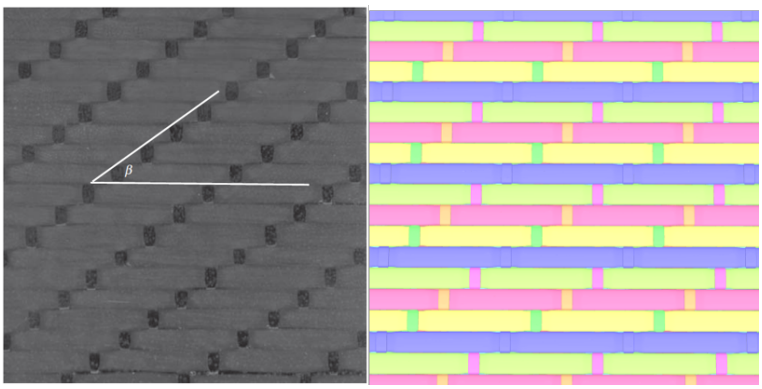

Figure 4: Top view of the material

The dispersion curves are calculated using the geometric model and the methodology presented in [20] that combines the WFEM and the CMS methods.

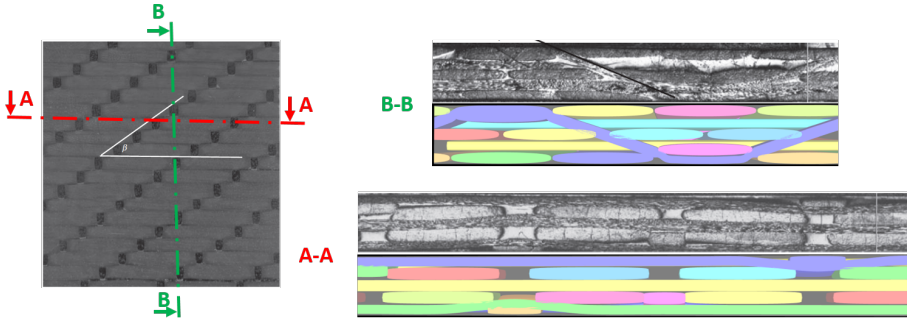

Figure 5: Cross sections of the material

4.3 WFE/CMS method

The nodal DOFs of the unit cell are partitioned in the following way: bottom, top, left, right, left-bottom corner, right-bottom corner, left-top corner, right-top corner and internal DOFs, which gives:
$\mathbf{q} = \left\{\mathbf{q_B^T} \quad \mathbf{q_T^T} \quad \mathbf{q_L^T} \quad \mathbf{q_R^T} \quad \mathbf{q_{LB}^T} \quad \mathbf{q_{RB}^T} \quad \mathbf{q_{LT}^T} \quad \mathbf{q_{RT}^T} \quad \mathbf{q_I^T}\right\}^T$. The equation of motion of the unit cell can be written as

$$\left[\mathbf{K} + \mathrm{i}\omega\mathbf{C} - \omega^2\mathbf{M}\right]\mathbf{q} = \mathbf{F} \tag{1}$$

In order to reduce the complexity of the structural dynamic model, a Component Mode Synthesis (CMS) method is applied. It is mostly used to reduce the use of CPU time and memory.
The key to this method is the reduction of the relative DOFs (internal nodes), whereas the boundary DOFs are kept as physical coordinates [21]. In the fixed interface CMS, a set of 'fixed boundary modes', also called component modes are selected among a subset of the local modes of the unit cell when the boundary DOFs are fixed and no force is acting on the internal nodes.
Once this reduction method has been applied, the periodic structure theory (PST) is employed. The PST states that when a free wave travels along a waveguide, the displacements between two opposite boundary sides of a cell differ only by a propagation factor. The unit cell needs however to be meshed in a similar way on its opposite boundaries, so that continuity in displacements and forces equilibrium is respected [22].
In our case the wave motion is in the Oxy plan, which gives

$$\begin{gathered}\mathbf{q_R} = \lambda_x\mathbf{q_L}; \qquad \mathbf{q_T} = \lambda_y\mathbf{q_B} \\ \mathbf{q_{RB}} = \lambda_x\mathbf{q_{LB}}; \quad \mathbf{q_{LT}} = \lambda_y\mathbf{q_{LB}}; \quad \mathbf{q_{RT}} = \lambda_x\lambda_y\mathbf{q_{LB}}\end{gathered} \tag{2}$$

λ_x and λ_y being respectively the propagation factors along the axis x and y.
The propagation factors are calculated using the following formula

$$\lambda_x = e^{-\mathrm{i}k_x\Delta}; \quad \lambda_y = e^{-\mathrm{i}k_y\Delta} \tag{3}$$

and the direction of propagation θ is computed using the following relations

$$k_x = kcos(\theta); \quad k_y = ksin(\theta) \tag{4}$$

Combining the CMS reduction method with the periodicity relation, allows us to reduce drastically the number of unknown in the equations and thus the calculation time.

5 RESULTS

A comparison is presented in Fig.6.

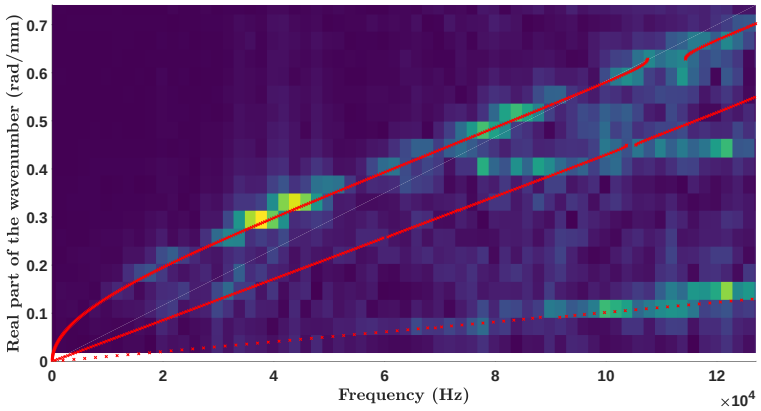

Figure 6: Dispersion curves of the material in the y-direction - background image results from the experimental B-scan - 'x' numerical results computed with the methodology presented in [20] - '+' numerical results computed with a classic WFE method and homogenised mechanical properties

A good agreement can be observed betweeen the numerical results and the experimental results. However the resolution of the experimental results doesn't allow to conclude wether the agreement is excellent or not. Also both numerical methods seem to give similar results.

6 CONCLUSIONS

- It is shown that this methodology has a good accuracy for determining the dispersion relations of complex woven composites.
- It is efficient time wise and provides more information on the dispersion relations than experimental testing.
- It is difficult to conclude whether the methodology provides more information than using a standard WFE method on a model with homogenized mechanical properties.

7 ACKNOWLEDGEMENT

- This work is funded by the INNOVATIVE doctoral programme. The INNOVATIVE programme is partially funded by the Marie Curie Initial Training Networks (ITN) action (project number 665468) and partially by the Institute for Aerospace Technology (IAT) at the University of Nottingham.
- We are grateful for access to the University of Nottingham High Performance Computing Facility.
- Special thanks go to the Composites Research Group members and especially to Louise Brown who gave us advices on TexGen, to Andreas Endruweit who gracefully provided us the dry fabrics and to the lab technicians Paul and Harry who helped us manufacture the composite samples.
- These experiments were conducted at the CEA List in France and we want to thank them for the help and opportunity provided on these.

REFERENCES

[1] C. Soutis, "Fibre reinforced composites in aircraft construction," *Progress in Aerospace Sciences*, vol. 41, no. 2, pp. 143–151, 2005.

[2] S. Mead, D. J.; Parthan, "Free wave propagation in two-dimensional periodic plates," *Journal of Sound and Vibration*, 1979.

[3] D. . J. Mead, "Wave propagation in continuous periodic structures: research contributions from southampton, 1964-1995," *Journal of Sound and Vibration*, 1996.

[4] L. Hinke, B. R. Mace, and M. J. Brennan, "Finite element analysis of waveguides," *Institute of Sound and Vibration Research*, 2004.

[5] C. Barbarosie and M. M. Neves, "Periodic structures for frequency filtering: analysis and optimization," *Computers & Structures*, vol. 82, no. 17-19, pp. 1399–1403, 2004.

[6] C. Droz, C. Zhou, M. N. Ichchou, and J. P. Lain, "A hybrid wave-mode formulation for the vibro-acoustic analysis of 2d periodic structures," *Journal of Sound and Vibration*, vol. 363, pp. 285–302, 2016.

[7] S. H. S. Gopalakrishnan, M. Ruzzene, *Computational Techniques for Structural Health Monitoring*. Springer, 2011.

[8] S. S. K. S. M. S. C. Soutis, "Damage detection in composite materials using lamb wave methods," *Institute of Physics Publishing*, 2002.

[9] V. Giurgiutiu, *Structural Health Monitoring of Aerospace Composites*. Academic Press, 2015.

[10] D. Chronopoulos, "Wave steering effects in anisotropic composite structures: Direct calculation of the energy skew angle through a finite element scheme," *Ultrasonics*, vol. 73, pp. 43–48, 2017.

[11] A. Endruweit and A. C. Long, "Analysis of compressibility and permeability of selected 3d woven reinforcements," *Journal of Composite Materials*, vol. 44, no. 24, pp. 2833–2862, 2010.

[12] D. Alleyne and P. Cawley, "A two-dimensional fourier transform method for the measurement of propagating multimode signals," *The Journal of the Acoustical Society of America*, vol. 89, no. 3, pp. 1159–1168, 1991.

[13] H. Yuanchen, J. Kyo Kook, and H. Sung Kyu, "Effects of fiber arrangement on mechanical behavior of unidirectional composites," *Journal of Composite Materials*, vol. 42, no. 18, pp. 1851–1871, 2008.

[14] M. Ansar, W. Xinwei, and Z. Chouwei, "Modeling strategies of 3d woven composites: a review," *Composite structures*, vol. 93, no. 8, pp. 1947–1963, 2011.

[15] X. Zeng, L. P. Brown, A. Endruweit, M. Matveev, and A. C. Long, "Geometrical modelling of 3d woven reinforcements for polymer composites: Prediction of fabric permeability and composite mechanical properties," *Composites Part A: Applied Science and Manufacturing*, vol. 56, pp. 150–160, 2014.

[16] M. Sherburn, *Geometric and mechanical modelling of textiles*. PhD thesis, University of Nottingham, 2007.

[17] H. Lin, L. P. Brown, and A. C. Long, "Modelling and simulating textile structures using texgen," *Advanced Materials Research*, vol. 331, pp. 44–47, 2011.

[18] N. Naouar, E. Vidal-Sall, J. Schneider, E. Maire, and P. Boisse, "Meso-scale fe analyses of textile composite reinforcement deformation based on x-ray computed tomography," *Composite Structures*, vol. 116, pp. 165–176, 2014.

[19] R. D. B. Sevenois, D. Garoz, F. A. Gilabert, S. W. F. Spronk, S. Fonteyn, M. Heyndrickx, L. Pyl, D. Van Hemelrijck, J. Degrieck, and W. Van Paepegem, "Avoiding interpenetrations and the importance of nesting in analytic geometry construction for representative unit cells of woven composite laminates," *Composites Science and Technology*, vol. 136, pp. 119–132, 2016.

[20] V. Thierry, L. Brown, and D. Chronopoulos, "Multi-scale wave propagation modelling for two-dimensional periodic textile composites," *Composites Part B: Engineering*, 2018.

[21] L. G. J. Becker, "Cms methods for efficient damping prediction for structures with friction," 2008.

[22] J. M. Mencik and M. N. Ichchou, "Multi-mode propagation and diffusion in structures through finite elements," *European Journal of Mechanics - A/Solids*, vol. 24, no. 5, pp. 877–898, 2005.

COMPDYN 2019

Proceedings of the
7th International Conference on
Computational Methods in Structural Dynamics and Earthquake Engineering

M. Papadrakakis, M. Fragiadakis (Eds)

First Edition, October 2019

ISBN (set): 978-618-82844-5-6
ISBN (vol III): 978-618-82844-8-7

Institute of Structural Analysis and Antiseismic Research
National Technical University of Athens, Greece